



Composition Gradients in Molten Salt Binary Mixtures during Electrolysis at High Current Density

C. E. Vallet,* D. E. Heatherly, and J. Braunstein*

Chemistry Division, Oak Ridge National Laboratory, Oak Ridge, Tennessee 37830

ABSTRACT

Separation of components has been measured in binary molten salt mixtures, $\text{AgNO}_3\text{-KNO}_3$, subjected to electrolysis between silver electrodes. The analysis of thin slices of frozen mixture contained in silica frits gives qualitatively the composition changes between anode and cathode and shows the expected enrichment of potassium ions at the cathode. Changes in concentration at the electrodes are measured electrochemically in free electrolytes and in electrolytes contained in frits. The time dependence of concentration at the electrodes is obtained both during electrolysis and during relaxation following electrolyses of different durations. The experimental results confirm the predictions from a mass transport model proposed previously for systems analogous to mixed molten salt batteries operated at high current densities.

Electrolyte composition gradients in aqueous fuel cells and electrolyzers have been observed (2, 3) and explained in terms of electrode reactions, diffusion, and migration (4-6). Previously derived equations for (one dimensional) diffusion and migration in molten salt binary mixtures during current flow predicted the establishment of concentration gradients in the electrolytes of molten salt batteries and fuel cells (7). Such gradients have been reported, but not analyzed, in an $\text{Al/NaCl-KCl-AlCl}_3/\text{Cl}_2$ battery (8) and in the electrolysis of LiBr-KBr mixtures for isotope separation (9). [Isotope separation by electrolysis of "pure" molten salt ${}^6\text{LiCl-}{}^7\text{LiCl}$ is itself an example of the development of composition gradients by virtue of difference of mobility (of ${}^6\text{Li}^+$, ${}^7\text{Li}^+$)] (10). These gradients, although potentially of significant magnitude and consequence in actual batteries (or fuel cells), are difficult to observe. Rapid back-diffusion during cooling imposes severe constraints on the sampling of such gradients for chemical analysis. In molten salt batteries (11, 12), variations of the potential between LiAl and FeS_x electrodes for reasons other than changes of the Li/K ratio of the LiCl-KCl electrolyte tend to obscure *in situ* potentiometric measurement of the composition changes. Consequently, there is a need for suitable analog experiments to test the validity of the predictions.

This paper presents the results of an experimental test of the predictions of the previously derived one dimensional equation for a system in which the electrode reaction, ion flows, and conditions of operation are analogous to those in a molten salt battery, but which is more amenable to quantitative analysis. We describe measurements of the composition changes in molten $\text{AgNO}_3\text{-KNO}_3$ mixtures subjected to electrolysis between two silver electrodes. Since silver, one of the two like-charged ions in the binary mixture, reacts at both electrodes, the ion flows are analogous

to those in the LiCl-KCl electrolyte of a Li/S battery, in which Li^+ ion enters the electrolyte at the anode and leaves at the cathode (11, 12). Experiments were done both with free electrolyte and with electrolyte contained in a coarse silica frit, the latter configuration resembling the containment of the electrolyte in a molten salt battery. Two kinds of measurements were made of composition changes: first, chemical analysis, following electrolyses for differing lengths of time and at differing current densities, in sections of rapidly cooled frits; second, *in situ* potentiometric analysis in cells with free and with frit-contained electrolytes. The results of both kinds of experiment and both kinds of analysis demonstrate the depletion of silver ions at the cathode, and confirm the predictions of our model under the conditions studied.

Ion Flows in $\text{AgNO}_3\text{-KNO}_3$

The ion flows considered in our previous analysis (7) of mass transport in electrolyzed molten salt mixtures were: (i) the faradaic flow across the electrode-electrolyte interface arising from the electrode reactions; (ii) the electromigrational flow of ions carrying the current through the electrolyte; and (iii) the diffusional flow driven by the concentration changes produced by the two preceding flows. In a constant volume system the diffusion-migration equation derived for the ion not reacting at the electrodes (cation K^+) was shown to be, neglecting convection

$$\frac{\partial C_K}{\partial t} = \frac{\partial}{\partial x} \left(D \frac{\partial C_K}{\partial x} \right) - \frac{I}{F} \frac{dt_K^{\text{NO}_3}}{dC_K} \frac{\partial C_K}{\partial x} \quad [1]$$

C_K is the ionic concentration of K^+ in eq cm^{-3} , x is the distance from the anode ($x = d$ at cathode), I is the current density, D is the binary diffusion coefficient in the $\text{AgNO}_3\text{-KNO}_3$ mixture, and $t_K^{\text{NO}_3}$ is the transference number of the cation K^+ relative to the nitrate anion; the boundary conditions at both electrodes ($x = 0, x = d$) are

* Electrochemical Society Active Member.
 Key words: molten salt, transport, battery.

$$\frac{\partial C_K}{\partial x} = \frac{It_K^{NO_3}}{FD} \quad [2]$$

Although convection terms and frit porosity may alter the predictions, and are being treated currently, our experimental results indicate that these effects are probably not large under the conditions studied here.

Equation [1] together with Eq. [2] can be numerically solved (13) for the cases where D and (or) $t_K^{NO_3}$ are composition dependent. The computation gives the entire composition profile between the two electrodes at any time and the time dependences of concentration at both electrodes. Figure 1 shows the analogy of the three ion flows considered in the model in a Li/S battery on charge or on discharge and in the KNO_3 - $AgNO_3$ mixture during electrolysis with silver electrodes. Only the two like-charged cations are indicated, since the common anions (Cl^- or NO_3^-) are taken as reference frame.

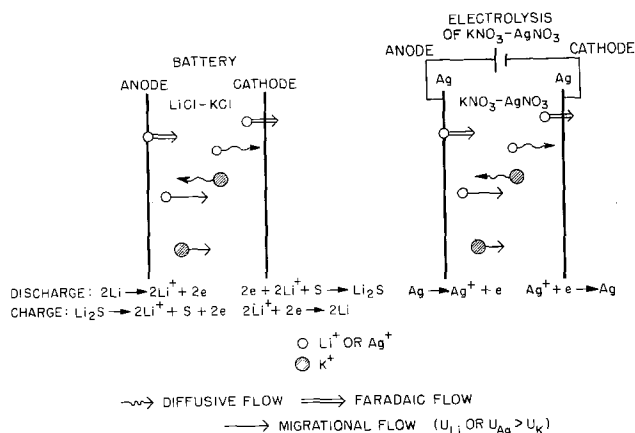


Fig. 1. Ion flow analogies in battery and in electrolysis cell

Experimental

Chemicals.—The silver nitrate was crystal certified A.C.S. from Fisher Scientific Company. The potassium nitrate was analytical reagent crystal from Mallinckrodt, Incorporated. It was dried in an oven at 300°C prior to weighing. The solutions were prepared by weighing the appropriate amounts of both components.

Electrolysis cells.—A typical silica cell for electrolysis of free electrolyte and electrochemical measurement of the concentration changes at both electrodes is shown in Fig. 2. The silver electrodes 1 and 2 are mounted in two pieces of Macor¹ (or of Teflon in experiments at temperature below 250°C) A and B in order to provide geometrically well-defined areas. The holders A and B are placed in the silica tube C, whose bore is machined to provide a tight fit to the bottom electrode support A. Two apertures, E and F, in the tube C, permit filling of all the space between the two electrodes with the molten salt when the tube C (maintained at the temperature of the melt) is inserted in the large tube D containing the binary nitrate melt. The silver electrode 3, dipping in the outer tube, is used as a reference electrode relative to the electrodes 1 and 2. The electrode separations were of the order of 1-2 cm and the electrode areas were of the order of 0.5 cm². The height of the melt in tube D was of the order of 4-5 cm. Uniformity of the temperature in the melt was obtained by inserting the assembly in an aluminum block G. A Leeds and Northrup Electromax Controller was used to maintain the furnace to within $\pm 0.1^\circ C$ of the desired temperature.

¹ Machinable Glass-Ceramic from Corning.

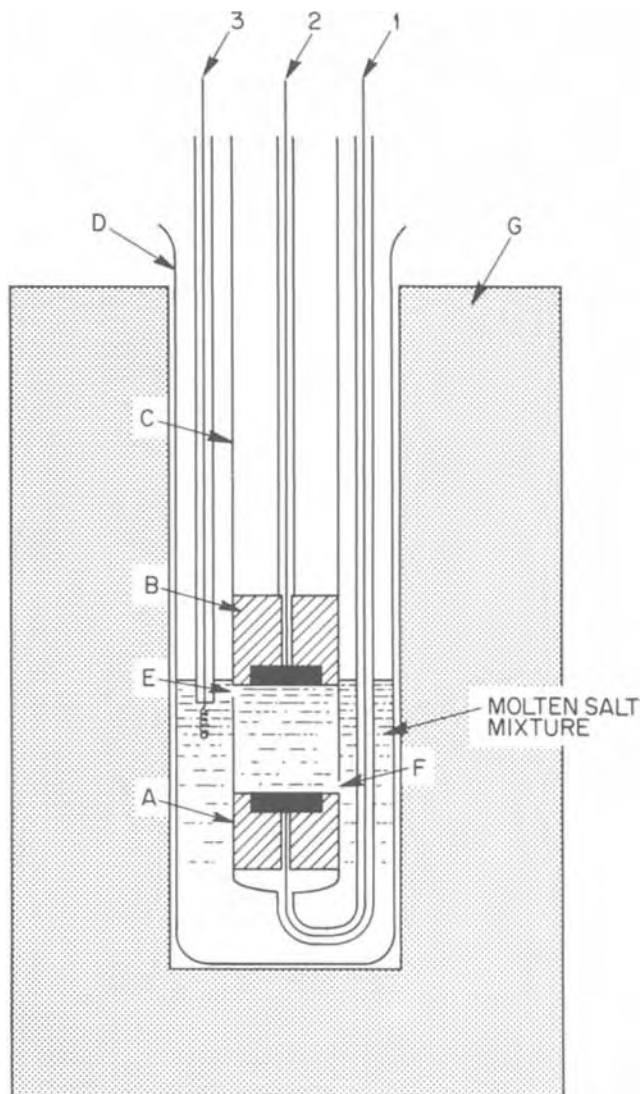


Fig. 2. Electrolysis cell with free electrolyte: A, B, Macor insulators; C, inner silica tubing; D, outer silica tubing; E, F, apertures in the internal silica tubing; G, aluminum block; 1, 2, silver electrodes for electrolysis; 3, silver reference electrode.

Figure 3 shows an electrolysis cell with the molten electrolyte contained in a coarse silica frit B. Silica frits 0.25-0.4 cm thick are sealed at one end of the silica tube A. Two planar silver electrodes 1 and 2, of 0.5 cm² area are placed against opposite faces of the frit. Electrode 2, introduced into tube A, has a known area in contact with the melt which impregnates the frit. Electrode 2 is used as anode or as cathode. The electrolyses are done between the electrodes 1 and 2. Silver electrode 3, dipping in the melt contained in the outer tube B, is used as a reference electrode. The level of the molten mixture in tube C is adjusted to touch the bottom of the upper electrode 2. This cell also is contained in an aluminum block for uniformity of the temperature.

Composition Changes

Measurements were made of the composition changes at the electrode surfaces and across the electrolyte between anode and cathode (concentration profiles) induced by electrolyses at 0.15 A-cm⁻² of 1-2 min duration. Both kinds of measurements showed the trend towards separation of the mixture components predicted by the mass transfer analysis. The concentration profiles, which we discuss first, show this effect qualitatively, and higher analytical precision is needed for a more quantitative test of the model. The con-

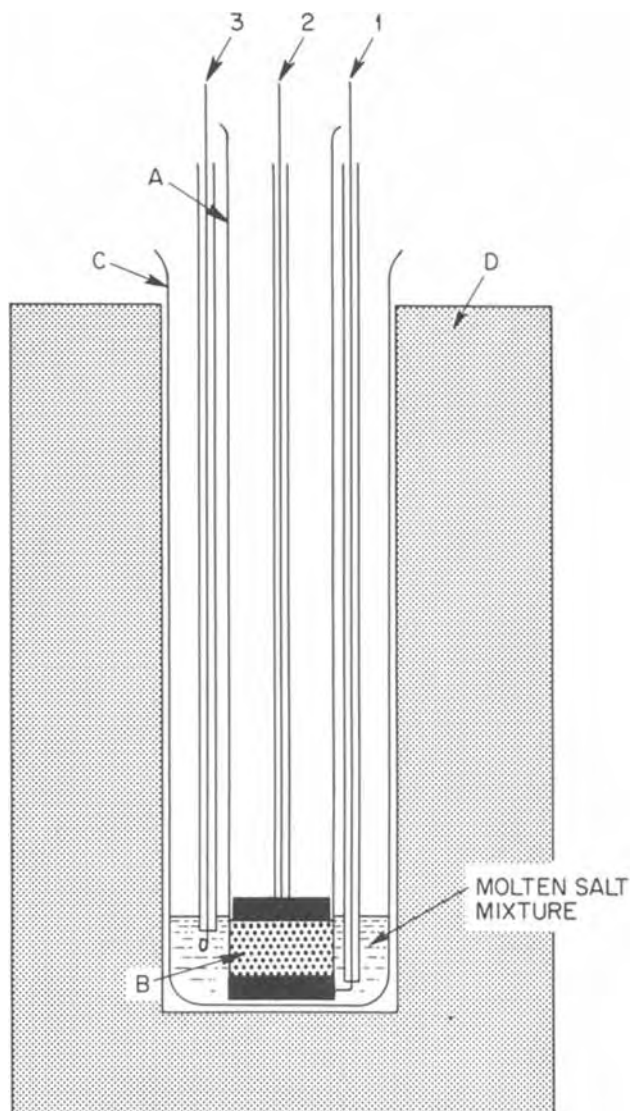


Fig. 3. Electrolysis cell with the electrolyte contained in a silica frit. A, Inner silica tubing; B, coarse silica frit sealed at the end of A; C, outer silica tubing; D, aluminum block; 1, 2, silver electrodes for electrolysis; 3, silver reference electrode.

centrations at the electrode surfaces and their change with time, however, are very well explained by the predictions of the mass transport model.

Experimental procedure.—A direct determination of the composition changes across the electrolyte was attempted after electrolyzing the $\text{AgNO}_3\text{-KNO}_3$ mixture, contained in the porous matrix in the cell shown in Fig. 3, at constant current for differing times. As soon as the current is cut off, the tube A (Fig. 3) is removed from the melt and rapidly cooled in a cold helium flow. The frit, B, is then sectioned into slices 15-20 thousandths of an inch thick using a Buehler low speed saw equipped with a diamond-faced blade 15 thousandths of an inch thick. A silicone cutting oil is used to increase the cutting speed. The slices are washed with cold benzene to remove the silicone cutting oil. The nitrate mixture is extracted from the frit slices by a hot (90°C) 0.01N HNO_3 solution. The hot solution is dropped onto the slice in a Buchner funnel as vacuum is applied to the collecting flask. The frit slices, dried in an oven, were weighed, and then reweighed after each washing. Table I gives typical weight losses (in mg) observed for four slices. Usually three washings are sufficient to reach a steady weight. The total weight loss of the slice is identified with the total weight of $\text{AgNO}_3\text{-KNO}_3$ mixture con-

Table I. Weight losses (mg) of frit slices during extraction by hot 0.01N HNO_3 solution

Washing No. / Slice No.	1	2	3	4
1	60.4	30.8	45.5	58.2
2	0.1	0.6	0.7	-0.1
3	—	0.1	0.1	—

tained in the slice. The water solutions, which typically contained $1 \times 10^{-3}\text{g}$ of salt per cm^3 , are analyzed both for potassium and for silver. The potassium analysis is done by flame spectroscopy, silver by spark source spectroscopy. The accuracy of these methods is usually estimated to be $\pm 5\%$. In order to test the analytical results and the extraction procedure from the frit, standard samples were prepared for analysis by diluting in 0.01N HNO_3 solution either a previously molten mixture of known composition or the mixture extracted from a quartz frit impregnated with a molten mixture of known composition. In most of the cases, both Ag and K analyses indicate a lower concentration of potassium. The results from silver analysis are found to be within 6% of the known compositions. Results from potassium analysis are within 10% of the known compositions. The extraction of the salt from the frit does not increase significantly the discrepancy between the results of the analysis and the known composition of the melt.

Composition profiles in $\text{AgNO}_3\text{-KNO}_3$.—A 0.2 $\text{AgNO}_3\text{-0.8 KNO}_3$ mixture at 310°C was electrolyzed at 0.15 A-cm^{-2} during 40 sec. The upper part of Table II gives the results of the analysis of the salt in five slices of the 0.5 cm-thick frit. Slice 1 was adjacent to the anode and slice 5 was closest to the cathode. The thickness of frit lost from each cut has been estimated to be about 0.05 cm, and the subsequent positions (relative to the anode) of the midpoints of the slices are reported in the third column. The lower part of Table II gives the results of the analysis of potassium and of silver in four slices of a 0.378 cm-thick frit in which a 0.5 $\text{KNO}_3\text{-0.5 AgNO}_3$ mixture has been electrolyzed for 90 sec at 0.15 A-cm^{-2} . The results in Table II for both initial compositions show a clear trend of increasing Ag/K ratio from cathode to anode. This is strengthened by a comparison of standard deviations of fit calculated for two models: (a) no effect of electrolysis, i.e., the analytical results for

Table II. Composition from analysis of potassium and of silver in slices of electrolyzed frits

$\bar{X}_{\text{K}} = 0.8$; time of electrolysis = 40 sec, current density = 0.15 A-cm^{-2} ; thickness of the frit = 0.5 cm

Slice No.	Thick-ness (cm)	Distance of midpoint from anode (cm)	X_{K}	
			From K analysis	From Ag analysis
1	0.065	0.0325	0.75	0.81
2	0.079	0.154	0.77	0.82
3	0.053	0.270	0.81	0.85
4	0.061	0.377	0.84	0.88
5	0.040	0.478	0.87	0.91

$\bar{X}_{\text{K}} = 0.5$; time of electrolysis = 90 sec, current density = 0.15 A-cm^{-2} ; thickness of the frit = 0.378 cm

Slice No.	Thick-ness (cm)	Distance of midpoint from anode (cm)	X_{K}	
			From K analysis	From Ag analysis
1	0.066	0.033	0.48	0.45
2	0.034	0.133	0.513	0.43
3	0.058	0.229	0.539	0.49
4	0.054	0.335	0.527	0.53

sections at differing positions are randomly distributed about the mean value, and (b) a systematic change of composition with position; for this, a least squares fit with a linear dependence on distance was assumed, although the solution of the diffusion-migration equation is not linear, since uncertainties in the data did not warrant a more complex function. Table III summarizes the standard deviation, σ_{N-1} , about the mean composition $\langle X_K \rangle$ of the different sections, and the standard deviation of fit, σ_{N-2} , based on the linear least squares fit. Table III also lists the difference, ΔX_K , between the values of X_K at the cathode and at the anode as calculated from the linear regression. In all the cases the standard deviation of fit of a linear dependence on distance are smaller than the standard deviation about an assumed constant value. For 0.8 KNO₃-0.2 AgNO₃, σ_{N-2} is sixfold smaller for the silver analysis and twentyfold smaller for the potassium analysis than σ_{N-1} . For 0.5 KNO₃-0.5 AgNO₃, σ_{N-2} is about half σ_{N-1} . Figure 4 shows the least squares fits to both K and Ag analyses in the two melts together with the experimental results reported for the midpoint of each slice. (The middle lines are the fits to the average of the data from both analyses.) The differences in composition at the cathode and at the anode calculated from the linear regression are larger than twice the standard deviations of fit (σ_{N-2}), the electrolyte near the cathode being richer in KNO₃.

The results thus show that the direction and magnitude of the composition changes at the two electrodes are consistent with those predicted (7) from solution of the diffusion migration equation in a binary melt with electrode reactions involving one of the like-charged ions. A more accurate measurement of the composition profile, requiring both better resolution of the distance and improved analytical accuracy, is under way.

Concentration changes at electrode surfaces.—The most striking evidence for the predicted gradients is obtained from measurements of the composition changes at the electrodes during electrolysis, and of their rates of decay after electrolysis.

In this second kind of experiment, the concentrations at the electrode surfaces and their time dependence were measured potentiometrically. The composition (X_{Ag}) at the silver cathode (or anode) of the concentration cell with transference containing molten AgNO₃-KNO₃ mixtures, Ag/AgNO₃-KNO₃ (X_{Ag}°): AgNO₃-KNO₃(X_{Ag})/Ag, is related to the open-circuit potential difference between the cathode (or anode) and a reference electrode dipped in a mixture of known composition (X_{Ag}°) by (14)

$$E = \frac{1}{F} \int_{X_{Ag}^\circ}^{X_{Ag}} \frac{t_{KNO_3}}{1 - X'_{Ag}} \frac{d\mu_{AgNO_3}}{dX'_{Ag}} dX'_{Ag} \quad [3]$$

where X'_{Ag} is the mole fraction of AgNO₃ in the melt and μ_{AgNO_3} the chemical potential of AgNO₃. The needed internal transference number may be calculated from the external mobilities of the Ag⁺, K⁺, and NO₃⁻ ions which have been determined by Duke and Owens (15) at 350°C. They report that the external mobility of nitrate ion is composition-independent, with absolute value 1.55×10^{-4} cm² sec⁻¹ V⁻¹, and that the mobilities of all the three ions are

Table III. Standard deviation about the average value $\langle X_K \rangle$, and of the linear regression

\bar{X}_K	X _K from Ag analysis			X _K from K analysis			ΔX_K
	(a) σ_{N-1}	(b) σ_{N-2}	$2\sigma_{N-2}$	(a) σ_{N-1}	(b) σ_{N-2}	$2\sigma_{N-2}$	
0.8	0.0416	0.007	0.014	0.0492	0.0026	0.0052	0.13
0.5	0.0465	0.024	0.048	0.0255	0.017	0.034	0.091

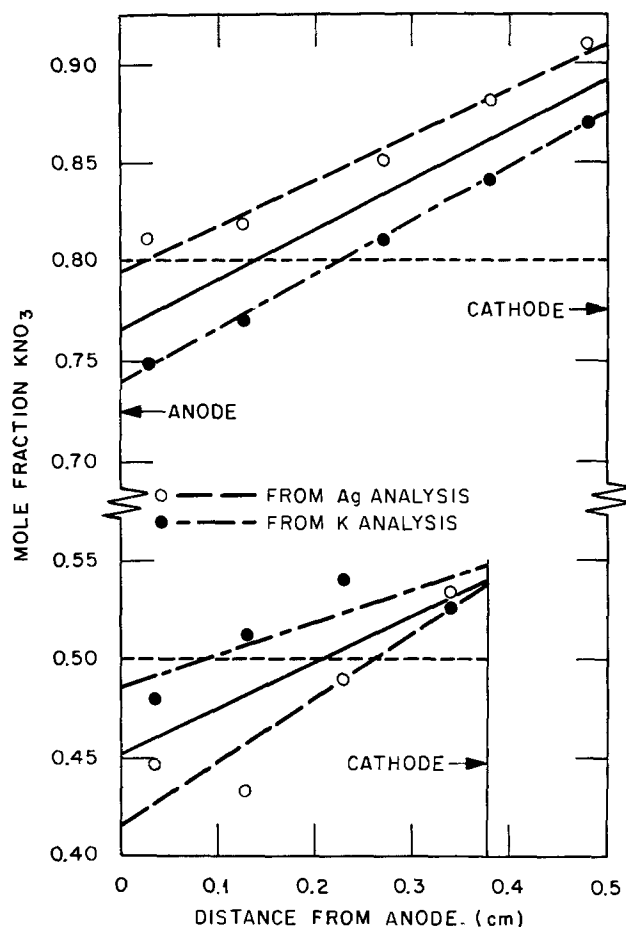


Fig. 4. Least squares fit of a linear dependence on distance to compositions from silver analysis (○) and from potassium analysis (●).

temperature-independent (15). A least squares fit of a second-order polynomial that represents the absolute values of the K⁺ and Ag⁺ mobilities, in cm² sec⁻¹ V⁻¹, was reported (16) as

$$u_K = (4.83 X_K^2 - 6.86 X_K + 4.49) \times 10^{-4} \quad [4a]$$

$$u_{Ag} = (-3.87 X_K^2 + 2.73 X_K + 3.71) \times 10^{-4}$$

The transference number of the potassium cation relative to nitrate ions is

$$t_{KNO_3} = \frac{C_K(u_K + u_{NO_3})}{C_K(u_K + u_{NO_3}) + C_{Ag}(u_{Ag} + u_{NO_3})} \quad [4b]$$

Figure 5 shows, in curve 1, the transference number t_{KNO_3} calculated from Eq. [4]. These values are confirmed by more recent measurements (17) of concentration cells with transference. The transference number of potassium relative to nitrate anions differs slightly from the KNO₃ mole fraction, ~20% at $X_K = 0.5$, and ~10% at $X_K = 0.7$. Its composition dependence is well represented in the composition range $0 < X_K < 0.55$ by a second degree polynomial

$$t_{KNO_3} = 0.6 X_K + 0.4 X_K^2 \quad [5]$$

or by the assumption of a constant mobility ratio (18) $u_{Ag}/u_K = 1.5$, as shown in curve 2 of Fig. 5.

The activity coefficients of KNO₃ and AgNO₃ have been found (19) to be larger than 0.8 at all concentrations. They are virtually unity around $X_K = 0.8$, the composition studied here. Therefore, in our calculations of the emf of the concentration cells (with $X_{Ag}^\circ = 0.2$) we may assume with very little error that the mixture is ideal. The emf of the concentration cell with transference becomes

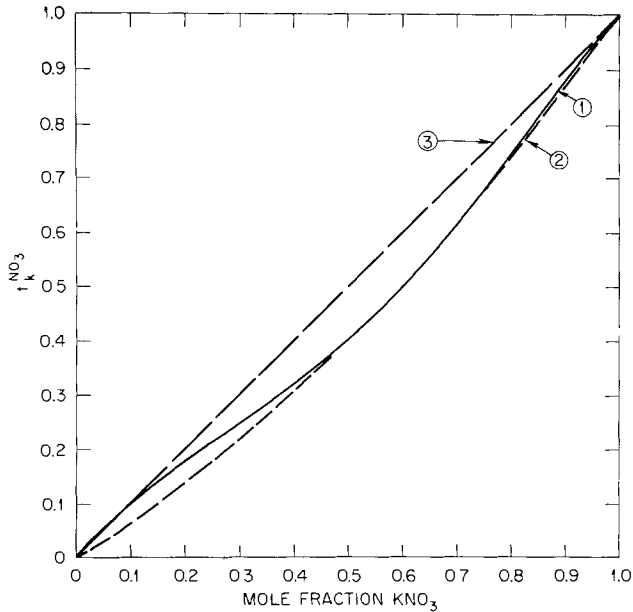


Fig. 5. Composition dependence of transference number of potassium relative to nitrate in $\text{AgNO}_3\text{-KNO}_3$. Curve 1, calculated from the external mobilities of Ref. (15); curve 2, fit assuming a constant mobility ratio $u_{\text{Ag}}/u_{\text{K}} = 1.5$; curve 3, transference number assumed equal to the mole fraction ($u_{\text{Ag}} = u_{\text{K}}$).

$$E' = \frac{RT}{F} \ln \frac{X_{\text{Ag}}}{X_{\text{Ag}}^0} + 0.4 \frac{RT}{F} (X_{\text{Ag}}^0 - X_{\text{Ag}}) \quad [6]$$

Note that the second term on the RHS results from the difference of the transference number from the mole fraction.

Time dependence of concentration in free electrolyte.—A 0.8 $\text{KNO}_3\text{-0.2 AgNO}_3$ mixture was electrolyzed at constant currents of 0.2 and 0.4A in the cell shown in Fig. 2. During electrolysis, the current was interrupted periodically for short periods of time in order to record the open-circuit potential of cathode and anode (electrodes 1 and 2) relative to the reference electrode, 3, in the melt of initial composition. The separation between the electrodes was 1.5 cm and the temperature 200°C. Figure 6 shows concentrations of potassium calculated with Eq. [6] from the measured potentials. As the electrolysis progresses, the concentration of potassium increases at the cathode and decreases at the anode. The dashed curves are the concentrations predicted by the model assuming an interdiffusion coefficient of $5 \times 10^{-5} \text{ cm}^2 \text{ sec}^{-1}$ and the transference number $t_{\text{K}}^{\text{NO}_3}$ given in Eq. [4]. The experimental points fall on the predicted curves initially, but for times longer than 3 min the concentration at the anode is closer to the initial concentration than the predicted values. This may arise partly from cumulative errors introduced by the successive current interruptions, but is in the direction expected for convective mixing in the free electrolyte. Figure 7 is a recording of the potentials of the anode and of the cathode during the current interruptions shown in the upper part of the figure. After current interruption, the potential decreases rapidly with time, hence there is a very fast concentration change at the electrodes. At the end of a current interruption step the concentration profile between the two electrodes, consequently, is different from that at the beginning of the interruption, and leads to a different concentration at the electrodes at the time of the next current interruption. Few experimental points were obtained at the cathode because of silver dendrite formation. The initial portion of the curves yields a high value of the apparent interdiffusion coefficient (5×10^{-5}

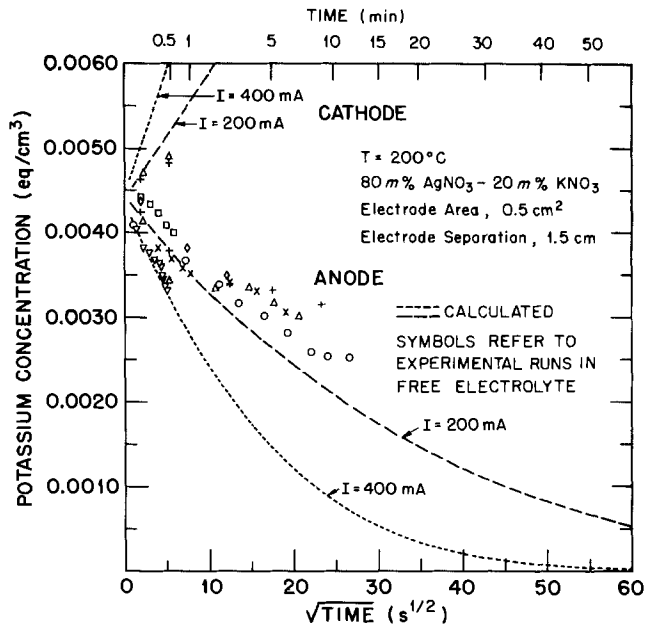


Fig. 6. Time dependence of concentration at electrodes during the electrolysis of 0.8 $\text{AgNO}_3\text{-0.2 KNO}_3$ free electrolyte, with constant current. +, Δ , \times , \circ current = 200 mA; ∇ current = 400 mA.

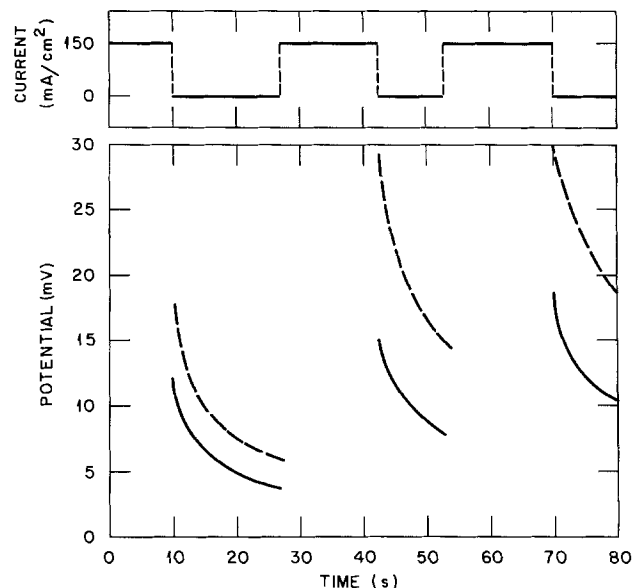


Fig. 7. Time dependence of potential of (+) anode (—) and of (—) cathode (---) during interruptions of electrolysis with constant current in 0.2 $\text{AgNO}_3\text{-0.8 KNO}_3$ at 310°C.

$\text{cm}^2 \text{ sec}^{-1}$), which is in the direction expected for errors resulting from convection in the melt. Results from analogous experiments using silica frits (Fig. 3) to reduce convection yield a more reasonable,² lower, interdiffusion coefficient, $1.5\text{-}2 \times 10^{-5} \text{ cm}^2 \text{ sec}^{-1}$.

Relaxation of the polarization emf in frits.—Since successive current interruptions disturb the development of concentration gradients in the electrolyte, another, related experiment was performed. The melt confined in a frit is electrolyzed at constant current for a known period of time, the current is cut off,

² At 300°C, the interdiffusion coefficient in $\text{AgNO}_3\text{-NaNO}_3$ mixtures has been reported as $2 \times 10^{-5} \text{ cm}^2 \text{ sec}^{-1}$ (20).

and the relaxation to the uniform initial composition is followed by measuring the potentials of cathode and of anode (relative to a reference electrode in the melt of initial composition) as they decay back towards zero. The recording on a X-Y recorder starts a few seconds after the cutoff, allowing complete discharge of the double layer. Extrapolation of the recorded curves to zero time of relaxation, and the use of Eq. [6], gives the composition at both electrodes at the end of each electrolysis. Typical relaxations, at 320°C, are indicated by the emf measurements, shown as points in Fig. 8, of anode and cathode after 1 min of electrolysis of a 0.2 AgNO₃-0.8 KNO₃ melt at 0.15 A-cm⁻². The lines in Fig. 8 are the calculated diffusional relaxations (Fick's second law) from the concentration profiles at the end of electrolysis. These transient concentration profiles during electrolysis were calculated by numerical solution of Eq. [1] and [2], with Eq. [3] for the emf at the end of electrolysis and during the relaxation. A square root of time scale is used in order to separate the points in the fast initial portion of the relaxation curve. The solid line curves are predicted potentials, with Eq. [5] for the transference number, the dashed curves are the predictions with the assumption of a transference number equal to the mole fraction, which provides a simpler but slightly less accurate computation. In all the computations the interdiffusion coefficient is taken to be 1.5×10^{-5} cm² sec⁻¹. In the three experiments, shown in Fig. 8, the thickness of the frit was about 0.5 cm. Extrapolation of the experimental curves to zero relaxation time leads to a composition of $X_{Ag} = 0.30$ at the anode and of $X_{Ag} = 0.08$ at the cathode at the end of electrolysis. The experimental curves have the general shape of the predicted curves and the time scale of the predicted curves agrees with the time scale of the experimental curves. Neglecting the deviations of the transference number from the mole fraction (dashed line curves) gives predicted composition changes slightly larger than those observed. At short times of relaxation, the measured emf values at the cathode differ more from the predictions than those at the anode. The measured curves correspond to less negative potentials, i.e., the com-

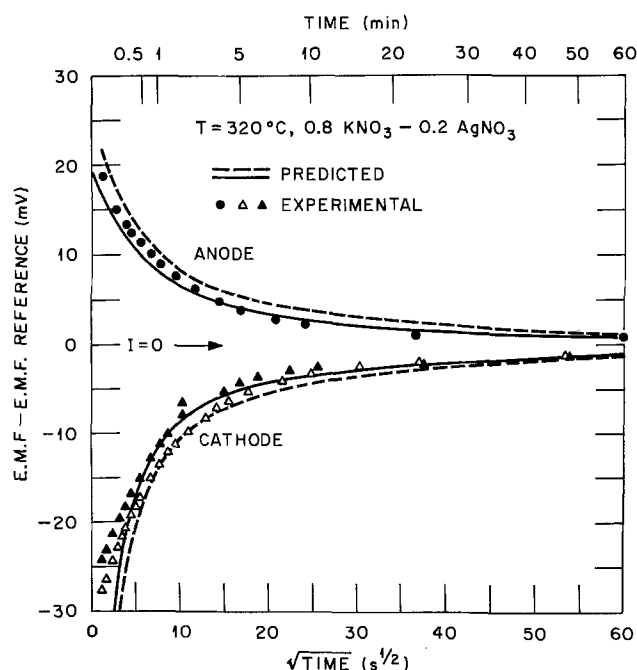


Fig. 8. Relaxation of polarization emf following electrolysis in 0.2 AgNO₃-0.8 KNO₃ at 0.15 A-cm⁻² for 1 min. Effect of the transference number on the predicted curves: — with emf calculated from Eq. [6]; --- with emf calculated assuming $t_{K^{NO_3}} = X_K$. Frit thickness: 0.5 cm.

position change at the cathode seems to be smaller than predicted. Possible causes of the deviation may include convection, dendrite formation at the cathode reducing the real current density, formation of a saturated solution, or the onset of a mixed electrode reaction. At 320°C, the liquidus composition is $X_{Ag} = 0.08$ (21), corresponding to an emf of -44 mV. The extrapolated emf at zero time from the two sets of experimental points is close to the emf corresponding to saturation. In order to eliminate the possibility of saturation, similar experiments were carried out at a higher temperature, 350°C.

The experimental results obtained at 350°C after 5, 10, and 20 sec of electrolysis are presented in Fig. 9, together with the corresponding predicted emf curves calculated as above, with Eq. [5] for the transference number and $D = 2 \times 10^{-5}$ cm² sec⁻¹. The compositions corresponding to the emf's are shown on the right-hand ordinate. After 20 sec of electrolysis at 0.15 A-cm⁻² with a 0.4 cm electrode separation, the measured silver nitrate concentration has increased by 60% at the anode and decreased by 42% at the cathode. Table IV compares the predicted compositions at anode and cathode at the end of electrolysis with the experimental compositions, the latter obtained by extrapolation to zero relaxation times. Experimental and predicted composition agree within 4-15%. As with the 320° results, the predicted anolyte composition changes at 350°C are smaller than those observed while the predicted catholyte changes are larger. This trend appears to increase with increasing electrolysis time, and cannot be attributed to saturation at the cathode (at 350°C) nor to convection or uncertainty in D , which would affect predicted cathode and anode composition changes in the same direction. The difference between predicted and observed composition changes is in a direction that could correspond to a higher current density at the anode than at the cathode,

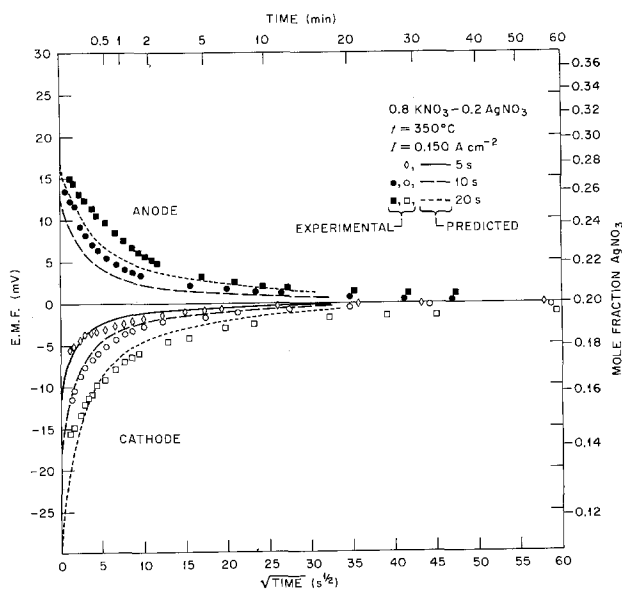


Fig. 9. Relaxation of polarization emf following electrolysis in 0.2 AgNO₃-0.8 KNO₃ at 0.15 A-cm⁻² for three different times. Temperature, 350°C. Experimental:

Electrolysis time: 5 sec ;
 Electrolysis time: 10 sec ● anode; ○ cathode
 Electrolysis time: 20 sec ■ anode; □ cathode

Predicted (anodic and cathodic):
 Electrolysis time: 5 sec —
 Electrolysis time: 10 sec ---
 Electrolysis time: 20 sec - - -

Table IV. Measured and predicted compositions at the anode and at the cathode from electrochemical measurement after electrolyses at 0.15 A-cm⁻² of a 0.2 AgNO₃-0.8 KNO₃ mixture at 350°C*

Time of electrolysis (sec)	Composition at the anode (X _{Ag})		Composition at the cathode (X _{Ag})	
	Measured	Predicted**	Measured	Predicted**
0	—	0.200	—	0.200
5	—	—	0.16	0.154
10	0.27	0.257	0.14	0.135
20	0.30	0.279	0.123	0.107

* These experiments were made with frits of thickness between 0.35 and 0.5 cm.

** Calculated with $D = 2 \times 10^{-5}$ cm² sec⁻¹ and the geometric electrode area.

which could result from dendrites at the cathode. Experiments are under way to determine the effects of frit porosity (i.e., tortuosity, partial blocking of the electrode, etc.) and longer electrolysis times on the validity of the model predictions, in a system for which the interdiffusion coefficient (as well as the transference number) is better known.

Conclusions

Electrolysis of AgNO₃-KNO₃ mixtures between silver electrodes, under conditions similar to those in a molten salt battery (e.g., Li(Al)/LiCl-KCl/FeS₂), demonstrates the development of significant current-induced composition gradients, as predicted from a consideration of the migrational, diffusional, and faradaic processes in binary molten salt mixtures. Chemical analysis of sections of salt quenched after electrolysis shows composition changes of direction and magnitude predicted, but with insufficient resolution for a rigorous test of the one dimensional model. Potentiometric analysis of compositions at the electrode surfaces after electrolysis and during diffusional relaxation are more precise than the chemical analysis; for short electrolysis times, they confirm strikingly the predicted end points of the composition profiles, but they cannot test the predicted shape of the profile in the bulk electrolyte. For longer electrolysis times, deviations occur between the predicted relaxations and the measurements, although the general features of the predicted gradients are observed. The deviations at long times are not attributable to convection alone, but probably also entail contributions from frit porosity, dendrite formation, and other effects. Work is in progress to resolve these contributions to the observed composition gradients and to incorporate them into the model, as well as to improve the analytical precision. The experimental demonstration of electrochemical composition changes in binary molten salt mixtures and the test of the model for predicting their extent are of importance because composition changes of the magnitude observed here may affect significantly the performance of fuel cells or batteries (8, 22).

Acknowledgments

We are pleased to acknowledge for their assistance W. H. Farmer (Metals and Ceramics Division) for cutting the frits, J. C. Franklin (Analytical Chemistry Division) for the analysis of silver, and P. L. Howell (Analytical Chemistry Division) for the analysis of potassium. Research sponsored by the Division of Materials Sciences, Office of Basic Energy Sciences, U.S. Department of Energy under Contract W-7405-eng-25 with the Union Carbide Corporation.

Manuscript submitted June 14, 1978; revised manuscript received July 9, 1979.

Any discussion of this paper will appear in a Discussion Section to be published in the December 1980

JOURNAL. All discussions for the December 1980 Discussion Section should be submitted by Aug. 1, 1980.

Publication costs of this article were assisted by Oak Ridge National Laboratory.

LIST OF SYMBOLS

C _K	ionic concentration of K ⁺ (eq cm ⁻³)
D	binary diffusion coefficient (cm ² sec ⁻¹)
d	distance between cathode and anode (cm)
E	open-circuit potential difference (V)
F	faraday (96,487C)
I	current density (A-cm ⁻²)
R	gas constant
T	temperature (°K)
t _K ^{NO₃}	transference number of K ⁺ relative to NO ₃ ⁻
u _i	absolute value of mobility of ion i
X ^o _{Ag}	mole fraction of AgNO ₃ (reference)
X _{Ag}	mole fraction of AgNO ₃ at anode (or cathode)
X' _{Ag}	mole fraction of AgNO ₃ in the melt
X _K	mole fraction of KNO ₃
<X _K >	mean composition (mole fraction of KNO ₃)
X _K	initial composition (mole fraction of KNO ₃)
x	distance from electrodes
μ _{AgNO₃}	chemical potential of AgNO ₃
σ _{N-1}	standard deviation about the mean composition
σ _{N-2}	standard deviation based on the linear least squares fit

REFERENCES

- D. E. Heatherly, Preliminary results presented at the Council Committee on Technician Activities, American Chemistry Society Meeting, Chicago, Aug. 28-Sept. 2, 1977.
- M. L. Miller and H. J. Fornasan, *This Journal*, **115**, 330 (1968).
- J. T. Lundquist and M. Vogel, *ibid.*, **116**, 1066 (1969).
- F. R. McLarnon, R. H. Muller, and C. W. Tobias, *Electrochim. Acta.*, **21**, 101 (1976).
- L. Hsueh and J. Newman, *Ind. Eng. Chem. Fundam.*, **10**, 4, 615 (1971).
- C. G. Smith and R. H. Muller, Lawrence Berkeley Laboratory Annual Report LBL-6016, p. 209 (1976).
- C. E. Vallet and J. Braunstein, *This Journal*, **125**, 1193 (1978); C. E. Vallet and J. Braunstein, *ibid.*, **126**, 527 (1979).
- G. L. Holleck and J. Giner, *ibid.*, **119**, 1161 (1972).
- Y. Yamamura, *J. Nucl. Sci. Technol.*, **6**, 698 (1969); Y. Yamamura and S. Suzuki, *ibid.*, **7**, 36 (1970).
- M. Chemla, *Discuss. Faraday Soc.*, **32**, 63 (1961).
- Progress Report, Argonne National Laboratory, ANL 76-98 (Dec. 1976).
- R. K. Steunenbergh and M. F. Roche, in "Electrode Materials and Processes for Energy Conversion and Storage," J. D. E. McIntyre, S. Srinivasan, and F. G. Will, Editors, p. 869, The Electrochemical Society Proceedings Series, Princeton, N.J. (1977).
- C. E. Vallet and J. Braunstein, *J. Phys. Chem.*, **81**, 2438 (1977).
- J. Braunstein and H. Braunstein, in "Experimental Thermodynamics," B. LeNeindre and B. Vodar, Editors, Chap. 18, p. 915, Butterworths, London (1975).
- F. R. Duke and B. Owens, *This Journal*, **105**, 476 (1958).
- G. L. Duret, R. J. Hassan, Jr., and M. P. Rill, Oak Ridge National Laboratory, ORNL/MIT-249 (Feb. 1977).
- M. Okada and K. Kawamura, *Electrochim. Acta.*, **15**, 1 (1970).
- C. E. Vallet and J. Braunstein, *This Journal*, **126**, 960 (1979).
- Y. Doucet and C. Naccache, *C. R. Acad. Sci. Fr.*, **259**, 2838 (1964).
- J. Richter, *Ber. Bunsenges. Phys. Chem.*, **80**, 92 (1976).
- A. Ussow, *Z. Anorg. Chem.*, **38**, 419 (1904).
- C. A. Melendres, C. C. Sy, and B. Tani, *This Journal*, **124**, 1060 (1977).

The Kinetics and Mass Transfer of Zinc Electrode in Acidic Zinc-Chloride Solution

Jung Taek Kim^{*1} and Jacob Jorné*

Department of Chemical Engineering, Wayne State University, Detroit, Michigan 48202

ABSTRACT

The kinetics, mass transfer, and surface roughness of zinc electrode in acidic zinc chloride solutions have been investigated in order to understand and optimize its performance in the zinc-chlorine hydrate battery. Polarization and limiting currents were measured using a rotating hemispherical zinc electrode. Exchange current densities and Tafel slopes are reported and the cathodic zinc deposition is confirmed to be first order. A cathodic mechanism of two consecutive one-electron transfer steps are postulated where the first step is the rate-determining step. A diffusion coefficient of zinc ion in 0.05M $ZnCl_2 + 1.0M$ KCl, $D_{Zn^{2+}} = 0.89 \times 10^{-5}$ cm²/sec, is obtained from the kinetics-diffusion mixed behavior. The surface roughness during the deposition depends strongly on the zinc-chloride concentration, the fraction of the limiting current i/i_L , and the deposition time. Two regions are observed: (i) at appreciable fraction of the limiting current where the roughness is determined by the hydrodynamic conditions, and (ii) at well below the limiting current where the roughness is governed by the microthrowing power of the zinc deposit. The growth of zinc dendrites at the edges of a rotating disk electrode was investigated potentiostatically. After an initiation period the current increased sharply and dendrites were detected. The growth direction of the dendrites is explained in terms of the hydrodynamic flow and the level of zinc ion concentration.

The zinc-chlorine hydrate battery is currently under development for utility peak-shaving and electric vehicle applications (1, 2). It is a flowing aqueous zinc chloride electrolyte battery which utilizes porous graphite flow-through chlorine electrode and dense graphite zinc-electrode substrate. The interelectrode gap is typically 2-4 mm and no separator is employed.

The individual overpotentials of the zinc and chlorine electrodes in the battery have been measured (3). The electrode kinetics and mass transfer effects have to be investigated in order to understand the source of the voltaic and coulombic inefficiencies in the battery. The kinetics of the chlorine electrode has been investigated in a previous paper by Kim and Jorné (4). The convective diffusion of the dissolved chlorine to the zinc surface which is responsible for the coulombic inefficiency has been investigated by Kim and Jorné (5), and by Kermani, Jorné, and Kodali (6). In this paper the kinetics, mass transfer, and the surface roughness of the zinc electrode are reported. Polarization measurements, limiting currents, coulombic efficiencies, and surface roughness effects were measured and the kinetics, transport parameters, and the reaction mechanism are discussed.

Although the deposition of zinc in aqueous solution has been extensively studied, most of the work dealt with its kinetics and postulated mechanisms. No general agreement has been reached pertaining to the kinetics, roughness of the deposition, and dendrite formation.

The kinetics of zinc deposition in acidic solution has been reported by a number of authors. Gaiser and Heusler (7) showed that zinc deposition is first order. Eriksurd (8) investigated the effect of halides and alkali cations on the Zn(Hg)/Zn(II) electrode reaction. Hulen and Eriksurd (9) studied the kinetics of the Zn(Hg)/Zn(II) electrode in acidic chloride solution. Sierra Alcazar and Harrison (10) suggested a cathodic reaction scheme in $ZnCl_2$ and KCl solution (pH = 3.0) of two consecutive one-electron transfer

steps where the first one is the rate-determining step. Weber and Tomassi (11) investigated the mechanism of zinc electrodeposition from its sulfate and chloride solutions. In chloride solutions the proposed mechanism involves various zinc chloride complexes: $ZnCl_3^-$, $ZnCl_4^{2-}$, $(ZnCl_2)_{ads}$, and H^+_{ads} . Epelboin and his co-workers (12-16) suggested a more complex scheme in which adsorbed H atoms catalyze the zinc reduction. The model involves an autocatalytic step in which Zn^+_{ads} is being generated. The adsorption at the interface involves three species, hydrogen, an anion, and Zn^+ cation which may be complexed. Multiple steady states are predicted and verified based on an "S" shaped current-potential curve. Moreover, the presence of an autocatalytic step at the interface plays an important role in the appearance of spongy, compact or dendritic deposits which are successively obtained when the current density is increased. The spatial configuration of the deposit is explained in terms of a coupling between the interfacial reactions and the surface diffusion of the adsorbed Zn^+ species (13, 15, 16). Regular spatial structures are claimed to be observed and explained in terms of dissipative structures. The detailed mechanism of the electrodeposition process is rather complicated.

The quality of metal deposition generally depends on the intermediate reactions and on several process variables, such as current density, concentration, fluid velocity, temperature, additives, and hydrogen reaction.

Experimental

Cell arrangement, rotator, preparation of zinc hemispherical electrode, and graphite disk electrode were reported previously (4, 5). A constant current supply (Electronic Measurement Model 620) and a potentiostat (PAR Model 173) were used in the galvanostatic and the potentiostatic experiments, respectively. The potential and the current were measured with an electrometer (PAR Model 136).

Faradaic efficiency tests were performed galvanostatically in 37% $ZnCl_2$ solution. A rotating zinc hemispherical electrode (99.999% New Jersey Zinc) was used. The surface of the electrode was polished with waterproof Al_2O_3 paper (Grid No. 600) and de-

* Electrochemical Society Active Member.

¹ Present address: Bell Laboratories, Murray Hill, New Jersey 07974.

Key words: zinc-chlorine battery, battery, rotating hemisphere, roughness, diffusion, faradaic efficiency, dendrite.

greased with spectroscopic grade pentane. The zinc electrode was weighed on a Mettler balance (H80) and transferred into the cell. After the experiment, the deposited (or dissolved) zinc electrode was rinsed with double distilled water, washed with spectroscopic grade pentane, and weighed.

The measurements of the kinetic parameters were performed potentiostatically in various zinc chloride solutions. A universal programmer (PAR Model 175) was used in conjunction with the potentiostat in order to sweep the potential of the zinc hemispherical electrode anodically or cathodically. The sweep rate was 10 mV/sec. The potential-current data was recorded on a recorder (HP Model 7046A).

The experiments of zinc deposition on a zinc hemispherical electrode and the dendritic growth on non-porous graphite disk electrode (Union Carbide ATJ) were performed in various zinc chloride concentrations galvanostatically and potentiostatically, respectively. The current-time data were recorded on Honeywell recorder (Electronik 194).

Solutions were prepared by direct reaction of dissolved chlorine and pure zinc rods (99.999%, New Jersey Zinc) in triply distilled water. The desired concentrations were achieved by dilution. All experiments were performed in deaerated solutions. The electrolyte was deaerated by bubbling N_2 gas prior to the experiments. The pH of the solution was measured with Orion pH meter (Model 701A). Pure zinc rod (99.999% New Jersey Zinc) was used as a counterelectrode for all experiments. Conductivities of the solutions were measured at 25°C using an a-c bridge, Generator Detector, Model 861A, Electro Scientific Industries, Portland, Oregon. The cell resistance and capacitance were balanced with an Impedance Bridge, Model 290B, and variable Decade Capacitors, Model DC57, Electro Scientific Industries, Portland, Oregon. A "U" type conductance cell was used. It contained two parallel platinum disk electrodes and all electrical wires were shielded. The cell was filled with solution and then transferred into a constant temperature bath. The viscosity of the solution was measured with Ostward Viscometer in a constant temperature bath.

Results and Discussion

Faradaic efficiency of Zn electrode.—The faradaic efficiency and the number of electrons transferred were obtained galvanostatically by weight measurements. Faraday's law is given by

$$\frac{\Delta W}{M} = \frac{It}{nF} \quad [1]$$

ΔW is the weight gained (or lost) by the electrode. M is the molecular weight of zinc, I is the current, t is the time, n is the number of electrons, and F is Faraday's constant.

The over-all cathodic reaction of the zinc ion is $Zn^{+2} + 2e \rightarrow Zn^0$. In order to verify the number of electrons transferred for the anodic dissolution or the cathodic deposition of zinc, weight loss or gain measurements were performed in 37% $ZnCl_2$ (pH = 1.0) solution. All variable factors, such as current, rotational speeds, time, concentration of solution, and pH were kept constant.

The number of electrons transferred was calculated from Eq. [1]. The obtained average values of the number of electrons transferred during the anodic and cathodic reactions are $n_a = 1.98$ and $n_c = 2.13$, respectively. These values represent an average of six experiments. The cathodic number of electrons transferred is slightly higher than the anodic number due to hydrogen evolution, although hydrogen overpotential is high on pure zinc surface. Sorensen, Davidson, and Klinberg (17) obtained the number of electrons for anodic zinc in various solutions at 30°C. The obtained values were $n_a = 1.77$ in 2.5M NaCl and 0.2M

$NaNO_3$ solution, $n_a = 2.02$ in 2.5M NaCl and 0.2M $KClO_3$ solution. It was also observed that the number of electrons transferred decreased as the temperature increased and on addition of an oxidizing agent (e.g., nitrate ion): in 0.2M $NaNO_3$ solution, $n_a = 1.90$ at $T = 30^\circ C$ and $n_a = 1.40$ at $T = 80^\circ C$ (17); $n_a = 2.0$ in 5M NaCl and in the absence of nitrate ion; $n_a = 1.72$ in 5M $NaNO_3$ and in the absence of the chloride ion; and $n_a = 1.62$ in 2.5M NaCl and 2.5M $NaNO_3$ at $T = 30^\circ C$. The lower value of n_a in the 2.5M NaCl and 2.5M $NaNO_3$ solution was attributed by Sorensen *et al.* (17) to the oxidation of unipositive zinc ion by nitrate ion which is catalyzed by chloride ion. Libby (18) proposed a catalytic effect based on the formation of a complex ion containing chloride ion, and Taube *et al.* (19-21) proposed a bridge transfer mechanism wherein the added chloride ion is coordinated between oxidant and reductant to form a bridge which serves as a path for the electrons.

The present value $n_a = 1.98$ in 37% $ZnCl_2$ in the absence of an oxidant at $T = 22^\circ C$ is in general agreement with the results of Sorensen *et al.* (17). It might indicate that unipositive zinc ion is formed during anodic dissolution. The unipositive zinc ion (Zn^+) thus postulated is very reactive and readily forms the bipositive zinc ion (Zn^{+2}) in the absence of an oxidant.

The kinetics of Zn electrode.—The polarization measurements of zinc metal in zinc chloride solution were performed on a rotating hemispherical zinc electrode. In order to eliminate the concentration overpotential, the rotational speed of the electrode was sufficiently high, $\omega = 3000$ rpm. The results are plotted according to the Tafel equation and are shown in Fig. 1. The data was corrected for the ohmic drop using Newman's method (22) for the case where the reference electrode is located far away (3.50 cm)

$$R = \frac{1}{4\pi\kappa r} \quad [2]$$

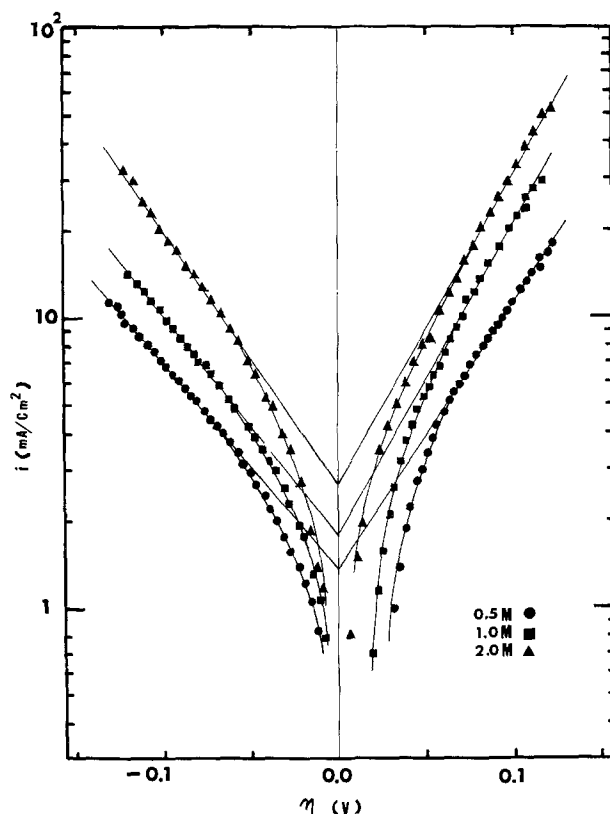


Fig. 1. Anodic and cathodic Tafel polarizations of zinc electrode in various $ZnCl_2$ and 1M KCl solutions. Electrode area: 0.752 cm^2 . Rotational speed: 3000 rpm.

R is the resistance (Ω), κ is the conductivity ($\Omega^{-1} \text{cm}^{-1}$) of the solution, and r is the radius of the electrode (cm). The conductivities of the various solutions are 0.0820, 0.0943, and 0.0980 $\Omega^{-1} \text{cm}^{-1}$ for 0.5, 1.0, and 2.0M ZnCl_2 solutions, respectively. The obtained exchange current densities and anodic and cathodic Tafel slopes are summarized in Table I. The theoretical cathodic Tafel slope is $b_c = -2.3RT/(1-\beta)nF$. If a symmetric transfer coefficient $\beta = 0.5$ and one-electron transfer $n = 1.0$, are assumed, then the Tafel slope is $b_c = -120 \text{ mV}$. The obtained experimental cathodic Tafel slopes (see Table I) are in agreement with the theoretical value. Sierra Alcazar and Harrison (10) measured Tafel slope of 120 mV using an a-c impedance technique.

The exchange current density (i_0) was calculated from the intercepts of the anodic and the cathodic branches in Fig. 1, and the obtained data are also summarized in Table I. An exchange current density of $\text{Zn}(\text{Hg})/\text{Zn}^{2+}$ in KCl is reported by Sierra Alcazar and Harrison (10): $i_0 = 2.0 \text{ mA/cm}^2$ for 0.1M $\text{ZnSO}_4 + 1.0\text{M KCl}$ (pH = 3.0). However, the exchange current also varies with the pH; in $3 \times 10^{-3}\text{M ZnSO}_4$ $i_0 = 2.4 \times 10^{-2} \text{ mA/cm}^2$ for pH = 3.5 and $i_0 = 1.8 \times 10^{-2} \text{ mA/cm}^2$ for pH = 2.5.

In general, the exchange current density depends on the concentration of reactants and products and can be written as (23)

$$i_0 = nFk_c^{(1-\beta)} k_a^\beta \pi C_1^{(Z_1 + \beta S_1)} \quad [3]$$

S_1 is the stoichiometric coefficient: $S_1 > 0$ for anodic reaction and $S_1 < 0$ for cathodic reaction. Clearly, the exchange current density increases if either the reactant's or product's concentration is increased. Figure 2 shows the log-log plot of the exchange current density vs. the zinc ion concentration. From the slope of the plot, the fractional power of the concentration in Eq. [3] is obtained, $Z + \beta S = 0.459$. If the reaction order $Z = 1.0$ and the stoichiometric coefficient $S_{\text{Zn}^{2+}} = 1.0$ are assumed, then the symmetric transfer coefficient β is 0.541 which is in agreement with the previous assumption $\beta = 0.5$ in the theoretical Tafel slope.

The reaction order of the zinc deposition process is obtained by

$$Z = \left[\frac{\partial(\log i_0)}{\partial(\log[\text{Zn}^{2+}])} \right] \quad [4]$$

Figure 3 shows the cathodic current density vs. the zinc concentration at various fixed potentials ($E = -1.065, -1.040, \text{ and } -1.015\text{V vs. SCE}$). The obtained reaction order is $Z = 0.75$. As shown previously, the reaction order is $Z = 1.0$ for $\beta = 0.5$. Thus, the zinc

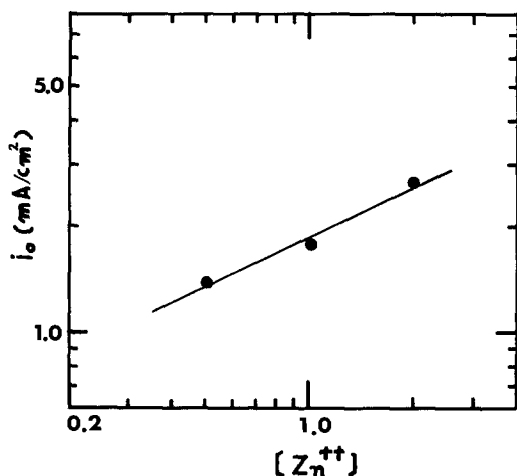


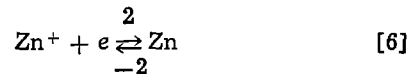
Fig. 2. The exchange current density vs. the molar concentration of zinc ion.

Table I. The kinetic Tafel parameters of zinc in zinc chloride solution (pH = 2.0)

ZnCl_2 (M)	i_0 (mA/cm ²)	b_a (mV)	$-b_c$ (mV)
0.5	1.36	108.5	139.5
1.0	1.75	94.4	131.3
2.0	2.65	90.6	113.7

cathodic reaction order is believed to be first order.

The obtained kinetic parameters suggest the following kinetic mechanism of zinc deposition



If Eq. [5] is the rate-determining step, the rate expression for the above reaction is

$$i_c = nFk_1 [\text{Zn}^{2+}] \exp \left[\frac{-(1-\beta)FE}{RT} \right] \quad [7]$$

Equation [7] yields a Tafel slope $b_c = -120 \text{ mV}$ (for $\beta = 0.5$) and a reaction order with respect to the concentration of the zinc ion $Z = 1.0$.

If Eq. [6] is the rate-determining step, the rate expression is

$$i_c = nFk_2 \theta \exp \left[\frac{-(1-\beta)FE}{RT} \right] \quad [8]$$

$$\frac{d\theta}{dt} = k_1(1-\theta) [\text{Zn}^{2+}] \exp \left[\frac{-(1-\beta)FE}{RT} \right] - k_{-1}\theta \exp \left[\frac{\beta FE}{RT} \right] - k_2\theta \exp \left[\frac{-(1-\beta)FE}{RT} \right] \quad [9]$$

θ is the fractional coverage of Zn^+ ion. At steady state and under the assumption of $k_{-1} \gg k_2$, Eq. [9] reduces to

$$\frac{\theta}{1-\theta} = \left(\frac{k_1}{k_{-1}} \right) [\text{Zn}^{2+}] \exp \left(\frac{-FE}{RT} \right) \quad [10]$$

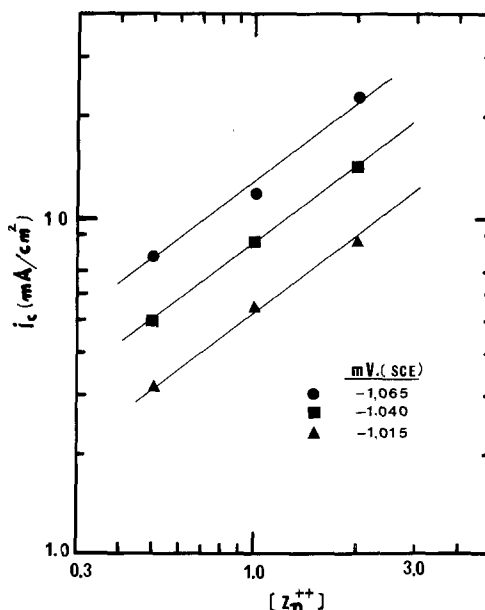


Fig. 3. The cathodic current density vs. the molar concentration of zinc ion at different fixed potentials.

θ is assumed to be very small ($1 - \theta \cong 1$) and substituting Eq. [10] into Eq. [8], results

$$i_c = nF \left(\frac{k_1 k_2}{k_{-1}} \right) [\text{Zn}^{++}] \exp \left[\frac{-(1 - \beta)FE}{RT} \right] \quad [11]$$

Equation [11] yields a Tafel slope $b_c = -40$ mV (for $\beta = 0.5$) and a reaction order $Z = 1.0$. If the fractional coverage is assumed to approach unity, then Eq. [8] yields a Tafel slope $b_c = -120$ mV and a reaction order $Z = 0$.

Thus, if Eq. [6] is the rate-determining step, the theoretical kinetic parameters contradict the experimental results. The present experimental results confirm that Eq. [5] is the rate-determining step.

The diffusion coefficient of zinc ion.—Cathodic polarization of zinc electrode in 0.05M ZnCl₂ and 1M KCl solution is shown in Fig. 4. Accurate zinc deposition limiting currents cannot be observed. The polarization shows a mixed kinetics behavior: partly controlled by mass transfer and partly controlled by kinetics. The steep rise in the current which appears at about -1.85 V vs. SCE is due to hydrogen evolution. A similar result was reported by Justinijanovic and Despić (24) in 0.5M alkaline zincate solution. The zinc reaction is diffusion controlled and hydrogen evolves simultaneously, therefore, the effective limiting current for zinc deposition alone is lower than the experimental value.

Figure 5 shows the plot of the current vs. the square root of the rotational speed under a fixed potential ($E = -1.654$ V vs. SCE). At low rotational speeds, the reaction is diffusion controlled and the current is proportional to the square root of the rotational speed, in agreement with the convective diffusion equation for a rotating hemispherical electrode

$$i_l = 0.451 nFD^{2/3} \nu^{-1/6} C_b \omega^{1/2} \quad [12]$$

At high rotational speeds, the reaction is kinetics controlled and the current becomes independent of the rotational speed

$$i_k = nFkC_b^z \quad [13]$$

From Fig. 5 the true limiting current of zinc deposition is obtained from which the diffusion coefficient of zinc ion is calculated

$$D_{\text{Zn}^{++}} = 0.89 \times 10^{-5} \text{ cm}^2/\text{sec}$$

The kinematic viscosity is $\nu = 0.935 \times 10^{-2}$ stokes. Diffusion coefficients of Zn(Hg) and Zn²⁺ were reported previously (8) using chronopotentiometric measurements: 1.5×10^{-5} and 0.7×10^{-5} cm²/sec, respectively, in general agreement with the present value.

Surface roughness during zinc electrodeposition.—It has been suggested that the surface roughness during metal electrodeposition is determined by the fraction of the limiting current at which the electrodeposition is performed, Landau (25).

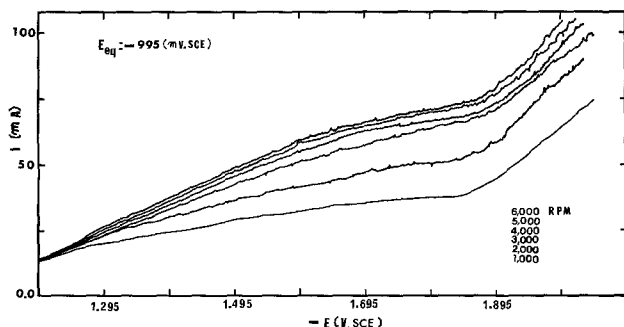


Fig. 4. Cathodic polarization of zinc hemispherical electrode in 0.05M ZnCl₂ + 1.0M KCl solution at various rotational speeds. Electrode diameter: 0.736 cm.

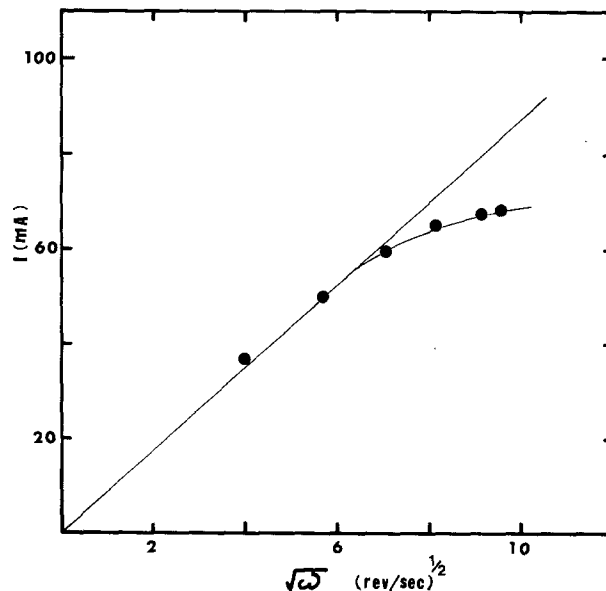


Fig. 5. Determination of the diffusion coefficient of zinc ion: the current vs. the square root of the rotational speed. Fixed potential $E = -1.654$ V vs. SCE. 0.05M ZnCl₂ + 1.0M KCl. Electrode diameter: 0.736 cm.

In the present investigation the appearance of roughness during zinc electrodeposition in ZnCl₂ solution is investigated and correlated to factors such as the fraction of the limiting current I/I_l , the zinc ion concentration, and the deposition time. In order to investigate these effects, the current was fixed at various regions: above the limiting current, near the limiting current, and below the limiting current. Figure 6 shows zinc deposits on rotating hemispherical zinc electrodes at various rotational speeds in 0.5M ZnCl₂ and 1M KCl solution. The fixed current was 200 mA and the deposition time was 30 min for each electrode. The limiting current of zinc deposition in 0.5M ZnCl₂ solution can be estimated from the obtained limiting current in 0.05M ZnCl₂ (Fig. 5). The estimated limiting currents in 0.5M ZnCl₂ are 360, 620, and 800 mA for rotational speeds, $\omega = 1000, 3000,$ and 5000 rpm, respectively. The fraction of the limiting current (I/I_l) is 0.55 for 1000 rpm, 0.32 for 3000 rpm, and 0.25 for 5000 rpm. Clearly, at higher rotational speeds (or at small fractions of the limiting current), the surface of the deposit is smoother than at lower rotational speeds.

The roughness of the zinc deposit is influenced also by the deposition time as shown in Fig. 7. The fraction of the limiting current was $I/I_l = 0.44$ and the time varied from 3.44 to 45 min. Obviously, more roughness developed over the longer period of time. In Fig. 8, the current was fixed at the limiting current region ($I = 62$ mA) and at 50% of limiting current ($I = 31$ mA). As the fraction of the limiting current approaches unity, the surface becomes rougher. Also, above the limiting current region ($I/I_l = 1.53$), the zinc surface was rougher than under the limiting current ($I/I_l = 0.65$) as shown in Fig. 9, although the applied current was identical in both cases.

The mechanism of roughness formation can be separated into two regions: near the limiting current, and at well below the limiting current. The roughness is determined by the local current distribution. At well below the limiting current the current distribution is governed primarily by electrical, electrochemical, and crystallographical factors rather than by mass transfer processes. However, at the limiting current, the surface concentration is zero, and the current density is simply proportional to the mass transfer coefficient. The local current density depends on the initial surface profile. At peaks, the mass transfer coefficient is high and the local current density is high too. On



Fig. 6. Zinc deposition at different fractions of the limiting current. 0.5M ZnCl₂ + 1.0M KCl solution

	A	B	C
I/I_1	0.55	0.32	0.25
I (mA)	200	200	200
I_1 (mA)	~360	~620	~800
Diameter (cm)	0.76	0.76	0.76
ω (rpm)	1000	3000	5000
t (min)	30	30	30

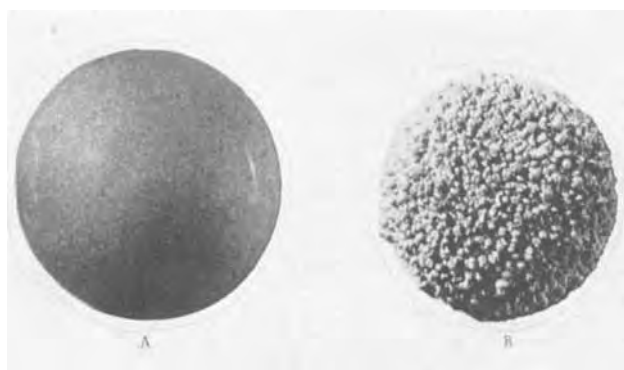


Fig. 7. Zinc deposition at different deposition times. 0.5M ZnCl₂ + 1.0M KCl solution.

	A	B
I/I_1	0.44	0.44
I (mA)	200	200
I_1 (mA)	~450	~450
Diameter (cm)	0.79	0.79
ω (rpm)	1500	1500
t (min)	3.44	45.0

the contrary, since the mass transfer coefficient at recesses is smaller than at the peak, the deposition rate is slow. Thus, if a current is applied near the limiting current, roughness can be amplified due to varying local mass transfer rates.

The interesting phenomenon of spiral formation at a rotating disk and a rotating hemisphere has been observed elsewhere during the process of metal dissolution or deposition (5, 26-28, 30-31). Figure 10 shows zinc deposits on a rotating zinc hemisphere electrode in 0.05M ZnCl₂ and 1M KCl solution. The current was fixed well below the limiting current ($I/I_1 = 0.16$) and the deposition process was examined at different times: $t = 20$ min and $t = 110$ min. After a short time of 20 min, a smooth deposit which contained many traces of hydrogen bubbles was observed. After a long period of 110 min, spiral tracings can be observed. At a higher current ($I = 20$ mA), less bubble tracing was observed. Since the rate of hydro-



Fig. 8. Zinc deposition at and below the limiting current. 0.05M ZnCl₂ + 1.0M KCl solution.

	A	B
I/I_1	1.0	0.5
I (mA)	62	31
I_1 (mA)	62	62
Diameter (cm)	0.72	0.72
ω (rpm)	3000	3000
t (min)	20	20

gen evolution is higher at high currents, the residence time of the hydrogen bubbles on the surface is short. Kadija and Nakic (29) confirmed that the space between the bubbles on the surface decreases by increasing the current. The dark lines show probably trajectories of hydrogen bubbles and zinc deposition is not observed at these lines, because of the shielding effect of the bubbles and the low rate of deposition under the bubbles. The appearance of these spiral markings is discussed by Rogers and Taylor (30) and results from the appearance of tiny protrusions on the rotating electrode. These may be, for example, hydrogen bubbles or rough deposits at the electrode surface. Spiral markings are observed frequently at the transitional flow region, and it is quite possible that the bubbles follow the secondary flow and are carried outward in logarithmic spiral trajectories. Jaksic and Tobias (31) observed striated profiles during zinc electrodeposition from its chloride or bromide solutions. The grooves follow the direction of flow and on rotating disk elec-

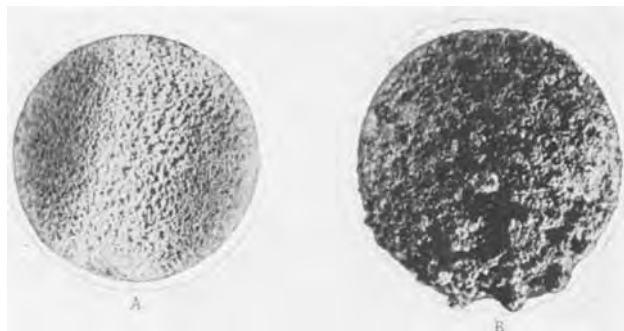


Fig. 9. Zinc deposition below and above the limiting current. 0.05M ZnCl₂ + 1.0M KCl solution.

	A	B
I/I_1	0.65	1.53
I (mA)	40	40
I_1 (mA)	62	26
Diameter (cm)	0.675	0.74
ω (rpm)	3000	500
t (min)	41.7	50



Fig. 10. Zinc deposition: the evolution of spiral markings. 0.05M ZnCl₂ + 1.0M KCl solution.

	A	B
I/I_1	0.16	0.16
I (mA)	10	10
I_1 (mA)	62	62
Diameter (cm)	0.75	0.75
ω (rpm)	3000	3000
t (min)	20	110

trodes this resulted in spiral patterns. This phenomenon is explained by a secondary flow which results in alternating regions of higher and lower interfacial concentrations (31).

Dendritic growth.—Deposition and dendritic growth on a rotating graphite disk electrode were performed potentiostatically in zinc chloride solution. Figure 11 shows the current-time behavior of the zinc deposition on a rotating graphite disk electrode. During the first 10–15 min the current did not change with time. During this period the process involved zinc deposition far below the limiting current and the initiation of dendrites at the disk edges. After this initiation period the current increased with time and dendritic growth was observed simultaneously at the disk edges. The current increased faster in 0.4M ZnCl₂ than in 4.3M ZnCl₂ solution as shown in Fig. 11.

If the reaction is partially limited by mass transport, the surface concentration (C_o) is related to the bulk concentration (C_b) by

$$C_o = C_b \left(1 - \frac{i}{i_1} \right) \quad [14]$$

where i is the applied current density and i_1 is the

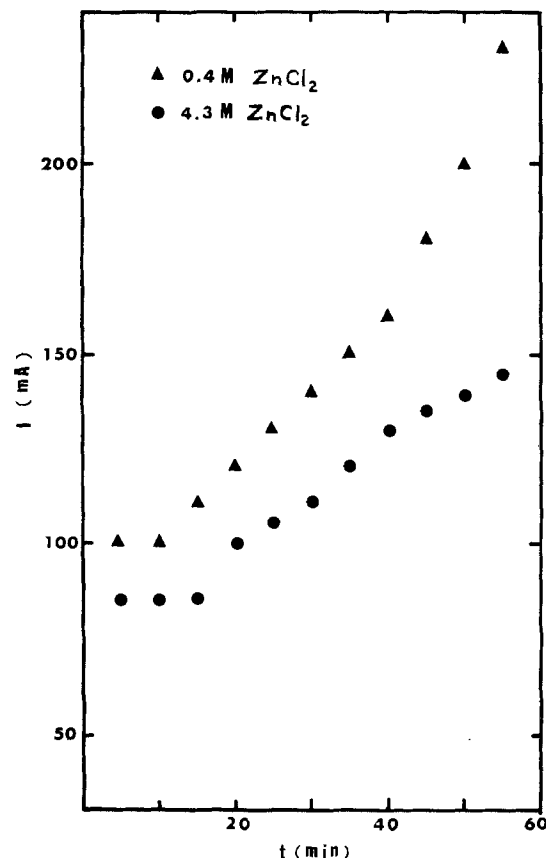


Fig. 11. The initiation and propagation of zinc dendrites at the edge of a rotating disk electrode under potentiostatic conditions. \blacktriangle 0.4M ZnCl₂, $E = -2.0V$ vs. SCE. \bullet 4.3M ZnCl₂, $E = -1.4V$ vs. SCE. $\omega = 4000$ rpm, area = 0.71 cm².

limiting current density. The limiting current was estimated from the plot of I vs. $\omega^{1/2}$ in Fig. 5. In 0.4 and 4.3M ZnCl₂ solutions the total currents during the initiation periods were 100 and 80 mA, respectively, and the estimated limiting currents at $\omega = 4000$ rpm are 0.42 and 4.5A, respectively (Fig. 5). The average fractions of the limiting current are $I/I_1 = 0.24$ and 0.018 and the surface concentrations during the initiation period are roughly 0.34 and 4.22M for the 0.4 and 4.4M ZnCl₂ solutions, respectively.

In both cases the currents were well below the limiting currents during the initiation period and as a result the initial current distributions were highly nonuniform. The local current densities at the edge of the disk electrode were much higher than in the center and dendrites initiated at the edges. The zinc deposition rate at the tips of the dendrites is very high and limited by mass transfer (spherical diffusion). Consequently, the surface concentration at the tip of the dendrite approaches zero. Since the deposition process is now diffusion limited the hydrodynamic condition becomes an important factor.

The effects of the hydrodynamic conditions and the concentration on the direction of the dendritic growth at the edge can be seen in Fig. 12 and 13. In the high zinc chloride concentration (4.3M) the dendrites grew in a vertical direction to the disk surface (Fig. 12). When the zinc chloride concentration was reduced by an order of magnitude (0.4M) the direction of dendritic growth changed drastically and the dendrites grew parallel to the Teflon disk and followed the flow direction (Fig. 13). The direction of the dendritic growth is an exact continuation of the spiral markings which have been observed before and can be seen also in Fig. 12 at the central region of the disk electrode.

The qualitative explanation to the change in direction of the dendritic growth is as follows: Initially,

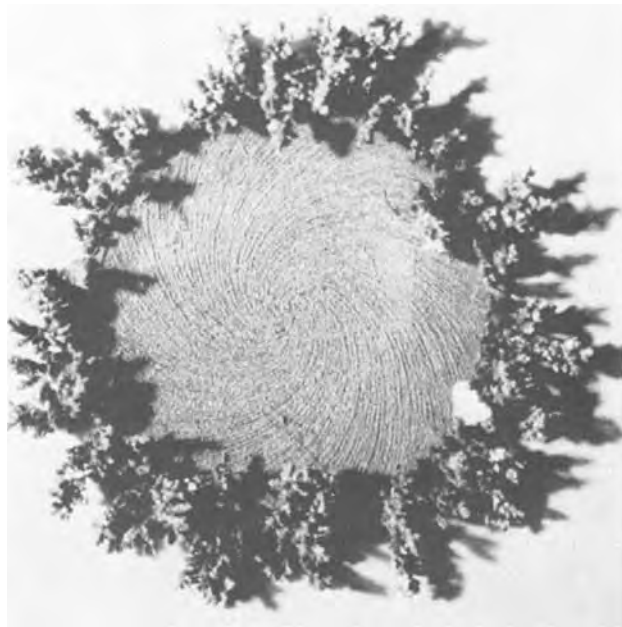


Fig. 12. Zinc dendrites on rotating disk graphite electrode (note vertical direction of growth). 4.3M ZnCl_2 . $E = -1.4\text{V}$ vs. SCE. $\omega = 4000$ rpm. Area = 0.71 cm^2 .

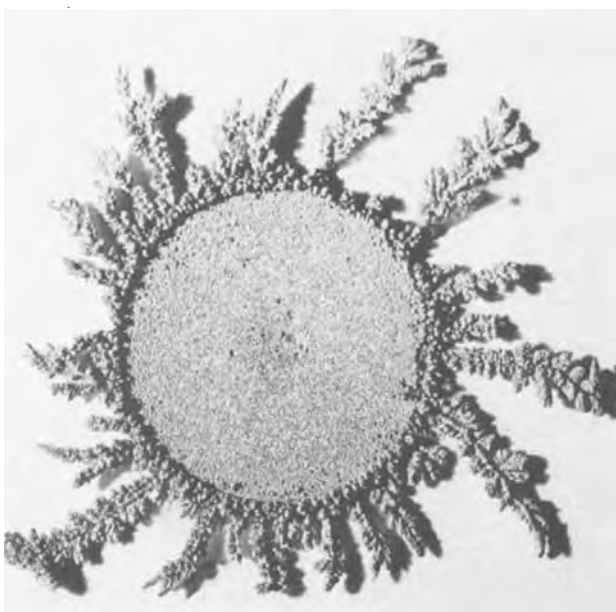


Fig. 13. Zinc dendrites on rotating disk graphite electrode (note horizontal direction of growth). 0.4M ZnCl_2 . $E = -2.0\text{V}$ vs. SCE. $\omega = 4000$ rpm. Area = 0.71 cm^2 .

zinc deposition is higher at the edge of the rotating disk electrode because of nonuniform current distribution. The zinc deposition reaction is fast and exhibits relatively high exchange current density which results in highly nonuniform current distribution below the limiting current. As a result, roughness develops at the edge and dendrites are initiated subsequently. The growth of the dendrites is mass transfer limited and the dendrites tend to grow toward a region of high zinc ion concentration. The dendrites also serve as large protrusions which interfere with the flow near the disk. The flow interaction reaches its full extent when the dendrites are about equal or slightly exceed the thickness of the hydrodynamic boundary layer. This effect results from flow separation at the tips of the dendrites and produces local eddies which transport small volumes of bulk liquid to the vicinity of the solid surface. Consequently, a narrow region

behind the dendrites near the insulator surface of the disk has a higher concentration of zinc ions which is quite close to the bulk concentration. Similar observations and explanation are given by Jaksic and Tobias (31). In the case of the low ZnCl_2 concentration (0.4M) the dendrites grew in the direction of the wakes behind the dendrites because the zinc concentration there was significantly higher than elsewhere on the disk surface. However, when the zinc bulk concentration was ten-fold higher, the effect became negligible and the dendrites grew vertically toward the bulk solution.

Summary

The kinetics of a zinc electrode in acidic zinc chloride solution was investigated. The postulated mechanism for the cathodic reaction indicates two consecutive one-electron transfer steps where the first one is the rate-determining step. The reaction is quite fast as indicated from its high exchange current densities. The morphology of the zinc deposit depends on the current density, the deposition time, and the hydrodynamic conditions (through the fraction of the limiting current). At low zinc ion concentration the deposit is generally smoother. At well below the limiting current the surface roughness depends on the microthrowing power. At appreciable fraction of the limiting current, the roughness is proportional to the fraction of the limiting current, and the surface becomes very rough at or above the limiting current. Zinc dendrites initiate at the edges of a rotating disk where the local current density is high. The dendritic growth is diffusion limited and is influenced by the flow especially at lower concentrations. The dendrites interact with the flow because they serve as protrusions and generate wakes behind them.

Manuscript submitted March 23, 1979; revised manuscript received June 19, 1979.

Any discussion of this paper will appear in a Discussion Section to be published in the December 1980 JOURNAL. All discussions for the December 1980 Discussion Section should be submitted by Aug. 1, 1980.

Publication costs of this article were assisted by Wayne State University.

REFERENCES

1. P. Carr, C. H. Chi, and P. C. Symons, in The 28th Power Sources Symposium, June 1978.
2. C. J. Warde, P. C. Symons, C. C. Whittlesey, and H. A. Catherino, in Proceedings of the 13th IECEC, Vol. 1, pp. 755-766 (1978).
3. J. Jorné, J. T. Kim, and D. Kralik, *J. Appl. Electrochem.*, In press.
4. J. T. Kim and J. Jorné, *This Journal*, **124**, 1473 (1977).
5. J. T. Kim and J. Jorné, *ibid.*, **125**, 89 (1978).
6. A. Kermani, J. Jorné, and S. Kodali, Paper 378 presented at the Electrochemical Society Meeting, Boston, Massachusetts, May 6-11, 1979.
7. L. Gaiser and K. E. Heusler, *Electrochim. Acta*, **15**, 161 (1970).
8. E. Eriksrud, *J. Electroanal. Chem.*, **76**, 27 (1977).
9. T. Hurlen and E. Eriksrud, *Electroanal. Chem. Interfacial Electrochem.*, **45**, 405 (1973).
10. H. B. Sierra Alcazar and J. A. Harrison, *Electrochim. Acta.*, **22**, 627 (1977).
11. J. A. Von Weber and P. Tomassi, *Metalloberflache*, **31**, 259 (1977).
12. I. Epelboin, M. Ksouri, E. Lejay, and R. Wiart, *Electrochim. Acta*, **20**, 603 (1975).
13. I. Epelboin, M. Ksouri, and R. Wiart, *J. Electroanal. Chem.*, **65**, 373 (1975).
14. I. Epelboin, M. Ksouri, and R. Wiart, *This Journal*, **122**, 1206 (1975).
15. I. Epelboin, M. Ksouri, and R. Wiart, *J. Electroanal. Chem.*, **58**, 433 (1975).
16. I. Epelboin, M. Ksouri, and R. Wiart, *J. Less-Common Metals*, **43**, 235 (1975).
17. D. T. Sorensen, A. W. Davidson, and J. Klinberg, *J. Inorg. Nucl. Chem.*, **13**, 64 (1960).

18. W. F. Libby, Abstracts of papers presented at the 115th Meeting of ACS, Division of Physical and Inorganic Chemistry, San Francisco, Calif. (1949).
19. H. Taube, H. Myers, and R. L. Rich, *J. Am. Chem. Soc.*, **75**, 4118 (1953).
20. H. Taube and J. Myers, *ibid.*, **76**, 2103 (1954).
21. H. Taube and E. L. King, *ibid.*, **76**, 4053 (1954).
22. J. Newman, *This Journal*, **113**, 501 (1966).
23. J. Newman, "Electrochemical Systems," Prentice-Hall, Englewood Cliffs, N.J. (1973).
24. I. N. Justinijanovic and A. R. Despic, *Electrochim. Acta*, **18**, 709 (1973).
25. U. Landau, Ph.D. Thesis, Department of Chemical Engineering, University of California, Berkeley, Lawrence Berkeley Laboratory, LBL 2702 (1976).
26. D. Johnson and D. R. Turner, *This Journal*, **109**, 918 (1962).
27. I. R. Krichevskii and Yu. V. Cehanskaya, *Zh. Fiz. Khim. SSSR*, **33**, 2331 (1959).
28. D. P. Gregory and A. C. Riddiford, *This Journal*, **107**, 950 (1960).
29. I. V. Kadija and V. M. Nakic, *J. Electroanal. Chem.*, **35**, 177 (1972).
30. G. T. Rogers and K. J. Taylor, *Nature, London*, **200**, 1062 (1963).
31. M. M. Jaksic and C. W. Tobias, Extended Abstracts, pp. 1164-1166, 29th ISE Meeting, Budapest (1978).

Influence of Accelerated Weathering on the Corrosion of Low-Alloy Steels

H. Schwitter and H. Böhni

Swiss Federal Institute of Technology, Institute of Materials Chemistry and Corrosion, 8093 Zürich, Switzerland

ABSTRACT

In low-alloy steels under accelerated atmospheric corrosion conditions the type of weathering, particularly the ratio of the time of wetness to the drying time, has a greater influence on the corrosion behavior than does the composition of the alloys. Electrochemical measurements show that the rust protection is not only due to the formation of compact macroscopic protective layers, but also to passivation effects. Passivation occurs for a prolonged period only at favorable accelerated weathering conditions. We propose a model for the interpretation of the corrosion behavior of low-alloy steels.

Weathering steels exposed to the atmosphere form, as is well known, compact and well-adhering protective layers which inhibit a further attack by corrosion. Depending on the composition of the alloy a more or less decreasing corrosion rate can be observed. Numerous papers have been published which support this observation (1-3).

Although these steels have been used throughout the world for a long period of time, the corrosion protective properties of the formed rust layers are not well enough understood. Most of the atmospheric corrosion tests performed until today do not allow any conclusions in this direction, because the different parameters, which are important for the corrosion behavior, have not been varied systematically in these tests.

The practical experiences with this material as well as the results of long-time tests obtained by Larrabee and Coburn (4) in the USA and Eduards (5) in England show, however, that considerable differences can occur between the different test sites. In England comparable steels corroded 5-10 times faster than in the USA, suggesting that the type of weathering is at least as important as the alloy composition.

It was therefore the aim of this study to examine the influence of weathering as well as the importance of the alloying elements on the corrosion behavior of low-alloy steels by means of appropriate accelerated weathering tests. Additionally, natural exposure tests, light and electron-optical studies, x-ray diffraction, and electrochemical measurements were carried out.

Experimental

Materials.—Materials examined were plain carbon steel and low-alloy steels with variable composition. Table I shows the analysis of these steels.

All low-alloy steels tested have the same basic composition. In three different groups, however, the alloy-

ing elements copper, chromium, and phosphorus were systematically varied.

Before exposure the steels were sandblasted and degreased in benzene.

Weathering.—The samples were exposed to three different types of accelerated weathering tests. Figure 1 gives a schematic survey of these weathering conditions. In the first weathering (3x) the samples were wetted and dried three times within 12 hr. In one week the samples were exposed 12 times to these 3x cycles and twice in 12 hr to a SO₂-containing atmosphere. In the weathering type 2x the specimens were exposed to two dry/wet cycles within 12 hr, in weathering type 1x they were wetted and dried only once in the same time. The average total time of wetness increased from 46% in the 3x cycle to 77% in the 1x cycle.

The specimens were wetted by means of aerosol spraying and sprinkling, dried at 42°C and at a relative humidity of 55%. During the SO₂-exposure the SO₂-concentration was 20 ppm and the relative humidity 85%. Before each SO₂-exposure the samples were also dried. For the natural exposure test in a suburban area near Zurich the samples were oriented towards the south at an angle of 45°.

Electrochemical experiments.—The electrochemical experiments were carried out in an air saturated 0.1M Na₂SO₄ solution. The current-potential curves were obtained potentiostatically by the usual electronic devices (potentiostat, function generator, potentialmeter). The sweep rate was 15 mV/min. As reference electrode a saturated calomel electrode was used. The surface of the sample examined was 4 cm².

Results

Weight losses.—Figure 2 gives a survey of the results obtained by the accelerated weathering tests. The copper as well as the chromium series clearly show the influence of weathering. The samples weathered with

Key words: accelerated weathering tests, weathering steel, atmospheric corrosion, wet/dry cycles, rust layers.

Table I. Chemical analysis of the steels used

Steel	C	S	Si	Mn	Cr	P	Cu	Ni	
Plain carbon steel S	0.02	0.011	0.005	0.29	0.015	0.042	0.018	0.04	
Low alloy	E	0.09	0.009	0.36	0.50	0.061	0.053	0.27	
	P	0.10	0.008	0.37	0.42	0.074	0.18	0.28	
	M	0.11	0.010	0.34	0.49	0.081	0.47	0.30	
	H	0.10	0.006	0.34	0.42	0.01	0.079	0.34	0.29
	F	0.11	0.010	0.34	0.49	0.28	0.067	0.34	0.30
	K	0.11	0.007	0.42	0.50	0.75	0.075	0.45	0.31
	J	0.10	0.007	0.36	0.45	0.54	0.014	0.44	0.31
	Q	0.11	0.011	0.39	0.50	0.51	0.074	0.41	0.30
N	0.11	0.012	0.38	0.50	0.51	0.101	0.47	0.30	

the 3x cycle have smaller weight losses than those with 2x and 1x cycle. The difference in the 2x and 1x type weathering, however, is not very pronounced. In the weathering 3x the influence of the alloying elements is weak. In addition, the unalloyed steel S shows only a very small corrosion rate after 9 weeks. The influence of the alloying elements in the weathering types 2x and 1x is slightly greater. In Fig. 2 the results of the most highly alloyed steels are at the lower limit, the ones of the less alloyed steels at the upper limit of the value band.

Figure 3 shows additionally the weight loss of the S and M-type steels as a function of total time-of-wetness t^* instead of exposure time. The results indicate that the lower weight losses of the 3x-type weathering are not only due to the shorter time-of-wetness during these weathering conditions but also due to the more protective properties of the rust layer.

From these results the following statement can be made: Frequent drying/wetting changes in the 3x weathering have a favorable influence on the corrosion behavior. After a large corrosion rate at the beginning of the exposure the samples corrode only slightly. This behavior is almost independent of the concentration of

the alloying elements. For the unalloyed steel S the corrosion rate decreases significantly also.

When the samples are weathered with longer wetting periods (2x, 1x), the corrosion rate does not decrease so much. Moreover, the total metal loss is two to three times as high compared to weathering 3x. During these

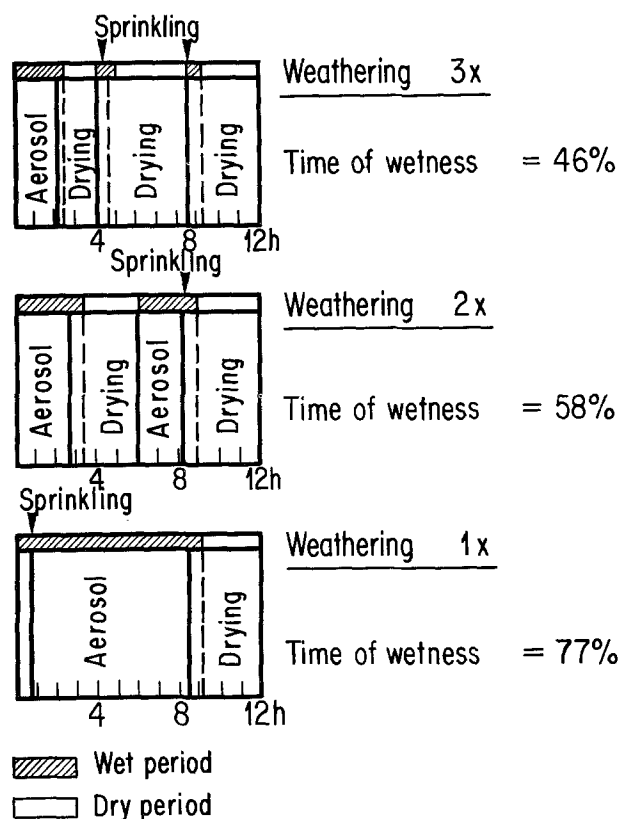


Fig. 1. Schematic survey of the types of accelerated weathering

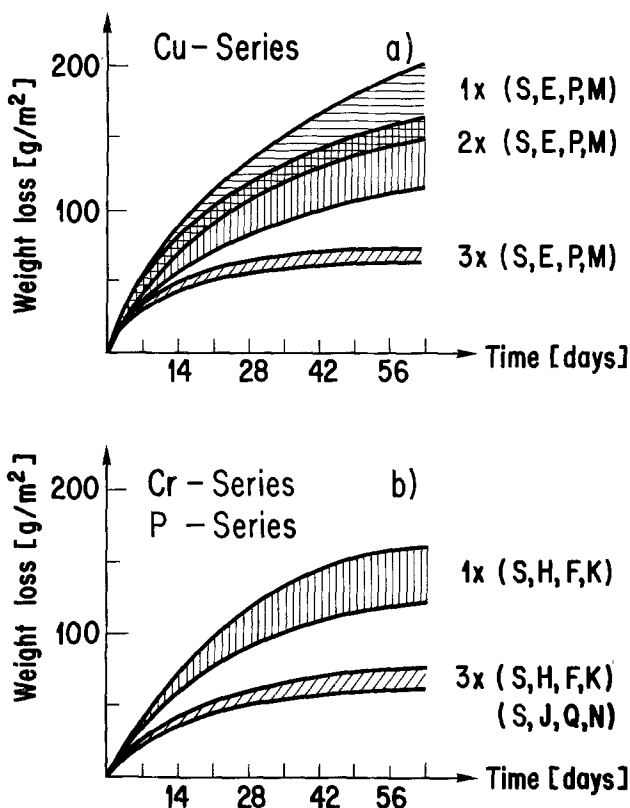
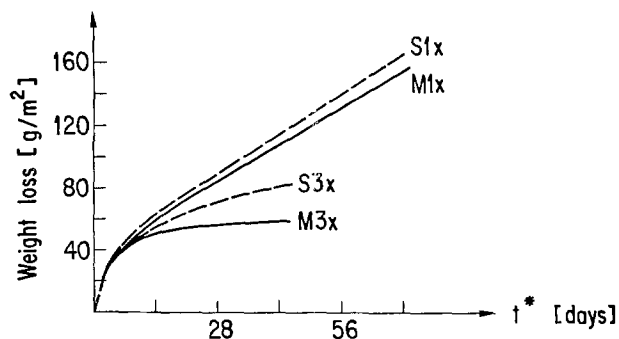


Fig. 2. Results of the accelerated weathering tests: a) copper-series; b) chromium and phosphorus series.

Fig. 3. Weight loss, x-axis reduced to time of wetness t^*

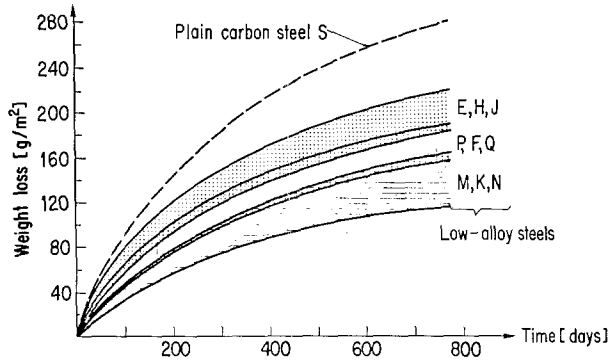


Fig. 4. Results of the natural weathering in suburban area

weathering conditions a beneficial influence of the alloying elements is observed.

Figure 4 shows the results of the natural exposure tests. In spite of the large scatter a similar influence of the alloying elements is obtained as in the case of the accelerated weathering 1x and 2x. Generally, the most alloyed steels have the lowest and the unalloyed carbon steels have the highest weight losses. Moreover, after two years exposure none of the steels tested formed the completely protective rust layers observed during 3x-type accelerated weathering.

Metallographic tests.—For the description of the further tests only the results of the carbon steel S and the copper containing steel M are used. Also, the 2x weathering is not mentioned any more because the results are similar to those in 1x weathering.

Examined macroscopically, the samples of the 3x-type weathering have a relatively dark, homogeneous-looking surface. No real rust blisters are visible. On the other hand, the rust layers formed on the 1x-type samples have a lighter color. Moreover the surface is covered with numerous big blisters.

Scanning electron microscopy (SEM).—Figure 5 shows the surface of the samples M3x and S3x taken with SEM. Here the rust layer is very homogeneous and compact. The single blisters are very small and of about the same size. The surface of the M3x sample has no visible cracks and on the S3x sample only few thin cracks can be seen.

On the other hand, the pictures of the M1x and S1x samples show a rather inhomogeneous rust surface, as may be seen in Fig. 6. Beside numerous small rust blisters there are also big ones covered with relatively large cracks.

Light microscope tests.—Microscopic observations show the structure of the rust layer. Figure 7 illustrates the metallographic micrographs of samples M3x and S3x. Figure 7a is taken by means of a light microscope, Fig. 7b under polarized light and crossed nicols. The rust layer of the M3x sample consists of two layers: the dark one covering the metal surface and the light one above it. The optical behavior of the dark layer is isotropic. The other layer shows an anisotropic behavior caused by double refraction and is bright orange-colored in the microscope. Electron probe microanalysis showed that in the dark layer the alloying elements and sulfur are accumulated. X-ray diffraction analysis indicated that a large amount of rust has an x-ray amorphous structure. From these results can be con-

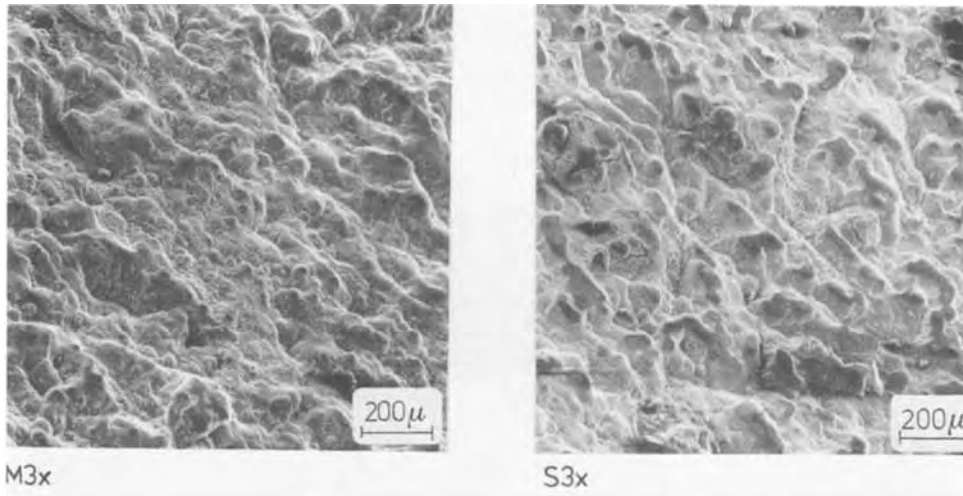


Fig. 5. Rust surface, weathering type 3x, scanning electron microscope.

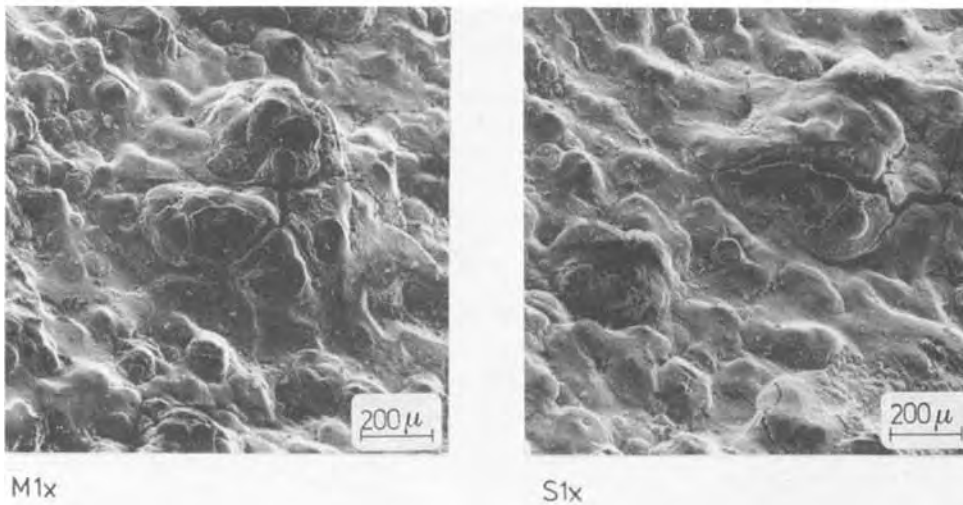


Fig. 6. Rust surface, weathering type 1x, scanning electron microscope.

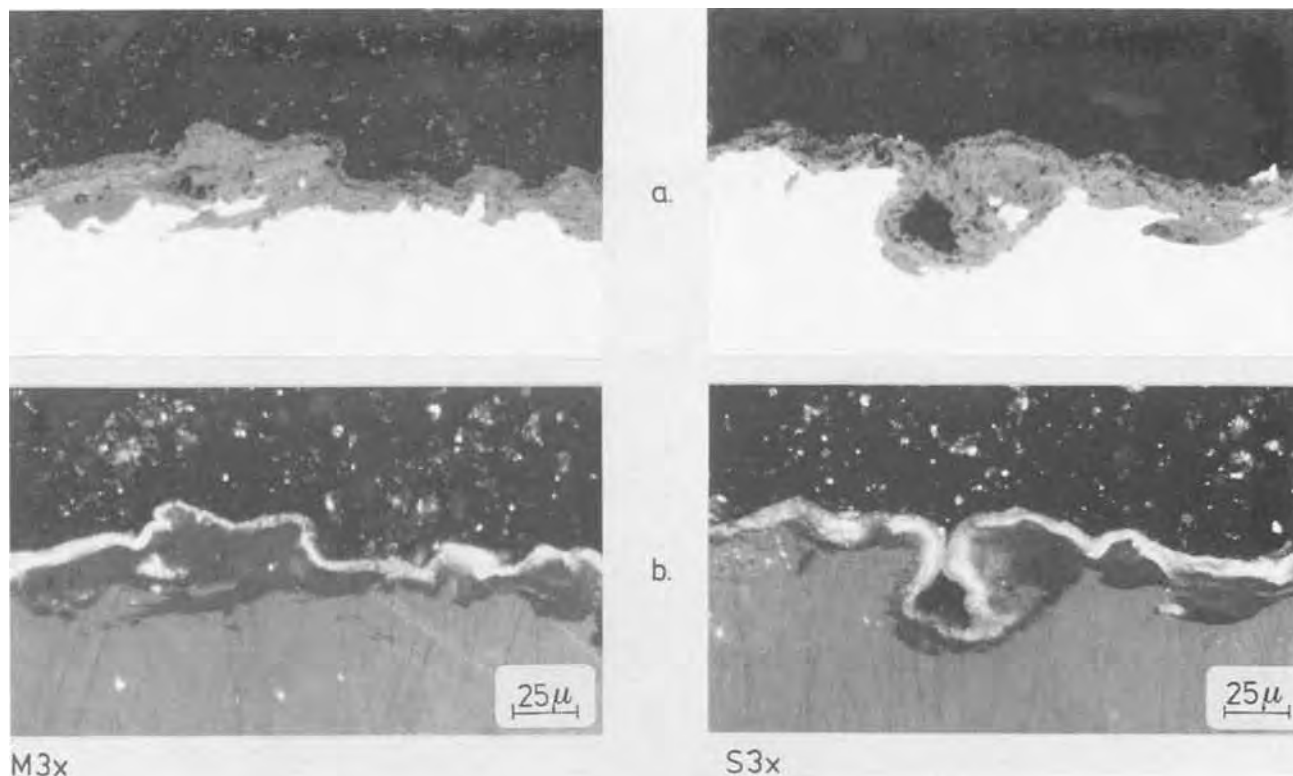


Fig. 7. Cross sections of the rust layers, weathering type 3x: a) light microscope; b) polarized light and crossed nicols

cluded that the dark parts in the cross sections consist of the amorphous $\text{FeO}_x(\text{OH})_{3-2x}$ as was already described by Misawa (6).

The surface of the M3x sample is covered at 80-90% with the dark, amorphous layer. The cross section through the rust layer of sample S3x shows a slightly less ordered structure. The light anisotropic layer is a little thicker compared with the dark layer. Yet, the metal surface is largely covered with the gray rust phase.

Figure 8 shows cross sections of the rust layer of the samples M1x and S1x. In the case of 1x-type weathering, the rust layer does not have the same ordered structure as with the 3x-type weathering. The light rust phases also appear directly on the metal surface. The dark rust layer covers here only 50-60% of the whole metal surface. Furthermore, the thickness of the rust layer is not uniform. The rust layer beside the big blisters is usually very thin and consists mainly of the light-colored anisotropic rust phase. Additionally, sul-

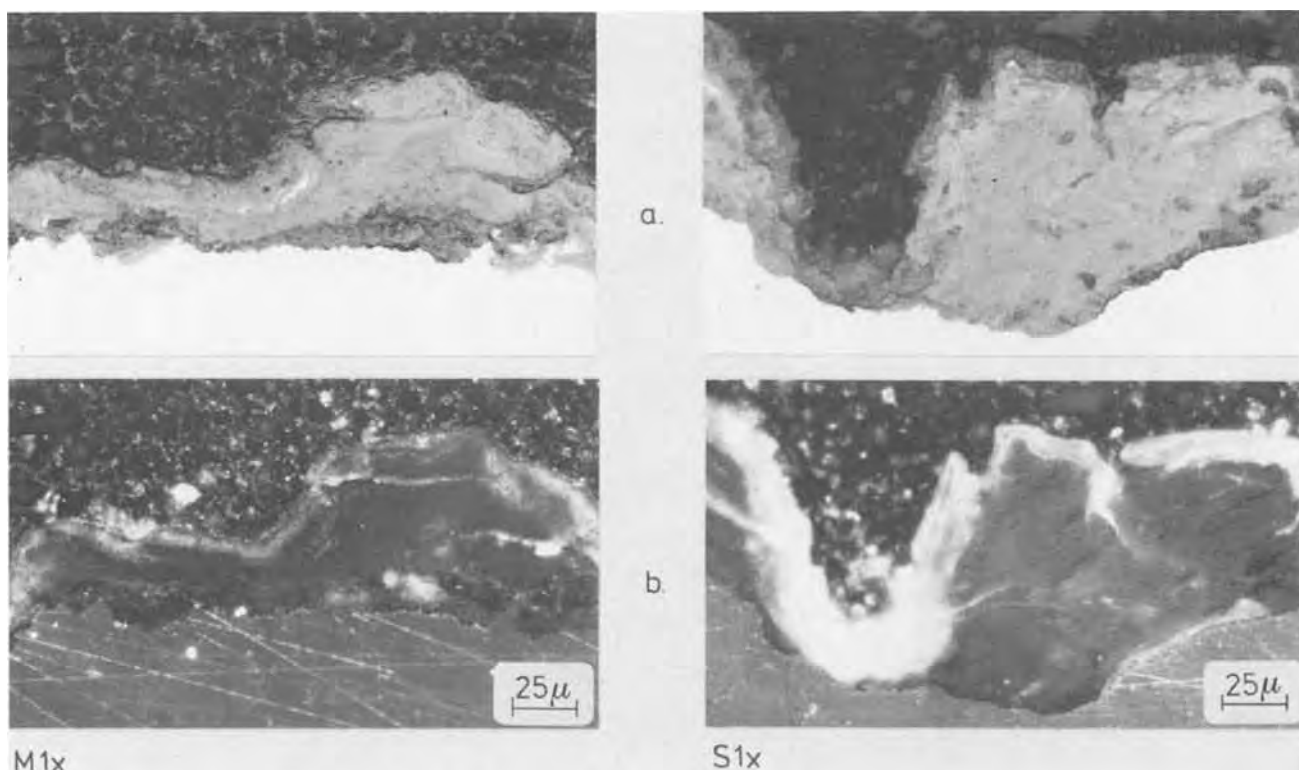


Fig. 8. Cross sections of the rust layers, weathering type 1x: a) light microscope; b) polarized light and crossed nicols

fate pockets are formed as can be seen in Fig. 8 (S1x) right underneath the big rust blister.

When preparing the metallographic cross sections, the light phases proved to be very brittle and tended to break out easily. The dark layers on the other hand are very compact and can easily be handled. This difference in the mechanical properties is very evident and points to the protective effect of the gray isotropic layer.

Electrochemical measurements.—Potential decay during immersion.—The dry samples were immersed in the electrolyte and the potential was continuously recorded.

Figure 9 shows the potential-time curves of the differently weathered alloyed and unalloyed samples after immersion. The potentials of the 1x-type weathered samples decrease in both cases within a few minutes by 300-400 mV and quickly reach a constant value. In the well-weathered samples this value is reached only after several hours. The constant potential value is nevertheless approximately the same in all the experiments. A rapid potential decay is also achieved by scratching the surface of the well-weathered sample (3x) with a needle (dotted line in Fig. 9).

Furthermore, the low-alloy steel M as well as the unalloyed steel S exposed to natural weathering conditions show quite similar potential-time curves as the 1x weathered samples (curves MA and SA in Fig. 9). This confirms the results already obtained by weight loss measurements where the natural exposure tests were also comparable with the 1x and 2x-type accelerated weathering.

Anodic polarization.—After having been immersed in the electrolyte for 20 min, the samples were anodically polarized.

Figure 10 shows such polarization curves which are similar to current-potential curves of passive metals. It can be demonstrated that the more the potential decreases during immersion, the larger is the value of the peak current in the anodic polarization curve. Poorly weathered samples always show accordingly high peak-current densities, whereas in well-weathered samples they are extremely small or do not exist at all.

Figure 11 shows the anodic polarization curve of the sample M3x which was scratched during immersion. The peak current density for the passivation of the samples is remarkably higher than in the sample which was only immersed. The passivation potential ϵ_p , however has the same value.

The reduction curves, starting in the passive state, also show an activation process in the same potential range, as is shown in Fig. 12. As is expected from the anodic polarization curves, this phenomenon appears more clearly in poorly weathered samples than in well-weathered ones.

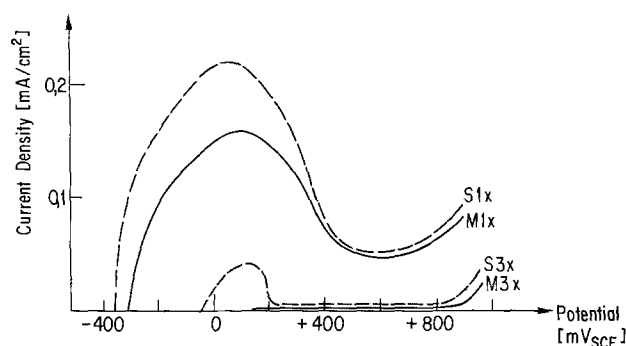


Fig. 10. Anodic current density-potential-curve after 20 min of immersion in 0.1M Na₂SO₄, sweep rate 15 mV/min.

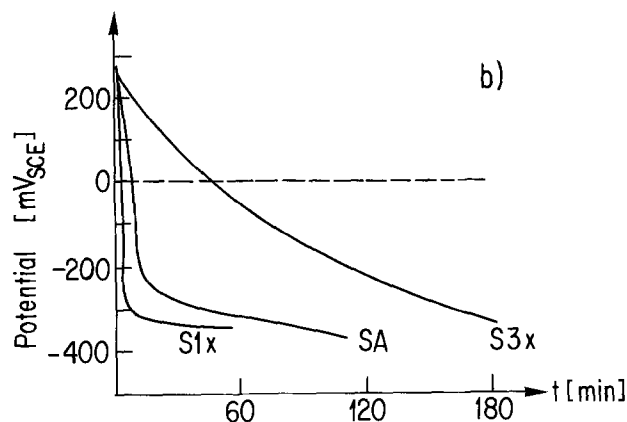
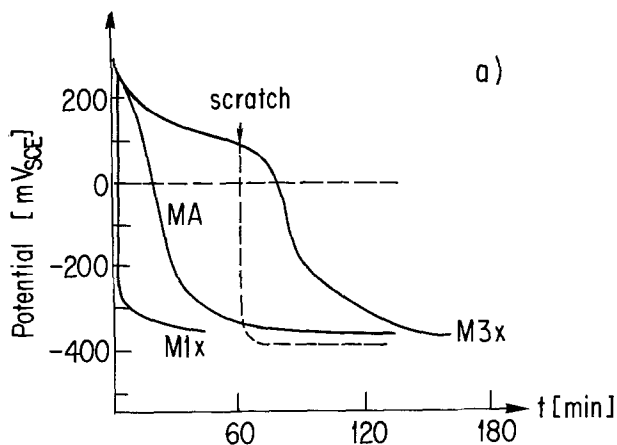


Fig. 9. Potential decay during immersion: a) weathering steel M; b) plain carbon steel S.

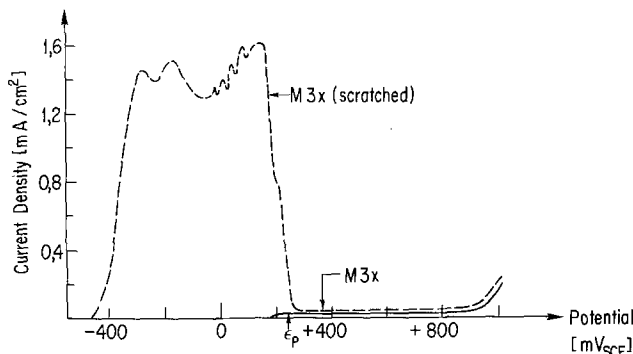


Fig. 11. Anodic current density-potential-curve of a scratched and an undamaged sample, 3x type weathering.

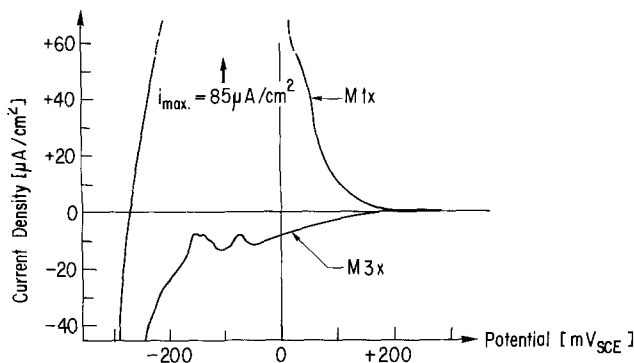


Fig. 12. Cathodic current density-potential-curve of different weathered (1x, 3x) steels immediately after immersion in 0.1M Na₂SO₄, sweep rate 15 mV/min., start at +400 mV.

Discussion

From the results of the electrochemical experiments one can conclude that the weathered samples are in a true passive state at the beginning of the immersion period. But with time the potential decreases to lower values and reactivation of the passive surface occurs. In order to maintain passivity, an easily reducible oxidizing agent has to be present in the rust of the weathered samples. This oxidizing agent keeps the potential of the system in the passive range until it is used up. Nothing can be said from this experiment concerning the quantity and the type of this oxidizing agent. As the different alloying elements do not influence the passivation within the different types of weathering, it may be concluded that an easily reducible part of the ordinary rust is responsible for maintaining passivity. In this experiment such a rust phase could be determined neither by cathodic reduction curves nor by x-ray diffraction analysis. This indicates that the amount is either very small and/or that the structure of the oxidizing agent is not much different from the structure of the ordinary rust.

The test with scratched samples showed that by increasing the active surface the anodic current increases as well. Therefore it can be supposed that the active surface of the poorly weathered samples 1x is much larger compared to the well-weathered ones. This fact explains also why the potential of the samples 1x decayed so much faster to lower values. Passivity is maintained here only until the oxidizing agent is used up.

Moreover the metallographic examinations show that the rust layer of the 1x weathered samples is covered by numerous cracks, in contrary to the rust obtained by 3x-type weathering which is almost free from cracks. In this case the metal surface is mostly covered with the dark compact rust phase. The cracks in the rust layer are supposed to be the sites of active corrosion on the metal surface. The better the steel is weathered, the more it is covered with the protective layer, i.e., the longer the oxidizing agent lasts to maintain passivity. Thus the potential decreases slower. During the drying periods reduced rust is reoxidized again by the atmospheric oxygen, so that the samples are passive again.

With the results obtained so far the following model for the formation of corrosion protective layers on low-alloy steels can be proposed: When the metal surface is exposed to frequent dry/wet cycles, the

whole surface corrodes rather evenly. In case of short wet periods no large sulfate pockets are formed. Due to precipitation of insoluble corrosion products and aging the metal surface is gradually covered by a rather compact and mainly amorphous rust layer which protects most of the surface from further attack. Finally the reduction current maintained by reducible rust components is sufficiently large to passivate the residual active areas during the wet periods. The growth of large rust blisters is therefore inhibited and the over-all corrosion rate decreases continuously. This process occurs not only on low-alloy but also on unalloyed steels.

When the metal surface is exposed to long wet periods, the corrosion rate increases and large sulfate pockets are formed. The surface is only partially covered by the corrosion inhibiting amorphous rust layer. In this case the residual active surface areas are considerably larger and can be passivated in the long wet period only for a short period of time. In this way localized corrosion processes are stimulated and due to the formation of voluminous corrosion products large cracks are formed. Finally the whole rust layer is peeled off. The corrosion inhibiting effect of these layers is therefore small.

Manuscript submitted Nov. 15, 1978; revised manuscript received May 18, 1979.

Any discussion of this paper will appear in a Discussion Section to be published in the December 1980 JOURNAL. All discussions for the December 1980 Discussion Section should be submitted by Aug. 1, 1980.

Publication costs of this article were assisted by the Swiss Federal Institute of Technology.

REFERENCES

1. F. Eisenstecken and W. Stinnes, *Arch. Eisenhuettenwes.*, **27**, 469 (1956).
2. W. Friehe and U. Tenhaven, *Stahl Eisen.*, **92**, 277 (1972).
3. S. G. Vedenkin, *Prot. Met.*, **11**, 259 (1975).
4. C. P. Larrabee and S. K. Coburn, First International Congress on Metallic Corrosion, p. 276, London (1962).
5. A. M. Edwards, Proc. Symp. on Developments in Methods of Prevention and Control of Corrosion in Buildings, British Iron and Steel Federation, London (1966).
6. T. Misawa, K. Hashimoto, and S. Shimodeira, *Corros. Sci.*, **14**, 131 (1974).

Reaction of Copper and Copper Oxide with H₂S

S. P. Sharma*

Bell Laboratories, Columbus, Ohio 43213

ABSTRACT

The lack of sulfidation of copper in indoor atmospheric corrosion has been attributed to the formation of copper oxide on copper, *i.e.*, the oxide which forms on the copper surface initially inhibits the growth of corrosion (sulfide films) on the surface. A permeation tube apparatus has been constructed with a quartz crystal microbalance (sensitivity $\sim 10^{-8}$ g) to elucidate the reaction of copper and copper oxide with H₂S. The film composition was measured with ESCA and Auger spectroscopy and the film thickness was measured with the quartz crystal microbalance to avoid the ambiguity of thickness estimation from sputter rate measurements in depth profiling. Results indicate that copper oxides grown in air (several hundred Å thick) provide good protection against H₂S at low relative humidities, but little protection at high relative humidities. Oxides grown in pure oxygen provide more protection, but still tarnish rapidly at higher relative humidities.

The atmospheric corrosion of copper is of significant interest to the electronic industry. Copper and its alloys are used as substrate materials for gold plated contacts. Porosity and wear processes may expose base metal, and in addition, diffusion of copper to the gold surface may take place. The tarnishing of the exposed copper may cause contact resistance increase and device failure.

Vernon (1, 2) has shown that a thin oxide film on Cu protects the metal from further attack by H₂S in air at room temperature but a sulfide film offers no protection. Baker (3) has studied the migration of corrosion products (sometimes referred to as creep) over the gold surface when copper and gold are in lateral contact and showed that the rate of migration increases with relative humidity. Tierney (4) showed recently that high relative humidity lessens the protective effect of oxide films towards sulfidation in the flowers of sulfur test. Frankenthal (5) has studied the tarnishing of copper in air with sulfur vapors at various humidities using Auger electron spectroscopy. It has been shown that in dry atmospheres the oxide films on copper protect the copper from sulfidation in flowers of sulfur environments (5). However, at higher relative humidities (>70%), the oxide films break down and the sulfide films keep on growing over the oxide.

The concentration of sulfur in the atmosphere generated from flowers of sulfur is much higher than that observed in the field. Also, gaseous pollutants in air normally include more H₂S and SO₂ than free sulfur. In order to understand the behavior of copper oxide films when exposed to gaseous pollutants, a study was conducted to determine the composition and the thickness of the tarnish films developed in an H₂S environment at ~ 5 ppm level. The effect of relative humidity and H₂S was observed on the tarnishing of Cu metal and Cu covered with oxides of various thicknesses and prepared by two different modes (air and oxygen environment). The exposure of material systems was done in a permeation tube apparatus. The film analyses were made by electron spectroscopy for chemical analysis (ESCA) and Auger electron spectroscopy (AES) in conjunction with argon ion sputtering. The film thicknesses were measured by quartz crystal oscillators (6) and by sputter-back profiling in AES and ESCA. Results indicate that copper oxides grown in air (several hundred Å thick) provide a good protection against H₂S at low relative humidities but provide little protection against H₂S at high relative humidities. Oxides grown in pure oxygen environments provide more protection than air grown oxides.

Experimental

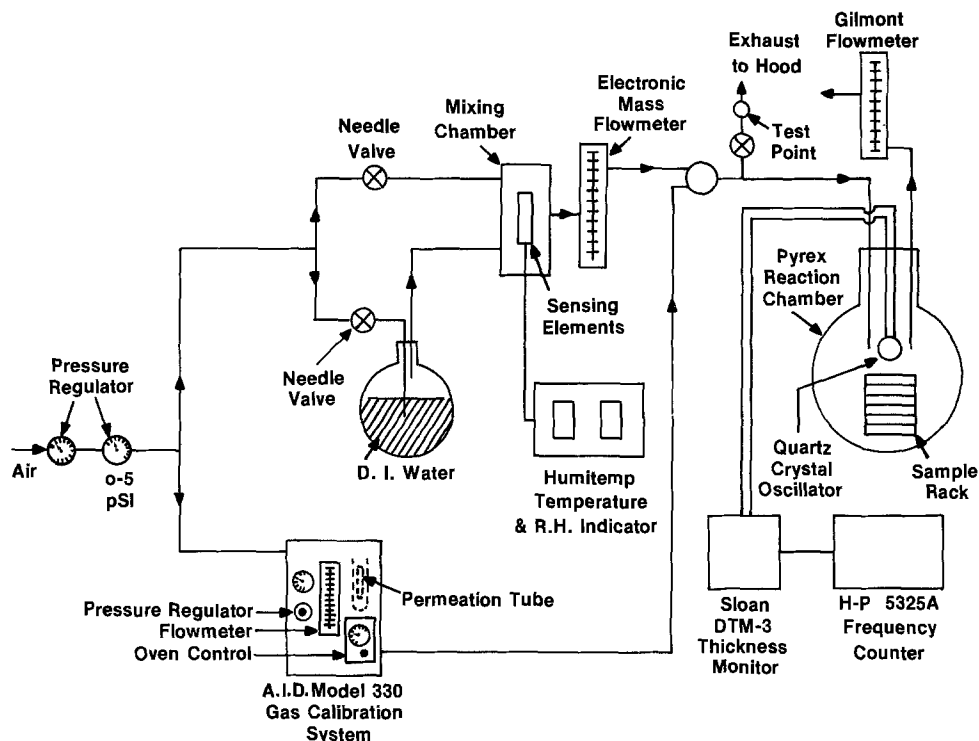
Coupons 15 mm square were cut from a 2.5 mm thick OFHC copper sheet. The coupons were degreased, finished to 600 grit and ultrasonically cleaned in distilled water and dried in air. In addition, 5 MHz AT-cut quartz crystals were coated with an electron beam evaporated Cu 1 μ m thick, and were also used as samples. Some coupons and Cu-evaporated quartz crystals were preoxidized in air at 125°C for 18 hr to give an oxide film of ~ 250 Å in thickness. At this oxide thickness, SEM analysis shows that the original surface features are closely reproduced, *i.e.*, the morphology of the films is similar (7). There may, however, be some difference in the structure and composition. Another set of coupons and quartz crystal samples were preoxidized in oxygen for one hour at 150°C to give an oxide film ~ 300 Å in thickness. A third set of coupons and quartz crystal samples were not preoxidized. All samples were exposed to air containing H₂S at various relative humidities.

The exposure was done in a permeation tube apparatus schematically shown in Fig. 1. An FEP (fluorinated ethylene propylene) Teflon tube is filled with H₂S in the liquid state and sealed. After an initial induction period, permeation of the chemical through the tube proceeds at a very constant rate (8). Dry air containing low levels of impurities is obtained from a commercial supplier. All traces of grease, water, and sulfur compounds are removed by filtering the air through activated charcoal and phosphorous pentoxide. The pressure in the incoming air line is maintained at ~ 5 psig. A double pressure regulator minimizes the pressure fluctuations in the incoming air line. Part of the dry air flows over a permeation tube which is maintained at a constant temperature of 30°C. A measured amount of this air containing H₂S enters the reaction chamber. Another part of the air from the incoming air line flows through a bubbler and is mixed with dry air in a mixing chamber. The amount of the wet air is measured with an electronic mass flowmeter and also enters the reaction chamber. The relative humidity in the reaction chamber can be varied by altering the humidity and the flow rate of wet air. The system flow rates were adjusted so that the H₂S concentration in the chamber was ~ 5 ppm and the relative humidity was zero or 80%. All measurements were made at room temperature and the flow rate was maintained at 75 ml/min.

The sample coupons were mounted in a rack suspended from the top of the reaction chamber. Quartz crystals 5 MHz, AT-cut, were also suspended from the top. The frequency was measured with an HP-5325A frequency counter. The decrease in the frequency of

* Electrochemical Society Active Member.
Key words: corrosion, growth, surfaces.

Fig. 1. Schematic diagram of the experimental apparatus.



the quartz crystal is related to the weight gain due to copper corrosion. Weight gain for a given frequency shift is obtained from the crystal constant (6) ($1.77 \times 10^{-8} \text{ g cm}^{-2} \text{ Hz}^{-1}$). This technique provides a sensitivity of $\sim 10^{-8} \text{ g/cm}^2$.

The corrosion films were analyzed for the elements present on a Physical Electronics scanning Auger system (AES) and ESCA system. ESCA measurements were made using Mg K_{α} radiation at 400W input power as described earlier (9). In order to correct for instrumental drift and to obtain an accurate energy calibration, data were referenced to the Au $4f_{7/2}$ line at 84.0 eV using a gold standard. Normal operating conditions for Auger analysis were 3 kV electron gun voltage, 1200V electron multiplier voltage, 1 eV/sec sweep rate, 0.3 sec time constant on the lock-in amplifier, 3 eV modulation amplitude and 1.6 mA emission current. For sputtering, the argon pressure was 5×10^{-5} Torr. Film thickness can also be determined by knowing the sputter rate and the time to sputter through the film. Since the sputter rates of various oxides and sulfides of copper are not known accurately, this process does not yield unambiguous absolute thickness. Thicknesses measured by the quartz crystal oscillator method were therefore employed in this study. The sputter rates were calculated by knowing measured thicknesses (by the quartz crystal microbalance) and sputter times. Some films on quartz crystals were sputtered back and their frequency change was continuously monitored to further check the sputter rates. In addition, the films on the copper coupons exposed for the same amount of time as the quartz crystals were sputtered back. These films on the coupons took the same time to sputter completely at the equivalent settings on the ion gun as the films on the quartz crystals, further supporting the conclusion that the film thicknesses on the coupons and the crystals are the same.

Results

The specimens that were not preoxidized had a measured oxide film $< 60 \text{ \AA}$ thick. This is the film which rapidly grows on copper at room temperature and is always present on copper surfaces. The rate of further growth of copper oxide (Cu_2O) at room temperature is very slow and during the time of our experiment very little film growth beyond this value

will take place. Preoxidized copper samples in air at 125°C for 18 hr were measured to have $\sim 250 \text{ \AA}$ thick film, while Cu_2O films grown on copper in a flowing oxygen environment at 150°C for one hour were measured to have $\sim 300\text{-}400 \text{ \AA}$ thick film. The preoxidized or unoxidized copper samples when exposed to sulfur-free air at various RH showed no further film growth. Preoxidized samples exposed to air containing 5 ppm H_2S at 0% RH also showed no further film growth and AES and ESCA analysis showed that the sulfur is present only as an adsorbed species. Figure 2 shows the Auger depth profile of a film on an air oxidized sample exposed to 5 ppm H_2S at 0% RH for 24 hr. By quantitative Auger analysis, it can be shown that most of the film is Cu_2O . It is also seen from this figure that the sulfur is present only as an adsorbed surface

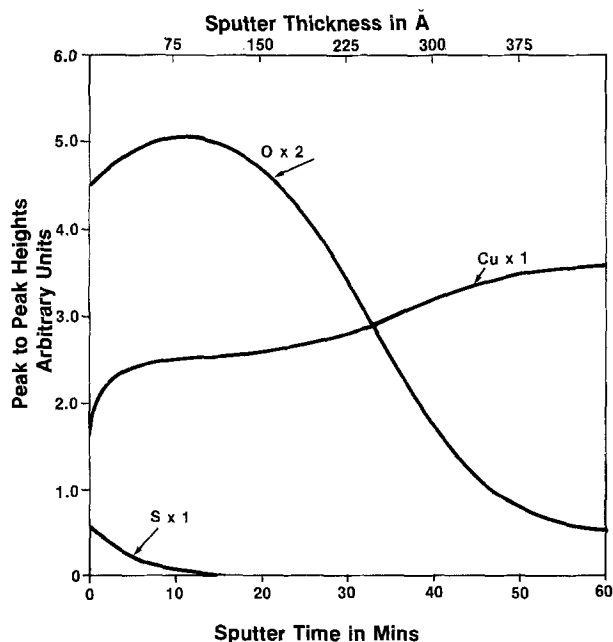


Fig. 2. Auger depth profile of the sulfided sample preoxidized in air and then exposed for 24 hr to H_2S at 0% RH ~ 5 ppm.

species. A similar kind of depth profile is obtained from O_2 -oxidized sample. The situation is quite different on an unoxidized sample. Figure 3 shows the depth profile of a film grown on an unoxidized copper sample exposed to ~ 5 ppm H_2S , 0% RH for 8 hr. It is obvious that the sulfide film grows on copper and no inhibition of tarnish films occurs in this case.

Figure 4 shows the Auger depth profile obtained from an air-oxidized sample exposed to ~ 5 ppm H_2S at 80% RH for 20 hr. As seen from this figure, the sulfide film grows over the oxide film. Initially, the surface film is a mixture of oxide and sulfide, for example, at 3 hr exposure (not shown) the elemental composition of the surface film is $Cu_{0.63}O_{0.12}S_{0.25}$. As the exposure increases (>8 hr), the film becomes a layered structure, the top film being the sulfide film. The com-

position of the surface film is $Cu_{0.65}S_{0.35}$. The surface composition does not change with the exposure time. This kind of layered structure with oxide sandwiched between a mixed sulfide layer and the metal is seen at almost all exposures (>8 hr). Interestingly enough, apart from the sulfide layer growth, the sandwiched oxide layer also increases in thickness with the exposure time. The compositional analysis of the sandwiched oxide layer reveals that this film becomes richer in Cu, i.e., this composition no longer corresponds to Cu_2O , instead it becomes $Cu_{0.82}O_{0.18}$. This suggests that the Cu_2O at higher relative humidities is no longer completely protective when exposed to H_2S .

Figure 5 shows a typical depth profile of a film which grew on a copper sample that has not been pre-oxidized (exposure time to H_2S —50 hr, 5 ppm, 80% RH). If this film is compared to the film which grows on air-oxidized copper in the same time period (not shown), the film which grows on bare Cu is thicker than the film on air-oxidized samples.

Another set of samples that were preoxidized in an oxygen environment ($150^\circ C$, 1 hr), were also exposed to 5 ppm H_2S for 8 hr at 80% RH. These samples show less sulfiding than air-oxidized or unoxidized copper (Fig. 6). The composition of the sulfide film is $Cu_{0.66}S_{0.34}$ and the sandwiched oxide composition remains at $Cu_{0.68}O_{0.32}$ (Cu_2O). This suggests that the oxide film grown in oxygen is more protective to H_2S exposure than air-oxidized copper samples.

The kinetic film growth rate data from the quartz crystal microbalance have been plotted in Fig. 7. The x-axis shows the time of exposure in hours and the y-axis is the frequency shift in Hz. The frequency shift can be converted to the total weight of the corrosion product by knowing the crystal constant. The thickness of the sulfide film can be calculated by knowing the density of Cu_2S (from the CRC Handbook), the area of the exposed material on the quartz crystal, and the total weight gain. We can also calculate the rate of film growth for various samples at different relative humidities. It is seen that at 0% RH, the sulfide film growth on copper follows a linear law, while air-oxidized samples show very little corrosion (the linear law may change as the film thickens). At 80% RH, the growth rate is initially linear but becomes parabolic as the thickness increases for both kind of samples, oxidized and unoxidized. This figure can also be utilized

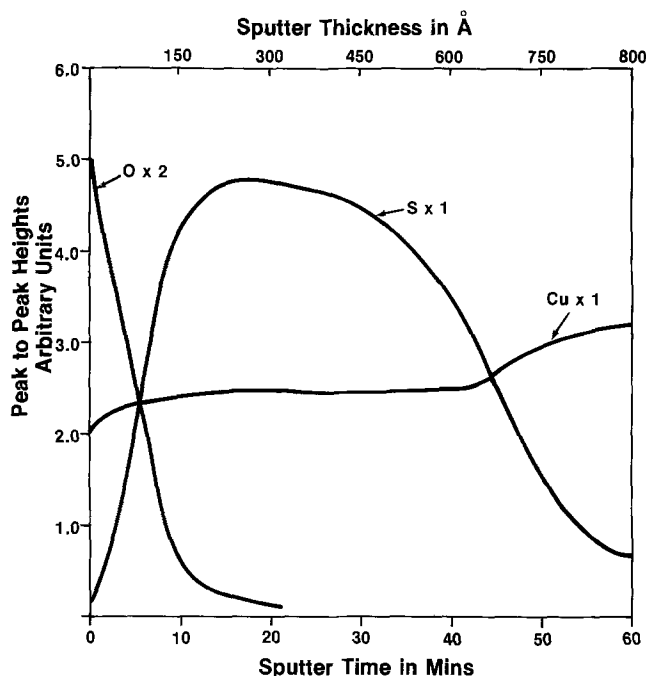


Fig. 3. Auger depth profile from the unoxidized Cu sample exposed for 8 hr to 5 ppm H_2S at 0% RH.

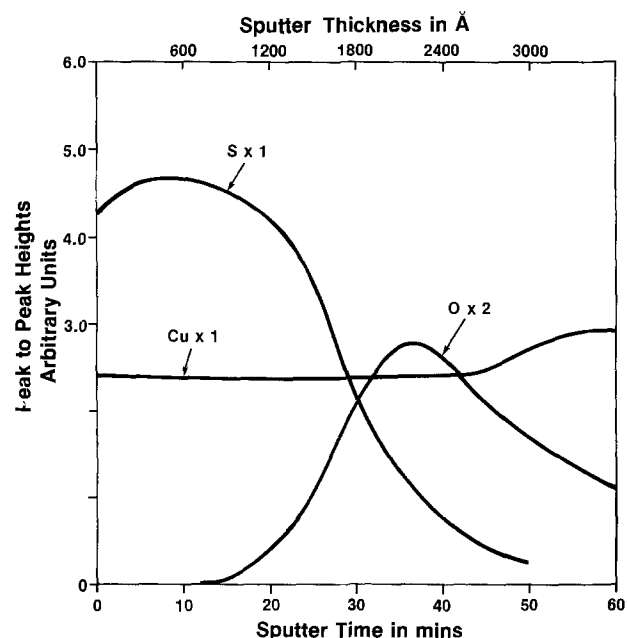


Fig. 4. Auger depth profile from an air-oxidized Cu exposed for 20 hr to 5 ppm H_2S at 80% RH.

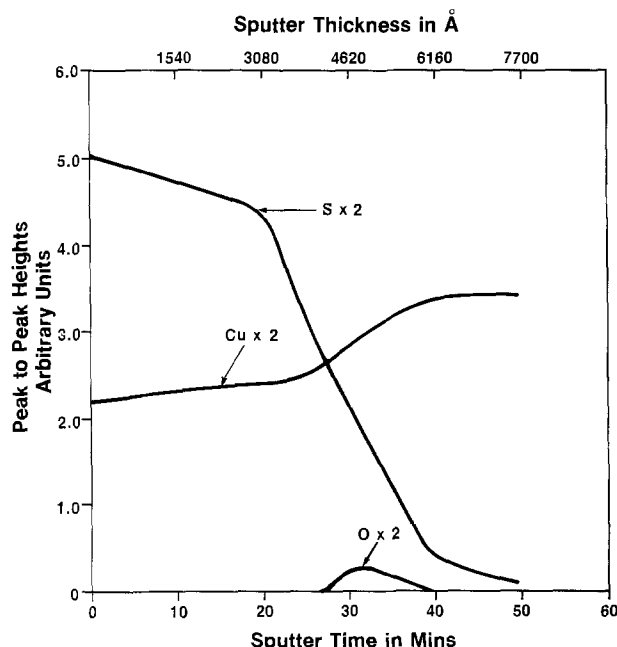


Fig. 5. Auger depth profile from the unoxidized Cu exposed for 50 hr to 5 ppm H_2S at 80% RH.

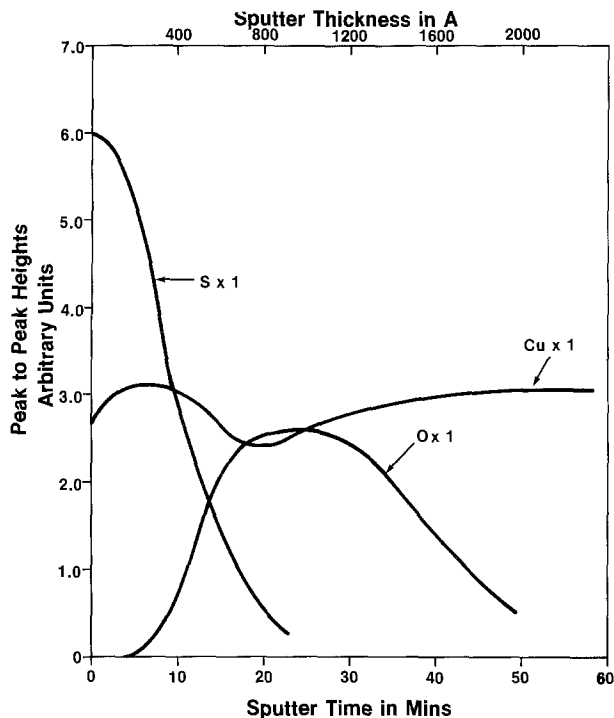


Fig. 6. Auger depth profile from the O₂-oxidized sample exposed for 8 hr to 5 ppm H₂S at 80% RH.

as a quantitative measure of amount of protection offered against sulfidation by various oxidized samples (the density difference between Cu₂S and Cu₂O is not appreciable and the density of the film can be assumed in between Cu₂S and Cu₂O). Figure 7 shows as an inset the film growth rates in the linear region for various samples. In the linear range the film growth on bare copper at 80% RH, is four times the rate of

Kinetic Growth Rate for Cu and Cu₂O Samples (5 ppm H₂S)

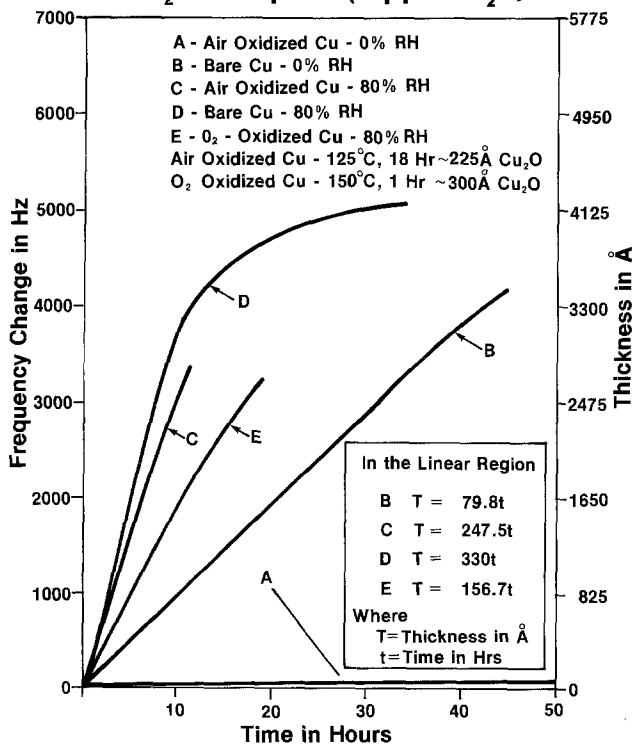


Fig. 7. Kinetic growth rate data obtained from quartz crystal microbalance is shown for various samples.

growth at 0% RH. The O₂-oxidized samples offer more protection against sulfidation than air-oxidized samples. Thus, in the linear region at 80% RH, the film thickness on air-oxidized copper is 75% of the film on bare copper, while the film thickness on O₂-oxidized copper is 47% of the film on copper. The film thickness determined from depth profiling will be the total film which has grown on the sample (oxide and sulfide) and can be compared to thicknesses from Fig. 7.

Interestingly, the sulfur Auger peak on bare Cu samples shows a fine structure (at 0% and 80% RH). There are three distinct peaks in the sulfur spectrum at 146, 151, and 156 eV as shown in Fig. 8. The air-oxidized Cu shows the same sulfur peak structure at 80% RH but the 146 eV peak is much less pronounced at 0% RH. Oxygen-oxidized Cu shows the sulfur peak at 146 but it is not very pronounced at either relative humidity. Finally, Fig. 9 shows an ESCA spectra from a typical sulfided Cu sample at 80% RH with insets showing the Cu and S peak structure. The binding energy peak for Cu occurs at 932.5 eV and the sulfur peak structure has been deconvoluted to yield two peaks, one at 161.7 eV and the other at 162.5 eV. ESCA spectra showed no difference in the sulfur peak structure on air-oxidized or bare copper samples at 80% RH. The ESCA analysis confirms the composition to be primarily Cu₂S (Cu at 932.5 eV and S at 161.7 eV). The peak at 162.5 eV in ESCA spectrum suggests

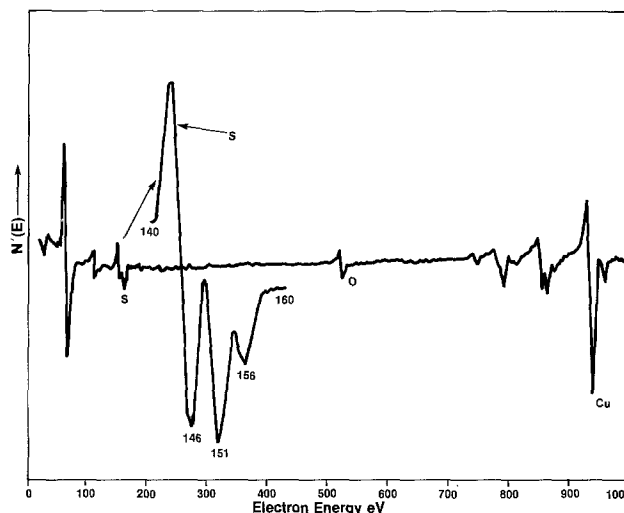


Fig. 8. A typical Auger spectra obtained from bare copper is shown. The three peak structure in the sulfur spectra is clearly visible.

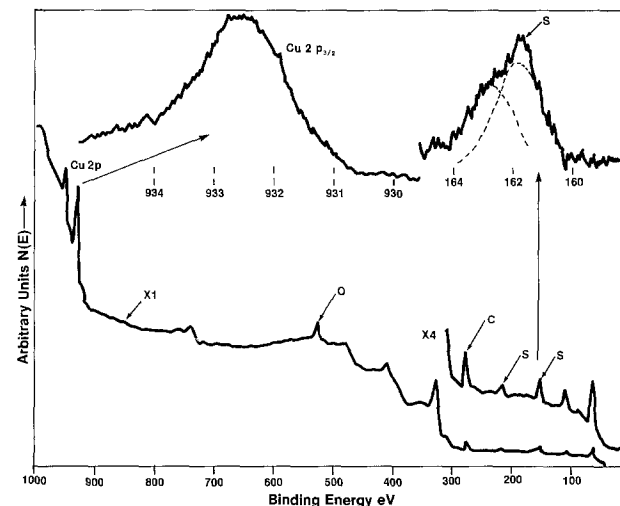


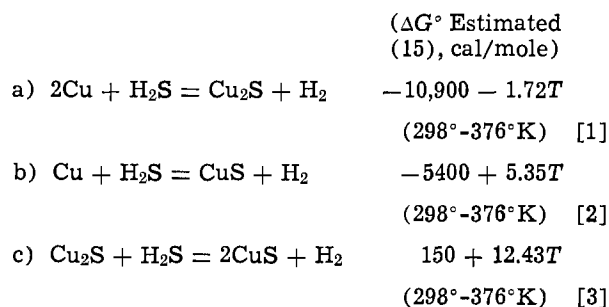
Fig. 9. ESCA spectra from a typical sulfided Cu sample is shown

the presence of free sulfur. At 0% RH, the 161.7 eV peak is not very pronounced on oxidized (air and O₂) samples.

Discussion

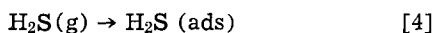
Low relative humidity.—In the absence of high relative humidity, the H₂S reaction with bare copper proceeds at a slower rate and the rate is observed to be linear. On preoxidized samples, no significant growth of tarnish films occurs at low RH. This can be explained as follows. Since the oxide thickness on preoxidized samples is considerably greater than the thickness (~60Å) of the oxide present at room temperature (10, 11), and Cu₂O is thermodynamically more stable than Cu₂S or CuS [standard free energy of formation at room temperature for Cu₂O, Cu₂S, and CuS are -34.98, -20.6, and -11.7 kcal/mole respectively (12)], oxide films are protective against further attack at low relative humidities.

Bare copper reacts with dry H₂S (0% RH) as well as with H₂S at a high relative humidity. The reaction rate of H₂S with bare copper at 0% RH is smaller (Fig. 7) than at high RH. Other investigators have observed this before (13, 14). Cu can react with H₂S according to one of the following schemes



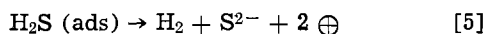
The first reaction has a lower standard free energy of reaction and is thermodynamically more favorable. In actual experiments, the sulfide on copper is found to be Cu₂S with some free sulfur (16). The activation energy of sulfidation (for Cu₂S) has been measured to be between 17.6 kcal/mole (13) to 21.3 kcal/mole (17). Our experiment and the experiments of others (13, 17) (at higher temperatures) revealed that the rate of tarnishing follows a linear rate law. Earlier authors (13, 17) have also observed that the sulfidation rate (or more specifically, the linear rate constant) increases with increasing concentration of H₂S. From this it can be argued that on bare copper, the rate-determining process is most likely to involve a phase boundary reaction at the gas/film interface (18). At this interface, the following reaction is most probable (13, 17)

- 1) adsorption of H₂S on the sulfide film

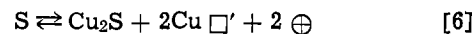


and

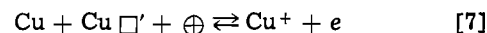
- 2) dissociation of adsorbed H₂S



where \oplus represents a positive hole in the sulfide. This dissociative adsorption reaction has been observed on nickel, tungsten, and iron at low temperatures (19). The activation energy of H₂S adsorption is very low for these materials (<1 kcal/mole). On other metals such as Ag and Pb, adsorption of H₂S also occurs but is reversible and nondissociative. This may explain why silver does not react with dry H₂S while Cu and Ni do. Since the process of dissociation is more difficult than adsorption, step 2 is likely to be rate-determining. Formation of S²⁻ ion at the gas/sulfide interface results in the depletion of cuprous ions. The usual defect equilibrium for Cu₂S at the gas/sulfide interface can be written as



The cation vacancies (Cu□') and positive holes \oplus will diffuse inward to the metal/sulfide interface where they will be annihilated as

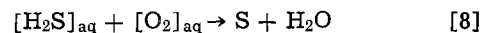


forming cuprous ion Cu⁺ and electron (e) which will diffuse outward to the gas/sulfide interface.

The copper sulfide which grows on copper is much more porous than Cu₂O. This is related to the fact that the volume quotient (that is, the ratio of the volume of the sulfide divided by the volume of the equivalent quantity of metal), which should always be larger than unity, assumes a very high value of 1.95 (18). This leads to high stresses at the metal/sulfide boundary resulting in cracks and fractures in the sulfide layer. Through the appearance of porous layers, the free sulfur may also migrate into the sulfide and come in direct contact with the metal. The three peak structure of sulfur on bare Cu observed in Auger spectra can be interpreted in the light of the above discussion. The most probable explanation is that the peak at 146 eV is due to Cu₂S while the peaks at 151 and 156 eV are due to adsorbed or free sulfur (20). More kinetic energy will be lost for sulfur in a bound chemical state and therefore a chemical shift towards lower kinetic energy might occur for Cu₂S resulting in a peak at 146 eV. The peaks at 151 and 156 eV arise from Auger transitions involving electrons in surface molecular orbitals formed by chemisorption of sulfur or free sulfur not strongly bound to copper (21). The above explanation is only suggestive and needs to be confirmed by further experimentation. In the case of oxidized copper exposed to H₂S at low relative humidity, the peak at 146 eV is not pronounced, confirming the depth profile analysis that sulfur does not react with Cu₂O. ESCA analysis in conjunction with ion sputtering also confirms that free sulfur is present in the entire Cu₂S film on bare copper. The peak at 161.7 eV is due to Cu₂S and at 162.5 eV is due to free sulfur.

Cu₂O does not react with H₂S at low RH because Cu₂O is thermodynamically more stable than Cu₂S as explained earlier and because the oxide thickness hinders the cation migration. In addition the rate of dissociative adsorption of H₂S on Cu₂O may be very small.

High relative humidity.—At high relative humidities Cu₂O reacts with H₂S. The rate of reaction with bare Cu is also much greater. The kinetic growth law starts as a linear law but becomes parabolic as the film thickness increases. This suggests that a different kind of reaction involving H₂S and Cu occurs at high relative humidities, i.e., a reaction involving the aqueous solution at the gas/sulfide interface is important in understanding the kinetics in this case. It is known that H₂S easily dissolves in water. The H₂S therefore goes into aqueous phase in adsorbed water layers on Cu and Cu₂O. From measurements of water adsorption by the author (22), it was found that several monolayers of water are adsorbed on Cu and Cu₂O at 80% RH. For a given relative humidity the amount of [H₂O] adsorbed is greater on Cu₂O than on Cu (22). The oxidation of H₂S to sulfur in aqueous solution takes place with dissolved oxygen according to the following reaction



as suggested by Lilienfeld and White (23), Campbell and Thomas (14), and Sneed *et al.* (24).

The composition of the sulfide film at the surface in all exposed samples is Cu_{0.65}S_{0.35} (after an exposure of 8 hr). For air-oxidized Cu, it is also seen that the sandwiched oxide layer increases in thickness with the exposure time and the composition of the oxide film becomes Cu_{0.82}O_{0.18} instead of Cu₂O. A model of

film growth can be proposed to account for these observations. The growth occurs at the sulfide/oxide interface but not at the oxide/metal interface. Copper ions migrate from the metal/oxide interface through the oxide and this accounts for increasing the ratio of Cu to O₂ in the oxide layer. This may also account for the increase in the thickness of the oxide layer, i.e., some migrating Cu ions may interact with O₂ ions and increase the thickness of oxide layer while increasing the ratio of Cu to O₂. Sulfur ions migrate inwards to the sulfide/oxide interface and it appears that the reaction occurs at the sulfide/oxide boundary.

The copper which has been preoxidized in oxygen offers slightly more protection against sulfidation than air-oxidized copper (Fig. 7). This may partly be due to the fact that the oxide thickness of the O₂-oxidized sample is greater than an air-oxidized sample. In addition, the oxide grown in the oxygen environment is expected to be more compact, i.e., structurally less porous. Cation migration through this oxide may be hindered and the rate of sulfidation will therefore be less. The above argument is strengthened by the fact that most of the sandwiched oxide layer after sulfidation in this case corresponds to Cu₂O, i.e., the rate of oxide breakdown is less.

Conclusions

An experimental permeation tube apparatus has been constructed. By utilizing the quartz crystal microbalance with a sensitivity of 10⁻⁸ g/cm²/Hz, ESCA and Auger spectroscopy, the reaction of copper and its oxides with H₂S, has been investigated at various relative humidities. The kinetic growth rate laws have been derived from the thickness measurements. It is concluded that cuprous oxide protects copper against further oxidation or sulfidation in H₂S environment in dry air. Dry H₂S attacks copper and the rate of reaction is linear. The film composition in this case is Cu₂S. At higher relative humidities the rate of reaction with bare copper starts as linear but becomes parabolic as the film thickness increases. In the linear range, the rate of reaction with bare copper at 80% RH is four times the rate of 0% RH. At higher RH, the oxide film breaks down and is attacked by H₂S. The films grown in oxygen offer slightly more protection than those grown in air. Thus in the linear region at high RH, the air-grown and oxygen-grown films have 75% and 47% of the film tarnish rates of bare copper. This difference may partly be due to thicker oxide on the oxygen-grown sample but is most probably due to the fact that these films are structurally less porous. In general, a layered tarnish film structure with an oxide film sandwiched between the metal and the sulfide film (Cu₂S) grows on preoxidized coupons.

Acknowledgments

The author wishes to thank F. E. Bader and J. H. Thomas for invaluable discussions. He is also thankful to L. L. Hines for experimental assistance.

Manuscript submitted Jan. 16, 1979; revised manuscript received June 2, 1979.

Any discussion of this paper will appear in a Discussion Section to be published in the December 1980 JOURNAL. All discussions for the December 1980 Discussion Section should be submitted by Aug. 1, 1980.

Publication costs of this article were assisted by Bell Laboratories.

REFERENCES

1. W. H. J. Vernon, *Trans. Faraday Soc.*, **23**, 113 (1927).
2. W. H. J. Vernon, *ibid.*, **27**, 255 (1931).
3. R. G. Baker, *Ann. Conf. Marine Tech. Soc.*, Vol. 2, p. 1265 (1970).
4. V. Tierney, Paper presented at the Ninth International Conference on Electrical Contact Phenomena, IIT, Chicago, Illinois, September 11-15, 1978.
5. R. P. Frankenthal, Abstract 8, p. 29, The Electrochemical Society Extended Abstracts, Philadelphia, Pennsylvania, May 8-13, 1977.
6. C. S. Lu and O. Lewis, *J. Appl. Phys.*, **43**, 4385 (1972). Also see S. P. Sharma and J. H. Thomas, *ibid.*, **14**, 825 (1977) and *ibid.*, **13**, 549 (1976).
7. S. P. Sharma, *This Journal*, **125**, 2005 (1979).
8. A. E. O'Keeffe and G. C. Ortman, *Anal. Chem.*, **38**, 760 (1966).
9. J. H. Thomas and S. P. Sharma, *J. Vac. Sci. Technol.*, **14**, 1168 (1977) and *Anal. Chem.*, **49**, 987 (1977).
10. T. N. Rhodin, *J. Am. Chem. Soc.*, **72**, 5120 (1950).
11. W. E. Campbell and U. B. Thomas, *Trans. Electrochem. Soc.*, **91**, 623 (1947).
12. "Handbook of Chemistry and Physics," Chemical Rubber Company, 49th ed., P. D-41 (1968-69).
13. B. Chattopadhyay and S. Sadigh-Esfandiary, *Corros. Sci.*, **13**, 747 (1973).
14. W. E. Campbell and U. B. Thomas, *Proc. Holm Seminar Elec. Cont. Phenom.*, p. 233, IIT, Chicago, Ill., Nov. 11-15, 1968.
15. F. D. Richardson and J. H. E. Jeffes, *J. Iron Steel Inst., London*, **171**, 165 (1952).
16. J. C. Bailar et al., Editors, A. G. Massey, "Comprehensive Inorganic Chemistry," Vol. 3, p. 29, Pergamon Press, Oxford (1973). Also see J. W. Evans and G. D. Fearnough, *J. Appl. Chem.*, **9**, 307 (1959).
17. M. Takeda, K. Fueki, and T. Mukaibo, *J. Electrochem. Soc. Jpn.*, **36**, 95 (1968).
18. K. Hauffe, "Oxidation of Metals," p. 253, Plenum Press, New York (1965).
19. J. R. Anderson and B. G. Baker, in "Chemisorption and Reactions on Metallic Films," Vol. 2, J. R. Anderson, Editor, p. 79, Academic Press, New York (1971).
20. C. C. Chang and J. M. Morabito, Private communication.
21. J. P. Cadd and J. C. Riviere, *Proc. Royal Soc. London, Ser. A*, **331**, 403 (1972).
22. S. P. Sharma, *J. Vac. Sci. Technol.*, In press.
23. S. Lilienfeld and C. White, *J. Am. Chem. Soc.*, **52**, 885 (1930).
24. M. C. Sneed, J. L. Maynard, and R. C. Brasted, "Comprehensive Inorganic Chem.," Vol. III, p. 68, D. Van Nostrand (1954).

Electrochemical Formation of Sulfur at Stainless Steel Surfaces

D. W. Shoosmith, T. E. Rummery, M. G. Bailey, and D. G. Owen

Research Chemistry Branch, Atomic Energy of Canada Limited,
Whiteshell Nuclear Research Establishment, Pinawa, Manitoba, R0E 1L0, Canada

ABSTRACT

The electrochemical formation of elemental sulfur at stainless steel electrodes has been studied in aqueous H_2S solutions at temperatures between 298° and 373°K and a total pressure (with H_2S) of 1.4 MPa. A deposit of sulfur was found only in solutions containing a low concentration of soluble iron ($\lesssim 10^{-6}$ mole dm^{-3}); at higher iron concentrations, pyrite and marcasite formation occurred. All three deposits formed from a common polysulfide intermediate, the nature of the deposit depending on the relative concentrations of soluble iron and polysulfide at the surface of the stainless steel.

In a previous paper (1), formation of iron disulfides, pyrite, and marcasite, on stainless steel surfaces from aqueous H_2S solutions at a total pressure of 1.4 MPa, was shown to occur via an electrocrystallization mechanism. Oxidation of H_2S to polysulfide species occurred as an anodic reaction at the stainless steel, followed by deposition of ferrous ion (as FeS_2) transported from a corroding carbon steel surface. Marcasite was formed only when the concentration of S_2^{2-} was increased by applying an anodic current to the stainless steel. From these results, it was concluded that marcasite can form when the concentration of S_2^{2-} is high relative to the concentration of Fe^{2+} .

This mechanism offers an explanation for the observation of pyrite and marcasite deposits on stainless steel surfaces at temperatures $\gtrsim 353^\circ\text{K}$ in heavy water (D_2O) production plants utilizing the Girdler sulfide process (2, 3). However, small quantities of elemental sulfur can also form on the stainless steel sieve trays in the Girdler sulfide process and the purpose of this communication is to show that a similar mechanism to that previously described (1) could be, at least in part, responsible for these sulfur deposits.

Experimental

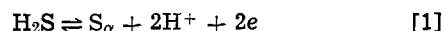
Experiments were performed in a thermostatted titanium autoclave containing aqueous solution pressurized with H_2S . The details have been discussed previously (1). To prevent charging and poor resolution during scanning electron microscopic examination, the sulfur deposits were coated with a thin gold film. Unless otherwise stated, all experiments were carried out for 160-170 hr at a total pressure (with H_2S) of 1.4 MPa. A temperature of 373°K or lower was used to avoid significant thermal cracking of the H_2S on the autoclave walls in the vapor space above the aqueous solution.

Results

The potential of the stainless steel electrode varied with the Fe^{2+} concentration as shown in Fig. 1. The datum for the intermediate soluble iron concentration (open circle in Fig. 1) was obtained using a small carbon steel electrode (5 cm^2) to supply soluble iron; data at higher iron concentrations (solid circles in Fig. 1) were obtained using a larger electrode (32 cm^2). The most anodic point (x in Fig. 1) was measured in an "iron-free" system. In this experiment no carbon steel electrode was included in the autoclave. The residual iron in solution resulted from dissolution from the autoclave walls of traces of iron disulfides deposited during previous experiments. The

Key words: hydrogen sulfide, stainless steel, sulfur.

vertical dashed line in Fig. 1 represents the equilibrium potential for the reaction



under the conditions used. This value was taken from the calculations of MacDonald and Hyne (4).

In Fig. 2, the potential of the stainless steel electrode in "iron-free" solution is plotted as a function of applied anodic current and compared to the data previously recorded for pyrite and marcasite deposition (1). The dashed lines in Fig. 2 represent the equilibrium potentials for reaction [1] and for the further oxidation of sulfur to sulfate via reaction [2]



Table I summarizes the nature and location of the deposits found in the autoclave. At 373°K and with zero applied current (experiment 1), no sulfur was detected in the autoclave. At an anodic current of

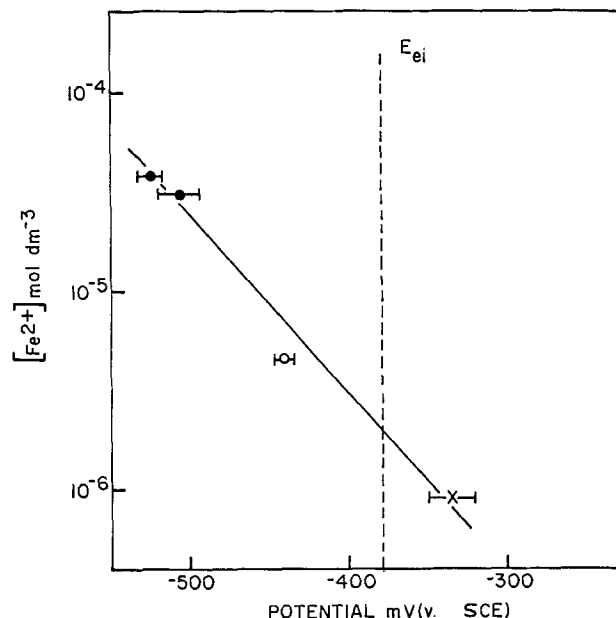


Fig. 1. Potential of stainless steel electrode as a function of the concentration of Fe^{2+} in the autoclave at 373°K and 1.4 MPa total pressure (with H_2S). Dashed line represents the equilibrium potential, E_{ei} , for reaction [1] (see text); ●—previously published data from Ref. (1); ○—recorded in the presence of a small carbon steel electrode (area = 5 cm^2); ×—recorded in "iron-free" solution (see text).

Table I. Summary of data on sulfur deposition* from H₂S aqueous solutions (1.4 MPa total pressure)

Experiment No.	I (μA)	T (°K)	Sulfur deposit location		E (mV vs. SCE)
			Stainless steel electrode	Titanium autoclave	
1	0	373	ND	ND	-335 ± 15
2	100	373	Trace	Upper rim	-275 ± 25
3†	100	373	ND	ND	-275 ± 20
4	250	373	ND	ND	-205 ± 20
5	50	323	Large deposit	ND	-360 ± 12
6	0	298	ND	ND	-570 ± 8
	100		Large deposit	Large deposit on all surfaces	> +2.0V

* Identified by x-ray powder diffraction and/or x-ray energy dispersive spectroscopy.

† Autoclave periodically vented and recharged with H₂S.

ND Nothing detected.

100 μA (experiment 2), a deposit of sulfur¹ was obtained around the upper rim of the autoclave. A trace deposit of what was probably sulfur also formed on the stainless steel electrode. When the 100 μA experiment was repeated and the autoclave periodically vented and recharged with H₂S (experiment 3), no sulfur deposit was obtained. This indicated that the deposit on the upper rim of the autoclave in experiment 2 was formed from sulfur in the H₂S vapor when the autoclave was cooled prior to opening. The periodic venting in experiment 3 removed this sulfur vapor and consequently no deposit was formed. Its formation by reaction of H₂S with O₂ can be ruled out since O₂ was carefully excluded from the autoclave (1). When the current was increased to 250 μA, no sulfur deposit was obtained (experiment 4).

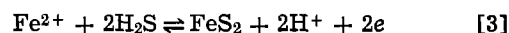
When both the current and the temperature were reduced (experiment 5), a large deposit of elemental

¹ Only S₈, the low temperature, orthorhombic form, was observed. Any sulfur deposited at > 96°C would probably be monoclinic, but unless very careful annealing or rapid quenching is performed, this transforms rapidly to α-S₈.

sulfur was obtained on the stainless steel electrode. The morphology of this deposit is shown in Fig. 3. X-ray spectroscopy showed that both the upper layer chain-like deposit [Fig. 3(b)] and the nodular base layer [Fig. 3(c)] were sulfur. No deposit was obtained on the autoclave walls at this temperature. An unpolarized stainless steel electrode situated close to the anodically polarized electrode in the autoclave showed only faint traces of a sulfur deposit. A further reduction in temperature to ≈ 298°K (experiment 6, Table I) resulted in the formation of substantial deposits of sulfur on all surfaces throughout the autoclave, including those above the surface of the liquid. In this case the potential of the stainless steel electrode rose to greater than 2.0V and became erratic. Figure 4 shows a photomicrograph of the stainless steel surface. The x-ray energy spectrum of the surface indicated that the deposit was essentially all sulfur.

Discussion

The data of Fig. 1 show that as the soluble Fe²⁺ concentration was decreased the potential of the unpolarized stainless steel shifted to more anodic values. This is as expected from the potential-pH diagram for the Fe-H₂S-H₂O system (1, 4) if the potential of the stainless steel is governed by the reaction



as previously demonstrated (1). For potentials greater than the equilibrium potential for reaction [1], the formation of elemental sulfur becomes thermodynamically possible. This condition was achieved in the "iron-free" solution (point x in Fig. 1). The fact that no elemental sulfur, or at the most only traces, were found (experimental, Table I) showed that the reaction was very slow at 373°K in the absence of an applied current.

The application of an anodic current (cf. experiments 1 and 2 in Table I) accelerated the formation of sulfur. However at 373°K transfer of sulfur from the liquid to the vapor phase occurred, sulfur being deposited on the autoclave walls. The mechanism of this transfer has not been studied but one possibility is that the sulfur deposit on the electrode [or a polysulfide intermediate (1)] dissolved to give aqueous polysulfide species and, subsequently, gas phase sulfanes (H₂S_x). Entrainment of sulfur in H₂S gas streams has been shown to occur for temperatures above the melting point of sulfur (5, 6), but not at the temperatures used in the present work. However there will be a finite concentration of polysulfide in solution [≈ 10⁻⁸ mole dm⁻³ under the conditions used (7)] and the sulfane H₂S₂ has a high vapor pressure, boiling at 343°K at normal pressure (8). Consequently the proposed pathway for the transfer of sulfur from liquid to vapor is not unreasonable. The fact that the transfer occurred suggested that the rate of such a process was significant at 373°K.

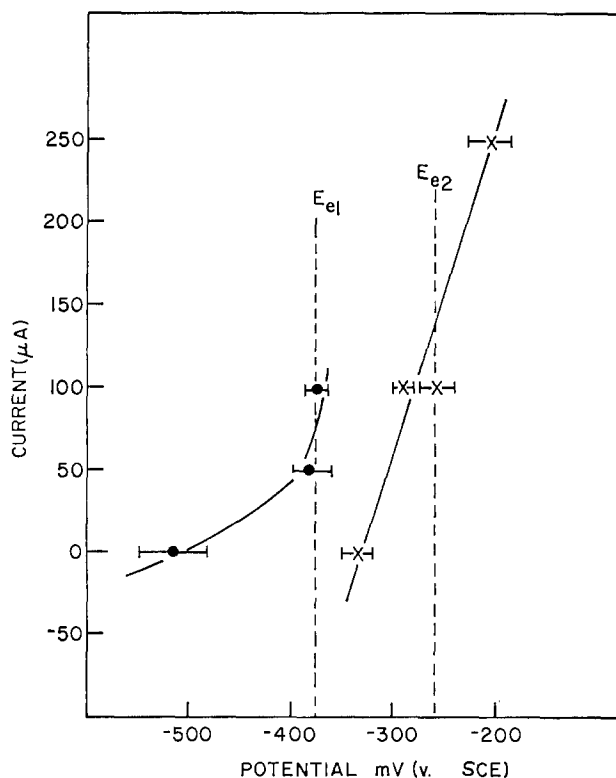


Fig. 2. Potential of stainless steel electrode as a function of applied current at 373°K and 1.4 MPa total pressure (with H₂S); —x— data recorded in "iron-free" solutions; —●— previously published data from Ref. (1); ---- equilibrium potentials for reaction [1] (E_{e1}) and reaction [2] (E_{e2}).

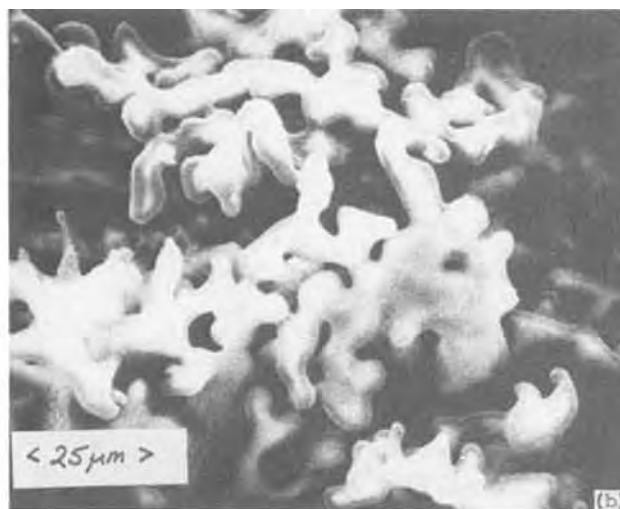
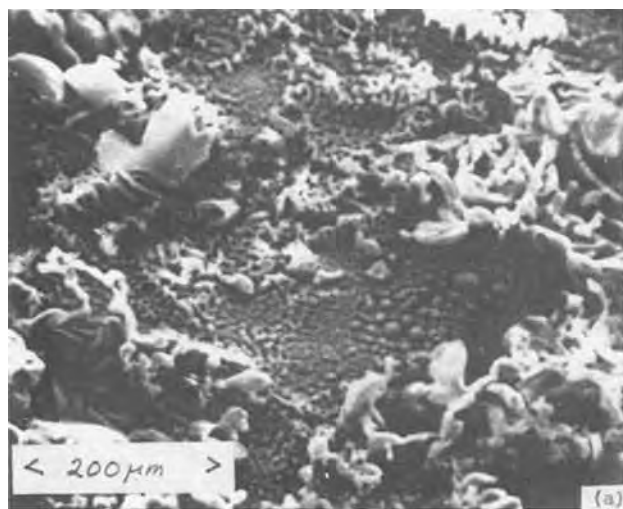


Fig. 3. Scanning electron photomicrographs of the elemental sulfur deposit on the stainless steel electrode after experiment 5 of Table I; (a) general surface, (b) upper layer deposit, (c) base layer deposit.

Dissolution and transfer of sulfur to the vapor was negligible at 323°K as shown by experiment 5 in Table I. The deposit remained localized on the stainless steel surface. The reason for the variations in morphology of the sulfur deposit is not known. One possibility was that the upper layer deposit [Fig. 3(b)] resulted from a precipitation reaction due to the finite solubility of the sulfur under these conditions.

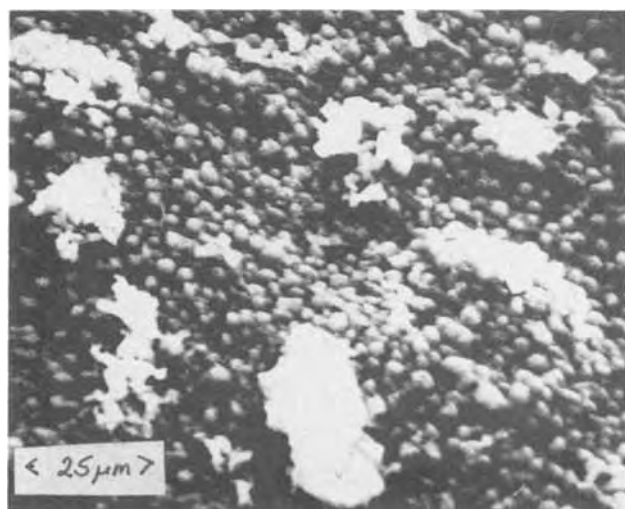
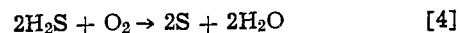


Fig. 4. Scanning electron photomicrograph of the elemental sulfur deposit on the stainless steel electrode after experiment 6 of Table I.

If the current was increased to 250 μ A at 373°K (experiment 4, Table I) no elemental sulfur was formed in the autoclave. Under these conditions the potential at the stainless steel electrode was more positive than the equilibrium potential for reaction [2] (Fig. 2) and it is likely that further oxidation of the sulfur to sulfate (or some intermediate oxidized state) occurred.

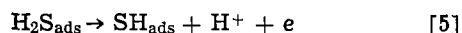
No attempt was made, in the present work, to characterize the nature of the corrosion film occurring on the stainless steel. However the current-potential data of Fig. 2 suggest that for the major part, the electrode potential was set by reactions 1 or 3. The one obvious exception is experiment 6 (Table I) where the potential of the stainless steel was >2.0 V and all surfaces in the autoclave were covered with elemental sulfur. In this case the stainless steel was passivated either by the deposit of spherical sulfur particles (Fig. 4) or by an underlying film of iron and chromium oxides or sulfides. The potential of the stainless steel was sufficiently positive to cause the decomposition of water to O_2 , which leads to the oxidation of H_2S via the reaction



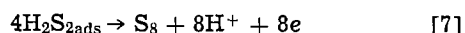
both in solution and in the gas phase (9, 10). The elemental sulfur so formed settled on any convenient surface. The ill-formed, larger particles shown in Fig. 4 were probably sulfur particles formed in aqueous solution, via reaction 4, which subsequently settled on the stainless steel surface.

The formation of elemental sulfur on anodically polarized metal surfaces in sulfide solutions has been

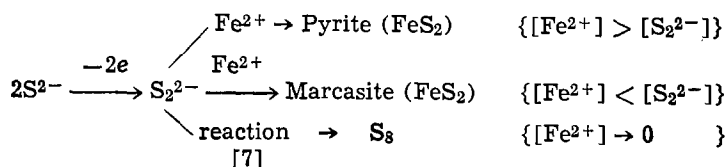
observed in a number of situations. Thus sulfur can be deposited on platinum from aqueous sulfide solutions (11, 12) and from polysulfide solutions in potassium thiocyanate melts (13). It has also been deposited on vitreous carbon and pyrolytic graphite electrodes from polysulfide melts (14). Little information is available on the mechanism of formation of elemental sulfur. The nodular nature of the base layer deposit [Fig. 3(c)] suggested the nucleation and growth of individual centers. A mechanism consistent with the present observations, and with the previously observed formation of iron disulfides in the presence of soluble iron, involves a polysulfide intermediate (1)



The further oxidation of this intermediate would lead to the formation of sulfur



As shown in the previous paper (1) the presence of soluble iron leads to the formation of pyrite and marcasite and the prevention of further oxidation via reaction [7]. The alternate processes can be summarized in the following reaction scheme



Protons have not been included in this reaction scheme although they are probably involved. Their production during the anodic reactions [5] to [7] will not lead to pH variations since an equivalent number will be consumed in the cathodic reaction.

Thus in the absence of soluble iron, the formation of elemental sulfur could occur via an electrochemical mechanism in heavy water production plants using the Girdler sulfide process. However at 373°K the rate of sulfur production would be very slow. Finally

both disulfide and elemental sulfur formation appear to proceed through the same polysulfide intermediate.

Manuscript submitted Aug. 8, 1978; revised manuscript received Sept. 20, 1979.

Any discussion of this paper will appear in a Discussion Section to be published in the December 1980 JOURNAL. All discussions for the December 1980 Discussion Section should be submitted by Aug. 1, 1980.

Publication costs of this article were assisted by Atomic Energy of Canada Limited.

REFERENCES

1. D. W. Shoesmith, T. E. Rummery, M. G. Bailey, and D. G. Owen, *This Journal*, **126**, 911 (1979).
2. H. K. Rae, Atomic Energy of Canada Limited Report, AECL-2555 (1966).
3. L. R. Haywood and P. B. Lumb, *Chem. Can.*, **27**, 19 (1975).
4. D. D. MacDonald and J. B. Hyne, Atomic Energy of Canada Limited Report, AECL-5811 (1977).
5. T. K. Wiewiorowski and F. J. Touro, *J. Phys. Chem.*, **70**, 234 (1966).
6. S. C. Swift, F. S. Manning, and R. E. Thompson, *J. Soc. Pet. Eng.*, **16**, 57 (1976).
7. W. F. Giggenbach, *Inorg. Chem.*, **13**, 1730 (1974).
8. K. W. C. Burton and P. Machmer, in "Inorganic Sulphur Chemistry," G. Nickless, Editor, p. 353, Elsevier, Amsterdam (1968).

9. K. Y. Chen and J. C. Morris, *Environ. Sci. Technol.*, **6**, 529 (1972).
10. G. G. Strathdee, Private communication.
11. H. Gerischer, *Z. Elektrochem.*, **54**, 540 (1950).
12. N. Ramasubramanian, *J. Electroanal. Chem. Interfacial Electrochem.*, **64**, 21 (1975).
13. B. Cleaver, A. J. Davies, and D. J. Schiffrin, *Electrochim. Acta*, **18**, 747 (1973).
14. M. P. J. Brennan, *ibid.*, **22**, 279 (1977).

Stress Corrosion Cracking and Electrochemical Behavior of AISI 304 Stainless Steel in Chloride-Containing Sulfate Solutions

H. S. Tong and D. J. Swartz

Allied Chemical Corporation, Morristown, New Jersey 07960

ABSTRACT

The slow strain rate testing technique was used to study the stress corrosion cracking (SCC) susceptibility of AISI 304 stainless steel in chloride-containing 35% $(\text{NH}_4)_2\text{SO}_4$ solutions at 104°C. The SCC susceptibility was evaluated from experimentally obtained quantitative expressions for the decreases of ultimate tensile strength and reduction of area in these solutions compared to inert conditions. The inhibiting effect of nitrates was also studied. Electrochemistry of the alloy-environment system is presented, and correlation between SCC susceptibility and the electrochemical parameters was established. Results are summarized as follows: (i) SCC of 304 SS may occur in the chloride-containing sulfate solutions at 104°C, (ii) the critical chloride concentration is 2000 ppm or less, above which SCC will occur, (iii) the threshold nitrate concentration is 1000 ppm or less, above which SCC can be inhibited, and (iv) the results are consistent with the view that SCC and pitting initiate in the same way.

The austenitic stainless steels are extensively used in chemical plant construction because of their general resistance to many common corrodents. They are used in the area of vessels, piping, valves, heat exchangers, and supporting hardware. Type 304 has been extensively used because of its economy and relative ease of fabrication, taking proper precautions to minimize the deleterious precipitation of carbides in the heat affected zone. A continuing problem with the use of the austenitic alloys has been the danger of stress corrosion cracking (SCC) in certain environments and stress situations. One of the well-known and probably most widely encountered form of SCC is that caused by the presence of chloride ion (1-5). Consequently many studies have been performed to determine mechanisms (6, 7), and to obtain data in specific systems on concentration and temperature (8, 9) bounds below which these alloys could be confidently applied. Considerable efforts have also been expended to determine the inhibiting effect of anions on the SCC of stainless steels in the chloride-containing media. For example, Uhlig and Cook (10) have shown that the addition of small amounts of nitrate, acetate, iodide, and benzoate inhibit SCC in MgCl_2 at 130°C. Okada (11) also reported that SCC propagation in the MgCl_2 solution may be halted by the presence of sodium nitrate.

The present paper presents data on a specific system which has been known to exhibit SCC in an operating chemical plant. The inhibiting effect of nitrate was also studied. Several observations were made which support empirical knowledge obtained in large scale use and the electrochemical characteristics of the system was examined.

Experimental Procedure

The test alloy was prepared in a form of 0.635 cm ($\frac{1}{4}$ in.) diam rods. The rods were quench annealed. Chemical analysis [weight percent (w/o)] of the steel was Ni-8.9, Cr-18.3, C-0.04, Si-0.02, Mo-0.2, and Cu-0.4. Specimens were pickled in 10% oxalic acid and cleaned with acetone and deionized water prior to testing. Round specimens with a reduced testing gauge of approximately 3 mm diam were used to facilitate uniform deformation and allow complete immersion, which negates problems associated with the liquid-vapor

interface and cell seals. The test solution was 35% w/o $(\text{NH}_4)_2\text{SO}_4$ with various chloride and nitrate concentrations, to which chloride was added as NaCl and nitrate was added as NH_4NO_3 .

The constant strain rate tensile testing technique was used in this test and the assembly is shown in Fig. 1, which is similar to that used elsewhere (12). The specimen is threaded at both ends to connect both supporting rods. The lower supporting rod is fixed to the lower plate of the metal frame by two stainless nuts to provide firm support during the specimen

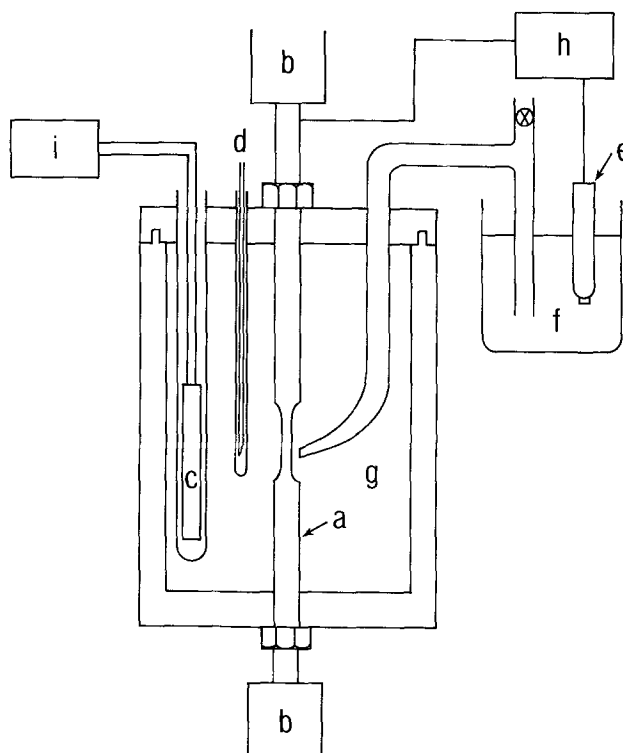


Fig. 1. Schematic assembly for SCC test: (a) specimen, (b) slow strain rate test machine, (c) heating rod, (d) thermocouple, (e) calomel electrode, (f) saturated KCl solution, (g) test solution, (h) potentiostat, and (i) heat control system.

Key words: stress corrosion, strain rate, fractography, inhibitors, pitting.

straining experiment. A Teflon corrosion cell of 500 ml capacity is used with the specimen sealed at the point of entry into the cell by passing it through a Teflon fitting. The top of the cell was sealed by a removable Teflon cover with a loosely fitted Teflon fitting through which the specimen emerged from the cell. A salt bridge capillary was located near the surface of the test specimen, leading to a saturated calomel electrode. A heating rod and a thermocouple were inserted into the cell to heat the solution and monitor the temperature of the solution, respectively. Air at about 7.0×10^4 Pa (10 psi) was bubbled through the solution during the test.

After the specimen was mounted inside the test cell, the test cell was heated to the desired temperature, i.e., 104°C . The specimens were not strained until a stable equilibrium testing temperature was reached. It was gradually pulled until the load cell on the straining machine registered a slight load, indicating the absence of slack between the pull rod, universal joint, and the specimen. Straining was then continued at a crosshead speed of $7.00 \times 10^{-5} \text{ min}^{-1}$. The load, elongation, and open-circuit potential (OCP) being monitored continuously until fracture occurred. The reduction of area (ROA) of the fractured specimen was then measured, and the fracture morphology was studied by means of scanning electron microscopy (SEM).

Anodic polarization was also studied on each alloy/environment system at a scan rate of 6 mV/min. The solution was saturated with air. The anodic polarization curves were obtained starting from the corrosion potential. Potentials were measured against a saturated calomel electrode, as were all potentials in this investigation. The ASTM recommended (13, 14) practice was taken into account in making the electrochemical measurements.

Results

Stress-elongation curves.—Stress-elongation curves obtained in various environments at a strain rate of $7.00 \times 10^{-5} \text{ min}^{-1}$ are shown in Fig. 2. The constant strain rate tensile test was initiated when the temperature reached a constant value, i.e., $104^\circ \pm 1^\circ\text{C}$. A little variation was observed at the initial stage because of the sliding resistance of the pull rod. From the results, it can be seen that there was relatively little difference between stress-elongation curves in controlled 35% $(\text{NH}_4)_2\text{SO}_4$ solution (no chloride) and those in the solution containing 1000 ppm chloride. However, relatively severe decreases in elongation were observed in the solutions containing 2000 ppm Cl^- and above.

The crack velocity was estimated from the measured crack depth and the time to failure. Cracking was assumed to have initiated when the load exceeded the yield strength of the material. It is interesting to note that the crack velocity increases slightly with increasing chloride concentration (for example, see Table I).

It is known that the SCC severity can be evaluated from the decrease in the ultimate tensile strength (UTS) and the decrease in the reduction of area

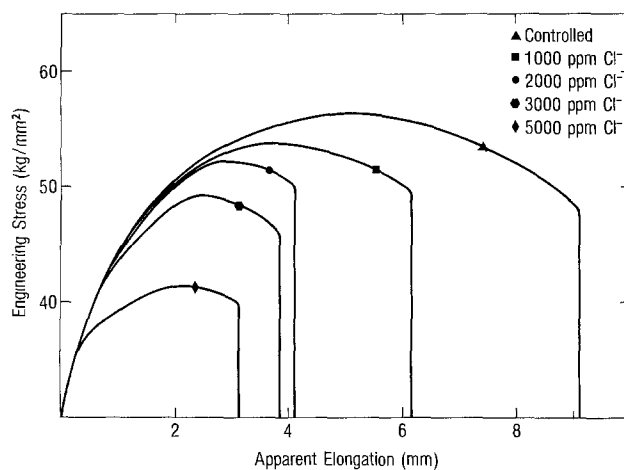


Fig. 2. Engineering stress-apparent elongation curves obtained in 35% $(\text{NH}_4)_2\text{SO}_4$ solutions with different Cl^- concentration at 104°C .

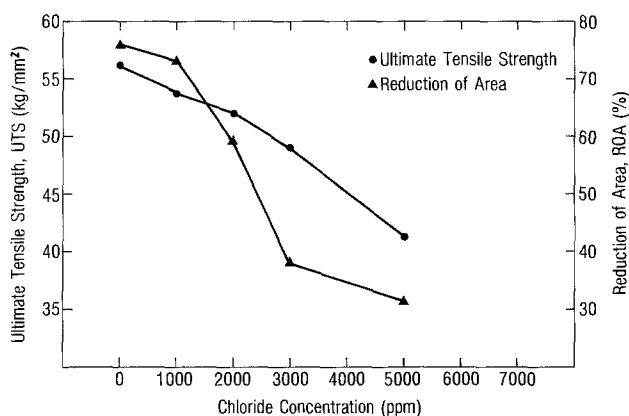


Fig. 3. Effect of Cl^- concentration on reduction of area (ROA) and ultimate tensile strength (UTS) in 35% $(\text{NH}_4)_2\text{SO}_4$ solutions at 104°C .

(ROA) in these solutions compared to the controlled conditions. The effect of chloride concentration on UTS and ROA is shown in Fig. 3. Results indicated that significant decreases in UTS and ROA occur in the solutions containing 2000 ppm Cl^- or above, which suggests that SCC may occur in those solutions. Visual examination of specimen surfaces confirmed the presence of rapid stress corrosion cracking at 2000 ppm Cl^- and the absence of cracking in the controlled condition. Cracks are clearly visible in the specimen side faces exposed to the sulfate solution containing 2000 ppm Cl^- (Fig. 4).

Scanning electron microscopic (SEM) studies have been carried out to examine the fracture morphology after each test, and the results are consistent with the slow strain rate test results. A typical transgranular

Table I. Some typical mechanical results for AISI 304 stainless steel in 35% $(\text{NH}_4)_2\text{SO}_4$ solutions at 104°C

Solution	Total time to failure (hr)	Time for crack propagation (hr)	Average crack velocity (cm/sec)	Remarks
35% $(\text{NH}_4)_2\text{SO}_4$	86.4	42.4	4.1×10^{-7}	Ductile
35% $(\text{NH}_4)_2\text{SO}_4$ + 1000 ppm Cl^-	57.1	27.0	6.8×10^{-7}	Ductile
35% $(\text{NH}_4)_2\text{SO}_4$ + 2000 ppm Cl^-	37.0	13.3	1.7×10^{-6}	TGSCC
35% $(\text{NH}_4)_2\text{SO}_4$ + 3000 ppm Cl^-	36.2	14.8	1.9×10^{-6}	TGSCC
35% $(\text{NH}_4)_2\text{SO}_4$ + 5000 ppm Cl^-	28.5	8.7	3.4×10^{-6}	TGSCC
35% $(\text{NH}_4)_2\text{SO}_4$ + 3000 ppm Cl^- + 100 ppm NO_3^-	32.1	15.4	1.3×10^{-7}	TGSCC
35% $(\text{NH}_4)_2\text{SO}_4$ + 3000 ppm Cl^- + 1000 ppm NO_3^-	63.8	33.7	2.3×10^{-7}	Ductile
35% $(\text{NH}_4)_2\text{SO}_4$ + 3000 ppm Cl^- + 8000 ppm NO_3^-	65.1	37.2	1.8×10^{-7}	Ductile

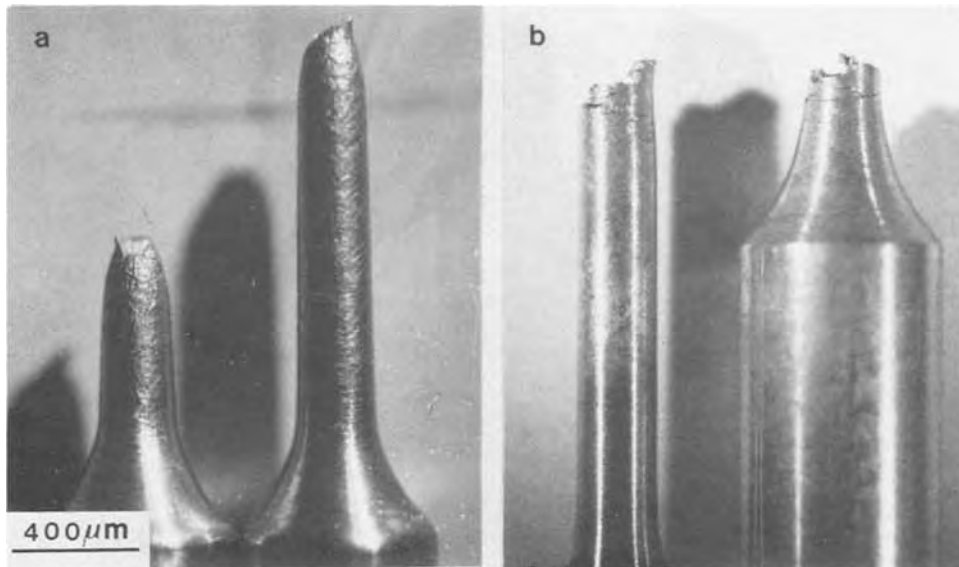


Fig. 4. Photomicrographs of specimens after slow strain rate experiment: (a) ductile failure in 35% $(\text{NH}_4)_2\text{SO}_4$ solution, and (b) SCC in 35% $(\text{NH}_4)_2\text{SO}_4 + 3000$ ppm Cl^- (original diam 2.54 mm).

cleavage-like fracture surface was observed in the specimens tested in the solution containing 2000 ppm Cl^- or above (see Fig. 5c-5e), while only dimple-like fracture structure was evident throughout the fracture surfaces in those solutions containing lower chloride concentrations (see Fig. 5a and 5b). In the case of the transgranular-type morphology multiple cracks were commonly observed. Figure 6 shows the typical multiple branching associated with SCC. Combining the above results suggests that SCC in this alloy/environment system will occur in the solution containing Cl^- somewhere in the range of 1000-2000 ppm.

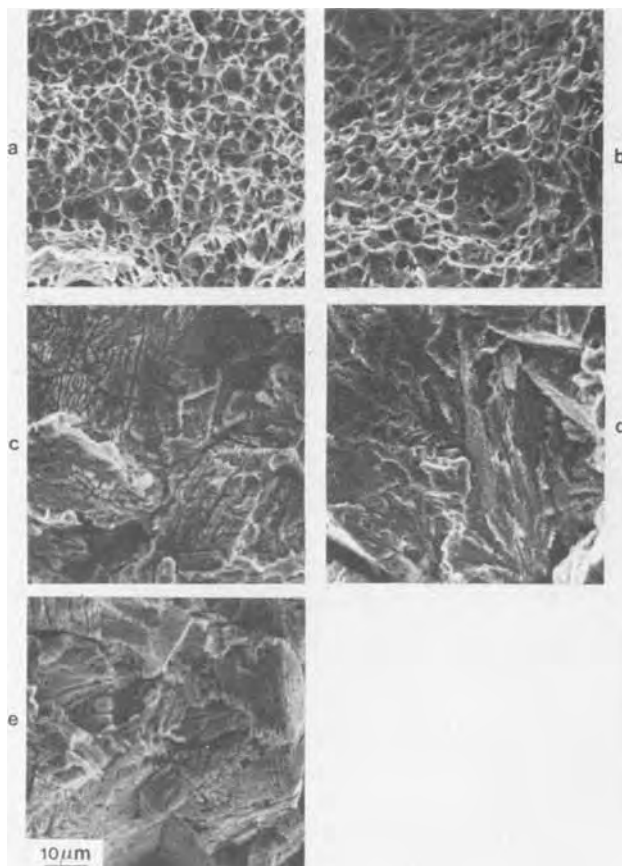


Fig. 5. SEM fractographs of specimens after a slow strain rate experiment in 35% $(\text{NH}_4)_2\text{SO}_4$ solution containing (a) 0 ppm Cl^- , (b) 1000 ppm Cl^- , (c) 2000 ppm Cl^- , (d) 3000 ppm Cl^- , and (e) 5000 ppm Cl^- at 104°C .

Since it has been reported (10) that the presence of nitrate may have a beneficial effect on the resistance to SCC, nitrate was added to the 35% ammonium sulfate solution containing 3000 ppm Cl^- in order to determine the approximate threshold nitrate concentration above which SCC can be inhibited at 104°C . In the absence of nitrate, this environment, as indicated above, had caused the onset of SCC in the alloy tested. Figure 7 shows the stress-elongation curves in the solutions with various nitrate concentrations. The addition of nitrate caused an increase in elongation, as expected, and the UTS and ROA increased significantly above 1000 ppm nitrate (see Fig. 8). ROA increased significantly even at 100 ppm nitrate. SEM studies showed that the presence of 1000 ppm nitrate or above inhibited SCC (see Fig. 9). In the case where 100 ppm nitrate was added to the solution, the crack mode was predominantly ductile (see Fig. 9a). However, at higher magnification, a transgranular and cleavage-like fracture morphology was evident in some limited regions, see Fig. 10. The crack velocity was found to decrease with increased nitrate concentration (see Table I).

Anodic polarization curves.—It is accepted that the SCC of a metal is governed, at least to some extent, by electrochemical reactions. Therefore, the electrochem-

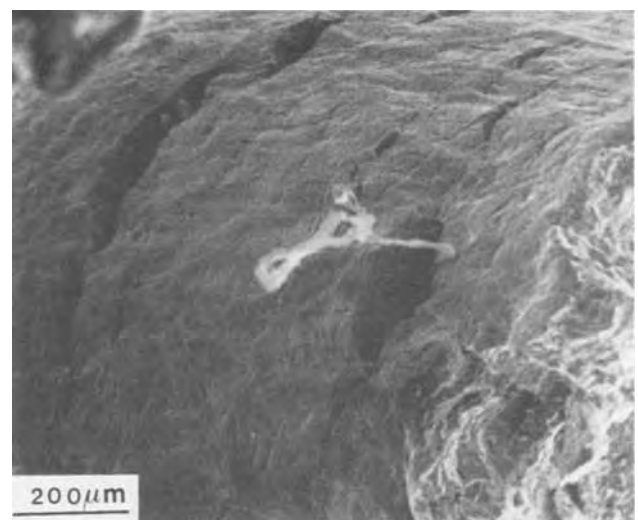


Fig. 6. SEM picture of a side view of the specimen after a slow strain rate experiment in 35% $(\text{NH}_4)_2\text{SO}_4$ solution containing 3000 ppm Cl^- at 104°C .

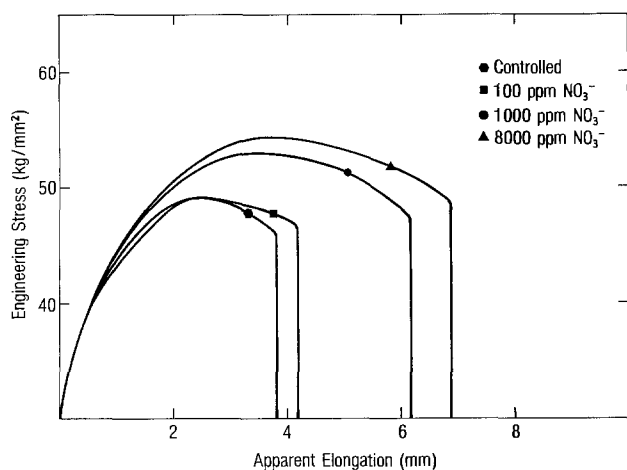


Fig. 7. Engineering stress-apparent elongation curves obtained in 35% $(\text{NH}_4)_2\text{SO}_4 + 3000 \text{ ppm Cl}^-$ solutions with different NO_3^- concentration at 104°C .

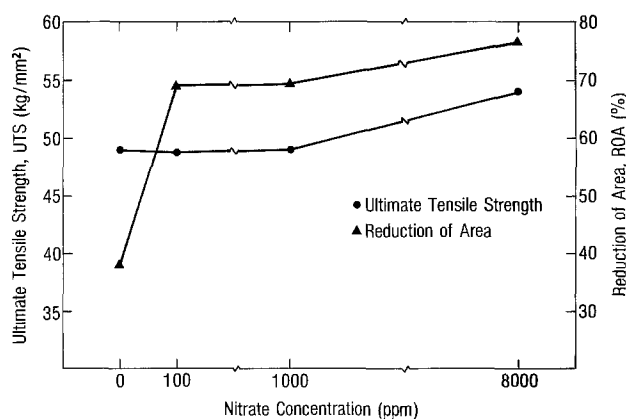


Fig. 8. Effect of NO_3^- concentration on reduction of area (ROA) and ultimate tensile strength (UTS) in 35% $(\text{NH}_4)_2\text{SO}_4 + 3000 \text{ ppm Cl}^-$ solution at 104°C .

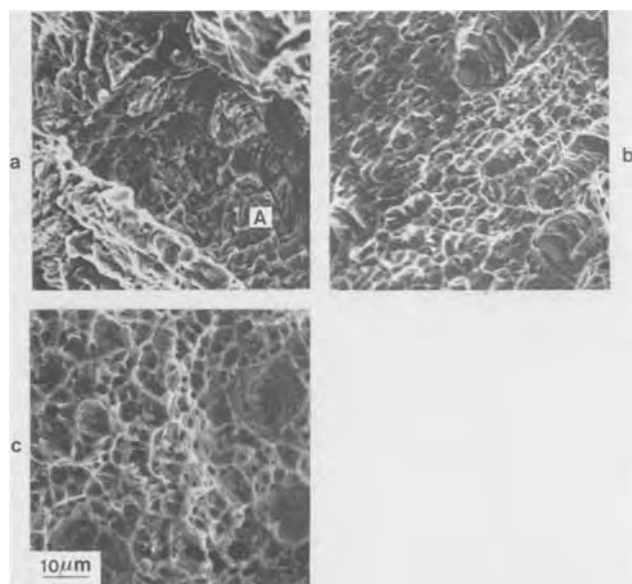


Fig. 9. SEM fractographs of specimens after a slow strain rate experiment in 35% $(\text{NH}_4)_2\text{SO}_4 + 3000 \text{ ppm Cl}^-$ solution containing (a) 100 ppm NO_3^- , (b) 1000 ppm NO_3^- , and (c) 8000 ppm NO_3^- at 104°C .

istry of the system has been studied to determine if any correlation can be established between SCC susceptibility and its electrochemical characteristics. Po-

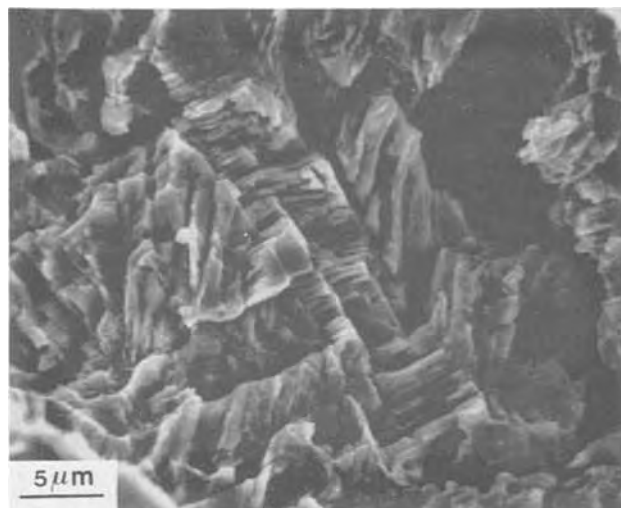


Fig. 10. The enlargements of region A of Fig. 9 (a)

larization curves were determined on unstressed specimens in each solution at 104°C , and the results are illustrated in Fig. 11. These figures illustrate the effect of chloride concentration in the sulfate solution on the electrochemical behavior of the metal. Some electrochemical parameters such as open-circuit potential (OCP), active-passive transition potential (E_{pp}), pitting initiation potential (E_b), are of great interest.

The current responses in Fig. 11 are typical for polarization runs in the various Cl^- solutions. In the solutions containing 0 ppm Cl^- and 1000 ppm Cl^- , an anodic current maximum was observed at $\sim +700 \text{ mV}$, which is probably due to the compositional change of the oxide film on the specimen's surface. A transpassive potential was obtained at even more noble region. Results indicate that the potential differences between the metastable OCP and E_b , above which pitting corrosion is initiated, decreases with increasing Cl^- content of the solution. Most significantly, a dramatic decrease of the potential difference occurs in the solution containing 2000 ppm Cl^- or above. These electrochemical results are consistent with the results obtained above that SCC will occur in the solution containing approximately 2000 ppm Cl^- or above. Furthermore, the results are consistent with the view (1) that pitting may be responsible for the initiation of SCC in this alloy/environment system.

The effect of nitrate in the chloride-containing sulfate solutions was also investigated, and the results are shown in Fig. 12. The anodic polarization curves were determined in the solution containing 3000 ppm

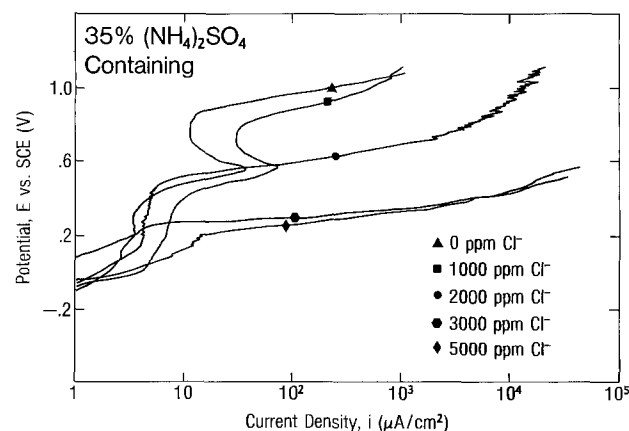


Fig. 11. The anodic polarization behavior of Type 304 stainless steel in 35% $(\text{NH}_4)_2\text{SO}_4$ solution containing different Cl^- concentration at 104°C .

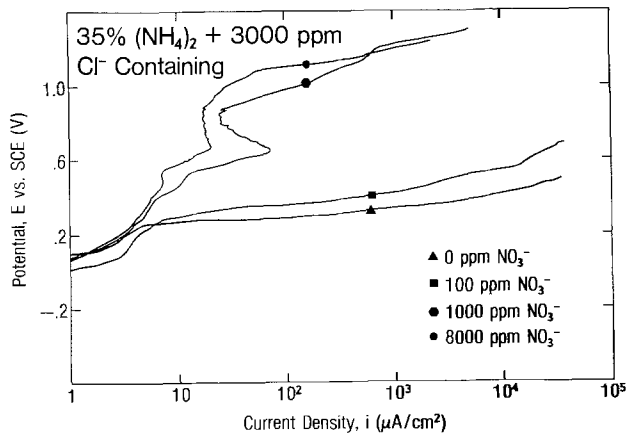


Fig. 12. The anodic polarization behavior of Type 304 stainless steel in 35% $(\text{NH}_4)_2\text{SO}_4 + 3000 \text{ ppm Cl}^-$ solution containing different NO_3^- concentration at 104°C .

chloride with various nitrate concentrations. From the results, it is obvious that nitrate has a beneficial effect on the noble shift of pitting potentials in the chloride-containing sulfate solution. Significantly, the addition of 1000 ppm nitrate or above results in a dramatic increase in the potential difference. This result correlates well with the constant strain rate results that the presence of approximately 1000 ppm nitrate or above may inhibit SCC.

Open-circuit potential-time curves.—The open-circuit potential (OCP) of the alloy was monitored as a function of immersion time at 104°C , and the resulting curves are illustrated in Fig. 13. The curves were obtained from tests in 35% $(\text{NH}_4)_2\text{SO}_4$ solutions containing various chloride concentrations. Note that, in general, OCP of the specimen shifts to a more noble direction as a function of immersion time. Comparing the results with the anodic polarization curves, Fig. 11, indicates that, in the solution containing 3000 ppm chloride or above, relatively long time immersion of the specimen results in a noble shift of OCP, which is eventually close to or more noble than the E_b , and pits formed subsequently.

Figure 14 shows the effect of nitrate in the sulfate solutions containing approximately 3000 ppm chloride. It can be seen from the figure that in the solution containing 1000 ppm NO_3^- or above, the OCP after 48 hr immersion is still much more active than the E_b (see Fig. 12).

Discussion

The results given above clearly demonstrate that Type 304 stainless steel may experience SCC in an ammonium sulfate solution containing chloride ion at

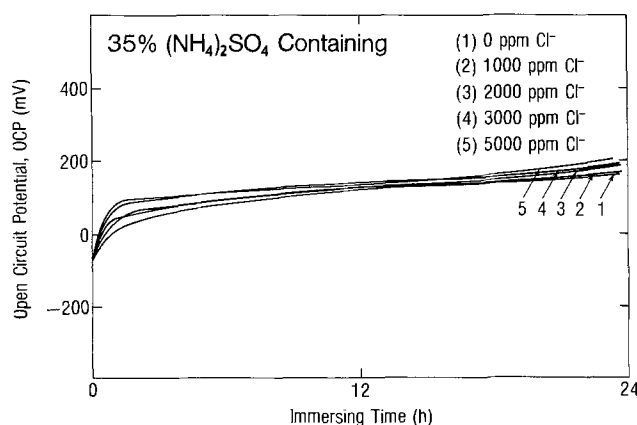


Fig. 13. The change in open-circuit potential (OCP) of Type 304 stainless steel in 35% $(\text{NH}_4)_2\text{SO}_4$ solution with different Cl^- concentration as a function of immersing time.

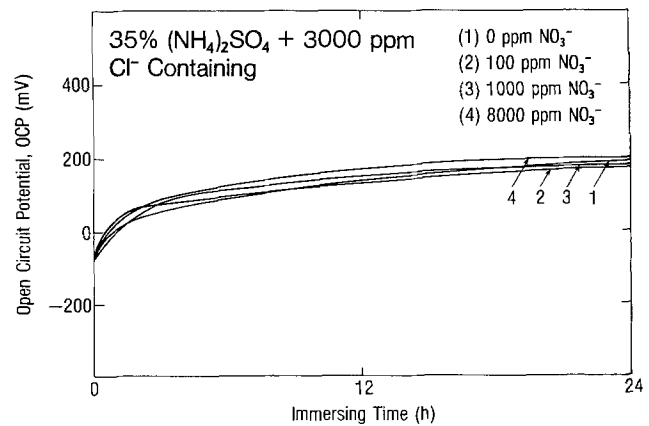


Fig. 14. The change in open-circuit potential (OCP) of Type 304 stainless steel in 35% $(\text{NH}_4)_2\text{SO}_4 + 3000 \text{ ppm Cl}^-$ solution with different NO_3^- concentration as a function of immersing time.

104°C . Evidently, the electrochemistry of the alloy/environment plays an important role in determining the SCC behavior.

Anodic polarization curves suggest that the metal is essentially passive in all the solutions tested, and the OCP shifts to a more noble direction with increasing chloride concentration. An interesting point with respect to SCC is that, as shown in the anodic polarization curves, the potential difference between OCP and E_b decreases substantially in the solution containing 2000 ppm chloride or more. Monitoring the OCP against the immersion time further indicated that in the solution containing 2000 ppm chloride or more, the OCP after 48 hr immersion became close to or more noble than E_b . This result is consistent with the suggestion that the pitting is responsible for the initiation of SCC, where the effect of chloride is to destroy the protectiveness of the surface film through the formation of active pits, which subsequently act as initiation sites of SCC.

Several authors have suggested that the critical factor in SCC is the rate at which a metal surface repassivates after the original passive film has been ruptured by slip-step emergence, etc., and therefore metals in the potential regions near the active-passive (17) and passive-transpassive transitions (17, 18), where the surface is still filmed but the impetus for passive film renewal is somewhat slow, should be more susceptible to SCC. The present results from fractographic and anodic polarization studies may represent another instance where SCC occurs near the passive-transpassive transition regions. This will, however, reemphasize the importance of the passive film and repenetration process SCC.

It has been reported that the SCC morphology in strongly acidic solutions is dependent on the $\text{SO}_4^{2-}/\text{Cl}^-$ ratio (19); the higher ratios favoring intergranular cracking and the lower ratios producing a mixture of transgranular and intergranular cracking. In the weakly acidic solutions of the present study, however, the fractures were always transgranular. The mechanism of the SCC propagation is not understood nor is such investigation the intent of this study. However, based on the fractographic observation that the river patterns, which are often thought to be associated with cleavage, were commonly seen on the fracture surfaces, it can be suggested that the SCC propagation is mechanical in nature.

The inhibiting effect of nitrate was clearly demonstrated by the slow strain rate testing and anodic polarization results. Similar results have been reported by Uhlig and Cook (10) in boiling MgCl_2 solution. They suggested that the addition of nitrate shifted the critical potential, above which cracking occurs, in a noble direction, and when the shift exceeds the corro-

sion potential for the alloy in the same solution, cracking is apparently inhibited. The present results indicated that the addition of nitrate essentially shifted the E_b value in a noble direction, and consequently widened the potential difference between OCP and E_b . In other words, the nitrate plays a role to prevent pitting initiation of the alloy in the solution. These results are consistent with the view that pitting may be responsible for the initiation of SCC. However, since no correlation between the critical SCC potential and other electrochemical parameters, such as pitting potential, were made, further experiments are essential to pursue this goal.

Another significant feature of this study is that a good correlation between SCC susceptibility and the electrochemical behavior of the alloy/environment system has been developed from which a better understanding of the mechanism of SCC can be obtained. Similar experiments are in progress (20) in our laboratory for Type 316 stainless steel. However, it should be emphasized that the theory derived from our present observations has only been explored for the ammonium sulfate system, as it exists in our production operation at 104°C, and the applicability of the conclusions from this study to other systems remains to be demonstrated.

Conclusions

The test results presented above may be summarized as follows:

1. AISI 304 stainless steel is susceptible to SCC at 104°C in the 35% $(\text{NH}_4)_2\text{SO}_4$ solution with the critical chloride concentration of approximately 2000 ppm or above.
2. Addition of 1000 ppm nitrate or above to the 35% $(\text{NH}_4)_2\text{SO}_4$ + 3000 ppm Cl^- solution inhibited SCC of the test steel at 104°C.
3. Results are consistent with the view that pitting may be responsible for the initiation of SCC.

Acknowledgment

The authors would like to thank Dr. J. Macur and Miss P. Brady for conducting the SEM studies and Allied Chemical Corporation for permission to publish the data.

Manuscript submitted March 15, 1979; revised manuscript received July 9, 1979. This was Paper 34 pre-

sented at the Boston, Massachusetts, Meeting of the Society, May 6-11, 1979.

Any discussion of this paper will appear in a Discussion Section to be published in the December 1980 JOURNAL. All discussions for the December 1980 Discussion Section should be submitted by Aug. 1, 1980.

Publication costs of this article were assisted by the Allied Chemical Corporation.

REFERENCES

1. R. L. Jones, *Corrosion (Houston)*, **31**, 424 (1975).
2. K. Hashimoto, *ibid.*, **31**, 398 (1975).
3. H. L. Logan, *J. Res. Nat. Bur. Stand.*, **48**, 99 (1952).
4. J. A. Davis and B. E. Wilde, *This Journal*, **117**, 1348 (1970).
5. G. Bianchi, F. Mazza, and S. Torchio, *Corros. Sci.*, **13**, 165 (1973).
6. R. W. Staehle, in "The Theory of Stress Corrosion Cracking in Alloys," J. C. Scully, Editor, p. 223, NATO, Brussels (1971).
7. J. R. Galvele, S. B. de Wexler, and I. Gardiazabal, *Corrosion (Houston)*, **31**, 352 (1975).
8. P. Engseth and J. C. Scully, *Corros. Sci.*, **15**, 505 (1975).
9. M. Kowaka and T. Kudo, *Tetsu To Hagane*, **62**, 390 (1976).
10. H. H. Uhlig and E. W. Cook, *This Journal*, **116**, 173 (1969).
11. H. Okada, Y. Hosai, and S. Abe, *J. Jpn. Inst. Met.*, **36**, 464 (1972).
12. J. H. Payer, W. E. Berry, and W. K. Boyd, *Special Technical Publication 610*, ASTM, p. 82 (1976).
13. 1978 Book of ASTM Standard, Conventions Applicable to Electrochemical Measurements in Corrosion Testing, ASTM Description G3-74, p. 693 (1978).
14. 1978 Book of ASTM Standard, Standard Reference Method for Making Potentiostatic and Potentiodynamic Measurements, G5-72, p. 715 (1978).
15. R. E. Bryant and J. B. Greer, *Mater. Proc. Perform.*, **9**, 19 (1970).
16. A. Couper, Minimizing Stress Corrosion Cracking of Austenitic Stainless Steels, Presented at Annual Conference, NACE, Cleveland, Ohio, March 1968.
17. R. N. Parkins, *Br. Corros. J.*, **7**, 15 (1972).
18. R. L. Jones, *Corrosion (Houston)*, **31**, 431 (1975).
19. J. D. Harston and J. C. Scully, *ibid.*, **25**, 494 (1969).
20. H. S. Tong, Unpublished results, Allied Chemical Corp. (1979).

Infrared and Raman Spectroscopy of Aqueous Corrosion Films on Lead

Richard J. Thibeau¹ and Chris W. Brown

Department of Chemistry, University of Rhode Island, Kingston, Rhode Island 02881

and Arnon Z. Goldfarb² and Robert H. Heidersbach*

Department of Ocean Engineering, University of Rhode Island, Kingston, Rhode Island 02881

ABSTRACT

The use of Raman and infrared spectroscopy to analyze surface films on metals is described. Surface films formed on lead by reaction with aqueous buffer solutions were examined. The composition of each film was determined by Raman spectroscopy while the sample was in the solution. Multiple reflection infrared spectra of dry samples confirmed the Raman results. The Pourbaix diagram for lead in water was calculated, and potentiostatic exposures were conducted to see if the compounds corresponded to those predicted in the diagram. Tetragonal PbO was found to occur over a much greater range of potentials than thermodynamic stability would indicate.

Passive films play an important role in corrosion and other electrochemical phenomena. Passive film studies frequently emphasize either the kinetics of film growth, breakdown, and repair or else they emphasize the structure and composition of the film. A number of techniques have been developed for both purposes.

This investigation was aimed at demonstrating the use of infrared (IR) and Raman spectroscopy for studying passive films formed on lead. The advantages of these techniques for passivation film studies are also discussed.

Surface analysis techniques.—A number of techniques are available for the study of passive film composition and structure. Recent reviews by Vermilyea (1) and Leidheiser (2) discuss most of the important surface analysis techniques available for use in studying passive films. Table I summarizes the techniques used in corrosion studies.

The ideal surface analysis technique would be able to provide structural information, *in situ*, on a variety of substrates. It should require no vacuum, work on amorphous as well as crystalline films, and be confirmable by other techniques. It should cover the entire atomic spectrum and not be limited, as is the case with Mössbauer spectroscopy, to certain elements (3-4). It is clear that Raman spectroscopy, with its

capability for *in situ* analysis of passive films as they form in aqueous media, has several important advantages over other surface analysis techniques. The combination of infrared and Raman spectroscopy offers structural analysis possibilities which cannot be met by other surface analysis techniques with the possible exception of differential reflectometry (5).

Vibrational Spectroscopy

Infrared and Raman spectroscopy.—Infrared and Raman spectroscopy are two similar structural analysis techniques. They are complementary in that one technique will often be highly sensitive to certain structures at the same time that the other technique will provide little, or no, information. For this reason they are usually used together, and the term vibrational spectroscopy is used to cover both techniques.

The optical schematic of a typical infrared spectrometer used for surface studies is shown in Fig. 1. Instruments of this type for use in corrosion studies were first described by Hannah (6), and subsequently have been used by Poling (7, 8), Mertens (9, 10), and others. Light from a single infrared source is split and directed along two parallel light paths. The sample(s) of interest are inserted into one light path (m_3 in Fig. 1), and the combination infrared reflection-absorption spectrum obtained from the sample is compared with the spectrum obtained in the reference beam, which is identical to the sample path in all aspects except the identity of the sample mirror. Comparison of the sample and reference beams eliminates source and light path artifacts from the spec-

* Electrochemical Society Active Member.

¹ Present address: Betz Laboratories, Trevose, Pennsylvania 19047.

² Present address: Neptune Oil Company, Tel Aviv, Israel.

Key words: lead, corrosion, spectroscopy, Pourbaix diagrams.

Table I. Characteristics of surface analytical techniques

Analytical method	Typical background pressure (Torr)	Analysis in aqueous solution	Min. film thickness observed (Å)	Information obtained
Raman spectroscopy	760	Yes	50 (19)	Compound identification
Infrared spectroscopy	760	No	10 (5)	Compound identification
X-ray diffraction	760	No	500	Compound identification
Ellipsometry (2)	760	Yes	10	Film thickness
Low energy electron diffraction (2) (LEED)	10 ⁻¹⁰	No	Monolayer	Compound identification
Auger electron spectroscopy (2) (AES)	10 ⁻⁹ -10 ⁻¹⁰	No	Monolayer	Elemental composition
Secondary ion mass spectrometry (2) (SIMS)	10 ⁻¹⁰	No	Monolayer	Elemental composition
Electron microprobe analyzer (2)	10 ⁻⁵ -10 ⁻¹⁰	No	200	Elemental composition
Scanning electron microscope (2) (SEM)	10 ⁻⁴ -10 ⁻⁹	No	50	Surface topography
Electron spectroscopy for chemical analysis (2) (ESCA)	10 ⁻⁷ -10 ⁻¹⁰	No	5	Elemental composition, electronic states
Differential reflectometry (5)	760	Yes	5	Compound identification

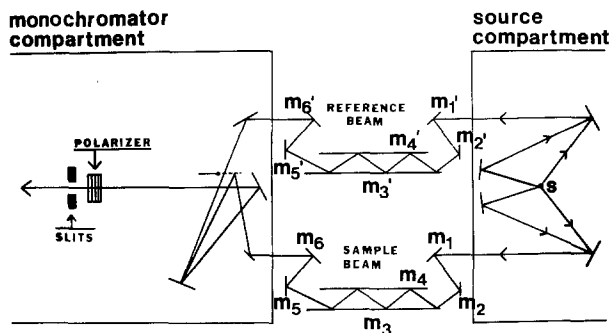


Fig. 1. Optical schematic of the infrared reflection-absorption setup used. S is the infrared source, reflecting surfaces are labelled m, and the sample is at position m_3 .

trum (11). It is beyond the purposes of this paper to discuss the reflection-absorption nature of the infrared spectra obtained using this technique. Detailed discussions of this are available (12-15).

Infrared spectra of liquids and solids are due to transitions between vibrational energy levels of the compound under investigation. Absorption bands are associated with the resonant energies of the chemical bonds in the material (11).

The optical schematic of a modern Raman spectrometer is shown in Fig. 2. The spectrometer consists of a laser, a sample compartment, an optical monochromator, and a detection system. The laser acts as a source of monochromatic light which strikes the sample. Most of the incident light is reflected from the sample surface and undergoes no change in wavelength. However, some of the incident light interacts with the surface, loses some of its energy, and causes scattering of light at wavelengths different from the incident radiation. It is this scattered light which is measured in Raman spectroscopy.

The transitions responsible for Raman scattering are shown in Fig. 3. Consider a molecule in the ground ($v = 0$) vibrational state. The incident radiation in the visible range (e.g., $\nu_0 = 20,000 \text{ cm}^{-1}$) excites the molecule to a pseudoenergy level by inducing a temporary dipole in the molecule. In a short time period ($\sim 10^{-14}$ sec) the molecule emits a photon at the same frequency (Rayleigh scattering) and returns to the ground state, or it emits a photon at a lower frequency and returns to a higher vibrational level, e.g., $v = 1$. In the latter case, the energy of the photon will correspond to a frequency $\nu_0 - \nu_1$; this type of transition is referred to as Stokes Raman scattering.

There is a Boltzmann distribution of molecules at all possible vibrational energy levels. Thus, even at room temperature there are molecules in the $v = 1$

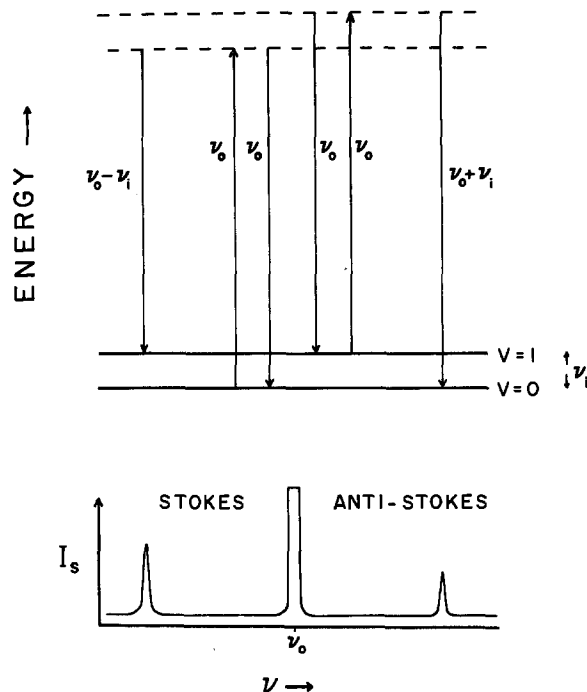


Fig. 3. Energy level diagram for a typical vibrational Raman transition and the Raman spectrum resulting from such a transition.

level. These can also be excited by the incident radiation to a pseudoenergy level. These molecules can then return to the same level and emit a photon of ν_0 , or they can return to $v = 0$ and emit a photon of $\nu_0 + \nu_1$. These latter transitions are also Raman, and are referred to as anti-Stokes Raman scattering.

A typical Raman spectrum of a diatomic molecule is shown in the bottom of Fig. 3. The intensity of the anti-Stokes Raman bands depends upon the magnitude of ν_1 , i.e., the greater ν_1 , the smaller the number of molecules in the level (Boltzmann distribution) and the smaller the intensity of the transition. Thus, in conventional Raman spectroscopy only the Stokes transitions are measured, and only the left half of the spectrum is used. Furthermore, it is conventional to plot the frequency difference, i.e., $\nu_0 - (\nu_0 - \nu_1) = \nu_1$, or the frequency corresponding to the differences between vibrational levels. For polyatomic molecules, Raman transitions to some or all of the possible vibrational levels can take place.

For a Raman transition to occur, the geometry of the molecule in the excited state must be such that a change in polarizability has taken place, i.e., the electron density about the molecule must be distorted

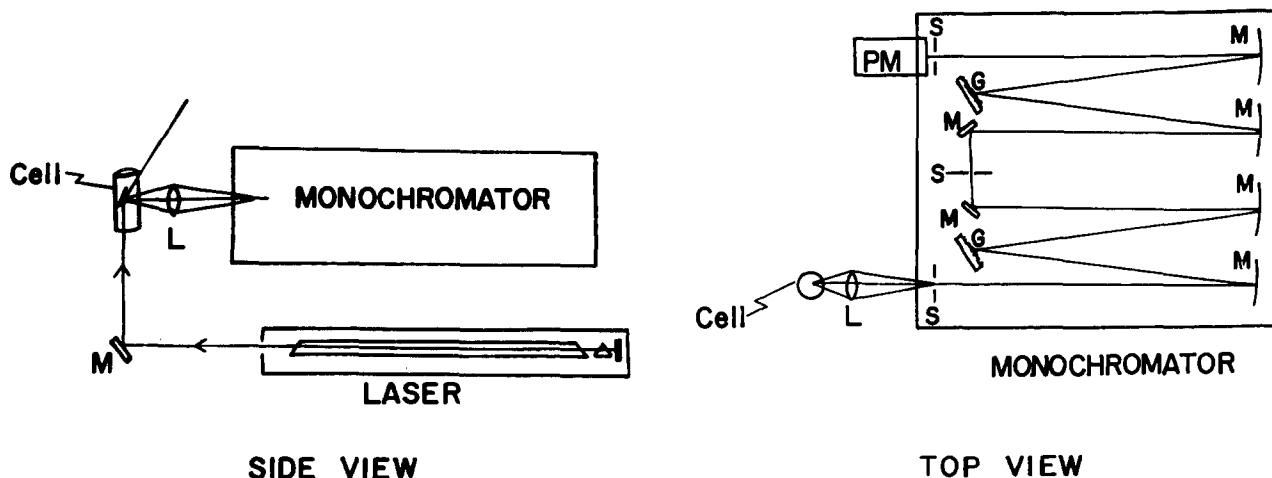


Fig. 2. Schematic drawing of a laser Raman spectrometer. Mirrors are labelled M, gratings, G, and slits, S

by the transition. For an absorption of infrared radiation to occur, the geometry of the molecule in the excited state must be such that a change in the dipole moment has taken place. Thus, both Raman and infrared absorption spectra provide data on vibrational transitions which in turn provide information on the bonding and the structure of the molecule. However, the two processes are entirely different, and one may occur without the other. Generally they provide complementary information, and both spectra are needed to completely understand the vibrational properties of the chemical species in the material.

Every molecule has its own characteristic infrared and Raman spectrum which can be used to identify the molecule (exceptions are homonuclear diatomic molecules which do not absorb infrared radiation). The primary use of these techniques has been in identification. The spectrum of an unknown chemical can be identified by comparing its infrared or Raman spectral "fingerprint" to those of known chemicals. It is this method that we have used to identify the composition of films on the surface of metals, *i.e.*, we compare spectra from surface films with spectra of known chemicals.

Pourbaix diagrams.—Potential-pH diagrams (Pourbaix diagrams) are available for a wide variety of metals (16), and they have found wide application in corrosion research (17, 18). The Pourbaix diagram of lead (16) was used as a basis for choosing exposure conditions for forming passive films on lead surfaces which were subsequently analyzed by Raman and infrared spectroscopy in this study. The lead diagram also contains a number of different insoluble species and is similar in many respects to the diagram for iron, the most important structural metal (16).

Experimental

Raman spectra were recorded with a Spex Industries Model 1401 double monochromator using a photon counting detection system. A simplified optical schematic of a spectrometer of this type is shown in Fig. 2. A Coherent Radiation Laboratories Model CR-3 argon ion laser is located beneath the monochromator, and the laser beam is directed by a mirror to the bottom of the sample cell. Some of the light scattered by the sample is collected by the lens (L), positioned 90° from the vertical laser beam, and is focused onto the entrance slits of the monochromator. Light passing through the slits is collimated by a mirror and dispersed by the first grating. The light, spread out according to frequency, is then directed by a second collimating mirror and a plane mirror to the intermediate slits. The narrow frequency band of light which has passed through the first monochromator then passes through a second identical monochromator, to maximize rejection of stray light, and reaches the detector, a photomultiplier tube. Each photon reaching the photomultiplier is converted to an electrical pulse which is amplified and counted. The number of counts (number of photons) per selected time interval is converted to an analog signal which drives the pen on a strip chart recorder. A frequency range is scanned by turning the two gratings in the monochromator simultaneously so the frequency of light reaching the detector is changed. The Raman spectrum recorded is thus a plot of light intensity *vs.* frequency difference from the excitation frequency.

The electrochemical cell shown in Fig. 4 is used in the sample compartment of the spectrometer to allow Raman spectra to be recorded while the sample is undergoing oxidation in an aqueous solution. The cell is designed for potentiostatic exposures of fairly large samples. The working electrode is a flat 2.8×5.7 cm rectangular sample held in a Teflon sample holder. The auxiliary electrode is platinum mesh, and the potential is maintained relative to a saturated calomel electrode by a potentiostat. The sample is held close

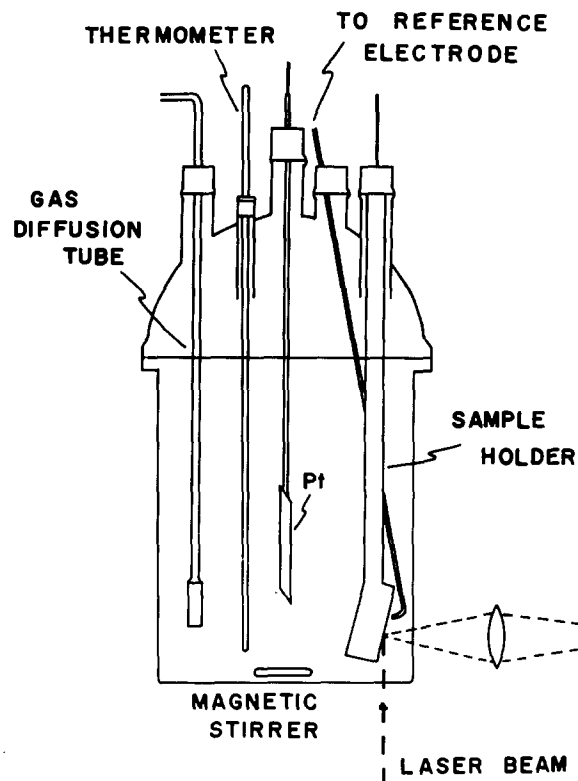


Fig. 4. Drawing of the electrochemical cell used for *in situ* Raman spectroscopy.

to the bottom and side of the cylindrical glass cell and at an angle of 20° from vertical so that it is in the optimum position for observation of Raman spectra. The angles between the sample surface and the incident beam, and between the surface and the axis of the collection optics are important in optimizing the efficiency of collecting Raman scattered light (19). The angles are chosen so that the electric vector of the incident beam may interact most strongly with the film and produce the maximum Raman scattering.

The sample size (2.8×5.7 cm) was selected so that the sample, after *in situ* examination by Raman spectroscopy, can be placed in the holder of a Wilks Scientific Corporation Model 9 multiple specular reflection attachment for infrared reflection-absorption analysis. An optical schematic of the reflection attachments in the Perkin-Elmer Model 521 infrared spectrophotometer is shown in Fig. 1. Two multiple reflection attachments are used in the spectrophotometer, one in the sample beam holding the oxidized metal sample and one in the reference beam holding an aluminum mirror.

Each time the infrared beam reflects off of the sample surface some radiation is absorbed by the surface film at frequencies of infrared absorption bands. Some light is also lost at all frequencies with each reflection so the mirrors are adjusted to provide the optimum angle of incidence (65°-88°, depending on film thickness) and the optimum number of reflections (1-3) for recording the spectrum of a film on a lead substrate. After the sample and reference beams are combined in the monochromator portion of the instrument, the light must pass through a polarizer which transmits only that light with its electric vector in the plane parallel to the plane of incidence with the sample surface. Only the parallel polarized light will interact with a thin film (13) so the extra light not in this plane, and containing no information, is filtered out to increase the sensitivity of the instrument.

Lead foil (Alfa Products, Incorporated, Danvers, Massachusetts), 1 mm thick and 99.9995% pure, was

Table II. Electrolyte solutions used in this investigation

Composition	pH
2.3M HBr	
0.063M KH_2PO_4 , 0.037M NaOH	7.0
0.041M NaHCO_3 , 0.018M NaOH	10.0

cleaned by immersion in warm, concentrated ammonium acetate solution for 5 min and rinsed with distilled water before being placed in solution in the electrochemical cell. The solution was purged of reactive dissolved gases by bubbling dry nitrogen through it for an hour before and throughout the period of sample exposure. For a few exposures, the lead sample was not connected to the potentiostat but was allowed to react at its equilibrium potential. For other exposures, the potentiostat was turned on immediately after placing the sample in solution, and it maintained the potential at a constant value throughout periods of exposure ranging from 6 min to 24 hr.

Some exposures were conducted on lead films which were vapor deposited onto gold substrates on glass microscope slides. These samples, similar to those used by Poling in his infrared studies of high temperature oxidation of iron and copper (7), allowed the lead to be completely oxidized leaving a nonreacted gold mirror substrate.

Table II lists the electrolytes used in this investigation. They are similar to those used by Pourbaix, Verink, and co-workers at the University of Florida (20) and have been used in other electrochemical studies in these laboratories (21). The exposures performed in this investigation are summarized in Table III.

Results and Discussion

Spectra.—A lead sample was immersed in 2.3M hydrobromic acid and allowed to corrode freely (no connection to the potentiostat). After 8 days the *in situ* Raman spectrum of the surface shown in Fig. 5a was recorded. The spectrum of the gray surface layer clearly indicates that it consists of PbBr_2 . The six strongest bands in the spectrum of pure PbBr_2 (Fig. 5c) are present in the spectrum of the film. Furthermore, the band shapes and frequencies in the spectra of the film and the powder are identical.

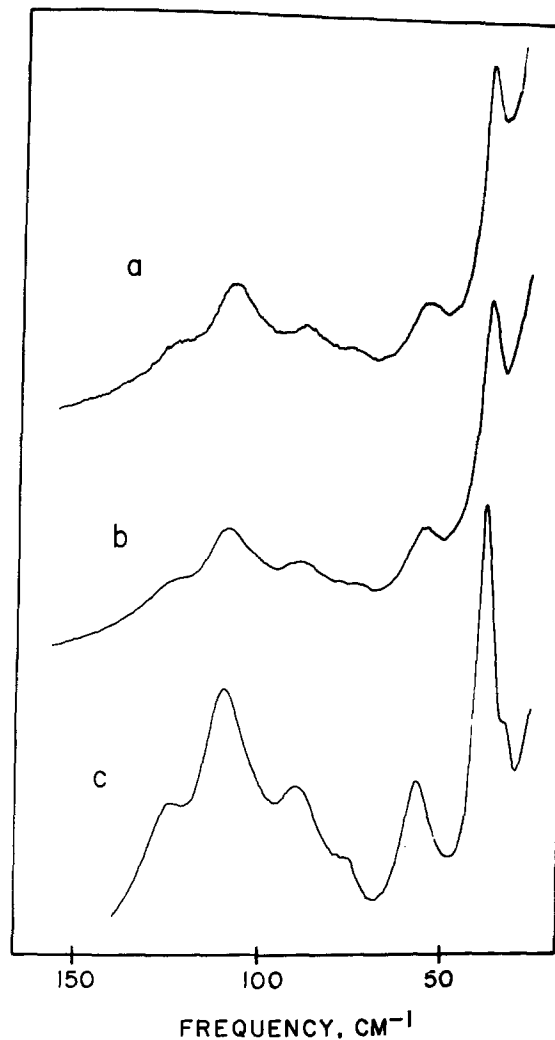


Fig. 5. Raman spectra of (a) the surface of lead foil immersed in deaerated 2.3M HBr solution for 8 days, (b) PbBr_2 powder from crystals formed on lead in 2.3M HBr after 34 days, (c) reagent grade PbBr_2 powder.

The sample was allowed to continue reacting undisturbed in the solution and white needle-like crys-

Table III. Controlled potential-pH exposures of lead in aqueous solutions

Solution pH	Potential V vs. NHE	Duration of exposure (hr)	Current density, $\mu\text{A}/\text{cm}^2$ ^(a)	Surface species	
				Predicted	Exper. observed
7	-0.62	17	1.7 ^(b)	Pb	None
7	-0.62	19	1.2 ^(b)	Pb	None
7	-0.16	20	6.3	Pb	None
7	-0.12	18	61	PbO	Tetragonal PbO
7	+0.06	2.8	112	PbO	Tetragonal PbO
7	+0.48	21		PbO	Tetragonal PbO
7	+0.58	3		PbO	Tetragonal PbO
7	+0.67	2	310	Pb ₂ O ₄	Tetragonal PbO
7	+0.74	23.5	397	Pb ₂ O ₃	Tetragonal PbO
7	+1.08	1.5	310	PbO ₂	Tetragonal PbO
7	+1.08	18	294	PbO ₂	Tetragonal PbO
10	-0.80	20.5	139 ^(b)	Pb	None
10	-0.42	18	24	Pb	(PbCO ₃) ₂ · Pb(OH) ₂
10	-0.28	4		Pb	Tetragonal PbO and (PbCO ₃) ₂ · Pb(OH) ₂
10	-0.26	21	14.3	PbO	Tetragonal PbO
10	-0.03	17	46	PbO	Tetragonal PbO
10	+0.02	23		PbO	Tetragonal PbO
10	+0.24	17	54	PbO	Tetragonal PbO
10	+0.34	2	455	PbO	Tetragonal PbO
10	+0.46	2.5	210	Pb ₂ O ₄	Tetragonal PbO
10	+0.75	0.75		PbO ₂	Tetragonal PbO
10	+0.75	18		PbO ₂	Tetragonal PbO
10	+0.84	1.5	115	PbO ₂	Tetragonal PbO
10	+0.94	6 min	175	PbO ₂	Tetragonal PbO
10	+0.94	17.5	91	PbO ₂	Tetragonal PbO
10	+1.24	17	1200	PbO ₂	Tetragonal PbO

^(a) Final or steady current.

^(b) Current flow in reducing direction.

tals formed on the surface. After immersion for 34 days, the sample was removed and dried. The white crystals were scraped off and ground into powder. The Raman spectrum of the resulting powder was identical to that of the surface film. It is clear that the Raman spectrum of a thick film is identical to that of a bulk sample. Possibly a spectrum of an extremely thin film might differ due to changes in the bonds because the surface compound is bound to the underlying metal, but for relatively thick films (hundreds or thousands of angstroms) the spectra are the same as that of a powder.

At this point it should also be pointed out that the films analyzed in this investigation were surface reaction products. No attempt was made to separate precipitated deposits, such as those discussed above, from adherent conversion products which may have acted as passive films and altered metal-environment reaction kinetics.

Analysis of surface films by infrared spectroscopy gives somewhat different results. While the entire range of vibrational bands, from lattice modes at 20 cm^{-1} to overtones beyond 6000 cm^{-1} , are easily observed with a Raman spectrometer, normally two different instruments are required to scan that range in the infrared. For this study, infrared spectra were obtained in the region $1500\text{--}250\text{ cm}^{-1}$. The low frequency bands of a compound like lead bromide could not be observed. Nearly all infrared spectra found in the literature are transmission spectra, observations of the amount of light passing through a partially absorbing sample. By combining absorption with reflection at the surface film-metal interface, the resulting absorption spectrum from the multiple reflections has a different appearance from a pure absorption spectrum. An infrared reflection-absorption spectrum results from changes in the extinction coefficient and the index of refraction, both of which can change radically in the vicinity of an absorption frequency, whereas a transmission spectrum is due to changes in extinction coefficient alone (11, 15). The result, as demonstrated in Fig. 6, is that a reflection-absorption spectrum usually has bands of slightly different

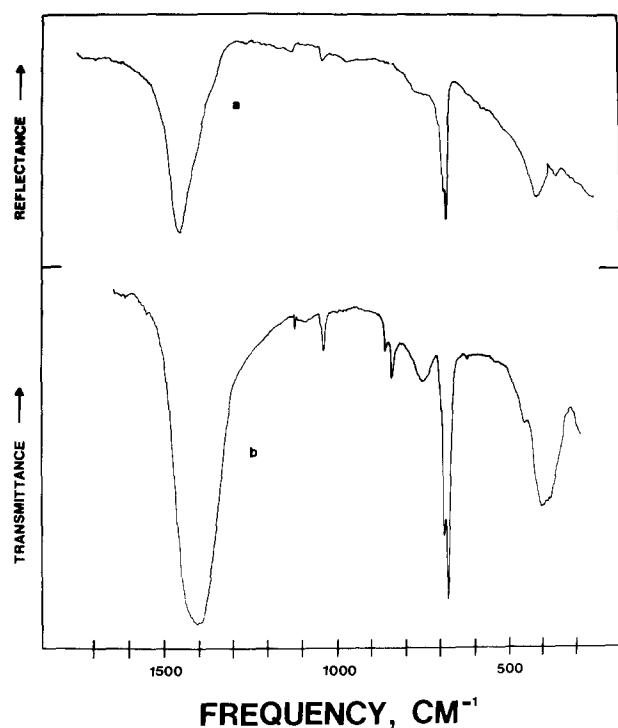


Fig. 6. (a) Infrared reflection-absorption spectrum of a lead sample after exposure in pH 10 solution at -0.42V vs. NHE for 24 hr, (b) transmission infrared spectrum of $(\text{PbCO}_3)_2 \cdot \text{Pb}(\text{OH})_2$ in a KBr pellet.

shape and frequency from a transmission spectrum (13, 14). The magnitude of the differences depends on such variables as angle of incidence of the infrared beam, film thickness, and number of reflections used. Since the spectra are sensitive to instrumental conditions, identification of compounds with infrared reflection-absorption alone is sometimes difficult. Infrared reflection-absorption, combined with Raman spectroscopy, permits much more accurate identification of the species present.

Some compounds have vibrational transitions which are much stronger in the infrared than in Raman, and some have vibrations which are much stronger in Raman spectra. Such is the case for the conditions in Fig. 6. The basic lead carbonate, $(\text{PbCO}_3)_2 \cdot \text{Pb}(\text{OH})_2$, on the lead surface that produced the strong infrared spectrum of Fig. 6 produced only a weak Raman band at 1050 cm^{-1} to indicate the presence of carbonate. Although $(\text{PbCO}_3)_2 \cdot \text{Pb}(\text{OH})_2$ can give the Raman spectrum shown in Fig. 7, it was necessary to use the complementary technique, infrared absorption, to specify which carbonate compound was present.

Water is a strong infrared absorber so samples must be dried before a spectrum can be observed. This is not the case with Raman spectroscopy; water poses little problem in obtaining a Raman spectrum. For potentiostatically exposed samples, Raman spectra were recorded with the sample in the solution with a potential applied. After obtaining a spectrum the sample was removed from the electrochemical cell, washed with distilled water, and dried at room temperature. The dry sample was then returned to the spectrometer sample compartment and another Raman spectrum recorded. This was done to identify any changes that might occur in the surface film upon drying. In the present investigation no significant differences between *in situ* and dry sample Raman spectra were found. Spectra obtained under both conditions are very similar as demonstrated in Fig. 8. Both spectra contain the three strongest bands of tetragonal PbO, enough to conclusively identify the compound as the surface species present. After removal from the cell and drying of the sample, the spectrum is slightly stronger. In this investigation the intensity of the Raman spectra recorded with samples in solution in the electrochemical cell was approximately half the spectral intensity of dry samples. The reasons for the decrease in intensity are scattering and reflection from the solution and sides of the cell and the difficulty of focusing light scattered in the cell onto the monochromator entrance.

Figure 9 shows the Raman spectrum of orthorhombic PbO (12). The thickness of the film that produced the spectrum was measured at 1600Å using a Taylor-step-1 stylus instrument. From the PbO spectra ob-

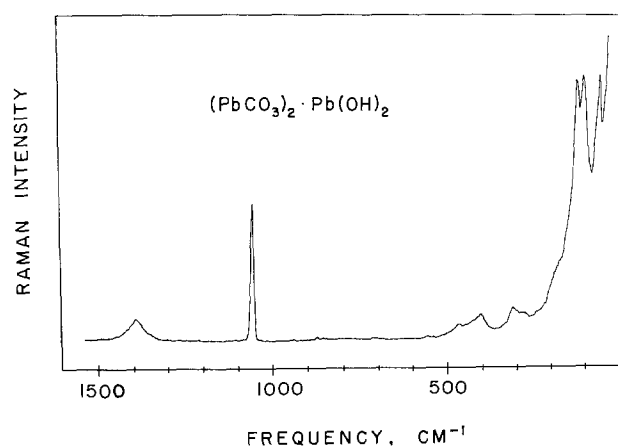


Fig. 7. Raman spectrum of reagent $(\text{PbCO}_3)_2 \cdot \text{Pb}(\text{OH})_2$ in a KBr pellet.

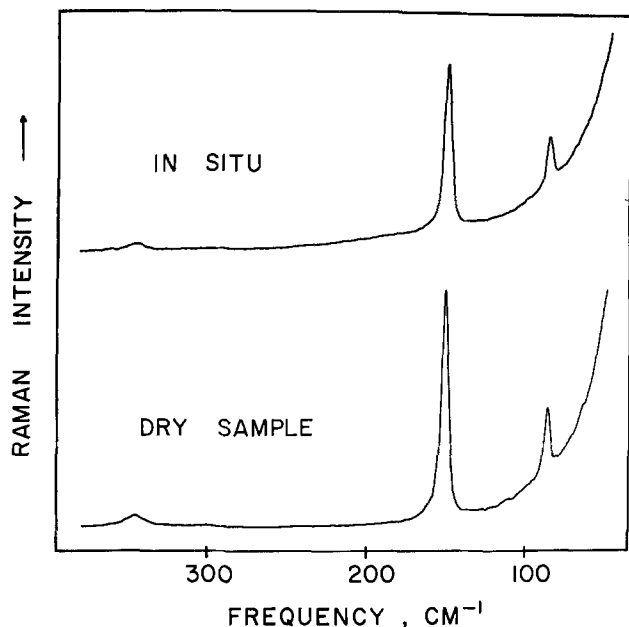


Fig. 8. Raman spectra of a lead surface in pH 7 solution at +0.06V vs. NHE after 2 hr 50 min exposure and of the same sample after washing with distilled water and drying.

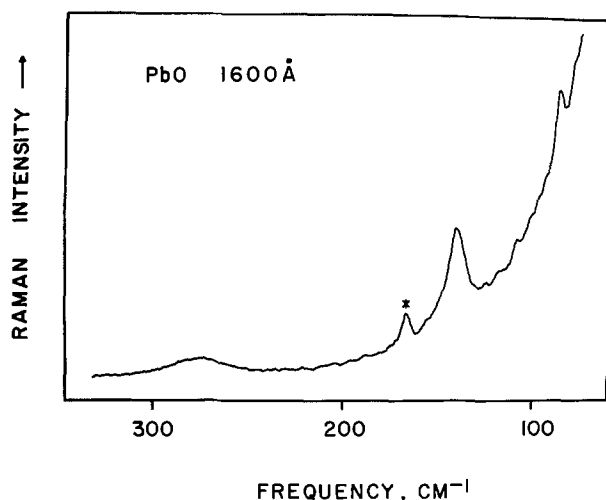


Fig. 9. Raman spectrum of a 1600 Å thick film of orthorhombic PbO made from a vacuum deposited lead sample. Grating ghost marked with an asterisk.

tained in this investigation for vapor-deposited samples, it is estimated that a minimum film thickness of approximately 200 Å is necessary to obtain usable spectra using the infrared and Raman instruments employed. Other oxides should have different minimum detectable thicknesses. Other researchers have reported infrared spectra from thinner films formed on nonlead substrates (6-10).

Single spectrometer scans were used to record the spectra recorded in this investigation. Signal averaging of multiple scans should increase the signal to noise ratio and reduce the minimum detectable thicknesses (22).

The lead-water Pourbaix diagram.—Most available potential-pH (Pourbaix) diagrams are based on the same type of thermodynamic calculations employed by Pourbaix in compiling his original atlas (16). Several experimental Pourbaix diagrams have appeared (17, 18, 20-26), and these are normally based on electrochemical polarization techniques which emphasize electrode kinetics.

Vibrational spectroscopy seems especially suited to analyze, *in situ*, films formed on metals under passivating conditions as predicted by Pourbaix diagrams. In this manner, experimental determinations of the composition of films formed in the passive region of a Pourbaix diagram should be possible.

The Pourbaix diagram of lead was chosen to test this hypothesis. Lead was chosen because its high atomic weight means that lead compounds should be relatively strong Raman scatterers (27). The lead diagram also contains a number of different insoluble species and is similar in many respects to iron, the most important structural metal (16). A report of similar attempts to verify some portions of the lead Pourbaix diagram using Raman spectroscopy was published during the course of this investigation (28). Hendra and co-workers used chloride-containing electrolytes in their investigation. Thus, a comparison with their results is beyond the scope of this paper. Studies of the effects of anions on the corrosion films formed on lead have been conducted (12, 29) and will be summarized in subsequent papers (30).

The lead-water equilibrium diagram published by Pourbaix is shown in Fig. 10. Initial attempts to verify this diagram using infrared and Raman spectroscopy led to a number of discrepancies between predicted and experimentally determined passive species. Recalculation of the Pb-H₂O equilibria using the most recent thermodynamic data from the National Bureau of Standards (31) resulted in the diagram of Fig. 11. It was hoped that fewer differences between predicted and observed species would be noted when this new data was used. The free energies of formation for the species in question in Fig. 10 and 11 are listed in Table IV. Figure 11 was used, in conjunction with potentiodynamic polarization curves run in the solutions of interest, to identify potential-pH combinations to be used to form passive films for spectroscopic investigation.

The results of the immunity (low potential) region of the Pourbaix diagram agree with the thermodynamic predictions summarized in Fig. 11 except for the appearance of basic lead carbonate for some potentials at pH 10. Spectra of tetragonal PbO were observed in regions where PbO, Pb₃O₄, Pb₂O₃, and PbO₂ were predicted by thermodynamics. At lower potentials the sample surfaces remained shiny, oxidation was relatively slow, and the oxide films were apparently thin. At higher potentials the metallic

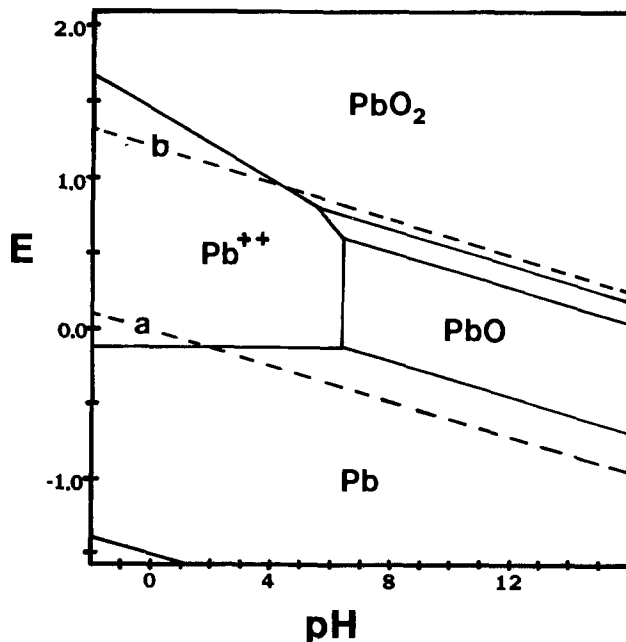


Fig. 10. Pb-H₂O Pourbaix diagram, Ref. (16)

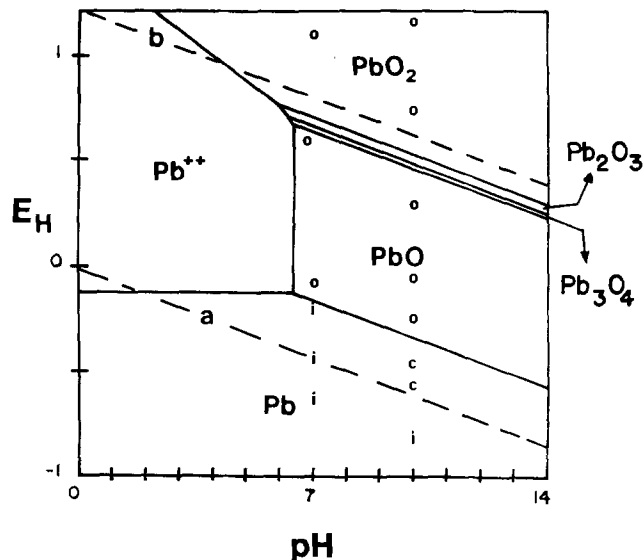


Fig. 11. Calculated Pb-H₂O Pourbaix diagram using the most recent NBS data (31). Experimental results, O = tetragonal PbO, i = apparent immunity, no spectrum observed, C = basic lead carbonate.

surface quickly became black. The black lead oxide has been previously described as PbO with a thin outer surface film of elemental lead (32). At the slower rates of oxidation occurring at lower potentials, the film did not become black.

The formation of tetragonal PbO under conditions where other oxides are predicted to be stable cannot be adequately explained. It must be noted, however, that, if PbO₂ were formed, it could probably not be detected using infrared and Raman spectroscopy. Lead dioxide has been reported to have no infrared absorption bands in the region 1500-250 cm⁻¹ (33), and no Raman spectra were observed from bulk samples of reagent grade PbO₂ (29).

Spectra have been obtained for orthorhombic PbO and Pb₃O₄ and are reported elsewhere (30, 32-35). The lack of observation of these species during the electrochemical exposures of the investigation may be due to errors in the theoretical Pourbaix diagram (Fig. 10 and 11). Another possibility is the presence of insufficient amounts of these compounds to be detectable by the instrumentation used. The possibility of a multilayered film with an outer layer, which is detectable spectroscopically, masking an inner film must also be considered (12).

Conclusions

Infrared and Raman spectroscopy can be used to identify surface films formed on electrodes in corrosive environments. Raman spectra can be obtained *in situ* in aqueous environments. There are only slight differences in intensity between *in situ* Raman spectra and those recorded on dry samples. Multiple reflection infrared spectroscopy complements *in situ* Raman spectroscopy.

Surface films identified on lead samples using infrared and Raman spectroscopy differed from those predicted by thermodynamics. Differences may be due

Table IV. Free energy data used to calculate the Pb-H₂O Pourbaix diagram

	ΔG_f° (cal/mole)	
	NBS (31)	Pourbaix (16)
Pb ⁺⁺	-5,830	-5,810
PbO (orthorhombic)	-44,910	-45,050
PbO (tetragonal)	-45,160	-45,250
PbO ₂ (orthorhombic)	-51,950	-52,340
Pb ₃ O ₄	-143,700	-147,600

to experimental limitations or may indicate deficiencies in thermodynamic prediction techniques such as anion effects which are not considered in the calculations for Fig. 10 and 11.

Acknowledgment

This work was supported by the Department of the Navy, Office of Naval Research, under contract N00014-76-C-0889. The idea for using Raman spectroscopy in corrosion studies was suggested by T. Rhodin of Cornell University.

Manuscript submitted Aug. 2, 1978; revised manuscript received Jan. 26, 1979.

Any discussion of this paper will appear in a Discussion Section to be published in the December 1980 JOURNAL. All discussions for the December 1980 Discussion Section should be submitted by Aug. 1, 1980.

Publication costs of this article were assisted by the University of Rhode Island.

REFERENCES

- D. A. Vermilyea, *Physics Today*, p. 23, September 1976.
- H. Leidheiser, in "Passivity of Metals (Proceedings of the 4th International Symposium on Passivity)," R. P. Frankenthal and J. Kruger, Editors, p. 223, The Electrochemical Society, Inc., Princeton, N.J. (1978).
- Lieng-Huang Lee, in "Characterization of Metal and Polymer Surfaces," L. H. Lee, Editor, Vol. 1, p. 1, Academic Press, New York (1977).
- U. Gonser, "Mossbauer Spectroscopy," Springer-Verlag, Berlin (1975).
- R. Hummel, C. Shanley, and E. Verink, Paper No. 22, Corrosion/77, NACE, San Francisco, March 1977.
- R. W. Hannah, *Appl. Spectros.*, **17**, 23 (1963).
- G. W. Poling, *This Journal*, **116**, 958 (1969).
- G. W. Poling, *J. Colloid Interface Sci.*, **34**, 365 (1970).
- F. P. Mertens, *Surf. Sci.*, **71**, 161 (1978).
- F. P. Mertens, *Corrosion*, **34**, 359 (1978).
- M. L. Hair, "Infrared Spectroscopy in Surface Chemistry," Marcel Dekker, New York (1967).
- A. Z. Goldfarb, M. S. Thesis, University of Rhode Island (1978).
- R. G. Greenler, *J. Chem. Phys.*, **44**, 310 (1966).
- R. G. Greenler, *ibid.*, **50**, 1963 (1968).
- T. Takamura and K. Takamura, in "Surface Electrochemistry," Japan, pp. 179-241, Scientific Societies Press (1978).
- M. Pourbaix, "Atlas of Electrochemical Equilibria in Aqueous Solutions," NACE, Houston (1969).
- K. D. Efrid, *Corrosion*, **31**, 77 (1975).
- E. D. Verink and T. Lee, in Proceedings of the Third International Conference on Marine Corrosion and Fouling, Gaithersburg, Md. (1972).
- R. G. Greenler and T. L. Slager, *Spectrochim. Acta, Part A*, **29**, 193 (1972).
- R. L. Cusamano, M.S. Thesis, University of Florida (1971).
- R. Turcotte, M.S. Thesis, University of Rhode Island (1977).
- C. H. Warren and L. Ramaley, *Appl. Opt.*, **12**, 1976 (1973).
- E. D. Verink and R. H. Heidersbach, Localized Corrosion—Cause of Metal Failure, ASTM STP 516, p. 303, American Society for Testing and Materials (1972).
- P. Parrish, M.S. Thesis, University of Florida (1970).
- R. Turcotte, M.S. Thesis, University of Rhode Island (1977).
- E. D. Verink and M. Pourbaix, *Corrosion*, **27**, 12 (1971).
- N. Colthup, L. Daly, and S. Wiberley, "Introduction to Infrared and Raman Spectroscopy," 2nd ed., Academic Press, New York (1975).
- E. S. Reid, R. P. Cooney, P. J. Hendra, and F. Fleischmann, *J. Electroanal. Chem.*, **80**, 405 (1977).
- R. J. Thibeau, Ph.D. Thesis, University of Rhode Island (1978).
- R. Thibeau, C. Brown, A. Goldfarb, and R. Heiders-

- bach, submitted to *This Journal*.
31. D. D. Wagman, W. H. Evans, V. B. Parker, I. Halow, S. M. Bailey, and R. H. Schummn, NBS Technical Note 270-3, U.S. Government Printing Office (1975).
32. E. W. Abel, in "Comprehensive Inorganic Chemistry," J. C. Bailar, H. J. Emeleus, R. Nyholm, and A. F. Trotman-Dickenson, Editors, Vol. 2, p. 119, Pergamon, Elmsford, N.Y. (1973).
33. N. T. McDevitt and W. L. Baun, *Spectrochim. Acta*, **20**, 799 (1964).
34. J. D. Donaldson, M. T. Donoghue, and S. D. Ross, *ibid.*, **30A**, 1967 (1974).
35. D. M. Adams and D. C. Stevens, *J. Chem. Soc. Dalton Trans.*, **1977**, 1096.

Effects of Target Materials on the Structural Properties of Sputtered SiC Films

Takao Tohda, Kiyotaka Wasa, and Shigeru Hayakawa

Materials Research Laboratory, Matsushita Electric Industrial Company, Limited, Kadoma, Osaka 571, Japan

ABSTRACT

SiC films were prepared either by direct sputtering of a SiC target in Ar or by reactive sputtering of a Si target in a mixture of Ar and hydrocarbon. Their chemical composition and structural properties were examined by Auger electron spectroscopy, infrared transmission, and reflection electron diffraction. It is seen that the chemical composition of the films sputtered from the Si target is strongly dependent on the deposition rate and the partial pressure of hydrocarbon. The sputtered films from the SiC target crystallize at lower deposition temperature than those from the Si target.

Silicon carbide, SiC, films have very promising electrical and chemical properties in high ambient temperature. For example, SiC thin films are found to be useful for making high temperature sensors (1). Reactive deposition of Si in hydrocarbon or direct sputtering of SiC is widely used for preparing SiC films. Learn and Haq prepared epitaxial β -SiC films by reactive evaporation of Si at 1100°C in a reactive gas of C₂H₂. They found that the ratio of the arrival rate of C₂H₂ to the arrival rate of Si at substrates should be more than 30 (2). Haq has studied reactive sputtering of Si in a mixture of Ar and C₂H₂ at a substrate temperature of 1150°C and suggests that there exists an optimum range in the partial pressure of the reactive C₂H₂ gas (3). Murayama and Takao have proposed an rf-ion plating method in C₂H₂ at 1000°C and concluded that the C₂H₂ pressure should be lower than 1.3×10^{-2} Pa and the deposition rate of Si should be higher than 200 Å min⁻¹ (4). Wasa, Nagai, and Hayakawa prepared polycrystalline SiC films by rf-sputtering of SiC in Ar and investigated the structural and mechanical properties (5). Nishino, Matsunami, Odaka, and Tanaka prepared epitaxial β -SiC films by rf-sputtering of β -SiC at 1200°C (6).

Recently we have studied the structural properties of rf-sputtered SiC films and found that the target materials used strongly affected the structural properties of the resultant SiC films. This paper describes the chemical composition and crystalline structure of rf-sputtered SiC films prepared from two different sputtering targets, SiC and Si.

Film Preparation

A conventional rf diode sputtering system was employed for the film deposition. Two different materials were used as a target: one was sintered 6H-SiC (diameter 100 mm, thickness 5 mm, purity 99.5%) and the other was single crystal Si (diameter 50 mm, thickness 0.25 mm, purity 99.9999%). Silicon (111) wafers were used for substrates. The substrates were etched in HF prior to sputtering deposition. The distance from the target to the substrates was 25 mm.

Key words: chemical composition, AES; SiC target, Si target.

The substrate temperature was controlled between 200°-740°C during film deposition.

For the SiC target, sputtering was done in Ar at a pressure of 2.7 Pa. A typical deposition rate was 0.3 $\mu\text{m/hr}$ with an rf power density of 2 W/cm². In this case the deposition rate increased linearly with the rf power. The substrate temperature had little effect on the deposition rate.

For the Si target, sputtering was done in a mixture of Ar and hydrocarbon (CH₄ or C₂H₂) at a pressure of 2.7 Pa. The partial pressure of CH₄ and C₂H₂ was varied from 4.1×10^{-2} to 1.3 Pa and from 9.2×10^{-3} to 5.9×10^{-2} Pa, respectively. In these cases the deposition rate varied with the partial pressure even at a constant rf power. A typical result for CH₄ at an rf power density of 3 W/cm² is shown in Fig. 1. At low CH₄ partial pressures, the deposition rate is independent of the partial pressure. At partial pressures above a critical pressure, 1.5×10^{-1} Pa, the

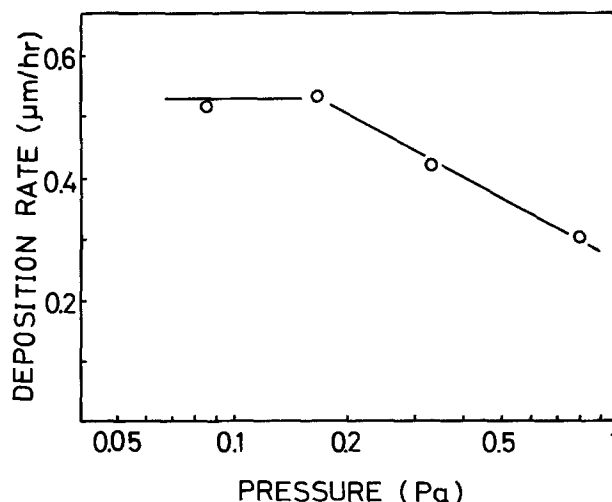


Fig. 1. Effect of CH₄ partial pressure on deposition rate at an rf power density of 3 W/cm².

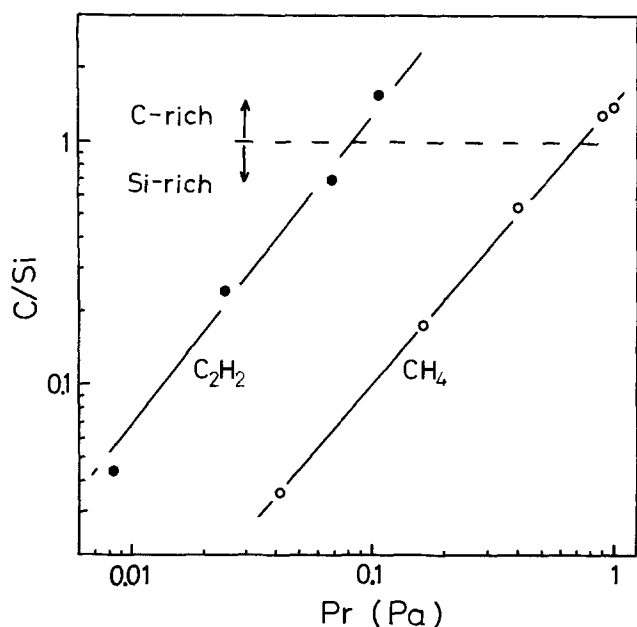


Fig. 2. Plots of C/Si vs. Pr ($\equiv P \times R_0/R$) for $R_0 = 0.5 \mu\text{m/hr}$

rate decreases with increasing partial pressure. The deposition rate for C_2H_2 showed a similar variation to that for CH_4 , although the critical pressure was much lower than for CH_4 being 1.6×10^{-2} Pa.

Results and Discussion

Auger electron spectroscopy (AES).—AES measurements were used to examine the chemical composition of the resultant films. A SiC bulk single crystal and the films sputtered from the SiC and Si targets were used for samples in the measurements. The ratio of the 272 eV C line intensity to the 92 eV Si line intensity of the samples, I_C/I_{Si} , was measured for all the samples after removal of surface layers of the samples by means of ion sputter-etching. The chemical composition ratio C/Si was estimated from I_C/I_{Si} assuming that C/Si is proportional to I_C/I_{Si} and C/Si is equal to unity for the bulk single crystal. I_C/I_{Si} and C/Si are listed in Table I for films together with their growth conditions and for the bulk single crystal. It is seen that the ratio C/Si of the films sputtered from the SiC target (samples 1-3) is not significantly affected either by the deposition rate or by the substrate temperature and is slightly larger than unity.

The ratio C/Si of the films sputtered from the Si target varies with the hydrocarbon partial pressure P and the deposition rate R . To examine the variation of C/Si with P and R , C/Si is plotted against Pr , which is defined by the relation

$$Pr \equiv P \times R_0/R$$

Table I. Chemical composition and deposition conditions of sputtered SiC films

Sample No.	Gas	Target material	Reactive gas pressure (Pa)	Deposition rate ($\mu\text{m/hr}$)	Rf power density (W/cm^2)	Substrate temp. ($^\circ\text{C}$)	Thickness (μm)	I_C/I_{Si}	C/Si
1	Ar	SiC	—	0.10	0.8	620	0.4	0.44	1.1
2	Ar	SiC	—	0.30	2.0	740	1.5	0.45	1.2
3	Ar	SiC	—	0.16	1.1	200	0.8	0.44	1.1
4	Ar + CH_4	Si	4.1×10^{-2}	0.52	3.0	600	1.6	0.014	0.036
5	Ar + CH_4	Si	1.7×10^{-1}	0.53	3.0	600	1.6	0.068	0.17
6	Ar + CH_4	Si	3.5×10^{-1}	0.43	3.1	600	1.4	0.21	0.54
7	Ar + CH_4	Si	3.5×10^{-1}	0.19	1.4	600	1.0	0.50	1.3
8	Ar + CH_4	Si	1.3	0.67	9.0	600	2.0	0.54	1.4
9	Ar + C_2H_2	Si	9.2×10^{-2}	0.57	3.0	600	1.7	0.017	0.044
10	Ar + C_2H_2	Si	2.0×10^{-2}	0.41	3.0	600	1.3	0.10	0.26
11	Ar + C_2H_2	Si	3.6×10^{-2}	0.27	3.0	600	0.8	0.27	0.69
12	Ar + C_2H_2	Si	5.9×10^{-2}	0.28	4.0	600	0.9	0.60	1.5
13		Bulk single crystal SiC						0.39	1.0

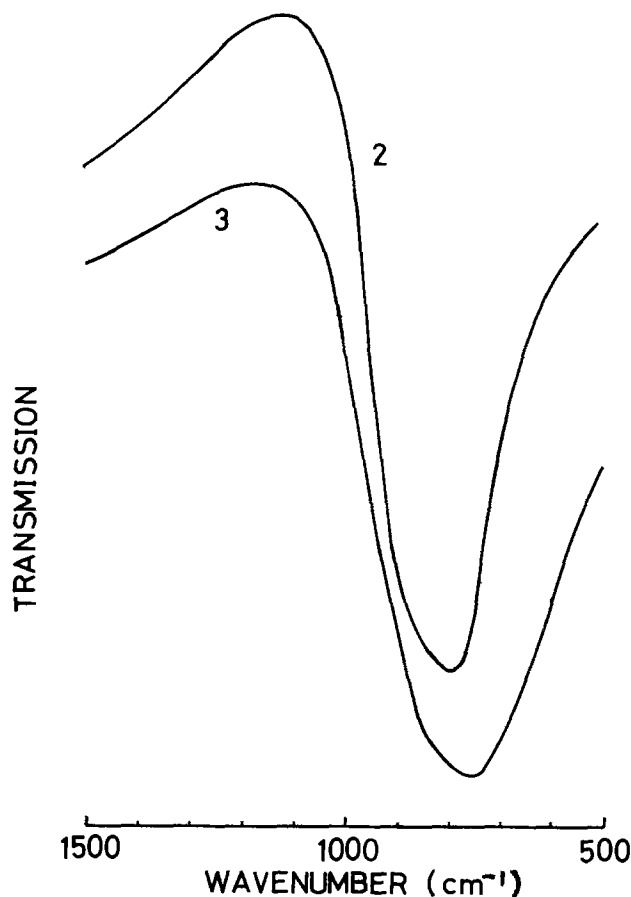


Fig. 3. Infrared transmission spectra of SiC films sputtered from a SiC target at 740°C (2) and at 200°C (3). Numbers in the figure indicate the sample number in Table I.

where R_0 is a normalization factor for the deposition rate. Figure 2 shows typical plots of C/Si vs. Pr for R_0 of $0.5 \mu\text{m/hr}$. It is found from the figure that stoichiometric SiC films are obtained at 8.0×10^{-2} Pa for C_2H_2 and 7.3×10^{-1} Pa for CH_4 when the films are prepared at a deposition rate of $0.5 \mu\text{m/hr}$. The straight lines with slope of unity imply that the ratio of the arrival rate of hydrocarbon molecules ($\propto P$) to the arrival rate of Si atoms ($\propto R$) at the substrate is proportional to C/Si . The fact that the CH_4 partial pressure to obtain stoichiometric SiC films is higher than the C_2H_2 partial pressure suggests that C_2H_2 has higher chemical reactivity with Si than does CH_4 .

Infrared transmission spectra.—Infrared transmission measurements were used to examine the formation of SiC. The films listed in Table I were used for the samples in the measurements. The spectra of the

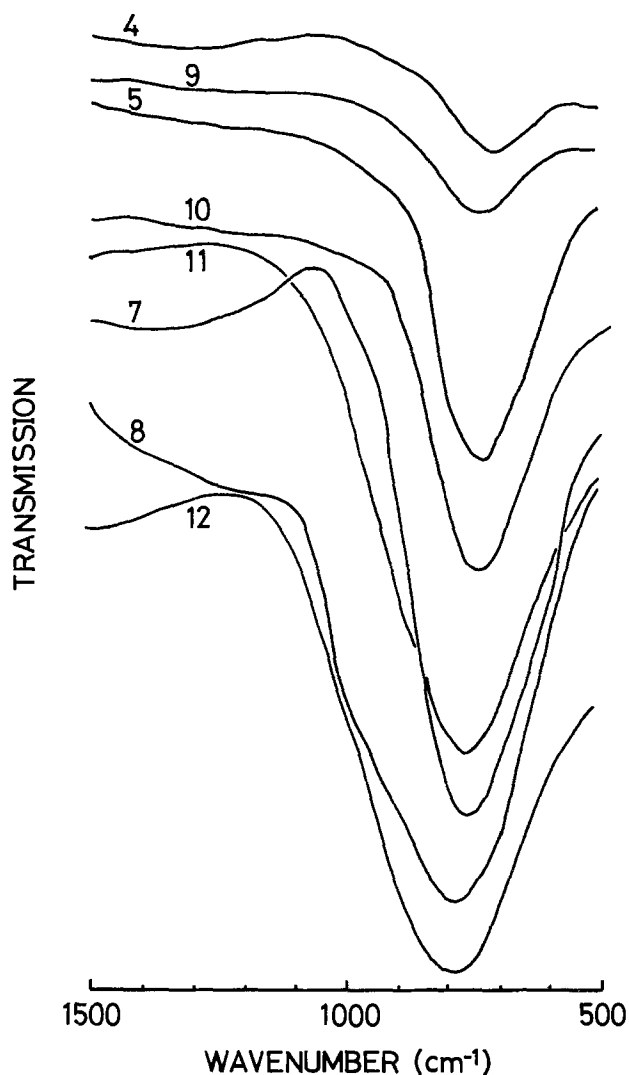


Fig. 4. Infrared transmission spectra of SiC films sputtered from a Si target at various partial pressures of CH_4 and C_2H_2 . Numbers in the figure indicate the sample number in Table I.

films sputtered from the SiC target (samples 2 and 3) at different deposition temperature are shown in Fig. 3. A large absorption band at about 800 cm^{-1} is due to the fundamental lattice vibration of SiC (7). The absorption band of sample 3 is broader than that of sample 2 and is shifted to lower frequency, i.e., about 770 cm^{-1} . This is due to the amorphous nature of the films prepared at low temperature (8).

The spectra of the films sputtered from the Si target in various partial pressures of CH_4 (samples 4, 5, 7, 8) and C_2H_2 (samples 9-12) are shown in Fig. 4. The position and the strength of the absorption band vary with the hydrocarbon partial pressure. The position shifts to higher frequency with increase of the ratio, C/Si. This may be caused by the difference in specific gravity between C-rich films and Si-rich films. The strength of the absorption band increases with the number of Si-C bonds. The largest absorption band at the same frequency as sample 2 is obtained in samples 7 and 11 for CH_4 and C_2H_2 , respectively. This fact agrees with the results obtained from the AES measurements, i.e., these samples are most stoichiometric among the samples listed in Table I.

Scanning electron microscopy (SEM) and reflection electron diffraction (RED).—SEM images and RED patterns of films of $0.6\text{ }\mu\text{m}$ thickness sputtered from the SiC target at a deposition rate of $0.3\text{ }\mu\text{m/hr}$ for various substrate temperatures are shown in Fig. 5. Epitaxial β -SiC films on Si (111) substrates were

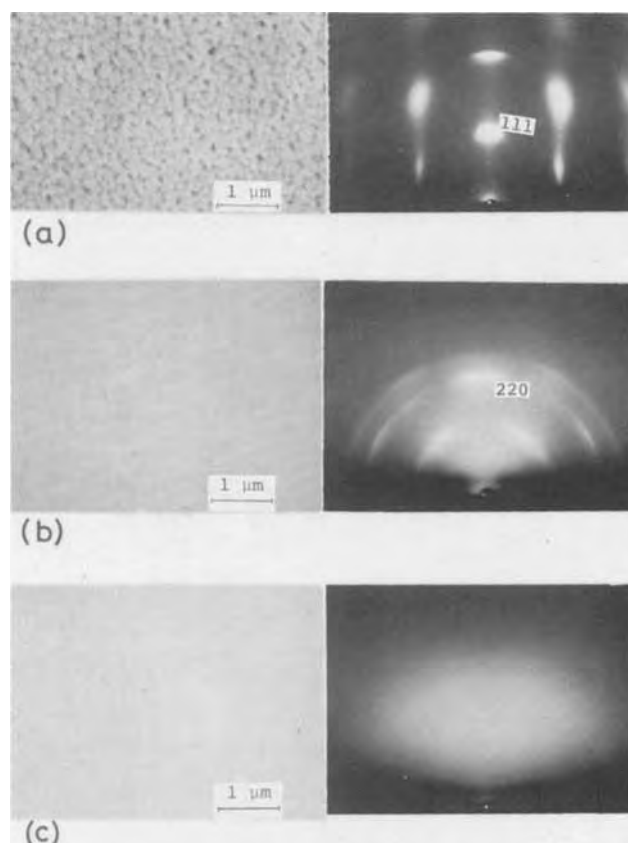
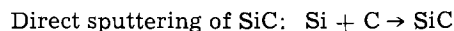


Fig. 5. SEM images and RED patterns of SiC films of $0.3\text{ }\mu\text{m}$ thickness on Si (111) substrates. The films were sputtered from a SiC target at a deposition rate of $0.3\text{ }\mu\text{m/hr}$ for substrate temperatures: (a) 740°C , (b) 600°C , (c) 200°C .

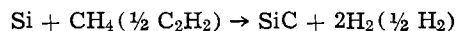
obtained at a substrate temperature of 740°C as shown in Fig. 5(a). The epitaxial relation is $\text{SiC}(111) // \text{Si}(111)$. Polycrystalline β -SiC films with the (220) plane parallel to the substrate surface were obtained for substrate temperatures higher than 550°C . A typical result is shown in Fig. 5(b). Amorphous SiC films with a specular surface were obtained below 500°C as shown in Fig. 5(c).

When SiC films were prepared by reactive sputtering from the Si target, the films showed halo RED patterns and specular surfaces even at a high substrate temperature of 650°C . These results indicate that the SiC films sputtered from the SiC target crystallize more easily than those sputtered from the Si target.

In sputtering processes, sputtered species are ejected from targets as atomic particles. The SiC films may be synthesized according to the following reactions



Reactive sputtering of Si:



The Si atoms react with the C atoms or the hydrocarbon molecules primarily on the substrate surface, since collisions between Si atoms and C atoms or hydrocarbon molecules in the space between target and substrate is less probable. Silicon atoms may react more easily with C atoms than hydrocarbon molecules because the C atoms sputtered from the SiC target have higher chemical activity and kinetic energy in comparison with the hydrocarbon molecules. In reactive sputtering, the higher chemical activity of C_2H_2 compared with CH_4 may not be inconsistent with the fact that CH_4 is more stable than C_2H_2 since CH_4

shows a negative Gibbs free energy (-51 kJ mole^{-1}) and C_2H_2 shows a positive one (209 kJ mole^{-1}).

Conclusions

Stoichiometric SiC films are obtained by reactive sputtering of a Si target under a suitable choice of hydrocarbon pressure and deposition rate, because the chemical composition ratio C/Si is proportional to the ratio of hydrocarbon pressure to deposition rate (P/R).

Although the chemical composition ratio C/Si is slightly larger than unity in the films sputtered from the SiC target, it is little affected either by deposition rate or by substrate temperature.

The crystallization temperature during film deposition differs for the target materials used. The SiC target gives lower crystallization temperature than the Si target: 550°C for the SiC target and above 650°C for the Si target.

Acknowledgment

The authors wish to thank Mr. K. Kusao for his help in the AES analysis.

Manuscript submitted April 2, 1979; revised manuscript received July 6, 1979.

Any discussion of this paper will appear in a Discussion Section to be published in the December 1980 JOURNAL. All discussions for the December 1980 Discussion Section should be submitted by Aug. 1, 1980.

Publication costs of this article were assisted by Matsushita Electric Industrial Company, Limited.

REFERENCES

1. K. Wasa, T. Tohda, M. Kasahara, and S. Hayakawa, *Rev. Sci. Instrum.*, To be published.
2. A. J. Learn and K. E. Haq, *Appl. Phys. Lett.*, **17**, 26 (1970).
3. K. E. Haq, *ibid.*, **26**, 255 (1974).
4. Y. Murayama and T. Takao, *Thin Solid Films*, **40**, 309 (1977).
5. K. Wasa, T. Nagai, and S. Hayakawa, *ibid.*, **31**, 235 (1976).
6. S. Nishino, H. Matsunami, M. Odaka, and T. Tanaka, *ibid.*, **40**, L27 (1977).
7. W. G. Spitzer, D. A. Kleinman, and C. J. Frosch, *Phys. Rev.*, **113**, 133 (1959).
8. B. Abeles and J. I. Gittleman, *Appl. Opt.*, **15**, 2328 (1976).

Electrode Kinetics of Copper Deposition from Copper Cyanide Solution

R. E. Sinitski, V. Srinivasan,¹ and R. Haynes*

Western Electric, Princeton, New Jersey 08540

ABSTRACT

Distinct limiting current densities can be observed in dilute acid copper cyanide solutions on both platinum and copper electrodes. The Levich equation is obeyed. Diffusion coefficients range (calculated from plots of limiting current densities vs. concentration and disk rotational speed) from 0.79 to $0.85 \times 10^{-6} \text{ cm}^2/\text{sec}$. These apparent diffusion coefficients are considered the lower limit due to an uncorrected concentration term. Tafel slopes range from 0.130 to 0.165V with a mean value of $0.144 \pm 0.016\text{V}$ and $\alpha = 0.40 \pm 0.03$. The exchange current density is $8 \pm 1 \times 10^{-5} \text{ A/cm}^2$. The copper deposition reaction is first order with respect to the copper-containing species. The decomposition of the copper-containing species responsible for the limiting current density is first order with a rate constant equal to $3.35 \pm 0.03 \times 10^{-6} \text{ sec}^{-1}$.

Fundamental electrokinetic studies of copper deposition from electrolytes containing cyanide are few in numbers (1-3). There is difficulty in identifying the discharging species among many possible complexes, such as $\text{Cu}(\text{CN})_2^-$, $\text{Cu}(\text{CN})_3^{2-}$, and assuring a unique separation between the hydrogen evolution reaction and copper deposition. No measurement of the diffusion coefficients of any of the copper cyanide complexes exists to date. Such a lack of emphasis is surprising since the copper cyanide plating system is of industrial importance and the copper cyanide complex may be significant in the electroless plating systems. The purpose of this study was to investigate electrode kinetics of copper deposition and to determine decomposition rates of the copper complex in acid copper cyanide solutions. Potentiodynamic sweeps were obtained using a Beckman Electroscan 30. An E.S.B. Model XLR-3A rotating assembly was used with a platinum rotating disk electrode. An electrolytic cell with a circular platinum mesh anode 3 cm in diam was used. The area of the platinum cathode was 0.3 cm^2 .

The stock solution was made of the following components at 160°F

CuCN	82.17 g/liter
NaCN	101.1 g/liter
KOH	32.8 g/liter

All test solutions were made by diluting with water, adding 7.8 g/liter of KCl and adjusting the pH by adding dilute nitric acid. pH valves were determined within ± 0.05 pH units.

The platinum rotating disk electrode was prepared by immersion in concentrated nitric acid for 5 min after each experiment to remove the deposited copper and activate the platinum.

The i - V curves were determined at a sweep rate of 50 mV/sec starting at the most anodic currents and sweeping cathodically.

Results and Discussion

Steady-state distinct limiting current densities are not observed in alkaline copper cyanide solutions. Figure 1 shows the effects on the current potential curves when the pH is changed from alkaline to acid. Changing the pH from 11.35 to 9.05 causes the current-voltage curve to shift uniformly to more anodic poten-

* Electrochemical Society Active Member.

¹ Present address: Amp, Incorporated, Colonial Park, Pennsylvania 17109.

Key words: copper plating, copper cyanide, electrode kinetics, copper cyanide decomposition.

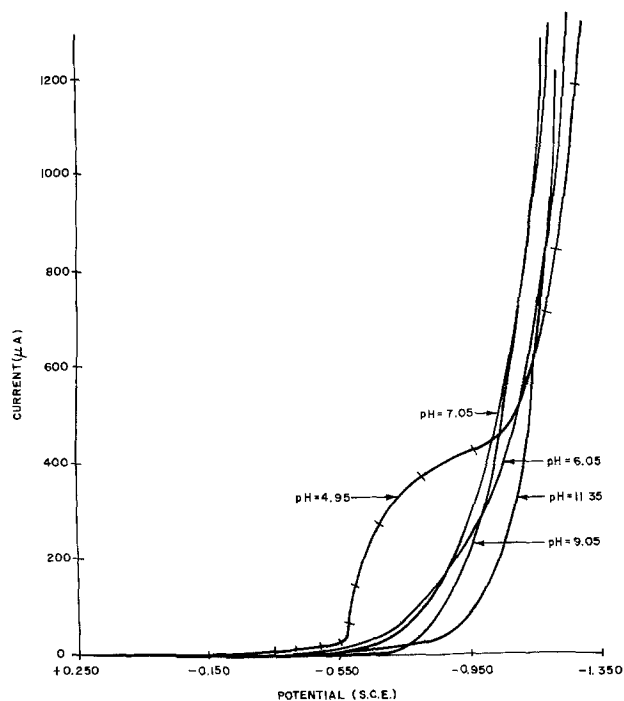


Fig. 1. Potential sweep: pH variation

tials. On decreasing the pH further the lower current densities begin to increase rapidly at a given potential. At the higher current densities the curve is shifted to more cathodic potentials. By decreasing the pH to 4.95 a distinct limiting current density is observed. The initial decrease in pH from 11.35 to 9.05 causes the free cyanide ion concentration to decrease from approximately 98% to 30% through an increase in the ion pair formation producing hydrocyanic acid (4). Further decreases in pH to 7.05 cause the fraction of ion pairs to approach 99%. Decreasing the cyanide ion concentration causes the concentration of the species $\text{Cu}(\text{CN})_3^{-2}$ to increase at the expense of $\text{Cu}(\text{CN})_4^{-3}$. The equilibrium potential for $\text{Cu}(\text{CN})_4^{-3}$ is -0.75V and $\text{Cu}(\text{CN})_3^{-2}$ is -0.40V (NHE). Decreasing the pH to 4.95 shifts both the concentration of copper to a higher fraction of $\text{Cu}(\text{CN})_3^{-2}$ and the equilibrium potential closer to -0.40V . At this lower pH the deposition can occur at a higher rate from the $\text{Cu}(\text{CN})_3^{-2}$ species and thus be separable from the hydrogen evolution reaction. At pHs less than about 3.0 CuCN begins to precipitate. Figure 2 shows current-voltage curve where a distinct limiting current density is observed. The residual current-voltage curve for the supporting electrolyte is also included in Fig. 2. Potentiodynamic sweeps starting at $+0.250$ and stopping at -1.350 were repeated on the same electrode three times. The results are shown in Fig. 3. The magnitude of the limiting current density is equal for the three repetitive sweeps. The peak at -0.560V that appears on the second sweep and whose amplitude increases on the third sweep is due to reduction of the copper oxide formed at potentials anodic to -0.150 . The limiting current density is diffusion-limited with respect to diffusion of ions to the electrodes from the solution. The limiting current occurs on platinum, copper, and copper electrodes partially covered with copper oxides. Figures 4-7 give data showing adherence to the Levich equation where either the concentration of the discharging species is varied or the rotational speed of the electrode is changed.

The plot of limiting current density vs. concentration of discharging species is linear up to 6×10^{-3} M/liter (see Fig. 7). The limiting current density plateau above this concentration at this rotational speed becomes of questionable usage for analytical purposes. The plot of limiting current density vs. the square root

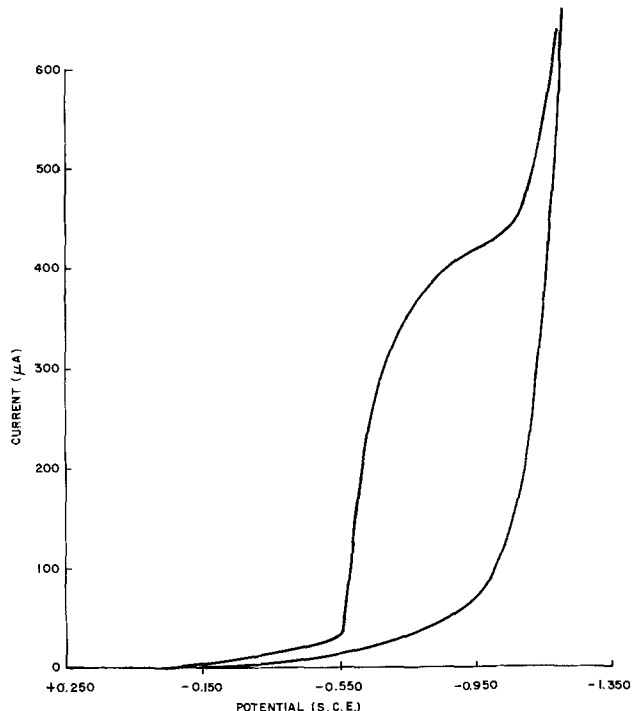


Fig. 2. Potential sweep: comparison with residual current

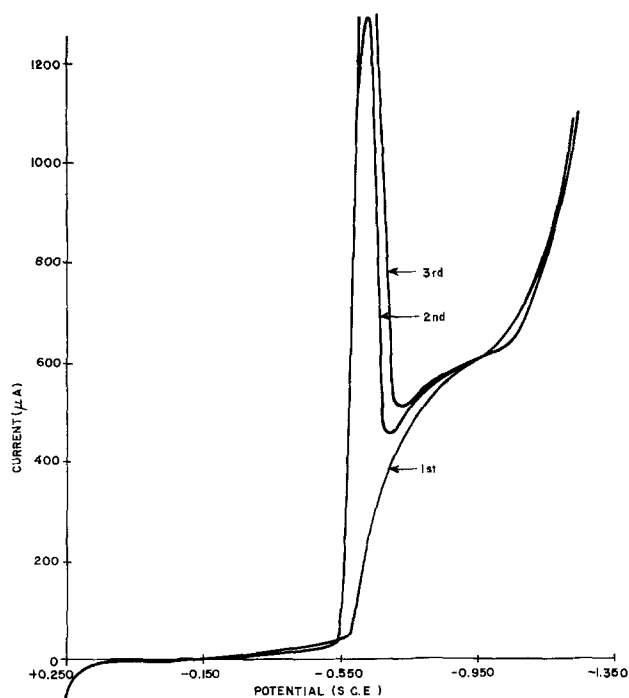


Fig. 3. Potential sweep: copper and platinum

of the rotational speed, given in Fig. 5 is valid up to 20 rps which is the limit of this study. Apparent diffusion coefficients calculated from the plots i_L vs. concentration are $0.85 \pm 0.09 \times 10^{-6}$ cm^2/sec (95% confidence limits). Apparent diffusion coefficients from plots of i_L vs. $w^{1/2}$ are $0.79 \pm 0.08 \times 10^{-6}$ cm^2/sec (95% confidence limits). The discharging species in these systems (1) is usually considered to be $\text{Cu}(\text{CN})_2^-$. Diffusion coefficients for $\text{Au}(\text{CN})_2^-$ in similar systems (5) range from 1.63×10^{-5} cm^2/sec to 1.68×10^{-5} cm^2/sec . These diffusion coefficients are calculated on the basis of the total copper metal content and are to be considered a lower limit. To calculate Tafel slopes current-voltage curves have been obtained over a wide range of concentrations of cop-

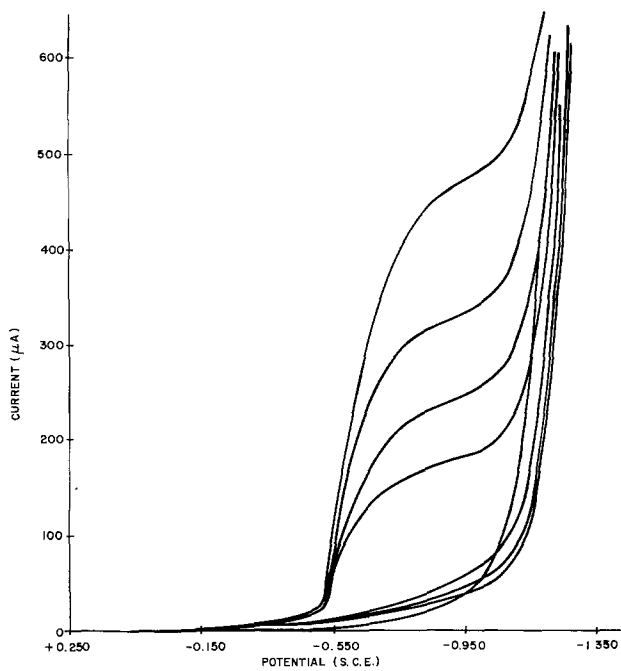


Fig. 4. Potential sweep: disk rotational speed

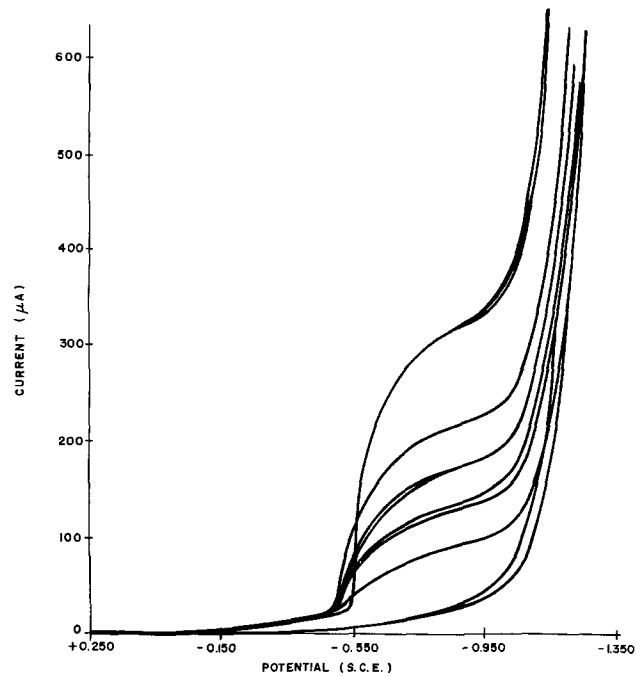


Fig. 6. Potential sweep: concentration variation

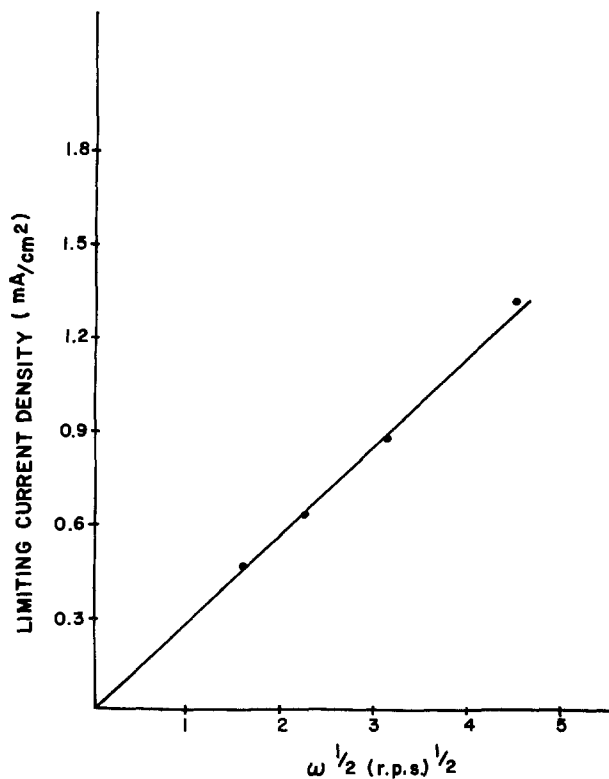


Fig. 5. Limiting current density vs. the square root of disk rotational speed.

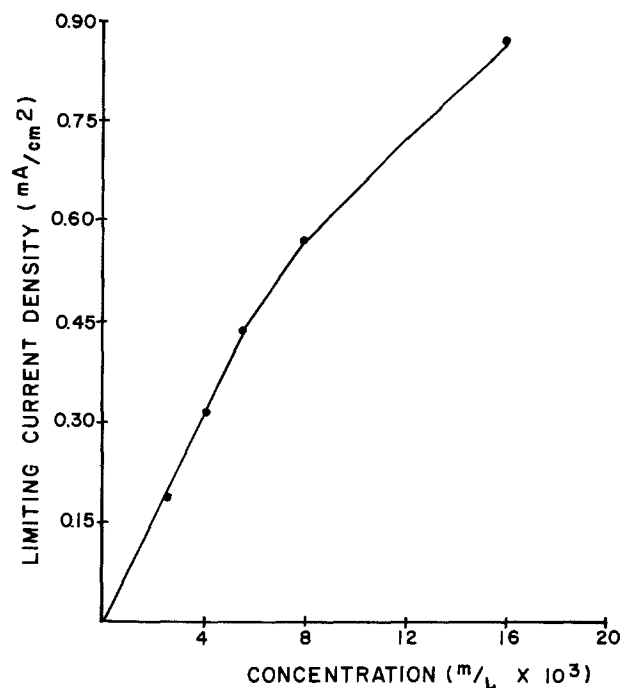


Fig. 7. Limiting current density vs. concentration

per cyanide with additional free cyanide yielding a constant ratio of copper cyanide to free cyanide and several diffusion layer thicknesses. Figure 8 shows a Tafel plot corrected for the effects of mass transfer for several different diffusion layer thicknesses corresponding to rotational speeds varying from 2.5 to 20 rps. Figure 9 gives data for Tafel plots corrected for effects of mass transfer for several concentrations of copper cyanide with added free cyanide. The ratio of copper cyanide to free cyanide is kept constant. Tafel slopes calculated from data in Fig. 8 and 9 yield an average value of the Tafel slope equal to 0.144V with a sample standard deviation of 0.016V. The trans-

fer coefficient is equal to 0.40 ± 0.03 for 95% confidence limits. This value of the transfer coefficient is essentially equal to that reported in the literature $\alpha = 0.38 \pm 0.04$ (1).

An approximate exchange current density can be obtained from the linear polarization curve. For a concentration of copper cyanide equal to 8×10^{-3} M/liter (with $\text{CuCN}/\text{CN} = 2.5$) $i_0 = 8 \pm 1 \times 10^{-5}$ A/cm². The equilibrium potential measured for the solution of copper cyanide concentration equal to 8×10^{-3} m/liter (with $\text{CuCN}/\text{CN} = 2.5$) at pH = 4.75 is equal to -0.430V (SCE). The order of the deposition reaction with respect to the copper-containing species is obtained (6) from the transfer coefficient and the slope of the log-log plot of the current-copper concentration at a constant potential. The order of the deposition reaction with respect to copper is 1.12 ± 0.05 .

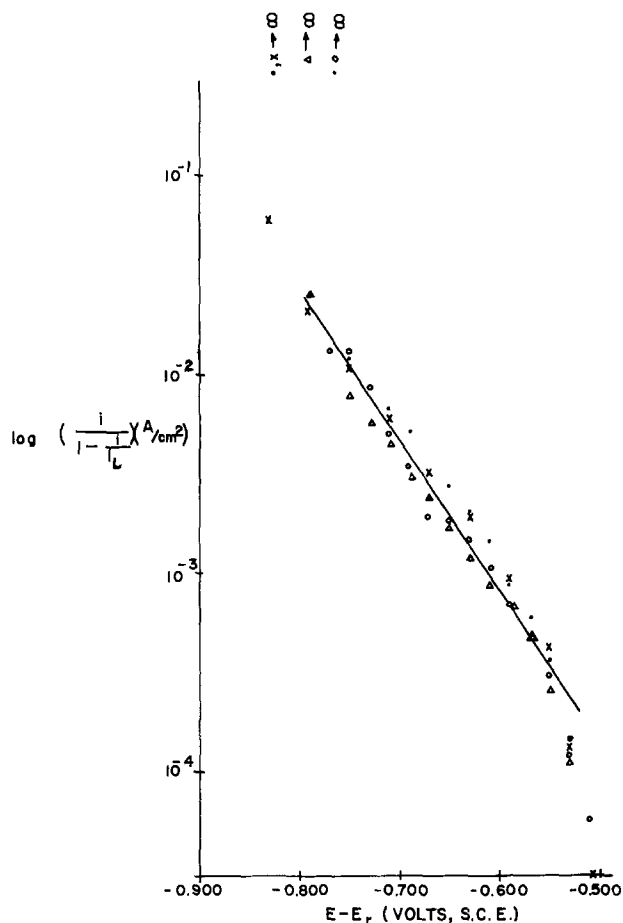


Fig. 8. $E - E_r$ vs. $\log (i/1 - i/i_L)$ for rotational speed dependence; symbol \times \cdot Δ \circ

rps	20	10	5	2.5
symbol	\times	\cdot	Δ	\circ

Dilute solutions of copper cyanide at pH equal to 4.75 decompose on standing. Figure 10 shows the current-potential curves of a solution containing 8×10^{-3} M/liter (with $\text{CuCN}/\text{CN} = 2.5$). The decomposition of the copper cyanide complex follows first order kinetics with a rate constant equal to $3.35 \pm 0.03 \times 10^{-6} \text{ sec}^{-1}$. During the period that decomposition takes place an increase in the turbidity takes place with an increase in hydrocyanic acid above the solution.

Conclusions

1. A distinct limiting current density can be observed in dilute acid copper cyanide solutions on both platinum and copper electrodes. The Levich equation is obeyed for copper deposition from dilute acid copper cyanide solutions. The limiting current density is proportional to the concentration and to the square root of the rotational speed of the disk electrode.

2. Electrode kinetic parameters have been determined for copper deposition from dilute acid copper cyanide solutions. Apparent diffusion coefficients considered to be a lower limit range from $0.79 \times 10^{-6} \text{ cm}^2/\text{sec}$ to $0.85 \times 10^{-6} \text{ cm}^2/\text{sec}$. Tafel slopes range from 0.130 to 0.165V with a mean value of $0.144 \pm 0.016\text{V}$ and $\alpha = 0.40 \pm 0.03$. The copper deposition reaction is first order with respect to the copper-containing species. The exchange current density determined for one concentration is $8 \pm 1 \times 10^{-5} \text{ A/cm}^2$ and the equilibrium potential for this condition is -0.430 (SCE) .

3. The decomposition of the copper-containing species responsible for the limiting current density is first order with a rate constant of $k = 3.35 \pm 0.03 \times 10^{-6} \text{ sec}^{-1}$.

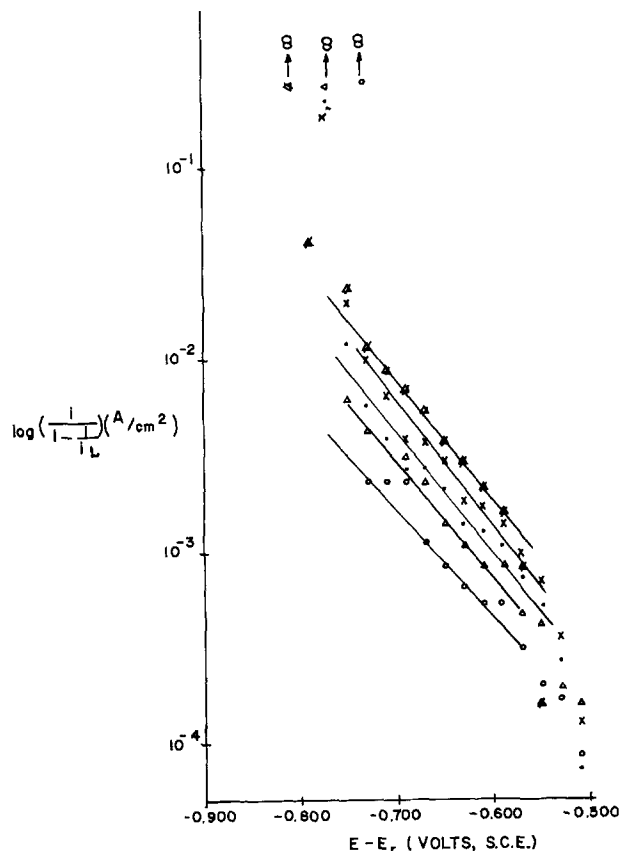


Fig. 9. $E - E_r$ vs. $\log (i/1 - i/i_L)$ for concentration dependence

concentration $\times 10^3 \text{ m/g}$	16	8	5.6	4	2.4
symbol	Δ	\times	\cdot	Δ	\circ

Manuscript submitted Sept. 25, 1978; revised manuscript received June 7, 1979. This was Paper 290 presented at the Atlanta, Georgia, Meeting of the Society, Oct. 9-14, 1977.

Any discussion of this paper will appear in a Discussion Section to be published in the December 1980

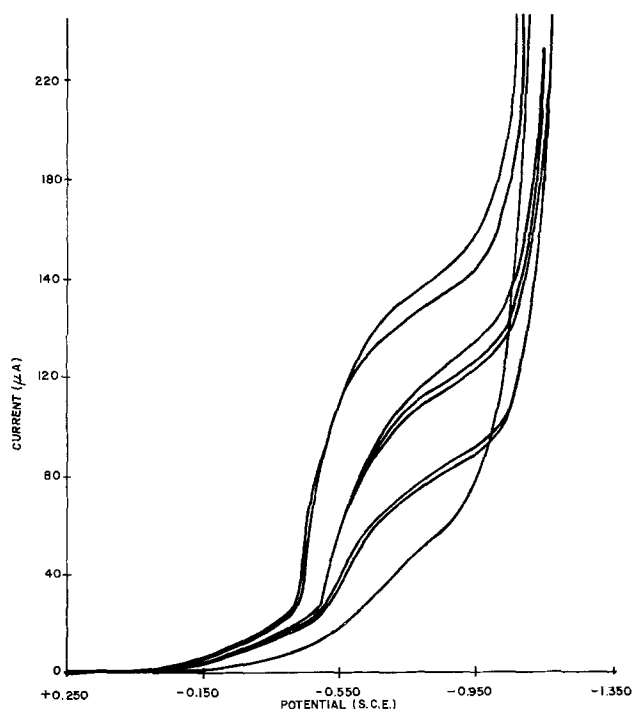


Fig. 10. Time dependence: potential sweep vs. concentration

JOURNAL. All discussions for the December 1980 Discussion Section should be submitted by Aug. 1, 1980.

Publication costs of this article were assisted by Western Electric.

REFERENCES

1. M. Costa and J. Rech, *C.N.R.S.*, **64**, 285 (1963).
2. G. G. Simulin, S. B. Lebed, V. D. Domashich, and V. V. Kosenko, *Electrokhimiya*, **8**, 816 (1972).
3. V. Bertocci and D. R. Turner, in "Encyclopedia of Electrochemistry," Vol. 2, A. J. Bard, Editor, p. 383, Marcel Dekker, Inc., New York (1974).
4. Robert P. Frankenthal, in "Handbook of Analytical Chemistry," 1st ed., L. Meites, Editor, p. 1-15, McGraw-Hill Book Co., New York (1963).
5. H. Y. Cheh and R. Sard, *This Journal*, **118**, 1737 (1971).
6. K. J. Vetter, "Electrochemical Kinetics," p. 436, Academic Press, New York (1967).

Kinetics of Electroless Copper Plating

III. Mass Transport Effects

Francis M. Donahue*

Department of Chemical Engineering, The University of Michigan, Ann Arbor, Michigan 48109

ABSTRACT

Gas bubble formation and evolution at the plating surface for electroless copper produces a microconvection condition which influences the mass transfer rate. The interfacial concentrations of the reactant species in the absence of forced convection are computed from this model and are found to be dependent on the plating rate and the bulk concentrations, diffusivities, and reaction stoichiometry. Analyses of published rate studies show that the interfacial concentrations of cupric ions were less than the bulk values and that the apparent reaction order based on the interfacial concentration was approximately constant. Two different correlations for superposed micro and macroconvection were found to be indistinguishable and consistent with the microconvection model when applied to published plating rate data at rotating cylinders.

Dumesic, Koutsky, and Chapman (1) have shown that the apparent reaction order of cupric ion in electroless copper plating solutions is dependent upon the rate of mass transport to rotating copper-plated cylinders. Since most technical practice and research studies operate at vertical surfaces in the virtual absence of forced convection, it is prudent to ascertain the nature of the transport process and to obtain a mathematical description of the mass transfer coefficient under these conditions. Further, the mechanism of the electroless copper plating reaction is accessible only if the interfacial concentrations of the species involved can be estimated.

This paper will discuss the nature of the transport process in the absence of forced convection and present the mathematical expressions describing the relationships among experimental conditions and mass transfer coefficients and interfacial concentrations. These results will be used to analyze the data from published kinetic studies. Finally, the effects of forced convection superimposed on the microconvection process will be analyzed.

General Remarks: Mass Transport

The flux of a transporting species, "j", in the absence of migration and bulk flow (conditions which prevail for the reactants in electroless copper plating) is

$$N_j = (10^{-3} D_{jm}/\delta) (c_{sj} - c_{bj}) \quad [1a]$$

or

$$N_j = 10^{-3} k_{cj} (c_{sj} - c_{bj}) \quad [1b]$$

where N_j is the flux of the transporting species "j" (mole/cm² sec), D_{jm} is the diffusivity of the species in the solution mixture (cm²/sec), δ is the mass transfer boundary layer thickness (cm) and c_{sj} and c_{bj} are the interfacial and bulk concentrations of the transporting

species, respectively, (M) and k_{cj} is the mass transfer coefficient of the species ($= D_{jm}/\delta$) (cm/sec). The diffusivity is a property of the transporting species-solution system and can be estimated (2-4) or measured. Mass transfer coefficients can be estimated from mass transfer correlations for particular system geometries and flow regimes (5-12). Similarly, boundary layer thicknesses for some system geometries and flow regimes are available (8, 10, 12).

If the flux of the transporting species is known along with its mass transfer coefficient or its diffusivity and boundary layer thickness, the interfacial concentration can be computed from

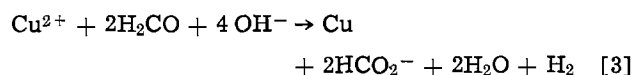
$$c_{sj} = c_{bj} + 10^3 N_j \delta / D_{jm} \quad [2a]$$

or

$$c_{sj} = c_{bj} + 10^3 N_j / k_{cj} \quad [2b]$$

General Remarks: Kinetics of Electroless Copper Plating

The over-all chemical reaction for the process is



The relationships among the fluxes of the transporting reactant species and the measured plating rate based on this equation are

$$N_{\text{Cu}^{2+}} = \frac{N_{\text{H}_2\text{CO}}}{2} = \frac{N_{\text{OH}^-}}{4} = -3.9 \times 10^{-9} \tau_p \quad [4]$$

where τ_p is the plating rate ($\mu\text{m/hr}$). Therefore, the fluxes of the reactant species can be computed from the measured plating rate(s) and used in Eq. [2a] or [2b] to estimate the interfacial concentrations.

Mass Transport in the Absence of Forced Convection

The evolution of hydrogen gas at the reaction surface (see Eq. [3]) provides a unique mass transfer

* Electrochemical Society Active Member.

Key words: electroless copper plating, gas evolution, kinetics, macroconvection, mass transport, microconvection.

condition in the absence of forced convection. Mass transfer coefficients and boundary layer thicknesses have been shown to be dependent on the volumetric flux of evolved gas (13-21). Although the bulk of the data presented in these publications is in the range of gas volumetric fluxes (current densities) of interest in industrial electrolytic cells (*i.e.*, one or more orders of magnitude greater than those for electroless copper plating), the lower end of the data of Ibl and Venczel (14, 16) is in the region of electroless copper plating. Therefore, a correlation obtained from their data for the diffusion boundary layer thickness will be used in this analysis, *i.e.*

$$\delta = 1.6 \times 10^{-3} v^{-0.53} \quad [5]$$

where v is the volumetric flux of hydrogen gas ($\text{cm}^3/\text{cm}^2 \text{ min}$). From Eq. [3] the gas volumetric flux is related to the plating rate by

$$v = 5.2 \times 10^{-3} r_p \quad [6]$$

Inserting Eq. [6] in [5]

$$\delta = 2.6 \times 10^{-2} r_p^{-0.53} \quad [7]$$

The interfacial concentrations of the respective reactant species can be estimated by inserting Eq. [7] and [4] in [2a] using estimates of the species diffusivities (*i.e.*, $\text{Cu}^{2+} = 9.3 \times 10^{-6} \text{ cm}^2/\text{sec}$, $\text{OH}^- = 6.8 \times 10^{-5} \text{ cm}^2/\text{sec}$ and $\text{H}_2\text{CO} = 10^{-5} \text{ cm}^2/\text{sec}$)

$$[\text{Cu}^{2+}]_s = [\text{Cu}^{2+}]_b - 1.1 \times 10^{-2} r_p^{0.47} \quad [8]$$

$$[\text{OH}^-]_s = [\text{OH}^-]_b - 5.8 \times 10^{-3} r_p^{0.47} \quad [9]$$

$$[\text{H}_2\text{CO}]_s = [\text{H}_2\text{CO}]_b - 2.0 \times 10^{-2} r_p^{0.47} \quad [10]$$

where the terms in brackets represent the concentrations of the species.

Plots of the absolute values of the differences between interfacial and bulk concentrations of the respective species with respect to the plating rate according to Eq. [8]-[10] are shown in Fig. 1. In addition, the plating rate range for published electroless copper plating rate studies (22-30) is shown. Inspection of Fig. 1 and the plating rates and compositions of plating baths found in the literature reveal that the concentration differences for formaldehyde and hydroxyl ion are less than ten percent of the bulk concentrations. Therefore, mass transport of these species cannot be expected to play a significant role in the control of the over-all process, as observed by Dumesic (1). On the other hand, the data indicate that for

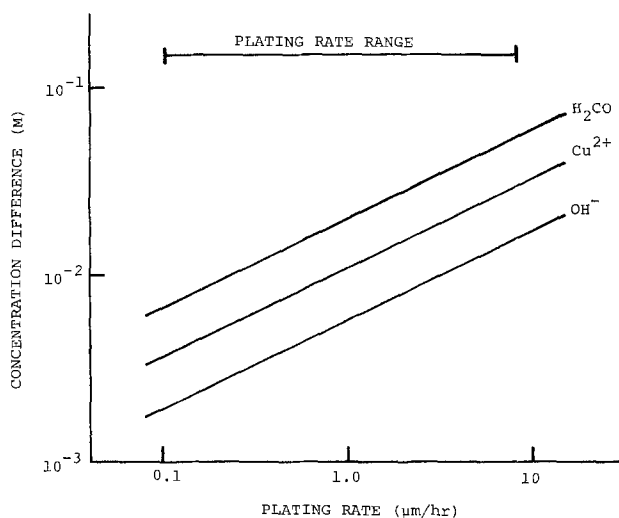


Fig. 1. Differences between bulk and interfacial concentrations for reactant species as functions of the electroless copper plating rate under microconvection conditions. The range of plating rates reported in the literature is shown.

baths which are dilute in cupric ion (*i.e.*, $[\text{Cu}^{2+}]_b < 10^{-2} \text{ M}$) with low plating rates (rates less than $0.5 \mu\text{m/hr}$ are characteristic of these copper-poor baths) the role of mass transport is decisive. Even in the more concentrated baths ($0.01 \text{ M} < [\text{Cu}^{2+}]_b < 0.2 \text{ M}$) the interfacial concentrations are between twenty and eighty percent of the bulk values—a region which is intermediate between mass transport and chemical or electrochemical control of the process.

Figure 2 shows plots of the plating rates as a function of bulk and interfacial cupric ion concentrations for five extensive rate studies (1, 22, 25, 27, 28). The lines through the data points (with the exception of the curved portion for the bulk concentration data of Molenaar (27)) are least squares fit of the respective data. Where data points are not shown for interfacial concentrations (open symbols), the estimated concentration differences were negative, zero, or smaller than the estimates of the bulk concentrations.¹

¹ With the exceptions of Ref. (25) and (28), the data had to be estimated from published graphs.

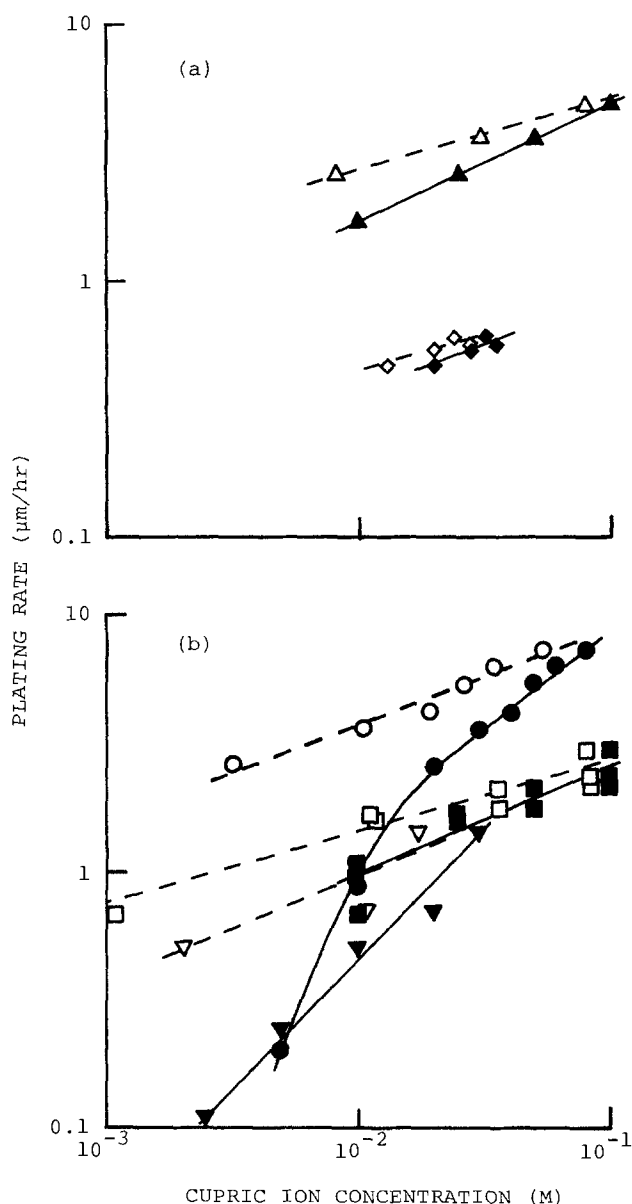


Fig. 2. Electroless copper plating rates as functions of cupric ion concentration. Filled symbols are for bulk concentrations; open symbols, interfacial concentrations. (a) Rochelle salt as complexing agent: diamonds, Ref. (22); triangles, Ref. (25). (b) EDTA as complexing agent: inverted triangles, Ref. (1); circles, Ref. (27); squares, Ref. (28).

Table I. Apparent reaction orders of cupric ion in electroless copper plating solutions

Reference No.	Basis concentration	
	Bulk	Interfacial
(22)*	0.36	0.28
(23)	0.6	—
(25)	0.47	0.27
(26)	0.37	—
(1)**	1.0	0.43
(27)	0.78	0.37
(28)	0.43	0.27

* Partial analysis of Goldie's data for "strong" solutions by the author.

** "Final" deposition rate at 0 rpm.

Table I shows the apparent reaction orders for cupric ion in electroless copper plating solutions. When the bulk concentration is used as the basis for the reaction order computation, the reaction orders exhibit a range from 0.36 to 1.0. On the other hand, when the interfacial concentration is used, the range is substantially diminished and, considering that the interfacial concentrations are only estimates and the data are from four different laboratories, the agreement is good. This agreement for the cupric ion reaction order, after allowing for mass transport effects, strongly suggests a mechanistic role for cupric ion which is independent of the complexing agent.

One can intuit the effect of mass transport on the empirical rate law (25) by noting that the higher the "bulk" reaction order, the greater is the "correction" when mass transport is taken into account (see Table I). Thus, the data of Dumesic (1) and Molenaar (27) were taken under conditions which were substantially influenced by mass transport while Goldie (22) and El-Raghy (26) evidently were operating in a region where mass transfer effects were minimal.

According to the mixed potential theory of electroless copper plating (31), the limiting value² of the apparent reaction order for cupric ion is 0.26. Three of the "interfacial" reaction orders given in Table I are approximately equal to this value.

Traditionally, when forced convection is absent from a system, it is prudent to evaluate the possible role of natural convection as the mode of mass transport (9). To this end, mass transfer coefficients for cupric ion due to natural convection were estimated for the data of Wong and Bhalla (28). In all cases, the mass transfer coefficients were smaller than those estimated for gas evolution (see below). Therefore, it can be concluded that the mode of mass transport in electroless copper plating baths at vertical surfaces is that due to microconvection (gas bubble formation and evolution).

Mass Transport in the Presence of Forced Convection

Vogt (20) has proposed a method of estimating the mass transfer coefficient in the presence of superposed microconvection (gas bubble formation and evolution at low gassing rates) and macroconvection (forced convection or convection induced by high gassing rates). His correlation can be written

$$k_c = (k_{cg}^2 + k_{cf}^2)^{0.5} \quad [11]$$

where k_c is the "net" mass transfer coefficient, k_{cg} is the microconvection coefficient, and k_{cf} is the macroconvection coefficient. Beck (13) has suggested a linear combination, i.e.

$$k_c = k_{cg} + k_{cf} \quad [12]$$

for the same situation.

² This value is based on Paunovic's values of Tafel slopes (32) corrected for temperature, a reaction order of one for cupric ion in the cathodic partial process and no interaction by cupric ion in the anodic partial process.

Since electroless copper plating operates at relatively low gassing rates, it can be assumed that the conditions discussed above represent microconvection. Therefore, the microconvection mass transfer coefficient can be computed by substituting (in turn) Eq. [4], [8], [9], and [10] in [1b] and rearranging to obtain equations of the form

$$k_{cgj} = A_j r_p^{0.53} \quad [13]$$

where k_{cgj} is the microconvection coefficient for species "j" and A_j is a constant for each "j". Figure 3 shows the dependence of microconvection mass transfer coefficients on plating rate for the reactant species.

The experiments of Dumesic (1) should provide a means of evaluating the relative merits of the correlations of Beck (13) and Vogt (20) since their experimental conditions with rotating cylinders represent a superposition of hydrodynamic flows. Unfortunately, their estimated mass transfer coefficients are too large due to an error in calculating the values of the Reynolds number. The Reynolds number should have been defined (10, 33)

$$Re = \Omega d^2 / 2\nu = 0.052 \omega d^2 / \nu \quad [14]$$

where Ω is the cylinder angular velocity (rad/sec), d is the cylinder diameter (cm), ν is the kinematic viscosity (cm²/sec), and ω is the cylinder rotation rate (rpm). Using their values of physicochemical properties and the correct form of the Reynolds number, the computed values of the macroconvection mass transfer coefficients for cupric ion, k_{cf} , were 6.2×10^{-4} cm/sec at 150 rpm, 1.6×10^{-3} cm/sec at 600 rpm, and 2.5×10^{-3} cm/sec at 1100 rpm. Table II shows the computed "net" mass transfer coefficients for cupric ion, k_c , based on the respective correlations. For Vogt's correlation (20), the coupling of the flows produces a moderate enhancement of the mass transfer rate at the lowest rotation speed while at the other rotation speeds macroconvection predominates. The correlation of Beck (13), on the other hand, predicts enhancement due to the superposed flows for all experimental conditions.

The interfacial concentrations of cupric ion can be computed from (inserting Eq. [4] in [2b])

$$[Cu^{2+}]_s = [Cu^{2+}]_b - 3.9 \times 10^{-6} r_p / k_c \quad [15]$$

Figure 4 represents the computed cupric ion interfacial concentrations for all of the data given in Dumesic Fig. 8. The data for zero rpm were computed from Eq. [8] while the rotating cylinder data were computed from Eq. [15] using the "net" mass transfer coefficients from Table II. If the reaction mechanism does not change with rotation speed and cupric ion

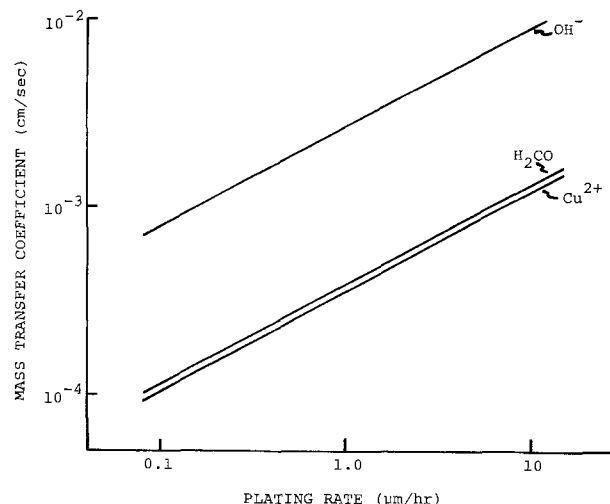


Fig. 3. Mass transfer coefficients for reactant species as functions of electroless copper plating rate under microconvection conditions.

Table II. Computed values of "net" mass transfer coefficients using data of Dumesic and Co-workers (1)

Rotation speed (rpm)	[Cu ²⁺] _b × 10 ² (M)	r _p (μm/hr)	k _{cg} × 10 ^{4*} (cm/sec)	k _c × 10 ^{4**} (cm/sec)	k _c × 10 ^{4***} (cm/sec)
150	0.25	0.27	1.8	6.5	8.0
150	0.5	0.47	2.4	6.6	8.6
150	1.0	0.81	3.2	7.0	9.4
150	2.0	1.2	3.9	7.3	10.1
150	3.0	1.6	4.6	7.7	10.8
600	0.25	0.47	2.4	16	18.4
600	0.5	0.57	2.6	16	18.6
600	1.0	0.87	3.2	16	19.2
600	2.0	1.34	4.1	17	20.1
600	3.0	1.75	4.8	17	20.8
1100	0.25	0.74	3.0	25	28.0
1100	0.5	0.94	3.4	25	28.4
1100	1.0	1.08	3.7	25	28.7
1100	2.0	1.41	4.2	25	29.2

* Computed from Eq. [13] (Fig. 3).
 ** Computed from Eq. [11].
 *** Computed from Eq. [12].

concentration, the data should fall on a single line. The "filled" symbols represent computations based on Beck's correlation (13) while the "open" symbols are for the correlation of Vogt (20). The least squares lines for both correlations are virtually indistinguishable with identical correlation coefficients. Therefore, although the correlations give different values of "net" mass transfer coefficients (see Table II), one cannot discriminate between the two on the basis of interfacial concentration computations for this study.

Conclusions

In the absence of forced convection, the mode of mass transport of reactant species in electroless copper plating is microconvection induced by gas bubble formation and evolution from the reaction surface. Equations describing the interfacial concentrations of the reacting species and the microconvection mass transfer coefficients have been developed and have been shown to depend on the plating rate, reaction stoichiometry, and species diffusivity.

The dependence of the plating rate on the interfacial concentration of cupric ion, *i.e.*, the apparent cupric

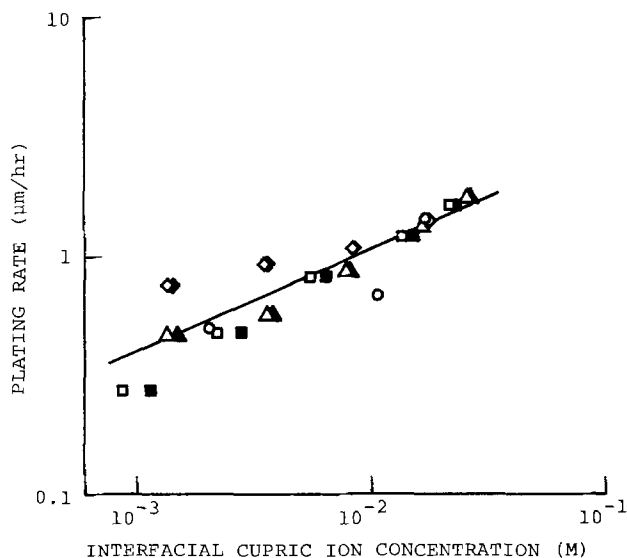


Fig. 4. Electroless copper plating rates at cylindrical electrodes as a function of interfacial concentration computed from Eq. [15] using mass transfer coefficients from Fig. 3 (0 rpm) and Table II for rotating experiments. Circles, 0 rpm; squares, 150 rpm; triangles, 600 rpm; diamonds, 1100 rpm. Open symbols, Vogt correlation (20); filled symbols, Beck correlation (13).

ion reaction order, has been found to be approximately constant for five electroless plating systems.

The interfacial concentration of cupric ion has been found to be smaller than the bulk concentration for all published electroless plating rate studies where sufficient information has been provided to effect an analysis. At low cupric ion concentrations and low plating rates (in the absence of forced convection) the effect of this concentration difference approaches mass transport control of the process.

No significant difference could be found between two correlations for mass transfer coefficients in superposed micro and macroconvection flows when data for electroless copper plating in a well-defined forced convection system were analyzed. Both correlations gave results which were consistent with the microconvective analysis presented here.

Acknowledgments

This material is based upon work supported by the National Science Foundation under Grant No. ENG 7511869. The author also wishes to express his gratitude to all his co-workers (past and present) who have provided good data and stimulating discussions.

Manuscript submitted June 21, 1979; revised manuscript received Aug. 1, 1979. This was Paper 158 presented at the Pittsburgh, Pennsylvania, Meeting of the Society, Oct. 15-20, 1978.

Any discussion of this paper will appear in a Discussion Section to be published in the December 1980 JOURNAL. All discussions for the December 1980 Discussion Section should be submitted by Aug. 1, 1980.

Publication costs of this article were assisted by The National Science Foundation.

LIST OF SYMBOLS

A_j	coefficient for species "j" (cm/sec (μm/hr) ^{0.53})
c_{bj}	bulk coefficient of species "j" (M)
c_{sj}	interfacial concentration of species "j" (M)
D_{jm}	diffusivity of species "j" in the solution (cm ² /sec)
d	cylinder diameter (cm)
k_c	"net" mass transfer coefficient (cm/sec)
k_{cf}	macroconvection mass transfer coefficient (cm/sec)
k_{cg}	microconvection mass transfer coefficient (cm/sec)
k_{crl}	microconvection mass transfer coefficient for species "j" (cm/sec)
k_{cj}	mass transfer coefficient for species "j" (cm/sec)
N_j	molar flux of species "j" (mole/cm ² sec)
Re	Reynolds number (= $\Omega d^2/2\nu$) (dimensionless)
r_p	plating rate (μm/hr)
v	volumetric flux of gas (cm ³ /cm ² min)
δ	mass transfer boundary layer thickness (cm)
ν	kinematic viscosity of solution (cm ² /sec)
Ω	cylinder angular velocity (rad/sec)
ω	cylinder rotation rate (rpm)
[]	concentration (M)

REFERENCES

- J. Dumesic, J. A. Koutsky, and T. W. Chapman, *This Journal*, **121**, 1504 (1974).
- J. R. Welty, C. E. Wicks, and R. E. Wilson, "Fundamentals of Momentum, Heat and Mass Transfer," pp. 461-465, Wiley, New York (1969).
- C. O. Bennett and J. E. Myers, "Momentum, Heat and Mass Transfer," 2nd ed., pp. 486-487, McGraw-Hill, New York (1974).
- R. E. Treybal, "Mass Transfer Operations," 2nd ed., pp. 29-31, McGraw-Hill, New York (1968).
- J. R. Welty, C. E. Wicks, and R. E. Wilson, "Fundamentals of Momentum, Heat and Mass Transfer," pp. 578-589, Wiley, New York (1969).
- C. O. Bennett and J. E. Myers, "Momentum, Heat and Mass Transfer," 2nd ed., pp. 561-580, McGraw-Hill, New York (1974).
- R. E. Treybal, "Mass Transfer Operations," 2nd ed., p. 63, McGraw-Hill, New York (1968).
- C. W. Tobias, M. Eisenberg, and C. R. Wilke, *This*

- Journal*, **99**, 359c (1952).
9. C. R. Wilke, C. W. Tobias, and M. Eisenberg, *Chem. Eng. Prog.*, **49**, 663 (1953).
 10. M. Eisenberg, C. W. Tobias, and C. R. Wilke, *This Journal*, **101**, 306 (1954).
 11. J. Newman, *Ind. Eng. Chem.*, **60**, 12 (1968).
 12. J. Newman, "Electrochemical Systems," pp. 305-334, Prentice-Hall, Englewood Cliffs, N.J. (1973).
 13. T. R. Beck, *This Journal*, **116**, 1038 (1969).
 14. N. Ibl and J. Venczel, *Metalloberflaeche*, **24**, 365 (1970).
 15. L. J. Janssen and J. G. Hoogland, *Electrochim. Acta*, **15**, 1013 (1970).
 16. N. Ibl, E. Adam, J. Venczel, and E. Schalch, *Chem. Ing. Techn.*, **43**, 202 (1971).
 17. M. G. Fouad and G. H. Sedahmed, *Electrochim. Acta*, **17**, 665 (1972).
 18. L. J. Janssen and J. G. Hoogland, *ibid.*, **18**, 543 (1973).
 19. L. J. Janssen, *ibid.*, **23**, 81 (1978).
 20. H. Vogt, *ibid.*, **23**, 203 (1978).
 21. K. Stephan and H. Vogt, *ibid.*, **24**, 11 (1979).
 22. W. Goldie, *Plating*, **51**, 1069 (1964).
 23. E. I. Saranov, N. K. Bulatov, and S. G. Mokrushin, *Prot. Met. (Engl. Transl.)*, **4**, 142 (1968).
 24. L. N. Schoenberg, *This Journal*, **118**, 1571 (1971).
 25. F. L. Shippey and F. M. Donahue, *Plating*, **60**, 43 (1973).
 26. S. M. El-Raghy and A. A. Abo-Salama, *This Journal*, **126**, 171 (1979).
 27. A. Molenaar, M. F. E. Holdrinet, and L. K. H. van Beek, *Plating*, **61**, 238 (1974).
 28. F. M. Donahue, K. L. M. Wong, and R. V. Bhalla, To be published.
 29. S. Ohno, *Plating*, **58**, 350 (1971).
 30. F. Pearlstein and R. F. Weightman, *ibid.*, **60**, 474 (1973).
 31. F. M. Donahue and F. L. Shippey, *ibid.*, **60**, 135 (1973).
 32. M. Paunovic, *ibid.*, **55**, 1161 (1968).
 33. J. Newman, "Electrochemical Systems," p. 325, Prentice-Hall, Englewood Cliffs, N.J. (1973).

Investigation of Two- and Three-Phase Fields in the Ga-As-Sb System

Michel F. Gratton¹ and John C. Woolley

Physics Department, University of Ottawa, Ottawa, Ontario, Canada K1N 6N5

ABSTRACT

The technique of annealing samples at a temperature at which both liquid and solid phases occur, followed by quenching to freeze-in the solid phase, has been used to investigate equilibrium conditions off the pseudobinary section. It has been found that large three-phase liquid-solid-solid fields occur corresponding to the two-phase solid-solid field of the pseudobinary section. The tie-lines of the various two-phase liquid-solid fields have been determined together with the boundaries of the three-phase fields at various temperatures in the range 600°-730°C. The locus of the cusp in the liquidus sheet corresponding to the liquidus point of the three-phase field has also been found. Finally, the two solid phases of the three-phase fields give the ranges of immiscibility in the pseudobinary section $\text{GaAs}_y\text{Sb}_{1-y}$, and hence the variation of the miscibility gap with temperature has been determined. This gap is found to be very asymmetric even at temperatures a little below the peritectic horizontal, the solubility limits at 700°C being $y = 0.30$ and 0.95 . The results are compared with the predictions of the simple solution model which give reasonable agreement with the liquidus data but poor agreement with the miscibility gap values.

The increased interest in ternary III-V alloys for various technological applications has resulted in considerable work being done on the form of the general ternary diagrams which contain these alloys in a pseudobinary section. Thus, experimental measurements have been made and calculations carried out to determine such quantities as liquidus and solidus isotherms and solidus isoconcentration lines [see, for example, Ref (1)]. The ternary system Ga-As-Sb is more complicated than some of the others because a miscibility gap occurs in the solid solution region of the section GaAs-GaSb and hence there must be three-phase, liquid-solid-solid, fields in the general diagram. Although some data are available concerning the liquidus sheet (2-7), little information has been obtained concerning the behavior of solid phases in the various isothermal sections (4, 7).

Here, experimental measurements have been made to determine as a function of temperature the boundaries of these three-phase fields, the position of tie-lines in the adjacent two-phase, liquid-solid, fields,

and the position of the cusp in the liquidus sheet corresponding to the liquid vertex of the three-phase field. These results give immediately the variation with temperature of the solid-solid miscibility gap in the GaAs-GaSb pseudobinary section. These experimental data have then been compared with the predictions of the simple solution model (1).

Experimental Method and Results

The presence of peritectic form in the pseudobinary section $\text{GaAs}_y\text{Sb}_{1-y}$ (4, 7) indicates that at temperatures below the peritectic horizontal, three-phase (liquid-solid-solid) fields must occur in the general ternary diagram in addition to the two-phase (liquid-solid) fields which terminate on the single-phase solid solution fields in the pseudobinary section. In order to investigate the boundaries of these fields and the tie-lines of the two-phase fields, it is necessary to investigate samples at various compositions well away from the pseudobinary section.

The samples used in the work were prepared from the required weights of GaAs, GaSb, and antimony or gallium as appropriate; this method being convenient and avoiding the necessity of dealing with elemental arsenic. The sample treatment was as de-

¹ Present address: Bell Northern Research Company, Ottawa, Ontario, Canada.

Key words: ternary phase diagram, $\text{GaAs}_y\text{Sb}_{1-y}$ alloys, miscibility gap.

scribed previously (8) using the anneal and quench technique. Thus each sample was weighed, sealed in a quartz ampul under reduced argon pressure, and held for 1-2 hr at 1250°C while being agitated to give good mixing of the components. The sample was then cooled to the required annealing temperature where it was allowed to attain equilibrium. It was found that, for the range of composition used in the work, annealing times of 3 days were quite sufficient for the sample to reach an equilibrium condition. Tests showed that annealing times of up to 60 days did not change the conditions attained after 3 days. The samples were then quenched in order to freeze-in the equilibrium solid phase. This technique is well suited to the present work since, provided the composition of the samples is appropriately chosen, an appreciable part of the mixture is liquid during the annealing, thus allowing a reasonable speed of diffusion. However, during the quench, the diffusion rate in the solid is very low and hence the solid phase (or phases) at the annealing temperature is retained unchanged. This phase (or phases) can be identified from an x-ray powder photograph using the known lattice parameter *vs.* composition relation (4) for the $\text{GaAs}_y\text{Sb}_{1-y}$ section. In the present work, the homogeneity of the required solid phase was clearly demonstrated by the sharpness of the high angle x-ray lines.

Conditions for equilibrium were investigated at various temperatures and the choice of starting compositions was guided by a preliminary theoretical estimate of the boundaries of the three-phase fields as described below plus the requirement that sufficient liquid phase be present during annealing to allow equilibrium to be attained rapidly. Firstly, the GaSb-rich side of the diagram was investigated, specimen compositions being chosen so that they would cover both the two-phase field and the three-phase field at the particular temperature of anneal. For convenience, two series of compositions were chosen, each with a fixed value of gallium concentration (*i.e.*, $N_{\text{Ga}} = 0.65$ and $N_{\text{Ga}} = 0.40$) and the compositions investigated

at 700°C are shown in Fig. 1. Thus, for example with the $N_{\text{Ga}} = 0.65$ series, three samples gave tie-lines in the two-phase field and four samples were in the three-phase field and, within the limits of experimental error, gave identical phases. For samples in both fields, the liquid phase on quenching gave almost pure GaSb plus some gallium-rich phase and the lines due to these phases could be easily observed in the x-ray photograph and discarded. The two-phase samples gave the required equilibrium solid while in the three-phase field two equilibrium solids, one GaSb-rich and one GaAs-rich, occurred. With the above choice of compositions, the GaSb-rich solid could be easily determined but the amount of the GaAs-rich phase was sufficiently small that only weak lines were obtained and these were not used in this section of the work. Similar results were obtained for the series with $N_{\text{Ga}} = 0.40$. The data obtained from these measurements plus those obtained similarly at other temperatures are given in Table I.

In order to determine the boundaries of the three-phase fields for any given temperature, graphs were plotted of the composition *y* of the equilibrium solid (determined from lattice parameter) against the arsenic content N_{As} of the annealed samples. The results for the cases of 700° and 675°C are shown in Fig. 2. For each temperature, the samples occurring in either three-phase field should all have the same value of *y* and a mean horizontal line has been drawn through these. It can be seen that in the two-phase field the variation of *y* with N_{As} can, within the limits of experimental error, be taken as a straight line, separate lines being drawn for the two sets of samples with different N_{Ga} . These lines will pass through the origin for temperatures below the melting point of GaSb. The point of intersection of each of these lines with the line from the three-phase field gives the parameters determining the three-phase boundary, *i.e.*, the *y* value gives a point on the pseudobinary section and the N_{As} value together with the appropriate N_{Ga} value gives a second point on the boundary. Lines showing the boundaries in the 700°C case are shown

Fig. 1. 700°C isothermal section of Ga-As-Sb diagram. ●, initial composition of annealed sample; △, composition of equilibrium solid in annealed sample; ○, 700°C liquidus points in Ga-As binary diagram (9); —, calculated 700°C liquidus isotherm (This work); - - -, experimentally determined tie-line; - · - ·, experimentally determined boundary of three-phase field.

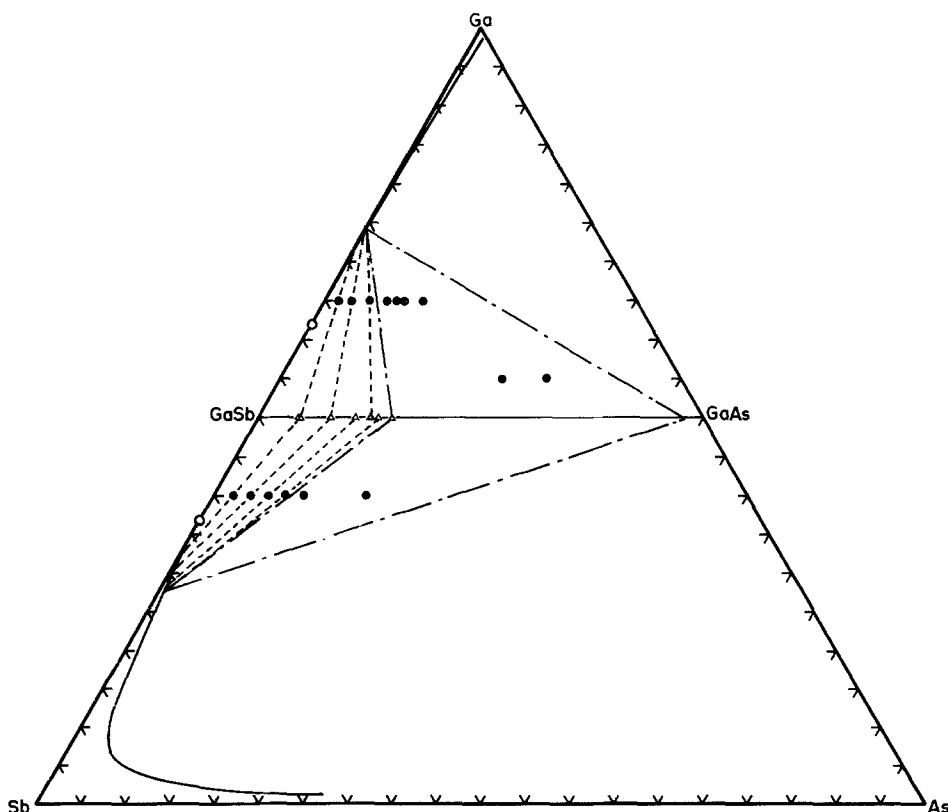


Table I. Composition of samples annealed at temperature T and lattice parameter and composition of resulting equilibrium solid phases

T ($^{\circ}\text{C}$)	Initial composition			a (nm)	Solid composition (y)	
	N_{Ga}	N_{As}	N_{Sb}			
600	0.400	0.010	0.590	0.6084	0.026	
	0.400	0.020	0.580	0.6076	0.045	
	0.400	0.030	0.570	0.6066	0.068	
	0.400	0.040	0.560	0.6063	0.073	
	0.400	0.050	0.550	0.6048	0.108	
	0.400	0.060	0.540	0.6047	0.110	
	0.400	0.120	0.480	0.6000	0.215	
	0.600	0.010	0.390	0.6084	0.026	
	0.600	0.020	0.380	0.6072	0.052	
	0.600	0.030	0.370	0.6058	0.084	
	0.600	0.040	0.360	0.6048	0.108	
	0.600	0.050	0.350	0.6058	0.084	
	0.600	0.060	0.340	0.6033	0.140	
	0.600	0.100	0.300	0.5991	0.235	
	625	0.400	0.010	0.590	0.6084	0.026
		0.400	0.025	0.575	0.6071	0.055
0.400		0.040	0.560	0.6064	0.070	
0.400		0.055	0.545	0.6052	0.098	
0.400		0.070	0.530	0.6032	0.144	
0.400		0.150	0.450	0.5985	0.249	
0.600		0.010	0.390	0.6083	0.028	
0.600		0.020	0.380	0.6070	0.058	
0.600		0.030	0.370	0.6065	0.069	
0.600		0.040	0.360	0.6048	0.108	
0.600		0.080	0.320	0.6013	0.188	
645		0.400	0.020	0.580	0.6075	0.048
		0.400	0.040	0.560	0.6053	0.095
		0.400	0.060	0.540	0.6034	0.138
		0.400	0.075	0.525	0.6028	0.152
		0.400	0.090	0.510	0.6022	0.166
	0.400	0.150	0.450	0.5983	0.256	
	0.650	0.010	0.340	0.6079	0.036	
	0.650	0.025	0.325	0.6057	0.086	
	0.650	0.035	0.315	0.6041	0.123	
	0.650	0.045	0.305	0.6028	0.152	
	0.650	0.055	0.295	0.6013	0.187	
	0.650	0.100	0.250	0.5978	0.265	
	675	0.400	0.020	0.580	0.6070	0.058
		0.400	0.040	0.560	0.6049	0.105
		0.400	0.060	0.540	0.6031	0.146
		0.400	0.080	0.520	0.6011	0.190
0.400		0.100	0.500	0.5975	0.272	
0.400		0.170	0.430	0.5972	0.279	
0.650		0.010	0.340	0.6079	0.036	
0.650		0.025	0.325	0.6047	0.110	
0.650		0.040	0.310	0.6023	0.164	
0.650		0.050	0.300	0.6001	0.214	
0.650		0.085	0.265	0.5964	0.298	
700		0.400	0.020	0.580	0.6056	0.090
		0.400	0.040	0.560	0.6026	0.159
		0.400	0.060	0.540	0.6001	0.214
		0.400	0.080	0.520	0.5976	0.270
		0.400	0.100	0.500	0.5970	0.283
	0.400	0.170	0.430	0.5970	0.283	
	0.650	0.015	0.335	0.6052	0.098	
	0.650	0.030	0.320	0.6025	0.160	
	0.650	0.050	0.300	0.5985	0.250	
	0.650	0.070	0.280	0.5957	0.312	
	0.650	0.080	0.270	0.5958	0.315	
	0.650	0.090	0.260	0.5956	0.308	
	0.650	0.110	0.240	0.5957	0.312	

in Fig. 1 and tie-lines for the two-phase fields are also shown. Similar results have been obtained for various temperatures in the range 600°-700°C.

While the pseudobinary section clearly defines one end of this three-phase boundary, the liquidus point is still undetermined. (These liquidus points will form a cusp across the liquidus sheet and so the point will, for convenience, be referred to as the cusp point.) It was hoped to determine the boundary on the GaAs side of the three-phase field by the same method, so that the two lines, together with the pseudobinary section, would completely define the three-phase triangle. However, it was found that a construction like that used in Fig. 2 was not possible in this case, since the range of solid solution of GaSb in GaAs was found to be very small for temperatures below 720°C. Thus the value of y for the equilibrium solid phase was in the range 0.95-1.00 for all annealed samples. Hence, although a figure could be obtained for the limiting y value, no N_{As} value could be found to give a second point on the limiting tie-line.

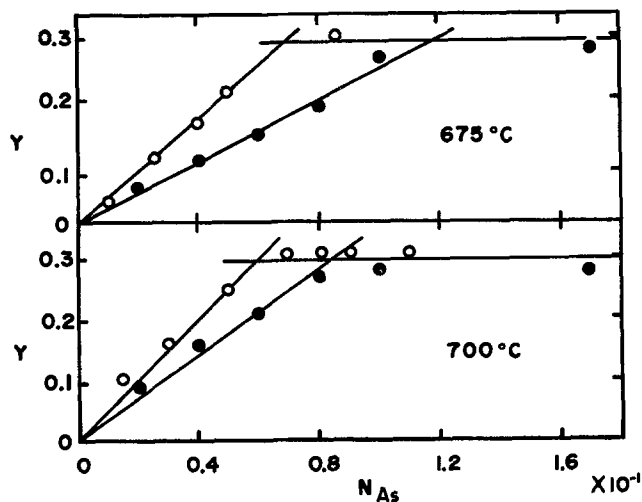


Fig. 2. Variation of composition y of equilibrium phase with arsenic concentration N_{As} of annealed sample. ●, $N_{\text{Ga}} = 0.40$ and ○, $N_{\text{Ga}} = 0.65$.

The cusp point has therefore been determined as the point of intersection of the GaSb-rich three-phase boundary and the appropriate liquidus isothermal curve. As was shown previously (1, 8), the simple solution model gives good agreement with experiment when used to calculate liquidus isotherms in these ternary systems. Thus, this model has been used here to calculate the appropriate liquidus isotherms, as is discussed further below. Figure 1 shows the calculated isotherm for 700°C, and it is seen that it lies very close to the Ga-Sb boundary of the diagram. For lower temperatures, the isotherms will be even closer to the boundary and, since the temperature gradient is relatively large in this range, little error should occur in the compositions of the points determined from these curves. However, problems occur for samples with N_{Ga} less than 0.5 at temperatures below about 650°C. In these cases, the cusp point is found to be close to the Sb apex of the main diagram. In this range, the calculated isotherms are not satisfactory as they do not indicate the position of the eutectic valley which must run out from the Ga-Sb eutectic [at $N_{\text{Ga}} = 0.12$ (9)] probably towards the minimum in the As-Sb liquidus curve [at $N_{\text{As}} = 0.25$ (10)]. Thus, the cusp point of the three-phase triangle has not been determined in this range.

As indicated above, the GaAs-rich sides of the three-phase triangles could not be determined by the same method as the GaSb-rich sides. However, annealing of samples in the GaAs-rich region of the three-phase fields gave the GaAs-rich equilibrium solid phase, and again, x-ray powder photographs gave the corresponding point of the pseudobinary section, thus completing the information needed to specify the three-phase fields. Figure 3 shows the three-phase fields for three different temperatures, 730°, 700°, and 600°C. It is seen that the position of the cusp point moves appreciably with temperature in the range 600°-745°C and Fig. 4 shows the variation of the values of N_{Ga} at the cusp point as a function of temperature. The N_{As} values at the cusp point were very much smaller, except in the Sb-rich region, as discussed above, and so could not be determined with any accuracy.

The other important information which is obtained immediately from the three-phase field data is the variation with temperature of the range of solid solution in the pseudobinary section. The experimental values are shown in Fig. 5. In the initial work on this question, samples with compositions on the pseudobinary section were annealed to equilibrium in the solid-solid two-phase field (7). The main difficulty

Fig. 3. Boundaries of three-phase fields at various temperatures. (a) 730°C, (b) 700°C, (c) 600°C.

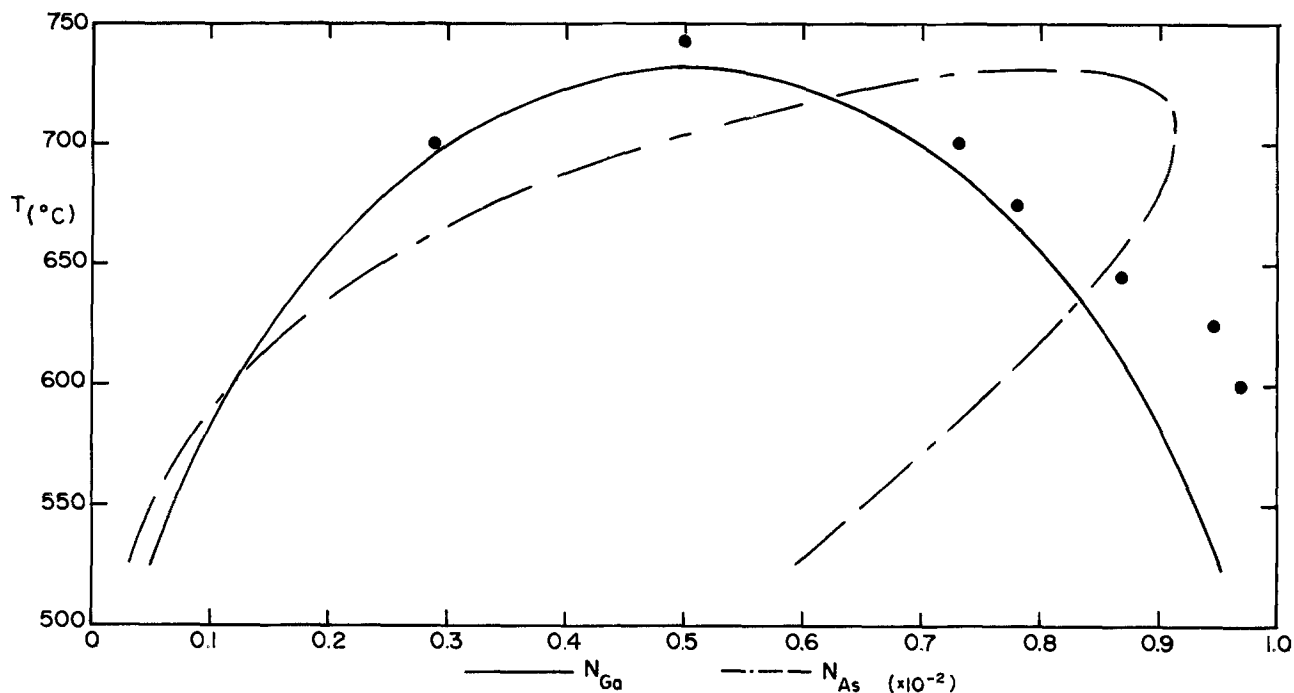
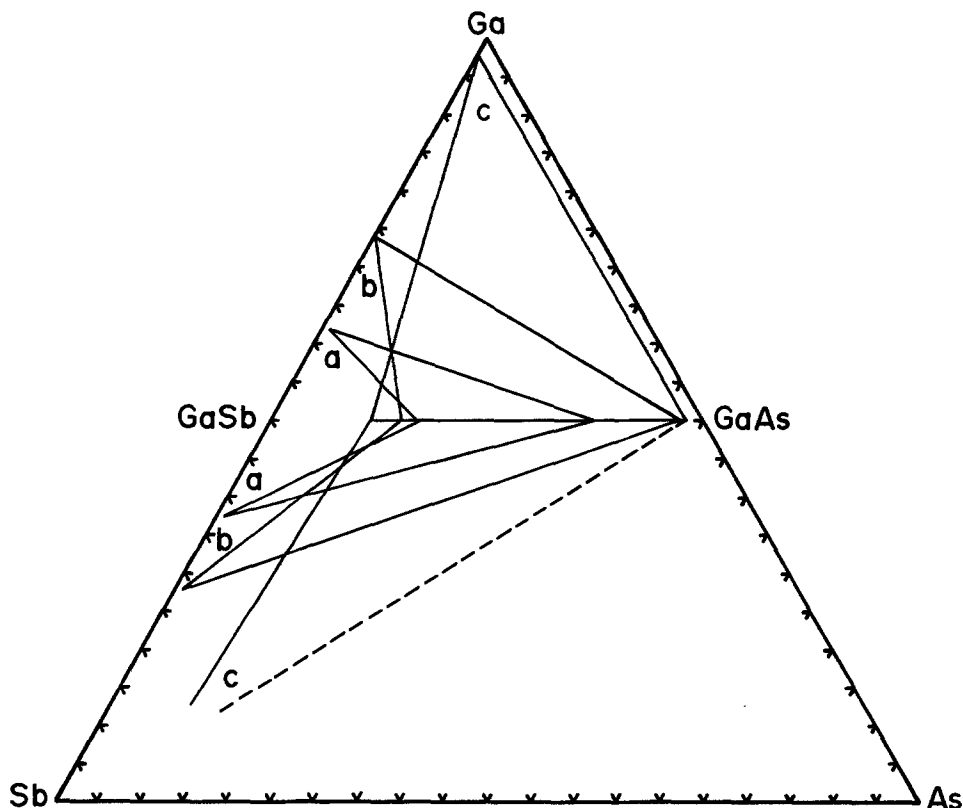


Fig. 4. Variation of position of cusp point as a function of temperature T :

●, experimental points, } N_{Ga} values
 —, calculated curve }
 ---, calculated curve } N_{As} values

with this method is that the diffusion rates are so slow that very long annealing times are required. Figure 5 shows results obtained in this way for samples annealed for three months or longer. These results confirm the data obtained from the three-phase field work, giving good agreement at both ends of the miscibility gap. It is worth noting that samples in the three-phase field needed less than three days annealing to attain equilibrium while samples in the

solid-solid two-phase field required at least three months.

Theoretical Analysis and Discussion

Little work has been published on calculations for this system. Panish and Ilegems (1) and Stringfellow (11) have calculated the liquidus and solidus curves of the pseudobinary section, and Antypas and James (3) have used Darken's quadratic formalism for a

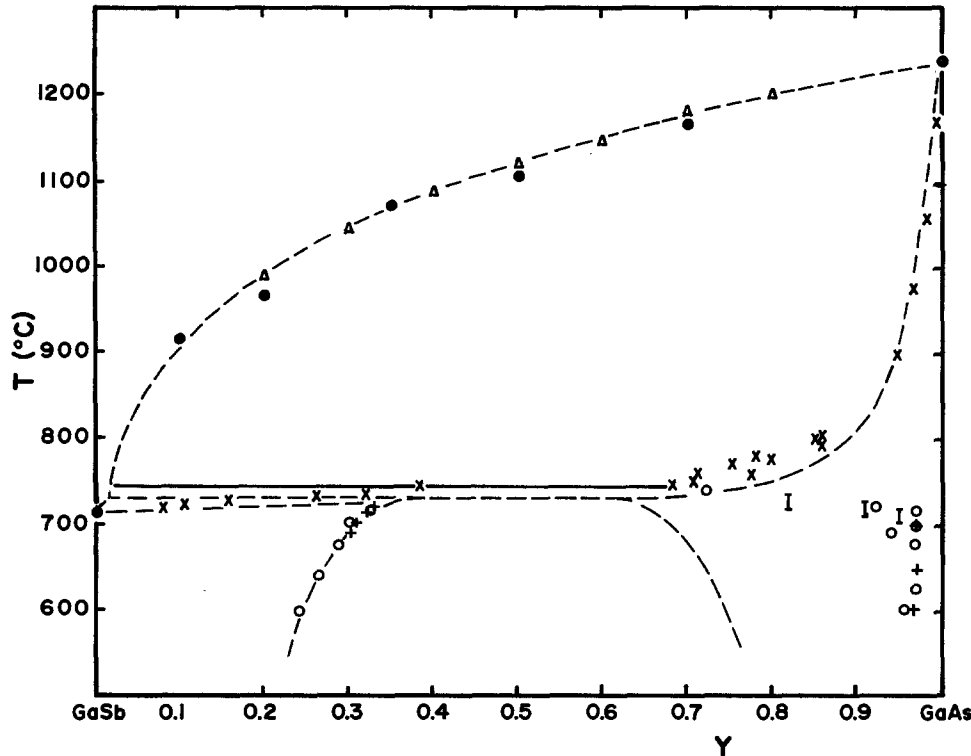


Fig. 5. Pseudobinary section GaSb-GaAs. Δ (24) and \bullet (25), experimental liquidus points; \times , solidus point from sample annealed in two-phase liquid-solid field; $+$, limits of miscibility gap from samples annealed in two-phase solid-solid field; \circ , limits of miscibility gap from samples annealed in three-phase field; —, experimental peritectic horizontal; ---, diagram calculated from simple solution model (This work).

ternary liquid and assumed a regular solid solution to calculate liquidus data for compositions with $N_{\text{Ga}} > 0.5$. More recently, Nahory *et al.* (5) have made an analysis based on the simple solution model, but treating the $\alpha_{\text{As-Sb}}$ interaction parameter as composition dependent rather than making the usual assumption of linear temperature dependence. Here, the simple solution model has been used to predict values for comparison with the various data determined experimentally.

The theory used for the simple solution model was summarized in a previous work on the Ga-In-Sb diagram (8) and the final equations necessary for the calculations are repeated here.

$$\ln \gamma_{\text{AC}} = \ln \frac{\gamma_{\text{A}}\gamma_{\text{C}}}{\gamma_{\text{A}}^s\gamma_{\text{C}}^s} + \ln 4 \frac{N_{\text{A}}N_{\text{C}}}{x} + \frac{\Delta S_{\text{FAC}}^{\text{F}}}{RT} (T_{\text{FAC}}^{\text{F}} - T) \quad [1a]$$

$$\ln \gamma_{\text{BC}} = \ln \frac{\gamma_{\text{B}}\gamma_{\text{C}}}{\gamma_{\text{B}}^s\gamma_{\text{C}}^s} + \ln 4 \frac{N_{\text{B}}N_{\text{C}}}{1-x} + \frac{\Delta S_{\text{FBC}}^{\text{F}}}{RT} (T_{\text{FBC}}^{\text{F}} - T) \quad [1b]$$

$$RT \ln \gamma_{\text{AC}} = \alpha_{\text{AC-BC}}(1-x)^2 \quad [2a]$$

$$RT \ln \gamma_{\text{BC}} = \alpha_{\text{AC-BC}}x^2 \quad [2b]$$

$$RT \ln \gamma_{\text{A}} = \alpha_{\text{AB}}N_{\text{B}}^2 + \alpha_{\text{AC}}N_{\text{C}}^2 + (\alpha_{\text{AB}} + \alpha_{\text{AC}} - \alpha_{\text{BC}})N_{\text{B}}N_{\text{C}} \quad [3a]$$

$$RT \ln \gamma_{\text{B}} = \alpha_{\text{AB}}N_{\text{A}}^2 + \alpha_{\text{BC}}N_{\text{C}}^2 + (\alpha_{\text{AB}} + \alpha_{\text{BC}} - \alpha_{\text{AC}})N_{\text{A}}N_{\text{C}} \quad [3b]$$

$$RT \ln \gamma_{\text{C}} = \alpha_{\text{AC}}N_{\text{A}}^2 + \alpha_{\text{BC}}N_{\text{B}}^2 + (\alpha_{\text{AC}} + \alpha_{\text{BC}} - \alpha_{\text{AB}})N_{\text{A}}N_{\text{B}} \quad [3c]$$

where the γ 's are activity coefficients, the α 's interaction parameters, N_{A} , N_{B} , and N_{C} concentrations of the three elements, x the mole fraction of AC in the solid phase, and $\Delta S_{\text{Fj}}^{\text{F}}$ and T_{Fj}^{F} the entropy of fusion and melting temperature of the compound j .

Vieland's equation [12] giving the relation for the liquidus curve of a binary system A-C with a line compound AC is

$$\alpha_{\text{AC}} = - \frac{RT}{2(0.5-c)^2} \left[\ln 4c(1-c) + \frac{\Delta S_{\text{FAC}}^{\text{F}}}{RT} (T_{\text{FAC}}^{\text{F}} - T) \right] \quad [4]$$

where c is the atomic fraction of C.

The binary phase diagram data for the Ga-Sb system of various workers (9, 12-15) have been used in Vieland's equation [16] (Eq. [4]) to give values of $\alpha_{\text{Ga-Sb}}$, the melting point and entropy of fusion of GaSb being taken as 712°C and 66.1 J mol⁻¹ K⁻¹, respectively (17). The values were fitted to a linear temperature dependence and the resulting parameters are given in Table II. A similar least squares fit to the Ga-As data gave an expression for $\alpha_{\text{Ga-As}}$ slightly different from that of Thurmond (18) and the value of $\alpha_{\text{Ga-As}}$ used here is also given in Table II. Jordan and Weiner (19) have questioned the validity of Vieland's method, but their improved formulation reduces to that of Vieland when a linear dependence on temperature is obtained, as in this case.

The other interaction parameters required for the analysis are $\alpha_{\text{As-Sb}}$ and $\alpha_{\text{GaAs-GaSb}}$. As in the case of the Ga-In-Sb diagram (8), values of these parameters have been determined here as a function of temperature by simultaneous solution of the experimental values for points on the liquidus and solidus curves of the pseudobinary section. Again, these α values were least squares fitted to a linear temperature variation and the resulting forms for $\alpha_{\text{As-Sb}}$ and $\alpha_{\text{GaAs-GaSb}}$ are shown in Table II.

Equations [1]-[3] were then solved simultaneously for T and y for various combinations of N_{Ga} , N_{As} , and N_{Sb} covering the complete ternary diagram, and liquidus isotherms were determined by appropriate interpolation of the data. These isotherms are shown in Fig. 6, together with the values predicted previously by Antypas and James (3), and the pseudobinary experimental values. The present results differ somewhat from those of this earlier work, but give a better fit to the known values on the pseudobinary section, as is to be expected from the method of $\alpha_{\text{GaAs-GaSb}}$ determination.

The isotherms at temperatures below 800°C are crowded together at low arsenic concentrations and these are shown separately in Fig. 7 using an orthog-

Table II. Interaction parameters for the ternary system Ga-As-Sb

$\alpha_{\text{Ga-As}}$	19828-36.617	J mol ⁻¹
$\alpha_{\text{Ga-Sb}}$	23624-32.387	J mol ⁻¹
$\alpha_{\text{As-Sb}}$	14.147-18715	J mol ⁻¹
$\alpha_{\text{GaAs-GaSb}}$	17154	J mol ⁻¹

Fig. 6. Calculated liquidus isotherms for Ga-As-Sb diagram. Calculated curves, — (This work); ---, (3); experimental points, □ (24), ○ (13), △ (12), + (9), ▽ (26).

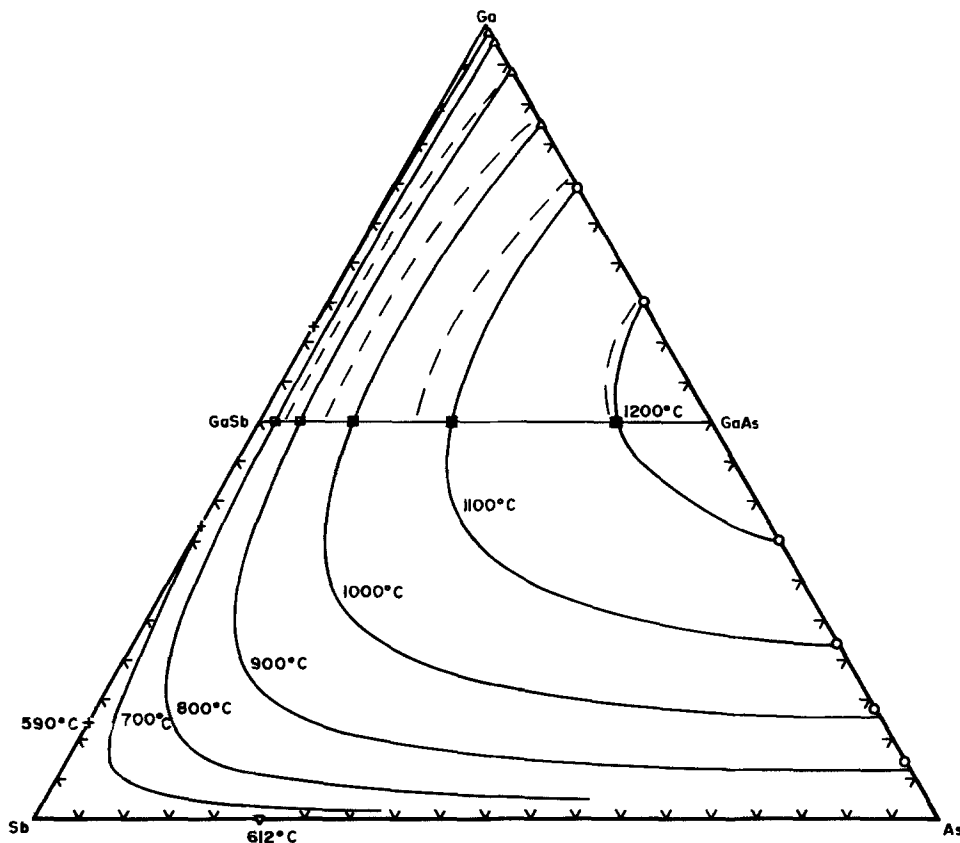
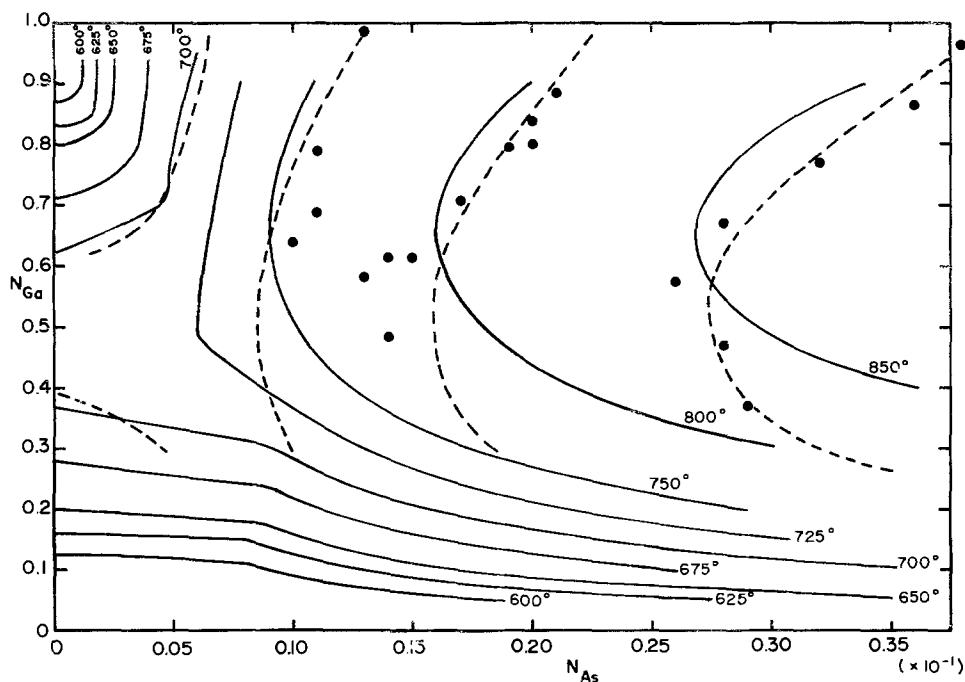


Fig. 7. Calculated liquidus isotherms for $T < 900^\circ\text{C}$. — (This work); ---, (5); ●, experimental points (5).



onal plot rather than the conventional one. The calculated isotherms of Nahory *et al.* (5) are also shown in Fig. 7 together with the experimental values obtained from liquid phase epitaxy work. In the calculations of Nahory *et al.*, $\alpha_{\text{As-Sb}}$ was treated as linearly dependent on N_{Sb} , and $\alpha_{\text{GaAs-GaSb}}$ was adjusted to give the best fit to the experimental data. The present curves show reasonable agreement with those of Nahory *et al.* Here, a better fit to the experimental points in the range $N_{\text{Ga}} > 0.50$ could be obtained by changing the constants in the expression for $\alpha_{\text{As-Sb}}$ while still retaining a linear temperature variation. However, such an expression for $\alpha_{\text{As-Sb}}$ gave a considerably poorer fit to the pseudobinary data.

From the calculated liquidus curves, the position of the cusp associated with the three-phase field can be predicted. Figure 8 shows the variation of the liquidus temperature T as a function of N_{As} for constant values of N_{Ga} (with $N_{\text{Ga}} < 0.5$), the calculated cusp point being given by the cross. These results are compared with the experimental data in Fig. 4 where the calculated values of T vs. N_{Ga} and those of T vs. N_{As} are shown. For the range $0.3 < N_{\text{Ga}} < 1.0$, there is good agreement between the calculated and experimental values for T vs. N_{Ga} . As indicated above, in the range $0 < N_{\text{Ga}} < 0.3$, the problem is complicated by the presence of a eutectic valley and experimental points have not been obtained.

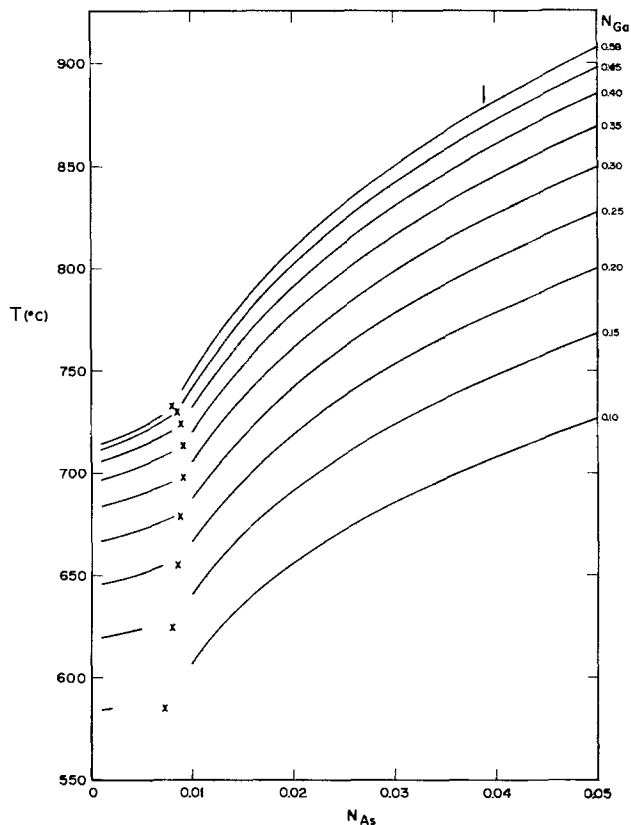


Fig. 8. Variation of temperature T with arsenic concentration N_{As} on liquidus sheet for various fixed values of gallium concentration N_{Ga} . X, cusp point.

Other results obtained from the simple solution analysis are the form of the pseudobinary section shown in Fig. 8. As is to be expected from the method of determining the α parameters, the fit to the liquidus and solidus curves is good, although the predicted peritectic temperature is 732°C as compared with the experimental value of 745°C (7). However, the case of the boundary of the two-phase solid-solid field is very different. The agreement between experiment and predicted value is very good for the GaSb-rich side of the miscibility gap, but is very poor for the GaAs-rich alloys. Some disagreement in this range is to be expected since it can easily be shown that any solid-solid miscibility gap predicted by the simple solution model using α 's, which are linear functions of T , will be symmetrical about $y = 0.5$. Since the experimental values show appreciable asymmetry, the simple solution model is bound to give poor agreement in this case.

The parameter of importance in the two-phase solid-solid field is $\alpha_{GaAs-GaSb}$. It is clear that to obtain an asymmetrical form for the miscibility gap, $\alpha_{GaAs-GaSb}$ must vary with y . It is of interest to check what form of expression is required for $\alpha_{GaAs-GaSb}$ to give the present experimental results. For two compounds, M and N, in equilibrium, the chemical potentials μ are given by

$$\mu_M = \mu_M^\circ + RT \ln \gamma_M y$$

$$\mu_N = \mu_N^\circ + RT \ln \gamma_N (1 - y)$$

where μ° is the chemical potential of the pure compound, γ the activity coefficient, and y the mole fraction of M. If the limits of solid solution occur at compositions y_1 and y_2 , then

$$\mu_{M1} = \mu_{M2} \quad \text{and} \quad \mu_{N1} = \mu_{N2}$$

giving

$$\ln \gamma_{M1} y_1 = \ln \gamma_{M2} y_2$$

$$\ln \gamma_{N1} (1 - y_1) = \ln \gamma_{N2} (1 - y_2)$$

The relation between the activity coefficients and the interaction parameters is

$$RT \ln \gamma_M = \alpha (1 - y)^2$$

$$RT \ln \gamma_N = \alpha y^2$$

Hence, if α_1 and α_2 are the values of α at y_1 and y_2 it can be shown that

$$\alpha_1 = \frac{RT \left\{ y_2^2 \ln y_2/y_1 - (1 - y_2)^2 \ln \frac{(1 - y_2)}{(1 - y_1)} \right\}}{(y_2 - y_1)(y_2 + y_1 - 2y_1 y_2)}$$

$$\alpha_2 = \frac{RT \left\{ y_1^2 \ln y_2/y_1 - (1 - y_1)^2 \ln \frac{(1 - y_2)}{(1 - y_1)} \right\}}{(y_2 - y_1)(y_2 + y_1 - 2y_1 y_2)}$$

In the present case, for each value of T , α_1 and α_2 have been determined from the experimental values of y_1 and y_2 , and the resulting variation of $\alpha_{GaAs-GaSb}$ is shown in Fig. 9. The values of α_1 and α_2 obtained are sensitive to the values of y_1 and y_2 used, and since the y_2 values are uncertain to a few percent, the resulting values of $\alpha_{GaAs-GaSb}$ are approximate only. In an attempt to fit these values to a relatively simple form, the relation $\alpha_{GaAs-GaSb} = 17,200 + 9000 y^4 \text{ J} \cdot \text{mol}^{-1}$ has been used, giving the curve shown in Fig. 9. This expression for $\alpha_{GaAs-GaSb}$ will, of course, give a good prediction of the solid miscibility gap but is inconsistent with that given in Table II from the pseudobinary liquidus-solidus data. It is clear that no simple form for $\alpha_{GaAs-GaSb}$ will allow the simple solution model to fit all of the experimental results.

Modifications to the simple solution model to include the effects of association of atoms in the liquid phase have been proposed by Jordan (20) and by Osamura and Murakami (21). As will be shown elsewhere, various possibilities of association in the liquid phase have been considered and none make any appreciable difference to the predicted values of the solid phase miscibility gap in this system. In no case can agreement with the experimental values be obtained without arbitrarily including an $\alpha_{GaAs-GaSb}$ variation of the form given above.

Conclusions

The work described here, together with that in a previous paper (7), indicates clearly that the pseudobinary section $GaAs_y Sb_{1-y}$ of the Ga-As-Sb system shows peritectic behavior, and that no equilibrium solid phase occurs in the pseudobinary section in the range $0.38 < y < 0.68$. This explains the problems that various workers (5, 22) have encountered in attempting growth of the alloys by liquid phase epitaxy. Samples in the above range have been produced by molecular beam epitaxy (6, 23) and, as indicated previously (7), it is suggested that these must represent a metastable condition.

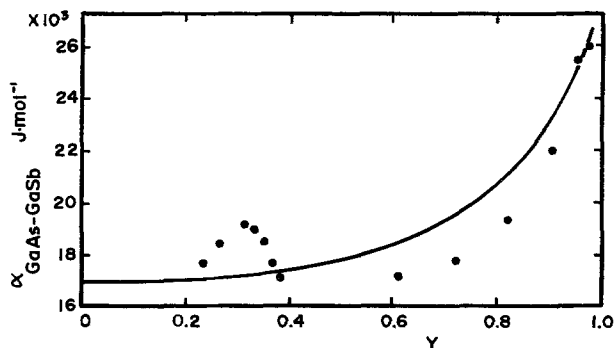


Fig. 9. Variation of interaction parameter $\alpha_{GaAs-GaSb}$ with composition y . ●, values determined from limits of pseudobinary miscibility gap; — $\alpha_{GaAs-GaSb} = 17,200 + 9000 y^4 \text{ J} \cdot \text{mole}^{-1}$.

The problems of liquid phase epitaxy are further illustrated by the diagrams in Fig. 3 and 5. For the composition range $0.67 < y < 1.00$, the temperature range in which certain alloys can be grown is very small, e.g., for $y = 0.80$ growth is possible only in the temperature range $735^{\circ}\text{--}785^{\circ}\text{C}$. As is also indicated in Fig. 3, the possible composition range of liquid solution from which alloys can be grown is very limited since compositions in the three-phase fields cannot be used for this purpose.

Acknowledgments

The authors wish to thank Dr. M. B. Panish and Dr. G. B. Stringfellow for useful discussions.

Manuscript submitted March 3, 1979; revised manuscript received June 26, 1979.

Any discussion of this paper will appear in a Discussion Section to be published in the December 1980 JOURNAL. All discussions for the December 1980 Discussion Section should be submitted by Aug. 1, 1980.

Publication costs of this article were assisted by John C. Woolley.

REFERENCES

1. M. B. Panish and M. Ilegems, in "Progress in Solid State Chemistry," Vol. 7, H. Reiss and J. O. McCaldin, Editors, p. 39, Pergamon Press, Oxford (1972).
2. J. C. Woolley, in "Compound Semiconductors," Vol. 1, R. K. Willardson and H. L. Goering, Editors, p. 3, Reinhold Publishing Corp., New York (1962).
3. G. A. Antypas and L. W. James, *J. Appl. Phys.*, **41**, 2165 (1970).
4. M. F. Gratten and J. C. Woolley, *J. Electron. Mater.*, **2**, 455 (1973).
5. R. E. Nahory, M. A. Pollack, J. C. DeWinter, and K. M. Williams, *J. Appl. Phys.*, **48**, 1607 (1977).
6. T. Waho, S. Ogawa, and S. Maruyama, *Jpn. J. Appl. Phys.*, **16**, 1875 (1977).
7. M. F. Gratten, R. G. Goodchild, L. Y. Juravel, and J. C. Woolley, *J. Electron. Mater.*, **8**, 25 (1979).
8. M. F. Gratten and J. C. Woolley, *This Journal*, **125**, 657 (1978).
9. I. G. Greenfield and R. L. Smith, *J. Met.*, **7**, 351 (1955).
10. W. F. Schottky and M. B. Bever, *Acta Metall.*, **6**, 320 (1958).
11. G. B. Stringfellow, *J. Phys. Chem. Solids*, **33**, 665 (1972).
12. R. N. Hall, *This Journal*, **110**, 385 (1963).
13. W. Koster and B. Thoma, *Z. Metallkd.*, **46**, 291 (1955).
14. A. G. Kalyuzhnaya, I. K. Polushina, and D. N. Tretyakov, *Russ. J. Inorg. Chem.*, **9**, 813 (1964).
15. M. H. Maglione and A. Potier, *J. Chim. Phys. Phys.-Chim. Biol.*, **65**, 1595 (1968).
16. L. J. Vieland, *Acta Metall.*, **11**, 137 (1963).
17. B. D. Lichter and P. Sommelet, *Trans. Am. Inst. Min. Metall. Pet. Eng.*, **245**, 99 and 1021 (1969).
18. C. D. Thurmond, *J. Phys. Chem. Solids*, **26**, 785 (1964).
19. A. S. Jordan and M. E. Weiner, *J. Phys. Chem. Solids*, **36**, 1335 (1975).
20. A. S. Jordan, *Metall. Trans.*, **7**, 191 (1976).
21. K. Osamura and Y. Murakami, *J. Phys. Chem. Solids*, **36**, 931 (1975).
22. C. G. Fonstad, M. Quillec, and S. Garone, *J. Appl. Phys.*, **49**, 5920 (1979).
23. C. A. Chang, R. Ludeke, L. L. Chang, and L. Esaki, *Appl. Phys. Lett.*, **31**, 759 (1977).
24. L. M. Foster and J. E. Woods, *This Journal*, **119**, 504 (1972).
25. J. Inoue, K. Osamura, and V. Murakami, *Suiyokwai-Shi*, **17**, 71 (1970).
26. C. H. Shih and E. A. Peretti, *Trans. Am. Soc. Met.*, **48**, 709 (1956).

Differential Infrared (DIR) Studies of CVD Borosilicate Films

Joe Wong

General Electric Company, Corporate Research and Development, Schenectady, New York 12301

ABSTRACT

Room temperature infrared transmission spectra in the range $4000\text{--}250\text{ cm}^{-1}$ of binary borosilicate glass (BSG) films vapor-deposited by reacting nitrogen-diluted $\text{B}_2\text{H}_6\text{--SiH}_4\text{--O}_2$ mixtures on heated Si substrates at 350°C have been obtained across the whole composition range. A differential infrared (DIR) technique has been used to identify a new B-O-Si stretching mode at $\sim 1130\text{ cm}^{-1}$. The intensity variation of this mode with composition is very similar to the well-characterized B-O-Si mode at 930 cm^{-1} , and lends further support to the structural model proposed earlier for the $\text{B}_2\text{O}_3\text{--SiO}_2$ glass system in which the boron and silicon are three-fold and four-fold coordinated with oxygen, respectively, and each oxygen is bridging a pair of B and/or Si atoms to form a 3-dimensional random network. The effect of thermal history on the structure of CVD glasses deposited above the glass transition temperature, T_g , as in the case of B_2O_3 is contrasted with that of CVD SiO_2 deposition at temperatures far below the T_g of the bulk material. Furthermore, it is shown by annealing experiments that the B-O-Si mode at 930 cm^{-1} is a very sensitive probe for structural changes in the borosilicate system.

Glassy solids are commonly formed by continuous cooling from the liquid state. The procedure consists of quenching a normal liquid into the supercooled liquid range at such a rate so as to bypass its equilibrium crystallization point. Finally, at T_g , the glass transition temperature, the system falls out of its internal equilibrium. The supercooled liquid now transforms to a glass, carrying with it the structural configuration at

Key words: infrared, CVD, films.

T_g . However, the essential requirement for glass formation is that the thermal energy of an ensemble of particles, whether molecules, ions, atoms, etc., can be removed at a rate which for kinetic reasons precludes the organization of these particles into a crystal lattice. For this purpose an initially liquid state of the glassy system is by no means necessary. In fact a more efficient procedure for removing the molecular thermal energy is to deposit the molecules sequen-

tially from a vapor onto a cold substrate (cold with respect to T_g of the deposited material).

Thus, the vapor-phase route provides not only another way of arriving at the glassy state of matter, but oftentimes allows preparation of novel amorphous materials unattainable by conventional techniques of quenching the liquid state. Binary B_2O_3 - SiO_2 glasses of composition not readily obtained by melt-quenching can be prepared by chemical vapor deposition (CVD) techniques (1) from one end component to the other (2). In the CVD technique, a preset mixture of the desired gases and vapors containing constituents of the desired material is passed over and allowed to react at a heated substrate, thereby producing a solid-phase reaction product in the form of a thin film (3). These CVD materials in the form of thin film are ideal for transmission spectroscopy in the frequency region where the materials exhibit high absorption coefficient, e.g., $\sim 10^4$ cm^{-1} in the infrared (4). Technologically, these binary glass films have wide applications as diffusion sources in the planar technology of microelectronic fabrication (2, 5) and, more recently, as cladding materials for low-loss SiO_2 -core fibers in optical waveguides (6, 7).

In this paper the infrared transmission spectra of binary borosilicate glass films vapor-deposited at low temperatures (350°-600°C) from N_2 -diluted reactive mixtures of B_2H_6 , SiH_4 , and O_2 are studied in some detail as a function of thermal history and composition. The spectra and structure of CVD B_2O_3 deposited above its T_g ($\sim 260^\circ C$) are contrasted with those of CVD SiO_2 deposited far below its T_g ($\sim 1159^\circ C$). In addition, taking advantage of the ease of control of film thickness during deposition, a differential technique has been used to elucidate some of the complex spectral features in the vibrational spectra of the binary glasses. The analysis and understanding of the infrared spectra of this simple binary borosilicate glass system form a basis of interpretation of the vibration spectra of other complex borosilicate glasses.

Experimental

The glass films studied were deposited on chemically polished 10 Ω -cm n-type (100)-oriented silicon wafers, 2.5 cm in diam and 0.05 cm thick. The technique of chemical vapor deposition was used for the pyrolytic oxidation of nitrogen-diluted mixtures of silane, diborane, and oxygen in the presence of excess oxygen such that the molar ratio of O_2 to total hydride in the reaction mixture was always greater than 10:1. The gas flow system and reactor used were identical to those employed by Brown and Kennicott (2) from this laboratory. The substrate temperature varied from 350° to 600°C. For example, with flow rates of 3800 cm^3 min^{-1} N_2 , 20 cm^3 min^{-1} O_2 ; 320 cm^3 min^{-1} SiH_4 (1% in Ar); and 80 cm^3 min^{-1} B_2H_6 (1% in Ar), a 25 mole percent (m/o) B_2O_3 glass film can be deposited at a rate of 700 Å min^{-1} at a substrate temperature of 350°C.

Since the refractive indexes of vitreous SiO_2 and B_2O_3 are very similar (~ 1.46) (9), one can use the color-thickness of Plisken and Conrad (10) for thermal SiO_2 to monitor film thickness of the borosilicate films during deposition. Film thicknesses used in the present study vary from 4000 to 6000 $\text{Å} \pm 200\text{Å}$.

Films containing more than 20 m/o B_2O_3 are hygroscopic and are prevented from atmospheric moisture degradation during infrared measurement with a covering layer of pure SiO_2 ($\sim 400\text{Å}$ thick) deposited sequentially from a preset SiH_4 - O_2 mixture. The covering layer of SiO_2 is compensated quantitatively in a Perkin-Elmer double-beam spectrophotometer (Model 457) with an identical SiO_2 layer deposited on a reference Si substrate. Film compositions were determined from the intensity ratio of the bands at ~ 1300 cm^{-1} and ~ 1000 cm^{-1} using a composition calibration curve of Tenney (9).

A differential infrared (DIR) technique applicable to transmission measurement of thin films has been described in some detail elsewhere (11). For clarity the essential steps will be outlined in the section on DIR data.

Films were heat-treated in the deposition reactor to a maximum temperature of 700°C for 10 min. Under this condition the free-carrier absorption arising from the diffusion of boron into the silicon substrate is negligible so that the infrared spectra below 1000 cm^{-1} are not obscured.

Results and Discussion

In this section the infrared data of as-deposited and heat-treated pure B_2O_3 and SiO_2 is first presented and discussed. This is followed by DIR data on the binary B_2O_3 - SiO_2 films using B_2O_3 and SiO_2 separately as a reference. Finally, the effects of annealing at 700°C on the binary glass spectra will be discussed.

Pure components.—CVD B_2O_3 .—The room temperature infrared transmission spectrum of pure B_2O_3 deposited at 350°C is shown in Fig. 1. Two prominent absorption bands at 1265 cm^{-1} and 715 cm^{-1} are evident. Using the relationship $A = \alpha t$ where A is the absorbance, α the absorption coefficient, and t film thickness, the absorption coefficients at these two frequencies are found to be $(2.1 \pm 0.1) \times 10^4$ cm^{-1} and $(0.32 \pm 0.02) \times 10^4$ cm^{-1} , respectively. With isotopic substitution of ^{10}B for ^{11}B the 1265 cm^{-1} band exhibits a 21 cm^{-1} upshift (12) and is associated with B-O bond stretching modes in the glassy lattice, while the lower frequency band exhibits only a 6 cm^{-1} upshift and is associated with bond bending modes.

When deposited above its equilibrium melting point in the range 450°-600°C (so that B_2O_3 is now deposited as liquid films) the resultant infrared spectra remain invariant and are directly superimposed onto that of the film of the same thickness deposited at 350°C shown in Fig. 1. However, when the as-deposited films are subsequently heat-treated at 700°C for 10 min in N_2 , a large change in the shape of the B-O band at 1265 cm^{-1} is observed, as indicated by the dotted scan in Fig. 1. The absorbance at band maximum decreases from 0.90 to 0.66 while the bandwidth at half height increases from 65 cm^{-1} to 120 cm^{-1} . The integrated intensity (area under the band) remains constant indicating that the total number of oscillators responsible for this absorption remain unchanged after heat-treatment. The increase in bandwidth after annealing at 700°C is indicative of a quenching-in of high temperature liquid configurations which, in general, have a broader distribution.

CVD SiO_2 .—The above observation in B_2O_3 is contrasted with that of CVD SiO_2 films deposited at tem-

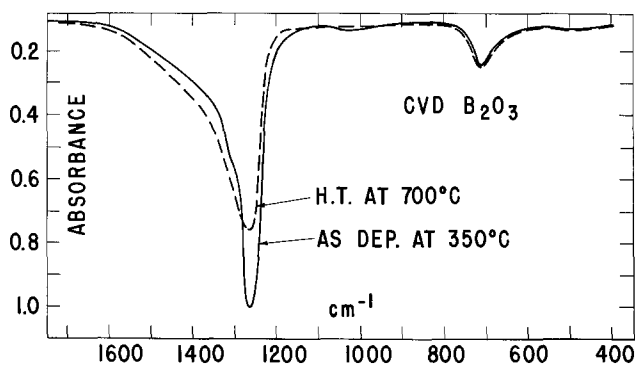


Fig. 1. Room temperature infrared transmission spectra of B_2O_3 vapor-deposited on Si. The solid curve denotes that of the as-deposited film deposited at 350°C while the dashed curve is that of the same film heat-treated at 700°C. The film was 4000 Å thick and was covered with a 400 Å thin layer of SiO_2 which was compensated in the reference beam with an identical SiO_2 film deposited on a bare Si wafer.

peratures much below its T_g (1159°C) (13). When heat-treated to 800°C and above, the infrared spectrum of SiO_2 deposited at 450°C from $\text{SiH}_4\text{-O}_2$ mixtures exhibits a progressive bandwidth narrowing (14) accompanied by an increase in both the absorbance and frequency at band maxima (Fig. 2) (15).

According to the dynamical calculation of Bell *et al.* (16) using a physically realistic random network model for vitreous SiO_2 , the observed bands at ~ 1060 , 800, and 450 cm^{-1} shown in Fig. 2 can be assigned to the Si-O bond stretching, O-Si-O bond bending, and Si-O-Si bond rocking modes in the glass structure. The integrated intensity of each band upon annealing remains invariant as in the case of the B-O absorption. The infrared data are correlated with a decrease in the root mean squared deviations of atomic distances in the radial distribution function (14). Together with the changes in other physical properties such as density, refractive index, etch rate, etc. (5) the combined vibrational and structural variations are indicative of a densification process brought about in as-deposited SiO_2 as a result of thermal annealing above its deposition temperature. Angular reorientation of the Si-O-Si centers (17) and/or further condensation of hydrogen-terminating Si-O chains (18) are possibilities of these structural changes.

Binary glasses.—The room temperature infrared spectra of as-deposited borosilicate glasses (BSG) have been studied systematically as a function of composition across the whole binary system (8). A distinct absorption at 930 cm^{-1} not present in either of the pure component spectra appears in the spectra of the binary glasses, and is associated with a vibration of the B-O-Si linkages in the borosilicate structure (19). The composition variation of the intensity of this band has been used quantitatively to construct a structural model of random networks of BO_3 triangles and SiO_4 tetrahedra bridged by oxygens. Above 1000 cm^{-1} , the absorptions are more complex and will be studied here with a DIR technique that has been proven useful in unraveling the vibrational spectra of CVD $\text{P}_2\text{O}_5\text{-SiO}_2$ glasses (11).

Differential Infrared Spectra

The vibrational spectra of impurities in a solid can often be masked and overshadowed by that of the host material. This is more so in the case of glassy solids which have broad absorption spectra of their own arising from structural disorder. The normal infrared spectra of binary and multicomponent glasses are usually more diffuse and sometimes featureless. Meaningful interpretations of these spectra are difficult if not impossible (20). Recently, a DIR technique has been applied by Smith (21) to study the vibrational modes arising from impurities such as C, B, Na, and Ti doped in bulk vitreous silica. The technique consists simply of measuring the transmission spectrum of a sample

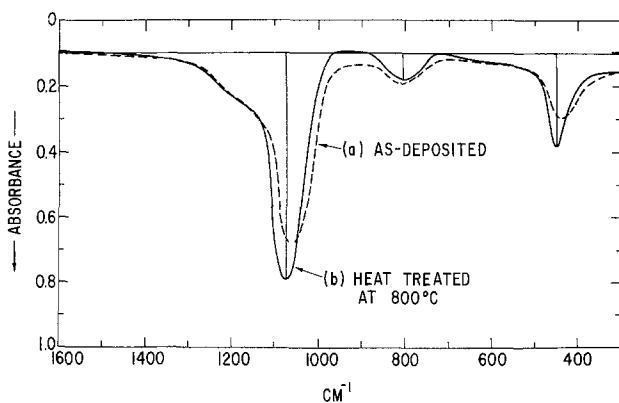


Fig. 2. Room temperature infrared transmission spectra of CVD SiO_2 film, 5200 Å thick: (a) as-deposited at 450°C and (b) the same film heat-treated at 800°C for 15 min.

vs. that of a host "pure" sample having the same effective absorption thickness placed in the reference beam of a double-beam spectrophotometer. Provided that both the sample and pure reference are sufficiently thin so that total absorption does not occur in the frequency range scanned, differential vibrational absorptions characteristic of the impurities can be isolated from the host spectrum. The DIR method has frequently been employed to eliminate solvent interference in organic systems (22).

The thickness of vapor-deposited films can easily be controlled during the CVD process by simply monitoring the time of deposition so that zero transmission in the absorption region 1600-250 cm^{-1} is avoided. The results for an as-deposited BSG film containing 24 m/o B_2O_3 are shown in Fig. 3. The curve labeled "BSG" is the normal infrared spectrum taken *vs.* an identical covering layer of SiO_2 (~ 400 Å thick) deposited on a bare Si in the reference beam. The curve labeled " SiO_2 " corresponds to the normal infrared spectrum (compensated by the same reference) of a pure SiO_2 film deposited under the same conditions of temperature, time, and flow rate of SiH_4 , O_2 , and N_2 carrier gas as the BSG film. The curve labeled "DIR" was obtained by rescanning the BSG spectrum but now using the SiO_2 film in the reference beam. From the DIR spectrum, in addition to the B-O-Si mode at 930 cm^{-1} , a band at 1125 cm^{-1} can clearly be differentiated from the broad absorption at 1100 cm^{-1} in the BSG spectrum. The position and half-width (110 $\text{cm}^{-1} \pm 5 \text{ cm}^{-1}$) of this differential band remain constant with composition across the binary system, as shown in Fig. 4. The intensity of this band, measured as peak absorbance with respect to point X in the DIR spectrum, shown in Fig. 3, and normalized to a 1 micron film absorption exhibits a maximum in the vicinity of 40 m/o B_2O_3 as shown in Fig. 5. This variation is very similar to the behavior of the well-defined Si-O-B vibration at 930 cm^{-1} studied previously (8). The constancy in frequency and bandwidth suggests that this mode is intrinsic of the borosilicate structure and its intensity variation with composition in analog to that of the 930 cm^{-1} band strongly indicates that it is a bond-stretching vibration of the Si-O-B linkages in the borosilicate lattice. In addition, the broad absorption at 450 cm^{-1} in the BSG spectrum in Fig. 3 can be seen to consist of overlapping contributions of the Si-O-Si and B-O-B bending modes in the binary mixtures.

Similarly, DIR spectra have been recorded *vs.* pure B_2O_3 . The results for the same 24 m/o B_2O_3 film discussed above is shown in Fig. 6. The curve labeled " B_2O_3 " is that for a pure B_2O_3 film deposited under identical conditions of temperature and time flow rates of B_2H_6 , O_2 , and N_2 to those of the BSG film. The DIR spectrum in this case consists simply of a differential band at $\sim 1360 \text{ cm}^{-1}$. The DIR spectra *vs.* pure B_2O_3 as a function of B_2O_3 content in the film are

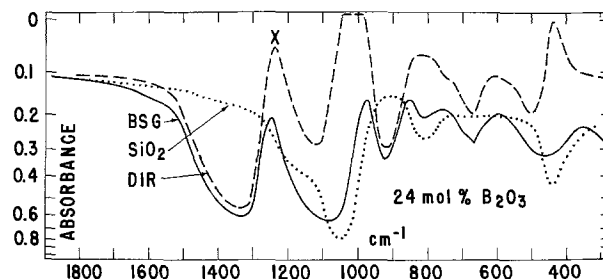


Fig. 3. DIR spectrum of an as-deposited borosilicate film containing 24 m/o B_2O_3 *vs.* a corresponding SiO_2 film deposited under identical conditions of temperature and flow rates of SiH_4 , O_2 , and N_2 . The curves labeled "BSG" and " SiO_2 " are the normal infrared spectra taken *vs.* an identical covering layer of 400 Å SiO_2 deposited on a bare Si wafer in the reference beam.

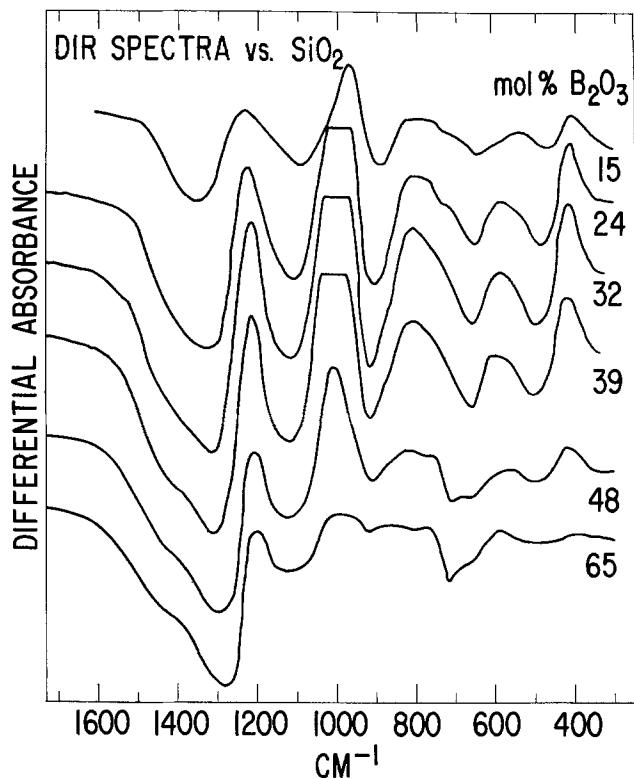


Fig. 4. DIR spectra of a series of as-deposited BSG films containing 15-65 m/o B_2O_3 ; each spectrum was taken vs. the corresponding SiO_2 film and covering layer.

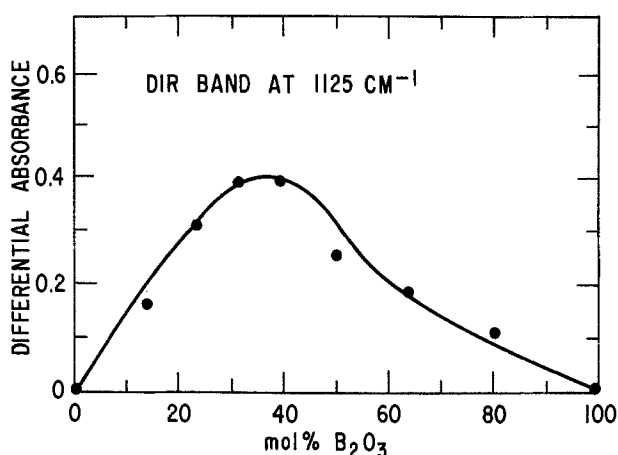


Fig. 5. Compositional variation of the intensity of the DIR band at 1125 cm^{-1} shown in Fig. 3. The plotted differential absorbance is normalized for 1 micron film in all cases.

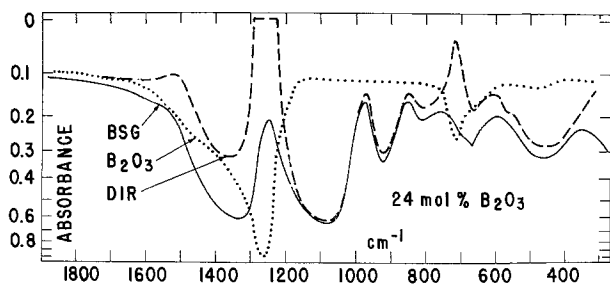


Fig. 6. DIR spectrum of an as-deposited borosilicate film containing 24 m/o B_2O_3 vs. a corresponding pure B_2O_3 film deposited under identical conditions of temperature and flow rates of B_2H_6 , O_2 , and N_2 . The curves labeled "BSG" and " B_2O_3 " are the normal infrared spectra taken vs. an identical layer of 400 \AA SiO_2 deposited on a bare Si wafer in the reference beam.

shown in Fig. 7. With increased B_2O_3 concentration, there is a gradual increase in both the halfwidth and intensity of the differential band at $\sim 1300\text{ cm}^{-1}$, exhibiting in both cases a maximum around 40 m/o B_2O_3 . The frequency of maximum absorption, however, decrease continuously from 1380 cm^{-1} at 85 m/o B_2O_3 to 1260 cm^{-1} for pure B_2O_3 . This mode is clearly associated with the stretching vibration of the B-O sublattice and is perturbed by the presence of the less polarizing Si^{4+} cation substituting for an equally polarizing B^{3+} cation as the next-nearest neighbor; thus effectively increasing the force constant of the B-O bond in the mixture. The spectral variations of this differential B-O mode lend further support to the existence of the B-O-Si linkage in CVD B_2O_3 - SiO_2 films and its distribution as a function of film composition deduced earlier in a described analysis of the 930 cm^{-1} band in the normal infrared spectrum (8).

Effects of Annealing at 700°C on Binary Films

Because of the metastable nature of materials in the glassy state, their properties are very much dependent on the mode of preparation as well as on thermal history. This is more so in the case of glass films that can be made by a variety of methods and at various deposition temperatures. In fact, the deviation from the most stable equilibrium state, *i.e.*, the crystalline state, can be much greater in vapor deposition than in melt-quenching processes. Technologically, CVD films are often heat-treated at temperatures above their deposition temperature during processing (2). The effects of annealing on the structure and hence properties of these films are therefore of fundamental interest. In the case of pure CVD B_2O_3 discussed above, annealing at 700°C for 10 min in N_2 brought about $\sim 100\%$ increase in the half-width of the B-O band at 1260 cm^{-1} in the infrared spectrum. We proceeded to study the effect of similar annealing on the binary films.

In Fig. 8 the normal infrared spectra of a 24 m/o B_2O_3 film before and after annealing at 700°C for 10 min in N_2 are given. Changes in bandwidth $\Delta\nu_{1/2}$ and/or absorbance at band maximum A are observed at

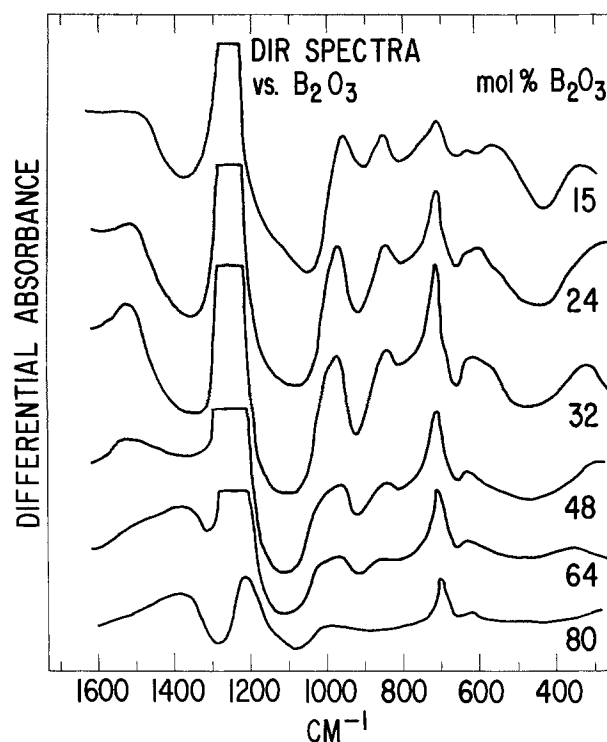


Fig. 7. DIR spectra of a series of as-deposited BSG films containing 15-80 m/o B_2O_3 ; each spectrum was taken vs. the corresponding B_2O_3 film and covering SiO_2 layer.

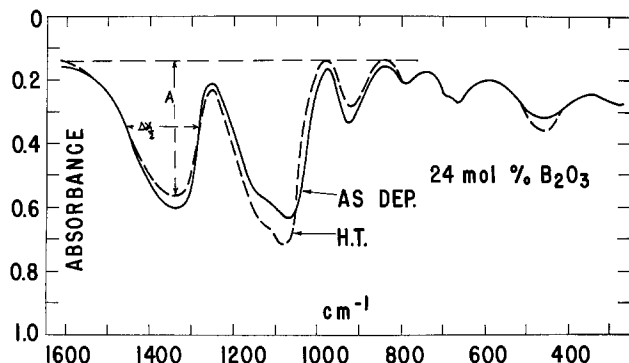


Fig. 8. Room temperature infrared spectra of a BSG film containing 24 m/o B_2O_3 before and after being heat-treated at $700^\circ C$ for 10 min in N_2 . Measurements of band absorbance A and band-width $\Delta\nu_{1/2}$ of the B-O band at $\sim 1300\text{ cm}^{-1}$ for the heat-treated film (dotted trace) are illustrated.

$\sim 1300\text{ cm}^{-1}$, 1100 cm^{-1} , 930 cm^{-1} , and to a lesser extent at 450 cm^{-1} . These spectral variations were studied as a function of film composition and are summarized as follows.

Upon annealing at $700^\circ C$, the B-O band at $\sim 1300\text{ cm}^{-1}$ in all films containing up to 48 m/o B_2O_3 shows an increase in $\Delta\nu_{1/2}$ accompanied by a corresponding decrease in A so that, within an experimental accuracy of $\pm 5\%$, there is no change in (integrated) band intensity due to heat-treatment, (Table I). The increase in $\Delta\nu_{1/2}$ is indicative of a "quenching-in" of high temperature B-O configurations having a broader distribution.

As shown in the section of DIR spectra, the absorption in the region 1100 cm^{-1} is complex and consists at least of two types of oscillators: Si-O and B-O-Si. With annealing the width of this band remains essentially constant for all compositions studied. However, the absorbance at band maximum and, hence, the integrated intensity, increases. The ratio of band intensity of heat-treated to that of the as-deposited is given in Table I as a function of B_2O_3 content.

On the other hand, the absorbance of the B-O-Si band at 930 cm^{-1} decreases at constant bandwidth upon annealing. The ratio of the band intensity of heat-treated to that of the as-deposited decreases with increased B_2O_3 content in the film. Since the intensity decreases at constant bandwidth, this implies that there is an apparent decrease in the number of B-O-Si oscillators upon annealing, which in turn may be brought about by phase separation, resulting in a change of the distribution of the B-O-B, Si-O-Si, and B-O-Si linkages from the ideal distribution (8). This qualitatively correlates with the increase of band intensity of the Si-O band at 1100 cm^{-1} . Thus, the B-O-Si band at 930 cm^{-1} is a very sensitive probe to structural changes in the borosilicate system.

Finally, a two-layer thin-film structure consisting of a 400 \AA CVD film of pure SiO_2 on a 4000 \AA film of

Table I. Effect of annealing on band intensities expressed as ratio of integrated intensities ^(a), ^(b) of heat-treated and as-deposited film

Film composition (m/o B_2O_3)	B-O band at $\sim 1300\text{ cm}^{-1}$	Si-O band at $\sim 1100\text{ cm}^{-1}$	B-O-Si band at 930 cm^{-1}
15	0.95	1.09	1.13
24	0.97	1.19	0.84
32	1.04	1.26	0.77
39	0.94	1.15	0.65
48	1.05	1.11	1.03

^(a) Integrated intensities are approximated by the product $\Delta\nu_{1/2} \times A$ where $\Delta\nu_{1/2}$ is the half-width and A is absorbance of band maximum. (Cf. Fig. 8.)

^(b) Estimated accuracy of intensity ratio $\pm 5\%$.

pure B_2O_3 vapor-deposited sequentially at $350^\circ C$ in a single crystal Si substrate was annealed *in situ* in the CVD reactor at $700^\circ C$. At this temperature the expansivity of B_2O_3 is large enough to cause material ejection through pinholes in the SiO_2 layer which is rigid and has almost zero expansivity, thus resulting in the "exploded" flow pattern shown in Fig. 9. This is a color micrograph taken with reflected white light. The dark fringes in the middle of the pinhole indicate a "punch-through" of the glass layers exposing the surface of the Si substrate. The band of jagged circular color fringes indicates a radial thickness gradient of the B_2O_3 layer about the center of the pinhole. The green and yellow regions in the radial pattern correspond to ridges and valleys respectively of the ejected B_2O_3 . This multilayer of configuration constitutes a novel method of pinhole detection in thin films and is applicable to a variety of thin films, whether metallic, dielectric, or semiconducting with thickness ranging from 100 \AA to $1\text{ }\mu\text{m}$ or more.

Concluding Remarks

The infrared transmission spectra of thin borosilicate glass films vapor-deposited on Si from B_2H_6 - SiH_4 - O_2 source at low temperatures have been studied systematically across the whole composition of the binary system. The effect of thermal history on the structure

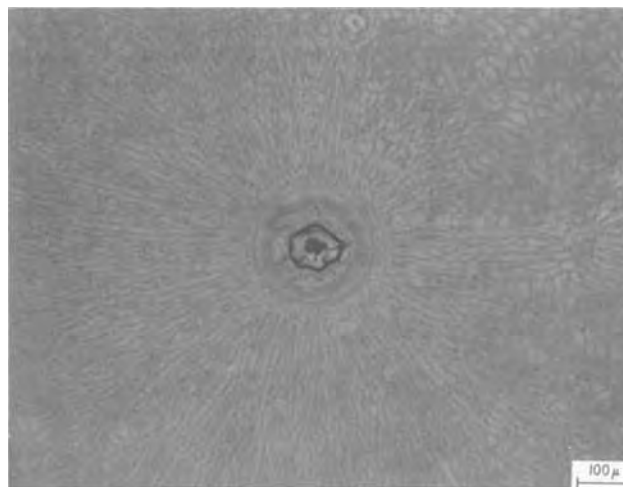


Fig. 9. Reflected light micrograph of an "exploded" flow pattern of liquid B_2O_3 through a pinhole defect in a covering layer of SiO_2 . See text for description of the thin film structure.

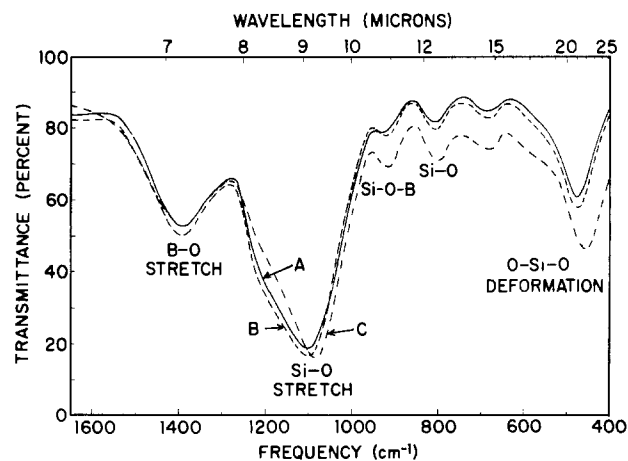


Fig. 10. Infrared spectra of Corning Pyrex films (23) illustrating the similarity and usefulness of the binary borosilicate spectra in understanding more complex borosilicate system. (A) Sedimented powder; (B) annealing (A) at $450^\circ C$; (C) fusing (A).

of CVD glasses deposited above T_g as in the case of B_2O_3 is contrasted with that of CVD SiO_2 deposited at temperatures far below the T_g of the bulk material. In the former case, where configurational relaxation is possible at deposition temperatures, the infrared spectrum and hence the structure of as-deposited B_2O_3 is not dependent on deposition temperature even when deposited as a liquid film at 600°C. Heat-treating the as-deposited film further to 700°C, however, results in an increase in the bandwidth of the B-O band at 1265 cm^{-1} , suggestive of a quenching-in of high temperature liquid configurations which in general exhibit a broader distribution. In the latter case, the infrared spectrum of as-deposited CVD SiO_2 exhibits broader absorption bands which progressively narrow with increasing heat-treatment temperature and finally approach the bulk values after heat-treating at 1000°C. The spectral observation is associated with a densification process in glass films deposited far below its T_g and is substantiated by other physical property changes such as increases in density, refractive index, etch rate, etc.

Differential infrared data on the binary glasses lead to the resolution of a band at $\sim 1130\text{ cm}^{-1}$ assigned to a bond-stretching vibration of the Si-O-B linkages in the glass structure. The intensity variation of this band with composition lends further support to the structural model proposed earlier for the B_2O_3 - SiO_2 glass system in which the boron and silicon are three-fold and four-fold coordinated with oxygen, respectively, and each oxygen is bridging a pair of B and/or Si atoms to form a three-dimensional random network. Deviation from this ideal distribution was observed for glasses containing 15-48 m/o B_2O_3 upon annealing at 700°C, as a result (possibly) of phase separation. It is also concluded that the B-O-Si at 930 cm^{-1} is a very sensitive probe to structural changes in the borosilicate system.

Finally, the analysis of the infrared spectra of the binary B_2O_3 - SiO_2 system may serve as a basis of interpreting and understanding the vibrational spectra of more complex borosilicate glasses such as those studied by Pliskin (23) shown in Fig. 10. It is clear from the present DIR data that in Fig. 10 the absorption at 1100 cm^{-1} has in addition to the Si-O stretch, a B-O-Si band at $\sim 1125\text{ cm}^{-1}$ (cf. Fig. 3-5 and discussion thereof). Similarly, in the absorption at $\sim 450\text{ cm}^{-1}$ in the complex borosilicate glass shown in Fig. 10 has a O-B-O deformation mode at 500 cm^{-1} superimposed on the O-Si-O band (cf. Fig. 3).

Manuscript submitted Feb. 20, 1979; revised manuscript received July 22, 1979.

Any discussion of this paper will appear in a Discussion Section to be published in the December 1980

JOURNAL. All discussions for the December 1980 Discussion Section should be submitted by Aug. 1, 1980.

Publication costs of this article were assisted by General Electric Company.

REFERENCES

1. W. Kern and R. C. Heim, *This Journal*, **117**, 568 (1970).
2. D. M. Brown and P. R. Kennicott, *ibid.*, **118**, 293 (1971).
3. W. M. Feist, S. R. Steele, and D. W. Readey, *Phys. Thin Films*, **5**, 239 (1967).
4. J. Wong and C. A. Angell, "Glass: Structure by Spectroscopy," Chap. 8, Marcel Dekker Inc., New York (1976).
5. J. Wong, *J. Electron. Mater.*, **5**, 113 (1976).
6. L. G. Van Uitert, D. A. Pinnow, J. C. Williams, T. C. Rich, R. E. Jaeger, and W. G. Grodkiewicz, *Mater. Res. Bull.*, **8**, 469 (1973).
7. W. G. French, A. D. Pearson, G. W. Tasker, and J. B. MacChesney, *Appl. Phys. Lett.*, **23**, 338 (1973).
8. A. S. Tenney and J. Wong, *J. Chem. Phys.*, **56**, 5516 (1972).
9. A. S. Tenney, *This Journal*, **118**, 1658 (1971).
10. W. A. Plisken and E. E. Conrad, *IBM Syst. J.*, **8**, 43 (1964).
11. J. Wong, *J. Non-Cryst. Solids*, **20**, 83 (1976).
12. T. A. Sodorov and N. N. Sobolev, *Opt. Spectrosc. USSR*, **3**, 360 (1957).
13. E. H. Fontana and W. A. Plummer, *Phys. Chem. Glasses*, **7**, 139 (1966).
14. N. Nagasima, *J. Appl. Phys.*, **43**, 3378 (1972).
15. J. Wong, *J. Appl. Phys.*, **44**, 5629 (1973).
16. R. J. Bell, N. F. Bird, and P. Dean, *J. Phys. C.*, **1**, 299 (1968).
17. R. C. Mozzi and B. E. Warren, *J. Appl. Crystallogr.*, **2**, 164 (1969).
18. M. L. Barry, in "Chemical Vapor Deposition, 2nd International Conference," J. M. Blocher, Jr., and J. C. Withers, Editors, pp. 598-617, The Electrochemical Society Softbound Proceedings Series, New York (1970).
19. P. E. Jellyman and J. P. Proctor, *J. Soc. Glass Technol.*, **39**, 173T (1955).
20. J. Wong and C. A. Angell, "Glass: Structure by Spectroscopy," Chap. 7, Marcel Dekker, Inc., New York (1976).
21. C. F. Smith, Jr., Ph.D. Thesis, Alfred University (1973) and *Appl. Spectrosc.*, **29**, 79 (1975).
22. W. J. Potts, Jr., "Chemical Infrared Spectroscopy," Vol. 1, p. 165, John Wiley and Sons, Inc., New York (1963).
23. W. A. Plisken, in "Physical Measurement and Analysis of Thin Films," E. M. Must and W. G. Guldner, Editors, p. 168, Plenum Press, New York (1969).

Anodic Oxidation of GaP in N-methylacetamide for Electrical Profiling of Ion-Implanted GaP

Taroh Inada* and Yasuhide Ohnuki

College of Engineering, Hosei University, Koganei, Tokyo 184, Japan

ABSTRACT

The anodic oxidation of gallium phosphide in properly pH-adjusted NMA solutions was carried out under constant current conditions. Uniform oxides have been reproducibly grown in NMA with 10% H₂O. The pH was adjusted to 12 using NH₄OH and readjusted to 8.5-10 using citric acid. The oxide thickness-forming voltage relationship is linear, with a slope of approximately 11 Å · V⁻¹, independent of current density from 0.125-4.0 mA · cm⁻². The thickness of GaP consumed during the oxide growth (x_c)-forming voltage (V_f) relationship is also linear, but its slope varies with current density (J , mA · cm⁻²) and is described empirically as $dx_c/dV_f = 5 \cdot J^{-0.12}$ (Å · V⁻¹). Electrical carrier-concentration and mobility profiles in Zn-implanted GaP were obtained by differential Hall-effect and sheet-resistivity measurements combined with an oxide growth-stripping process, where anodization is performed under optimum defined conditions.

Investigation of electrical properties of ion-implanted semiconductors (1-3) is an important requirement for device application. This is due to the many crystal defects introduced by ion implantation into structure-sensitive semiconductors. Measurements of both carrier concentration and mobility profiles in ion-implanted semiconductors are needed. Many researchers have dealt with electrical profile measurements as functions of implantation parameters such as ion species, dose, implant energy and temperature, and annealing conditions (4-6).

Electrical profiling was performed by Hall-effect and sheet-resistivity measurements followed by a layer removal technique. In layer removal, a very thin layer (100Å or less) must be stripped reproducibly at every step. Two different semiconductor-layer removal techniques have been employed. One is a chemical etch (7) and the other is anodic oxidation stripping (8). The chemical etch rate varies over a wide range depending on temperature, and changes in composition of the etchant due to volatile components such as HF, H₂O₂, and H₂O. The effect of crystallinity of semiconductor to be removed on the etch rate is not small (9), and can affect the layer stripping of ion-implanted samples, where concentrations of impurities and defects are not uniform in the thickness direction.

An anodic oxidation may provide a uniform thickness oxide layer and thickness control can be achieved electrically if a proper electrolyte is used. Much data has been published on the anodization of GaAs (8, 10-13), and layer stripping has been employed in electrical profiling of ion-implanted GaAs (2, 3). Lorenzo *et al.* (14) reported on the use of anodic oxidation as a means of layer stripping in profiling electrical carrier concentration of ion-implanted InP. Few publications report on the anodization of GaP (15-17) and none report on electrical profiles in ion-implanted GaP. In this paper we will report the anodization conditions of GaP and the properties of the anodically oxidized layers. Optimum conditions or the anodization of GaP are proposed for the oxide growth-stripping cycle.

Experimental

The anodic oxidation of GaP was carried out in a Teflon beaker, which had a 4 mm diam opening in the bottom. A rubber gasket was placed between the beaker bottom and the GaP wafer to prevent leakage of electrolyte. The GaP wafer was placed on a copper

contact plate. The GaP wafers used in this experiment were either undoped or sulfur-doped n-type (111)-oriented single crystals with net carrier concentrations of $0.5-1.2 \times 10^{16}$ or $1.6-2.8 \times 10^{17}$ cm⁻³, respectively. Anodization was also done on p-type GaP layers formed by Zn implantation and annealing in these n-type substrates.

Prior to anodization chemical-mechanically polished GaP wafers were cleaned ultrasonically in TCE and methanol, dipped in dilute H₃PO₄, rinsed in deionized water, and dried in N₂ gas flow. All anodic oxidations were done by a constant current method at current densities from 0.125 to 4.0 mA · cm⁻². Voltage applied between the copper contact plate and a platinum cathode (cell voltage) was monitored on a high impedance (1000 MΩ) recorder.

Electrolyte solutions were N-methylacetamide (NMA) containing 10 weight percent (w/o) H₂O adjusted to a pH between 6.8 and 14 by adding NH₄OH and citric acid. A conventional pH meter with a glass electrode was used for the pH measurement. Electrical conductivity of the electrolyte was measured by an a-c method using separated platinum electrode plates (1 cm²). After anodization, half the grown oxide area was removed from the sample by masking and etching in dilute H₃PO₄. The thickness of the oxide layer was determined as a depth difference between the unetched oxide surface and the GaP surface using an interferometer. To get high resolution, the sample surface was coated with a vacuum-deposited Al layer prior to the interferometric measurement.

The thickness of GaP layer consumed during the oxide growth was measured as a depth difference between the original GaP surface (nonoxidized area) and the GaP surface exposed after the oxidation and oxide stripping. If the anodization was terminated at a low predetermined voltage of 10V, the GaP thickness consumed during the oxide growth was too thin to measure by interferometric technique. Therefore the oxidation and the oxide layer removal process was repeated until the total forming voltage reached 200V.

Concentration profiles of Ga, P, and O in grown oxide layers were measured by Auger electron spectroscopy (AES) combined with an Ar ion-sputter etching. The AES depth profiling was carried out using a Physical Electronics Industries cylindrical mirror-analyzer (Model 10-234G). The primary electron current and energy were 5 μA and 3 keV, respectively. After pumping to a pressure of 5×10^{-8} Torr, high purity argon (99.9995%) was introduced into the AES chamber until the pressure reached 5×10^{-5} Torr. The Ar

* Electrochemical Society Active Member.

Key words: gallium phosphide, anodization, composition profile, ion implantation, electrical profile.

ion energy used for sputter-layer stripping was 0.5 keV.

Carrier-concentration and mobility profiles of Zn-implanted GaP layers were measured by a differential Hall-effect and sheet-resistivity method. The implantation was carried out into the sulfur-doped n-type GaP with mass-separated Zn ions at an energy of 100 keV and at room temperature. After implantation, samples were annealed at 900°C in flowing N₂. Both front and rear surfaces were coated with sputter-deposited 1500Å thick SiO₂ films to prevent the thermal dissociation of the GaP surface layers during annealing. The van der Pauw configuration (18) for the Hall measurements was made by a standard photoresist technique with hot aqua regia (~55°C) etchant. Ohmic contacts were made by vacuum evaporation of Au metal (19). These contacts were used as anode contact during the anodic oxidation of Zn-implanted layers.

Results and Discussion

Anodic oxidation of GaP.—The anodic oxidation of GaP was carried out in NMA solutions having a pH of 6.8–14. Since pure NMA has a melting point of around 27°C, 10 w/o of H₂O was introduced into the pure NMA to lower the melting point before pH adjustment. The pH of NMA varied from 7.0 to 6.8 on adding H₂O, indicating that the NMA solution became acid.

Cell voltage vs. anodization time obtained from oxidations in different pH NMA solutions at a constant current density of 1.0 mA·cm⁻² are shown in Fig. 1. The numbers in parentheses show the pH used. The pH adjustment was achieved through two different procedures. The pH of Type A solutions was obtained by adding NH₄OH and that of Type B solutions was obtained by adding NH₄OH and citric acid. Type B solutions can be considered as “buffered solutions”. A linear relationship between cell voltage and anodization time was obtained when the anodization was done in a solution with a pH between 8.0 and 10. However, as seen in Fig. 1, many spikes appeared on the cell voltage-time curves for solutions of pH between 6.8 and 7.5, independent of electrolyte type.

Surface morphology of oxide layers grown in solutions of different pH were examined in an optical microscope. A distinct relationship was found between the creations of spikes on cell voltage-time curves and of surface pits on oxide layers. A very smooth surface,

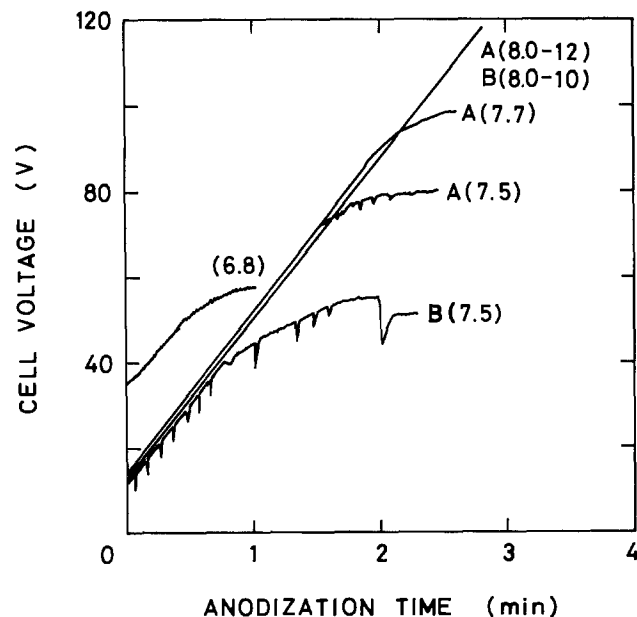


Fig. 1. Cell voltage vs. anodization time in NMA solutions with pH varied with NH₄OH, A, and NH₄OH and citric acid, B, and water, pH = 6.8.

and linear cell-voltage time curves, were obtained by anodization in solutions of pH between 8.5 and 10. Typical smooth surface of an oxide grown in Type A solution with a pH of 9.0 is given in Fig. 2(a). However a number of surface pits were observed on oxide layers grown both in Type A and B solutions with pH below 7.5 as shown in Fig. 2(b). Many spikes were observed on the cell voltage-time curve for this growth (see Fig. 1). When surface pits were formed in oxide layers, deep pits were also produced on the surface of the GaP substrate.

Electrical resistance of NMA solution was measured as a function of pH. Figure 3 shows the decrease in the electrical resistance observed on increasing the pH from 7.2 to 8.3 (Type A solution). Electrical resistance tended to be relatively insensitive to pH above 8.5 and homogeneous or pit-free oxide layers could be grown. Reduction in electrical resistance with increasing pH of NMA has also been reported by Muller *et al.* (8).

In preparing Type B solution, NH₄OH was added to the NMA solution to a pH of 12 and then citric acid was added. As the pH of the solution was decreased by citric acid, the electrical resistance decreased as illustrated in Fig. 3. The electrical resistance of Type B solution (pH = 7.5) was ~30 times less Type A solution (pH = 7.2). Anodization of GaP in this solution (Type B, pH = 7.5), gave a nonhomogeneous oxide layer, indicating that pH is a more critical factor than electrical resistance of the solution. A 20% reduction

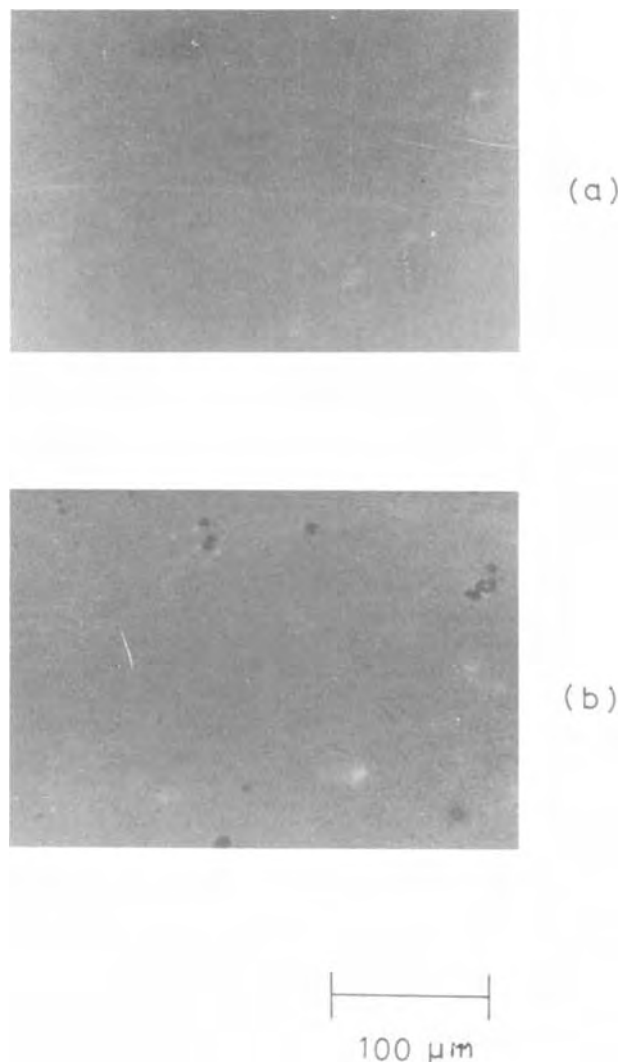


Fig. 2. Surface morphologies of oxidized GaP anodized at 1.0 mA·cm⁻² in Type A solution, pH = 9.0 (a), and in Type B solution, pH = 7.5 (b).

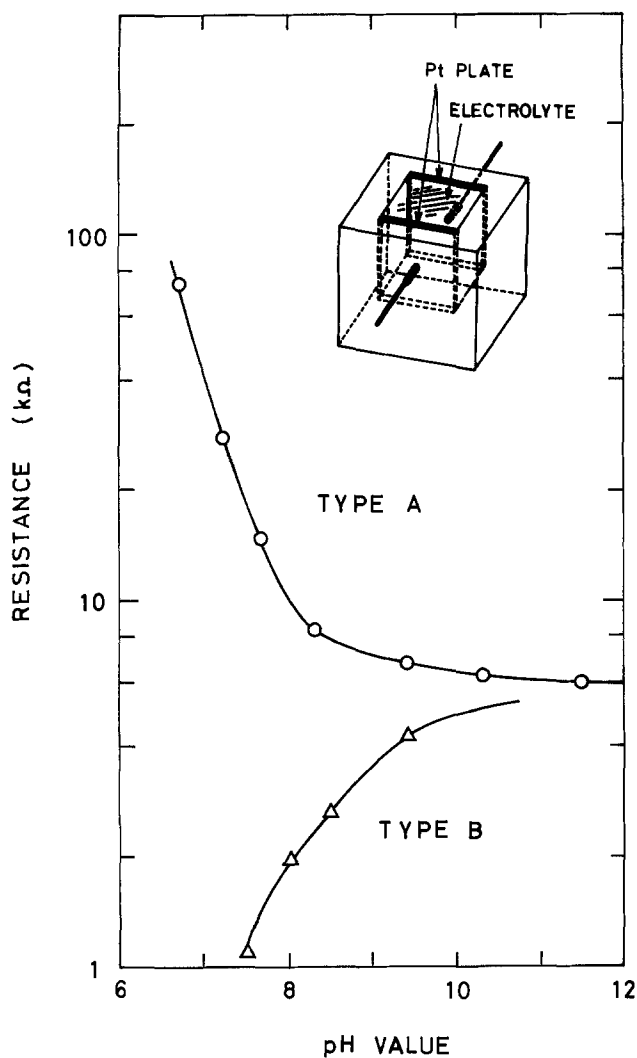


Fig. 3. Electrical resistance of NMA solutions vs. pH for Types A and B solutions measured with 1 cm^3 electrode configuration sketched in the figure.

in the pH of Type A solutions within several hours after these solutions were prepared was attributed to evaporation of volatile NH_4OH from the electrolyte. Thus, experimental data for Type A solutions shown in Fig. 1 and 3 were obtained by using freshly prepared solutions. No detectable change in the pH of Type B solutions was observed for at least two months.

It was concluded that the use of Type B solution with a pH between 8.5 and 10 was essential to achieve reproducible anodization of GaP with a homogeneous oxide layer. All experimental data given in the following section were obtained from the anodization in Type B solution with a pH of 9.0.

If anodic oxidation is carried out at constant current density, measured cell voltage can be divided into the following two components, i.e., a forming voltage (V_f) and another voltage drop (V_i). The V_f is a voltage drop due to oxide growth and increases with thickness of the oxide. The V_i depends on such external parameters as contact resistance originating from the interface between electrolyte and GaP surface, resistance of electrolyte, contact resistance between the rear surface of GaP and the copper contact plate, and bulk resistance of GaP substrate. Therefore, V_i is independent of anodization time or thickness of the oxide layer and can be estimated as an initial voltage appearing at anodization time = 0 on a cell voltage-time characteristic curve.

Figure 4 shows measured initial voltages as a function of current density. The effect of illumination on

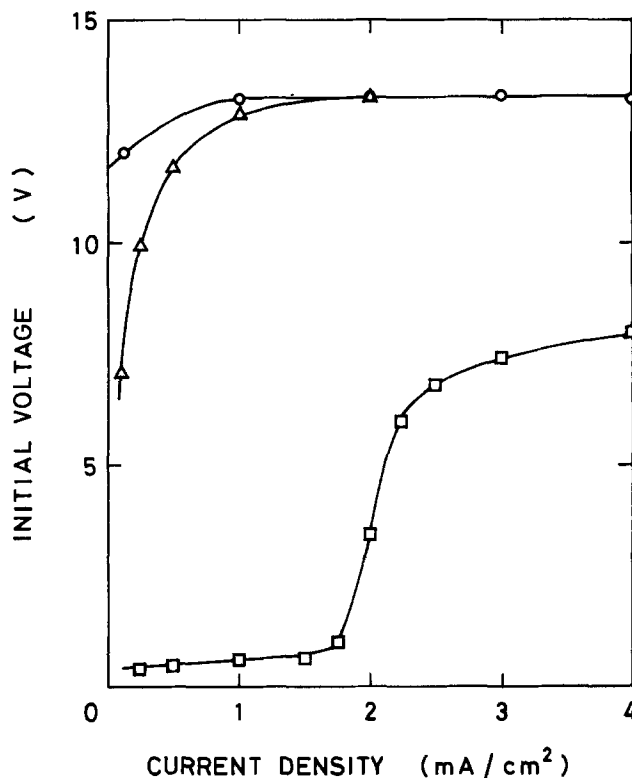


Fig. 4. Initial voltage vs. anodization current density for anodization in Type B solution pH = 9.0 under dark (\circ), and illuminated conditions; Δ : light intensity of 3.3×10^{16} quanta $\cdot \text{cm}^{-2} \cdot \text{sec}^{-1}$, and \square : light intensity of 1.7×10^{17} quanta $\cdot \text{cm}^{-2} \cdot \text{sec}^{-1}$.

the initial voltage was also examined using white light (2854°K) from tungsten lamps having different wattages. The light was focused to a 5 mm spot by a condensing lens and passed through the 4 mm diam opening in the bottom of the anodization cell. The light intensity was measured by replacing the GaP wafer with a standard GaP p-n junction photodetector whose absolute quantum efficiency had been calibrated as a function of wavelength. The initial voltage was reduced from 13.2 to 0.5V by illuminating the GaP surface at a light intensity of 1.7×10^{17} quanta $\cdot \text{cm}^{-2} \cdot \text{sec}^{-1}$, where the anodization was done on n-type GaP at a current density of $1.0 \text{ mA} \cdot \text{cm}^{-2}$. Note that the photon flux density gives intensity of light with energy above the bandgap of GaP. The results in Fig. 4 indicate that the major part of the initial voltage occurs at the GaP surface-electrolyte interface, since it is a highly photosensitive parameter.

The forming voltage (V_f) is plotted in Fig. 5 as a function of anodization time, and at current densities ranging from 0.125 to $4.0 \text{ mA} \cdot \text{cm}^{-2}$. The V_f was obtained by subtracting the initial voltages from measured cell voltages. The forming voltage increased linearly with anodization time for the current densities studied. The rate of increase with time (dV_f/dt) was approximately proportional to current density.

Oxide thickness and GaP consumed during the oxide growth at a current density of $1.0 \text{ mA} \cdot \text{cm}^{-2}$ are shown in Fig. 6 as a function of V_f . Growth rate of the oxide layer was defined as dx_o/dV_f , where x_o is the thickness of the oxide layer. From the slope shown in Fig. 6, the growth rate was found to be $11 \text{ A} \cdot V_f^{-1}$. The ratio of the thickness of oxide to thickness of GaP consumed was 2.2 at this current density over the forming voltage range studied.

As shown in Fig. 7, the oxide layer growth rate was independent of anodization current density from 0.125 to $4.0 \text{ mA} \cdot \text{cm}^{-2}$ and no Tafel slope (20) could be calculated. However, the amount of GaP consumed during the oxide growth within an increase of unit forming voltage (dx_c/dV_f) slightly increased with increasing

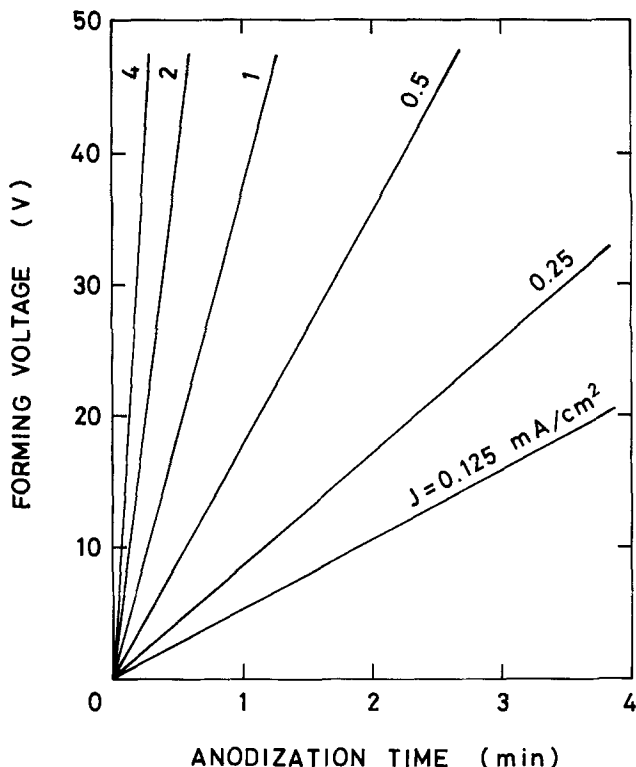


Fig. 5. Forming voltage vs. anodization time in Type B solution, pH = 9.0, at various current densities.

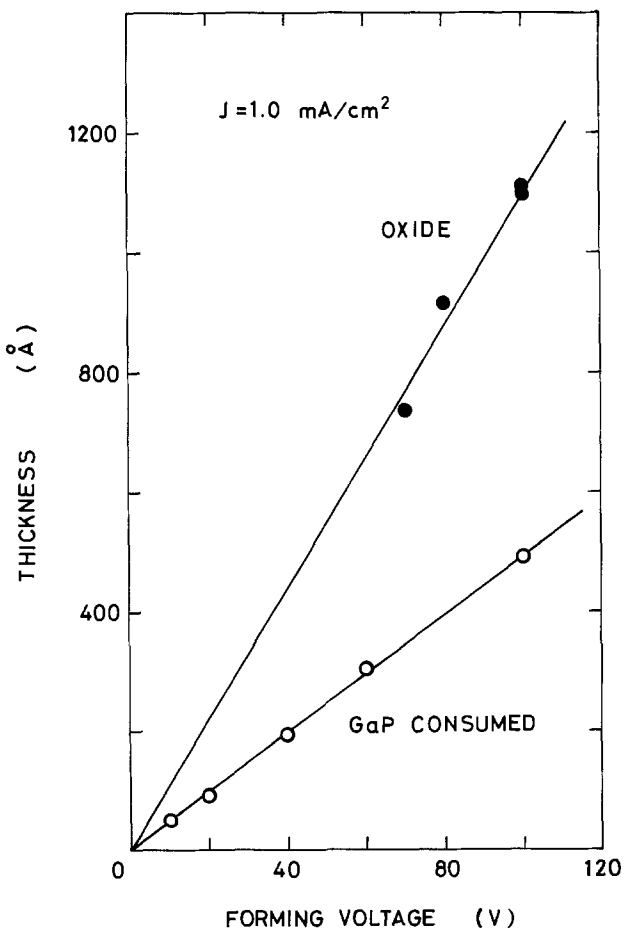


Fig. 6. Oxide thickness and amount of GaP consumed vs. forming voltage during anodization in Type B solution, pH = 9.0.

anodization current density and was described empirically as follows

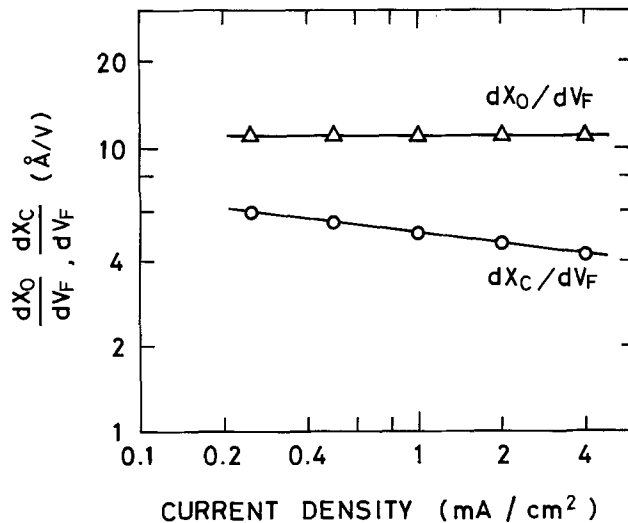


Fig. 7. Oxide growth rate (dx_0/dV_f) and amount of GaP consumed per unit forming voltage (dx_c/dV_f) vs. anodization current density for anodization in Type B solution, pH = 9.0.

$$\frac{dx_c}{dV_f} = 5 \cdot J^{-0.12} \quad (\text{Å} \cdot \text{V}^{-1})$$

where J is an anodization current density in $\text{mA} \cdot \text{cm}^{-2}$.

When anodic oxidation is used to thin GaP for differential electrical profiling, it is extremely important to know exactly the thickness of GaP removed at each stripping step. In general, the thickness of the GaP layer removed is calculated from the increase in V_f if the anodic oxidation is carried out at constant current. The results shown in Fig. 7 indicate that the layer stripping of GaP has to be carried out at a given current density throughout the in-depth electrical profile measurements when forming voltage is used to calculate the thickness of GaP removed.

AES measurements on anodically oxidized GaP layers.—Atomic concentration profiles in anodically grown oxide layers on GaP wafers were examined using Auger electron spectroscopy (AES) with an Ar ion-sputter stripping. The concentrations of oxygen, gallium, and phosphorus were measured by peak-to-peak height of Auger signals originated from O KLL-transition at 505 eV, the Ga LMM-transition at 1068 eV, and the P LMM-transition at 117 eV, respectively. The Auger signal due to the P KLL-transition at 1858 eV was also measured.

Figure 8(a) displays typical depth profiles for 500Å thick oxide layers grown at a current density of $2.0 \text{ mA} \cdot \text{cm}^{-2}$. The O concentration decreases with depth while the Ga concentration (LMM) and P concentration (KLL) are almost constant throughout the oxide layer. However, P LMM level increases gradually, corresponding to the decrease of O level, and becomes constant in the GaP bulk region. Previous work has shown that the variation of P LMM level with depth can be attributed to the chemical shift in the P LMM (21). Thus oxidized P atoms decrease along with decrease of the O concentration while nonoxidized P atoms increase in the oxide. The atomic ratio of P/Ga is uniform throughout the oxide layer. Concentrations observed by AES after the oxide layer was removed by dipping in a dilute H_3PO_4 solution are shown in Fig. 8(b). The trace O signal is believed to be a native oxide grown during sample handling.

Auger depth profiles from a 500Å thick oxide layer grown on n-type GaAs ($n = 1 \times 10^{18} \text{ cm}^{-3}$, Si-doped) using the same electrolyte (Type B, pH = 9.0) are shown in Fig. 9. The signals of Ga, As, and O were constant through the oxide layer with no decrease in O KLL level with depth.

Depth profiles of oxide layers formed on GaP at a current density of $0.25 \text{ mA} \cdot \text{cm}^{-2}$ are illustrated in Fig.

Fig. 8. Auger depth profiles for GaP anodically oxidized in Type B solution, pH = 9.0, $J = 2.0 \text{ mA} \cdot \text{cm}^{-2}$: (a) as-grown, (b) after dipping in dilute H_3PO_4 .

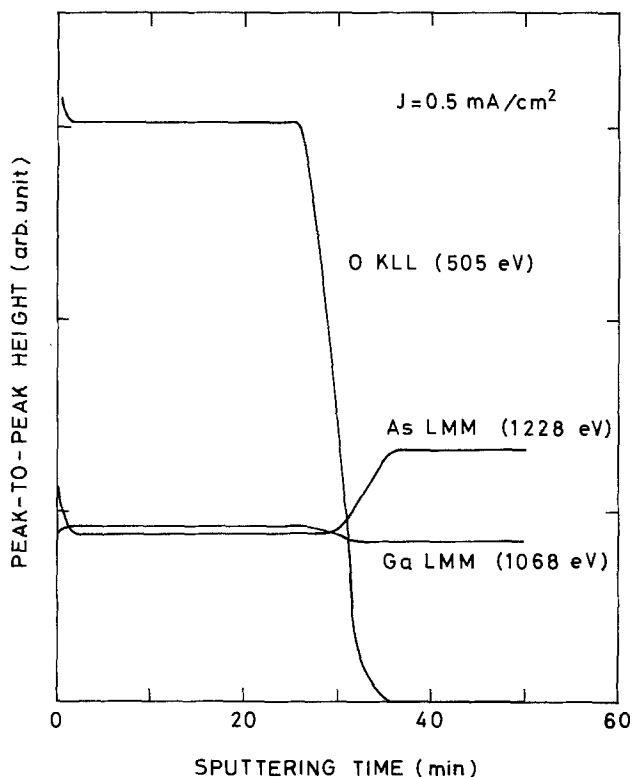
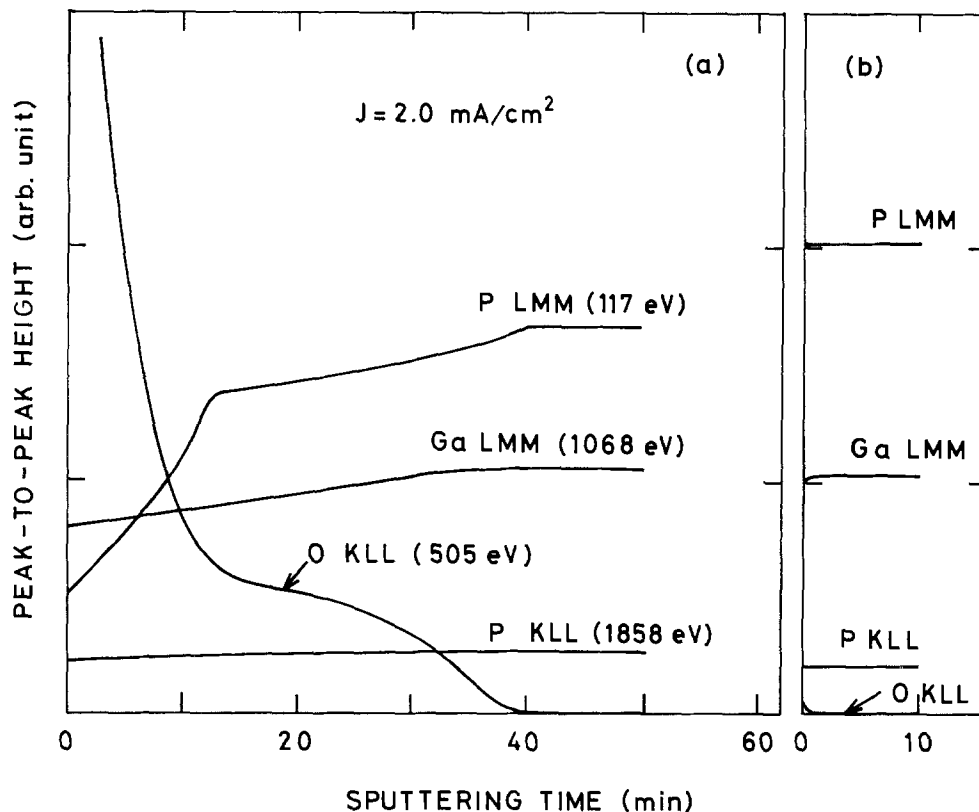


Fig. 9. Auger depth profiles for GaAs anodically oxidized in Type B solution, pH = 9.0, $J = 0.5 \text{ mA} \cdot \text{cm}^{-2}$.

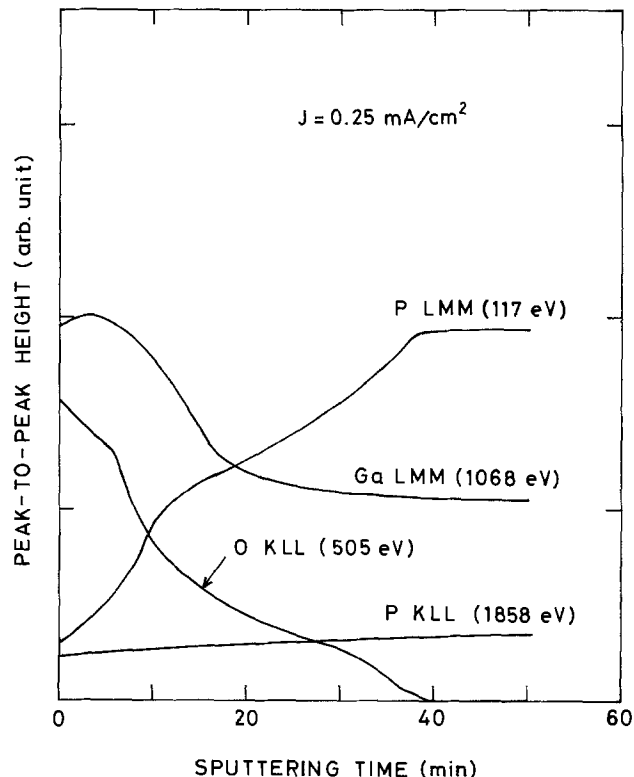


Fig. 10. Auger depth profiles for GaP anodically oxidized in Type B solution, pH = 9.0, $J = 0.25 \text{ mA} \cdot \text{cm}^{-2}$.

10. A decrease of O with depth was also observed in this sample. However the Ga profiles differ from those in oxide layers grown at higher current density. The Ga LMM levels near the surface are approximately two times higher than that in GaP bulk region, indicating an accumulation of Ga near the surface, after which the Ga and O KLL levels decreased in a similar way to oxide grown at a current density of $2.0 \text{ mA} \cdot \text{cm}^{-2}$. The reduction in P KLL level, which origi-

nates from total P atoms, was observed in this sample. This reduction was greater near the oxide surface, particularly at low anodization current density. These results suggest that the relative increase of Ga is related with preferential dissolution of the P oxide during anodization, and is consistent with the observation that oxide thickness is independent of anodization current while the thickness of GaP consumed increases at low current density.

Aging effect of anodically oxidized GaP.—To use anodically oxidized layers for surface passivation, a stable oxide is desired. Examination of surfaces of anodic oxide layers on GaP showed deterioration of oxide layers, which was attributed to a localized increase of the oxide thickness after storage in a laboratory atmosphere.

Anodic oxide layers on GaP of 1100Å thickness were prepared at six different current densities in the range from 0.125 to 4.0 mA·cm⁻². As-grown oxide surfaces were uniform and showed an interference color of blue. Typical surface morphologies of an oxide grown at 2.0 mA·cm⁻² are shown in Fig. 11. The as-grown surface is shown in (a) with the appearance of mesas after one day (b), which increased after two weeks (c), and 6 months (d). Almost all of the original oxide surface was covered with additional oxide after six months. Maximum thickness of the oxide layer was around 1400Å, in agreement with a change of color from blue to golden yellow.

Formation of mesa on anodically oxidized GaP layers strongly depended on the anodization current density used. Oxides grown at 0.25 mA·cm⁻² had no mesas after two weeks storage, although mesas were observed after one month which grew as the storage time was prolonged [see Fig. 11(e)]. Results obtained from a series of surface observations for oxide films

grown at different current densities are summarized in Fig. 12.

To obtain more stable oxides, anodic oxidation of GaP in NMA should be done using a low current density. However, the amount of oxide dissolved during the oxidation increases at low current density. To employ anodic oxidation thin layer removal for differential Hall-effect measurements on GaP, a knowledge of the exact thickness of the GaP removed *vs.* forming voltage and suppressed oxide dissolution are desired.

Electrical profiling of Zn-implanted GaP.—Carrier-concentration and mobility profiles in Zn-implanted GaP layers were obtained from successive Hall-effect and sheet-resistivity measurements following anodized layer stripping. The Zn-implanted GaP layers were anodized in Type B solution, pH = 9.0, at 1.0 mA·cm⁻². The thickness of the GaP layer stripped at each removal step was 50Å, obtained at a forming voltage of 10V. No difference in the ratio x_o/x_c was observed between S-doped n-type and Zn-implanted p-type layers. The initial voltage for the anodization of p-type GaP was small (0.6V at $J = 1.0$ mA·cm⁻²) even if the anodization was done under a dark condition. The illumination effect of reducing the initial voltage could not be observed in p-type GaP.

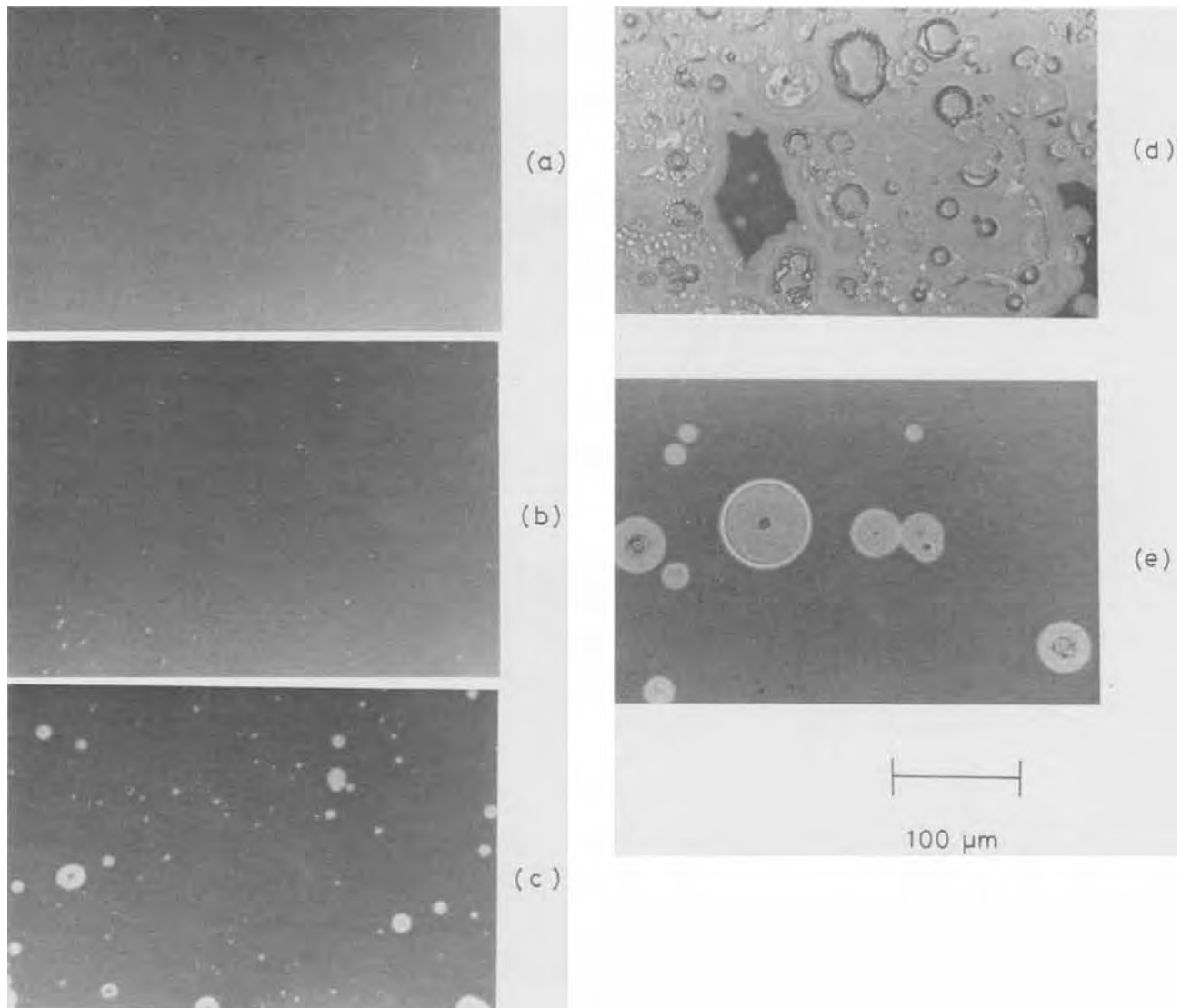


Fig. 11. Photographs showing changes of surface morphology of GaP anodically oxidized in Type B solution, pH = 9.0, after storage: (a) as-grown surface, (b) after one day, (c) after two weeks, (d) and (e) after six months. The sample shown in (a)-(d) was anodized at $J = 2.0$ mA · cm⁻² and (e) was anodized at $J = 0.25$ mA · cm⁻².

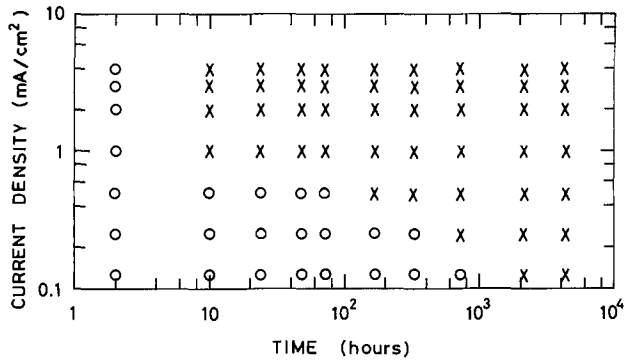


Fig. 12. Relationship between anodization current density and storage time when surface morphology changed from as-grown (O) to deteriorated (X). Anodization was done in Type B solution, pH = 9.0.

Typical carrier-concentration and mobility profiles for samples implanted at a Zn ion dose of $2.0 \times 10^{14} \text{ cm}^{-2}$ are shown in Fig. 13. From the carrier-concentration profile, the p-n junction depth can be estimated to be around $0.35 \mu\text{m}$ which agreed with that measured by angle-lap ($\theta = 1.5^\circ$) and staining. The measured carrier-concentration profile differed from the profile predicted by the LSS range-energy theory (22, 23). Apparently, diffusion of Zn during annealing determines the final carrier-concentration profile as previously reported for GaP (24), GaAs (25), and GaAsP (26). Mobility in the Zn-implanted layer agreed with mobility in bulk GaP for hole concentrations equal to the measured carrier concentrations (27). Electrical profiles and electrical characteristics of Zn-implanted p-n junction diodes will be separately reported.

Summary

Conditions for anodic oxidation of GaP in electrolytes consisting of NMA, water, NH_4OH , and citric acid were defined for reproducible differential electrical profiling of GaP. The best conditions were: (i) NMA with 10% H_2O adjusted to pH = 12 with NH_4OH and readjusted to 8.5-10 with citric acid, (ii) 0.5-1.0 $\text{mA}\cdot\text{cm}^{-2}$ anodic current density, (iii) 10-100V forming voltage, consuming 50-500Å GaP at $J = 1.0 \text{ mA}\cdot\text{cm}^{-2}$, (iv) oxide growth rate 11Å per unit forming voltage, and (v) illuminated sample to reduce the initial voltage. Since the amount of GaP consumed depends on current density a constant current density is required.

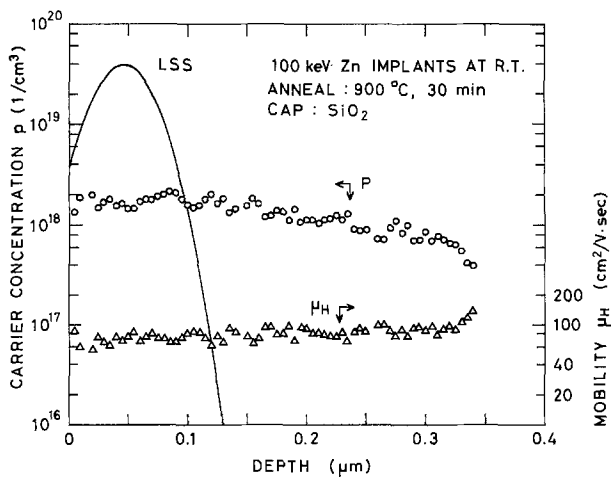


Fig. 13. Electrical carrier-concentration and mobility profiles in GaP Zn-implanted at $2.0 \times 10^{14} \text{ ions}\cdot\text{cm}^{-2}$ and annealed 30 min at 900°C . Anodization for layer stripping was done in Type B solution, $J = 1.0 \text{ mA}\cdot\text{cm}^{-2}$.

Surface deterioration of the grown oxide occurred during storage and was worse for oxides grown at a higher current density. This limits the use of grown oxide for passivation and diffusion masks but does not affect electrical profiling as was shown in this work.

Acknowledgments

We would like to express our appreciation to A. Okada of RCA Research Laboratories, Inc. for the use of the AES analyzer and for his fruitful discussion on the AES data.

Manuscript submitted March 19, 1979; revised manuscript received June 18, 1979.

Any discussion of this paper will appear in a Discussion Section to be published in the December 1980 JOURNAL. All discussions for the December 1980 Discussion Section should be submitted by Aug. 1, 1980.

Publication costs of this article were assisted by Hosei University.

REFERENCES

1. J. P. Donnelly, "Gallium Arsenide and Related Compounds," p. 166, The Institute of Physics, London and Bristol (1977).
2. K. Gamo, T. Inada, S. Krekeler, J. W. Mayer, F. H. Eisen, and B. M. Welch, *Solid-State Electron.*, **20**, 213 (1977).
3. T. Inada, H. Miwa, S. Kato, E. Kobayashi, T. Hara, and M. Mihara, *J. Appl. Phys.*, **49**, 4571 (1978).
4. J. W. Mayer, L. Eriksson, and J. A. Davies, "Ion Implantation in Semiconductors," Academic Press, New York and London (1970).
5. G. Dearnaley, J. H. Freeman, R. S. Nelson, and J. Stephen, "Ion Implantation," North-Holland Publishing Co., Amsterdam and London (1973).
6. R. G. Wilson and G. R. Brewer, "Ion Beams," John Wiley and Sons, New York and London (1973).
7. S. S. Kular, B. J. Sealy, and K. G. Stephens, *Electron. Lett.*, **14**, 2 (1978).
8. H. Muller, F. H. Eisen, and J. W. Mayer, *This Journal*, **122**, 651 (1975).
9. J. F. Gibbons, E. O. Hechtel, and T. Tsurushima, *Appl. Phys. Lett.*, **15**, 117 (1969).
10. S. M. Spitzer, B. Schwartz, and G. D. Weigle, *This Journal*, **122**, 397 (1976).
11. H. Hasegawa and H. L. Hartnagel, *ibid.*, **123**, 713 (1976).
12. L. C. Feldman, J. M. Poate, E. Ermanis, and B. Schwartz, *Thin Solid Films*, **19**, 81 (1973).
13. T. Ishii and B. Jeppson, *This Journal*, **124**, 1784 (1977).
14. J. P. Lorenzo, D. E. Davies, and T. G. Ryan, *ibid.*, **126**, 118 (1979).
15. F. Ermanis and B. Schwartz, *ibid.*, **121**, 1665 (1974).
16. J. M. Poate, P. J. Silverman, and J. Yahalom, *ibid.*, **120**, 844 (1973).
17. B. Schwartz, F. Ermanis, and M. H. Brastad, *ibid.*, **123**, 1089 (1976).
18. L. van der Pauw, *Phillips Res. Rep.*, **13**, 1 (1958).
19. T. Inada and Y. Ohnuki, "Ion Implantation in Semiconductors," p. 107, Plenum Press, New York and London (1974).
20. J. O'M. Bockris, Editor, "Modern Aspects of Electrochemistry," No. 4, p. 176, Butterworth, London (1966).
21. A. Okada, Y. Ohnuki, and T. Inada, *Appl. Phys. Lett.*, **33**, 447 (1978).
22. J. Lindhard, M. Scharff, and H. Schitt, *K. Dan. Vidensk. Selsk. Mat. Fys. Medd.*, **33**, 1 (1963).
23. J. F. Gibbons, W. S. Johnson, and S. W. Mylroie, "Projected Range Statics," Dowden, Hutchinson and Ross, Stroudsburg, Pennsylvania (1975).
24. T. Inada and Y. Ohnuki, *Appl. Phys. Lett.*, **25**, 228 (1974).
25. M. C. Boissy and D. Diguët, *This Journal*, **125**, 1505 (1978).
26. T. Itoh and Y. Oana, *Appl. Phys. Lett.*, **24**, 320 (1974).
27. H. C. Casey, J. F. Ermanis, and K. B. Wolfstrin, *J. Appl. Phys.*, **40**, 2945 (1969).

Vapor Transport of Zirconium and Silicon during Heat-Treatment of Zircaloy in Silica

D. R. Knittel and D. Cubicciotti*

SRI International, Menlo Park, California 94025

ABSTRACT

When pieces of Zircaloy are heated above 600°C in sealed silica capsules, silicon is deposited on the Zircaloy surface as zirconium silicides and zirconium is deposited on the silica in two forms: as an oxide layer in the high temperature region and as a metallic mirror on lower temperature surfaces. Samples of Zircaloy were heated in silica capsules under various conditions and analyzed by scanning electron microscopy. The results indicate that the deposits resulted from vapor transport processes involving volatile zirconium and silicon fluorides. Residual fluoride on Zircaloy surfaces, remaining from acid pickling treatments, was observed by Auger electron spectroscopy and mass spectroscopy in amounts sufficient to cause the transport. The thermodynamics of the vapor transport reactions are in accord with the fluoride mechanism.

Heat-treatment of small pieces of zirconium or its alloys is often performed in sealed silica capsules; however, that procedure results in significant changes. In particular, the metal surfaces become contaminated with silicon. Demant and Wanklyn (1) observed that Zircaloy samples become contaminated during heat-treatment in silica capsules and this leads to an increase in the initial oxidation rate of the metal. Cox (2) ascribed this contamination to a deposit of Si transported by gaseous SiO during the heat-treatment.

In addition to silicon deposition on the Zircaloy, zirconium-containing compounds form on the silica. Feuerstein (3) found that when Zircaloy was heated to 600°C and higher in evacuated silica tubes a white-gray deposit formed on the silica wall around the capsule. Neutron activation analysis showed the deposit contained Zr and traces of Sn (3). Feuerstein (3) also found that when open Zircaloy capsules containing ZrI₄ were heated to 800°C in evacuated silica tubes, a mirror-like metallic deposit formed on the silica around the open capsule. The deposit also formed on surfaces of ZrO₂ and Al₂O₃. Analysis showed the mirror deposit to be Zr with a few percent Sn (3). During the process, the Zircaloy capsule turned gray and the surface became roughened. Feuerstein associated the transport of zirconium with small amounts of adventitious iodine remaining in the system.

These examples show that when Zircaloy is heated in silica there is transfer of Zircaloy to the silica surface and silicon to the metal. As Cox (2) has noted, the silicon on the Zircaloy surface probably has a significant influence on corrosion rates. Silicon on the Zircaloy surfaces may have influenced corrosion results obtained on samples heat-treated in silica.

We have investigated reactions that occur during heat-treatment of zirconium alloys in silica. Our results indicate that silicon and zirconium are vapor-transported by volatile fluorides of these elements under the conditions of our experiments. Residual fluoride is found on the surfaces of zirconium alloys after bright-dipping or pickling treatments. [Under other experimental conditions, especially in the absence of fluoride, vapor transport by SiO may be important, as suggested by Cox (2).]

Experimental

Pieces of Zircaloy-4 sheets 1 × 3 × 0.08 cm obtained from Teledyne Wah Chang Albany (batch number Ht. 393533Q Zr-4) were used. The samples

* Electrochemical Society Active Member.

Key words: evaporation, mass transport, ceramics, metals.

were cleaned in acetone, methanol, and water in an ultrasonic cleaner. They were then tested: (i) as received and after the following treatments: (ii) heating in a dynamic vacuum at 900°C to remove volatile surface species, (iii) argon ion etching for 2 hr, which removed a surface layer of about 2 μm, and (iv) chemical etching in HF-HNO₃-H₂O₂ pickling solution. Each sample was inserted into a silica capsule (1.5 cm in diam, 14 cm long), which was evacuated and sealed. The end of the capsule containing the Zircaloy foil was then heated to 900°C, and the other end heated to 650°C. A photograph of a typical capsule and a diagram of the temperature gradient is shown in Fig. 1. In other experiments the whole capsule was heated at a uniform temperature of 900°C. Transport of zirconium and silicon was also observed when capsules were maintained at 700°C. Samples were heated for times varying from 2 min to 50 hr. Shorter time experiments showed less pronounced effects.

Physical and chemical characteristics of the samples were studied in a scanning electron microscope (SEM). A Cambridge Research Laboratory instrument was used in which x-ray fluorescence analyses were performed with a wavelength dispersive detector (Microscope Corporation, Sunnyvale, California), and an energy dispersive analyzer (Kevex Corporation, Burlingame, California). With that system we could detect oxygen, carbon, nitrogen, and heavier elements. It was not possible to detect fluorine, since its peaks were masked by those of zirconium.

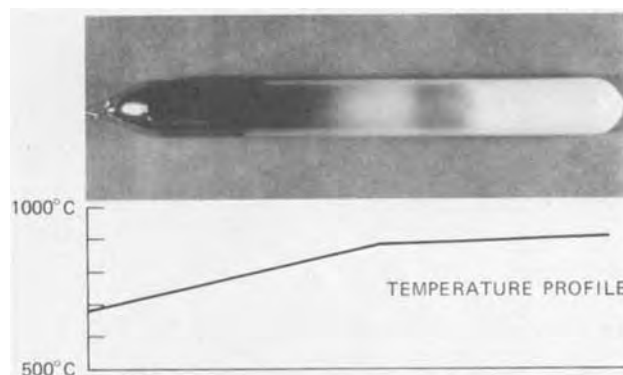


Fig. 1. Photograph of a sealed silica tube containing Zircaloy foil which had been heated in a temperature gradient for 6 hr. The Zircaloy foil is difficult to discern but is inside the white region at the right end. The metallic mirror deposit extends over about 4 cm at the left end. The tube had an inside diameter of 1.5 cm and is 14 cm long.

Surface analyses for fluorine were performed with an Auger electron spectrometer (Varian Cylindrical Mirror Analyzer). To investigate the volatile species a surface layer was machined from the inner surface of a Zircaloy-4 tube (Sandvik Special Metals Corporation) and those turnings were heated in a molybdenum effusion cell in a direct-inlet, high temperature mass spectrometer. The mass spectrometer system is described elsewhere (4).

Results

The effects of heating as-received Zircaloy (6 hr at 900°C) in an evacuated silica capsule are illustrated in Fig. 1. There were three distinct regions on the inner wall of the capsule: (i) a white (sometimes gray) deposit around the Zircaloy foil in the 900°C region, which was heaviest on the side of the foil closest to the silica, (ii) a region in which there was no deposit, in the 800°-900°C temperature zone, and (iii) a metal-mirror deposit, heaviest in the 750°-800°C region and becoming thinner towards the cooler end of the capsule. No metallic deposit was observed when the cooler end of the capsule was maintained at 400°C.

SEM analyses showed the presence of Zr on the silica in both the white deposit and the metal-mirror deposit regions and the presence of Si on the Zircaloy foil. The ratio of the peak height in SEM of Zr to Si was ~ 4 in the white deposit region and 3-4 in the metal-mirror deposit region. No other elements besides Zr and Si (and oxygen) were observed on the silica. Figure 2 shows the structure of the white deposit. X-ray diffraction of that deposit showed it was primarily monoclinic ZrO_2 . In a one hour experiment the white deposit was found by SEM to be about 0.3 μm thick from which we estimate that about $1.5 \times 10^{-3} g$ of Zr had been deposited. The metal-mirror deposit was thinner and less dense than the white deposit. In the same one hour experiment the metallic deposit was found to be about 0.1 μm thick and contained about $0.5 \times 10^{-3} g$ of Zr (assuming the metallic deposit was $ZrSi$ and had a density of 4 g/cm^3). The electrical resistance of the mirror deposit, as determined by a simple two-probe test, was low in

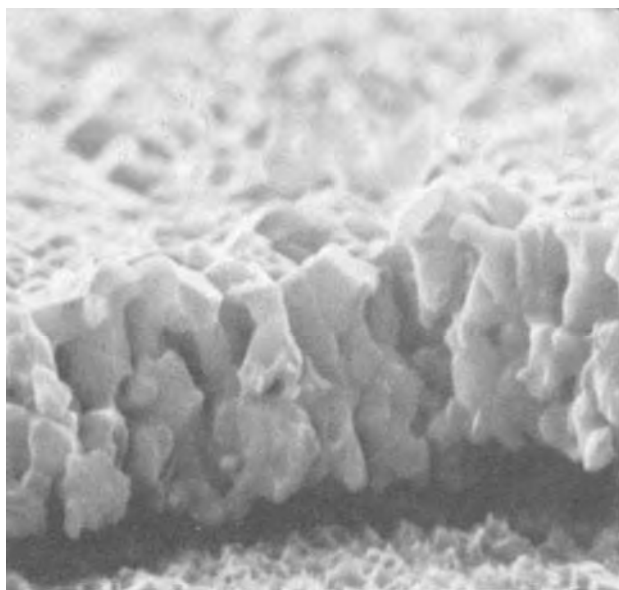


Fig. 2. SEM photograph of the fractured edge of white deposit on the silica in the 900°C temperature range. The silica capsule had been heated in the temperature gradient described in Fig. 1 for 50 hr. Analysis of the layer in the middle of the photograph showed mainly Zr with some Si and x-ray diffraction showed it to be ZrO_2 . The layer is very porous so that volatile species could readily permeate it. The layer near the bottom of the photo was silica.

keeping with its metallic appearance. The x-ray diffraction pattern of the metal mirror deposit could not be identified with the ASTM patterns.

The Zircaloy surface of the sample exposed in the same one hour experiment, was found in SEM to have a coating which was about 1 μm thick and had a Zr to Si ratio of about 1.5. Figure 3 shows the surface of a Zircaloy sample heated under similar conditions for 50 hr. The surface had a honeycomb structure and had a silicon to zirconium ratio of about one. It was found to be from 10 to 15 μm thick. The x-ray diffraction pattern of the surface showed the presence of small amounts of Zr_2Si but the more intense peaks could not be identified with the ASTM (5) patterns. We believe they were due to zirconium silicides whose diffraction patterns have not been reported (6). No oxygen was detected on the surface of the foil (however oxygen transported could have diffused into the bulk and not been detected).

When a silica capsule containing a Zircaloy sheet was heated in a constant temperature zone, no metallic deposit was found. A large amount of a white deposit of ZrO_2 , compared with the temperature gradient experiments described above, formed on the silica wall. In a 12 hr experiment, SEM observation of the metal surface showed that it was covered with a layer of material having a columnar structure 3-5 μm thick. X-ray diffraction analysis showed that Zr_2Si was the major species present.

The surface of a Zircaloy sample heated in a silica capsule at a uniform temperature of 900°C for 15 min is shown in Fig. 4. We analyzed the ridges which apparently decorated grain boundaries and found they contained only Zr and Si. The surface regions between the ridges also had silicon.

Some Zircaloy foils were heated in silica capsules that were not sealed but were kept under dynamic vacuum for 6 hr at 900°C. SEM examination showed no zirconium deposited on the silica walls and no silicon on the Zircaloy. One of these capsules was subsequently sealed under vacuum and heated an additional 6 hr at 900°C. SEM examination showed a little transfer of zirconium to the silica and some silicon on the Zircaloy. This suggested that only a small fraction of the transporting species remained after the heat-treatment in the dynamic vacuum.

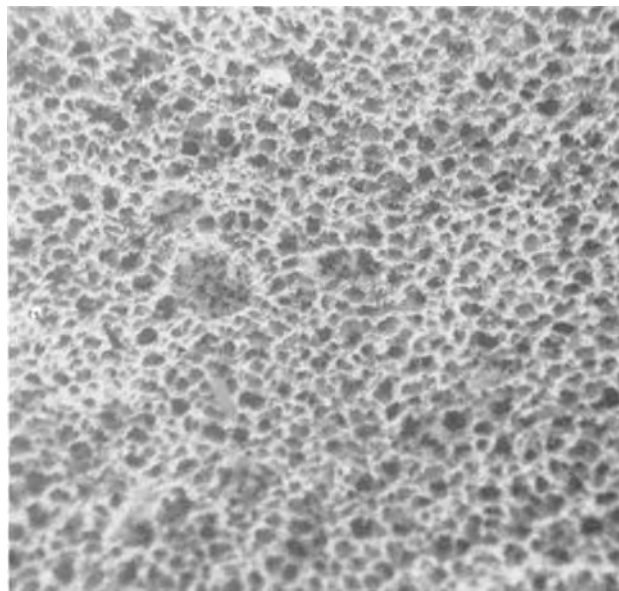


Fig. 3. SEM photograph of the surface of a Zircaloy-4 sample that had been treated in the temperature gradient described in Fig. 1 for 50 hr. Analysis of the surface showed Zr and Si in a ratio of ~ 1 . Width of photograph = 0.1 mm.

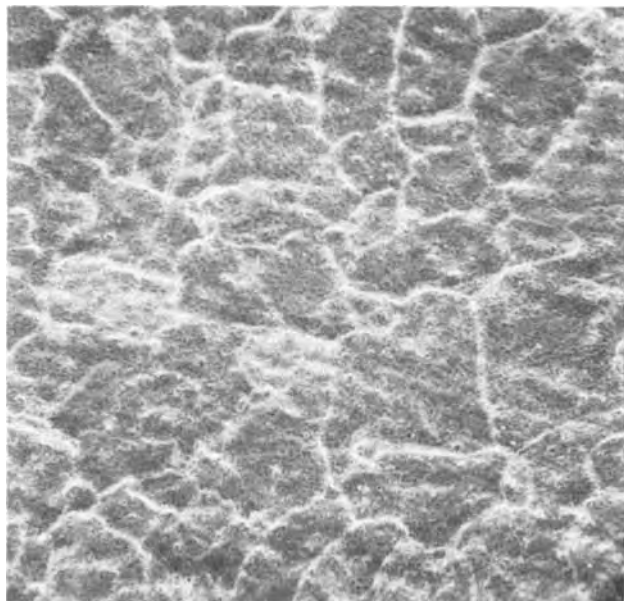


Fig. 4. SEM photograph of the surface of a Zircaloy-4 sample that had been heated at uniform temperature of 900°C for 15 min in a silica capsule. Analysis of the surface showed Si and Zr in both the ridges and valleys at a ratio of about 0.7. Width of the photograph = 0.1 mm.

To learn whether the species causing the transport was initially on the Zircaloy surface, we removed a 2 μm surface layer from a sample by Argon ion-etching for 2 hr. That treatment was presumably enough to remove the fluoride since others have shown that residual fluoride occurs only in the first 0.5 μm of a surface (7, 8). The sample was sealed in a silica tube and heated at 900°C for 6 hr. No transport of silicon to the Zircaloy or zirconium to the silica was observed.

Another sample was chemically etched with HF-HNO₃-H₂O₂ solution. Transport similar to that described for the as-received Zircaloy foil was observed after a 6 hr test. These results suggest that the species that causes the transport is on the Zircaloy surface. It is removed by heat-treatment in a dynamic vacuum, but remained after chemical etching. Thus we suspected that the transport was due to residual fluoride in the Zircaloy surface.

Zircaloy surfaces were examined by Auger electron spectroscopy (AES) for surface impurities. Fluorine (as well as O, C, Sn, and Zr) was found by AES on the surfaces of both the as-received and the chemically etched samples at about the same concentration and equivalent to about 2% of the surface atoms. The surfaces were ion etched in the AES apparatus to examine subsurface layers. Fluoride was detectable until about 0.1 μm of the surface had been removed. A rough estimate of the surface concentration of fluoride, based on these AES results, indicates there was about 0.2 $\mu\text{g}/\text{cm}^2$ of F on the Zircaloy surface. This compares well with Mackintosh (7) and Golicheff *et al.* (8). On the sample that had been heated in a dynamic vacuum, the AES study showed that about 0.1% of the surface atoms were F, which indicates that the dynamic vacuum heat-treatment removed most of the surface fluorine. We calculate that all the fluoride (0.2 $\mu\text{g}/\text{cm}^2$ of metal surface) in one of our typical experiments would produce a total pressure of about 1.3×10^{-5} atm of volatile metal tetrafluoride in the capsule.

Mass spectrometry was used to identify the volatile species. A surface layer was machined (without cutting oils) from the inside surface of a 50 cm length of 1 cm diam Zircaloy-4 tubing. The cuttings were placed in a molybdenum effusion cell and heated slowly in

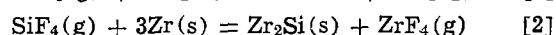
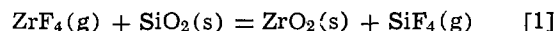
a direct-inlet mass spectrometer. When the temperature of the cell reached 370°C, ion peaks corresponding to ZrF₄ were observed. The major ion peak observed was Zr⁹⁰F₃⁺. Relative isotope intensities were in accord with natural isotopic abundances. No other vapor species were observed. The sample was heated at 900°C and ZrF₃⁺ disappeared in about one hour.

We then tried to establish whether there was a volatile species containing both zirconium and silicon which could have caused the transport of zirconium because the vapor pressure of zirconium itself was too small to account for the transport. A sample of Zircaloy was heated in a sealed silica capsule for 50 hr. A Zr-Si coating was found on the surface by SEM. That sample was then heated at 900°C for 50 hr in a silica tube open to a dynamic vacuum (10^{-5} Torr). A thin mirror-like deposit was formed on the cool walls of the tube; SEM examination showed that deposit contained no zirconium but was rich in chromium. Apparently the chromium component of the Zircaloy had evaporated. However, no zirconium had been transported. The partial pressures of any zirconium-bearing species must have been quite small, we estimate less than 10^{-13} atm. Therefore the transporting gas species was not a Zr-Si molecule.

Discussion

The experiments described showed that zirconium and silicon were both transported in sealed capsules but were not transported in capsules open to the vacuum system. That result and the uniformity of the deposits over a wide area indicate that vapor transport was the primary mechanism. In the temperature gradient experiments two kinds of deposits contained zirconium (a ceramic deposit near the Zircaloy and a metallic Zr-Si deposit at the cooler end of the capsule), presumably formed by different mechanisms. The mass spectrometer study showed that ZrF₄ was the principal volatile species formed when Zircaloy was heated. Auger surface analyses showed that fluoride was present on surfaces of as-received Zircaloy, and that samples that had been treated to remove the original surface fluoride (ion milling or heating in dynamic vacuum) did not show Zr/Si transport. From those results, we conclude that the observed transfer of zirconium and silicon occurs by vapor transport, with gaseous fluorides acting as transporting species under the conditions of these experiments.

In the chemistry of the Zr-Si-F-O system, there are several gaseous species known: ZrF₄, ZrF₃, SiF₄, SiF₃, SiO, and that the divalent and monovalent fluorides of Zr and Si that are not important here. There are also several potential solid phases: ZrO₂, SiO₂, and several binary Zr-Si compounds. The following two-step cycle could cause vapor transport of zirconium and silicon and not consume the small amounts of fluoride available



When the capsule is first heated, the surface fluoride evaporates as ZrF₄. In this scheme, reactions [1] and [2], the surface coating formed on the Zircaloy is Zr₂Si (observed by x-ray diffraction of foil heated in constant temperature zone of 900°C). For other experimental conditions (higher temperature or temperature gradients described in Fig. 1) compounds richer in Si are formed (SEM showed Zr/Si \approx 1.5 to 1). Reaction [2] should be rewritten for these situations, but the same principles apply.

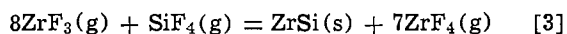
The free energy changes for these reactions can be evaluated from available data (JANAF (9), Kubaschewski *et al.* (10), and our estimate of the absolute entropy of Zr₂Si at 298°K to be 30 cal/mole deg) with the result

$$\Delta G^\circ (\text{reaction [1], cal}) = -30,600 + 6.6T$$

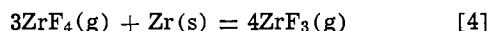
$$\Delta G^\circ (\text{reaction [2], cal}) = -64,000 - 10.9T$$

At 1200°K the free energy changes are -23 and -77 kcal, respectively. Thus both reactions have favorable free energies, and the net result will be formation of a ZrO_2 deposit on the silica walls and a Zr_2Si deposit on the Zircaloy. Those reactions can occur only if the capsule is sealed so that the volatile fluorides (ZrF_4 and SiF_4) are not removed. The temperature coefficients of the free energies are small and, thermodynamically, the process should occur at any reasonable temperature. We observed that transport was slow below 600°C.

The second type of coating containing zirconium was observed on the silica wall at the cooler end of the capsule, for temperatures below 800°C when the foil end was 900°C. That transport must have occurred by a different chemical mechanism, because the deposit was metallic and formed only at lower temperatures. (X-ray diffraction patterns showed that it was not a zirconium oxide and SEM showed $Zr/Si \approx 1$). To deposit a metallic film, the transporting vapor species must be a species lower valent than tetrafluoride to allow disproportionation to occur. ZrF_3 and SiF_3 are the most likely candidates since the divalent and monovalent species would occur only at much lower pressures than the trifluorides. If the species is ZrF_3 , then the deposition reaction (in the cool end, 800°C or lower) would be



and regeneration of trifluoride would occur at the hot end (900°C) by



The equilibrium constants for these two reactions can be combined to give the following condition

$$\frac{P(ZrF_4)}{P(SiF_4)} = K_3 \text{ (at } 800^\circ\text{C)} \times K_4^2 \text{ (at } 900^\circ\text{C)}$$

which can be evaluated from thermodynamic data (JANAF (9) and estimate of 20 cal/mole deg for the entropy of $ZrSi$), so that when $P(ZrF_4)/P(SiF_4) = 10^{16.6}$, deposition of $ZrSi$ can occur (hot end 900°C, cool end 800°C). If the cool end temperature is above 800°C for that pressure ratio, no deposition can occur.

If the lower valent fluoride is SiF_3 , a comparable set of transport reactions can be derived. For either case, it is possible to understand from the thermodynamic data why the mirror deposit forms only below a certain temperature, not throughout the tube. At the present state of our knowledge, we have no way of knowing whether the predominant vapor species in the capsules is ZrF_4 or SiF_4 (and whether ZrF_3 or

SiF_3 accounts for the mirror). The relative rates of reactions [1] and [2] would determine which species dominated. That species might be different for different capsule conditions or geometries.

Cox (2) suggested that $SiO(g)$ may be important in transporting Si to the zirconium surface. Our results suggest that transport of Si via $SiO(g)$ is small compared to the fluoride mechanism because transport was greatly reduced when the residual fluoride was removed by heating in a dynamic vacuum or by ion etching. Under conditions for which SiO transport was dominant there would be no mechanism for zirconium transport because the volatilities of the zirconium oxides are very small.

Acknowledgments

This work was supported under Contract No. EY-76-S-03-1339 by the Division of Basic Energy Science, Department of Energy, Dr. Robert P. Epple, Technical Monitor. The authors thank Dr. Kai Lau for the mass spectrometry measurements, Dr. G. N. Krishnan for Auger spectra, and Mr. Jan Terry for the scanning electron microscopy.

Manuscript submitted April 3, 1979; revised manuscript received July 3, 1979.

Any discussion of this paper will appear in a Discussion Section to be published in the December 1980 JOURNAL. All discussions for the December 1980 Discussion Section should be submitted by Aug. 1, 1980.

Publication costs of this article were assisted by SRI International.

REFERENCES

1. J. T. Demant and J. N. Wanklyn, UKAEA Report AERE-R4788 (1965).
2. B. Cox, in "Advances in Corrosion Science and Technology," Vol. 5, M. G. Fontana and R. W. Staehle, Editors, pp. 173-391, Plenum Press, New York (1976).
3. H. Feuerstein, USAEC Report ORNL-4543 (1970); also Private communication (1975).
4. D. L. Hildenbrand, *J. Chem. Phys.*, **66**, 3526 (1977); **48**, 3657 (1968); **52**, 5751 (1970).
5. ASTM, Publ. SMA-27, JCPDS International Center for Diffraction DATA, Swarthmore, Pennsylvania (1977).
6. G. L. Miller, "Zirconium," pp. 363-366, Academic Press, Inc., New York (1957).
7. W. D. Mackintosh, *Nucl. Technol.*, **13**, 65 (1972).
8. I. Golicheff and Ch. Engelmann, *J. Radioanal. Chem.*, **16**, 503 (1973).
9. JANAF Thermochemical Tables, The Dow Chemical Co., Midland, Mich. (1965).
10. O. Kubaschewski, E. Evans, and C. Alcock, "Metallurgical Thermochemistry," 4th ed, Pergamon Press, New York (1967).

A Performance and Current Distribution Model for Scaled-Up Molten Carbonate Fuel Cells

V. Sampath and A. F. Sammells*

Institute of Gas Technology, Chicago, Illinois 60616

and J. R. Selman*

Department of Chemical Engineering, Illinois Institute of Technology, Chicago, Illinois 60616

ABSTRACT

The performance of scaled-up (100 cm²) fuel cells with cross flow of fuel and oxidant has been modeled using the polarization characteristics of small-scale (3 cm²) fuel cells. The model also yields the two-dimensional (superficial) current distribution. The performance predicted by the model approximates to within 4% the experimental data if a suitable average value is assigned to the effective cell impedance. The latter depends on the inlet gas composition but does not vary much with the current; its value may be estimated from small-scale cell data. Carbon monoxide conversion contributes appreciably to the performance of low Btu cells; it tends to make the current distribution less uniform. The presence of methane must be considered in pressurized cells, but it does not appear to be formed to a significant extent. The relative contribution of mass transfer and kinetic resistance to the cell impedance are discussed in light of recent experimental results.

Mathematical modeling of cell performance has two distinct objectives:

1. To identify the rate-limiting factors in cell performance.

2. To predict the performance of scaled-up cells from small-scale cell data.

The present work concerns the latter type of modeling; the specific objective is to predict the current distribution in, and the performance of, 100 cm² molten-carbonate fuel cells in which the fuel gas and the oxidant gas (Table I) flow at right angles to each other and in which the fuel conversion is 75%. The ohmic resistance of such cells may be measured using conventional current-interruption techniques. Polarization, however, is not usually measured in scaled-up cells because reference electrodes are not easy to build into these cells. Also, polarization, as well as current density, varies over the electrode surface as a function of conversion, therefore, a single polarization measurement yields only limited information.

However, polarization data are available for small-scale (3 cm²) cells equipped with reference electrodes (1, 2) which operate at differential conversion. These data are specific for the input gas composition and may

* Electrochemical Society Active Member.

Key words: molten carbonate fuel cells, modeling, cell performance, current distribution.

Table I. Compositions (in mole fractions) of fuel gas and oxidant used in modeling cell performance at 1 atm and 650°C. Gases have been saturated with H₂O at room temperature and equilibrated at 650°C. Outlet conditions refer to 75% conversion based on CO and H₂

Fuel	Reformed natural gas		Low Btu coal gasification	
	Inlet	Outlet	Inlet	Outlet
H ₂	0.600	0.099	0.186	0.038
CO ₂	0.074	0.400	0.114	0.355
CO	0.100	0.044	0.140	0.039
H ₂ O	0.23	0.457	0.078	0.176
N ₂	—	—	0.482	0.392
Oxidant	Standard oxidant			
	Inlet	Outlet		
O ₂	0.145	0.094		
CO ₂	0.291	0.186		
H ₂ O	0.030	0.038		
N ₂	0.534	0.682		

be used as input for the cross-flow cell performance model.

Small-Scale Cell Polarization

Figure 1 illustrates the IR-free overpotential at a porous nickel anode and at a porous nickel cathode in a 3 cm² cell, for 7.5% conversion of 80% H₂-20% CO₂ fuel gas with standard oxidant (70% air-30% CO₂) (1). Typically, these polarization curves are approximately linear. Quasi-linear polarization behavior of a porous electrode in molten carbonate was observed at IGT as early as 1967 by Argano *et al.* (3) using a nickel anode of appreciably larger pore size and smaller internal area than the electrodes of Fig. 1. An example is shown in Fig. 2.

Because the overpotential is well above $RT/2F$ (40 mV at 650°C), this linear polarization behavior cannot be explained exclusively by kinetic rate limitations. Also, it is only approximate; the linear fit is usually less than satisfactory near the origin, and for some gas compositions the cathode polarization is better represented by two straight lines, with a transition in the range of 150-200 mA/cm², than by a single line. These features suggest that the porous electrodes operate under combined control of kinetics and mass transfer, while ohmic potential drop in the pores may also be significant.

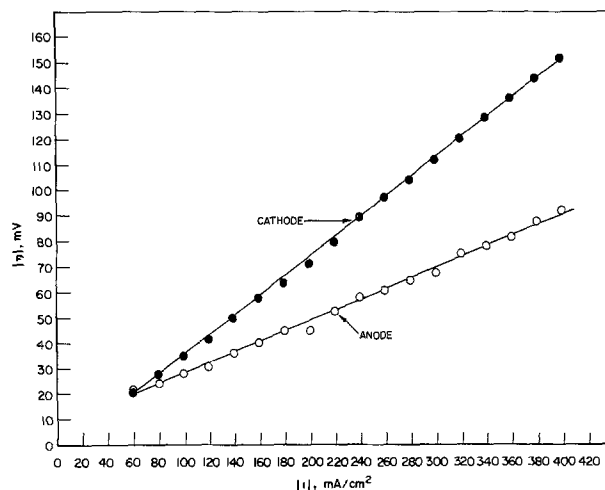


Fig. 1. Polarization (IR free) in a 3 cm² fuel cell [from Ref. (1)]

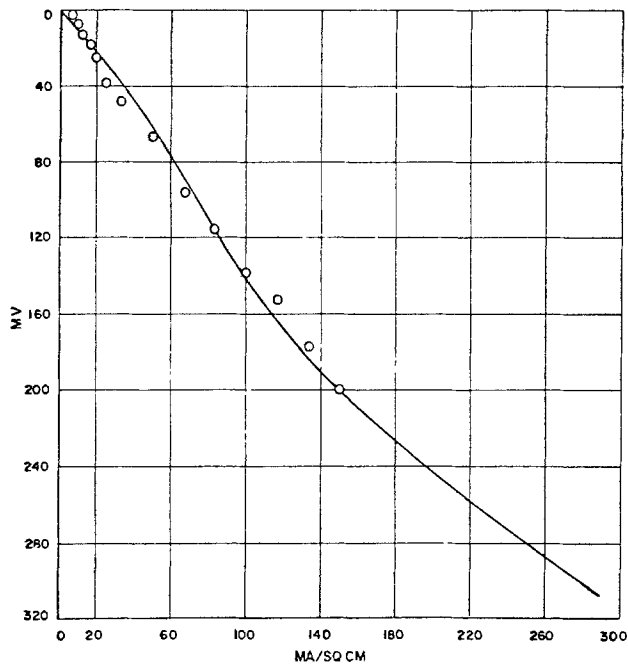


Fig. 2. Anode polarization (iR free) in a 3 cm^2 fuel cell [from Ref. (3)].

A porous electrode model may be used to interpret the rate processes in the electrodes. Porous electrode models applied to fuel cells have been reviewed by Bockris and Srinivasan (4) and by Austin (5). Although such models have been fairly successful in correlating or predicting the performance of room-temperature fuel cells, there have been few publications concerning molten-carbonate fuel cell modeling (6-9).

Wasan *et al.* (6) and Sood (7) modeled the oxidation of hydrogen in a porous anode, using a thin-film model of the electrode pores. In Fig. 2, the solid line indicates the polarization predicted by the model of Wasan. The flooded-pore model was rejected because it predicted a limiting current of hydrogen oxidation, which was not observed.

Recent calculations (10, 11) suggest that a limiting current would probably not be observed in a flooded pore because of factors such as hydrogen transport in the metal (nickel) and the relatively important ohmic drop in the electrolyte film. Thus, a more appropriate physical representation may be a composite of flooded and filmed pores (agglomerate model). However, there is no reliable information about the nature and extent of the active surface in each of the porous electrodes. Thus, the film model remains the most acceptable simple representation of the electrode operation.

Although the film model is relatively simple, several of its input parameters are not known and need to be estimated. At least three dimensionless parameters are to be adjusted in fitting the experimental curve to the film model in addition to Butler-Volmer transfer coefficients and stoichiometric coefficients of the electrode reaction (11). This leaves one a considerable latitude in the assignment of parameter values or reaction mechanisms, without any guarantee of physical realism.

Therefore, the present work aims to predict cell performance and current distribution without resort to a microscopic model. Whereas at least three adjustable parameters are used in most porous electrode models, Fig. 1 and 2 show that, as a first approximation, a linear polarization expression adequately represents the data for the purpose of cell performance modeling. This conclusion was also reached by Dharia (8) who utilized an "effective cell resistance" to model the performance of a cell in which fuel and oxidant gas flow co-cur-

rently (co-flow). In the present work, the linear-polarization assumption is combined with mass balances for a cross-flow configuration of fuel and oxidant gases, as employed currently in scaled-up cells.

Basic Model

Figure 3 is a schematic diagram of the gas flows to the cell. It also shows how the cell is divided into sections for computation purposes.

Mass balances on the anode and the cathode result in one equation each for local hydrogen and CO_2 conversion. The two equations are coupled by the local current density. In the initial modeling, only hydrogen was assumed to react. The water-gas shift reaction was not considered, and CO was not assumed to be electrochemically active. In this case, mass balance equations at the anode are obtained as follows

$$\text{H}_2: \frac{P}{RT L_C/n} \frac{\partial}{\partial x} \left(\frac{\Phi_A}{n} X_H \right) = -\frac{i_A}{2F} = -\frac{i}{2F} \quad [1]$$

$$\text{CO}_2: \frac{P}{RT L_C/n} \frac{\partial}{\partial x} \left(\frac{\Phi_A}{n} X_{CA} \right) = \frac{i_A}{2F} = \frac{i}{2F} \quad [2]$$

$$\text{H}_2\text{O}: \frac{P}{RT L_C/n} \frac{\partial}{\partial x} \left(\frac{\Phi_A}{n} X_W \right) = \frac{i_A}{2F} = \frac{i}{2F} \quad [3]$$

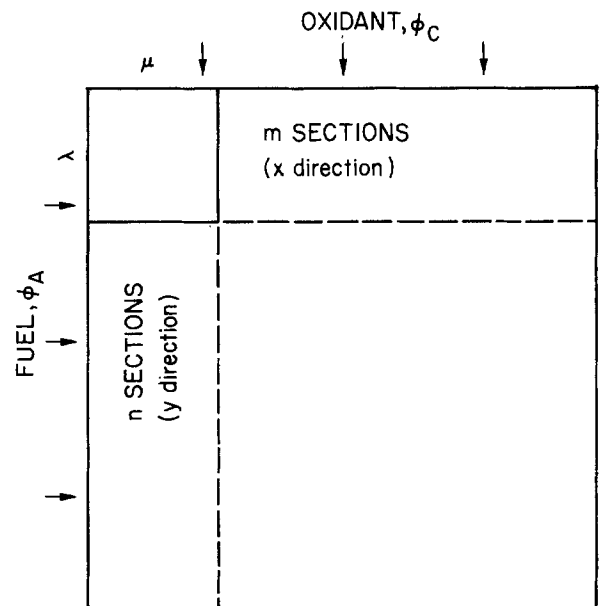
$$\text{CO}: \frac{P}{RT L_C/n} \frac{\partial}{\partial x} \left(\frac{\Phi_A}{n} X_{CO} \right) = 0 \quad [4]$$

The corresponding cathode mass balances are

$$\text{CO}_2: \frac{P}{RT L_A/m} \frac{\partial}{\partial y} \left(\frac{\Phi_C}{m} X_{CC} \right) = \frac{i_C}{2F} = -\frac{i}{2F} \quad [5]$$

$$\text{O}_2: \frac{P}{RT L_A/m} \frac{\partial}{\partial y} \left(\frac{\Phi_C}{m} X_O \right) = \frac{i_C}{4F} = -\frac{i}{4F} \quad [6]$$

$$\text{N}_2: \frac{P}{RT L_A/m} \frac{\partial}{\partial y} \left(\frac{\Phi_C}{m} X_N \right) = 0 \quad [7]$$



Φ_A = FUEL FLOW RATE

Φ_C = OXIDANT FLOW RATE

λ = ANODE GAS CONVERSION

μ = CATHODE GAS CONVERSION

Fig. 3. Schematic diagram of the fuel and oxidant flows to the cell.

By defining conversion of hydrogen, λ , as

$$\lambda = \frac{\text{moles of H}_2 \text{ consumed}}{\text{moles of H}_2 \text{ in}} = \frac{\Phi_A^\circ X_{H^\circ} - \Phi_A X_H}{\Phi_A^\circ X_{H^\circ}} \quad [8]$$

where the $^\circ$ superscript refers to the inlet conditions; and conversion of CO₂, at the oxygen electrode μ , as

$$\mu = \frac{\text{moles of CO}_2 \text{ consumed}}{\text{moles of CO}_2 \text{ in}} = \frac{\Phi_C^\circ X_{CC^\circ} - \Phi_C X_{CC}}{\Phi_C^\circ X_{CC^\circ}} \quad [9]$$

the mass balances (1-4) can be combined in one equation

$$\frac{Pm}{RTL_{CLA}} \Phi_A^\circ X_{H^\circ} \frac{\partial \lambda}{\partial \xi} = \frac{i}{2F} \quad [10]$$

and the cathodic-side mass balances (5-7) in a second equation

$$\frac{Pn}{RTL_{ALC}} \Phi_C^\circ X_{CC} \frac{\partial \mu}{\partial \eta_d} = \frac{i}{2F} \quad [11]$$

Here ξ and η_d are dimensionless distances in the x and y direction, respectively, as defined by

$$\xi = \frac{x}{L_A/m} \quad \eta_d = \frac{y}{L_C/n} \quad [12]$$

$$\frac{V + V_A^\circ - V_C^\circ}{RT/2F} - \ln \left[\frac{X_{CC^\circ} (X_{O^\circ})^{1/2} X_{H^\circ}}{X_W^\circ X_{CA^\circ}} \right] = \ln \left\{ \frac{(1 - \mu) \left(1 - 1/2\mu \frac{X_{CC^\circ}}{X_{O^\circ}} \right)^{1/2} (1 - \lambda) (1 + \lambda X_{H^\circ})}{(1 - 3/2\mu X_{CC^\circ})^{3/2} \left(1 + \lambda \frac{X_{H^\circ}}{X_W^\circ} \right) \left(1 + \lambda \frac{X_{H^\circ}}{X_{CA^\circ}} \right)} \right\} - \frac{JZA}{RT/2F} \quad [24]$$

L_A/m is the length of one section in the x direction and L_C/n is the length of one section in the y direction (Fig. 3).

For the purpose of computation, Eq. [10] and [11] were further simplified by defining a dimensionless current density

$$J = \frac{i}{A} = \frac{i}{I_{\max} m} \quad [13]$$

where

$$A = \frac{2FP\Phi_A^\circ X_{H^\circ} m}{RTL_{CLA}} \quad [14]$$

and I_{\max} is the current density that would result if 100% conversion of the anode gas took place and the resulting current were uniformly distributed over the entire cell.

Then, the mass-balance equations reduce to

$$\frac{\partial \lambda}{\partial \xi} = J \quad [15]$$

and

$$\frac{\partial \mu}{\partial \eta_d} = \frac{i}{SA} = \frac{J}{S} \quad [16]$$

where S denotes the stoichiometric ratio of CO₂ flow in the cathode to H₂ flow in the anode

$$S = \frac{X_{CC^\circ} \Phi_C^\circ n}{X_{H^\circ} \Phi_A^\circ m} \quad [17]$$

The local current density, i , is also dependent on the conversion via the cell potential balance; at each point in the cell the sum of the local equilibrium potentials, overpotentials, and ohmic potential drop must equal the cell terminal potential. The latter is considered uniform in the x and y directions. The cell potential is thus given by

$$V = (V_{CN} - V_{AN}) - iZ_{\text{ohm}} + \eta_C - \eta_A \quad [18]$$

where the equilibrium potentials at the electrodes are

$$V_{AN} = V_A^\circ + \frac{RT}{2F} \ln \left(\frac{X_W X_{CA}}{X_H} \right) \quad [19]$$

and

$$V_{CN} = V_C^\circ + \frac{RT}{2F} \ln (X_{O^{1/2}} X_{CC}) \quad [20]$$

Here the CO₃⁼ activity gradient through the cell is considered to be zero. V_A and V_C are the standard anode and cathode potentials. Assuming a linear current-overpotential relationship

$$\eta_A = i_A Z_A = i Z_A \quad [21]$$

$$\eta_C = i_C Z_C = -i Z_C \quad [22]$$

where Z_A and Z_C are effective electrode resistances ($\Omega\text{-cm}^2$). The dependence of overpotential and ohmic potential drop on the current density may now be represented by an effective resistance

$$Z = R_{\text{ohm}} + \frac{\eta_{\text{an}}}{i} - \frac{\eta_{\text{cath}}}{i} \quad [23]$$

Using the definition of conversions λ and μ from Eq. [8] and [9], Eq. [18] can be written as

The first term on the right-hand side is the "Nernst loss" compared to inlet conditions. The second term is the overpotential and ohmic loss.

Equations [15], [16], and [24] are solved simultaneously to give λ , μ , and the current density. The computation starts at $\xi = 0$, $\eta_d = 0$ (fuel and oxidant inlet) and marches down the fuel flow and oxidant flow directions simultaneously. The fuel conversion, λ , is adjusted following each step in the ξ direction; so is the CO₂ conversion, μ , following each step in the η_d direction. Computations were carried out for a 10×10 cm fuel cell (100 cm² electrode area) using 10 sections in each direction. No significant differences were found when the number of sections was increased to 20 each; thus a 10×10 grid appeared to yield sufficient accuracy.

Experimental

The equations were solved simultaneously using a Harris System 120 computer.

The predicted current distributions were compared with experimental data generated on 100 cm² fuel cells (94 cm² electrode area). Here the anode consists of porous nickel, having a thickness of 30 mils and a mean pore size of around 5 μm . The cathode also initially consists of porous nickel which, under operating potential (to which it is subjected), oxidizes to NiO. This electrode has a 15 mil thickness and a mean pore size of between 12 and 14 μm . The electrolyte tile typically consists of a eutectic mixture of 62% Li₂CO₃-38% K₂CO₃ supported on a LiAlO₂ matrix.

Results and Discussion

In the computations reported here, Z was assigned an average value for the entire cell. Initially, this value was based on polarization measurements at small-scale fuel cells, as in Fig. 1, using reformed natural gas. Fairly good agreement was obtained between prediction and experimental data for this gas (Fig. 4). However, the fuel conversion predicted by the model exceeded 75% at most current densities;

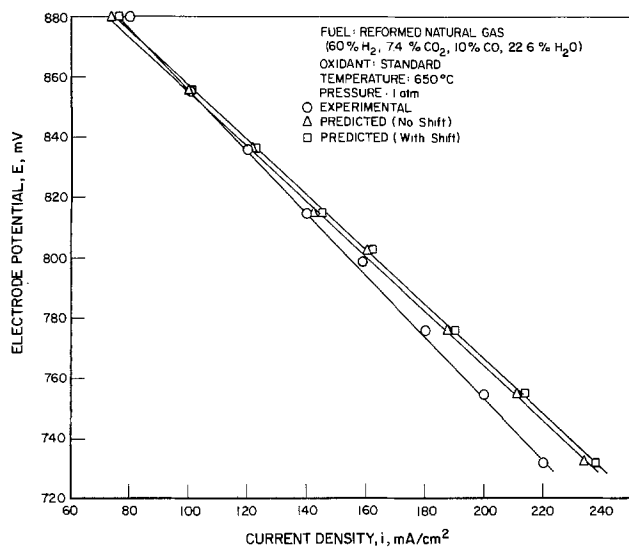
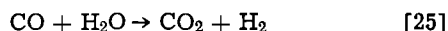


Fig. 4. Predicted polarization curves for reformed natural gas compared with experimental data. The effective resistance, Z , was assigned the value of $1.00 \Omega\text{-cm}^2$.

thus it appeared that the impedance was underestimated by the value based on the feed gas composition. This point was therefore investigated in more detail (see "Effective cell resistance" below).

Water-gas shift reaction.—In the case of low-Btu feed gas, the model's prediction was quite unsatisfactory. Here, conversion of CO to hydrogen



may be presumed to occur as H_2O product is formed in the cell. Therefore, local equilibrium conversion was assumed and included in the model. The results, using the same resistance value as before,¹ show that the effect of CO conversion is negligible in the case of reformed natural gas, but important for low Btu gas (Fig. 5) and other CO-rich feed gases. Here too, it became evident that resistance values based on polarization measurements with reformed natural gas yield unsatisfactory predictions for CO-rich, H_2 -lean feed gases; fuel conversion is overestimated.

Effective cell resistance.—To investigate the dependence of the effective cell resistance on current density and gas composition, the performance of the fuel cell was simulated for three different gas compositions (see Table II), at 75% conversion with respect to H_2

¹Except for an adjustment of the ohmic component using experimental data.

Fig. 5. Predicted polarization curves for low Btu coal gas compared with experimental data. The effective resistance, Z , was assigned the value of $1.046 \Omega\text{-cm}^2$.

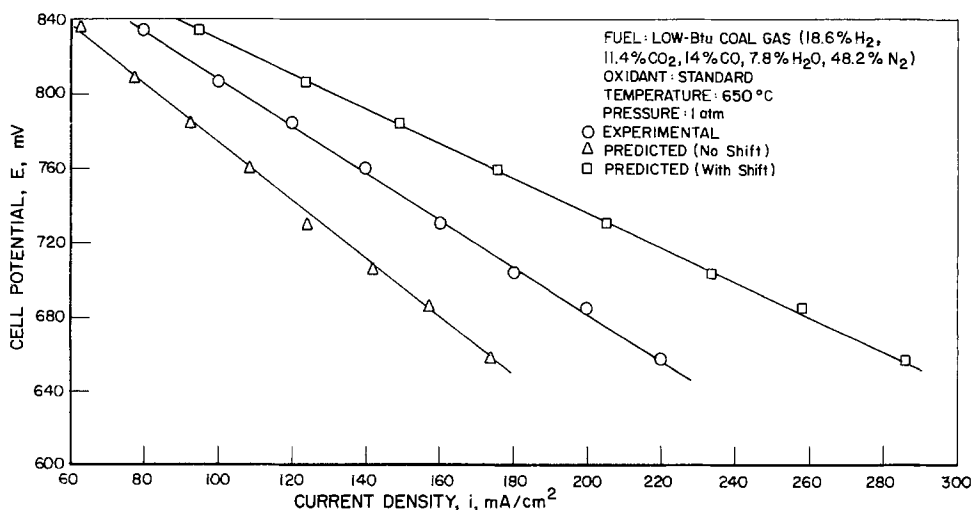


Table II. Estimated and measured cell resistance values

Gas composition (in mole percent) averaged between inlet and outlet, at 75% conversion

	Fuel electrode		Oxygen electrode		
	RNG	Low Btu	Standard	Standard	
	H_2	35.0	11.2	O_2	11.9
	CO_2	23.7	23.5	CO_2	23.9
	CO	7.2	9.0	N_2	60.8
	H_2O	34.1	12.7	H_2O	3.4
Estimated resistance					
Z_a or Z_c	Z_a :	0.315	0.455	Z_c :	0.428
$Z_a + Z_c$		0.743	0.883		
R_{ohmic}		0.400	0.446		
Z_{total}		1.14	1.33		
Measured resistance	at 200 mA/cm ² (computed from exp. data)				
		1.05	1.49		

and CO. The value of Z was adjusted at each cell potential until 75% conversion resulted.

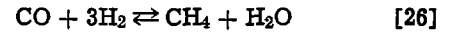
The current densities thus obtained agree to within 4% with experimental results. Figure 6 illustrates this for reformed natural gas and low Btu coal gas. Apparently, the assumption that CO is completely converted to hydrogen is justified. Figure 7 shows that the CO conversion makes a major contribution to the current in the case of low Btu gas.

For a particular feed gas, the effective cell resistance (Z) values at 75% conversion do not change by more than 10% as the total cell current is increased (Fig. 8). This finding gives support to the assumption that cell performance may be modeled satisfactorily by using an average Z value, rather than adjusting Z from point to point to account for local fuel oxidant gas compositions. In Table II, the effective resistance values found by fitting experimental curves are compared with estimates obtained by using small-cell polarization data. From the latter, the electrode impedances corresponding to the average gas compositions in the fuel and oxidant electrodes are calculated. Although small-cell data are not available for the full range of fuel and oxidant gas compositions, preliminary estimates can be made based on the fraction hydrogen in the fuel gas and oxygen in the oxidant (2). Ohmic resistances are added as determined *in situ* for the crossflow cell. Table II shows that in this manner, adequate predictions ($\pm 10\%$) of the effective cell resistance of scaled-up cells may be made, solely on the basis of small-scale cell polarization data and *in situ* ohmic resistance measurements (see Fig. 8). As more data become available for the polarization of small cells and the dependence of the anode polarization on the CO, CO_2 , and H_2O concentrations is accounted for, one may expect that the estimates will become more accurate, especially for low Btu gases.

Current distribution.—The current distribution as expected shows a maximum at the inlet of both fuel and oxidant, and a minimum at the outlet of the fuel,

though not necessarily at the outlet of the oxidant. Figure 9 illustrates this for reformed natural gas at 160 mA/cm² (0.8V cell potential). As the value of Z increases, the current distribution for the same conversion becomes more uniform. Thus, for low Btu gas it is more uniform than for reformed natural gas.

Pressurized operation.—Increasing the operating pressure of the fuel cell results in increased emf, because of the increase in partial pressure of the reactants. Higher pressures may also be expected to produce increases in gas solubilities and, hence, additional improvements in cell performance. However, pressure also favors methane formation



and carbon deposition



The latter is prevented by humidifying the gas following compression, before it enters the cell. So far, there is not sufficient evidence to establish whether or not equilibrium [26] is actually attained, either after compression or inside the fuel cell.

In the model calculations, the gas composition at the fuel cell entrance was at first assumed at equilibrium with respect to Eq. [26]. Table II illustrates this

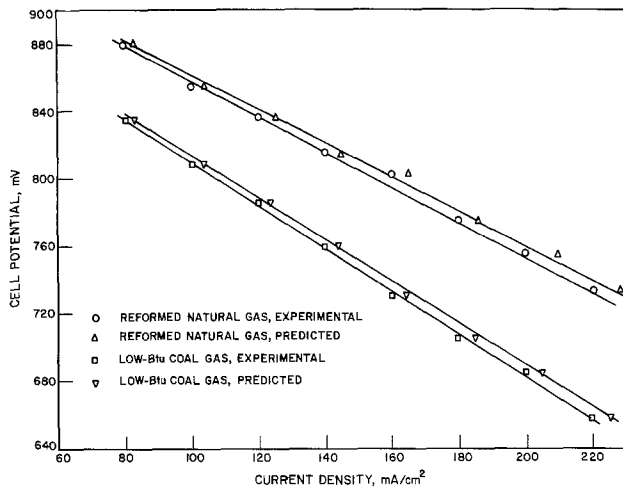


Fig. 6. Comparison of predicted and experimental polarization curves. The effective resistance, Z, has been adjusted for 75% conversion.

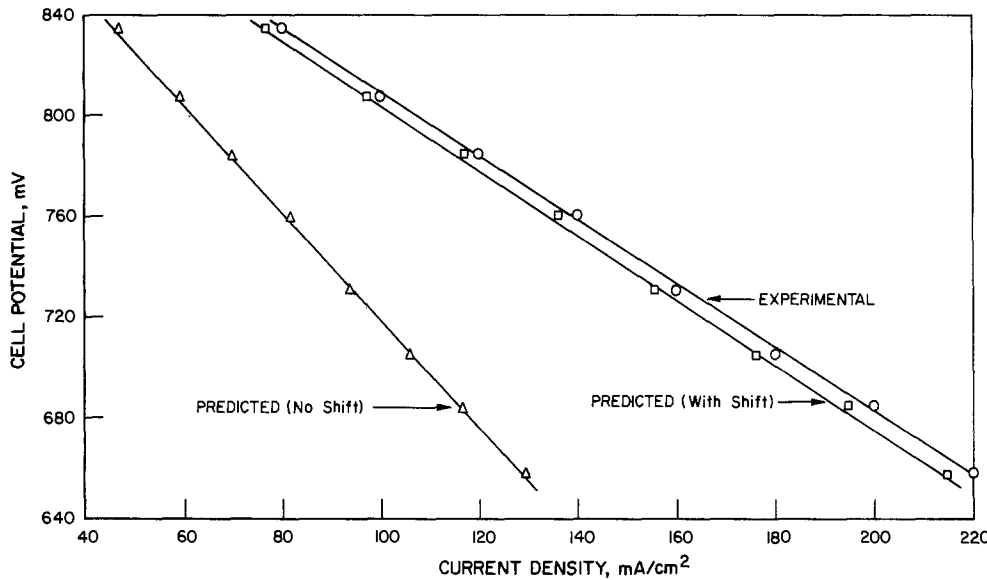


Fig. 7. Comparison of the experimental current density with computed current densities (fuel: low Btu coal gas). The Z value has been adjusted for 75% conversion (1.40-1.55 Ω-cm²).

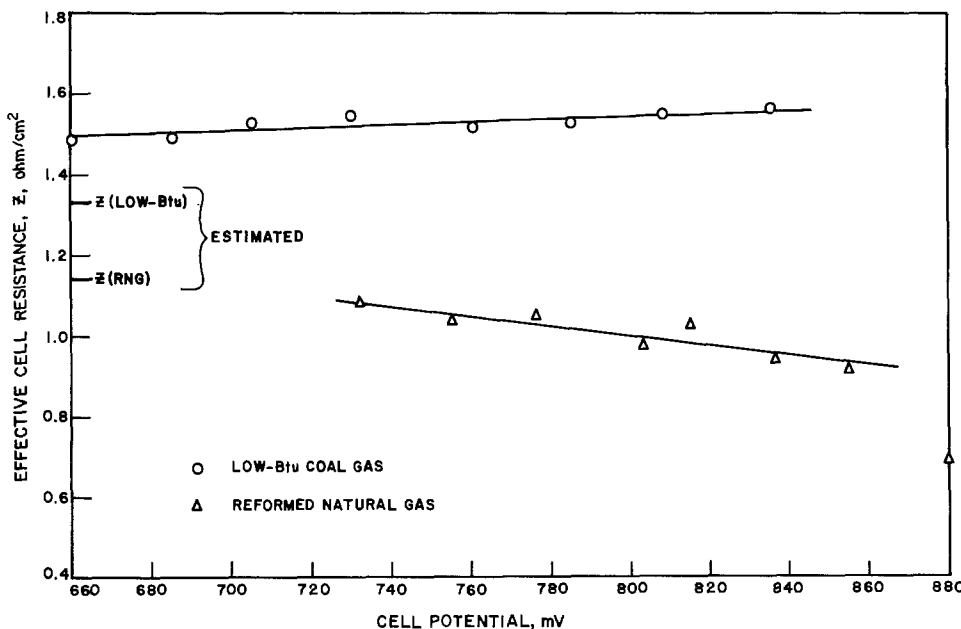


Fig. 8. Effective resistance as a function of current load in cell operation.

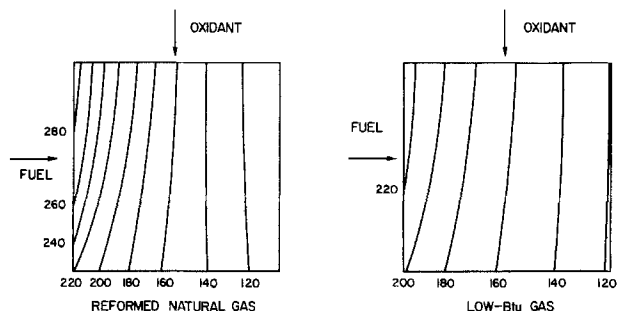


Fig. 9. Current distributions calculated for reformed natural gas and low Btu gas, both with standard oxidant, at 75% conversion and average current density of 165 mA/cm².

for steam-reformed naphtha. Since H₂O is produced by anodic oxidation of hydrogen, some steam-reforming of CH₄ may take place. Therefore, equilibrium 26 has been included in the model for pressurized cell operation.

The predicted average current density (or conversion) was compared with experimental data (11) obtained for a pressurized cross-flow cell at constant flow rate (rather than at constant 75% conversion, as in the cells operated at atmospheric pressure). The cell resistance, Z , was varied until good agreement was obtained at an arbitrary cell potential, e.g., 0.830V, and the same Z value was then used to generate a complete performance curve.

For a flow rate identical to that used in the cell, an average current density of 120 mA/cm² was the maximum that could be generated by the cell at 0.830V, even for very low values of Z . Thus, it appears that equilibrium [26] is far from complete at the entrance to the cell; the compressed gas contains more hydrogen than equilibrium [26] would predict (31 m/o) and this excess is, at least initially, responsible for the better than predicted performance of the cell.

This is also evident from the result obtained when one uses the composition equilibrated only with respect to the water-gas shift reaction, as input to the pressurized operation model. The current density then agrees with the experimental value (160 mA/cm² at 0.83V) for a cell resistance not very different from that at atmospheric pressure (see Table III and Fig. 10).

The current distribution is not significantly altered by increasing the pressure. The ratio of highest to lowest current density is 2.11 at 1 atm and 1.94 at 10 atm for reformed naphtha.

Conclusion

A linear-polarization model has been used successfully to compute performance and current distribution

Table III. Gas composition (in mole fractions) and cell performance of steam-reformed naphtha at 650°C (constant flow rate)

Mole fraction	1 atm*	10 atm**	10 atm*
H ₂	0.497	0.310	0.497
CO ₂	0.107	0.111	0.107
CO	0.096	0.041	0.096
H ₂ O	0.285	0.434	0.285
CH ₄	0.015	0.104	0.015

Flow rates (cm ³ /sec)	1 atm Exp.	1 atm* Model	10 atm Exp.	10 atm* Model
Fuel	12.6	12.6	1.26	1.26
Oxidant	39.9	39.9	3.99	3.99
Current density (mA/cm ²)	160	162.8	160	159.8
Cell voltage (V)	0.785	0.785	0.830	0.830
Effective resistance (Ω-cm ²)		1.088		1.14

* Equilibrated with respect to water-gas shift reaction.

** Equilibrated with respect to water-gas shift and methane formation reactions.

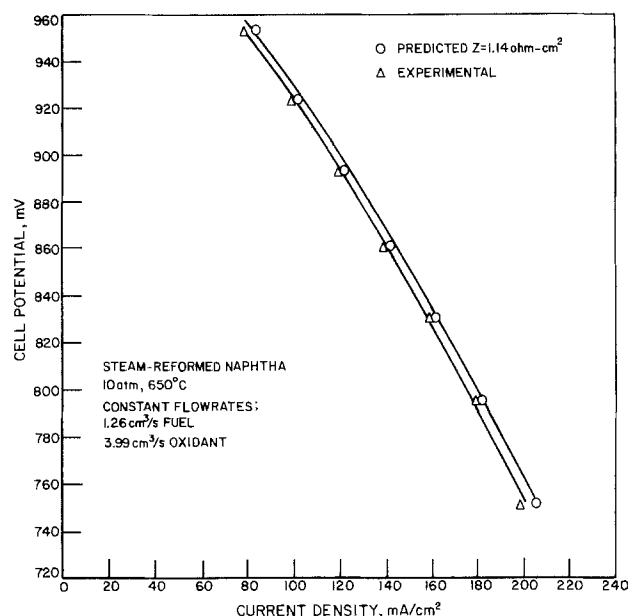


Fig. 10. Experimental and predicted current density in pressurized operation using steam-reformed naphtha at constant flow velocity. Prediction is based on inlet gas in equilibrium with respect to water-gas shift, but not methanation. Resistance Z was assigned a constant value of 1.14 Ω-cm².

of a scaled-up fuel cell as a function of gas compositions, flow rates, and operating pressure. The effective cell resistance used in the linear-polarization model may be estimated with satisfactory accuracy from small-scale cell polarization data and ohmic resistance measurements *in situ*. In pressurized operation, the formation of CH₄ may be accounted for, as well as CH₄ steam reforming in the fuel cell, but, at least for steam-reformed naphtha, the composition of the compressed gas at the fuel cell inlet appears not to be in equilibrium with respect to CH₄ formation. The highest local current density in a fuel cell is approximately two times the lowest local current density, both in atmospheric and in pressurized operation.

LIST OF SYMBOLS

A	dimensionless current density, Eq. [14]
F	Faraday's constant, 96,501 C/equiv.
i_A	anodic current density (>0), mA/cm ²
i_C	cathodic current density (<0) mA/cm ²
i	current density ($i = i_A = i_C $), mA/cm ²
J	dimensionless current density, Eq. [13]
L_A	total length of the fuel gas channel, cm
L_C	total length of the oxidant gas channel, cm
m	number of sections in the anode flow direction
n	number of sections in the cathode flow direction
P	pressure, atm
R	gas constant, 82.06 atm-cm ³ /g-mole-°K
R_{ohm}	ohmic cell resistance, Ω
T	temperature, °K
V	cell terminal potential, V
V_{CN}	equilibrium (Nernst) potential at the cathode, V
V_{AN}	equilibrium (Nernst) potential at the anode, V
V_A°	standard anode potential, V
V_C°	standard cathode potential, V
X_k	mole fraction of the gas component k
x	distance in the fuel flow direction, cm
y	distance in the oxidant flow direction, cm
Z	effective cell resistance, Ω-cm ²
Z_A	effective anode resistance, Ω-cm ²
Z_C	effective cathode resistance, Ω-cm ²

Greek symbols

η_C	cathodic overpotential (<0), V
η_A	anodic overpotential (>0), V
Φ_A	total fuel flow rate, cm ³ /sec
Φ_C	total oxidant flow rate, cm ³ /sec

Subscript

A	anode
C	cathode

H	hydrogen
CA	CO ₂ in anode gas
CC	CO ₂ in cathode gas
W	water
CO	carbon monoxide
O	oxygen
N	nitrogen

REFERENCES

1. J. R. Selman, H. C. Maru, V. Sampath, and L. G. Marianowski, in "Electrode Materials and Processes for Energy Conversion and Storage," S. Srinivasan, J. D. E. McIntyre, and F. G. Will, Editors, p. 656, The Electrochemical Society Softbound Proceedings Series, Princeton, N.J. (1978).
2. Institute of Gas Technology, Project 8984 Final Report, July 1976-September 1977.
3. E. S. Argano, T. Schmidt, and D. T. Wasan, *Chem. Eng. Progr. Symp. Ser.*, No. 77, 63, 26 (1967).
4. J. O'M. Bockris and S. Srinivasan, "Fuel Cells: Their Electrochemistry," McGraw-Hill Book Co., New York (1969).
5. S. Srinivasan and E. Gileadi, in "Handbook of Fuel Cell Technology," C. Berger, Editor, p. 221, Prentice Hall, Englewood Cliffs, N.J. (1968).
6. D. T. Wasan, T. Schmidt, and B. S. Baker, *Chem. Eng. Progr. Symp. Serv.*, No. 77, 63, 16 (1967).
7. S. K. Sood, M.S. Thesis, Illinois Institute of Technology, Chicago (1968).
8. D. I. Dharia, Paper 77905, *I.E.C.E.C.*, 337 (1977).
9. V. Sampath, J. R. Selman, and A. F. Sammells, Paper 372 presented at The Electrochemical Society Meeting, Pittsburgh, Pa., Oct. 15-20, 1978.
10. J. R. Selman, V. Sampath, and A. F. Sammells, Paper presented at Molten Carbonate Fuel Cell Workshop, Oak Ridge, Tennessee, October 31-November 2, 1978.
11. "Fuel Cell Research on Second-Generation Molten Carbonate Systems," Annual Report, October 1977-September 1978, Institute of Gas Technology, Chicago, Illinois.

Capacitance Study of Thermally Grown Oxide Films on Iron

K. S. Yun,* S. M. Wilhelm,* S. Kapusta,** and N. Hackerman***

Department of Chemistry, Rice University, Houston, Texas 77001

ABSTRACT

The dielectric properties of thermally grown oxide films on iron were determined by measuring the frequency and the temperature dependence of the capacitance in aqueous electrolyte solutions. The oxide films behave similarly to n-type semiconductors. The ionization energy of donor states in the oxide was obtained from calculation of the conductivity profile (0.64 eV) and from Mott-Schottky plots (0.69 eV).

Recently the current-potential characteristics and the photoresponse of thermally grown iron oxide were studied in this laboratory (1, 2). Thermal iron oxide electrodes were shown to be potentially useful as photoanodes in photoassisted electrolysis of water because of their relatively low bandgap (2.1 eV) and good corrosion stability.

The physical properties and the crystal structure of thermally formed iron oxide have been reported in detail by a number of authors (3-8). Up to about 570°C the high temperature oxidation of iron leads to formation of a two-layer scale of Fe₃O₄ and Fe₂O₃. A three-layer scale of FeO, Fe₃O₄, and α -Fe₂O₃ is formed at higher temperatures. The latter oxide film consists mainly of FeO and Fe₃O₄, the outer layer of α -Fe₂O₃ accounting for only 1-5% of the total thickness. The two inner layers have a metal-like conductivity (9) so that the semiconducting properties of the iron oxide are due only to the nonstoichiometry of the α -Fe₂O₃ layer. The oxide film is structurally highly disordered and may be described as glassy with short range crystalline order. The mean diameter of the crystal grains is approximately 1-2 nm.

A capacitance investigation is useful for obtaining information on the electronic structure of semiconducting oxide films in contact with an electrolyte. Recently, Kennedy and Frese (10) reported on a capacitance study of high purity polycrystalline α -Fe₂O₃ and discussed the flatband potentials and the donor densities. From the change in slope of the Mott-Schottky plots they suggested a deep donor level. A similar

effect was observed for thermally grown oxide films (2).

The change in slope of the Mott-Schottky plot also can be observed for thin film covered metal electrodes without any deep donor levels and therefore the capacitance change alone is not a sufficient criterion for a second donor level. In order to clarify the semiconducting behavior and deep donor levels of thermally grown iron oxide, films of the oxides have been studied here via the frequency and temperature dependence of the capacitance.

Experimental

The procedure for growing the oxide films on iron has been reported (1, 2). Electrodes were made from zone-refined iron. Impurities higher than 5 ppm were Cu (10 ppm) and Ca (5 ppm). An oxide-covered iron rod (diameter 0.7 cm, length 1 cm) was embedded in a Teflon cylinder which was preheated (120°C) in an oven. After cooling, the edge was coated with silicon adhesive (Dow Corning) so that a circular area (approximately 0.3 cm²) was exposed. Electrical contact was made by an iron rod inserted through a glass tube into the Teflon holder. The same electrode was used for each experiment.

The electrolyte was a 0.1M H₃BO₃ + NaOH buffer solution with 1M NaNO₃ supporting electrolyte (pH = 8.4). All chemicals were reagent grade and the water was triply distilled. A saturated calomel electrode (SCE) was used as a reference electrode and all potentials are referred to SCE. For the temperature studies the cell was placed in a constant temperature water bath ($\pm 0.5^\circ\text{C}$).

Capacitance measurements were made with a General Radio Type 1603-A Z-Y Bridge, with a Type 1323-P

* Electrochemical Society Active Member.

** Electrochemical Society Student Member.

*** Electrochemical Society Honorary Member.

Key words: differential capacitance, iron oxide films, donor levels.

Preamp and a Type 1232-A Tuned Amp and Null Detector. A Model 505B Exact Waveform Generator was used as an oscillator and the amplitude was adjusted to 10 mV with an HP Model 350B Attenuator Set. Most capacitance measurements were carried out under potentiostatic conditions at 1 kHz. The bias voltage was supplied by a Princeton Applied Research Model 373 Potentiostat. To prevent oscillation of the potentiostat a variable frequency filter was placed between the counter and the reference electrode outputs of the potentiostat. The time constant of the filter (0.5 sec) was such that the open-circuit condition could be duplicated in the frequency range of 500 Hz-10 kHz. The series capacitance (C_s) and resistance (R_s) could be measured directly by balancing the working electrode against the internal components of the bridge.

To measure the capacitance a potential pulse technique was used. The electrode potential was changed in a 1 μ sec risetime to the potential of measurement, the bridge balanced (< 5 sec), and the potential returned to initial condition (usually 0.0V). The pulse was alternately anodic and cathodic, with the same amplitude. The measured differential capacitance of a particular electrode could be reproduced within 1% after 24 hr immersion in the electrolyte solution. During the initial 24 hr period, the capacitance values varied randomly within 5% of their initial values.

Results and Discussion

Film thickness.—The experimentally accessible total capacitance, C , consists of the space charge capacitance, C_{sc} , and the Helmholtz capacitance, C_H , in series

$$1/C = 1/C_{SC} + 1/C_H \quad [1]$$

C can be equated with C_{SC} as long as C_H is much larger than C . The situation is then analogous to a parallel plate condenser between metal and electrolyte with a semiconducting film as a dielectric. All capacitance values were corrected by Eq. [1] by assuming a constant Helmholtz capacitance of 20 μ f cm^{-2} (11-13).

At sufficiently positive electrode potentials, low donor densities, and with thin surface films, the charge necessary to change the electrode potential is predominantly stored in the metal. The differential capacitance is then independent of the electrode potential and is a measure of effective film thickness, d . It can be expressed as

$$1/C_{SC} = d/\epsilon\epsilon_0 A \quad [2]$$

where ϵ and ϵ_0 are the dielectric constants of the oxide and of vacuum and A is electrode area.

The dependence of reciprocal capacitance on film growing time is shown in Fig. 1. Capacitance values were taken at an electrode potential of +0.5V and a frequency of 1 kHz. The growing rate of the oxide films is a parabolic function with time (4, 7-9). This is substantiated by the linear dependence between C_{SC}^{-1} and $t^{1/2}$. The proportionality factor (6.94 nm/sec $^{1/2}$) was found by using $\epsilon = 80$.

The value $\epsilon = 80$ was estimated from the capacitance value by assuming a thickness (10.3 nm) based on a golden brown oxide interference color (14). For thicker gray films, however, ϵ assumed values up to 120. This discrepancy is due to the fact that thicker films contain a lower percentage of oxygen in the film. The minimum value was taken as the dielectric constant and is in good agreement with the value given in Ref. (10). It should be noted that the dielectric constant of α -Fe $_2$ O $_3$ has also been measured as 8 at 1 kHz (15) and 120 at 1 MHz (16).

Frequency dependence.—Randomly oriented microcrystalline oxides such as anodic and thermally produced oxide films are asymmetric. The concentration of oxygen vacancies (or metal excess) as compared with a strict stoichiometry is greater near the metal than near the surface. This asymmetric constitution results in rectification, photoeffects, and other semiconducting

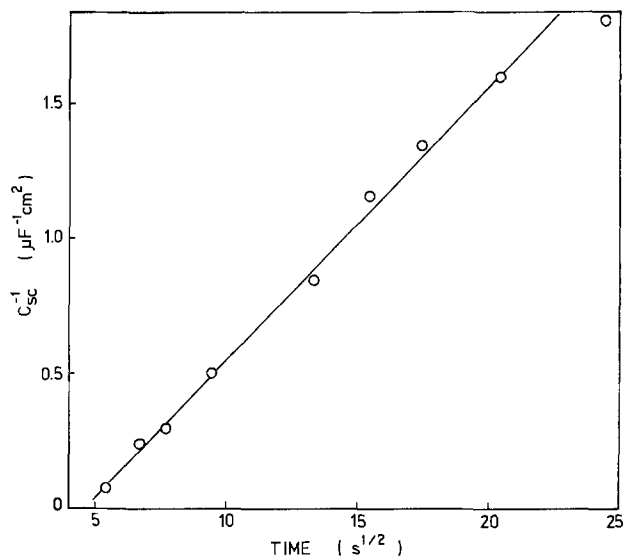


Fig. 1. Reciprocal space charge capacitance, C_{SC}^{-1} , vs. square root of time, $T = 25^\circ C$, $f = 1$ kHz, $pH = 8.4$.

properties. The impedance of an asymmetric oxide layer is approximated by a resistance R_s and a capacitance C_s in series and can be directly measured with an a-c bridge as a function of frequency (17).

Young (17) derived the frequency dependence of $R_s(f)$ and $C_s(f)$ under the assumption that the oxide film consists of an infinite number of parallel RC units in series. Within certain frequency limits ($f = 50$ Hz-8 kHz) and at room temperature the following relationships were found to hold for an anodically formed niobium oxide film

$$R_s = R_0 + a/f \quad [3]$$

$$1/C_s = 1/C_\alpha + b \log f \quad [4]$$

$$b/a = 9.2 \quad [5]$$

where R_0 , C_α , a , and b are constants.

The compliance of the thermal iron oxide with these relationships is demonstrated in Fig. 2 and 3. The ratio, b/a , is 9.8 which is in good agreement with Young's theoretical value. A relationship equivalent to Eq. [3], [4], and [5] was derived independently by Winkel and de Groot (18) by assuming relaxation of the dielectric under the influence of an external field

$$d(C_s^{-1})/d \ln f = 4R_s f \quad [6]$$

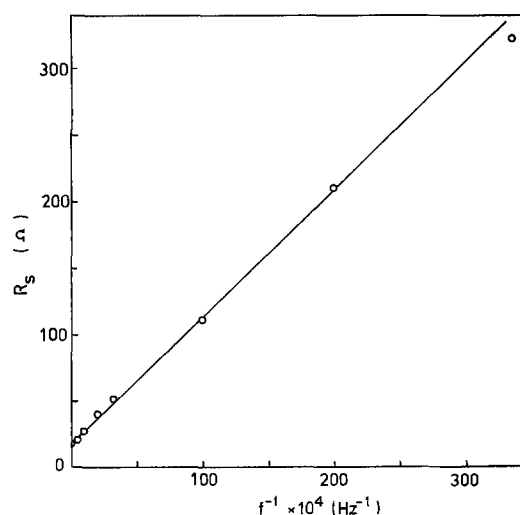


Fig. 2. Series resistance vs. reciprocal frequency, $T = 25^\circ C$, $pH = 8.4$, open circuit.

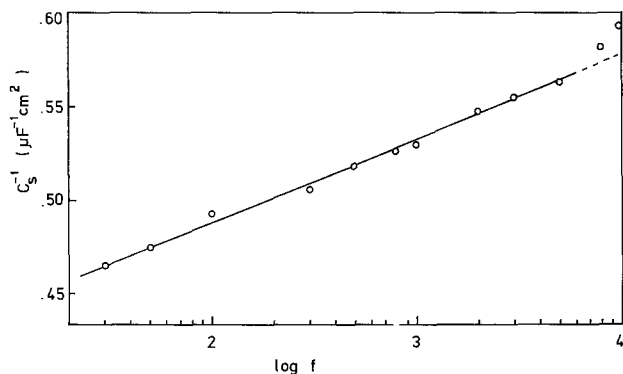


Fig. 3. Reciprocal capacitance vs. logarithm of frequency, $T = 25^\circ\text{C}$, $\text{pH} = 8.4$, open circuit.

As Winkel and de Groot suggested, the equivalency of the two derivations is related to the exponential relationship of the conductivity defined by

$$\sigma = \sigma_0 \exp(d/d_0) \quad [7]$$

which was Young's theoretical basic concept¹ and of the relaxation time, τ , of polarizable particles in the dielectric defined by

$$\tau = \tau_0 \exp(q/kT) \quad [8]$$

where σ_0 , d_0 , and τ_0 are constants and q is the depth of the potential valley. There is a linear correlation between σ and τ (19). Recently Van Meirhaeghe *et al.* (20) also reported that the equivalency should be a consequence of the validity of Eq. [4].

R_0 can be obtained by extrapolation of R_s to $f^{-1} \rightarrow 0$ in Fig. 2. At sufficiently high frequencies, R_s corresponds to the ohmic resistance of the electrolyte. R_0 was found to be 17Ω from Fig. 2.

Equation [7] can be rewritten with $d/d_0 = C_0/C$ via Eq. [2] as

$$\sigma = \sigma_0 \exp(C_0/C) \quad [9]$$

According to Smyth *et al.* (21) the conductivity is directly proportional to the frequency of measurement

$$\sigma = 2\pi f \epsilon \epsilon_0 \quad [10]$$

Using Eq. [9] and [10] σ can be calculated as a function of position in the dielectric film. The frequency therefore determines the conductivity and the capacitance determines the position in the oxide. In order to determine this position it is necessary to have the absolute value of C_0 . C_0 can be obtained at high frequency, where the dielectric behaves like an ideal parallel plate condenser. It was not possible, however, to measure the capacitance at frequencies above 10 kHz. However, it was possible to obtain C_0 from the temperature dependence of the capacitance.

Temperature dependence.—In Fig. 4 the temperature dependence of capacitance is shown. The capacitance is corrected for the Helmholtz capacitance (assuming $20 \mu\text{F cm}^{-2}$) using Eq. [1]. The capacitance is directly proportional to the temperature

$$C_{\text{SC}} = C_0 + B(T - T_0) \quad [11]$$

where B is a proportionality factor and T_0 is defined as a critical temperature at which C_{SC} approaches C_0 . The accessible temperature is not sufficient to observe C_0 and extrapolation of C_{SC} to $T \rightarrow T_0$ (Fig. 4) is not possible because T_0 is undetermined.

C_0 and T_0 can be obtained by varying the proportionality factor B . It was found experimentally that B depends on the electrode potential. The results are shown in Fig. 5. The extrapolation of C_{SC} for different electrode potentials to low temperatures intersect the same point ($C_0 = 1.5 \mu\text{F cm}^{-2}$ and $T_0 = -26^\circ\text{C}$). Smyth

¹ The original equation was expressed in terms of resistivity.

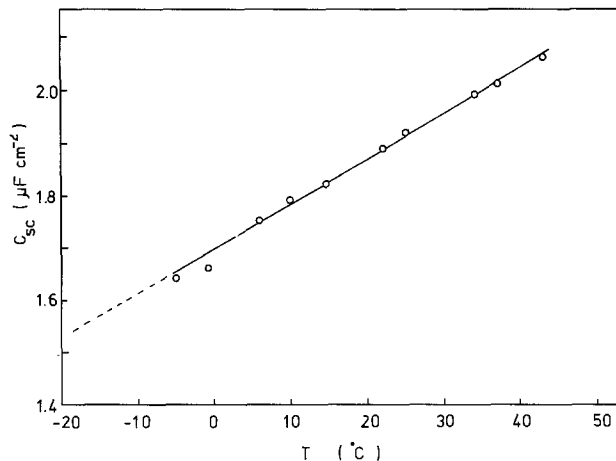


Fig. 4. Space charge capacitance vs. temperature, $f = 1 \text{ kHz}$, $\text{pH} = 8.4$.

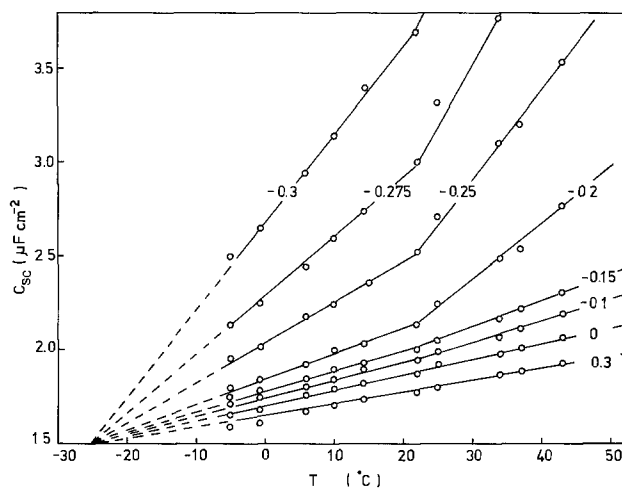


Fig. 5. Capacitance vs. temperature for different electrode potentials, $f = 1 \text{ kHz}$, $\text{pH} = 8.8$.

et al. (21) also found the value of T_0 to be around -30°C for heat-treated anodic tantalum oxide films.

The dependence of B on electrode potential could be explained by local dissociation equilibria of the donors



where O_V is an oxygen vacancy (or Fe^{2+}) and O_V^+ is a singly ionized donor. At negative electrode potentials the local dissociation equilibrium is shifted to the left resulting in a higher temperature sensitivity. At strong anodic potentials the donors are more dissociated and the total amount of the charge in oxide is less affected by temperature. The capacitance is then constant and the effective thickness d approaches the actual thickness d_0 .

The abrupt slope increase at around 20°C suggests that the polycrystalline iron oxide has two donor levels, i.e., shallow and deep donor levels as suggested by Kennedy and Frese (10) from their Mott-Schottky plots. The deep donors affect the total amount of charge at this temperature. Mott-Schottky plots also show an abrupt change in slope at this temperature (see next section). The extrapolation of the higher slopes in Fig. 5 also intersect at $C_0 = 1.5 \mu\text{F cm}^{-2}$. Thus C_0 is independent of the deep donor concentration as expected, since C_0 represents the actual thickness of the oxide film. Having determined C_0 , d_0 can be calculated from Eq. [2] ($d_0 = 67 \text{ nm}$).

Using Eq. [9] it is possible to calculate the conductivity, σ , at the reduced position C_0/C_{SC} . The results are shown in Fig. 6. The calculated values of σ at fre-

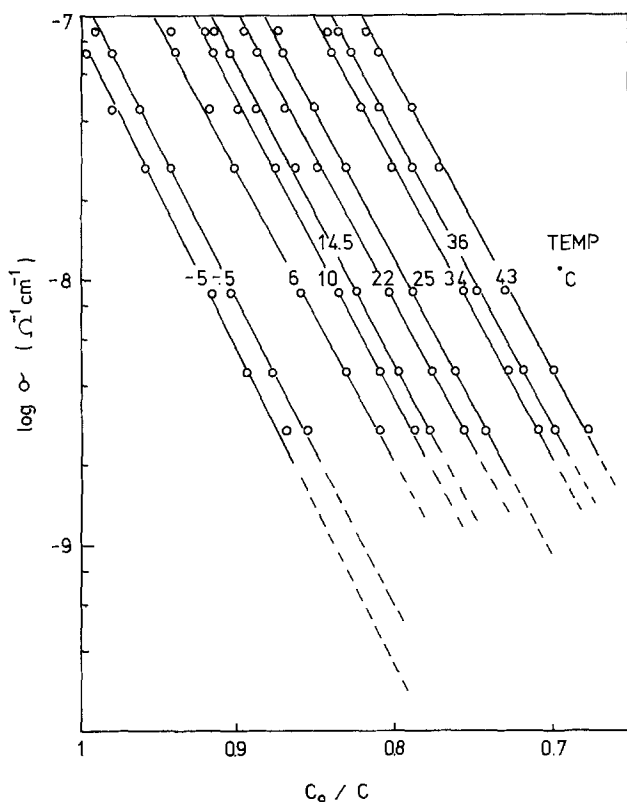


Fig. 6. Conductivity profile for different temperature, pH = 8.4

quencies lower than 200 Hz are not shown, because in this range σ does not follow Eq. [9]. The uniformity in slope suggests that the oxide is homogeneous for at least 30% of the total film thickness. The ionization energy, E_D , of donors does not depend on oxide position, ionized donor concentration, N_D^+ , or the electron concentration in the conduction band.

The electron concentration, n , of an n-type impurity semiconductor can be expressed as

$$n = (N_D N_C)^{1/2} \exp(-E_D/2kT) \quad [13]$$

where N_C is the effective density of states in the conduction band. Hence the conductivity is

$$\sigma = \sigma_0 \exp(-E_D/2kT) \quad [14]$$

A plot of $\ln \sigma$ vs. T^{-1} gives a straight line, where the slope corresponds to the half of the ionization energy (Fig. 7). The value of σ was taken at the point $C_o/C_{sc} = 0.8$ (from Fig. 6). The slope gives $E_D = 0.64$ eV. This value is in good agreement with the value $E_D = 0.69$ eV obtained from the Mott-Schottky plots (see next section) and with reported values (10, 22, 23).

Mott-Schottky plots.—The simplified Mott-Schottky relation (24) is

$$C_{sc}^{-2} = (2kT/e^2 \epsilon_0 N_D) (-y - r + \ln r) \quad [15]$$

where y is the reduced potential drop in the space charge layer (V_{sc}) expressed as

$$y = eV_{sc}/kT = (V - V_f)e/kT \quad [16]$$

and r is the degree of dissociation of donors expressed as

$$r = N_D^+/N_D \quad [17]$$

V_f is the flatband potential.

A plot of C_{sc}^{-2} vs. V_{sc} , if linear, yields the donor density, N_D , from the slope and a characteristic potential V_o at $C_{sc}^{-2} \rightarrow 0$. In Fig. 8 and 9 the effects of frequency and temperature on Mott-Schottky plots are shown. The characteristic potential, V_o , as well as the slopes are a function of temperature and frequency. The potential at which the slope changes has been de-

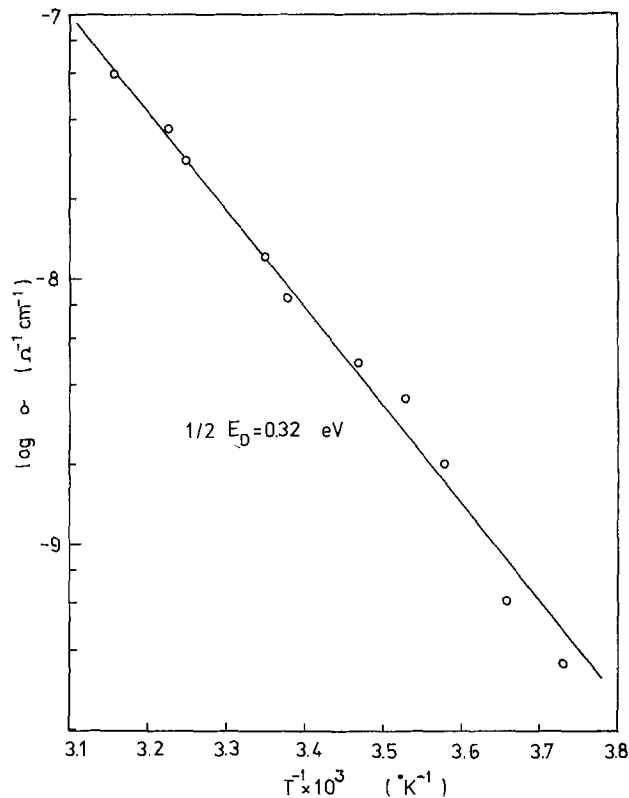


Fig. 7. Temperature dependence of conductivity at $C_o/C = 0.8$, pH = 8.4.

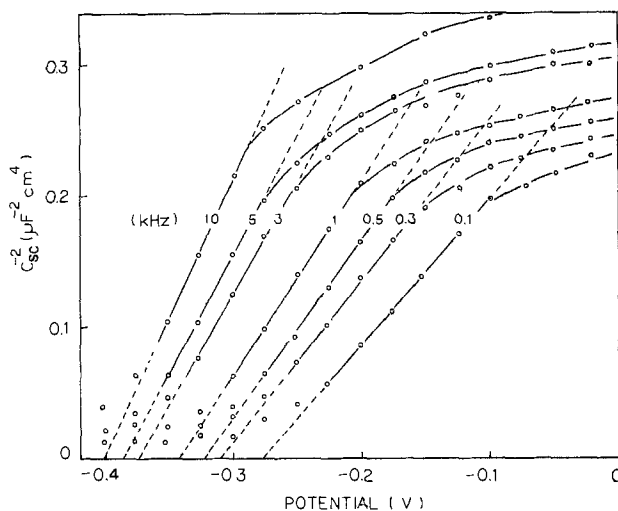


Fig. 8. Mott-Schottky plots for different frequencies, $T = 25^\circ\text{C}$, pH = 8.4.

scribed by Kennedy and Frese as a "critical potential" for ionization of deep donors. However, it should be noted that in this case the film thickness is also a factor.

For $C_{sc}^{-2} \rightarrow 0$, Eq. [15] can be rewritten as

$$V_o - V_f = (-r + \ln r)kT/e \quad [18]$$

If $r = 1$, i.e., the donors are completely dissociated, the potential difference, $V_o - V_f$, has its minimum value (kT/e) so that V_o is approximately equal to the flatband potential, V_f . If $r \ll 1$, as would be expected for deep donors, V_o is cathodic with respect V_f , i.e., a one-order decrease in r corresponds to 60 mV cathodic shift of V_o at room temperature. The frequency dependence of V_o is linear with logarithm of f (Fig. 10) and the slope $dV_o/d \log f$ is -63 mV. From the theory and the experimental results there should be a correlation between r and f in a manner consistent with $r \propto f^{-1}$. This is not unusual for impurity semiconduc-

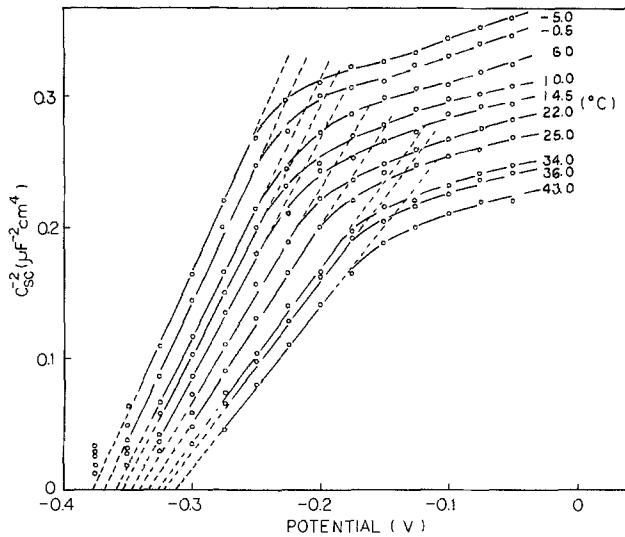


Fig. 9. Mott-Schottky plots for different temperatures, $f = 1$ kHz, $\text{pH} = 8.4$.

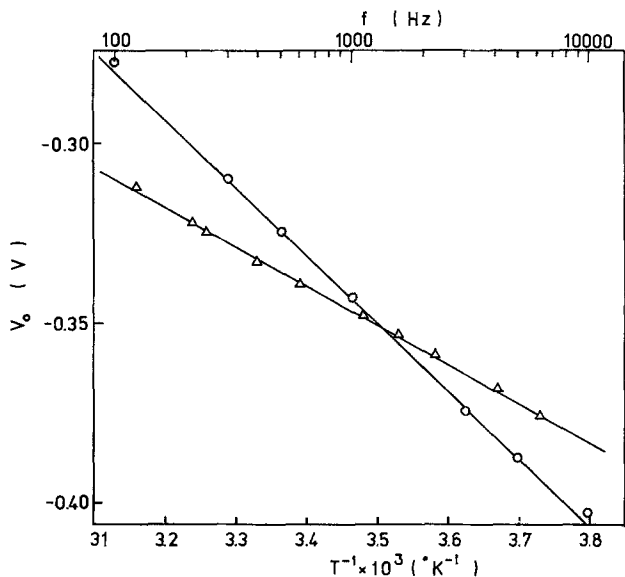


Fig. 10. Characteristic potential vs. frequency (\circ symbol) from Fig. 8 and vs. reciprocal temperature (Δ symbol) from Fig. 9.

tors, because the local ionization equilibrium of donors is influenced by the measurement frequency. The experimental result ($dV_0/d \log f = -63$ mV) is not general, since it can be dependent on pH, the frequency dependence of the dielectric constant, the Helmholtz layer capacitance, the contact potential at the metal-semiconductor interface, etc.

Bockris and Uosaki (25) have observed for p-SiC that V_0 depends differently on frequency in acidic and alkaline solutions. Their results show that in 1N NaOH, V_0 is shifted to anodic potentials with increasing frequency and in 1N H₂SO₄, V_0 is not affected by frequency. No explanation was given for this observation. As would be expected, however, the pH value can change the shape of band bending. In strong acidic solution the band bending is large enough that the donors can be completely dissociated. In this case V_0 is not affected by frequency. On the other hand, in strong alkaline solution, the band bending is small or even inverted. V_0 is then shifted to anodic potential with increasing frequency. For n-type semiconductors the situation is reversed. Observations on anodic niobium oxide films by Stützel and Heusler (26) substantiate this suggestion. V_0 can also be independent of frequency (27, 28) without regard to pH, if $r = 1$.

The measurement of V_f from Mott-Schottky plots is somewhat uncertain, especially for a highly doped impurity semiconductor electrode. For the exact determination of V_f several methods have been reported (2, 29-31). In this paper the flatband potential is defined as the potential where the photocurrent vanishes. This potential corresponds to V_0 , when measured at 1 kHz at any pH. This will be discussed in detail in a future paper.

The temperature dependence of V_0 shows that V_0 is directly proportional to T^{-1} (Fig. 10). According to Eq. [13] and [17] the degree of dissociation, r , can be reexpressed as

$$r = (N_C/N_D)^{1/2} \exp(-E_D/2kT) \quad [19]$$

under the assumption that $E_D \gg 2kT$ and $n = N_D^+$. For $r \ll 1$ and from Eq. [18] and [19] the potential difference ($V_0 - V_f$) is directly proportional to T^{-1} and expressed as

$$(V_0 - V_f)e/kT = \frac{1}{2} \ln(N_C/N_D) - E_D/2kT \quad [20]$$

The plot V_0 vs. T^{-1} yields a straight line and E_D can be calculated from the slope. The slope in Fig. 10 yields $E_D = 0.69$ eV at $T = 300^\circ\text{K}$. This value is in good agreement with the value obtained from the conductivity. This method, however, has several advantages. The experimental technique and the theoretical treatment are simpler. Also the experiment can be carried out at fixed frequency so that the frequency dependence of adsorbed species or dipoles is eliminated.

The frequency and the temperature dependences of the donor density, N_D , are shown in Fig. 11. The apparent break around $T = 20^\circ\text{C}$ is similar to the already observed potential dependence of the capacitance (Fig. 5). This reinforces the previous assumption that the deep donors begin to affect the total amount of the space charge at this temperature. On the other hand, the frequency dependence of N_D shows a linear relationship to $\log f$. However, it cannot be fully ruled out that the slope change of Mott-Schottky plot is mainly due to the frequency response of the dielectric constant. This can be assured only if V_0 is not frequency dependent.

Acknowledgment

The authors wish to thank the Robert A. Welch Foundation of Houston, Texas, for financial support of this research. They also wish to thank the American Iron and Steel Institute and Battelle Memorial Institute for the generous donation of the zone-refined iron used in this study.

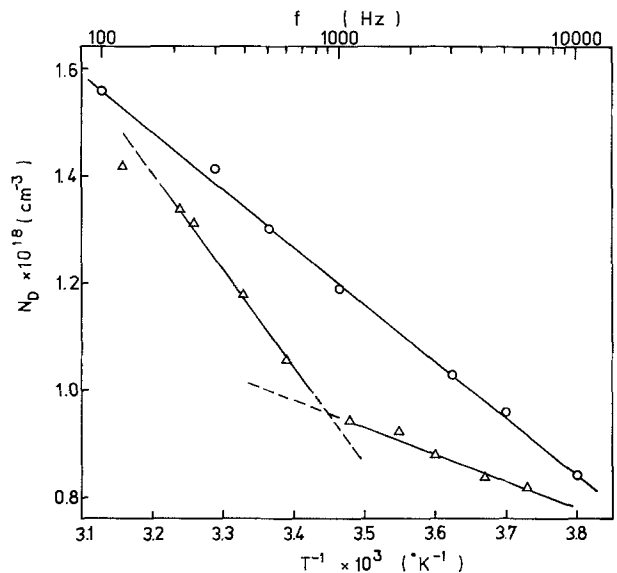


Fig. 11. Donor density vs. frequency (\circ symbol) from Fig. 8 and vs. reciprocal temperature (Δ symbol) from Fig. 9.

Manuscript submitted Oct. 16, 1978; revised manuscript received June 20, 1979.

Any discussion of this paper will appear in a Discussion Section to be published in the December 1980 JOURNAL. All discussions for the December 1980 Discussion Section should be submitted by Aug. 1, 1980.

Publication costs of this article were assisted by Rice University.

REFERENCES

- Lun-Shu Ray Yeh and N. Hackerman, *This Journal*, **124**, 833 (1977).
- S. M. Wilhelm, K. S. Yun, L. Ballenger, and N. Hackerman, *ibid.*, **126**, 419 (1979).
- N. Ramasubramanian, P. B. Sewel, and M. Cohen, *ibid.*, **115**, 12 (1968).
- R. Francis and D. G. Lees, *Corros. Sci.*, **16**, 867 (1976).
- D. Caplan and M. Cohen, *ibid.*, **6**, 321 (1966).
- R. J. Hussey, G. I. Sproule, D. Caplan, and M. J. Graham, *Oxid. Met.*, **2**, 65 (1977).
- A. G. Goursat and W. Smeltzer, *ibid.*, **6**, 101 (1973).
- P. Kofstad, "High Temperature Oxidation of Metals," John Wiley & Sons, Inc., New York (1966).
- J. B. Goodenough, in "Progress in Solid State Chemistry," Vol. 5, H. Reiss, Editor, p. 145, Pergamon Press, Oxford (1971).
- J. H. Kennedy and K. W. Frese, *This Journal*, **125**, 723 (1978).
- P. C. Grahme, *Chem. Rev.*, **41**, 441 (1947).
- F. Möllers, H. J. Tolle, and R. Memming, *This Journal*, **121**, 1160 (1974).
- D. M. Tench and E. Yeager, *ibid.*, **121**, 318 (1974).
- U. R. Evans, "The Corrosion and Oxidation of Metals," p. 56, Edward Arnold, London (1960).
- O. Jantzen, *Z. Agnew. Phys.*, **18**, 5601 (1965).
- R. K. Quinn, R. D. Nashy, and R. J. Baugham, *Mater. Res. Bull.*, **11**, 1011 (1976).
- L. Young, *Trans. Faraday Soc.*, **51**, 1250 (1955).
- P. Winkel and D. G. de Groot, *Philips Res. Rep.*, **13**, 489 (1958).
- D. Greig, "Electrons in Metal and Semiconductors," p. 100, McGraw-Hill Book Co., London (1969).
- R. C. Van Meirhaeghe, E. C. Dutoit, F. Cardon, and W. P. Gomes, *Electrochim. Acta*, **20**, 995 (1975).
- D. M. Smyth, G. A. Shirn, and T. B. Tripp, *This Journal*, **111**, 1331 (1964).
- F. J. Morin, *Phys. Rev.*, **93**, 1195 (1954).
- R. F. G. Gardner, F. Swett, and D. W. Tanner, *J. Phys. Chem. Solids*, **24**, 1183 (1963).
- J. F. Deward, *Bell Syst. Tech. J.*, **39**, 615 (1960).
- J. O'M. Bockris and K. Uosaki, *This Journal*, **124**, 1348 (1977).
- O. Stütze and K. E. Heusler, *Z. Phys. Chem. N. F.*, **65**, 201 (1969).
- E. C. Dutoit, R. L. Van Meirhaeghe, F. Cardon, and W. P. Gomes, *Ber. Bunsenges. Phys. Chem.*, **29**, 1209 (1975).
- K. S. Yun, Dissertation, Clausthal (1977).
- K. E. Heusler and K. S. Yun, *Electrochim. Acta*, **22**, 977 (1977).
- M. A. Butler, *J. Appl. Phys.*, **48**, 1914 (1977).
- R. N. Noufi, P. A. Kohl, and A. J. Bard, *This Journal*, **125**, 375 (1978).

Effect of Ruthenium Ions on Grain Boundaries in Gallium Arsenide Thin Film Photovoltaic Devices

W. D. Johnston, Jr.*

Bell Laboratories, Holmdel, New Jersey 07733

and H. J. Leamy, B. A. Parkinson,*¹ A. Heller,* and B. Miller*

Bell Laboratories, Murray Hill, New Jersey 07974

ABSTRACT

Chemisorption of ruthenium ions decreases both the rate of carrier recombination at grain boundaries and the surface recombination velocity on thin film, polycrystalline n-GaAs grown by chemical vapor deposition. Charge collection scanning electron microscopy reveals a pronounced improvement in charge collection at gold n-GaAs Schottky barriers following ruthenium treatment. After chemisorption of ruthenium ions, a solar to electrical conversion efficiency of 4.8% was reached in the n-GaAs/0.8M K₂Se-0.1M K₂Se₂-1M KOH/C liquid junction cell with semiconductor grains of 3-7 μm diameter. The ruthenium effect here is much more dramatic than that shown in single crystal substrates, increasing the power conversion efficiency by up to a factor of four over etched specimens.

It is particularly advantageous to fabricate solar cells based on polycrystalline, direct gap semiconductors with a liquid, rather than solid-state, junction as the active element. The formation of a rectifying junction by immersion of the semiconductor into an electrolyte solution is almost trivially simple. The complex requirements for forming matched expansion, or matched lattice, solid-state p-n or Schottky barrier junctions on the polycrystalline material are thus bypassed. Schottky barrier solar cells formed on micron crystalline sized GaAs films at present have reported solar to electrical conversion efficiencies such as 1.3 (1), 2.8 (2), 5 (3), and 6.3% (4). These values are

all low with respect to the 17% range (5) achieved with single crystal or large crystallite devices. On the other hand, efficiencies of 5.1%, or 70% relative to single crystal values, have been obtained for hot-pressed polycrystalline CdSe in a semiconductor-liquid junction (SCLJ) cell (6). The failure to obtain efficiencies in polycrystalline GaAs solid-state cells closer to those in single crystal cells has variously been ascribed to excessive surface recombination velocities, recombination at grain boundaries, and/or shunting from heavily doped grain boundaries.

Recent results from this laboratory demonstrated a 12% solar to electrical conversion efficiency for a single crystal semiconductor n-GaAs/Se⁻-Se_x⁻-OH⁻/C cell with a hillock surface topography achieved through appropriate etching and with modification of

* Electrochemical Society Active Member.

¹ Present address: Ames Laboratory, Iowa State University, Ames, Iowa 50011.

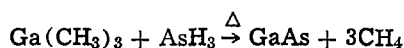
Key words: semiconductor, solar, energy conversion.

the interfacial chemistry by Ru(III) chemisorption (7, 8). These efforts encouraged us to evaluate some polycrystalline thin film materials as photoanodes. This paper is concerned with chemically vapor deposited films from $(\text{CH}_3)_3\text{Ga-AsH}_3$ reactions which form an n-type layer on graphite substrates, the characteristics of electrodes so formed in selenide-polyselenide regenerative electrolytes, and the effect of Ru(III) treatment on the electrode properties. Besides observing the consequences of Ru chemisorption by voltammetry of the redox electrolyte-GaAs junction cells, we studied, by charge collection scanning electron microscopy (CCSEM), the effect of the Ru treatment prior to Au deposition on these films to form Au-GaAs Schottky barriers.

In CCSEM an energetic, focused electron beam is scanned over the thin barrier metallization and penetrates the semiconductor to produce carrier pairs. These are collected by the barrier field and the resultant current is employed as the video signal of a synchronously scanned CRT display (9). In this way, an image of local charge collection is formed and the influence of the Ru treatment on this process can be examined.

Experimental

The GaAs films were grown on substrates of high density graphite from Carbone-Lorraine (Type 5890-PT) after evaporative deposition of 500Å of germanium which ensured an ohmic contact. In one case (sample 70) a smooth molybdenum substrate, also precoated with 500Å of Ge, was employed. The GaAs layer is formed by the pyrolytic reaction (10)



The $\text{Ga}(\text{CH}_3)_3$ was Alfa-Ventron Electronic grade, 99.9995%, with detected impurities of Si and Al, 2 ppm each, and Cu and Mg not detected. AsH_3 was Matheson Electronic grade, 99.995%, supplied as a 2% dilution in ultrahigh purity H_2 (99.999%, total hydrocarbon < 0.5 ppm). The substrate was held at 700°C on a Mo or graphite susceptor with rf induction heating.

A flow of 5-20 cm^3/min of palladium-diffused hydrogen was passed through the trimethyl gallium bubbler, held at -11°C . The mole fractions of trimethyl gallium and arsine were approximately 10^{-4} and 10^{-3} , respectively. These conditions resulted in a growth rate of 10-12 $\mu\text{m}/\text{hr}$. The total flow rate of H_2 was 4 liters/min.

Photoelectrodes were constructed with GaAs films 10-30 μm thick by attaching a copper wire with conductive silver epoxy to the back of the graphite substrate and masking all nonsemiconductor surfaces with epoxy. The electrodes were etched in either 1:1 H_2SO_4 -30% H_2O_2 , or in the same etchant diluted 1:4 with distilled water. The electronics, light measurement systems, and cell geometries were similar to those described previously (11). The ruthenium treatment solution was 0.01M RuCl_3 -0.1M HNO_3 . The preparation of the 1M KOH -1M K_2Se electrolyte and adjustment of polyselenide content have been described elsewhere (12).

Surfaces of polycrystalline GaAs subjected to the various treatments described below were evaluated by charge collection scanning microscopy after vacuum deposition of 200-500Å of Au to form a Schottky barrier. Prior to the deposition the specimens were simply washed and air dried. Nonblocking contacts to the graphite substrates were made with silver paint.

Results and Discussion

Table I summarizes some of the physical properties of the polycrystalline GaAs prepared by organic pyrolysis. The surface topography of the materials that exhibited the best solar conversion efficiencies was dominated by columnar grains of 3-7 μm dimensions,

Table I.

Specimen	Thickness (μm)	Mobility ($\text{cm}^2 \text{V}^{-1} \text{sec}^{-1}$)	Dopant conc. (cm^{-3})	Avg. crystallite grain size (μm)	Misc.
37	15	—	—	—	500Å Ge
49	10	3400	1×10^{17}	1-3	Some O_2
53	12	1460	4×10^{17}	3-5	O_2
63	24	2900	4×10^{16}	3-5	No O_2
70	12	—	2×10^{15}	1-3	Mo, no pinholes
93	23	2900	4×10^{16}	3-5	Pinholes
105	30	4000	4×10^{16}	3-7	Cracks, little O_2

as measured from SEM photographs. The thickness of the films was kept at 10-30 μm , both to examine the efficiency of thin films and to minimize the number of grain boundaries perpendicular to the carrier drift field. Mobilities and dopant concentrations were estimated from Hall measurements made on single crystal substrate films grown in the same run as the polycrystalline samples.

The film (sample 70) grown on a molybdenum surface exhibited a uniform, pinhole-free structure in SEM photographs, with relatively small, partly columnar grains 1-3 μm in size. This specimen was grown to evaluate the combined effects of fewer leaks (via pinholes) to the substrate and a more electrochemically passive substrate material.

Oxygen contamination may pose a problem during the growth of the films due to the tendency of oxygen to form deep donors in GaAs (13). The extent of the contamination is small and difficult to characterize accurately. For present purposes, it was qualitatively estimated from the perfection of the single crystal epitaxy.

The current-voltage curves for an illuminated anode (sample 63) in a selenide-polyselenide liquid junction cell are shown in Fig. 1, as a function of surface treatment. This set of curves is representative of the voltammetric behavior of all the films relative to surface treatment, independent of their relative effectiveness for light to electrical energy conversion. Curve 1 shows the response of a film immersed in the cell without prior treatment. Curve 2 indicates the improved behavior shown after a short exposure (1-5 sec) to sulfuric acid-hydrogen peroxide etchants. [Neither the exact composition of the etchant nor the time the electrode is etched have any effect on this curve so long as the etch is not prolonged (> 10 sec) or overly repeated.] Substantial improvement in the characteristics following etching is seen in all the semiconductor samples.

Curve 3 results after the electrode of curve 2 is removed from the selenide electrolyte, washed, dipped for 30-60 sec in the 0.01M $\text{Ru}(\text{III})$ -0.1M HNO_3 solution, washed again, and returned to the cell. Dramatic improvements are found in the short-circuit current, open-circuit voltage, and fill factor, beyond those reached by etching alone. The relative improvements (curve 3 vs. curve 2) are even more substantial than those seen with ruthenium-treated single crystal GaAs electrodes in the same system. Ruthenium enhancement of the single crystal performance is manifest as an increased operating voltage and fill factor of the cell. In that case, no increase (or decrease) in short-circuit current was observed, as the voltage bias on most single crystal electrodes at short circuit is sufficient to collect the photogenerated carriers at high quantum efficiency (a light-limited current region is reached). For the particular example in Fig. 1 the power output was increased by a factor of four after the ruthenium treatment. Substantial improvements using the ruthenium treatment were observed in all the polycrystalline materials examined in this study, with the exact level a function of both substrate and experimental conditions. The fill factor and power

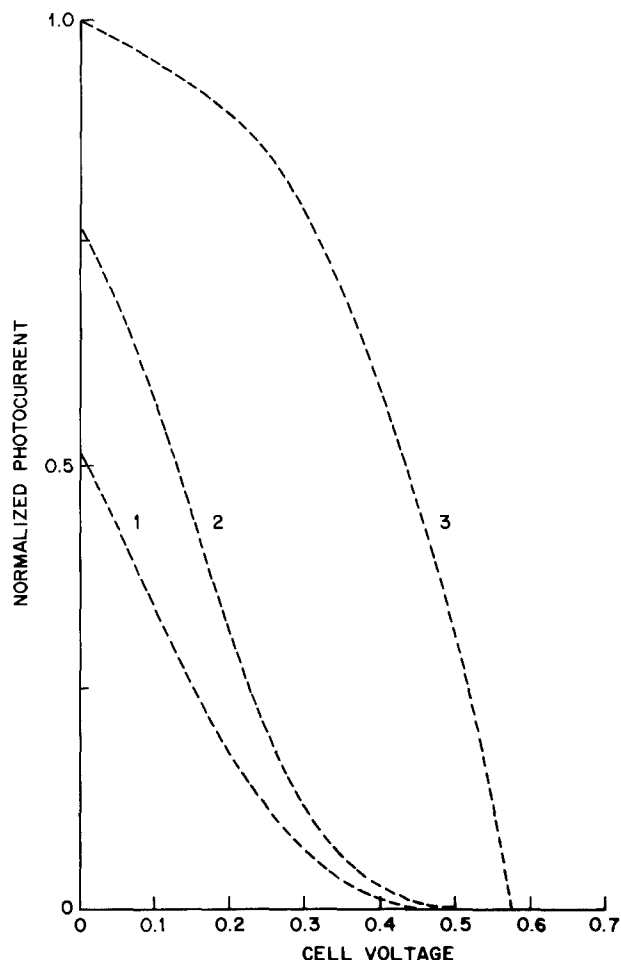


Fig. 1. Current-voltage curves for sample 63 n-GaAs electrode in the 0.8M K_2Se -0.1M K_2Se_2 -1M KOH electrolyte as a function of prior surface treatment. Illumination level fixed. Photocurrent is normalized to maximum value. Curve 1, Electrode as received; curve 2, two second etch in 1:1 H_2SO_4 -30% H_2O_2 ; curve 3, dip in 0.01M $RuCl_3$ -0.1M HNO_3 for 30 sec after curve 2 tracing.

conversion efficiency, as determined from Fig. 1 for which limiting current is not attained, ought to be sensitive to current (illumination) level. The relative performances of untreated and Ru-treated specimens under varying intensity are shown in Fig. 2 and 3, respectively, for the same set of normalized light intensities, all other factors being kept constant. The 105 electrode was used untreated and then the same set of data was repeated after it was ruthenium treated. Although this sample does not show as large an overall increase in power output from ruthenium chemisorption as sample 63, the fill factor is clearly maintained at high intensities much better in the electrode after it has been treated with ruthenium. The maximum power outputs from these curves are plotted vs. intensity in Fig. 4. These plots show more clearly that the ruthenium-treated electrode has a better relative efficiency than the untreated one under the higher kinetic stress of increased illumination level.

Table II contains a summary of open-circuit voltages (OCV), fill factors (ff), and qualitative ranking (poor to very good) of short-circuit current (ISC) for the specimens physically characterized in Table I. Tungsten-halogen illumination of approximately one-sun equivalent intensity was used for these measurements. Comments on the dark currents refer to the cathodic (forward diode) current observed in the unilluminated cell at potentials of the semiconductor that are negative with respect to that of the selenide-polyselenide couple at carbon. High dark currents mean more metallic-like behavior of the electrode (forward conduction at potentials more positive than that of the expected flatband level) and are related both to

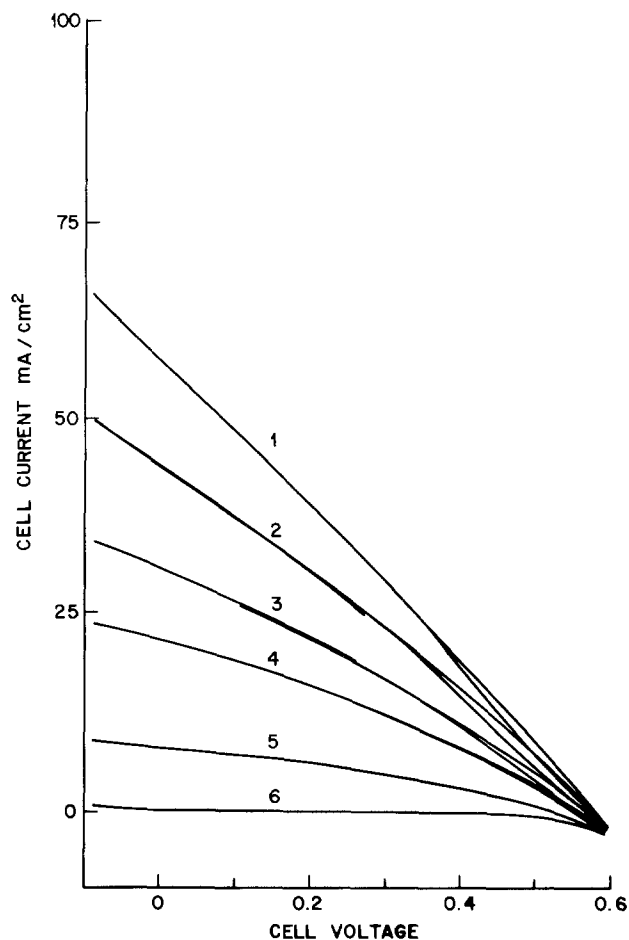


Fig. 2. Effect of varying intensity on current-voltage curves of untreated sample 105 electrode in cell of Fig. 1. Curve 1 corresponds to focused 100W tungsten-lamp. Successive curves refer to nominal absorbance of neutral density filter in beam. Curve 2, 0.2; curve 3, 0.4; curve 4, 0.6; curve 5, 1.0; curve 6, ∞ (dark behavior).

film properties and the activity of pores which may reach through to the substrate.

The solar efficiency values quoted in Table II were measured using natural sunlight for the samples (63, 93, and 105) which had the better laboratory characteristics. The current-voltage curve obtained for the best specimen (sample 63) at an insolation of 96 mW/cm² is shown in Fig. 5. The power conversion efficiency is 4.8% as compared to 12% for single crystal n-GaAs electrodes that were handled and measured similarly.

Under tungsten-halogen laboratory illumination producing a similar power output as the solar runs, the efficiency decreased by about 15% after 11,000 C/cm² of charge passage. Doubling the light intensity at that time increased the rate of decline which was associated with the appearance of gas evolution. Failure appears to be associated with attack at pores. Cross-sectional examination showed a much reduced rate of over-all material loss than the approximately 25 μ m annual rate estimated earlier for single crystal electrodes not treated with ruthenium. Further work would be required to refine photocorrosion rates this low in magnitude and suggest or estimate the long term stability.

For the CCSEM experiment, the 63 photoanode described above was removed from the liquid junction cell, metallized with gold, and examined along with a parallel metallized sample not otherwise exposed. Figure 6 compares results obtained from ruthenium-treated and untreated material. In both cases the light, rod-like feature is that of the silver contact to the top layer. The darker the image of the barrier area, the higher the local collection efficiency. The improved

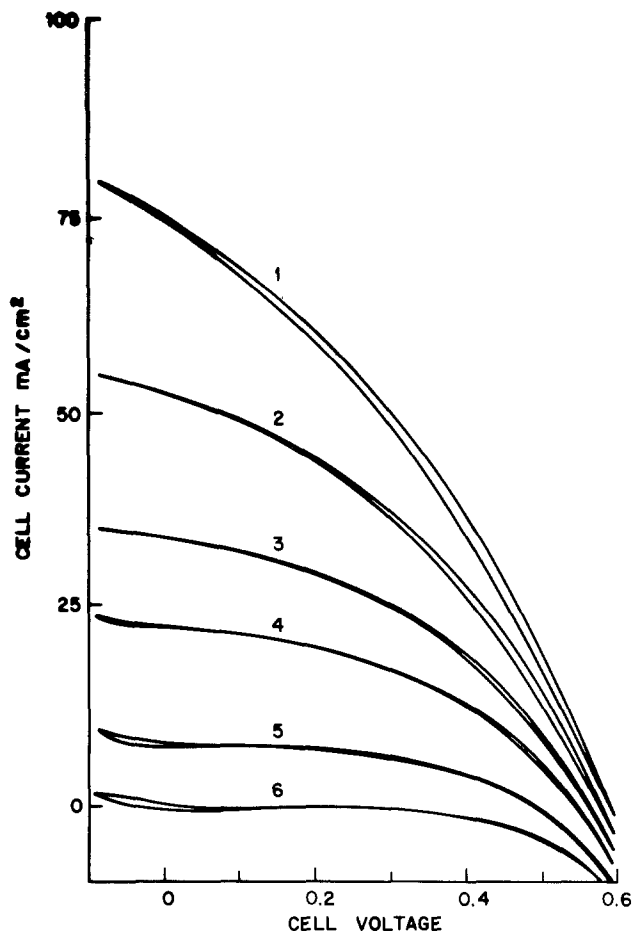


Fig. 3. Experiment and notations of Fig. 2 except that sample 105 electrode was given full ruthenium treatment.

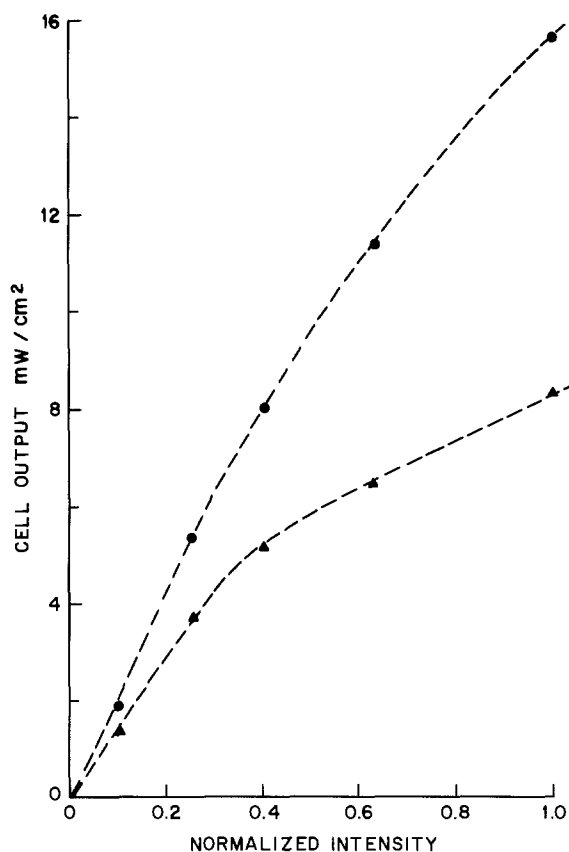


Fig. 4. Maximum power outputs from curves of Fig. 2 (▲) and Fig. 3 (●) plotted vs. normalized intensity (1 = no filter).

Table II.

Specimen	OCV	SSC*	ff	Solar efficiency (%)	Comments
37	0.52	p	0.43	—	
49	0.45	g	0.43	—	High dark current with H ₂
53	0.4	f	0.35	—	As 49
63	0.575-0.625	vg	0.42	4.8	
70	0.3	p	0.4	—	
93	0.6	g	0.39	3.5	Low dark current
105	0.55	vg	0.42	3.8	High dark current

* SSC: qualitative comparison, p = poor, f = fair, g = good, vg = very good.

collection efficiency of the ruthenium-treated barrier is readily apparent.

The contrast between the untreated barrier (a) and the background region (i.e., the silver contact) is nearly zero, indicating a low collection efficiency. In comparison, the ruthenium-treated material (b) exhibits substantial collection over the entire device area. The Schottky barriers in both cases exhibit uniform contrast except in the regions of cracks in the GaAs films and contaminants on the surface of the Au Schottky barrier metallization. These macroscopic defects are observed in secondary electron micrographs as regions of reduced emission, and their contrast in the charge collection micrographs is at least partially accounted for by the variations in absorbed energy that accompany the topographical features of the defects.

A higher magnification comparison of the samples shown in Fig. 6 is presented in Fig. 7. In this figure, the improvement in collection efficiency of the ruthenium-treated device is observed to be associated with an increase in both the number of individual crystallites that are active and a decrease in the propensity of the intercrystallite boundaries to act as recombination sites. Although collection efficiency is reduced at the grain boundaries in both devices, the decrease is smaller in the ruthenium-treated chemical.

The improved quantum efficiency that is qualitatively apparent in Fig. 6 and 7 was investigated more quantitatively by measurement of the local charge collection currents. For this experiment a freshly prepared GaAs film was sequentially etched and exposed

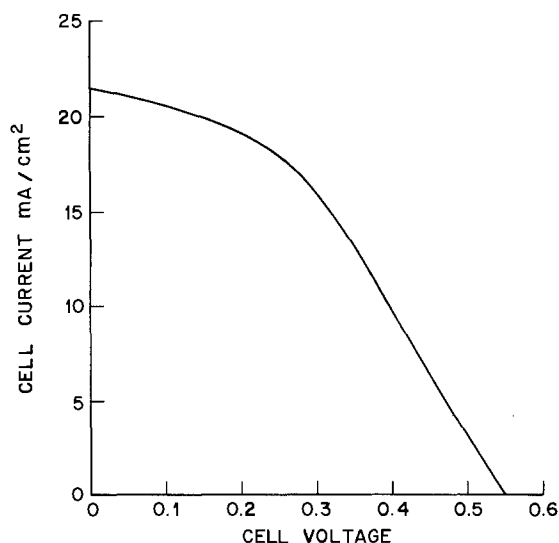


Fig. 5. Current-voltage curve under solar irradiance of 96 mW/cm² for n-GaAs/0.8M K₂Se-0.1M K₂S₂-1M KOH/C cell with sample 63 polycrystalline thin film electrode given ruthenium treatment. Power conversion efficiency is 4.8%.

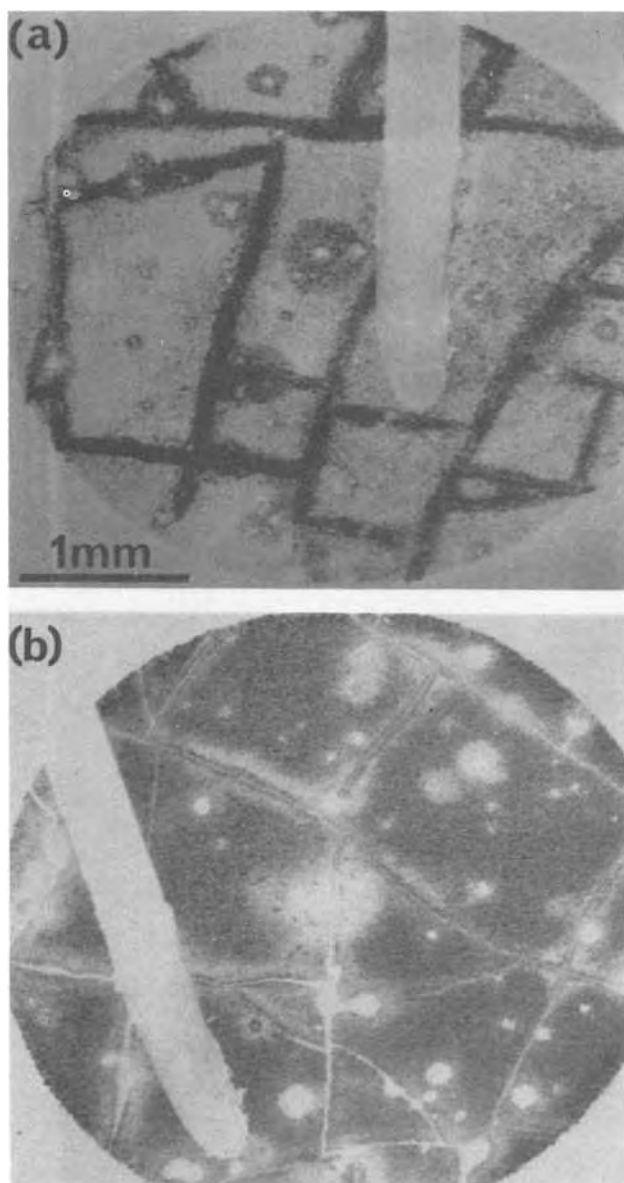


Fig. 6. CCSEM micrographs of gold metallized sample 63 electrodes with GaAs surface given (a) no prior treatment and (b) ruthenium treatment.

to the selenide and Ru(III) solutions, each operation being performed on a successively smaller portion of the sample. In this way, the final sample contained exposed areas of untreated, etched, etched and selenide-treated, and finally etched, selenide- and Ru(III)-treated material. A single Schottky barrier was fabricated over the entire sample and the charge collection was determined in each region by recording the current collected during a single linear scan of the electron beam over a 1 mm portion of each region.

As seen in Fig. 7, the current collected during each scan varied from maximum values at the grain interiors to lower levels at the grain boundaries. The average value of the current was taken for the determination of collection efficiency.

The results, normalized to the electron beam current,² are plotted vs. electron beam energy in Fig. 8. This plot shows that the average collected current is markedly affected by the various surface treatments. The untreated surface is essentially inactive while the Ru dipped material exhibits the largest collection effi-

²The measurement of collection current was conducted with beam currents in the 10^{-10} A range to insure low injection level conditions.

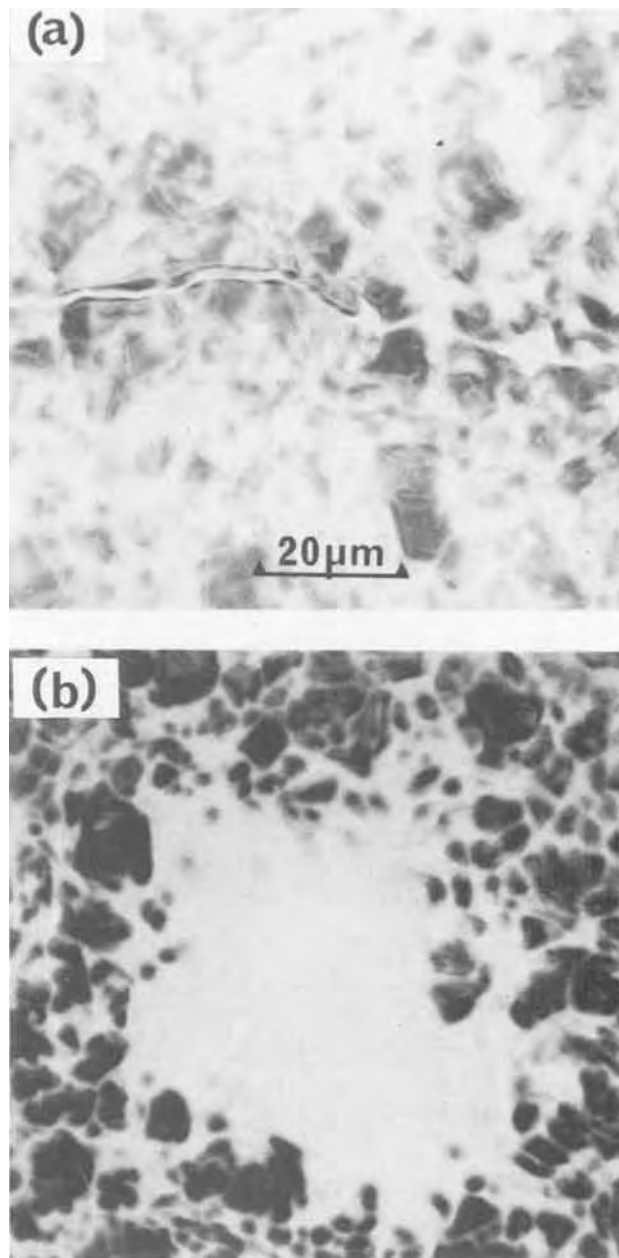


Fig. 7. Higher magnification micrograph of Fig. 6 specimens

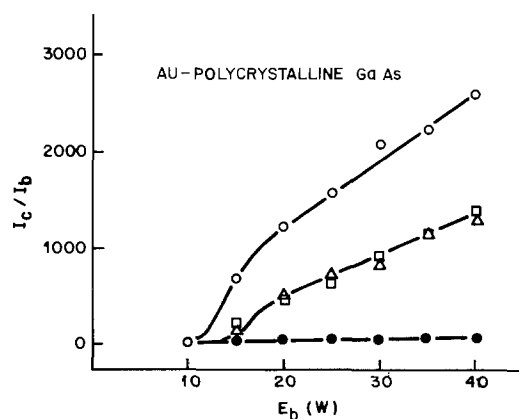


Fig. 8. Average scan current, I_c , normalized by electron beam current, I_b , plotted vs. electron beam energy as a function of GaAs treatment prior to gold metallization. ●, Untreated; □, etched; △, etched and selenide dipped; ○, etched, selenide dipped, and ruthenium dipped.

ciency at all accelerating voltages. Furthermore, while etching the surface improves the collection efficiency of the device, a subsequent selenide dip alone does not cause further improvement, in agreement with our experience with the liquid junction cells. We note, however, that ruthenium is not effectively adsorbed without the preceding selenide step.

Charge collection in all instances declines to zero at electron beam accelerating voltages below 10 kV. This is attributable to absorption of the beam electrons by the 500Å Au metallization. At higher voltages, the linear rise in collected current indicates a constant charge collection efficiency that is independent of the depth distribution of injection up to $\sim 5 \mu\text{m}$.³ This suggests that charge collection is not diffusion length limited in this experiment. Although all of the treated areas are similar in this regard, the improvement imparted by the Ru(III) step amounts to an approximately 100% increase in collected current relative to the freshly etched surface on which no ions were intentionally chemisorbed. If the standard value for pair generation energy, 4.6 eV, is employed, an approximately 50% increase in quantum efficiency (from 20 to 33%) may be obtained from the data of Fig. 8.⁴

Summary and Conclusions

The solar efficiencies and cell parameters under laboratory illumination, when related to other data of Table I and II, allow certain conclusions about film properties. For example, oxygen contamination appears deleterious. Porosity, while it introduces metallically behaving shunts, is clearly not the only source of reduced voltage and fill factor. The sample grown on the smoother Mo substrate, which should have negligible leakage due to pores, behaved poorly. Grain size distribution plus the level of recombination at, or current shunting through, the boundaries appears to be important as well.

The effect of ruthenium in enhancing the current-voltage behavior of the cells is much more prominent than it is in the single crystal material described previously, consistent with the CCSEM data on the Au-GaAs Schottky barrier after the various stages of chemical treatment. That the effect is due to chemisorbed Ru and not to the removal of deleterious impurities was shown (14) by direct detection with Rutherford backscattering. The chemisorption of ruthenium raises the current collection efficiency of the device. The maximum observed solar conversion efficiency of 4.8% is 40% of that which we have reported for cells with single crystal photoanodes. We feel that better film quality for this application should be possible and this goal should be pursued. The results also suggest that the chemisorption of ruthenium might improve the current collection and over-all conversion efficiency of n-GaAs based Schottky junction (metallized) solar cells.

³ The electron range, R , in GaAs is given by $R = 0.027E_b^{1.40} \mu\text{m}$ with E_b in kV.

⁴ These figures were computed following correction for absorption within the gold metallization.

Ruthenium treatment appears to further reduce the already low level of photocorrosion in the GaAs-selenide system but extensive measurements of the stability of the more efficient film anodes must be made before conclusions on the viability of these materials can be drawn. The failure mode of the film electrodes is related to the pore structure and the polycrystalline cells consequently exhibit greater variability in output than the single crystal cells.

The model previously outlined for the reduction by ruthenium chemisorption of carrier traps or of output reducing shunts as the origin of the beneficial effects is consistent with the independent CCSEM data. Recent observations by luminescence methods (14) of a reduction in surface recombination velocity at single crystal GaAs-air interfaces with the ruthenium treatment further strengthens the case for such interpretation.

Manuscript submitted May 17, 1979; revised manuscript received June 25, 1979.

Any discussion of this paper will appear in a Discussion Section to be published in the December 1980 JOURNAL. All discussions for the December 1980 Discussion Section should be submitted by Aug. 1, 1980.

Publication costs of this article were assisted by Bell Laboratories.

REFERENCES

1. A. E. Blakeslee and S. M. Vernon, *IBM J. Res.*, **22**, 346 (1978).
2. S. S. Chu, T. L. Chu, H. T. Yang, and K. H. Hong, *This Journal*, **125**, 1668 (1978).
3. P. Vohl, D. M. Perkins, S. G. Ellis, R. R. Addis, W. Hui, and G. Noel, *IEEE Trans. Electron Devices*, **ed-14**, 26 (1967).
4. S. S. Chu, T. L. Chu, and H. T. Yang, *Appl. Phys. Lett.*, **32**, 557 (1978).
5. C. J. Wu and Y. C. M. Yeh, cited in Y. C. M. Yeh and R. J. Stirn, *ibid.*, **33**, 401 (1978).
6. B. Miller, A. Heller, M. Robbins, S. Menezes, K. C. Chang, and J. Thomson, Jr., *This Journal*, **124**, 1019 (1977).
7. B. Parkinson, A. Heller, and B. Miller, in Conf. Rec. 13th IEEE Photovoltaic Spec. Conf., Washington, D.C., p. 1253 (1978).
8. B. Parkinson, A. Heller, and B. Miller, *Appl. Phys. Lett.*, **33**, 521 (1978).
9. See, e.g., H. J. Leamy, L. C. Kimerling, and S. D. Ferris, in "Scanning Electron Microscopy/1976," Part IV, Vol. I, O. Johari, Editor, pp. 529-538, ITT Research Inst., Chicago (1976).
10. H. M. Manasevit, *This Journal*, **118**, 647 (1971).
11. A. Heller, K. C. Chang, and B. Miller, *ibid.*, **124**, 697 (1977).
12. K. C. Chang, A. Heller, B. Schwartz, S. Menezes, and B. Miller, *Science*, **196**, 1097 (1977).
13. A. G. Milnes, in "Deep Impurities in Semiconductors," Wiley-Interscience, New York (1973) and references therein.
14. R. J. Nelson, J. S. Williams, H. J. Leamy, B. Miller, H. C. Casey, Jr., B. A. Parkinson, and A. Heller, *Appl. Phys. Lett.*, in press.

Doping Density Dependent Attachment of RhB on TiO₂ Electrodes

R. Schumacher,¹ R. H. Wilson,* and L. A. Harris

General Electric Company, Corporate Research and Development, Schenectady, New York 12301

ABSTRACT

In this study a technique to sensitize TiO₂ electrodes with rhodamine B bonded to the surface is presented. To study both the attachment process and the mechanisms of spectral sensitization the system TiO₂/dye/electrolyte/Pt was investigated. The photocurrent produced by visible light illumination was studied as a function of electrolyte pH, illumination time, wavelength, and doping density. The observed photoresponse increased with doping density by a factor of 8 over the range investigated. Dye states were not removed from the surface during the course of illumination. The oxidized dye states were observed to be re-reduced after biasing at sufficiently negative voltage. The observation that the amount of dye deposited on the TiO₂ surface is affected by the doping density of the samples used is discussed in terms of the nature of the bonding between dye and surface. The photocurrent quantum efficiency per absorbed photon was calculated to be about 0.01.

There has been much interest in photochemical work on sensitized semiconductor electrodes with dyes in solution (1-3). Also of interest are dye-modified semiconductor electrodes because of their response to visible light quanta. Excited dye molecules sitting at the surface are able to transfer an electron to the conduction band of the semiconductor if both energy levels are in the same range. In order to link those molecules at the surface different types of bonding are described in the literature up to now: monolayer assemblies generated by the Langmuir-Blodgett technique (3-7) and covalently bonded dye molecules on semiconductor electrodes (8, 9). Even in the case of dyes in solution, most of the photocurrent is due to an adsorbed layer of dye on the surface of the electrode, at least for dyes with short excited-state lifetimes (10, 11). Photoresponses in the visible light range have been reported for all of these.

In this work we present a new technique to fix rhodamine B on the surface of TiO₂ electrodes. A correlation of the amount of dye deposited on the semiconductor surface and the doping density of the samples was observed. The electrodes were characterized by electrochemical and/or optical measurements. The attachment process of the dye on the surface is discussed in terms of (i) an influence of the electric field strength, (ii) adsorption sites, and (iii) the presence of negatively charged species, at the surface of TiO₂.

When the dye-coated electrode is illuminated with light that is absorbed by RhB a photocurrent is observed. The current decreases in time as the RhB becomes oxidized. The dye can be reduced by applying a negative bias so that the initial current level is regained. This indicates that the attachment is stable.

Experimental and Sample Preparation

Materials and measuring setups.—Two different types of rhodamine B (RhB) coated TiO₂ samples were used in this work: single crystals and polycrystalline material deposited on fused silica substrates. The rutile single crystal slabs about 1 mm thick were sliced from a boule obtained from NL Industries. The (001) faces of these samples were coated with RhB after polishing, cleaning, and reduction as have been described previously (12).

The polycrystalline samples were prepared by using the chemical vapor deposition (CVD) technique. Fused

silica disks 4 mm thick were used as substrates. Thin films in the range of 500-1000Å were deposited via the hydrolysis reaction of TiCl₄ in the presence of water vapor at approximately 500°C. In order to bring these samples to a uniform starting condition they were oxidized in a dry oxygen stream for 30 min at 900°C. Various doping densities N_D were made by reduction in a dry hydrogen-stream for 30 min but at different temperatures.

The experimental setup for characterizing the photoresponse of the RhB-coated single crystals in the visible range was the same as previously described (13, 14). Second order light quanta >3 eV (<400 nm) were eliminated from the grating monochromator output by using an appropriate filter (Corning CS3-74). All electrochemical measurements were carried out in 0.5M Na₂SO₄ aqueous solution in which the pH was adjusted by adding sulfuric acid or sodium hydroxide. The exposed sample area (0.125 cm²) remained constant as the crystal was pressed against a gasketed opening in the side of the cell.

Absorption measurements of dye molecules coated on polycrystalline samples were carried out in a Perkin-Elmer Spectrophotometer Model 575. An untreated fused silica disk was used as reference. The reported absorbance data were obtained by comparison of spectra recorded before and after RhB coating. Absorption measurements in aqueous RhB solutions were carried out using RhB solution of 10⁻⁴M/liter. Different pH values were adjusted as described above.

The rhodamine B was obtained commercially. The electrolytes were prepared using distilled water and reagent grade chemicals.

Coating technique.—The coatings of TiO₂ single crystal samples as well as the polycrystalline samples were achieved by simple immersion in an about 0.02 M/liter RhB/CH₃OH solution. A typical reaction time was 5 min. Thereafter the samples were immersed in distilled water for 5 sec to remove the excess dye molecules from the surface, followed by a short rinse under flowing distilled water. Finally the specimens were dried in a slight air stream.

Reproducible results for both kinds of TiO₂ materials were obtained only with freshly reduced samples. Prior to each coating process the samples were cleaned in hot conc sulfuric acid (50°C) for 5 min.

Results

Typical photocurrent *vs.* wavelength behavior obtained from the difference between data recorded before and after RhB coating is shown in Fig. 1. For this measurement the RhB coated single crystal used

* Electrochemical Society Active Member.

¹ Present address: Institut für Physikalische Chemie der Universität Kiel, Olshausenstr. 40-60, D-2300 Kiel, West Germany.

Key words: semiconductor, surface, coatings, electrode, bonding.

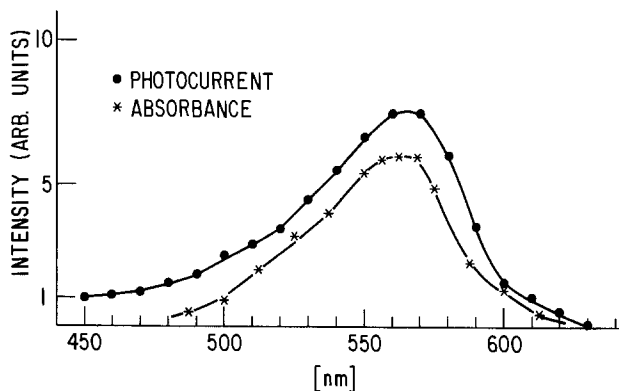


Fig. 1. Comparison of initial photocurrent spectrum obtained from coated single crystal (—●—) and absorbance spectrum obtained from coated polycrystalline (—*—) TiO₂ samples.

was maintained at a bias of 0.5V (SCE) with an 0.5M Na₂SO₄ electrolyte of pH 1. The doping density of the sample was $N_D = 5 \times 10^{19} \text{ cm}^{-3}$ as determined from capacitance-voltage measurements. As seen from the graph the initial anodic photocurrent of a freshly prepared sample shows a single peak with its maximum value around 565 nm but with a shoulder at about 520 nm. The absorbance of a dye-coated polycrystalline sample is also included in this figure. The data were obtained using a specimen which was reduced at 615°C (see below). As can be seen, the maximum intensity of photocurrent and absorbance are observed at identical wavelengths. Similar results were reported for covalently (8, 9) bonded RhB on SnO₂ as well as for simply adsorbed (11, 15) dye molecules on ZnO surfaces.

Except for the shoulder in the photocurrent response curve the present results do not clearly indicate the presence of a distinct dimer peak at 520 nm as reported by others (8, 11). The coating technique used in the present work, however, differs from those used in this earlier work.

The influence of the hydrogen ion concentration on the photoprocess on dye-sensitized TiO₂ single crystals was investigated. The results can be seen in Fig. 2 along with the pH dependence of the absorbance in an aqueous RhB solution. All points are taken from measurements at $\lambda = 560 \text{ nm}$.

The distinct structure of the absorbance characteristic for pH < 2 shown on the graph was explained by Ramette and Sandell (16) as being due to different molecular arrangements in strong acid solutions. The slightly decreasing absorbance for pH > 2 has been explained by the same authors as dilution effect.

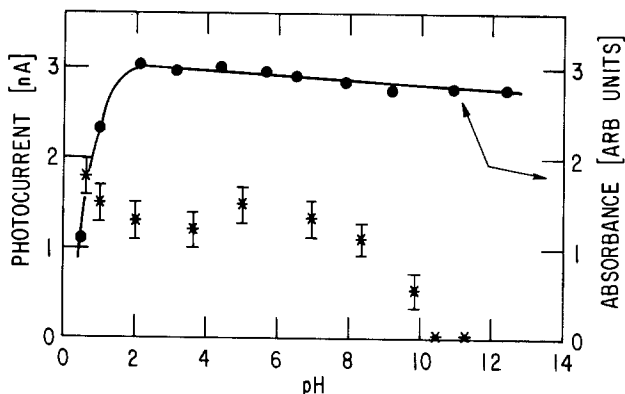


Fig. 2. Dependence of initial photocurrent and absorbance data on pH. The currents were taken from measurements of a dye-sensitized single crystal sample (*) and the absorbance in aqueous 10⁻⁴M RhB solution (●).

Unlike the absorbance results described above, the behavior of the electrochemically observed photocurrent shows little change in the range pH 0.6-8. No sharp decrease of the photocurrent intensity for pH < 2 was observed. Apparently, the attachment of an additional proton which blocks the ring resonance and which causes the drop in absorbance at low pH is impeded if the dye is attached to the surface. For pH values > 10 the photocurrent fell below the sensitivity range of the experimental setup.

This fall off in photocurrent at high pH can be explained using Fig. 3. This graph shows the energy situation of TiO₂ and RhB in terms of a Pourbaix-like diagram. The data shown, taken from the literature (17), are valid when semiconductor surface and dye are not in contact. As shown by the diagram the energy level for rhodamine B in its excited state, RhB*, lies above the TiO₂ conduction band edge as long as the pH is smaller than 12. In this region electron transfer from excited dye molecules to the conduction band is possible. This argument to explain the pH dependence of dye-sensitized semiconductors has been used frequently (11, 15). The coating process apparently does not affect the band situation at the TiO₂ surface because a shift in the flatband potential could not be measured.

According to the theory of photoprocesses on dye-sensitized semiconductor electrodes, illumination leads to a decrease of photocurrent intensity as the surface dyes become oxidized (1, 2). At a bias of 0.5V (SCE) the course of this bleaching process with time is shown in Fig. 4 using a sensitized TiO₂ single crystal sample with $N_D = 10^{19} \text{ cm}^{-3}$. The time dependence of a freshly prepared sample is characterized by the symbol (●); the decay rates depicted as (*, ◇) were observed after biasing for 60 sec at -0.5V (SCE) and then returning to +0.5V (SCE) for measuring the

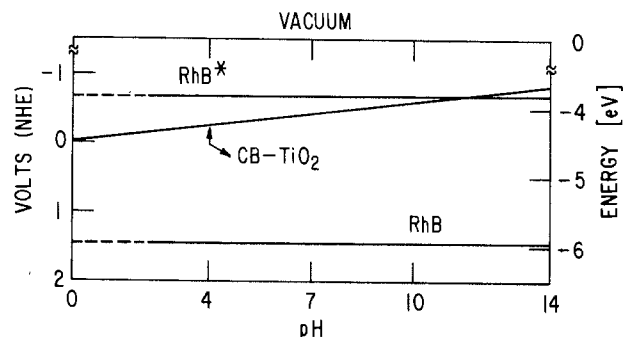


Fig. 3. Electron energy levels for rhodamine B in the ground and the excited state. The energy level of the TiO₂ conduction band edge is also shown.

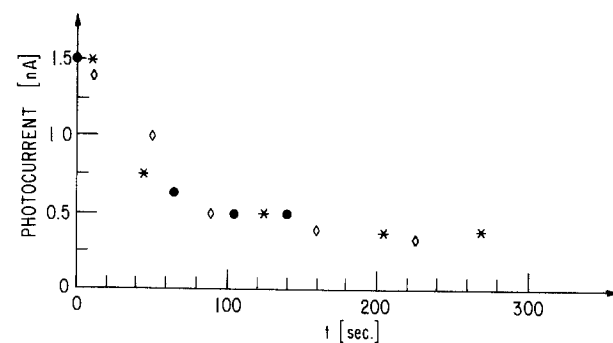


Fig. 4. Time dependence of the photoresponse under illumination at 560 nm in pH 1 electrolyte. The points describe the decay at a potential of 0.5V (SCE). The initial decay of a freshly prepared sample is characterized by the symbol (●); for the same sample points (*, ◇) were obtained subsequently after reduction at -0.5V (SCE).

photocurrent. As can be seen from the figure all three plots follow similar decay laws. Furthermore it is worth noting that after applying a negative potential of $-0.5V$ (SCE) the photocurrent returned to its initial value of 1.5 nA [point (●) on the ordinate]. From these observations it can be deduced that no dye molecules were lost from the surface when illuminated, but the oxidized surface dye was reduced by operation of the electrode at $-0.5V$ (SCE).

Variable photocurrents were observed when TiO_2 single crystals of different doping densities N_D coated with RhB were used. The results for samples with N_D ranging from 5×10^{17} – $5 \times 10^{22} \text{ cm}^{-3}$ are shown in Fig. 5. In this range the photocurrent changes by about a factor of 8. The points are obtained from the difference in measurements in acid solution of $\text{pH} = 1$ and at $\lambda = 560 \text{ nm}$ taken before and after RhB coating. Furthermore, at the applied voltage of $0.5V$ (SCE) for the samples investigated the initial photocurrent was found to be independent of potential.

In order to clarify this observation, absorption measurements were made to quantify the amount of surface coverage as a function of doping density. For this purpose fused silica disks coated with thin films of TiO_2 as described above were used. Prior to coating with dye the doping density of those quartz TiO_2 samples was changed by hydrogen treatment at different temperatures. The quantitative determination of the doping density for such thin films is difficult because the film thickness may not exceed that of the space charge region. A typical visible absorption spectrum for the sample reduced at 615°C has already been shown in Fig. 1.

The data taken from the maximum intensity of the absorbance spectra at 560 nm are listed in Table I along with the surface layer thickness of RhB calculated in fractions of a monolayer coverage. The calculations were made by using the molar absorption coefficient of 1.05×10^5 for a near-neutral aqueous RhB solution (18) and a dye molecule area of 100\AA^2 as reported by Spittler and Calvin (11). The reduction temperatures of the specimens range from 475°C – 615°C . A sample sensitized just after the course of oxidation at 900°C yielded an absorbance of 2×10^{-3} but not listed in the table.

To check whether thermal etching during the course of reduction affected the results reported in Table I the samples marked (*) were reoxidized and again coated with dye. The absorbance for both samples after reoxidation was 2×10^{-3} . Thus, a change in effective surface area cannot be used to explain the observations in Table I.

Discussion

As was shown in the experimental section the doping density N_D of the semiconductor samples affects the amount of dye deposited on its surface. The density of the dye layer was determined by absorption mea-

² The unrealistically high doping density of $N_D = 5 \times 10^{22} \text{ cm}^{-3}$ obtained from capacitance-voltage measurements is most likely due to surface roughness caused by etching.

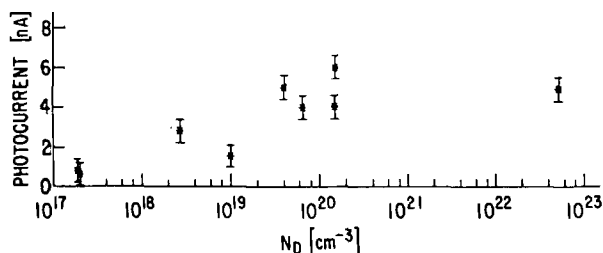


Fig. 5. Dependence of the photoresponse on the TiO_2 doping density N_D . The data were obtained in $\text{pH} 1$ electrolyte and for an illumination wavelength of 560 nm .

Table I. Absorbance and dye layer thickness for sensitized polycrystalline TiO_2 material prepared after reduction at different temperatures

Reduction temperature ($^\circ\text{C}$)	475	510	560*	590	615*
Absorbance (10^{-3})	2	4	5.2	7.2	11.2
Dye layer thickness (monolayer)	0.12	0.23	0.30	0.42	0.64

surements on polycrystalline material. Although the amount of dye deposited on single crystals was not measured optically, the results shown in Table I suggest that the coverage would increase with doping density since the doping density is known to increase with temperature during reduction. This increased dye coverage readily explains the increased photocurrent seen in Fig. 5.

As can be seen from Fig. 4, the photocurrent decreases with time to some lower value. It is instructive to calculate the surface density of RhB that is represented by the decaying portion of the current. For the data in Fig. 4 this is approximately $6 \times 10^{12} \text{ cm}^{-2}$ assuming one electron per RhB molecule. For comparison, the absorbance value in Table I for 510°C gives a RhB surface density of $2.3 \times 10^{13} \text{ cm}^{-2}$ if the solution molar extinction coefficient of 1.05×10^5 is used (18). This suggests that only a fraction of the RhB on the surface is participating in the rapid decay and that the remainder has a much lower probability of electron transfer and is responsible for the photocurrent remaining after 5 min.

Of course, the surface density of RhB on the electrode is only inferred from measurements on the TiO_2 films. Without some method to determine the density of RhB on the surface of the electrode itself it is not possible to be more quantitative in discussing the current decay. In this preliminary report, the point that should be emphasized in Fig. 4 is the ability to return to the initial current by applying a negative voltage. This illustrates the stable nature of the RhB attachment. Based on the data in Table I the calculated over-all quantum efficiency per absorbed photon is less than 0.01.

Now the question arises on the nature of the linkage between dye molecules and the semiconductor surface and how it is affected by the doping density. The reactivity of highly doped TiO_2 samples was the subject of a number of investigations in recent years (19-27). The affinity of those samples to interact with chemicals is a well-known phenomenon. It was shown (24, 26, 27) that small molecules such as O_2 , NO_2 , and N_2O undergo a reaction upon exposure to activated TiO_2 surfaces. For example, the reaction with air or oxygen leads to the formation of O_2^- . Such reaction products were identified by ESR spectroscopy.

As our results have shown, rhodamine B does not lose its dye character when coated on reduced TiO_2 surfaces. This observation excludes a chemical reaction with the dye center of the molecule as the attachment process. On the other hand a negatively charged ion, such as the O_2^- described above could attract the positive ring system of the dye molecules, thus giving rise to an ionic bond. This ionic bonding would not be expected to change the character of the dye. This mechanism can explain the influence of reduction temperature on the density of RhB since the generation of the negative surface species depends on the reduction of the TiO_2 (27).

On the other hand it is known that the doping density affects the electric field strength, E_s , at the semiconductor surface. The value of E_s is proportional to the one-half power of the doping density N_D . Thus an increase of the amount of dye molecules deposited on the surface caused by an increase in field strength seems possible.

It is also possible that an increase of active adsorption sites accompanies an increase in N_D . Making the

reasonable assumption that all sites within 20Å of the surface are able to interact with the attached surface states, a density of sites can be estimated to be 10¹³ sites/cm² for a sample with $N_D = 5 \times 10^{19}$ cm⁻³. Thus, the predicted density of surface sites due to donors is about one-tenth of a monolayer at this doping density yet this is approximately the doping density at which monolayer coverage by RhB occurs. On the other hand, due to the approximate nature of this comparison, the introduction of surface adsorption sites by donors cannot be excluded as an explanation for the RhB attachment process.

Conclusion

Two results of the present work are considered to be the main features: the dependence of the attachment process on the semiconductor doping density and the complete reduction of oxidized dye states after a cathodic sweep.

As already argued in the discussion a final answer on the nature of the bonding between dye molecules and TiO₂ that is based on experimental results cannot be given. The bonding is most likely due to several contributions. Further experiments using different solvents, dyes, and electrode materials would provide additional information about this process.

It is supposed that the reduction of oxidized dye states occurs via conduction band electrons which return the RhB to its initial condition. This illustrates the stability of the bond between the dye and the surface.

Acknowledgment

This work was supported in part by the Department of Energy, Office of Basic Energy Science.

Manuscript submitted April 30, 1979; revised manuscript received June 25, 1979.

Any discussion of this paper will appear in a Discussion Section to be published in the December 1980 JOURNAL. All discussions for the December 1980 Discussion Section should be submitted by Aug. 1, 1980.

Publication costs of this article were assisted by General Electric.

REFERENCES

1. R. Memming, "Electroanalytical Chemistry," Vol. 11, A. J. Bard, Editor, p. 1, Marcel Dekker, Inc., New York (1979).

2. H. Gerischer, *Photochem. Photobiol.*, **16**, 243 (1972); R. Memming, *ibid.*, **16**, 325 (1972).
3. R. Memming, *Faraday Discuss. Chem. Soc.*, **58**, 261 (1974).
4. K. Hauffe and U. Bode, *ibid.*, **58**, 281 (1974).
5. H. Kuhn, D. Möbius, and H. Bücher, in "Physical Methods of Chemistry," Vol. 1, Part 3B, A. Weissberger and B. W. Rossiter, Editors, pp. 577-702, Wiley, New York (1972).
6. T. Miyasaka, T. Watanabe, A. Fujishima, and K. Honda, *J. Am. Chem. Soc.*, **100**, 6657 (1978).
7. T. Miyasaka, T. Watanabe, A. Fujishima, and K. Honda, *Nature*, **277** (1979).
8. M. Fujihira, N. Ohishi, and T. Osa, *ibid.*, **268**, 226 (1977).
9. M. Fujihira, T. Osa, D. Hursh, and T. Kuwana, *J. Electroanal. Chem. Interfacial Electrochem.*, **88**, 285 (1978).
10. M. T. Spitler and M. Calvin, *J. Chem. Phys.*, **66**, 4294 (1977).
11. M. T. Spitler and M. Calvin, *ibid.*, **67**, 5193 (1977).
12. R. H. Wilson, L. A. Harris, and M. E. Gerstner, *This Journal*, **126**, 844 (1979).
13. L. A. Harris, D. R. Cross, and M. E. Gerstner, *ibid.*, **124**, 839 (1977).
14. L. A. Harris and R. H. Wilson, *ibid.*, **123**, 1010 (1976).
15. T. Watanabe, A. Fujishima, O. Tatsuoki, and K. Honda, *Bull. Chem. Soc. Jpn.*, **49**, 8 (1976).
16. R. W. Ramette and E. B. Sandell, *J. Am. Chem. Soc.*, **78**, 4872 (1956).
17. T. Takizawa, T. Watanabe, and K. Honda, *J. Phys. Chem.*, **82**, 139 (1978).
18. M. E. Gal, G. R. Kelly, and T. Kurucsev, *J. Chem. Soc. Faraday Trans.*, **269**, 395 (1973).
19. V. B. Kazansky, O. V. Nikitina, G. B. Paryisky, and B. F. Kiselev, *Dokl Akad. Nauk Uzb.SSR*, **151** (2), 369 (1963).
20. M. Che, C. Naccache, and B. Imelik, *J. Chim. Phys. Chimie. Biol.*, **65**, 1301 (1968).
21. S. Fukuzawa, K. M. Sancier, and T. Kwan, *J. Catal.*, **11**, 364 (1968).
22. V. V. Nikisha, B. N. Shelimov, and V. B. Kazansky, *Kinet. Kata.*, **12**, 332 (1971).
23. C. Naccache, P. Meriaudeau, M. Che, and A. J. Tench, *Trans. Faraday Soc.*, **67**, 506 (1971).
24. R. D. Iyengar and Kellermann, *J. Colloid Interface Sci.*, **35**, 424 (1971).
25. R. D. Iyengar and M. Codell, *Adv. Colloid Interface Sci.*, **3**, 365 (1972).
26. J. Cunningham and A. L. Penny, *J. Phys. Chem.*, **78**, 870 (1974).
27. Chr. Dyrek and R. N. Schindler, *Z. Naturforsch. Teil A*, **32**, 501 (1977).

Surface States Formation due to Impregnated Hydrogen at p-Type Gallium Phosphide Electrodes with Metal Adatoms

Hiroyuki Uchida, Hiroshi Yoneyama,* and Hideo Tamura

Department of Applied Chemistry, Faculty of Engineering, Osaka University, Yamadakami, Suita, Osaka, Japan

ABSTRACT

p-Type GaP electrodes with and without metal adatoms showed noticeable photoresponse at wavelengths longer than the intrinsic absorption threshold, if surface states were formed by hydrogen impregnation. The formation mechanism of the surface states was analyzed and the role of metal adatoms was evaluated. The energy levels of the surface states formed are determined by analysis of the cathodic current in the dark.

In a recent paper (1) we reported that the spectral response of p-type GaP electrodes was successfully extended to longer wavelengths by depositing a mono-

layer of any of several kinds of metal such as gold, silver, palladium, or copper onto the electrode surface and then cathodically polarizing the electrode under illumination. Impregnated hydrogen seemed to be responsible for the enhanced photocurrent spectra.

* Electrochemical Society Active Member.

Key words: semiconductor, photocathode, spectra, catalysis.

However, a detailed mechanism of the hydrogen impregnation and the nature of surface states formed has remained ambiguous. In order to develop more information on these points, the present study has been conducted.

Experimental

The same p-type GaP ($N_A = 4 \times 10^{17}/\text{cm}^3$) as reported previously (1) was used as the electrode material. The surface pretreatment of GaP and metal deposition on it were also the same as in the previous study, except for the deposition of Pb. The deposition potential of Pb was set at 0.25V vs. SCE in the present study, which was found to be more suitable than the potential selected in the previous study, although no appreciable difference was observed in results obtained.

A 500W xenon lamp was used as a light source, and a monochromator with a 600 lines/mm grating (JASCO, Model CT-25) was employed to obtain monochromatic light. The second-order diffraction was eliminated by employing suitable colored glass filters, and the slit width chosen was 2 mm, by which the resolution of monochromatic light was ± 6 nm. The intensity of light was measured by using a calibrated thermopile (The Eppley Laboratory, Incorporated). The number of photons incident on the electrode surface was determined by correcting the absorption in the electrolyte. For this purpose, absorption in a quartz cell of 1 cm path length was measured, and the incident photons were estimated by taking into account the distance between a quartz window and the electrode surface.

Measurements of photocurrent in the order of nA was made by employing the lock-in amplifier technique. A lock-in amplifier (N. F. Circuit Design Block Company, Model LI-572B) was tuned to a light chopper of 30 Hz for this purpose, and a photocurrent signal was monitored by an oscilloscope (Iwatsu, Model 056). The minimum photocurrent detected was 10 Pa.

All the measurements were carried out in the dark room at room temperature. Prior to measurements, purified nitrogen was bubbled into electrolytes for more than 30 min.

Cathodic polarization to cause hydrogen evolution was essential to obtain enhanced photocurrent spectra at p-type GaP electrodes covered with the monolayer amount of deposited metal ($M(\theta = 1)/\text{p-GaP}$). This treatment was termed here as "activation treatment" as in the previous study for the purpose of convenience. The activation treatment was made in 0.5M H_2SO_4 . After the activation treatment, the electrode was repeatedly subjected to potential sweep polarization at 1 V/min in the dark in a potential range between -1.0V vs. SCE and the potential at which the cathodic current commenced, until stable current-potential curves were obtained. The electrode was then subjected to a variety of measurements. Where the nature of electrolytes for measurements was different from 0.5M H_2SO_4 , the electrode was shortly immersed in distilled water and then inserted in the electrolyte of interest. The other details were already reported (1).

Results and Discussion

Quantum yield of p-type GaP.—In our previous paper (1), we did not discuss the quantum yield of activated electrodes, because of poor purity of the monochromatic light. Figure 1 shows spectra of quantum yield of saturated cathodic photocurrent giving the hydrogen evolution reaction (HER) at p-type GaP electrodes with and without the monolayer of deposited gold, which were obtained in 0.5M H_2SO_4 at -0.5V vs. SCE. As already described previously (1), the developed photoresponse covered wavelengths between 500 and 1200 nm. The maximum quantum yield in the developed spectra, which was observed between 600 and 850 nm, was about 1%.

The shape of spectra of the quantum yield in the intrinsic absorption region was in good agreement with

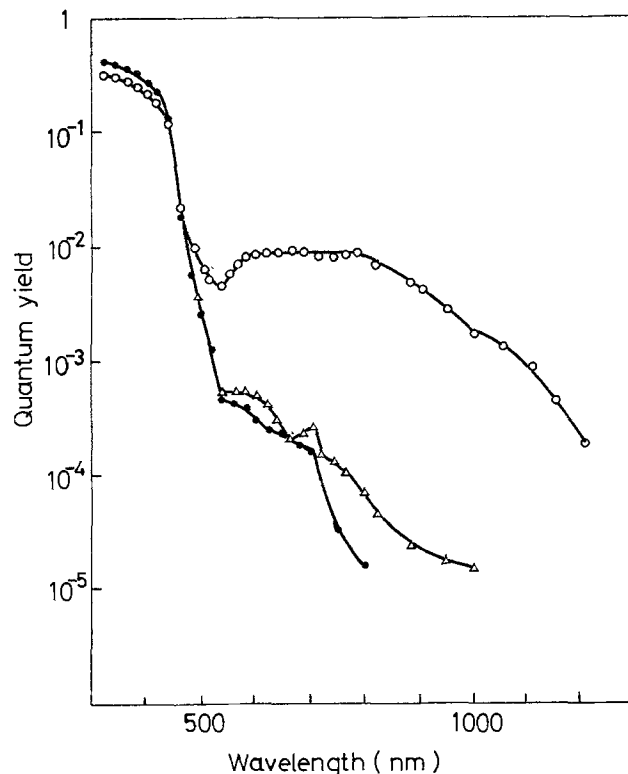


Fig. 1. Spectra of quantum yield of saturated cathodic photocurrent at p-type GaP electrodes in 0.5M H_2SO_4 at -0.50V vs. SCE. (—●—) nonactivated p-type GaP, (—△—) nonactivated Au($\theta = 1$)/p-GaP, (—○—) 1 hr activated Au($\theta = 1$)/p-GaP.

the results by Duchais *et al.* (2), but not with our previous results (3). Since the absolute value of the maximum quantum yield obtained at the present electrode ($N_A = 4 \times 10^{17}/\text{cm}^3$) agreed very well with that of Ref. (3), the inaccordance of the previous spectrum is attributable to the difference of purity of light.

It is seen in Fig. 1 that GaP shows weak photoresponse up to about 800 nm (1.55 eV) even if no activation treatment was made. Referring to the bandgap of GaP (4, 5), the result is not understandable from band-band transitions. Therefore, the phenomenon seemed to be caused by band-original surface states transition. The results in this figure indicate that the concentration of surface states is enhanced by the activation treatment with almost the same energetic distribution.

As already described, the magnitude of photoresponse of activated $M(\theta = 1)/\text{p-GaP}$ electrodes depends on the kind of the deposited metal (Au, Ag, Pd > Cu >> Pb, none). In order to elucidate the nature of this phenomenon, it will be useful to obtain information on (i) the energy levels of the deposited metals and (ii) the role of the deposited metal on the activation treatment.

Surface states formed by metal adatoms.—Kolb, Przasnyski, and Gerischer (6) showed that the energetic position of metal adatoms on n-type semiconductors can be determined by measuring photocurrent caused by excitation from the adatoms into the conduction band under anodic bias. If the situation for n-type semiconductors is similar to that for p-type semiconductors, it may be possible to observe cathodic current caused by excitation either from the valence band into the metal adatoms, or from the metal adatoms into the conduction band. Attempts to measure photocurrent of this nature were made in 10^{-3}M $\text{K}_3\text{Fe}(\text{CN})_6/3\text{M}$ NaOH for nonactivated $M(\theta = 1)/\text{p-GaP}$ at the potential at which preferential reduction of $\text{Fe}(\text{CN})_6^{3-}$ occurs, i.e., at -0.35V vs. Hg/HgO (7). Since the cathodic current via the va-

lence band, which is observed in the dark, was large in this electrolyte (7), the lock-in amplifier technique was employed to detect the cathodic photocurrent of interest. The results obtained are shown in Fig. 2, for the deposition of Ag and Au. In this figure, photocurrent is given in a relative scale in such a manner that it was unity when a photocurrent of 1 nA/cm^2 was measured for photon incidence of $1 \times 10^{13}/\text{cm}^2 \cdot \text{sec}$. According to this figure, the shapes of photocurrent spectra of $\text{Au}(\theta = 1)/\text{p-GaP}$ and $\text{Ag}(\theta = 1)/\text{p-GaP}$ are quite similar to the electrode with no metal adatoms, and hence no determination of energetic positions of metal adatoms is possible from the results obtained. It is evident that original surface states play a more significant role in appearance of the observed photoresponse than metal adatoms.

Activation process of electrodes and role of deposited metals.—As already described, both activated and non-activated electrodes show photoresponse to light of wavelength longer than the intrinsic absorption threshold, but the intensity of the response is different between these, which must be the result of concentration differences in surface states. Therefore, if the non-activated electrodes are cathodically polarized at a constant potential under illumination with monochromatic light of wavelength longer than the intrinsic threshold, then the concentration of surface states sensitive to this light must be increased with polarization time.

Figure 3 shows increasing trends of photocurrent with polarization time under illumination with monochromatic light of 620 nm for a variety of non-activated $\text{M}(\theta = 1)/\text{p-GaP}$ electrodes, which were obtained by the lock-in technique. The cathodic polarization was made at -0.5V vs. SCE in $0.5\text{M H}_2\text{SO}_4$. The results show that illumination with 620 nm light produced surface states sensitive to this light. If one rearranges

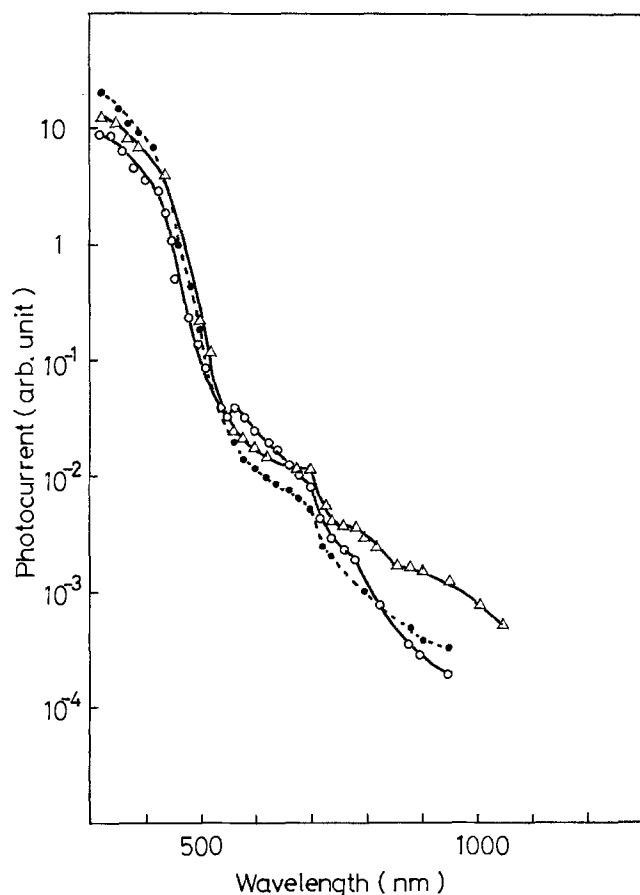


Fig. 2. Relative photocurrent spectra of nonactivated GaP having the monolayer amount of various metals in $10^{-3}\text{M K}_3\text{Fe}(\text{CN})_6/3\text{M NaOH}$ at -0.35V vs. Hg/HgO . (—○—) Ag, (—△—) Au, (---●---) none.

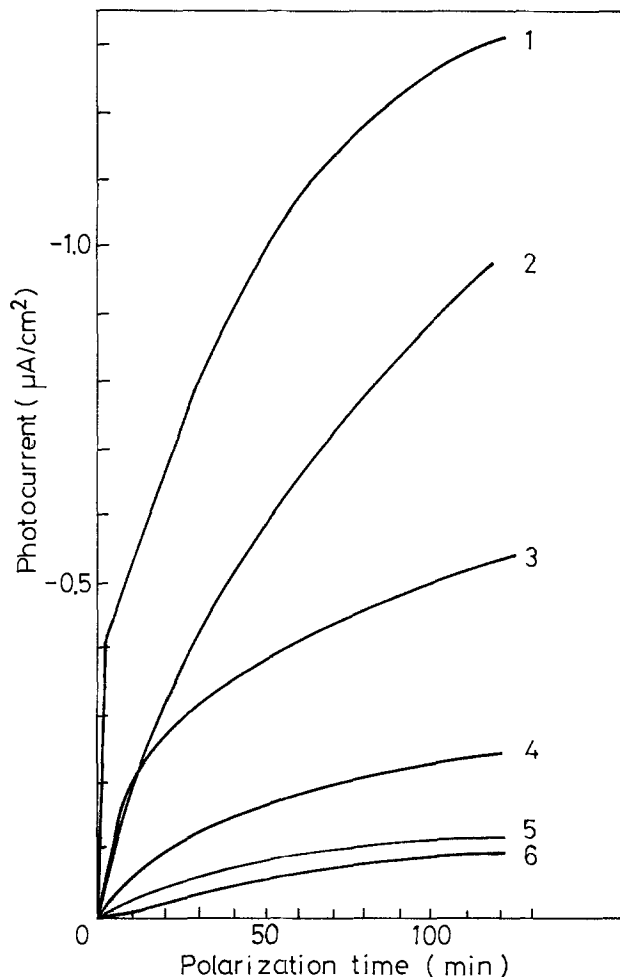


Fig. 3. Increases in photocurrent with polarization time under illumination with 620 nm light for a variety of nonactivated $\text{M}(\theta = 1)/\text{p-GaP}$ electrodes. Curve 1, Pd; curve 2, Au; curve 3, Ag; curve 4, Cu; curve 5, none; curve 6, Pb. Solution = $0.5\text{M H}_2\text{SO}_4$, $E = -0.50\text{V vs. SCE}$.

the results in this figure in the form of photocurrent at any time vs. the charge consumed up to this time, then linear relations are found to be established between the two. Typical examples are given in Fig. 4 for the cases of p-GaP and $\text{Au}(\theta = 1)/\text{p-GaP}$. This result implies that the photocurrent at 620 nm is proportional to the charge consumed, Q , which leads to discharge of water into hydrogen.

Considering that the photocurrent at $\lambda = 620 \text{ nm}$ is proportional to the surface states concentration, N , and

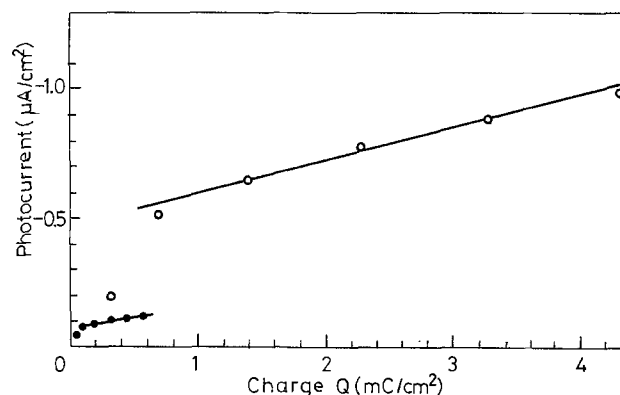


Fig. 4. Dependency of photocurrent on the amount of charge consumed during the activation treatment. (—○—) $\text{Au}(\theta = 1)/\text{p-GaP}$, (—●—) p-type GaP. Solution = $0.5\text{M H}_2\text{SO}_4$, $E = -0.50\text{V}$, $\lambda = 620 \text{ nm}$.

that the magnitude of the photocurrent was proportional to the charge consumed during the cathodic polarization, then one is led to believe that the discharged species are impregnated into the electrode to form effective surface states; impregnation of atomic hydrogen is the most likely source of these surface states. Since the amount of charge to cover the monolayer of GaP is 0.38 mC/cm², the charge consumed up to the polarization time of 120 min corresponds to about two and ten monolayers for p-GaP and Au($\theta = 1$)/p-GaP, respectively. Judging from $I-t$ traces in Fig. 3, the activation has not been completed within 120 min, although in the case of irradiation of full light from the xenon lamp, the polarization for 1 hr was sufficient.

The impregnation of hydrogen must proceed via a diffusion process, according to Eq. [1]

$$i_{\text{diff}} \propto (AD^{1/2}FC_s\tau^{-1/2}) \cdot t^{-1/2} \quad [1]$$

where i_{diff} is the diffusion current, D the diffusion coefficient, C_s the surface concentration, A the surface area, and t is the polarization time. Since Q almost corresponds to diffusion current times t , the following relation should hold

$$N \propto i_{\text{diff}} \cdot t = (kC_sD^{1/2}) \cdot t^{1/2} \quad [2]$$

If an assumption is made that photocurrent at $\lambda = 620$ nm is proportional to N , then one can expect that the photocurrent at $\lambda = 620$ nm is proportional to the square root of the polarization time with the gradient of $kC_s\sqrt{D}$. Figure 5 shows that such a relation holds for the present results except for initial stages. In the initial stage, at least some portion of photocurrent must be consumed in the adsorption process of hydrogen to cover the electrode. The degree of the steady-state coverage must be dependent on the kind of metal adatoms (8). Table I shows the charge consumed in the initial stages in which the deviation from a photo-

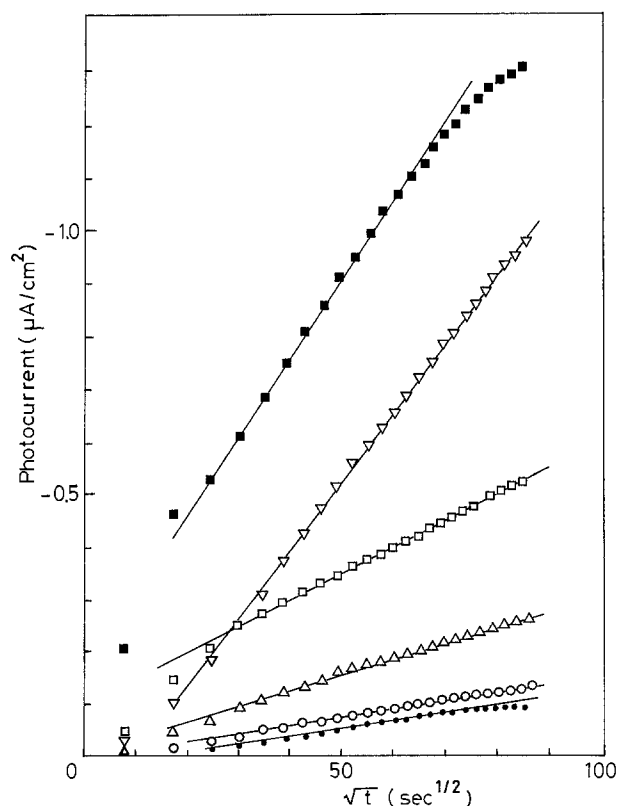


Fig. 5. Plots of photocurrent against square root of the polarization time for $M(\theta = 1)/p\text{-GaP}$ electrodes. (—■—) Pd, (—▽—) Au, (—□—) Ag, (—△—) Cu, (—○—) none, (—●—) Pb. Solution = 0.5M H_2SO_4 , $E = -0.50\text{V}$, $\lambda = 620$ nm.

Table I. The charge consumed in the initial stages in which the deviation from a i_{photo} vs. \sqrt{t} relation was observed

$M(\theta = 1)/p\text{-GaP}$	Charge ($\mu\text{C}/\text{cm}^2$)
Pd	111
Au	15
Ag	69
Cu	8
None	9
Pb	8

current vs. \sqrt{t} relation was observed. If the adsorption of hydrogen preferentially occurs in the initial stage, the photocurrent should be invariant, which was different from the observed results. Therefore, both impregnation and adsorption of atomic hydrogen must compete with each other in this stage.

It is seen in this figure that the gradient of the linear relations is different from one another. This implies that $kC_s\sqrt{D}$ is different depending on the kind of deposited metal. Since the diffusion coefficient of hydrogen atoms in GaP, D , must be the same independently of the kind of metal, the difference in the gradient must reflect differences in the surface concentration of atomic hydrogen among the deposited metals.

It is well known that the rate of the HER at metal electrodes is dependent upon the kind of substrate. If one plots $kC_s\sqrt{D}$ against $\log i_0$ (9) of deposited metal for the HER, a fairly good relation is found to hold (Fig. 6). Although the magnitude of $\log i_0$ for the HER is not necessarily related to the surface concentration of atomic hydrogen which is formed as a reaction intermediate (8), the results in Fig. 6 indicate that C_s at metal adatoms of $M(\theta = 1)/p\text{-GaP}$ is empirically related to $\log i_0$.

Energy levels of the surface states due to impregnated hydrogen.—For charge transfer via surface states, two models can be imagined (Fig. 7). In one of the models, "model 1," which was discussed previously (1), electrons are photoexcited to the surface states from the valence band, and then are transferred to the electrolyte. In the other model, "model 2," electrons are photoexcited to the conduction band from the occupied

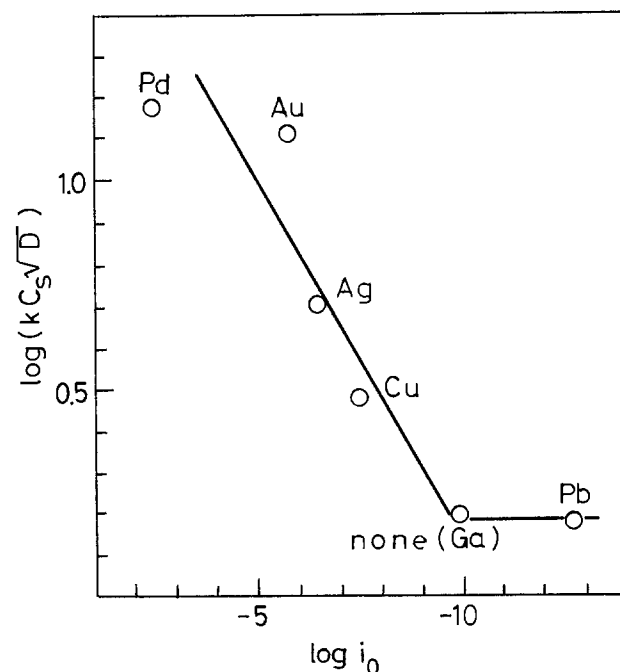


Fig. 6. Relation between $\log(kC_s\sqrt{D})$ and $\log i_0$ for hydrogen evolution reaction of deposited metals.

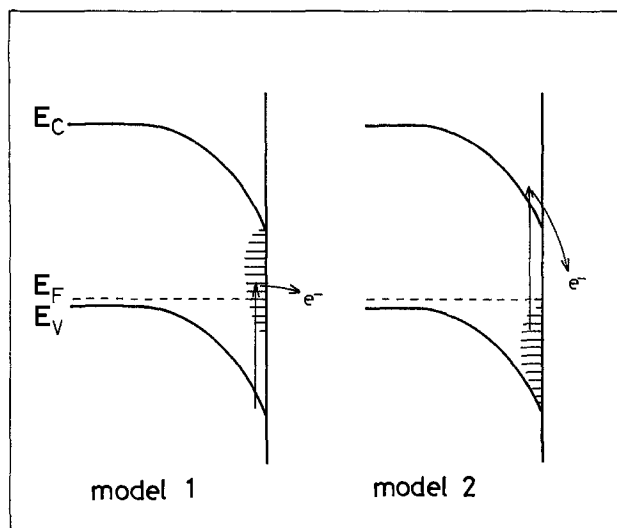


Fig. 7. Schematic diagrams of the charge transfer via the surface states for p-type GaP electrodes.

surface states and then are transferred to the electrolyte. The spectral response obtained is very broad, and hence, it seems difficult to definitely determine the fixed energetic positions of the surface states. Therefore, we assume that the energy levels of the surface states are distributed according to the spectral response obtained. Thus, for "model 1," surface states are distributed from just below the conduction band (2.3 eV above the valence bandedge) to the middle of the forbidden band (1.2 eV above the valence bandedge). For "model 2," the states are distributed between the top of the valence bandedge and the middle of the forbidden band. In order to draw a definite answer to which model is more appropriate, the following experiments were conducted.

Figure 8 shows the cathodic polarization curves in the dark for p-type GaP and Ag($\theta = 1$)/p-GaP in 10^{-3} M $K_3Fe(CN)_6/3M$ NaOH. For this measurement, the electrodes were polarized at $-0.4V$ vs. Hg/HgO and after 2 min, the potential sweep was started towards the negative potential region. The sweep rate was 20 mV/sec and the first cathodic sweep is shown in this figure. One can determine from the results the potentials E_t at which appreciable cathodic current commenced to flow, and these are given in Table II together with flatband potentials E_{fb} of the electrodes. In this table, potential drop in the space charge layer at E_t ,

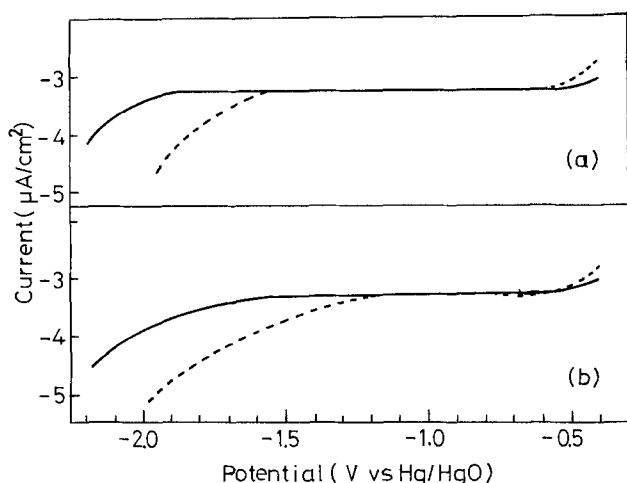


Fig. 8. Current-potential curves for p-type GaP (a) and Ag($\theta = 1$)/p-GaP (b) in the dark in 10^{-3} M $K_3Fe(CN)_6/3M$ NaOH. (—) nonactivated, (----) activated.

Table II. Flatband potential E_{fb} in 3M NaOH and onset potential of cathodic current in the dark E_t in 10^{-3} M $K_3Fe(CN)_6/3M$ NaOH at p-GaP and Ag ($\theta = 1$)/p-GaP electrodes

		E_{fb} (V vs. Hg/HgO)	E_t (V vs. Hg/HgO)	$\Delta\phi_{sc}$ (V)
p-GaP	Nonactivated	-0.03	-1.90	1.87
	Activated	-0.20	-1.60	1.40
Ag ($\theta = 1$)/ p-GaP	Nonactivated	0.10	-1.50	1.60
	Activated	0.00	-1.20	1.20

$\Delta\phi_{sc}$, is also given. Although the $Fe(CN)_6^{3-}$ solution was used as the electrolyte, the hydrogen evolution seemed to take part in the cathodic current flow, because the current-potential characteristics of the non-activated electrodes became near to that of the activated electrodes by repeating the sweeps.

It is noticed from Fig. 8 and Table II that E_t was shifted towards anodic potentials by the activation treatment, in spite of the fact that E_{fb} became negative by the activation [1]. As a result, the cathodic current at the activated electrodes commenced to flow with small bandbending compared to that of the nonactivated electrodes. Considering that the activation treatment enhances the concentration of surface states alone without changing energetic distribution profiles, a conclusion is drawn that the cathodic behavior of the electrodes was greatly affected by the surface-state density.

By analyzing the nature of the cathodic current on the basis of this knowledge, we can determine which model of the surface states, "model 1" or "model 2," is more reasonable. If the cathodic current is due to conduction band electrons, which is very scarce, E_t will not be influenced by enhancement of the surface-state concentration. To date, many studies have suggested participation of surface states in electrode reactions at semiconductors, but none has shown that such a small current as several $\mu A/cm^2$ is influenced by the surface-state concentration. The bandbending can assist electrons in reaching the surface from the bulk, and so the depth of surface states is not primarily important at least at a very small current.

On the other hand, if the cathodic current is due to the valence band mechanism, growth of the surface states into the interior of the electrode is feasible for valence band electrons to be transferred into the electrolyte. An electronic interaction between the valence band and surface states becomes large with an increase in the depth of impregnated hydrogen when the band is bent downwards. One can have a clear image on this point by illustrating bandbending profiles at the potential of E_t . Examples are given in Fig. 9 for the activated and nonactivated Ag($\theta = 1$)/p-GaP. The figure was obtained by using Eq. [3] (10) and [4] (11)

$$x_0 = (2\epsilon\epsilon_0\Delta\phi_{sc}/e_0N_A)^{1/2} \quad [3]$$

$$\phi_b - \phi = [e_0(N_D - N_A)/2\epsilon\epsilon_0](x - x_0)^2 \quad [4]$$

where N_A and N_D are acceptor and donor concentration of the electrode, respectively, x_0 is the thickness of the space charge layer, x is the distance from the electrode surface, and ϕ_b is the bulk potential of the electrode.

Thus, the cathodic current in the dark is likely to be brought about by electron transfer from the valence band into the electrolyte via the surface states probably with "electron tunneling" mechanism (12). From discussion described here, "model 2" is more reasonable for the energy level of surface states than "model 1."

Acknowledgment

The authors would like to acknowledge the valuable discussion with Dr. A. Moritani of Osaka University.

Manuscript submitted Nov. 27, 1978; revised manuscript received July 10, 1979.

Any discussion of this paper will appear in a Discussion Section to be published in the December 1980 JOURNAL. All discussions for the December 1980 Discussion Section should be submitted by Aug. 1, 1980.

Publication costs of this article were assisted by Osaka University.

REFERENCES

1. H. Yoneyama, S. Mayumi, and H. Tamura, *This Journal*, **125**, 68 (1978).
2. J. O'M. Bockris and K. Uosaki, *ibid.*, **124**, 1348 (1977).
3. H. Tamura, H. Yoneyama, C. Iwakura, H. Sakamoto, and S. Murakami, *J. Electroanal. Chem. Interfacial Electrochem.*, **80**, 357 (1977).
4. J. C. Phillips, "Bonds and Band in Semiconductors," p. 169, Academic Press, New York (1973).
5. R. Memming, *This Journal*, **125**, 117 (1978).
6. D. M. Kolb, M. Przasnyski, and H. Gerischer, *Z. Phys. Chem.*, **93**, 1 (1974).
7. K. H. Beckmann and R. Memming, *This Journal*, **116**, 368 (1969).
8. S. Trasatti, *J. Electroanal. Chem. Interfacial Electrochem.*, **39**, 163 (1972).
9. H. Kita and T. Kukisu, *J. Res. Inst. Catal., Hokkaido Univ.*, **21**, 200 (1973).
10. H. Gerischer, *J. Electroanal. Chem. Interfacial Electrochem.*, **58**, 263 (1975).
11. S. R. Morrison, "The Chemical Physics of Surfaces," p. 30, Plenum Press, New York (1977).
12. J. W. Gadzuk, *J. Appl. Phys.*, **41**, 286 (1970).

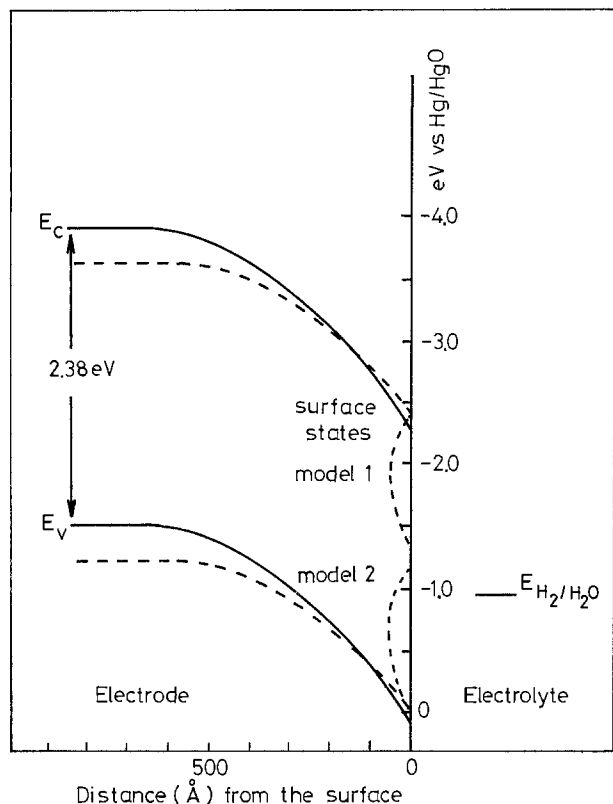


Fig. 9. Profile of the bandbending for nonactivated (—) and activated (---) $\text{Ag}(\theta = 1)/\text{p-GaP}$ electrodes at the onset potential of electron tunneling in $10^{-3}\text{M K}_3\text{Fe}(\text{CN})_6/3\text{M NaOH}$.

Electrogenerated Chemiluminescence

XXXVI. The Production of Steady Direct Current ECL in Thin Layer and Flow Cells

George H. Brilmyer* and Allen J. Bard**

Department of Chemistry, The University of Texas at Austin, Austin, Texas 78712

ABSTRACT

Studies of the ECL of rubrene in thin layer cells containing two gold electrodes separated by 20–500 μm and viewed parallel to the electrode surface are reported. The agreement between calculated and experimental currents and intensities was good and operating lifetimes of 30 min to 4 hr were observed. Flow cells in which solution is recirculated through two mesh electrodes into a mixing chamber where electron transfer and emission occurs are also described. Higher light intensities were obtainable with the flow cells, which appear to be a more favorable configuration for application to ECL devices.

Electrogenerated chemiluminescence (ECL), in which an electron transfer reaction of electrogenerated species produces an electronically excited state (1–2), has been proposed for several types of electrochemical devices, including displays (3), lasers (4–7), and up-conversion devices (8–9). The practical applications of ECL to such devices have been largely hindered by lifetime problems. For directly pumped ECL lasers, which have been discussed but never reduced to practice, two other problems exist. For most ECL cells the reaction zone thickness, which is governed by the dis-

tance the reactants can interdiffuse before reaction, is too narrow to utilize because of optical constraints in laser design. Moreover the current densities achieved with ECL cells have been judged insufficient to generate the needed level of excited states, even with fairly efficient ECL systems (5).

One possible configuration of an ECL laser device involves a thin layer cell in which the solution is confined between closely spaced generating electrodes. A previous study of this cell configuration utilizing transparent tin oxide electrodes spaced a fixed distance (50 μm) (3) apart, with the ECL observed through the electrode, demonstrated the feasibility of this type of cell. To utilize such a cell for a laser in a

* Electrochemical Society Student Member.

** Electrochemical Society Active Member.

Key words: electrochemiluminescence, rubrene, thin layer electrochemistry, electrochemiluminescent devices.

waveguide mode, interelectrode spacings of 500-1000 nm are required. We report here experiments with a thin layer cell employing solid electrodes and an adjustable gap, with ECL viewed end-on (*i.e.*, parallel to the electrode surfaces) and an investigation of the effect of interelectrode spacing on ECL intensity, risetime, and lifetime.

An approach to obtaining a wider ECL zone and the required higher current densities (*i.e.*, reactant fluxes) for a laser involves the use of a flow cell arrangement in which the precursor species are brought to the electrodes by convection (as well as diffusion) and the reactants flow together to cause ECL. The construction of flow ECL flow cells is difficult, because the high purity requirements of the solutions and the necessary pretreatment procedures preclude the use of large solution volumes and many solution pumping arrangements. To date the only flow cells reported have been those utilizing the rotating ring-disk electrode (10); this configuration is not useful for the desired applications. We report here the construction of an all-glass recirculating flow cell in which the solution containing the electroactive species is circulated through oppositely polarized Pt mesh electrodes where the reactant radical ions are generated. The solution streams are then mixed in the area just beyond the electrodes and the resulting emission intensity studied as a function of interelectrode voltage and solution flow velocity. The operation, current densities, and lifetime of such a cell is described.

Experimental

Chemicals.—Rubrene, obtained from Aldrich Chemical Company, was recrystallized from hot xylene (under subdued red light) with cold methanol. The orange-red crystals obtained were dried under vacuum at 10^{-5} Torr for 24 hr. Tetra-*n*-butylammonium perchlorate (TBAP) (polarographic grade, obtained from Southwestern Analytical Chemical Company) was recrystallized from ethanol and dried under vacuum at 100°C . The solvent system used for all thin layer experiments was benzonitrile (BZN) and benzene (BZ). BZN (reagent grade, purchased from Eastman Organic Chemicals) was purified by a previously reported procedure (11) and then distilled from calcium hydride under vacuum. BZ (spectrograde, obtained from Mallinckrodt Chemical Company) was purified as previously reported (12) and then vacuum distilled on to a sodium mirror, permitted to stand for 2 hr, and then distilled into a flask containing Woelm Alumina (Research Organic/Inorganic Chemical Company, Sun Valley, California). Both BZN and BZ were then stored in a Vacuum Atmospheres Corporation (Hawthorne, California) glove box. 1,2-Dimethoxyethane (DME) (Eastman Chemical Company) was vacuum distilled several times from lithium aluminum hydride and then into a clean flask. AN was purified as previously reported (8). Both the AN and DME were stored on a vacuum line and distilled directly into the electrochemical cell.

Apparatus.—The electrochemical cells used are shown in Fig. 1 and 2. The adjustable thin layer cell contained two gold disk electrodes and a platinum quasi-reference electrode. The disk electrodes were constructed by silver soldering a 4 mm diameter, 1 mm thick gold disk to the head of a 2 mm brass bolt. The disk was then machined into a conical shape with the face of the cone perpendicular to the bolt. The electrode could be wrapped with Teflon tape and pressure fit into a Teflon holder. The adjustable holder employed a modified Teflon needle valve (Fischer-Porter Company). The arms of the cell were aligned to ensure that the electrodes were parallel when in position. The electrode separation was determined by measuring the distance between the external electrode contacts with a 4-5 in. micrometer (J. T. Slocomb Company) and normalizing this to the distance mea-

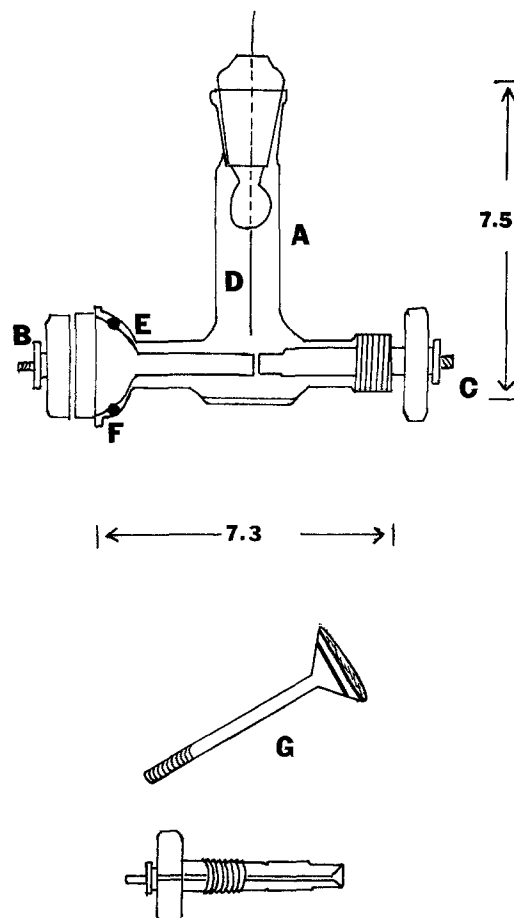


Fig. 1. Thin layer cell. (A) Cell body, (B) stationary disk electrode, (C) adjustable disk electrode, (D) platinum quasi-reference electrode, (E) Teflon O-ring, (F) 18-9 female socket, (G) gold disk (4 mm) soldered onto brass bolt, machined to fit Teflon holder.

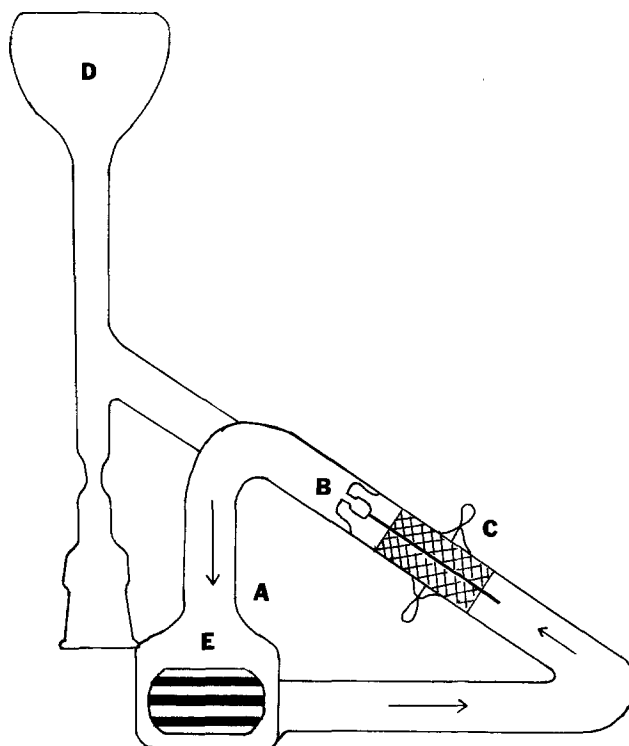


Fig. 2. Pump cell. (A) Cell body with pump, (B) reaction chamber, (C) platinum gauze electrodes with all platinum leads, (D) side arm, and (E) pump with stirring disk.

sured when the separation was zero. All wire and disk electrodes were mechanically polished prior to use with a 0.3 μm polishing alumina (Precision Scientific Company). A Bausch and Lomb dissecting microscope was used to observe the position of the reaction zone and the emission between the electrodes. The flow cell was designed to permit the use of vacuum techniques for solution preparation as well as continuous circulation of the solution. An integral part of the cell is the pump which was made by sealing a Teflon stirring disk (Markson Science Incorporated, Del Mar, California) into a glass cylinder whose dimensions permitted constrained rotation of the stirrer. The solution enters the pump normal to the plane of rotation of the stirrer and exits off-axis and parallel to this plane. The solution is then electrolyzed by two platinum mesh electrodes which are separated by a coarse frit. These two separate streams containing the radical ions then mix efficiently to produce the emission in a confined area (Fig. 3).

All electrochemical experiments were conducted with a combination of a PAR Model 175 universal programmer and a PAR Model 173 potentiostat (Princeton Applied Research Corporation, Princeton, New Jersey). Photometric measurements were conducted with the cell inside of a dark box, using an EG & G Radiometer/Photometer (Model 550-1). The cell current and light intensity were monitored simultaneously on a Moseley Model 7100B dual pen recorder. The rotation rate of the magnetic stirring bar was measured with a Type K53K-AB Strobotac (General Radio Corporation, Concord, Massachusetts).

Procedure

A solution consisting of 4 mM rubrene (R), 0.05M TBAP in a 1:1 mixture of BZN/BZ was used for all thin layer experiments. Although the thin layer cell was air tight, it could not be placed under high vacuum. Thus the solution was prepared in a separate vessel, freeze-pump-thawed several times and returned to the dry box. The cell was then filled, removed from the dry box and reproducibly positioned

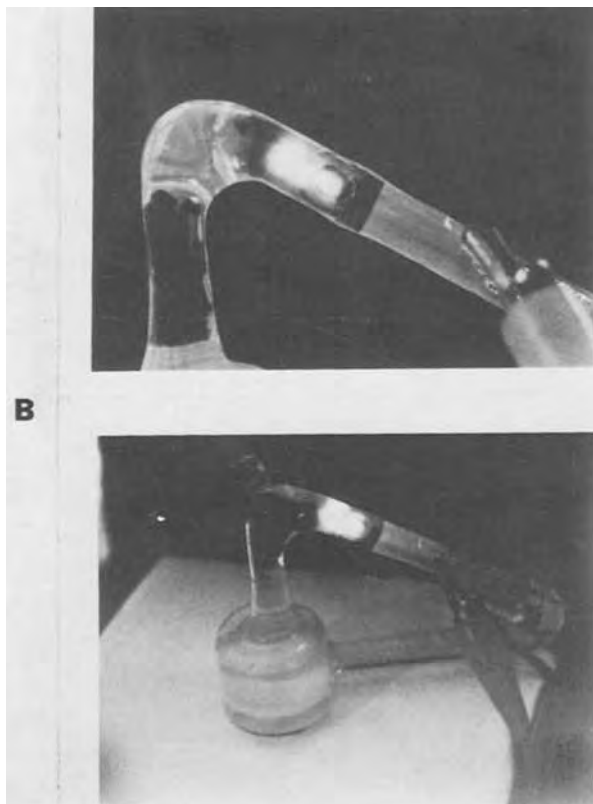


Fig. 3. Flow cell in operation. (A) Reaction chamber, (B) entire pump cell.

above the radiometer inside the dark box. The thin layer experiment consisted of first using cyclic voltammetry to characterize the solution and insure system purity. ECL was generated in the two electrode mode by applying a potential, ΔE , between the electrodes

$[\Delta E \cong E_{pa}(R^{\cdot+}/R) - E_{pc}(R^{\cdot-}/R) + iR_s]$ (where E_{pa} and E_{pc} are the cyclic voltammetric peak potentials for the anodic and cathodic waves, i is the current, and R_s is the cell resistance). The equal areas of the electrodes yields equal current densities at anode and cathode and the chosen ΔE value prevents formation of the very reactive dication or dianion species. Because the process involved is diffusion controlled, the cell current, ECL intensity and diffusion time can be studied as a function of the distance separating the electrodes. These experiments were carried out and results compared to the theoretically expected values.

Flow cell experiments were conducted using 4 mM rubrene and 0.1M TBAP in AN/BZ solutions. The flow cell was equipped with a side arm where the solution was prepared, freeze-pump-thawed and then gravity transferred to the cell itself. The solution could then be circulated through the cell and the potential difference (ΔE) applied to the two electrodes.

Results and Discussion

Thin layer cell.—Typical results of thin layer cell experiments are shown in Fig. 4-9. When the voltage step ΔE is applied, current flow begins and quickly attains a steady-state value; the emission commences when the diffusing reactant streams merge after a time controlled by the interelectrode separation (Fig. 4). Experimental values obtained for the steady-state

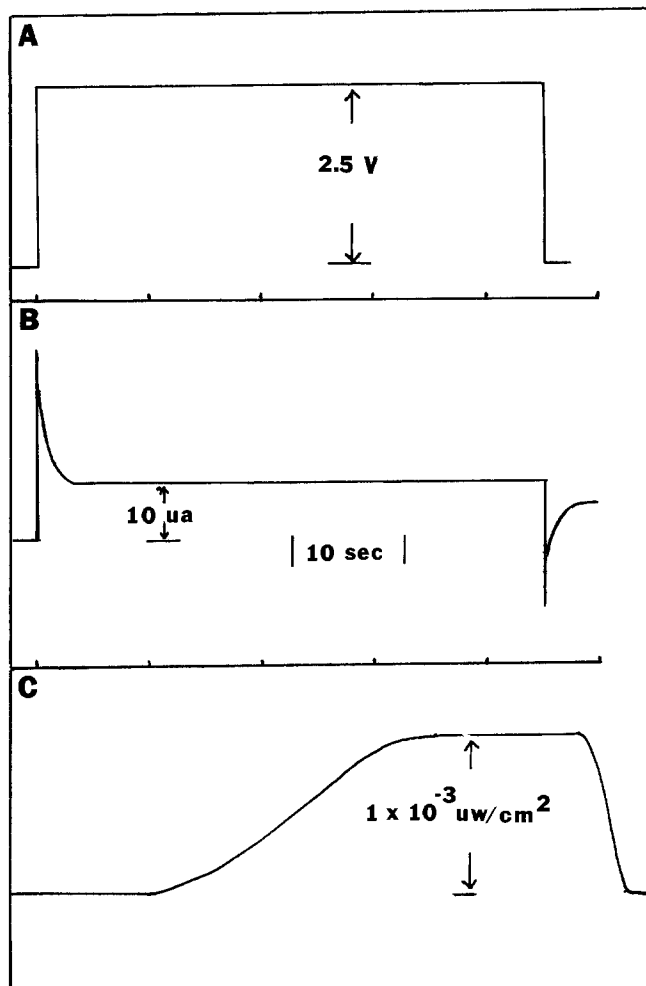


Fig. 4. Typical thin layer experiment. (A) Potential program, (B) current response, (C) resulting ECL intensity. 4 mM rubrene 0.05M TBAP in 1:1 mixture of BZN:BZ, electrode separation = 0.02 cm.

current, i_{ss} , compared to those calculated as a function of electrode separation by Eq. [1] are shown in Fig. 5

$$i_{ss} = nFAD (\Delta C/\Delta X) \quad [1]$$

where n is the number of electrons consumed per molecule in the electrode reaction; F is the Faraday (96,487 C/equiv.); A , the average electrode area (0.141 cm²); D , the diffusion coefficient of rubrene; $\Delta C/\Delta X$, the concentration gradient of radical species at steady state. D for rubrene was determined by chronoamperometry (14) to be 3.1×10^{-6} cm²/sec; this value agrees with that previously found for rubrene in BZN (15) and was used in all theoretical calculations. The i_{ss} values were calculated by assuming that a complete annihilation reaction occurs at the center of the cell so that the rubrene concentration there is equal to its initial value, C (4 mM), while the concentration at each electrode was essentially zero. Thus $\Delta C = C$ for $\Delta X = d/2$ or

$$i_{ss} = 2nFAD C/d \quad [2]$$

The experimental results obtained are in good agreement with those calculated from [2] at electrode separations above 200 μ m. At smaller separations the deviation from the theoretical behavior can be rationalized by uncertainties in the determination of the interelectrode distance, d .

The d-c emission that appeared was less intense than that found with 1 Hz alternating pulses in the same solutions but was easily visible. As expected the intensity and time for the appearance of the ECL resulting from d-c electrolysis was a function of the electrode separation. The ECL intensity can be related to cell current by Eq. [3] (16)

$$I_{ss} = \phi_{ECL} i_{ss}/nF \quad [3]$$

where ϕ_{ECL} is the ECL efficiency and I_{ss} the total emission from the cell at steady state. I_{ss} can be calculated from the measured ECL intensity by using a detector of known area and then making the appropriate geometric corrections (for the amount of emission which does not strike the detector).

In this experiment the geometric corrections are based on the fact that the emission is formed in a very thin disk-shaped reaction zone sandwiched between two zones of highly absorbing radical ions which are in turn bounded by the gold disk electrodes. The presence of such high concentrations of radical ions on either side of the reaction zone has several effects on the geometry of the system. First, no corrections need be made for electrode reflectivity effects. Second, a correction must be made for the fraction of

the ECL absorbed by the radical ions. This was estimated to be 97% based on the dimensions of the area between the electrodes. Finally, one must realize that the emission which is not absorbed leaves the reaction zone at a very restricted, slightly diverging, angle. Therefore, the photodiode (area = 1 cm², diam 1.13 cm) was placed 3.6 cm below the cell to insure that the width of the emission was smaller than that of the diode. For this reason the projected image was taken as a ring (radius = 3.6 cm, width = 1.13 cm) and a surface area correction (25.6 cm² : 1 cm²) could be made. No corrections were made for solution absorbance or inner filter effects because the fluorescence efficiency was taken as unity (15) and the photodetector was wavelength independent. The resulting ECL intensity (μ W/cm²) was converted to number of photons using Eq. [4] (17)

$$I \text{ (photons/sec)} = \frac{\text{(total watts)} (6.24 \times 10^{18})}{1239.8/\lambda \text{ (nm)}} \quad [4]$$

and plotted vs. electrode separation in Fig. 6. A plot of i_{ss} vs. I_{ss} for different values of electrode separation is shown in Fig. 7. Although the data are very scattered the slope of the line (least squares) corresponds to $\phi_{ECL} = 0.013$, which is within the accepted range of reported values for the rubrene system.

The time required [after the application of the voltage (ΔE) to the cell] for the reactants to diffuse together and for ECL to appear can be approximated by Eq. [5] (3)

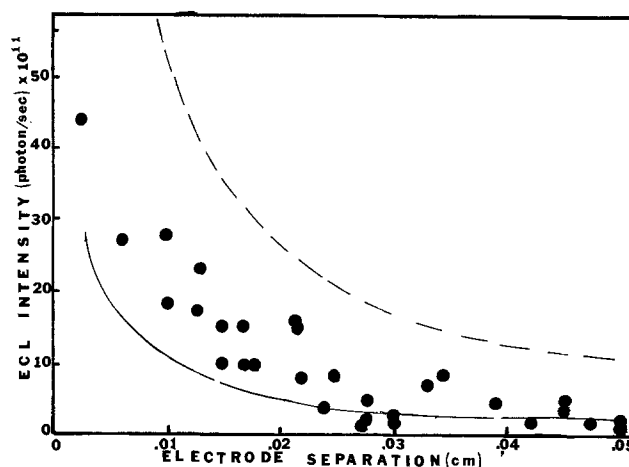


Fig. 6. Plot of ECL intensity vs. electrode separation. ---, Theory ($\phi_{ECL} = 0.025$); ●, experimental; —, theory ($\phi_{ECL} = 0.005$). Solution the same as in Fig. 4.

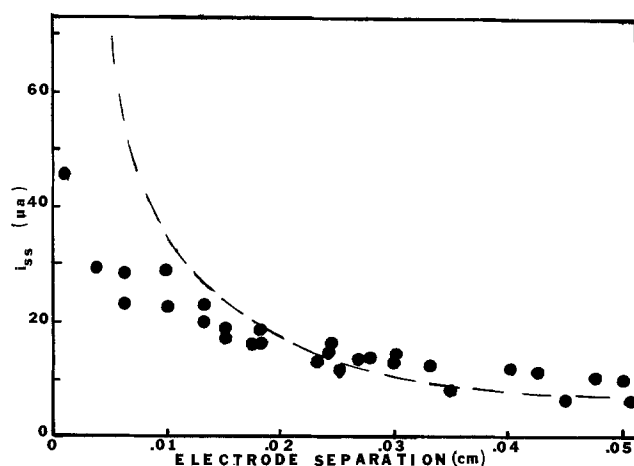


Fig. 5. Plot of steady-state current (i_{ss}) vs. electrode separation. ---, Theoretical; ●, experimental. Solution the same as in Fig. 4.

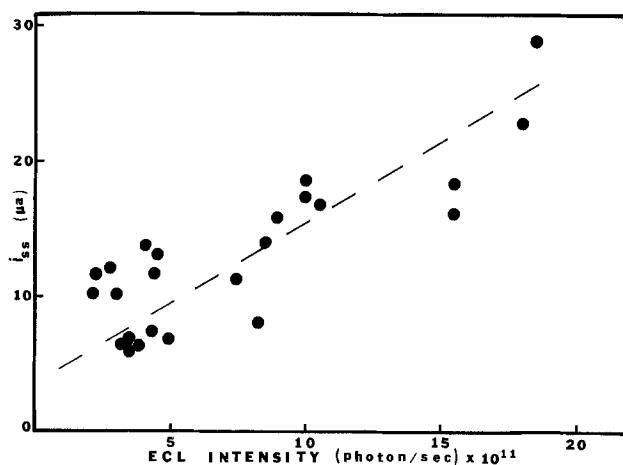


Fig. 7. Plot of steady-state current (i_{ss}) vs. steady state ECL intensity for various values of electrode separation. Solution same as in Fig. 4.

$$t(\text{sec}) = \frac{d^2(\text{cm})}{16D} \quad [5]$$

From this equation and the previously calculated diffusion coefficient, a comparison can be made between the calculated time needed for ECL to appear and the experimental results at different values of d . The results given in Fig. 8 show quite good agreement with the approximate equation. When the thin layer gap was observed under $8\times$ magnification with a simple dissecting microscope, we found that the ECL did not occur in the exact center of the spacing between the electrodes. The reaction zone was clearly closer to the cathode with BZN/BZ as solvent and closer to the anode with DME. This can be explained by the slight instability of the anion or cation in the various solvents.

The operating lifetime of a single thin layer experimental cell was studied because of the great interest in application of the technique for displays or for use as a laser. The solutions were first subjected to cyclic voltammetry and fluorescence measurements before the experiment was actually begun. An initial cyclic voltammogram is shown in Fig. 9. The experiments were then conducted as described. The cell was permitted to remain on until the light intensity reached its steady-state value (200 sec). The cell was then turned off, and the ECL intensity decayed to zero. The results were very reproducible (within 5%) for repetitive experiments (ca. 30) over a period of 4 hr. When the cell was kept turned on and the experiment was permitted to continue well beyond 200 sec, the light intensity would remain relatively constant for 30 min. After this time the light would decrease at a constant rate until it finally dropped below a detectable level (~ 5 hr). When another experiment was attempted immediately, no light was detected. If the electrodes were separated, the solution stirred, and the electrodes repositioned with fresh solution from the reservoir in the gap, ECL was obtained but the intensity was about an order of magnitude smaller than the original experiment. Cyclic voltammetry revealed a reducible impurity with this solution, and fluorescence measurements showed a small amount of product that emits a 420 nm. If these experiments are continued, eventually all the electroactive species is consumed. Note also that successful long duration electrolysis in a solution containing 0.05M TBAP was accomplished here, while in a previous study (3) lifetimes of only 3-5 min were found.

Flow cell.—The results of the flow cell experiments showed this technique to be capable of producing stronger and longer lasting emission. In this mass transfer controlled system, the cell current and ECL intensity attained their limiting values very quickly

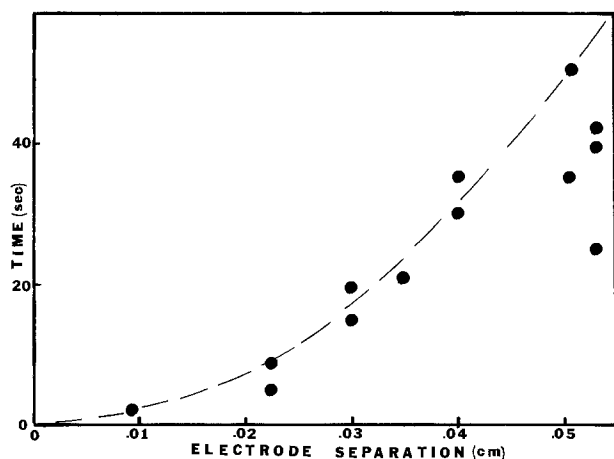


Fig. 8. Effect of electrode separation on time of ECL appearance. ---, Theoretical; ●, experimental. Solution same as in Fig. 4.

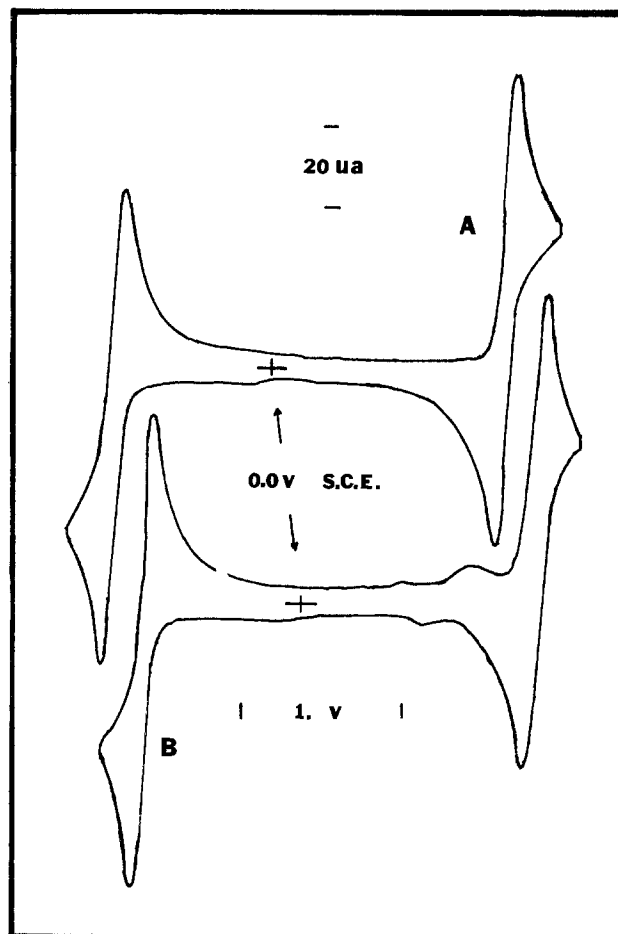


Fig. 9. Cyclic voltammograms of 4 mM rubrene/0.05M TBAP/BZN/BZ solution; (A) before thin layer experiment, (B) after 4 hr of thin layer experiments. Scan rate (v) = 100 mV/sec. Solution same as in Fig. 4.

after application of the d-c voltage (Fig. 10). Both of these quantities oscillated slightly because of fluctuations in the flow rate of the solution. This effect is also seen in Fig. 11 and 12 which show the dependence of the cell current and ECL intensity on the stirring rate and cell potential. The operating lifetime of this system greatly exceeded that of the thin layer cells. This can be attributed to the larger flux of radical ions and shorter lifetime required for the radical ions before the electron transfer reaction. In a typical experiment the ECL initially occurred solely in the mixing chamber. The emission produced was continuous and could be controlled by the flow rate of the solution. During electrolysis, if the flow rate was stopped for 30 sec and then restarted, light pulses an order of magnitude more intense than the continuous level were obtained. At this point in the experiment the radical ions were very stable. In fact, during a stop flow experiment, the electrolysis could be stopped for several minutes before the pump was restarted and the light pulse obtained was relatively unchanged. After about 2 hr when the ECL began to fail, the emission was observed to stream from one of the electrodes. This can be attributed to a difference in the radical ion stabilities, as observed also in the thin cell experiments. In this case, an instability of one of the species causes an excess of the opposite species after the mixing process. This excess is circulated throughout the whole solution volume, and results in emission at the electrode where the less stable radical ion is formed as the more stable radical ion reaches it. This was verified by producing an excess of the less stable species (using a 3 electrode system). By purposeful generation at an excess of one species the

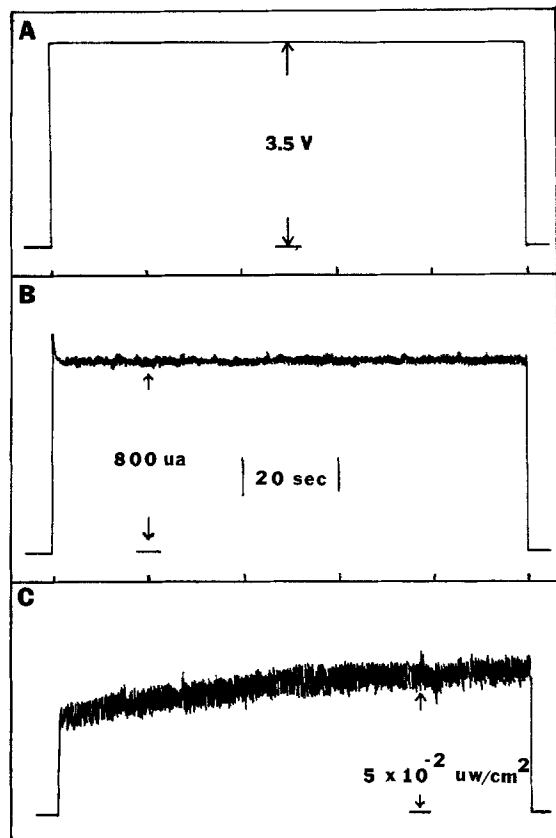


Fig. 10. Typical flow experiment. (A) Potential program, (B) current response, (C) resulting ECL intensity. Stirring rate \cong 500 rpm, 4 mM rubrene/0.1M TBAP/ACN/BZ.

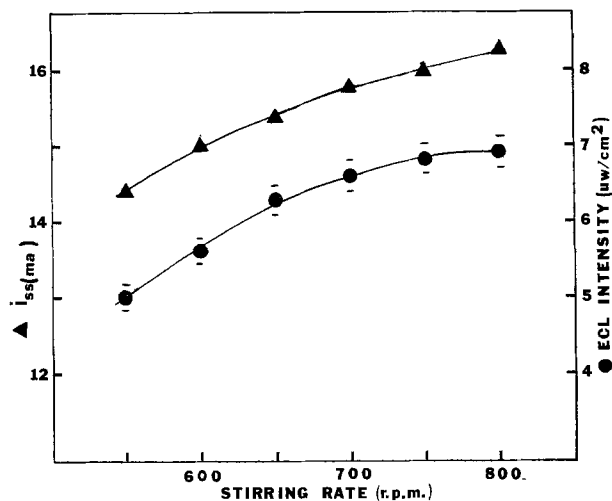


Fig. 11. Flow rate dependence of ECL. No geometric corrections made. Solution same as in Fig. 10.

streaming effect could not only be eliminated but it could be forced to occur at the opposite electrode. Such an ion degradation process tends to cascade and eventually all of the emission appeared at one electrode and not in the mixing chamber. Finally after about 30 hr the ECL ceased.

Fluorescence analysis showed only a trace amount of rubrene remained while revealing a large amount of product emitting at 420 nm. Further extraction shows two crystalline products (yellow and brown) with fluorescent maxima corresponding to 400 and 425 nm. Mass spectroscopic data showed that the products were isomers of dihydrorubrene. This finding is in agreement with that described by Moreu *et al.* (18) in the synthesis of dihydrorubrene.

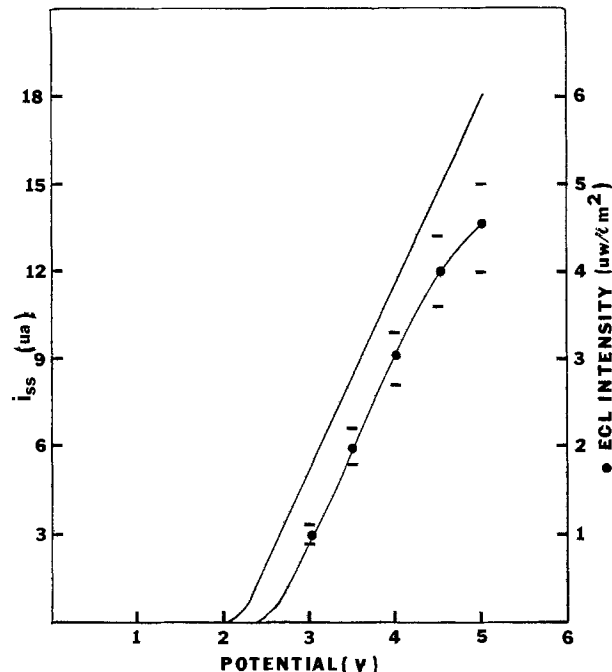


Fig. 12. Potential dependence of ECL. No geometric correction made. Stirring rate \cong 600 rpm. Solution same as in Fig. 10.

Conclusions

In this paper the feasibility of the development of an ECL device has been studied. Parameters affecting the electrically induced emission have been examined in both diffusion and convective modes. The results show that flow techniques do indeed have advantages over thin layer techniques for the production of continuous ECL. The thin layer mode of ECL formation is seen to be an impractical source of emission for an ECL device. The emission from this diffusion-controlled process is weak and is confined to a very narrow area, sandwiched between two zones of the highly colored radical ions. The lifetime of this d-c emission (5 hr) proved to be much greater than that previously published (3), but still unsatisfactory for any practical application. A major problem with this configuration appears to be the very small volume of solution confined between the electrodes. This volume is very susceptible to impurities which are either initially introduced or electrochemically generated. Detrimental side reactions which occur under these conditions, cause depletion of the electroactive species or formation of species which can effectively quench the ECL. These findings, along with the reaction zone geometry problem, suggest that the thin layer cell will not be useful for laser applications.

A better approach to this problem would be to utilize a flow system for the production of ECL. This method produces stronger emission due to the larger radical ion flux and the shorter radical lifetimes necessary for anion-cation annihilation. Buildup of impurities is minimized, and they are distributed through a much larger volume of solution. By making physical improvements on cell design (*e.g.*, larger electrodes, faster mixing) one could perhaps increase the ECL intensity an order of magnitude but probably not much more than this.

These experiments were performed using one of the better chemical systems known for the production of ECL. Even this system eventually failed. The mechanism for this failure is still not well understood, but at least partially occurs because of degradation of the parent molecule.

Acknowledgment

We would like to thank Mr. John Somerville and Mr. William Bruton whose artful glass work made this

project possible. The support of the research by the U.S. Army Research Office is gratefully acknowledged.

Manuscript submitted Feb. 15, 1979; revised manuscript received July 12, 1979.

Any discussion of this paper will appear in a Discussion Section to be published in the December 1980 JOURNAL. All discussions for the December 1980 Discussion Section should be submitted by Aug. 1, 1980.

Publication costs of this article were assisted by the University of Texas at Austin.

REFERENCES

1. L. R. Faulkner and A. J. Bard, in "Electroanalytical Chemistry," Vol. 10, A. J. Bard, Editor, pp. 1-95, Marcel Dekker, New York (1977).
2. D. M. Hercules, *Acc. Chem. Res.*, **2**, 301 (1969).
3. D. Laser and A. J. Bard, *This Journal*, **122**, 632 (1975).
4. R. M. Measures, *Appl. Opt.*, **13**, 1121 (1974).
5. C. A. Heller and J. L. Jernigan, *ibid.*, **16**, 61 (1977).
6. R. M. Measures, *ibid.*, **14**, 909 (1975).

7. C. P. Keszthelyi, *Spectros. Lett.*, **8**, 25 (1975).
8. J. D. Luttmmer and A. J. Bard, *This Journal*, **125**, 1423 (1978).
9. D. Laser and A. J. Bard, *Chem. Phys. Lett.*, **34**, 605 (1975).
10. J. T. Maloy and A. J. Bard, *J. Am. Chem. Soc.*, **93**, 5968 (1971).
11. A. Weissberger, E. S. Proskauer, J. A. Riddick and E. E. Toops, Jr., "Organic Solvents," 2nd ed., p. 438, Wiley, Interscience, New York (1955).
12. L. S. R. Yeh and A. J. Bard, *Chem. Phys. Lett.*, **44**, 339 (1976).
13. J. D. Luttmmer and A. J. Bard, *ibid.*, **55**, 493 (1978).
14. M. Von Stackelberg, M. Pilgrim, and V. Toome, *Z. Elektrochem.*, **57**, 342 (1953).
15. A. Pighin, Personal communication.
16. A. J. Bard, C. P. Keszthelyi, H. Tachikawa, and N. E. Tokel, in "Chemiluminescence and Bioluminescence," M. J. Cormier, D. M. Hercules and J. Lee, Editors, pp. 193-208, Plenum Press, New York (1973).
17. C. P. Keszthelyi, N. E. Tokel-Takvoryan, and A. J. Bard, *Anal. Chem.*, **47**, 249 (1975).
18. C. Moureau, C. DuFraisie, and P. Lotte, *Bull. Soc. Chim., Fr.*, **47**, 221 (1930).

The Warburg Impedance in the Presence of Convective Flow

Daniel A. Scherson and John Newman*

Department of Chemical Engineering, University of California, Berkeley, California 94720

ABSTRACT

The Warburg impedance of a rotating disk electrode is analyzed by means of an inverse Laplace transformation of the governing differential equation. This new formulation reduces the problem to a partial differential equation for which approximate solutions are known. The results obtained agree with exact numerical values for a wide range of low and high frequencies.

The impedance associated with changes in concentration induced by sinusoidally varying boundary conditions at the electrode surface was first analyzed by Warburg (1) and Kruger (2). Later Rosebrugh and Lash-Miller (3) extended these studies to account for a diffusion layer of finite thickness. Based on this model, Schuhmann (4) derived an analytic expression for the impedance which predicts more realistic values in the low frequency regime. Recently Levart and Schuhmann (5) proposed a general method for evaluating the concentration impedance of a uniformly accessible rotating disk electrode. By defining a frequency related complex variable, these authors obtained an asymptotic solution valid for high frequencies and any finite value of the Schmidt number found in electrochemistry. Homsy and Newman (6) analyzed this specific problem by a regular perturbation expansion showing that the stagnant Nernst diffusion layer concept is valid only for very high frequencies. A comparison of these solutions (7) concluded that the expression derived by Levart and Schuhmann best represents the behavior of the system for a wide range of frequency values.

This contribution constitutes a new approach, establishing an interesting connection between transient convective diffusion and the Warburg impedance of a rotating disk electrode.

Radial diffusion and convection, as well as migration effects, will be neglected. Furthermore, it will be

assumed that the Schmidt number is large, and that dilute-solution theory, with constant transport and thermodynamic properties, is applicable.

Mathematical Formulation

According to Homsy and Newman (6) the time varying concentration, \tilde{c} , for an alternating current of frequency ω , can be expressed as

$$\tilde{c} = a\theta \exp(jKt^*) \quad [1]$$

where

$$K = \omega\nu \left(\frac{3D}{\alpha\nu} \right)^{2/3} \bigg| \Omega D$$

and

$$t^* = t\Omega D \left(\frac{\alpha\nu}{3D} \right)^{2/3} \bigg| \nu$$

are the dimensionless frequency and time respectively.

By substituting Eq. [1] into the convective diffusion equation [Eq. [1], Ref. (6)] these authors arrived at the following complex equation

$$\theta'' + 3\zeta^2\theta' - jK\theta = 0 \quad [2]$$

subject to the boundary conditions

$$\theta = 1 \text{ at } \zeta = 0, \quad \theta \rightarrow 0 \text{ as } \zeta \rightarrow \infty \quad [3]$$

where $\zeta = y\sqrt{\Omega/\nu} (\alpha\nu/3D)^{1/3}$ is a dimensionless distance from the disk. A generalization of Eq. [2] can be obtained by defining a complex parameter, $p = \zeta$

* Electrochemical Society Active Member.

Key words: rotating disk, convective diffusion, alternating current.

+ jK, where the real part, ξ , can be understood as arising from some simple homogeneous reaction at the surface

$$\theta'' + 3\xi^2\theta' = p\theta \quad [4]$$

It can be shown that a formal inverse Laplace transformation of Eq. [4] yields the following partial differential equation

$$\frac{\partial^2 \tilde{\theta}}{\partial \xi^2} + 3\xi^2 \frac{\partial \tilde{\theta}}{\partial \xi} = \frac{\partial \tilde{\theta}}{\partial \tau} \quad [5]$$

and boundary conditions given by

$$\begin{aligned} \tilde{\theta} &\rightarrow 0 \text{ as } \xi \rightarrow \infty \\ \tilde{\theta} &= 1 \text{ at } \xi = 0, \tau > 0 \\ \tilde{\theta} &= 0 \text{ at } \xi \geq 0, \tau = 0 \end{aligned} \quad [6]$$

If the real variables $\tilde{\theta}$ and τ are regarded as a dimensionless concentration and time respectively, it becomes clear that Eq. [5] describes transient convective diffusion to a rotating disk. Moreover the boundary conditions specified in Eq. [6] refer to a buildup case after a step increase in the concentration at the surface.

The problem, so stated, has been analyzed independently by Krylov and Babak (8) and Selman (9) yielding results valid for short times in terms of parabolic cylinder functions. Nisancioglu and Newman (10) have derived a long-time series by solving numerically for the eigenvalues and eigenfunctions of a Sturm-Liouville system. Excellent agreement with the short time series cited above was found for a wide interval of time.

It is interesting to note that the function that prescribes the Warburg impedance for this particular system [Eq. [6], Ref. (6)] is precisely the Laplace transform of the flux at the surface. Therefore, an expression valid for high frequencies, $\theta_{HF}'(0)$, can be obtained from the short-time series (8, 9)

$$\begin{aligned} \mathcal{L}\left(-\frac{\partial \tilde{\theta}}{\partial \xi} \Big|_{\xi=0}\right) &= -\theta_{HF}'(0) \\ &= p^{1/2} + \frac{3}{4p} + \frac{9}{32}p^{-5/2} + 0(p^{-4}) \end{aligned} \quad [7]$$

and correspondingly the long-time series (10) determines a relation applicable in the low frequencies regime, $\theta_{LF}'(0)$

$$\begin{aligned} \mathcal{L}\left(-\frac{\partial \tilde{\theta}}{\partial \xi} \Big|_{\xi=0}\right) &= -\theta_{LF}'(0) \\ &= \frac{1}{\Gamma(4/3)} + p \sum_{n=0}^{\infty} \frac{B_n}{p + \lambda_n} \end{aligned} \quad [8]$$

where B_n and λ_n are the coefficients and eigenvalues of the Sturm-Liouville system respectively.

In the absence of mechanistic complications ($\xi = 0$), the frequency dependent part of the Warburg impedance will be simply given by replacing the value of p in Eq. [8] and Eq. [9] by jK where K is the original dimensionless frequency

$$-\theta_{HF}'(0) = \sqrt{jK} - \frac{3j}{4K} + \frac{9}{32}(jK)^{-5/2} \quad [9]$$

$$-\theta_{LF}'(0) = \frac{1}{\Gamma(4/3)} + jK \sum_{n=0}^{\infty} \frac{B_n}{jK + \lambda_n} \quad [10]$$

The result obtained in Eq. [9] is identical to that reported by Homsy and Newman (6) [Eq. [12], Ref.

Table I. Solutions for the real and imaginary parts of $-1/\theta_{HF}'(0)$

K	High frequency solution		Levart and Schuhmann		Exact solution		Nernst layer solution	
	Re $\left\{ \frac{-1}{\theta'(0)} \right\}$	-Im $\left\{ \frac{-1}{\theta'(0)} \right\}$	Re $\left\{ \frac{-1}{\theta'(0)} \right\}$	-Im $\left\{ \frac{-1}{\theta'(0)} \right\}$	Re $\left\{ \frac{-1}{\theta'(0)} \right\}$	-Im $\left\{ \frac{-1}{\theta'(0)} \right\}$	Re $\left\{ \frac{-1}{\theta'(0)} \right\}$	-Im $\left\{ \frac{-1}{\theta'(0)} \right\}$
3.5	0.4417	0.3755	0.4392	0.3780	0.4561	0.3474	0.48538	0.37104
5.0	0.3469	0.3155	0.3462	0.3162	0.3556	0.3115	0.36685	0.34060
7.5	0.2717	0.2560	0.2715	0.2510	0.2735	0.2588	0.26868	0.27945
10.0	0.2311	0.2235	0.2311	0.2236	0.2314	0.2240	0.22266	0.23537
20	0.1600	0.1581	0.1600	0.1581	0.1600	0.1581	0.15656	0.15788

(6)]. However, these authors arrived at an erroneous expression for the real and imaginary part of $(-\theta_{HF}'(0))^{-1}$. The correct components are given by

$$\operatorname{Re} \left\{ -\frac{1}{\theta_{HF}'(0)} \right\} = \frac{a}{a^2 + b^2},$$

$$-\operatorname{Im} \left\{ -\frac{1}{\theta_{HF}'(0)} \right\} = \frac{b}{a^2 + b^2} \quad [11]$$

where

$$a = \frac{\sqrt{2}}{2} \left(K^{1/2} - \frac{9}{32} K^{-5/2} \right) \quad [12]$$

$$b = \frac{\sqrt{2}}{2} \left(K^{1/2} + \frac{9}{32} K^{-5/2} \right) - \frac{3}{4K} \quad [13]$$

Similarly, from Eq. [10]

$$\operatorname{Re} \left\{ -\frac{1}{\theta_{LF}'(0)} \right\} = \frac{r}{s^2 + r^2},$$

$$-\operatorname{Im} \left\{ -\frac{1}{\theta_{LF}'(0)} \right\} = \frac{s}{s^2 + r^2} \quad [14]$$

where

$$r = \frac{1}{\Gamma(4/3)} + K^2 \sum_{n=0}^{\infty} \frac{B_n}{\lambda_n^2 + K^2} \quad [15]$$

$$s = K \sum_{n=0}^{\infty} \frac{B_n \lambda_n}{\lambda_n^2 + K^2} \quad [16]$$

Numerical values obtained from Eq. [11], [12], and [13] are listed in Table I. As it can be clearly seen, the analytic results derived from the high frequency series are in excellent agreement with the exact solution and do not differ significantly from those reported by Levart and Schuhmann (7).

The first ten eigenvalues, λ_n , and the related coefficients, B_n , of the eigenfunctions [Table I, Ref. (10)] were used to calculate the corresponding components for the low frequency spectrum from Eq. [14], [15], and [16]. These are given in Table I where the few available exact results are also shown for comparison.

In addition, Table I and Table II contain values for $(-\theta'(0))^{-1}$ obtained from an analysis based on a stagnant Nernst diffusion layer (4, 6) i.e.

$$-\frac{1}{\theta_N'(0)} = \Gamma\left(\frac{4}{3}\right) \frac{\tanh \sqrt{j\omega\delta^2/D}}{\sqrt{j\omega\delta^2/D}} \quad [17]$$

where the Nernst diffusion layer thickness, δ , is given by

$$\delta = \Gamma\left(\frac{4}{3}\right) \sqrt{\frac{\nu}{\Omega}} \left(\frac{3D}{\alpha\nu}\right)^{1/3} \quad [18]$$

Table II. Solutions for the real and imaginary parts of $-1/\theta_{LF}'(0)$

K	Low frequency solution		Exact solution		Nernst layer solution	
	$\operatorname{Re} \left\{ \frac{-1}{\theta'(0)} \right\}$	$-\operatorname{Im} \left\{ \frac{-1}{\theta'(0)} \right\}$	$\operatorname{Re} \left\{ \frac{-1}{\theta'(0)} \right\}$	$-\operatorname{Im} \left\{ \frac{-1}{\theta'(0)} \right\}$	$\operatorname{Re} \left\{ \frac{-1}{\theta'(0)} \right\}$	$-\operatorname{Im} \left\{ \frac{-1}{\theta'(0)} \right\}$
0	0.89298	0.0000	0.89298	0.0000		
0.05	0.89278	0.01134			0.89279	0.01186
0.1	0.89219	0.02266			0.89222	0.02371
0.2	0.88985	0.04516			0.88996	0.04727
0.5	0.87397	0.11010			0.87453	0.11570
0.7	0.85679	0.14988			0.85768	0.15817
1.0	0.82333	0.20229			0.82442	0.21523
1.5	0.75542	0.26748	0.72406	0.30195	0.75500	0.28926
2.0	0.68409	0.30641	0.64160	0.33934	0.67925	0.33682
3.5	0.51238	0.32695	0.45610	0.34736	0.48538	0.37104

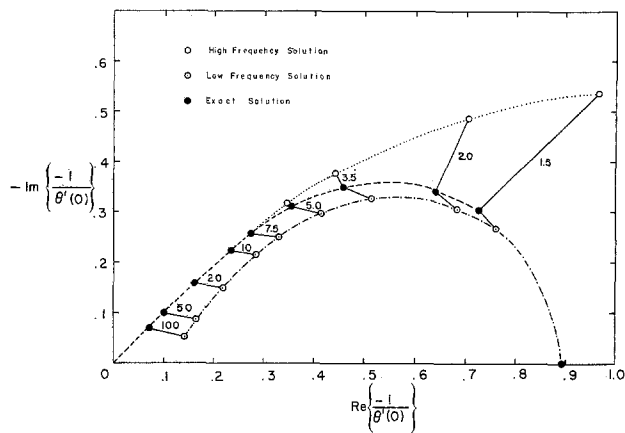


Fig. 1. Representation of the function $(-\theta'(0))^{-1}$ in the complex plane.

A graphical representation of $(-\theta'(0))^{-1}$ in the complex plane is depicted in Fig. 1, where solid lines connect equal values of the dimensionless parameter K . It is interesting to note that although in the real space the short-time (8, 9) and the long-time series (10) overlap within a few tenths of a percent in a wide interval of time, that behavior is not reproduced in the complex plane after a Laplace transformation. This problem is presently under investigation in this laboratory.

Summary

Laplace transform techniques have been utilized in order to determine the Warburg impedance of a rotating disk. The solution obtained for high frequencies has been shown to reproduce within one percent exact numerical results for values of K greater than 7.5.

Acknowledgment

This work was supported by Sandia Laboratories, Albuquerque, New Mexico.

Manuscript submitted Feb. 5, 1979; revised manuscript received Aug. 1, 1979.

Any discussion of this paper will appear in a Discussion Section to be published in the December 1980 JOURNAL. All discussions for the December 1980 Discussion Section should be submitted by Aug. 1, 1980.

Publication costs of this article were assisted by the University of California.

LIST OF SYMBOLS

α	0.51023
a	see Eq. [12]
A	amplitude of time-varying concentration, mole/cm ³
b	see Eq. [13]
B_n	coefficients of Sturm-Liouville system [see Ref. (10)]
\tilde{c}	time-varying concentration of reactant, mole/cm ³

D	diffusion coefficient cm ² /sec
j	$\sqrt{-1}$
K	$\omega\nu(3D/\alpha\nu)^{2/3}/\Omega D$, dimensionless frequency
p	generalized complex parameter
r	see Eq. [15]
s	see Eq. [16]
t	time, sec
t^*	$t\Omega D(\alpha\nu/3D)^{2/3}/\nu$, dimensionless time
y	normal distance from the disk, cm
$\Gamma(4/3)$	0.89298, gamma function of 4/3
δ	$\Gamma(4/3)\sqrt{\nu/\Omega}(3D/\alpha\nu)^{1/3}$, Nernst diffusion layer thickness
ζ	$y\sqrt{\Omega/\nu}(\alpha\nu/3D)^{1/3}$, dimensionless distance normal to the disk
ξ	real part of p
θ	complex, dimensionless, time-varying concentration
\sim	
θ	inverse Laplace transform of θ
λ_n	eigenvalues of Sturm-Liouville system [see Ref. (10)]
τ	inverse Laplace transform of p
ω	frequency of alternating current, rad/sec
Ω	rotation speed of disk, rad/sec

<i>Subscripts</i>	
HF	high frequency approximation
LF	low frequency approximation
N	Nernst formalism

REFERENCES

1. E. Warburg, *Wied. Ann.*, **67**, 493 (1898).
2. F. Kruger, *Z. Phys. Chem.*, **45**, 1 (1903).
3. T. R. Rosebrugh and W. Lash-Miller, *J. Phys. Chem.*, **14**, 816 (1910).
4. D. Schuhmann, *Compt. Rend.*, **262C**, 624 (1966).
5. E. Levart and D. Schuhmann, *J. Electroanal. Chem. Interfacial Electrochem.*, **53**, 77 (1974).
6. R. V. Homsy and J. Newman, *This Journal*, **121**, 521 (1974).
7. E. Levart and D. Schuhmann, *ibid.*, **122**, 1082 (1975).
8. V. S. Krylov and V. N. Babak, *Sov. Electrochem.*, **7**, 626 (1971).
9. J. R. Selman, Ph.D. Thesis, University of California, Berkeley (1971).
10. K. Nisancioglu and J. Newman, *J. Electroanal. Chem. Interfacial Electrochem.*, **50**, 23 (1974).

Polarization Phenomena Associated with Reduction of a Doped Ceria Electrolyte

Da Yu Wang* and A. S. Nowick*

Henry Krumb School of Mines, Columbia University, New York, New York 10027

ABSTRACT

The steady-state and transient polarization behavior of doped ceria solid electrolyte cells at 700°-900°C was studied in the current range above the cathodic limiting current, where electrolyte reduction sets in. The current interruption method was used together with a reference electrode, to measure separately the anodic and cathodic overpotentials (η_a and η_c) and the ohmic polarization for various oxygen pressures, types of electrodes, and dopant levels. The cathodic steady-state curves ($\ln I$ vs. η_c) show a linear region of slope e/kT which is interpreted in terms of the Wagner polarization cell theory, and it is shown that this theory is applicable to the cathodic polarization even when ionic blocking is incomplete. Values of the electronic transference number are obtained for various electrolyte compositions and temperatures which agree well with values obtained by other methods. The observed anodic steady-state overpotential is related to a residual ionic current. The transient anodic curves following current interruption show behavior in which $\eta(t)$, starting positive, changes sign and eventually joins the cathodic curve; subsequently both decay to zero. At higher initial overpotentials, a very slow decay occurs in which both decay curves show anomalous humps after long time periods. These phenomena have been interpreted in terms of simple models which involve primary diffusion of electrons (from cathode to anode), secondary diffusion (into the region of the reference electrode), and oxygen uptake from all of the electrodes.

The present study was carried out to obtain a fuller understanding of polarization phenomena occurring in systems that use solid electrolytes. In previous papers (1, 2), we made use of the current interruption method in combination with a reference electrode, to study the nature of electrode phenomena at relatively low overpotentials occurring at platinum paste electrodes on a doped CeO₂ electrolyte. This method makes it possible to determine separately the anodic and cathodic overpotentials as well as the ohmic polarization of the electrolyte. It was shown that, at high oxygen partial pressures (p_{O_2}), data for the steady-state current (I) vs. overpotential (η) obey the Butler-Volmer equation both for anodic and cathodic polarizations. This behavior was interpreted as controlled by a charge trans-

fer (or activation) mechanism, and the nature of the rate-determining step of this process was studied. At relatively low p_{O_2} , on the other hand, the cathodic polarization showed limiting-current behavior, characteristic of concentration polarization. It is believed that the limiting process is the rate at which oxygen adatoms can be supplied at the cathode.

As reported in the previous papers, when η is made sufficiently cathodic, I rises above the limiting current I_l , and the IR drop in the electrolyte is no longer ohmic. Previous workers (3-5) have shown that reduction of the electrolyte sets in at such high cathodic potentials. The present work was carried out to explore this behavior more quantitatively. In so doing, we have applied Wagner's treatment (6) of current-voltage behavior, for a polarization cell in which ionic current is blocked. This treatment was, in fact, derived for the idealized case in which one electrode is totally block-

* Electrochemical Society Active Member.

Key words: electrode polarization, solid electrolytes, cerium dioxide, electronic diffusion.

ing to ions while the other is an electronic conductor which is completely reversible to ionic flow, and at which no overpotential is developed. Nevertheless, it is shown that the present experimental method, which permits the separate determination of the two electrode overpotentials and the IR drop in the electrolyte, makes it possible to apply the Wagner treatment even under less ideal conditions.

In addition to steady-state (I vs. η) behavior, we have also studied the transient overpotential following interruption of the current. While several unusual aspects were observed, it was found that they could all be explained in terms of the reduction of the electrolyte, the diffusion of electrons, and the uptake of oxygen from the electrodes.

Ceria doped with calcia or yttria was chosen for the present work, because its high oxygen-ion conductivity above 600°C make it suitable for many electrochemical applications, and because its electrical properties have been well studied, particularly its ionic and electronic conductivity as a function of temperature and p_{O_2} .

Theory

We present a modification of the Wagner treatment (6) suited to the type of cell used in these experiments. By employing an electrode which is blocking to ionic flow (the cathode, in the present case), ionic conduction is suppressed under steady-state conditions and conduction takes place only because of the migration of electronic carriers. Wagner assumes that the electronic carriers are dilute enough to obey ideal solution laws and to have a mobility that is constant. He then obtains, for the electronic conductivity at any position x in an oxide electrolyte

$$\sigma_e = \sigma_e^0 \exp[(\mu_{O_2}^0 - \mu_{O_2})/4kT] \quad [1]$$

where μ_{O_2} is the chemical potential of oxygen and super 0 refers to values at a reference position which is in equilibrium with the ambient gas. Wagner further shows that the electronic current density across an electrolyte of thickness L is

$$J_e = \frac{1}{4eL} \int_{\mu_{O_2}^a}^{\mu_{O_2}^c} \sigma_e d\mu_{O_2} \quad [2]$$

where $\mu_{O_2}^a$ and $\mu_{O_2}^c$ are values at the anode and cathode, respectively. Substituting Eq. [1] into [2] and integrating gives

$$J_e = (kT\sigma_e^0/eL) \{ \exp[(\mu_{O_2}^0 - \mu_{O_2}^c)/4kT] - \exp[(\mu_{O_2}^0 - \mu_{O_2}^a)/4kT] \} \quad [3]$$

The Nernst equation gives for the cathodic and anodic overpotentials, respectively (both defined as positive quantities)

$$4e\eta_c = \mu_{O_2}^0 - \mu_{O_2}^c; \quad 4e\eta_a = \mu_{O_2}^a - \mu_{O_2}^0 \quad [4]$$

which combined with Eq. [3] gives

$$J_e = J_e^0 [\exp(e\eta_c/kT) - \exp(-e\eta_a/kT)] \quad [5]$$

where

$$J_e^0 = kT\sigma_e^0/eL \quad [6]$$

Wagner considered the idealized case in which the non-blocking electrode (here, the anode) is reversible to the conducting ions, so that $\eta_a = 0$, and any IR drop in the current leads and contacts is negligible. In that case

$$\eta_c = E \quad [7]$$

where E is the total potential across the cell, and Eq. [5] becomes

$$J_e = J_e^0 [\exp(eE/kT) - 1] \quad [8]$$

(The validity of Eq. [8] also requires that E never exceed the decomposition potential of the electrolyte.) However, it is clear that even if $\eta_a \neq 0$, Eq. [5] takes

on the useful asymptotic form when a sufficiently large cathodic potential is applied

$$\ln J_e = \ln J_e^0 + (e/kT)\eta_c \quad [9]$$

i.e., a plot of $\ln J_e$ vs. η_c should give a straight line with slope e/kT and intercept determined by Eq. [6]. The advantage of a direct measurement of η_c by the current interruption method is that η_c can be obtained separately from η_a and the IR drop in the current leads so that Eq. [9] can be utilized even when η_a and IR are not zero. For the case where the normal conductivity is primarily ionic so that the equilibrium electronic transference number, $t_e^0 \ll 1$, we can insert $\sigma_e^0 \cong t_e^0\sigma_i^0$ (σ_i^0 being the ionic conductivity) into Eq. [6] to obtain

$$J_e^0 = (kT/eL)\sigma_i^0 t_e^0 \quad [10]$$

Thus, the intercept of Eq. [9] can be used to determine t_e^0 under the conditions where this equation is valid.

In considering the type of polarization cell with which we will be dealing, it is advantageous to be able to relax the requirement of complete blocking of ions. Brook *et al.* (3) have considered the case in which ionic blocking is incomplete, but nevertheless, large, so that a residual ionic current density J_{ir} is present. They show that Wagner's Eq. [8] then becomes

$$J_e = J_e^0 \left[\exp \left\{ \left(1 - \frac{J_{ir}}{J_i} \right) \frac{eE}{kT} \right\} - 1 \right] \quad [11]$$

where J_i is the ionic current in the absence of polarization. If we assume that J_{ir} is invariant over a large range of E , while $J_i = E/R_i S$, S being the electrode area and R_i the corresponding resistance, we obtain for large E

$$\ln J_e = [\ln J_e^0 - eJ_{ir}R_i S/kT] + eE/kT \quad [12]$$

i.e., the correction term goes into the intercept. However, if the current interruption method is used, the additional term enters only in the IR drop, which is separately measured, so that a relation of the type of Eq. [9], involving the cathodic overpotential, is unaffected. At the same time, if $\eta_a > 0$ because of the ionic flow, Eq. [9] will be unchanged. It may be concluded that Eq. [9] should be valid even with only partial blocking of the ionic current. The validity of this equation can be verified experimentally in several ways: (i) from the e/kT slope; (ii) from the correct determination of t_e^0 from the value of the intercept combined with Eq. [10]; (iii) by the shift in the $\ln J_e$ vs. η_c plots for two samples of the same electrode but different electrolyte thicknesses, L_1 and L_2 , given by

$$\Delta\eta_c = \eta_{c2} - \eta_{c1} = (kT/e) \ln(L_2/L_1) \quad [13]$$

and (iv), by the shift in the same plots with a change in the ambient p_{O_2}

$$\Delta\eta_c = (kT/4e) \ln(p_{O_2}^{(2)}/p_{O_2}^{(1)}) \quad [14]$$

This last equation comes from the pressure dependence of σ_e^0 for doped ceria (as well as stabilized zirconia) which has been shown (7, 8) to obey

$$\sigma_e^0 \propto p_{O_2}^{-1/4} \quad [15]$$

Experimental Methods

Doped ceria electrolytes and platinum paste electrodes were prepared as described previously (1). Three electrodes were applied to the samples in the geometrical arrangement shown schematically in Fig. 1. The arrangement for the current interruption method is also described in Ref. (1). Most of the transient studies were carried out with the aid of a storage oscilloscope (Tektronix 564). For those cases in which the decay time was longer than 5 sec, however, a Hewlett-Packard 7128A two-pen strip chart recorder was used. The two pens were connected to the outputs of Keithley 640 and Keithley 150A voltmeters, the first voltmeter connected between the electrode under investigation

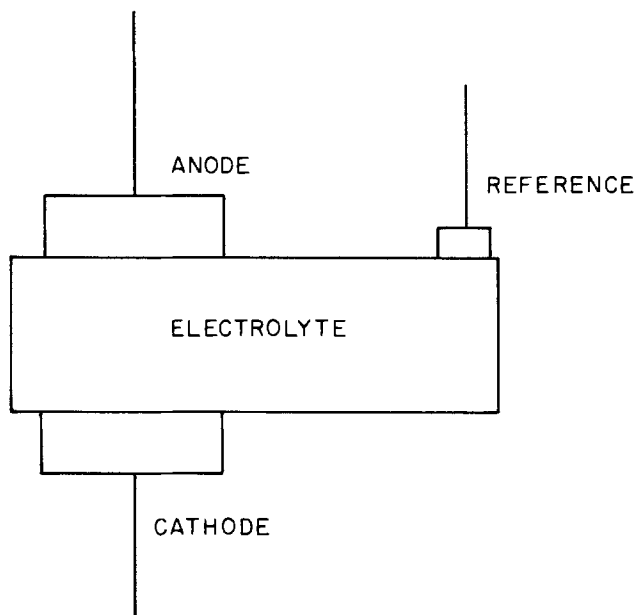


Fig. 1. Schematic diagram of the electrode arrangement

and the reference electrode with input impedance $> 10^{12}\Omega$, and the second one connected between the anode and cathode with an input impedance $10^9\Omega$. The response time of the recorder is $\frac{3}{4}$ sec.

In addition to Pt paste electrodes, two new types of electrodes were used in this study: gold paste (Engelhard A-2123) and platinum foil ($120\ \mu\text{m}$ thickness). Gold paste was brushed onto the surface of the electrolyte, then fired at 800°C for 4 hr. For the platinum foil electrode, an unfluxed Pt paste (Engelhard 6926) was first applied, the platinum foil was pressed on under an alumina disk weighing 23g, and this combination was fired at 1400°C in an argon atmosphere for 3 hr.

The gases and the gas treatments are as described previously (1), except that in this study we added one stopcock just before the gas enters the sample chamber. By controlling this valve, we can rapidly change the ambient gas composition during an experiment. Argon-oxygen gas mixtures were used in this study, covering the range of p_{O_2} from 10^{-5} to 10^{-2} atm, as well as CO/CO₂ mixtures whose p_{O_2} was measured with the aid of a cell utilizing a calcia-stabilized zirconia electrolyte.

The absence of polarization of the reference electrode was demonstrated by varying the input impedance of the oscilloscope and observing that the voltage readings are unchanged [see Ref. (1)].

Steady-State Behavior

The "instantaneous" potential drop, which occurs in a time $\sim 10^{-7}$ sec after current interruption, is taken as the IR drop, while the initial value after this drop is taken as the steady-state overpotential, η , at the electrode under investigation. This overpotential, measured as a function of the current, I , that flowed prior to interruption, constitutes the steady-state data.

Figure 2 shows typical examples of plots of $\log I$ vs. η_c (cathodic overpotential) at low p_{O_2} , showing the limiting-current region and the current increase at higher cathodic values. Data are presented for electrolytes of two thicknesses at temperatures of 700° and 800°C . In each case a straight line of slope $e/2.3 kT$ (represented by the solid line) is obtained at high η_c . The dashed lines in the lower η_c region are fitted curves based on the assumption that concentration polarization dominates this region. [Detailed analysis can be found in Ref. (1)]. Figure 2 shows that the position of the straight-line region depends on the

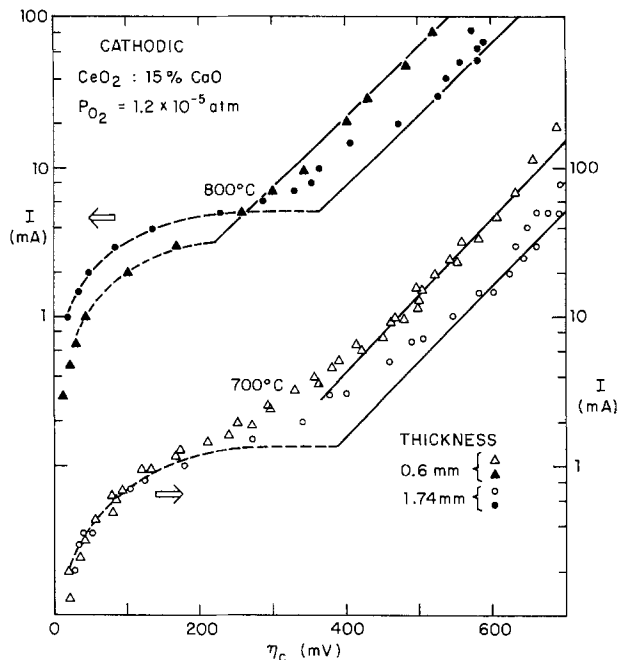


Fig. 2. Plots of steady-state cathodic overpotential as a function of $\log I$ for two different temperatures and sample thicknesses, showing the increase in current above the limiting-current range and the fit to straight lines of slope $e/2.3 kT$ (solid lines).

thickness of the electrolyte, for samples having the same electrode area. The observed overpotential difference of the two samples with electrolyte thickness 0.6 and 1.74 mm is 95 mV at 800°C , and 90 mV at 700°C ; these results compare favorably with the values 98.5 mV for 800°C and 89.4 mV for 700°C calculated from Eq. [13]. This electrolyte thickness dependence is also observed with other electrolyte samples containing different dopants and dopant concentrations, and Eq. [13] always fits the data well.

In the region of the $e/2.3 kT$ slope, the electrolyte resistance is no longer constant. An example is shown in Fig. 3, where the departure from ohmic behavior (represented by the 45° line) at high currents is apparent, indicating that the electrolyte is being reduced. As further evidence that reduction of the electrolyte is indeed taking place in this range, we showed that the

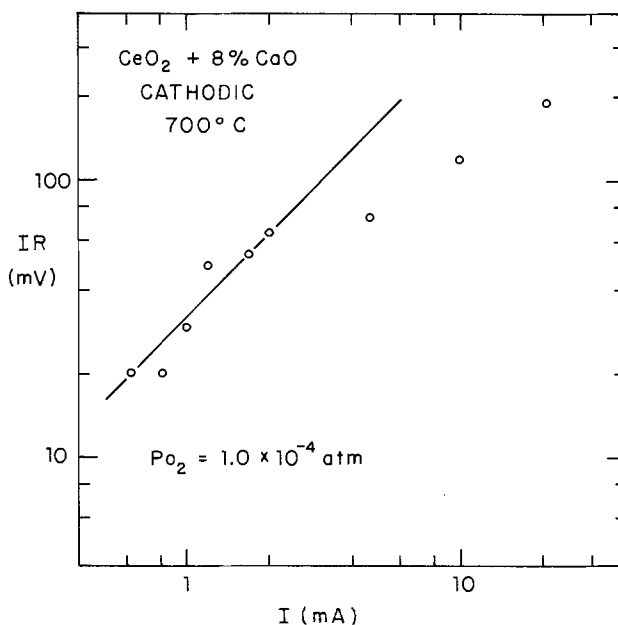


Fig. 3. A log-log plot of cathodic IR drop vs. I . The 45° line represents a constant resistance, R .

total resistance of the cell ($\sim 4\text{-}6\Omega$) in this range is mainly that of the Pt leads.

Since reduction occurs at the cathode, it is a matter of concern as to whether the reference electrode is also reduced. As verification that it is not, we note that the steady-state curves were independent of separation of the reference from the adjacent electrode (for separation greater than 5 mm), and also independent of whether the reference is on the same side of the sample as the cathode or as the anode.

To block ionic flow at the cathode more effectively than is obtained with the porous Pt paste electrode, a similar experiment was carried out using a Pt foil electrode at the cathode and Pt paste at the anode—both with the same nominal area. The result, shown in Fig. 4 at $p_{O_2} = 1.2 \times 10^{-5}$ atm, shows that the cathodic overpotential can be fitted with the Wagner Eq. [8] over a much more extended region than for the case where the cathode is Pt paste. (The comparison shown in Fig. 4 was made simply by reversing the polarity of the same sample.) However, the more important result is that the linear regions for the two cases closely overlap each other. (The observed 10 mV difference between them is probably not significant when we consider the possible error in attempting to match the actual electrode areas of the two electrodes.) This result shows that the behavior at high η_c is independent of whether only partial ionic blocking or more-or-less complete blocking takes place.

Figure 4 also shows that the linear region can be shifted by changing p_{O_2} . The observed shift of cathodic overpotential is 250 mV between p_{O_2} values of 2.3×10^{-10} and 1.2×10^{-5} atm. Comparison with the calculated value 251.3 mV based on Eq. [14], shows that there is very good agreement.

By changing the electrode material from Pt paste to Au paste, it was demonstrated that the reduction phenomenon is unrelated to the type of metal used for the cathode. We first prepared a sample with both sides having Pt paste electrodes, and then in turn, replaced each electrode with Au paste, measuring the

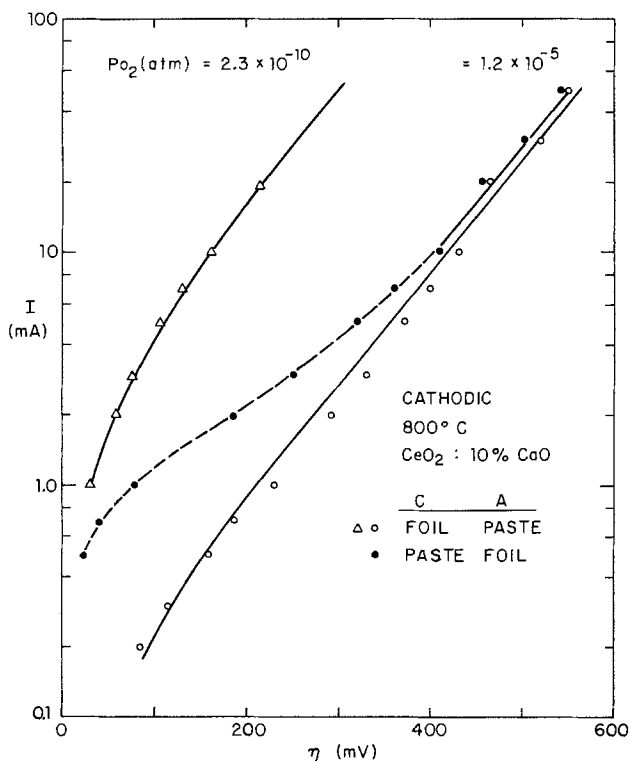


Fig. 4. Comparison of cathodic overpotential curves for Pt paste and Pt foil cathodes at two different oxygen partial pressures. The reference electrode is always Pt paste. Solid lines are the fit to the Wagner equation.

cathodic I - η curve in each case. The results are shown in Fig. 5, which demonstrates that Pt paste and Au paste give the same cathodic curve in the linear region. (The deviation from linearity at the upper current limit will be discussed later.) On the other hand, Fig. 5 shows that the anodic overpotential is very dependent on the type of metal electrode. Figure 6 shows that it also depends strongly on the structure of the electrode and on the p_{O_2} of the ambient gas. The corresponding cathodic curves, however, consistently show

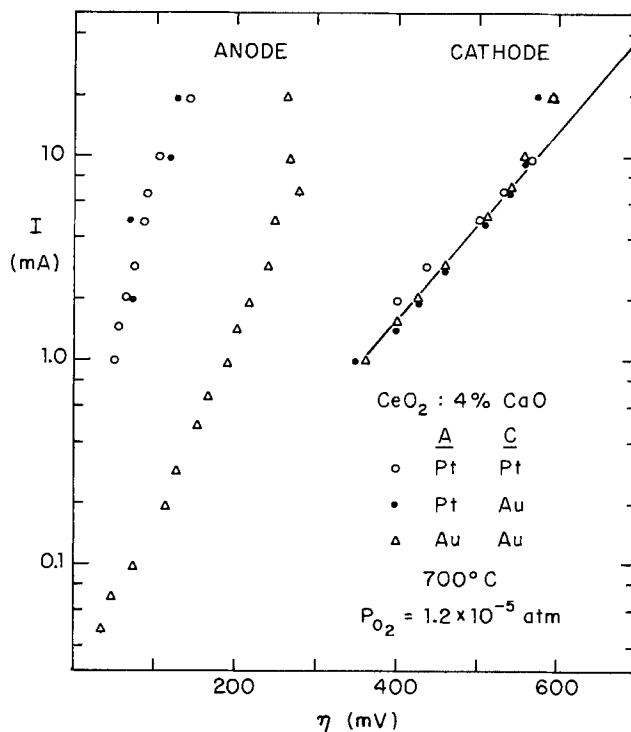


Fig. 5. Anodic and cathodic I vs. η curves for different combinations of Pt paste and Au paste electrodes. (For clarity of the figure, cathodic data at lower overpotentials are omitted.)

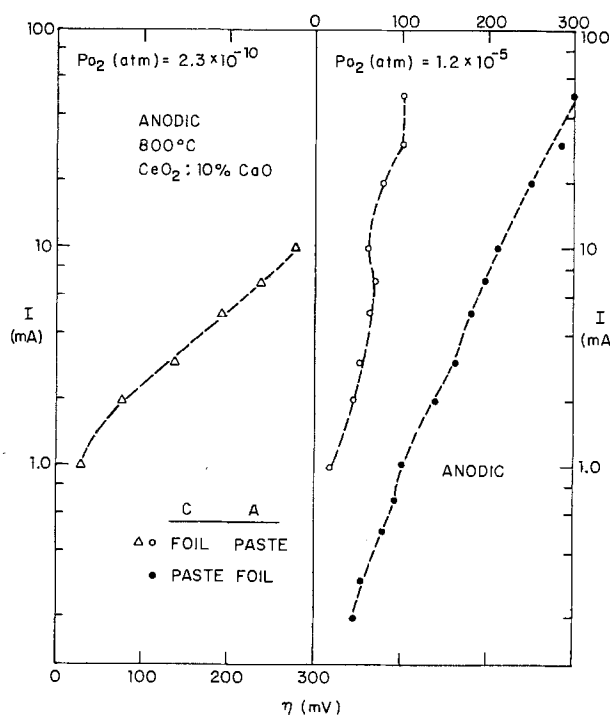


Fig. 6. Anodic I vs. η curves for different electrode materials and different oxygen partial pressures.

the linear region with slope $e/2.3 kT$ and intercept determined by Eq. [13] and [14].

As a final test of the applicability of the Wagner model to cathodic behavior in the reduction range, we employed Eq. [10] to calculate values of t_e^0 from the intercepts, $\ln J_e^0$, of the linear plots, after obtaining σ_1^0 either from d-c four-probe measurements or from the IR drop in regions where the Butler-Volmer equation is obeyed (1). In this way, t_e^0 was obtained over the temperature range 500°-900°C with calcia concentration in the electrolyte ranging from 1 to 15%. These t_e^0 values are collected in Fig. 7 and compared with values from other sources (7, 9), obtained by using Eq. [15] and the fact that σ_1^0 is independent of p_{O_2} . In general, good agreement is obtained.

In these experiments, the use of the reference electrode was very important for the correct determination of t_e^0 . In fact, if the cathode-to-anode potentials were used to determine t_e^0 , values at least three times smaller would have been obtained, and much of the good agreement in Fig. 7 would be lost. It would therefore appear that the failure of Brook *et al.* (10, 11) to obtain satisfactory values of t_e^0 relates to their application of the theory with the full anode-to-cathode potential, E .

In view of the fact that all four tests suggested at the end of the Theory section have given the predicted results, we conclude that it is valid to apply the modified Wagner theory (Eq. [9] and [10], or [8] with η_c substituted for E) to the present experiments, even though blocking is not complete and $\eta_a \neq 0$.

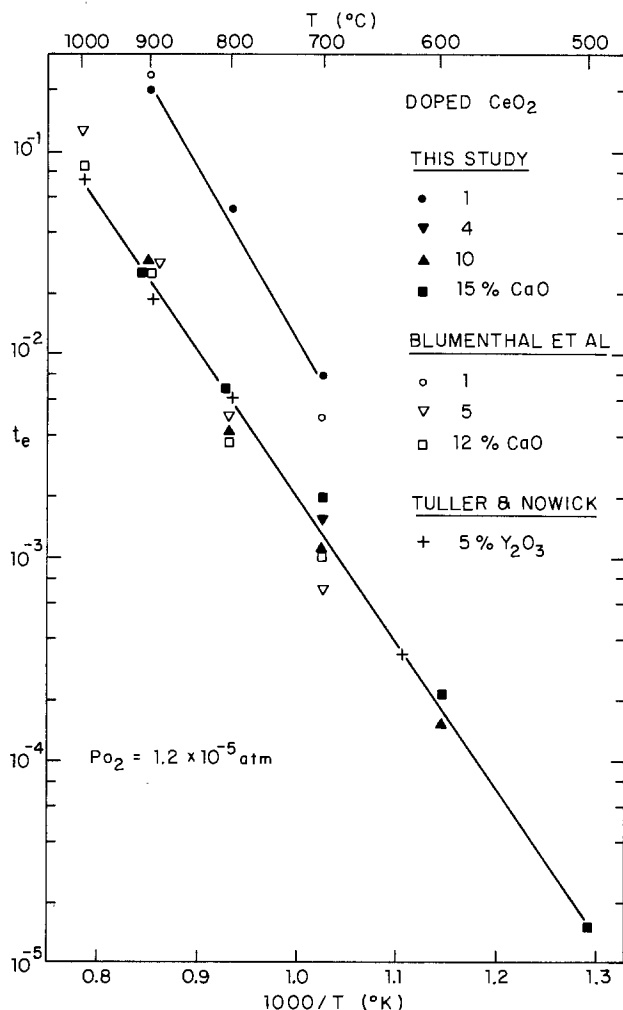


Fig. 7. Values of the equilibrium electronic transference number t_e^0 as a function of temperature for various doped ceria electrolytes. Results obtained from the present work are compared with those obtained previously by other methods.

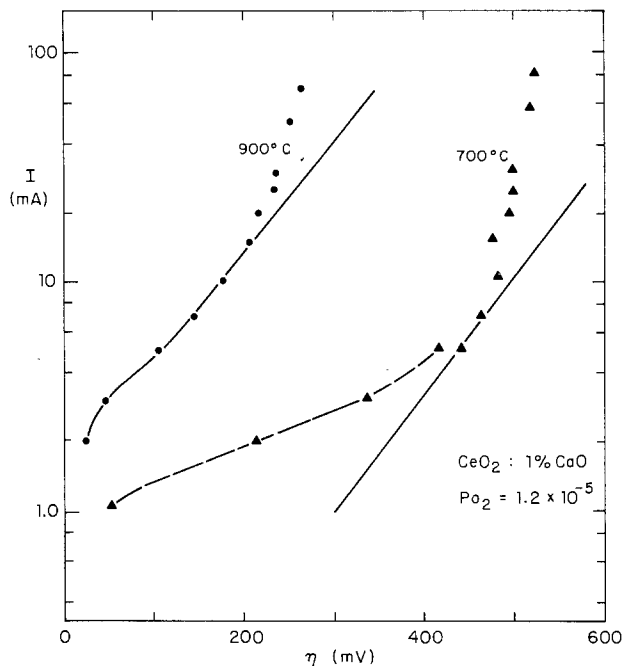


Fig. 8. Cathodic I vs. η curves for a $\text{CeO}_2:1\% \text{CaO}$ electrolyte at two temperatures, showing early departure from the straight lines of slope $e/2.3 kT$ (the solid lines).

If we consider the straight-line region with slope $e/2.3 kT$ as the first increase of current beyond the cathodic limiting-current region, then, as already noted in Fig. 5, a second increase of current (to values above the straight line) occurs at still higher overpotentials. This phenomenon manifests itself more strikingly the lower the dopant concentration in the electrolyte. For example, Fig. 8 shows the cathodic results for a 1% calcia-doped ceria sample at 700° and 900°C, compared against straight lines of slope $e/2.3 kT$ (the solid lines). Clearly, the departure from linearity occurs sooner in this case than for the electrolytes with higher CaO content. Table I further demonstrates that the point of departure from Eq. [9] occurs earlier the lower the CaO dopant concentration in the electrolyte, and that this departure is correlated with the ionic conductivity. The reason for this second increase of current is still somewhat obscure, although it may be related either to a nonconstant chemical potential of oxygen ions (12) or to electrons no longer obeying ideal solution theory (13).

It is desirable next to discuss the substantial anodic polarization that is observed in these experiments. Undoubtedly, such polarization must be traced to the presence of a residual ionic current, for it has been shown (1) that the charge transfer process gives rise to an anodic overpotential obeying a Tafel equation. Relating the anodic overpotential to a residual ionic current is also consistent with the observation that the anodic overpotential is larger with Au paste or Pt foil at the anode than with Pt paste (see Fig. 5 and 6). According to a separate study of polarization phenomena at lower overpotentials with Au paste and Pt foil electrodes (14), both of these electrodes yield anodic

Table I. Effect of CaO content on the value of η_c at which departure from the Wagner equation occurs, and comparison with ionic conductivity (σ_1^0). (All results obtained at 700°C and $p_{O_2} = 10^{-5}$ atm.)

% CaO in CeO_2	η_c (mV)	$\sigma_1^0 T$ ($\Omega\text{-cm})^{-1} \text{K}$
1	475	4.8
4	575	14
15	650	27

currents considerably lower than that obtained with Pt paste electrodes for a given anodic overpotential, because the electrode reaction is limited by lateral diffusion along the interface rather than by the charge transfer reaction.

Transient Behavior

Moderate time-scale effects.—The anodic and cathodic decay curves, $\eta(t)$, following current interruption behave quite differently in the reduction range than they do in the concentration-polarization range (2). Most strikingly, while the decay occurs in periods less than 10^{-2} sec for the lower overpotentials, in the reduction range the cathodic overpotential remains close to its initial value after current interruption for periods as long as 10^0 - 10^2 sec, depending on the degree of polarization, the ambient gas, and the temperature. Typical cathodic recovery curves for the reduction range are shown as solid circles in Fig. 9 on a log time scale and in Fig. 10 on a linear time scale. The time for complete recovery, τ_R , is dependent on the thickness of the electrolyte, and, in fact, increases approximately in proportion to the thickness. Thus, in Fig. 10, τ_R

is 60 and 200 sec for lines A (thickness 0.60 mm) and B (thickness 1.74 mm), respectively.

In the same polarization range, the anodic overpotential decay curve behaves abnormally, relative to its behavior at lower overpotentials (2). Starting from a positive overpotential, it decays across the zero line and then becomes negative. After reaching a maximum negative value, it then recovers to the zero line, as shown by the open circles in Fig. 9. Usually, we observe that the maximum negative value reached by the anode is close to the corresponding cathodic value at the same time, and that the subsequent course of recovery is almost the same for both electrodes. Correspondingly, the decay curve from anode to cathode (which we call the "total decay curve") stays at or close to zero during this recovery period.

The return of the anodic overpotential to zero following interruption of the current is attributed to the discharge of the double layer associated with the anodic polarization (2). The subsequent crossing of the zero line, with the anodic overpotential going substantially negative before decaying back to zero, suggests that

Fig. 9. Cathodic and anodic decay behavior in the reduction range for a CeO_2 :15% CaO electrolyte at 800°C . ● cathodic for electrolyte thickness 0.06 cm; ○ anodic for 0.06 cm; △ anodic for 0.174 cm (early part only). Note that in this figure the cathodic overpotential is shown as negative. The solid curves are calculated.

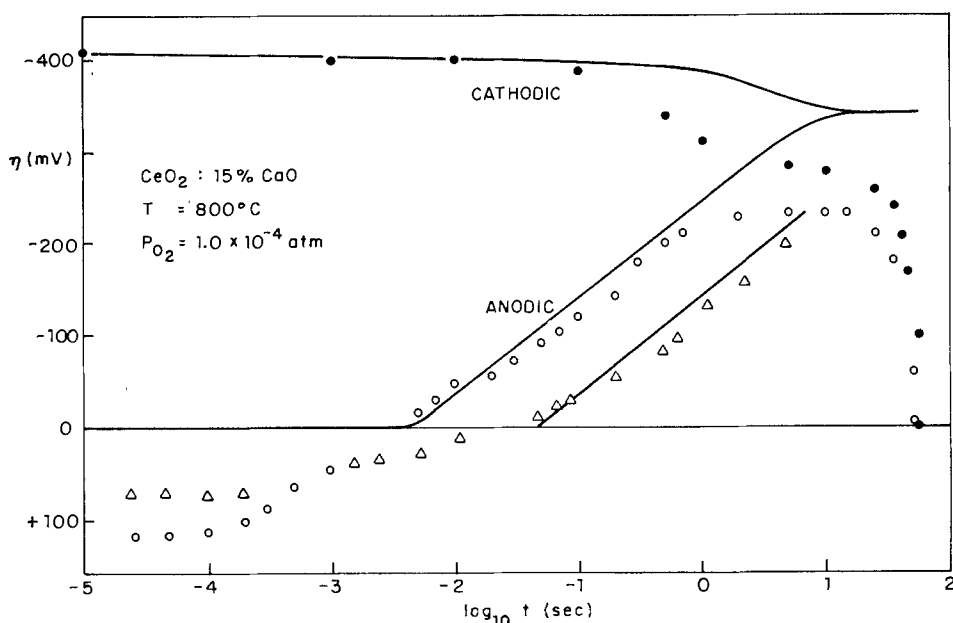
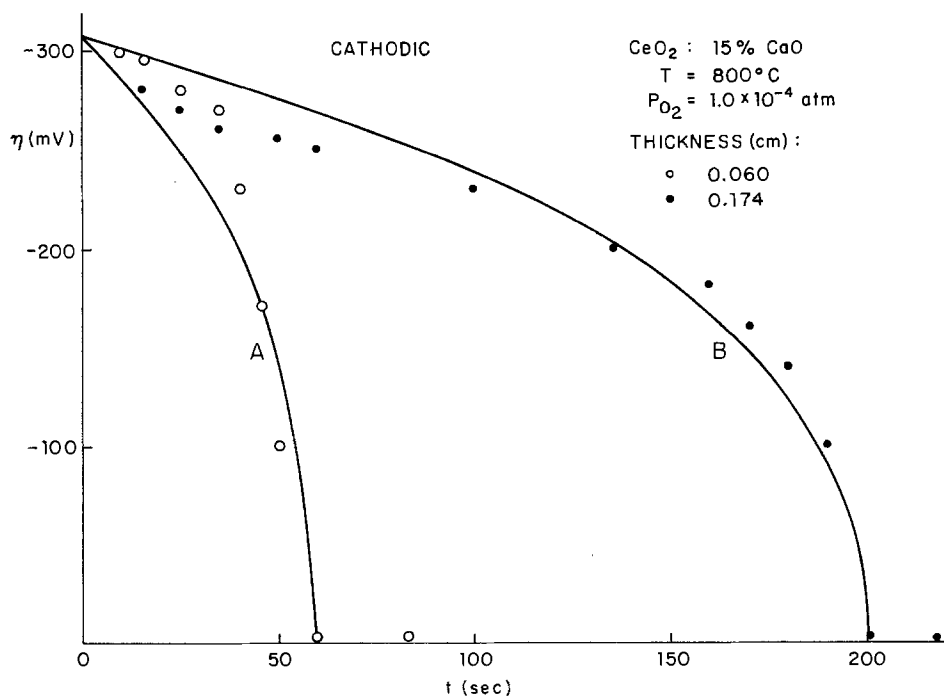


Fig. 10. Cathodic decay curves (on a linear time scale) for two different electrolyte thicknesses. Curve A is the same run as in Fig. 9. The solid curves are the fitted functions described in the text.



the oxygen activity at the anode falls below the thermal equilibrium value.

At steady state, the region of the electrolyte adjacent to the cathode is reduced, and, after the interruption of the current, the concentration of oxygen must return to its original thermal equilibrium value. The results of Fig. 9 suggest that, on a short time scale, the uptake of oxygen from the gas phase proceeds very slowly, *i.e.*, the cathode is effectively baffled from the oxygen gas. Therefore, in the meantime, oxygen diffuses across from the anode (which also has essentially no uptake of oxygen on this time scale). Thus, the concentration of oxygen at the anode will first be depleted until it reaches approximately the same value as that of the cathode, at which point diffusion will cease. This explains qualitatively why the anodic decay curve crosses over the zero line and goes negative to the point where it joins the cathodic curve. In attempting to develop this concept more quantitatively, we employ a model similar to that of Weiss (15), except that the boundary conditions involved are different.

There are two types of charge carriers inside the reduced electrolyte: oxygen vacancies and electrons, and these must diffuse together to maintain charge balance (ambipolar diffusion). Since the concentration of electrons is much smaller than that of the oxygen vacancies (when the current is not too great), the redistribution of oxygen activity is controlled by the diffusion of the electrons (16). Considering the structural arrangement of the electrodes (Fig. 1), we initially use the one-dimensional diffusion equation. Assuming $f(x, t)$ is the electron concentration at position x and time, t , Fick's equation is then given as

$$\partial f(x, t) / \partial t = D_e \partial^2 f(x, t) / \partial x^2 \quad [16]$$

D_e being the diffusion coefficient of the electrons.

For complete blocking at the electrodes, the boundary conditions at the anode ($x = L$) and cathode ($x = 0$) are

$$\partial f(0, t) / \partial x = \partial f(L, t) / \partial x = 0 \quad [17]$$

In order for the diffusion flux to be constant across the sample, the initial distribution of electron concentration must be linear along the sample and given by

$$f(x, 0) = f(0, 0) + [f_0 - f(0, 0)]x/L \quad [18]$$

where f_0 is the thermal equilibrium concentration of electrons at the anode. With these conditions, Eq. [16] can be easily solved to obtain, for $x = L$ and $x = 0$, the respective solutions

$$f\left(\frac{L}{0}, t\right) = [f_0 + f(0, 0)]/2 \pm (4/\pi^2) [f_0 - f(0, 0)] \sum_{\substack{n \\ \text{odd}}} (1/n^2) \exp(-D_e n^2 \pi^2 t / L^2) \quad [19]$$

Now, using the Nernst law together with Eq. [15] we find that the anodic and cathodic transient overpotentials (relative to a reference electrode in equilibrium) are given, respectively, by

$$\eta_a(t) = (kT/e) \ln f_0 / f(L, t) \quad [20]$$

$$\eta_c(t) = (kT/e) \ln f(0, t) / f_0 \quad [21]$$

Inserting Eq. [19] into Eq. [20] and [21] gives the desired expressions for the decay curves. For numerical computation, the ratio $j(0, 0) / f_0$ is determined from the value of the initial cathodic overpotential following interruption. This leaves only the diffusion coefficient D_e as an adjustable parameter. The fitted curves to the data of Fig. 9, both for the anode and cathode, are presented by the solid lines. This fitting was obtained with the value $D_e = 10^{-4}$ cm²/sec, which, for 800°C, is consistent with the results of a previous study (17). We see that the calculated cathodic overpotential re-

mains almost constant, decaying only slightly, while the anodic overpotential changes rapidly until it finally joins the cathodic curve. The data of Fig. 9 also show that for two different electrolyte thicknesses, $L_1 = 0.06$ cm and $L_2 = 0.174$ cm, the two anodic curves are shifted in their time scales by an amount proportional to $(L_2/L_1)^2$, as required for a diffusion process.

Figure 9 shows fair agreement between the calculated curve and the initial negative anodic data. At the tail end of the region of fitting, however, the result is poor, showing that the total number of electrons remaining at the end of this stage is lower than calculated. Possible reasons for such a departure are related to electrolyte reoxidation as well as to the occurrence of secondary diffusion out of the region of the electrodes (as will be discussed later). On the other hand, because of the porous structure of the electrodes, some lateral diffusion must be required, so that treatment in terms of one-dimensional diffusion must inevitably be too idealized.

Thus far, we have attempted to interpret only the first stage of decay curves such as those of Fig. 9. The recovery that takes place after the anodic curve has joined the cathodic is considered to be the second stage. As found in Fig. 10, the total time, τ_R , needed for recovery in this stage is approximately proportional to the thickness of the electrolyte. The simplest assumption we can make for this stage is that the rate of uptake of oxygen from the electrodes is a constant. (Clearly, this condition must break down at some point before the electrolyte is completely reoxidized.) Since, during the first stage, the concentration gradient between anode and cathode levels out, we can describe the recovery stage in terms of an average electron concentration, say $c(t)$, instead of $f(x, t)$. Thus, the equation for $c(t)$ can be given as

$$SLdc(t)/dt = -2KS \quad [22]$$

the solution for which is

$$c(t) = c(0) - (2Kt/L) \quad [23]$$

where S is the surface area of the electrode and K is the constant rate of uptake oxygen atoms per unit area of either electrode. The quantity $c(0)$ is the initial value of $c(t)$, which is obtained from Eq. [19], setting $t \rightarrow \infty$. Thus, the predicted recovery curve is

$$\eta(t) = -(kT/e) \ln \left\{ \frac{c(0) - (2Kt/L)}{f_0} \right\} \quad [24]$$

As soon as $c(t) = f_0$ the recovery process must stop. Therefore the time to complete recovery, τ_R , is given by

$$\tau_R = (L/2K) [c(0) - f_0] \simeq (L/2K) c(0) \quad [25]$$

where the last inequality holds because $c(0) \gg f_0$. At $t = \tau_R$, $\eta(t)$ must abruptly become zero.

The data of Fig. 10 have been fitted to Eq. [24] with the initial value and τ_R as the only parameters. The results of this fitting are shown by the solid lines. Considering the simplicity of the assumptions made, the fit is quite good, and the data indeed show a discontinuity in $d\eta/dt$ at $t = \tau_R$. The K values obtained for curves A and B differ slightly from each other, K for curve B being 15% smaller than that for curve A.

In order to obtain a numerical value for K , an estimate of f_0 is required. Using $D_e = 10^{-4}$ cm²/sec and the values of t_e^0 and σ_1^0 determined for this sample, allows a rough calculation of f_0 . The corresponding value of K , expressed as a current density, is ~ 4 mA/cm² which is similar in magnitude to the limiting current, I_l . This is not surprising, since both quantities are manifestations of the limiting rate at which the electrodes can furnish oxygen.

In all cases of transient behavior reported thus far, we have made every effort to keep both anode and cathode alike in both structure and geometry. If, how-

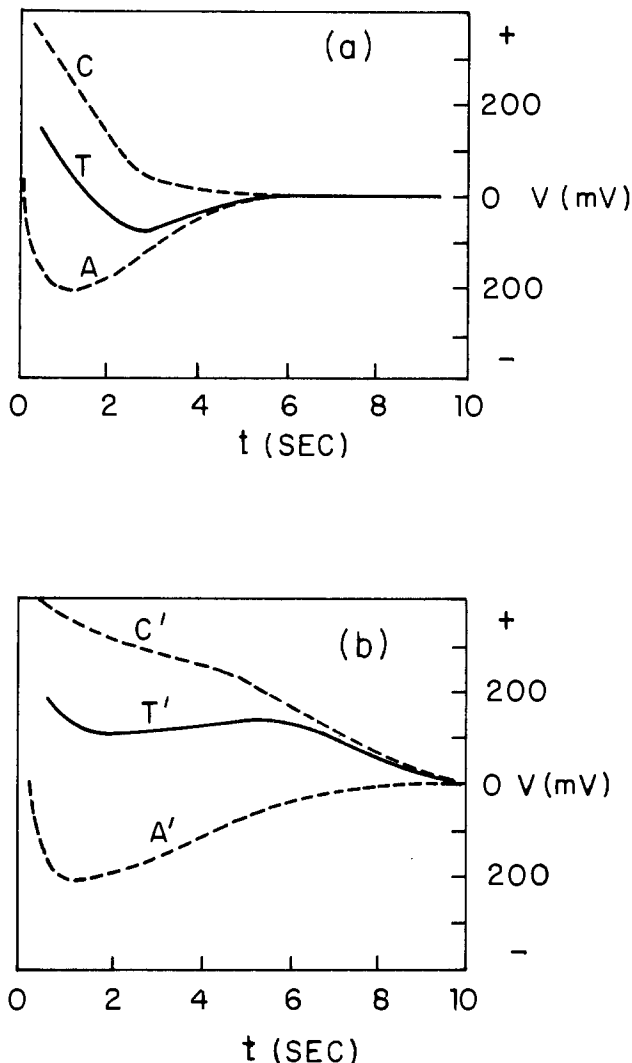


Fig. 11. Decay curves for anodic (A and A'), cathodic (C and C') and total (T and T') overpotential for a CeO_2 : 8% CaO electrolyte at 900°C and $p_{\text{O}_2} = 0.94 \times 10^{-3}$ atm. Polarization current had been 30 mA. Two electrodes are used: Pt paste and a composite (Pt paste/Pt foil): (a) case where anode is the composite electrode; (b) cathode is the composite.

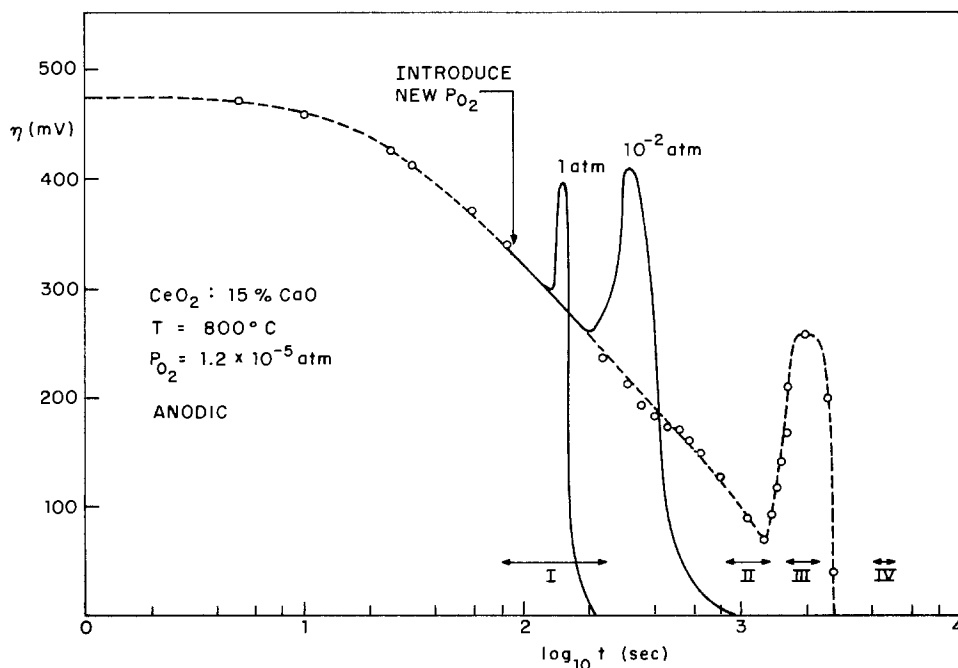
ever, one of the electrodes is baffled to the ambient oxygen gas, its recovery proceeds more slowly than that of the other one. For example, for the data of Fig. 11a, the anode was composed of two layers: platinum paste/platinum foil, while the cathode was the usual platinum paste. As shown in this figure, the second-stage recovery of line A (anodic) was much slower than that of line C (cathodic). Therefore, the total decay curve (line T) now crossed the zero line and became negative. With reversed polarity, the result is shown in Fig. 11b; the cathodic overpotential (line C') now decayed more slowly than the anodic (line A'), while the total decay curve (line T') showed a hump and did not cross the zero line. (In both cases, lines A and A' started from a positive potential, but the initial decay was so rapid that only the part of decay curve after the sign reversal can be seen.) Such results indicate that the uptake of oxygen is a property of the electrode, which functions as a catalyst. At this point we cannot say what is the rate-determining step for this process, but the similarity between K and I_1 , suggests that it may be related to adsorbed oxygen on the Pt surface.

Results such as these, especially the possibility for the total decay curve to become negative are of interest because such observations are occasionally reported (18) and questioned (19).

Long time-scale effects.—If we polarized the electrolyte at higher currents, but still in the straight line (e/kT slope) region, the decay curve for both anode and cathode could persist beyond 10^3 sec. Also, as shown in Fig. 12, the pattern of the curves changed dramatically in the tail of the decay, *viz.*, $\eta(t)$ rose to produce a hump. Both anode and cathode gave the same type of decay curve, except that the hump did not appear at exactly the same time for the two electrodes. Thus, the total decay curve, after remaining at zero for some time, rose to give a hump owing to this asymmetry.

Because the decay proceeded over such a long time, it became possible to use a small a-c signal to study the conductivity of the electrolyte at various stages. Four different regions (as marked in Fig. 12) were studied. The results are in Table II, where the parallel resistance measured at 10 Hz is listed. As shown, this resistance, R , increased steadily to region IV. This continuous increase in R suggests that reoxidation of the reduced electrolyte is taking place over the time period of the hump.

Fig. 12. Anodic decay curve for 0.174 cm thick electrolyte originally polarized to $I = 44$ mA, $\eta = 100$ mV. Points are the data for $p_{\text{O}_2} = 1.2 \times 10^{-5}$ atm after crossover to negative overpotentials. The regions I-IV refer to this data. Solid curves show the behavior observed when gases of higher p_{O_2} are introduced after 10^2 sec.



Because of the long decay time, it was also possible to study the effect of a change in the partial pressure of oxygen, by introducing new gas into the sample chamber during the course of the decay. As shown in Fig. 12, the hump could be shifted, such that the higher the p_{O_2} , the earlier it appeared. Also, the size of the hump was smaller, the higher the p_{O_2} of the introduced gas. In addition, the response of the decay to the changed gas was very much dependent on the flow rate of the gas, a greater flow rate giving the same effect as a higher p_{O_2} .

In our interpretation of the first stage of the decay curves as electronic diffusion and the second stage, or recovery, as the uptake of oxygen from the electrodes, we neglected to consider secondary diffusion, by which electrons migrate out of the region between the two working electrodes, causing partial reduction of the area adjacent to the reference electrode. This process clearly involves a longer time constant than the primary (cathode-to-anode) diffusion because the electrode separation is larger (~ 6 -10 mm as against 1 mm from cathode to anode). It is this process that we believe is responsible for the long time decay in samples carried to higher overpotentials, as in Fig. 12.

In order to see why secondary diffusion enters in this case and not in those for lower overpotentials, we make a comparison of various relevant time constants. For primary diffusion a time constant τ_D may be defined by

$$\tau_D = L^2/D_e\pi^2 \quad [26]$$

based on Eq. [19], where L is the cathode-to-anode distance. A similar quantity τ_D' , for secondary diffusion may be defined by the same expression, except that L' , the distance from reference to working electrode, replaces L . Finally, for the recovery process we have defined the time, τ_R , to complete recovery by Eq. [25]. In Table III, these three time constants are compared for three cases: A and B are the corresponding two runs in Fig. 10, while C is the run represented by open circles in Fig. 12. In the latter case, the calculation of τ_R is made using the same K value as for A and B; however, since p_{O_2} is substantially lower in this case, K should actually be lower, and therefore τ_R larger than the value calculated. For cases A and B, Table III shows that $\tau_D \ll \tau_R$, and that τ_D' is large enough that appreciable secondary diffusion is not expected before recovery is complete. This result vindicates our pre-

vious neglect of the secondary diffusion process. In case C, however, τ_R is so large [because $\eta(0)$, and therefore $c(0)$ is large], that there is sufficient time for secondary diffusion to occur prior to the recovery process. In fact, the value of τ_D' is consistent with the observed decay time in Fig. 12. Accordingly, we interpret the decay process prior to the hump in Fig. 12 as due to secondary diffusion.

It then remains to explain the hump. The fact that the time of occurrence of the hump depends on p_{O_2} (Fig. 12) and on the rate of gas flow, all suggest that the hump is related to the uptake of oxygen from the electrodes. The results of the a-c study (Table II), showing that the resistance continues to increase throughout the range of the hump, is also consistent with the idea that reoxidation of the electrolyte is taking place.

In interpreting the hump, we propose that uptake of oxygen occurs at the reference as well as the working electrodes. Since secondary diffusion is incomplete, the chemical potential of oxygen at the reference electrode is closer to that of the ambient gas than that of either the cathode or anode. Thus, the reference starts at a lower value of $c(0)$ and will reach equilibrium before the working electrodes. The result is that $|\eta|$ increases as long as the reference is being reoxidized; once it reaches equilibrium, however, the decay process continues in the usual way. Therefore, a hump is produced. A more quantitative examination of this model gives a good fit to the data of Fig. 12 for the time period $>10^3$ sec.

Summary

The results for the steady-state behavior show that the Wagner polarization cell treatment describes well the cathodic data (η_c vs. I) even though blocking of the ionic flow is incomplete. From these data, reliable values of the electronic transference number have been obtained.

The transient behavior following current interruption can be interpreted according to the following concepts:

1. Primary diffusion of electrons from cathode to anode constitutes the first stage of the decay curves, in which the anodic overpotential crosses the zero line and goes negative to join the cathodic overpotential.
2. Secondary diffusion of electrons out of the region of the working electrodes causes reduction in the region near the reference electrode. This stage only occurs if $\eta(0)$ is sufficiently high that $\tau_D' > \tau_R$.
3. Recovery of both working electrodes takes place by means of a constant rate of uptake of oxygen through the electrodes. This stage can be a monotonic decrease in $|\eta|$, or it can give rise to a hump if partial reduction of the region near the reference electrode had occurred.

Acknowledgments

The authors are deeply indebted to Dr. D. O. Raleigh whose extensive comments led to a great improvement of this paper. Part of the experimental work was carried out under a grant (DMR 76-80157) from the National Science Foundation. The later experiments and much of the interpretation was sponsored by the Department of Energy, under contract ER-78-S-02-4693.

Manuscript received June 14, 1979. This was Paper 146 presented at the Seattle, Washington, Meeting of the Society, May 21-26, 1978.

Any discussion of this paper will appear in a Discussion Section to be published in the December 1980 JOURNAL. All discussions for the December 1980 Discussion Section should be submitted by Aug. 1, 1980.

Publication costs of this article were assisted by Columbia University.

REFERENCES

1. Da Yu Wang and A. S. Nowick, *This Journal*, **126**, 1155 (1979).

Table II. Values of a-c parallel resistance measured at 10 Hz in the four regions shown on Fig. 12

(a) from anode to cathode	
Region	R (Ω)*
I	11.3
IV	102.1
(b) from reference electrode to anode	
Region	R (Ω)*
II	138
III	175
IV	413

* Not corrected for the resistance of the Pt leads.

Table III. Calculated time constants for primary diffusion (τ_D), secondary diffusion (τ_D'), and recovery (τ_R) for three cases of a CeO_2 :15% CaO electrolyte at 800°C. (In each case, L' is taken to be 8 mm, and $D_e = 10^{-4}$ cm^2/sec .)

	$\eta(0)$ (mV)	L (mm)	p_{O_2} (atm)	τ_D (sec)	τ_D' (sec)	τ_R (sec)
A	310	0.60	10^{-4}	3.6	650	60
B	310	1.74	10^{-4}	31	650	200
C	480	1.74	10^{-5}	31	650	>1255

2. Da Yu Wang and A. S. Nowick, *ibid.*, **126**, 1166 (1979).
3. R. J. Brook, W. L. Pelzmann, and F. A. Kröger, *ibid.*, **118**, 185 (1971).
4. C. J. Kevane, E. L. Holverson, and R. D. Watson, *J. Appl. Phys.*, **34**, 2083 (1963).
5. R. E. W. Casselton, *J. Appl. Electrochem.*, **4**, 25 (1974).
6. C. Wagner, in "Proc. Seventh Meeting Int. Comm. of Electrochem. Thermod. and Kinetics (CITCE) Lindau 1955," p. 361, Butterworths, London (1957).
7. H. L. Tuller and A. S. Nowick, *This Journal*, **122**, 255 (1975).
8. J. W. Patterson, E. C. Bogren, and R. A. Rapp, *ibid.*, **114**, 752 (1967).
9. R. N. Blumenthal, F. S. Brugner, and J. E. Garnier, *ibid.*, **120**, 1230 (1973).
10. F. A. Kröger, "The Chemistry of Imperfect Crystals," Vol. III, 2nd ed., p. 147, North-Holland Publishing Co., Amsterdam (1974).
11. T. H. Etsell and S. N. Flengas, *This Journal*, **119**, 1 (1972).
12. A. V. Joshi and C. C. Liang, *J. Phys. Chem. Solids*, **36**, 927 (1975).
13. T. Jow and J. B. Wagner, Jr., *This Journal*, **125**, 613 (1978).
14. Da Yu Wang and A. S. Nowick, Paper 3 presented at The Electrochemical Society Meeting, Boston, Massachusetts, May 6-11, 1979.
15. K. Weiss, *Z. Phys. Chem. [N.F.]*, **59**, 242 (1968).
16. C. Wagner, *J. Phys. Chem. Solids*, **29**, 1925 (1968).
17. H. L. Tuller and A. S. Nowick, *ibid.*, **38**, 859 (1977).
18. E. L. Holverson and C. J. Kevane, *J. Chem. Phys.*, **44**, 3692 (1966); *J. Appl. Phys.*, **38**, 5421 (1967).
19. R. N. Blumenthal and B. A. Pinz, *J. Appl. Phys.*, **38**, 2376 (1967).

The Electrochemical Behavior of Aluminum in the Low Temperature Molten Salt System n Butyl Pyridinium Chloride: Aluminum Chloride and Mixtures of This Molten Salt with Benzene

J. Robinson¹ and R. A. Osteryoung^{*2}

Department of Chemistry, Colorado State University, Fort Collins, Colorado 80523

ABSTRACT

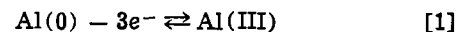
The aluminum deposition and stripping processes at tungsten, platinum, and glassy carbon electrodes in the low temperature molten salt system, n butyl pyridinium chloride:aluminum chloride, and the 50 volume percent (v/o) mixture of this molten salt with benzene have been investigated, using a variety of electrochemical techniques. At all three electrodes, and in both solvent systems, the deposition reaction in slightly acidic melts, the reduction of Al_2Cl_7^- ions, was found to involve a nucleation process while at the tungsten and platinum electrodes underpotential deposition was also observed. Reduction of the n butyl pyridinium cation was found to occur at $-1.1\text{V vs. Al}(2:1 \text{ melt})$ which is positive of the reduction potential of AlCl_4^- ions and therefore aluminum deposition in basic melts was not observable. Studies of the stripping of aluminum from inert substrates showed that aluminum is very slowly corroded in acidic melts, and melt-benzene mixtures, by traces of oxidizing impurities while in basic systems aluminum reduces the n butyl pyridinium cation. Potentiometric titration of the 50 v/o melt-benzene mixture showed that the acid-base properties of this system are defined, as in the pure melt, by the equilibrium



with an equilibrium constant of 2.2×10^{-13} at 30°C .

Chloroaluminate melts (alkali metal chloride- AlCl_3 mixtures), in view of their interesting acid-base properties, have recently received considerable attention from molten salt chemists, and a number of reports of electrochemical and spectroscopic studies of both organic, and inorganic, species in these media have appeared in the literature. One of the most thoroughly investigated areas has been the electrochemistry of aluminum, both at aluminum electrodes (1-5) and also at foreign substrates (6). Initial reports of the anodic dissolution of aluminum in molten $\text{NaCl}:\text{AlCl}_3$ (7, 8) indicated that at low current densities the observed current efficiencies, as determined by weighing the electrode, were significantly greater than required

for the three electron oxidation described by Eq. [1]



This behavior was attributed to the formation of univalent aluminum which was in some way stabilized by the melt. A subsequent study (5) has however shown that the dissolution current efficiencies in excess of 100% were in fact caused by corrosion of the aluminum electrode by impurities in the melt, and that by careful melt purification procedures current efficiencies very close to 100% can be achieved for both the aluminum deposition and the anodic stripping process.

It is well known (9) that as the alkali metal chloride: AlCl_3 ratio in a chloroaluminate melt is varied the nature of the aluminum containing ion changes; in basic melts (excess alkali metal halide) mainly AlCl_4^- ions are present whereas in acid melts the Al_2Cl_7^- ion

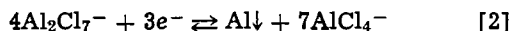
* Electrochemical Society Active Member.

¹ Present address: Department of Chemistry, University of Southampton, Southampton, SO9 5NH, England.

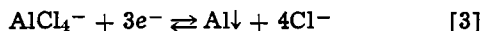
² Present address: Department of Chemistry, State University of New York at Buffalo, Buffalo, New York 14214.

Key words: anode, voltammetry, metals.

becomes predominant. Letisse and Tremillon (1) have proposed that aluminum deposition is possible from either of these ions. In acidic melts the reaction is

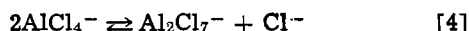


whereas in basic melts it becomes



Rolland and Mamantov (6) have observed both these deposition reactions at glassy carbon, platinum, and tungsten electrodes and have made a thorough study of the reduction of Al_2Cl_7^- ions in slightly acidic melts. They have shown that nucleation processes are important at all three electrodes and also that alloy formation occurs on the platinum electrode.

In this laboratory we have recently been particularly interested in the development of low temperature nonprotonic molten salt systems analogous to the alkali metal chloroaluminates. This work has shown that suitable solvents can be made from mixtures of alkyl pyridinium halides and aluminum halides. The first such system studied was the 2:1 AlCl_3 :ethyl pyridinium bromide mixture, which was molten at room temperature, and it was demonstrated that this solvent, and its mixtures with benzene, could be successfully used for organic and organometallic electrochemistry (10-12), as well as for photochemical investigations (13). Unfortunately as the AlCl_3 :ethyl pyridinium bromide ratio was varied from 2:1 the melting point of this system increased sharply, the mixture being molten at room temperature only for the 2:1 system. It has recently been shown (14) that mixtures of *n* butyl pyridinium chloride (BuPyCl) and AlCl_3 are molten at, or near, room temperature for the entire composition range from 2:1 to 0.75:1 (AlCl_3 :BuPyCl). This system should therefore be very useful for studying the Lewis acidity dependent chemistry and electrochemistry of a variety of inorganic species and of organic species which are too volatile to be studied in the alkali metal chloroaluminates. As with these latter melts, variations in the composition of the low temperature molten salt system cause changes in the aluminum-containing species in the melt. This behavior has been investigated by Raman spectroscopy (15) and potentiometric techniques (16) and it has been shown that the acid-base properties of the melt are fully described by the equilibrium in Eq. [4] (16)



for which the equilibrium constant, K , was shown to be less than 3.83×10^{-13} at 30°C. The exact determination of K from potentiometry with an Al electrode is precluded as Al reduces the butylpyridinium cation in basic melts; however use of a NiCl_2 electrode (17) to measure the Cl^- ion concentration in basic melts suggests that the true value of K lies close to the above value (18). This very low value for K implies that in the 1:1 melt nearly all the aluminum is present as AlCl_4^- ions with only very small concentrations of Cl^- and Al_2Cl_7^- ions being present; any AlCl_3 added to a 1:1 melt complexes with AlCl_4^- ions, according to Eq. [4] to form Al_2Cl_7^- ions such that in the 2:1 system the Al is present almost entirely as Al_2Cl_7^- . Any BuPyCl added to a 1:1 melt results in an increase in the free Cl^- ion concentration. This is in contrast to the behavior observed in alkali metal chloroaluminates where large concentrations of free Al_2Cl_6 molecules are also present in acid melts (9).

Low temperature baths for the electrolytic deposition of aluminum have long been of interest and Hurley and Weir (19) have shown that bright aluminum deposits, several tenths of a millimeter thick, can be formed by electrolysis of a 2:1 mixture of AlCl_3 and ethyl pyridinium bromide to which either benzene or toluene has been added until a two-phase system

starts to form. By careful engineering and the use of addition agents the deposition of even thicker layers is possible (20). Recent work in this laboratory (21) has shown that the addition of benzene to AlCl_3 :BuPyCl melts results in an increase in the conductivity of the medium due to a sharp reduction in the viscosity, but ^1H and ^{13}C NMR studies (21) indicate that the benzene does not complex with any species in the melt. This present paper is concerned with an investigation of the electrochemical behavior of Al in the AlCl_3 :BuPyCl and the 50 v/o benzene- AlCl_3 :BuPyCl systems. A variety of electrochemical techniques have been used including cyclic and pulse voltammetry, potentiometry, and coulometric techniques at three different electrodes, tungsten, glassy carbon, and platinum. The results obtained are compared to those observed in the alkali metal chloroaluminates.

Experimental

The procedure for the preparation of *n* butyl pyridinium chloride from *n* butyl chloride and pyridine (Fisher ACS) has been given in a previous publication (14) and consists essentially of refluxing the two reactants together and purifying the resulting product by recrystallization from acetonitrile-ethyl acetate mixtures. The AlCl_3 :BuPyCl melts are then prepared by adding carefully sublimed AlCl_3 (Fluka A.G. iron-free) to the BuPyCl. This mixing is highly exothermic and care must be taken to ensure that the temperature does not rise above 100°C or decomposition may occur. The melt-benzene mixtures were drilled to permit the introduction of the reference and secondary electrode compartments which were isolated from the bulk of the melt by fine porosity glass frits. Holes were also drilled in the cap for the working electrode and the thermocouple well. Unless otherwise stated the reference electrode was an Al wire (5N Alfa inorganics) immersed in a 2:1 AlCl_3 :BuPyCl melt, and all potentials are quoted with respect to this electrode. The secondary electrode was also a coiled Al wire. The essential details of the experimental techniques, electrochemical instrumentation, construction of electrodes, and operation of the dry box (Vacuum Atmospheres Company), in which all experiments were carried out have been presented in an earlier publication (22).

In order to achieve reproducible electrochemical results, great care had to be taken in preparing the electrode surfaces. All the electrodes were polished to a mirror-like finish using alumina (Type B Fisher), washed and dried, and then transferred into the dry box where they were again polished on alumina to remove any surface oxide films. The platinum and glassy carbon electrodes were then introduced into the melt and held at 1.5V vs. Al for about 20 min prior to commencing experiments. To obtain reproducible results on the tungsten electrode, the electrode potential was cycled into aluminum deposition several times before voltammograms were recorded.

Previous studies (15, 16) indicate that any AlCl_3 added to a 1:1 melt will complex with tetrachloroaluminate ions to form Al_2Cl_7^- . Melts of known Al_2Cl_7^- concentration were therefore prepared by adding volumes of a 2:1 melt (all aluminum present as Al_2Cl_7^-) to a 1:1 melt or a 1:1 melt to which 50% by volume of benzene had been added.

The titration of Cl^- ions in a 50 v/o benzene-melt mixture with Al_2Cl_7^- ions was carried out in the following manner. A 46:54 AlCl_3 :BuPyCl melt was prepared and benzene was added to give a 50 v/o mixture (attempts to make 50 v/o benzene mixtures with melts more basic than this resulted in the precipitation of BuPyCl). An Al indicator electrode was then introduced into the melt and the potential between this and an Al reference electrode in a 50 v/o benzene-2:1 melt was measured using a high impedance voltmeter. Weighed amounts of 50 v/o benzene-2:1

melt were then added and the potential difference between the indicator and reference electrodes was recorded after each addition. From this data the potentiometric titration curve was constructed.

Results and Discussion

Potentiometric titration of the benzene-containing melt.—The titration of Cl^- with Al_2Cl_7^- in chloroaluminates has proved a useful technique for determining the equilibria that govern the acid-base properties of these melts (9, 16). It was decided therefore that this would be a useful approach for investigating the properties of AlCl_3 :BuPyCl melt diluted to 50 v/o with benzene. Figure 1 shows such a potentiometric titration which was performed in such a way as to maintain the volume percentage of benzene constant. The circles represent the experimental points and the solid line is the 'best fit' theoretical curve, *vide infra*.

The equilibrium potential of an Al wire in an acid melt is determined by the equilibrium in Eq. [2] and the potential difference between two Al wires in melts of different composition is given by Eq. [5]

$$\Delta E = \frac{4}{3} \frac{RT}{F} \ln \frac{[\text{Al}_2\text{Cl}_7^-]_1}{[\text{Al}_2\text{Cl}_7^-]_2} + \frac{7}{3} \frac{RT}{F} \ln \frac{[\text{AlCl}_4^-]_2}{[\text{AlCl}_4^-]_1} \quad [5]$$

while a similar expression exists for Al wires in basic melts. If it is assumed that the benzene only dilutes the melt and does not complex with any of the species present it is possible, from the experimental data of Fig. 1 and Eq. [5], to calculate a value for the equilibrium constant, K , for the equilibrium described by Eq. [5]. The value of K determined in this way was 2.2×10^{-13} , which is very similar to the value determined for the pure AlCl_3 :BuPyCl melt (16). The solid line in Fig. 1 is the potentiometric curve calculated using the above value for K ; the agreement is excellent in the acid region and fairly good for basic melts. The experimental potential values for the basic melts were found to be rather unstable since, as in the pure melt the Al wire indicator electrode reduces the melt. The reduction potential of the melt is -1.1V vs. Al and therefore all experimental potentials greater than this (the first five points of Fig. 1) represent mixed potentials; thus, as with the pure melt the calculated value for K is only an upper limit. [The mechanism of the melt reduction process will be the subject of a future publication (23).]

That the potentiometric data can be fitted successfully using the single equilibrium in Eq. [4] provides proof that the assumption that the benzene is not involved in any complexation equilibria with any of the aluminum-containing ions or Cl^- is justified. Further support for this assumption comes from the potential difference between Al wires in a 2:1 melt and a 50 v/o

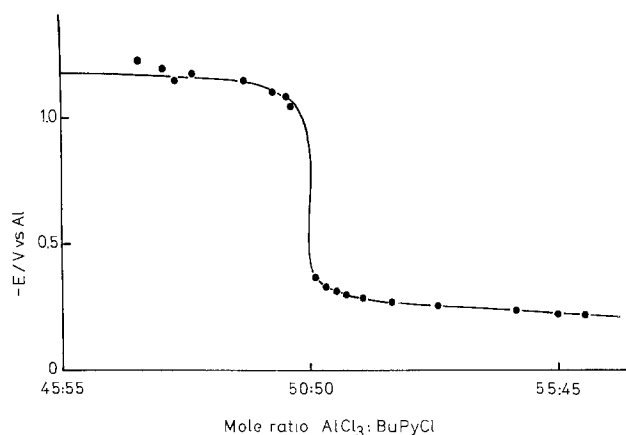


Fig. 1. The potentiometric titration of Al_2Cl_7^- with Cl^- in the 50 v/o benzene- AlCl_3 :BuPyCl system at 30°C .

benzene-2:1 melt mixture which is 12 ± 1 mV; assuming that the liquid junction potential is negligible (using the redox potential of the ferrocene-ferrocinium couple as a reference it appears that this assumption is justified) the experimental potential difference agrees very well with the value of 13 mV calculated for the potential difference between an Al wire in a 2:1 melt and an Al wire in a melt in which the concentrations of Al_2Cl_7^- , AlCl_4^- and Cl^- ions are half their values in the 2:1 system. On the basis of this evidence it can be concluded that any AlCl_3 added to a 50 v/o benzene-1:1 melt will complex with AlCl_4^- to form Al_2Cl_7^- ions as in the pure melt.

The aluminum deposition reaction.—The deposition behavior observed in the pure melt and the melt + benzene was qualitatively the same and therefore the two solvents will be discussed simultaneously. Figure 2 shows a typical cyclic voltammogram for the deposition of aluminum at a tungsten electrode in a slightly acidic melt. The large peak observed at -0.43V (I) can be attributed to the reduction of Al_2Cl_7^- ions. Table I shows the dependence of the peak current and peak potential (at a sweep rate of 100 mV sec^{-1}) of this peak on the concentration of Al_2Cl_7^- ions. It can be seen that the peak current is proportional to the concentration of this species while, as predicted for the formation of an insoluble product, the peak potential varies linearly with $\log[\text{Al}_2\text{Cl}_7^-]$. The peak labelled II corresponds to the anodic stripping of the Al deposit. This behavior is essentially the same as was observed by Rolland and Mamantov (6) in the NaCl - AlCl_3 system except that in the present case there is also a small peak, III, positive of the main deposition process and a corresponding stripping wave IV. The nature of these peaks is more readily investigated when the potential sweep is restricted to the potential region of peaks III and IV and is not permitted to go into bulk Al deposition; Fig. 3 shows such voltammograms at various sweep rates. It can be seen that the peak heights are directly proportional to the sweep rate and it was also observed that provided the melt remained acidic the peak height, at a fixed sweep rate, was independent of the concentration of Al_2Cl_7^- . When the melt was made basic the peaks III and IV disappeared. From this behavior it can be concluded that these peaks correspond to the formation and stripping of a

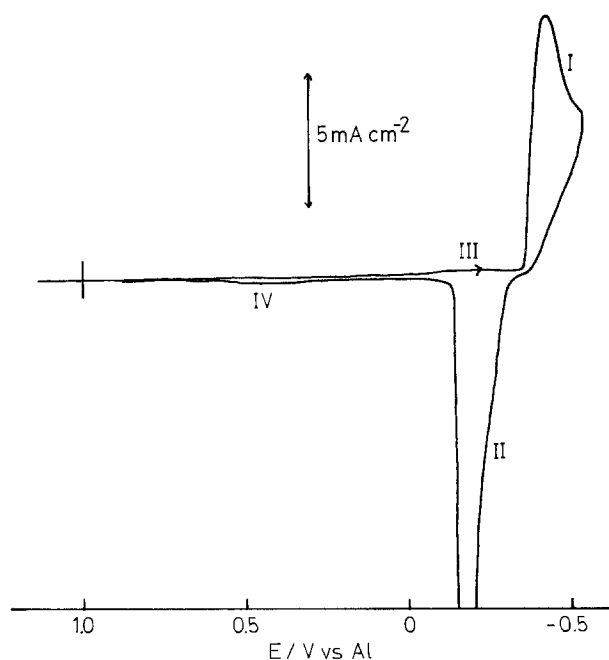


Fig. 2. Cyclic voltammogram at a tungsten electrode of $2.32 \times 10^{-1}\text{M}$ Al_2Cl_7^- in the AlCl_3 :BuPyCl melt at 60°C . Sweep rate = 0.1 V sec^{-1} .

Table I. The concentration dependence of the cyclic voltammetry peak current and peak potential for the deposition of Al from Al_2Cl_7^- on a tungsten electrode in a $\text{AlCl}_3:\text{BuPyCl}$ melt at 60°C . The sweep rate was 100 mV sec^{-1}

$[\text{Al}_2\text{Cl}_7^-]/\text{M} \times 10^2$	$i_p/\text{mA cm}^{-2}$	E_p/V
0.60	0.25	-0.575
3.08	1.34	-0.515
5.29	2.48	-0.480
7.49	3.50	-0.455
11.16	5.22	-0.435
15.9	7.13	-0.425
32.0	14.20	-0.395

surface layer. Since the activity of the aluminum metal is not fixed at the start of the reduction process it is possible that underpotential deposition, i.e., deposition at potentials positive of the bulk deposition, can occur. The charge, Q_m , under either of the peaks III or IV is approximately $2.4 \times 10^{-4} \text{ C cm}^{-2}$, which if it is assumed that peak III corresponds to the underpotential deposition of Al accounts for about 1/3 of a monolayer (this value was calculated assuming the electrode to be perfectly smooth, i.e., to have its geometric area. Any roughness would reduce the calculated degree of coverage). It therefore appears that a surface phase is formed which consists either of a 1/3 of a monolayer of Al or alternatively a greater degree of surface coverage occurs but only partial charge transfer takes place.

A similar type of behavior is observed at platinum electrodes, Fig. 4, except that now the underpotential deposition process appears as a slowly rising current prior to bulk deposition rather than a distinct peak. The behavior at platinum electrodes is also different in the respect that the underpotential deposition corresponds to several monolayers of aluminum and if the potential is held at a value corresponding to the underpotential deposition region for long periods of time the number of monolayers deposited can be increased somewhat. It is probable that this process at platinum electrodes corresponds therefore to alloy formation. A similar conclusion was reached concerning the deposition of Al from $\text{AlCl}_3:\text{NaCl}$ melts at platinum electrodes (6). No underpotential deposition processes were observed at glassy carbon electrodes.

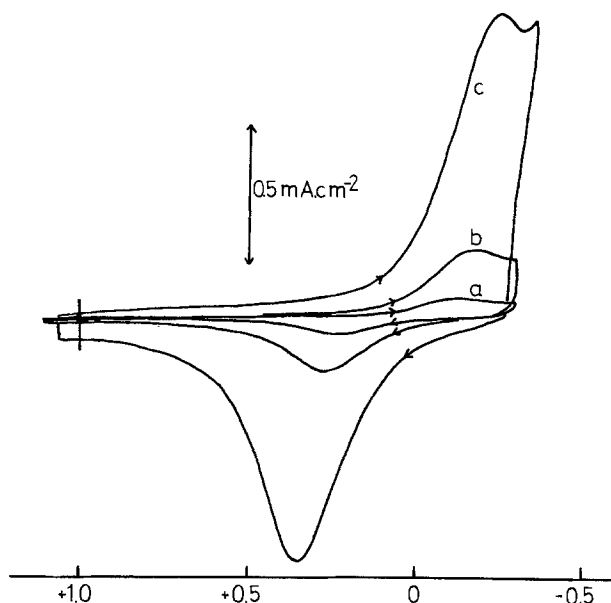


Fig. 3. Cyclic voltammograms at a tungsten electrode of $2.32 \times 10^{-1} \text{ M Al}_2\text{Cl}_7^-$ in the $\text{AlCl}_3:\text{BuPyCl}$ melt at 60°C . Sweep rates (a) 0.05 V sec^{-1} ; (b) 0.2 V sec^{-1} ; (c) 1 V sec^{-1} .

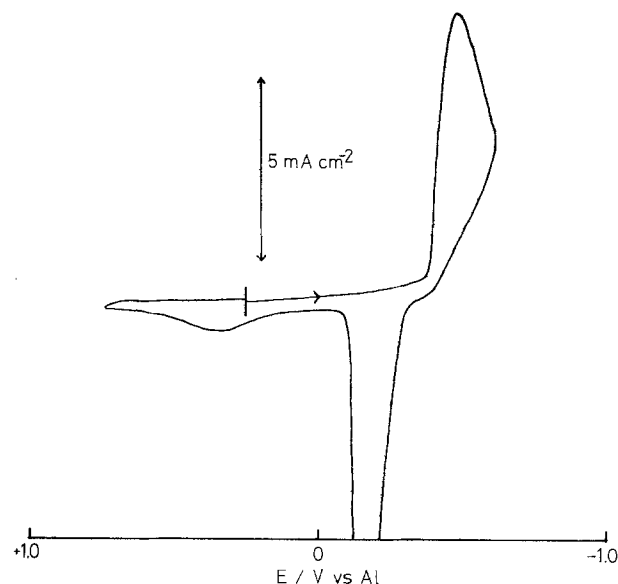


Fig. 4. Cyclic voltammogram at a platinum electrode of $1.72 \times 10^{-1} \text{ M Al}_2\text{Cl}_7^-$ in the $\text{AlCl}_3:\text{BuPyCl}$ melt at 60°C . Sweep rate = 0.1 V sec^{-1} .

Analysis of the voltammograms at all three electrodes and in both solvent systems shows that the peak currents for bulk Al deposition were proportional to the concentration of Al_2Cl_7^- ions and the value of the peak potential became more negative as the sweep rate increased. As shown in Table II the value of the function $i_p/\nu^{1/2}$ was a constant at slow sweep rates (less than 1 V sec^{-1}) but decreased with increasing sweep rate. This type of behavior is identical to that observed by Rolland and Mamantov (6) in NaAlCl_4 and was attributed to the presence of nucleation processes in the deposition reaction. That this is true can readily be shown by chronoamperometry, *vide infra*, and also by the potential difference between an Al wire in the melt and the potential at which the cyclic voltammetry current increases rapidly due to bulk Al deposition. The values of this voltage difference, the nucleation overpotential, are 40 mV for tungsten and about 80 mV for platinum and glassy carbon in the pure melt at a temperature of 60°C , and are between 40 and 70 mV higher in the melt + benzene. These overpotentials are significantly greater than those observed in $\text{AlCl}_3:\text{NaCl}$ melts at 175°C (6). From the peak currents at low sweep rates ($<500 \text{ mV sec}^{-1}$), assuming that the deposition reaction proceeds according to Eq. [2], it is possible to calculate the value of the diffusion coefficient, D , of Al_2Cl_7^- . This calculation was made assuming that the peak corresponds to the reversible formation of an insoluble product and that the electrodes had their geometric areas. The values

Table II. The sweep rate dependence of the function $i_p/\nu^{1/2}$ for the deposition of Al at tungsten, platinum, and glassy carbon electrodes from a $\text{AlCl}_3:\text{BuPyCl}$ melt at 60°C containing $1.56 \times 10^{-1} \text{ M Al}_2\text{Cl}_7^-$

$\nu/\text{V sec}^{-1}$	$i_p/\nu^{1/2}/\text{mA cm}^{-2} \text{ V}^{-1/2} \text{ sec}^{1/2}$		
	Tungsten	Platinum	Carbon
0.01	20.9	25.4	17.9
0.02	21.1	25.5	17.9
0.05	21.0	25.8	18.2
0.1	21.1	25.6	18.2
0.2	21.0	25.7	18.2
0.5	20.9	25.1	18.1
1.0	21.0	25.2	17.9
2.0	19.8	23.6	16.6
5.0	17.7	21.7	15.4
10.0	16.1	20.3	14.2

of D calculated from the data obtained at the three different electrodes in the melt, and in the melt-benzene mixture, are given in Table III. It can immediately be seen that there is a lack of agreement between the values obtained at the three electrodes for both solvents. Similar behavior was observed for the D values calculated for Al_2Cl_7^- ions in NaAlCl_4 at 175°C (6) and was attributed to the presence of the nucleation process. The difference in the D values calculated for the melt and the melt + benzene is very similar to the difference found for the diffusion coefficient of ferrocene in pure 2:1 AlCl_3 :ethyl pyridinium bromide and the 50 v/o benzene-melt mixture (11). Higher values are observed in the benzene mixtures due to the much lower viscosity of this medium compared to the pure melt (21).

It can be seen in Table III that no value of D was determined when using glassy carbon electrodes in the melt-benzene mixtures. This is because reproducible cyclic voltammograms could not be recorded. This was also true of the pure melt at 40°C , with the glassy carbon electrodes, but increasing the temperature to 60°C appeared to overcome this problem and therefore all experiments in the pure melt were carried out at this temperature. A lower temperature had to be used for the melt-benzene mixtures to minimize the benzene evaporation losses. It was also observed that the glassy carbon electrode had to be maintained at a potential of about 1.5V for at least 15 min between voltammograms if reproducible results were to be obtained. This presumably allows the electrode surface to return to its initial state, a process which was accelerated by increasing the temperature. The tungsten and platinum electrodes did not require such prolonged treatment between experiments, about a minute sufficing.

As was stated earlier, chronoamperometry provides an excellent means of observing nucleation processes. At all three electrodes, rising transients were observed in both the melt and the melt + benzene when the electrode potentially was pulsed cathodically from a value of 1.0V to a value corresponding to Al deposition, indicating that the Al deposition at all the electrodes involves a nucleation step. Figure 5 shows such transients in AlCl_3 :BuPyCl melt at the three electrodes for the same overpotential while Fig. 6 shows the result of analyzing the rising portions of some of these transients at a tungsten electrode in a slightly acidic melt-benzene mixture. It can be seen that the current varies linearly with $t^{1/2}$ which indicates that instantaneous three-dimensional nucleation is occurring followed by hemispherical diffusion controlled growth of the nuclei (24). Similar behavior was observed in the pure melt and with the other two electrodes. From Fig. 5 it can be seen that the time between the application of the pulse and the current maximum, t_{max} , was greatest for the glassy carbon electrode and least for the tungsten; the t_{max} values observed in the benzene-melt mixture were about twice those observed in the pure melt at the same overpotential.

At times greater than t_{max} the current shows the usual i proportional to $t^{-1/2}$ behavior and from a series of such chronoamperograms at a tungsten electrode it is possible to construct pulse voltammograms as is shown in Fig. 7 for the pure melt. (The larger nucleation effects observed at platinum and carbon electrodes

Table III. Diffusion coefficient values, D , for the Al_2Cl_7^- ion calculated from cyclic voltammetry

Electrode	Melt (60°C) $D \times 10^7/\text{cm}^2 \cdot \text{sec}^{-1}$	Melt + benzene (30°C) $D \times 10^6/\text{cm}^2 \cdot \text{sec}^{-1}$
Tungsten	4.26	1.09
Glassy carbon	3.67	
Platinum	5.19	1.17

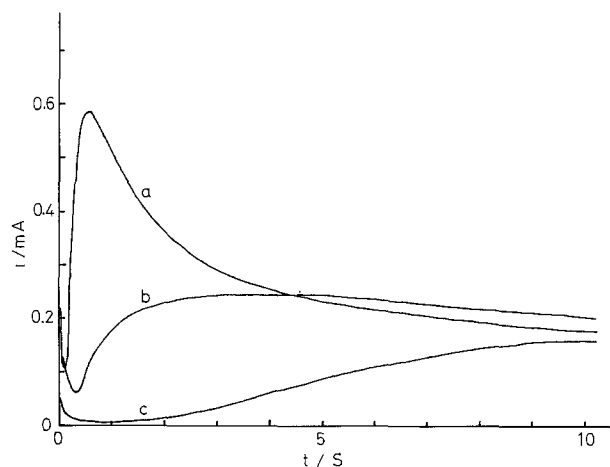


Fig. 5. Chronoamperograms for Al deposition from AlCl_3 :BuPyCl at 60°C . The electrode materials were: (a) tungsten (0.00785 cm^2), (b) platinum (0.0612 cm^2), and (c) glassy carbon (0.0707 cm^2). The current axis for the tungsten electrode has been expanded by a factor of 10. The Al_2Cl_7^- concentration was $3.6 \times 10^{-1} \text{ M}$. The potential step was from +1.0V to an overpotential of -85 mV .

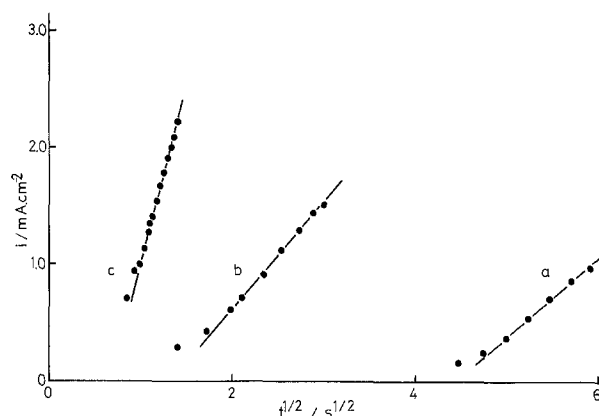


Fig. 6. i vs. $t^{1/2}$ plots for chronoamperometric data obtained at a tungsten electrode in the 50 v/o benzene- AlCl_3 :BuPyCl system at 30°C . The Al_2Cl_7^- concentration was $1.13 \times 10^{-1} \text{ M}$ and the overpotentials were (a) 80 mV ; (b) 100 mV ; and (c) 120 mV .

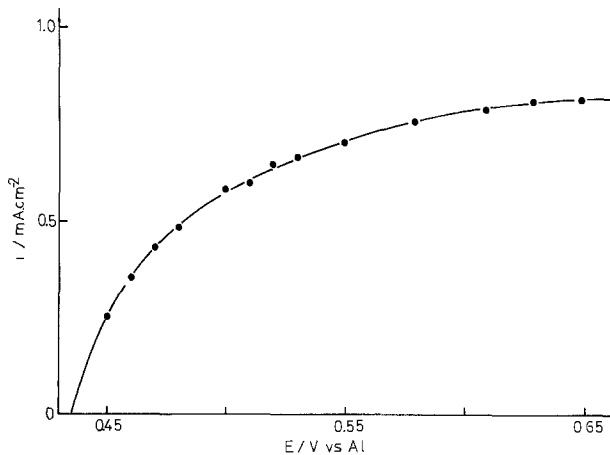


Fig. 7. Reconstructed pulse voltammogram at a tungsten electrode in a solution of $1.17 \times 10^{-1} \text{ M}$ Al_2Cl_7^- in the AlCl_3 :BuPyCl melt at 60°C . The pulse length was 17.5 sec .

and in the melt-benzene mixture precluded the construction of voltammograms for these conditions.) The shape of this curve is as would be predicted for the deposition of an insoluble product and a plot of $\log(i_d - i)$ vs. E (where i is the current at the potential E and i_d is the limiting plateau current) is linear

with a slope of 144 ± 2 mV. At 60°C RT/F has a value of 66 mV therefore the observed slope corresponds to an αn_α value of 0.46. In the $\text{AlCl}_3:\text{NaCl}$ melt at 175°C the deposition reaction was, on the basis of the pulse voltammetric data, found to be perfectly reversible; the quasi reversibility found in the $\text{AlCl}_3:\text{BuPyCl}$ system is probably in part due to the lower temperature of the solvent. At potentials corresponding to the plateau current the current at the three electrodes shows a linear dependence on $t^{-1/2}$, for pulse times greater than about 1 sec and less than about 20 sec, indicating that the process is diffusion controlled (the high viscosity of these molten salts permits diffusion control to be maintained for much longer times than in more conventional solvents before convection effects are observed). From these straight line plots it is possible to calculate the value of D for Al_2Cl_7^- ions. The values calculated for the three electrodes in both solvents are given in Table IV. As observed in the cyclic voltammetric results, there are differences in the values calculated for the three electrodes, and also between the values calculated from the chronoamperometry and cyclic voltammetry for the same electrode. The values of D calculated from diffusion controlled $i-t$ transients (those showing linear i vs. $t^{-1/2}$ behavior) should not be affected by nucleation effects. The reason for the poor agreement between the values obtained with the different electrodes is not known.

It will have been observed from the above discussion that the behavior at glassy carbon electrodes is rather irreproducible at temperatures below 60°C whereas this was not true of the other electrode materials studied. In previous studies (14) where both the reactant and product were soluble in the melt this problem was not, however, observed. Even at temperatures above 60°C it was required to hold the glassy carbon electrode at 1.0V for long periods to achieve reproducible behavior. This pretreatment presumably removed any oxide films, adsorbed oxygen, or previously deposited Al from the electrode surface. The lack of reproducible behavior at the lower temperatures is probably due to incomplete removal of these layers. In view of this evidence it is perhaps better to use tungsten and platinum electrodes when studying deposition processes in these media.

The aluminum stripping reaction.—While studying the $\text{NaCl}:\text{AlCl}_3$ system Gale and Osteryoung (5) employed a totally electrochemical method for investigating the anodic stripping efficiencies of Al. A known amount of Al was deposited on an inert electrode and this was then stripped off at known current densities. The stripping time was determined by monitoring the electrode potential on a $y-t$ recorder. While the Al was being stripped the electrode potential changed very little but when this process was complete, the potential rose rapidly to that of Cl_2 evolution. The transition time, τ , was determined from the potential-time curves by extrapolation of the maximum gradient value at the completion of the stripping. This same technique was used in the present work to investigate the Al stripping in the $\text{AlCl}_3:\text{BuPyCl}$ system. Aluminum was plated on the tungsten electrode at $10 \mu\text{A}$ for 100 sec and then it was immediately stripped off at anodic currents of 50, 20, 10, 5, 2, and $1 \mu\text{A}$. The apparent stripping efficiencies determined in this way are given in Table V, as percentages of the deposition charge, both for the pure 2:1 $\text{AlCl}_3:\text{BuPyCl}$ melt and the 50 v/o

Table V. Variation of aluminum anodic stripping efficiencies, as percentage of the cathodic deposition charge,* with stripping current density at tungsten electrodes

Stripping current density/ mA cm^{-2}	Melt (60°C) $\tau/\%$	Melt + benzene (30°C) $\tau/\%$
6.37	99.1	99.5
2.54	99.0	99.5
1.27	98.6	99.0
0.637	98.0	97.7
0.254	95.0	96.5
0.127	93.7	95.0

* 0.127 C cm^{-2} ($1.27 \text{ mA} \cdot \text{cm}^{-2}$ plate for 100 sec).

2:1 melt mixture. At high stripping current densities the stripping charge as a percentage of the deposition charge is close to 100% but on reducing the stripping current the percentage drops. A similar reduction in this percentage was observed in the $\text{NaCl}:\text{AlCl}_3$ system (5) and was attributed to corrosion processes (the lower stripping currents require longer times and hence more corrosion can occur). It was readily shown that similar corrosion was occurring in the low temperature systems. Aluminum was deposited on the tungsten electrode at $10 \mu\text{A}$ for 100 sec and the electrode was then left on open circuit for periods of 500, 1000, and 2000 sec before stripping at an anodic current of $10 \mu\text{A}$. The stripping charges as percentages of the deposition charge were 95.7, 93.7, and 89.5, respectively, for the pure melt and 97.5, 96.5, and 94.5 for the melt + benzene. The above results imply that when left for long periods of time impurities in the melt will corrode Al, the corrosion rate in the 2:1 $\text{AlCl}_3:\text{BuPyCl}$ melt being $2.1 \times 10^{-11} \text{ moles cm}^{-2} \text{ sec}^{-1}$ and for the melt + benzene $1.1 \times 10^{-11} \text{ moles cm}^{-2} \text{ sec}^{-1}$. That the corrosion rate in the melt + benzene is approximately one half the value obtained for the pure melt suggests that the benzene does not introduce any corroding impurities.

All the above corrosion results refer to the tungsten electrode and very similar results were also obtained with platinum but rather lower stripping percentages were obtained with the glassy carbon electrodes. Similar behavior in the $\text{NaCl}:\text{AlCl}_3$ system was attributed to there being higher impurity levels in the glassy carbon than in the tungsten resulting in an increased corrosion rate (5). A more probable explanation is that, as was observed earlier in the cyclic voltammetry experiments, there are some slow kinetic steps involved in the Al stripping process at glassy carbon resulting in low τ values being determined from the potential-time curves. It was observed that the 'end points' of the curves for carbon were considerably less sharp than for tungsten and platinum. The corrosion rates observed in this work are very similar to those observed in the pre-electrolyzed $\text{NaCl}:\text{AlCl}_3$ system (5); the $\text{AlCl}_3:\text{BuPyCl}$ melts have, however, not been pre-electrolyzed and it is therefore possible that such treatment could reduce the corrosion rate significantly.

All the above stripping data was obtained using either the 2:1 $\text{AlCl}_3:\text{BuPyCl}$ melt or the 50 v/o mixture of this melt with benzene. Similar results were found with other acidic melts but if the concentration of Al_2Cl_7^- was below that required to maintain the applied plating current density low apparent stripping percentages were observed. This is because the efficiency of the plating process is reduced. In the high temperature alkali metal chloroaluminate deposition is also possible from the AlCl_4^- ions and therefore if the Al_2Cl_7^- concentration drops below that required for the applied current density then deposition from AlCl_4^- will also occur. 100% plating efficiencies are therefore observed for all melt compositions (5). In the $\text{AlCl}_3:\text{BuPyCl}$ system the next most readily reduced species after the Al_2Cl_7^- ions is the butyl

Table IV. Diffusion coefficient values, D , for the Al_2Cl_7^- ion calculated from chronoamperometry

Electrode	Melt (60°C) $D \times 10^7/\text{cm}^2 \cdot \text{sec}^{-1}$	Melt + benzene (30°C) $D \times 10^6/\text{cm}^2 \cdot \text{sec}^{-1}$
Tungsten	5.10	1.10
Glassy carbon	8.00	1.72
Platinum	8.00	1.65

pyridinium cation. Therefore if the Al_2Cl_7^- ion concentration drops below that required to sustain the applied current density, reduction of the butyl pyridinium cation occurs and the plating efficiency drops below 100% hence resulting in the apparently low stripping percentages.

In conclusion it can be said that, as anticipated, the aluminum deposition and stripping reactions in the low temperature $\text{AlCl}_3\text{:BuPyCl}$ melts and mixtures of the melt with benzene are very similar to those observed in the $\text{AlCl}_3\text{:NaCl}$ system. As was suggested many years ago by Hurley and Weir (19), these low temperature aprotic systems, particularly the benzene mixtures, are worthy of investigation as potential Al plating baths.

Acknowledgment

This work was supported by the Air Force Office of Scientific Research under Grant No. AFOSR-76-2978.

Manuscript submitted Dec. 6, 1978; revised manuscript received June 1, 1979.

Any discussion of this paper will appear in a Discussion Section to be published in the December 1980 JOURNAL. All discussions for the December 1980 Discussion Section should be submitted by Aug. 1, 1980.

Publication costs of this article were assisted by Colorado State University.

REFERENCES

1. B. Tremillon and G. Letisse, *J. Electroanal. Chem. Interfacial Electrochem.*, **17**, 387 (1968).
2. K. Schulze and H. Hoff, *Electrochim. Acta.*, **17**, 119 (1972).
3. G. L. Holleck and J. Giner, *This Journal*, **119**, 1161 (1972).
4. B. Gilbert, D. L. Brotherton, and G. Mamantov, *ibid.*, **121**, 773 (1974).
5. R. J. Gale and R. A. Osteryoung, *ibid.*, **121**, 983 (1974).
6. P. Rolland and G. Mamantov, *ibid.*, **123**, 1299 (1976).
7. Yu. K. Delimarski, V. F. Makogan, and A. Ya. Zhigailo, *Sov. Electrochem., Engl. Transl.*, **5**, 98 (1969).
8. V. N. Storozhenko, *ibid.*, **8**, 942 (1972).
9. L. G. Boxall, H. L. Jones, and R. A. Osteryoung, *This Journal*, **120**, 223 (1973).
10. H. L. Chum, V. R. Koch, L. L. Miller, and R. A. Osteryoung, *J. Am. Chem. Soc.*, **97**, 3264 (1975).
11. V. R. Koch, L. L. Miller, and R. A. Osteryoung, *ibid.*, **98**, 5277 (1976).
12. H. L. Chum, D. Koran, and R. A. Osteryoung, *J. Organomet. Chem.*, **140**, 349 (1977).
13. H. L. Chum, D. Koran, and R. A. Osteryoung, *J. Am. Chem. Soc.*, **100**, 310 (1978).
14. J. Robinson and R. A. Osteryoung, *ibid.*, **101**, 323 (1979).
15. R. J. Gale, B. Gilbert, and R. A. Osteryoung, *Inorg. Chem.*, **17**, 2728 (1978).
16. R. J. Gale and R. A. Osteryoung, *ibid.*, **18**, 1603 (1979).
17. B. Gilbert and R. A. Osteryoung, *J. Am. Chem. Soc.*, **100**, 2725 (1978).
18. R. J. Gale, B. Gilbert, and R. A. Osteryoung, *Inorg. Chem.*, **18**, 2723 (1979).
19. F. H. Hurley and T. P. Wier, *This Journal*, **98**, 207 (1951).
20. W. H. Safranek, W. C. Schickner, and C. L. Faust, Battelle Memorial Inst. Report to Navy Bureau Aeronautics. Contr. No. NOa(s) 9409.
21. J. Robinson, R. C. Bugle, H. L. Chum, D. Koran, and R. A. Osteryoung, *J. Am. Chem. Soc.*, **101**, 3776 (1979).
22. J. Robinson and R. A. Osteryoung, *This Journal*, **125**, 1454 (1978).
23. R. J. Gale and R. A. Osteryoung, submitted to *This Journal*.
24. G. J. Hills, D. J. Schiffrin, and J. Thompson, *Electrochim. Acta.*, **19**, 657 (1974).



A Method of Forming Thin and Highly Reliable Gate Oxides Two Step HCl Oxidation

C. Hashimoto, S. Muramoto, N. Shiono, and O. Nakajima

*Musashino Electrical Communication Laboratory,
Nippon Telegraph and Telephone Public Corporation, Tokyo, 180, Japan*

ABSTRACT

A new two step HCl oxidation has been developed as a method of forming thin and highly reliable gate oxides used in MOS LSI's. It consists of initial HCl oxidation at low temperature with low HCl concentration and following HCl treatment at high temperature in a mixture of N_2 , O_2 , and HCl gases. This report mainly covers oxide defect reduction effect and passivation effect of oxides formed by the two step HCl oxidation. The oxide defect density depends on the condition of the initial oxidation and following heat-treatment. Concretely, it is effective, for defect reduction, to use HCl oxide as the initial oxide and give it high temperature treatment for over 20 min. The passivation effect depends on the HCl concentration and the treatment time at the HCl treatment. It became evident that over 90 min treatment is necessary for passivation at 1150°C with 3% HCl. According to SIMS analysis, the mechanism of this passivation is fundamentally similar to that of a usual HCl oxidation. Many applications may be expected for this two step HCl oxidation.

Recent remarkable improvements in electron beam lithographic techniques, in addition to other developments such as ion implantation and dry etching techniques, will ensure that far smaller dimensions in silicon semiconductor device fabrication than those made today are achieved. Therefore, attempts to develop very large integrated circuits are now being advanced in the field of MOS technology. According to the scaling method (1), which is an effective principle to realize smaller devices, gate oxide needs to be far thinner. For this reason, techniques to form thin and highly reliable oxides are required. The oxides must have good uniformity and reproducibility in thickness, high dielectric breakdown voltage, small defect density such as pinholes, small surface charge and interface state density, and large passivation ability.

In recent years, oxidation of Si in a mixture of O_2 and HCl gases has attracted special interest. It has been made clear that this so-called HCl oxidation has many benefits: a reduction of instabilities due to the presence of mobile ions in the oxide (2), a reduction in oxide defects, an improvement in dielectric breakdown characteristics of the oxide (3), a reduction in surface charge density in the oxide, a reduction in interface state density at the oxide-silicon interface (4), an increase in minority carrier lifetime in the underlying silicon (5), and a reduction in stacking fault density in the underlying silicon (6).

Therefore, it was attempted to form thin and highly reliable oxides by use of HCl oxidation. After some investigation, however, it became evident that usual HCl oxidation methods were not suitable for forming thin and highly reliable oxides. This problem was

solved by two step HCl oxidation and highly reliable thin oxides were obtained. First, an oxide of considerable thickness was formed, using usual HCl oxidation at relatively low temperatures and containing relatively low HCl concentrations in the atmosphere. The oxide formed under this condition has good uniformity and reproducibility in thickness, and small defect density (3). Then, passivation ability was furnished to the oxide and, simultaneously, desired thickness oxide was obtained by heat-treatment in a mixture of N_2 , O_2 , and HCl gases at relatively high temperature. This paper reports why the two step HCl oxidation was proposed and characteristics of the oxides formed by the two step HCl oxidation.

Problems in HCl Oxidation for Thinner Oxides

The preceding section gave some benefits of HCl oxidation. However, all those benefits are not obtained under the same oxidizing conditions. For instance, the oxide defect density obtained from the dielectric breakdown voltages of MOS capacitors becomes smaller as oxidation temperature becomes lower. Conversely, it becomes as large as that of dry O_2 oxides in a temperature range of over 1100°C (3). On the other hand, only oxides grown at over that temperature have passivation effects (7). So, it is necessary to choose the most suitable method according to each purpose when forming a thin oxide.

Self-aligned gate structures are already indispensable for smaller devices in the MOS LSI fabrication technology. For their gate electrode materials, polysilicon and refractory metals (Mo, W, etc.) are used today. When polysilicon is used, it is mainly required for the gate oxide to have small defect density, because electrical stabilization of MOS structures is

Key words: MOS, silicon dioxide, reliability, chlorine oxidation.

achieved by use of passivation ability of P or As contained in polysilicon as an impurity. On the other hand, when one of the refractory metals is used, passivation ability is also required for the gate oxide because the gate electrode material has no passivation ability.

In spite of the demerit mentioned above, refractory metals may be still favorable for achieving higher speed and higher density MOS LSI's because of their lower resistivity and better manufacturing precision than polysilicon. Experiments were made concerning forming thin and highly reliable gate oxides keeping refractory metal, Mo, in mind as a gate electrode. (100), 8-12 Ω -cm, p-type Si slices were used in most of the investigations described below.

As indicated in Fig. 1, the oxidation rate of silicon is increased in the presence of HCl over 900°C. So, it is difficult to control the thicknesses of thin oxides growing at over the 1100°C necessary for passivation effects, because of too short an oxidation time. Two methods are considered fundamentally to solve this problem: (i) To decrease the oxidation rate by diluting a given HCl/O₂ mixture by N₂; and (ii) to give the HCl treatment in the HCl/N₂ mixture at a high temperature for achieving passivation ability for oxides prepared beforehand.

The passivation effects of the oxides grown by the two methods mentioned above were examined. However, it became evident that the oxide grown by method (i) appeared "grainy" when the HCl concentration was large enough to get a passivation ability, and that method (ii) was not applicable as the substrate silicon was etched by the chlorine species passed through the oxide pinholes and reached the substrate surface during HCl treatment.

It is obvious from the above examination that the problems occurring when forming thin oxides by HCl oxidation are mainly due to the very strong reaction between silicon and chlorine at over 1100°C. Therefore, the following method is proposed to solve these problems and form thin oxides. First, a uniform oxide of which the thickness is under the desired thickness and near it, is formed using another method. Then a passivation ability is given to the oxide using the HCl treatment at over 1100°C and making the chlorine species diffuse into the oxide. In this case, etching of substrate silicon is prevented by making the atmosphere a little oxidizing. The desired oxide thickness is obtained simultaneously by doing so. It is considered that highly reliable oxides can be obtained by employing this method, because the reaction between substrate silicon and chlorine can be made more indirect and the oxides can be stabilized electrically, while retaining their uniform thickness.

In practice, it was possible to obtain thin and highly reliable oxides using HCl oxides, as initial oxides,

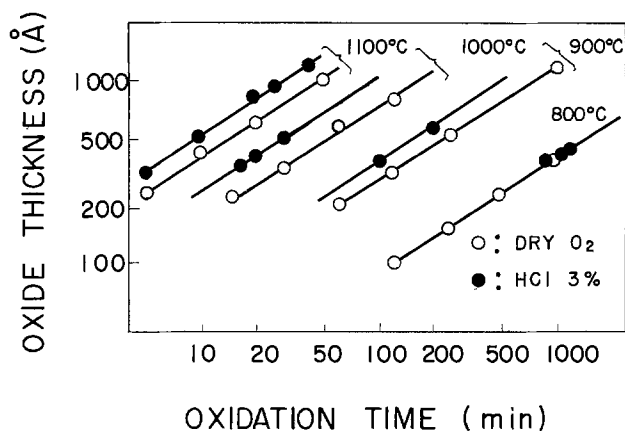


Fig. 1. Oxide thickness vs. oxidation time in dry O₂ and O₂/HCl mixture at various temperatures.

grown at low temperature (under 1000°C) and with low HCl concentration (a few percent) which are known to have small oxide defect densities, and using HCl treatments as following treatments, which are the treatments in the mixture of N₂, HCl, and O₂ gases where mixing a little O₂ gas is necessary to protect the silicon substrates from etching. Hereafter, we call this method "Two Step HCl Oxidation." Investigation results for the characteristics of the two step HCl oxidation are reported in the following.

Characteristics of Two Step HCl Oxidation

Thickness vs. time for two step HCl oxidation.—The two step HCl oxidation consists of two processes and oxide thickness increases at the HCl treatment as well as the initial oxidation. Therefore the relation between thickness and time must be known, not only for initial oxidation but also for HCl treatment. This HCl treatment is a kind of oxidation in very low oxygen partial pressures. The oxidation kinetics of silicon in an O₂/N₂ mixture have been studied (8) and it is said that the Deal-Grove relationship (9) cannot be applied under an oxygen partial pressure range of 10⁻² atm. However, no detailed study about the growth kinetics of SiO₂ films while adding HCl gas to the above atmosphere, as in the present work, is found. Probably, the mechanism will become more complicated. Moreover, the thickness we need to know is that of the oxide increased by HCl treatment after initial oxidation by another method. So it is difficult to analyze the mechanism systematically.

In this study, the following simple power law was assumed to first approximation

$$X = kt^n \quad [1]$$

where X = oxide thickness, t = virtual HCl treatment time which means the summation of the time necessary to form the same thickness as the initial oxide, assuming the use of HCl treatment and the time of the practical following HCl treatment. Both k and n are complex functions of temperature, mixing ratio of gases, and oxide thickness. The HCl oxides grown at 1000°C with 3% HCl were used as initial oxides. Two kinds of oxides, ~350 and ~500Å thick, were prepared, referring to Fig. 1. Then, HCl treatments under several conditions were given to these oxides for 60 or 120 min and the final thicknesses were measured. In this study, an ellipsometer was used to determine oxide thickness. k and t were determined to give the nearest values to the measured thicknesses for HCl treatment conditions. Examples of the results are shown in Fig. 2.

As seen from this figure, the values obtained from the experimental equations agreed with the measured values within $\pm 5\%$ errors in this experimental range. Using one of these equations for the desired HCl treatment condition, and deciding the final oxide thickness and the HCl treatment time, one can obtain the initial oxide thickness and the oxidation time from Fig. 2 and Fig. 1, respectively.

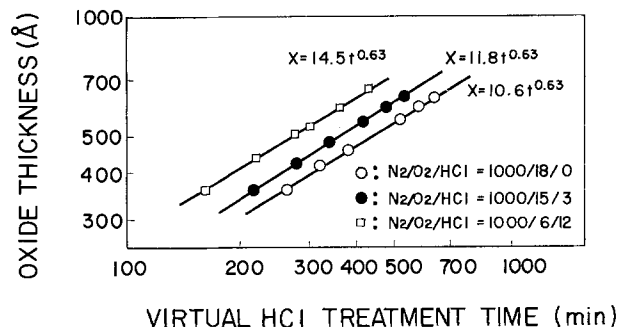


Fig. 2. Oxide thickness vs. virtual HCl treatment time at 1150°C in various N₂/O₂/HCl mixtures.

Here, it is very interesting that n is constant for all treatment atmospheres and only k increases as HCl concentration increases within the experimental range shown in Fig. 2. However, it is considered that n may change when oxide thickness becomes much thinner. Therefore, it is necessary to accumulate more data to explain the oxidation kinetics in detail.

Reduction of oxide defect density.—According to data reported by Osburn (3), oxide defect density is reduced by HCl oxidation at low temperatures with low HCl concentration, in comparison with that of dry O₂ oxides.

In this report oxide defects were detected by the copper decoration method, using methanol as the bath medium (10). This method has a merit to detect not only pinholes in insulator films but also defects other than so-called "pinholes," since the defect density changes depending on the applied electric field. It was confirmed experimentally that the copper decoration density at 1 MV/cm applied electric field and above roughly corresponds respectively to the oxide pinhole density and to the other defect density.

Figure 3 shows the copper decoration density dependence on the applied electric field for dry O₂ oxide, HCl oxide, and two step HCl oxide. From this figure, it was confirmed that the defect density of a HCl oxide grown at low temperatures with low HCl concentration is less than that of a dry O₂ oxide and that the defect density of a two step HCl oxide is still more reduced by a high temperature HCl treatment.

Since oxide defect density considerably depends on the surface condition of the prepared wafer, the evaluation of the defect density in this report was performed by comparison among wafers cut from the same ingot so as to reduce the influence of initial wafer condition. The wafers were prepared and cleaned simultaneously and only oxidation conditions were changed.

The experiment to vary the atmosphere of the high temperature treatment was carried out to investigate the cause of this newly discovered effect of the two step HCl oxidation to reduce oxide defect density. The results are shown in Fig. 4.

This figure shows that every oxide which received the high temperature treatment had a smaller defect density than the as-grown oxide. In addition, the higher the HCl concentration in the treatment at-

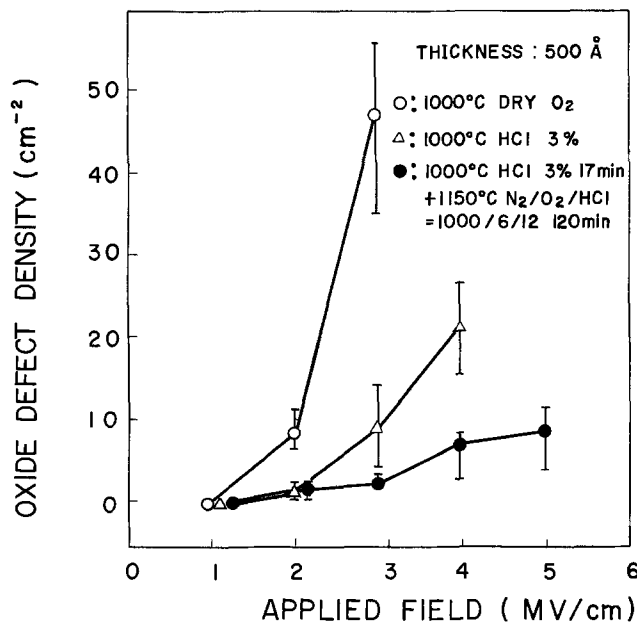


Fig. 3. Relation of oxide defect density vs. applied electric field on SiO₂ under evaluation for dry O₂, HCl, and two step HCl oxide.

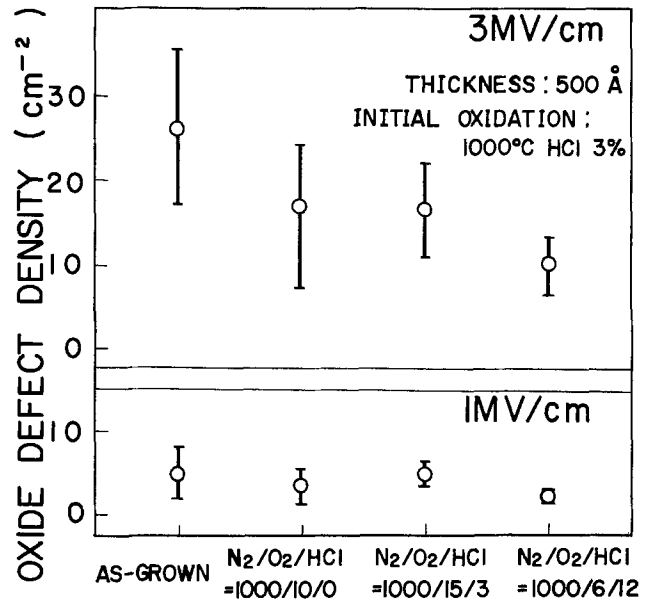


Fig. 4. Ambient effect on oxide defect density during following heat-treatment at 1150°C for 30 min.

mosphere becomes, the smaller the oxide defect density becomes.

In this case, however, differences in initial oxide thickness among these oxides may affect these results, because the initial oxide thickness was controlled to make the final thickness of every oxide 500Å. Therefore, defect density dependence was investigated for HCl oxides grown at low temperatures with low HCl concentration on the oxide thickness. As indicated in Fig. 5, little dependence was found within the thickness range from 250 to 500Å. Therefore, the results in Fig. 4 depend only on the atmosphere of the high temperature treatment.

As the above corroboration was obtained, the oxide defect density dependence was investigated for HCl treatment time under the same condition as to make the final oxide thickness 500Å. The atmosphere is that in which the smallest oxide defect density was gotten in Fig. 4. Figure 6 indicates results where rapid effect appears at a treatment time of between 10 and 20 min above 2 MV/cm applied field, and that

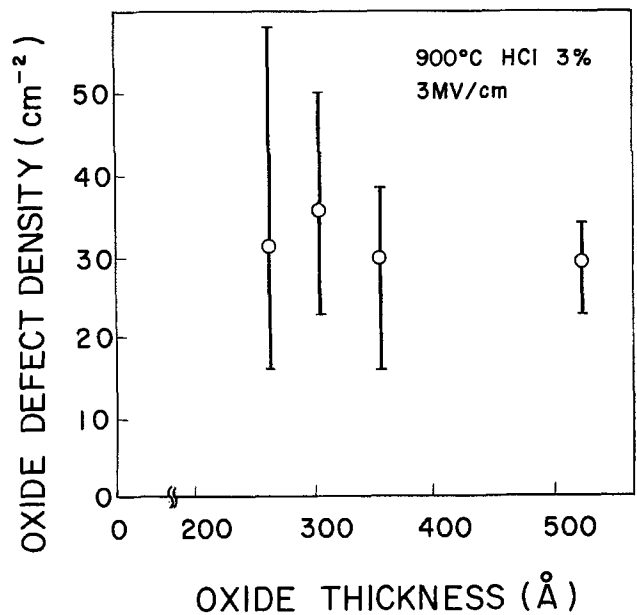


Fig. 5. Oxide thickness dependence of oxide defect density for HCl oxide.

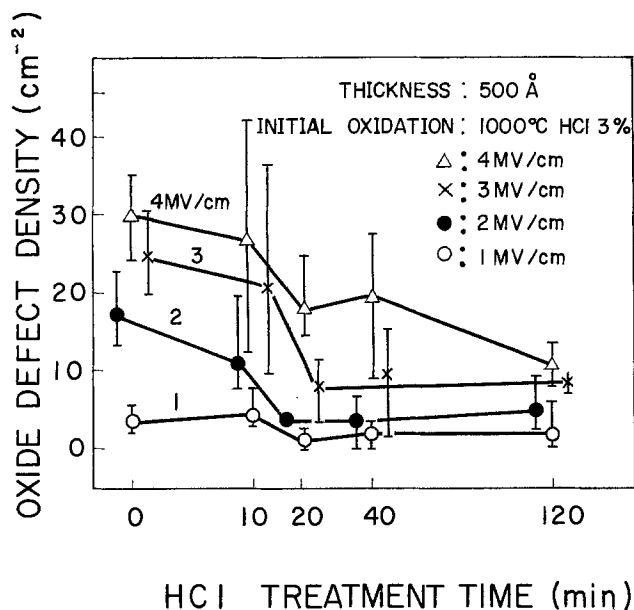


Fig. 6. Treatment time effect on oxide defect density during following HCl treatment at 1150°C in $\text{N}_2/\text{O}_2/\text{HCl} = 1000/6/12$ mixture.

more effect appears as the treatment time becomes longer at 4 MV/cm. From this, it became evident that the HCl treatment, at least over 20 min, is practically necessary to obtain an oxide with small defect density by two step HCl oxidation.

According to the results of the above investigation, the following two factors are assumed as the cause of this oxide defect density reduction effect by high temperature treatment. (i) Since the treatment is a very slow oxidation at high temperature, the oxidation of the parts proceeds where sufficient oxidation has not been accomplished at the initial oxidation for some unknown reasons. (ii) The composition of the parts which have been weak electrically, for some reasons other than the thickness nonuniformity changes being strong due to the high temperature treatment.

To separate these two factors, the size of the defect densities was compared between the oxide receiving the high temperature treatment in N_2 gas which is not an oxidizing atmosphere and the as-grown oxide. Both oxides were formed by HCl oxidation at low temperature with low HCl concentration. If factor (i) is dominant, the oxide defect density must not reduce by the high temperature treatment in N_2 gas, because oxidation cannot proceed.

It is obvious, from Fig. 7, that the defect density of the oxide receiving the high temperature treatment is smaller than that of the as-grown oxide. Therefore, it may be said that the change in oxide composition by high temperature treatment is dominant as the cause of the oxide defect reduction effect. The fact that a certain reduction effect exists for the treatment in pure N_2 gas suggests that HCl gas contained in high temperature treatment atmosphere has a rather secondary effect and the composition of the initial oxide has an essential effect.

As is shown in Fig. 8, the result was also obtained that oxide defect density detected by copper decoration method decreases as the oxidation temperature increases within the temperature range from 800° to 1100°C. There is much probability that this phenomenon is due to the same cause as above.

These tendencies are contrary to that of the defect density which Osburn obtained from the measurement of the initial dielectric breakdown voltage distributions, and rather agree with his results obtained for the wear-out characteristics (3). This improved wear-out reliability was attributed to the presence of hydrogen rather than halogens.

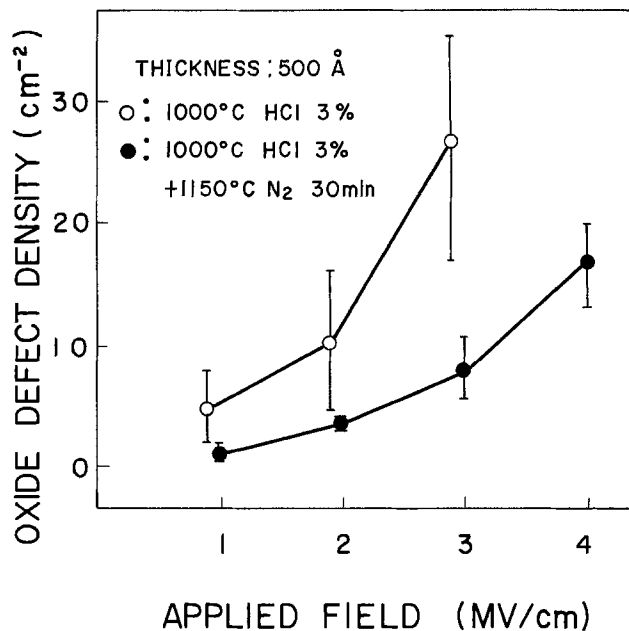


Fig. 7. High temperature N_2 treatment effect on 3% HCl oxide defect density.

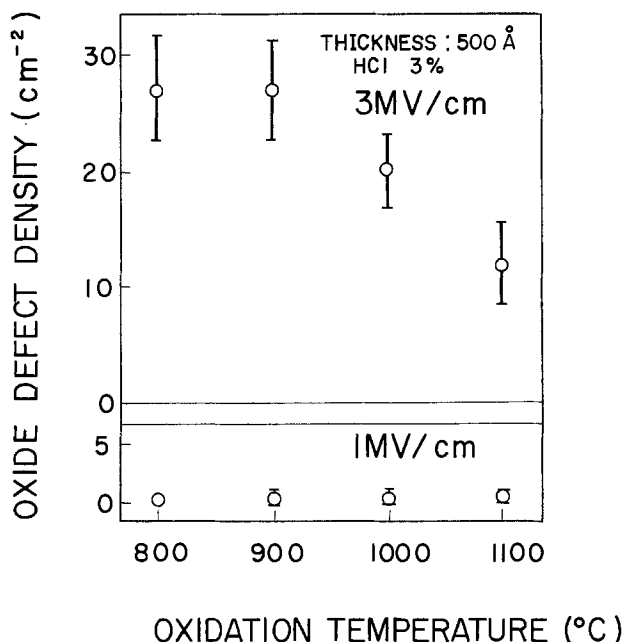


Fig. 8. Oxidation temperature dependence of oxide defect density for 3% HCl oxide.

It is necessary, for analyzing completely the oxide defect density reduction effect of the high temperature treatment mentioned in this report, to determine details about defects detected by copper decoration method. For the first step, an investigation was made to clarify which attributes to this reduction effect, hydrogen or chlorine. The results of the investigation performed so far are indicated in the following.

First, dry O_2 oxides were prepared which contain neither hydrogen nor chlorine within themselves, and then gave high temperature N_2 treatments for some of them and high temperature HCl treatments for others. The size of the defect densities was compared between oxides receiving these heat-treatments and as-grown oxides. The results are shown in Fig. 9 and Fig. 10. For both cases, the defect density increases by heat-treatment for 30 min. A report was published that the oxide breakdown field is degraded by N_2 anneal at high temperature (11), and the above

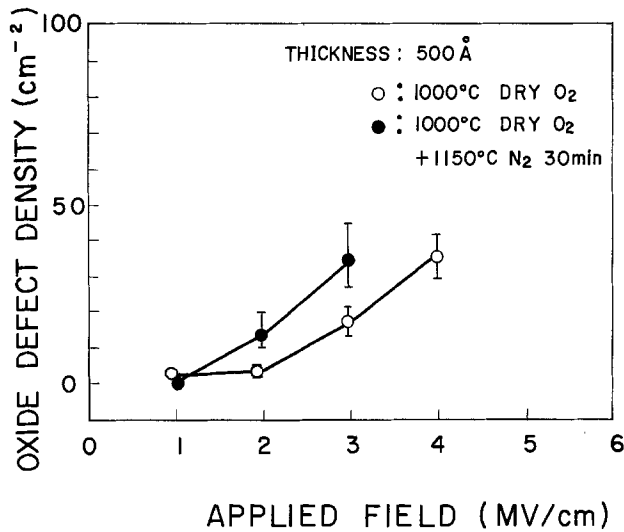


Fig. 9. High temperature N₂ treatment effect on dry O₂ oxide defect density.

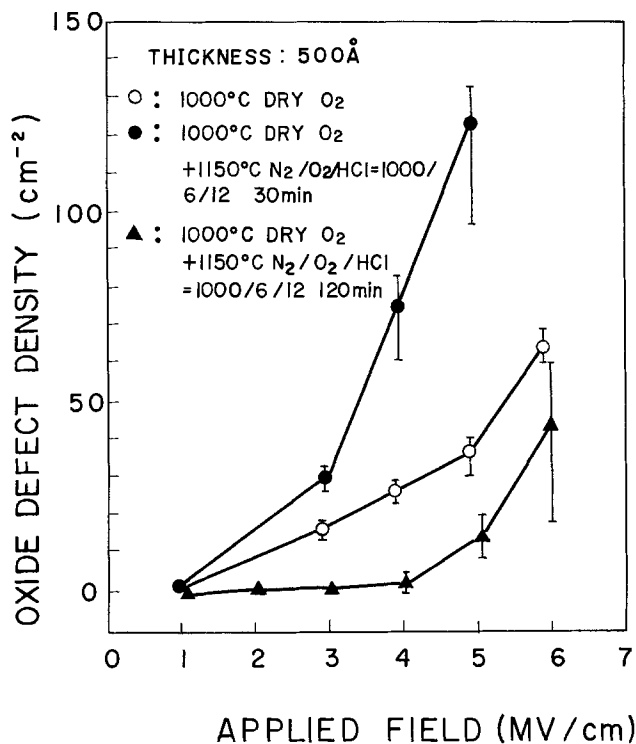


Fig. 10. High temperature HCl treatment effect for 30 and 120 min on dry O₂ oxide defect density.

phenomenon may be caused by the same reason as in the report. The result shown in Fig. 10 especially supports the previously mentioned assumption that HCl gas contained in high temperature treatment atmosphere has only a secondary effect. The defect density, however, decreases when the HCl treatment time extends to 2 hr. This property is not that of dry O₂ oxide, but that of the oxide grown in the term of the HCl treatment.

Next, an investigation was made on wet O₂ (95°C H₂O) oxide and steam (H₂ burning) oxide containing hydrogen but no chlorine. As in the case of the wet O₂ oxide, the defect density of the as-grown oxide is very large, but decreases by N₂ anneal at high temperature, as is shown in Fig. 11. On the other hand, Fig. 12 indicates that the defect density of the steam oxide is relatively small and still decreases by high temperature N₂ treatment.

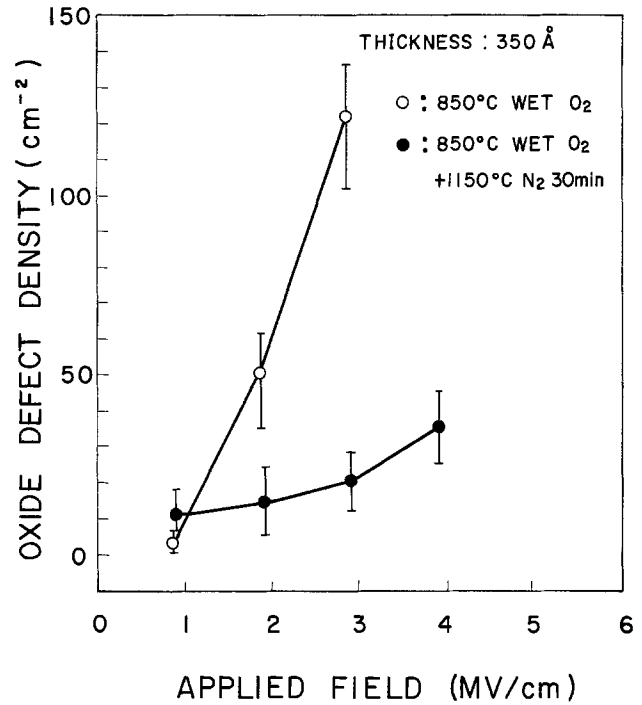


Fig. 11. High temperature N₂ treatment effect on wet (95°C) O₂ oxide defect density.

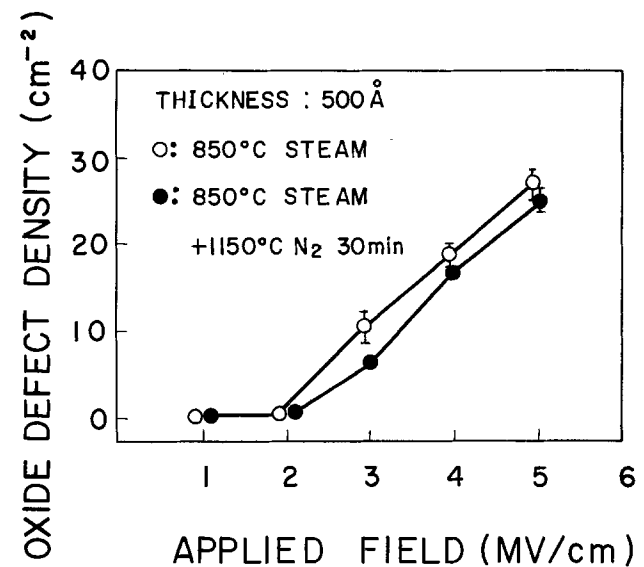


Fig. 12. High temperature N₂ treatment effect on steam (H₂ burning) oxide defect density.

Finally, a comparison is made on the size of the defect density between the as-grown Cl₂ oxide and that with a following high temperature N₂ anneal, where Cl₂ oxide means the oxide grown in a mixture of O₂ and Cl₂ gases. Not hydrogen but chlorine is contained within Cl₂ oxide. As is shown in Fig. 13, the defect density of the Cl₂ oxide is considerably small and further decreases by N₂ anneal at high temperature. Therefore, the defect density reduction effect of high temperature treatment is proved to not be limited to one oxidation method or the behavior of a certain element.

The results of the above investigation are summarized as follows. (i) The defect densities of HCl oxide, steam oxide, and Cl₂ oxide are smaller than that of dry O₂ oxide. In addition, the oxide defect density decreases as the oxidation temperature increases within the 800°-1100°C range. (ii) The defect densities of HCl oxide, wet O₂ oxide, steam oxide, and Cl₂ oxide decrease by high temperature treatment on the order of 1150°C.

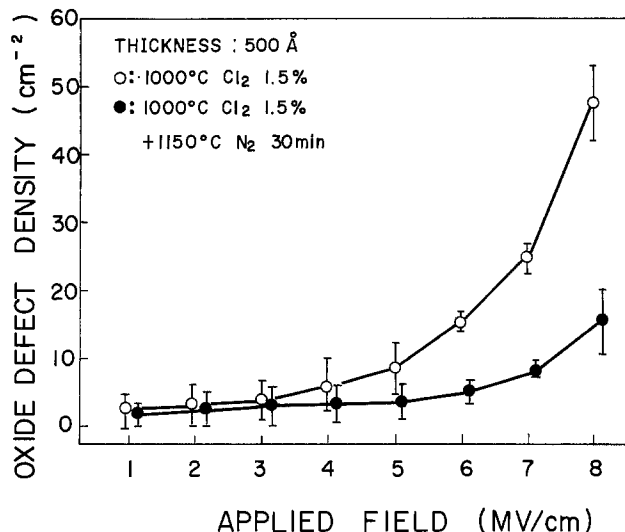


Fig. 13. High temperature N₂ treatment effect on Cl₂ oxide defect density.

It is difficult to explain these phenomena systematically by only one factor. It is necessary to consider at least two factors. The phenomenon described in (i) is a problem during oxidation. Since defect density decreases by oxidation mixing of very corrosive gases such as HCl or Cl₂, it is assumed that certain impurities that have strong resistance against oxidation, such as heavy metals, exist at the surface or inside of the substrate silicon, which act as nuclei of oxide defects at oxidation and are gettered by existence of the corrosive gases. On the other hand, the phenomenon described in (ii) is a problem after oxidation, and cannot be explained without the concept of the change in the oxide composition caused by heat-treatment. Unfortunately, it is not yet possible to clarify the mechanism.

Passivation effect.—Recently, purification of work environment in the semiconductor technology has been developed, and contamination at a gate oxidation process in the MOS fabrication process almost need not be taken into consideration. Therefore, there only remains the photolithography processes of gate electrodes patterning and later processes as possible processes for incorporating contaminations into MOS structures. Especially, as in the case of a self-aligned gate structure, contaminations can easily diffuse into a gate oxide during the heat-treatment to form source and drain regions after the photolithography. So it is desirable that the gate oxide has a passivation ability prepared for an unexpected situation when using an Mo gate electrode for which no stabilization effect is expected from a diffusion source. Many investigations on passivation effect of HCl oxidation have been performed by several persons, but it cannot be asserted that passivation effects have been sufficiently studied for thinner oxides and for contaminations incorporated into oxides during heat-treatment accompanying a self-aligned gate process. The passivation effect was investigated using two step HCl oxidation.

To fabricate the evaluation MOS diodes, Mo evaporated from an E-gun heated source was used as gate electrodes, 500 μm □ electrodes were formed by photolithography and annealed for 15 min in N₂ at 1000°C, assuming the annealing process activates the source and drain-implanted impurity layers, where the quantities of contamination on the wafers were controlled by omitting a step in the washing process, usually carried out after the photolithography process, in order to clarify the passivation effect.

500Å thick dry O₂ oxide was prepared as the standard reference oxide, and "passivation efficiency," P ,

was defined as

$$P = \frac{\Delta N_{\text{FBD}} - \Delta N_{\text{FBH}}}{\Delta N_{\text{FBD}}} \quad [2]$$

where ΔN_{FBD} and ΔN_{FBH} are, respectively, mobile ion density in the dry O₂ oxide and that in the two step HCl oxide after positive BT stress. Both oxides were manufactured in the same lot after the Mo evaporation process.

Figure 14 shows the HCl concentration effect on passivation efficiency in oxides grown at 1000°C with 3% HCl to 350Å thick and received HCl treatments for 2 hr. It is seen that the passivation effect takes place rather suddenly between N₂/O₂/HCl = 1000/6/18 and N₂/O₂/HCl = 1000/6/24. This HCl concentration is less than 3% to the carrier gas, and smaller than about 4% necessary for a usual HCl oxide to gain a passivation effect (12). However, there are only a few studies about O₂-adding HCl treatment. Especially, no investigation has been reported about the oxides receiving as long as 2 hr HCl treatment and receiving heat-treatment after forming electrodes. There is sufficient possibility that these factors exert some influence on passivation effect, that a more detailed investigation will be needed.

Next, an investigation was made on treatment time dependence of passivation effects of oxides grown under the same initial condition as the above oxides and which received HCl treatment at 1150°C in the mixture of N₂/O₂/HCl = 1000/6/24. As indicated in Fig. 15, the passivation effect appears suddenly at between 60 and 90 min treatment time. As in the case of usual HCl oxidation, 20-30 min are needed for an

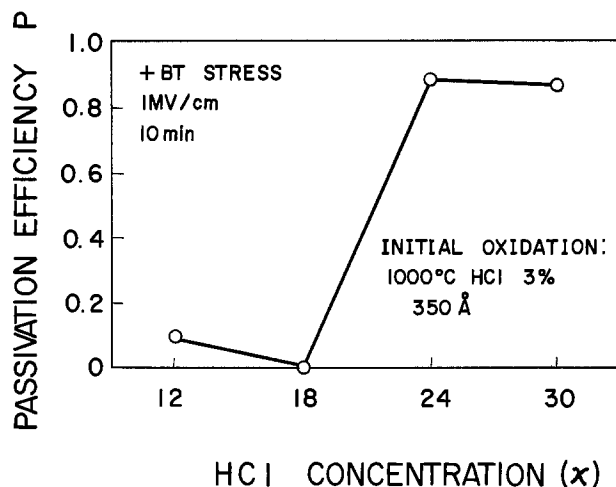


Fig. 14. HCl concentration = x dependence of passivation efficiency during HCl treatment at 1150°C in N₂/O₂/HCl = 1000/6/ x mixture for 120 min.

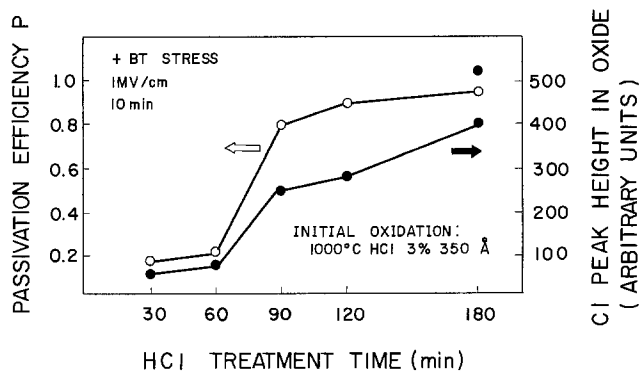


Fig. 15. Treatment time dependence of passivation efficiency and Cl peak height in oxide during HCl treatment at 1150°C in N₂/O₂/HCl = 1000/6/24 mixture.

oxide to obtain a sufficient passivation effect (12). It is considered that this difference is due to the relatively low HCl concentration of the above HCl treatment.

An attempt was made to measure Cl distribution in two step HCl oxides by use of secondary ion mass spectroscopy (SIMS) to investigate the passivation mechanism of those oxides. The results show that Cl piles up in SiO₂ close to the Si interface and the size of the peak height corresponds well to the passivation effect as shown in Fig. 15. These phenomena are very similar to that of usual HCl oxides. Also, the following results were obtained by SIMS analysis. No pile-up of Cl in the oxides exists after initial oxidation at 1000°C within the HCl concentration range from 0 to 6%. These pile-up phenomena depend completely on following HCl treatment at 1150°C. Therefore, it is only necessary to consider the following HCl treatment condition in regard to passivation.

As there are many parameters in the two step HCl oxidation, such as HCl concentration, O₂ concentration, and treatment time at the HCl treatment, many variations are expected in the method of forming an oxide having a passivation effect.

Summary

A method has been reported, called two step HCl oxidation, to form a thin and highly reliable gate oxide used in the MOS LSI fabrication process. First, an oxide of considerable thickness is formed using usual HCl oxidation at relatively low temperature with relatively low HCl concentration. Then, the oxide is given an HCl treatment in a mixture of N₂, O₂, and HCl gases at relatively high temperature. Forming an oxide like this, oxide surface roughness, which is a drawback of the HCl oxidation with high HCl concentration, does not arise. Oxide defect density decreases and electrically stabilized oxide is obtained.

It was clarified that HCl oxide as initial oxide, followed by high temperature treatment for over 20 min, is necessary to reduce oxide defect density. It also became clear that passivation effect is sufficiently obtainable for an oxide by HCl treatment with about 3% HCl concentration for over 90 min. However, clarification of the detailed oxidation kinetics and the

mechanisms of the above mentioned effects are retained as the subject for a future study.

This two step HCl oxidation is considered to be widely applicable by choosing a proper oxidizing condition according to individual requirements, because of its many changeable parameters.

Acknowledgments

The authors would like to thank Drs. M. Hirai, M. Kondo, H. Araki, and T. Yashiro for their advice and encouragement through the present work. They are also indebted to a number of colleagues for sample preparations and measurements, in particular to Mr. M. Seki for performing Cl analysis of oxides, Mr. T. Amazawa for evaporating Mo, and Mrs. E. Watanabe for measuring oxide thickness.

Manuscript received Aug. 11, 1978.

Any discussion of this paper will appear in a Discussion Section to be published in the December 1980 JOURNAL. All discussions for the December 1980 Discussion Section should be submitted by Aug. 1, 1980.

Publication costs of this article were assisted by Nippon Telegraph and Telephone Public Corporation.

REFERENCES

1. R. H. Dennard, F. H. Gaensslen, H. N. Yu, E. Basso, and A. LeBlanc, *IEEE J. Solid-State Circuits*, **9**, 256 (1974).
2. R. J. Kriegler, Y. C. Cheng, and D. R. Colton, *This Journal*, **119**, 388 (1972).
3. C. M. Osburn, *ibid.*, **121**, 809 (1974).
4. M. Severi and G. Soncini, *Electron. Lett.*, **8**, 402 (1972).
5. D. R. Young and C. M. Osburn, *This Journal*, **120**, 1578 (1973).
6. H. Shiraki, *Jpn. J. Appl. Phys.*, **14**, 747 (1975).
7. K. Kobayashi, K. Tanabashi, K. Ohta, and T. Kubota, *Denki Kagaku*, **42**, 294 (1974).
8. B. E. Deal and A. S. Grove, *J. Appl. Phys.*, **36**, 3770 (1965).
9. Y. Kamigaki and Y. Itoh, *ibid.*, **48**, 2891 (1977).
10. O. Nakajima, N. Shiono, and C. Hashimoto, 8th Symposium on Reliability and Maintainability, Union of Japanese Scientists and Engineers, Tokyo, May 31-June 2, 1978.
11. B. H. Vromen, *Appl. Phys. Lett.*, **27**, 152 (1975).
12. R. J. Kriegler, A. Aitken, and J. D. Morris, in "Proceedings of the 5th Conference on Solid State Devices," p. 341, Tokyo (1973).

Silver Halide-Chalcogenide Glass Inorganic Resists for X-Ray Lithography

K. D. Kolwicz¹ and M. S. Chang^{*2}

Moore School of Electrical Engineering, University of Pennsylvania, Philadelphia, Pennsylvania 19104

ABSTRACT

Silver halide-chalcogenide glass composite thin film structures are evaluated as inorganic x-ray resists at Al K_α line. The sensitivity is shown to be a factor of 2 better than the PMMA 2041 for a 300 nm thick resist layer. A comparable contrast is indicated. A high resolution capability is expected because of the amorphous nature of the composite. A possible mechanism of this inorganic resist action is discussed.

Current integrated circuit technology restricts itself to the use of organic polymer resists (OPR) in routine photolithographic processes. Success with these materials has precluded the consideration of alternatives to OPR by the solid-state electronics industry on the grounds that OPR could be modified to meet all re-

* Electrochemical Society Active Member.

¹ Present address: Bell Laboratories, Allentown, Pennsylvania 18103.

² Present address: Hewlett Packard Laboratories, Palo Alto, California 94304.

Key words: inorganic resists, x-ray lithography, negative x-ray resists.

quirements. The new submicron technologies such as electron and ion beam processing and x-ray or synchrotron radiation sources are resist dependent. Organic materials tend to have low Z numbers and low stopping cross sections for electrons and x-rays. Inorganic materials are far more flexible and are used extensively as sensitizers in OPR. For x-ray lithography (1), current activity on resist technology (2-8) is concentrated on incorporating heavy atoms into existing resists to achieve higher sensitivity. Polymethyl methacrylate (PMMA) has the highest resolu-

tion of all existing resists and has a very high contrast. Its sensitivity, however, is low. Other new x-ray resists such as Bell Laboratories' DCPA (5) and Texas Instrument's XR79 (6) have a much higher sensitivity but their resolution is poor, limited to 0.5 μm . In this paper, we report a novel inorganic thin film composite structure that shows promise as an x-ray resist with high sensitivity as well as high resolution and contrast.

Inorganic resists (9-13) have received some attention in the past for metallic and oxide pattern delineation for direct device fabrication. Recently, chalcogenide glasses (14, 15) have been employed as inorganic resists, but poor sensitivity limits these materials in practical applications. By photodoping with silver, chalcogenide glasses are made insoluble in alkaline solutions (16) which makes them attractive for lithographic applications (17), and a high contrast electron beam resist has been reported (18). Most recently, the compatibility of inorganic resists with plasma etching for pattern development has been demonstrated (19). The utilization of this dry processing technique for microstructure fabrication is very attractive.

In this work, a silver halide-chalcogenide glass composite thin film structure is considered, and an inorganic x-ray resist is described, for the first time. Silver halides are chosen for the following reasons: they can be vacuum deposited; they do not decompose during evaporation; they dissociate into metallic silver and halogen gases upon irradiation, providing a source of silver for the photodoping effect; and they readily dissolve in solutions of sodium thiosulfate, well known to the photographic industry as a fixing agent (20). Pure silver films are not used because autodoping (21) into the chalcogenides prior to irradiation has been noticed, apparently due to the procedure of vacuum deposition. Very recently, silver halide emulsions have been reported independently as highly sensitive resists but defects remain as serious limitations (22).

Experimental

Exposure systems.—The x-ray exposures were carried out using a converted electron beam evaporator with an aluminum anode, giving the resulting emission of the Al K_{α} line at 8.34Å. The electron beam power used to excite x-ray emission was 4 kV at 25 mA, and the target to substrate distance was 6 cm. A 2.5 μm thick Al filter was placed between the anode and the target to reduce infrared heating and the Bremsstrahlen. The mask used was a 6.25 μm thick Mylar membrane stretched over a quartz ring with a 0.5 μm thick gold absorber patterned by photolithography. The optimum x-ray exposure time for PMMA 2041 was determined to be 5 hr (corresponding to approximately 4 J/cm² energy) as a reference.

The light source used for the photolithographic characterization was a Kasper Model 17A mask aligner equipped with a 200W high pressure Hg lamp. The intensity at the sample plane was 90 mW/cm².

Thin film preparation.—Thin films of As_2S_3 chalcogenide glass were evaporated using a hot wall deposition system. Glassy chunks of Servofrax® were melted in a molybdenum boat in a vacuum system at pressures of 1×10^{-6} Torr or less. Deposition rates were typically 10-20 Å/sec. Initial As_2S_3 film thicknesses were all 300 nm. Substrates were cleaned borosilicate slides for photolithography and freshly oxidized silicon wafers for x-ray lithography. On top of the As_2S_3 film, an overlayer of AgCl 20 nm thick was then evaporated to form the composite. Thereafter, the composite structure was stored in darkness or handled in a red safe-light. After exposure, the remaining AgCl was removed in a standard solution of Kodak rapid fixer solution A mixed with water at a ratio of 1:3 for 10 min, and the undoped As_2S_3 was then etched in a 0.03N NaOH solution. The lithographic process is shown schematically in Fig. 1.

Etch rate and thickness determination.—An optical *in situ* monitoring technique (23) was used to determine the etch rate. In the 0.03N NaOH solution at room temperature, an etch rate of 41 Å/sec for the unexposed As_2S_3 film and 23 Å/sec for the exposure-saturated As_2S_3 film without any AgCl overlayer has been obtained. Silver-doped As_2S_3 has essentially zero etch rate in the NaOH solution. The remaining film thickness of the delineated image was measured with a Sloan Angstrommeter.

Results and Discussions

The AgCl- As_2S_3 composite is evaluated first as a photoresist. It was found to possess the negative resist property that the exposed region remains after development. The characteristic curve of percent remaining film thickness as a function of the exposure energy is shown in Fig. 2; a threshold for the onset of insolubilization was observed. The resist sensitivity is defined as the minimum exposure to obtain 100% film thickness remaining. For the composite the sensitivity was 3 J/cm², which is a factor of 5 less sensitive than the common Kodak negative polymer photoresist KPR (24).

The simple As_2S_3 layer is also photosensitive, as shown in Fig. 2. Its etch rate decreased when exposed to light and reached a saturated but nonzero value when fully exposed. Since the exposed and unexposed portions of the film etch concurrently, a maximum of 38% of the initial 30 nm film thickness remains after etching when the unexposed layer has just been removed by a 75 sec etch in 0.03N NaOH at room temperature. The etch rate characteristics of As_2S_3 have been studied in detail elsewhere (23). If the corresponding exposure is taken as the reciprocal sensitivity, an improvement in sensitivity by a factor of 10 is obtained by going to the AgCl- As_2S_3 composite structure.

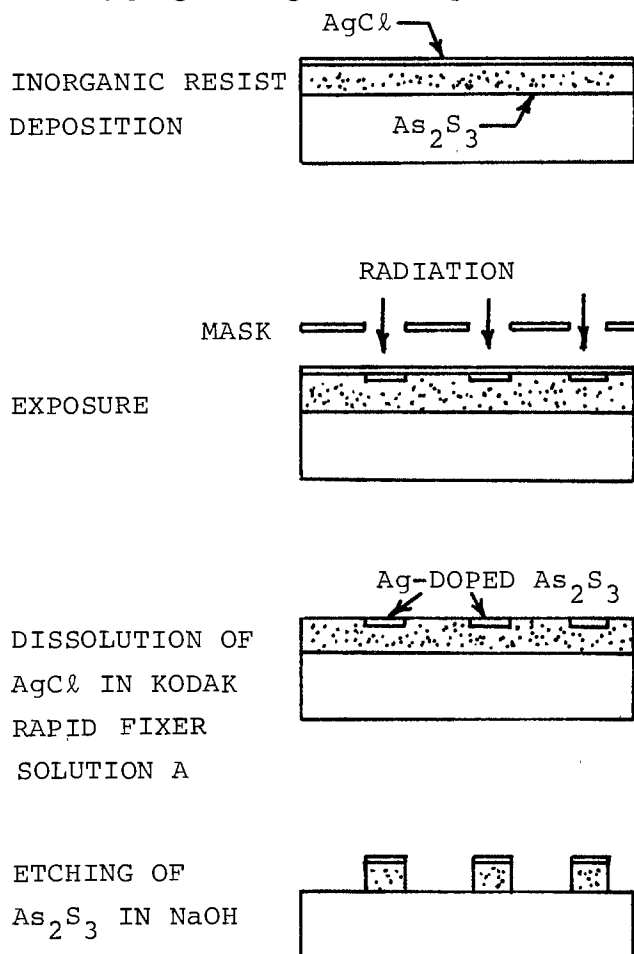


Fig. 1. Schematic relief pattern generation in AgCl- As_2S_3 composite inorganic resist.

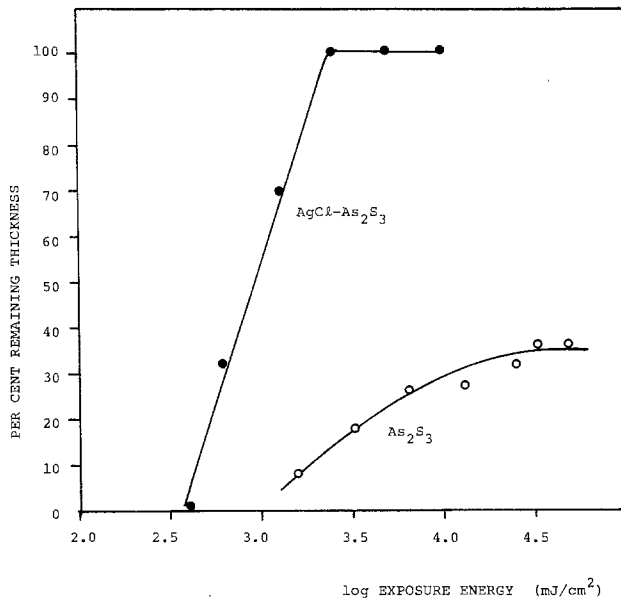


Fig. 2. Percent remaining thickness as a function of the log exposure energy for AgCl-As₂S₃ (●) and As₂S₃ (○). The light source power density was 90 mW/cm². The saturation energy for the AgCl-As₂S₃ corresponds to a 30 sec exposure. The larger saturation exposure in the simple As₂S₃ system reduces the etch rate to 38% of the rate without exposure.

Encouraged by this observation, we attempted to evaluate the composite as an x-ray resist. The characteristic curve of remaining film thickness as a function of the exposure time with our x-ray system is shown in Fig. 3 A. A similar curve for the well-known PMMA 2041 x-ray resist was also obtained under the same exposure conditions followed by development in a 1:3 solution (1) of methyl isobutyl ketone (MIBK) and isopropyl alcohol (IPA) for 1 min. With a remaining film thickness of 300 nm as a criterion, a 5 hr x-ray exposure time was required for PMMA. Compared to the 2.5 hr required for the AgCl-As₂S₃ composite, we have an improvement in sensitivity of a factor of two. The slopes of the two curves are approximately the same, indicating equally high resist contrast obtainable in this inorganic resist. Figure 4 shows a pattern delineated by x-ray lithography in this inorganic resist. The linewidth is about 6 μm. From the published data (1), an exposure of about 4 J/cm² is required to give a PMMA dissolution rate of 300 nm/min. Assuming linear time dependence of delivered x-ray energy for our lithographic system, we obtain an optimum exposure of 2 J/cm² for the composite resist.

Using available data (25) for the x-ray cross sections of arsenic and sulfur, it is estimated that 30% of the x-ray energy is absorbed by an As₂S₃ film 300 nm thick, the thickness being arbitrarily chosen for this study.

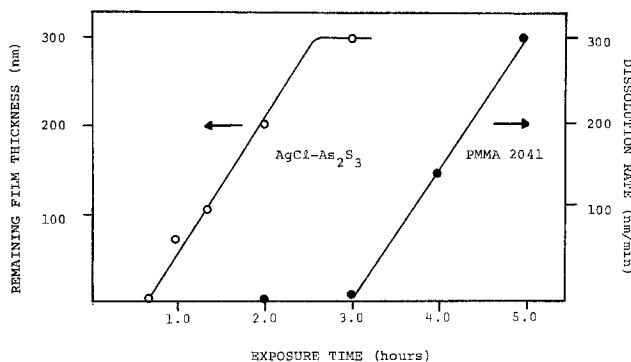


Fig. 3. X-ray resist characteristics for AgCl-As₂S₃ composite inorganic resist (○) and for PMMA 2041 (●) as a function of exposure time. The 5 hr exposure time corresponds to an x-ray energy of approximately 4 J/cm².

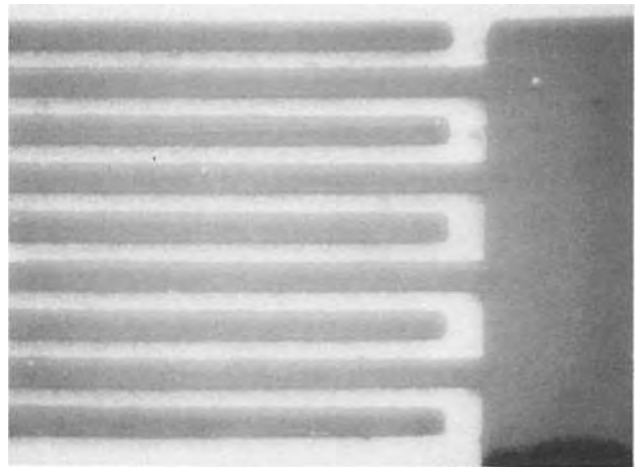
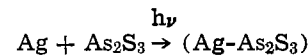
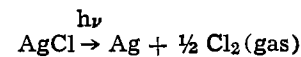


Fig. 4. A scanning electron micrograph of a pattern generated by x-ray lithography in AgCl-As₂S₃. The remaining film thickness is 100 nm and the linewidth is 6 μm. The material remaining between the lines is an artifact due to the x-ray lithography system (i.e., penumbral blurring and vibration) and is not related to the resist properties.

Optimization of film thickness along with other exposure parameters (e.g., wavelength, etc.) could result in improved performance. The comparison with PMMA in MIBK:IPA = 1.3 developed is also arbitrarily chosen. One is a positive resist, while the other is a negative resist. Nevertheless, the x-ray inorganic resist property is clearly demonstrated, and a different concept to achieve more sensitive x-ray resists is established.

The mechanism that permits the AgCl-As₂S₃ composite to form relief structures is tentatively attributed to the silver doping effect (16, 21). The process can be represented by two equations



The silver halide decomposes into metallic silver and halogen gas upon absorption of irradiation, and thus provides the source for silver doping. The silver-doped As₂S₃ is insoluble in the NaOH solution thereby generating a pattern. The linear relationship between the doping depth and the square root of exposure time has been established (16), typical of a diffusion-controlled process. An x-ray photon absorbed by the inorganic resist produces a shower of secondary electrons which will carry most of the energy of the incident photon and is responsible for the silver doping process.

To obtain information about the doping depth required for resist application, the following experiment was performed. A layer of metallic Ag 20 nm thick was sandwiched between the 300 nm As₂S₃ and the glass substrate as shown by the insert in Fig. 5. Several samples were exposed to the mask aligner light source for different exposure times. Then, all the samples were etched at the same time in a 0.03N NaOH solution for 2 min, which is a little more than enough time to remove the 300 nm of exposure saturated As₂S₃. The thickness of the resulting insoluble Ag-doped layer formed in the exposed area was measured. Figure 5 shows the doping depth as a function of exposure time. It is seen that with a limited source of silver (i.e., 20 nm), the doping depth consists of only a fraction of the bulk, even for long exposure times. This depth is reached in a relatively short exposure, and further exposures do not drive the silver further into the bulk. This observation lends credence to the idea that the x-ray resist action of AgCl-As₂S₃ is due to the formation of a thin layer of As₂S₃ into which silver has penetrated and changed its chemical solubility. The re-

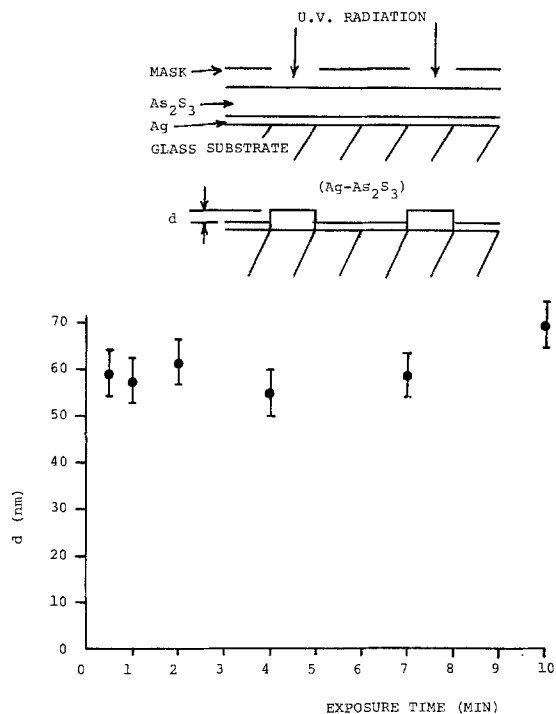


Fig. 5. Establishment of doping depth with a limited silver source of 20 nm thickness. The inserts show the procedure for establishing the doping depth. The exposure source is the mask aligner with a power density of 90 mW/cm².

sulting thin "cap" about 80 nm thick or less protects the underlying undoped As_2S_3 film from being etched. The pattern of this thin cap gives the pattern of the final image. It is anticipated that a thinner cap would suffice for the protective action. In an isotropic etching environment this would be a problem in fine line lithography, but it is not insurmountable as As_2S_3 has been shown (19) to be suitable for plasma etching. The minimum cap thickness is yet to be determined.

Since both the silver halide and chalcogenide glass are amorphous, the resolution capability of this composite inorganic resist is expected to be extremely high. We are at present limited by our mask making capability to 6 μ m linewidth as shown in Fig. 4. Since the pattern-forming layer is thin (50 nm or less), in an anisotropic etching medium the ultimate resolution should be very good for a reasonable height-to-width aspect ratio. Recently, a minimum linewidth of 100 nm has been delineated through the holographic exposure technique in this laboratory (26, 27). A similar high resolution capability is expected through the x-ray replication process. The resolution limit may fall in the 10 nm range, which is the diffusion length of the excited carriers (17).

Conclusion

The composite thin film structure $AgCl-As_2S_3$ has been characterized as a photoresist and an x-ray resist. As a photoresist, it is found to be about 5 times less sensitive than organic resists in popular use, while as an x-ray resist, it is shown to be about twice as sensitive as PMMA. In both cases, the sensitivity cannot at this point favorably compete with the sensitivities of organic resists now being used in practice, but sensitization techniques for silver halides known by the photographic industry and optimization of resist thickness parameters provide room for improvement. The resist action is shown to be essentially due to the radiation enhanced reaction at the interface of the $AgCl-As_2S_3$ thin films, with the subsequent pattern defining layer being of the order of tens of nanometers. This fact coupled with the compatibility of the As_2S_3 to plasma etching and the amorphous nature of the resist materials would mean a high resolution capability for pattern generation.

Acknowledgment

This work was supported by the National Science Foundation under Grant Number ENG 76-80140.

The authors wish to thank Prof. Jay N. Zemel for interesting discussions and to Sperry-Univac for the loan of the electron gun used in the x-ray system.

Manuscript submitted Dec. 27, 1978; revised manuscript received July 18, 1979.

Any discussion of this paper will appear in a Discussion Section to be published in the December 1980 JOURNAL. All discussions for the December 1980 Discussion Section should be submitted by Aug. 1, 1980.

Publication costs of this article were assisted by the University of Pennsylvania.

REFERENCES

- E. Spiller and R. Feder, in "X-Ray Optics," H. J. Queisser, Editor, Chap. 3, Springer-Verlag, New York (1977).
- L. F. Thompson, E. D. Feit, M. J. Bowden, P. V. Lenzo, and E. G. Spencer, *This Journal*, **121**, 1500 (1974).
- S. Imamura, S. Sugawara, and K. Murase, *ibid.*, **124**, 1139 (1977).
- M. Kakuchi, S. Sugawara, K. Murase, and K. Matsuyama, *ibid.*, **124**, 1648 (1977).
- G. N. Taylor, G. A. Coquin, and S. Somekh, *Poly. Eng. Sci.*, **17**, 420 (1977).
- R. K. Watts, K. E. Bean, and T. L. Brewer, Electron and Ion Beam Science and Technology, Eighth International Conference, Robert Bakish, Editor, p. 453, The Electrochemical Society Soft-bound Proceedings Series, Princeton, N.J. (1978).
- I. Haller, R. Feder, M. Hatzakis, and E. Spiller, *This Journal*, **126**, 154 (1979).
- J. N. Helbert, C. F. Cook, Jr., C.-Y. Chen, and C. U. Pittman, Jr., *ibid.*, **126**, 694 (1979).
- T. W. O'Keefe and R. M. Handy, *Solid-State Electron.*, **11**, 261 (1968).
- B. H. Hill, *This Journal*, **116**, 668 (1969).
- E. T. Fitzgibbon and W. H. Hartwig, Abstract 12, p. 38, The Electrochemical Society Extended Abstracts, Spring Meeting, Washington, D.C., May 9-13, 1971.
- W. R. Sinclair, D. L. Rousseau, and J. J. Stancavish, *This Journal*, **121**, 925 (1974); and G. W. Kamm-lott and W. R. Sinclair, *ibid.*, **121**, 929 (1974).
- J. P. Ballantyne and W. C. Nixon, *J. Vac. Sci. Technol.*, **10**, 1094 (1973).
- H. Nagai, A. Yoshikawa, Y. Toyoshima, O. Ochi, and Y. Mizushima, *Appl. Phys. Lett.*, **28**, 145 (1976).
- M. S. Chang and T. W. Hou, *Opt. Commun.*, **24**, 220 (1978).
- T. Shirakawa, I. Shimizu, H. Kokado, and E. Inoue, *Photogr. Sci. Eng.*, **19**, 139 (1975).
- A. Yoshikawa, O. Ochi, H. Nagai, and Y. Mizushima, *Appl. Phys. Lett.*, **29**, 677 (1976).
- A. Yoshikawa, O. Ochi, H. Nagai, and Y. Mizushima, *ibid.*, **31**, 161 (1977).
- M. S. Chang and J. T. Chen, *ibid.*, **33**, 892 (1978).
- "The Theory of the Photographic Process," 3rd ed., J. H. Hames, Editor, Chap. 1, MacMillan, New York (1966).
- H. Kokado, I. Shimizu, and E. Inoue, *J. Non-Cryst. Solids*, **20**, 131 (1976).
- R. B. Marcus, T. Shankoff, D. Smith, C. D. Capio, T. F. Retajczyk, and A. Timko, in "International Electron Devices Meeting Technical Digest," p. 591, Institute of Electrical Engineers (1978).
- M. S. Chang and T. W. Hou, *Thin Solid Films*, **55**, 463 (1978).
- M. R. Goldrick and L. R. Plauger, *Photogr. Sci. Eng.*, **17**, 386 (1973).
- W. H. McMaster, N. Kerr Del Grande, J. H. Mallett, and J. H. Hubbell, "Compilation of X-ray Cross Sections," Lawrence Radiation Laboratory, UCRL-50174, Sec. II, Rev. 1.
- T. W. Hou and M. S. Chang, *Appl. Opt.*, **18**, 1753 (1979).
- M. S. Chang, in "Conference of Third Biennial University/Industry/Government Microelectronics Symposium," p. 124, Institute of Electrical and Electronics Engineers, (1979).

Electrical Breakdown

I. During the Anodic Growth of Tantalum Pentoxide

V. Kadary¹ and N. Klein

Faculty of Electrical Engineering, Technion-Israel Institute of Technology, Haifa, Israel

ABSTRACT

Observations are presented on breakdown events during the anodic growth of tantalum pentoxide in characteristics which plot the rate of breakdown as function of oxide thickness at constant field, F . The characteristics shift to lower thicknesses for an increase in field, or a decrease in temperature. The breakdown process is interpreted by the stochastic succession of avalanche breakdown model. An approximate relation was derived for the rate of breakdown as function of insulator thickness. This relation could be well fitted to experimental data at various fields. The fitting procedure permits the evaluation of the coefficient of impact ionization α , finding for a set of anodizations $\alpha = 4.4 \times 10^6 \exp(-21.5/F)/\text{cm}$ with F in MV/cm, in the range of fields 6.1-6.7 MV/cm. There is an uncertainty of roughly $\pm 10\%$ in α , due to shallow minima in fitting procedures, to fluctuations in the rate of breakdown, and to some uncertainty in the magnitude of F .

Since the extensive studies of Güntherschulze and Betz (1), electrical breakdown during the anodization of "valve metals" has been the subject of many investigations. Recent reviews found difficulties both in the definition of breakdown and in the interpretation of the processes (2-4). Several mechanisms were proposed to explain breakdown, such as fissure formation in the oxide (5), or local crystallization in the amorphous insulator. Evidence was not found, however, in support of these mechanisms and it was shown that crystallization does not precede breakdown, but is a side effect caused by local heating (6).

Already Güntherschulze and Betz (1) suggested that breakdown during anodization is connected with electronic impact ionization and avalanching. This view was shared by other investigators (3, 7), and recently an avalanche breakdown theory was developed by Ikonopisov (8). The feasibility of the avalanche breakdown mechanism is supported by observations on electroluminescence and anodic growth. Van Geel *et al.* (9) observed in aluminum oxide that the intensity of electroluminescence accompanying anodization increases as some exponential function of oxide thickness. The nature of this increase was interpreted with the assumption of electronic avalanche formation. Fritzsche (10) investigated the rate of oxide growth and current transients during the anodic growth of silicon dioxide, also interpreting observations with avalanche formation.

It has been more difficult to obtain experimental evidence for avalanche mechanisms from breakdown observations. This may in part be due to the fact that even the definition of breakdown is subject to discussion (3, 4). Since the electric field is constant during anodization, breakdown has been defined by some voltage value. As such, various voltages were proposed: the voltage at which sparking starts, the maximum voltage which can be reached on anodization, or the voltage at which a deflection from linearity arises in the voltage *vs.* time curve.

These voltages certainly describe, more (or less) important aspects related to breakdown during anodic growth. They do not account, however, for individual observations of numerous breakdown events. To provide this information, new approaches were proposed for the description of breakdown properties during anodization. These are based on the measurement of the total number of breakdowns as a function of anodization voltage in the work of Orlov *et al.* (11) and Albella *et al.* (12), and on the determination of

the rate of breakdown as a function of thickness by Kadary and Klein (13).

This paper applies the latter approach, plotting the rate of breakdown *vs.* voltage, or thickness in breakdown characteristics. Detailed experimental data are presented on the characteristics as a function of anodization field. Results are examined for interpretation by thermal or by electronic impact ionization mechanisms. Examination shows that, applying the stochastic succession of avalanche breakdown theory (14), good agreement is found between calculations and experimental data. Agreement is found also for breakdown during the anodization of aluminum and will be described in Part II (15), the companion paper.

Samples and the Experimental System

Anodizations were carried out on 5000Å thick, sputtered, lightly nitrogen-doped, β tantalum layers, supplied by courtesy of the Bell Telephone Laboratories, Allentown, Pennsylvania. The layers were deposited on borosilicate glass covered with about 150Å thick tantalum pentoxide for better adherence.

Samples were needed for the observations in which breakdown and light emission were not enhanced at the edges of the tantalum layer, and which could be placed horizontally in the electrolytic bath for ease of light measurement. This was achieved with the samples shown in Fig. 1: These had photolithographically delineated tantalum areas which were 9 mm in

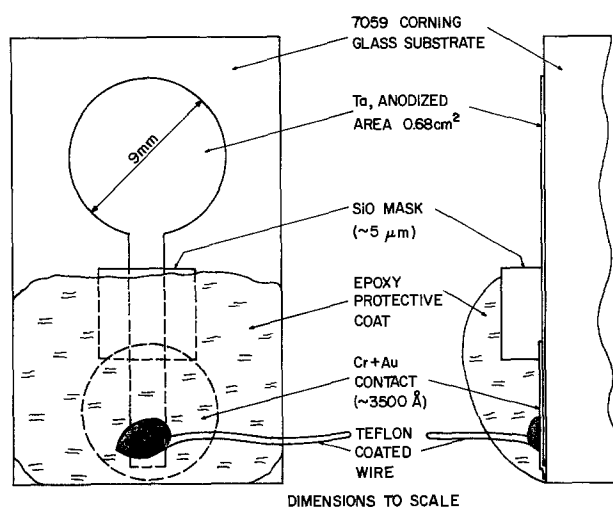


Fig. 1. Tantalum sample for anodization

¹ Present address: Israel Aircraft Industries, Yahud, Israel.

diameter and contained a contact strip. The latter was contacted by a Cr-Au land, to which a Teflon-coated wire was soldered. For insulation from the electrolyte, the contact strip and land were covered by a 5 μm thick vapor-deposited silicon oxide layer and by a thick epoxy coat. The tantalum area exposed to anodization was 0.68 cm^2 .

The electrolytic bath was contained in a Pyrex dish 37 mm deep and 74 mm diam. The sample was held at the bottom center of the dish with silicone grease. A tantalum ring 15 mm wide and 0.1 mm thick served as cathode. The electrolytic bath was an aqueous solution of citric acid with a range of concentrations from 2.5×10^{-3} to 1.8 weight percent (w/o), the corresponding resistivities at 1 kHz varying from 21,000 to 260 $\Omega\text{-cm}$. All the anodizations were carried out at constant current densities ranging from 0.5 to 10 mA/cm^2 ; temperature rises were reduced by magnetic stirring.

The experimental setup for the measurement of breakdown events and light emission is illustrated in Fig. 2. The events, as discussed later, are detected by a current pulse in the external circuit and often also by a spark at the breakdown spot. For the detection of the current pulses in the system a parallel capacitor C_p of a few μF capacitance and a series resistor $R_s = 10 \text{ k}\Omega$ were added to the anodization circuit. On breakdown, discharge of C_p through the breakdown filament produced a current pulse, which was monitored on the series resistor R_s .

The source of anodization was a constant current Elscint HVS power supply for the current range 10^{-4} - 10^{-1}A . A low-pass filter reduced current ripples from the supply to about 0.01% of the anodization current. This prevented the transmission of external current pulses to the $C_p R_s$ detecting circuit, except in the case of extremely large breakdown events, which usually occurred beyond the range of useful observations.

The light emitted from the sample was measured with an RCA Type 1P28 photomultiplier which was coupled to the sample with a 100 mm long, 10 mm diam quartz light guide. The collecting face of the light guide was concentric with and 10 mm above the sample. This distance was a compromise of the opposing requirements of uniform anodization and maximum light collection. The sensitivity of the photomultiplier extended over the spectral range 2200-6200 \AA , with a maximum close to 3300 \AA . The photomultiplier had potted leads and was cooled with solid CO_2 . The electrolytic bath, the light guide, and the photomultiplier were enclosed in an aluminum box, impervious to external light.

To register the anodization voltage, the voltage across the parallel capacitor C_p was measured with a

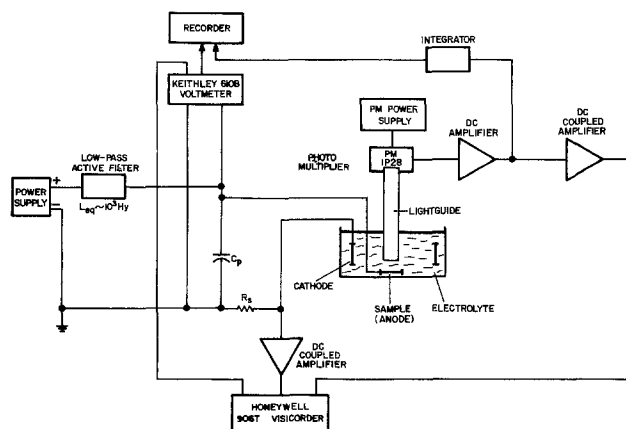


Fig. 2. Experimental setup for breakdown and light emission measurements.

Keithley 610B voltmeter and the voltage across the oxide layer was obtained by subtracting voltage drops in the electrolyte and the series resistor R_s .

Four quantities were recorded during each anodization run: the oxide voltage, current pulses associated with breakdown, the intensity of electroluminescence, and sparks. The electroluminescence (not discussed in this paper) was recorded against time of anodization on a pen-type Moseley 7100 BM, Hewlett Packard strip-chart recorder. The current pulses, sparks, and voltage *vs.* time of anodization were recorded on a Honeywell 906T visicorder oscillograph equipped with Heiland M8000 plug-in galvanometers. The response of the galvanometers was flat within 5% in the frequency range from 0 to 4800 Hz. Chart speeds varied from 5 to 100 mm/sec. A typical anodization run to 350-400V as function of time was recorded on roughly 6m length of chart paper.

Records of Breakdown Events

Güntherschulze and Betz (1) established that an individual breakdown event during anodization is due to temporary current runaway through a filament in the oxide. Such breakdown events can be studied with oscillograms of the current pulse arising in the series resistor R_s and the pulse due to a spark as function of time. This is illustrated by the oscillogram of Fig. 3, showing two events, one of which was accompanied by a spark.

Records of the sequence of breakdown events *vs.* time during anodization were obtained with the visicorder and are illustrated by three typical sections of a chart record in Fig. 4. In this chart spikes protruding from the noise on the upper trace denote current pulses on a compressed time scale. The slowly rising line is the trace of the anodization voltage, while the noisy bottom trace is due to the photomultiplier output current. On the latter trace, spikes are of interest, denoting sparks. The anodization recorded in Fig. 4 was carried out in an electrolyte of 2.3 $\text{k}\Omega\text{-cm}$ resistivity, at a current density of 1 mA/cm^2 . The three chart sections represent the voltage ranges (a) 35-48V, (b) 245-247V, and (c) 305-305.5V. In these sections, the time scales change. The typical anodic growth represented by Fig. 4 produced no current pulses below 30V, and the few current pulses between 30 and 100V were not accompanied by light pulses as indicated by the chart of Fig. 4(a). Figure 4(b) characterizes the voltage range in which the rate of current pulses begins to rise rapidly with voltage, in this case above 220V. In this chart, light pulses coincident with current pulses are observed in part of the events. Occasionally light pulses without coincident current pulses are found. Visual observation of the breakdown sparks suggests that events occur at random places, and the traces of Fig. 4(b) indicate inde-

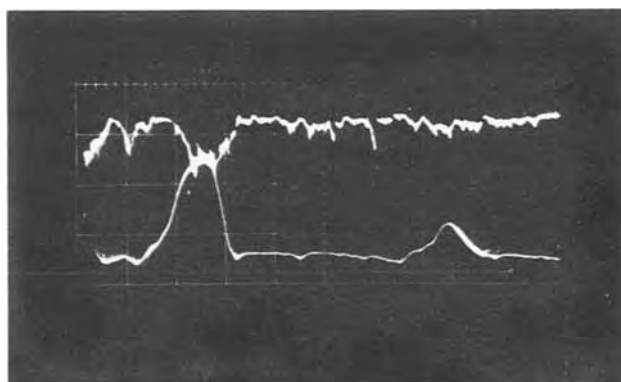


Fig. 3. Oscillogram of two current pulses (lower trace), and one of light pulse (upper trace) during anodization. Horizontal scale time, 2 msec/div; vertical scale, pulse amplitudes in relative units.

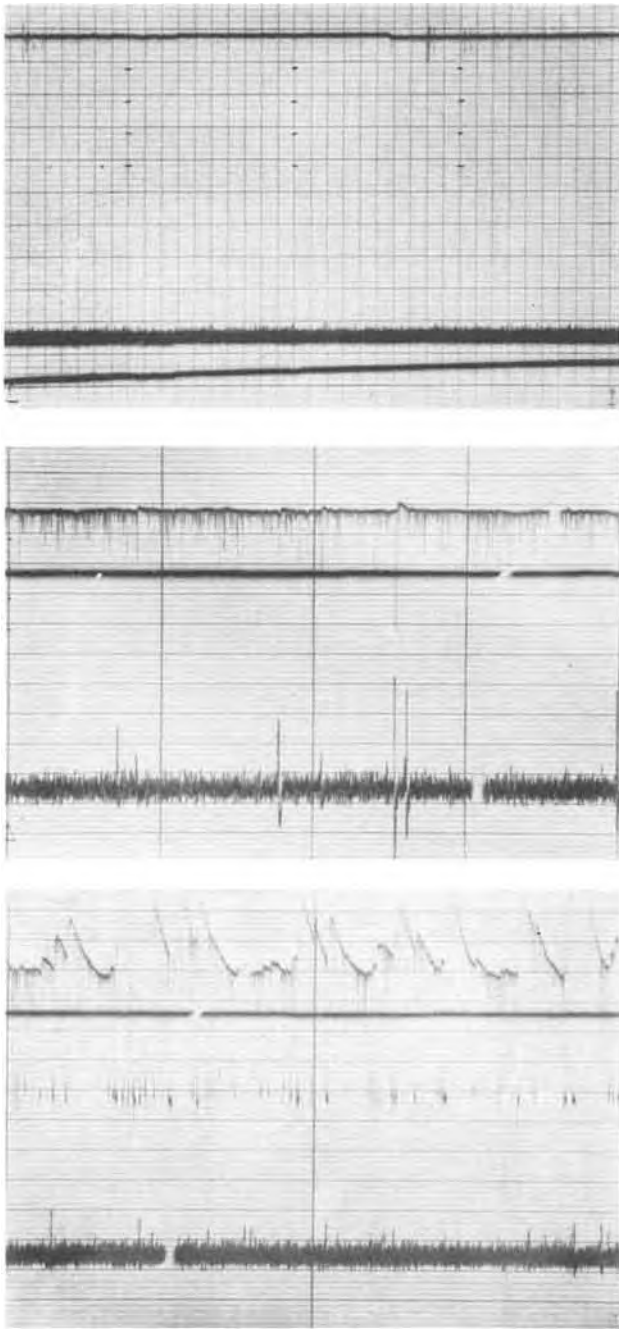


Fig. 4. Three visicorder charts vs. time during anodization. Upper traces, current pulses, $3.3 \mu\text{A}/\text{large vertical division}$. Slowly rising traces voltage, $30 \text{ V}/\text{large vertical division}$; bottom traces, sparks and a-c component of electroluminescent light. Voltage range of charts: (a) 35-48V, (b) 245-247V, and (c) 305-305.5V. Chart speeds: (a) 5 mm/sec; (b) 35 mm/sec; (c) 100 mm/sec.

pendent events of varying magnitudes occurring at random times.

Roughly above 300V prolonged events begin to appear, illustrated by the current pulse traces in the chart of Fig. 4(c). Oscillograms show that subsequent pulses are not independent, but overlap. Visual observations reveal persistent sparking, involving large areas. Breakdowns are propagating in this upper voltage range, events follow each other at adjacent places and are often the consequence of changes produced in the properties of the oxide by the prior breakdown. Since we were interested in the causes of the initiation of breakdown, determined by the original properties of the oxide, we made use of observations in the two lower voltage ranges only, where events appear to be random and independent.

To evaluate the information of the chart records, the current pulses were counted in small time intervals in which the effect of voltage changes could be considered small. With these data the rate of current pulses as function of anodization voltage, or insulation thickness, was calculated and the relationship plotted in a current pulse characteristic. Since any point of the characteristic was determined from a limited number of events, the standard deviation of the pulse rate was added, denoted by bars on the characteristics where feasible. When the time intervals for the counting of current pulses were very small, considerable fluctuations were found in the characteristics. This will be illustrated for the anodic growth of aluminum oxide in Fig. 1 of the companion paper (15). The rate of sparks was determined in the same manner as the rate of current pulses.

The characteristics were usually based on the count of current pulses of all sizes. Occasionally counts were classified according to the amplitude range of the current pulses and classified characteristics were obtained, as shown in Fig. 5. In this case the anodization was carried out with a current density $j = 1 \text{ mA}/\text{cm}^2$ in an electrolytic bath of $2.3 \text{ k}\Omega\text{-cm}$ resistivity. The pulse rate is plotted vs. anodization voltage for five groups of current pulses indicating an increase in mean pulse size with increasing voltage.

Current Pulses due to Filamentary Current Runaway

Breakdown events revealed by sparks are clearly the consequence of filamentary current runaway. Examination of spark-affected breakdown spots shows structural changes with a pit in the tantalum, one to a few micrometers in diameter. This pit seems to indicate the final size of the breakdown filament. The event appears to be a destructive breakdown, followed by some anodic regrowth of the damaged spot (1).

The question that arises immediately relates to the nature of the events unaccompanied by a spark. In such a case is the current pulse also due to local current runaway or due to a different process?

A direct answer is not available since for sparkless events structural changes were not detected in the oxide. Examination of breakdown charts as presented in Fig. 4b and comparison of current pulse charac-

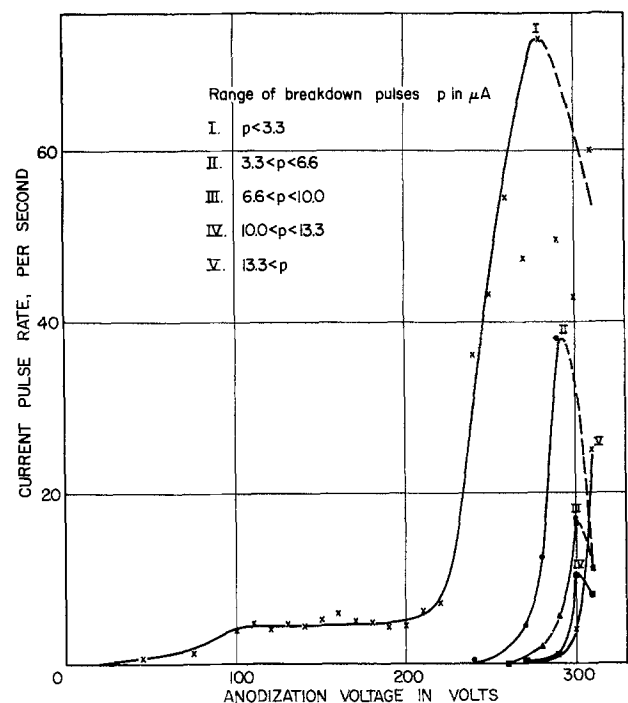


Fig. 5. Rate of current pulse vs. anodization voltage characteristics, classified by pulse amplitude.

teristics as shown in Fig. 5 with spark characteristics indicated in all cases that: (i) sparkless and spark-accompanied events are intermixed in a random manner; (ii) the likelihood of the occurrence of a spark increased with current pulse size, and (iii) the fraction of spark-accompanied events gradually increased with voltage to near unity, as the average current pulse amplitude increased.

These observations can be explained with the assumption that sparkless and spark-accompanied events have the same origin but differ in their development. This implies that not only events accompanied by a spark, but also sparkless events start with filamentary current runaway. Very large drops are expected, therefore, in the resistivity ρ_f of filaments during current pulses; to examine the validity of this assumption drops in ρ_f were calculated with the help of experimental results. Data were needed for this purpose on the magnitude of the filament radius, r_f , but were not available. Bounds were assessed instead on the magnitude of r_f . A lower bound was indicated by the oxide thickness during breakdown observations, roughly 5000Å, and this assessment is confirmed by the breakdown model developed later. An upper bound for r_f was indicated by the size of breakdown pits on spark accompanied events. The calculations were extended, therefore, over the range $0.5 < r_f < 5 \mu\text{m}$.

For the calculation of ρ_f the sample and the experimental setup were represented by the simplified equivalent circuit of Fig. 6. In this figure, C_i and R_i are insulator capacitance and resistance, respectively, and R_e is the electrolyte series resistance. R_f is the resistance of a breakdown filament, R_{ef} is the electrolyte resistance in series with the filament, and R_c is the resistance of the ionic charge layer at the oxide interface for cylindrical current flow into the filament. The resistance, R_c , is calculated with

$$R_c = \frac{w}{2\pi\epsilon_0\epsilon\mu V} \ln \frac{r_c}{r_f} \quad [1]$$

where r_c is the sample radius, w the oxide thickness, μ the ionic mobility, ϵ_0 the permittivity of empty space, ϵ the relative permittivity of the oxide, and V the voltage across the oxide. The resistance R_{ef} is calculated as a hemispherical spreading resistance and

$$R_{ef} = \rho_e/2\pi r_f \quad [2]$$

with ρ_e the resistivity of the electrolyte. A local breakdown is represented by a temporary closure of the switch. On breakdown the capacitors C_p and C_i discharge through the filament.

R_s was 10 k Ω and R_0 in ohms was numerically about equal to ρ_e in $\Omega\text{-cm}$ in the experiments. Drops in the values of ρ_f on the occurrence of current pulses are illustrated by calculations with $V = 300\text{V}$ as a representative voltage and $j = 1 \text{ mA/cm}^2$ as current density of anodization. For these values of V and j , $w \simeq 4.8 \times 10^{-5} \text{ cm}$, $C_i = 3.1 \times 10^{-8} \text{ F}$ with $\epsilon = 25$ and the oxide resistivity $\rho_i = 6.3 \times 10^{-9} \Omega\text{-cm}$. The sample radius $r_c = 0.45 \text{ cm}$; assuming for the ionic mobility in the electrolyte $\mu = 3 \times 10^{-4} \text{ cm}^2/\text{Vsec}$, the resistances R_c and R_{ef} were evaluated with Eq.

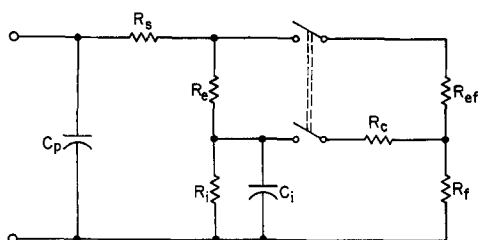


Fig. 6. Equivalent circuit for the interpretation of a breakdown event.

[1] and [2]. The calculations were carried out for four limiting cases, when $2r_f = 1$ and $10 \mu\text{m}$ and $\rho_e = 260$ and $21,000 \Omega\text{-cm}$, respectively. Results are presented in Table I showing that both R_c and R_{ef} are much larger than R_e or R_s .

Since $C_p \gg C_i$, the voltage drops on the capacitors were in most current pulse observations small and ρ_f was calculated neglecting these voltage drops. The smallest current pulses which could be discerned above the noise of the measurements were $5 \times 10^{-7} \text{ A}$. Calculation of ρ_f for $5 \times 10^{-7} \text{ A}$ pulses with the switch closed in the circuit of Fig. 6 resulted in the values presented in the last line of Table I.

Comparison of these ρ_f values with the oxide resistivity of $6.3 \times 10^9 \Omega\text{-cm}$ shows that the resistivity in a filament drops by several orders of magnitude even for the smallest current pulse and largest filament size. The resistivity drops increase as the filament size decreases and as the current pulse size increases. Therefore, it appears clearly that current pulses represent temporary current runaway processes. For smaller current pulses events are largely sparkless and such events can be considered as nondestructive breakdowns. Since for the understanding of the initiation of breakdown all current runaway processes are of interest, irrespective of whether the event is destructive or nondestructive, the investigation is based on the study of current pulse breakdown counts and characteristics

The values calculated for the electrolyte resistances R_e and R_{ef} are in the $10^8 \Omega$ range (Table I), showing that breakdown filaments are protected by large series resistances during anodic growth. This is in marked contrast to conditions in samples flanked by solid electrodes. In such samples a small resistance is in series with filaments, a few ohms when aluminum electrodes are 1000Å thick (16).

Reliable counting of the insulator current pulses depends on the parameters of the detecting circuit. The circuit of Fig. 6 indicates that for this purpose a capacitance C_p is needed, which is much larger than that of the sample C_i . This was found also experimentally, shown by the current pulse characteristics in Fig. 7a. The current pulse rate increases with increasing C_p and saturates for $C_p > 10^{-6} \text{ F}$. Usually a $2 \times 10^{-6} \text{ F}$ capacitor was selected for C_p .

It is interesting to note from curve c of Fig. 7a that some current pulses on R_s were observed even in the absence of a parallel capacitor. In this case only the most powerful breakdown events were observed with unusually large voltage drops of more than 10V on C_i . It was found that in the case of largest voltage drops small current pulses penetrated the low-pass filter from the power supply and were detected on R_s .

Figure 7b presents the spark rates measured at the same time as the current pulses of Fig. 7a. Relative to the current pulse characteristics the spark characteristics are shifted to higher voltages. It appears that the magnitude of the external capacitor affects but little the spark pulse characteristics and the occurrence of a spark depends mainly on the local development of the breakdown event.

Experimental Results

Experimental observations were made mainly at anodization current densities $j = 0.5, 1, 5, \text{ and } 10$

Table I. Filament resistivity

Filament diameter, $2r_f, \mu\text{m}$	1	1	10	10
Electrolyte resistivity, $\rho_e, \Omega\text{-cm}$	260	21,000	260	21,000
Resistance R_e, Ω	3.5×10^8	3.5×10^8	2.6×10^8	2.6×10^8
Resistance R_{ef}, Ω	8.3×10^7	6.7×10^9	8.3×10^8	6.7×10^8
Resistivity, $\rho_f, \Omega\text{-cm}$	9.7×10^4	6.1×10^4	9.9×10^8	9×10^8

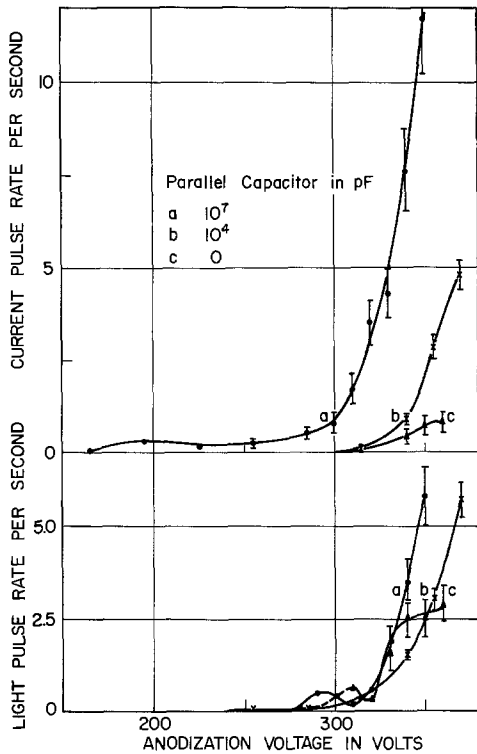


Fig. 7. Current and light pulse vs. anodization voltage with parallel capacitor size as parameter. $j = 1 \text{ mA/cm}^2$, $\rho_e = 7000 \text{ } \Omega\text{-cm}$.

mA/cm^2 . The magnitude of mean oxide fields, F , which produce these current densities is not known accurately. For the anodization of sputtered β tantalum films at a temperature $T = 298^\circ\text{K}$ and $j = 1 \text{ mA/cm}^2$ Mills *et al.* (17) found $F = 6.45 \times 10^6 \text{ V/cm}$, but Simmons *et al.* (18) arrived at $6.0 \times 10^6 \text{ V/cm}$. Nitrogen doping of the tantalum by 2 atomic percent (a/o) N was observed to increase the field by about 1% (18).

For present purposes a relationship giving j as function of F and T is needed. Such a relationship was obtained by Young (19) for the anodization of bulk tantalum giving j in A/cm^2 as function of both F and T in V/cm and $^\circ\text{K}$, respectively, and

$$j = 1.74 \times 10^8 \exp \left[\frac{1.16 \times 10^4}{T} (-2.185 + 3.497 \times 10^{-7}F - 1.675 \times 10^{-14}F^2) \right] \quad [3]$$

Since with this relation $F = 6.17 \times 10^6 \text{ V/cm}$ is obtained for $j = 1 \text{ mA/cm}^2$ at $T = 298^\circ\text{K}$ and since the slopes of the j - F characteristics $d(\ln j)/dF$ differ little for the anodizations of bulk and sputtered β tantalum (17), Eq. [3] was used for the calculation of the fields in the experiments. Results for the temperature of anodizations of 292°K are presented in Table II. At breakdown voltages $4^\circ\text{--}5^\circ\text{C}$ temperature rises were found at current densities of 5 and 10 mA/cm^2 and for these conditions corrected field values were calculated shown in the third line of Table II. While there is some uncertainty in the absolute field values of Table II, the relative magnitudes of fields for varying current densities agree well with the experimental results for sputtered β tantalum (17).

Table II. Anodization fields

Current density, mA/cm^2	0.5	1	5	10
Mean electric field, MV/cm	6.14	6.26	6.56	6.70
Fields corrected for temperature rise in the breakdown range, MV/cm	6.14	6.26	6.50	6.63

The effect of the uncertainty in field values on the evaluation of experimental results are discussed later.

The observations that are presented are characteristics giving R_r the rate of the total number of current pulses. Typical current pulse characteristics as function of voltage are presented in Fig. 8a with the current density of anodization as parameter. Since for the discussion on the breakdown mechanism the thickness dependence of the characteristics are of prime interest the data of Fig. 8a are replotted *vs.* thickness in Fig. 8b. The figures show that with increasing current density and thicknesses the current pulse rates increase rapidly. At the upper end of the characteristics, the slope of the curves tends to decrease. This may be unexpected, the slope decrease is however

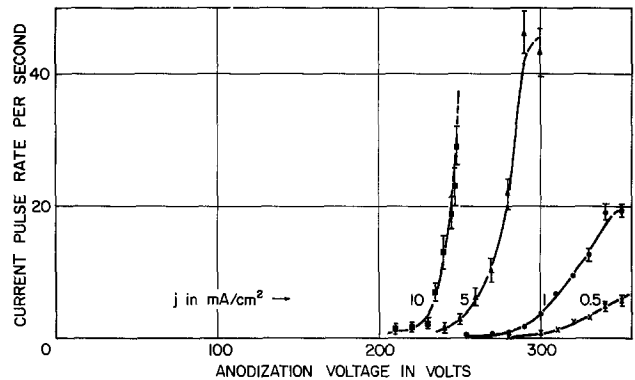


Fig. 8a. Current pulse rate vs. anodization voltage with current density as parameter. Experimental data are connected by full lines. Electrolyte resistivity $7000 \text{ } \Omega\text{-cm}$.

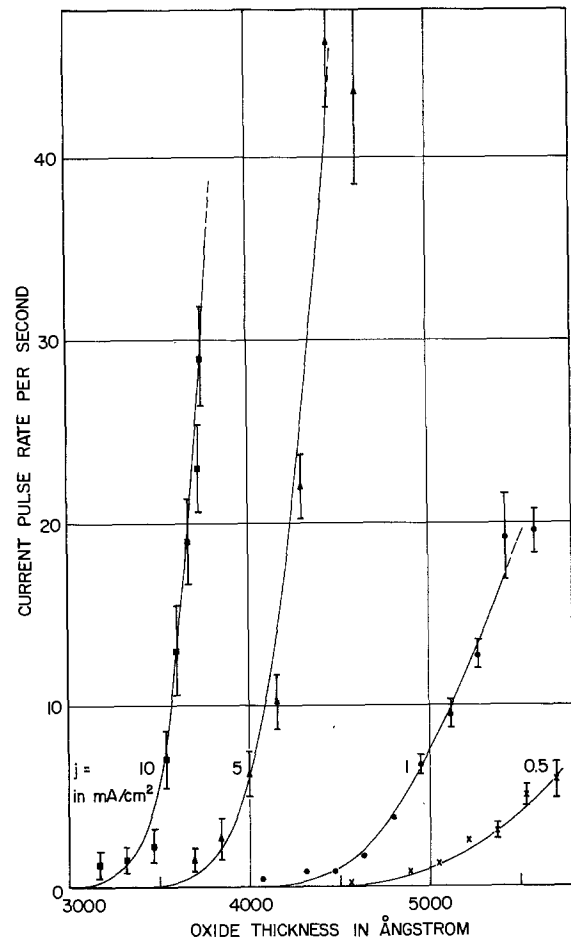


Fig. 8b. The experimental data of Fig. 8a vs. insulator thickness, plotted as dots with bars. Full lines represent calculated results.

consistently observed, when propagating breakdowns do not interfere in the measurements. The characteristics were found to be reproducible within a few percent on the thickness scale. The rate of breakdown could not be determined for $R_r > 30$ /sec for the characteristic of $j = 10$ mA/cm², because breakdowns were propagating.

The rate of breakdown was measured not only at constant field and growing insulator thickness, but also at practically constant thickness and varying field conditions. To obtain such results, the anodic growth was stopped at some voltage and the rate of current pulses measured at decreasing voltages with the sample remaining in the electrolyte. This is illustrated by the experiment of Fig. 9 for a 5700Å thick oxide, anodized with 0.5 mA/cm² current density to 350V. The rate of current pulses was found to decrease with increasing inverse field exponentially. Such a behavior was observed also in tantalum pentoxide films flanked by solid electrodes (16).

A series of experiments were carried out to study the influence of electrolyte concentration on the breakdown characteristic. The measurements extended over a range of resistivities from 260 to 2.1×10^4 Ω-cm, with a maximum citric acid concentration of 1.8 w/o. The breakdown characteristics as a rule were not much influenced by variations in ρ_e , although often inconsistent behavior was observed. On the whole a small tendency for shifts of the characteristics to lower voltages appeared with decreasing ρ_e . Earlier workers found larger decreases of the sparking voltage with decreasing ρ_e and increasing concentration (1, 3, 20, 21). These differences may in part be due to the larger range of concentrations in earlier work and also to the possible inclusion of sparks at weak spots, when the sparking voltage was determined.

A few experiments were carried out at electrolytic bath temperatures varying from 3° to 50°C, and characteristics for a given current density were found to shift to higher voltages with increasing temperature. Since the anodization field decreases with increasing temperature, the field decrease appears to be the dominant factor determining the shift in the characteristic.

The characteristics of Fig. 5 and 7 show small flat peaks for the rate of breakdowns at relatively low voltages, below the rising range of the characteristics. An unusually large peak of this kind was obtained for an anodization with $j = 1$ mA/cm² in an electrolyte of 2340 Ω-cm resistivity, illustrated by Fig. 10.

On many anodizations such low voltage peaks were not observed. They seem, however, to occur more frequently on anodizations in a low resistivity electrolyte and the magnitude of the peak and its voltage

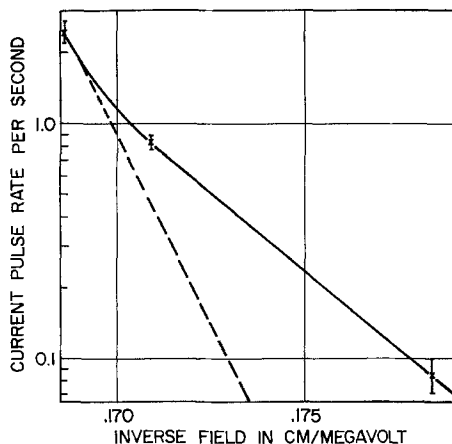


Fig. 9. Current pulse rate vs. inverse field below the anodization field for a 5700Å thick oxide sample. Full line, measurements; broken line, calculated results.

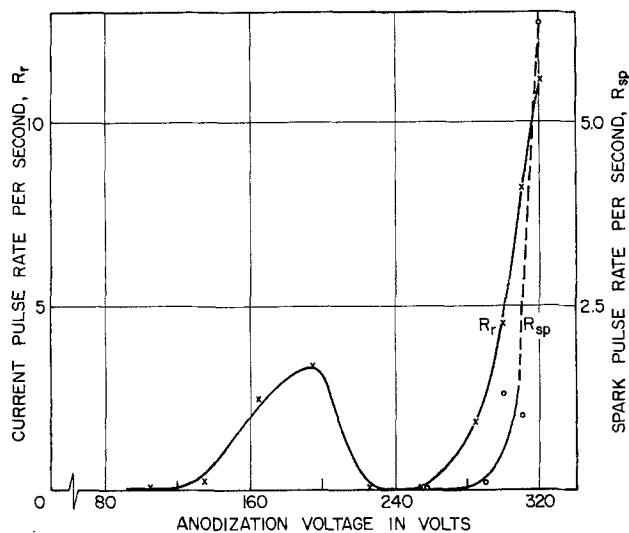


Fig. 10. Breakdown characteristics for a sample with a large current pulse rate peak at low voltages. $j = 1$ mA/cm² and $\rho_e = 2340$ Ω-cm.

range were found to vary widely. The low voltage peak events thus do not exhibit regularity, in contrast to the events observed in the rising part of the characteristics. It is possible that the events in the low voltage peaks of the characteristics are breakdown pulses at defects, indicating that breakdown characteristics could provide information for quality control.

Breakdown Mechanism

Identification of the breakdown mechanism is usually a complex problem. Difficulties arise for experimental and also for theoretical reasons. Experimental problems are connected with weak spots, fluctuations, and shorting breakdowns, although shorting does not disturb observations during anodic growth. Theoretically a good understanding of the high field conduction properties, of the energy band structure of the insulator, and of the relevant breakdown mechanisms is needed but is often only incompletely available. Such difficulties are found also in the discussion of breakdown in tantalum pentoxide.

The bandgap of tantalum pentoxide was found to be 4.6 eV from measurements of photoconduction (22), and the Fermi level of the parent tantalum metal was located 1.1 eV below the conduction bandedge of very thin oxides (23). In samples flanked by metallic electrodes, high field conduction in the range 0.5-3 MV/cm proved to be bulk limited and interpreted at room temperature by the Poole-Frenkel mechanism (24). Electrons were believed to be the dominant charge carriers. The Poole-Frenkel conduction mechanism was connected with coulombic trapping centers of 3×10^{18} /cm³ density, located 1.0 eV below the conduction bandedge (25, 26). The Fermi level of the oxide was estimated to be 1.4 eV below the conduction bandedge (26). No information seems to be available on conduction by holes and on their trapping properties in the insulator.

Conduction processes are very complex during anodic growth since in principle two ionic and two electronic species transport the current (27). In tantalum pentoxide the oxide field for a given current density remains constant during anodic growth and the ionic current component is two to three orders of magnitude larger than the electronic component (2). Models for the ionic current mechanism were therefore developed independently of the electronic current flow. No satisfactory model was established however (2), and it is as yet unclear whether the ionic current is bulk or interface limited, and whether space charges influence the ionic current flow. The

nature of the electron injection process from the electrolyte into the insulator has not been clarified either.

Diverse mechanisms were proposed for the explanation of breakdown events (28). Some of them like the electromechanical, the high temperature ionic, and the mechanism connected with asperities do not seem to be appropriate to the present case. Theories were not elaborated for mechanisms based on low temperature ionic, bond-breaking, and double injection processes and their relevance for tantalum pentoxide cannot be assessed. The mechanisms examined here are the thermal, because some temperature rises were observed in the oxide in the breakdown range of voltages, and that due to impact ionization, which was proposed by several earlier investigators (1, 3, 7, 8, 12).

Thermal breakdown.—The slope of the voltage vs. time curves was found to decrease roughly 1% at voltages close to the breakdown range, when anodizations were carried out at 5 and 10 mA/cm² current densities. The decrease in the slope was interpreted as a field decrease, the consequence of temperature rise by Joule heat (29). The temperature rise was calculated for a field decrease of 1% with Eq. [3]. A temperature rise of 4°–5°C was found, raising the question whether thermal instability was the cause of breakdown events during anodic growth at higher current densities.

Equation [3] shows that for anodic growth at a constant field, the conductivity of the oxide σ can be expressed in the form $\sigma = N \exp(-M/T)$, M and N being constants. For this conductivity relation thermal instability arises at a temperature T_m , calculated with (30)

$$T_m = \frac{M}{2} [1 - \sqrt{1 - 4T_0/M}] \quad [4]$$

Here T_0 is the ambient temperature and for a selected field M is determined with Eq. [3]. Calculations result in $T_m - T_0 = 11.7^\circ\text{C}$ for a field $F = 6.1$ MV/cm and $T_m - T_0 = 13.5^\circ\text{C}$ at $F = 6.7$ MV/cm. These results remain practically unaltered in more accurate constant current calculations which account for the small field decreases, when the temperature rises to T_m . Since the calculated values of $T_m - T_0$ are much larger than observed in the experiments, thermal instability cannot be the cause of the breakdown events at $j \leq 10$ mA/cm². This finding is reinforced by the circumstance that current runaway can only be localized and filamentary because the total current is constant and thermal filamentary current runaway occurs usually at temperatures larger than T_m (30).

Deterministic models of breakdown by impact ionization.—A number of mechanisms were proposed to explain breakdown by impact ionization (16, 28). Early theories of "intrinsic" breakdown ascribed it to the onset of impact ionization; Forlani and Minnaja (31) ascribed it to the destructive effect of large current flow. Newer theories based on O'Dwyers' (32) model interpret breakdown as an instability process causing current runaway.

Intrinsic theories cannot interpret the observations during anodic growth, because theories postulate that breakdown is independent of thickness. Ikonopisov (8) applied recently Forlani and Minnaja's model to interpret breakdown during anodization. This model assumes that carriers injected from the electrolyte into the oxide multiply by avalanching and breakdown arises, when the current density becomes high enough to cause destruction. Simple relations were derived which give the breakdown voltage V_b and the oxide thickness at breakdown and explain the dependence of V_b on current density, j . The theory was not developed further to account quantitatively for the spread in V_b values with thickness and for

the localization of breakdown events and the theory could not be verified by comparison with experiments.

This model does not account for current instability effects, which arise far below the temperature rise required for destruction. In case that the current increases with temperature, thermal instability and current runaway arise at a few tens of degrees temperature rise of the insulator (16). When the current runaway is connected with nearly immobile holes left by avalanches (32), the initial temperature rise can be insignificant.

Thus some form of instability is expected to trigger breakdown at a lower field than found with Ikonopisov's theory stipulating temperature rise to destruction (8). Since thermal instability was discounted, breakdown observations are examined with models based on instability by electronic impact ionization. To make the treatment tractable, we assume that the low mobility ionic current components do not influence the rapid breakdown events, except by determining the average field.

Theories of breakdown due to instability by electronic impact ionization are based on O'Dwyers' (32) positive feedback model. The model assumes that electrons injected into an insulator multiply by impact ionization leaving trapped holes behind. The holes increase the cathode field increasing electron injection and carrier multiplication. This regenerative process is successfully opposed below the critical current runaway field, F_r , by hole-electron recombination and/or by hole drift to the cathode. For fields larger than F_r breakdown arises after a time t_r , decreasing rapidly with increasing field. On anodization at constant field breakdown occurs only above a critical thickness, w_r .

This positive feedback process was elaborated for three models: (i) The IR model, applicable when the effect of ionization is opposed by recombination (33, 34). (ii) The small ionization ID model, when hole drift opposes ionization and the product of the ionization coefficient α and insulator thickness w , $\alpha w < 1$ (32, 35). (iii) The large ionization ID model; as described under (ii), but with $\alpha w > 1$.

Relations were derived for F_r , w_r , and t_r (34, 35) assuming that electron injection into the insulator is by Fowler-Nordheim tunneling and the electron current density, j_e

$$j_e = AF^2 \exp(-B/F) \quad [5]$$

with A and B constants. For the ionization coefficient the expression

$$\alpha = \alpha_0 \exp(-H/F) \quad [6]$$

was used with α_0 and H constants.

For the IR and the small ionization ID model the relation for the time to runaway t_r was found to be approximately (34)

$$t_r \approx \frac{2\epsilon_0\epsilon}{AB\alpha_0 w} \exp\left(\frac{B+H}{F_r}\right) \quad [7]$$

The relation is applicable above the critical thickness w_r , predicting that the rate of breakdown R_r , the inverse of t_r , is proportional to w . Examining the experimental results of Fig. 8b, we assume that w_r , the critical thickness for current runaway, is found where the R_r vs. w curve starts to rise. The rise of the curve above w_r is seen to be much steeper than predicted by Eq. [7] and this model does not fit the experimental results.

For the large ionization ID model (35) with $w > w_r$

$$t_r \approx \frac{2\epsilon_0\epsilon \exp[(B/F) - \alpha w]}{AB} \quad [8]$$

To test this model the data of Fig. 8 were replotted on a semilogarithmic scale in Fig. 11. The curves do not fit an exponential relationship between R_r and w well, except at a current density of 5 mA/cm².

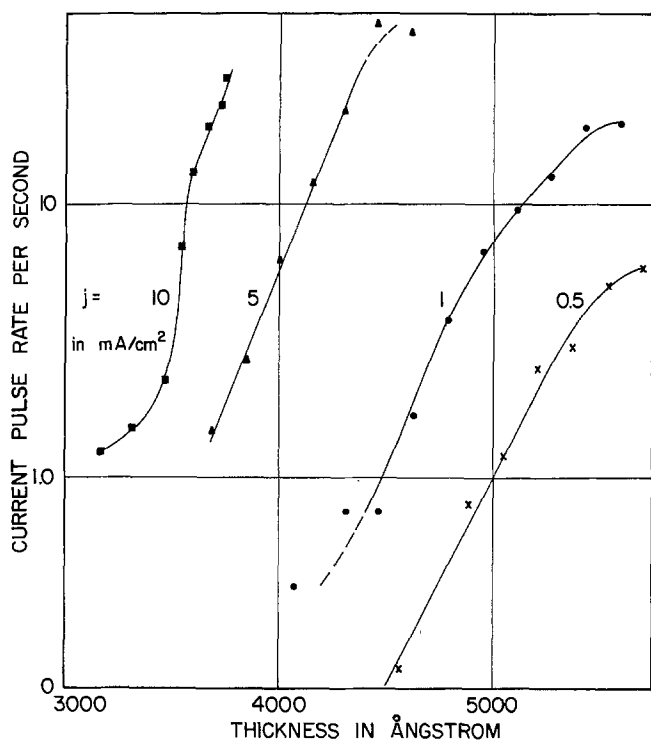


Fig. 11. Semilogarithmic plot of the experimental results of Fig. 8b vs. thickness.

We calculated α from the straight line sections of the curves for 0.5, 1, and 5 mA/cm², but as an average value for the curve at 10 mA/cm². α was found to increase from 3.5 to 5.5 $\times 10^5$ /cm for a field increase from 6.14 to 6.63 MV/cm. The αw products at the upper ends of the straight line sections were close to 20 implying avalanche sizes of $\exp 20 \approx 5 \cdot 10^9$. Such avalanche sizes are impossibly large. Owing to the effect of positive charges opposing the development of avalanches, their sizes are restricted to magnitudes, smaller by about six orders of magnitude (36, 14). The α values derived from Fig. 11 are therefore unrealistic and the oxide observations cannot be interpreted with the model of Eq. [8].

The relations presented in this section were derived by a continuum treatment of the breakdown models. The equations for F_r , w_i , and t_r are deterministic, not accounting for the effects of the finite properties of the electronic charge and of fluctuations. These effects can have significant influence on breakdown events: They can cause localization and randomness of breakdown events, breakdown fields lower, and times to breakdown shorter than given by the deterministic relations (14). Since the deterministic models did not explain observations a stochastic breakdown model is examined in the continuation.

The stochastic succession of avalanche breakdown model.—Account is taken of the finite properties of the electronic charge in the succession of avalanche model (14). This is a stochastic large ionization ID model also based on O'Dwyers' (32) instability mechanism by one carrier impact ionization. We recount here the essential features of the model and modify it for the purposes of this work.

In the succession of avalanche model, primary electrons injected produce avalanches by impact ionization leaving very low mobility holes in the insulator. The positive charges are centered in avalanche clusters spaced apart, and the hole density is grossly nonuniform. This is illustrated in the cross-sectional sketch of an insulator in Fig. 12a. The vast majority of the hole clusters drift out of the insulator without further effect. There is, however, a chance that a second electron is injected into a hole cluster before it leaves

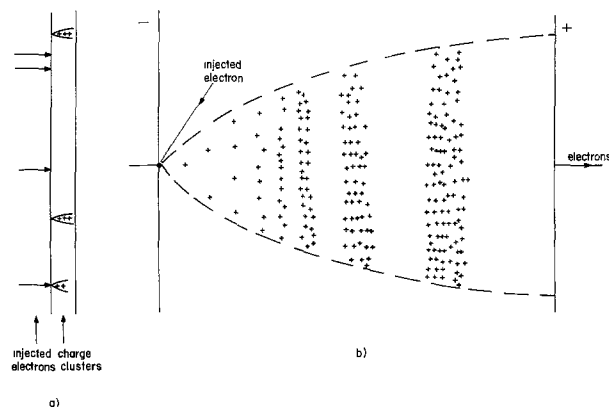


Fig. 12. (a) Cross-sectional sketch of an insulator with positive avalanche clusters spaced apart; (b) Schematic picture of positive charges produced in an avalanche (neglecting large fluctuations).

the insulator. A second avalanche arises, which locally enhances the cathode field, greatly increasing the chance for the injection of a third electron, etc. The regenerative effect of successive avalanches leads to current runaway and local breakdown, when an additional electron is always injected before the hole cluster leaves the insulator.

The average number of electrons, n , in an avalanche produced by an electron injected at the cathode is

$$n = \exp \left(\int_0^w \alpha dw' \right) \quad [9]$$

Alternatively, considering individual ionizations

$$n = 2^i \quad [9a]$$

i being the average number of ionizing collisions. There is an upper limit to the avalanche size, since the positive charges produced and left behind keep decreasing the field at the progressing front of the avalanche, until impact ionization stops (36, 14). Since the avalanche size is an exponential function of i , the effect of the positive charges becomes significant for the last few ionizing steps only. This is illustrated in Fig. 12b by the schematic picture of the positive charges of an avalanche produced by a primary electron. When the effect of holes is negligible the mean avalanche size produced by a primary electron

$$n = \alpha w \quad [9b]$$

The largest possible avalanche contains N_1 carriers, has a length w_1 and a cross section A_v at the front. Approximate relations derived for N_1 , w_1 , and A_v are (14)

$$N_1 = 4\pi\epsilon_0\sigma\kappa i_1 e l_p V_1 / 3q = 2^{i_1} \quad [10]$$

$$w_1 = \kappa i_1 V_1 / F \quad [11]$$

$$A_v = 4\pi\kappa i_1 l_p V_1 / 3F \quad [12]$$

Here $\sigma < 1$ is a form factor accounting for the localized effect of the opposing field of the positive charge; κ accounts for the average increase of the mean free path of impact ionization toward the anode (see Fig. 12b); i_1 is the number of impact ionizations by the injected electron producing the avalanche of size N_1 ; l_p is the mean free path for electron-optical phonon collisions, and V_1 is the mean voltage drop for an impact ionization in the vicinity of the cathode.

A relation for N_1 as function of field will be needed below. This is obtained by replacing $V_1 = F \ln 2/\alpha$ and $i_1 = \ln N_1 / \ln 2$ in Eq. [10] resulting in

$$N_1 / \ln N_1 = 4\pi\epsilon_0\sigma\kappa e l_p F / 3q\alpha \quad [10a]$$

Relations were derived (14) for the rate of breakdown, when fluctuations in the size of the avalanche

$N \leq N_1$ produced by a primary electron are disregarded. We denote in this case the rate of breakdown by R_{rN} , in distinction from R_r , which will apply when account is taken of fluctuations in the avalanche size N . For the case of electron injection by Fowler-Nordheim tunneling (Eq. [5])

$$R_{rN} = K \exp(-L_f B/F) \quad [13]$$

was obtained. Relative to the exponential factor, K depends weakly on F in this relation and will be assumed constant here. L_f is larger than unity and increases with the number of successive avalanches required for current runaway. The number of successive avalanches is the larger, the smaller the cathode field enhancement by the individual avalanches. The slope of the $\ln R_{rN}$ vs. $1/F$ plot is L_f times larger than that of the $\ln j_e$ (Eq. [5]) plot and L_f is denoted the slope enhancement factor.

L_f is a complex function of the primary avalanche size N (14) and will for present purposes be roughly approximated by

$$L_f = 1 + \gamma/N \quad [14]$$

with γ a constant. Replacing in Eq. [13]

$$R_{rN} = K \exp \left[-\frac{B}{F} \left(1 + \frac{\gamma}{N} \right) \right] \quad [13a]$$

A form better suited for calculations is used below

$$R_{rN} = C \exp(-B/F) \exp(bFN) \quad [13b]$$

with C and b constants. These two equations show a rapid increase in R_{rN} with increase in N , the size of the primary avalanches.

The increase in R_{rN} is limited by the maximum value of the avalanche size N_1 . We denote R_{rN} by R_{r1} and L_f by L_{f1} , for the case, when $N = N_1$ and obtain with Eq. [13] and [13a]

$$R_{r1} = K \exp \left[-\frac{B}{F} \left(1 + \frac{\gamma}{N_1} \right) \right] = K \exp(-L_{f1} B/F) \quad [15]$$

For thicknesses $w > w_1$ the avalanche size remains N_1 and R_{r1} is constant.

We show in the Appendix that calculations with Eq. [13a] can be well fitted to the experimental data of Fig. 8b. The fitting procedure, however, results in insignificant magnitudes for γ/N_1 representing the effect of field enhancement on the breakdown process for N_1 size avalanches. The value of γ/N_1 has to be at least 10 times larger according to the succession of the avalanche breakdown model and Eq. [13a] is not applicable to the observations.

We will show in the continuation that the succession of avalanche model becomes applicable, if account is taken of the effect of fluctuations in the avalanche size N and a modified relation will be derived for R_r as function of F and w . The treatment is based on approximations, because a rigorous derivation seems to be prohibitively complex.

The effect of fluctuations in the avalanche size on the rate of breakdown equation.—Fluctuations in avalanche size around a mean avalanche size n at a thickness w were investigated by Wijsman (37). The probability density $p(N, w)$ for the production of an avalanche of N electrons by an electron injected at the cathode into a w thick insulator is given by

$$p(N, w) \simeq \frac{1}{n} \exp(-N/n) \quad [16]$$

The relation is valid for $n \gg 1$, which is usually the case and in the thickness range in which the field distortion by positive charges is unimportant. An analytical relation is not available for thicknesses in which the effect of positive charges is significant. At

thicknesses larger than w_1 fluctuations in N are expected to be small and avalanches tend to grow to the size N_1 .

In the thickness range in which Eq. [16] is valid $p(N, w)$ has a broad exponential distribution and fluctuations in avalanche size are considerable. Breakdown events can therefore be initiated at a given thickness w by primary avalanche sizes N varying from the smallest size to N_1 and the rate of breakdown R_r is obtained by summing the breakdown contributions at all primary avalanche sizes. A first approach in finding the breakdown contribution dR_r at a thickness w and at primary avalanches between the sizes N and $N + dN$ is to equate dR_r with $p(N, w)dN \times R_{rN}$, with the product of the differential fraction of N size avalanches and of the rate of breakdown by N size avalanches at the thickness w_N . Such an assumption, however, overestimates the contribution dR_r at a thickness $w < w_N$, since the avalanches succeeding the N size primary avalanche at w are smaller than at w_N . The contribution dR_r is therefore smaller at w than at w_N and to account for this, the product for dR_r is multiplied by a function $c(n)$ and

$$dR_r = c(n) R_{rN} p(N, w) dN \quad [17]$$

$c(n)$ increases with w and hence with the mean avalanche size. The relationship $c(n)$ is not known and the simplest assumption is that

$$c(n) = \eta n \quad [18]$$

with η a constant.

Replacing for the factors of Eq. [17] from Eq. [13b], [16], and [18] and integrating over all primary avalanche sizes from $N \simeq 0$ to $N = N_1$ we obtain

$$R_r = \frac{\eta C \exp(-B/F)}{bF - 1/n} [\exp(bFN_1) \exp(-N_1/n) - 1] \quad [19]$$

In this expression the product $C \exp(-B/F) \exp(bFN_1) = R_{r1}$, the value of R_{rN} for $N = N_1$ (see Eq. [13b]). Numerical results obtained from experimental data show that at thicknesses in which breakdown events are registered $1/n$ can be neglected in the denominator and unity in the square brackets. Equation [19] obtains then the simple form

$$R_r \simeq \frac{\eta}{bF} R_{r1} \exp(-N_1/n) \quad [19a]$$

Since the field changes little η/bF is approximately constant and

$$\eta/bF = k \quad [20]$$

Replacing for n in Eq. [19a] from Eq. [9b] the relation for the rate of breakdown is obtained for thicknesses in which R_r is not affected significantly by positive charges

$$R_r \simeq k R_{r1} \exp[-N_1 \exp(-\alpha w)] \quad [21]$$

Alternatively replacing for R_{r1} from Eq. [15]

$$R_r = kK \exp \left[-\frac{L_{f1} B}{F} - N_1 \exp(-\alpha w) \right] \quad [21a]$$

These two relations are based on the approximations contained in Eq. [13b], [16], [18], and [20]. Comparison of Eq. [21a] with Eq. [5] shows that R_r increases strongly with the rate of electron injection into the insulator.

Since the probability density $p(N, w)$ is not known at thicknesses with significant positive charges, a relation for R_r is not available in this thickness range. We may extend, however, the validity of Eq. [19a] for this range in rough approximation by replacing for n from Eq. [9], obtaining

$$R_r \approx kR_{r1} \exp \left[-N_1 / \exp \left(\int_0^w \alpha dw' \right) \right] \quad [22]$$

The dependence of R_r on thickness expressed by Eq. [22] is schematically illustrated in Fig. 13 by a solid line curve. The lower part of the curve rising at increasing slopes corresponds to the range of validity of Eq. [21]. Beyond the range of its validity Eq. [21] is represented by the broken line curve. When the effect of positive charges becomes significant the slope of the solid line curve decreases with increasing thickness and the rate of breakdown saturates at $R_r = kR_{r1}/e$ for $N = N_1$.

Comparison of the succession of avalanche breakdown theory with experiments.—Breakdown characteristics, illustrated by Fig. 8a, were found to have slopes increasing with thickness, except at largest R_r values. Experimental data were compared therefore with Eq. [21] and [21a], examining the fit of the functional relationship and evaluating the breakdown coefficients α , N_1 , and kR_{r1} . The field dependence of α and kR_{r1} was determined too and compared with the functional relationships of Eq. [6] and [15].

Examinations started with a modified form of Eq. [21] obtained by taking logarithms twice

$$\ln [\ln (kR_{r1}/R_r)] = \ln N - \alpha w \quad [21b]$$

Equation [21b] predicts a linear relationship between $\ln [\ln (kR_{r1}/R_r)]$ and w . This relationship was found to be reasonably well observed. We illustrate this with the experimental data of Fig. 8b, which are replotted in Fig. 14, using α , kR_{r1} , and N_1 values evaluated below. The bars of standard deviations were omitted in Fig. 14 for clarity. Good linearity was found for the data of anodizations especially at 0.5, 1, and 10 mA/cm². The linear range of the data is connected by solid lines, but by broken line curves at extreme values of R_r , where deviations from linearity are observed. The deviations at the upper ends of the characteristics indicate that Eq. [21] is not applicable for very small values of R_r . These deviations may, however, be due also to very rare breakdown events at defects. Deviations at the largest w values are expected from theory and will be shown to result from the effect of positive charges.

Using double logarithmic plots and Eq. [21b] best fit straight lines to experimental data were computed by the least squares method. The coefficients α , N_1 , and kR_{r1} were determined with the straight lines and the following results were obtained from a large series of anodizations of tantalum layers produced in different sputtering runs:

1. kR_{r1} was found to increase with $1/F$ as shown in Fig. 15, bars indicating a spread in R_{r1} values. This spread may be partly due to variations in electron injection properties from the electrolyte into the

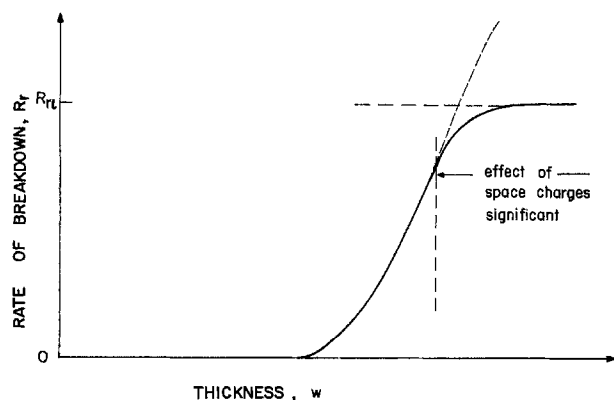


Fig. 13. Schematic representation of rate of breakdown vs. thickness according to Eq. [22].

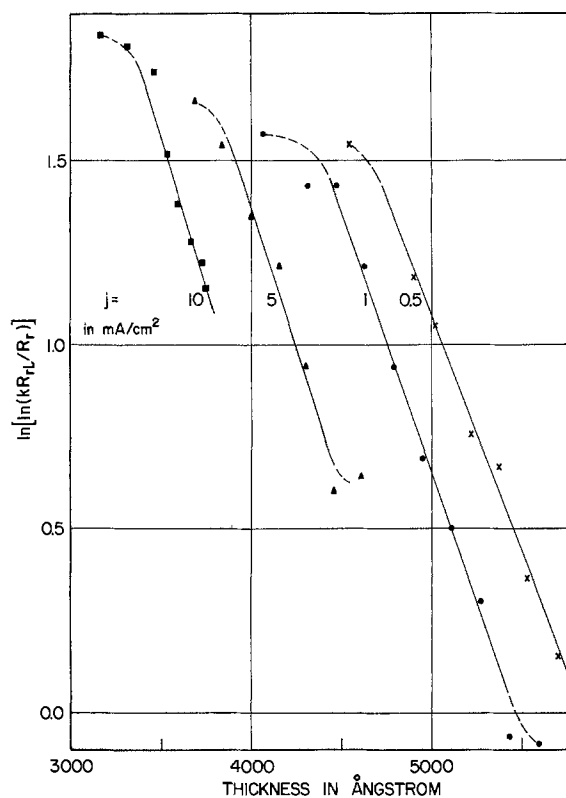


Fig. 14. Double-logarithmic plot of the experimental results of Fig. 8b vs. thickness as dots. Straight lines are calculated.

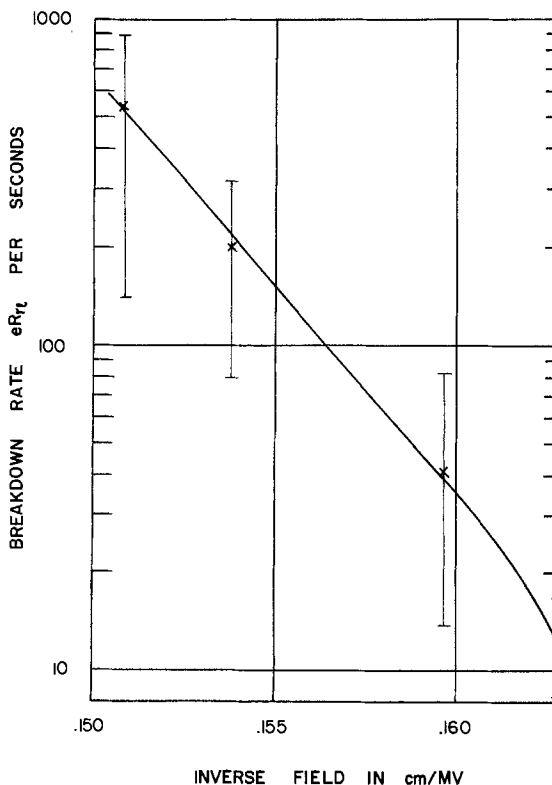


Fig. 15. The coefficient kR_{r1} vs. the inverse field

oxide. The functional relationship of the plot in Fig. 15 agrees fairly well with that predicted by Eq. [15] and the slope of the straight line part of the plot gives $L_{t1}B \approx 290$ MV/cm.

2. The coefficient of impact ionization was determined from the slope of the straight lines. A set of ten anodizations of randomly selected tantalum layers resulted in $\alpha = (1.58 \pm 0.21) \times 10^5/\text{cm}$ at a field of

6.26 MV/cm. Values of α found for other fields differed little and since the variance of the α values was large, the field dependence of α could not be established with anodic growths on randomly selected tantalum layers.

3. A large uncertainty was experienced in the determination of N_1 with the double logarithmic plots, values varying between 1500 and 3500 for anodizations at 6.26 MV/cm.

Variations found in the values of the coefficients were in part due to experimentation with tantalum layers from differing sputtering runs. An important part of the variations was, however, due to shallow minima in the best fit procedures and to fluctuations in the rate of breakdown, which diminish the accuracy of the best fit procedure. The shallow minima manifested themselves in fairly reasonable fits of calculated curves and experimental data for a range of variation in α by roughly $\pm 10\%$. Such changes in α resulted in slightly larger changes of opposite sign in R_{r1} and in much larger changes in N_1 . The nature of these changes are illustrated numerically with the example of the characteristics of Fig. 8b in Table III.

To find the field dependence of the coefficient of impact ionization α , the coefficients were determined with anodizations carried out at increasing fields on tantalum layers from the same sputtering run. Results of such anodizations are presented by the data of Fig. 8b. In the calculations best fit procedures were applied only to the determination of the coefficients for anodization at one field. These coefficients were used for the calculation of the coefficients at other fields providing an additional test for the validity of the theory. The calculations are illustrated with the data of Fig. 8b.

The best fit procedure was applied to the 6.26 MV/cm characteristic in Fig. 8b resulting in $\alpha = 1.4 \times 10^5/\text{cm}$, $kR_{r1} = 48.9/\text{sec}$, and $N_1 = 2082$. With these data the curve marked $j = 1 \text{ mA/cm}^2$ was obtained in Fig. 8b, agreeing well with observations, except at the upper R_r values. To calculate the coefficients at other fields changes of the thickness w with field F at a constant rate of breakdown were investigated.

Equation [21a] shows that when R_r is constant, the exponent in the expression

$$\frac{L_{fl}B}{F} + N_1 \exp(-\alpha w) = C \quad [23]$$

is a constant, C . C is determined from data at a given field and thickness and for calculations of α and N_1 at other fields and thicknesses Eq. [23] gives

$$\alpha = \frac{1}{w} \ln \frac{N_1}{C - L_{fl}B/F} \quad [24]$$

A second relation for the calculation of α and N_1 , is presented by Eq. [10a], which shows that $N_1/\ln N_1$ is proportional to F/α . A third relation for the evaluation of kR_{r1} is presented by Eq. [21].

Using the three relations the coefficients were determined by numerical methods. As an example we

Table III. Variations in the coefficients for the characteristic of $j = 1 \text{ mA/cm}^2$ in Fig. 8b

				The uncertainty
$\alpha \times 10^{-5}/\text{cm}$	1.26	1.4	1.54	$\pm 10\%$
N_1	1130	2082	3850	+85 -46
kR_{r1}/sec	56.8	48.9	43	-12 +16
$H, \text{ MV/cm}$	21.1	21.5	21.9	+1.9 -2.1
$\alpha_0 \times 10^{-6}/\text{cm}$	3.7	4.4	5.1	+16 -17
$i_0, \text{ A}$	3.7	6.9	13	

quote figures calculated with data for $R_r = 6/\text{sec}$ in the observations of Fig. 8b: For $j = 1 \text{ mA/cm}^2$ $R_r = 6/\text{sec}$ is found at a thickness $w = 4910\text{\AA}$. Using the previously determined values $\alpha = 1.4 \times 10^5/\text{cm}$, $N_1 = 2082$, and $L_{fl} = 290 \text{ MV/cm}$, $C = 48.5$ is obtained with Eq. [23]. With this value of C the coefficients were evaluated for $j = 0.5, 5, \text{ and } 10 \text{ mA/cm}^2$ anodization current densities and the results are tabulated in Table IV. Changes in the value selected for R_r did not alter the results significantly.

The breakdown characteristics calculated with the values derived for the coefficients are plotted as solid line curves in Fig. 8b. Except at the upper ends of the curves, good agreement is found with experimental results at 0.5 and 10 mA/cm^2 , but the agreement is not as good for 5 mA/cm^2 current density. The straight lines of Fig. 14 were also obtained with the α and R_{r1} values of Table IV, although for better fit the N_1 values were altered by a few percent.

The values presented for α in Table IV fit reasonably well the relationship of Eq. [6] for the coefficient of impact ionization, which can be expressed by $\alpha = 4.4 \times 10^6 \exp(-21.5/F)/\text{cm}$ with F in MV/cm . Comparison of the magnitude of $H = 21.5 \text{ MV/cm}$ with the fields of anodization indicates a "high field range of ionization," in which α increases relatively slowly with field.

To examine the reason for the deviations of experimental results from Eq. [21] at the upper end of the breakdown characteristics, avalanche sizes, n_m , unaffected by positive charges were calculated. With Eq. [9b] $n_m = \exp(\alpha w_m)$, w_m being the largest oxide thickness at which R_r was observed. The magnitudes of n_m were compared with N_1 and the ratios n_m/N_1 are presented in Table IV. The ratios show clearly that positive charges affect the breakdown rate at the upper ends of the characteristics, that avalanche sizes are smaller than n_m and should be calculated with Eq. [9]. It follows from Eq. [22] that a decrease in the slope of the characteristics is expected at the upper ends, as indeed demonstrated by the experimental data of Fig. 8b.

In the case of the 5 mA/cm^2 characteristic even a decrease was found in R_r at w_m and this may be a fluctuational effect. Propagating breakdowns prevented observations in tantalum pentoxide at thickness larger than w_m . It will be shown in Part II (15) that observations could be extended to larger thicknesses during the anodic growth of aluminum oxide. The results show a saturation in the rate of breakdown with increasing w , as predicted by Eq. [22].

The coefficients of the characteristics of Fig. 8b could be determined with good accuracy basing calculations on the value $\alpha = 1.4 \times 10^5/\text{cm}$ at 6.26 MV/cm . This value of α was, however, found by best fit procedure, involving an uncertainty in its magnitude. To study the effect of this uncertainty we recalculated the parameters kR_{r1} , N_1 , α_0 , and H for Fig. 8b assuming an uncertainty of $\pm 10\%$ in the value of α at 6.26 MV/cm . Results of the calculations presented in Table III show that the constant H is little affected, the effect on R_{r1} and α_0 is somewhat larger than on α , and that the value of N_1 is subject to a considerable uncertainty.

The magnitude of the field, known to a few percent accuracy only (see section on Experimental Results) is another source of uncertainty. A change in the field value assumed produces an inversely proportional change in the oxide thickness calculated from

Table IV. Parameters derived from data of Fig. 8b

$F, \text{ MV/cm}$	6.14	6.26	6.5	6.63
$\alpha \times 10^{-5} \text{ cm}$	1.31	1.40	1.57	1.70
N_1	2195	2082	1909	1788
kR_{r1}/sec	20.9	48.9	288	688
n_m/N_1	0.78	1.1	0.56	0.41

voltage observations. The effect of the thickness change is eliminated in Eq. [21a] by a change in α proportional to the change in field and the uncertainty in the field produces an uncertainty of the same magnitude in α .

The uncertainty in the value of the parameters is largely removed, when one constant is well known at a given field. While such a value is not available for Ta₂O₅ some independent indication of bounds for α and N_1 is obtained by calculating the mean free path for phonon collision, l_p , with Eq. [10a]. We replace for this purpose the α and N_1 values found in Table III and the approximate values $\sigma = 0.85$ and $\kappa = 1.8$ (14) in Eq. [10a] and evaluate data presented in the last line of Table III for l_p .

Information does not seem to be available on l_p in Ta₂O₅ for comparison. A value of about 6Å was found for l_p in amorphous aluminum oxide films at high fields (38, 39) and 1.7Å was derived for l_p in thermally grown silicon dioxide films at breakdown fields (33). It is likely that a few angstroms is the length of l_p also in amorphous tantalum pentoxide and Table III indicates that the calculations from breakdown observations resulted in reasonable values for l_p .

It is of interest to consider further avalanche properties. An individual avalanche of size N_1 produces a temperature pulse θ at the breakdown spot. Assuming that θ is due to the instantaneous heating effect of electrons, θ can be evaluated with the relation $\theta \approx \sigma_e e F^2 / 4c$ (14), with c the specific heat of the oxide, 0.8 W/cm³·K. For a field of 6.26 MV/cm $\theta \approx 23^\circ\text{C}$ is found. Such a temperature pulse cannot result in breakdown, because the pulse dissipates within nanoseconds (14) and calculations show that thermal instability cannot arise within this short time interval (30).

The stochastic properties of the succession of avalanche model were shown to be connected with the wide spacing between positive charge avalanche cones drifting toward the cathode (Fig. 12a). A fraction f of the oxide volume only is assumed to be occupied by avalanche cones. Stipulating a maximum value in f for the validity of the model, a lower bound can be estimated for the hole mobility, μ_p with the equations

$$f = j_e A_v t_t / q \quad \text{and} \quad t_t = w / \mu_p F \quad [25]$$

where j_e is the electron current density injected from the electrolyte, A_v is the largest avalanche cross section, and t_t is the transit time for holes through the oxides. Assuming that j_e is one thousandth of the ionic current density, 10^{-6} A/cm², $f = 0.1$, $w = 5 \times 10^{-5}$ cm, $F = 6.26$ MV/cm, and $A_v = 2.8 \times 10^{-11}$ cm² from Eq. [12] using data of Tables III and IV, a hole mobility of 1.4×10^{-8} cm²/Vsec is obtained with Eq. [25]. This value of μ_p indicates deep trapping of holes.

We examined also whether trapping of electrons influences the development of avalanches. The electron trapping levels are 1 eV below the conduction band-edge (24), and calculation of the trap occupancy τ at room temperature (40) shows that τ is 50% at 3.1 mV/cm. The trap occupancy drops rapidly with increasing field and electron trapping appears to have no significance in the range of the breakdown experiments during anodic growth.

The breakdown observations of Fig. 9 at constant thickness and at fields varying below fields for anodic growth were also examined with Eq. [21]. For the calculation of the field dependence of R_r , $w = 5700\text{\AA}$, $L_{FI}B = 290$ MV/cm, $N_1 = 2082$, and $\alpha = 4.4 \times 10^6 \exp(-21.5/F)/\text{cm}$ (F in MV/cm) were replaced in Eq. [21a]. The results are plotted by a broken line curve in Fig. 9. This curve agrees with the experimental data at highest values for R_r only, but drops off rapidly below experimental data at lower fields. It appears that Eq. [21a] is not applicable at lower

fields, when the rate of breakdown becomes very small. Figures 8b and 14 show that Eq. [21b] is not applicable at anodization fields either, when R_r is very small. The field dependence of the rate of breakdown is not known in this range of R_r .

It should be noted that as the field drops, the mean avalanche size and probably the hole mobility drop rapidly. The law governing electron injection into the oxide may alter too and these effects may change the mode of the breakdown mechanism. This may be illustrated by breakdown observations on 2300Å thick tantalum pentoxide films flanked by metallic electrodes at fields as low as 4.5 MV/cm (14). Avalanches are hardly expected to arise at such low fields, but mainly single ionizations by collision. The IR or the small ionization ID model may explain breakdown events in this case.

Summary

Breakdown observations made during the anodic growth of tantalum pentoxide were presented in characteristics, which plot the rate of breakdown as a function of oxide thickness at constant field. The breakdown events could not be interpreted by thermal instability or by mechanisms based on impact ionization at low rates, but by the stochastic succession of avalanche breakdown model.

An approximate relation derived for this model, giving the rate of breakdown, R_r , as function of insulator thickness, shows that R_r depends strongly on the electron current injected from the electrolyte and on electron multiplication in the oxide. The relation explains the observed shifts of the breakdown characteristics to lower thicknesses, with increasing field, or with decreasing temperature.

Characteristics calculated with the relation for R_r could be well fitted to experimental observations at various fields. Theory predicts a decrease in the slope of breakdown characteristics at larger R_r values, when the effect of the positive charges of the avalanches becomes significant. This has been consistently observed. The relation for R_r is not applicable at very low rates of breakdown, observed at relatively small insulator thicknesses, or at fields lower than those for anodic growth.

The coefficients in the relation for R_r were evaluated by best fit methods and with data on the variation of oxide thickness with field at a constant rate of breakdown. We found for the set of samples of Fig. 8b the mean values $\alpha = 1.4 \times 10^5/\text{cm}$ and $N_1 = 2082$ at a field of 6.26 MV/cm, and for the coefficient of impact ionization the relation $\alpha = 4.4 \times 10^6 \exp(-21.5/F)/\text{cm}$, with F in MV/cm for the range of fields 6.1-6.7 MV/cm.

These results are subject to uncertainties owing to shallow minima in the best fit procedures, to fluctuations in R_r , and to some uncertainty in the value of the electric field. Assessing the uncertainty in the magnitude of the coefficient of impact ionization to $\pm 10\%$, a somewhat larger uncertainty is found for the saturation value of $R_r = kR_{r1}/e$, but a large uncertainty in N_1 , the largest avalanche size. The uncertainty in the magnitude of the parameters could be largely removed, if one coefficient was known at one field.

Acknowledgments

Thanks are due to Dr. H. Basseches, Bell Laboratories, Allentown, Pennsylvania, for valuable help in supplying tantalum-coated substrates, and to Dr. M. Shatzkes, I.B.M., for careful reading of the manuscript and detailed comments. This work was submitted to Technion by V. K. in partial fulfillment of the requirements for the D. Sc. degree.

Manuscript submitted July 31, 1978; revised manuscript received June 1, 1979.

Any discussion of this paper will appear in a Discussion Section to be published in the December 1980

JOURNAL. All discussions for the December 1980 Discussion Section should be submitted by Aug. 1, 1980.

APPENDIX

The Magnitude of the Slope Enhancement Factor in Eq. [13a]

Equation [13a] does not account for the effect of fluctuations in avalanche size. Replacing for $N = n$ from Eq. [9b] into Eq. [13a]

$$R_{rN} = K \exp \left[-\frac{B}{F} - \frac{B}{F} \gamma \exp(-\alpha w) \right] \quad [13c]$$

is obtained. This equation has the same formal dependence on F and w as Eq. [21b], which accounts for the effect of fluctuations in N . Equation [13c] can therefore be fitted to the experimental data of Fig. 8b just as well as Eq. [21b] and the numerical results of the section Comparison of the Succession of Avalanche Breakdown Theory with Experiments can be applied to the coefficients of Eq. [13c].

B and $B\gamma/F$ in Eq. [13c] correspond to $L_f B$ and N_1 in Eq. [21b], respectively. Thus in Eq. [13c] $B = 290$ MV/cm and $B\gamma/F = 2082$ for a field of 6.26 MV/cm (see Table IV), resulting in $\gamma \approx 45$. The slope enhancement factor $L_f = 1 + \gamma/N$ (Eq. [14]) is smallest for the largest avalanche size N_1 and $L_{f1} \approx 1.045$, assuming $N_1 \approx 1000$ with Eq. [10] and Table III.

The relation derived for L_f in Ref. (14) is

$$L_f = 1 + (1 - R)(1/\beta_1 + 1/\beta_2 + \dots + 1/\beta_{n-1}) \quad [26]$$

$(1 - R)$ is close to unity and accounts for the effects of the removal of positive charge by drift. The coefficients β_1, β_2, \dots are the factors of field enhancement at the cathode after the first, second, etc. avalanche at the breakdown spot. The magnitude of the coefficients β falls between 1 and 2 and $\beta_1 < \beta_2 < \beta_3 \dots$. The number of the $1/\beta$ terms resulting in breakdown are smallest when $N = N_1$. For this case the slope enhancement term $(1 - R)(1/\beta_1 + 1/\beta_2 + \dots + 1/\beta_{n-1})$ can hardly be less than 0.5 and may reach 2.5 (14). The upper limit 0.045 found for this term from experimental results contradicts therefore, the succession of avalanche breakdown model and Eq. [13a] is not applicable to the observations.

REFERENCES

1. A. Güntherschulze and H. Betz, "Elektrolytkondensatoren," Krayn, Berlin (1937).
2. C. J. Dell'Oca, D. L. Pulfrey, and L. Young, in "Physics of Thin Films," Vol. 6, M. H. Francombe and R. W. Hoffman, Editors, pp. 1-79, Academic Press, New York (1971).
3. J. Yahalom, in "Oxide-Electrolyte Interfaces," R. S. Alwitt, Editor, pp. 288-301, The Electrochemical Society Softbound Proceedings Series, Princeton, N.J. (1973).
4. W. D. Westwood, N. Waterhouse, and P. S. Wilcox, "Tantalum Thin Films," Academic Press, London (1975).
5. N. N. Axelrod and N. Schwartz, *This Journal*, **116**, 460 (1969).
6. J. Yahalom and J. Zahavi, *Electrochim. Acta*, **16**, 603 (1971).
7. A. K. Vijh, *Corros. Sci.*, **11**, 411 (1971).
8. S. Ikonopisov, *Electrochim. Acta*, **22**, 1077 (1977).
9. W. Ch. van Geel, A. C. Pistorius, and B. C. Bouma, *Philips Res. Rep.*, **12**, 6 (1957).
10. C. R. Fritzsche, *J. Phys. Chem. Solids*, **30**, 1885 (1969).
11. V. M. Orlov, L. L. Odyneets, and T. I. Ryungenen, *Sov. Electrochem.*, **9**, 783 (1973).
12. J. M. Albella, I. Monter, and J. M. Martinez-Duart, *Thin Solid Films*, **58**, 307 (1979).
13. V. Kadary and N. Klein, in 8th Convention IEEE, Tel-Aviv, 27-36/VII, 1973; Abstract 118, p. 299, The Electrochemical Society Extended Abstracts, Fall Meeting, Boston, Massachusetts, Oct. 7-11, 1973.
14. N. Klein, *Adv. Phys.*, **21**, 605 (1972).
15. N. Klein, V. Moskovici, and V. Kadary, *This Journal*, **127**, 152 (1980).
16. N. Klein, in "Advances in Electronics and Electron Physics," Vol. 26, L. Marton, Editor, pp. 309-424, Academic Press, New York (1969).
17. D. Mills, L. Young, and F. G. R. Zobel, *J. Appl. Phys.*, **37**, 1821 (1966).
18. R. T. Simmons, P. T. Morzenti, D. M. Smyth, and D. Gerstenberg, *Thin Solid Films*, **23**, 75 (1974).
19. L. Young, *Proc. R. Soc. London, Ser. A.*, **258**, 496 (1960).
20. F. J. Burger and J. C. Wu, *This Journal*, **118**, 2039 (1971).
21. G. C. Wood and C. Pearson, *Corros. Sci.*, **7**, 119 (1967).
22. L. Apker and E. A. Taft, *Phys. Rev.*, **88**, 58 (1952).
23. W. E. Flannery and S. R. Pollack, *J. Appl. Phys.*, **37**, 4417 (1966).
24. P. L. Young, *ibid.*, **46**, 2794 (1975); *ibid.*, **47**, 235 (1976).
25. J. H. Thomas III, in Proceedings of Conference on Electric Insulation and Dielectric Phenomena, 1975, Gaithersburg, Md.
26. J. H. Thomas III, *J. Appl. Phys.*, **45**, 835 (1974).
27. A. T. Fromhold, Jr., "Theory of Metal Oxidation," Vol. 1, North Holland, New York (1976).
28. N. Klein, *Thin Solid Films*, **50**, 233 (1978).
29. L. Young, *Trans. Faraday Soc.*, **53**, 229 (1957).
30. L. Altcheh and N. Klein, *IEEE Trans. Electron Devices*, **ed-20**, 801 (1973).
31. F. Forlani and N. Minnaja, *Phys. Status Solidi*, **4**, 311 (1964).
32. J. J. O'Dwyer, *J. Appl. Phys.*, **40**, 3887 (1969).
33. T. M. DiStefano and M. Shatzkes, *Appl. Phys. Lett.*, **25**, 685 (1974); *J. Vac. Sci. Technol.*, **12**, 37 (1975); *ibid.*, **13**, 50 (1976).
34. N. Klein and P. Solomon, *J. Appl. Phys.*, **47**, 4364 (1976).
35. I. Kashat and N. Klein, *ibid.*, **48**, 5217 (1977).
36. J. J. O'Dwyer, *J. Phys. Chem. Solids*, **28**, 1137 (1967).
37. R. A. Wijsman, *Phys. Rev.*, **75**, 833 (1949).
38. R. M. Handy, *J. Appl. Phys.*, **37**, 4620 (1966).
39. E. D. Savoye and D. E. Anderson, *ibid.*, **38**, 3245 (1967).
40. P. C. Arnett, *ibid.*, **46**, 5236 (1975).

Electrical Breakdown

II. During the Anodic Growth of Aluminum Oxide

N. Klein, V. Moskovici,¹ and V. Kadary²

Faculty of Electrical Engineering, Technion-Israel Institute of Technology, Haifa, Israel

ABSTRACT

Breakdown characteristics found during the anodic growth of aluminum oxide start with a range of rapid increase in the rate of breakdown R_r . This is followed by a range of saturation, when observations are not disturbed by propagating breakdowns. The mean value of R_r can be subject to some variations in the saturation range. The breakdown characteristics shift to lower voltages with increasing field of anodization. The observations agree with predictions of the succession of avalanche breakdown theory. The reason for variations of R_r in the saturation range is not clear. The coefficient of impact ionization at a field of 8.7 MV/cm was found to be roughly 2×10^5 mcm. Compared with tantalum pentoxide the breakdown characteristics of aluminum oxide show a relatively poor reproducibility.

Samples and Some Oxide Properties

Investigations of Part I of this paper (1) were extended to electrical breakdown during the anodic growth of aluminum oxide. Experimental setup and methods applied were the same as in the tantalum pentoxide observations (1). The samples had the dimensions and buildup shown in Fig. 1 of Part I (1) for tantalum samples. The samples produced in vacuum by thermal vaporization of high purity aluminum were deposited on borosilicate glass substrates. The aluminum layers, 5000Å thick, had a mirror-like surface.

We were interested in examining nonporous films, which are not attacked by the electrolyte (2). The pH of the electrolytes used was limited, therefore, to the range of 5.5-6.5 (3). The anodic growths were performed with an electrolyte of an aqueous solution of 0.1M ammonium tartarate adjusted with tartaric acid to a pH of 6. Deionized water with a resistivity of several MΩ-cm was used. The resistivity of the electrolyte measured at 1 kHz was 70 Ω-cm. Electron diffraction showed that the oxide layers grown were amorphous.

We review briefly data on the properties of anodic aluminum oxide relevant for this work: Experimental results published on the electric field of formation, F , as function of current density of anodization, j , vary, roughly within $\pm 7\%$ (4-6) and this spread introduces some uncertainty in the evaluation of experimental results. We use here the F - j relation obtained by Siejka *et al.* (7) for room temperature

$$j = 1.72 \times 10^{-25} \exp(5.76 \times 10^{-6} F) \quad [1]$$

with j in A/cm² and F in V/cm. Table I presents values of F at the current densities selected for the observations. Equation [1] was obtained for polished sheet samples and we assume its applicability to the mirror-like thin film samples of this work.

Optical measurements of Arakawa and Williams (7) for the determination of the bandgap of anodically grown Al₂O₃ showed the onset of appreciable absorption at 6.8 eV. This was connected with excitonic transitions, while band to band transitions were ascribed to energies above 9.4 eV. Powell (8) found band to band transitions with photoconduction experiments in chemi-

cally vapor-deposited (CVD) films with photon energies larger than 7.8 eV. Measurements of the barrier at the aluminum-CVD aluminum oxide interface resulted in energies of 3-3.5 eV (9-11). Conduction experiments at high fields in CVD films were interpreted with trapping of injected electrons roughly 1.35 eV below the conduction bandedge (12). Observations indicated deep trapping of holes, but quantitative data were not obtained (13). The electronic current component during anodization was found to amount to less than 2% of the ionic current on polished aluminum samples (6).

Experimental Results

Experimental observations are illustrated by the breakdown characteristics plotted in Fig. 1-3. Figure 1 presents the characteristic for an anodization at 1 mA/cm² current density at room temperature. Dots with bars of standard deviation in the figure represent experimental results and the solid line is calculated. The characteristic rises rapidly between 200 and 230V. This range is followed by one of saturation, in which the rate of breakdown R_r fluctuates around a mean of about 7/sec.

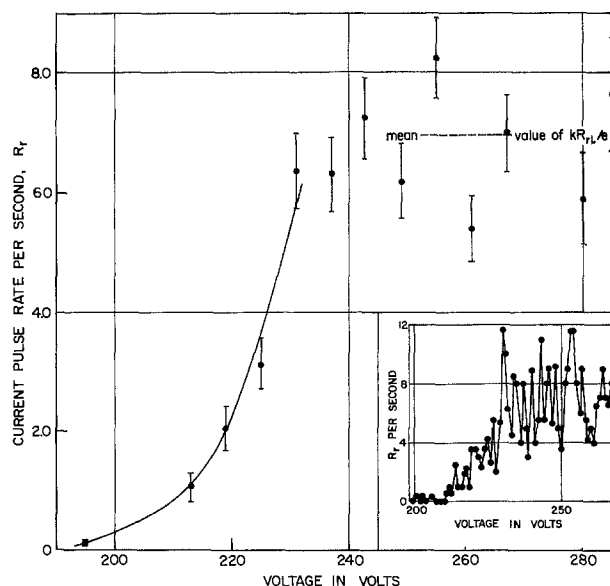


Fig. 1. Rate of breakdown vs. anodization voltage at a current density of 1 mA/cm². Dots are experimental results and the solid line curve is calculated. The insert gives part of the characteristic counting breakdown events in 1V intervals; dots are connected by lines for clarity.

Table I. Anodization fields

Current density, mA/cm ²	0.5	1	2	5
Mean electric field of formation, MV/cm	8.58	8.7	8.82	8.98

¹ Present address: Israel Electric Corporation, Haifa, Israel.

² Present address: Israel Aircraft Industries, Limited, Yehud, Israel.

A saturation range for R_r could not be observed in tantalum pentoxide owing to the prevalence of propagating breakdowns above the voltage, where the slope of the characteristic begins to decrease. In contrast, propagating breakdowns were usually not numerous in the saturation range of aluminum oxide. In the case of the experiment of Fig. 1, for instance, propagating breakdowns occurred only over 10% of growth time and the frequency of such breakdowns was roughly constant over the saturation range. The great majority of breakdowns were individual, randomly distributed events. The rate of breakdown could therefore be determined in good approximation for Fig. 1, counting all current pulses, including those found in the traces of propagating breakdowns. To assess the error due to this counting procedure, we determined R_r also by disregarding current pulses found in the traces of propagating breakdowns and by correcting for the time lost to observation by the propagating breakdowns. These R_r values were a few percent smaller than those plotted in Fig. 1.

Fluctuations in R_r were considerable and to illustrate their nature, R_r is plotted vs. the anodization voltage V in the inset of Fig. 1, counting breakdown events in 1V intervals. For clarity, successive R_r values are connected by solid lines. This plot indicates a periodic variation in the mean value of R_r over periods of 10-12V. Other kinds of variations in the mean value of R_r in the saturation range were observed as well, such as a peak in R_r at the beginning of the range, or a decrease in R_r in the middle of the range. The saturation range was followed by a range filled by propagating breakdowns. Owing to prevalence of propagating breakdowns, a saturation range was not observed in all experiments. This was experienced especially with samples in which breakdowns started at voltages lower than the average starting voltage.

Figure 2 presents breakdown characteristics for anodizations at 1 and 5 mA/cm² on two samples produced in one production run. The characteristic shifts to a lower voltage range and R_r increases with increase of field, as found also for tantalum pentoxide (1). The rate of breakdown in the saturation range for $j = 1$ mA/cm² is roughly 2/sec. This is about three and one-half times smaller than found for R_r in the saturation range in Fig. 1. Such a spread in observations was frequently found with anodic growth experiments of aluminum oxide. Characteristics obtained shifted on the anodization voltage scale around a mean by $\pm 15\%$ for anodization current densities of $j = 0.5$ and 1 mA/cm² and $\pm 10\%$ for $j = 2$ and 5 mA/cm².

Stopping anodic growth, the rate of breakdown was measured at fields lower than fields of formation, with the sample remaining in the electrolyte. Results of such an experiment are presented in Fig. 3 for a 2700Å thick oxide sample.

Discussion

The examination of the experimental results was performed in the same manner as for tantalum pentoxide (1). The observations could not be interpreted by thermal breakdown or with the deterministic impact ionization breakdown theories. We examined, therefore, the applicability of the succession of avalanche model. For this model the rate of breakdown is given by Eq. [21] of Part I (1), valid in the thickness range in which the effect of positive charge is not important and

$$R_r = kR_{r1} \exp[-N_1 \exp(-\alpha w)] \quad [2]$$

The notation of the symbols of Eq. [2] is the same as in Part I (1).

Calculations with Eq. [2] based on $w \propto V$ resulted in reasonably good fits to experimental data and this is illustrated in Fig. 1 and 2 by the solid line curves. However, the fitting procedure was within limits successful for differing sets of the coefficients α , N_1 , and kR_{r1} ; the uncertainty found in the determination of the

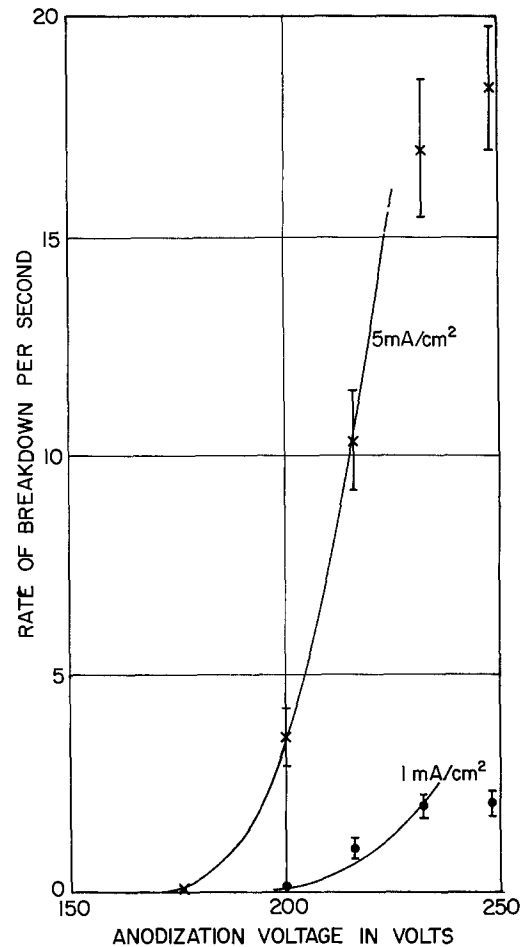


Fig. 2. Rate of breakdown vs. anodization voltage at current densities of 1 and 5 mA/cm². Dots are experimental results and the solid line curves are calculated.

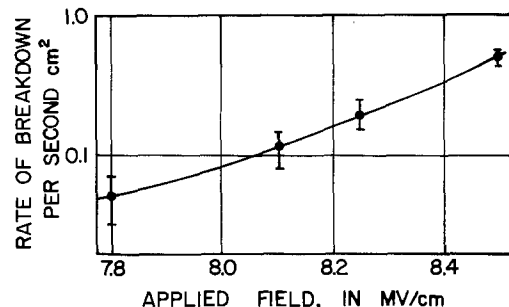


Fig. 3. Rate of breakdown as function of fields smaller than fields of formation in an oxide approximately 2700Å thick.

coefficients for tantalum pentoxide was enhanced in the case of aluminum oxide owing to poorer experimental reproducibility and less accurate knowledge of the magnitude of the field.

Fortunately Eq. [12a] of Part I (1) for the size of the largest avalanche N_1 could also be applied to the determination of α , N_1 , and kR_{r1} , since experimental data are available on l_p , the mean free path of electron-phonon scattering in aluminum oxide. Equation [12a] has the form

$$\frac{\alpha N_1}{\ln N_1} = \frac{4\pi\epsilon_0}{3q} \epsilon F \sigma l_p \kappa \quad [3]$$

The notation of the symbols is given in Part I (1). The coefficients α , N_1 , and kR_{r1} can, in principle, be accurately calculated with Eq. [2] and [3] and the experimental results. The magnitude of the factors σ , l_p , and κ of Eq. [3] is, however, not well known and only

bounds could be estimated for the coefficients α , N_1 , and kR_T .

The magnitude of the factors σ and κ was discussed in Ref. (14). $\sigma < 1$ is a form factor accounting for the localized effect of the positive charges opposing further ionization by an N_1 size avalanche. The magnitude of σ was estimated to vary between 0.7 and 0.9. $\kappa > 1$ is a factor accounting for the average increase of the mean free paths of impact ionization toward the anode. The magnitude of κ depends strongly on the field dependence of the coefficient of impact ionization α . κ was estimated to vary between 1.4 and 2.

Several experimental methods were applied to find the magnitude of l_p . A number of investigators attempted to determine l_p from observations of hot electron transport in very thin aluminum oxide films in a range of fields which include fields of anodization (15-18). Handy (15) found near isotropic electron-optical phonon scattering with an energy loss of 0.12 eV and 4Å free travel in the field direction. In reasonable agreement with these results, Savoye and Anderson (16) found isotropic scattering with an energy loss of 0.1 eV and a mean free path $l_p = 6\text{Å}$. The determination of l_p by observations of internal photoemission (19) resulted in $l_p = 10\text{Å}$ near an aluminum-aluminum oxide interface.

Accounting for the uncertainties in the magnitudes of σ , κ , and l_p , breakdown characteristics were calculated with Eq. [2] and [3], fitting experimental results. We assumed for the product $\sigma\kappa l_p$ the bounds $6 \leq \sigma\kappa l_p \leq 18$ in angstroms and $\epsilon = 8.5$. The coefficients of the characteristics evaluated for the experiments of Fig. 1 and 2 are presented in Table II. The columns marked M contain the coefficients for the arithmetic mean of the calculated bounding α values. The bounds of the α values differ by $\pm 13\%$ from the mean value of α .

The mean avalanche size n_m was evaluated at w_m , at the thickness corresponding to the upper end of the calculated characteristics, assuming that n_m is not affected by positive charges and $n_m = \exp(\alpha w_m)$. The ratios n_m/N_1 were formed and tabulated in Table II. The magnitude of the n_m/N_1 ratios indicate that positive charges are significant at w_m and that Eq. [2] is not applicable for thicknesses $w > w_m$.

The last line of Table II presents $V_i = F \ln 2/\alpha$, the mean voltage drop for an impact ionization. The qV_i values found are more than three times larger than the oxide bandgap (7, 8).

The rate of breakdown is kR_T/e in the saturation range according to Eq. [22] of Part I (1). Since the magnitude of k is not known, R_T could not be calculated in the saturation range. The fluctuations in R_T were examined by plotting in Fig. 4 the histogram of the number of current pulses which were observed in 1 sec growth intervals. The observations extended over 110 sec from the anodization voltage 233 to 273V. The average number of current pulses was 6.86/sec in this voltage range. Using this average, the Poisson distribution of the number of pulses in 1 sec intervals was calculated and plotted as a solid line in Fig. 4. Comparison of this curve with the histogram reveals a surplus of intervals observed with low and large numbers of current pulses, but some lack in intervals below the peak of the curve.

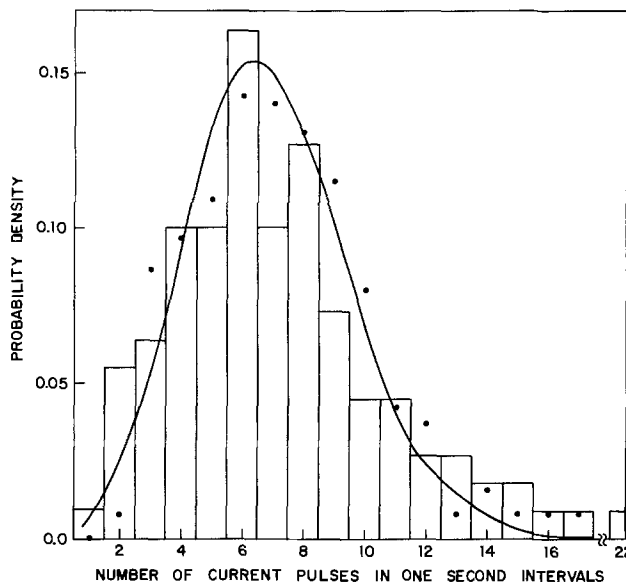


Fig. 4. Histogram of the number of current pulses in 1 sec intervals for the data of Fig. 1 in the saturation range. Solid line curve the Poisson distribution with an average number of current pulses of 6.86 in a 1 sec interval. Dots represent the corrected histogram.

At first sight, the results of Fig. 4 indicate that the breakdown events in the saturation range are not random and independent. This may be partly due to the occurrence of propagating breakdowns. A more significant cause may be the periodic variation of the mean breakdown rate (see Fig. 1) which enhances the histogram at low and large numbers of current pulses. To test the latter assumption the periodic variations were subtracted from the observed R_T values, representing the variation in R_T by $\Delta R_T = 1.2 \cos [2\pi(t - 590)/30]$ per second, with t time in seconds and $t \approx 590$ sec at 233V. The correction decreased the average number of current pulses, but by 1% only. The histogram of the corrected R_T values is represented by dots in Fig. 4. A chi-square test for the corrected histogram resulted in a P -value of 0.6, indicating a good fit to the Poisson distribution.

The reason for the periodic variations in the mean of R_T has not been ascertained. If it is assumed that the periodic variations are not directly connected with the breakdown mechanism, the corrected histogram indicates that the breakdown events are likely to be random and independent, as expected with the succession of avalanche breakdown theory.

Avalanche properties were examined in the manner described for tantalum pentoxide. We found that trapping by 1.35 eV deep traps (12) does not affect conduction band electrons at fields of anodization and the hole mobility was estimated to be larger than $3 \cdot 10^{-8} \text{cm}^2/\text{Vsec}$. The temperature pulse produced by an avalanche was calculated to be 15°C .

Equation [21a] of Part I (1) for the rate of breakdown could not be fitted to the experimental results of Fig. 3 for aluminum oxide at fields lower than fields

Table II. The coefficients of the anodic growths of Fig. 1 and 2

Experiments	Fig. 1			Fig. 2			Fig. 2		
	M			M			M		
Current density, mA/cm ²	1	1	1	1	1	1	5	5	5
The product $\sigma\kappa l_p$, Å	6	10.4	18	6	10.2	18	6	10.6	18
$\alpha \times 10^{-5}/\text{cm}$	1.66	1.91	2.16	1.75	2.0	2.26	1.95	2.25	2.54
N_1	359	590	985	338	548	919	310	513	846
kR_T/sec	507	259	154	47	27	18	178	102	68
$\exp(\alpha w_m)/N_1 = n_m/N_1$	0.23	0.27	0.31	0.31	0.38	0.45	0.35	0.44	0.53
V_i , V	36	32	28	34	30	27	32	28	24

of anodization. The rate of breakdown is very small in such experiments. As with tantalum pentoxide, it was found also with aluminum oxide that Eq. [21a] is not applicable, when R_r is very small.

In conclusion it is found that the succession of avalanche breakdown theory agrees with observations during the anodic growth of aluminum oxide, predicting a rising range in the rate of breakdown followed by one of saturation in R_r . The reason for the variations in the mean value of R_r in the saturation range is not clear. A magnitude of roughly $2 \times 10^5/cm$ is obtained for the coefficient of impact ionization α at a field of 8.7 MV/cm. Compared with the breakdown characteristics of tantalum pentoxide, the characteristics of aluminum oxide show a relatively poor reproducibility.

Acknowledgments

Thanks are due to Dr. P. Feigin for fruitful discussions and to E. Yashchin for help with the statistical calculations. This work was submitted to Technion by V. M. in partial fulfillment of requirements for the M.Sc. degree.

Manuscript submitted July 31, 1978; revised manuscript Aug. 10, 1979.

Any discussion of this paper will appear in a Discussion Section to be published in the December 1980 JOURNAL. All discussions for the December 1980 Discussion Section should be submitted by Aug. 1, 1980.

Low Resistivity CdTe-Te Films by a Combined Hot-Wall-Flash Evaporation Technique

Cornelius A. Menezes

Department of Physics, Centro de Investigacion y de Estudios Avanzados
del Instituto Politécnico Nacional, Apartado, Mexico

ABSTRACT

We have developed a new technique utilizing a combination of hot-wall chamber and flash evaporation for the preparation of low resistivity ($10-100 \Omega^{-1} \text{ cm}^{-1}$) p-type CdTe-Te films. Both thin and thick films can be produced by this technique. The films are characterized by excellent stability during heating and cooling cycles and high reproducibility of resistivity values from batch to batch. Potential probe measurements indicate excellent homogeneity. An optimum hot-wall and substrate temperature has been determined for obtaining low resistivity specimens. We have also studied electrical and optical characteristics like contact characteristics, thermoelectric power, and optical transmission. The high stability and low resistivity CdTe-Te films obtained by this technique may have wide ranging applications in solid-state devices.

We describe in this paper a rather novel deposition technique, which we call the hot-wall-flash evaporation technique (HWFE), involving the combined use of high vacuum flash evaporation and a hot-wall precondensation chamber for preparation of low resistivity CdTe-Te films. These films have the following electrical and mechanical properties: Low electrical resistivity with either gold or indium-gallium contacts. Resistivities are in the range $10^2-10^{-2} \Omega\text{-cm}$. The film surfaces are metallic gray and specular in aspect. On well-cleaned substrates pin-hole free films can be obtained. Film adhesion on glass substrates was remarkably good. This was evaluated by pressing adhesive (Scotch) tape and attempting to strip off the film (8). Reproducibility of resistivity values was good. In measurements made on different runs under similar conditions, the resistivity values in $\Omega^{-1} \text{ cm}^{-1}$ were within 10% of each other.

REFERENCES

1. V. Kadary and N. Klein, *This Journal*, **127**, 139 (1980).
2. D. A. Vermilyea, *Acta Metall.*, **2**, 482 (1954).
3. M. Pourbaix, "Atlas of Electrochemical Equilibria in Aqueous Solutions," Pergamon Press, New York (1966).
4. W. J. Bernard and J. W. Cook, *This Journal*, **106**, 643 (1959).
5. A. C. Harkness and L. Young, *Can. J. Chem.*, **44**, 2409 (1966).
6. J. Siejka, J. P. Nadai, and G. Amsel, *This Journal*, **118**, 727 (1971).
7. E. T. Arakawa and M. W. Williams, *J. Phys. Chem. Solids*, **29**, 735 (1968).
8. R. J. Powell, *Appl. Phys. Lett.*, **28**, 643 (1976).
9. N. Szydlo and R. Poirier, *J. Appl. Phys.*, **42**, 4880 (1971).
10. D. J. DiMaria, *ibid.*, **45**, 5454 (1974).
11. M. Kleefstra, A. T. van Zanten, and P. Ceriolo, *Thin Solid Films*, **30**, 225 (1975).
12. C. A. T. Salama, *This Journal*, **118**, 1993 (1971).
13. R. J. Powell, *J. Appl. Phys.*, **47**, 4598 (1976).
14. N. Klein, *Adv. Phys.*, **21**, 605 (1972).
15. R. M. Handy, *J. Appl. Phys.*, **37**, 4620 (1966).
16. E. D. Savoie and D. E. Anderson, *ibid.*, **38**, 3245 (1967).
17. H. Kanter and W. A. Feibelman, *ibid.*, **33**, 12, 3580 (1962).
18. R. E. Collins and L. W. Davies, *Solid-State Electron.*, **1**, 445 (1964).
19. F. L. Schuermeyer, C. R. Young, and J. M. Blasingame, *J. Appl. Phys.*, **39**, 1791 (1968).

Electron microprobe analysis of the lowest resistivity films has revealed the presence of 25-50% free tellurium in these films. No data are yet available on the composition of higher resistivity films prepared by the HWFE technique.

Though thin films of CdTe have been investigated before, previous attempts to evaporate CdTe by conventional high vacuum techniques have produced films with very high resistivity ($10^7-10^8 \Omega\text{-cm}$ at room temperature) (1-7). Glang *et al.* (8) state that "regardless of deposition temperature all films have resistivities of $10^7 \Omega\text{-cm}$ or higher, even if impurities are added to the source material." Cusano's method (9) which uses a hydrogen ambient cannot be described as a high vacuum technique for reproducible preparation of low resistivity high stability CdTe films. It was recently shown by Wald (10) that one of the major impediments to the wider use of CdTe based

devices was the lack of techniques whereby problems of (i) erratic and nonreproducible behavior of thin films of CdTe and (ii) lack of good contacts to low resistivity CdTe p-type material could be solved. In this context there appears to be a need for an improved understanding of the physical mechanism of CdTe deposition. The HWFE technique has the potential to substantially change the composition of the film with respect to the starting material through control of the temperature of the hot-wall or substrate or both of these. There is a possibility that the results obtained with hot-wall flash evaporation of CdTe may help in solving the problem of obtaining low resistivity CdTe, though the present results show that a gross excess of Te is incorporated in the CdTe films.

The hot-wall technique has been used to grow thick films of ZnTe by Behrndt and Moreno (11). Though the actual physics of the process remains uncertain, it appears that a kind of molecular beam is formed by exchange of energy of the Cd and Te atoms with the hot-wall. Thus the beam that impinges on the substrate has a much higher incident energy and a higher pressure compared with that in a normal evaporation process.

The great (approximately 20%) increase in the substrate temperature on initiation of the flash deposition through the hot-wall points to such an increase in the energy of the incident Cd and Te atoms. This high energy could lead to the relocation of Cd and Te atoms to more favorable positions (of minimum lattice energy, corresponding to greater symmetry) after first impinging on the substrate. We believe that this is partly responsible for obtaining the low resistivity CdTe-Te films with highly stable characteristics.

In our experiments we used two brands of high purity CdTe powder as the evaporant, Balzers CdTe specified to be 99.999% pure and Eagle-Pitcher CdTe powder (High Purity). Both these powders, being undoped with In, Ga or Cd, produced p-type layers.

Previous attempts to obtain low resistivity CdTe have relied upon ion implantation or high temperature annealing of high resistivity p-CdTe in an atmosphere of Cd-P or Te-P (12). There is no report on the stability of these films with regard to thermal cycling. The hot-wall flash evaporation technique, however, enables the reproducible and direct preparation of low resistivity p-CdTe-Te with conductivities about two orders of magnitude higher than those reported (12) for CdTe including those that have been intentionally doped by In, Ga, Al or subjected to high temperature annealing treatment in a Cd-P or Te-P atmosphere.

Experimental

The basic vacuum system used was of an unusual design (a Balzers Model B300). It has a cross-shaped work chamber with 4 ports, covered by demountable aluminum vacuum covers, sealed by O-ring seals. A cross section of the chamber is shown in Fig. 1. The flash evaporation system consists of an a-c solenoid-powered vibrating feeder, 1, into which the material to be evaporated is placed.

The funnel attached to the vibrating bowl, 2, is aligned above a rectangular chute, 3, inclined over the molybdenum trough, 7, which forms the evaporation source. We have used two such feeders opposite to each other in two parts of the vacuum chamber. The evaporation source (a molybdenum trough of rectangular shape) is supported on electrical feed throughs mounted on the lower part.

The feed chutes (Fig. 1, 3) are mounted on a stainless steel disk just above the molybdenum trough and are adequately baffled to prevent spattering of the evaporant material from the trough. The hot-wall, 4, is a quartz tube around which is a heating spiral of 0.6 mm diam tungsten wire. This spiral is electrically isolated from the source heating circuit and has electrical feed throughs in the top part. The hot-wall has

a diameter of 28 mm and a height of 60 mm. The lower end of the hot-wall fits over a hole of 18 mm diameter in the baffle surrounding the evaporation trough. Thus, a well-defined beam of vapor is obtained when evaporant material impinges upon the heated trough and this beam then proceeds to the substrate axially through the hot-wall chamber. The substrate mounting, 6, is just above the top end of the hot-wall and allows a circular area of 200 sq mm to be deposited at a time. Thermocouples of Chromel-Alumel were used to monitor the trough temperature, the hot-wall temperature and the substrate temperature. Substrate heating was accomplished by a molybdenum radiant strip heater mounted 10 cm above the plane of the substrate. An important feature of the assembly is the provision of a pair of polished semicircular stainless-steel reflectors, 5, coaxial with the hot-wall chamber but situated at a distance of 50 mm (radially) from it. This virtual radiation concentrator helps to focus the radiant energy at the center of the hot-wall chamber. The temperature rise in the axial center of the hot-wall chamber was nearly doubled by the use of these reflecting mirrors, besides avoiding the troublesome and unnecessary heating of the glass walls of the vacuum chamber. Typical power input to the hot-wall heater was 100W; the temperature that could be attained very easily with this input was about 600°C. All metal surfaces were molybdenum or stainless-steel.

Liquid nitrogen cooled traps (both, of the Miessner type, and above the diffusion pump) were in use at all times during heating and evaporation cycles. The residual air pressure in the chamber was better than 3×10^{-6} Torr. Pyrex microscope slides were the preferred substrates for deposition, though other substrates like quartz or soda glass could also be used.

Temperatures at all relevant points were monitored during trial runs. The hot-wall temperature was measured under the same vacuum conditions at its axial center, and a calibration was obtained between the heating current and the average hot-wall temperature. This is the temperature referred to in the course of this work. The current passing through the molybdenum trough was 250A for a temperature of 930°-950°C. The preheater current was 22A, while the current through the hot-wall heater was 9A. The operation of the vibrating feeder has to be done skillfully to prevent too much charge from falling in a short time into the trough. Too rapid charging of the heating trough can cause unevaporated powder to impinge upon the substrate and seriously impair the surface.

Because of the multiple heating circuits and the possibility of internal shorts between the various heaters, isolation transformers are used in all the heater circuits. These serve the dual purpose of giving good isolation of each circuit and providing high currents at low voltage for individual heaters in the system.

Film thickness of the films was measured with a Varian Model 980-8000 Interferometer. Films used for resistivity measurements had a thickness of 0.41 μm .

A specific problem that is often encountered in the flash evaporation technique is the sudden increase in pressure in the evaporation chamber when the particles of CdTe impinge upon the heated molybdenum boat. This was suspected to be due to degassing from the interstices of the granular CdTe powder. It was found that the use of an additional preheater positioned about 8 cm above the CdTe feeder to heat the powder in vacuum for 10-25 min, prior to evaporation by flashing, eliminated this undesirable pressure rise.

Figure 2 shows the plot of pressure rise in the chamber before and after the use of the preheater above the CdTe feeder.

We have thus eliminated, by the use of the charge preheater, an important drawback to the flash evap-

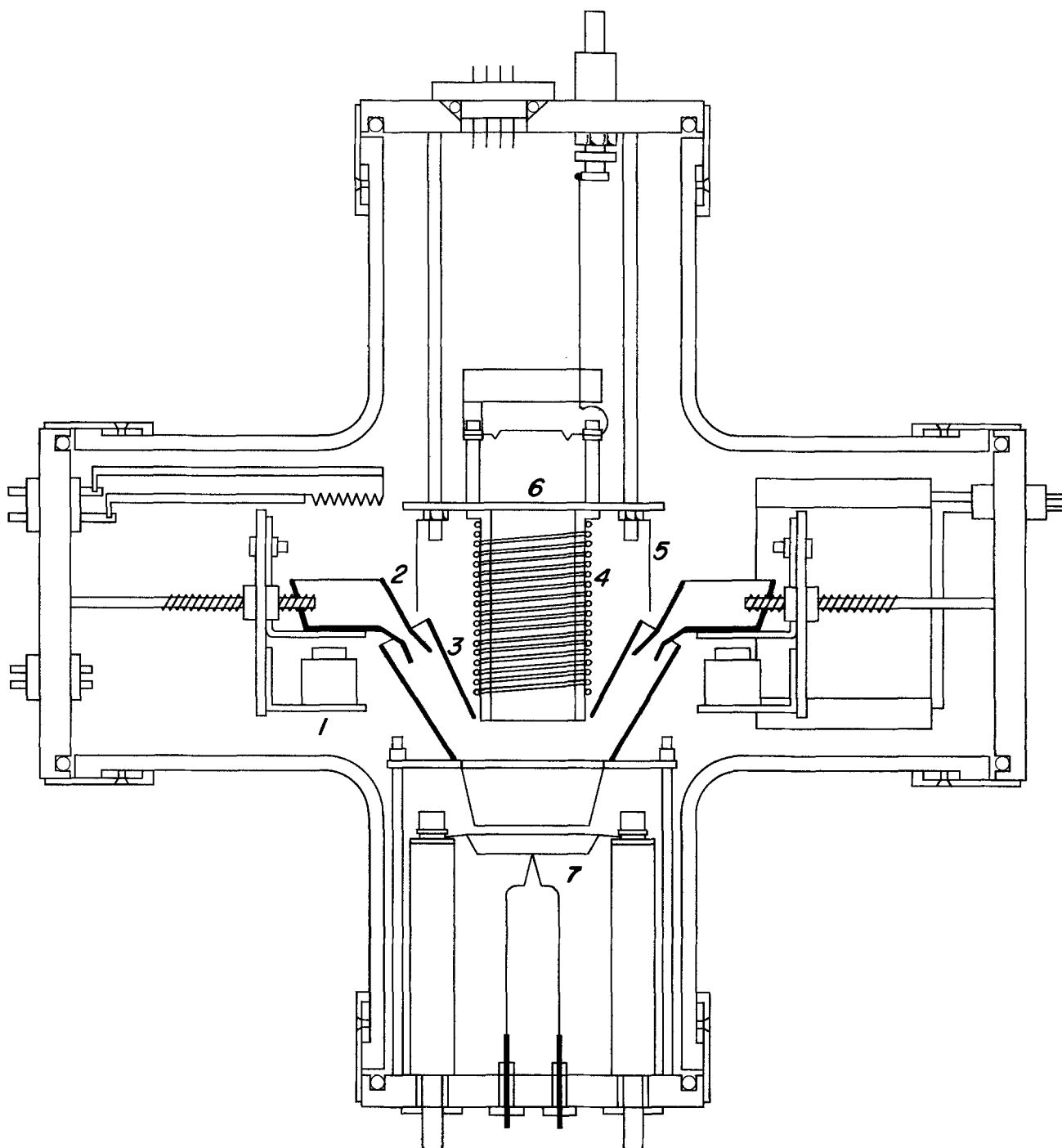


Fig. 1. Cross-section drawing of cross-shaped vacuum chamber showing the vibrating feeders, 1, vibrating bowl, 2, feed chutes, 3, hot-wall chamber, 4, substrate holder, 6, stainless-steel reflectors, 5, and molybdenum heater trough, 7.

oration technique which has been well recognized by previous workers in this field. For instance, Chopra (13) states that, "Since the large amount of rapidly released gas produces spattering of particles from the evaporant this method (flash evaporation) is not easily controllable."

The amount of gas released during evaporation is inversely proportional to the preheating time and temperature. By keeping a constant heater temperature (around 1000°C) and changing the heating time, we have found that heating times of 10-15 min are adequate (for a charge of up to 1g) to reduce pressure rise on flashing to negligible amounts.

Results

The cadmium telluride-tellurium films produced by this technique have extremely smooth and shiny surfaces. Typically these films are free from pinholes and

are dense in appearance. We have studied the effect of hot-wall and substrate temperature and have found that both the hot-wall temperature and the substrate temperature have a pronounced influence on the properties of the films produced. In a series of experiments, Balzers high purity CdTe powder was evaporated under as similar conditions as possible, while the substrate temperature and hot-wall temperature were systematically changed. With low substrate temperatures (100°C or lower) and hot-wall temperatures below 450°C the resulting films had a very high resistivity ($10^7 \Omega\text{-cm}$ or higher). However, when the substrate temperatures were raised to 200°C and the hot-wall temperature was in the range 500°-600°C we were consistently able to obtain films with resistivity of $10^{-3} \Omega\text{-cm}$.

Still higher substrate temperatures are possible, but the efficiency of deposition in terms of thickness

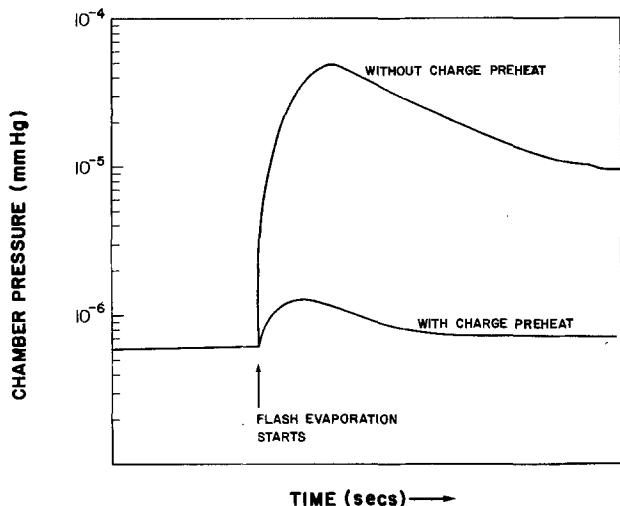


Fig. 2. Plot of pressure rise in the vacuum chamber as a function of time from initiation of flash evaporation for (i) without (CdTe) charge preheater and (ii) with charge preheater.

of deposit per unit weight of starting material used, is impaired. We thus feel that the optimum temperature of hot-wall and substrate for obtaining low resistivity ($10^{-3} \Omega\text{-cm}$) CdTe-Te films is 560° and 200°C , respectively. Table I gives a few examples of conductivity values obtained for various substrate and hot-wall temperatures. It is clear from the data that low resistivity CdTe-Te can be obtained using a hot-wall temperature in the range $500^\circ\text{--}600^\circ\text{C}$ and substrate temperatures in the range $100^\circ\text{--}250^\circ\text{C}$.

Control experiments where either flash evaporation alone or hot-wall was used alone (with conventional evaporation from a heated boat) showed that the desired low resistivity films with optimum properties (physical and electrical) were obtained only when both flash evaporation and the hot-wall were used together. In either of the above cases where only one of the two techniques (hot-wall or flash evaporation) was used alone, the result was high resistivity ($\sim 10^7 \Omega\text{-cm}$) CdTe.

Stability during thermal cycling.—Since the instability and erratic behavior of vacuum deposited CdTe films has often been cited as a major drawback in device applications (10), we decided to study the stability behavior of these films.

The high stability of resistivity of these films became apparent first during measurements of conductivity vs. temperature. In order to establish the high stability further, a sample of $10 \Omega^{-1} \text{cm}^{-1}$ CdTe-Te film ($1\text{--}2 \mu\text{m}$ thick) was placed on the lower end of a cold finger projecting into a high vacuum chamber. The specimen could thus be cycled repeatedly and rapidly by electrical heating and cooled by liquid nitrogen to about 80°K .

In our experiments the specimen was cycled over 25 times. At the end of the cycling as well as during it, the resistivity at 25°C was within 1% of its initial value. The specimens were also completely stable against changes in the ambient pressure or gas composition. There was no measurable change in the resistance values when rapidly evacuated to 10^{-6} mm

Table I.

Substrate temp ($^\circ\text{C}$)	Hot-wall temp ($^\circ\text{C}$)	Conductivity ($\Omega^{-1}\text{-cm}^{-1}$)	
200	560	6.5	High conductivity
166	560	2.5×10^{-1}	High conductivity
130	560	1.2×10^{-1}	High conductivity
95	425	$\sim 10^{-7}$	Very low conductivity

Hg from atmospheric pressure. A typical plot of resistivity values for several consecutive cycles is shown in Fig. 3.

Contact characteristics.—Because of the established difficulty in making ohmic contacts to p-type low resistivity material, as recently reviewed by Wald (10), we have specially investigated the nature of contacts made to films produced by the hot-wall flash evaporation system (HWFE). The linearity of an $I\text{-}V$ characteristic in the case of a suspected blocking contact is only a necessary but not sufficient condition (14) for true ohmic behavior. It is also necessary to probe the potential distribution along the length of the film to make sure that there is no abnormal potential drop at the extremities where current contacts are made.

We have measured both the $I\text{-}V$ characteristics, down to millivolt levels, using a variety of contact metals. For the potential probe, a special mask with several very thin (0.6 mm) probes was fabricated by photolithographic techniques. The interprobe spacing was 3 mm. The measurements of potential were done with a Keithley 610 electrometer to ensure that no loading of the probes occurred. The metals used for the contacts were indium, indium-gallium, gold, nickel, chromium. We found that good contacts could be obtained with the first three metals, but only when the CdTe was evaporated onto the predeposited contact metals. The linear plots obtained with the potential probe technique (Fig. 4) show the absence of contact barriers and also demonstrate the good electrical homogeneity of the specimens.

For specimens with indium or gold end contacts, the linear $I\text{-}V$ plot of Fig. 5 shows that the contacts are reasonably ohmic down to the millivolt level.

Electrical conductivity.—Electrical conductivity was measured in CdTe-Te films evaporated by the HWFE technique. Films were deposited on Pyrex substrates through molybdenum masks which defined the resistive pattern in the form of a bar. Evaporated indium contacts were used. Measurements were carried out in a low temperature vacuum cryostat down to about 90°K . A feature of the measurements was that the values of resistivity at any temperature were extremely reproducible (within 1%) and the specimen showed no drift or hysteresis on heating and cooling. The plot of conductivity vs. reciprocal temperature is shown in Fig. 6.

Thermoelectric power.—Thermoelectric power measurements were carried out in a vacuum cryostat with

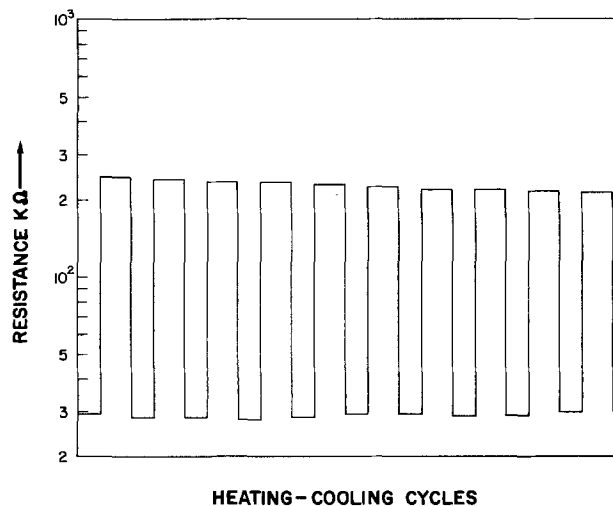


Fig. 3. Plot of resistance of a (HWFE) CdTe-Te thin film specimen during part of continuous thermal cycling experiments. Steady base line indicates return to initial value after each cycle. Total change after all cycles was less than 1%.

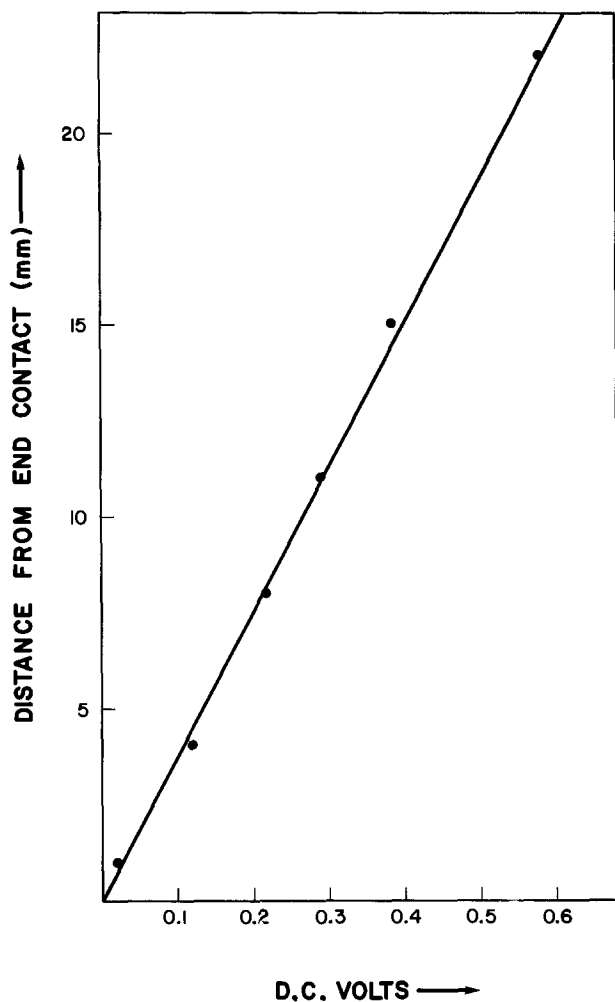


Fig. 4. Plot of distance from an end contact as a function of potential drop in the CdTe-Te film (potential probe experiment).

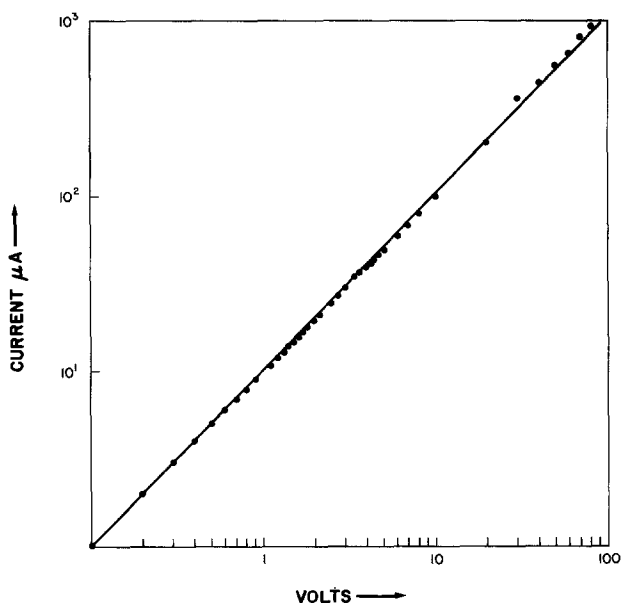


Fig. 5. Electrical contact characteristics for CdTe-Te films prepared by hot-wall flash evaporation technique.

the sample of CdTe-Te mounted on a copper strip with the hot end heated by a 5W wire-wound resistor of 575Ω . Power to the heater was supplied from an HP regulated supply. The cold end was in contact with a large copper sink which could be cooled to -180°C .

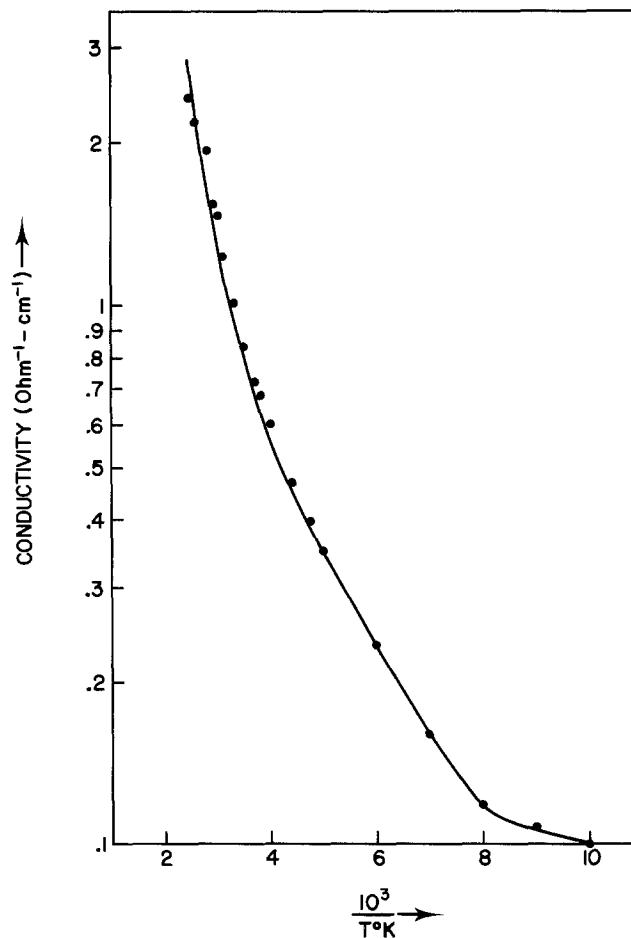


Fig. 6. Electrical conductivity of CdTe-Te film prepared by hot-wall-flash evaporation.

Typical gradients were of the order of $5^\circ\text{-}7^\circ\text{C}$. Thermoelectric power measurements showed conclusively that the specimens were p-type with a thermoelectric power of $173\ \mu\text{V}/^\circ\text{K}$ at 223°K . The temperature gradient was constant within 0.1% during the experiments.

Optical transmission.—Optical transmission data were obtained for typical CdTe-Te HWFE specimens evaporated onto Pyrex glass slides. A typical transmission spectrum is shown in Fig. 7 for a low resistivity ($10^{-1}\ \Omega\text{-cm}$) CdTe-Te film. The spectrum is uncorrected for reflectance effects.

The spectrum shows considerable absorption at wavelengths beyond the absorption edge of CdTe and this can be attributed to the presence of excess Te in the films.

Stoichiometry and structure.—Electron microprobe measurements on three specimens of the lowest resistivity ($10^{-3}\ \Omega\text{-cm}$) have revealed the presence of from 25 to 50% free tellurium in the CdTe-Te films. In this context some of the comments on the stoichiometry of CdTe films by previous workers may be pertinent. According to Glang *et al.* (8) CdTe films deposited at temperatures below 150°C had excess tellurium, but these authors go on to say that regardless of deposition temperature, all films had resistivities higher than $10^7\ \Omega\text{-cm}$. Further, according to these authors (8), deviations from stoichiometry in CdTe films condensed between 25° and 250°C must be considerably smaller than $10^{16}\ \text{cm}^{-3}$. Apparently, under hot-wall conditions the equilibrium between the elemental species, Cd and Te condensing on to the substrate shifts appreciably towards Te, resulting in a CdTe matrix with Te in considerable excess. The exact nature of the distribution of Te in the CdTe matrix is not yet known but would seem to warrant further

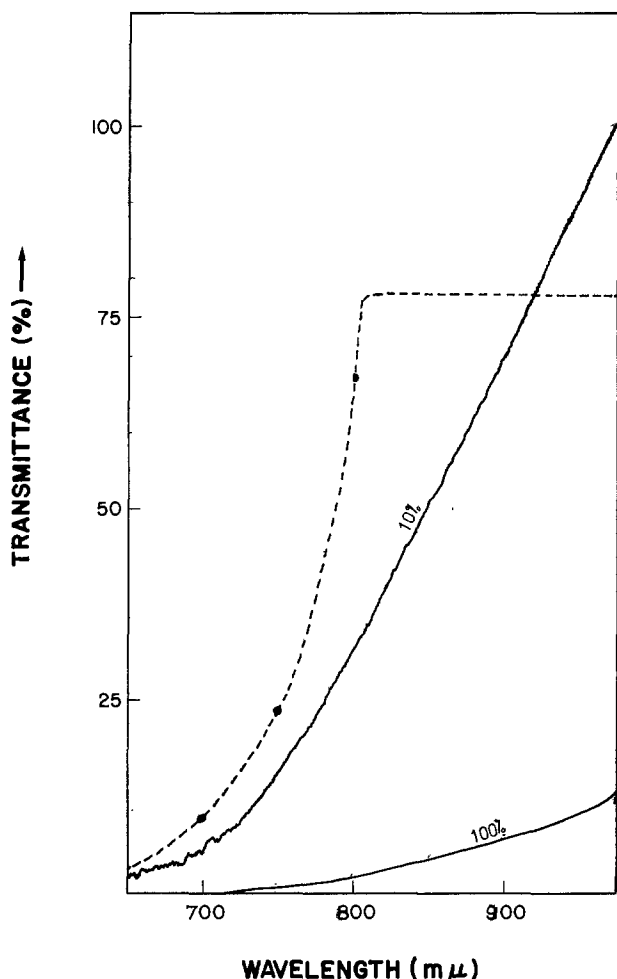


Fig. 7. Optical transmission spectrum for a CdTe-Te film (0.5) prepared by hot-wall-flash evaporation technique, drawn in full-scale corresponding to 10% transmission and to 100% transmission. The dashed curve is a calculated curve for single crystal CdTe using appropriate optical constants.

study. Since very little is known about the exact mechanism of condensation of CdTe, it is hoped that the fact that a considerable stoichiometric excess of Te can be introduced into CdTe in a more or less controlled manner, would help advance the understanding of CdTe deposition. It remains to be seen if the HWFE technique can be adapted or modified to provide CdTe films with only a slight (10^{17}) excess of Te, sufficient to give a substantial p conductivity at room temperature. It is interesting to note that even after prolonged heat-treatment under inert gas conditions the CdTe-Te films retain some of their conductivity. Further studies are in progress on such films, which show sharp x-ray reflections, to determine their carrier concentration, mobility and contact behavior.

X-ray diffraction was utilized in an attempt to determine the structure of the CdTe-Te films. No spectrum could be obtained for an as-deposited film on a glass substrate. However on heat-treatment in a neutral atmosphere sharp reflection patterns were obtained. Figure 8 shows an x-ray spectrogram of a CdTe film. Comparison of the data with A.S.T.M. 19-193 indicates that the structure corresponds to that of hexagonal CdTe, prepared by the sublimation of the cubic modification onto a glass substrate between 500° and 800°C in argon.

It is noteworthy that no lines corresponding to Te appear which indicates that Te has sublimed during the heat-treatment (300°C) or is in an amorphous state. Most films showed a great increase in the I/I_0 ratio after heat-treatment.

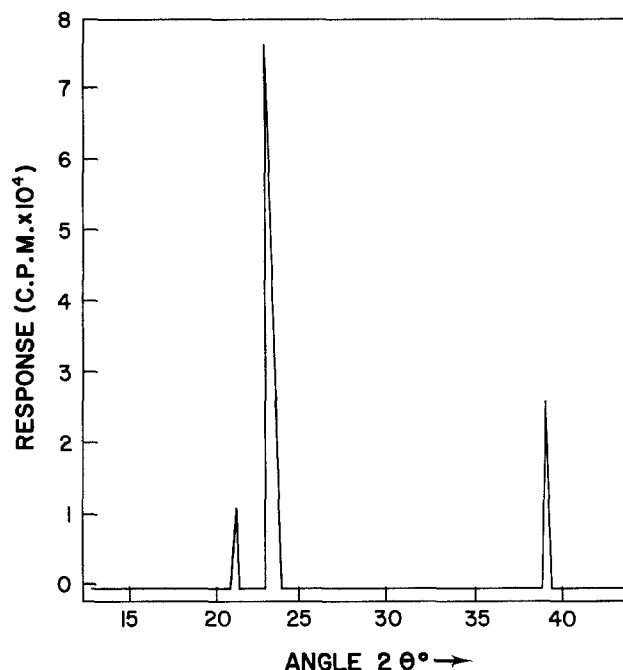


Fig. 8. X-ray spectrogram of a well-oriented HWFE CdTe film showing hexagonal structure.

Summary

The hot-wall-flash evaporation technique is described in detail. It has been applied to the preparation of CdTe-Te films which are characterized by low resistivity, ohmic contacts to common contact metals, specular surfaces, and stability during rapid thermal cycling between 250° and 350°K. A notable improvement in flash evaporation technique has been the incorporation of a charge preheater to eliminate troublesome outgassing during flash evaporation. Electron microprobe analysis has revealed that up to 50% free tellurium may be present in the films. The optical absorption spectrum shows a shift in absorption towards longer wavelengths, consistent with the microprobe data. X-ray data for heat-treated films show good orientation of CdTe with hexagonal structure.

Acknowledgments

The author is grateful to Dr. Feliciano Sánchez-Sinencio for useful discussions in the course of the work. The interest and guidance of Dr. Richard H. Bube are also gratefully acknowledged. The author is indebted to Dr. Richard H. Bube and Dr. Alan L. Fahrenbruch for obtaining the optical transmission data and electron microprobe analysis at Stanford University. The author would like to thank Ricardo A. Chávez for help in preparing specimens. Lastly, I thank Dr. Alfonso Lastras-Martínez, Dr. Juan Luis del Valle, and Mr. Manuel Saucedo for useful discussions.

This work was partially supported by CONACyT, PNCB, and Comisión Nacional de Energéticos (SEPAFIN).

Manuscript submitted Nov. 16, 1978; revised manuscript received May 2, 1979.

Any discussion of this paper will appear in a Discussion Section to be published in the December 1980 JOURNAL. All discussions for the December 1980 Discussion Section should be submitted by Aug. 1, 1980.

Publication costs of this article were assisted by the Centro de Investigacion y de Estudios Avanzados del Instituto Polytechnico.

REFERENCES

1. V. M. Lyubin and G. A. Fedorova, *Sov. Phys. Dokl.*, **135**, 1343 (1960).
2. P. P. Konorov and I. B. Shevchenko, *Sov. Phys.*

- Solid State*, 2, 1027 (1960).
3. B. Goldstein and L. Pensak, *J. Appl. Phys.*, 30, 155 (1959).
 4. G. Rudowski, *Electron. Technol. Poland*, 7, 103 (1974).
 5. K. K. Muravjeva, I. P. Kalinkin, V. B. Aleskovsky, and N. S. Bogomolov, *Thin Solid Films*, 5, 6 (1970).
 6. S. Miersschaut, *Thin Films*, 2, 53 (1971).
 7. A. R. Hutsin, *Bull. Am. Phys. Soc.*, 6, 110 (1961).
 8. R. Glang, J. G. Kren, and W. J. Patrick, *This Journal*, 110, 407 (1963).
 9. D. A. Cusano, *Solid-State Electron.*, 6, 217 (1963).
 10. F. V. Wald, *Rev. Phys. Appl.*, 12, 272 (1977).
 11. M. E. Behrndt and S. C. Moreno, *J. Vac. Sci. Technol.*, 8, 494 (1971).
 12. R. Ludeke, *ibid.*, 8, 204 (1971).
 13. K. L. Chopra, in "Thin Film Phenomena," p. 18, McGraw Hill, New York (1969).
 14. L. B. Valdes, *Proc. IRE*, 42, 420 (1954).

The Intermediate Role of Gd^{3+} in the Energy Transfer from a Sensitizer to an Activator (Especially Tb^{3+})

J. Th. W. de Hair and W. L. Konijnendijk

Philips Lighting Division, Eindhoven, The Netherlands

ABSTRACT

Energy transfer from a sensitizer to an activator via Gd^{3+} ions is discussed. This is done for the $Bi^{3+} \rightarrow Dy^{3+}$ and $Sb^{3+} \rightarrow Dy^{3+}$ transfer in $GdPO_4$, and for the $Bi^{3+} \rightarrow Tb^{3+}$ transfer in GdB_3O_6 . The phosphor $Gd_{0.95}Bi_{0.01}Tb_{0.01}B_3O_6$ shows Tb^{3+} luminescence with a quantum efficiency of 80% for excitation of Bi^{3+} . After excitation of Bi^{3+} , energy transfer takes place to Gd^{3+} ions. Then the energy may migrate from one Gd^{3+} to another until energy transfer from Gd^{3+} to Tb^{3+} occurs. Compared to the energy transfer in other sensitized Tb^{3+} phosphors, this process has a high efficiency at relatively low activator concentrations. The energy transfer from Bi^{3+} to Gd^{3+} and between Gd^{3+} ions mutually has been investigated for $Gd_{0.99-x}La_xBi_{0.01}B_3O_6$. For $x < 0.4$ energy transfer between Gd^{3+} ions is observed. The quantum efficiency of the Gd^{3+} luminescence for Bi^{3+} excitation of $Gd_{0.59}La_{0.4}Bi_{0.01}B_3O_6$ amounts to 75% and decreases for increasing Gd concentrations.

Trivalent gadolinium can act as a sensitizer in processes of energy transfer. Brill and Wanmaker (1) describe the energy transfer from Gd^{3+} to Tb^{3+} in $CaNaBO_3$. Ozawa and Nishikawa (2) report the energy transfer to other rare earths in $(Y,Gd)_2O_3$ solid solutions, whereas Reisfeld *et al.* (3) have investigated the transfer of energy from Gd^{3+} to Tb^{3+} in borate glass. Bozhevovnov *et al.* (4) give evidence of energy transfer from Gd^{3+} to Mn^{2+} in CaF_2 . In all these cases the excitation spectra of the activator (A) luminescence show up excitation lines of Gd^{3+} . The optical transitions of Gd^{3+} occur within the 4f shell and are observed in the ultraviolet region. These transitions are parity and spin forbidden and have a very low absorption strength. Thus, sensitization with Gd^{3+} ($Gd^{3+} \rightarrow A$ transfer) where the energy must be absorbed by Gd^{3+} , does not result in phosphors which luminesce with high intensity.

On the other hand, sensitization of Gd^{3+} luminescence ($S \rightarrow Gd^{3+}$ transfer) is also known. Blasse and Brill (5) have observed energy transfer from TaO_4^{3-} groups to Gd^{3+} in $GdTaO_4$. Reisfeld and Morag (6) report the energy transfer from Tl^+ to Gd^{3+} in borax and phosphate glasses. In these cases, the intensity of the Gd^{3+} luminescence is enhanced, due to the strong absorption by Tl^+ or TaO_4^{3-} groups followed by energy transfer to Gd^{3+} .

So far the sensitization of Gd^{3+} ($S \rightarrow Gd^{3+}$) and the energy transfer from Gd^{3+} to a sensitizer ($Gd^{3+} \rightarrow A$) have been considered separately. It seems worthwhile to investigate the possibilities of the combination of both processes in phosphor luminescence. We have studied, therefore, the intermediate role of Gd^{3+} in the energy transfer from a sensitizer to an

activator. Recently, we have shown (7) that the energy transfer from Bi^{3+} to Tb^{3+} in GdB_3O_6 occurs almost exclusively via the Gd^{3+} ions. Before that, only indications of a possible intermediate role of Gd^{3+} can be found in the literature. Blasse and Brill (5) have suggested that energy transfer from TaO_4^{3-} groups to Dy^{3+} , Sm^{3+} , and Er^{3+} in $GdTaO_4$ occurs via Gd^{3+} . Indications can also be found in a paper by Grisafe and Fritsch (8) on the luminescence of Eu^{3+} and Tb^{3+} in $LnNbO_4$ ($Ln = La, Gd, Y$). Recently, Blasse (9) has described how in $GdNbO_4:Eu^{3+}$ the Gd^{3+} ions play an important role.

In this paper we discuss in more detail the energy transfer in GdB_3O_6 activated with Bi^{3+} and Tb^{3+} . First, we describe the $Bi^{3+} \rightarrow Gd^{3+}$ transfer in $Gd_{1-x}La_xB_3O_6$ activated with Bi^{3+} . Next, we will show that thanks to the intermediate role of Gd^{3+} the energy transfer to Tb^{3+} is complete at relatively low Tb concentrations. Low Tb concentrations have a great advantage for commercial Tb^{3+} phosphors since the price of these phosphors is determined mainly by the Tb contents. Finally, we show the intermediate role of Gd^{3+} in the energy transfer from Bi^{3+} or Sb^{3+} to Dy^{3+} in $GdPO_4$.

Experimental

Powder samples were prepared by the usual solid-state reaction techniques. Stoichiometric proportions of the starting compounds were intimately mixed together and then heated twice at 1040°C. The metaborates were prepared starting with an excess of 10 mole percent (m/o). The samples activated with terbium were heated in a nitrogen atmosphere.

Formation of the compounds was checked by x-ray analysis with a Philips diffractometer using $CuK\alpha$ radiation.

All optical measurements were performed at room temperature with equipment described elsewhere (10). The spectra given in Fig. 1-3 have been corrected for the characteristics of the experimental setup.

Results and Discussion

The compound GdB_3O_6 shows very weak Gd^{3+} luminescence. This luminescence can be excited at the ${}^6\text{I}_7$ (~ 273 nm) or ${}^6\text{D}_7$ (~ 250 nm) levels of Gd^{3+} . Because of the forbidden nature of $4f \rightarrow 4f$ transitions, the absorption strength is very low (see Fig. 1a for the diffuse reflection spectrum of GdB_3O_6).

The luminescence of Gd^{3+} is more intense when GdB_3O_6 is activated with Bi^{3+} . The emission spectrum of $\text{Gd}_{0.99}\text{Bi}_{0.01}\text{B}_3\text{O}_6$ is shown in Fig. 1b. The Gd^{3+} luminescence consists of the ${}^6\text{P}_{7/2} \rightarrow {}^8\text{S}_{7/2}$ transition (near 312 nm) and the ${}^6\text{P}_{5/2} \rightarrow {}^8\text{S}_{7/2}$ transition (near 306 nm). The excitation spectrum of the Gd^{3+} luminescence of $\text{Gd}_{0.99}\text{Bi}_{0.01}\text{B}_3\text{O}_6$ is shown in Fig. 1a. This spectrum consists of the ${}^8\text{S}_{7/2} \rightarrow {}^6\text{I}_7$ transitions of Gd^{3+} at 273 nm and two strong and broad excitation bands which correspond to electronic transitions of Bi^{3+} . The band with a maximum at 240 nm is due to the ${}^1\text{S}_0 \rightarrow {}^3\text{P}_1$ transition, whereas the one peaking near 200 nm corresponds to the ${}^1\text{S}_0 \rightarrow {}^1\text{P}_1$ transition. The ${}^8\text{S}_{7/2} \rightarrow {}^6\text{D}_7$ excitation of Gd^{3+} near 250 nm is hidden under the ${}^1\text{S}_0 \rightarrow {}^3\text{P}_1$ band of Bi^{3+} . The presence of Bi^{3+} excitation bands in the excitation spectrum of the Gd^{3+} luminescence indicates the occurrence of energy transfer from Bi^{3+} to Gd^{3+} . We did not observe any Bi^{3+} emission from Bi^{3+} -activated GdB_3O_6 . The quantum efficiency of the Gd^{3+} luminescence of $\text{Gd}_{0.99}\text{Bi}_{0.01}\text{B}_3\text{O}_6$ amounts merely to 20%, which is due to concentration quenching of the Gd^{3+} luminescence. On replacing a part of Gd by La according to the formula $\text{Gd}_{0.99-x}\text{La}_x\text{Bi}_{0.01}\text{B}_3\text{O}_6$ we find that the quantum efficiency of the Gd^{3+} luminescence upon excitation at the maximum of the Bi^{3+} excitation

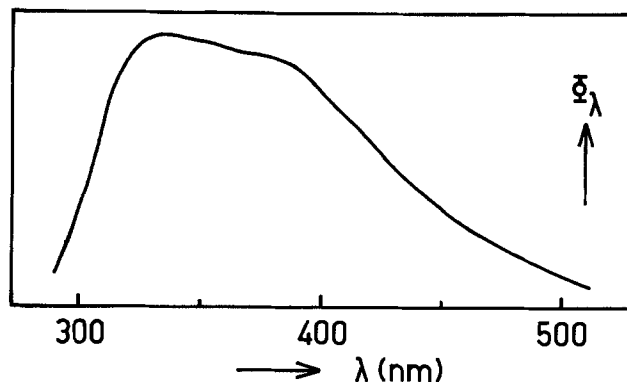


Fig. 2. Spectral energy distribution of the luminescence of $\text{La}_{0.99}\text{Bi}_{0.01}\text{B}_3\text{O}_6$ for 254 nm excitation.

band (${}^1\text{S}_0 \rightarrow {}^3\text{P}_1$) increases up to 75% when $x = 0.4$. For higher La contents both Gd^{3+} and Bi^{3+} luminescence is observed. The intensity of the Gd^{3+} luminescence decreases whereas that of the Bi^{3+} luminescence increases. The Bi^{3+} luminescence in the lanthanum-rich region of $\text{Gd}_{0.99-x}\text{La}_x\text{Bi}_{0.01}\text{B}_3\text{O}_6$ is given in Fig. 2 for $\text{La}_{0.99}\text{Bi}_{0.01}\text{B}_3\text{O}_6$. In the light of current theories on nonradiative energy transfer (11), the emission band of Bi^{3+} in GdB_3O_6 must overlap the energy levels of the Gd^{3+} ion (${}^6\text{P}_{7/2}$, ${}^6\text{P}_{5/2}$, and ${}^6\text{P}_{3/2}$). Reisfeld and Morag (6) describe the energy transfer from Tl^{3+} to Gd^{3+} in inorganic glasses. The emission of Tl^{3+} in these glasses peaks between 300 and 330 nm. Blasse and Brill (5) have found that in the solid solutions series $\text{Y}_{1-x}\text{Gd}_x\text{TaO}_4$, the Gd^{3+} luminescence is sensitized by the TaO_4^{3-} groups. The emission band of YTao_4 peaks at 335 nm. One of us (7) has described the energy transfer from Bi^{3+} to Gd^{3+} in $\text{YAl}_3\text{B}_4\text{O}_{12}$. The Bi^{3+} emission in $\text{YAl}_3\text{B}_4\text{O}_{12}$

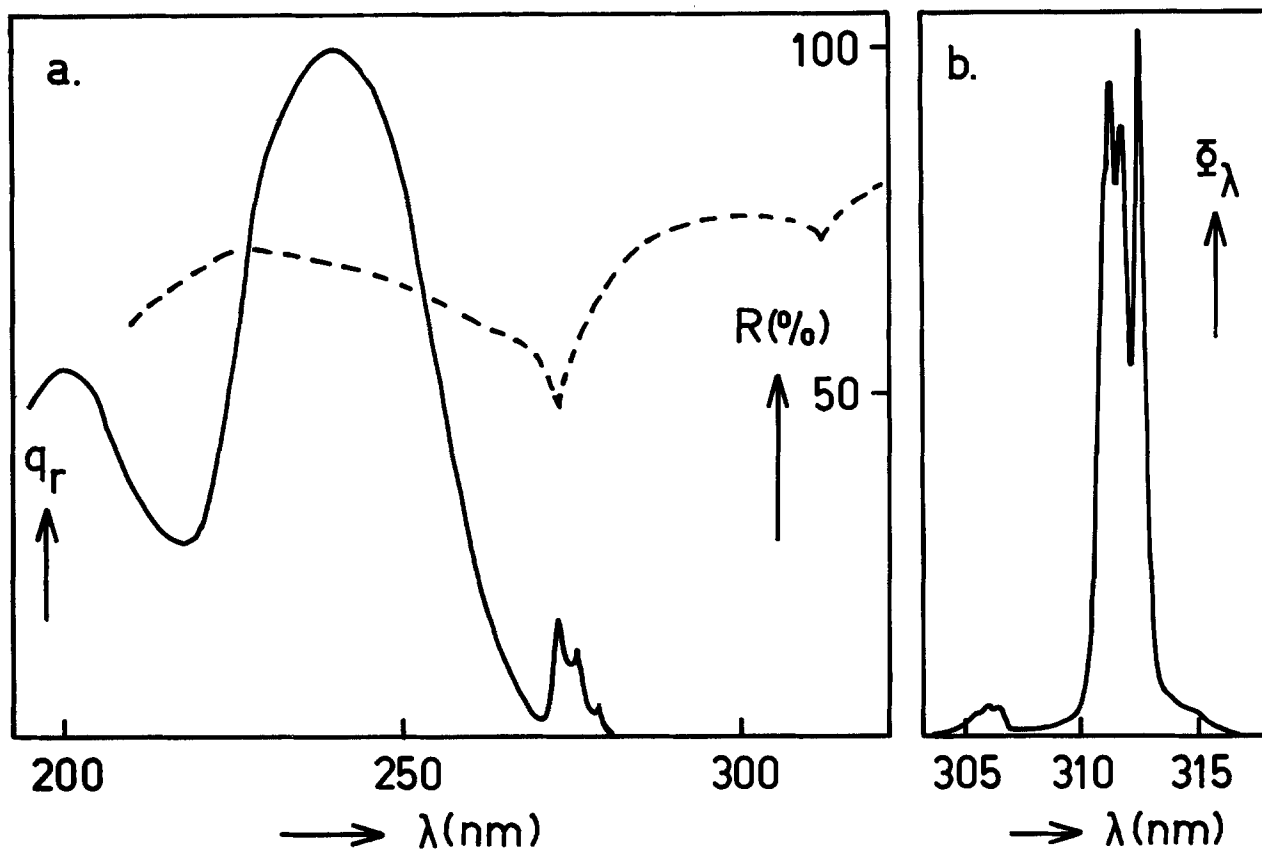


Fig. 1. (a) Diffuse reflection spectrum of GdB_3O_6 (broken line) and excitation spectrum of the Gd^{3+} luminescence of $\text{Gd}_{0.99}\text{Bi}_{0.01}\text{B}_3\text{O}_6$ (solid line), q_r in this and other figures denotes the relative quantum output, R gives the percentage reflectance. (b) Spectral energy distribution of the luminescence of $\text{Gd}_{0.99}\text{Bi}_{0.01}\text{B}_3\text{O}_6$ for 254 nm excitation. Φ_λ in this and other figures denotes the radiant power per constant wavelength interval.

peaks at 300 nm. Energy transfer also occurs from Ce^{3+} to Gd^{3+} in CeF_3 (12) (Ce^{3+} emission peaking near 290 nm). In all these examples complete energy transfer to Gd^{3+} occurs since the sensitizer emission shows a considerable overlap with the 6P_J energy levels of Gd^{3+} . The Bi^{3+} emission in LaB_3O_6 (Fig. 2), however, is situated at too long wavelengths to have a good overlap. According to Blasse (13), the Bi^{3+} emission is influenced by a variation in the size of the site occupied by Bi^{3+} . Van der Steen *et al.* (14) have reported on the luminescence of Bi^{3+} in $NaLaO_2$ and in $NaGdO_2$. $NaLaO_2-Bi^{3+}$ emits in the red, $NaGdO_2-Bi^{3+}$ in the blue region. Possibly the virtual emission of Bi^{3+} in GdB_3O_6 will be at shorter wavelengths than in LaB_3O_6 .

The compound with composition $Gd_{0.98}Bi_{0.01}Tb_{0.01}B_3O_6$ shows very intense, characteristic Tb^{3+} luminescence at room temperature under 254 nm excitation (7). The quantum efficiency of this luminescence is 80% for excitation of Bi^{3+} . This value is remarkably high for the low Tb^{3+} concentration present, since direct $Bi^{3+} \rightarrow Tb^{3+}$ transfer is very improbable. The virtual emission of Bi^{3+} in GdB_3O_6 does not show overlap with the $4f \rightarrow 5d$ band of Tb^{3+} which is observed near 200 nm in this host lattice. There is only overlap with the $4f \rightarrow 4f$ transitions of Tb^{3+} . In such a case, the probability of $Bi^{3+} \rightarrow Tb^{3+}$ transfer is low and the transfer distance short. A high Tb concentration would be required for efficient, direct $Bi^{3+} \rightarrow Tb^{3+}$ transfer in GdB_3O_6 . The high transfer efficiency in GdB_3O_6 at low Tb concentrations must be accounted for with a different transfer process. We have proven (7) that the Gd^{3+} ions play an important role in the energy transfer from Bi^{3+} to Tb^{3+} . Excitation of Bi^{3+} will be followed mainly by $Bi^{3+} \rightarrow Gd^{3+}$ transfer. The energy can now migrate from Gd^{3+} to Gd^{3+} until it reaches a Tb^{3+} ion.

Because of the involvement of Gd^{3+} in the energy transfer, efficient transfer in $Gd_{0.98}Bi_{0.01}Tb_{0.01}B_3O_6$ is observed for relatively low Tb concentrations. Let us now compare some sensitized Tb^{3+} phosphors listed in Table I. In this table, we indicate the presence of energy transfer between the sensitizers (S — S) and the occurrence of spectral overlap between the sensitizer emission and the $4f \rightarrow 5d$ excitation bands of Tb^{3+} ($4f \rightarrow 5d$). We also give the quantum efficiency of the Tb^{3+} luminescence for excitation in the maximum of the sensitizer-excitation band. Generally speaking, the energy transfer from a sensitizer to Tb^{3+} is efficient when the sensitizer emission overlaps the $4f \rightarrow 5d$ absorption band of Tb^{3+} , as in $Y_{1-x}Tb_xTaO_4$, or when energy transfer between the sensitizers occurs, as in $Ce_{1-x}Tb_xB_3O_6$. In both cases, a low Tb concentration is sufficient to obtain an efficient energy transfer. When there is no energy transfer between the sensitizers and there is no overlap with the $4f \rightarrow 5d$ band, as in $Ce_{1-x}Tb_xB_3O_6$, $Ce_{1-x}Tb_xF_3$, and $Ce_{1-x}Tb_xMgAl_{11}O_{19}$, then a high Tb concentration is necessary to achieve efficient energy transfer. With Gd^{3+} as the intermediate the $Ce^{3+} \rightarrow Tb^{3+}$ trans-

fer in CeF_3 is complete at lower Tb concentrations (compare $Ce_{0.8}Tb_{0.2}F_3$ and $Ce_{0.75}Gd_{0.2}Tb_{0.05}F_3$). We have already mentioned that energy transfer from Bi^{3+} to Tb^{3+} in GdB_3O_6 is complete for 1 atomic percent (a/o) Tb (compare the Tb concentration in the isostructural phosphor $Ce_{0.67}Tb_{0.33}B_3O_6$). In $Gd_{0.98}Bi_{0.01}Tb_{0.01}B_3O_6$ the direct energy transfer $Bi^{3+} \rightarrow Tb^{3+}$ over relatively long distances (maximum $\sim 13\text{\AA}$) cannot compete with the energy transfer from Bi^{3+} to a Gd^{3+} ion as nearest neighbor ($\sim 4\text{\AA}$). After the energy transfer from Bi^{3+} to the 6P_J levels of Gd^{3+} , the losses of energy at Gd^{3+} are small. The energy-level scheme of Gd^{3+} shows a large gap of about $32 \cdot 10^3 \text{ cm}^{-1}$ (the difference between the ${}^6P_{7/2}$ and ${}^8S_{7/2}$ states of Gd^{3+}). Radiationless relaxation of Gd^{3+} is very improbable. Mutual energy transfer between Gd^{3+} ions may occur by interaction between the 6P_J levels of different Gd^{3+} ions. After this energy transfer there remains, however, an energy gap of $32 \cdot 10^3 \text{ cm}^{-1}$. The only way of losing energy is by transfer from Gd^{3+} to "killer sites." This explains why the quantum efficiency of the Gd^{3+} luminescence of $Gd_{0.99}Bi_{0.01}B_3O_6$ amounts merely to 20%. In view of the high quantum efficiency of the Tb^{3+} luminescence of $Gd_{0.98}Tb_{0.01}Bi_{0.01}B_3O_6$ ($\sim 80\%$) $Gd^{3+} \rightarrow Tb^{3+}$ transfer competes successfully with the losses of energy from Gd^{3+} to "killer sites." On substituting La for Gd up to the composition $Gd_{0.55}La_{0.4}Bi_{0.01}Tb_{0.01}B_3O_6$ the quantum efficiency of the Tb^{3+} luminescence decreases slightly to 75% for excitation of Bi^{3+} . If energy transfer between Gd^{3+} ions can in fact be ignored with this composition (as we have assumed above), this means that $Gd \rightarrow Tb$ transfer can take place over nearly 13\AA . This result is in fair agreement with those of Reisfeld *et al.* (3). They found that the efficiency of $Gd^{3+} \rightarrow Tb^{3+}$ transfer in borate glasses is 50% for transfer over 13\AA .

Evidence of the intermediate role of Gd^{3+} has also been obtained for energy transfer from Sb^{3+} and Bi^{3+} to Dy^{3+} in $GdPO_4$. In this compound complete energy transfer from Sb^{3+} and Bi^{3+} to Gd^{3+} is observed. The excitation spectra of the Gd^{3+} luminescence are pictured in Fig. 3a for $Gd_{0.99}Bi_{0.01}PO_4$ and $Gd_{0.99}Sb_{0.01}PO_4$. The excitation bands of the sensitizer (Bi^{3+} or Sb^{3+}) are well separated from the Gd^{3+} excitation lines at 273 nm. Upon coactivation with Dy^{3+} , the emission consists of Gd^{3+} and Dy^{3+} luminescence for excitation of the sensitizer (see Fig. 3b for the emission spectrum of $Gd_{0.985}Bi_{0.01}Dy_{0.005}PO_4$ for 254 nm excitation). The ratio of the intensities of Gd^{3+}/Dy^{3+} luminescence does not depend on whether the sensitizer or Gd^{3+} is excited. Moreover, this ratio is the same for $Gd_{0.985}Sb_{0.01}Dy_{0.005}PO_4$ and $Gd_{0.985}Bi_{0.01}Dy_{0.005}PO_4$ upon excitation of the sensitizers. These observations demonstrate unambiguously the intermediate role of Gd^{3+} in the energy transfer. Note that the height of the sensitizer-excitation band relative to the height of the Gd^{3+} -excitation lines in Fig. 3a depends on the nature of the sensitizer. Probably the nonradiative losses in Bi^{3+} are larger than in Sb^{3+} .

In this paper, we have paid attention only to Tb^{3+} - or Dy^{3+} -activated phosphors. We have also found, however, that Gd^{3+} can play an intermediate role in energy transfer to Eu^{3+} , Sm^{3+} , and Mn^{2+} . This will be the subject of further investigations.

In conclusion, we have illustrated the intermediate role of Gd^{3+} in energy transfer from a sensitizer to an activator. This energy transfer can occur almost exclusively via Gd^{3+} and can have a high efficiency even for relatively low activator concentrations. In this way, highly efficient Tb^{3+} phosphors can be obtained with much lower Tb concentrations than the hitherto known sensitized Tb^{3+} phosphors with high efficiency, such as $Ce_{0.65}Tb_{0.35}MgAl_{11}O_{19}$ (17). The involvement of Gd^{3+} in the energy transfer opens up new possibilities for the development of phosphors.

Table I. The occurrence of energy transfer between sensitizers (S — S), the overlap of sensitizer emission with $4f \rightarrow 5d$ absorption bands of Tb^{3+} ($4f \rightarrow 5d$), and the quantum efficiencies (q.e.) for some sensitized Tb^{3+} phosphors

Composition	S — S ¹	$4f \rightarrow 5d$ ²	q.e. ³	Reference
$Y_{0.97}TaO_4$	—0.03Tb	—	+	70 (5)
$Ce_{0.99}BO_3$	—0.01Tb	+	—	40 (15)
$Ce_{0.67}B_3O_6$	—0.33Tb	—	—	75 (16)
Ce_2F_3	—0.20Tb	—	—	50 (15)
$Ce_{0.65}MgAl_{11}O_{19}$	—0.35Tb	—	—	80 (17)
$Ce_{0.75}Gd_{0.2}F_3$	—0.05Tb	Gd^{3+}	—	70 This work
$Gd_{0.98}Bi_{0.01}B_3O_6$	—0.01Tb	Gd^{3+}	—	80 This work

¹ Energy transfer (+), no energy transfer (—).

² Overlap (+), no overlap (—).

³ q.e. of Tb^{3+} for excitation of the sensitizer.

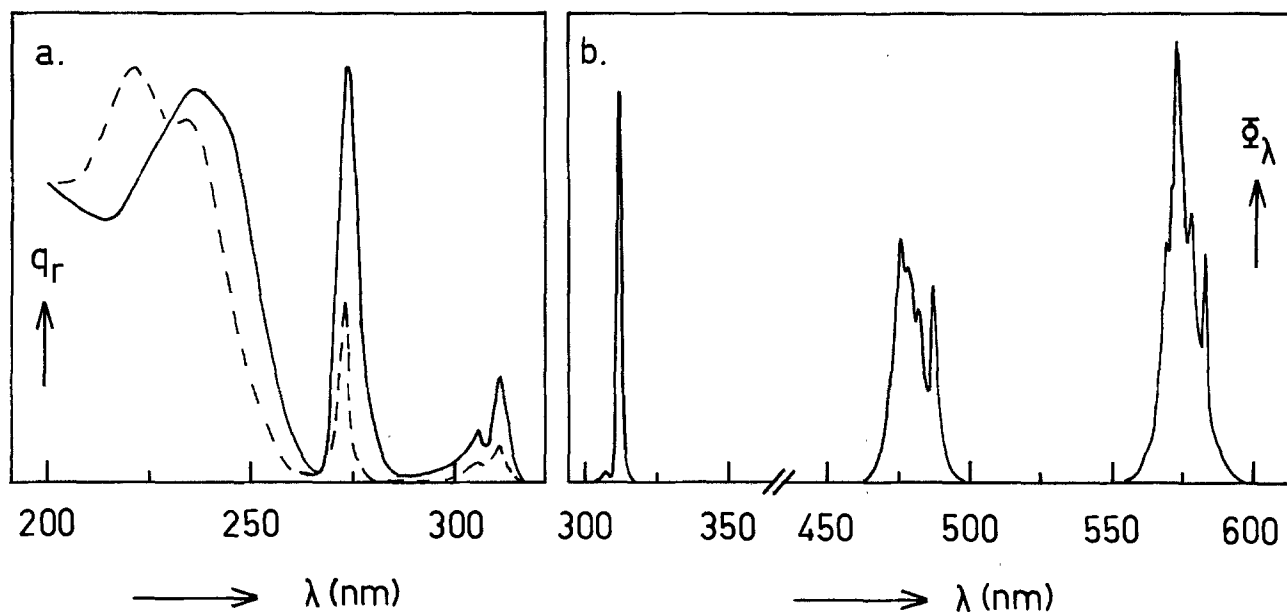


Fig. 3. (a) Excitation spectrum of the 480 nm Dy^{3+} luminescence of $Gd_{0.985}Bi_{0.01}Dy_{0.005}PO_4$ (solid line) and $Gd_{0.985}Sb_{0.01}Dy_{0.005}PO_4$ (broken line). (b) Spectral energy distribution of the luminescence of $Gd_{0.985}Bi_{0.01}Dy_{0.005}PO_4$ for 254 nm excitation. Note the break in the wavelength scale.

Acknowledgments

The authors are indebted to Mr. L. B. A. Spijkerman and Mr. C. W. A. Schetters for the preparation of the materials and for performing optical measurements.

Manuscript submitted April 24, 1979; revised manuscript received Aug. 1, 1979.

Any discussion of this paper will appear in a Discussion Section to be published in the December 1980 JOURNAL. All discussions for the December 1980 Discussion Section should be submitted by Aug. 1, 1980.

Publication costs of this article were assisted by Philips Lighting Division.

REFERENCES

1. A. Bril and W. L. Wanmaker, *J. Chem. Phys.*, **43**, 2559 (1965).
2. L. Ozawa and S. Nishikawa, *Jpn. J. Appl. Phys.*, **7**, 1354 (1968).
3. R. Reisfeld, E. Greenberg, and R. Velapoldi, *J. Chem. Phys.*, **56**, 1698 (1972).
4. V. E. Bozhevolnov, L. N. Ivanov, V. K. Kozlov, Yu. V. Voronov, Yu. P. Timofeev, and V. V. Karelin, *Phys. Status Solidi B*, **78**, 483 (1976).
5. G. Blasse and A. Bril, *J. Lumin.*, **3**, 109 (1970).
6. R. Reisfeld and Sh. Morag, *Appl. Phys. Lett.*, **21**, 57 (1972).
7. J. Th. W. de Hair, *J. Lumin.*, **18/19**, 797 (1979).
8. D. A. Grisafe and C. W. Fritsch, *J. Solid State Chem.*, **17**, 313 (1976).
9. G. Blasse, *J. Lumin.*, **14**, 231 (1976).
10. W. L. Wanmaker, J. W. ter Vrugt, and E. P. J. de Meester, *This Journal*, **119**, 1237 (1972).
11. D. L. Dexter, *J. Chem. Phys.*, **21**, 836 (1953).
12. G. M. Boogerd, Unpublished results.
13. G. Blasse, *J. Chem. Phys.*, **48**, 217 (1968).
14. A. C. van der Steen, J. J. A. van Hesteren, A. Roos, and G. Blasse, *J. Lumin.*, **18/19**, 235 (1979).
15. G. Blasse and A. Bril, *J. Chem. Phys.*, **51**, 3252 (1969).
16. W. L. Konijnendijk and R. C. Peters, Private communication.
17. J. M. P. J. Verstegen, J. L. Sommerdijk, and J. G. Verriet, *J. Lumin.*, **6**, 425 (1973).

Heavy Metal Gettering in Silicon-Device Processing

Livio Baldi, Gianfranco Cerofolini, and Giuseppe Ferla*

Direzione Tecnica, Divisione MOS, SGS-ATES, Milano, Italy

ABSTRACT

Heavy metal gettering in silicon devices has been investigated. The best results have been obtained with $POCl_3$ predeposition followed by annealing at moderate temperature. A model, previously developed for gold, is applied to the description of heavy metal gettering. Once inserted into a standard device process, our gettering step allows us to obtain leakage currents about 100 pA/cm² and 1 pA/cm for diodes and storage time around 10³ sec for capacitors.

A whole class of LSI devices, dynamic RAM's, is based on low reverse currents in junctions and high storage times in capacitors. In addition, all other LSI

devices (static RAM's, ROM's, microprocessors) have dynamic nodes whose behavior depends also on leakage current in junctions and capacitors. The leakage current in junctions is also responsible for the quiescent dissipation of CMOS devices (essentially produced for their low dissipation) so that, especially in MSI-CMOS

* Electrochemical Society Active Member.
Key words: phosphorus gettering, silicon defects, diode, capacitor.

devices, the leakage current must be kept low enough.

Since dissipation is the main factor which limits size and complexity of large systems (fast computers, electronic switching systems), it is of great interest to reduce these leakages. As dissipation is an activated process (activation energy ≈ 0.5 eV), the most obvious approach to its reduction is to operate at low (liquid nitrogen) temperature (1). In view of the great technological difficulties that this approach implies, it is highly desirable to reduce leakages in MOS devices without lowering temperature. In the next section we show that this objective can be accomplished almost completely if heavy metals are removed from the active zones of the devices.

Techniques to selectively remove atoms of a given class are known as gettering, and various gettering procedures for heavy metals have been proposed. Many of them are based on the high affinity of heavy metals toward damaged regions. The damage was produced far from the active regions (*i.e.*, on the wafer back surface) in many ways: mechanical damage (2), ion implantation (3), heavy phosphorus diffusion (4), and stress by mechanical mismatch (5). Other techniques are based on phosphorus deposition followed by high temperature annealing (6-8). In this work we show that a very effective gettering effect can be obtained by phosphorus deposition followed by segregation annealing at moderate temperature: this process must be performed before metal deposition and allows heavy metals to segregate in the contacts or at the back surface.

This paper contains a short description of the principal causes of leakage current; describes three experiments where gettering by phosphorus and by damage are compared; presents a simple description of the gettering theory by segregation annealing; gives the experimental details of our main test-vehicle, the diode; considers the effect of our gettering technique on another device, the capacitor; and finally, contains a discussion of our procedure in comparison with other known processes.

Leakages

We confine ourselves to the n^+/p junction, though, *mutatis mutandis*, the following discussion can be extended to the p^+/n junction and to the MOS capacitor. Leakage current can be ascribed to the following causes: diffusion current, extended defects, and generation/recombination phenomena on Shockley-Read-Hall (SRH) centers.

The diffusion current depends on temperature (through the intrinsic carrier concentration), doping, and trap density; this current can be thought of as the unavoidable contribution to the leakage current.

Extended defects (dislocations, stacking faults, etc.) in active zones once decorated by metal atoms are responsible for a strong increase of reverse current, soft junctions, and so on. Their presence in a device is often catastrophic and may influence both process yield and device performances. Extended defects either are present in the starting slice or are introduced during wafer processing. Care must be used to avoid the second possibility. For instance, high temperature HCl treatment (9,10) and argon or nitrogen annealing before oxidation (11) have lately been proposed to remove stacking fault nuclei. Thermal or mechanical stresses must be avoided so as not to generate dislocations in active zones. This is easily obtained if high temperature ($\gtrsim 1000^\circ\text{C}$) process steps are avoided. If high temperature steps, such as reflow annealing (12), are required then one must use slow push/pull.

The third quantity, generation/recombination on SRH centers, can largely be varied during device processing. Chemically, SRH centers are heavy metal atoms that can exchange both electrons and holes with the lattice; the current they produce is proportional to the atom concentration in the active zone.

The program previously outlined can operatively be restated as follows: to reduce heavy metal concentration in active zone by a procedure (gettering) compatible with the MOS process.

Before describing in short our gettering procedure and how we arrived at it, we would point out that the parameter to test quality of a procedure was the leakage current in suitably prepared diodes. This choice has a clear operative meaning; its physical relevance is discussed later.

Gettering by Damaging

A first idea to reduce SRH center concentration comes directly from tables of the segregation coefficient between solid and liquid silicon (Table I) (13). According to this table we attempted to simulate the liquid structure by damage and to getter heavy metals by the damaged zones.

Initially, we damaged the back side by lapping. Leakage currents and defect density in wafers with damaged back sides were found to be lower than in as-received wafers (polished back sides), in spite of the unwanted front damage introduced during the lapping step. Residual defect density was, however, rather high, and leakage currents still were above the diffusion current limit.

Therefore, we considered two other ways to create largely defective zones: (i) deposition on the back side of a layer of CVD polycrystalline silicon, and (ii) damaging by formation of SiP precipitates.

In the first experiment, shown in Fig. 1, we prepared diodes in the "standard" (see section on Diode Test) way and simulated the liquid silicon structure by depositing a $2\ \mu\text{m}$ thick layer of poly-Si. Poly-Si is actually composed of many grains (ranging in size from 100 to 10,000 Å) in which lattice order is maintained. We may suppose that only the atoms in the first 2-3 layers at the surface of the crystallites are in a quasi-liquid state, *i.e.*, active for gettering. Total surface area is

$$A = aV/R$$

where a is a shape factor (6 for cubic and spheric grains), R a suitable linear dimension of grains (diameter for spheric, edge for cubic ones), and V the total volume. For a layer of thickness t the number of active atoms is given by

$$n = saN_{\text{Si}}^{2/3}t/R$$

where s is the number of liquid-like layers ($s = 2-3$) and N_{Si} the atomic density of silicon ($N_{\text{Si}} = 5 \times 10^{22}\ \text{cm}^{-3}$). Letting $a = 6$ and $R = 1500\ \text{Å}$, we have for a $2\ \mu\text{m}$ thick poly-Si layer $n \approx (2 \div 3) \times 10^{17}\ \text{cm}^{-2}$. Using the segregation coefficient given above, the poly-Si layer should be able to getter as much as 80% of gold from 500 μm thick wafers. Annealing temperatures, 700° and 800°C , and duration, 60 min, were chosen because they are high enough to allow the migration of fast diffusing, metal impurities from one side of the wafer to the other. The resulting gettering activity was negligible (see Fig. 1) showing that the Si-damaged layer (formed by chemical vapor deposition) does not succeed in simulating the liquid layer in the considered temperature range.

In a second experiment the lattice damage was produced by phosphorus predeposition. In our deposition conditions electrically inactive phosphorus is surely formed; indeed V/I after predeposition is typically

Table I.

Metal	Segregation coefficient (solid to liquid)
Au	2.5×10^{-5}
Cr	$< 10^{-8}$
Cu	4×10^{-4}
Fe	8×10^{-8}
Ta	10^{-7}

Fig. 1. Structure of the first experiment: gettering by poly-Si on the back side.

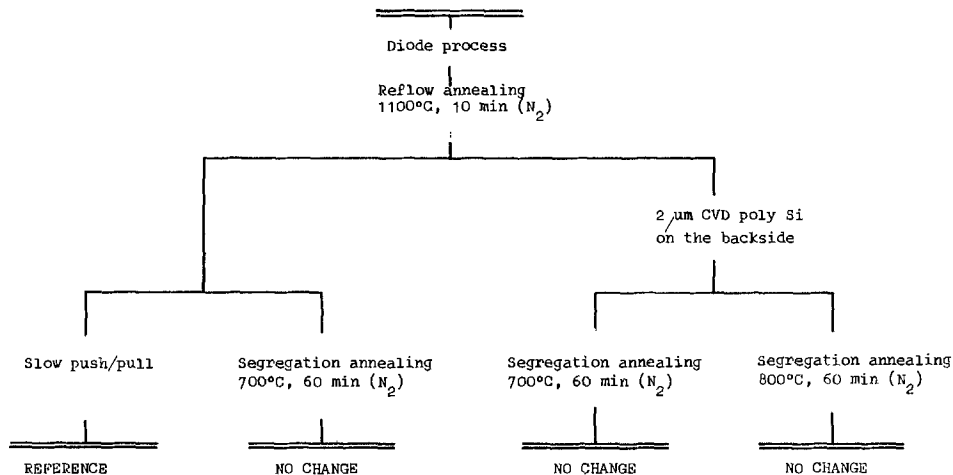
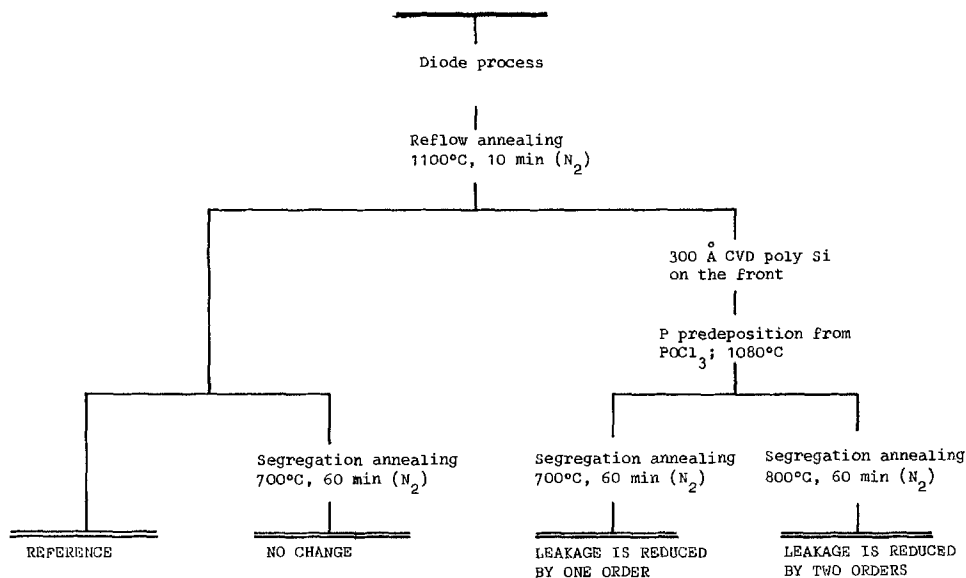


Fig. 2. Structure of the second experiment: gettering by POCl_3 predeposition and moderate temperature annealing.



5 \div 6 Ω and decreases to about 3 Ω after the drive-in step. LAMEL researchers have clearly described how during phosphorus deposition from POCl_3 in oxidizing environment SiP orthorhombic precipitates are formed inside the silicon matrix (14). Because of the lattice mismatch, the SiP precipitates are the source of a complex network of dislocations and defects of various kinds which can be thought of as simulating the liquid structure. The experiment, shown in Fig. 2, was carried out with the same annealing conditions as the first experiment; in spite of this, the results (Fig. 3) were completely different. Since it looked unlikely that the amount of damage introduced by SiP precipitates was greater than that contained in poly-Si, we tentatively admitted that, at the considered temperatures, gettering takes place preferentially by phosphorus rather than by damage. That phosphorus is able to getter impurities was recognized in earlier work (6, 15).

To clarify if gettering was due to single P atoms or to SiP precipitates we performed an experiment where gettering in n^+ regions without precipitates was compared with gettering in n^+ regions with precipitates. As the leakage current was low and practically the same in the two cases¹ (Fig. 4), we could deduce that gettering requires phosphorus atoms and segregation annealing at moderate temperature.

We have arrived at this statement according to the results of only three experiments; actually we per-

formed about thirty different experiments which can be explained, in their generality, only by the previous model.

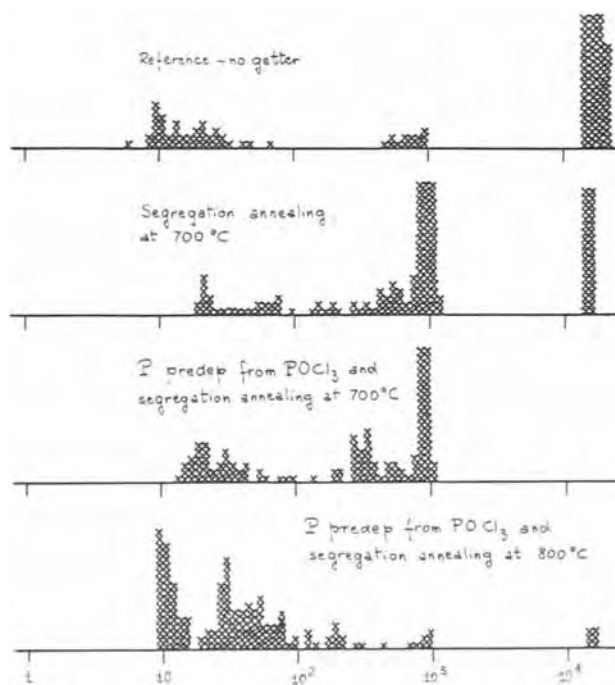


Fig. 3. Leakage current distributions for diodes processed during the second experiment.

¹ However, recently, Tseng et al. (16) at the California Institute of Technology have clearly given evidence for gold gettering by dislocations in addition to gettering by single phosphorus atoms. In fact, they observed that after annealing at 800°C for 100 hr the Au profile roughly follows the P concentration except in a dislocation-rich region, where Au concentration is higher.

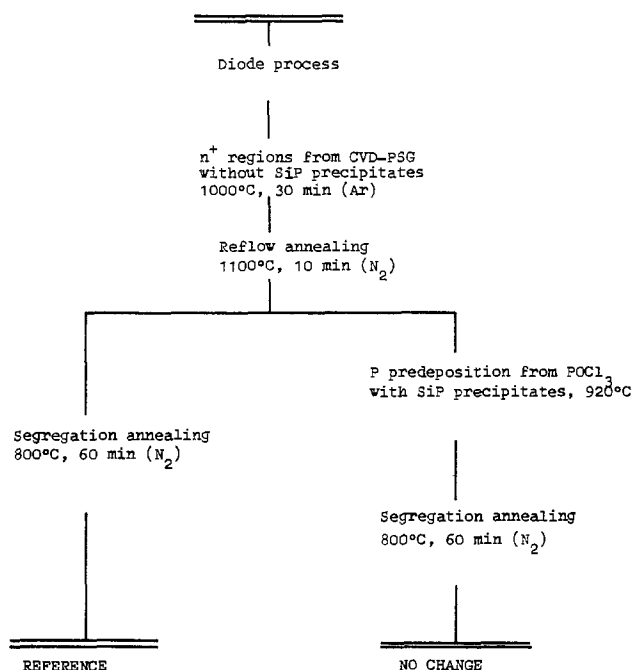


Fig. 4. Structure of the third experiment: gettinger by POCl₃ predeposition with precipitates compared with gettinger by predeposition without precipitates.

A Model for Gettinger by Phosphorus Atoms

The conclusions of the previous section suggest that gettinger takes place preferentially on sites associated with phosphorus atoms, in agreement with the theoretical analysis of Meek and Seidel (7).

In equilibrium conditions atomic concentration of metals in undoped silicon is given in Ref. (17)²

$$N = N_{\text{Si}} \exp(-E/k_B T)$$

where E is a suitable energy factor and k_B is the Boltzmann constant.

If phosphorus produces getter sites, metal dissolution in phosphorus-doped silicon is described by

$$N' = N_{\text{Si}} \exp(-E/k_B T) + N_P \exp(-E_*/k_B T) \quad [1]$$

where the number of getter sites is supposed to increase in proportion to the atomic concentration of phosphorus through an activated process (activation energy E_*) (17). It is supposed that, once formed, the getter site is filled. Formula [1] is the limiting case, for low phosphorus concentration and temperature not too high, of the result obtained by Meek and Seidel for copper and gold.

The segregation coefficient between doped and intrinsic silicon is given by the ratio of N' to N

$$K = 1 + (N_P/N_{\text{Si}}) \exp[(E - E_*)/k_B T] \quad [2]$$

Relationship [2] suggests that gettinger by segregation annealing is feasible only if $E_* < E$, and, in this case, the upper temperature where it is effective is given by this condition: $k_B T < E - E_*$. The lower temperature limit is determined by the annealing duration: The temperature must be high enough to allow a complete segregation.

For a particular impurity, gold, the calculation of $E - E_*$ was possible from known thermodynamic data, suggesting an annealing temperature in the range 700°-800°C³ (17). Graphs of the segregation coefficient vs. temperature for various phosphorus concentrations (metal impurity: gold) are shown in Fig. 5. The con-

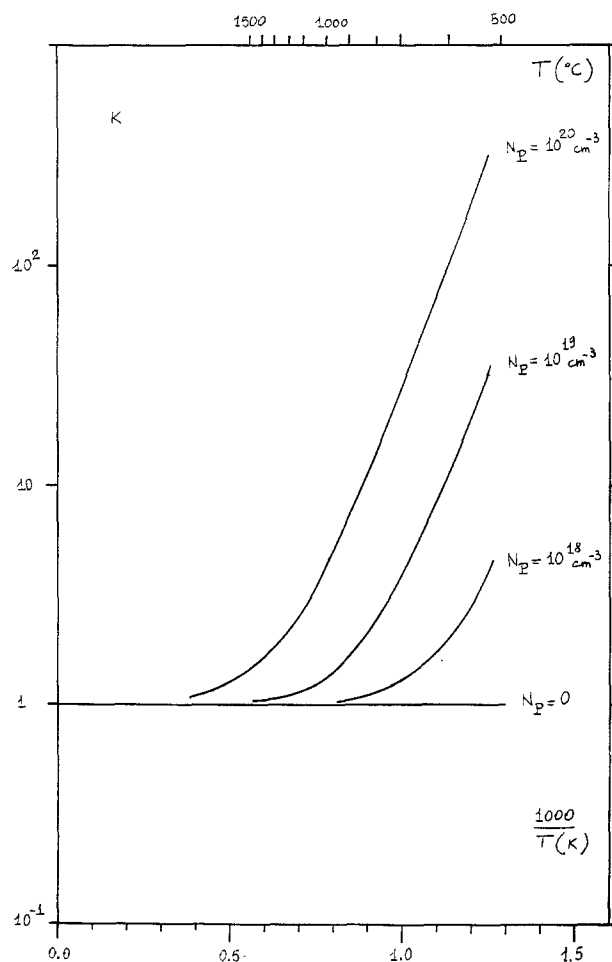


Fig. 5. Segregation coefficient of gold in P-doped silicon vs. temperature for various phosphorus concentrations.

clusion obtained for gold can tentatively be assumed to hold for other heavy metals (7, 15).

The Diode Test

The gettinger procedure previously described can be applied to any standard n-channel MOS or CMOS process and allows us to obtain diodes which at room temperature currently have leakages in the range 50-150 pA/cm², irrespective of substrate growth method (CZ or FZ). Leakage current is low enough to be close to the diffusion value so that some indications on the process are required.⁴

This process requires a boron field implantation to avoid surface inversion in high resistivity materials. The various steps are reported in Table II (no cleaning is indicated) and are taken from an n-channel silicon-gate process simplified by avoiding gate oxide growth and poly-Si deposition. We hope that further published reductions in leakages will be accompanied by the associated diode process.

As previously stated, diodes processed in this way reproducibly have at a reverse bias of 15V an area leakage current of about 100 pA/cm²; in addition, the perimeter leakage current is of the order of 1 pA/cm and typical electric defect density on good materials is less than 1 defect/cm² (19). The diffusion limits are roughly the following: area leakage current is 35 pA/cm² [calculated by the equation $J = e\sqrt{D_n/\tau_n} n_i^2/N_A$ (20), assuming an electron diffusion coefficient $D_n = 30 \text{ cm}^2/\text{sec}$, a minority electron carrier lifetime⁵ $\tau_n = 10 \mu\text{sec}$,

² Metal atoms are supposed to reach this concentration coming from a source at unit activity.

³ Obviously, annealing time must increase as temperature decreases to permit heavy metals to diffuse. The results of the experiments of Fig. 2 can be explained by observing that annealing at 700°C for 1 hr is a time shorter than that required for full segregation.

⁴ Leakage current of the same order has been reported by Brotherton and Gill in a recent communication (18). This paper is also of interest for the estimate of the value of the diffusion current.

⁵ This value is typical for CZ-grown silicon slices with resistivity in the MOS range. However, this parameter is continuously increasing with the development of the technology of silicon production.

Table II. Diode process*

1.	Initial oxidation (HCl-steam), 875°C, 500A
2.	Silicon nitride deposition, 920°C
3.	Active zone mask-nitride etch (plasma)
4.	B ¹¹ field implantation, 10 ¹³ ions/cm ²
5.	Field oxidation (steam), 920°C, 1.1 μm
6.	Thin oxide etch (HF)
7.	Nitride etch (plasma)
8.	Front mask, back oxide etch (HF)
9.	P predeposition (POCl ₃), 920°C, V/I = 6Ω
10.	P diffusion (O ₂), V/I = 3Ω
11.	PSG deposition
12.	Contact mask, PSG etch (buffered solution)
13.	Reflow annealing (1100°C)
14.	P predeposition (POCl ₃), 920°C, V/I = 6Ω
15.	Segregation annealing (N ₂), 800°C
16.	Al/Si deposition, 1 μm
17.	Metal mask, Al/Si etch (H ₂ PO ₄ , plasma)
18.	Alloy (H ₂) 450°C

* Diodes prepared according to this process currently have a reverse current in the range 50-150 pA/cm² at a bias of 15V. Diodes prepared simultaneously are distributed very sharply around the mean value, and only a small portion of the whole population (about 5%) has high leakages (1 nA/cm² or more). We ascribe this portion to electrically active defects (19).

an intrinsic carrier concentration $n_i = 1.6 \times 10^{10} \text{ cm}^{-3}$, and an acceptor concentration $N_A = 2 \times 10^{15} \text{ cm}^{-3}$; e is the proton charge], perimeter leakage current is $5 \times 10^{-3} \text{ pA/cm}$ (calculated considering the perimeter as a 90° arc of cylindrical junction with radius equal to the junction depth, 1.5 μm, and assuming the same current density calculated for area). Incoming slices were declared dislocation free by the producer and the claim was found true by incoming inspection.

From the comparison we easily realize that the attempt to reduce the defect density and area leakage current have been accomplished to a great extent; but the objective to reduce the gap for the perimeter leakage current has not yet been reached. At present we do not know if the high perimeter leakages must be ascribed to the ion-implant damage, to the vicinity to the field oxide, or to the competitive gettering action of the boron-implanted region (we are indebted to one referee for this suggestion). The perimeter leakage current is a parameter of increasing relevance as the device complexity increases and the feature sizes decrease.

A Review of Gettering Effects on Dynamic RAM's

Though diodes are both conceptually and operatively a good vehicle for testing a gettering efficiency, it is always possible that the efficiency of a getter procedure is lost in a complete (dynamic RAM) process. This process is roughly the same as the one previously described for diodes, with the addition of gate oxidation and annealing (1100°C), poly-Si deposition (660°C), and masking between steps 8 and 9.

For this kind of device, the most important contributions to the over-all leakage current are given by perimeter leakage current and recombination current in MOS capacitors. A typical parameter depending on the latter current and of significance in dynamic RAM's is the storage time of MOS capacitors. In Fig. 6 we have plotted this parameter measured on capacitors processed in our facility as test patterns on the same wafers as 4 K dynamic RAM's. The graph starts with the storage time after the introduction of a rough back side for wafers. This constituted an improvement over the previously used back-polished wafers since the rough back side behaved as a getter region for impurities and prevented the formation of etch pits on the wafer front. The next increase in storage time took place when the P diffusion was also allowed to take place on the back side of the wafers thus improving the getter efficiency at the back side. A third increase in storage time took place when automatic pullers were introduced for all high temperature annealing. This avoided wafer warping and reduced the density of crystal defects induced by processing. A decrease in storage time took place simultaneously with the intro-

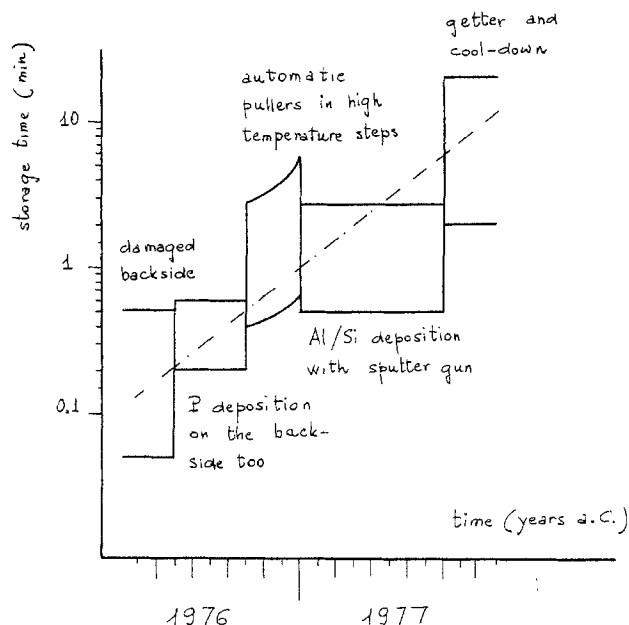


Fig. 6. Improvement in storage time after process changes

duction of sputter-gun deposition of Al/Si. Since the previously used process required the deposition of a thin layer of poly-Si at the temperature of 660°C before Al deposition, we now assume that this step acted as segregation annealing. The last improvement shown took place with the introduction of the cool-down for reflow annealing (19) and of the above-mentioned gettering step.

In conclusion, the results of this figure provide strong evidence that our gettering procedure, though set up to reduce area leakage currents in diodes, is also efficient in reducing recombination current in gate oxide capacitors.

Discussion

The gettering technique we have described is based on phosphorus deposition followed by segregation annealing at moderate temperature.

In the short history of microelectronics several other gettering techniques have been proposed. Many of them, irrespective of the mechanism proposed to explain the gettering activity, were based on phosphorus deposition followed by high temperature ($\geq 1000^\circ\text{C}$) annealing (6-8). This does not agree with our results that the final annealing should be performed at moderate ($\approx 800^\circ\text{C}$) temperature. This discrepancy can be overcome by the following argument.

Considering Eq. [1], it is seen that the solid solubility of metal impurities increases quickly as temperature increases. Thus, if heavy metals are present in the slice in the (catastrophic) form of precipitates, phosphorus deposition followed by high temperature annealing dissolves them. This mode of gettering (i.e., removing metal precipitates) is clearly recognized even in the early work of Goetzberger and Shockley (6) but is not effective in modern materials. Silicon is now furnished with a very low content of heavy metals, especially if float-zone grown. Accordingly, no precipitates are present in the slice and dissolved atoms must be segregated far from the active zones. The phenomenon to be used is selective segregation which is effective at moderate temperature.

If the silicon slice contains metal precipitates, the two processes can be carried out in this order: phosphorus deposition plus high temperature annealing and segregation annealing at moderate temperature. Thus, the objective outlined at the beginning of this work can be considered almost reached, with the remarkable exception of the periphery leakage current. The decrease of this quantity is the obvious, next objective.

Manuscript submitted Feb. 22, 1979; revised manuscript received Aug. 3, 1979.

Any discussion of this paper will appear in a Discussion Section to be published in the December 1980 JOURNAL. All discussions for the December 1980 Discussion Section should be submitted by Aug. 1, 1980.

Publication costs of this article were assisted by SGS-ATES.

REFERENCES

1. R. W. Keyes, *Science*, **195**, 1230 (1977).
2. R. B. Herring, 18th Annual Electronic Materials Conference (1976).
3. A. G. Nassibian, V. A. Browne, and K. D. Perkins, *J. Appl. Phys.*, **47**, 992 (1976).
4. G. A. Rozgonyi, P. M. Petroff, and M. H. Read, *This Journal*, **122**, 1725 (1975).
5. P. M. Petroff, G. A. Rozgonyi, and T. T. Sheng, *ibid.*, **123**, 565, 570 (1976).
6. A. Goetzberger and W. Shockley, *J. Appl. Phys.*, **31**, 1821 (1960).
7. R. M. Meek and T. E. Seidel, *J. Phys. Chem. Solids*, **36**, 731 (1975).
8. M. J. J. Theunissen, J. Snel, and P. H. M. Willemse, *Philips Res. Rep.*, **32**, 429 (1977).
9. T. Hattori, *Jpn. J. Appl. Phys.*, **17**, 69 (1978).
10. H. Shiraki, in "Semiconductor Silicon, 1977," H. R. Huff and E. Sirtl, Editors, p. 546, The Electrochemical Society Softbound Proceedings Series, Princeton, N.J. (1977).
11. S. Kishino, S. Isomae, H. Tamura, and M. Maki, *Appl. Phys. Lett.*, **32**, 1 (1978).
12. G. F. Cerofolini, G. Ferla, and C. Rovere, *Thin Solid Films*, **50**, 73 (1978).
13. H. Hermann, H. Herzer, and E. Sirtl, *Festkörperprobleme*, **15**, 279 (1975).
14. A. Armigliato, D. Nobili, M. Servidori, and S. Solmi, *J. Appl. Phys.*, **47**, 5489 (1976).
15. R. N. Hall and J. C. Racette, *ibid.*, **33**, 379 (1964).
16. W. F. Tseng, T. Koji, J. W. Mayer, and T. E. Seidel, *Appl. Phys. Lett.*, **33**, 441 (1978).
17. L. Baldi, G. F. Cerofolini, G. Ferla, and G. Frigerio, *Phys. Status Solidi A*, **48**, 523 (1978).
18. S. D. Brotherton and A. Gill, *Appl. Phys. Lett.*, **33**, 890 (1978).
19. L. Baldi, G. F. Cerofolini, and G. Ferla, *Surf. Technol.*, **8**, 161 (1979).
20. S. M. Sze, "Physics of Semiconductor Devices," p. 100, John Wiley & Sons, Inc., New York (1969).

Study of Anodization Process on GaAs by *In Situ* Differential Reflectance

C. Yamagishi, A. Moritani, and J. Nakai

Department of Electronics, Faculty of Engineering, Osaka University, Osaka 565, Japan

ABSTRACT

The anodic film growth on GaAs during the anodization process and the dissolution process of the grown film in the open-circuit condition have been observed with the *in situ* differential reflectance technique. The initial phase of anodic oxidation process has also been investigated in this study. The experimental results strongly suggest that the two-dimensional growth of the anodic nuclei takes place in the initial phase and that the substrate-dissolution process is controlling the film formation. A "less soluble region" has been observed in the dissolution curve. The film keeps growing in the open-circuit transient region due to the residual ions within the grown film. It is also shown that the dissolution curve of the grown film is useful in characterization of the film rather than the anodization curve. The obtained value of parameter from the best-fitting to the dissolution curve is 0.2 \AA sec^{-1} for the dissolution rate at pH 2.4 in tartaric acid-water-propylene glycol electrolyte and 1.79 ± 0.05 for the refractive index of the anodically grown film at 6328 \AA .

In recent years oxidation of GaAs has been studied for preparation of the passivation film and gate-insulating film for GaAs-MOSFET. The anodic oxidation has been considered to be one of the most promising techniques to form the native oxide film on GaAs and several performances of the GaAs-MOSFET devices with the anodic films have been reported (1).

The fundamental study of the anodic oxidation on GaAs, however, has not been extensively studied yet. In recent publications, Hasegawa and Hartnagel (2) have shown that Anodization of GaAs in Glycol and Water (AGW process) can provide a stable and reproducible process in forming the anodic oxide films on GaAs and the films possess low conductivity and high dielectric breakdown field-strength. Another interesting report on the initial phase of anodic oxidation on GaAs has been made by Szpak (3). His experimental observation with the use of scanning electron microscope (SEM) indicates that the two-dimensional growth of the oxide film takes place in the initial phase of film formation. We have also shown in our previous report (4) that different type of film formation from that in the region of passive film formation takes place in the initial phase of anodic oxidation.

It is the purpose of this paper to show some further investigations on the anodic oxidation of GaAs using

the new technique of *in situ* differential reflectance with a double beam-single detector system and double specimens (4). It will be shown in this paper that the present technique is available to the study of anodic oxide film formation of thick films grown on GaAs or on the other semiconductors. The initial anodization process and dissolution process of the grown film will also be discussed in this paper.

Theory

We consider the thickness modulation with uniform-film growth on a substrate. The description with the Jones matrix representation for a stratified media is very convenient and gives the generalized form for the system in question (5). The intermediate layer is only the anodic film as shown in Fig. 1, so that the basic vector in the electrolyte is represented by

$$\begin{bmatrix} E_{r1} \\ E_{i1} \end{bmatrix} = \begin{bmatrix} (1 + n_2/n_1)/2 & (1 - n_2/n_1)/2 \\ (1 - n_2/n_1)/2 & (1 + n_2/n_1)/2 \end{bmatrix} \times \begin{bmatrix} \exp(ikd) & 0 \\ 0 & \exp(-ikd) \end{bmatrix} \times \begin{bmatrix} (1 + n_3/n_2)/2 & (1 - n_3/n_2)/2 \\ (1 - n_3/n_2)/2 & (1 + n_3/n_2)/2 \end{bmatrix} \begin{bmatrix} E_{r3} \\ E_{i3} \end{bmatrix} \quad [1]$$

Key words: semiconductor, anode, reflectance, passivity.

where E_{rj} and E_{lj} are the complex amplitudes of the rightward and leftward propagating plane-wave states in the j th layer, n_j is the complex refractive index of the j th layer, (the subscripts 1, 2, and 3 mean the electrolyte, the film, and the substrate, respectively), k is the complex propagation constant in the film, and d is the film thickness. The boundary condition is $E_{r3} = 0$ which means that energy propagates only to the left in the substrate. The complex reflectance ratio, r , is defined as

$$r = E_{r1}/E_{l1} \quad [2]$$

and the reflectance, R , for the system follows from the definition

$$R = |r|^2 = r^*r \quad [3]$$

The relative change in r , $\Delta r/r$, resulting from the thickness change is expressed by Eq. [4], using Eq. [1] and [2]

$$\begin{aligned} \frac{\Delta r}{r} &= \frac{r(d) - r(0)}{r(0)} = \frac{r(d)}{r(0)} - 1 \\ &= \frac{(n_1 + n_3)}{(n_1 - n_3)} \times \frac{(n_1 + n_2)(n_2 - n_3)\exp(ikd) + (n_1 - n_2)(n_2 + n_3)\exp(-ikd)}{(n_1 - n_2)(n_2 - n_3)\exp(ikd) + (n_1 + n_2)(n_2 + n_3)\exp(-ikd)} - 1 \end{aligned} \quad [4]$$

It follows that the relative change of reflectance, $\Delta R/R$, observed experimentally is given by

$$\begin{aligned} \frac{\Delta R}{R} &= \frac{R(d) - R(0)}{R(0)} = \frac{(r + \Delta r)^*(r + \Delta r) - r^*r}{r^*r} \\ &= 2 \operatorname{Re} \left(\frac{\Delta r}{r} \right) + \left| \frac{\Delta r}{r} \right|^2 \end{aligned} \quad [5]$$

For a very small change, or, a very thin surface film in the thickness modulation, the last term in the right-hand side of Eq. [5] is negligible and the linear approximation theory becomes valid (6). Now, $\Delta R/R$ in the thickness modulation can be evaluated by Eq. [4] and [5] for relatively thick films.

Experimental

Zn-doped p-GaAs wafers with carrier concentration of $1 \times 10^{18} \text{ cm}^{-3}$ and (100) face were used in the present experiment. The effect of illumination on the cell voltage, V_C , may be negligible when p-GaAs samples with high carrier concentration are used since holes play an important role in the anodization process. The ohmic contact was formed by deposition of In-Ag alloy in vacuum, followed by a brief annealing in hydrogen atmosphere at 500°C . A typical size of the sample surface area was $7 \times 7 \text{ mm}^2$. Samples were chemomechanically polished and etched by the etchant of $3\text{H}_2\text{SO}_4:1\text{H}_2\text{O}_2:1\text{H}_2\text{O}$ for one minute. Each sample was subjected to a series of cleaning procedures with organic solvents and boiling in HCl in order to get rid of the native oxide which might have grown during the sample preparation. All the measurements were made in 3 weight percent (w/o) aqueous solution of tartaric acid mixed with propylene glycol in the volume ratio

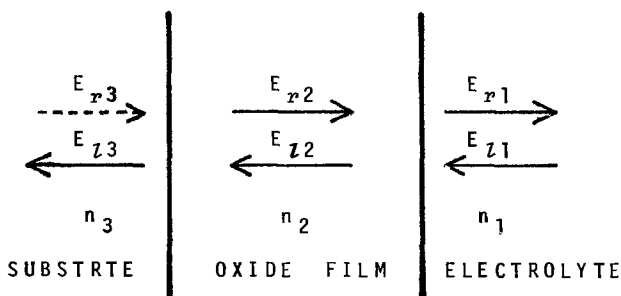


Fig. 1. Schematic diagram of thickness modulation on three-phase model. Semi-infinite substrate is at left, transparent electrolyte at right.

1:2, buffered by NH_4OH to obtain a desired pH-value, if necessary (2). The pH-value of the electrolyte without adjustment was typically 2.4. Distilled water was used to prepare the electrolyte. The electrolyte was not agitated in the experiment since agitation causes the noise in the optical signal. The experimental setup and measurement techniques on the differential reflectance measurement are as follows.

A double beam-single detector system as shown in Fig. 2 was introduced in order to minimize the drift caused by the optical components. The light beam is divided into the sample and reference channels by a half-circular chopper mirror. A 1 mW He-Ne laser with the wavelength of 6328\AA was used as the light source. The polarizers were used only for the attenuation of the light intensity, since the measurements were made in the normal incident configuration at present. We put a reference electrode of GaAs (GaAs-1 in

Fig. 2) prepared in the same way as the sample electrode (GaAs-2 in Fig. 2) in order to minimize the difference in the reflected light intensities between the two and then set it to zero prior to the anodization by adjusting the gate width of the delay-gate switching circuit, which has been reported elsewhere (7). The waveform of the signal obtained from the photomultiplier is also shown in the insert of Fig. 2. The gate width was adjusted such that only the flat portion of the signal was picked up to avoid any spike signal which had resulted from the edges of the chopper mirror, and each gate width is adjustable independently so that the initial difference in the light intensities between the two, if it exists, can be set to zero. The output signal in the reference channel was kept constant by a servo-system which controls the high voltage of the photomultiplier. The mirrors and electrodes were set such that the two beams were near-normally in-

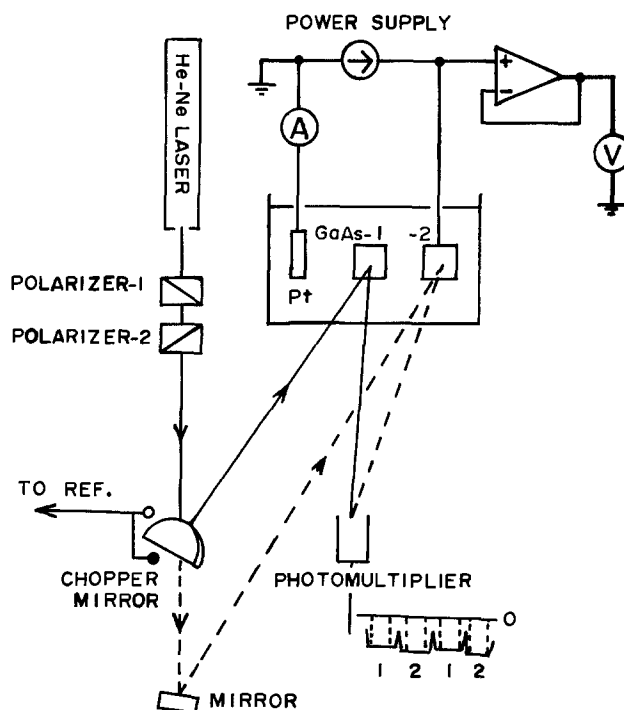


Fig. 2. Experimental setup for the double beam-single detector system using the differential reflectance technique. The polarizers are used for the attenuation of the light intensity in this case.

cident onto the sample and reference electrodes and that the reflected-light beams struck the same area of the photocathode of the photomultiplier. We were careful to set the electrodes near the window of the cell as much as possible in order to minimize the noise caused by contaminants or bubbles in the electrolyte used, and all the measurements were made on the table which was made to absorb the ground vibration. Thus, the $\Delta R/R$ vs. time ($\Delta R/R - t$), $\Delta R/R$ vs. cell-voltage ($\Delta R/R - V_c$), cell-voltage vs. time ($V_c - t$), and/or current-density vs. time ($J_d - t$) characteristics were simultaneously measured and recorded with a two pen recorder. The magnitude of the drift in this system was estimated below 1% of the signal.

Results and Discussion

Outline of $\Delta R/R$ characteristics.—In the first place, we point out the stability of the electrolyte used. The $V_c - t$ characteristics measured above the critical current-density needed for the initiation of film formation in two electrolytes of the same composition are shown in Fig. 3, where F-electrolyte is freshly prepared just before the anodization and O-electrolyte was prepared a week before. Such fresh and old electrolytes show a difference in the $V_c - t$ curves under the condition of constant current (c.c.); in the F-electrolyte the duration time in the initial portion of the $V_c - t$ curve with smaller gradient is longer than that in the O-electrolyte under the same constant current condition. The experimental data, except Fig. 3 and 10, shown in the following were obtained with the F-electrolyte.

Typical experimental results of the $\Delta R/R$ characteristics under the three important situations for practical production of the anodic oxide film for GaAs-MOS devices are shown in Fig. 4-6. Figure 4 shows the $\Delta R/R - t$ (solid line) and $V_c - t$ (broken line) curves under the condition of c.c.-to-open-circuit. The point designated as "OFF" is the time when the circuit was opened. The current-density was $295 \mu A cm^{-2}$ in this case. In the initial phase of anodization both $\Delta R/R - t$ and $V_c - t$ curves have slowly varying portions with the duration time t_c followed by steeply changing portions. The observation of the $\Delta R/R$ signal in the initial phase indicates a "nonpassive" film growth (8) or the quasi-two-dimensional growth of the passive film which is recently reported by Szpak (3). After the circuit was opened, the $\Delta R/R$ signal increased to the initial zero value indicating the dissolution of the anodically grown film. The film is found to be in "less soluble region" for the time t_d and to complete the dissolution in the time t_p as shown in Fig. 4.

The $\Delta R/R - t$ (solid line) and $J_d - t$ (broken line) curves under the condition of constant voltage (c.v.)-to-open-circuit are shown in Fig. 5, where J_{df} is the

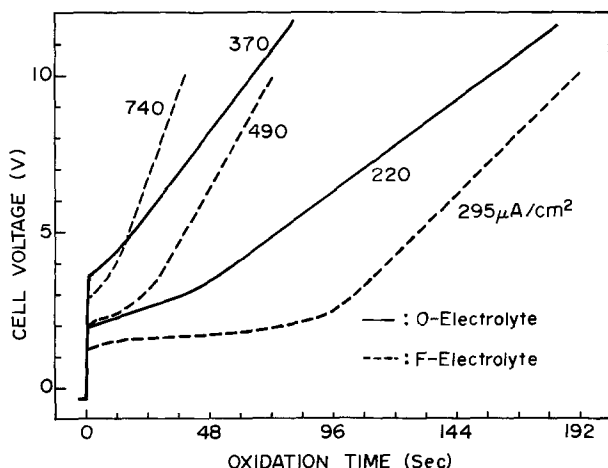


Fig. 3. $V_c - t$ characteristics under the c.c. condition in old- and fresh-electrolyte.

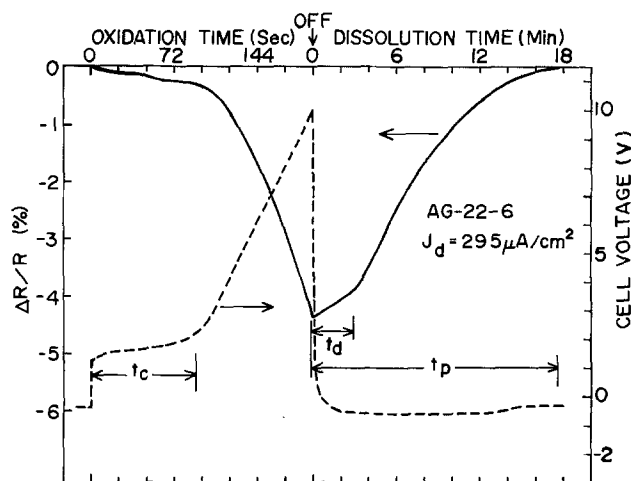


Fig. 4. $\Delta R/R - t$ (—) and $V_c - t$ (---) characteristics under the condition of c.c.-to-open-circuit.

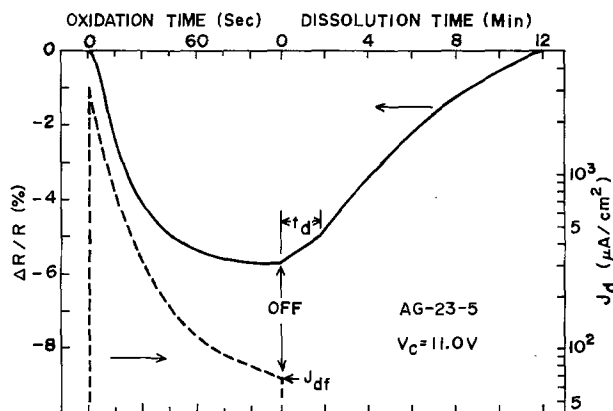


Fig. 5. $\Delta R/R - t$ (—) and $J_d - t$ (---) characteristics under the condition of c.v.-to-open-circuit. J_{df} is the final current-density.

final current-density. The applied constant voltage was 11.0V in this case. It is found in Fig. 5 that the $\Delta R/R$ signal decreases to a constant value defined by the formation voltage V_f which is the difference between the final cell-voltage and initial voltage drop and corresponds to the grown film thickness, and then it increases in the open-circuit condition in the same manner as in Fig. 4. The "less soluble region" also appeared in this case though the initial flat portion is hardly observed in $\Delta R/R - t$ characteristics.

Lastly, the result under the condition of c.c.-to-c.v.-to-open-circuit is shown in Fig. 6. This condition is commonly applied to the anodic oxidation for the practical use. It is noted that the film formation still continues after the change from the c.c. condition to the c.v. condition.

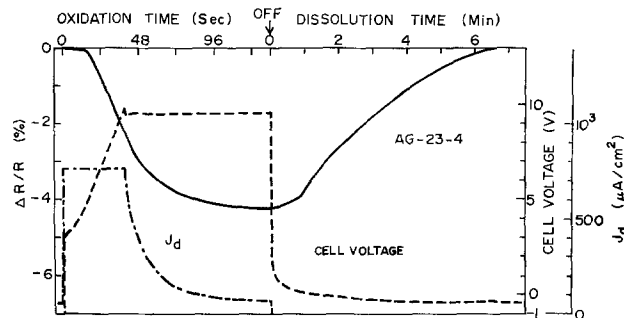


Fig. 6. $\Delta R/R - t$ (—), $V_c - t$ (---), and $J_d - t$ (-·-·-) characteristics under the condition of c.c.-c.v.-open circuit.

After the complete dissolution we repeated the experiments with the same sample and the same electrolyte. Such experimental results under the condition of c.c.-to-open-circuit are shown in Fig. 7, where it is seen that the reproducibility of this experiment is excellent. It is also suggested that the dissolution rate varies with the final thickness of the grown film; it increases as the grown film thickness increases.

Initial phase of anodization process.—A few investigations on the initial phase of anodization of GaAs have been reported. Harvey and Kruger (8) studied the behavior of GaAs anode and observed the active-passive transition under a certain condition. They also observed nonpassive film growth in the active region. Hasegawa and Hartnagel (2) studied the anodic oxidation of GaAs in the AGW process and also observed the active-passive transition. More recently Szpak (3) studied the initial phase of anodization of GaAs in the AGW process with SEM and suggested that the quasi-two-dimensional growth from nucleation site is taking place in the initial phase.

In this section, we will explain the observation of the surface coverage-*vs.*-time ($\theta - t$) derived from the $\Delta R/R - t$ curves in the initial phase of anodic oxidation in terms of the two-dimensional growth assuming that cylindrical nuclei grow in two dimensions in the initial phase. For the growth of an anodic film at constant thickness, the value of $\Delta R/R$ may be determined by an "average thickness $d_0\theta$ ", where d_0 is the constant thickness of the cylindrical nuclei and θ the surface coverage which is a ratio of the area covered with anodic film to the whole area of electrode, since the wavelength of light used is so long as compared with the dimensions of the nuclei. Thus one may be able to argue the surface coverage as described in the following. The first derivative of the surface coverage θ may be written by

$$\frac{d\theta}{dt} = \frac{J_f M}{z F \rho d_0} = \frac{J_f}{q_m} \quad [6]$$

where J_f is the current-density consumed for the film formation, M the average molecular weight of the anodic oxide film, ρ the density of the film, z the number of ionic charge, F the Faraday constant, and $q_m = z F \rho d_0 / M$ the charge amount which is necessary to have the full surface coverage. The problem in the two-dimensional growth of anodic film is what is the slowest process which controls the rate of film formation. Two situations of interest may exist for the two-dimensional growth; (A) the dissolution of the anode material into the electrolyte is the slowest process, called "metal-dissolution-controlling," (B) the growth of anodic film

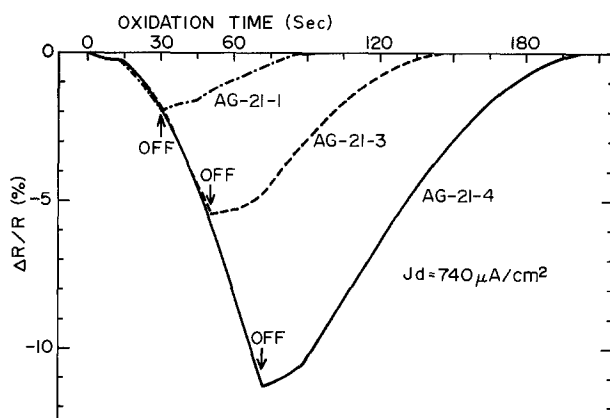


Fig. 7. Reproducibility of the $\Delta R/R$ characteristics with the same sample under the condition of c.c.-to-open-circuit. The initial phase of anodization is reproduced well under the same current-density condition. Time scale after OFF for each curve refers to dissolution time, and has been multiplied by a constant factor 1/10.

is the slowest process, called "film-formation-controlling" (9). In each case, the surface coverage θ is given by Eq. [7] or [8]

(A) metal-dissolution-controlling case

$$\theta = 1 - \exp\left(-\frac{t}{\tau_d}\right) \quad [7]$$

(B) film-formation-controlling case

$$\theta = 1 - \exp(-at^2) \quad [8]$$

where τ_d and a are constants. The metal-dissolution-controlling is more likely in the present experimental results than the film-formation-controlling since it is found in Fig. 8 that the film thickness, which refers to θ below the full surface coverage, has similar time dependence of type (A) of Eq. [7], as written by Eq. [9]

$$\theta = 1 - \exp\left(-\frac{t}{\tau}\right) \quad [9]$$

In Fig. 8, the theoretical curve (broken line) is drawn assuming that the time constant τ is 6.5 sec and the thickness of cylindrical nuclei d_0 is 35Å. Both curves coincide with each other though the coincidence is broken near the critical time from which the passive film starts to grow in three dimensions. According to Eq. [6], J_f is given by the first derivative of θ so that differentiating the experimental equation, Eq. [9], gives

$$J_f = \frac{q_m}{\tau} \exp\left(-\frac{t}{\tau}\right) = J_1(1 - \theta) \quad [10]$$

Equation [10] is likely to correspond to the concept of the metal-dissolution-controlling (9), so that $J_1 = q_m/\tau$ may be considered to be the current-density on the uncovered surface at $t = 0$ and nearly equal to the applied current-density J_d at $t = 0$, if any current-loss is negligible at $t = 0$. Value of q_m is estimated as 4.8 mC cm⁻² from the time constant τ and current-density J_d in Fig. 8. This value corresponds to the charge amount which four atomic layers of (100) face of GaAs have. If it is assumed that four atomic layers

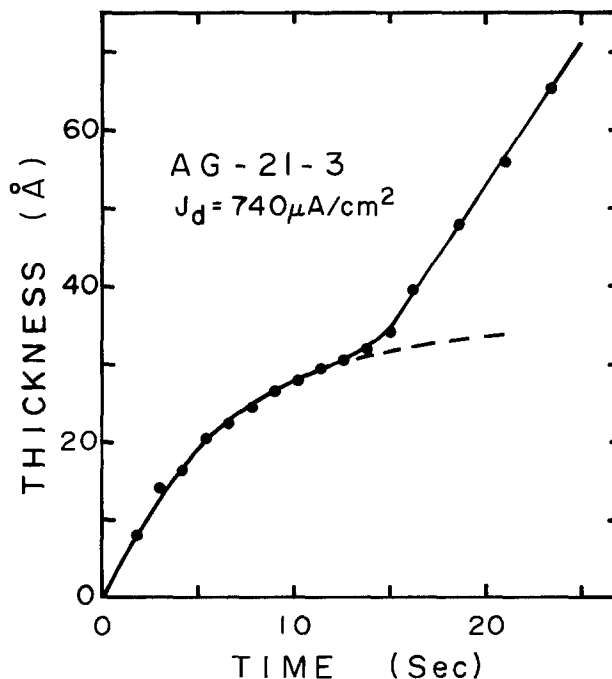


Fig. 8. Comparison of the experimental curve (—) with theoretical curve (----) in the initial phase of the film thickness *vs.* time characteristics under the c.c. condition. The theoretical curve of the two-dimensional growth fits well with the experimental curve.

dissolve into the electrolyte as ions of Ga^{3+} and As^{3+} and their whole charges are consumed for the formation of oxide film with thickness of 35\AA in this case, the consumption ratio was estimated to be 1.55. This value is in good agreement with that calculated using the previously reported data of the growth rate and consumption rate (2).

Next we will derive the velocity of radial growth v , cm sec^{-1} , assuming that the nucleation of anodic film is taking place progressively under the c.c. condition. The contribution of nuclei which generated at time u to the surface coverage θ at time t , with no consideration of overlapping is given by

$$d\theta_{ex} = Z\{1 - \theta(u)\}du\pi \left\{ \int_u^t v(t)dt \right\}^2 \quad [11]$$

where Z is the nucleation rate, $\text{cm}^{-2} \text{sec}^{-1}$, and θ_{ex} is the surface coverage with no account taken of overlapping. Integrating Eq. [11] gives

$$\theta_{ex} = \int_0^t Z\pi\{1 - \theta(u)\} \left\{ \int_u^t v(t)dt \right\}^2 du \quad [12]$$

Substituting Eq. [9] into Eq. [12] with use of Abrami's equation (10), $\theta = 1 - \exp(-\theta_{ex})$, gives,

$$\frac{t}{\tau} = \int_0^t Z\pi \exp\left(-\frac{u}{\tau}\right) \left\{ \int_u^t v(t)dt \right\}^2 du \quad [13]$$

Differentiating Eq. [13] twice and rearranging gives

$$\begin{aligned} \left(\frac{1}{v}\right) \frac{d}{dt} \left(\frac{1}{v}\right) &= 2\pi Z \int_0^t \exp\left(-\frac{u}{\tau}\right) du \\ &= 2\pi Z \left\{ 1 - \exp\left(-\frac{t}{\tau}\right) \right\} \end{aligned} \quad [14]$$

Solving Eq. [14] with boundary condition, $1/v = 0$ at $t = 0$, which means that there is almost infinite space for nucleation and radial growth at the start of anodization under the constant current condition so that the velocity of radial growth should be substantially large at $t = 0$ (11), one may obtain

$$v(t) = (4\pi Z^2)^{-1/2} \left\{ \exp\left(-\frac{t}{\tau}\right) + \frac{t}{\tau} - 1 \right\}^{-1/2} \quad [15]$$

or in another form of v as a function of θ

$$v(\theta) = (4\pi Z^2)^{-1/2} \left(\ln \frac{1}{1-\theta} - \theta \right)^{-1/2} \quad [16]$$

Figure 9 shows the plots of $v(\theta)$ given by Eq. [16]. In Fig. 9, the work by Armstrong and Harrison (11) is also shown for reference. They assumed no current-loss and instantaneous nucleation. On the other hand, Szpak (3) considered that the velocity of radial growth has a linear relationship with the available surface area and gets substantially higher as critical time is approached.

In our present case it is found that the fundamental Eq. [9] is valid and the derived $v - \theta$ curve of the solid line in Fig. 9 gives qualitative understanding of the kinetics of the surface coverage on GaAs until the critical time. However, the velocity of radial growth v will substantially increase so as to fill the small pores among the nuclei as the critical time is approached.

"Less soluble region".—The region where the dissolution rate appears to be small is found in the dissolution curves and we call it "less soluble region." The dependences of the two parameters, t_d and t_p , upon the formation voltage V_f are shown in Fig. 10. It is observed that t_p has linear dependence upon V_f , while t_d has little dependence upon V_f , though t_d is dependent on the pH-value of the electrolyte used and current-

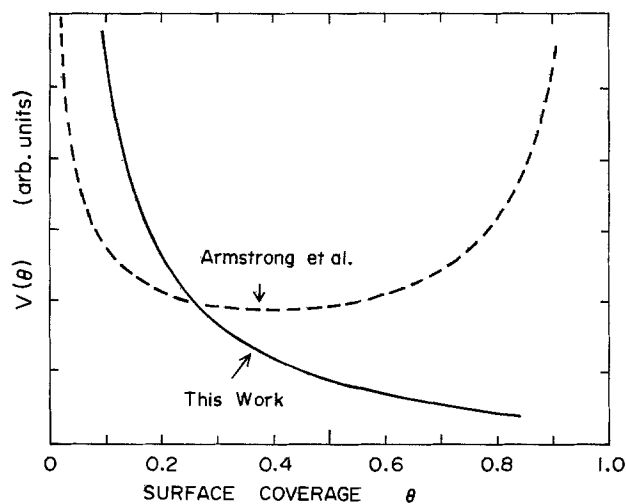


Fig. 9. Outline of the velocity of radial growth v as function of the surface coverage θ . This work; —, work by Armstrong and Harrison; ----.

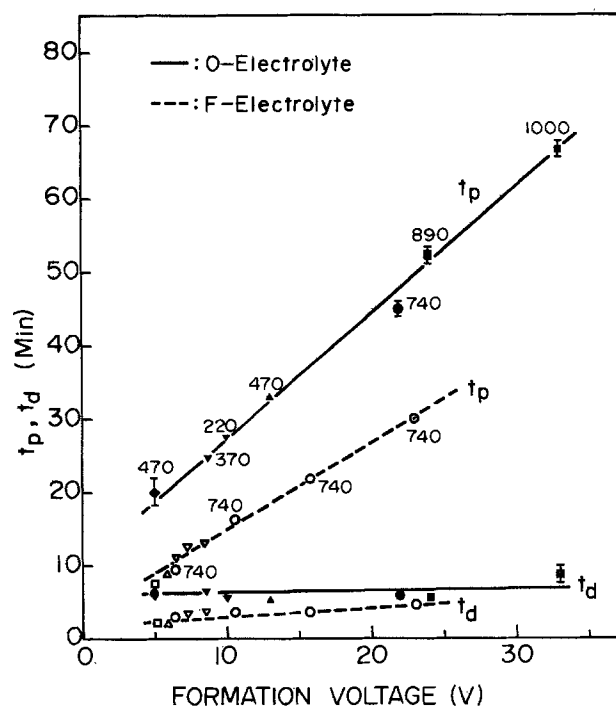


Fig. 10. Dependences of the parameters, t_d and t_p upon the formation voltage V_f . Their dependences on the electrolyte used are also shown. Different symbols refer to different samples. The same symbols refer to different runs with the same sample. The current-densities are denoted with the numbers on the figure in the dimension $[\mu\text{A cm}^{-2}]$.

density. It is also observed that the dissolution rate appears to be smaller in the O-electrolyte than in the F-electrolyte. Figure 11 shows the dependence of t_d upon the final current-density J_{df} which was already indicated in Fig. 5. It seems that t_d is proportional to the square root of J_{df} . This result strongly suggests that the anodic film keeps growing after the circuit is opened due to the residual ions within the anodically grown film and thus "less soluble region" appears. Figure 12 shows the thickness and dissolution rate of the grown film after the open-circuit derived from the best-fitting to the $\Delta R/R - t$ curve. The extrapolation of the linear portion to the zero dissolution time yields the thickness $d = 190\text{\AA}$ which is in good agreement with that calculated using the previously reported data of the growth rate (2). This fact also suggests the

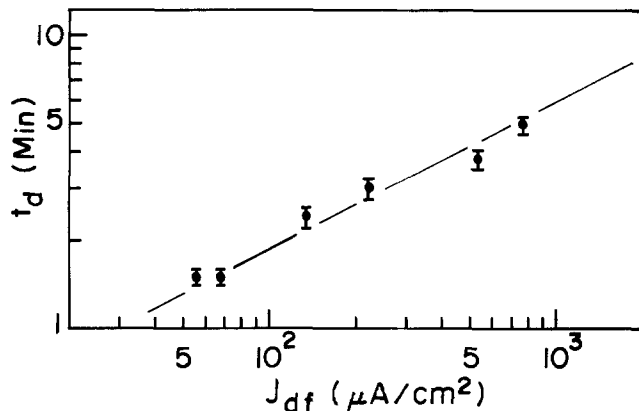


Fig. 11. Dependence of t_d upon the final current-density J_{df}

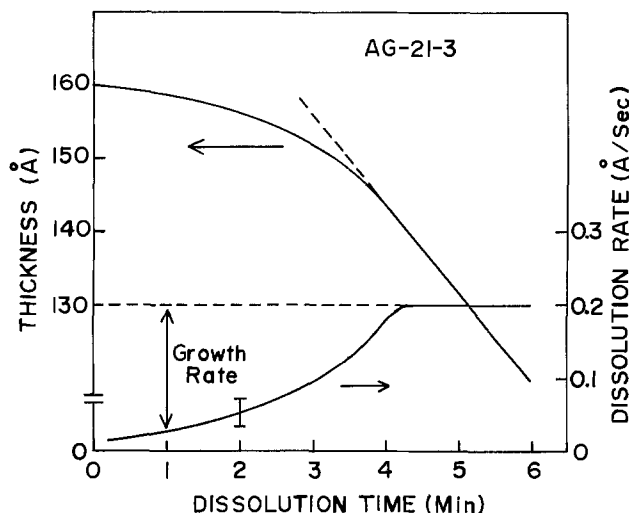


Fig. 12. Thickness and dissolution rate as function of the dissolution time.

passive film growth in the open-circuit transient region. The dissolution rate is found to be constant, 0.2 Å sec^{-1} , in this sample beyond t_d . The growth rate in the transient region would be represented as marked in Fig. 12 assuming that the dissolution takes place at constant rate throughout the reaction process.

Best-fit calculation.—The dissolution curve is considered to be little influenced by the initial condition of anodization so that it is available to apply a best-fit calculation to one of the dissolution curves apart from the "less soluble region" in order to obtain the optical constant and dissolution rate. The anodization curve of $\Delta R/R - t$ (or $-V_f$) characteristics contains in the initial stage the contribution of the nonpassive film, or the two-dimensional growth of the passive film which depends on the surface treatment, current-density, and electrolyte used. On the other hand, the dissolution curve may result from the clean surface of the substrate at the anodic film-GaAs interface so that it is much less dependent upon the surface treatment. The best-fit calculation for the dissolution curve was made with inversely considering that the film grows on the clean surface of the substrate and assuming that the growth rate (the dissolution rate, in truth) is constant during the process. It is shown in Fig. 13 that the theoretical curve fits well with the experimental $\Delta R/R - t$ curve. In Fig. 13, the circles represent the experimental points and the solid line is the theoretical curve of the three-phase model, electrolyte-anodic film-substrate, with use of Eq. [4] and [5] assuming $n_1 = 1.40$ (the average value of the refractive indexes of water and propylene glycol) and $n_3 = 3.85 + 0.19i$ (12). It is found that the dissolution rate is surely constant from $t = t_d$ to t_p and its value is obtained to be

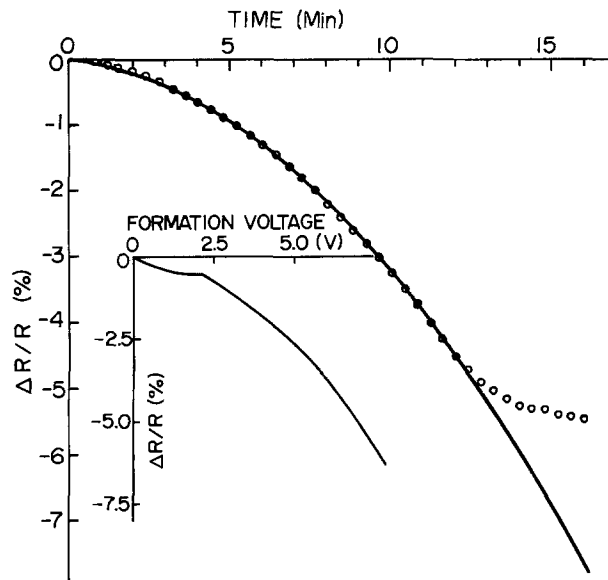


Fig. 13. Result of best-fitting to one of the dissolution curves of the $\Delta R/R - t$ characteristics. Open circles represent the experimental data, and solid line the theoretical curve.

0.2 Å sec^{-1} in this sample. This value is about one order of magnitude larger than that obtained in the AGW process and one order smaller than that obtained in the AAS (anodization in aqueous solution without glycol) process by Hasegawa and Hartnagel (2). The value of the other parameter obtained from this best fitting is 1.79 ± 0.05 for the refractive index of the anodic oxide film at 6328Å . This value seems to be in good agreement with the previously reported data of the refractive index (13-17).

Summary and Conclusions

We have observed the anodic oxide film growth and dissolution on GaAs in the *in situ* differential reflectance measurements and demonstrated its availability to the investigation of the anodization process. The main conclusions are summarized in the following:

1. The initial shoulder has been observed in the anodization curve of the film thickness *vs.* time characteristics. This initial shoulder is due to the two-dimensional growth rather than due to the deposition of the nonpassive film which has a different refractive index. The time dependence of the surface coverage $\theta(t)$ suggests that the substrate-dissolution is the rate-determining process of the film formation in the initial phase of anodization on GaAs. The time dependence of the velocity of radial growth has also been derived assuming the progressive nucleation.

2. The "less soluble region" has been observed in the dissolution curve of $\Delta R/R$ *vs.* time characteristics. The duration time t_d for which the "less soluble region" exists is proportional to the square root of the final current-density J_{df} and has weak dependence upon the formation voltage V_f . These observations suggest that the "less soluble region" appears due to the anodic film formation by the residual ions within the grown film.

3. It is clarified that the growth or dissolution rate is constant except in the initial phase or the "less soluble region" from the best-fitting to one of the dissolution curves of the $\Delta R/R - t$ characteristics. The value of the parameter obtained from the best-fitting is 0.2 Å sec^{-1} for the dissolution rate and 1.79 ± 0.05 for the refractive index of the anodic oxide film at 6328Å . It is also shown that the dissolution curve is more suitable for characterization of the anodically grown film than the anodization curve since the former is considered to be produced with the clean film-substrate interface.

Acknowledgment

The authors would like to acknowledge H. Kubo, S. Tachi, and A. Shimano for their important assistance

and useful discussions. They would like to thank Professor H. Hasegawa of Hokkaido University for his useful suggestions and sending the preprint prior to publication. They wish to express their gratitude to K. Matsumoto of Sumitomo Electric Industries, Limited for providing the GaAs single crystals. This work is partially supported by the Grant-in-Aid for Scientific Research on Surface Electronics from the Ministry of Education of Japan.

Manuscript submitted Oct. 11, 1978; revised manuscript received July 22, 1979.

Any discussion of this paper will appear in a Discussion Section to be published in the December 1980 JOURNAL. All discussions for the December 1980 Discussion Section should be submitted by Aug. 1, 1980.

Publication costs of this article were assisted by Osaka University.

REFERENCES

1. B. Bayraktaroglu, E. Kohn, and H. L. Hartnagel, *Electron. Lett.*, **12**, 53 (1976).
2. H. Hasegawa and H. L. Hartnagel, *This Journal*, **123**, 713 (1976).
3. S. Szpak, *ibid.*, **124**, 107 (1977).
4. A. Moritani, H. Kubo, and J. Nakai, *J. Appl. Phys.*,

- 48, 2638 (1977).
5. D. E. Aspnes, *J. Opt. Soc. Am.*, **63**, 1380 (1973).
6. J. D. E. Mcntyre and D. E. Aspnes, *Surf. Sci.*, **24**, 417 (1971).
7. A. Moritani, K. Kondo, and J. Nakai, *Jpn. J. Appl. Phys.*, **15**, 1549 (1976).
8. W. W. Harvey and J. Kruger, *Electrochim. Acta*, **16**, 2017 (1971).
9. D. A. Vermilyea, in "Advances in Electrochemistry and Electrochemical Engineering," Vol. 3, P. Delahay, Editor, p. 211, John Wiley & Sons, New York (1963).
10. M. Abrami, *J. Chem. Phys.*, **7**, 1103 (1939); **8**, 212 (1940); **9**, 177 (1941).
11. R. D. Armstrong and J. A. Harrison, *This Journal*, **116**, 323 (1969).
12. R. C. Eden, Ph.D. Thesis, Stanford University, Palo Alto, California (1976).
13. R. A. Logan, B. Schwartz, and W. J. Sundburg, *This Journal*, **120**, 1385 (1973).
14. C. J. Dell'Oca, G. Yan, and L. Young, *ibid.*, **118**, 89 (1971).
15. A. Shimano, A. Moritani, and J. Nakai, *Jpn. J. Appl. Phys.*, **15**, 939 (1976).
16. D. E. Aspnes, B. Schwartz, A. A. Studna, L. Derick, and L. A. Koszi, *J. Appl. Phys.*, **48**, 3510 (1977).
17. P. A. Barnes and D. P. Schinke, *Appl. Phys. Lett.*, **30**, 26 (1977).

Liquid Phase Growth of HgCdTe Epitaxial Layers

C. C. Wang,* S. H. Shin, M. Chu, M. Lanir, and A. H. B. Vanderwyck

Rockwell International Science Center, Thousand Oaks, California 91360

ABSTRACT

Epitaxial layers of mercury cadmium telluride ($\text{Hg}_{1-x}\text{Cd}_x\text{Te}$) with Cd composition (x value) from 0.17 to 1.0 have been grown in Te solution by a liquid phase epitaxial (LPE) technique. The layers are grown on CdTe substrates with (100), (110), (111)Cd, and (111)Te orientations. The best surface is obtained on the (111)Cd surface. Typical hole concentration of HgCdTe layers with Cd composition of 0.2 is on the order of $5 \times 10^{16}/\text{cm}^3$ with a Hall mobility of $400 \text{ cm}^2/\text{Vsec}$ at 77°K . X-ray topographic analysis indicates that these epilayers have as good a crystalline structure as that of the substrates.

A number of crystal growth techniques have been developed with varying degrees of success in the preparation of bulk and epitaxial HgCdTe crystals (1-8). Because of difficulties associated with the epitaxial crystal growth techniques, the development of HgCdTe device technology has been restricted to that of bulk photovoltaic and photoconductive detectors. Although charge-coupled devices in bulk HgCdTe (9) have recently been realized, these devices are limited to a frontside-illuminated mode (10), unless back-side-thinned (11). This limitation, however, will be alleviated by the development of HgCdTe epitaxy on CdTe substrates, from which back-side-illuminated heterostructure HgCdTe/CdTe detectors can be made. This paper reports on results on liquid phase epitaxy (LPE) of HgCdTe layers on CdTe substrates.

LPE is a relatively low temperature growth process that has been developed extensively in preparing high quality III-V (12) and IV-VI (13) semiconductors. LPE growth of II-VI compounds has not been widely studied (14) in the past, mainly because of the high vapor pressure of column II elements and the low solubility of column VI species in column II solutions at low temperatures. In the work reported here, a modified LPE dipping technique is used, from which HgCdTe layers with Cd composition from 0.17 to 0.4 have been grown in Te solutions. Pure CdTe epilayers have also been grown when Hg is not added to the system. As a result, it was possible to fabricate the first

back-side-illuminated HgCdTe/CdTe heterostructure diodes using these epilayers (15).

The high pressure system is utilized to control the high mercury vapor pressure over the molten materials, and the growth system is shown in Fig. 1. The apparatus consists of an inner quartz reaction tube and an outer quartz tube that is mounted between two stainless steel flanges to keep high argon gas pressure. The pressure inside the tube is maintained at 200-300 psi during growth. We have not determined the Hg vapor pressure during the growth which is found not to be a critical parameter in growing a 20% HgCdTe layer reproducibly under high external pressure. The outer quartz tube is mounted in a vertical furnace that is controlled to within $\pm 0.05^\circ\text{C}$. A thermocouple is inserted into the melt to monitor the actual melt temperatures. The inner reaction tube is plugged with high purity quartz wool to prevent excess mercury evaporation from the melt. A cold zone is established just below the quartz wool in order to condense mercury vapor.

In a typical growth, CdTe substrates are first lapped and chemically polished in a $\text{Br}_2:\text{HBr}$ solution (10% Br_2 in volume) followed by a $\text{Br}_2:\text{CH}_3\text{OH}$ etch (5% Br_2 in volume) before loading in the growth chamber. Prior to growth, appropriate amounts of high purity (99.9999%) Hg and Cd are reacted in the Te melt at $\sim 700^\circ\text{C}$ for an hour. For example, a typical ratio of CdTe:Hg:Te for 20% HgCdTe growth is 0.004:0.251:0.745. Subsequently, the melt and the oriented substrate are brought to the saturation temperature, typically at $\sim 500^\circ\text{C}$. The saturation tempera-

* Electrochemical Society Active Member.

Key words: liquid phase epitaxy, epitaxial layers, II-VI compound semiconductors, heterostructures.

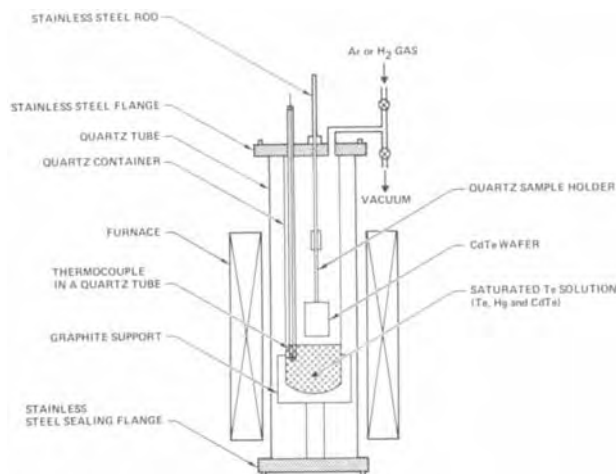


Fig. 1. Schematic of the liquid phase epitaxy growth system

ture is determined empirically in the growth system shown in Fig. 1. The epilayers grown from solutions initially are either saturated or unsaturated by as much as $\sim 15^\circ\text{C}$. In the latter case, examination of the epilayers shows that the substrates are melted back by the solution prior to growth. Through an interaction process it is possible to determine the liquid composition by dipping the known weight of CdTe into the melt of Hg and Te solutions at growth temperatures. The growth temperature normally drops at a rate of from 0.2 to $1^\circ\text{C}/\text{min}$ with a typical value on the order of $0.25^\circ\text{C}/\text{min}$. In order to eliminate an Hg vapor diffused layer obtained during the heat-up cycle, the substrate is melted back at 550°C for 15 sec in the growth solution prior to growth. A temperature profile of LPE is shown in Fig. 2. The actual LPE growth time takes about an hour for a $\sim 20\ \mu\text{m}$ epilayer on the (111) oriented substrates, resulting in a growth rate of $\sim 1\ \mu\text{m}/^\circ\text{C}$.

Table I provides a summary of growth conditions of HgCdTe with a Cd composition of 0.2. The HgCdTe epilayers are nominally p-type when undoped CdTe substrates are used. These layers exhibit n-type conduction when grown on In-doped CdTe presumably as a result of indium diffusion from the substrate.

The HgCdTe epilayers are grown on CdTe substrates with (100), (110), (111)Cd, and (111)Te orientations. Layers with thickness of from 1 to $300\ \mu\text{m}$ have been grown. Under normal growth conditions, the deposition rate in (100) orientation is about $2\ \mu\text{m}/^\circ\text{C}$, which is twice as fast as that in (111) orientation.

Figure 3 shows the surface of an HgCdTe epilayer grown on a (111)Cd oriented substrate. The surface is mirror-like and free of residual melt. The size of the wafer is on the order of $1.5 \times 1.5\ \text{cm}$ and the layer is about $30\ \mu\text{m}$ thick. Notice the surface quality of this

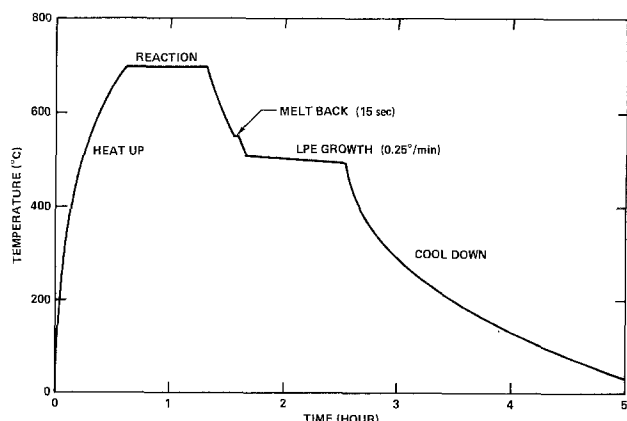


Fig. 2. Temperature profile for LPE growth

Table I. Growth conditions and properties of as-grown HgCdTe epilayers

(I) Growth conditions		
Melt composition	CdTe:Hg:Te = 0.004:0.251:0.745	
Container pressure	200 psi	
Substrate orientations	(111) A	
Growth temperature	$\sim 500^\circ\text{C}$	
Reaction temperature	$\sim 700^\circ\text{C}$	
Growth time	60 min	
Cooling rate	$0.25^\circ\text{C}/\text{min}$	
(II) Epilayer characteristics		
Cd composition	0.2	
Thickness	$20\ \mu\text{m}$	
CdTe/HgCdTe transition	$0.5\text{--}1\ \mu\text{m}$	
Carrier concentration (n-type)	$2 \times 10^{15}/\text{cm}^3$	{ In-doped Substrate
Electron mobility	$1 \times 10^5\ \text{cm}^2/\text{Vsec}$	
Carrier concentration (p-type)	$5 \times 10^{18}/\text{cm}^3$	{ Undoped Substrate
Hole mobility	$400\ \text{cm}^2/\text{Vsec}$	

layer. The inch scale of a ruler is clearly shown. As in all the other LPE growth of semiconductors, the surface quality is dependent on the orientation of the substrate (16). It is found that the epilayer on (111)Cd oriented substrate always has a better surface morphology than that on the (111)Te oriented surface. In fact, the quality of (111)Cd oriented surface is also better than that on (110) and (100) surfaces.

Detailed examination of the epilayer surface quality on the (111)Cd face reveals that it is mirror smooth for a thickness of less than $10\ \mu\text{m}$ and shows facets and sometimes terrace substructures for layers thicker than $30\ \mu\text{m}$. The terrace surface may be due to the substrate being slightly off the (111)Cd orientation (16) and/or liquid-solid interface instabilities (17); it becomes more pronounced as the thickness increases. The surface of a (111)Te epilayer usually exhibits voids across the wafer, and the density of these voids increases as the layer becomes thicker. Figure 4(a) shows the surface morphology of a thick HgCdTe layer grown on the (111)Cd surface and Fig. 4(b) is that of a layer grown on the (111)Te surface. It is not clear what mechanisms are responsible for the voids on the (111)Te surface. It appears, however, that these defects may originate from the Te metal atoms on the (111)Te surface. Indeed, a similar development of void defects was observed on GaAs LPE layers (18), and it was hypothesized that the defects on the surface were caused by small particles which induce the formation of depressions and voids in the epilayers. The remainder of this paper presents properties of HgCdTe epilayers grown on the (111)Cd face of the substrate.

Figure 5 is the cross section of a typical HgCdTe single layer. Notice the planarity of the interface. The etchant used for delineating the interface attacks CdTe, not HgCdTe; and as a result, HgCdTe shows a white stripe while CdTe exhibits a gray color. Electron microprobe analysis indicates that a major transition region



Fig. 3. The surface of an HgCdTe epilayer grown on an (111)Cd oriented substrate. The number scale is 0.1 in.

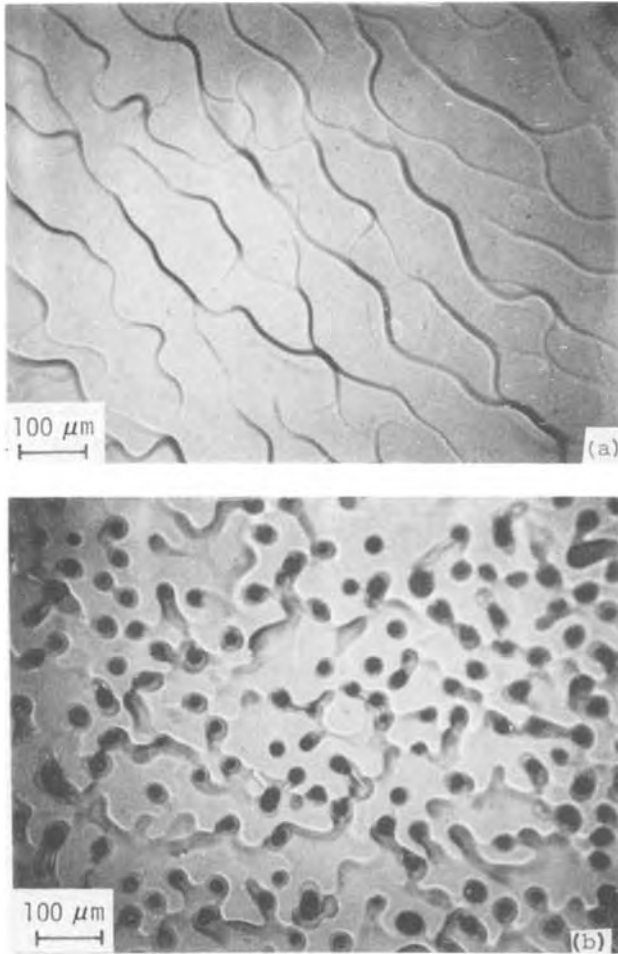


Fig. 4. (a) The surface morphology of an HgCdTe layer grown on the (111)Cd surface; (b) the surface morphology of an HgCdTe layer grown on the (111)Te surface.

between the HgCdTe epilayer and the substrate is on the order of $2 \mu\text{m}$ for thick layers ($d \approx 100 \mu\text{m}$), and is less than $0.5 \mu\text{m}$ for thin layers ($d \approx 15 \mu\text{m}$). An electron microprobe analysis of an HgCdTe layer with a Cd composition on the order of 0.2 is shown in Fig. 6. A major transition is observed within $0.5 \mu\text{m}$ region at the metallurgical interface. The gradual compositional change in the epilayer and the substrate may be due to interdiffusion during growth and has been found to have no direct effect on device performance, *e.g.*, uniformity, since the ion-implanted junction is formed in less than a micron from the surface.

The infrared transmission at 300°K is usually used for determining the layer composition in addition to the electron microprobe analysis. Figure 7(a) shows the transmission edge of five typical HgCdTe epilayers for Cd compositions from 0.17 to 0.28. This nondestructive test provides a rapid feedback to assess and improve the LPE growth parameters. A typical infrared transmission spectrum for a HgCdTe epilayer with a Cd composition of 0.3 is shown in Fig. 7(b). The spec-

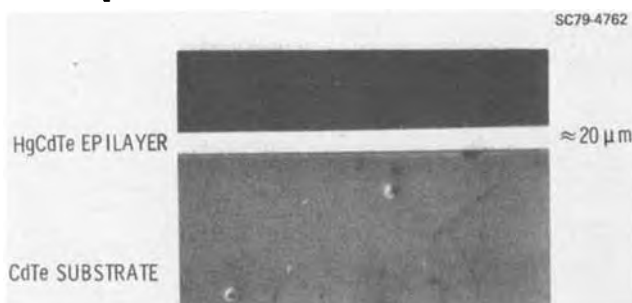


Fig. 5. The cross section of a typical HgCdTe epilayer

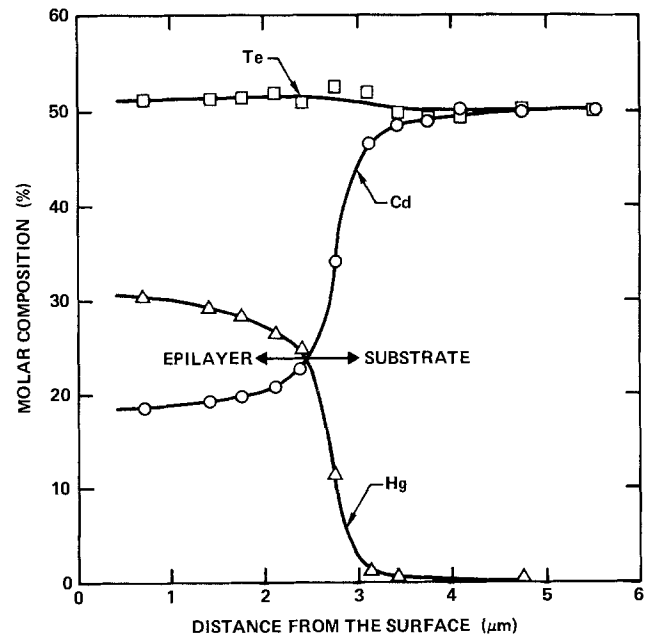


Fig. 6. The composition profile of an HgCdTe epilayer

trum exhibits a sharp cut-on at $4.2 \mu\text{m}$ and also oscillates beyond that wavelength due to infrared interference in the HgCdTe epilayer. It is not clear at this time what causes the short wavelength tail; it may be due to the gradual compositional change in the epilayer. Since the epilayer has a refractive index that is different from that of the substrate, these oscillations are interference fringes produced by the superposition of light transmitted through the layer and the internal reflection from the interface of HgCdTe and CdTe. If N is a positive integer, then the interference satisfies the equation $2nd = N\lambda$, where d is the thickness of the epilayer and λ is the wavelength at which the transmission maximum occurs. From this information, we can calculate the average index of refraction, n , of these HgCdTe epilayers. The results give a value of 3.33 for HgCdTe with a Cd composition of 0.3, which is in good agreement with reflectance measurements (19).

Typical electrical characteristics of as-grown n-type and p-type HgCdTe epilayers are shown in Table I. In Table I, properties of HgCdTe layers with a Cd composition of 0.2 and a thickness on the order of $20 \mu\text{m}$ are given. Since the CdTe substrate can be made semi-insulating, the conventional Van der Pauw-Hall measurement technique provides unambiguous results if HgCdTe layers are grown on these substrates. Typical hole concentration is on the order of $5 \times 10^{16}/\text{cm}^3$ with a Hall mobility of $400 \text{ cm}^2/\text{Vsec}$ at 77°K . From a device point of view, this as-grown carrier concentration is suitable for fabricating high performance photovoltaic detectors (15).

X-ray topography was used for analyzing the HgCdTe film crystallinity and for comparing it with the CdTe substrate. This kind of study is important since dislocations generated due to difference in thermal expansion coefficient, lattice mismatch, or significant difference in doping levels between the substrate and the epilayer have been observed by x-ray topography in a variety of crystal systems (20-22). We used an AMR Hart Topographic camera with $100 \times 1000 \mu\text{m}$ source. The $\text{CuK}\alpha_1$ microfocussed beam take-off angle is 6° and the divergence slit is $100 \mu\text{m}$. Figure 8 shows an x-ray topograph of a CdTe wafer with an HgCdTe epilayer grown on a section of it. This photograph represents a wafer of the size of $1.5 \times 1.5 \text{ cm}$. The x-ray picture shown is a (440) reflection. Other reflections were also examined, but no additional information was obtained. In Fig. 8, the band in the center is due to edge solidification of the melt. The bubbles near the bottom of the epilayer (left of photograph) are due to residual melts on the surface. The substructure near

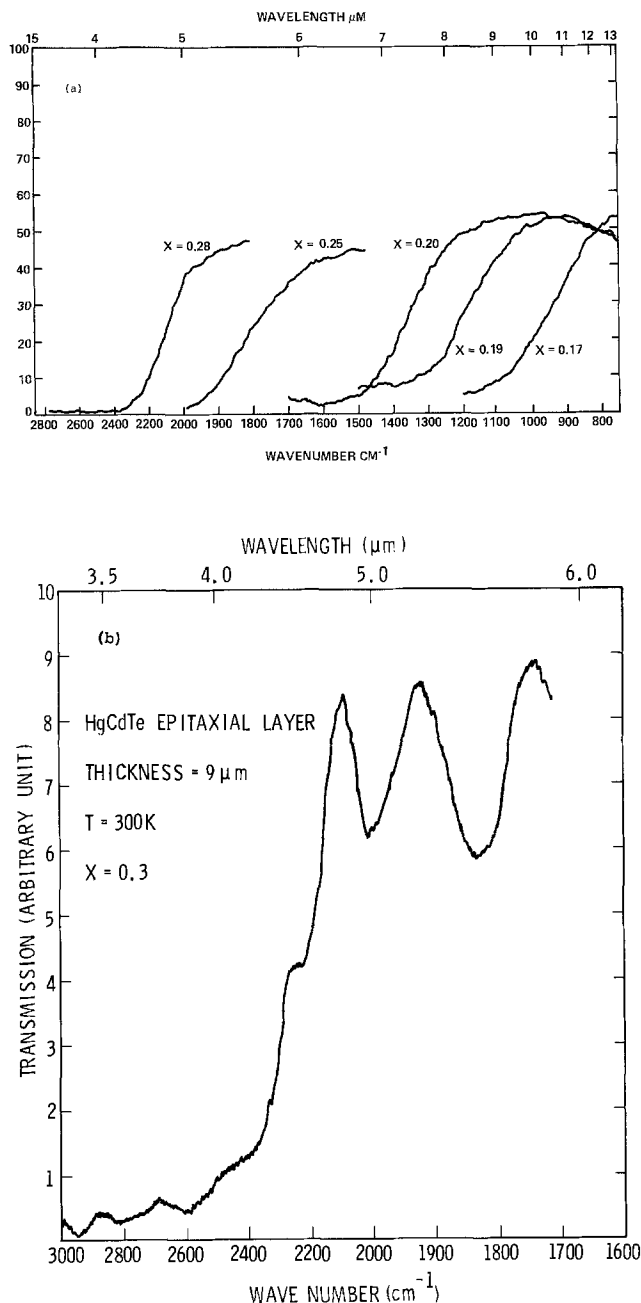


Fig. 7. (a) Infrared transmission spectra of five selected HgCdTe epilayers with various x at room temperature; (b) an infrared transmission spectrum which exhibits interference fringes due to HgCdTe epilayer.

the top of the CdTe substrate (right of photograph) is due to the gripping from the sample holder. Since the diffracted x-ray comes almost entirely from a surface region about $5 \mu\text{m}$ thick, the epilayer image on the left of photograph represents only diffraction from the HgCdTe. Careful examination of Fig. 8 reveals no dislocation pattern; the substructure of the layer can be seen to be very similar to that of the substrate. It may be concluded, therefore, that the crystalline perfection of the epilayer is currently limited by the CdTe quality.

In summary, we have demonstrated that device quality HgCdTe epilayers can be grown by liquid phase epitaxy. The best surface is obtained with the (111)Cd orientation; this surface is mirror smooth to the naked eye and free of residual melts. The metallurgical interface between the substrate and the epilayer is planar; the major interdiffusion region is less than $0.5 \mu\text{m}$ for thin HgCdTe epilayers ($d \approx 15 \mu\text{m}$). Finally, the crystalline quality of HgCdTe is as good as that of the CdTe substrate. The results presented here indicate that the LPE technique offers a viable approach to preparation

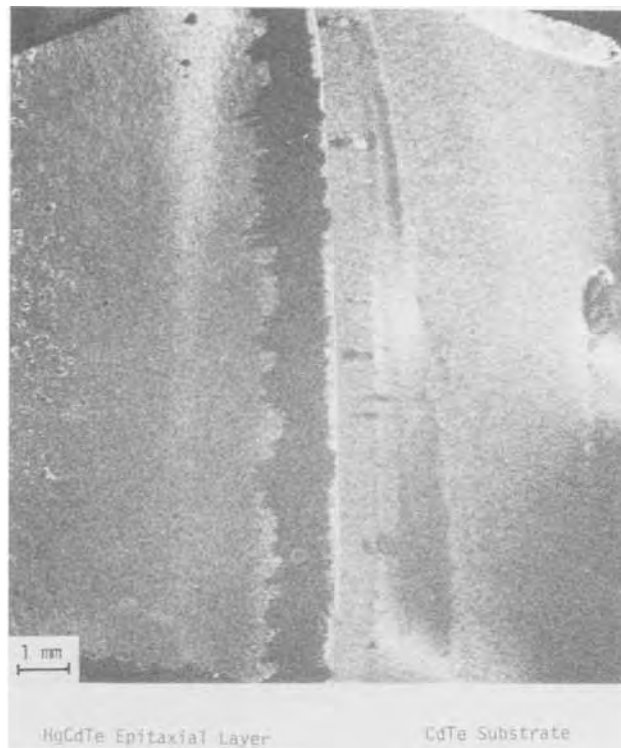


Fig. 8. X-ray topograph of a CdTe substrate with a HgCdTe epilayer grown on a section of it.

of device grade HgCdTe epitaxial materials and advanced device structures (15).

Manuscript submitted Jan. 16, 1979; revised manuscript received July 25, 1979.

Any discussion of this paper will appear in a Discussion Section to be published in the December 1980 JOURNAL. All discussions for the December 1980 Discussion Section should be submitted by Aug. 1, 1980.

Publication costs of this article were assisted by Rockwell International.

REFERENCES

1. T. C. Harman, in "Physics and Chemistry of II-VI Compounds," M. Aven and J. S. Premer, Editors, p. 767, North Holland Publishing Company, Amsterdam (1967).
2. J. Steininger, *J. Electron. Mater.*, **5**, 299 (1976).
3. T. C. Harman, *ibid.*, **1**, 230 (1973).
4. O. N. Tufte and E. L. Stelzer, *J. Appl. Phys.*, **40**, 4559 (1969).
5. P. Becla and J. M. Pawlikowski, *Infrared Phys.*, **18**, 457 (1976).
6. P. Vanier, F. H. Pollak, and P. M. Raccah, *J. Electron. Mater.*, To be published.
7. G. Fiorito, G. Gasparini, and D. Pasonni, *This Journal*, **125**, 315 (1978).
8. P. Vohl and C. M. Wolfe, *J. Electron. Mater.*, **7**, 659 (1978).
9. R. A. Chapman, M. A. Kinch, A. Simmons, S. R. Borrello, H. B. Morris, J. S. Wrobel, and D. D. Buss, *Appl. Phys. Lett.*, **32**, 434 (1978).
10. J. Marine and C. Motte, *Appl. Phys. Lett.*, **23**, 450 (1973).
11. P. R. Bratt, A. H. Lockwood, and K. J. Riley, Paper presented at IRIS Specialty Group Meeting on Infrared Detectors, Annapolis, Maryland, June, 1978.
12. R. R. Dawson, in "Progress in Solid State Chemistry," Vol. 7, H. Reiss and J. I. McCaldin, Editors, pp. 117-139, Pergamon Press, Oxford (1972).
13. J. T. Longo, J. S. Harris, Jr., E. R. Gertner, and J. C. Chu, *J. Cryst. Growth*, **15**, 107 (1972).
14. LPE growth of II-VI compounds can be found in the following representative papers: (a) A. Kanamori, T. Ota, and K. Takahashi, *This Journal*, **122**, 1117 (1975). (b) A. V. Simashevich and R. L. Tsiulyann, *J. Cryst. Growth*, **35**, 269 (1976). (c) R. Widner, D. P. Bortfeld, and H. P. Klein-

- knecht, *J. Cryst. Growth*, **6**, 237 (1970).
 15. M. Lanir, C. C. Wang, and A. H. B. Vanderwyck, *Appl. Phys. Lett.*, **34**, 59 (1979).
 16. R. H. Sauland and D. D. Roccasecca, *J. Appl. Phys.*, **44**, 1983 (1973).
 17. R. F. Sakerka, *J. Cryst. Growth*, **3**, 4, 71 (1968).
 18. E. Bauser, *Appl. Phys.*, **15**, 243 (1978).
 19. R. Dornhaus and J. Nimtz, "Solid State Physics," p. 93, (Springer Tracts in Modern Physics: 78) Springer-Verlag, Berlin (1976).
 20. G. H. Schwuttke, *J. Appl. Phys.*, **36**, 2716 (1965).
 21. E. S. Meieran, *This Journal*, **114**, 292 (1967).
 22. H. Holloway and L. C. Bobb, *J. Appl. Phys.*, **38**, 2711 (1967).

Quantitative Measurement of Stress in Silicon by Photoelasticity and Its Application

H. Kotake and Shin. Takasu*¹

Toshiba Research and Development Center, Saiwai-ku, Kawasaki 210, Japan

ABSTRACT

Quantitative evaluation method for stress in crystal was established by photoelasticity. It consists of three procedures: measurement by plane polarized light, measurement by circularly polarized light, and piezo-optical coefficients calculation. The last method is indispensable for stress evaluation in crystal. Piezo-optical coefficients for silicon in the [110] $\bar{1}10$ [001] and [112] $\bar{1}10$ $\bar{1}\bar{1}1$ coordinate system were calculated from the values in the [100] [010] [001] coordinate system measured by Giardini. Practical approximation was made to correlate each isochromatic line directly to the difference between two principal stresses. This method was applied to the evaluation of the stress in silicon semiconductor pellet caused in the mounting and molding process. Observation of isochromatic lines according to temperature was practical for determination of the zeroth order of retardation.

Photoelastic measurement is one of the important methods used for crystal characterization. However, crystal anisotropy makes its application to quantitative evaluation rather difficult. Photoelastic study of silicon crystals was started by Bond and Andrus (1) and Giardini (2). Application of photoelasticity to silicon processing was reported by Laderhandler (3), Hornstra (4), DeNicola (5), and Takasu (6). Except for the reports by Takasu and Edmonds (7), these were reports on crystal defects due to crystal growth or grinding. Quantitative measurement was made by Laderhandler (3) for silicon. However, there is no complete report on piezo-optical coefficients in various coordinate systems for the purpose of crystal characterization, although there are some reports on the experimental determination of these values (8).

Quantitative measurement has been made easy by piezo-optical coefficients calculation in various measurement coordinate systems. A slight approximation was made to correlate each isochromatic line directly to the difference between the two principal stresses perpendicular to the observation direction.

This quantitative evaluation method can be applied to various fields of crystal characterization, such as crystal growth and its processing. Among those, silicon semiconductor pellet stress measurement in the mounting and molding process is very important from the device fabrication reliability viewpoint.

Evaluation Procedure

The ultimate photoelastic measurement aim is to determine the principal stress directions and magnitudes. Quantitative evaluation procedure of stress distribution in crystal by photoelasticity is shown in Fig. 1.

Principal stress line can be obtained through the measurement by plane polarized light, because the isoclinic line obtained by this method corresponds to the region where principal stress directions coincide with those of polarizer and analyzer. Isochromatic lines, which correspond to stress magnitude, can be obtained through the measurement by circularly polarized light.

The apparatus used in these observations is schematically illustrated in Fig. 2. The quarter wave plates were used only in the observation by circularly polarized light. Silicon was observed by infrared radiation of 1.1 μm wavelength with 0.2 μm bandwidth, which was obtained by the combination of tungsten lamp, silicon filter, and PbO-PbS vidicon. Therefore, it is effectively monochromatic.

Piezo-optical coefficients have to be determined to correlate each isochromatic line to a stress value. This is indispensable in crystal study, for piezo-optical coefficients in the same sample coordinate system have to be used. Calculations of these values are shown in the following section.

Another important point is to determine the isochromatic line of the zeroth order of retardation, which becomes the standard for stress determination. This must be done according to circumstances by assuming sample stress distribution.

For more accurate measurement, Tardy's method can be used to determine the suborder of retardation.

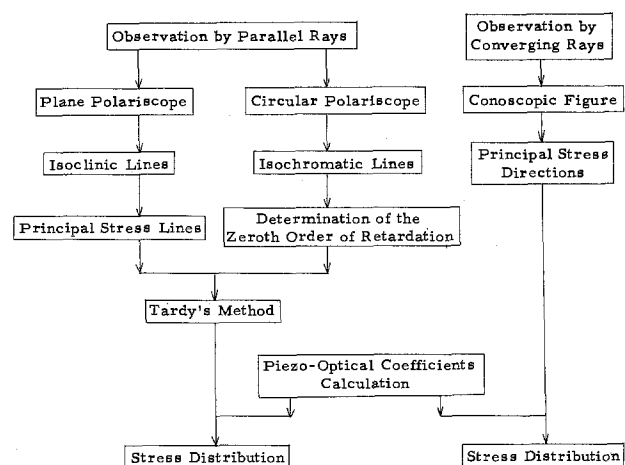


Fig. 1. Quantitative evaluation procedure of stress distribution in crystal by photoelasticity.

* Electrochemical Society Active Member.

¹ Present address: VLSI Cooperative Laboratories, Takatsu-ku, Kawasaki 213, Japan.

Key words: infrared equipment, birefringence, semiconductors.

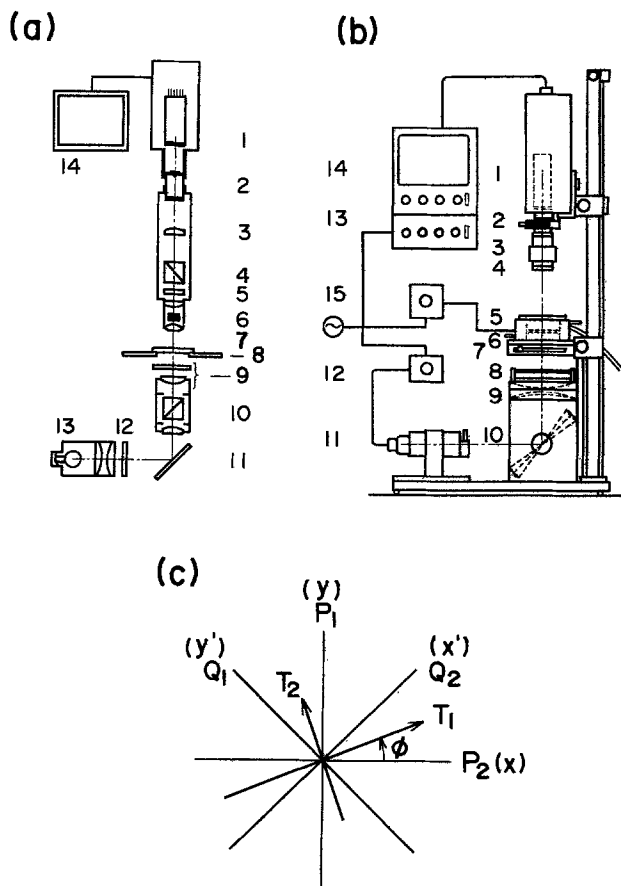


Fig. 2. Infrared photoelastic apparatus. (a) Microscope, 1: IR vidicon camera, 2: ocular, 3: Bertrand lens, 4: analyzer, 5: 1/4 wave plate, 6: objective, 7: sample, 8: stage, 9: condenser and 1/4 wave plate, 10: polarizer, 11: mirror, 12: Si filter, 13: light source, 14: monitor TV. (b) Macro apparatus, 1: IR vidicon camera, 2: IR polarizer, 3: lens, 4: 1/4 wave plate, 5: heating stage, 6: sample, 7: 1/4 wave plate, 8: IR polarizer, 9: condenser, 10: mirror box, 11: light source, 12: light source controller, 13: camera controller, 14: monitor TV, 15: heating stage controller. (c) Principal axes directions, P_1 : IR polarizer, P_2 : IR polarizer (analyzer), Q_1 : 1/4 wave plate, Q_2 : 1/4 wave plate, T_1, T_2 : Sample principal stresses, ϕ : angle between T_1 and P_2 .

The conoscopic figure, obtained in the observation by converging rays, gives three-dimensional stress information. It is especially helpful for the determination of principal stress directions.

Piezo-Optical Coefficients Calculation

Piezo-optical coefficient.—There is a relation between refractive index n_i and stress T_i , where subscript i means the i th component in the coordinate system, as follows

$$\Delta \left(\frac{1}{n_i^2} \right) = \sum_j \pi_{ij} T_j \quad [1]$$

π_{ij} in this formula is called the piezo-optical coefficient and can be described in the next equation for cubic crystals in the [100] [010] [001] coordinate system

$$\pi_{ij} = \begin{pmatrix} \pi_{11} & \pi_{12} & \pi_{12} & & & \\ \pi_{12} & \pi_{11} & \pi_{12} & & & \\ \pi_{12} & \pi_{12} & \pi_{11} & & & \\ & & & \pi_{44} & & \\ & & & & \pi_{44} & \\ & & & & & \pi_{44} \end{pmatrix} \quad [2]$$

These values were measured for silicon by Giardini (2)

$$\begin{aligned} \pi_{11} - \pi_{12} &= -14.4 \times 10^{-14} \text{ cm}^2/\text{dyne} \\ \pi_{44} &= -10.0 \times 10^{-14} \text{ cm}^2/\text{dyne} \end{aligned} \quad [3]$$

In the case that two principal stress directions are [100] and [010], and the sample is observed from [001], T_1 is

$$T_1 = \begin{pmatrix} T_1 \\ T_2 \\ 0 \\ 0 \\ 0 \\ 0 \end{pmatrix} \quad [4]$$

From Eq. [1]

$$\Delta \left(\frac{1}{n_i^2} \right) = \begin{pmatrix} \pi_{11} T_1 + \pi_{12} T_2 \\ \pi_{12} T_1 + \pi_{11} T_2 \\ \pi_{12} T_1 + \pi_{12} T_2 \\ 0 \\ 0 \\ 0 \end{pmatrix} \quad [5]$$

Then, the difference between refractive indexes of light waves vibrating in [100] and [010] directions is

$$\Delta \left(\frac{1}{n_1^2} \right) - \Delta \left(\frac{1}{n_2^2} \right) = (\pi_{11} - \pi_{12}) (T_1 - T_2) \quad [6]$$

The same relations can be obtained in other observations.

Transformed values of piezo-optical coefficients.—When coordinate axes are transformed from [100], [010], and [001] to other directions, corresponding piezo-optical coefficients π_{ij} , stresses T_i , and refractive indexes n_i are also transformed. Results were summarized in Table I in the case of [110] $[\bar{1}10]$ [001] and [112] $[\bar{1}10]$ $[\bar{1}\bar{1}1]$ coordinate systems. The primed values are with respect to the new system of axes. In this table, transformed refractive indexes n_i' were expressed by original piezo-optical coefficients π_{ij} and transformed stresses T_i' . The value of $\{\Delta(1/n_i'^2) - \Delta(1/n_i^2)\}$ is not always proportional to the difference between the principal stresses $(T_i' - T_j')$. It is very convenient to make a slight approximation. Coefficient of $(T_i' - T_j')$ was obtained from the average of coefficients of T_i' and T_j' , in some cases, in Table I.

Retardation.—Phase difference between two light waves which travel, vibrating parallel to the two principal stress directions (T_k and T_l), can be defined as

$$h = \frac{d}{\lambda} (\Delta n_k - \Delta n_l) \quad [7]$$

where h is the retardation measured in wavelength unit λ and d is the light path distance in the crystal. On the other hand

$$\begin{aligned} \Delta n_k - \Delta n_l &= \frac{n_0^3}{2} \left\{ \Delta \left(\frac{1}{n_l^2} \right) - \Delta \left(\frac{1}{n_k^2} \right) \right\} \\ &= \frac{n_0^3}{2} A (T_l - T_k) \end{aligned} \quad [8]$$

where n_0 is the refractive index in crystal free from stress and value A is shown in Table I. Then, the relation between the difference in principal stresses and retardation is

$$T_l - T_k = \frac{2}{n_0^3 A} \frac{h\lambda}{d} \quad [9]$$

The value $T_l - T_k$ in the case of $\lambda = 1.1 \mu\text{m}$, $h = 1$, $d = 10 \text{ mm}$ are shown in Table II for various cases of observation.

Stress Gradient Direction

It is important and helpful to know the stress gradient direction in a sample. Tardy's method, which is used for the determination of the suborder of retarda-

Table I. Calculated values of silicon piezo-optical coefficients

Coordinate axes		Change in refractive indexes (T: dyne/cm ²)
Suffix	* Principal stress ** Observation	
1	* [100]	$\Delta\left(\frac{1}{n_1^2}\right) - \Delta\left(\frac{1}{n_2^2}\right) = (\pi_{11} - \pi_{12})(T_1 - T_2)$
2	* [010]	$= -14.4 \times 10^{-14} (T_1 - T_2)$
3	** [001]	
1	* [110]	$\Delta\left(\frac{1}{n_1'^2}\right) - \Delta\left(\frac{1}{n_2'^2}\right) = \pi_{44} (T_1' - T_2')$
2	* $\bar{[110]}$	$= -10.0 \times 10^{-14} (T_1' - T_2')$
3	** [001]	
1	* [110]	$\Delta\left(\frac{1}{n_1'^2}\right) - \Delta\left(\frac{1}{n_2'^2}\right) = \left(\frac{1}{2}\pi_{11} - \frac{1}{2}\pi_{12} + \frac{1}{2}\pi_{44}\right) T_1' - (\pi_{11} - \pi_{12}) T_2'$
2	** $\bar{[110]}$	$\approx \frac{1}{2} \left\{ \left(\frac{1}{2}\pi_{11} - \frac{1}{2}\pi_{12} + \frac{1}{2}\pi_{44}\right) + (\pi_{11} - \pi_{12}) \right\} (T_1' - T_2')$
3	* [001]	$= -13.3 \times 10^{-14} (T_1' - T_2')$
1	* [112]	$\Delta\left(\frac{1}{n_1'^2}\right) - \Delta\left(\frac{1}{n_2'^2}\right) = \left(\frac{1}{3}\pi_{11} - \frac{1}{3}\pi_{12} + \frac{2}{3}\pi_{44}\right) (T_1' - T_2')$
2	* $\bar{[110]}$	$= -11.5 \times 10^{-14} (T_1' - T_2')$
3	** $\bar{[111]}$	
1	* [112]	$\Delta\left(\frac{1}{n_1'^2}\right) - \Delta\left(\frac{1}{n_2'^2}\right) = \left(\frac{1}{6}\pi_{11} - \frac{1}{6}\pi_{12} + \frac{5}{6}\pi_{44}\right) T_1' - \pi_{44} T_2'$
2	** $\bar{[110]}$	$\approx \frac{1}{2} \left\{ \left(\frac{1}{6}\pi_{11} - \frac{1}{6}\pi_{12} + \frac{5}{6}\pi_{44}\right) + \pi_{44} \right\} (T_1' - T_2')$
3	* $\bar{[111]}$	$= -10.4 \times 10^{-14} (T_1' - T_2')$
1	** [112]	$\Delta\left(\frac{1}{n_2'^2}\right) - \Delta\left(\frac{1}{n_1'^2}\right) = \left(\frac{1}{6}\pi_{11} - \frac{1}{6}\pi_{12} + \frac{5}{6}\pi_{44}\right) T_2' - \pi_{44} T_1'$
2	* $\bar{[110]}$	$\approx \frac{1}{2} \left\{ \left(\frac{1}{6}\pi_{11} - \frac{1}{6}\pi_{12} + \frac{5}{6}\pi_{44}\right) + \pi_{44} \right\} (T_2' - T_1')$
3	* $\bar{[111]}$	$= -10.4 \times 10^{-14} (T_2' - T_1')$

tion, is one way to do this. However, before that, it is desired to consider the circular polariscope first.

Light wave electric field vector in circular polariscope is shown in Fig. 3, when a quarter wave plate pair is placed such that the x' component in Fig. 2(c) increases by $\pi/2$ in phase after the first quarter wave plate (Q_1), and decreases by $\pi/2$ in phase after the second quarter wave plate (Q_2).

In Tardy's method, the sample is placed so that principal stress directions (T_1, T_2) at the point in problem in the sample coincide with those of polarizer (P_1) and analyzer (P_2) in Fig. 2(c), and the angle between T_1 and P_2 is zero ($\phi = 0$). Then, analyzer (P_2) is rotated clockwise or counterclockwise until the intensity at the point becomes a minimum. The analyzer rotation angle corresponds to the suborder of retardation. The shift direction of the dark isochromatic line means that of the increase in ($T_1 - T_2$) or that of the decrease in retardation (h) when the analyzer is rotated clockwise. The result becomes opposite if the directions of the quarter wave plate pair are changed with each other.

Table II. The principal stress difference which causes 1λ ($\lambda = 1.1 \mu\text{m}$) retardation in 1 cm light path

Observation directed	Principal stress directions	Principal stress difference for 1λ retardation (kg/cm ²)
[001]	[100] [010]	36
[001]	[110] $\bar{[110]}$	52
$\bar{[110]}$	[110] [001]	43
$\bar{[111]}$	[112] $\bar{[110]}$	45
$\bar{[110]}$	[112] $\bar{[111]}$	50
[112]	$\bar{[110]}$ $\bar{[111]}$	50

It is very convenient to use a standard sample whose stress gradient direction is well-known, to check the optical system of the apparatus. A standard sample example is a beam bent at four points, as shown in Fig. 4. In this case, the upper half is under compressive stress and the lower half is under tensile stress.

Application

This quantitative evaluation method was applied to stress measurements on IC pellets in Dual In-line Package with 42 pins ($53 \times 13 \times 3.5 \text{ mm}$). A silicon pellet obtained from (100) wafer had the orientation of [110] $\bar{[110]}$ [001] and $5 \times 5 \times 0.5 \text{ mm}$ dimensions. The pellet was mounted on a Kovar metal frame (230 μm thick) by epoxy resin at 175°C. This was molded in epoxy resin by a transfer molding machine at 165°C and cured.

Photoelastic measurement of silicon pellet stress after mounting was made through optically polished parallel side surfaces [Fig. 5(a)]. For the molded pellet, epoxy resin was removed to the size of the pellet by cutting and grinding and a pair of side surfaces on the pellet were optically polished [Fig. 5(b)]. Observation was made through these parallel side surfaces by placing the sample so that these surfaces were perpendicular to the observation direction.

It was ascertained by the conoscopic figure in the observation by converging rays that two principal stresses were in the plane parallel to the optically polished surfaces.

Observed isochromatic lines by parallel rays are shown in Fig. 6 for a mounted pellet and in Fig. 7 for a molded pellet. Evaluated stress values are also shown in these figures although they are only approximate ones. In these measurements, isochromatic lines of the zeroth order of retardation had to be determined. This was done by observing the change in isochromatic lines

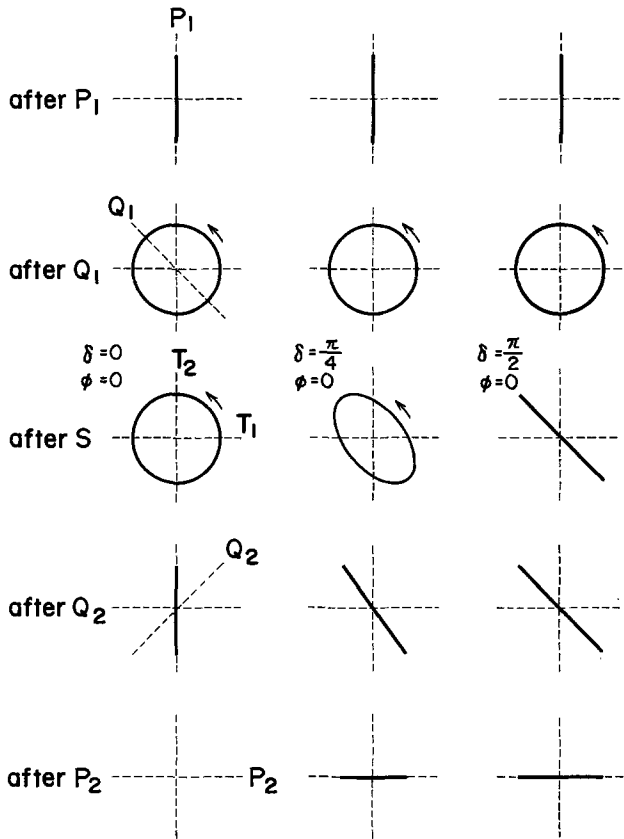


Fig. 3. Electric field vector after each plate of circular polariscope. P_1 : polarizer, P_2 : analyzer, Q_1 : 1st 1/4 wave plate, Q_2 : 2nd 1/4 wave plate, S : sample, T_1, T_2 : sample principal stresses, ϕ : angle between P_2 and T_1 , δ : retardation for $T_1 - T_2$ ($\delta = 2\pi h$).

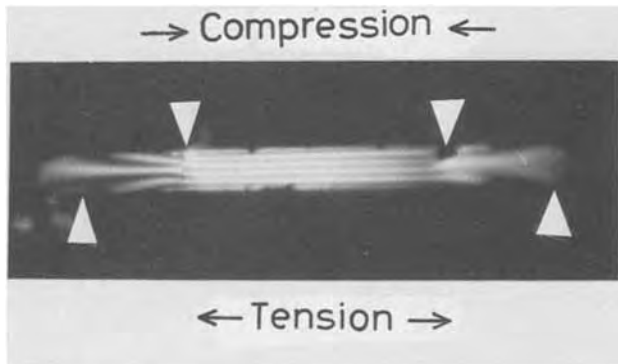


Fig. 4. Standard sample for determination of stress gradient directions.

according to the temperature (Fig. 8). Silicon pellet is thought to be free from stress at the mounting and molding temperature as it was observed to be dark at these temperatures. Stress is induced and the number of isochromatic lines increases as the sample is cooled to room temperature. It is natural to think that the first dark isochromatic line corresponds to the zeroth order of retardation.

The results in Fig. 6 and 7 show that the pellet became upward convex after mounting whereas it became concave after molding. It is clear that stress distribution changes drastically during the molding process. This information is important for semiconductor device fabrication reliability concerned with the pellet crack problem. Proper structure design and assembling technique would reduce silicon pellet stress and photoelastic measurement can be applied in these studies.

In molded IC pellet observation, sample preparation by epoxy resin cutting and grinding is not thought to

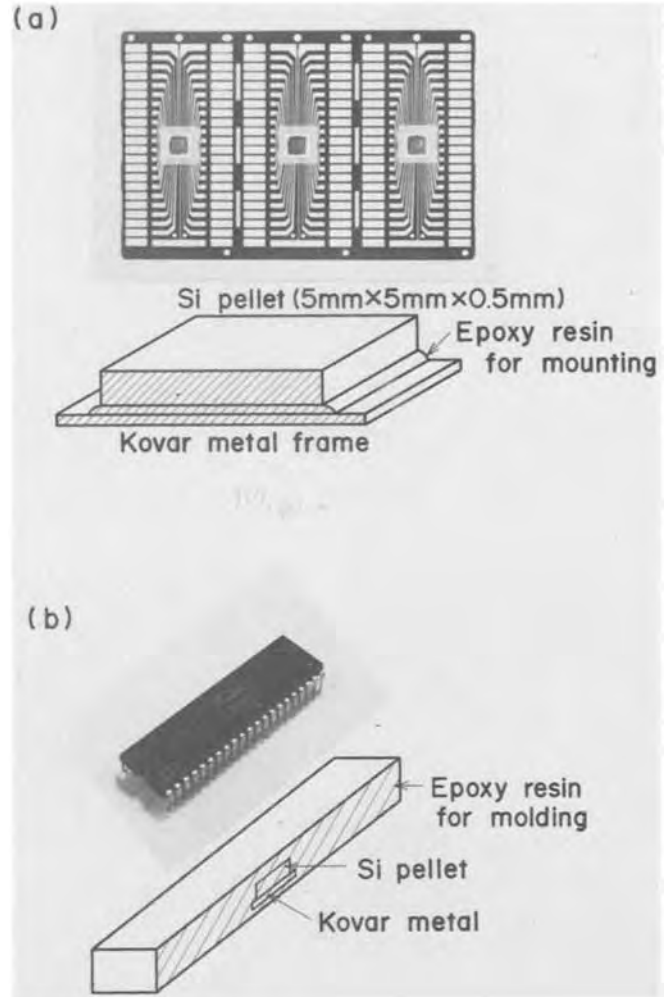


Fig. 5. Sample preparation. (a) Mounted silicon pellet and photoelastic measurement sample, (b) molded silicon pellet and photoelastic measurement sample. Optically polished side surfaces are shown by hatching.

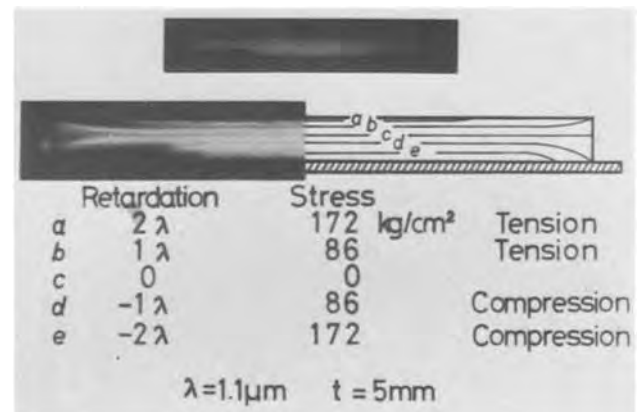


Fig. 6. Silicon pellet stress distribution after mounting. Stress values are approximate ones.

change the stress distribution very much, for it was ascertained that stress distribution was more dependent on epoxy resin thickness than on its lateral size.

Discussion

A slight approximation was made to correlate each isochromatic line directly to the two principal stress differences. This approximation is practical, for it makes stress distribution easy to understand. Calculated values of piezo-optical coefficients in three coordinate systems $[100] [010] [001]$, $[110] [\bar{1}10] [001]$, and $[112] [\bar{1}10] [\bar{1}\bar{1}1]$, shown in Table I, will cover

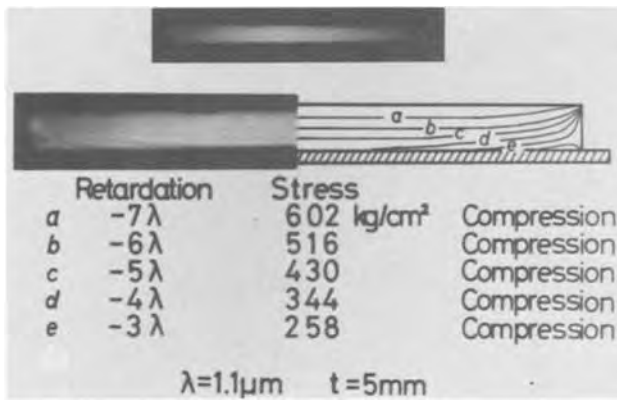


Fig. 7. Silicon pellet stress distribution after molding. Stress values are approximate ones.

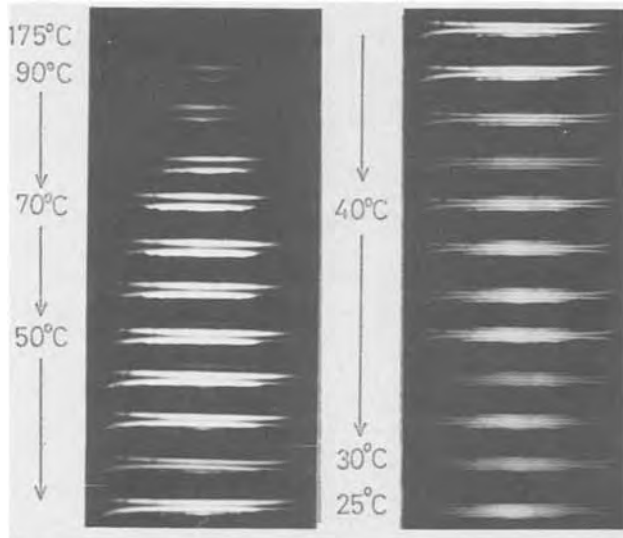


Fig. 8. Temperature dependence of isochromatic lines in silicon pellet mounted on Kovar metal by epoxy resin.

nearly all the cases of semiconductor crystal measurement in the usual device fabrication process although those in other coordinate systems can be calculated in the same way.

Changes in isochromatic lines according to temperature were observed to determine the zeroth order of retardation. Another method for this is to observe with more than two light waves with different wavelengths. In this case, an isochromatic line of the zeroth order of retardation remains in the same position of the sample, but other isochromatic lines change their positions according to the wavelengths. Nevertheless, this method is thought to be impractical for silicon, because it is transparent only to infrared radiation, and the choice of wavelength is limited.

From the result in Fig. 6 and 7, stress distribution in silicon pellet after mounting or molding can be understood as bending of flat plate. In the case of mounting, an experimental value can be compared with a theoretical one calculated from bimetal theory. According to the bimetal theory stress σ at the point z mm apart from the interface in material a in Fig. 9 is

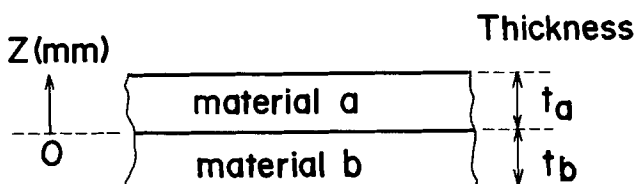


Fig. 9. Bimetal structure

$$\sigma = \frac{(C_1 - C_2 z) (\gamma_b - \gamma_a) (T - T_0)}{C_3} \frac{E_a}{1 - \nu_a} \quad [10]$$

where

$$C_1 = \frac{1 - \nu_a}{1 - \nu_b} \frac{E_b}{E_a} \left(\frac{t_b}{t_a} \right)^2 + 4 \frac{t_a}{t_b} + 3$$

$$C_2 = 6 \left(\frac{1}{t_a} + \frac{1}{t_b} \right)$$

$$C_3 = \frac{1 - \nu_b}{1 - \nu_a} \frac{E_a}{E_b} \left(\frac{t_a}{t_b} \right)^2 + \frac{1 - \nu_a}{1 - \nu_b} \frac{E_b}{E_a} \left(\frac{t_b}{t_a} \right)^2 + 4 \frac{t_a}{t_b} + 4 \frac{t_b}{t_a} + 6$$

and t_a and t_b are thickness of material a and b respectively, E_a and E_b are Young's modulus of material a and b respectively, ν_a and ν_b are Poisson's ratio of material a and b respectively, γ_a and γ_b are thermal expansion coefficients of material a and b respectively, T_0 is the temperature at which the plate is flat and free from stress, and T is the temperature at which stress is calculated. In this case, material a is (100) silicon pellet and material b is Kovar, $t_a = 0.05$ cm and $t_b = 0.023$ cm, $E_a = 1.69 \times 10^{12}$ dyne/cm² and $E_b = 1.40 \times 10^{12}$ dyne/cm², $\nu_a = 0.361$ and $\nu_b = 0.3$, $\gamma_a = 2.4 \times 10^{-6}$ 1/deg and $\gamma_b = 5.0 \times 10^{-6}$ 1/deg, $T_0 = 175^\circ\text{C}$ and $T = 25^\circ\text{C}$. Then $\sigma = -540 + 17,500z$ [kg/cm²].

Experimental values were compared with these calculated ones in Fig. 10. Calculated values were twice or three times larger than the experimental ones. The reason for this difference may come from the neglect of the epoxy resin layer between silicon and Kovar and the temperature dependency of mechanical properties.

Quantitative measurement of crystal stress distribution by photoelasticity can be applied to various engineering fields. IC pellet stress measurement done here is just one application. Other applications are to stress distribution of as-grown crystals and crystal processing such as cutting, grinding, and scribing. This method can also be used in the study of other crystals, such as GaP, GaAs, etc., using their piezo-optical coefficients.

Conclusion

A quantitative measurement procedure for stress in silicon by photoelasticity was established by calculating piezo-optical coefficients in various coordinate systems for observation. A slight approximation was made in the calculation for practical purposes. This method was applied to the study of semiconductor pellet stress distribution in the mounting and molding process, and important information was obtained for semiconductor device fabrication reliability.

Acknowledgment

During this study, valuable discussions and encouragement were received from Y. Matsushita and T. Wada. The authors wish to express their gratitude to Dr. S. Nagakura and Dr. O. Nittono for valuable discussions and critical reading of the manuscript. They also thank T. Sugahara for his helpful work with the apparatus and sample making.

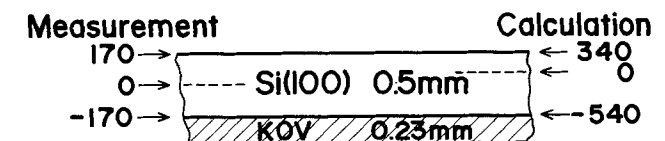


Fig. 10. Induced stress by adhesion, measurement: photoelastic method, calculation: 2-dimensional bimetal theory, stress unit: kg/cm², sample: (100) pellet, 5 × 5 × 0.5 mm.

Manuscript submitted May 1, 1979; revised manuscript received July 2, 1979.

Any discussion of this paper will appear in a Discussion Section to be published in the December 1980 JOURNAL. All discussions for the December 1980 Discussion Section should be submitted by Aug. 1, 1980.

Publication costs of this article were assisted by Toshiba Research and Development Center.

LIST OF SYMBOLS

n_1	refractive index
n_0	refractive index in crystal free from stress
π_{ij}	piezo-optical coefficient, cm^2/dyne
T_1	stress, dyne/cm^2
λ	wavelength
d	light path distance in crystal
h	retardation measured in wavelength unit λ
δ	retardation in phase, $2\pi h$

ϕ angle between analyzer axis (P_2) and sample principal stress direction (T_1)

REFERENCES

1. W. L. Bond and J. Andrus, *Phys. Rev.*, **101**, 1211 (1956).
2. A. A. Giardini, *Am. Mineral*, **43**, 249 (1958).
3. S. R. Laderhandler, *J. Appl. Phys.*, **30**, 1631 (1959).
4. J. Hornstra and P. Penning, *Philips Res. Rep.*, **14**, 237 (1959).
5. R. O. DeNicola and R. N. Tauber, *J. Appl. Phys.*, **42**, 4262 (1971).
6. S. Takasu and Y. Matsushita, *Jpn. J. Appl. Phys.*, **44**, *Suppl.*, 259 (1975); S. Takasu, "Crystal Growth and Characterization," R. Ueda and J. B. Mullin, Editors, p. 317, North Holland Publishing Co., (1975).
7. H. D. Edmonds, Abstract 321, p. 823, The Electrochemical Society Extended Abstracts, Las Vegas, Nevada, Oct. 17-22, 1976.
8. A. A. Giardini, *J. Opt. Soc. Am.*, **47**, 726 (1957).

Power Conversion Efficiency Monitoring in Photoelectrochemical and Other Solar Cells

B. Miller*

Bell Laboratories, Murray Hill, New Jersey 07974

ABSTRACT

A device is described which incorporates a superimposed a-c voltage signal, current-voltage product generation, synchronous detection, and a feedback loop to bias a photovoltaic converter to its point of maximum power output. Examples of its operation as a continuous monitor of power conversion efficiency are given for p-n junction and photoelectrochemical cells. Applications to studying the design fundamentals of the latter are illustrated, based on control derived with two- and three-electrode configurations to evaluate response to efficiency determining parameters such as light intensity and mass transport in the cell. The circuit stably responds with the average values of power output under periodically interrupted light up to at least 10 Hz. These characteristics open the way to external power conversion spectroscopy in the ultraviolet to near infrared range.

The power output characteristics of photovoltaic devices are easily obtained with two-terminal current (I) or voltage (V) scanning circuits. From these curves one calculates the maximum deliverable power ($V_m I_m$) between the zero limits at open-circuit voltage (V_{oc}) and short-circuit current (I_{sc}), and divides by the radiant input to get the maximum conversion efficiency. Since the external efficiency is obviously crucial to these converters, a scheme for its continuous monitoring under varying illumination and as a function of other experimental conditions would benefit evaluation of basic relations and design parameters of such cells. Apparatus to such ends is described in this paper.

Immediate motivation for providing this capability rose from recent active development of an electrochemical class of photovoltaic converters, semiconductor-liquid junction cells (1) (SCLJ), application to which we stress. In these systems determination of maximum power output and efficiency may be subject to greater experimental restraints than that of solid-state junction cells because redox chemistry must occur at both cell electrodes for current passage. Net local chemical alteration of the interfacial region, reflected in V-I curve hysteresis or long term trends, may result if the system deviates from the ideal of cancelling chemical reactions at the two electrodes or displays

surface modification or cumulative mass transfer effects such as concentration overpotentials or varying light absorption.

Holding the electrode at the maximum power point during a series of experimental variations reduces the possibility of extraneous conditions changing the comparative results and gives a closer picture to steady state. Thus it provides the most realistic way to evaluate design and environmental factors for which E_{oc} and I_{sc} monitoring are insensitive and for which the recording of full current-voltage curves may cause a perturbation of the experiment in liquid junction systems. Given $V_m I_m$ capacity, a further extension would be direct spectroscopic examination of wavelength response for this quantity of primary interest. Conventional spectroscopies with I_{sc} (quantum efficiency) or V_{oc} (difficult to interpret) inputs vs. wavelength to analyze the quality of the semiconductor and the junction would be usefully supplemented by this method. Some preliminary measurements are cited in this regard.

A circuit for tracking the maximum power output, and thus efficiency when simultaneous light input measurements are made, is described here with data illustrating its functions. Although the above discussion is oriented toward photoelectrochemical cells, the method is obviously applicable to other photovoltaics and a p-n silicon cell was first used to establish its claimed performance. A photoanode arrangement of good re-

* Electrochemical Society Active Member.

Key words: energy conversion, servo systems, synchronous detection.

producibility involving metallized semiconductors was employed to illustrate the electrochemical applications.

Circuit Design

A schematic of the voltage controlled circuit is given in Fig. 1, and its operation first described for two terminal operation. In summary, the peak power output is found through superimposing a sinusoidal voltage of 10-20 mV at 800 Hz on the cell, synchronously detecting the VI product of the cell at that frequency, and returning the phase sensitive d-c output of the synchronous detector in a servo loop minimizing the a-c signal, i.e., finding the operating point at which $d(VI)/dV \rightarrow 0$ or VI is a maximum. Some of these quantities are shown schematically in the Fig. 1 inset. (800 Hz provides a sufficient cell amplitude response at a frequency significantly above both those generated in rotating disk electrodes by geometric asymmetries and by the light chopping experiments. No further optimization of this value was sought.)

Amplifier 1 applies the a-c and feedback d-c voltages to the positive output terminal of the solar cell. The negative electrode (the n-type semiconductor photoanode in the liquid junction cell example) is held at virtual ground by the current measuring amplifier 2. Product VI from the multiplier X is recorded and also fed to the signal input of the synchronous detector (PAR 128). $V_m I_m$ tracking is initiated from a zero or bias condition (bias input not indicated on schematic) by applying the small a-c signal of 10-20 mV at 800 Hz from an internal oscillator to amplifier 1 while using the same source for the lock-in reference channel.

The feedback from the lock-in output to amplifier 1 is adjustable with the variable resistor to provide gain of 1-100. With no feedback ($V < V_m$), the phase is adjusted for maximum negative lock-in output. Closing the loop at the lowest gain setting then moves V toward V_m . The gain, for a suitable lock-in sensitivity and time constant, is increased to a level at which VI is acceptably unchanging, say within 1%, or $VI \cong 0.99V_m I_m$. Excessive over-all gain leads to oscillation.

With phase and gain adjusted, the circuit will track $V_m I_m$ over a wide range of input radiation or other output modifying variable. A lock-in time constant of 0.3 sec and capacitive damping for amplifiers 1 and 2, ≤ 0.1 msec, provide stable operation and speed of response adequate to most solar cell operating needs.

If the light intensity is simultaneously monitored, the quotient of output to input power, P_o/P_i , can be obtained from the analog divider arrangement shown. Since the multiplier output is VI/10, an unshown preceding V follower with selectable gain (usually 10) is inserted to compensate. Initial amplifier 2 load is set so that the maximum anticipated current will provide several volts to maximize the range over which the circuit will respond to the above limits.

Isolation from counterelectrode effects in electrolytic cells is normally done by three electrode operation with a reference electrode added. The reference electrode in these cases is conveniently the dark electrode material in a geometric position to sense the minimum feasible fraction of the cell electrolyte IR drop. The reference level is thus very close to the redox potential corresponding to the common point of an idealized cell at short circuit with no electrolyte resistance or counterelectrode losses. Three electrode operation gives the maximum power output possible with the photovoltaic electrode without counterelectrode or almost all cell IR drop. Power loss sources may be analyzed both by comparing two and three electrode operation and by examining the three electrode configuration, altering photovoltaic electrode conditions such as light intensity and stirring. Thus the maximum power monitoring circuitry was made adaptable to two working electrode or working electrode-reference electrode potential differences as a voltage signal, simply by switching the input to the multiplier from the reference electrode follower instead of the counterelectrode lead from amplifier 1, as shown in Fig. 1.

Experimental

The practical version of the schematic circuitry of Fig. 1 was constructed with additional switching to provide direct reading of V_{oc} and I_{sc} as well as $V_m I_m$ so as to obtain fill factors or monitor these other parameters as a function of experimental variables. The apparatus also contains a conventional analog ramp generator with input to amplifier 1 to run conventional scanned voltage I-V curves (with simultaneous VI multiplier output) to compare the accuracy of $V_m I_m$ found by the servo loop procedure.

Input irradiance for these experiments was obtained from a 10 mW He-Ne laser (Hughes Industrial Products) combined with a three Glan Laser prism polarizer based optical attenuator (Karl Lambrecht Corporation) containing a rotatable element driven by an added 1 rpm motor for intensity scanning experiments (2). A quartz plate in the beam directed about 4% of the light to a Metrologic Corporation silicon power detector whose analog output, proportional to the actual P_i incident on the cell, was used for the analog divider denominator in efficiency monitoring experiments. Since the experiments here were only used for relative efficiency comparisons, calibration was not performed and the input called P_i is the reflected part of the beam in the figures.

The silicon p-n cell was standard and its area was only partially illuminated by the laser beam, diffused to about 0.5 cm diam in these experiments.

The electrolytic cell utilized as photoanode a gold plated n-GaAs electrode whose preparation and properties are elsewhere described (2). The redox electrolyte was 0.2M $K_4Fe(CN)_6$ -0.05M $K_3Fe(CN)_6$ in a pH 5 acetate buffer (0.5M). These hybrid electrodes (3, 4) have the metal-semiconductor Schottky junction isolated from the electrolyte to inhibit photocorrosion but otherwise are light-controlled and are sensitive to cell resistance, surface kinetics, and transport just

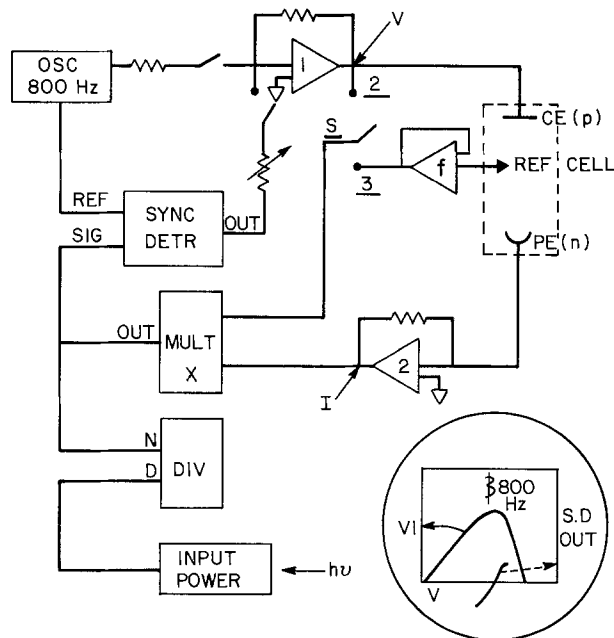


Fig. 1. Schematic of maximum power detection circuitry. CE = counterelectrode, PE = photoelectrode, Ref = reference electrode. p and n refer to contacts to respective Si cell regions. Multiplier X = Burr-Brown 4204, Divider = Burr-Brown 4291, Synchronous Detector = PAR 128, Input Power Meter = Metrologic 60-530 Radiometer, Amplifiers 1 and 2 = Burr-Brown 3440, Amplifier f = Burr-Brown 3420. Inset shows schematic relation of VI and synchronous detector output, with 800 Hz signal on voltage axis.

as electrolyte-exposed semiconductor cells. These electrodes were used for the demonstration experiments here because of their stable voltammetric behavior. Exposed semiconductor electrodes have been used with the system equally well. These electrodes, however, often show time dependent features. Although the circuitry is designed to study such characteristics, to give confidence in its performance for that work it was decided to use systems here in which $V_m I_m$ measured from repeated V-I scans and from the steady-state servo scheme data ought normally to be identical and could be more rigorously compared.

The electrode was mounted as a rotating disk in a cell with an optical flat bottom into which the light beam was reflected by a mirror. Counter and reference electrodes were spectroscopic grade carbon rods. Air was not excluded from the cell which was at ambient temperature.

Results and Discussion

Voltage scans plotting I-V and VI-V for four normalized light irradiances (as read from the calibrated attenuator) are shown for the p-n Si cell in Fig. 2. Superimposed on the curves are noted the recorder pen points for the correspondingly determined I_m - V_m and $I_m V_m$ - V_m points for the same light settings found separately by the servo loop circuitry. The tracking of maximum product was initiated as described above with phase and gain adjustment only at the $P_i = 1$ point. The correspondence between the scan $I_m V_m$ maxima and the servo maxima is within chart reading error for the decade range of power input and confirms the circuit function. The unity normalized value of average P_i here is about 10 mW/cm². The power with the small beam size is not spatially uniform, but not disturbing to this test.

A similar experiment but with motorized intensity scanning and direct recording of both P_o and the conversion efficiency P_o/P_i vs. P_i for the p-n Si cell is shown in Fig. 3. The efficiency follows input intensity in this range, as is known (5). This experiment corresponds to the use of the circuit to monitor cell efficiency continuously under fluctuating light, such as sunlight. The circuit easily handles a decade change in P_i or P_o without any I range resistor change and is, in fact, stable down to zero current.

The current-voltage characteristics of the Au-n-GaAs/Fe(CN)₆⁻⁴-Fe(CN)₆⁻³/C cell with an additional 220Ω resistance in the counterelectrode lead are shown in Fig. 4 from a single voltage scan (a fritted disk separating the counterelectrode already contributes about 130Ω; the series external resistor emphasizes the IR

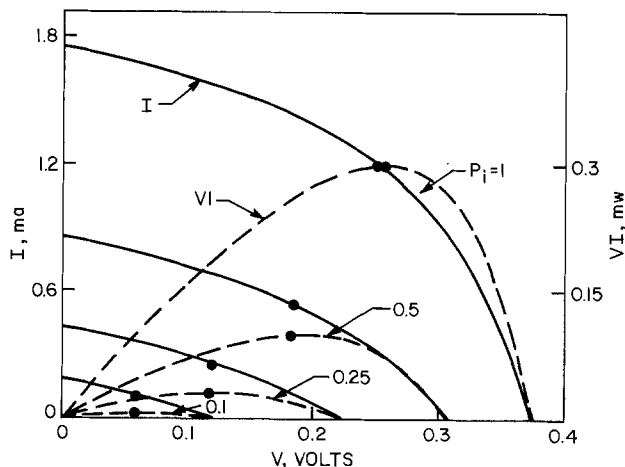


Fig. 2. Current, voltage, and power recorded under voltage scan for silicon p-n cell at four different relative light power levels (P_i), as indicated for each pair of curves. Points are V_m , I_m , and $V_m I_m$ found by maximum power circuitry for same conditions. 800 Hz signal is 17 mV pk-pk.

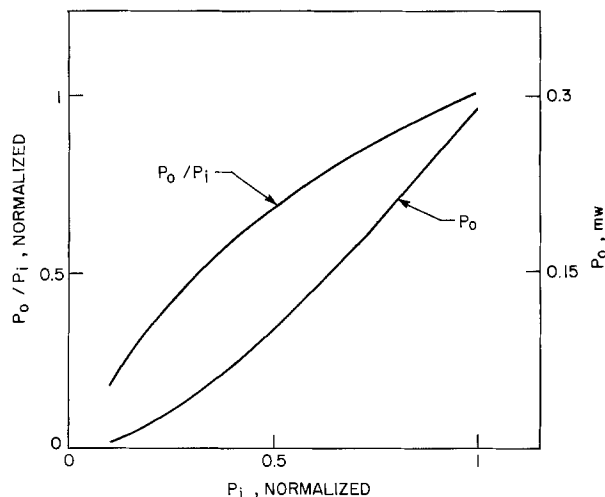


Fig. 3. Normalized maximum power efficiency (P_o/P_i) and power output (P_o) vs. normalized light input power (P_i) for silicon p-n cell.

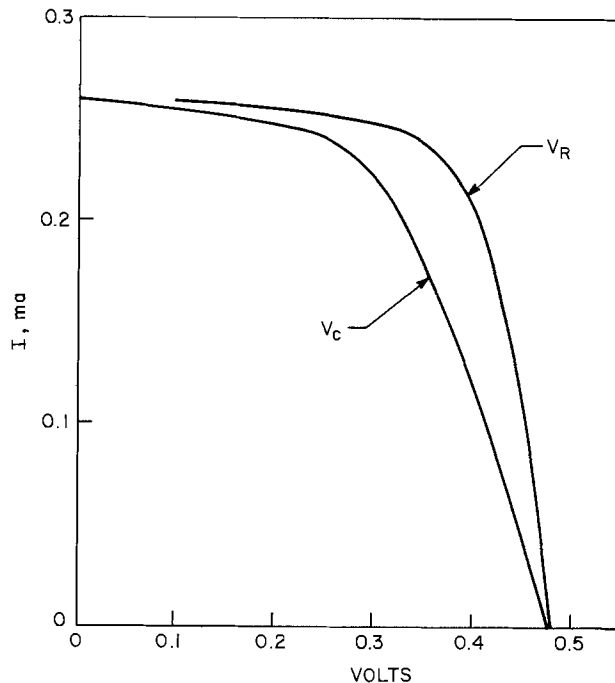


Fig. 4. Current vs. cell voltage (V_c) and reference electrode-photoelectrode potential difference (V_R) with V_c scan control in Au on n-GaAs/Fe(CN)₆⁻⁴-Fe(CN)₆⁻³/C cell with C reference electrode, laser illumination. External 220Ω resistor drop included in V_c . Photoelectrode rotated at 900 rpm.

loss effect). Both cell voltage, V_c , including external resistor drop, and the difference of reference and photoanode potentials, V_R , were recorded vs. cell current.

Approximately 100 mV difference exists between these two voltages at the short-circuit condition of the two current passing electrode leads ($V_c = 0$) and the maximum power represented by the V_R curve is 30% greater than that of the V_c curve. This translates to a nearly 30% higher fill factor since V_{oc} , as measured in both cases, is identical and I_{sc} at $V_r = 0$ will only be slightly greater (~2%) than at $V_c = 0$. The V_{oc} and I_{sc} parameters are thus not different, or only slightly so, in a case with simulated large internal losses and their monitoring may be poorly indicative of cell performance.

With the same gold plated n-GaAs electrode, cell configuration, and initial intensity level, a further comparison of two- and three-electrode cell ($V_c I$ and $V_R I$) behavior was made in Fig. 5. This plot is anal-

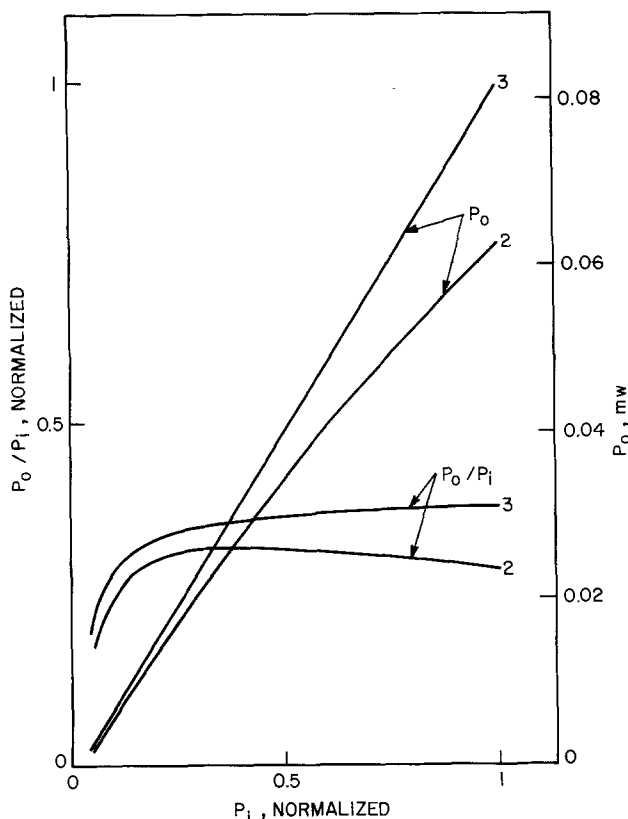


Fig. 5. Plot as in Fig. 3 for cell and conditions of Fig. 4. $P_i = 1$ is illumination level of Fig. 4. Curves marked 2 and 3 have maximum power controlled from V_c and V_R , respectively. 800 Hz signal is 20 mV pk-pk.

ogous to that of the solid-state junction experiment in Fig. 3, but here with the two different SCLJ cell maximization arrangements selected by switch *S* in Fig. 1. The ratio of the initial ($P_i = 1$) values of $V_R I_m$ and $V_c I_m$ from Fig. 5 is 1.31, within experimental error of the value calculated (1.30) from the V-I plots in Fig. 4, again confirming the circuit accuracy.

The limiting efficiency of the photoanode expressed by the maximum $V_R I$ product increases monotonically with intensity and only levels off at the highest P_i . Current densities at this point (5 mA/cm²) correspond closely to those a gold plated electrode generates in approximately AM2 (75 mW/cm²) sunlight (6). Because of the combined electrolyte and external resistor losses, the two current-carrying terminal $V_c I$ maximum efficiency peaks at about $P_i = 0.4$. The two efficiencies approach most closely when the IR drops become minimal and overpotential ascribable to the large counterelectrode is nil.

Application of such cell design analysis data to study of the mass transport parameter is shown in Fig. 6. The P_o/P_i ratio, under the $V_R I$ maximization condition to be essentially free of IR or counterelectrode effects, is displayed vs. time as a function of rotation speed, starting at 900 rpm. An increase to 1600 rpm raises P_o less than 1%. A decrease to 400 rpm from 1600 rpm (factor of two for a mass transport limited current) produces a 1% decline. At 100 rpm the power is 3% less than the initial 900 rpm value, but when rotation is stopped efficiency drops steadily, reaching about an additional 18% loss after only 80 sec when the 900 rpm speed was resumed. The output then returned to within 1% of its initial 900 rpm level.

Even with a 0.2M solution of ferrocyanide reducing agent, the 4 mA/cm² current density causes substantial concentration gradient effects at the electrode surface when convective diffusion assistance (stirring) is absent. Such effects become more important as cells achieve higher efficiencies, even when redox electro-

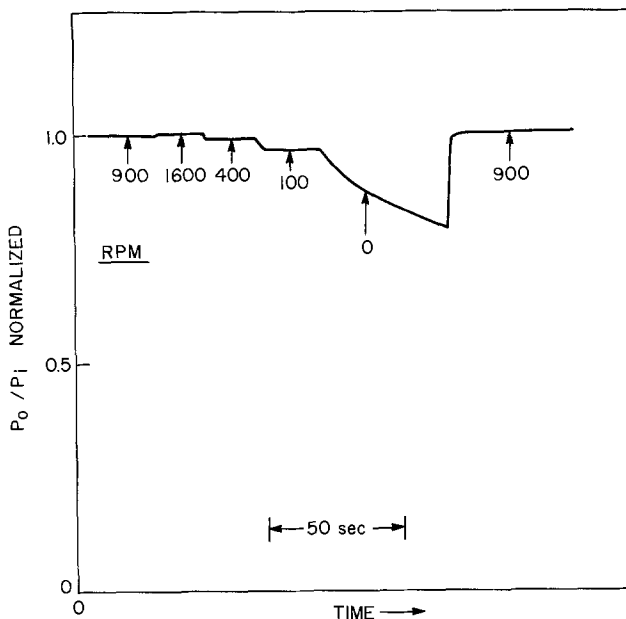


Fig. 6. Normalized maximum power efficiency for Fig. 4 cell and illumination level as a function of photoelectrode rotation speed, as marked, with time. Circuitry conditions of Fig. 5.

lytes are quite concentrated. The 12% n-GaAs/Se=Se₂=-OH-/C cell with a 1M total selenium concentration has a fill factor detectably sensitive to stirring at high solar irradiance (7). Experiments such as shown here will be useful to analyze operating parameter influences on mass transport at the photoanodes, both alone and combined with counterelectrode effects.

The circuitry shown is capable of measuring average maximum cell power in two- or three-electrode configurations for practical alternating light intensity frequencies. An experiment similar to that of Fig. 5 was performed along with one in which the same scanned intensity laser beam was modulated by square wave chopping with a two sector wheel driven at 10 Hz by a PAR 192 variable speed chopper. The lock-in time constant was increased to 1 sec to enhance the averaging process. In both cases here the multiplier (P_o) and light power detector (P_i) outputs were heavily filtered to produce d-c averaged outputs and a steady P_o/P_i reading even in the chopped light case. The two (d-c and 10 Hz) efficiency vs. average P_i scans are shown in Fig. 7.

The 10 Hz chopped light trace starts at $P_i = 0.5$ because of the 50% duty factor. Otherwise the curves are essentially superimposable. Proper processing of the chopped signals (preferably originally sinusoidal) by bandpass filters with gain prior to analog division, then rectification, would permit power conversion efficiency spectroscopy to be done directly with a scanned monochromatic beam as light source. Although this process does not eliminate d-c effects on the multiplier output, extraneous light can be experimentally reduced. Of course where chopping offers little advantage the d-c response spectroscopy could be obtained.

The advantages of direct P_o/P_i recording vs. wavelength, as opposed to that of I_{sc} or V_{oc} , are considerable for the analysis of photoelectrode characteristics since P_o/P_i is the deciding factor in their over-all performance possibilities and thus in diagnostic examination. The results of Fig. 7 are sufficient to show that the method is feasible. At 40 Hz the circuit remains stable with only the sacrifice of a fraction of the response which may not affect the relative shape of a spectrum.

Summary and Conclusions

A circuit for monitoring the maximum power of a photovoltaic device has been constructed and demon-

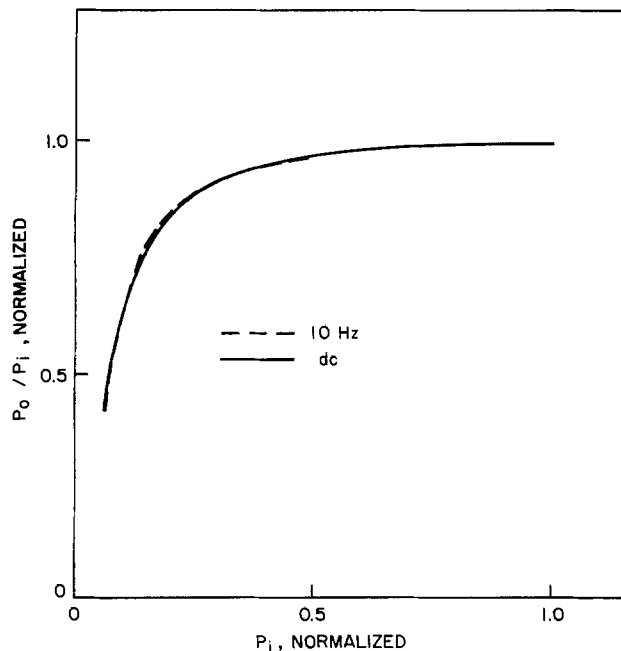


Fig. 7. Normalized maximum power efficiency (P_o/P_i) vs. normalized light input power (P_i) with 10 Hz chopped input (dashed line) and d-c illumination (solid line). Other conditions as with V_R multiplier input of Fig. 5.

strated to serve this function under a variety of conditions. In semiconductor-liquid junction configurations its use with both current-carrying terminals and with semiconductor plus reference terminal as voltage input allows analysis of efficiency loss mechanisms in the cell. Mass transport, light intensity, and internal resistance effects were viewed clearly in a well-controlled system by the maximum power tracking circuit. When combined with analog division by the input power, the quotient of conversion efficiency is directly

monitored. The latter will be useful for continuous solar measurements, light concentrator experiments, and for long-term stability studies. The frequency response of the circuitry combined with proper averaging permits light chopping and shows stability even with square wave light intensity transitions. Application of either the d-c or chopped light methods with the maximum power circuitry to an external power conversion efficiency vs. wavelength spectroscopy has interesting advantages for photovoltaic studies.

Acknowledgments

The author is grateful to S. H. Glarum for essential suggestions on the maximum power circuitry, to S. Menezes for preparation of the metallized semiconductor electrodes, and to A. Heller for numerous discussions.

Manuscript submitted June 4, 1979; revised manuscript received July 7, 1979.

Any discussion of this paper will appear in a Discussion Section to be published in the December 1980 JOURNAL. All discussions for the December 1980 Discussion Section should be submitted by Aug. 1, 1980.

Publication costs of this article were assisted by Bell Laboratories.

REFERENCES

1. "Semiconductor—Liquid Junction Solar Cells," A. Heller, Editor, The Electrochemical Society Soft-bound Proceedings Series, Princeton, N.J. (1977).
2. B. Miller, S. Menezes, and A. Heller, *This Journal*, **126**, 1483 (1979).
3. Y. Nakato, S. Tonomura, and H. Tsubomura, *Ber. Bunsenges. Phys. Chem.*, **80**, 1289 (1976).
4. R. H. Wilson, L. A. Harris, and M. E. Gerstner, *This Journal*, **124**, 1233 (1977).
5. R. K. Yasui and L. W. Schmidt, Conf. Rec. IEEE 8th Photovoltaic Spec. Conf., Seattle, Washington, pp. 110-122 (1970).
6. S. Menezes, Private communication.
7. B. A. Parkinson, A. Heller, and B. Miller, *This Journal*, **126**, 954 (1979).

High-Efficiency GaAs Photoanodes

Rommel Noufi* and Dennis Tench**

Rockwell International Science Center, Thousand Oaks, California 91360

ABSTRACT

The photoresponse of large-grained polycrystalline and single crystal n/n^+ -GaAs in aqueous selenide/polyselenide solution is compared with that of single crystal n -GaAs. Use of the n/n^+ -structure is shown to significantly improve performance, and the power conversion efficiency for the large-grained n/n^+ -material is found to approach that for n/n^+ -single crystals. For single crystal n/n^+ -GaAs, the measured conversion efficiencies for white light from a xenon lamp were 14% (uncorrected) and 19% (corrected for absorption in the solution).

Considerable attention has been focused recently on n -GaAs as a candidate photoanode for use in electrochemical solar cells (1-3). This material has an ideal bandgap for utilization of the solar spectrum (1.4 eV), but like other common narrow-bandgap semiconductors is prone to photodissolution in ionizing solutions. Although significant progress has been made in stabilizing GaAs against photodecomposition (1, 2), only single crystal electrodes have been considered. Polycrystalline materials, however, will almost certainly

* Electrochemical Society Student Member.

** Electrochemical Society Active Member.

Key words: n/n^+ -GaAs, polycrystalline, photoelectrochemical cell, efficiency.

be required for any practical solar conversion device not involving concentrators.

Since the photosensitive junction in electrochemical solar cells is extremely abrupt compared to a p-n junction and one side is practically transparent to the solar spectrum, more of the incident light is absorbed within the region of high electric field at the interface where charge carriers are more efficiently separated and collected. Thus, in electrochemical cells, the efficiencies of polycrystalline films can more closely approach those of single crystals (4, 5). For the semiconductors studied to date, however, this promise has only been realized to a limited extent, e.g., 5% solar

conversion efficiencies for polycrystalline CdSe (5) compared to 7.2% for single crystals (6), and considerable improvement is needed. The present work was undertaken to provide a comparison between large-grained polycrystalline and single crystal GaAs photoanodes, and to determine the extent to which internal losses in the electrodes can be mitigated by utilizing layered n/n^+ -material.

Experimental Details

Electrode materials investigated were large-grained polycrystalline and single crystal n/n^+ -GaAs and single crystal n -GaAs. The designation n/n^+ denotes a layered structure of a lightly doped film deposited on a more heavily doped substrate of the same material. One advantage of this arrangement is that the film can be doped at the level that provides optimum separation and collection of photogenerated charge carriers at the interface ($\sim 10^{16}$ carriers/cm³ for GaAs) without paying the penalty of a high resistive loss in the bulk of the electrode. Also, since the Fermi level of the n^+ -material is slightly higher, a back surface field (BSF) is created at the n/n^+ -junction which opposes diffusion of holes from the n -layer to the n^+ -bulk, while favoring transport of electrons (7). Thus, the BSF enhances charge carrier separation and tends to confine holes to the surface n -region away from the ohmic back contact (where the recombination rate is infinite). The net result is an improvement in the conversion efficiency for the n/n^+ -material compared to n -type. Details of the effect of a BSF on the short-circuit current and open-circuit voltage are given in Ref. (7).

To prepare the polycrystalline and single crystal n/n^+ -GaAs, Sn-doped n -layers were grown epitaxially on 0.5 mm thick polycrystalline or single crystal substrates, respectively, doped with Si ($\sim 10^{18}$ carriers/cm³). The polycrystalline epilayer, which had a grain size of 100-1000 μm , was grown by molecular beam epitaxy and was 2.5 μm thick with $\sim 10^{17}$ carriers/cm³ having a mobility of $\sim 3100 \text{ cm}^2\text{V}^{-1}\text{sec}^{-1}$. The single crystal epilayer was grown by liquid phase epitaxy and was 3 μm thick with $\sim 10^{16}$ carriers/cm³ having a mobility of $\sim 6000 \text{ cm}^2 \text{V}^{-1} \text{sec}^{-1}$. The n -GaAs single crystal, which was investigated for comparison, was Si-doped to 3×10^{16} carriers/cm³. Ohmic contacts were made using indium/gold alloy and the GaAs electrodes were sealed in epoxy resin. In each case, the area of electrode exposed to the solution was 0.3 cm².

Electrochemical measurements were made in nitrogen-saturated selenide/polyselenide solution (1M K₂Se + 0.1M Se + 1M KOH) which has been shown to be effective in suppressing photodecomposition of GaAs (1). The counter and reference electrodes were platinum (10 cm²) and saturated calomel (SCE), respectively. The cell was sealed and had a flat quartz window to admit the light from a 1000W xenon lamp, the spectrum of which is shown in Fig. 1. The light intensity falling on the cell was measured by a Hewlett-Packard radiant flux meter to be 115 mW/cm² (unless otherwise noted). Absorption losses by a 5 mm layer of the polyselenide solution reduced the intensity at the electrode surface to 85 mW/cm². The n -GaAs electrode was etched in a 1:1 sulfuric acid-hydrogen peroxide mixture (3), whereas the n/n^+ -materials were used as grown.

Results and Discussion

The photocurrent response in selenide/polyselenide solution for polycrystalline and single crystal n/n^+ -GaAs and single crystal n -GaAs is shown as a function of the electrode potential in Fig. 2. It is evident from the higher currents at the same electrode potential (approximately the same degree of band bending) that the separation and subsequent collection of photogenerated charge carriers is more efficient for the n/n^+ -materials. Furthermore, the conversion efficiency for

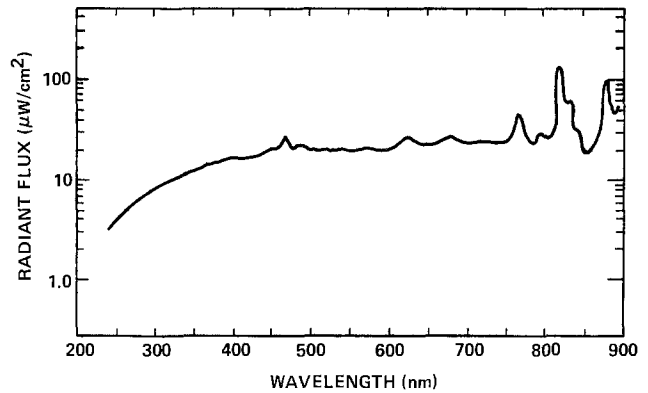


Fig. 1. Spectral output of a 1000W xenon lamp as measured with a Hewlett-Packard radiant flux meter.

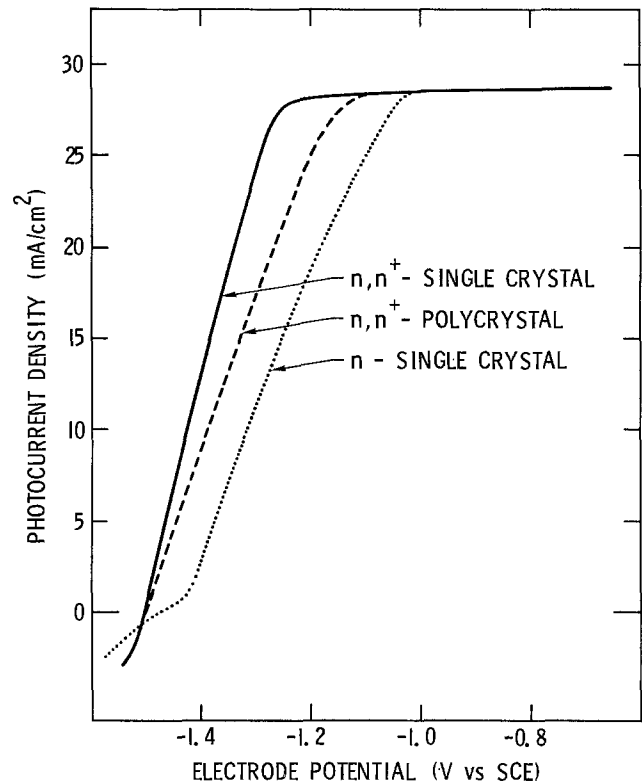


Fig. 2. Photocurrent vs. electrode potential for GaAs photoanodes illuminated with white light of 115 mW/cm² (uncorrected for solution absorption) in aqueous selenide/polyselenide solution.

the polycrystalline n/n^+ -electrode approaches that for the n/n^+ -single crystal. As discussed above, the efficiency enhancement for the n/n^+ -electrode is attributable to the effect of the BSF in enhancing charge carrier separation and hindering the diffusion of the holes to the ohmic back contact.

Figure 3 shows the relationship between the current density and the cell voltage for cells based on polycrystalline and single crystal n/n^+ -GaAs. The polycrystalline material compares favorably with the single crystal, yielding practically the same short-circuit current (29 mA/cm²) and an only slightly smaller open-circuit voltage (0.68V). The fill factor for the polycrystalline electrode is also somewhat smaller (0.67) than that for the single crystal (0.80), presumably because of the lower parallel resistance due to leakage along grain boundaries (7).

Characteristics of the two cells are summarized in Table I. The 19% value is 45% of that theoretically attainable for this system under xenon lamp illumination from 250 to 885 nm (42%). These efficiency values have not been corrected for Carnot limitations arising

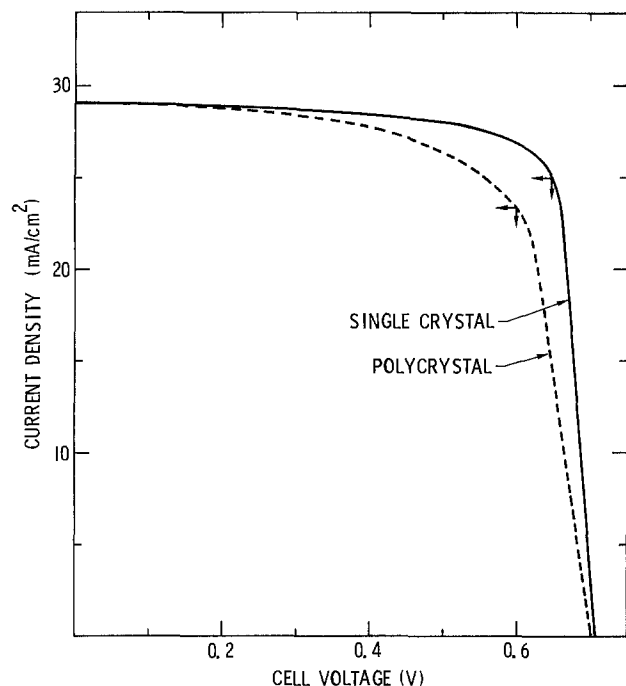


Fig. 3. Current density vs. cell voltage for n/n^+ -GaAs photoanodes under illumination with white light of 115 mW/cm^2 (uncorrected for solution absorption). Curves are the average of forward and reverse scans at 100 mV/sec .

from the temperature difference between the source and the converter (8). The conversion efficiencies for the n/n^+ -polycrystalline material are only slightly less (2-3%), as might be expected when the grain size is large (100-1000 μm) compared to the thickness of the space charge layer ($\sim 0.1 \mu\text{m}$).

Conclusions

The results reported here demonstrate that the conversion efficiency for large-grained polycrystalline GaAs in photoelectrochemical cells approaches that for single crystals. In either case, the use of a layered n/n^+ -structure significantly improves the performance which approaches that theoretically attainable. The challenge in attaining a practical solar conversion de-

Table I. Characteristics of photoelectrochemical cells based on n/n^+ -GaAs in selenide/polyselenide solutions under illumination with white light (115 mW/cm^2) from a xenon lamp

Parameter	Poly-crystalline	Single crystal
Open-circuit voltage	0.68V	0.7V
Short-circuit current	29 mA/cm^2	29 mA/cm^2
Fill factor	0.67	0.80
Maximum power output	14 mW/cm^2	16 mW/cm^2
Power conversion efficiency		
Uncorrected	12%	14%
Corrected for solution absorption	16%	19%

vice is to duplicate such results for materials fabricated economically on a large scale.

Acknowledgments

The authors are indebted to Mr. Dennis Edwall and Dr. David Miller for providing the n/n^+ -GaAs used in this work.

Manuscript submitted April 23, 1979; revised manuscript received July 23, 1979.

Any discussion of this paper will appear in a Discussion Section to be published in the December 1980 JOURNAL. All discussions for the December 1980 Discussion Section should be submitted by Aug. 1, 1980.

Publication costs of this article were assisted by Rockwell International.

REFERENCES

1. K. C. Chang, A. Heller, B. Schwartz, S. Menezes, and B. Miller, *Science*, **196**, 1097 (1977).
2. P. Kohl and A. J. Bard, *This Journal*, **126**, 603 (1979).
3. B. Parkinson, A. Heller, and B. Miller, *Appl. Phys. Lett.*, **33**, 521 (1978).
4. R. Noufi, P. Kohl, and A. J. Bard, *This Journal*, **125**, 375 (1978).
5. B. Miller, A. Heller, M. Robbins, S. Menezes, K. C. Chang, and J. Thomson, Jr., *ibid.*, **124**, 1019 (1977).
6. A. Heller, K. C. Chang, and B. Miller, *ibid.*, **124**, 697 (1977).
7. H. J. Hovel, "Semiconductors and Semimetals," Vol. 11 (Solar Cells), Academic Press, New York (1975).
8. R. G. Mortimer and R. M. Mazo, *J. Chem. Phys.*, **35**, 1013 (1961).

The Effect of Hot Electron Injection on Interface Charge Density at the Silicon to Silicon Dioxide Interface

Yoshio Miura, Kikuo Yamabe, Yoshio Komiya, and Yasuo Tarui

VLSI Technology Research Association, Cooperative Laboratories, Kawasaki, Japan

ABSTRACT

The avalanche injection of hot electrons at the silicon to silicon dioxide interface causes an anomalous N-shaped shift of flatband voltage in accordance with the injected charge density and generates an interface state with widely distributed time constants. To explain the N-shaped behavior, we propose a model which assumes electron trapping in the silicon dioxide and the generation of the donor-type interface state. It is also observed that the orientation of silicon substrate strongly affects the generated interface-state density. The generated interface-state density of a (100) capacitor has a value approximately half that of a (111) capacitor. The energy level of the generated interface state is distributed near the middle of the energy gap of silicon. The dominant electron capture cross sections are approximately $1 \times 10^{-18} \text{ cm}^2$ for both (100) and (111) capacitors.

With the development of short channel MOS devices, significant instability due to the emission of electrons from the silicon into the silicon dioxide has become an important problem. Subsequent trapping of the hot electrons in the silicon dioxide causes instabilities in the form of threshold voltage shift and transconductance degradation (1-4). A large amount of work has been done on hot electron instability in MOS structure (5-11). It has been shown that some of the injected electrons are trapped in the silicon dioxide and that the flatband voltage increases in proportion to the number of injected electrons. The flatband voltage has a tendency to saturate in relation to the filling of the electron traps in the silicon dioxide. But a reversal of the flatband voltage shift for a larger number of injected electrons is reported by Gdula (6) and is explained likely due to fast surface-state generation. There are few reports about the interface state density generated by the hot electron injection (7).

In the present study, hot electrons are injected by the avalanche injection technique (8) in order to examine the interface charge density at the silicon to silicon dioxide interface.

The results confirm the reversal of the flatband voltage shift (6). Furthermore, we observe that the flatband voltage appears to increase again after a large number of electrons have passed through the silicon to silicon dioxide interface. It is also observed that the injection of hot electrons generates interface states with widely distributed time constants. The interface-state density is strongly affected by the orientation of the silicon substrate in the same manner as the fixed charge density at the thermally oxidized silicon surface (12). The purpose of this paper is to clarify the changes of flatband voltage which occur with the avalanche injection of hot electrons at the silicon to silicon dioxide interface.

Experiments

Sample preparation.—MOS capacitors are fabricated using p-type silicon wafers with an approximately $0.3 \text{ } \Omega\text{-cm}$ (100) plane, and $2 \text{ } \Omega\text{-cm}$ (100) and (111) planes. The thickness of the silicon dioxide film is about 800 \AA for the $0.3 \text{ } \Omega\text{-cm}$ capacitor, 850 \AA for the $2 \text{ } \Omega\text{-cm}$ (100) capacitor, and 1000 \AA for the $2 \text{ } \Omega\text{-cm}$ (111) capacitor. The oxidation is performed in an all-quartz system at 1000°C in dry oxygen. All oxide growth is followed by 30 min of annealing in dry nitrogen at growth tem-

perature. Aluminum electrodes are evaporated from an electron gun source, followed by postmetallization at 450°C for 30 min in dry nitrogen.

Measurement technique and condition.—Starting with a previously unused capacitor, the complete capacitance-voltage (C-V) characteristic is measured at various frequencies (1 MHz-17 Hz) with low amplitude signals. Hot electrons are injected into the silicon dioxide by the avalanche injection technique. The avalanching field is provided by a 100 kHz constant-voltage square wave generator. The square waves are interrupted periodically to automatically measure the flatband voltage at 1 MHz as a means for monitoring the interface charge density at the silicon to silicon dioxide interface. The capacitor is then reconnected to the C-V measuring apparatus and complete C-V data at various frequencies is determined. The avalanche injection current density is in the range from 10^{-5} to 10^{-4} A/cm^2 . As the variation of pulse width for the avalanche injection at 100 kHz shows little effect on the injected current density, most of the injected electrons will be hot electrons. The generated interface-state density is obtained from the C-V data before and after the capacitor is avalanched for specified injected electronic charges. The estimated flatband voltage shift due to the generated interface state, V_{FBI} , is obtained from

$$V_{\text{FBI}} = N_{\text{ss}}/C_{\text{ox}}$$

where N_{ss} is the generated interface-state density and C_{ox} is the oxide capacitance of the MOS capacitor. An electron capture cross section is obtained from the flatband voltage data as a function of the injected charge density (13).

Results

The characteristic shown in Fig. 1 is a typical result of the variation of the flatband voltage as a function of the injected charge density for the $0.3 \text{ } \Omega\text{-cm}$ (100) capacitor with a pulse bias of 37V. The flatband voltage typically increases for some initial range of injected charge and then gradually decreases as injected charge increases. However, the flatband voltage appears to increase again when large number of electrons are injected. This is called "N-shaped" behavior. Figure 2 shows a typical set of complete C-V characteristics at various injected charge levels with the signal frequency as a parameter. Figure 2 [A]-[D] are results for injected charge levels of 0, $0.75 \times 10^{18}/\text{cm}^2$, $4.5 \times$

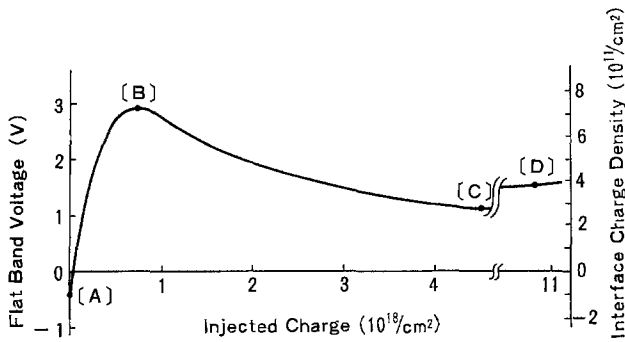


Fig. 1. Flatband voltage as a function of injected charge density for the 0.3 Ω -cm (100) capacitor.

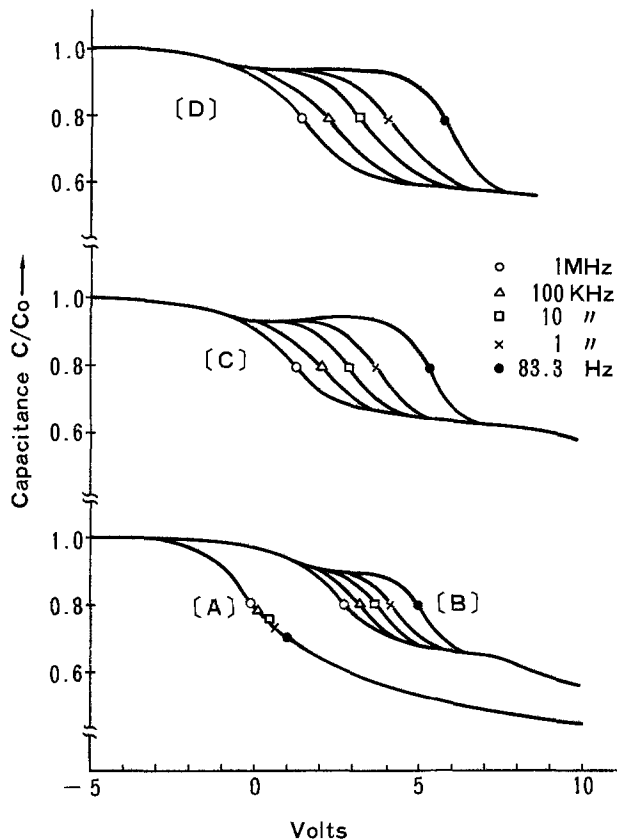


Fig. 2. Typical set of C-V characteristics at various injected charge levels with signal frequency as a parameter. [A] = 0; [B] = $0.75 \times 10^{18}/\text{cm}^2$; [C] = $4.5 \times 10^{18}/\text{cm}^2$; [D] = $10.8 \times 10^{18}/\text{cm}^2$.

$10^{18}/\text{cm}^2$, and $10.8 \times 10^{18}/\text{cm}^2$, respectively. We can see large increases in interface-state density with widely distributed time constants as the injected charge density increases. But a smaller increase is noted in Fig. 2 [D] in comparison with [C].

Similar experiments are also carried out for the 2 Ω -cm (100) and (111) capacitors with a pulse bias of 95V. The characteristic of the flatband voltage vs. the injected charge density of the (100) and (111) capacitors is similar to Fig. 1. However, for the (100) capacitor, the maximum is approached more slowly than for the (111) capacitor. The dominant electron capture cross sections obtained from the data are $1.3 \times 10^{-18}/\text{cm}^2$ for the (100) capacitor, and $1.0 \times 10^{-18}/\text{cm}^2$ for the (111) capacitor. The generated interface-state density obtained from the C-V characteristics is shown in Fig. 3 for the (100) and (111) capacitors with the injected charge density as a parameter. It is seen that the (100) capacitor has approximately half the generated interface-state density of the (111) capacitor at equivalent injected charge densities.

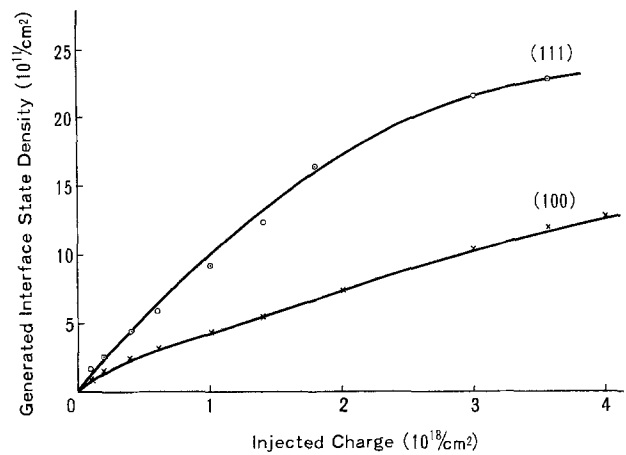


Fig. 3. The generated interface-state density as a function of the injected charge density for 2 Ω -cm (100) and (111) capacitors.

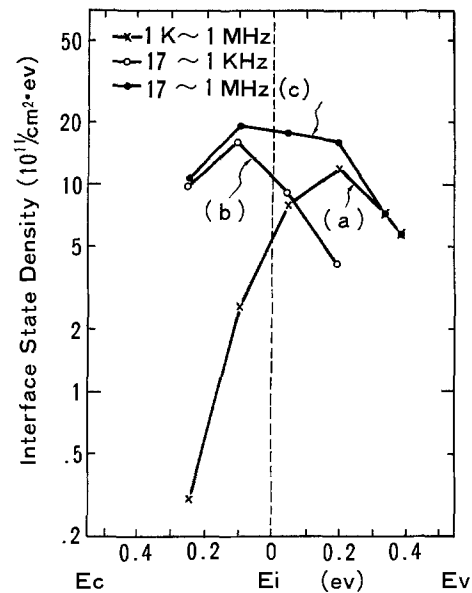


Fig. 4. Energy distribution of generated interface state for the (100) capacitor at injected charge density of $3 \times 10^{18}/\text{cm}^2$; at signal frequency ranges: (a) = 1 kHz-1 MHz, (b) = 17 Hz-1 kHz, and (c) = 17 Hz-1 MHz.

Figure 4 shows the energy distribution of the generated interface states for the 2 Ω -cm (100) capacitor at the injected charge density of $3 \times 10^{18}/\text{cm}^2$. The results given in Fig. 4 (a)-(c) are obtained from the C-V characteristics in response to the frequency range of (a) 1 kHz-1 MHz, (b) 17 Hz-1 kHz, and (c) 17 Hz-1 MHz, respectively, where (a) + (b) = (c). The energy level of the interface state for (c) is distributed near the middle of the energy gap of silicon; however the energy level of the interface state for (a), with the shorter time constant, is distributed on the valence band side; while (b) with the longer time constant is on the conduction band side. Similar characteristics of the energy distribution are obtained for the different injected charge levels as predicted from Fig. 2. And approximately the same distributions are obtained for the (111) capacitor, except for the density distribution.

Discussion

As seen in Fig. 1, the flatband voltage exhibits N-shaped behavior in proportion to the avalanche injection of hot electrons. This N-shaped behavior cannot be explained by detrapping because hot electrons are injected at a constant applied voltage. It is observed that the interface states with widely distributed time

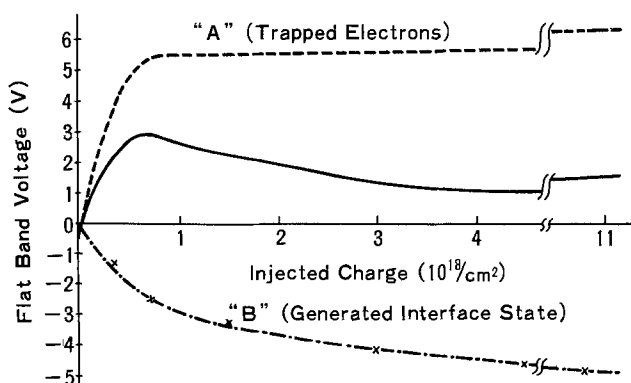


Fig. 5. Resultant N-shaped behavior with flatband voltage shift due to trapped electrons and the generated interface state.

constants are generated by hot electron injection at the silicon to silicon dioxide interface and that density increases with increasing injected electronic charge (Fig. 2).

The N-shaped behavior can be explained by the following model. As some of the injected electrons are trapped in the silicon dioxide, the flatband voltage increases in proportion to the number of injected electrons (denoted as "A" in Fig. 5). If the generated interface is assumed to be the donor type of interface state, the shifting direction of the flatband voltage is opposite to the direction resulting from the electron trapping in the silicon dioxide ("B" in Fig. 5); thereby decreasing the flatband voltage. Thus, the anomalous N-shaped phenomenon shown in Fig. 1 can be explained by considering the above two factors; i.e., by summing the shift of the flatband voltage due to electron trapping in the silicon dioxide with that due to the generation of a donor-type interface state at the silicon to silicon dioxide interface. These two factors are illustrated in Fig. 5 by "A" and "B" along with the N-shaped resultant variation.

It is also observed in Fig. 3 that the generated interface-state density with widely distributed time constants is strongly affected by the orientation of the silicon substrate. The interface-state density values of the (100) capacitor are about half the values for the (111) capacitor. Since the interface state is considered a result of a broken or strained bond in the vicinity of the silicon to silicon dioxide interface, the generated interface-state density can be expected to have a strong dependence on the orientation of the silicon substrate, in a similar way to the fixed charge density at the thermally oxidized silicon surface (12). Thus it may be said that the reliability of short channel V-MOS devices which are composed on the (111) plane must be inferior to (100) plane devices, assuming that the same amount of hot electrons are injected.

To determine the true (corrected) electron capture cross section, it must be obtained from curve "A" in Fig. 5 which shows the flatband voltage shift only due to electron trapping in the silicon dioxide. The electron capture cross section obtained from the N-shaped characteristic is not true, because it includes the shift of the flatband voltage due to the generated interface state. The dominant electron capture cross section obtained from the N-shaped variation (uncorrected) is about 1.5 times larger than the corrected capture cross section obtained from curve "A" in Fig. 5. The corrected and uncorrected electron capture cross sections for (100) and (111) capacitors are given in Table I for the dominant electron traps. As an e-gun is used for aluminum evaporation, there will be neutral traps having a capture cross section of about 10^{-14} - 10^{-15} cm^2 as pointed out by Aitken *et al.* (14). But the neutral trap density of the capacitor used is much smaller (less than $5 \times 10^{10}/\text{cm}^2$) than the density of dominant trap (about $2.5 \times 10^{12}/\text{cm}^2$). Then the neu-

Table I. Corrected and uncorrected electron capture cross sections of dominant electron traps for (100) and (111) capacitors

	(100) (cm^2)	(111) (cm^2)
Corrected	8.6×10^{-19}	6.7×10^{-19}
Uncorrected	1.3×10^{-18}	1.0×10^{-18}

tral trap will affect the flatband voltage shift and the capture cross section.

The physical cause of the generated interface state with widely distributed time constants has not been determined, and the correlation between e-gun aluminum and interface-state generation by injected electron current is not clear yet. More detailed studies are warranted.

Summary

The avalanche injection of hot electrons at the silicon to silicon dioxide interface causes an anomalous N-shaped shift of flatband voltage.

Interface states with widely distributed time constants are generated by the avalanche injection of hot electrons.

The N-shaped shift of the flatband voltage is explained by a model assuming a combination of electron trapping and the generation of a donor-type interface state.

The orientation of the silicon substrate strongly affects the generated interface-state density.

The generated interface-state density of the (100) capacitor has a value approximately half that of the (111) capacitor. Short channel V-MOS devices which are composed on the (111) plane are less reliable than (100) plane devices, assuming the same amount of hot electrons are injected.

The energy level of the interface state is distributed near the middle of the energy gap of silicon. The energy level of the interface state with the shorter time constant is distributed on the valence band side and that with the longer time constant is on the conduction band side.

The dominant electron capture cross sections are approximately 1×10^{-18} cm^2 for both (100) and (111) capacitors.

Acknowledgment

The authors wish to thank Koichiro Hoh for many helpful discussions and Kyozo Shimizu for his encouragement.

Manuscript submitted March 16, 1979; revised manuscript received May 21, 1979.

Any discussion of this paper will appear in a Discussion Section to be published in the December 1980 JOURNAL. All discussions for the December 1980 Discussion Section should be submitted by Aug. 1, 1980.

Publication costs of this article were assisted by VLSI Technology Research Association.

REFERENCES

- H. Hara, Y. Okamoto, and H. Ohnuma, *Jpn. J. Appl. Phys.*, **9**, 1103 (1970).
- S. A. Abbas and R. C. Dockerty, *Appl. Phys. Lett.*, **27**, 147 (1975).
- T. H. Ning, C. M. Osburn, and H. N. Yu, *J. Electron. Mater.*, **6**, 65 (1977).
- T. H. Ning, P. W. Cook, R. H. Dennard, C. M. Osburn, S. E. Schuster, and H. N. Yu, *Tech. Digest*, p. 472, International Electron Device Meeting (1978).
- D. J. DiMaria. A review paper given at the Proceedings of the International Topical Conference, 1978, p. 160.
- R. A. Gdula, *This Journal*, **123**, 42 (1976).
- E. H. Nicollian, A. Goetzberger, and C. N. Bergund, *Appl. Phys. Lett.*, **15**, 174 (1969).
- E. H. Nicollian, C. N. Bergund, P. F. Schmidt, and J. M. Andrews, *J. Appl. Phys.*, **42**, 5654 (1971).

9. T. H. Ning, C. M. Osburn, and H. N. Yu, *ibid.*, **48**, 286 (1977).
10. K. Nagai, Y. Hayashi, and Y. Tarui, *Bull. Electrochem. Lab.*, **40**, 23 (1976).
11. J. F. Verwey and A. Heringa, *IEEE Trans. Electron Devices*, **ed-24**, 519 (1977).
12. Y. Miura, *Jpn. J. Appl. Phys.*, **4**, 958 (1965).
13. T. H. Ning and H. N. Yu, *J. Appl. Phys.*, **45**, 5373 (1974).
14. J. M. Aitken, D. R. Young, and K. Pan, *ibid.*, **49**, 3386 (1978).

The Nucleation of CVD Silicon on SiO₂ and Si₃N₄ Substrates

I. The SiH₄-HCl-H₂ System at High Temperatures

W. A. P. Claassen and J. Bloem*

Philips Research Laboratories, Eindhoven, The Netherlands

ABSTRACT

The grain size in polycrystalline silicon layers is subject to various external conditions among which the initial nucleation of silicon on the substrate may play a decisive role. This article describes experiments with silicon on SiO₂ and Si₃N₄ substrates in the SiH₄-HCl-H₂ system for temperatures between 925° and 1200°C. The saturation cluster densities are determined as a function of gas phase composition and temperature and could be varied between 10⁴-10¹¹ cm⁻². The experimental results are compared with predictions of existing nucleation theories using analysis of the monomer silicon adatom concentration. In this way the nucleation can be described satisfactorily and approximate values for the size of the critical cluster can be derived.

Polycrystalline silicon layers, which are grown by pyrolysis of silane, are widely used in the electronic industry, e.g., in the fabrication of MOS (metal-oxide-silicon) field effect transistors and integrated circuits. The electrical properties of these layers closely depend on the size of the polysilicon grains in the layers (1). It is not very well known how the grain size depends on the total number of nuclei and whether nucleation of new grains continues in the course of further growth.

Nucleation experiments with silicon on amorphous, polycrystalline, and monocrystalline substrates have been reported (2-15), but attempts to make a more systematic study and quantitative evaluation of the results are relatively scarce. Joyce and Bradley (3) (pyrolysis of silane in vacuum) and Brooker and Unvala (4) (vacuum-evaporation) observed three-dimensional nuclei in the deposition of silicon on a monocrystalline silicon substrate. However, in a more recent article Joyce *et al.* (5) in collaboration with Charig and Skinner (6) showed that the initial growth becomes two dimensional if surface contaminants such as C and O are removed by heat-treatment up to 1300°C in UHV. Nishizawa and co-workers (7) formed perfect {111} facets on nearly {111} oriented silicon substrates. By hydrogen reduction of SiCl₄ at 1200°C nuclei in the form of pyramids are formed on the perfect {111} facet, with a density depending on growth temperature and SiCl₄ concentration. Since these pyramids are distributed homogeneously on the facet and have a uniform size, the conclusion was drawn that they correspond to growth nuclei without lattice defects. Abrahams *et al.* (8), Blank and Russell (9), Mercier (10), Bicknell *et al.* (11), and Cullen *et al.* (12) investigated nucleation processes of silicon on monocrystalline Al₂O₃ substrates. They observed three-dimensional islands. However, at temperatures higher than 800°C, the Al₂O₃ surface reacts with the deposited silicon. High temperatures and relatively low silane pressures, or a silicon compound containing chlorine, favor this etching reaction. Brown *et al.* (13) have

reported a similar etching reaction for low silane input concentration on a monocrystalline quartz substrate. On amorphous and polycrystalline substrates, such as given by Si₃N₄ and SiO₂, three-dimensional nuclei are observed as shown by Alexandrov *et al.* (14) (pyrolysis of silane on Si₃N₄ and SiO₂ substrates in vacuum) and Kamins and Cass (15) (pyrolysis of silane in an H₂ atmosphere on SiO₂ substrates). It has been shown that nucleation of silicon on a foreign substrate like SiO₂ or Si₃N₄ needs a higher supersaturation than nucleation on a clean silicon surface. This prompted studies on selective epitaxial growth of silicon on silicon slices partly coated with an oxide or nitride layer. Selective epitaxial growth of Si has been studied by Ogawa *et al.* (16) on windows in Si₃N₄ layers (SiCl₄-H₂ system), by Ray-Choudhury and Schroder (17) on windows in SiO₂ layers (SiCl₄-H₂ and SiH₄-H₂ systems), by Druminski and Gessner (18) on windows in SiO₂ and Si₃N₄ layers (SiH₄-HCl-H₂ system), and by Sirtl and Seiter (19) on windows in SiO₂ layers (SiCl₄-Br₂-H₂ system). Ogawa *et al.* determined a critical SiCl₄ pressure for the nucleation on Si₃N₄ substrates as a function of growth temperature. In the SiH₄-H₂ system it was necessary to use a relatively high deposition temperature (>1200°C) in order to prevent growth on the SiO₂ mask. In the SiCl₄-H₂ system the SiO₂ was entirely removed for high SiCl₄ concentrations (>1200°C), while the Si₃N₄ film was not deteriorated at all for any growth condition. Sirtl and Seiter used Br₂ instead of HCl because the purity of Br₂ is much higher than that of HCl. The bromine added to the SiH₄-H₂ mixture is converted to HBr by the hydrogen, while thermodynamically HBr acts as HCl.

In order to obtain a more coherent picture of the nucleation of silicon as a function of gas phase composition and temperature a systematic experimental study was started to study nucleation and growth of silicon on SiO₂ and Si₃N₄ substrates. It was found that the total number of nuclei could be varied between 10⁴-10¹¹ cm⁻² by variation of temperature, input con-

* Electrochemical Society Active Member.

centration of silane, and by the addition of small quantities of HCl to the carrier gas.

Experimental

Most of the nucleation experiments were performed in a horizontal epitaxial rf heated reactor, consisting of a rectangular water-cooled fused silica tube, provided with a pyrographite-coated carbon susceptor covered with a thin layer of silicon. Nucleation of silicon was performed on silicon slices (2 in. wafers) covered with amorphous, 1500Å thick LP-CVD SiO_2 and Si_3N_4 layers. The effective cross section of the reactor was about 13 cm^2 . The gas system was provided with AFC 550 automatic flow controllers for the H_2 carrier gas and the SiH_4 source (5% SiH_4 in H_2). The flow rate of pure undiluted HCl was determined by a conventional Brooks flowmeter. Some experiments were performed in a horizontal air-cooled rf heated reactor. The system was also equipped with a mass flow controller for HCl. The equipment is shown schematically in Fig. 1. The carrier gas was purified of H_2O (<1 ppm) and O_2 (<1 ppm) with a A.S.M. gas purifier. Before each experiment the slices were cleaned by etching with 0.2 volume percent (v/o) HCl in H_2 at about 1000°C for 5 min. After this the reactor was flushed with a stream of H_2 , while the substrate was brought to the desired nucleation temperature. During the nucleation experiment hydrogen loaded with SiH_4 and HCl was passed over the slices. To ensure stable gas flow conditions a room temperature gas velocity of about 50 cm/sec was chosen. Because of the rapid nucleation only short pulses of specific SiH_4 -HCl mixtures were often sufficient. It was found that reproducible results could be obtained with a constant HCl flow and a short additional pulse of SiH_4 gas. This procedure was followed throughout, including the experiments in which longer deposition times were used. The temperature of the slices was measured with an optical pyrometer focused on the surface of an uncoated silicon slice; the readings were corrected for the emissivity of silicon and the absorption and reflection of the system. SEM and TEM photomicrographs were made from each slice in order to determine the morphology of the layer during the initial stage of deposition. These photomicrographs provided an easy means of measuring the density of observed silicon islands.

Experimental Results

To study the initial stages of deposition of polycrystalline silicon on SiO_2 and Si_3N_4 substrates, we carried out a series of short depositions at different temperatures and different combinations of SiH_4 and HCl concentrations. For a constant substrate temperature and fixed SiH_4 and HCl concentrations the density of nuclei was measured as a function of the time of growth. After an incubation period the density of Si clusters very quickly reached a saturation value with respect to exposure time where the exposure time is defined as the duration of the SiH_4 pulse in the mass flow controller. After this hardly any new clusters were formed. The existing clusters showed a very narrow size distribution. The initial

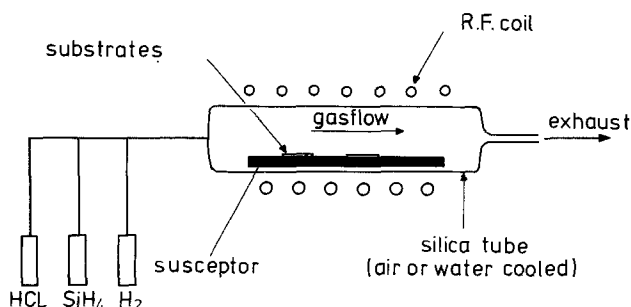


Fig. 1. Schematic view of the equipment

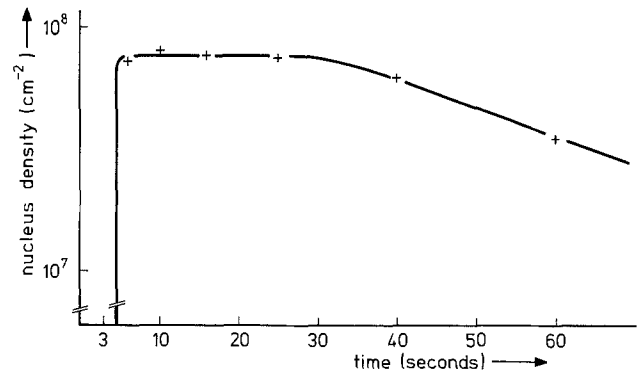


Fig. 2. The nucleus density as a function of the exposure time for $p_{\text{SiH}_4} = 8.8 \cdot 10^{-4}$ bar and $p_{\text{HCl}} = 4.4 \cdot 10^{-3}$ bar at 1000°C on an SiO_2 substrate.

nucleation took place in a short time, after which the clusters merely increased in size until coalescence occurred. Figure 2 gives a typical example for a constant ratio of SiH_4 and HCl at 1000°C and a SiO_2 substrate, where the nucleus density is plotted as a function of growth time. A corresponding SEM photomicrograph is shown in Fig. 3. Up to 3 sec no clusters were observed on SEM (Fig. 2) or TEM photomicrographs. In the case of TEM the detection limit is 150Å. A constant nucleus density is present between 6 and 25 sec in which time the mean radius of the nuclei increases from 0.1 to $0.25 \mu\text{m}$ (Fig. 3), after which coalescence occurs. It could be observed that the existing clusters show a narrow size distribution which supports the argument that the initial nucleation takes place in a very short period of time. It was also observed that the time needed to reach the saturation density is shorter for a Si_3N_4 substrate than for a SiO_2 substrate, also these periods are longer for high HCl concentrations and low SiH_4 concentrations. Further these periods decrease with increasing temperature. It is found that, for the SiH_4 -HCl- H_2 system in the temperature range of 925°C - 1200°C , this incubation time is of the order of 1-60 sec.

If we assume that the clusters are hemispherical, we can calculate the number of deposited atoms. From the experiments it can be concluded that the total deposited volume is small until coalescence is reached. After this the deposited volume increases linearly with time with the same slope as obtained on silicon substrates. In the latter case no incubation time is observed. This behavior is an additional indication of the incomplete condensation in the early

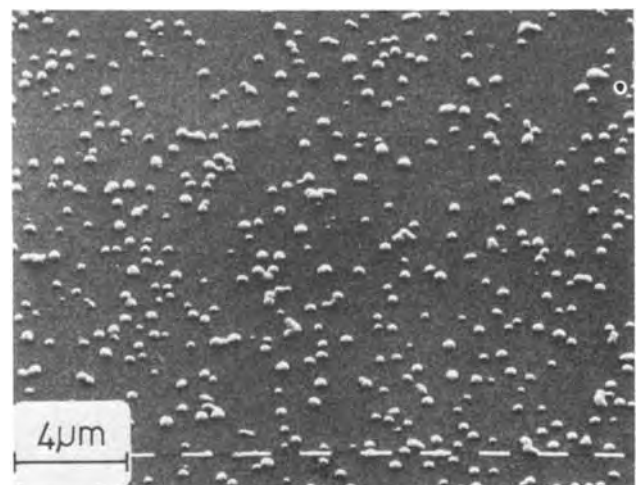


Fig. 3. SEM pictures of the nucleus density for $p_{\text{SiH}_4} = 8.8 \cdot 10^{-4}$ bar and $p_{\text{HCl}} = 4.4 \cdot 10^{-3}$ bar at 1000°C on an SiO_2 substrate after an exposure time of 10 sec.

Table I. Saturation nucleus density (cm^{-2}) for the $\text{SiH}_4\text{-HCl-H}_2$ system on SiO_2 and Si_3N_4 substrates between 1200° and 925°C (water-cooled rf reactor): x means coalescence takes place and 0 means no nucleation is observed. t is the exposure time.

p_{HCl} (bar)	p_{SiH_4} (bar)	1200°C				1100°C				1000°C				925°C			
		t (sec)	SiO_2	Si_3N_4		t (sec)	SiO_2	Si_3N_4		t (sec)	SiO_2	Si_3N_4		t (sec)	SiO_2	Si_3N_4	
—	$2.8 \cdot 10^{-4}$	5	—	$1.7 \cdot 10^9$	8	—	$2.7 \cdot 10^9$		15	$3 \cdot 10^9$	$7 \cdot 10^9$		20	$1.1 \cdot 10^9$	$1.6 \cdot 10^{10}$		
—	$7.3 \cdot 10^{-4}$	5	$4.7 \cdot 10^8$	$2.2 \cdot 10^9$	5	$1.4 \cdot 10^9$	$3.9 \cdot 10^9$		5	$6 \cdot 10^9$	10^{10}		5	$8 \cdot 10^9$	$2 \cdot 10^{10}$		
$1.8 \cdot 10^{-3}$	$3.7 \cdot 10^{-4}$	5	$3.3 \cdot 10^8$	—	10	$1.3 \cdot 10^7$	$6.8 \cdot 10^8$		15	$1.2 \cdot 10^8$	10^9		30	$3.2 \cdot 10^8$	$1.0 \cdot 10^9$		
$1.8 \cdot 10^{-3}$	$7.3 \cdot 10^{-4}$	5	$2.2 \cdot 10^7$	$2.5 \cdot 10^8$	5	$6.0 \cdot 10^7$	$1.4 \cdot 10^9$		5	$3.9 \cdot 10^8$	$2.2 \cdot 10^9$		5	$1.5 \cdot 10^9$	$3.5 \cdot 10^9$		
$1.8 \cdot 10^{-3}$	$2.6 \cdot 10^{-3}$	3	$6.7 \cdot 10^7$	$3.1 \cdot 10^8$	3	$2.8 \cdot 10^8$	$7 \cdot 10^8$		5	$8.5 \cdot 10^8$	x		10	x	x		
$3.6 \cdot 10^{-3}$	$2.8 \cdot 10^{-4}$	20	$6 \cdot 10^8$	$1.0 \cdot 10^9$	30	$1.6 \cdot 10^4$	$1.0 \cdot 10^7$		60	0	0		120	$3 \cdot 10^8$	0		
$3.6 \cdot 10^{-3}$	$7.3 \cdot 10^{-4}$	5	$3 \cdot 10^7$	$5.4 \cdot 10^7$	5	$9 \cdot 10^5$	$5.3 \cdot 10^8$		5	$7 \cdot 10^7$	$1.3 \cdot 10^9$		15	$7.2 \cdot 10^8$	$1.8 \cdot 10^9$		
$3.6 \cdot 10^{-3}$	$1.4 \cdot 10^{-2}$	5	$1.4 \cdot 10^6$	$2.1 \cdot 10^8$	10	$7.9 \cdot 10^9$	x		15	$2.9 \cdot 10^8$	x		25	$9.5 \cdot 10^8$	x		
$3.6 \cdot 10^{-3}$	$2.6 \cdot 10^{-3}$	3	$3.1 \cdot 10^7$	$1.1 \cdot 10^8$	5	$6.5 \cdot 10^7$	x		8	$6.1 \cdot 10^8$	—		13	$1.9 \cdot 10^9$	x		
$5.5 \cdot 10^{-3}$	$7.3 \cdot 10^{-4}$	5	$8 \cdot 10^4$	$2.3 \cdot 10^7$	30	$2 \cdot 10^4$	10^9		30	$3.0 \cdot 10^7$	$6.0 \cdot 10^8$		30	$2.5 \cdot 10^8$	$5 \cdot 10^8$		
$7.2 \cdot 10^{-3}$	$7.3 \cdot 10^{-4}$	5	$3 \cdot 10^8$	$5.4 \cdot 10^7$	60	$8 \cdot 10^8$	$1.5 \cdot 10^7$		30	$9 \cdot 10^4$	$3 \cdot 10^9$		240	$2.4 \cdot 10^8$	—		
$7.2 \cdot 10^{-3}$	$1.4 \cdot 10^{-3}$	5	$6 \cdot 10^8$	—	10	$1.1 \cdot 10^5$	$1.4 \cdot 10^8$		15	$1.4 \cdot 10^7$	$5 \cdot 10^8$		30	$3.9 \cdot 10^8$	$1.9 \cdot 10^9$		

stages of nucleation and growth on the foreign substrates.

Nucleation on a SiO_2 substrate.—The experimentally observed saturation densities of Si clusters are collected in Tables I and II. Figure 4 presents SEM photomicrographs for different input concentrations of SiH_4 and HCl and a SiO_2 substrate at 1000°C . In Fig. 5 the saturation density of Si clusters is plotted as a function of temperature for different input concentrations of SiH_4 and HCl on a SiO_2 substrate. It is apparent that the introduction of HCl reduces the number of nuclei and increases the temperature dependence of the formation process. It is also observed, but not shown here, that the nucleus density decreases at temperatures below 925°C . In a later publication this feature will be discussed. Further it was measured that at 1200°C the SiO_2 surface partly deteriorates when relatively low input concentrations of SiH_4 and long exposure times are used. It will be shown in the discussion that between 925° and 1200°C the experimental data on the saturation density of nuclei (N_s) as a function of temperature and gas phase compositions can be described by

$$N_s = A \left\{ \frac{B^\circ p_{\text{SiH}_4}}{C^\circ p_{\text{HCl}}^{2+1}} \right\}^a \exp \frac{E}{kT} \quad [1]$$

where $C^\circ = 6 \cdot 10^6$ when p_{SiH_4} and p_{HCl} are expressed in bars. The exponent a and the activation energy E still depend on gas phase composition. In Fig. 6 the saturation density of clusters at 1000°C is plotted as a function of $p_{\text{SiH}_4}/(6 \cdot 10^6 p_{\text{HCl}}^{2+1})$. For SiH_4 the equilibrium vapor pressure (above which decomposition of SiH_4 can be expected) is $\sim 10^{-6}$ bar (20). This value is nearly independent of temperature in the range of interest and in good agreement with the results given

Table II. Saturation nucleus densities (cm^{-2}) for the $\text{SiH}_4\text{-HCl-H}_2$ system (air-cooled rf reactor) on SiO_2 and Si_3N_4 substrates at 1000°C . t is the exposure time and x means that coalescence occurs (7).

p_{HCl} (bar)	p_{SiH_4} (bar)	t (sec)	Substrate	
			SiO_2	Si_3N_4
—	$1 \cdot 10^{-5}$	370		$2.7 \cdot 10^9$
—	$9 \cdot 10^{-5}$	35	$6.6 \cdot 10^8$	$1.7 \cdot 10^{10}$
—	$2.2 \cdot 10^{-4}$	15	$1.4 \cdot 10^9$	$1.4 \cdot 10^{10}$
—	$4.4 \cdot 10^{-4}$	5	$5.0 \cdot 10^8$	$2.8 \cdot 10^{10}$
—	$8.8 \cdot 10^{-4}$	3	$6.5 \cdot 10^8$	$4.0 \cdot 10^{10}$
—	$1.7 \cdot 10^{-3}$	3	$8 \cdot 10^9$	x
$4.4 \cdot 10^{-4}$	$8.8 \cdot 10^{-4}$	5	$2.5 \cdot 10^9$	$1.1 \cdot 10^{10}$
$8.8 \cdot 10^{-4}$	$8.8 \cdot 10^{-4}$	5	$1.6 \cdot 10^9$	$9.1 \cdot 10^9$
$1.3 \cdot 10^{-3}$	$8.8 \cdot 10^{-4}$	5	$8.0 \cdot 10^8$	$7.1 \cdot 10^9$
$2.2 \cdot 10^{-3}$	$8.8 \cdot 10^{-4}$	5	$3.8 \cdot 10^8$	$5.0 \cdot 10^9$
$4.4 \cdot 10^{-3}$	$8.8 \cdot 10^{-4}$	10	$8.0 \cdot 10^7$	$1.1 \cdot 10^9$
$6.6 \cdot 10^{-3}$	$8.8 \cdot 10^{-4}$	30	$9 \cdot 10^5$	$4.0 \cdot 10^7$

in Fig. 6. From experiments as given in Fig. 5 ($\log N_s$ vs. $1/T$) for temperatures above 925°C an apparent activation energy can be obtained from the Arrhenius plot. The experimental values of E are given in Fig. 7 as a function of the gas phase composition, the latter expressed as $p_{\text{SiH}_4}/(6 \cdot 10^6 p_{\text{HCl}}^{2+1})$. It is observed that at high supersaturations the activation energy comes to a limiting value of 1.9 eV. At lower supersaturations the activation energy increases, this behavior is accompanied by a strong decrease in the number of nuclei.

Nucleation on a Si_3N_4 substrate; difference compared with a SiO_2 substrate.—Tables I and II also present experimental data for the saturation densities of stable clusters in the $\text{SiH}_4\text{-HCl-H}_2$ system for Si_3N_4 substrates. From the tables it can be observed that the saturation density of Si clusters is always larger for a Si_3N_4 substrate than for a SiO_2 substrate (other things being equal). This means that coalescence takes place much earlier on a Si_3N_4 substrate than on a SiO_2 substrate. In spite of the rapid nucleation and coalescence we were able to observe the saturation cluster density by choosing an appropriate exposure time. Figure 8 gives a plot of the saturation nucleus density for two different mixtures of SiH_4 and HCl as a function of temperature for both substrates. In the case of the Si_3N_4 substrate, too, the addition of HCl reduces the number of clusters and increases the temperature dependence of the saturation density, though to a smaller degree than for the SiO_2 substrate. The experimentally found expression for the saturation nucleus density (Eq. [1]) as a function of gas phase composition for the SiO_2 substrate can also be used for a Si_3N_4 substrate between 1200° – 925°C , as will be shown in the discussion. The nucleus density as a function of $p_{\text{SiH}_4}/(6 \cdot 10^6 p_{\text{HCl}}^{2+1})$ for a Si_3N_4 substrate at 1000°C is plotted in Fig. 6. For temperatures above 925°C an apparent activation energy can be obtained from the Arrhenius plot ($\log N_s$ vs. $1/T$). The experimental values of E for Si_3N_4 substrates are included in Fig. 7 which also gives E values for SiO_2 substrates. It is observed that with increasing supersaturation the activation energy decreases and this decrease is stronger for the SiO_2 substrate than for the Si_3N_4 substrate.

Discussion

Nucleation theory.—The growth of thin films on a substrate starts with the formation of small cap-shaped clusters if the cohesive forces between the atoms in the cluster are greater than the adhesive forces between adsorbed atoms (adatoms) and the substrate. The formation of the small clusters begins with the arrival of atoms or molecules from the vapor. After adsorption, and perhaps chemical reaction, adatoms are formed on the surface. These adatoms diffuse across the surface where, through statistical fluctuations in local con-

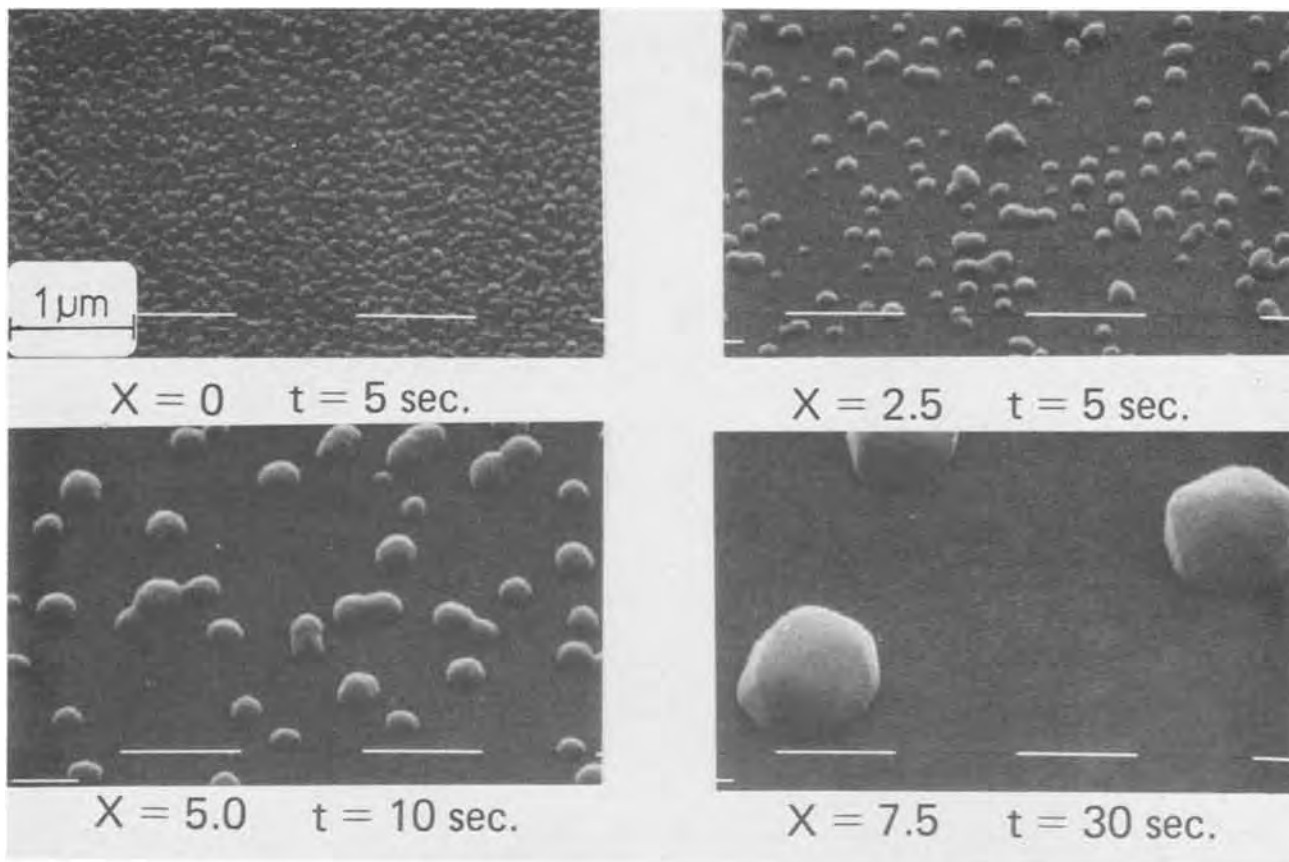


Fig. 4. SEM pictures of the nucleus densities for $p_{SiH_4} = 8.8 \cdot 10^{-4}$ bar and $p_{HCl} = X \cdot p_{SiH_4}$ (where $X = 0, 2.5, 5.0,$ and 7.5) at 1000°C on an SiO_2 substrate. t is the exposure time.

centration, they form small clusters of atoms which grow and decay by addition or loss of single atoms. If the cluster exceeds a critical size (supercritical cluster) further growth becomes energetically favorable. Clusters that are smaller than the critical size (subcritical) can decay.

In the chemical thermodynamic approach we can write for the radius r^* of the critical cluster

$$r^* = \frac{2\delta v}{kT \ln p/p_e} \quad [2]$$

where δ is the surface free energy which is taken isotropic, v is the atomic volume, and $kT \ln p/p_e$ is the supersaturation function giving the gain in free

energy on crystallization. Using the experimental results we can give an estimation of r^* . In Fig. 6 the saturation density of Si clusters is plotted as a function of the gas phase composition. This gives us the opportunity to calculate the supersaturation p/p_e , where $p_e \sim 10^{-6}$ bar is the equilibrium vapor pressure of SiH_4 . Using Eq. [2] with $v = 2 \cdot 10^{-21}$ cm³ and $\delta = 10^{-4}$ J/cm² (21) gives $r = 1.5$ nm for $p/p_e = 5$ and $r = 0.4$ nm for $p/p_e = 10^3$. This means that for high supersaturation the radius of the critical cluster approaches molecular dimensions, but in that case the

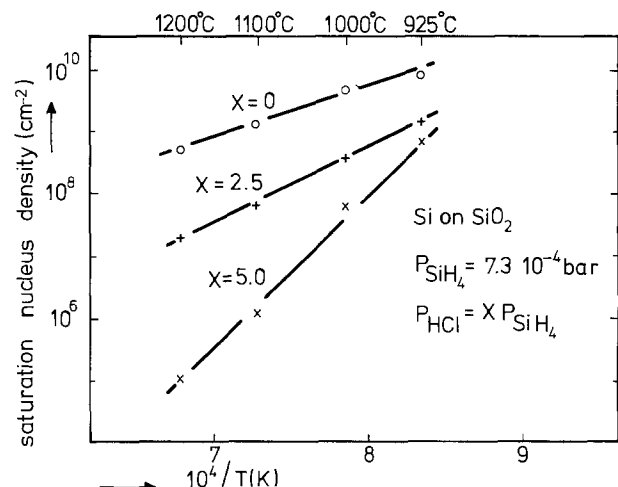


Fig. 5. The saturation nucleus density as a function of the reciprocal temperature for different mixtures of SiH_4 and HCl on SiO_2 substrates.

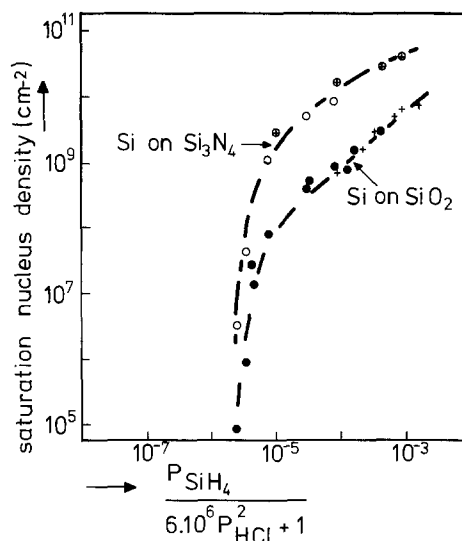


Fig. 6. The saturation nucleus density of Si clusters on an SiO_2 and Si_3N_4 substrate at 1000°C for different input concentrations of SiH_4 and HCl (+, \oplus only SiH_4 ; \circ, \bullet mixture of SiH_4 and HCl).

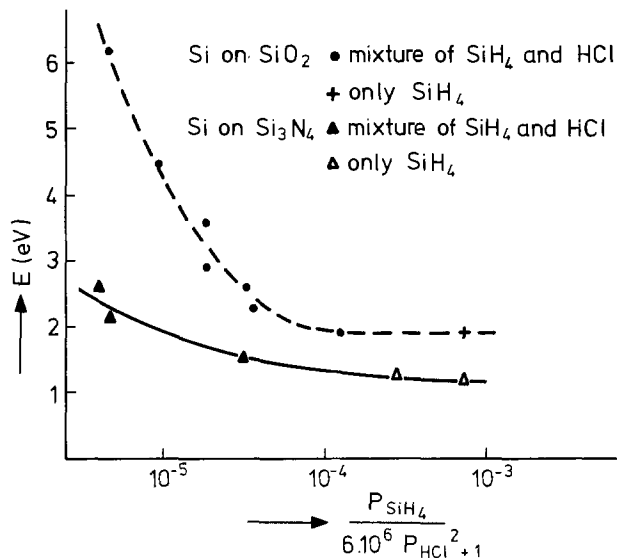


Fig. 7. The relation between the activation energy for cluster formation and the input concentrations of SiH_4 and HCl for SiO_2 and Si_3N_4 substrates.

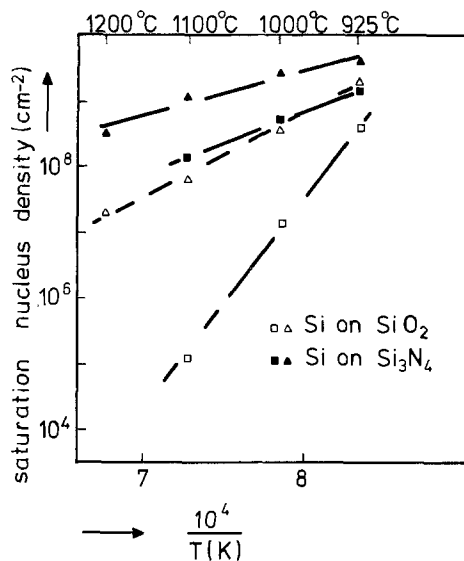


Fig. 8. The saturation cluster density of Si clusters as a function of temperature for two SiH_4 - HCl mixtures on SiO_2 and Si_3N_4 substrates (Δ , \blacktriangle : $p_{\text{SiH}_4} = 7.3 \cdot 10^{-4}$ bar and $p_{\text{HCl}} = 1.8 \cdot 10^{-3}$ bar. \square , \blacksquare : $p_{\text{SiH}_4} = 1.4 \cdot 10^{-3}$ bar and $p_{\text{HCl}} = 7.2 \cdot 10^{-3}$ bar).

thermodynamic interpretation of surface energies is no longer justified. These difficulties are avoided when the nucleation process is treated by writing the partition function and potential energies for the adatoms and clusters as is done in the atomistic nucleation theory. Walton (22), in an approximate treatment, considered the potential energy difference E_i between i adatoms and a cluster of i atoms. For the reaction on the surface



he found for the density of critical clusters n_i if no stable clusters are present and $n_1 > n_i$

$$\frac{n_i}{n_0} = C_i \left(\frac{n_1}{n_0} \right)^i \exp \frac{E_i}{kT} \quad [3]$$

where n_1 is the concentration of adatoms, n_0 is the number of surface sites, C_i is a statistical weighting factor, and E_i is the heat of formation of the cluster consisting of i atoms. Equation [3] is generally used in the atomistic nucleation theories to find a general expression for the saturation density of stable clusters.

The rate of formation of adatoms as a function of exposure time t and the incoming flux J_1 can be given by

$$\frac{dn_1}{dt} = J_1 - \frac{n_1}{\tau_{ev}} - \frac{n_1}{\tau_r} - \frac{n_1}{\tau_g} \quad [4]$$

where τ_{ev} is the mean residence time before evaporation, τ_r is the τ value if adatoms are removed by chemical reaction, and τ_g is the τ value for the capture of adatoms by stable clusters. In the case of complete condensation the τ_{ev} and τ_r values are supposed to be so great that no desorption or etching of adatoms occurs. The adatom concentration increases with time until the diffusional flux has grown sufficiently to substantially reduce the value of n_1 . Evaporation or reaction comes into play for incomplete condensation and the smallest τ values in the series determines the value of τ_s and therefore the value of n_1 giving

$$n_1 = J_1 \tau_s \quad \text{for } t \gg \tau_s \quad [5]$$

The surface concentration n_1 is attained before nucleation starts. As nucleation proceeds τ_s will decrease because adatoms also disappear by incorporation in stable clusters. Between the clusters the value of n_1 eventually drops below the initial steady-state concentration, whereupon the production of new nuclei ceases. The maximum cluster density is one of the easily measurable quantities when the nucleation rate is too high to be measured. Following Venables (23) we can write for the formation rate of stable clusters

$$\frac{dn_x}{dt} = U_i - U_c - U_m \quad [6]$$

where n_x is the density of stable clusters at the time t . U_i is the nucleation rate and U_c and U_m are the rates at which stable clusters are lost due to coalescence and cluster mobility, respectively. In the SiH_4 - HCl - H_2 system at temperatures between 925° and 1200°C, n_x reaches a saturation value N_s long before coalescence occurs (see Fig. 2), hence $U_c \ll U_m$. Stowell's analysis of data on the nucleation of Au and Ag on alkali halide substrates shows that cluster mobility becomes important at temperatures above 400°C (24). Lewis (25) assumes that the detachment of peripheral atoms of hemispherical clusters determines the activation energy of the mobility process. In that case the activation energy for cluster diffusion is independent of cluster size, while the actual cluster mobility strongly depends on the size, viz., via a preexponential entropy term.

Masson *et al.* (26) measured relatively large diffusion coefficients, which are probably caused by non-epitaxial orientation of the clusters. According to Behrndt (27) liquid nuclei, with consequently a relatively high surface mobility, are also possible at temperatures which are much lower than the melting point of the condensate. For the case where all stable clusters are mobile, at least initially until n_x saturates, Venables gives an expression describing the maximum cluster density N_s for incomplete condensation

$$\frac{N_s}{n_0} \approx \left(\frac{J}{n_0 v} \right)^{(i+1)/2} \exp \frac{(i+1)E_a + E_i + E_m - E_d}{2kT} \quad [7]$$

where E_a is the activation energy of desorption, E_x the activation energy for surface diffusion of mobile clusters, E_d the activation energy for surface diffusion of adatoms, n_0 the number of surface sites, and v the adatom vibration frequency; the other parameters have already been defined (Eq. [3] and [5]). In the SiH_4 - HCl - H_2 system there is an incubation period for the formation of a significant number of stable clusters and a nonlinear increase of the deposited volume in the early state of growth (see above) which supports

the arguments for incomplete condensation. The relation deduced by Venables (Eq. [7]) can be compared with the experimentally found relationship between the saturation cluster density and the supersaturation with the help of Eq. [5] and the calculated adatom concentration (n_1) as given in Eq. [A-16] of the Appendix.

Adatom concentration and surface coverages.—To arrive at an expression determining the adatom concentrations of Si on the substrate the main processes responsible for formation and removal are summarized in the Appendix. It is concluded that the following steps may be important: (a) diffusion of silane toward the surface; (b) adsorption of silane, diffusion across the surface, and chemical reaction (formation of adatoms); (c) etching reactions of HCl, H₂, and SiO₂ with silicon adatoms; (d) desorption of reaction products; and (e) diffusion of reaction products away from the surface. Since the value of the diffusion coefficient in the gas phase is rather insensitive to temperature (ideal gas $D \propto T^{3/2}$) the processes (a) and (e) will have a low activation energy.

In order to obtain realistic information about the concentration of adatoms and free surface sites some additional information may be helpful:

(i) From nucleation experiments in the SiH₂Cl₂-H₂-N₂ system at temperatures between 900° and 1100°C on SiO₂ and Si₃N₄ substrates (28) it is found that hydrogen strongly influences nucleation on SiO₂ substrates. In the case of Si₃N₄ substrates there is hardly any difference in saturation density between the results in H₂ or N₂ ambient.

(ii) The saturation cluster density in the SiH₂Cl₂-N₂ system is equal for both substrates at temperatures between 925° and 1100°C.

(iii) From nucleation experiments in the SiH₄-H₂ system at temperatures between 900° and 600°C (28) we know that for SiO₂ substrates the saturation density decreases with decreasing temperature, whereas Si₃N₄ substrates show the opposite behavior.

The observations mentioned above suggest that the adsorption of hydrogen has a great influence on the nucleation kinetics, especially for the SiO₂ substrates. Under normal operating conditions (925°-1200°C, $p_{H_2} \cong 1$ bar) it is thus likely that hydrogen adsorption will occur, but it is only below 900°C that hydrogen adsorption will influence nucleation on SiO₂ substrates by limiting the number of surface sites where SiH₄ adsorption may occur.

For the silicon adatom concentration on a SiO₂ substrate Eq. [A-16] can be used. If hydrogen adsorption does not limit the number of surface sites and with $n_0 \gg [\text{SiH}_4^*]$, $[\text{Cl}^*]$ one obtains

$$\frac{n_1}{n_0} = \frac{K_1 k_2 p_{\text{SiH}_4}}{(k_{-2} p_{\text{H}_2}^2 + k_6 p_{\text{HCl}}^2 + k_9)} \quad [8]$$

For nucleation on Si₃N₄ substrates also, Eq. [A-16] can be used. In that case k_9 can be disregarded on thermodynamic grounds as reaction of Si with Si₃N₄ will be slow, also hydrogen adsorption is not rate limiting. It is observed, moreover, that the number of stable clusters saturates at high concentrations and $[\text{SiH}_4^*]$ cannot be neglected. Therefore n_1 can be given as

$$\frac{n_1}{n_0} = \frac{K_1 k_2 p_{\text{SiH}_4}}{(k_{-2} p_{\text{H}_2}^2 + k_6 p_{\text{HCl}}^2) (1 + K_1 p_{\text{SiH}_4})} \quad [9]$$

For $p_{\text{HCl}} = 0$ and $K_1 p_{\text{SiH}_4} < 1$ the temperature dependence of n_1 is determined by $K_1 K_2$ which, in the temperature region of interest, is nearly independent of temperature. According to the JANAF Tables (20), $d(\ln K_p)/d(1/T) \cong 0$ around 1000°C.

Interpretation of results.—In this section we compare the expression obtained by Venables (Eq. [7]) with the results of the nucleation experiments in the

SiH₄-HCl-H₂ system on SiO₂ and Si₃N₄ substrates in the temperature region of 925°-1200°C. Equation [7] can be modified by introducing $n_1 = J_1 \tau_s$, where n_1 is given by Eq. [8] or [9] and τ_s is defined as $\tau_s = v^{-1} \exp E_a/kT$, E_a being the enthalpy of desorption and v the adatom vibration frequency. The modified expression (Eq. [7]) then reads for SiO₂ substrates

$$\frac{N_s}{n_0} \cong \left\{ \frac{K_1 k_2 p_{\text{SiH}_4}}{(k_{-2} p_{\text{H}_2}^2 + k_6 p_{\text{HCl}}^2 + k_9)} \right\}^{(i+1)/2} \exp \frac{E_i + E_m - E_d}{2kT} \quad [10]$$

It should be realized that the expression between curly brackets already presents a simplified version of a more complex expression. A possible activation energy from this relation has to be added to the exponential term. This, however, depends on which of the terms in the denominator prevails and whether HCl is present or not. In order to put Eq. [10] into a form that permits evaluation of the experimental data we can write

$$N_s = A \left\{ \frac{B p_{\text{SiH}_4}}{C p_{\text{HCl}}^{i+1}} \right\}^{(i+1)/2} \exp \frac{E_i + E_m - E_d}{2kT} \quad [11]$$

in which A is a constant (equal to n_0)

$$B = \frac{K_1 k_2}{(k_{-2} p_{\text{H}_2}^2 + k_9)} = B^0 \exp \frac{-E_{r,1}}{kT} \quad [12]$$

$$C = \frac{k_6}{(k_{-2} p_{\text{H}_2}^2 + k_9)} = C^0 \exp \frac{-E_{r,2}}{kT} \quad [13]$$

The values of i , B , and C thus depend on temperature and gas phase composition and will be different for nucleation on different substrates. For the SiO₂ substrate the constants A , B^0 , and C^0 can be calculated as follows. From Fig. 6 we know that, for pure SiH₄, N_s is proportional to p_{SiH_4} . This means that $(i+1)/2 = 1$ for p_{SiH_4} ranging from $9 \cdot 10^{-5}$ to $1.7 \cdot 10^{-3}$ bar. Making use of the corresponding values of E (Fig. 7) we find $AB^0 = 2 \cdot 10^5$. The mixture $p_{\text{SiH}_4} = 2.6 \cdot 10^{-3}$ bar and $p_{\text{HCl}} = 1.8 \cdot 10^{-3}$ bar gives a cluster density higher than the corresponding one for the lowest pure SiH₄ concentration. This leads to the conclusion that $(i+1)/2 = 1$ for this SiH₄-HCl mixture as well. Inserting $AB^0 = 2 \cdot 10^5$, $(i+1)/2 = 1$, and $E = 1.9$ eV (the activation energy for this special SiH₄-HCl mixture) in Eq. [11] we obtain $C^0 = 6 \cdot 10^6$. The linear relationship [$(i+1)/2 = 1$] between N_s and p_{SiH_4} for silane pressures between $9 \cdot 10^{-5}$ and $1.7 \cdot 10^{-3}$ bar leads to a critical cluster size of $i = 1$. In that case ($p_{\text{HCl}} = 0$) the experimentally found activation energy for cluster formation (E) becomes

$$E = \frac{1}{2} (E_i + E_m - E_d - 2E_{r,1}) = 1.9 \text{ eV} \quad [14]$$

As to the value of E_i , a cluster can be called stable when half of the possible bonds are formed between atoms in the cluster and between cluster and substrate (29). For silicon, therefore, two bonds have to be realized per silicon atom. In order to arrive at a relation between the binding energy E_i of a cluster of i atoms on SiO₂ and the Si-Si bond energy (E_b) a triangular lattice of oxygen atoms on the substrate is shown schematically in Fig. 9. For amorphous SiO₂ a triangular lattice is acceptable because short-range order (regions of crystallinity 10-100Å in size) may exist (30). Amorphous SiO₂ forms a random three-dimensional network where each silicon atom is tetrahedrally surrounded by four oxygen atoms and each oxygen atom is bonded to two silicon atoms with an average Si-O distance of 1.62Å, an average O-O distance of 2.65Å, and an average Si-Si distance of 3.00Å (31). At the surface, however, a silicon atom can be

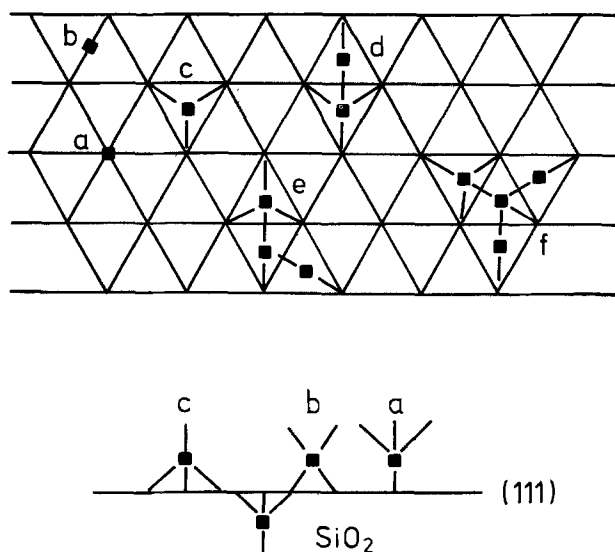


Fig. 9. Binding energies of atoms and clusters on a nearest neighbor bond model of nucleation on a triangular oxygen lattice: (a) single bonded, (b) double bonded, (c) triple bonded, (d) critical cluster size, $i = 1$, (e) critical cluster size $i = 2$, (f) critical cluster size $i = 3$.

bonded in three different ways to the oxygen lattice. In the first place a Si atom can have a single bond to an oxygen atom (Si-adatom). Further a double and a triple bonding of a Si atom with the oxygen lattice is possible. The triple bonding, which is the most stable one, can be seen in Fig. 9(c). In this simple model a Si-Si bond is formed only when a Si atom [(a) in Fig. 9] on the surface forms a bond with the triple-bonded Si atom [giving (d) in Fig. 9]. In this case the critical cluster consists of one atom only (the triple-bonded Si atom belongs to the SiO_2 lattice). This model can be extended to clusters containing more than two Si atoms [(e) and (f) in Fig. 9 for $i = 2$ and $i = 3$], so that for the critical cluster it leads to an energy gain over the binding energy of one Si-Si bond

$$E_i \cong iE_{\text{Si-Si}} \quad [15]$$

For $i = 1$ and $E_{\text{Si-Si}} = 2 \text{ eV}$ (32) Eq. [14] leads to

$$E_m - E_d - 2E_{r,1} = 1.8 \text{ eV} \quad [16]$$

If we compare the results for the Si_3N_4 substrate and the SiO_2 substrate in the temperature region 925°C to 1200°C we see that the composition of the gas phase where nucleation is no longer observed (Fig. 6) is almost the same for both substrates. This justifies the use of Eq. [11] for the saturation density on Si_3N_4 also. From Fig. 7 we know that E is nearly constant at silane pressures between $5 \cdot 10^{-5}$ and 10^{-3} bar. This means that the cluster size is constant in this region. From Fig. 6 ($\log N_s$ vs. $p_{\text{SiH}_4\text{eff}}$) it can be observed that in this particular region the tangent changes from 1 to $1/2$. At high supersaturation N_s probably saturates because the concentration of free surface sites is a function of the SiH_4 pressure (Eq. [9]). Thus, at silane pressures between $5 \cdot 10^{-5}$ and 10^{-3} bar we have $i = 1$, and in that case E becomes

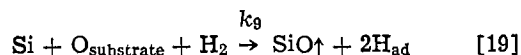
$$E = 1/2 (E_1 + E_m - E_d - 2E_{r,1}) = 1.2 \text{ eV} \quad [17]$$

With $E_{\text{Si-Si}} = 2 \text{ eV}$ (32) this gives

$$E_m - E_d - 2E_{r,1} = 0.4 \text{ eV} \quad [18]$$

Introducing $E_{r,1} \cong 0 \text{ eV}$ for Si_3N_4 (as discussed above) into Eq. [18] gives $E_m - E_d = 0.4 \text{ eV}$. Lewis expects $E_m \cong 2E_d$ (25), which then should give $E_m \cong 0.8 \text{ eV}$ and $E_d \cong 0.4 \text{ eV}$ as maximum values.

Coming back to the nucleation on SiO_2 substrates, we note that Eq. [16] with $E_m - E_d = 0.4 \text{ eV}$, as obtained above, leads to $E_{r,1} = -0.7 \text{ eV}$. The difference between $E_{r,1}$ for SiO_2 (-0.7 eV) and $E_{r,1}$ for Si_3N_4 ($E_{r,1} \cong 0 \text{ eV}$) can be explained as being due to reactions with the substrate and the formation of SiO (k_9 in Eq. [8]), but for Si_3N_4 substrates this reaction is absent. This means that k_9 has an activation energy of 0.7 eV , and the formation of SiO is promoted by the presence of hydrogen. The reaction between a silicon adatom and the SiO_2 substrate can be described as



In this way the coverage of the substrate with the first silicon layer is impeded, the more so the higher the temperature, as found experimentally for SiO_2 substrates in hydrogen, where at 1200°C the SiO_2 surface partly deteriorates.

If $6 \cdot 10^6 p_{\text{HCl}}^2 > 1$, the activation energy for cluster formation becomes

$$E = 1/2 [E_1 + E_m - E_d - (i + 1)(E_{r,1} - E_{r,2})] \quad [20]$$

In the experiment on SiO_2 with $p_{\text{SiH}_4} = 2.6 \cdot 10^{-3}$ bar and $p_{\text{HCl}} = 1.8 \cdot 10^{-3}$ bar, where $i = 1$ as discussed before, the activation energy equals that of pure silane (Fig. 7). From this it can be expected that $E_{r,2}$ is small and can be disregarded in the first approximation. For low supersaturations the activation energy increases because of the increasing value of i and E_i .

The highest value found for E_i of 6.2 eV , with $E_m - E_d \cong 0.4 \text{ eV}$, $E_{r,2} \cong 0$, and $E_{r,1} \cong -0.7 \text{ eV}$ and using Eq. [15], gives a critical cluster with $i = 4$.

For Si_3N_4 the highest E value is $E \cong 2 \text{ eV}$ and a similar approach then leads to a critical cluster of $i = 2$.

Conclusions

In an attempt to understand and be able to monitor the crystallite size in polycrystalline silicon layers we have studied the nucleation of silicon on various substrates. Experiments on the nucleation of Si on SiO_2 and Si_3N_4 substrates are reported for the SiH_4 - HCl - H_2 system in the temperature range of 925°C to 1200°C .

The differences and conformities between the two substrates are discussed. It is observed that the saturation nucleus density increases with decreasing temperature for both substrates. This effect, which is stronger for the SiO_2 than for the Si_3N_4 substrate, is attributed to the size and the formation energy of the initial critical cluster and to the reaction with the substrate, especially in the case of SiO_2 in which the H_2 ambient plays an important role. The introduction of HCl strongly reduces the nucleus density, resulting in an increased grain size in the polycrystalline material. The experimental results can be explained by the application of an expression as obtained by Venables, together with an analysis of the silicon adatom concentration on the substrate as a function of gas phase composition. It is found that the number of silicon atoms in the critical cluster varies between 1 and approximately 4 in the experimental range under discussion. It will be obvious that the values of the activation energies are open to criticism, because slightly different assumptions could change the picture. However, the impression remains that nucleation of silicon on SiO_2 and Si_3N_4 substrates at temperatures higher than 900°C can be explained semiquantitatively on the basis of existing statistical nucleation theory supplemented by arguments of a chemical and kinetics nature.

Acknowledgments

The authors wish to thank Mrs. C. W. T. Bulle and Mrs. G. v. Leeuwen for the SEM and TEM photomicrographs and Mr. C. F. W. Flinsenbergh for making available his water-cooled rf reactor.

Manuscript submitted March 20, 1979; revised manuscript received July 19, 1979.

Any discussion of this paper will appear in a Discussion Section to be published in the December 1980 JOURNAL. All discussions for the December 1980 Discussion Section should be submitted by Aug. 1, 1980.

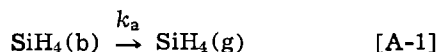
Publication costs of this article were assisted by Philips Research Laboratories.

APPENDIX

Calculation of Adatom Concentrations

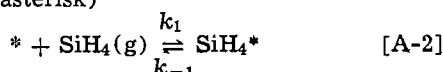
The main process responsible for nucleation and growth of silicon on a monocrystalline silicon substrate in the SiH₄-HCl-H₂ system is described by Bloem and Giling (33). Nucleation of silicon on a SiO₂ substrate will differ from that on a monocrystalline silicon substrate, but the processes which take place are approximately of the same nature.

(a) Supply of SiH₄ by means of gas phase diffusion

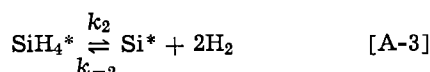


where SiH₄(b) is the concentration of SiH₄ in the bulk of the gas phase and SiH₄(g) the concentration of SiH₄ near the surface.

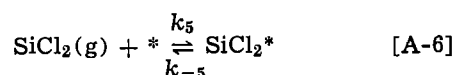
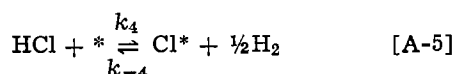
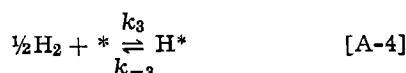
(b) Adsorption of SiH₄ on a free site on the surface (denoted by an asterisk)



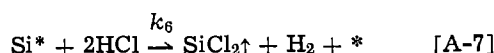
(c) The reaction of SiH₄ at the surface



(d) Adsorption of hydrogen, chlorine, and SiCl₂



(e) Etching of adatoms by chlorine



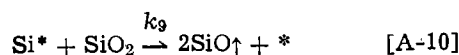
(f) Growth of silicon by diffusion of Si adatoms on the surface and incorporation into a stable cluster



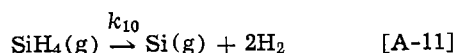
(g) Evaporation of silicon adatoms



(h) Reaction of Si adatoms with the substrate



(i) Reaction of SiH₄ in the gas phase



Formation of silicon-containing compounds other than SiCl₂, such as SiH₂Cl₂, SiHCl₃, and SiCl₄, can be disregarded on the grounds of thermochemical data available in literature (34, 35).

In a steady-state situation the Si* and SiH₄* concentrations are constant, given by

$$n_1 = [\text{Si}^*] = \frac{k_1[\text{SiH}_4^*]}{k_{-2}p^2_{\text{H}_2} + k_6p^2_{\text{HCl}} + k_7 + k_8 + k_9} \quad [\text{A-12}]$$

$$[\text{SiH}_4^*] = \frac{k_1p_{\text{SiH}_4}(\text{g})[*] + k_{-2}n_1p^2_{\text{H}_2}}{k_2 + k_{-1}} \quad [\text{A-13}]$$

In [A-13] the second term in the numerator can be expected to be small compared with the first term, in which case

$$n_1 = \frac{k_1k_2[*]p_{\text{SiH}_4}(\text{g})}{(k_2 + k_{-1})(k_{-2}p^2_{\text{H}_2} + k_6p^2_{\text{HCl}} + k_7 + k_8 + k_9)} \quad [\text{A-14}]$$

For nucleation of Si on a SiO₂ substrate in the SiH₄-HCl-H₂ system, several approximations can be made. We have seen that, after an incubation period, the nucleus density very quickly reached a saturation value. On the basis of these experiments it will be assumed that the time taken to attain the population of adatoms is short, so that n_1 reaches a constant value before nucleation occurs. Then k_7 can be omitted until nucleation takes place. The existence of an incubation period further means that the reaction is surface-controlled and the greater part of the silane will desorb before reacting ($k_{-1} > k_2$). Because of the surface-controlled reaction, and provided gas phase nucleation can be left out of account, we can put $p_{\text{SiH}_4}(\text{g}) = p_{\text{SiH}_4}(\text{b})$ during the induction period ($k_1 < k_a$). The presence of a carrier gas prevents evaporation ($k_8 < k_{-2}p^2_{\text{H}_2}$). The desorption of SiCl₂ in the initial stage before nucleation is not expected to be rate limiting, and therefore the surface coverage of SiCl₂ will be low and can be disregarded. In that case we can write for the concentration of free surface sites

$$[*] = n_0 - [\text{SiH}_4^*] - [\text{H}^*] - [\text{Cl}^*] - n_1$$

where n_0 is the total number of sites at the surface. In adsorption equilibrium for every species an expression can be found as for [H*], where Eq. [A-4] leads to

$$[\text{H}^*] = K_3p^{1/2}_{\text{H}_2}[*]; \quad K_3 = k_3/k_{-3}$$

For $n_1 \ll n_0$ this gives

$$[*] = \frac{n_0}{1 + K_1p_{\text{SiH}_4} + K_3p^{1/2}_{\text{H}_2} + K_4p_{\text{HCl}}/p^{1/2}_{\text{H}_2}} \quad [\text{A-15}]$$

With the above approximation the steady-state Si adatom concentration becomes

$$\frac{n_1}{n_0} = \frac{K_1k_2p_{\text{SiH}_4}}{(k_{-2}p^2_{\text{H}_2} + k_6p^2_{\text{HCl}} + k_9) \cdot \frac{1}{\left(1 + K_1p_{\text{SiH}_4} + K_3p^{1/2}_{\text{H}_2} + \frac{K_4p_{\text{HCl}}}{p^{1/2}_{\text{H}_2}}\right)}} \quad [\text{A-16}]$$

In this equation the formation of silicon adatoms is governed by the equilibrium adsorption of SiH₄ (K_1), the rate of reaction of SiH₄ (k_2), and the total amount of free surface sites (as given by Eq. [A-15]), divided by the ways in which adatoms are removed from the surface in the initial stages before the actual nucleation starts, i.e., etching by HCl and H₂ and reaction with the SiO₂ substrate (k_9).

REFERENCES

- J. Y. W. Seto, *J. Appl. Phys.*, **46**, 5247 (1975).
- See for example, B. A. Joyce, *Rep. Prog. Phys.*, **37**, 363 (1974).
- B. A. Joyce and R. R. Bradley, *This Journal*, **110**, 1235 (1963).
- G. R. Booker and B. A. Unvala, *Philos. Mag.*, **11**, 11 (1965).
- B. A. Joyce, J. H. Neave, and B. E. Watts, *Surf. Sci.*, **15**, 1 (1969).
- J. M. Charig and D. J. Skinner, *ibid.*, **15**, 277 (1969).
- J. Nishizawa, T. Terasaki, and M. Shimbo, *J. Cryst. Growth*, **17**, 241 (1972).
- M. S. Abrahams, C. J. Buiocchi, R. T. Smith, J. F. Corboy, Jr., J. Blanc, and G. W. Cullen, *J. Appl. Phys.*, **47**, 5139 (1976).
- J. M. Blank and V. A. Russell, *Trans. Metall. Soc. AIME*, **236**, 291 (1966).
- J. Mercier, *This Journal*, **118**, 962 (1971).
- R. W. Bicknell, B. A. Joyce, J. H. Neave, and G. V. Smith, *Philos. Mag.*, **14**, 31 (1966).

12. G. W. Cullen, J. F. Corboy, and J. T. McGinn, in "Semiconductor Silicon 1977," H. R. Huff and E. Sirtl, Editors, p. 235, The Electrochemical Society Softbound Proceedings Series, Princeton, N.J. (1977).
13. A. S. Brown, B. A. Joyce, J. H. Neave, and D. J. Stirland, *J. Appl. Crystallogr.*, **1**, 70 (1968).
14. L. N. Alexandrov, F. L. Edelmann, and V. V. Voskoboinikov, *Thin Solid Films*, **32**, 241 (1976).
15. T. I. Kamins and T. R. Cass, *ibid.*, **16**, 147 (1973).
16. G. Ogawa, T. Nishinaga, M. Kasuga, and T. Arizumi, *Jpn. J. Appl. Phys.*, **10**, 1675 (1971).
17. P. Rai-Choudhury and B. K. Schroder, *This Journal*, **118**, 107 (1971); *ibid.*, **120**, 664 (1973).
18. M. Druminski and R. Gessner, *J. Cryst. Growth*, **31**, 312 (1975).
19. E. Sirtl and H. Seiter, in "Semiconductor Silicon 1969," R. R. Haberecht and E. L. Kern, Editors, p. 189, The Electrochemical Society Softbound Proceeding Series (1969).
20. JANAF Thermochemical Tables, 2nd ed. NSRDS-NBS-37 (June 1971).
21. R. J. Jaccodine, *This Journal*, **110**, 524 (1963).
22. D. Walton, *J. Chem. Phys.*, **37**, 2182 (1962).
23. J. A. Venables, *Philos. Mag.*, **27**, 697 (1973).
24. M. J. Stowell, *Thin Solid Films*, **21**, 91 (1974).
25. B. Lewis, *Surf. Sci.*, **21**, 289 (1970).
26. A. Masson, J. J. Métois, and R. Kern, *ibid.*, **27**, 463 (1971).
27. K. H. Behrndt, in "Techniques of Metals Research," Vol. I, Part 3 (1968).
28. W. A. P. Claassen and J. Bloem, To be published.
29. D. Turnbull, "Thermodynamics in Physical Metallurgy," p. 282, American Society for Metals, Nov-ely (1950).
30. E. H. Fontana and W. A. Plummer, *Phys. Chem. Glasses*, **7**, 139 (1966).
31. R. L. Mozzi and B. E. Warren, *J. Appl. Crystallogr.*, **2**, 164 (1969).
32. S. R. Gunn and L. G. Green, *J. Phys. Chem.*, **65**, 779 (1961).
33. J. Bloem and L. J. Giling, in "Current Topics in Materials Science," Vol. I, E. Kaldis, Editor, chap. 4, North-Holland Publishing Co. (1978).
34. P. van der Putte, L. J. Giling, and J. Bloem, *J. Cryst. Growth*, **41**, 133 (1977).
35. V. S. Ban and S. L. Gilbert, *This Journal*, **122**, 1382 (1975).

AZ1350J as a Deep-U.V. Mask Material

B. J. Lin

IBM Thomas J. Watson Research Center, Yorktown Heights, New York 10598

ABSTRACT

The conventional near-u.v.-and-visible(310-430 nm) resist AZ1350J is found to be useful as a mask opaque material for deep-u.v.(200-260 nm) lithography because of increased optical absorption at wavelengths below 300 nm. Only 0.2 μm is required to obtain a contrast of 100 using a Xe-Hg arc lamp and polymethyl methacrylate(PMMA) as the photoresist. The AZ mask does not deteriorate when exposed to light if kept in a vacuum below 10^{-2} Torr. Otherwise, about 300 passes can be expected. Experimental printing results show 1 μm images in 1.5 μm of PMMA. Special applications in projection printing, contact printing, and the portable conformable mask technique are discussed.

As the minimum feature size of integrated circuit patterns approaches the one micrometer range the near-u.v. and visible spectral region 310-430 nm used in conventional u.v. lithography becomes inadequate. The deep-u.v. wavelengths 200-260 nm make it possible to print 0.5 μm features spaced 0.25 μm apart in 1.8 μm of resist (1). Polymethyl methacrylate (PMMA) and many other E-beam resists are used as deep-u.v. resists instead of AZ1350J. Conventional Hg sources and the more efficient deuterium lamp supply the deep-u.v. exposing light. Quartz and sapphire are good transparent materials for the mask substrate. Conventional mask opaque materials such as chromium and iron oxide are also satisfactory for deep u.v.

In this paper, the use of the near-u.v. photoresist AZ1350J as a deep-u.v. mask opaque material is reported. The photoresist can be easily spun onto the substrate for pinhole-free coverage and can be stripped, permitting reuse of substrate without repolish. The developed image is readily used, thus eliminating the extra etching step and the rough edges caused by it. Being transparent in the visible region, the AZ mask facilitates alignment just as the dichroic iron oxide mask (2). However, because of less resistance to abrasion, it is most suited for projection printing and specific applications in contact printing.

Key words: photoresists, mask material, deep u.v. lithography, lithography, IC fabrication.

Spectral Transmission Characteristics

The spectral transmission of 0.2 μm of AZ1350J spun on a 0.25 mm quartz substrate was evaluated with a Beckman GT spectrophotometer in the region 200-460 nm. Considering that it is a photoresist and would be affected by exposure to light, measurements were taken at different exposure levels. The exposing light source was a 1 kW Xe-Hg arc lamp with a 0.07 NA condenser consisting of quartz and lithium fluoride elements. The power level is estimated to be of the order of 20 mW/cm² in near-u.v. and 1 mW/cm² in deep-u.v. An exposure of 0.5 sec adequately exposes the 0.2 μm of AZ1350J for a 1 min development in a 1:1 mixture of AZ developer and deionized water. An exposure time of 7 min is required to expose 1 μm of PMMA for a 1 min development in methyl isobutyl ketone (MIBK).

The measurements were taken at 0, 0.5, and 1 sec, then 1, 10, 40, and 100 min, and 3.7, 5.7, 9.7, 16.7, 33.3, 53.5, and 60 hr of near-u.v. and deep-u.v. exposure of the AZ resist to simulate the radiation effects on the mask during its lifetime. The 0, 1 sec, 10 min, 5.7, 33.3, and 60 hr curves are shown in Fig. 1. From an unexposed resist to that of 1 sec exposure, the transmission increases in the regions 310-460 nm and 245-295 nm. The former is due to bleaching of the photoactive compound in the near-u.v. region and the latter accounts for the deep-u.v. sensitivity of AZ1350J observed by Nakane and Mifune (3). With further u.v.

Table I. System parameters for wavelengths between 205 and 255 nm

Wavelength (nm)	205	215	225	235	245	255
Xe-Hg arc lamp (relative)	2	8	13	22	30	29
Deuterium lamp (relative)	0.363	0.431	0.467	0.440	0.386	0.363
Photosensitivity of PMMA (cm ² /W-min)	255	131	62.5	15.6	3.22	0.214
Transmission of quartz	0.880	0.891	0.898	0.902	0.910	0.913
Transmission of unexposed AZ	0	0	0	0.015	0.18	0.285
AZ after 5.7 hr	0	0.002	0.007	0.015	0.026	0.039
AZ after 60 hr	0.06	0.062	0.07	0.09	0.11	0.14
AZ after 51 hr in vacuum	0	0	0	0	0.007	0.016

exposure, the transmission decreases to a minimum after 5.7 hr then increases indefinitely. This latter bleaching effect is probably due to oxidation during exposure, because it is eliminated and the absorption becomes even higher for another wafer exposed 51 hr in 10^{-2} Torr of vacuum.

Figure 2 shows the change of transmission as a function of exposure time at 220, 258, 280, and 340 nm. From 230 nm and below, AZ1350J is not photosensitive as indicated by the absence of the first bleaching and it is also very opaque making it suitable to mask off deep-u.v. light. After 5.7 hr, it starts to bleach out if left exposed in the atmosphere, implying that the masking property would be lost if the mask is not used in a vacuum environment. The 258 and 280 nm lines are respectively the local maximum and minimum transmission points in the spectrum. The 340 nm line represents a typical line in the near-u.v. region and was chosen for convenience.

System Spectral Response

Because PMMA is not sensitive above 260 nm, any contribution to partial exposure through the AZ mask is in the region 200-260 nm. The local transmission peak at 258 nm may reduce contrast, especially when the 254 nm Hg line is present. Fortunately the photosensitivity of PMMA at 250 nm is two orders of mag-

nitude lower than that at 220 nm (1), thus, offsetting the strong 254 nm emission. To gain a better insight, the total system response which includes the radiation spectrum of the light source, the transmission spectrum of the 0.2 μ m AZ mask, and that of a 0.25 mm quartz substrate, and the spectral photosensitivity of PMMA, is evaluated quantitatively.

The spectra used are shown in Table I in increments of 10 nm. The spectra of the Xe-Hg and deuterium lamps are taken from manufacturer's manuals. The photosensitivity of PMMA is taken from Ref. (1). For the transmission spectrum of AZ1350J, the unexposed case and those exposed 5.7 and 60 hr as well as that aged 51 hr in vacuum are chosen.

The spectral response with the opaque part of the mask is obtained by multiplying the respective components at each wavelength interval. The transmission of quartz is not included since it has been already taken into account in the transmission measurements. For the transparent part of the mask, the transmission of AZ is replaced by that of quartz. Then, a summation in wavelength is taken for each response. Taking the ratio of the sum for the transparent part to the sum of the opaque part results in the contrast that can be achieved with the AZ mask. It is shown in Table II. A discussion of implications of Table II and printing results is given in the following section.

Printing Results

The C-bar magnetic bubble propagation circuit pattern is used for our printing experiment. The C-bars have 1 μ m arms spaced 1 μ m apart. The original mask was delineated by E-beam in chromium on quartz substrate. AZ copies, with 0.2 and 1 μ m of AZ1350J were made with near-u.v. light by con-

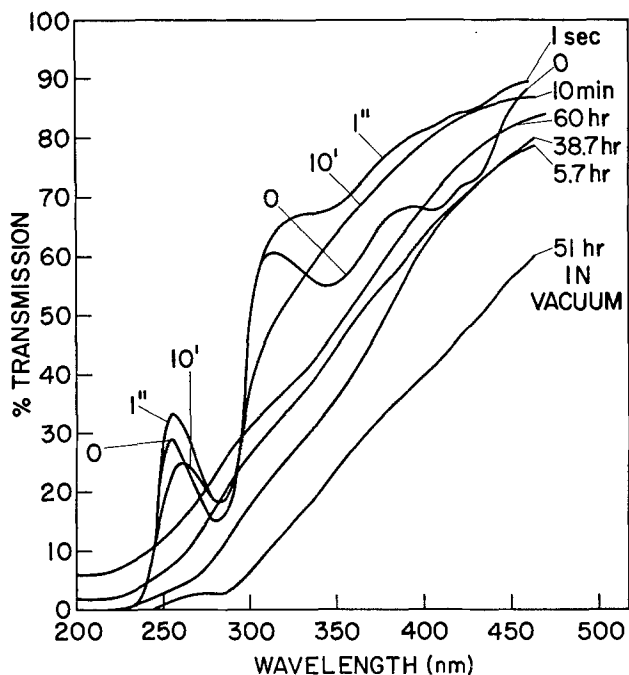


Fig. 1. The transmission spectrum of 0.2 μ m of AZ1350J in different aging conditions.

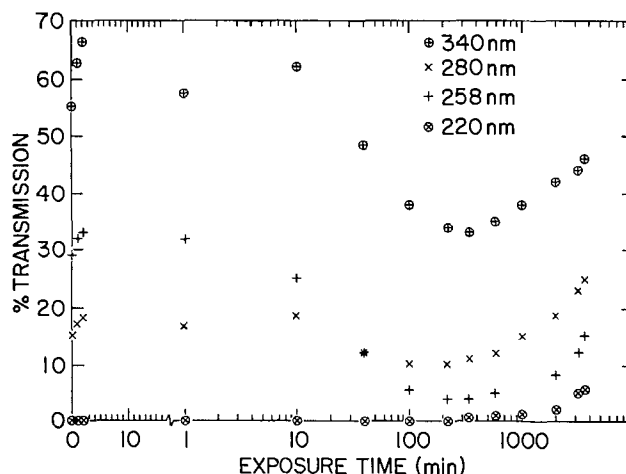


Fig. 2. Optical transmission of 0.2 μ m of AZ1350J as a function of exposure time.

Table II. The contrast obtained with the AZ mask under different aging conditions and different light sources. The spectral characteristics of the sources, the mask, and the deep-u.v. resist are included

	Unexposed AZ	After 5.7 hr	After 60 hr	51 hr in vacuum
Mercury lamp	104	160	13	3,244
Deuterium lamp	474	363	14	16,600

formable printing. A layer of 1.5 μm of PMMA 2041 was spun on Si wafers with 0.6 μm of SiO_2 . Then, deep-u.v. conformable printing (4) was done with the original chromium mask and the two AZ masks, using an exposure of 8.3 min and a development of 1 min in MIBK. This exposure-development level is chosen so that the exposed resist is just completely developed.

The image delineated by the chromium mask is seen in Fig. 3a and 3b, at angles of 45° and 90° respectively. The side view Fig. 3b shows the line between the C's. The 0.1 μm aluminum evaporated for SEM purpose is also seen above the oxide layer. These are typical PMMA images that are routinely obtained by deep-u.v. conformable printing. The opened lines are slightly larger than the spacing exactly like those on the mask. Figures 3c and 3d show the image obtained with the 0.2 μm AZ mask aged by exposing for 0.5 sec. Though the calculated contrast is in the order of 100, the resist covered by AZ is still slightly exposed and appears as faint ghost lines in the corners and pinholes in the corners. This exposure penetrates only 0.1 μm into PMMA as seen in the little indentation at the top of the 1 μm line between the arms of the C's in Fig. 3d. Therefore, in spite of the less appealing appearance, the image is usable. The image obtained with the 1 μm AZ mask is shown in Fig. 3e and 3f. Now, because of higher contrast in the mask, the ghost lines and pinholes are eliminated. However, the opened lines are much smaller when compared to that of the original mask, because the resist image in AZ has a natural overcut profile (5). When the pattern at the top of the AZ resist is controlled to resemble that of the original mask, the pattern at the bottom of the AZ resist is much smaller. This effect is useful for the AZ mask technique, because it offers a means to change the width-space ratio when copying from an existing mask. The method is easy to control as the resist thickness can be precisely varied by changing the spin speed. The range of control well exceeds the usual method of exposure-development manipulation.

When absolutely no ghost lines are allowed, a deuterium lamp can be used instead of the mercury lamp. From Table II, a 4.6 time increase in contrast is obtained. This is sufficient to eliminate the low contrast ghost lines as seen in Fig. 4 where 0.8 μm lines spaced 0.8 μm apart are delineated in 1.5 μm of PMMA. With a 200W deuterium lamp, an exposure time of 30 min is required for a 57 mm wafer to develop in a minute.

For conventional mask applications where the mask is prepared independently of the wafer, the contrast can be improved by aging the mask with a blanket exposure longer than 1 min. As seen in Fig. 2, the transmission maximum at 258 nm is eliminated to improve the contrast. It can be dramatically improved, if the mask is aged in a vacuum. In fact, if the mask is used in the atmosphere, the service life is limited to less than 300 passes because of the decrease in contrast due to bleaching. If the mask is used always in vacuum, its contrast ratio continues to increase.

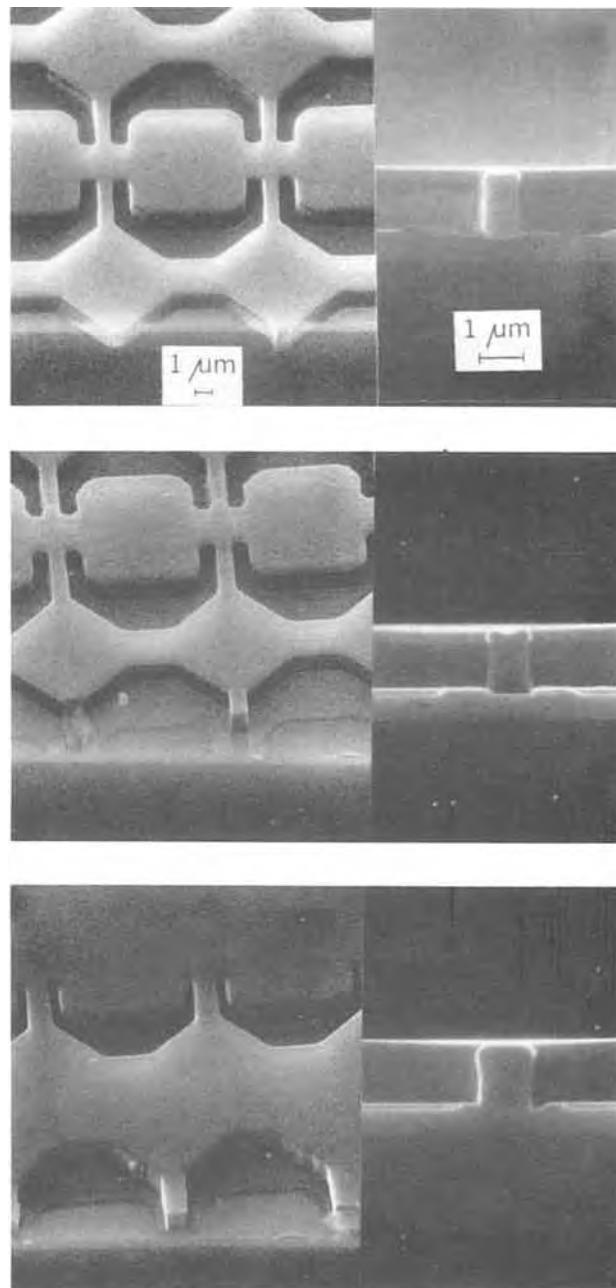


Fig. 3. (a) top left, 1 μm C-bar images in 1.5 μm of PMMA made with deep-u.v. conformable printing using a regular chromium mask and a Xe-Hg arc lamp; (b) top right, side view of 3 (a); (c) middle left, same pattern obtained with a 0.2 μm AZ mask; (d) middle right, side view of 3 (c); (e) bottom left, same pattern obtained with a 1 μm AZ mask; (f) bottom right, side view of 3 (e).

Applications

Projection printing.—In a projection system, the mask does not come in contact with the wafer, therefore, it can be soft. The AZ mask is potentially very suitable for a Perkin-Elmer-type (6) all mirror system using deep-u.v. light to expose. The surface of the mask would be flooded with nitrogen or a simple vacuum fixture would be used to protect the mask from deterioration. If an optical window is used, the imaging optics has to be corrected for the extra window introduced. In this type of 1:1 system, an identical window can be placed at the wafer side to be symmetrical to that at the mask side.

The projection printer can also be used to make near-u.v. working master masks from a master AZ

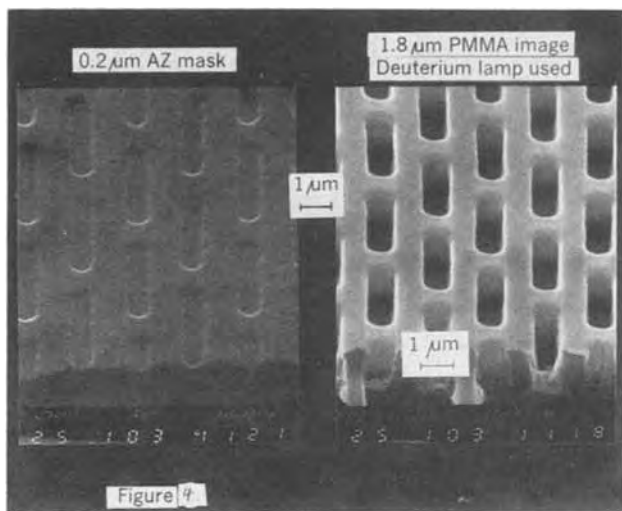


Fig. 4. $0.8 \mu\text{m}$ lines spaced $0.8 \mu\text{m}$ apart delineated in $1.5 \mu\text{m}$ of PMMA with a deuterium lamp.

mask directly fabricated with a photorepeater or an E-beam machine. Copying in deep-u.v. ensures adequate resolution on the working masks for near-u.v. applications. Using noncontact mask replication eliminates defects generated by the usual contact replication method.

Proximity printing.—With a mask-to-wafer gap of over $10 \mu\text{m}$ and flushing of nitrogen in between, AZ mask can be used for mass production in proximity printing. However, it is not feasible to use AZ mask when physical contact between the mask and wafer is inevitable. Then it can only serve as an intermittent mask to change the polarity, create a mirror image, or fine tune the width-to-space ratio of an existing mask.

Portable conformable masks.—The AZ layer can be directly spun on PMMA. After exposing in near-u.v. light, the AZ layer is developed to become an intimately contacted mask on PMMA for blanket exposure.

An amplification of aspect ratio by a factor of 10 can easily be obtained. Existing near-u.v. machines can expose faster, with better resolution, and produce width-to-height aspect ratios only attainable with deep-u.v. lithography. A detailed report was published elsewhere (7).

Conclusion

The conventional mask opaque materials such as chromium and iron oxide cannot be completely substituted with AZ1350J, due to differences in durability. However, the advantages associated with the AZ mask are very desirable. It eliminates the etching of chromium and iron oxide which has long been troublesome. Evaporation or sputtering which requires a vacuum system and extreme cleanliness to prevent pinhole defects is no longer necessary. Substrate recycling is done by simply stripping the photoresist instead of an additional etching and expensive re-polishing. Alignment becomes easier because of the dichroic property. Therefore, it is preferred whenever softness is not disadvantageous.

Acknowledgment

The author is indebted to C. Lapadula for technical assistance. Support and encouragement from J. S. Wilczynski and A. N. Broers are deeply appreciated.

Manuscript submitted May 2, 1979; revised manuscript received Aug. 13, 1979.

Any discussion of this paper will appear in a Discussion Section to be published in the December 1980 JOURNAL. All discussions for the December 1980 Discussion Section should be submitted by Aug. 1, 1980.

Publication costs of this article were assisted by IBM Thomas J. Watson Research Center.

REFERENCES

1. B. J. Lin, *J. Vac. Sci. Technol.*, **12**, 1317 (1975).
2. W. R. Sinclair, M. V. Sullivan, and R. A. Fastnacht, *This Journal*, **118**, 341 (1971).
3. Y. Nakane and T. Mifune, Sony Corp., publication in Japanese.
4. B. J. Lin, *IBM J. Res. Dev.*, **20**, 215 (1976).
5. B. J. Lin, *J. Vac. Sci. Technol.*, **15**, 1012 (1978).
6. D. A. Markle, *Solid State Technol.*, 50 (June 1974).
7. B. J. Lin, *SPIE Proceedings*, 174 (1979).

Arsenic Ion Channeling through Single Crystal Silicon

Yasuo Wada, Shigeru Nishimatsu,* and Norikazu Hashimoto

Hitachi Limited, Central Research Laboratory, Kokubunji, Tokyo, 185 Japan

ABSTRACT

The main mechanism of anomalous tail generation in arsenic ion implanted layers is examined using silicon gate MOS capacitance flatband voltage and MOSFET threshold voltage measurements. Primarily, this approach measures the quantity of arsenic ions incorporated in silicon substrates as functions of polycrystalline silicon grain size. This method can measure ion amounts as low as 10^{11} cm⁻² in the substrate. Only samples with large grains which extend across the polycrystalline silicon layer show flatband and threshold voltage shifts. Therefore, the mechanism of anomalous tail generation is attributed to arsenic ion channeling through single crystal silicon. Variations in the implant angle, as well as formation of a surface amorphous layer, are not sufficient to prevent channeling.

High dose arsenic ion implantation technology has attracted attention recently for the fabrication of high packing density MOS LSI source and drain regions (1, 2), due to its precise control and flexible application. Nevertheless, designers continue to ask for higher packing density LSI's. Therefore, it is necessary to fabricate even better-controlled source and drain regions than ever.

In order to control precisely the arsenic profile in these regions, it is imperative to control the initial arsenic profile, as well as diffusion conditions such as temperature, time, and ambient. However, arsenic ion implantation into single crystal silicon has been reported to generate an anomalous tail in deep substrate regions which exceeds the main peak profile (3, 4). This phenomenon has been observed using the neutron activation analysis. The possible causes were attributed to channeling (3), and to anomalous diffusion (4) through single crystal silicon. The concentration of the anomalous tail was reported to be less than 10^{17} cm⁻³, which is almost too low a concentration to be detected by conventional analyses other than neutron activation analysis. Therefore, in order fully to investigate and identify this phenomenon, it was necessary to develop a new method which enables the determination of anomalous profiles in impurity implanted silicon layers.

This paper describes a highly sophisticated, yet simple method to determine the cause of anomalous arsenic profile in silicon. This new method utilizes conventional silicon gate MOS LSI technology (5), combined with controlled polycrystalline silicon grain growth phenomenon (6).

Fundamental Concept

In order to determine whether the arsenic incorporation mechanism is anomalous diffusion or channeling, polycrystalline silicon (poly-Si) gate MOS capacitor (MOS C) was used. The crystalline state of poly-Si can be controlled by impurity doping and annealing (6). Therefore, arsenic ions can be implanted through a gate, with the crystalline state between small grain poly- and single crystal. A schematic representation of the MOS C is shown in Fig. 1. If ion channeling takes place in the poly-Si layer with large crystals which extend across the thickness, some fractions of the implanted ions would reach the substrate and change the flatband voltage (V_{FB}) of the MOS C. On the other hand, V_{FB} would not shift, regardless of the implantation conditions, if the main cause of the anomalous profile in arsenic ion implanted layers is diffusion through single crystal silicon. This is because the gate oxide layer under-

neath the poly-Si layer prevents the arsenic ions from diffusing into the silicon substrate.

Experimental Procedures

MOS capacitor fabrication and capacitance-voltage measurements.—An MOS C was fabricated on a p-type, (100) oriented, 10 Ω -cm silicon wafer. The gate oxide thickness was 50 nm, and the poly-Si gate was 0.4 μ m thick. Phosphorus (P) ions were implanted at a 50 keV acceleration energy to doses of between 0.4×10^{16} cm⁻². The dose rate was less than 3 μ A/cm², keeping the substrate temperature during ion implantation less than 150°C (7). Therefore, anomalous effects due to substrate heating do not occur. The samples were then annealed at 1000°C for 20 min.

A 1 mm square poly-Si gate was delineated by conventional photolithographic technology. Then, arsenic (As) ions were implanted between 50-180 keV, to a dose of between 1×10^{15} - 3×10^{16} cm⁻². The dose rate was also less than 3 μ A/cm². Therefore, the substrate temperature rise during ion implantation was less than 150°C (7). The implantation angle was varied from 0 to 15 degrees in order to examine the channeling effect. Annealing, at 1000°C for 20 min in dry nitrogen, was performed to activate the implanted As ions. Low temperature annealing in a hydrogen atmosphere was carried out to eliminate unnecessary surface states almost completely.

The As ions in the anomalous tail distribute within less than 5 times as deep as the projected range (R_p) of the Gaussian distribution (3, 4). In this experiment, R_p was less than 0.1 μ m (9). Therefore, considering the sample dimensions shown in Fig. 1, As ions should

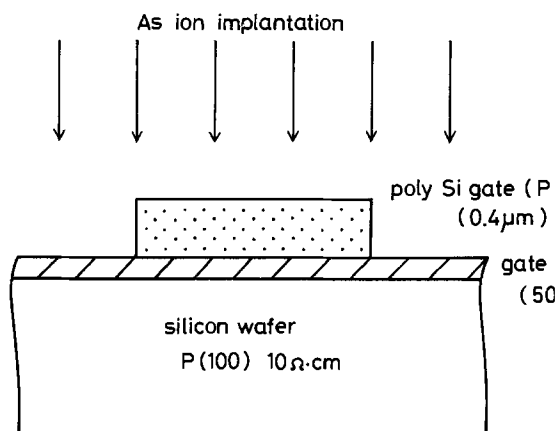


Fig. 1. Schematic representation of poly-Si gate MOS C utilized in this experiment: poly-Si thickness, 0.4 μ m; gate oxide thickness, 50 nm.

* Electrochemical Society Active Member.

Key words: poly-Si grain growth, ion implantation, channeling, MOS LSI.

distribute within $0.1 \mu\text{m}$ from the gate oxide-silicon substrate interface. In addition, As ions have a diffusion coefficient as low as $3 \times 10^{-2} \mu\text{m/hr}^{1/2}$ at 1000°C (8); these experimental conditions do not cause As ions to diffuse into silicon substrate. Therefore, the implanted ions can be measured in terms of surface states (Q_{ss}). Furthermore, these thermal treatments after ion implantation almost completely eliminated the parasitic effects that might affect the flatband voltage shifts.

High frequency capacitance-voltage ($C-V$) measurements were carried out to evaluate flatband voltage shift (ΔV_{FB}) of the MOS C thus fabricated. The amount of ions incorporated into the substrate (N_i) is derived from the following equation (11)

$$N_i = \Delta V_{FB} C_{ox} / qA \quad [1]$$

where, C_{ox} and A are oxide capacitance and the area of the MOS C, respectively.

MOSFET fabrication.—MOSFET's were fabricated using conventional silicon gate technology (5). The gate oxide thickness was 50 nm , and the poly-Si gate was $0.4 \mu\text{m}$ thick. The poly-Si gate was doped with various concentrations of phosphorus, and annealed in dry nitrogen in order to control the grain size. As ions were implanted at 150 keV acceleration energy to a dose of $1 \times 10^{16} \text{ cm}^{-2}$. Then the samples were annealed at 1000°C for 20 min in dry nitrogen. After metallizing with aluminum, the samples were annealed in hydrogen to minimize the surface states.

The electrical characteristics of MOSFET's thus fabricated were then measured. These characteristics, such as threshold voltage and tailing current, were measured under the conditions listed in Table I.

Results and Discussion

Phosphorus doping concentration dependence of grain growth.—The crystalline state of heavily phosphorus-doped poly-Si is briefly reviewed first to provide a common reference point. Typical transmission electron micrographs (Hitachi HU 12A type) are shown in Fig. 2. These results indicate that, in the case of less than $2.5 \times 10^{20} \text{ cm}^{-3}$ phosphorus doping, the film consists of $0.1 \mu\text{m}$ mean grain diameter poly-Si. Therefore, there are four separate grains stacked vertically in $0.4 \mu\text{m}$ thick films. On the other hand, the poly-Si layer contains large crystals which extend throughout the thickness with more than a $5 \times 10^{20} \text{ cm}^{-3}$ doping. Although the mean grain diameter of the grains is approximately $0.8 \mu\text{m}$, the poly-Si films are equivalent to single crystal silicon with regard to the masking effect against implanted ions.

Therefore, it is possible to examine the behavior of the arsenic ions implanted into various crystalline states from poly- to single crystal. The main orientation of the grown grains measured by electron diffraction was (110). The surface roughness of the poly-Si film remained almost the same as in as-deposited samples even after thermal annealing at 1100°C for 30 hr . A typical cross-sectional scanning electron micrograph is shown in Fig. 3. Therefore, implanted ion leakage through the thinner part of the gate need not be taken into consideration.

Flatband voltage shift.—Phosphorus doping concentration dependence of flatband voltage shift (V_{FB} shift) was measured for poly-Si gate samples with various grain sizes. Arsenic ions (As ions) were implanted at a 150 keV acceleration energy where the projected range and deviation are 0.0845 and 0.0292

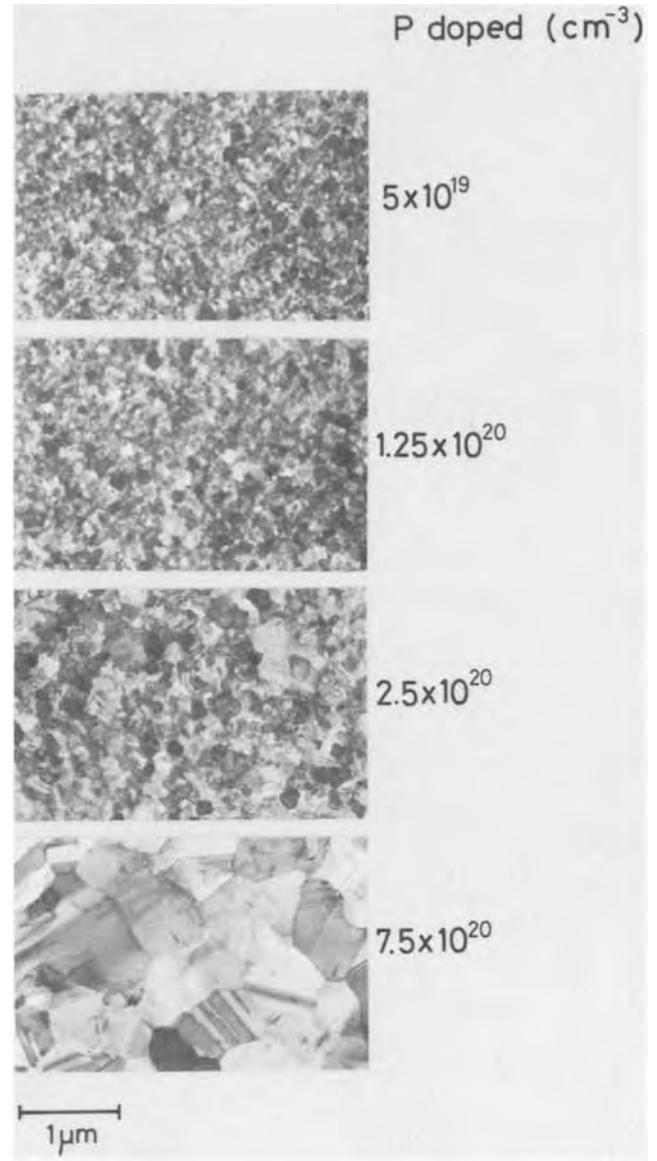


Fig. 2. Transmission electron micrograph showing phosphorus doping concentration dependence of grain growth: poly-Si thickness, $0.4 \mu\text{m}$, annealed at 1000°C for 20 min .

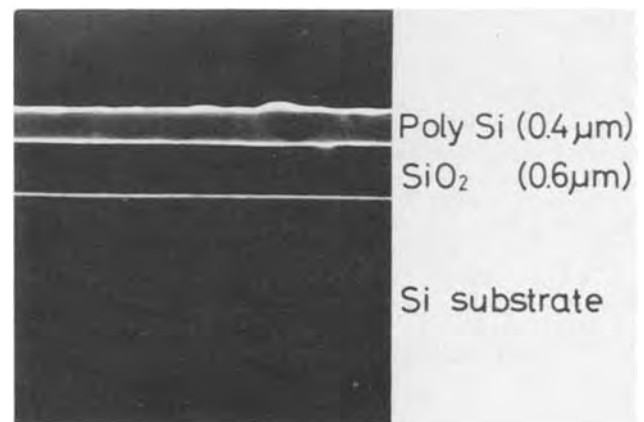


Fig. 3. Scanning electron micrograph of poly-Si cross section annealed at 1100°C for 3 hr .

Table I. Typical measuring conditions of MOSFET's

Drain voltage (V_{DD})	8V
Substrate bias (V_{BB})	-2V
Threshold voltage (V_{TH})	$I_{DS} = 10 \text{ nA}$
Measuring temperature	25°C

μm , respectively, in silicon (9). The calculated profile was located well within the poly-Si layer, as shown in Fig. 4.

Typical results are shown in Fig. 5, in which the phosphorus doping concentration dependence of poly-

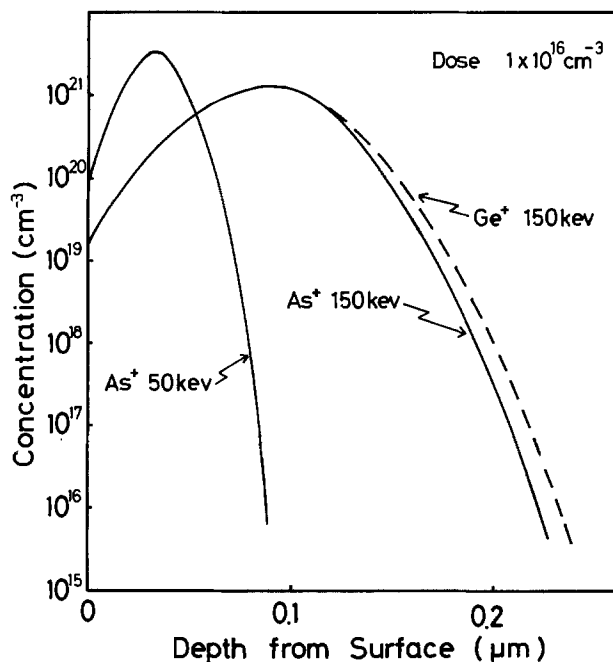


Fig. 4. Calculated ion profiles in Si

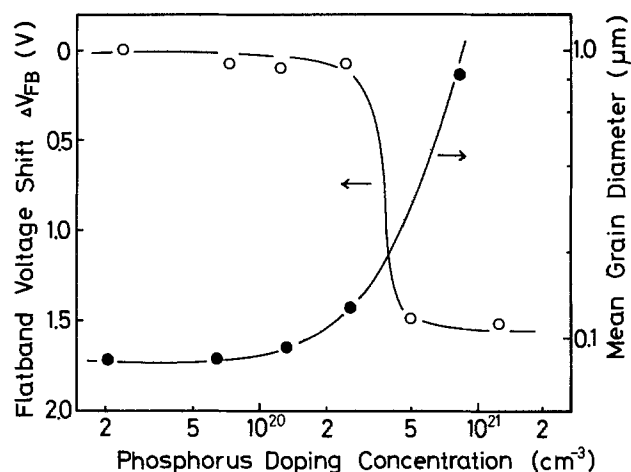


Fig. 5. Phosphorus doping concentration dependence of flatband voltage shift and mean grain diameter: poly-Si thickness, $0.4 \mu\text{m}$; gate oxide thickness, 50 nm ; arsenic ion implantation condition, $150 \text{ keV } 1 \times 10^{16} \text{ cm}^{-2}$.

Si grain growth is also depicted. The results clearly indicate that there is a correspondence between V_{FB} shift and poly-Si grain diameter. The samples with poly-Si grains extending across the gates show a V_{FB} shift of about 1.5 V . The As^+ ion dose incorporated in the silicon substrate was approximately 10^{12} cm^{-2} , which is 10^{-4} of the total As dose.

These results indicate that anomalous diffusion in the large grain poly-Si layer does not take place. One possible reason for this phenomenon is As ion channeling through the large crystal poly-Si gate. However, some other mechanisms, which could contribute to the phenomenon, are considered in the following sections.

V_{FB} shift mechanism identification.—Possible reasons for the V_{FB} shift, or donor incorporation into substrate, are as follows:

(i) As^+ ion penetration through poly-Si region with single crystals extending across the thickness (channeling); (ii) Knock-on of P atoms into the silicon substrate by the implanted As^+ ions; (iii) Enhanced diffusion of donor ions through the gate oxide.

The following experiments were conducted to clarify the phenomenon and make identification of the mech-

anism possible: (i) Ge^+ or As^+ ion implantation, with the same profiles, in silicon; (ii) As^+ ion implantation at lower implantation energies.

The calculated As and Ge profiles are shown in Fig. 3. They show that nearly all the implanted ions in the profile are located well within the poly-Si layer. Therefore, if only the high energy As^+ ion implanted sample shows V_{FB} shifts, the cause of the V_{FB} shift is As^+ ion penetration through the large crystal poly-Si gate. If As and Ge implanted samples both show a V_{FB} shift, the main mechanism is P knock-on by the implanted ions. If all As^+ implanted samples show a V_{FB} shift, the cause must be anomalous diffusion through the gate oxide.

The experimental results revealed that only high energy As ion implanted samples exhibited V_{FB} shifts. Typical results for the acceleration energy dependence of V_{FB} shift are shown in Fig. 6. As^+ ions penetrate into the substrate when implanted at more than 140 keV . These experimental results indicate that the main mechanism of this phenomenon is As channeling through the large crystal poly-Si gates.

Location of arsenic ion penetration.—The TEM micrographs shown in Fig. 1 tend to indicate that some fraction of As^+ ions would channel through the grain boundaries and change the flatband voltage. Therefore, in order to define the location of As ion penetration, the tailing current of MOSFET's was measured.

The tailing current of a MOSFET (I_t) is expressed as (15)

$$\log I_t = \alpha V_g \quad [2]$$

Where, V_g is the gate voltage and α is the tailing factor, given by the following equation

$$\alpha = k \cdot T / q \cdot \log(1 + k_s t_{\text{ox}} / k_{\text{ox}} W_d) \quad [3]$$

where, the notations are listed in Table II.

The tailing current was then compared with conventional channel doping technology (10). If As ion penetration occurred uniformly over the poly-Si gate, these two results should coincide. On the other hand, if the As ions penetrate along specified paths, such as grain boundaries, then these two results should differ. This is because the effective channel width, W_d in Eq. [3], differs between these samples. Therefore, the gradient of the $\log I_t - V_g$ relationship (α) should be different.

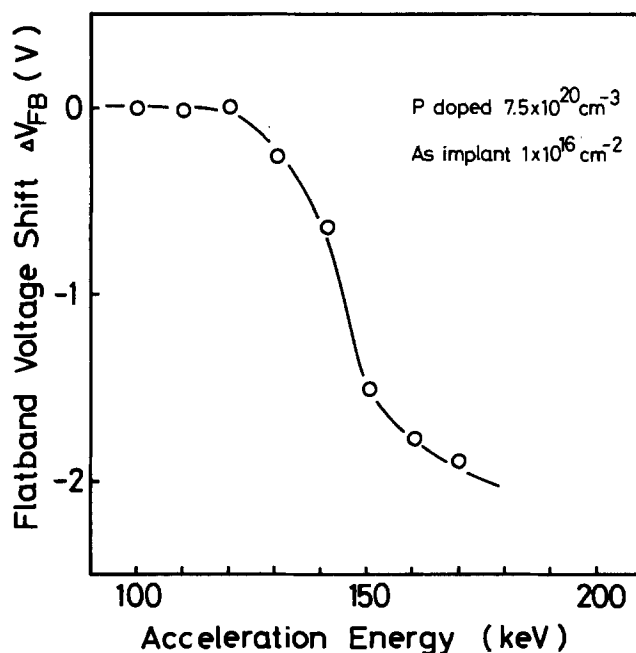


Fig. 6. Arsenic acceleration energy dependence of flatband voltage shift: poly-Si thickness, $0.4 \mu\text{m}$; gate oxide thickness, 50 nm ; arsenic ion dose, $1 \times 10^{16} \text{ cm}^{-2}$.

Table II. Symbols in Eq. [3]

k	Boltzmann constant	$1.38 \times 10^{-23} \text{ JK}^{-1}$
T	temperature	298°K
q	elementary charge	$1.60 \times 10^{-19} \text{ C}$
k_s	dielectric constant of silicon	11.7
k_{ox}	dielectric constant of oxide	3.9
t_{ox}	oxide thickness	50 nm
W_d	channel width	15 μm

Typical results are shown in Fig. 7. They clearly reveal that the tailing current of the As-incorporated MOSFET's, shown by solid lines, is almost the same as that of the depletion-mode MOSFET's, calculated using Eq. [2], shown by the broken line. The larger the As incorporation amount becomes, the smaller becomes the gradient of the line. This is due to the residual current effect in heavily doped MOSFET's (15).

These results show that the As penetration occurs uniformly in the channel region. Therefore, the As incorporation into the silicon substrate is caused by As channeling through large poly-Si grains extending across the poly-Si gate.

Arsenic ion channeling through single crystal silicon.—The As ions incorporated by channeling into the substrate amount to as much as 10^{-1} of the total dose (3). In this experiment, the As ions in the substrate come to about 10^{-4} of the total dose. Therefore, the channeling phenomenon reported here should differ from that of previous reports.

The critical angle for As channeling is less than 8° (4), which is as low as that of P (13, 14). The implantation angle dependence of V_{FB} shift was mea-

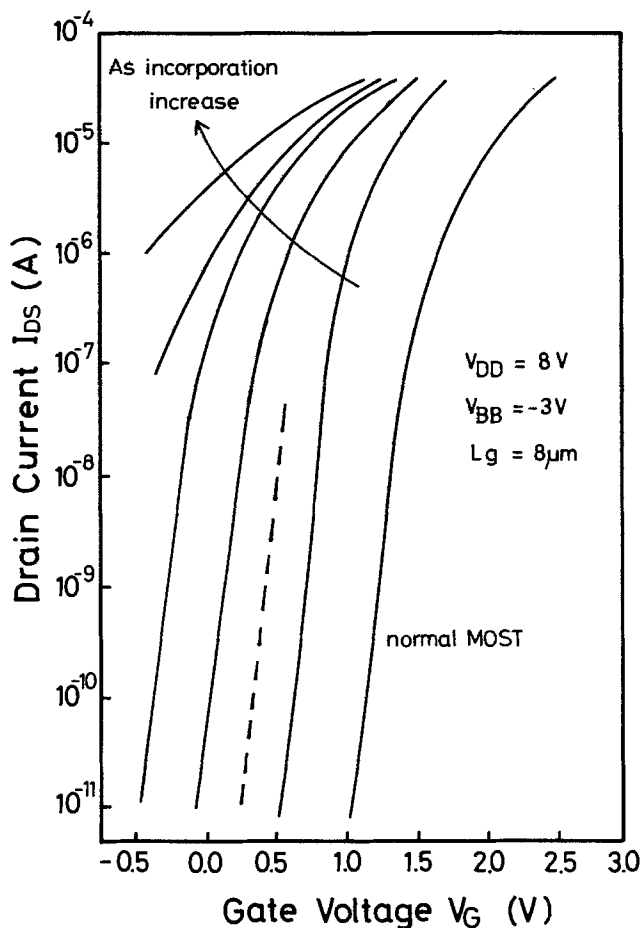


Fig. 7. Arsenic incorporation amount dependence of MOSFET tailing current, measured under the conditions listed in Table I. —, experiment; ---, calculation.

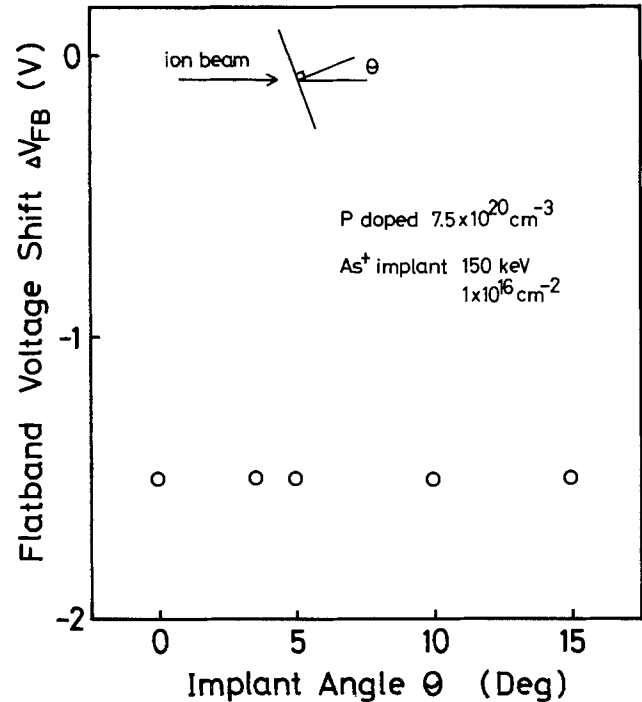


Fig. 8. Arsenic ion implantation angle dependence of flatband voltage shift: poly-Si thickness, 0.4 μm ; gate oxide thickness, 50 nm; implanted at 150 keV to $1 \times 10^{16} \text{ cm}^{-2}$ dose.

sured and the results are shown in Fig. 8. They depict that V_{FB} shift does not depend on an implantation angle of less than 15° . Similar results were also reported, where the implantation angle was varied from 0 to 50° (4). Such off-angle channeling also takes place in the case of P or B ion implantation (12). This off-angle channeling should cause nonuniform sheet resistivity in ion implanted-annealed samples, and can be attributed to planar channeling in the silicon crystals (16).

In addition to these phenomena, dose dependence of V_{FB} shift was observed in this experiment. As expressed in the previous section, the substrate heating was less than 150°C . Therefore, an amorphous layer was formed under these heavy ion implantation conditions. Typical results are shown in Fig. 9, which indicate that the surface amorphous layer, generated by more than a 10^{14} cm^{-2} As⁺ ion dose (3), does not prevent implanted ion channeling. The generally reported channeling phenomena are impeded by the surface amorphous layers, such as a silicon dioxide films or implanted-amorphized layers (3).

These results clearly show that the measurement method reported here is highly sensitive for measuring ion channeling through single crystal silicon. With large grains extending across the polycrystalline silicon layer, a kind of planar channeling could take place (16).

As shown in Fig. 6, the poly-Si gate, composed of single crystals, reduces the apparent stopping power for implanted ions. The reduction was approximately 30% in the case of samples with a 0.4 μm thick poly-Si gate and 50 nm thick gate oxide. Therefore, every precaution is necessary to prevent implanted ions from channeling, or being incorporated into the substrate. This might limit the practical application of ion implantation technology for source and drain region formation in silicon gate MOS LSI fabrication.

Conclusion

The anomalous profile of As⁺ ion implanted layers was investigated by silicon gate MOS LSI technology, combined with the effect of the poly-Si grain growth phenomenon. The main mechanism of the anomalous

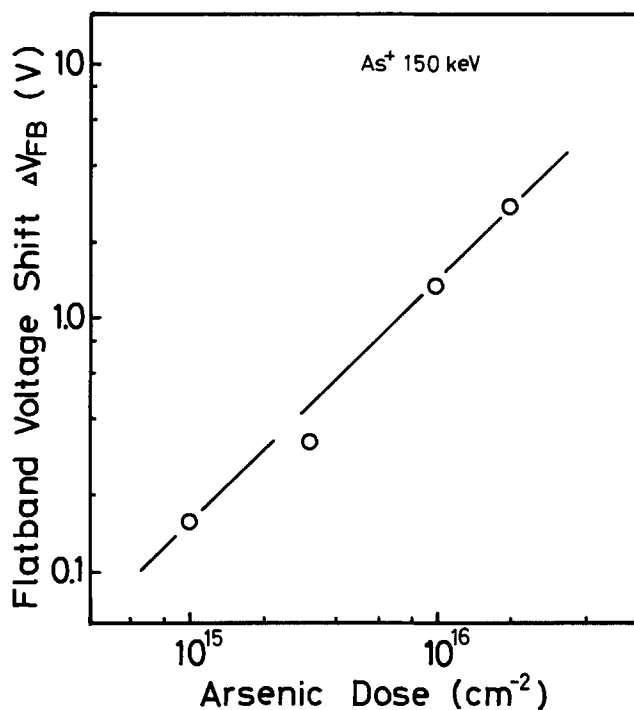


Fig. 9. Arsenic ion dose dependence of flatband voltage shift: poly-Si thickness, 0.4 μm ; gate oxide thickness, 50 nm; implanted at 150 keV.

As profile was found to originate from As^+ ion channeling.

This channeling phenomenon at the 10^{-4} level is beyond the scope of channeling generally investigated. The surface amorphous layer generated by heavy As ion implantation, as well as by larger implantation angles, could not prevent this channeling phenomenon. Therefore, every care is necessary to control the As profile in single crystal silicon, such as source and drain regions of MOS LSI's and bipolar LSI emitters.

In addition, this phenomenon might limit the practical application of ion implantation technology when employing the self-aligned gate structure. This is because of the reduction of the singly crystallized poly-Si gate stopping power against the implanted As ions.

Acknowledgments

The authors wish to express their thanks to Mr. Shinji Ohnishi for promoting this work, Dr. Takashi

Tsuchimoto is thanked for participating in valuable discussions. They are also grateful to Dr. Takashi Tokuyama for his continuous encouragement and contributions. The authors also appreciate the TEM micrographs taken by Dr. Fumio Nagata and the experimental assistance provided by Mr. Hiroo Usui.

Manuscript submitted Feb. 8, 1979; revised manuscript received July 27, 1979.

Any discussion of this paper will appear in a Discussion Section to be published in the December 1980 JOURNAL. All discussions for the December 1980 Discussion Section should be submitted by Aug. 1, 1980.

Publication costs of this article were assisted by Hitachi, Limited.

REFERENCES

1. R. H. Dennard, F. H. Gaensslen, H. N. Yu, V. L. Rideout, E. Bassons, and A. R. LeBlanc, *IEEE J. Solid-State Circuits*, **sc-9**, 256 (1974).
2. Y. Wada, S. Nishimatsu, and K. Sato, *Solid-State Electron.*, **21**, 513 (1978).
3. J. M. Fairfield and B. L. Crowder, *Trans. Metall. Soc. AIME*, **245**, 469 (1969).
4. M. Iwaki, K. Gamo, K. Masuda, S. Namba, S. Ishihara, and I. Kimura, in "Ion Implantation," B. L. Crowder, Editor, p. 111, Plenum Press, New York (1973).
5. F. Fagin and T. Klein, *Solid-State Electron.*, **13**, 1125 (1970).
6. Y. Wada and S. Nishimatsu, *This Journal*, **125**, 1499 (1978).
7. Y. Wada, H. Usui, and M. Ashikawa, *Jpn. J. Appl. Phys.*, **14**, 1351 (1975).
8. R. K. Jain and R. J. Van Overstraeten, *This Journal*, **122**, 552 (1975).
9. J. F. Gibbons, W. S. Johnson, and S. W. Mylroie, "Projected Range Statistics," Dowder, Hutchinson, and Roth, Inc., Stroudsburg, Pa. (1975).
10. F. F. Fang, *IEEE J. Solid-State Circuits*, **sc-10**, 205 (1975).
11. A. S. Grove, "Physics and Technology of Semiconductor Devices," John Wiley and Sons, New York (1967).
12. D. E. Davies, *Solid-State Electron.*, **13**, 229 (1970).
13. J. W. Mayer and O. J. Marsh, "Ion Implantation in Semiconductors," p. 239, Academic Press, New York (1969).
14. G. Dearnaley, J. H. Freeman, G. A. Gard, and M. A. Wilkins, *Can. J. Phys.*, **46**, 587 (1968).
15. T. Masuhara and J. Etoh, *IEEE Trans. Electron Devices*, **ed-20**, 799 (1974).
16. D. V. Morgan, Editor, "Channeling," John Wiley and Sons, London (1973).

The Liquid Phase Epitaxial Growth of High Purity $\text{Ga}_{1-x}\text{Al}_x\text{As}$

Amitabh Chandra and Lester F. Eastman

School of Electrical Engineering, Cornell University, Ithaca, New York 14853

ABSTRACT

We report the obtainment of high purity in the LPE growth of n $\text{Ga}_{1-x}\text{Al}_x\text{As}$ ($0 \leq x \leq 0.3$) at 700°C . Carrier concentrations at or below $1 \times 10^{15} \text{ cm}^{-3}$ have been consistently obtained, the lowest value achieved being under $3 \times 10^{14} \text{ cm}^{-3}$ at $x = 0.15$. It has been shown that these low carrier concentrations do not result from a high compensation ratio. In fact, $(N_D + N_A)$ has been measured to lie in the range $1-2 \times 10^{15}$ for all but one of the ten samples examined. The Hall mobilities of these samples drop gradually from $\approx 100,000 \text{ cm}^2 \text{ Vsec}$ for $x = 0$ to 24,000 for $x = 0.18$ at 77°K , and from 8600 for $x = 0$ to 5100 for $x = 0.18$ at 295°K . We believe that a dominant shallow donor impurity (thought to be sulfur) is introduced into the melt with the aluminum. We find that the second epitaxial growth from a melt is significantly purer than the first, presumably due to the extra baking.

Gallium Aluminum Arsenide [$\text{Ga}_{1-x}\text{Al}_x\text{As}$, or $(\text{Ga,Al})\text{As}$] was first prepared in the late sixties by both a vapor transport technique (1) and liquid phase epitaxy (2), and its usefulness in electroluminescent devices was demonstrated (2,3). Its importance as an electronic material was established in 1969-1970 with the development of the heterostructure laser (4-6), and later, the $\text{GaAs}-(\text{Ga,Al})\text{As}$ solar cell (7). For these applications, the $(\text{Ga,Al})\text{As}$ is required to be heavily doped, so that the background purity is not critical. Most reports of background net doping in $(\text{Ga,Al})\text{As}$ range from mid- 10^{15} to mid- 10^{16} cm^{-3} (8-12). In contrast, GaAs has been grown, with $(N_D + N_A) \lesssim 10^{14} \text{ cm}^{-3}$ (13-15).

High purity and high quality $(\text{Ga,Al})\text{As}$ is desirable for fundamental studies such as alloy scattering and n - n heterojunction current rectification (16). Also, new device concepts such as the heterojunction FET (17) have arisen that require $(\text{Ga,Al})\text{As}$ of higher purity.

In this paper the growth of high purity $\text{Ga}_{1-x}\text{Al}_x\text{As}$ by LPE is reported. We use the term high purity to denote material with $(N_D - N_A) \lesssim 10^{15} \text{ cm}^{-3}$, that is not heavily compensated. Our approach to obtaining purity has been to (i) start with a clean growth environment, (ii) grow at a relatively low temperature (700°C), and (iii) study the effect, on the layer purity, of the amount of aluminum in the melt, and of baking the melt.

LPE Procedures

The horizontal sliding boat LPE growth system used in these experiments is similar to the one described by Morkoc and Eastman (15,18), with a continuously flushed nitrogen glove box added for substrate and melt loading. During the loading and unloading operations, the boat and melts are hence exposed only to trace amounts of oxygen. Substrates and melt components are transferred across the glove box walls through a $1\frac{1}{2}$ in. diam hole that is normally kept sealed. During the transfer operation, a high N_2 flow rate (50-100 ft^3/hr) minimizes the introduction of air into the glove box.

Standard procedures (15,18) for purifying the growth environment were followed. The quartzware was cleaned in electronic grade organic solvents and deionized water, and then soaked in aqua regia before a final rinse in deionized water and drying in a laminar flow hood. After assembly, the furnace tube and the pushrods were baked under flowing hydrogen at 950°C

for 4 hr and at 900°C overnight. The graphite boat was Rf baked to 1200°C in a 10^{-7} Torr vacuum (followed by backfilling the vacuum chamber with ultrahigh purity nitrogen). The boat, loaded with gallium, was then hydrogen baked in the assembled tube at 850°C for 24 hr. The boat was used for several LPE experiments with several melts before conducting the experiments reported here.

Two series of $(\text{Ga,Al})\text{As}$ epilayers were grown. In the first (series F), ten layers of $\text{Ga}_{1-x}\text{Al}_x\text{As}$ were grown on semiinsulating GaAs :Cr substrates from five melts, with x ranging from 0.02 to 0.18. Each melt was used for growing two layers before being discarded. The first layer grown from each melt is called a 'type-A' layer, the second is called a 'type-B' layer.

The second series of layers (series H) were grown at $x \approx 0.3$, and will be discussed later.

Practical thermodynamic calculated data for the Ga-Al-As system was obtained from the techniques described in Ref. (19) and (20). Figure 1 shows the equilibrium value of x as a function of the amount of Al added to a 10g gallium melt at 700°C . Shown also is the mass of GaAs required to saturate the Ga-Al melt.

0.01 in. MARZ grade Al wire supplied by Materials Research Corporation was used. The thin wire allowed the weight to be carefully selected by measuring the length (1.33 mg/cm). Crystal Specialities undoped

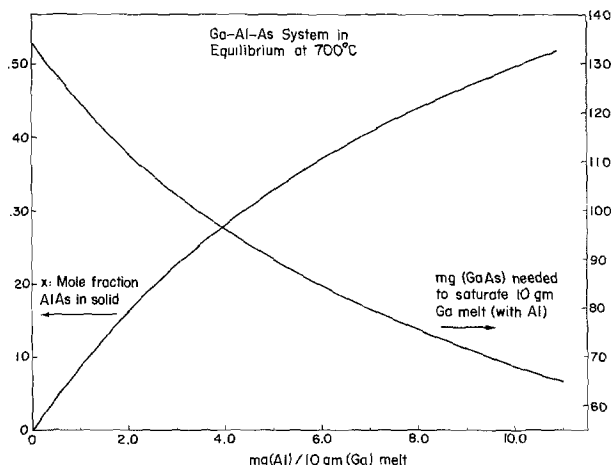


Fig. 1. Solidus isotherms for the Ga-Al-As system at 700°C , [from Ref. (19) and (20)].

Key words: $\text{Al}_x\text{Ga}_{1-x}\text{As}$, high purity, LPE, III-V alloy semiconductor.

GaAs (with $\mu_{300} = 5500 \text{ cm}^2/\text{Vsec}$) was used as the source of arsenic. About 95% of the amount of GaAs required for saturation was added to the melt.

Growth melts were prepared as follows. The amounts of Al and GaAs required were first weighed out. Two pieces of aluminum, each of the required mass, were taken. The GaAs source material was standard cleaned, etched, and loaded into the growth well of the boat with a 10g ingot of six nines gallium (supplied by Alusuisse). The Ga + GaAs melt was baked for 36 hr at 700°C before adding the aluminum. Both pieces of aluminum were ultrasonically cleaned in organic solvents, and then etched in HF: methanol (1:1) in a plastic beaker at room temperature for 3 min. After the etching step, the Al oxidation was minimized by rinsing in methanol, and transferring under methanol into the nitrogen atmosphere of the glove box, where one of the pieces was dried in a flowing stream of dry nitrogen and added to the melt. The second piece of aluminum was weighed to estimate the weight loss of the loaded piece due to etching.

Types A and B epilayers were grown from the melts according to the following steps: (i) Load first set of source-seed substrate (s-s, undoped GaAs) and main substrate (m-s, nonconverting S.I. GaAs) in the boat at the same time the Al is added to the melt. (ii) After purging reactor with H_2 for 75 min (flow rate = 750 ml/min), bake at 700°C for 23 hr. (iii) Bring s-s under melt to saturate melt for 1 hr. (iv) Start ramp cooling (at 12°/hr). (v) After 15 min of growth on the s-s, initiate growth on m-s. (vi) Grow on m-s for 135 min, then end growth and cool reactor. (vii) Unload m-s and s-s. Load new m-s and s-s for 2nd run (type B) from melt. (viii) Repeat steps 2 through 6. (ix) Unload m-s and s-s. Discard melt. Prepare next melt.

It was not established whether or not it was necessary to reduce the air exposure of the etched aluminum. Dawson (21) and others (22) have emphasized the need to prevent any aluminum oxide being formed in the melt if good quality epitaxial layers are desired. They accomplish this by using techniques described in Ref. (21) and (22) and obtain shiny oxide-free melts. In our experience, a thin light brown oxide scum was observed on the Ga-Al-As melts, although it did not interfere with the growth of epilayers, which always had excellent surface morphologies (Fig. 2). However, the s-s's usually attained poor surface morphologies showing incomplete wetting (Fig. 3). We believe that the s-s was instrumental in wiping clean any oxide slag present at the bottom of the melt, thus providing a clean melt interface to the m-s.

As expected, the slag increased with each run. One melt (not of the F-series) was used for four growth

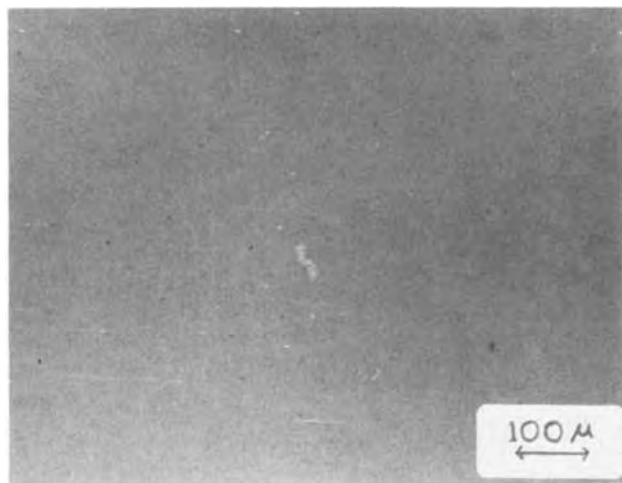


Fig. 2. Photomicrograph of the typical surface morphology of grown $\text{Ga}_{1-x}\text{Al}_x\text{As}$ layers.

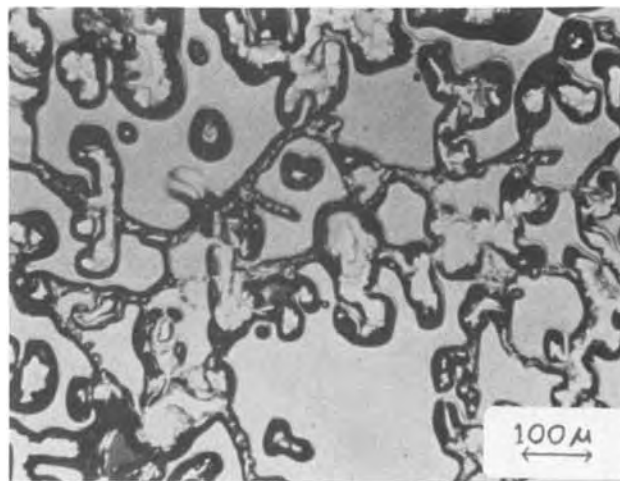


Fig. 3. Photomicrograph of the source-seed after a growth run, showing incomplete wetting presumably caused by oxide under the melt.

runs. Only in the fourth run were any major morphology problems observed, and that over less than half the substrate area.

Composition Determination

Layer compositions were obtained from 5°K photoluminescence (PL) measurements. Radiative efficiencies were found to be significantly lower than normally observed for $\text{Ga}_{1-x}\text{Al}_x\text{As}$. A likely cause was the postgrowth immersion in concentrated HCl to dissolve small melt droplets. It was suspected that HCl affected surface stoichiometry to greatly enhance the nonradiative recombination processes.

Values of x measured by PL correspond to the layer surface. We studied the uniformity of x with depth for sample F-18, using secondary ion mass spectroscopy (SIMS). The Al response was found to increase almost linearly by ~12% from the layer surface to the substrate interface, over a thickness of 9.2 microns.

Results of composition measurements are compared in Table I with values predicted theoretically from Fig. 1. For simplicity, layer compositions were assumed constant and equal to the surface values measured by PL. The theoretical compositions for type A layers correspond to the weight of Al added to the melt. For type B layers, the lowering of the aluminum content of the melt was estimated from the composition and thickness of the corresponding type A layer. Good agreement between theory and experiment supports the validity of the thermodynamic calculations of Ref. (19) and (20).

Carrier Density and Mobility Determination

Van der Pauw Hall samples were made from each $\text{Ga}_{1-x}\text{Al}_x\text{As}$ epilayer with x below 0.2, and tin dots were alloyed in a hydrogen atmosphere using a strip heater. Good ohmic contacts were easily obtained. However, this technique did not work for the series of $x \approx 0.3$ samples, with a native oxide on the surface preventing the tin from alloying with the semiconductor.

The results of room temperature and 77°K electron concentrations and mobilities determined by Hall measurements at $B = 2000\text{G}$ are presented in Table II, which also lists the n_{295} determined by C-V profiling using Au Schottky barriers. "Uncorrected" Hall carrier densities were obtained by assuming the electrical thickness of the epilayers to be equal to their metallurgical thickness. Fairly large discrepancies were observed between the uncorrected n_{Hall} and $n_{\text{C-V}}$. However, by accounting for the depletion of free carriers near the surface and the substrate interface of the epilayers (23), so that the electrical thickness was lower

Table I. Composition data on Ga_{1-x}Al_xAs layers grown at 700°C

Melt No.	Sample No.	Wt of Al in 10g Ga (mg)	Thickness (microns)	x_{theory} (%)	Wt of Al depleted (mg)	Photolum (5°K) peak energy (eV)	x from photoluminescence† (%)
I	A	F-10	0.25	11.1	2.1	1.545	2.0
	B	F-11	0.22*	11.1	1.75	1.541	1.75
II	A	F-12	0.56	12.0	5.1	1.581	4.6
	B	F-13	0.48*	13.9	4.3	1.577	4.2
III	A	F-14	1.0	11.4	8.8	1.632	8.2
	B	F-15	0.87*	13.0	7.7	1.625 (uncertain)	7.8
IV	A	F-16	1.5	11.1	12.6	1.682	11.8
	B	F-17	1.31*	10.3	11.3	1.670	11.0
V	A	F-18	2.13	9.3	17.1	1.744	17.7
	B	F-19	1.92*	9.5	15.6	1.726	15.4

* Estimated

† Best estimated value

Table II. Carrier density measurements on Ga_{1-x}Al_xAs samples

Melt	Type	Run No.	$x\%$ (approx)	μ_{77} (cm ² /Vsec)	μ_{295} (cm ² /Vsec)	n_{Hall} Uncorrected ($\times 10^{14}$ cm ⁻³)	$n_{\text{C-V}}$ ($\times 10^{14}$ cm ⁻³)	n_{Hall} Corrected ($\times 10^{14}$ cm ⁻³)
I	A	F10	2.0	74,200	8,080	3.2	6.2	4.6
	B	F11	1.75	80,950	8,070	4.5	7.2	6.0
II	A	F12	4.6	57,550	7,225	5.9	7.8	7.4
	B	F13	4.2	70,450	7,770	4.3	7.6	5.3
III	A	F14	8.2	43,000	6,500	5.7	7.4	7.2
	B	F15	7.8	56,600	7,190	4.7	5.9	6.0
IV	A	F16	11.8	32,200	5,840	7.6	8.4	9.0
	B	F17	11.0	45,650	6,655	3.5	6.8	4.6
V	A	F18	17.7	23,850	5,130	8.0	9.8	9.6
	B	F19	15.4	30,650	5,680	1.7	2.7	2.6

than the metallurgical thickness, this discrepancy was reduced significantly.

Carrier freezeout in these samples, on cooling from 295° to 77°K, was well within experimental error, and was therefore not considered to be significant. This indicated that the donors in the Ga_{1-x}Al_xAs epilayers were predominantly shallow, thereby ruling out the possibility that the main donor species was oxygen.

The electron mobility of Ga_{1-x}Al_xAs was found to drop rapidly with x . Figures 4 and 5 show the μ_{77} and μ_{295} of the F series layers plotted against x . At both temperatures, the experimental points fall along two distinct curves, one for the type A samples, and the other for the type B samples. For each A-B pair grown from the same melt, the type B sample has a significantly higher mobility than the type A sample, at both temperatures. The decrease in x can account for only a small fraction of the increase in μ , as is clearly seen in Fig. 4 and 5. It is therefore reasonable to infer that the type B samples are significantly purer than the type A samples.

The large reduction of μ_{77} with x cannot be accounted for by the relatively small increase in the electronic effective mass m^* in the range $0 < x < 0.2$ (24). Hence the decrease in mobility must be largely caused by increased electron scattering. Upper valley transport and intervalley scattering at low fields are negligible for $x < 0.2$ at 77°K (9), while phonon scattering is expected to remain approximately constant as x increases. That leaves ionized impurity scattering and alloy (25) space-charge (26) scattering.

To determine the cause of the increase in scattering with x in our samples, we undertook a study of the intravalley scattering mechanisms in Ga_{1-x}Al_xAs. The details of this investigation will be described elsewhere (27). Use was made of the different temperature dependence of alloy scattering and ionized impurity scattering. Hall data was taken on the Ga_{1-x}Al_xAs

samples at 25°-110°K at B = 2000G. Figure 6(a) and (b) show the plots of μ_H vs. temperature measured. By fitting this data to our theoretical model, we were able to obtain estimates of N_A and N_D , as well as information on alloy scattering for each sample.

The alloy and space charge scattering mechanisms were grouped together because two scattering cross sections have the same energy and temperature dependence (28). Kaneko *et al.* (28) and Stringfellow (29) have found space charge scattering to dominate over alloy scattering in their samples. The same empirical x -dependent space charge scattering factor

$$N_s Q = 5 \times 10^3 + 6.3 \times 10^5 x \text{ (cm}^{-1}\text{)} \quad [1]$$

is used by both authors to obtain good agreement between theory and experiment. In our layers, however, the extent of alloy/space-charge scattering was only a fraction (7-15%) of that suggested by Eq. [1], and could be accounted for by alloy scattering alone. We could therefore conclude that our (Ga,Al)As samples were high quality with a minimal density if any of the space-charge scatterers described in Ref. (26).

The increase of phonon and alloy scattering and the decrease of ionized impurity scattering with increasing temperature causes the μ vs. T curves to peak at a temperature T_{max} , which is lower for purer samples. The curves in Fig. 6 show T_{max} to be in the range 50°-60°K, indicating that (i) these samples are pure, rather than heavily compensated, and (ii) the type B samples are purer than their type A counterparts.

Values of N_A and N_D obtained from this analysis are plotted in Fig. 7. The heavy lines connect values of type A samples, while thin lines connect type A points to corresponding (same melt) type B points. The following observations are clear: (i) For type A samples, N_D increases with x , while N_A remains approximately constant, (ii) For each A-B pair, both N_A and

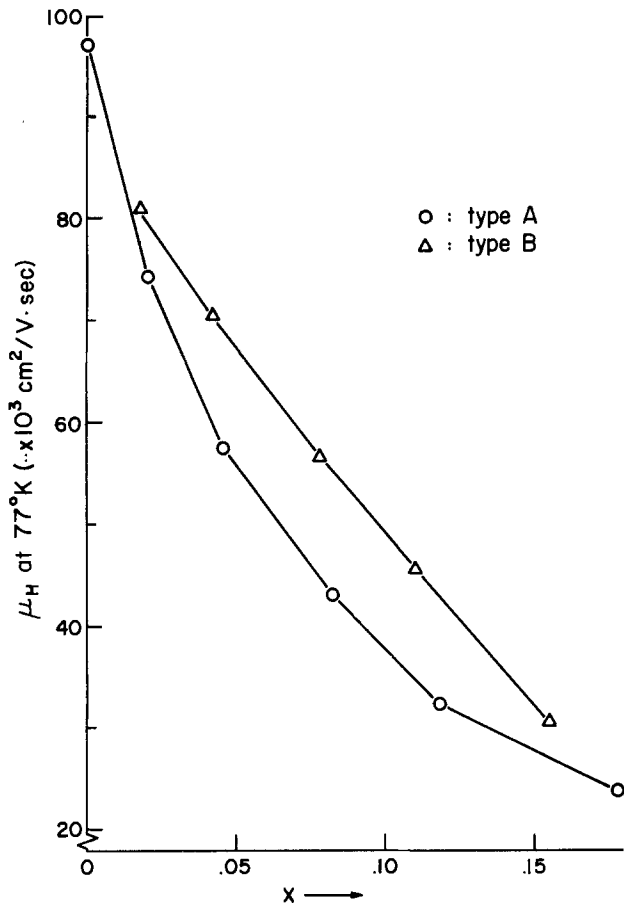


Fig. 4. 77°K Hall mobility data (at 2 KG) of $Ga_{1-x}Al_xAs$ layers, plotted against x .

N_D are lower for the type B sample. However, the decrease in N_D is larger, resulting in a lower net car-

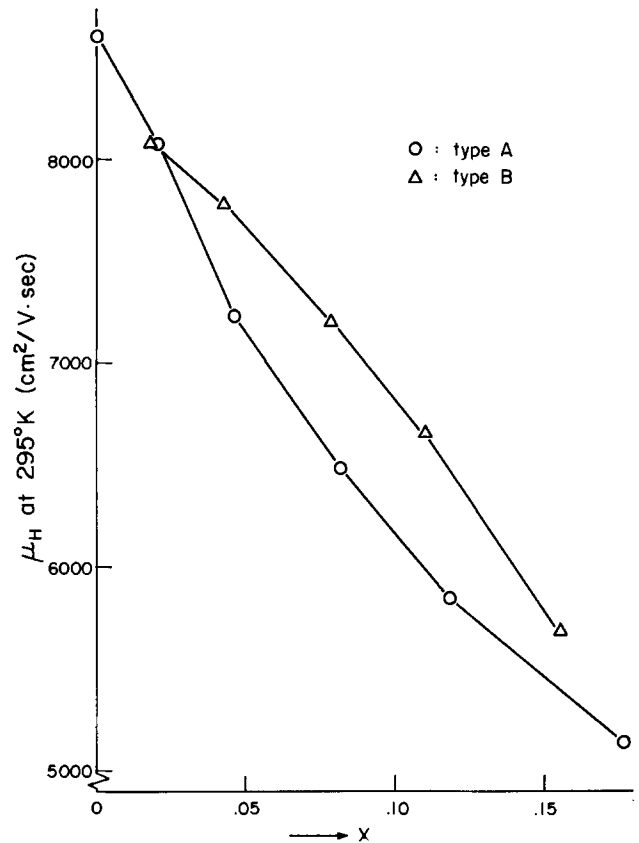


Fig. 5. Room temperature Hall mobility data (at 2 KG) of $Ga_{1-x}Al_xAs$ layers, plotted against x .

rier concentration, and (iii) The compensation ratio $(N_D + N_A)/(N_D - N_A)$ is ≈ 2 for most samples, and < 4 for all samples, as is typically observed in undoped GaAs.

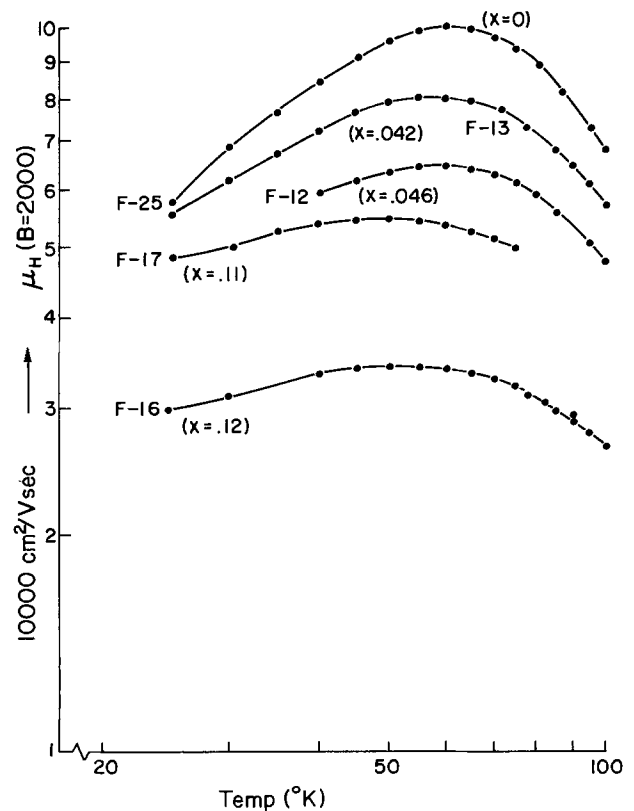
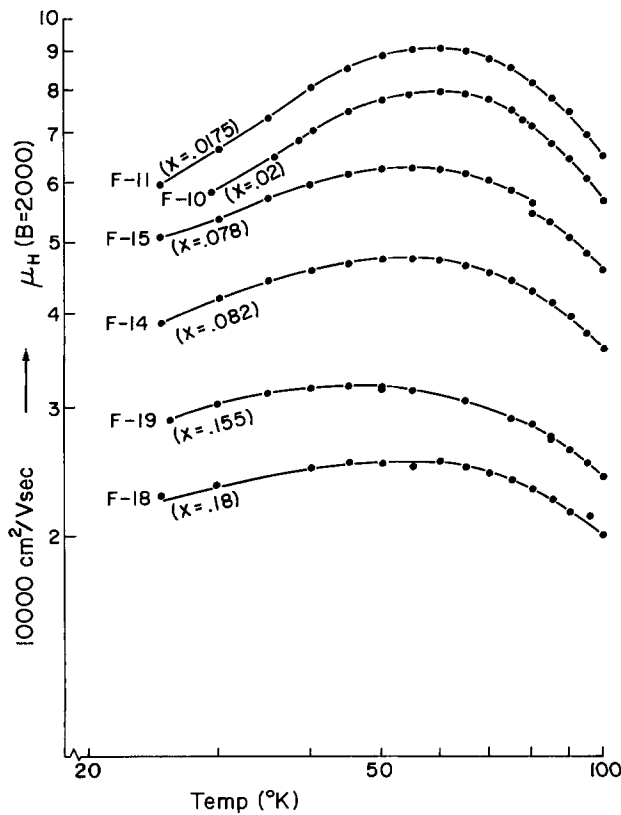


Fig. 6 (a), left (b), right, Temperature variation of Hall mobility (at 2 KG) for the $Ga_{1-x}Al_xAs$ layers

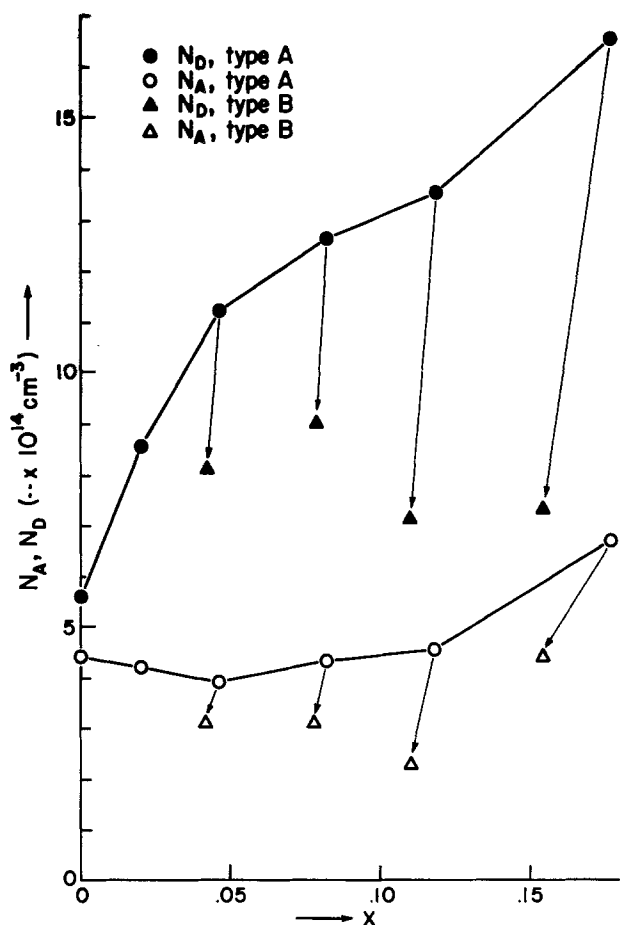


Fig. 7. Donor and acceptor densities vs. x for type A and type B $\text{Ga}_{1-x}\text{Al}_x\text{As}$ layers.

Discussion

An explanation of these experimental results is that a donor species is introduced into the melt with the aluminum. Examining the supplier's material analysis (30) reveals that the major impurities present in the aluminum are O (30 ppm), C (20 ppm), N (5 ppm), S (5 ppm), H (3 ppm), Ca (0.3 ppm), and Mg (0.26 ppm). All other impurities have quoted concentrations below 0.1 ppm. Segregation coefficients of Sn and Si in GaAs are too low to account for the increase in the donor densities. The group VI donors, however, namely S, Se, and Te, have estimated segregation coefficients (K) of ~ 45 , 14, and 4.5 (31, 32) respectively at 700°C . We have already ruled out oxygen as a possibility. Thus the donor introduced with the aluminum is most likely to be sulfur.

A simple calculation for sample F-14 (for example) shows that there is approximately one atom of Al present in the melt for every 3870 atoms of Ga, and 5 ppm S in Al corresponds to one atom of sulfur for every 7.8×10^8 atoms of gallium. Using $K = 45$ gives a donor incorporation of about $1.3 \times 10^{15} \text{ cm}^{-3}$, which is the correct order of magnitude. (The close agreement of this number with the experimental value of N_D for F-14 is, of course a coincidence.) Thus our contention that the donor is sulfur is quite plausible.

The donor density in the melt drops quite significantly for the second (type B) epigrowth. Donor incorporation into the type A epilayer can account for only a 1% reduction of the donor concentration in the melt. Some other mechanism of donor loss from the melt must therefore exist.

Further experiments (H-series) were conducted in an effort to obtain purity in $\text{Ga}_{1-x}\text{Al}_x\text{As}$ at $x = 0.3$. With a total bake time of 40 hr at 700°C after the addition of aluminum, the carrier concentration obtained

in the first epilayer (type A) was $2.5 \times 10^{15} \text{ cm}^{-3}$ ($\pm 25\%$). For a second melt, a total bake time of 92 hr at 700°C after adding aluminum gave a first epilayer with $n = 1.4 \times 10^{15} \text{ cm}^{-3}$. A third melt was baked after adding aluminum at 900°C for 13 hr followed by 92 hr at 700°C , before growing the first epilayer. The carrier concentration obtained was $1.1 \times 10^{15} \text{ cm}^{-3}$. In each of the three cases, the substrates were loaded and baked along with the melt for 22 hr prior to growth.

In their study of Cr doping of high purity n GaAs epilayers grown at 700°C , Woodard and Eastman (32) have used the technique of baking the Ga-As-Cr melt at 900°C for 15 hr to remove a volatile donor impurity that is introduced with the chromium. This, however, increases the silicon contamination of the melt, which must then be baked at 700°C to lower the silicon concentration. They have shown that about 96 hr of baking at 700°C brings the total Si incorporation to $\lesssim 2 \times 10^{14} \text{ cm}^{-3}$. Our observations on growth from Ga-Al-As melts show the positive effect of such baking techniques on layer purity, but also indicate that the purification process is slower than in the Ga-As-Cr case. This is probably because the oxide on the melt prevents the sulfur from escaping, except through cracks.

We suspect that the oxide slag itself is responsible for gettering the impurities from the melt. We speculate that each time the boat is taken out of the furnace tube into the glove box, trace amounts of oxygen are trapped between the surfaces of the boat. On baking, some oxygen diffuses to the melt forming aluminum oxide which collects at the melt's surfaces. The extent of impurity gettering by the slag is limited by the amount (of slag) produced; hence the correlation between the number of previous epi-runs from a melt and the layer purity.

In conclusion, we have obtained the highest purity in $\text{Ga}_{1-x}\text{Al}_x\text{As}$ ($x < 0.3$) reported so far to our knowledge by growing at 700°C in a clean environment, and by following baking procedures after adding aluminum to the melt. These layers were grown in a reactor which gives a μ_{77} of only 100,000 cm^2/Vsec for undoped GaAs, compared with 150,000-170,000 cm^2/Vsec obtained in the best systems in our laboratory, indicating room for further improvement. Also, the possibility exists of using Woodard's (33) $900^\circ + 700^\circ\text{C}$ baking technique to obtain even higher purity, provided oxide slag formation can be prevented by using Dawson's methods (21).

Acknowledgments

We are indebted to Dr. Ron Nelson of Bell Labs for the photoluminescence measurements, to Dr. David Hodul of Cornell for the SIMS profiles, and to our colleague Dr. Colin Wood for his critical appraisal and helpful comments with the manuscript. This work was supported by the Office of Naval Research under Contract No. N00014-75-C-0739.

Manuscript submitted April 6, 1979; revised manuscript received June 29, 1979.

Any discussion of this paper will appear in a Discussion Section to be published in the December 1980 JOURNAL. All discussions for the December 1980 Discussion Section should be submitted by Aug. 1, 1980.

Publication costs of this article were assisted by Cornell University.

REFERENCES

1. J. F. Black and F. M. Ku, *This Journal*, **113**, 249 (1966).
2. H. Rupprecht, J. M. Woodall, and G. D. Pettit, *Appl. Phys. Lett.*, **11**, 81 (1967).
3. K. J. Linden, *J. Appl. Phys.*, **40**, 2325 (1969).
4. Zh. I. Alferov, V. M. Andreyev, V. I. Korol'kov, E. L. Portnoi, and D. N. Tret'yakov, *Sov. Phys. Semicond.*, **2**, 1289 (1969).
5. H. Kressel and H. Nelson, *RCA Rev.*, **30**, 106 (1969).

6. I. Hayashi, M. B. Panish, and P. W. Foy, *IEEE J. Quantum Electron.*, **5**, 211 (1969).
7. J. M. Woodall, U.S. Pat. 3,675,026 (1972).
8. M. S. Saidov, V. V. Nikitin, B. Sadaev, G. N. Kovardakova, and A. S. Saidov, *Sov. Phys. Semicond.*, **10**, 1038 (1976).
9. T. Sugeta, A. Majerfeld, A. K. Saxena, P. N. Robson, and G. Hill, Proceedings of 6th Biennial Cornell Elec. Engineering Conf., p. 45, Cornell University, Ithaca, New York (1977).
10. D. V. Lang and R. A. Logan, *Appl. Phys. Lett.*, **31**, 683 (1977).
11. C. M. Garner, Y. D. Shen, C. Y. Su, G. L. Pearson, and W. E. Spicer, *J. Vac. Sci. Technol.*, **15**, 1480 (1978).
12. D. Cheung, Ph.D. Thesis, Stanford University (1975).
13. C. S. Kang and P. E. Green, *Appl. Phys. Lett.*, **11**, 171 (1967).
14. H. G. B. Hicks and D. F. Manley, *Solid State Commun.*, **7**, 1463 (1969).
15. H. Morkoc and L. F. Eastman, *J. Cryst. Growth*, **36**, 109 (1976).
16. A. Chandra and L. F. Eastman, *Electron. Lett.*, **15**, 90 (1979).
17. A. Chandra and L. F. Eastman. "The Use of a $\text{Ga}_{1-x}\text{Al}_x\text{As}$ -GaAs Interface for Electron Confinement in Low Noise FETs," presented at the Workshop on Compound Semiconductor Materials and Devices, San Francisco, Feb. 1978, proceedings unpublished.
18. H. Morkoc and L. F. Eastman, *This Journal*, **123**, 906 (1976).
19. M. Ilegems and G. L. Pearson, Proceedings of the 1968 International Symposium on Gallium Arsenide, p. 3, Institute of Physics and Physical Society Conference Series No. 7, London (1969).
20. M. B. Banish and M. Ilegems, in "Progress in Solid State Chemistry," Vol. 7, H. Reiss and J. O. McCaldin, Editors, p. 39, Pergamon Press, Oxford (1972).
21. L. R. Dawson, *J. Cryst. Growth*, **27**, 86 (1974).
22. J. M. Woodall and H. J. Hovel, *ibid.*, **39**, 108 (1977).
23. A. Chandra, C. E. C. Wood, D. Woodard, and L. F. Eastman, *Solid State Electron.*, To be published.
24. R. Dingle, R. A. Logan, and J. R. Arthur, Jr., Gallium Arsenide and Related Compounds (Edinburgh, 1976), p. 210, Institute of Physics Conference Series No. 33a, London (1977).
25. J. W. Harrison and J. R. Hauser, *Phys. Rev. B*, **13**, 5347 (1976).
26. L. R. Weisberg, *J. Appl. Phys.*, **33**, 1817 (1962).
27. A. Chandra and L. F. Eastman, Submitted to *J. Appl. Phys.*
28. K. Kaneko, M. Ayabe, and N. Watanabe, Gallium Arsenide and Related Compounds (Edinburg, 1976), p. 216, Institute of Physics Conference Series No. 33a, London (1977).
29. G. B. Stringfellow, *J. Appl. Phys.*, To be published.
30. Materials for Research Catalogue, Materials Research Corporation, Orangeburg, New York 10962.
31. C. S. Kang and P. E. Greene, Proceedings of the 1968 International Symposium on Gallium Arsenide, p. 18, Institute of Physics and Physical Society Conference Series No. 7, London (1969).
32. H. G. B. Hicks and P. D. Greene, Private communication.
33. D. Woodard, Ph.D. Thesis, Cornell University (1979).

Bird's Beak Configuration and Elimination of Gate Oxide Thinning Produced during Selective Oxidation

T. A. Shankoff, T. T. Sheng, S. E. Haszko, R. B. Marcus, and T. E. Smith

Bell Laboratories, Murray Hill, New Jersey 07974

ABSTRACT

In the selective oxidation scheme for processing Si MOS devices, Si_3N_4 is used to mask gate oxide areas against the isolation oxidation. After removing the Si_3N_4 , gate oxide is grown. This scheme produces three topographical features which have ramifications in subsequent processing and in device properties: a notch in the isolation oxide, penetration of the isolation oxide under the masking Si_3N_4 , and thinning of the gate oxide at the isolation oxide edge; the first two features form the bird's beak configuration. The transmission electron microscope was applied to thin film ($<1 \mu\text{m}$) cross sections through the bird's beak in order to obtain an accurate description of these features. The bird's beak extended typically 1.5 and 0.8 μm in the n- and p-channel structures, respectively, leading to a corresponding decrease in the active device length of 3.8 and 2.3 μm for the 1.4 μm thick isolation oxide. Gate oxide at the edge of the bird's beak was thinned 35-100% in the n-channel samples and 20-50% in the p-channel samples. It was found that oxidation subsequent to the isolation oxidation and Si_3N_4 removal destroys the oxidation barrier (wet oxidation seemingly more effective than dry and more convenient). Thus, a method which incorporates an additional, short, sacrificial wet oxidation step between isolation and gate oxidations, in order to overcome the thinning phenomenon, is described.

One of the Si IC device processing schemes designed to minimize surface texture is the selective oxidation process. According to this method the initial isolation oxide is formed by selective thermal oxidation using a Si_3N_4 mask over regions of the chip that will later become active device areas. In this manner, the SiO_2 step at the surface is reduced by $\sim 50\%$ compared with the step height in conventional processing.

It has been observed that this processing scheme produces a bird's beak configuration (1-4) at the edge of the isolation oxide, and that subsequent gate oxidation (after removal of masking Si_3N_4) often results in a thinning of the gate oxide next to the isolation oxide. The thinning of the gate oxide has been attributed to the presence of a thin layer of a Si nitride (or oxynitride) on the Si which serves as a barrier to oxida-

tion; the nitride is believed to occur as a result of NH_3 generation from the masking Si_3N_4 during isolation oxidation followed by interaction of the NH_3 with the Si substrate (2). One processing procedure that has been introduced in an attempt to minimize the frequency of occurrence or magnitude of this anomalous thinning is the use of an additional Si_3N_4 etch (4). After the isolation oxide is grown, the masking oxide or oxynitride over the Si_3N_4 , the Si_3N_4 , and the underlying oxide layer (called the "pad oxide") are removed by BHF, hot H_3PO_4 , and BHF, respectively. An additional hot H_3PO_4 treatment is used to dissolve any Si nitride that might exist on the Si surface. However, oxide thinning is sometimes observed even after the additional Si_3N_4 etch is used and is sometimes not observed without the second etch. Gate oxide thinning has an important influence on the properties of the transistor subsequently built in that region, and the fact that the magnitude of the oxide thinning is variable only emphasizes the serious nature of the problem.

This study was initially intended to describe in some detail the configuration at the bird's beak region which results from selective oxidation processing, with particular attention directed to gate oxide thinning.¹ During this work, sufficient understanding of the thinning phenomenon was generated so as to result in the development of a convenient method for its elimination. We will address this topic after an initial discussion of the typical selective oxidation structure.

Experimental

Samples were examined at various stages of selective oxidation processing by making thin film cross sections through the bird's beak using a technique described earlier (6) and performing the examination with the transmission electron microscope. Some studies were also made by scanning electron microscopy. Seven p-channel (111) wafers were studied. These wafers were processed through the intermediate dielectric stage; they were then sectioned and examined in the TEM. Six samples from three (100) wafers receiving n-channel processing also were examined; these samples represented five stages in processing. The processing sequence is outlined in Table I; a list of samples is shown in Table II.

The samples studied with the transmission electron microscope were sections through the bird's beak along a plane orthogonal to both the sample surface and the edge of the isolation oxide on the device surface. The samples were prepared by (i) cleaving small pieces from the wafer, (ii) mounting 6-8 pieces on their sides, embedding in epoxy, (iii) lapping the composite to a thickness of 100-150 μm , and (iv) ion mill thinning to a final thickness of $< 1 \mu\text{m}$. Studies were performed on a JEM200A transmission microscope at 200 keV. In some cases the device surfaces of samples were coated with $\sim 0.5 \mu\text{m}$ polysilicon before thinning to protect the surfaces during handling.

Some samples were also examined with a Cambridge Stereoscan scanning electron microscope at 20 keV.

Results and Discussion

Structural study.—The main features of the isolation and gate oxides formed during both n- and p-channel processing are shown in the low magnification electron micrographs of samples A and B in Fig. 1. Figure 1(a) shows the 1.5 μm isolation oxide at the sides, and 1000Å SiO_2 under the 1200Å Si_3N_4 at the center. The isolation oxidation left notches in the oxide at the edges of the Si_3N_4 (N). After removal of the Si_3N_4 and the underlying oxide, the notch features are made softer [Fig. 1(b)] and after gate oxidation, some

¹A similar study of a gate oxide thinning was just concluded for the case of conventional processing, where it was shown that thinning results from the slower oxidation rate at the instep at the Si-isolation oxide interface, in turn controlled by the steepness of the field oxide wall and the angle of the instep (5).

Table I. Processing*

Clean wafers
1100°C dry oxide, 300-1000Å
1200Å CVD Si_3N_4 (masking nitride)
1000Å CVD SiO_2 (masking oxide) or wet oxidation to form oxynitride mask
Isolation oxide P-L; BHF etch: resist strip and clean
H_3PO_4 etch
BHF, 1 min (if 1000Å CVD SiO_2 used)
1000°C wet, 460 min (isolation oxidation)
BHF, 1 min (oxynitride removed)
H_3PO_4 etch (masking Si_3N_4 removed)
This is the point in processing where additional oxidation to eliminate the thinning phenomenon is inserted
BHF, 2 min (or less)
H_3PO_4 etch (second Si_3N_4 etch** (an option))
Clean wafers
1000°C, 30 min dry O_2 (gate oxidation)
Polysilicon gate level processing
Intermediate oxide deposition, processing
Metallization

* This is the typical processing scheme used for all samples; some processing steps used such as chanstop implant are omitted for the sake of brevity.

** This step was omitted in the processing of samples I and K.

Table II. Samples used in study

Sample	Process	Sample removed after step	Wafer
A	p-channel	isolation oxidation	1
B	p-channel	gate oxidation	2
C	p-channel	intermediate oxide deposition	3
D	p-channel	intermediate oxide deposition	3
E	p-channel	intermediate oxide deposition	3
F	n-channel	isolation oxidation	4
G	n-channel	Si_3N_4 etch	4
H	n-channel	gate oxidation	4
I	n-channel	gate oxidation	5*
J	n-channel	gate oxidation	4
K	n-channel	intermediate oxide deposition	6*
L	n-channel	gate oxidation	7

* Did not receive second Si_3N_4 etch.

thinning of the gate oxide is seen (T) at the typical location, just outside the bird's beak (B).

Higher magnification electron micrographs of the bird's beak region in three samples (C, D, E) from a p-channel wafer are shown in Fig. 2. The length of the bird's beak (measured from the lowest point of the notch) is shown for the three samples, and the average value is $\sim 0.8 \mu\text{m}$. Gate oxide thinning produces a dip only in the upper surface of the gate oxide (at the

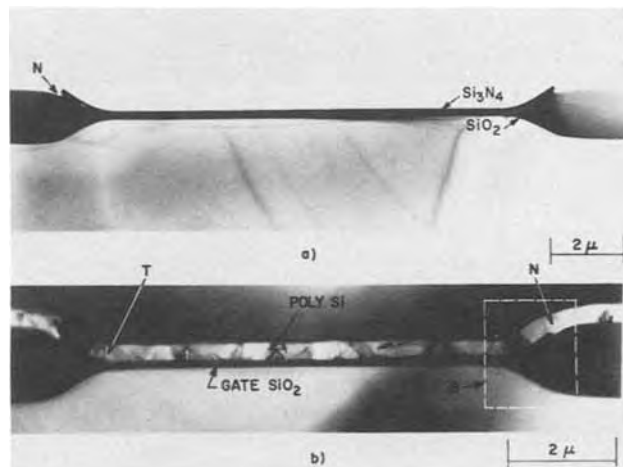


Fig. 1. TEM of cross section of p-channel samples (a) after isolation oxidation (sample A) and (b) after gate oxidation (sample B). The notch left in the isolation oxide following oxidation (N) and the site of gate oxide thinning (T) are shown. The region commonly referred to as the bird's beak is outlined (B).

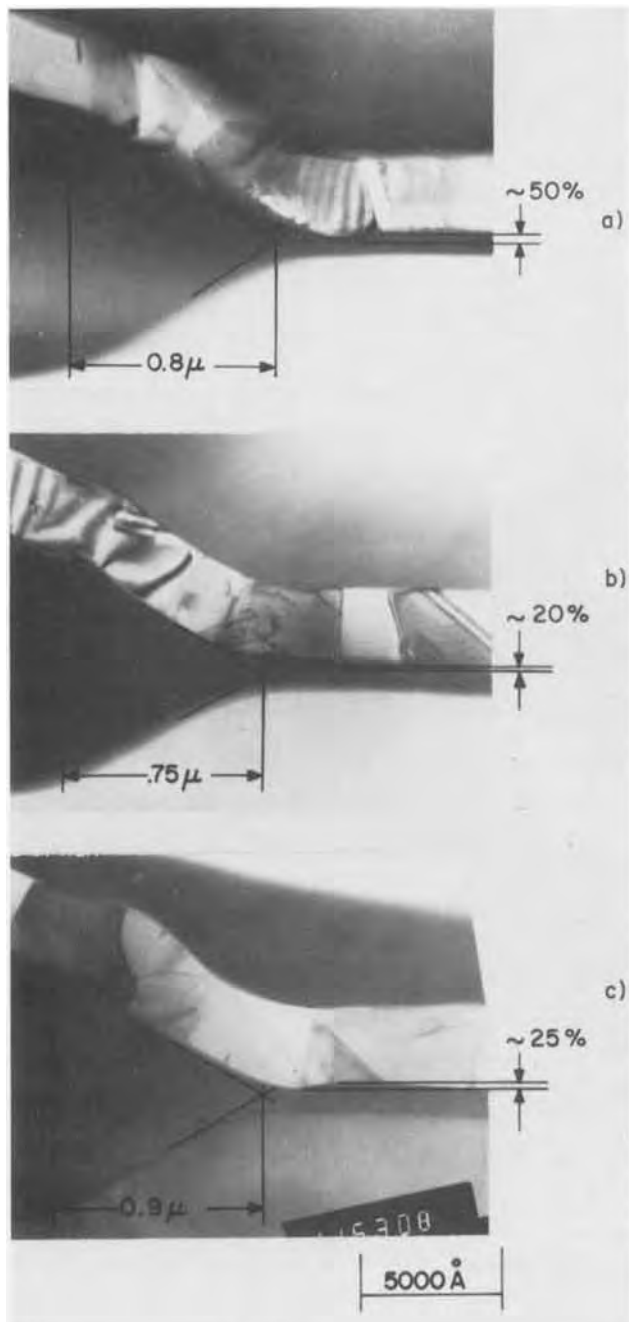


Fig. 2. TEM of cross section of p-channel samples at bird's beak. Figures 2(a), (b), and (c) show samples C, D, E, respectively. The bird's beak length is 0.7-0.9 μm and the percent gate oxide thinning at the sites T are shown.

gate oxide-poly-Si interface) on all the p-channel samples examined. The percentage thinning is indicated for these samples, and the average value is $\sim 30\%$. This value is only approximate since the samples were tilted to varying degrees while being photographed making it difficult to take accurate measurements.

Cross sections of n-channel structures are shown in Fig. 3(a)-(d) (samples F-I, respectively). Figure 3(a)-(c) show parts of the same wafer after the wafer has undergone successive processing treatments. The distance from the point of the bird's beak to the notch [Fig. 3(b)] is 1.5 μm . It is noteworthy that nearly 100% gate oxide thinning was found on sample H [Fig. 3(c)] which had received the second Si_3N_4 etch, while sample I which did not get the second Si_3N_4 etch showed only $\sim 35\%$ gate oxide thinning [Fig. 3(d)]. It should be pointed out that the thinning seen on the n-channel samples is symmetrical, e.g., both surfaces of the gate oxide move together, as would be expected if a barrier

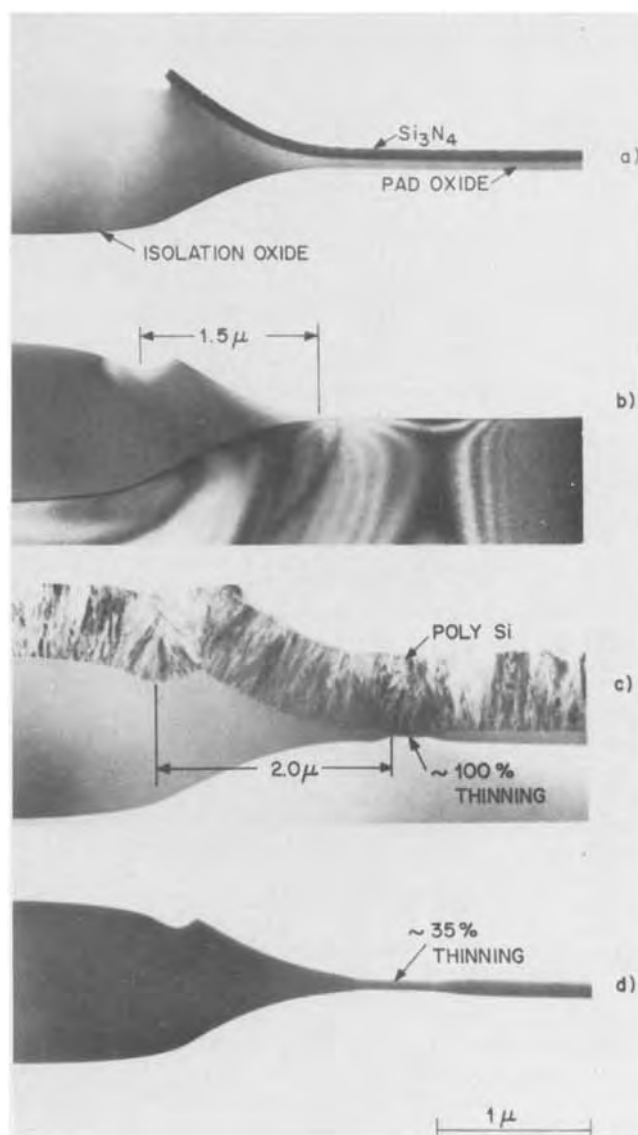


Fig. 3. TEM of cross sections of n-channel samples at bird's beak. Figures 3(a)-(c) show samples F, G, H taken from wafer 4 at different stages of processing; Fig. 3(d) shows sample I. The length of the bird's beak in 3(b) is 1.5 μm , and $\sim 100\%$ and $\sim 35\%$ gate oxide thinning are seen in Fig. 3(c) and (d), respectively.

caused slower oxidation at that site. This is contrary to the case observed with the p-channel samples (Fig. 2) where thinning was one-sided.

Another sample from wafer No. 4 is shown at higher magnification in Fig. 4. Superimposed on the micrograph is an outline of the bird's beak obtained from Fig. 3(d). It is clear that the 0.38 μm oxide thinned region ($\sim 90\%$ thinning) begins near the tip of the beak of the isolation oxide. Some further oxidation at the isolation oxide edge of the beak clearly has occurred during gate oxidation, and it would therefore seem that the barrier to gate oxidation extended only over a distance of $\sim 0.38 \mu\text{m}$ on the Si surface and was not present over most of the bird's beak region. The lack of coincidence of the superposition at the notch is attributed to the undulating character of the notch as one moves along the surface, shown in the scanning electron micrographs of Fig. 5. A top view of wafer K is shown in 5(a) and two parallel lines corresponding to the notch (N) and oxide thinning (T) are visible even through the 1 μm thick P-glass and through the 6000 Å polysilicon. SEM photographs of a cross section of sample L and a top view of the same sample are shown in Fig. 5(b) and 5(c), respectively; the undulating nature of the notch is due to the shape of the masking

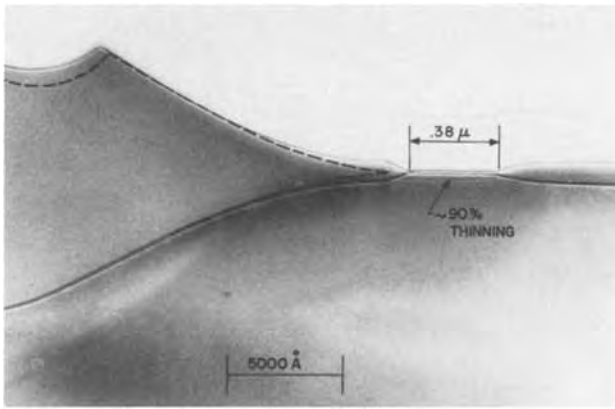


Fig. 4. TEM of cross section of sample J showing $\sim 90\%$ gate oxide thinning and superpositioning of bird's beak profile prior to gate oxidation [obtained from Fig. 3(b)].

Si_3N_4 edge which in turn is a result of photolithographic processing.

The bird's beak can be defined as the horizontal distance between the site where the isolation oxide begins to thicken and the projection of the notch minimum. This value is $1.5 \mu\text{m}$ (Fig. 3(c), 3(d), 4). The

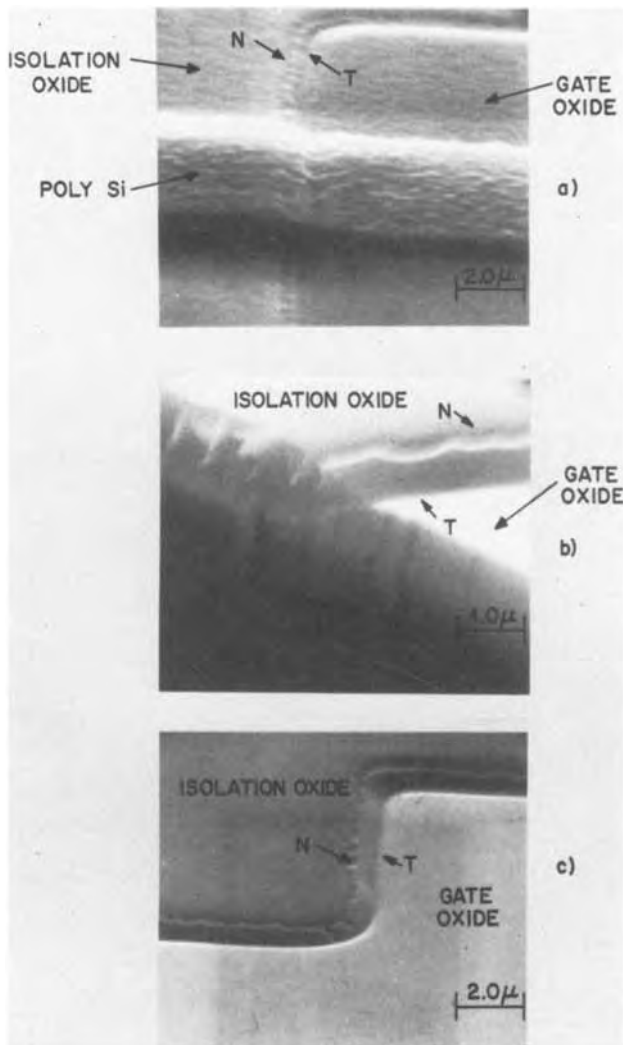


Fig. 5. SEM of samples K (a) and L (b), (c). The isolation oxide notch (N) and gate oxide thinning (T) are indicated. The undulating shape of the notch is partially responsible for the lack of coincidence of the notch in Fig. 4 with the superimposed profile of Fig. 3(b).

source and drain region will be shorter than the measured length of the masking Si_3N_4 before isolation oxidation by $1.5 \mu\text{m} \times$ radial factor. For samples used in the present study with $1.4 \mu\text{m}$ isolation oxide, the shortening is 1.9 and $1.2 \mu\text{m}$ per edge for the n- and p-channel samples, respectively.

The bird's beak length in the p-channel samples is $0.8 \mu\text{m}$ (Fig. 2) and the pad oxide thickness under the 1200\AA Si_3N_4 was 730\AA . In a published study on geometrical features at the bird's beak in a selective oxidation processing scheme (1), a direct correlation was found between beak length and thickness of underlying pad oxide; for a Si_3N_4 thickness of 500\AA and isolation oxide thickness of $0.65 \mu\text{m}$, the bird's beak length changed from 0.55 to $0.75 \mu\text{m}$ as the underlying oxide thickness varied from 100 to 500\AA . The data in Ref. (1) do not permit an easy extrapolation to the thicknesses of isolation oxide and Si_3N_4 used in the present study, and work is in progress to determine the relationship between Si_3N_4 thickness, pad oxide thickness, and beak length.

It is obvious that a barrier to oxidation is present of a type described by Kooi *et al.* (2). The mechanism proposed for formation of the barrier involves reaction of steam and the masking Si_3N_4 in the formation of SiO_2 and NH_3 (or NH_3 -like species) followed by NH_3 diffusion through the oxide pad beneath the Si_3N_4 to the Si substrate at the boundary of the thick and thin oxide regions; subsequent reaction produces some form of Si nitride or oxynitride. The present study shows that in the processed n-channel selective oxidation structure the barrier forms a band which begins near the tip of the bird's beak and extends less than one micron away from the tip. Additional oxidation occurs at the isolation oxide edge during gate oxidation, and the barrier does not extend in a direction into the beak. Sample H [Fig. 3(c)] was from a wafer which received a second Si_3N_4 etch which was added to dissolve the oxidation barrier which is presumed to be a Si nitride or an oxynitride. Sample I shows more gate oxide thinning than sample I [Fig. 3(d)] which did not receive the second etch. It is clear that the gate oxide thinning phenomenon is variable and not predictable, at least for the samples studied here.

A solution of the thinning problem.—Tentatively making the assumption that NH_3 , or a closely related species, is responsible for formation of the oxidation barrier, (100) Si wafers were exposed to various NH_3 ambients, and the subsequent oxidation behavior was noted (7). In that study it was shown that oxidation, though impeded, would commence once the barrier was overcome. In particular, steam oxidation was found to be more effective than dry oxidation in breaking down the NH_3 induced barrier. It was also shown that, once the barrier layer is consumed by oxidation, a normal wet or dry oxide growth curve is obtained. Experiments were continued on patterned wafers processed according to a typical selective oxidation schedule.

After a 1050°C wet isolation oxidation masked by a composite 1200\AA $\text{Si}_3\text{N}_4/1000\text{\AA}$ pad oxide layer, a 3 in. B-doped $\langle 100 \rangle$ wafer was treated in 160°C H_3PO_4 for 60 min and BHF for 90 sec to expose the Si substrate in the gate regions. After dry oxidation at 1000°C to a 1000\AA thickness (typical gate oxide), the wafer was evaluated to determine the degree of oxide thinning. The photograph in Fig. 6(a) is a TEM profile of this wafer after this first gate oxidation, while Fig. 6(b) shows a TEM micrograph of the same wafer after a second 90 sec BHF treatment and dry reoxidation to 1000\AA . It is clear that the initially present thinning is completely eliminated by the reoxidation process. In addition, the profile has approached planarity because of the additional etchback step, but some thick oxide has been lost.

Having found that a certain amount of oxidation either removes the barrier or renders it ineffective as an oxidation inhibitor, we endeavored to identify the

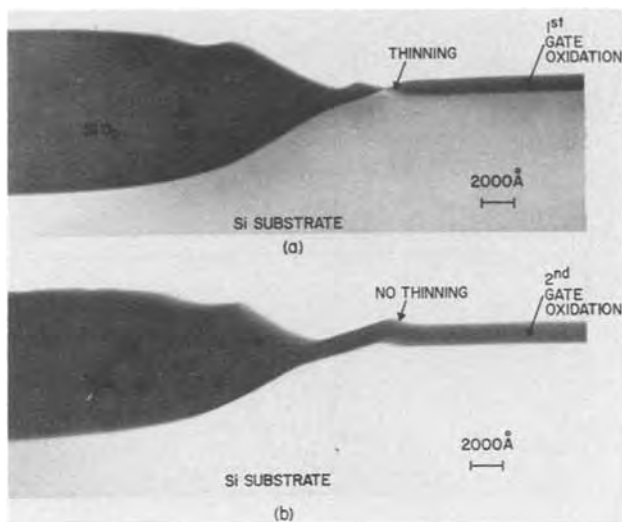


Fig. 6. TEM profiles of the isolation oxide edge as seen on a test wafer. In (a) the initial 1000Å oxide pad was removed in BHF in a 90 sec etch just after the masking Si_3N_4 etch, and a 1000Å dry gate oxide was grown. The thinned region in the gate oxide is clearly seen. In (b) the initial gate oxide was removed by etching for another 90 sec in BHF, and a second 1000Å dry gate oxide was grown. Absence of a thinned region is obvious on this sample.

various processing conditions required to minimize or eliminate the thinning phenomenon. The parameters and processing procedures studied included initial pad oxide thickness, type and degree of oxidation to be used between the isolation and gate oxidations, possible etching alternatives to the intermediate oxidation, and viable etchback schedules.

Because of the tedious nature of the TEM method of study (see experimental section), another means was used to evaluate each experimental sample. It was found that the Talystep surface profilometer with a 1000Å stylus could trace the Si wafer surface at the bird's beak and graphically detail the surface features defined by a TEM photograph. The only ambiguity which arose was definition of oxide thinning for cases where pad oxide etchback was used. In the etchback step, some isolation oxide is removed, and a dip is produced at the edge of the isolation oxide. After subsequent gate oxidation, it is impossible to resolve the oxide thinning because of the overpowering Si dip. For this reason the bulk of our work dealt with samples which did not receive an etchback of the initial pad oxide in processing.

Two different initial pad dry oxidation thicknesses and two types of thermal oxidation were selected for study. Both wet (950°C) and dry oxidations (1000°C) respectively were used for pad oxide thicknesses of 300 and 1000Å. After isolation oxidation (1.2 μm wet at 1050°C), the Si_3N_4 oxidation mask was stripped in BHF (1 min, removes oxynitride surface) and 160°C H_3PO_4 (45 min); the underlying initial pad oxide was left in place. The wafers were cleaned and reoxidized in 500Å steps and were evaluated using the Talystep surface profilometer to determine the degree of oxide thinning in each case.

The control oxidation curves shown in Fig. 7 and 8 were determined from the wafers being measured, by thickness measurement of large thin oxide regions. The curves in each figure for oxidation over the barrier were obtained from Talystep data assuming equal oxide growth both above and below the silicon surface. Thus, where the control data shows that an additional 500Å of oxide was grown, a Talystep depression of 150Å would be taken as only 200Å growth in the barrier region (500Å less $2 \times 150\text{Å}$). Examples of the detail of the Talystep trace in this application may be seen in Fig. 9. From the data it can readily be seen that the

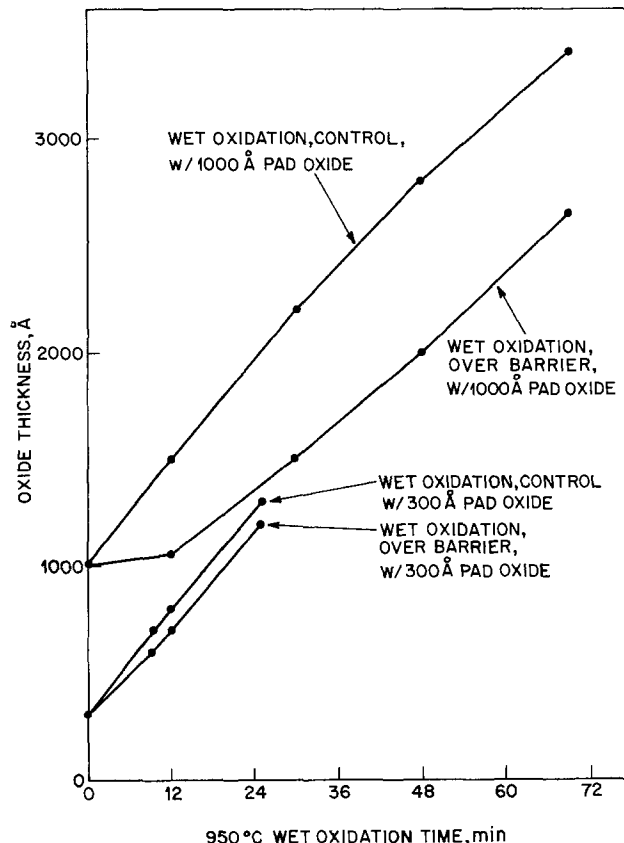


Fig. 7. Wet oxidation curves for wafers having initial pad oxide thicknesses of 300 and 1000Å. Since the pad oxides were in place at the onset of the additional wet oxidation, the curves begin at the respective pad oxide thicknesses. Additional oxidation with time is readily noted in the figure. Control data are from Si regions outside the oxidation barrier regions, while the lower curves in each pad oxide set are within the barrier regions.

wet oxidation is more effective than the dry oxidation, and the presence of the thin initial oxide pad makes removal of the barrier easier than with the thicker pad oxide. Thus, even an additional 300Å wet oxidation of a 300Å pad oxide sample brings the oxidation curve

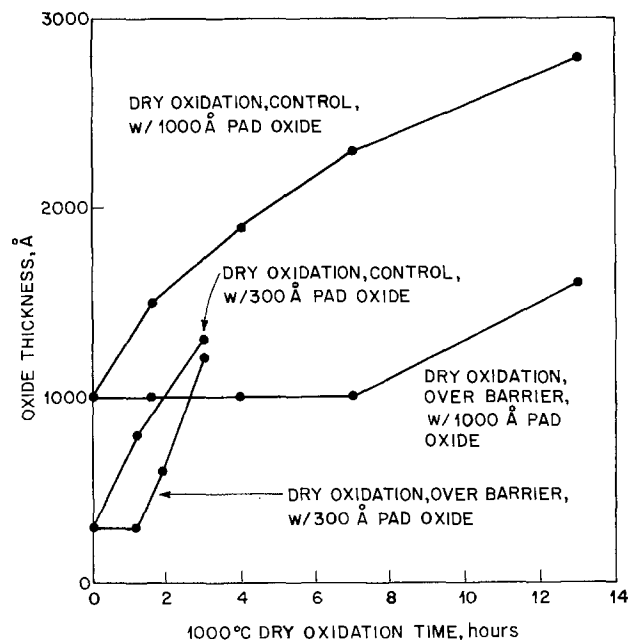


Fig. 8. Dry oxidation curves for wafers having initial pad oxide thicknesses of 300 and 1000Å.

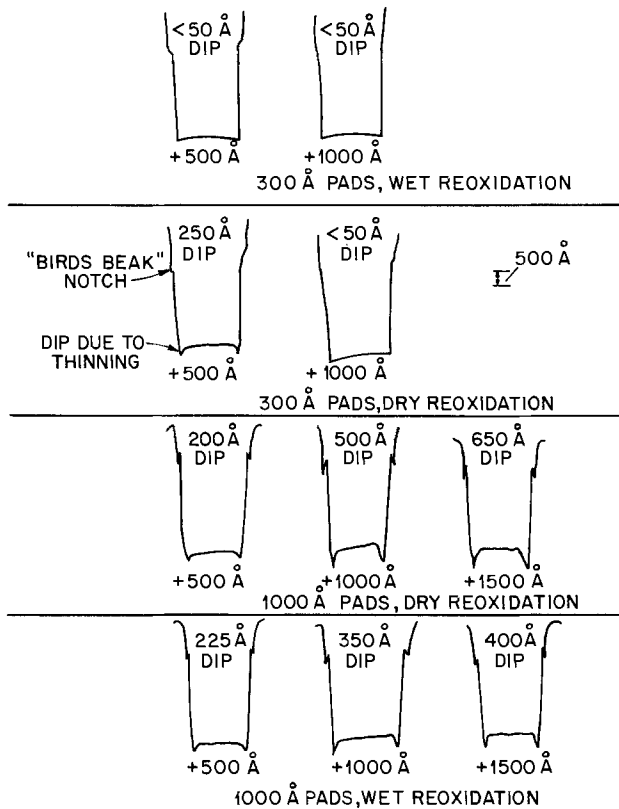


Fig. 9. Typical Talystep traces used to obtain oxidation curves in Fig. 9 and 10. Noted "Dips" must be multiplied by 2 to determine total oxidation inhibition since thinning is symmetrical above and below the Si surface for these samples.

parallel to the control curve, where nearly 2000Å additional dry oxidation is required for a thick 1000Å pad oxide wafer. In three of the four pad oxide thickness-oxidation type curve sets, the onset of normal sample oxidation in the barrier region is indicated by a growth curve which becomes parallel to the control curve, while in the dry oxidation of a 300Å pad oxide, the barrier oxidation appears to "catch up" to the control.

Since the thin pad oxide seemed to be so much more effective in facilitating subsequent removal of the oxidation barrier, the question arose as to whether the thin oxide appeared to be more effective simply because the gaseous oxidation species could reach the barrier layer in the silicon in much higher concentration than in the thicker pad oxide samples. It seemed possible that for the same degree of barrier, the thick oxide simply acted as a much more effective oxidation block. In order to answer this, a thick pad sample was thinned from 1000 to 300Å in BHF just after nitride removal and was halved for wet and dry oxidation treatments. In both the wet and dry oxidations, the samples gave oxidation curves in the barrier region exactly the same as for a thick pad oxide wafer. We are forced to conclude that a thick oxide pad results in an oxidation barrier which is more severe than for thinner pad oxides. Other experiments with samples having no oxide pads which were shown to have no oxidation barrier at all are consistent with this result. Unfortunately, processing without a pad oxide (a stress buffer) generally results in dislocation growth at feature edges due to high Si_3N_4 stress.

As mentioned earlier the underlying oxide pad was not removed in order to facilitate the use of the Talystep as a diagnostic tool. An even more important point is that etching of the pad oxide, no matter how minimal the overetch, will always expose the Si barrier region to chemical attack and thus confuse the data. This had perhaps been noted in our earlier diagnostic

work as evidenced by the variability in the percent thinning of samples oxidized after the pad was removed in BHF. As will be mentioned later, extended BHF treatment can minimize the thinning effect. However, experiments with the pad oxide left in place become complicated by the possibility of an additional oxidation barrier which might form in the pad oxide itself, making the thicker pad appear anomalously worse than the thin one. The last described experiments in which the 1000Å pad, thinned to 300Å, behaved exactly like the thick pad on reoxidation, tends to discount this possibility because the etchback step in BHF should certainly etchback an in-pad barrier layer along with the oxide in the uppermost 700Å layer.

As a result of these experiments, the recommended selective oxidation processing sequence includes a thin pad oxide (200-400Å) with a wet reoxidation step after nitride removal. This is most easily achieved by leaving the thin initial dry oxide pad in place for the wet oxidation step. An initial pad oxide thick enough to survive early cleaning steps is recommended as well as wet reoxidation of a minimum of 1000Å to insure statistical success of the procedure. A 90 sec BHF etchback prior to gate oxidation is the only additional requirement. This removes all oxide in the gate region but does not overly consume the isolation oxide.

A final note must be made regarding the alternative method of barrier etching from the substrate after initial etchback of the selective oxidation Si_3N_4 and pad oxide layers. We have tried several times to evaluate the method using a second 160° or 180°C H_3PO_4 etch to remove the barrier. What was found is that the Si substrate is etched at a rate varying from 3-10 Å/min. The variability depends on temperature, the particular Si wafer, and the H_3PO_4 used. Talystep data show much less etching at the oxidation barrier position (supposedly a type of Si nitride) than on the remainder of the exposed Si surface. This indicates either that the barrier is not attacked by H_3PO_4 or is attacked more slowly than is the Si surface. We have found, however, that a correlation exists between amount of exposure of the Si substrate in the gate regions to BHF and subsequent oxide thinning. Exposure of the Si to BHF beyond the time required to strip the pad (1-2 additional min) generally reduces the potential for thinning. Since the second etch procedure incorporates exposure of the Si surface to BHF prior to H_3PO_4 treatment, it is possible that the combination of the two etchants proves effective. At any rate, excessive exposure to BHF loses isolation oxide, and our proposed procedure, which involves only 90 sec BHF treatment, results in loss of only 1500Å isolation oxide.

Conclusions

TEM and SEM studies of n-channel and p-channel selective oxidation processed wafers show a bird's beak shape of the edge of the isolation oxide, with a notch at the top at the site of the edge of the masking Si_3N_4 , and bird's beak lengths of 1.5 and 0.8 μm on n-channel and p-channel samples respectively. The bird's beak length is defined as the distance between the site where the isolation oxide begins to thicken and the horizontal projection of the minimum in the isolation oxide notch. The active device length is decreased due to the presence of two beaks bordering the active region. For a given isolation oxide thickness, this decrease is greater for n-channel samples than for p-channel samples by about 50% (here 3.8 μm compared to 2.3 μm).

There is a barrier on the Si surface to gate oxidation. This barrier forms a band beginning near the tip of the bird's beak and extending a short distance (<1 μm) away from the tip on the n-channel samples. Gate oxide thinning of 20-50% was found on processed p-channel selective oxidation wafers, and 35-100% oxide thinning was found on processed n-channel wafers.

A convenient means for elimination of the thinning phenomenon is presented. Since it was found that wet oxidation subsequent to the isolation oxidation and

Si_3N_4 removal rapidly destroys the oxidation barrier, a method which incorporates an additional, short wet oxidation step between isolation and gate oxidations is described and recommended for selective oxidation processing.

Acknowledgments

We are indebted to H. J. Levinstein and S. P. Murarka for many interesting and helpful discussions regarding this work.

Manuscript submitted May 17, 1979; revised manuscript received June 10, 1979.

Any discussion of this paper will appear in a Discussion Section to be published in the December 1980 JOURNAL. All discussions for the December 1980 Discussion Section should be submitted by Aug. 1, 1980.

Publication costs of this article were assisted by Bell Laboratories.

REFERENCES

1. E. Bassous, H. N. Yu, and V. Maniscalco, *This Journal*, **123**, 1729 (1976).
2. E. Kooi, J. G. van Lierop, and J. A. Appels, *ibid.*, **123**, 1117 (1976).
3. T. T. Sheng, S. E. Haszko, and T. A. Shankoff, Unpublished results.
4. J. T. Clemens, R. H. Doklan, and J. J. Nolen, Unpublished results.
5. T. T. Sheng and R. B. Marcus, *This Journal*, **125**, 432 (1978).
6. T. T. Sheng and C. C. Chang, *IEEE Trans. Electron Devices*, **ed-23**, 531 (1976).
7. S. P. Murarka, C. C. Chang, and A. C. Adams, *This Journal*, **126**, 996 (1979).

Applications of Electrochemical Methods for Semiconductor Characterization

I. Highly Reproducible Carrier Concentration Profiling of VPE "Hi-Lo" n-GaAs

Thomas Ambridge, John L. Stevenson,¹ and R. Martin Redstall

Post Office Research Centre, Martlesham Heath, Ipswich, IP5 7RE, Great Britain

ABSTRACT

Factors which influence the accuracy and reproducibility of semiconductor carrier concentration profiling via capacitance-voltage measurements and dissolution at an electrolytic Schottky barrier are critically examined. Attention is centered upon the capacitance contributions from the edge regions of the electrolyte contact area. It is shown that several properties of the electrolyte, and the measurement frequency, as well as the physical means of electrolyte confinement have an important influence. In particular, a suitable combination of electrolyte conductivity, wetting, and dissolution behavior can be met by 0.1M Tiron, for the profiling of GaAs using the "Post Office Profile Plotter." Examples are given which demonstrate the high degree of reproducibility, both short- and long-term, attainable for the profiling of "hi-lo" structures. Optimization of the approach for other semiconductor materials, for which an "ideal" electrolyte may not be available, is also discussed.

The Post Office Profile Plotter² (1, 2) has been shown to provide an uncomplicated and convenient method for measurements of carrier concentration in GaAs and some other III-V compound semiconductor materials. It employs the semiconductor specimen as one electrode in an electrochemical cell, under controlled conditions where the differential capacitance of the Schottky barrier formed at the semiconductor/electrolyte interface is measured to give carrier concentration, and where, simultaneously, anodic dissolution is arranged, yielding a continuous depth profile of this parameter. Uniform illumination of the interface is required, to promote the dissolution reaction for n-type material. The sample wafer needs no pretreatment whatsoever, and the profile is obtained in one continuous, automatic sequence. These are notable advantages compared with most conventional "measure and strip" practices including capacitance-voltage profiling using metal/electrolyte Schottky barriers, where individual steps are limited by reverse-bias breakdown.

In principle, the electrochemical technique can be applied over wide ranges of carrier concentration and depth, and should be particularly advantageous for "hi-lo" profiling (1, 3), where the conventional approach would be especially tedious, due to the early

onset of breakdown in "hi"-doped material. Special care is needed, however, in relation to the area of electrolyte contact with the semiconductor specimen. A molded plastic sealing ring is used to define the area of contact and illumination. In practice the limits of the wetted area may extend somewhat beyond those of the illuminated area. The difference is termed "excess area," and needs to be taken into account for accurate profiling, since, whereas dissolution is restricted to the illuminated zone, the whole of the wetted area may contribute to the capacitance measurement.

In this paper, after a brief reminder of details of the profiling technique, we shall first describe experiments aimed at defining, precisely, the actual area(s) of electrolyte/semiconductor contact. Following this, the specific roles of electrolyte conductivity and measurement frequency are examined. Some detailed profiles obtained from "hi-lo" VPE n-GaAs (modified Read IMPATT material) are also presented. Emphasis is placed on the very high levels of reproducibility required from the profiling technique in this area of application (4, 5).

Experimental Technique

The principles of the profile measurement technique, and the prototype automatic instrument have already been described in detail (1, 2). For convenience, however, some of the essential information is briefly repeated here, and recent refinements highlighted. Ini-

¹ Present address: Intelsat, Washington, D. C. 20024.

Key words: capacitance, Schottky, wetting, frequency, Tiron.

² The Post Office Profile Plotter is manufactured by Polaron Limited, Watford WD1 8XG, Herts, England.

tially, we restate the profiling equations, and related instrumental parameters

I. Net donor concentration

$$N_D - N_A = \frac{2\epsilon\epsilon_0}{q} \frac{\delta V}{\delta(W_D^2)}$$

where ϵ_0 = permittivity of free space, ϵ = relative permittivity of the semiconductor, δV = modulation component of potential (100 mV rms, 30 Hz).

II. Depletion width

$$W_D = \frac{\epsilon\epsilon_0 A}{C}$$

where A = barrier area, C = capacitance (test signal: 50 mV rms, 3 kHz).

III. Width removed

$$W_R = \frac{M}{NFDA} \int Idt$$

where M = molecular weight, D = density of the semiconductor, N = the number of charge carriers transferred per molecule dissolved (= 6 for GaAs, this work), F = the Faraday, I = instantaneous dissolution current.

IV. Plotted depth

$$x = W_D + W_R$$

The electrochemical cell used in this work was the commercially supplied unit, which incorporated several changes from that earlier described. Several of the essential features, including the vertical specimen mounting arrangements are depicted in Fig. 1. Also incorporated, but not shown, are a saturated calomel electrode (SCE), as a reference, a carbon d-c working cathode, a platinum wire secondary cathode (for a-c measurements) close to the specimen, and a nozzle device for the initial clearance of bubbles. The electrolyte is stationary, in this design, but is refreshed for each profile measurement.

As before, the illumination provided for hole generation in n-type material is restricted to short wavelengths (below about 550 nm) corresponding to strong absorption, within a region of the semiconductor much narrower than the depletion width, in all but the most highly doped specimens ($\geq 10^{18} \text{ cm}^{-3}$). This ensures that, in most epitaxial material, the availability of holes at the surface, for the dissolution reaction, is independent of lateral variations in carrier concentration (and diffusion length); thus at a well-chosen

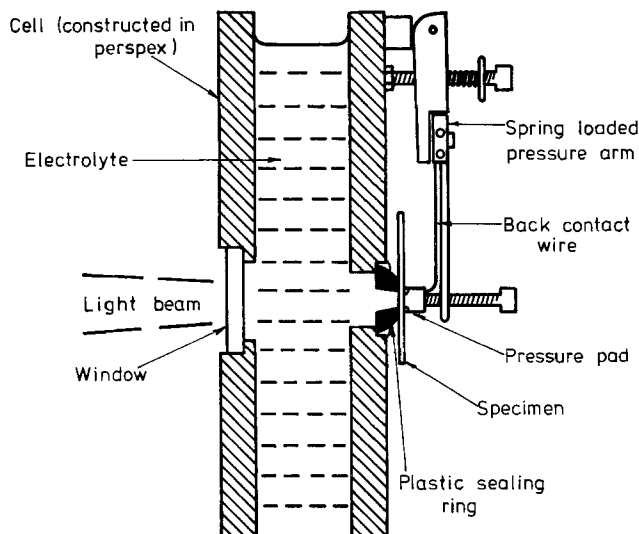


Fig. 1. Part of the electrochemical cell unit, showing specimen mounting. (Polaron Limited).

anodic potential microscopically smooth dissolution is usually obtained (1, 2).

Over-all uniformity of illumination has been substantially improved through the use of an optical lens system, and aperture arrangement, giving a slightly convergent (4°) beam. With proper alignment, a near-ideal etched well is obtained, as depicted in the "Talysurf"³ profile of Fig. 2, which indicates a maximum variation of $\pm 3\%$. The final intensity of illumination typically used is about 6.0 mW cm^{-2} , yielding a dissolution rate of approximately $3.0 \mu\text{m hr}^{-1}$.

The electronic instrumentation of the Post Office Profile Plotter has remained much as described earlier. However, an important recent refinement has been the incorporation of an automatically controlled electronic shutter. This provides an operational mode whereby dissolution under illumination is interrupted, at frequent intervals, by short periods of darkness during which the capacitance analysis, and point plotting of carrier concentration, is automatically performed. (The profile remains essentially continuous, comprising up to 300 points.)

In the present work, during profiling, both measurement and dissolution were performed, under potentiostatic control, at a common potential of about 0.3V anodic ("reverse biased") with respect to the dark rest value, regardless of the electrolyte employed. This choice of potential was based on criteria, aimed at avoiding defect-sensitive dissolution modes, and departures from ideal barrier characteristics, as discussed in previous publications (1, 2). Briefly, the main practical requirements are that the dissolution current should be negligible in the dark, and that dI/dV (both under illumination, and in the dark) should be minimal, whenever possible. For separate, frequency-dependent electrochemical C-V measurements, confined to high quality epitaxial material, a potential range from rest to about 1.5V anodic was spanned; standard phase-sensitive techniques were used for capacitance determination.

Contacted Area Definition

Physical area determination.—The accuracies of all carrier concentration profiles obtained from measurements of Mott-Schottky capacitance characteristics are critically dependent on the area of semiconductor contact and its edge definition (6). Where the conducting medium is a liquid, the problem is particularly severe (7).

Direct observation of the contact outline at the electrolyte/semiconductor interface has been aided by the use of samples upon which a uniform anodic native oxide has been formed (8) specially for this purpose. In the worst cases the area of electrolyte contact comprises several zones, as shown in Fig. 3(a). Here the n-GaAs test sample oxide was subjected, after loading onto the sealing ring, to open-circuit dissolution in an electrolyte of 2M KOH in aqueous solution. This was followed by anodic dissolution, under illumination, of $0.5 \mu\text{m}$ of GaAs.

The innermost boundary which appears on the photograph is that of A_C , the "central" area, which received illumination and thus was the only region within which

³The "Talysurf" moving stylus surface measuring instrument is manufactured by Rank Taylor Hobson, Leicester LE2 0SP, England.

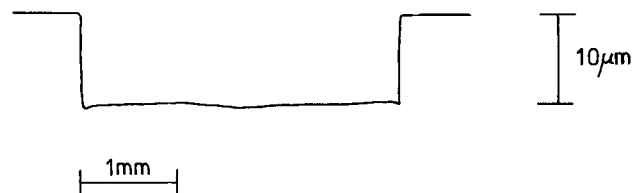


Fig. 2. "Talysurf" trace over an area, electrochemically stripped to an average depth of $10 \mu\text{m}$.

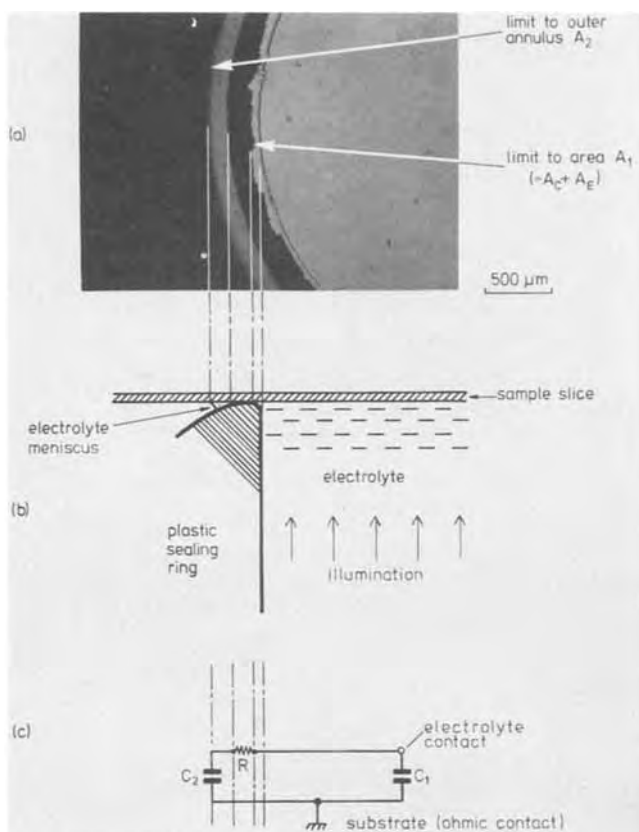


Fig. 3. The electrolyte/sample contact: (a) Contact zones observed for 2M KOH/n-GaAs, (b) physical model, and (c) electrical model.

GaAs dissolved. A_E is that excess wetted area which arises from simple shadowing of the illumination, due to slight rounding of the edge profile of the sealing ring. The existence of this has long been recognized (2), and the facility to compensate for the excess capacitance contribution (assumed to remain constant during dissolution profiling) is incorporated within the Profile Plotter. The sum of the areas, $A_C + A_E$, has been designated A_1 , and is approximately 0.1 cm^2 in the present work.

The existence of an outer excess wetted area A_2 , also revealed by the dissolution of oxide, requires an extension of our earlier model for the contact. Figure 3(b) shows the probable model for the formation of the additional zone A_2 ; this "meniscus contact" is particularly invidious, being potentially highly variable both in radial and circumferential extent. In the depicted circumstances its formation may be envisaged as a result of seepage across the flattened rim of the sealing ring, although, clearly, individual imperfections in the rim could provide a direct path.

Frequency-dependent "excess capacitance" model.—The electrical "interface circuit" model of Fig. 3(c) was adopted in order to investigate the participation of the specimen area A_2 in capacitance measurements. The resistive element R is proposed to represent a thin film of electrolyte present at the sealing rim, and as a result should have a conductance dependent on the dimensions of the peripheral capillary, and the electrolyte conductivity. In contrast, the capacitance C_2 depends upon the specimen doping only. An immediate consequence of a contact such as shown in Fig. 3 is that the apparent carrier concentration will show a variation with the measurement frequency, depending upon the relative impedances of R and C_2 .

Experimental confirmation was obtained by making electrochemical C-V measurements on uniformly doped specimens (with $N_D - N_A \approx 3 \times 10^{15} \text{ cm}^{-3}$)

at both 3 kHz (as used in the Profile Plotter) and 100 kHz, which revealed marked frequency dependence, especially for the lowest doped specimens. No frequency dependence was detected, over the range 30 Hz-1 MHz for the same specimens subjected to C-V measurements via conventional metal Schottky barriers; fairly close agreement with the higher frequency electrochemical measurements was obtained.

By assuming that 100 kHz electrochemical measurements gave a "correct" value for $N_D - N_A$, for a specimen doped at about 10^{17} cm^{-3} , a value for R was estimated (at about $25 \text{ k}\Omega$) by comparing the additional capacitance measured at 3 kHz with that calculated directly on the basis of the measured value of area A_2 . A calculation was then made of the percentage error in carrier concentration, over a wide range due to the effective excess capacitance (limited by R) at the two frequencies. The result is shown in Fig. 4. Note that the error becomes small (less than 5%) at 100 kHz for carrier concentration values greater than about $3 \times 10^{15} \text{ cm}^{-3}$ in uniformly doped material. For measurements at 3 kHz the model predicts much larger errors than those shown, for material in the "lo" region of a typical "hi-lo" structure (e.g., as demonstrated later and depicted in Fig. 5). However the corresponding errors should be negligible at 100 kHz, since the condition $R = \omega C_2^{-1}$, at which the absolute value of effective excess capacitance is at a maximum, occurs at a very low value of carrier concentration.

It is worth reemphasizing here that we have modelled frequency-dependent capacitance-voltage behavior entirely on the basis of peripheral contact phenomena in the electrochemical system. Certain other possible sources of frequency dependence, such as the presence of deep states, which may be invoked (9) are ruled out in the present investigation by the "solid-state" measurements. Thus, clearly, although other sources may dominate in other reported studies of capacitance behavior at the semiconductor/electrolyte interface (10-12), a frequency-dependent contribution related to that of the present model should not be overlooked entirely in such cases, even though the precise details of area definition may differ.

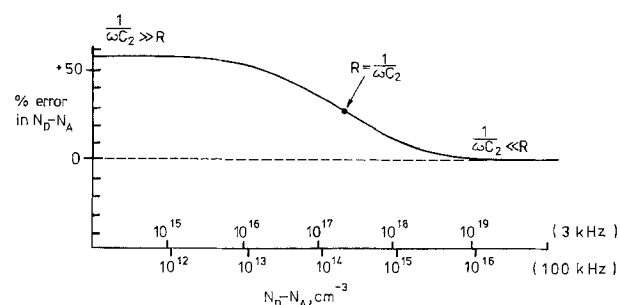


Fig. 4. The calculated dependence of error in carrier concentration upon absolute values, at measurement frequencies of 3 and 100 kHz, for the contact system of Fig. 1.

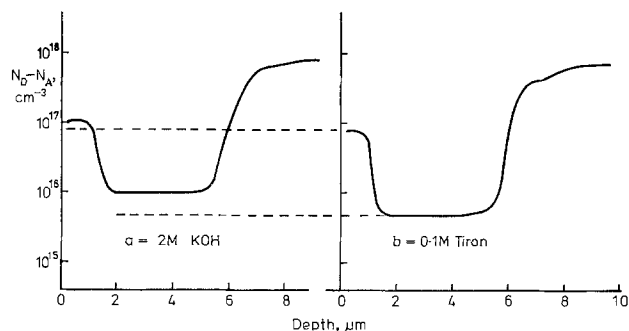


Fig. 5. "Hi-lo" profiles obtained from the same VPE n-GaAs specimen, using (a) 2M KOH and (b) 0.1M Tiron electrolyte.

Choice of Electrolyte

It is apparent from the model that two principal options exist for reducing the measurement errors of Fig. 4: (i) a decrease in electrolyte conductance, and (ii) an increase in measurement frequency. For GaAs it has proved to be sufficient simply to pursue (i) alone while retaining the standard Profile Plotter frequency of 3 kHz (which is most suited to measurements of the absolute values of capacitance encountered); it is not yet clear that this approach would be successful for other materials however (see Discussion).

Some initial attempts were made to increase R by employing KOH electrolyte of reduced concentration, or alternative alkaline solutions. These attempts were unsuccessful, due to the accumulation at the interface of insoluble (and only slowly soluble) hydrated oxides during anodic etching (8), causing a loss of Mott-Schottky capacitance characteristics. However, complexant electrolytes, in which the GaAs is reacted electrochemically to produce soluble chelated compounds, have proved to be suitable alternatives, even in quite dilute form. We have made specific use of Tiron (1,2 dihydroxybenzene-3,5 disulfonic acid, disodium salt) (13), which in 0.1M solution has a conductance approximately 4% of that of 2.0M KOH solution as used earlier. Assuming that R is proportional to the electrolyte resistivity, the substitution of 0.1M Tiron for 2.0M KOH should produce a change in impedance ratio ($\omega C_2^{-1} : R$), and hence in the over-all carrier concentration measurement error, approaching that obtained from the frequency increase as previously explored, as depicted in Fig. 4.

The effect of changing the electrolyte is shown by the two profiles of Fig. 5; each was recorded for an adjacent area on a "hi-lo" VPE n-GaAs structure. The discrepancy between the two measurements of $N_D - N_A$ for the "hi" avalanche region is 33% in this case, whereas the data of Fig. 4 would predict an error approaching 38% (for 2.0M KOH at 3 kHz). Thus, in this region at least, it appears that the use of Tiron has virtually eliminated the effective capacitance contribution from any outer excess area, A_2 . Clearly the influence on the "lo" region is even more marked, although a more rigorous experimental approach is required (see the following section) to allow quantitative assessment. The validity of the electrical isolation model has been further reinforced by measurements in the presence of gross leakage of electrolyte (promoted by temporarily reducing the loading pressure of the specimen onto the sealing ring); even here relatively small, although somewhat variable, effects were noted when using 0.1M Tiron, compared with extreme changes when using 2M KOH.

Subsequent investigations, employing oxide dissolution tests, have shown that, under suitable loading conditions, over-all peripheral seepage can apparently be avoided when Tiron is used as the electrolyte. The remaining mechanism for outer excess area formation is then via small individual imperfections in the sealing ring edge. As shown in Fig. 6, the extent of the excess area may be quite restricted in this case. Although electrical isolation is apparently still fairly effective in this situation, the distinction between A_E and A_2 in the model is less clear. Thus, for the high accuracy measurements described in the following section, employing Tiron electrolyte, only selected sealing rings, having no imperfections detectable by oxide dissolution tests, were utilized. Nevertheless it must be emphasized that for less demanding tasks (e.g., routine profiling of fairly uniformly doped material with better than 10% reproducibility), the use of Tiron provides a considerable degree of immunity from minor imperfections in the seal, due to its reduced electrical conductivity.

It should be pointed out that the increased series path resistance within the electrochemical cell, when

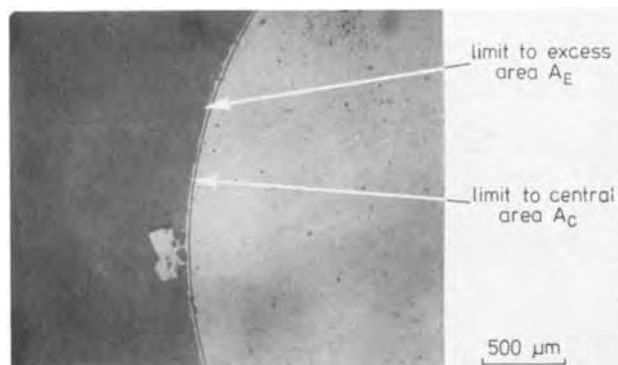


Fig. 6. Modified electrolyte/sample contact, for 0.1M Tiron/n-GaAs, under conditions where the outer contact zone is related to an individual imperfection in the seal.

using 0.1M Tiron, should not normally introduce significant error (i.e., more than 5%) into the measured carrier concentration, for values below about $3 \times 10^{18} \text{ cm}^{-3}$ (at the measurement frequency of 3 kHz). This assumes that the semiconductor barrier impedance is predominantly capacitive, which is generally true for high quality VPE layers. Under certain circumstances however, abnormally high parallel leakage conductance within the semiconductor depletion region can introduce complications, which will be discussed in a later contribution (14).

Application to High Accuracy Measurements

Surface uniformity mapping.—Lateral uniformity is an important requirement in material grown for device fabrication, and where comparative measurements are made on different areas of a given slice, for assessment of measurement techniques (as in Fig. 5). The Post Office Profile Plotter can be used to assess the lateral uniformity of doping, by determination of carrier concentration under conditions of negligible dissolution. Two uniformity maps made in this way (again for the "avalanche" layer of Read IMPATT material), are shown in Fig. 7. The two slices used here were produced in successive growth experiments, but at different vertical locations in the VPE horizontal furnace tube, and receiving different patterns of gas flow during epitaxy. The marked improvement in geographical uniformity in slice B corresponded with its having been centrally placed in the furnace tube.

This form of measurement provides the simplest useful test situation in which the electrochemical contact can be assessed. For reproducible measurements, the physical contact area must be kept constant over the duration of the experiment. By repeated remapping of slice B, it was established that the distribution of carrier concentration could indeed be reproduced closely. This implies that short-term area redefinition is significantly better than 2%, and is probably comparable with that typical of the mercury probe contact system (also used for Schottky barrier capacitance measurement), which was claimed initially by Hammer to be



Fig. 7. Surface carrier concentration uniformity maps (using 0.1M Tiron electrolyte) for VPE n-GaAs specimens grown under different conditions. The figures represent percentage deviations from the mean values of 6.9 and $9.7 \times 10^{16} \text{ cm}^{-3}$ for A and B respectively.

about 1% of the total area (7). We note that the indicated total variation in carrier concentration is about $0.5 \times 10^{16} \text{ cm}^{-3}$ for the avalanche region of slice B. This is a substantial improvement over work reported by Niehaus and Schwartz (5) where minimum non-uniformities amounting to a total variation of $1 \times 10^{16} \text{ cm}^{-3}$ were reported on Read IMPATT material of similar specification.

"Hi-Lo" profiles.—Two profiles, obtained from neighboring areas of an IMPATT slice, are shown in Fig. 8. The inset shows the $N_D - N_A$ measurements made initially at the surface. One full profile, as shown (designated "a") was taken of the complete "hi-lo" structure (and was virtually indistinguishable from one taken to a depth of $5 \mu\text{m}$ at position "c"). The second shown profile (labelled "b") was recorded after removal of $1 \mu\text{m}$ of epitaxial material from the whole surface area of the slice, using an electrochemical trimming procedure previously termed replication etching (13). The two values of $N_D - N_A$ obtained for the drift region are in good agreement, the maximum difference between the plots being 5% at the point where the profile "b" was initiated. These results clearly demonstrate the elimination of any significant contribution to the measurement from an outer area A_2 . The same conclusion has been arrived at from comparisons with results from mercury probe measure and strip procedures applied to "hi-lo" structures.

In the absence of significant errors due to "outer excess area" the major remaining influence on accuracy is the reproducibility of the central area A_C , and the "inner excess area" A_E . The errors in $N_D - N_A$ in the "hi" and "lo" sections of a profile, due to differences between the assumed and actual values of A_C and A_E can easily be shown to be given by

$$\frac{(N_D - N_A)_{\text{HI actual}}}{(N_D - N_A)_{\text{HI plotted}}} = \left[\frac{A_1 \text{ assumed}}{A_1 \text{ actual}} \right]^2 \quad [1]$$

and

$$\frac{(N_D - N_A)_{\text{LO actual}}}{(N_D - N_A)_{\text{LO plotted}}} = \left[\frac{(N_D - N_A)^{1/2}_{\text{LO plotted}} + \left(\frac{A_E}{A_1} \text{ assumed} - \frac{A_E}{A_1} \text{ actual} \right)}{(N_D - N_A)^{1/2}_{\text{HI plotted}}} \right]^2 \left[\frac{A_C \text{ assumed}}{A_C \text{ actual}} \right]^2 \quad [2]$$

The derivation assumes that the measured capacitance is machine-corrected for the contribution of that proportion of the initial capacitance corresponding to the area A_E assumed. Also, second order effects (such as carrier concentration dependent band bending) are neglected.

The expression [2] for $(N_D - N_A)_{\text{LO}}$ can be simplified by taking typical values $(N_D - N_A)_{\text{HI}} / (N_D - N_A)_{\text{LO}}$

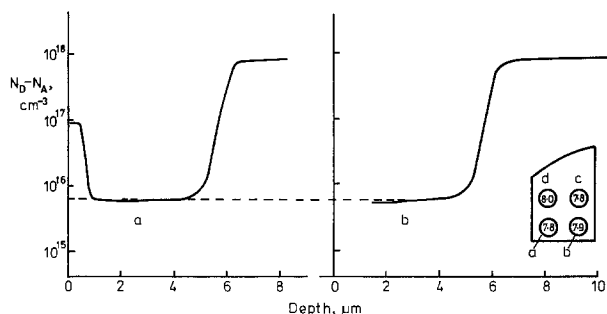


Fig. 8. (a) A full "hi-lo" profile and (b) the profile for an adjacent area of the same n-GaAs specimen after independent removal of $1 \mu\text{m}$ of material. The inset shows the locations, and initial surface carrier concentration measurements over the slice, in units of 10^{16} cm^{-3} . 0.1M Tiron was used as the electrolyte.

$= 25$ and $A_C = 0.1 \text{ cm}^2$, to give the approximation

$$\frac{(N_D - N_A)_{\text{LO actual}}}{(N_D - N_A)_{\text{LO plotted}}} \simeq [1 + 100 (A_E \text{ assumed} - A_E \text{ actual})] \left[\frac{A_C \text{ assumed}}{A_C \text{ actual}} \right]^2 \quad [3]$$

Thus, for example, an error of 5% in $(N_D - N_A)_{\text{LO}}$ could arise from an error of 2.5% in A_C , or 10% in A_E (having an actual value of 0.005 cm^2), or a combination of errors in both. Successive measurements, using the oxide dissolution procedure, have shown that while area variations can be much less than this in the short term (as confirmed by profile reproducibility), these values can be exceeded in the longer term (periods exceeding a few days), depending on the exact conditions of instrumental use. In practice we have been able to maintain a profiling reproducibility of this order, on "hi-lo" structures over a period of many months by regular daily monitoring of areas, using oxide-coated specimens, and if necessary applying corrections to plotted data, on the basis of the above formulas.

It is useful to note that electrochemical profiles showing geographically systematic variations of less than $0.25 \times 10^{15} \text{ cm}^{-3}$ have been obtained in the "lo" region ($N_D - N_A = 5.5 \times 10^{15} \text{ cm}^{-3}$) of samples similar to slice B (Fig. 7), with data taken at six locations covering a total area of 2 cm^2 . This compares favorably with the work of Niehaus and Schwartz (5) who reported that a target value of $(N_D - N_A)_{\text{LO}} = (2.0 \pm 0.24) \times 10^{15} \text{ cm}^{-3}$ could not be met over a complete grown wafer. We also note earlier work by Wissemann *et al.* (4) who reported on the attainment of abrupt transitions between $(N_D - N_A)_{\text{HI}}$ and $(N_D - N_A)_{\text{LO}}$. Profiles taken using a mercury probe system showed that the total level change required (from $1 \times 10^{17} \text{ cm}^{-3}$ to $5 \times 10^{15} \text{ cm}^{-3}$) could be achieved within $0.3 \mu\text{m}$, but only by performing the epitaxy in a complicated furnace, with two deposition zones, and involving the mechanical resiting of the substrate in each zone during growth. Although such a technique was not used during the production of the layers examined here, equally sharp transitions have been obtained according to the electrochemical profiles [see, for example, profile a in Fig. 8, and also the work of Bass (3)].

Discussion

Successful profiling, with a negligible influence from an "outer excess area" capacitance has been demonstrated for GaAs, through an optimization of electrolyte characteristics. Unfortunately it cannot be foreseen that a similar combination of electrical conductivity, wetting, and dissolution behavior will be attainable in electrolytes applicable to other semiconductor materials. For example, Tiron is unsuitable for profiling either InP or GaP, due to the accumulation of phosphorus at the semiconductor surface.

A viable approach is much needed here, due to important applications which include profiling of the quaternary GaInAsP, as well as InP, in double heterostructure laser material, and also because alternative measurement techniques are limited; considerable difficulty is encountered in the fabrication of simple metal Schottky barriers suitable for carrier concentration measurement on InP (15). It must be anticipated that it may be necessary to resort to fairly concentrated (high conductivity) electrolytes for satisfactory dissolution.

The possible use of a higher measurement frequency (e.g., 100 kHz), in order to exclude the capacitance contribution from A_2 , has already been introduced. However, for the presently employed barrier area, the sample impedance at high carrier concentrations ($N_D - N_A \cong 10^{18} \text{ cm}^{-3}$) would approach the same order as the simple "ohmic" contact impedances, leading to significant errors. Nevertheless, for much smaller areas,

higher frequency operation would be more appropriate to the sample impedances encountered. This would also be compatible with a requirement to reduce the area in order to minimize material consumption, such as has been applied to the profiling of LPE GaAs/GaAlAs heterostructures, with $A_C \leq 0.01 \text{ cm}^2$ (16). Unfortunately, the relative size of A_E tends to increase as A_C is reduced, so that the reproducibility of "hi-lo" profiling must suffer.

Electrolytic contact area definition has also been obtained by masking using evaporated wax films (10), or photoresist (17). However, for accurate measurements at low carrier concentration levels the mask would need to be quite thick (e.g., 100 μm) in comparison with the maximum depletion width (e.g., $> 1 \mu\text{m}$ for $N_D - N_A \leq 10^{15} \text{ cm}^{-3}$); otherwise an "excess" capacitance would be measured through the mask. The thickness requirement could lead to difficulty in achieving sharp edge definition of the masking material; in addition undercutting of the mask during dissolution profiling would be a problem unless the mask could be made opaque. The masking material would of course need to be impervious to the electrolyte employed. The approach would always suffer the disadvantage of the additional amount of preparation required, compared with the inherent simplicity of the sealing ring method.

Taking into account the various factors discussed above, perhaps the best approach to elimination of outer excess area contributions for other semiconductors, and to improved reproducibility of absolute area, lies in the optimization of the geometry, surface finish, and material composition of the sealing ring. In conjunction with this, given that it may not be practicable to tailor the electrical conductivity of the electrolyte, consideration should be given at least to the wetting characteristics, with the objective of avoiding seepage, as was apparently achieved for Tiron under "ideal" conditions. Reliable results would then depend upon the preservation of the sealing edge, to be confirmed by regular monitoring, in the manner already described in detail.

The influence of illumination on accurate profiling deserves some comment. As pointed out, the present system allows the carrier concentration measurement data to be obtained in the dark. In practice, the computed carrier concentration has usually been found to have negligible dependence upon illumination (at the "standard" level), for high quality epitaxial material, as in this work. However in certain classes of "imperfect" material, departures from ideal barrier behavior, under illumination, have provided useful qualitative information, as will be discussed in a forthcoming paper (14). In principle, depth scale information does not depend upon the precise level of illumination, or in-depth variations in corresponding dissolution photocurrent, since the depth removed is determined electronically from the dissolution rate integral. Lateral variations in dissolution rate will, however, introduce a loss of resolution, especially at the deepest interfaces. The precautions taken to minimize this problem have already been mentioned, and the experimental evidence suggests that it is insignificant in the present work. Nevertheless, this is an aspect of the technique where vigilance is needed. In particular, exceptional situations can arise, for example when profiling damaged material, where significant in-depth variations in photocurrent do occur, and could compound the effects of any lateral nonuniformity in illumination (14).

We have so far not referred to any possible long-term variability of results due to drift in the analogue electronics of the Profile Plotter. In practice the commercial instrument is easily maintained in precise calibration on a day-to-day basis using readily accessible front panel trimmers; over-all reproducibility of the combined analogue functions can be spot-

checked over a wide carrier concentration range, using a specimen simulator (comprising solid-state varactors) and generally confirmed to be everywhere within about 2%. Thus contact area definition remains the major potential source of irreproducibility.

Note that throughout the present work, we have limited the consideration of measurement accuracy and reproducibility to technological aspects of the electrochemical system. Other aspects generally applicable to capacitance-voltage based profiling techniques, e.g., concerning the possible influence of deep levels, and Debye spreading limitations on the resolution of interfaces, have been considered at length elsewhere (9, 18-20).

Conclusion

With the widening realization that successful fabrication of many advanced devices in GaAs, and other semiconductor materials, will require an exact and consistent knowledge of carrier concentration profiles, we have demonstrated here that the electrochemical technique can be entrusted with the determination of accurate and highly reproducible data. The necessary attention to choice of electrolyte, contact area definition, and simple well-defined routine checks have been fully discussed.

In forthcoming papers we shall describe further extensions of the electrochemical technique applicable to: (i) "damage" profiling in relatively imperfect material, including, specifically, ion-implanted layers; (ii) compositional, as well as carrier concentration (both n- and p-type), profiling of heteroepitaxial material, including LPE double heterostructures grown for laser fabrication; and (iii) Hall mobility, and carrier concentration profiling, in MBE, VPE, and ion-implanted layers, including those produced for microwave FET fabrication.

Acknowledgments

The authors wish to thank Dr. R. H. Moss for providing epitaxial structures, P. J. O'Sullivan for making available measurements using solid-state Schottky diodes, J. C. Regnault and C. J. Allen for performing some of the other measurements, and Dr. M. M. Faktor for helpful discussions. Acknowledgment is made to the Director of Research of the British Post Office for permission to publish this paper.

Manuscript submitted April 16, 1979; revised manuscript received Aug. 13, 1979.

Any discussion of this paper will appear in a Discussion Section to be published in the December 1980 JOURNAL. All discussions for the December 1980 Discussion Section should be submitted by Aug. 1, 1980.

Publication costs of this article were assisted by the Post Office Research Centre.

REFERENCES

1. T. Ambridge and M. M. Faktor, *Inst. Phys. Conf. Ser.*, **24**, 320 (1975).
2. T. Ambridge and M. M. Faktor, *J. Appl. Electrochem.*, **5**, 319 (1975).
3. S. J. Bass, *J. Cryst. Growth*, **44**, 29 (1978).
4. W. R. Wisseman, R. L. Adams, D. W. Shaw, and T. E. Hasty, *IEEE Trans. Electron Devices*, **ed-21**, 317 (1974).
5. W. C. Niehaus and B. Schwartz, *Solid-State Electron.*, **19**, 175 (1976).
6. F. D. Hughes, *Acta Electron.*, **15**, 43 (1972).
7. R. D. Hammer, *Rev. Sci. Instrum.*, **41**, 292 (1970).
8. B. Schwartz, F. Ermanis, and M. H. Brastad, *This Journal*, **123**, 1089 (1976).
9. L. C. Kimerling, *J. Appl. Phys.*, **45**, 1839 (1974).
10. A. Yamashita, T. Aoki, and M. Yamaguchi, *Jpn. J. Appl. Phys.*, **14**, 991 (1975).
11. A. Wolkenberg, *Surf. Sci.*, **50**, 580 (1975).
12. W. H. Lafiere, R. L. Van Meirhaeghe, F. Cardon, and W. P. Gomes, *ibid.*, **59**, 401 (1976).
13. M. M. Faktor and J. L. Stevenson, *This Journal*, **125**, 621 (1978).
14. T. Ambridge, To be submitted to *This Journal*.

15. S. Guha and F. Hasegawa, *Solid-State Electron.*, **20**, 27 (1977).
 16. T. Ambridge, J. L. Stevenson, and R. M. Redstall, To be submitted to *This Journal*.
 17. D. L. Lile and D. A. Collins, *Electron. Lett.*, **14**, 457 (1978).
 18. W. C. Johnson and P. T. Panousis, *IEEE Trans. Electron Devices*, **ed-18**, 965 (1971).
 19. K. Hesse and H. Strack, *Solid-State Electron.*, **15**, 767 (1972).
 20. C. P. Wu, C. W. Mueller, and E. C. Douglas, *IEEE Trans. Electron Devices*, **ed-22**, 319 (1975).

Observation and Analysis of Surface States on TiO₂ Electrodes in Aqueous Electrolytes

R. H. Wilson*

General Electric Company, Research and Development Center, Schenectady, New York 12301

ABSTRACT

When a TiO₂ electrode in an aqueous electrolyte is biased enough positive of its flatband potential and then photoexcited with light of wavelength shorter than 400 nm, photocurrent is observed. If the electrode is subsequently swept to more negative voltages in the dark a negative current is observed which is in excess of the normal dark current observed on a subsequent sweep with no photoexcitation between sweeps. The excess current is observed to have a maximum at a voltage positive of the flatband potential. In this paper, the growth and decay of this reduction peak are investigated experimentally. The peak is analyzed as a reduction by conduction band electrons of surface states that were oxidized by valence band holes during the photoexcitation. The observations favor the interpretation that these states are intermediates of the reaction leading to O₂ evolution. This interpretation, however, is not unequivocally established. It is clear that the conduction-band electron reduction of a state that was previously oxidized by a valence-band hole is in effect an electron-hole recombination. This recombination controls the onset of photocurrent with voltage. There are 10¹³-10¹⁴ of these states per cm² and the cross section for electron interaction with this surface state is estimated to be 10⁻¹⁶-10⁻¹⁷ cm² based on the analysis used to describe the peak. The usefulness of this analysis in investigating these states and surface states due to surface coatings is discussed.

Since the first report (1) of stable, photoelectrochemical oxygen evolution on TiO₂, a substantial effort has been made to improve on those early results. This work has been the subject of several recent reviews (2-5). The work reported here is part of a continuing effort to understand the processes that occur on TiO₂ during O₂ evolution as a guide to the use of narrower bandgap semiconductors for that purpose.

In a previous report (6) observation of a reduction current peak produced by photoexcitation of a TiO₂ electrode was discussed briefly. In this paper the experimental measurement of this peak is reported in more detail and a model to describe the effect is developed. Data are presented to support the view that this reduction current is due to an electron transfer to a relatively stable surface species that was produced by a reaction with a hole in the valence band of the TiO₂ during illumination. A model for this process is presented. The possibility that this stable surface species is an intermediate of the series of reactions leading to oxygen evolution is discussed. It is further argued that this reduction by a conduction band electron is a reversal of a previous oxidation by a valence band hole. The net results of these two processes is an electron hole recombination and this recombination is the controlling factor in the onset of photocurrent with increasing positive voltage applied to the n-type TiO₂ electrodes.

Experimental Procedures

All measurements were made using a cell with a 4 mm diam opening to which a larger single crystal TiO₂ electrode was pressed using a thin silicone gasket

* Electrochemical Society Active Member.

Key words: photoelectrolysis, semiconductor, interfaces, photoelectrochemistry.

as a seal. A saturated calomel electrode (SCE) connected by a Luggin capillary was used as a reference electrode. The counterelectrode was a platinized platinum electrode. Light to the TiO₂ electrode entered the cell through a vitreous silica window and passed through 1 cm of electrolyte before falling on the electrode. The light source was a 150W xenon lamp with a Bausch and Lomb grating monochromator. The measurements were made using a PAR Model 173 potentiostat and a Model 175 universal programmer. The current-voltage curves were recorded on an X-Y recorder. The TiO₂ electrodes were prepared using methods previously described (7). The electrolytes were prepared using distilled water and reagent grade chemicals.

Observations

The nature of the observations to be described is illustrated in Fig. 1 where the current-voltage characteristics of a TiO₂ electrode are shown when the voltage is swept from zero volts (SCE) at -200 mV/sec in 1M KOH under the following conditions: (i) in the dark with no illumination subsequent to the previous negative voltage sweep; (ii) illuminated with 350 nm light; (iii) in the dark after 30 sec illumination with 350 nm light at 0 volts (SCE). As can be seen in curve 3 of Fig. 1, additional cathodic current occurs as a result of the short period of illumination at 0 volts. The principal features of this reduction peak are observed to be independent of the crystal face of the TiO₂ (they are also observed on SrTiO₃) and the doping density of the TiO₂. Factors that do affect the reduction peak will be discussed here.

The growth of the reduction peak as a function of illumination time is illustrated in Fig. 2(a). In each case there is a 5 sec delay between the light-off and

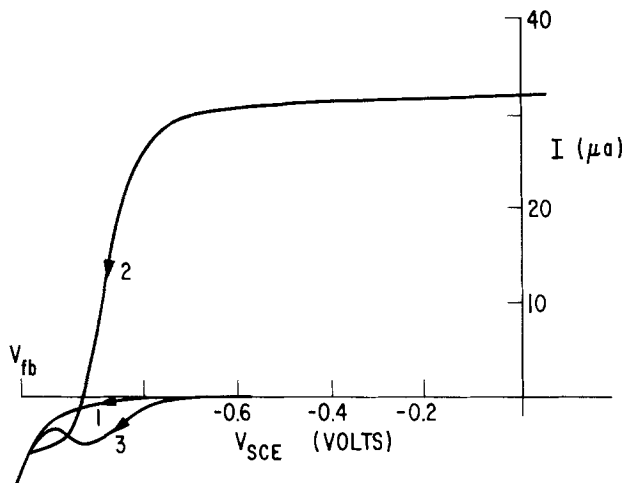


Fig. 1. Current-voltage curves of a TiO_2 electrode in 1.0M KOH with -200 mV/sec scan from 0 volts (SCE). Curve 1, in dark; curve 2, with 350 nm light on; curve 3, in dark after 30 sec illumination with 350 nm light at 0 volts (SCE).

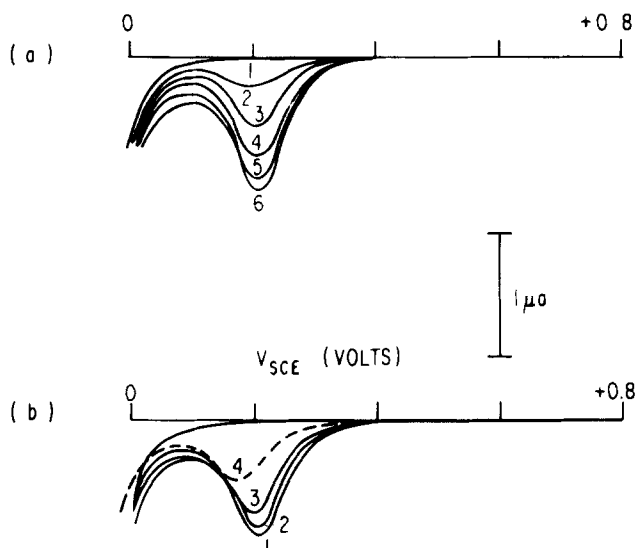


Fig. 2. Current-voltage curves of a TiO_2 electrode in 0.5M H_2SO_4 with a -200 mV/sec scan from $+0.8\text{V}$ (SCE) in dark (a) after exposure to 350 nm light for curve 1, 0 sec; curve 2, 0.1 sec; curve 3, 1.0 sec; curve 4, 5 sec; curve 5, 30 sec; curve 6, 180 sec with 5 sec delay before initiating voltage sweep; and (b) after exposure to 350 nm light for 30 sec and curve 1, 5 sec; curve 2, 30 sec; curve 3, 120 sec; curve 4, 6000 sec delay before initiating voltage sweep.

the beginning of the sweep. As can be seen, there is a rapid initial growth with a subsequent saturation. The growth can be approximated by

$$N = N_0(1 - e^{-t/\tau}) \quad [1]$$

where t is the time of exposure to light, N is the area under the peak (to be expressed as the number of electrons per unit electrode area), N_0 is its saturation value and τ is a time constant which is inversely proportional to the photocurrent density during illumination. An approximate empirical relationship is

$$\tau = 2 \times 10^{-4} \frac{C}{\text{cm}^2} / j \quad [2]$$

where j is the current density during illumination. Greater precision in this measurement is not considered to be justified at this time. The value of N_0 was observed to be independent of light intensity and current density.

The decay of the peak for different delay times before the sweep is initiated is shown in Fig. 2(b).

In each case the electrode was illuminated for 30 sec before the beginning of the delay period. No functional relationship was found to describe the remaining peak size as a function of time. It is readily seen from the figure that the rate of decay decreases with time and a substantial fraction of the peak is left after 100 min. The decay rate was the same at $+0.8$ or $+0.6\text{V}$ during the delay period.

The rates of growth and decay of the peak were independent of the electrolyte, stirring of the electrolyte, and the presence or absence of dissolved O_2 in the electrolyte. As will be discussed, some features of the current during the sweep do depend on the electrolyte and stirring.

Figure 3 shows the effect of scan rate on the reduction peak. The solid curves were made at -500 mV/sec and the dashed curves were made at -50 mV/sec both in 0.5M H_2SO_4 . Note that the current scale differs by a factor of ten for the two sets of curves. Curves 1 were after illumination with 350 nm light at $+0.8\text{V}$ for 30 sec and then a 30 sec delay before initiating the voltage sweep. Curves 2 were subsequent sweeps in the dark with no illumination at $+0.8\text{V}$. It is obvious that the area under the peaks is approximately proportional to the scan rate, i.e., the amount of charge transferred is independent of scan rate. The shift in peak position is noteworthy and will be discussed in the next section.

All of the following observations of the reduction peak were made using a -200 mV/sec sweep rate, 30 sec illumination with 350 nm light at 0 volts in 1M KOH or $+0.8\text{V}$ in 0.5M H_2SO_4 with a 5 sec delay between light-off and the beginning of the voltage sweep.

Figure 4 shows a series of measurements made on a TiO_2 electrode. Figure 4(a) shows measurements made in 1M KOH. The solid curves were initial measurements and the dashed curves after 0.1C of charge was passed by illuminating the electrode with 350 nm light at 0 volts (SCE) (current about $18 \mu\text{A}$). Curves 1 were made after 30 sec illumination at 0 volts after a previous sweep to -1.2V . Curves 2 were made after curve 1 with no intervening illumination. Several features can be noted in these curves. One is the development of a second peak at -0.95V after 0.1C. This peak continues to grow with further passage of photocurrent. Its rate of growth is nonlinear with current density growing more per unit of charge passed at higher current density. While this extra reduction peak is interesting, it will not be discussed in detail in this report. As will be seen, it slowly disappears in 0.5M H_2SO_4 .

Another feature is a shift of the initial peak at -0.85V to a slightly more positive voltage. This shift is probably due to a change in the flatband potential during the 0.1C charge transfer, since a corresponding

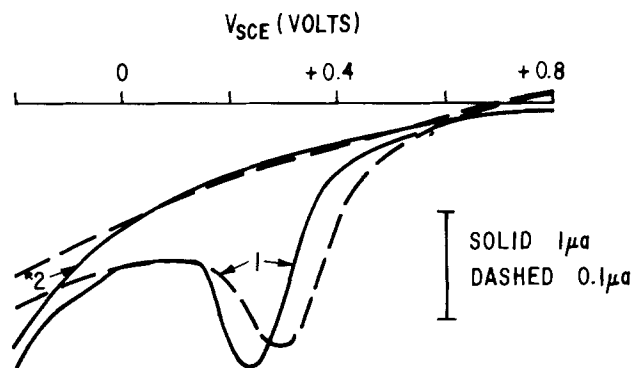


Fig. 3. Current-voltage curves of a TiO_2 electrode in 0.5M H_2SO_4 in dark after curves 1, 30 sec exposure to 350 nm light with 30 sec delay before initiating voltage sweep at: solid curve 500 mV/sec; dashed curve 50 mV/sec; curve 2, no exposure before sweep.

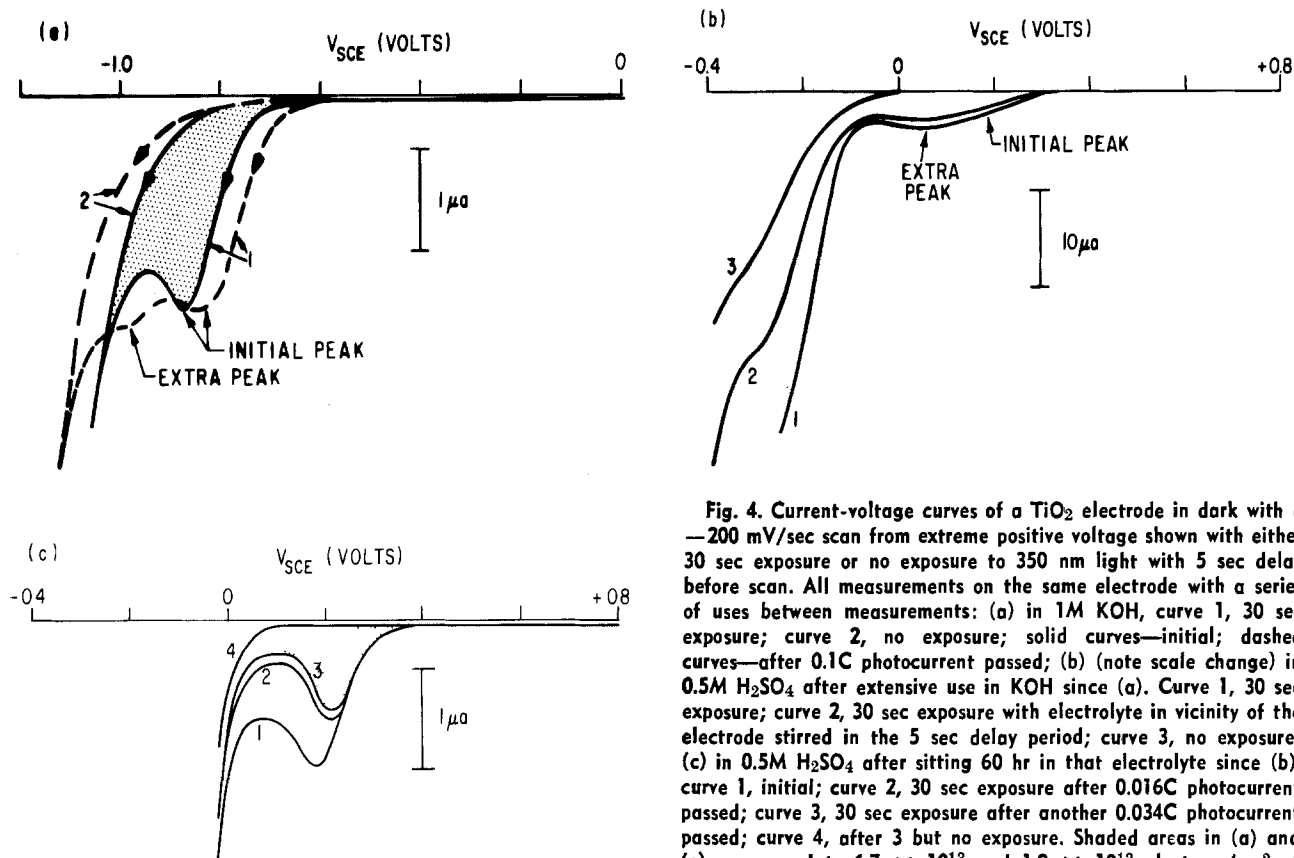


Fig. 4. Current-voltage curves of a TiO_2 electrode in dark with a -200 mV/sec scan from extreme positive voltage shown with either 30 sec exposure or no exposure to 350 nm light with 5 sec delay before scan. All measurements on the same electrode with a series of uses between measurements: (a) in 1M KOH, curve 1, 30 sec exposure; curve 2, no exposure; solid curves—initial; dashed curves—after 0.1C photocurrent passed; (b) (note scale change) in 0.5M H_2SO_4 after extensive use in KOH since (a). Curve 1, 30 sec exposure; curve 2, 30 sec exposure with electrolyte in vicinity of the electrode stirred in the 5 sec delay period; curve 3, no exposure; (c) in 0.5M H_2SO_4 after sitting 60 hr in that electrolyte since (b), curve 1, initial; curve 2, 30 sec exposure after 0.016C photocurrent passed; curve 3, 30 sec exposure after another 0.034C photocurrent passed; curve 4, after 3 but no exposure. Shaded areas in (a) and (c) correspond to 6.7×10^{13} and 1.9×10^{13} electrons/cm² of TiO_2 respectively.

shift occurs in the capacitance-voltage curve. The shift is reversible in the dark. This can be seen in the position of curve 4 in Fig. 2(b). Again, this shift, while interesting, will not be discussed further here. In addition, it should be noted that this shift and the associated capacitance change come after long periods of photocurrent. There is no change in capacitance at 0 volts as a result of the 30 sec illumination responsible for the reduction peak.

The existence, location, and size of the initial peak are the features of interest here. These features will be considered further in the discussion section.

After more use in KOH during which the extra peak grew further, the electrode of Fig. 4(a) was measured in 0.5M H_2SO_4 . The results are shown in Fig. 4(b) and 4(c). The observations in Fig. 4(b) were made shortly after the removal of KOH and the addition of H_2SO_4 . Note that a less sensitive current scale is used in 4(b). Curve 1 is after 30 sec illumination with 350 nm light at +0.8V with no stirring of the electrolyte. Curve 2 is for the same conditions but with the electrolyte stirred in the vicinity of the electrode during the 5 sec delay between illumination and voltage sweep. Curve 3 was with no illumination before the sweep. The current increase at more negative voltages in curve 3 is a function of the amount of dissolved oxygen in the electrolyte. Oxygen is unavoidable since it is produced during the period of illumination. Figure 4(b) is intended to illustrate the effect of stirring and the additional structure at -0.3 V and to point out that these features are not those under consideration here. In addition, some of the extra peak that grew in KOH can still be seen at +0.05V.

Figure 4(c) shows the behavior of the same electrode after sitting over a weekend in 0.5M H_2SO_4 . Curve 1 is an initial measurement. Curve 2 is after 0.016C passed through the electrode using 350 nm illumination at +0.8V, a subsequent sweep to -0.4 V, and then the usual 30 sec illumination at +0.8V

before the sweep. Curve 3 is after another 0.034C with the same procedure. Curve 4 is a sweep with no illumination after curve 3.

Again, several features can be noted in Fig. 4(c). One is the absence of the second peak that developed in Fig. 4(a) and was still evident in 4(b). The states responsible for the peak are apparently removed by 0.5M H_2SO_4 .

A second feature is the shift in peak position to more positive potentials similar to that seen in Fig. 4(a). It also is accompanied by a corresponding shift in the capacitance-voltage curve and is probably due to a change in flatband voltage.

A third feature is the variable background current from which the peak at +0.2V rises. This current is apparently the tail of some of the effects seen in Fig. 4(b) at more negative voltages.

The features of interest in this report are the size and location of the peak itself. These will be dealt with quantitatively in the discussion section. There is an obvious difference in the size of this peak in H_2SO_4 and KOH. When the 0.5M H_2SO_4 was removed after curve 3 of Fig. 4(c) and was replaced by 1M KOH, the peak was very similar to the initial peak shown in Fig. 4(a).

The behavior of the reduction peak described in this section has been reproduced on many TiO_2 electrodes with different preparation and different doping densities. The peak, however, is not always as clean and sharp as illustrated thus far. This is seen in Fig. 5 where initial measurements on a TiO_2 electrode which had sat in the laboratory several weeks between the time it was prepared and the time it was first measured are shown in the solid curves. No cleaning procedure was used prior to the measurement.

The dashed curves are measurements on the same electrode after further use in 1M KOH, subsequent measurement in 0.5M H_2SO_4 , and then measurement in 1M KOH. Sharpening of the reduction peak (curves 3) is obvious. This sharpening developed gradually

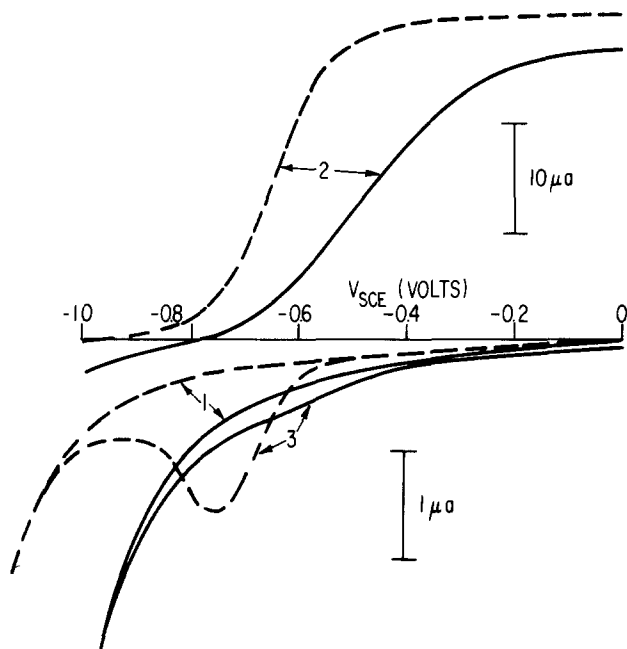


Fig. 5. Current-voltage curves of a TiO_2 electrode in 1.0M KOH with -200 mV/sec scan from 0 volts (SCE), curve 1, in dark, no light exposure; curve 2, with 350 nm light on; curve 3, in dark after 30 sec illumination with 350 nm light and 5 sec delay before voltage scan: solid curves—initial measurement on electrode with no cleaning before use; dashed curves—after 0.02C photocurrent in KOH and 0.01C photocurrent in H_2SO_4 .

as more photocurrent was passed in both 1M KOH and 0.5M H_2SO_4 . The photocurrent-voltage curves (curves 2) shown in Fig. 5 show corresponding changes as do the background dark current curves (curves 1) on which the reduction peak rides. Similar changes were produced by cleaning the electrode in concentrated H_2SO_4 at temperatures above 50°C . No attempt was made to analyze the surface to establish the cause of this behavior. It is described here to emphasize the importance of surface cleaning and to point out the correspondence between the reduction peak and the photocurrent-voltage curves.

Discussion

Peak size and position.—Few quantitative treatments have been published of charge transfer processes between electrolyte species and the bands of semiconductors when the electrolyte energy levels are in the range of the bandgap of the semiconductor. A tunneling analysis (8) has been applied to explore the distribution of electrolyte energy levels. The strong doping density dependence of the tunneling analysis precludes that as an explanation of the observations presented here. The brief, small polaron treatment published (9) does not seem to apply to the present case.

A number of investigators have used localized states at the interface in a qualitative way to explain this charge transfer process. Quantitative treatments using an interaction cross section between semiconductor carriers and interface/electrolyte states have been made for majority carriers (10, 11) and photoexcited minority carriers (12) and the applicability of this approach to a variety of interface states has been suggested (6). It will be applied to the observations reported here.

Assume a surface density of empty electron states, N , at the surface of an n-semiconductor with a bulk electron density, n_b . The density of electrons at the surface of the semiconductor, n_s , is given by

$$n_s = n_b \exp[-q(V - V_{fb})/kT] \quad [3]$$

where V is the voltage applied to the semiconductor

relative to some reference in the electrolyte and V_{fb} is the flatband potential of the semiconductor relative to the same reference, q is the magnitude of the electron charge, T is absolute temperature, and k is Boltzmann's constant. The discussion will be restricted to $V > V_{fb}$ where the value of V_{fb} will be considered independent of V . The current density, j , of electrons reacting with the surface states is given by

$$j = qn_s N \sigma v \quad [4]$$

where v is the thermal velocity of the electrons (about 10^7 cm/sec) and σ is the cross section for interaction between the electrons and the surface states. If it is further assumed that each state that is filled by this electron current is not reemitted then

$$\frac{dN}{dt} = \frac{dN}{dV} \frac{dV}{dt} = -\frac{j}{q} \quad [5]$$

If the initial voltage is large enough so that n_s is very small and the voltage is swept negative at a constant dV/dt , Eq. [3], [4], and [5] can be combined and approximately integrated as

$$\int_{N_1}^N \frac{dN}{N} = -\frac{v\sigma n_b}{\frac{dV}{dt}} \int_{\infty}^V e^{-\frac{q(V - V_{fb})}{kT}} dV \quad [6]$$

to get

$$N = N_1 \exp\left\{ \frac{v\sigma n_b kT}{q} \exp[-q(V - V_{fb})/kT] / q \frac{dV}{dt} \right\} \quad [7]$$

Combining Eq. [3], [4], and [7] an expression for $j(V)$ can be determined.

The voltage, V_p , for the maximum in the $j(V)$ expression can readily be obtained as

$$V_p - V_{fb} = \frac{kT}{q} \ln\left(-\frac{n_b \sigma v kT}{q dV/dt}\right) \quad [8]$$

Using Eq. [8], the current density can be written as a function of $(V - V_p)$.

$$j = qN_1 \left(-\frac{q}{kT} \frac{dV}{dt}\right) e^{-\frac{q(V - V_p)}{kT}} \exp\left[-e^{-\frac{q(V - V_p)}{kT}}\right] \quad [9]$$

Thus, the shape of the reduction peak is fixed and its size determined by N_1 and the voltage sweep rate. Equation [8] can be rearranged to give

$$\sigma = -\frac{dV}{dt} \frac{q}{kT n_b v} \exp\left[\frac{q(V_p - V_{fb})}{kT}\right] \quad [10]$$

from which the cross section for electron capture can be calculated from V_p if V_{fb} and n_b can be determined.

In Fig. 6 calculated $j(V - V_p)$ curves are compared with experimental results taken from the shaded areas of Fig. 4(a) and 4(c). For the calculations the values of N_1 were determined from the areas under the experimental curves. These were 6.7×10^{13} and 1.9×10^{13} per cm^2 respectively. The position of the peak in the calculated curve was matched to the experimental peak. As can be seen the experimental curves are broader than the calculated curves. This does not necessarily indicate that the model used to describe the charge transfer process is not appropriate. The calculations assume a single value for σ , a uniform doping density, and a uniform flatband voltage across the surface of the electrode. A spread in the value for any of these could explain the width of the experimental peaks. The very broad peak in Fig. 5 is probably due to a spread in flatband voltage due to surface contamination. Since this effect can be elim-

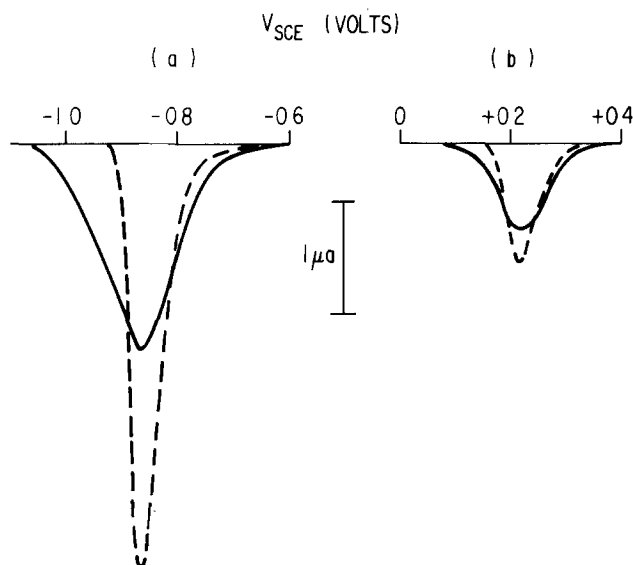


Fig. 6. Comparison of experimental reduction peaks (solid curves) corresponding to the shaded areas of (a) Fig. 4(a); and (b) Fig. 4(c) with curves calculated (dashed curves) from Eq. [9] using $N_i = 6.7 \times 10^{13} \text{ cm}^{-2}$ and $1.9 \times 10^{13} \text{ cm}^{-2}$ respectively and matching the peak position to the experimental curve.

inated by proper surface preparation it will not be considered further here.

The model correctly describes the effect of voltage sweep rate illustrated in Fig. 3. Equation [9] shows the current proportional to the sweep rate. Equation [8] shows the peak position decreasing 0.06V for a factor of 10 increase in sweep rate. Both of these effects are readily seen in Fig. 3. The background current on which the peak rides also increases with scan rate as expected since it is capacitive current due to a changing voltage across the depletion region of the semiconductor.

Frequency dependent capacitance and nonuniform doping density prevent precise flatband voltage determination. The capacitance vs. voltage measurements at 1000 Hz that were made in conjunction with the experimental reduction peak measurements in Fig. 6 show nonuniform doping density with depth. Using capacitance-voltage measurements it is possible, however, to determine a difference in flatband potential of more than 1V for the electrode in 1M KOH and 0.5M H_2SO_4 corresponding to the two measurements in Fig. 6. This differs from the 0.8V difference expected from the 0.059V/pH shift usually attributed to TiO_2 . This discrepancy could be due to surface effects determined by the sequence of measurements. It could affect the relative values for σ but does not affect the principal conclusions of this report. Using $V_{fb} = -0.3\text{V}$ and $V_p = +0.21\text{V}$ in 0.5M H_2SO_4 and $V_{fb} = -1.3\text{V}$ and $V_p = -0.85\text{V}$ in 1M KOH the values of $\sigma = 3.6 \times 10^{-16} \text{ cm}^2$ and $3.6 \times 10^{-17} \text{ cm}^2$ respectively are obtained. [A value of $n_b = N_d = 7 \times 10^{17} \text{ cm}^{-3}$ was used. It can be shown that for nonuniform doping with depth the appropriate value for n_b in Eq. [3] is its value at the edge of the depletion region. This value for n_b can be determined from the slope of A^2/C^2 vs. V at the voltage corresponding to the peak (13).]

No attempt has been made to determine values of σ with greater precision to see if there are sample to sample and electrolyte to electrolyte variations or if σ is approximately the same under all conditions. A better understanding of the origin of the states responsible for the peak will provide the driving force for more precise measurements. The values for σ determined here are smaller than the geometric cross section of a state localized on a single atom. This suggests that the state is not positively charged (the

coulombic attraction could make the cross section much larger than geometric). A cross section smaller than geometric could be due to poor electronic or phonon coupling between the state and the semiconductor. The model developed here could be used to study factors that affect this coupling in the experimental situation described here or in other experimental circumstances involving charge transfer between surface coatings and semiconductors.

Growth of peak.—Two possible circumstances will be analyzed to describe the observed growth of the reduction peak. One of these assumes a fixed density, N_s , of electron states on the surface of the electrode. After a negative voltage sweep and before illumination these states are assumed to be filled with electrons. When the illumination is started the density of holes at the surface increases by p_s . These holes move with a thermal velocity, v (assuming the same effective mass as electrons gives $v = 10^7 \text{ cm/sec}$ for both holes and electrons), and interact with the filled states with a cross section, σ_h . The density of empty states, N , grows according to

$$\frac{dN}{dt} = p_s(N_s - N)\sigma_h v - n_s N \sigma v - Nr \quad [11]$$

where r is the spontaneous hole emission constant, i.e., Nr is the capture rate of electrons from the valence band (n_s and σ were defined at Eq. [3] and [4]). Neglecting hole emission and operating at a voltage well positive of the flatband voltage (in the saturation region of curve 2, Fig. 1) so that n_s can be neglected

$$N = N_s[1 - \exp(-p_s\sigma_h vt)] \quad [12]$$

is readily obtained if p_s is assumed constant and t is the time the electrode is illuminated. If the light is stopped at time t and a negative voltage sweep is started the N of Eq. [12] becomes the N_i of Eq. [9] if spontaneous decay of N during the initial period of the sweep is neglected. Neglecting hole emission and assuming p_s constant in time are probably not precisely justified but are acceptable in this semiquantitative treatment intended to contrast different approaches to describe the processes involved. It will be noted that Eq. [12] and Eq. [1] are of the same form. Furthermore, p_s is proportional to light intensity (12) and consequently to j in the saturation region of the photocurrent for the current densities used here. This is consistent with Eq. [2].

Another approach to describe the origin of the reduction peak is to treat it as due to an intermediate of the water splitting reaction



where h^+ is a hole in the valence band of the semiconductor. If S_1 is a rate constant for the rate-limiting step of a series of reactions in which a hole produces an intermediate with surface density, N , and σ_p is the cross section for a hole to react with this intermediate as a next step in O_2 evolution the rate equation for this process is

$$\frac{dN}{dt} = p_s S_1 - p_s N \sigma_p v - n_s N \sigma v - Nr \quad [14]$$

where the other terms are as before. Using the same assumptions as for Eq. [12], ($r = 0$; $n_s = 0$)

$$N = \frac{S_1}{\sigma_p v} [1 - \exp(-p_s \sigma_p vt)] \quad [15]$$

is obtained. All the caveats applied to Eq. [12] should be used for Eq. [15] also. The interesting comparison is that the saturation value of N in Eq. [15] comes naturally as a result of the relative rates of a first and second oxidation by photoexcited holes. The larger value for the reduction peak in KOH compared to H_2SO_4 is readily explained as an increase in S_1 due

to some difference, e.g., the Helmholtz layer, between KOH and H₂SO₄. N_s in Eq. [12] is purely ad hoc.

In most other respects the two approaches give similar results. Both predict saturation values of N independent of light intensity but growth rates dependent on light intensity.

The fact that the observed capacitance is independent of the states being filled or empty, however, suggests that the states are neutral in both cases. This favors the reaction-intermediate model in which a chemical process such as H⁺ leaving the surface after hole capture or OH⁻ leaving the surface after electron capture could maintain this neutrality.

More precise analysis of the processes and/or new experimental observations are necessary to distinguish between the two approaches analyzed here.

Decay of peak.—The process by which the reduction peak decreases during the delay period between turning the light off and initiating the voltage sweep is probably hole emission to the valence band. Some alternative explanations can be eliminated, others seem too arbitrary.

Electron capture from the conduction band can be eliminated by noting that the decay rate is the same at +0.6V and +0.8V in 0.5M H₂SO₄ as noted in the observation section. The electron density at the surface changes by more than three orders of magnitude for that voltage change.

Electron capture from an impurity can be eliminated since the decay rate is independent of stirring during the delay. Other electrolyte levels are not able to donate an electron. Furthermore, the decay rate is approximately the same in 1M KOH and 0.5M H₂SO₄.

Electron capture from H₂O in the electrolyte is a possible explanation if a thermal activation to surface states distributed in energy is assumed to explain the long term stability of some of the states. The subsequent chemistry implied by this water oxidation step makes this process seem untenable.

A straightforward explanation is contained in the last term of both Eq. [11] and [14]. With the light off and at high voltages both p_s and n_s are negligible and the equation can be integrated to

$$N(E) = N_0(E)e^{-\tau t} \quad [16]$$

where a distribution in energy is emphasized. Since hole emission from a surface state of energy, E , above the valence band is an endoenergetic process, thermal activation is required and τ can be written in the form

$$\tau = v\sigma_e\eta_v e^{-E/kT} \quad [17]$$

where $\eta_v = 10^{19} \text{ cm}^{-3}$ is the estimated effective density of states in the valence band and σ_e is the cross section for a valence band electron to react with the surface state. Using a decay constant $\tau = 100 \text{ sec}$ and $\sigma_e = 10^{-16} \text{ cm}^2$ a value of $E = 0.7 \text{ eV}$ is obtained. As can be seen from Fig. 2(b) about 30% of the peak area is lost in 120 sec. Under the above assumptions 70% of the states would be more than 0.7 eV above the valence band. The numbers used for σ_e and η_v are only estimates, however, the logarithmic dependence makes the value of E weakly dependent on these parameters. This explanation is plausible and if the states involved are intermediates of O₂ evolution it suggests that they are 2-2.5 eV below the hydrogen potential.

Summary and Conclusions

In this report experimental results have been presented which indicate that oxidized states are produced on the surface of TiO₂ electrodes in aqueous electrolytes when the TiO₂ is illuminated under conditions which produce a photocurrent in the cell. Most of these states are still there after several minutes. They decrease at a rate consistent with thermally activated hole emission from states several tenths

of an eV above the valence band with at least a tenth of a volt distribution in energy. Measurements on other stable electrodes with valence bands higher in energy could test this hypothesis.

The observed reduction peak produced by these states during a negative voltage sweep has been analyzed as a reaction with electrons in the conduction band at the surface of the semiconductor. They interact with a cross section which can be determined by the position of the reduction peak. Preliminary measurements indicate that the cross section is about 10^{-16} cm^2 , i.e., smaller than the geometric cross section. This model describes all of the observed behavior and can be used to analyze other surface state interactions with semiconductor electrons, e.g., attached surface layers. A correlation between electron-capture cross section and attachment process of the layer could be very useful.

The saturated density of these oxidized states was explained as an intrinsic density of surface states or as the result of the relative rate of production and consumption of intermediate states of the O₂ evolution process. Kinetic considerations in the growth in density of these oxidized states were discussed but a detailed analysis was not developed.

Evidence supporting the view that the surface state is an intermediate in the O₂ evolution process was discussed. The argument in favor of this view is not conclusive at this point. Measurements in other solvents such as acetonitrile might be useful in resolving this question.

What is clear is that the surface state produced by oxidation by a hole from the valence band can also be reduced by an electron from the conduction band. The net effect is an electron hole recombination. It is this recombination that controls the onset of photocurrent with voltage in a manner previously described (12). If the state is an intermediate of the O₂ evolution process it represents an inherent limitation in attempts to use narrower bandgap semiconductors if its cross sections and energy levels are the same for other semiconductors.

Acknowledgments

This work was supported in part by the Office of Basic Energy Sciences of the Department of Energy. I am indebted to L. A. Harris and R. Schumacher for critical reading of the manuscript.

Manuscript submitted March 22, 1979; revised manuscript received June 5, 1979.

Any discussion of this paper will appear in a Discussion Section to be published in the December 1980 JOURNAL. All discussions for the December 1980 Discussion Section should be submitted by Aug. 1, 1980.

Publication costs of this article were assisted by General Electric Company.

REFERENCES

1. A. Fujishima and K. Honda, *Bull. Chem. Soc. Jpn.*, **44**, 1148 (1971); *Nature (London)*, **238**, 37 (1972).
2. L. A. Harris and R. H. Wilson, *Annu. Rev. Mater. Sci.*, **8**, 99 (1978).
3. H. P. Maruska and A. K. Ghosh, *Sol. Energy*, **20**, 443 (1978).
4. A. J. Nozik, *Annu. Rev. Phys. Chem.*, **29**, 189 (1978).
5. M. Tomkiewicz and H. Fay, *Appl. Phys.*, **18**, 1 (1979).
6. R. H. Wilson, Abstract 415, p. 1038, The Electrochemical Society Extended Abstracts, Seattle, Washington, May 21-26, 1978.
7. R. H. Wilson, L. A. Harris, and M. E. Gerstner, *This Journal*, **126**, 844 (1979).
8. R. Memming and F. Mollers, *Ber. Bunsenges. Phys. Chem.*, **76**, 475 (1972).
9. G. Beni, in "Semiconductor Liquid-Junction Solar

Cells," A. Heller, Editor, p. 108, The Electrochemical Society Softbound Proceedings Series, Princeton, N.J. (1977).

10. T. Freund and S. Roy Morrison, *Surf. Sci.*, **9**, 119 (1968).

11. A. Many, *CRC Crit. Rev. Solid State Sci.*, **4**, 515 (1974).

12. R. H. Wilson, *J. Appl. Phys.*, **48**, 4292 (1977).

13. J. Hilibrand and R. D. Gold, *RCA Rev.*, **21**, 245 (1960).

Technical Notes



End Point Detection in Plasma Etching by Optical Emission Spectroscopy

Kadou Hirobe and Takashi Tsuchimoto*

Computer Development Laboratories Limited, Kodaira, Tokyo 187, Japan

Optical emission spectroscopy has been applied to precise end point detection in plasma etching (1-4) and the method has many advantages superior to the others such as mass spectroscopy (5), visual observation of change in interference colors, and ellipsometry (6). The purpose of this paper is to introduce a measure for the end point detection method using an optical emission and to evaluate the lower limit of detection for etching polycrystalline silicon (poly-Si) and silicon nitride (Si_3N_4).

Figure 1 shows a block diagram of etching apparatus and optical emission observation system which has been used in the experiment. Plasma etching was carried out in a volume loading, barrel type apparatus (Model 2005-1813 SC from International Plasma Corporation). Wafers were placed in a quartz wafer boat inside a quartz chamber. $\text{CF}_4 + \text{O}_2$ (4%) was used as an etching gas. Typical etching condition was 100W rf power and 0.5 Torr (66.5 Pa). Poly-Si and Si_3N_4 films were prepared using the reaction of chemical vapor deposition on thermally oxidized silicon substrates. The optical emission observation system was composed of a spectrometer (Model 139 from Hitachi, Limited), a photomultiplier, an amplifier, and a recorder. The resolution of the system was 0.5 nm. The emission was viewed through the thick quartz window at one end of the chamber. No optical lens was used. In the experimental measurement, the wavelengths of 674 and 777 nm were selected for those spectra which were most useful for Si_3N_4 and poly-Si etching, respectively. It is considered that the 674 nm line is from N_2 molecule and the 777 nm is from SiF molecule, and N_2

* Electrochemical Society Active Member.

Key words: rf discharge, barrel type etching apparatus, polycrystalline silicon, mass spectroscopy, carbon tetrafluoride.

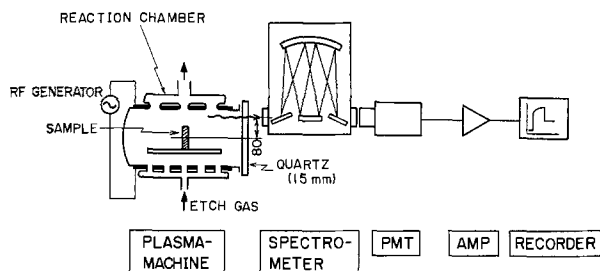


Fig. 1. Block diagram of the etching apparatus and optical emission observation system.

and SiF come from the reaction products of Si_3N_4 and poly-Si with CF_4 in the plasma, respectively.

Figure 2 shows a typical change in emission intensity of the 674 nm line during etching Si_3N_4 films. The emission intensity increased gradually with increasing temperature of the chamber and of wafers which were warmed up by rf discharge, and then decreased rapidly as the surface area of the remaining Si_3N_4 film decreased, and finally leveled off after etching was completed. The end point was clearly detected at the point where the curve suddenly drops off in the figure. Similar characteristic changes in the intensity of the 777 nm line emission were obtained for etching poly-Si film.

A new measure is introduced for expressing the lower limit of detection of the end point. The measure is defined as the ratio of the change in emission intensity at the end point (B) to the maximum emission intensity (A), namely B/A . In order to evaluate the lower limit of detection of the method for poly-Si and Si_3N_4 , the relations between B/A and the area

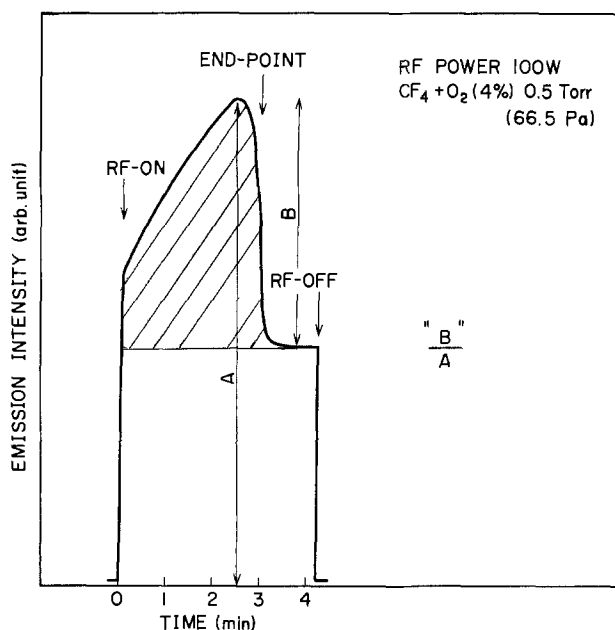


Fig. 2. Typical emission intensity of 674 nm as a function of time.

of the sample were examined. The experimental results are presented in Fig. 3. The intensity ratio B/A was dependent on materials to be etched. The B/A for Si_3N_4 was much greater than that for poly-Si. The end point was precisely detected on the recorder chart when B/A was larger than 1%. Therefore, the end point could be precisely detected when the surface area of the samples was larger than 0.3 cm^2 for Si_3N_4 and 2 cm^2 for poly-Si.

In order to explain the differences in the lower limit of detection between poly-Si and Si_3N_4 , the relations between photons emitted from the plasma and the surface area of samples were investigated using the following assumptions. (i) The number of photons emitted from SiF or N_2 is proportional to the volume of etched area, (ii) the volume is proportional to the surface area, (iii) the number of photons detected is proportional to integrated emission intensity, (iv) the integrated intensity is proportional to the area shown as the shaded area in Fig. 2. From these assumptions, the integrated intensity can be expressed by the equation

$$\int I dt = K \cdot S^n \quad [1]$$

where I is the emission intensity (photons sec^{-1}), t is the etching time (sec), K is a constant (photons cm^{-2}) and S is the surface area of sample (cm^2). Experimental relations are shown in Fig. 4. The integrated intensity of 674 nm spectrum was linear with the area of sample and the value of n was nearly unity, while for 777 nm the integrated intensity was not proportional to the surface area and n was 1.71. The deviation of n from unity in case of monitoring poly-Si etching by 777 nm spectrum will be explained as the SiF molecule also comes from the reaction between the quartz chamber and the CF_4 plasma. On the other hand, for Si_3N_4 etching N_2 molecules are formed only by the reaction of Si_3N_4 with the plasma. Therefore, the change in the 674 nm emission intensity is thought to be proportional to the change of amount of N_2 .

Experimental results obtained in this study have shown that optical emission spectroscopy is able to

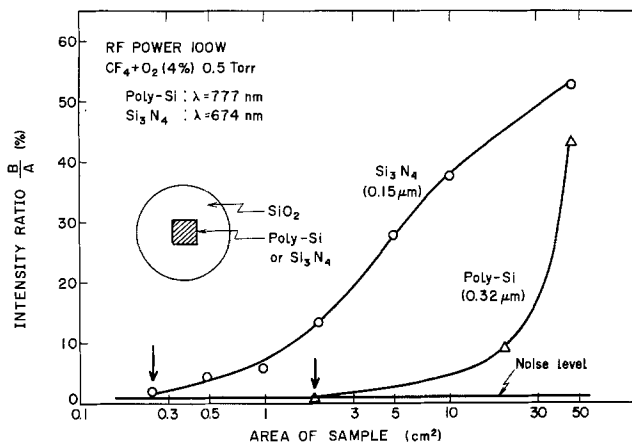


Fig. 3. Intensity ratio B/A as a function of area of sample

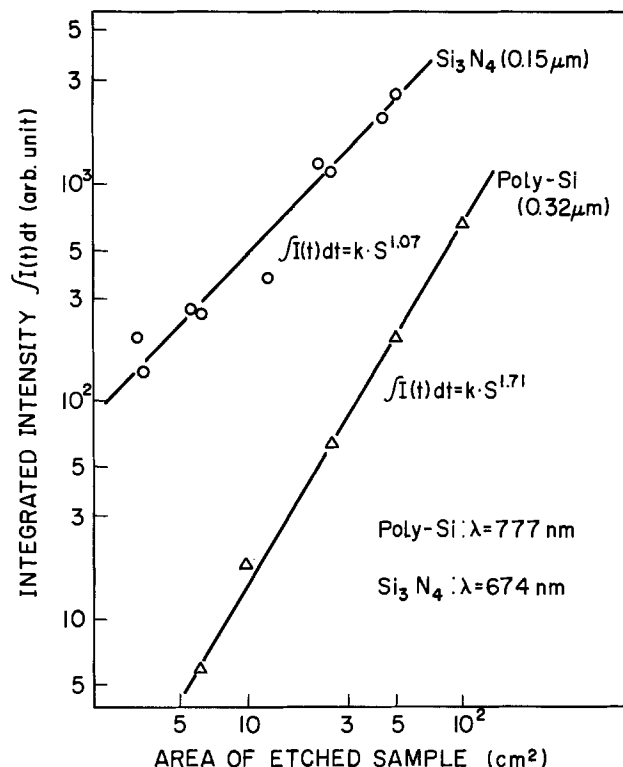


Fig. 4. Integrated intensity as a function of area of sample

detect the end point in etching small surface areas of poly-Si and Si_3N_4 films precisely and the method has wide applications in the control of plasma etching.

Manuscript submitted Nov. 16, 1978; revised manuscript received May 30, 1979.

Any discussion of this paper will appear in a Discussion Section to be published in the December 1980 JOURNAL. All discussions for the December 1980 Discussion Section should be submitted by Aug. 1, 1980.

Publication costs of this article were assisted by Computer Development Laboratories Limited.

REFERENCES

1. W. R. Harshbarger, R. A. Porter, T. A. Miller, and P. Norton, Kodak Microelectronics Seminar Proceedings, p. 43 (1976).
2. R. G. Poulsen and G. M. Smith, in "Semiconductor Silicon 1977," H. R. Huff and E. Sirtl, Editors, p. 1058, The Electrochemical Society Softbound Proceedings Series, Princeton, N.J. (1977).
3. R. G. Poulsen, *J. Vac. Sci. Technol.*, **14**, 266 (1977).
4. E. O. Degenkolb, C. J. Mogab, M. R. Goldrick, and J. E. Griffiths, *Appl. Spectrosc.*, **30**, 520 (1976).
5. Y. Horiike and M. Shibagaki, in "Proc. 7th Conference Solid State Devices," Tokyo, 1975; *Jpn. J. Appl. Phys.*, **15** (1976) Suppl., p. 13 (1975).
6. H. H. Busta and R. E. Lajos, IEEE 1977 International Electron Devices Meeting (IEDM), p. 12, Dec. 5-7, 1977.

The Effects of Different Environments on the Thermal Stability of Powdered Samples of LiAlO₂

P. A. Finn*

Argonne National Laboratory, Argonne, Illinois 60439

The second generation fuel cell presently being developed by the Department of Energy is the molten carbonate fuel cell (1). The system, which will be coal-fueled, is anticipated to be a high-efficiency electric generator. Lithium aluminate is used in molten-carbonate fuel cells as the matrix support material for the carbonate electrolyte (1-3). Powdered mixtures of LiAlO₂ and alkali carbonate are blended and then hot-pressed into a thin electrolyte structure (tile) which is sandwiched between the two electrodes. Changes in the physical form of LiAlO₂ at the cell operating temperature (925°K) will alter both the strength and the electrolyte-retention properties of the tile.

The three allotropic forms of LiAlO₂ (α -, β -, and γ -) belong to the following crystal groups, hexagonal (4), orthorhombic (5), and tetragonal (6), and have densities of 3400 (4), 2610 (7), and 2615 (6) kg/m³, respectively. Lehmann and Hesselbarth (8) and Lejus (9) found that in air in the absence of carbonate, γ -LiAlO₂ was the stable allotrope at temperatures $\geq 1173^\circ\text{K}$. In the presence of lithium carbonate in air, the temperature at which α -LiAlO₂ transforms to γ -LiAlO₂ is lowered to $\leq 973^\circ\text{K}$ (10, 11). Fischer noted that the transformation of β - to γ -LiAlO₂ occurred at 1173°K (7) (no details were given); however, the effect of lithium carbonate on the phase transformation of β - to γ -LiAlO₂ was not reported. Studies on the crystal growth of LiAlO₂ as a function of time, temperature, or gas environment were not found in the literature. To increase our knowledge of the LiAlO₂ system, the thermal stability of α -, β -, and γ -LiAlO₂ to both allotropic transformation and crystal growth has been studied as a function of time, temperature, and environment.

Experimental

To obtain information useful to fuel-cell operation, we have heated powdered samples in gold crucibles for 24-1000 hr at 875°-1200°K, in three gas environments—air, CO₂, and 80% H₂-20% CO₂ saturated with H₂O at 295°K. All samples containing alkali carbonate consisted of 45 weight percent (w/o) LiAlO₂ and 55 w/o Li₂CO₃-K₂CO₃ [(62-38 mole percent (m/o)], the electrolyte composition presently being used in molten-carbonate fuel cells. The three allotropic forms of LiAlO₂ were prepared in this laboratory (see Table I). Clump-shaped particles of α -LiAlO₂ were prepared by heating a mixture of Degussa γ -Al₂O₃ and reagent grade Li₂CO₃ (1:1.5 mole ratio) at 873°K for 24 hr in air enriched in CO₂. To produce β -LiAlO₂, an aqueous slurry of γ -Al₂O₃-LiOH-KOH in the mole ratio of 1.0:4.1:1.2 was evaporated to dryness. The residue was ground before exposure to air enriched in CO₂ for 6 hr at 295°K, and then 4 hr at 873°K (12). The γ -LiAlO₂ was obtained by heating α -LiAlO₂ in the presence of Li₂CO₃ at 973°K for 17 hr in air. Carbonate was removed from samples by washing with a 50:50 volume mixture of glacial acetic acid and acetic anhydride, followed by a methanol wash. Samples were characterized by x-ray diffraction, scanning electron microscopy, and BET surface areas.

* Electrochemical Society Active Member.

Key words: molten carbonate, fuel cell, allotropic transformation, crystal growth, LiAlO₂.

Experimental Results

A summary of the test results for the allotropic transformation of α - or β -LiAlO₂ to γ -LiAlO₂ are presented in Table II. Initial tests were conducted in the absence of carbonate to verify the temperatures at which the transformation of either α - or β - to γ -LiAlO₂ occurred. A sample of α -LiAlO₂ that was heated at 1110°K for 64 hr remained α -LiAlO₂. Another sample that was heated at 1210°K for 40 hr transformed to γ -LiAlO₂; a minor amount of LiAl₅O₈ (a decomposition product formed by the loss of Li₂O) was also present. The material after transformation to γ -LiAlO₂ consisted of small bipyramidal-shaped particles with a surface area of 15 m²/g. Our results are consistent with Hesselbarth (8) and Lejus (9) who found that α -LiAlO₂ transformed to γ -LiAlO₂ at $\sim 1173^\circ\text{K}$. A sample of β -LiAlO₂ that was heated at 1030°K for 23 hr remained β -LiAlO₂. Another sample of β -LiAlO₂ that was heated at 1110°K for 24 hr transformed to γ -LiAlO₂, and a minor amount of β -LiAlO₂ remained. The particles, after transformation to γ -LiAlO₂, retained the rod configuration. The transformation of β - to γ -LiAlO₂ thus occurs in air in <24 hr at temperatures <1110°K but >1030°K. Our results complement those of Fischer (2) which were obtained at 1173°K. In air in the absence of carbonates, β -LiAlO₂ transformed to γ -LiAlO₂ at a temperature lower than that at which α -LiAlO₂ transforms to γ -LiAlO₂. This result would indicate that β -LiAlO₂ is less stable to allotropic transformation than α -LiAlO₂.

Table I. Physical characteristics of untreated LiAlO₂

Allotrope	Surface area (m ² /g)	Particle shape	Particle dimension (μm)
α -LiAlO ₂	60	Clumps of small particles	< 0.25
β -LiAlO ₂	12	Rods	1 \times 0.2
γ -LiAlO ₂	3	Bipyramids	0.5

Table II. The stability of α - and β -LiAlO₂ to allotropic transformation to γ -LiAlO₂

Allotrope	Environment	Temp (°K)	Time (hr)	Product
α	Air	1110	64	α
α	Air	1210	40	γ
α	Air, Li/K ¹	875	24	γ (ma) ² , α (me) ³
α	HCH ⁴ , Li/K	875	160	α (ma), γ (mi) ⁵
α	CO ₂ , Li/K	975	442	α
α	CO ₂ , Li/K	975	1062	γ
β	Air	1030	23	β
β	Air	1110	24	γ , β (mi)
β	Air, Li/K	945	352	γ
β	HCH, Li/K	945	787	β
β	HCH, Li/K	975	107	γ
β	CO ₂ , Li/K	975	991	γ

¹ Li/K = 62 m/o Li₂CO₃ - 38 m/o K₂CO₃ (55 w/o).

² ma = major

³ me = medium

⁴ HCH = 80% H₂-20% CO₂ saturated with H₂O at 295°K.

⁵ mi = minor

In further thermal tests, powdered samples containing LiAlO_2 and 55 w/o carbonate were heated for 24 hr to ~ 1000 hr at temperatures of $875^\circ\text{--}975^\circ\text{K}$ in three gas environments—air, CO_2 , and 80% H_2 -20% CO_2 saturated with water at 295°K . The test results are summarized in Table II. A sample of α - LiAlO_2 that was held for 24 hr at 875°K in air, transformed to γ - LiAlO_2 , a medium amount of α - LiAlO_2 remained. The sample after heat-treatment consisted of small bipyramidal-shaped particles with a surface area of <5 m^2/g . At 925° and 975°K , only very minor amounts of α - LiAlO_2 remained after ~ 24 hr, and the shape of the particles, small bipyramids, was similar to that observed at 875°K . Thus, in the presence of carbonates, a sample of α - LiAlO_2 with high surface area (60 m^2/g) was unstable when heat-treated in air above 875°K . In an environment consisting of 80% H_2 -20% CO_2 saturated with water at 295°K , a sample of α - LiAlO_2 contained a minor amount of γ - LiAlO_2 after either 160 hr at 875°K or 24 hr at 925°K . However, after 121 hr at 975°K , significant amounts of both α - and γ - LiAlO_2 were present. The samples after heat-treatment at 875° , 925° , or 975°K consisted of small bipyramidal-shaped particles with surface areas of ~ 5 m^2/g . These results indicate that, in the presence of carbonates, α - LiAlO_2 is unstable when heat-treated in a 80% H_2 -20% CO_2 - H_2O environment. A sample of α - LiAlO_2 held in CO_2 for 140 hr at 875°K remained α - LiAlO_2 . A second sample held 442 hr at 975°K did not transform to γ - LiAlO_2 ; but after 1062 hr at 975°K , γ - LiAlO_2 was the major species present. Bipyramidal-shaped particles were produced with surface areas of <5 m^2/g . Evidently, a long period is required in the presence of CO_2 to accomplish the transformation of α - to γ - LiAlO_2 . The samples held in CO_2 exhibited crystal growth, but the rate of growth was slower in CO_2 than in air or 80% H_2 -20% CO_2 - H_2O . In the presence of carbonate, pure CO_2 slows both the transformation of α - to γ - LiAlO_2 and the rate of loss of surface area of the samples.

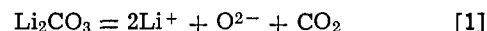
In air, β - LiAlO_2 in the presence of 55 w/o carbonate was stable for 2400 hr at 925°K to allotropic transformation; crystal growth was minimal. At 945°K , β - LiAlO_2 was still present after 112 hr but γ - LiAlO_2 was the only species present after 352 hr. At 975°K , more than 100 hr was required to transform completely β - to γ - LiAlO_2 . The γ - LiAlO_2 consisted of bipyramidal-shaped particles with a surface area of <2 m^2/g . In the 80% H_2 -20% CO_2 - H_2O environment, β - LiAlO_2 was stable for 2400 hr at 925°K and for 787 hr at 945°K ; but after 107 hr at 975°K , only γ - LiAlO_2 was present. Thus, as the temperature is increased, γ - LiAlO_2 becomes the only stable allotrope in 80% H_2 -20% CO_2 - H_2O . In CO_2 , β - LiAlO_2 was present after 212 hr at 925°K . After 991 hr at 975°K , only γ - LiAlO_2 was present; a minor amount of γ - LiAlO_2 was detected after 211 hr at 975°K . The γ - LiAlO_2 product consisted of bipyramidal-shaped particles. From these results, it appears that β - LiAlO_2 transforms to γ - LiAlO_2 at a lower temperature in the presence of carbonates than in their absence. In all the environments studied, β - LiAlO_2 transformed to γ - LiAlO_2 when held at temperatures of 945°K or greater for periods of ≥ 1000 hr.

No transformations of γ - LiAlO_2 in the presence of carbonates to either α - or β - LiAlO_2 were detected under the conditions studied (*i.e.*, powders held at 875° , 925° , and 975°K for times of 24-1000 hr in the three gas environments). Because the γ - LiAlO_2 sample had a low initial surface area, 3 m^2/g , crystal growth was detectable only at 975°K in all three gas environments. The growth rate was highest in air and lowest in CO_2 .

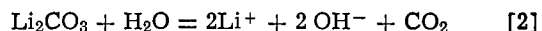
Discussion

A solubility of LiAlO_2 (form unspecified) of $3 \times 10^{-4}\text{M}$ at 975°K in the ternary carbonate (Li_2CO_3 - Na_2CO_3 - K_2CO_3) has been reported (3). At this con-

centration, an appreciable amount of LiAlO_2 is in solution in the form of Li^+ and AlO_2^- . The mobility of these dissolved species would play an important role in the growth mechanism of LiAlO_2 particles. Therefore, a solution-deposition mechanism is quite feasible in the LiAlO_2 -carbonate system. The carbonates themselves are subject to both thermal decomposition and reaction with water. The dissociation constant of Li_2CO_3 at 925°K is $\approx 9 \times 10^{-6}$ (13)



The hydrolysis constant of Li_2CO_3 at 925°K is $\approx 4 \times 10^{-4}$ (14)



The constants for K_2CO_3 are two orders of magnitude smaller. High concentrations of CO_2 would suppress both these reactions. However, in an air environment, the low partial pressure of CO_2 and high partial pressure of H_2O would favor the production of significant amounts of Li^+ and O_2^- in reaction [1] and Li^+ and OH^- in reaction [2]. Preliminary experiments in this laboratory indicate that, in the presence of large amounts of LiOH and KOH , in an air atmosphere, the transformation of α - and β - LiAlO_2 to γ - LiAlO_2 at 925°K proceeds rapidly. Crystal growth is extensive in less than 5 hr, producing γ - LiAlO_2 with surface areas <5 m^2/g . These data suggest that LiAlO_2 is more soluble in hydroxide-containing melts than in pure carbonate melts. The presence of hydroxide species in the carbonate melts facilitates both crystal growth and the transformation of either α - or β - to γ - LiAlO_2 .

Conclusions

The experimental data on the behavior of the three forms of LiAlO_2 in the presence of molten carbonate suggest the following conclusions. First, the transformations of both α - and β - LiAlO_2 to γ - LiAlO_2 occur at lower temperatures in the presence of carbonate than in its absence, *i.e.*, 873°K vs. 1173°K for α - and 945°K vs. 1110°K for β -. Thus, in the presence of carbonate at fuel cell operating temperatures, the β -form is stabilized relative to the α -form at temperatures $\leq 945^\circ\text{K}$. Second, in the presence of carbonate, both α - and β - LiAlO_2 transform to γ - LiAlO_2 , the rate being greatest in air and lowest in CO_2 . This suggests that CO_2 slows the transformations of α - and β - to γ - LiAlO_2 by suppressing the hydrolysis of Li_2CO_3 and/or K_2CO_3 , thus limiting the formation of Li^+ and OH^- . Third, crystal growth occurs with all three allotropes and proceeds at a much higher rate in the presence of the carbonate melt, thereby suggesting a solution-deposition mechanism. The rate of crystal growth for all three allotropes of LiAlO_2 is highest in air and lowest in CO_2 . Therefore, by suppressing OH^- formation, CO_2 decreases the solubility of LiAlO_2 in the carbonate melt and reduces both crystal growth and the transformation of α - and β - to γ - LiAlO_2 . On the other hand, a large partial pressure of H_2O would increase the solubility of LiAlO_2 in the carbonate melt increasing crystal growth and the rate of transformation of α - and β - to γ - LiAlO_2 .

Acknowledgment

The author would like to acknowledge B. S. Tani for conducting the x-ray analyses.

Manuscript submitted April 16, 1979; revised manuscript received June 6, 1979. This was Paper 259 presented at the Pittsburgh, Pennsylvania, Meeting of the Society Oct. 15-20, 1978.

Publication costs of this article were assisted by Argonne National Laboratory.

REFERENCES

1. J. P. Ackerman, in "Electrode Materials and Processes for Energy Conversion and Storage," J. D. E. McIntyre, S. Srinivasan, and F. G. Will,

- Editors, p. 634-641, The Electrochemical Society Softbound Proceedings Series, Princeton, N. J. (1977).
- H. E. Huynink, *Energy Conv.*, **12**, 139 (1972).
 - G. H. J. Broers and H. J. J. van Ballegoy, "Proceedings of the 3rd International Symposium on Fuel Cells," p. 77, Brussels (1969).
 - M. Marezio and J. P. Remeika, *J. Chem. Phys.*, **44**, 3143 (1966).
 - K. Dorhofer, *J. Appl. Crystallogr.*, **12**, 240 (1979).
 - M. Marezio, *Acta Crystallogr.*, **19**, 396 (1965).
 - A. K. Fischer, *Inorg. Chem.*, **16**, 974 (1977).
 - H. A. Lehmann and H. Hesselbarth, *Z. Anorg. Allg. Chem.*, **313**, 117 (1961).

- A. M. Lejus, *Rev. Hautes Temp. Refract.*, **1**, 72 (1964).
- N. N. Semenov, *Izv. Sib. Otd. Akad. Nauk SSR, Ser. Khim. Nauk*, **1**, 156 (1967).
- S. Gal, K. Tomor, E. Pungor, G. Sooki-Toth, and P. Horvath, *J. Therm. Anal.*, **9**, 241 (1976).
- K. Kinoshita, J. W. Sim, and J. P. Ackerman, *Mater. Res. Bull.*, **13**, 445 (1978).
- B. K. Anderson, Ph.D. Thesis, The Technical University of Denmark (1975).
- JANAF Thermochemical Tables, published by U.S. Department of Commerce (1971).

The Use of Etching Techniques in the Characterization of Degraded GaAs-GaAlAs Lasers

T. van Dongen, R. P. Tijburg, and J. Bakker

Philips Research Laboratories, Eindhoven, The Netherlands

The appearance of nonluminescent areas in stripe geometry GaAs-GaAlAs double heterostructure (DH) lasers has previously been identified by Deloach and co-workers as related to a major degradation mechanism (1). The correlation between the dark lines and dislocations in the active layer itself or the adjacent GaAlAs layers has been demonstrated by means of transmission electron microscopy (TEM) (2) and subsequent use of a dislocation etchant and a selective etchant (3). The authors of the latter reference used bars of DH material in which dark line patterns were generated by optical pumping with a krypton laser. With etching, they only found textured patterns correlated with the degradation-related dark features in the GaAlAs layer close to the interface with the active layer.

In the study of degraded lasers it may be useful to detect in which layer degradation-related phenomena are present and what may be their starting point. With a combination of selective etching and photoetching, we are able to reveal the presence of degradation-related phenomena in several layers of a DH laser including the active layer.

Selective etching of the various compounds present in DH material has already been described in Ref. (4) and (5). For the selective etching of the GaAs capping layer we used a rough copy of the pH-7 etchant consisting of 25 ml H₂O₂, 25 ml H₂O, and 8 drops NH₄OH. The p-type GaAlAs layer was removed selectively with a solution of 50 mg Ce(SO₄)₂·4H₂O, 50 mg Ce(NO₃)₃·6H₂O, and 500 mg Fe₂(SO₄)₃·H₂O in 50 ml H₂O. The Fe₂(SO₄)₃ was added to keep the pH of the solution lower than or equal to two.

Selective photoetching has been shown to be a sensitive technique for the determination of crystal imperfections in GaAs. Recently, Kuypers and van Gils of this laboratory (7) showed a one-to-one correlation between nonluminescent spots in epitaxial (100) GaP and features revealed by selective photoetching. Their etchant, consisting of 20 ml H₂SO₄ (96%), 20 ml H₃PO₄ (85%), and 0.2 ml H₂O₂ (30%), was used for our experiments.

The time needed to reveal defects depends on the incident light intensity; 30 sec to 1 min is generally sufficient to reveal the desired features at room temperature, using a tungsten 45W microscope lamp, focused to a spot of 1 cm².

The degraded lasers studied were cleaved from a standard double heterostructure composed of four epilayers

grown by liquid phase epitaxy on a (100) substrate. The lasing area was restricted by a proton bombardment or a pyrolytic silicon dioxide layer on top of the capping layer. In most cases, the dimensions of the stripes were 10 × 300 μm².

After life test a laser was desoldered from the mounts. The indium solder had been removed from the surface with concentrated HCl. The chromium-platinum contact on the capping layer had been removed also in the etchant since the chromium dissolves readily when it is in contact with platinum. Next, each subsequent layer was treated with the photoetchant in order to reveal any defect present. After photoetching, the appropriate selective etchant was used to remove the whole layer. In the diodes studied, we found with photoetching the same degradation-related pattern as was present in the spontaneous emission as viewed through the substrate and as revealed by EBIC. Mostly, the textured pattern became visible only in the active layer. Only crystal defects generated during the growth could be revealed in the matching GaAlAs layers. Figure 1a shows the EBIC pattern of a degraded oxide stripe laser diode. Figure 1b shows the same diode with a similar pattern revealed by photoetching of the active layer.

Figure 2a shows a dark line pattern in the spontaneous emission viewed through a window in the substrate contact. The same pattern revealed by etch-

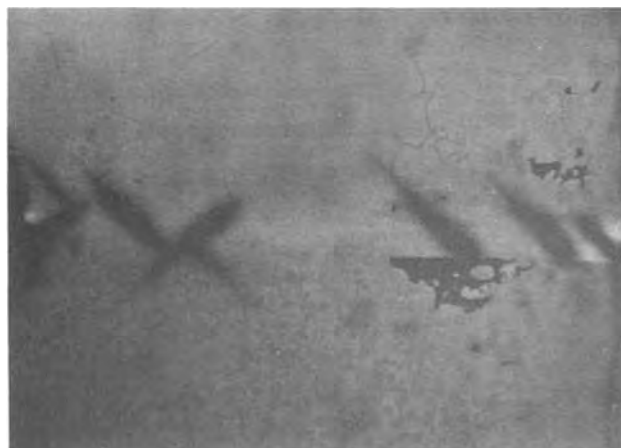


Fig. 1a. Electron beam induced current topograph of a degraded oxide stripe double heterostructure laser diode.

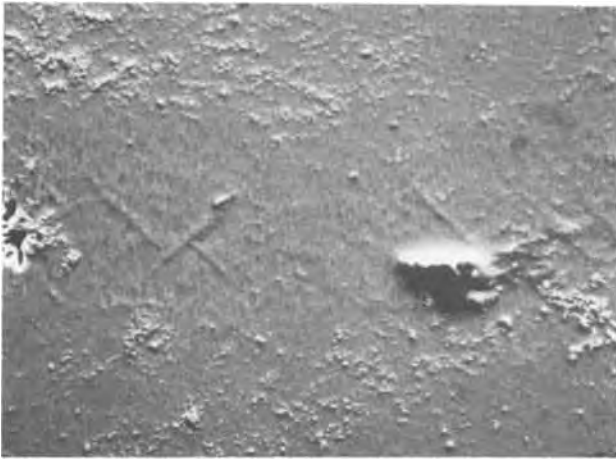


Fig. 1b. The dark lines of 1a revealed by photoetching of the active layer. The etch rate of the dark lines is lower than that of the undisturbed material.

ing of the active layer under illumination is shown in Fig. 2b. Since this figure gives a view of the surface opposite to that of the spontaneous emission, the direction of the etched pattern is opposed to that of the dark lines.

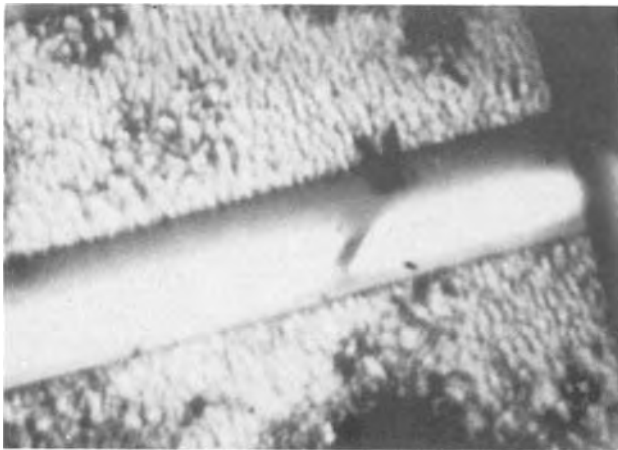


Fig. 2a. Dark lines in the spontaneous emission of a laser diode viewed through a window in the substrate contact.

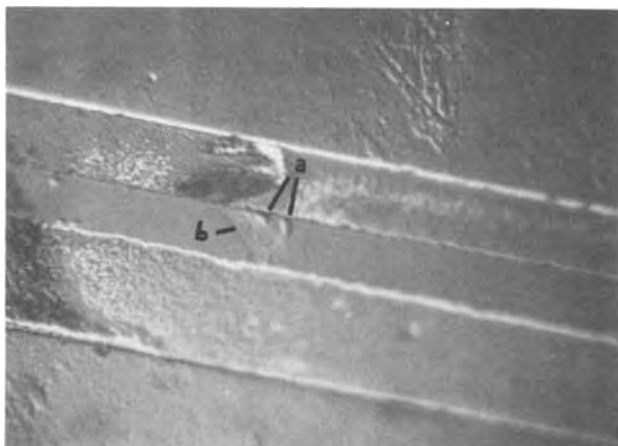


Fig. 2b. The dark lines of Fig. 2a revealed by photoetching of the active layer. This figure gives a view of the surface opposite to that of the spontaneous emission. The direction of the etched pattern is opposed to that of the dark lines. The crystal imperfections, a, show a higher etch rate than the dark lines, b.



Fig. 3. This dark line structure revealed by photoetching is typical for a dark line initiated at a mirror of a GaAs-AlGaAs double heterojunction laser.

In the textured pattern of Fig. 2b obtained with photoetching, we see a difference between the dark lines and the crystal imperfections. The dark lines show a lower etch rate than the adjacent undisturbed material. The crystal imperfections, however, show a higher etch rate than the adjacent undisturbed material. This latter behavior is in accordance with the results observed by Kuhn-Kuhnenfeld on dislocations in p-type GaAs [Ref. (6)]. As yet, the lower etch rate of the dark lines remains unexplained.

If we study the etched samples with secondary emission in a scanning electron microscope, the resolving power is many times better than that of pictures obtained from the spontaneous emission through the substrate. Since details of micron size are clearly observable, the resolution is also better than that of EBIC pictures. As is already known, the dark features initiated at the mirror and associated with catastrophic failure are attributed to crystallographic damaged regions (8). With photoetching of the active layer, it can be made visible that these defects are of different structure than the dark lines which arise elsewhere in the active layer (see Fig. 3).

Acknowledgments

The authors are indebted to Mr. P. de Waard for providing the picture of the luminescence pattern and to Mr. J. de Poorter for his contribution in making the SEM photographs.

Manuscript submitted Nov. 27, 1978; revised manuscript received April 2, 1979.

Any discussion of this paper will appear in a Discussion Section to be published in the December 1980 JOURNAL. All discussions for the December 1980 Discussion Section should be submitted by Aug. 1, 1980.

Publication costs of this article were assisted by Philips Research Laboratories.

REFERENCES

1. B. C. Deloach, B. W. Hakki, R. L. Hartman, and L. A. D'Asaro, *Proc. IEEE*, **61**, 1042 (1973).
2. P. Petroff and R. L. Hartman, *Appl. Phys. Lett.*, **23**, 469 (1973).
3. W. D. Johnston and W. M. Callahan, *J. Appl. Phys.*, **45**, 505 (1974).
4. R. Tjburg and T. v. Dongen, *This Journal*, **123**, 687 (1976).
5. R. A. Logan and F. K. Reinhart, *J. Appl. Phys.*, **44**, 4172 (1973).
6. F. Kuhn-Kuhnenfeld, *This Journal*, **119**, 1063 (1972).
7. F. P. J. Kuypers and W. van Gils, Private communication.
8. B. W. Hakki and F. R. Nash, *J. Appl. Phys.*, **45**, 3907 (1974).



Electrochromism at Niobium Pentoxide Electrodes in Aqueous and Acetonitrile Solutions

Benjamin Reichman* and Allen J. Bard*

Department of Chemistry, The University of Texas at Austin, Austin, Texas 78712

Display devices based on electrochromic effects on metal oxides are currently being investigated intensively. For example a number of studies on the electroreduction of WO_3 to form the blue hydrogen tungsten bronze, H_xWO_3 , which can be reversibly bleached upon oxidation have been reported (1-4). However the slow dissolution of WO_3 in the aqueous sulfuric acid solutions used as the electrolytes in most cells has prevented application of this system to practical devices. Systems with WO_3 based on nonaqueous solvents, such as glycerol and acetonitrile, with formation of H- or Li-bronzes have also been described (5-8), but these also have problems (dissolution, irreversible coloring, or slow response). We report here preliminary experiments demonstrating electrochromic behavior of Nb_2O_5 in both aqueous and acetonitrile (AN) solutions. This oxide, which is insoluble in many media, shows reasonable response times and reversible coloring and bleaching, and so appears to be a promising system for electrochromic devices. Moreover the excellent stability of Nb towards corrosion in mineral acids because of the protective Nb_2O_5 layer (9) suggests that this material should form stable systems.

The Nb_2O_5 electrodes were prepared by heating a niobium metal disk (12.7 mm dia., cut from a rod of 99.8% Nb obtained from Alfa Ventron) in air to $\sim 500^\circ\text{C}$ for about 10 min which produced a white layer of Nb_2O_5 about 15 μm thick. Electrical contact was made to the Nb metal by scraping off part of the oxide and connecting a Cu wire to the Nb with silver epoxy cement. A typical current-potential curve recorded with this electrode in 1 M H_2SO_4 with a Pt wire as a counter electrode and vs. a $\text{Hg}/\text{Hg}_2\text{SO}_4/1\text{ M H}_2\text{SO}_4$

reference electrode, is shown in Fig. 1. The cathodic current which started at $\sim 0\text{ V}$ vs. NHE is associated with coloration of the Nb_2O_5 layer and the anodic current, which appeared after reversal of the potential scan direction, is associated with the bleaching process. Upon reducing this electrode in the aqueous 1 M H_2SO_4 with a potential step to -0.6 V vs. NHE, a dark blue color appeared on the electrode surface. The blue color disappeared upon oxidation by a step to $+1\text{ V}$ vs. NHE. The electrochromic process was reversible with a response time of less than 1 sec.

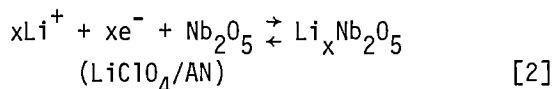
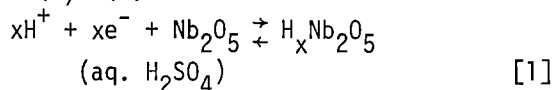
Electrochemical reduction and coloration of the Nb_2O_5 electrode could also be carried out in AN solution containing 0.8 M LiClO_4 . All solutions were prepared in an inert atmosphere glove-box by dissolving the LiClO_4 (dried by heating under vacuum at 110°C for three days), in AN (distilled before use by a previously described procedure (10)). The electrochemical cell containing a Pt counter electrode and bleached Nb_2O_5 quasi-reference electrode was filled in the glove box, then sealed with vacuum grease and removed for the electrochemical experiments. A current-potential curve of the Nb_2O_5 electrode in the AN/ LiClO_4 solution is shown in Fig. 2. The cathodic current which started at about 0 V vs. the Nb_2O_5 reference electrode is associated with coloration of the film. The electrode surface was bleached during passage of the anodic current which appeared following potential scan reversal. Upon stepping the electrode potential between -0.8 V and $+1.5\text{ V}$ in these solutions, the electrode could be colored and bleached reversibly with a response time of 1 to 2 sec. Continuous coloring and bleaching (1 sec steps) was carried out three days with no apparent changes in behavior.

The Nb_2O_5 appeared to be stable in the aqueous-sulfuric acid and the AN solutions

*Electrochemical Society Active Member. Key words: semiconductors, displays, voltammetry.

under cycling and at open circuit, although in the case of the aqueous solutions some hydrogen evolution appeared during the coloration process.

While we have not yet investigated the mechanism of this reaction in any detail, as a working hypothesis we propose that the coloring process in aqueous and AN solutions occurs either by niobium bronze formation (by analogy to the tungsten bronzes) or by reduction of niobium(V) (9):



Acknowledgment.--The support of this research by Texas Instruments is gratefully acknowledged.

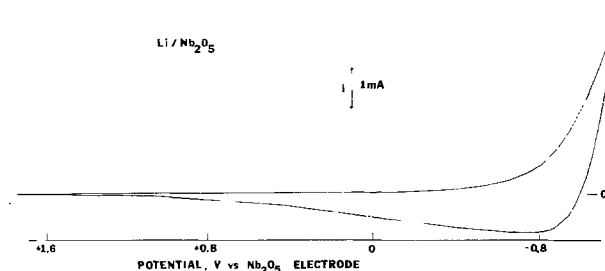


Fig. 2. Current-potential curve recorded with Nb_2O_5 electrode in 0.82 M LiClO_4/AN solution; scan rate: 100 mV/sec.

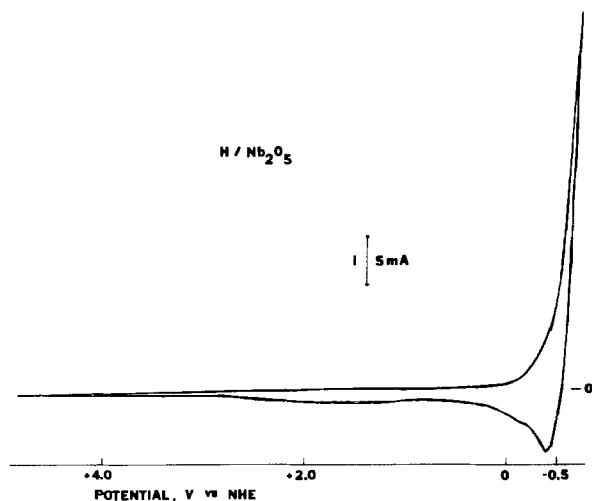


Fig. 1. Current-potential curve recorded with Nb_2O_5 electrode in aqueous 1 M H_2SO_4 solution; scan rate: 100 mV/sec.

Manuscript received Nov. 13, 1979.
Publication costs of this article were assisted by The University of Texas.

REFERENCES

1. S. K. Deb, *Philos. Mag.* **27**, 801 (1973).
2. B. W. Faughnan, P.S. Crandall, and P.M. Heyman, *RCA Review*, **36**, 177 (1975).
3. H. N. Hersch, W.E. Kramer, and J.H. McGee, *Appl. Phys. Lett.*, **27**, 646 (1975).
4. I. F. Cheng, B.L. Gilbert, and T.I. Sun, *This Journal*, **122**, 955 (1975).
5. J. P. Randin, *J. of Electronic Materials*, **2**, 42 (1978).
6. B. Reichman and A.J. Bard, *This Journal*, **126**, 583 (1979).
7. T. B. Reddy and E.A. Battistelli, Abstr. G-4, The 95th Conf. on Electronics Materials, Cornell Univ., Ithaca, N.Y., June 1977.
8. T. J. Knowles, H.N. Hersch, and W. Kramer, *ibid.*, Abstr. I-3.
9. H. V. K. Udupa and V.K. Venkatesan, in "Encyclopedia of the Electrochemistry of the Elements," A.J. Bard, Ed., Marcel Dekker, N.Y., Vol. 2, Chap. 3, 1974.
10. C. P. Keszthelyi and A.J. Bard, *This Journal*, **120**, 241 (1973).

The Advantages of RHEED over LEED for Surface Studies of Emerged Electrodes

D. M. Kolb and G. Lehmppuhl

Fritz-Haber-Institut der Max-Planck-Gesellschaft, D-1000 Berlin 33, Germany

Investigations on the structural properties of bare and adsorbate covered electrode surfaces by electron diffraction are among those which cannot be performed directly in situ. The most obvious approach to this problem which has been chosen in the past by several groups (1-5) is the removal of the electrode from the electrochemical environment and subsequent transfer into a vacuum chamber where highly structure-sensitive electron diffraction methods can be employed. The obvious choice at first thought for structural investigations in vacuo is LEED (low energy electron diffraction) and this technique has been used nearly exclusively for the study of the structure of removed electrode surfaces. The results obtained so far show definite promise, although they differ somewhat from group to group. We have chosen an alternative approach. In two recent publications we reported first results on structural investigations of electrode surfaces and adsorbates using RHEED (reflected high energy electron diffraction) (6,7). In the present communication we reemphasize those advantages of RHEED over LEED which are of crucial importance to these combined electrochemical and vacuum studies to effect genuine information transfer.

In diffraction experiments we observe a section through the reciprocal lattice. In case of a surface lattice due to a two-dimensional array of atoms the reciprocal lattice consists of reciprocal lattice rods. In LEED we observe the vertical section through these rods, while in RHEED only a nearly tangential (or horizontal) section by the Ewald sphere through a reduced number of rods is observed.

LEED requires ultra high vacuum (UHV) conditions while RHEED does not. Usually a LEED pattern is not observed from a newly inserted sample unless it is annealed or/and ion bombarded. This is well documented in many sur-

face science articles. Such a pretreatment, however, inevitably destroys the "electrochemical" information of the surface, i.e., with LEED we no longer view that surface which experienced electrochemical manipulation. E.g. in ref. (5) it is stated that no LEED pattern is obtained by observation directly after removal of the Pt electrode and transfer into the UHV chamber. Therefore a 500 eV Ar bombardment was employed until reasonably sharp diffraction spots appeared. It was assumed that this procedure removed the adsorbed impurities only (mainly C and O containing species) leaving the underlying Pt surface unchanged. This is a highly disputable assumption which we question, since a 250-500 eV ion bombardment is standard procedure not only to clean but also to renew surfaces by removing several substrate surface layers. It seems therefore that after such a treatment the surface is no longer the same as that which was in the electrolyte.

RHEED, on the other hand, is not bound to UHV conditions since impurity layers are easily penetrated by the high energy electrons and are not observed as long as they are arranged randomly. The latter, however, is the usual case. If it were not, it would be interesting information in itself. The grazing angles of incidence yield an information depth of about five atomic substrate layers for perfectly flat surfaces, which makes RHEED comparable with LEED in surface sensitivity. While information on the surface structure and on facets can be gained about equally well with LEED and RHEED, the latter technique can yield additional information on the bulk properties of the sample and on the smoothness of the surface, which is not accessible by LEED (8). Besides, the efficiency of ordinary high vacuum RHEED in terms of time and expenditure is also a significant advantage over LEED.

In the following some examples are given which demonstrate the power of RHEED for surface analyses of emerged electrodes. We have stated in a recent publication (7) that the pronounced desorption peak at -0.14 V (SCE) in the

Key words: electrode emersion, surfaces, RHEED.

current-potential curve for Pt in 1 N H₂SO₄ is due to hydrogen on Pt(110), while H₂ on Pt(111) yields a rather unstructured desorption spectrum. Furthermore, we found that several potential excursions into the oxide region with an initially perfect Pt(111) surface gives rise to the peak at -0.14 V, characteristic for the (110) face (see e.g. Fig. 4 in ref. (7) and compare with Fig. 11 in ref. (5)). Obviously a surface change occurs and our RHEED data support this view. The shape of the diffraction spots which contains information on the size and surface orientation of the coherent scattering areas, indicates faceting of the (111) surface during these potential excursions, with (110) facets being the most likely ones, in agreement with the electrochemical finding.

Drastic surface distortions on the Pt(111) surface by repetitive potential cycling into the oxide region, have also been observed with LEED, however, only as an increase in the angular width of the LEED spots and their gradual disappearance (5). More subtle changes on electrode surfaces, such as superstructures from bare reconstructed or adsorbate covered surfaces, will certainly not be found in LEED after the ion bombardment. Using RHEED we have observed such reconstructions on Au and Ag single crystal surfaces due to adsorption or surface reactions (e.g. Cu adsorption on Au(111) (6) or AgCl formation on Ag(111) (9)). Such reconstructions proved to be very delicate. Some of the superstructure features disappeared slowly during observation because of the electron bombardment. It is clear that weakly bound states would not withstand the ion bombardment pretreatment which is required for observation of LEED patterns.

In the very interesting and beneficial combination of electrochemical and surface physics techniques the transfer of the electrode from the electrochemical cell into the vacuum chamber is a crucial and delicate step. To be sure that the surface is changed as little as possible after electrochemical manipulation the choice of a diffraction technique is important which accepts the electrode surface as it is and does not demand further preparation cycles. This seems to be the case with RHEED rather more than with LEED.

REFERENCES

- (1) W. E. O'Grady, M.Y.C. Woo, P. L. Hagans, and E. Yeager, *J. Vac. Sci. Technol.*, **14**, 365 (1977).
- (2) E. Yeager, W. E. O'Grady, M. Y. C. Woo, and P. L. Hagans, *This Journal*, **125**, 348 (1978).
- (3) A. T. Hubbard, R. M. Ishikawa, and J. Katekaru, *J. Electroanal. Chem.*, **86**, 271 (1978).
- (4) R. N. Ross, Jr., *J. Electroanal. Chem.*, **76**, 139 (1977).
- (5) R. N. Ross, Jr., *This Journal*, **126**, 67 (1979).
- (6) H. O. Beckmann, H. Gerischer, D. M. Kolb, and G. Lehmpfuhl, *Symp. Faraday Soc.*, **12**, 51 (1977).
- (7) K. Yamamoto, D. M. Kolb, R. Kötzt, and G. Lehmpfuhl, *J. Electroanal. Chem.*, **96**, 233 (1979).
- (8) S. Ino, *Japan. J. Appl. Phys.*, **16**, 891 (1977).
- (9) G. Lehmpfuhl and D. M. Kolb, to be published.

Synthesis of Diamond

Shigeto Yamaguchi* and Nobuo Setaka

National Institute for Researches in Inorganic Materials, Sakura-mura Niihari-gun Ibaraki-ken, 300-31 Japan

It was attempted to produce fine particles of diamond by means of chemical explosion. A mechanical mixture of carbon monofluoride and copper in their powdered states was submitted to a shock-wave compression in a closed vessel of steel. The ratio of both materials was 1:9 by weight. The maximum pressure of this shock-wave compression amounted to about 0.6 mega-bars, whose duration was about one pico-sec. The technique and the apparatus for generating this shock-wave and for transmitting it to the steel vessel should be referred to the report published (1). The reaction vessel reached over 1000°C in temperature during the shock-wave compression concerned. In fact, one discerned the surface of the steel vessel sintered. The reaction products found in the vessel were immersed in conc. nitric acid containing potassium chlorate for several hours in order to dissolve carbon, copper and copper fluoride. The yellowy residue obtained after this chemical treatment has been scrutinized in terms of electron diffraction. The diffraction pattern observed is reproduced in Fig.1. Fig.2 is a double exposure, in which Fig.1 is superimposed onto the reference pattern of gold in order to measure the interplanar spacings of the sample in question. The spacings and the Miller indices determined for the reflections on Fig.1 coincide with those of diamond crystal registered (2). Carbon fluoride was converted

*Electrochemical Society Active Member. Key words: diamond, carbon monofluoride, explosion.

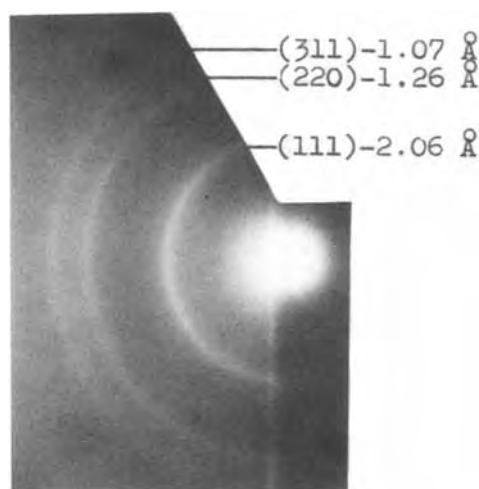


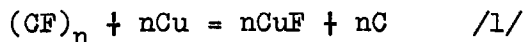
Fig. 1. Electron diffraction pattern from the diamond crystallites produced by exploding a powdered mixture composed of carbon fluoride and copper. Wave-length: 0.0349 Å. Camera distance: 50 cm. Positive enlarged 2.3 times.



Fig. 2. Double exposure, in which Fig. 1 is superimposed onto the reference pattern of gold for measuring the interplanar spacings of the sample.

into diamond by about twenty percent by weight. The mean particle size of the diamond crystallites here synthesized is estimated to be about 100 Å from the half-width value of the reflections in Fig.1. The powder sample corresponding to Fig.1 was able to scratch the surface of sapphire when used as an abrasive. This also demonstrated that the sample contained diamond.

The chemical reaction that allowed to produce diamond under the conditions laid down can be expressed by the equation



Here the copper powder acted on carbon fluoride not only as a defluorinator, but also as a thermal medium for quenching the diamond powder formed to the purpose. Carbon atoms in the $(\text{CF})_n$ crystal are characterized by the same sp^2 -bond as in diamond (3). This implies that carbon in a nascent state as produced by the reaction /1/ can readily be converted into diamond circumstances permitting. Thus the result obtained in this work suggests another way for preparing diamond. Carbon tetrachloride and the Na-K alloy should be employed instead of $(\text{CF})_n$ and Cu, respectively. It is known that the liquid alloy is formed easily at room temperature when sodium and potassium are brought into contact with one another, and that this alloy wetted with carbon tetrachloride explodes violently when shocked mechanically. It is therefore plausible that a mixture of both reagents which is enclosed in a firm vessel gives rise to diamond as the product of an internal explosion when triggered by means of shock-wave. The present experiment corresponds to a preliminary to the diamond preparation by the explosion method.

There are the reports regarding the procedures of preparing diamond with carbon halogenides and metals at high temperature and under high static pressure (4). They differ from the present method, however, insofar as the latter employs the instantaneous dynamic compression.

REFERENCES

1. T. Akashi, A. Sawaoka, S. Saito and M. Araki, Japan J. Appl. Phys., 15, 891 (1976).
2. ASTM X-Ray Diffraction Data Cards Card Number 6-0675.
3. Holleman-Wiberg, "Lehrbuch der anorganischen Chemie", p. 452, Walter de Gruyter, Berlin (1971).
4. J. L. Margrave, R. G. Bautista and P. J. Ficalora, Chem. Abs., 78, 99841v (1973); De Beers Industrial Diamond Div. Ltd., 88, 172966c (1978).

Manuscript submitted Feb. 12, 1979;
revised manuscript received April 3, 1979.

Publication costs of this article
were assisted by National Institute for
Researches in Inorganic Materials.

Electrostatic Binding of Metal Complexes to Electrode Surfaces Coated with Highly Charged Polymeric Films

Noboru Oyama* and Fred C. Anson*

Arthur A. Noyes Laboratory, California Institute of Technology, Pasadena, California 91125

Previous reports in which metal complexes have been attached to electrode surfaces coated with polymeric molecules have depended upon the formation of covalent or coordination bonds in the attachment procedure (1-4). Such schemes can be quite successful but depending, as they do, on rather specific surface chemistry, they are not applicable to as wide a variety of metal complexes as might be desirable. We have observed that coating graphite electrodes with polymers bearing charged ionic groups produces surfaces which strongly bind multiply-charged metal complexes bearing charges opposite to that on the attached ionic polymer. By exploiting this observation it is entirely possible that virtually any desired metal ion can be attached in large quantities to electrode surfaces by coordinating the metal ion with ligands that produce a multiply-charged complex ion.

EXPERIMENTAL

The source and mounting of the pyrolytic graphite electrodes and procedures for coating them with adherent films of poly (4-vinylpyridine) (M.W. = 7.4×10^5) have been previously described (1,4) along with the electrochemical measuring techniques employed. Potentials are quoted vs. a sodium chloride saturated calomel electrode.

RESULTS AND DISCUSSION

The effective pK values of polyelectrolytes such as poly (4-vinylpyridine) (PVP) depend somewhat upon molecular weight. However, it is likely that

PVP is largely protonated at pH values below ca. 3 and essentially neutral at

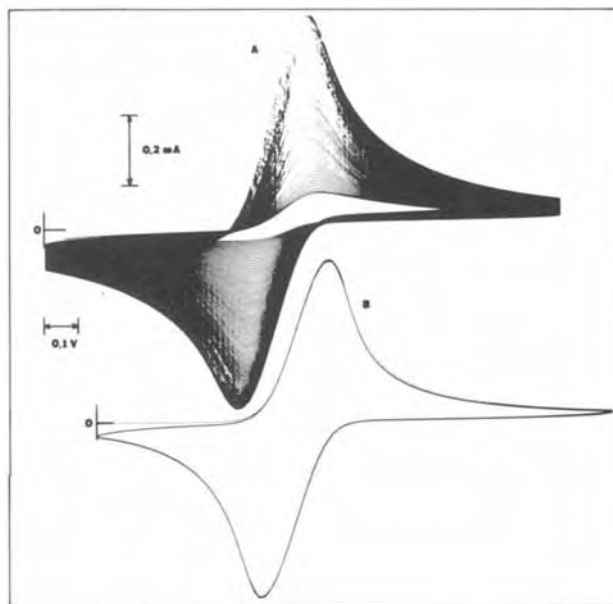


Figure 1: A - Cyclic voltammograms of 5 mM $\text{Fe}(\text{CN})_6^{3-}$ at a pyrolytic graphite electrode (0.17 cm^2) coated with 4.6×10^{-7} moles cm^{-2} of pyridine as PVP. Supporting electrolyte: 0.2 M CF_3COONa at pH 3.8. The potential was cycled continuously at 200 mV s^{-1} between +0.8 and -0.7 volt. The voltammogram reached a steady state after 20 minutes of cycling. B - Cyclic voltammogram resulting after the electrode used in A was washed with water and replaced in 0.2 M CF_3COONa at pH 2.9.

*Electrochemical Society Active Member
Key Words: Electrode coatings, polyelectrolyte films, ion incorporation

pH values above ca. 8 (5). To prepare a highly positively charged electrode surface a graphite electrode was coated with PVP and exposed to supporting electrolyte at pH 3.8. The resulting electrode was used to record the series of cyclic voltammograms for $\text{Fe}(\text{CN})_6^{3-}$ shown in Figure 1A.

The peak current obtained immediately after the electrode was introduced into the solution is somewhat smaller than the current at uncoated electrodes because the polymer film retards the $\text{Fe}(\text{CN})_6^{3-/4-}$ electrode reaction somewhat (4). However, in sharp contrast with uncoated electrodes, the voltammetric currents increase as the potential is cycled continuously and they reach extraordinarily large values. (The currents also increase, although somewhat less rapidly, if the electrode potential is not cycled.) If the electrode is removed from the solution, rinsed and transferred to an acidic solution containing only supporting electrolyte the voltammogram shown in Figure 1B is obtained and its magnitude is virtually unaffected by repeated cycling for periods up to one hour. The voltammogram in Figure 1B disappears if the electrode is removed, washed with electrolyte at pH 10 and replaced in the supporting electrolyte. These observations seem clearly to demonstrate that the protonated PVP film on the electrode surface preferentially incorporates the multiply-charged ferricyanide as the counter ion, even though much larger concentrations of singly-charged trifluoroacetate anions are present in the supporting electrolyte. The behavior is quite analogous to that of polyelectrolytes in homogeneous solutions under conditions where the polyion is highly charged (6). The fact that multiply-charged counter ions incorporated into PVP films are not replaced rapidly by ion exchange upon exposure to simple univalent electrolytes containing none of the multiply-charged ion indicates that a significant activation barrier impedes the break-up of the electrostatic binding within the polyionic film.

Figure 2 emphasizes this point for the case in which the dinegative anion, IrCl_6^{2-} , is held electrostatically within a protonated PVP film. Initially after transfer of the coated electrode

from the solution of IrCl_6^{2-} to a solution containing only supporting electrolyte at pH 2.8 there is a fairly rapid loss of a fraction of the IrCl_6^{2-} from the surface - presumably from the portion of the polymer most accessible to the electrolyte. However, after a few minutes of repetitive scanning the voltammogram settles down to the one shown in Figure 2 which undergoes no further change during several additional minutes of scanning. If the pH of the supporting electrolyte is raised to 4.5 the release of IrCl_6^{2-} from the surface resumes as revealed by a steadily diminishing voltammetric response.

The extent of the electrostatic attachment is not related simply to the charge carried by the counter ion being attached. For example, exposing a PVP coated electrode to a solution containing both 5 mM $\text{Fe}(\text{CN})_6^{3-}$ and 5 mM IrCl_6^{2-} leads to greater binding of the less highly charged anion. Thus, chemical differences among the incorporated ions appear to modulate purely electrostatic factors in controlling the extent of incorporation.

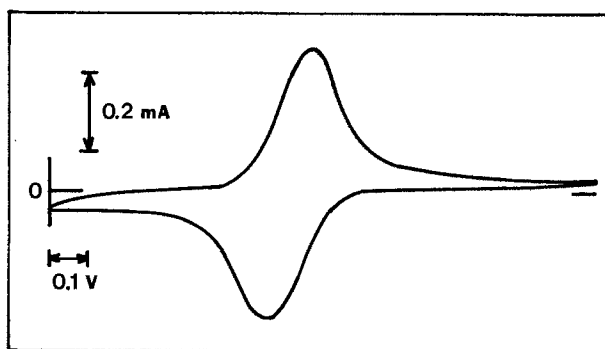


Figure 2: Steady-state cyclic voltammogram for an electrode coated with 4.6×10^{-7} moles cm^{-2} of PVP, soaked in a 5mM solution of $(\text{NH}_4)_2\text{IrCl}_6$ at pH 2.8 (CF_3COOH) for 60 seconds, rinsed with water and transferred to supporting electrolyte solution (0.2 M CF_3COONa at pH 2.6). Scan rate: 200 mVs $^{-1}$. Potential range: +1.3 to -0.1 volt.

Electrostatic Binding of Metal Complexes to Electrode Surfaces Coated with Highly Charged Polymeric Films

Noboru Oyama* and Fred C. Anson*

Arthur A. Noyes Laboratory, California Institute of Technology, Pasadena, California 91125

Under pressing conditions (high concentrations of incorporated ion, low concentration of supporting electrolyte, long exposure times) it is possible to incorporate greater quantities of ferricyanide into protonated PVP films than would correspond to electrostatic neutralization of all of the positive charge present on the fully protonated pyridine groups. For example, a PVP film containing 4.6×10^{-7} moles cm^{-2} of pyridine incorporated as much as 2×10^{-7} moles cm^{-2} of ferricyanide. We presume that under these conditions the $\text{Fe}(\text{CN})_6^{3-}$ is incorporated in the form of an ion pair with a cation of the supporting electrolyte. With IrCl_6^{2-} the maximum quantity incorporated into films never exceeded ca. 30% of the total possible cationic charge in the polyionic film.

Multiply-charged cationic complexes can also be incorporated electrostatically into polyanionic films. For example, Figure 3 shows voltammograms

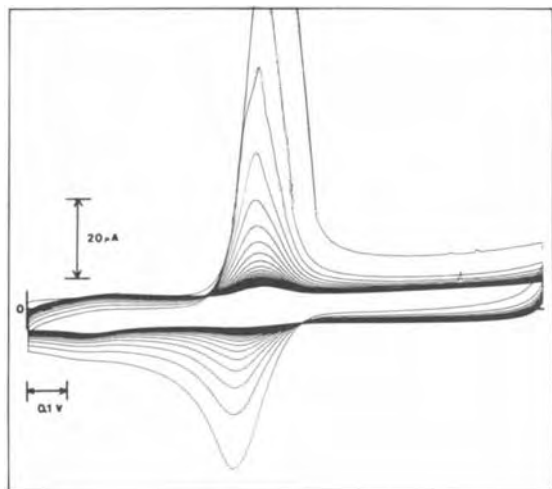


Figure 3: Cyclic voltammograms for $\text{Ru}(\text{NH}_3)_6^{3+/2+}$ attached to a pyrolytic graphite electrode coated with ca. 4×10^{-7} moles cm^{-2} of carboxylic acid as polyacrylic acid (M.W. = 2.2×10^5). The coated electrode was soaked for 5 min. in 1 mM $\text{Ru}(\text{NH}_3)_6^{3+}$ at pH 6.1, washed for 10-20 s. with water, transferred to supporting electrolyte (0.2 M CF_3COONa + 5 mM $\text{Na}_2\text{B}_4\text{O}_7$; pH 8.1) and the potential cycled continuously between +0.3 and -1.0 volt at 200 mV s^{-1} . The time elapsed between the first and last scans was ca. 7 min.

for an electrode that was coated with polyacrylic acid, soaked in a 1 mM solution of $\text{Ru}(\text{NH}_3)_6^{3+}$ at pH 6.1 (where the polymer is converted to a polyanion) and transferred to pure supporting electrolyte solution. Large quantities of the tripositive cation are clearly incorporated into the polyanionic film (ca. 10^{-8} moles cm^{-2} of $\text{Ru}(\text{NH}_3)_6^{3+}$) but repetitive cycling of the potential leads to continuous departure of the $\text{Ru}(\text{NH}_3)_6^{3+}$ from the film. The loss of $\text{Ru}(\text{NH}_3)_6^{3+}$ occurs whether or not the potential is cycled but the rate of loss is greater during cycling when the charge on the incorporated cation is diminished by one unit during each half-cycle. The less permanent binding of $\text{Ru}(\text{NH}_3)_6^{3+}$ by the polycarboxylate coating may be associated with the more hydrophilic nature of this film compared with PVP: The latter polymer is insoluble in aqueous acid while polysodium acrylate is water soluble (although films deposited on pyrolytic graphite resist dissolution). The activation barriers for entry or departure of cationic reactants from the polycarboxylate layer are apparently considerably smaller than for PVP.

The attractive simplicity of the electrostatic binding procedure for holding large quantities of metal complexes on electrode surfaces is complemented by the variety of ionic polymers that are available to serve as anchoring matrices. In addition, the procedure allows complexes to be introduced on electrode surfaces without change in their primary coordination sphere, a factor that could be of considerable importance with catalytically active complexes. These attributes have encouraged us to explore more broadly the combinations of charged complexes and ionic polymers that may be exploited to produce electrode surfaces laden with desired ionic reactants.

ACKNOWLEDGMENTS

This work was supported by the National Science Foundation and the U. S. Army Research Office.

REFERENCES

1. N. Oyama and F. C. Anson, *J. Am. Chem. Soc.*, 101, 739, 3450 (1979) and earlier references cited therein.
2. K. Itaya and A. J. Bard, *Anal. Chem.*, 51, 1487 (1978).
3. R. Nowak, F. A. Schultz, M. Umaña, H. Abruña and R. W. Murray, *J. Electroanal. Chem.*, 94, 219 (1978).
4. N. Oyama and F. C. Anson, *J. Electrochem. Soc.*, in press.
5. H. Nishikawa and E. Tsuchida, *J. Phys. Chem.*, 79, 2072 (1975).
6. F. Oosawa, "Polyelectrolytes", Ch. 2, 4, 6, Marcel Dekker, Inc., New York (1971).

Manuscript submitted July 31, 1979;
revised manuscript received Oct. 22, 1979.

Publication costs of this article were
assisted by the California Institute of
Technology.



NH₄Cu₄Cl₃(I_{2-x}Cl_x), a New Highly Conducting Solid Electrolyte

S. Geller, J. R. Akridge,*¹ and S. A. Wilber

Department of Electrical Engineering, University of Colorado, Boulder, Colorado 80309

ABSTRACT

A new solid electrolyte, with a very narrow solid solution range, NH₄Cu₄Cl₃(I_{2-x}Cl_x), 0.09 ≤ x ≤ 0.13, isostructural with RbAg₄I₅ and RbCu₄Cl₃I₂ is reported. The corresponding lattice constant range is 9.985–9.982 ± 0.003 Å. The new solid electrolyte is thermodynamically stable between 130° and 170°C. Certain formulations which are not phase pure appear to have improved stability below 130°C. Room temperature conductivities as high as 0.21 (Ω-cm)⁻¹ have been attained. At 150°C, conductivities as high as 0.73 (Ω-cm)⁻¹ have been attained.

Recently, Takahashi *et al.* (1) have reported a new solid electrolyte Rb₄Cu₁₆Cl₁₃I₇ with a high electrolytic conductivity. We have reported (2) the crystal structure and conductivity of RbCu₄Cl₃I₂ and our continued investigation has shown that there is a solid solution range RbCu₄Cl₃(I_{2-x}Cl_x) with 0.0 ≤ x ≤ 0.4 (3). This range includes the composition reported by Takahashi *et al.* which should be written RbCu₄Cl₃(I_{1.75}Cl_{0.25}).

We write the general formula RbCu₄Cl₃(I_{2-x}Cl_x), because there is clear evidence² that the twelvefold sites are filled with chloride ions exclusively, and when excess chloride ions are present, they replace iodide ions in the eightfold sites. That is to say, in the solid solutions, none of the iodide ions appear to be in the twelvefold sites. Crystals of these substances are isostructural with RbAg₄I₅ for which structural details are given in several papers (2, 4-6).

The highest solid electrolyte conductivities in the moderate range of temperature 70°–450°K have been reported by us (2) for RbCu₄Cl₃I₂; at room temperature the value is at least 0.47 (Ω-cm)⁻¹. The analogous value reported for RbCu₄Cl₃(I_{1.75}Cl_{0.25}) by Takahashi *et al.* (1) is 0.34 (Ω-cm)⁻¹.

In this paper we report a new highly conducting solid electrolyte. For simplicity, we give the formula as NH₄Cu₄Cl₃(I_{1.9}Cl_{0.1}) in the title of the paper, even though a narrow solid solution range exists close to this formula. This solid electrolyte is closely related to the materials discussed above.

Preparation of the Materials

Preparation and purification of CuI and CuCl have been given in Ref. (2). NH₄I was used without further purification, but was carefully dried, after which it was stored over P₂O₅ in a desiccator.

The materials studied in this investigation were prepared by first melting appropriate amounts of reactants in an evacuated, then sealed Pyrex tube, quenching,

grinding the sample in a nitrogen-filled glove box, pelletizing, heating at some temperature below the melting point, and continuing by solid-state reaction (*i.e.*, further regrinding, repelletizing, reheating when found necessary as judged from x-ray powder diffraction photographs). Alternatively, the mixture of reactants was not premelted; that is, all steps were carried out in the solid state. It was found that an optimum reaction temperature is 150°C.

Numerous attempts to prepare stoichiometric NH₄Cu₄Cl₃I₂ were unsuccessful. Furthermore, unlike the case for the RbCu₄Cl₃(I_{2-x}Cl_x) system, the range of composition we were able to attain was very narrow; the measured range of lattice constant is 9.982–9.985 Å. In the next section, we show how the estimate of composition was made.

Determination of the Composition

Because it did not seem possible to prepare the stoichiometric compound NH₄Cu₄Cl₃I₂, and because it is not a simple matter to ascertain the phase purity of these materials from powder diffraction data, we resorted to the following method of estimating the composition.

The values of the lattice constants of RbAg₄I₅ (4, 7) and of NH₄Ag₄I₅ (7) have been reported: 11.24 and 11.19 Å, respectively. However, these were not sufficiently precise for the purpose. New samples of these materials were prepared; powder photographs were taken with CrK radiation. The lattice constants obtained are 11.244 and 11.204 Å, respectively, giving a difference of 0.040 Å. The lattice constant of RbCu₄Cl₃I₂ is 10.032 Å (2). If a linear dependence on the ionic size is assumed, then we might expect a lattice constant of 9.992 Å for stoichiometric NH₄Cu₄Cl₃I₂. In the RbCu₄Cl₃(I_{2-x}Cl_x) system, we have found (3) that the substitution of 0.1 Cl⁻ for 0.1 I⁻ produces a decrease of 0.0075 Å in lattice constant. Our measured lattice constants have a range of 9.982–9.985 ± 0.003 Å. If we take 9.992 Å as the lattice constant of the stoichiometric compound, these measured values give a "most probable" solid solution range: NH₄Cu₄Cl₃I_{1.87}Cl_{0.13} to NH₄Cu₄Cl₃(I_{1.91}Cl_{0.09}).

This approach has been corroborated as follows. An unsuccessful attempt was made to produce the material

* Electrochemical Society Active Member.

¹ Present address: Union Carbide Corporation, Parma Research Center, Parma, Ohio 44130.

Key words: electrolyte, thermodynamics, conduction.

² This comes from an experiment carried out during investigation of the RbCu₄Cl₃(I_{2-x}Cl_x) system (3) which indicates that a content of more than two iodides per formula unit is unattainable, at least under the conditions of preparation described in the text.

with formula $[\text{Rb}_{0.5}(\text{NH}_4)_{0.5}]\text{Cu}_4\text{Cl}_3\text{I}_2$; unreacted CuI was present even after five regrindings and a total of 80 hr of heating at 150°C. The lattice constant of the solid electrolyte material was 10.008Å. If it is assumed that the ratio of Rb^+ to NH_4^+ is 1 and attribute the low lattice constant (it should be 10.012Å) to dissolved Cl^- , the formula should be $[\text{Rb}_{0.5}(\text{NH}_4)_{0.5}]\text{Cu}_4\text{Cl}_3(\text{I}_{1.95}\text{Cl}_{0.05})$. Such a specimen was prepared; it appears to be single phase and it still has the lattice constant 10.008Å. This, therefore, implies a lattice constant of 9.992Å for a hypothetical $\text{NH}_4\text{Cu}_4\text{Cl}_3\text{I}_2$, equal to the predicted value. It should be mentioned that in the $\text{RbCu}_4\text{Cl}_3(\text{I}_{2-x}\text{Cl}_x)$ system (3), the lattice constant is linear in x .

Crystal Structure Analysis

A very small crystal (largest dimension 0.10 mm; smallest dimension, 0.06 mm) was obtained by heating a specimen of nominal composition $\text{NH}_4\text{Cu}_4\text{Cl}_3(\text{I}_{1.5}\text{Cl}_{0.5})$ which was clearly not single phase, at 150°C for 14 days. The solid electrolyte in this material has a lattice constant of 9.982Å implying the composition $\text{NH}_4\text{Cu}_4\text{Cl}_3(\text{I}_{1.87}\text{Cl}_{0.13})$ as discussed earlier. Photographs taken with a Buerger precession camera confirmed that the crystal is isostructural with $\alpha\text{RbAg}_4\text{I}_5$ (4) (space group, P4_132 or P4_332).

The intensity data were collected with an automated Buerger-Supper single crystal diffractometer; Zr-filtered, $\text{MoK}\alpha$ radiation was used, with 0.5°/min scanning rate and scan width (1.5 + 0.5 Lp), where L is the Lorentz and p the polarization factor. No corrections were made for absorption. Calculations were made with computer programs and with atomic scattering factors for which references are given in Ref. (2).

Only highlights of the results need be given here. Tables of parameters, of interionic distances and of calculated and observed structure amplitudes are given in Tables I, II, and III. The agreement factor $\Sigma\Delta F/\Sigma F_{\text{obs}}$, where $\Delta F = ||F_{\text{obs}}| - |F_{\text{calc}}||$, for 125 observed intensities is 5.3%. The low total number of observed reflections results from the very small size of the crystal. However, the data were of sufficient number to give convergence of parameters.

Over-all, there is really no statistically significant difference of positional and occupancy parameters between $\text{NH}_4\text{Cu}_4\text{Cl}_3(\text{I}_{1.87}\text{Cl}_{0.13})$ and $\text{RbCu}_4\text{Cl}_3\text{I}_2$ and the same is true essentially of the interionic distances. One should expect, of course some difference between the $(\text{NH}_4)^+ - \text{Cl}^-$ and $\text{Rb}^+ - \text{Cl}^-$ distances in $\text{NH}_4\text{Cu}_4\text{Cl}_3(\text{I}_{1.87}\text{Cl}_{0.13})$ and $\text{RbCu}_4\text{Cl}_3\text{I}_2$. The results, 3.368 ($\sigma = 0.005$) and 3.381 ($\sigma = 0.003$) Å are in the right direction, even though the difference does not have statistical significance. [It should be recalled (2) that in

both compounds, only chloride ions surround the large cations.]

For completeness, the following results should be mentioned. At one point in this investigation, we thought that the crystal had the stoichiometric formula $\text{NH}_4\text{Cu}_4\text{Cl}_3\text{I}_2$, and the structure was refined on this basis. The agreement factor was only slightly higher, 5.6%, and the parameters and interionic distances were almost identical with those of the aforementioned analysis. It is somewhat disappointing that the data and method of calculation could not make a better distinction in this case.

Stability of $\text{NH}_4\text{Cu}_4\text{Cl}_3(\text{I}_{1.87}\text{Cl}_{0.13})$

The compound $\text{NH}_4\text{Cu}_4\text{Cl}_3(\text{I}_{1.87}\text{Cl}_{0.13})$ is not thermodynamically stable except at temperatures above 130°C and below its melting point of approximately 170°C, indeed a narrow stability range. The compound could not be made by solid-state reaction below 130°C. Several other experiments also showed that although the compound could be quenched to room temperature where it would remain for considerable time (>1 month), it was not thermodynamically stable. For example, a material made to have nominal composition $\text{NH}_4\text{Cu}_4\text{Cl}_3(\text{I}_{1.67}\text{Cl}_{0.33})$, containing the solid electrolyte $\text{NH}_4\text{Cu}_4\text{Cl}_3(\text{I}_{1.86}\text{Cl}_{0.14})$, that is, not phase pure but not containing excess CuI, when quenched from 120°C, showed the presence of CuI in the powder photograph.

A powder photograph taken of material with nominal composition $\text{NH}_4\text{Cu}_4\text{Cl}_3(\text{I}_{1.67}\text{Cl}_{0.33})$ at a temperature of 100°C (8 hr exposure) showed complete decomposition of the material.

The conductivity measurements also showed that the material is not thermodynamically stable at temperatures below 130°C. However, the presence of excess CuCl and other unidentified phases, not readily seen in the powder photographs, did seem to increase the stability and, in one case, substantially.

Conductivity

This material is unusual in several respects. It is not unique, however, in the respect that only a solid solution is attainable. [See for example Ref. (8, 9).] It is possible that under conditions we have not tried, the stoichiometric compound is attainable; it does not seem to be quenchable to room temperature in any case. (Needless to say, we have tried such experiments.) We have not been able to make conductivity measurements on the material with the formula given.

Our approach is as follows: We prepare a pellet of dimensions approximately 0.64 cm diam by 0.44 cm long with copper electrodes. The copper powder is freshly prepared and compressed onto the ends of

Table I. Positional and thermal parameters of $\text{NH}_4\text{Cu}_4\text{Cl}_3(\text{I}_{1.87}\text{Cl}_{0.13})$

Ion position	Ammonium 4a	(Iodide, chloride) 8c	Chloride 12d	Copper (cuprous)		
				24e	24e	8c
Multiplier	1/6	1/3	1/2	0.306	0.326	0.031
σ				0.028	0.031	0.006
x	3/8	0.0109	3/8	0.5196	0.0010	0.161
$\sigma(x)$		0.0002		0.020	0.0020	
y	3/8	= x	-0.1497	0.2306	0.8354	= x
$\sigma(y)$			0.0008	0.0031	0.0025	
z	3/8	= x	= (3/4 - y)	0.7994	0.2150	= x
$\sigma(z)$				0.0020	0.0024	
β_{11}	0.0124	0.0079	0.0111	0.0111	0.0093	0.0111
$\sigma(\beta_{11})$		0.0002	0.0017	0.0026	0.0025	
β_{22}	= β_{11}	= β_{11}	0.0087	0.0305	0.0325	= β_{11}
$\sigma(\beta_{22})$			0.0009	0.0055	0.0060	
β_{33}	= β_{11}	= β_{11}	= β_{22}	0.0101	0.0187	= β_{11}
$\sigma(\beta_{33})$				0.0026	0.0040	
β_{12}	0	0.0001	-0.0007	0.0059	0.0001	-0.0011
$\sigma(\beta_{12})$		0.0002	0.0008	0.0031	0.0025	
β_{13}	0	= β_{12}	= β_{12}	-0.0015	0.0017	= β_{12}
$\sigma(\beta_{13})$				0.0019	0.0022	
β_{23}	0	= β_{12}	0.0011	0.0013	-0.0014	= β_{12}
$\sigma(\beta_{23})$			0.0011	0.0026	0.0035	

Note: Parameters given without standard errors were held constant throughout the calculation.

Table II. Interionic distances and standard errors

Atom types and symmetry	No. of distances	Distance (Å)
(I,Cl)-I	3	4.200 (3)
(I,Cl)-I	3	3.955 (10)
(I,Cl)-I	3	4.124 (1)
(I,Cl)-I	3	4.275 (11)
Cl-(I,Cl)	2	3.955 (10)
Cl-(I,Cl)	2	4.124 (1)
Cl-(I,Cl)	2	4.275 (11)
Cl-Cl	4	3.716 (7)
Cl-Cl	2	5.509 (20)
Chloride octahedron about NH ₄ ⁺		
NH ₄ -Cl	6	3.368 (5)
Cl-Cl	6	3.716 (7)
Cl-Cl	3	5.504 (20)
Cl-Cl	3	5.738 (11)
Tetrahedron about Cu ⁺ (c)		
Cu-(I,Cl)	1	2.59
Cu-Cl	3	2.41
(I,Cl)-Cl	3	4.275 (11)
Cl-Cl	3	3.716 (7)
Tetrahedron about Cu ⁺ (e) (0.520, 0.291, 0.799) II		
Cu-(I,Cl)	1	2.74 (3)
Cu-Cl	1	2.33 (2)
Cu-(I,Cl)	1	2.66 (2)
Cu-Cl	1	2.42 (3)
(I,Cl)-(I,Cl)	1	4.200 (3)
Cl-Cl	1	3.716 (7)
Cl-(I,Cl)	3	4.275 (11)
Cl-(I,Cl)	1	4.125 (1)
Tetrahedron about Cu ⁺ (e) (0.001, 0.835, 0.215) III		
Cu-Cl	1	2.52 (3)
Cu-(I,Cl)	1	2.69 (3)
Cu-(I,Cl)	1	2.53 (2)
Cu-Cl	1	2.29 (2)
(I,Cl)-(I,Cl)	1	4.200 (3)
Cl-(I,Cl)	1	3.955 (10)
Cl-(I,Cl)	2	4.124 (1)
Cl-Cl	1	3.716 (7)
Cl-(I,Cl)	1	4.275 (11)
Nearest neighbor Cu ⁺ tetrahedral sites		
Cu (c)-Cu (II)	3	1.55
Cu (II)-Cu (c)	1	1.55
Cu (II)-Cu (III)	1	1.52 (3)
Cu (II)-Cu (III)	1	1.44 (3)
Cu (II)-Cu (II)	1	1.72 (5)
Cu (III)-Cu (II)	1	1.52 (3)
Cu (III)-Cu (II)	1	1.44 (3)

solid electrolyte. That is to say, first the copper powder is put into the die and smoothed, then the solid electrolyte, and then the copper powder. The composite is then compressed at 500 bars. The resulting pellet is then placed between the electrodes of the measuring device and heated uniformly to 150°C. We have found that this results in improved contact of the electrodes and in densification of the solid electrolyte.

In the case of samples made up with nominal composition NH₄Cu₄Cl₃(I_{1.67}Cl_{0.33}) (but we emphasize, not single phase), we first obtain a conductivity of approximately 0.21 (Ω-cm)⁻¹ at room temperature. As the sample is heated we notice a substantial decrease in the conductivity, undoubtedly a result of decomposition. On heating to above 130°C, there is a large increase in the conductivity. On further heating to 150°C, the conductivity increases as shown in Fig. 1(a). On decreasing the temperature, the conductivity decreases normally until 130°C is reached, and then substantially as shown in Fig. 1(a). Powder photographs taken of the material after such experiments show, as expected, a decomposition of the solid electrolyte that was present. Between 130° and 150°C, the solid electrolyte is surely present.

With a sample of the composition which we have deduced for the solid electrolyte and which we believe to be single phase, the above procedure fails. At room temperature, we obtained an initial value of 0.13 (Ω-cm)⁻¹, but as the sample was heated the conductivity decreased markedly and did not increase again even above 130°C. Powder photographs showed that the solid electrolyte had decomposed considerably. This experiment was repeated with Ag electrodes with similar results.

On the other hand, with a sample made up with nominal composition NH₄Cu₄Cl₃(I_{1.5}Cl_{0.5}) which ob-

Table III. Observed vs. calculated structure amplitudes

H	K	FO	FC	H	K	FO	FC	H	K	FO	FC
—	L = 0	—	—	7	7	32	39	9	7	28	36
2	2	200	203	8	2	42	44	11	3	39	32
4	0	263	272	8	7	26	22	11	5	28	25
4	2	45	46	9	1	60	54	—	L = 4	—	—
4	3	97	94	9	2	40	45	—	—	—	—
4	4	302	307	9	3	61	61	4	4	97	97
5	1	130	126	9	4	43	38	5	5	71	77
5	2	22	23	9	5	51	53	6	6	98	97
5	3	41	44	9	7	33	27	7	4	37	38
5	4	42	42	9	9	28	30	7	6	30	30
5	5	66	62	10	2	31	35	7	7	33	43
6	1	49	52	10	4	27	26	8	4	87	87
6	2	145	135	11	1	51	46	8	5	44	36
6	3	21	17	11	3	32	32	8	8	39	36
6	6	108	108	11	5	28	27	10	6	40	33
7	2	20	19	—	L = 2	—	—	—	L = 5	—	—
7	3	66	64	—	—	—	—	—	—	—	—
7	5	32	36	2	2	116	117	5	5	96	94
7	6	23	32	3	3	44	35	6	5	38	42
7	7	28	30	4	2	253	251	7	5	41	44
8	0	167	163	4	3	69	67	7	6	28	28
8	1	55	60	5	3	45	48	7	7	41	39
8	4	73	69	6	2	74	68	9	5	35	38
8	7	29	22	6	4	123	127	9	7	36	31
8	8	46	51	6	4	26	23	—	L = 6	—	—
9	3	25	21	7	2	35	27	—	—	—	—
9	5	52	52	7	4	35	27	—	—	—	—
10	2	52	55	7	5	32	28	6	6	31	30
10	6	54	55	8	2	144	137	—	L = 7	—	—
11	1	37	34	8	3	49	60	—	—	—	—
11	7	29	25	8	6	68	74	7	7	47	44
12	0	42	40	9	3	44	48	—	—	—	—
12	4	31	30	9	7	35	33	—	—	—	—
12	5	36	28	10	4	51	54	—	—	—	—
—	L = 1	—	—	12	2	41	44	—	—	—	—
2	2	59	61	—	L = 3	—	—	—	—	—	—
3	1	269	264	3	3	265	268	—	—	—	—
3	3	138	140	4	3	79	80	—	—	—	—
4	1	21	21	4	3	126	130	—	—	—	—
4	2	38	44	5	3	100	101	—	—	—	—
4	4	72	72	5	5	22	20	—	—	—	—
5	1	221	215	6	3	30	31	—	—	—	—
5	2	67	67	6	4	114	110	—	—	—	—
5	3	63	65	7	3	34	27	—	—	—	—
5	5	107	112	7	4	45	45	—	—	—	—
6	1	28	28	7	5	51	53	—	—	—	—
6	2	33	33	7	7	29	26	—	—	—	—
6	4	23	23	8	3	52	52	—	—	—	—
6	5	23	25	8	4	33	32	—	—	—	—
6	6	73	74	8	6	30	33	—	—	—	—
7	1	80	87	9	3	36	33	—	—	—	—
7	3	112	109	9	4	35	36	—	—	—	—
7	4	41	48	9	5	35	36	—	—	—	—
7	5	86	90	9	6	33	28	—	—	—	—

viously (as seen in powder photographs) contains a marked excess of CuCl (and therefore other phases, not readily identifiable), the situation is considerably different. Again the specimen first shows a high initial room temperature conductivity of 0.23 (Ω-cm)⁻¹. On heating, there does not appear to be the strong indication of decomposition observed in the two other cases. On cooling, there appears to be a transition at 130°C [see Fig. 1(b)], but it is much unlike the other two cases and substantial conductivities are observed down to 10°C. A sudden decrease in conductivity occurs on cooling to 5°C. On reheating to room temperature from 5°C, there is still a substantial conductivity, 0.13 (Ω-cm)⁻¹, but markedly lower than obtained either before or after heating. A powder photograph showed the presence of CuI.

Other experiments show that excess CuCl by itself does not stabilize the material as does preparation of solid solutions as though they really did exist. We emphasize that the solid electrolyte has a very narrow composition range and that materials with compositions containing more Cl⁻ ion are not single phase.

The conductivities were measured with the vector impedance meter³ used to make the measurements on RbCu₄Cl₃I₂ (2). In Fig. 1(a), below 130°, experiments were run at two different cooling rates. The lower curve is for the slower cooling rate; it is seen that under the slower cooling rate, the decomposition is greater as would be expected. Above 130° the slope

³The frequency range has been expanded from 10⁻¹ Hz to 650 kHz.

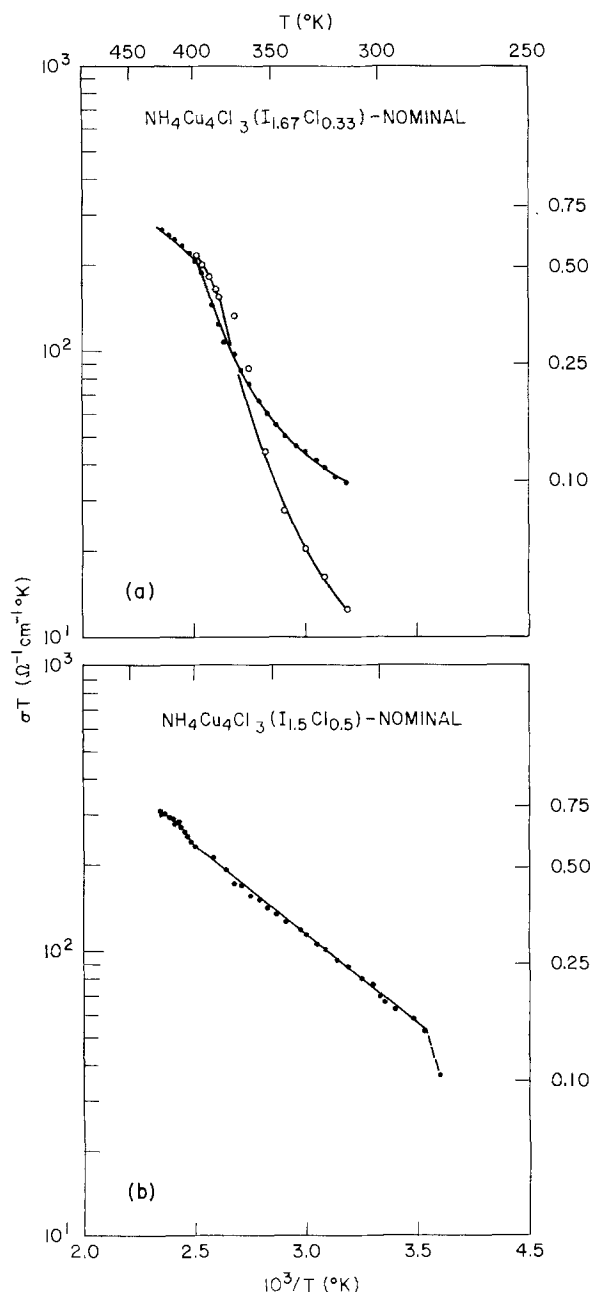


Fig. 1. (a) Specific conductivity multiplied by absolute temperature vs. reciprocal temperature for the nominal composition $\text{NH}_4\text{Cu}_4\text{Cl}_3(\text{I}_{1.67}\text{Cl}_{0.33})$ (not single phase). Also shown are the absolute temperature and specific conductivity. The upper and lower curves are the results for faster and slower cooling, respectively. Note that the curves meet at $T = 400^\circ\text{K}$ where the solid electrolyte phase is thermodynamically stable. (b) Specific conductivity multiplied by absolute temperature vs. reciprocal temperature for the nominal composition $\text{NH}_4\text{Cu}_4\text{Cl}_3(\text{I}_{1.5}\text{Cl}_{0.5})$ (not single phase). Instability appears at 280°K .

of $\log(\sigma T)$ vs. $1000/T$ yields 0.15 eV for the enthalpy of activation of motion.

Figure 1(b) shows a small anomaly at 130°C , indicating perhaps an onset of decomposition of the solid electrolyte present, but this is not confirmed by x-ray powder photography. The slope of $\log(\sigma T)$ vs. $1000/T$ gives 0.13 eV for the enthalpy of activation of motion.

Additional Discussion

The instability of the new solid electrolyte prevents an exact determination of its electrical transport properties. One should expect the conductivity to behave similarly to that of the analogous rubidium materials. In any case, there is no doubt that the solid electrolyte $\text{NH}_4\text{Cu}_4\text{Cl}_3(\text{I}_{1.87}\text{Cl}_{0.13})$ has high conductivity, and that from a practical viewpoint it has been proved that the solid electrolyte can be stabilized at least down to 5°C . Further experiments toward stabilizing this solid electrolyte are in progress. Needless to say, such experiments are worthwhile from an economic point of view because NH_4I is much less expensive than RbI and CuI and CuCl are much less expensive than AgI .

Acknowledgment

This work was supported by the National Science Foundation under Grant No. DMR-11378-A01.

Manuscript received May 30, 1979.

Any discussion of this paper will appear in a Discussion Section to be published in the December 1980 JOURNAL. All discussions for the December 1980 Discussion Section should be submitted by Aug. 1, 1980.

Publication costs of this article were assisted by the National Science Foundation.

REFERENCES

1. T. Takahashi, O. Yamamoto, S. Yamada, and S. Hayashi, Paper No. 6-2, Extended Abstracts of Second International Meeting on Solid Electrolytes, St. Andrews, Scotland (1978).
2. S. Geller, J. R. Akridge, and S. A. Wilber, *Phys. Rev. B*, **19**, 5396 (1979).
3. S. Geller and J. R. Akridge, Unpublished.
4. S. Geller, *Science*, **157**, 310 (1967).
5. S. Geller, *Phys. Rev. B*, **14**, 4345 (1976).
6. S. Geller, in "Solid Electrolytes," S. Geller, Editor, pp. 41-66, Springer-Verlag, Heidelberg (1977).
7. B. B. Owens and G. R. Argue, *Science*, **157**, 308 (1967).
8. S. Geller and M. D. Lind, *J. Chem. Phys.*, **52**, 3782 (1970).
9. A. A. Colville and S. Geller, *Acta Crystallogr. Sect. B*, **27**, 2311 (1971); *Acta Crystallogr. Sect. B*, **28**, 3196 (1972).

Selective Dissolution of Cd-Mg Alloys

I. Static Samples

J. I. Gardiazábal¹ and J. R. Galvele*

Comisión Nacional de Energía Atómica, Departamento de Materiales, 1429 Buenos Aires, Argentina

ABSTRACT

The susceptibility to selective dissolution of Cd-Mg alloys in deaerated 0.5M NaClO₄ solutions, at room temperature to 75°C, was studied. The range of compositions studied was Cd-11 a/o Mg (Cd-2.6 w/o Mg) to Cd-50 a/o Mg (Cd-18 w/o Mg). Between -0.9 and -0.5V_(NHE), selective dissolution of magnesium was found. Cadmium was accumulated on the surfaces as a soft, crystalline, metallic film, most probably as a porous layer. The selective dissolution rate was four orders of magnitude faster than that reported in literature for similar compositions of Cu-Zn brass in NaCl solution. The selective dissolution became faster as the temperature and the magnesium content of the alloy increased.

One important type of corrosion of alloys is the selective dissolution or dealloying. By this process the more active component is leached away from the alloy. The nobler metal remains on the corroded alloy surface, usually as a sponge-like product. Although extensive work has been done on the subject, there is still considerable disagreement about the mechanism of selective dissolution. While some authors have suggested that both metals dissolve, and the nobler of the two is redeposited (1, 2), others have suggested that only the less noble of them is dissolved. In the latter case, the nobler metal is rearranged on the alloy surface, either by volume diffusion (3, 4) or by some type of surface diffusion (5). Arguments against the volume diffusion stem from the fact that at room temperature dealloying is observed in high melting point alloys. The diffusion coefficients at room temperature, if extrapolated from high temperature measurements, seem to be too low to account for the dealloying process by volume diffusion.

In the present work, a low melting point alloy was selected for the investigation in the expectancy that fast dealloying processes would be observed. To avoid the difficulties introduced by the formation of intermetallics, an alloy with a complete solid solubility range was selected. The system chosen was cadmium-magnesium. This alloy shows complete solubility at all the compositions (6). From the dealloying point of view, the alloy seemed to be promising because of the difference of almost 2V in the standard equilibrium potentials of the two components. On the other hand, since hydrogen evolution on cadmium shows a high overvoltage, no strong interference was expected by this cathodic reaction. This was confirmed in Part II, where calibration measurements were made with Cd-disk, Cu-ring rotating electrodes. The collection factor, *N*, showed a difference of less than 1%, compared to the theoretical value. This showing that if there was a cathodic reaction of hydrogen evolution, its contribution to the current density was a minor one.

This work is divided into two parts. The first one shows that a dealloying process takes place in this system. In the second part, ring-disk rotating electrodes are used. This part attempts to determine if a process of simultaneous dissolution of Cd and Mg, with the redeposition of cadmium, is operating.

Experimental

The samples were prepared by melting 99.99% cadmium and 99.99% magnesium in an iron crucible, as described in (7). The melting was done under an argon

* Electrochemical Society Active Member.

¹ Present address: Universidad Católica de Valparaíso, Casilla 4059, Valparaíso, Chile.

Key words: alloy, anode, corrosion, dissolution.

atmosphere, and the melt was made homogeneous by mechanical stirring. Eight mm diameter ingots of samples were cast in graphite crucibles, which were previously dried for 24 hr at 110°C. The as-cast ingots were etched in a 5% HNO₃ solution and sealed in quartz tubes, with a 400 mm Hg argon pressure. To make the ingots homogeneous, they were annealed for 40 hr at the temperatures indicated in Table I, followed by water quenching. Finally, the ingots were machined down to 6 mm diameter rods, and stored in a desiccator. Five different compositions were used, with the nominal values of Cd-50Mg; Cd-31Mg; Cd-26Mg; Cd-23Mg; and Cd-11Mg, in atomic percentage (a/o). The analytical compositions are shown in Table I.

Polarization samples were prepared from the 6 mm diameter rods cut into pieces 10 mm long. A copper electric lead was fastened to one end of the rod. The electric lead and the rod surface were covered with an epoxy resin (ARALDIT "D" CY 230 plus HY 951), leaving one end of the rod exposed. The exposed face was abraded with 600 silicon carbide paper immediately before exposing the sample to the test solution.

Polarization measurements were made in a double-walled Pyrex glass cell, with a platinum counterelectrode. The temperature of the cell was controlled with a Haake FS thermostat. A saturated calomel electrode was used as reference. All the potentials are reported in the normal hydrogen electrode scale (NHE). The potential was controlled by means of a LYP-Electronica potentiostat, and the current recorded with a Honeywell Elektronik 19 recorder.

The electrolyte used was 0.5M NaClO₄, pH 5.5, made up from a HClO₄ solution, and with the pH adjusted with an NaOH solution. This electrolyte was chosen to minimize the formation of Cd complexes in the solution. For the same reason, no buffers were used in the present work.

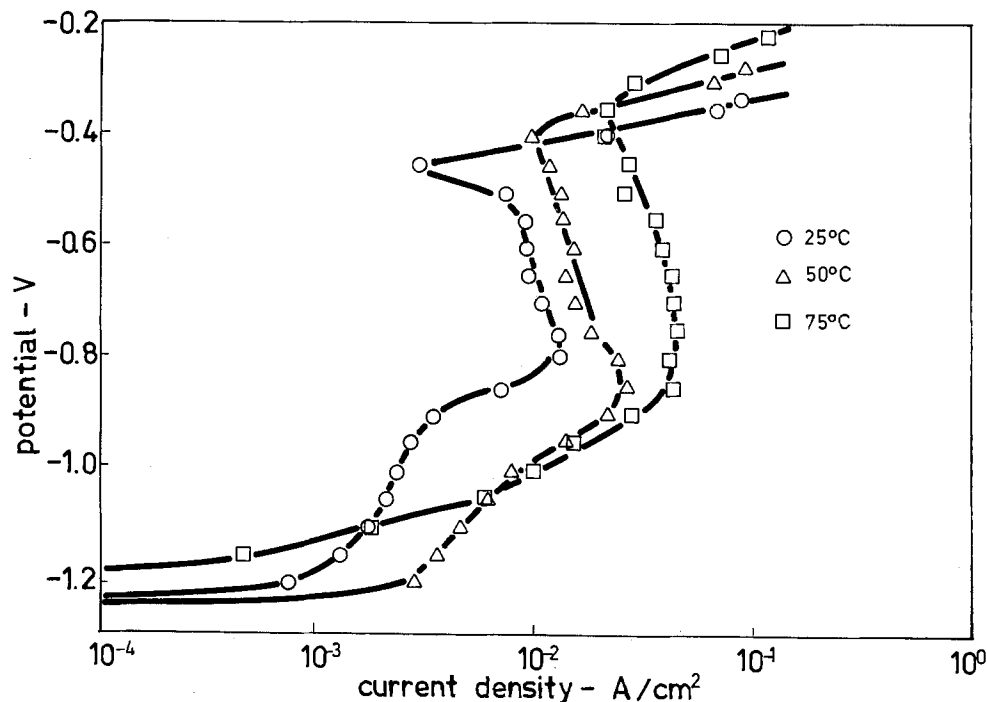
Results

Polarization curves.—Anodic polarization curves were drawn for Cd-50Mg and Cd-26Mg alloys in 0.5M NaClO₄ solution at 25°, 50°, and 75°C. The measure-

Table I. Chemical composition and annealing temperatures of the Cd-Mg alloys

Alloy	Magnesium content		Annealing temperature (°C)
	w/o	a/o	
Cd-11Mg	2.6	11.0	270
Cd-23Mg	6.1	23.1	290
Cd-26Mg	7.0	25.8	310
Cd-31Mg	8.9	31.1	320
Cd-50 Mg	17.7	50.1	380

Fig. 1. Anodic polarization curves of Cd-50Mg alloy in de-aerated 0.5M NaClO₄ solution, pH 5.5.



ments were performed in steps of 50 mV, waiting 5 min at each potential. Figure 1 shows the results for Cd-50Mg alloy, similar results were obtained with the Cd-26Mg alloy. Above the corrosion potential the current increased to a potential around -0.9 to -0.8 V. Above this potential there was a region where the current was potential-independent. Around -0.4 V, a new current increase was found. As confirmed by separate experiments which are described below, up to about -0.5 V selective dissolution of magnesium was taking place. Above -0.5 V, the current increase was followed by the simultaneous dissolution of magnesium and cadmium. The exact potential at which cadmium begins to dissolve simultaneously was measured in the second part of this work by using ring-disk rotating electrodes. An increase in the temperature increased the rate of selective dissolution of the alloy at potentials lower than -0.5 V. After the polarization experiments, a thick, poorly adherent film was covering the samples.

The curves in Fig. 1 are similar in shape to those reported by Pickering and Byrne (8) for the selective dissolution of Cu-Zn brass. However, the dissolution rates in Cd-Mg are considerably higher. The Cd-Mg system seems to dealloy at a rate about four orders of magnitude higher than Cu-Zn. Pickering and Byrne reported for gamma-brass (Cu 65 a/o Zn) a potential-independent dissolution rate of the order of 10^{-6} A/cm². On the other hand, Cd-50Mg showed a potential-independent dissolution rate of the order of 10^{-2} A/cm².

From the anodic polarization curves three potentials (-0.51 , -0.71 , and -0.91 V) were chosen for the study of the dealloying process. These were the potentials used in most of the remaining experiments.

Surface film composition.—Samples of the Cd-Mg alloys were exposed to the NaClO₄ solution at 25°C for 3 hr at constant potentials. The potentials used were the three reported above. The corroded samples were mounted for metallographic cross sectioning. The cross-sectioned samples were polished down to $\frac{1}{4}$ μ m diamond powder, observed under the optical microscope, and analyzed with a CAMECA M.S. 46 Microprobe Analyzer.

Figure 2 shows the cross-section micrograph of a sample of Cd-31Mg exposed for 3 hr at -0.51 V and 25°C in the 0.5M NaClO₄ solution. Figure 3 shows the microprobe analysis of the same sample. The identification of the various regions is as follows: R, mounting resin; F, surface film; A, alloy. The cps number shows

the full-scale range of the meter, in counts per second. The number of counts per second is proportional to the concentration of the analyzed element in the sample. The cadmium analysis (top of Fig. 3), shows that the cadmium content in the film was higher than that in the alloy. The magnesium content in the film, on the other hand, was very low. There was no concentration gradient of magnesium in the film.

Since the number of counts per second is proportional to the concentration of the analyzed element, an estimate can be made of the composition of the film. From the count-reading for cadmium in the alloy and that in the film, a semi-quantitative estimate of the cadmium content in the film was made (Table II). No similar estimate of the Mg content could be made, because the Mg readings in the film were in the range of the background noise of the equipment. In all the cases, the Mg content in the film was smaller than 1 weight percent (w/o). As shown in Table II, the surface film was mainly composed of cadmium. The film could either be Cd metal, or some Cd oxide or hydroxide.

The nature of the film was determined by means of a Debye-Scherrer x-ray diagram. A sample of Cd-50Mg exposed for 3 hr at -0.71 V in the NaClO₄ solution at

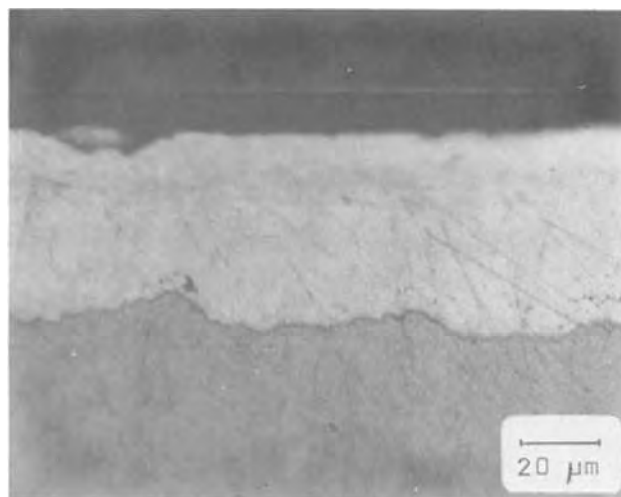


Fig. 2. Cross-section micrograph of corroded Cd-31Mg alloy after 3 hr dissolution in 0.5M NaClO₄ solution, at -0.51 V and 25°C.

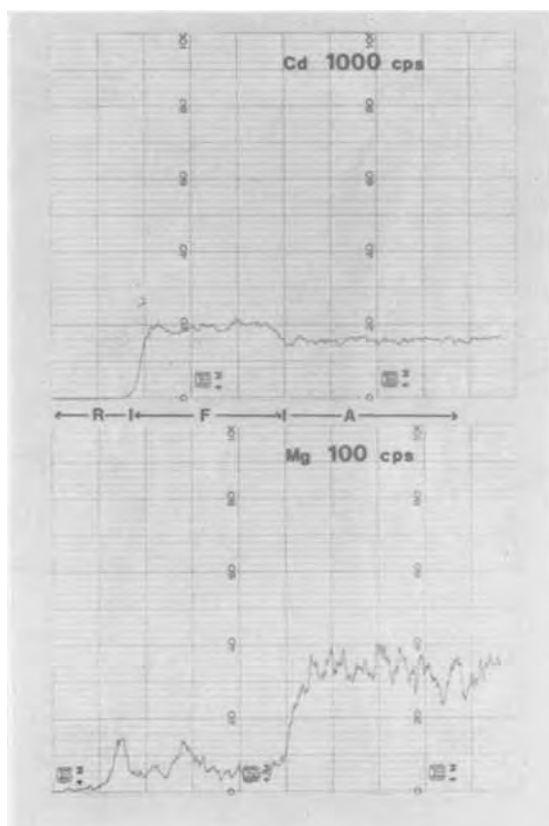


Fig. 3. Cd and Mg concentration profiles on the sample in Fig. 2. R, mounting resin; F, surface film; A, cadmium-magnesium alloy; cps, counts per second from the Electron Microprobe Analyzer.

25°C, was used for this purpose. The surface film was carefully peeled off and ground to powder. A Debye-Scherrer diagram was obtained after a 4 hr exposure with a cobalt x-ray tube and an iron filter. The calculated spacings are reported in Table III, and compared with those for metallic Cd (9). The diagram showed that the film was crystalline, and that it was composed of metallic Cd. The possibility of an oxide or some other Cd compound was ruled out.

Effect of temperature on the dealloying.—Constant potential measurements were performed at the three mentioned potentials at 50° and 75°C, for Cd-11Mg, Cd-26Mg, and Cd-31Mg. Figure 4 shows the cross-section micrograph of a Cd-26Mg sample exposed for 3 hr at -0.71V and 75°C. Figure 5 is the concentration profile for cadmium and magnesium for the same sample. In general, it was observed that at higher temperatures the dealloyed region was thicker. At the same time, numerous cracks were found in the film, which were filled by magnesium corrosion products. No cadmium was found inside those cracks.

Current-time curves.—Duplicate current-time measurements were made for every one of the alloys and at each of the three chosen potentials. The exposure

Table II. Surface film composition of Cd-Mg alloys exposed at 25°C for 3 hr to 0.5M NaClO₄ solution, pH 5.5, at constant potentials. The composition, in weight percent, was estimated ±1%.

Alloy Number	Compo-sition	Surface film		
		-0.51V	Potential -0.71V	-0.91V
Cd-50Mg	82.3% Cd	100% Cd	100% Cd	100% Cd
Cd-31Mg	91.1% Cd	100	—	99
Cd-26Mg	93.0% Cd	99	100	100
Cd-23Mg	93.9% Cd	99	99	100
Cd-11Mg	97.4% Cd	—	99	—

Table III. Spacing data obtained with a Debye-Scherrer diagram for the film produced in Cd-50Mg at -0.71V and 25°C. Spacings were compared with the values reported in (9)

d_{Cd} (Å)	hkl	d_{sample} (Å)
2.345	101	2.340
1.316	112	1.317
1.290	200	1.284
1.258	201	1.262
1.062	203	1.053
1.030	105	1.041
1.022	114	1.013
0.975	210	1.005
0.950	204	0.953
		0.956

time was 20 hr. At the end of each exposure, the pH of the solution was measured. It was found that the pH of the solution changed considerably during the experiment, reaching values close to pH 10. The anodic reaction product was Mg²⁺, while on the counterelectrode hydrogen evolution was taking place. These reactions lead to the formation of Mg(OH)₂ in the bulk solution. This process explains the observed pH increase. The high pH values produced incipient precipitation of magnesium corrosion products on the samples. This magnesium precipitation explained the presence of regions rich in magnesium observed in Fig. 5. The effect of pH changes on the dealloying process is currently being studied (10).

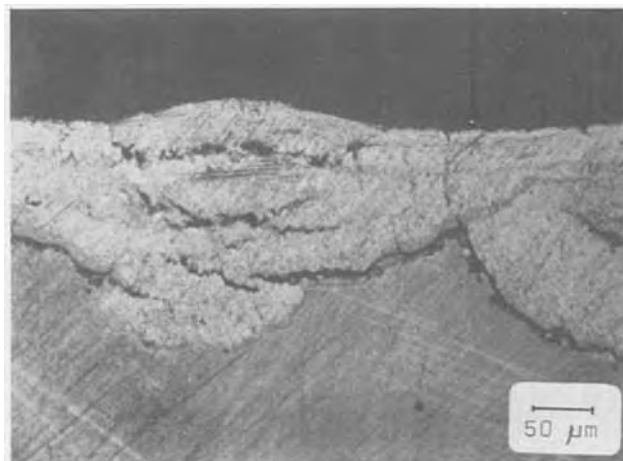


Fig. 4. Cross-section micrograph of corroded Cd-26Mg alloy after 3 hr dissolution in 0.5M NaClO₄ solution, at -0.71V and 75°C.



Fig. 5. Cd and Mg concentration profiles on the sample in Fig. 4. R, mounting resin; F, surface film; A, cadmium-magnesium alloy; cps, counts per second from the Electron Microprobe Analyzer.

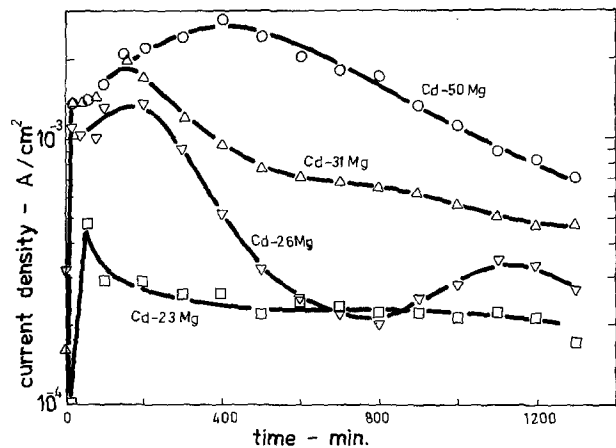


Fig. 6. Current-time curves for Cd-Mg alloys in 0.5M NaClO₄ solution at $-0.71V$ and $25^{\circ}C$.

Figure 6 shows typical current-time curves observed with the different alloys. A current decay is observed, although the current decreases at a much lower rate than that predicted by the Pickering and Wagner mechanism (3). Fluctuations in the current during the run were observed. These were attributed to the cracking of the surface film. In general, the lower the content of magnesium, the lower the dealloying rate. The potential had no noticeable effect on the dealloying rate at the potentials tested.

According to the dealloying mechanism by Pickering and Wagner, a linear relation should be found between the current density and I/\sqrt{t} . But, in Fig. 6 almost stationary currents are observed. However, as it was pointed out by Pchel'nikov *et al.* (11) that relation should be found only at the very early stages of dealloying, or in very dilute solid solutions. Deviations of the linear behavior will be due to crystal lattice parameter changes, or to the formation of new phases. In the particular case of the Cd-Mg alloys used in the present work, considerable changes in volume should take place. After the dissolution of magnesium, the remaining cadmium should undergo volume shrinkage of the order of 20-50%. If the criterion introduced by Pilling and Bedworth (12) is used in the present case, the corrosion product will be found to have a Pilling and Bedworth relation considerably lower than one. This would indicate that no protective film should be formed by the cadmium on the surface.

Conclusions

It was found that Mg-Cd alloys show selective magnesium dissolution in NaClO₄ solutions. The rate of selective dissolution increases with the increase of magnesium content in the alloy, as well as with the increase of the temperature in the solution. A soft porous layer of cadmium is formed on the dealloyed alloy. X-ray analysis shows that the film is crystalline. This film has been identified as metallic cadmium.

Due to the important volume shrinkage of the corrosion product, no protective film is formed on the dealloyed alloy for composition between Cd-50Mg and Cd-11Mg. Cd-Mg alloys seem to be a very promising system for the study of the mechanism of dealloying of metals. The high mobility of cadmium atoms at room temperature could account for the high dealloying rate found in these alloys.

Acknowledgments

This research has been supported by the Comisión de Investigaciones Científicas (Provincia de Buenos Aires) and by the Programa Multinacional de Metalurgia—Programa Regional de Desarrollo Científico y Tecnológico, O.E.A.

Manuscript submitted Dec. 28, 1978; revised manuscript received May 11, 1979.

Any discussion of this paper will appear in a Discussion Section to be published in the December 1980 JOURNAL. All discussions for the December 1980 Discussion Section should be submitted by Aug. 1, 1980.

REFERENCES

1. V. F. Lucey, *Br. Corros. J.*, **1**, 9 (1965).
2. H. Sugawara and H. Ebiko, *Corros. Sci.*, **7**, 513 (1967).
3. H. W. Pickering and C. Wagner, *This Journal*, **114**, 698 (1967).
4. H. W. Pickering, *ibid.*, **115**, 143 (1968).
5. H. G. Feller, *Corros. Sci.*, **8**, 259 (1968).
6. M. Hansen, "Constitution of Binary Alloys," 2nd ed., p. 425, McGraw Hill, New York (1958).
7. H. Steeple, *Acta Crystallogr.*, **5**, 247 (1952).
8. H. W. Pickering and P. J. Byrne, *This Journal*, **116**, 1492 (1969).
9. X-ray Powder Data File, Inorganic Volume, American Society for Testing and Materials, 2nd Ed. (1967).
10. R. Mizrahi and J. R. Galvele, Research in progress.
11. A. P. Pchel'nikov, L. I. Krashinkaya, A. D. Sitnikov, and V. V. Losev, *Electrokhimiya*, **11**, 37 (1975).
12. N. B. Pilling and R. E. Bedworth, *J. Inst. Met.*, **29**, 529 (1923).

Selective Dissolution of Cd-Mg Alloys

II. Rotating Ring Disk Electrode

J. I. Gardiazabal and J. R. Galvele*

Comisión Nacional de Energía Atómica, Departamento de Materiales, 1429 Buenos Aires, Argentina

ABSTRACT

Selective dissolution was found for Cd-Mg alloys in 0.5M NaClO₄ solutions, pH 5.5. Below -0.51V (NHE) the anodic dissolution of the alloys led to the formation of Mg²⁺ ions. No evidence of formation of Cd²⁺ ions, under the same conditions, was found. The anodic current densities were high, showing a fast dealloying process. In addition, they became higher at higher temperatures, and with a higher magnesium content of the alloy. The results are discussed in view of the published mechanisms of selective dissolution. A selective dissolution process is assumed, where a collapse in the cadmium film leads to a nonprotective surface layer. The anodic current density dropped to zero for alloys in the range of Cd-7.4 (±1.7) a/o Mg. This indicates that for lower magnesium contents a continuous protective film of metallic cadmium is formed on the alloy surface.

The rotating ring disk electrode is a powerful research technique. It has been frequently used in the study of selective dissolution of alloys. With this technique, it is possible to detect and collect on the inert ring electrode the dissolution products from the alloy disk electrode. An approximate solution to the theory of transfer of the rotating ring disk electrode is due to Ivanov and Levich (1). The exact solution was derived later by Albery (2). A fundamental parameter in this technique is N , the collection efficiency. N is defined as the proportion of material electrochemically produced on the disk electrode, which reaches the ring electrode

$$N = \text{ring current/disk current} = -i_R/i_D$$

The negative sign is included because i_R and i_D have opposite signs. Tables for N , for different ring disk radius ratios have been published by Albery and Bruckenstein (3).

The rotating ring disk electrode has been used in the study of selective dissolution of alloys by the following authors: Pickering and Wagner (4) for Cu-Au and Cu-Zn; Feller (5) for Cu-Zn; Miller (6) for Cu-Zn; Taylor (7) for Cu-Zn; and Marshakov, Bolychev, and Potapova (8) for Cu-Zn, Ag-Zn, and Ag-Cd alloys.

As shown by Pickering and Byrne for Cu-Zn alloys (9), and for Au-Cu alloys (10), two different regions are observed in the anodic polarization curves of alloys during the dealloying process: one, at low potentials, where only the active metal dissolves; the other, at higher potentials, where both metals dissolve. Most rotating ring disk studies of dealloying were done with galvanostatic control (4, 5, 7). In this way, since the potential was not fixed, it was not evident in what region of potentials the disk was dissolving. For this reason, in the present work it was decided to use simultaneous potential control of the ring and disk.

Following the study of dealloying of Cd-Mg alloys with stationary electrodes by the authors (11), the selective dissolution was studied with the rotating ring disk electrode. The results show no evidence of simultaneous dissolution of cadmium and magnesium, during dealloying, below -0.51V. Only magnesium was dissolving, leaving a film of metallic cadmium on the alloy surface. The activation energy values for dealloying are in the range of those expected for volume diffusion in the metal. It was also observed that the anodic dissolution current dropped to zero for magnesium contents below 7.4 atomic percent (a/o). This

change is assumed to be related to a change in the nature of the metallic cadmium surface film.

Experimental

Several designs of rotating ring disk electrodes were tested. Those based on metal plus Teflon had to be discarded, because crevices could not be avoided between metal and Teflon. Those crevices gave collection efficiency factors, N , different from the theoretical N values. The best results were obtained with rotating ring disk electrodes based on a metal-epoxy resin design. Figure 1 shows schematically the electrodes used in the

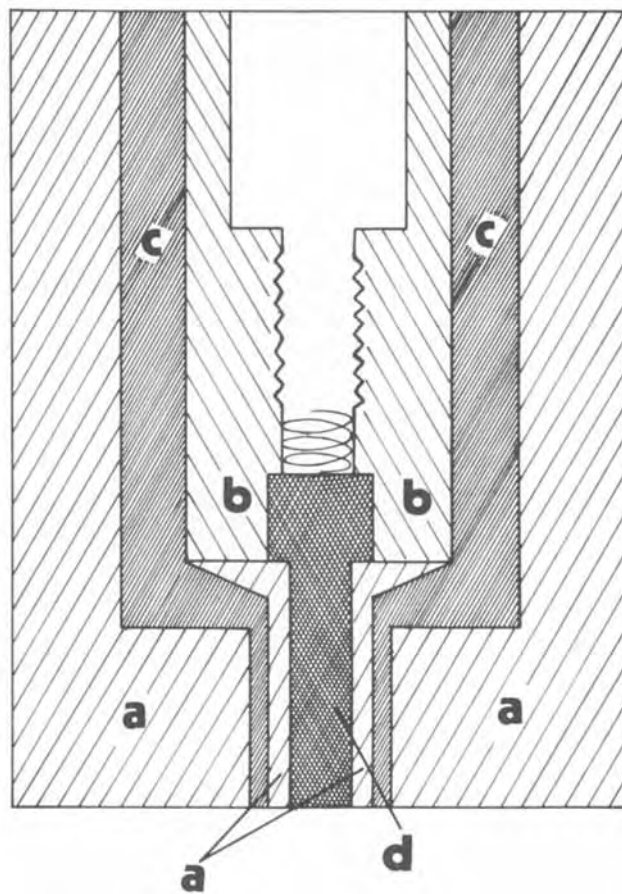


Fig. 1. Cross section of the rotating ring disk electrode, schematic, not in scale: a, Epoxy-resin support; b, acrylic-resin isolator; c, copper-ring electrode; d, alloy-disk electrode.

* Electrochemical Society Active Member.

¹ Present address: Universidad Católica de Valparaíso, Casilla 4059, Valparaíso, Chile.

Key words: alloy, anode, corrosion, dissolution.

Table I. Electrode dimensions and collection efficiency values, N , for the various rotating ring disk electrodes used

Electrode No.	Disk compos. (a/o)	R_d (cm)	R_r^i (cm)	R_r^e (cm)	A_d (cm ²)	A_r (cm ²)	N^*
0	Cadmium	0.1047	0.1163	0.1531	0.033	0.031	0.4017
1	Cd-11Mg	0.1043	0.1134	0.1250	0.034	0.0087	0.2263
2	Cd-11Mg	0.1044	0.1163	0.1519	0.034	0.030	0.4044
3	Cd-23Mg	0.1050	0.1153	0.1463	0.035	0.026	0.3757
4	Cd-26Mg	0.1037	0.1130	0.1225	0.034	0.007	0.2050
5	Cd-26Mg	0.1031	0.1175	0.1513	0.033	0.029	0.3783
6	Cd-31Mg	0.1050	0.1137	0.1524	0.035	0.032	0.4224
7	Cd-50Mg	0.1020	0.1100	0.1202	0.033	0.0072	0.2158
8	Cd-50Mg	0.1075	0.1150	0.1525	0.036	0.032	0.4206
9	Copper	0.1034	0.1183	0.1533	0.034	0.030	0.3843

R_d , radius of the disk; R_r^i , internal radius of the ring; R_r^e , external radius of the ring; A_d , area of the disk; A_r , area of the ring.
* Values from Albery and Bruckenstein (3).

present work. With these electrodes, the difference between the theoretical and the experimental N values was found to be less than 1%. Table I shows the dimensions of some of the electrodes used in the present work. Electrodes with lower N values were initially prepared, but the final measurements were done with the electrodes described in Table I. The same electrode was used several times, after abrading the corroded surface with 600 silicon carbide paper.

The ring metal was copper. The disk metal was composed of some of the alloys reported in Part I (11), with the following nominal compositions, in a/o: Cd-11Mg; Cd-23Mg; Cd-26Mg; Cd-31Mg; and Cd-50Mg. Rotating ring disk electrodes with copper and cadmium disks were also used for calibration purposes.

The measurements were made in a double-walled Pyrex glass cell. The temperature in the cell was regulated by circulation of water through a Haake FS thermostat. The Luggin capillary was positioned close and normal to the disk electrode (12). The cell contained approximately 360 ml of solution. The Luggin capillary was connected, through a salt bridge, to a saturated calomel reference electrode. All the potentials are reported in the normal hydrogen electrode scale (NHE).

The potentials of ring and disk were independently controlled by using a double potentiostat based on the circuits published by Napp *et al.* (12). The electrolyte used was 0.5M NaClO₄, pH 5.5, made up from HClO₄ solution, and with the pH adjusted with NaOH solution. No buffers were used in the present work. Prior to the measurements, the solutions were deaerated by bubbling prepurified nitrogen for 7 hr (13). During the measurements a stream of purified nitrogen was maintained above the solution. The potential of the disk was scanned with a LYP-Electronica potential scanner, with a scanning range from 1×10^{-4} to 1×10^3 V/sec. The currents on the ring and disk were simultaneously recorded with a 2 FAM X-Y Hewlett-Packard Recorder. The rotation speed of the electrodes was regulated with a LYP-Electronica electronic controller.

The experimental parameters were determined with a rotating cadmium-disk copper-ring electrode, in a deaerated 0.5M NaClO₄ solution, with pH values ranging from 3.0 to 7.0. A pH dependent cathodic reaction interference was found on the ring and disk electrodes at low pH values. This interference was attributed to H₂O₂ produced by the platinum counterelectrode (14). The interference was found to be negligible for pH values above 5.0.

At potentials above -0.49 V, the cadmium-disk dissolved actively, with a Tafel slope of about 0.050V. However, at pH values above 6 the active anodic dissolution was replaced by an active-passive transition. Since the effect of such an active-passive transition on the dealloying process was unknown, it was decided to work at pH 5.5.

Cathodic deposition experiments were performed with a rotating copper-disk electrode, in a deaerated 0.5M NaClO₄ solution, pH 5.5, containing 0.001M Cd⁺⁺ ions. The electrode potential was changed at a scanning rate of 6 mV/sec and various rotation speeds were used. The results are shown in Fig. 2. A limiting cathodic current was found for cadmium deposition. The linear relation between this limiting current and the square root of the rotation speed showed it to be a pure diffusion process (15). From all these measurements, a potential of -0.76 V was chosen for the deposition of cadmium on the ring electrode in all the rotating ring disk electrode experiments with the Cd-Mg alloys.

Results

Polarization curves.—Figures 3-7 show ring disk electrode measurements for Cd-50Mg, Cd-31Mg, Cd-26Mg, Cd-23Mg, and Cd-11Mg alloys in deaerated, pH 5.5, 0.5M NaClO₄ solution at various temperatures. The initial potential of the disk alloy electrode was -1.56 V, and it was increased with a scanning rate of 0.001 V/sec, while the potential of the copper ring electrode was kept at -0.76 V. The electrode was rotated at a speed of 314 radians/sec.

The alloys showed a corrosion potential below which the cathodic reaction of hydrogen evolution was predominant. Above the corrosion potential, the anodic currents observed were the result of alloy dissolution. The corrosion potential was not clearly affected by the temperature, but it was a function of the cadmium content of the alloy. The higher the content of cadmium, the higher the corrosion potential. It went from

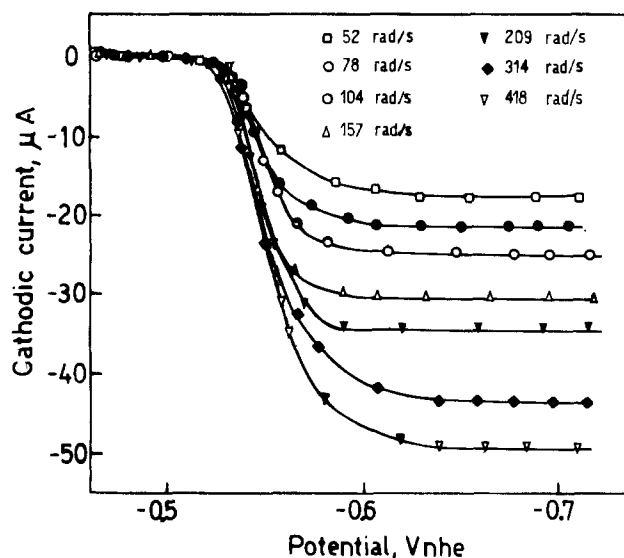


Fig. 2. Cathodic electrodeposition of cadmium on a rotating copper disk electrode, at various rotation speeds. Deaerated 0.5M NaClO₄ solution, pH 5.5, containing 0.001M Cd⁺⁺ ions.

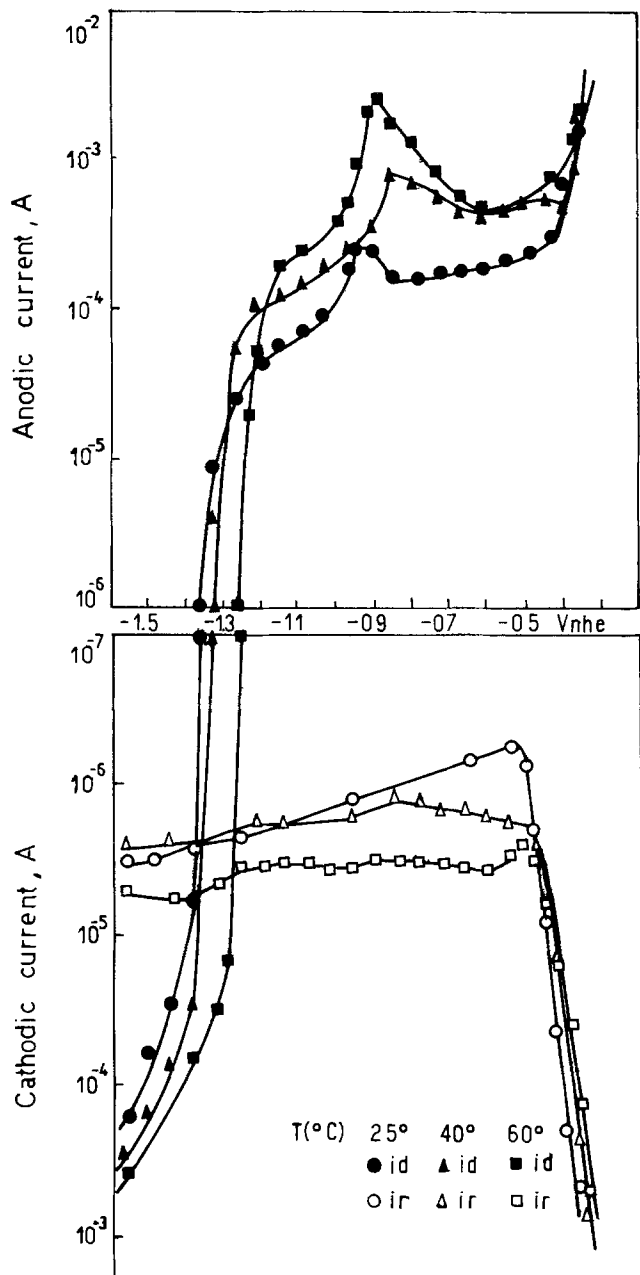


Fig. 3. Potentiokinetic polarization curves of Cd-50Mg disk electrode alloy in deaerated 0.5M NaClO₄ solution, pH 5.5, at various temperatures. i_d , disk electrode current; i_r , ring electrode current; rotation speed of the electrode, 314 radians/sec; potential scanning rate of the disk, 0.001 V/sec; potential of the ring, $-0.76V$; electrode No. 8.

$-1.36V$ for the Cd-50Mg alloy, to $-0.91V$ for the Cd-11Mg alloy.

Above the corrosion potential the measured anodic current increased, showing a maximum somewhere between -0.92 and $-0.84V$. In the Cd-11Mg alloy (Fig. 7), on the other hand, if such a maximum existed it was obscured by the cathodic reaction. This maximum current was a function of the temperature of the solution and the composition of the alloy. From the temperature effect, an estimate of the activation energy of the process could be made. Table II shows the activation energy values found for the various alloys. These values are in the range of those expected for volume diffusion in metals. For example, the activation energy reported for diffusion of cadmium in disordered Mg₃Cd alloy is 12.8 kcal/mole (16).

The anodic current density was equal to that found on static samples (11), and was not affected by the speed of the rotating electrode. This current was a

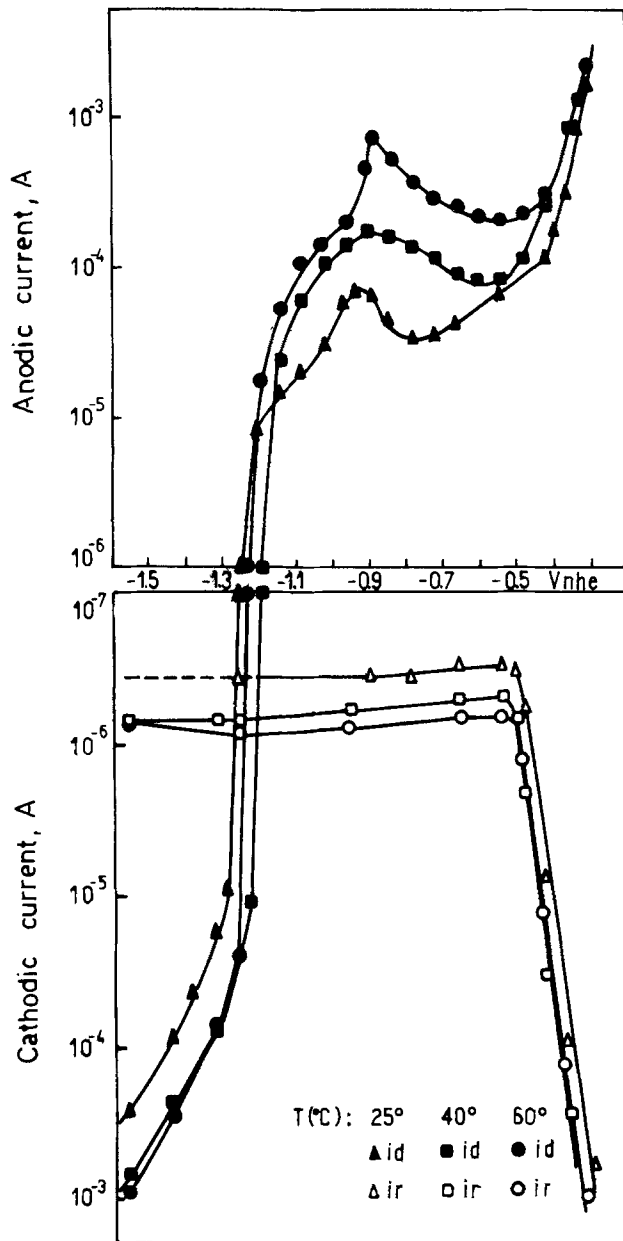


Fig. 4. Potentiokinetic polarization curves of Cd-31Mg disk electrode alloy in deaerated 0.5M NaClO₄ solution, pH 5.5, at various temperatures: i_d , disk electrode current; i_r , ring electrode current; rotation speed of the electrode, 314 radians/sec; potential scanning rate of the disk, 0.001 V/sec; potential of the ring: $-0.76V$, electrode No. 6.

function of the composition of the alloy: the higher the content of cadmium, the lower the anodic current density. An empirical relation was found between the current density and the alloy composition. A linear relation between the square root of the current density and the alloy composition was observed (Fig. 8). This linear relation was found at all the temperatures tested, and was checked for -0.61 , -0.71 , and $-0.81V$. By extrapolation, an alloy composition was found, for which the current density should be zero. This would indicate that either no selective dissolution occurs for lower magnesium contents, or that there is a change in the mechanism of selective dissolution. Table III shows the extrapolated values, and a good coincidence was found between them, for all the temperatures and potentials tested. Potentiostatic values, from the cadmium stripping experiments described below, were also included. The mean value of the extrapolated composition was Cd-7.4 (± 1.7) a/o Mg.

If the potential was increased (Fig. 3-7), the current, after reaching a maximum, showed little change

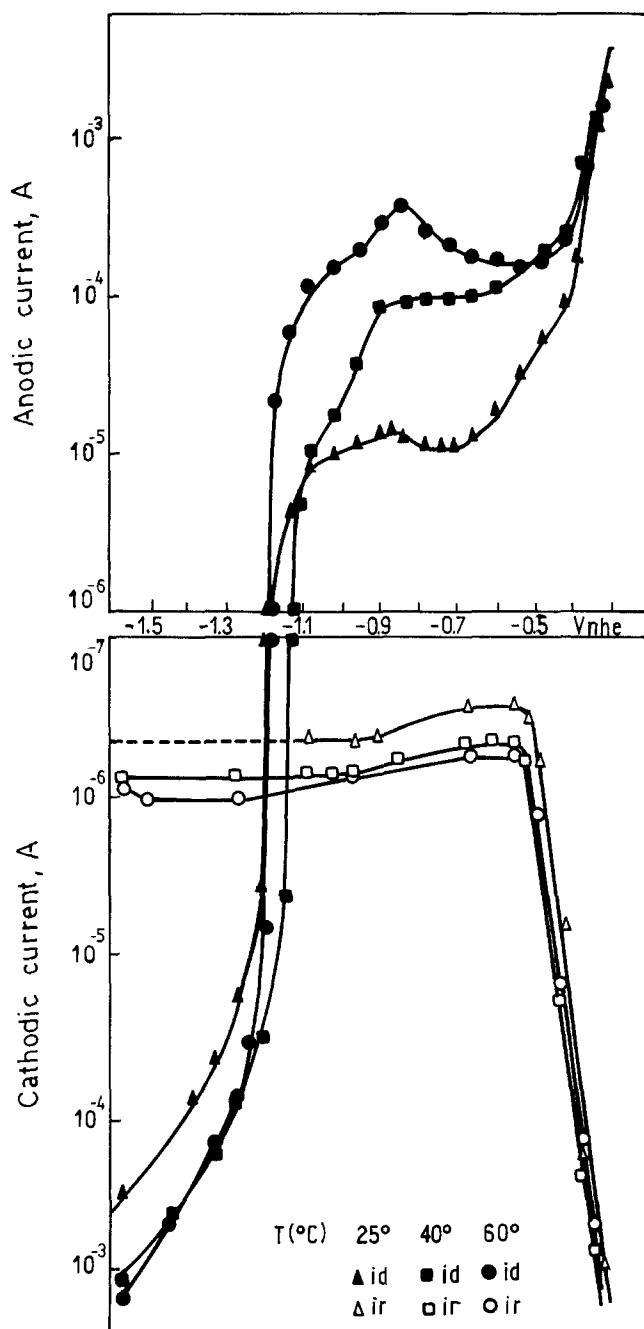


Fig. 5. Potentiokinetic polarization curves of Cd-26Mg disk electrode alloy in deaerated 0.5M NaClO₄ solution, pH 5.5, at various temperatures: i_d , disk electrode current; i_r , ring electrode current; rotation speed of the electrode, 314 radians/sec; potential scanning rate of the disk, 0.001 V/sec; potential of the ring: $-0.76V$, electrode No. 5.

with the potential up to about $-0.42V$. At this potential, for all the alloys tested and for all the temperatures used, a sharp increase in the current was found, leading to severe corrosion of the disk.

If the ring is kept at a potential of $-0.76V$, the presence of dissolved cadmium in the solution should be detected as a cathodic current on the ring. For disk electrode potentials between -1.56 and $-0.51V$ a potential independent background current was observed on the ring. As shown in experiments described below, no cadmium was found on the ring for this range of potentials. It was concluded, then, that between -1.56 and $-0.51V$ no soluble cadmium was produced during the anodic dissolution of the Cd-Mg alloy. At and above $-0.51V$ the cathodic current on the ring showed a sharp increase, and deposition of cadmium was detected on the ring. This shows that between -1.56 and

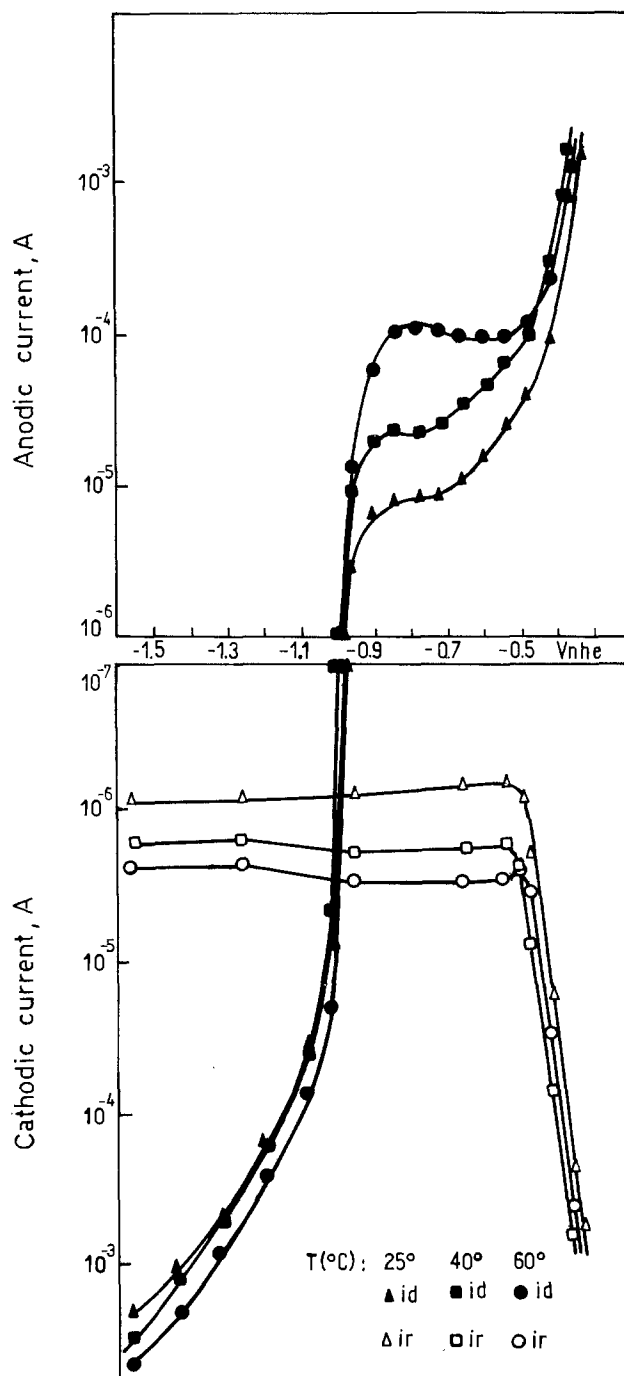


Fig. 6. Potentiokinetic polarization curves of Cd-23Mg disk electrode alloy in deaerated 0.5M NaClO₄ solution, pH 5.5, at various temperatures. i_d , disk electrode current; i_r , ring electrode current; rotation speed of the electrode, 314 radians/sec; potential scanning rate of the disk, 0.001 V/sec; potential of the ring, $-0.76V$; electrode No. 3.

$-0.51V$ the anodic current on the disk was solely due to the dissolution of magnesium. At $-0.51V$ and above, on the other hand, the anodic current on the disk was the result of the simultaneous anodic dissolution of magnesium and cadmium. Below $-1.56V$, dissolution of magnesium was, most probably, to be found too, but it was obscured by the cathodic reaction of hydrogen evolution. The potential at which dissolution of cadmium from the disk began, $-0.51V$, was not affected either by the composition of the alloy or by the temperature. The independence of the potential with respect to the composition of the alloy was due to the fact that the cadmium ions were produced by the dissolution of the dealloyed film, the composition of which should be the same for all the alloys tested.

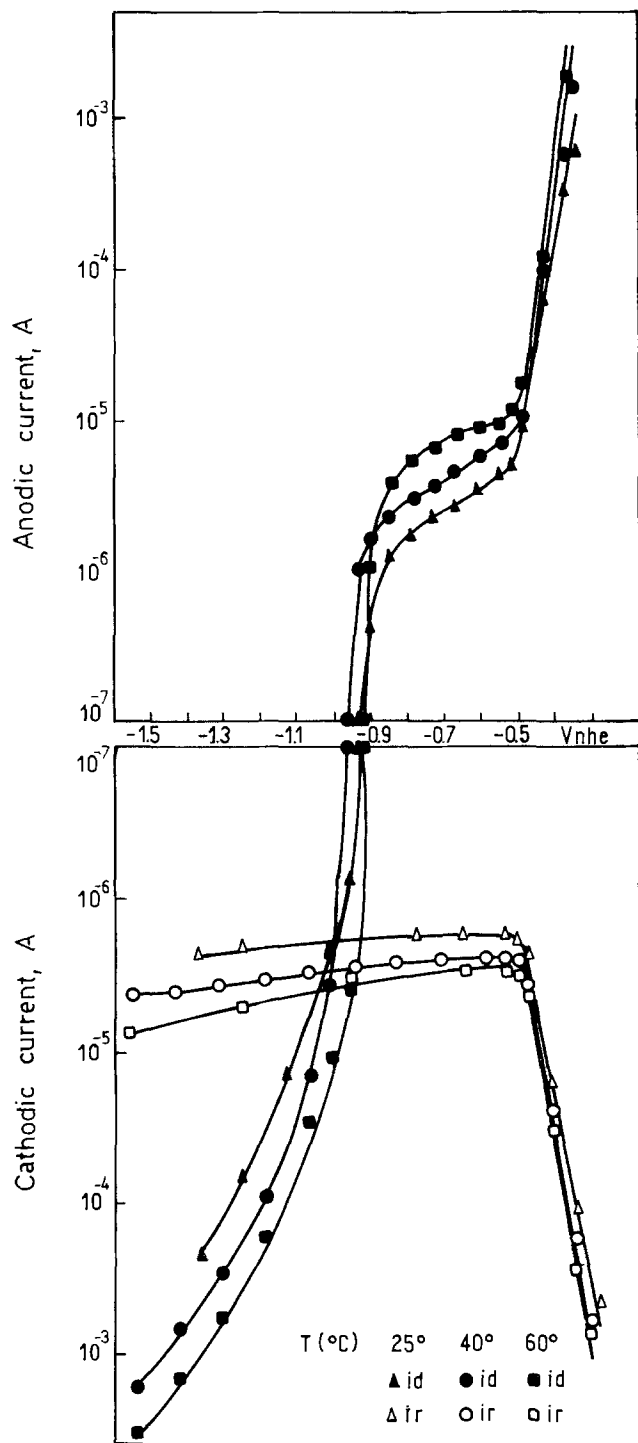


Fig. 7. Potentiokinetic polarization curves of Cd-11Mg disk electrode alloy in deaerated 0.5M NaClO₄ solution, pH 5.5, at various temperatures. *i_d*, disk electrode current; *i_r*, ring electrode current; rotation speed of the electrode, 314 radians/sec; potential scanning rate of the disk, 0.001 V/sec; potential of the ring, -0.76V, electrode No. 2.

Cadmium deposition on the ring electrode.—Electron microprobe analysis was used to confirm the observations made in the electrochemical measurements. The presence of cadmium, electrodeposited on the ring electrode, was investigated with the electron microprobe. The ring disk electrode was introduced in the electron microprobe analyzer through a specially designed sample holder. In one set of experiments, samples of all the alloys were exposed to the deaerated 0.5M NaClO₄ solution, for 3 hr at -0.51V for the disk electrode, and -0.76V for the ring electrode. After the 3 hr exposure, the ring disk electrode was retrieved from the cell and taken to the electron microprobe analyzer. The analy-

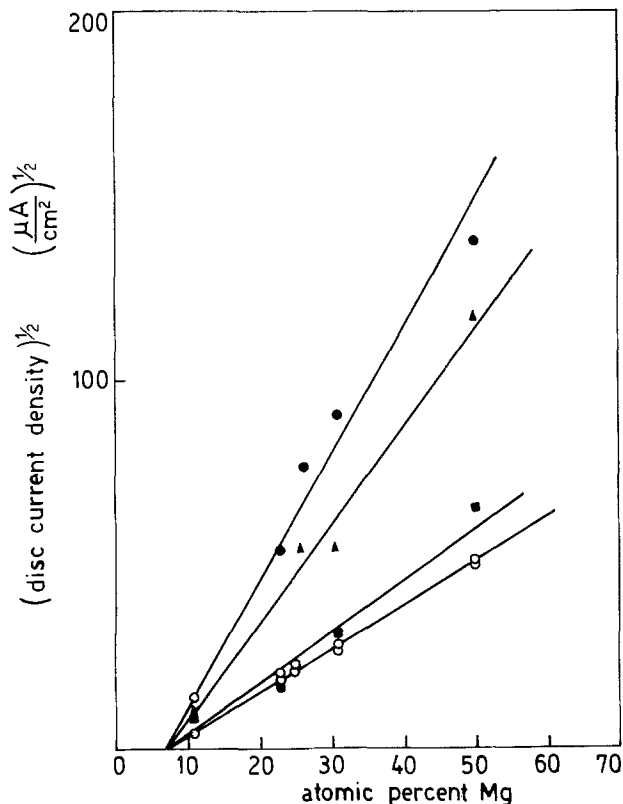


Fig. 8. Effect of the alloy composition on the anodic current density of Cd-Mg alloys in deaerated 0.5M NaClO₄, pH 5.5, at -0.71V, and various temperatures. Potentiokinetic measurements: ●, 60°C; ▲, 40°C; and ■, 25°C. Potentiostatic measurements: ○, 25°C.

sis showed the presence of cadmium on the ring electrode. Similar results were obtained with all the other alloys.

The deposition of cadmium on the ring at lower disk potentials was also investigated. To prevent air-formed films from being chemically dissolved in the solution and redeposited on the ring, a double set of experiments was made. In all these experiments the potential of the alloy-disk was kept at -0.71V. In a first set of experiments, the potential of the ring was first maintained at -0.76V for 2 hr and then at -0.26V for another 2 hr. In this way, any cadmium deposited

Table II. Activation energy values calculated for the dissolution rate of Cd-Mg alloys in deaerated 0.5M NaClO₄, pH 5.5, at -0.88V

Alloy	Activation energy (kcal/mole)
Cd-50Mg	12.3
Cd-31Mg	12.8
Cd-26Mg	19.2
Cd-23Mg	14.1

Table III. Extrapolated values of magnesium content for which the anodic dissolution current density is zero

Temp. (°C)	Potential		
	-0.61V	-0.71V	-0.81V
25	7.7	8.8	9.3
40	5.2	7.5	9.5
60	6.2	4.6	8.2
25*	—	7.4*	—

* Potentiostatic measurements.

during the first two hours was anodically stripped at the higher potential. The initial 2 hr exposure was chosen to allow the system to reach a stationary state. After this treatment, the electrodes were taken to the electron microprobe and analyzed for cadmium on the ring. In this way, the background current for cadmium analysis on the ring was found. In a second set of experiments, after exposing the ring at -0.76V for 2 hr and then at -0.26V for 2 hr, the ring electrode was exposed for another 2 hr at -0.76V . After it, the ring-disk electrodes were taken to the electron microprobe and an analysis was made for cadmium deposited on the ring. No difference was found for any of the alloys between the cadmium-deposited and the cadmium stripped ring electrodes. In both cases only the background current on the ring was observed with no discernible difference between the two treatments. It was concluded that no cadmium ions were liberated to the solution when the disk was anodically corroding at -0.71V . Confirming the electrochemical results reported above, and those described in Part I of this paper (11), selective dissolution of magnesium was found to take place during the anodic polarization of Cd-Mg alloys. Up to -0.51V the only anodic reaction product was dissolved magnesium, while at and above -0.51V , simultaneous dissolution of cadmium and magnesium was found.

Discussion and Conclusions

From the results in Part I (11) and those reported in the present work, it is concluded that Cd-Mg alloys are susceptible to selective dissolution in NaClO_4 solutions. Between the corrosion potential and -0.51V , magnesium leaches away from the alloy, leaving a surface film of pure metallic cadmium. No soluble cadmium ions are produced during this dealloying process. Cadmium ions are produced only when the potential of the alloy is -0.51V or higher. The dealloying process rate is accelerated by an increase in the temperature. And an estimation of the activation energy for the process gives values close to those found for volume diffusion in similar alloys. This dealloying rate is a function of the alloy composition. The higher the magnesium content, the higher the dissolution rate, at a fixed potential. A linear relation was found between the square root of the current density and the magnesium content of the alloy. By extrapolation, this current density would be zero for an alloy of Cd-7.4 Mg.

Several mechanisms have been proposed for the dealloying process (4, 5, 17-21). These mechanisms are usually divided into three groups: (i) dissolution of the entire alloy, followed by redeposition of one of the components (20); (ii) selective dissolution of one of the species, leaving the nobler species on the alloy surface (4, 5, 18, 21); and (iii) a combination of (i) plus (ii), where both mechanisms are active at different potentials (17, 19). Mechanism (ii) requires a redistribution of the noble metal on the alloy surface. Various possibilities have been suggested. According to Pickering and Wagner (4), the noble metal remains as a continuous film on the alloy surface, and selective dissolution proceeds by volume diffusion of the active metal through the noble metal layer. Feller (5), on the other hand, suggested that the redistribution of the noble metal atoms takes place through surface diffusion and clustering. For low noble metal contents, this surface diffusion will lead, according to Swan (18), to tunneling. Pchel'nikov *et al.* (21) showed experimental evidence supporting the Pickering and Wagner mechanism, while Fort and Verink (17), raised doubts about such a mechanism.

As for the results of the present work, we will concentrate on the measurements below -0.51V where dealloying is found. The ring-disk measurements showed that in this range of potentials no soluble cadmium ions are formed. Otherwise, they should be

detectable on the ring electrode. This means that a mechanism of dissolution and redeposition is not operative at a macroscopic level. It could be argued that it takes place at a microscopic level, not detectable by the ring disk electrode experiments. But in that case, it would not be discernible from mechanism (ii).

As pointed out by Pchel'nikov *et al.*, a mechanism of selective dissolution by volume diffusion through a solid film is easily detectable. This mechanism should give a linear relation between the dealloying current density and I/\sqrt{t} . But, as these authors pointed out, such a relation is only found either in solid solutions with a very low content of the negative component, or in the very early stages of dealloying. Otherwise, too high stresses would be created in the dealloyed surface film, and it will therefore not remain continuous.

For the Cd-Mg alloys studied in the present work, the dealloying current density does not decay linearly with I/\sqrt{t} (11), but almost remains constant with time. A criterion, similar to that introduced by Pilling and Bedworth (22) for oxidation of metals, can be applied to the surface dealloyed film. According to this criterion, a corrosion product film will be continuous and protective only when it has at least the same volume as the metal consumed. If the relative volume of the product film is lower, the film will not be protective. For the case of Cd-Mg alloys, the Pilling and Bedworth relation would be

$$\frac{W \cdot d}{w \cdot D} = K$$

where w is the weight of the alloy containing one atom gram of cadmium, W is the atomic weight of cadmium, D the film density, and d the alloy density. The film, as shown in Part I, is pure cadmium. The values of alloy density were taken from (23). According to Pilling and Bedworth, K values lower than one will give nonprotective films. The calculated values were: Cd-15 Mg, $K = 0.86$; Cd-10 Mg, $K = 0.91$; and Cd-5 Mg, $K = 0.95$. If allowance is made for some redistribution of stresses in the film, for values close to one, it is concluded that no continuous film should be expected for alloys with magnesium contents above 10 a/o.

From the results of the present work, it is concluded that Cd-Mg alloys show selective dissolution, most probably by a volume diffusion mechanism. Due to differences in the relative volume between the alloy and the corrosion product, the cadmium film formed on the surface becomes discontinuous and nonprotective. This film becomes protective when formed on high cadmium alloys, thus explaining the current zero found for the Cd-7.4 Mg alloy. Further studies are being made to detect the initial dealloying stages, where the linear relation with I/\sqrt{t} should be found. The morphology of the nonprotective film is also being studied.

Acknowledgments

This work was sponsored by the Programa Multinacional de Metalurgia (O.E.A.), and by the Comisión de Investigaciones Científicas, Pcia, Buenos Aires.

Manuscript submitted April 25, 1979; revised manuscript received Sept. 14, 1979.

Any discussion of this paper will appear in a Discussion Section to be published in the December 1980 JOURNAL. All discussions for the December 1980 Discussion Section should be submitted by Aug. 1, 1980.

Publication costs of this article were assisted by the Comisión de Investigaciones Científicas, Pcia, Buenos Aires.

REFERENCES

1. V. G. Levich, "Physicochemical Hydrodynamics," pp. 60, 328, Prentice-Hall, Inc., Englewood Cliffs, N.J. (1962).
2. W. J. Albery, *Trans. Faraday Soc.*, **62**, 1915 (1966).

3. W. J. Albery and S. Bruckenstein, *ibid.*, **62**, 1920 (1966).
4. H. W. Pickering and C. Wagner, *This Journal*, **114**, 698 (1967).
5. H. G. Feller, *Corros. Sci.*, **8**, 259 (1968).
6. B. Miller, *This Journal*, **116**, 1117 (1969).
7. A. H. Taylor, *ibid.*, **118**, 854 (1971).
8. I. K. Marshakov, V. S. Bolychev, and O. P. Potapova, *Z. Metallov*, **9**, 3 (1973).
9. H. W. Pickering and P. J. Byrne, *This Journal*, **116**, 1492 (1969).
10. H. W. Pickering and P. J. Byrne, *ibid.*, **118**, 209 (1971).
11. J. I. Gardiazabal and J. R. Galvele, *ibid.*, **126**, 255 (1979).
12. D. T. Napp, D. C. Johnson, and S. Bruckenstein, *Anal. Chem.*, **39**, 481 (1967).
13. D. Gilroy and J. E. O. Mayne, *J. Appl. Chem.*, **12**, 382 (1962).
14. J. I. Gardiazabal, Ph.D. Thesis, Universidad Nacional de La Plata, La Plata, Argentina (1977).
15. K. J. Vetter, "Electrochemical Kinetics," Academic Press, New York (1967).
16. Y. Adda and J. Philibert, "La Diffusion dans les Solides," Vol. II, p. 1156, Presses Universitaires de France, Paris (1966).
17. W. C. Fort III and E. D. Verink, 4th Int. Conf. Marine Corrosion and Fouling, pp. 179-185 (1976).
18. P. R. Swann, in "Localized Corrosion," R. W. Staehle, B. F. Brown, J. Kruger, and A. Agrawal, Editors, p. 104, N.A.C.E., Houston, Texas (1974).
19. R. H. Heidersbach and E. D. Verink, *Corrosion*, **28**, 397 (1972).
20. H. Sugawara and H. Ebiko, *Corros. Sci.*, **7**, 513 (1967).
21. A. P. Pchel'nikov, L. I. Krasinskaya, A. D. Sitnikov, and V. V. Losev, *Elektrokhimiya*, **11**, 37 (1975).
22. N. B. Pilling and R. E. Bedworth, *J. Inst. Met.*, **29**, 529 (1923).
23. N. Ridley, *J. Inst. Met.*, **93**, 46 (1964-65).

Contamination of Electronic Equipment after an Extended Urban Exposure

G. B. Munier, L. A. Psota, B. T. Reagor,* B. Russiello, and J. D. Sinclair*

Bell Laboratories, Holmdel, New Jersey 07733

ABSTRACT

Water soluble contaminants on electromechanical telephone switching equipment exposed for up to 40 years to the New York City environment have been chemically analyzed by a combination of methods, and their moisture pickup characteristics have been monitored by instrumental gravimetric techniques. Samples were collected from structural surfaces by extraction with filter paper squares moistened with distilled water. Elements with atomic numbers greater than 11 were identified by energy dispersive x-ray analysis. Selected anions were identified by microchemical tests and infrared spectroscopy. Nitrate and sulfate concentrations of 46 samples from one location were measured using nitrate and lead ion selective electrodes (the latter for titration of sulfate). Several hundred samples from this and four other locations were analyzed using a chloride ion selective electrode. On zinc surfaces, chloride concentrations averaged 27 $\mu\text{g}/\text{cm}^2$ for typical locations, while sulfate and nitrate concentrations averaged 48 and 6 $\mu\text{g}/\text{cm}^2$, respectively. On aluminum surfaces, chloride concentrations averaged <2 $\mu\text{g}/\text{cm}^2$, while sulfate and nitrate concentrations averaged 25 and 3 $\mu\text{g}/\text{cm}^2$, respectively. Moisture pickup by contaminants on zinc and aluminum surfaces was found to occur above 26 and 46% RH, respectively.

The cumulative contamination of electronic devices and equipment during long term exposure to urban atmospheres is a continuing concern for the electronics industry. In some cases, the contamination consists of dusts that have collected on surfaces and that may have reacted chemically with the surfaces. In other situations, the contamination consists of the products of attack by pollutant gases, such as SO_2 , NO_x , H_2S , mercaptans, organic sulfides and disulfides, ozone, and chlorine-containing species. Gases generated by the equipment itself can also contaminate and produce corrosion. These gases may be volatile components of plastics or other insulating or packaging materials that evolve after equipment installation for periods ranging from a few hours to many years, or they may be volatile degradation products from oxidation or from photochemical processes. Generally a combination of dusts and complex films containing oxides, sulfides, sulfates, oxyanions of nitrogen, chlorides, oxyanions of chloride, and other substances is found. Passive oxide films are usually not appropriately classified as contaminants.

The composition of the dusts will be determined by contributions from outdoor aerosols and aerosols

generated within the equipment room by human activity, equipment operation (wear products), and deterioration of equipment and building surfaces due to a variety of aging processes, including oxidation and thermal or photochemical degradation. The composition of the outdoor component will be modulated by the air handling and filtration system for the equipment room. Modern high efficiency filters (85% NBS dust spot rating) remove most particles with diameters greater than 1 μm (1), in which case the contribution from the typical outdoor component in the New York metropolitan area will be primarily anthropogenic in origin (except along the seacoast) and rich in ammonium and sulfate ions (2-4). At seacoast locations, the submicron aerosols can have sodium and chloride ion concentrations (3, 4) that approach those of the ammonium and sulfate ions. Many buildings, however, are equipped with air filtration systems of much lower efficiency, in which case dusts of mineralogical origin will become prevalent. Equipment that has been in operation for 40 years has generally experienced exposures to unfiltered air during its first 10-20 years of operation. Most of the equipment studied in this work falls in this category. Even in recent years the equipment has generally not had the benefits of air purified by high efficiency filters. Thus, particles in the one to

* Electrochemical Society Active Member.

Key words: condensation, contamination, pollution, water.

ten micron range will be common, and a high percentage of these will have originated naturally from local crustal materials.

Internally generated dust will have a high carbon content from human activity. Weschler (5) has found that the dust generated in the Bell Laboratories facility at Holmdel, New Jersey, which is equipped with high efficiency filters, contains 40% carbon by weight. There may also be incidents of high sodium chloride influx when winter salting activity is prevalent (2). Particles generated by the equipment will often include phenolic plastics, ABS, calcium carbonate (which is used as a filler in many types of insulation and plastics), glass fibers (from reinforced plastics and insulation), and textile materials (from wire insulation, carpeting, etc.).

The water soluble components of contamination are of particular concern to the electronics industry because they may form electrolyte solutions in the presence of moisture, as occurred in Los Angeles when airborne nitrates, which tend to be hygroscopic at relative humidity (RH) levels above 50%, caused electrolytic stress corrosion cracking of nickel brass (6). Similarly, the corrosion rates of exposed substrate material in gold-plated connector contacts in the presence of various pollutants have been related to RH (7-10). In other situations, degradation may be caused by electrical leakage through the electrolyte (11-15). The leakage itself may be the cause of circuit failure, or coincidental corrosion of the circuit member serving as the anode in a leakage pathway may disrupt current flow. Metallic dendrite growth will often occur in this situation.

Electrical leakage is enhanced at high relative humidity, particularly if a hygroscopic contaminant is present. Vernon (16) first called attention to the importance of the concept of critical relative humidity (CRH) in assessing the corrosion hazards associated with contamination. In many cases a CRH can be identified, either through knowledge of the composition of the contaminant or through experimental measurement, as with instrumental gravimetric methods (17). Exposure of contaminated devices to an environment in which the CRH of the contaminant is exceeded may lead to moisture acquisition, followed by electrical leakage, disruption of current flow, and eventual device failure.

Convenient procedures for analyzing water-soluble contaminants and measuring their moisture pickup characteristics are valuable in assessing the causes of equipment failure and in determining procedures for dealing with the failure mechanism. For large equipment installations, correlations between contaminant distributions and equipment problems can often be found. In some cases it is possible to specify humidity ranges or improved air filtration equipment that can be expected to alleviate the problem. In other cases device modification may be necessary.

This paper presents the methods that were used to analyze problems occurring in electromechanical switching equipment that has been exposed for up to 40 years to the New York City (Manhattan) environment at five locations. Contamination data for equipment in one location (hereafter designated as Location I), which developed switching problems during and after a high humidity event, are discussed in some detail.

The most difficult aspect of analyzing equipment surfaces is the selection of a sampling procedure, because the equipment must usually be sampled while it is operating. Since the water-soluble contaminants are of principle concern, surfaces must be water extracted in a way that will permit complete removal of the soluble species from a fixed surface area, without allowing moisture to come in contact with active equipment components. Structural or otherwise inactive surfaces that can be expected to provide the

necessary chemical information to appraise contaminant effects on active surfaces must therefore be selected. In this study, structural surfaces that were zinc plated and surfaces of aluminum equipment covers were chosen. A sampling procedure suited to the requirements of this work has been investigated by Hermance *et al.* (6). In their work, nitrate salts were extracted from equipment surfaces with small sections of filter paper that had been moistened with distilled water, laid on the surfaces, and allowed to dry. The soluble components of the contamination remain in the paper after the water evaporates and can be readily transported to the laboratory for analysis. In this work, chemical identification was accomplished by x-ray techniques, standard microchemical tests, and infrared spectroscopy. For the urban environment of this study, chloride, nitrate, and sulfate were the anions of particular concern. These were determined quantitatively using ion selective electrodes (18). Clyster and Adams (19) and Ross and Frant (20) have described procedures for the analysis for sulfate. Baucke (21) has discussed chloride selective electrodes. Nitrate selective electrodes are described in a compilation of selected analytical methods by Gallay *et al.* (22). In the studies by Weschler (2, 5), chloride, nitrate, and sulfate extracted from indoor dust particles were determined by these methods.

In combination with the chemical analysis, knowledge of the CRH and the moisture pickup characteristics of the water-soluble contaminants can provide a basis for assessing the cause of equipment problems and for devising methods to deal with these problems. One of the authors has developed instrumental gravimetric procedures for determining the CRH and total moisture pickup characteristics of dusts, contaminants, and corrosion products (17). These methods have been applied to several types of samples from Location I.

Experimental

Surface extractions were accomplished with square sections (one-half in. on a side) of Whatman 3MM filter paper. The papers were moistened with triply distilled water (18 m Ω resistivity) that had been equilibrated with atmospheric carbon dioxide. The papers were briefly drained to eliminate excess water that otherwise would significantly increase the effective area of the sampled surface. The volume of water in each paper was determined to be approximately 0.06 ml. The papers were placed on flat surfaces in either a horizontal or vertical plane and were removed from the surfaces after drying. The sampling interval was approximately 30 min but was somewhat dependent on the relative humidity. The procedure was carried out three times on each sampled area to insure complete removal of water-soluble contaminants.

The sample papers were then stored in separate containers and transported to the laboratory. Ten ml portions of distilled water were used to extract the contaminants from the papers in the laboratory. In most cases, the three papers from each sampled area were extracted together, but in a few cases each paper was extracted separately. The samples were divided into several groups for several types of quantitative and qualitative analysis. The residue remaining after evaporation of several of the extracts was analyzed by SEM/x-ray techniques using an AMR-1000 scanning electron microscope in conjunction with a Princeton Gamma Tech Si(Li) energy dispersive x-ray analyzer and a Tracor Northern NS-880 multichannel analyzer. The technique is capable of identifying elements having atomic numbers greater than 11. Samples were analyzed for multielement anions by standard microchemical tests (nitrate and chlorate by the nitron test, sulfate by barium chloride precipitation, carbonate and bicarbonate by hydrochloric acid in glycerine) and by infrared spectroscopy (on silver chloride crystals). Quantitative analyses for chloride, nitrate, and sulfate

were carried out with Orion ion selective electrodes. A 90-02 double junction electrode, using the Orion proprietary solution for the inner chamber and 10% KNO_3 in the outer chamber, was employed as the reference electrode (except the outer solution for nitrate analysis was 0.1M KF). The 10 ml extract from the papers was directly analyzed for chloride with a 90-17 solid-state chloride electrode. The extract was then split into two 5 ml portions. Nitrate analysis was accomplished on one portion with a 90-07 nitrate electrode after a 5 ml portion of 0.2M KF solution was mixed with it to provide a constant ionic strength. Phenylmercuric acetate was included as a preservative. Sulfate analysis was carried out on the other 5 ml portion by titration with 0.001M $\text{Pb}(\text{ClO}_4)_2$ after adding 5 ml of methanol. A 94-82 solid-state lead specific electrode was used to monitor the end point.

Paper blanks were analyzed for chloride, nitrate, and sulfate. The average quantities of these anions per paper were 2, 4, and 2 μg , respectively. The hydrogen ion concentrations of the distilled water extracts from blank paper squares and from moistened squares that had been placed in contact with equipment surfaces for brief periods were measured with Tridicator pH paper.

Moisture pickup characteristics of the residues of some of the paper extracts from aluminum and zinc plated surfaces and of a green corrosion product contaminating electrical contact surfaces (collected by brushing) were measured by gravimetric methods using a du Pont 951 Thermogravimetric Analyzer coupled to a 990 Thermal Analyzer. Samples were equilibrated for several days or weeks with the laboratory atmosphere (RH approximately $40 \pm 10\%$) before they were analyzed in the microbalance.

Continuous pickup rates for the various materials were determined by passing a stream of air (maintained at approximately 23°C), which had been humidified by bubbling it through distilled water maintained at 23°C , through the microbalance sample tube (2.5 cm diam by 12 cm long). The relative humidity of the airstream was close to 100%. Weight was recorded graphically as a function of time, and each run was allowed to proceed until the rate of weight gain approached zero or reached an extended steady state.

CRH measurements were made using the same balance with a modified airstream apparatus. A minimum RH in the balance housing (maintained at 23°C) of 22% was achieved by passing a stream of dry air through a dispersion frit submerged in distilled water cooled to 0°C . The water was warmed from 0°C to nearly 23°C at a rate of $0.25^\circ\text{C}/\text{min}$, thereby increasing the RH from 22 to nearly 100%. A recording of weight *vs.* time was translated to weight *vs.* RH. The relative humidity at which an onset in weight gain occurred was taken to be the CRH. Further details on these methods for measuring moisture pickup characteristics are given elsewhere (17).

Results and Discussion

Microchemical tests on several dust samples from Location I and on residues remaining after extraction of several papers with distilled water established the presence of significant amounts of nitrate ion and sulfate ion. Carbonate was detected in the dust samples but not in the extract residues. Chlorate ion was not detected. Other multielement anions such as sulfite and nitrite were presumed to be present only at very low levels, which would not contribute significantly to equipment problems. Infrared spectroscopy confirmed the presence of nitrate and sulfate. SEM/x-ray analysis of the extracts from zinc surfaces established the presence of large amounts of sulfur, chlorine, calcium, and zinc, a small amount of potassium, and traces of iron. Similar analyses of the extracts from aluminum surfaces showed that sulfur and calcium were present in large amounts, chlorine and potassium in small amounts, and iron, copper, and zinc in trace amounts.

SEM/x-ray analysis of the residue remaining after extraction of several papers with distilled water and evaporation of the resulting solution to dryness indicated that the paper contained low but significant levels of sulfur, chlorine, calcium, potassium, copper, and iron.

The approximate pH of the solution associated with the filter paper squares during sampling was determined with pH paper. The pH paper was placed over moist filter paper squares that had been laid on the appropriate surfaces. Distilled water that had been equilibrated with the atmosphere (pH approximately 5.7) was used for all procedures. The approximate pH's observed for zinc and aluminum surfaces were 6.0-6.5 and 5.0-5.5, respectively. These pH's are a result of the combined effects of the atmosphere equilibrated distilled water and the sampled surface. Separate measurements with pH paper in the absence of filter paper squares indicated the filter paper had no detectable effect on the pH. The somewhat less acidic pH of the zinc surface is consistent with the solubility products of the hydroxides of zinc and aluminum, which are 10^{-16} and 2×10^{-32} , respectively, and with our experimental observation that solutions created by exposing distilled water (with dissolved carbon dioxide eliminated) to excess zinc oxide are somewhat alkaline. The oxide film on zinc surfaces is a weak buffer, which will tend to drive the surface solution towards the alkaline pH range, whereas the oxide film on aluminum surfaces will have a negligible effect compared to the atmospheric influence of carbon dioxide with moisture on the surface.

Based on the chemical analyses, the extracted species of greatest concern in terms of potential for equipment degradation were the anions chloride, nitrate, and sulfate. Since these appeared to be the major anions present, it was felt the quantitative measurements of surface concentrations of these species could be used to estimate cation concentrations from charge and mass balance requirements. Proportions for the cations present could be approximated from qualitative results determined in this work, coupled with data on New York City air quality that were available in the literature (2-6, 23, 24) and from the Environmental Protection Agency (25).

Forty-six samples (each consisting of three papers) from Location I were selected for chloride, nitrate, and sulfate analysis from the more than 75 samples that were collected. Several hundred samples from four other locations in Manhattan (hereafter designated Locations II-V) were analyzed for chloride. Experimentation indicated that extraction of water-soluble contaminants was generally 80-90% complete after two extractions. On this basis, three samplings of each area were considered to provide complete extraction of the surface.

Table I summarizes the types of surfaces extracted, the year of their manufacture (vintage), and the measured chloride, sulfate, and nitrate concentration levels for the 46 samples from Location I. For samples 1 to 5, the three papers used to extract the surface were stored and measured separately to verify that nearly complete extraction of the surface was achieved with three papers. For all other samples, the three papers were combined for storage and measurement. In the cases of nitrate and chloride, this procedure reaffirmed that three papers provide essentially complete surface extraction, but in the case of sulfate another problem was found. The usual procedure for end-point determination when titrating with $\text{Pb}(\text{ClO}_4)_2$ is to plot electrode potential *vs.* quantity of titrant added, the end point being taken as the point of greatest inflection. Ross and Frant (20), using dioxane rather than methanol to sharpen end points (through decreased PbSO_4 solubility), found the minimum titratable sulfate concentration for standard solutions was about 10^{-6}M . However, the time required to reach equilibrium after each

Table I. Concentrations of surface contaminants at Location I

Sample No.	Surface metal	Year of manufacture of sampled surface	Chloride concentration ($\mu\text{g}/\text{cm}^2$)	Sulfate concentration ($\mu\text{g}/\text{cm}^2$)	Nitrate concentration ($\mu\text{g}/\text{cm}^2$)
1	Zn	47	39	127 (65) *	<31
2	Zn	47	28	136 (56)	<31
3	Zn	47	27	102 (38)	<31
4	Zn	47	22	94 (47)	<31
5	Zn	47	49	131 (64)	<31
6	Zn	47	34		<31
7	Zn	47	29		<31
8	Zn	47	41	41	<31
9	Zn	47	22		<31
10	Zn	64	7	33	<31
11	Zn	64	6	40	<31
12	Zn	64	8	39	<31
13	Zn	64	6	34	<31
14	Zn	47	42	60	<31
15	Zn	47	30	58	<31
16	Zn	47	27	28	<31
17	Zn	47	21	46	<31
18	Zn	47	35	58	<31
19	Zn	47	21	57	<31
20	Zn	47	52	50	15
21	Zn	47	37	63	18
22	Al	47	4	27	5
23	Al	56	<2	26	2
24	Al	56	7	39	7
25	Al	57	<2	28	3
26	Zn	47	45	64	8
27	Zn	47	42	50	8
28	Al	47	<2	29	2
29	Al	47	<2	29	2
30	Al	56	<2	26	0
31	Al	56	<2	15	8
32	Zn	47	41	51	6
33	Zn	47	58	99	15
34	Al	56	<2	16	0
35	Al	56	<2	14	0
36	Zn	57	5	27	2
37	Zn	57	11	40	4
38	Zn	57	10	39	0
39	Zn	57	14	27	4
40	Zn	56	5	39	0
41	Zn	56	10	52	1
42	Zn	56	12	27	0
43	Zn	56	10	51	4
44	Zn	47	48	51	7
45	Zn	47	27	39	4
46	Zn	47	45	51	8

* Values in parentheses are the concentrations extracted by the first paper.

addition of titrant was considered impractically long for sulfate concentrations less than $5 \times 10^{-5}M$. Their data on the effect of interferences indicate that NaCl, which is a significant contaminant in the samples studied in this work, can obscure the end point. For the range of concentrations found in this study ($7 \pm 4 \times 10^{-5}M$), the point of greatest inflection was not always readily apparent or, in some cases, was ambiguous. Experimentation with standard solutions indicated that if the end point was selected to be -200 mV, satisfactory agreement between known and measured concentrations was obtained. An error of 25-50% for the lowest concentrations of sulfate was considered acceptable for this work. The total sulfate levels from the three papers for samples 1-5 were, however, very high relative to other 1947 vintage surfaces. In the case of chloride, the concentrations of samples 1-5 were not extraordinary. This suggests that an interfering effect, caused by a species other than sulfate (possibly sodium chloride), increased the apparent concentrations to unrealistically high levels. The effect appeared to have a similar magnitude for each titration, whether the three papers were run simultaneously or separately. The sulfate concentrations indicated for samples 6-46 thus include this effect only one time, while samples 1-5 include it three times, once for each paper. A correction factor for the effect was not readily derivable, and thus it was decided that the sulfate concentrations for samples 1-5 should be based on the extract from the first paper only. These values are given in parentheses in Table I. Concentrations for samples 6-46 are high by perhaps 7-15 $\mu\text{g}/\text{cm}^2$. Concentrations for samples 1-5 may or may not be high, but they are certainly lower than they would have

been had all three papers been analyzed simultaneously.

Nitrate concentrations were found to be very low, approaching the sensitivity limit of the method. Samples 1-19 were analyzed and found to have concentrations below the region of linearity in the potential-concentration electrode calibration plots from which concentrations were determined. It was originally anticipated that most of the samples would have concentrations in the linear regime, but it was apparent after completing these 19 analyses that this would probably not be the case. For the remaining samples, concentrations were determined by extrapolation into the nonlinear regime. The data were treated very conservatively, based on results for standard solutions, so the concentrations listed are lower limits for nitrate. Unfortunately, only an upper limit can be set for samples 1-19 because the solutions were discarded before the extrapolation procedure was initiated. In retrospect, it appears that in situations in which nitrate surface concentrations are likely to be less than 30 $\mu\text{g}/\text{cm}^2$, the spectroscopic procedure with chromotropic acid described by West (26) would be a preferable method of analysis. The nitrate selective electrode is somewhat more convenient and faster but is at least one order of magnitude less sensitive and tends to drift.

Average concentrations of chloride, sulfate, and nitrate on 1947 vintage equipment are shown in Table II, along with average contamination rates for the 30 year exposure period. Indiscriminate application of these contamination rates to locations outside the New York City area is not advised, but for environments comparable to that of New York City, the contamination rates are probably reasonable guides for locations that have not, except for perhaps a brief period, been equipped with high efficiency air filtration systems. It also should be kept in mind that the implicit assumption that contamination rates are constant is probably not strictly valid. Some surfaces will tend to passivate as corrosion processes occur or dust layers collect, while others will be activated. Fine dust particles (less than 1 μm diam) tend to be mobile and may serve as a continuing source of a contaminant until the accumulation of less mobile particles restricts their interaction with the surface. Furthermore, pollution levels have varied substantially over the past 30 years. Evidence of these complicating factors is provided in Table III, which shows chloride and sulfate contamination rates on zinc surfaces for 1947, 1956-1957, and 1964

Table II. Contamination data for 1947 vintage equipment at Location I

	Chloride	Sulfate	Nitrate
Zinc surfaces:			
Concentration ($\mu\text{g}/\text{cm}^2$)	36	54	10
Contamination rate ($\mu\text{g}/\text{cm}^2$ yr)	1.2	1.8	0.33
Aluminum surfaces:			
Concentration ($\mu\text{g}/\text{cm}^2$)	<2*	28	3
Contamination rate ($\mu\text{g}/\text{cm}^2$ yr)	<0.07	0.93	0.1

* This number is based on all values $<2 \mu\text{g}/\text{cm}^2$ being 0; if all values less than 2 are assumed to be 1, the average is 2.

Table III. Contamination rates on zinc surfaces of various equipment vintages from the vintage year through 1977

	($\mu\text{g}/\text{cm}^2$ yr)		
	1947	1956-1957	1967
Sulfate	1.8	1.9	2.8
Chloride	1.2	0.5	0.5

vintage equipment based on concentration averages for each vintage group. Only four samples were available for the calculation of 1964 rates, and thus the averages are very approximate. The results suggest, however, that sulfate contamination rates have increased over the past 30 years, while chloride contamination rates have decreased. Keeping these complicating factors in mind, the contamination rates provide estimations of contaminant concentrations.

Concentrations of chloride, sulfate, and nitrate in airborne particulates taken from the data of Hermance (6), The National Air Sampling Network (NASN) (24), The National Air Surveillance Network Summary (NASNS) (25), Patterson and Wagman (P + W) (3), and Leaderer (4) are compared in Table IV with the average concentrations found on the zinc and aluminum surfaces (computed for all samples neglecting vintage effects). The similarities are striking. Except for comparisons involving chloride on zinc surfaces, the relative proportions of these anionic species are roughly the same in the airborne particulates and on the surfaces tested. The scavenging ability of zinc for chlorine-containing species obviously plays a dramatic role in the contamination of zinc surfaces. The data also suggest that the surface texture and moisture content of surfaces may be important factors affecting the collection and retention of dust particles. The higher sulfate and nitrate concentrations on zinc as compared to aluminum surfaces are consistent with the unpolished nature and higher surface area of the zinc surfaces relative to those of aluminum and with the lower CRH associated with the zinc surfaces (to be discussed later). The differences are probably not related to surface configuration, because approximately the same number of horizontal and vertical surfaces were sampled for both zinc and aluminum, and the concentrations on horizontal and vertical surfaces of the same metal were quite similar.

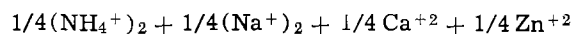
In order to determine if the total anion concentration can be accounted for by the combination of the average chloride, nitrate, and sulfate concentrations found on the surfaces, it is necessary to select an approximate composition for the associated cations and to obtain an average extract weight per sample. The latter was accomplished with another set of samples, also from Location I, with very similar vintage distributions. Contamination levels for this group of samples were assumed to be similar to the levels of the group used for chloride, nitrate, and sulfate determinations. Twenty-six paper extract samples that had been collected from zinc surfaces were combined and extracted with 10 ml of distilled water. The extract was filtered and then evaporated to dryness and weighed. An identical procedure was followed for 12 samples from aluminum surfaces. From these weighings, it was determined that the average weight of material extracted from a single sampling location on zinc surfaces (after subtracting an experimentally determined value of 21 $\mu\text{g}/\text{cm}^2$ for the solids extracted from three paper

blanks) was 117 $\mu\text{g}/\text{cm}^2$, while the average for aluminum surfaces was 61 $\mu\text{g}/\text{cm}^2$.

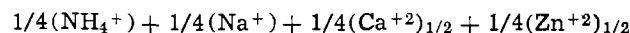
SEM/x-ray analysis was also carried out on these extracts and makes possible, in conjunction with information available in the literature and reasonable assumptions about likely surface chemistry, an estimate of the predominant cations associated with chloride, nitrate, and sulfate on zinc surfaces and on aluminum surfaces.

The SEM/x-ray results on extracts from zinc surfaces established the presence of large amounts of sulfur and chlorine, consistent with the presence of sulfate and chloride, in addition to large amounts of calcium and zinc. Potassium and iron were identified as minor components. As discussed above, zinc is an excellent scavenger for chlorine-containing species and thus chlorine was presumed to be present exclusively as zinc chloride. While some of the chlorine may have originated from the marine influence on this seacoast location and thus would have sodium associated with it, the very low chloride levels found on aluminum surfaces suggest the sea salt influence is small. (It should be noted that the lack of appreciable chloride on aluminum surfaces in spite of the seacoast influence may be due in part to the submicron size of sea salt aerosol. Such particles will tend to be mobile and could serve as a continuing source of chloride on reactive zinc surfaces but would have little effect on less reactive aluminum surfaces. This potential effect was assumed to be unimportant in this work, but further study is needed on this point, particularly on the reaction mechanism and the fate of the sodium. Sulfate is a major water soluble component of the outdoor aerosols at this urban location, as are ammonium, calcium, and sodium ions.) Morrow and Brief (23), using emission spectrography, found ambient concentrations of calcium and sodium in the New York metropolitan area in 1969-1970 of 1.17 and 1.08 $\mu\text{g}/\text{m}^3$, respectively. Hermance *et al.* (6) reported ambient concentrations for ammonium, calcium, and sodium ions of 4.9, 1.9, and 2.7 $\mu\text{g}/\text{m}^3$ for samples collected in New York City in 1959. Patterson and Wagman (3) found ammonium ion concentrations ranging from 1.8 to 11.4 $\mu\text{g}/\text{m}^3$, while the survey compiled by Leaderer *et al.* (4) reports a range of <0.11-11.5 $\mu\text{g}/\text{m}^3$. The National Air Surveillance Network Summary for 1971 through 1974 (25) reported an average ambient concentration of 0.9 $\mu\text{g}/\text{m}^3$ for ammonium ion.

While the available data show a range of concentrations for the various cations, as a rough approximation it seems reasonable to describe the "composite" cation associated with sulfate on zinc surfaces as



Zinc is included because it is the surface metal, and it was found in high concentration in the surface extract. The proportions of some of the cations may be in error, but examination of the cation formula weights that would react with one formula weight of SO_4^{-2} indicates that substantial deviations will not have a major effect on the composite cation formula weight. If the cation formula weights, which are 36.0, 46.0, 40.0, and 65.4, respectively, are each weighted by 1/4, as above, the composite equivalent weight is 46.8. If, instead, the proportions of the cations were 2/6, 1/4, 1/4, and 1/6, respectively, the composite cation equivalent weight would be 44.4. Using similar reasoning for the cations associated with nitrate on zinc surfaces, the composite cation can be approximated as



Average Cl^- , NO_3^- , and SO_4^{-2} concentrations were used for comparing the experimental weight measurements with the weights calculated from the concentrations of anions and cations, since the vintage distributions of the two sample sets were comparable. Using the surface concentrations of Cl^- , NO_3^- , and

Table IV. Concentration comparisons

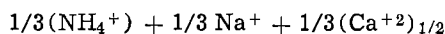
Airborne particulate:	Chloride	Sulfate	Nitrate
Hermance (1959)	2.5 ($\mu\text{g}/\text{m}^3$)	18.3 ($\mu\text{g}/\text{m}^3$)	2.6 ($\mu\text{g}/\text{m}^3$)
NASN (1958)		22.8	2.4
NASN (1963-1964)		32.2	2.5
NASNS (1971-1974)		15.9	0.9
P + W (1970)	0.3-1.9	2-21	0.8-9.7
Leaderer (1976)	0.1-0.5	2-41	0-4
Water extractable contaminants:			
Zinc surfaces	27 ($\mu\text{g}/\text{cm}^2$)	48 ($\mu\text{g}/\text{cm}^2$)	6 ($\mu\text{g}/\text{cm}^2$)
Aluminum surfaces	<2*	25	3

* This number is based on all values <2 $\mu\text{g}/\text{cm}^2$ being 0; if all values less than 2 are assumed to be 1, the average is 2.

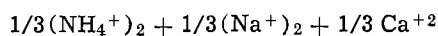
SO₄⁻² given in Table IV, the average extract from zinc surfaces was calculated to weigh 128 μg/cm², which is judged not to be significantly different from the 117 μg/cm² value measured experimentally for a different set of samples collected from the same location. Alternatively, if the extreme case is considered in which no mixing of cations and anions occurs on the surface, it is reasonable to associate Zn⁺² exclusively with Cl⁻, NH₄⁺ with SO₄⁻², and Na⁺ with NO₃⁻. If the role of Ca⁺² is ignored, the average extract from zinc surfaces is calculated to weigh 126 μg/cm². The fact that a consistent number is obtained even if Ca⁺² is ignored is important because of solubility limitations for Ca⁺² in the presence of SO₄⁻². Based on the solubility product of CaSO₄ (1.2 × 10⁻⁶), Ca⁺² cannot be a 25% contributor to the composite cation except for the lower range of SO₄⁻² concentrations.

The reasonably close agreement between measured extract weights and those calculated from a range of models is evidence that the water-extractable matter can be accounted for as chloride, sulfate, and nitrate salts. Perhaps more importantly, the fact that close agreement is attained, almost regardless of how the cations are apportioned or distributed, serves to emphasize that quantifying the anions will usually provide sufficient information to quantify total contamination levels for water soluble species.

The SEM/x-ray analyses of extracts from aluminum surfaces indicated that the major element present having atomic numbers greater than 11 were sulfur and calcium. The presence of sulfur is consistent with the sulfate analysis. The aluminum oxide surface on aluminum metal is relatively nonreactive and tends to protect the underlying metal from chemical attack. On the basis of the SEM/x-ray data, the literature data cited above on the ambient aerosol composition in New York City, and the nonreactive nature of aluminum surfaces, the composite cation associated with Cl⁻ and NO₃⁻ as presumed to be



while the composite cation for SO₄⁻² was approximated as



On this basis, the weight of extract contributed by all the salts is calculated to be 42 μg/cm². The total extract weight of 61 μg/cm² measured experimentally indicates that most of the extractable material can be accounted for as chloride, sulfate, and nitrate salts. It is not certain whether the 30% difference in these numbers represents unaccounted for species, inappropriate assumptions in the calculations, experimental error, or a combination of these, although, in view of some of the experimental difficulties and the fairly crude nature of the approximations, the first seems unlikely. Other inorganic anions would very likely

have been detected if they and their associated cations were present in sufficient quantity to account for 30% of the total weight.

Several other locations in the same urban environment as Location I, which have equipment with similar vintage distributions, were sampled and analyzed for chloride ion concentrations on surfaces. The results for zinc surfaces, based on the average concentrations, are as follows: Location II — 34 μg/cm²; Location III — 23 μg/cm²; Location IV — 27 μg/cm²; and Location V — 24 μg/cm². The value for Location I (27 μg/cm²) is identical to the average from the other locations (27 μg/cm²), indicating that the chloride contamination in Location I is typical for this urban environment.

Knowledge of the composition of a surface contaminant is important not only for understanding and predicting the reaction chemistry of a surface but also for evaluating the tendency of the contaminated surface to pick up moisture. A number of compilations of the CRH of common salts exist, the most extensive of which is a listing of 140 pure substances by Balarev *et al.* (27). Contaminants that are rich in a salt with a low CRH will have moisture pickup characteristics that are dominated by the influence of the salt. In many cases, however, a complex mixture of cations and anions exists, and it is not possible to predict with certainty which, if any, of the possible salts will dominate. Furthermore, a mixture often will not exhibit the reversible behavior typical of a pure salt. In any event, even if the CRH can be estimated, the rate of moisture pickup will be unknown. To deal with complex mixtures it is necessary to measure the CRH and moisture pickup rates experimentally. Instrumental gravimetric techniques (17) have been used for these measurements in this work.

The moisture pickup characteristics of a green corrosion product that contaminated the springs and contacts of switching equipment and of the residues from the moistened paper extracts from zinc surfaces and aluminum surfaces at Location I are summarized in Table V, along with similar data for some pertinent pure salts. A detailed explanation of the parameters used to characterize hygroscopicity and an expanded listing containing 41 different substances and materials appear elsewhere (17).

The CRH was determined experimentally, except where indicated in Table V. Measurements were made by passing an air stream over the sample at a sufficiently rapid flow rate (1500 ml/min) to cause rapid weight gain as the RH in the flow chamber was raised above the CRH of the sample. In a separate experiment, the sample was exposed to a water-saturated atmosphere flowing at a rate of 10 ml/min over the sample. Weight gain was monitored as a function of time from which the moisture pickup rate parameters indicated in columns 3-5 in the table could be calculated. The

Table V. Moisture pickup characteristics of various samples

Sample	Critical RH (%)	Initial rate of moisture pickup at 100% RH (%/min)	Rate of moisture pickup at termination at 100% (%/min)	Average weight gain rate at 100% RH (%/min)	Total weight gain (%)	Sample weight (mg)
Green corrosion product	80					
Nickel sulfate	91†			0.001	0.144	
Extract from zinc surfaces	26	0.49	0.048	0.060	153	5.1
Zinc chloride	<10	0.28	0.19	0.256	8.7	34
Extract from aluminum surfaces	46 (35)	0.79	0.02	0.075	84	1.9
Calcium sulfate		0.17	0.07	0.123	4.9	107
Calcium chloride	31↓	0.34	0.34	0.338	8.1	53
Sodium chloride	76↓	0.03	0.04	0.035	3.8	87
Dust (Location I)	27	0.10	0.01	0.012	36.0	20

* A minor component was responsible for a slight moisture pickup at this RH.

† From Ref. (26).

↓ "Handbook of Chemistry and Physics," 56th ed. (1975).

experiment was continued until the moisture pickup rate stabilized at a constant value. Generally speaking, the average weight gain rate throughout the experiment is an indication of the relative hygroscopicity of the sample. In some situations it may be more important to know the rate of moisture pickup in the first few minutes of exposure to elevated RH, in which case the initial rate of moisture pickup may be a more appropriate index of relative hygroscopicity.

The major problem that the switching equipment in Location I experienced was caused by the green corrosion product, which was found on the surfaces of the noble metal contacts. From the contamination data on the zinc and aluminum surfaces, sulfate or possibly chloride salts are likely causes of the corrosion products. SEM/x-ray analysis indicated that the green substance was rich in nickel and sulfur. This result was consistent with the observation that the corrosion product was always observed in the vicinity of the nickel base on which the electrical contacts were mounted. The effective CRH of the green corrosion product was approximately 82%. The CRH of a pure sample of nickel sulfate was measured to be 91%, which is reasonably consistent with the chemical analysis. This rather high CRH indicates that the nickel sulfate corrosion product will not pose a moisture hazard in normal building environments. Consideration of the temperature-humidity conditions that existed during a series of equipment malfunctions in a high humidity period indicates, however, that the 91% RH level was exceeded at equipment surfaces. The acquired moisture resulted in the creepage of the corrosion product onto the electrical contact surfaces and also provided low resistance leakage paths that led to equipment problems. Insulating films resulted as the moisture evaporated when normal humidity levels were restored. Unfortunately, an insufficient amount of the green corrosion product was available to measure the rate of moisture pickup at 100% RH.

The water-soluble contaminants extracted from zinc surfaces exhibited a low critical RH and a moderate rate of moisture pickup at 100% RH. The moisture pickup of zinc chloride, a major contaminant on these surfaces, has also been measured and is shown in Table V. The CRH for zinc chloride is known to be <10%, though it has not been measured precisely. Unfortunately, the apparatus used for CRH measurements in this work is currently limited to RH levels above 22%. Nevertheless, the low upper limit that has been reported for the CRH and the rapid and large moisture pickup observed at high RH in this work readily account for the moderate tendency of the extract from zinc surfaces to acquire moisture.

The water extract from aluminum surfaces, which was found to be a mixture of several salts, as discussed above, is moderately hygroscopic. The measured CRH is lower than that for several of the salts that could be present and for which data are available (17, 27), including ammonium sulfate (80%), ammonium chloride (77%), sodium sulfate (approximately 90%), sodium chloride (75%), sodium nitrate (74%), and calcium sulfate (65%). Calcium chloride, which is also likely to be present, has a CRH of approximately 31% and may be the major contributing factor to the low CRH of the extract. Hydration to form the various hydrates of calcium sulfate occurs at low RH but the formation of hydrates usually does not produce a sudden surge in weight gain as the RH is increased. Data are lacking on calcium and ammonium nitrate, but the nitrate salts for which information is available generally have CRH's well above 50%.

A dust sample that was brushed from equipment surfaces at Location I was analyzed for comparison to the extracts from the zinc and aluminum equipment surfaces. The dust included fibers, hairs, and organic substances that are not water-soluble. Consequently, the average weight gain rate (0.012%/min) was sub-

stantially lower than those of the zinc and aluminum extracts (0.060 and 0.075%/min, respectively). The low CRH is attributable to adsorption processes on the dust with its large surface area rather than the salt dissolution event normally associated with CRH.

Summary and Conclusions

Water-soluble contaminants existing on zinc and aluminum switching equipment surfaces that have been exposed for up to 40 years to typical New York City indoor environments have been identified and to some extent quantified. The major water-soluble contaminants on zinc surfaces include Zn^{+2} , Ca^{+2} , Na^+ , NH_4^+ , Cl^- , and SO_4^{-2} , with somewhat lesser amounts of NO_3^- . The most prevalent water-soluble contaminants on aluminum surfaces include Ca^{+2} , Na^+ , NH_4^+ , and SO_4^{-2} , with lesser amounts of Cl^- and NO_3^- . In the case of aluminum, only roughly 70% of the total amount of extractable material could be accounted for by Cl^- , NO_3^- , and SO_4^{-2} and an approximated composite cation. The discrepancy may be caused by a combination of experimental errors and inappropriate assumptions, or it may indicate that there is another anion that is a significant component.

The anions Cl^- , NO_3^- , and SO_4^{-2} are often associated with corrosion susceptibility, which can lead to electrical leakage in many types of devices and can cause open circuits, particularly with thin film conductors. The device hazard associated with their presence is often a result of moisture acquisition. The CRH's determined in this work for the extracts from the zinc and aluminum surfaces were sufficiently low (26 and 46%, respectively) and the moisture pickup rates were sufficiently high to warrant concern about the potential for equipment degradation at the higher humidity levels (55-65%) that are encountered for indoor environments with typical air handling equipment. During the high humidity incident that occurred at Location I, the RH at equipment surfaces rose to nearly 100% for a brief period. In this situation, the CRH of nickel sulfate (91%), which is a "normal" contaminant on nickel surfaces in New York City and ordinarily does not pose a serious equipment hazard, was exceeded, leading to dissolution and redistribution of nickel sulfate at critical equipment surfaces, such as relay contacts.

This study has shown that a thorough analysis of contaminant concentrations on operating electrical equipment can be accomplished using paper sampling methods and routine analytical procedures. By combining analytical results with knowledge of the CRH, which can be readily determined by instrumental gravimetric methods or found in one of several compilations, and the moisture pickup rates, which can also be experimentally determined, useful conclusions about the environmentally induced causes of equipment malfunction and recommendations about environmental parameters that will reduce equipment degradation can be made.

Acknowledgments

The authors wish to express their appreciation to C. J. Weschler, C. A. Russell, and P. C. Milner for very helpful discussions during the course of this work.

Manuscript submitted Feb. 16, 1979; revised manuscript received Aug. 7, 1979.

Any discussion of this paper will appear in a Discussion Section to be published in the December 1980 JOURNAL. All discussions for the December 1980 Discussion Section should be submitted by Aug. 1, 1980.

Publication costs of this article were assisted by Bell Laboratories.

REFERENCES

1. E. J. Bauer, B. T. Reagor, and C. A. Russell, *ASHRAE J.*, Oct., 53 (1973).
2. (a) C. J. Weschler, Paper 225 presented at the an-

- nual meeting of the American Chemical Society, Miami, September 1978; (b) C. J. Weschler and M. V. Walker, submitted to *Environ. Sci. Technol.*
3. R. K. Patterson and J. Wagman, *J. Aerosol Sci.*, **8**, 269 (1977).
 4. B. P. Leaderer, *J. Air Pollut. Control Assoc.*, **28**, 321 (1978).
 5. C. J. Weschler, *Environ. Sci. Technol.*, **12**, 923 (1978).
 6. H. W. Hermance, C. A. Russell, E. J. Bauer, T. F. Egan, and H. V. Wadlow, *ibid.*, **5**, 781 (1971).
 7. N. R. Stalica, Paper presented at the Eleventh Annual Connector Symposium, Cherry Hill, N.J., October 25-26, 1978.
 8. F. E. Bader, S. P. Sharma, and M. Feder, Proc. at the Ninth International Conference on Electrical Contact Phenomena, Chicago, pp. 341-351, Illinois Institute of Technology, September 11-15, 1978.
 9. R. P. Frankenthal, Paper 8 presented at The Electrochemical Society Meeting, Philadelphia, Pennsylvania, May 8-13, 1977.
 10. W. H. Abbott, Paper 244 presented at the Electrochemical Society Meeting, Pittsburgh, Pennsylvania, October 15-20, 1978.
 11. R. P. Frankenthal and W. H. Becker, Paper 246 presented at The Electrochemical Society Meeting, Pittsburgh, Pennsylvania, October 15-20, 1978.
 12. D. W. Rice, P. B. P. Phipps, and R. F. Tremoureux, Paper 9 presented at The Electrochemical Society Meeting, Philadelphia, Pennsylvania, May 8-13, 1977.
 13. W. B. Wargotz, Paper 11 presented at The Electrochemical Society Meeting, Philadelphia, Pennsylvania, May 8-13, 1977.
 14. I. Trachtenberg, Paper 14 presented at the Electrochemical Society Meeting, Philadelphia, Pennsylvania, May 8-13, 1977.
 15. R. P. Kozakiewicz and N. L. Sbar, Paper 44 presented at The Electrochemical Society Meeting, Philadelphia, Pennsylvania, May 8-13, 1977.
 16. W. H. J. Vernon, *Trans. Faraday Soc.*, **27**, 255 (1931).
 17. J. D. Sinclair, *This Journal*, **125**, 734 (1978).
 18. R. P. Buck, *Anal. Chem.*, **50**, 17R (1978).
 19. H. Clyster and F. Adams, *Anal. Chim. Acta*, **92**, 251 (1977).
 20. J. W. Ross and M. S. Frant, *Anal. Chem.*, **41**, 967 (1969).
 21. F. G. K. Baucke, *J. Electroanal. Chem. Interfacial Electrochem.*, **67**, 277, 291 (1976).
 22. W. Gallay, H. Egan, J. L. Monkman, R. Truhaut, P. W. West, and G. Widmark, "Environmental Pollutants Selected Analytical Methods (Scope 6)," pp. 236, 248, Ann Arbor Science Publishers Inc., Ann Arbor, Michigan.
 23. N. L. Morrow and R. S. Brief, *Environ. Sci. Technol.*, **5**, 786 (1971).
 24. U. S. Department of Health, Education and Welfare, Robert A. Taft Sanitary Engineering Center, "Air Quality Data from the National Air Sampling Network, 1957-61," Cincinnati, Ohio, 1962; "Air Quality Data from the National Air Sampling Network, 1964-65," Cincinnati, Ohio, 1966.
 25. EPA-600/4-77-003, January, 1977.
 26. P. W. West and G. E. Lyles, *Anal. Chim. Acta*, **23**, 227 (1960); P. W. West and P. L. Sarma, *Mikrochim. Acta*, **4**, 506 (1957).
 27. Kh. Balarev, Kh. Stoeva, and Kh. Stoev, *God. Viss. Khim-Tekhnol. Inst., Burgas, Bulg.*, **10**, 623 (1973).

The Anodic Rhodium Oxide Film: A Two-Color Electrochromic System

S. Gottesfeld*¹

Bell Laboratories, Murray Hill, New Jersey 07974

ABSTRACT

The oxide film grown on a rhodium metal substrate in alkaline solutions by potential multipulsing behaves as a fast two-color electrochromic system. Reversible yellow \rightleftharpoons dark green or yellow \rightleftharpoons brown-purple coloration changes are obtained in either 1M or 5M KOH solutions. The films suffer very small charge losses after 10^5 cycles in either 1M or 5M KOH electrolytes. The response is faster, but the open-circuit memory is shorter in the more concentrated alkaline solution. The response time of the Rh oxide film in alkaline solutions is comparable to that of the Ir oxide electrochromic in acid solutions, but the open-circuit memory is longer in the latter system. A loss of electrochromic activity was found to be caused in both rhodium and iridium oxide films by excessive cathodic pulse potentials.

The electrochromic properties of anodic iridium oxide films grown on iridium substrates by potential multicycling in acid electrolytes were described in several recent publications (1-4). These oxide films were shown to exhibit fast coloration and bleaching ($\tau = 50-80$ msec), excellent open-circuit memory and very satisfactory stability when subjected to coloration-bleaching multicycles in sodium sulfate electrolytes. In a recent paper Burke and O'Sullivan reported the growth of oxide layers on rhodium electrodes in alkaline solutions by a similar potential multicycling procedure (5). The last authors also reported a color change which could be observed during film growth, from yellow at the cathodic end of the potential range

scanned to green at the anodic end. Such coloration changes were reported to be detectable only for thin films while thicker films were reported to maintain a dark green color during potential cycling (5).

In this communication some measurements of the electrochromic properties of anodic rhodium oxide films will be described. The results show that rhodium oxide films grown and pulsed in alkaline solutions can exhibit a reversible coloration change with response times similar to those reported for the anodic iridium oxide films.

Experimental

Measurements of electrochemical characteristics and reflectance changes were performed with the spectroelectrochemical apparatus used previously (1, 2): The Rh sample was mounted from the top and along the axis of a Teflon cylindrical cell equipped with two

* Electrochemical Society Active Member.

¹ On leave from the Department of Chemistry, University of Tel-Aviv, Tel-Aviv, Israel.

Key words: electrochromic oxides, iridium oxide, display.

quartz windows for light incidence and reflection at 45°. A stabilized monochromated light source and a photomultiplier served to monitor the reflectance variations. Electrolytes were prepared from reagent grade KOH and conductivity water. The rhodium disk electrode employed had an area of 0.45 cm². It was cut from a 0.015 in. thick Rh foil (Engelhard, >99.9%) mechanically polished to a mirror finish and spot welded to a Rh wire lead. Potentials were measured relative to a Hg/HgO electrode in the same KOH solution, separated by a Teflon stopcock from the main cell compartment. All potentials are reported relative to the reversible hydrogen electrode (RHE). [In KOH solutions $E_{\text{Hg}/\text{HgO}} = +0.926\text{V vs. RHE}$ (6).] A Pt foil served as a counterelectrode. To dissolve the oxide film grown in a previous experiment, the Rh disk electrode was immersed for 3 hr in 5M H₂SO₄ at 80°C. Following such a treatment the large current peaks due to the reversible conversion of the oxide layer disappeared completely.

Results and Discussion

The nature of the electrochromic process.—A rhodium electrode completely free of oxide exhibits a very small charge capacity in the anodic potential region prior to O₂ evolution. On continuously pulsing the potential of the Rh electrode immersed in 1M KOH at a frequency of 0.5 Hz between 0.03 and 1.58V an oxide layer developed, in accordance with the results of Burke and O'Sullivan (5). It could be recognized by the large current peaks which developed in the cyclic voltammogram between ca. 0.9V and the onset of oxygen evolution at ca. 1.55V. Figure 1 shows voltammograms for a "bare" Rh electrode in 1M KOH and for the same electrode following alternating growth pulses of 1 sec width applied between 0.03 and 1.58V. Voltammograms of the shape shown in Fig. 1 were obtained immediately following oxide growth, but were modified later to show a well-resolved and more reversible early anodic process [similar to that observed in the voltammogram of Ir oxide (1, 2)], as demonstrated in Fig. 2. This type of modification could be usually detected after leaving the oxide-covered Rh electrode in the KOH solution for 24 hr at open circuit, and could be accelerated by alternating coloration pulses in which the applied cathodic potential was less negative than during film growth, e.g., 1.58 \rightleftharpoons 0.5V (see discussion of these effects below). The pseudocapacitive currents which increase with oxide growth on Rh are the result of a redox process within the oxide layer, of the nature previously described for anodic Ir oxide

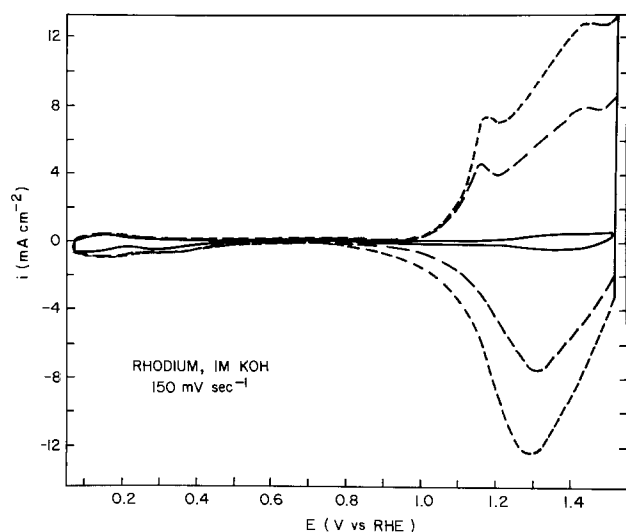


Fig. 1. Growth of oxide on Rh by potential multipulsing in 1M KOH. Solid curve, the "bare" electrode. Dashed curves, following 900 and 1800 pulse cycles applied at 0.5 Hz between 0.03 and 1.58V.

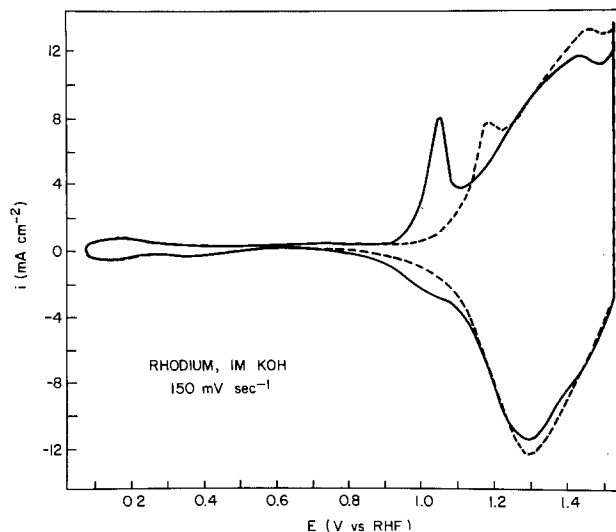
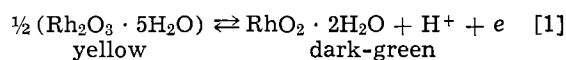
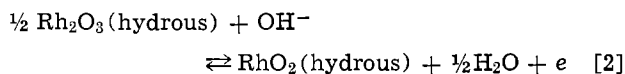


Fig. 2. Changes in the form of the voltammogram following a long immersion in the electrolyte at open circuit. Dashed curve, as-grown. Solid curve, following 24 hr at open circuit.

films (1, 2). Burke and O'Sullivan suggested that the over-all electrocoloration process probably proceeds by a double ejection and injection of protons and electrons according to



An equivalent equation for the same over-all process, which takes into account that water molecules have to be the proton donors at this pH level and that the exact water content of the film is unknown, may be written as



The water molecules required for the cathodic process may be a part of the structure of the oxide film, in the form of water of hydration in excess of the stoichiometric formulas as well as "free" water molecules which reside in pores within the oxide layer (2). In both Eq. [1] and [2] a single electron process is assumed, while the voltammogram in Fig. 2 shows clearly an additional limited redox process at less positive potentials, which results in a shoulder during the cathodic half-cycle and in a relatively sharp peak during the anodic half-cycle at 1.0V. The charge under this early peak is smaller than that associated with the major reversible process, as found also in the voltammograms of iridium oxide. It is possible that it is due to a further lowering of the oxidation state (e.g., from +3 to +2) in some specific regions (e.g., grain boundaries) under stronger cathodic polarizations, which cannot advance further because of a severe lowering of the electronic conductivity in the reduced form of the oxide. The suggestion (5) that Eq. [1] describes the over-all process was based on colors of known hydrous bulk Rh oxides: The color of the bulk sesquioxide $\text{Rh}_2\text{O}_3 \cdot 5\text{H}_2\text{O}$ is reported to be light yellow, while hydrous rhodic oxide $\text{RhO}_2 \cdot 2\text{H}_2\text{O}$ is dark green (7). These particular colors were observed during this work at some oxide thicknesses, while at other film thicknesses the changes observed were yellow \rightleftharpoons brown or yellow \rightleftharpoons purple. In 1M KOH the color of the anodic form changed periodically during film growth from green to brown-purple and back to green, while the cathodic form was always yellow-gold. Such periodic changes of color with film thickness suggest that the observed colors may be caused in this case by both absorption in the film and interference effects (8). It is doubtful, therefore, if identification of the cathodic and anodic forms as known stoichiometric

bulk hydrous oxides can be made on the basis of the observed colors alone. The yellow \rightleftharpoons dark green coloration change seemed, however, to be the more pleasant to the eye and could be always obtained by growing the oxide in 1M KOH up to a stage where the perceived contrast viewed at normal incidence (with scattered light illumination) has reached a satisfactory level, while these particular colors were observed. Following the termination of film growth the observed colors of the oxide were not modified even after 10^5 cycles between the cathodic and anodic forms.

Color modulation at 100% charge efficiency in alkaline solutions.—Just as in the case of oxide growth on Ir (2) there are both anodic and cathodic potential thresholds for the growth of Rh oxide on Rh by alternating potential multipulsing. These growth characteristics are described in detail in Ref. (5). As a result of this behavior, an oxide-covered Rh electrode immersed in 1M KOH solutions can be cycled so as to induce coloration changes without further film growth, provided the potential limits are properly selected. In the selection of these limits the following factors had to be considered in the case of the Rh oxide film: (i) Since the potential of the color forming redox reaction lies in this case close to the anodic limit of the water stability range, the highest anodic coloration potential which can be applied without significant co-evolution of oxygen has to be used to obtain good contrast. (ii) Although the available overpotential for the cathodic coloration is very large, the cathodic applied potential should not be more negative than 0.2V to avoid further film growth (5). An even less negative cathodic voltage is advisable to prevent the deactivation of the electrochromic film (see below). Considering these factors the pulsing potentials selected in both 1M and 5M KOH were $0.43 \rightleftharpoons 1.48\text{V}$ ($-0.50 \rightleftharpoons +0.55\text{V vs. Hg/HgO}$). Figures 3 and 4 show the electrochemical and optical characteristics recorded for an oxide-covered Rh electrode immersed in 1M and 5M KOH, respectively, in the limited potential region employed for the alternating coloration cycles. The reflectance of the oxide-covered rhodium electrode at the cathodic end of the region was designated as R_0 , and is close to that of the metal substrate. The film thickness was selected so as to obtain the well perceived yellow \rightleftharpoons dark green coloration change, as explained above. The closed form of the charge vs. potential curves demonstrates that coloration cycles could be run at a 100% charge efficiency. The charge injection level required to produce a reflectance attenuation of 70% at 546 nm (viewed at 45°) was of the order of

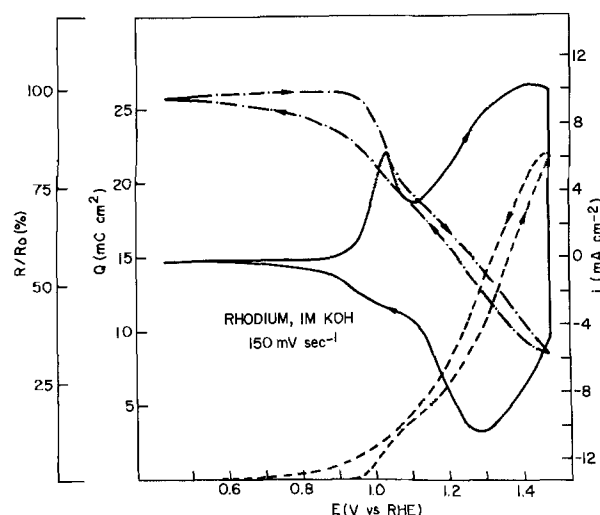


Fig. 3. Variations of the current (solid) charge (dashed) and reflectance at 546 nm, 45° (dashed-dotted) for the oxide-covered Rh electrode in 1M KOH during a triangular modulation of the potential in the range employed for the coloration cycles.

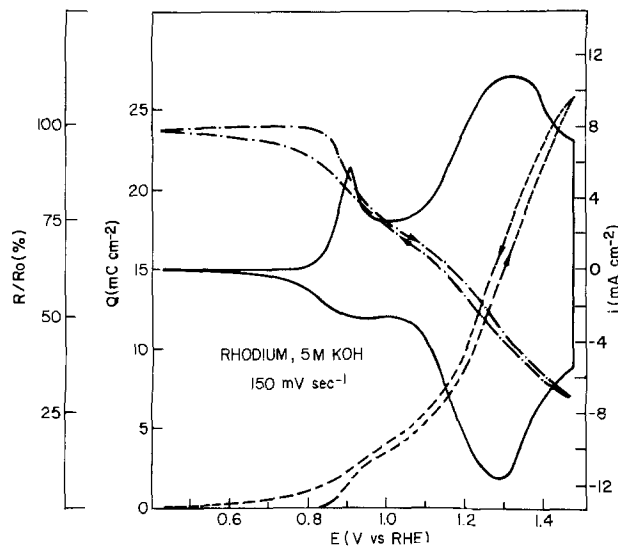


Fig. 4. Variations of the current (solid) charge (dashed) and reflectance at 546 nm, 45° (dashed-dotted) for the oxide-covered Rh electrode in 5M KOH during a triangular modulation of the potential in the range employed for the coloration cycles.

20 mC cm^{-2} , i.e., comparable to that required to color the Ir oxide film (1, 2). Assuming a density of 5 g cm^{-3} for the hydrous oxide and a molecular weight of 344 ($\text{Rh}_2\text{O}_3 \cdot 5\text{H}_2\text{O}$), this level of charge injection amounts to a uniform one-electron process throughout a film 1400 \AA thick. Since the Rh oxide film is a two-color electrochromic system, the reflectance attenuation (or contrast ratio) may not be a very satisfactory figure of merit for its evaluation. The strong reversible reflectance variations associated with the coloration change demonstrate, however, that there is also a large decrease in brightness going from the cathodic (yellow) to the anodic (dark green) form, which enhances the perceived contrast. (Similar reflectance changes were recorded at other wavelengths throughout the visible region.) The R vs. V curves show some hysteresis at the cathodic end of the cycle associated with a similar hysteresis in the Q vs. V curve. A similar behavior is found in the case of the Ir oxide film in acid solutions. In both cases the last stage of the cathodic process is the slowest step in the complete cycle when ohmic drops in solution are eliminated. Comparison of Fig. 3 and 4 reveals that the main process seems to be more reversible in 5M KOH and the major anodic peak is better developed prior to the onset of O_2 evolution. This is due in part to the smaller iR drop in 5M KOH, but may be also associated with a cathodic shift of the potential of the electrochromic reaction vs. RHE, as found for Ir in alkaline solutions (2).

Response, stability, and memory.—Figure 5(a) demonstrates the response of the Rh oxide electrochromic in 1M KOH to alternating coloration pulses of 1 sec width. In this case the response of the system to the anodic pulse can be seen to be relatively slow. This is due to a combination of a small effective coloration overvoltage and limited conductivity in solution. The cathodic process occurs relatively more rapidly (except for the slower tail) thanks to the larger allowed overvoltage. As shown in Fig. 5(b) both the anodic and cathodic steps were significantly enhanced in 1M KOH by compensating the iR drop in solution using the positive feedback circuit of the PAR potentiostat. Such an enhancement means that a solution of a higher conductivity (or an improved cell geometry) should allow a better response in this case. This was indeed verified by transferring the oxide grown in 1M to a 5M KOH solution. The response in 5M KOH without iR compensation is demonstrated in Fig. 6(a) and 6(b) on two different time scales. It is clear from Fig. 6

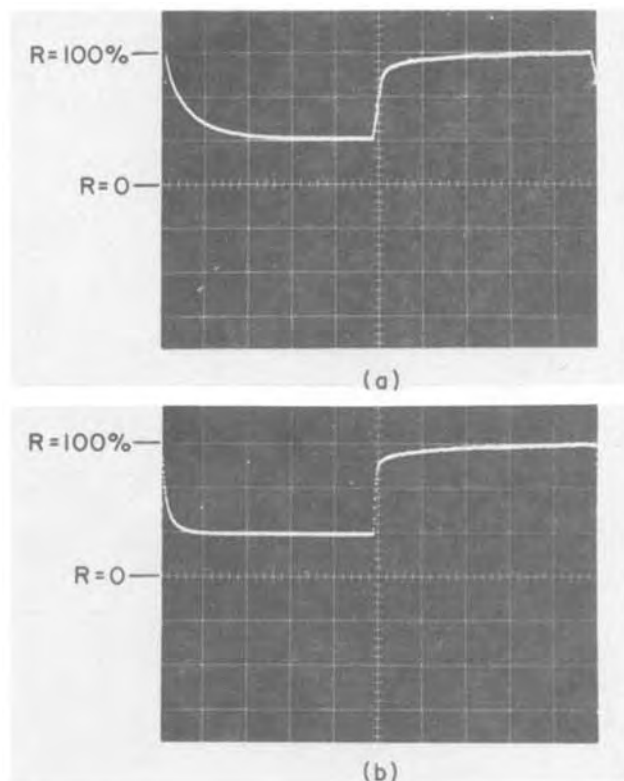


Fig. 5. Variations of the reflectance at 546 nm (45°) with time during alternating potential pulses $0.43 \rightleftharpoons 1.48\text{V}$ of 1 sec width, applied to an oxide-covered Rh electrode in 1M KOH: (a) without iR compensation; (b) with iR compensation.

that the inherent response of the Rh electrochromic oxide is as fast as that found for Ir oxide.

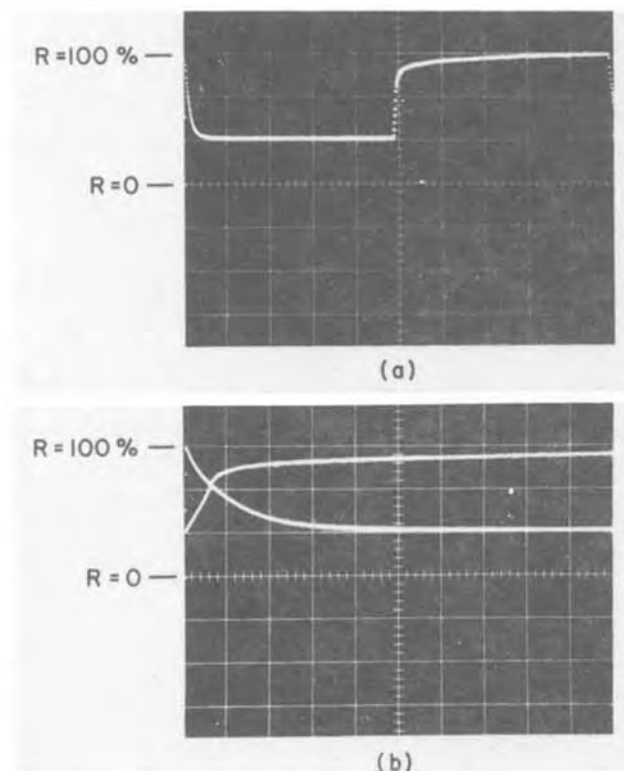


Fig. 6. Variation of the reflectance at 546 nm (45°) with time during alternating potential pulses $0.43 \rightleftharpoons 1.48\text{V}$ of 1 sec width, applied to an oxide-covered Rh electrode in 5M KOH (without iR compensation): (a) complete cycle shown (2 sec full scale); (b) the onsets of anodic and cathodic reflectance variations are shown on an expanded time scale (200 msec full scale).

Multipulsing experiments which lasted 30 hr each showed that the increased concentration of KOH did not cause any increase in the rate of charge loss: Following ca. 10^5 coloration cycles at 0.5 Hz between $0.42 \rightleftharpoons 1.47\text{V}$ the observed contrast and the monitored reflectance variations were practically unchanged in both 1M and 5M KOH, while the charge losses ranged in both electrolytes between 0-3%. The good stability found for Rh oxide film in these multipulsing experiments in spite of the relatively high anodic coloration potentials which have to be applied is in accordance with the reported difficulty in removing this film by anodizing it at high potentials (5). [The electrochromic Ir oxide film tends to dissolve under high anodic potentials (9).]

The rate of color loss at open circuit ("open-circuit memory") is demonstrated for the Rh oxide electrochromic in Fig. 7. The decay curves given in Fig. 7 should be compared with a loss of only 10% in light absorption after 5 hr at open circuit as measured for the Ir oxide electrochromic film in acid solutions (1). Thus, while the memory of the Rh oxide electrochromic may be satisfactory for some purposes (especially when immersed in 1M KOH), it is shorter than that found for Ir oxide. The shorter memory is a direct result of the high redox potential of the electrochromic reaction: The anodic form of the oxide [most probably Rh(IV) and perhaps partially Rh(VI) (5)] is formed at a very anodic potential and is expected thermodynamically to react with water. Furthermore, since the $\text{Rh(IV)} \rightleftharpoons \text{Rh(III)}$ conversion is quite reversible (see the major peaks in the voltammograms) the decay of anodic coloration may indeed proceed at open circuit by the reaction of the higher oxide with the aqueous solution to yield the lower oxide and molecular oxygen. This reaction can be written as a sum of two electrochemical half-processes

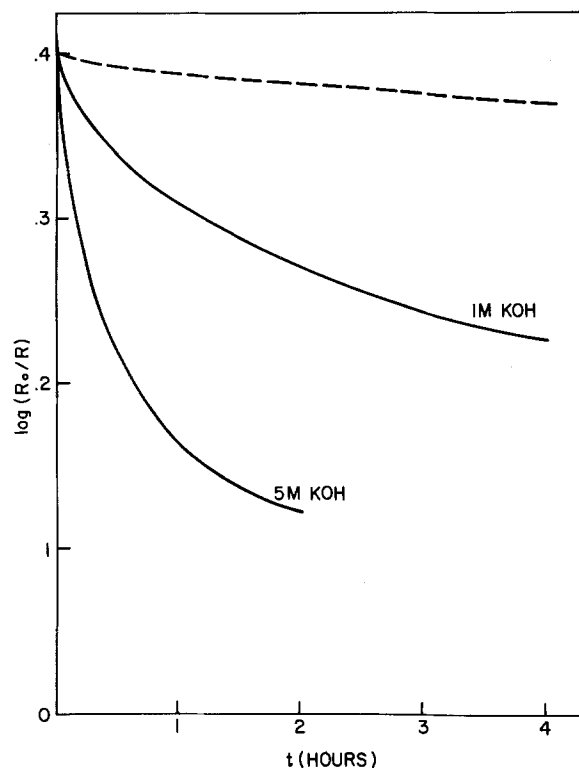
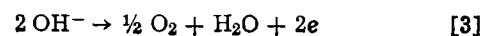
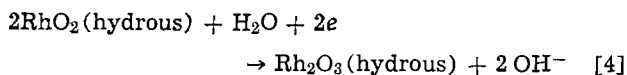
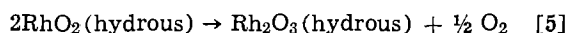


Fig. 7. The open-circuit decay of light absorption in the Rh oxide film immersed in 1M and 5M KOH electrolytes, following the application of a potential pulse of 1.48V. (Measured at 546 nm, 45°). The behavior of Ir oxide in 0.5M H_2SO_4 is given for comparison by the dashed curve.



with the net result being



When the rate is determined, as expected, by half-process [3], the open-circuit decay will be enhanced by a higher concentration of OH^- ions, as found experimentally (Fig. 7). Comparison of the open-circuit memories reported for the Ir, Rh, and W electrochromic oxides in aqueous solutions demonstrates the importance of the location of the electrochromic redox reaction on the potential scale: In the case of Ir oxide the potential range of the electrochromic reaction is located close to the middle of the water stability range. Thus, no component of a pure aqueous sulfate solution, even when open to the atmosphere, is expected to react with the colored form of Ir oxide. On the other hand, in the case of Rh oxide, where anodic coloration is obtained at a potential close to that of O_2 evolution, as well as in the case of WO_3 where coloration is obtained close to the onset of H_2 evolution, the colored forms are reactive in contact with water or dissolved oxygen, respectively, thus leading to shorter open-circuit memories.

The cathodic deactivation of the electrochromic Rh oxide film.—The Rh oxide films were found to lose their electrochromic activity following a short application of excessive cathodic pulse potentials. This behavior is demonstrated in Fig. 8 for a film pulsed in a 5M KOH electrolyte: Following the extension of the cathodic pulse potential down to 0.08V for only 2 min (60 cycles), while keeping the anodic pulse potential unchanged, the response during the cathodic half-cycle became very sluggish. Under such conditions the color of the film remained dark-green (or dark-brown)

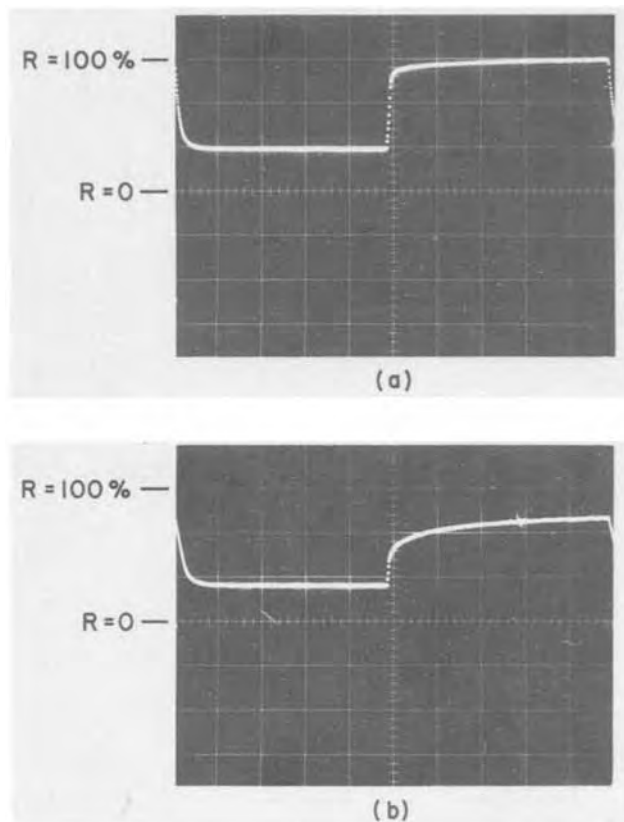


Fig. 8. The effect of an excessive cathodic pulse potential applied for 2 min (60 coloration cycles) on the response of the electrochromic Rh oxide film in 5M KOH. (a) Regular response at 633 nm (45°) recorded during pulsing between 1.48 and 0.43V. (b) Recorded during pulsing between 1.48 and 0.08V 2 min after the cathodic overvoltage had been extended.

during alternating pulsing, as described by Burke and O'Sullivan for the thicker Rh oxide films which they observed during growth. Figure 9 shows the associated effects recorded in the voltammogram and in the charging curve: The early anodic peak seems to have disappeared completely at this scan rate, while the charging curve exhibits a stronger hysteresis. Following such a short deactivating treatment, the changes in the electrochromic response and in the form of the voltammogram could be reversed by the reapplication of the regular pulses between $0.43 \rightleftharpoons 1.48\text{V}$, i.e., by employing less negative cathodic pulse voltages. In other experiments it was found that a similar "rejuvenation" of cathodically deactivated Rh oxide films could be achieved by immersing the oxide-covered Rh electrode in a hot (75°C) KOH solution for ca. 15 min. It is clear from the charging curves in Fig. 9, as well as from the successful attempt to reverse the deactivating effect by immersion in hot KOH, that the cathodic deactivation is not associated with a permanent loss of charge but rather with some change in the structure of the film. [The term "deactivation" in the sense used here should be thus clearly distinguished from the terms "activation" and "deactivation" of Ir electrodes which were used before in the literature to describe the growth and the complete loss of the oxide layer (10).] It thus seems that the applied cathodic overvoltages have to be limited to prevent a loss of electrochromic activity. Fortunately, the cathodic process proceeds rapidly even at the lower overvoltages which were regularly employed (see Fig. 6), and the higher cathodic overpotentials associated with deactivation can be avoided without loss of speed. In fact no rate enhancement is recorded for an active Rh oxide film when the cathodic pulse potential is temporarily extended, because the cathodic process seems to reach a limiting rate which is probably controlled by diffusion in the film. This behavior is demonstrated in Fig. 10.

Very similar effects to those described in Fig. 8-10 were observed for the iridium oxide electrochromic film as well, in H_2SO_4 solutions, and will be described in more detail elsewhere. It should be stressed, however, that no loss of activity was encountered if the cathodic pulse potentials previously prescribed (1, 2)

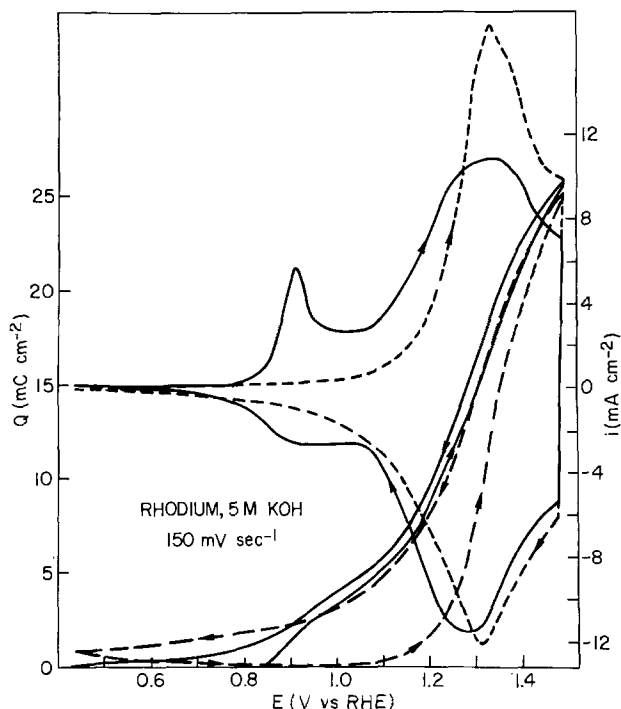


Fig. 9. The effects of cathodic deactivation on the voltammogram and the charging curve. Solid curves recorded for the active form. Dashed curves, recorded for the cathodically deactivated film.

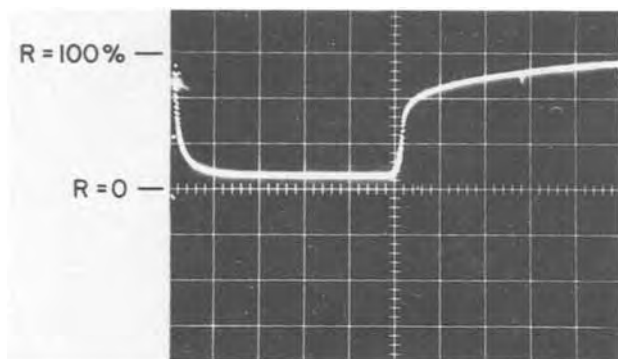


Fig. 10. The limiting rate of cathodic coloration in the Rh oxide film. The figures show two superimposed reflectance time curves recorded at 440 nm (45°) during two cycles with different cathodic pulse potentials: $+1.48 \rightleftharpoons +0.53\text{V}$ and $1.48 \rightleftharpoons +0.23\text{V}$. (Pulse width, 1 sec).

were not exceeded. Restoration of the activity by lowering the cathodic overvoltage (while increasing temporarily the anodic applied voltage) was effective in the case of the Ir oxide films as well. Beni and Shay have described before a heat-treatment (immersion in hot electrolyte) for anodic iridium oxide films, which was reported to improve their electrochromic response (3). The results presented here indicate that a direct cause of deactivation in Ir oxide as well as Rh oxide electrochromic films is the use of excessive cathodic pulse potentials. If the cathodic potential is properly controlled no deactivation should occur. Furthermore, reactivation by immersion in a hot solution will not solve the problem if excessive cathodic potentials are further applied, because deactivation will occur again in exactly the same way, as found in this work for heat-treated Rh oxide films. The electrochromic response recorded following sufficiently long periods of multicycling will be thus determined by the electrochemical parameters of the display cell for both heat-treated and nontreated electrodes. In particular, since the growth of these films does require the application of potentials close to 0V vs. RHE, the as-grown films may be, in principle, somewhat less active (although the higher anodic potentials which are used during growth tend to continuously reactivate the film). However, with film thicknesses normally employed in this work, as well as before (1, 2), the stable rapid response was found to be established

during the first few alternating coloration cycles. Examination of the voltammograms presented by Burke and O'Sullivan (5) reveals that the early anodic peak is very small compared with the one obtained for active Rh oxide films as presented in Fig. 3. Continuous cycling with the cathodic potential extended down to the onset of H_2 evolution (5) may have resulted in their case in a partially deactivated film, causing the decay of the reversible coloration changes.

One possible reason for the deactivation by excessive cathodic pulse potentials could be an irreversible lowering of the electronic conductivity in the film. Preliminary measurements of the electrical properties of these electrochromic oxide films suggest that this is indeed the case. Details of such measurements will be described in a forthcoming report.

Acknowledgment

Thanks are due to J. D. E. McIntyre and S. H. Glarum for helpful discussions, and to W. F. Peck, Jr. for technical assistance.

Manuscript submitted May 29, 1979; revised manuscript received Aug. 28, 1979.

Any discussion of this paper will appear in a Discussion Section to be published in the December 1980 JOURNAL. All discussions for the December 1980 Discussion Section should be submitted by Aug. 1, 1980.

Publication costs of this article were assisted by Bell Laboratories.

REFERENCES

1. S. Gottesfeld, J. D. E. McIntyre, G. Beni, and J. L. Shay, *Appl. Phys. Lett.*, **33**, 208 (1978).
2. S. Gottesfeld and J. D. E. McIntyre, *This Journal*, **126**, 742 (1979).
3. G. Beni and J. L. Shay, *Appl. Phys. Lett.*, **33**, 567 (1978).
4. J. L. Shay, G. Beni, and L. Schiavone, *ibid.*, **33**, 942 (1978).
5. L. D. Burke and E. J. M. O'Sullivan, *J. Electroanal. Chem.*, **93**, 11 (1978).
6. D. J. G. Ives and G. J. Janz, "Reference Electrodes," p. 335, Academic Press, New York (1961).
7. M. Pourbaix, "Atlas of Electrochemical Equilibria in Aqueous Solutions," p. 351, Pergamon, London (1966).
8. J. D. E. McIntyre, S. Gottesfeld, and W. F. Peck, Jr., Unpublished results.
9. D. N. Buckley and L. D. Burke, *J. Chem. Soc. Faraday I*, **71**, 1447 (1975).
10. J. O. Zerbino, N. R. de Tacconi, and A. J. Arvia, *This Journal*, **125**, 1266 (1978).

Solution Growth of CdSe and PbSe Films

R. C. Kainthla, D. K. Pandya, and K. L. Chopra

Department of Physics, Indian Institute of Technology, Delhi, New Delhi 110029, India

ABSTRACT

Cadmium selenide and lead selenide films have been deposited by a solution growth technique on single crystal germanium and silicon, glass, mica, and copper substrates. The effect of bath parameters (pH, temperature, and relative concentration of reactants) and the nature of the substrate on the rate of deposition and terminal thickness has been established. The structure of the films has also been studied. Based on the experimental results, a growth model has been proposed.

Metal chalcogenides (sulfides, selenides, and tellurides) are important materials for such applications as photoconducting cells, photovoltaic cells, and other electrooptical devices. These materials can be obtained

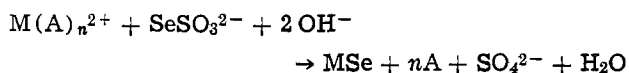
Key words: chemical deposition, semiconductor films, metal-selenide films, growth kinetics.

in thin film form by evaporation, sputtering, pyrolysis, and chemical deposition techniques (1). Of all these techniques, chemical solution growth is relatively inexpensive, simple, and convenient for large area deposition of II-VI and IV-VI compounds. By this technique, films can be deposited on a variety of sub-

strates (insulators, semiconductors, and metals) by allowing them to remain in an aqueous solution of the appropriate chemicals for a predetermined time. For example, films can be obtained by the reaction of a metal salt solution with an aqueous solution of a compound capable of giving chalcogenide ions under suitable conditions. Thiourea and selenourea are the commonly used compounds which furnish sulfur and selenium ions by hydrolysis in alkaline solution (2-5). Selenourea solution is very unstable and has to be stabilized using antioxidants like sodium sulfite. In addition, the compound cannot be synthesized easily. Another compound which can generate selenium ions is sodium selenosulfate. It can be synthesized easily by dissolving selenium in a sodium sulfite solution; the resulting solution is fairly stable. As the hydrolysis constants of selenourea and selenosulfate are different, the conditions under which film formation takes place are different in the two cases. To optimize conditions for deposition of selenide films using selenosulfate solution, a detailed study of film formation under different conditions is necessary. Second, although the technique has been used by some workers for preparing selenide films of cadmium (6) and lead (7), the growth mechanism is not understood clearly. With this in mind, we have studied the rate of growth of cadmium and lead selenide films on different substrates under different conditions.

Experimental Details

Cadmium and lead selenide films have been prepared by using the following over-all reaction



where M is a metal (Cd or Pb) and A is a complexing agent [NH_3 , OH^- , or $C_6H_5O_7^{3-}$].

The experimental setup to deposit the films was the same as described by Kaur *et al.* (8). The reaction mixture was prepared from 0.5M cadmium acetate, 7M ammonia solution, 5M potassium hydroxide, and 0.125M sodium selenosulfate solution in the case of cadmium selenide films and 0.5M lead acetate, 0.820M trisodium citrate, 5M potassium hydroxide, and 0.125M sodium selenosulfate solution in the case of lead selenide films. Appropriate volumes of salt solution, ammonia or trisodium citrate and distilled water were mixed at room temperature and stirred continuously. Substrates were immersed vertically in the solution which was then heated to the required temperature of deposition. Potassium hydroxide was added to adjust the pH of the solution in the case of lead selenide films. For cadmium selenide film deposition, in one case potassium hydroxide was added to adjust the pH, while in the other case the pH was determined by the ammonia concentration. Appropriate volume of sodium selenosulfate solution was then added. The final concentrations of the reagents in the solution used to coat the substrate have been mentioned in the figure captions. Substrates were taken out at different times and the films washed with distilled water and dried. The substrates used in our study were (i) glass slides boiled in chromic acid and distilled water and cleaned ultrasonically before use, (ii) freshly cleaved mica, (iii) polished slices of silicon and germanium, and (iv) freshly cleaned copper foils or vapor-deposited thin films of copper on glass substrates. Mirror-like films of metal selenide are obtained on both sides of the substrate.

The film thickness was measured by Taylor Hobson Talystep instrument. For electron microscopy studies, the films were floated off the substrate in dilute nitric acid and lifted onto copper grids. The films were then transferred to the electron microscope specimen holder and examined in AEI-EM 802 electron microscope. The electron diffraction patterns were analyzed using conventional methods.

Results

Figures 1 and 2 show typical curves for film thickness as a function of dip time, for different pH values of the bath in the case of PbSe and for different ammonia concentrations in the case of CdSe films, respectively. In the initial stages of growth, the thickness increases at a fast rate. Subsequently the rate decreases resulting in a terminal thickness. To get larger thicknesses, the films, after cleaning in distilled water (to remove any precipitate adhering to the film), are immersed again in a fresh bath. The film thickness as a

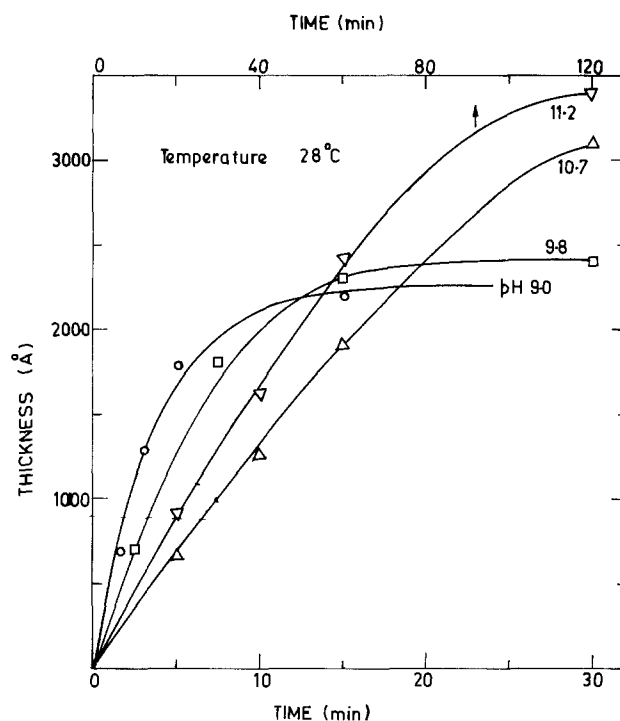


Fig. 1. PbSe film thickness as a function of time for a reaction mixture at 28°C and of composition: $7 \times 10^{-2}M Pb(CH_3COO)_2$, $1.2 \times 10^{-1}M Na_3C_6H_5O_7$, $5 \times 10^{-2}M Na_2SeSO_3$, and various pH values (glass substrate).

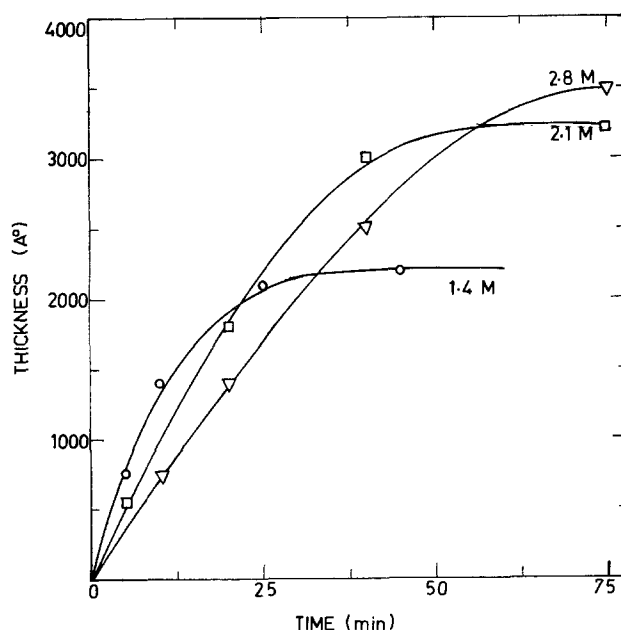


Fig. 2. CdSe film thickness as a function of time for a reaction mixture at 77°C and of composition: $4.8 \times 10^{-2}M Cd(CH_3COO)_2$, $5.3 \times 10^{-2}M Na_2SeSO_3$, and various NH_3 concentrations (glass substrate).

function of time shows a similar behavior in subsequent dips. The rate of deposition, obtained from the initial part of the curves, and the terminal thickness depend sensitively on the pH of the bath, concentration of the reactants, temperature of deposition, and the nature of the substrate. The effect of various parameters on the rate of deposition and terminal thickness of the films is discussed in detail in the following.

Effect of pH.—As is clear from Fig. 1, the rate of deposition decreases while the terminal thickness increases with increase in pH value. Figure 3 shows the rate of deposition as a function of pH for films deposited at 28° and 60°C. At 28°C, good quality (uniform, adherent, and specularly reflecting) films are obtained for pH between 9.0 and 11.4. Below pH 9.0, nonuniform and nonadherent films are obtained. Above pH 11.4 no reaction is observed to take place. Between pH 9.0 and 11.4, the amount of precipitate accumulated in the solution decreases with increasing pH value. The terminal thickness of the films increases with increase in pH value as shown in Fig. 4.

In the case of CdSe films, when potassium hydroxide is added to adjust the pH of the bath, the solution has a suspension of $\text{Cd}(\text{OH})_2$. From this solution thin (terminal thickness $\sim 800\text{\AA}$) films of CdSe are obtained. The terminal thickness decreases while the rate of deposition increases with increase in the pH value. Above a certain pH value, where precipitation dominates, film formation does not take place.

When potassium hydroxide is not added to the solution, the solution is clear and has to be heated to high temperatures ($> 45^\circ\text{C}$) to obtain CdSe films. The rate of deposition decreases while the terminal thickness increases with increase in ammonia concentration. The rate of deposition and terminal thickness as a function of ammonia concentration are plotted in Fig. 5.

Effect of temperature.—In Fig. 3, the rate of deposition of the PbSe films is plotted as a function of pH for two different temperatures. For a particular pH value, the rate of deposition increases on increasing the temperature of the bath. At 60°C, the lower limit of pH to get good quality films is increased to 9.6 while the upper limit changes to 12.0. Similarly, at 5°C, the limiting pH values are 8.7 and 9.9. For CdSe films also, the rate of deposition increases with increase in temperature of deposition (Fig. 6).

Figure 4 shows the terminal thickness of PbSe films as a function of the pH for two different temperatures

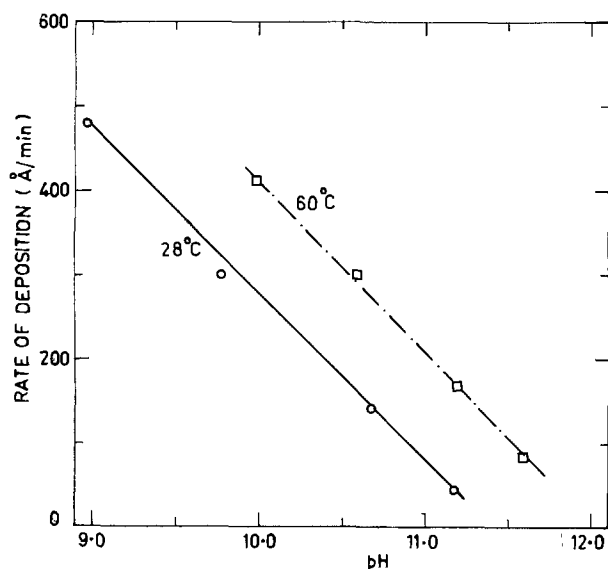


Fig. 3. Rate of deposition of PbSe films as a function of pH value for a reaction mixture of composition: $7 \times 10^{-2}\text{M Pb}(\text{CH}_3\text{COO})_2$, $1.2 \times 10^{-1}\text{M Na}_3\text{C}_6\text{H}_5\text{O}_7$, $5 \times 10^{-2}\text{M Na}_2\text{SeSO}_3$ (glass substrate).

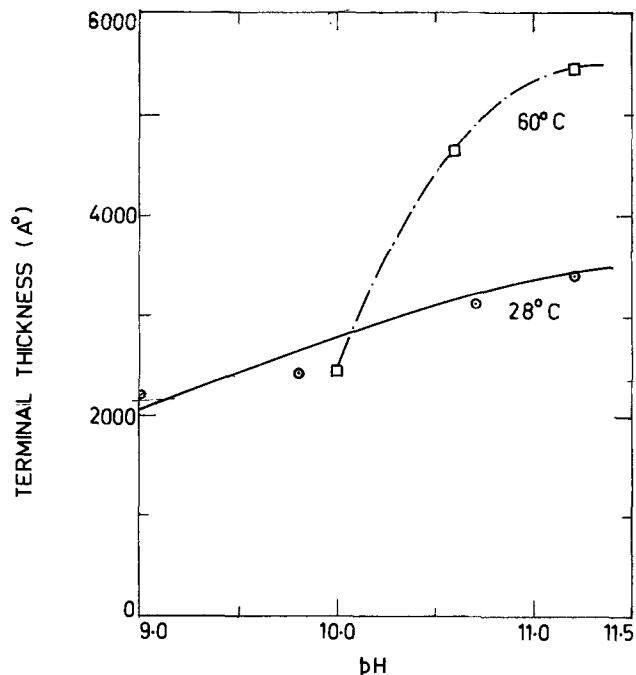


Fig. 4. Terminal thickness of PbSe films as a function of pH value for a reaction mixture of composition: $7 \times 10^{-2}\text{M Pb}(\text{CH}_3\text{COO})_2$, $1.2 \times 10^{-1}\text{M Na}_3\text{C}_6\text{H}_5\text{O}_7$, $5 \times 10^{-2}\text{M Na}_2\text{SeSO}_3$ (glass substrate).

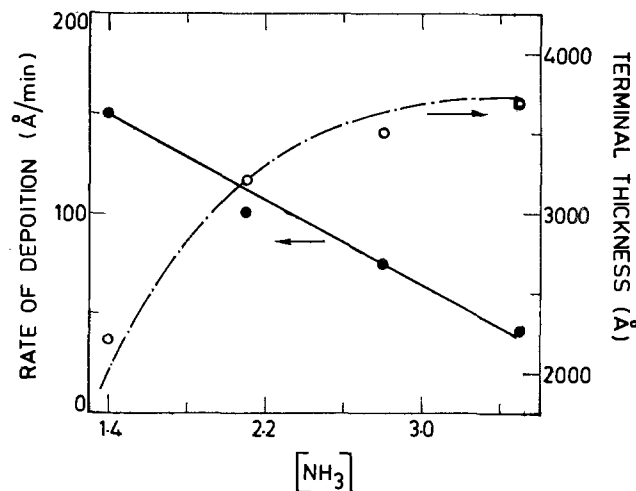


Fig. 5. Rate of deposition and terminal thickness of CdSe film as a function of NH_3 concentration for a reaction mixture of composition: $4.8 \times 10^{-2}\text{M Cd}(\text{CH}_3\text{COO})_2$ and $5.3 \times 10^{-2}\text{M Na}_2\text{SeSO}_3$ at 77°C (glass substrate).

of deposition. The terminal thickness increases with increase in temperature of deposition at high pH values, whereas at low pH values, the terminal thickness decreases with increase in the temperature of deposition. For example, terminal thickness of the film deposited at 60°C is higher at pH 10.7 and lower at pH 10.0 as compared to the terminal thickness of the film deposited at 28°C. In the region of less precipitation, for CdSe films the terminal thickness also increases with increase in temperature of deposition (Fig. 6).

Effect of sodium selenosulfate concentration.—The effect of sodium selenosulfate concentration on the rate of deposition and terminal thickness is shown in Fig. 7 for CdSe films. The rate of deposition increases with increase in selenosulfate concentration. The terminal thickness first increases, passes through a maximum, and then decreases with increasing concentration of selenosulfate. Similar results are obtained for PbSe films.

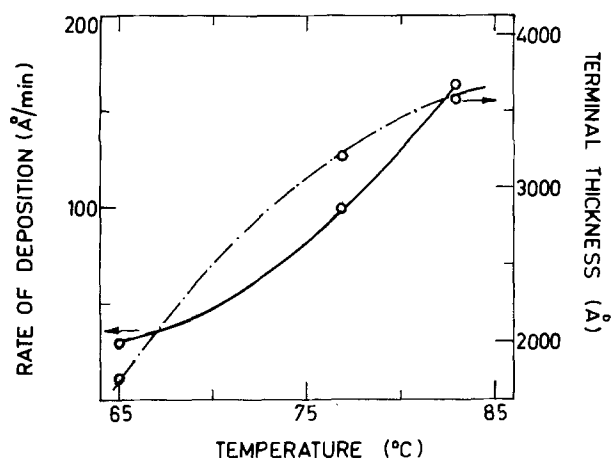


Fig. 6. Rate of deposition and terminal thickness of CdSe films as a function of temperature of deposition for a reaction mixture of composition: $4.8 \times 10^{-2} \text{M Cd}(\text{CH}_3\text{COO})_2$, $5.3 \times 10^{-2} \text{M Na}_2\text{SeSO}_3$, and 2.1M NH_3 (glass substrate).

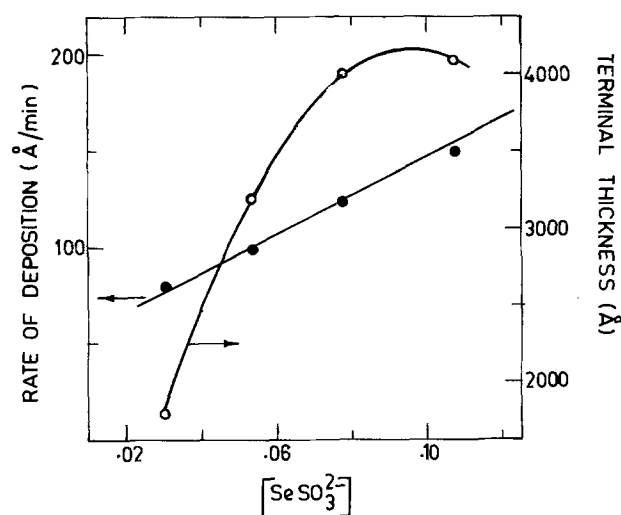


Fig. 7. Rate of deposition and terminal thickness of CdSe films as a function of Na_2SeSO_3 concentration for a reaction mixture of composition: $4.8 \times 10^{-2} \text{M Cd}(\text{CH}_3\text{COO})_2$ and 2.1M NH_3 concentration at 77°C (glass substrate).

Effect of substrate.—The effect of different substrates on the kinetics of growth of PbSe films deposited on glass, copper, polished slices of single crystal silicon, and germanium at 28°C and pH 10.4 is shown in Fig. 8. The rate of deposition and terminal thickness are maximum for single crystal germanium followed by silicon, copper, and glass. Similar results are obtained for CdSe also. The results are similar to that observed for PbS and $\text{Pb}_{1-x}\text{Hg}_x\text{S}$ films deposited by the same technique (9).

Structure.—The lead selenide films deposited are polycrystalline (grain size depending on the deposition conditions) and have fcc (NaCl-type) structure with lattice parameter $a = 6.08 \text{Å}$ which agrees well with the ASTM value of $a = 6.124 \text{Å}$. The grain size increases with increase in temperature of deposition and pH value of the bath.

Cadmium selenide films, when deposited from a bath having a suspension of $\text{Cd}(\text{OH})_2$, have mixed hexagonal and cubic phases. Films obtained from clear solution have cubic (sphalerite) structure with lattice parameter $a = 6.063 \text{Å}$. The hexagonal phase has lattice parameters, $a = 4.20 \text{Å}$, $c = 7.01 \text{Å}$.

Discussion

Sodium selenosulfate (Na_2SeSO_3) hydrolyzes in alkaline solution to give Se^{2-} ions according to

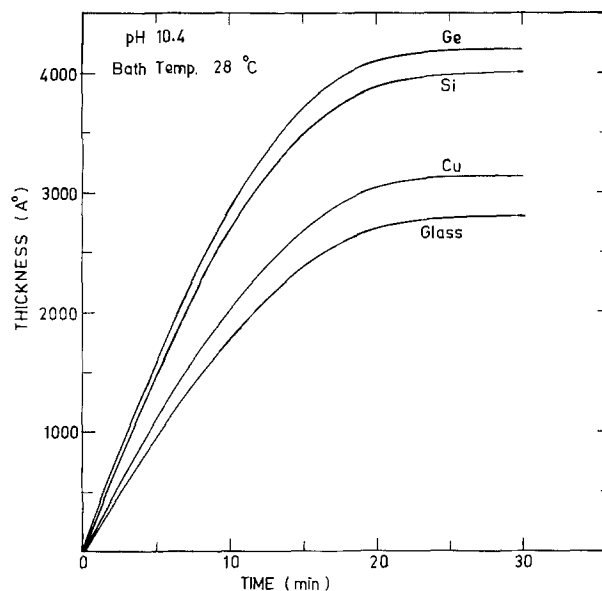
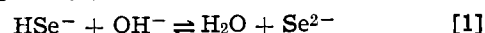
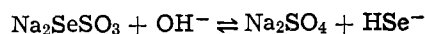


Fig. 8. PbSe film thickness as a function of time for a reaction mixture at 28°C and pH 10.4 of composition: $7 \times 10^{-2} \text{M Pb}(\text{CH}_3\text{COO})_2$, $1.2 \times 10^{-1} \text{M Na}_3\text{C}_6\text{H}_5\text{O}_7$, and $5 \times 10^{-2} \text{M Na}_2\text{SeSO}_3$ on different substrates.

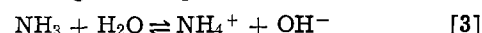


In the presence of metal ions (M^{2+}) in the solution, metal selenide (MSe) will be formed if the ionic product of M^{2+} and Se^{2-} exceeds the solubility product of MSe



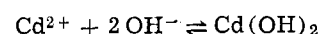
To control the number of ions and hence rate of reaction, the metal ions are taken in the form of a fairly stable complex $\text{M}(\text{A})_n^{2+}$. The complex dissociates to give controlled number of M^{2+} ions which then combine with Se^{2-} ions to form MSe. In the present study, the systems Cd salt (acetate)- NH_3 - Na_2SeSO_3 -KOH and Pb salt (acetate)- $\text{Na}_3\text{C}_6\text{H}_5\text{O}_7$ -KOH- Na_2SeSO_3 have been taken for the deposition of CdSe and PbSe films, respectively.

CdSe film growth.—Ammonia hydrolyzes in water to give OH^- according to the equation



with hydrolysis constant $K_{\text{hyd}} = 1.8 \times 10^{-5}$.

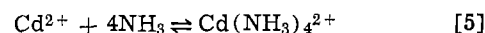
When ammonia solution is added to Cd-salt solution, $\text{Cd}(\text{OH})_2$ starts precipitating when solubility product (SP) of $\text{Cd}(\text{OH})_2$ is exceeded, i.e.



with

$$\text{SP} = [\text{Cd}^{2+}][\text{OH}^-]^2 = 2.2 \times 10^{-14} \quad (p\text{SP} = 13.66) \quad [4]$$

The $\text{Cd}(\text{OH})_2$ precipitate dissolves in excess ammonia solution to form the complex cadmium tetra-ammine ion $[\text{Cd}(\text{NH}_3)_4^{2+}]$



The stability constant of $[\text{Cd}(\text{NH}_3)_4^{2+}]$, $pK = 7.12$, i.e.

$$\frac{[\text{Cd}^{2+}][\text{NH}_3]^4}{[\text{Cd}(\text{NH}_3)_4^{2+}]} = 7.56 \times 10^{-8} \quad [5a]$$

Conversion to logarithmic concentrations and elimination of $p[\text{Cd}^{2+}]$ from Eq. [4] and [5] leads to

$$\text{pH} = 10.73 + \frac{1}{2} p[\text{Cd}(\text{NH}_3)_4^{2+}] - 2p[\text{NH}_3]$$

If excess ammonia is added to dissolve the $\text{Cd}(\text{OH})_2$ precipitate, $p[\text{Cd}(\text{NH}_3)_4^{2+}]$ can be approximated by pC_{salt} . Hence

$$\text{pH} = 10.73 + \frac{1}{2} pC_{\text{salt}} - 2p[\text{NH}_3]$$

In the present case, $pC_{\text{salt}} = -\log(4.8 \times 10^{-2}) \simeq 1.3$.
Therefore

$$pH = 11.38 - 2p[\text{NH}_3] \quad [6]$$

Equation [6] when plotted is a straight line A as shown in Fig. 9. Points lying on the line and in region I represent a homogeneous system consisting of stable $\text{Cd}(\text{NH}_3)_4^{2+}$ complex in equilibrium with Cd^{2+} ions. In region II, which can be reached by the addition of an alkali to the solution, conditions for the spontaneous formation $\text{Cd}(\text{OH})_2$ exist so that the points lying in region II represent a heterogeneous system consisting of the complex $\text{Cd}(\text{NH}_3)_4^{2+}$ and a solid phase of $\text{Cd}(\text{OH})_2$ simultaneously in equilibrium with Cd^{2+} ions.

CdSe films have been obtained in region II and for conditions corresponding to the points on the line A. In the heterogeneous system of $\text{Cd}(\text{OH})_2$ and $\text{Cd}(\text{NH}_3)_4^{2+}$, the region enclosed by the two dotted lines B and C represents conditions for obtaining films of measurable thickness. The film formation in this region is explained on the basis of heterogeneous nucleation. $\text{Cd}(\text{OH})_2$ present in the solution and that formed on the substrate act as nuclei for the formation of CdSe. More of CdSe is formed in the bulk of the solution and on the substrate surface by the addition of more Cd^{2+} and Se^{2-} ions from the solution to the initially formed CdSe and consequently with time a precipitate of CdSe is formed in the bulk and a film on the substrate. As the pH of the solution is further increased most of the Cd^{2+} and OH^- ions spontaneously react to form $\text{Cd}(\text{OH})_2$ in the bulk of the solution and hence on addition of sodium selenosulfate most of the CdSe is precipitated resulting in lower terminal thicknesses at high pH values of the bath.

From clear solutions (i.e., homogeneous system) at room temperature ($\sim 28^\circ\text{C}$) no film or precipitate is formed even when the solution is kept for a very long time. This is due to the fact that as most of Cd^{2+} ions are in the bound complex form $\text{Cd}(\text{NH}_3)_4^{2+}$, ionic product of Cd^{2+} and Se^{2-} does not exceed the solubility product of CdSe. To get higher concentrations of Cd^{2+} , the solution has to be heated. The heating results in dissociation of the complex and selenosulfate and, therefore, higher concentrations of Cd^{2+} and Se^{2-} are available for reaction. Also the increased kinetic energy of the ions with increasing temperature results in more frequent collisions so that the probability of CdSe formation increases. Thus from clear solutions containing 2.1M ammonia, CdSe films can be obtained only at temperatures above 45°C . The mechanism of film growth from clear solution is discussed in the following section.

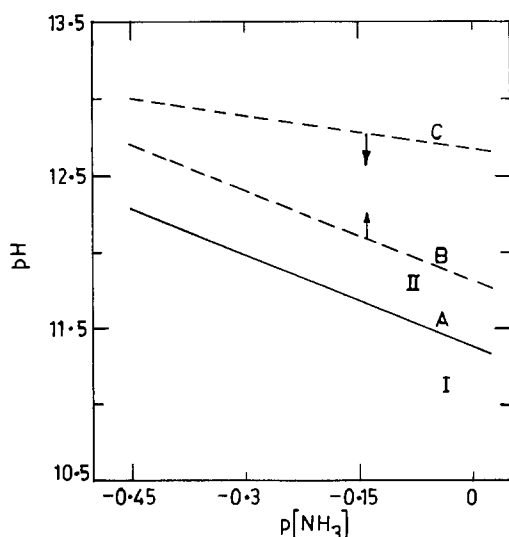
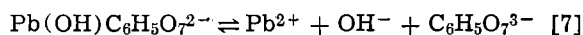


Fig. 9. Plot of Eq. [6]

Growth of PbSe films.—For PbSe film growth, the Pb^{2+} ions are complexed with $\text{C}_6\text{H}_5\text{O}_7^{3-}$ ions to give $\text{Pb}(\text{OH})\text{C}_6\text{H}_5\text{O}_7^{2-}$ which dissociates to give Pb^{2+} according to the reaction



The complex has stability constant $K = 1.4 \times 10^{-19}$ so that

$$\frac{[\text{Pb}^{2+}][\text{OH}^-][\text{C}_6\text{H}_5\text{O}_7^{3-}]}{[\text{Pb}(\text{OH})\text{C}_6\text{H}_5\text{O}_7^{2-}]} = 1.4 \times 10^{-19} \quad [8]$$

The Pb^{2+} ions formed according to Eq. [7] react with Se^{2-} ions formed in Eq. [1] to give PbSe.

The concentration and the rate of generation of Pb^{2+} , Cd^{2+} , and Se^{2-} ions is determined by reactions [7], [5], and [1], respectively. Metal selenide is formed (according to reaction [2]) when the ionic product (IP) of M^+ and Se^{2-} exceeds the solubility (SP) of MSe. The ratio $IP/SP = S$ defines the supersaturation of the ions over the MSe and can be varied by choosing the appropriate initial concentrations of the reactants. When $S > 1$, the ions combine on the substrate and in the solution to form MSe nuclei which grow with time to give film and precipitate, respectively. Once MSe is formed it acts as catalyst for further deposition of fresh portions of MSe preferentially. The rate of deposition and terminal thickness is dependent on the reaction mixture since the latter determines the rate of formation and growth of nuclei. As the catalytic MSe surface develops both on the surface and in the volume of the solution, the proportion of MSe formed on substrate is determined by the ratio of nuclei formed on the substrate and in the over-all solution.

In their studies on the growth of PbSe films using selenourea in place of sodium selenosulfate, Lundin *et al.* have found that the initial induction period required to form PbSe nuclei from the initially homogeneous system on the substrate surface is not observed in the kinetic curves if the substrates are covered with a seeding layer of $\text{Sn}(\text{OH})_2$ (5). As our thickness *vs.* time plots (Fig. 1 and 2) also do not show the initial induction period, we assume that the surface which is in contact with the solution has suitable impurities or foreign particles which initiate nucleation and growth of the MSe. Although the exact nature of these impurities/particles is not known, the assumption is supported by the known fact that in any precipitation system there are many particles of different nucleating efficiencies (10, 11). At low supersaturations, the most efficient group of particles will act as nuclei for MSe formation, which then grow to larger sizes. The experimental observation of large grain sizes at high pH values, where Pb^{2+} concentration is small and hence supersaturation low, suggests the existence of foreign particles on the nucleating surface. The nuclei grow and coalesce to form a continuous film. The nucleation and growth mechanism of formation of MSe films is supported by the electron microscopic investigations as seen in a series of electron micrographs in Fig. 10.

The above model of nucleation and growth of thin films is supported by our earlier observation that alloys of PbS and HgS can be prepared over a wide composition range ($\text{Pb}_{1-x}\text{Hg}_x\text{S}$, $0 \leq x \leq 0.33$) and the films can be grown epitaxially on a suitable substrate under controlled conditions (9). The observation that $\text{Pb}_{1-x}\text{Hg}_x\text{S}$ films containing α phase or β phase of HgS and CdS films with cubic, hexagonal, or mixed structure can be obtained by simply changing the deposition conditions also supports the mechanism of film formation by combination of ions on the substrate (8, 9). Note that the process of ion by ion deposition on the substrate is analogous to the atom by atom condensation process during vapor deposition.

Our observations can be understood on the basis of this mechanism of film growth as discussed in the following. The rate of deposition is high in the initial

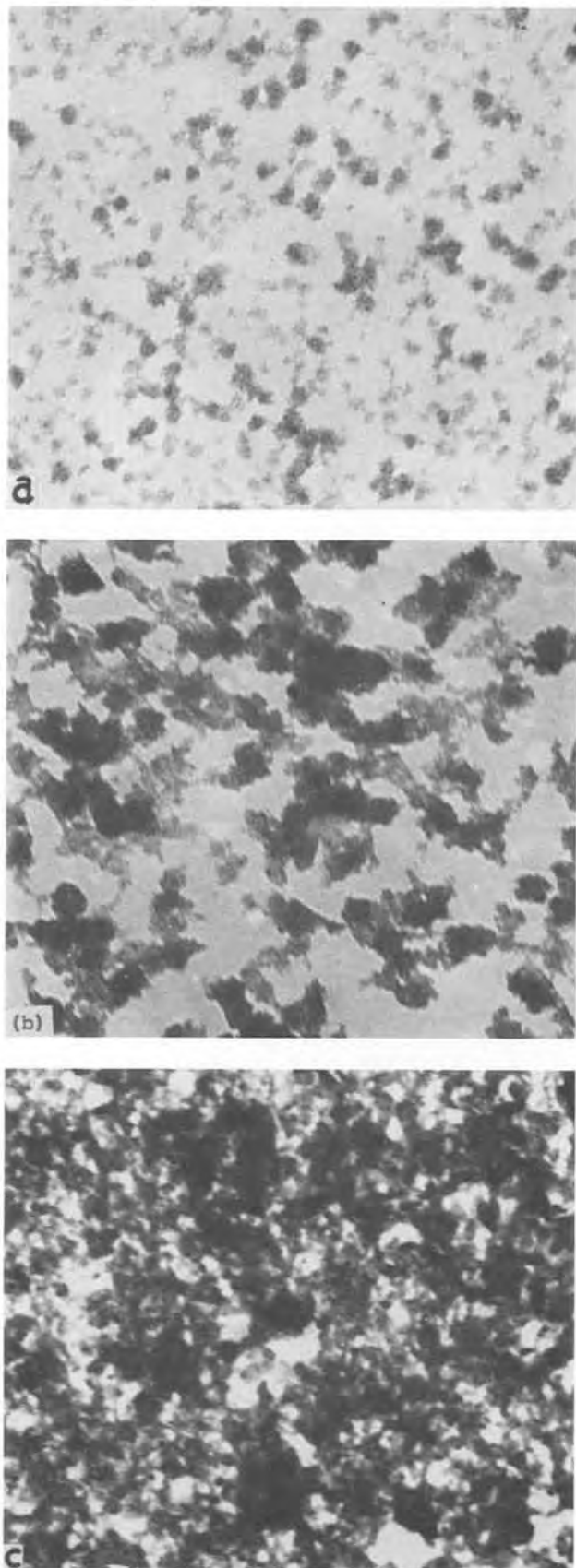


Fig. 10. Electron micrographs showing growth of PbSe films after (a) 3 min, (b) 6 min, and (c) 12 min. ($\times 80K$.)

stages of growth because the concentration of M^{2+} and Se^{2-} ions is high. As more and more of MSe is formed, the solution becomes depleted of ions, resulting in a lower rate of deposition. The rate of deposition becomes zero, resulting in a terminal thickness, when

the concentration of M^{2+} and Se^{2-} ions decrease to a value such that $S < 1$.

Effect of pH.—The reaction rate and the rate of deposition depend on the supersaturation S . The lower the supersaturation, the slower is the formation of MSe. From Eq. [8], if the concentration of OH^- is more in the solution, the Pb^{2+} concentration is small resulting in low S and slow rate of reaction. With increase in pH as the Pb^{2+} concentration decreases, the rate of formation of PbSe is reduced. Above a certain pH, depending on the bath temperature (11.4 at 28°C), the concentration of Pb^{2+} decreases to a level such that the ionic product of Pb^{2+} and Se^{2-} becomes less than the solubility product of PbSe ($S < 1$). Above this pH value, PbSe is not formed. Thus the decrease in the rate of deposition with increase in pH value and no reaction above a certain pH value is explained. Similarly, in the case of CdSe film deposition, where Cd^{2+} concentration decreases with increase in NH_3 concentration, the rate of deposition decreases on increasing the NH_3 concentration.

In the clear solution, the formation of MSe takes place by homogeneous nucleation which takes place at relatively higher supersaturations than that for heterogeneous nucleation. With increase in pH/ammonia concentration, for the case of PbSe/CdSe, as the supersaturation decreases, the precipitation is decreased resulting in more MSe on the substrate and hence higher terminal thickness.

Effect of temperature.—The dissociation of the complex and selenosulfate depends on the temperature of the bath. At higher temperatures, the dissociation is greater and gives higher concentration of M^{2+} and Se^{2-} ions. This results in higher rates of deposition. Due to thermal dissociation being higher at higher temperatures, the pH value above which ionic product of Pb^{2+} and Se^{2-} decreases to a value below the solubility product of PbSe is more, resulting in an increase in the limiting pH value for PbSe formation from 11.4 at 28°C to 12.0 at 60°C. The increased kinetic energy of the ions and hence the increased interaction between them at high temperatures are also responsible for the increase in the rate of deposition.

The terminal thickness decreases or increases with increase in the bath temperature depending on the conditions under which films are prepared. At low pH values supersaturation is high even at low temperatures. Further increase in the temperature increases the supersaturation resulting in precipitation of most of the PbSe and consequently lower terminal thickness. At high pH values where supersaturation is low, precipitation is limited, and most of the PbSe is formed on the substrate surface. Further, the thermal dissociation of complex and selenosulfate is increased at higher temperatures so that more Pb^{2+} and Se^{2-} ions are available for PbSe formation and thus higher terminal thicknesses are obtained.

Figure 6 shows results for CdSe films deposited at different temperatures for 2.1M ammonia concentration. At this concentration, the supersaturation being low the precipitation is small and hence the terminal thickness increases with increase in temperature of deposition in agreement with the above argument.

Effect of selenosulfate concentration.—The increase in the selenosulfate concentration leads to an increase in Se^{2-} ion concentration. As the rate of any chemical reaction is proportional to the concentration of the reacting species, the rate of deposition increases with increasing selenosulfate concentration. The maximum in terminal thickness is obtained because of lower selenosulfate concentrations, the number of Se^{2-} ions being insufficient to combine with all the available M^{2+} ions. As selenosulfate concentration increases, more Se^{2-} ions become available to form MSe leading to larger thicknesses. Above a certain concentration, when rate of reaction becomes high, precipitation also

becomes important leading to a lesser amount of MSe on the substrate and hence lower terminal thicknesses.

Effect of substrate.—Film formation can take place only under certain conditions, that is, either under optimum conditions for MSe formation or when the substrate has special properties facilitating the formation of single crystal films. The second condition favors film formation because when the lattice of the deposited materials matches well with that of the substrate, the free energy change of nucleation is smaller thereby facilitating nucleation. As Si and Ge have the same lattice (cubic) as CdSe and PbSe, the nucleation on these substrates is facilitated leading to higher rates of deposition and larger terminal thicknesses.

Conclusions

1. Uniform, adherent, and specularly reflecting PbSe and CdSe films can be deposited on an insulating, metallic, and semiconducting substrates by a simple chemical growth technique.

2. The film formation takes place by the recombination of the ions on the substrate surface via a nucleation and growth process.

3. The rate of deposition of the films and the terminal thickness depend sensitively on pH, composition, and temperature of the bath and the nature of the substrate.

Manuscript submitted April 27, 1979; revised manuscript received July 27, 1979.

Any discussion of this paper will appear in a Discussion Section to be published in the December 1980 JOURNAL. All discussions for the December 1980 Discussion Section should be submitted by Aug. 1, 1980.

REFERENCES

1. K. L. Chopra, "Thin Film Phenomena," chap. 2, McGraw-Hill Book Co., New York (1969).
2. D. O. Skovlin and R. A. Zingaro, *This Journal*, **111**, 42 (1964); D. E. Bode, in "Physics of Thin Films," Vol. 3, G. Hass and R. E. Thun, Editors, p. 275, Academic Press, New York (1966).
3. G. A. Kitaev, S. G. Mokrushin, and A. A. Üritskaya, *Colloid J. USSR*, **27**, 38 (1965).
4. T. M. Racheva, I. D. Dragieva, D. H. Djoglev, and P. P. Dimitrova, *Thin Solid Films*, **17**, 85 (1973).
5. A. B. Lundin and G. A. Kitaev, *Inorg. Mater.*, **1**, 2107 (1965).
6. G. A. Kitaev and T. S. Terekhova, *Russian J. Inorg. Chem.*, **15**, 25 (1970).
7. G. M. Fofanov and G. A. Kitaev, *ibid.*, **14**, 322 (1969).
8. I. J. Kaur, D. K. Pandya, and K. L. Chopra, Submitted to *This Journal*.
9. N. C. Sharma, D. K. Pandya, H. K. Sehgal, and K. L. Chopra, *Thin Solid Films*, **59**, 157 (1979).
10. D. H. Klein and J. A. Driy, *Talanta*, **13**, 289 (1966).
11. A. E. Nielsen, "Kinetics of Precipitation," pp. 23-25, Pergamon Press, London (1964).

The Influence of Solution pH on Microstructure of Electrodeposited Cobalt

S. Nakahara* and S. Mahajan*

Bell Laboratories, Murray Hill, New Jersey 07974

ABSTRACT

In this study we have attempted to elucidate the influence of pH on microstructures of electrodeposited cobalt using transmission electron microscopy. It is observed that at low pH (~ 1.6), the microstructure mostly consists of highly faulted fcc regions, and electron diffraction patterns are very complex. On the other hand, at high pH (~ 5.7) hcp phase is observed, and the density of faults is greatly reduced. From these observations together with results of chemical analysis, it is proposed that at low pH, the formation of fcc cobalt, probably in the form of metastable cobalt hydride, is greatly facilitated by the adsorption and subsequent incorporation of atomic hydrogen into the electrodeposits. However, later on these hydrogen atoms rapidly diffuse out of the film, thereby the resulting "fcc cobalt" (cobalt hydride) becomes unstable at room temperature and transforms martensitically into hcp cobalt.

It has long been known that the high temperature ($>417^\circ\text{C}$) phase of cobalt (fcc) can be obtained by electrodeposition at ambient temperature. Polukarov (1) and Goddard and Wright (2) have reported that the pH of an electrolyte has a marked influence on the formation of the fcc phase. Electrodeposition from solutions with $\text{pH} < 2.4$ results in fcc cobalt, whereas from solutions with $\text{pH} > 2.9$, hcp cobalt is produced (2). However, it remained unresolved as to how fcc cobalt can be produced at room temperature.

Recently, Wright (3) and Gaigher and van der Berg (4) have reported on the influence of pH on the fcc \rightleftharpoons hcp phase transition during the early stages of cobalt electrodeposition. Wright (3) has suggested that fcc cobalt grows epitaxially onto fcc metal substrates, and, in addition, the incorporation of hydrogen into the fcc lattice during the deposition at low pH may make the fcc \rightarrow hcp phase transition, based on energy considerations, unlikely. This conclusion strongly implies that

the formation of fcc cobalt is characterized as the hydrogen-assisted state of extended pseudomorphism, which is similar in principle to that observed in vapor-deposited cobalt/copper bimetallic films (5). These suggestions, however, do not seem to be consistent with the fact that very thick fcc cobalt films, which are not affected by epitaxial growth, can be produced at low pH (2). With respect to the occurrence of the hcp cobalt at high pH, Gaigher and van der Berg (4) have suggested an association with the presence of colloidal hydroxides at the cathode surface during the deposition.

In this study, we have investigated the influence of pH on the microstructures of electrodeposited cobalt films by transmission electron microscopy, and these results constitute the present paper. A plausible explanation for the formation of fcc cobalt at low pH has been developed.

Experimental

Cobalt films were electrodeposited on a sheet of annealed OFHC copper. The composition of the plat-

* Electrochemical Society Active Member.
Key words: pH, electrodeposition, electron.

ing solution was 300 g/liter CoSO_4 , 3 g/liter NaCl , and 6 g/liter boric acid (2). The pH was lowered and raised by the addition of H_2SO_4 and NaOH , respectively. Plating was conducted without any mechanical agitation at the current density of 10 mA/cm^2 and at room temperature (20°C).

Cobalt films were prepared from two solutions with pH = 1.6 and 5.7. This choice of pH values is based upon the previous investigation (2). For the purpose of convenient terminology, cobalt films obtained in these low and high pH solutions will be called, hereafter, low pH cobalt (LP-Co) and high pH cobalt (HP-Co) films, respectively. After masking the front surface of the plated films, the film-substrate composite was prepared for TEM examination by electropolishing from the substrate side using the conventional window technique. In this way, viewing can be done on the region in which the effect of the substrate on the microstructure of deposits would be minimal. Furthermore, as the thickness of all the films was well in excess of $50 \mu\text{m}$, the role of substrate in inducing epitaxial growth should be negligible.

All TEM micrographs were obtained using a JEM 200 microscope operated at an accelerating voltage of 200 kV. Images of small inclusions in the deposits were taken using the defocus contrast technique, which has been described previously (6).

Results

The plating characteristics in the low and high pH solutions were quite different. In the low pH solution, plating was accompanied by the evolution of a large amount of hydrogen gas and, consequently, the current efficiency for the metal deposition was extremely low. It was apparent that both cobalt and hydrogen are depositing simultaneously at the cathode. In the high pH solution, on the other hand, only a small amount of hydrogen gas was seen to evolve at the cathode and the current efficiency for the metal deposition was nearly 100%.

Transmission electron microscopy studies have revealed that the microstructures of LP-Co films were markedly different from those of HP-Co films. In particular, the most dramatic structural difference was observed in their electron diffraction patterns. Figures 1(a) and (b) show electron diffraction patterns for LP-Co and HP-Co films, respectively. It is noted that the diffraction pattern for the LP-Co film is extremely complicated as compared to that of the HP-Co film. The observed streaking in the diffraction pattern, in fact, was found to originate from extensive faulting within individual grains. An example of the extensively faulted grains in the LP-Co film is shown in Fig. 2; trace of the fault plane is delineated by the dotted line AA'. From the analysis of electron diffraction patterns, it was found that the LP-Co film primarily contains faulted fcc cobalt with a small amount of hcp phase, whereas the HP-Co film consists entirely of the hcp phase. A summary of the diffraction analysis is shown in Table I. The present results confirm the earlier observations that fcc cobalt can be produced during electrodeposition from the low pH solution. Typical microstructures of the LP-Co film are further illustrated in Fig. 3. In most of the grains, faulting is observed only on one variant, but some grains, such as the one marked with a symbol, FCC, contain faults lying on two variants. In view of the fact that in fcc structure, faulting can occur on four $\{111\}$ planes, the observed faulting on two planes within one grain appears to be consistent with the above electron diffraction results.

Figure 4 shows the structure of HP-Co film. The noticeable difference from the LP-Co films is that almost all grains are of hcp cobalt without any appreciable faulting, but contain a high density ($\sim 1.4 \times 10^{17}/\text{cm}^3$) of small ($\sim 10\text{\AA}$) inclusions. Very few faults are present. The three fine arrows point out three typical

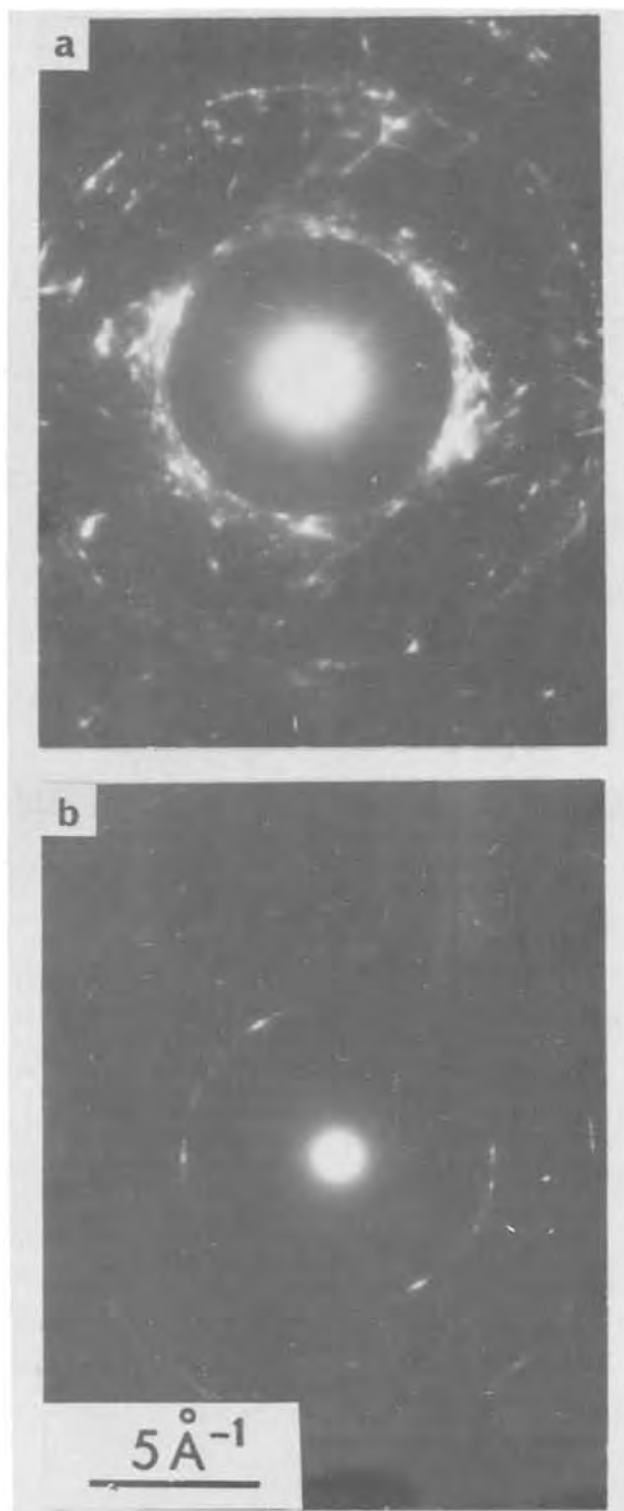


Fig. 1. Electron diffraction patterns from electrodeposited cobalt films obtained in a solution with (a) pH = 1.6 and (b) 5.7.

inclusions which are made visible using the defocus contrast technique (6). The fact that these inclusions are seen as white dots surrounded by black rings in the underfocused condition suggests that the inclusions have smaller mean inner potential than does the surrounding cobalt matrix. It is further noted that these inclusions are incorporated systematically along the (0001) basal plane of each grain. Figure 5 shows some zigzag steps due to slight misorientation in the film plane, in which lines of incorporated inclusions also follow systematically along the basal planes as indicated with a symbol, TT'. This crystallographic alignment of inclusions strongly suggests that they must

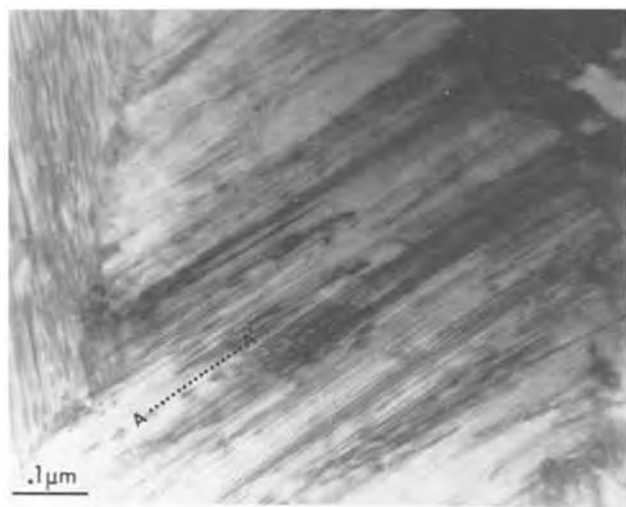


Fig. 2. Microstructure of electrodeposited cobalt film (LP-Co) obtained in a solution with $\text{pH} = 1.6$. A high density of faults is seen and the trace is indicated with symbols, AA'.

have been incorporated during the deposition on the (0001) basal plane which is also the growth plane for the cobalt metal.

In order to determine the amount of probable impurity content in the deposits, the LP-Co and HP-Co films were analyzed using vacuum fusion technique and mass spectrometry.¹ The LP-Co film was found to contain 33 ppm H_2 and 35 ppm O_2 . On the other hand, the HP-Co film contained 230 ppm H_2 and 890 ppm O_2 . The higher content of both hydrogen and oxygen in the HP-Co film suggests that these gases may have originated from cobalt hydroxides.

Discussion

It has been shown that fcc cobalt can be obtained during the electrodeposition from the low pH solution. It should be noted, however, that these cobalt grains observed in the LP-Co film are highly faulted. It is well known that the $\text{fcc} \rightarrow \text{hcp}$ structural transformation can be accomplished by faulting on alternate

¹This analysis was made by Gollob Analytical Service Corporation, Berkeley Heights, New Jersey 07922.

Table I. Analysis of electron diffraction patterns

Electron diffraction from LP-Co film		
d_{obs} (Å)	Identification*	
	d (Å)	HKL
2.000	2.0467	111 _{fcc}
2.158	2.165	1010 _{hcp}
1.918	1.910	101 _{fcc}
1.755	1.7723	200 _{fcc}
1.501	1.48	1012 _{hcp}
1.262	1.252	1120 _{hcp}
1.158	1.149	1013 _{hcp}
1.065	1.083	2020 _{hcp}
Electron diffraction from HP-Co film		
d_{obs} (Å)	Identification*	
	d (Å)	HKL
2.109	2.165	1010
2.053	2.023	0002
1.472	1.48	1012
1.266	1.252	1120
1.176	1.149	1013
1.085	1.083	2020

* For hcp cobalt, data from ASTM Diffraction File 5-0727 and for fcc cobalt, data from ASTM Diffraction File 15-806.

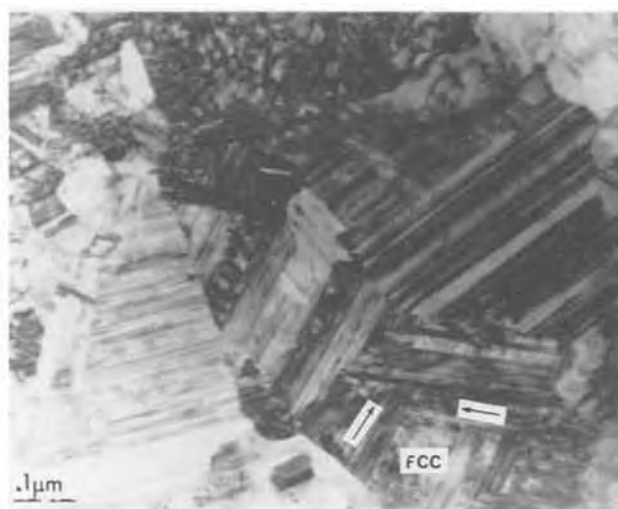


Fig. 3. Structure of an electrodeposited cobalt film (LP-Co) obtained in a solution with $\text{pH} = 1.6$. The film contains primarily fcc grains as indicated with a symbol, FCC, in which two faulting systems (see two arrows) are activated, indicative of fcc structure.



Fig. 4. Microstructure of an electrodeposited cobalt film (HP-Co) obtained in a solution with $\text{pH} = 5.7$. Three arrows indicate the presence of inclusions (seen as white dot surrounded by a black ring), trapped in the (0001) basal plane of hcp cobalt grains. The micrograph is slightly underfocused to reveal the image of inclusions using the defocus contrast technique.

{111} planes (7). The microstructure of the LP-Co film, therefore, suggests that the fcc structure was originally formed during the deposition, but due to its instability at room temperature transformed into the more stable hcp phase via $\{111\}_{\text{fcc}}$ faulting. A question, then, can be raised as to how fcc cobalt is produced in the low pH solution, but not in the high pH.

In order to understand the basic mechanism of fcc cobalt formation, it is important to understand the electrochemical aspects of cobalt electrodeposition. A number of investigations (8-10) have discussed the peculiarities in the electrochemical behavior generally common to the iron group metals, i.e., Fe, Co, and Ni. The electrolytic reduction of the iron group metal ions from aqueous solutions is accompanied by substantial overvoltage, and markedly varies with the pH of the solution. This high overvoltage is generally attributed to the high adsorption of foreign substances (hydrogen, hydroxide) on the electrode surface, which, in turn, influences the reduction rate of metal ions. In particular, when the deposition is made at low temperature (20°C), both the cathode potential and current effi-

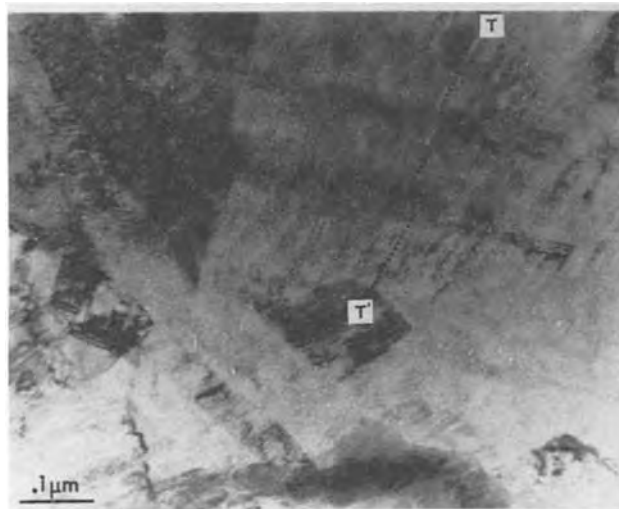


Fig. 5. Microstructure of an electrodeposited cobalt film (HP-Co) prepared in a solution with $\text{pH} = 5.7$. A dotted line, traced with symbols, TT', follows the systematic directional change in the line of inclusions. It is seen that these hcp cobalt grains are slightly misoriented to each other, forming a fan-shaped morphology.

ciency for the metal deposition sharply decrease with decreasing pH . This phenomenon can also be explained by the increasingly high adsorption and subsequent codeposition of hydrogen atoms with decreasing solution pH . At high temperature (150°C), however, the irreversible adsorption of hydrogen or hydroxide is drastically decreased, and hence the inhibiting action of these foreign substances and the overvoltage for the metal reduction are also decreased. From these investigations, the following observations emerge. At low pH ($<2.0 \sim 2.2$) and low temperature, the current is used up chiefly for the reduction of hydrogen ions. At high pH (>3.0), the current is mainly consumed for the reduction of metal ions, but some retardation of the reduction of metal ions is due to the adsorption of hydroxide.

From the above electrochemical results, it is now clear that the effect of solution pH on the microstructures of cobalt electrodeposits can be closely related to the incorporation of foreign substances (hydrogen, hydroxide). In our experiment, hydrogen is likely to be incorporated in the LP-Co film, whereas hydroxide may be codeposited into the HP-Co film. Our microstructural results then can be conveniently discussed in terms of the codeposition of hydrogen and hydroxide.

The cobalt film prepared from the low pH solution is expected to contain an appreciable amount of hydrogen at least within a short period of time immediately after the film is formed. It is then conceivable that the film could have been cobalt hydride prior to the outdiffusion of hydrogen. Although cobalt hydrides or their complexes are reported to be prepared in the form of CoH (11) and CoH_2 (12) during chemical reactions involving cobalt salt under hydrogen, cobalt hydrides are predicted (13) to be nonexistent or, if any, very unstable. Thus, if cobalt hydrides can be produced, they will be extremely unstable. The assumption that metastable cobalt hydride may be produced during the cobalt electrodeposition is consistent with the fact that nickel, one of the iron group metals, is converted into metastable nickel hydride by cathodic charging with hydrogen (14). The cathodic charging of nickel with hydrogen produced nonstoichiometric nickel hydride NiH_n ($n = 0.7 \sim 1.0$) which has the same Bravais-type lattice as that of nickel, but has the lattice spacing by about 6% larger (15). This nickel hydride was apparently unstable under ambient conditions, but was stable enough to permit x-ray diffraction studies (14, 16). The cobalt electrodeposition mode

at low pH resembles effectively the cathodic charging of nickel with hydrogen, as most of the current is used up for the reduction of hydrogen ions. In analogy to the nickel hydride, cobalt hydride can be assumed to have a fcc structure.

The stability of hydrogen in cobalt or alternatively cobalt hydride can be argued from the point of hydrogen solubility and diffusivity in cobalt. The solubility of hydrogen at room temperature is known to be extremely small (17). According to Vagramyan and Petrova (18), the hydrogen solubility in cobalt at 20°C is $\ll 0.05 \text{ cm}^3/\text{g}$ ($\ll 4.46 \text{ ppm}$). The data obtained by Stafford and McLellan (19) show that the solubility of hydrogen in cobalt at 300°C is about 0.63 ppm. If we extrapolate their solubility curve to room temperature (20°C), it amounts to 0.041 ppm, consistent with the Vagramyan and Petrova data. Furthermore, in case nonequilibrium hydrogen is incorporated into cobalt during the deposition, it could escape out of the film very rapidly as it has a high diffusivity at room temperature. From the data obtained by Caskey *et al.* (20), the diffusivity of hydrogen in cobalt, extrapolated to room temperature (20°C), is $1.71 \times 10^{-11} \text{ cm}^2/\text{sec}$ for fcc cobalt. These diffusivities are extremely high, and, for example, a simple calculation based upon the random walk theory indicates that hydrogen included in cobalt films, $50 \mu\text{m}$ thick (our film thickness is about $75 \mu\text{m}$), can diffuse out of the film between 51 hr and 18 days at room temperature after the film preparation. The fact that the gas analysis in the cobalt electrodeposits has been made 5 months after the film preparation suggests that dissolved atomic hydrogen has diffused out of the film, and, therefore, the origin of appreciable amount of hydrogen obtained in the analysis should be different. The amount of hydrogen found in this experiment probably originates from the decomposition of cobalt hydroxide.

It appears that the observed hydrogen content in both the LP-Co and HP-Co films originates from the decomposition of some form of cobalt hydroxide and not from dissolved atomic hydrogen. The observed ratio of H_2/O_2 (33/35) for the LP-Co film is consistent with the preceding suggestion. However, to rationalize the result for the HP-Co film, the existence of oxygen-rich cobalt hydroxide has to be invoked. The pH dependence of both hydrogen and hydroxide occlusion in cobalt electrodeposits obtained in cobalt chloride solution has been studied by Vagramyan and Petrova (20). Their results are shown together with our results in Fig. 6. Curves A and B represent hydrogen gas and gas arising from the decomposition of cobalt hydroxide, respectively, and a black dot with an arrow denotes our data. It is seen that our data follow the trend of curve B, suggesting that our gas content comes primarily from the decomposition of cobalt hydroxide. It is interesting to note that the amount of dissolved hydrogen at $\text{pH} = 1.6$ is very large, but it is negligibly small at $\text{pH} = 5.7$. Their results again confirm the electrochemical observation that a large amount of hydrogen is codeposited at low pH .

Inclusions observed in the HP-Co film are probably particles of cobalt hydroxide. From an electron diffraction analysis, however, we could not find any diffraction lines corresponding to crystalline cobalt hydroxide. These noncrystalline inclusions are probably in a colloidal form, as they are seen to have a much smaller mean inner potential than the cobalt matrix. That these inclusions are crystallographically aligned closely resembles the morphology of O-phenanthroline molecules incorporated into copper electrodeposits (21). It was found (21) that organic additives are generally first adsorbed at growth steps and subsequently incorporated into a deposit. The manner in which these molecules are incorporated, therefore, follows the geometry of growth steps. The crystallographic arrangement of cobalt hydroxide inclusions on the (0001) growth plane of hcp cobalt (see Fig. 7 for a schematic

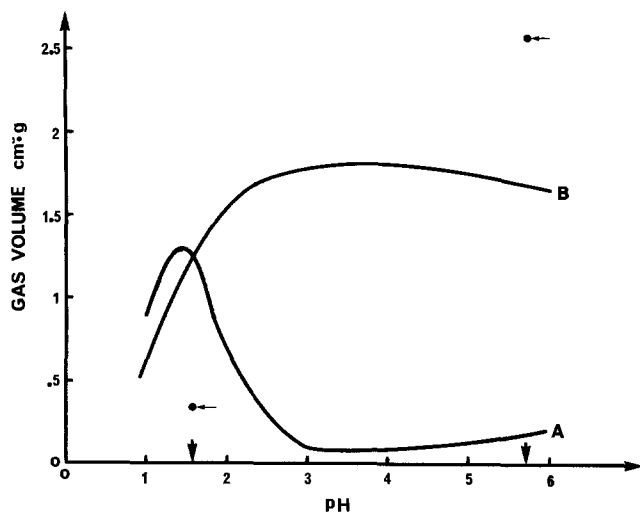
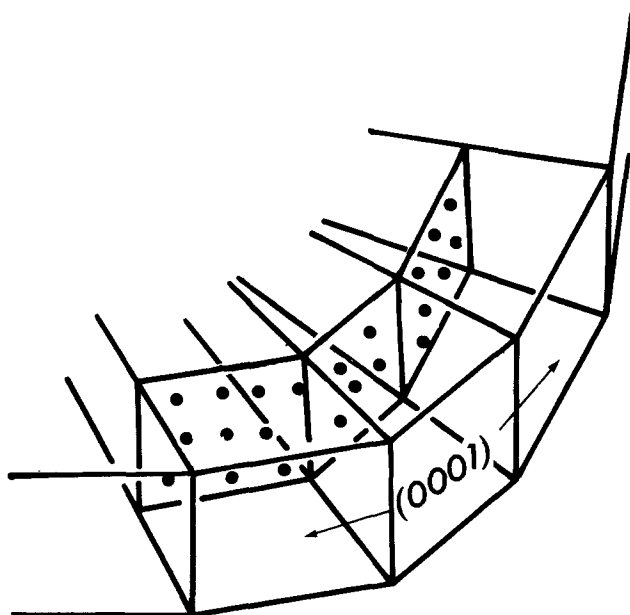


Fig. 6. The relation between the pH of the electrolyte and the amount of hydrogen present in cobalt electrodeposits. Curves A and B represent the amount of hydrogen and the amount of gas arising from the decomposition of hydroxides in cobalt electrodeposits obtained from 1N CoCl_2 at 25°C and a current density of 20 mA/cm² (due to Vagramyan and Petrova, 1962). The amount of hydrogen in cobalt electrodeposits in this experiment is indicated with black circles with fine arrows and is seen to follow closely with curve B.



• Cobalt hydroxide

Fig. 7. Growth model illustrating the structure of hcp cobalt obtained at pH = 5.7. The incorporation of spherical cobalt hydroxides in the (0001) basal planes is also shown.

view) thus suggests that they behave very much like an organic additive. It should be pointed out that contrary to the previous conclusion (4), these colloidal inclusions do not contribute to the stability of hcp phase, but simply act as an addition agent, which generally inhibits a lateral growth and may promote a vertical growth by being adsorbed at advancing growth steps.

For the sake of comparison with the gas analysis, we listed the population density and volume percent (v/o) of inclusions which are determined from the TEM micrographs. These data, together with the estimated amount of cobalt hydroxide, $\text{Co}(\text{OH})_2$, are summarized in Table II. It is noted that the trend of the amount also follows that of curve B in Fig. 6, lending

Table II. TEM analysis of inclusions in cobalt electrodeposits

Specimen	Population density of inclusions (cm ⁻³)	Volume density (%)	Calculated $\text{Co}(\text{OH})_2$
LP-Co	2.3×10^{15}	0.01	0.04
HP-Co	1.4×10^{17}	0.48 ~ 1.88	2 ~ 8

further support to the idea that the inclusions are cobalt hydroxide particles. The calculated amount of $\text{Co}(\text{OH})_2$ from the v/o of the inclusions is somewhat smaller than that determined by the gas analysis. This difference is probably due to smaller inclusions which are not detectable by TEM.

Conclusions

It has been shown that at low pH (~1.6), the microstructures of cobalt electrodeposits consist of highly faulted fcc regions with some hcp regions. At high pH (~5.7), on the other hand, the density of faults is greatly reduced and the microstructures consist entirely of hcp phase. Furthermore, a high density of inclusions, probably cobalt hydroxide, was observed in the high pH deposits. From these observations together with a chemical analysis, it is suggested that during the cobalt electrodeposition at low pH, the formation of apparent fcc phase, actually metastable cobalt hydride (fcc), is greatly promoted by the codeposition of atomic hydrogen, but during and after the deposition, the rapid diffusion of atomic hydrogen causes the fcc hydride phase to decompose and partially transform to hcp cobalt. This transformation involves the formation of faults on {111} planes.

Acknowledgment

The authors would like to thank Dr. G. Y. Chin for his constructive comments on this manuscript.

Manuscript submitted April 9, 1979; revised manuscript received July 30, 1979.

Any discussion of this paper will appear in a Discussion Section to be published in the December 1980 JOURNAL. All discussions for the December 1980 Discussion Section should be submitted by Aug. 1, 1980.

Publication costs of this article were assisted by Bell Laboratories.

REFERENCES

1. Yu. M. Polukarov, *Russ. J. Phys. Chem.*, **34**, 68 (1960).
2. J. Goddard and J. G. Wright, *Br. J. Appl. Phys.*, **15**, 807 (1964).
3. J. G. Wright, *Thin Solid Films*, **22**, 197 (1974).
4. H. L. Gaigher and N. G. van der Berg, *Electrochim. Acta*, **21**, 45 (1976).
5. W. A. Jesser and J. W. Matthews, *Philos. Mag.*, **17**, 461 (1968).
6. S. Nakahara and Y. Okinaka, in "Properties of Electrodeposits—Their Measurement and Significance," R. Sard, H. Leidheiser, Jr., and F. Ogburn, Editors, p. 50, The Electrochemical Society Softbound Proceeding Series, Princeton, N.J. (1975).
7. J. W. Christian, *Proc. R. Soc. (London), Ser. A*, **206**, 51 (1951).
8. A. T. Vagramyan, V. N. Kuznetsova, A. P. Popkov, V. A. Savostin, and L. A. Uvarov, *Russ. J. Phys. Chem.*, **35**, 694 (1961).
9. A. T. Vagramyan and M. A. Zhamagortsyan, *ibid.*, **38**, 427 (1964).
10. Yu. P. Balakin, A. T. Vagramyan, and L. A. Uvarov, *Izv. Akad. Nauk SSSR, Ser. Khim.*, **3**, 398 (1966).
11. R. C. Ray and R. B. N. Sahai, *J. Indian Chem. Soc.*, **23**, 67 (1946).
12. B. Sarry, *Z. Anorg. Allg. Chem.*, **288**, 48 (1956).
13. T. R. P. Gibb, Jr., *Prog. Inorg. Chem.*, **3**, 315 (1962).
14. B. Baranowski and M. Smialowski, *J. Phys. Chem. Solids*, **12**, 206 (1959).
15. A. Janko, *Naturwissenschaften.*, **47**, 225 (1960).

16. S. Majchrzak, *Bull. Acad. Pol. Sci., Ser. Sci. Chim.*, **15**, 485 (1967).
 17. T. V. Lipets, Zh. L. Vert, and I. P. Tverdovskii, *Russ. J. Phys. Chem.*, **43**, 740 (1969).
 18. A. T. Vagramyan and Yu. S. Petrova, "The Mechanical Properties of Electrolytic Deposits," Consultant Bureau, New York (1962).
 19. S. W. Stafford and Rex B. McLellan, *Acta Metall.*, **22**, 1463 (1974).
 20. G. R. Caskey, Jr., R. G. Derrick, and M. R. Louthan, Jr., *Scr. Metall.*, **8**, 481 (1974).
 21. S. Nakahara and A. Staudinger, Paper 262 presented at the Electrochemical Society Meeting, Las Vegas, Nevada, Oct. 17-22, 1976.

Primary Potential and Current Distribution Around a Bubble on an Electrode

Paul J. Sides* and Charles W. Tobias**

Materials and Molecular Research Division, Lawrence Berkeley Laboratory
and Department of Chemical Engineering, University of California, Berkeley, California 94720

ABSTRACT

An analytical solution for the primary potential and current distribution around a spherical bubble in contact with a plane electrode is presented. Zero at the contact point, the current density reaches only 1% of its undisturbed value at 30% of the radius from that point and goes through a shallow maximum two radii away. The solution obtained for spherical bubbles is shown to apply for bubbles having contact angles smaller than 17.5°. The incremental resistance caused by dilute arrays of bubbles is evaluated.

The evaluation of effective thermal or electrical conductance of heterogenous systems from the conductivities of the individual phases is a commonly occurring problem in science and technology. For suspensions of gas bubbles generated by discharge processes at electrodes, the problem is tractable because the discontinuous phase consists of spherical, nonconducting particles. As early as 1892 Maxwell (1) presented an analytical solution for the effective conductivity of a dilute random suspension of spherical particles. Rayleigh (2) developed an exact solution for a cubic array of spheres. Using an ingenious approximate treatment by Bruggeman (3), Tobias and co-workers (4, 5) proposed useful approximations for treating concentrated, random suspensions of spheres and applied these results in the evaluation of the effect of gas bubbles on the resistance and current distribution in electrolytic gas generators (6). Hine and co-workers (7) differentiated between a relatively concentrated dispersion of gases near the electrodes and the more dilute suspension in the bulk electrolyte. These semi-empirical models, however, do not consider the effect of bubbles attached to the electrode surface. The effect of this layer of bubbles, present during electrolysis, differs from that of bubbles dispersed in the bulk electrolyte because the environment of a bubble sitting on the surface is asymmetric; the electrode, an equipotential surface, is in contact with a planar array of bubbles, while the electrolyte extends to a large distance on the opposite side of this array.

In the following, an analytical solution is presented which describes the potential field around a spherical bubble in point contact with a planar equipotential surface when the field far from the sphere is linear. The current distribution on the electrode plane and the incremental resistance caused by a dilute array of bubbles are also evaluated.

Theoretical

We use tangent sphere coordinates to solve Laplace's equation for the potential field and current distribution on the planar electrode around the insulating sphere. The coordinate planes are spheres tangent to a

plane and toroids without center openings; they are related to Cartesian coordinates by

$$z = \frac{\nu}{\nu^2 + \mu^2}, \quad x = \frac{\mu}{\mu^2 + \nu^2} \quad [1]$$

The coordinates and their relations to the geometry appear in Fig. 1. ν corresponds to the inverse of radial distance from the contact point while μ is analogous to an angular coordinate. Infinity of both coordinates specifies the contact point. Moon and Spencer (8) present a rather complete discussion of various coordinate systems, including the one above, in their "Field Theory Handbook."

The variables, defined in dimensionless form, are as follows

$$\begin{aligned} z^* &= z/2a \\ x^* &= x/2a \\ \nu^* &= 2a\nu \\ \mu^* &= 2a\mu \\ \phi^* &= \phi/2a\phi_0 \\ i^* &= i/\kappa\phi_0 \end{aligned} \quad [2]$$

The distance variables are normalized to the bubble diameter; therefore, $x^* = 1$ defines a plane parallel to the y^*z^* plane and located one bubble diameter from the axis passing through the center of the bubble and the contact point.

We write the potential as the sum of a disturbance and a linear term

$$\phi^* = \phi_d^* + z^* \quad [3]$$

The second term already satisfies Laplace's equation and all boundary conditions except the one on the bubble surface; therefore

$$\nabla^2 \phi_d^* = 0 \quad [4]$$

The disturbance must vanish both on the electrode and far away; the potential must be symmetric about an axis passing through the center of the bubble and the contact point; finally, no current passes through the bubble. In tangent sphere coordinates Eq. [4] and these boundary conditions are

* Electrochemical Society Student Member.

** Electrochemical Society Active Member.

Key words: potential field, current distribution, electrolytic gas evolution.

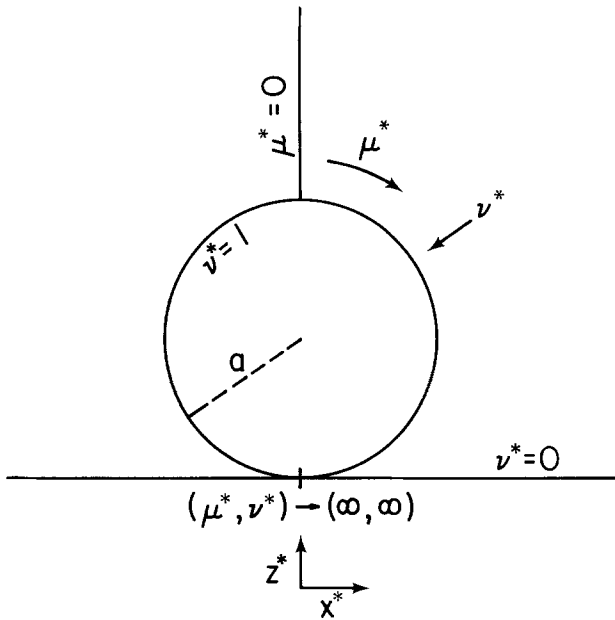


Fig. 1. Tangent sphere coordinates in two dimensions

$$\frac{(\mu^{*2} + \nu^{*2})^3}{\mu^*} \left[\frac{\partial}{\partial \mu^*} \left(\frac{\mu^*}{\mu^{*2} + \nu^{*2}} \frac{\partial \phi_d^*}{\partial \mu^*} \right) + \mu^* \frac{\partial}{\partial \nu^*} \left(\frac{1}{\mu^{*2} + \nu^{*2}} \frac{\partial \phi_d^*}{\partial \nu^*} \right) \right] = 0 \quad [5]$$

$$\phi_d^* |_{\nu^*=0} = 0 = \phi_d^* |_{\nu^*=0} \quad \mu^*=0 \quad [6]$$

$$\left. \frac{\partial \phi_d^*}{\partial \mu^*} \right|_{\mu^*=0} = 0 \quad [7]$$

$$\left. \frac{\partial \phi^*}{\partial \nu^*} \right|_{\nu^*=1} = 0 \quad [8]$$

Moon and Spencer (8) give the separation criteria, the separated equations, and their general solutions. After applying conditions [6] and [7], we obtain

$$\phi_d^* = A \sinh(q\nu^*) J_0(q\mu^*) (\mu^{*2} + \nu^{*2})^{1/2} \quad [9]$$

Because the domain is infinite, the solution must include all values of q ; therefore, [9] passes to an integral

$$\phi_d^* = (\mu^{*2} + \nu^{*2})^{1/2} \int_0^\infty A \sinh(q\nu^*) J_0(q\mu^*) dq \quad [10]$$

The insulation condition [8] determines A as a function of q . Upon differentiating the complete potential ϕ^* , evaluating this expression at $\nu^* = 1$, and equating it to zero, we obtain

$$0 = \frac{1}{(\mu^{*2} + 1)^{1/2}} \int_0^\infty A \sinh q J_0(q\mu^*) dq + (\mu^{*2} + 1)^{1/2} \int_0^\infty A q \cosh q J_0(q\mu^*) dq + \frac{(\mu^{*2} - 1)}{(\mu^{*2} + 1)^2} \quad [11]$$

Following Witze, Schrock, and Chambré (9), we use the differential equation satisfied by J_0 and integrate twice by parts to obtain

$$\frac{1 - \mu^{*2}}{(\mu^{*2} + 1)^{3/2}} = \int_0^\infty q H J_0(q\mu^*) dq \quad [12]$$

where

$$H(q) = \frac{1}{q} \left\{ -\frac{d}{dq} \left[q \frac{d}{dq} (A \cosh q) \right] + A(q \cosh q + \sinh q) \right\} \quad [13]$$

After inverting the transform with the help of the Erdelyi Tables (10) and rearranging the equations, we obtain

$$\frac{dA}{dq} = \frac{1 - q + e^{-2q}}{2 \cosh^2 q} + \frac{C}{2q \cosh^2 q} \quad [14]$$

C must be zero for the derivative to remain finite at $q = 0$

$$A = \int_\infty^q \frac{1 - q + e^{-2q}}{2 \cosh^2 q} dq \quad [15]$$

The potential is now given by

$$\phi^* = (\nu^{*2} + \mu^{*2})^{1/2} \int_0^\infty A J_0(q\mu^*) \sinh(q\nu^*) dq + \frac{\nu^*}{(\mu^{*2} + \nu^{*2})} \quad [16]$$

and the primary current distribution is

$$i^* = \mu^{*2} \frac{\partial \phi^*}{\partial \nu^*} \Big|_{\nu^*=0} = \mu^{*3} \int_0^\infty q A J_0(q\mu^*) dq + 1 \quad [17]$$

Equations [16] and [17] were numerically evaluated by routines that calculated the Bessel functions and integrated their products with the hyperbolic functions over the appropriate domains.

Discussion

The potential map appears in Fig. 2(a) and (b). The potential is normalized so that equipotentials far from the bubble coincide with distance from the electrode (see Eq. [3]). As required by the insulation condition, Eq. [8], the equipotentials meet the bubble at right angles; they approach their undisturbed values far away. One can see from Fig. 2(a) that the displacement of equipotentials caused by the insulating sphere becomes negligibly small beyond one and a half diameters from its contact point along the electrode and three diameters perpendicular to the electrode.

The current distribution as a function of dimensionless distance appears in Fig. 3(a) and (b). The current density is normalized to be 1.0 at a great distance from the sphere; we call this the "undisturbed" value. The value 0.5 on the abscissa of Fig. 3 marks the outer-

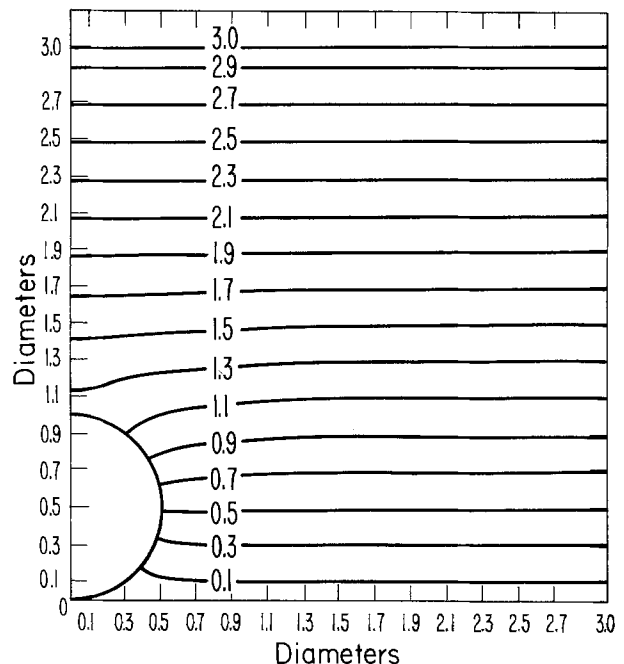


Fig. 2(a). Potential around an insulating sphere tangent to an electrode.

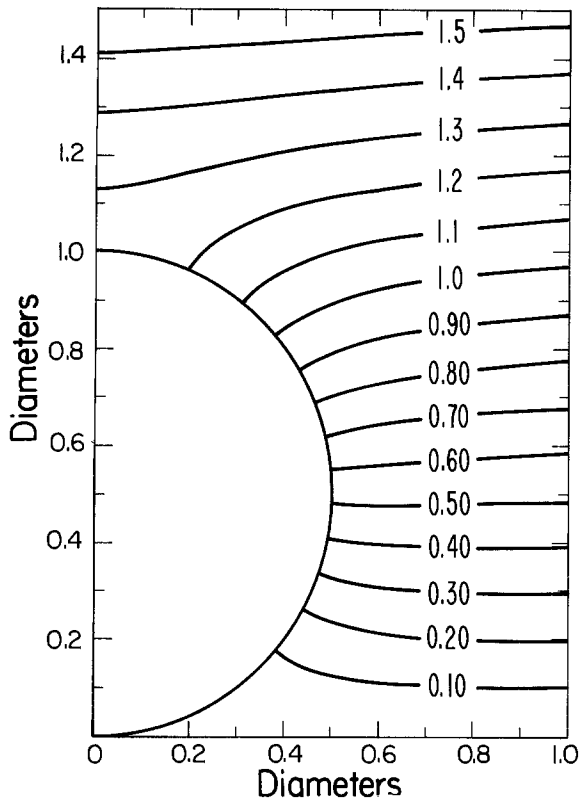


Fig. 2(b). Detail of potential close to sphere

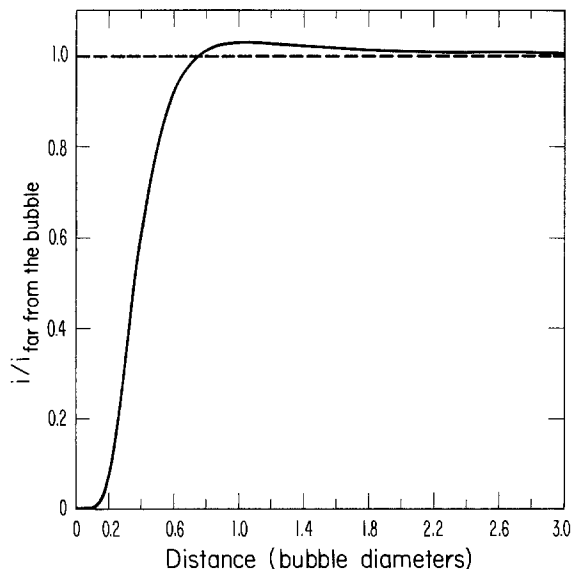


Fig. 3(a). Current distribution near a spherical insulator tangent to a surface.

most circle on the electrode shadowed by the bubble; here, the current density is 80% of its undisturbed value. The current density farther from the bubble exceeds 1.0 because the upper half of the sphere deflects the flux and thereby creates a maximum current density 2% greater than the undisturbed value at one diameter from the contact point. We conclude that fields around spheres separated by more than three diameters affect each other negligibly.

A detail of the current distribution near the contact point appears in Fig. 3(b). Zero at the axis, the current density reaches only 1% of its undisturbed value at 30% of the radius from the contact point; therefore, we can insulate the area inside this distance with a surface which coincides with a surface of flow. Thus the effect of a tangent insulating sphere on the current distribution approximates that of a bubble having a nearly

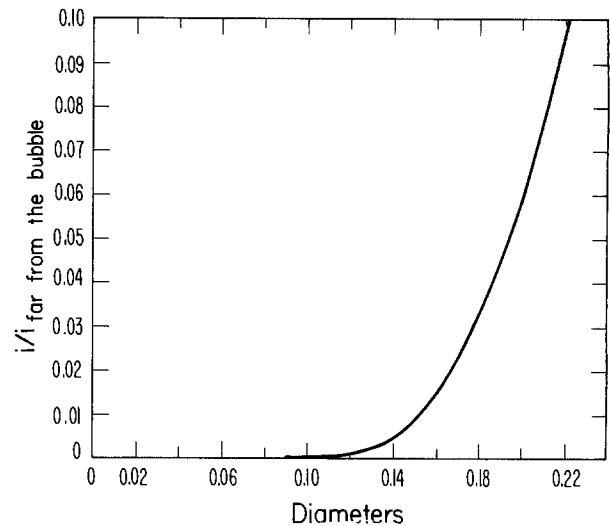


Fig. 3(b). Detail of current distribution near the contact point

spherical shape and a contact area less than $0.09 \pi a^2$. Calculating the contact angle for this base area according to the geometry in Fig. 4

$$\theta = 90^\circ - \cos^{-1}(b/a) = 17.5^\circ \quad [18]$$

we conclude that the effect of a sphere on a plane approximates that of a nearly spherical bubble having a contact angle less than 17.5° .

The bubble increases the resistance by deforming the otherwise straight lines of current. We evaluate the effect by integrating the potential disturbance over a plane far from the electrode and parallel to it

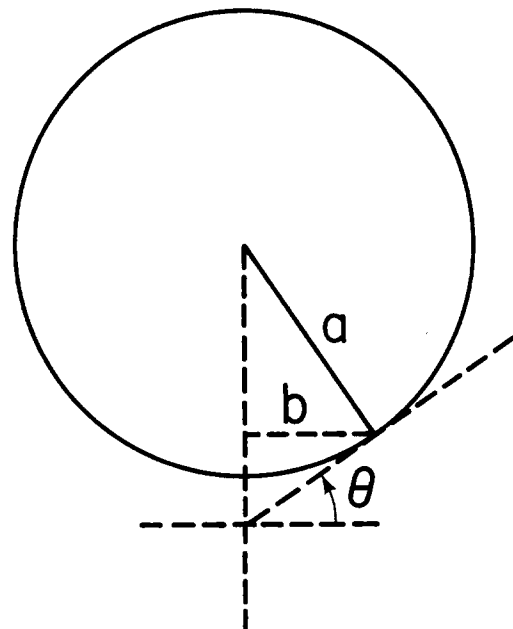
$$\Delta\phi = 4a^2 \int_0^\infty 2\pi x^* \phi_d^* |_{z^* \rightarrow \infty} dx^* = A_o \pi a^2 \quad [19]$$

where

$$\begin{aligned} A_o &= 8 \int_0^\infty q A dq \\ &= 0.9015 \end{aligned} \quad [20]$$

$\Delta\phi$ does not depend on distance from the electrode; it is the net disturbance of potential integrated with area. "n" bubbles per unit area, distributed such that their contributions are independent, cause a net potential disturbance

$$\Delta\phi^* = n A_o \pi a^2 \quad [21]$$

Fig. 4. Geometry for calculation of contact angle θ

One cannot deduce a conductivity analogous to Maxwell's because the layer of bubbles is two dimensional; the effect must be characterized as a polarization at the electrode surface. The increment of resistance caused by the bubbles on an electrode of area S is the net potential disturbance, [21], divided by the total current to the electrode, $\kappa\phi_0 S$

$$\Delta R = \frac{\Delta\phi^*}{\kappa S\phi_0} = \frac{2A_0 n\pi a^3}{\kappa S} \quad [22]$$

ΔR is a resistance increment related only to the disturbance caused by the bubbles. Its sum with the cell's resistance in the absence of gas gives the net cell resistance.

Bubbles whose contact points are three diameters apart in a planar hexagonal array give a number density $0.0321/a^2$. If the bubble diameter is a tenth of the interelectrode gap in a parallel plane cell geometry, Eq. [22] predicts a resistance increase of only 1%. This means that the resistance caused by a sparse collection of small bubbles is negligible. When closer than three diameters, the bubbles interact significantly and thereby disturb the potential more than predicted by Eq. [22]; nevertheless, this equation establishes that when the diameters are a tenth of the interelectrode spacing, the minimum added resistance caused by a close-packed array of bubbles on a surface is at least 8% of the cell resistance. In reality, because of the severe pinching of the field between bubbles, the effect must be substantially larger than this, perhaps by a factor of two to three. Experiments and additional theory are in progress which will determine the effect of dense single and multiple surface layers of bubbles on the resistance at electrodes.

Acknowledgment

This work was supported by the Division of Materials Sciences, Office of Basic Energy Science, U.S. Department of Energy under contract No. W-7405-Eng-48.

The authors wish to express their appreciation for fruitful suggestions by John Newman.

Manuscript submitted April 16, 1979; revised manuscript received Aug. 22, 1979.

Any discussion of this paper will appear in a Discussion Section to be published in the December 1980

JOURNAL. All discussions for the December 1980 Discussion Section should be submitted by Aug. 1, 1980.

Publication costs of this article were assisted by the University of California.

LIST OF SYMBOLS

a	bubble radius, cm
A_0	0.9015, dimensionless
A	Fourier constant, dimensionless
b	radius of bubble base, cm
C	constant of integration
i	current density, A/cm ²
n	number density of bubbles, cm ⁻²
q	separation parameter, dimensionless
ΔR	net resistance increase caused by the layer of bubbles, Ω
S	area of electrode, cm ²
x	distance parallel to electrode, cm
z	distance perpendicular to electrode, cm
ϕ	potential, V
ϕ_0	slope of linear potential field far from the bubble, V/cm
$\Delta\phi$	net potential disturbance far from the electrode integrated with area, V·cm ²
ν	tangent sphere coordinate, cm ⁻¹
μ	tangent sphere coordinate, cm ⁻¹
κ	conductivity, ($\Omega\cdot\text{cm}$) ⁻¹
θ	contact angle, degrees

Subscripts and superscripts

d	disturbance
\bullet	dimensionless quantity

REFERENCES

1. J. C. Maxwell, "Electricity and Magnetism," Vol. 1, 3rd ed., p. 440, Oxford (1892).
2. Lord Rayleigh, *Phil. Mag.*, **34**, 381 (1892).
3. D. A. Bruggeman, *Ann. Physik.*, **24**, 636 (1935).
4. R. E. Meredith and C. W. Tobias, *Advances in Electrochemistry and Electrochem. Engr.*, **2**, 15, Wiley Interscience, New York (1970).
5. R. M. De La Rue and C. W. Tobias, *This Journal*, **106**, 827 (1959).
6. C. W. Tobias, *ibid.*, **106**, 833 (1959).
7. F. Hine, M. Yasuda, R. Nakamura, and T. Noda, *ibid.*, **122**, 1185 (1975).
8. P. Moon and D. E. Spencer, "Field Theory Handbook," p. 104, Springer-Verlag, Berlin (1961).
9. C. P. Witze, V. E. Schrock, and P. L. Chambre, *Int. J. Heat Mass Transfer*, **11**, 1637 (1968).
10. A. Erdelyi, W. Magnus, F. Oberhettinger, and F. G. Tricomi, "Tables of Integral Transforms," Vol. 2, McGraw-Hill, New York (1954).

Bubble Effects on the Solution IR Drop in a Vertical Electrolyzer Under Free and Forced Convection

Fumio Hine* and Koichi Murakami¹

Nagoya Institute of Technology, Nagoya 466, Japan

ABSTRACT

Effects of electrolytic bubbles on the IR drop of caustic soda solution in a vertical cell of one meter height were studied under both free and forced convection. Three pairs of Luggin-Haber probes were positioned near the anode and the cathode to determine the solution IR drop during electrolysis. A sectioned electrode having 10 segments was employed to obtain the current distribution from the bottom to the top of cell. The superficial resistivity of the solution containing gas bubbles agreed well with the Bruggemann equation. The solution IR drop decreased significantly when adequate conditions or cell geometry for solution circulation were provided. The anode-to-cathode gap was found to be the most important parameter for reduction of the solution IR drop in a vertical cell.

An important item in the voltage balance of an industrial electrolytic cell is the IR drop in the electrolyte across the gap between the electrodes. When the electrode reaction evolves gas, the presence of gas bubbles dispersed in the electrolyte may greatly increase the IR drop. This is particularly true if the electrode is not perforated, in which case all the evolved gas must pass through the electrolysis gap.

There are several ways of minimizing the unwanted "bubble effects."

1. Use of perforated electrodes, which permit some, if not all, of the evolved gas, to be removed from the electrolysis gap.

Thus, in amalgam-type chlorine cells equipped with horizontal block anodes of graphite, these blocks may be machined and perforated in various ways to minimize accumulation of chlorine gas bubbles on the underside of these blocks (1-4). Also, modern amalgam cells equipped with "spaghetti"-type metal anodes almost eliminate the bubble effect.

In modern diaphragm-type chlorine cells equipped with vertical dimensionally stable anodes (DSA), which are usually perforated, a major part of the evolved chlorine is removed from the electrolysis gap by passing through the perforations. This also permits closer spacing between anode and diaphragm. Thus the IR drop can be minimized.

2. Recirculation of electrolyte decreases the gas void fraction in the electrolysis zone, and thus improves the conductivity of the two phase mixture of electrolyte and gas in the gap.

Thus, in older diaphragm-type chlorine cells, equipped with solid graphite blade anodes, a return path is provided which allows the anolyte brine to recirculate freely. The recirculation is driven by the gas lift effect in the anode-diaphragm gap (5, 6).

In newer diaphragm-type chlorine cells, equipped with box-type DSA's, the inside of the DSA can be utilized as a downcomer for recirculating the anolyte.

Box-type electrodes can also be used in cells for water electrolysis, to improve the circulation of caustic potash electrolyte, thus decreasing the void fraction of hydrogen on one side of the diaphragm, and of oxygen on the other (7, 8).

3. Miscellaneous, such as electrolysis under high pressure, which decreases the volume of the gas bubbles, and improves conductivity (7, 9).

This paper is concerned with Item 2, the effect of electrolyte circulation on the performance of gas-evolving cells, particularly with reference to current distribution and voltage drop in the electrolysis gap. The experiments were designed to reveal fundamental relationships, and thus to be useful in the design of industrial electrochemical cells.

In the previous report, an empirical equation for the conductivity of the gas-solution mixture as a function of the current density and the solution velocity in a narrow channel was presented (10). In addition to the articles quoted in Ref. (10), useful papers with respect to the bubble effects on the current distribution and the voltage balance in electrolytic cells can be found (11-13). Funk and Thorpe studied the void fraction and the current distribution in a water electrolysis cell (11). They concluded that the slip ratio, u_g/u_l , in this case was nearly unity, which was of great importance in defining the void fraction and in the analysis of hydrodynamics or pressure drop in electrolytic cell.

Although there is no doubt that the IR drop and the overvoltage near the electrode are affected by bubbles, enhancement of mass and heat transfer is also of importance to electrolytic gas evolution. The thickness of the hydrodynamic film or the boundary layer along the electrode is reduced, and hence the heat transfer coefficient in the cell is increased by circulation of the electrolytic solution (14-22). MacMullin *et al.* studied the enhancement of heat transfer in an electrolyzer, where hydrogen evolution took place at the cathode (17). The gas evolution promotes rapid circulation of the electrolyte resulting in a significant increase of the fluid film heat transfer coefficient, by a factor of 2 to 3.

Flow of the gas-electrolyte mixture along the vertical electrode during cell operation is a "two-phase flow" or a "backmix flow" depending on the liquid flow velocity and the void fraction of bubbles (23-25). In some cases, gas bubbles grow in size, and cover the electrode surface; thus the overvoltage becomes high. On the other hand, some gas bubbles leaving the electrode disperse in the solution, and the IR drop between two electrodes increases. That is, the "bubble effects" are classified into (i) the surface reduction of the working electrode, and (ii) increase in the resistivity of the electrolytic solution.

Tobias and his collaborators published a series of excellent papers on the effect of bubbles on the current distribution and the ohmic resistance (26-28). They propose Bruggemann's equation

* Electrochemical Society Active Member.

¹ Present address: Research Laboratory, The Japan Carlit Company, Sibukawa, Japan.

Key words: gas, cell, resistivity, convection.

$$\rho/\rho_0 = (1 - \epsilon)^{-3/2} \quad [1]$$

to correlate the resistivity *vs.* gas void fraction in electrolytic cells. The gas void fraction is closely related to the bubble size, *i.e.*, the larger the bubble size the smaller is the void fraction in general. Bubbles in water grow in size, but coalescence of electrolytic bubbles is very limited, and is affected greatly by the solution composition (29,30), for reasons that are unclear at present.

The experiments described in this paper were conducted in a vertical cell, one meter high, to determine the bubble effects on the operating conditions and the cell geometry. Solution circulation by gas lift action and forced flow is also discussed.

Experimental Procedure

A vertical Lucite cell one meter high, as shown in Fig. 1, was fabricated. The anode and the cathode, each 89 cm long and 3 cm wide, were made of 304 stainless steel (SS) plate 3 mm thick. Heavy copper bus bars were employed to minimize the IR drop in the SS electrodes. The anode-to-cathode gap was adjusted by the lead-in shafts with PTFE spacers of different lengths in the range 0.5-3 cm. A PVC back-plate was positioned to provide a space of an adequate size for the electrolyte. For experiments under forced circulation, a shield plate was provided at the cell bottom as shown in Fig. 1B. The electrolytic solution was pumped up from the inlet to the cell top through the interelectrode gap, and sent back to the reservoir.

Three pairs of the Luggin-Haber probes made of PTFE were positioned at the cell bottom, the center, and at the top to obtain the solution IR drops at these respective points. The potential was referred to the Hg/HgO electrode. The Luggin probes were inserted into the electrode plate from the back side so as to avoid disturbance to solution flow. Because the outer diameter of the Luggin tip was thick (6 mm), an equation proposed by Barnartt was used to calibrate the potential deviation (31).

A sectioned electrode with 10 segments, also made of SS, was used to determine the current distribution. The distance of the segments from a flat plate counter-electrode was adjusted carefully to equalize the elec-

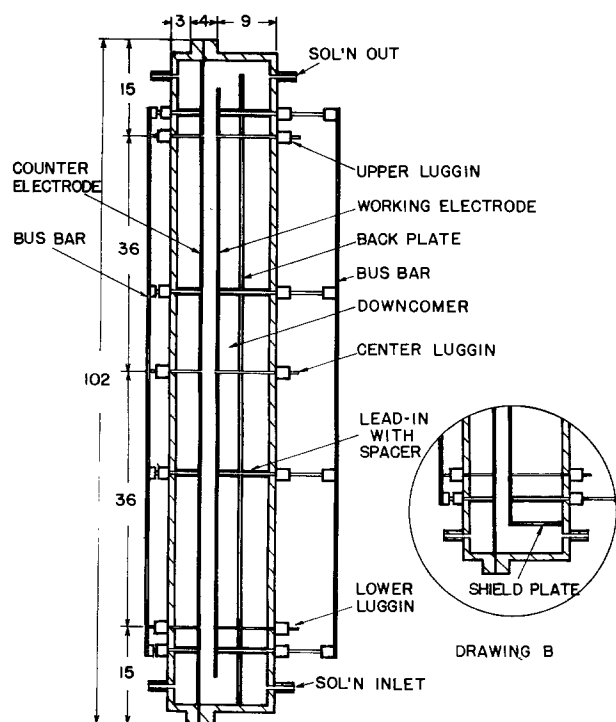


Fig. 1. A vertical cell. Drawing B shows a shield plate for experiments under forced circulation.

trode gaps prior to the experiment. This procedure was important for obtaining reproducible results.

Each electrode segment had a shunt in series, and was connected to a common copper bus bar. The voltage drop in a shunt was measured to obtain the current passing. The gas void fraction and the solution resistance increase with the level from the bottom to the top of the cell. Therefore, the current distribution along the vertical electrode is demonstrated by the variation of the currents carried by the different electrode segments.

Electrolytic solution, mostly 2N NaOH at 40°C, was circulated between the thermostated reservoir and the space behind both electrodes to keep the temperature constant, even in the case of blocked convection.

Oxygen and hydrogen were liberated at the anode and the cathode respectively, during electrolysis, and were mixed because there was no separator in the cell. Thus, for one Faraday passed, 1/4 mole O₂ plus 1/2 mole H₂ were evolved.

The polarization curves on a small SS electrode were obtained in a separate cell containing NaOH solution. The potential *vs.* current density was found to be a straight line over a wide range of current density above 2 A/dm². The sum of the slopes of both anodic and cathodic polarization curves was 0.340 Ω-cm² in 2N NaOH at 40°C.

Results and Discussion

Solution resistivity vs. gas void fraction.—Figure 2 illustrates three types of flow pattern in a vertical cell: blocked convection (mode 1), natural circulation (mode 2), and forced circulation (mode 3). In mode 1, the gas-liquid mixture rises to the cell top, and the solution freed of gas bubbles comes down through a part of the electrode gap, thus complicating the flow pattern. In mode 2, the gas-solution mixture rises through the electrode gap by gas lift action and the solution flows down through the downcomer when the circulation path is provided. Separation of gas bubbles from the solution is stimulated by rapid flow, and hence the gas void fraction decreases in this case. On the other hand, when the solution containing gas bubbles is forced into the reservoir from the cell top by pump, the gas void fraction may be still further reduced, as in mode 3.

In Fig. 2, *H* represents the level of electrolyte before the current is turned on. With current on, the level increases by ΔH , due to hold-up of gas bubbles in the electrolyte.

For mode 1, $b = 0$, and the average gas void fraction ϵ_a is

$$\epsilon_a = \Delta H/[H + \Delta H], \text{ approximately} \quad [2]$$

For mode 2

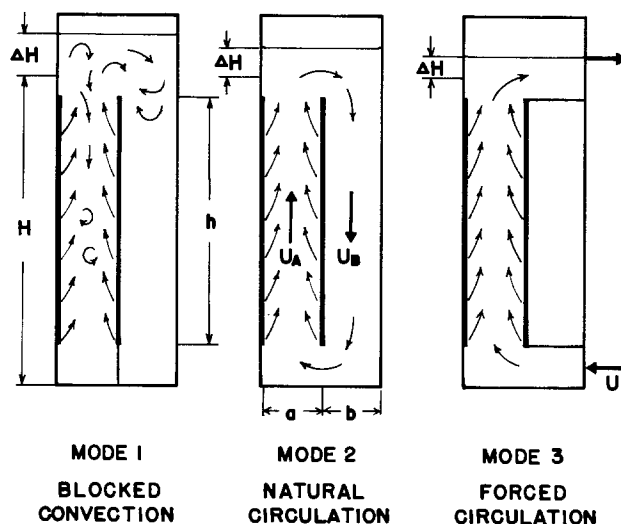


Fig. 2. Flow pattern in vertical cells

$$\epsilon_a = \frac{a + b}{a} \frac{\Delta H}{H + \Delta H}, \text{ approximately} \quad [3]$$

In this case, the solution in the downcomer is assumed to be bubble-free.

Suppose that the gas void fraction at the center level is ϵ_a . The current density at the center Luggin was confirmed to be almost average. Figure 3 shows the reduced resistivity ρ/ρ_0 at the center Luggin as a function of ϵ_a calculated by Eq. [2] (open points for mode 1).

The gas void fraction with a cell in mode 3 was also obtained. The solution level comes down by ΔH from the outlet when the polarizing current and the pump are turned off, thus, ϵ_a can be obtained by a similar manner. Although the experimental results fluctuated more in comparison with mode 2, the solution resistivity vs. average gas void fraction fitted roughly with Eq. [1] and was independent of the flow rate of solution. Therefore, Bruggemann's equation is valid for all cases.

In a previous work (10), we reported that the Bruggemann relation may not work well, especially under forced convection. That result differed from the present conclusion, probably due to different methods of experimentation. The solution IR drop was obtained from the voltage drop between the anode Luggin and the cathode Luggin in the present study, whereas the potential difference between the working electrode and the Luggin probe located on the front of the counterelectrode was measured in the previous work. The overvoltage of the working electrode was calibrated by the current interruption technique in this case, but the IR drop through a thin layer in the vicinity of the working electrode was, of course, involved. A solution layer near the electrode might be crowded with electrolytic gas bubbles just leaving the electrode surface, and the condition in this region differs from the bulk of solution. This may be the major reason for the different conclusions in the two papers.

Current distribution.—Figure 4 shows examples of the current distribution obtained with the sectioned electrode. At small current, the current distribution is quite uniform, and solution circulation is not required because the gas void fraction is small. On the other hand, the local current density varies with height at high currents. Variation of the current density without solution circulation is very large compared to that with circulation. Also, this figure shows that the average current density is achieved at about 40-50% of the electrode height from the bottom end, and is independent of the total current and solution circulation.

Tobias obtained a theoretical equation for the local current density i_x (26). With his equation, we have

$$i_x/i_a = 8(K + 2)^2 / (K + 4)(KX + 2)^3 \quad [4]$$

where K is the gas effect parameter, and X is the dimensionless vertical height, x/h . We confirm that this equation can be fitted to our data, if we make suitable corrections for the humid volume of the gas bubbles at local estimated pressures. Equation [4] is also valid for cells of different height as shown in Fig. 5, that is, the i_x/i_a vs. x/h is almost independent of the electrode height. The thick line shows the empirical equation obtained by the method of least squares with the data plotted. The thin line is the curve calculated by Eq. [4] with $K = 0.6$. However, in the experiments described, K varied in the range 0.2-0.7 depending on the electrode gap: the larger the electrode gap the smaller was the value of K .

Natural circulation.—In most of these experiments, the flow pattern was clearly a dispersion of gas bubbles in flowing electrolyte. However, at high current den-

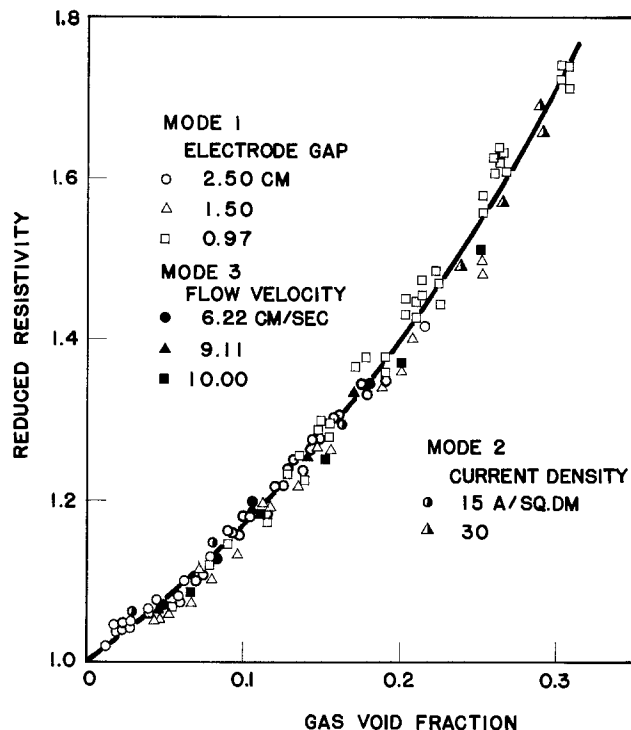


Fig. 3. Relationship between the reduced resistivity and the gas void fraction under blocked convection and forced circulation.

sity in narrow channels (0.5 cm gap), slug flow could be observed.

It is evident that the reduced resistivity is related to the current density and the flow velocity of the electrolyte. The open points in Fig. 6 show the experimental results obtained in the cell with forced circulation. The closed points are the results obtained with natural circulation, mode 2. The flow velocity by gas lift action increases when the gas void fraction increases at high current densities. From Fig. 6, flow velocity under natural circulation, mode 2, can be estimated to be about 14 cm/sec at 15 A/dm² and 20 cm/sec at 37 A/dm², for example. These estimates are valid because the ρ/ρ_0 vs. ϵ curve is independent of the solution flow as shown in Fig. 3. Figure 7 illustrates the estimated velocity of solution circulation as a function of the current density and the gap, which is obtained by the method described above. The velocity increases with decrease of the electrode gap, but is limited in narrow channels, less than 1 cm gap. In this discussion, and in Fig. 6-9, flow velocity is defined as the velocity of the gas-free electrolyte as it enters the gap; that is, it is the flow in cm³/sec divided by the area of the gap in cm².

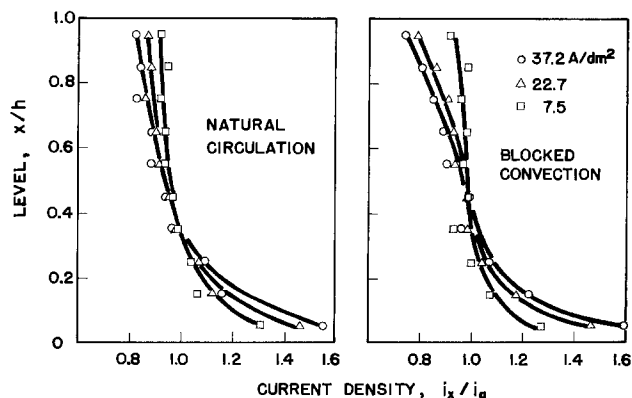


Fig. 4. Current distribution curves under natural circulation and blocked convection conditions. Electrode gap = 1.90 cm.

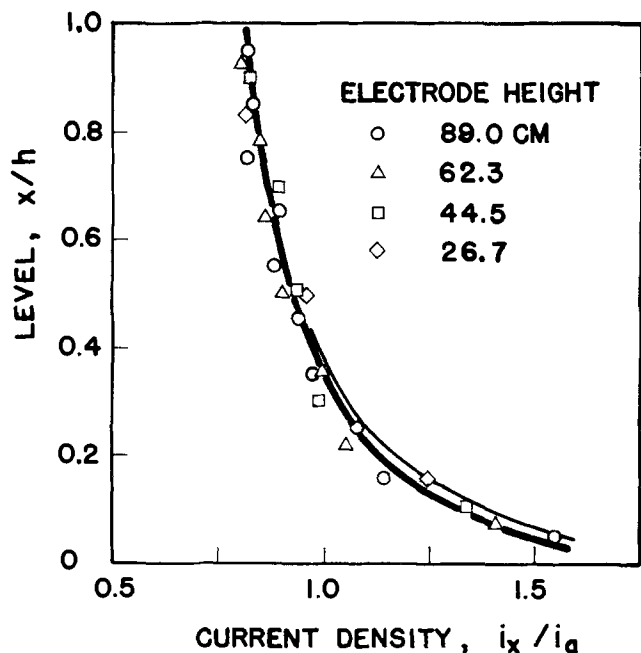


Fig. 5. Current distribution curve with electrodes of different heights. Electrode gap = 3.90 cm. Average current density = 37.4 A/dm². Thin line calculated by Eq. [3] with $K = 0.6$.

The solution flow velocity u_1 is represented by

$$u_1 = V_1/ac (1 - \epsilon) \quad [5]$$

Since the volumetric flow rate of solution, V_1 , remains constant, u_1 is only a function of ϵ .

Now, the current density i is a function of ϵ

$$i = \frac{\Delta E}{\rho a} = \frac{\Delta E}{\rho_0 a} (1 - \epsilon)^{3/2} \quad [6]$$

The voltage drop in the electrolyte, ΔE , is

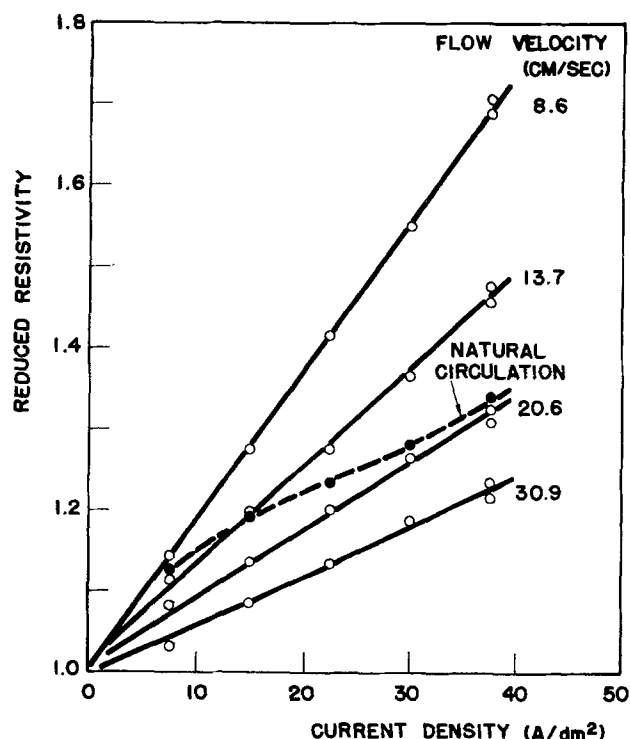


Fig. 6. Reduced resistivity vs. current density curves as functions of the flow velocity with forced circulation. The dotted line is a curve obtained under natural circulation conditions. Electrode gap = 0.97 cm.

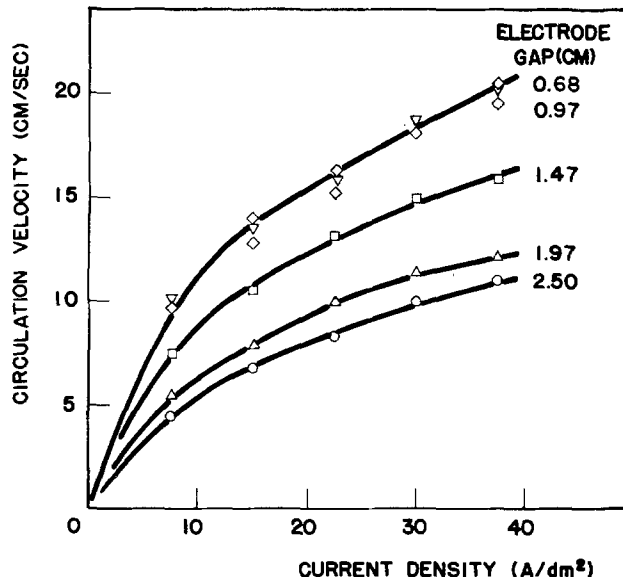


Fig. 7. Circulation velocity as a function of the current density and the electrode gap in a cell, mode 2.

$$\Delta E = E_T - E_0 - \Sigma \eta \quad [7]$$

where E_T is the terminal voltage, E_0 the decomposition voltage, and $\Sigma \eta$ is the sum of the overvoltage at anode and cathode. Suppose that E_T remains constant from the top to the bottom of the cell because heavy copper bus bars are employed in both anode and cathode sides, and E_0 is, of course, constant. On the other hand, $\Sigma \eta$ and ΔE are functions of the current density. In practical cells, however, E_T is sometimes shown by a simple equation

$$E_T = A + B i^n \quad [8]$$

where A is the superficial decomposition voltage, B and n are coefficients depending on the overvoltage characteristics, the solution conductivity, and the cell geometry. Although n is unity in many cases, sometimes we see values of n ranging from 1.0 to 2.0 in electrolytic cells where gas evolution takes place. Generally, the overvoltage and its increment with the current density are relatively small compared to the IR drops in the solution containing gas bubbles, as was shown in Fig. 3 in the previous paper (10). Thus, we estimate that $E_0 + \Sigma \eta$ in Eq. [7] is roughly equal to A in Eq. [8], and hence, $\Delta E \approx B i^n$. Substituting it and Eq. [6] into Eq. [5], we have

$$u = C i^m \quad [9]$$

where

$$C = \frac{V_1}{ac} \left(\frac{B}{\rho_0 a} \right)^{2/3} \quad \text{and} \quad m = \frac{2(n-1)}{3}$$

Figure 8 shows the log-log plots of the flow velocity vs. average current density in a cell, mode 2, with different gaps. Straight lines with a slope of about 0.5 were obtained, and hence, $u_1 \propto \sqrt{i}$. Also, $n \approx 1.75$.

The flow velocity reaches a maximum at an electrode gap of 0.75 cm as shown in Fig. 9. The figure also shows the effect of solution flow on the reduction of the IR drop or the reduced resistivity of the solution (center).

The terminal voltage was a minimum electrode gap of 5-7 mm. In a narrow channel, less than 5 mm, the flow pattern becomes slug, and ρ/ρ_0 is large. On the other hand, ρ/ρ_0 is almost independent of the electrode gap when the gap is larger than 10 mm. Consequently, the solution IR drop and the terminal voltage at constant current density increases with the increase of the electrode gap (top figure).

The reduced resistivity in a cell without circulation, mode 1, is shown by the closed points. Since convection

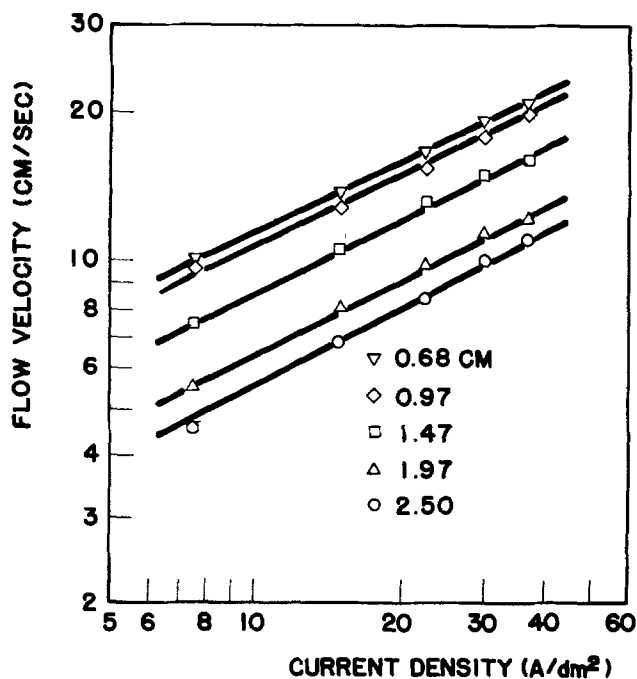


Fig. 8. Log-log plots of the flow velocity vs. current density at different gaps between two electrodes. Natural circulation, mode 2.

occurs only in the space between two electrodes, the larger the electrode gap the smaller is the resistivity. Also the ρ/ρ_0 is affected greatly by the current density, which indicates difficulty of separation of gas bubbles from the electrolytic solution.

In this connection, the size of the downcomer seems to be an important factor for natural circulation. According to experiments, the gap of 12-15 mm was sufficient for solution circulation.

A more exact mathematical approach to the problem of *a priori* calculation of the gas void fraction in the electrolysis gap, as a function of the various independent variables, would no doubt be desirable. However, this would depend on the ability to predict the gas rise velocity relative to the local liquid velocity, for swarms of bubbles of varying size, as generated at the electrodes. The problem is indeed complicated, and for its proper solution, additional experimental techniques must be developed. In the meantime, the present simplified approach has revealed interesting relationships in cells with gas-evolving electrodes.

The experiments described in this paper were conducted with solid electrodes, and hence the electrolysis zone was crowded with evolved gases. This was the case for the old style diaphragm-type chlorine cells using graphite blade anodes. In the new type cells using DSA's, the anodes are perforated, so that the evolved chlorine passes through the electrodes to the outer space, and hence, the gas void fraction in the electrode gap is reduced considerably, resulting in low voltage drops. This, of course, is of great interest to us, and will be investigated in the future.

Conclusion

Effect of the electrolytic gas bubbles on the solution IR drop and the terminal voltage of a vertical cell, one meter high, was studied. Experiments were conducted under blocked convection, natural circulation, and forced circulation conditions. The anode-to-cathode gap, the space of the downcomer, and the electrode height were varied. The superficial resistivity of electrolytic solution containing gas bubbles was confirmed to be a function of the gas void fraction, and agreed well with the Bruggemann equation.

The average gas void fraction in the gap is a measure of the gas hold-up in the gap, and depends strongly on the volumetric liquid flow rate in the gap.

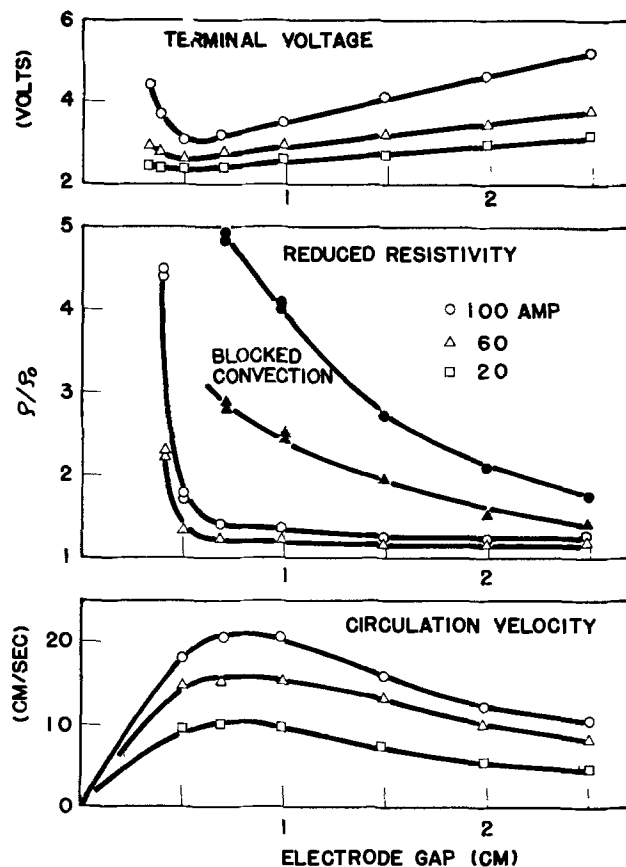


Fig. 9. Terminal voltage, reduced resistivity, and circulation velocity as functions of the electrode gap and the current. Average current density: 37.2 A/dm² at 100A, 22.7 A/dm² at 60A, and 7.5 A/dm² at 20A. Closed points = blocked convection (mode 1).

Other factors include the rate of rise of bubble swarms relative to the liquid rate, current density, overvoltage, etc.

The gas lift effect may be utilized to promote natural circulation of liquid through the gap, and thus to improve conductivity in the gap. The optimum area of downcomer used for recirculation should be about twice the area of the electrode gap.

The anode-to-cathode gap is, of course, a major component of the terminal cell voltage. The gas void fraction in a narrow channel is large and it causes a large increase in the solution IR drop. On the other hand, the solution IR drop increases with increase of the electrode gap. An optimum gap between anode and cathode is about 5-7 mm depending on the operating conditions such as current density and solution composition.

The local current density varies from the bottom to the top of cell due to the change of the gas void fraction along the electrode. But the current distribution is improved significantly by solution circulation. The current density near the center of electrode then takes the average value.

In conclusion, design of the cell configuration and choice of the operating conditions to yield sufficient flow of solution between the two electrodes are useful for reducing the gas void fraction, and thus the cell voltage.

Acknowledgments

The authors wish to extend many thanks to Mr. R. B. MacMullin, Niagara Falls, New York, for his review and suggestions, and also for preparation of the paper. We thank Dr. M. Yasuda for his discussion.

Manuscript submitted March 19, 1979; revised manuscript received July 31, 1979. This was Paper 281 presented at the Boston, Massachusetts, Meeting of the Society, May 6-11, 1979.

Any discussion of this paper will appear in a Discussion Section to be published in the December 1980 JOURNAL. All discussions for the December 1980 Discussion Section should be submitted by Aug. 1, 1980.

Publication costs of this article were assisted by Fumio Hine.

LIST OF SYMBOLS

a	anode-to-cathode gap (m)
b	electrode-to-backplate (size of downcomer) (m)
c	electrode width (m)
h	electrode height (m)
i	current density (A/m ²)
m	number of charge transfer (—)
m and n	coefficients in Eq. [8] and [9], respectively
u	flow velocity (m/sec)
u_A	flow velocity in electrode gap (see Fig. 2) (m/sec)
u_B	flow velocity in downcomer (see Fig. 2) (m/sec)
x	level from the bottom end of electrode (m)
A and B	coefficients in Eq. [8]
C	coefficient in Eq. [9]
E_0	decomposition voltage (V)
E_T	terminal voltage (V)
ΔE	voltage drop in electrolyte (V)
F	Faraday (96,500 C/g-equiv.)
H	height of bubble-free solution (m)
ΔH	increment of height due to dispersion of gas bubbles (m)
K	parameter in Eq. [4] [= $hi_x (\beta + \rho_x a) / mFP\rho_0 u_g a^2$]
P	pressure of gas (Pa)
V	volumetric flow rate (m ³ /sec)
X	reduced height [= x/h] (—)
β	slope of polarization curve (Ω -m ²)
ϵ	gas void fraction (—)
ρ	resistivity of gas-solution mixture (Ω -m)
ρ_0	resistivity of bubble-free solution (Ω -m)
$\Sigma\eta$	sum of overvoltage at anode and cathode (V)

Subscripts

a	average
x	local
g	gas
l	liquid

REFERENCES

- F. Hine, S. Yoshizawa, S. Okada, and T. Uesugi, *Kogyo Kagaku Zasshi*, **58**, 554 (1955).
- F. Hine, S. Yoshizawa, and S. Okada, *Denki Kagaku*, **24**, 370 (1956).
- S. Okada, S. Yoshizawa, F. Hine, and Z. Takehara, *ibid.*, **26**, 165, 211 (1958).
- S. Yoshizawa, F. Hine, Z. Takehara, and M. Yamashita, *ibid.*, **28**, 205 (1960).
- R. B. MacMullin, *Electrochem. Technol.*, **1**, 5 (1963).
- R. B. MacMullin, *Denki Kagaku*, **38**, 570 (1970).
- C. L. Mantell, "Electrochemical Engineering," p. 308, McGraw-Hill, New York (1960).
- "Denki Kagaku Binran" (Handbook of Electrochemistry), p. 732, Maruzen Publishers, Tokyo (1964).
- Y. Hinonishi, "High Pressure Water Electrolysis, Kogyo Butsuri Kagaku" (Physical Chemistry of Chemical Industry), Vol. 4, p. 73, Corona Publishers, Tokyo (1949).
- F. Hine, M. Yasuda, R. Nakamura, and T. Noda, *This Journal*, **122**, 1185 (1975).
- J. E. Funk and J. F. Thorpe, *ibid.*, **116**, 48 (1969).
- N. D. Koshel' and O. S. Ksenzhek, *Sov. Electrochem.*, **8**, 436 (1972).
- P. A. Danna, *This Journal*, **121**, 1286 (1974).
- N. Ibl, *Chem.-Ing.-Tech.*, **35**, 353 (1963).
- L. J. J. Janssen and J. G. Hoogland, *Electrochim. Acta*, **15**, 1013 (1970); **18**, 543 (1973).
- N. Ibl, J. Venczel, E. Schalch, and E. Adam, *Chem.-Ing.-Tech.*, **43**, 202 (1971).
- R. B. MacMullin, K. L. Mills, and F. N. Ruehlen, *This Journal*, **118**, 1582 (1971).
- M. G. Fouad, G. H. Sedahmed, and H. A. El-Abd, *Electrochim. Acta*, **18**, 279 (1973).
- M. G. Fouad and G. H. Sedahmed, *ibid.*, **20**, 615 (1975).
- I. Rousar and V. Cezner, *ibid.*, **20**, 289 (1975).
- I. Rousar, J. Kacin, E. Lipper, F. Smirous, and V. Cezner, *ibid.*, **20**, 295 (1975).
- H. Vogt, *ibid.*, **23**, 1019 (1978).
- D. S. Scott, "Properties of Cocurrent Gas-Liquid Flow, Advances in Chemical Engineering," Vol. 4, T. B. Brew *et al.*, Editors, p. 199, Academic Press, New York (1963).
- "Chemical Engineers' Handbook," J. H. Perry, Editor, 4-21 and 5-38, McGraw-Hill, New York (1963).
- T. Z. Fahidy, *Can. J. Chem. Eng.*, **174**, June 1966.
- R. E. De La Rue and C. W. Tobias, *This Journal*, **106**, 827 (1959).
- C. W. Tobias, *ibid.*, **106**, 833 (1959).
- R. E. Meredith and C. W. Tobias, *ibid.*, **110**, 1257 (1963).
- R. R. Lessard and S. A. Zieminski, *Ind. Eng. Chem. Fundam.*, **10**, 260 (1971).
- F. Hine and T. Sugimoto, Paper 459 presented at The Electrochemical Society Meeting, Seattle, Washington, May 21-26, 1978.
- S. Barnartt, *This Journal*, **99**, 549 (1952).

Gas-Diverting Electrodes in the Chlor-Alkali Membrane Cell

Jacob Jorne*

Department of Chemical Engineering, Wayne State University, Detroit, Michigan 48202

and Joseph F. Louvar*

BASF Wyandotte Corporation, Wyandotte, Michigan 48192

ABSTRACT

The purpose of this investigation was to find an effective means of removing gas bubbles from the interelectrode space of a new chlor-alkali membrane cell. Gas evolution increases the ohmic resistance of the electrolyte and the current distribution becomes nonuniform in the vertical direction. It was observed that by using a gas-diverting electrode the gas bubbles were diverted to the back of the vertical electrode. Various expanded steel cathodes were very effective in diverting the H₂ gas, which resulted in a significant drop of the cell potential. The effectiveness was tested as a function of the spacing between the cathode and the membrane, the current density, the temperature, and the geometry of the expanded metal electrodes. An increase in current efficiency is reported as well, due to the induced turbulence at the surface of the membrane facing the cathode. In addition, the gas-diverting electrode removes the restriction on the cell's height and can result in capital investment savings. Membrane over-potentials are reported as well.

This investigation was aimed at evaluating new electrode geometries (expanded steel cathodes) as an effective means of removing the evolving hydrogen gas and reducing the terminal voltage of a new chlor-alkali membrane cell.

The overpotential and current distribution on vertical gas-evolving electrodes (chlorine and hydrogen) are affected by the bubbles, the hydrodynamics and the geometry of the cell. It is well accepted that gas evolution enhances mass transfer of reactants and products to and from the electrode's surface. However, an additional factor is the nonuniform increase of the resistivity of the electrolytic solution in the interelectrode space with the undesired consequence of increased ohmic drop and nonuniform current distribution in the vertical direction.

The theoretical effects of gas evolution on the ohmic resistance and current distribution are discussed by Tobias (1), Nagy (2), Hine *et al.* (3), and De La Rue and Tobias (4); experimental results are reported as well (5-11) concerning mass transfer and bubble effects. Tobias (1) presents a theoretical treatment for stagnant electrolyte and obtains analytical solutions of the void fraction, current distribution, and ohmic loss under restricted and simplified conditions. A general and qualitative understanding of the problem is thereby obtained. Nagy (2) extends the analysis for more realistic conditions by including linear kinetic polarization for an electrode built of vertical blades.

The studies mentioned above, utilized standard flat electrode configurations which did not divert the gas bubbles to the back of the vertical electrode. These results implied, however, that if it were possible to remove the gas from the interelectrode space, the result could be a substantial decrease in the terminal voltage. Taking the simple case of a flat sheet electrode, and following the approaches of Tobias (1) and Nagy (2), the effective solution resistance is given by

$$R_{\text{eff}} = \frac{2RT\rho I_T}{hW^2PmFS} \frac{1}{f_{\text{av.}}(1-f_{\text{av.}})(2-f_{\text{av.}})^2} \quad [1]$$

where I_T is the total constant current, $f_{\text{av.}}$ is the average void fraction, ρ is the resistivity of a gas free elec-

trolyte, h is the electrode height, W is the electrode width, P is the pressure, m is the number of electrons, S is the bubble rise velocity.

Minimum resistance is obtained at

$$f_{\text{av.}} = 0.36 \quad [2]$$

The interelectrode spacing corresponding to $f_{\text{av.}} = 0.36$ is given by

$$\delta_{\text{min}} = 1.69 \frac{RT}{PmF} \frac{i_{\text{av.}} h}{S} \quad [3]$$

This important result deserves some illustrative calculations: If we consider an experimental cell of height $h = 10$ cm operating under current density $i_{\text{av.}} = 200$ mA/cm² and assume the bubble rise velocity $S = 1$ cm/sec (following Stokes' law), then

$$\delta_{\text{min}} = 0.4 \text{ cm}$$

For a realistic industrial cell of height $h = 100$ cm and current density of $i_{\text{av.}} = 200$ mA/cm² the optimal spacing is

$$\delta_{\text{min}} = 4.0 \text{ cm}$$

To illustrate the advantage of close proximity let us take an example where the distance between the membrane and the two electrodes is 0.4 cm. The approximate resistivities of NaCl and NaOH are 2 and 1 Ω -cm, respectively. The ohmic resistance of this geometry is approximately

$$R = (\rho_{\text{NaCl}} + \rho_{\text{NaOH}}) \delta = (2 + 1) 0.4 = 1.2 \Omega\text{-cm}^2$$

If we operate under a typical current density of 200 mA/cm² then the total ohmic drop is 0.24V. If by introducing gas-removing electrodes we can reduce the spacing to 0.1 cm then the ohmic drop is 0.06V, and a substantial decrease in the cell's terminal voltage can be achieved.

The treatments of Tobias (1) and Nagy (2) are presented under restrictive assumptions, nevertheless the above examples demonstrate the desirability of finding a more efficient way to remove the gases from the interelectrode spaces.

Gas-diverting electrode.—As a possible solution to the adverse effect of the gas void volume on the resistance of the interelectrode spacing, it was proposed

* Electrochemical Society Active Member.
Key words: gas evolution, chlor-alkali cell, bubbles, membrane, Nafion, chlorine, hydrogen, caustic.

to investigate several electrode geometries which can divert the evolving gases (Cl_2 and H_2) to behind the electrodes. Inspecting commercially available unflattened expanded carbon steels it was expected that screens of special three-dimensional structure might promote the removal of the evolving gas. This would allow designing the cell in such a way that the electrodes could be placed in a very close proximity to the membrane and the ohmic drop would be reduced substantially. Promising geometries are the Standard Diamond, Standard Louver, Standard Honeycomb, and the Ramona Grid (see catalogs of Niles Expanded Metals, Chandler Expanded Metals Corporation, and Keen Penmetal Products).

The principle is illustrated in Fig. 1 where a schematic representation of an unflattened expanded metal electrode is presented.

It is generally accepted in the chlor-alkali industry that any saving over 50 mV is significant and worth looking into. The general approach was to test cathode geometries that divert the gas to the rear of the electrode, and decrease the interelectrode spacing and the resultant ohmic loss.

Due to the fact that expanded steel screens are commercially available, the experimental investigation concentrated only on the geometry of the cathode. However, it is believed that the same consideration can be applied to the chlorine anode in the form of an expanded ruthenized titanium anode.

Experimental

Various expanded metal geometries were tested. In general the unflattened expanded metals were preferred because it seemed that the three-dimensional structure diverts the evolving gas to the rear.

A Plexiglas cell was used throughout the investigation. The cell consisted of two identical compartments attached together with stainless steel bolts and clamps. A Nafion membrane (du Pont Type 031) was placed between the two compartments and the cell was sealed with $\frac{1}{2}$ in. Gore-Tex type gasket material. The cell is shown schematically in Fig. 2. In the bottom of the cell grooves were located in order to place the electrodes at a fixed distance from the membrane. Six spacings were used on each side; the cathodic spacings were: 0.33, 0.85, 1.32, 1.85, 2.42, and 2.98 cm; the anodic spacings were: 0.30, 0.86, 1.37, 1.88, 2.42, and 2.98 cm. The electrodes were 7.6 cm wide and 10.2 or 15.2 cm high.

The electrodes were held and electrically connected from the top by a movable piece of Plexiglas. The area of the membrane was 155 cm^2 . Each cell compartment was 10 cm wide, 20 cm high, and 5 cm deep. The gases (H_2 and Cl_2) were released to the hood through $\frac{1}{2}$ in. holes at the top of the cell. The top of the anode compartment was flushed continuously with an air stream to remove the chlorine gas. The cell was heated by an

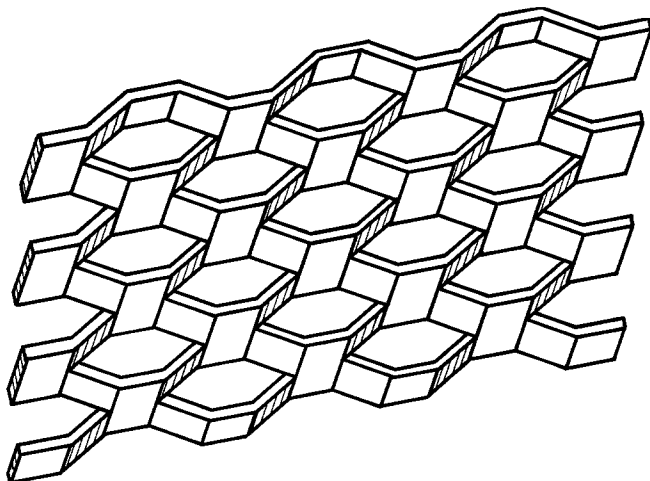


Fig. 1. Gas-diverting electrode

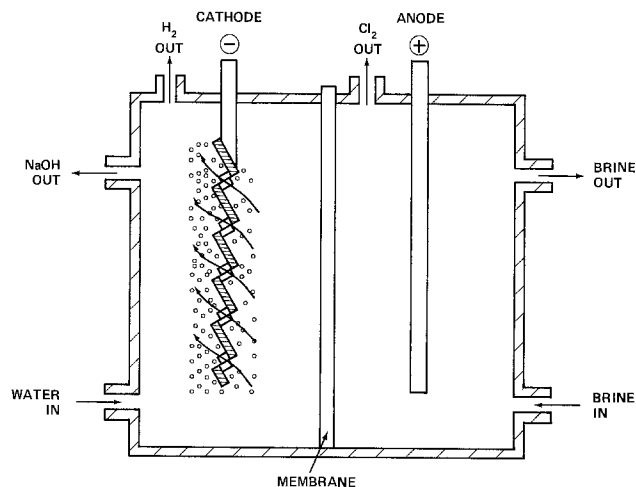


Fig. 2. The experimental cell with a diverting gas cathode (schematic).

electrical heater located in the anolyte, and the temperature was measured by a Weston thermometer No. 104 located in the catholyte.

The 5.5M NaCl and 3.5M NaOH solutions were prepared by dilution. The concentrations were measured gravitationally and by titration. The pH of the solutions was measured at the beginning and end of the experiment. The pH in the anolyte varied between 3 and 3.5. The solutions were fed into the cell through two funnels connected to the two compartments. During the experiments the solutions were replaced every hour in order to minimize concentration and pH changes. There was no flow-through of NaOH or NaCl through the cathode and anode compartments during the runs. Two standard calomel electrodes (Corning No. 104) were used and placed in syringe compartments connected by small Teflon capillaries (AWG No. 24, Penntube Plastics Company, Clifton Heights, Pennsylvania) to the catholyte and the anolyte solutions. The tips of the Luggin capillaries were located firmly in the middle of the electrodes facing the membrane. The tips were cut at an angle facing up to avoid accumulation of gas bubbles.

Constant current was supplied by 6261B d-c power supply, 0-20V, 0-50A (Hewlett Packard). The current was measured by a shunt and digital multimeter Fluke Model 8000A (Fluke, Seattle, Washington). The cell potential and the various potentials between the working electrodes and the two reference electrodes were measured by Electrometer Model 1455 (Data Precision Corporation, Wakefield, Massachusetts). Ohmic drops were measured using the current interrupter technique where the current is interrupted and the potential drop is followed on a fast oscilloscope. Current interrupter Model 101 (Electrolytic Research Division, BASF Wyandotte) was used, and the pulse was applied by Universal Programmer Model 175, (PAR, Princeton, New Jersey) (pulse width 100 V/sec, 1 msec). The potential drop was followed on a Nicolet 1090 AR Explorer Digital Oscilloscope (1 $\mu\text{sec}/\text{point}$, 4V range), and the oscilloscope traces were copied directly to an XY recorder, Ohmigraphic 2000 Recorder (Houston Instrument). In all cases the potential drop was read directly from the digital oscilloscope.

Procedure.—The steel electrodes were degreased and cleaned in concentrated HCl. The cell was assembled with the electrodes under consideration and was placed in the hood. Electrical connectors were attached and the reference electrode compartments were filled with the corresponding solutions and pumped through the capillaries. The cell was filled with NaCl and NaOH solutions and different constant currents were applied at various cathode and anode positions. The electrodes were moved from one groove to the next and the measurements were repeated. Potentials were measured

between the various electrodes and across the membrane, and ohmic losses were estimated from the current interrupter measurements. The catholyte and anolyte solutions were replenished every hour so the changes in concentrations were kept below $\pm 0.5M$ for NaOH and NaCl, respectively.

At the end of the day, the cell was drained, washed thoroughly, and the membrane was left overnight in distilled water. The membrane was always left in distilled water prior to the experiment, and in this way it remained stretched throughout the experiments. In all the experiments the same piece of membrane was used.

In some experiments the cell over-all impedance was measured by an impedance meter, Model 251 (Electro Scientific Industries, Portland, Oregon). The resistance measurements were conducted in the LR mode because of the range limitation of the instrument. The leads of the impedance meter were attached to noncurrent-carrying connectors. The frequency of measurements was held constant at 1 kHz.

The expanded metals are characterized by the following dimensions: SWD—nominal short way of design, LWD—nominal long way of design, SWO—short way of opening (actual), LWO—long way of opening (actual).

The following flattened and unflattened steel cathodes were tested:

1. The conventional flattened steel cathode. Design size: 0.25 in. SWD, 0.5 in. LWD. Opening size: $\frac{1}{8}$ in. SWO, $\frac{5}{16}$ in. LWO.

2. $\frac{1}{4}$ in. No. 18 std. Ca., unflattened, Niles Expanded Metals. 114 lb/ft². Design size: 0.25 in. SWD, 1.00 in. LWD. Opening size: 0.11 in. SWO, 0.718 in. LWO.

3. $\frac{3}{16}$ in. No. 22, No. 104 louver (large structure) Niles Expanded Metals. Design size: $\frac{3}{16}$ in. SWD, $\frac{7}{16}$ in. LWD. Opening size: $\frac{3}{16}$ in. SWO, $\frac{3}{8}$ in. LWO.

4. $\frac{1}{8}$ in. No. 24, No. 104 louver (fine structure) Niles Expanded Metals. Design size: $\frac{1}{8}$ in. SWD, $\frac{5}{16}$ in. LWD. Opening size: $\frac{1}{8}$ in. SWO, $\frac{1}{4}$ in. LWO.

5. Ramona Grid, Keen Penmetal Products, Parkersburg, West Virginia 26101. Design size: $\frac{1}{2}$ in. SWD, 1.0 in. LWD. Opening size: $\frac{1}{16}$ in. SWO, $\frac{3}{4}$ in. LWO.

In all experiments the anode was made of flattened ruthenized titanium anode (coated on both sides).

The following parameters were investigated: (i) The effectiveness of expanded metal cathodes in moving the gas to the rear (visual observations). (ii) The effect of the spacing between the membrane and the cathode on the ohmic resistance of the cell. (iii) Effect of current density. (iv) Ohmic drop across the membrane. (v) Effect of temperature. (vi) Over-all cell terminal voltage and its dependence on the cathode structure, cathode spacing, current density, and temperature.

Results and Discussion

Visual observations.—All the new cathode geometries showed the ability to release the evolving gas to the rear. With Ramona Grid, Niles $\frac{1}{4}$ in. No. 18 std. Ca., Niles louver $\frac{1}{8}$ in. and $\frac{3}{16}$ in., even when placed far away from the membrane (3 cm spacing) the gas evolution was almost entirely at the back. The gas evolved smoothly through the inclined planes and there was no evidence of accumulation of gas in the inter-electrode spacing.

The separation of the gas bubbles was quite slow in the catholyte compartment. Very fine H₂ bubbles were formed and the catholyte turned very quickly into a finely dispersed opaque suspension. It is quite possible that this behavior is due to the relatively large volume of the compartments and the back mixing of the gas in the volume behind the electrode. The gas-liquid separation was easier at the anolyte where the Cl₂ gas separated smoothly from the brine.

Figure 3 shows the cell potential as a function of the cathode-membrane spacing for the various expanded

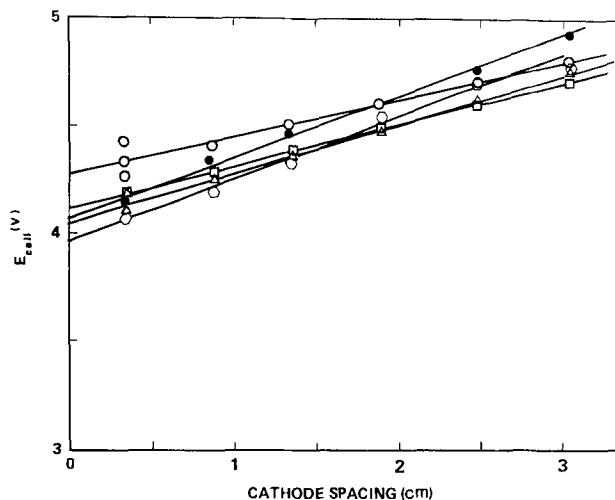


Fig. 3. Cell potential vs. cathode spacing for various cathodes. $i = 215 \text{ mA/cm}^2$, $T = 35^\circ\text{C}$. \circ , Flattened conventional cathode; \triangle , Niles std. Ca. $\frac{1}{4}$ in. cathode; \square , std. Louver $\frac{3}{16}$ in. cathode; \circ , std. Louver $\frac{1}{8}$ in. cathode; \bullet , Ramona grid cathode. The anode spacing is 0.30 cm.

steel cathodes as well as for the flattened conventional cathode. The lines are extrapolated to zero spacing, and the cell potential at zero cathode spacing is taken as a measure of the cathode's ability to divert gas to the rear. The cell potential at zero cathode spacing is summarized in Table I. The anode spacing was kept constant at $d_a = 0.30$ cm. Comparing the results at 35°C indicates that all the new geometries show a significant drop in the cell potential of about 100–200 mV. The saving is less significant at higher temperature because the conductivity is higher and the saving is smaller. The crossing of lines in Fig. 3 indicates the changing abilities of the various electrodes to divert gas at various cathode spacings.

Good results were obtained in particular with Ramona Grid and the std. louver $\frac{1}{8}$ in. (fine structure) cathodes, however, the Niles $\frac{1}{4}$ in. std. Diamond also gave improved results and should be considered equal.

The electrode geometry is even more important in the design of the anode since the resistance of the solution is higher in the anolyte (NaCl solution). Therefore, it is expected that higher saving can be achieved by testing anodes of similar geometries. Since the conductivity of the caustic (catholyte) increases by a factor of about 2 by going from 35° to 80°C , the voltage saving on the anode side is expected to be of the order of 50–100 mV at 80°C . The conductivity of the brine (NaCl) is about half that of NaOH; therefore, the saving in voltage on the anode side by replacing the anode with a new geometry is expected to be of the order of 100–200 mV. These estimations are quite qualitative and based on the concept that the new geometries can be located very close to the membrane while the gas evolves from the rear. However, the dispersion and the void fraction of the chlorine bubbles are quite different from those of hydrogen.

Ohmic resistance of cell.—The cell resistance was measured using a current-interruption technique. Fig-

Table I. Cell potentials at zero cathode spacing

Cathode	Temperature ($^\circ\text{C}$)	E_{cell} ($d_c = 0$)
Flattened conventional	35	4.26
Ramona grid	35	3.95
	37	4.05
	80	3.65
Std. Louver $\frac{1}{8}$ in.	25	4.02
	35	3.96
	75	3.45
Std. Louver $\frac{3}{16}$ in.	35	4.10
Niles $\frac{1}{4}$ in. std. Diamond	35	4.02

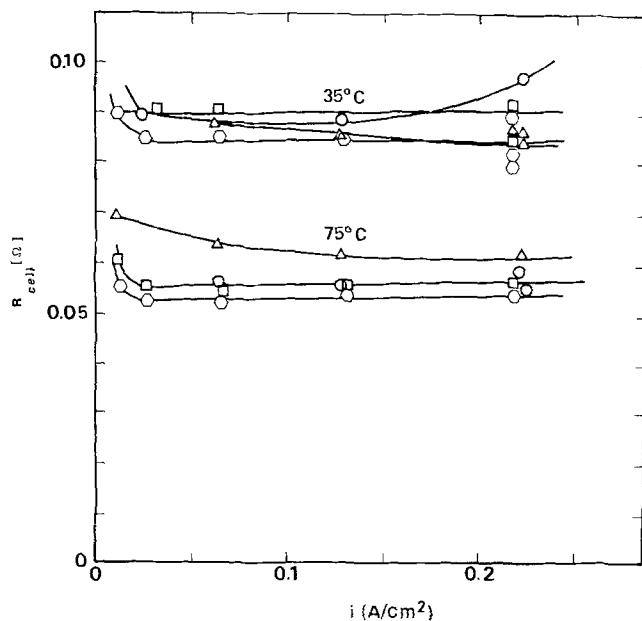


Fig. 4. Current interruptor measurements: Cell ohmic resistance vs. apparent current density. Electrode area, 77.4 cm²; cathode spacing, 0.33 cm; anode spacing, 0.30 cm. ○, Flattened conventional cathode; △, Niles std. Ca. 1/4 in. cathode; □, std. Louver 1/8 in. cathode; ◇, std. Louver 3/16 in. cathode; ○, std. Louver 1/8 in. cathode.

ure 4 shows the dependence of the cell's ohmic resistance on the current. The ohmic resistance is independent of the current over a wide range for all the gas diverting electrodes. The lack of increase of ohmic resistance at high current indicates the effectiveness of the new cathode geometries in diverting the gas from the electrode-membrane space. The ohmic resistance increases, however, for the conventional flattened cathode at 35°C, indicating a buildup of void fraction in front of the cathode. At low current densities the ohmic resistance increases with a decrease in the current density. This unexpected effect occurs at apparent current densities below ~30 mA/cm². It is speculated that the hydrogen bubbles at low current density are very small and their rising velocity is low. Consequently the electrolyte is cloudy due to insufficient coalescence of the bubbles and the void fraction is higher than expected. Hine and Sugimoto (11) showed that the hydrogen void fraction deviates from the straight line passing through the origin at low current density probably due to the small bubble and insufficient coalescence.

Figure 5 shows the ohmic voltage drop (IR) of a 77.5 cm² cell with various cathodes as a function of the cathode spacing. Linear dependence is observed for all the gas-diverting electrodes, which indicates that the gas evolution is from the rear and the ohmic resistance of the catholyte is not changing with the cathode-membrane spacing. The parallel lines indicate that the ohmic resistance is due mostly to the electrolytic resistance and not to buildup of void fraction. An exceptional case is that of the flattened conventional cathode at 35°C where a minimum can be observed at 1.02 cm spacing and the ohmic loss increases at smaller spacing, probably due to gas evolution and high void fraction in front of the cathode. For the same electrode the resistance of the cell increases with the current (see Fig. 4), indicating again that a flattened electrode is inefficient in diverting the hydrogen gas to the rear. In all other unflattened geometries the cell resistance drops linearly with the cathode spacing, which indicates an effectiveness in diverting the gas to the rear of the cathode. The best location of the electrode is in a very close proximity to the membrane. The cell's ohmic resistance for the Ramona Grid 116 cm² cell is linear with cathode spacing and increases the confi-

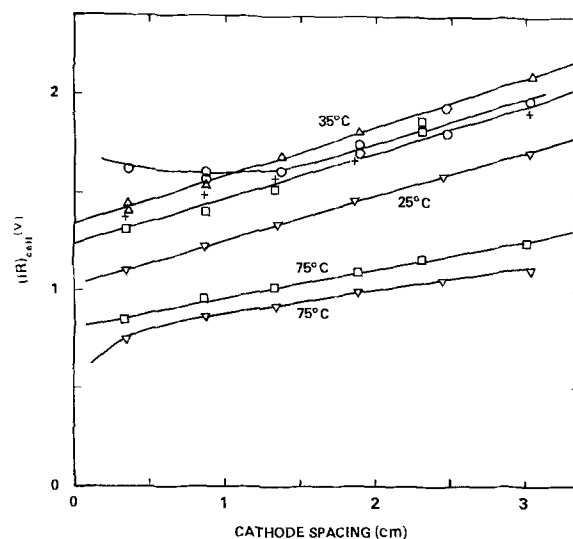


Fig. 5. Current interruptor measurements: Cell ohmic drop vs. cathode spacing at various temperatures. Electrode area, 77.4 cm²; total current, 16.7A. ○, Flattened conventional cathode 35°C; △, Niles std. Ca. 1/4 in. cathode 35°C; □, std. Louver 1/8 in. cathode 35° and 75°C; +, std. Louver 3/16 in. cathode 35°C; ▽, Ramona grid cathode 25° and 75°C, area, 18 in.². The anode spacing is 0.30 cm.

dence in our current interrupting technique. The linear dependence indicates that the gas evolves at the rear and does not contribute significantly to the ohmic loss of the cell. Figure 5 shows again that the cell resistance increases monotonically with the cathode spacing, again due to the effectiveness of the Ramona Grid cathode in moving the gas to the rear of the electrode.

Similar results were obtained for the louver-type cathodes, although a slight increase in resistance can be observed at small spacing, a possible indication of some gas evolution in the cathode-membrane space.

The Niles 1/4 in. std. Ca. Diamond cathode shows similar behavior: however, the cell resistance decreases slightly with current at 35°C (Fig. 4).

Cathode polarization.—The individual cathodic polarizations were measured using a Luggin capillary reference electrode located in the center of the cathode. The surface overpotential, free of ohmic drop, at 215 mA/cm² and 80°C is about 300-400 mV. The polarizations of std. louver 3/16 in. and 1/8 in. and the Ramona Grid cathodes are quite similar to that of the flattened cathode.

In general all the cathodes show similar polarization curves and the cathodic overpotential is of the order of 300-400 mV. As expected, a rise in the temperature does not change the surface overpotential much, and the difference is due mainly to ohmic drop.

Impedance measurements.—Typical impedance measurements are shown in Fig. 6 for std. Louver 3/16 in. cathode and DSA anode. The potential, resistance, and inductance of the cell are plotted vs. the apparent current density. Similar behavior was observed for cells with different cathodes. The increase in the resistance of the cell at low currents can be explained by the higher charge-transfer resistance at lower overpotentials. The cell potential increases with the current and the larger slope at low currents corresponds to the higher resistance at this range. The inductance increases monotonically with the applied current although in some measurements a small minimum could be observed at a low current density of around 25 mA/cm². Generally as the resistance decreases with increasing current, the inductance increases. No explanation is available presently for these phenomena. The agreement between the resistances obtained by the a-c impedance measurements and the d-c inter-

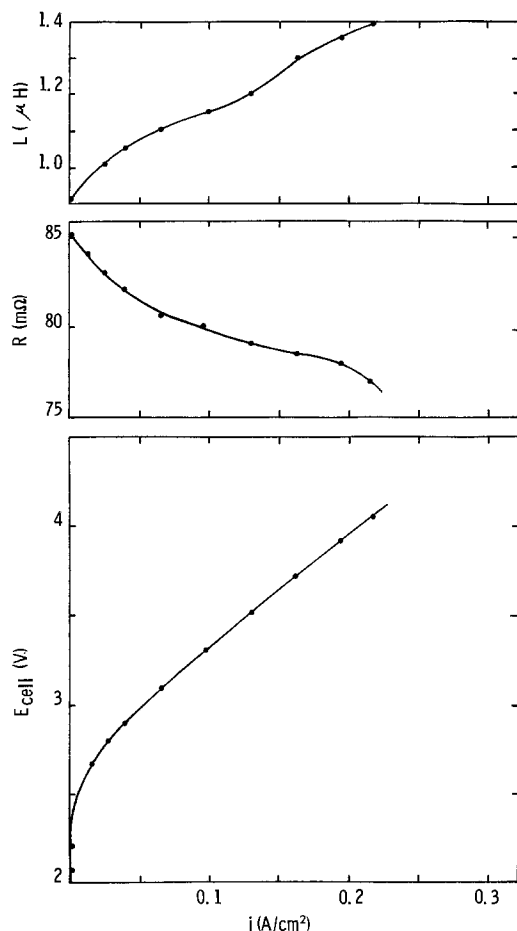


Fig. 6. A-C impedance measurements: cell potential, resistance, and inductance vs. apparent current density. Electrode area, 77.4 cm²; temperature, 40°C; cathode spacing, 0.33 cm; anode spacing, 0.30 cm; cathode, std. Louver 3/16 in.

ruption measurements is qualitatively reasonable: The resistance in Fig. 6 falls in the same range as the resistances in Fig. 4 which were obtained by d-c interruption. The qualitative agreement indicates that most of the cell resistance is ohmic in nature.

Membrane potential and resistance.—The potential across the membrane was measured using two calomel reference electrodes. It is important to realize that the potential difference E_{rr} includes some ohmic drop of the brine and the caustic solutions. However, these ohmic contributions are relatively small due to the close proximity of the Luggin capillary tips to the membrane.

The membrane potential E_{rr} shows generally linear dependence with the current at the practical range (see Fig. 7) although some kind of Tafel behavior can be observed at lower currents, probably due to the membrane activation potential and liquid junction contributions. The measurements were quite difficult due to the capture of the gas bubbles in the liquid junction, and the capillaries had to be flushed periodically.

In order to estimate the membrane resistance, free of the adjacent solution resistance, the potential between the two reference electrodes was measured at various cathode spacings (the cathodic reference electrode moved with the cathode). A linear dependence of E_{rr} on the cathodic spacing was obtained. The increase in E_{rr} is due to the increase in the catholyte resistance associated with the larger spacing. The potential E_{rr} can be extrapolated to zero spacing and the ohmic drop of the catholyte can be eliminated. Similarly the ohmic drop of the anolyte was estimated from the dependence of the cell's potential on the anolyte spacing and subtracted from E_{rr} in order to obtain the true potential difference across the membrane.

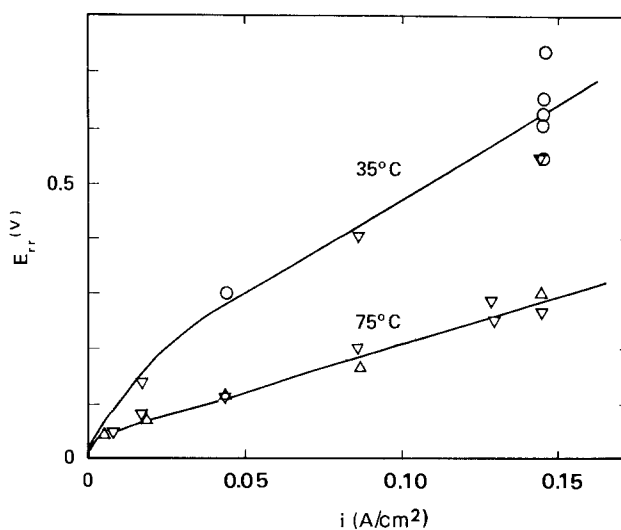


Fig. 7. Potential across Nafion membrane vs. apparent current density. Area, 77.4 cm²; cathode spacing, 0.33 cm; anode spacing, 0.30 cm; membrane, Nafion 031, effective area = 116 cm²; cathode, Δ flattened conventional cathode, 75°C, ∇ std. Louver 1/8 in., 35° and 75°C, \circ std. Louver 3/16 in., 35°C.

The membrane potential drop is roughly 300 mV at a current density of about 215 mA/cm² at 75°C. At 35°C the membrane potential is about 600 mV.

The average extrapolated value for zero spacings is 0.43V at 35°C, so the IR-free potential difference across the membrane at 35°C is approximately 0.43V. The effective exposed area of the membrane is 116 cm². The resistance per 1 cm² membrane is therefore

$$r_{\text{membrane, 35°C}} = \frac{0.43\text{V}}{25\text{A}} (116\text{ cm}^2) = 2.0\ \Omega\text{cm}^2$$

Similar estimation at 75°C show that the specific resistance of the membrane (per 1 cm²) is roughly

$$r_{\text{membrane, 75°C}} = \frac{0.27\text{V}}{25\text{A}} (116\text{ cm}^2) = 1.3\ \Omega\text{cm}^2$$

It is not clear from the present measurements whether the resistance of the membrane is mostly ohmic or contains activation overpotential. Current-interruption measurements were not successful in determining the nature of the membrane potential.

A practical conclusion, however, can be made: The Nafion 031 membrane behaves like an ohmic resistance under industrial conditions, and the potential drop across the membrane can be estimated from the specific resistance obtained in the present report.

Current efficiency.—Additional advantage of using gas-diverting cathodes is reported by Creamer, Krumpelt, and Jorne (12). High current efficiency can be obtained by inducing turbulence in the catholyte by utilizing a gas-diverting cathode in close proximity to the membrane. An increase in the average current efficiency from 77 to 82% is reported by replacing the flattened cathode by an expanded-metal cathode which directed the gas away from the membrane. The cell was operated with Nafion membrane Type 313, under current density of 200 mA/cm², temperature of 82°–85°C and the pH in the anolyte varied from 3 to 3.5. The increase in current efficiency is due to the induced turbulence at the membrane surface and the resulting decrease in the hydroxide concentration at the surface of the membrane. The current efficiency of Nafion membranes is a strong function of the hydroxide concentration.

Conclusions

The three-dimensional structure and the inclined surfaces of the gas-diverting electrode enable the diversion of the gas to the rear of the electrode. This

results in ohmic drop saving because the electrode can be placed in a very close proximity to the membrane. In addition, an increase in the current efficiency is reported due to the induced turbulence at the surface of the membrane facing the cathode. The gas-diverting electrode can eliminate limitations on the electrode height with resultant capital investment savings.

Acknowledgment

The support of BASF Wyandotte Corporation is gratefully acknowledged.

Manuscript submitted March 23, 1979; revised manuscript received Aug. 1, 1979.

Any discussion of this paper will appear in a Discussion Section to be published in the December 1980 JOURNAL. All discussions for the December 1980 Discussion Section should be submitted by Aug. 1, 1979.

Publication costs of this article were assisted by BASF Wyandotte Corporation.

REFERENCES

1. C. W. Tobias, *This Journal*, **106**, 833 (1959).
2. Z. Nagy, *J. Appl. Electrochem.*, **6**, 171 (1976).
3. F. Hine, M. Yasuda, R. Nakamura, and T. Noda, *This Journal*, **122**, 1185 (1975).
4. R. E. De La Rue, and C. W. Tobias, *ibid.*, **106**, 827 (1959).
5. M. G. Fouad, G. H. Sedahmed, and H. A. El-Abd, *Electrochim. Acta*, **18**, 55, 279 (1973).
6. M. G. Fouad and G. H. Sedahmed, *ibid.*, **19**, 861 (1974).
7. M. G. Fouad and G. H. Sedahmed, *ibid.*, **20**, 615 (1975).
8. L. J. J. Janssen and J. G. Hoogland, *ibid.*, **18**, 543 (1973).
9. D. Jennings, A. T. Kuhn, J. B. Stepanek, and R. Whitehead, *ibid.*, **20**, 903 (1975).
10. I. Rousar and V. Cezner, *ibid.*, **20**, 289 (1975).
11. F. Hine and T. Sugimoto, Abstract 459, p. 1143, The Electrochemical Society Extended Abstracts, Vol. 78-1, Seattle, Washington, May 21-26, 1978.
12. E. D. Creamer, M. Krumpelt, and J. Jorne, U.S. Pat. 4,142,950 (1979).

Sodium Ion Diffusion in Nafion[®] Ion Exchange Membranes

H. L. Yeager and B. Kipling

Department of Chemistry, University of Calgary, Calgary, Alberta, Canada T2N 1N4

and R. L. Dotson*

Olin Corporation, Charleston, Tennessee 37310

ABSTRACT

Development of membrane chlor-alkali cells during this past decade represents a major advancement for commercial electrochemical technology. Chemical engineering applications of separation processes such as this involve diffusional mass transfer that can be treated as a rate process. The chlor-alkali application includes sodium, chloride, and hydroxyl ions plus water as mobile species in caustic soda and brine solutions and also between immiscible membrane and solution phases. These immiscible phases are brought into contact to allow selective transfer of sodium and water from brine to the caustic solutions. Previous data reported on NaOH diffusion through Nafion[®] membranes, D_{NaOH} , are difficult to interpret because not only do they involve hydroxide and sodium ion fluxes to give average diffusion coefficients, but also unknown gradients of electrolyte and water concentration are present in the membrane phase. This present work greatly simplifies these problems encountered by isolating and measuring the precise sodium ion self-diffusion coefficient, D_{Na^+} , with radio-tracer techniques in various du Pont Nafion[®] and EDA modified membranes. It then relates the D_{Na^+} to equivalent weight, surface treatment, and fabric backing in these membranes. These data for D_{Na^+} are very important in chlor-alkali cells because the sodium ion is the major current carrier; therefore, its value can be related to the relative activation energy and voltage drop among similar membranes.

The development of chlor-alkali cells which employ permselective ion exchange membranes as separators represents a major advancement in electrochemical technology. Nafion[®] perfluorosulfonic acid ion exchange membranes have the necessary chemical stability and ionic transport properties which are needed for this application as well as for fuel cells of various designs. In order to bring these technologies to full commercialization, it is important to develop a thorough understanding of the physical and chemical properties of the membrane for solution environments in which it is to be used. Recently, several studies of Nafion have been reported which relate to funda-

mental properties (1-10) and its application to chlor-alkali (11-16) or fuel cell systems (17-20). The central morphological feature of Nafion is the aggregation of exchange sites and counterions into clusters, with a Bragg spacing of about 50Å (1, 13). Gierke discusses the ion clustering phenomenon with regard to ion transport and hydroxide rejection in chlor-alkali cells (13). The transport properties of Nafion have been found to vary considerably with external solution concentration (12, 16-18), presumably due to changes in membrane water and electrolyte content.

Membranes which are produced by du Pont for chlor-alkali applications are generally composites of two equivalent weights of polymer or of one equivalent weight where one surface has been chemically modified to change the nature of the ion exchange grouping

* Electrochemical Society Active Member.

Key words: transport, polymer, chlor-alkali.

¹ Registered trademark of E. I. du Pont de Nemours and Company.

(12, 14-16). These modifications alter the membrane's dynamic properties; it has been found for experiments in which NaCl and NaOH solutions are separated by such membranes that the properties of the membrane side which is in contact with NaOH solution dominate the over-all membrane performance (16). Apparent membrane diffusion coefficients of NaOH have been measured for such systems (12, 16). Diffusion increases with lower equivalent weights and increasing NaOH concentration. Surface modification to produce sulfonamide exchange sites lowers diffusion rates by a factor of fifty while doubling the activation energy of diffusion (16).

A difficulty in the interpretation of these apparent NaOH diffusion coefficients is that not only are hydroxide and sodium ion fluxes coupled to produce an averaged diffusion coefficient, but unknown gradients of electrolyte and water concentration exist in the membrane phase. In order to remove these problems, we have measured the self-diffusion coefficient of Na⁺ in various Nafion samples using a tracer method under equilibrium conditions. We wish to determine the influence of equivalent weight, surface treatment, and fabric backing on the membrane diffusion of Na⁺, which is the major current-carrying species in the chlor-alkali membrane cell. Membrane water and NaOH concentrations have been determined also as a function of temperature and solution concentration. Finally, the membrane voltages of two Nafion materials which are produced for chlor-alkali applications have been measured in an operating cell.

Experimental

The properties of Nafion membranes which were studied are presented in Table I. Nafion 214 and 295 are manufactured for commercial chlor-alkali use and have one surface converted to sulfonamide exchange sites (14). This is accomplished by treating one surface of the polymer with ethylenediamine (EDA) while in the sulfonyl fluoride form. Open weave Teflon fabrics are used with these membranes to improve strength. The T-900 fabric, used in No. 295, provides a large open area because rayon threads present in the fabric can be chemically removed after lamination to the membrane. In practice the sulfonamide side of the membrane is exposed to NaOH solution in a chlor-alkali cell.

Membranes were pretreated by equilibration of the material for several hours in NaOH solution of given concentration and temperature to be used in the experiment. Equilibration times were 8 hr or longer. Since Nafion's properties are not completely reversible with temperature cycling (6, 18), data were taken using membrane samples which had not been heated to temperatures above that of the experiment. Water sorption measurements were made by a weight-drying method. Samples were dried at 150°C in vacuum before weighing, and completeness of drying was checked by measuring the infrared spectra of the dried materials. Corrections for sorbed electrolyte were applied to weight changes.

Table I. Properties of Nafion membranes

Membrane designation	Equiv. wt.	EDA conversion	Thickness, mm	Fabric (% open area)
1150 EW	1150	—	0.25	—
1200 EW	1200	—	0.25	—
1150 (EDA)	1150	~0.04 mm	0.18	—
EDA	1150	total	0.18	—
No. 214	1150	~0.04 mm	0.18	"T-24" (32%)
No. 295	1150	~0.04 mm	0.18	"T-900" (70%)

Membrane Na⁺ concentrations were determined using a radiotracer method. Membrane samples were equilibrated with a NaOH solution which had been doped with ²²Na⁺. The membrane was then removed, carefully blotted, and counted using a well-counter with associated electronics. The radiotracer was obtained as a carrier-free aqueous solution from commercial sources, and was used as received. For membranes without fabric backing, dimensional changes with temperature and concentration were measured and used to calculate membrane Na⁺ molarities. A wide flange micrometer (L. S. Starrett Company, Athol, Massachusetts) was used to measure the thickness of membrane samples, with a repeatability of about 0.01 mm. Fabric backed membranes showed minimal dimensional changes (<3%).

Sodium ion self-diffusion coefficients were also determined using ²²Na⁺ radiotracer. In this procedure, the membrane separates NaOH solutions of identical composition, and the radiotracer is added to one solution to initiate the experiment. At periodic intervals, 1 ml samples are withdrawn from the second solution. Steady-state conditions prevail as long as a small fraction of the total amount of tracer has been transferred (<2%). A diagram of the diffusion cell is shown in Fig. 1. The cell is constructed of borosilicate glass, with Teflon stirring paddles in each 100 ml compartment. Constant speed motors are used to drive the stirrers at 500 rpm. Silicone rubber gaskets hold the membrane in place; the exposed membrane area is 10 cm². Cold water condensers are mounted on the ports to prevent evaporation, Ascarite-filled drying tubes are used to prevent CO₂ uptake from the atmosphere, and the cell is thermostatted to ±0.1°C using a glass water jacket.

The steady-state flux of Na⁺ is given by

$$J = -\overline{DC}/d(1 + 2\overline{DC}\delta/DCd) \quad [1]$$

where J is the flux in mole cm⁻² sec⁻¹, D is the diffusion coefficient, C is molar concentration, d is membrane thickness, δ is the thickness of the unstirred liquid film at each membrane surface, and barred quantities refer to values within the membrane phase (21). With reasonable stirring and the high solution concentrations used here, the second term in the denominator is much less than unity and the expression simplifies to

$$J = -\overline{DC}/d \quad [2]$$

A few experiments were performed in dilute solution. In these cases, δ was estimated from values which have been determined in the same cell under similar solution conditions (3, 5). The change in \overline{D} from that neglecting film diffusion was about 20% in the most extreme case.

The voltage drop across Nafion 214 and 295 under conditions which duplicate an operating chlor-alkali cell was measured using a Teflon laboratory-scale cell. A steel cathode and a TiO₂-RuO₂ coated titanium anode were the working electrodes. Membrane area was 60 cm², the NaCl solution concentration was fixed at 4.8M, and the cell temperature was controlled at 85°C. The membrane voltage drop was measured using two probe electrodes and Luggin capillaries which extended to

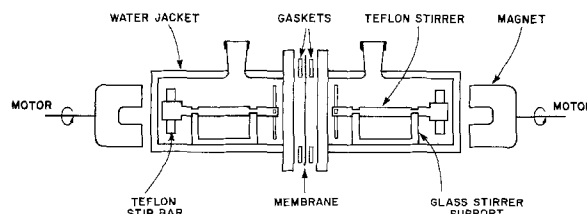


Fig. 1. Cell for membrane diffusion studies

each membrane surface. Current density was set at 2 kA m^{-2} .

Results and Discussion

Membrane water sorption and Na^+ concentration at several temperatures and NaOH solution concentrations are given in Tables II and III. The higher exchange capacity of 1150 equivalent weight (EW) produces higher sorption compared to 1200 EW, as expected. A comparison of results for the two backed membranes reveals the influence of the fabric. The much larger Na^+ and water concentrations for No. 295 probably result from void spaces within the membrane which are produced when rayon strands are chemically dissolved. It is also seen that membrane water contents are very sensitive to external solution concentration. The Na^+ membrane concentrations are essentially constant; this may be because the increasing tendency for NaOH sorption is balanced by lowered water contents as solution concentration increases.

Plots of typical tracer flux data are shown in Fig. 2 for the No. 214 membrane. At lower temperatures, transport is often extremely slow and only upper limits to Na^+ membrane diffusion coefficients can be made in some cases. Self-diffusion coefficients of Na^+ in all membrane samples are given in Table IV. Very similar trends can be seen for these diffusion coefficients as compared to membrane water concentrations, with higher water sorption producing enhanced diffusion. Self-diffusion coefficients for the two fabric backed membranes must be compared to those of the unbacked materials with caution, however. The measured area and thickness of No. 214 and No. 295 are not the effective values for a diffusing sodium ion. Errors in \bar{C} and J which are caused by area measurements cancel in Eq. [2], but the error in d , and in \bar{C} which employs d , will multiply. The presence of fabric approximately doubles the measured thickness; therefore we estimate that the actual Na^+ self-diffusion coefficients for these fabric backed membranes are about a factor of four smaller than the values listed in Table IV. This means that Na^+ diffusion in the fabric

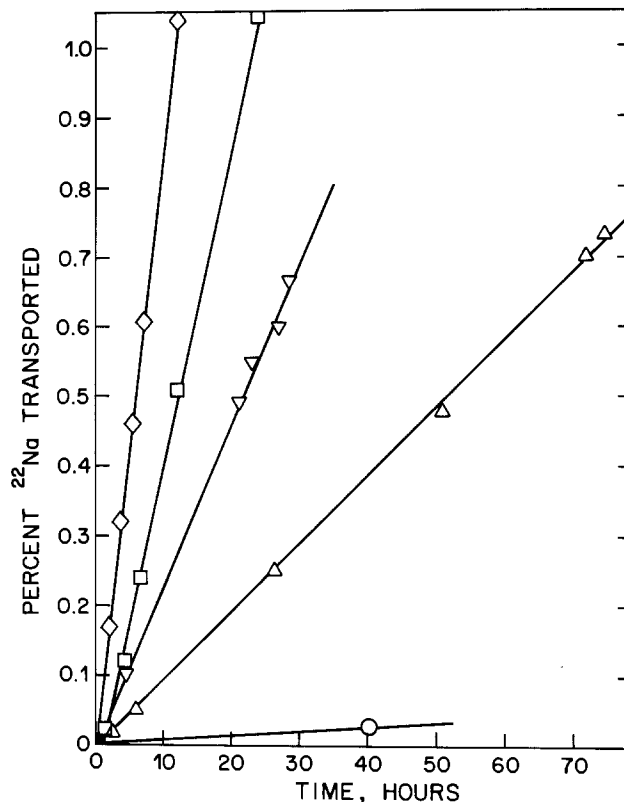


Fig. 2. Na^+ tracer flux in Nafion 214, 9.4M NaOH external solution. 25°C, ○; 40°C, △; 55°C, ▽; 70°C, □; 85°C, ◇.

backed membranes is more restricted than in their unbacked analogs, 1150 EW or 1150(EDA).

If ionic diffusion in Nafion can be treated as a simple kinetic process with a characteristic activation energy, then

$$\bar{D}_{\text{Na}^+} \propto \exp(-E_{\text{ACT}}/RT) \quad [3]$$

and a plot of $\log \bar{D}$ vs. $1/T$ should be linear. This is found to be true for the unbacked membranes between 60° and 90°C, as shown in Fig. 3. Activation energies of diffusion were calculated from the slopes of these lines and are given in Table V. Values of 3-5 kcal mole⁻¹ are typical of ionic activation energies in aqueous solution, and therefore Na^+ diffusion may be solution-like in 1150 and 1200 EW. Conversion of some sulfonate exchange sites to weakly acidic sulfonamide groupings approximately doubles the activation energy. This is probably due not only to the reduced water content with 1150(EDA) but more importantly to the enhanced attraction of sulfonamide sites to counterions. This might be expected because of the much stronger basic properties exhibited by ionized sulfonamides relative to sulfonates in aqueous solution. Full conversion to the sulfonamide form with the (EDA) membrane

Table II. Water sorption, g $\text{H}_2\text{O}/\text{g}$ dry membrane

Membrane	Concentration	Temperature				
		60°C	70°C	80°C	90°C	
1200 EW	9.5M	0.072	0.097	0.082	0.069	
1150 EW	9.5M	0.080	0.111	0.098	0.091	
1150 (EDA)	9.5M	0.079	0.096	0.087	0.081	
No. 295	9.5M	0.151	0.200	0.175	0.161	
	11.0M	0.101	0.113	0.108	0.157	
	12.5M	0.070	0.075	0.081	0.087	
No. 214	5.9M	25°C	40°C	55°C	70°C	85°C
		0.075	0.074	0.081	0.085	0.091
	9.4M	0.032	0.031	0.041	0.055	0.065
	11.0M	0.023	0.024	0.026	0.030	0.046
	12.5M	0.024	0.028	0.027	0.025	0.034
	15.1M	0.020	0.020	0.018	0.024	0.025

Table III. Membrane Na^+ concentration, mole liter⁻¹

Membrane	Concentration of NaOH	Temperature				
		60°C	70°C	80°C	90°C	
1200 EW	9.5M	2.54	2.29	2.32	2.48	
1150 EW	9.5M	2.95	2.83	2.61	2.56	
1150 (EDA)	9.5M	2.61	2.52	2.57	2.35	
EDA	9.5M	1.64	1.64	1.50	1.49	
No. 295	9.5M	2.99	3.04	2.80	2.72	
	11.0M	2.90	2.52	2.70	2.83	
	12.5M	2.81	3.31	3.01	2.82	
No. 214	5.9M	25°C	40°C	55°C	70°C	85°C
		1.48	1.61	1.77	1.76	1.71
	9.4M	1.98	1.96	2.03	2.02	1.91
	11.0M	2.02	2.26	2.37	2.41	2.25
	12.5M	2.26	2.63	2.33	2.20	2.13
	15.1M	2.75	2.99	2.80	2.37	2.38

Table IV. Self-diffusion coefficient of Na^+ , $\text{cm}^2 \text{ sec}^{-1} (\times 10^6)$

Membrane	Concentration of NaOH	Temperature				
		60°C	70°C	80°C	90°C	
1200 EW	9.5M	19.1	26.3	30.9	34.5	
1150 EW	9.5M	29.6	31.5	35.2	39.8	
1150 (EDA)	9.5M	17.2	24.7	30.6	40.8	
EDA	9.5M	4.4	7.6	12.5	19.9	
No. 295	9.5M	28.6	42.7	59.5	83.0	
	11.0M	18.5	30.7	38.3	46.0	
	12.5M	6.2	9.9	13.5	18.5	
No. 214	5.9M	25°C	40°C	55°C	70°C	85°C
		11.8	23.1	54.4	102	154
	9.4M	0.1	4.7	10.8	21.9	44.9
	11.0M	<0.06	1.12	5.7	10.5	19.2
	12.5M	<0.03	<0.03	1.70	5.1	10.0
	15.1M	<0.06	<0.06	0.1	0.45	0.53

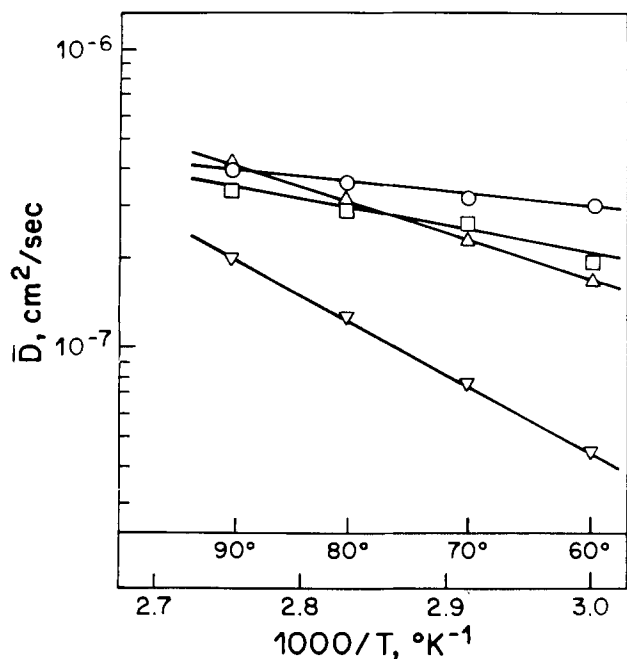


Fig. 3. Arrhenius plots for Na^+ diffusion in Nafion membranes, 9.5M NaOH external solution. \circ , 1150 EW; \square , 1200 EW; \triangle , 1150 (EDA); ∇ , EDA.

yields greatly reduced diffusion coefficients and a very high energy of activation.

Arrhenius plots for Nafion 214 and 295 are shown in Fig. 4 and 5. Linear relationships are again seen above 60°C. Results which were obtained for No. 214 at lower temperatures indicate that the activation energy of diffusion increases abruptly, especially at higher NaOH solution concentrations. This suggests that the mechanism of diffusion changes below a given temperature and solution concentration. This is similar to the results of ionic self-diffusion measurements in dilute solutions for Nafion 120 EW using water and other swelling solvents (5). Activation energies of diffusion for Na^+ were 7 and 4 kcal mole⁻¹ for water and methanol systems, respectively. However for Na^+ in acetonitrile or Cs^+ in all three solvent systems, activation energies were 15-20 kcal mole⁻¹. These much higher values were attributed to the inability of counterions to transport between ion clusters. This may explain the changes in slopes for the lines in Fig. 4 as well.

Activation energies calculated from the higher temperature data for No. 213 and No. 295 are larger than that of the analogous membrane without fabric backing, 1150 (EDA). Also, the two fabrics yield different increments to the activation energy. This suggests that the polymer morphology may be altered in the fabric lamination step of manufacturing such membranes, for in the absence of such changes the activation energy

Table V. Activation energy of Na^+ diffusion in Nafion, kcal mole⁻¹

Membrane	NaOH conc. (M)	Temperature range (°C)	E_{ACT}
1150 EW	9.5	60-90	2.5
1200 EW	9.5	60-90	4.7
1150 (EDA)	9.5	60-90	6.9
EDA	9.5	60-90	12.1
No. 295	9.5	60-90	8.5
	11.0	60-90	7.2
	12.5	60-90	8.7
No. 214	5.9	25-70	9.7
	9.4	40-85	10.9
	11.0	55-85	9.1
	12.5	70-85	10.2

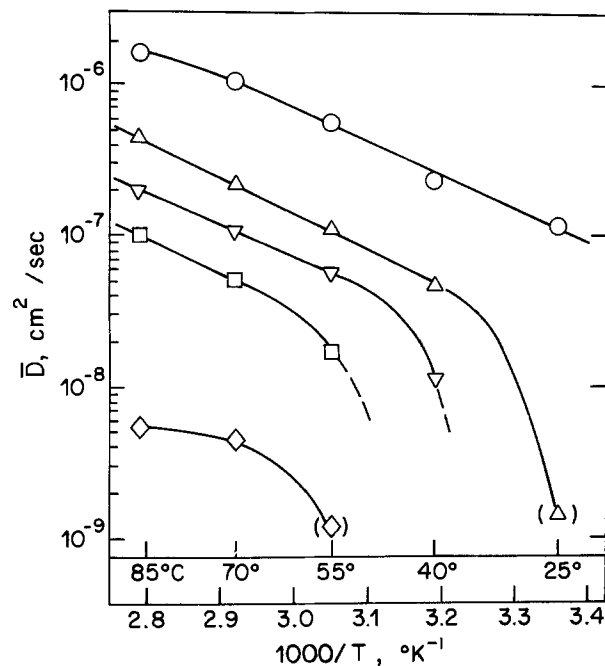


Fig. 4. Arrhenius plots for Na^+ diffusion in Nafion 214, NaOH external solution. \circ , 5.9M; \triangle , 9.4M; ∇ , 11.0M; \square , 12.5M; \diamond , 15.1M.

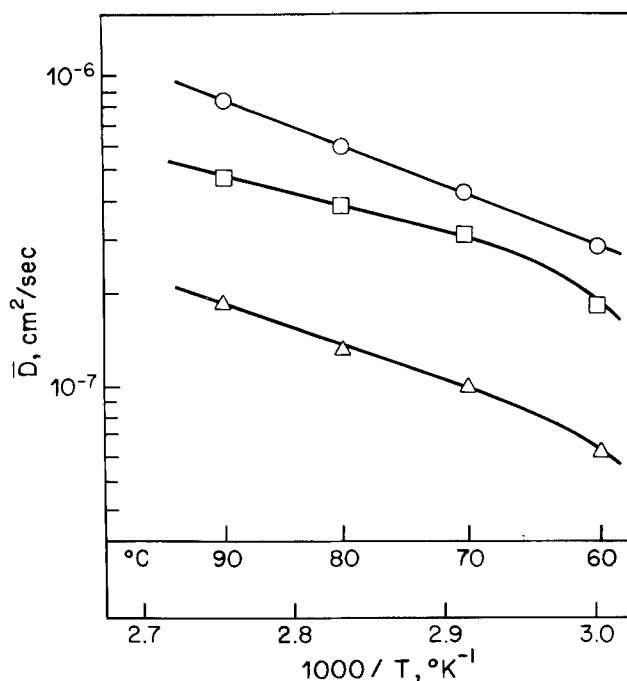


Fig. 5. Arrhenius plots for Na^+ diffusion in Nafion 295, NaOH external solution. \circ , 9.5M; \square , 11.0M; \triangle , 12.5M.

of diffusion should remain constant. The lowering of E_{ACT} near 11M NaOH solution concentration for both membranes is interesting. These values were remeasured with the same result. This suggests that an optimum NaOH concentration may be found with regard to the transport properties of Nafion membranes in chlor-alkali cells.

The dependence of the Na^+ self-diffusion coefficient on solution pH for Nafion 295 is shown in Fig. 6. Also plotted here is the change in the molarity of water in NaOH solution as a function of NaOH concentration, using standard chemical handbook data. The pronounced decrease of the diffusion coefficient in concentrated solution for No. 295 can be attributed to the dehydrating effect of the drop in solution water content, as illustrated in Fig. 6. At intermediate solution

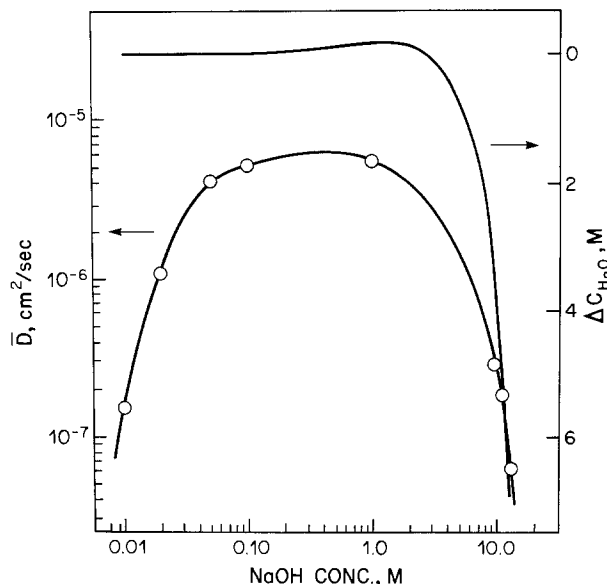


Fig. 6. Na^+ diffusion coefficient in Nafion 295 at 60°C , NaOH external solution; and change in water molarity in NaOH solution.

concentrations, membrane water contents increase and the diffusion of Na^+ rises by a factor of about 50. The reduction in diffusion coefficient in more dilute solutions is attributable to the sulfonamide exchange site layer in the membrane. These sites are weakly acidic, and if the internal membrane pH is not sufficiently high, the sites will protonate to remove the ion exchange capability of this layer of membrane. This would greatly reduce Na^+ diffusion. This result has relevance to the chlor-alkali cell. The pH gradient across the membrane separator will be affected by the adjustable brine acidity; the results in Fig. 6 suggest that brine pH may have a pronounced effect on membrane transport properties. We conclude that the operating properties of membranes such as Nafion 214 and 295 may be very sensitive to gradients in membrane pH and water content.

Membrane voltage drops for these membranes in a laboratory scale chlor-alkali cell are shown in Fig. 7. It is seen that the membrane voltage for No. 214 is about double that of No. 295, as would have been predicted from their respective Na^+ diffusion coefficients.

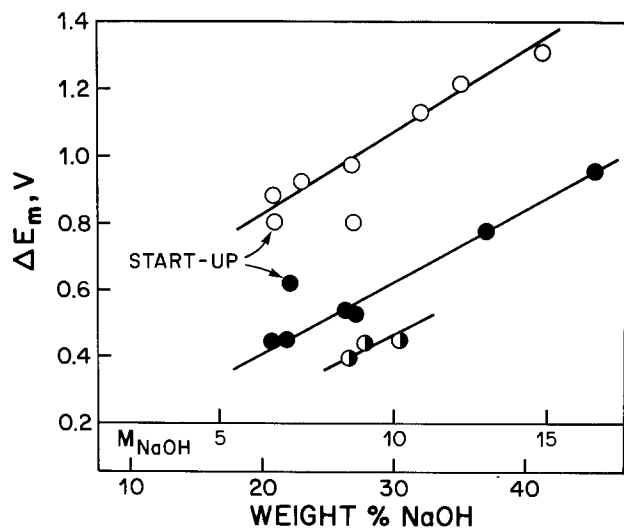


Fig. 7. Membrane voltage drop in operating chlor-alkali cell; 4.8M NaCl, 2 kA m^{-2} current density, 85°C . \circ , Nafion 214; \bullet , Nafion 295; \bullet , Nafion 295 after use.

Several other factors would need to be considered for more detailed comparisons of cell membrane voltages, however. These include the respective membrane Na^+ and OH^- concentrations, current efficiencies, and electro-osmotic water transport. Another feature of the operating properties of these membranes is shown in Fig. 7, where the membrane voltage of No. 295 has dropped by 0.15V after several weeks of operation. However this is accompanied by a decrease in current efficiency from 87 to 73%. Polymer degradation, long term morphological changes, or the slow accumulation of brine impurities are seen as possible contributing factors. Future work will examine the effect of gradients in membrane pH and water content, and imposed electrical current on the transport properties of these membranes.

Acknowledgment

Dr. N. Cyr, R. Huntrods, and H. C. Kuo performed experimental portions of this work. The authors wish to thank E. I. du Pont de Nemours and Company for providing membrane samples. Financial support for this research was provided by the Olin Corporation.

Manuscript submitted June 12, 1979; revised manuscript received Aug. 29, 1979.

Any discussion of this paper will appear in a Discussion Section to be published in the December 1980 JOURNAL. All discussions for the December 1980 Discussion Section should be submitted by Aug. 1, 1980.

Publication costs of this article were assisted by the Olin Corporation.

REFERENCES

- S. C. Yeo and A. Eisenberg, *J. Appl. Polym. Sci.*, **21**, 875 (1977).
- M. Lopez, B. Kipling, and H. L. Yeager, *Anal. Chem.*, **48**, 1120 (1976).
- M. Lopez, B. Kipling, and H. L. Yeager, *ibid.*, **49**, 629 (1977).
- H. L. Yeager and A. Steck, *ibid.*, **51**, 862 (1979).
- H. L. Yeager and B. Kipling, *J. Phys. Chem.*, **83**, 1836 (1979).
- W. G. F. Grot, G. E. Munn, and P. N. Walmsley, Paper 154 presented at The Electrochemical Society Meeting, Houston, Texas, May 7-11, 1972.
- R. A. Komoroski and K. A. Mauritz, *J. Am. Chem. Soc.*, **100**, 7487 (1978).
- K. A. Mauritz, C. J. Hora, and A. J. Hopfinger, *Polym. Prepr., Am. Chem. Soc. Div. Polym. Chem.*, **19**, 324 (1978).
- K. A. Mauritz and S. R. Lowry, *ibid.*, **19**, 336 (1978).
- R. A. Komoroski, *ibid.*, **19**, 341 (1978).
- S. G. Cutler, *ibid.*, **19**, 330 (1978).
- T. Berzins, Paper 437 presented at The Electrochemical Society Meeting, Atlanta, Georgia, Oct. 9-14, 1977.
- T. D. Gierke, Paper 438 presented at The Electrochemical Society Meeting, Atlanta, Georgia, Oct. 9-14, 1977.
- C. J. Hora and D. E. Maloney, Paper 441 presented at The Electrochemical Society Meeting, Atlanta, Georgia, Oct. 9-14, 1977.
- D. E. Maloney and C. J. Molnar, Paper presented at the 71st Annual Meeting, American Institute of Chemical Engineers, Miami Beach, Florida, Nov. 12-16, 1978.
- T. Berzins, Paper presented at the 71st Annual Meeting, American Institute of Chemical Engineers, Miami Beach, Florida, Nov. 12-16, 1978.
- F. G. Will, *This Journal*, **126**, 36 (1979).
- R. S. Yeo and J. McBreen, *ibid.*, **126**, 1682 (1979).
- R. S. Yeo and D-T. Chin, Paper 249 presented at The Electrochemical Society Meeting, Boston, Massachusetts, May 6-11, 1979.
- F. G. Will and H. S. Spalci, Paper 14 presented at The Electrochemical Society Meeting, Pittsburgh, Pennsylvania, Oct. 15-20, 1978.
- F. Helfferich, "Ion Exchange," Chap. 8, p. 348, McGraw-Hill, New York (1962).

Reduction of Cd_2SnO_4 and $\text{Cd}_2\text{SnO}_4/\text{CdO}$ Thin Film Electrodes in Sulfuric Acid Electrolytes

D. E. Hall*

The International Nickel Company, Incorporated,
INCO Research and Development Center, Sterling Forest, Suffern, New York 10901

ABSTRACT

The reductive decomposition of cadmium stannate thin film semiconductor electrodes in sulfuric acid electrolytes results in extensive depletion of cadmium from the electrodes. This was established from composition vs. depth profiles of Cd_2SnO_4 films obtained using Auger electron spectroscopy combined with sputter-etching of the Cd_2SnO_4 films at a controlled rate. The reduction process occurs at potentials positive of the estimated flatband potential of Cd_2SnO_4 . When CdO is present in the Cd_2SnO_4 films, reduction is greatly accelerated. The effect is similar to that caused by increasing the acid concentration of the electrolyte. Scanning electron micrographs show that the films are preferentially attacked at grain boundaries, where CdO is believed to be concentrated.

Recently, the use of cadmium stannate thin film electrodes in iron-thionine photogalvanic cells was described (1). The power output of cells with Cd_2SnO_4 cathodes declined slowly with use. This was attributed to reductive decomposition of the Cd_2SnO_4 cathodes in their operating potential range, which was evident from current vs. potential curves of Cd_2SnO_4 in the supporting electrolyte. In this preliminary investigation of the electrochemical properties of Cd_2SnO_4 , the flatband potential was estimated from Schottky-Mott plots of capacitance data, and the potentials of anodic and cathodic limiting processes were established. Cadmium stannate was found to reduce at potentials several tenths of a volt positive of the limiting cathodic process; the extent of reduction was dependent on acid concentration in the electrolyte.

The electrochemical behavior of other highly conductive oxide semiconductors has also received recent attention. Stannic oxide is the best characterized of these, having been used for many years as a working electrode in photoelectrochemical studies. Laitinen and co-workers (2) investigated the behavior of SnO_2 in strong acid solutions and provided evidence for surface electrolysis of SnO_2 at potentials positive of the cathodic limit, where SnO_2 is reduced to metallic tin. The surface reduction of SnO_2 was enhanced by increasing the acid concentration in the electrolyte, and also by the presence of specifically adsorbed anions such as chloride. A calculation was presented to show that the charge involved in the reduction process was considerably greater than that available from the first atomic layer of the electrode surface. The authors speculated that the surface roughness factor was greater than one and/or more than a monolayer of tin atoms was reduced.

Additional information on thin film semiconductor electrochemistry can be obtained by using instrumental techniques suitable for analysis of thin film composition and surface structure. Recently, Armstrong *et al.* (3) investigated the behavior of tin oxide and indium tin oxide thin films in acid electrolytes. Using Auger electron spectroscopy and ESCA, direct evidence of electrochemically induced changes in electrode stoichiometry was obtained. By depth-profiling SnO_2 electrodes which had been subjected to controlled-

potential electrolysis, it was shown that the ratio of oxygen to tin in SnO_2 decreased as the electrolysis potential was made more negative. The O/Sn ratio was lowered in a region extending quite deeply into the film, supporting the observation by Laitinen and co-workers that several atomic layers of the electrode surface are probably involved in the electrochemistry of SnO_2 .

In the present paper, the reduction of Cd_2SnO_4 in sulfuric acid electrolytes is described. It is shown that reduction of Cd_2SnO_4 causes compositional changes in the film which extend to great depths below the film surface. A mechanism for this effect is suggested, based on structural and compositional analyses of electrochemically etched films.

Experimental

Cadmium stannate thin films, with and without significant amounts of CdO, were sputter-deposited on low-alkali glass substrates and characterized by G. Haacke of American Cyanamid Company. The sputter deposition and characterization procedures have been discussed recently in detail by Haacke and co-workers (4). All Cd_2SnO_4 films had been annealed at 650°C after deposition and had sheet resistances between 2.5 and 3 Ω/\square . A Cd_2SnO_4 film containing $\geq 10\%$ CdO was annealed at 670°C; its sheet resistance was 3.6 Ω/\square . This film was noticeably yellower than the others, which typically have a pale gray-green cast. [The adsorption-edge shift caused by the presence of CdO in Cd_2SnO_4 films has been reported by Haacke (5).] Each thin film was cut down to make electrodes approximately 0.3 cm² in area. Electrical contact was made to one edge of each electrode using indium metal or silver paint. The contact and connecting wires were then coated with silicone rubber sealant. Electrochemical measurements were made at 23°C in a cell containing a SCE reference and a platinum foil counterelectrode. The H_2SO_4 and Na_2SO_4 electrolyte solutions were made from reagent grade chemicals, using distilled water. Potential-cycling experiments were performed using a Princeton Applied Research 173 potentiostat and 175 universal programmer. The negative limit of potential cycles was not allowed to reach the cathodic limiting process, in order to study the reductive decomposition of Cd_2SnO_4 at more positive potentials which was reported in an earlier paper (1).

* Electrochemical Society Active Member.
Key words: cadmium stannate, semiconductor electrodes, Auger electron spectroscopy.

Auger electron spectroscopy (AES) was performed using a Physical Electronics Model 545 Scanning Auger Microprobe under a vacuum of 10^{-9} Torr. A 5 keV electron beam was rastered over an area of roughly 4×10^{-3} mm². To establish the composition of the film as a function of distance from its surface, a 2 kV argon ion beam was used to sputter-etch the film at a controlled rate. This rate was calibrated by an independent thickness measurement obtained by scanning electron microscopy. As described below, some Cd₂SnO₄ electrodes were visibly damaged by exposure to H₂SO₄ electrolytes and potential-cycling experiments, with the result that their composition changed. The sputtering rates of these electrodes were, by necessity, assumed to be equal to those of new Cd₂SnO₄ films. Spectra were recorded at preselected intervals during sputtering, until a strong silicon signal indicated complete removal of the film. Initial analyses of elemental composition used Cd, Sn, and O sensitivity factors obtained from other oxide materials, but these were found to be unsatisfactory. Accordingly, sensitivities were renormalized from data obtained midway through the depth-profile of a new Cd₂SnO₄ film, where the composition was nearly constant. In the AES results reported below, Cd + Sn + O + final Si analyses were used as the basis for normalization; carbon and small amounts of other surface impurities such as chlorine were subtracted from the raw data. A three-point smoothing treatment was used on the resulting normalized data. None of the major features of the depth profiles were significantly altered by this treatment, although minor ripples in compositional analysis were reduced.

During the AES investigation of Cd₂SnO₄ and Cd₂SnO₄/CdO films, it was discovered that the primary electron beam caused the Sn/Cd ratio to increase slightly with time (6). It was not determined whether this was caused by migration of Sn to the beam spot, or by Cd migration away from it. An investigation of this effect indicated that, during the time required for each depth profile to be made, this change in the Sn/Cd ratio was not large enough to interfere with the features of the depth-profile plots or the conclusions drawn from them.

The surface topographies of Cd₂SnO₄ films were examined with a Cambridge Stereoscan 180M scanning electron microscope. A 26 keV primary beam energy was used with 30k magnification. Lower magnifications were also used to examine prominent surface features. The elemental compositions of selected sites on Cd₂SnO₄ and Cd₂SnO₄/CdO electrodes were obtained by energy-dispersive x-ray spectrometry (EDS).

Results

Cd₂SnO₄ thin films in sulfuric acid electrolytes. The AES depth profile of a new Cd₂SnO₄ thin film is shown in Fig. 1. The expected analysis of stoichiometric Cd₂SnO₄ is 55 weight percent (w/o) Cd, 29 w/o Sn, and 16 w/o O. SEM photomicrographs showed that the Cd₂SnO₄ surface had a uniform structure consisting of ~ 0.2 μ m diam knobs. The large surface defects on the SnO₂ films examined by Armstrong *et al.* (3) were not evident on Cd₂SnO₄, reflecting differences in film preparation methods.

The initial cyclic potential sweeps of Cd₂SnO₄ in 0.01M H₂SO₄ showed no distinctive features between 1.0 and 0.4 V/SCE. However, successive sweeps often showed a small but noticeable reduction wave at ~ 0.4 V/SCE. The reduction wave, shown in Fig. 2 (solid line), persisted in potential sweeps recorded at short intervals during a period of a few hours, but the reduction current gradually declined until a distinct wave was no longer observed (Fig. 2, dotted line). Between potential sweeps, the rest potential drifted slowly to ~ 0.4 V/SCE, indicating spontaneous decom-

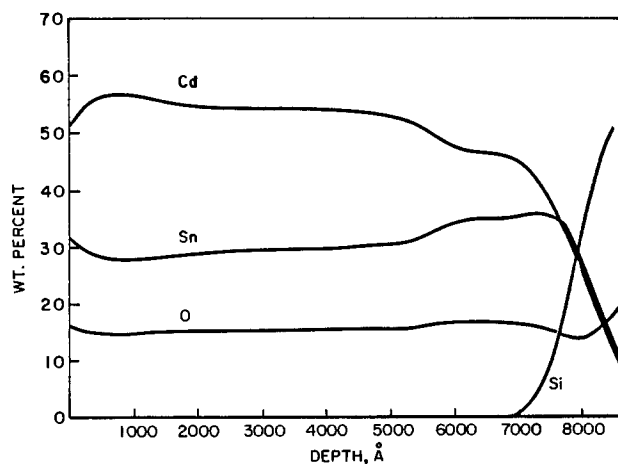


Fig. 1. Composition vs. depth profile of a Cd₂SnO₄ thin film (as-received).

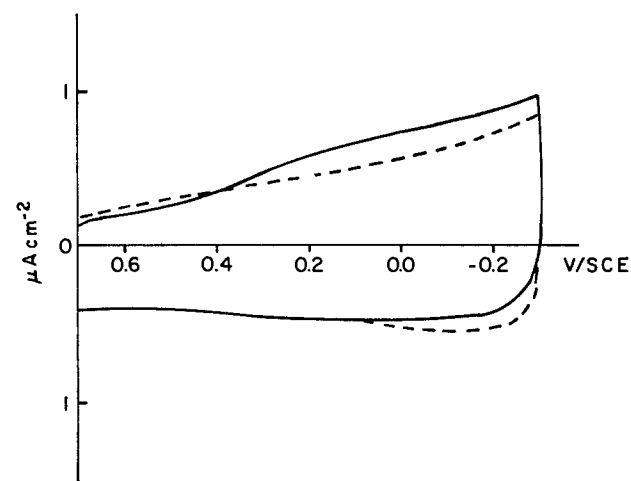


Fig. 2. Cd₂SnO₄ electrode in 0.01M H₂SO₄. Potential sweep rate = 5 mV sec⁻¹. Solid line: 4th cycle, 35 min after insertion of electrode into cell. Dotted line: after 148 min of exposure to electrolyte.

position of the film. Current-potential curves similar to the dotted-line curve of Fig. 2 were also obtained in 0.2M Na₂SO₄.

To determine more accurately the onset potential for Cd₂SnO₄ reduction, cyclic potential sweeps were performed with regular increases of the negative switching potential ($E_{sp,c}$) until no faradaic current could be detected on the positive sweep, thus indicating that no reduction had occurred on the previous negative sweep. It was necessary to obtain these measurements at slow sweep rates (5-10 mV sec⁻¹) because of the slowness of the faradaic process (1). Initially, no oxidation current was observed for $E_{sp,c}$ greater than approximately 0.4 V/SCE. After continued cycling, oxidation currents were observed for $E_{sp,c}$ as positive as ~ 1.0 V/SCE (Fig. 3), indicating that Cd₂SnO₄ reduction occurs over a much wider potential range than previously reported (1). The rest potential of the Cd₂SnO₄ electrode showed a similar shift. The observed reduction of Cd₂SnO₄ at potentials as positive as 1.0 V/SCE shows that Cd₂SnO₄ is apparently reduced at potentials positive of the flatband potential (1). Armstrong *et al.* (3) reported similar behavior for SnO₂ thin film electrodes.

When the Cd₂SnO₄ electrode was removed from the electrolyte, the film had a uniform reddish-green color at the electrode center, gradually changing to the original color of the Cd₂SnO₄ film at the edges, where the electrode had been partially shielded by the silicone resin. SEM photomicrographs showed that the electrode surface structure was essentially unchanged.

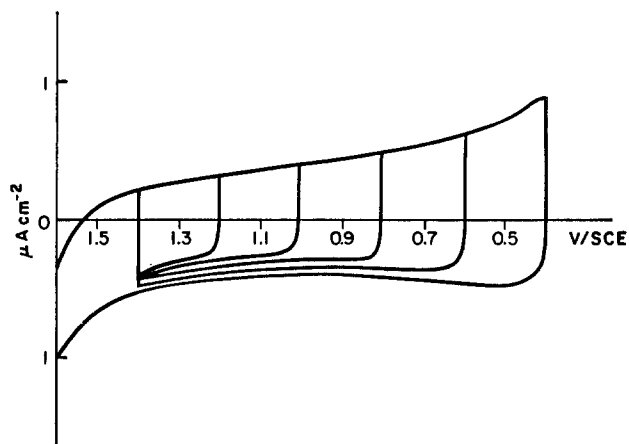


Fig. 3. Cd_2SnO_4 electrode in $0.01\text{M H}_2\text{SO}_4$. Same electrode as in Fig. 2, after 192 min of exposure to electrolyte. Potential sweep rate = 10 mV sec^{-1} .

Thus, it appeared that fairly uniform surface electrolysis had taken place. The AES depth profile of the electrode (Fig. 4) showed a small decrease in film thickness, as well as extensive removal of Cd from the top 1000Å of the film. The drop in Cd content in the film surface region was apparently responsible for the lower reduction currents observed on the last cyclic potential sweeps, as shown in Fig. 2.

Reduction waves were established rapidly when potential sweeps were performed in $0.1\text{M H}_2\text{SO}_4$, as shown in Fig. 5. These waves were similar to those reported previously when $0.05\text{M H}_2\text{SO}_4$ was used [Fig. 2 of Ref. (1)], but were much sharper and at more positive potentials in the stronger acid. Laitinen *et al.* (2) also found that peak current definition at SnO_2 electrodes increased with increasing acid concentration. Using lattice constants for Cd_2SnO_4 from Haacke *et al.* (4), it was determined that the charge passed on the cathodic sweep from Fig. 5 (solid line) would be sufficient to reduce completely the cadmium content of ~ 2 molecular layers of Cd_2SnO_4 , assuming a surface roughness factor of one. This supports the above-mentioned observation of Laitinen *et al.* (2) that the electrochemical reduction of oxide semiconductors may well involve more than one molecular layer at the electrode surface concurrently. The abrupt truncation of reduction waves, and the erratic currents encountered with continued cycling, may be caused by the decreased accessibility of cadmium in succeeding layers of the electrode. The corresponding oxidation process was observed as a broad wave at $\sim 0.6\text{ V/SCE}$. A strong oxidation wave was also associated with the limiting cathodic process (Fig. 5, dotted line). With

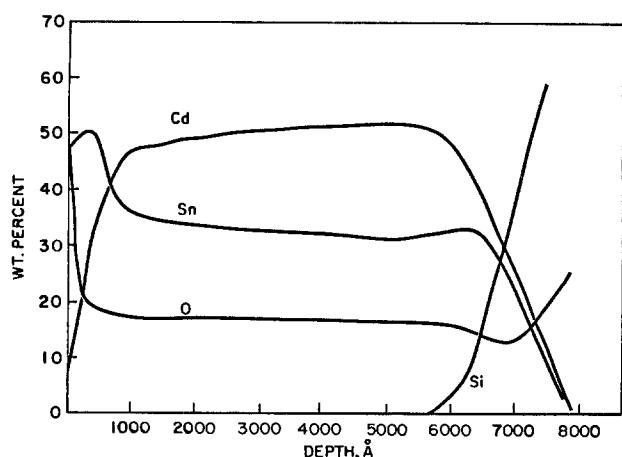


Fig. 4. Composition vs. depth profile of a Cd_2SnO_4 thin film after potential cycling in $0.01\text{M H}_2\text{SO}_4$.

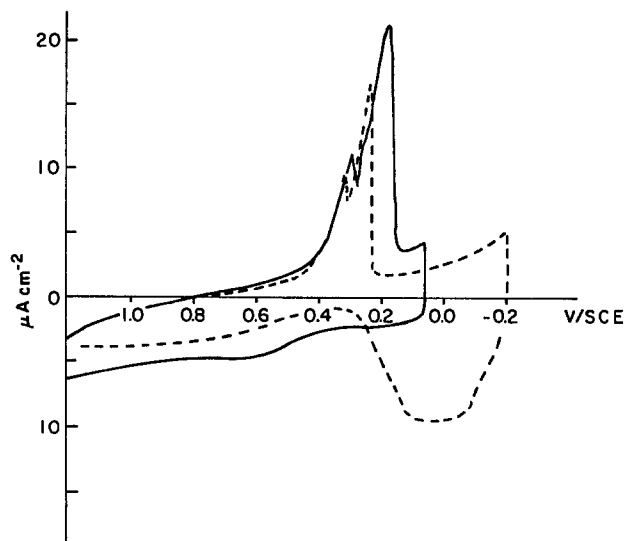


Fig. 5. Cd_2SnO_4 electrode in $0.10\text{M H}_2\text{SO}_4$. Solid line: potential sweep rate = 10 mV sec^{-1} . Dotted line: potential sweep rate = 5 mV sec^{-1} .

continued cycling, the reduction waves became less well-defined and currents were erratic.

Examination of the electrodes following potential sweeps in $0.1\text{M H}_2\text{SO}_4$ showed that the Cd_2SnO_4 films were unevenly colored and contained many highly etched areas. The AES depth profile (Fig. 6) showed extensive Cd depletion in the top 2500Å of the film. Near the film surface, the composition was nearly that of SnO_2 (79 w/o Sn, 21 w/o O). The AES depth profile of a Cd_2SnO_4 film exposed to $0.1\text{M H}_2\text{SO}_4$ for the same length of time without potential cycling was similar to Fig. 6, indicating that acid-induced decomposition of Cd_2SnO_4 was much more rapid than in $0.01\text{M H}_2\text{SO}_4$.

The above results, taken with those from Ref. (1), describe the reduction and current vs. potential behavior of Cd_2SnO_4 in 0.01 - $0.25\text{M H}_2\text{SO}_4$. Distinct cathodic waves are either absent or very small in $0.01\text{M H}_2\text{SO}_4$, and the Cd_2SnO_4 surface is reduced uniformly. Considerable cadmium is removed from the film surface region, although this process occurs slowly. Similar current-potential curves are obtained in $0.2\text{M Na}_2\text{SO}_4$. In the absence of potential cycling, open-circuit reduction occurs at a rate which is appreciable, but slower than that resulting from applying more negative potentials which do not reach the cathodic limiting process. Higher acid concentrations greatly accelerate the reduction of Cd_2SnO_4 . In $0.05\text{M H}_2\text{SO}_4$, two distinct

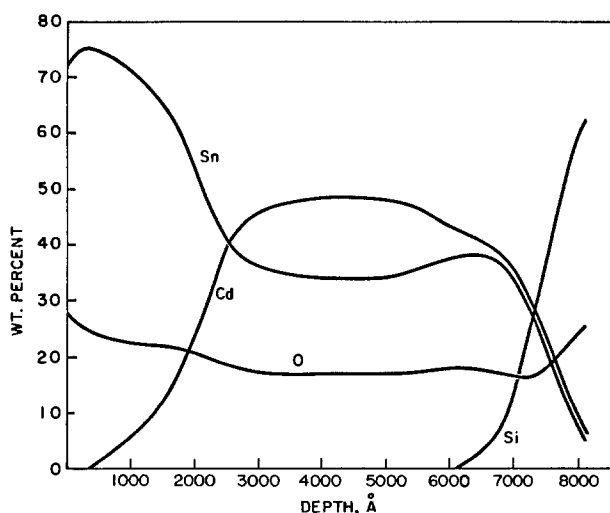


Fig. 6. Composition vs. depth profile of a Cd_2SnO_4 thin film after potential cycling in $0.10\text{M H}_2\text{SO}_4$.

cathodic waves appear, and shift to more positive potentials as the H_2SO_4 concentration is raised to 0.1M. The Cd_2SnO_4 films are visibly etched, indicating more aggressive decomposition occurring preferentially at certain sites on the films. Reduction is also rapid at open circuit. In both cases, AES depth profiling shows deep Cd removal and the electrode composition approaches SnO_2 . In 0.25M H_2SO_4 , reduction waves are similar to those observed in 0.1M H_2SO_4 , but are larger; the electrode film is rapidly destroyed.

The complexity of the depth profiles of reduced Cd_2SnO_4 films makes it difficult to draw conclusions regarding the reduction products (which could include CdSnO_3 , for example). However, a reasonable interpretation of the above data is that Cd_2SnO_4 is converted ultimately to SnO_2 . The time-dependent composition of the electrode surface region also makes it difficult to assign a particular electrode process to the anodic and cathodic current peaks observed in cyclic potential sweeps, as in Fig. 5. Laitinen *et al.* (2) ascribed similar peaks at SnO_2 electrodes to the slow reduction and oxidation of surface tin species. However, while the current peaks observed in the present work are at approximately the same potentials, they are larger than similar peaks observed by Laitinen at pure SnO_2 , and occur in much weaker acid. In addition, cathodic current peak truncation, and the reduction of peak currents with continued potential cycling, both suggest depletion of electroactive material while the SnO_2 content of the Cd_2SnO_4 film surface is increasing. (This current-potential behavior might also be caused by mechanical breakdown of the film.) Thus, although the current *vs.* potential curves at SnO_2 and Cd_2SnO_4 thin film electrodes in the two studies have similarities, it is doubtful whether their current peaks in strong acids can be attributed to the same processes.

$\text{Cd}_2\text{SnO}_4/\text{CdO}$ thin films in sulfuric acid electrolytes.

—The AES depth profile of a Cd_2SnO_4 film containing CdO is shown in Fig. 7. The elemental composition of the film is similar to that found in Fig. 1 for Cd_2SnO_4 , with a slightly higher percentage of Cd in the $\text{Cd}_2\text{SnO}_4/\text{CdO}$ film.

When potential sweeps were imposed on $\text{Cd}_2\text{SnO}_4/\text{CdO}$ thin films in 0.01M H_2SO_4 , two distinct reduction waves at 0.4 and 0.3 V/SCE were obtained immediately, as shown in Fig. 8 (solid line). A corresponding, well-defined oxidation wave was present at 0.6 V/SCE. Repeated potential cycling caused the reduction waves to shift to more negative potentials, merging to form a single, sharp peak (Fig. 8, dotted line). The oxidation wave became less distinct. At the conclusion of potential sweep experiments, the $\text{Cd}_2\text{SnO}_4/\text{CdO}$ films were visibly etched, in the same manner as Cd_2SnO_4 films in 0.1M H_2SO_4 . Scanning electron microscopy

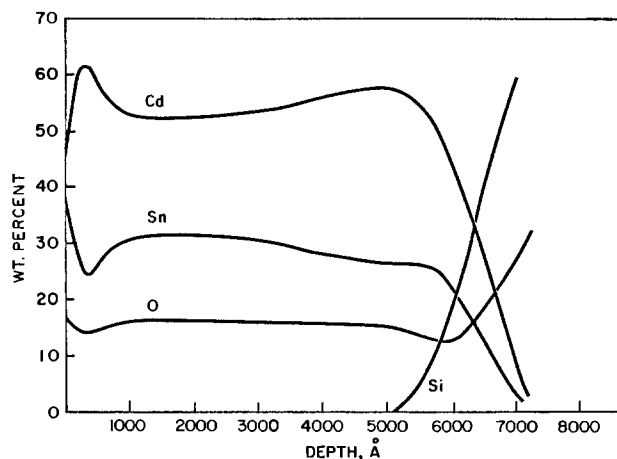


Fig. 7. Composition vs. depth profile of a $\text{Cd}_2\text{SnO}_4/\text{CdO}$ thin film (as-received).

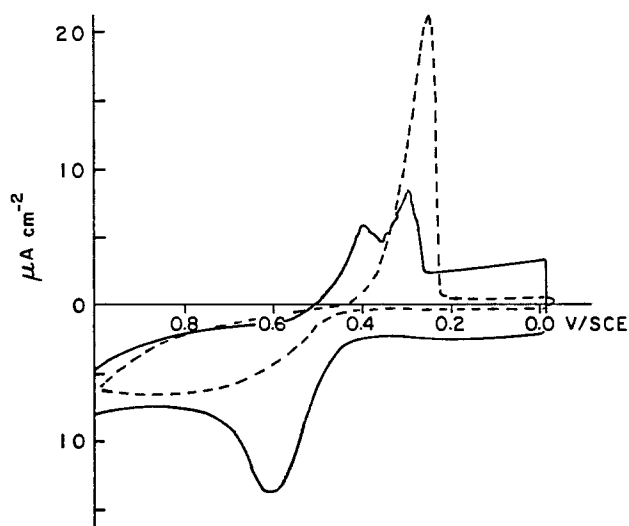


Fig. 8. $\text{Cd}_2\text{SnO}_4/\text{CdO}$ thin film electrode in 0.01M H_2SO_4 . Potential sweep rate = 5 mV sec^{-1} . Solid line: 3rd cycle. Dotted line: after repeated cycling.

revealed that the entire film surface was covered with deep crevices, separating the film into angular plates approximately 2-3 μm across [Fig. 9(A)]. In addition, larger eruptions of the film were observed, as shown in Fig. 9(B). An elemental analysis was performed by EDS at each of the numbered sites. In the crevice (site 1), a strong silicon signal together with the absence of any Sn or Cd signal indicated total loss of the film. At site 2, silicon and tin were both detected; the Cd signal was very weak. The majority of the film surface, represented by site 3, showed a strong tin signal and a very weak Cd signal.

The composition change of $\text{Cd}_2\text{SnO}_4/\text{CdO}$ is much more extensive than for any similar reductive decomposition of thin film semiconductor electrodes reported to date. A typical AES depth profile of $\text{Cd}_2\text{SnO}_4/\text{CdO}$ after potential cycling as described above is shown in Fig. 10. The decreased film thickness shows that a substantial amount of material was removed by the reduction process. More striking, however, is the nearly complete removal of Cd from the film. At depths of 1500-3500 Å, the composition of the etched film is nearly that of SnO_2 .

The behavior of $\text{Cd}_2\text{SnO}_4/\text{CdO}$ thin film electrodes is probably due to film structure. Evidence has been obtained which suggests that the CdO phase is concentrated at Cd_2SnO_4 grain boundaries (7). The CdO phase is attacked more vigorously than the Cd_2SnO_4 , resulting in the segmented appearance of electrochemically etched $\text{Cd}_2\text{SnO}_4/\text{CdO}$ films [Fig. 9(A)]. Subsequent electrolyte penetration into the intergranular crevices results in removal of Cd from the Cd_2SnO_4 phase to a greater extent than in Cd_2SnO_4 films not containing CdO, which are attacked mainly at the surface. The EDS analyses given above, for example, show that Cd depletion is most extensive near the large crevice in Fig. 9(B), where electrolyte penetration occurs most readily. The quantity of Cd depleted from $\text{Cd}_2\text{SnO}_4/\text{CdO}$ films, as seen from AES depth profiling, indicates that Cd_2SnO_4 within the film bulk is indeed reduced, for the amount of Cd removed is obviously much greater than that contained in the amounts of CdO present. The effect of CdO, therefore, is to provide sites at the grain boundaries which are more readily attacked at low acid concentrations. Equivalent results are obtained by exposing Cd_2SnO_4 films (without CdO) to higher acid concentrations.

During the course of this study and an earlier one (1), erratic current-potential curves with higher than normal reduction peaks were sometimes obtained at Cd_2SnO_4 electrodes in 0.01M H_2SO_4 . Those curves were

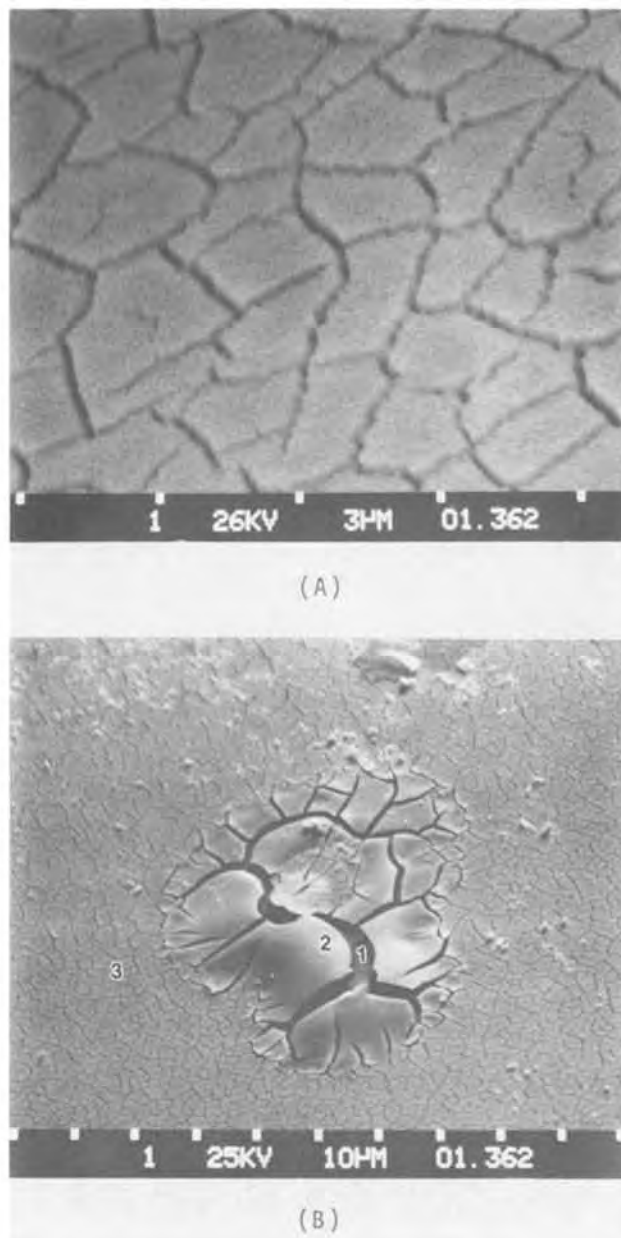


Fig. 9. Scanning electron micrographs of electrochemically etched $\text{Cd}_2\text{SnO}_4/\text{CdO}$ thin film electrodes. (A) Network of crevices covering most of electrode surface, $7500\times$. (B) Large eruption of $\text{Cd}_2\text{SnO}_4/\text{CdO}$ film, showing areas where EDS analyses were made, $1000\times$.

similar to ones obtained in the present work with electrodes known to contain CdO. Because of the difficulty in preparing truly single-phase films (4, 8); it is therefore likely that Cd_2SnO_4 electrodes displaying unusually vigorous reduction contained undetected quantities of CdO sufficient to promote intergranular attack.

Discussion

Changes in metal oxide electrode stoichiometry affect the semiconductor properties of the electrode surface region by changing its charge carrier density, conductivity, and even the oxide compounds present, as suggested in the present work. Both the composition of the oxide surface and the thickness of the oxide region are important. Armstrong *et al.* (3) have demonstrated the importance of composition changes at optically transparent thin film electrodes. Recent work, notably by Srinivasan and co-workers (9) has also emphasized the importance of obtaining an adequate description of the surface oxide layer at electrodes used for oxygen evolution and reduction.

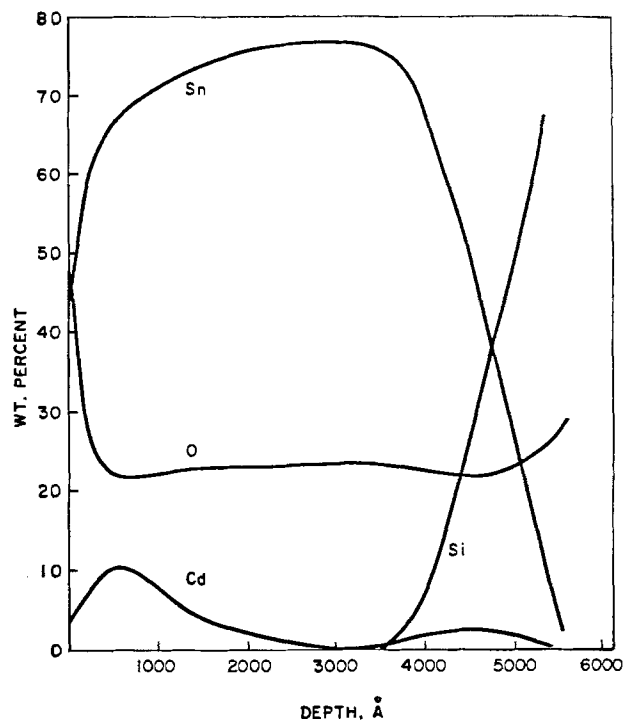


Fig. 10. Composition vs. depth profile of $\text{Cd}_2\text{SnO}_4/\text{CdO}$ thin film after potential cycling in $0.01\text{M H}_2\text{SO}_4$.

An important difference between tin oxide and cadmium stannate is that electrode processes at Cd_2SnO_4 which occur positive of the cathodic limit are not confined to charging and discharging of surface species. When the process is slow enough (as in weak acid electrolytes), the conversion of relatively unstable Cd_2SnO_4 to the more stable SnO_2 can be monitored, making it possible to observe stoichiometry changes to great depths. At higher acid concentrations, or when CdO is present at grain boundaries, the reduction process is accelerated, providing a physical picture of the electrode reduction. The grain-boundary corrosion of the thin film oxide semiconductor can be clearly seen.

The use of surface analysis techniques such as Auger electron spectroscopy, combined with sputter-etching to determine depth profiles of electrodes, involves certain assumptions. Following earlier practice (3), an equal sputtering rate was assumed for all elements in Cd_2SnO_4 thin films. An additional assumption was also made: thin films reduced to the point of having structure defects and large compositional differences were assumed to have the sputtering characteristics of unetched films. It is doubtful that truly quantitative data can be obtained under such circumstances. However, in the present work, such a method has proved useful in determining the essential features of Cd_2SnO_4 thin film reduction. These assumptions, and others which will be made in future studies, will doubtless be investigated in more detail as AES and other surface analysis techniques are used increasingly to study mixed metal oxide and other electrode surfaces.

Acknowledgments

The cadmium stannate electrodes used in this work were generously supplied by Dr. G. Haacke, whose interest in this work and useful information are gratefully acknowledged. Valuable discussions of depth profile results were held with Dr. H. L. Yeh and Mr. D. J. Hunt. This work was supported by the INCO Creative Research Program.

Manuscript submitted Nov. 20, 1978; revised manuscript received Aug. 30, 1979.

Any discussion of this paper will appear in a Discussion Section to be published in the December 1980

JOURNAL. All discussions for the December 1980 Discussion Section should be submitted by Aug. 1, 1980.

Publication costs of this article were assisted by INCO.

REFERENCES

1. D. E. Hall, *This Journal*, **124**, 804 (1977).
2. H. A. Laitinen, C. A. Vincent, and T. M. Bednarski, *ibid.*, **115**, 1024 (1968).
3. N. R. Armstrong, A. W. C. Lin, M. Fujihira, and T.

- Kuwana, *Anal. Chem.*, **48**, 741 (1976).
4. G. Haacke, W. E. Mealmaker, and L. A. Seigel, *Thin Solid Films*, **55**, 67 (1978).
5. G. Haacke, *Appl. Phys. Lett.*, **28**, 622 (1976).
6. D. J. Hunt, Personal communication.
7. G. Haacke and L. C. Burton, NTIS Report No. PB 261 850 (Sept. 1976).
8. G. Haacke, Personal communication.
9. P. W. T. Lu and S. Srinivasan, *This Journal*, **125**, 1416 (1978).

Determination of the Liquid Interaction Parameters of InP, InAs, GaAs, and GaP in the Range 580°-670°C

Ernesto H. Perea and Clifton G. Fonstad

Department of Electrical Engineering and Computer Science and Center for Materials Science and Engineering, Massachusetts Institute of Technology, Cambridge, Massachusetts 02139

ABSTRACT

The liquid interaction parameters for InP, GaAs, InAs, and GaP have been measured in the 580°-670°C range. The procedure followed to determine these parameters, together with an account of the conditions under which the measurements were carried out in order to obtain reproducibility of the results, are described.

The III-V quaternary, $\text{In}_u\text{Ga}_{1-u}\text{P}_v\text{As}_{1-v}$, has recently received much attention because of its importance for optoelectronic and hot electron device applications (1-4). The accurate determination of the liquid interaction parameters (5) for InP, InAs, GaAs, and GaP is an important step towards the determination of the complete set of parameters that govern solid-liquid equilibrium of $\text{In}_u\text{Ga}_{1-u}\text{P}_v\text{As}_{1-v}$. In this work, a systematic determination of these parameters is reported, together with a complete description of the conditions under which the measurements were carried out in order to secure the reproducibility of the results.

Published data (6) is typified by high dispersion and least squares fits made over a large range of temperatures yield parameters that are inadequate in the restricted range of temperatures used in quaternary growths. Differences between experimentally measured liquidus temperatures and those calculated using liquid interaction parameters previously reported (6, 7) are in some cases quite significant. Using the parameters determined in this work, binary liquidus temperatures can be predicted to within $\pm 0.5^\circ\text{C}$ between 580° and 670°C.

The Binary Liquid Interaction Parameter

The solid-liquid equilibrium for a binary consisting of elements i and j is given in the simple solution model by (5)

$$\Delta S_{F^{ij}}(T_{F^{ij}} - T_1) + RT_1 \ln(4x_i^l x_j^l) - \alpha_{ij}^l [0.5 - (x_i^l)^2 - (x_j^l)^2] = 0 \quad [1]$$

where $\Delta S_{F^{ij}}$ and $T_{F^{ij}}$ are the entropy and temperature of fusion, respectively, T_1 is the liquidus temperature, and x_i^l and x_j^l are the atomic fraction of components i and j in the liquid. We note that $x_i^l + x_j^l = 1$.

The liquid interaction parameter α_{ij}^l is then given in terms of measurable quantities by

$$\alpha_{ij}^l(T_1) = \frac{\Delta S_{F^{ij}}(T_{F^{ij}} - T_1) + RT_1 \ln(4x_i^l x_j^l)}{0.5 - (x_i^l)^2 - (x_j^l)^2} \quad [2]$$

In general α_{ij}^l is a function of T_1 which as a first ap-

proximation is taken to be of the form (8)

$$\alpha_{ij}^l(T_1) = a - bT_1 \quad [3]$$

This is a good approximation only if a limited temperature range is involved (typically less than 100°C). An example of this limitation can be seen in the data of Ilegems *et al.* for GaP (9).

Measurement Conditions

The conditions under which the liquidus temperature was measured have been carefully standardized in order to secure their reproducibility. All measurements were carried out in a pyrolytic graphite boat with three $8 \times 8 \times 10$ mm wells, separated 10 mm from each other. A semitransparent, movable furnace with a flat temperature profile over the length of the boat was used with a temperature controller capable of stabilizing the temperature to within $\pm 0.01^\circ\text{C}$. A programmer was used to produce the desired rates of temperature increase or decrease. The temperature was accurately measured by means of a calibrated Chromel-Alumel thermocouple with reference junction in DI ice and water. The liquidus temperatures were measured by direct visual inspection of the solutions (melts) through a microscope attached to the furnace.

The ability to slide the furnace was very useful in drastically reducing to total times the solutions were at elevated temperature because the furnace could be preheated initially and then moved over the boat, and after each run the boat could be cooled down very quickly by sliding the furnace away and directly cooling the boat with a fan.

The solutions were prepared by weighing both of the components of each melt, In and InP, Ga and GaAs, In and InAs, and Ga and GaP for InP, GaAs, InAs, and GaP, respectively. The binary compounds were weighed with an accuracy of $\pm 0.5\%$.

The liquidus temperature measurement technique was standardized as follows:

Initially, the solution was quickly heated to approximately $T_1 + 10^\circ$ and periodically shaken in order to dissolve all the components completely in the least possible time. The solution was then cooled down so it solidified by sliding the furnace away; it was then reheated and stabilized at approximately $T_1 - 3^\circ\text{C}$.

Key words: semiconductor, solubility, equilibrium.

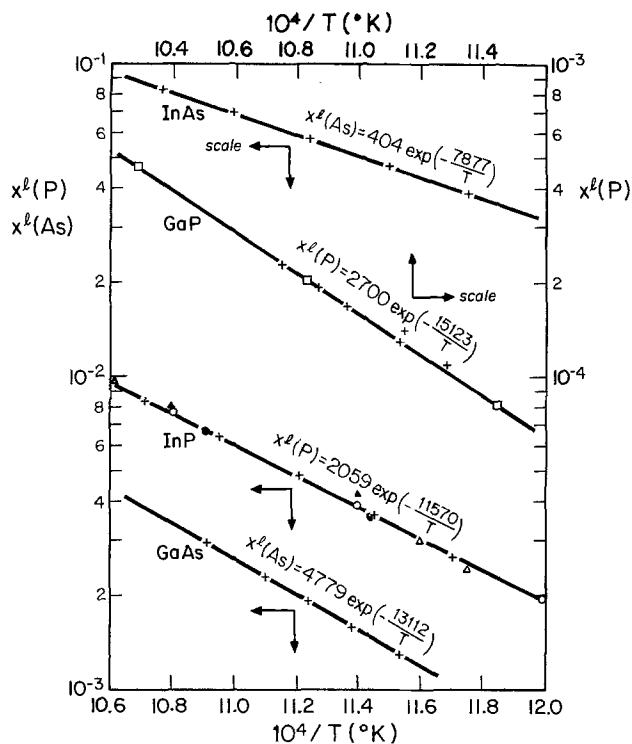


Fig. 1. In-P, Ga-As, In-As, and Ga-P solubility curves. Ref: +, This work; □, M. Ilegems *et al.* (9); ○, J. J. Hsieh (10); ●, N. Sol *et al.* (11); △, J. P. McVittie (12); ▲, R. N. Hall (13).

From there the temperature was increased slowly at 0.03°/min until the last piece of solid was observed to dissolve completely. The temperature at which this occurred was the measured value of T_l . The rate of decrease of T_l with time due to P evaporation was found to be in good agreement with the values reported for InP in Ref. (10). The heating rate used in the measurements reported here, 0.03°C/min, is slow enough so that there is thermodynamic equilibrium between the solid and liquid phases in the solution.

Table I. Measured liquidus temperatures, T_l , for (Ga-As), (In-As), (Ga-P), and (In-P) solutions containing the atomic fraction of arsenic or phosphorous indicated in the first column. The last column lists the liquid interaction parameter calculated from this data using Eq. [2].

Ga-As	x^l (As)	T_l (°C)	α_{12} (cal/mole)
	0.001574	606.0	-3319.57
	0.001918	613.3	-3455.06
	0.002285	624.6	-3507.30
	0.002959	641.9	-3652.11
In-As	x^l (As)	T_l (°C)	α_{12} (cal/mole)
	0.03801	576.0	-4843.51
	0.04745	596.0	-5035.67
	0.05821	616.3	-5240.04
	0.07025	636.3	-5446.11
	0.08353	656.5	-5641.85
Ga-P	x^l (P)	T_l (°C)	α_{12} (cal/mole)
	0.0001307	625.0	-724.1
	0.0001694	639.0	-783.9
	0.0001962	647.0	-825.0
	0.0002317	657.0	-859.47
In-P	x^l (P)	T_l (°C)	α_{12} (cal/mole)
	0.002672	580.5	792.46
	0.003637	600.3	682.47
	0.004884	618.8	518.13
	0.006478	640.3	488.48
	0.008491	660.4	397.82

Liquidus Temperature Data and Liquid Interaction Parameter Values

The measured liquidus temperatures T , in the range 580°-670°C are listed in Table I and are presented in Fig. 1 together with data points in this temperature range from other workers. The agreement of our data with the few previously published points (9-13) is seen to be very good. A linear least squares fit to the experimental points in Fig. 1 yields the following expressions

$$\text{InP: } x^l(\text{P}) = 2059 \exp(-11570/T) \quad [4]$$

$$\text{GaAs: } x^l(\text{As}) = 4779 \exp(-13112/T) \quad [5]$$

$$\text{InAs: } x^l(\text{As}) = 404 \exp(-7877/T) \quad [6]$$

$$\text{GaP: } x^l(\text{P}) = 2700 \exp(-15123/T) \quad [7]$$

Values of the liquid interaction parameter were calculated at each liquidus temperature measured μs -

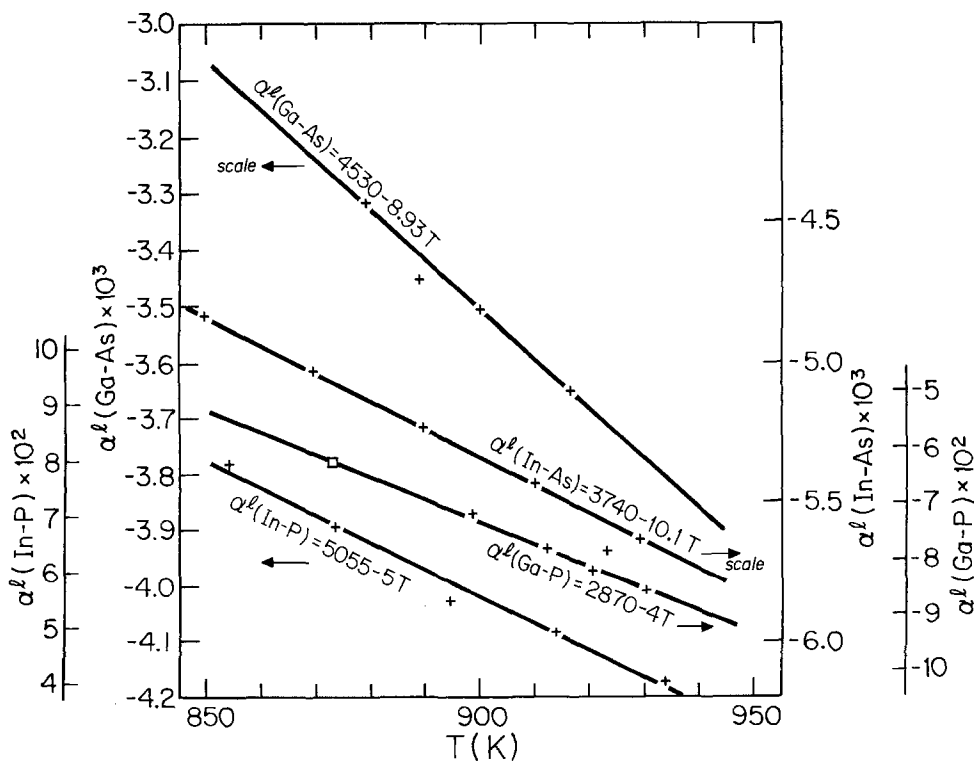


Fig. 2. The liquidus interaction parameters $\alpha^l(\text{In-P})$, $\alpha^l(\text{Ga-As})$, $\alpha^l(\text{In-As})$, and $\alpha^l(\text{Ga-P})$. The crosses are data measured in this work and the solid lines represent a least squares fit to a linear dependence on temperature.

Table II. Entropies and temperatures of fusion and liquid interaction parameters for InP, GaAs, InAs, and GaP.

	$\Delta S_{F^{ij}}$ (cal/mole-°K)	$T_{F^{ij}}$ (°C)	α_{ij}^1 (cal/mole)
InP	15.2 [Ref. (6)]	1062 [Ref. (6)]	5055-5T
GaAs	16.64 [Ref. (5)]	1238 [Ref. (5)]	4530-8.93T
InAs	14.52 [Ref. (7)]	942 [Ref. (7)]	3740-10.1T
GaP	16.4 [Ref. (9)]	1470 [Ref. (9)]	2870-4T

ing Eq. [2]. The entropies and temperatures of fusion ($S_{F^{ij}}$, $T_{F^{ij}}$) used in this calculation, together with the resulting least squares linear fits of α_{ij} are presented in Table II, and Fig. 2.

While the data presented in Fig. 1 agree well with previously reported results, the interaction parameters presented in Table II differ significantly from previously reported values. This is true because the fit of a simple linear temperature variation for α_{ij} can only be made over a limited temperature range, as has been done here.

Acknowledgments

The authors wish to acknowledge the excellent technical assistance of Mr. Anthony Colozzi, Mr. Joseph Walsh, and Mr. Anthony Santangelo. This work was sponsored by International Telephone and Telegraph Electro-Optical Products Division. This work was supported by the National Science Foundation, Grant DMR 76-80895.

Manuscript submitted March 19, 1979; revised manuscript received July 24, 1979.

Any discussion of this paper will appear in a Discussion Section to be published in the December 1980 JOURNAL. All discussions for the December 1980 Discussion Section should be submitted by Aug. 1, 1980.

Publication costs of this article were assisted by the Massachusetts Institute of Technology.

REFERENCES

- C. J. Neuse, *J. Electron. Mater.*, **6**, 253 (1977).
- G. A. Antypas and R. L. Moon, *This Journal*, **120**, 1574 (1973).
- G. A. Antypas, *ibid.*, **117**, 1393 (1970).
- M. A. Littlejohn, J. R. Jauser, and T. H. Glisson, *Solid-State Electron.*, **21**, 107 (1978).
- A. S. Jordan and M. Ilegems, *J. Phys. Chem. Solids*, **36**, 329 (1975).
- M. B. Panish, *J. Cryst. Growth*, **27**, 6 (1974).
- M. B. Panish and M. Ilegems, in "Progress in Solid State Chemistry," Vol. 7, H. Reiss and J. O. McCaldin, Editors, p. 39, Pergamon, New York (1972).
- C. D. T. Thurmond, *J. Phys. Chem. Solids*, **26**, 785 (1965).
- M. Ilegems, M. B. Panish, and J. R. Arthur, *J. Chem. Thermodyn.*, **6**, 157 (1974).
- J. J. Hsieh, *Inst. Phys. Conf. Ser.*, **33b**, 74 (1976).
- N. Sol, J. R. Clariou, N. T. Link, and M. Moulin, *J. Cryst. Growth*, **27**, 325 (1974).
- J. P. McVittie, Ph.D. Thesis, Stanford University (1972).
- R. N. Hall, *This Journal*, **110**, 385 (1963).

Rotating Ring Disk Electrode Study of the Hydrogen Peroxide Oxidation of Fe(II) and Cu(I) in Hydrochloric Acid

James F. Skinner

Department of Chemistry, Williams College, Williamstown, Massachusetts

Arnold Glasel, Li-chien Hsu, and B. Lionel Funt

Department of Chemistry, Simon Fraser University, Burnaby, Vancouver, British Columbia, Canada

ABSTRACT

The kinetics of the oxidation of electrochemically generated Fe(II) and Cu(I) by H_2O_2 in 2.0M HCl has been studied with a platinum rotating ring disk electrode over a range of concentrations and temperatures. The data have been analyzed with a digital simulation technique to give values of k_1 the rate constant for the rate-determining initial step in the oxidation. The value in the case of Fe(II) is $(2.2 \pm 0.5) \times 10^2 M^{-1} sec^{-1}$ at 25°C, considerably larger than the literature values of this reaction. Possible reasons for this discrepancy both in the experimental results and in the simulation technique are discussed. For the Cu(I) reaction, $10^2 k_1 = 1.5, 2.6, \text{ and } 4.0 M^{-1} sec^{-1}$, at 15°, 25°, and 35°C, respectively, giving an activation energy of 8.5 kcal. These are the first reported values for k_1 for the Cu(I) reaction.

The rotating ring disk electrode (RRDE) has been used in the investigation of diverse chemical systems (1-6) and a recent article (7) gave a very thorough review of the applications of this electrode system. Our previous results (8-10) have demonstrated the utility of such an electrode for the study of the steps in electrochemically initiated polymerizations. One of the most thoroughly investigated (11-14) redox polymerization initiators is the iron(II)-hydrogen peroxide system (Fenton's reagent), which generates the highly reactive hydroxyl radical.

Key words: oxidation, polymerization, kinetics.

Haberland and Landsberg (15) have reported a study of the kinetics of the iron(II)-hydrogen peroxide reaction using a gold rotating disk electrode (RDE), while Opekar and Beran (16) have studied this reaction on palladium, gold, and glassy carbon RDE. Bard and Prater (17) have used an RRDE for a limited study of the kinetics of this reaction, and they suggested a method (18) for determining rate constants based on a computer simulation of the appropriate hydrodynamic and reaction parameters. Bard and co-workers have subsequently analyzed the kinetics of a variety of reactions using the RRDE and the computer simulation.

The original purpose of the present study was to apply the RRDE to redox initiators other than Fenton's reagent, but our preliminary efforts to duplicate Bard's results suggested that a more thorough RRDE investigation of this system was necessary. An error in the numerical analysis led to a specific rate constant in apparently better agreement with the literature than was actually the case.¹ Data are reported here for an RRDE study of the iron(II)-hydrogen peroxide reaction over a range of concentrations and, in addition, the first kinetic data on the copper(I)-hydrogen peroxide reaction are reported over a range of concentrations and temperatures. The importance of certain experimental variables is discussed and the accuracy of the computer simulation method for analysis of RRDE data for kinetic parameters is reviewed.

Experimental

Apparatus.—The potentiostat used was similar to that described by Bruckenstein (19) and provided independent control of both electrodes. A Hewlett-Packard 3300A function generator was used to sweep the disk voltage and the currents were measured on a Hewlett-Packard T046A X-Y/Y' recorder. The rotation speed, ω , was controlled to within 1% by a Carter motortachometer assembly with an electronic feedback circuit.

The cell has been described (8) and was thermostated to $\pm 0.1^\circ\text{C}$. The ring and disk electrodes were constructed of bright platinum with dimensions $r_1 = 0.30$ cm, $r_2 = 0.33$ cm, and $r_3 = 0.43$ cm, where r_1 , r_2 , and r_3 are the outer radii of the disk, the insulating spacer, and ring, respectively. A heavy gauge, coiled platinum wire, was the counterelectrode in a side chamber isolated from the test solution by a porous glass frit. A saturated calomel electrode (SCE) was used as the reference electrode, in contact with the test solution through a Luggin capillary positioned 1 mm below the RRDE surface. The electrode was preconditioned immediately before each run, spinning for 5 min with zero potential applied in each of the following: 6M HCl, 2M H₂SO₄ saturated with FeSO₄, distilled water, and 2.0M HCl (the solvent used in the run). This treatment optimized the reproducibility of the electrode response.

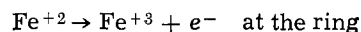
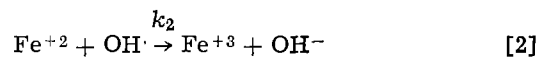
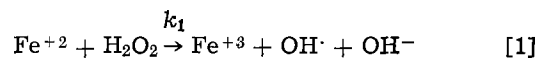
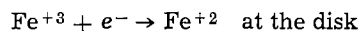
For the measurements on the Fe(III) solutions, the ring was potentiostated at 1.00V (*vs.* SCE) while the disk was swept from 0.7 to 0.0V. The ring and disk currents were measured when the disk voltage was 0.20V, corrections being made for the residual solvent currents. For the Cu(II) solutions, the ring was held at 0.50V, while the disk was swept from 0.50 to -0.25 V, with the currents being measured when the disk voltage was -0.2 . The disk voltage was swept at approximately 10 mV/sec, the collection efficiency being essentially independent of sweep rate over the range 5-50 mV/sec for the test solutions. Currents were measured from the recorder traces with a precision of about 1%.

Reagents.—Certified reagent grade FeCl₃·6H₂O and CuCl₂·2H₂O were used as received. The 2.0M HCl solvent was prepared volumetrically from standardized concentrated reagent, and the 3% H₂O₂ was vigorously flushed with nitrogen and titrated against KMnO₄ before each run. The test solution containing the metal chloride was flushed with nitrogen before the run and nitrogen was passed over the surface of the solution in the cell during a run. Unless specifically noted as otherwise, currents were measured as a function of ω on the solution containing the metal ion, the H₂O₂ was then added with a syringe, the solution mixed, and purged with nitrogen. Currents were then measured in the presence of the H₂O₂.

Digital simulation.—The authors are indebted to Professor Bard for supplying a copy of the computer

program for the digital simulation. The details of the technique have been presented (17, 20) and the same notation will be used here. The solution below the electrode is subdivided vertically and radially into small volume elements or boxes. The disk and ring currents depend on the concentrations of the electroactive species in the volume elements immediately below the electrode surfaces. The simulation takes into account changes in concentration resulting from convective flow due to the rotating electrode, from diffusion due to concentration gradients, and from the reactions occurring in the solution just below the electrode.

The relevant reactions are



where the following rate equations can be written for Eq. [1] and [2]

$$\begin{aligned} \frac{-d[\text{Fe}^{+2}]}{dt} &= k_1[\text{Fe}^{+2}][\text{H}_2\text{O}_2] + k_2[\text{Fe}^{+2}][\text{OH}\cdot] \\ &= \frac{d[\text{Fe}^{+3}]}{dt} \end{aligned} \quad [3]$$

$$\frac{-d[\text{H}_2\text{O}_2]}{dt} = k_1[\text{Fe}^{+2}][\text{H}_2\text{O}_2] \quad [4]$$

$$\frac{-d[\text{OH}\cdot]}{dt} = k_2[\text{Fe}^{+2}][\text{OH}\cdot] - k_1[\text{Fe}^{+2}][\text{H}_2\text{O}_2] \quad [5]$$

If a steady-state approximation can be applied to [OH·], Eq. [5] can be equated to zero, and Eq. [3] rewritten as

$$\frac{-d[\text{Fe}^{+2}]}{dt} = 2k_1[\text{Fe}^{+2}][\text{H}_2\text{O}_2] = \frac{-d[\text{Fe}^{+3}]}{dt} \quad [6]$$

In Eq. [1]-[6], Fe³⁺, and Fe²⁺ may be replaced by Cu²⁺ and Cu⁺, respectively.

Defining $FA(J,K)$, $FB(J,K)$, and $FC(J,K)$ as the fractional concentrations of Fe³⁺, Fe²⁺, and H₂O₂, respectively, in a given volume element (J,K), the change in concentration due to the reaction within that volume element will be DEL, Eq. [7], and the corrected concentrations will be given by Eq. [8]-[10]

$$\text{DEL} = XKTC * FB * FC \quad [7]$$

$$FA(J,K) = FA(J,K) + \text{DEL} \quad [8]$$

$$FB(J,K) = FB(J,K) - \text{DEL} \quad [9]$$

$$FC(J,K) = FC(J,K) - 0.5 * \text{DEL} \quad [10]$$

where XKTC is a dimensionless rate parameter given as

$$XKTC = (2k_1 C_A^0 \nu^{1/3}) / (\omega D^{1/3} (0.51)^{2/3}) \quad [11]$$

C_A^0 is the bulk concentration of Fe³⁺, ν is the kinematic viscosity, ω is the rotation speed, and D is the diffusion coefficient of Fe³⁺. The result of the simulation is the solid curve shown in Fig. 1 where m is the bulk molarity ratio, [H₂O₂]/[Fe³⁺], and N , the collection efficiency, is the ratio of the ring current to the disk current at a given ω .

To simplify comparison of the present results with those of Bard and Prater (17), their values of 5.0×10^{-6} cm²/sec and 1.0×10^{-2} cm²/sec have been used for D and ν , respectively, in calculating k_1 [for both Fe(III) and Cu(II) at 25°C] from the interpolated values of XKTC using Eq. [11]. Diffusion coefficients are not available for Cu(II) and Fe(III) in 2.0M HCl.

¹ Communication between the authors and Professors Bard and Prater confirm this error.

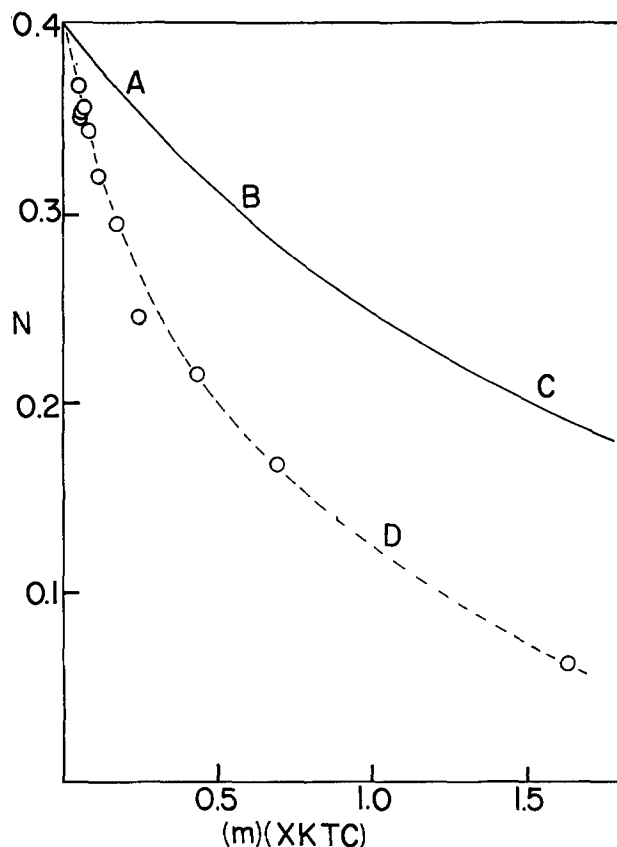


Fig. 1. Simulated collection efficiency vs. (m) (XKTC). See Discussion for explanation of curve D and of points A, B, and C.

Jahn and Vielstich reported (21) a value (at 25°C) of 6.5×10^{-6} for Fe(III) in 1M HClO₄ using an RDE. Beran (16) reported a value of 5.2×10^{-6} in 0.1M HCl using an RDE. Kolthoff and Lingane (22) give a value of 7.2×10^{-6} for Cu(II) in 1M KCl, while Bruckenstein (23) reported a value of 5.7×10^{-6} for Cu(II) in 0.2M H₂SO₄.

An attempt has been made to correct both D and ν for the Cu(II) results at 15° and 35°C. Delahay (24) reported values for D for Fe(III) in 0.25M H₂SO₄ at two temperatures. The temperature dependence represented by these two values was used to correct the 25° value of 5.0×10^{-6} to 3.4×10^{-6} , and 6.6×10^{-6} at 15° and 35°C, respectively. Kinematic viscosities for 2.0M HCl have been measured (25) which allowed correction of the 1.0×10^{-2} value at 25° to 1.25×10^{-2} , and 0.82×10^{-2} for ν at 15° and 35°C, respectively.

Results and Discussion

The detailed results for one run are shown in Table I while the results for runs at other concentrations are shown in condensed form in Table II for Fe(III)-H₂O₂ and in Table III for Cu(II)-H₂O₂. An average value for k_1 , with an average deviation, is given for each run as well as values, in parentheses, for additional runs at the same concentrations. Figure 2 shows current-voltage sweeps for the disk and the ring for the 2.0M HCl solvent, for the solvent with H₂O₂, and for an Fe(III)-H₂O₂ solution. In this case, the H₂O₂ was added first and then the FeCl₃ · 6H₂O was added to the same aliquot of solvent.

Figures 3 and 4 show the effect produced by the solution reactions (Eq. [1] and [2]) on the disk and ring currents for Fe(II)-H₂O₂ and Cu(II)-H₂O₂ (only the one-electron reduction of Cu(II) is shown). Figure 5 shows both the one-electron and two-electron Cu(II) disk reductions for the Cu(II)-H₂O₂ solution. The ring current disappears over the range of disk voltages where the Cu(II) is completely reduced and plated out

Table I. RRDE results in 2.0M HCl at 25°C

ω (rad sec ⁻¹)	6.48 mmole FeCl ₃				6.40 mmole H ₂ O ₂			
	i_{R^w} (μ A)	i_{D^w} (μ A)	i_{R^w} (μ A)	i_{D^w} (μ A)	N^1	XKTC	k_1 (M ⁻¹ sec ⁻¹)	
9.4	85	206	25	380	0.064	5.18	191	
22	136	336	80	474	0.167	1.99	173	
36	172	423	119	543	0.215	1.34	187	
62	220	557	158	653	0.246	1.01	246	
90	258	652	216	740	0.295	0.60	210	
137	313	806	276	872	0.320	0.43	228	
182	349	902	328	978	0.344	0.28	199	
222	380	996	362	1064	0.356	0.21	185	
258	400	1054	383	1140	0.353	0.23	232	
290	418	1106	403	1218	0.350	0.25	281	
299	414	1130	407	1214	0.367	0.16	184	

¹ Calculated from Eq. [15] $10^3 k_1 = 2.1 \pm 0.3$
($10^3 k_1 = 2.5 \pm 0.3, 2.7 \pm 0.5, 2.3 \pm 0.3, 2.5 \pm 0.5, 2.6 \pm 0.4$)

on the disk. The sharp rise in disk current at -0.2V in Fig. 3 and -0.5V in Fig. 5 indicates the onset of solvent decomposition. Figure 6 gives the linear dependence (without H₂O₂) of the currents on $\omega^{1/2}$ as predicted by the Levich equation. Figures 3-6 are in good general agreement with what has been previously reported (15-17, 19). Figure 7 shows the dependence of the collection efficiency on H₂O₂ concentration for fixed Fe⁺³ concentration.

The kinetics of the oxidation of metal cations by hydrogen peroxide has received considerable attention, with Fe(II) being the most thoroughly investigated. It is generally accepted that the reaction proceeds through the two one-electron transfer steps given in

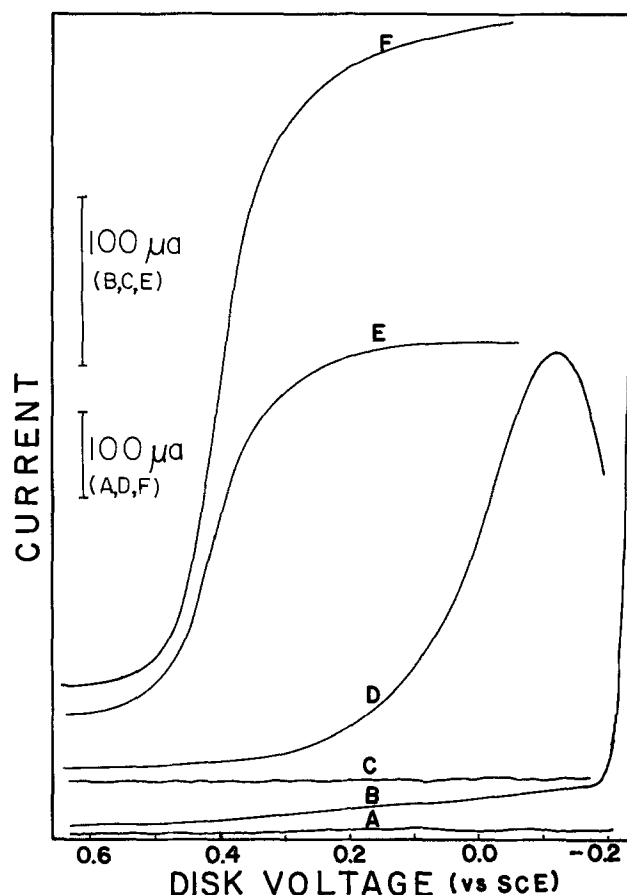


Fig. 2. Current-voltage sweeps in 2.0M HCl at 25°C: A and B for ring and disk, respectively, solvent only, $\omega = 143$ rad sec⁻¹; C and D for ring and disk, respectively, 6.40 mmole H₂O₂, $\omega = 87$; E and F for ring and disk, respectively, for 6.4 mmole FeCl₃-6.4 mmole H₂O₂, $\omega = 87$. Ring at 1.00V (vs. SCE). The sweeps have been shifted vertically for clarity so that the current base lines do not coincide.

Table II. RRDE results for 2.0M HCl at 25°C

3.30 mmole FeCl ₃		3.30 mmole H ₂ O ₂	6.45 mmole FeCl ₃		12.8 mmole H ₂ O ₂
ω	N	k_1	ω	N	k_1
9.5	0.125	205	9.5	0.0173	178
20	0.229	176	22	0.077	178
32	0.274	189	36	0.121	192
56	0.310	210	62	0.174	212
80	0.327	233	88	0.207	233
122	0.357	192	134	0.254	237
161	0.361	232	179	0.264	285
200	0.367	237	221	0.288	273
233	0.363	317	259	0.288	320
262	0.379	192	289	0.301	306
270	0.374	247	299	0.305	303
$10^2 k_1 = 2.2 \pm 0.2$			$10^2 k_1 = 2.5 \pm 0.5$		
6.45 mmole FeCl ₃		1.28 mmole H ₂ O ₂	12.94 mmole FeCl ₃		1.28 mmole H ₂ O ₂
ω	N	k_1	ω	N	k_1
9.5	0.273	169	9.4	0.308	122
22	0.341	137	23	0.347	132
36	0.340	226	37	0.359	158
61	0.364	214	62	0.367	204
88	0.369	262	90	0.377	194
134	0.381	236	138	0.380	245
174	0.380	217	182	0.385	241
216	0.386	271	219	0.386	258
257	0.380	494	254	0.383	373
300	0.389	306	284	0.390	239
$10^2 k_1 = 2.5 \pm 0.7$ (2.2 ± 0.1)			$10^2 k_1 = 2.3 \pm 0.6$ (1.6 ± 0.5)		
1.31 mmole FeCl ₃		12.8 mmole H ₂ O ₂			
ω	N	k_1			
13.7	0.0324	176			
25	0.069	208			
47	0.130	224			
75	0.172	258			
102	0.200	279			
149	0.236	299			
192	0.248	342			
232	0.261	359			
271	0.267	393			
293	0.268	420			
297	0.269	420			
$10^2 k_1 = 3.1 \pm 0.7$					

Eq. [1] and [2]. At relatively high peroxide concentrations, the following additional reactions may need to be considered

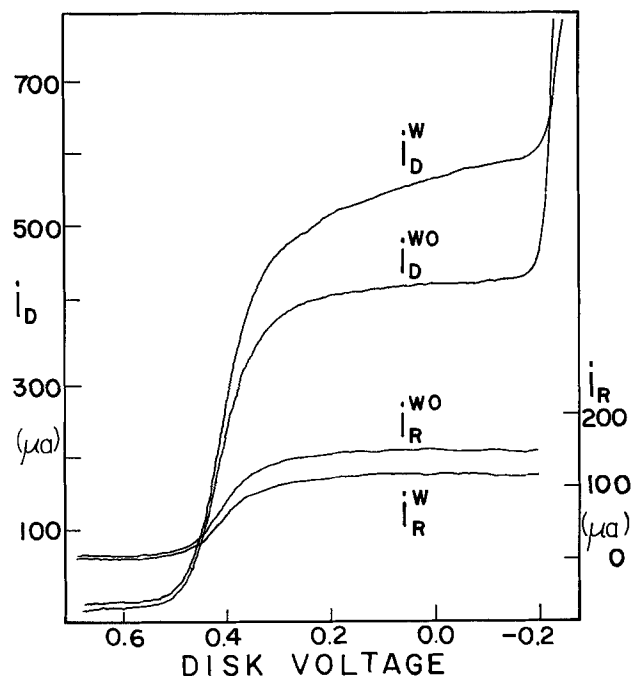
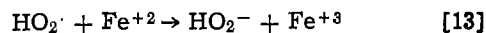
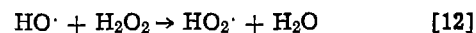


Fig. 3. Current-voltage sweeps in 2.0M HCl at 25°C: i_D^{wo} and i_R^{wo} are disk and ring currents, respectively, in 6.0 mmole FeCl₃; i_D^{w} and i_R^{w} are disk and ring currents, respectively, in 6.0 mmole FeCl₃-6.0 mmole H₂O₂. $\omega = 37 \text{ rad sec}^{-1}$.

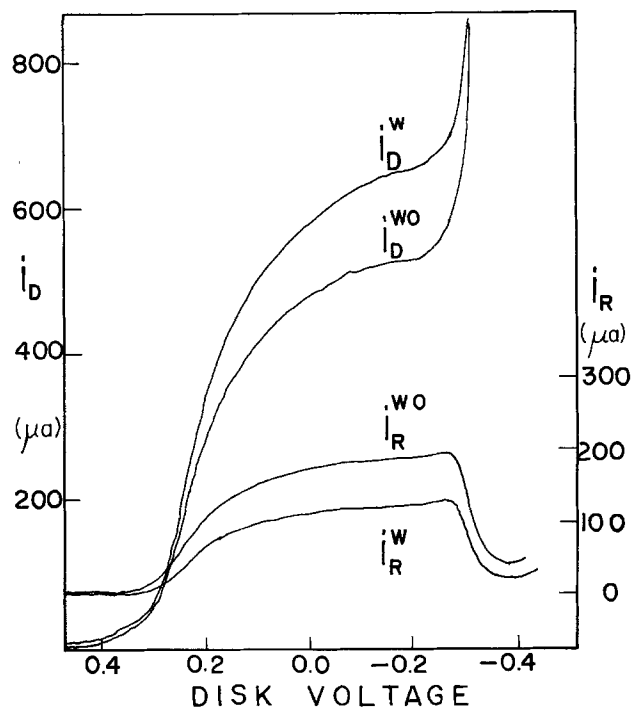


Fig. 4. Current-voltage sweeps in 2.0M HCl at 25°C: i_D^{wo} and i_R^{wo} are disk and ring currents, respectively, in 6.0 mmole CuCl₂; i_D^{w} and i_R^{w} are disk and ring currents, respectively, in 6.0 mmole CuCl₂-6.0 mmole H₂O₂. $\omega = 37 \text{ rad sec}^{-1}$.

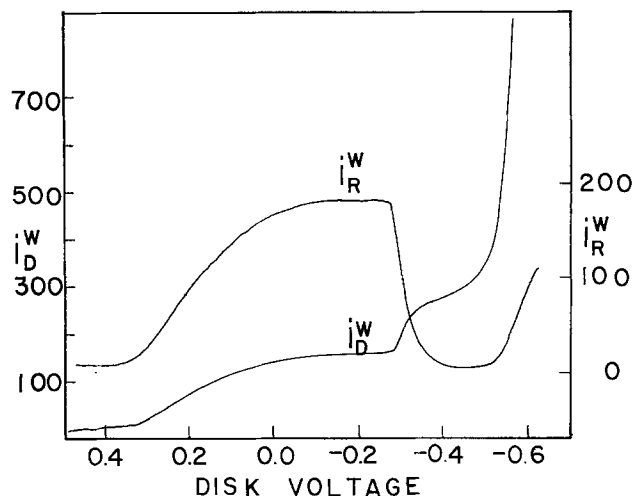


Fig. 5. Current-voltage sweeps in 2.0M HCl at 25°C: i_D^w and i_R^w are disk and ring currents, respectively, in 6.66 mmole CuCl_2 -6.66 mmole H_2O_2 , $\omega = 47 \text{ rad sec}^{-1}$.

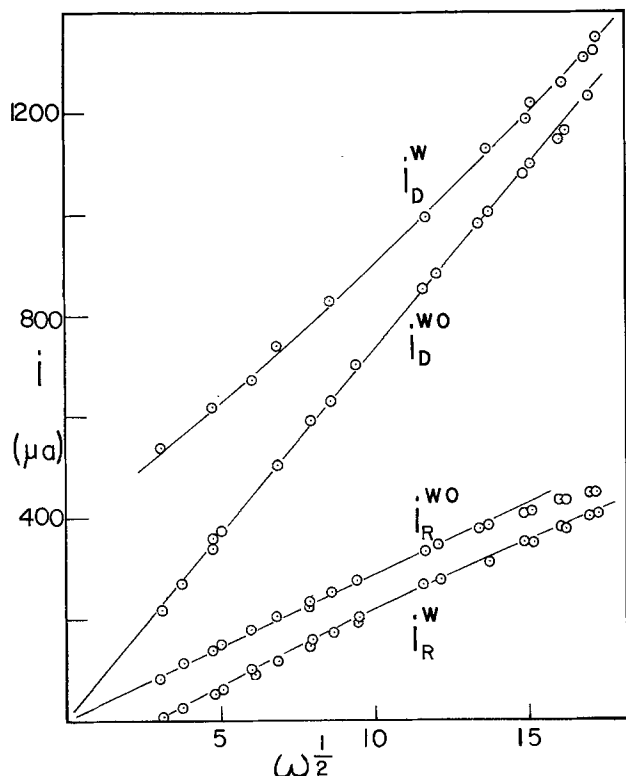
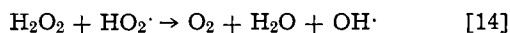


Fig. 6. Current vs. $\omega^{1/2}$ in 2.0M HCl at 25°C: i_D^{wO} and i_R^{wO} are the disk and ring currents, respectively, in 6.4 mmole FeCl_3 ; i_D^w and i_R^w are the disk and ring currents, respectively in 6.4 mmole FeCl_3 -12.8 mmole H_2O_2 .



There are numerous literature values for k_1 for the Fe(II)- H_2O_2 reaction in a wide variety of supporting electrolytes. For the purpose of using the present results to test rigorously the digital simulation, a careful review of the literature has been made.

Baxendale (26) reported a value of $53\text{M}^{-1} \text{sec}^{-1}$ at 25°C in acidic perchlorate, sulfate, or chloride. Sutin (27, 28) reported values of 58-64 in chloride-perchlorate mixtures, while Wells (29) gave values of 50, 54, and 69 in 1M NaClO_4 , 1M HClO_4 , and 1M NaCl , respectively.

There have been four studies reported where Fe(II) was generated electrochemically from Fe(III), with the peroxide reaction catalytically regenerating the Fe(III). In a polarographic study at the dropping mer-

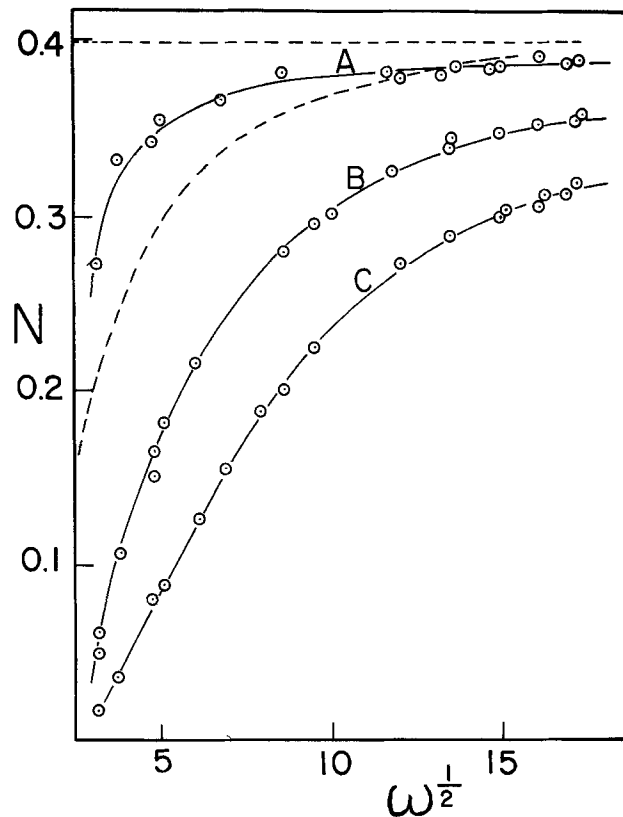


Fig. 7. Experimental collection efficiencies at 25°C for 6.45 mmole FeCl_3 in 2.0M HCl: A, 1.28 mmole H_2O_2 ; B, 6.45 mmole H_2O_2 ; and C, 12.8 mmole H_2O_2 . See Discussion for explanation of dashed curve.

cury electrode, Delahay (24) reported values at 0.6° and 31.4°C in 0.25M H_2SO_4 from which a value of approximately 59 can be interpolated for 25°C. At a gold rotating disk electrode, Haberland (15) calculated a value of 73 in 1M KCl at 25°C, using a graphical method of analysis, while Beran (16), using a method of moments developed by Bruckenstein (30), calculated a value of 92 at 25°C in 0.1M HCl using a rotating palladium disk electrode. In the publication of their digital simulation technique for the analysis of RRDE data, Bard and Prater (17) reported a value of $105 \pm 5\text{M}^{-1} \text{sec}^{-1}$ for k_1 at 25°C for a 6.4 mmole FeCl_3 , 3.2 mmole H_2O_2 solution in 2M HCl. Their calculations were incorrectly based on the $m = 1.0$ working curve (Fig. 1) rather than on the $m = 0.5$ curve (see Footnote 1). Recalculation of their data with the authors' form of the program (see Experimental) using an $m = 0.5$ working curve with the dimensions of their electrode gave $k_1 = 202 \pm 15$, in agreement with the values in Tables I and II.

The authors are not aware of a literature value for k_1 for Cu(I) in either an aquo or chloro complex. This may reflect the well-known lack of stability of this oxidation state of copper in aqueous medium. An advantage of the present technique is that Cu(I) is generated immediately prior to its reaction with H_2O_2 . Anbar (31) reported a value of $k_1 = 850\text{M}^{-1} \text{sec}^{-1}$ in the case of the bis(bipyridyl) copper (I) complex ion at 25°C. There have been numerous studies (14, 32-34) of the catalytic role played by the more stable Cu(II) in a variety of reactions, in some instances in the presence of Fe(II) and H_2O_2 .

Czapski (35) reported values of k_1 of 2.8×10^4 , 2.7×10^2 , and $5.8\text{M}^{-1} \text{sec}^{-1}$ for chromium (II), titanium(III), and vanadium (IV) in HClO_4 at 25°C.

To use the simulated working curve in Fig. 1, a corrected collection efficiency is calculated from Eq. [15] at each ω

$$N = 0.3994(N^w/N^{wo})$$

$$= 0.3994((i_{R^w}/i_{D^w})/(i_{R^{wo}}/i_{D^{wo}})) \quad [15]$$

where the superscripts w and wo indicate iron or copper solutions with H₂O₂ and without H₂O₂, respectively, and 0.3994 is the value of the collection efficiency calculated from electrode dimensions. Although N^{wo} should be independent of ω, there appeared a small decrease in N^{wo} at the higher ω, from a value close to 0.3994. Equation [15] eliminates this dependence on ω, presumably due to turbulence from irregularities in the construction of the electrode.

Several points need to be made in regard to the rate constants presented in Tables I-III. Reaction concentrations have been varied from having a ten-fold excess of cation (*m* = 0.1), to concentrations equimolar in cation and peroxide (*m* = 1.0), to having a ten-fold excess of peroxide (*m* = 10). Assuming that the reaction is first order in each reactant, a one hundred-fold increase in reaction rate would be expected between the slowest and fastest cases. The computer simulation gives *k*₁ values (averaged over a run) in general agreement over this wide range of concentrations. However, the over-all average value of 240 ± 40M⁻¹ sec⁻¹ for the Fe(II)-H₂O₂ reaction is three to four times the literature values. On closer examination of the *k*₁ values for a given run, it can be seen that there is an increase in *k*₁ with increasing ω.

Figure 8 includes the Cu(I)-H₂O₂ results (*m* = 1.0) from Table III as well as literature values (26, 36) for the Fe(II)-H₂O₂ reaction. It is interesting to note that an activation energy of 8.5 kcal is found for the Cu(I) reaction, in general agreement with the 9.6 kcal found for the Fe(II) reaction (37). This satisfactory temperature dependence suggests strongly that *k*₁ values calculated for the copper reaction using the digital simulation are indeed rate constants for a homogeneous solution reaction and not for some more complicated process occurring at the electrode surface. The fact remains, however, that the absolute value of *k*₁ is high, at least in the iron case where good literature values are available.

Reasons for this discrepancy could be experimental in origin or could result from some of the approximations made in deriving the computer simulation. Both of these possibilities will now be discussed.

There is a question as to the state of complexation of the Fe(III)/Fe(II) and Cu(II)/Cu(I) during both the electrode processes and the homogeneous solution reactions. The formation constants of chloro complexes of Fe(III) and Cu(II) in aqueous solution (38-40) are in the range of 1-10, suggesting that several complexed species will be present in the 2.0M HCl: FeCl²⁺, FeCl₄⁻, CuCl⁺, and CuCl₃⁻. There is less information

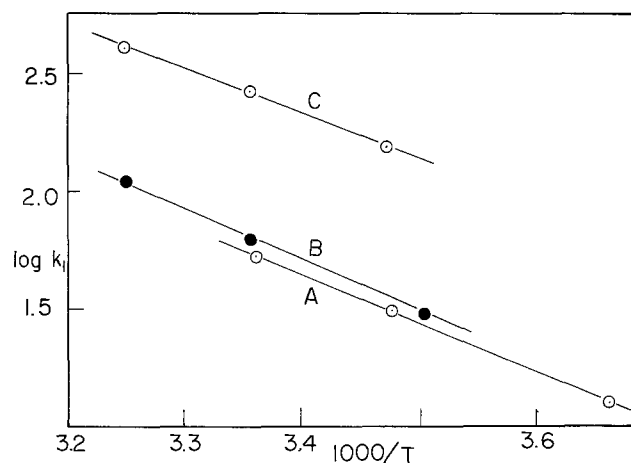


Fig. 8. Arrhenius plot: A, Fe(II)-H₂O₂, Ref. (27); B, Fe(II)-H₂O₂, Ref. (37); C, Cu(I)-H₂O₂, This work.

Table III. RRDE results in 2.0M HCl

15°C ω	6.70 mmole CuCl ₂ N	6.70 mmole H ₂ O ₂ k ₁	15°C ω	6.22 mmole CuCl ₂ N	62.4 mmole H ₂ O ₂ k ₁
9.1	0.086	113	9.1	0.000	—
22	0.182	121	22	0.0042	106
36	0.235	124	36	0.0143	117
63	0.281	137	63	0.040	127
90	0.304	149	90	0.064	134
138	0.327	162	138	0.105	139
182	0.340	171	182	0.133	147
224	0.342	204	224	0.154	153
257	0.353	180	257	0.168	158
282	0.360	167	282	0.179	159
286	0.360	170	286	0.181	157
k ₁ = 154 ± 20			k ₁ = 140 ± 15		
25°C ω	6.83 mmole CuCl ₂ N	6.83 mmole H ₂ O ₂ k ₁	25°C ω	6.37 mmole CuCl ₂ N	63.7 mmole H ₂ O ₂ k ₁
9.1	0.0500	202	9.1	0.000	—
21	0.137	203	21	0.000	—
35	0.189	211	35	0.0045	192
60	0.257	204	60	0.0153	218
86	0.275	239	86	0.037	205
132	0.302	270	132	0.067	216
174	0.326	254	174	0.082	232
214	0.330	291	214	0.098	248
247	0.334	310	247	0.106	247
273	0.337	328	273	0.110	251
285	0.336	349	285	0.110	261
k ₁ = 260 ± 45 (10% <i>k</i> ₁ = 2.5 ± 0.4, 2.6 ± 0.4)			k ₁ = 230 ± 2.0		
35°C ω	6.66 mmole CuCl ₂ N	6.67 mmole H ₂ O ₂ k ₁	35°C ω	6.25 mmole CuCl ₂ N	58.0 mmole H ₂ O ₂ k ₁
9.0	0.0319	296	9.0	0.000	—
22	0.112	308	22	0.00099	344
35	0.165	317	35	0.024	315
60	0.225	330	60	0.055	317
87	0.247	390	87	0.076	336
134	0.290	381	134	0.111	353
179	0.301	441	179	0.121	360
226	0.318	446			
254	0.320	486			
280	0.317	557			
287	0.329	473			
k ₁ = 402 ± 71			k ₁ = 338 ± 15		

on the stability of the chloro complexes of Fe(II) and Cu(I). Both Sutin (28) and Wells (29) have found a small dependence of *k*₁ for the Fe(II)-H₂O₂ reaction in going from 0-1M Cl⁻ at constant ionic strength, but nothing large enough to explain the discrepancy in the present results. It is unclear as to whether the complexation will change for the cation following its being reduced at the disk but before it reacts with the H₂O₂, and if such a change would affect the calculated rate constants.

Another possible source of error, most serious for the Fe(II)-H₂O₂ data at low ω, comes from the fact that in measuring the disk currents at 0.2V, conditions of limiting current flow were not always satisfied. This was not a problem with the ring currents which did level out (see Fig. 2-4). (While the ring and disk currents are anodic (-) and cathodic (+), respectively, the absolute magnitudes are shown in the figures). This is frequently a problem in polarographic investigations and, indeed, the current-voltage curves for Beran's RDE study (16) of the Fe(II)-H₂O₂ reaction showed considerable slope. The digital simulation is based on the assumption that ring and disk currents are measured under conditions of diffusion limited current flow. In selecting a less positive voltage, say 0.1V for measuring the currents, to insure better that a limiting current is being measured, the question of direct reduction of H₂O₂, in the case of iron, becomes more serious (see below). Going to a lower voltage would have the greatest effect on *i*_D^w in Eq. [15], giving a slightly larger value of *N* and, in turn, a smaller *k*₁.

The slope of the disk current trace is greatest for low ω and hence this error in N would be greatest at low ω , but it is in the range of low ω that the N -XKTC working curve is least sensitive to change in N . On balance, it is felt that this is probably not a serious source of error in k_1 .

The most serious question that can be raised about the experimental validity of the results in Tables I-III concerns whether the H_2O_2 , in addition to being reduced by Fe(II) in solution, is partially or completely reduced directly at the disk electrode, giving a larger disk current than would be found for the disk reduction of Fe(II) alone. The electrochemical reduction of both hydrogen peroxide and oxygen has been thoroughly studied as a function of pH at different metal electrodes, with particular emphasis on elucidating the role of the peroxide in the complete reduction of oxygen.

In some of the earliest applications of the RRDE, Nekrasov and Myuller (41) reduced O_2 to H_2O_2 at the disk and were able to detect the H_2O_2 at the ring electrode. The nonlinear dependence of the ring and disk currents on $\omega^{1/2}$ led them to postulate that the electrode reactions of O_2 and H_2O_2 are slow, not diffusion controlled, and generally irreversible. Extensive investigation by Bockris and Damjanovic (42, 43) on the electrochemical reduction of O_2 has confirmed these results in acidic and basic solution and pointed to the importance of the pretreatment of platinum electrodes in determining the degree of adsorption of H_2O_2 . In the RDE study of the Fe(II)- H_2O_2 reaction, Beran (16) found such considerable reduction of H_2O_2 at a platinum electrode in 0.1M HCl that satisfactory measurements could not be made, while neither Haberland [(15), using a gold RDE] nor Bard [(17), using a carbon paste RRDE] made any reference to the problem for the solutions studied. Bard did report the appearance of bubbles at the electrode for very high H_2O_2 concentrations.

The current-voltage sweep for H_2O_2 in HCl in Fig. 2 clearly shows evidence of H_2O_2 reduction at the disk. Although the magnitude of this current, at a fixed H_2O_2 concentration and ω in the absence of Fe(III), was reproducible for a given solution, it did vary for a series of runs under apparently identical conditions. In the acidic medium used, there was never a ring current simultaneous with the increased disk current. Figure 9 shows that the magnitude of the disk current is proportional to the H_2O_2 concentration, but in Fig. 9 the maximum, present in Fig. 2 at $-0.1V$, is not apparent. Figure 10 shows that the electrochemical reduction of H_2O_2 is clearly quite different from the reduction of Fe(III), in that the former depends very markedly on the rate at which the disk potential is varied, at constant ω , while the disk current for the Fe(III) reduction is independent of this sweep rate. Different rates of electron transfer and degrees of adsorption of the electroactive species are indicated.

Figure 11 shows a current-voltage sweep of both the disk and ring in solution containing both reducible species, Fe(III) and H_2O_2 . While the maximum in i_D^w at $-0.1V$ is clearly the result of H_2O_2 reduction (probably irreversible because of the absence of any corresponding increase in ring current), the authors suggest that at $+0.2V$, the predominant contribution to the disk current is the Fe(III) reduction.

Although the disk currents for H_2O_2 without Fe(III) were somewhat variable, Fig. 12 shows the largest disk currents that were obtained at 0.2V for 6.4 mmole H_2O_2 . Two aspects of Fig. 12 are important. The currents are small in comparison to the disk current given in Tables I-III. At 6.4 mmole $FeCl_3$ in 2M HCl, a disk current of 423 μA was obtained at 0.2V at $\omega = 36$ radians sec^{-1} , while for 6.4 mmole H_2O_2 under the same conditions the disk current was about 50 μA . The second point is that the disk currents in Fig. 12 decrease with increasing ω , in marked contrast to the behavior pre-

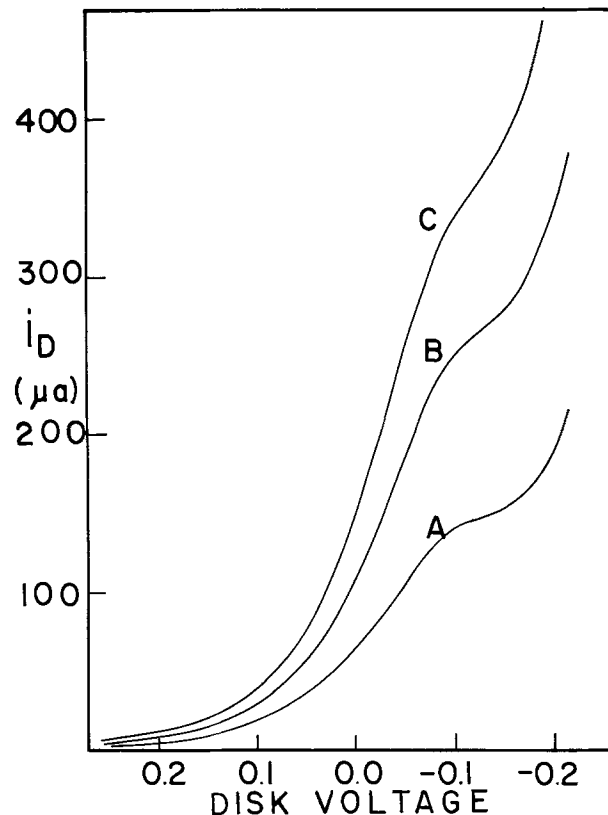


Fig. 9. Current-voltage sweeps in 2.0M HCl at 25°C: A, 5.95 mmole H_2O_2 ; B, 11.8 mmole H_2O_2 ; and C, 17.6 mmole H_2O_2 . $\omega = 45$ rad sec^{-1} and ring at 0.25V.

dicted for diffusion-controlled current flow. For the run shown in Table I, for example, there is no certainty that there was a peroxide current of this magni-

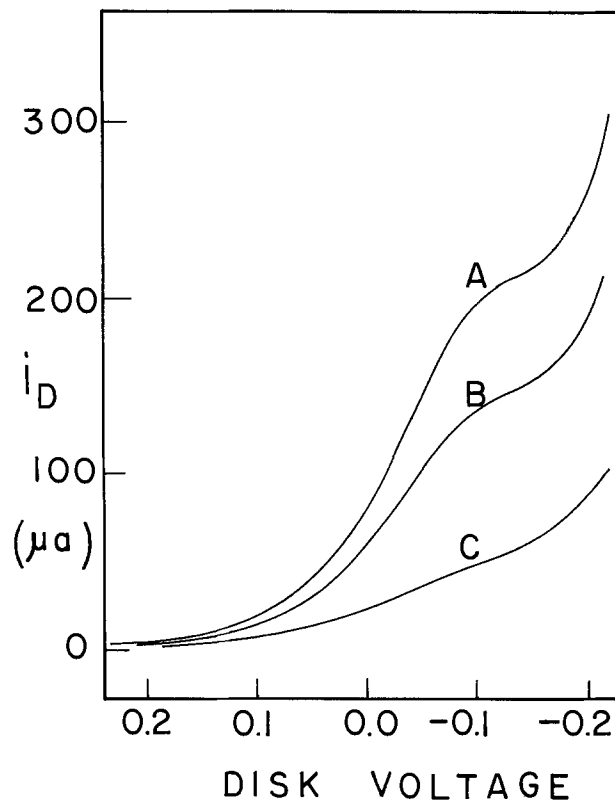


Fig. 10. Current-voltage sweeps for 5.95 mmole H_2O_2 in 2.0M HCl at 25°C at different sweep rates: A, 22 $mV sec^{-1}$; B, 9 $mV sec^{-1}$; and C, 4 $mV sec^{-1}$. $\omega = 45$ rad sec^{-1} and ring at 0.25V.

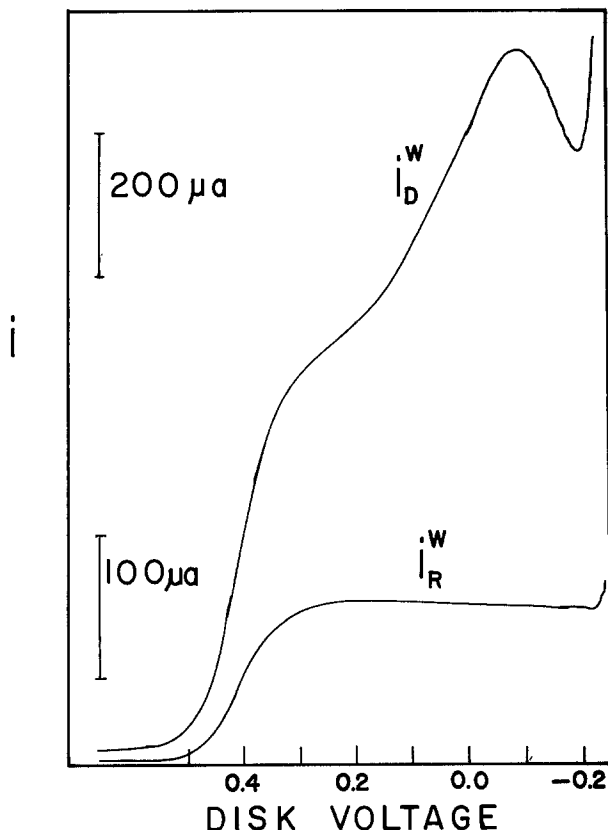


Fig. 11. Current-voltage sweeps 6.4 mmole H_2O_2 -6.4 mmole FeCl_3 in 2.0M HCl at 25°C. $\omega = 87 \text{ rad sec}^{-1}$.

tude, but our experience suggests that the values given in Fig. 12 represent the largest contribution that could have been expected. In all the runs given in Tables I-III, the FeCl_3 or CuCl_2 was dissolved first, with currents measured, and then the H_2O_2 was added and the resultant currents measured. It was not possible to measure the disk current for just the H_2O_2 for such a run. The disk currents given in Table IV are taken from Table I, corrected for the direct electrode reduction of H_2O_2 of a magnitude indicated by the data in Fig. 12. New values of N and k_1 are given in Table IV. The correction does decrease k_1 from 210 to 160, but this value remains considerably larger than the values 50-70 $\text{M}^{-1} \text{ sec}^{-1}$ reported in the literature. It must be also emphasized that the $i_{\text{D}}^{\text{H}_2\text{O}_2}$ values in Table IV may

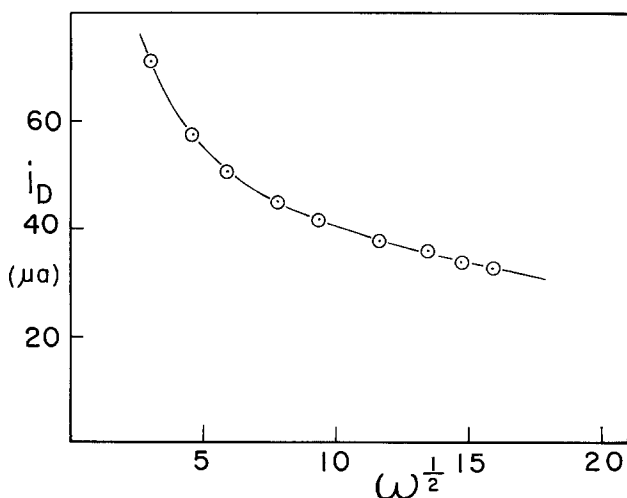


Fig. 12. Disk currents for 6.4 mmole H_2O_2 in 2.0M HCl at 25°C. Current measured at a disk voltage of 0.2V.

represent too large a correction.

In the case of the $\text{Cu(I)}-\text{H}_2\text{O}_2$ reaction, a much stronger case can be presented for arguing that in the presence of both the Cu(II) and H_2O_2 , only Cu(II) is reduced at the disk. In Fig. 2, the onset of solvent decomposition (H_2 evolution) at the disk becomes very pronounced in the 2.0M HCl at a disk voltage just negative of -0.2V . In Fig. 5, with Cu(II) and H_2O_2 in the 2.0M HCl, the solvent decomposition is shifted cathodically to about -0.5V , with the one electron reduction of Cu(II) occurring near -0.2V where the ring and disk currents were measured. Again in Fig. 2 and 9, the contribution to the disk current from the H_2O_2 reaches a maximum at about -0.1V , but in Fig. 5 there is no evidence of a maximum in the disk current which could be attributed to H_2O_2 reduction in the region of -0.1V .

In Fig. 13, the disk currents (all measured at -0.2V) are given as a function of $\omega^{1/2}$ for CuCl_2 in 2.0M HCl, for H_2O_2 in the same solvent, and for both CuCl_2 and H_2O_2 in this solvent. The current in the third case is clearly not the sum of the currents in the first two cases. In the presence of HCl, H_2O_2 , and Cu(II) , the only species that is reduced to a significant extent at -0.2V on the disk is the Cu(II) . Bruckenstein (44) has suggested that Cu(I) is strongly absorbed on a platinum RRDE and this may be the cause of the elimination of the two other electrode reactions which clearly occur in the absence of Cu(II) . In summary, there is little reason to believe that the $\text{Cu(II)}-\text{H}_2\text{O}_2$ data in Table III need to be corrected for direct reduction of H_2O_2 at the disk electrode.

While the authors believe that the direct reduction of H_2O_2 at the disk is not a major source of error, the direct disk reduction of the highly reactive hydroxyl radical, $\cdot\text{OH}$, produced in Eq. [1], is possible. An increase in the disk current as the result of reduction of $\cdot\text{OH}$ would probably be offset by a decrease in disk current from reduction of Fe(III) as less of the latter will be produced in reaction [2]. Reaction [2] is extremely fast so the concentration of the radical will be low.

Included in Fig. 7 is a hypothetical curve calculated on the assumption that $m = 1.0$ working curve in Fig. 1 is correct and that $k_1 = 60\text{M}^{-1} \text{ sec}^{-1}$. The discrepancy between actual data ($m = 1.0$) and this calculated curve is very great and far exceeds any reasonable experimental error.

Having reviewed the possible sources of experimental uncertainty which might explain the high k_1 values, we would now like to look closely at the digital simulation which is used to generate the working curve (Fig. 1) from which k_1 is calculated from an experimental collection efficiency. An uncertainty of $\pm 1\%$ in each of the four currents used in Eq. [15] is realistic for the present work, which would result in a maximum uncertainty of $\pm 4\%$ in N . On the $m = 1.0$ curve in Fig. 1, an uncertainty of $\pm 4\%$ in N produces, on interpolation to the curve, values of $XKTC$ (and k_1) with uncertainties of ± 45 , 18, and 5% at points A, B,

Table IV. Results corrected for H_2O_2 reduction current

ω	i_{D}^{w}	$i_{\text{D}}^{\text{H}_2\text{O}_2}$	$i_{\text{D}}^{\text{w}} - i_{\text{D}}^{\text{H}_2\text{O}_2}$	N	$N_{\text{H}_2\text{O}_2}$	$k_1 \pm$	$k_1^{\text{H}_2\text{O}_2}$
9.4	380	71	309	0.064	0.079	191 (6)	161
22	474	57	417	0.167	0.189	173 (10)	143
36	543	51	492	0.215	0.237	187 (15)	152
62	653	45	608	0.246	0.263	246 (25)	212
90	740	42	698	0.25	0.312	210 (33)	166
137	872	38	834	0.320	0.340	228 (45)	163
182	978	36	942	0.344	0.357	199 (52)	148
222	1064	34	1030	0.356	0.369	185 (59)	127
258	1140	33	1107	0.353	0.363	232 (74)	176
290	1218	31	1187	0.350	0.359	281 (81)	226
299	1214	31	1183	0.367	0.375	184 (74)	132

$$10^3 k_1 = 2.1 \pm 0.3 \quad 1.6 \pm 0.2$$

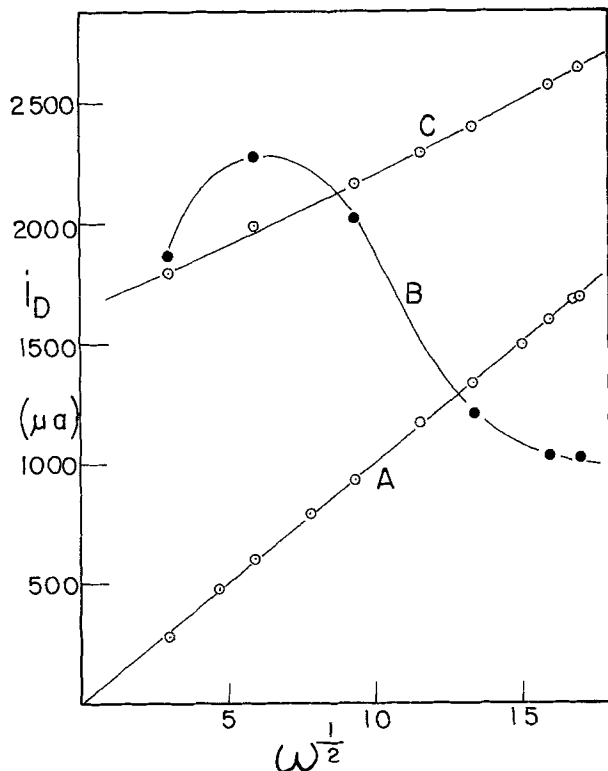


Fig. 13. Disk currents in 2.0M HCl at 35°C: A, 6.25 mmole CuCl₂; B, 63 mmole H₂O₂; and C, 6.25 mmole CuCl₂-58 mmole H₂O₂. Ring at 0.50V. All currents measured at a disk voltage of -0.2V.

and C, respectively. Therefore, the uncertainty in the k_1 values in Table I-III increases markedly in going to higher ω . This uncertainty, based on the use of the working curves, is given in Table IV in parentheses for the k_1 values. Within these limits of uncertainty, k_1 values are relatively constant over the range of ω values, although in some runs there does appear to be a more consistent increase in k_1 with increasing ω .

To generate a curve (Fig. 1) simulating the dependence of collection efficiency on the rate of the following reaction in solution, the program must calculate the time dependence and the location dependence of the concentrations of the electroactive species in a manner that closely resembles the actual reaction mechanism occurring in the solution. Equations [1] and [2] give what is generally assumed to be the reaction mechanism. It should be noted that k_2 is of the order of $10^8 \text{M}^{-1} \text{sec}^{-1}$, making Eq. [1] the rate-determining step (45, 46). The computation steps specific to the kinetic processes are given by Eq. [8-10]. Bard (17) used neither the factor of 2 in Eq. [11] nor the factor of 0.5 in Eq. [10], and made no reference to the detailed reaction mechanism. The authors present what they believe to be a more consistent treatment.

Figure 1 shows both the simulated dependence of collection efficiency on the rate constant (solid curve) and the dependence of the observed collection efficiency (data from Table I) on rate constant (circles), using the literature value of $60 \text{M}^{-1} \text{sec}^{-1}$ for k_1 . Although there is no experimental evidence to support the idea, if one introduces a factor of 2 or 3 before the DEL terms in Eq. [8] and [9], a steeper working curve results, giving smaller k_1 values for a given ω . This arbitrary change has the effect of increasing the rate of change of the concentrations of Fe(III) and Fe(II), relative to the rate of disappearance of [H₂O₂], in the reaction volume beneath the electrode.

The digital simulation (17) gives not only the dependence of N on the kinetic parameter, XKTC, but also the dependence of the limiting disk and ring currents on XKTC. At a given ω , the disk current in-

Table V. Calculation of k_1 from $i_R^w/i_R^{w_0}$, $i_D^w/i_D^{w_0}$ and N

25°C ω	6.65 mmole CuCl ₂ k_1 (from $i_R^w/i_R^{w_0}$)	6.65 mmole H ₂ O ₂ k_1 (from $i_D^w/i_D^{w_0}$)	k_1 (from N)
9.0	173	432	202
22	157	354	191
35	165	335	202
61	184	284	209
89	194	328	233
134	227	373	274
179	218	402	278
217	137	455	228
253	228	466	234
280	251	572	336
288	275	412	308

$$10^3 k_1 = 2.0 \pm 0.4 \quad 10^3 k_1 = 4.0 \pm 0.6 \quad 10^3 k_1 = 2.3 \pm 0.4$$

$$25^\circ\text{C} \quad 6.48 \text{ mmole FeCl}_3 \quad 6.40 \text{ mmole H}_2\text{O}_2$$

$$10^3 k_1 = 1.4 \pm 0.3 \quad 10^3 k_1 = 4.0 \pm 1.1 \quad 10^3 k_1 = 2.1 \pm 0.3$$

Literature values: $50-70 \text{M}^{-1} \text{sec}^{-1}$

creases while the ring current decreases with increasing XKTC. For a given m , say 1.0, one can generate curves of $i_R^w/i_R^{w_0}$ vs. XKTC, and $i_D^w/i_D^{w_0}$ vs. XKTC. Table V shows the k_1 values calculated using just the ring currents, just the disk currents and, finally, both currents through Eq. [15]. A Cu(II)-H₂O₂ run was chosen for this analysis to minimize the possibility of an error in i_D^w resulting from reduction of H₂O₂ at the electrode. Findings very similar to those in Table V have been found for a recalculation of an Fe(III)-H₂O₂ run. Somewhat lower k_1 values are found when just the ring currents are used, while using just the disk currents gives much larger values of k_1 , further from the literature values in the case of Fe(II). These results suggest that in the simulation, the dependence of the disk current on the reaction kinetics may need further study, specifically the treatment of the volume of solution immediately below the disk electrode as a single "box" in the (J,K) grid. It may be that in the catalytic mechanism, the current resulting from the repeated reduction of Fe(III) or Cu(II) at the disk is not being correctly calculated.

Acknowledgment

The authors thank the National Research Council of Canada for financial support of this work (B.L.F.) and Simon Fraser University for the provision of a graduate scholarship (L.H.).

Manuscript received Nov. 27, 1978; revised manuscript received Aug. 15, 1979.

Any discussion of this paper will appear in a Discussion Section to be published in the December 1980 JOURNAL. All discussions for the December 1980 Discussion Section should be submitted by Aug. 1, 1980.

REFERENCES

1. F. R. Shu and G. S. Wilson, *Anal. Chem.*, **48**, 1679 (1976).
2. J.-M. Nigretto and A. J. Bard, *This Journal*, **123**, 1303 (1976).
3. I. V. Shimonis and L. N. Nekrasov, *Electrokhimiya*, **12**, 1756 (1976).
4. M. Wu, W. I. Higuchi, J. L. Fox, and M. Friedman, *J. Dent. Res.*, **55**, 496 (1976).
5. L. R. Yeh, *J. Electroanal. Chem. Interfacial Electrochem.*, **84**, 159 (1977).
6. W. J. Albery and M. L. Hitchman, "Ring-Disc Electrodes," Oxford University Press, Oxford (1971).
7. S. Bruckenstein and B. Miller, *Acc. Chem. Res.*, **10**, 54 (1977).

8. B. L. F. Funt, W. Severs, and A. Glasel, *J. Polym. Sci., Polym. Chem. Ed.*, **14**, 2763 (1976).
9. B. L. Funt and V. Verigin, *Can. J. Chem.*, **52**, 1643 (1974).
10. L.-C. Hsu, A. Glasel, J. F. Skinner, and B. L. Funt, *This Journal*, **126**, 939 (1979).
11. J. H. Baxendale, *Ad. Catal.*, **4**, 31 (1952).
12. J. Weiss, *ibid.*, **4**, 343 (1952).
13. C. F. Wells and M. A. Salam, *Trans. Faraday Soc.*, **63**, 620 (1967).
14. C. Walling and S. Kato, *J. Am. Chem. Soc.*, **93**, 4275 (1971).
15. V. D. Haberland and R. Landsberg, *Ber. Bunsenges. Phys. Chem.*, **70**, 724 (1966).
16. F. Opekar and P. Beran, *J. Electroanal. Chem.*, **32**, 49 (1971).
17. K. B. Prater and A. J. Bard, *This Journal*, **117**, 1517 (1970).
18. K. B. Prater, *Chemical Instrumentation*, **3**, 259 (1972).
19. D. T. Napp, D. C. Johnson, and S. Bruckenstein, *Anal. Chem.*, **39**, 481 (1967).
20. K. B. Prater and A. J. Bard, *This Journal*, **117**, 207, 335 (1970).
21. D. Jahn and W. Vielstich, *ibid.*, **109**, 849 (1962).
22. I. M. Kolthoff and J. J. Lingane, "Polarography," Vol. 1, p. 52, Interscience Publishers Inc., New York (1952).
23. G. N. Tindall and S. Bruckenstein, *Anal. Chem.*, **40**, 1402 (1968).
24. P. Delahay and G. L. Stiehl, *J. Am. Chem. Soc.*, **74**, 3500 (1952).
25. J. F. Skinner, Unpublished results.
26. W. G. Barb, J. H. Baxendale, P. George, and K. R. Hargrave, *Trans. Faraday Soc.*, **47**, 462 (1951).
27. T. J. Conocchioli, E. J. Hamilton, Jr., and N. Sutin, *J. Am. Chem. Soc.*, **87**, 926 (1965).
28. H. N. Po and N. Sutin, *Inorg. Chem.*, **7**, 621 (1968).
29. C. F. Wells and M. A. Salam, *Trans. Faraday Soc.*, **63**, 620 (1967).
30. P. Beran and S. Bruckenstein, *J. Phys. Chem.*, **72**, 3630 (1968).
31. I. Pecht and M. Anbar, *J. Chem. Soc. A*, 1902 (1968).
32. N. Uri, *J. Phys. Chem.*, **53**, 1070 (1949).
33. G. M. Coppinger, *J. Am. Chem. Soc.*, **79**, 2758 (1957).
34. Y. I. Skarlatov and A. P. Purmal, *Zh. Fiz. Khim.*, **51**, 3140 (1977).
35. A. Samuni, D. Meisel, and G. Czapski, *J. Chem. Soc., Dalton Trans.*, 1273 (1972).
36. J. H. Baxendale, M. G. Evans, and G. S. Park, *Trans. Faraday Soc.*, **42**, 155 (1946).
37. T. J. Hardwick, *Can. J. Chem.*, **35**, 428 (1957).
38. L. G. Sillen, "Stability Constants of Metal-Ion Complexes, Section I: Inorganic Ligands." Special Publication No. 17, The Chemical Society (London) (1964).
39. H. A. Schwarz and R. W. Dodson, *J. Phys. Chem.*, **80**, 2801 (1976).
40. D. W. Smith, *Coord. Chem. Rev.*, **21**, 93 (1976).
41. L. N. Nekrasov and L. Myuller, *Dokl. Akad. Nauk SSSR*, (in English), **149**, 1107 (1963); **154**, 437 (1964); **157**, 416 (1964).
42. A. Damjanovic, A. Dey, and J. O'M. Bockris, *Electrochim. Acta*, **11**, 791 (1966).
43. A. Damjanovic, M. A. Grenshaw, and J. O'M. Bockris, *This Journal*, **114**, 466, 1107 (1967).
44. S. Bruckenstein and D. T. Napp, *J. Am. Chem. Soc.*, **90**, 6303 (1968).
45. M. Anbar and P. Neta, *Int. J. Appl. Rad. Isot.*, **18**, 493 (1967).
46. G. V. Buxton and R. M. Sellers, *Coord. Chem. Rev.*, **22**, 195 (1977).

Investigation on the Kinetics of Electroreduction Processes at Dark TiO₂ and SrTiO₃ Single Crystal Semiconductor Electrodes

J. Vandermolen and W. P. Gomes

Laboratorium voor Fysische Scheikunde, Rijksuniversiteit Gent, Krijgslaan 271, B-9000 Gent, Belgium

and F. Cardon

*Laboratorium voor Kristallografie en Studie van de Vaste Stof,
Rijksuniversiteit Gent, Krijgslaan 271, B-9000 Gent, Belgium*

ABSTRACT

The cathodic dark current at n-type Nb-doped TiO₂ and H₂-treated SrTiO₃ electrodes in Fe(CN)₆³⁻, Fe⁺³, or IrCl₆²⁻ aqueous solution was measured as a function of applied voltage, concentration of oxidizing agent, and pH. Two distinct current regimes were observed, differing by their Tafel slopes and by their concentration dependence. The most marked feature of the results was the saturation of the current as a function of concentration in the high current-density region. The experimental data were interpreted on the basis of a model involving electron transfer through surface states.

The study of the cathodic dark current-voltage behavior at n-type semiconductor electrodes is important from both the fundamental and the practical point of view. The fundamental importance lies in the possibility of testing the direct electron transfer model and in the elucidation of the reaction mechanism. This kind of study may lead to an extension of our knowledge on electrochemical reaction mechanisms on semiconductor electrodes in general and may hence

Key words: semiconductor, cathode, interface, voltammetry, kinetics.

also have a certain significance to photoelectrochemical reactions which are being used for solar energy conversion. A more direct connection between the cathodic dark current at n-type semiconductors and the problem of electrochemical solar energy conversion is that the cathodic current characteristics may enter into the expression for the open-circuit photovoltage as a function of light intensity [see, e.g., Ref. (1)].

Cathodic dark current-voltage studies on n-ZnO in the presence of several oxidizing agents have revealed a behavior which is essentially in accordance with the

simple direct electron transfer model (Tafel slopes of nearly 0.06V, proportionality between current density and oxidizing agent concentration) (2-4). More complicated behavior, including higher Tafel slopes and fractional powers in the relationship between current density and concentration, has been reported for n-CdS and n-CdSe and has been interpreted by assuming the participation of surface states in the electrode reactions (5). In a recent article (6), Schmickler interpreted several literature results on cathodic currents at oxide electrodes by assuming tunneling of electrons through a thin space charge layer. The present cathodic study pertains to n-TiO₂ and n-SrTiO₃ electrodes. Preliminary results on TiO₂ in aqueous solution by ourselves and other groups (7-9) led to Tafel slopes, considerably higher than the 0.06V expected by simple theory. In Ref. (9), this phenomenon was associated with the presence of surface states. The existence of such states has been assumed in order to interpret luminescence measurements as well in the case of TiO₂ (9, 10) as of SrTiO₃ (11) electrodes. The single crystal TiO₂ samples used in the present work were made semiconducting by doping with Nb during growth. Such samples were preferred to crystals reduced in H₂ with the idea of avoiding the possible complications of nonuniform doping. Since only insulating SrTiO₃ crystals were available to us, they were made semiconducting by partial reduction in hydrogen.

Experimental

Preparation of the electrodes.—A synthetic monocrystalline boule of Nb-doped rutile (TiO₂ + 0.05 weight percent (w/o) Nb₂O₅) and one of undoped SrTiO₃ were purchased from National Lead Industries (South Amboy, New Jersey). Several samples were cut perpendicularly to the growth direction. In what follows, the TiO₂ samples will be indicated as (a), (b), (c), (d), the SrTiO₃ samples as (v), (w), (x), (y), and (z). By x-ray analysis, it was established that the faces exposed to the electrolyte were (001) for rutile and (311) for SrTiO₃. The preparation of the electrodes of both substances was similar and consisted of sandpapering, followed by polishing with alumina powder of decreasing grain size. The samples were etched for 1 hr in molten NaOH and subsequently rinsed in HCl or HNO₃ and in distilled water. In order to make the SrTiO₃ crystals semiconducting, they were heated between 900° and 1000°C in a H₂ flow for several hours. The rear side of each specimen was connected to a metallic lead by means of In, which was melted onto the surface. Further details on the mounting of the samples have been given in a previous paper (12).

Donor concentrations, determined by capacitance measurements (13), were of the order of 10¹⁸-10¹⁹ cm⁻³. For TiO₂, this concentration range is in agreement with the value, calculated from the concentrations of Nb₂O₅ specified by the furnisher, whereas for SrTiO₃, it is consistent with the values deduced from Hall measurements by Perluzzo and Destry (14) under the same conditions of reduction in H₂. From impedance measurements, carried out on specimen (d), the flat-band potential V_{fb} at pH = 0 was established to be at -0.30V vs. SHE for Nb-doped TiO₂. It has not been established yet whether the difference between this value and that for H₂-treated TiO₂ [+0.15V vs. SHE (7)] is significant or not. Frequency-independent capacitance results on SrTiO₃ were obtained by our group (13) and by Tench and Raleigh (15), the V_{FB} values at pH = 0 being -0.60 and -0.20V vs. SHE, respectively. Hitherto, no satisfactory explanation is available for the rather large discrepancy between both values. For the following discussion, the mean value (-0.40V vs. SHE) will be adopted.

Apparatus.—The cell was identical to that described in a previous paper (12) and contained the electrode

under investigation, a Pt counterelectrode, and a saturated mercurous sulfate reference electrode. Before each experiment, the electrodes were immersed for 12 hr in indifferent electrolyte solution of the same pH as the redox solution used in the cathodic experiment and for 3 hr in the redox solution at a voltage close to the region where the measurements were to be performed. Current measurements were carried out potentiostatically and potentiodynamically. Using a potentiostatic arrangement, the currents were read after a stabilization time which, in the case of measurements with varying concentration, could amount to 1 hr. Potentiodynamic measurements were performed with an apparatus allowing variable rate of potential sweep. In order to avoid hysteresis in the potential/current plot, the sweep rate was kept at a low value ($\leq 70 \mu\text{V} \cdot \text{sec}^{-1}$). The potentiodynamic results obtained this way were identical with potentiostatic measurements. All measurements were performed in darkness at room temperature while bubbling high purity nitrogen through the solution.

Electrolyte solutions.—All solutions used in the present work were prepared with deionized water and reagent grade chemicals. They all contained 0.25M K₂SO₄ as the indifferent electrolyte. The proton concentration was fixed at pH = 9.4 or 4.6 by making solutions of 0.1M Na₂B₄O₇ · 10 H₂O and 0.05M HAc/0.05M KAc, respectively; pH values in the neighborhood of 2 or 12 were adjusted by adding H₂SO₄ or KOH. The concentration of Fe³⁺ was determined after reduction with a Jones reductor by titration with KMnO₄. The concentration of the oxidizing agents will be specified in the results.

Results

The cathodic dark current was measured for Nb-doped TiO₂ and for H₂-treated SrTiO₃, in a voltage range corresponding to the presence of a depletion region, as a function of applied voltage, of the nature and concentration of oxidizing agents in solution, and of pH.

j -V relationship.—Without any oxidizing agents added, the current density j within the voltage range of our experiments was negligibly low. Hence, effects due to the reduction of protons, mentioned in the literature for TiO₂ (16, 17), are not to be considered in our case.

In Fig. 1, typical log $|j|$ vs. V plots are shown, as observed on samples (a), (c), and (d) for TiO₂ and on samples (v), (w), (x), and (y) for SrTiO₃ upon addition of sufficiently large concentrations of Fe(CN)₆³⁻, Fe³⁺, or IrCl₆²⁻. At high current densities, the relationship appeared to be linear. The corresponding Tafel slopes $|dV/d \log |j||$ were found for a given simple

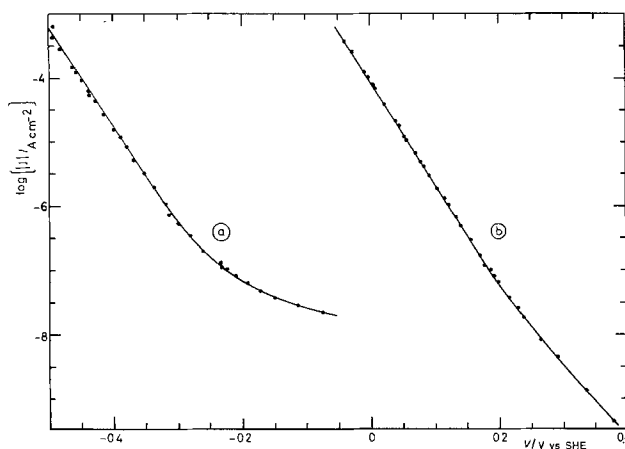


Fig. 1. Logarithm of the cathodic dark current density $|j|$ as a function of electrode potential. TiO₂ specimen (d): curve a pH = 12.3, curve b pH = 4.8.

and electrolyte composition, to be reproducible to within 2 mV, and to have values ranging around 63 mV. For the highest current densities ($> 10^{-4}$ A-cm $^{-2}$), dependence on nitrogen bubbling was observed, indicating diffusion limitation in the solution; in what follows, only those results will be considered which did not show this effect. For TiO $_2$ sample (b) and SrTiO $_3$ sample (z), higher and less reproducible Tafel slopes were found in this region (70-80 mV).

At low current densities, deviation from Tafel behavior was observed, in the sense opposite to that which would be expected from the anodic contribution to the total current (see Fig. 1). The current range corresponding to this deviation extends towards higher current densities when the pH increases (compare curves a and b in Fig. 1).

The log $|j|$ vs. V behavior at lower concentrations of oxidizing agent differs from that at higher concentrations in the values of $|dV/d \log |j||$ at high current densities, which are higher.

j-c relationship.—The relationship between the current density j and the oxidizing agent concentration c_{ox} appeared to depend, at given pH, on the electrode potential. Two extreme types of behavior exist.

At potentials which are rather positive with respect to flatband potential, i.e., at sufficiently small current densities in the low current density region just mentioned, j at constant voltage depends linearly on c_{ox} (see, e.g., Fig. 2).

In the high current density region (Tafel region), the current density at given voltage saturates as a function of concentration (see, e.g., Fig. 3). Saturation due

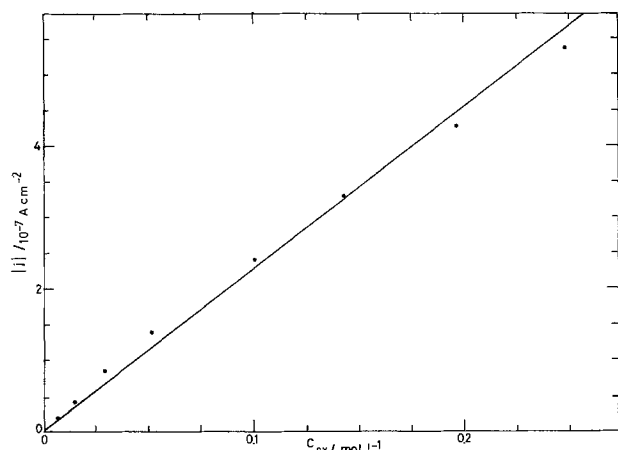


Fig. 2. Cathodic dark current density $|j|$ as a function of concentration of oxidizing agent c_{ox} . TiO $_2$ specimen (d), pH = 9.4, $V = 0.150V$ vs. SHE, ox = Fe(CN) $_6^{3-}$.

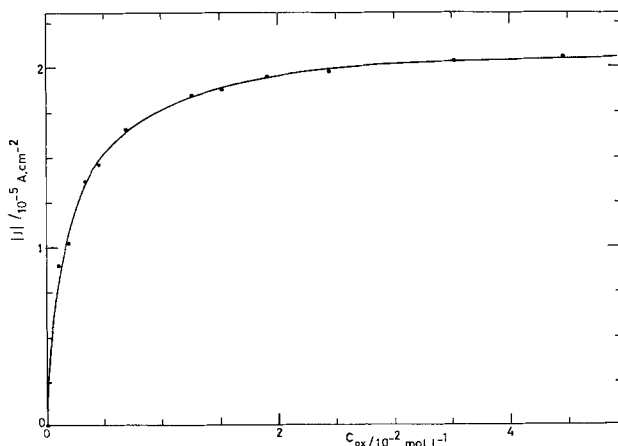


Fig. 3. Cathodic dark current density $|j|$ as a function of concentration of oxidizing agent c_{ox} . TiO $_2$ specimen (d), pH = 4.7, $V = 0.056V$ vs. SHE, ox = Fe(CN) $_6^{3-}$.

to slow diffusion from the electrode of products formed electrochemically can be excluded since the current density depends exponentially on applied voltage and since it was found to be independent of bubbling nitrogen through the solution.

The j vs. c_{ox} relationship can here be represented by

$$j = \frac{j_{sat} \cdot c_{ox}}{A + c_{ox}} \quad [1]$$

as appears from Fig. 4, where the data of Fig. 3 have been replotted as j vs. j/c_{ox} . Indeed, from Eq. [1], it follows that

$$j = j_{sat} - A(j/c_{ox}) \quad [2]$$

Values of j_{sat} and A have been experimentally determined under various circumstances.

The saturation current density j_{sat} was studied for Nb-doped TiO $_2$ and H $_2$ -treated SrTiO $_3$ as a function of applied voltage V , of the nature of the oxidizing agent, of the identity of the sample, and of the pH.

The j - V relationship can be described by

$$\ln |j_{sat}| = \{\ln |j_{sat}|\}_{V=0} - \frac{\alpha F V}{RT} \quad [3]$$

with α close to unity. In the results which follow, a given j - V curve will be characterized by $(\ln |j_{sat}|)_{V=0}$, the saturation current density extrapolated to 0V vs. SHE. In Fig. 5 curve a and b, values of $(\ln |j_{sat}|)_{V=0}$ are plotted for TiO $_2$ and SrTiO $_3$, respectively, as a function of pH for different samples and oxidizing agents. The results show that the saturation current density is roughly independent of the sample and of the nature of the oxidizing agent, but is different for TiO $_2$ and for SrTiO $_3$ and varies over one order of magnitude per pH unit.

Additional experiments have been performed in which the saturation current, measured with a given oxidizing agent, was observed upon addition of another oxidizing agent; this addition was found to cause no significant change in the current, proving again that j_{sat} is independent of the nature of the oxidizing agent.

The coefficient A in Eq. [1] and [2] was found to depend on applied voltage, on the sample used, on the nature of the oxidizing agent, and on the pH. No attempts have been made yet to describe this complex behavior by analytical expressions.

Discussion

Although at first glance a relationship such as Eq. [1], which is of the Langmuir type, might suggest that the electroreduction mechanism would involve adsorption of the oxidizing agent, several arguments can be raised against this hypothesis. Firstly, one does not see

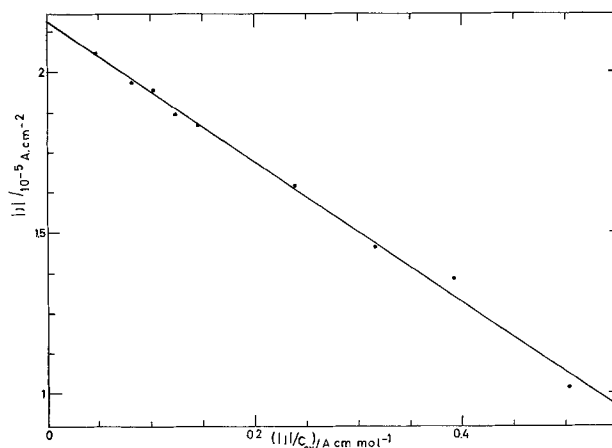


Fig. 4. $|j|$ vs. $|j|/c_{ox}$. TiO $_2$ specimen (d), pH = 4.7, $V = 0.056V$ vs. SHE, ox = Fe(CN) $_6^{3-}$.

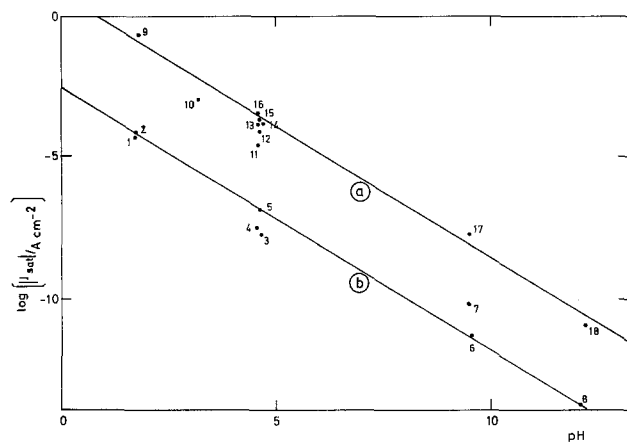


Fig. 5. Logarithm of the cathodic dark saturation current density j_{sat} at $V = 0$ vs. SHE as a function of pH.

Oxidizing agent: $\text{Fe}(\text{CN})_6^{3-}$ [3, 4, 6, 7, 8, 10, 12, 14, 15, 17, 18]

$\text{Fe}(\text{H}_2\text{O})_6^{3+}$ [1]

IrCl_6^{2-} [2, 5, 9, 11, 13, 16]

Specimen: curve a: TiO_2 ; (b) [10, 12, 14, 15, 17, 18]

(d) [9, 11, 13, 16]

curve b: SrTiO_3 ; (v) [8]; (w) [4, 5];

(y) [1, 2, 3, 6]; (z) [7]

how an adsorption model would explain the fact that a given concentration corresponds to current saturation at high current densities and not at low current densities. Secondly, an adsorption model does not imply a saturation current which is independent of the nature of the reactant. Thirdly, in the case of TiO_2 , it has been shown by capacitance measurements that the flatband potential is not influenced by the presence of the oxidizing agents used (7), indicating that they are not significantly adsorbed.

Tunneling of electrons through the space charge layer can hardly be responsible for the observed behavior, in view of the relatively low donor densities involved here; moreover, such a mechanism would be difficult to reconcile with the validity of Eq. [1] as well as Eq. [3].

In order to explain our results, it appears necessary to postulate a mechanism involving at least two consecutive steps. Tentatively, we will assume a two-step mechanism in which surface states act as intermediates. In the first step, an empty surface state is filled by a conduction band electron; in the second step, this electron is transferred to an empty redox level (see Fig. 6). We will represent the forward and reverse rate constants for the first and second steps by k_1 , k_{-1} , k_2 , and k_{-2} , respectively. We will further represent the density of surface states and their occupation factor by N and f , respectively. The net filling rate $N df/dt$ of the surface states is then given by

$$N \frac{df}{dt} = k_1(1-f)Nn_s - k_{-1}fN - k_2fNc_{\text{ox}} + k_{-2}(1-f)Nc_{\text{red}} \quad [4]$$

n_s being the conduction band electron density at the surface and c_{ox} and c_{red} the concentration of oxidizing and corresponding reducing agent, respectively.

It is assumed here that the electron level distribution in the redox electrolyte is at equilibrium. Since the experiments are made under steady-state conditions, $N(df/dt) = 0$, we have from Eq. [4]

$$f = \frac{k_1 \cdot n_s + k_{-2} \cdot c_{\text{red}}}{k_{-1} + k_2 \cdot c_{\text{ox}} + k_1 \cdot n_s + k_{-2} \cdot c_{\text{red}}} \quad [5]$$

The current density j is given by

$$j = -eN [k_2 \cdot f \cdot c_{\text{ox}} - k_{-2} \cdot (1-f) \cdot c_{\text{red}}] \quad [6]$$

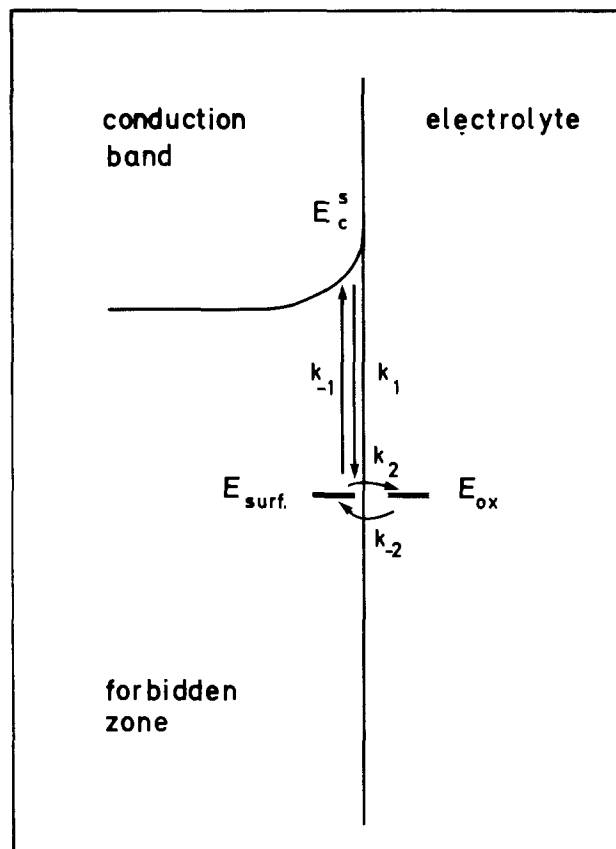


Fig. 6. Charge transfer through surface states. E_{surf} : energy of surface level; E_{ox} : energy of empty redox level in solution; E_c^s : energy of the conduction band edge at the surface; k_1 , k_{-1} , k_2 , k_{-2} : rate constants of filling and emptying processes.

with e the absolute value of the elementary charge. Substituting Eq. [5] into Eq. [6], we obtain

$$j = -eN \frac{k_1 \cdot n_s \cdot c_{\text{ox}} - (k_{-1} \cdot k_{-2} / k_2) c_{\text{red}}}{(k_{-1} + k_1 \cdot n_s + k_{-2} \cdot c_{\text{red}}) / k_2 + c_{\text{ox}}} \quad [7]$$

The relationship between j and c_{ox} as expressed in Eq. [7] reduces to the experimental one, expressed in Eq. [1], when the first term in the numerator of Eq. [7] is sufficiently large, i.e., when n_s largely exceeds the value corresponding to electrode equilibrium. In this case, the value of j_{sat} is given by

$$j_{\text{sat}} = -eN k_1 n_s \quad [8]$$

Since n_s varies over one order of magnitude per 0.06 eV band bending, the theoretical expression for j_{sat} (Eq. [8]), is in agreement with the experimental Eq. [3] describing the voltage-dependence, as well as with the observed pH dependence of j_{sat} at a given applied voltage which can then be ascribed to the pH shift of the flatband potential. Equation [8] also explains the experimental observation that j_{sat} is independent of the nature of the oxidizing agent if it is assumed that the same surface states are involved in the reduction of different oxidizing agents. It can be remarked here that Eq. [8] corresponds to the situation in which the capture of electrons by the surface states is rate-limiting. Moreover, since for a given material, j_{sat} was found to vary very little from sample to sample, acceptance of the validity of Eq. [8] leads to the implication that $N k_1$ is constant for a given material within the well-determined conditions of doping and pretreatment in our experiments. Numerical values of $N k_1$ can be obtained from our results, basing upon Eq. [8]; e.g., for SrTiO_3 at pH = 0, $j_{\text{sat}} = 3 \cdot 10^{-3} \text{ A} \cdot \text{cm}^{-2}$ at 0V vs. SHE (see Fig. 5), i.e., at a band bending of 0.4 eV. Hence, a value of $N k_1 \approx 10^5 \text{ cm} \cdot \text{sec}^{-1}$ is found. From

solid-state considerations, it follows that

$$k_1 = v S_n \quad [9]$$

v being the mean thermal speed of conduction band electrons and S_n the electron capture cross section of the surface states. Accepting $v = 10^7$ cm·sec⁻¹, we obtain $N S_n = 10^{-2}$. Assuming that the surface states are of the donor type, which implies $S_n \sim 10^{-12}$ cm², a reasonable value for the density of surface states is found, i.e., $N = 10^{10}$ cm⁻². In an analogous way, $N k_1 = 4 \cdot 10^6$ cm·sec⁻¹ is obtained for TiO₂ corresponding to $N = 4 \cdot 10^{11}$ cm⁻². It should be remarked that these values may be subject to a certain error, due to the uncertainty in the determination of the flatband potential (see the section "Preparation of the electrodes") and of S_n .

Still under conditions where $k_1 \cdot n_s \cdot c_{ox} \gg (k_{-1} \cdot k_{-2} / k_2) c_{red}$ but at values of c_{ox} which are below the range corresponding to current saturation as a function of c_{ox} , the contribution of n_s in the denominator of Eq. [7] qualitatively explains the observed lowering of the voltage dependence of j , i.e., the increase of the experimental Tafel slopes. The high Tafel slopes, observed by Dutoit *et al.* (7) on H₂-treated TiO₂ electrodes at relatively low c_{ox} , might be attributed to the same reason.

As mentioned in the results, the change in current-voltage behavior at increasing positive voltage (low current density range) cannot be interpreted on the basis of the anodic contribution to the total current, i.e., referring to Eq. [7], to the term $(k_{-1} \cdot k_{-2} / k_2) c_{red}$ in the numerator.

Different mechanisms may lead to such behavior. For example, a small contribution of the valence band to the cathodic current (hole injection), which is voltage-independent, might be involved here. Another possibility is that two parallel current paths, j and j' , over surface states of different types participate to the reaction, the first one being already described by Eq. [7], the second one by an analogous expression in which the corresponding rate constants will be denoted by k'_1 , k'_{-1} , k'_2 , and k'_{-2} and the density of states by N' (the same situation might result from an energetic distribution of surface states). In view of the facts that the current increases over much less than one decade per -0.06 V voltage shift and is proportional to c_{ox} (see Fig. 2), it can be assumed then that the term $(k'_1 / k'_2) n_s$ in the denominator of the expression for j' predominates. In the limiting case where all other terms in the denominator are negligible with respect to $(k'_1 / k'_2) n_s$, i.e., at relatively high n_s , the expression for j' reduces to

$$j' = -e N' k'_2 c_{ox} \quad [10]$$

in agreement with the observed concentration dependence and corresponding to rate-limiting charge transfer from the surface state to the reactant. This current might constitute a constant and negligible contribution to the total cathodic current in the high current-density range. The influence of pH upon the low current-density behavior, as demonstrated in Fig. 1, can be ascribed to the change in the relative position of energy levels at the semiconductor surface with respect to those in solution, causing a change in the value of k'_2 . It may be remarked here that the hole injection mechanism, mentioned above, can be formally described by an expression similar to Eq. [10].

The current-voltage and current-concentration results mentioned above are not interpretable on the basis of the direct electron transfer model, in which conduction band electrons at the surface tunnel directly through the interfacial barrier toward empty redox levels. Indeed, the direct electron transfer model leads to a current, directly proportional to n_s and c_{ox} , a behavior which was not observed in any current range of our experiments. Especially in acid medium, this result

is somewhat surprising, in view of the relative position of energy levels at the interfaces involved. Indeed, from V_{fb} values mentioned in the section "Preparation of the electrodes," the position of the conduction band edge at the surface E_c^s can be estimated to be at $+0.5$ eV for Nb-doped TiO₂ and at $+0.6$ eV for SrTiO₃ at pH = 1.5, being the lower pH limit of our experiments. Common literature values for the maximum of the empty level density curve E_{ox}^m of the hexacyanoferrate couple are between $+0.1$ eV (18) and $+0.4$ eV (1). Accepting a value of about 1 eV for the rearrangement energy of the Fe³⁺/Fe²⁺ couple (18), the corresponding E_{ox}^m value may be located at about $+0.2$ eV. Hence, at least in acid medium, a noticeable contribution of the direct transfer mechanism would be expected; in other cases, the surface state model can be rationalized by the fact that E_{ox}^m is markedly below E_c^s . Apparently, the reduction over surface states is fast enough so that the direct transfer mechanism is unable to compete under any circumstances of our experiments. Any discussion on this point is hampered by the lack of quantitative data on the parameters involved.

Acknowledgment

One of us (J.V.) thanks the "Instituut ter Aanmoediging van het Wetenschappelijk Onderzoek in Nijverheid en Landbouw" (I.W.O.N.L.) for a scholarship.

Manuscript submitted April 19, 1979; revised manuscript received Aug. 26, 1979.

Any discussion of this paper will appear in a Discussion Section to be published in the December 1980 JOURNAL. All discussions for the December 1980 Discussion Section should be submitted by Aug. 1, 1980.

Publication costs of this article were assisted by Rijksuniversiteit-Gent.

REFERENCES

1. W. P. Gomes and F. Cardon, in "Semiconductor Liquid-Junction Solar Cells," A. Heller, Editor, p. 120, The Electrochemical Society Softbound Proceedings Series, Princeton, N.J. (1977).
2. T. Freund and S. R. Morrison, *Surf. Sci.*, **9**, 119 (1968).
3. S. R. Morrison, *ibid.*, **15**, 363 (1969).
4. R. A. L. Vanden Berghe, F. Cardon, and W. P. Gomes, *ibid.*, **39**, 368 (1973).
5. V. A. Tyagai and G. Ya. Kolbasov, *Surf. Sci.*, **28**, 423 (1971).
6. W. Schmickler, *Ber. Bunsenges. Phys. Chem.*, **82**, 447 (1978).
7. E. C. Dutoit, F. Cardon, and W. P. Gomes, *ibid.*, **80**, 475 (1976).
8. E. N. Paleolog and A. Z. Fedotova, *Elektrokhimiya*, **5**, 1336 (1969).
9. R. N. Noufi, P. A. Kohl, S. N. Frank, and A. J. Bard, *This Journal*, **125**, 246 (1978).
10. H. Morisaki and K. Yazawa, *Appl. Phys. Lett.*, **33**, 1013 (1978).
11. J. G. Mavroides, in "Semiconductor Liquid-Junction Solar Cells," A. Heller, Editor, p. 84, The Electrochemical Society Softbound Proceedings Series, Princeton, N.J. (1977).
12. E. C. Dutoit, R. L. Van Meirhaeghe, F. Cardon, and W. P. Gomes, *Ber. Bunsenges. Phys. Chem.*, **79**, 1206 (1975).
13. F. Vanden Kerchove, J. Vandermolen, W. P. Gomes, and F. Cardon, *ibid.*, **83**, 230 (1979).
14. G. Perluzzo and J. Destry, *Can. J. Phys.*, **56**, 453 (1978).
15. D. M. Tench and D. O. Raleigh, *Nat. Bur. Stand. (U.S.) Spec. Publ.*, **455**, 229 (1976).
16. M. L. Knotek and D. S. Ginley, *This Journal*, **125**, 160C (1978).
17. L. A. Harris, M. E. Gerstner, and R. H. Wilson, *ibid.*, **126**, 850 (1979).
18. R. Memming, in "Semiconductor Liquid-Junction Solar Cells," A. Heller, Editor, p. 38, The Electrochemical Society Softbound Proceedings Series, Princeton, N.J. (1977).

Surface Properties of Sodium Tungsten Bronzes

Michael Francis Weber,* H. R. Shanks, A. J. Bevolo, and G. C. Danielson

Ames Laboratory-USDOE and Department of Physics, Iowa State University, Ames, Iowa 50011

ABSTRACT

The surfaces of sodium tungsten bronze crystals have been examined by using cyclic voltammetry and Auger electron spectroscopy before and after electrochemical treatments. Compositional depth profiles of the sodium depletion layers were obtained and the formation of hydrogen tungsten bronze was observed and studied. Hydrogen tungsten bronze was found to form on the anodized cubic sodium tungsten bronze at two separate potentials, corresponding to the formation of semiconducting and metallic phases of H_xWO_3 .

Sodium tungsten bronzes are members of a general class of nonstoichiometric compounds with the formula M_xWO_3 where M is a metal and $0 < x < 1$. The compound WO_3 is a semiconductor with a bandgap of 2.6 eV (1) and a monoclinic structure. The addition of increasing concentrations of different metal atoms, such as the alkali elements, results in a series of crystal structures with increasing symmetry and with differing electronic properties. For $x > 0.5$, Na_xWO_3 has a nearly cubic structure at room temperature (2). At a slightly elevated temperature, the material undergoes a phase transition to the true cubic perovskite structure. The crystals in this range of x -values will be referred to here as in the cubic phase. The unit cell of the cubic bronze structure consists of a tungsten atom at the cube center, oxygen atoms on the cube faces, and the sodium atoms at the cube corners. The oxygen atoms form an octahedron around the tungsten atom, so that the compound is composed of corner bonded WO_6 octahedra surrounding the sodium atoms.

Recent investigations (3-5) have shown that anodization of Na_xWO_3 in acid solutions removes sodium atoms to a depth of several hundred angstroms, leaving a semiconducting layer of low x -value Na_xWO_3 on the surface. After anodization, a reversal of the electrode polarity causes the crystal surface to change color from a light green to a deep blue. This color change has been shown to be associated with the movement of hydrogen into the empty sodium sites (4-6) and the formation of H_xWO_3 .

Hydrogen tungsten bronzes have crystallographic and electrical properties similar to the other bronzes (7). Crystals of the orthorhombic and tetragonal II phases are semiconductors, and crystals of the tetragonal I and cubic phases exhibit metallic conductivities. The ranges of x -values corresponding to each phase is not well-known.

Two processes studied by cyclic voltammetry were the anodic dissolution of the bronze, and formation of hydrogen tungsten bronzes on the surface. The cubic sodium tungsten bronzes have been studied for both of these reactions (4, 8, 9). However, several questions still remain concerning the hydrogen bronze formation on cubic Na_xWO_3 and the crystal structure of the sodium depletion layer on this compound. Even though hydrogen bronze formation has been studied on cubic Na_xWO_3 , the x -value of the resulting hydrogen bronze (H_xWO_3) surface has not been determined. Since the hydrogen x -value is unknown, the electronic state of the surface, semiconducting or metallic as a function of potential is also unknown.

Experimental

The sodium tungsten bronze crystals were prepared by the electrolysis of a fused salt of sodium tungstate and tungsten trioxide as described by Shanks. (10). Crystal growth was initiated from the tip of a

gold wire drawn up a few millimeters into the end of a 2 mm OD quartz tube. Single crystals, approximately 2 cm or more on an edge, were normally obtained. Spark source mass spectroscopy showed total impurity concentrations of about 400 ppm with Mo being the major impurity.

For the electrochemical studies, the crystals were either cleaved or cut on a high speed diamond saw to a typical sample size of $4 \times 4 \times 6$ mm. Cleaved crystals were cleaned in boiling conductivity water, while the crystals cut on the diamond saw were first cleaned in boiling ethyl acetate, followed by hot concentrated NaOH, and finally in boiling conductivity water. The cut samples were then either polished or cleaved away on one end to ensure a fresh bronze surface. The crystals were mounted in Teflon using the method described by Nagy and McHardy (11). Details of the sample mounting and electrical connection are illustrated in Fig. 1. Polishing of the cut surface consisted of mechanical polishing with $0.05 \mu\text{m}$ alumina powder. The area of each sample was determined from a photomicrograph of the mounted crystal, with no corrections being made for surface roughness.

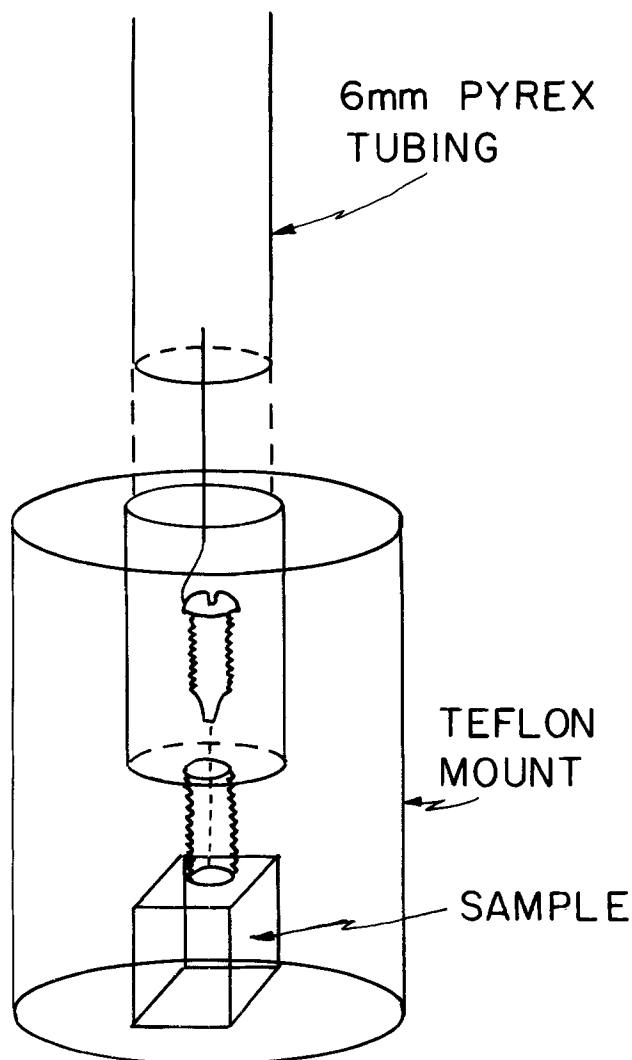
The experiments were conducted in a three compartment cell constructed of quartz and Teflon. Water used in the solutions was distilled directly into the test cell from an all-quartz still. Complete technical details of this equipment can be found elsewhere (12, 13). The only solution used in the cell for this study was 0.1N H_2SO_4 (pH 1.2) mixed *in situ* from Apache Chemicals 99.9999% pure (distilled in Vycor) sulfuric acid. The solution was not preelectrolyzed for any of these experiments. A palladium hydride electrode (14) was used as a reference electrode. The Pd-H electrode was repeatedly checked against a saturated calomel reference electrode since its potential tended to drift for a long time after recharging with hydrogen. Thus, all potentials were referenced to the normal hydrogen electrode using the relation $V_{NHE} = V_{SCE} + 0.242V$.

Immediately before insertion into the test cell, all samples were washed with acetone, and then with isopropyl alcohol, followed by a final cleaning with an isopropyl vapor phase degreaser. After insertion into the cell, the potential on each electrode was cycled between 0.1V and 1.6V NHE for approximately 20 min to clean the surface further. Only small changes in the cyclic voltammetry curves were observed during this time. Unless otherwise noted, all cyclic voltammetry curves shown in this paper are steady-state curves. A Keithley Model 640 electrometer was used to measure the potentials while a Princeton Applied Research Model 173/176 potentiostat/galvanostat was used to control the three electrodes. Anodization of the bronze surfaces were carried out galvanostatically, a given anodization treatment was specified by the applied current density, and the final voltage attained after a given time.

Chemical composition of the electrode surfaces was determined by Auger electron spectroscopy (AES).

* Electrochemical Society Active Member.

Key words: films, electrode, potential, sputtering.



SAMPLE MOUNTING

Fig. 1. Sample mounting and electrical connection for the tungsten bronze samples.

The primary electron beam current for the Auger analysis was $5 \mu\text{A}$ at 4 keV with a spot diameter of $40 \mu\text{m}$. Elemental abundances were determined from the peak to peak AES signals after correction for the Auger sensitivity factor for each element. The Auger analysis was carried out during continuous sputtering of the crystal surface by argon ions at 2.5 keV. To eliminate any crater edge effects, the ion beam was rastered over a 3 mm^2 area, and the Auger electron beam was centered in this area. The sputtered depth was calculated by assuming an average sputtering yield of 2 for sodium tungsten bronze. The Auger electron energies monitored were: for tungsten, 38 eV, 48 eV, and a doublet of 163-179 eV; for oxygen 510 eV; and for sodium, 990 eV. Compositions were obtained by comparison with the observed stoichiometry of a bronze crystal of known composition which had been cleaned in the surface analysis vacuum chamber, since both electron beam induced desorption and preferential sputtering of the alkali metal can occur. In addition to the AES measurements, SEM photographs were used to reveal the surface morphology of some crystals. These studies were performed both before and after the electrodes

were subjected to strong anodic and cathodic polarizations. All measurements were made at $25^\circ \pm 2^\circ\text{C}$.

Results and Discussion

Polished crystals of cubic Na_xWO_3 were found to have little or no sodium depletion layer when Auger depth profiled. Anodizing the crystals, however, resulted in sodium depletion at the surface. A polished $\text{Na}_{0.7}\text{WO}_3$ crystal which was anodized at 0.5 mA/cm^2 for 3 hr, during which time the potential slowly increased to 5.5V NHE, had a surface x -value of about 0.25 which extended for some 800Å into the crystal. Another crystal with an x -value of 0.6 was anodized at 1 mA/cm^2 for 9 hr with a final potential of 9.0V NHE. Sodium depletion extended to a depth of 1500Å with a surface x -value of about 0.1. Similar results were obtained on a number of crystals with comparable anodizing times.

Considering the high potentials needed to create the depletion layer, reports of depletion layers over $100 \mu\text{m}$ thick (15) must be viewed with considerable skepticism. The ion microprobe results of Bockris and McHardy (3) indicated depletion layers over 1000Å thick on samples anodized to only 2V. In view of the consistency of our measurements, a 1000Å depletion layer formed by only 2V seems excessive.

The C-V curve for an anodized $\text{Na}_{0.9}\text{WO}_3$ crystal is shown in Fig. 2. The redox reaction occurring at +0.15V (NHE) has several features. First, the potentials at which the peak current, i_p , occur approach a difference of 60 mV as the sweep rate, S , approaches zero. Second, i_p increases linearly with S . All cubic Na_xWO_3 , with $0.6 < x < 0.9$, that had been anodized, exhibited C-V curves nearly identical to those shown in Fig. 2.

These data present a dilemma that was first resolved by Randin and co-workers (4). The peak current separation approaching 60 mV as S approaches zero implies that a diffusion-limited redox couple is occurring. But such a reaction should have i_p proportional to the square root of S , whereas the data have i_p proportional

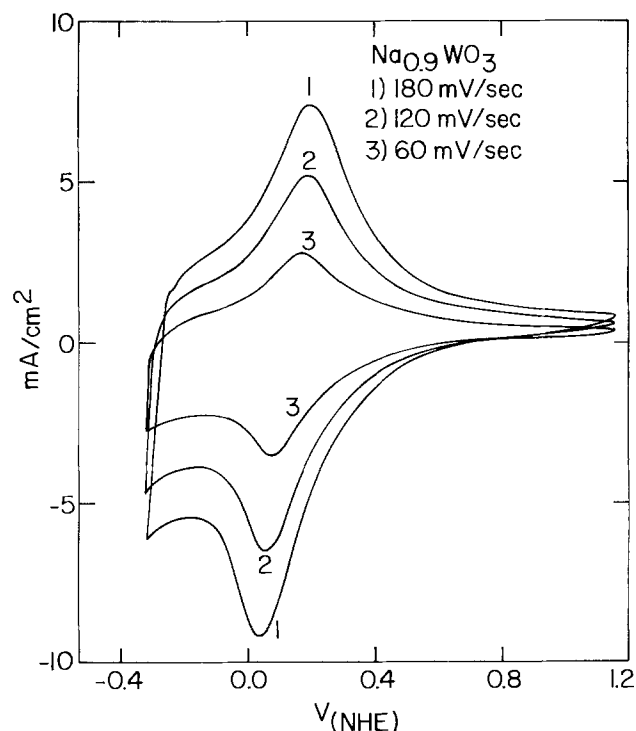
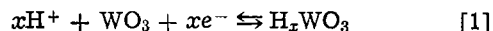


Fig. 2. C-V curves for an anodized cubic sodium tungsten bronze. The redox reaction at 0.15V is the formation of hydrogen tungsten bronze in the sodium depletion layer. The reaction is reversible and the surface undergoes no net change. No anodic corrosion currents were observed at anodic potentials up to 2.0V.

to S. This latter result implies that a surface reaction is occurring limited only by the activation energy and the surface coverage fraction (16, 17). Randin was able to reconcile these facts by assuming that the redox couple represents the formation of hydrogen bronze by



This reaction was occurring on the surface of an anodized bronze with the diffusing species being the hydrogen ions. The key notion is that the hydrogen ions are diffusing through the empty sodium sites in the sodium depletion layer of the bronze electrode, rather than the electrolyte.

Freshly polished crystals of cubic Na_xWO_3 have C-V curves of the same form as those for anodized crystals, but the peak currents are an order of magnitude smaller at similar sweep rates. The C-V curve for such a crystal is shown in Fig. 3. These curves are further evidence that the large current peaks, centered around 0.15V, are due to Eq. [1], because a hydrogen bronze can be formed at 0.15V only if empty sodium sites are available for the hydrogen atoms to occupy. Some sodium is probably lost from the surface just by etching from the acid and by the C-V experiment itself, when potentials above 1V are reached on the C-V trace. The amount of sodium depleted by these processes is much smaller than the amount of sodium lost by anodizing the crystal at 5-10V, and the differences in the current peak heights in Fig. 2 and 3 are obvious.

On both anodized and unanodized crystals, the current approaches zero as the potential becomes more positive. Extended potential scans out to 2.0V show that no reactions occur in this potential region, or more specifically, the cubic Na_xWO_3 surface does not dissolve at these high potentials. Also, the integrated current on the positive going scan equals the integrated current on the reverse scan. This equality implies that a totally reversible reaction is occurring, with no net change of the bronze surface. However, the first scans on all freshly polished crystals exhibited a corrosion current above 1.2V, which disappeared after several voltage cycles. The corrosion reaction above 1.2V is probably the removal of sodium atoms from the first few layers of the crystal surface. The initial C-V traces on some crystals did not have well-defined peaks, but only broad current maxima. One explanation of the

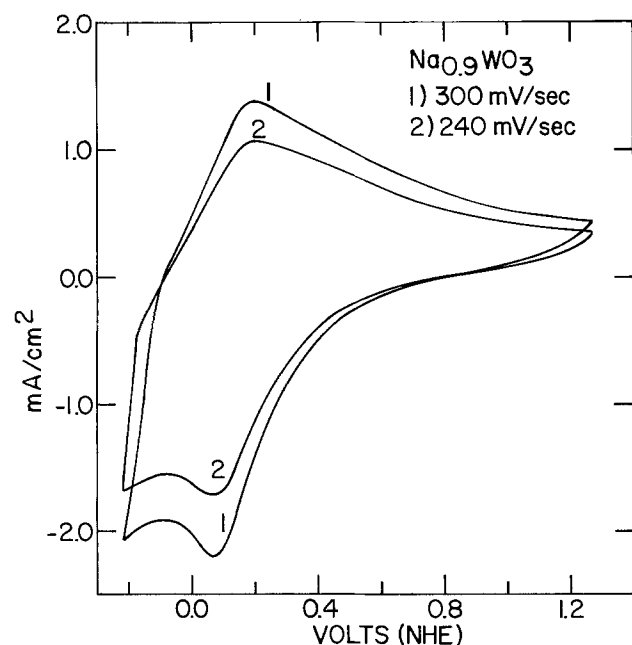


Fig. 3. C-V curve for a freshly polished cubic sodium tungsten bronze crystal. The peak currents are an order of magnitude lower than those on an anodized crystal because hydrogen occupies only the vacant sodium sites.

broadening is simply a dirty surface. On most samples, the peaks sharpened up after several voltage scans. The reason for the difference is unknown. After a strong anodization, 5V or greater, a cubic sodium tungsten bronze exhibited the curve shown in Fig. 2.

The hydrogen bronze formation peak (cathodic current peak) in Fig. 3 is only a shoulder on a larger background current, which introduces the question of the origin of this background current. One possibility was hydrogen evolution, but the high overvoltages on a hydrogen Tafel plot (12, 18-20) show that this background current cannot be hydrogen evolution. The extended cyclic voltammetry scan in Fig. 4 also shows this to be the case. Hydrogen evolution does not begin until about -0.6V , but a second reaction is occurring, with broad peaks, near -0.3V . The reaction at -0.3V could be greatly enhanced by holding the crystal at a potential below -0.3V . Figure 5 shows the C-V curves of a crystal after anodization to 2V, reduction at -0.7V for 3 hr, and reanodization to 6.8V. The C-V curves of this crystal show enhanced currents at -0.3V compared to those of an unreduced crystal such as those shown in Fig. 4. The second anodization did not restore the crystal to its original state, implying that the reduction process has irreversibly changed the surface of the electrode.

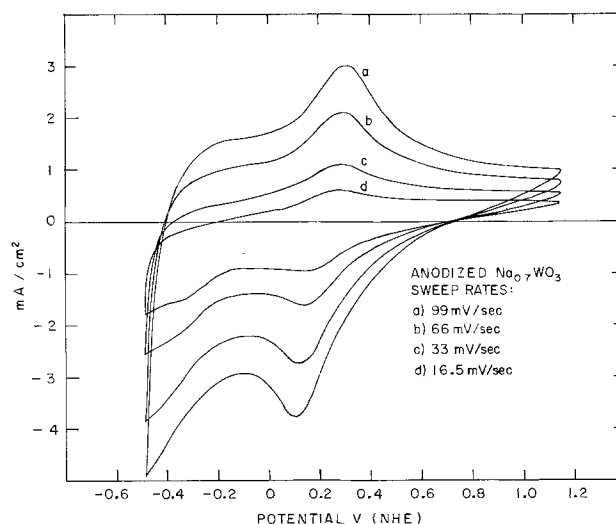


Fig. 4. C-V scans over an extended range of potentials. A second reaction is observed near -0.3V . The reaction near 0.15V is unaffected by the extended scan. Both reactions are shown to be due to hydrogen bronze formation.

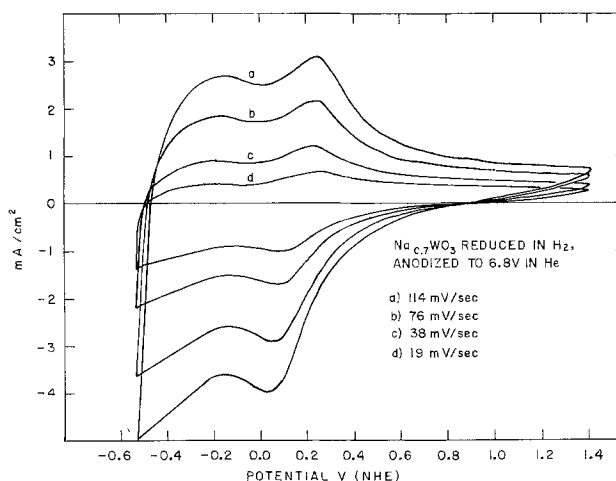


Fig. 5. C-V curves for the reduced crystal after it was anodized to 6.8V. The anodization process increased the peak currents at 0.15V as usual, but did not greatly affect the reaction at -0.3V . The reduction process irreversibly changed the crystal surface.

The positive current sections of the curves shown in Fig. 5 are almost identical to the curves obtained by Vondrak and Balej in their study of hydrogen absorption by sodium tungsten bronzes (9). Contrary to Randin (4), they did not attribute the current peak at 0.15V to hydrogen bronze formation, but attributed only the peak at -0.3V to that process. All researchers agree that a strong reduction of a sodium tungsten bronze crystal results in a severe blistering or cracking of the crystal surface. Such stresses must be associated with changes in the crystallographic properties of the crystal and are obviously irreversible. An SEM photograph of such a surface is shown in Fig. 6. The C-V curves in Fig. 4 and 5 indicate that the stresses on the crystal have caused a permanent change in the crystal which allows more hydrogen to enter the crystal at -0.3V.

The two reactions on the sodium tungsten bronze surface at 0.15 and -0.3V are thought to be the formation of the semiconducting and metallic phases of hydrogen tungsten bronze. There is both experimental and theoretical support for this hypothesis. First, Siclet *et al.* (21) studied the reduction of powdered WO_3 on a mercury electrode. By x-ray analysis of the powders, they found that orthorhombic $\text{H}_{0.1}\text{WO}_3$ was formed at potentials near +0.340V, and that either the tetragonal I or cubic phase, corresponding to $0.33 \leq x \leq 0.5$, was formed at potentials near -0.136V. The resolution of their equipment was insufficient to give an exact x -value for the latter compound.

The second clue to the nature of the two reactions on the surface of Na_xWO_3 is a simple visual observation made during C-V scans on all the anodized cubic sodium tungsten bronzes. The normal color of this oxide surface is a light green. As the electrode potential passes 0.15V on the cathodic scan, the surface turns dark blue and highly absorbing in appearance. When the potential passes through the region of the current peak around -0.3V, the surface turns orange and highly reflecting in appearance. The change in the observed reflectance is indicative of a semiconductor-

metal transition between 0.15 and -0.30V. The band-gap of semiconducting H_xWO_3 is low enough, probably <1 eV, to absorb all visible light, and the reflectance at more negative potentials is due to metallic H_xWO_3 . A sodium-depleted surface initially has a high band-gap close to that of WO_3 (3). This normal state of the anodized surface can be reinstated simply by returning to potentials more positive than 0.15V. The higher potentials drive out the hydrogen by means of the oxidation process described by Randin *et al.* (4). That the electronic nature of H_xWO_3 is similar to that of Na_xWO_3 is remarkably demonstrated by the succession of colors seen with progressively more negative potentials. The hydrogen tungsten bronze on the crystal surface proceeds through all the colors of the sodium tungsten bronzes corresponding to sodium x -values of zero, to higher sodium x -values of about 0.6 or 0.7. The separation in energy between the two reactions at 0.15 and -0.3V is 0.45 eV, which is consistent with our estimates of the bandgaps of semiconducting hydrogen tungsten bronzes.

Formation of the low x -value or semiconducting H_xWO_3 involves electron transfer to sites that are spatially well-separated but are at similar energy levels. The energy required to add more hydrogen is therefore constant at low x -values. On this basis, the current peaks around 0.15V would be expected to be rather sharp and well-defined, which we have observed to be the case. However, after the semiconductor-metal transition has occurred, the conduction electron wave functions overlap. The energy required to increase the electron density increases continuously as more electrons are added because of the increased electronic repulsive energy. Therefore, the current peaks at -0.3V associated with the formation of metallic H_xWO_3 can be expected to be very broad, as is observed experimentally (see Fig. 5).

Conclusions

Anodized sodium tungsten bronzes were shown by Auger depth profiling to have a greatly depleted sodium content on the crystal surface. The sodium depletion layer was 1500Å thick samples anodized to 9V, with a sodium x -value of between 0.05 and 0.1. The cyclic voltammetry curves provide strong evidence that the sodium depletion layer on Na_xWO_3 retains the crystal structure of the bulk. Hydrogen tungsten bronze is formed in the sodium depletion region of a sodium tungsten bronze crystal at low potentials. The hydrogen bronze is formed in two steps, one at 0.15 and the other at -0.3V, corresponding to the formation of semiconducting and metallic hydrogen tungsten bronze.

Acknowledgments

This work was supported in part by the U.S. Department of Energy contract No. W-7405-Eng-82, Division of Materials Sciences budget code AK-01-02-02-2, and in part by the National Science Foundation. The authors would like to thank O. M. Sevde and Dr. Erwin Buck for their help in the early stages of this work.

Manuscript submitted March 7, 1979; revised manuscript received Aug. 27, 1979.

Any discussion of this paper will appear in a Discussion Section to be published in the December 1980 JOURNAL. All discussions for the December 1980 Discussion Section should be submitted by Aug. 1, 1980.

Publication costs of this article were assisted by Iowa State University.

REFERENCES

1. S. Sawada and G. C. Danielson, *Phys. Rev.*, **113**, 803 (1959).
2. R. Clarke, *Phys. Rev. Lett.*, **39**, 1550 (1977).
3. J. O'M. Bockris and J. McHardy, *This Journal*, **120**, 53 (1973).
4. J. P. Randin, A. K. Vijh, and A. B. Chughtai, *This Journal*, **120**, 1174 (1973).



Fig. 6. SEM photograph of the cracked surface of a strongly reduced $\text{Na}_{0.6}\text{WO}_3$ crystal. Here the cracks can be seen to be only in the sodium depletion layer which is flaking off the crystal.

5. M. F. Weber and H. R. Shanks, *Natl. Bur. Std. Spec. Publ.* 455, Alan D. Franklin, Editor, p. 297, Government Printing Office, Washington, D.C. (1976).
6. R. J. Colton, A. M. Guzman, and U. Wayne Rabalais, *J. Appl. Phys.*, **49**, 409 (1978).
7. P. G. Dickens and R. J. Hurditch, in "Chemistry of Extended Defects in Non-Metallic Solids," L. Eyring and M. O'Keeffe, Editors, p. 555, Amsterdam-North Holland (1970).
8. Jean-Paul Randin, *This Journal*, **120**, 378 (1973).
9. J. Vondrak and J. Balej, *Electrochim. Acta*, **18**, 1017 (1973).
10. H. R. Shanks, *J. Cryst. Growth*, **13/14**, 433 (1972).
11. Z. Nagy and J. McHardy, *This Journal*, **117**, 1222 (1970).
12. M. F. Weber, Ph.D. Thesis, Iowa State University, Ames, Iowa (1977).
13. M. F. Weber, *IS Report*, **IS-4437** (1978).
14. J. McHardy, Ph.D. Thesis, University of Pennsylvania, Philadelphia, Pa. (1972).
15. M. McHardy and P. Stonehart, in "Electrochemistry," Series 2, Vol. VI, A. D. Buckingham and J. O'M. Bockris, Editors, p. 171, Butterworths, London (1976).
16. S. Srinivasan and E. Gileadi, *Electrochim. Acta*, **11**, 321 (1966).
17. B. E. Conway and H. Anderstein-Kozlowska, *Natl. Bur. Std. Spec. Publ.* 455, A. D. Franklin, Editor, p. 107, U.S. Government Printing Office, Washington, D.C. (1976).
18. J. Vondrak and B. Alej, *Electrochim. Acta*, **20**, 283 (1975).
19. D. B. Sepa, D. S. Ovcin, and M. V. Vojnovic, *This Journal*, **119**, 1285 (1972).
20. R. J. Mannan, Ph.D. Thesis, University of Pennsylvania, Philadelphia, Pa. (1967).
21. G. Siclate, J. Chevrier, J. Lenoir, and C. Eyraud, *Compt. Rend.*, **C 277**, 227 (1973).

Semiconductor Electrodes

XXV. The p-GaAs/Heptyl Viologen System. Photoelectrochemical Cells and Photoelectrochromic Displays

Benjamin Reichman, Fu-Ren F. Fan, and Allen J. Bard*

Department of Chemistry, The University of Texas at Austin, Austin, Texas 78712

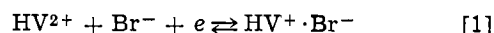
ABSTRACT

The photoreduction of aqueous solutions of 1,1'-diheptyl-4,4'-bipyridyl (heptyl viologen, HV^{2+}) bromide on p-GaAs was investigated. Under irradiation with light of wavelengths below 885 nm, the photoreduction of HV^{2+} to form a precipitate of violet $HVBr$ occurs on p-GaAs at a potential of ~ 400 mV more positive than the reversible potential of the $HV^{2+}/HVBr$ couple on Pt. Oxidation of $HVBr$ back to soluble HV^{2+} occurs in the dark at more negative potentials. Photoelectrochemical low capacity storage cells based on this reaction with Cu, Ni, or $H_xNb_2O_5$ counterelectrodes were constructed. In such cells, under illumination, the p-GaAs electrode behaves as the cathode, a photovoltage develops, and current flows in the external circuit, while $HVBr$ precipitates on the electrode surface, and the counterelectrode is oxidized. In the dark, the current flows in the opposite direction, the p-GaAs is the anode, and reduction occurs at the counterelectrode. Such a cell also produces an alternating electrical output under periodic illumination. Photoelectrochromic cells based on this reaction and utilizing simultaneous addressing with light and electrical signals are also proposed.

A number of photoelectrochemical (PEC) cells employing semiconductor electrodes for the conversion of radiant to electrical energy (liquid junction photovoltaic cells) have been described (1-17). Most have employed n-type semiconductors and have been used for the instantaneous production of electricity without chemical storage. The possibility of a photochargeable PEC cell using a third storage electrode or with production of soluble reactants has been discussed, however (8, 10-11). PEC cells employing p-type electrodes are less common (8-9, 15-17). Studies of aqueous systems with p-GaAs and p-GaP have been reported (15-16, 18), but the observed efficiencies of these were usually quite small and in many cases problems with electrode stability were encountered. Investigations of p-GaAs electrodes in acetonitrile solutions suggest good stability under strict water-free conditions (19).

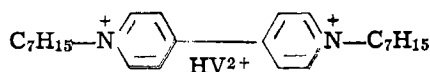
We report here investigations of the p-GaAs electrode immersed in aqueous solutions containing 1,1'-diheptyl-4,4'-bipyridyl (heptyl viologen, HV^{2+}) bromide. The reduction of HV^{2+} bromide on metal electrodes yields a precipitate of the violet radical cation

salt (Eq. [1]) and this has been suggested as the basis



of electrochromic displays (20-22). The formation of such a precipitate by photoreduction at a p-type semiconductor would allow low capacity energy storage via a solid material, just as occurs in secondary batteries. We will show that such a photoreduction does occur at p-GaAs at potentials ~ 400 mV less negative than that observed at a platinum electrode and that dark oxidation of the $HVBr$ precipitate is possible. Moreover, the p-GaAs electrode is stable both in the dark and under illumination in the HV^{2+} solution so that PEC cells using suitable counterelectrodes (e.g., Cu/CuO) which show a periodic electrical output under chopped illumination can be constructed.

A second aspect of these studies concerns the application of reaction [1] on p-GaAs for display purposes. Several devices for active displays based on combining electrogenerated chemiluminescence and semiconductors have been described (23). A passive photoactivated display based on metal deposition on a semiconductor electrode was recently reported (24). The principles of a similar display based on precipitation of $HVBr$ at a point on a semiconductor electrode simultaneously



* Electrochemical Society Active Member.
Key words: cell, photoelectricity.

addressed by light and an electrical signal is described here.

Experimental

The single crystal p-GaAs was obtained from Atomergic Chemicals (Long Island, New York) with acceptor concentration $3 \times 10^{18} \text{ cm}^{-3}$ (Zn-doped) and was mounted as an electrode as previously described (13). The surface (face 111) was first polished with $0.5 \mu\text{m}$ alumina powder and then etched for 10-15 sec in a solution which contained $\text{H}_2\text{SO}_4:\text{H}_2\text{O}:30\% \text{H}_2\text{O}_2$ in concentration ratio 3:1:1. In some experiments single crystal p-GaP was also employed. The surface of this crystal was etched in 11M HCl for 10 sec before use.

As light sources either a 450W xenon lamp or a He-Ne laser (1.6 mW power) was used. The potentiostatic measurements were carried out with a Princeton Applied Research (PAR) potentiostat Model 173, with a cell consisting of an aqueous saturated calomel reference electrode (SCE) and a Pt wire as the counter-electrode. The electrochemical cell was provided with Pyrex windows for the passage of light. Nitrogen gas was passed through the solution before the experiments and above the solution during the experiments, since viologen radical cations are very sensitive to oxygen.

In the two electrode PEC cell experiments the voltage of the photocell between the p-GaAs and the oxide counterelectrode was measured on an x-t recorder through a voltage follower. The photocell current was measured on an x-t recorder through a current-to-voltage converter. For short time measurements of the cell short-circuit current, a Nicolet Model 1090A digital oscilloscope was used. The light intensity at the semiconductor surface was varied by means of neutral density filters.

Results

Cyclic voltammetry.—The i - V curve at a p-GaAs electrode of an unstirred solution of 0.01M HV^{2+} and 0.2M KBr at a scan rate of 100 mV/sec is shown in Fig. 1. In the dark (curve a) there was only a small current in the cathodic region with a very small peak on scan reversal. Under illumination of the p-GaAs electrode surface with the full power of the 450W xenon lamp, a larger cathodic current beginning at $\sim 0.1\text{V vs. SCE}$ appeared (curve b). Simultaneously with the appearance of this cathodic current, the precipitation of the violet HVBr was observed on the electrode surface. On reversing the scan direction, a sharp anodic current peak occurred, either in the dark or under illumination. During the passage of the anodic current the violet precipitate on the semiconductor surface disappeared. Thus the overall process is that shown in [1], with illumination necessary for the reduction process, as is usual for p-type semiconductors.

These cyclic voltammograms could be repeated many (at least 100) times with only a small change in the peak height of the cathodic photocurrents, demonstrating good chemical reversibility of the deposition and stripping process. Upon illuminating the electrode with the narrow beam of a He-Ne laser, violet spots appeared on the electrode surface at exactly the location and of the size of the laser beam spot. The response time of the process was investigated by potential steps under illumination or by irradiation with chopped light with the electrode held at a constant potential (Fig. 2). A good coloration was observed on the electrode surface within $\sim 0.5 \text{ sec}$ after illumination of the electrode. Although the intensity ratio for HVBr deposited on dark p-GaAs is not very high, the deposition was easily discernable and this type of process can be considered for use as an electrochromic display controlled by both light and electrode potential and may also be applicable to photoimaging purposes (24, 25).

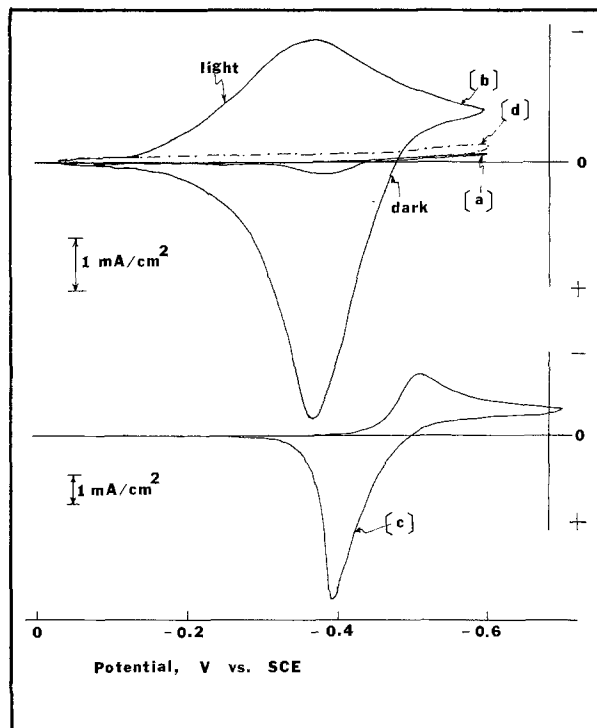


Fig. 1. Cyclic voltammograms recorded with p-GaAs at 100 mV/sec with aqueous solution containing 0.01M HVBr_2 and 0.2M KBr : (a) in the dark; (b) under illumination; (c) cyclic voltammogram recorded with the same solution on a Pt disk electrode (100 mV/sec); (d) cyclic voltammogram recorded with p-GaAs in solution containing only 0.2M KBr . Light source, 450W Xe lamp.

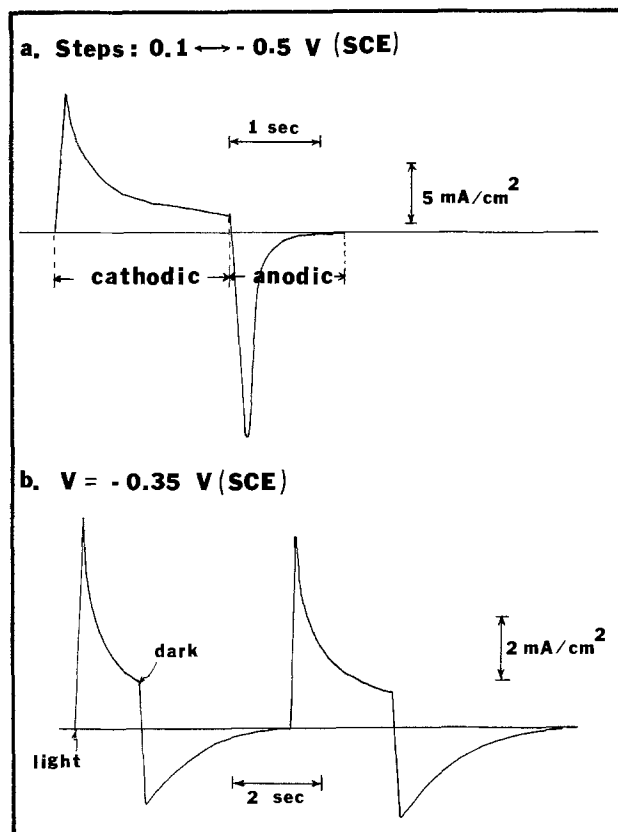


Fig. 2. Current-time transients in potential step experiments on p-GaAs in solution containing 0.01M HVBr_2 and 0.2M KBr : (a) potential stepped between -0.5 to $+0.1\text{V}$ under constant illumination; (b) the potential held at -0.35V vs. SCE under chopped illumination. Light source, 450W Xe lamp.

The cyclic voltammograms of the solution of 0.01M HV^{2+} dibromide and 0.2M KBr at a Pt electrode is shown in Fig. 1c. By comparison of this voltammogram with that obtained with p-GaAs under illumination, one can see that significant photoreduction of HV^{2+} can occur on p-GaAs at potentials ~ 400 mV less negative than on Pt. The photocurrent attributable to the reduction of protons on the p-GaAs in a KBr solution not containing HV^{2+} was very small (Fig. 1d). Photoreduction of HV^{2+} was also investigated with a p-GaP photocathode. In this case, the underpotential for the reduction process was even larger than in the case of p-GaAs, but the process was not very reversible and the back oxidation occurred only at more positive potentials than on a Pt electrode. Thus, upon scanning a p-GaP electrode over roughly the same potential region (Fig. 3), a gradual accumulation of HVBr occurred on the electrode surface and the cathodic current gradually decreased.

With the light intensity used in the experiments described above, the photoreduction current on p-GaAs was limited by the rate of diffusion of HV^{2+} to the electrode surface, as demonstrated by the proportionality of the cathodic photocurrent to the square root of the scan rate, v (Fig. 4). Moreover, as shown in Fig. 5, while the potential for photocurrent onset and the current at the foot of the wave depended upon the light intensity, at more negative potentials the maximum current was almost independent of intensity and was limited by the rate of diffusion of HV^{2+} to the electrode surface.

PEC cells.—Since the photoreduction of HV^{2+} occurs on p-GaAs with an underpotential of about 400 mV while the back-oxidation in the dark on p-GaAs occurs at the same potentials as on Pt, one can envision a sort of solar storage cell composed of a p-GaAs and another chemically reversible electrode (Fig. 6). This counterelectrode should have a redox potential between the potential for the photoreduction of HV^{2+} on p-GaAs and the potential for oxidation of HVBr in the dark (Fig. 6c). In such a cell, when light irradiates the p-GaAs, it is the cathode of the cell and HVBr precipitates (Fig. 6a). The HVBr precipitate on the p-GaAs is stable at open circuit, and can be oxidized in the dark back to the original HV^{2+} , while the counterelectrode becomes the cathode of the cell (Fig. 6b). Three counterelectrodes with redox potentials suitable for such a photocell, Cu/Cu-oxide, $H_xNb_2O_5/Nb_2O_5$, and Ni/Ni-oxide, were used. The open-circuit voltages, and the short-circuit currents of such cells composed of p-GaAs, and the three counterelectrodes under periodic illumination are shown in Fig. 7. The relative polarity of the p-GaAs shows the expected changes (Fig. 6) as the semiconductor is subjected to the chopped beam. In

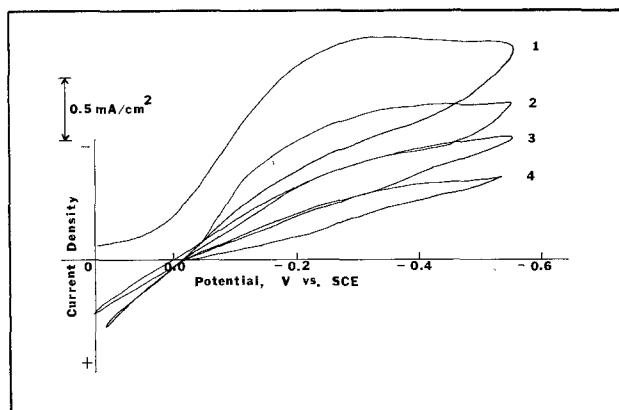


Fig. 3. Consecutive cyclic voltammograms at irradiated p-GaP solution containing 0.01M $HVBr_2$ and 0.2M KBr. Scan rate, 100 mV/sec. Light source, 450W Xe lamp.

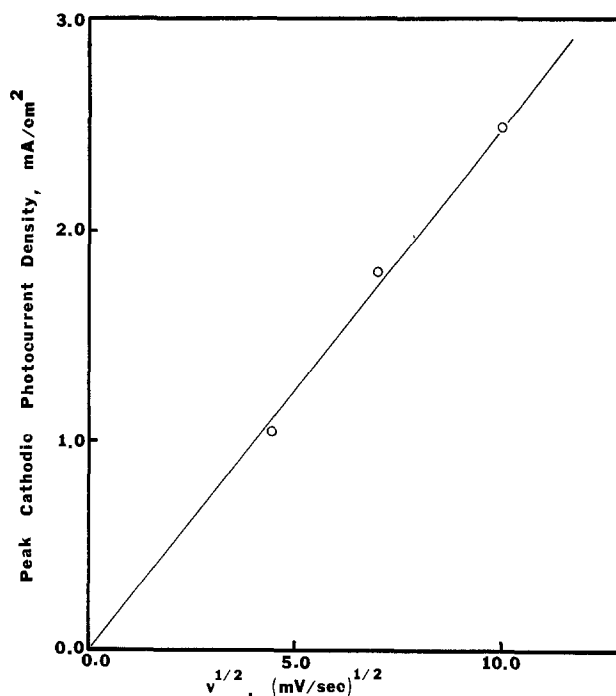


Fig. 4. Scan rate v dependence of the peak cathodic photocurrent at irradiated p-GaAs in a solution containing 0.1M $HVBr_2$ and 0.2M KBr. Light source, 450W Xe lamp.

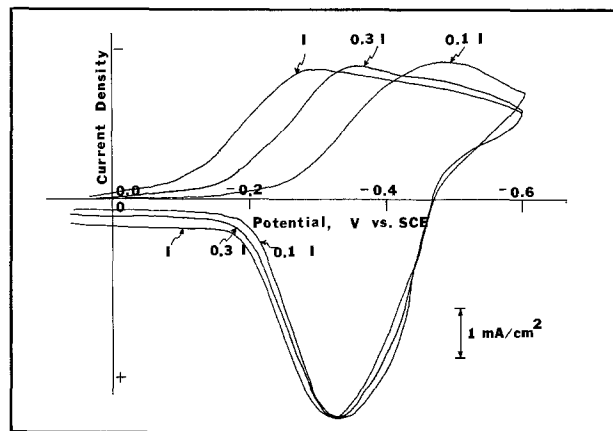


Fig. 5. Cyclic voltammograms at p-GaAs in solution of Fig. 4 with different relative light intensities. Light source, 450W Xe lamp.

the photocharged condition, the HVBr remained on the electrode surface and the open-circuit voltage was stable for at least 2 hr. The maximum open-circuit voltages were found with the Cu counterelectrode with potential excursions of up to 0.4V observed (Fig. 7A). The short-circuit currents of these cells are shown in Fig. 7B. In the light, current flows in the external circuit during which precipitation of the purple HVBr on the surface of the p-GaAs occurs. The current decays almost to zero in about 10 sec because a thick opaque film of HVBr builds up on the electrode surface and the HV^{2+} concentration is depleted near the electrode surface. The cell can be regarded as a storage battery. The precipitate of HVBr can be stored on the p-GaAs, and then oxidized in the dark to yield a current in a direction opposite to that observed under illumination. Obviously, the capacity of such a cell is very small; the maximum charge in the form of HVBr which can precipitate on the p-GaAs before the current drops to zero is about 10 mC/cm². Alternately, the cell can be considered as a type of a-c device under periodic illumination. In this mode the p-GaAs cell performance was very stable with all three cells and no deteriora-

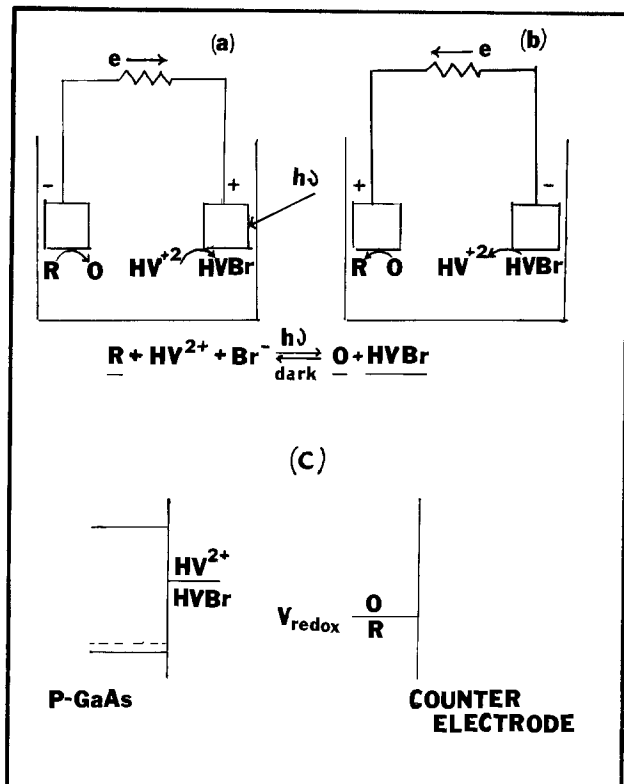


Fig. 6. Schematic description of the HVBr_2 -based photoelectrochemical cell operating: (a) under illumination (photocharge); (b) in the dark (discharge); (c) relative energy levels and potentials at the counterelectrode, and at the p-GaAs, required for operation of the cell shown in (a) and (b).

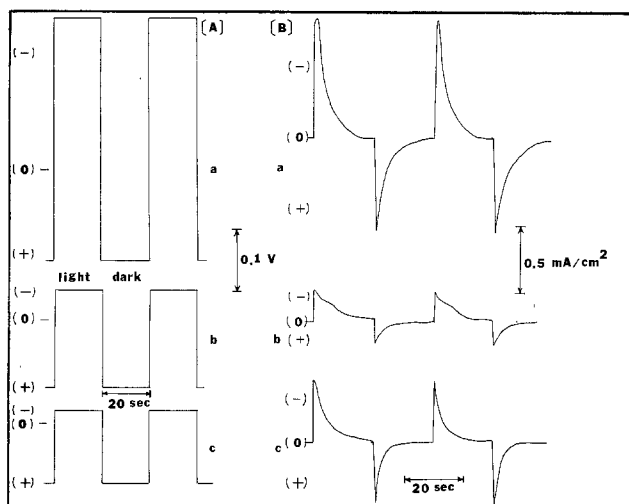


Fig. 7. (A) Open-circuit potentials and (B) short-circuit current under chopped illumination for the cells: (a) p-GaAs/HVBr/HVBr₂, KBr/Cu; (b) p-GaAs/HVBr/HVBr₂, KBr/Nb₂O₅; (c) p-GaAs/HVBr/HVBr₂, KBr/Ni. Light source, 450W Xe lamp.

tion or decrease in the current was observed after 4 days of continuous operation with 20 sec period illumination by the 450W xenon lamp. The open-circuit voltage, the current, and the amount of charge involved were all reproducible and stable to within 10%. The variation of the initial short-circuit current on light intensity under irradiation with the He-Ne laser (1.6 mW power) was examined with all three cells (Fig. 8). A linear dependence of the short-circuit current on light intensity was observed at the lower intensity levels. In the case of Cu counterelectrode, saturation of the current occurred at $\sim 2.5 \text{ mA/cm}^2$. With Ni as the counterelectrode, no saturation of the short-circuit

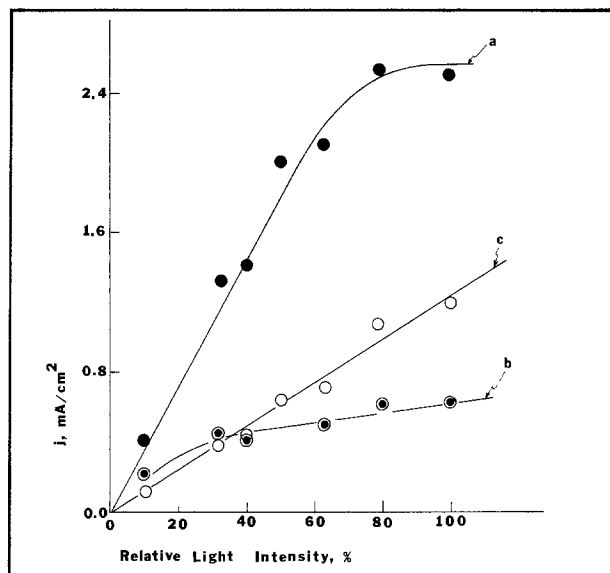


Fig. 8. Initial short-circuit photocurrents for the three cells described in Fig. 7 as a function of light intensity (He-Ne laser).

current occurred even at the highest intensity used, while with Nb_2O_5 as a counterelectrode a linear dependence was observed only at very low light levels. In all cases, the currents obtained were the highest for the Cu electrode. The current saturation observed in this case can probably be ascribed to the limitation by diffusion of HV^{2+} to the p-GaAs surface, since the magnitude of the saturation current density in Fig. 8a is similar to the limiting current found in the voltammograms, Fig. 1b, with identical HV^{2+} concentrations. With the Nb_2O_5 electrode, the short-circuit current reaches saturation earlier than in the case of Cu and was clearly limited by the oxidation reaction taking place on the Nb_2O_5 electrode. The maximum quantum efficiencies for the photocells were calculated from the slopes of the linear portions of the curves in Fig. 8, yielding values of $\sim 20\%$ (Cu), $\sim 10\%$ (Ni), and 2% (Nb_2O_5).

Discussion

The behavior of the p-GaAs/solution interface and a rationalization of the observed PEC cell behavior can be presented in terms of the surface controlled model for GaAs proposed elsewhere (26) (Fig. 9). In this model, the Fermi level of the semiconductor is pinned by surface states located about one-third of the way up in the gap (i.e., $\sim 0.4\text{-}0.5\text{V}$ above the valence band-edge) (Fig. 9a). The maximum open-circuit photopotential, V_{on} , observed under intense illumination would then be $\sim 0.4\text{V}$, and the open-circuit photovoltage would be the difference between V_{on} and V_{redox} of the counterelectrode reaction (Fig. 9b). In the dark after deposition of HVBr, oxidation of HVBr occurs via the surface states and the p-GaAs essentially behaves as an inert contact to the layer (Fig. 9c). The counterelectrode in a two-electrode PEC cell must have a redox potential between V_{on} and that of the $\text{HV}^{2+}/\text{HVBr}$ system, so that only couples in a relatively narrow range of potentials are suitable.

Storage cells based on this type of electrode reaction will necessarily have small capacities, unless films which deposit on the electrode surface can be found which are both transparent to the wavelengths absorbed by the semiconductor and are electrical conductors. Moreover, higher concentrations of the soluble form are required to prevent mass transfer limitations to the photocurrent even before film formation causes current decay. Such cells may, however, find application in very low capacity batteries or as a-c devices under periodic illumination.

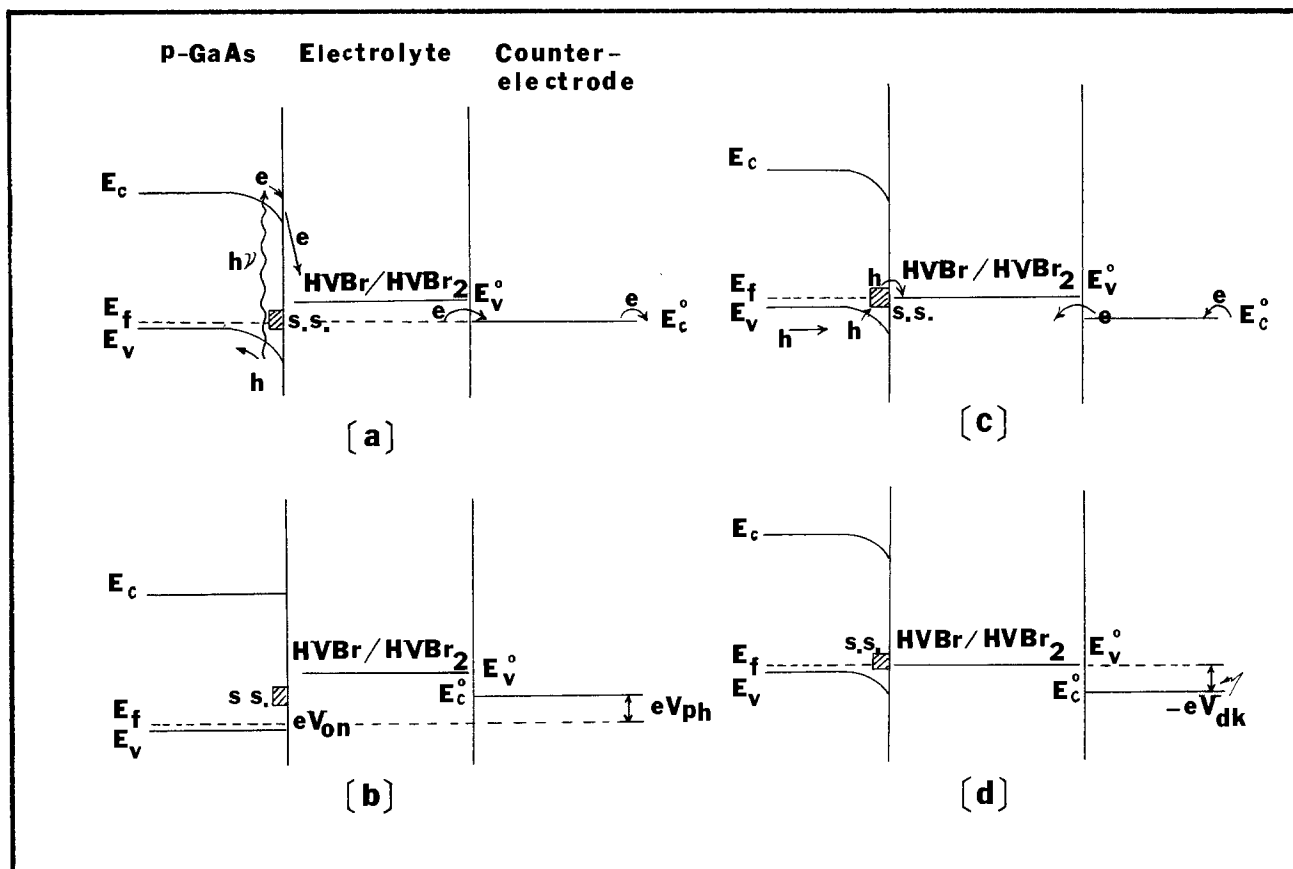


Fig. 9. Schematic description of the energy levels of the HVBr_2 -based photoelectrochemical cells in the light at (a) short circuit, no HVBr film on p-GaAs initially, and (b) open circuit, no HVBr film on p-GaAs initially. In the dark at (c) short circuit, with HVBr film on p-GaAs, and (d) open circuit, with HVBr film on p-GaAs. E_c = conduction band edge of p-GaAs; E_f = Fermi energy of p-GaAs; E_v = valence band edge of p-GaAs; s.s. = surface state; E_v° = energy corresponding to the redox potential of heptyl viologen couple; E_c° = energy corresponding to the redox potential of the counterelectrode; V_{ph} = open-circuit voltage in the light; V_{dk} = open-circuit voltage in the dark; V_{on} = onset potential of photocurrent.

The application of such a system to produce a display addressable both optically and electrically (a photoelectrochromic display) is perhaps of greater interest (Fig. 10). One can envision the operation of such a device in which a light beam produces a raster on the electrode surface, and the electrode potential is switched to (i) the deposition potential (coloring), (ii) open circuit (hold), or (iii) the stripping potential (erase). The advantage of such a display, compared to the more familiar electrochromic ones, is that only two leads need be provided to the cell rather than the multiple leads and complicated electrical addressing required for a large screen or multi-character display. While the contrast ratio for HVBr on GaAs is not very good, in principle a wide bandgap semiconductor (e.g., > 3 eV), which would appear white and would be addressed with an ultraviolet beam could be employed. For a display involving rapid scanning, a system with a faster response time is also required. Similar concepts involving semiconductors and metal depositions for photoimaging have been reported (24, 27).

Acknowledgment

The support of this research by the Office of Naval Research, which is a joint project with Professor A. B. P. Lever of York University, and the National Science Foundation is gratefully acknowledged.

Manuscript submitted July 25, 1979; revised manuscript received Sept. 17, 1979.

Any discussion of this paper will appear in a Discussion Section to be published in the December 1980 JOURNAL. All discussions for the December 1980 Discussion Section should be submitted by Aug. 1, 1980.

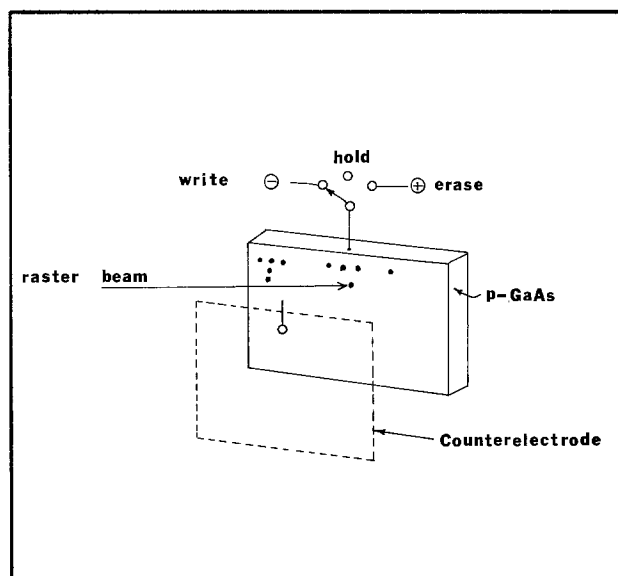


Fig. 10. Schematic description of a photoelectrochromic display device based on HVBr_2 reduction on p-GaAs electrode.

Publication costs of this article were assisted by The University of Texas at Austin.

REFERENCES

1. R. Memming, in "Electroanalytical Chemistry," Vol. 11, A. J. Bard, Editor, pp. 1-84, Marcel Dekker, New York (1979).
2. A. J. Nozik, *Ann. Rev. Phys. Chem.*, **29**, 189 (1978).
3. H. Gerischer, *J. Electroanal. Chem.*, **58**, 263 (1979).
4. A. J. Bard, *J. Photochem.*, **10**, 59 (1979).

5. D. Laser and A. J. Bard, *This Journal*, **123**, 1027 (1976).
6. T. Inoue, T. Watanabe, A. Fujishima, K. Honda, and K. Kohayakawa, *ibid.*, **124**, 719 (1977).
7. A. B. Ellis, J. M. Bolts, S. W. Kaiser, and M. S. Wrighton, *J. Am. Chem. Soc.*, **99**, 2848 (1977).
8. R. Memming, in "Proceedings of Conference on Electrochemistry and Physics of Semiconductor-Liquid Interface under Illumination," A. Heller, Editor, pp. 38-48, Airlie, Virginia.
9. J. M. Bolts, A. B. Ellis, K. D. Legg, and M. S. Wrighton, *J. Am. Chem. Soc.*, **99**, 4826 (1977).
10. G. Hodes, J. Manassen, and D. Cahen, *Nature*, **261**, 403 (1976).
11. J. Manassen, G. Hodes, and D. Cahen, *This Journal*, **124**, 533 (1977).
12. R. N. Noufi, P. A. Kohl, and A. J. Bard, *ibid.*, **125**, 375 (1978).
13. P. A. Kohl and A. J. Bard, *ibid.*, **126**, 59, 603 (1979).
14. B. A. Parkinson, A. Heller, and B. Miller, *ibid.*, **126**, 954 (1979).
15. R. Memming, *ibid.*, **125**, 117 (1978).
16. H. Yoneyama, H. Sakamoto, and H. Tamura, *Electrochim. Acta*, **20**, 341 (1975).
17. R. E. Malpas, K. Itaya, and A. J. Bard, *J. Am. Chem. Soc.*, **101**, 2535 (1979).
18. M. Tomkiewicz and J. M. Woodall, *This Journal*, **124**, 1436 (1977).
19. P. A. Kohl and A. J. Bard, *ibid.*, **126**, 59 (1979).
20. C. J. Schoot, J. J. Ponjee, H. T. Van Dam, R. A. Van Doorn, and P. T. Bolneijn, *Appl. Phys. Lett.*, **23**, 64 (1973).
21. R. J. Jasinski, *This Journal*, **124**, 637 (1977).
22. J. Bruinind and C. G. A. Kregting, *ibid.*, **125**, 1397 (1978).
23. J. D. Luttmer and A. J. Bard, *ibid.*, **126**, 414 (1979).
24. T. Inoue, A. Fujishima, and K. Honda, *Chem. Lett.*, **11**, 1197 (1978).
25. M. Yamana, *Appl. Phys. Lett.*, **29**, 571 (1976).
26. Fu-Ren F. Fan and A. J. Bard, *J. Am. Chem. Soc.*, Submitted.
27. G. L. McLeod, *Photogr. Sci. Eng.*, **13**, 93 (1969).

Semiconductor Electrodes

XXIII. The Determination of Flatband Potentials from Differential Stress Measurements with Attached Piezoelectric Detectors

Lee J. Handley and Allen J. Bard*

Department of Chemistry, The University of Texas at Austin, Austin, Texas 78712

ABSTRACT

A new method for the determination of the flatband potential, V_{fb} , of semiconductor electrodes by differential stress measurements of a piezoelectric detector bonded to the semiconductor is reported. Values of V_{fb} for single crystal n-SrTiO₃ and p-GaAs, and polycrystalline n-TiO₂ in 1N NaOH and 1N H₂SO₄ are shown to be in good agreement with previously determined values. Possible application of such measurements to the study of surface changes and breakdown is suggested.

The flatband potential, V_{fb} , of a semiconductor/electrolyte solution interface is an important parameter in explaining the electrochemical characteristics of the system in the dark and under illumination (1-3). V_{fb} is a function of both the semiconductor material and the solution composition, and is measured to determine the locations of the semiconductor valence and conduction bandedges with respect to solution energy levels. Usually V_{fb} -values are determined by direct measurements of the space charge differential capacity, C_{sc} , (Schottky-Mott plots) or by determinations of the open-circuit photopotential (or the potential for the onset of the photocurrent) under intense irradiation. Both of these methods often suffer from difficulties which result in large uncertainties in the V_{fb} -values estimated by them. In C_{sc} measurements the Schottky-Mott plots are frequently nonlinear and yield V_{fb} -values which are functions of the frequency used. This has been attributed to the effect of surface states and other factors (4). The estimation from photopotentials can also be perturbed by the existence of surface states or intermediate levels as well as by recombination effects which, for an n-type semiconductor, will yield onset photopotentials less negative than the actual V_{fb} -value (5).

V_{fb} can also be determined by observing the voltammetric response in the dark of couples spanning a potential range above and below V_{fb} (5, 6). Such measurements usually yield a V_{fb} -value with considerable uncertainty and may also be perturbed by electron transfers occurring via surface states. In this paper, we

propose a method for the determination of V_{fb} , based on the measurement of differential stress (with a piezoelectric crystal attached to the semiconductor electrode) as a function of potential, which is experimentally simple and theoretically direct.

There have been several previous reports of the application of piezoelectric materials (which are materials which produce a potential when placed under a stress) to measurements at metal electrodes (7-10).

From a modified form of the Lipmann equation that was used by Gokhstein (7) for metal electrodes, the differential surface stress ($\partial\sigma_s/\partial E$) is related to the surface charge density (q) and deformation by

$$\partial\sigma_s/\partial E = -q - \partial q/\partial\theta \quad [1]$$

where θ is the ratio of the surface area before and after deformation. For an ideally polarized electrode, the term $\partial q/\partial\theta$ is zero, since the charge density does not depend upon the deformation of the electrode surface. Even for nonpolarizable electrodes this term may be small and is equal to zero at the flatband potential, because at V_{fb} there is no charge on the electrode.

For semiconductor electrodes, the excess charge q is distributed in the space charge region. At potentials negative of the flatband potential, the space charge region has an excess of electrons and the differential stress measurements will be positive. At the flatband potential there is no excess charge and the differential stress is zero. For potentials positive of the flatband potential there is an accumulation of holes in the space charge region and the differential stress will be negative. Thus, as implied by Eq. [1], the differential stress tracks the space charge, and the intercept of the dif-

* Electrochemical Society Active Member.
Key words: piezoelectricity, capacitance.

ferential stress as a function of potential will be at the flatband potential.

Experimental

The experimental technique used for semiconductor electrodes is the same as the technique developed for metal electrodes (8-10). Three electrodes were prepared by bonding a ceramic piezoelectric disk (Edo Western Corporation, Salt Lake City, Utah) to the back of the semiconductor with Devcon 5-minute epoxy cement. The piezoelectric disk was electrically insulated from the semiconductor and the electrolyte with silicone cement (Fig. 1). The face next to the semiconductor was maintained at ground potential to insure that a-c potentials on the semiconductor would not affect the potential measured across the piezoelectric disk.

The three semiconductors studied were single crystal n-type SrTiO_3 (2 mm thick), which had been reduced in hydrogen at 800°C for 5 hr; single crystal p-type GaAs (1 mm thick), which was doped with Zn; and polycrystalline n- TiO_2 (0.2 mm thick), which was prepared by oxidizing titanium foil in an open flame. The electrolytes used were stock solutions of 1N NaOH and 1N H_2SO_4 .

The measurement procedure generally followed that used with metal electrodes (8-10). An a-c modulating signal superimposed on a potential ramp generated the piezoelectric signal (see Fig. 2). For this experiment both the in-phase ($\phi = 0^\circ$) and quadrature ($\phi = 90^\circ$) piezoelectric signals were recorded simultaneously for each potential scan.

Results and Discussion

Separation of quadrature and in-phase signals.—If the semiconductor/electrolyte interface is represented as an equivalent circuit composed of a resistor and capacitor in series (where the resistor represents the bulk resistance of the semiconductor and the capacitance is that of the space charge region), then the a-c modulation voltage will produce two components of electrode stress. The first, attributable to the IR heating caused by the a-c current that flows through the bulk of the semiconductor, is proportional to the potential difference across the bulk resistance. It will be in-phase and proportional to the modulating signal amplitude. The second is due to the surface stress caused by a change in the charge density in the space charge region. This component is proportional to the potential difference across the space charge capacitance and will be 90° out of phase with, but still proportional to, the modulating signal. The assumption has been made that $\omega RC \gg 1$, so that $\tan^{-1}(\omega RC) \sim 90^\circ$. All of the data supports this assumption. This proportionality of the in-phase and quadrature signals to the modulating signal amplitude is shown in Fig. 3. Under these conditions, the in-phase signal is about an order of magnitude larger than the quadrature signal.

The determination of flatband potentials.—The in-phase signal should always have the same sign at all electrode potentials while the quadrature signal should change sign at the flatband potential. This is shown in Fig. 4 for n- SrTiO_3 . At very positive potentials ($\sim +11\text{V}$) the quadrature signal again changes sign, probably because of a breakdown phenomenon since this potential corresponds to the onset of d-c anodic current.

The quadrature signals near the flatband potentials for n- SrTiO_3 and n- TiO_2 in 1N H_2SO_4 and 1N NaOH are shown in Fig. 5 and 6. The V_{fb} -values determined from such differential stress measurements are listed in Table I. These results agree very well with values previously reported (3, 11, 12) and have an uncertainty of only ± 25 mV or less, which is better than the usual methods for determining flatband potentials. The pH shift for these materials is near 59 mV/pH unit, as expected (3, 11, 12).

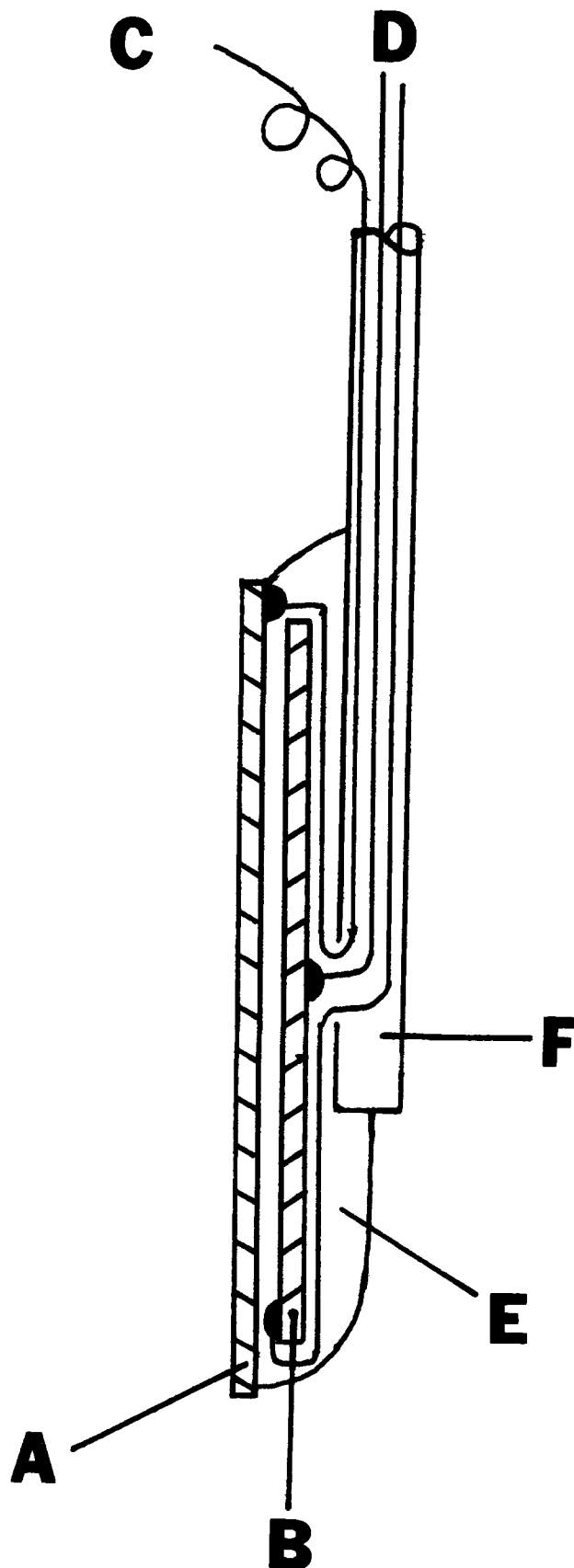


Fig. 1. The working electrode. A: semiconductor; B: piezoelectric ceramic disk ($\phi = 16$ mm; thickness = 0.2 mm); C: lead to potentiostat; D: leads from piezoelectric to lock-in amplifier pre-amplifier; E: epoxy cement; F: Pyrex glass tube.

Frequency dependence.—The frequency dependence of the differential stress measurements is shown in Fig. 7 for the quadrature signal at three different frequencies and in Fig. 8 for the in-phase signal at the

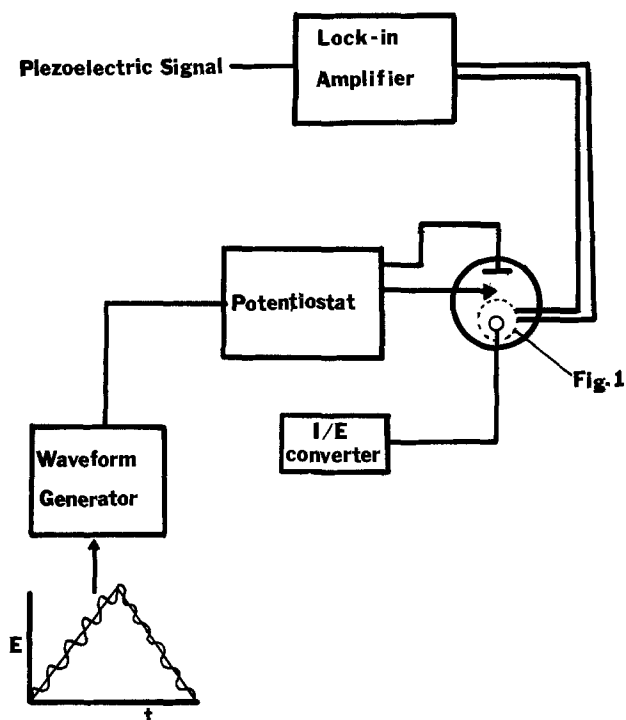
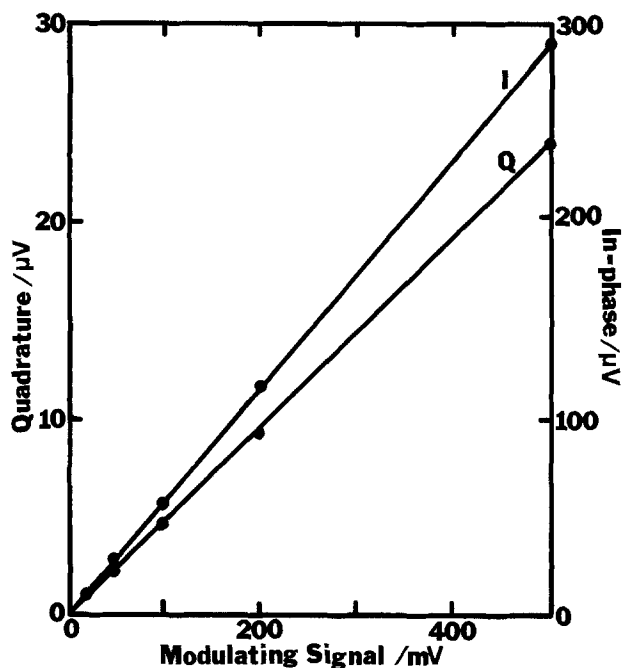
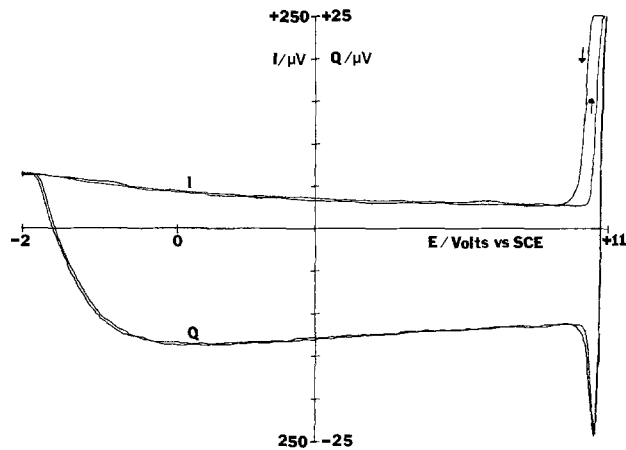
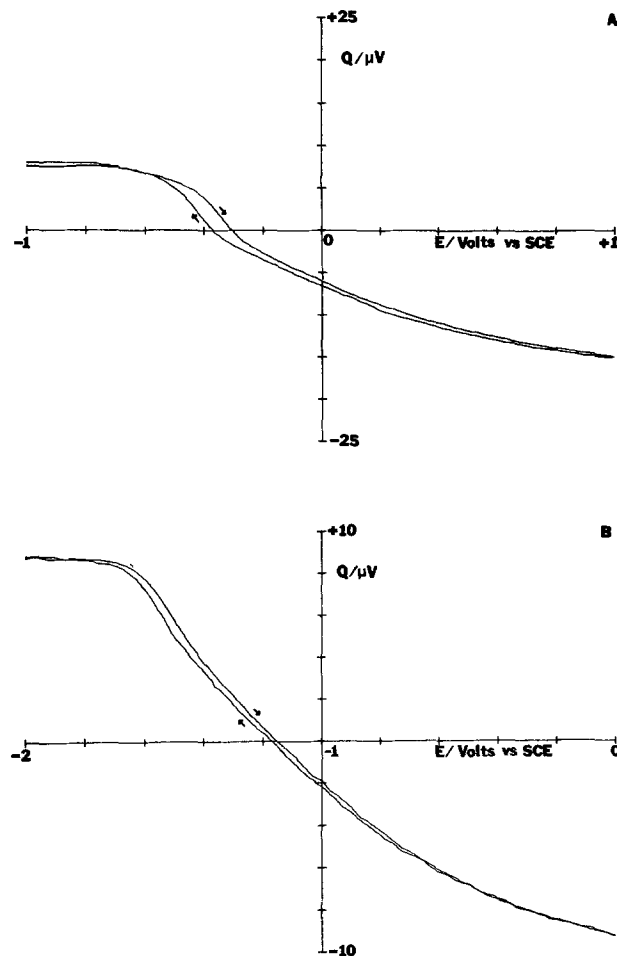


Fig. 2. Block diagram of the apparatus

Fig. 3. (A) In-phase and (B) quadrature differential stress measurements for n-SrTiO₃ in 1N NaOH at 0V vs. SCE with a modulating frequency of 1 kHz.

same three frequencies for n-SrTiO₃ in 1N H₂SO₄. The capacitive impedance of the space charge region increases with a decrease in frequency, therefore, increasing the absolute value of the quadrature signal at potentials other than the flatband potential. The intercepts for all three frequencies are within a range of 40 mV. Since the IR stress (in-phase) signal is an order of magnitude larger than the space charge (quadrature) signal, the changes in the quadrature signal have only a small effect on the in-phase signal.

Effects of chemical changes at the electrode surface.—The quadrature differential stress measurements for p-GaAs are shown in Fig. 9 and 10 for 1N H₂SO₄ and 1N NaOH, respectively. The extent of frequency de-

Fig. 4. In-phase (*I*) and quadrature (*Q*) differential stress signals for n-SrTiO₃ in 1N NaOH for cyclic potential sweep from -2 to +11V vs. SCE at 20 mV/sec with a modulating signal of 50 mV at 1 kHz. The in-phase signal scale is an order of magnitude larger than that for the quadrature signal.Fig. 5. A: Quadrature differential stress measurement for n-SrTiO₃ in 1N H₂SO₄ from -1 to +1V vs. SCE with a modulating signal of 50 mV at 1 kHz. B: Quadrature differential stress measurement for n-SrTiO₃ in 1N NaOH from -2 to 0V vs. SCE with a modulating signal of 50 mV at 1 kHz.

pendence of intercept was similar to that for n-SrTiO₃. The V_{fb} -values, listed in Table I, are in reasonable agreement with previous measurements (13). An interesting point to note is the difference in hysteresis for p-GaAs for the acidic and alkaline electrolytes when the potential is scanned between +1.5 and -0.5V vs. SCE. The data for 1N H₂SO₄ show almost no hysteresis, while there is approximately 0.1V difference

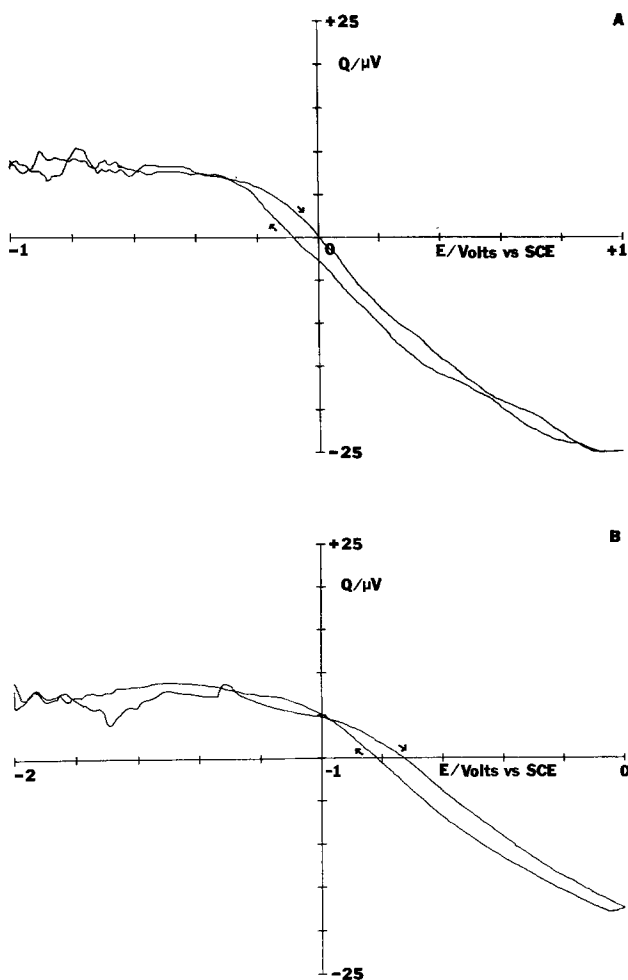


Fig. 6. A: Quadrature differential stress measurement for n-TiO₂ in 1N H₂SO₄ from -1 to +1V vs. SCE with a modulating signal of 50 mV at 1 kHz. B: Quadrature differential stress measurement for n-TiO₂ in 1N NaOH from -2 to 0V vs. SCE with a modulating signal of 50 mV at 1 kHz.

between the forward and reverse sweeps for V_{fb} in 1N NaOH. This can probably be attributed to instability of p-GaAs in alkaline solutions at potentials positive of the flatband potential. When the potential was scanned from -0.4 to +1V vs. SCE, the hysteresis was still present (Fig. 11). However, for a potential scan from -0.4 to 0V, the hysteresis near V_{fb} disappeared (Fig. 12). This suggests that differential stress measurements may also be useful for studying stability and changes in the surface of semiconductor electrodes.

Effects of illumination.—Since the space charge region will have an excess of majority carriers on one side of the flatband potential, and an excess of negative charge on the other side, the effects of illumina-

Table I. Comparison of V_{fb} -values obtained by differential stress measurements to previously reported results.

Semiconductor	This work		Previous measurements		
	Electrolyte	V_{fb} (V vs. SCE)	pH ^a	V_{fb} (V vs. SCE)	Reference
n-SrTiO ₃	1N H ₂ SO ₄	-0.35	0.0	-0.30	(11)
	1N NaOH	-1.15	13.3	-1.19	(3)
			13.5	-1.10	(11)
n-TiO ₂	1N H ₂ SO ₄	-0.05	0.0	-0.01	(11, 14)
	1N NaOH	-0.80	13.3	-0.90	(3, 12)
			13.5	-0.80	(11, 14)
p-GaAs	1N H ₂ SO ₄	0.5	2.1	0.10	(13)
	1N NaOH	-0.30	9.2	-0.24	(13)

^a As reported or estimated to ±0.1 pH unit.

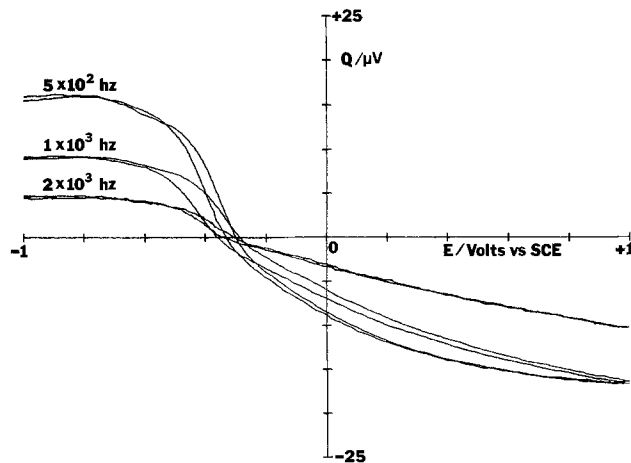


Fig. 7. Quadrature differential stress measurements for n-SrTiO₃ in 1N H₂SO₄ from -1 to +1V vs. SCE. The modulating signal was 50 mV at the three frequencies indicated.

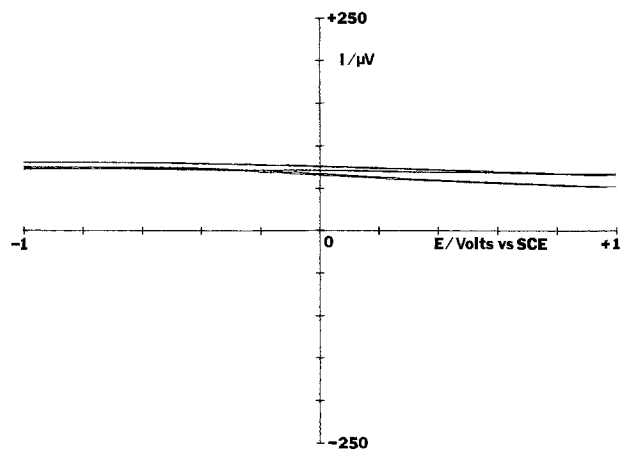


Fig. 8. In-phase differential stress measurements under the same conditions as Fig. 7.

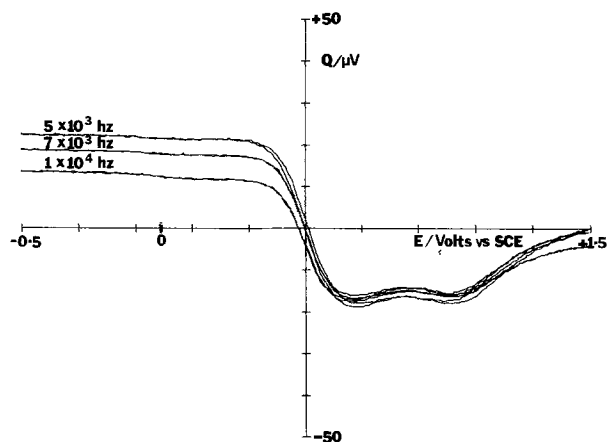


Fig. 9. Quadrature differential stress measurements for p-GaAs in 1N H₂SO₄ from -0.5 to +1.5V vs. SCE. The modulating signal was 50 mV at the three frequencies indicated.

tion should be different for potentials positive and negative of V_{fb} . For p-GaAs at potentials more positive than V_{fb} , there is an accumulation of majority carriers in the space charge region and illumination should not substantially change the differential stress measurements. For potentials negative of V_{fb} the bands are bent downwards, and the effects of illumination should be much larger. The differential stress measurements for p-GaAs in the dark and under

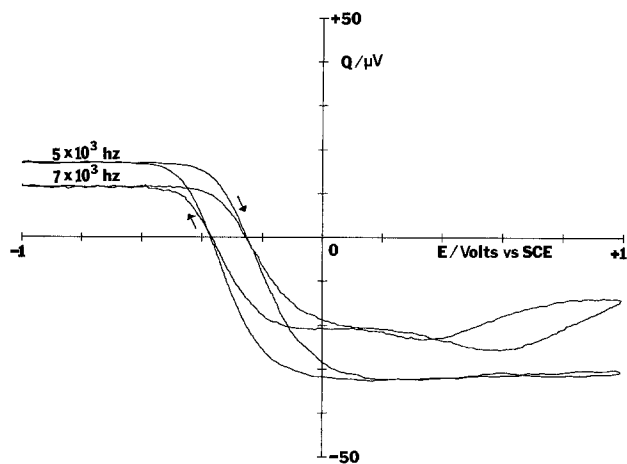


Fig. 10. Quadrature differential stress measurements for p-GaAs in 1N NaOH from -1 to $+1$ V vs. SCE. The modulating signal was 50 mV at the two frequencies indicated.

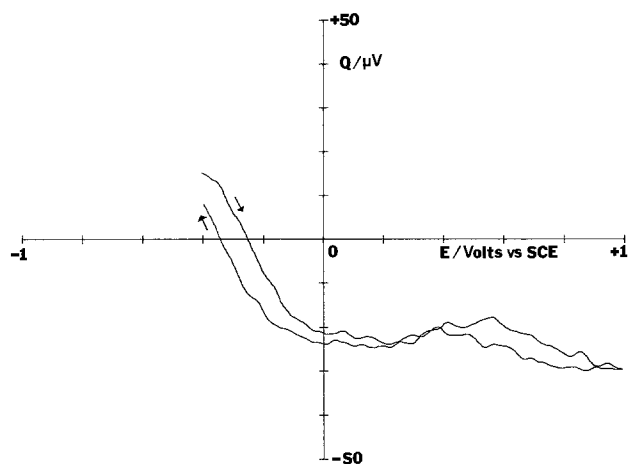


Fig. 11. Quadrature differential stress measurements for p-GaAs in 1N NaOH from -0.4 to $+1$ V vs. SCE with a modulating signal of 50 mV at 5 kHz.

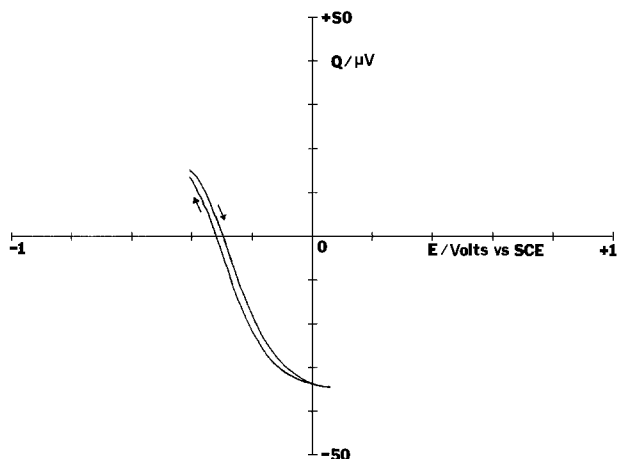


Fig. 12. Quadrature differential stress measurement for p-GaAs in 1N NaOH from -0.4 to 0 V vs. SCE with a modulating signal of 50 mV at 5 kHz.

illumination (Fig. 13) agree with this prediction. The effect of illumination is to decrease the extent of band bending, thereby reducing the surface stress.

Conclusions

Preliminary experiments have demonstrated that V_{fb} -values of both p- and n-type semiconductor electrodes, single crystal and polycrystalline, can be determined from differential stress measurements as a

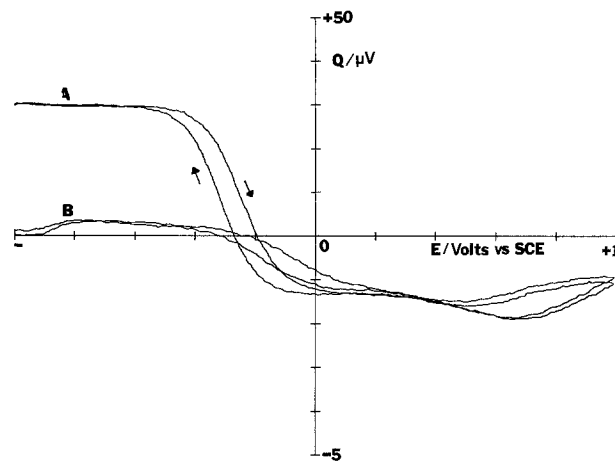


Fig. 13. Quadrature differential stress measurements for p-GaAs in 1N NaOH from $+1$ to -1 V vs. SCE: (A) in dark and (B) under illumination. The modulating signal was 50 mV at 5 kHz.

function of potential. The only assumption that has been made is that a semiconductor electrode can be represented as an equivalent circuit consisting of a resistor and capacitor in series. The V_{fb} -values from the differential stress measurements are in excellent agreement with independent previous measurements and show the expected pH shift of 59 mV/pH unit for n-SrTiO₃ and n-TiO₂.

In addition to determination of V_{fb} , the sharp change in the differential stress observed near the breakdown potential may be of use in elucidating the phenomena occurring in this region. As seen in Fig. 4, the quadrature signal has a sharp minimum near the breakdown potential; there is definite hysteresis in the in-phase signal but none for the quadrature signal. The dependence of the differential stress signals on frequency and illumination is in qualitative agreement with the experimental results. Preliminary results also suggest that differential stress measurements may be useful in studying the stability and changes in the surface of semiconductor electrodes. Work is in progress to obtain a better understanding for these latter effects as well as extending V_{fb} measurements to other semiconductors and other solvent/electrolyte systems.

Acknowledgment

The support of the research by the National Science Foundation is gratefully acknowledged. We are indebted to Drs. Rolf Hülhagen and Richard Malpas for helpful suggestions during the course of this research.

Manuscript submitted July 6, 1979; revised manuscript received Aug. 27, 1979.

Any discussion of this paper will appear in a Discussion Section to be published in the December 1980 JOURNAL. All discussions for the December 1980 Discussion Section should be submitted by Aug. 1, 1980.

Publication costs of this article were assisted by The University of Texas at Austin.

REFERENCES

1. R. Memming, in "Electroanalytical Chemistry," Vol. 11, A. J. Bard, Editor, pp. 1-84, Marcel Dekker, New York (1979).
2. H. Gerischer, in "Physical Chemistry—An Advanced Treatise," Vol. IXA, H. Eyring, D. Henderson, and W. Jost, Editors, p. 463, Academic Press, New York (1970).
3. M. A. Butler and D. S. Ginley, *This Journal*, **125**, 228 (1978).
4. E. C. Dutoit, F. Cordon, and W. P. Gomes, *Ber. Bunsenges. Phys. Chem.*, **80**, 475 (1976).
5. P. A. Kohl and A. J. Bard, *J. Am. Chem. Soc.*, **99**, 7531 (1977).

6. S. N. Frank and A. J. Bard, *ibid.*, **97**, 7427 (1975).
7. A. Ya. Gokhshtein, *Sov. Electrochem. Engl. Trans.*, **7**, 13 (1971).
8. R. E. Malpas, R. A. Fredlein, and A. J. Bard, *J. Electroanal. Chem. Interfacial Electrochem.*, **98**, 171 (1979).
9. R. E. Malpas, R. A. Fredlein, and A. J. Bard, *ibid.*, **98**, 339 (1979).
10. R. E. Malpas and A. J. Bard, *Anal. Chem.*, In press.
11. J. F. McCann and L. J. Handley, Submitted to Faraday Society Meeting (1979).
12. Y. G. Berube and P. L. DeBruyn, *J. Colloid. Interface Sci.*, **27**, 305 (1968).
13. W. H. Laflere, R. L. Van Meirhaeghe, F. Cardon, and W. P. Gomes, *Surf. Sci.*, **59**, 401 (1976).
14. H. Yoneyama, H. Sakamoto, and H. Tamura, *Electrochim. Acta*, **20**, 341 (1975).

Application of A-C Techniques to the Study of Lithium Diffusion in Tungsten Trioxide Thin Films

C. Ho,* I. D. Raistrick,* and R. A. Huggins*

Stanford University, Stanford, California 94305

ABSTRACT

The small signal a-c impedance of the cell

Li|LiAsF₆ (0.75M) in propylene carbonate|
Li_yWO₃ thin film on tin oxide covered glass substrate

has been measured at room temperature as a function of frequency from 5×10^{-4} Hz to 5×10^3 Hz at various open-circuit voltages. The diffusion equations have been solved for the appropriate finite boundary conditions, and analysis of the impedance data by the complex plane method yields values for the chemical diffusion coefficient, the component diffusion coefficient, the partial ionic conductivity of lithium, and the thermodynamic enhancement factor for Li_yWO₃ as a function of *y*. The films of WO₃ were prepared by vacuum evaporation and were largely amorphous to x-rays. The chemical diffusion coefficient has a value of 2.4×10^{-12} cm²/sec at *y* = 0.1, increasing to 2.8×10^{-11} cm²/sec at *y* = 0.26. At short times (*t* < 0.5 sec) the interfacial charge transfer reaction is important, but at longer times the rate of lithium injection is determined by the diffusion kinetics.

Considerable interest has developed recently in the possibility of fabricating display devices based on the electrochemical injection of metal or hydrogen atoms into transition metal oxides, usually WO₃. The reaction may be written



For each atom injected an electron enters the conduction band of the host oxide and a deep blue coloration develops. At the same time, the electronic conductivity of the oxide rapidly increases. The range of solid solubility of M in WO₃ may be quite extensive; typically a *y* value of about 0.1-0.2 is necessary for good optical contrast. The activity of M in M_yWO₃, and hence the electrode potential of the electrochromic oxide will vary continuously with *y* as long as a single phase solid solution is formed. If the reaction proceeds rapidly and reversibly, then the metal atoms may be repeatedly injected and removed by controlling the electrode potential of the oxide electrode with respect to a counterelectrode which acts as a source and sink of M.

Although reactions of this type have been known for several years, few data are available on basic electrochemical parameters, such as diffusion coefficients of M in the oxide or exchange current densities, even though the eventual response time of the device will be largely determined by these parameters. It is not even clear whether the rate of injection is limited by diffusion or by charge transfer at times of interest for display applications.

* Electrochemical Society Active Member.

Key words: diffusion, WO₃, lithium injection, electrochromic films, a-c technique.

This paper describes a steady-state a-c technique which may be used to determine the rate-limiting process and the important kinetic parameters of an electrochromic system. It is illustrated by results obtained for the lithium-tungsten trioxide system.

Although any of several transient techniques could, in principle, be used to study this system, an a-c method was chosen since it seemed likely that, using complex plane methods, data analysis could be much simplified, especially since semi-infinite diffusion conditions cannot be assumed for the case of thin film electrodes.

Few studies of the electrochromic effect of alkali metals in WO₃ have been reported (1-10). Green *et al.* have studied sodium and lithium injection in WO₃ using both liquid and solid electrolytes (2-5, 10). The diffusion coefficient of lithium was estimated to be 2×10^{-12} cm²/sec (3). Mohapatra (8), however, has recently reported a much higher value of 5×10^{-9} cm²/sec. Thermodynamic data for lithium in amorphous WO₃ films have recently also appeared (9, 10).

Theory of the A-C Method

Alternating-current and voltage methods have, of course, been extensively used in many kinds of electrochemical systems, and several review articles are available (11-13).

In general, either current or voltage may be the controlled variable, and the phase and magnitude of the dependent variable (voltage or current, respectively) are determined with respect to this. If measurements are made over a wide-enough frequency

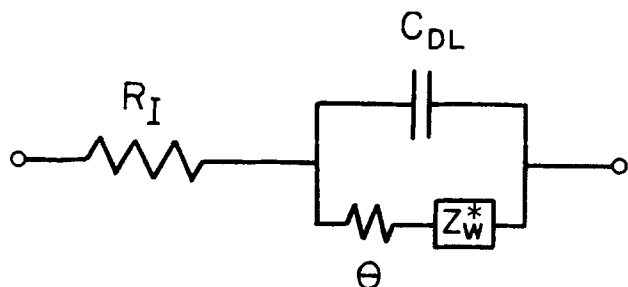


Fig. 1. The Randles equivalent circuit for the a-c response of a system with charge transfer and diffusion of the electroactive species.

range, then different physical processes may be separated through their different time constants.

The problem of the a-c response of a simple electrochemical system with either charge transfer or diffusion-limited kinetics has been considered by several authors. The equivalent circuit for this situation is due to Randles (14) and is shown in Fig. 1. This circuit will also be valid for the diffusion of a metal into an oxide electrode, if it can be assumed that diffusion is driven by a gradient in composition and not by an electric field.

In Fig. 1, R_I is the uncompensated ohmic resistance of the electrolyte and electrode, C_{DL} is the double layer capacitance of the electrode-electrolyte interface, θ is the charge transfer resistance, and Z_W^* is a complex impedance arising from the diffusion of the electroactive species.

For the case of semi-infinite diffusion

$$Z_W^* = A\omega^{-1/2} - jA\omega^{-1/2} \quad [1]$$

where ω is the radial frequency, $j = \sqrt{-1}$, and A is a constant which contains a concentration independent diffusion coefficient. Z_W^* is often known as the Warburg impedance (15). The explicit form of A , and a more general expression for Z_W^* , which is also valid for a finite diffusion situation, are derived below.

The charge transfer resistance θ , is related to the exchange current density (I_0), through a linearization of the Butler-Volmer equation for small overpotentials (δE)

$$\theta = \frac{\delta E}{i} = \frac{RT}{nI_0F} \quad \delta E \ll \frac{RT}{F} \quad [2]$$

It is assumed in the derivation of this equivalent circuit that small signal conditions are met, since C_{DL} , θ and A are in general voltage or concentration dependent and lead to nonlinear behavior.

The frequency response of this circuit will be governed by the relative importance of charge transfer and diffusion in determining the current: for very slow diffusion $Z_W^* > \theta$, and for very slow charge transfer kinetics $Z_W^* < \theta$. Since Z_W^* is a function of frequency and θ is not, then an electrode reaction rate may be controlled by diffusion at low frequencies (long times) and by charge transfer at high frequencies (short times).

Derivation of Z_W^ for a thin film electrode.*—The magnitude of the Warburg impedance Z_W^* is determined by the chemical diffusion coefficient of the neutral electroactive species (A) in the electronically conducting oxide electrode (B), and the explicit form of Z_W^* can be derived by solving Fick's laws with suitable initial and boundary conditions. The situation is fully analogous to the determination of chemical diffusion coefficients in solid solution electrodes by a transient galvanostatic technique discussed previously by Weppner and Huggins (16, 17).

Experimentally, the electrode is held at a constant potential E , with respect to a reference electrode of pure A , until equilibrium is reached. The composition of the sample at equilibrium is uniform and equal to A_yB . The chemical potential of A in A_yB is

$$\mu_A = \mu_A^\circ + RT \ln \gamma_A X_A \quad [3]$$

Here X_A is the mole fraction of A , and γ_A is its activity coefficient. If we choose $\gamma_A \rightarrow 1$ as $X_A \rightarrow 1$ then μ_A° is the chemical potential of pure A at the same temperature. Thus

$$E = -\frac{RT}{zF} \ln \gamma_A X_A \quad [4]$$

z is the charge carried by A cations, F and R are the gas constant and Faraday, respectively.

A small alternating voltage

$$\delta E = v_0 \sin \omega t \quad [5]$$

is now applied between the A_yB working electrode and the reference electrode, which drives the surface of the working electrode to a new time dependent concentration $X_A + \delta X_A$ (which corresponds to a stoichiometry of $A_{y+\delta y}B$). Eventually, a steady state is reached and we require an expression for the amplitude and phase of the current flowing through the cell. Since the current density depends on the gradient in concentration at the interface, through Fick's law, and the voltage depends on the chemical potential at the interface, it is necessary to either make dilute solution assumptions or else to have knowledge of the activity coefficient of A in A_yB . Since the solid solutions under consideration here are quite concentrated (X_A may be as high as 0.3) dilute solution behavior cannot be assumed and an alternative approach is adopted here which is equivalent to a knowledge of γ_A as a function of y . If we can assume that for very small changes in voltage

$$\frac{\delta E}{\delta X_A} \cong \frac{dE}{dX_A} \quad [6]$$

We can substitute Eq. [6] into Eq. [5] and obtain

$$\delta X_A(t) = (dE/dX_A)_{X_A}^{-1} \cdot v_0 \sin \omega t \quad [7]$$

This equation describes the change in mole fraction of A at the electrode-electrolyte interface for a very small change in applied alternating voltage. $(dE/dX_A)_{X_A}$ may be obtained by differentiation of the coulometric titration curve at the appropriate composition (X_A), or as will be seen later, may, in the present case, be obtained directly from very low frequency measurements. Equation [7] represents a linearization of the dependence of concentration on voltage. The mole fraction of A at the interface is therefore a sinusoidal function of time as long as $(dE/dX_A)_{X_A}$ is constant over the range of composition δX_A .

For a diffusion experiment it is convenient to write Eq. [7] in terms of the number of atoms per unit volume (C_A), and the stoichiometry (y)

$$\delta C_A(t) = \frac{N}{V_M} \cdot \left(\frac{dE}{dy} \right)_y^{-1} \cdot v_0 \sin \omega t \quad [8]$$

Here N is Avogadro's number and V_M is the molar volume of A_yB , assumed constant over the range δy .

We therefore seek solutions of the equation

$$\frac{\partial[\delta C_A(x,t)]}{\partial t} = D \frac{\partial^2[\delta C_A]}{\partial x^2} \quad [9]$$

with the initial condition of uniform concentration

$$\delta C_A(x,0) = 0 \quad [10]$$

and the $x = l$ boundary condition given by Eq. [8]. Here l is the thickness of the oxide electrode; the coordinate system used is shown in Fig. 2. The second boundary condition is

$$\partial[\delta C_A(0,t)]/\partial x = 0 \quad [11]$$

corresponding to an interface impermeable to A. The diffusion coefficient used here is the chemical diffusion coefficient, which is appropriate for the diffusion of a species in an activity gradient (16). With certain assumptions, it can be related to the particle diffusion coefficient of the components (A^{z+} ions and electrons).

The solution of Eq. [9] for these conditions is given by Carslaw and Jaeger (18)

$$\delta C_A(x,t) = \alpha B \sin(\omega t + \phi) \quad [12]$$

with

$$\alpha = \frac{N}{V_M} \cdot \left(\frac{dE}{dy}\right)^{-1} v_o \quad [13]$$

$$B = |f| \quad [14]$$

$$\phi = \arg(f) \quad [15]$$

and

$$f = \frac{\cosh kx \cdot (1+j)}{\cosh kl \cdot (1+j)} \quad [16]$$

with

$$k = (\omega/2\tilde{D})^{1/2} \quad [17]$$

Note that this is the steady-state solution. There is also a transient caused by starting the sinusoidal oscillation at $t = 0$. The form of this transient is given in Ref. (18).

In order to determine the current density in the system, it is necessary to evaluate $(\partial[\delta C_A]/\partial x)_{x=l}$. From Eq. [12] it may be shown that

$$\left(\frac{\partial[\delta C_A]}{\partial x}\right)_{x=l} = \tau \sin(\omega t + \beta) \quad [18]$$

where

$$\tau = (\alpha k / \sqrt{2d}) (h^2 + s^2)^{1/2} \quad [19]$$

and

$$\beta = \arctan\left(\frac{h+s}{h-s}\right) \quad [20]$$

with

$$h = \sinh(2kl) \quad [21]$$

$$s = \sin(2kl) \quad [22]$$

$$d = \cosh^2(kl) \cdot \cos^2(kl) + \sinh^2(kl) \cdot \sin^2(kl) \quad [23]$$

Thus, the current density

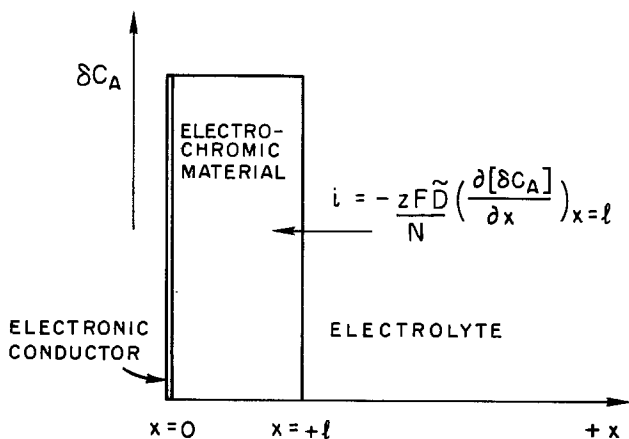


Fig. 2. The coordinate system used for the solution of the diffusion equations.

$$i_d = -\tilde{D} \left(\frac{\partial[\delta C_A]}{\partial x}\right)_{x=l} \cdot \frac{zF}{N} \quad [24]$$

has an amplitude

$$i_o = -\frac{zF}{2V_M} \left(\frac{dE}{dy}\right)^{-1} \cdot v_o (\omega\tilde{D})^{1/2} \left(\frac{h^2 + s^2}{d}\right)^{1/2} \quad [25]$$

and a phase of β with respect to the applied voltage. Note that both the phase and the amplitude are frequency dependent.

Two extreme cases are of interest. First, consider the value of i_o for high frequencies, small \tilde{D} , or thick samples, i.e., $kl \gg 1$. Under these conditions $(h^2 + s^2)^{1/2}/d = 2$, and so

$$i_o = -\frac{zFV_o}{V_M} \left(\frac{dE}{dy}\right)^{-1} \cdot (\omega\tilde{D})^{1/2} \quad [26]$$

and

$$\beta = \arctan(1) = \pi/4 \quad [27]$$

Thus, the phase difference between the current and the voltage is independent of frequency and is equal to 45° . Expressing this result as a complex impedance

$$\begin{aligned} Z_W^* &= |Z| \cos\left(\frac{\pi}{4}\right) - j|Z| \sin\left(\frac{\pi}{4}\right) \\ &= \frac{|Z|}{\sqrt{2}} \cdot (1-j) \end{aligned} \quad [28]$$

where

$$|Z| = \left| \frac{v_o}{i_o a} \right| = \left| \frac{V_M (dE/dy)}{zF\tilde{D}^{1/2} a} \cdot \omega^{-1/2} \right| \quad [29]$$

where a = surface area.

Comparison of Eq. [28] with Eq. [1] shows that for these conditions the preexponential factor A in the Warburg impedance has the form

$$A = \left| \frac{V_M (dE/dy)}{\sqrt{2} zF\tilde{D}^{1/2} a} \right| \quad [30]$$

The other limiting case occurs at very low frequencies, for very thin samples or for large \tilde{D} . If

$$kl \ll 1 \quad (\text{i.e., } \omega \ll 2\tilde{D}/l^2) \quad [31]$$

$$i_o = -\frac{zFv_o}{V_M} \left(\frac{dE}{dy}\right)^{-1} l \omega \quad [32]$$

$$\beta = \arctan(\infty) = \frac{\pi}{2} \quad [33]$$

Thus, under these conditions the current is 90° out of phase with the voltage and is independent of the diffusion coefficient.

Expressed as the imaginary (X) and real (R) parts of the complex impedance for these conditions

$$X = |Z| \sin \beta = |Z| = |V_M (dE/dy) / zF\omega l a| = \frac{1}{\omega C_L} \quad [34]$$

$$R = |Z| \cos \beta = |Z| 2k^2 l^2 / 3a \quad [35]$$

$$= R_L = \left| \frac{V_M}{zFa} \left(\frac{dE}{dy}\right) \left(\frac{l}{3\tilde{D}}\right) \right| \quad [36]$$

where C_L and R_L are the limiting low frequency capacitance and resistance. An interesting consequence of Eq. [34] and [36] is that for thin samples, it is not necessary to obtain a coulometric titration curve since simultaneous solution of these equations yields values for both the diffusion coefficient and $(dE/dy)_y$. Alternatively, if this last quantity is known independently, then the sample thickness may be calculated. Of course, no information about $(dE/dy)_y$ or l may be obtained

from the high frequency data since the diffusion is then semi-infinite in nature, and only \tilde{D} may be determined.

At intermediate frequencies, when neither of the two limiting cases can be applied, the frequency response of the electrode must be analyzed using the full impedance expressions

$$Z_W^* = R_W - jX_W \quad [37]$$

with

$$X_W = |Z| \sin \beta \quad [38]$$

$$R_W = |Z| \cos \beta \quad [39]$$

where β is given by Eq. [20], and

$$|Z_W| = |v_o/i_o a| \quad [40]$$

where i_o is given by Eq. [25].

Complex plane representation.—Since the form of Z_W^* is now known, the impedance of the entire circuit of Fig. 1 can be computed as a function of frequency. The most useful way of representing this result is by plotting the real (R) and imaginary (X) components of the total circuit impedance *vs.* one another in the complex plane as functions of frequency. Three such computer generated plots are shown in Fig. 3.

In Fig. 3(a), the diffusional impedance is large and a straight line of 45° slope is seen over most of the frequency range. The kinetics of the system are limited almost entirely by the rate of the diffusional process. The high frequency real axis intercept gives the value of R_I and \tilde{D} may be found by analysis of the straight line portion of the curve using Eq. [28] and [29].

In Fig. 3(b) a transition is obtained such that the kinetics pass from diffusion control at low frequencies to charge transfer control at high frequencies. The semicircle at high frequencies is due to the parallel combination of C_{DL} and θ , the values of which may in principle be obtained by analysis of the high frequency data. The extrapolated real intercept of the straight line region lies at [11]

$$R_S = R_I + \theta - r \quad [41]$$

with

$$r = 2C_{DL}A^2 \quad [42]$$

where A is given by Eq. [30].

At very low frequencies the phase angle begins to increase due to the onset of finite length effects. This process is complete in Fig. 3(c), where R has reached its limiting value given by the sum of R_L (Eq. [36]) and $(R_I + \theta)$. If the diffusion kinetics are in the proper range, there can be good separation between the charge transfer semicircle at high frequencies, the 45° line of Z_W^* at intermediate frequencies, and the vertical line at very low frequencies, due to the finite thickness effect. \tilde{D} may be obtained from either the 45° portion of the line or from R_L , determined from the limiting resistance, and Eq. [36].

Experimental Procedures

Sample preparation.—The diffusion experiments were carried out on thin films of tungsten trioxide deposited on tin oxide (700Å thick) covered glass substrates. Amorphous WO_3 films were prepared by thermal evaporation of the oxide at a rate of 30 Å/sec. The substrate temperature during evaporation was 100°C, and the pressure was maintained at 2×10^{-4} Torr of air. The method of preparation and the characterization of these films was discussed in Ref. (19), where it was also demonstrated that such films are stable in the electrolyte/solvent system used in the present experiments.

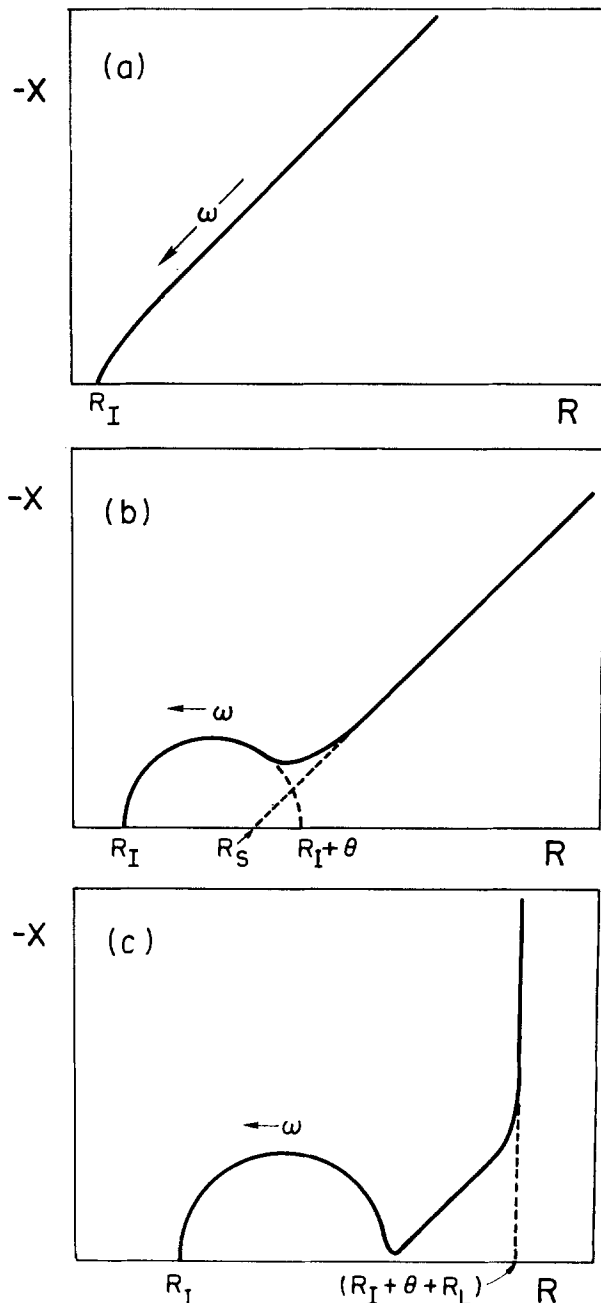


Fig. 3. Computer simulation of the complex impedance of the circuit shown in Fig. 1 for various values of the diffusion coefficient.

The results reported below were obtained on 1500Å thick films which had been heat-treated in pure oxygen for 6 hr at 350°C. This procedure was adopted in order to dry the films and to ensure that the stoichiometry was in fact WO_3 . X-ray diffraction experiments indicated that the initially amorphous films, which showed only a broad diffuse scattering centered on a d value of 3.6Å, developed some crystallinity on undergoing this heat-treatment. Several sharp reflections developed, which could be indexed on the same unit cell as the high temperature tetragonal modification of WO_3 (in agreement with the observations of Green [10], but with slightly reduced lattice parameters). The sharp reflections were superimposed on a diffuse background similar to that of the unheated, treated films.

A density of 5.2 g/cm³ was used in the calculation of the results below, based on a comparison of the measured film volume (using interferometry) and chemical analysis (19).

Electrochemical measurements.—Measurements were made using a three electrode configuration. Both

counter and reference electrodes were pure lithium metal, and the electrolyte was 0.75M LiAsF_6 in propylene carbonate. The electrolyte was dried by prolonged agitation with lithium chips. All materials and the electrochemical cell were kept in a helium-filled dry box. Measurements were made at 300°K.

The thin film working electrode was held at constant voltage (and hence composition) by a Princeton Applied Research Model 173 potentiostat. A small alternating signal from a Hewlett Packard HP3110B oscillator was then superimposed on the constant voltage and the current flowing in the counter-working electrode circuit was monitored via a standard resistance. The circuit is shown in Fig. 4. The amplitude of the signal applied to the sample was always less than 10 mV and the frequency range covered extended from 5×10^{-4} Hz up to 5 kHz.

Above 20 Hz, the amplitude and phase of the current with respect to the applied voltage were measured directly using a PAR Model 5204 two-phase lock-in analyzer. Above about 100 Hz, small corrections were made to compensate for the attenuation and phase shift introduced into the signal by the potentiostat. This was achieved by comparing the a-c perturbation of the potential difference between the reference and working electrodes directly with the output of the oscillator.

Below 20 Hz, the signals corresponding to current and voltage were amplified using a PAR Model 113 preamplifier and fed to the analog-to-digital converters of a Digital Equipment Corporation Lab 8e computer, where the two signals were averaged over several cycles and compared.

Results

The change in open-circuit voltage (E) with composition (y) is plotted in Fig. 5. The order in which the points were taken is indicated, showing that the measurements were in fact made at equilibrium. Results of the two other thermodynamic studies are also shown for comparison (9, 10).

The complex impedance data are summarized in Fig. 6 and 7. In Fig. 6, the higher frequency data are shown for four open-circuit voltages. At the highest voltage (2.6V with respect to pure lithium), a straight line of slope 45° was obtained from about 0.01 Hz up to 5 kHz, corresponding to complete diffusion control of the electrochemical insertion reaction over the whole of the available frequency range. At lower open-circuit voltages (corresponding to higher lithium concentrations in the film), the separation of a semicircular region is evident at higher frequencies and, at the same time at lower frequencies, the 45° line begins to give way to a vertical line under the influence of finite length effects. The 5 Hz points are marked on the plots, and it can be seen that at this frequency a gradual transition from diffusion-controlled to charge transfer-controlled kinetics takes place as lithium is added to the film.

Complex impedance data for the lowest frequencies are shown in Fig. 7. In this frequency range, the rate

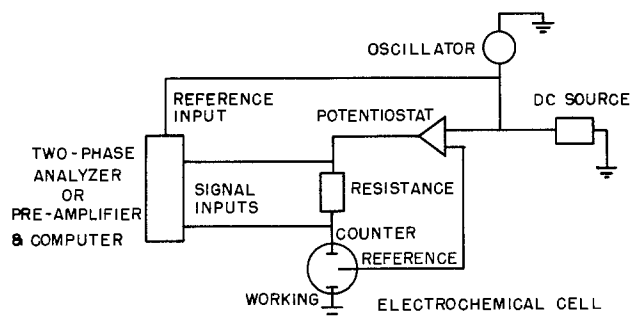


Fig. 4. Experimental circuit used for the A-C impedance measurements.

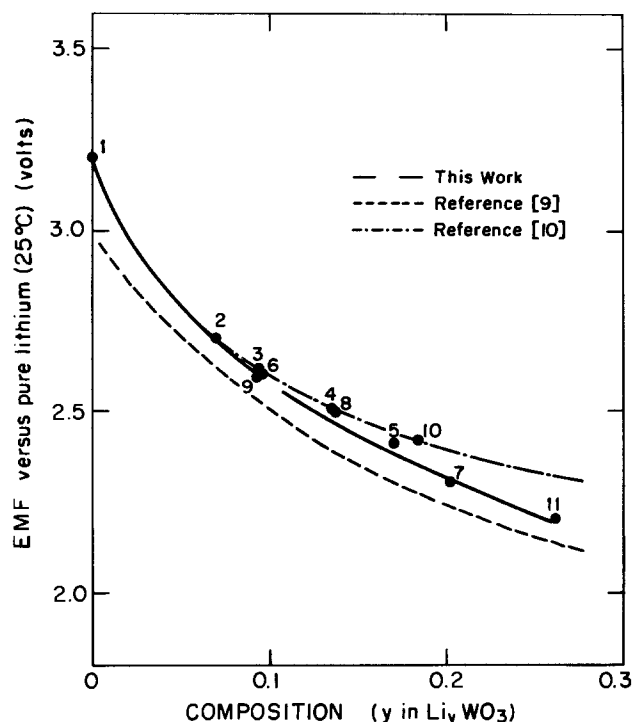


Fig. 5. Coulometric titration curve for Li_yWO_3 . The numbers indicate the order in which the data were taken. Results of Mohapatra and Wagner (9) and Green (10) are shown for comparison.

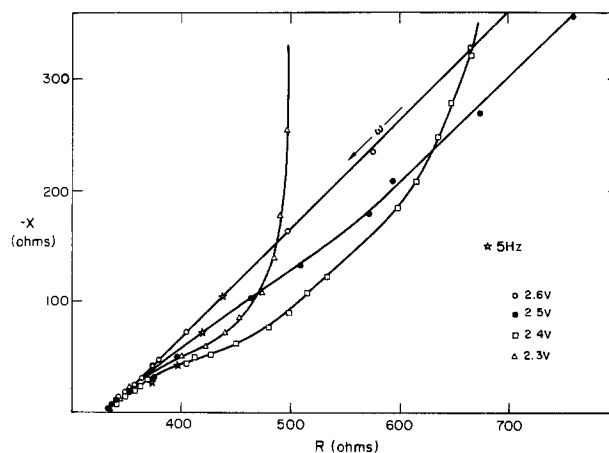


Fig. 6. High frequency complex impedance data

of lithium injection is always diffusion-controlled. The onset of finite length effects shifts to higher frequencies and the low frequency limiting resistance decreases as more lithium is added to the film, indicating that the diffusion coefficient is steadily increasing. Values of the chemical diffusion coefficient, \tilde{D} , were obtained from either the 45° straight line region or else from the low frequency limiting behavior. At high voltages, in the semi-infinite diffusion regime, data analysis presented no problems. Both the real and the imaginary parts of the impedance are proportional to $\omega^{-1/2}$. This is illustrated in Fig. 8 for the highest voltage case. \tilde{D} was calculated from such plots using Eq. [28] and [29]. Alternatively, \tilde{D} can be calculated from the low frequency limiting resistance (Eq. [36]). The low frequency limiting capacitance (obtained from Eq. [34]) yields values of $(dE/dy)_y$ which were used in the computation of \tilde{D} . Relevant data are given in Table I.

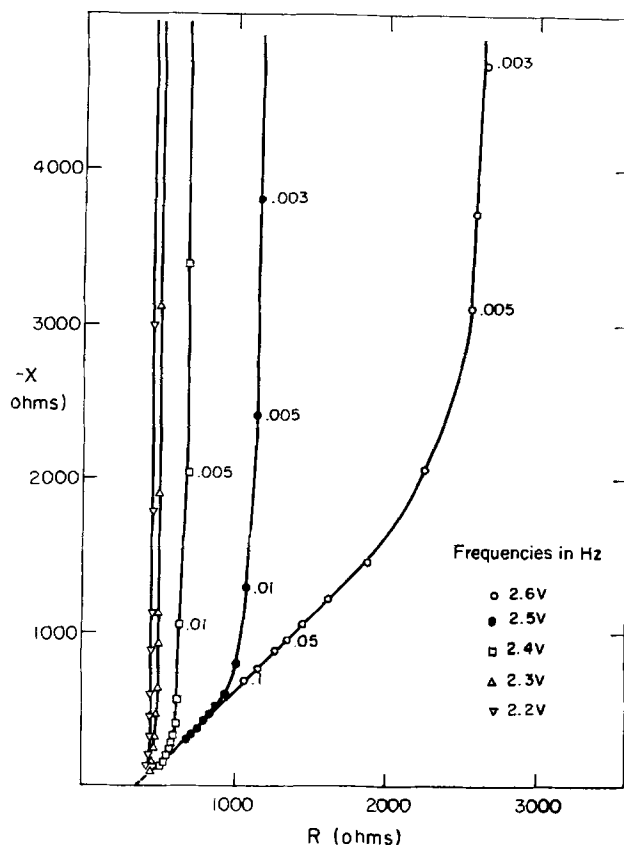


Fig. 7. Low frequency complex impedance data

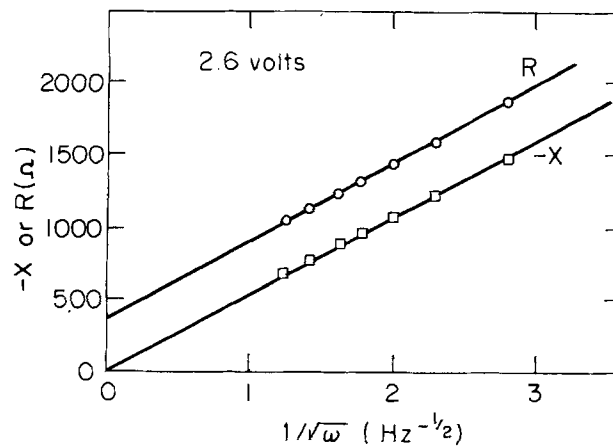
Use of R_L for the calculation of \tilde{D} , however, has a disadvantage in the particular case of the data under consideration here. R_L is measured from the point at which the 45° straight line would intercept the real axis (see Fig. 3b), and thus, if this point is not well-defined, due to overlap of the diffusion- and charge transfer-controlled regions, an inaccuracy is introduced into the calculation of \tilde{D} . The overlap also prevents accurate evaluation of C_{DL} and θ .

These difficulties could, in principle, be overcome by fitting the low frequency impedance data to the full impedance expression (Eq. [38] and [39]). However, the complicated nature of these functions makes this a difficult task which was not attempted here.

Values of the diffusion coefficients calculated for lower voltages (2.2 and 2.3V) are, therefore, of lower accuracy than those for higher voltages.

Discussion

The a-c method.—The technique described in this paper shows itself to be a useful tool for the study of diffusion in thin film solid electrodes, although it is by no means limited in application to such systems. The method appears to have a number of advantages over alternative, transient techniques (such as voltage

Fig. 8. Real and imaginary parts of the complex impedance plotted vs. $\omega^{-1/2}$.

or current step experiments), the most important being that more information is obtained through relatively simple data analysis procedures using the complex impedance plane method. Even in situations where there is extensive overlap of the charge transfer- and diffusion-controlled regions, or where the diffusion coefficient is sufficiently high to introduce finite length effects, much important information can be obtained by inspection of the complex impedance plot. The same information is, of course, also contained in the transient response of linear systems, but data acquisition (particularly at short times) and integral transform analysis so complicate the procedure that often only data obtained over a limited time period (for example, when the change in dependent variable is proportional to \sqrt{t}) are actually useful. As may be seen from the present results, the region in which the impedance is proportional to $\omega^{1/2}$ (or in which E would be proportional to $t^{1/2}$ in a current step experiment) may be very limited or nonexistent. Under these circumstances, the complex impedance method at the very least gives an indication of the experimentally important phenomena contributing to the time response of the system. Often a useful limiting region can be identified (for example, the very low frequency response for thin films) which can be used to extract numerical values for kinetic parameters.

A further advantage of using a steady-state method is that the response signal can be critically evaluated at each frequency, and further averaging (at low frequencies) or filtering (at high frequencies) can be employed.

Like the galvanostatic intermittent titration technique described by Weppner and Huggins (16), the a-c method is capable of very high resolution with respect to composition and is therefore applicable to phases with rather narrow ranges of stoichiometry.

The application of this method is, of course, dependent on the validity of a number of assumptions.

Table I. Thermodynamic and kinetic data

Composition* (y in L_xWO_3)	Open circuit voltage (vs. Li)	\tilde{D} ($\text{cm}^2 \text{sec}^{-1}$)	$\left(\frac{dE}{dy}\right)_y^{**}$	$\frac{d \ln \alpha_{L_1}}{d \ln C_{L_1}}$	D_K ($\text{cm}^2 \text{sec}^{-1}$)	σ_{L_1} ($\Omega^{-1} \text{cm}^{-1}$)
0.097	2.60	$2.4 \times 10^{-12}\dagger$	5.0	18.9	1.3×10^{-13}	1.04×10^{-9}
0.138	2.50	$4.9 \times 10^{-12}\dagger$	3.6	19.4	2.5×10^{-13}	3.0×10^{-9}
0.170	2.40	$1.5 \times 10^{-11}\dagger\dagger$	4.0	26.5	5.7×10^{-13}	8.1×10^{-9}
0.201	2.30	$2.6 \times 10^{-11}\dagger\dagger$	3.8	29.8	8.7×10^{-13}	1.5×10^{-8}
0.260	2.20	$2.8 \times 10^{-11}\dagger\dagger$	3.6	36.5	7.7×10^{-13}	1.7×10^{-8}

* Calculated assuming a density of 5.2 g cm^{-3} .

** Calculated from Eq. [34].

† \tilde{D} calculated from Eq. [29].

†† \tilde{D} calculated from Eq. [36].

The first of these is that the boundary conditions used in the solution of Fick's diffusion equation are correct. The greatest difficulty will usually lie in the assumption that the potential of the cell is a measure of the lithium activity at the interface between the electrolyte and the electrode. This is only true if the electrode is a predominantly electronic conductor. In the present case, there seems to be good evidence that this is so. The high electronic conductivity of tungsten bronze phases is well-established (20); values are much higher than ionic conductivities calculated from previous or present measurements of diffusion coefficients, although direct measurements of partial ionic conductivities have not been made.

A second assumption implicit in the derivation given above is that the driving force for diffusion is only a gradient in composition, and that the electric field in the electrode is negligible. This, of course, will be true in view of the high electronic conductivity mentioned above.

Thirdly, in order for the solution of the diffusion equations to be correct, it must be assumed that the system is linear. In other words, the diffusion coefficient is assumed to be independent of concentration over the range of alternating voltage applied. In practice, the applied voltage can be made very small, so that the measured impedance becomes independent of amplitude. This test is very easy to carry out due to the steady-state nature of the experiment. It seems likely that the diffusion coefficient will change rather slowly with composition, and hence voltage, except in very narrow phases where rapid variation of the thermodynamic enhancement factor may be expected (16). Similar considerations of linearity also apply of course at higher frequencies where the double layer capacitance and charge transfer resistance might also show voltage dependent behavior.

Kinetic properties of WO₃ thin film electrochromic electrodes.—The primary observation concerning the kinetics of lithium incorporation into WO₃ thin films is that both diffusion and interface kinetics are important. At long times (low frequencies), the interface is essentially at equilibrium, and diffusion of neutral lithium in a concentration gradient limits the rate of coloration of the oxide. At times shorter than about 0.5 sec however, charge transfer kinetics limit the rate of injection. The following considerations are relevant.

(i) Firstly, the thermodynamic and kinetic properties of WO₃ thin films are very dependent on the method of preparation (6), and in particular are dependent on the degree of crystallinity of the films. The results given here, although typical of films which show relatively rapid coloration on lithium injection, must not be regarded as applying to all WO₃ films. A detailed study of the thermodynamics and kinetics of different kinds of films is currently underway and the results will be published separately.

(ii) Secondly, the experiments reported here are small signal experiments. In a practical device much larger voltages or currents will be applied to the samples with several consequences. First, the reaction resistance θ will change with applied voltage due to both the change in lithium concentration at the interface and the inherent voltage dependence of the heterogeneous charge transfer reaction. Secondly, large voltage differences across the interface will have important effects on the rate of bleaching as discussed by Faughnan *et al.* (21). If the potential of the surface layer of WO₃ is increased beyond about 3V with respect to lithium, then the surface will become depleted of lithium and, since the electronic conductivity falls as lithium is removed, an electric field will develop in the electrochromic which will tend to increase the rate of lithium removal. This might happen, for example, when the WO₃ is bleached under constant current conditions, when the diffusion process

cannot indefinitely support the current. A third effect of higher voltages will occur under rapid coloration conditions where the voltage falls to such low values that a concentration driven phase change on the surface of the oxide might be irreversible. Mohapatra and Wagner (9), for example, found that the chemical potential of lithium in amorphous Li_yWO₃ was constant for $y > 0.4$ (approximately 2V vs. Li). If this constant activity corresponds to a two- or three-phase region, then the new phase(s) formed may have very slow or irreversible kinetics.

In summary, therefore, small signal results should not be taken as a definitive measure of how an electrochromic device would operate under large signal conditions.

The charge transfer resistance of the interface was found to be 100-150 Ω/cm^2 . As discussed in the Results section, an overlap of the diffusion response and the charge transfer response prevents an accurate evaluation of this resistance and its voltage dependence. The corresponding exchange current density is 8×10^{-5} - 1.3×10^{-4} A/cm², a value which will depend on the concentration of Li⁺ in the liquid electrolyte as well as electrode material parameters. Mohapatra (8) has suggested a value as high as 2×10^{-3} A/cm² for lithium injection. Somewhat smaller values (5×10^{-6} - 3×10^{-5} A/cm²) have been found by Crandall and Faughnan (22) for the injection of hydrogen into amorphous WO₃.

Chemical diffusion coefficients for low lithium concentrations are in good agreement with the value of 2×10^{-12} cm²/sec suggested by Green (3). An increase with increasing lithium concentration of about one order of magnitude is observed, but the values are still much lower than the 5×10^{-9} cm²/sec reported by Mohapatra (8). The thermodynamic results given by Mohapatra and Wagner in Ref. (9), however, were in very good agreement with the results of the present study. More recent results by Green (10)

show a slightly smaller value for \tilde{D} of 4×10^{-13} cm²/sec on films which also have similar coulometric titration curves. Green also suggested that rapid diffusion along grain boundaries is followed by much slower diffusion into the bulk of the grains, with an associated diffusion coefficient of about 6×10^{-16} cm²/sec. In the present study, no evidence for two diffusion processes, either in series or in parallel has been found, as the form of the results is adequately explained by a single diffusion coefficient.

As discussed by Weppner and Huggins (16), the chemical diffusion coefficient \tilde{D} is related to the component diffusion coefficient D_k by the relation

$$\tilde{D} = D_k \frac{d \ln a_{\text{Li}}}{d \ln C_{\text{Li}}} \quad [43]$$

for the case where the electronic transference number is close to unity. In this equation the activity and concentration terms refer to neutral lithium. Hence

$$\tilde{D} = -D_k \frac{dE}{dy} \frac{zF}{RT} y \quad [44]$$

and since

$$D_k = kTb \quad [45]$$

and

$$\sigma_{\text{Li}} = z^2 F^2 C_{\text{Li}} b \quad [46]$$

where b is the general mobility and σ the partial conductivity of Li⁺ ions

$$\sigma_{\text{Li}} = \frac{zF\tilde{D}}{V_M} \left(\frac{dE}{dy} \right)^{-1} \quad [47]$$

Numerical values for D_k and σ_{Li} are given in the table. Like the chemical diffusion coefficient, these quantities appear to increase with increasing lithium con-

tent, the most rapid rate of increase occurring around $y = 0.17$.

In summary, a general steady-state a-c method has been described which allows the diffusion coefficient of a species in an electronically conducting thin film electrode to be determined. In addition, qualitative information about the kinetics of the interface charge transfer reaction has been obtained, and it is believed that in some situations detailed interfacial kinetic data could be obtained. The method has a number of advantages over transient current or voltage step techniques, stemming partly from the method of analysis in the frequency domain which allows a clear distinction to be drawn between interface and bulk processes.

Acknowledgment

The computer program for the low frequency measurements was conceived and written by Dr. B. A. Boukamp of this laboratory, to whom the authors are most grateful.

Manuscript submitted July 30, 1979; revised manuscript received Aug. 28, 1979.

Any discussion of this paper will appear in a Discussion Section to be published in the December 1980 JOURNAL. All discussions for the December 1980 Discussion Section should be submitted by Aug. 1, 1980.

Publication costs of this article were assisted by Stanford University.

REFERENCES

1. H. N. Hersh, W. E. Kramer, and J. H. McGee, *Appl. Phys. Lett.*, **27**, 646 (1975).
2. R. J. Colton, A. M. Guzman, and J. Wayne Rabalais, *J. Appl. Phys.*, **49**, 409 (1978).
3. M. Green, W. C. Smith, and J. A. Weiner, *Thin Solid Films*, **38**, 89 (1976).
4. M. Green and K. S. Kang, *ibid.*, **44**, L19 (1977).
5. W. C. Dautremont Smith, M. Green, and K. S. Kang, *Electrochim. Acta*, **22**, 751 (1977).
6. H. R. Zeller and H. U. Beyeler, *J. Appl. Phys.*, **13**, 231 (1977).
7. T. J. Knowles, *Appl. Phys. Lett.*, **31**, 817 (1978).
8. S. K. Mohapatra, *This Journal*, **125**, 284 (1978).
9. S. K. Mohapatra and S. Wagner, *ibid.*, **125**, 1603 (1978).
10. M. Green, *Thin Solid Films*, **50**, 145 (1978).
11. M. Sluyters-Rehbach and J. H. Sluyters, in "Electroanalytical Chemistry," Vol. 4, A. J. Bard, Editor, pp. 1-128, Marcel Dekker, New York (1970).
12. D. D. Macdonald, "Transient Techniques in Electrochemistry," p. 229, Plenum Press, New York (1977).
13. D. E. Smith, in "Electroanalytical Chemistry," Vol. 1, A. J. Bard, Editor, pp. 1-155, Marcel Dekker, New York (1966).
14. J. E. B. Randles, *Discuss. Faraday Soc.*, **1**, 11 (1947).
15. E. Warburg, *Ann. Physik*, **67**, 493 (1899); **6**, 125 (1901).
16. W. Weppner and R. A. Huggins, *This Journal*, **124**, 1569 (1977).
17. W. Weppner and R. A. Huggins, *Annual Review of Materials Science*, R. A. Huggins, Editor, p. 269, Annual Reviews Inc., Palo Alto (1978).
18. H. S. Carslaw and J. C. Jaeger, "Conduction of Heat in Solids," 2nd Ed., p. 105, Oxford Univ. Press, Oxford (1959).
19. J. P. Randin, *J. Electron. Mater.*, **7**, 47 (1978).
20. P. J. Wiseman and P. G. Dickens, in "MTP International Review of Science." Inorganic Chemistry. Series II. Vol. 10, L. E. J. Roberts, Editor, p. 211, London (1975).
21. B. W. Faughnan, R. S. Crandall, and M. A. Lampert, *Appl. Phys. Lett.*, **27**, 275 (1975).
22. R. S. Crandall and B. W. Faughnan, *Appl. Phys. Lett.*, **28**, 95 (1976).

Development of Sulfur-Tolerant Components for the Molten Carbonate Fuel Cell

A. F. Sammells,* S. B. Nicholson, and P. G. P. Ang*

Institute of Gas Technology, Chicago, Illinois 60616

ABSTRACT

The sulfur tolerance of candidate anode and anode current collector materials for the molten carbonate fuel cell were evaluated in an electrochemical half-cell using both steady-state and transient potentiostatic techniques. Hydrogen sulfide was introduced into the fuel at concentrations of 50 and 1000 ppm. At the higher sulfur concentration using low BTU fuel, both nickel and cobalt were observed to undergo a negative shift in their open-circuit potentials, and high anodic and cathodic currents were observed compared with clean fuels. Exchange currents measured using the transient potentiostatic technique were not greatly affected by 50 ppm H₂S introduced into the fuel. However, at higher sulfur concentrations, higher apparent exchange currents were observed, indicating a probable sulfidation reaction. Of the new anode materials evaluated, Mg_{0.05}La_{0.95}CrO₃ and TiC showed good stability in the anodic region. With the former material, exchange current densities in low BTU fuel were calculated to be ≈ 8 mA/cm² at 650°C, lower values than found for either nickel or cobalt anodes under similar conditions. Of the anode current collector materials evaluated, high stabilities were found for 410 and 310 stainless steels. The implications and relevance of these results on fuel cell performance are discussed.

The essential components which comprise the molten carbonate fuel cell are a porous nickel or cobalt anode, and a porous nickel oxide cathode, which are separated by an ionically conducting molten carbonate mixture

* Electrochemical Society Active Member.

Key words: sulfur-tolerant anode, current collectors, molten carbonate fuel cell.

supported on a lithium aluminate matrix. These components together are commonly referred to as the tile. To date, these fuel cell components have shown good electrochemical performance and corrosion stability under cell operating conditions over several thousand hours in the absence of sulfur-containing species in the fuel and oxidant. However, commercialization of this

system for electric utility power plants will dictate that the fuel cell must operate on fuel oils in the short term and on the products of coal gasification in the longer term, all of which can be expected to contain sulfur.

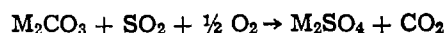
Two general approaches can be followed towards solution of the sulfur problem in the molten carbonate fuel cell. The first approach is to remove completely the sulfur contaminants from the fuel cell before entry into the fuel cell anode. The second approach is to determine the sulfur tolerance of currently used cell components. When degradation in cell performance and materials stability becomes evident, the next step is to identify, characterize, and develop sulfur-tolerant components that show acceptable long-term electrochemical performance under defined sulfur concentrations within the overall system. The second of these two approaches is discussed here. Previous literature (1) has indicated that the catalytic activity of nickel may be poisoned because of the H_2S chemisorption at the temperatures of the molten carbonate fuel cell ($\sim 650^\circ C$). This sulfur uptake may result in the formation of nickel sulfide (1) at the porous nickel anode, possibly resulting in a loss of both structural integrity and electrocatalytic activity (2, 3). This requirement will introduce to the cathode sulfur originating from the anode inlet. Under the oxidizing conditions of the cathode, this SO_2 can be expected to absorb readily into the molten carbonate mixture present.

No work has been reported on the corrosion of nickel by sulfide or sulfate while in the presence of molten carbonate under conditions representative of those in the molten carbonate fuel cell. Most work reported to date has focused on nickel in contact with various sulfur-containing gases. For example, the corrosion rate of nickel either in pure SO_2 or in SO_2/O_2 mixtures has shown parabolic gravimetric kinetics, which can result in the growth of external NiO and internal Ni_3S_2 scales. At temperatures above $645^\circ C$ the eutectic sulfide in contact with nickel becomes liquid. Even at $603^\circ C$, an inner Ni_3S_2 layer is formed on nickel (4) via diffusion of SO_2 through open channels or crevices in the initial NiO oxide layer. The overall rate of this process is probably controlled by diffusion of nickel through the continuous Ni_3S_2 phase in the nickel oxide matrix.

Chromium oxide (Cr_2O_3) was also selected for evaluation as an anode material. Relatively pure Cr_2O_3 is an n-type semiconductor material at temperatures above $1000^\circ C$. However, at temperatures below this, the concentration of intrinsic defects will be less than the concentration of extrinsic defects present from impurity dopants. By the addition of monovalent (5) or divalent (6) cationic impurities at temperatures below $1000^\circ C$, p-type conduction can be promoted. But the reducing environment present at the anode of the molten carbonate fuel cell can be expected to favor a donor dopant such as Ti^{4+} rather than an acceptor such as Mg^{2+} . Sintered compacts of TiO_2 -doped Cr_2O_3 were found susceptible to cracking in the course of this work.

Although extensive data are available on the free energy of formation for metal sulfides (7), as are Ellingham-type plots (8), no data appear to be available under conditions representative of those present in the molten carbonate fuel cell. Consequently, discussion of such thermodynamic data in reference to the equilibrium potential values obtained in this work during anode sulfidation can be considered too speculative and is therefore not covered.

Large-scale molten carbonate fuel cells will require the implementation of a catalytic burner between the anode outlet and the cathode inlet for CO_2 management to maintain the desired electrochemical process. This requirement will introduce to the cathode sulfur originating from the anode inlet. Under the oxidizing conditions of the cathode, this SO_2 can be expected to absorb readily into the molten carbonate mixture present both at the porous nickel oxide cathode and within the tile by the equilibrium reaction



which can be expected to favor strongly the formation of the alkali metal sulfate. The concentration of sulfur species at the anode may be influenced by electrochemical transport of sulfur species (initially present as sulfate) from the sulfur-contaminated cathode, and may have an impact on the long-term stability of the anode.

This work reports on electrochemical half-cell measurements on presently used anode and anode current collector materials with both clean and sulfur-containing fuels. By this means, the effect of such sulfur-containing species on the anode stability and electrode kinetics can be evaluated. The initial selection of candidate sulfur-tolerant components for the molten carbonate fuel cell included materials which had previously shown evidence of extended stability when used in applications such as methanation catalysis, positive electrode current collector components of high-temperature metal/sulfur batteries, and interconnect materials used in solid-oxide fuel cells. The latter materials, which included $Mg_{0.05}La_{0.95}CrO_3$, were of particular interest because they had shown high stability to both oxidizing and reducing conditions in the high-temperature solid oxide fuel cell. These materials were initially subjected to preliminary corrosion testing by simulating those chemical conditions expected in the anode environment of the system. Materials evaluated as sulfur-tolerant anodes in the electrochemical half-cell have included nickel, cobalt, CoMo, CoW, WC, TiC, $Mg_{0.05}La_{0.95}CrO_3$, Cr_2O_3 (doped with TiO_2), and NbN. Materials for the anode current collector have included Hastelloys, Kanthal, 400 and 300 stainless steels, and iron-aluminum-manganese and iron-aluminum-molybdenum alloys. The relative stabilities of these materials at the anode and anode current collectors for the molten carbonate fuel cell and a comparison of the electrocatalytic behavior of these candidate anodes will be discussed.

Experimental

The preliminary corrosion screening of selected materials was performed by partially submersing coupons in a lithium/potassium carbonate mixture at $650^\circ C$ in ceramic boats. These boats were placed in an alumina tube through which the desired fuel composition could be passed. The corrosion stability of materials was evaluated with the molten carbonate equilibrated with both clean and sulfur-containing fuels.

Materials for the anode and anode current collectors were obtained from commercial sources (Materials Research Corporation, Orangeburg, New York, and CERAC, Incorporated, Milwaukee, Wisconsin). Electrochemical parameters were measured using an electrochemical half-cell. Working electrodes were attached to an alumina-sheathed lead wire of 316 stainless steel. For nickel and cobalt, however, the lead wires were made from nickel and cobalt, respectively. A gold wire bubbled with 33.3% O_2 -66.7% CO_2 inside an alumina tube served as a reference electrode. The gold was in contact with the melt via a small hole (0.015 in. diam) at the bottom of the tube. All measurements were performed in an electrolyte of composition 62 Li_2CO_3 -38 mole percent (m/o) K_2CO_3 at $650^\circ C$. The counter-electrode used in this work consisted of "Palau" of nominal composition 80% Au, 20% Pd, which proved to have a higher sulfur tolerance than a pure gold counterelectrode, the usual material used at IGT when clean fuels are used in electrochemical half-cell work. Fuels with a predetermined high sulfur content or pure H_2S were mixed into the primary fuel after the humidification step at the rate required to achieve the desired sulfur content. Experimental observations in this work indicated some apparent sensitivity of the open-circuit potential obtained at both nickel and cobalt electrodes to the presence of H_2S introduced into the fuel gas. At concentrations of 50 ppm and below, such variations in the open-circuit potential

were found to be somewhat erratic and not completely reproducible. Apart from some variations in the open-circuit potential, steady-state polarization curves for clean fuel and fuel containing 50 ppm H_2S exhibited an almost identical slope, indicating little evidence of electrode poisoning. Polarization data were performed in both low BTU fuels corresponding to the respective compositions 21.4% H_2 , 17.7% CO , 9.2% CO_2 , 1.1% CH_4 , 45% N_2 , 5.6% H_2O , and to high BTU fuel of 68.1% H_2 , 23.4% CO , 3.39% CO_2 , and 5.03% H_2O . Emphasis on this work was placed, however, on the low BTU fuels corresponding to coal gasification.

The potential of the working electrode was controlled by a Wenking Model 66TSI potentiostat. Steady-state currents were recorded on a Hewlett-Packard 7046A X-Y recorder. To eliminate errors caused by mass-transfer effects, transient potentiostatic techniques were employed using a Wenking ST72 potentiostat. This instrument has a risetime of about 7 μsec when a step voltage is applied. A Tacussel Type GSTP2B pulse-sweep generator was used to control this potentiostat with the output voltage being monitored with a Fluke Type 8020A digital voltmeter. Signals from the transient techniques were displayed and photographed on a Tektronix Type 547 oscilloscope. Electrodes made with this transient potentiostatic technique were performed using appropriate IR compensation within the potentiostat. Without such compensation, a large transient capacitive current was usually seen. Such an effect can cause some error in the current extrapolated to time zero. In order to achieve IR compensation, part of the voltage at the current recorder terminal of the potentiostat was picked up from an external potentiometric voltage divider (250 Ω) and fed back into one of the potentiostat control inputs. The feedback voltage was then adjusted until the system almost started to oscillate. The positive feedback resulted in an increase of the control voltage proportional to the cell current. The temperature of the melt was maintained with an alumina-sheathed, Chromel-Alumel thermocouple.

Results and Discussion

To determine the effect of sulfur-containing fuels on the electrochemical performance of nickel and cobalt anodes, both steady-state and potential-step type measurements were performed in an electrochemical half-cell. Steady-state techniques were used to identify the enhanced currents caused by the anodic sulfidation reactions and changes that may occur in the open-circuit potential as a result of such reactions. Figures 1 and 2 compare steady-state polarization curves for nickel and cobalt anodes in low BTU fuel with and without 50 ppm H_2S . In both cases, introduction of sulfur as H_2S into the fuel was observed to perturb the open-circuit potential.

In the case of nickel (Fig. 1), the shift was 15 mV positive of the initial -1154 mV open-circuit potential, whereas in the case of cobalt (Fig. 2), the shift was in the cathodic direction by only around 7 mV. Other than these minor shifts in the open-circuit potential, the current voltage characteristics are very similar in each case.

In the fuel cell, sulfur can be expected to enter the cathode as SO_2 , resulting in the formation of sulfate. Sulfate may then be available for migration to the anode, where it could be reduced to sulfide species under the reducing conditions present. Thus, sulfur introduced into the fuel cell by this means could result in locally high accumulations of sulfide in the proximity of the anode. Consequently, H_2S introduced at concentrations of around 50 ppm with low BTU fuel in the half-cell may not simulate the local high sulfur content that may occur in the real fuel cell.

The observation of erratic open-circuit potential readings with both nickel and cobalt anodes may be caused either by a mixed potential effect due to the formation of a metal sulfide species on the anode, or

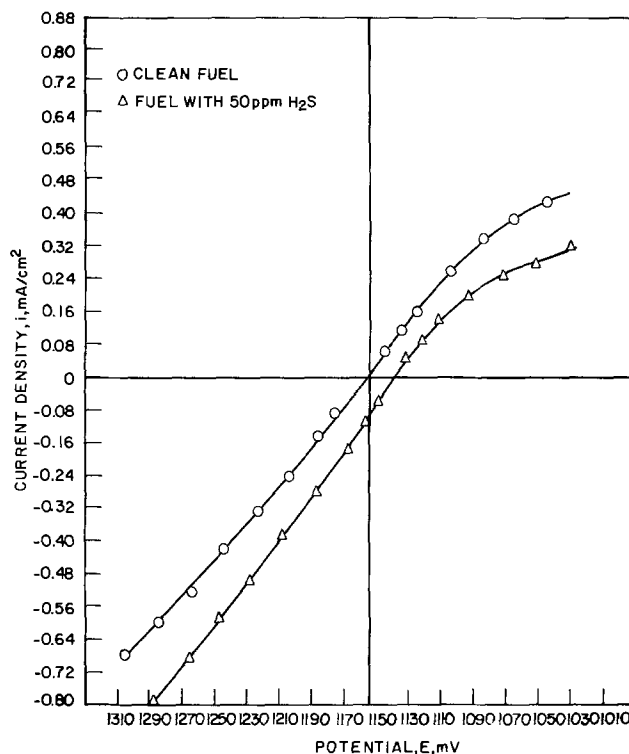


Fig. 1. Steady-state polarization curves for nickel using low BTU fuel with and without 50 ppm H_2S added (Li/K electrolyte, 650°C).

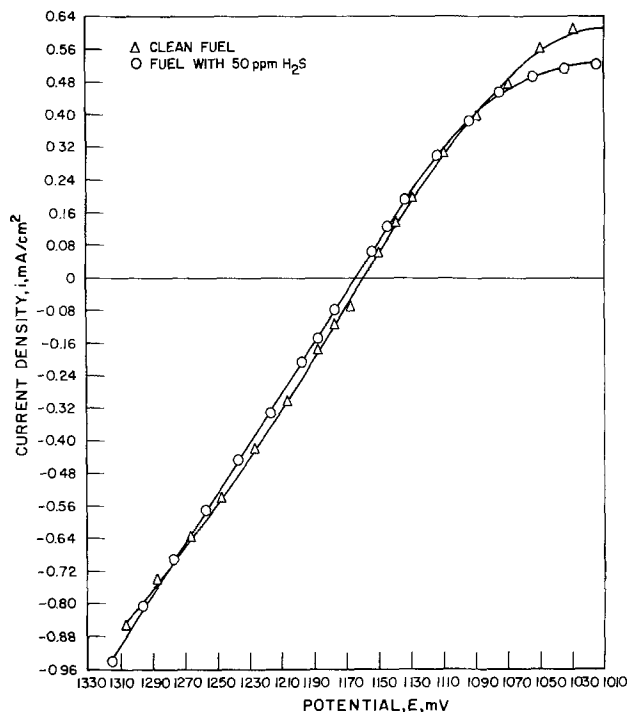


Fig. 2. Steady-state polarization curves for cobalt using low BTU fuel with and without 50 ppm H_2S added (Li/K electrolyte, 650°C).

due to some subtle changes in the fuel composition from one measurement to another.

Introduction of H_2S at concentrations of approximately 1000 ppm into low BTU fuel resulted in extensive sulfidation of both nickel and cobalt upon potentiostating anodically as shown in Fig. 3. In each case, the open-circuit potential was observed to be shifted to more negative values, possibly indicating a mixed-potential effect caused by the fuel oxidation



Fig. 3. Anodes from electrochemical half-cell after they had been potentiostated in Li/K carbonate melt in low BTU fuel containing 1000 ppm H₂S at 650°C

reaction and the presence of metal sulfide on the anode surface. For nickel at 650°C (in low BTU fuel), the open-circuit potential was shifted from -1154 to -1185 mV and for cobalt the shift was -1160 to -1200 mV. Clearly, neither of these two anode materials is stable at such high sulfur levels. With the electrochemical conditions present in the half-cell, the rate of the overall electrochemical reaction was found to be dependent not only upon fuel bubbling rate, but also on the voltage sweep rate used. Such observations indicated diffusion or mixed control. To assess the impact of introducing sulfur species into the electrolyte from the fuel, the electrode kinetics were compared for both nickel and cobalt with clean and sulfur-containing fuels to indicate whether any electrocatalytic poisoning effects occurred by the introduction of such sulfur impurities.

Transient potentiostatic measurements (9, 10) were performed for the separation of kinetic data under the probable diffusion (or mixed) control condition present in the half-cell. By this technique, the time dependency of the current for a given applied potential will be given by

$$i = i(0) \cdot \left(1 - \frac{2}{\sqrt{\pi}} \cdot \lambda \sqrt{t} \right) \quad [1]$$

for the conditions $\sqrt{t} \ll 1$, where

$$\lambda = \frac{i_0}{2F} \left[\frac{1}{\bar{C}_r D_r} \exp\left(\frac{\alpha z F}{RT} \eta\right) + \frac{1}{\bar{C}_o D_o} \exp\left(\frac{(1-\alpha) z F}{RT} z F \eta\right) \right] \quad [2]$$

and $i(0)$ the current density at time zero given by

$$i(0) = i_0 \left[\exp\left(\frac{\alpha z F}{RT} \eta\right) - \exp\left(\frac{-(1-\alpha) z F}{RT} z F \eta\right) \right] \quad [3]$$

where \bar{C}_o and \bar{C}_r are the equilibrium concentrations of the oxidized and reduced species, and D_o and D_r are the corresponding diffusion coefficients, and the other symbols have their usual significance. By plotting i vs. \sqrt{t} in Eq. [1] above, a current density at time zero, $i(0)$, can be extrapolated from the intercept with the current axis. In practice, however, excellent agreement was found between activation currents extrapolated from reaction [1] above and those $i(0)$ values obtained from the extrapolation of currents between 0.8 and 1.2 msec to time zero. Consequently, the majority of activation currents recorded were obtained using the latter technique with periodic comparison with those values obtained from relationships [1]-[3]. A voltage step was applied to the nickel or cobalt working electrode and the current was recorded as a function of time. Under such conditions of diffusion (or mixed) control, the assumption was made that at time zero, only activation control will be present, that is, sufficient supply of electroactive species will be present

together with minimal reaction products, so that any mass transfer effects will be minimized. Figure 4 shows a typical oscillogram for nickel with and without 50 ppm H₂S in low BTU fuel, showing the decay of current with time for an applied anodic pulse of 40 mV for the equilibrium potential (two time scales shown).

Here, the exchange current density calculated from the $i(0)$ value was found to be around 25 mA/cm² in both cases, indicating that such low levels of sulfur (50 ppm H₂S) appear to have little effect upon the electrode kinetics for fuel oxidation, in essential agreement with the steady-state data.

A series of progressively more anodic and cathodic potential steps were applied to both nickel and cobalt in fuel with and without 50 ppm H₂S introduced into low BTU fuel at 650°C. The respective activation polarization curves for these two anodes are shown in Fig. 5 and 6, where they are compared with such data obtained using clean fuel. As was indicated earlier, 50 ppm H₂S does not appear to affect drastically the electrode kinetics for either the anodic or cathodic processes, although some small lowering in electrode activity does become apparent at higher applied overpotentials. Upon introduction of 50 ppm H₂S, the exchange current density was observed to become slightly lower, reducing from 26 to 25 mA/cm², and from 19.5 to 18.5 mA/cm², respectively, for nickel and cobalt, although such small variations in activation data can be considered to be well within the experimental error of this work. When potential step techniques are performed on these anode materials in fuel containing 1000 ppm H₂S, anodic and cathodic currents appear to be dominated by the sulfidation reaction as indicated in Fig. 7 and 8, respectively, for nickel and cobalt.

When high sulfide concentrations build up in the proximity of the anode, either directly from sulfur-

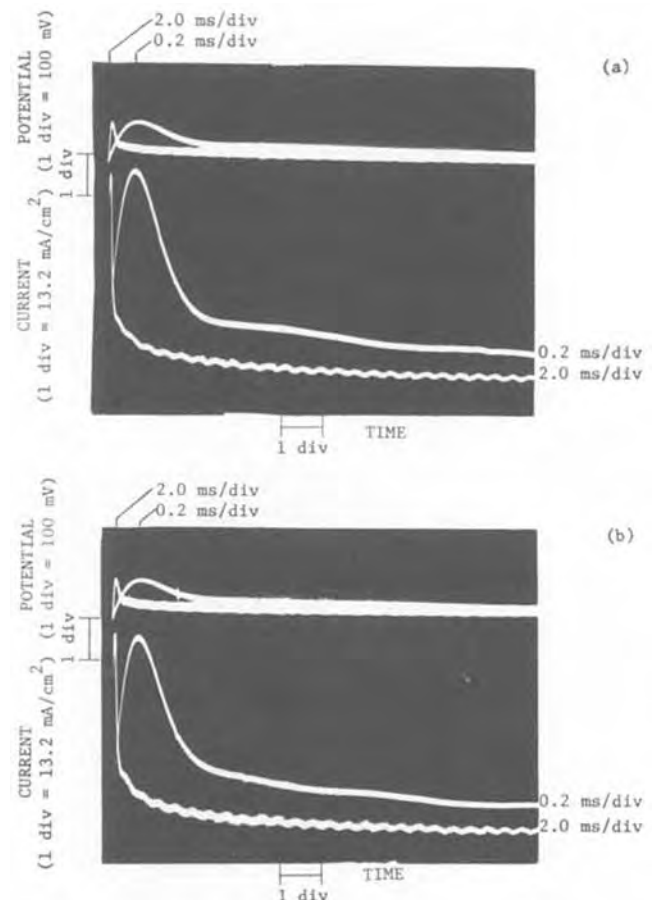


Fig. 4. Transient potentiostatic measurements on nickel in lithium-potassium melt at 650°C [low BTU fuel used both (a) with and (b) without 50 ppm H₂S introduced with fuel].

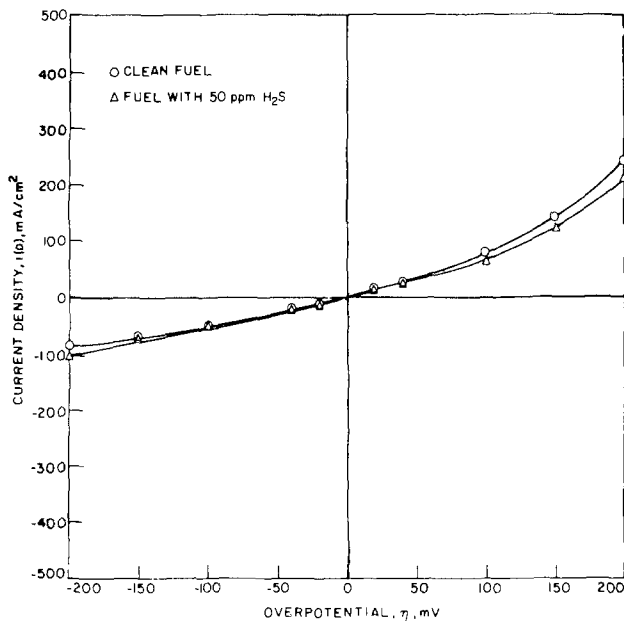


Fig. 5. Comparison of activation polarization curves for nickel in clean low BTU fuel and low BTU fuel with 50 ppm H₂S added.

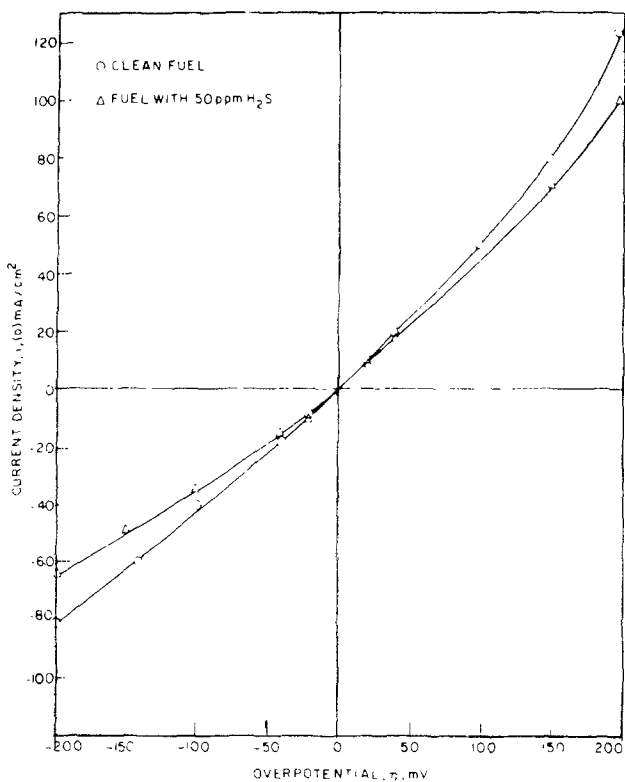


Fig. 6. Comparison of activation polarization curves for cobalt in clean low BTU fuel and low BTU fuel with 50 ppm H₂S added.

containing fuel or indirectly from SO₂ introduced into the cathode, neither nickel nor cobalt appear to be viable anode candidates. There is considerable incentive, therefore, to identify potentially sulfur-tolerant anode materials for this fuel cell system.

Preliminary corrosion results for selected sulfur-tolerant candidate anodes are shown in Table I. Materials which showed apparent stability in this corrosion test were then subjected to steady-state potentiostatic polarization evaluation in the electrochemical half-cell. These results are summarized in Table II, where open-circuit potentials and anodic currents at 50 mV overpotential are compared.

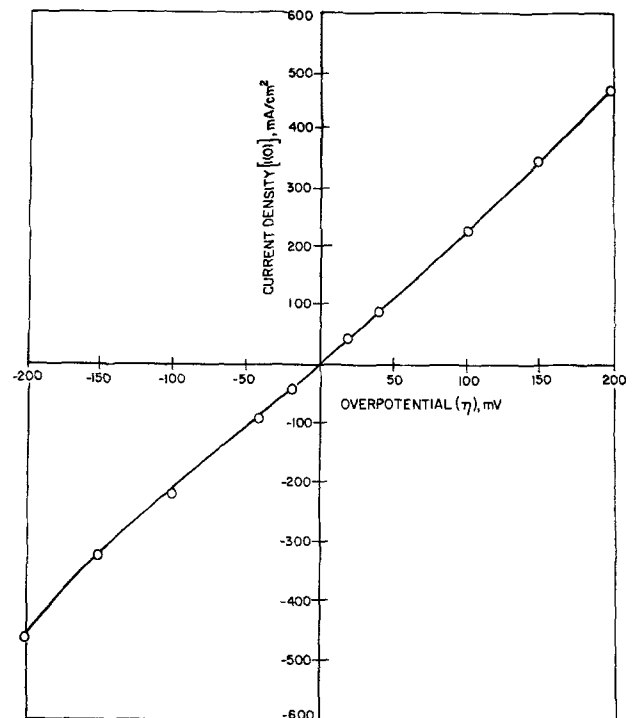


Fig. 7. Apparent activation polarization curve for nickel during sulfidation.

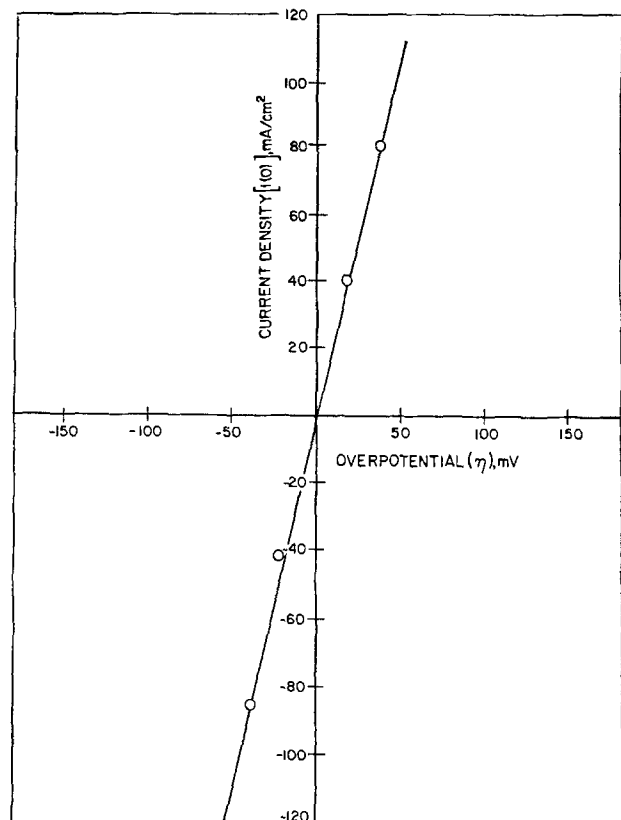


Fig. 8. Apparent activation polarization curve for cobalt during sulfidation.

Apart from nickel and cobalt anodes, which have already been discussed, highest stabilities were found for Mg_{0.05}La_{0.95}CrO₃ and TiC. Figure 9 compares steady-state polarization data on Mg_{0.05}La_{0.95}CrO₃ in low BTU fuel with and without 50 ppm H₂S. No shift in the open-circuit potential was observed, and current voltage characteristics were very similar in both cases, particularly in the anodic region. Introduction of fuel containing 1000 ppm of H₂S did not shift the open-circuit potential to negative values as observed with

Table I. Corrosion results for candidate anode materials

Composition, %	Total exposure to low-BTU fuel, hr	Period in H ₂ S (274 ppm), hr	Total weight change, %	Comments
WC—10; CO—90	1588	1301	-3.3	
TaC	1122	1122	—	Completely corroded
TiB ₂	432	432	—	Completely corroded
ZrC	168	none	—	Completely corroded
TiC	1506	1051	-1.0	
VC	355	187	-24.7	
NbN	1506	1051	+10.1	
Mg _{0.05} La _{0.95} CrO ₃	1506	1051	+0.1	
TiO ₂ (Ta-doped)	1343	1080	+0.7	
TiO ₂ (Nb-doped)	1343	1080	-1.1	
Mo—90; Ti—10	1080	1080	-32.4	
Co—64.8; Mo—35.2	1554	1554	-27.8	
Co—38.1; Mo—61.9	432	432	-53.2	
Nickel	1554	1554	-0.9	
Fe—90.0; Cr—9.0; Mo—1.0	432	432	-48.5	
Cr—30.6; Co—69.4	648	648	—	Completely corroded
Co—49; 51—W	648	648	—	Completely corroded
Co—24.3; 75.7—W	648	648	—	Completely corroded
Co—63.0; Cr—30.0; Mo—7.0	1122	1122	—	Completely corroded
Co—22.1; Cr—77.9	1122	1122	+13.7	
Cobalt	1122	1122	+0.3	
Cr ₂ O ₃ (1 mole TiO ₂)	1122	1122	+7.0	Sample broken
Tungsten	1122	1122	-44.7	
Molybdenum	1122	1122	—	Completely corroded
FeB	474	474	—	Completely corroded
Ni—50; Co—50	474	474	+3.5	
CoPS	474	474	—	Completely corroded
WS ₂	474	474	—	Completely corroded
CoF ₃	474	474	—	Completely corroded
Ni—50; Al—50	474	474	+25.9	
CoAs ₂	474	474	+0.9	
MoS ₂	474	474	—	Completely corroded
Cr ₃ Co ₂	474	474	—	Completely corroded
WC	648	648	—	Completely corroded
MnS	648	648	-27.0	Sample broken

nickel and cobalt anodes. Examination of this material afterwards indicated no surface corrosion even after anodic potentiostating.

Figure 10 compares activation data performed on this material using the potential step technique with that obtained for nickel. For Mg_{0.05}La_{0.95}CrO₃ exchange current densities of around 8 mA/cm² were obtained in low BTU fuel. As seen in Fig. 10, exchange current densities for fuel oxidation on nickel are greater than with Mg_{0.05}La_{0.95}CrO₃. On the basis of the kinetic data and the apparently high-sulfur tolerance of Mg_{0.05}La_{0.95}CrO₃, this material may be an interesting candidate as an anode material for the molten carbonate fuel cell, although the present high cost of this material would not favor its use in the immediate future.

Steady-state polarization measurements have been performed on TiC, Cr₂O₃ (1 m/o of TiO₂), WCo (75.5% W, 24.3% Co), Nichrome (80% Ni, 20% Cr), and NiAl

in the lithium/potassium carbonate electrolyte at 650°C in low BTU fuel. Upon examination of all of these materials, evidence of surface corrosion became evident. Candidate anode current collector materials were subjected to an initial screening corrosion test as described previously for the selected anodes. The materials selected, together with the corrosion results, are shown in Table III. From these results, good corrosion stability was found for 446 and 310 stainless steels, together with Uniloy. More promising materials were subjected to steady-state potentiostatic evaluation. Figure 11 shows the steady-state current voltage characteristics obtained with 446 stainless steel. The results of such potentiostatic testing for the selected anode current collector materials are summarized in Table IV. Materials were anodically potentiostated at 75 mV in low BTU fuel with and without H₂S and the currents recorded as a function of time. A decay in current with time was taken as indicative of surface oxide

Table II. Potentiostatic evaluation of anode materials using low BTU fuel gas in binary carbonate melt at 650°C

Composition, %	Clean fuel		Fuel with 50 ppm H ₂ S		Comments
	Open-circuit potential, mV	Current <i>i</i> (at 50 mV from rest potential) mA/cm ²	Open-circuit potential, mV	Current <i>i</i> (at 50 mV from rest potential) mA/cm ²	
Cr ₂ O ₃ —99; TiO ₂ —1	-1032	0.122			Electrode badly cracked
Nickel—50; cobalt—50	-1138	0.383	-1102	0.202	Trace of current very noisy
Tungsten carbide	-1368	2.918	-1305	1.134	Indicates corrosion; not run cathodically
Tungsten cobalt	-1402	2.299			Electrode corroded; not run in H ₂ S
Titanium carbide	-1142*	0.166*	-1135	0.167	
Mg _{0.05} La _{0.95} CrO ₃	-1130	0.040	-1132	0.041	
Ni—50; Al—50	-1160	0.918			Electrode corroded; not run in H ₂ S
TiO ₂ (Ta doped)			-1106**	0.157**	
TiO ₂ (Nb doped)	-1097	0.114	-1134**	0.105**	Very large cathodic current
Nickel	-1154	0.250	-1141	0.193	
Nickel			-1185**	17.51**	Indicates corrosion
Cobalt	-1158	0.304	-1163	0.304	
Cobalt			-1201**	8.47**	
Niobium nitride	-1104	0.493			Indicates corrosion; not run in H ₂ S
Chromium—77.9; cobalt—22.1	-1290	0.0			No anodic current
CoAs ₂	-1136	0.32			

* High BTU fuel.
** 1000 ppm H₂S.

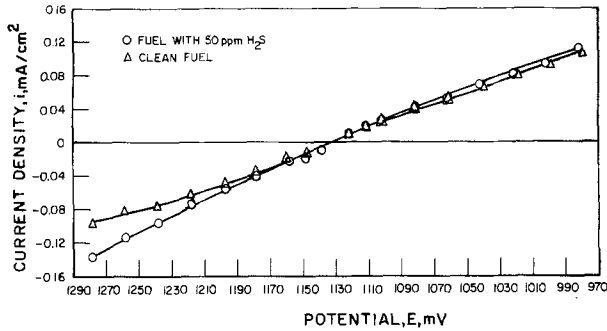


Fig. 9. Steady-state polarization curve for $Mg_{0.05}La_{0.95}CrO_3$ using low BTU fuel with and without 50 ppm H_2S added (Li/K electrolyte, $650^\circ C$).

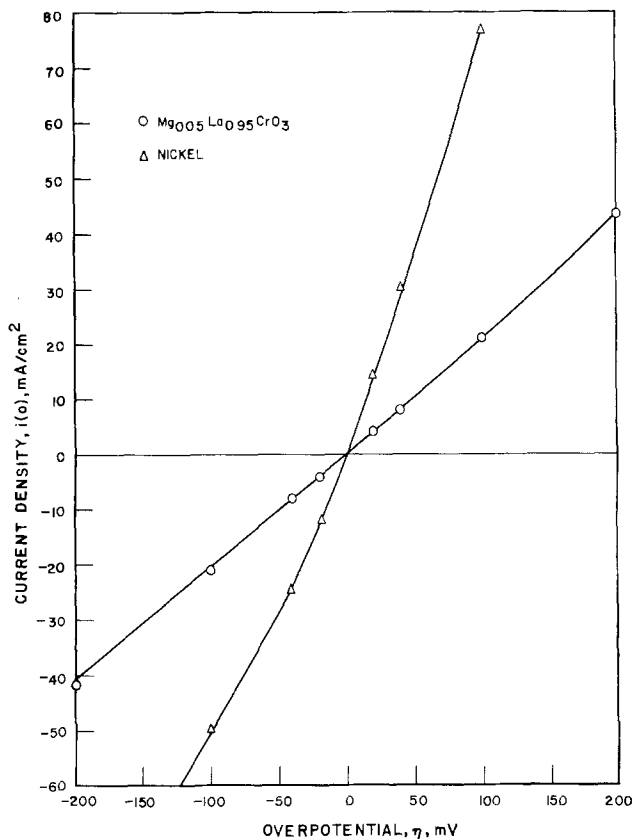


Fig. 10. Activation polarization curves for $Mg_{0.05}La_{0.95}CrO_3$ and nickel using low BTU fuel (Li/K carbonate electrolyte, $650^\circ C$).

formation as shown in Fig. 12 for 446 stainless steel. All materials were examined visually for evidence of corrosion after such potentiostating.

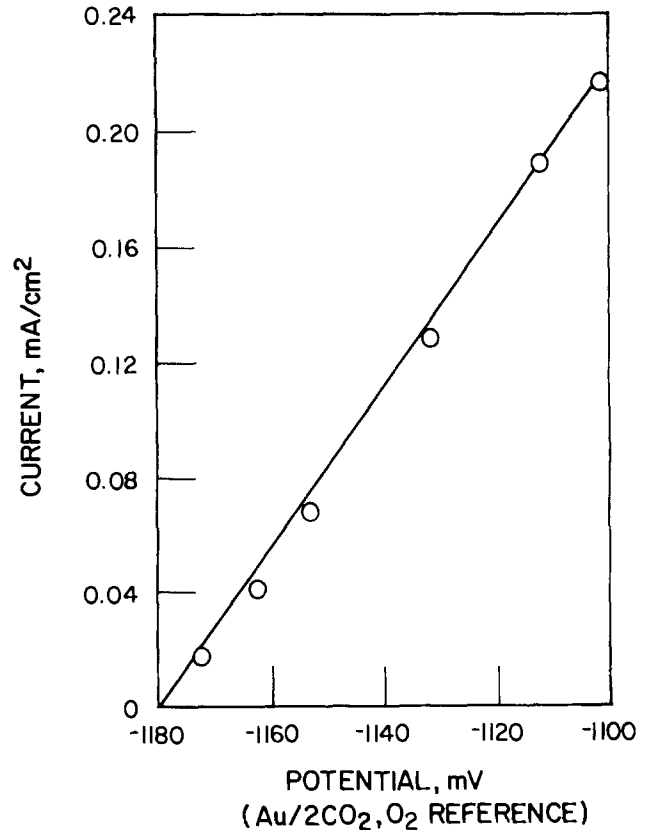


Fig. 11. Steady-state polarization curve for 446 stainless steel in low BTU fuel at $650^\circ C$.

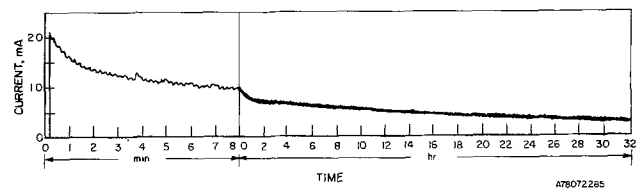


Fig. 12. Variation of current with time at an applied anodic overpotential of 75 mV for 446 stainless steel (low BTU fuel used).

Of those materials evaluated, high stabilities were found for 410 and 310 stainless steels. Open-circuit potentials were found for the stainless steels in low-BTU fuel were fairly close to those expected; nevertheless, some of the other candidates that readily corroded showed somewhat more cathodic potentials.

Conclusion

At low-sulfur concentrations (≈ 50 ppm) the electrode kinetics for fuel oxidation on both nickel and cobalt anodes do not appear to be effected in an im-

Table III. Corrosion results for candidate anode current collector materials

Composition, %	Total exposure to low BTU fuel, hr	Period in H_2S (274 ppm), hr	Total weight change, %	Comments
C—0.25; Mn—2.0; Si—1.5; Cr—25.0; Ni—20; Fe—51.25 (SS—303)	1588	1301	+0.2	
Cr—50.0; Ni—49.0; Ti—1.0 (Uniloy)	1588	1301	+0.5	
Co—50.0; Cr—28.0; Fe—16.5; W—5.5	355	187	-20.3	
Fe—81.8; Al—15; Mo—3.2 (VE—441)	648	648	+82.9	
Cr—21.0; Mn—9.0; Ni—6.0; Fe—64	1588	1301	+0.5	
Fe—70; Al—10; Mn—20 (EX—20)	648	648	+26.7	
C—0.2; Cr—25.0; Ni—0.5; Fe—74.3 (SS—446)	1588	1301	+0.6	
Cr—22.0; Co—0.5; Al—5.0; Fe—73.5 (Kanthal)	258	258	—	Completely corroded
C—0.18; Mn—2.0; Si—1.0; P—0.2; S—0.15; Cr—18.0; Ni—9.0; Mo—0.6; Fe—Bal. (SS—303)	1554	1554	-5.3	
C—0.08; Cr—17.0; Ni—12; Mo—3.0; Fe—Bal. (SS—316)	1554	1554	+2.2	

Table IV. Potentiostatic evaluation of anode current collector materials using low BTU fuel gas in binary carbonate melt at 650°C

Composition, %	Clean fuel		Fuel with 50 ppm H ₂ S		Comments
	Open circuit potential mV	Current <i>i</i> (at 50 mV from rest potential) mA/cm ²	Open circuit potential, mV	Current <i>i</i> (at 50 mV from rest potential) mA/cm ²	
C-0.2; Cr-25.0; Ni-0.5; Fe-74.3 (SS 446)	-1182	0.128	-1137	0.147	
C-0.25; Mn-2.0; Si-1.5; Cr-25.0; Ni-20; Fe-51.25 (SS 310)	-1186	0.063	-1145	0.089	Black coating after test
C-0.08; Cr-17.0; Ni-120; Mo-3.0; Fe Bal. (SS 316)	-1173	0.156	-1164	0.197	Black coating after test
Co-0.15; Mn-1.0; Si-1.0; Cr-12.5 Fe-Bal. (SS 410)	-1173	0.184	-1148	0.157	
C-0.15; Mn-1.0; Si-1.0; Ni-45.45; Fe-18.5; Cr-21.8; Co-2.5; Mo-9.0; W-0.6 (Hastelloy X)	-1167	0.236	-1147	0.207	
Ni-80.0; Cr-20.0 (Nichrome)	-1257	3.508			Corroded
Cr-22.0; Co-0.5; Al-5.0; Fe-73.5 (Kanthal)	-1330	0.0			Corroded
Fe-70; Al-10; Mn-20 (Ex 20)	-1347	0.218	-1222	0.911	
Fe-81.8; Al-15.0; Mo-3.2 (VE 441)	-1382	0.413			Crusted with thick black oxide

portant way. At high-sulfur concentrations (≈ 1000 ppm) shifts in the open-circuit potential of both these materials occurred together with evidence of sulfidation.

Promising anode materials which may show long-term sulfur tolerance include $Mg_{0.05}La_{0.95}CrO_3$ and TiC. However, their long-term performance as porous sintered anodes has yet to be evaluated. Anode current collectors showing the greatest stability included 410 and 310 stainless steels.

Acknowledgment

This work was performed for the Electric Power Research Institute under Contract No. RP-1085-2. The authors acknowledge the support and contribution of their colleagues at IGT.

Manuscript submitted Feb. 8, 1979; revised manuscript received July 19, 1979.

Any discussion of this paper will appear in a Discussion Section to be published in the December 1980 JOURNAL. All discussions for the December 1980 Discussion Section should be submitted by Aug. 1, 1980.

Publication costs of this article were assisted by the Institute of Gas Technology.

REFERENCES

1. E. A. Gulbransen and S. A. Jansson, in "High Temperature Metallic Conversion of Sulfur and Its Compounds," Z. A. Foroulis, Editor, pp. 3-51, The Electrochemical Society Softbound Proceedings Series, New York (1970).
2. J. R. Rostrup-Nielsen, *J. Catal.*, **11**, 220 (1968).
3. R. B. Pannell, K. S. Chung, and C. H. Bartholomew, *ibid.*, **46**, 340 (1977).
4. K. Luthra and W. Worrell, in "Properties of High-Temperature Alloys," Z. A. Foroulis and F. S. Pettit, Editors, p. 318, The Electrochemical Society Softbound Proceedings Series, Princeton, N.J. (1976); *Metall. Trans.*, **10A**, 621 (1979).
5. W. S. Hagel, *J. Appl. Phys.*, **36**, 2586 (1965).
6. W. A. Fischer and H. Dietrich, *Phys. Chem., NF*, **41**, 205 (1964).
7. S. R. Shatynski, *Oxid. Met.*, **11**, 307 (1977).
8. H. J. T. Ellingham, *J. Soc. Chem. Ind. London*, **63**, 125 (1944).
9. H. F. Gerischer, *Z. Electrochem.*, **59**, 604 (1955).
10. H. F. Gerischer and W. F. Vielstich, *Z. Phys. Chem., NF*, **3**, 16 (1955).

Mass Transport Phenomena in the Molten Sulfur-Sodium Polysulfide System

J. Divisek, F. G. Bodewig,* J. Mergel, and H. Lippert

Institute of Chemistry, Institute 4: Applied Physical Chemistry, Nuclear Research Center (KFA), Juelich, Germany

and B. Kastening

Institute of Physical Chemistry, University of Hamburg, Hamburg, Germany

ABSTRACT

The exchange rate for mass transfer of sulfur across the sulfur-sulfur saturated sodium pentasulfide interface was investigated by S-35 tracer studies and found to be 0.19 ± 0.04 g S/cm²/hr at 300°C. The self-diffusion coefficients of sulfur in Na₂S₄ and Na₂S_{5.2} as determined by the capillary method using S-35 labeling were $2.3 \pm 1.1 \times 10^{-5}$ and $1.5 \pm 0.4 \times 10^{-5}$ cm² sec⁻¹, respectively, at 300°C. The diffusion coefficient of the electroactive species in Na₂S₄ was determined by chronopotentiometry at a rotating disk electrode. Its value is 7×10^{-7} cm² sec⁻¹ at 300°C. Approximate values of the activation energy of diffusion and nC_{ox} in Na₂S₄ are given. A first attempt is made, in terms of a mechanistic model of the mass-transfer processes, to explain the different data obtained for *D* from tracer and electrochemical experiments, respectively.

During the discharge of the sodium-sulfur battery sulfide is transferred across the sulfur-sodium polysulfide interface to the melt and transported as poly-

sulfide through the melt to the electrode where it is electrochemically reduced to a lower polysulfide (1-3). No data for the mass transfer of sulfur between the sulfur pool and the melt are available in the literature, and for its diffusion through the melt the

* Electrochemical Society Active Member.

Key words: fused salts, battery, diffusion, chronopotentiometry.

data are conflicting (1, 4). In the course of some work done on the Na/S battery in this laboratory it was therefore deemed desirable to study these transport phenomena and, if possible, determine whether the diffusion or the sulfur transfer is the rate-determining step in the sulfur transport to the electrode.

Experimental

Chemicals.—Sulfur flower (Merck) was purified according to the method of Bacon and Fanelli (5). Reagent grade sodium metal (Merck) was used as received after having been cleaned in ethanol.

Radioactive sulfur (isotope S-35, half-life 87d) was obtained from Amersham Buchler or prepared from purified sulfur by irradiation in the DIDO reactor of the Nuclear Research Center, Juelich. The activity of this stock supply was determined as described below and was between 15 and 100 $\mu\text{Ci/g}$ at the time of use. All experiments were performed under argon gas passed through a purification unit (Oxisorb; Messer Griesheim).

Polysulfide preparation.—Sodium tetrasulfide was prepared from the elements according to the method of Fehér and Berthold (6) in a glove box with a circulated and purified argon atmosphere ($\text{O}_2 < 10$ volume ppm; $\text{H}_2\text{O} < 15$ volume ppm). Its composition was determined as described by Fehér and Berthold (7). The ethyl alcohol content remaining after the product had been dried under vacuum was determined by gas chromatography to be below the detection limit of 0.01 weight percent (w/o).

Sulfur-saturated sodium pentasulfide ($\text{Na}_2\text{S}_{5.2}$) was prepared from Na_2S_4 by the addition of an excess of sulfur followed by mixing the liquid constituents at about 300°C with a vibrator (Vibro-Mixer E1 Chemap) for 15 min. The excess sulfur separates overnight from the pentasulfide melt and can be removed after solidification. The composition of the product thus prepared was determined analytically (7) to be $\text{Na}_2\text{S}_{5.2}$ within experimental error. Measurements of potential with respect to a sodium/ β -alumina electrode confirmed the composition.

The active and inactive sulfide melts for the capillary experiments were prepared as follows. A charge of tetrasulfide was divided into two portions to one of which radioactive sulfur was added. To the other portion an equivalent amount of inactive sulfur was added so that both portions had the same composition differing only slightly from that of the starting material (1-2g of sulfur were added per 100g of tetrasulfide). The labeled pentasulfide was prepared as above except that the sulfur used contained S-35. The inactive pentasulfide was prepared from the same charge of tetrasulfide using an equivalent amount of inactive sulfur.

Equipment and Procedures

Sulfur transfer and self-diffusion coefficients.—The exchange of sulfur across the sulfur-sulfur saturated pentasulfide system was determined by labeling the sulfur phase with radioactive sulfur and measuring the increase of the activity of the sulfide phase with time.

The experiments were carried out in a Pyrex vessel (diam 3.5 cm) in a vertical tube furnace at temperatures between 297° and 305°C . First, molten pentasulfide (80g) and sulfur (50g) were left in contact at 300°C for 48 hr under slow stirring of both phases to ensure that equilibrium conditions had been established. Radioactive sulfur (40-85 μCi) was then added to the sulfur phase and samples of about 1-2 ml were taken from the bulk of the pentasulfide phase at intervals of usually 1 hr. Sulfur was precipitated from these samples and prepared for liquid scintillation counting as described below. During the 5-6 hr, which each run lasted, one or two samples were also taken from the sulfur phase to determine its activity. The pentasulfide and sulfur originally charged into the vessel and all samples taken from it were weighed

since the amount of material left in the vessel during the course of the experiment as well as the activity removed from it by taking the samples were needed for the calculations.

The mass transfer of sulfur across the interface was alternatively determined by measuring the decrease of the activity in a capillary filled with radioactive sulfur and immersed in molten pentasulfide. This method has been used frequently to determine self-diffusion coefficients (8). The apparatus is shown in Fig. 1. The capillaries had an inside diameter of 0.08 cm, a length of 4.0 cm, and their upper end was closed by a flat seal. The capillary was filled by evacuating the Pyrex vessel, lowering the capillary into the radioactive sulfur (in position 1), and admitting argon into the vessel. The capillary was then raised and the sulfur pot replaced by the pot with the pentasulfide previously held in position 2. To start the experiment the capillary was lowered into the pentasulfide melt and the rotation of the pot was started. The decrease of the activity was determined after 3-4 hr and the experiments were carried out at $300^\circ \pm 2^\circ\text{C}$. The apparatus shown in Fig. 1 has the advantage over other arrangements [cf., e.g., Ref. (9)] that the material in the capillary remains liquid throughout the experiment. This is especially advantageous for sulfur and compounds such as polysulfides, which form bubbles in the capillary on remelting.

The same procedure was followed for the determination of the self-diffusion coefficients of sulfur in its melt and in Na_2S_4 and $\text{Na}_2\text{S}_{5.2}$, the only difference being that the substances in the capillary again contained the labeled material.

Electrochemical measurements.—The chronopotentiometric measurements were performed on a tetrasulfide melt with a rotating disk electrode driven by a rotator with speed control (Model ASR; Pine Instru-

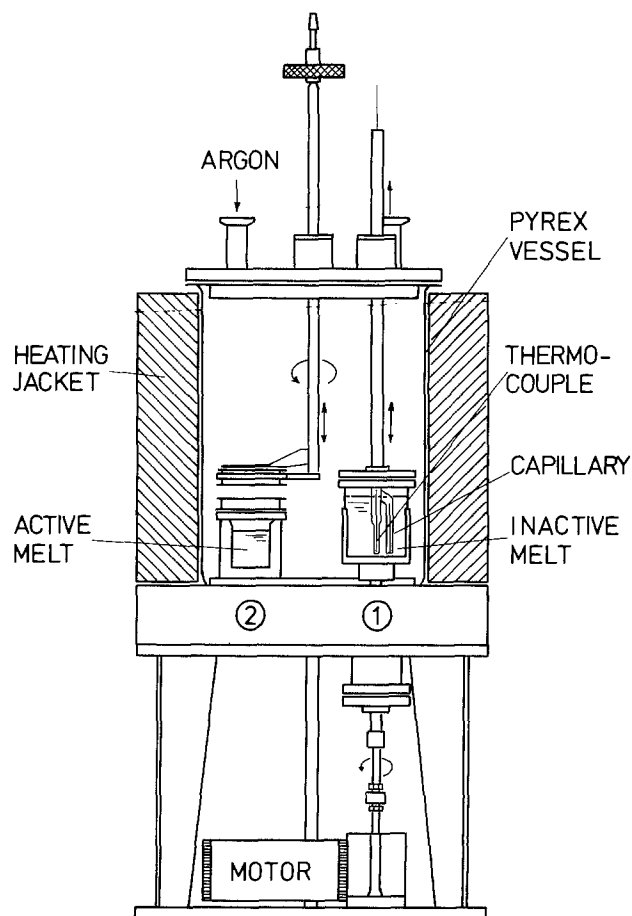


Fig. 1. Diffusion apparatus

ment Company). A disk electrode was constructed which proved to be suitable for high temperature work. Details are shown in Fig. 2. A PAR universal programmer (Model 175) served as pulse generator. The curves were drawn on an X-Y recorder (Model 7046 A; Hewlett Packard) from the memory of a digital oscilloscope (Model 1090 A with a Model 96 A Plug-In; Nicolet). A graphite rod in the melt served as reference electrode. It behaves reversibly and has a stable potential (2).

The voltammetric curves were obtained with the rotating disk electrode described above, employing a potentiostat with a continuous and automatic IR compensation built in this laboratory (10) in principle according to the method of Britz and Brocke (11). At a sufficiently large double-layer time constant the accuracy of the IR compensation of this instrument is about 1%. This condition was met here since the time constant in this melt system [(4), and own measurements] is about a factor of 100 larger than the current interruption period of the potentiostat.

Activity measurement.—The activity of the samples was determined by liquid scintillometry. The following is a short description of the procedure adopted. A weighed sulfide sample was dissolved in water from which sulfur was precipitated by adding HCl. Although one sulfur atom per molecule polysulfide escapes as H_2S , this can be accounted for in the calculations since S-35 is distributed proportionally among the decom-

position products as was shown here by checking the radioactivity balance in some experiments [see also Ref. (12)]. The precipitated sulfur was dissolved in toluene (CS_2 could not be used due to its high degree of quenching). A mixture of this solution with Instagel (Hewlett Packard) was counted for one minute on a Corumat-2700 (INC Tracerlab). Since only the ratio of the activities of the samples in question was required for the calculations it was not necessary to determine the counting efficiency as long as the quenching due to sulfur itself remained constant. This was assured by always having the same amount of sulfur present in the solutions counted.

Results and Discussion

Mass transfer of sulfur.—A total of six runs were performed to determine the exchange of sulfur across the sulfur-sulfur saturated pentasulfide interface.

The amount of sulfur (in g) transferred during a measurement period was obtained by dividing the increase of the activity in the sulfide phase during that period by the activity of the sulfur phase per gram of sulfur at the beginning of the period. The calculations are straightforward. The following approximations were made. The activity of the sulfur phase was considered constant during the period and the transfer of radioactive sulfur in the reverse direction (*viz.*, from the sulfide to the sulfur phase) was neglected. Both approximations are justified since they produce errors of less than 3%. The overall accuracy of the measurements (estimated to be 15%) was considered such that it seemed unwarranted to correct for these changes.

The results obtained at various stirring rates are shown in Fig. 3. The least squares line of all data points with its confidence interval (13) was determined to check whether or not the transfer of S-35 is influenced by the stirring rate. It is, however, a moot point to decide this solely on the basis of these data although the values at 110 and 205 rpm are somewhat

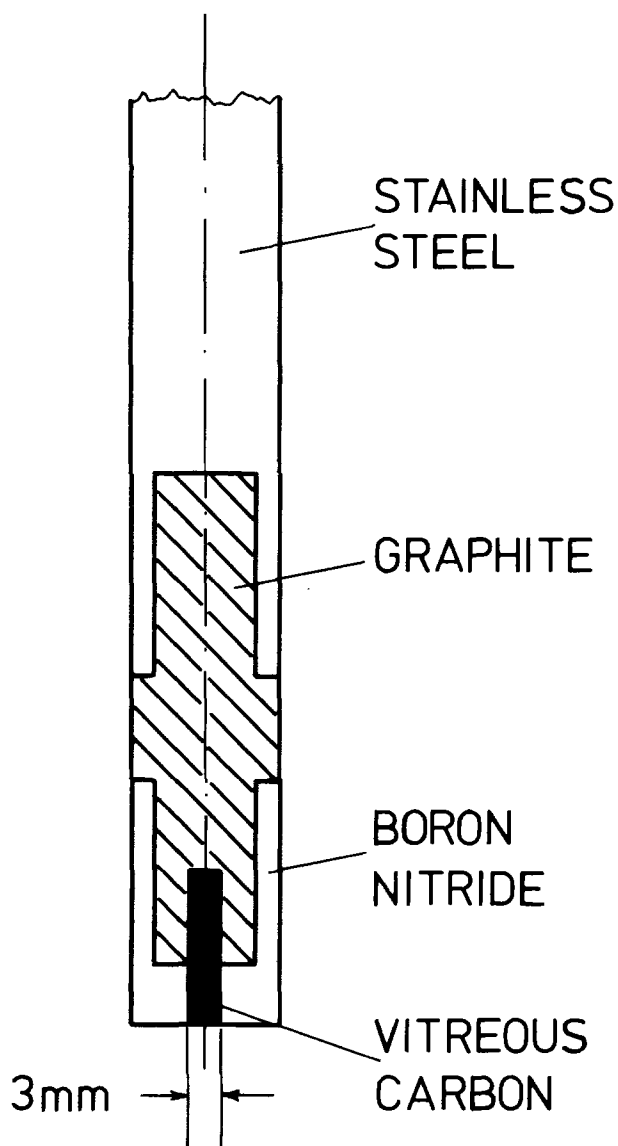


Fig. 2. Rotating disk electrode for high temperature studies

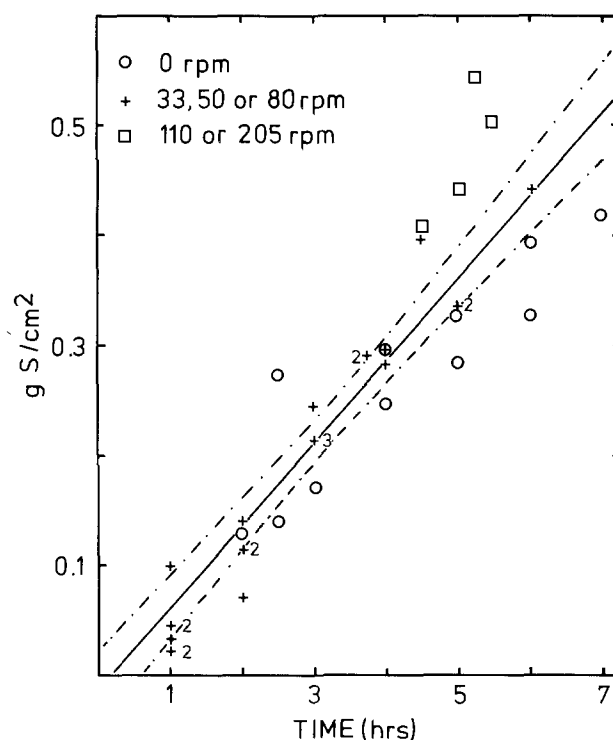


Fig. 3. Sulfur transferred in g/cm^2 sulfur-pentasulfide interface as a function of time and stirring speed (at $300^\circ C$). Least squares line of all data points (6 runs with a total of 43 points including 6 points, 0, 0). Dashed curve is 95% joint confidence hyperbola [Ref. (13)]. Number indicates multiple points.

higher (0.10 g/cm²/hr) than those obtained from the least squares line (0.075 g/cm²/hr), while those in the unstirred melt are somewhat lower (0.06 g/cm²/hr). Increasing the stirring rate above 200 rpm was not possible without disturbing the interface and obtaining an undefined area. It was therefore decided to carry out the same measurements with the aid of capillaries whereby a diffusion layer of labeled pentasulfide is essentially prevented. To calculate the amount of sulfur transferred in these experiments, Fick's second law with the appropriate boundary conditions

$$D \frac{\partial c(x,t)}{\partial x} = kc(x,t), c(x,0) = c^b, c(\infty,t) = c^b$$

has to be solved. The solution, for a cylinder of infinite length, has been given by Delahay (14) as

$$c(x,t) = c(x,0) \left[\operatorname{erfc} \left(\frac{x}{2D^{1/2}t^{1/2}} \right) + \exp \left(\frac{Qx}{D^{1/2}} + Qt \right) \operatorname{erfc} \left(Qt^{1/2} + \frac{x}{2D^{1/2}t^{1/2}} \right) \right]$$

where

$$Q = \frac{k}{D^{1/2}}$$

That the equation is also valid for a capillary with a length of 4 cm as long as the diffusion time is kept short (3-4 hr) is shown by the concentration profile of S-35 in the capillary calculated for a diffusion time of 4 hr and an infinite value of k (Fig. 4, curve a). A finite value of k only improves the situation since the section at the end of the capillary, where the concentration of S-35 remains at its initial value, becomes even longer (Fig. 4, curve b representing a typical run). The value of the self-diffusion coefficient (D) of sulfur in its melt required for calculating the curve was determined in other experiments (see below). With the values of D and t known the value of k was determined in the following manner. The concentration profile at time t was calculated for the experimentally determined amount of tracer at time $t = 0$ and a likely value of k . Then the amount of tracer remaining at time t was obtained by numerically integrating the area under the curve and compared with the amount experimentally determined at time t . The value of k was changed until these two values agreed to within 0.1%. The values of k determined in four experiments with $D = 5.07 \times 10^{-5}$ cm²/sec (see Table I)

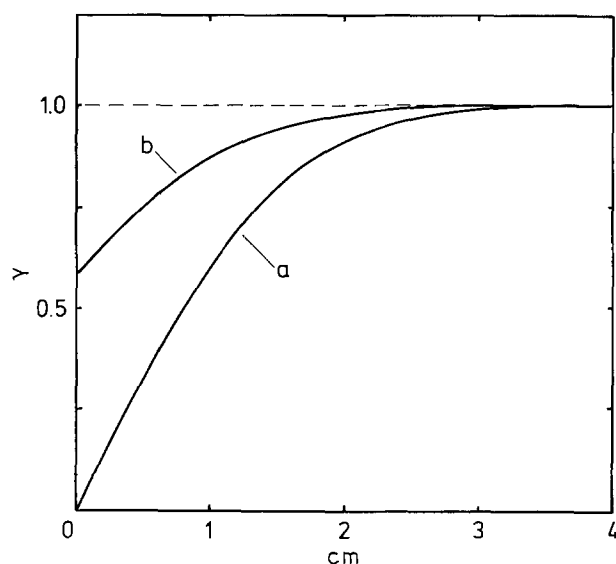


Fig. 4. Fraction of S-35 (γ) remaining in capillary as a function of the distance from the mouth of the capillary. Curve a, for an infinite value of k , curve b, represents a typical run.

Table I. Self-diffusion coefficients in liquid sulfur, Na₂S₄, and Na₂S_{5,2} at about 300°C

	Temperature (°C)	$D \times 10^5$ (cm ² sec ⁻¹)
Sulfur	298	5.56
	296	5.54
	298	4.12
Average (std dev)	—	5.1 (0.9)
Sodium tetrasulfide	296	1.57
	300	3.57
	300	1.33
	304	3.54
	307	1.39
Average (std dev)	—	2.47
Sodium pentasulfide	297	1.18
	297	1.42
	300	0.95
	300	1.20
	300	1.81
Average (std dev)	—	2.12
Average (std dev)	—	1.4 (0.5)

were: 2.69, 2.81, 3.18, and 4.00×10^{-5} cm/sec at 296°C. The amount of sulfur transferred was calculated from

$$\frac{dN}{qdt} = kc$$

where $c = 1.69$ g/cm³ and q is the area of the interface, here taken equal to the cross section of the capillary since visual inspection with a magnifying glass showed a practically flat interface between the two phases. The values thus obtained were 0.16, 0.17, 0.19, and 0.24 g/cm²/hr with an average value of 0.19 ± 0.04 g/cm²/hr. This value seems more justified than the one determined above since in those experiments a diffusion layer of S-35 must have been present.

The calculations of the mass transfer of sulfur from the capillary experiments depend on the condition that no convection disturbances occur inside the capillary since these would cause some of the liquid to be dragged out (15). If the liquids in the capillary and bath are the same (which is the case if self-diffusion coefficients are measured), the length of the region where the disturbances occur can be evaluated (16). This " Δl -region" leads to a diffusion path shorter than the geometric length of the capillary but the experiments can be carried out such that Δl becomes negligible compared to the length of the capillary as will be shown below in the section "Self-diffusion coefficients." If the liquids are not the same and form an interface the disturbances in the capillary will be smaller, if not all together absent, especially if the lighter liquid is in the capillary. It is, therefore, also justified to neglect the " Δl -effect" in the calculations of the mass transfer of sulfur since the same experimental conditions prevailed, except that an interface existed between the two liquids.

The net rate of sulfur transfer across the interface S/Na₂S_x, which is zero at equilibrium conditions ($x = 5.2$), will be positive or negative according to whether $x > 5.2$ or $x < 5.2$. However, the assumption seems to be reasonable that the net rate under such conditions is always smaller than the exchange rate at $x = 5.2$ ($k = 3$ cm/sec corresponding to 0.19 g S/cm²/hr, see above). A distinct transfer rate has nevertheless been observed in a qualitative manner under conditions where the x value, in the immediate vicinity of the interface, is not far from equilibrium, as shown by the following experiment. An open ended Pyrex tube (diam 2 cm) was placed vertically in a large bath of tetrasulfide Na₂S₄ (350g) which effectively served as a sulfur sink. Some sulfur was added on top of the melt inside the tube so that it just covered the highest of four gold plated Pt wires which were sealed into the wall of the tube at a distance of about 1.5 mm of each other along the tube's vertical axis. The rest potentials of these wire electrodes was measured against a reference electrode consisting of a

graphite rod in the tetrasulfide bath. When steady-state conditions had been reached, there always existed a rather thick diffusion layer (several mm) the composition of which corresponded to $5.2 > x > 5$ within the range where the wires were placed (the error of the potential measurement was estimated at 5...10 mV so that a more accurate determination of the composition was not possible). Both the transport through the diffusion layer and the limited rate of transfer across the interface must therefore in general be taken into consideration.

Self-diffusion coefficients.—The self-diffusion coefficients of sulfur in its melt and in tetrasulfide and pentasulfide melts were calculated with the simplified formula of McKay (17, 9)

$$D = \frac{7.7476l^2(1-\gamma)^2}{\pi^2 t}$$

where γ is the fraction of tracer remaining at time t in a capillary of length l , closed at one end and immersed in a diffusion sink where the tracer concentration is effectively zero at all times. The formula can be applied if $1 > \gamma > 0.5$ which was achieved in these experiments by keeping the diffusion time between 3 and 4 hr.

The Reynolds number given by

$$N_{Re} = \frac{R\omega\rho d}{60\eta}$$

where R (radius of rotation) = 0.8 cm, ω (angular frequency) = $2\pi \times 33$ rpm, ρ (density of melt) = 1.8–1.9g cm⁻³ [from Ref. (18)], d (ID of capillary) = 0.08 cm, and η (viscosity of melt) = 0.43–0.57g cm⁻¹ sec⁻¹ from Ref (18)] had a maximum value of about 1 in these experiments. This results in a “ Δl -region” (16)

$$\Delta l = d(1.35 \times 10^{-2} + 1.69 \times 10^{-1}N_{Re} - 1.30 \times 10^{-2}N_{Re}^2) = 0.014 \text{ cm (max.)}$$

which can be neglected here compared to the length of the capillary (4 cm). The value of γ was determined by taking the ratio of the experimentally measured activity remaining in the capillary at time t and that present initially at time $t = 0$. The results are listed in Table I.

The self-diffusion coefficient in liquid sulfur has been determined previously by Saxton and Drickamer (19), also with S-35. At 300°C they reported a value of about 2×10^{-6} cm²/sec. The agreement is poor. This may be due to the method of analysis used at that time, *viz.*, of counting solid samples under a Geiger counter. This certainly presents problems regarding the counting geometry although the authors reported having taken considerable care in this respect. Furthermore, the experiments were carried out with a frit of which the effective pathlength had to be determined in another set of experiments and this may have introduced another source of error, especially since the latter experiments had to be carried out at a much lower temperature.

The self-diffusion coefficients in polysulfide melts have not been determined previously. The values here are in the usual range found in other melts.

Electrochemicals diffusion coefficients.—The chronopotentiometric measurements for determining the diffusion coefficient of the electroactive species in the tetrasulfide melt were carried out with a rotating disk electrode. This method has the advantage that no prior knowledge of the concentration of the electroactive species and no assumptions regarding the actual reaction(s) at the electrode are required. The only conditions are that the mass transport of the electroactive species must be controlled by convective diffusion according to Levich (20) and any equilibria in which the electroactive species may be involved with-

in the diffusion layer must be kinetically sufficiently fast. The former condition is fulfilled as shown in Fig. 5 by the fact that the cathodic current at the disk electrode varied linearly with $\sqrt{\omega}$, while the anodic current was a quasi-linear (21) function of $\sqrt{\omega}$, due to blocking of the electrode surface by sulfur above certain anodic current densities (about 1 A/cm² in Fig. 7). The latter condition is met because the diffusion coefficient determined by this method at several rotational speeds remained constant within experimental error (see Table II).

At the anodic current densities used here the rotating electrode remains free of deposit. A stationary electrode, on the other hand, becomes blocked in both the anodic and cathodic directions by sulfur and an insoluble polysulfide, respectively, (1, 2), and is therefore less suitable for measuring diffusion coefficients in this melt system.

The calculations were carried out according to the mathematical solution derived by Hale (22) and by Nanis and Klein (23) whereby the general equation for convective diffusion

$$\frac{\partial c}{\partial t} = D \frac{\partial^2 c}{\partial x^2} - V_x \frac{\partial c}{\partial x}$$

is solved for the galvanostatic boundary conditions

$$c(x,0) = c^b, \quad c(\infty,t) = c^b, \quad \text{and} \quad \left(\frac{\partial c}{\partial x} \right)_{x=0} = \text{constant}$$

by introducing the dimensionless variables

$$y = \frac{c - c^b}{c^b - c_{0,\tau}}, \quad \theta = \frac{Dt}{\delta^2}, \quad \text{and} \quad z = \frac{x}{\delta}$$

where δ is a normalized form of the Levich layer ($1.62D^{1/3}\nu^{1/6}\omega^{-1/2}$), $c_{0,\tau}$ the concentration at the electrode surface at transient time τ , and c^b the time independent bulk concentration. If a galvanostatic pulse is applied to the electrode the potential changes with time. At the transient time τ the potential becomes constant and the function θ reaches a value of 2.5 according to the normalization of Hale (22). The diffusion coefficient can then be calculated from $\theta = D\tau/\delta^2$ with the experimentally determined value of τ . In the experiments the current of the pulse in both anodic and cathodic directions was varied between 0.8 and 0.6 of the limiting current as measured with the disk electrode. The temperature was varied between 300° and 370°C. In all cases a double pulse was em-

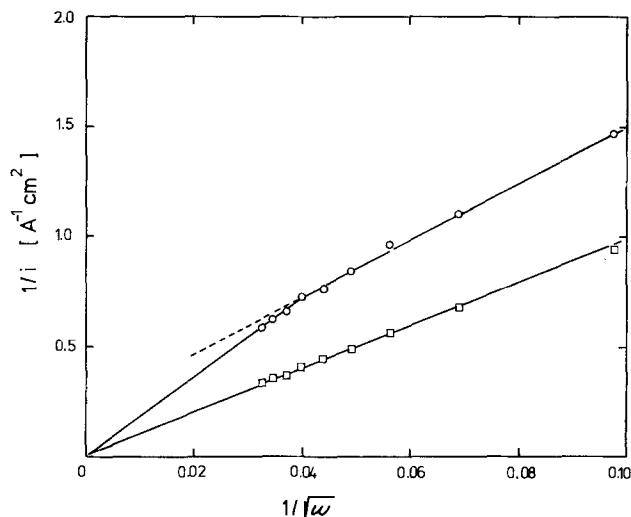


Fig. 5. Dependence of $1/i$ on $1/\sqrt{\omega}$ at the rotating disk electrode in Na_2S_4 at 340°C (\square — \square cathodic current, \circ — \circ anodic current).

Table II. Diffusion coefficients ($\text{cm}^2 \text{sec}^{-1}$) measured in Na_2S_4 with the rotating disk electrode between 300° and 370°C at various speeds of rotation. Values in brackets not used for least squares analysis.

Temp. (°C)	Current direction	$D \times 10^6$ (rpm) at			From least squares line:		
		4000	6000	8000	$D \times 10^6$	Lower	Upper
300	Cathodic	(2.1)	0.76	0.88	0.7	0.5	1.0
	Anodic						
320	Cathodic	1.34	0.77	1.10	1.0	0.8	1.2
	Anodic	1.10	0.77	0.57	0.9	0.6	1.3
330	Cathodic	0.96	0.88	0.96	1.2	1.0	1.4
	Anodic	(3.94)	1.60	0.96	1.1	0.8	1.4
340	Cathodic	1.23	1.00	1.95	1.4	1.1	1.6
	Anodic	1.95	1.38	1.23	1.2	1.0	1.6
350	Cathodic	1.74	1.23	1.58	1.6	1.3	1.9
	Anodic	(3.00)	1.75	1.10	1.4	1.1	1.3
370	Cathodic	2.39	2.57	2.39	2.1	1.6	2.8
	Anodic	1.79	2.06	1.38	1.9	1.2	2.8

ployed (24) although the charging of the double layer within the transient time was almost negligible. Typical curves are shown in Fig. 6.

As a check the transient times were also measured when the diffusion layer decayed after the current had been shut off. The values of τ thus measured were always equal to those of the "buildup" experiments.

The values of D thus obtained are listed in Table II where the values given in the last column are those obtained from the least squares curve. The lower and upper limits of D correspond to a 95% joint confidence interval [for details see Ref. (13)]. The correlation was 72% for the cathodic points and 48% for the anodic ones. The scatter of the latter points is relatively large and may be due to the fact that even with this method of measurement the problems associated with anodic deposition of sulfur cannot always be totally eliminated.

From the temperature dependence of the diffusion coefficients in Na_2S_4 the activation energy of diffusion can be calculated. The least squares line gives an approximate value of 12 and 11 kcal/mole for the cathodic and anodic diffusion, respectively, in the temperature range 300°-370°C. These values are in good agreement with those obtained from viscosity data (18) which give an activation energy of viscosity of 10.3 kcal/mole.

By combining the values of the cathodic limiting currents at the rotating disk electrode with the least squares values of D the values of nC_{ox} (number of electrons \times concentration of reducible species) were found to be 6.5 (300°C), 7.7 (320°C), 6.5 (330°C), 8.1 (340°C), and 8.6 (350°C) mole/liter. Since the anodic

"limiting" currents are due to blocking of the electrode surface by a deposit of sulfur they cannot be used to calculate values of nC_{red} . Attempts to determine the degree of blocking by applying the theory of Landsberg and Thiele (21) were undertaken but did not lead to unambiguous results.

Diffusion coefficients and nC values have been previously determined in polysulfide melts. Ludwig [Ref. (1), p. 430] combined various electrochemical measurements reported by different authors and obtained a value of $D = 6.3 \times 10^{-7} \text{ cm}^2/\text{sec}$ and $nC = 18.2$ moles/liter for Na_2S_5 at 350°C. For Na_2S_4 he found $D = 2 \times 10^{-7} \text{ cm}^2/\text{sec}$ at 300°C. From the Nernst-Einstein equation he estimated the latter value to be $7.9 \times 10^{-7} \text{ cm}^2/\text{sec}$. Armstrong, Dickinson, and Reid (4) found values of $D = 9.8 \times 10^{-6} \text{ cm}^2/\text{sec}$ for Na_2S_3 at 350°C and of $D = 1.4 \times 10^{-5} \text{ cm}^2/\text{sec}$ for Na_2S_5 at 350°C. These authors also report values for the concentration of the oxidized and reduced species.

The values calculated by Ludwig (1) are in rather good agreement with those found here. A direct comparison of the results of Armstrong *et al.* (4) with ours, which are in a tetrasulfide melt, is not possible. However, since it seems unlikely that the values in Na_2S_3 and Na_2S_5 , which lie close together, would differ much from those in Na_2S_4 it can nevertheless be said that the results do not agree. Their diffusion coefficients are an order of magnitude larger and the concentrations of the oxidized species lie between 1.3 and 1.7 mole/liter (for $n = 1$). The discrepancy must be due to the assumptions on which these authors base their calculations. In both Na_2S_3 and Na_2S_5 they postulate a reversible diffusion controlled reaction of the type $\nu_{\text{ox}}\text{Ox} + ne^- \rightarrow \nu_{\text{red}}\text{Red}$. It seems plausible that the same situation should then also exist in the tetrasulfide melt. However, IR compensated voltammetric curves obtained in our laboratory with Na_2S_4 melts clearly show that there are two coupled redox systems present (Fig. 7). Other investigations (1) also point in this direction. The above assumptions seem, therefore, of questionable validity. Moreover, the diffusion coefficient of the electroactive polysulfide species has been determined in fused LiCl-KCl eutectic at 420°C by chronopotentiometry to be $3.1 \times 10^{-6} \text{ cm}^2/\text{sec}$ (25). From the Stokes-Einstein equation it is hard to imagine how the diffusion coefficient of a polysulfide species in Na_2S_3 or Na_2S_5 could be an order of magnitude larger when the viscosity is so much larger (approximately 20-40 cp vs. 2-3 cp in LiCl-KCl) and the temperature 70°C lower. The ratio of the radii of the two diffusing ionic species would have to be about 35. This seems unreasonable, even considering the fact that the diffusion of the ion takes place under different conditions (*viz.*, in a solvent in one case and in its molten salt in the other).

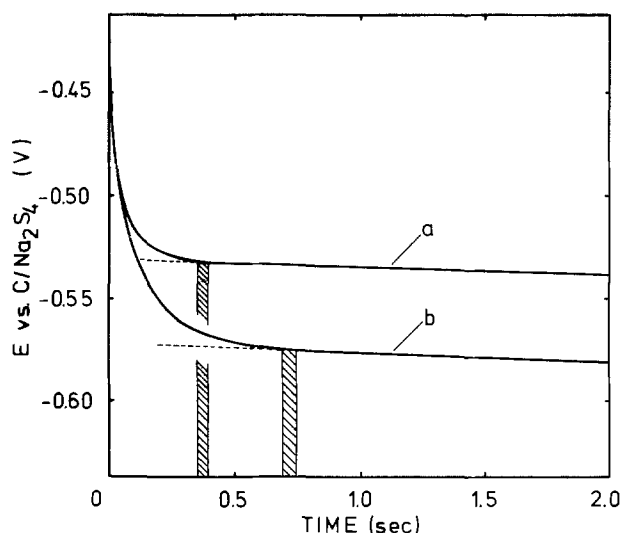


Fig. 6. Chronopotentiometric curves at the rotating disk electrode in Na_2S_4 at 350°C. Curve a, at 8000 rpm, curve b, at 4000 rpm. Shaded area indicates estimated error on τ .

Conclusions

The rate of sulfur exchange under equilibrium conditions across the $\text{S}/\text{Na}_2\text{S}_{5.2}$ interface was determined

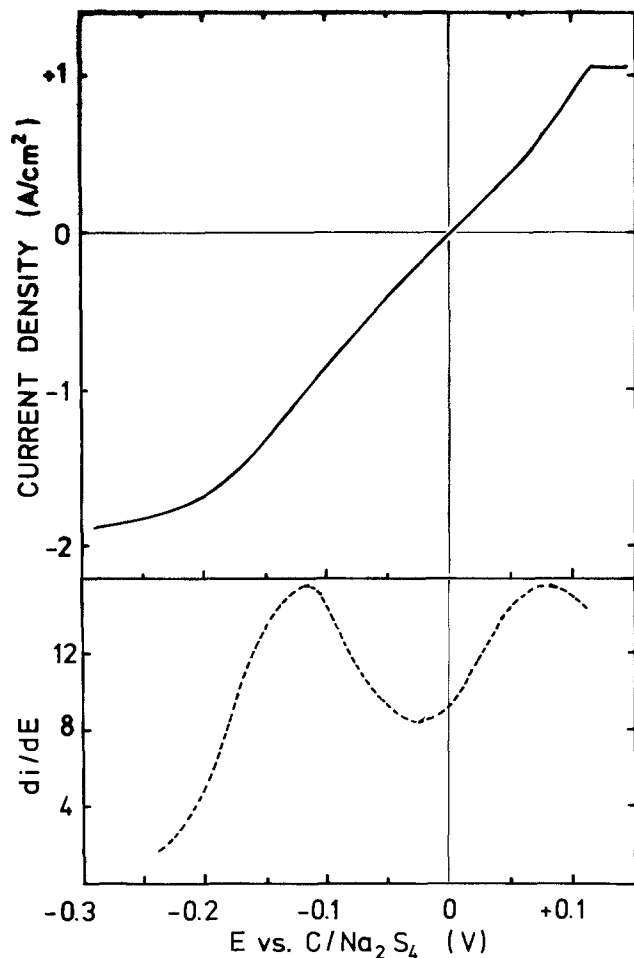


Fig. 7. Voltammetric curve (a, top) of Na_2S_4 at 340°C at the rotating disk electrode (4000 rpm). The differentiated curve (b, bottom) (di/dE vs. E) is drawn in to show the points of inflection of curve (a).

from the capillary experiments to be about $0.19\text{ g S/cm}^2/\text{hr}$. The experiments with a large $\text{S}/\text{Na}_2\text{S}_{5.2}$ interface exhibiting lesser transfer rates of $\text{S}-35$ (about $0.06\text{ g S/cm}^2/\text{hr}$ at conditions of thermal convection and up to about $0.1\text{ g S/cm}^2/\text{hr}$ at slow stirring) suggest the formation of diffusion layers on either side of the interface. Since the diffusion coefficient of $\text{S}-35$ in $\text{Na}_2\text{S}_{5.2}$ is markedly lower than in liquid sulfur (Table I), the effect of diffusion in the pentasulfide melt on the transfer rate will be even more pronounced than that in the sulfur phase.

Under practical conditions in a sodium-sulfur battery, with an actual mass transfer across the interface during charging or discharging, stirring is absent and convection will not be very vigorous. The transport through the convective diffusion layer and the transfer rate across the interface will then simultaneously limit the rate of charge or discharge. In general the transfer rate is expected to be lower than the exchange rate of $0.19\text{ g S/cm}^2/\text{hr}$ which would correspond to a current density of 0.06 A/cm^2 of $\text{S}/\text{Na}_2\text{S}_x$ interface. At large cell currents a sufficiently large interface must, therefore, be provided.

The diffusion coefficients which govern the mass transfer at the electrode/ Na_2S_x interface (Table II) are more than one order of magnitude lower than those governing the sulfur exchange at the $\text{S}/\text{Na}_2\text{S}_x$ interface. This difference is obviously due to different transport mechanisms. Apart from the question of which species are actually moving, the matter transported in both cases is different. While it is an uncharged sulfur species at the sulfur side of the melt, it is some sort of sulfide ion (and simultaneously sodium ion) at the electrode side of the melt.

A possible explanation could be as follows. The transport of sulfur takes place by a rapid exchange of sulfur atoms between the polysulfide ions, or "hopping" from one polysulfide ion to another without being strongly bound to and immediately incorporated into the ionic structure. These mechanisms do not necessarily lead to detectable amounts of free sulfur atoms and are not in contradiction with investigations by Cleaver and Davies (3) which showed that no free sulfur is present in polysulfide melts. On the other hand, the transport of sulfide (and sodium ions) requires the movement of complete ions because the exchange of S with charge does not occur for some reason.

Acknowledgment

We wish to thank Brown, Boveri and Cie. AG (Heidelberg) for supplying the β -alumina tubes.

Manuscript submitted Sept. 25, 1978; revised manuscript received July 15, 1979.

Any discussion of this paper will appear in a Discussion Section to be published in the December 1980 JOURNAL. All discussions for the December 1980 Discussion Section should be submitted by Aug. 1, 1980.

Publication costs of this article were assisted by the Nuclear Research Center, Juelich.

REFERENCES

1. R. P. Tischer and F. A. Ludwig, in "Advances in Electrochemistry and Electrochemical Engineering," Vol. 10, H. Gerischer and C. W. Tobias, Editors, p. 391, John Wiley and Sons, New York (1977).
2. K. D. South, J. L. Sudworth, and J. G. Gibson, *This Journal*, **119**, 554 (1972).
3. B. Cleaver and A. J. Davies, *Electrochim. Acta*, **18**, 733 (1973).
4. R. D. Armstrong, T. Dickinson, and M. Reid, *ibid.*, **21**, 935 (1976).
5. R. F. Bacon and R. Fanelli, *Ind. Eng. Chem.*, **34**, 1043 (1942).
6. F. Fehér and H. J. Berthold, *Z. Anorg. Allg. Chem.*, **273**, 144 (1953).
7. F. Fehér and H. J. Berthold, *Fresenius' Z. Anal. Chem.*, **138**, 245 (1953).
8. J. S. Anderson and K. Saddington, *J. Chem. Soc. (Supl. No. 2)*, S 381 (1949).
9. A. Z. Borucka, J. O'M. Bockris, and J. A. Kitchener, *Proc. R. Soc. London, Ser. A*, **241**, 554 (1957).
10. W. A. Brocke, Nuclear Research Center, Juelich; Private communication.
11. D. Britz and W. A. Brocke, *J. Electroanal. Chem. Interfacial Electrochem.*, **58**, 301 (1975).
12. E. N. Gur'yanova, Ya. K. Syrkin, and L. S. Kuzina, *Dokl. Akad. Nauk S.S.S.R.*, **86**, 107 (1952); *Chem. Abstr.*, **47**, 1475 (1953).
13. J. Mandel and F. J. Linning, *Anal. Chem.*, **29**, 743 (1957).
14. P. Delahay, *J. Am. Chem. Soc.*, **75**, 1430 (1953).
15. J. H. Wang, *ibid.*, **74**, 1182 (1952).
16. L. Nánis, S. R. Richards, and J. O'M. Bockris, *Rev. Sci. Instrum.*, **36**, 673 (1965).
17. A. T. McKay, *Proc. Phys. Soc. London*, **42**, 547 (1930).
18. B. Cleaver and A. J. Davies, *Electrochim. Acta*, **18**, 727 (1973).
19. R. L. Saxton and H. G. Drickamer, *J. Chem. Phys.*, **21**, 1362 (1953).
20. V. G. Levich, "Physicochemical Hydrodynamics," pp. 60-72, Prentice-Hall, Inc., Englewood Cliffs, N.J. (1962).
21. R. Landsberg and R. Thiele, *Electrochim. Acta*, **11**, 1243 (1966).
22. J. M. Hale, *J. Electroanal. Chem.*, **6**, 187 (1963).
23. L. Nánis and I. Klein, *This Journal*, **119**, 1683 (1972).
24. H. Gerischer and M. Krause, *Z. Phys. Chem. N.F.*, **10**, 264 (1957).
25. F. G. Bodewig and J. A. Plambeck, *This Journal*, **116**, 607 (1969).



Possible Use of Honeycomb-Type Structures for High Power Batteries and Fuel Cells

J. T. Kummer

Ford Motor Company, Research Staff, Dearborn, Michigan 48121

This note describes a possible method for constructing a Kapitza-type battery that differs from the usual thin plate approach, and may be simpler to make, and a possible method for constructing a fuel cell that may offer an economic advantage over present methods of construction.

One type of honeycomb structure that has been used by the Ford Motor Company as a substrate for auto exhaust catalysts has ~ 47 openings per cm^2 of front face surface and is manufactured for the most part by an extrusion process. The passageways which run the axial length of the honeycomb have a square cross section with an inside dimension of 1.1 mm, and are separated from one another by walls that are 150-250 microns thick and 35-40% porous (~ 10 micron pore diam) (1). When the porous walls are filled with electrolyte they can act as battery separators. The present ceramic material is essentially corderite ($2\text{MgO} \cdot 2\text{Al}_2\text{O}_3 \cdot 5\text{SiO}_2$), however, other ceramic or plastic materials could be used for the devices described here if they are chemically resistant to the electrolyte used and possess sufficient thermal stability. Passageway cross sections other than square can be extruded, the passageway wall thickness can be varied, and the diameter of the pores in the passageway walls can be varied (1).

If the alternate passageways in the honeycomb contain a positive and a negative electrode, respectively, the structure allows for a high interface area between electrodes with considerable strength. The power available, if it were limited only by the electrolyte resistance in the passageway walls, would be high. The resistance of the electrolyte in the porous walls (250 microns thick) of the passageways has been measured for 35% H_2SO_4 and is such that a 0.2V potential between alternate passageways of a round honeycomb 6 in. diameter (8500 openings total on front face) and 6 in. tall (weight 4.1 lb dry and 9.8 lb full of acid) would allow 9000A to flow between alternate passageways. If the electrodes were sufficiently active to allow the cell voltage to remain at 2V at the high current density represented by the 9000A ($\sim 2\text{A}$ per passageway or ~ 320 mA per cm^2 of passageway wall surface) one could obtain 18 kW from this size honeycomb. In order to construct a battery of cells with an output voltage of 12V and to increase heat removal during charge and discharge, the honeycomb could be cut into six cells 1 in. thick, 6 in. diameter to be connected in series. A plate would be required to seal the bottom of each section. In order to construct a high power lead acid battery, the passageways would have to be filled with a Pb-PbO mixture (prilled powder), acid added, and a top structure attached which pushed lead contacts into each opening. Every other lead contact would be connected together to complete the cell. An alter-

native design would have lead wires in the bottom seal plate project up into the honeycomb holes. This would require two metal (Pb alloy) sheets each with either a wire projection or a hole arranged in alternate sequence (47 per cm^2). The two sheets would be placed together separated by an insulator with the wires from the lower sheet passing through the holes in the upper. The two sheets would represent the battery terminals. For honeycombs ~ 1 in. thick the current in each wire would be ~ 400 mA. The use of a wire for the positive current collector could present a corrosion problem. Such metal sheets would simplify the construction of this device. Such a cell could be charged and discharged at the power level dictated by the electrode activity. As a high power cell with a limited amount of electrolyte, it would not have a high energy density. The 6 in. \times 6 in. honeycomb + acid + PbO + terminals would weigh 25-30 lb.

Experimental

Battery.—Two adjacent honeycomb passageways 1.1 mm inside size were cut out of a honeycomb and sealed at the bottom with black wax. A Cu wire was put in one passageway (–) and a Pt wire in the other (+) passageway. A fine PbO powder was added to both passageways to a depth of 1.5 cm. This required some patience since the powder was not free-flowing but rather caked up. The cell was wrapped with masking tape, painted with waterproof cement at a small bottom section, and placed in 35% H_2SO_4 . It was charged at 1/2 mA overnight. The open-circuit voltage was 2.13V.

When shorted with 47Ω (40 mA) the voltage dropped from 2.13 to 1.9V and slowly dropped to 1.8V after 1.4 min. This corresponds to 27 mA/cm length of passageway at a ΔV of 0.23V. The 18 kW cell required 143 mA/cm of passageway length.

When shorted with 22Ω (80 mA) the voltage dropped rapidly from 2.13 to 1.75V and then to 1.7V after 0.33 min. This corresponds to 55 mA/cm length of passageway at an overall voltage drop of 0.4V (IR + polarization).

The short-circuit current with a 1.6A meter was 0.26A. At a discharge current of 10 mA the cell voltage was 2V after 7 min and 1.95V after 10 min.

It is estimated that the first case represents 3.5 kW for the 6 \times 6 in. honeycomb at 1.9V and the second case 6.7 kW for the 6 \times 6 in. honeycomb at 1.75V. These values would improve somewhat if the cells had been surrounded by counter cells instead of only being adjacent and if a Pb-PbO mixture had been used (better positive electrode conductivity). These tests say nothing about durability or allowable charging rate. The benefits, if any, of this way to make a high power cell could best be evaluated by a battery company since the battery performance is determined princi-

Key words: battery, electrolyte, fuel cell.

pally by the electrode material, an area in which they have considerable expertise.

In addition to its use as a possible battery separator, the honeycomb structure can also be used for the construction of a fuel cell. The material from which the honeycomb is made need not be ceramic (although the ceramic allows high temperature processing of the electrode materials on the honeycomb before use) but must be an insulator, resistant to acid or base, and the walls must be porous. It is thought that the use of the honeycomb structure could reduce the cost of fuel cell construction.

Because the pore structure of the walls is small ($\sim 10\mu$) in size (1) the wicking action of the walls will cause the electrolyte to fill the pores.

In fuel cell use, each alternate passageway of the honeycomb would contain either fuel or oxidant. A plastic header attached to one end of the honeycomb is necessary to distribute the fuel and oxidant to the required passageway. The walls of the passageway would have to be coated with a catalytic material to promote the electrode reactions. This can be done by a simple dip procedure such as is used in applying a catalytic washcoat to the honeycomb for auto exhaust service. For the fuel cell, a washcoat would be a conductive electrode catalyst. If necessary, a different washcoat could be applied to different channels by the use of a suitable plug to block off alternate passageways.

In the case of fuel cells, however, the particle size of the washcoat as compared to the honeycomb pore size is quite critical. If the washcoat particle size is too small, it will penetrate from one side of the passageway wall to the other through the pores. Since the electrode catalyst must possess electrical conductivity, it may give a partial short to the fuel cell. If the washcoat particle size is too large, it may not adhere well. This problem can be alleviated by applying a coarse particle washcoat to the honeycomb of the honeycomb material and resintering to give a passageway wall of dual pore size, the outer layer having the larger pores to accommodate and hold a large particle size electrode catalyst.

It is necessary to make electrical contact to the washcoat by means of a small metal wire inserted into each

opening with every other wire connected together. If the electrode catalyst is poorly conducting, a highly conductive washcoat would have to be applied before applying the electrode catalyst. In this case electrical connection need only to be made at one end of the passageway.

Fuel cell.—Two adjacent honeycomb cells, 1.1 mm inside size, of a Corning corderite honeycomb of ~ 47 openings per cm^2 with a 250 micron wall thickness, and a length of 3.8 cm were sealed with collodion and coated with a slurry of Ni powder (Sheritt NF-1M-P240) in water, and sintered in H_2 at 850°C for 1 hr. This gave an adherent, porous, and very conductive Ni coating to the inside of the passageways. NiO powder would be just as effective as Ni since it reduces to Ni. A mixture of NiO + MgO could also be used so that after reduction the MgO could be leached out with acid to give a more porous Ni coating. The honeycomb structure withstands the high temperature exposures without any difficulty.

A chloroplatinic acid solution (8 mg/cm^3) was added to the Ni containing honeycomb until the honeycomb walls were wet and then the honeycomb was dried at 110°C .

H_2 was passed through one passageway and air in the surrounding passageways. The electrolyte was 25% NaOH solution in the passageway walls. The open-circuit voltage was $\sim 1\text{V}$ and the short-circuit current was $\sim 19\text{ mA}$.

Manuscript submitted Nov. 27, 1979; revised manuscript received Sept. 8, 1979.

Any discussion of this paper will appear in a Discussion Section to be published in the December 1980 JOURNAL. All discussions for the December 1980 Discussion Section should be submitted by Aug. 1, 1980.

Publication costs of this article were assisted by Ford Motor Company.

REFERENCE

1. A. J. Goodsel, *Powder Technol.*, **9**, 191 (1974).

Note Added in Proof: It has been brought to the authors attention that a somewhat similar structure for a Zn-AgO and a Zn-air battery has been proposed by F. C. Arrance and C. Berger (USP 3647 542 and 3661 644).

An Electrochemical Control System for Electroless Copper Bath

Milan Paunovic*

Kollmorgen Corporation, PCK Technology Division, Glen Cove, New York 11542

Electroless deposition of copper was studied from the chemical (1-3), electrochemical (4-7), kinetic (7, 8-16), and mechanistic (4-7, 17-22) aspects. The subject was reviewed in a number of articles (23-26) and books (27, 28). The number of chemical and electrochemical publications on electroless deposition of copper is relatively small (about twenty-two papers in the period 1948-1979) The number of publications is even smaller when automatic analysis and control of a production electroless copper bath is considered.

So far, as we know, there is no published paper describing a complete control system (an automatic analyzer) for the analysis of the composition and performance of the production electroless copper bath. The published papers on this subject describe only control of limited number of variables, the rate of

deposition (29-31), and concentration of some reacting components (32). However, more complete control systems have been described at the fall meetings of The Electrochemical Society, 1976 (32, 33), and 1978 (34-36), and a brief description of these systems is available in the form of extended abstracts.

The subject of this paper is the application of electrochemical methods of analysis in study and control of the electroless copper bath. Duration of an electrochemical analysis is in the range of milliseconds, or seconds. This short time of analysis makes these methods very attractive.

Chronopotentiometry (37, 38), voltametry (4, 19, 20, 22, 38-40), and polarography (32) can be used to analyze (manually or automatically) an electroless copper bath. Polarographic method has been applied successfully for analysis of copper, formaldehyde, and cyanide (32, 34). This paper describes the applications of chronopotentiometry and voltametry (developed

* Electrochemical Society Active Member.

Key words: copper, formaldehyde, electroless plating, chronopotentiometry, sodium 2-mercaptobenzothiazole

1968-1971) in the study and control of the electroless copper bath. The same techniques can be used to analyze electroless deposition of other metals.

Experimental

An all-glass, two (or single) compartment cell with three electrodes was used. Platinum sheets of 1.1 cm², electroplated with copper, served as cathode and anode. Plating was done in an acid copper solution (CuSO₄ · 5H₂O-188 g/liter, H₂SO₄-74 g/liter) at 10 mA/cm² for 5 min. A saturated calomel electrode (SCE), in a separate reference electrode compartment (at room temperature), was employed as a reference electrode. A platinum sheet electroplated with copper in a single compartment cell can be used as a reference electrode.

An EDTA (ethylenediaminetetraacetic acid) type electroless copper bath was used for these studies. This bath (41) contained: Na₄EDTA-52 g/liter, CuSO₄ · 5H₂O-9-12 g/liter, CH₂O-5-10 ml (37%)/liter, NaCN-1-30 mg/liter, and NaOH to the desired pH. The solutions were prepared with analytical grade reagents and deionized water.

The mixed potential was measured with a vacuum tube voltmeter (pH meter) using the SCE as a reference electrode.

The voltammograms were obtained with a PAR (Princeton Applied Research, Princeton, New Jersey) Model 174A Polarographic Analyzer, and the current-voltage curves recorded on a Houston Instruments (Austin, Texas) Model RE0074 X-Y Recorder.

The chronopotentiograms were obtained with a transistorized constant current power supply, made in this laboratory. The potential-time curves were recorded on the Tektronix 564B storage oscilloscope. Oscilloscope traces were photographed with a Polaroid Camera C-27.

Results and Discussion

Chronopotentiometric determination of cupric ions.—Chronopotentiograms.—A typical chronopotentiogram for the reduction of cupric ions in the EDTA bath is shown schematically in Fig. 1. The starting potential of the chronopotentiogram is the mixed potential, E_{mp} . The current is switched on at the time $t = 0$. Reduction of cupric ions with measurable rate starts at the potential $E_{t=0}$ (defined according to Fig. 1). At the transition time τ the concentration of cupric ions at the electrode equals zero and the potential is E_{τ} .

After the elapse of time τ a part of the current at the test electrode is used for charging the double layer until the potential reaches the value when water is reduced.

The characteristic potentials of a chronopotentiogram at 20 mA/cm², 68°C, pH 11.90, 9.0 g/liter CuSO₄ ·

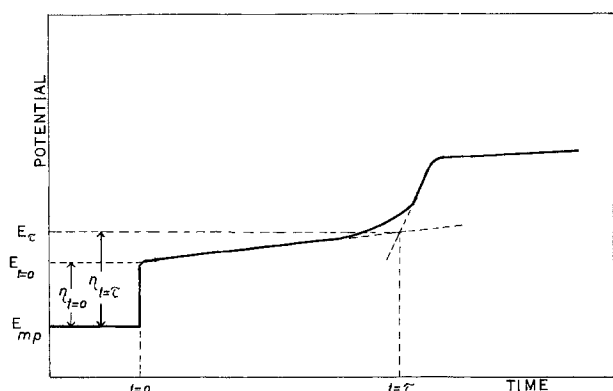


Fig. 1. Variation of the potential of the test electrode with time in cathodic chronopotentiometry of the EDTA electroless copper bath.

5H₂O, 5.5 ml/liter CH₂O are: $E_{mp} = -0.78$, $E_{t=0} = -1.06$, and $E_{t=\tau} = -1.24$ V vs. SCE.

Reproducibility of transition time measurements.—Change of potential in the vicinity of transition time is fast and large. This large increase of potential allows very precise determination of the transition time. The reproducibility studies on 27 chronopotentiograms show that the transition time of 0.87 sec can be reproduced with a ± 0.02 sec deviation from the mean value.

Transition time as a function of cupric ion concentration.—Dependence of the transition time on the concentration of CuSO₄ was studied at pH 11.70, 11.80, and 11.90. When the concentration of CuSO₄ · 5H₂O varies from 9 to 12 g/liter, the transition time varies from 0.38 to 0.84 sec. The plot of $\tau^{1/2}$ vs. the concentration is shown in Fig. 2. It is seen from Fig. 2 that τ depends considerably on pH.

Chronopotentiometric determination of formaldehyde.—Chronopotentiograms.—Anodic chronopotentiogram at 4.5 mA/cm² at a copper anode exhibits two steps. A typical chronopotentiogram is shown schematically in Fig. 3. The starting potential of a chronopotentiogram is the mixed potential of the copper electrode, E_{mp} . The transition time τ_2 is measured from the first transition time, τ_1 , to the second inflection point. Oxidation in the first step starts at the potential E_1 which is about +0.13V with respect to the mixed potential at the bath composition given for the cathodic chronopotentiograms. At the transition time τ_1 and τ_2 the potential is +0.21 and +0.33V with respect to the mixed potential, respectively. It is seen that there is a clear distinction between these two steps. E_2 is +0.22V with respect to the mixed potential.

Transition time as a function of formaldehyde concentration.—The dependence of transition time on the

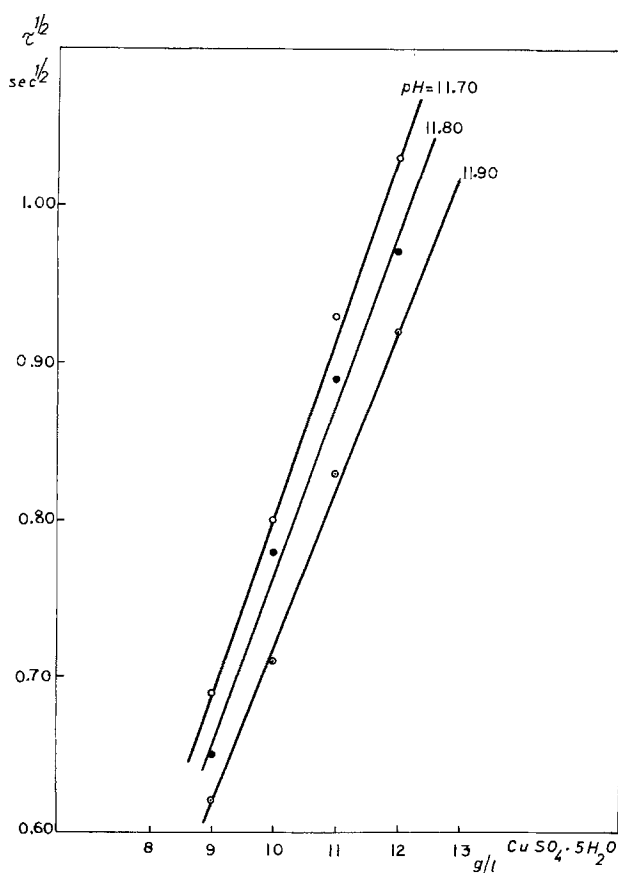


Fig. 2. Variation of $\tau^{1/2}$ with CuSO₄ · 5H₂O; $i = 20.0$ mA/cm², 68°C.

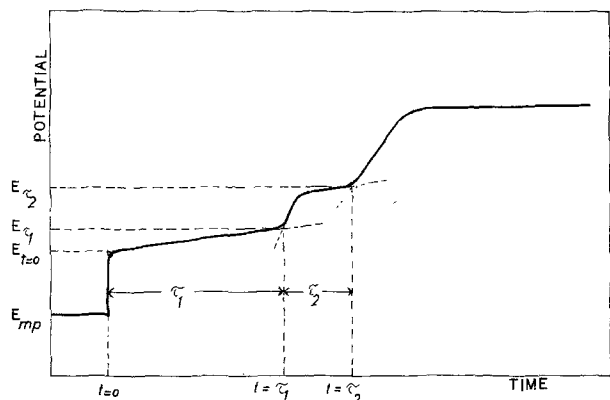


Fig. 3. Variation of the potential of the test electrode with time in anodic chronopotentiometry of the EDTA electroless copper bath.

concentration of formaldehyde in the bath is shown in Fig. 4. It is seen that for constant conditions when only the formaldehyde is a variable, $\tau_1^{1/2}$ and $\tau_2^{1/2}$ are proportional to the concentration of formaldehyde in the solution. Transition times τ_1 and τ_2 show differences in the following properties: the transition time τ_1 depends, and τ_2 does not, in practical limits, on the concentration of other components of the bath; the rate of change of the transition time τ_1 with the concentration of formaldehyde, $\Delta\tau_1/\Delta C$ (CH_2O) is faster than that for τ_2 ; $\tau_2^{1/2}$ is proportional to the concentration of formaldehyde in the bath, irrespective of the concentration of additives (in practical limits) and $\tau_1^{1/2}$ is proportional to the formaldehyde concentration only if other components of the bath are constant.

On the basis of the above observations, our present interpretation is that the first step in the anodic chronopotentiogram (τ_1) is due to oxidation of adsorbed species (H , CH_2O^-), or simultaneous oxidation of adsorbed and diffusing species (since the first step is sloping and not horizontal); the second step (τ_2) is due to oxidation of diffusing species. If the value of τ_1 depends on the amount of adsorbed formaldehyde, or adsorbed and diffusing formaldehyde, it could be a measure of the activity of the bath. The transition time τ_1 reflects the status of the competitive adsorption between additives, fragments of the dissociative adsorp-

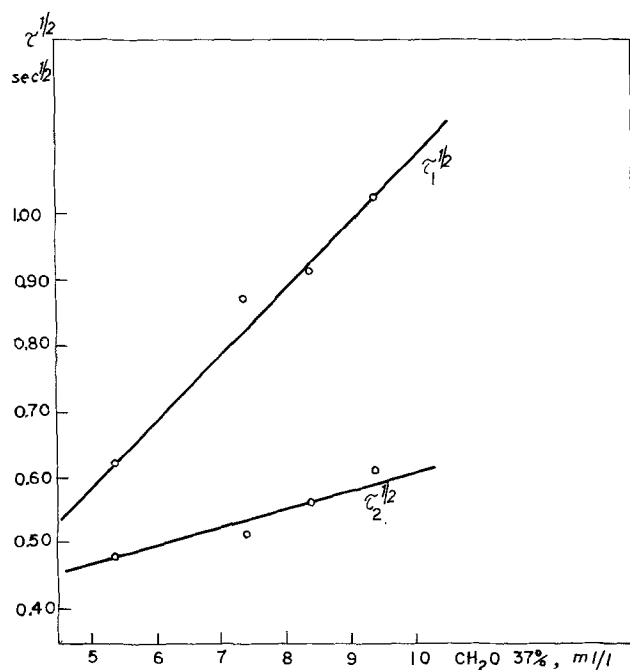


Fig. 4. Chronopotentiometric $\tau^{1/2}$ function for the first and second transition time; $i = 4.5 \text{ mA/cm}^2$, 68°C .

tion of formaldehyde (H , CH_2O^-), OH^- , ligand, complexed copper ions, and water. Situation at the electrode is even more complicated due to the partial surface oxidation, Cu to Cu_2O , starting at -0.54 V vs. SCE. Since E_2 is about -0.45 V vs. SCE, it follows that oxidation of formaldehyde in the time interval τ_2 occurs at the partially oxidized surface.

Adsorption effects.—Absence of additives.—At 20 mA/cm^2 and higher current densities chronopotentiograms show only one transition time due to the anodic oxidation of formaldehyde. This transition time will be called τ . The two transition times, τ_1 and τ_2 , are recorded at current densities lower than 20 mA/cm^2 .

Variation of τ with the current density i can be used to estimate the amount of the adsorbed electroactive species (37). The transition time τ varies from 5 to 41 msec when the current density varies from 20 to 87 mA/cm^2 . The linear relationship was obtained for the plot of $i\tau$ vs. $1/i$ and $i\tau$ vs. $\tau^{1/2}$. Since both functions yield a straight line, it is not possible to make a conclusion on the mechanism of reactions, but it is possible to estimate the surface concentration of formaldehyde, Γ , from the intercepts (42). Γ , estimated from the intercepts, as a function of pH is shown in Fig. 5.

Presence of additives.—Effect of additives can be studied by recording potential time curves in the milliseconds (msec) or microseconds (μsec) range. In the msec range the usual chronopotentiograms exhibit the transition time, whereas in the μsec range the linear relationship, with the slope characteristic of the double layer capacity, is obtained.

Chronopotentiograms.—The partial coverage of the electrode by the adsorbed addition agents that are neither reduced nor oxidized at the electrode causes an increase in the actual current density i due to a decrease in the available surface area A ($i = I/A$, where I is the current). An increase in current density causes a decrease in τ . This change in the available surface area and the resulting change in the transition time is

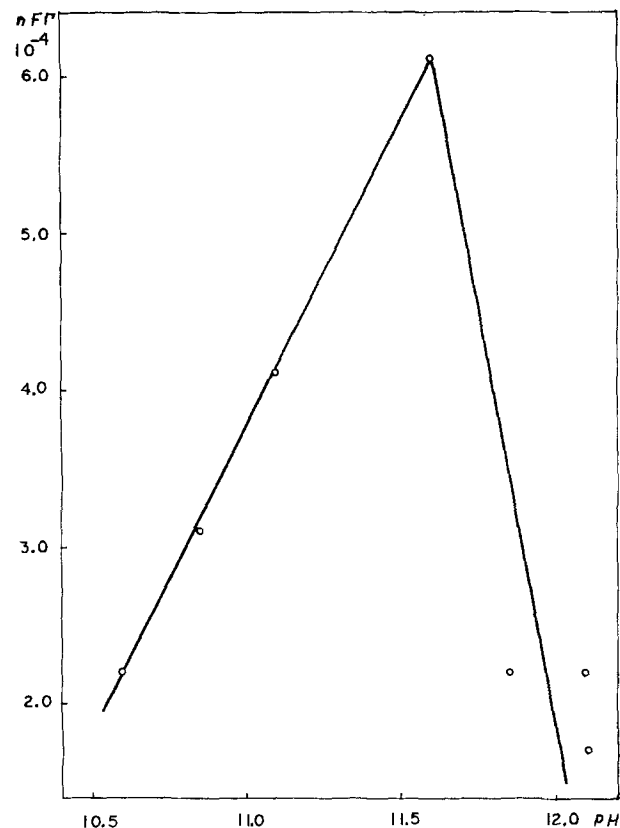


Fig. 5. The surface concentration of formaldehyde (Γ) as a function of pH.

a function of the bulk concentration of the addition agent. Thus, by determining the change in the transition time $\Delta\tau = \tau^\circ - \tau$, where τ° is the transition time in the absence, and τ in the presence of the adsorbed additive, one can obtain information on adsorption conditions at the electrode and, under certain conditions, the bulk concentration of the addition agent (43).

The difference $\Delta\tau$ caused by 30 mg/liter of NaCN, in the absence of other additives, at pH 11.60 and 12.10 is 51 and 9 msec, respectively. The difference $\Delta\tau$ caused by the adsorption of sodium 2-mercaptobenzothiazole as a function of pH is shown in Fig. 6.

Double layer capacity.—Galvanostatic potential time curves in the microseconds range can be used to estimate level of additives in an electroless bath (38). The slope of the recorded linear potential-time relationship is related to the electrode double layer capacity, $C_{dl} = i(dt/dV)$. Double layer capacity for the EDTA electroless copper bath varies from 200 $\mu\text{F}/\text{cm}^2$, for the bath in the absence, to 100 $\mu\text{F}/\text{cm}^2$ in the presence of additives. Double layer capacity for the supporting electrolyte and the ligand only, e.g., 0.01M Na_2SO_4 , and 0.01M EDTA at pH 13.0 and 70°C, is 58.8 $\mu\text{F}/\text{cm}^2$.

Polarization resistance.—The current-potential relationship in the range of the mixed potential (e.g., from $/E_{mp}/-50$ to $/E_{mp}/+50$ mV) can be used for testing of the presence of impurities or general activity of the bath. In the vicinity of the mixed potential, the current-potential relationship is linear. The slope of this linear plot (44), the polarization resistance ($R_p = (d\eta/di)_{i=0}$), can be used as a characteristic parameter of a bath. An EDTA electroless copper bath plating at the mixed potential of -530 mV vs. SCE had the polarization resistance of 128 Ω . The same bath after contamination showed the polarization resistance of 4200 Ω . The potential sweep in these measurements was 1 mV/sec.

Summary

The data presented in this note show that the chronopotentiometry and voltametry can be used to analyze and control the operation of an electroless copper bath.

In our preliminary investigations the complete chronopotentiograms have been recorded. However, in the analytical applications this is not necessary. It is sufficient to detect the transition time only. This can be done automatically (45) by introducing a time interval counter into the electrolysis circuit. In automatic determination of the transition time, the electrolysis and the counter are started simultaneously by means of a switch. Electrical signal for the counter, to terminate counting, can be the potential of the test

electrode at which the transition time is measured or the peak value of the first derivative curve at the transition time. The reading at the counter directly gives the transition time. The scale of the timer can be calibrated directly in concentrations of the species being determined.

An instrument based on the above-presented principles was constructed and used in the control of the production electroless copper bath. This control system is applicable to other electroless and electroplating baths.

It was shown that the transition time values for a specific bath component depend on pH and the concentration of other components of the bath. For this reason, it is necessary to have for each component a family of curves corresponding to the specific set of other parameters. A microprocessor, or a computer, can select the correct value of the observed component and use this value for the bath control instructions.

Acknowledgments

The author would like to thank Dr. Karl Egerer, President, Kollmorgen Technologies and J. McCormack, Director of Research, PCK Technology Division for permission to publish this paper.

REFERENCES

- H. Narcus, *Tech. Proc. Am. Electroplat. Soc.*, **35**, 157 (1948).
- A. E. Cahill, *ibid.*, **44**, 130 (1957).
- R. M. Lukes, *Plating*, **51**, 1066 (1964).
- M. Saito, *Met. Surf. Technol.*, **16**, 300 (1965); **17**, 15 (1965); **17**, 260 (1965).
- M. Paunovic, *Plating*, **55**, 1161 (1968).
- F. Donahue, *This Journal*, **119**, 72 (1972).
- S. M. El-Raghy and A. A. Abo-Salama, *ibid.*, **126**, 171 (1979).
- W. Goldie, *Plating*, **51**, 1069 (1964).
- F. L. Shippey and F. M. Donahue, *ibid.*, **60**, 43 (1973).
- F. M. Donahue and F. L. Shippey, *ibid.*, **60**, 135 (1973).
- A. Molenaar, J. E. A. M. v. d. Meerakker, and J. Boven, *ibid.*, **61**, 649 (1974).
- A. Molenaar, M. F. E. Holdrinet, and L. K. H. van Beek, *ibid.*, **61**, 238 (1974).
- J. Dumesic, J. A. Koutsky, and T. W. Chapman, *This Journal*, **121**, 1405 (1974).
- L. G. Bhatgadde and S. Mahapatra, *Met. Finish.*, **75** (12), 28 (1977).
- F. M. Donahue and K. L. M. Wong, Abstract 173, p. 460, The Electrochemical Society Extended Abstracts, Vol. 78-2, Pittsburgh, Pennsylvania, October 15-20, 1978.
- F. M. Donahue, Abstract 167, p. 447, The Electrochemical Society Extended Abstracts, Vol. 78-2, Pittsburgh, Pennsylvania, October 15-20, 1978.
- R. Sard, *This Journal*, **117**, 804 (1970).
- L. N. Schoenberg, *ibid.*, **118**, 1571 (1971); **119**, 1491 (1972).
- M. Paunovic, *ibid.*, **124**, 349 (1977).
- R. E. Acosta and L. T. Romankiw, Abstract 277, p. 736, The Electrochemical Society Extended Abstracts, Vol. 77-2, Atlanta, Georgia, October 9-14, 1977.
- M. Paunovic, *This Journal*, **125**, 173 (1978).
- M. Saito and H. Honma, *Met. Surf. Technol. Japan*, **29**, 403 (1978).
- E. B. Saubestre, *Tech. Proc. Am. Electroplat. Soc.*, **46**, 264 (1959).
- E. B. Saubestre, *Plating*, **59**, 563 (1972).
- F. M. Donahue, *Oberflaeche-Surf.*, **13** (12), 301 (1972).
- Y. Okinaka, Abstract 269, p. 692, The Electrochemical Society Extended Abstracts, Vol. 76-2, Las Vegas, Nevada, October 17-22, 1976.
- W. Goldie, "Metal Coating of Plastics," Chap. 6, Electrochemical Publications Ltd., Hatch End, Middlesex, Great Britain (1968).
- "Modern Electroplating," F. A. Lowenheim, Editor, Chap. 31, John Wiley & Sons, New York (1974).
- G. Herrmann, *Metalloberflaeche-Angew. Elektrochem.*, **26**, 334 (1972).

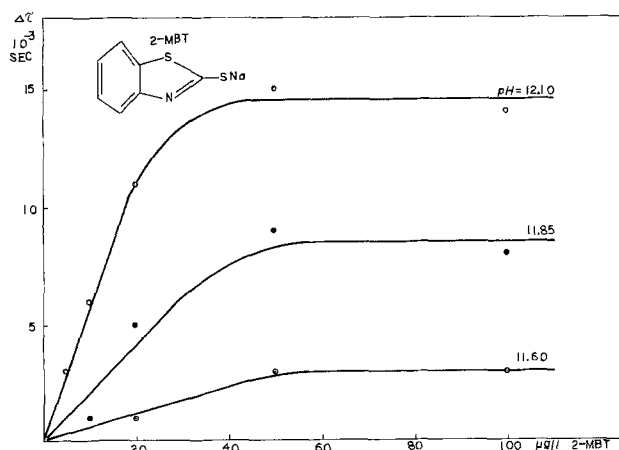


Fig. 6. Change of $\Delta\tau$ with the concentration of sodium 2-mercaptobenzothiazole (2-MBT).

30. F. L. Shippey, C. U. Yu, and F. M. Donahue, *Plating*, **59**, 762 (1972).
31. M. J. Brown, *Insulation/Circuits*, **21** (11), 17 (1975).
32. Y. Okinaka, D. R. Turner, C. Wolowodiuk, and D. W. Graham, Abstract 275, p. 704, The Electrochemical Society Extended Abstracts, Vol. 76-2, Las Vegas, Nevada, October 17-22, 1976.
33. S. Stokes, *ibid.*, Abstract 276, p. 706.
34. D. R. Turner and Y. Okinaka, Abstract 164, p. 441, The Electrochemical Society Extended Abstracts, Vol. 78-2, Pittsburgh, Pennsylvania, October 15-20, 1978.
35. J. DeBrita and E. Ozolins, Abstract 165, p. 443, The Electrochemical Society Extended Abstracts, Vol. 78-2, Pittsburgh, Pennsylvania, October 15-20, 1978.
36. T. Rau, Abstract 166, p. 445, The Electrochemical Society Extended Abstracts, Vol. 78-2, Pittsburgh, Pennsylvania, October 15-20, 1978.
37. M. Paunovic, *J. Electroanal. Chem.*, **14**, 447 (1967).
38. M. Paunovic, Abstract 146, p. 390, The Electrochemical Society Extended Abstracts, Fall Meeting, Detroit, Michigan, October 5-9, 1969.
39. R. S. Nicholson and I. Shain, *Anal. Chem.*, **36**, 706 (1964).
40. E. Yeager and J. Kuta, in "Physical Chemistry, An Advanced Treatise," Vol. IXA, H. Eyring, Editor, Chap. 4, Academic Press, New York (1970).
41. R. J. Zablisky, J. F. McCormack, J. D. Williamson, and F. W. Schneble, Jr., U.S. Pat. 3,095,309 (1963).
42. M. Paunovic, *J. Electroanal. Chem.*, **14**, 454, 469 (1967).
43. M. Paunovic and R. Oechslein, *Plating*, **58**, 602 (1971).
44. K. J. Vetter, "Electrochemical Kinetics," p. 154, Academic Press, New York (1967).
45. M. Paunovic, *J. Electroanal. Chem.*, **14**, 472 (1967).



Photosensitization of Semiconductor Electrode by Cyanine Dye in Lipid Bilayer

W. Arden and P. Fromherz

*Max-Planck -Institut für Biophysikalische Chemie, Molekularer Systemaufbau,
 D 34 Göttingen-Nikolausberg, Germany*

ABSTRACT

A thin film electrode is prepared by evaporation of indium-tin-oxide. It is covered by a bimolecular layer of lipid doped with a cyanine dye in direct contact to the electrode. The assembly is investigated in an electrochemical cell. The bilayer lowers the voltage dependent capacitance corresponding to the effect of a thin homogeneous dielectric with a hole fraction of about one percent. Illumination leads to a sensitized photocurrent which is enhanced by thiourea. The maximal yield at saturating potential and 3M thiourea is 0.7. The electron is transferred at a rate of about 10^{10} sec^{-1} and a yield of 0.8. An intermediate is formed consisting of the oxidized dye and an electron at the electrode surface. Supersensitization is due to the reduction of this intermediate by thiourea, the drop of current at low potentials is assigned to a reduction by occupied surface states.

Photocurrent through a semiconductor/electrolyte interface may be enhanced by organic dyes. The mechanism of such photosensitization process has been studied extensively because of its relevance to the photoelectric conversion of solar energy and to the electrophotographic process (1-4). The primary process of sensitization is generally assumed to be an electron transfer to the electrode from an excited state of the dye with a donor level above the edge of the conduction band (5, 6).

Prerequisite for electron transfer is a close contact of chromophore and semiconductor which may be achieved by four methods: (i) adsorption of the dye from the electrolyte (1-4), (ii) evaporation of a non-aqueous solution of the dye (7), (iii) deposition of an insoluble monolayer of the dye by the Blodgett technique (8, 9), and (iv) covalent binding of a reactive dye (10). Close contact may be indicated by a modification of the spectrum of absorption or of the sensitized current itself as compared to the absorption spectrum of the free dye (5, 6). The active state of the dye involved in transferring an electron may be the first excited singlet or triplet state (11).

Prerequisite for an observable sensitized photocurrent is, in the case of an n-type semiconductor, anodic polarization of the electrode such that the electric field in the space charge removes the transferred electron to the bulk of the semiconductor (2, 12). Photocurrent may be enhanced by supersensitizers which induce the electron transfer by reducing the excited dye (2, 13). Such type of supersensitization is connected with the quenching of fluorescence of the dye (14-16). Additional cosensitization is achieved by auxiliary dyes which enhance the excitation of the sensitizer by energy transfer (17, 18). The photocurrent is lowered by recombination mediated by surface states of the electrode (19).

Key words: membrane, capacitance, photoconductivity.

Photo-oxidation of the sensitizer leads to a decay of sensitized current under steady illumination (7, 14, 20). The photobleaching of the dye is observed directly by fluorescence or Raman spectroscopy (18, 21). Bleaching may be suppressed by addition of a redox couple which regenerates the oxidized dye (7, 14, 18, 20).

Sensitization of photocurrent in an electrochemical cell is in close relation to the photographic sensitization of silver halides (22). Of some relevance to the present study are the various modifications of spectral features by the adsorption of sensitizing dyes (23), the correlation of sensitizing efficiency and redox potential of the dyes (24), and the photographic sensitization by dye monolayers (25, 26).

The present paper is concerned with the sensitization of photocurrent through an interface made from an indium-tin-oxide electrode and a cyanine dye incorporated into an insoluble bilayer of lipids deposited onto the electrode. A schematical drawing of the structure of the electrode/electrolyte interface as well as of the energy levels of the components is given in Fig. 1. The reproducible preparation of immobilized sensitizer in the bilayer by monolayer deposition allows a rather detailed analysis of sensitization by simultaneous detection of photocurrent and fluorescence. The elementary processes involved in sensitization such as electron transfer, activation by supersensitizer, and inhibition by surface states are characterized and comprised in a kinetic scheme. The quantum yields of electron transfer, supersensitization, and recombination are evaluated quantitatively.

An extension of the present investigation is the construction of an antenna system of dye molecules located at the bilayer/water interface, which has been presented in a previous paper (18). These studies are elements of a more involved project considering the coupling of electron, photon, and proton in an

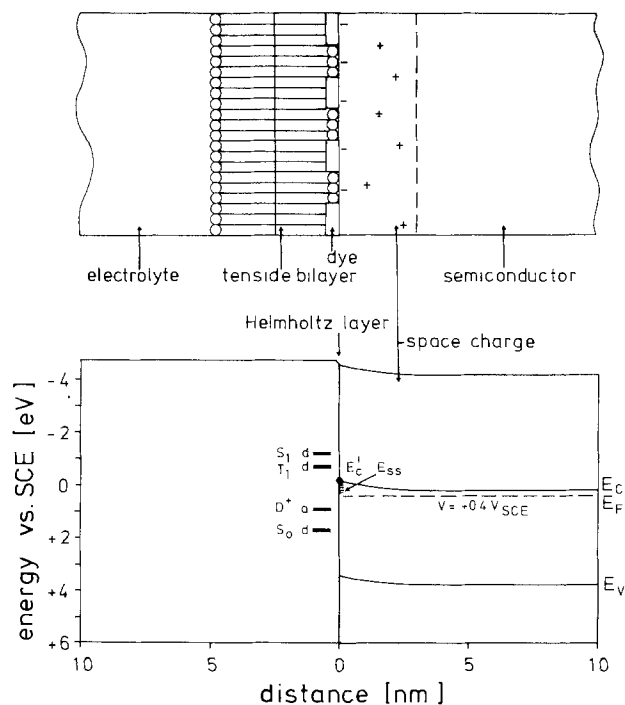


Fig. 1. Structure and energy levels of the dye-bilayer-semiconductor system. For the assignments of the energy levels see the sections on "Flatband potential" and "Photosensitization". The figure is drawn for pH 10 and an electrode potential $V = 0.4V_{SCE}$. Notations in the text.

artificial membrane doped with appropriate dyes and enzymes (27).

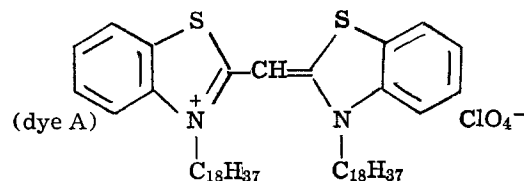
After a description of technical details, the present paper continues with the characterization of the electrode/bilayer system by determination of the edge of the conduction band, of the distribution of surface states, and of imperfections of the bilayer. Subsequently the mechanism of sensitized photocurrent is derived on the basis of a set of qualitative observations. Finally the quantum yields of some elementary processes of the sensitization such as electron transfer, recombination, and supersensitization are evaluated. The main results are stated in the summary.

Experimental

The semiconductor electrode.—Transparent polycrystalline films of indium-tin-oxide are prepared by thermal vacuum evaporation from pressed pellets (Merck) onto freshly cleaned glass slides ($38 \times 12 \times 1$ mm) using an alumina-coated tantalum boat. The vacuum unit is equipped with a diffusion pump and liquid nitrogen trap. Evaporation source current (300A) and evaporation rate (1.5 nm/sec) are carefully controlled such that reproducible electrodes are obtained. The thickness of the film as checked during evaporation by a quartz monitor is about 30 nm. The films are oxidized in air at 400°C for 15 min. The conductivity is 30–300 mho/cm, the mobility as determined by the Hall effect is 10–20 cm^2/Vsec . Thus the density of charge carriers is $2 \cdot 10 \times 10^{19} \text{ cm}^{-3}$. The fraction of Sn atoms in the Sn/In-oxide is 30% as determined by x-ray fluorescence measurements. The donor action of most Sn-atoms is lost since they are bound as $(\text{SnO}_2)_2$ groups in the In_2O_3 (28). The bandgap of indium oxide is 3.6 eV (29) and the absorption coefficient at 350 nm is $7 \times 10^4 \text{ cm}^{-1}$ (29).

Lipid bilayers.—Monomolecular films are prepared by spreading arachidic acid at the air/water interface (pH 5.5, $5 \times 10^{-4} \text{ M CdCl}_2$) (8). Two monolayers are transferred onto the hydrophilic electrode at a surface

pressure of 30 dyne/cm and a speed of 25 cm/min within a few hours after preparation of the semiconductor electrodes. A Teflon trough with automatic control of surface pressure and film area and a precision transferring lift are applied (30). The lipid bilayers are doped with the monomethine-thia-cyanine dye (dye A) (31), by mixing the dye with arachidic acid in a molar ratio of 1:5 in a 10^{-3} M solution in chloroform before spreading. For the sensitization experiments the first monolayer transferred is doped, the second is undoped such that a structure is obtained as sketched in Fig. 1.



Electrochemical cell.—The electrochemical cell is a boring (diameter 9 mm, depth 15 mm) in a block of black PVC. The slide with the semiconductor-bilayer system is fixed onto the opening of this boring filled with electrolyte. The electrode is mounted in a trough under water in order to avoid damage to the transferred bilayer (27, 30). Electrical contact is made to the electrode by soldering with indium outside of the cell. A saturated calomel electrode serves as a reference. The pH is controlled by a glass electrode fitted into the cell. The electrolyte may be replaced during the measurements. Usually 10^{-3} M TRIS buffer of various pH is applied. Thiourea is used as a supersensitizer at concentrations up to 3M. For measurements of capacitance 10^{-2} M KCl is applied and a mask is introduced at the opening of the cell to reduce the area of the electrode to 0.1 cm^2 .

Capacitance.—For determination of the capacitance of the electrode a sine wave signal (amplitude 10 mV, angular frequency $\omega = 10^3 \text{ sec}^{-1}$) is superposed onto the d-c-potential of the electrode by means of a potentiostat (PAR). The output of a current-voltage converter is fed into a lock-in amplifier set on a phase difference of 90° between signal and reference. The output of the lock-in amplifier (being proportional to effective capacitance times frequency) is inverted and squared so that C^{-2} may be plotted continuously vs. applied voltage on a X-Y recorder as the electrode potential is scanned by a sweep generator (sweep time 10–100 sec). The series resistance of the semiconductor film (about 1 k Ω) is compensated by the internal resistance mode of the potentiostat. The whole circuit is calibrated with a set of capacitors with parallel and series resistances, with an accuracy better than 3% in the frequency range 0.05–5 kHz.

Photocurrent.—The semiconductor is illuminated through its glass support by a 150W Xe-lamp (Hanovia) through a monochromator (Bausch and Lomb, slit width 5 nm) driven by a stepping motor. The intensity at 400 nm is about 100 $\mu\text{W}/\text{cm}^2$. The light is chopped at a frequency of 2 sec^{-1} . The photocurrent is fed into a current voltage converter and amplified with a lock-in amplifier. Current spectra are recorded continuously on a X-Y recorder and corrected for constant photon flux.

Fluorescence and absorption.—The fluorescence emission from the semiconductor/bilayer system is detected through a monochromator (Jarrel and Ash, slit width 4 nm) with a photomultiplier (EMI 9558QB) simultaneously with the measurement of photocurrent (18). The signal is amplified with a lock-in amplifier and recorded as a function of excitation or emission wavelength. Absorption spectra of the dye/electrode system are measured wet and dry in a special vibrating high sensitivity photometer without applied voltage (8).

Semiconductor and Bilayer

Flatband potential.—The edge of the conduction band E_C^i at the interface of the semiconductor (cf. Fig. 1) is derived from the flatband potential V_{FB} , according to Eq. [1]. e_0 is the elementary charge, kT is the thermal energy, N_D is the density of donors in the n-type semiconductor, and N_C is the density of states in the conduction band

$$E_C^i = e_0 V_{FB} - kT \ln N_C/N_D \quad [1]$$

The condition of zero space charge is determined from the dependence of the capacitance C_{EL} of the electrode on the potential V of the electrode: C_{EL} is given by the capacitances C_H and C_{SC} of the Helmholtz layer and of the space charge, respectively, according to Eq. [2], where C_{SC} is a function of the potential drop in the space charge V_{SC} (32) [$\epsilon\epsilon_0$ permittivity of the semiconductor, for indium oxide $\epsilon = 3.6$ (29)]

$$\frac{1}{C_{EL}} = \frac{1}{C_H} + \frac{1}{C_{SC}} = \frac{1}{C_H} + \sqrt{\frac{V_{SC} - kT/e_0}{\epsilon\epsilon_0 e_0 N_D/2}} \quad [2]$$

Elimination of V_{SC} (33) leads to Eq. [3]

$$\frac{1}{C_{EL}^2} = \frac{1}{C_H^2} + \frac{V - V_{FB} - kT/e_0}{\epsilon\epsilon_0 e_0 N_D/2} \quad [3]$$

In the limit of a very large capacitance C_H , V_{SC} may be replaced by $V - V_{FB}$ directly in Eq. [2].

The data of C_{EL}^{-2} (V) are given in Fig. 2 for a series of pH values. The flatband potential is obtained from the linear extrapolation of the data to the abscissa considering the contribution of the Helmholtz layer $C_H^{-2} = 4.4 \cdot 10^{-3}$ [$\text{cm}^2/\mu\text{F}$]² and the thermal potential $kT/e_0 = 25$ mV according to Eq. [3]. (The slopes of the interpolating lines correspond to a density of donors $N_D = 1 \times 10^{20}$ cm^{-3} , which is in agreement with the density of free electrons in the bulk as obtained from the Hall effect if a correction for surface roughness is not considered.) At pH 10 one extrapolates $V_{FB} = 0.02V_{SCE}$. From this value one obtains $E_C^i = -0.15$ eV according to Eq. [1] considering $N_C = 3 \cdot 10^{22}$ cm^{-3} as given by the density of In-atoms (28).

This value of E_C^i is the basis of the construction of Fig. 1. The vacuum levels in Fig. 1 are drawn with an electron affinity for In_2O_3 of 4.4 eV (34, 35), a normal potential of the saturated calomel electrode of 0.25V (36), and a Fermi level of the normal hydrogen electrode referred to vacuum of 4.5 eV (37). Lowering of pH leads to an increase of the flatband potential (Fig. 2), i.e., to a lower "attachment" E_C^i of the conduction band to the interface (Eq. [1]). This shift has to be attributed to a modification of the Helmholtz potential

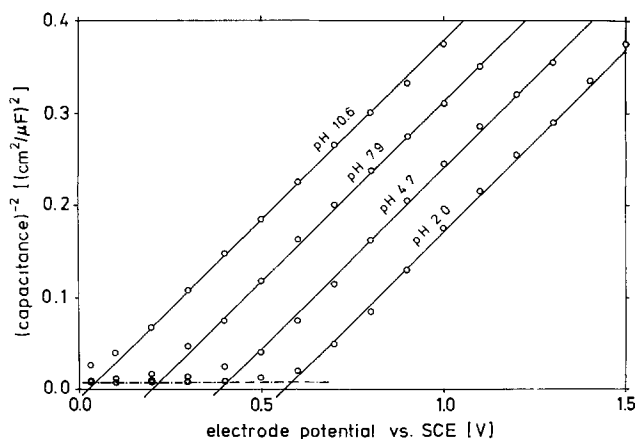


Fig. 2. Square of reciprocal capacitance C_{EL}^{-2} of the uncovered electrode vs. potential V for a series of pH values. Solid lines according to Eq. [3] with $N_D = 1 \cdot 10^{20}$ cm^{-3} . Dotted line indicates $C_H = 15$ $\mu\text{F}/\text{cm}^2$.

caused by chemical reaction or adsorption at the surface of the oxide (38-40).

Surface states.—The distribution of surface states is derived from the dependence of the intrinsic photocurrent on the electrode potential. Neglecting the contribution of the field-free region, the photocurrent per incident photon, i_{SC} , depends on the light absorption in the space charge layer (a_{SC}) and on the reaction of the photogenerated holes which diffuse to the interface (41). Considering that the fraction of charges which cross the electrolyte/electrode interface (rate S_t) in competition to the recombination reaction with occupied surface states (rate S_r) is $S_t/(S_t + S_r)$ the photocurrent is given by Eq. [4] (41)

$$i_{SC} = \frac{1}{1 + S_r/S_t} \cdot a_{SC} \quad [4]$$

An increase in the electrode potential leads on one hand to an enhanced absorption in the growing thickness d_{SC} of the space charge according to Eq. [5], where α is the absorption coefficient of the semiconductor and where d_{SC} is replaced by $\epsilon_0\epsilon/C_{SC}$ from Eq. [2] neglecting the slight difference of V_{SC} and $V - V_{FB}$

$$a_{SC} = \alpha d_{SC} = \alpha \cdot \sqrt{\frac{V - V_{FB} - kT/e_0}{e_0 N_D/2\epsilon\epsilon_0}} \quad [5]$$

On the other hand, lowering the Fermi potential e_0V reduces the number of occupied surface states. Assuming an exponential decrease of the density of surface states in the bandgap from E_C^i (41) with a depth ϵ_s and considering that S_r is proportional to the number of occupied states (41), i.e., approximately to the number of states up to the Fermi level e_0V , one obtains S_r as a function of V according to Eq. [6], where S_r^m is the maximal rate of recombination, when all surface states are involved

$$S_r = S_r^m \exp\left(\frac{E_C^i - e_0V}{\epsilon_s}\right) \quad [6]$$

Thus $i_{SC}(V)$ depends on V_{FB} , E_C^i , ϵ_s , and S_r^m/S_t if Eq. [5] and [6] are inserted into Eq. [4]. The data of the intrinsic photocurrent for a wavelength of excitation of 350 nm and pH 10 are shown in Fig. 3. The absorption in the space charge drawn in the figure is calculated according to Eq. [5] with $V_{FB} = 0.02V_{SCE}$, $N_D = 6 \cdot 10^{19}$ cm^{-3} , and $\alpha = 7 \cdot 10^4$ cm^{-1} (28). The data of current are fitted by Eq. [4] with the two parameters $S_r^m/S_t = 500$, and $\epsilon_s = 0.15$ eV considering $E_C^i = -0.15V_{SCE}$. Addition of thiourea enhances somewhat the photocurrent, which can be fitted by $S_r^m/S_t = 70$, i.e., an enhanced S_t with unchanged ϵ_s (Fig. 3).

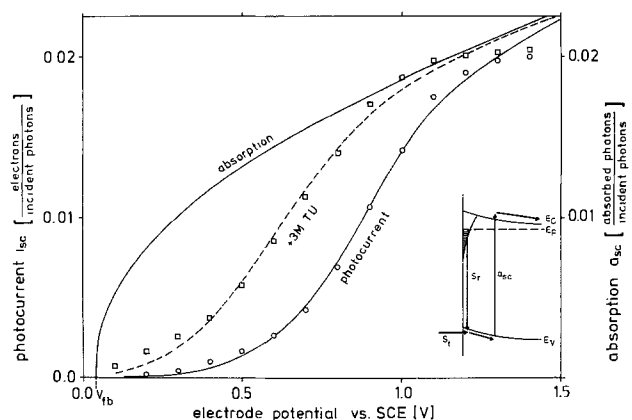
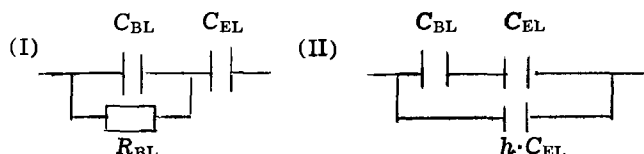


Fig. 3. Intrinsic photocurrent of uncovered electrode vs. potential V at pH 10 with illumination at 350 nm [action spectrum see Ref. (18)]. The data without and with thiourea are fitted according to Eq. [4]. The optical absorption of the space charge is calculated according to Eq. [5].

It is important to consider that the shape of a current-voltage relation as calculated from Eq. [4] depends critically on the character of the distribution of the surface states. A contribution of states of only one sharp energy or of a homogeneous distribution would not even lead to a rough fit of the data.

Bilayer.—The quality of the bilayer on top of the semiconductor is reflected in the effective capacitance of the covered electrode C_{eff} as a function of the potential applied. The modification of C_{eff}^{-1} by a bilayer as referred to C_{EL}^{-1} is considered for two limiting cases (I) a homogeneous bilayer of capacitance C_{BL} and loss resistance R_{BL} , and (II) a bilayer with C_{BL} perforated by holes such that a fraction of area h of the semiconductor remains in contact with the electrolyte. The two models are described by the equivalent circuits I and II. For model II the fraction of free electrode is assumed to appear in addition to the geometrical surface, e.g., by roughness



C_{eff}^{-1} for the two cases is given by Eq. [7] and [8], where C_{EL} is given by Eq. [2], (ω is the angular frequency of the probing a.c.)

$$\frac{1}{C_{\text{eff}}^{\text{I}}} = \frac{1}{1 + (\omega R_{\text{BL}} C_{\text{BL}})^{-2}} \cdot \frac{1}{C_{\text{BL}}} + \frac{1}{C_{\text{EL}}} \quad [7]$$

$$\frac{1}{C_{\text{eff}}^{\text{II}}} = \frac{1}{1 + h(1 + C_{\text{EL}}/C_{\text{BL}})} \cdot \left(\frac{1}{C_{\text{BL}}} + \frac{1}{C_{\text{EL}}} \right) \quad [8]$$

The data of C_{eff}^{-1} with and without bilayer are shown in Fig. 4 for pH 6. The data of the uncovered electrode are fitted according to Eq. [2] with $V_{\text{SC}} = V - V_{\text{FB}}$, using the values $C_{\text{H}}^{-1} = 0.07 \text{ cm}^2/\mu\text{F}$, $V_{\text{FB}} = 0.28 \text{ V}_{\text{SCE}}$, and $N_{\text{D}} = 1 \times 10^{20} \text{ cm}^{-3}$ as obtained from a C^{-2}/V plot.

C_{BL} is obtained from measurements with multibilayers on top of the electrode below flatband potential as shown in Fig. 5. C_{eff}^{-1} increases linearly with the number of the bilayers starting from C_{H}^{-1} . The capacitance per bilayer in the multibilayer system as derived from the slope in Fig. 5 is found to be $C_{\text{BL}} = 0.42 \mu\text{F}/\text{cm}^2$ in good agreement to data for dry multilayer systems (42, 43).

C_{eff}^{-1} of an electrode covered by one ideal multilayer-like bilayer ($R_{\text{BL}} = \infty$, $h = 0$) is obtained by addition of $C_{\text{BL}}^{-1} = 2.4 \text{ cm}^2/\mu\text{F}$ to C_{EL}^{-1} . As shown in Fig. 4 the data approach this theoretical curve only at high potentials whereas a large discrepancy is found at low potentials. Fitting the data by Eq. [7] at low potentials with $R_{\text{BL}} = 3.8 \text{ k}\Omega$ ($\omega = 1 \text{ kHz}$) leads to a large disparity of theory and experiment at high potentials as shown in Fig. 4. Apparently the data cannot be fitted by model I, since Eq. [7] implies a constant increment to C_{eff}^{-1} for the bilayer. This disparity cannot be due to voltage drop in the bilayer. The d-c-resistance of the bilayer as estimated for cathodic polarization of the electrode is in the range of $10^5 \Omega$, which is by two orders of magnitude lower than the blocking resistance of the electrode itself in anodic polarization.

The data, however, may be fitted by model II: The solid line in Fig. 4 is obtained from Eq. [8] with $h = 0.012$ and C_{EL} calculated from Eq. [2] with unchanged values of V_{FB} and C_{H} . The dotted line at low potentials is obtained when the measured C_{EL} is inserted into Eq. [8] still with $h = 0.012$. The agreement between theory and experiment is now very good over the whole voltage range: At low potentials the high capacitance of the blank regions of the electrode dominate such that large deviations occur as compared to the capacitance

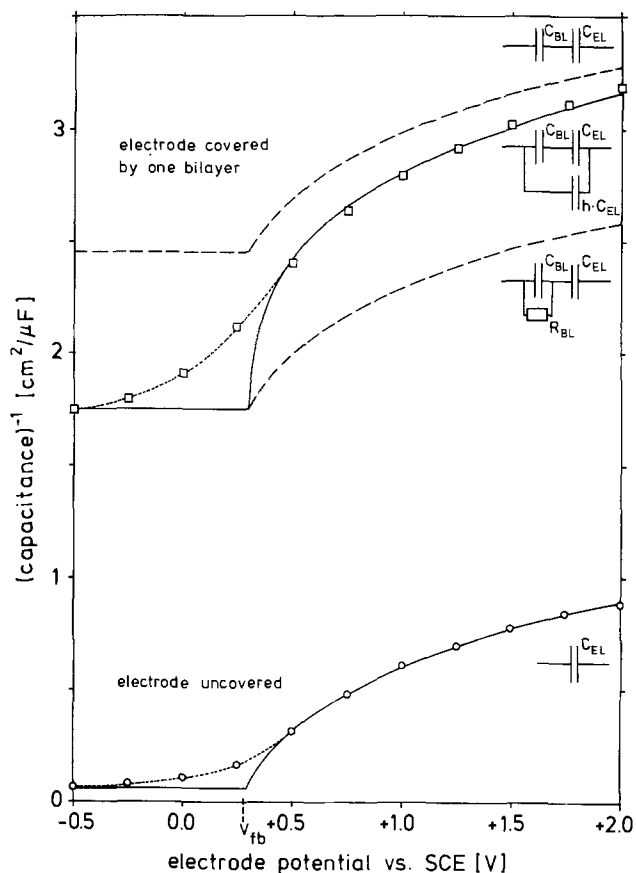


Fig. 4. Reciprocal capacitance vs. potential V at pH 6 for electrode uncovered and covered by one bilayer of Cd-arachidate. The solid and dotted curves represent theoretical C - V relations for the indicated equivalent circuits. Details in the text.

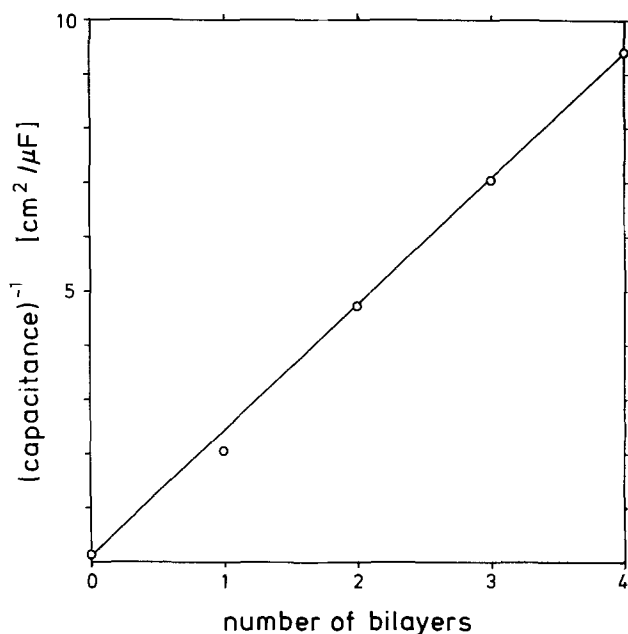


Fig. 5. Reciprocal capacitance of electrode as a function of the number of deposited bilayers at pH 6 and electrode potential $V = -0.5 \text{ V}_{\text{SCE}}$.

of an electrode covered by an ideal bilayer. At high potentials the low capacitance of the semiconductor reduces this contribution of the holes.

The value of the fraction of holes as assigned to the bilayer by fitting the capacitance according to Eq. [8] varies from 0.005 to 0.05 depending on the preparation of the semiconductor. Doping of the bilayer with

cyanine dye A does not change the hole fraction significantly. In any case the area of the bilayer equals the geometrical area at the air/water interface during coating (transfer ratio equals one). We attribute thus the free area h to roughness of the electrode. The rather small value of h indicates a very smooth nature of the surface. Bridging of roughness by the bilayer must be negligible, since chromophores incorporated at the bilayer/semiconductor interface reflect a direct contact of the bilayer with the surface by their features of optical absorption as discussed in the next section.

Mechanism of Photosensitization

Doping of the bilayer on top of the electrode by the cyanine dye A leads to an enhancement of photocurrent through the interface electrolyte/semiconductor. Structure and energy levels of the system are shown in Fig. 1.

The oxidation potential of the ground state S_0 of the dye is $E_{A/A+S_0} = 1.4V_{SCE}$ (44) (Table 1 and Fig. 2 in that reference). The oxidation energies of the first excited singlet and triplet state are constructed by subtracting the spectroscopic excitation energies. With an energy of optical absorption of 2.9 eV (cf. Fig. 7) the oxidation potential of S_1 is $E_{A/A+S_1} = -1.5V_{SCE}$. Considering a singlet-triplet splitting of 0.5 eV (45, 46) the oxidation potential of T_1 is $E_{A/A+T_1} = -1.0V_{SCE}$. The kinetic levels of electron donation for S_0 , S_1 , and T_1 and of electron acceptance for the oxidized doublet D^+ are assumed to be 0.4 eV higher and lower respectively than the corresponding equilibrium potentials as caused by reorganization (5).

It is apparent that the donor levels of both excited states $E_{dS_1} = -1.1V_{SCE}$ and $E_{dT_1} = -0.6V_{SCE}$ are well above the edge of the conduction band which is $E_{C^i} = -0.15V_{SCE}$ for indium-tin-oxide electrode at pH 10. The acceptor level of the oxidized state $E_{aD^+} = +1.0V_{SCE}$ is on one hand far above the edge of the valence band at $E_{V^i} = +3.45V_{SCE}$ due to the large band-gap of 3.6 eV (29). On the other hand it is far below the surface states which are mainly distributed in the range of $0.0V_{SCE}$ according to the depth of 0.15 eV of their exponential distribution below E_{C^i} .

The sensitization of photocurrent by the cyanine dye A is characterized by seven observations as described below. These observations lead to a mechanism of sensitization as depicted in Fig. 6.

Absorption spectrum.—The absorption spectrum of dye A in the bilayer in contact to the indium-tin-oxide, as shown in Fig. 7, is characteristic for dye-monomers, with the 0-0 transition at 430 nm and a 0-1 vibronic transition at 410 nm (23). The typical absorption band of dimers at 410 nm, as observed usually in dye monolayers in contact to water (8, 47), is suppressed, although little contribution of dimer absorption to the shoulder at 410 nm cannot be excluded. Thus the interaction of the dye with the elec-

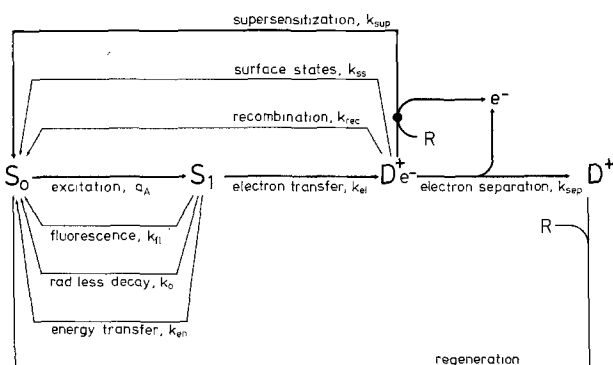


Fig. 6. Kinetic mechanism of photosensitization of indium-tin-oxide electrode by cyanine dye. Notations in the text.

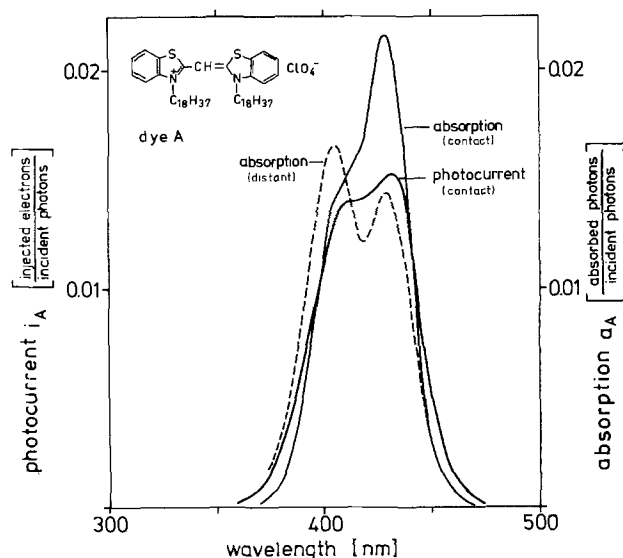


Fig. 7. Spectra of optical absorption and of photocurrent for thiacyanine dye A. The spectra refer to chromophores in direct contact to the electrode and on the aqueous side of the bilayer (cf. Fig. 1). The contribution of the electrode itself is subtracted [cf. Ref. (18)].

trode breaks the stacking interaction of the chromophores without shifting the electronic transition of the monomers (Fig 7). This observation indicates close contact of the dye molecules with the semiconductor, presumably with flat orientation of the chromophores, without any significant modification of their electronic structure.

Photocurrent spectrum.—The photocurrent through an electrode coated with a dye-doped bilayer exhibits a component with a spectral maximum at 430 nm as shown in Fig. 7. Thus excitation of the dye monomer to its first excited singlet state S_1 induces charge transfer through the interface. Whether the shoulder at 410 nm, which is enhanced as compared to the absorption spectrum, has to be assigned to the action of the higher excited state of the monomer or to excited dimers cannot be decided at the present moment. The following experiments are all concerned with the maximum at 430 nm which can be assigned unequivocally to the $S_0 - S_1, 0-0$ transition of the monomer.

Chromophore variation.—Substitution of the monomethin-thiacyanine A by analogous dyes, a monomethin-oxacyanine, a trimethin-thiacyanine, and trimethin-carbocyanine (31), with absorption maxims from 360 nm up to 560 nm does not affect the efficiency of photocurrent, which is under optimal conditions (see below) about 0.7 (Fig. 7). The action spectrum of photocurrent of the free electrode extends up to 460 nm (18). Photosensitization by energy transfer from excited dyes to surface states of the electrode would be possible only for chromophores with some overlap of their emission spectrum with this action spectrum of the electrode. The constant efficiency for the homologous series of cyanine dyes up to an emission wavelength as long as 600 nm excludes this mechanism of sensitization. On the other hand the redox-potentials of the excited dyes are all far above the edge of the conduction band (Fig. 1) (44) such that sensitization by electron transfer from the excited dyes to the conduction band is consistent with the observations.

Bleaching.—Sensitization (without addition of thiourea) is connected with a fast reversible bleaching of the dye, as has been shown by fluorescence measurements in a previous paper (18). This result indicates the formation of an oxidized dye, the radical doublet D^+ , having transferred an electron to the semiconductor (cf. Fig. 6).

Contacting.—The binding of the dye to the surface of the electrode leads to a quenching of fluorescence as compared to a dye incorporated at the aqueous side of the bilayer [Fig. 8(c)]. The quantum yield of the decay process of S_1 as induced by direct contact is 0.8. (The evaluation of this yield is discussed in the next section.) The induced decay of S_1 reflects the primary process of sensitization: The upper limit of the quantum yield of photocurrent, as observed at high potential and high supersensitization, is near 0.8 as well (Fig. 9 and 10). A significant induction of an unproductive decay has not been considered.

This primary process is not intersystem crossing as caused by a heavy atom effect followed by electron transfer (48): Contacting dye A in the bilayer to an evaporated thin layer of lanthanumfluoride breaks the dimers of the dye as in the case of indium-tin-oxide, but does not lead to any quenching of fluorescence. Lanthanum resembles indium and tin with respect to atomic number and ion radius such that the heavy

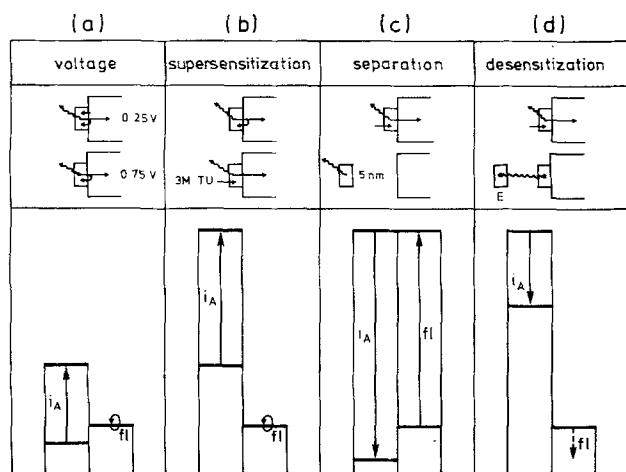


Fig. 8. Photocurrent and fluorescence as induced and emitted resp. by thiocyanine dye A in contact to electrode. (a) potential: $0.25V_{SCE}$ and $0.75V_{SCE}$, (b) thiourea (TU): 0M and 3M, (c) dye location: direct contact and separation by one bilayer (5 nm) from electrode, (d) energy transfer: no acceptor and acceptor E at a distance of 5 nm. The schemes at the top of the figure illustrate the mechanistic effects as assigned in the text.

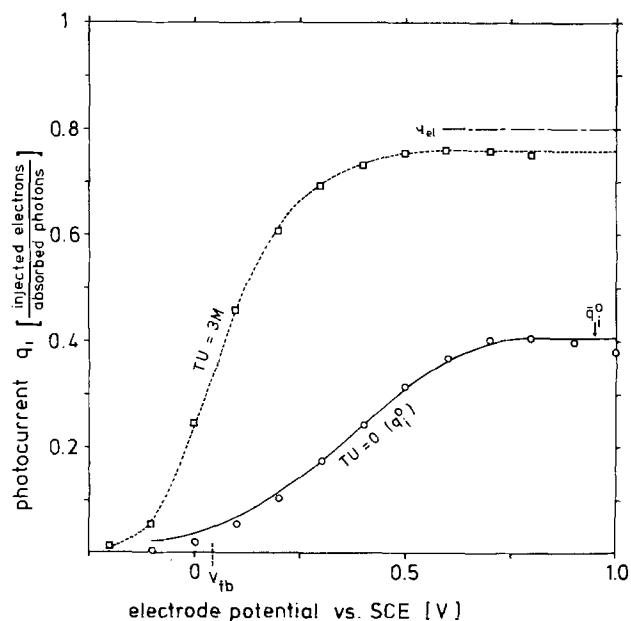


Fig. 9. Quantum yield q_i of sensitized photocurrent vs. potential V at pH 10 without and with 3M thiourea (TU). The data without thiourea are fitted according to Eq. [10].

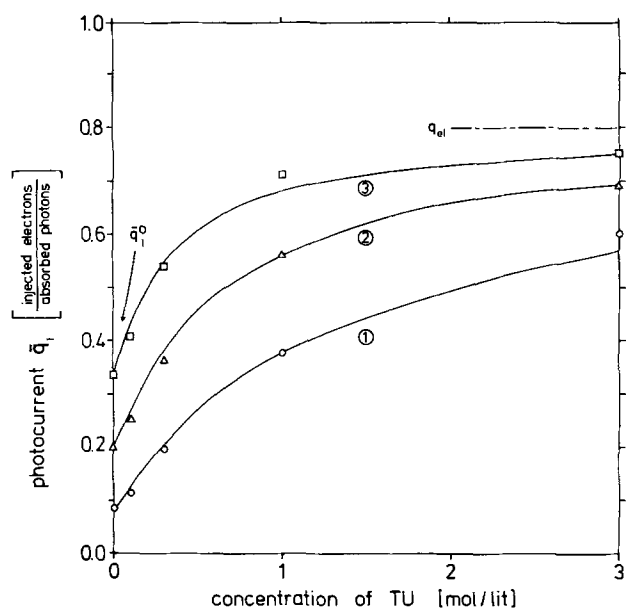


Fig. 10. Quantum yield q_i of sensitized photocurrent at saturating potential $V = 0.8V_{SCE}$ vs. concentration of thiourea (pH 10). The theoretical fit for the three samples is obtained according to Eq. [17].

atom effect of LaF_3 should be comparable to that of In_2O_3/SnO_2 . However electron transfer from the dye is excluded in the case of LaF_3 due to the large band-gap of that insulator (6.7 eV) (49). These observations indicate that the primary process of sensitization is electron transfer directly from S_1 to the indium-tin-oxide.

Supersensitization.—Addition of thiourea to the electrolyte enhances the photocurrent [Fig. 8(b)]. This enhancement is observed from the very beginning of illumination. It is not only a suppression of bleaching during illumination. Thus the effect cannot be assigned to regeneration of the photo-oxidized D^+ (cf. Fig. 6). On the other hand the enhancement is not connected with any quenching of fluorescence [Fig. 8(b)]. Thus the supersensitization cannot be assigned to reduction of S_1 with subsequent induced electron transfer.

The observation indicates the existence of another intermediate formed by the primary process of electron transfer. This intermediate must consist of the photo-oxidized dye and the transferred electron at the surface of the electrode as symbolized by D^+e^- in Fig. 6: Supersensitization is due to reduction of the dye in the intermediate, as induced by thiourea, with subsequent removal of the electron to the bulk of the electrode as indicated in Fig. 6. This process competes with the unproductive recombination of D^+e^- back to S_0 . Without supersensitization the photocurrent is caused by spontaneous separation of the electron in D^+e^- to the bulk of the electrode producing the bleached radical D^+ (Fig. 6).

Electrode potential.—Lowering the applied potential of the electrode leads to a lowering of photocurrent far above flatband potential [Fig. 8(a) and 9]. This inhibition as caused by lifting the Fermi potential may be due to electron donation from occupied surface states of the electrode back to the chromophore. Electron donation to S_1 is excluded, since no potential dependence of fluorescence is observed.

The drop of current is suppressed by supersensitization (Fig. 9). Thus the potential dependent inhibition is related to the intermediate D^+e^- . It reflects the antisensitizing reduction of the oxidized dye by occupied surface states with subsequent release of the electron (Fig. 6). This assignment is discussed in detail in the next section.

Quantum Yield of Photosensitization

The quantum yield of sensitized current q_i is the ratio i_A/a_A of sensitized photocurrent i_A per incident light intensity and the optical absorption (a_A) of the dye. Considering the reaction scheme of Fig. 6, q_i is determined by the quantum yield q_{el} of electron transfer leading to the intermediate D^+e^- and the quantum yields of release of the electron q_{sep} and q_{sup} corresponding to the spontaneous separation leading to the oxidized D^+ and to the supersensitization as induced by thiourea, according to Eq. [9]

$$q_i = i_A/a_A = (q_{sep} + q_{sup}) \cdot q_{el} \quad [9]$$

The present section considers the estimation of q_{el} and the evaluation of q_{sep} and q_{sup} as a function of electrode potential and thiourea concentration, respectively. All measurements refer to the very beginning of illumination, where bleaching of the dye by formation of D^+ has not to be considered, i.e., the absorption a_A is always the absorption of the unperturbed dye layer.

Electron transfer.—Incorporation of an energy acceptor E at the interface bilayer/water perturbs the sensitizing process exclusively by the competition of energy transfer with electron transfer from S_1 . Thus the ratio of current i_A/i_A^E without and with acceptor equals the ratio of quantum yields q_{el}/q_{el}^E without and with acceptor according to Eq. [9]. q_{el} and q_{el}^E are defined by the rate constants of electron transfer k_{el} , of fluorescence k_{fl} , of radiationless deactivation k_o , and of energy transfer k_{en} according to Eq. [10a] and [10b]

$$q_{el} = \frac{k_{el}}{k_{el} + k_{fl} + k_o} \quad [10a]$$

$$q_{el}^E = \frac{k_{el}}{k_{el} + k_{fl} + k_o + k_{en}} \quad [10b]$$

By straightforward algebra the ratio q_{el}/q_{el}^E may be expressed in terms of the unknown q_{el} and a parameter $k_{en}/(k_{fl} + k_o)$, which characterizes the energy transfer system, according to Eq. [11]

$$\frac{q_{el}}{q_{el}^E} = 1 + \frac{k_{en}}{k_{fl} + k_o} (1 - q_{el}) \quad [11]$$

The ratio $k_{en}/(k_{fl} + k_o)$ may be determined from fluorescence quenching in a bilayer arrangement without semiconductor. If the contact of the semiconductor does not affect the rate constants, q_{el} may be determined from Eq. [11]. This procedure has been used previously in the case of sensitization of silver bromide (25).

With dye A as an acceptor, using an analogous oxacyanine as a sensitizer, k_{en} is found to be two times faster than $(k_{fl} + k_o)$ (18). With the quenching of current $q_{el}^E/q_{el} = 0.7$ [Fig. 8(d)] one obtains $q_{el} = 0.8$. The oxacyanine, used as a sensitizer in this experiment, behaves in all aspects as the original thiocyanine (18).

A similar result is obtained by evaluating the quenching of fluorescence as observed when the sensitizer is brought from the aqueous side of the bilayer to the semiconductor [Fig. 8(c)]. The ratio of fluorescence intensity of the dye in contact I_c and of the dye at a distance of 5 nm to the semiconductor I_d is related directly to q_{el} according to Eq. [12] as may be easily derived from a consideration of the rate constants

$$\frac{I_c}{I_d} = 1 - q_{el} \quad [12]$$

With $I_c/I_d = 0.2$ one obtains $q_{el} = 0.8$. This determination is less reliable than the previous one since the optical surroundings of the dye differ for the two different locations in front of the reflecting electrode.

The evaluation of q_{el} as considered is in fact an evaluation of the quantum yield of that decay process

of S_1 which is induced by a semiconductor. Identification with the quantum yield of electron transfer implies that no other decay channels are opened by the electrode. This assumption is justified a posteriori by the fact that the quantum yield of current under optimal conditions of supersensitization approaches also the value of 0.8 (Fig. 10) and that no induced formation of the triplet state is observed. k_{el} may be expressed by k_{fl} : With the quantum yield of fluorescence without semiconductor $k_{fl}/(k_{fl} + k_o) = 0.2$ (18) and with $q_{el} = 0.8$ considering Eq. [10a] one obtains $k_{el} = 20 \cdot k_{fl}$. The radiative lifetime of the cyanine dye A is 3 nsec (50, 51). Electron transfer to the electrode from S_1 occurs thus with a rate constant of about $k_{el} = 7 \times 10^9 \text{ sec}^{-1}$.

Inhibition by surface states.—The quantum yield of current without addition of thiourea, q_i^0 , becomes significant only far above the flatband potential (Fig. 9). Such a characteristic has been reported previously for polycrystalline electrodes of SnO_2 (52). The removal of the transferred electron from the interface by the field in the space charge should lead, however, to a sharp increase of current at the flatband potential as reported for single crystalline electrodes of ZnO (5). In the present case such a characteristic is observed after addition of thiourea (Fig. 9). We attribute the depression of current in the absence of supersensitization to the action of occupied surface states of the semiconductor, donating an electron with rate constant k_{ss} to the intermediate D^+e^- , i.e., reduction of D^+ to S_0 with subsequent release of the electron (Fig. 6). Supersensitization inhibits this deactivation process by competition. Without supersensitization Eq. [9] becomes $q_i^0 = q_{sep}^0 q_{el}$, where q_{sep}^0 is defined by the rate constants of separation, recombination, and reduction by surface states, i.e., k_{sep} , k_{rec} , and k_{ss} , respectively, according to Eq. [13] (see Fig. 6)

$$q_{sep}^0 = \frac{k_{sep}}{k_{sep} + k_{rec} + k_{ss}} \quad [13]$$

The experimental results of Fig. 9 indicate a decrease of k_{ss} with increasing potential of the electrode. With $q_{el} = 0.8 q_{sep}^0$ in saturation ($k_{ss} = 0$) is $q_{sep}^0 = 0.5$. This result means that the release of the electron to the bulk of the semiconductor with formation of D^+ occurs with a similar rate as the recombination to S_0 . The value of q_{sep}^0 varies considerably from sample to sample (cf. Fig. 10).

The voltage dependence of q_i^0 may be described in terms of q_{sep}^0 , q_{el} , and the parameter k_{ss}/k_{sep} characterizing the reduction by surface states according to Eq. [14] which is obtained from Eq. [9] and [13]

$$q_i^0 = \frac{q_{sep}^0}{1 + q_{sep}^0 \cdot k_{ss}/k_{sep}} \cdot q_{el} \quad [14]$$

Assuming k_{ss} to be proportional to the number of occupied surface states, the experimental data of Fig. 9 reflect the decrease of the number of states involved when the Fermi level is lowered. The smooth decrease of the current q_i^0 excludes electron donation only from a narrow range of surface states of energies, e.g., near the acceptor energy of the dye, $E_a^{D^+}$. This behavior is described, however, if one assumes that all occupied surface states above the acceptor level are involved considering the exponential distribution of states as determined above. Integrating over this distribution up to the Fermi e_0V and denoting the maximal rate of donation, when all states would contribute to reduction, by k_{ss}^m one obtains k_{ss} as a function of the potential according to Eq. [15], which is analogous to Eq. [6]

$$k_{ss} = k_{ss}^m \exp \frac{E_0^i - e_0V}{e_s} \quad [15]$$

Best fit of the experimental data in Fig. 9 is obtained by Eq. 14 with $k_{ss}^M = 40 \cdot k_{sep}$. The other parameters are $\bar{q}_{sep}^0 = 0.5$ and $q_{el} = 0.8$ as determined above. The values of $E_C^1 = -0.15 \text{ eV}_{SCE}$ and $\epsilon_s = 0.15 \text{ eV}$ are as in the case of intrinsic photocurrent.

Supersensitization induced by thiourea.— \bar{q}_i is enhanced by thiourea as shown in Fig. 10. In order to act as a supersensitizer thiourea has to cross the bilayer in the intact regions or through the holes such that it reduces the D^+ in direct contact. The primary photochemical process may be followed by secondary dark reactions. According to Eq. [9] \bar{q}_i depends on the sum ($\bar{q}_{sup} + \bar{q}_{sep}$) of quantum yields in saturation which is expressed by the rate constants according to Eq. [16] where k_{sup} is the rate constant of supersensitization (Fig. 6)

$$\bar{q}_{sep} + \bar{q}_{sup} = \frac{k_{sep} + k_{sup}}{k_{rec} + k_{sep} + k_{sup}} \quad [16]$$

The data of Fig. 10 indicate an increase of k_{sup} with increasing concentration TU of thiourea, i.e., an increase from $(\bar{q}_{sup} + \bar{q}_{sep}) = \bar{q}_{sep}^0$ for $TU = 0$ to $(\bar{q}_{sup} + \bar{q}_{sep}) = 1$ for $TU \rightarrow \infty$. Assuming a linear proportionality of supersensitization with the concentration of thiourea, i.e., $k_{sup} = k_{sup}^M \cdot TU$ where k_{sup}^M is the rate constant for 1M thiourea, \bar{q}_i is given by Eq. [17], which is obtained from Eq. [9] and [16] introducing \bar{q}_{sep}^0 as in the previous section

$$\bar{q}_i = \frac{\bar{q}_{sep}^0 + \bar{q}_{sep}^0 \cdot \frac{k_{sup}^M}{k_{sep}} TU}{1 + \bar{q}_{sep}^0 \frac{k_{sup}^M}{k_{sep}} TU} \cdot q_{el} \quad [17]$$

Supersensitization is characterized by the parameter k_{sup}^M/k_{sep} . The two summands of Eq. [17] reflect the enhanced contribution of supersensitization and the suppressed contribution of spontaneous separation when the concentration of thiourea is increased.

As shown in Fig. 10 the data of \bar{q}_i scatter for different samples of the electrode. A fit of all data is obtained by Eq. [17] with $q_{el} = 0.8$ using a single parameter of supersensitization $k_{sup}^M/k_{sep} = 6.5M^{-1}$, if the samples are characterized by individual $\bar{q}_i^0 = \bar{q}_{sep}^0 q_{el}$. Accordingly, supersensitized injection with 3M thiourea is 20 times faster than spontaneous separation. The reduction of D^+e^- induced by thiourea may thus compete effectively with the reduction by surface states which is found to be up to 40 times faster than k_{sep} . This result is consistent with the modification of the potential dependence of current as induced by thiourea shown in Fig. 9. The variability of \bar{q}_i^0 ($0.05 < \bar{q}_i^0 < 0.5$) is due to a variability of \bar{q}_{sep}^0 since q_{el} is found to be constant. In the expression $\bar{q}_{sep}^0 = (1 + k_{rec}/k_{sep})^{-1}$ the variability has to be assigned to k_{rec} . A variation of k_{sep} such that the ratio k_{sup}^M/k_{sep} remains constant appears to be improbable. The recombination rate may depend on slight variations of the type and number of surface states which may be caused by irreproducible slight variations of the preparation conditions of the evaporated electrode.

Summary

The present paper includes the following results.

1. A lipid bilayer is deposited onto a semiconductor electrode rather homogeneously, but not without imperfections, where electrode and electrolyte are in direct contact. The fraction of free area is in the order of 0.01.

2. Electrons from an excited chromophore in a membrane structure are transferred to the semiconductor with a quantum yield of 0.8. The electron transfer from the first excited singlet state of the monomer of

a thiocyanine dye occurs at a rate of about 10^{10} sec^{-1} . The rate does not depend on the electric field in the space charge.

3. Sensitization of photocurrent is connected with a kinetic intermediate consisting of the oxidized chromophore and the transferred electron at the surface of the electrode.

4. Supersensitization by thiourea is not due to reduction of the first excited singlet state but to reduction of the oxidized chromophore in the intermediate with subsequent release of the electron into the bulk of the semiconductor. This process competes with unproductive recombination.

5. The voltage dependence of sensitized current is due to reduction of the oxidized chromophore in the intermediate by occupied surface states in the electrode. All occupied states above the acceptor level of the dye, up to the Fermi potential, appear to be effective. The energetic distribution of the states corresponds to the distribution of surface states involved in surface recombination of holes in the case of intrinsic photocurrent.

Acknowledgments

We thank Prof. Th. Hehenkamp, Institut für Metallphysik der Universität Göttingen, for the determination of the composition of the electrode by an x-ray microprobe and Dr. E. E. Polymeropoulos for critical reading of the manuscript.

Manuscript submitted May 22, 1979; revised manuscript received Sept. 10, 1979.

Any discussion of this paper will appear in a Discussion Section to be published in the December 1980 JOURNAL. All discussions for the December 1980 Discussion Section should be submitted by Aug. 1, 1980.

Publication costs of this article were assisted by the Max Planck-Institut für Biophysikalische Chemie.

REFERENCES

- H. Gerischer and H. Tributsch, *Ber. Bunsenges. Phys. Chem.*, **72**, 437 (1968).
- H. Tributsch and H. Gerischer, *ibid.*, **73**, 251 (1969).
- K. Hauße, H. Pusch, and J. Range, *Z. Phys. Chem.*, **64**, 122 (1969).
- K. Hauße, H. J. Danzmann, H. Pusch, J. Range, and H. Volz, *This Journal*, **117**, 993 (1970).
- H. Gerischer and F. Willig, in "Topics in Current Chemistry," Vol. 61, F. L. Boschke, Editor, p. 31, Springer, Berlin (1976).
- K. H. Hauße, *Photogr. Sci. Eng.*, **20**, 124 (1976).
- H. Tributsch and M. Calvin, *Photochem. Photobiol.*, **14**, 95 (1971).
- H. Kuhn, D. Möbius and H. Bücher, in "Physical Methods of Chemistry," A Weissberger and B. W. Rossiter, Editors, Vol. I, part 3B, pp. 577-702, Wiley, New York (1972).
- R. Memming, *Faraday Discuss. Chem. Soc.*, **58**, 261 (1974).
- M. Fujihira, N. Ohishi, and T. Osa, *Nature (London)*, **268**, 226 (1977).
- M. Spittler, M. Lübke, and H. Gerischer, *Chem. Phys. Lett.*, **56**, 557 (1978).
- R. Memming and H. Tributsch, *J. Phys. Chem.*, **75**, 562 (1971).
- R. Memming, *Photochem. Photobiol.*, **16**, 325 (1972).
- U. Bode, K. Hauße, Y. Ishikawa, and H. Pusch, *Z. Phys. Chem.*, **85**, 144 (1973).
- T. Watanabe, A. Fujishima, and K. Honda, *Ber. Bunsenges. Phys. Chem.*, **79**, 1213 (1975).
- U. Bode and K. Hauße, *This Journal*, **125**, 51 (1978).
- K. Hauße and U. Bode, *Faraday Discuss. Chem. Soc.*, **58**, 281 (1974).
- W. Arden and P. Fromherz, *Ber. Bunsenges. Phys. Chem.*, **82**, 868 (1978).
- T. Yamase, H. Gerischer, M. Lübke, and B. Pettinger, *ibid.*, **82**, 1041 (1978).
- B. Pettinger, H.-R. Schöppel, and H. Gerischer, *ibid.*, **77**, 960 (1973).
- H. Yamada, T. Amamiya, and H. Tsubomura, *Chem. Phys. Lett.*, **56**, 591 (1978).

22. H. Gerischer and H. Selzle, *Electrochim. Acta*, **18**, 799 (1973).
23. A. H. Herz, *Adv. Colloid. Interface Sci.*, **8**, 237 (1977).
24. P. B. Gilman, Jr., *Pure Appl. Chem.*, **49**, 357 (1977).
25. L. V. Szentpaly, D. Möbius, and H. Kuhn, *J. Chem. Phys.*, **52**, 4618 (1970).
26. D. Möbius, *Photogr. Sci. Eng.*, **18**, 413 (1974).
27. P. Fromherz, Habilitationsschrift, Fachbereich Physik. Chemie, Universität Marburg (1977).
28. H. Köstlin, R. Jost, and W. Lems, *Phys. Status Solidi A*, **29**, 87 (1975).
29. H. K. Müller, *ibid.*, **27**, 723 (1968).
30. P. Fromherz, *Rev. Sci. Instrum.*, **46**, 1380 (1975).
31. J. Sondermann, *Liebigs Ann. Chem.*, **749**, 183 (1971).
32. W. Schottky, *Z. Phys.*, **118**, 539 (1939).
33. R. DeGryse, W. P. Gomes, and J. Vennick, *This Journal*, **122**, 711 (1975).
34. E. Wang and L. Hsu, *ibid.*, **125**, 1328 (1978).
35. D. L. Feucht, *J. Vac. Sci. Technol.*, **14**, 57 (1977).
36. H. H. Willard, L. L. Merritt, I. R. Dean, and I. A. Dean, "Instrumental Methods of Analysis," 4th ed., Princeton, New Jersey (1967).
37. F. Lohmann, *Z. Naturforsch Teil A*, **22**, 843 (1967).
38. H. Gerischer, M. Hofmann-Perez, and W. Mindt, *Ber. Bunsenges. Phys. Chem.*, **69**, 130 (1965).
39. F. Lohmann, *ibid.*, **70**, 428 (1966).
40. M. A. Butler and D. S. Ginlay, *This Journal*, **125**, 228 (1978).
41. R. H. Wilson, *J. Appl. Phys.*, **48**, 4292 (1971).
42. B. Mann and H. Kuhn, *ibid.*, **42**, 4398 (1971).
43. E. Polymeropoulos, *ibid.*, **48**, 2404 (1977).
44. R. F. Large, in "Photographic Sensitivity," R. J. Cox, Editor, p. 241, Academic Press, London (1973).
45. S. P. McGlynn, T. Azumi, and M. Kinoshita, "Molecular Spectroscopy of the Triplet State," p. 174, Prentice-Hall, N.J. (1969).
46. V. A. Kuzumin, A. S. Tabikolov, and Yu. E. Borisevich, *Chem. Phys. Lett.*, **53**, 52 (1978).
47. P. Fromherz, *Z. Naturforsch. Teil C*, **28**, 144 (1973).
48. E. Clementi and M. Kasha, *J. Chem. Phys.*, **26**, 956 (1957).
49. M. P. Wirick, *Appl. Opt.*, **5**, 1966 (1966).
50. N. J. L. Roth and A. C. Craig, *J. Phys. Chem.*, **78**, 1154 (1974).
51. L. D. Derkacheva, V. A. Petukhov, and E. G. Treneva, *Opt. Spectrosk.*, **41**, 574 (1976).
52. H. Kim and H. A. Laitinen, *This Journal*, **122**, 53 (1975).

In Situ Measurement and Analysis of Plasma-Grown GaAs Oxides with Spectroscopic Ellipsometry

J. B. Theeten,¹ R. P. H. Chang,* D. E. Aspnes, and T. E. Adams²

Bell Laboratories, Murray Hill, New Jersey 07974

ABSTRACT

A versatile ellipsometer with variable energy (1.5-5.6 eV) and angle of incidence (60°-75°) has been constructed for *in situ* thin film diagnostics on a linear plasma reactor. This instrument has been used to study the plasma oxidation of GaAs (100) surfaces. During oxidation the ellipsometer is set at a fixed wavelength and a fixed angle of incidence for monitoring the thickness of the oxide. Such information as the rate of oxidation, transient effects, uniformity, and optical absorption of the oxide layer are obtained during plasma processing. The oxidation process can be interrupted at any moment for examining the sample as a function of energy and angle of incidence. A multilayer analysis is presented to determine (i) the dielectric function and the thickness of the oxide layer, and (ii) the composition and the thickness of the interface region between the oxide and the GaAs substrate. The effect of the rate of plasma oxidation on the oxide properties is also discussed.

The use of plasma oxidation for obtaining oxide films with good electrical properties on a GaAs substrate has been actively investigated in the past few years (1). These oxide films have been analyzed by a variety of techniques (1-4). Of these, spectroscopic ellipsometry has proved to be suitable not only for determining the nature and the thickness of the oxide layer but also for nondestructively analyzing the interface region between the oxide and the substrate (2).

To investigate further the influence of plasma processing parameters on the characteristics of the oxide films during plasma exposure, we have constructed a versatile ellipsometer for *in situ* thin film diagnostics on a linear plasma reactor. The system not only will improve our knowledge of plasma-grown GaAs oxides, but also it will be applicable to films of more complex structure such as those involving both metallic aluminum and GaAs. In this paper we describe the system and various applications. The optical and the

electronic aspects of the system are discussed. Kinetic measurements of the oxides and their interpretation are given and spectroscopic measurements with variation of the angle of incidence are illustrated. Both the modeling of our ellipsometry data and a complete multilayer analysis of two samples oxidized at very different rates are discussed. The analysis reveals marked differences between the two oxides, both in the oxide layer and at the interface with the GaAs substrate.

Description of the System

A simplified schematic diagram of the experimental configuration is shown in Fig. 1. It consists of a spectroscopic ellipsometer attached to a linear plasma reactor (5). The ellipsometer is a photometric type related to Fourier-transform rotating-analyzer ellipsometers described previously (6). The main difference in the present design is that the source and detector are interchanged. The sequence of optical elements is therefore lamp, rotating polarizer, sample, fixed analyzer, monochromator, and photomultiplier. The advantage of this configuration is that it places the monochromator between the reactor and the detector. Therefore, the light generated by the reactor is essentially

* Electrochemical Society Active Member.

¹ Present address: Laboratoires d'Electronique et de Physique, 94450 Limeil-Brevannes, France.

² Present address: Cornell University, Ithaca, New York 14850.

Key words: plasma oxides, GaAs oxides, ellipsometry, thin films, plasma processing.

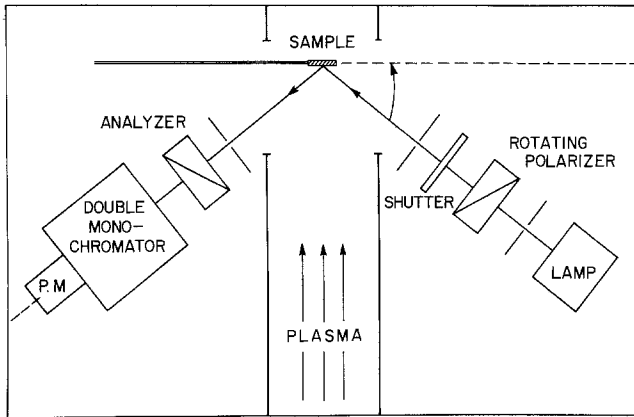


Fig. 1. Schematic view of the automatic spectroscopic and variable-angle ellipsometer for *in situ* measurement of plasma-exposed samples.

eliminated before reaching the detector, thus greatly improving the signal to noise ratio. An added feature with respect to previous systems is that the angle of incidence can be varied continuously.

In oxidation measurements, the sample is placed in a vacuum chamber such that its surface is nearly normal to the oxygen plasma column. The plasma is produced at an O_2 pressure of 10^{-3} Torr by a pair of rf electrodes. A typical rf power is 300W at 27 MHz. A magnetic field up to 1 kG confines the plasma along the axis of the vacuum chamber. The sample is biased positively at 50-100V with respect to the plasma. Typical currents collected during the oxidation process are a few 10 mA/cm².

The optical components are as follows. The light source is a feedback-stabilized high brightness 500W Xe arc lamp³ which has an essentially line-free continuum over the accessible energy range of 1.5-5.6 eV that is ideally suited for this spectroscopic method. A quartz Rochon prism is used as the rotating polarizer to provide combined depolarizer/polarizer functions and thus greatly reduce the effects of any residual polarization in the lamp flux as well as providing approximately linearly polarized light to illuminate the sample. The shutter chops the incident beam to provide a background reference to eliminate effects of drift in electronic components and to isolate the fraction of light detected by the photomultiplier that originates by reflection from the sample. Strain-free fused-quartz windows mounted on standard 2 $\frac{3}{4}$ in. conflat flanges provide optical access to the plasma reaction chamber. To minimize oxide nonuniformity effects in optical data, as discussed later, the illuminated area on the sample is restricted to 0.3×0.6 mm² by an 0.3 mm diameter aperture.

A u.v. calcite Glan-Thompson prism is used as the fixed analyzer to reduce over-all system length. Absorption by this prism determined the 5.6 eV upper limit of the spectral range. Wavelength filtering is provided by a quarter-meter double grating monochromator⁴ operated at a typical resolution of 1 nm. An S20 photomultiplier⁵ is used as the detector and determines the low energy spectral limit of 1.5 eV.

The polarizer is mounted in a hollow-shaft d-c motor⁶ that is feedback stabilized to operate at speeds typically near 25 rps. An attached hollow-shaft optical encoder⁷ is used to trigger a 14-bit analog-to-digital converter (ADC) giving 1024 conversions per revolution. The entire lamp, polarizer, and shutter assembly is mounted on Teflon-supported rails designed to slide on the optical table to provide any angle of incidence from 60°-76°. The angle of incidence is determined geometrically by laser alignment and further

checked by ellipsometric measurements on a reference SiO₂-Si sample.

The detector output voltage has a Fourier spectrum related to the optical configuration and sample properties as follows. If the complex reflectance ratio of the sample is

$$\rho = r_p/r_s = \tan \psi e^{i\Delta} \quad [1]$$

where r_p and r_s are the complex field reflectance coefficients for p- and s-polarized light, respectively, then the detector output is proportional to the intensity incident upon it, or

$$I(t) = I_{av} [\sin^2 P \sin^2 A + \cos^2 P \cos^2 A \tan^2 \psi + \frac{1}{2} \tan \psi \cos \Delta \sin 2P \sin 2A] \quad [2]$$

where I_{av} is the average intensity and the azimuth angles P and A are measured from the plane of incidence. In operation $A = A_0$ is fixed, and $P = \omega t$ where ω is the mechanical angular frequency. Under these conditions the harmonic spectrum of Eq. [2] can be written

$$I(t) = a \cos 2P + b \sin 2P + C \quad [3]$$

where the coefficients a , b , and c can be determined by Fourier analysis of the measured intensity. It follows from Eq. [2] that

$$\tan \psi = \tan A_0 \sqrt{\frac{c+a}{c-a}} \quad [4]$$

$$\cos \Delta = b/\sqrt{c^2 - a^2} \quad [5]$$

The angle of incidence dependence enters through P .

Fourier analysis of the data and over-all control of both plasma and optical systems are provided by the data processing and control system outlined in block form in Fig. 2. The system features two processors: (i) a fast acquisition and control interface for local control of peripherals, on-line data accumulation, and establishing the proper sequence of operations, and (ii) a central processing unit⁸ to reduce and analyze the data and to interact with the control terminal and various input/output and long-term data storage devices. The interface frees the main CPU from operational details and with 1024 circulating locations accumulates on-line the output of the ADC to allow the main CPU to Fourier transform the previous set of data while the next data are being recorded.

A typical time sequence of operation is given in Table I. In this sequence, the plasma is turned on during the display and storage operation of the CPU by an interface-controlled bias change on a PIN-diode switch in the rf generator. A real-time clock accurately determines the time of exposure. The plasma is turned off during data and background acquisition. In this mode of operation data acquisition takes about 1 sec, corresponding to 24 turns of the polarizer, fol-

⁸ PDP 11-03 system manufactured by DEC.

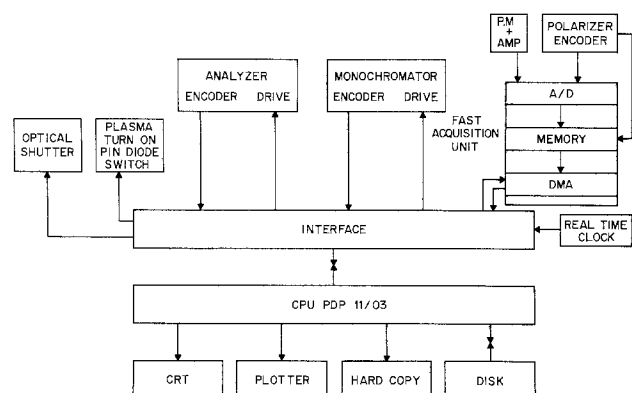


Fig. 2. Block diagram of the data processing and control system, showing interconnections among the peripherals, interface, and on-line computer.

³ Manufactured by the Oriel Company.

⁴ Model 82-410 manufactured by Jarrell Ash.

⁵ Model 9558 QA manufactured by EMI.

⁶ Model 1500C-50-060 manufactured by Magnetic Tech.

⁷ Model 5V670 manufactured by Baldwin.

Table I. Typical time sequence of computer operations during a plasma experiment

TIME SEQUENCE	CPU JOB STATUS	FAST ACQUISITION UNIT	PLASMA	SHUTTER
1	REDUCES PREVIOUS DATA	ACCUMULATES DATA	OFF	OPEN
2	TRANSFER DATA		OFF	CLOSED
3	REDUCES PREVIOUS BGD	ACCUMULATES BGD	OFF	CLOSED
4	TRANSFER BGD		ON	OPEN
5	COMPUTES PREVIOUS (Δ , ψ) DISPLAYS AND STORES; CONTROLS THE PLASMA EXPOSURE TIME	NO ACCUMULATION	ON	OPEN
RETURN TO STEP #1				

lowed by 1 sec of data processing and plasma exposure. In fact, chopping the plasma exposure allows the processing to be slowed down so that the ellipsometer can follow fast kinetic phenomena. For slow reactions such chopping is not necessary and measurements can be taken with uninterrupted plasma exposure. It is thus always possible to obtain spectroscopic ellipsometry data under quasi-equilibrium conditions.

Kinetics

A typical series of measurements during plasma oxidation are shown on Fig. 3. In this case, the wavelength of light and the angle of incidence were kept constant. The plasma exposure was stopped for spectroscopic measurements at various angles of incidence at times 1, 2, and 3. The $\cos \Delta$ curve oscillates between -1 and $+1$ as the thickness of the oxide increases. For the 3000\AA , 63.7° conditions of Fig. 3, the period in the $\cos \Delta$ oscillations corresponds to approximately 800\AA of oxide. The rate of growth is thus obtained directly from the $\cos \Delta$ curve. Here, it is about $100\text{\AA}/\text{min}$. We compare samples grown at 30 and $3000\text{\AA}/\text{min}$ in the next section. As seen in Fig. 3, the rate of growth decreases as the oxide thickness increases. The second oscillation takes about 570 sec to complete as to about 440 sec for the first one. This is

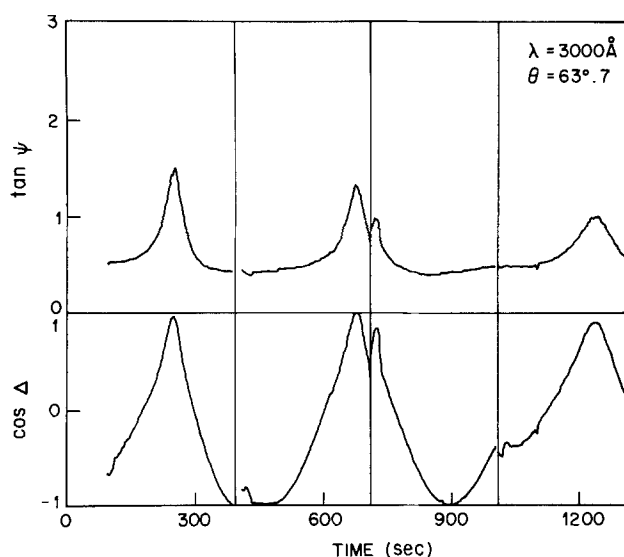


Fig. 3. Typical real-time kinetic measurements. The $\tan \psi$ and $\cos \Delta$ values were recorded at a fixed wavelength (3000\AA) and a fixed angle (63.7°) as a function of the time of plasma exposure. The plasma exposure was interrupted at 1, 2, and 3 for spectroscopic and angular analysis.

due to the fact that the bias voltage of the sample is kept constant. The oxide growth behavior is in agreement with previously published kinetic curves (4).

The $\tan \psi$ curve exhibits a series of peaks associated with each $\cos \Delta$ oscillation. The interesting fact is that the heights of these peaks are not constant but decrease as the oxide thickness increases. As illustrated schematically in Fig. 4, the decrease indicates that the oxide is optically absorbing at 3000\AA . If the plasma oxide were like the anodic oxide, which does not absorb below 4.8 eV (7), then both $\tan \psi$ and $\cos \Delta$ curves would be cyclic with a repeat thickness of about 800\AA as shown in Fig. 4a. In particular, the height of the $\tan \psi$ peaks would be constant. If one now assumes that the plasma-grown oxide is equivalent to an anodic oxide but containing 2% unoxidized As, then the $\tan \psi$ peak heights decrease as shown in Fig. 4b. To obtain Fig. 4b, we calculated the dielectric function of a 98% oxide-2% amorphous As (aAs) mixture in the Bruggeman effective-medium approximation (EMA) (8) using reported data (9) for aAs. Here, the effective dielectric function $\langle \epsilon \rangle$ of the mixture is given by

$$\sum_i v_i \frac{\epsilon_i - \langle \epsilon \rangle}{\epsilon_i + 2\langle \epsilon \rangle} = 0 \quad [6]$$

where ϵ_i represents the (complex) dielectric function of the i th constituent and v_i the relative volume fraction, where

$$\sum_i v_i = 1 \quad [7]$$

The calculated $\tan \psi$ curve shows a decrease in the peak heights because the oxide layer is absorbent, so the constructive interference regimes that give rise to the $\tan \psi$ maxima are less and less effective as the light has to propagate further and further into the layer. A comparison between Fig. 3 and 4 indicates that 2% aAs incorporated into the oxide is a reasonable estimate. The dielectric function of the plasma-grown oxide is discussed more extensively later. The $\tan \psi$ kinetic curve can thus be used as an indication of the oxide layer composition.

Inspection shows that ($\cos \Delta$) does not exactly reach $+1$ in its third oscillation in Fig. 3. This is a much smaller effect than the decrease in the $\tan \psi$ and is related to the nonuniformity of the oxide layer thickness within the area probed by the beam. It is seen most clearly in the very narrow positive extrema of $\cos \Delta$ and is discussed in the next section. Kinetic measurements thus can also be used to estimate the uniformity of the deposit without changing either the wavelength or the angle of incidence or the position of the sample.

Another interesting feature in Fig. 3 is the anomalous behavior of $\tan \psi$ and $\cos \Delta$ when plasma oxidation is restarted at 1, 2, and 3. Generally speaking, when the plasma is restarted after a sufficiently long shutdown (typically 15 min), the oxide thickness tends

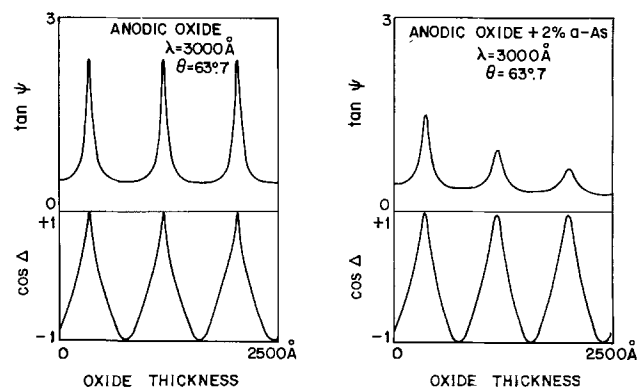


Fig. 4. Simulated kinetic data for (a, left) an anodic oxide and (b, right) a mixture of 98% anodic oxide and 2% amorphous arsenic.

to decrease before increasing again. A more detailed example of this phenomenon is shown in Fig. 5. At the onset of the plasma, $\cos \Delta$ decreases before increasing. We speculate that when the plasma is on, the oxide layer has to charge up before a breakdown voltage is reached, enabling O^- ions to migrate toward the oxide-substrate interface (or the Ga^+ and As^+ ions to migrate from the substrate toward the oxide-vacuum interface) before oxidation will start. Thus before breakdown occurs, the bombardment of the oxide-vacuum interface by the plasma ions tends to sputter off some of the oxide. A detailed study of this effect will be reported later.

Spectroscopy and Angular Variation

The capability of varying both angle and energy continuously is a very important improvement with respect to conventional ellipsometry. If the dielectric functions of the constituents of a complex multilayer structure are known or can be measured independently, then the only unknowns in a modeling of the ellipsometric data for the structure are the thicknesses of the various layers and the composition of each layer. We assume here that a multilayer description is reasonable (that is, the boundaries between layers are sharp, and in the case of heterogeneous layers, the Bruggeman EMA is valid). By contrast to the conventional ellipsometer, which gives only two independent data $\tan \psi$ and $\cos \Delta$ at the operating energy and angle, our system gives a very large number of independent data. This allows a very refined model to be fitted to the experiment. We have achieved fits up to 5 parameters, as will be shown in the next section. A qualitative discussion of optimizing sensitivity to interfaces or nonuniformities is given below.

In general at a fixed angle of incidence our spectroscopic ellipsometer yields $\tan \psi$ and $\cos \Delta$ curves exhibiting a series of resonances if the overlayers are transparent and at least 1000\AA thick. A detailed study of the nature of these resonances has been reported previously (10). In short, for energies at $\tan \psi$ peaks, the s-polarized component of the incident light is transmitted through the top layer and into substrate with maximum efficiency (minimum reflected inten-

sity) for a given configuration. The top layer(s) therefore develop an interference condition to impedance match the s-polarized light from the ambient to the substrate. The height of the $\tan \psi$ peak is a measure of the minimum of r_s at the "resonance," because when $r_s \rightarrow 0$, $|r_p/r_s| = \tan \psi \rightarrow \infty$. Under these conditions a possible thin interface layer between substrate and overlayer(s) can modify the multiple interference regime established in the top layer(s) and can be detected with great sensitivity. It is clear that the sensitivity to interfaces is greatest when the "resonance" is sharpest, i.e., when the height of the $\tan \psi$ peak is greatest. Since r_s is a rapidly varying function of the angle of incidence, it is possible by varying this angle to "tune" or "detune" the s-wave antireflection condition and thus increase or decrease the sensitivity to the interface region. The sensitivity can be enhanced by a judicious choice of energy. For example, Fig. 6 shows spectroscopic data for a 2100\AA thick plasma-grown oxide for various angles of incidence. The peak in $\tan \psi$ near 2.7 eV increases when the angle of incidence is decreased from 72° to 61° . At the same time, the $\cos \Delta$ curve narrows. The other peaks near 4.1 and 5 eV show less variation because the oxide here is more absorbent in these regions. Thus the multiple interference regime is most effective, or the sensitivity to an interface layer the greatest, at 2.7 eV and 61.5° . The height of the $\tan \psi$ peaks can thus be used to monitor in a very sensitive way the presence and the nature of an interface layer. However, another effect has to be considered which may also affect the apparent "quality" of the s-wave matching. If the top layer is not uniform in thickness, resonances for beams coming from different areas will not occur at the same angle or energy, causing an apparent broadening or lowering of the resonance.

To demonstrate this effect experimentally, we have examined the Si-SiO₂ system where the interface region is known to be extremely sharp (11) and therefore have eliminated any possible strong influence of an interface layer. An 8900\AA thick SiO₂ layer thermally grown on a single crystal Si substrate was nonuniformly etched with CF₄ in our plasma reactor to a thickness of about 6000\AA . By probing the various regions of the sample with a 0.3 mm diameter beam, a nonuniformity in thickness of about $175\text{\AA}/\text{min}$ is estimated. The $\tan \psi$ and $\cos \Delta$ curves obtained for various beam diameters on the same spot are given in Fig. 7. If the thickness were constant over the sample, then a calculation shows that the $\tan \psi$ peak should be about 4.7 and the $\cos \Delta$ cusp should reach -1 at about 2.3 eV. For our smallest beam diameter of 0.3 mm the illuminated sample area is an ellipse of $0.3 \times 0.7\text{ mm}$ at 67° . The thickness of the oxide therefore varies by

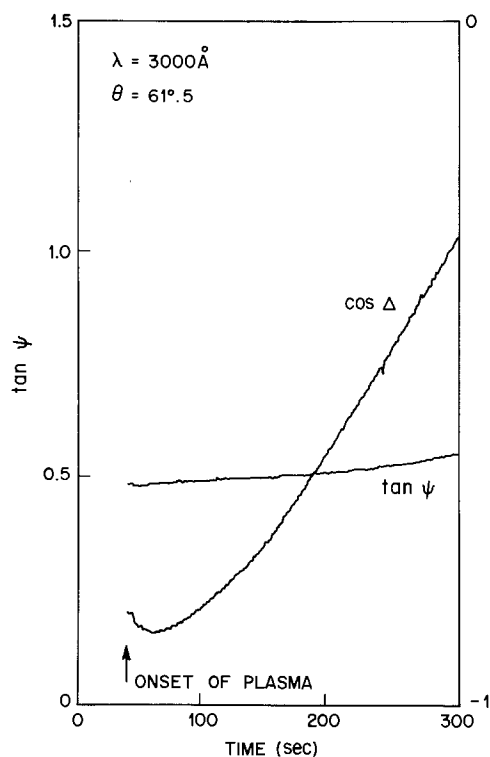


Fig. 5. Real-time data showing a typical transient regime at the onset of plasma oxidation.

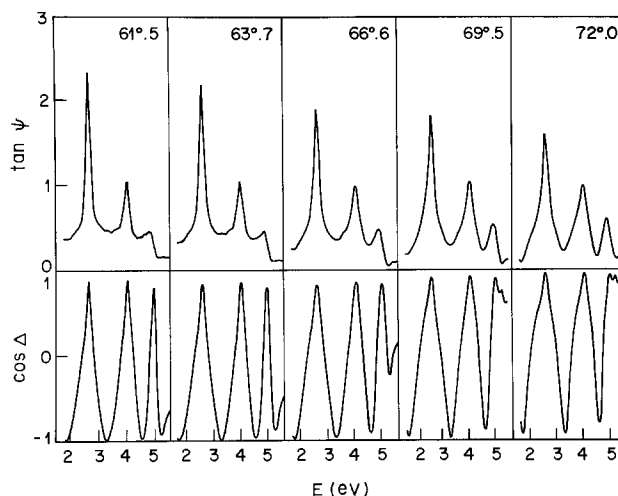


Fig. 6. Spectroscopic data for various angles of incidence for a 2100\AA plasma-grown oxide on GaAs.

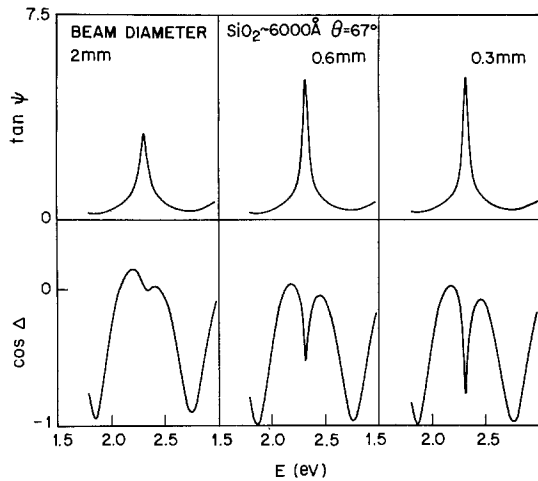


Fig. 7. The effect of nonuniformity of oxide thickness on $\tan \Psi$ and $\cos \Delta$. The sample is a 6000Å SiO_2 layer on a crystalline Si substrate. The nonuniformity is about 175 Å/mm.

about 120Å, or 2%, over the beam spot. Although the $\tan \psi$ peak height is close to its calculated value, Δ only reaches -0.8 . For a 0.6 mm diameter beam, corresponding to about 4% thickness variation over the beam spot, $\tan \psi$ is still acceptable while $\cos \Delta$ only reaches -0.5 . For a 2 mm aperture that includes about a 14% thickness variation, both $\tan \psi$ and $\cos \Delta$ are affected. These measurements show that a few percent of nonuniformity in the top layer can be detected. As also discussed in connection with Fig. 4, the effect of the nonuniformity is more pronounced on $\cos \Delta$ than on $\tan \psi$.

Modeling

In this section we treat the analysis of raw data such as those shown in Fig. 6. Everything is based on the assumption that films can be represented as a superposition of distinct, uniform layers. The validity of this assumption should be tested where possible by an independent technique such as depth profile Auger spectroscopy. The AES studies reported earlier (12) on these plasma-grown oxides indicate that Ga, As, and O concentrations are uniform to within a few percent throughout the entire oxide layer. A narrow interface, less than 100Å wide, is generally detected between the oxide and the substrate. Describing this interface region as a single layer of uniform composition is obviously an approximation, but if its thickness is much less than the wavelength the optical effect of the actual interface will be similar to that of a unique layer. Therefore, in the subsequent discussion a four-phase system consisting of air, a top layer, an interface layer, and a substrate is considered. We also show that this simple four-phase structure fails when the interface region is sufficiently wide.

The four-phase model requires for its complete definition the complex dielectric functions $\epsilon_s(E)$, $\epsilon_I(E)$, $\epsilon_L(E)$, and $\epsilon_a = 1 + i0$ of the substrate, interface, top layer, and (air) ambient, respectively, the thicknesses d_I and d_L of the interface and top layer, and the angle of incidence, θ_0 . From these parameters a complex reflectance ratio

$$\rho = \rho(\epsilon_s, \epsilon_I, d_I, \epsilon_L, d_L, \theta_0, E) \quad [8]$$

can be calculated using standard equations (13). At any given energy and angle of incidence, an experimental value of ρ can be determined to be compared with the calculated value. This provides two constraints on the eight variables in Eq. [8] [we assume E and θ_0 , like ρ , are input data].

Taken at face value, the parameters in Eq. [8] are still highly underdetermined. However, it is always possible to measure the substrate dielectric function ϵ_s independently, either before film growth or by stripping after the oxide has been grown. [We note that

the plasma reactor is ideally suited for this purpose.] Because ϵ_s is usually much more rapidly varying in energy than ϵ_I and ϵ_L , it is more difficult to determine in a multilayer system and hence more important to know *a priori* and to be able to treat as data. We therefore assume that ϵ_s is known.

Further constraints can be obtained from the energy dependence of ρ , using the fact that d_I and d_L are independent of energy, and that ϵ_I and ϵ_L are usually slowly varying. If the film is known to be transparent in a certain region of the spectrum, then at least $\text{Im}(\epsilon_L) = 0$. If also $d_I = 0$, then the only remaining unknowns are d_L and $\text{Re}(\epsilon_L)$ and Eq. [8] can be solved exactly for these quantities. Having d_L , it is now possible under this restriction to calculate ϵ_L at all energies. This approach was used in fact with two sets of ellipsometric data, taken on samples with very thin natural and very thick anodically grown oxides, which were reduced simultaneously to obtain both ϵ_s and ϵ_L for GaP, GaAs, and GaSb (7).

We are concerned here with interface layers, so we cannot assume that d_I is zero. Two possibilities now exist. First, we may make "educated guesses" about the probable composition of interface and layer, and then model ϵ_I and ϵ_L in the EMA. By so doing, the number of free parameters is substantially reduced if the dielectric functions of all constituents are known over the available spectrum. This follows because the energy dependence of ϵ_I and ϵ_L is now determined by the data for their constituents, and the model parameters remaining are layer thicknesses and constituent volume fractions, all of which are independent of energy. The validity of the model must be inferred by how well it fits the entire experimental spectrum. This approach was used recently to investigate effective-medium representations of surface roughness on aSi samples grown by CVD (14).

The second approach is to assume $d_I = 0$ and solve for d_L and ϵ_L as if the interface did not exist. The question then arises as to how ϵ_L and d_L will differ from their correct values. Remembering that the effect of the interface is greatest at energies where $\tan \psi$ is maximum, it may be expected that ϵ_L will be fairly close to its correct value away from the $\tan \psi$ peaks, particularly if $d_I \ll d_L$, and that d_L will be too large by approximately d_I . Rapid, unphysical variations or discontinuities in ϵ_I may appear near peaks of $\tan \psi$ where the interface cannot be ignored.

To examine these points, we use the simulated spectra given in Fig. 8a. Here, we plot the $\tan \psi$ and $\cos \Delta$ energy dependence calculated from the following

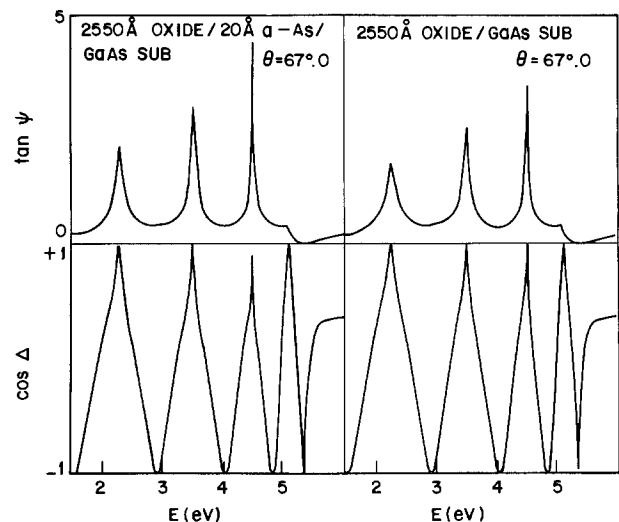


Fig. 8. Calculated $\tan \Psi$ and $\cos \Delta$ curves as a function of energy: (a, top) for a 2550Å anodic GaAs oxide on a GaAs substrate with a 20Å interface layer of aAs, and (b, bottom) same as (a) but without the aAs interface layer. The angle of incidence is 67°.

data: top layer, 2550Å of anodic oxide on GaAs with $\epsilon_L(E)$ taken from Ref. (7); transition layer, 20Å of aAs with $\epsilon_I(E)$ taken from Ref. (9); substrate, cGaAs with $\epsilon_S(E)$ taken from Ref. (15). The angle of incidence is 67°. For comparison, the curves with no transition layer, but otherwise unchanged, are given in Fig. 8b. Note that the presence or the absence of the transition layer can only be seen in the height of the $\tan \psi$ peaks, as we have previously emphasized. We consider now reducing the simulated data of Fig. 8a, calculated in a four-phase system, by means of a three-phase model.

Using the constraint that $\text{Im}(\epsilon_I)$ must be nearly zero in the long wavelength region (specifically at 1.5 eV) gives $d_L = 2540\text{Å}$ and the ϵ_I spectrum as curves 1 in Fig. 9a. Curves 2 give the true values used for generating the data of Fig. 8a. The value of d_L obtained in this model is not the actual one since the assumed absence of the transition layer has to be compensated by a modification of the top layer. Comparing curves 1 and 2 of Fig. 9a indicates that the real part of ϵ_L obtained in this three-phase model is very close to the actual value. In fact, the deficiency of this model can be only seen in the oscillations of $\text{Im}(\epsilon_L)$ and its negative value in the region where it should be zero. The fact that the calculated $\text{Im}(\epsilon_L)$ becomes negative comes from the assumed absence of a rejecting interface layer. Thus, the top layer has to "generate" light to compensate for this absence.

Apart from the small deviations of $\text{Im}(\epsilon_L)$ the agreement between curves 1 and 2 in Fig. 9a is satisfactory. We therefore conclude that a three-phase analysis of the experimental data is a reasonable way to obtain the dielectric function of the top layer.

Having determined ϵ_L , it is now tempting to try to determine ϵ_I as well. In this case Eq. [8] contains 4 unknowns: ϵ_I , d_I , and d_L . As already noted, d_L as deduced from the three-phase model is not valid and it also must be varied for the contribution of the transition layer to be determined. Since the interface region represents the transition from an absorbing substrate to a dielectric it is not likely to be a dielectric and that $\text{Im}(\epsilon_I)$ might be small is not valid. To obtain ϵ_I from Eq. [8], one must guess the values of d_L and d_I . Unfortunately, as illustrated in Fig. 9b, the calculated ϵ_I is too strongly dependent on these parameters, especially d_L . In Fig. 9b we have plotted the results of inverting Eq. [8] for ϵ_I with an improper guess of $d_L = 2570\text{Å}$ and $d_I = 20\text{Å}$ as curves 1. Curves 2 give the proper result for $d_L = 2550\text{Å}$ and $d_I = 20\text{Å}$, which is of course the dielectric function of aAs. The

disagreement between curves 1 and 2 indicates that a minor error in d_L totally modifies the calculated ϵ_I . In fact, this result was expected by comparing Fig. 8a and 8b, because the interface layer only influences the resonance regions. Outside these energy regions, a small error in the top layer parameters requires a large change in the parameters of the interface layer to compensate it.

It therefore appears very difficult to obtain ϵ_I from the experiment, at least when d_I is small compared to d_L . We must limit ourselves to the less general model discussed, making some further assumptions on the nature of this interface and modeling its dielectric function appropriately. Since the various possible constituents of this layer are cGaAs, aGaAs, aAs, aGa, and oxide, an EMA mixture of these constituents is assumed. Then, only a limited number of energy-independent parameters need be determined. As already mentioned, we used a five-parameter model for this purpose. Although this procedure is less general than desired, the examples discussed in the next section show that it gives a good qualitative picture of the nature of this interface layer, which allows us to investigate films grown by different rates of oxidation.

Results and Discussion

The capabilities of our system for a multilayer analysis are now demonstrated by studying the effect of the rate of growth on the characteristics of the oxide layer. The $\tan \psi$ and $\cos \Delta$ spectroscopic curves given in Fig. 10 represent data from two samples of comparable thickness ($\sim 1600\text{Å}$) but grown at very different rates. The first was oxidized in about 30 sec, while the second, in a lower density plasma, was oxidized in 50 min.

A three-phase model reduction of the data of Fig. 10 yields the dielectric function ϵ_L shown in Fig. 11a and 11b. As already mentioned, d_L is adjusted to minimize the imaginary part of ϵ_L . For the slow grown oxide, Fig. 11a, the oscillations in the $\text{Im}(\epsilon_L)$ curve are more pronounced, indicating as discussed above the inadequacy of a three-phase description. If we now consider the fast-grown oxide results of Fig. 11b, the oscillations are much smaller, indicating that the interface region is much thinner. In both cases, we note the striking feature that the $\text{Im}(\epsilon_L)$ curve is greater than zero even at low energies. Since the anodic oxide film is totally transparent below 4.8 eV (7) the long absorption tails in Fig. 11 are a clear indication of unoxidized material in the plasma-grown oxide. To obtain a quantitative estimate of the amount of absorbing material, we use the anodic GaAs oxide as a reference and insert via an EMA calculation a small fraction of aAs. The result for 98% anodic oxide and 2% aAs is also plotted in Fig. 11. Interestingly, the agreement between ϵ_L and the composite dielectric function

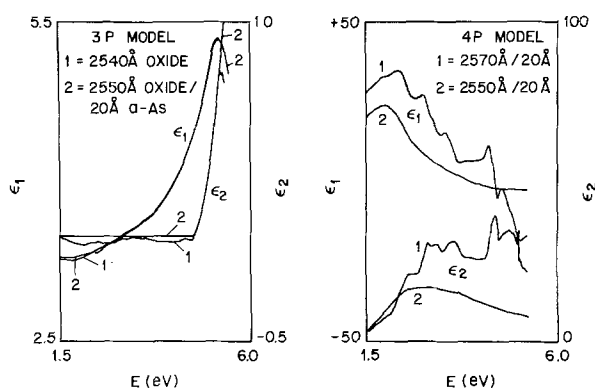


Fig. 9. (a, left) Real (ϵ_1) and imaginary (ϵ_2) parts of the dielectric function ϵ of the top layer as calculated in a three-phase model reduction of the calculated four-phase spectra of Fig. 8a. The results are given as curves 1. The true dielectric function of the anodic GaAs oxide is given as curves 2. (b, right) Real (ϵ_1) and imaginary (ϵ_2) parts of the dielectric function ϵ_I of the interface layer, obtained in a four-phase data reduction of Fig. 8a but using the incorrect thickness. The calculated values, shown as curves 1, are compared to the actual dielectric function of aAs shown as curves 2.

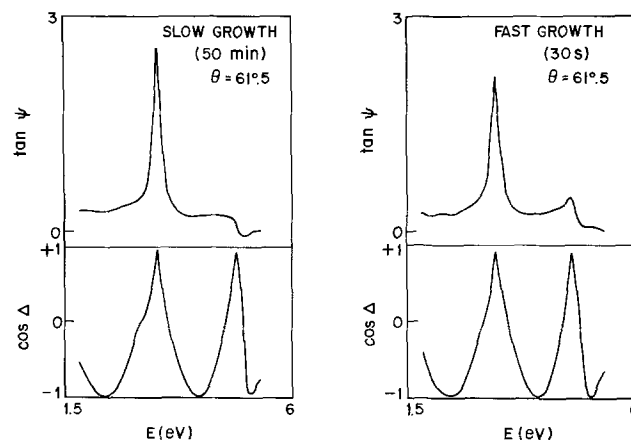


Fig. 10. Experimental $\tan \Psi$ and $\cos \Delta$ spectra for two plasma-grown oxides with very different rates of growth. The angle of incidence is 60.5°.

is satisfactory to 4.8 eV. Above 4.8 eV, deviations occur indicating that the plasma-grown oxide and the anodic oxide are different materials. To choose one as a reference for the other is no longer justified. However, below 4.5 eV the description of the plasma-grown oxide as a mixture of anodic oxide and aAs is a good approximation and can be used to estimate the amount of absorbing material.

The effect of aAs in Fig. 11 is not unique. A similar effect would be obtained by mixing the anodic oxide with aGaAs or aGa, and the amount of absorbing material will differ slightly from one mixture to the other. On chemical grounds aGa is unlikely, but the existence of aGaAs cannot be ruled out by our analysis in the 1.5-4.5 eV region. Nevertheless, the use of aAs appears more reasonable from the greater stability of Ga_2O_3 compared to As_2O_3 (16). Furthermore, the presence of aAs in these oxides has recently been observed via Raman scattering (17).

To obtain a complete five-parameter representation, we will therefore use as adjustable parameters d_T , d_L , the percentage of aAs in the top layer, the percentage of aAs in the interface layer, and the angle of incidence. We use the angle of incidence because the actual value might differ slightly from earlier alignment measurements.

To give an estimate of the relative effect of the various parameters, Table II gives the least squares deviations between experiment and the four-phase model calculations when only the thicknesses are allowed to vary and the compositions are changed by finite increments. From Table II, it is seen that the agreement is significantly improved by incorporating aAs into the top layer and including a transition layer. The fit is very sensitive to the composition of the top layer and to a lesser extent to the composition of the interface layer. The best fit in Table II occurs for a 1558Å top layer of 98% anodic oxide and 2% aAs, a 32Å interface layer of 75% anodic oxide and 25% aAs, and an angle of incidence of 61°. The least squares residual is 0.67. If all five parameters are allowed to vary independently, the statistical analysis gives the following results: the angle of incidence is $60.50^\circ \pm 0.02^\circ$, the top layer thickness is $151 \pm 2\text{Å}$ with a composition of anodic oxide with $(1.5 \pm 3.6\%)$ aAs, the unbiased estimator δ of the mean squares deviation (18) for this fit is $\delta = 7.06 \cdot 10^{-2}$. The comparison between this model and the data is shown in Fig. 12. As expected, the curves differ above 4.5 eV, indicating that the mixture assumption is no longer valid.

A similar five-parameter fit to the slow-growth data is given in Fig. 13. In this case, the fit is less satisfactory. The unbiased estimator is now $\delta = 16.5 \cdot 10^{-2}$. The following structure is obtained: the angle of incidence is $60.45^\circ \pm 0.02^\circ$, the top layer thickness is $1502 \pm 210\text{Å}$ with a composition of anodic oxide with $(1.9 \pm 0.2\%)$ aAs, the interface layer thickness is

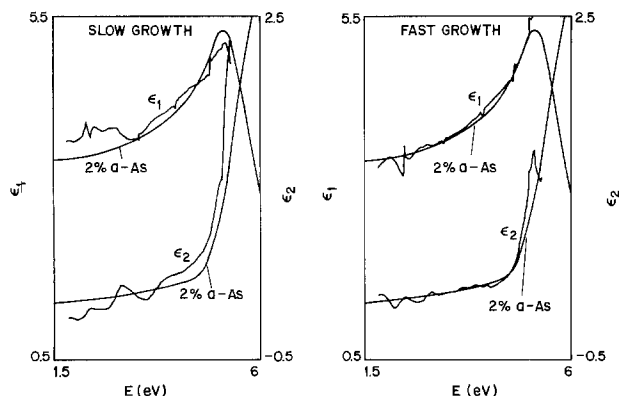


Fig. 11. Dielectric functions of the top layers of the samples measured in Fig. 10 calculated in a three-phase model. For comparison, the dielectric function of an EMA mixture of 98% anodic oxide with 2% aAs is also given.

Table II. Least squares analysis of the data of Fig. 10 for a fast-grown plasma oxide. To illustrate the relative influence of the various parameters, only the thicknesses are varied for this table while compositions (percentage of aAs) of the layers are incremented. The minimum deviations as well as the best thicknesses for each set of compositions are given.

TOP LAYER INTERFACE LAYER	PURE ANODIC OXIDE	1% a As	2% a As	3% a As
	NO FILM	7.19 1589Å	3.52 1597Å	0.78 1585Å
25% a-As	5.80 1590Å/350Å	0.95 1504Å/118Å	0.67 1558Å/32Å	1.69 1566Å/0Å
50% a-As	2.80 1570Å/400Å	1.23 1539Å/112Å	0.73 1566Å/29Å	1.69 1566Å/0Å

$400 \pm 210\text{Å}$ with a composition of pure aAs. The fact that the $\tan \psi$ data are not reproduced very well even below 4.5 eV, in the energy region where the mixture approximation was found reasonable for the fast-grown sample, indicates that a four-phase model is not correct. In fact, the thickness and the composition obtained for the transition layer indicate that this region is broad and very absorbent. A gradual variation of its composition from the top layer to the substrate is therefore more likely, in which case a multi-layer analysis is improper. Also, the top layer itself is

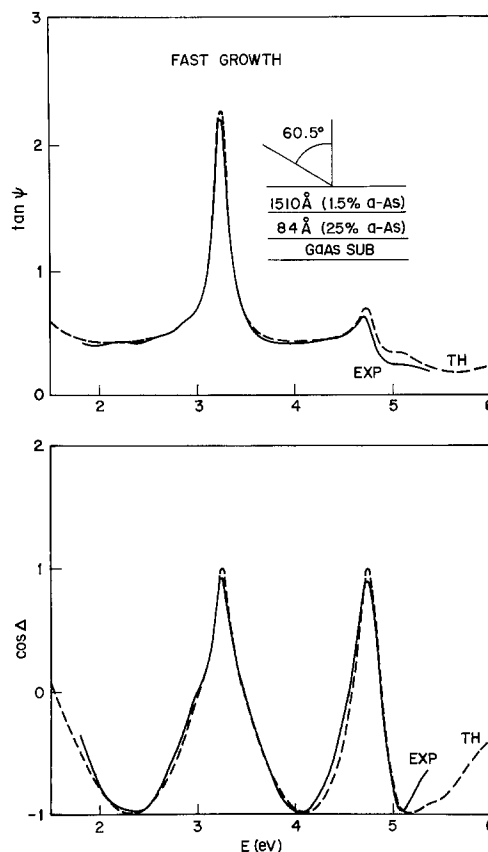


Fig. 12. Best five-parameter fit for the fast-grown sample

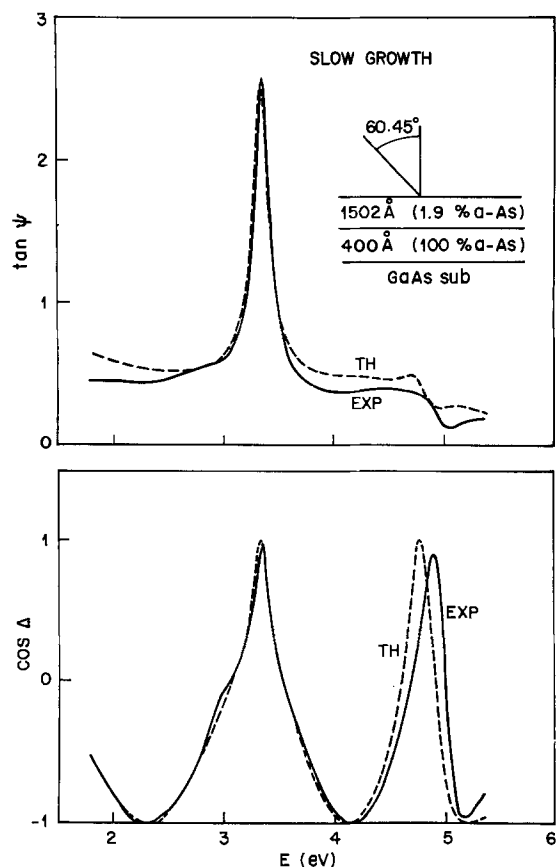


Fig. 13. Best five-parameter fit for the slow-grown sample

more absorbent than for the fast-grown oxide, making an analysis of the interface more difficult.

Although a four-phase model is not completely satisfactory, the values of the parameters obtained in the analysis of the two samples give some insight into the mechanism of plasma oxidation of GaAs. Whatever the rate of growth, some unoxidized material is present in the oxide, and it tends to accumulate at the interface between the oxide layer and the substrate. As already mentioned, the relative instability of As_2O_3 with respect to Ga_2O_3 can be invoked to speculate that unoxidized arsenic is left in the oxide during the plasma oxidation.

If the process is very fast, the dynamics tend to favor a stoichiometric oxide. However, if the rate of oxidation is slow, more As atoms will be left unoxidized. More quantitatively, the total amount of unoxidized As in the fast-grown sample is equivalent to a layer of 42 Å of aAs, while the same thickness for the slow-grown sample would be 410 Å. The fact that unoxidized material is mainly located at the oxide-substrate interface is probably due to segregation. To obtain a good quality oxide, the above analysis stresses the importance of a fast rate of oxidation.

Conclusion

In situ analysis of plasma-grown oxides with spectroscopic ellipsometry has been demonstrated. The

present system is capable of evaluating the rate of oxidation during plasma processing, the uniformity of the oxide, as well as the composition of the oxide through a multilayer analysis. One of the unique features of our system is the ability to monitor the amount of unoxidized aAs in the oxide during processing.

We have also shown that the technique for the multilayer film analysis is quite powerful in assessing the interface structure of the oxide films. This technique can certainly be extended to study the oxidation mechanism of layered films (e.g., Al on GaAs). The present study on the oxidation of GaAs is by no means conclusive. There are still many facets (such as the transient effect at the onset of the oxidation) that remain to be understood.

Manuscript received Feb. 26, 1979.

Any discussion of this paper will appear in a Discussion Section to be published in the December 1980 JOURNAL. All discussions for the December 1980 Discussion Section should be submitted by Aug. 1, 1980.

Publication costs of this article were assisted by Bell Laboratories.

REFERENCES

1. R. P. H. Chang, *Thin Solid Films*, **56**, 89 (1979) and references therein.
2. J. B. Theeten, D. E. Aspnes, and R. P. H. Chang, *J. Appl. Phys.*, **49**, 6097 (1978).
3. R. P. H. Chang, T. T. Sheng, C. C. Chang, and J. J. Coleman, *Appl. Phys. Lett.*, **33**, 341 (1978).
4. R. P. H. Chang, A. J. Polak, D. L. Allara, C. C. Chang, and W. A. Landford, *J. Vac. Sci. Technol.*, **16**, 888 (May/June 1979).
5. R. P. H. Chang, *ibid.*, **14**, 278 (1977).
6. P. S. Hauge and F. H. Dill, *IBM J. Res. Dev.*, 472 (November 1973); D. E. Aspnes and A. A. Studna, *Appl. Opt.*, **14**, 220 (1975); *Rev. Sci. Instrum.*, **49**, 291 (1978).
7. D. E. Aspnes, B. Schwartz, A. A. Studna, L. Derick, and L. A. Koszi, *J. Appl. Phys.*, **48**, 3510 (1977).
8. D. A. G. Bruggeman, *Ann. Phys. (Leipzig)*, **24**, 636 (1935); D. Stroud, *Phys. Rev. B*, **12**, 3368 (1975).
9. G. N. Greaves and E. A. Davis, *Philos. Mag.*, **34**, 265 (1976).
10. J. B. Theeten and D. E. Aspnes, *Thin Solid Films*, In press.
11. See for instance, O. L. Krivanek, D. C. Tsui, T. T. Sheng, and A. Kamgar, in "Proceedings of the Conference on the Physics of SiO_2 and Its Interface," S. T. Pantelides, Editor, p. 356, Pergamon, New York (1978).
12. C. C. Chang, R. P. H. Chang, and S. P. Murarka, *This Journal*, **125**, 481 (1978).
13. See, for instance, R. M. A. Azzam and N. M. Bashara, "Ellipsometry and Polarized Light," North Holland, Amsterdam (1977).
14. D. E. Aspnes, J. B. Theeten, and F. Hottier, *Phys. Rev. B*, To be published.
15. D. E. Aspnes and A. A. Studna, Unpublished.
16. See, for instance, C. W. Wilmsen, *Thin Solid Films*, **39**, 105 (1976).
17. M. Rhinewine, R. P. H. Chang, and R-E. Slusher, Unpublished.
18. E. S. Keeping, "Introduction to Statistical Inference," Chap. 12, Van Nostrand, Princeton (1962).

Residues from Wet Processing of Positive Resists

L. H. Kaplan and B. K. Bergin

IBM Data Systems Division, East Fishkill Facility, Hopewell Junction, New York 12533

ABSTRACT

An ellipsometric study has been made of the residues left from the development and stripping of several positive resists as a function of surface treatment, development, and stripping variables. Residues of up to nearly 5 nm have been ellipsometrically observed in the development of AZ-1350J and AZ-111, using commonly employed developer solutions under conditions which yield positive print biases. The use of adhesion promoters HMDS, BSA, and BSTFA generally appeared to increase the amount of residue. The stripping effectiveness of organic solvents such as acetone was found to be extremely sensitive to post-baking, with temperatures as low as 130°C causing detectable residues after stripping. The use of a postdevelopment exposure helps prevent this problem. High temperature inorganic strippers, such as sulfuric/nitric acid mixtures, are highly effective, but unexplained "negative residues" are observed. Also, for resist that is cross-linked by ion bombardment, considerable residue is observed at patterned edges and can be removed only by a 400°C bake before stripping. Caro's acid, evaluated as a room temperature inorganic stripper, is fully equivalent to the high temperature acids. In addition, it shows superior stripping properties for cross-linked resists and minimal attack on Cu-Al-Si metallization. A persulfate-based stripper, similar in composition and properties to Caro's acid but whose makeup does not involve the handling of concentrated hydrogen peroxide, was also evaluated. This type of stripper appears best suited to commonly used process technology, from considerations of safety, effectiveness, and pollution control.

Modern semiconductor technology makes use of positive-type resists for the definition of patterns that are subsequently etched or otherwise defined into the substrate material. The pattern definition involves the formation of a resist film, exposure of the film in a pattern by energetic radiation, and the dissolution of the exposed regions by a suitable "developer" liquid. After defining the pattern in the substrate, the resist must be completely removed to avoid adversely affecting subsequent processing steps.

The most commonly used positive resists consist of mixtures of novolak resins with naphthodiazquinone sulfonic acid esters, generally referred to as the photoactive compound (PAC). The two-component mixture in a cast film has aqueous basic solution dissolution rates less than those of the films of the novolak resin alone. Exposure to suitable radiation decomposes the diazo groups and results in a basic aqueous solution dissolution which is faster than for the novolak resin alone. It is known that, as a result of exposure to radiation, the PAC is transformed into a carboxylic acid which contributes to increasing the dissolution rate of the resist film (1). After immersion in a basic aqueous solution (developer), the remaining patterned material is generally baked to enhance its resistance to subsequent processing. It can then be used as a mask for performing various chemical (generally etching) and physical operations on the exposed portions of the underlying substrate material.

A basic premise of the photolithographic process is that the photoresist will be evenly and completely removed from all areas defined as open by the patterned light distribution. These areas must be fully etchable in a uniform manner. Even a partial blockage of an area to be etched by resist residue would require extra etching time, during which some feature dimensions could be unacceptably widened. On the other hand, if the etch is terminated on dimensional criteria, the random resist residues will give rise to random residues of the material being etched. This could adversely affect the contact resistance in via holes or could cause shorts between adjacent metal lines. In the case of FET gates, resist residues can introduce undesirable surface states and charge.

Key words: photoresist, residue, stripper, develop, ellipsometry.

After being used to protect delineated areas of the substrate material from a particular operation, the resist must be removed to allow further processing. This is often accomplished by immersion of the working piece in a "stripping solution." [The use of oxygen plasma, or "ashing," is also a well-known means of removing resist but has not been evaluated in the present work. It has, however, been adequately covered elsewhere (2, 3).]

Four general requirements are associated with performance of resist stripping solutions. First, the stripper must be effective in completely removing all resist films of interest, including those which have been subjected to conditions that dramatically change their chemical properties. This removal should be complete, down to the limits of detectability. Second, the stripping liquid must not attack anything other than the resist. For example, it should be inert to reactive metallurgies. Third, preparation and handling of the stripper should be as safe as possible. It is generally accepted, in this connection, that room temperature is more desirable than elevated temperatures. Consideration must also be given here to the hazard potential of the materials used in preparation of the stripper, if it is prepared *in situ*. Finally, there is the matter of pot-life and the subsequent method of disposal required. Clearly, the most ideal disposal technique is the ability to flush the spent stripper down the industrial waste drain, if this is feasible from an ecological viewpoint.

Probably the most popular type of stripper for unmodified positive resists is also the most ecologically undesirable. This is the phenol-based hot stripper. Strippers such as this must generally be used at about 100°C or higher. At this temperature, their pot-life is short and the disposal becomes a problem. This is especially true because "clean water" environmental standards for phenol content are extremely rigorous (4). The use of phenol-type strippers is rapidly becoming untenable and, consequently, this class of stripper was ignored in the present work.

The most widely used room-temperature organic stripper is acetone, which, because of its very active solvent action, is quite efficient in visually removing normal photoresist. Unfortunately, it is quite volatile

and flammable, leading to safety as well as air contamination problems. Further, as will be seen later, it has limitations in its stripping abilities.

Most inorganic strippers are mixtures of sulfuric acid with certain other ingredients. The two most popular mixtures are those containing some form of oxidized chromium and those containing nitric acid. The former type has been suspected of causing electrical defects in circuits. The sulfuric/nitric acid mixtures now appear to be the most widely used inorganic strippers. This type of mixture is effective only at elevated temperatures (e.g., 100°C) and, under these conditions, it is capable of ruining metallurgy by its severe chemical attack. Hot acid strippers, then, can only be used in situations where metal is absent (e.g., after oxidation, diffusion, CVD, etc.).

There exist very few examples of a fourth type of stripper, the room temperature inorganic solution. The two evaluated in this work are "Caro's acid," as defined herein (5), and a related stripper using $K_2S_2O_8$ in H_2SO_4 . Aside from temperature, these systems have the advantages of low metal attack and simple disposability. On the other hand, there have been some objections raised regarding the safety aspects of their formulation.

In the present work, we were concerned with the effectiveness of the develop and strip processes, in terms of how well the original surface was regenerated. The characterization of any surface has ambiguity. When we ask how well a given stripper or developer cleans a surface, we must become involved, not only with residual resist which remains, but also with changes to the original surface which the resist application and/or removal might have made. This may not be too important if we are willing to neglect everything below, say, the 10 nm range. If, however, we are interested in monolayers and submonolayers, we are forced to become involved with questions of surface state, bound water, etc., and the effects of these on our measurement method.

For the thickness range (e.g., up to 10 nm) indicated, there are actually only three types of quantitative measurement methods available: ellipsometry, plasma chromatography, and high energy spectroscopy. The last, consisting mainly of ESCA and ISS, is useful for carbonaceous materials only when coupled with ultrahigh vacuum, oil-free pumping systems which only recently became available in commercial equipment. Plasma chromatography is an extremely sensitive method (6) for detection of volatile residues on surfaces. At this point, however, its quantitative capabilities are undemonstrated for applications such as we have here and chemical identification requires generation of a library of reference spectra. In addition, mention should be made here of a more qualitative residue test, commonly known as the "breath test." This is highly sensitive to very thin surface layers but generally requires these layers to be spatially nonuniform in order to form visible breath figures.

For the purposes of this study, ellipsometry was most heavily employed, with some use being made of plasma chromatography. Classically, if an ellipsometric measurement (e.g., of a resist residue) is to be made on a reflecting surface, such as Si or Al, a knowledge of the optical constants of the surface is necessary, as well as a knowledge of at least one optical constant of the residue. This is not always available, and a technique involving residue on a transparent surface, such as thermally grown SiO_2 , is much more amenable to approximating the thickness of the residue. In this case, the procedure is to make a preliminary measurement of the oxide thickness before resist is applied and remeasure the apparent "oxide" thickness after stripping. Naturally, the location of the measurement site must be extremely accurate. The method described yields an "equivalent oxide" thickness of the residue. That is, it gives the thickness which the residue layer

would have if it were thermal oxide. Since calculations by So (7) have shown that the computed thickness is a very weak function of refractive index, this method gives a very good approximation of the true residue thickness, although it admittedly says nothing about the chemical identity of the residue or its physical/optical characteristics (other than approximate thickness).

Experimental

Several resists were investigated in this study. Single lots of each of two commercially available resists, AZ-1350J¹ and AZ-111¹, were evaluated.

The photoresists were applied and processed as follows.

AZ-1350J: (1000 nm). 4 parts resist: 1 part AZ thinner¹ (by volume); spin 30 sec at 3600 rpm; bake 15 min at $85^\circ \pm 5^\circ C$ (hot plate).

AZ-111: (1250 nm). Neat; spin 30 sec at 3300 rpm; bake 20 min at $85^\circ \pm 5^\circ C$ (hot plate).

Exposure times were established in preliminary testing to yield zero print bias (2500 nm line) in 60 sec (180 sec for AZ-111) of development. Resist layers were blanket-exposed for these times and developed for various periods of time in the following developers.

AZ-1350J: AZ developer¹ (undiluted), or AZ developer (1:1 dilution with water), or tetramethyl ammonium hydroxide (5% in water).

AZ-111: AZ-303 developer¹ (1:5 with water).

All studies were done using thermally oxidized (nominal 80 nm SiO_2) 57 mm silicon substrates. Where utilized, adhesion promoter precoats were applied in one of the following ways.

Hexamethyldisilazane (HMDS):

HMDS, vapor: Immerse wafer (in carrier) for desired time in vapor over boiling mixture of HMDS/Freon TF.² Withdraw slowly. Preliminary experimentation suggested the following optimum parameters for each of the resists used: AZ-1350J: 4 min, 10% HMDS (b.v.); AZ-111: 10 min, 4% HMDS (b.v.).

HMDS, puddle: statically apply HMDS (neat); spin 15 sec at 3600 rpm; dynamically apply Freon TF during first 10 sec of a 90-sec spin at 3600 rpm.

Bis-N,-O-(trimethylsilyl)acetamide (BSA):

BSA, puddle: statically apply (0.1% in Freon TF); spin 30 sec at 3600 rpm; bake 45 min at 130°C (hot plate).

Bis-N,O(trimethylsilyl)trifluoroacetamide (BSTFA):

BSTFA, puddle: statically apply (neat); spin 30 sec at 3600 or 6000 rpm; A-1100 silane primer,³ 0.1% in H_2O , dip; DI water rinse, 15 sec; spin dry.

Four stripping processes were characterized in this work. The procedures are as follows.

Acetone: Immerse in ultrasonically agitated acetone at room temperature for 5 min. Repeat two additional times with fresh acetone. Rinse in DI water for minimum of 5 min. Blow dry with filtered N_2 .

H_2SO_4/HNO_3 : Immerse in 12% $HNO_3/88\% H_2SO_4$ (b.v.) for 5 min at 100°C. Rinse in DI water (5 min). Blow dry with filtered N_2 .

Caro's acid:

Preparation: Measure 85 p.b.v. of 90% H_2O_2 into a Teflon² tank. Add 5 p.b.v. of DI water. Quickly add 1900 p.b.v. H_2SO_4 with stirring. Monitor temperature and keep peak $T < 50^\circ C$. After cooling to room temperature, do functional cotton swab test. Cotton swab test: Dip a cotton swab into the solution, start timer. Place cotton swab immediately into a clean dry beaker. Observe time for cotton swab to suddenly blacken and smoke violently. This time should be < 12 sec for satisfactory stripping.

Strip: Immerse for 5 min. Without rinsing, immerse in a second bath of the same material for 5 min.

¹ Product of Shipley Corporation, Newton, Massachusetts.

² Product of E. I. du Pont de Nemours & Company, Incorporated, Wilmington, Delaware.

³ Product of Ohio Valley Specialty Chemicals, Incorporated, Marietta, Ohio.

Rinse in DI water for 5 min. Blow dry in filtered N₂.

Potassium persulfate stripper:

Preparation: Add 700g K₂S₂O₈ to 2000 ml H₂SO₄.

Stir (magnetic stirrer) for several hours or until dissolved.

Strip: Immerse 5 min in a first bath. Immerse 5 min in a second bath of the same solution. Rinse in DI water. Blow dry.

Residues from both development and stripping were measured using ETA, an automated ellipsometer which has been previously described elsewhere (8). The thicknesses of the nominal 80 nm oxide films were measured before and after the complete resist process, at 10 premapped 3 mm spots on each wafer. The differences were corrected for instrumental drift via a control wafer and were then averaged. For most of the work reported, each thickness measurement was repeated 5 times to reduce measurement error.

Development Residues

AZ-1350J development.—The characterization of the residues from this resist covered the areas of developer type, concentration, exposure time, and adhesion promotion. Five exposure levels (in addition to no exposure) were used. In the case of optimum exposure (arbitrarily chosen as that yielding zero print bias on a 2.5 micron line in 60 sec development time), wafers were run with 2 modes of HMDS precoat, as well as without precoat. For the optimum exposure and for zero exposure, additional wafers were run with the 2 HMDS modes but without overlying resist. Two developers were used: AZ developer and a 5% solution of tetramethyl ammonium hydroxide (TMAH). The AZ developer was used both neat and in dilution with an equal volume of water (1:1).

Figure 1 shows the variation of residue thickness with development time for the three developer solutions investigated. The curves shown are for the case of optimum exposure with no adhesion promoter, but analogous curves for other conditions are similar. The general trend of residue thickness vs. development time is predictably down. However, the slope of the curves is strongly influenced by the specific developer solution, the TMAH developer showing much faster residue decay than the AZ developer. The diluted AZ de-

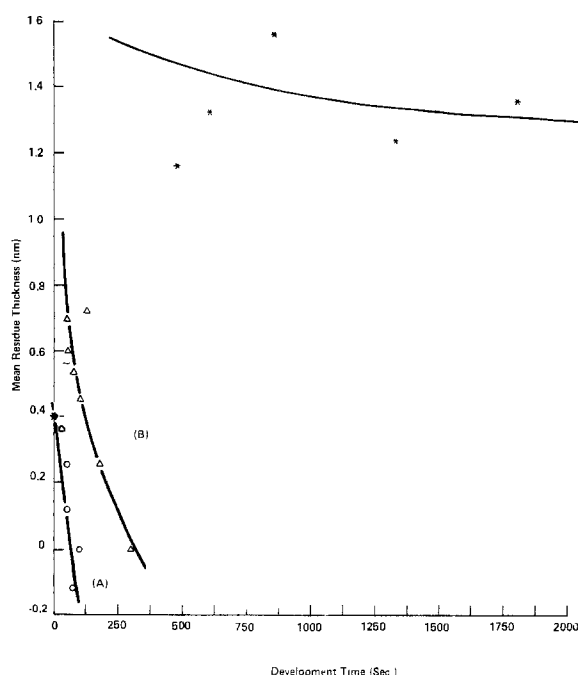


Fig. 1. AZ-1350J development curves for no adhesion promoter. Exposure optimum. (A) TMAH, 5%; (B) AZ dev., neat; (C) AZ dev., 1:1.

veloper shows especially tenacious residues, which remain at significant levels even after long development times.

Figure 2 illustrates the variation of residue thickness with exposure time for AZ developer and TMAH. The particular curves shown are for 45 sec development time without an adhesion promoter, but are typical of other situations. The exposure time is shown as a percent of the optimum exposure. As with development, the residues are seen to decrease with exposure time, with the AZ developer showing significantly higher residues than TMAH.

The effect of the use of adhesion promoters on the residues left by neat AZ developer is shown in Fig. 3. The residues shown by the HMDS (vapor) case are significantly higher than those shown by the HMDS (puddle) case, which is statistically indistinguishable (at 90% confidence) from the no-promoter case. The corresponding plot for TMAH, shown in Fig. 4, indicates the same relative positions for the two HMDS cases but a distinguishably lower residue for no promoter.

To further study the difference between puddle and vapor processes with AZ developer, residues for the two processes were measured without applying a photoresist layer after HMDS treatment. In this way, the effect of liquid resist solubility of the HMDS would be eliminated. Interestingly enough, in this case, the two processes yielded substantially equivalent residues, as shown in Table I. Thus, the larger residue shown by the resist using the vapor process cannot be explained by postulating a larger initial HMDS layer. Rather, it would appear that the HMDS layer deposited by the vapor process is capable of bonding the lowest resist layers more effectively. Such bonding is indicated by the fact that, regardless of the precoat process, more residue is left (after any given development time) by the resist-coated samples than by samples coated with HMDS only. This is shown in Tables II and III for the vapor and puddle processes, respectively.

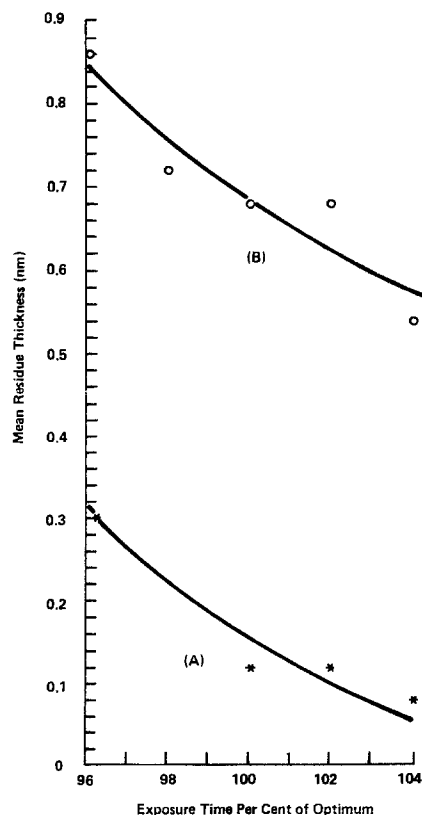


Fig. 2. AZ-1350J exposure curves for 45 sec development and no adhesion promoter. (A) 5% TMAH; (B) AZ dev., neat.

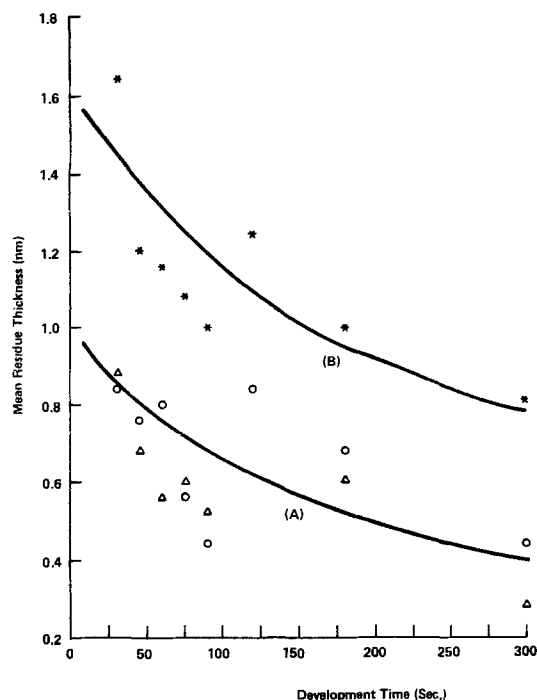


Fig. 3. AZ-1350J development curves for optimum exposure and neat AZ developer. (A) HMDS (puddle) and no promoter; (B) HMDS (vapor).

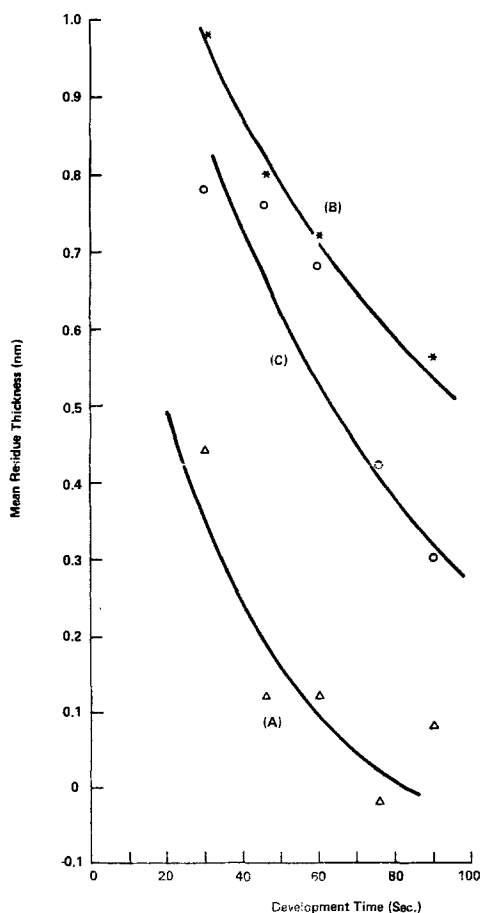


Fig. 4. AZ-1350J developer curves for optimum exposure and 5% TMAH. (A) No promoter; (B) HMDS (vapor); (C) HMDS (puddle).

After selected development steps, the various wafers were analyzed by plasma chromatography in an attempt to gain insight into the chemical nature of the residues. Figures 5 and 6 show several plasmagrams for the various residues. System blanks are included in each figure as references. Note, from Fig. 5, that the

Table I. Comparison of HMDS (vapor) with HMDS (puddle) (no resist) (undiluted AZ developer)

Dev. time (sec)	HMDS (vapor)			HMDS (puddle)			Difference	
	Mean (nm × 10)	σ	N	Mean (nm × 10)	σ	N	F (means)	F (var)
30	3.1	1.4	8	4.4	1.4	8	3.1	1.0
45	3.3	4.1	10	2.1	2.0	8	0.6	3.9
60	2.9	4.9	10	1.9	2.3	9	0.3	4.5
75	2.4	3.9	9	1.5	5.2	10	0.2	0.6
90	1.3	4.7	9	0	2.2	9	0.5	4.5
120	3.4	4.7	9	1.6	2.9	9	1.0	2.6
180	3.0	6.5	10	-0.8	0.6	7	2.3	102.0
300	1.4	5.7	10	-3.2	1.4	8	4.8	17.3

Table II. Effect of resist application on residue with vapor HMDS (undiluted AZ developer)

Dev. time (sec)	No resist			AZ-1350J			Difference	
	Mean (nm × 10)	σ	N	Mean (nm × 10)	σ	N	F (means)	F (var)
30	3.1	1.4	8	16.3	4.9	10	52.7	0.1
45	3.3	4.1	10	12.1	1.8	7	28.5	4.9
60	2.9	4.9	19	11.7	4.1	10	19.0	1.4
75	2.4	3.9	9	10.7	2.9	9	26.3	1.8
90	1.3	4.7	9	10.1	2.7	9	23.7	3.1
120	3.4	4.7	9	12.3	1.7	9	25.8	7.6
180	3.0	6.5	10	10.0	3.2	10	9.2	4.0
300	1.4	5.7	10	8.2	2.3	8	10.1	6.2

Table III. Effect of resist application on residue with puddle HMDS (undiluted AZ developer)

Dev. time (sec)	No resist			AZ-1350J			Difference	
	Mean (nm × 10)	σ	N	Mean (nm × 10)	σ	N	F (means)	F (var)
30	4.4	1.4	8	8.5	5.4	8	4.4	0.1
45	2.1	2.0	8	7.6	4.2	9	11.3	0.2
60	1.9	2.3	9	8.1	3.8	9	17.2	0.4
75	1.5	5.2	10	5.8	4.2	9	3.7	1.6
90	0	2.2	9	4.3	4.1	9	7.5	0.3
120	1.6	2.9	9	8.3	3.7	9	18.4	0.6
180	-0.8	0.6	7	6.7	5.5	9	12.4	0
300	-3.2	1.4	8	4.3	5.8	9	12.6	0.1

plasmagrams for vapor and puddle HMDS alone (no resist) are almost identical for AZ developer. Reference to the figures indicates that the HMDS, with or without resist, produces a pair of peaks at 7.1 and 9.5 msec of drift time. For situations involving resist, additional peaks at 6.4 and 8.6 msec are evident. A distinct difference seems to exist between residues from "HMDS only" situations and those from cases without promoters. In the case of HMDS (puddle) with resist, the only peaks in evidence are the same peaks (7.1 and 9.5 msec) seen for HMDS alone. But, for HMDS (vapor) these peaks are accompanied by residual peaks at 6.4 and 8.6 msec, thus indicating the presence of resist-related components in the larger residue found with vapor HMDS.

Another material used for adhesion promotion is BSTFA. Figure 7 presents the results of examining this material as a function of development time in neat AZ developer. Also shown for reference is the curve of Fig. 1, corresponding to no adhesion promoter. Note that, with AZ-1350J, BSTFA yields a significant residue, which does not reduce with further development.

AZ-111 development.—This resist showed rather interesting results in terms of the individual lots of developer used. Figure 8 shows data for this resist, using two different lots of developer designated "good" and "bad" to reflect the residue situation. Without the use of HMDS, the developer lot used has no effect. A single curve may be drawn through the experimental points for both curves. For the cases involving HMDS

Fig. 5. Plasmagrams. (A) System blank; (B) HMDS (vapor), no resist, 30 sec dev.; (C) HMDS (puddle), no resist, 30 sec dev.; (D) AZ-1350J, no promoter, 30 sec dev., opt. exp.; (E) AZ-1350J, no promoter, 30 sec dev. underexp.

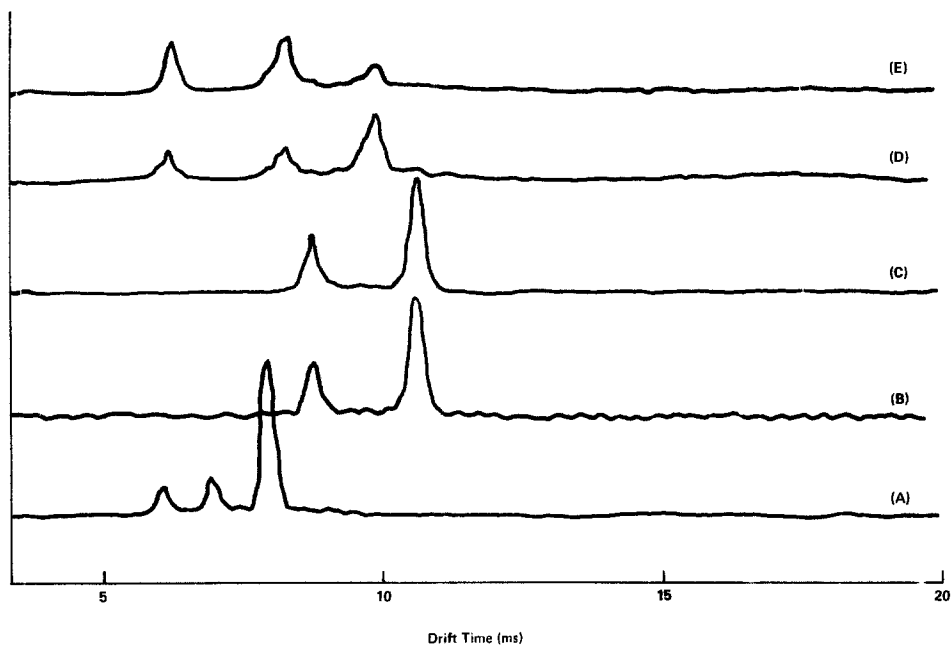
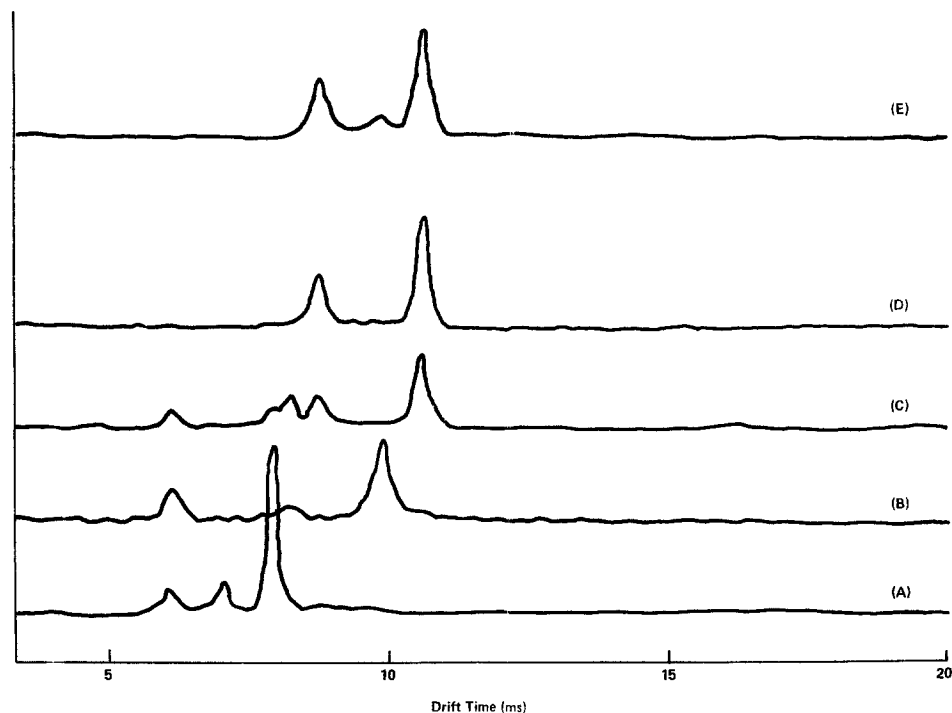


Fig. 6. Plasmagrams. (A) System blank; (B) AZ-1350J, no promoter, opt. exp.; (C) AZ-1350J, HMDS (vapor), opt. exp.; (D) AZ-1350J, HMDS (puddle), opt. exp.; (E) AZ-1350J, no promoter, overexposed.



precoating, however, a substantial difference exists between the lots of developer. Thus, it would appear that residues formed by the interaction of the HMDS with components of the resist are particularly sensitive to small changes in developer.

Stripping Residues

Acetone.—The behavior of acetone in stripping normally processed AZ-1350J resist is shown in Table IV. Here, several processes were used, including BSA and HMDS adhesion promotion as well as no adhesion promoter at all. The mean values and standard deviations for the effective oxide thicknesses of the residues are shown along with the statistical evidence that they are different from the control wafer. Note that in many cases the residue was so thick that it could not be measured by ETA in the configuration utilized (*i.e.*, combined thickness > 140 nm).

The origin of these catastrophic residues is strongly suggested by our knowledge of the resist process and mechanism. In the above work, a postbake of 30 min at 130°C has been used. It is well known that ex-

posure to elevated temperatures, especially in the presence of reactive compounds such as diazo, can cause polymers to cross-link (9). Such cross-linking can result in more difficult removal of the resist after postbake. Further, a normal laboratory hotplate, such as is commonly utilized for postbakes, has a relatively unstable temperature, with excursions of $\pm 20^\circ$ about the mean being common.

The mechanism just proposed for the occurrence of catastrophic residue failure suggests its own cure. It was indicated previously that cross-linking is favored by thermal treatment in the presence of free-radical initiators, such as the diazo containing molecules of the photoactive compound. A simple approach toward alleviating the residue difficulty would then be to eliminate the diazo groups once the pattern has been formed. This could be accomplished easily by a post-development exposure thorough enough to harmlessly convert all diazo groups into carboxyl groupings so that no initiating groups remain to cause cross-linking during the postbake. It has been previously shown (10) that such exposed resist does not begin to in-

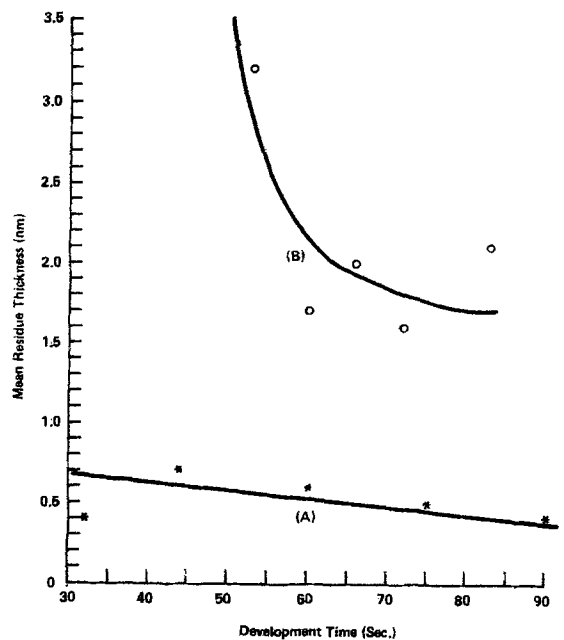


Fig. 7. AZ-1350J development curve for optimum exposure and neat AZ developer. (A) No promoter; (B) BSTFA/A-1100.

solubilize until temperatures in excess of 170°C are reached. Therefore, use of a postdevelopment exposure should eliminate the necessity of precise control and limitation of postbake temperature.

Accordingly, an experiment was carried out in which several wafers, having each of the three adhesion promotion treatments used previously, were either exposed or not exposed to u.v. after development.

Table IV. Acetone stripping

Group	Mean (nm × 10)	σ	N	F	95% confid.	99% confid.
HMDS, dev. Control	72.4 0.8	35.2 4.5	10 10	36	Diff.	Diff.
No prom., no dev., Control	164.4 0.8	26.2 4.5	10 10	340	Diff.	Diff.
BSA, dev. Control	THTM* 0.8	— 4.5	10 10		Obviously different	
No prom., dev. Control	THTM 0.8	— 4.5	10 10		Obviously different	
No prom., dev. Control	THTM	—	10		Obviously different	
No prom., no dev.	164.4	26.2	10			

* THTM = Too high to measure.

Table V. Effect of postdevelopment exposure on acetone stripping

No adhesion promoter	5 min acetone				10 min acetone				40 min acetone			
	Mean (nm × 10)	σ	N	F	Mean (nm × 10)	σ	N	F	Mean (nm × 10)	σ	N	F
Exposed	-0.4	3.9	10	—								
Not exp.	THTM*	—	10	—								
Diff. ?	Obviously different											
% confid.	Diff. at 99% confid.											
BSA												
Exposed	12.0	7.2	10	26	9.7	3.9	10	22	10.6	4.2	10	23
Not exp.	29.1	7.0	10		17.1	2.5	10		21.3	5.1	10	
Diff. ?	Diff. at 99% confid.											
% confid.	Diff. at 99% confid.											
HMDS												
Exposed	-2.1	15.2	10	1.3	-1.0	5.3	8	5				
Not exp.	8.9	1.6	10		4.0	2.8	10					
Diff. ?	Diff. at 95% confid.											
% confid.	Not different											

* THTM = Too high to measure.

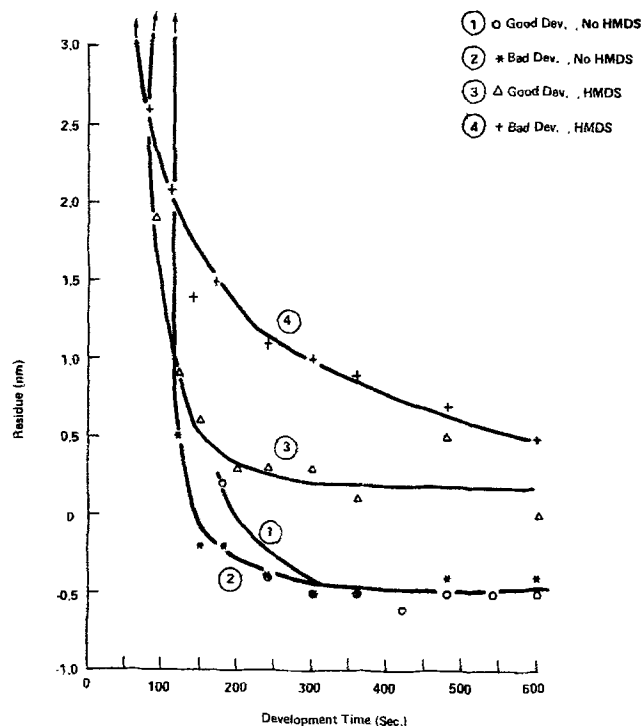


Fig. 8. Development curves for AZ-111

After postbaking, stripping was carried out with acetone, but, unlike the previous work, the films were measured after time increments of 5, 10, and 40 min (total) in ultrasonically agitated acetone. The mean and standard deviations for the apparent residue thicknesses are shown in Table V. Note that, as before, in some cases the residue was too thick to measure. Where the residue was reduced to approximately zero by a given acetone treatment, of course, no further processing was done. The efficacy of the exposure treatment appears to be a function of the adhesion promoter used. The method appears to give best results with no adhesion promoter and worst results with BSA-promoted resist.

Since it was suspected that the catastrophic residues reported for acetone were caused by excessive temperature excursions during postbake, an experiment was carried out in which the occurrence of residue was studied as a function of carefully controlled ($\pm 1^\circ\text{C}$) postbake temperature from 130° to 138°C. All 130°C samples appeared clean to the naked eye, as did all control samples (no processing) for each temperature. All experimental samples baked at 138°C showed residues over the entire substrate. Wafers baked at

intermediate temperatures showed varying residue coverage, depending on the adhesion promoter used.

Ellipsometric measurements confirmed these observations. Wherever a visible residue existed, the ETA indicated residue thicknesses in excess of 50 nm, i.e., out of range of the normal mode for the instrument. Spot checks of such sites with interference measurements, however, often showed residue thickness ranges of several hundred nanometers.

The amount of residue after acetone stripping is plotted in Fig. 9 against the postbake temperature. It is evident that residue is a very strong function of temperature, rising from barely above detectable limits at 130°C to visible thicknesses at 138°C. It will be noted from Table VI that the controls in all cases indicate "residues" of less than 5 nm, indicating minimal ambient contamination to the samples. For the processed substrates, statistically significant residues were found even for the 130°C postbake. Since such residue levels might eventually prove to be process-compatible, however, it is more important to consider results for the higher temperatures. For the 138°C postbake, all processed sample residues were unmeasurably high using ETA. Even at 135°C, catastrophic failure still results in cases involving either BSA or HMDS. Thus, for postbakes in the range of 130°C, acetone must be looked upon as a marginal stripper, requiring very precise control of postbake temperature.

Evaluation of a High Temperature Inorganic Stripper

As previously mentioned, 12% HNO₃ in H₂SO₄ at 100°C was chosen as representative of this stripping category. Table VII shows the results observed on a particular set of processed wafers using this stripping technique. Each wafer here is statistically compared with the group control. These results indicate the occurrence of negative "residue" for certain cases. That is, the measured oxide thickness is smaller after processing than it was originally. The origins of these "negative residues" can be sought in two directions. First, of course, is the possibility that the hot acid stripper is active enough to remove surface layers from the oxide film, or at least to change the surface optically (e.g., Si-O-Si to Si-OH) in a way which would be interpreted as lower oxide thickness. On the other hand, another explanation would be that an original impurity layer was measured as the initial oxide thickness and that this layer was removed by the application and spinning of the adhesion promoter or resist.

In order to test this last hypothesis, a separate experiment was run, in which HMDS and BSA, respectively, were applied to separate wafers, with measure-

Table VI. Ellipsometric measurements of residues (mean/ σ in nm \times 10)

	Postbake temperature (°C)				
	130	132	133	135	138 \pm 1
HMDS	10.6/2.8	21.7/3.5	9.2/4.9	>1400	>1400
BSA	3.4/3.5	23.2/3.8*	15/2.3	>1400	>1400
No promoter	14.5/1.4	28.7/2.6	19.3/3.3*	41.1/7.5*	>1400
No development	13.2/2.4	8.8/22.4*	18.1/2.2	42.3/7.5*	>1400
Control	-0.6/1.8	1.2/1.5	-1.2/1.5	1.4/3.7	-4.7/0.9

* Means and standard deviations (σ) taken on measurable data only.

Table VII. Acid stripping

Group	Mean (nm \times 10)	σ	N	F	95% conf.	99% conf.
HMDS, dev.	-1.2	1.0	10	18	Diff.	Diff.
Control	0.8	0.9	10			
BSA, dev.	-1.3	0.7	10	27	Diff.	Diff.
Control	0.8	0.9	10			
No promoter, dev.	-4.1	2.4	10	33	Diff.	Diff.
Control	0.8	0.9	10			
No promoter, no dev.	-4.2	0.7	10	168	Diff.	Diff.
Control	0.8	0.9	10			

ments being made before and after application. The above hypothesis suggests that the "oxide" thickness should diminish as a result of this process. However, as shown by Table VIII, the adhesion promoters each leave a very real residue. This does not, of course, preclude the possibility that an original impurity layer is solubilized by the promoter layer and is removed during subsequent stripping.

A further evaluation of the hot acid technique involved removal of the highly cross-linked resist formed when AZ-1350J is used as a mask for ion implant operations. In typical situations (e.g., 50-80 kV, 7.5 \times 10¹⁵ As ions/cm², 1 mA), a 15 min immersion in the hot H₂SO₄/HNO₃ stripper produced rather poor stripping, with much of the resist remaining intact (see Fig. 10). Use of a bake in air for 1 hr at 400°C prior to stripping improved the results markedly. However, residue still tended to remain at the edges of resist openings, where (because of the resist profile) the full ion flux impinged on the resist/oxide interface (see Fig. 10b). The effect of this high temperature bake probably is to oxidize and crack the resist structure,

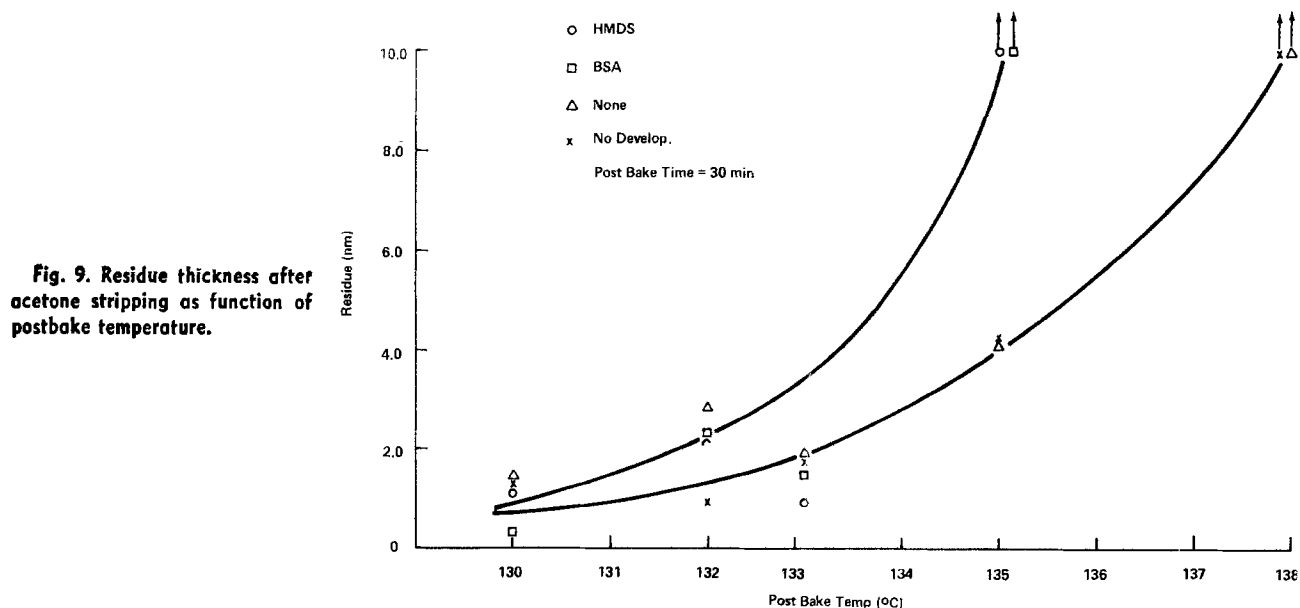


Fig. 9. Residue thickness after acetone stripping as function of postbake temperature.

Table VIII. Effect of adhesion promoter application on "oxide thickness"

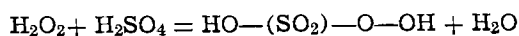
	Mean (nm × 10)	σ	N
HMDS*	+16.3	2.3	10
ESA*	+22.7	3.8	10
Control	-1.3	2.2	10

* Applied as in processing resist. See Experimental.

rendering it more easily removable by the acid. However, the resist cross-linked in the immediate vicinity of the oxide surface apparently is firmly bound and not removed.

Evaluation of Caro's Acid

"Caro's acid," a solution of peroxymonosulfuric acid in concentrated sulfuric acid, was first seriously proposed as a resist stripper by Beck *et al.* (5). The stripping solution is created by a mixture of concentrated H₂SO₄ with highly concentrated (85-90%) hydrogen peroxide. The reaction is said to proceed as follows



While the reaction itself is not highly exothermic, substantial heat can be developed by dilution of the sulfuric acid medium with water contained in the peroxide, as well as that formed by the reaction. Since the H₂SO₅ species is not particularly heat-stable, excessive amounts of water in the peroxide can lead to thermal decomposition of the H₂SO₅. This makes it necessary to use the peroxide in highly concentrated form. Use of the usual laboratory "concentrated" H₂O₂ will lead to an overheated solution on mixing and little or no H₂SO₅ concentration. An additional deleterious effect of excess water is, of course, its potential for shifting the equilibrium in the above reaction, since water is a by-product.

Caro's acid has several major advantages as a stripper. First, it is used at room temperature. Its mode of action is understood to be dehydration coupled with oxidation. In general, organic materials such as photoresist are oxidized to CO₂ and H₂O, thus avoiding a buildup of intermediate products. This leads to a pot-life of the order of 3 weeks or more and ecologically acceptable disposal may be made by aspirating into an industrial waste drain, since only sulfate remains.

The residues left by AZ-1350J as a function of immersion time in Caro's acid are shown for several sets

Table IX. Thermal SiO₂-AZ-1350J-Caro's acid. Effect of multiple cycles (ten sites/wafer, all wafers developed).

Adhesion promoter	Number of cycles*	Residue (nm × 10)	
		Mean	σ
HMDS	1	11.4	1.1
	2	-3.8	2.3
BSA	1	14.2	3.4
	2	-0.7	1.4
	3	-3.1	15.5
None	1	5.0	2.2
	2	-0.9	1.9

* Each cycle consisting of 5 min dip into Caro's acid which had not been disturbed for previous 5 min.

Table X. Comparative stripping of various positive resists by Caro's acid

Resist*	Time for visual cleanliness (min)
AZ-1350J	5
AZ-111	20
PR 102	15

* Applied to obtain approximately 1000 nm thickness in each case.

of process parameters in Table IX. It is obvious that normally processed resist is completely stripped by a total of 10 min in Caro's acid.

In addition to evaluation of AZ-1350J resist, some observations were also made on the ability of Caro's acid to strip several other positive resists. Table X gives comparative results in terms of stripping time necessary to obtain visually clean surfaces, using AZ-111, and Microline PR 102⁴ resists.

As in the case of hot acid stripping, the capability of Caro's acid with respect to highly cross-linked resist was evaluated. Three types of cross-linking were used. In the first, the resist film over thermal oxide was subjected to a CF₄ plasma (simulated dry etch of SiO₂) for sufficient time to strip about one-half the thickness of resist, and the remaining film was then stripped in Caro's acid. The experiment was repeated two times, inserting a 130°C bake once before the plasma, and once after the plasma. Ellipsometric re-

⁴ Product of GAF Corporation, New York, New York.

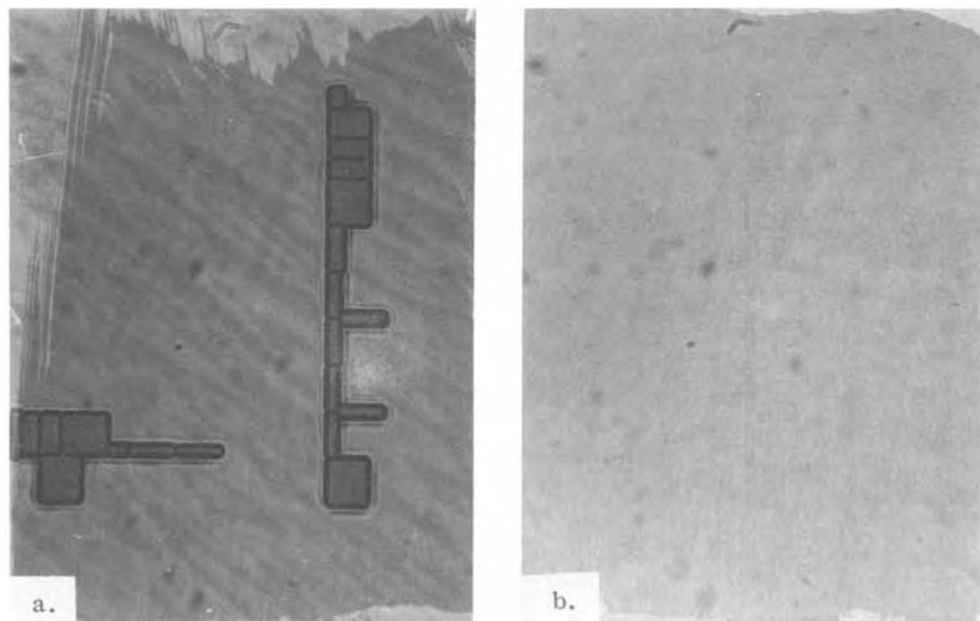


Fig. 10. Micrographs of acid-stripped ion implant patterns. (A) After 15 min strip; (B) 1 hr at 400°C followed by 15 min strip.

sults on this experiment, given in Table XI, show that no significant residue remains after a 10 min strip.

In the second cross-linking procedure, AZ-1350J with an added thermal-free radical initiator (Lupersol 101,⁵ an organic peroxide) was applied to a premeasured oxidized Si wafer and then subjected to an arsenic ion bombardment (80 kV, 5×10^{15} ions/cm²). The results of Caro's acid stripping of this wafer are also shown in Table XI, and here we see that a 10 min immersion proved insufficient to produce a clean surface. Table XII presents residue data for further immersions in Caro's acid. Extrapolation of these results suggests that the ion implant process forms an approximately 15 nm residual film, which is not removable by Caro's acid treatment alone. Inclusion of a high temperature bake prior to stripping, however, renders the residue removable in Caro's acid, although not without difficulty (see Table XII). It was desired to isolate the cause of this residue and, to this end, two additional samples (for which the actual ion bombardment was removed from the process) were characterized. The first sample consisted of the postbaked, peroxide-modified resist, while the other was postbaked (see Experimental section) but contained no peroxide. The results clearly indicate that the ion bombardment is necessary for formation of the previously mentioned 15 nm residue.

As a final attempt at cross-linking, a film of AZ-1350J (applied by the standard process through 130°C postbake) was bombarded with 15 kV electrons for various periods of time in raster patterns by "looking" at it with an SEM at various magnifications. After stripping, an interference contrast microscope was used to search for residual patterns, using scribed marks as locating aids. The results here are necessarily qualitative since we cannot calculate with any accuracy

⁵ Product of Lucidol Division, Pennwalt Corporation, Buffalo, New York.

Table XI. Stripping residues for highly cross-linked resist

Treatment	Residue after 10 min in Caro's acid		Time in Caro's acid to reduce residue to control (99.5% conf.) (min)
	Mean (nm × 10)	σ	
As ion implant	150.3	28.3	
CF ₄ plasma etch			
Bake before etch	-0.7	1.0	<10
Bake after etch	-0.7	2.2	<10
Control	0.4	1.0	—
Electron beam (relative exposure)			
100			>87
83			>87
67			>87
50			>87
33			>87
17			>87
6			~87
3			16
1			2

Table XII. Removal of ion-implanted resist*

Time (min)	Strip treatment	Residue (nm × 10)	
		Mean	σ
10	Caro's acid	150	28
15	Caro's acid	142	27
35	Caro's acid	149	27
75	At 400°C (air) then 20 min Caro's acid	Excessive (>1400)	
75	At 400°C (air) then 30 min Caro's acid	2	5
10	Caro's acid, no implant	4	5
10	Caro's acid, no implant, unmodified resist	2	4

* 80 kV, 5×10^{15} As ions/cm². Blanket AZ-1350J + Lupersol 101.

either the cross-linking efficiency or the flux density of the SEM primary electrons. Table XI summarizes the results obtained in terms of relative electron exposures. These results indicate that increasing electron beam exposure rapidly insolubilizes AZ resist so that, after some degree of exposure, even 1.5 hr of Caro's acid immersion will not remove it, nor will any other wet strip process we have studied. Although it is likely that such exposures would never be experienced by resist in any reasonable process, the data gives us insight into the action of Caro's acid on organic materials, i.e., the solubilizing action does not arise from simple oxidation alone but requires that the carbon atoms be relatively free.

Persulfate Stripper

Caro's acid stripper has as its active ingredient peroxymonosulfuric acid, H₂SO₅. This rendition of the formula is somewhat misleading in that it appears to indicate a higher oxidation number for sulfur than the maximum of six allowed by its electronic structure. The proper rendition, HO—(SO₂)—O—OH, indicates correctly that the molecule retains the sulfur in its +6 state but has incorporated an atom of oxygen in a peroxide configuration. Thus, the oxidizing ability of this species rests with its (extra) active oxygen.

With this in mind, the question might well be asked as to why a molecule with a similar configuration on the opposite side of the sulfur (i.e., persulfuric acid, or HO—O—(SO₂)—(SO₂)—O—OH) would not be equally or more effective. Although the acid itself is not readily available, its potassium salt, K₂S₂O₈, is a commonly used analytical compound. Admixture of this salt with sulfuric acid should produce substantial quantities of the acid species. Although it is difficult to predict the change in activity of the active oxygen due to the dimeric molecule (e.g., resonances, inductive effects), it is certainly reasonable to assume that there will be some similarity in activity of such a persulfate solution to the Caro's acid system with which we have been working.

Such a stripper, if effective, would have a very substantial advantage over Caro's acid. The latter can only be produced by use of highly concentrated hydrogen peroxide. This material is potentially detonatable (upon admixture of only small amounts of organics) and can also present a serious fire hazard. For improperly clothed personnel, it can present further danger in the form of severe chemical burns.

Accordingly, the evaluation procedure used earlier for other strippers was carried out with a persulfate/sulfuric acid mixture as stripper. After some preliminary work, the composition and makeup described under Experimental was chosen. Results of this evaluation are shown in Table XIII. Note that all means for the 5 min strip are significantly larger (95% confidence) than the control, whereas the mean residues after 10 min are equivalent to, or lower than, the control. Thus, for normally processed and baked resist, the persulfate/H₂SO₄ combination gives results which are equivalent to those obtained previously with Caro's acid.

Evaluation with respect to highly cross-linked resist was made comparatively using only electron-beam as a cross-linking vehicle. Recall that previously stated results with Caro's acid showed that most of the elec-

Table XIII. Persulfate/H₂SO₄ stripping of normal AZ-1350J

Adhesion promoter	Devel.	Residue (nm × 10)			
		After 5 min		After 10 min	
		Mean	σ	Mean	σ
HMDS	Yes	26.4	11.5	-11.7	2.1
BSA	Yes	18.6	11.3	-13.4	3.0
None	Yes	25.3	9.4	-11.0	1.8
None	No	32.7	10.2	-10.3	1.8
Control	—	0	3.2	-7.2	3.3

tron dosages used produced far greater cross-linking effects than a typical ion-implant operation. Thus, use of such electron dosages will certainly provide a "worst-case" comparison of strippers.

In these experiments, a resist-coated sample was exposed by sweeping with the raster of an SEM using a different (but known) magnification for each sweep and keeping the exposure time constant. The process was then repeated (without turning off the beam or breaking vacuum) with a second sample having similar resist thickness. The result is two samples, each having an identical set of resist patches which have increasing cross-link density through the set. When these two pieces were subjected respectively to Caro's acid and to the persulfate/H₂SO₄ mixture, areas of lowest cross-link density were removed first, and higher density patches were removed as immersion time increased. The time necessary to remove a patch of given density is an indication of the relative effectiveness of the strippers.

Table XIV shows the lowest density patch remaining for each of the strippers as a function of stripping time. The numbers shown are only relative and are obtained by squaring the magnification factor. Two complete experiments were performed and the table shows the results of both. It is important to note that there is a steady decrease in residue as stripping time is increased. It is evident from the table that for a given stripping time the persulfate stripper is effective against only about half of the cross-link density that is stripped by Caro's acid. This must, however, be viewed against the virtual ineffectiveness of most organic strippers on this relatively huge level of cross-linking.

Conclusion

The data that have been presented here demonstrate the marked sensitivity of commonly used photoresists to processing, when one is concerned with extreme cleanliness of pattern exposed and stripped surfaces. Especially with regard to development, the occurrence of residues appears to be due to a very complex interaction of a number of parameters. (Consider, for example, the differences among the various resists studied and how this ranking changes when HMDS is used as an adhesion promoter).

It is of interest to note the effect, observed in most instances here, of higher residues with adhesion promoters. This appears to be especially true of HMDS when applied from vapor. The relative residue effects of the various adhesion promoters used cannot be simply tabulated. There would appear to be specific interactions with the various resists, leading, for example, to higher HMDS residues on AZ-111 but larger BSTFA residues with AZ-1350J. The choice of adhesion promoter must be made specifically for each specific resist.

We have also examined the effectiveness and suitability of a number of wet stripping processes to a

variety of stripping situations. In general, we have seen that normally processed AZ-1350J resist, with proper control on bake cycles, offers no problem to almost any stripping system. If we consider "harder" resists, we find that ecologically acceptable organic stripping modes are essentially nonexistent. If we apply the further restriction that we wish our system to be universal for all substrate layers in general use, we find ourselves limited to essentially one class of strippers: that comprising Caro's acid and its related variations. As a direct and universal substitute for conventional Caro's acid, the persulfate modification cannot be claimed to be completely successful. Its area of deficiency is, of course, in the stripping of very highly cross-linked resist. It must be recalled that even Caro's acid is incapable of stripping resist with a high enough degree of cross-linking. The advantages of the persulfate system in ease of preparation would seem to more than make up for what may well be an irrelevant disadvantage in terms of speed of stripping highly cross-linked resist.

Finally, there remains the question of just what a permissible level of residue really is, both for development and for stripping. In the latter case, this would be determined by considerations involving the particular processing step which follows removal. However, unless the resist has been subjected to an extreme amount of high energy particle bombardment, it should be possible to reduce residues essentially to zero. For development, however, if we insist on a level which cannot statistically be distinguished from zero, then we cannot hope to achieve zero print bias in almost any of the resist/developer/promoter combinations studied. A practical process can then be achieved only by relaxing either the required residue level or the acceptable print bias. The trade-off between these two items must be carefully considered, along with the possible alternative of implementing an additional process step (e.g., a brief O₂ plasma exposure) to remove trace residues without increasing resist image openings.

Acknowledgments

The authors wish to express thanks to the following individuals for their advice and technical help in the collection of data and preparation of this paper: T. Hayden, G. Henderson, J. Lounsbury, and S. Zimmerman.

Manuscript submitted May 14, 1979; revised manuscript received Aug. 3, 1979.

Any discussion of this paper will appear in a Discussion Section to be published in the December 1980 JOURNAL. All discussions for the December 1980 Discussion Section should be submitted by Aug. 1, 1980.

Publication costs of this article were assisted by IBM.

REFERENCES

1. O. Sus, *Ann.*, **556**, 65 (1944).
2. H. G. Hughes, W. L. Hunter, and K. Ritchie, *This Journal*, **120**, 99 (1973).
3. P. H. Holloway and D. W. Bushmire, *Annu. Proc. Reliab. Phys. (Symp.)*, **12**, 180 (1974).
4. Federal Water Pollution Act Amendment of 1972, 33 U.S. Code, 1251-1356.
5. W. Beck *et al.*, U.S. Pat. 3,900,337 (1975).
6. F. W. Karasek, *Anal. Chem.*, **46**, 710A (1974).
7. S. S. So and S. M. Zimmerman, *Polarized Light (SPIE)*, **88**, 119 (1976).
8. P. S. Hauge and F. H. Dill, *IBM J. Res. Dev.*, **17**, 472 (1973).
9. F. W. Billmeyer, "Textbook of Polymer Science," pp. 468, 539, John Wiley & Sons, Inc., New York (1971).
10. R. S. Horst *et al.*, U.S. Pat. 3,873,813 (1975).

Table XIV. Persulfate/H₂SO₄ stripping of highly cross-linked AZ-1350J resist

Experi- ment	Strip time (min)	Lowest cross-link density remaining	
		Caro's acid	Persulfate/ H ₂ SO ₄
1	5	2.5 × 10 ^{7*}	4 × 10 ⁴
	10	2.5 × 10 ^{7*}	2.5 × 10 ^{7*}
	15	—	2.5 × 10 ^{7*}
2	5	4.9 × 10 ⁷	2.5 × 10 ⁷
	10	4.9 × 10 ⁷	2.5 × 10 ⁷
	15	—	2.5 × 10 ⁷

* Highest density available in experiment.

Residual Stress, Chemical Etch Rate, Refractive Index, and Density Measurements on SiO₂ Films Prepared Using High Pressure Oxygen

E. A. Irene* and D. W. Dong

IBM Thomas J. Watson Research Center, Yorktown Heights, New York 10598

and R. J. Zeto*

U. S. Army Electronics Technology and Devices Laboratory (ERADCOM), Fort Monmouth, New Jersey 07703

ABSTRACT

Dry oxygen pressure at 500 atm is used to grow SiO₂ films 10³ nm thick on silicon at 800°C. The residual film stress, chemical etch rate, refractive index, and density of the pressure-oxide films is measured and compared with measurements of thermal oxide films prepared at 1 atm dry oxygen pressure. The high pressure/low temperature films exhibited higher refractive indexes, slower chemical etch rates, and higher measured densities compared to 1 atm thermal oxides prepared at 1000°C. These results are attributed to the lower oxidation temperature rather than the higher oxidation pressure of the pressure-oxide films. It is concluded that the formation of higher density SiO₂ films is a specific result of low temperature processing. The use of high pressure oxidation provides a convenient technique to prepare the low temperature high density SiO₂ films of sufficient thickness for further study.

Recently, Zeto *et al.* (1, 2) reported enhanced oxidation rates for single crystal silicon thermally oxidized in dry oxygen at elevated oxygen pressures up to 500 atm. It was shown (1) that the silicon oxidation rate obtained by using oxygen at 140 atm (*i.e.*, the pressure of oxygen in commercially available oxygen tanks) and 800°C was comparable to the rate obtained by using 1 atm oxygen at 1200°C. Therefore, the use of elevated oxygen pressures enables a reduction of the oxidation temperature and/or time for an oxidation step. This temperature/time reduction has great technological importance because of the need to maintain sharp dopant profiles and minimize the creation of thermally induced defects in modern small devices. The use of steam (3) and high pressure steam (4) for the thermal oxidation of silicon also offers considerable kinetic enhancement, however, the quality of the SiO₂ and Si may be degraded based on reports of increased electron trapping in SiO₂ due to H₂O (5) and increased Si defects resulting from exposure of the Si to steam oxidation (6).

Whether the MOS industry will accept a new process, such as the use of increased oxidant pressures, will depend both on the need for the lower temperature processing and the demonstration that the SiO₂ quality is not degraded by the new process. It is clear from the industry trend towards smaller devices that lower processing temperatures are required and therefore this study is aimed toward demonstrating that important aspects of the SiO₂ quality resulting from high pressure dry oxidation of silicon can be equivalent to the SiO₂ grown in the conventional 1 atm processes.

As with any new process, the dry high pressure oxidation process has problems associated with reproducibility and optimization. Notwithstanding these anticipated difficulties, Zeto *et al.* (2) reported that mobile and fixed charge levels were acceptably low (in the low 10¹⁰ charges/cm² range) on many samples. These promising results have provided the impetus to improve the process through equipment evolution and to obtain more physical properties data on the resulting SiO₂ films.

* Electrochemical Society Active Member.

Key words: high pressure oxidation, silicon, silicon dioxide, density, film stress.

The present study reports the results of several physical properties measurements on SiO₂ grown by the high pressure dry oxidation of silicon: residual film stress, chemical etch rates, density, refractive index, and film morphology as obtained by transmission electron microscopy (TEM). Collectively, these measurements show that the films have increased density as compared with 1 atm films prepared at conventional oxidation temperatures of 1000°C. The higher refractive indexes, slower etch rates, and higher measured densities of the high pressure low temperature films are attributable to the lower processing temperatures rather than the higher oxygen pressures. Thus a specific advantage of high pressure oxidation methods is that these higher density low temperature SiO₂ films can be prepared in practical oxidation times.

Experimental Procedures

Sample preparation.—Four high pressure dry oxygen oxidation runs were performed as described below to grow oxides about 10³ nm thick on six Si substrates. The Si slices were nominally 2 Ω-cm p-type, 2.54 cm diam, and 0.02 cm thick. Three each of <111> and <100> orientations were used and designated 111, 112, and 113 for the <111> samples and 012, 013, and 014 for the <100> samples. Control oxides were grown at 1 atm, 1000° or 800°C in pure dry O₂ on <100> silicon to similar thicknesses and were used in the film stress, etch measurements, and refractive index measurements to obtain meaningful comparisons with the high pressure grown samples. Prior to any oxidation all Si slices were thoroughly cleaned by a previously described procedure (7). The six samples for high pressure oxidation were initially oxidized at 1000°C in 1 atm ultradry O₂ to obtain 100 nm SiO₂. This was done to obtain a reproducible initial curvature in the Si substrates for the stress measurements.

Pressure oxidation.—The apparatus used for the high pressure dry oxidation was described previously (1) with the exception that a larger pressure vessel was used to accommodate the 2.54 cm diam Si slices noted above. For each of the experimental oxidations, the Si slices were heated to about 800°C while a vacuum was drawn on the vessel. Then, 500 atm dry oxygen pressure was applied within several minutes. After the de-

sired oxidation time the pressurized vessel was withdrawn from the furnace and cooled by radiation. All samples were oxidized at 800°C to yield about 10^3 nm SiO_2 . The oxidation rates for the $\langle 100 \rangle$ samples were about 87 and 132 nm/hr for the $\langle 111 \rangle$ Si. The H_2O content of the pressurized gas was measured as less than 1 ppm.

Film stress.—The residual room temperature stress was calculated from a measurement of the curvature of a Si wafer before and after the SiO_2 film growth by dry pressure-oxidation. The change in Si curvature was measured by an optical interference technique. The apparatus, appropriate equations, and elastic constants used for the calculations as well as the procedures were previously described (8) for a study of Si_3N_4 film stress. Only a small difference (less than 10%) is anticipated in the residual stress for $\langle 100 \rangle$ for $\langle 111 \rangle$ orientations due to the difference of elastic constants for the different Si orientations and we ignored this difference in the present study. The pressure-oxide samples had about 5% thickness nonuniformity across the sample as compared with about 1% for the 1 atm SiO_2 oxides. The direct implication of this on the measured film stress has not been determined but it may contribute to the over-all scatter of the pressure-oxide stress data.

Chemical etch rates.—Chemical etch rates have been shown to be a very sensitive measure of SiO_2 film density (12). The temperature, composition, and extent of agitation of the etchant solution can all alter chemical etch rates. In order to preclude obscuring comparisons between high pressure oxides, controls, and low temperature oxides due to experimental difficulties, samples and controls for a given comparison were etched simultaneously in the same solution. For the comparison of high pressure oxides with 1 atm 1000°C standards, two samples of each were etched together in a commercially available 9/1: $\text{NH}_4\text{F}/\text{HF}$ mixture at $\sim 22^\circ\text{C}$. For this comparison (Fig. 1) more scatter was seen for the pressure oxides. The scatter was due to the larger nonuniformity of the SiO_2 thickness for these samples and the problem of returning to the same spot on the sample for ellipsometric thickness measurements after each exposure to etchant. However, the results to be reported are outside this scatter. Similarly, the comparison of etch rates for the 1 atm 800° and 1000°C grown SiO_2 was made on samples etched in a 9/1: NF_4/HF simultaneously and together at $\sim 22^\circ\text{C}$. The differences in the 1000°C 1 atm controls are presumably due to the above-mentioned temperature, agitation, and etchant batch differences.

Density.—The SiO_2 film density, ρ was calculated from measured values for the mass change of the samples before and after removal of the film by etching and the volume of the film as obtained from the area of the Si wafer and the film thickness. Only the

film on the polished side of the Si was used and a correction was made for the area lost as the Si wafer flat. The weighing accuracy was better than $3 \times 10^{-6}\text{g}$ while the oxide mass was about 10^{-3}g . The average film thickness accuracy was estimated to be better than about 3% based on multiple ellipsometric measurements taken across the wafers and the surface area was known to better than 3%. Based on these values, the error in ρ , $\Delta\rho$, is calculated to be about 10^{-2} . Therefore, the higher density measured for the high pressure grown and the 800°C, 1 atm oxides as compared with 1000°C, 1 atm is a real difference but the absolute values are somewhat uncertain to better than several percent.

Film thickness and refractive indexes.—The SiO_2 thickness and refractive indexes were measured by ellipsometry. A description of the instrument with the various constants used was previously published (9). The reported measurements of refractive index were made near one-half of an ellipsometric period, i.e., at odd multiples of ~ 140 nm for the 632.8 nm light and ~ 120 nm for 546.1 nm light. Near these thicknesses the ellipsometric measurement is most sensitive to different refractive indexes. The index measurements were made during the course of the etching experiments and the index values corresponding to half-period thicknesses were tabulated.

TEM.—Samples were prepared for microscopy by removal of the Si with an $\text{HF}-\text{HNO}_3$ etchant. Since the SiO_2 was too thick ($\sim 1 \mu\text{m}$) for penetration by the 100 keV electrons, the etchant was also used to etch away most of the SiO_2 leaving about 100 nm for examination by TEM.

Experimental Results

Residual stress measurements.—A comparison of the SiO_2 film stress for the high pressure oxides, controls (1 atm O_2 , 1000°C) and literature values are shown in Table I. All of the stresses shown in Table I both measured in this study and from the literature are compressive stresses. The high pressure oxides show more scatter in the stress values than the controls and this may be due to the greater thickness nonuniformity found for these films (about 5% across the wafers). Considering the scatter in the stress values, the film stress for the high pressure oxides is the same as for the controls. Optical microscopic examination revealed no evidence for Si slip due to stress on any of the substrates.

Chemical etch rates.—Figure 1 shows the combined etching results from two pressure-oxide and two control samples 1 atm O_2 , 1000°C. Individually the etch rates were 50.0 and 48.2 nm/min for the pressure samples and 58.6 and 58.7 nm/min for the controls. The spread in the pressure-oxide samples was due to thickness nonuniformity which required returning to

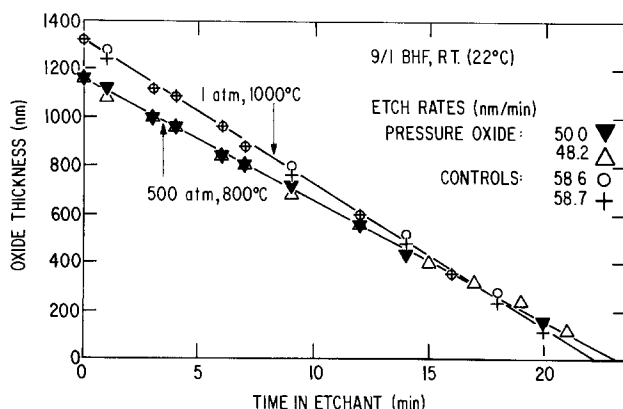


Fig. 1. Plot of SiO_2 thickness vs. time in etchant for two pressure-oxide and two control samples.

Table I. Residual film stress results for pressure-oxide SiO_2 , normal 1 atm SiO_2 and literature values. All stresses shown are compressive

Sample ID	Stress (dynes/cm ² · 10 ⁻⁹)
Pressure oxides (500 atm, 800°C)	
012	1.5
013	4.0
014	4.0
111	2.3
112	4.0
113	2.8
Average: 3.1	
Controls (1 atm, 1000°C)	
005	4.1
006	4.2
Literature	
Jaccodine and Schlegel (10)	2.0 for 875°C SiO_2 2.7 for 1000°C SiO_2 3.7 for 1200°C SiO_2
Whelan <i>et al.</i> (11)	

the exact same spot on the SiO_2 film for the repeated thickness measurements. However, the difference in etch rate between pressure-oxides and controls was well outside the scatter and is therefore considered significant. Pliskin and Lehman (12) reported that a more dense SiO_2 can give rise to a slower etch rate in an HF-based etchant.

Index of refraction.—Table II shows that the high pressure grown samples have a significantly higher refractive index than the controls. This may be caused by pressure oxides having a higher density since it was reported that a higher SiO_2 film density will yield a measurably higher refractive index (12). The measurements associated with sample 013 are particularly interesting, since this sample has an initial oxide thickness near one-half an ellipsometric period. The initial oxide thickness is about 1000 nm, of which 100 nm is a 1 atm 1000°C SiO_2 and the remaining SiO_2 has been grown at 800°C with 500 atm oxygen. Since oxidation takes place at the Si- SiO_2 interface, the 1 atm SiO_2 is always on top of the high pressure SiO_2 and hence it would be removed after the first etching. However, before etching the composite index is larger than for 1 atm 1000°C SiO_2 but smaller than the high pressure SiO_2 while after the removal of this outer SiO_2 that has a lower index, the index returns to the pressure oxide value. This is a predictable result based on the fact that 1 atm, 1000°C SiO_2 has a lower index than the 500 atm 800°C films and this result demonstrates the sensitivity of the ellipsometric measurement.

Film density.—Since both the etch rate and index of refraction measurements showed the possibility that pressure-oxide SiO_2 samples have higher density, the direct measurement of density was performed. Table III shows that indeed the pressure-oxide films have a higher density than the 1 atm oxides.

TEM.—Figure 2 shows an area of a pressure-oxide film which had an unusually large amount of particulate. Diffraction showed the particulate to be amorphous and the electron contrast appeared to be about the same as for the 1 atm SiO_2 . The pressure vessel used to prepare these samples contained a fused silica test tube liner to hold the silicon slices. We believe that the particulate is SiO_2 dust from the fused silica

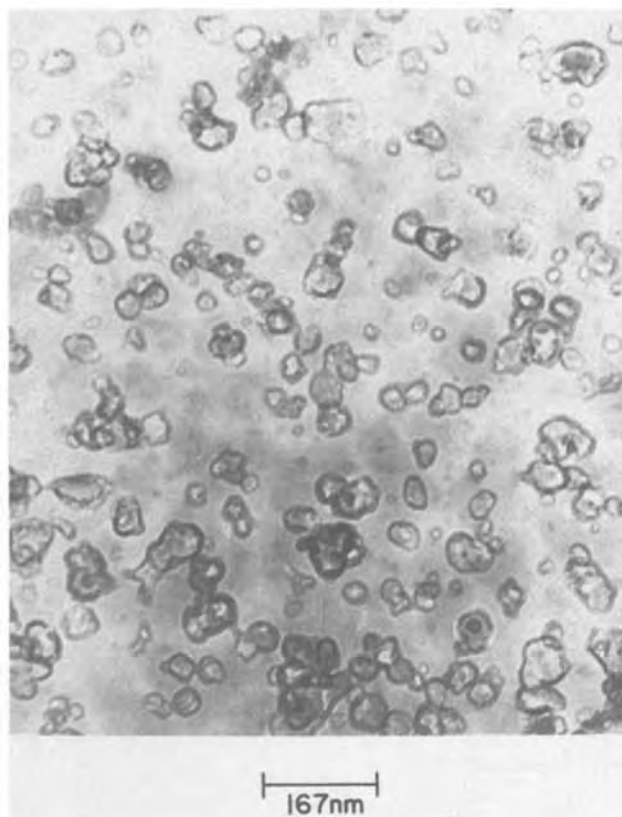


Fig. 2. TEM micrograph of pressure-oxide area which has a large number of amorphous SiO_2 inclusions.

Table II. Refractive index results for pressure-oxide SiO_2 and control samples for 632.8 light

Sample ID	SiO_2 thickness (nm)	Refractive index (at $\lambda = 632.8$ nm)
Pressure oxides (500 atm, 800°C)		
112	947.6	1.476
	153.3	1.475
014	983.0	1.473
	941.4	1.473
	685.7	1.475
113	129.8	1.478
	960.0	1.475
013	967.2 (No etch)	1.467
	684.6	1.477
Average pressure-oxide = 1.475		
Controls (1 atm, 1000°C)		
001	959.0	1.461
002	951.4	1.461
	1293.0	1.462
Average control = 1.461		

Table III. Density results for pressure-oxide and control samples

Sample ID	Density (g/cm^3)
Pressure-oxides (500 atm, 800°C)	
113	2.41
013	2.35
Control (1 atm, 1000°C)	
005	2.26

insert since procedures required that it be thermally cycled, physically handled, and mechanically vibrated in every experiment. Undoubtedly this particulate would contribute to various dielectric failure modes, therefore a second generation high pressure oxidation system has been designed to eliminate this problem.

800°C 1 atm SiO_2 film.—Up to this point the properties measurements on the high pressure oxides taken collectively indicate that these films have a higher density than the 1 atm 1000°C controls. However, in view of a recent study by Taft (13) which shows that a higher refractive index results from lower oxide growth temperatures, the higher density found for the high pressure oxides in this study may be due to the 800°C oxidation temperature and therefore independent of the higher oxidation pressure. To check this possibility, measurements of the refractive index, etch rates, and density using the same techniques described above were done on 800°C, 1 atm oxygen-grown SiO_2 films. The results shown in Table IV, while not extensive, clearly show that the lower temperatures produce a more dense oxide film. When an 800°C 1 atm SiO_2 film was heated in flowing N_2 at 1000°C for 2 hr, the refractive index returned to the 1000°C value. This suggests that higher defect concentrations produced at higher temperatures are responsible for the lower densities. Further work to clarify this situation is in progress.

Table IV. Refractive index, etch rate, and film density results for 1 atm 800°C SiO_2

Refractive index:	1.468 at 632.8 nm light 1.476 at 546.41 nm light
Etch rate:	800°C—1 atm—72 nm/min 1000°C—1 atm—81 nm/min Control
Film density:	Two samples 2.47 g/cm^3 2.42 g/cm^3

Summary and Conclusions

It was previously demonstrated that a significant oxidation rate enhancement is obtained by using high dry O_2 pressures and that acceptable oxide charge and interface state levels could also be obtained. The present study extends the property measurements to include film stress, chemical etch rate, refractive index, density, and TEM morphology. These measurements show that: (i) there is no significant difference in the residual Si/SiO₂ film stress for high pressure and 1 atm thermal oxides, (ii) high-pressure/low-temperature thermal oxide SiO₂ films have a significantly higher density than films prepared at conventional oxidation temperatures such as 1000°C, and (iii) 1 atm thermal oxides prepared at 800°C have a higher density than films prepared at 1000°C.

The formation of high density SiO₂ films on silicon is therefore a specific merit of reduced oxide growth temperatures. The preparation of these higher density SiO₂ films is an advantage afforded by high pressure oxidation methods since higher pressures allow the oxides required in IC devices to be prepared at reduced temperatures in practical oxidation times. It remains to be determined whether or not the higher density material has other interesting properties, such as improved dielectric strength.

Acknowledgment

The portion of this research conducted at IBM was partially supported by the Defense Advanced Research Projects Agency and monitored by the Deputy for

Electronic Technology, RADC, under Contract F19628-76-C-0249.

Manuscript submitted May 23, 1979; revised manuscript received July 25, 1979.

Any discussion of this paper will appear in a Discussion Section to be published in the December 1980 JOURNAL. All discussions for the December 1980 Discussion Section should be submitted by Aug. 1, 1980.

Publication costs of this article were assisted by IBM Thomas J. Watson Research Center.

REFERENCES

1. R. J. Zeto, C. G. Thornton, E. Hryckowian, and C. D. Bosco, *This Journal*, **122**, 1409 (1975).
2. R. J. Zeto, C. D. Bosco, E. Hryckowian, and L. L. Wilcox, Abstract No. 82 presented at the Electrochemical Society Meeting, Philadelphia, Pennsylvania, May 8-13, 1977.
3. B. E. Deal, *This Journal*, **110**, 527 (1963).
4. J. R. Ligenza, *ibid.*, **109**, 73 (1962).
5. R. A. Gdula, *ibid.*, **123**, 41 (1976).
6. S. M. Hu, *J. Appl. Phys.*, **45**, 1567 (1974).
7. E. A. Irene, *This Journal*, **121**, 1613 (1974).
8. E. A. Irene, *J. Electron. Mater.*, **5**, 287 (1976).
9. E. A. Irene and Y. J. van der Meulen, *This Journal*, **123**, 1380 (1976).
10. R. J. Jaccodine and W. A. Schlegel, *J. Appl. Phys.*, **37**, 2429 (1966).
11. M. V. Whelan, A. H. Groemans, and L. M. C. Goossens, *Appl. Phys. Lett.*, **10**, 262 (1967).
12. W. A. Pliskin and H. S. Lehman, *This Journal*, **112**, 1013 (1965).
13. E. A. Taft, *ibid.*, **125**, 968 (1978).

The Chemical Deposition of Boron-Nitrogen Films

A. C. Adams* and C. D. Capio

Bell Laboratories, Murray Hill, New Jersey 07974

ABSTRACT

Films containing boron, nitrogen, and hydrogen have been deposited at reduced pressure by reacting diborane and ammonia at 250°-600°C. Deposition rates as high as 15 nm/min (150 Å/min) have been achieved with thickness uniformities and reproducibilities better than ±3%. The films have been characterized by measuring infrared spectra, refractive index, optical absorption in the ultraviolet and visible, stress, chemical inertness, etch rates in a plasma, step coverage, and adhesion.

Boron nitride is a high resistivity semiconductor with a large bandgap. Several papers have been published describing the preparation of thin boron nitride films, the physical and chemical properties of these films, and potential applications to silicon integrated circuits (1-4). The possible applications include using the boron nitride film as a diffusion source (1-2), as a protective coating (1), as a sodium barrier (1), and as a dielectric (1). The previous films have been prepared by reacting diborane and ammonia at temperatures of 600°-1250°C (1, 2), by reacting these same gases in a plasma with substrate temperatures of 750°-1000°C (3), by reacting boron trichloride and ammonia at 600°-900°C (4), and by reactive sputtering at 250°-900°C (5). In this paper we describe the characterization of films containing boron, nitrogen, and hydrogen chemically deposited at low temperatures (250°-600°C).

Experimental

The deposition equipment is similar to other low pressure reactors that have been recently described (6,7), and is shown schematically in Fig. 1. The reaction takes place in a round quartz tube, 170 cm long,

with an inside diameter of 11.5 cm. The tube is heated with a three-zone furnace (Lindberg Model 54677 with a Model 59754-A controller). All depositions are

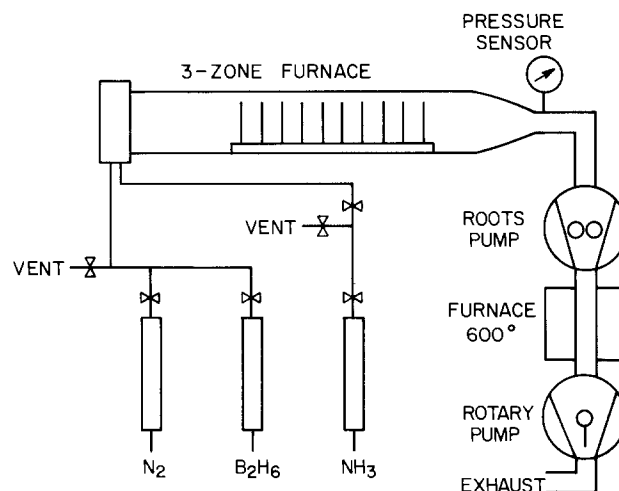


Fig. 1. Schematic diagram of the low pressure deposition reactor

* Electrochemical Society Active Member.

Key words: CVD, dielectrics, infrared, insulator.

made with a flat temperature profile, $\pm 0.5^\circ\text{C}$, over the central 55 cm of the furnace. The ends of the quartz tube are sealed by O-rings in water-cooled flanges. Silicon wafers stand vertically, perpendicular to the gas flow, with a 5 mm spacing between adjacent wafers. The total capacity is 110 wafers. The samples are loaded and unloaded at the gas inlet end of the tube to avoid contamination from solid products that deposit at the exhaust. Diborane, ammonia, and nitrogen are individually metered through calibrated rotameters and introduced into the reaction tube. Separate lines are used for the diborane and the ammonia to prevent the formation of solid compounds in the gas lines. The reduced pressure is obtained with a Roots pump (Leybold-Heraeus, Model WS-250) backed by a mechanical pump (Sargent-Welch, Model 1397). The exhaust gases pass through a small furnace at 600°C to decompose any boron hydrides before they reach the mechanical pump. The pressure is measured with a capacitance manometer (MKS Baratron, Type 222) located at the exhaust end of the reaction tube. Valves are located at the inlet and exhaust of the reactor so gas samples can be taken to measure the reactant concentrations.

In a typical deposition, samples are loaded, the reactor tube sealed, and the system evacuated to 0.002 Torr. This pressure is maintained for 10 min while the samples reach thermal equilibrium. During this time, the gases are allowed to flow through the rotameters to a vent. The deposition is started at the end of the warm-up cycle by switching the gases from the vent to the reactor. Typical pressures during the deposition are 0.3-0.5 Torr. At the end of the deposition, the gases are switched from the reactor to the vent, the reaction tube evacuated to 0.002 Torr for 5 min, and then backfilled to atmospheric pressure with nitrogen.

For comparisons, some samples have been prepared at atmospheric pressure at $650^\circ\text{--}775^\circ$ using a radiantly heated reactor (A model AMN-715 Nitrox reactor manufactured by Applied Materials, Incorporated). The substrates are 75 mm diam silicon wafers, (100) orientation, phosphorus-doped, with a resistivity of 1-10 $\Omega\text{-cm}$. Prior to deposition, the samples are cleaned by a sequence of acidic and basic hydrogen peroxide solutions (8). The gases used are 15% diborane in nitrogen or argon, electronic grade ammonia, both obtained from Matheson Gas Products, Incorporated, and nitrogen, obtained from a liquid nitrogen source.

Film thickness is measured by ellipsometry (9), reflectance spectroscopy (10), or prism coupling (11). The film refractive index is measured by ellipsometry at $\lambda = 0.5461 \mu\text{m}$ (9), or by prism coupling at $\lambda = 0.6328 \mu\text{m}$ (11). Film stress is measured by substrate bending using an optically levered laser beam to measure the radius of curvature. Infrared spectra are measured with a Perkin-Elmer Model 580 spectrophotometer using a bare silicon substrate in the reference beam.

Deposition

The films are formed by reacting diborane and ammonia. Attempts at determining the stoichiometry of the reaction by examining the composition of the gas leaving the reactor have not been successful. Infrared spectra of the exhaust gas shows the presence of unreacted diborane plus other species, probably higher boranes. These gases are not observed when the reaction temperature is above 550°C . Many chemical reactions appear to be taking place, and the complete system is very complex.

The deposition rate of the solid film depends on the square root of the diborane partial pressure (as shown in Fig. 2), is independent of the ammonia partial pressure (for ammonia partial pressures between 0 and 0.1 Torr), and is independent of the total pressure (at constant reactant partial pressures). This behavior differs from that observed for depositions at atmospheric pressure and at higher temperatures, where the rate

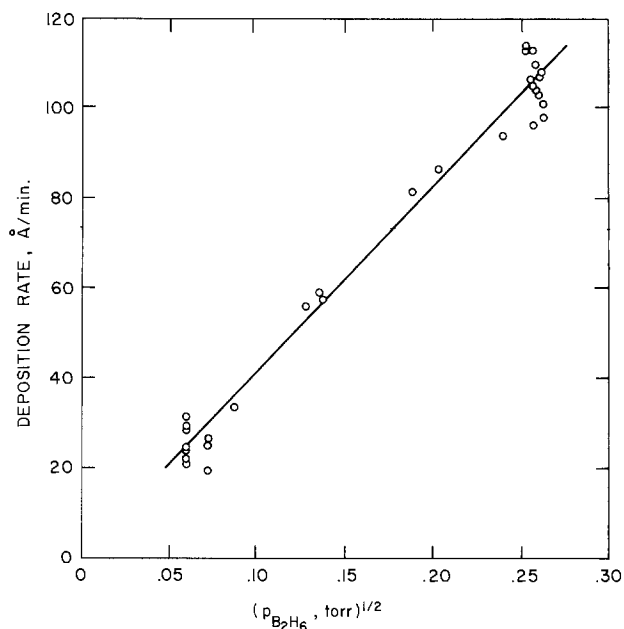


Fig. 2. Deposition rate vs. the square root of the diborane partial pressure for films deposited at 340°C ; the ammonia partial pressure varies from 0.001 to 0.1 Torr; the total pressure is 0.5 Torr.

is higher (50-1000 Å/min), is proportional to the diborane concentration, and decreases with increasing ammonia concentration (1).

The deposition rate is shown as a function of temperature in Fig. 3. At low temperatures, the rate increases with increasing temperature and an Arrhenius behavior is observed. The rate reaches a maximum at about 430°C , and then decreases rapidly with additional increases in temperature. The decreasing rate results from depletion of reactants (caused by reactions on the hot walls at the front of the furnace) which also causes the thickness uniformity across a sample to degrade, as shown in Fig. 3.

An Arrhenius plot is given in Fig. 4 showing data obtained at four different diborane partial pressures. The activation energies range from 20 to 26 kcal/mole,

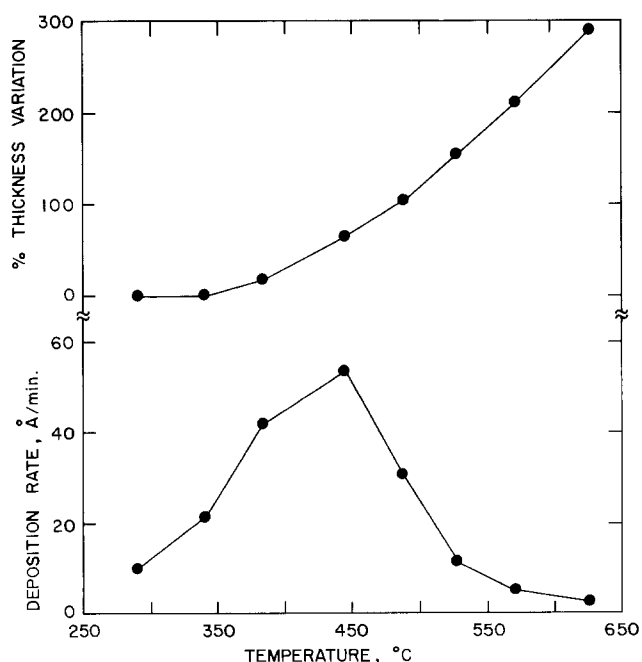


Fig. 3. Deposition rate and thickness uniformity vs. the deposition temperature. Pressures are: diborane, 0.005; ammonia, 0.006; total, 0.5 Torr.

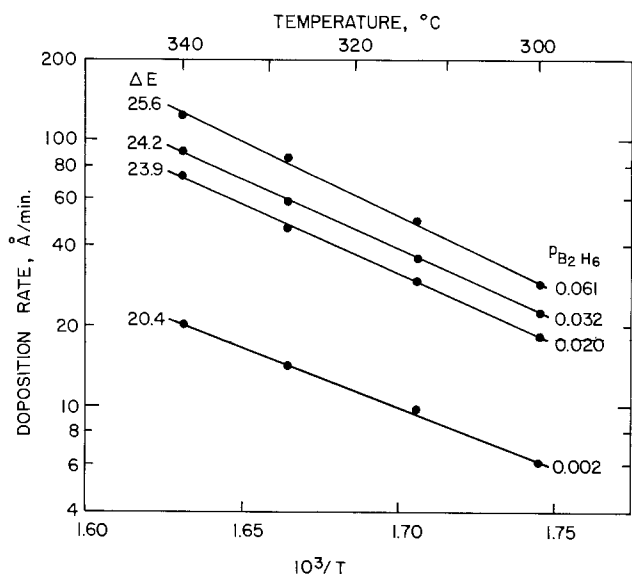


Fig. 4. Arrhenius plot; the total pressure is 0.5 Torr; the $\text{NH}_3/\text{B}_2\text{H}_6$ ratio is 2.

and a concentration dependence is suggested. Such a behavior is common for heterogeneous reactions, but further interpretation has not been attempted due to the lack of detailed kinetic information.

Film Properties

Infrared.—An infrared spectrum of a film deposited at 340°C is shown in Fig. 5. The assignments, which are tentative, are suggested by comparisons with spectra for cyclic boron-nitrogen compounds (12-16), in addition to comparisons with spectra for boron nitride (1-3, 17, 18). The infrared spectrum is insensitive to variations in the $\text{NH}_3/\text{B}_2\text{H}_6$ ratio in the reactant gas (for $0.5 < \text{NH}_3/\text{B}_2\text{H}_6 < 5$). This suggests that the film is a compound with a reasonably well-defined stoichiometry rather than a codeposited mixture. Films deposited at low temperatures ($250^\circ\text{--}400^\circ\text{C}$) have a strong B-N absorption at $1400\text{--}1415\text{ cm}^{-1}$. This frequency is higher than the range reported for boron nitride ($1315\text{--}1380\text{ cm}^{-1}$) (1, 17, 18), and is similar to the frequencies reported for cyclic B-N compounds ($1405\text{--}1440\text{ cm}^{-1}$) (12, 13, 16). The B-H frequency ($2510\text{--}2520\text{ cm}^{-1}$) and the NH_2 frequencies ($1540\text{--}1545$ and $3210\text{--}3240\text{ cm}^{-1}$) are similar to reported values (13-16). Thus the infrared spectra show that the deposited film contains boron and nitrogen, possibly bonded in a ring structure, and also contains hydrogen bonded to the boron (as BH) and bonded to the nitro-

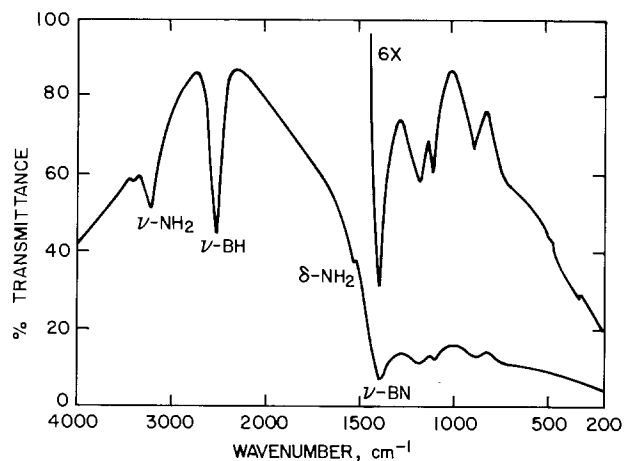


Fig. 5. Infrared spectrum of a boron nitride film deposited at 340°C with $\text{NH}_3/\text{B}_2\text{H}_6 = 1.3$.

gen (as NH_2). The weak absorption at 3400 cm^{-1} may be NH or may be an OH impurity.

The infrared spectrum is sensitive to the deposition temperature (Fig. 6). As the deposition temperature increases, the absorptions assigned to the NH_2 groups (at 3220 and 1540 cm^{-1}) quickly decrease in intensity and disappear. In addition, the BH absorption at 2500 cm^{-1} decreases in intensity and eventually disappears; the BN absorption at 1400 cm^{-1} shifts to lower frequencies; and, two well-defined absorptions appear at about 780 and 880 cm^{-1} . The spectrum in Fig. 6 for the material deposited at 600°C is essentially identical to that of boron nitride deposited at 600°C (1).

Structure and composition.—The films are amorphous as shown by electron diffraction and transmission electron microscopy. The maximum grain size, if grains exist, is estimated to be less than 25Å . Auger spectroscopy indicates a boron to nitrogen ratio of six for films deposited at 340°C with $\text{NH}_3/\text{B}_2\text{H}_6$ greater than 0.5. Quantitative measurements of the hydrogen content are not available. The films appear to have a composition of approximately B_6NH_x , where x is a strong function of the deposition temperature.

Refractive index.—The refractive index, as shown in Fig. 7 and 8, depends on the ratio of reactants and on the deposition temperature. The refractive index decreases rapidly from about 3.4 to 2.3 as the $\text{NH}_3/\text{B}_2\text{H}_6$ ratio increases from 0 to 0.5. Further increases in the $\text{NH}_3/\text{B}_2\text{H}_6$ ratio produce only small changes in the refractive index. This is another indication that the film composition is relatively constant for $\text{NH}_3/\text{B}_2\text{H}_6$ ratios greater than 0.5. The temperature dependence shown in Fig. 8 is more complex. The refractive index increases with increasing deposition temperature, goes through a broad maximum at about 400°C , and then decreases with further increases in temperature. For comparison, boron nitride deposited at atmospheric pressure at $600^\circ\text{--}900^\circ\text{C}$ has a refractive index between 1.7 and 1.8, and decreases with increasing deposition temperature (1). The high temperature data in Fig. 8 agree with this behavior. Polycrystalline boron nitride films deposited at $600^\circ\text{--}900^\circ\text{C}$ using boron trichloride

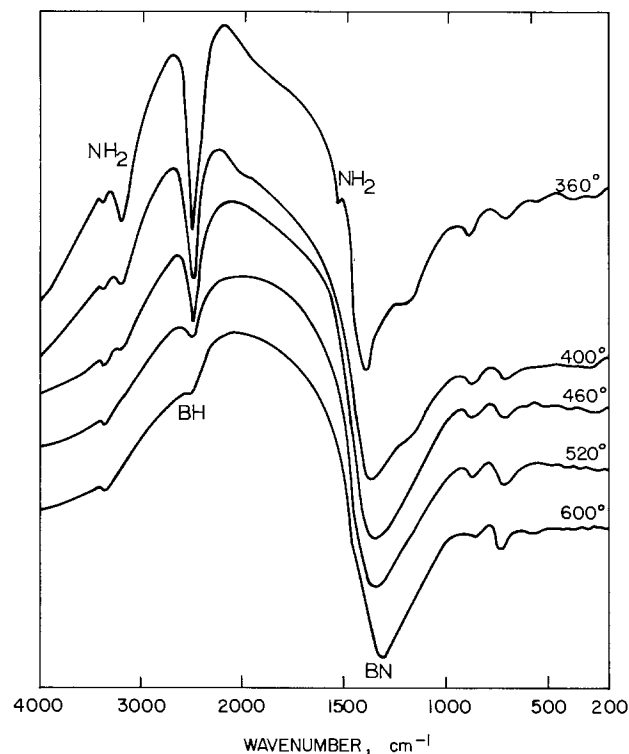


Fig. 6. Percent transmittance for films deposited at different temperatures with $\text{NH}_3/\text{B}_2\text{H}_6 = 1.3$.

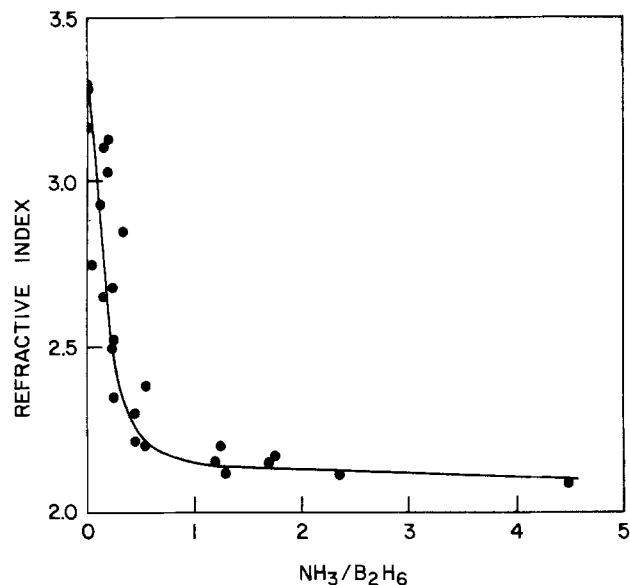


Fig. 7. Refractive index measured at $\lambda = 0.5461 \mu\text{m}$ for films deposited at 340°C .

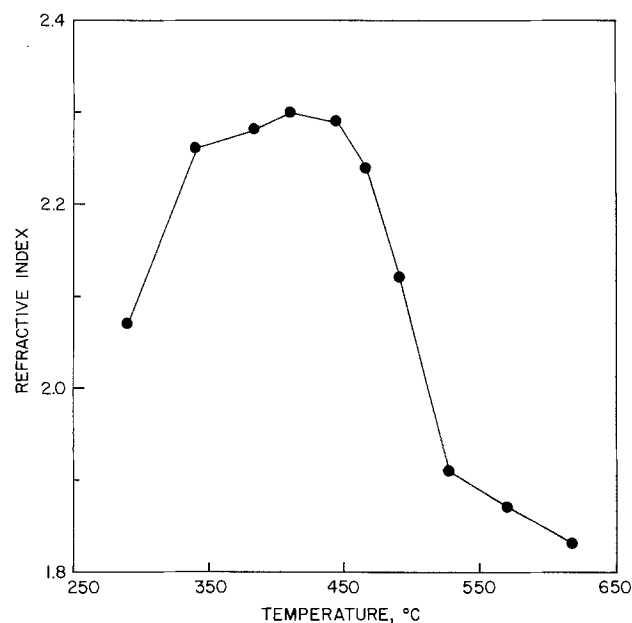


Fig. 8. Refractive index measured at $\lambda = 0.5461 \mu\text{m}$ for films deposited with $\text{NH}_3/\text{B}_2\text{H}_6 = 1.3$.

have a slightly higher refractive index, 1.9-2.0 (4), while cubic boron nitride has an index of 2.12 (19).

Absorption coefficient.—The optical absorption in the ultraviolet-visible region (190-900 nm) has been measured for samples deposited on fused silica disks. The maximum absorption occurs in the ultraviolet with a long tail extending throughout the visible (Fig. 9). Absorption coefficients have been calculated for a wavelength of 600 nm (considered as representative of the absorption in the visible region) and are plotted in Fig. 10 and 11. The absorption coefficient is high when the $\text{NH}_3/\text{B}_2\text{H}_6$ ratio is zero, is nearly constant when $\text{NH}_3/\text{B}_2\text{H}_6 > 0.5$, and increases with increasing deposition temperature. Plots of $\alpha^{1/2}$ vs. E or $\alpha^2 E^2$ vs. E , which have been used to measure the optical bandgap in boron nitride films (1,4), cannot be used with the present films because the curves are not linear. The absorption coefficients in Fig. 10 and 11 appear to be larger than those found for boron nitride deposited at high temperatures (1), but are similar to those found for sputtered boron nitride films (5).

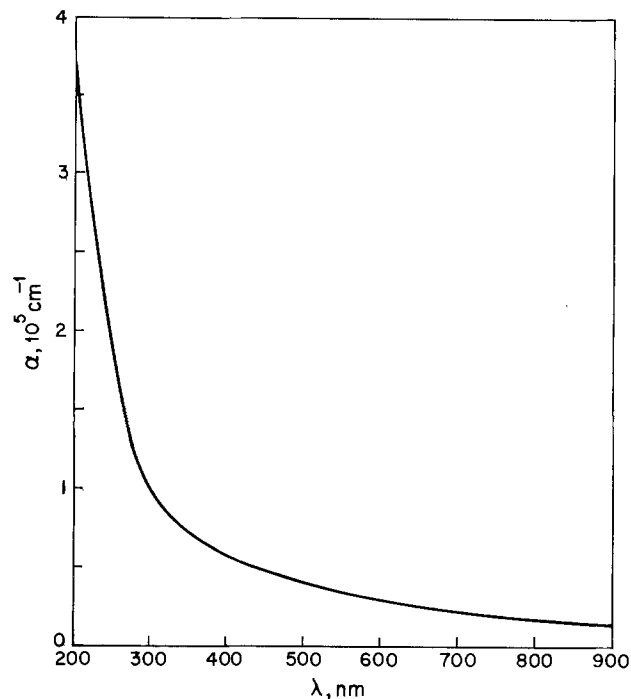


Fig. 9. Absorption coefficient for films deposited at 340°C with $\text{NH}_3/\text{B}_2\text{H}_6 = 1.3$.

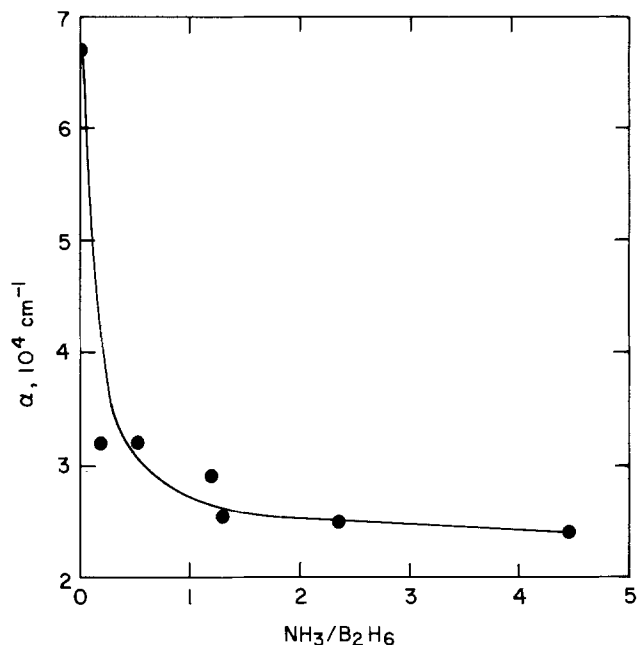


Fig. 10. Absorption coefficient at $\lambda = 0.6 \mu\text{m}$ for films deposited at 340°C .

Stress.—The film stress has been measured for different reactant ratios and is shown in Fig. 12. The solid points are from films deposited at 340°C at reduced pressure; the open points are from films deposited at 700°C at atmospheric pressure. Films from both depositions have a tensile stress when the $\text{NH}_3/\text{B}_2\text{H}_6$ ratio is less than about 0.3. At higher ratios, the film stress is compressive. The films deposited at reduced pressure at 340°C have a lower stress at all $\text{NH}_3/\text{B}_2\text{H}_6$ ratios.

Etch rate.—The films deposited at 290°C - 450°C are insoluble in wet etchants. Solutions that have been investigated are: concentrated hydrofluoric acid, concentrated phosphoric acid (25° and 155°C), 5M potassium hydroxide, buffered hydrofluoric acid, boiling water, aqua regia, and a mixture of nitric, hydrofluoric,

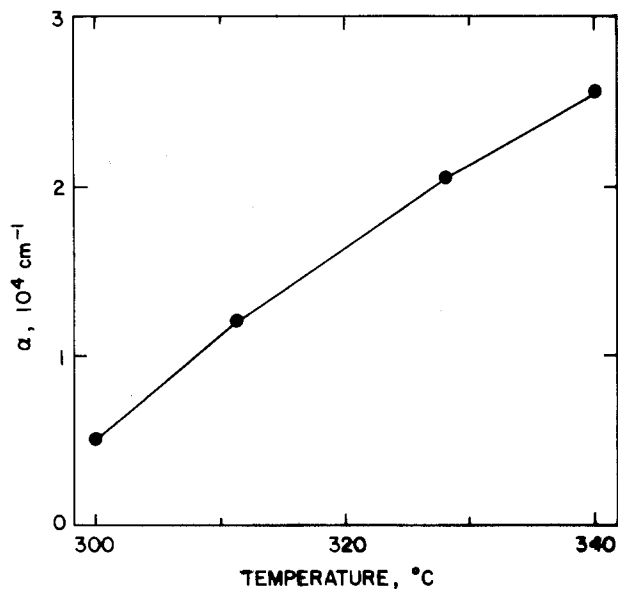


Fig. 11. Absorption coefficient at $\lambda = 0.6 \mu\text{m}$ for films deposited with $\text{NH}_3/\text{B}_2\text{H}_6 = 1.3$.

and acetic acids (5:1:1). Etching is not observed in any of these solutions. The minimum detectable etch rate is about 0.2 Å/min. For comparison, the etch rate of boron nitride films is 80 Å/min in phosphoric acid at 130°C (2), and 150 Å/min in phosphoric acid at 180°C (1). Although the films are insoluble in etching solutions, they are easily etched in a $\text{CF}_4\text{-O}_2$ plasma with etch rates of approximately 3000 Å/min. This is the same rate as observed for boron nitride films (2).

Step coverage.—Step coverage has been evaluated by depositing over metal steps and examining with a scanning electron microscope. In addition, depositions have been made on wafers that have grooves 50 μm deep and 5 μm wide etched in the silicon. In all cases the depositions are conformal, as shown in Fig. 13, even in the case of the very deep grooves. Step coverage has been further investigated by depositing films over wafers metallized with aluminum or with titan-

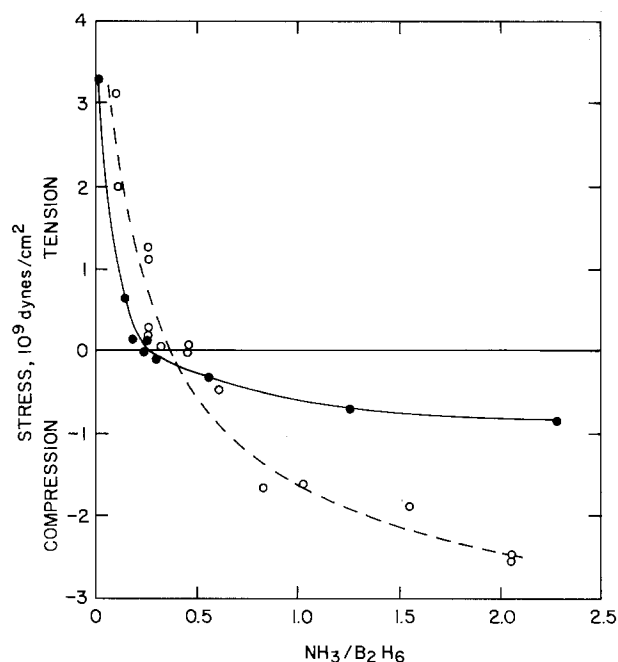


Fig. 12. Film stress vs. the $\text{NH}_3/\text{B}_2\text{H}_6$ ratio; open points: films deposited at atmospheric pressure at 700°C; closed points: films deposited at 0.5 Torr at 340°C.

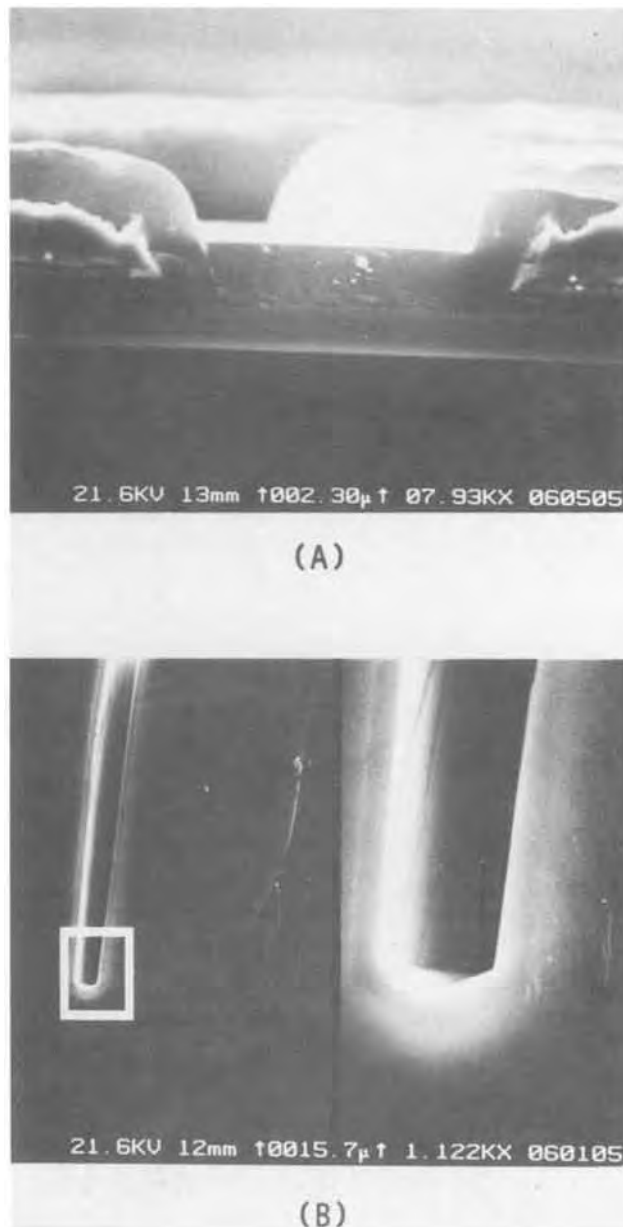


Fig. 13. Scanning electron micrographs showing step coverage of films deposited at 340°C; (A) over titanium-platinum-gold; (B) cross section showing deposition over very deep grooves etched in silicon.

ium-platinum-gold, and then subjecting the samples to a metal etch (hydrofluoric acid for the aluminum, and aqua regia for the gold). Pinholes, cracks, or incomplete step coverage are revealed by attack of the metal. No regions of attack have been observed, showing that the step coverage is complete.

Adhesion.—Quantitative measurements of the film adhesion have not been made. Generally the adhesion is satisfactory; peeling or cracking is not observed after etching patterns in a plasma, after various chemical treatments, or after standing in room ambient for several months. In addition, cracking of the film has not been observed for films over aluminum metallizations even after repeated temperature cycling between 25° and 450°C. Films deposited over gold metallizations show no signs of cracking after heating to 350°C. For both metallizations, cracking is evaluated by microscopic examination before and after decoration of any cracks with a metal etching solution.

However, there are a few exceptions to the generally good adhesion. Four samples (from more than

one hundred) have suffered adhesion loss after standing for 3-6 months. In one case, crystals (probably of boric acid) (1) have been observed on the film surface. Reasons for the adhesion loss on these four samples have not been determined. Auger analysis has detected oxygen in two of these films. This suggests that the adhesion loss may have been caused by a small leak in the reactor. Cracking and loss of adhesion also occur when the films on silicon substrates are annealed in steam at 2 atm pressure and 125°C. After 7 hr, cracking has started along the edge of the wafers. This cracking proceeds inward until the entire film is cracked after about 24 hr. The film thickness, refractive index, and infrared spectrum are unchanged by the steam anneal. It appears that the steam causes a reaction at the film-silicon interface leading to loss of adhesion and cracking, but the film itself does not react with the steam. Loss of adhesion is also observed after samples are annealed in vacuum at temperatures above 500°C. The annealing causes loss of hydrogen (determined from the decrease in intensity of the BH and NH₂ infrared absorptions) and causes changes in the BN bonds (the BN absorption shifts from 1400 to 1340 cm⁻¹). A few days after the anneal, the films start to crack. This phenomenon is not observed for films annealed at temperatures below 500°C.

Defects.—Films thicker than 0.1 μm are pinhole-free as shown by the inability of acids to attack metals (aluminum or gold) covered with the film. The major film defects are small round mounds or hillocks, which have been reported previously for films of boron nitride (1). The hillocks appear to have the same composition as the film and have a spherical shape (Fig. 14) ranging in size up to 1 μm in diam. The formation of the hillocks is independent of the substrate, independent of the NH₃/B₂H₆ ratio, and independent of the diborane partial pressure; however, the hillock density increases as the deposition temperature decreases. The cause of these hillocks and the mechanism of their formation are not understood.

Reproducibility.—An estimate of the deposition reproducibility has been obtained by measuring monitors from 13 consecutive depositions. The means and the standard deviations are: thickness, 0.582 and 0.014 μm; refractive index, 2.24 and 0.03; and stress, 0.05 × 10⁹ and 0.38 × 10⁹ dynes/cm². The reproducibility is very good.

Other Materials

During this work other materials have also been prepared and partially characterized. Depositions using diborane but no ammonia produce films containing boron and hydrogen, as shown by the BH infrared absorption at 2560 cm⁻¹. These films have a metallic appearance, have a refractive index of about 3.4, have a strong optical absorption near 200 nm, and have a high tensile stress, 3 × 10⁹ dynes/cm². Addition of acetylene instead of ammonia gives films containing boron, carbon, and hydrogen. These films are not soluble in acid solutions, are easily etched in a CF₄-O₂ plasma, have a refractive index of 2.7, have infrared absorptions at 2555 cm⁻¹ (BH) and 1105 cm⁻¹, and have a low tensile stress. Boron nitride films have been prepared by reacting boron trichloride and ammonia at reduced pressure at 700°-800°C. The films have a refractive index of 1.9-2.0 and have infrared absorptions at 3430, 1350, and 790 cm⁻¹. Crystals, probably of boric acid (1), form on the surface of these films within a few days.

Summary

Films of a boron-nitrogen compound with a composition of approximately B₆NH_x have been deposited at reduced pressure by reacting diborane and ammonia at 250°-600°C. The thickness uniformity and reproducibility are within ±3% for films deposited

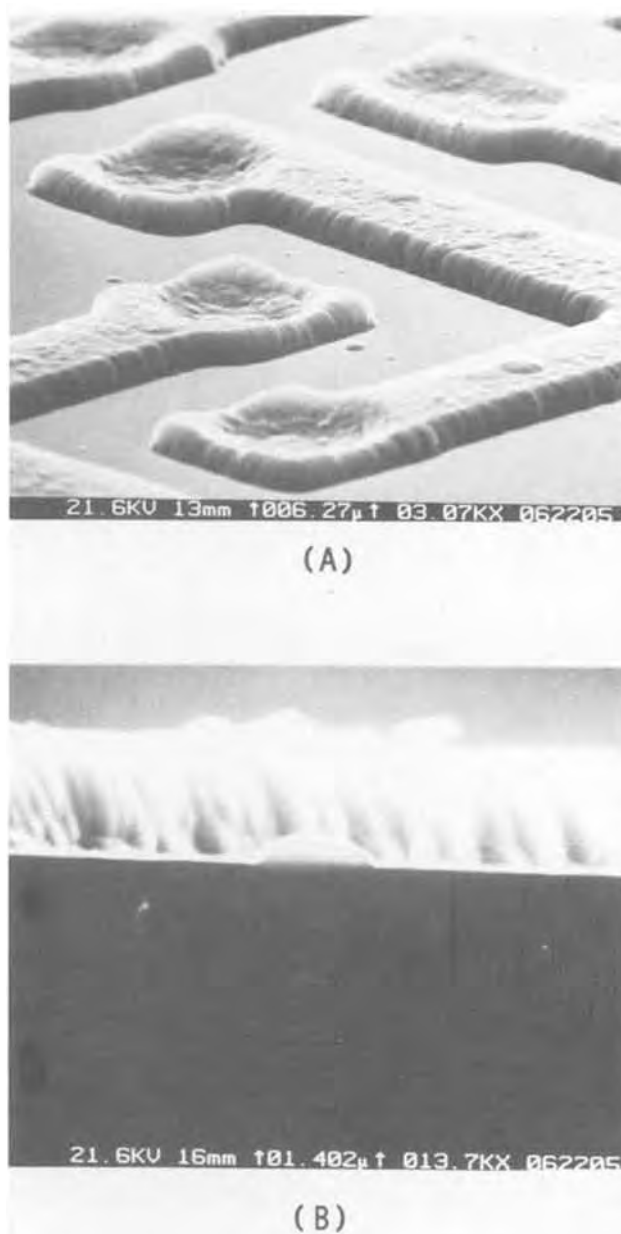


Fig. 14. Hillocks in films deposited at 340°C over aluminum metallization: (A) SEM of the surface; (B) SEM showing a cross section.

at 340°C. Infrared spectra show that the films contain boron and nitrogen, possibly bonded in a ring structure, and hydrogen bonded as BH, NH₂, and possibly NH. The film properties are nearly independent of the ratio of reactants (for 0.5 < NH₃/B₂H₆ < 5), but are affected by the deposition temperature. The film refractive index is about 2.2 for films deposited at 340°C. The films have an absorption maximum in the ultraviolet with a long tail extending throughout the visible region. At 600 nm, the absorption coefficient is about 2.5 × 10⁴ cm⁻¹ and increases with increasing deposition temperature. The films deposited in the reduced pressure reactor at 340°C have a lower stress than comparable films deposited at atmospheric pressure at 700°C. For NH₃/B₂H₆ ratios greater than 0.3, the films have a low compressive stress (0 to 1 × 10⁹ dynes/cm²). The films are in tension for lower values of the NH₃/B₂H₆ ratio and reach a maximum stress of about 3 × 10⁹ dynes/cm² for NH₃/B₂H₆ = 0. The films are chemically inert, being insoluble in all etching solutions investigated. However, the films are easily etched in a CF₄-O₂ plasma with an etch rate of

3000 Å/min. The step coverage is conformal with no pinholes or cracks, and the adhesion is satisfactory; although, adhesion problems develop if samples are annealed at temperatures greater than 500°C or are heated in steam at 125°C for several hours. The major defects are spherical hillocks ranging in size up to 1 μm in diam. The hillock density decreases as the deposition temperature increases.

Acknowledgment

The authors would like to thank W. W. Weick for the steam anneals, C. C. Chang for the Auger analysis, C. J. Mogab for the plasma etching, J. C. North for supplying the silicon samples for step coverage experiments, and H. J. Levinstein and S. Brogdo for their many comments and suggestions.

Manuscript submitted May 24, 1979; revised manuscript received July 31, 1979.

Any discussion of this paper will appear in a Discussion Section to be published in the December 1980 JOURNAL. All discussions for the December 1980 Discussion Section should be submitted by Aug. 1, 1980.

Publication costs of this article were assisted by Bell Laboratories.

REFERENCES

1. M. J. Rand and J. F. Roberts, *This Journal*, **115**, 423 (1968).
2. M. Hirayama and K. Shohno, *ibid.*, **122**, 1671 (1975).
3. S. B. Hyder and T. O. Yep, *ibid.*, **123**, 1721 (1976).
4. W. Baronian, *Mater. Res. Bull.*, **7**, 119 (1972).
5. A. J. Noreika and M. H. Francombe, *J. Vac. Sci. Technol.*, **6**, 722 (1969).
6. R. S. Rosler, *Solid State Technol.*, **20**, 63 (1977).
7. A. C. Adams and C. D. Capiro, *This Journal*, **126**, 1042 (1979).
8. W. Kern and D. A. Puotinen, *RCA Rev.*, **31**, 187 (1970).
9. R. J. Archer, *J. Opt. Soc. Am.*, **52**, 970 (1962).
10. F. Reizman and W. Van Gelder, *Solid-State Electron.*, **10**, 625 (1967).
11. A. C. Adams, D. P. Schinke, and C. D. Capiro, *This Journal*, **126**, 1539 (1979).
12. A. W. Laubengayer, P. C. Moews, Jr., and R. F. Porter, *J. Am. Chem. Soc.*, **83**, 1337 (1961).
13. K. W. Boddeker, S. G. Shore, and R. K. Bunting, *ibid.*, **88**, 4396 (1966).
14. K. Niedenzu, W. Sawodny, H. Watanabe, J. W. Dawson, T. Totani, and W. Weber, *Inorg. Chem.*, **6**, 1453 (1967).
15. O. T. Beachley, Jr., *ibid.*, **8**, 981 (1969).
16. G. A. Anderson and J. J. Lagowski, *Spectrochim. Acta, Part A*, **26**, 2013 (1970).
17. E. G. Brame, Jr., J. L. Margrave, and V. W. Meloche, *J. Inorg. Nucl. Chem.*, **5**, 48 (1957).
18. P. C. Li and M. P. Lepie, *J. Am. Ceram. Soc.*, **48**, 277 (1965).
19. P. J. Gielisse, S. S. Mitra, J. N. Plendl, R. D. Griffis, L. C. Mansur, R. Marshall, and E. A. Pascoe, *Phys. Rev.*, **155**, 1039 (1967).

Hydrogen Profiles of Anodic Aluminum Oxide Films

William A. Lanford¹

Wright Nuclear Structure Laboratory, Yale University, New Haven, Connecticut 06520

and Robert S. Alwitt* and Christopher K. Dyer*²

United Chemicon, Incorporated, Northbrook, Illinois 60062

ABSTRACT

The ¹⁵N hydrogen profiling technique is used to measure hydrogen concentration profiles in a variety of Al₂O₃ films including amorphous anodic barrier films grown in different electrolytes, pseudoboehmite, and composite oxide films grown by reaction with boiling water followed by anodic oxidation. Hydrogen profiles of the composite oxide films confirm that the "relaxation" which causes a large loss in field strength results from penetration of water deep into the oxide film. Comparison of our results with those obtained by SIMS is made where the SIMS data are available.

We have used a nuclear reaction technique to measure hydrogen concentration vs. depth in a representative group of aluminum oxide films including: amorphous barrier films grown in different electrolytes (phosphate, tartrate, glycol-borate), pseudoboehmite films formed by reaction of Al with boiling water, and composite oxides grown by reaction of Al with water followed by anodic oxidation. Composite oxides were examined both before and after a "relaxation" (1), which causes an order of magnitude loss of field strength. This "relaxation" seems to be associated with entry of water deep into the barrier oxide. Direct evidence for water within the barrier layer had not been available before the present study.

The presence of hydrogen in the form of protons or hydroxyl groups has been invoked by several investigators to explain the growth and properties of anodic aluminum oxide films. Hoar and Mott (2) suggested that porous Al₂O₃ growth involved transport

* Electrochemical Society Active Member.

¹ Present address: Department of Physics, SUNY, Albany, New York 12222.

² Present address: Bell Laboratories, Murray Hill, New Jersey 07974.

Key words: dielectrics, nuclear reactions, oxidation, water.

of oxygen as OH⁻ to the metal interface coupled with a counterflow of H⁺ to the solution; this idea was later expanded upon by Hoar and Yahalom (3). Heine and Pryor (4) proposed that an observed increase in the a-c conductivity of the outer portion of barrier Al₂O₃ films was due to OH⁻ in this part of the film. A-C resistivity profiles of anodic Al₂O₃ films were extensively measured by Brock and Wood (5) who ascribed all decreases in resistivity to the presence of protons or OH⁻. No attempts to measure the hydrogen content had yet been reported and all these authors seemed to consider that any hydrogen in the oxide was present at low but unspecified concentrations. A radically different proposal came from Dorsey (6), who interpreted the infrared spectra of *in situ* anodic alumina films as showing that the barrier layer was an alumina trihydrate. It was later shown that his conclusion was the result of incorrect interpretation of the spectra and that anodic alumina films prepared in boric acid electrolyte contained no appreciable amount of hydroxyl group (7).

The introduction of secondary ion mass spectroscopy (SIMS) provided a new tool for the study of oxide

composition, one that could give information on composition *vs.* depth. Dorsey compared SIMS spectra of gibbsite, boehmite, and anodic alumina formed in 2M boric acid and again concluded that the anodic oxide was a trihydrate (8). Since it is known that this oxide is not a trihydrate, it appears that the interpretation of SIMS data for analysis of oxides and hydroxides must be done with great caution. More recently, SIMS has been used to measure hydrogen profiles of anodic Al_2O_3 films formed in tartrate electrolytes (9). Hydrogen was detected throughout the film, and the concentration depended upon the pH of the electrolyte.

Because of the potential difficulty in interpreting SIMS data, we have used the ^{15}N resonant nuclear reaction technique (10) to measure hydrogen concentration profiles in the anodic oxide films of the present study. While this is a relatively new technique, it has already been used to profile hydrogen in thin film insulators—silicon nitride (11), semiconductors—amorphous SiH_x (12), and superconductors— Nb_3Ge (13), as well as in a variety of hydrated glasses (14). This technique uses a nuclear reaction as a probe for hydrogen and, as a result, is inherently a more quantitative technique than those such as SIMS whose signal may be sensitive to poorly understood atomic or solid-state effects. Most importantly, in the ^{15}N hydrogen profiling technique the region of the sample being analyzed for hydrogen is not exposed to the atmosphere of the instrument chamber. Hence, the procedure is much less susceptible to experimental artifacts than is the SIMS technique (9). Because this method is relatively new and may not be familiar to many of the readers, we will briefly review it below. More detailed discussions of the method and its application are available in the literature (10-14).

The purpose of this study was to see what could be deduced about oxide film structure and composition from H profile measurements by nuclear reaction and to learn about the advantages and limitations of the technique. The intent was to survey a range of film types rather than study particular films in detail. Since the only reported H profiles are for films formed at several pH values in tartrate electrolyte (8), we put some emphasis on the analysis of similar films.

Experimental

Sample preparation.—99.99% Al foil was cut into 20 cm^2 coupons and chemically polished in a mixture of 15 parts 70% HNO_3 + 85 parts 85% H_3PO_4 for 2 min at 85°C. The foil specimen was then immersed in stirred 1M NaOH for 10 min at room temperature to remove the polishing film.

Anodic oxide films were formed on these foils in the following ways:

1. At 1 mA/cm^2 , 95°C in 1.4 g/liter $\text{NH}_4\text{H}_2\text{PO}_4$ to 150V.
2. At 1 mA/cm^2 , 25°C in ethylene glycol containing 17% ammonium pentaborate to 150V.
3. At 1 mA/cm^2 , 25°C in 30 g/liter ammonium tartrate. Two sets of specimens were prepared. The first set was anodized to 60V at pH 4.26, 6.73, 9.08 and the second was anodized to 150V at pH 3.98, 6.27, 9.21.

4. By immersion of the specimen in boiling distilled water for 5 min to form a hydrous oxide film, followed by anodization ("formation") in 100 g/liter boric acid + 0.9 ml/liter 30% NH_4OH at 95°C. The formation was first at 1 mA/cm^2 to 220V and then at constant voltage until the current decayed to 25 $\mu\text{A}/\text{cm}^2$.

Procedure 4 gives a composite oxide film in which a largely crystalline barrier oxide layer forms between the Al substrate and the outer hydrous oxide (15). While there had been no direct evidence for water in these films, the barrier oxide layer contains voids and it has been suggested that these can become filled with water on open circuit in a nonaggressive electrolyte resulting in "relaxation" (1). To verify this, a composite oxide specimen was examined for hydrogen

both before and after a relaxation in $\sim 0.2\text{M}$ Na_2CO_3 at $\sim 35^\circ\text{C}$ for 10 min.

A second anodization (reformation) after a relaxation appears to fill the barrier layer voids with oxide (15). A foil which had been formed and relaxed was stabilized by a "reformation" at 25 $\mu\text{A}/\text{cm}^2$ to 220V in the boric acid electrolyte. This foil was also examined for hydrogen content.

Measurement of H content.—The ^{15}N hydrogen profiling technique (10) makes use of a narrow isolated resonance in the nuclear reaction $^{15}\text{N} + ^1\text{H} \rightarrow ^{12}\text{C} + ^4\text{He} + 4.43$ MeV gamma ray. The method is shown schematically in Fig. 1. Because this is a resonance reaction, there is a large probability for this reaction to take place only when the relative energy of the ^{15}N and ^1H is at the resonance energy. To use this reaction as a probe for hydrogen, the sample to be analyzed is bombarded with ^{15}N and the yield of the characteristic 4.43 MeV gamma rays is measured. If the ^{15}N is at the resonance energy, the yield of characteristic gamma rays is proportional to hydrogen on the surface of the sample. If the energy of the ^{15}N is raised above the resonance energy, there are essentially no reactions with hydrogen on the surface of the sample because the energy is too high. However, as the ^{15}N ions penetrate the sample, they lose energy and reach the resonance energy at some depth. Now the yield of gamma rays is proportional to hydrogen at this depth. Hence, by measuring the yield of 4.43 MeV gamma rays *vs.* ^{15}N energy, the hydrogen concentration *vs.* depth is determined. See Fig. 1. Further discussions of this technique and its application are available in the literature (10-14).

The sensitivity of the ^{15}N hydrogen profiling technique is determined by the amount of ^{15}N beam incident on the sample. In the present study, each data point required on the order of 100 sec of beam which resulted in a sensitivity limit of 1×10^{20} atoms cm^{-3} . The beam spot on the specimen was typically a few mm in diameter. The depth resolution near the surface of the sample is determined by the ratio of the width of the resonance over the rate of energy loss of the ^{15}N beam (dE/dx). For Al_2O_3 this depth resolution is 3 nm. However, as discussed below, the practical depth resolution for several of the films used in the present study is limited by the rather non-uniform outer layer of hydrous aluminum oxide.

The chamber used to measure the hydrogen profiles is shown schematically in Fig. 2. The samples to be analyzed were mounted on a "sample wheel" which could be remotely positioned and rotated to change samples. The ^{15}N beam is incident from the right and the gamma rays are detected by a sodium iodide detector placed directly behind the samples. No oil pumps are used in order to minimize hydrocarbon surface contaminations. Instead, the vacuum system is pumped only by ion pumps and liquid nitrogen cold

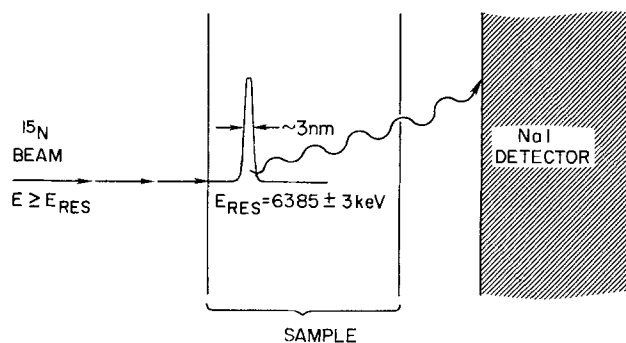


Fig. 1. A schematic representation of the ^{15}N hydrogen profiling method. Because of the narrow resonance at 6385 keV, the measured gamma ray yield is proportional to hydrogen content at a specific depth into the sample.

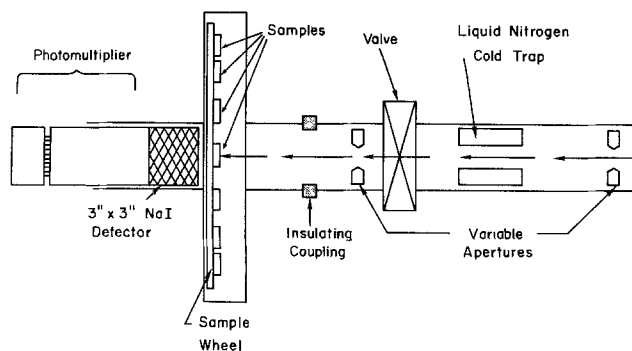


Fig. 2. A schematic representation of the experimental chamber used to measure hydrogen profiles.

traps. The vacuum is typically 10^{-6} Torr. The amount of ^{15}N beam incident on the samples is monitored by measuring the electrical current deposited on the target by the ^{15}N beam.

Determination of H profile.—The depth at which the ^{15}N reaches the resonance energy is given by

$$\text{depth} = (E - E_{\text{res}}) / (dE/dx)$$

where E_{res} is the resonance energy, 6.385 MeV, and dE/dx is the gradient of energy loss of the ^{15}N ions. The latter quantity was calculated (16) from the Northcliffe and Schilling stopping powers corrected for "Z₂ oscillations." The stopping powers were 7.31 MeV·mg⁻¹·cm² for Al₂O₃ and 8.34 MeV·mg⁻¹·cm² for pseudoboehmite (AlOOH·½ H₂O). Table I(a) shows the energy loss rates in units of MeV μm⁻¹ for the films used in this work. Each of the amorphous barrier films was assumed to have the same density as that found for glycol-borate films (17).

The hydrogen concentration (C_{H}) is given by

$$C_{\text{H}} = (\text{constant}) (\text{gamma ray yield}/\mu\text{C}) (dE/dx)$$

where the constant depends only on the resonant cross section and detector efficiency. For our system

$$C_{\text{H}} (\text{atoms cm}^{-3}) = (3.8 \times 10^{19})$$

$$(\text{counts per } 0.4 \mu\text{C}) (dE/dx)$$

This calibration had been previously established and is accurate to better than 10% (10, 18).

Total film thickness was estimated from reported values for films formed under similar conditions. These values are listed in Table I(b).

Results and Discussion

Amorphous barrier layers.—*Phosphate and glycol-borate films.*—Hydrogen concentrations at several depths are shown in Table II; for comparison consider that the oxide consists of $\sim 2 \times 10^{22}$ Al₂O₃ units cm⁻³. Both films have a surface region that is enriched in

Table I. Film properties

a. Density and energy loss	ρ (g cm ⁻³)	Ref.	dE/dx (MeV μm ⁻¹)
Amorphous barrier Al ₂ O ₃	3.17	(17)	2.32
Crystalline barrier Al ₂ O ₃	3.65	(15)	2.67
Crystalline barrier Al ₂ O ₃ (after reformation)	3.82	(15)	2.79
Pseudoboehmite	2.44	(19)	2.03
b. Total film thickness	Thick-ness (nm)	Ref.	
150V phosphate	210	(20)	
150V glycol-borate	170	(17)	
60V tartrate	70	(5)	
150V tartrate	175	(5)	
220V composite barrier	220	(15)	

Table II. H concentrations in phosphate and glycol-borate 150V films

Depth (nm)	C_{H} (10^{20} atoms cm ⁻³)	
	Phosphate	Glycol-borate
17	4.3	4.5
37	2.6	<1
56	2.8	1.4
75	<1	<1

hydrogen and, to a depth of about 60 nm, the phosphate film contains more hydrogen than the G-B film. The highest H concentration in both films is about one H atom for every fifty Al₂O₃ units. These films were not examined for hydrogen at depths greater than 75 nm but from the results obtained it seems likely that the remainder of the films contained less than 1×10^{20} H atoms cm⁻³. To offer another frame of reference, this concentration is equivalent to 0.04 weight percent (w/o) H₂O if the H were present as H₂O. Quite clearly, hydrogen is a trace constituent in these films.

Randall and Bernard (21) have measured the phosphorus content of anodic Al₂O₃ films formed in phosphate electrolytes. In the outer ~75% of the film there was a uniform concentration that depended only slightly on particular anodizing conditions and was independent of total film thickness. From their data for anodizations in 10^{-2}M NaH₂PO₄ at 98°C, we calculated a phosphorus concentration in the outer layer of 1.2×10^{21} atoms cm⁻³. This is more than four times the hydrogen concentration we have observed in a similar film, so it is likely that the incorporation of hydrogen and phosphorus are independent processes and not the result of HPO₄²⁻ or H₂PO₄⁻ incorporation.

Tartrate films.—These films formed at less than 100% current efficiency at all pH. Brock and Wood (5) estimated the current efficiency of film formation in 3% ammonium tartrate from dV/dt measurements. We made similar estimates, based on dV/dt for the G-B anodization which is 100% efficient. Their results at 0.1 and 10 mA/cm² compare in this way with our results at 1.0 mA/cm²:

pH	Current efficiency (%)			
	0.1	1.0		10
		60V	150V	
4-5	24	74	68	83
6-7	29	72	72	99
9	19	22	75	76

These figures are the percent of the total charge used for barrier oxide deposition. There was no significant gas evolution from the Al during anodization, so the balance of the charge presumably was used for Al dissolution.

Specimen capacitance was independent of pH. The 60V films had a capacitance in the range 2.16-2.22 μF and the 150V films were in the range 0.888-0.901 μF. From this we infer that the barrier layer thickness was independent of pH.

The hydrogen concentrations found in these films are summarized in Table III. The 150V pH 4 film was similar to the phosphate film. The high hydrogen concentration at a depth of 9 nm may not be a true measure of the concentration at that depth, but could be an artifact of surface contamination and surface roughness. Compared with the 150V pH 4 film, the 60V pH 4 and pH 7 films had 3-4 times higher hydrogen content throughout their thickness of about 70 nm. We do not know if the lower hydrogen content in the interior of the 150V pH 4 film as compared with the 60V pH 4 film is a true effect of film growth or merely due to specimen variation.

Table III. H concentrations in tartrate films

a. 60V films			
Depth (nm)	pH 4.3	C_H (10^{20} atoms cm^{-3}) pH 7.1	pH 9.1
17	7.1	4.2	115-132
37	—	—	36-100
56	9.9	6.7	28
75	<1	1.0	10
94	<1	<1	3.0
114	—	—	2.5

b. 150V films*			
Depth (nm)	pH 4.0	C_H (10^{20} atoms cm^{-3}) pH 6.3	pH 9.2
9	42	407-670	250-460
17	5.9	202-282	84-247
26	2.0	45-121	6-17
39	2.7	1.7-15.6	<1
83	2.4	3.8	1.7

* See Fig. 3.

The 60V pH 9 film had a surface layer greatly enriched in hydrogen. Repeated measurements at the same point in the film showed an apparent decrease of H with time indicating the ion beam was causing some of the hydrogen to be lost from the film. This behavior may be indicative of very weakly bound hydrogen, e.g., as molecular water, which can be lost to the vacuum system. At greater beam penetration the H content fell to low values typical of the other amorphous barrier films; but this occurred at apparent film depths of 94-114 nm. Since the barrier layer thickness appears to be about 70 nm for all the 60V films (based on capacitance), it seems likely that the pH 9 film had a nonbarrier deposit on top of the barrier film.

Because of the ease with which hydrogen appeared to be lost from this surface, the 150V films were analyzed several times at each ^{15}N beam energy and repositioned for each increase in beam energy to expose a fresh area. The outer part of the pH 9 film had a very high H content that varied during the analysis in the same way as the 60V pH 9 film. The 150V pH 6 film exhibited the same behavior and it seems that both films can be described as having H-rich nonbarrier deposits on their outer surface. All the 150V film analyses are shown in Fig. 3.

The 150V films were stripped from the metal substrate and examined by transmission electron microscopy. The pH 9 film showed dark patches arranged in a linear pattern [Fig. 4(a)], and at high magnification a high density of fine pores was seen [Fig. 4(b)]. The pH 6 film had about the same density of linear patches but no porosity was evident. The pH 4 film had dark patches on some areas but much of the film was free of this feature. The patches may be $Al(OH)_3$ precipitated from solution onto barrier oxide. The patches and porous oxide are certainly not characteristic of barrier oxide and it seems likely that they are the H-rich outer regions. Other surface regions may also be H-rich but free of distinctive structural features.

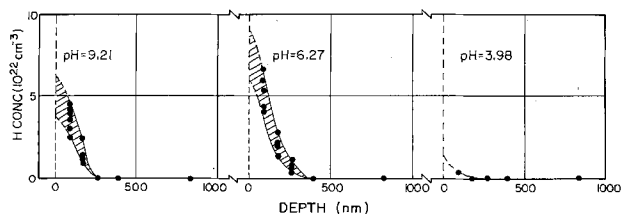


Fig. 3. Hydrogen profiles of 150V anodic Al_2O_3 films formed in tartrate electrolytes at different pH. The cross-hatched area indicates the range over which the hydrogen content decreased during the analysis at a given depth. See text.

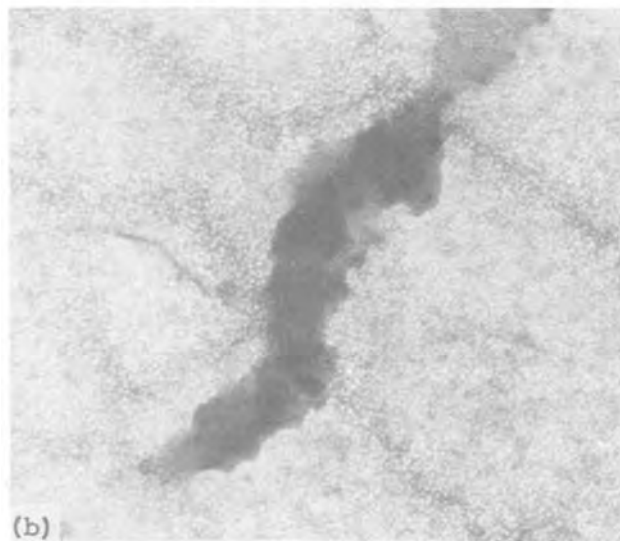
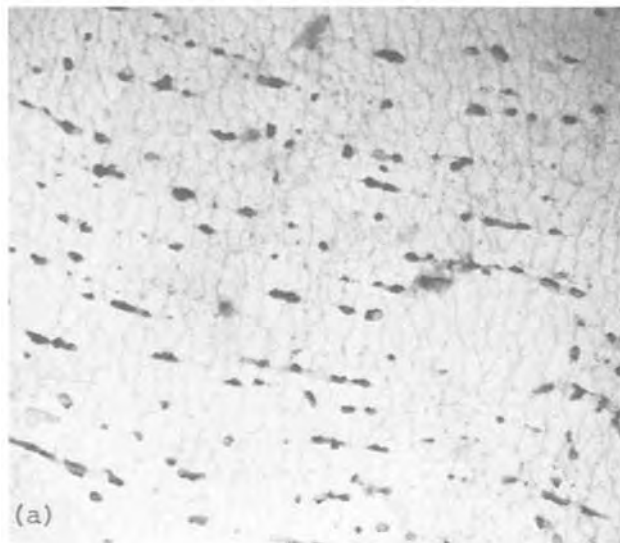


Fig. 4. Transmission electron micrographs of 150V pH 9 tartrate film at (a) 8,000 \times and (b) 75,000 \times magnification.

SIMS analysis of 60V tartrate films (8) also indicated an increase in film thickness at alkaline pH, but the profile of H-containing species was relatively flat across the layer formed at pH 9.9. Only at pH 10.6 was the outer film enriched in hydrogen, but the difference between surface and barrier oxide concentrations was no more than fivefold, far less than the hundredfold difference determined from nuclear resonance.

It is difficult to make a critical comparison of the two analytical techniques from these data because films formed in tartrate tend to be complex and perhaps difficult to reproduce. For example, Brock and Wood (5) observed $\sim 10^9$ pores cm^{-2} in films formed at pH 5, whereas we saw no pores in films formed at pH 4 or pH 6. Brock and Wood observed a decreased a-c resistivity in the surface region of films formed at pH 7, 10 mA/cm 2 , but Richardson, Wood, and Breen (22) saw no unusual resistivity change with films formed and measured at presumably identical conditions. Finally, in this present work we have the example of a 60V pH 7 barrier film growing at 22% current efficiency whereas a 150V film grew at 75% efficiency. A suitable comparison of the two techniques could only be done by making the measurements on the same specimens.

Hydrous oxide films.—The reaction of aluminum with boiling water produces a film of pseudoboehmite, a poorly crystallized form of boehmite (γ - AlOOH) containing excess water. The film typically has a composition of $\text{Al}_2\text{O}_3 \cdot 2.1 \text{H}_2\text{O}$, a specific density of 2.44 g cm^{-3} (19), and a duplex structure consisting of a dense inner layer and a porous fibrillar outer layer (23).

Al foil specimens were reacted with boiling water for either 5 or 30 min and, from the weight gain and previous thickness measurements on similar films (23), we estimated the structure to be the following:

Reaction time (min)	Avg film wt. ($\mu\text{g}/\text{cm}^2$)	Thickness (nm)	
		Inner	Outer
5	64.8	100	200-300
30	107.2	220	300

The H-profiles of these samples are shown in Fig. 5 and 6.

Before examining the profiles it will be helpful to first consider the effect of the film structure on the results. As the ^{15}N beam passes through the porous layer it loses energy only when in the solid phase, so it will always reach the resonance energy within the solid, and the correct value of dE/dx for calculating C_H is the local energy loss, which is the value shown for pseudoboehmite in Table I. Thus, the C_H values calculated for the porous layer will be specific concentrations for the solid phase in that layer and not bulk concentrations. Based on these same considerations, it can be seen that this profiling technique does not give the true thickness of the porous layer but will give a thickness equivalent to the weight and the specific density of pseudoboehmite. In other words, this technique does not distinguish between a porous structure and a dense structure if the solid phase in the two structures has the same composition and density.

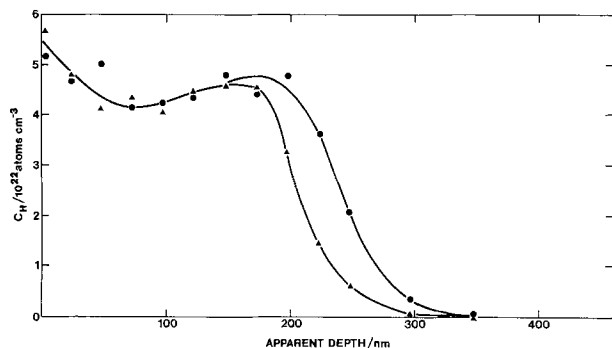


Fig. 5. The distribution of hydrogen in the surface film formed on Al during a 5 min reaction with boiling water. Results with two specimens are shown.

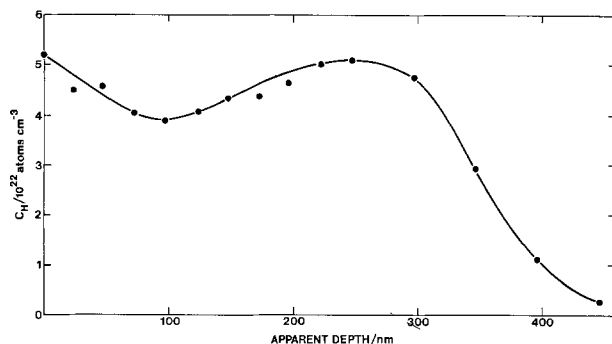


Fig. 6. The distribution of hydrogen in the surface film formed on Al during a 30 min reaction with boiling water.

Figures 5 and 6 show that the hydrogen content of the pseudoboehmite films was $4\text{--}5 \times 10^{22}$ atoms cm^{-3} . This is in excellent agreement with the figure of 4.5×10^{22} calculated from the average film composition and a specific density of 2.44 g cm^{-3} (19).

The H-profiles show a gradual decrease towards the metal surface whereas micrographs of film cross sections show this interface to be quite sharp (23). We think this tail is due to the effect of the rough, uneven texture of the outer film surface. Surfaces of constant ^{15}N beam energy will approximately follow the contour of the outer surface. As the beam energy is increased so that the resonance reaction occurs deeper in the film, a point is reached where for part of the specimen surface the resonance energy level is within the metal rather than the film. This marks the beginning of the tail, and further increase in beam energy increases the fraction of metal at the resonance energy.

The half-height of the tail gives an estimate of the position of the oxide-metal interface. Since the corresponding film thickness is for a layer free of porosity, we can compare the weight of pseudoboehmite calculated from this thickness with the actual film weight. For the 5 min boil films the average apparent thickness is 226 nm, and for the 30 min film it is 358 nm. The corresponding film weights are 55 and $87 \mu\text{g}/\text{cm}^2$, which are 15-20% lower than the measured values given earlier.

Thus, the rough porous nature of the outer film does not hinder an accurate measure of the H concentration of the film material, but it does effectively degrade the depth resolution for measurements inside the sample.

Composite oxide layers.—The H-profiles of 220V composite oxide films, before and after a relaxation, are shown in Fig. 7. The abscissa is presented as beam energy rather than a calculated depth.

For these films the pseudoboehmite tail extends into the barrier oxide and from the beam energy at half-height an apparent thickness of 167 nm was calculated for the hydrous oxide. This is about 60 nm less than the initial thickness because some of the hydrous oxide loses water and is converted to barrier Al_2O_3 (23, 24). From data reported for a 5 min boil + 175V composite oxide (24), it was calculated that 70 nm of pseudoboehmite was transformed, in reasonable agreement with these results.

No information can be obtained about H content in the barrier oxide close to the hydrous oxide. At greater depths C_H drops to a steady value in the range $2\text{--}3.5 \times 10^{20}$ atoms cm^{-3} for the specimen that was not relaxed. This is the same concentration as in the amorphous barrier oxides (Tables II and III);

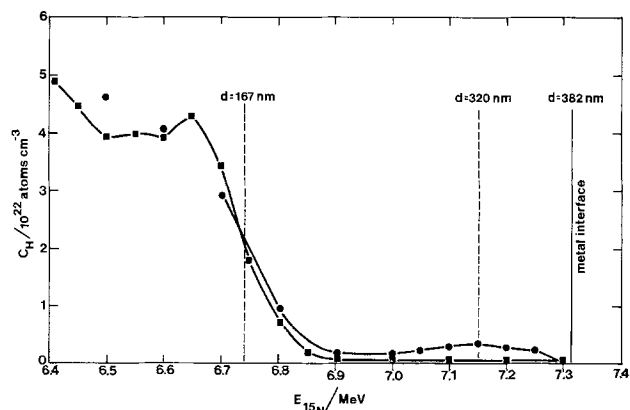


Fig. 7. The distribution of hydrogen in the composite films formed by 5 min reaction with boiling water and then anodizing to 220V. The hydrogen profiles are given both before (■) and after (●) inducing the "relaxation."

although the composite barrier layer is crystalline γ - Al_2O_3 .

After a relaxation there was a well-defined peak centered at 153 nm from the hydrous/barrier interface. (This depth was calculated using the dE/dx for crystalline barrier oxide shown in Table I and the half-height beam energy of 6.74 MeV as the reference plane.) The peak region is shown more clearly in Fig. 8. The peak width is broadened because of the spatial distribution of beam energy caused by outer surface roughness. The integrated area under the peak (which is not affected by the surface roughness) corresponds to $\sim 2.7 \times 10^{16}$ atoms cm^{-2} . A reformation removed the peak but left a residual hydrogen content slightly higher than in the film after formation. See Fig. 8.

The H-profile did not define the barrier oxide/metal interface because hydrogen was still detected at depths that must have been well within the metal. For example, ellipsometric measurements have shown this barrier layer thickness to be 215 nm (15) and this was used in Fig. 7 to delineate the oxide/metal interface. With the reformed specimen, C_H of 4.1 and 3.7×10^{20} atoms cm^{-3} were measured at beam energies of 7.43 and 7.65 MeV, and from the scale in Fig. 7 it can be seen that the resonance energy must have been within the metal. This situation did not arise with the amorphous barrier films where at beam penetrations greater than the oxide thickness the gamma ray yield dropped to the background level. This phenomenon may be due to preferential hydration along grain boundaries and at impurity sites during the boiling water reaction.

These results are in excellent agreement with a proposed model of Alwitt and Dyer (1) that explains the electrical instability that accompanies relaxation as the result of penetration of water into voids deep within the barrier oxide, while reformation subsequently fills the voids with anodic oxide and consumes the water. The H-profiles presented here are the first direct evidence for water penetration and accumulation in the barrier layer.

The area under the H peak corresponds to 0.4 μg cm^{-2} H_2O in the film, which compares with 0.6-1.5 μg cm^{-2} calculated from reformation charge with the assumption that the void volume occupied by the reformation oxide had been completely filled with water. Most of the reformation charge is consumed at low voltage, so it was inferred that the water accumulated near to the metal interface, in the lower $\sim 30\%$ of the barrier layer (1). This location of the voids is supported by the present results.

Summary

The ^{15}N nuclear resonance reaction can be used to measure H in Al_2O_3 at levels as low as 1×10^{20} atom cm^{-3} . The method easily gives quantitative results accurate to 10% and, because it measures H inside solids without the removal of the surface, it is free of ambient contamination effects.

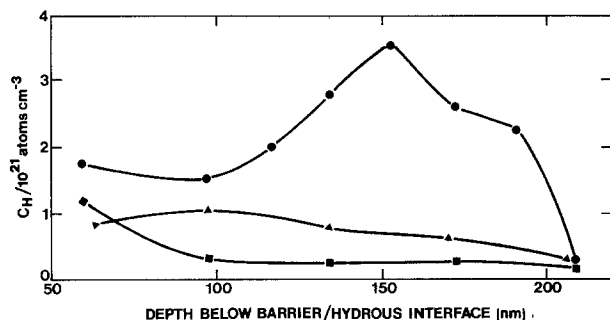


Fig. 8. Same specimen as in Fig. 7 but showing details of H-content in peak region; as formed (■), after inducing "relaxation" (●), and after reanodization (▲).

Ordinary amorphous anodic oxides, such as films formed in phosphate or glycol-borate electrolytes, contain only trace amounts of hydrogen. The G-B film had the lowest H content, but additional measurements would have to be made to test the significance of the connection between H content of the film and water content of the anodization electrolyte.

Films formed in tartrate electrolytes tended to have H-rich surface deposits, presumably containing precipitated $\text{Al}(\text{OH})_3$. The deposits had no effect on the barrier layer and were not detected by electrical measurements. These solutions have been used by different investigators to produce anodic oxides whose properties are then studied and presented as perhaps being typical of the general class of anodic Al_2O_3 layers. The tendency to precipitation from solution and incipient porosity suggests that caution should be exercised in using these films, as only layers formed at 100% current efficiency can be free of these effects.

There is a problem with depth measurement in films that are not compact and of uniform thickness. This was illustrated by the pseudoboehmite film, where the rough outer layer introduced an energy dispersion that was present throughout the specimen thickness. Even so, it was possible to learn that there is only a small variation in composition throughout the film.

The H-profiles of the composite oxides gave detailed information on the composition of a very complex structure and provided the first direct experimental evidence verifying previous ideas about the cause of field strength instability of the barrier layer.

Acknowledgment

The authors are grateful to Mrs. Judith Clini for assistance in preparing the specimens used in this work. This research was supported in part by U.S. Department of Energy Contract No. EY-76-C-02-3074.

Manuscript submitted May 23, 1979; revised manuscript received Aug. 3, 1979.

Any discussion of this paper will appear in a Discussion Section to be published in the December 1980 JOURNAL. All discussions for the December 1980 Discussion Section should be submitted by Aug. 1, 1980.

Publication costs of this article were assisted by Yale University.

REFERENCES

- R. S. Alwitt and C. K. Dyer, *Electrochim. Acta*, **23**, 355 (1978).
- T. P. Hoar and N. F. Mott, *J. Phys. Chem. Solids*, **9**, 97 (1959).
- T. P. Hoar and J. Yahalom, *This Journal*, **110**, 614 (1963).
- M. A. Heine and M. J. Pryor, *ibid.*, **110**, 1205 (1963).
- A. J. Brock and G. C. Wood, *Electrochim. Acta*, **12**, 395 (1967).
- G. A. Dorsey, Jr., *This Journal*, **113**, 169 (1966).
- T. Takamura, H. Kihara-Morishita, and U. Moriyama, *Thin Solid Films*, **6**, R17 (1970).
- G. A. Dorsey, Jr., *This Journal*, **119**, 1227 (1972).
- M. F. Abd Rabbo, J. A. Richardson, and G. C. Wood, *Electrochim. Acta*, **22**, 1375 (1977).
- W. A. Lanford, H. P. Trautvetter, J. Ziegler, and J. Keller, *Appl. Phys. Lett.*, **28**, 566 (1976); W. A. Lanford, *Nucl. Instrum. Methods*, **149**, 1 (1978).
- W. A. Lanford and H. J. Rand, *J. Appl. Phys.*, **49**, 2473 (1978).
- M. H. Brodsky, M. A. Frisch, J. F. Ziegler, and W. A. Lanford, *Appl. Phys. Lett.*, **30**, 561 (1977).
- W. A. Lanford, P. H. Schmidt, J. M. Rowell, J. M. Poate, R. C. Dynes, and P. D. Dernier, *ibid.*, **32**, 339 (1978).
- W. A. Lanford, K. Davis, P. LaMarche, T. Laursen, R. Groleau, and R. H. Doremus, *J. Non-Cryst. Solids*, In press.
- C. K. Dyer and R. S. Alwitt, *Electrochim. Acta*, **23**, 347 (1978).

16. L. C. Northcliffe and R. F. Schilling, *Nucl. Data Tables*, **A1**, 233 (1970), with corrections suggested by J. S. Foster *et al.*, *Nucl. Instrum. Methods*, **136**, 349 (1976).
17. W. J. Bernard and J. W. Cook, *This Journal*, **106**, 643 (1959).
18. J. F. Ziegler *et al.*, *Nucl. Instrum. Methods*, **149**, 19 (1978).
19. W. J. Bernard and J. J. Randall, Jr., *This Journal*, **107**, 483 (1960).
20. Y. Shibata, H. Takahashi, and M. Nagayama, Private communication.
21. J. J. Randall, Jr. and W. J. Bernard, *Electrochim. Acta*, **20**, 653 (1975).
22. J. A. Richardson, G. C. Wood, and A. J. Breen, *Thin Solid Films*, **16**, 81 (1973).
23. T. Kudo and R. S. Alwitt, *Electrochim. Acta*, **23**, 341 (1978).
24. R. S. Alwitt and W. J. Bernard, *This Journal*, **121**, 1019 (1974).

Nonsimultaneous Place Exchange: A Microscopic High Field Transport Mechanism in Solids

A. T. Fromhold, Jr.*

Department of Physics, Auburn University, Auburn, Alabama 36830

ABSTRACT

A nonsimultaneous place-exchange mechanism is postulated whereby ionic motion takes place by means of elemental excitations labeled "hopons." A hopon is defined to be the thermally activated electric field-modified motion of a localized place exchange between oppositely charged ionic constituents in a compound. The virtual defect associated with hopon motion is considered to be a highly localized disturbance which jumps statistically with time from place to place in the medium, although in certain cases it may be a somewhat more extended wavelike disturbance which propagates with a finite velocity through the medium. These two possibilities are referred to respectively as "noncollective" and "collective" hopon transport mechanisms. Some of the ramifications of hopons for the formation of anodic oxides on metals are examined, including consideration of where the new oxide layers are formed, the relative transport numbers for anions and cations through the oxide, the preservation of microscopic order in the anion and the cation sublattices in the oxide, and the energies and the kinetics for anodic oxide growth.

The classic mechanisms which have been proposed for ionic transport through insulators involve the concepts of lattice vacancies or ion interstitials (1-6). For metal oxides and similar compounds such as the alkali halides, the lattice vacancies or interstitials may involve either the cation species or the anion species, or both, depending on the system. As one example, in the superionic conductor α -AgI it has been concluded that ionic transport occurs primarily by the motion of silver ions in an essentially perfect anion lattice (7).

Other types of point defect motion have also been postulated in the literature. For example, Seitz (8) envisioned transport in metals by a lattice imperfection motion termed an interstitialcy that is the inverse counterpart of a lattice vacancy. Such motion occurs when an interstitial atom jumps into a normal lattice site while simultaneously forcing the atom which is there into a neighboring interstitial site. The activation energy for this type of motion was estimated to be less than that required for the simple hopping of interstitials between neighboring interstitial sites. Weber and Friauf (9) have interpreted their radioactive tracer data on the diffusion of Ag in single crystals of AgCl in terms of the interstitialcy motion of Ag.

Zener (10) also put forth a novel idea for diffusion in metals, namely, the simultaneous rotation of several metal atoms. This has been termed the "ring" mechanism.

For independent thermally activated motion of cation or anion species by any of the above mechanisms, a small difference in activation energies between possible mechanisms leads to the prediction of large differences in the mobilities. This leads to the conclusion that the relative transport numbers for cations and

anions should be nearly 0 and 1, or else 1 and 0, as the case may be. (For example, activation energies of 1.0 and 1.1 eV lead to Boltzmann probability factors of 1.58×10^{-17} and 3.30×10^{-19} at a temperature of 300°K, so the corresponding diffusion coefficients will differ by a factor of 48.)

Although the independent motion of point defect species is, without doubt, a viable concept, there is experimental evidence that for particular systems some other mechanism may be more important. For example, transport numbers for cations and anions are sometimes found to be of the same order of magnitude, despite the high improbability that the vastly different sized and chemically unlike components would have essentially the same activation energy for motion through the medium. One example is the anodic growth of Ta₂O₅ on parent tantalum metal, for which Pringle (11) finds by means of marker experiments utilizing radioactive noble gases that the transport numbers of the cation species and the anion species are 0.24 and 0.76, respectively. One is forced by such experimental results to search for some mechanism involving a correlated motion of cations and anions through the lattice.

One concept of a correlated motion of cations and anions has been proposed by Sato and Cohen (12) to explain their experimental observations of logarithmic growth of anodic oxide films on iron. The Sato-Cohen mechanism is based on the earlier place-exchange concept of Lanyon and Trapnell (13) for a permutation of cation and anion positions in a dipolar surface layer as illustrated in Fig. 1. Sato and Cohen visualized simultaneous place exchanges of this type along an entire line of atoms extending through a three-dimensional layer. Their development involves the relative probability for the simultaneous flipping of all electric dipoles extending through the layer. The activation energy for individual place-exchange events de-

* Electrochemical Society Active Member.

Key words: transport, mobility, diffusion, anodization, oxidation.

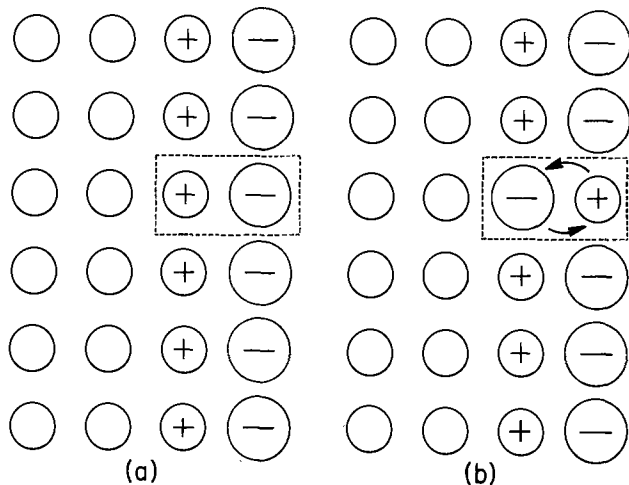


Fig. 1. Place exchange representing a permutation of cation and anion positions in a dipolar surface layer. (a) Before place exchange. (b) Configuration after place exchange.

duced by comparison of this model with the experimental data was about 3.5 kcal/mole, or equivalently, 0.15 eV. Brusić (14) has pointed out that this is probably too low by about an order of magnitude.

It recently occurred to me (15) that there is an alternative to the simultaneous place-exchange mechanism of Sato and Cohen which leads to a more realistic value for the activation energy. This alternative is a nonsimultaneous place-exchange (or hopon) mechanism, in which individual place-exchange events occur sequentially in time (see Fig. 2) along a chain of dipoles extending through the medium (16).

To illustrate the mechanism we chose the specific system of an oxide overlayer on a metal (17, 18) and follow individual oxygen atoms from their initial chemisorbed state on the oxide surface until they become incorporated as part of the growing oxide layer and subsequently as the oxide continues to grow thicker on the metal. Alternatively, we could think of affixing appropriate ion exchange electrodes at the interfaces of a static ionic conducting layer and applying a voltage (19, 20). In fact, the presently considered mechanism will be most likely to occur in the case of applied voltages leading to very large electric fields, as for example, in the case of anodic oxidation (21-25) where fields in the 10^5 - 10^6 V/cm range are common.

One-Hopon Mechanism

The physical model.—Let us examine our problem by carrying out a gedankenexperiment in which we follow the time evolution of a sequence of correlated (but nonsimultaneous) place-exchange events in an oxide layer. Consider first of all a single place exchange to occur at the surface of a stoichiometric oxide covered with some adsorbed oxygen species at the oxide-oxygen (or oxide-solution) interface. That is, a cation exchanges position with an adsorbed oxygen thereby changing the physical picture from (a) to (b) in Fig. 2. It can be noted from (b) that, as a consequence of this place exchange, at least two negative charges are side-by-side. (In one dimension, there are two, but in three dimensions, the number will be greater.) This constitutes an increase in the Coulomb energy of the configuration of the order of $e^2/4\pi\epsilon_0 d_0$, with d_0 being the atom spacing.¹ A more accurate estimate would involve a consideration of the change in the Coulomb energies of interaction with all other ions in the solid, which for a crystalline lattice would involve a type of Madelung sum (26). The static dielectric constant ϵ in the Coulomb energy expression

¹ The magnitude of the electronic charge is denoted by e ; the charge on the electron is then $-e$. The ionic charge is denoted by Z_e , where Z includes the sign of the ionic charge.

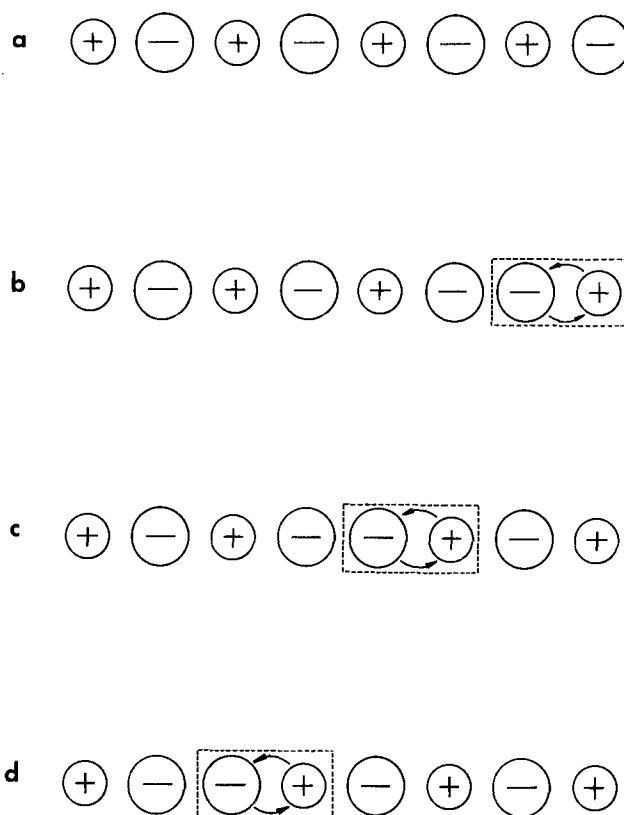


Fig. 2. Sequential nonsimultaneous place-exchange events which constitute hopon transport. (a) Before place exchange. (b) Configuration after the first place-exchange event. (c) Configuration after the second place exchange. (d) After the third place exchange.

for nearest neighbor ions is not really appropriate because the side-by-side charges are not separated by a macroscopic region of oxide which can polarize and thus provide the necessary electrostatic screening. In addition, the increase in the energy of the system required for the place exchange will actually be different from this Coulomb value, because there will be a modified chemical bonding of the pair of oxygen and metal ions with the surrounding atoms in both the oxide and the adsorbed oxygen in the new configuration (3). The amount of this modification will depend to a large extent on the energy of formation and the degree of covalency of the oxide, but the value and even the sign of the contribution are difficult to ascertain because there are contributions of the opposite sign which are of the same order of magnitude. The amorphous state of some insulator compounds constitutes a further uncertainty in the defect energies. For a discussion of some of the various factors involved in the semiquantitative calculation of defect energies, see Kröger (27, 28). Actually a difficult quantum-mechanical calculation would be required to carry out this part of the problem properly.

In lieu of a quantum-mechanical calculation involving atomic and molecular wave functions and taking into account the disorder within the region, let us simply use the Coulomb energy expression given above as some reasonable estimate of the free energy increase U_H required for this initial place-exchange event. That is, U_H is the formation energy of a single place-exchanged pair (referred to as a hopon) in the oxide. A reasonable order-of-magnitude average value for the static dielectric constant ϵ is $10\epsilon_0$, where ϵ_0 is the permittivity of free space. For $\epsilon \approx 10\epsilon_0$, the Coulomb energy expression leads to an estimate of the order of 0.35 eV for U_H in a one-dimensional system; the values for two- and three-dimensional systems are larger because of the greater number of nearest neigh-

bor ions. An activation energy W_H will also be involved due to lateral interactions, but first of all let us consider the equilibrium number of such place-exchanged pairs per unit area of the oxide surface. Considering a submonolayer coverage of the oxide surface denoted by the fraction θ , then for n_{cations} per unit surface area of the oxide we can expect the number $n_{\text{pairs}}^{(o)}$ of place-exchanged oxygens to be

$$n_{\text{pairs}}^{(o)} = \theta n_{\text{cations}} \exp(-U_H/k_B T) \quad [1]$$

For $n_{\text{cations}} = 6 \times 10^{15}/\text{cm}^2$, $\theta = 0.5$, $U_H \approx 0.35$ eV, and $T = 300^\circ\text{K}$, we find that $n_{\text{pairs}}^{(o)} \approx 4 \times 10^8/\text{cm}^2$. Since $n_{\text{pairs}}^{(o)}/n_{\text{cations}} \approx 7 \times 10^{-8}$, at least in this estimate, the mutual interaction between the place-exchanged pairs in the surface layer can be neglected in a first-order calculation.

At this point in our gedankenexperiment, let us consider a second place-exchange event which takes place within the oxide below one of the first place-exchanged pairs [see (c) in Fig. 2]. It is interesting to note that this second event involves neither member of the first pair. Although an activation energy W_H will be required for this second event, in the lowest order there will be no free energy change of the system. This is due to the fact that the Coulomb energy of the side-by-side (or nearest neighbor) charges of the same sign after the second flip (*i.e.*, place-exchange event) is the same as that of the corresponding configuration of charges of the same sign before the second flip, and likewise the modified bonding energy of the medium is essentially the same, though the position of the modified chemical bonds has been displaced in the medium (In higher order there will be some differences in the Madelung energy which may be neglected in view of the major uncertainties already discussed.)

Let us consider more closely the physical situation at this point in our gedankenexperiment. On balance, we have replaced one cation in the lattice by one anion, so we have a local nonstoichiometry, a local deviation from charge neutrality, and a localized density deviation. Any one of these three would constitute a "defect" in the amorphous (or crystalline) medium. Because the motion of this defect is not associated with any particular anion or cation, but instead, involves many such cations and anions in sequence along a path in the medium, such a defect is a "virtual defect" in the medium. We refer to this particular type of virtual defect as the "hopon." (The well-known lattice vacancy is likewise a virtual defect, since its motion similarly is unassociated with any particular ion, but instead, involves many different ions in sequence in its path through the medium.) The net charge deviation associated with the hopon is, at minimum, the charge on the anion; it can also be argued that the accompanying absence of a cation leads to an additional contribution to the effective charge having the same sign as that of the anion charge and having the magnitude of the cation charge. Let us denote the effective charge of this virtual defect by q_H . With an externally applied forward electric field E , there is an electric force $q_H E$ which acts on the virtual defect. The electric force tries to drive the virtual defect toward the metal interface.

From another viewpoint, the second place-exchange event described above leads to the movement of one cation through one atom distance d_o in the direction of the field, and simultaneously the event leads to the movement of one anion through one atom distance d_o in the opposite direction to that of the field. The change in electric potential energy $\Delta\mathcal{E}_P$ associated with the second place-exchange event is thus

$$\Delta\mathcal{E}_P = Z_c e E d_o + Z_a e E (-d_o) = (Z_c - Z_a) e E d_o \quad [2]$$

where $Z_c e$ is the charge of the cation and $Z_a e$ is the charge of the anion. Recognizing that this energy must

be the same as that denoted by $q_H E d_o$, we again reach the conclusion that the charge magnitude of the hopon is the sum of the magnitudes of the charges $Z_c e$ and $Z_a e$, namely

$$q_H = (Z_c - Z_a) e = (|Z_c| + |Z_a|) e \quad [3]$$

The equality involving the magnitudes in Eq. [3] follows because the anion and the cation species are of opposite sign. If, on the other hand, one considered the possibility of an interchange of ions of the same type, as, for example, in the ring diffusion mechanism of Zener (10) for elemental metals, the charges of the two ions would be identical so that q_H would be zero. This clarifies the point that hopon motion in an ionic compound will be strongly promoted by an applied electric field even though there is no analogous effect of a field on the diffusion rate of cations in an elemental metal (6).

The conclusion reached by means of the above arguments leading to Eq. [3] is that the free energy is lowered by an amount $q_H E d_o$ by the second place-exchange event. The activation energy W_H is likewise lowered. For example, if the maximum in the activation barrier is presumed to occur when the exchange is half completed, as for example in the case of exchange by means of a simple 180° rotation of a dipolar molecule, then to first order the exchange barrier maximum is reached when each member of the pair has moved a distance $a = \frac{1}{2} d_o$. Considering the distance d_o to be parallel to the direction of the field, the activation energy barrier maximum W_H is lowered by an amount $\Delta W = q_H E a$ in the forward direction by the electric field. Thus the net barrier for forward motion of the virtual defect is

$$W^{(f)} = W_H - q_H E a \quad [4]$$

If the exchanged pair is at angle θ with respect to the field, as might be the case for a three-dimensional oxide, then from elementary physics it is easily seen that this energy takes the form

$$W^{(f)} = W_H - q_H E a \cos \theta = W_H - q_H \vec{E} \cdot \vec{a} \quad [5]$$

Motion in the reverse direction would be quite analogous, except the displacement would be $-d_o$ instead of d_o with respect to the field direction. To first order the activation barrier for reverse motion of the virtual defect will be raised by the amount $q_H E a \cos \theta$; the net barrier for reverse motion of the virtual defect is thus

$$W^{(r)} = W_H + q_H \vec{E} \cdot \vec{a} \quad [6]$$

Formal similarity to the hopping model.—One cannot help but note the striking formal similarity between the activation energy expressions given by Eq. [5] and [6] which have been deduced for the presently considered nonsimultaneous place-exchange event and the activation energy expression for the movement of a vacancy or an interstitial in the hopping model (17, 18, 21, 29). The present activation energy expression deduced for nonsimultaneous place exchange is, in contrast, markedly different from the activation energy for the simultaneous place-exchange model of Sato and Cohen (12). This difference can be shown to be particularly significant insofar as it leads to a different functional dependence on oxide thickness with an attendant markedly different kinetics for growth of the layer.

Although the motion of the hopon, as we have developed above, is mainly due to the electric field force, a gradient of hopons leads also to a net motion of hopons along the gradient. Thus the formal similarity between nonsimultaneous place exchange and the defect hopping picture can be carried quite far. In fact, the role of concentration gradients (17, 29), space-charge effects (18, 30), stress effects (31, 32), and electric field effects (17, 18) carry over *in toto*, as

indicated in Appendixes A through D. The concepts of interfacial equilibrium and transport-limited rates are also apropos under the proper conditions. The shape of the kinetic curves will therefore be similar to that deduced (15, 18) on the basis of the hopping model. Nevertheless, there remain two areas where great differences exist between the nonsimultaneous place-exchange and the hopping models. The first is that of the microscopic energies involved in the formation and movement of the defects: Place-exchange energies will be different from the corresponding energies for vacancies and interstitials, though a quantum calculation taking into full account the mechanistic differences would be quite involved from a calculational standpoint. Second, the microscopic reordering of individual tracer cations and anions in the already formed oxide during growth of new oxide is quite different for the two models.

Hopon chains.—It has already been pointed out that neither member of the pair of ions involved in the initial place-exchange event is involved in the second place-exchange event. Whereas a radioactive (or similarly tagged) oxygen ion moving a distance of two lattice spacings by interstitial motion in a direction perpendicular to the oxide-oxygen interface would be found a depth of $2d_0$ below this interface, the motion of the hopon through a distance $2d_0$, when it initiates with a radioactive oxygen ion at the oxide interface, would result in the displacement of the radioactive ion to a depth of only d_0 below the interface.

Continuing now with our gedankenexperiment described previously, a third place-exchange event occurring in line with, and immediately below, the first two place-exchanged pairs would involve essentially the same activation energy as the second pair, but it would lead to no further displacement of the tagged oxygen ion [see (c) and (d) in Fig. 2], even though the total distance of transport of the hopon in a direction perpendicular to the surface would then be greater by d_0 .

In the present model of nonsimultaneous place exchange, each such place-exchange event is correlated in time and position with the preceding and succeeding place-exchange events; however, the place-exchange events do not occur simultaneously as they do in the case of the simultaneous place-exchange mechanism described by Sato and Cohen (12). Nevertheless, simultaneous and nonsimultaneous place exchanges both lead to the same microscopic arrangement of individual ions in the layer.

Continuing the above gedankenexperiment involving successive place-exchange events, one can visualize successive exchanges which follow a one-dimensional path of cations extending through the oxide to the metal interface. This leads us to the conclusion that the radioactive tracer oxygen ion would still have moved only a distance of d_0 , even though the hopon would have moved all of the way through the oxide.

One result of this sequence of place-exchange events along a path of ions extending from the oxygen interface to the metal interface is the transport of one oxygen anion from the oxygen interface through the oxide to the metal interface, which anion can react with the metal to form more oxide. The sequence of events involving the creation of the hopon, the subsequent movement of the hopon through the medium, and the annihilation of the hopon at the end of its journey, will be referred to as a "hopon chain," or simply a "chain." This sequence of events (the chain) is depicted in Fig. 3. The last step, namely, the chemical reaction with the metal, can likewise be viewed as a place-exchange event, with the oxygen anion exchanging places with a metal cation in the metal surface. This latter event differs from the very first place-exchange event in that some free energy due to Coulomb forces is now liberated instead of absorbed. Interfacial equilibrium at the metal interface should therefore be a very good approximation even during rapid growth of the layer. In the interest of characterizing the last step quantitatively, we can designate the energy released as U_A , the subscript A indicating annihilation of the hopon which was created at the oxide-oxygen interface. The difference $U_A - U_H$ is a quantity related to the free energy U_{oxide} liberated in the formation of the oxide.

In the case of externally applied voltages, the question of charge balance during hopon motion is easily resolved, since charge can then be transported by electrons through the external circuit employed to set up the electric field in the oxide. This is, whatever charge is transported through the oxide due to motion of hopons can be equivalently transported through the external circuit by electrons to maintain a uniform steady-state loop current in the closed electrical circuit. Since any net mass current due to the motion of hopons is accompanied by an attendant charge current, hopon transport will in general require either such externally applied voltages, or else will require a corresponding electronic current through the oxide itself equivalent to that given by the coupled currents condition (17) in thermal oxidation.

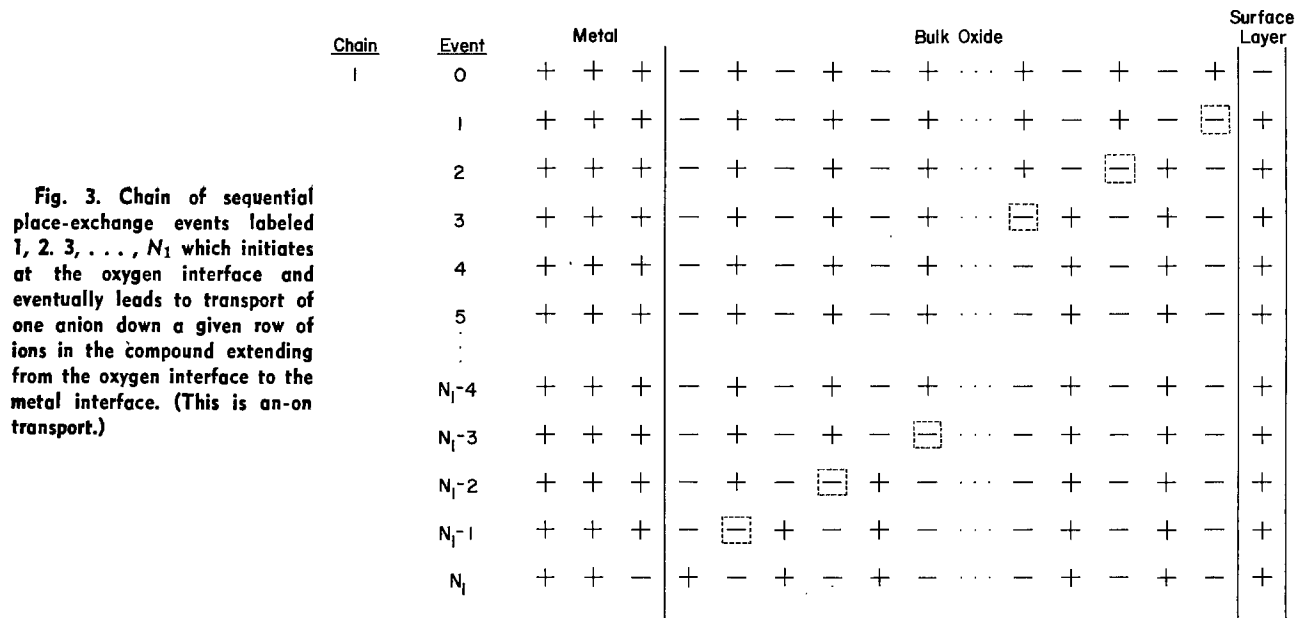


Fig. 3. Chain of sequential place-exchange events labeled 1, 2, 3, ..., N_1 which initiates at the oxygen interface and eventually leads to transport of one anion down a given row of ions in the compound extending from the oxygen interface to the metal interface. (This is an-on transport.)

Energies involved in bulk-limited place exchange.—

To review the energies which have been introduced, there is first of all the formation energy U_H of the hopon, then there are the activation energies $W^{(f)}$ and $W^{(r)}$ for forward and reverse place exchange leading to forward and reverse motion of the hopon through the amorphous or crystalline medium, and last there is the annihilation energy U_A of the hopon. To the free energies U_H and U_A might be added the electrostatic potential energies $q_H E_o d'$ and $q_H E_N d''$ due to the applied electric field, where d' and d'' represent in the present situation the atomic distances at the metal-oxide and the oxide-oxygen interfaces and the quantities E_o and E_N represent, respectively, the electric fields at these interfaces. [Although d' and d'' may be the same as d_o , the lattice constant within the oxide, we allow for the possibility that these lattice parameters at the interfaces can be different because of the different number of chemical bonds at the interfaces. This has been treated by Young and Dignam (33).] However, such electric-field modifications in the interfacial free energies represent a higher order effect which frequently can be neglected. The above energies represent the ones of primary interest for a nonsimultaneous place-exchange transport mechanism which is rate limited within the bulk three-dimensional oxide, with near equilibrium conditions prevailing at the two interfaces.

Possibility of rate limitation by place exchange at the interfaces.—Let us consider, on the other hand, the possibility that the bulk oxide is near equilibrium, with the interfaces representing the rate-limiting step for transport. Then the electrostatic free energy differences $\Delta G_P = q_H E d_o$ within the oxide (instead of the activation energy and the field modifications of such) become important. In addition, in this case the interfacial activation energy barriers and the field modifications $q_H E_o a'$ and $q_H E_N a''$ of such (instead of the free energies of place exchange at the interfaces) become quite important. The parameters a' and a'' are related to the hopping distances d' and d'' at the interfaces; to first order, $a_o' = \frac{1}{2} d'$ and $a_o'' = \frac{1}{2} d''$.

Microscopic order in the cation and anion arrays.—Let us now continue our earlier gedankenexperiment and ask what happens when a new series of place-exchange events takes place along the same path which the first virtual defect followed to the metal interface. To recall the physical situation at the end of the first chain, refer to the event labeled N_1 in Fig. 3. The initiation step in the second chain is depicted by the event labeled 1 in the center of Fig. 4. The next step in the second chain is the second place-exchange event depicted in chain 2 in Fig. 4, and the third and fourth place-exchange events in the second chain are likewise depicted in Fig. 4. It is interesting to note that a tagged tracer oxygen ion would have now moved a distance $2d_o$, which thereafter remains unchanged throughout the course of the second chain. Analogously, a tagged tracer metal ion in the metal surface participating in the two chains considered above would move a distance d_o in the direction of the oxide-oxygen interface at the end of the first chain, and would move an additional distance d_o in the same direction near the end of the second chain. (This can be deduced by studying the sequence of events depicted in Fig. 5.) A different tracer oxygen which adsorbs on the oxide at the site of origination of the second chain would move one unit (namely, d_o) toward the metal interface if it becomes involved in the initiation of the second chain (see Fig. 4). A second tagged metal cation in the metal surface directly underneath the first tracer metal cation involved in the first chain will participate in the second chain, moving one unit in the direction of the oxide-oxygen interface at the end of the second chain (see Fig. 5).

At Oxide-Oxygen Interface

Chain	Event	Bulk Oxide				Surface Layer	
		+	-	+	-	+	-
1	0	+	-	+	-	+	-
	1	+	-	+	-	□	+
	2	+	-	□	+	-	+
	3	□	+	-	+	-	+
	4	-	+	-	+	-	+
	5	-	+	-	+	-	+
	N	-	+	-	+	-	+
2	0	-	+	-	+	-	+
	1	-	+	-	+	-	□
	2	-	+	-	□	+	-
	3	-	□	+	-	+	-
	4	+	-	+	-	+	-
	5	+	-	+	-	+	-
	N	+	-	+	-	+	-
3	0	+	-	+	-	+	-
	1	+	-	+	-	+	-
	2	+	-	+	-	□	+
	3	+	-	□	+	-	+
	4	□	+	-	+	-	+
	5	-	+	-	+	-	+
	N	-	+	-	+	-	+

Fig. 4. Initiation of a series of sequential hopon chains (labeled 1, 2, 3) at the oxygen interface which lead to anion transport down a given row of ions in a compound, with the initiation of each chain leading to formation of new oxide at the oxygen interface.

Comparison of microscopic order for chains initiating at the gas interface with predictions of the hopping model.—Of very great interest is the order-preserving property of the nonsimultaneous place-exchange transport mechanism presently under consideration. Each successive chain initiating at the oxygen interface effectively marches each involved anion through one unit distance along the path toward the metal-oxide interface, and simultaneously marches each involved cation along the path through one unit distance toward the oxide-oxygen interface.

In contrast, consider the transport of other types of defect initiating at the oxygen interface in the hopping model. Each anion interstitial transported along a hopping path involves no individual movement of the ions in the already formed oxide; the new oxide formed as a consequence of transport to the metal interface is located at the metal interface, so it gradually shifts the layer of already formed oxide away from the metal interface. Each cation vacancy transported along a hopping path results in the shift of each cation on the path a distance of one unit toward the oxygen interface; the new oxide formed as a consequence of transport of the cation vacancy to the metal interface is formed at the oxygen interface. Thus, anion interstitial transport preserves the microscopic arrangements of both cations and anions within the already formed oxide, whereas cation vacancy transport preserves the microscopic arrangement of anions within the already formed oxide but shifts each cation along the path one unit nearer to the oxide-oxygen interface.

Initiation of chains at the metal interface and comparison of microscopic order with predictions of the hopping model.—Let us consider the alternate possi-

At Metal-Oxide Interface

Chain	Event	Metal			Bulk Oxide							
		+	+	+	-	+	-	+	-	+	-	
1	0	+	+	+	-	+	-	+	-	+	-	+
	1	+	+	+	-	+	-	+	-	+	-	+
	⋮											
	N_1-4	+	+	+	-	+	-	+	-	+	-	+
	N_1-3	+	+	+	-	+	-	+	-	+	-	+
	N_1-2	+	+	+	-	+	-	+	-	+	-	+
	N_1-1	+	+	+	-	+	-	+	-	+	-	+
N_1	+	+	-	+	-	+	-	+	-	+	-	
2	0	+	+	-	+	-	+	-	+	-	+	-
	1	+	+	-	+	-	+	-	+	-	+	-
	⋮											
	N_2-4	+	+	-	+	-	+	-	+	-	+	-
	N_2-3	+	+	-	+	-	+	-	+	-	+	-
	N_2-2	+	+	-	+	-	+	-	+	-	+	-
	N_2-1	+	+	-	+	-	+	-	+	-	+	-
N_2	+	-	+	-	+	-	+	-	+	-	+	
3	0	+	-	+	-	+	-	+	-	+	-	+
	1	+	-	+	-	+	-	+	-	+	-	+
	⋮											
	N_3-5	+	-	+	-	+	-	+	-	+	-	+
	N_3-4	+	-	+	-	+	-	+	-	+	-	+
	N_3-3	+	-	+	-	+	-	+	-	+	-	+
	N_3-2	+	-	+	-	+	-	+	-	+	-	+
N_3-1	+	-	+	-	+	-	+	-	+	-	+	
N_3	-	+	-	+	-	+	-	+	-	+	-	

Fig. 5. Termination at the metal interface of the series of sequential hopon chains (labeled 1, 2, 3) which initiated at a given row of ions in the compound at the oxygen interface (Fig. 3), with each termination of a chain leading to formation of new oxide at the metal interface.

bilities of the movement of hopons and other point defect species originating at the parent metal interface and subsequently moving in the direction of the oxygen interface. An initial place-exchange event at the parent metal interface is depicted by event 1 in Fig. 6. The second, third, and other successive events in the chain are likewise depicted in Fig. 6.

It is interesting to note that the excess charge in the oxide is positive for the present case. This is

opposite in sign to the excess charge produced in the oxide when a chain initiates at the oxygen interface. That is, when the chain initiates at the oxygen interface, a cation is thrust out of the oxide simultaneously while an adsorbed oxygen is thrust into the oxide as an excess anion, giving rise to an excess of negative charge within the oxide. However, when the chain initiates at the metal interface, a cation is thrust into the oxide simultaneously while an oxygen is thrust out of the oxide into the surface layer of metal ions, giving rise to an excess of positive charge within the oxide. The directions of motion of the two types of hopon are likewise opposite, since the hopon initiating at the oxygen interface moves toward the metal while the hopon initiating at the metal interface moves toward the oxygen. Because of the signs of the effective charges and the directions of motion, a hopon initiating at the oxygen interface will be referred to as an "an-on," in analogy with an excess anion, and a hopon initiating at the metal interface will be referred to as a "cat-on," in analogy with an excess cation.

The last event in the presently considered chain initiating at the metal interface is depicted as event N_1 in Fig. 6; this is the place-exchange event occurring at the oxide-oxygen interface. Thus a hopon chain originating at the metal interface (*viz.*, a cat-on) is merely the time-reversed version of a hopon chain originating at the oxygen interface (*viz.*, an an-on). (Compare, for example, Fig. 3 and Fig. 6.) In both situations, each cation in the path is marched one unit toward the oxide-oxygen interface, and each anion in the path is marched one unit toward the metal-oxide interface. One therefore cannot deduce the source interface for place exchange by an examination of the order within the ion arrays of the formed oxide. In other words, hopon chains initiating at either interface will lead to final results which are indistinguishable, namely, the formation of comparable amounts of new oxide at the two interfaces.

In the hopping model, on the other hand, each cation interstitial transported along a hopping path involves no individual movement of the ions in the already formed oxide; the new oxide which is formed at the oxide-oxygen interface as a consequence of transport of interstitial cations to that interface covers the layer of already formed oxide. Each anion vacancy transported along a hopping path results in the shift of each anion on the path a distance of one unit away from the oxide-oxygen interface; the new oxide is formed at the metal interface. Thus, cation interstitial

Fig. 6. Chain of sequential place-exchange events labeled 1, 2, 3, . . . , N_1 which initiates at the metal interface and eventually leads to transport of one cation down a given row of ions in the compound extending from the metal interface to the oxygen interface. (This is cat-on transport.)

Chain	Event	Metal			Bulk Oxide						Surface Layer		
		+	+	+	-	+	-	+	-	+		-	
1	0	+	+	+	-	+	-	+	-	+	-	+	-
	1	+	+	-	+	-	+	-	+	-	+	-	+
	2	+	+	-	+	-	+	-	+	-	+	-	+
	3	+	+	-	+	-	+	-	+	-	+	-	+
N_1	4	+	+	-	+	-	+	-	+	-	+	-	+
	N_1-3	+	+	-	+	-	+	-	+	-	+	-	+
	N_1-2	+	+	-	+	-	+	-	+	-	+	-	+
	N_1-1	+	+	-	+	-	+	-	+	-	+	-	+
N_1	+	+	-	+	-	+	-	+	-	+	-	+	

transport preserves the microscopic arrangements of both cations and anions within the already formed oxide, whereas anion vacancy transport preserves the microscopic arrangement of cations within the already formed oxide but shifts each anion along the path one unit away from the oxide-oxygen interface.

Our conclusion is that hopon chains can initiate at either interface. The oxygen interface may be favored because the free surface allows the strain energy to be minimized. The initiation of hopons at opposite interfaces will be independent because of the relatively large separation distance of the interfaces.

Distinguishing between various possibilities by means of marker and tracer experiments.—To summarize the over-all picture, the simultaneous motion of the cation and anion arrays in opposite directions is characteristic of the place-exchange mechanism, the independent motion of the cation array toward the oxygen interface is characteristic of the cation vacancy transport mechanism, the independent motion of the anion array away from the oxygen interface is characteristic of the anion vacancy mechanism, and the preservation of both cation and anion arrays in the already formed oxide is characteristic of the interstitial transport mechanism. In the latter situation of transport by interstitials, the new oxide forms at the oxygen interface for cation motion, but it forms at the metal interface for anion motion. These predictions are summarized in Table I along with the effective charges of the various defects.

Experimentally, then, it should be possible to distinguish between the place-exchange model and the hopping model by studying the changes in microscopic ordering of the cations and anions in the already formed oxide taking place during new oxide growth. Experiments involving tracers (34-44) and markers (11, 45, 46) should be especially helpful. Markers indicate the relative amounts of new oxide formed on each side of a given position in the oxide film following marker placement. The positions of tracers of oxygen and the metal forming new oxide after incorporation into the oxide are characteristic of the transport mechanisms producing oxide growth. A given radioactive decay is a singular event for each excited nucleus, so that a given ion is not tagged by its radioactivity in the same way as if it could be painted red or yellow and thus located over and over again. That is, each radioactive atom cannot be viewed as measurable more than once. Sophisticated techniques are now used for the actual experiments, as for example, the use of O^{18} as tracer atoms and their subsequent activation by proton bombardment to enable the determination of their average location in the oxide films. In this way the over-all order of the ions can be deduced and the time evolution of such followed by measuring the distribution of radioactivity within the ensemble. The predictions listed in Table I for

the hopon transport mechanism are in qualitative accord with the experimental tracer results of Pringle (34, 35), Amsel and Samuel (41), and also others (42). The quantitative agreement is discussed later in conjunction with relative ionic transport numbers predicted by the hopon model and the corresponding experimental results deduced by marker experiments (11).

Volume-preserving condition during oxide growth.—Another important aspect of the microscopic differences between the hopping and place-exchange models is the manner in which the new oxide volume-preserving condition is satisfied. A given chain in the place-exchange mechanism results in a cation being placed at the oxide-oxygen interface and an anion becoming buried within the first layer of metal at the metal-oxide interface. (See, for example, Fig. 4 and 5.) The associated chemical reaction of oxidation causes equal amounts of new oxide to be formed at both interfaces, assuming that the cations and anions have the same magnitude valence. This conclusion is independent of the source interface where the initial place-exchange event in the chain occurs. Already formed oxide thus becomes sandwiched between layers of new oxide which form subsequently by means of the place-exchange transport mechanism. There are some local strains at the metal interface as the new layer forms there, but these strains are gradually relieved as the monolayer of new oxide is completed. For equal magnitude valences, if the oxide molecular volume is greater than twice the volume of metal required for its formation, then the entire oxide layer will gradually be shifted sufficiently into the free region (containing only gaseous oxygen, or else the passivating or anodizing solution) to accommodate this extra volume; if the oxide molecular volume is less than twice the volume of metal required for its formation, then the entire oxide layer will gradually be shifted sufficiently toward the metal to accommodate this volume difference.

On the other hand, the volume-preserving condition is somewhat different in the case of vacancy or interstitial transport. For cation interstitial transport, the new oxide is formed at the oxygen interface. There need arise no large strains at that interface when the chemical reaction of new oxide formation occurs there, because it is a free (i.e., an unconstrained) interface. However, the voids left behind at the metal interface by cation interstitial motion away from this interface must somehow be eradicated if the metal is to remain in physical contact with the oxide. The microscopic voids may simply diffuse into the metal and be annihilated at the dislocations. At the other extreme, the microscopic voids may coalesce until the oxide finally separates from the metal. Vermilyea (47) has addressed this question. He concluded that there is no problem with void formation if the cations from

Table I. Ordering characteristics of oxide layers formed by different transport mechanisms

Transport mechanism	Charge q of the defect* effective for the electric force	Interface where new oxide layers are formed	Where are new M^+ ions incorporated as molecules in the oxide?	Where are new O^- ions incorporated as molecules in the oxide?	Distance† traveled by each M^+ ion involved in one chain	Distance† traveled by each O^- ion involved in one chain
Cation interstitial	$Z_{c1}e$	Oxygen interface	Oxygen interface	Oxygen interface	L	0
Cation vacancy	$Z_{cv}e$	Oxygen interface	Metal interface	Oxygen interface	d_o	0
Anion interstitial	$Z_{a1}e$	Metal interface	Metal interface	Metal interface	0	L
Anion vacancy	$Z_{av}e$	Metal interface	Metal interface	Oxygen interface	0	d_o
Hopon	$(Z_a + Z_c)e$	Both interfaces	Metal interface	Oxygen interface	d_o	d_o

* The charge is that which is acted on by the electric field E to produce the electric force $F = qE$. The Z values are derived from the valences, with subscripts c and a denoting some cation or some anion species, respectively; subscripts i and v denote specifically that the defect species is of the interstitial or vacancy type respectively.

† The oxide thickness is L , and d_o is the oxide lattice parameter.

the metal enter the oxide at kinks in a lattice step on the metal surface, since the step can move continuously across the metal surface until a complete layer of atoms has been removed.

For anion interstitial transport, the local strains created in accommodating the new oxide formed at the metal interface are vastly larger than for the place-exchange mechanism, since there is no simultaneous removal of a cation. The Pilling-Bedworth ratio is relevant here: If the oxide molecular volume is greater than the volume of metal required for its formation (the Pilling-Bedworth ratio being the ratio of the two), then the entire oxide layer will gradually be shifted sufficiently into the free region (containing the gaseous oxygen or the solution) to accommodate this extra volume; if the oxide molecular volume is less than the volume of metal required for its formation, then the entire oxide layer will gradually be shifted sufficiently toward the metal to accommodate this volume difference.

For cation vacancy transport, the new oxide forms at the oxygen interface; the vacancy is annihilated at the metal interface, and the void so created in the metal must be somehow eliminated if adherence of the oxide to the metal is to be maintained. Surface diffusion within the metal to a dislocation or to a surface step is a likely mechanism since the corresponding activation energy is favorably low.

For anion vacancy transport, the new oxide forms at the metal interface; the vacancy is annihilated at the oxygen interface without difficulty. However, large local strains will be created within the oxide at the metal interface if the Pilling-Bedworth ratio exceeds unity, since the new oxide must somehow be accommodated until gradually a monolayer is formed and the entire oxide has shifted sufficiently into the free region to eliminate the volume difference.

For cases of hopon transport in which the valences of the anion and cation involved in the simple exchange process are unequal, there will be unequal volumes of oxide formed at the two interfaces. The relative amounts are deduced quantitatively in one of the following subsections (*viz.*, Ionic transport numbers). Consider ΔL_a to be the volume of oxide formed at the metal interface due to oxygen anion interstitial or vacancy transport, and consider ΔL_c to be the volume of oxide formed at the oxygen interface due to metal cation interstitial or vacancy transport. Then it follows that whenever the ratio of oxide molecular volume to the corresponding volume of metal containing the same number of metal atoms exceeds $(\Delta L_a + \Delta L_c)/\Delta L_a$, then the entire oxide layer will be shifted outwardly from the metal into the free oxygen region by a sufficient amount to accommodate this extra volume. On the other hand, whenever the ratio of oxide molecular volume to the corresponding volume of metal containing the same number of metal atoms is less than $(\Delta L_a + \Delta L_c)/\Delta L_a$, then the entire oxide layer will be shifted inwardly toward the metal by a sufficient amount to accommodate the volume difference. It is shown in the subsection entitled "Ionic transport numbers" that the ratio $\Delta L_a/(\Delta L_a + \Delta L_c)$ can be identified as the relative anion transport number t_a for the ionic portion of the electrical conductivity. Thus the critical ratio referred to above is the reciprocal of t_a .

Hopon recombination.—The question arises as to whether or not there can be a correlation (or a coupling) of hopon chains initiating at opposite interfaces, and whether or not hopons moving in opposite directions (*viz.* an-ions and cat-ions) can recombine similarly to the way electrons and electron holes recombine in a solid. First of all it is intuitive that chains originating at opposite interfaces of the oxide will initiate independently because the separation distance between the two hopons is initially the entire

thickness of the oxide layer. The intuition is based on the fact that the molecular forces are simply not long range forces. Furthermore, it is intuitive that there will be no correlated motion (over long distances) of cat-ions and an-ions because the directions of motion are opposite. (This is to be carefully distinguished from the two-hopon transport process discussed in the section on Two-hopon processes.) On the other hand, if two hopons initiate independently at opposite interfaces but happen to travel down the same cation-anion line, then it is possible for them to annihilate at some intermediate point within the oxide. This is somewhat analogous to the way that an interstitial cation proceeding in one direction can annihilate a cation vacancy moving in the opposite direction. Thus cat-ions and an-ions can recombine within the oxide, quite analogous to the recombination of electrons and electron holes. The annihilation of two hopons can be visualized by considering the events depicted in Fig. 3 and 6 to occur simultaneously along the same line until the hopons meet at some point within the oxide layer. The hopon recombination process involves both a recombination of the virtual charges of opposite sign of the two hopons, as well as the uniform inversion of the cation-anion pairs along a continuous line through the oxide medium. The net result is a charge transport and a mass transport through the medium which is identical to that produced by single hopons of either type. The new oxide layers are located in the same places and have the same thicknesses as they would have for transport due to a single hopon process.

Ionic transport numbers.—Relative transport numbers for oppositely charged ionic species can be deduced in marker experiments such as those of Pringle (11). The relative quantities of new oxide formed at the two interfaces during a given time interval is measured; that oxide ΔL_a formed at the metal interface is attributed to anion transport (either interstitials or vacancies) and that oxide ΔL_c formed at the oxygen interface is attributed to cation transport (either interstitials or vacancies). Transport numbers traditionally provide a measure of relative charge transport, as opposed to relative mass transport or relative oxide volume formed at the two interfaces. However, in the usual situation in which the charge of a point defect during its motion through the oxide is the same as the product of its valence in the new oxide and the electronic charge magnitude, the quantities of oxide formed at the interfaces can be converted linearly to units related to the amounts Q_c and Q_a of the charge of the cations contained within each of the two respective quantities of new oxide ΔL_c and ΔL_a formed at the two interfaces (*i.e.*, $Q_c \propto \Delta L_c$ and $Q_a \propto \Delta L_a$). The ionic transport numbers t_c and t_a are then given by

$$t_a = Q_a/(Q_c + Q_a) = \Delta L_a/(\Delta L_c + \Delta L_a) \quad [7a]$$

$$t_c = Q_c/(Q_c + Q_a) = \Delta L_c/(\Delta L_c + \Delta L_a) \quad [7b]$$

The equations deduced in this section presume that the charges of the cation and anion during hopon transport are the same as their respective valences in the new oxide being formed. The alternate equations required whenever the charge of an ion during motion is different from that in the stoichiometric oxide are deduced in Appendix E.

The question which we now address is the following: What do we expect to obtain experimentally for t_c and t_a whenever transport occurs by hopons? First of all let us consider the simplest situation as depicted in Fig. 3 or Fig. 6, namely, individual place exchange events which involve a single anion and a single cation. (This is referred to as a "diatomic" hopon.) At the conclusion of a hopon chain originating at either interface, effectively one cation has been transported to the oxide-oxygen interface and one anion

has been transported to the metal-oxide interface. If Z_c represents the valence of the cation species and Z_a represents the valence of the anion species, the charge neutral oxide molecule composed of metal M and oxygen O can be characterized by the chemical formula $M_{|Z_a|}O_{|Z_c|}$. Thus one metal ion M is sufficient to form (on the average) a fraction $1/|Z_a|$ of a molecule of new oxide, and one oxygen ion O is sufficient (on the average) to form a fraction $1/|Z_c|$ of a molecule of new oxide. Therefore, considering that each transported oxygen ion is responsible for forming the new oxide at the metal interface and each transported metal ion is responsible for forming the new oxide at the oxygen interface, then in oxide growth resulting from place-exchange events involving single anion and cation pairs (*viz.*, the diatomic case), the relative amount of oxide formed at the metal interface to that formed at the oxygen interface will be in the ratio

$$\frac{1}{|Z_c|} \div \frac{1}{|Z_a|} = \left| \frac{Z_a}{Z_c} \right| \quad [8]$$

The ratio of the oxide formed at the metal interface to the total oxide formed will be given by

$$\frac{\Delta L_a}{\Delta L_c + \Delta L_a} = \frac{1/|Z_c|}{(1/|Z_a|) + (1/|Z_c|)} = \frac{|Z_a|}{|Z_c| + |Z_a|} \quad [9a]$$

and the ratio of the oxide formed at the oxygen interface to the total oxide formed will be given by

$$\frac{\Delta L_c}{\Delta L_c + \Delta L_a} = \frac{1/|Z_a|}{(1/|Z_a|) + (1/|Z_c|)} = \frac{|Z_c|}{|Z_c| + |Z_a|} \quad [9b]$$

The transport numbers experimentally determined by measurements of the relative quantities of oxide formed at the two interfaces are given by comparison of Eq. [9a] and [9b] with Eq. [7a] and [7b]

$$t_a = \frac{\Delta L_a}{\Delta L_c + \Delta L_a} = \frac{|Z_a|}{|Z_c| + |Z_a|} \quad [10a]$$

$$t_c = \frac{\Delta L_c}{\Delta L_c + \Delta L_a} = \frac{|Z_c|}{|Z_c| + |Z_a|} \quad [10b]$$

These predictions are summarized in Table II. As an example, consider Ta_2O_5 , for which $Z_c = +5$ and Z_a

$= -2$. The preceding expressions yield $t_a = 2/7$ and $t_c = 5/7$, as compared to the experimental values $t_a = 0.76$ and $t_c = 0.24$ of Pringle (11). Assuming the correctness of the experimental values, the discrepancy may be due to the existence of a more complex type of hopon transport mechanism (as described in the following sections), or else the difference may reflect additional contributions to transport by individual anion interstitials or vacancies.

Next, let us consider more complicated situations in which individual place-exchange events involve more than two ions. If the stoichiometric oxide is represented by the chemical formula $M_{|Z_a|}O_{|Z_c|}$, then an equivalent representation insofar as relative numbers of metal atoms and oxygen atoms is MO_{p_0} , where p_0 is the rational number defined by $p_0 \equiv |Z_c/Z_a|$. If rotation of the stoichiometric unit MO_{p_0} by place exchange constituted the mode of hopon transport, then equal volumes of oxide would be formed at the two interfaces. This follows from the fact that at the completion of each chain, one stoichiometric rotational unit of oxide would have been formed at each interface. (A special case of this is an oxide composed of neutral diatomic molecules.) Suppose, on the other hand, that the individual place-exchange events each involve a group having composition MO_p , where p is a rational number but in general $p \neq p_0$. (For example, if a place-exchange event involves one cation and two anions, then $p = 2$; if a place-exchange event involves two cations and one anion, then $p = 1/2$.) If p is less than p_0 , then for each molecule of stoichiometric oxide formed by the transport of one cation to the oxygen interface by a hopon chain, a lesser amount (namely, p/p_0 of a molecule, on the average) would be formed by place exchange of oxygen with atoms of the parent metal at the metal interface. If p exceeds p_0 , then for each molecule of stoichiometric oxide formed by the transport of one cation to the oxygen interface by a hopon chain, a greater amount (namely, p/p_0 molecules, on the average) would be formed by place exchange of oxygen with atoms of the parent metal at the metal interface. Hopon motion would then lead to stoichiometric oxide layers having thicknesses in the ratio of 1 to p/p_0 to be formed at the oxygen and metal interfaces, respectively. The ratio p/p_0 for the amount of oxide formed at the metal interface to that formed at the oxygen interface in turn leads to the experimental transport numbers

Table II. Prediction of experimental ionic transport numbers and the minimum ratio for (oxide volume)/(corresponding volume of metal) which can give compressive stresses at the metal interface due to volume conservation*

Type of defect	Relative ionic transport numbers		Minimum ratio of oxide volume to metal volume for compressive stresses
	t_c	t_a	
Cation	Interstitial	$\frac{Z_c J_{ci}}{J_{ionic}}$	∞
	Vacancy	$\frac{Z_c J_{cv}}{J_{ionic}}$	∞
Anion	Interstitial	$\frac{Z_a J_{ai}}{J_{ionic}}$	1
	Vacancy	$\frac{Z_a J_{av}}{J_{ionic}}$	1
Simple hopon	General diatomic case	$\frac{ Z_c }{ Z_c + Z_a }$	$\frac{ Z_a + Z_c }{Z_a}$
	Diatomic case for $ Z_c = Z_a $	$1/2$	2
Complex hopon	General multi-atom case	$\frac{ Z_c }{ Z_c + Z_a p}$	$\frac{ Z_a p + Z_c }{ Z_a p}$
	Multi-atom case with charge neutral rotational unit	$1/2$	2

* Notation is as follows: ci denotes cation interstitial; cv denotes cation vacancy; ai denotes anion interstitial; av denotes anion vacancy; J_{ionic} is the total ionic charge current in units of electrons- m^{-2} - sec^{-1} ; p is the ratio of O to M ions in the place exchange unit (e.g., MO_p), with $p = 1$ for the simple place exchange of an M with an O.

$$t_a = \frac{p/p_0}{(p/p_0) + 1} = \frac{p}{p + p_0} = \frac{p}{p + |Z_c/Z_a|} = \frac{|Z_a|p}{|Z_a|p + |Z_c|} \quad [11a]$$

$$t_c = \frac{1}{(p/p_0) + 1} = \frac{p_0}{p_0 + p} = \frac{|Z_c/Z_a|}{|Z_c/Z_a| + p} = \frac{|Z_c|}{|Z_c| + |Z_a|p} \quad [11b]$$

For the simple place-exchange mechanism involving a single anion and a single cation, $p = 1$ and the above formulas reduce to the results [10a] and [10b] already derived. For $p = 2$, however, these formulas yield for Ta_2O_5 the values $t_c = 5/9$ and $t_a = 4/9$. For $p = 1/2$, on the other hand, these formulas yield for Ta_2O_5 the values $t_c = 5/6$ and $t_a = 1/6$. From another viewpoint, if we assume $t_c = 1/4$ for Ta_2O_5 , in accordance with Pringle's results (11), then we have the relation

$$\frac{1}{4} = \frac{5}{5 + 2p} \quad [12]$$

which gives $p = 7\frac{1}{2}$. This would correspond (rightly or wrongly) to rotation of a group Ta_2O_{15} in each individual place exchange. In some respects this type of a rotation would be similar to the ring mechanism for diffusion in metals postulated by Zener (10), but as previously discussed, the hopon mechanism is promoted strongly by the electric field, whereas the ring mechanism is not influenced by the field.

Consider now the limiting case in which the value of p is the same as $p_0 = |Z_c/Z_a|$. Then the basic rotational unit is a neutral entity having the same composition as the stoichiometric oxide, and Eq. [11a] and [11b] yield straightaway $t_a = 1/2$ and $t_c = 1/2$. This result is in agreement with the above conclusions for this situation.

In Al_2O_3 and Nb_2O_5 , the experimental transport numbers for the cations have been reported to have the values $t_c \approx 0.37$ and 0.25 , respectively (48). The value 0.37 for aluminum is within the range 0.33 to 0.41 (49, 50) obtained in the electrolyte aqueous ammonium dihydrogen citrate, but it is outside of the range 0.54 - 0.63 given for the electrolyte sodium tetraborate in ethylene glycol. The value of 0.25 for niobium is within the range of values 0.22 - 0.33 given by other experiments (49) using 0.1 molar aqueous Na_2SO_4 as the electrolyte. It is evident that the unit of rotation for Nb in Nb_2O_5 cannot be the neutral molecule, since the relative transport numbers do not have the value 0.5 . It is quite interesting that $t_c \approx 1/4$ in both Ta_2O_5 and Nb_2O_5 , even though the chemical bonding of Ta and Nb is probably sufficiently different to yield significantly different values for the activation energy for cation motion. This lends credence to the place-exchange hypothesis that a molecular group is involved in some fundamental way in the transport mechanism. Since crystal structure is not such an important factor in amorphous oxides, one might expect an important factor to be the ratio of anions to cations in the neutral oxide molecule.

Applying the above formulas to Al_2O_3 , utilizing $t_c = 1/3$ together with $Z_c = +3$ and $Z_a = -2$, leads to the result $p = 3$. This would correspond to the rotation of the molecular group AlO_3 in each place-exchange event, which indeed differs from the results for Ta_2O_5 and Nb_2O_5 . (Using $t_c = 2/5$ leads to the result $p = 2.25$ for the aluminum oxide case, corresponding to the molecular group Al_3O_9 .)

It is to be recognized that the specific numbers deduced in this way depend on the experimental measurements available at the present time. The results are nevertheless quite suggestive of the idea that

transport under the presently considered conditions of high externally applied electric fields involves some type of cooperative motion between the cations and anions in the medium. In addition, it has been verified experimentally that the order of the oxygen ions is conserved (34, 39). [The oxygen atoms are fixed according to their order of arrival during the formation of amorphous compact layers on aluminum or tantalum, according to Cherki and Siejka (39), such that the oxygen atoms belonging to a new layer are located at the oxide-solution interface.] Likewise, in the case of Ta_2O_5 it has been found that the order of the tantalum ions is conserved (35, 42). For these reasons, the presently described hopon mechanism seems to provide the basis for a viable model of anodic oxidation.

Two-Hopon Processes for Transport in Three-Dimensional Systems

The Coulomb energy for hopon transport in a three-dimensional system (see Fig. 7 and 8) would increase continuously with successive place-exchange events because of the interaction between charges in the lateral directions. This undesirable feature can be essentially eliminated if a second hopon follows the first in a closely correlated manner down a single chain. (Possibly a mechanism involving laterally adjacent chains could also be envisioned.)

Consider, for example, the two-hopon process depicted in Fig. 9, and let us compare the Coulomb energy of this process with that of a one-hopon process for a three-dimensional system. It can be noted from Fig. 7 and 8 that the sequential reversal in the electric dipole orientation which can be accomplished without any additional energy input in a one-dimensional system (see Fig. 2) would require a linear increase in the energy due to lateral Coulomb interactions in the three-dimensional system, as mentioned above. This would quickly become prohibitive, so energetically it is favorable for the first place exchange to be closely followed spatially and temporally by a second place exchange which reinverts the orientation of the line of electric dipoles. The correlated motion of these two place exchanges through the oxide layer, as illustrated in Fig. 9, then requires no continuous input of energy, so in this respect the situation reverts energetically to that of the single place exchange moving down a line of atoms which is shown in Fig. 2.

Collective Hopon Transport

There are two closely related possibilities for the nonsimultaneous place exchange mechanism. First of all there is the situation already described in which it is implicit that each local place-exchange event has

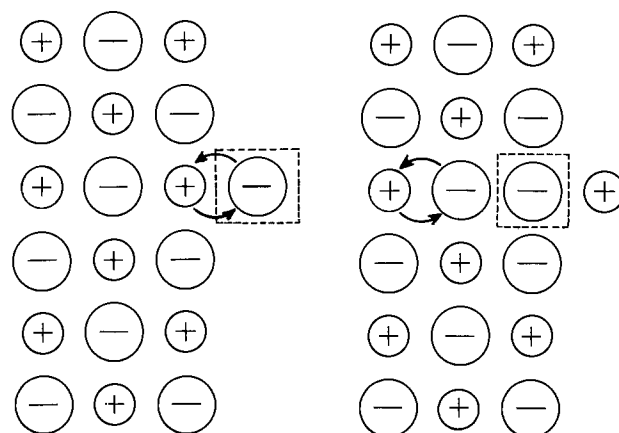


Fig. 7. Lateral Coulomb interactions produced by a one-hopon process down a row of ions extending through a three-dimensional oxide. (Left drawing: first place-exchange event; right drawing: second place-exchange event.)

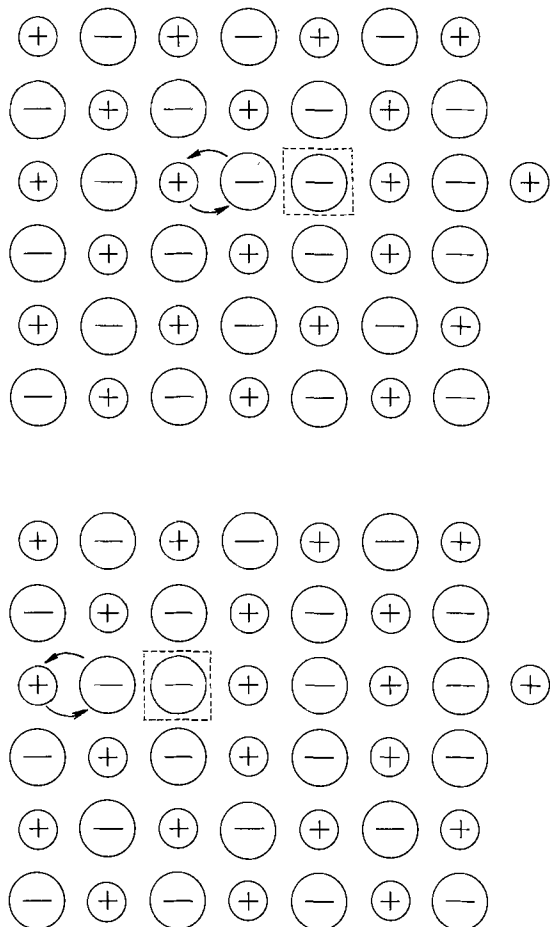


Fig. 8. Continuous Coulomb energy increase resulting from one-hopon transport down a row of ions extending through a three-dimensional oxide. (Upper drawing: third place-exchange event; lower drawing: fourth place-exchange event.)

been completed before the adjacent place-exchange event along the chain begins. This situation represents a time and spatial sequence of individual (but correlated) place-exchange events occurring one at a time which eventually lead to completion of a hopon chain. There is a second possibility, however, in which each locally adjacent place-exchange event begins even before the first place-exchange event has been completed. This constitutes a collective behavior amounting to extension of the place-exchange event over distances larger than the atomic spacing in the medium (see Fig. 10). Perhaps the easiest way to understand this latter proposal is to consider the wavelike propagation of the disturbance associated with a falling row of dominos triggered by an initial push at one end of the row. Each domino begins to fall at a different point in time; the sequential tipping over of the various dominos in the row is collective but not simultaneous. In the same way, a single place-exchange event which occurs at one interface (e.g., at the oxygen interface in an oxide film) may constitute the initiation of a time sequence of correlated partial place-exchange events which propagate at a finite speed down a chain.

We refer to the above two possibilities as "noncollective" and "collective" hopon transport mechanisms, respectively. Noncollective hopon transport is characterized by a thermally activated electric field-modified motion of a highly localized place-exchange disturbance which jumps statistically in time from place to place in the medium. Collective hopon transport is characterized by a thermally activated electric field-driven motion of an extended wavelike place-exchange disturbance which propagates at a finite velocity through the medium. The limit in which the propaga-

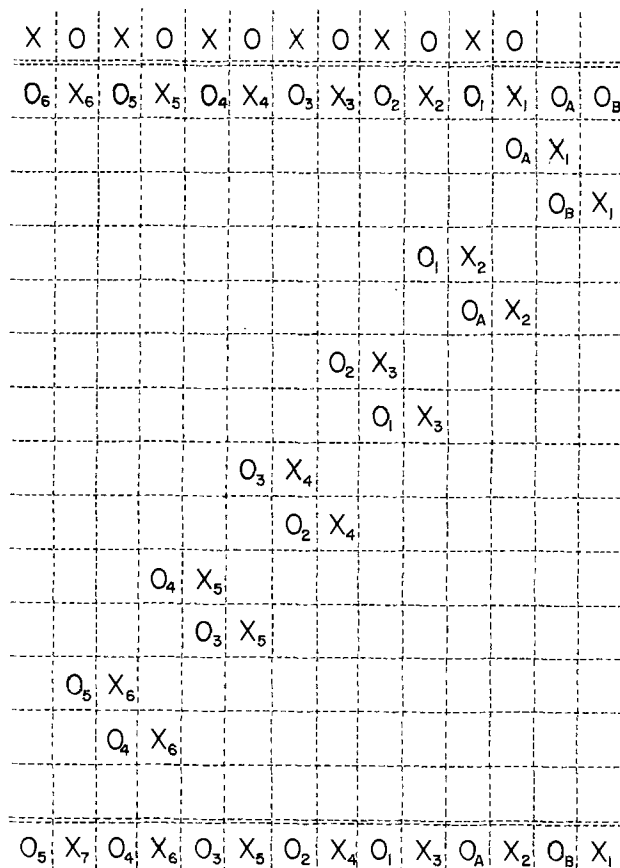


Fig. 9. Two-hopon transport process leading to temporal correlation of the transport of two anions (labeled O_A and O_B) through a compound made up of cations (labeled X_j , with $j = 1, 2, 3, \dots$) and anions (labeled O_j , with $j = 1, 2, 3, \dots$). [The top two rows indicate two lateral rows of ions in a compound, with adsorbed oxygens O_A and O_B at the end of one of the rows. Each successive row downward from the second in the configuration indicates the change in the preceding configuration produced by a single place-exchange event. A given row position thus indicates a given time. Each column indicates a given site in the lattice. At a given point in time (corresponding to a given row), the ion occupying any given column site is indicated by the nearest vertical entry upward in the column, beginning with the row in question. The second row indicates the starting configuration, and the bottom row indicates the final configuration. The important point to be noted is that the type of ion (cation or anion) occupying a given site is the same after completion of two-hopon transport down the row as it was initially. Furthermore, the Coulomb interaction energy remains constant during two-hopon transport once the two defect anions (O_A and O_B) enter the oxide.]

tion velocity approaches infinity provides the closest approximation to the Sato-Cohen model (12). There are still some differences, namely, different activation energies and the dependence of these energies on oxide layer thickness.

It is evident that the two-hopon process can involve either the collective or the noncollective mechanism. Perhaps the a-c response and corresponding frequency dependence of the dielectric loss (51) within the film can be employed to distinguish between the various possibilities for any specific experimental system.

Discussion

The purpose of this paper has been to develop in some detail a microscopic picture for a specific high field transport mechanism, viz., place exchange of oppositely charged ions in a solid. A quantitative basis is developed for deducing the transport rate due to this mechanism, which in turn can be applied to deduce the kinetics of anodic film formation on metals.

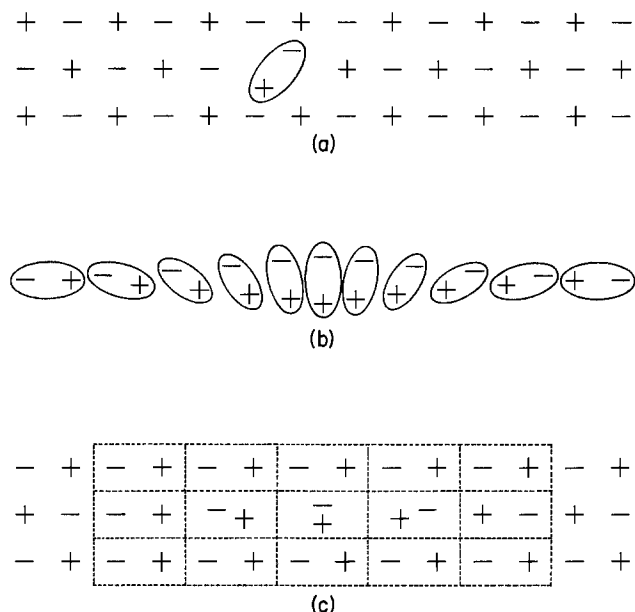


Fig. 10. Collective one-hopon transport [diagram (b)] contrasted with noncollective one-hopon transport [diagram (a)]. (In diagram (a), a single dipole consisting of a place-exchange pair is depicted in the process of flipping at some instant of time. In diagram (b) a group of adjacent dipoles are in various stages of flipping at a given instant of time. As time passes, the disturbance travels in one direction or the other with finite velocity. Diagrams (a) and (c) indicate the Coulomb interaction energy of the two types of disturbance with lateral rows of ions in the oxide.)

Although the basic idea that place exchange may give rise to transport through a three-dimensional layer dates back to the work of Sato and Cohen (12), it is only in the light of relatively more recent experimental results (11) indicating transport numbers of the same order of magnitude for oppositely charged ions that it seemed worthwhile to the present author to consider such a mechanism more seriously.

While it is relatively easy to compare the predictions of the presently considered hopon model with the predictions of other microscopic transport mechanisms (see Tables I and II, for example), it is more difficult to compare its predictions with phenomenological models which are not well defined from a microscopic viewpoint. One such model is the "network defect model" of Dignam (49) which was postulated to explain coupled cation and anion transport. Transport numbers, for example, are considered to be meaningless entities in the Dignam model, whereas these quantities are well defined in the hopon model. It is also difficult or impossible to estimate activation energies and the field modification of such in cases where the microscopic transport mechanism is unspecified. According to Dignam (49), the essence of the network defect model is a bond breaking and rearrangement, but this must indeed be characteristic of any transport mechanism because the motion of any defect involves a local modification in the chemical bonds of the surrounding atoms in the solid. Perhaps the unique features of Dignam's model are summarized in the following quotations:

Within the framework of the random-network model of the vitreous state as proposed by Zachariasen [(52)] a defect can be imagined to form by rupture of one of the metal-oxygen bonds, followed by separation of these "dangling bonds" through a succession of processes each of which may be described as an exchange of partners. Such defects may be described alternatively as regions of local nonstoichiometry bearing a single charge, positive in the case of cation-network de-

fects and negative in the case of anion-network defects, in order to satisfy valency requirements.

... as the disturbance moves through a given region of the vitreous network, the atoms are displaced irreversibly; no single atom, however, is displaced as far as one interatomic distance.

... ion transport by this mechanism maintains the order in both the anion and cation subnetworks, except for a small amount of reordering arising from the random nature of the transport process.

... there can be no such thing as a unique marker that can be inserted into the vitreous film to define a position against which to measure unique transport numbers.

The Dignam model does not appear to be specific in the sense that it postulates any given microscopic transport mechanism. Apart from the fact that the hopon model is based on a specific microscopic mechanism, namely, place exchange, there are clearly a number of important differences between the Dignam network model and the hopon model. Among these are the distances traveled by any given ion in the oxide matrix per transported ion, the value of the defect charge, the relative amounts of oxide formed at the two interfaces, the relevance of the concept of transport numbers, and the general intuitive picture of how transport takes place.

Pringle (11) has listed five possibilities for the growth of new oxide, namely, the following: (I) The metal alone migrates, and the reaction to form new oxide occurs only at the oxide/oxygen interface. (II) The oxygen alone migrates, so that the new oxide is formed only at the metal/oxide interface. (III) When both metal and oxygen migrate, these two mechanisms could occur together, so that new oxide would be formed at both interfaces. (IV) When both the metal and oxygen migrate, however, the new oxide does not have to be formed at the interfaces; it could be formed within the existing oxide through the transport of material from each side. (V) Since mechanisms III and IV are not mutually exclusive, the new oxide could be formed both within the existing oxide and at the interfaces.

Although these possibilities in no way constitute microscopic transport mechanisms, they do more or less categorize the various possibilities to be considered when interpreting the marker and tracer experiments (11, 34). It can be noted that hopon transport leads to mode III in the above listing; this is also the category chosen by Pringle (11) as being the one most in accord with his radioactive noble gas marker experiments. Pringle makes the point that radioactive noble gas marker experiments can only determine how much of the new oxide is being formed by metal and/or oxygen migration; they cannot determine how the individual atoms migrate. A marker for oxygen itself is required to delineate more specifically how the oxygen moves. The conclusion was reached on the basis of the tracer experiments (34) that the oxygen atoms jump a distance corresponding to not much more than one interoxygen distance. This again is in accord with the predictions of the hopon mechanism. Likewise, recently reported measurements (35) of the motion of the tantalum ion during anodic oxidation are in accord with the hopon mechanism.

The intuitive picture which Pringle (11) put forth for the transport mechanism through anodic oxides formed on tantalum is perhaps best summarized by the following quotation:

In this model ... each moving atom carries a fraction of the charge a fraction of a "lattice spacing" in such a way that the total effect is equivalent to one charged atom jumping one "lattice spacing." Both tantalum and oxygen take part in this process, so that the lattice loses its rigidity during the charge transfer event.

To quote from the later experimental paper by Pringle (34) on the oxygen tracer work:

The nature of the oxygen migration is thus rather obscure, but the present results are not inconsistent with the hypothesis put forward in a previous paper . . . that charge is transferred during the anodic oxidation of tantalum via the simultaneous movement of a group of atoms, both tantalum and oxygen.

It therefore seems apparent that Pringle did not have any specific microscopic transport mechanism in mind. It is not specified how the tantalum and oxygen are moving as a group, and it is not specified how the charges are distributed and how the net charge is carried through the medium. The above statements could be more or less consistent with a number of microscopic transport mechanisms.

Vermilyea (24) has speculated that in amorphous Ta_2O_5 the local configuration of ions surrounding each tantalum ion changes with the passage of current and thus depends on the conditions of formation (*i.e.*, the past history) of the oxide. This idea seems to be closely related to the intuitive picture underlying the network defect model (49) discussed earlier.

Young (53), in his paper on the steady-state kinetics of formation of anodic oxide films in sulfuric acid, pointed out the possible importance of the glassy structure (54) of the anodic oxide. This represented an early recognition of the relevance of the early work of Zachariassen (52) on glasses which others (55) since that time have cited as being relevant to metal oxidation.

Amsel and Samuel (41) discussed the possible transport mechanisms involved in anodic oxidation in the light of their experimental results using O^{18} isotopes. Because perfect conservation of order was observed for the oxygen in the oxide layer during growth, with the already formed oxide remaining at the metal interface and new oxygen being incorporated at the solution interface, it was concluded that the oxygen ions either did not move, or else that they move by highly correlated vacancy diffusion, the vacancies originating from the lattice plane in contact with the metal. From experiments using two metals simultaneously (Al and Ta), they concluded in addition that metal ions move by creation and subsequent annihilation of an atom or vacancy, with several possibilities discussed for this process. Cation vacancy diffusion coupled with exchange capture of cation interstitials were considered quite likely, the latter evidently being an interstitialcy mechanism (8).

Dewald (56) treated the effects of space charge on the ionic current. An extension of this single carrier model to include concentration gradients has been given by Fromhold and Kruger (57), and analytical results for the very high field limit have been deduced (58).

Fisher, Bean, and Vermilyea (59) have examined the role of the surface charge field in lowering the barriers for ionic hopping at the oxide interfaces, and Dignam (60) has examined the effects of asymmetry introduced into the potential energy barriers by the field. Dankov (61) has pointed out the role of stresses in thin oxide layers. Other creative ideas on transport mechanisms possibly relevant for anodic oxide formation have been summarized by Young (62).

The question of the experimental kinetics for anodic film formation is still being debated in the literature. Whereas Sato and Cohen (12) found a direct logarithmic growth law for the anodization of iron, Draper and Jacobs (63) found a space-charge modified growth law similar to that predicted by the work of Dewald (56). The latter would be in better accord with the theoretical predictions of the present model, which gives rise to the same kinetics as predicted by the space-charge gradient model (57, 58) for single carrier

transport. Moshtev (64) found that even in the case of iron, the steady-state growth kinetics in the passive region using neutral solutions could be best described by a field-assisted single carrier transport equation of the same basic type as the space-charge gradient model. Thus the present model of anodic film formation by hopon transport is reasonably consistent with much of the published experimental data.

The central points which have been made in the present development of hopon motion are the following: (a) The postulated hopon transport is a new type of place exchange (nonsimultaneous) which leads to a different kinetics of growth from the simultaneous place-exchange mechanism of Sato and Cohen. (b) The structural ordering of the cation and anion lattices resulting from this specific microscopic transport mechanism of hopon motion has been carefully delineated and compared with the ordering expected for transport by cation and anion vacancies and interstitials. (c) An electric field represents an important driving force for hopon transport.

Conclusions

The nonsimultaneous place-exchange mechanism has certain features (primarily the microscopic ordering of cations and anions) which are very similar to the collective place-exchange model of Sato and Cohen; nevertheless, this mechanism has other features (primarily the kinetics) which are more closely related to the hopping model of Verwey. In fact, the reason that the picture of nonsimultaneous place exchange is so attractive is that it incorporates the best features of the hopping transport mechanism and the place-exchange transport mechanism. The energetically most favorable mechanism for any particular system will of course prevail. In some systems, this may be a hopon mechanism; in others, it will be the pure hopping of interstitials or vacancies. Since the microscopic order preservation is quite different for the various models, as summarized in Table I, radioactive tracer experiments can aid in differentiating between the possibilities for a given system.

The following interesting conclusions have been reached regarding oxide growth by means of the above-described hopon transport mechanism:

1. The new metal ions are incorporated at the metal interface and the new anions are incorporated at the oxygen interface; hopons can, in principle, initiate at either interface.

2. The microscopic order of the cations and anions within the line of atoms involved in a hopon chain are individually preserved during subsequent transport, since each cation is marched one unit cell distance away from the metal interface and each anion is marched one unit cell distance toward the metal interface with each successful termination of a hopon chain.

3. The transport numbers for the oppositely charged ionic species will be of the same order of magnitude.

4. Hopons result in the transport of a net charge through the medium; the rate of such transport will be markedly dependent on any applied or built-in electric field.

5. Space charge effects are much the same as for interstitials or vacancies.

6. A hopon gradient acts as a driving force for transport.

7. Many stress effects are quite analogous to those predicted for the hopping of vacancies or interstitials, though some of the quantities (*e.g.*, the Pilling-Bedworth ratio) must be replaced by different values.

8. The kinetics of oxide formation for hopon transport are quite analogous to those predicted by the lattice interstitial or vacancy hopping model.

Acknowledgments

The author enjoyed interesting discussions of hopon transport with Dr. J. S. L. Leach and Dr. N. Sato

while at the Passivity Symposium in Airlie, Virginia, and he wishes to thank Dr. R. P. Frankenthal and Dr. J. Kruger for giving him the opportunity to present the work at that conference. The author also enjoyed discussing the hopon mechanism with Dr. G. Amsel at the Anodic Films Symposium in Seattle, Washington.

Manuscript submitted Aug. 7, 1978; revised manuscript received July 29, 1979. This was Paper 198 presented at the Seattle, Washington, Meeting of the Society, May 21-26, 1978.

Any discussion of this paper will appear in a Discussion Section to be published in the December 1980 JOURNAL. All discussions for the December 1980 Discussion Section should be submitted by Aug. 1, 1980.

Publication costs of this article were assisted by Auburn University.

APPENDIX A

Transport due to a Gradient of Hopons

A gradient in the density of hopons can also act as a driving force for transport. In zero electric field, for example, the particle current of hopons at the position of the potential barrier labeled k is

$$J_k = \nu \exp(-W_H/k_B T) [n_{k-1} - n_k] \quad (k = 1, 2, \dots, N) \quad [\text{A-1}]$$

where n_k is the number of hopons per unit area located in the potential minimum following the potential barrier labeled k . In this one-dimensional labeling scheme, there are N barriers across the oxide film, so that in terms of an atomic separation distance d_o , the thickness of the oxide film is Nd_o .

APPENDIX B

Space Charge due to Hopons

The existence of space charge in the hopon model follows from the charges associated with the virtual defects. After the initial place exchange between two ions of opposite sign, we have a situation in which an ion of one sign in the lattice is replaced by an ion of opposite sign. Thus the excess charge, relative to a stoichiometric situation of local space charge neutrality, has the magnitude

$$|q_H| = (|Z_c| + |Z_a|)e \quad [\text{B-1}]$$

The discrete form of Poisson's equation [Eq. (8.1) in Ref. (17)] then leads to a position-dependent electric field, which in SI units is

$$E_k = E_o + (q_H/\epsilon) \sum_{j=1}^k n_{j-1} \quad (k = 1, 2, \dots, N) \quad [\text{B-2}]$$

where E_o is the electric field at the source interface, E_k is the electric field at the potential barrier labeled k , and n_j is the number of hopons per unit area located in the potential minimum following the potential barrier labeled k .

APPENDIX C

Stress Effects due to an Electrochemical Potential Gradient of Hopons

An electrochemical potential difference for hopons can produce a stress somewhat analogous to the manner in which such a gradient for other types of point defects leads to such stresses (32). The general relation that the force is given by the gradient of the electrochemical potential \tilde{u} leads to

$$F = - \frac{d\tilde{u}}{dx} \quad [\text{C-1}]$$

for the force acting on each defect at position x in the oxide. For a bulk concentration C of hopons, a good approximation to the electrochemical potential \tilde{u} is given by

$$\tilde{u} = k_B T \ln C + q_H V \quad [\text{C-2}]$$

where V is the electrostatic potential determined in

the usual way by a spatial integral of the electric field in accordance with Poisson's equation [see Sec. 4, Chap. 3 in Ref. (17)].

APPENDIX D

Fundamental Kinetics Equation for Oxide Growth by Hopon Transport

The kinetics of oxide formation are determined from the differential expression (17)

$$\frac{dL}{dt} = R J_o \quad [\text{D-1}]$$

where L is the oxide thickness, t is the time, J_o is the steady-state current of hopons, and R is the volume of oxide formed per hopon which traverses the oxide film from $x = 0$ to $x = L$. The local steady-state particle current J_k at the potential barrier labeled k is determined by the hopon gradient and the electrical force $q_H E$ in accordance with the hopping expression

$$J_k = \nu \exp(-W_H/k_B T) [n_{k-1} \exp(q_H a_k^{(f)} E_k / k_B T) - n_k \exp(q_H a_k^{(r)} E_k / k_B T)] \quad (k = 1, 2, 3, \dots, N) \quad [\text{D-2}]$$

where $a_k^{(f)}$ is the forward hopping distance at barrier k , $a_k^{(r)}$ is the reverse hopping distance at barrier k , ν is an attempt frequency for place exchange, and all other parameters have been previously defined. The forward and reverse hopping distance $a_k^{(f)}$ and $a_k^{(r)}$ can differ because of the asymmetry introduced by superimposing the asymmetrical electrical potential energy on an otherwise symmetric potential energy barrier (29, 60). The integration of the above series of coupled difference equations can be carried out analytically or numerically in the limit of the steady state to obtain the hopon current density J_o required above for the kinetics. The results are the same as those obtained specifically for the case of one-species transport in the presence of space charge of the mobile species and a concentration gradient (57, 58).

APPENDIX E

Case of Transport by Ionic Defects Having a Variable Valence

Consider the situation in which new oxide having the stoichiometric composition MO_{p_o} is being formed, with the metal ion valence Z_c and the oxygen ion valence Z_a , with $p_o = |Z_c/Z_a|$. Consider simultaneously the basic rotational unit to have a composition described by MO_p , with the metal ion charge during transport being $Z_c'e$, and the oxygen ion charge during transport being $Z_a'e$. The transport numbers based on relative charge transport would then be given by

$$t_a' = \frac{p|Z_a'|}{p|Z_a'| + |Z_c'|} \quad [\text{E-1}]$$

$$t_c' = \frac{Z_c'}{p|Z_a'| + |Z_c'|} \quad [\text{E-2}]$$

whereas the transport numbers computed from the relative amounts of oxide formed at the two interfaces would be given by

$$t_a = \frac{p/p_o}{(p/p_o) + 1} = \frac{p}{p + p_o} = \frac{p}{p + |Z_c/Z_a|} = \frac{p|Z_a|}{p|Z_a| + |Z_c|} \quad [\text{E-3}]$$

$$t_c = \frac{1}{1 + (p/p_o)} = \frac{p_o}{p + p_o} = \frac{|Z_c/Z_a|}{p + |Z_c/Z_a|} = \frac{|Z_c|}{p|Z_a| + |Z_c|} \quad [\text{E-4}]$$

It is to be noted by comparing Eq. [E-1] with Eq. [E-3], and also comparing Eq. [E-2] with Eq. [E-4], that the experimental values for the transport numbers deduced on the basis of relative amounts of oxide formed at the two interfaces are not in accord with the true transport numbers as determined on

the basis of charge transport. Although it might seem unlikely that Z_c' and Z_a' would differ from Z_c and Z_a in hopon transport, nevertheless one should keep an open mind as to various possibilities.

It is interesting that even in the case of transport by a single type of interstitial (or single type of vacancy) with some attendant electron transport, the ionic and electronic transport numbers obtained by a comparison of mass and charge transport will only be correct if the actual charge of the ionic defect during transport can be ascertained. Otherwise, the correct transport numbers are obtained only if the defect charge during transport is the same as that determined from the valence in the oxide being formed. As a specific example, consider the transport of cation interstitials and electrons. The meter current and the oxide growth rate will be given by

$$I_{\text{meter}} = Z_{ci}'eJ_{ci} + |(-e)J_e| \quad [\text{E-5}]$$

$$\frac{dL}{dt} = R_{ci}J_{ci} \quad [\text{E-6}]$$

where R_{ci} is the volume of new oxide formed per cation interstitial transported through the oxide film. The above constitute two equations and two unknowns. If $Z_{ci}'e$ is assumed to be equal to $Z_{ci}e$, then knowing the left-hand sides from measurements of the meter current and the oxide growth rate, together with the constant R_{ci} computed from the oxide density, then we can solve the two equations simultaneously to obtain the values of J_{ci} and J_e . Then the true transport numbers are given by

$$t_i' = Z_{ci}'eJ_{ci} / (Z_{ci}'eJ_{ci} + |eJ_e|) \quad [\text{E-7}]$$

$$t_e' = |eJ_e| / (Z_{ci}'eJ_{ci} + |eJ_e|) \quad [\text{E-8}]$$

Since, however, the determination involves presuming a value for Z_{ci}' , which may in fact differ in certain cases from Z_{ci} , the determination of the relative charge transport numbers by employing the mass transport rate as indicated above can lead to error.

REFERENCES

- E. J. W. Verwey, *Physica*, **2**, 1059 (1935).
- C. Wagner, *Trans. Faraday Soc.*, **34**, 851 (1938).
- N. F. Mott and M. J. Littleton, *ibid.*, **34**, 485 (1938).
- N. F. Mott, *ibid.*, **34**, 500 (1938).
- N. F. Mott and R. W. Gurney, *ibid.*, **34**, 506 (1938).
- J. R. Manning, "Diffusion Kinetics for Atoms in Crystals," D. Van Nostrand Co., inc., Princeton, N.J. (1968).
- H. R. Zeller, P. Brüesch, L. Pietronero, and S. Strässler, in "Superionic Conductors: Chemistry, Physics and Applications," G. D. Mahan, Editor, Plenum Publishing Co., New York (1976).
- F. Seitz, *Acta Crystallogr.*, **3**, 355 (1950).
- M. D. Weber and R. J. Friauf, *J. Phys. Chem. Solids*, **30**, 407 (1969).
- C. Zener, *Acta Crystallogr.*, **3**, 346 (1950).
- J. P. S. Pringle, *This Journal*, **120**, 398 (1973).
- N. Sato and M. Cohen, *ibid.*, **111**, 512 (1964).
- M. A. H. Lanyon and B. M. W. Trapnell, *Proc. R. Soc. London, Ser. A*, **227**, 387 (1955).
- V. Brusić, in "Oxides and Oxide Films," Vol. 1, J. W. Diggle, Editor, pp. 1-89, Marcel Dekker, Inc., New York (1972).
- A. T. Fromhold, Jr., in "Passivity of Metals," R. P. Frankenthal and J. Kruger, Editors, p. 59, The Electrochemical Society, Inc., Princeton, N.J. (1978).
- A. T. Fromhold, Jr. and An-Ban Chen, *Phys. Status Solidi*, **90**, K21 (1978).
- A. T. Fromhold, Jr., "Theory of Metal Oxidation," Vol. I, "Fundamentals," North-Holland Publishing Co., Amsterdam (1976).
- A. T. Fromhold, Jr., in "Oxides and Oxide Films," Vol. 3, J. W. Diggle and A. K. Vijh, Editors, pp. 1-271, Marcel Dekker, Inc., New York (1976).
- A. T. Fromhold, Jr., *Phys. Status Solidi*, **36**, K129 (1969).
- A. T. Fromhold, Jr. and W. D. Foster, *Electrocomponent Sci. Technol.*, **3**, 51 (1976).
- L. Young, "Anodic Oxide Films," Academic Press, Inc., New York (1961).
- L. Young and F. G. R. Zobel, *This Journal*, **113**, 277 (1966).
- D. A. Vermilyea, *ibid.*, **102**, 655 (1955).
- D. A. Vermilyea, *ibid.*, **104**, 427 (1957).
- J. Kruger and J. P. Calvert, *ibid.*, **114**, 43 (1967).
- C. Kittel, "Introduction to Solid State Physics," 5th ed., p. 89, John Wiley & Sons, Inc., New York (1976).
- F. A. Kröger, *J. Phys. Chem. Solids*, **29**, 1889 (1968).
- F. A. Kröger, "The Chemistry of Imperfect Crystals," North Holland Publishing Co., Amsterdam (1964).
- A. T. Fromhold, Jr. and E. L. Cook, *J. Appl. Phys.*, **38**, 1546 (1967).
- A. T. Fromhold, Jr., in "Reaction Kinetics in Heterogeneous Chemical Systems," P. Barret, Editor, pp. 490-511, Proceedings of the 25th International Meeting of the Société de Chimie Physique, Dijon, France, July 8-12, 1974, Elsevier Scientific Publishing Co., Amsterdam (1976).
- A. T. Fromhold, Jr., *Surf. Sci.*, **22**, 396 (1972).
- A. T. Fromhold, Jr., in "Stress Effects and the Oxidation of Metals," J. V. Cathcart, Editor, pp. 2-74, Proceedings of the symposium held in Detroit, Michigan, Oct. 21-22, 1974, The Metallurgical Society of AIME, New York (1975).
- D. J. Young and M. J. Dignam, *J. Phys. Chem. Solids*, **34**, 1235 (1973).
- J. P. S. Pringle, *This Journal*, **120**, 1391 (1973).
- J. P. S. Pringle, Paper 195 presented at the Seattle, Washington, Meeting of The Electrochemical Society, May 21-26, 1978.
- S. Rigo, B. Maurel, and G. Amsel, Paper 176 presented at the Seattle, Washington, Meeting of The Electrochemical Society, May 21-26, 1978.
- J. Siejka, J. P. Nadai, and G. Amsel, *This Journal*, **118**, 727 (1971).
- S. Rigo and J. Siejka, *Solid State Commun.*, **15**, 259 (1974).
- C. Cherki and J. Siejka, *This Journal*, **120**, 784 (1973).
- B. Agius and J. Siejko, *ibid.*, **120**, 1019 (1973).
- G. Amsel and D. Samuel, *J. Phys. Chem. Solids*, **23**, 1707 (1962).
- B. Verkerk, P. Winkel, and D. G. DeGroot, *Philips Res. Rep.*, **13**, 506 (1958).
- W. J. Moore and B. Selikson, *J. Chem. Phys.*, **19**, 1539 (1951).
- J. Bardeen, W. H. Brattain, and W. Shockley, *ibid.*, **14**, 714 (1946).
- J. J. Randall, W. J. Bernard, and R. R. Wilkinson, *Electrochim. Acta*, **10**, 183 (1965).
- B. Maurel, D. Dieumegard, and G. Amsel, *This Journal*, **119**, 1715 (1972).
- D. A. Vermilyea, *Acta Metall.*, **5**, 492 (1957).
- F. A. Kröger, quoted in Paper 150 presented at the Seattle, Washington, Meeting of the Electrochemical Society, May 21-26, 1978.
- M. J. Dignam, in "Oxides and Oxide Films," Vol. 1, J. W. Diggle, Editor, pp. 91-286, Marcel Dekker, Inc., New York (1972).
- J. A. Davies and B. Domeij, *This Journal*, **110**, 84 (1963).
- D. M. Smyth, G. A. Shirn, and T. B. Tripp, *ibid.*, **111**, 1331 (1964).
- W. H. Zachariasen, *J. Am. Chem. Soc.*, **54**, 3841 (1932).
- L. Young, *Proc. R. Soc. London, Ser. A*, **258**, 496 (1960).
- D. A. Vermilyea, *This Journal*, **104**, 485 (1957).
- F. P. Fehlner and N. F. Mott, *Oxid. Met.*, **2**, 59 (1970).
- J. F. Dewald, *This Journal*, **102**, 1 (1955).
- A. T. Fromhold, Jr. and J. Kruger, *ibid.*, **120**, 722 (1973).
- A. T. Fromhold, Jr., *ibid.*, **124**, 538 (1977).
- C. P. Beañ, J. C. Fisher, and D. A. Vermilyea, *Phys. Rev.*, **101**, 551 (1956).
- M. J. Dignam, *Can. J. Chem.*, **42**, 1155 (1964).
- P. D. Dankov, C. R. (Dokl.) *Acad. Sci. URSS*, **LI**, 453 (1946).
- L. Young, *Can. J. Chem.*, **37**, 276 (1959).
- P. H. G. Draper and P. W. M. Jacobs, *Trans. Faraday Soc.*, **59**, 2888 (1963).
- R. V. Moshtev, *Ber. Bunsenges. Phys. Chem.*, **71**, 1079 (1967).

SiO₂ Particulates Dispersed in a CVD Reactor

II. Correlation with Film Characteristics

A. Shintani,* K. Suda, and M. Maki[†]

Hitachi, Limited, Central Research Laboratory, Kokubunji, Tokyo 185, Japan

ABSTRACT

The concentrations of vitreous silicate particulates dispersed in the CVD reactor measured by a laser light scattering technique are related to the characteristics of the deposited film. The larger particulates, 0.3-0.5 μm in diam, decrease in number with increase of gas flow rate with constant reactant concentrations, but smaller particulates show no change in number. When the reactants are diluted, the smaller particulates increase in number but the large particulates decrease. This confirms that the large particulates are formed by coagulation of small particulates. The 0.3-0.5 μm diam particulates cause pinholes which can be detected by generation of hydrogen bubbles in an appropriate electrolyte. The smaller particulates, 0.1-0.3 μm in diam, and the film deposition rate do not affect the pinhole formation. The pinhole density (D) is expressed in terms of the electric field strength (E), where $D \propto E^n$ ($0 < n < 1.5$). The particulate contamination of the films varies with reactant concentration but does not correspond well to the variation of the particulates dispersed in the reactor. Hillock-like patterns on film surface are not particulates.

Formation of vitreous silicate and phosphosilicate glass (PSG) films has frequently been carried out at low temperatures (450°C) using chemical vapor deposition (CVD) with silane and oxygen as reactants. Film formation is the result of a complex heterogeneous free-radical branching-chain reaction involving a surface reaction of SiH₄ and O₂ (1). A SiO₂ fog is simultaneously produced in the gas phase. This fog possibly contributes to pinholes in the film and to particulate contamination.

Recently, an aerosol measuring technique was developed which makes it possible to evaluate particulate dispersion in the reactor (3, 4). In Part I of this study (3), the size, number, and relative distribution of SiO₂ particulates with submicron diameters were measured for various conditions.

In Part II of this study, the possible correlations of pinholes and particulate contamination in CVD SiO₂ films with SiO₂ particulates in the gas phase have been investigated.

Experimental

The CVD apparatus, laser particulate monitor (LPM), and the experimental setup have been described in detail in Part I (3) and elsewhere (2).

Methods for detecting and characterizing localized defects in dielectric films have been surveyed by Kern and Comizzoli (4), and the electrolysis method used in this work is similar to that described by these authors. The specimen is made the cathode in 0.1N NaCl aqueous solution with a platinum wire as anode. Pinholes are detected by observation of hydrogen bubbles. Electrically weak points in the film cannot be distinguished from pinholes in this technique.

Particulate contamination density was estimated from the average value of the particulate flakes on 40-50 square patterns of area 0.25 cm². In addition, He-Ne laser light scattered by particulates was detected using a photomultiplier.

Results and Discussion

The size distribution of SiO₂ particulates dispersed in the CVD reactor varies with reaction time (3). Larger particulates, greater than 0.3 μm in diam, decrease in number with time, whereas smaller particulates gradually increase. These trends can be attributed to particulate coagulation in the gas phase.

* Electrochemical Society Active Member.

[†] Present address: Hitachi, Limited, Hitachi Research Laboratory, Hitachi, Ibaraki, Japan.

Key words: dielectric film, pinholes, particulate contamination, submicron particulates.

It can be easily understood that the particulate collisions in a CVD reactor are linearly proportional to gas contact time and particulate concentration. Contact time is defined by the reactor volume times the inverse of the total gas flow rate. The contact time decreases with the increase in the total gas flow rate admitted to the constant volume reactor. According to Eq. [3] in Part I

$$n = \frac{n_0}{1 + (cn_0 V R^3) t}$$

the contact time is implicitly involved in the coagulation time defined by $1/(cn_0 V R^3)$. The velocity gradient of the gas flow, $V = \partial V_x / \partial y$ included in the coagulation time, increases with total gas flow rate. This means that the decrease in coagulation time contributes to the particulate coagulation reduction trend. Therefore, large particulates decreased with the increase in gas volume when the reactant concentrations remained constant (Fig. 1). The figure shows the relation between particulate numbers and the inverse of total gas flow rate, $1/V$. While the number of large particulates increased with $1/V$, particulates smaller than 0.3 μm in diam showed no large change in number. The smallest measurable particulates, 0.1-0.2 μm , decreased in number with $1/V$.

Particulate collisions and hence coagulation is reduced when the reactant gas concentration is diluted. As shown in Fig. 2, 0.1-0.2 μm diam particulates increased in number with increased dilutions but 0.2-0.3 μm diam particulates decreased. The 0.1-0.2 μm diam particulates tended to saturate in number at dilution gas flow rates greater than 12 liters/min. The small particulate concentrations may indicate the nuclei or original particulate behavior.

The surfaces of deposited films show hillocks which increase in size with reaction time, as shown in Fig. 3. Hillock size and film thickness both rose linearly with reaction time. This result indicates that the particulates do not directly contribute to film growth. Although the behavior of particulates smaller than 0.1 μm in diam were not measured, these would be dispersed in a manner similar to the distribution of 0.1-0.2 μm diam particulates.

The particulates in the range of 0.1-0.5 μm in diam were observed because of the limitation of the LPM. On the other hand, the observed particulate flakes were larger than 1 μm in diam in both optical microscopic and laser light scattering technique measurements so that particulate contamination could not be directly

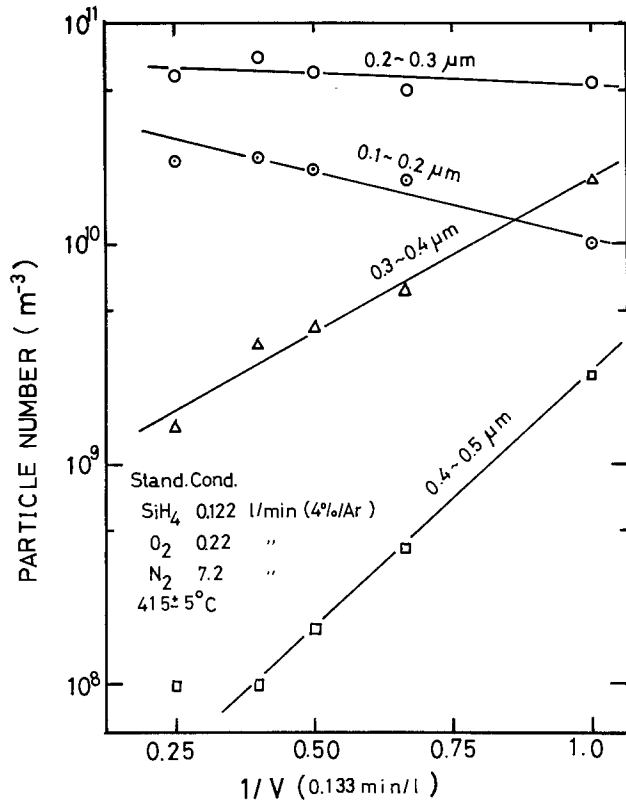


Fig. 1. Total-gas flow rate dependences of individual particulate sizes at 5 min after reaction start. Basic gas flow rates were 0.122 liter/min for SiH_4 (4% Ar), 0.22 liter/min for O_2 , and 7.2 liters/min for N_2 . Total gas flow rate was changed for the experimental conditions with these gas flow rate ratios remaining.

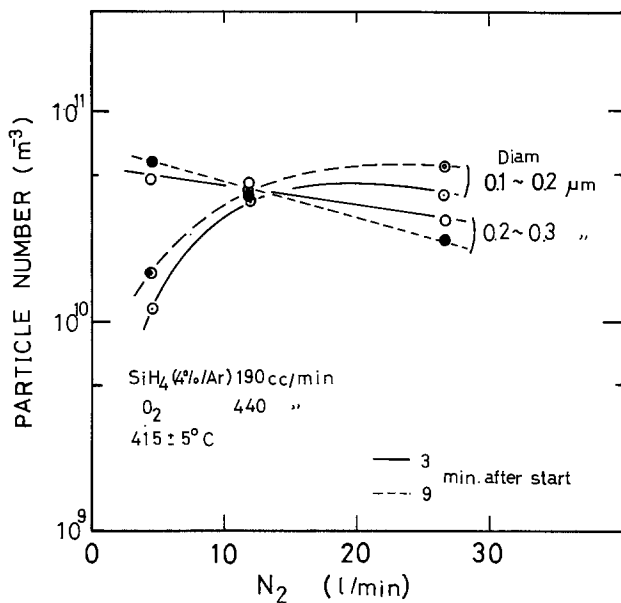


Fig. 2. Gas dilution effect on particulate distribution at 3 and 9 min after reaction start.

compared with variations of dispersed particulates. However, the behavior of particulates larger than $0.5 \mu\text{m}$ in diam can be estimated from that for particulates larger than $0.3 \mu\text{m}$ in diam as reported in Part I. Particulates larger than $0.3 \mu\text{m}$ in diam tend to decrease in number with reaction time. Judging from this, particulates larger than $1 \mu\text{m}$ in diam should be reduced in number with reaction time. The number of these larger particulates would be less than that of particulates with diameters between 0.3 and $0.5 \mu\text{m}$. If the particulates larger than $1 \mu\text{m}$ in diam contribute

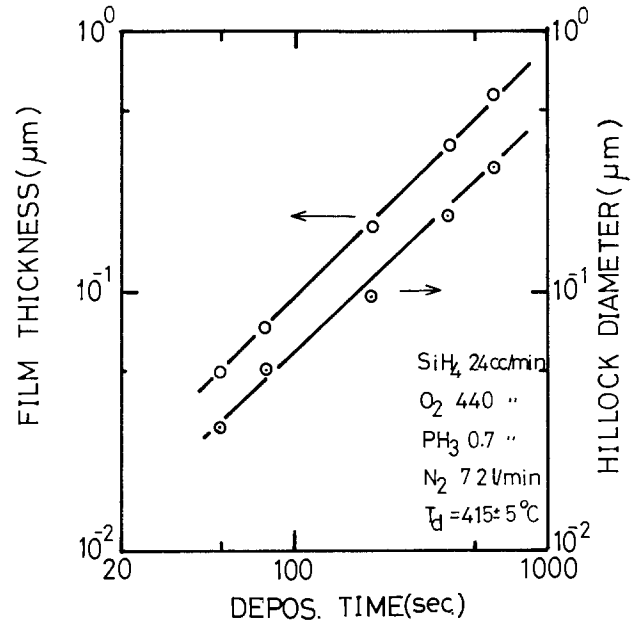


Fig. 3. Time dependences of film thickness and approximately largest hillock-like pattern sizes.

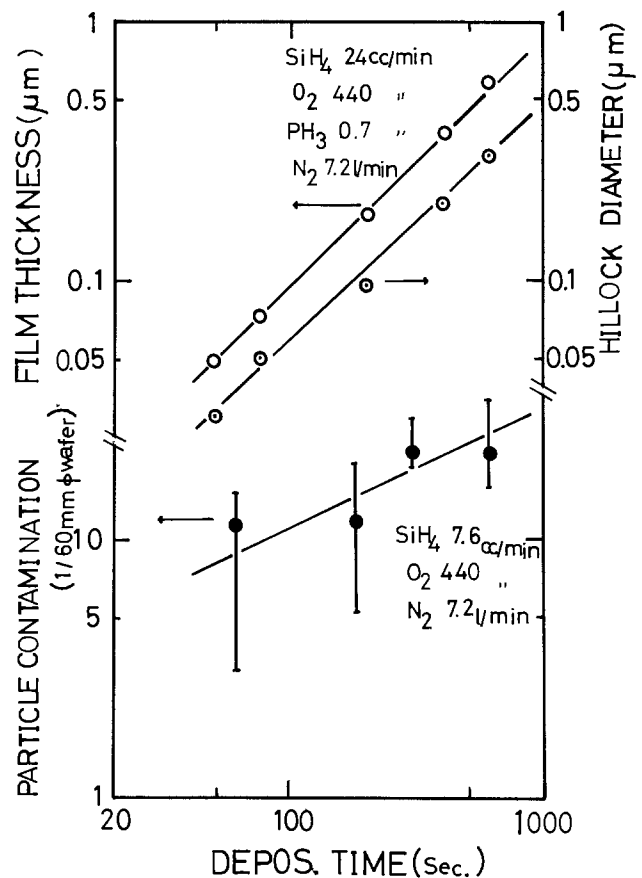


Fig. 4. Dependence of particulate contamination density on film formation time. The contamination was measured using the laser light technique.

to the observed particulate contamination, the contamination density should increase with reaction time with a power lower than one. The results were apparently consistent with this (Fig. 4).

The addition of PH_3 to the reactants inhibits particulate coagulation (3). The contamination density tended to decrease monotonically with increase in PH_3 flow rate, as revealed in Fig. 5. Comparing with Fig. 8 shown later, particulate contamination does not correspond well to particulates dispersed in the reactor.

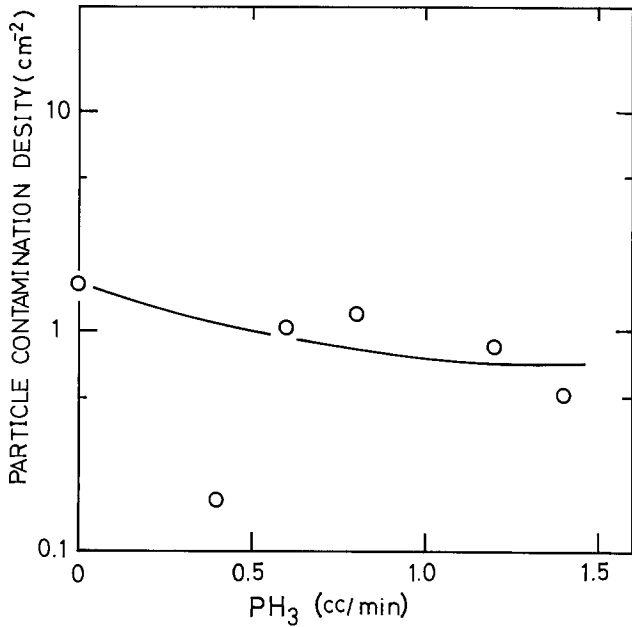


Fig. 5. PH_3 flow rate dependence of particulate contamination. The contamination was measured using a microscope.

Pinhole density measured by the electric technique depended on the strength of the electric field applied to the film, as shown in Fig. 6. Although each data point had large fluctuation, the mean pinhole density (D) can be experimentally expressed by

$$D \propto E^n \quad [1]$$

where E is the electric field strength applied to the film, and n is an appropriate constant. The figure shows that there is some difference in n between thermal and CVD oxide films.

Correlations between pinholes and film formation conditions are shown in Fig. 7 and 8. In a Si device, a vitreous silicate insulator sandwiched between evaporated Al layers is generally operated with an electric field of 10^6 V/cm. The densities plotted in the figures were obtained for films applied with electric fields of this magnitude. The number of 0.3-0.5 μm

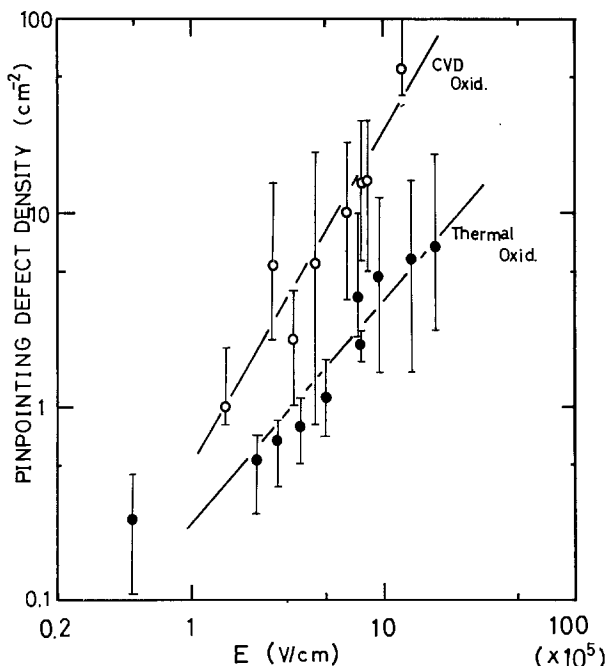


Fig. 6. Electric field strength dependences of pinholes in vitreous silicate films.

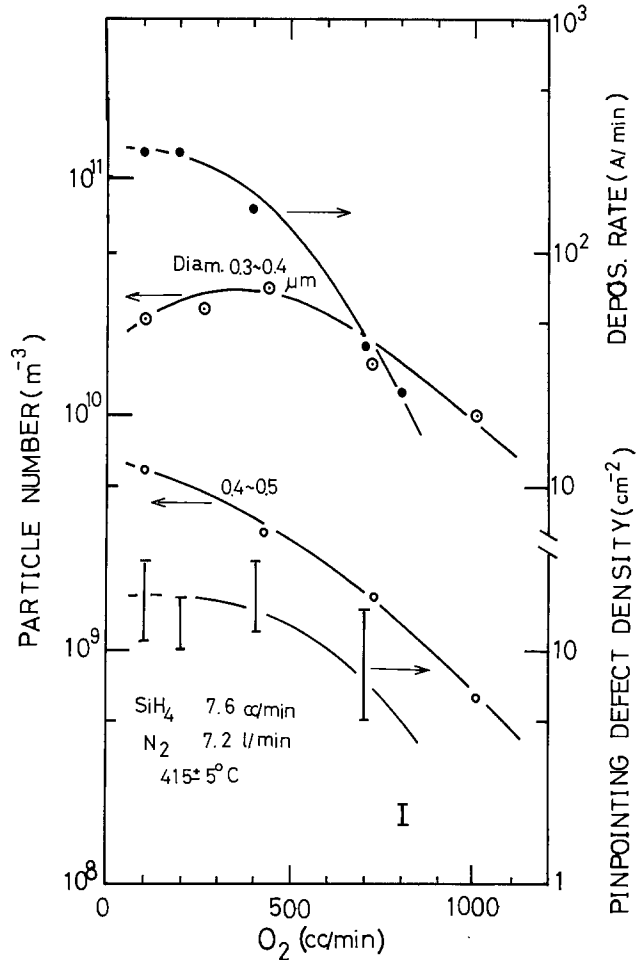


Fig. 7. O_2 flow rate dependences of 0.3-0.5 μm diam particulate number, pinhole density, and film deposition rate.

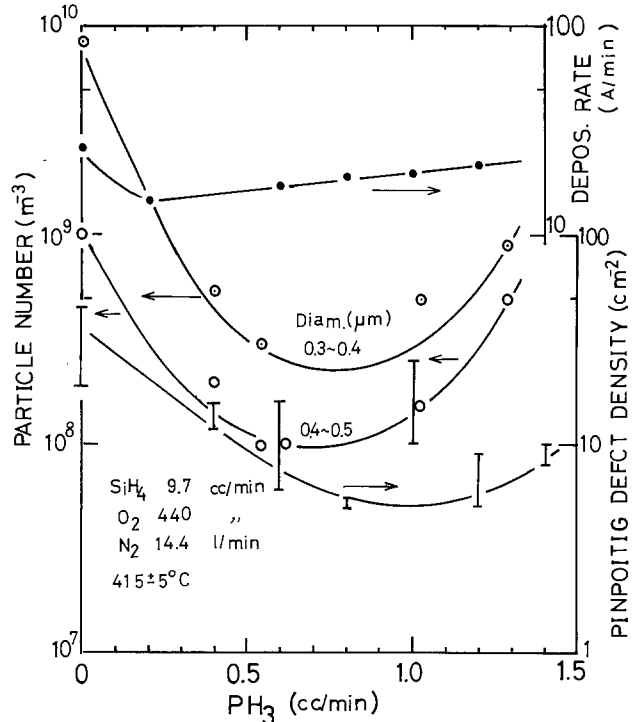


Fig. 8. PH_3 flow rate dependences of 0.3-0.5 μm diam particulate number, pinhole density, and film deposition rate.

diam particulates, the film deposition rate, and pinhole densities are illustrated. The variation in pinhole density with O_2 flow rate is in an approximate agreement

with the variations of both the film formation rate and number of particulates dispersed in the gas phase (Fig. 7). However, the variation of pinhole density with PH_3 flow rate follows that of particulate numbers, not that of film formation rate, as seen in Fig. 8. These results reveal that the pinholes and weak spots are extrinsically induced. If the local electrically weak characteristics were intrinsically generated during chemical vapor deposition, the pinhole density would undergo a major increase with the film deposition rate. When the plane formation of the film does not sufficiently develop, local irregularities in film thickness, which cause the electrically weak characteristics, occur. This can become extreme when the film surface consists of many hillock-like patterns and when the film deposition rate becomes fast. The dependence of pinhole density on PH_3 concentration is contrary to that of film deposition rate (Fig. 8).

Figures 7 and 8 show that particulates larger than $0.3 \mu\text{m}$ in diam are most likely to induce these defects. The distribution of particulates smaller than $0.3 \mu\text{m}$ in diam in the reactor contrast with those of large particulates, as mentioned previously [cf. Fig. 4, 5, and 7 in Ref. (4)]. These small particulates are accordingly not considered to be a primary cause of pinholes.

Film formation at 415°C is controlled by reactant diffusion through a stagnant gas layer over a substrate surface. Large particulates embedded on the substrate surface can act as a sink for adsorbed atoms moving on the surface and can perturb the gas phase boundary layer. Local thickness irregularities of the film, especially in the vicinity of very large particulates, is clearly visible even by eye as interference color variations. More drastic irregularities of the thickness can be seen with nondoped films than with PSG films. The addition of PH_3 to the reactants effectively inhibits the coagulation of small particulates, as discussed in Part I. The doped film surface is smoother than that of nondoped films.

Conclusions

Particulates, $0.3\text{--}0.5 \mu\text{m}$ in diam, decrease in number with increase of total gas flow rate with the reactant

concentration constant but smaller particulates show no change. Small particulates increase in number when the reactant concentrations are diluted with the ratio of reactants (O_2/SiH_4) constant but the large particulates decrease in number. This confirms that large particulates are formed by coagulation of small particulates.

Pinholes and other electrically weak points can be detected by generation of H_2 bubbles in an appropriate electrolyte. The pinhole density (D) is expressed in terms of the electric field strength (E) applied to the film, where $D \propto E^n$. The value of n is a measure of the electrical characteristics of the film. The pinholes vary in density with PH_3 concentration similar to variations of $0.3\text{--}0.5 \mu\text{m}$ diam particulates, but not to variations of smaller particulates and film deposition rate.

The hillock patterns on the surface are not attributable to particulates in $0.1\text{--}0.5 \mu\text{m}$ diam region. The variations of particulate contamination densities of the films with reactant concentrations do not correlate well with the variations in the number of particulates dispersed in the reactor.

Manuscript submitted April 3, 1979; revised manuscript received Sept. 20, 1979.

Any discussion of this paper will appear in a Discussion Section to be published in the December 1980 JOURNAL. All discussions for the December 1980 Discussion Section should be submitted by Aug. 1, 1980.

Publication costs of this article were assisted by Hitachi, Limited.

REFERENCES

1. W. Kern and R. S. Rosler, *J. Vac. Sci. Technol.*, **14**, 1082 (1977).
2. K. Suda, *J. Sci. Instrum.*, In press.
3. A. Shintani, K. Suda, M. Suzuki, M. Maki, and K. Takami, *This Journal*, **124**, 1771 (1977).
4. W. Kern, *RCA Rev.*, **34**, 655 (1973); W. Kern, *Solid State Technol.*, **17**, 35 (March, 1974); W. Kern, *ibid.*, **17**, 78 (April, 1974); W. Kern and R. B. Comizzoli, *J. Vac. Sci. Technol.*, **14**, 32 (1977).

Luminescence of Doped and Undoped $\text{Al}_2(\text{WO}_4)_3$, $\text{Sc}_2(\text{WO}_4)_3$, and $\text{Lu}_2(\text{WO}_4)_3$

G. Blasse and M. Ouwerkerk

Physical Laboratory, State University, 3508 TA Utrecht, The Netherlands

ABSTRACT

The luminescence of doped (Eu^{3+} , Cr^{3+}) and undoped $\text{Al}_2(\text{WO}_4)_3$, $\text{Sc}_2(\text{WO}_4)_3$, and $\text{Lu}_2(\text{WO}_4)_3$ has been investigated. The tungstate luminescence is not very efficient for reasons closely related to the packing of the crystal structure. $\text{Sc}_2(\text{WO}_4)_3$ and $\text{Lu}_2(\text{WO}_4)_3$ are very hygroscopic. The Eu^{3+} emission can be used as a tracer for the moisture amount of these tungstates. At 4.2°K the Cr^{3+} emission consists of ${}^2\text{E}$ line emission (R and N lines). In the vibronic structure coupling with tungstate vibrational modes have been observed. At higher temperatures the ${}^4\text{T}_2$ emission takes over.

Vanadates, niobates, tungstates, and similar compounds are known as potential efficient luminescent materials: Examples are $\text{Mg}_3(\text{VO}_4)_2$ (1), YNbO_4 (2), and CaWO_4 (3). Surprisingly enough the aluminum analogs have never been studied before in this respect. The luminescence of AlVO_4 (4) and AlNbO_4 (5) has been reported elsewhere by us. None of these materials has a high luminescent efficiency. This was ascribed to structural peculiarities.

Key words: tungstate, phosphors, crystal structure.

In this paper we report on the luminescence of doped and undoped $\text{Al}_2(\text{WO}_4)_3$, and extended our investigations to $\text{Sc}_2(\text{WO}_4)_3$ and $\text{Lu}_2(\text{WO}_4)_3$ because the three tungstates are isomorphous (6, 7). In this way we had available three host lattices in which the ionic radius of one of the constituents varies largely (Al^{3+} 0.535\AA , Sc^{3+} 0.745\AA , Lu^{3+} 0.861\AA ; radii according to Shannon and Prewitt (8) for six-coordination). As dopants we used Eu^{3+} and Cr^{3+} and, superficially, Bi^{3+} and U^{6+}

The crystal structure of these materials is rather complicated. The tungsten coordination is tetrahedral. There are two crystallographically different tungsten sites: W(1) has site symmetry C_2 and four equivalent positions in the orthorhombic unit cell, W(2) has C_1 and eight equivalent positions. The trivalent metal ion is in a distorted, octahedral coordination with site symmetry C_1 .

Borchardt (9) has reported the luminescence of $Sc_2(WO_4)_3$ and $Lu_2(WO_4)_3$ at 77°K. Stork *et al.* (10) reported the 300°K emission spectrum of Cr^{3+} in $Al_2(MoO_4)_3$ during a study of the catalytic properties of the system $Mo|\gamma-Al_2O_3$. This molybdate is isomorphous with $Al_2(WO_4)_3$ as is $Cr_2(WO_4)_3$ (6). Our investigations are considerably broader without entering into every detail.

Experimental

Samples were prepared by firing intimate mixtures of the starting materials ($Al(OH)_3$, Sc_2O_3 , Lu_2O_3 , Eu_2O_3 , Cr_2O_3 , and WO_3) in corundum crucibles at 800°C and, after a milling procedure, at 1000°C for several hours in air. In a few cases samples were prepared in a completely dry atmosphere and mounted in the cryostat in a dry box. X-ray powder patterns were run on a Philips diffractometer using $CuK\alpha$ radiation. The performance of the optical measurements has been described before (1, 5).

Results and Discussion

Vibrational spectra.—The infrared and Raman spectra were measured for $Al_2(WO_4)_3$, $Sc_2(WO_4)_3$, and $Lu_2(WO_4)_3$. Figure 1 presents the Raman spectra in the region of the W-O stretching vibrations. Figure 2 gives the infrared spectrum of $Al_2(WO_4)_3$ in that

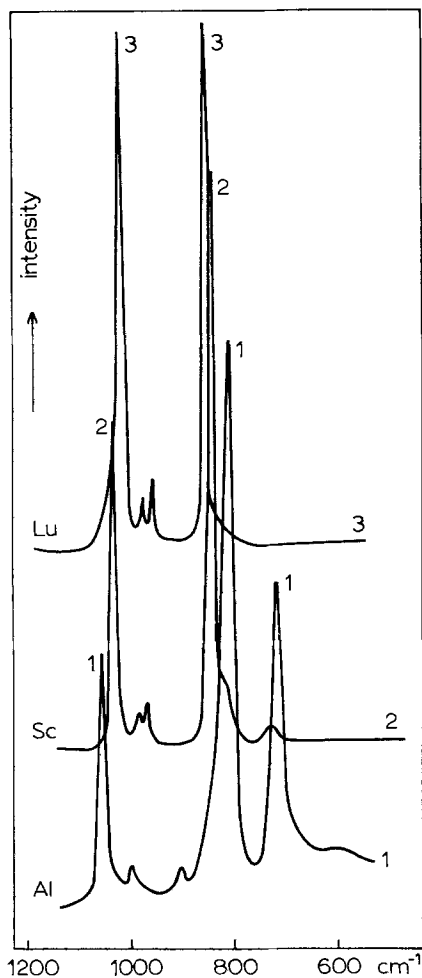


Fig. 1. Raman spectra of $Al_2(WO_4)_3$, $Sc_2(WO_4)_3$, and $Lu_2(WO_4)_3$ at room temperature in the W-O stretching region.

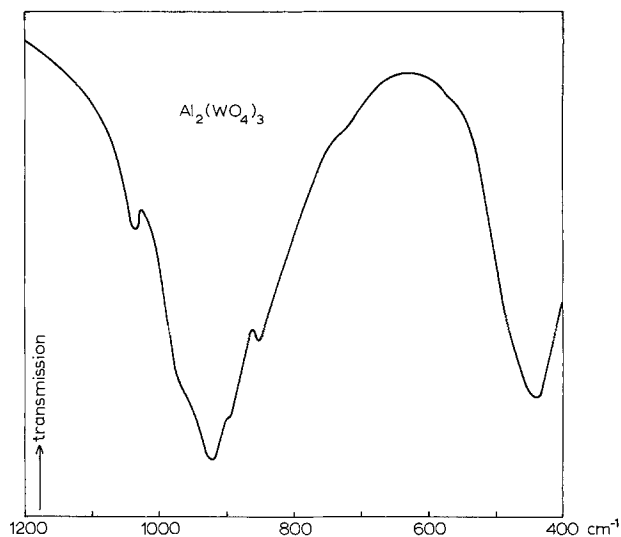


Fig. 2. Infrared spectrum of $Al_2(WO_4)_3$ at room temperature (KBr pellet).

region. Those of $Sc_2(WO_4)_3$ and especially $Lu_2(WO_4)_3$ show less subbands and are less broad. Figures 1 and 2 show two interesting facts, *viz.*, the number of lines or bands is large, and the spectral region which is covered by the W-O stretching vibrations is very large.

This is especially clear after comparison with the spectra for a tungstate with a simple crystal structure, *e.g.*, Na_2WO_4 , where the symmetric stretching mode (ν_1) is at 928 cm^{-1} and the asymmetric stretching mode (ν_3) at 811 cm^{-1} (11). The present complicated situation arises from the fact that the unit cell (with symmetry D_{2h}) contains four W(1) and eight W(2) ions. Under the low site symmetry of both ions the threefold degenerate ν_3 splits into components which, partly in the case of W(1) and completely in the case of W(2), have the same symmetry representation as ν_1 . As a consequence the symmetric and asymmetric modes mix and it is no longer useful to make a distinction between them. A similar situation has been reported for Mg_2SiO_4 (12).

On the basis of the site symmetry alone (neglecting interaction between equivalent tungstate tetrahedra) we expect eight allowed peaks in the Raman as well as in the infrared spectra. We find fewer peaks, but the large difference between the Raman and infrared spectra suggests that the interaction (factor group analysis) should be taken into account. This yields 24 Raman peaks and 18 infrared bands which, due to the exclusion principle, should be different. It is clear that the experimental results cannot be analyzed on this basis. Two remarks can be made. (i) The interaction between equivalent tungstate groups is expected to be stronger in the aluminum compound than in the other two compounds in view of the shorter W-W distances. In fact the spectra of the aluminum compound extend over the widest range, (ii) The presence of relatively high vibrational frequencies (> 1000 cm^{-1}) may be related to the occurrence of relatively short W-O distances in the crystal structure [*e.g.*, 1.70Å for W(1)-O(4) in $Sc_2(WO_4)_3$ to be compared with the tetrahedral W-O distance in $CaWO_4$ of 1.78Å (6)]. However, the more important reason for reporting the vibrational spectra here is that they are of use in the interpretation of the Cr^{3+} emission spectrum of $Al_2(WO_4)_3-Cr$.

Diffuse reflection spectra.—The reflection spectra of the three tungstates resemble the reflection spectrum of $Sc_2(WO_4)_3$ reported by Borchardt (9). There is an optical bandgap in the short wavelength ultraviolet: at 230 nm for $Lu_2(WO_4)_3$, at 235 nm for $Sc_2(WO_4)_3$,

and 240 nm for $\text{Al}_3(\text{WO}_4)_3$. This part of the spectrum is independent of sample history. Excitation into this region will be called i-excitation below. This is the same absorption as observed, for example, for the alkaline earth tungstates MWO_4 ($\text{M} = \text{Ca}, \text{Sr}, \text{Ba}$) where the edge is also below some 250 nm and shifts to shorter wavelengths the larger the alkaline earth ion (13).

In addition, the reflection spectra show a tail which extends down to some 360 nm. The shape of the tail depends on sample history. The tail in the spectra of our samples has lower intensity than that reported in Ref. (9). We will call this part the e-part of the spectrum.

The absorption in these spectral regions is ascribed to charge-transfer transitions in the tungstate groups. A more detailed assignment will be given below in connection with the luminescence emission spectra.

Tungstate luminescence.—None of the undoped compounds under consideration show luminescence at room temperature; at liquid nitrogen temperature they show a weak, blue-green emission under ultra-violet excitation; the emission intensity increases upon cooling to liquid helium temperature. In Fig. 3 we have given some representative examples of emission spectra for the case of $\text{Al}_2(\text{WO}_4)_3$. For i-excitation the emission consists of a broad band with a maximum at about 460 nm, for e-excitation the emission depends on excitation wavelength and peaks in the range between 500 and 550 nm.

Excitation spectra do not yield much additional information because the broad emission bands cannot be separated. The excitation spectra can also be divided into what we have called an i and an e region. These spectra extend down to some 360 nm. The 460 nm emission band has a short wavelength limit at about 360 nm.

The i-region is assumed to be the intrinsic tungstate absorption region corresponding with the shorter wavelength emission band. This compares favorably with the situation in CaWO_4 (3, 13). One may wonder what is the reason for the relatively low quenching temperature of the luminescence and the absence of a really intense emission at very low temperatures. It cannot be excluded that this is partly due to the fact that the 460 nm emission band "touches" the e-region excitation band, so that energy transfer may have a reasonable probability. The emission spectrum for i-excitation, however, contains only a minor amount of the long-wavelength emission, so that this cannot be the real explanation for the low quenching temperature and luminescence intensity.

The sharp decrease of luminescence intensity and quenching temperature in the series of scheelites CaWO_4 , SrWO_4 , BaWO_4 has been ascribed to the increase of the ionic radius of the alkaline earth ion so that the parabola offset in the configurational coordinate diagram will be largest for the largest ion resulting in the lowest luminescence intensity and quenching temperature (14). In the scheelites the oxygen ion is surrounded by one tungsten ion and two alkaline earth ions in a roughly triangular way. If the W-O distance increases upon excitation, oxygen ion movement will be inhibited by the alkaline earth ions. In the crystal structure of the present tungstates the oxygen ion is coordinated by one tungsten ion and only one trivalent metal ion in a nonlinear arrangement. As a consequence the trivalent metal ion essentially does not oppose expansion of the W-O distance. This runs parallel with the influence of the large divalent ions in the ordered perovskite structure upon the quenching temperature of luminescence. This influence is practically nonexistent (15). This model explains why the parabola offset of the tungstate tetrahedra in the compounds $\text{M}_2(\text{WO}_4)_3$ under

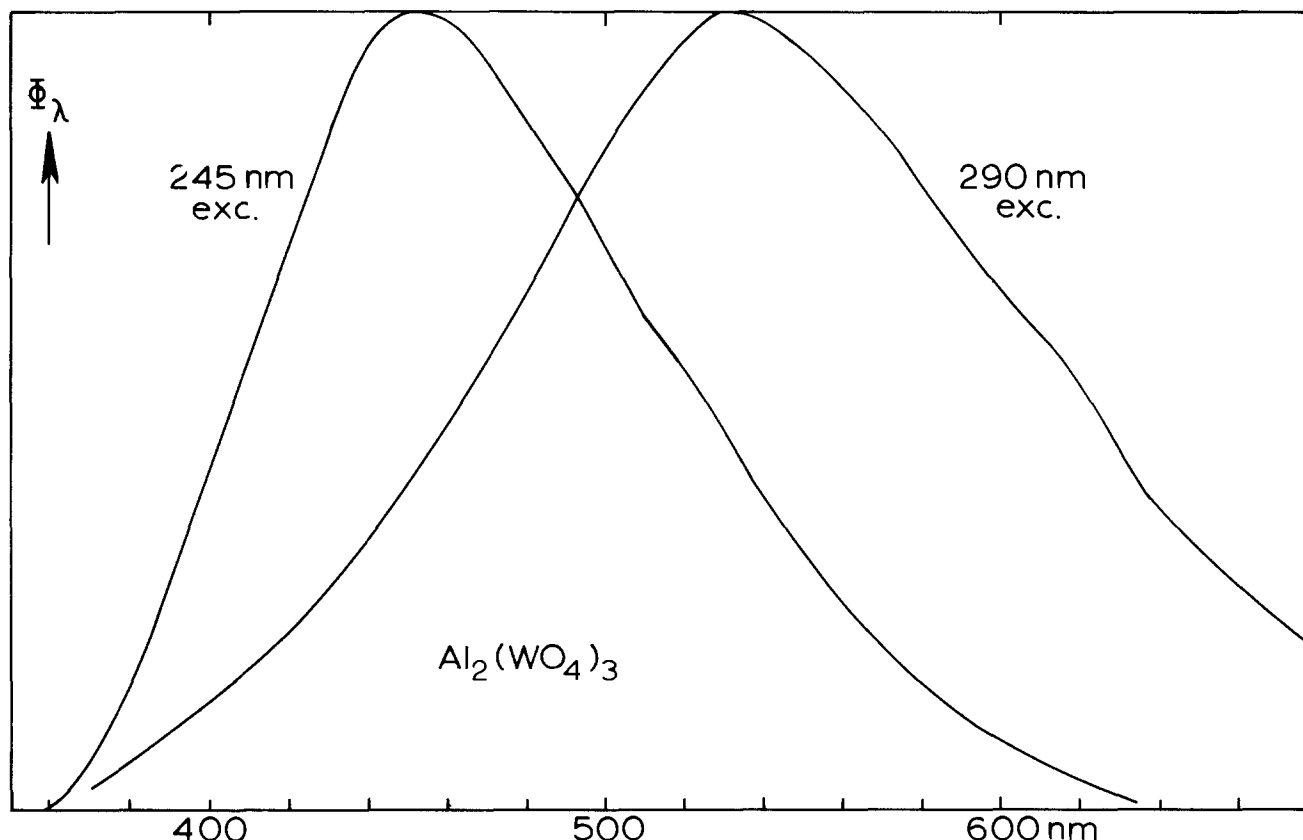


Fig. 3. Spectral energy distribution of the emission of $\text{Al}_2(\text{WO}_4)_3$ at 4.2°K . Φ_λ gives the spectral radiant power per unit wavelength interval in arbitrary units. Left-hand side: i-region excitation; right-hand side: e-region excitation (see also text).

consideration is large and, consequently, the luminescence intensity and quenching temperature low. The model has two implications. In the first place, the Stokes shift of the emission should be large. This is in fact observed. In the case of the efficient phosphor CaWO_4 the tungstate luminescence Stokes shift is some $16,000 \text{ cm}^{-1}$ (3). In the present compounds it amounts to at least some $20,000 \text{ cm}^{-1}$ (due to the short-wavelength limitation of our apparatus it is difficult to measure the i-excitation band maximum accurately). In the second place, the nature of the trivalent ion should not have a great influence on the quenching temperature. This also was observed.

Let us now turn to the e-excitation region with the longer wavelength emission band. Since the characteristics of this luminescence depends on sample history and on excitation wavelength, it is obvious to ascribe this luminescence to extrinsic tungstate groups, i.e., groups which are located near to imperfections in the crystal lattice. It is now well known that many tungstates (and also titanates, niobates) show an additional long wavelength emission which is due to tungstate groups near defects (16). Energy transfer from intrinsic to extrinsic groups has also been shown to occur. What is different in the tungstates under consideration is the high concentration of the extrinsic groups as appears from the diffuse reflection spectra. It may be that the complicated character of the crystal structure favors a high concentration of imperfections. In addition it should be mentioned that especially $\text{Sc}_2(\text{WO}_4)_3$ and $\text{Lu}_2(\text{WO}_4)_3$ are hygroscopic. The hydrated samples can be excited most efficiently in the e-region (see below). Even samples prepared and handled in a completely dry atmosphere showed the e-region absorption, so that it cannot be solely due to the presence of hydration. It is general experience, and not unexpected, that the extrinsic groups have quenching temperatures and efficiencies which are about equal to and often even lower than those of the intrinsic groups (16). This agrees with the present results.

The complicated nature of the host lattice luminescence makes these compounds very unsuitable for a study of energy transfer. Nevertheless we investigated several doped samples. Only Eu^{3+} and Cr^{3+} activation seems to be worthwhile to be reported separately. The activation with U^{6+} yielded weak green luminescence with a uranyl-type character (17), and the activation with Bi^{3+} yielded new, broad emission bands at longer wavelengths upon excitation in the e-region as reported before for similar Bi^{3+} -activated compounds (18).

Eu^{3+} emission.— Eu^{3+} -activated tungstates $\text{M}_2(\text{WO}_4)_3$ ($\text{M} = \text{Al}, \text{Sc}, \text{Lu}$) show at room temperature a red luminescence of medium intensity. At lower temperatures the tungstate emission bands are also present. Figure 4 shows the Eu^{3+} emission spectrum of $\text{Al}_2(\text{WO}_4)_3:\text{Eu}$ upon excitation into the Eu^{3+} ions. Figure 5 presents the emission spectrum of dry $\text{Lu}_2(\text{WO}_4)_3:\text{Eu}$ upon i-excitation, whereas Fig. 6 gives the emission spectrum of $\text{Lu}_2(\text{WO}_2)_3:\text{Eu}$ upon e-excitation. The latter sample was prepared and handled in an undried atmosphere.

First we consider the Eu^{3+} emission spectrum. Formally the Eu^{3+} ion occupies a site without any symmetry element, so that all degeneracy should be lifted and every transition allowed. Figure 4 shows that this is only partially the case. The ${}^5\text{D}_0\text{-}{}^7\text{F}_1$ transition is not clearly split into three components in $\text{Al}_2(\text{WO}_4)_3$, but in dry $\text{Lu}_2(\text{WO}_4)_3$ it is not split at all (Fig. 5). This suggests that the coordination of the Eu^{3+} ion is not distorted too strongly from regular octahedral. Such coordination has been reported for Al, Sc and Lu (6, 7). The fact that the Eu^{3+} ion is much larger than the trivalent host lattice ions does not obviously change this situation, although it can be concluded that the distortion around Eu^{3+} on Al^{3+} sites must be

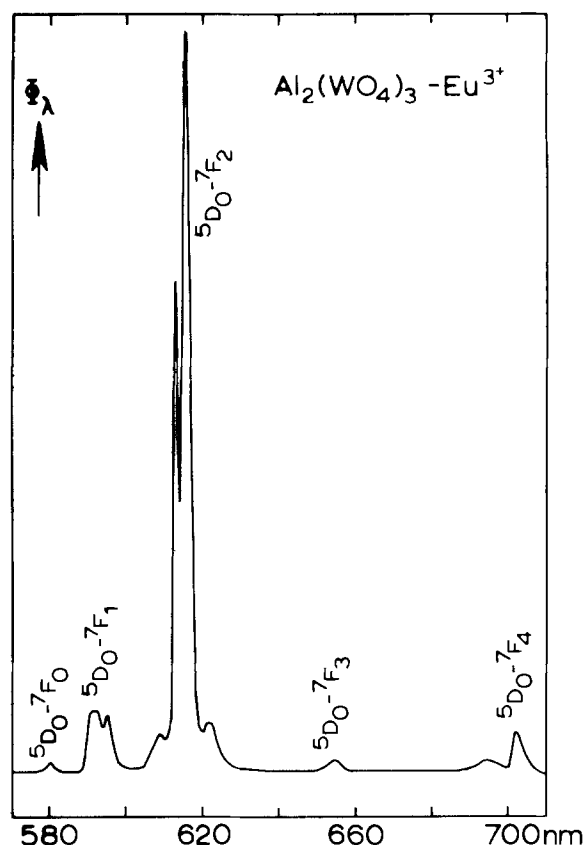


Fig. 4. Spectral energy distribution of the Eu^{3+} emission of $\text{Al}_{1.98}\text{Eu}_{0.02}(\text{WO}_4)_3$ at 4.2°K . Excitation into the Eu^{3+} ion at 395 nm .

larger than on the Sc^{3+} and Lu^{3+} sites. This is not too surprising. Note also that the Eu^{3+} emission is strongly concentrated in the red ${}^5\text{D}_0\text{-}{}^7\text{F}_2$ transition. This is another example of the influence of hypersensitivity on the ${}^5\text{D}_0\text{-}{}^7\text{F}_2$ transition (19-21). The small deviation from inversion symmetry (regular octahedron) is not enough to enforce the electric dipole transitions (${}^5\text{D}_0\text{-}{}^7\text{F}_4$) considerably, but enforces strongly the hypersensitive ${}^5\text{D}_0\text{-}{}^7\text{F}_2$ transition.

Excitation into the host lattice yields emission spectra like those given in Fig. 5 and 6. For Eu^{3+} concentrations of 1 atomic percent (a/o) the ratio of Eu^{3+} to tungstate emission is of the order one-half to one-third. At first sight this indicates efficient transfer from the host lattice to the activator, but this is incorrect since the tungstate emission has already been partly quenched as argued above. There is no sense in studying energy transfer phenomena more quantitatively in these systems because the extrinsic tungstate groups compete with the Eu^{3+} ions in trapping the host lattice emission and also the quenching temperature of the tungstate luminescence is low.

The results for $\text{Sc}_2(\text{WO}_4)_3:\text{Eu}^{3+}$ and $\text{Lu}_2(\text{WO}_4)_3:\text{Eu}^{3+}$ depend on whether the samples have been kept completely dry or not. In Fig. 6 the emission spectrum of Eu^{3+} in the "wet" sample is different from that in the dry sample (Fig. 5). All lines are much broader in the wet sample; further, the ${}^5\text{D}_0\text{-}{}^7\text{F}_1$ transition is now split and the ${}^5\text{D}_0\text{-}{}^7\text{F}_0$ transition (at about 580 nm), although weak, has a higher intensity. Even in the dry sample the "wet" Eu^{3+} emission can be obtained by exciting selectively in the e-region, viz., around 280 nm . The explanation of all this is that $\text{Sc}_2(\text{WO}_4)_3$ and $\text{Lu}_2(\text{WO}_4)_3$ are very hygroscopic [whereas $\text{Al}_2(\text{WO}_4)_3$ is not]. The hydrates are excited most efficiently at 280 nm . This is a very sensitive test for the humidity content of the samples. In fact not even our dry samples, prepared and mounted with great care, were completely water-free. The Eu^{3+} coordina-

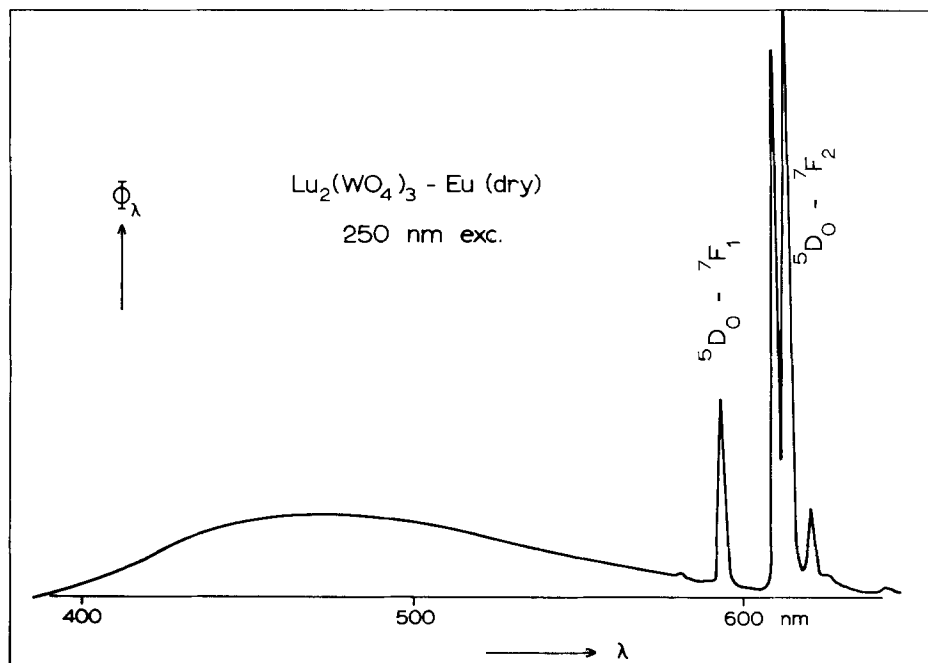


Fig. 5. Spectral energy distribution of the emission of $\text{Lu}_{1.98}\text{Eu}_{0.02}(\text{WO}_4)_3$ at 4.2°K under i-region excitation. Dry sample.

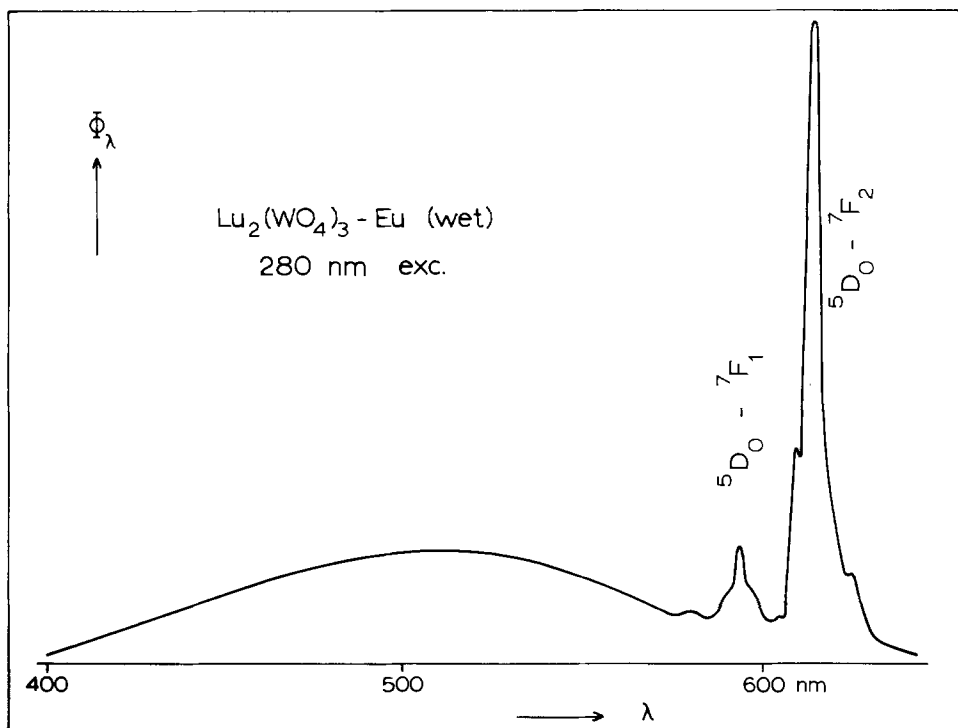


Fig. 6. Spectral energy distribution of the emission of $\text{Lu}_{1.98}\text{Eu}_{0.02}(\text{WO}_4)_3$ at 4.2°K under e-region excitation. Wet sample.

tion in the hydrate is different from that in the dry compound.

Cr^{3+} emission.—The Cr^{3+} ion yields deep-red to infrared emission in the present host lattices. The character of this emission depends on the temperature. The 4.2°K emission of Cr^{3+} in $\text{Al}_2(\text{WO}_4)_3$ is shown in Fig. 7 and consists of two lines at 719 and 723.5 nm followed by some weak vibronic structure which has been tabulated in Table I. In view of the low Cr^{3+} concentration (0.5 a/o) and the fact that there is only one crystallographic site for the trivalent metal ions, the occurrence at low temperature of two lines is surprising. The lines are undoubtedly due to the $^2\text{E} \rightarrow ^4\text{A}_2$ transition on the Cr^{3+} ion. The fact that there is more than one line can be ascribed to Cr^{3+} pair emission which has been studied intensively in other host lattices (22). The energy difference between the two lines, about 90 cm^{-1} , is well in line

with such an interpretation. In Table I the 719 nm line is called the R line and the 723.5 nm pair line the N line following the literature convention. Table I shows that the R and the N line are followed by similar vibronic lines. There is coupling with a low frequency mode which probably has mainly $\text{Me}^{3+}-\text{O}^{2-}$ character, but also with tungstate vibrational modes and especially with those which occur with high intensity in the infrared spectra. In view of the D_{2h} symmetry of the unit cell these have Ungerade symmetry as required for coupling to the parity-forbidden $^2\text{E} \rightarrow ^4\text{A}_2$ transition. It is interesting that the transition on the Cr^{3+} ion couples with the tungstate vibrational modes.

The excitation spectrum of this emission contains, in addition to the tungstate excitation bands, the well-known $^4\text{A}_2 \rightarrow ^4\text{T}_2$, $^4\text{T}_1(\text{F})$, $^4\text{T}_1(\text{P})$ transitions. These show also some vibrational structure in which the

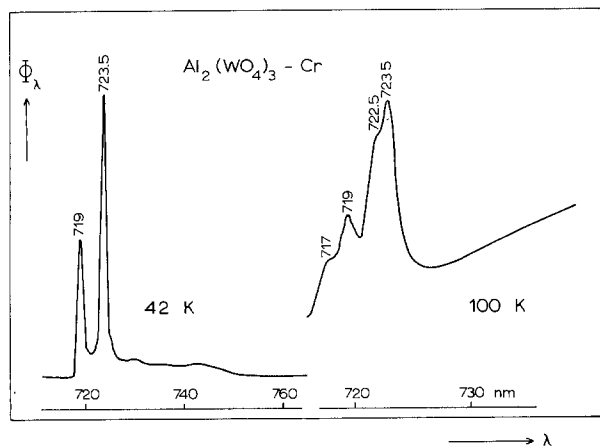


Fig. 7. Spectral energy distribution of the Cr^{3+} emission of $\text{Al}_{1.99}\text{Cr}_{0.01}(\text{WO}_4)_3$ at 4.2°K (left-hand side) and at 100°K (right-hand side) under 470 nm excitation [${}^4\text{A}_2 \rightarrow {}^4\text{T}_1(\text{F})$]. Note the change in wavelength scale. In the 100°K spectrum the highest energy part of the ${}^4\text{T}_2 \rightarrow {}^4\text{A}_2$ emission band (peaking at about 800 nm) is observable.

tungstate-vibrations can be recognized, but due to their vagueness the assignment cannot be made with much certainty.

The pair line (N) is much too strong for Cr^{3+} to be distributed at random among the aluminum lattice. Since our samples were made by solid-state reactions, we have to assume that the Cr^{3+} ions occur still in pairs in the lattice. This phenomena is well known for Cr^{3+} (23). In fact the samples mentioned in Ref. (10) were made from solution and show a higher R/N line intensity ratio than ours.

At higher temperatures the spectrum becomes rapidly more complex (see Fig. 7). The R as well as the N line are accompanied by a line at higher energy indicating the well-known splitting of the ${}^2\text{E}$ level (22). For the single ion this splitting amounts to some 40 cm^{-1} which is well in line with results on Cr^{3+} in other lattices (22). In addition, a broad-band emission develops peaking at roughly 800 nm . This is the ${}^4\text{T}_2 \rightarrow {}^4\text{A}_2$ emission from the thermally occupied ${}^4\text{T}_2$ level. The total emission intensity drops strongly from 4.2° to 300°K . This agrees with models proposed by Fonger and Struck (24) which state that the Cr^{3+} emission is quenched via the ${}^4\text{T}_2$ level. In ruby the ${}^4\text{T}_2$ level is high (2350 cm^{-1}) above the ${}^2\text{E}$ level, but in $\text{Al}_2(\text{WO}_4)_3$ the energy difference must be considerably smaller. From the position of the R line and the first peak in the vibrational structure of the ${}^4\text{A}_2 \rightarrow {}^4\text{T}_2(\text{F})$ excitation band (which is then considered to be the zero-phonon line) the energy difference is estimated to be 500 cm^{-1} .

Table I. Vibronic side band frequencies of $\text{Al}_2(\text{WO}_4)_3:\text{Cr}$ at 4.2°K

Vibronic side band frequency ($\pm 10\text{ cm}^{-1}$) ^b	Electronic origin ^c	Character	Vibrational spectrum (cm^{-1}) ^b
195 cm^{-1} (s)	R	} $\text{Me}^{3+}-\text{O}^{2-}$	
195 (m)	N		
450 (m)	R	} Tungstate deformation mode	440, IR, s
440 (m)	N		
870 (w)	R	} Tungstate stretching mode	~ 920 , IR, s
890 (w)	N		
980 (w)	R	} Tungstate stretching mode	1050, Ra, s
1030 (w)	N		

^a These vibronics coincide into a relatively broad peak.

^b s: strong, m: medium, w: weak, Ra: Raman, IR: infrared.

^c R: R line (single ion emission); N: N line (pair emission).

Concluding Remarks

The crystal structure of $\text{Al}_2(\text{WO}_4)_3$ is so complicated that it obviously allows a high concentration of defects which complicate the luminescence behavior. The thermal quenching temperature of the tungstate luminescence is low and composition independent which can be ascribed to a structural characteristic, viz., the oxygen coordination.

Consequently, efficient energy transfer to activators does not occur. The emission of Eu^{3+} can easily be explained and is at the same time sensitive to the moisture content of the samples. The Cr^{3+} emission can be explained following well-known models. The Cr^{3+} emission couples with tungstate vibrational modes. The ${}^4\text{T}_2(\text{F})$ level is rather close above the ${}^2\text{E}$ level resulting in broad-band emission and quenching at elevated temperatures.

Acknowledgments

The authors are indebted to Mr. J. Hop who performed a number of introductory experiments.

Manuscript received June 27, 1979.

Any discussion of this paper will appear in a Discussion Section to be published in the December 1980 JOURNAL. All discussions for the December 1980 Discussion Section should be submitted by Aug. 1, 1980.

Publication costs of this article were assisted by State University.

REFERENCES

- H. Ronde and G. Blasse, *J. Inorg. Nucl. Chem.*, **40**, 215 (1978).
- W. L. Wanmaker, A. Bril, J. W. ter Vrugt, and J. Broos, *Philips Res. Rep.*, **21**, 270 (1966).
- F. A. Kröger, "Some Aspects of the Luminescence of Solids," Elsevier, New York (1948).
- G. Blasse and J. Hop, *J. Solid State Chem.*, **27**, 423 (1979).
- G. Blasse and R. U. E. 't Lam, *ibid.*, **25**, 77 (1978).
- S. C. Abrahams and J. L. Bernstein, *J. Chem. Phys.*, **45**, 2745 (1966).
- J. J. de Boer, *Acta Crystallogr. Sect. B*, **30**, 1878 (1974).
- R. D. Shannon and C. T. Prewitt, *ibid.*, **26**, 1076 (1970).
- H. J. Borchardt, *J. Chem. Phys.*, **39**, 504 (1963).
- W. H. J. Stork, J. G. F. Coolegem, and G. T. Pott, *J. Catal.*, **32**, 497 (1974).
- A. Müller, E. J. Baran, and R. O. Carter, *Structure Bonding (Berlin)*, **26**, 112 (1976).
- M. Th. Paques-Ledent and P. Tarte, *Spectrochim. Acta, Part A*, **29**, 1007 (1973).
- G. Blasse and W. J. Schipper, *Phys. Status Solidi A*, **25**, K163 (1974).
- G. Blasse, *J. Chem. Phys.*, **51**, 3529 (1969).
- J. Th. W. de Hair and G. Blasse, *J. Solid State Chem.*, **19**, 263 (1976).
- J. A. Groenink and G. Blasse, *ibid.*, In press; *Phys. Status Solidi*, **54**, 477 (1979); A. J. H. Macke, *Phys. Status Solidi A*, **39**, 117 (1977).
- M. V. Hoffmann, *This Journal*, **117**, 227 (1970).
- G. Blasse and A. Bril, *J. Chem. Phys.*, **50**, 2974 (1969).
- C. K. Jørgensen and B. R. Judd, *Mol. Phys.*, **8**, 281 (1964).
- R. D. Peacock, *Structure Bonding (Berlin)*, **22**, 83 (1975).
- G. Blasse, *ibid.*, **26**, 43 (1976).
- G. F. Imbusch, in "Luminescence Spectroscopy," M. D. Lumb, Editor, Chap. I, Academic Press, New York (1978); "Luminescence of Inorganic Solids," B. Di Bartolo, Editor, pp. 115, 135, and 155, Plenum Press, New York (1978).
- A. Ellison and K. S. W. Sing, *J. Chem. Soc. Faraday Trans. 1*, **12**, 2807 (1978); F. Kellendonk, this laboratory, unpublished.
- W. H. Fonger and C. W. Struck, *Phys. Rev. B*, **11**, 3252 (1975).

U.V. Absorption Band in Ge-Doped Sodalite Powders

L. T. Todd, Jr. and F. M. Tranjan

Department of Electrical Engineering, University of Kentucky, Lexington, Kentucky 40506

ABSTRACT

A bright green luminescence, with an emission bandpeak at 5250Å and an excitation bandpeak at 3465Å, has been reported for germanium-doped sodalite powders. This article reports the results of an investigation of the properties of u.v. absorption band at 3450Å that is shown to be responsible for the luminescence. A settled slide technique was used to prepare samples so that small variations in the absorption band could be detected. Experimental results are presented that show the effect of the hydrogen annealing temperature, hydrogen annealing time, and F-center creation on the u.v. absorption band intensity. The results indicate a definite relationship between the u.v. absorption band and the luminescence. The results of the coloration experiments show that the luminescent centers are associated with thermally erasable F-centers while they are independent of photoerasable F-centers. The u.v. band was found to exist in sodalite: Cl, Br, and I. While the band intensities differ for those powders, the peak wavelengths are exactly the same. Possible models for both coloration and luminescence are discussed.

The luminescent properties of germanium-doped synthetic sodalite powders have been reported by Todd (1, 2). The luminescence is characterized by an emission bandpeak at 5250Å and an excitation bandpeak at 3465Å. Todd studied the effect of the hydrogen annealing temperature, the hydrogen annealing time, and F-center creation on the luminescent intensity. Information regarding the number of luminescent centers was obtained indirectly rather than by direct experimental observation. The intensity of the luminescence generated within the colored powders was calculated using data obtained from measurements of observed luminescence and diffuse reflectance spectra (2). That study found that F-center creation by electron beam coloration greatly reduces the observed luminescence. This reduction results partially from the absorption of generated luminescence by F-centers while further reduction results from actual quenching of luminescent centers. The quenching was shown to be associated with the creation of thermally erasable F-centers while the creation of optically erasable F-centers did not cause quenching.

This article reports the observation of a u.v. absorption band at 3450Å in germanium-doped sodalite powders. The purpose of this study was to determine if this band represents the absorption due to the luminescent centers reported earlier (2). If that were the case, one could directly observe the behavior of the luminescent centers under various experimental conditions rather than use indirect mathematical calculations to obtain the results. A technique for detecting small variations in the u.v. absorption spectra of sodalite powders is described. This technique is used to determine the effect of the hydrogen annealing temperature, hydrogen annealing time, and F-center creation on the u.v. absorption band intensity. The results of these experiments are compared to those reported by Todd (2).

Experimental

Material preparation and measurement techniques.—The materials used in this investigation were grown by a hydrothermal growth technique as described previously (2-4). The powders were annealed in a hydrogen atmosphere to sensitize them to permit both coloration and luminescence.

Samples for absorption measurements were made using a modified version of a technique described by Chang and Onton (5). Powders were settled onto glass slides (1 × 1/2 × 1/16 in.) using a conventional powder settling technique (6) rather than using the compressed powder technique used by Chang and

Key words: sodalite, u.v. absorption, luminescence cathodochromism.

Onton. The density of the settled powders was varied between 2.5-12.6 mg/cm². Samples were colored by electron beam exposure in a demountable CRT system using an accelerating voltage of 30 kV (7). Index matching liquid was added to the powder to reduce light scattering in order to permit transmission measurements. A second glass slide was placed over the powder surface to retain the index matching liquid.

Absorption spectra were obtained with a Cary-14 spectro-photometer. Two glass slides were placed in the path of the reference beam to nullify the absorption of the glass used for the sample holder. An index matching liquid with $n = 1.484$ was used for all experiments since it provided maximum light transmission. The absorption of this liquid is negligible in the wavelength region of interest (3100-8000Å).

Results

The u.v. absorption band reported in this investigation is shown in Fig. 1 centered at 3450Å. This spectrum was obtained using a bromine sodalite sample with 1 atomic percent (a/o) germanium substituted for silicon, $\text{Na}_6\text{Al}_6(\text{Si}_{0.99}\text{Ge}_{0.01})_6\text{O}_{24} \cdot 2\text{NaBr}$. The powder was annealed in hydrogen at 750°C for 15 min and the sample density was 12.6 mg/cm². This powder emits a very bright green luminescence when excited by long wavelength u.v. radiation. The spectrum for an undoped bromine sodalite sample annealed under the same conditions is also shown in Fig. 1. This material does not luminesce under u.v. excitation and does not possess the u.v. absorption band at 3450Å. These spectra suggest that the u.v. band at 3450Å is then related to the luminescent centers.

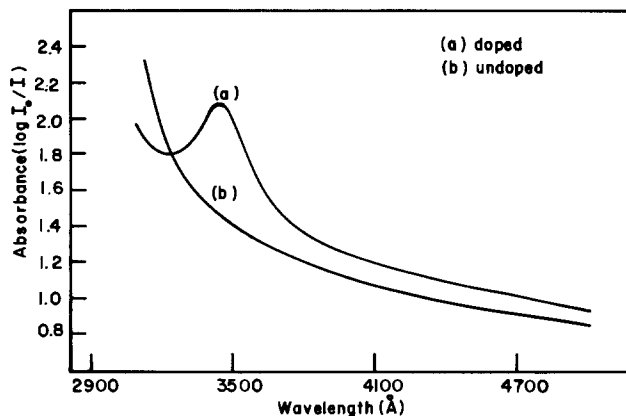


Fig. 1. Absorbance of Ge-doped (a) and undoped (b) bromine sodalite.

Effect of hydrogen annealing on the u.v. band intensity.—The effect of the hydrogen annealing temperature and time on the u.v. absorption band intensity was studied using a sample containing 1 a/o germanium. Figure 2 summarizes the results of an experiment in which samples were annealed at various temperatures for 15 min and their absorption bands measured. The absorption is negligible for anneal temperatures less than 650°C, but increases rapidly with increasing anneal temperature up to 750°C and then decreases sharply.

Figure 3 summarizes the results of an experiment in which samples were annealed at 750°C for various annealing times and their absorption bands were measured. The band intensity increases almost linearly with the annealing time between 0 and 15 min and then saturates for higher annealing temperatures.

The behavior of the u.v. band intensity as a function of hydrogen temperature and time is essentially identical to that reported by Todd (2) for the luminescent intensity as a function of the same parameters. The

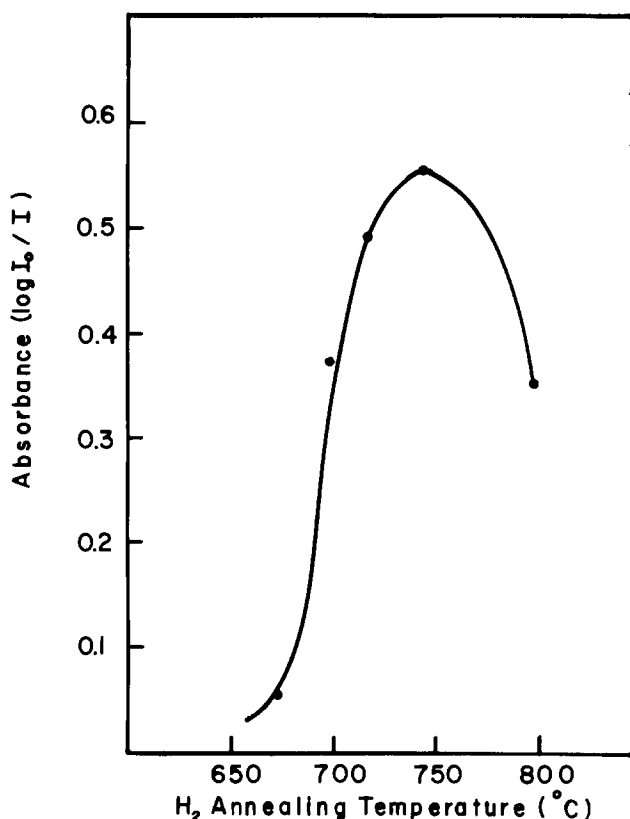


Fig. 2. Absorbance of the u.v. band as a function of H₂ annealing temperature.

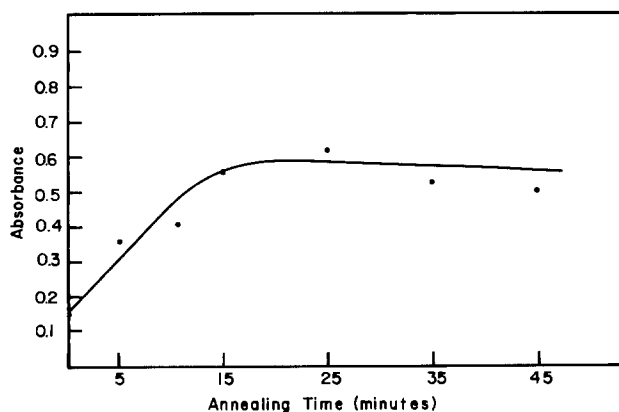


Fig. 3. Absorbance of the u.v. band as a function of H₂ annealing time at 750°C.

above results clearly indicate that the u.v. band is due to absorption by the luminescent centers.

Effect of F-center creation on the u.v. band intensity.—It has been reported (2) that coloration of germanium-doped sodalite powders quenches the luminescent intensity. Therefore, an experiment was conducted to determine the effect of coloration on the u.v. band intensity. Samples of powder with the composition Na₆Al₆(Si_{0.99}Ge_{0.01})₆O₂₄ · 2NaBr were settled with a density of 6.3 mg/cm². This density produced the optimum sample thickness for measuring small variations in the u.v. and F-band intensities. Thinner samples provided only small absorption bands while thicker samples could not be colored uniformly throughout the sample thickness.

The effect of photoerasable coloration on the u.v. band intensity was investigated. A sample was colored by electron beam exposure and its absorption spectrum was measured immediately after coloration. The sample was then optically bleached with white light for 1 hr and its spectrum remeasured. The resulting spectra, Fig. 4, show that the F-band intensity dropped considerably while the u.v. band intensity remained essentially unchanged. This result supports the earlier calculation (2) that indicated that photoerasable color centers were not involved in the quenching of luminescent centers.

The u.v. band intensity as a function of the formation of thermally erasable F-centers was also studied. In this experiment each colored slide was optically bleached before its spectrum was obtained. The absorption spectra, with backgrounds subtracted, of a colored and an uncolored sample are shown in Fig. 5. These spectra show that the u.v. band intensity does decrease upon coloration. Several samples were colored to different degrees of darkness and their spectra mea-

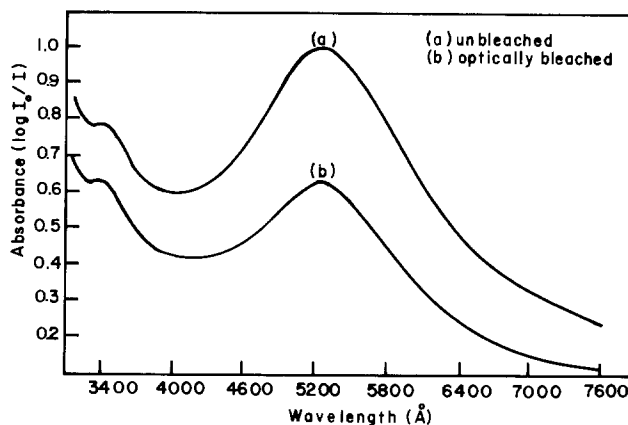


Fig. 4. Absorbance spectra of the u.v.- and F-bands for unbleached (a) and optically bleached (b) Ge-doped bromine sodalite.

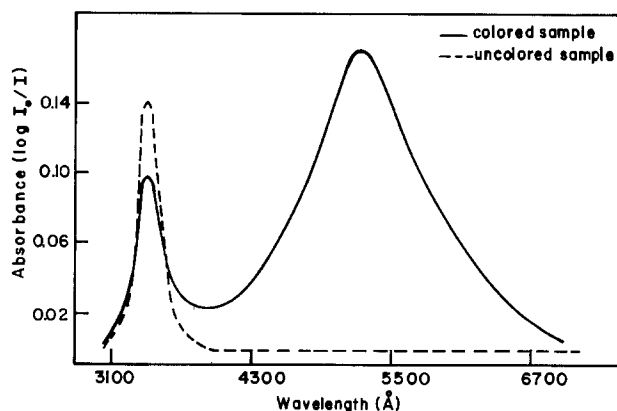


Fig. 5. Absorbance spectra, with background removed, of the u.v.- and F-bands for uncolored (---) and colored (—) Ge-doped bromine sodalite.

sured. The peak absorbance for both the F-band and the u.v. band were obtained. The absorbance is defined as $\log(I/I_0)$ where I is the sample beam intensity and I_0 is the reference beam intensity. The u.v. band fractional absorption $(1 - I/I_0)$ is plotted as a function of the F-band fractional absorption in Fig. 6. The graph shows that the u.v. band absorption decreases almost linearly with increasing F-band absorption. Also shown in Fig. 6 is a plot obtained by Todd (2) for the generated luminescent intensity as a function of the thermally erasable F-band fractional absorption. The generated luminescent intensities have been normalized to the same scale as the u.v. band fractional absorbance to permit an easier comparison. The slight difference in the slopes of the two plots is probably due to the constants assumed by Todd (2) to calculate the generated luminescence.

The results of the experiments discussed in this section clearly indicate that the u.v. band, and thus the luminescent center, is directly related to thermally erasable F-centers and is unaffected by the formation of optically erasable F-centers.

U.V. band intensity in sodalite: Cl, Br, and I.—Luminescent emission at 5250Å has been reported for Ge-doped sodalite: Cl, Br, and I (1). Hence the presence of the u.v. band in these sodalites was examined. The absorption bands for these three powders are shown in Fig. 7. The band intensity is most intense for sodalite: Cl and least for sodalite: I. The wavelength of the absorption bandpeak is unchanged by the halogen ion content.

Summary and Conclusions

Several experiments were conducted to show that the u.v. absorption band presented in this article is responsible for the luminescence reported for Ge-doped sodalite (2). It was found that the u.v. band exists in Ge-doped, luminescent powders but is not present in undoped sodalite samples that do not luminesce. The strong similarity in the behavior of the u.v. band intensity and the generated luminescent intensity (2), as a function of the hydrogen annealing temperature and time, indicates that the u.v. absorption band is directly related to the luminescent centers present in Ge-doped sodalite powders.

By directly observing the u.v. band intensity as a function of F-center creation, it is concluded that the creation of thermally erasable F-centers reduces the number of luminescent centers while the creation of optically erasable F-centers does not affect the luminescent center content. These experimental results support the mathematical calculations of generated lumin-

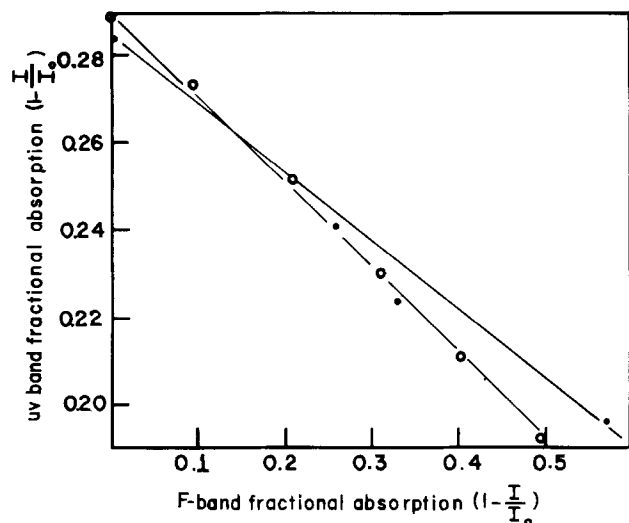


Fig. 6. Fractional absorbance of the u.v. band vs. F-band fractional absorbance (●) and normalized generated luminescence intensity vs. F-band fractional absorbance (○).

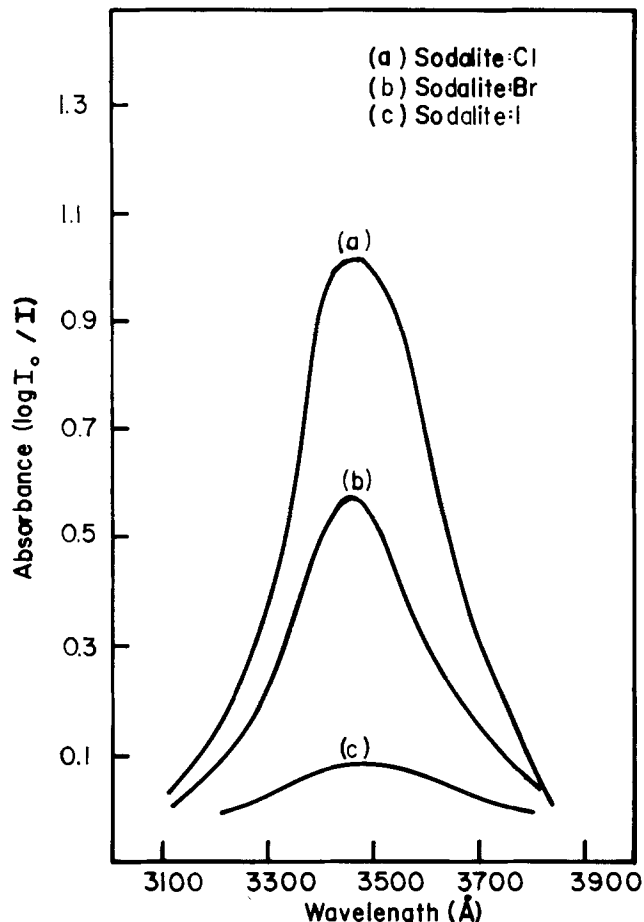


Fig. 7. Absorbance spectra of chlorine (a), bromine (b), and iodine (c) sodalite samples.

escence as a function of F-center formation reported previously (2).

The above results may provide a key to determining the difference between the optical- and thermal-modes of coloration present in sodalite. While several models (8-10) have been proposed, none has adequately accounted for the two modes of coloration. It is generally accepted that both the optically and thermally erasable F-centers are created when electrons are trapped at halogen ion vacancies in the centers of sodalite cages (11-14). However, the origins of the electrons that become trapped have not yet been determined. It is possible that the origin of electrons that form thermally erasable F-centers is different from that of the electrons responsible for optically erasable coloration. Another possibility is that the electrons that are captured to form thermally erasable centers may originate far from the halogen vacancies they occupy while the electrons that are captured to form optically erasable centers may originate within or near the cage where the optically erasable center resides. Therefore, since a recombination site is readily accessible, the electrons of the optically erasable centers would have a high probability of recombination when optically pumped.

While both the "different origin" and the "proximity" models may be operative in a given material, the results reported here support the "different origin" explanation. One implication of these results is that the electrons responsible for thermally erasable F-centers are also involved with the transition which produces the observed luminescence. Electron beam exposure of the material may dislodge these electrons from the luminescent sites and they may become captured at a halogen vacancy to form an F-center. This sequence, extinction of a luminescent center at the expense of thermally erasable F-center formation, is consistent with our observations. The origin of those electrons

that result in optically erasable F-centers would then be somewhere other than a luminescent site since the formation of optically erasable centers does not affect the generated luminescence.

The exact location of the luminescent site is not known but a strong possibility is that the absorption and subsequent luminescence may be due to a hole located on a bonding oxygen atom. The hole could result from the removal of a nonbonding electron from an oxygen atom during the sensitizing process. This center is similar to the Al center or Al (III) e^+ center present in fused silica and quartz (15). Two of our observations support this possibility. First, an inter-shell transition localized on an oxygen atom would be well protected from variations in the lattice. We observe, in fact, that the wavelength of the peak of the u.v. absorption band is absolutely insensitive to changes in the halogen content which also causes significant alterations of the lattice parameter. The location of the emission band has also been reported to be insensitive to changes in the lattice size (1). Our second observation is that the efficiency of the luminescence increases greatly when small amounts of Ge are substituted for Si. Since Ge may be reduced much more easily than Si during the hydrogen annealing step, it is possible that a larger number of nonbonding electrons may be removed from oxygen atoms thus creating more luminescent centers. It has been reported (1, 3) that luminescence exactly like that described above also occurs in sodalite samples that contain no Ge. Therefore, Ge is not essential for luminescent emission but does improve the efficiency. This observation is also consistent with the above model since a hole could exist on the oxygen atom even in the absence of Ge. Quenching of the luminescence by F-center formation would be consistent with the above model if the removal of an additional electron from a luminescent site is sufficient to cause the luminescent transition to become forbidden. Additional experiments are being conducted to gather more information regarding the luminescent site and its relationship to the coloration mode.

Acknowledgments

The authors wish to thank Dr. E. B. Bradley for the use of his laboratory equipment during part of the

experimental work, and Gary Grider and Debbie Shirley for their assistance in the preparation of the manuscript. This work was supported by the National Science Foundation under Grant No. DMR75-10620.

Manuscript submitted Feb. 1, 1979; revised manuscript received Sept. 5, 1979.

Any discussion of this paper will appear in a Discussion Section to be published in the December 1980 JOURNAL. All discussions for the December 1980 Discussion Section should be submitted by Aug. 1, 1980.

REFERENCES

1. L. T. Todd, Jr., E. F. Farrell, and A. Linz, *IEEE Trans. Electron Devices*, **ed-23**, 1183 (1976).
2. L. T. Todd, Jr., *This Journal*, **125**, 1133 (1978).
3. L. T. Todd, Jr., Ph.D. Thesis, M.I.T., Cambridge, Mass. (1973).
4. M. S. Perlmutter, L. T. Todd, Jr., and E. F. Farrell, *Mater. Res. Bull.*, **9**, 65 (1974).
5. I. F. Chang and A. Onton, *J. Electron. Mater.*, **2**, 17 (1973).
6. W. Espe, "Materials of High Vacuum Technology," Vol. 3, p. 122, Pergamon Press, Elmsford, N.Y. (1968).
7. F. M. Tranjan, M.S. Thesis, University of Kentucky, Lexington, Ky. (1976).
8. D. W. G. Ballentyne and K. L. Bye, *J. Phys. D.*, **3**, 1438 (1970).
9. J. S. Brinen and L. A. Wilson, *J. Chem. Phys.*, **56**, 6256 (1972).
10. B. W. Faughnan, I. Gorog, P. M. Heyman, and I. Shidlovsky, *Proc. IEEE*, **61**, 291 (1973).
11. W. G. Hodgson, J. S. Brinen, and E. F. Williams, *J. Chem. Phys.*, **47**, 3719 (1967).
12. E. F. Williams, W. G. Hodgson, and J. S. Brinen, *J. Am. Ceram. Soc.*, **52**, 139 (1969).
13. M. J. Taylor, D. J. Marshall, P. A. Forrester, and S. D. McLaughlan, *Radio Electron. Eng.*, **40**, 17 (1970).
14. S. D. McLaughlan and D. J. Marshall, *J. Phys. Chem.*, **74**, 1359 (1970).
15. T. W. Hickmott, *J. Appl. Phys.*, **45**, 1050 (1974).

Fast Decay U.V. Phosphor—YAlO₃:Ce

Takeshi Takeda, Takeo Miyata, Fumio Muramatsu, and Tetsuhiko Tomiki¹

Matsushita Research Institute Tokyo, Incorporated, Tamaku, Kawasaki 214, Japan

ABSTRACT

Samples prepared to obtain u.v.-emitting YAlO₃:Ce (YAP:Ce) by solid-state reactions up to 1600°C are never free of visible-emitting Y₃Al₅O₁₂:Ce (YAG:Ce). Furthermore, YAG cannot easily be removed from the products. By adding Ba compounds, the YAG content of the product can be minimized, and BaAl₂O₄ and other phases formed can be eliminated by HNO₃-treatment to yield "pure" YAP:Ce. The Ba compounds-fluxed YAP:Ce is moreover the most efficient of all trial samples. It has a radiant efficiency $\eta \sim 7\%$ and a decay time $\tau_{1/e} \sim 30$ nsec for CR excitation.

Ce³⁺-activated phosphors show a very fast luminescence decay and are useful for flying-spot scanner tubes and beam-indexing tubes (1). Many hosts activated with Ce³⁺ (2-5) have been explored, e.g., yttrium silicates and yttrium aluminates.

In the pseudobinary Y₂O₃-Al₂O₃ system, three compounds, Y₃Al₅O₁₂ [garnet: YAG (6)], YAlO₃ [perovskite: YAP (7)], and Y₄Al₂O₉ [monoclinic: YAM (8)],

are known: YAG:Nd is a well-known laser material. YAG:Ce is the commercially available P46 phosphor with emission peak λ_{\max} at 550 nm, radiant efficiency $\eta = 4\%$, and decay time $\tau_{1/e} = 70$ nsec for CR excitation (1). YAP:Ce single crystal is reported to show a luminescence with $\lambda_{\max} \sim 370$ nm, $\tau_{1/e} = 16$ nsec, and efficiency near unity for u.v. excitation (9). However, YAP is described as metastable (10-14), because crushed single crystals (11, 12) or polycrystals from the melt (13, 14), both of which are single phase YAP initially, convert to YAG and an unidentified phase (11,

¹Present address: The Department of Physics, University of the Ryukyus, Naha, Okinawa, Japan.

Key words: ultraviolet, luminescence, tubes.

12) or to YAG and YAM (13, 14) when subjected to heat-treatment. Powder samples prepared through solid-state reactions below 1600°C contain YAG and YAM also (13, 14).

The purpose of this work is to prepare the u.v.-emitting YAP:Ce free of other phases, especially YAG phase. This is because YAG:Ce emits in the yellow, and moreover, it is not easily removed from the products. The preparation method is mainly through the use of Ba compounds as a flux which simultaneously produces an efficient YAP:Ce as the main product, and second phases, mainly BaAl_2O_4 , which are mostly soluble in HNO_3 .

YAP:Ce phosphors are described in patent documents (15) as having $\lambda_{\text{max}} \sim 370 \text{ nm}$, $\eta = 2 \sim 3\%$, and $\tau_{1/e} \lesssim 40 \text{ nsec}$ for CR excitation. The properties of our phosphors are compared to these values below.

Phosphor Preparation

The starting materials were mainly Y_2O_3 , Al_2O_3 , and CeF_3 of 4N purity. Two kinds of attempts were carried out to investigate their influences on the solid-state reaction and luminescence properties. One was to add alkali or alkaline earth-compounds to the stoichiometric mixture and the other was to add excess Y_2O_3 to the stoichiometric mixture.

A designation $x\text{-}y(\text{CeF}_3)\text{-}z(\text{M})$ is used hereafter to specify the sample, which means that the sample is prepared from a mixture of $(1-0.01y)/2$ moles of Y_2O_3 , $0.01y$ moles of CeF_3 , $x/2$ moles of Al_2O_3 , and $0.01z$ g-equiv. of M; M stands for the additive as flux. The starting materials were mixed by ballmilling for 20 hr in ethanol. After having been dried, the mixture was fired in a platinum crucible at temperatures in a range from 800° to 1600°C typically for 4 hr in air. Fired samples were ground slightly in an alumina bowl. Several samples were treated with HNO_3 solution (3N) and then washed with distilled water to remove the undesirable phases. The particle size of ground powders was about 1-10 μm with the maximum distribution at around 5 μm when the starting mixture contained fluorides, e.g., CeF_3 , BaF_2 , YF_3 . Samples prepared from the mixtures without fluorides were slightly sintered and had larger particle sizes.

The products were examined by powder x-ray diffraction using $\text{CuK}\alpha$ radiation to identify the synthesized phases. To make a comparison easy of the relative amount of each phase in different samples, the operating parameters of the diffractometer were kept constant in all the measurements. The lines diffracted from the (121) plane of YAP, the (420) plane of YAG, the (221) plane of YAM, and the (222) plane of Y_2O_3 were marked.

Measurements

Emission spectra and intensities.—Measurements were made by employing a demountable CRT. The cathodoluminescent output emerging at 90° to the electron beam through a qualified fused silica window was focused by concave mirrors onto the entrance slit of a Leiss single-prism monochromator provided with a R666 photomultiplier (Hamamatsu TV Company, Limited). The correction factor for the instrumental response has been determined with the use of a D_2 arc lamp (Model UV-40, the Optronic Laboratory, Incorporated) and a tungsten lamp (EPI-1630, the Eppley Laboratory, Incorporated) which were both calibrated at NBS. Phosphors were settled on Al plates ($7 \times 13 \times 1 \text{ mm}^2$) with an area density of 8 mg/cm². The emission spectra were taken under the irradiation of a 10 kV beam modulated at 430 Hz (duty 1/2). The beam current was set to $\sim 0.3 \mu\text{A/cm}^2$ and the spot size to 6 mm ϕ .

The emission intensity from YAP:Ce was estimated by using a u.v. bandpass filter (Hoya U360), and the relative intensity in different samples was measured under the same irradiation conditions by use of a turntable in a demountable CRT.

The radiant efficiency measurements were made by use of a thermopile (Hilger Schwarz FT 3-1, 2.3 $\mu\text{V}/\mu\text{W}$). Phosphors were excited by a beam modulated at 12.5 Hz. The relative radiant efficiency η of YAP:Ce phosphor was determined by using a number of NBS standard phosphors (NBS-1020 to -1028, and -1032) and η -values reported by Brill (16) and Ludwig and Kingsley (17).

Decay times.—The cathodoluminescence decay times were measured by employing a sealed off 6 in. CRT and a pulsed 10 kV electron beam with a repetition frequency of 1 kHz. The pulse width was usually set to 20 nsec and was enlarged up to 500 nsec in the estimation of the afterglow level in the decay curve. The emission from the sample was detected by the R666 photomultiplier combined with the U360 filter, and the decay curve was displayed on an X-Y recorder via a sampling oscilloscope (Sony-Tektronix 7S14). The time constant of the measuring system has been estimated as about 5 nsec (i.e., pulse rise time ~ 1 nsec, photomultiplier transit time ~ 2 nsec, and RC-time constant ~ 2 nsec), and the 1/e decay time $\tau_{1/e}$ of P47 phosphor ($\text{Y}_2\text{SiO}_5\text{:Ce}$) measured here was about 4 nsec longer than the reported 30 nsec (1).

Results and Discussion

Solid-state reaction.—The formation profiles of various phases in the sample 1-1(CeF_3)-0 are shown against the firing temperature T_f in Fig. 1. The reaction is very sluggish and the product still contains YAG at $T_f = 1600^\circ\text{C}$. By treating the samples with HNO_3 , Y_2O_3 and YAM can easily be removed, but YAG cannot. Therefore, the suppression of YAG formation in the reaction process is important. As shown in Fig. 1, a remarkable dip occurs on the growth curve of YAP at $T_f = 1150^\circ\text{C}$, corresponding to the growth curve peak of YAG. Since this unusual YAG growth at 1150°C is observed also in the sample 1-0-0 or 1-1(CeO_2)-0 when a part of Y_2O_3 or Al_2O_3 is replaced by YF_3 or AlF_3 , it seems to have an intimate relation with the presence of fluorides in the starting mixture.

The addition of Ba compounds accelerates the formation of YAP and suppresses that of YAG. Figure 2 shows an example of the formation profiles of various phases in the sample 1-1(CeF_3)-1.5(BaF_2)-1.5(BaCO_3). Other Ba compounds, e.g., BaO , $\text{Ba}(\text{NO}_3)_2$, BaC_2O_4 , affected the reaction similarly. Although the effect of Ba compounds on the YAP formation is less marked than that of KF (cf. Fig. 3), the Ba compound-fluxed sample is the most efficient phosphor of all the trial

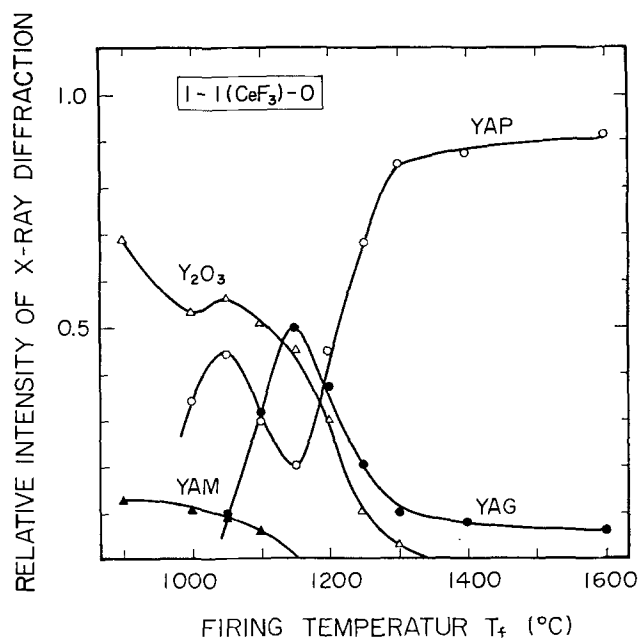


Fig. 1. Growth curves of YAP, YAG, and YAM in 1-1(CeF_3)-0

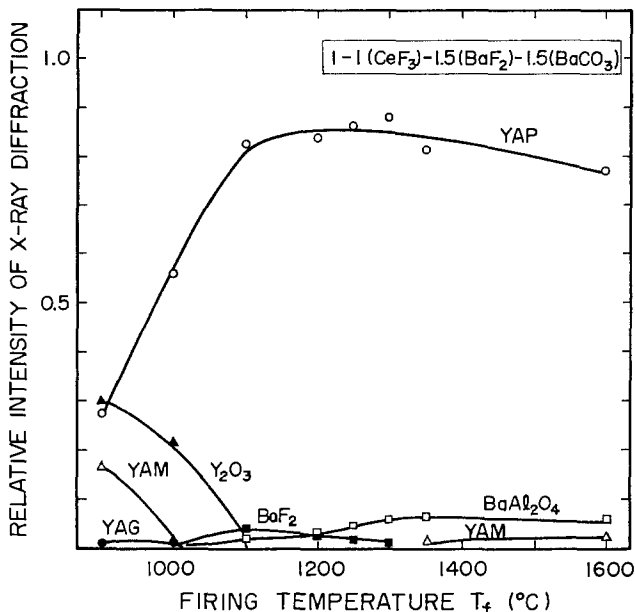


Fig. 2. Growth curves of YAP, YAG, YAM, and BaAl₂O₄ in 1-1(CeF₃)-1.5(BaF₂)-1.5(BaCO₃).

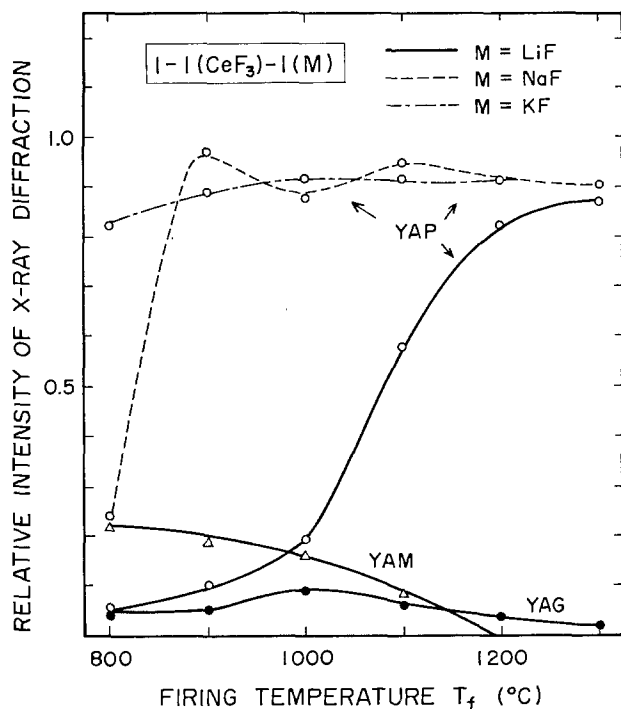


Fig. 3. Growth curves of YAP in 1-1(CeF₃)-1(M), M being LiF, NaF, or KF. Curves of YAG and YAM are shown only for 1-1(CeF₃)-1(LiF).

samples in this work. As is seen from Fig. 2, no YAG phase is detected in the samples fired at $T_f \geq 1100^\circ\text{C}$. BaAl₂O₄, BaF₂, and sometimes YAM are detected in these samples, but they can easily be removed by HNO₃-treatment to yield the x-ray diffraction pattern of "pure" YAP phase.

The above samples are prepared from the mixtures containing fluorides, i.e., CeF₃ and BaF₂. In the fluoride-free mixtures the reaction proceeds similarly, but the products, e.g., 1-1(CeO₂)-3(BaCO₃), are slightly sintered and have larger particle sizes. Moreover, the products are less efficient phosphors than those from the mixtures with fluorides. Thus, the practical YAP:Ce phosphor is synthesized from the mixture containing both barium compound and fluoride. Fluorides may be CeF₃, BaF₂, YF₃, or AlF₃. The addition of Mg, Ca, Sr compounds hardly affected the reaction.

In Fig. 3 is shown the effect of LiF, NaF, or KF on the YAP formation; KF gives the most remarkable effect to accelerate the YAP formation and in the sample 1-1(CeF₃)-1(KF) the YAP content in the product shows a nearly saturated value even at $T_f = 800^\circ\text{C}$. In these alkali compounds-fluxed samples, the YAG phase is almost equally suppressed and thus the growth curve of YAG phase is shown only for the case of LiF addition in Fig. 3.

The suppression of the YAG phase is observed also when excess Y₂O₃ is added to the mixture. According to Mizuno and Noguchi (13), the YAG phase is still detected in the sample prepared by firing a mixture with Y₂O₃:Al₂O₃ = 0.57 : 0.43 at 1600°C. This product is expressed as 0.754-0-0 in our designation. Figure 4(a) shows no YAG phase in the sample 0.78-1(CeF₃)-0 fired at $T_f \geq 1300^\circ\text{C}$. This difference might be caused by the presence of CeF₃ in the present mixture. The sample 0.5-1(CeF₃)-0 just corresponds to the product from the stoichiometric mixture for YAM. Figure 4(b) indicates that the formation of YAM is also sluggish. An attempt was made to obtain the single phase YAM by firing the mixture at 1600°C; this resulted in failure. Although a YAM:Ce phosphor is described (18) as having λ_{max} at 320 nm for the 254 nm excitation, we could not observe this emission. Only the YAP:Ce emission was detected in the sample 0.5-1(CeF₃)-0 fired at 1600°C for the 254 nm or the CR excitation.

X-ray diffraction lines which seem to be ascribed to CeO₂ or Ce₂Y₂O₇ are detected in the samples with $y \geq 0.5$. These lines also disappear when the samples are treated by HNO₃. The Ce concentration was determined by means of a mass spectrometer and a spectrochemical analysis on the samples 1-y(CeF₃)-z(BaF₂)-(3-z)(BaCO₃) with $y = 0.1, 0.5, 1,$ and 2 . Here, $3y + 2z = 6$ and $y \leq 2$. The samples were fired at 1300°C for 2 hr and treated by HNO₃. The joint use of BaF₂ and BaCO₃ is for the sake of keeping the fluorine amount constant in the starting mixture when y is varied in the above formula. The detected Ce concentration was in good agreement with each of y -values [doped Ce

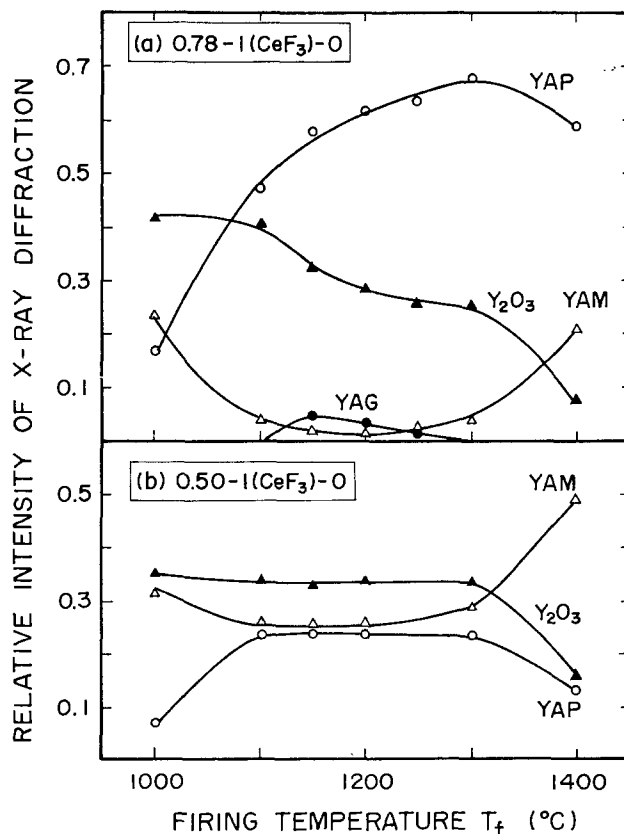


Fig. 4. Growth curves of YAP, YAG, and YAM in (a) 0.78-1(CeF₃)-0 and (b) 0.5-1(CeF₃)-0.

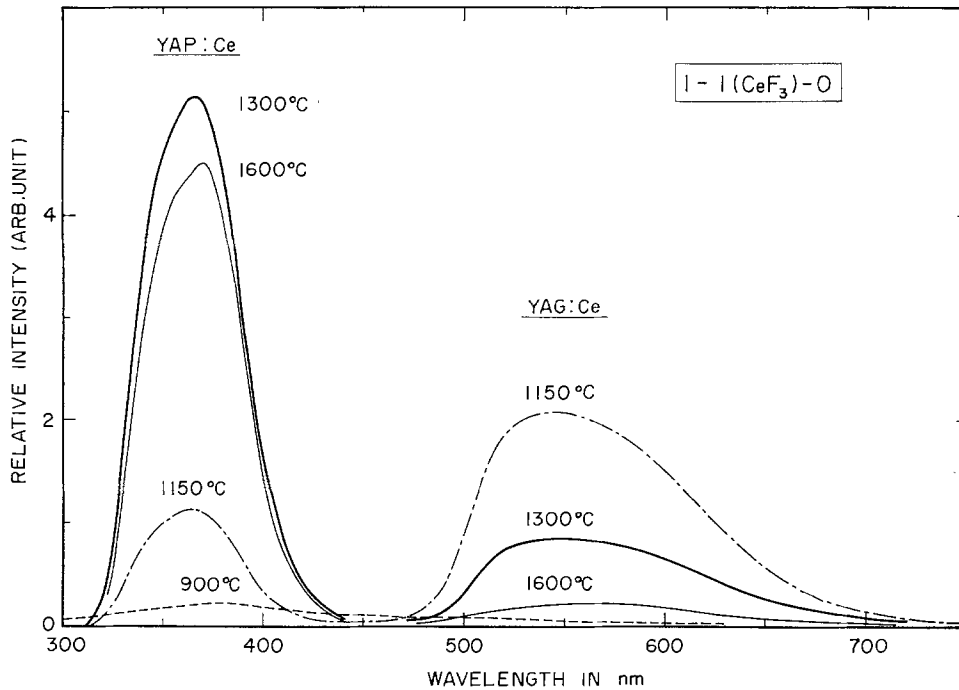


Fig. 5. Cathodoluminescence spectra in 1-1(CeF₃)-0 fired at 900°, 1150°, 1300°, and 1600°C.

concentration in atom percent (a/o)] for $y \leq 0.5$ and tended to a saturated value of $0.5 \sim 0.6$ a/o for $y \geq 1$. The agreement between the results obtained through the two methods was found to be sufficient. These results suggest that the solubility limit of Ce ions in YAP is around 0.5 a/o. This value is very close to the solubility limit of Ce ions in YAG (19).

Luminescence properties.—The emission spectra of the samples 1-1(CeF₃)-0 are shown in Fig. 5. Reflecting the unusual YAG growth in the 1150°C sample (cf. Fig. 1), the emission of YAG:Ce is much stronger than that of YAP:Ce in this sample. The emission color changes from yellow for $T_f = 1150^\circ\text{C}$ to white for 1300°C and further to whitish violet for 1600°C. As is seen from the figure, the apparent λ_{max} of YAP:Ce emission shifts to longer wavelengths as T_f increases, indicating an increase of absorption in the shorter wavelength region of the YAP:Ce emission spectrum.

The relative intensities of cathodoluminescence from samples with fluxes, 1-1(CeF₃)-1(M) and 1-1(CeF₃)-1.5(BaF₂)-1.5(BaCO₃), are displayed against T_f in Fig. 6, where M stands for Li₂CO₃, NaF, KF, K₂CO₃, RbCl, CsCl, MgCO₃, CaCO₃, and SrCO₃. The data of samples without flux, 1-1(CeF₃)-0, are also included for comparison (a broken curve). Since the U360 filter is employed here, the emission from YAP:Ce is dominantly detected. The emission intensity of P47 phosphor [$\lambda_{\text{max}} = 415$ nm and $\eta = 6\%$ (1)] measured through this system is taken as unity in the figure. One sees in Fig. 6 that the emission intensity enhancement is most prominent in the (BaF₂ + BaCO₃)-fluxed samples. A similar enhancement is observed also when the samples are prepared with other Ba compounds, e.g., BaO, Ba(NO₃)₂, BaC₂O₄. The 1100°C sample with Ba compounds is the most efficient of all the samples in Fig. 6 and has $\eta \sim 6\%$. The 1300°C sample without flux has $\eta \sim 3\%$; this value agrees well with the η -value of YAP:Ce in the patent documents (15b, 15c) where it is reported to be $0.8 \sim 0.9$ times the radiant efficiency of P16 phosphor [4% (4)].

As shown in Fig. 6, the emission intensity of Ba compounds-fluxed samples shows a pronounced decrease with T_f when it exceeds 1100°C; the intensity of the 1600°C sample is about one-half of that of the 1100°C sample. Decreases of the emission intensities are observed also in the samples with $y = 0.5$ and $y = 0.1$, as shown in Fig. 7. In the samples with $y \leq 0.01$, however, the emission intensity shows no decrease with increasing T_f . These results will be explained by

taking into account the emission line shape and the decay time mentioned below.

The dependence on y of the YAP:Ce emission line shape is shown in Fig. 8. The spectra are normalized with respect to their maxima. The apparent λ_{max} shifts to longer wavelengths as y increases; from 355 nm for $y = 0.01$ to 365 nm for $y = 1$ at $T_f = 1300^\circ\text{C}$.

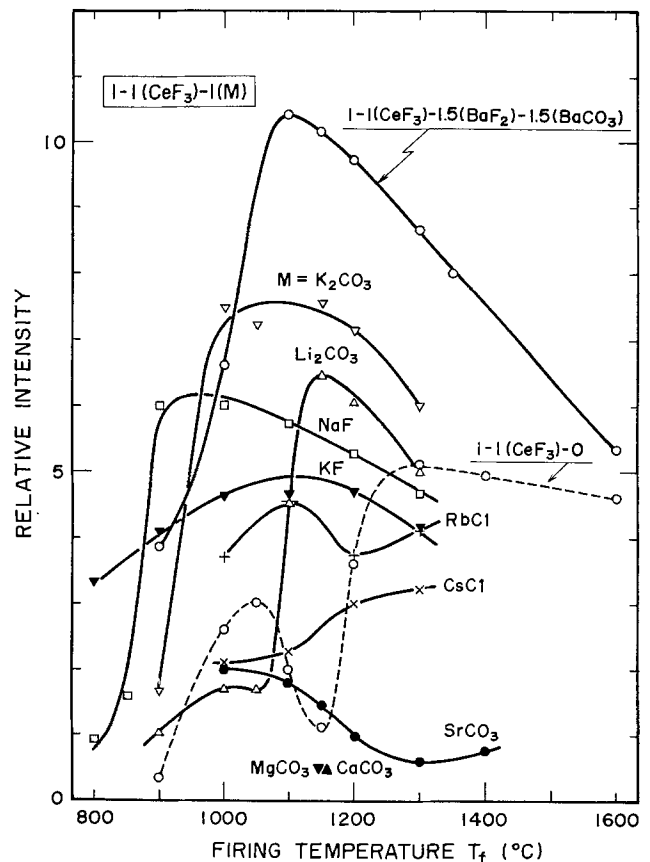


Fig. 6. Relative intensity of YAP:Ce cathodoluminescence in the samples 1-1(CeF₃)-0, 1-1(CeF₃)-1(M), and 1-1(CeF₃)-1.5(BaF₂)-1.5(BaCO₃). M = Li₂CO₃, NaF, KF, K₂CO₃, RbCl, CsCl, MgCO₃, CaCO₃, or SrCO₃.

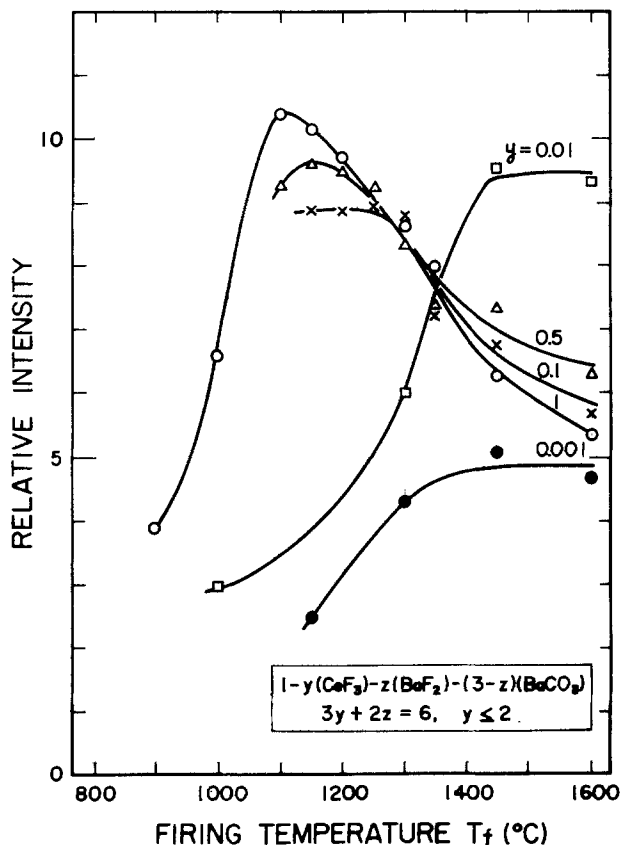


Fig. 7. Dependences on y and T_f of the relative intensity of YAP:Ce cathodoluminescence in Ba compounds-fluxed samples. Samples are treated with HNO_3 .

Since Ce^{3+} in YAP has an absorption band extending to ~ 350 nm (9), a self-absorption would occur in the shorter wavelength region of the emission spectrum, and thus the increase of y would cause the apparent λ_{max} -shift to longer wavelength. In the samples with $y \geq 0.1$, the apparent λ_{max} -shift to longer wavelength

is observed also with the increase of T_f . On the contrary, it is observed in samples with $y \leq 0.01$ that the emission line shape depends neither on y nor on T_f ; this indicates that the self-absorption is negligibly small in these samples. The progressive increase of absorption with T_f in samples with $y \geq 0.1$ will partly explain the decrease of the emission intensity in Fig. 7.

As shown in Fig. 8, the YAG:Ce emission becomes stronger with decreasing y . This means that not only barium ions, but also cerium ions play a role in suppressing the YAG formation.

The addition of Ba compounds is found not to cause an appreciable change in the YAP:Ce emission line shape.

The decay times are shown in Fig. 9. The data of the samples 1-1(CeF_3)-0 are included for comparison (a broken curve). As seen from this figure, $\tau_{1/e}$ for $y \geq 0.1$, which shows a nearly constant value of 27 \sim 28 nsec for low T_f , becomes shorter with T_f when it exceeds a certain threshold value. This value is $\sim 1150^\circ\text{C}$ for $y = 0.5$ and $y = 1$, and is $\sim 1350^\circ\text{C}$ for $y = 0.1$. The $\tau_{1/e}$ -values for $y < 0.1$ are greater than the above constant value, but tends to it as T_f increases. Since the $\tau_{1/e}$ -values for $y = 1$ almost agree with each other for the samples with and without Ba compounds for $T_f \geq 1150^\circ\text{C}$, it seems that the addition of Ba compounds yields only a small influence in $\tau_{1/e}$.

The influences of LiF and NaF on $\tau_{1/e}$ are also small, but the addition of KF makes $\tau_{1/e}$ considerably long; for example, the sample 1-1(CeF_3)-1(KF) fired at 1300°C has $\tau_{1/e}$ of about 30 nsec.

In the samples x -1(CeF_3)-0 with $x < 1$, a broad maximum of the emission intensity is observed for x between 1 and 0.5, and $\tau_{1/e}$ shows a gradual increase with decreasing x . For example, in the sample 0.78-1(CeF_3)-0 fired at 1300°C , an emission intensity of 8 in unit of the ordinate of Fig. 6 and $\tau_{1/e}$ of 24 nsec are obtained; that is, the emission intensity and $\tau_{1/e}$ increase by 60 and 10%, respectively, in comparison with those in 1-1(CeF_3)-0.

The luminescence decay of Ce^{3+} in YAP is not expressed with a single exponential function and shows an afterglow which is usually more pronounced for lower T_f or smaller y . An example of the decay curve is shown for the sample 1-1(CeF_3)-3(BaCO_3) fired at

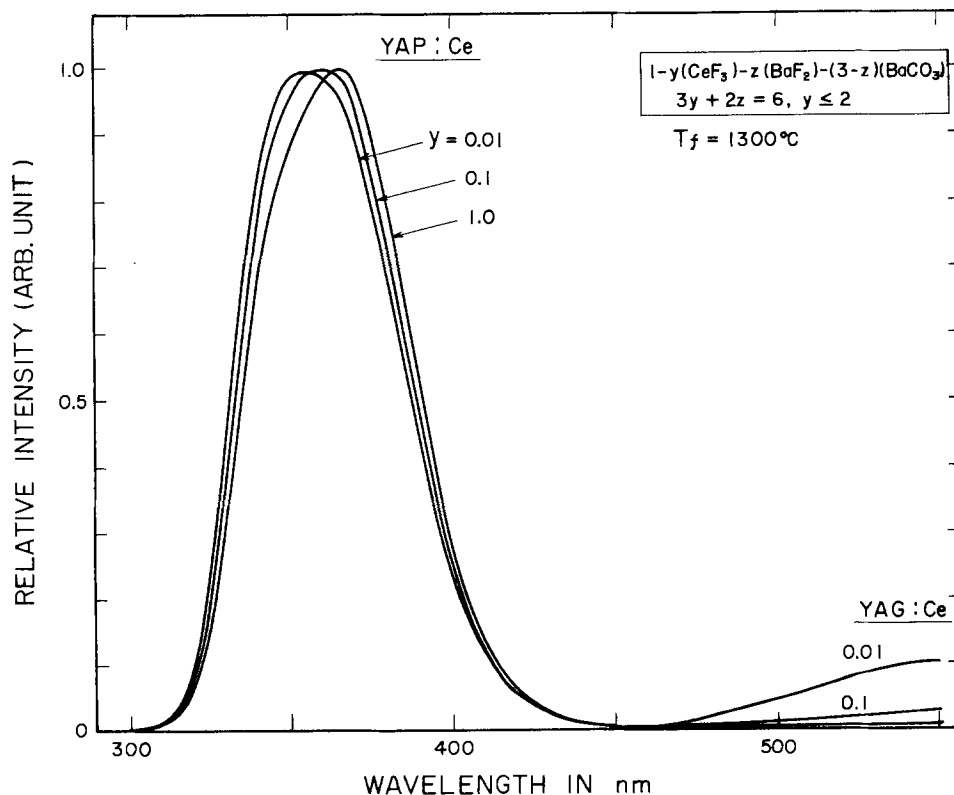


Fig. 8. Dependences on y of the cathodoluminescence spectrum in Ba compounds-fluxed samples. Samples are treated with HNO_3 .

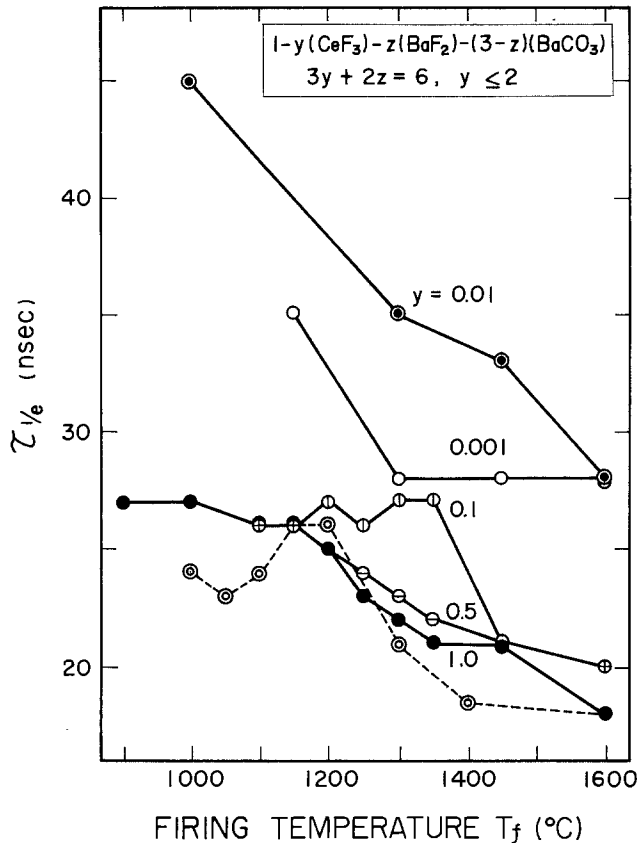


Fig. 9. Dependences on y and T_f of the cathodoluminescence decay time $\tau_{1/e}$ of YAP:Ce in the samples with and without Ba compounds as flux. Samples with Ba compounds are treated with HNO_3 .

1000°C in Fig. 10. Such decay curves have been observed in several Ce^{3+} -activated phosphors (20) and are explained in terms of energy traps which release their energy slowly to excite the emission center after the excitation pulse is turned off. As shown in the figure, the decay curve can be expressed by a sum of three different exponents (dashed lines) in a region of initial several hundreds nanoseconds. The decay function for this sample is

$$D(t) = \frac{\exp(-t/22) + 0.1590 \exp(-t/80) + 0.0217 \exp(-t/500)}{1 + 0.1590 + 0.0217} \quad [1]$$

Here, t is in nsec and the excitation pulse width (Δt) is 20 nsec. The full curve calculated by use of Eq. [1] is seen to fit the dots representing the experimental behavior. It will be reasonable to consider that the shortest decay constant (τ_1) corresponds to the lifetime of Ce^{3+} in the excited 5d level and that the longer ones represent the time constants of the process of energy release from energy traps. Since the greater number of energy traps are to be filled with the increase of Δt , the afterglow level would be more pronounced for longer Δt . Therefore, Eq. [1] is correct only for $\Delta t = 20$ nsec. To see the validity of Eq. [1], several decay behaviors with different values of Δt were analyzed. It was confirmed that each decay behavior observed could be well fitted only by changing the coefficients, i.e., 0.1590 and 0.0217 in Eq. [1], without varying the time constants.

Figure 11 shows the values of τ_1 in several samples. From this figure, the following can be pointed out. First, for $y \leq 0.01$, τ_1 depends neither on y nor on T_f and shows a constant value of 22 ~ 23 nsec. Second, for $y \geq 0.1$, τ_1 which is initially equal to this constant value becomes shorter with increasing T_f above a certain threshold value. These results seem to indicate that the constant value corresponds to the radiative transition probability of the 5d-4f Ce^{3+} emission. Our measuring system has a time constant of about 5 nsec. So, by simply subtracting this from the constant value,

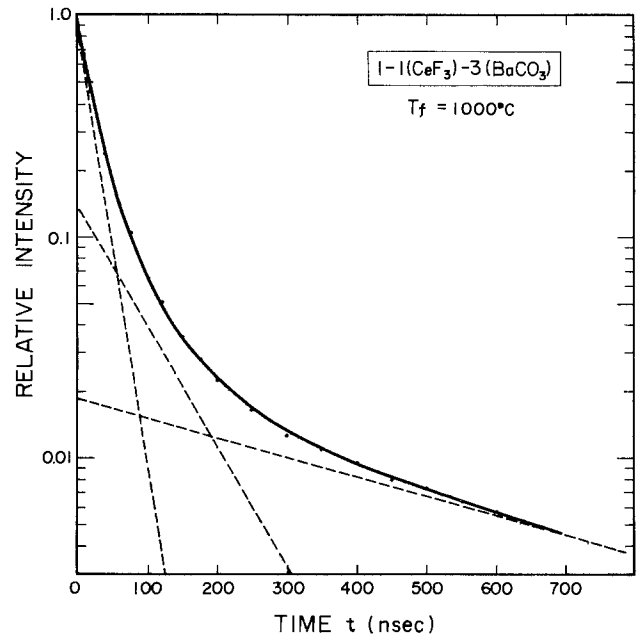


Fig. 10. An example of cathodoluminescence decay curve in $1-1(\text{CeF}_3) - 3(\text{BaCO}_3)$ fired at 1000°C.

we obtain 17 ~ 18 nsec. This is very close to 16 nsec obtained for the u.v. excitation (9).

The decrease of τ_1 in the samples with $y \geq 0.1$ and with higher T_f will be ascribed to a nonradiative transition. Energy sinks might be produced to cause a concentration quenching in these samples. These energy sinks will not affect τ_1 of the samples with $y \leq 0.01$, as the probability of energy transfer from Ce^{3+} to Ce^{3+} is negligibly small in these samples. The non-radiative transition causes the emission loss, and this as well as the absorption increase mentioned before will explain the decrease of emission intensity shown in Fig. 7.

As stated hitherto, Ce concentration, firing temperature, and combination of starting materials are interrelated in their effects on the emission intensity and the decay time. A partial replacement of Y_2O_3 or Al_2O_3 by YF_3 or AlF_3 is also effective. By optimizing

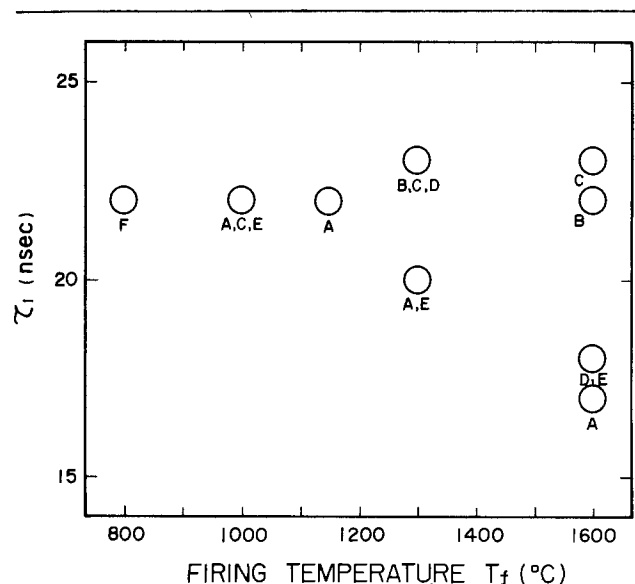


Fig. 11. Values of τ_1 in the samples $1-1(\text{CeF}_3) - 0$ (A), $1-y(\text{CeF}_3) - z(\text{BaF}_2) - (3-z)(\text{BaCO}_3)$ with $y = 0.001$ (B), 0.01 (C), 0.1 (D), 1 (E), and $1-1(\text{CeF}_3) - 1(\text{KF})$ (F). $3y + 2z = 6$ and $y \leq 2$. Samples except (A) are treated with HNO_3 .

preparation conditions, the highest η of 7 ~ 7.5% is obtainable; however, this accompanies a longer $\tau_{1/e}$ of 30 ~ 32 nsec.

Finally, as for the deterioration against a continuous electron beam bombardment, the present phosphor is not serious and superior to P47 phosphor.

Acknowledgment

The authors are much indebted to Dr. J. Nishida and the members of his group for their cooperation in this work and information concerning YAP:Ce characteristics as beam-indexing phosphor in color TV applications.

Manuscript submitted April 6, 1979; revised manuscript received Sept. 10, 1979. This was Paper 222 presented at the Boston, Massachusetts, Meeting of the Society, May 6-11, 1979.

Any discussion of this paper will appear in a Discussion Section to be published in the December 1980 JOURNAL. All discussions for the December 1980 Discussion Section should be submitted by Aug. 1, 1980.

Publication costs of this article were assisted by Matsushita Research Institute Tokyo, Incorporated.

REFERENCES

1. A. Bril, G. Blasse, A. H. Gomes de Mesquita, and J. A. de Poorter, *Philips Tech. Rev.*, **32**, 125 (1971).
2. G. Blasse and A. Bril, *Appl. Phys. Lett.*, **11**, 53 (1967).
3. A. H. Gomes de Mesquita and A. Bril, *Mater. Res. Bull.*, **4**, 643 (1969).
4. A. H. Gomes de Mesquita and A. Bril, *This Journal*, **116**, 871 (1969).
5. T. E. Peters, *ibid.*, **119**, 1720 (1972).
6. H. S. Yoder and M. S. Keith, *Am. Mineral.*, **36**, 519 (1951).
7. S. Geller and E. A. Wood, *Acta Crystallogr.*, **9**, 563 (1956).
8. J. W. Reed and A. B. Chase, *ibid.*, **15**, 812 (1962).
9. M. J. Weber, *J. Appl. Phys.*, **44**, 3205 (1973).
10. I. Warshaw and R. Roy, *J. Am. Ceram. Soc.*, **42**, 434 (1956).
11. J. S. Abell, I. R. Harris, and B. Cockayne, *J. Mater. Sci.*, **7**, 1088 (1972).
12. J. S. Abell, I. R. Harris, B. Cockayne, and B. Lent, *ibid.*, **9**, 527 (1974).
13. M. Mizuno and T. Noguchi, *Rep. Gov. Ind. Res. Inst. Nagoya*, **16**, 171 (1967).
14. M. Mizuno and T. Noguchi, *ibid.*, **16**, 210 (1967).
15. (a) M. R. Royce and J. S. Martin Jr., U.S. Pat. 3,623,994 (1971). (b) Y. Koga, Japanese Patent Document, Sho-49-3913 (1974). (c) K. Awazu, Japanese Patent Document, Sho-50-29833 (1975).
16. A. Bril, in "Luminescence of Organic and Inorganic Materials," H. P. Kallmann and G. W. Spruch, Editors, p. 479, John Wiley and Sons, New York (1962).
17. G. W. Ludwig and J. D. Kingsley, *This Journal*, **117**, 348 (1970).
18. G. Blasse and A. Bril, *J. Chem. Phys.*, **47**, 5139 (1967).
19. T. Y. Tien, E. F. Gibbons, R. D. DeLosh, P. J. Zacmanidis, D. E. Smith, and H. L. Stadler, *This Journal*, **120**, 278 (1973).
20. For example, E. F. Gibbons, T. Y. Tien, R. G. DeLosh, P. J. Zacmanidis, and H. L. Stadler, *ibid.*, **120**, 835 (1973).

The Interplay of Thermodynamics and Kinetics in Molecular Beam Epitaxy (MBE) of Doped Gallium Arsenide

R. Heckingbottom, C. J. Todd, and G. J. Davies

Post Office Research Centre, Martlesham Heath, Ipswich, IP5 7RE, Suffolk, England

ABSTRACT

Molecular beam epitaxy (MBE) is normally carried out with a substantial overpotential for growth. The generally accepted assumption, that as a consequence the thermodynamic framework describing chemical equilibrium is irrelevant, has been reexamined. The thermodynamic predictions for the behavior of the common dopants Si, Ge, Sn, Pb, Be, Mn, S, Se, Te, Zn, Cd, and Mg in GaAs under typical MBE conditions have been determined. Good agreement with observed behavior is found for all cases except Pb. Thus it is shown that when doping is unsuccessful it is because there is no overpotential for doping, even though the overpotential for growth of GaAs is maintained. The results show that there is no clear evidence for major kinetic barriers in MBE of GaAs, only the possibility of subtler effects of the kind found in VPE and LPE. The method should be predictive in the application of MBE to new systems.

It is generally assumed (1-3) that molecular beam epitaxy (MBE) of gallium arsenide is controlled by kinetic aspects of the crystal growth process. By this it is meant that the kinetic processes controlling the crystal growth are not those consistent with thermodynamic equilibrium being reached; rather that there are

kinetic barriers which prevent equilibrium from being reached and which prevent thermodynamics being used to predict sensible approaches to MBE.¹ As a typical example it is often quoted that Zn cannot be used to dope GaAs successfully under MBE conditions because its sticking coefficient is too low, a fact which is regarded as a kinetic observation that could not be predicted from thermodynamics.

In this conventional view MBE is to be contrasted strongly with alternative methods of crystal growth, vapor phase epitaxy (VPE) and liquid phase epitaxy (LPE), where an important interplay between thermodynamic framework and kinetic detail is assumed

Key words: equilibrium, impurity concentration, vapor pressure.
¹The authors would like to thank the referee for drawing a notable exception to these remarks to their attention. In their recent book (25) (not available in the U.K. at the time of writing) Casey and Panish outline an approach by Ilegems which starts from a similar standpoint to ours. The Ilegems approach accounts reasonably for the behavior of the low vapor pressure dopants but fails qualitatively for S, Se, and Te and quantitatively in the comparison of Zn and Mg.

Table I. Predicted and observed results of doping GaAs under MBE conditions

Dopant	Si	Ge	Sn	Pb	Be	Mg	Zn	Cd	S	Se	Te	Mn
Prediction	S	S	S	M	S	M	U	U	S	S	S	S
Observation	S	S	S	U	S	M	U	U	S	S	S	S

Where S = successful, M = moderately successful, U = unsuccessful.

(4, 5). It is pointed out here that it is layers grown by LPE and VPE that have proved suitable for semiconductor device fabrication. If MBE layers are to have a similar suitability, they must approach the equilibrium situation to a comparable extent and not contain large additional nonequilibrium concentrations of defects. In general MBE-grown layers of GaAs are proving suitable for device purposes with the implication that the approach to equilibrium is comparable in MBE, VPE, and LPE.

In this paper we examine closely what the predictions of the thermodynamic framework should be for MBE of GaAs, with particular emphasis on doping, and compare them with the experimental results. We have considered all the common dopants and the qualitative comparison is shown in Table I.

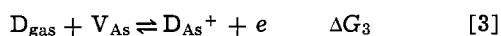
As can be seen from Table I, there is only one instance where the thermodynamic prediction is in error. In the first part of the paper we show, on a quantitative basis, how the qualitative summary in Table I is obtained. In the second part, the numerical results are compared with the experimental data and the implications of the close fit for the kinetics of doping in MBE of GaAs are outlined.

Theoretical Approach

The generally accepted approach to describing doping of GaAs under equilibrium conditions is illustrated by the following example of a donor impurity occupying a site on the arsenic sublattice



or overall



where D_{gas} is a donor atom in the vapor phase, D_{As} and D_{As}^+ represent donor atoms and ions respectively substitutional on As lattice sites; V_{As} is a vacant arsenic lattice site, and e is an electron in the conduction band of GaAs. ΔG_1 etc. are the partial molal free energies of the respective reactions, thus

$$\Delta G_1 = -RT \ln K_1 \quad [4]$$

where

$$K_1 = [D_{\text{As}}]/P_{\text{D}}[V_{\text{As}}] \quad [5]$$

and $[]$ represents concentration and P pressure in atmospheres, *i.e.*, assuming activity coefficients of unity. Similarly

$$K_2 = n[D_{\text{As}}^+]/[D_{\text{As}}] \quad [6]$$

where $n = [e]$ and

$$K_3 = K_1 K_2 = n[D_{\text{As}}^+]/P_{\text{D}}[V_{\text{As}}] \quad [7]$$

If all the carriers in the bulk semiconductor originate from reaction [2] then

$$n = [D_{\text{As}}^+] = K_3^{1/2} P_{\text{D}}^{1/2} [V_{\text{As}}]^{1/2} \quad [8]$$

Analogous treatments apply to donors on sites on the Ga sublattice and acceptors on both sublattices. In each case if we control the native defect concentration, *i.e.*, $[V_{\text{As}}]$ in the example illustrated by Eq. [8], via the arsenic pressure we may determine the carrier concentration in the GaAs (n in the above case) by the activity of the dopant outside the GaAs (P_{D} in the above case).

The basic problem therefore is to calculate what pressures of dopants are required to give useful concentrations of carriers under normal MBE conditions

for growth of GaAs, and to see how these compare with the pressures needed in practice. First, if we require specific results we must define our growth conditions. We will choose $P_{\text{Ga}} = 10^{-6}$ Torr, $P_{\text{As}_4} = 2 \cdot 10^{-6}$ Torr and $T_{\text{substrate}} = 560^\circ\text{C}$ ($\equiv 833^\circ\text{K}$) and calculate the dopant pressures required to give carrier concentrations of $2.2 \cdot 10^{19} \text{ cm}^{-3}$ and $2.2 \cdot 10^{16} \text{ cm}^{-3}$ (or 10^{-3} and 10^{-6} respectively when expressed as fractional concentrations of the relevant Ga or As sublattice sites). We can now consider the most effective way to make the quantitative estimates for the individual dopant elements.

Be, Si, Ge, and Sn.—It will be clear that we are concerned primarily with the interaction between the dopant atom and the GaAs lattice, *i.e.*, the enthalpies and entropies that contribute to ΔG_3 . However this significant group of dopants permit a simplification which means it is sufficient to consider their elemental vapor pressures. Thus we note that if we apply any pressure in the typical MBE range (10^{-6} - 10^{-10} Torr), these elements would condense at 560°C (6). In a non-growth experiment we would have the condensed element with a surface concentration in the GaAs equal to the solubility limit at 560°C . To obtain sensible doping levels with no surface condensation some measure of ΔG_3 would be required. However we have specified a significant growth rate and based on the thermodynamic prediction of a unit sticking coefficient we calculate that a pressure of 10^{-9} Torr will give a dopant concentration of 10^{-3} (*i.e.*, $P_{\text{D}}/P_{\text{Ga}}$) and a pressure of 10^{-12} Torr will give a dopant concentration of 10^{-6} . It will be noted that the value of 10^{-12} Torr lies below the vapor pressures of Sn and Be at 560°C , technically invalidating the approximation near this lower limit. A fuller consideration based on LPE growth (7) of GaAs shows that even for the worse case, Sn, the correction is negligible.

S, Se, and Te.—In contrast to the previous group, all these important conventional dopants for GaAs have elemental vapor pressures P_{D}^0 in excess of the MBE working range by several orders of magnitude at 560°C . Any MBE must be carried out therefore with dopant activities a_{D} ($\equiv P_{\text{D}}/P_{\text{D}}^0$) $\ll 1$. A most convenient source of data for determining whether the values of a_{D} available in MBE will be high enough to provide useful doping is provided by LPE and VPE. Before carrying out any extrapolations however it is necessary to consider that the treatment given in Eq. [1] \rightarrow [8] does not fit the experimental data. Thus the $n a P_{\text{D}}^{1/2}$ relationship given in [8] is often replaced in practice by a linear relationship (8, 9) $n a P_{\text{D}}$ or $n a a_{\text{D}}$, which is more readily applicable to growth from solution.

One interpretation is that the thermodynamic treatment is inapplicable. However this seems most unlikely. The linear dependence has now been reported for group II, group IV, and group VI elements involving substitution on both sublattices and in both VPE and LPE (4, 5, 8, 9). It is unlikely that the crucial kinetics will be almost identical in all these dissimilar situations; rather that some overall thermodynamic framework does apply, and the model of the defect chemistry is wrong in detail. Linear dependence of $[n] = [D_{\text{As}}^+]$ at room temperature can be obtained by a simple amendment to the model. During growth we assume that n is not dominated by the incorporated $[D]$ but is fixed at some higher value. In these circum-

stances n is constant and

$$[D_{As^+}] = K_3 P_D [V_{As}] / n = K_3' P_D [V_{As}] \quad [9]$$

showing the required linear dependence of dopant incorporation on P_D .

At least two important models for expecting n to be constant and $>[D_{As^+}]$ have already been described (5, 9). Casey and Panish (9) have proposed that a surface space-charge layer dominates the incorporation of S, Se, and Te while Hurlle (5) has recently suggested that a high value of n may result from the ionization of a native defect, like V_{As} , at the growth temperature. For present purposes we do not need to adopt the details of either model, simply to adopt the observed linear dependence of $[D^+]$ on P_D or a_D for our extrapolations from VPE or LPE conditions to those in MBE.

We may now consider doping with sulfur. Under practical VPE conditions (10) a ratio of 10^{-7} for H_2S/H_2 is sufficient to give $[S_{As^+}] \approx 10^{17} \text{ cm}^{-3}$ at 750°C . If we assume that the $P_{H_2S}/[S_{As^+}]$ ratio is not particularly temperature sensitive, we may calculate the value of P_{S_2} at 560°C which is in equilibrium with $P_{H_2} = 1 \text{ atm}$ and $P_{H_2S} = 10^{-7} \text{ atm}$ from standard free energy data (11). We then find that $[S_{As^+}] = 10^{17} \text{ cm}^{-3}$ is equivalent to a P_{S_2} value of only $6.5 \cdot 10^{-21} \text{ atm}$. Using Eq. [9] for the case of $D = S$

$$[S_{As^+}] = K_3' P_S [V_{As}] = K_3'' P_{S_2}^{1/2} [V_{As}] \quad [10]$$

we may calculate the values of P_{S_2} necessary to give $[S_{As^+}]$ of $2.2 \cdot 10^{16} \text{ cm}^{-3}$ and $2.2 \cdot 10^{19} \text{ cm}^{-3}$ as being $1.98 \cdot 10^{-20} \text{ Torr}$ and $1.98 \cdot 10^{-14} \text{ Torr}$ respectively. Clearly the situation degenerates to that of the first group of elements during growth. Then allowing for the diatomic nature of S_2 , the required pressures to obtain the upper and lower doping levels are $5 \cdot 10^{-10} \text{ Torr}$ and $5 \cdot 10^{-13} \text{ Torr}$ respectively. The assumption about the temperature dependence of the $P_{H_2S}/[S_{As^+}]$ ratio is unlikely to be poor enough to affect this conclusion.

For completeness we should also consider that there is a significant change in P_{As_4} in transferring from VPE to MBE conditions. From Ashen *et al.* (12) we may set the value of P_{As_4} in a typical VPE kit at $1.5 \cdot 10^{-3} \text{ atm}$ while we have chosen $2.6 \cdot 10^{-9} \text{ atm}$ for our MBE system. The effect of P_{As_4} is conventionally described as follows

$$\frac{1}{4} As_4 + V_{As} \rightleftharpoons 0 \quad [11]$$

$$K_{11} = P_{As_4}^{-1/4} [V_{As}]^{-1} \quad [12]$$

$$[V_{As}] = K_{11}^{-1} P_{As_4}^{-1/4} \quad [13]$$

Substituting in Eq. [10] we have

$$[S_{As^+}] = K_3''' P_{S_2}^{1/2} P_{As_4}^{-1/4} \quad [14]$$

where $K_3''' = K_3'' K_{11}^{-1}$. Thus the reduction in P_{As_4} increases the level of $[S_{As^+}]$ corresponding to a given value of $P_{S_2}^{1/2}$. In the case above the increase is by a factor of 24.9. As a result our calculated values of P_{S_2} should fall by a factor of 620, making the prediction that the ratio of arrival rates will dominate even more secure. Alternative schemes (5) where V_{As} is ionized to give V_{As}^+ and a controlling value of n would by

analogous treatment show a reduced dependence of $P_{As_4}^{-1/4}$ i.e., an increase of times 5 in $[S_{As^+}]$ due to the change of P_{As_4} between VPE and MBE conditions.

The only remaining doubt about the prediction for sulfur doping stems from a second reaction which is also thermodynamically possible. Ga_2S should not only be stable under the growth conditions but have a vapor pressure in excess of 10^{-6} Torr at 560°C . Thus the value of P_{S_2} needed in practice might differ from those shown in Table II due to a loss of both S and Ga due to the competing formation and reevaporation of Ga_2S molecules.

Tellurium is another member of the group where there is sufficient data, this time from LPE (13), to allow assessment of the likely position in MBE. Casey *et al.* (13) have shown that to obtain $[Te_{As^+}] = 10^{-6}$ at 1273°K one requires $[Te_{soln.}] = 2.85 \cdot 10^{-6}$, i.e., the segregation coefficient is 0.35, in a typical LPE system. An estimation of the position at 833°K can be obtained by extrapolation of the data of Greene (14). The segregation coefficient is ≈ 40 indicating that the required value of $[Te_{soln.}]$ has fallen to $2 \cdot 10^{-8}$. The next task is to determine the vapor pressure of tellurium in equilibrium with the solution. We may write

$$Te_{soln.} \rightleftharpoons \frac{1}{2} Te_2 \quad [15]$$

$$K_{15} = P_{Te_2}^{1/2} / [Te_{soln.}] \quad [16]$$

To obtain an over estimate of K_{15} we may assume Raoult's law, i.e., ignoring any stabilizing effect of Te-Ga interactions in the solution. Then for the limiting case of liquid Te we have at 560°C

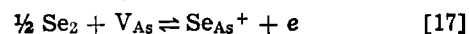
$$K_{15} = [3.29 \cdot 10^{-3}]^{1/2} / [1] = 5.7 \cdot 10^{-2} \text{ atm}^{1/2}$$

Substituting for K_{15} and $[Te_{soln.}]$ in [16] we obtain

$$P_{Te_2}^{1/2} = 5.7 \cdot 10^{-2} \cdot 2 \cdot 10^{-8} \text{ and } 5.7 \cdot 10^{-2} \cdot 2 \cdot 10^{-5} \text{ atm}^{1/2}$$

for our required doping levels of $2.2 \cdot 10^{16} \text{ cm}^{-3}$ and $2.2 \cdot 10^{19} \text{ cm}^{-3}$, respectively. The respective values of P_{Te_2} are thus $9.9 \cdot 10^{-16}$ and $9.9 \cdot 10^{-10} \text{ Torr}$. For our assumed growth conditions the lower value will again have to be increased to $5 \cdot 10^{-13} \text{ Torr}$. As with S doping there is the possibility of competing reactions giving Ga_2Te or similar volatile species, but in this case no firm data appear to be available.

Empirical data on the doping of GaAs with Se seem almost nonexistent. On general grounds its behavior is almost certain to be intermediate between that of S and Te. Comparison of the major enthalpy terms involving Se (heat of dissociation and heat of solution on V_{As}) in the incorporation equation



can be made with analogous reactions for S and Te, using electronegativity differences as shown later in the Zn/Mg comparison. These estimates show that there is likely to be little difference between Se and Te, which is a sufficient prediction for our present requirements.

Zn, Cd, and Mg.—The final important class of dopants are the group II elements Zn, Cd, and Mg which normally give p-type doping. Again, the elemental vapor pressures of 5, 50, and 0.4 Torr, respectively, at 560°C

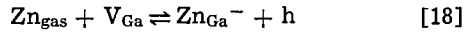
Table II. Predicted operating pressures (in Torr) of common dopants for GaAs under typical MBE conditions of $P_{Ga} = 10^{-6} \text{ Torr}$, $P_{As_4} = 2 \cdot 10^{-6} \text{ Torr}$, and $T_{\text{substrate}} = 833^\circ\text{K}$ (560°C)

Element	Si	Ge	Sn	Pb	Be	Mg	Zn	Cd	S*	Se*	Te*	Mn
Bulk dopant conc. $2.2 \cdot 10^{19} \text{ cm}^{-3}$	10^{-9}	10^{-9}	10^{-9}	$1.5 \cdot 10^{-6}$	10^{-9}	$1.6 \cdot 10^{-7}$	$3 \cdot 10^{-3}$	$8 \cdot 10^1$	$5 \cdot 10^{-10}$	10^{-9}	10^{-9}	10^{-9}
Bulk dopant conc. $2.2 \cdot 10^{16} \text{ cm}^{-3}$	10^{-12}	10^{-12}	10^{-12}	$1.5 \cdot 10^{-9}$	10^{-12}	$1.6 \cdot 10^{-10}$	$3 \cdot 10^{-5}$	$8 \cdot 10^{-2}$	$5 \cdot 10^{-13}$	$5 \cdot 10^{-13}$	$5 \cdot 10^{-13}$	10^{-14}

* Assuming diatomic molecules in the gas-phase.

mean that only activities much less than unity can be used in MBE work and the problem is to determine whether these activities are high enough to give useful doping levels.

Most information is available for Zn, both from LPE and VPE growth of GaAs. Unfortunately it is not all in good agreement. A straightforward treatment of p-type doping invokes the reaction



analogous to Eq. [3] with V_{Ga} representing a vacancy on the Ga sublattice of GaAs and h an electron hole. We may then write

$$p = [\text{Zn}_{\text{Ga}^-}] = K_{18}^{1/2} P_{\text{Zn}}^{1/2} [\text{V}_{\text{Ga}}]^{1/2} \quad [19]$$

with $p = [h]$ for the case where p is controlled by the addition of Zn. Further we may write

$$0 \rightleftharpoons \text{V}_{\text{Ga}} + \text{V}_{\text{As}} \quad [20]$$

so

$$K_{20} = [\text{V}_{\text{Ga}}][\text{V}_{\text{As}}] \quad [21]$$

and substituting for $[\text{V}_{\text{Ga}}]$ in [19] we have

$$p = K_{18}^{1/2} K_{20}^{1/2} P_{\text{Zn}}^{1/2} [\text{V}_{\text{As}}]^{-1/2} \quad [22]$$

Panish and Casey (15) have reported a hole concentration dependence on $X_{\text{Zn}(l)}^{1/2}$ where $X_{\text{Zn}(l)}$ is the atom fraction of Zn in the liquid phase. They also show that

$$P_{\text{Zn}} = P_{\text{Zn}^0} \gamma_{\text{Zn}(l)} X_{\text{Zn}(l)} \quad [23]$$

where $\gamma_{\text{Zn}(l)}$ is the activity coefficient of Zn and $\gamma_{\text{Zn}(l)} \simeq 1$ in Ga-rich conditions (despite the pressure ratio being in favor of arsenic species, the MBE conditions chosen represent a position close to the Ga-rich boundary of GaAs). Thus from Fig. 2 of Ref. (15) we obtain $P_{\text{Zn}}/P_{\text{Zn}^0} = 10^{-2}$ and 10^{-7} for doping levels of $2 \cdot 10^{19}$ and $2 \cdot 10^{16} \text{ cm}^{-3}$, respectively. With $P_{\text{Zn}^0} = 5 \text{ Torr}$ at 560°C the corresponding values of P_{Zn} are $5 \cdot 10^{-2}$ and $5 \cdot 10^{-7} \text{ Torr}$ suggesting that the lower doping levels might be obtainable.

The above analysis assumes that the segregation coefficient between Zn in GaAs and in the melt remained constant in the temperature range 560° to 1000°C . This is likely to be reasonable assumption as there is experimental support for the range 650° – 800°C from the work of Keller and Muench (16). However both this work (16) and the latest VPE work (17) show clearly that at these lower temperatures the hole concentration varies linearly with P_{Zn} . As with the n-type dopants the carrier concentration at the growth temperature becomes independent of the dopant concentration, and

$$[\text{Zn}_{\text{Ga}^-}] = K_{18} K_{20} P_{\text{Zn}} [\text{V}_{\text{As}}]^{-1/p} \quad [24]$$

analogous to Eq. [9]. Direct extrapolation of Sidorov's data (17) gives values of $4.8 \cdot 10^{-5}$ and $4.8 \cdot 10^{-2} \text{ Torr}$ for the two doping limits required. These values need to be corrected for the reduction in P_{As_4} on changing from VPE to MBE conditions. The dependence of $[\text{V}_{\text{As}}]$ on P_{As_4} was given in Eq. [13]. For Zn incorporation the pressures given above need to be increased by factors of 25 or possibly 5, see S doping earlier. These values apply strictly to 770°C . If we assume as above (16) that the segregation coefficient varies little with temperature, then we must allow for the fact that a given value of P_{Zn} represents a much higher activity of zinc in the gas-phase at the lower temperature of 560°C . As a result the zinc pressure required to give a fixed value of $[\text{Zn}_{\text{Ga}^-}]$ is reduced by a factor of 32 at the lower temperature. The final values are shown in Table II confirming that Zn is not a suitable dopant for GaAs using MBE.

Cadmium is expected to be an even less suitable dopant. Using Sidorov's data (17) the extrapolated values are $3.8 \cdot 10^{-2}$ and 38 Torr for our two required doping concentrations. These values need correcting for

the change in P_{As_4} as in the Zn analysis and the change in activity with temperature which in this instance gives a factor of 12.

Magnesium represents a more complex case as there appears to be no data on its use as a dopant for GaAs except in MBE experiments. However we may make a more approximate estimate of its behavior by the following comparison with Zn doping. We may assume Mg is incorporated onto the same sites as Zn so that the only significant change in comparison with Eq. [18] is in the enthalpy of solution to give Mg_{Ga^-} as compared with Zn_{Ga^-} . This difference we may estimate using Paulings method (18) to calculate the difference between Zn-As and Mg-As bond strengths. We have

$$\Delta H(\text{Zn-As}) = \frac{1}{2} \Delta H(\text{Zn-Zn})$$

$$+ \frac{1}{2} \Delta H(\text{As-As}) + 23(X_{\text{Zn}} - X_{\text{As}})^{1/2}$$

and

$$\Delta H(\text{Mg-As}) = \frac{1}{2} \Delta H(\text{Mg-Mg})$$

$$+ \frac{1}{2} \Delta H(\text{As-As}) + 23(X_{\text{Mg}} - X_{\text{As}})^{1/2}$$

where $X_{\text{Zn}} = 1.6$, $X_{\text{Mg}} = 1.2$, and $X_{\text{As}} = 2.10$ are the Pauling electronegativities of the elements. Now $\Delta H(\text{Zn-Zn}) \simeq \Delta H(\text{Mg-Mg})$ (19) so that the difference in bond strength depends only on the electronegativity term. The numerical value of 12.9 kcal/mole for $\Delta H(\text{Mg-As}) - \Delta H(\text{Zn-As})$ compares well with that of Naganuma and Takahashi (2) calculated by the same approach. The Pauling result only applies to the formation of a single bond, i.e., to the distribution of the first electron involved in bonding. As both Zn and Mg contribute two electrons to the valence band in GaAs we can expect the difference due to the electronegativity difference to lie between 12.9 and 25.8 kcal/mole and a value of 20 kcal/mole will be taken as a sensible guide.

Now, at fixed p and $[\text{V}_{\text{As}}]$ Eq. [24] becomes

$$K_{25} = [\text{Zn}_{\text{Ga}^-}]/P_{\text{Zn}} \quad [25]$$

where $K_{25} = K_{18} K_{20} [\text{V}_{\text{As}}]^{-1/p}$. Also $K_{25} = 10^{-6}/3 \cdot 10^{-5} = 3.3 \cdot 10^{-2} \text{ Torr}^{-1}$ under the chosen growth conditions, as indicated by the values in Table II. With the above assumptions the analogous constant $K_{\text{Mg}} = [\text{Mg}_{\text{Ga}^-}]/P_{\text{Mg}}$ is given by $K_{\text{Mg}} = \exp(+20,000/RT) K_{25}$.

At 833°K , $K_{\text{Mg}} = 1.85 \cdot 10^5 \cdot 3.3 \cdot 10^{-2} = 6.105 \cdot 10^3 \text{ Torr}^{-1}$ so that for $[\text{Mg}_{\text{Ga}^-}] = 10^{-6}$, $P_{\text{Mg}} = 1.64 \cdot 10^{-10} \text{ Torr}$ and for $[\text{Mg}_{\text{Ga}^-}] = 10^{-3}$ $P_{\text{Mg}} = 1.64 \cdot 10^{-7} \text{ Torr}$. If we consider reasonable limiting values of 16,000 and 24,000 cal/mole for the increase in enthalpy of solution for Mg we obtain values of P_{Mg} very close to one order of magnitude larger and one order of magnitude smaller, respectively. Thus Mg is clearly a possible dopant.

Mn and Pb.—The elements Mn and Pb have also been used as dopants for GaAs in MBE. These elements do not fit closely into any of the groups described so far and again there is little supporting data from other experiments. It is possible however to make some estimate of their expected behavior. Inspection of Pauling's equations (18) given for Zn and Mg in the previous section shows that the main variations between different substituents on the Ga sublattice derive from the metal-metal bond energy term and the electronegativity term. For metals forming monatomic vapors we may take the elemental vapor pressure as a measure of the bond energy term. The electronegativity term is then a measure of the additional stability conferred by the required incorporation in dilute solution in the GaAs lattice. We note (i) that for $[\text{Zn}_{\text{Ga}^-}] = 10^{-3}$ a value of $P_{\text{Zn}} \simeq 10^{-2} P_{\text{Zn}^0}$ was required and (ii) that $X_{\text{Zn}} \simeq X_{\text{Mn}} \simeq X_{\text{Pb}}$. Thus as a first estimate the pressures required to give our upper concentration value should be $\simeq 1\%$ of the elemental vapor pressures, i.e., $2 \cdot 10^{-10} \text{ Torr}$ for Mn and $1.5 \cdot 10^{-6}$ for Pb. In prac-

tice therefore Mn should behave like the first group of elements (Si, etc.) and Pb should be less suitable but possible.

Results

The results are collected in Table II. In considering the results the following observations need to be kept clearly in mind. Most of the values are based directly or indirectly on results from VPE and LPE. They are not therefore indisputably thermodynamic values. In fact they incorporate any intrusion of kinetic limitations found in VPE and LPE. They are therefore the predictions based on the assumption that kinetic effects are comparable in MBE, VPE, and LPE. Kinetic effects showing doping concentration dependence on crystal growth rate and orientation are well documented (4) and factors ≥ 10 are typically reported—significant, but small compared with the extrapolations involved in this work.

A similar perspective is required when considering the possible errors due to the detail of the extrapolations, where estimates of temperature variation for several quantities had to be made for some elements. A more significant level of uncertainty is involved where recourse has to be made to basic data such as electronegativity coefficients. As indicated in the text for the case of Mg, a further uncertainty of about an order of magnitude is possible.

The predicted results may now be compared with experiment. The results for the first group of elements, Si, Ge, Sn, and Be, are very much as expected. The elemental vapor pressures are sufficiently low (and it has become established that the sticking coefficients are unity, as assumed in the thermodynamic treatment), that the thermodynamic background is obvious, and the doping problem degenerates to a simple ratio of dopant and gallium beam fluxes.

The second group of elements S, Se, and Te represents a striking success for the present approach. The elemental vapor pressures are high and specific attention to the chemical interaction of dopant and GaAs matrix is required. The earlier incorporation of Te (1) and the recent report of doping by S and Se (20) are seen as part of the predicted framework and not as intricate kinetic exceptions. The latter results (20) also show that in practice the competing reaction of evaporation of Ga₂S is of negligible importance. Additionally, the successful use of a compound source (PbS) argues strongly for facile surface kinetics which would allow the thermodynamically predicted situation to be reached. Finally it should be emphasized that because of the chemical interaction (primarily Ga-S) the thermodynamically predicted sticking coefficient for these three dopants is unity.

The third group of elements Zn, Cd, and Mg are equally successfully described by the thermodynamic approach even though the outcome is in such marked contrast with that for the second group. The underlying reason is that the chemical interaction, *e.g.*, Zn-As is much weaker than, *e.g.*, Ga-S. Thus Zn and Cd are unsuitable as dopants for GaAs under MBE conditions and the thermodynamically predicted sticking coefficients are extremely low at $3.3 \cdot 10^{-8}$ and $1.25 \cdot 10^{-11}$, respectively. The result for Zn is strikingly close to that estimated by Naganuma and Takahashi (2) using the same basic approach and also close to their single measured value of $5 \cdot 10^{-7}$. It should be noted that though these authors (2) stressed the kinetics of the reactions, the kinetics were those consistent with the thermodynamic framework outlined here. Turning to Mg, it is predicted to be usable as indeed it is. Our thermodynamic sticking coefficient is $6.25 \cdot 10^{-3}$, significantly higher than the earlier calculated value (2) of $1.8 \cdot 10^{-5}$. This arises because we feel that in the bulk Mg must form more than the single bond considered for the surface reaction in the earlier work (2). Our value does not agree well with any of the experimental values for the sticking coefficient of 10^{-5} (21) or 10^{-4}

(2) based on electrical activity or unity (22) based on total chemical content. It is almost certain that the higher chemical figure (22) applies in general but that most of the Mg is not electrically active. This means most of it is not incorporated by the reaction considered here and so the prediction would not be expected to apply. One of the more likely competing reactions is the incorporation of Mg with O, as the CO and CO₂ pressures in a typical MBE system are thermodynamically sufficient to oxidize Mg at all the beam pressures explored.

Of the two remaining elements Mn is unexceptional, like the first group of elements, but Pb is the only example where the model prediction is wrong. Before concluding that Pb provides a clear case of kinetic dominance we must examine the grounds on which the prediction was made more closely. First we find that the data base was almost nonexistent in this case. A distribution coefficient of 10^{-1} was assumed based on the observed behavior of Zn. However there is some suggestion (7) that the true value for Pb is very low (at least like that for Sn) and in the region of 10^{-4} . In terms of our previous analysis the most likely term to have been ignored is a significant elastic term due to the large size of Pb which would reduce the enthalpy of solution of Pb in GaAs appreciably. With the lower segregation coefficient of 10^{-4} Table II would be amended to show $1.5 \cdot 10^{-3}$ and $1.5 \cdot 10^{-6}$ Torr. It is clear however that Wood (20) reports even less incorporation of Pb than this, suggesting that even with this revised thermodynamic framework there is evidence for additional kinetics barriers possibly also related to the large size of Pb atoms.

One final important aspect remains to be discussed. So far we have only considered the distribution of dopant atoms between gas-phase and bulk semiconductor. In any detailed treatment the surface must also be considered. In practical MBE this is particularly important as, in the growth of thin layers, the transient behavior at the start and finish of growth can determine the success or otherwise of the process. Thus in the cases of doping with Sn (23) and Te (1) and also Pb (20) high surface concentrations of the dopant have been established. In general these enhanced surface concentrations could arise from the thermodynamic basis or from kinetic barriers to further reaction. It should be stressed, however, that these complications do not invalidate the results of the bulk/gas-phase analysis described here. On the contrary these results can be used together with the experimental data to clarify the kinetic aspects of the doping reactions. The approach is described in more detail in the Appendix but the main conclusions are as follows. There is no evidence remaining for any kinetic barriers at the gas/surface interface. At the surface/bulk interface, the only cases where the experimental evidence suggests additional kinetic barriers may be important are for Pb doping, some of the transients observed in Sn doping, and for amphoteric doping by Ge.

Conclusions

The incorporation of all common dopants into GaAs under typical MBE conditions has been examined. It is found that in all cases except Pb the predictions based on the thermodynamic and chemical equilibrium framework fit the results observed in practice. The closeness of this fit indicates that any additional kinetic aspects of MBE growth are likely to be comparable to those found in VPE and LPE. In the light of these results it should be possible to obtain useful guidance in applying MBE to other systems by considering first the thermodynamic framework applying to them.

Acknowledgment

Acknowledgment is made to the Director of Research of the British Post Office for permission to publish this paper.

Manuscript submitted May 7, 1979; revised manuscript received July 26, 1979. This was Paper 123 presented at the Boston, Massachusetts, Meeting of the Society, May 6-11, 1979.

Any discussion of this paper will appear in a Discussion Section to be published in the December 1980 JOURNAL. All discussions for the December 1980 Discussion Section should be submitted by Aug. 1, 1980.

Publication costs of this article were assisted by the Post Office Research Centre.

APPENDIX

The Interplay of Kinetics and Thermodynamics in MBE

In general, different concentrations of dopant in the surface and the bulk GaAs are to be expected, so that occurrence of surface enrichment is not necessarily evidence for kinetic delays in the bulk incorporation step. In fact, in the particular case of doping during growth a complete kinetic freeze at the surface/bulk incorporation step would give a disordered solid with the dopant buried in the bulk. Surface enrichment therefore like the growth of good crystalline material, gives evidence of considerable kinetic mobility on the surface. Thermodynamic data for dopant adsorption on the surface of GaAs is almost nonexistent, however we can learn something about the situation from the implications of the results in Tables I and II.

The main situations that are possible are shown schematically in Fig. A-1. The figure shows the free energies of the dopant in the gas phase, on the surface, and in the bulk. Obviously the free energy is a func-

tion of concentration and we illustrate the position for concentrations which are accessible and desirable in MBE.

Thus we have the maximum convenient gas-phase pressure of 10^{-16} Torr, a likely maximum bulk concentration of $2.2 \cdot 10^{19} \text{ cm}^{-3}$, and exactly the same surface concentration of 10^{-3} expressed as a fractional surface coverage.

The abscissa is the reaction coordinate for doping from the gas-phase.

In the more normal situation of doping during growth there is direct access from the gas-phase to both the surface and the bulk. The kinetic routes in the two main stages of reaction surface/gas interaction and surface/bulk interaction are shown by (a), (b), (c), and (d). Routes (a) and (c) represent routes with kinetic barriers which dominate the outcome of the process while (b) and (d) represent facile kinetic routes which allow the outcome to be predicted by the thermodynamic framework. Before considering specific dopants we can consider an example of the application of Fig. A-1, e.g., case I. At 10^{-6} Torr there is a considerable gain in free energy if the dopant condenses on the surface to give a coverage of 10^{-3} and a further gain by incorporation at a bulk concentration of $2.2 \cdot 10^{19} \text{ cm}^{-3}$. If the kinetic paths are (b) and (d) then doping by MBE will work. In fact, to stop much higher doping concentrations than required from being obtained, the gas pressure will have to be reduced until either the free energy falls to that of the solid or simple considerations of arrival fluxes vs. the growth rate intervene. The concentration on the surface will then be lower than in the bulk. Alternatively, if path (a) applied, doping to the required level will not occur due to a low sticking coefficient due to kinetic factors. If route (b) (c) applies one is likely to get untidy incorporation of dopant, e.g., leading to compensation or deep traps or conceivably, by a more complex mechanism, some surface enrichment. It is interesting to note that in the case (not shown) where free energies in all three states are equal, one would expect a sticking coefficient of 10^{-3} on thermodynamic grounds, i.e., even though paths (b) and (c) were followed, and even lower values due to additional kinetic factors if path (a) was followed.

We may now consider the main groups of dopants in terms of Fig. A-1. Well-behaved dopants such as Si or Be clearly fit case I (b) (d) very well. Case II (b) (c) is conceivable if (c) gives direct burial of dopant, thus preventing surface segregation, but it must be considered unlikely. Dopants S and Se appear to be similar with the facile surface kinetics implied by I (b) (d) being even more likely, at least in Wood's experiments (20). Ge is also likely to fit I (b) (d). It is not clear whether the amphoteric doping by Ge is dominated by the thermodynamics of the stoichiometry variations in GaAs with P_{As_4} or by the dominance of path (c) at some values of P_{As_4} . Further study might increase our understanding of these factors considerably.

Turning to the usable but less satisfactory dopants, Sn and Te would appear to give a simple fit to II (b) (d). Possible alternatives are II (b) (c) or even I (b) (c) both of which would require sufficient mobility in the surface/bulk interaction to prevent burial of the dopant but insufficient to allow normal incorporation. This possibility cannot be ruled out but it should be noted that it involves the same kind of sophisticated growth modelling required to explain LPE and VPE, not some simpler kinetic limitation peculiar to MBE. In so far as the highest doping levels cannot be obtained using Mn (24) case V or VI is suggested converting to I at lower doping levels. However the thermodynamic framework would predict I. The empirical results at lower doping levels suggest route (b) (d) but as suggested by Ilegems *et al.* (24) it is possible that at the higher concentrations the Mn on the surface interferes with the growth of the host crystal, causing unacceptable crystal morphology. As Mg incorporation is probably affected by impurities it will not be considered in this section.

Finally we consider the unsuccessful dopants Zn, Cd, and Pb. For Zn and Cd cases V or VI are predicted by thermodynamics. For Zn routes (b) and (d) are suggested by the single result of modified MBE (2). This result means that one cannot attribute the Jack

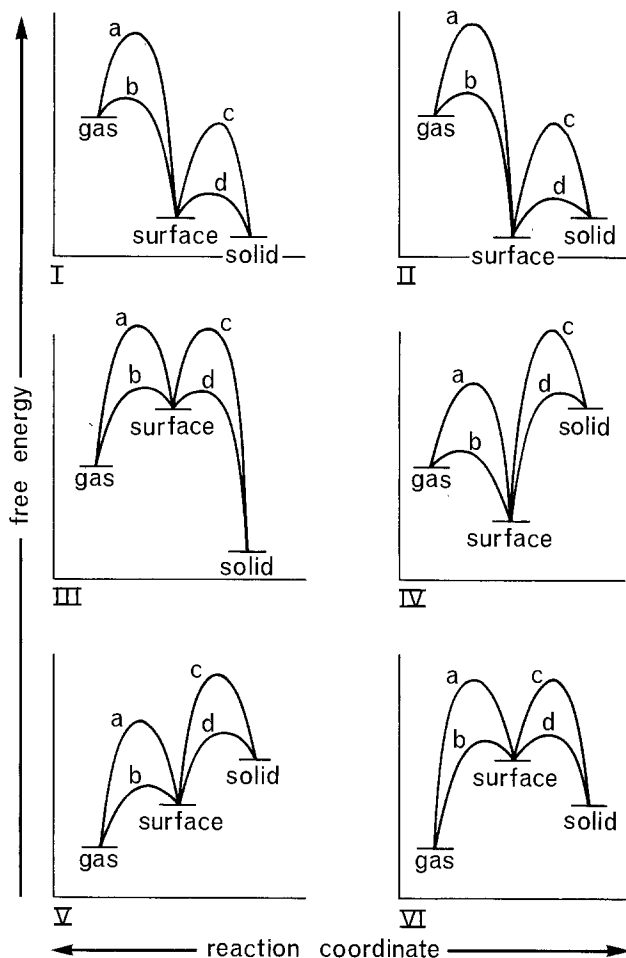


Fig. A-1. Dopant free energy vs. reaction coordinate diagrams for the important alternative possibilities in doping gallium arsenide from the gas-phase. Alternative reaction paths are shown as (a), (b), (c), and (d). The free energies refer to a pressure of 10^{-6} Torr in the gas-phase, a coverage of 10^{-3} on the surface, and a bulk concentration of $2.2 \cdot 10^{19} \text{ cm}^{-3}$.

of success in Zn doping simply to the occurrence of route (a) in any of the cases in Fig. A-1. There is no data on Cd but a parallel with Zn is to be expected. Pb is more complicated. The revised thermodynamic prediction suggests cases IV or V (the elastic term will have less effect on surface atoms) at the higher concentrations. In practice Wood's results favor case IV (with the beam on) and routes (b) and (d) are favored by the very completeness of the absence of Pb from the bulk. Here it seems likely that some kinetic barrier to incorporation also operates as discussed for Sn.

REFERENCES

1. A. Y. Cho and J. R. Arthur, in "Progress in Solid State Chemistry," Vol. 10, G. Somorjai and J. McCaldin, Editors, Pergamon Press, Oxford (1975).
2. M. Naganuma and K. Takahashi, *Phys. Status Solidi A*, **31**, 187 (1975).
3. L. L. Chang and R. Ludeke, in "Epitaxial Growth A," J. W. Matthews, Editor, p. 37, Academic Press, New York (1975).
4. J. B. Mullin, *J. Cryst. Growth*, **42**, 77 (1977).
5. D. T. J. Hurle, "Proc. 6th Int. Symp. on GaAs and Related Compounds," Inst. Phys. Conf. Series, **33a**, 113 (1977).
6. R. E. Honig and D. A. Kramer, *RCA Rev.*, **30**, 285 (1969).
7. H. Kressel and J. K. Butler, "Semiconductor Lasers and Heterojunction LEDs" Academic Press, New York (1977).
8. M. Heyen, H. Bruch, K. H. Bachem, and P. Balk, *J. Cryst. Growth*, **42**, 127 (1977).
9. H. C. Casey and M. B. Panish, *ibid.*, **13/14**, 818 (1972).
10. M. A. Savva, *This Journal*, **123**, 1498 (1976).
11. O. Kubaschewski and E. L. P. Evans, "Metallurgical Thermochemistry," 3rd ed., Pergamon Press, London (1958).
12. D. J. Ashen, P. J. Dean, D. T. J. Hurle, J. B. Mullin, A. M. White, and P. D. Greene, *J. Phys. Chem. Solids*, **36**, 1041 (1975).
13. H. C. Casey, M. B. Panish, and K. B. Wolfstirn, *ibid.*, **32**, 571 (1971).
14. P. D. Greene, *Solid State Commun.*, **9**, 1299 (1971).
15. M. B. Panish and H. C. Casey, *J. Phys. Chem. Solids*, **28**, 1673 (1967).
16. K. Keller and W. V. Muench, *Solid-State Electron.*, **14**, 526 (1971).
17. Yu. G. Siderov, L. F. Vasileva, I. V. Sabinina, and S. A. Duoretsky, *This Journal*, **123**, 698 (1976).
18. L. Pauling, "The Nature of the Chemical Bond," 3rd ed., Cornell University Press, New York (1960).
19. R. C. Weast, Editor, "Handbook of Chemistry and Physics," 53rd ed., p. F188 The Chemical Rubber Company, Cleveland (1973).
20. C. E. C. Wood, *Appl. Phys. Lett.*, **33**, 770 (1978).
21. A. Y. Cho and M. B. Panish, *J. Appl. Phys.*, **43**, 5118 (1972).
22. B. A. Joyce and C. T. Foxon, *Jpn. J. Appl. Phys.*, **16** (Supplement 16-1), 17 (1977).
23. A. Y. Cho, *ibid.*, **46**, 1733 (1975).
24. M. Ilegems and R. Dingle, "Proc. 5th Int. Symp. on GaAs and Related Compounds," Inst. Phys. Conf. Series, **24**, 1 (1975).
25. H. C. Casey and M. B. Panish, "Heterostructure Lasers, Part B," p. 132 Academic Press, New York (1978).

Properties of Sputtered Tungsten Silicide for MOS Integrated Circuit Applications

F. Mohammadi* and K. C. Saraswat**

Integrated Circuits Laboratory, Stanford University, Stanford, California 94305

ABSTRACT

Feasibility of the use of WSi_2 as gate electrode and electrical interconnecting material has been investigated. Properties of as-deposited and annealed thin films of WSi_2 have been studied to determine their compatibility with integrated circuit fabrication processes. Thin films of WSi_2 were deposited by sputtering on oxidized silicon, with and without a coating of poly-Si. As-deposited films were amorphous, with a resistivity of $6 \times 10^{-4} \Omega\text{-cm}$. Upon annealing above 900°C in N_2 , the films became polycrystalline. The resistivity decreased and the average grain size increased as a function of time and temperature. A minimum resistivity of $10^{-4} \Omega\text{-cm}$ was obtained. Chemical reagents commonly used for cleaning and etching, when used with WSi_2 , showed behavior similar to poly-Si. Al contacts to WSi_2 were stable up to 600°C for $WSi_2/SiO_2/Si$ structure and up to 550°C for $WSi_2/\text{poly-Si}/SiO_2/Si$ structure. These are significantly higher than the temperatures commonly used for sintering Al contacts to Si. Thermal oxidation of WSi_2 films in steam in the temperature range of 1000°C - 1200°C was performed and good quality SiO_2 was grown. Finally WSi_2 gate MOS devices were fabricated and characterized.

With the advances in the integrated circuit technology as the device dimensions are continuously decreasing, severe requirements are being imposed upon the materials. In MOS integrated circuits, the requirements for the material used to form the gate electrodes and the electrical interconnections are low resistivity, ability to withstand various chemicals and high temperatures encountered during fabrication process, and the capability to be defined into fine patterns. Poly-Si is widely used for this application, however, its inadequate properties are beginning to limit the per-

formance of the circuits. High resistivity of poly-Si causes degradation in the speed of the circuits because of R-C delay times. Although the grain size in as-deposited poly-Si can be very small, subsequent high temperature processing increases it markedly (1). This causes a problem in defining very fine lines. Refractory metals such as Mo and W can meet most of the above requirements, but they cannot withstand high temperature oxidizing ambients, because their oxides are generally volatile, and they cannot withstand chemical reagents commonly encountered during fabrication of integrated circuits. These two requirements can be met by the silicides of some of the refractory metals, such as $MoSi_2$ and WSi_2 . Feasibility of the use

* Electrochemical Society Student Member.

** Electrochemical Society Active Member.

Key words: tungsten silicide, annealing, resistivity, oxidation.

of MoSi_2 (2) and WSi_2 (3) has been demonstrated. In order to use these materials routinely to fabricate integrated circuits, a much more detailed knowledge of their properties is required. This will allow not only the determination of the compatibility of silicides with fabrication processes, but also will allow optimization of the process involving the use of silicides.

In this work we have studied the properties of thin films of WSi_2 deposited by sputtering. WSi_2 was deposited on oxidized silicon with and without an interlayer of poly-Si. Properties of as-deposited films, effect of high temperature annealing in N_2 atmosphere on resistivity and structure, thermal oxidation in steam, and stability of Al contacts to these films has been studied. Finally, MOS devices fabricated using WSi_2 as the gate material have been characterized.

Sample Preparation

Intermetallic refractory metal silicides can be obtained by the deposition of the refractory metal on silicon and subsequent conversion of the refractory metal to the desired intermetallic by reaction of the refractory metal with silicon at elevated temperatures (4). Formation of silicides by chemical vapor deposition (5), coevaporation of metal and Si (3), sputtering from a target made of silicide (2), and laser irradiation of metal deposited on Si (6) have been investigated. In this work the deposition of WSi_2 was done by rf diode sputtering from a hot-pressed target made of the silicide.

Single crystal Si wafers with (100) and (111) orientation were thermally oxidized in dry O_2 to grow 1000Å SiO_2 . The wafers were divided into two groups. On one group of wafers 4000Å thick undoped poly-Si was deposited by chemical vapor deposition. These wafers were further split into two subgroups by doping some of the poly-Si films with boron and phosphorus. The first set of poly-Si films was implanted with phosphorus, with dose varying from 10^{14} to 10^{16} ions/cm², at an energy of 100 keV. The samples were annealed for one hour at 1100°C, the first 15 min in dry O_2 and 45 min in dry N_2 atmosphere. The second set of poly-Si films was implanted with boron, with dose varying from 10^{14} to 5×10^{15} ions/cm², at an energy of 100 keV. The samples were thermally oxidized at 900°C wet oxygen for 30 min to grow a thin layer of SiO_2 and then annealed at 1100°C for 30 min

in dry N_2 atmosphere. The oxide layer was grown at a lower temperature to minimize the loss of boron by leaching. The third set was doped with boron by thermal diffusion, using B_2H_6 as the source of impurity, and the fourth set was doped with phosphorus using POCl_3 as the source of impurity. Both sets were doped for 30 min at 1000°C. A 4000Å thick WSi_2 film was deposited on top of all of the samples, i.e., SiO_2/Si and poly-Si/ SiO_2/Si structures and single crystal Si, using a Perkin-Elmer, rf diode sputtering system. The ambient was argon at a pressure of 20μ , the substrate temperature was kept below 300°C and the rate of deposition was 360 Å/min with a peak voltage of 1.5 keV, and an rf power of 280W. The target was made of hot-pressed WSi_2 . Prior to the deposition the samples were sputter-etched in order to obtain cleaner deposition interface and remove any residual SiO_2 . For all of the subsequent studies the three basic structures, WSi_2/Si , $\text{WSi}_2/\text{SiO}_2/\text{Si}$, and $\text{WSi}_2/\text{poly-Si}/\text{SiO}_2/\text{Si}$, were used.

Properties of As-Deposited Films

Auger electron spectroscopy and electron microprobe measurements showed that in the as-deposited WSi_2 films the ratio between the number of Si atoms to the number of W atoms was approximately 2:1. Glancing angle x-ray diffraction analysis did not show any specific peak of WSi_2 , indicating that the as-deposited films are amorphous. Figure 1(a) shows a transmission electron micrograph (TEM) of the films showing no specific grain structure, again strengthening the conclusion that the films are amorphous. An average resistivity of about 6×10^{-4} Ω-cm was measured for the films.

The films were not attacked by chemicals generally used in fabrication of IC's, e.g., H_2SO_4 , HNO_3 , HCl , HF , and mixtures of $\text{H}_2\text{SO}_4 + \text{H}_2\text{O}_2$, $\text{HCl} + \text{H}_2\text{O}_2$, and $\text{NH}_4\text{OH} + \text{H}_2\text{O}_2$, the common cleaning reagents for Si. Therefore in all of the experiments described subsequently the samples were cleaned using cleaning procedures commonly used for Si.

Properties of Annealed WSi_2 Films

Since the as-deposited films were amorphous, a study was conducted to investigate the effect of high temperature annealing, on the properties of WSi_2 films. $\text{WSi}_2/\text{SiO}_2/\text{Si}$ and $\text{WSi}_2/\text{poly-Si}/\text{SiO}_2/\text{Si}$ samples were

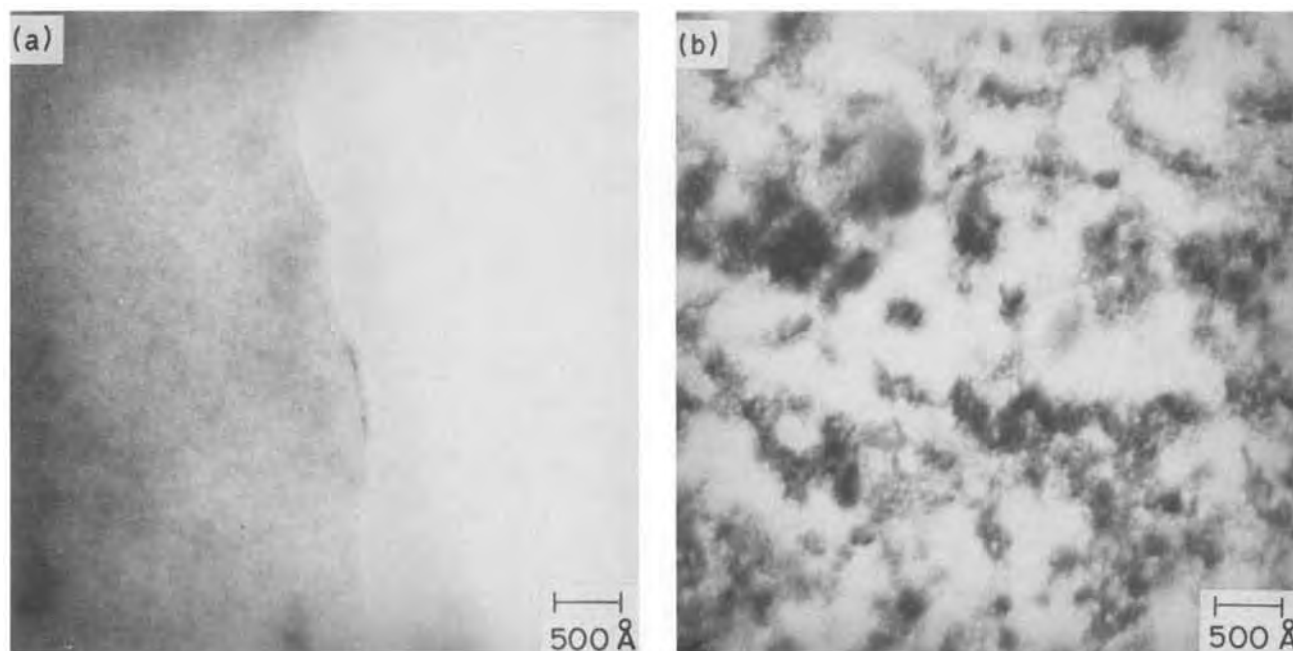


Fig. 1. TEM of WSi_2 films (a) as-deposited, (b) annealed at 1000°C for 120 min. In (a) the left side of the figure is the WSi_2 film and the right side is air.

annealed in N_2 , in the temperature range of 975°-1200°C, for times ranging from 30 to 180 min. Poly-Si was kept undoped and a fresh sample was used for each annealing experiment. Figure 2 shows the change in resistivity of the samples annealed for 30 min at temperatures between 975°-1200°C. As the annealing temperature increased the resistivity decreased. The resistivity of the WSi_2 films deposited on poly-Si was slightly lower than the films deposited on SiO_2 . Figure 3 shows the resistivity of the samples annealed at 975°C for times ranging from 30 to 180 min. Again the resistivity decreased as a function of time.

X-ray diffraction and TEM studies of the annealed samples showed that upon annealing the films became polycrystalline. Figure 1(b) shows the TEM of a WSi_2 film annealed for 120 min at 1000°C. There is a definite grain structure, with average grain size less than 500Å. Figure 4 shows results of x-ray diffraction of the same samples as used for TEM. Upon crystallization no specific preferred orientation of WSi_2 is observed. More x-ray diffraction studies showed that as the annealing temperature or time was increased the intensity of the diffraction peaks increased and the width decreased. This indicates that as the temperature or time of annealing is increased the degree of crystallization also increases.

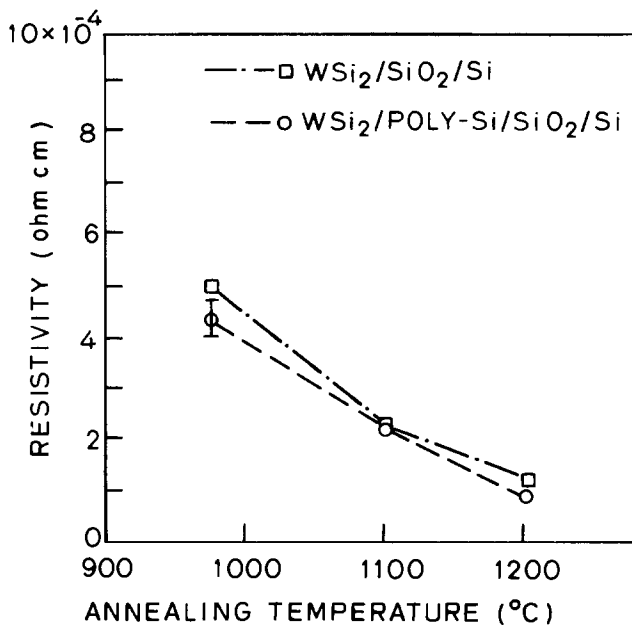


Fig. 2. Variation of resistivity as a function of annealing temperature for 30 min in N_2 ambient.

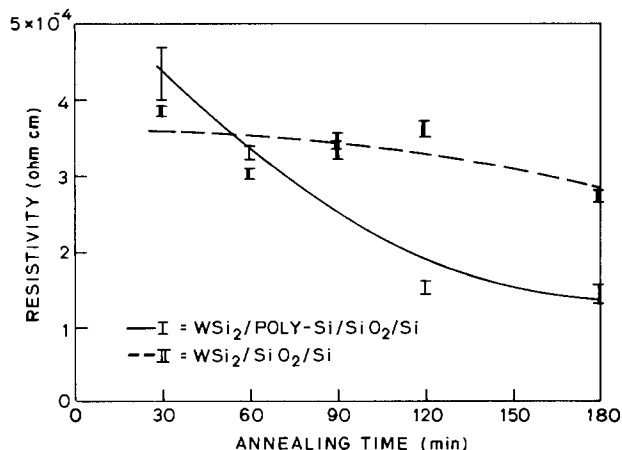


Fig. 3. Resistivity of $WSi_2/poly-Si/SiO_2/Si$ and $WSi_2/SiO_2/Si$ films as a function of annealing time for annealing temperature of 975°C in N_2 ambient.

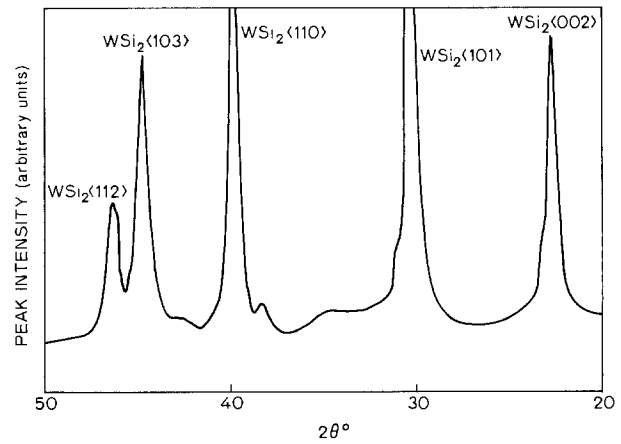


Fig. 4. X-ray diffraction pattern of the WSi_2 film annealed at 1000°C for 120 min. $Cu-K\alpha_1$ diffraction intensity is plotted as a function of twice the angle of incidence (2θ).

Finally compatibility of doped poly-Si with WSi_2 was investigated by studying the effect of annealing on $WSi_2/doped\ poly-Si/SiO_2/Si$ structures. The poly-Si layers were doped with boron and phosphorus as described in "Sample Preparation." After depositing WSi_2 all samples were annealed for one hour in N_2 at 1000°C. Figure 5 shows the resistivity variation of the combined WSi_2 and poly-Si layers as a function of doping density in poly-Si. For comparison the resistivity of the poly-Si layers alone is also given. It is evident that the resistivity of WSi_2 dominates the total resistivity and the presence of the dopant does not have any adverse effect on the resistivity of WSi_2 .

Thermal Oxidation

Formation of an insulator layer on top of the gate electrode and the interconnection layer is necessary so as to isolate it from subsequently deposited conducting layers. Vapor-deposited SiO_2 and Si_3N_4 can be used for this application. However, thermally grown

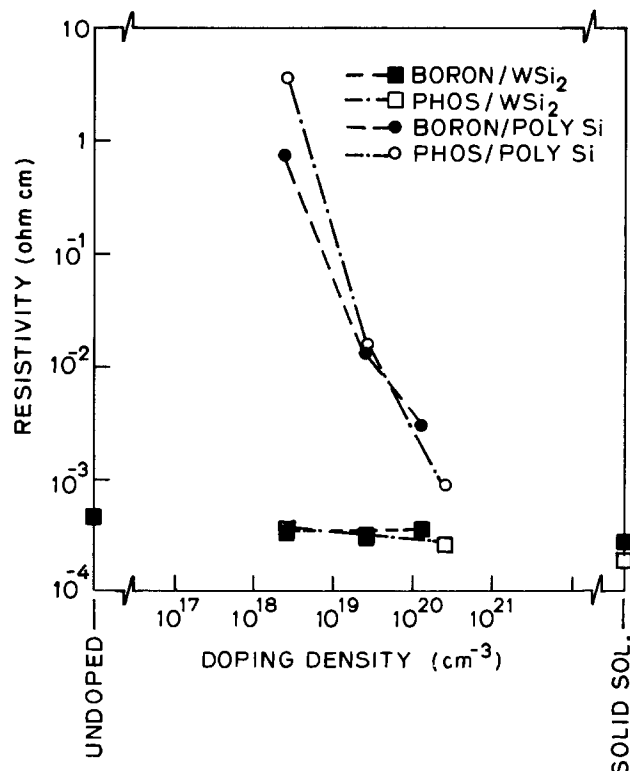


Fig. 5. Resistivity of $WSi_2/doped\ poly-Si/SiO_2/Si$ and doped $poly-Si/SiO_2/Si$ films as a function of dopant concentration.

SiO₂ is generally of superior quality. Therefore thermal growth of SiO₂ on WSi₂ is of extreme importance. The feasibility of thermal oxidation of WSi₂ was demonstrated by Zirinsky *et al.* (7) by oxidizing WSi₂/poly-Si/SiO₂/Si structure in steam at 1000°C. Their effort to oxidize WSi₂/SiO₂/Si structure was not as successful. In our work we have oxidized WSi₂ deposited on top of oxidized silicon as well as single crystal silicon (8). WSi₂/Si and WSi₂/SiO₂/Si samples were first annealed at 1000°C in N₂ for 60 min to crystallize the films. The annealed films were oxidized in steam with N₂ as the carrier gas, at 1000°, 1100°, and 1200°C, for periods of 5 to 30 min. After etching a step in the grown SiO₂, the thickness was measured with a Talystep. Figure 6 shows the thickness of SiO₂ as a function of time for the three temperatures of growth. It is seen that growth of SiO₂ is a stronger function of temperature for WSi₂ films deposited on Si. In order for SiO₂ to be used as an insulating layer in between conducting layers, it must have high electrical breakdown strength. For the oxides grown on WSi₂ the mean value of breakdown strength was about 4 × 10⁶ V/cm, which is comparable to the oxides grown on poly-Si.

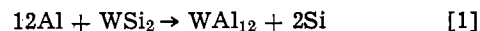
Stability of Aluminum Contacts

Aluminum is widely used as the last layer to provide electrical interconnections for multilayer structures. The last step in the Al metallization process generally is to anneal the wafers at 400°-500°C. This step improves the ohmic contact of Al to Si, removes the oxide damage caused during metal evaporation, and reduces the density of surface states at the oxide-silicon interface. It has been reported in the literature that at these temperatures Al can react with other silicide such as PtSi, MoSi₂, and CoSi₂ (9). In this reaction Al displaces Si from the silicide and forms compounds with metals, *e.g.*, PtAl₂, MoAl₁₂, and Co₂Al₉. In our work we have demonstrated the stability of the Al contacts to WSi₂ films.

After the deposition of 4000Å thick films of WSi₂, the WSi₂/SiO₂/Si and WSi₂/undoped poly-Si/SiO₂/Si samples were annealed at 1000°C for two hours in N₂ to crystallize the WSi₂ films. Following the anneal, 1.5 μm thick Al was deposited on top of the WSi₂ layers using an electron beam evaporation system. The resulting Al/WSi₂/SiO₂/Si and Al/WSi₂/poly-Si/SiO₂/Si structures were annealed for 30 min in dry N₂ at temperatures from 400° to 700°C. The quality of the annealing samples was examined by optical and scanning electron microscopes and x-ray diffraction.

The temperature up to which the Al/WSi₂ interface was stable was 600°C for the samples with WSi₂/SiO₂ interface and 550°C for the samples with WSi₂/Si interface. At and below these temperatures annealing did not affect the chemical and electrical properties of Al/WSi₂ layers. Average resistivity of the films was

about 3 × 10⁻⁶ Ω-cm dominated by Al. X-ray diffraction on Al/WSi₂/SiO₂/Si samples showed that after annealing at temperatures up to 600°C, the intensity of the diffraction peaks of various orientations of WSi₂ and Al remained unchanged. Above 600°C the WSi₂ peaks did not change much, but the Al peaks completely vanished and new peaks of WAl₁₂ and (111) Si appeared. This indicates a chemical reaction between Al and WSi₂ above 600°C



Similar reactions have been observed for MoSi₂, CoSi₂, and PtSi at 550°, 425°, and 300°C, respectively (9). An optical photograph of the surface of the sample annealed above 600°C is shown in Fig. 7, clearly showing the damage to the surface of the sample.

The Al/WSi₂/poly-Si/SiO₂/Si samples annealed up to 550°C were found to be stable and the intensity of the x-ray diffraction peaks of various orientations of WSi₂, Al, and (110) Si [this is the predominant orientation of LPCVD poly-Si deposited at 620°C (1)] remained unchanged. No surface damage could be detected by SEM and optical microscope. However, the samples annealed at 600°C and above showed severe surface damage. Although the x-ray diffraction peaks of WSi₂ did not change significantly except for slight increase in the intensity of (101) and (002) orientations, the (110) Si peak reduced markedly and Al peaks almost disappeared. No WAl₁₂ peak could be detected. This indicates that WSi₂ itself is not responsible for the instability; however, Al and poly-Si react above the eutectic temperature. It is known that diffusion of metals and Si can readily take place through a layer of silicide (9, 10). Therefore it is probable that upon annealing Al and Si diffuse through WSi₂ and at the eutectic temperature of 577°C cause the physical damage to the surface. The important point to be observed here is that both the structures were stable at the temperatures commonly used for sintering Al contacts to Si.

WSi₂ Gate MOS Devices

Using WSi₂ as the gate electrode, MOS capacitors of area 0.04 cm² were fabricated on (100)-oriented, n-type Si, with 5 × 10¹⁴ cm⁻³ doping density. Gate oxide of thickness 600Å was grown in dry O₂ at 1100°C. Following the WSi₂ deposition on the gate oxide, photolithography was done to define the gate electrodes and WSi₂ was etched in a HF-HNO₃ solution. The samples were annealed at 1000°C in N₂ for 30 min to crystallize WSi₂ and then annealed at 450°C in forming gas for 30 min to minimize surface states. Capacitors

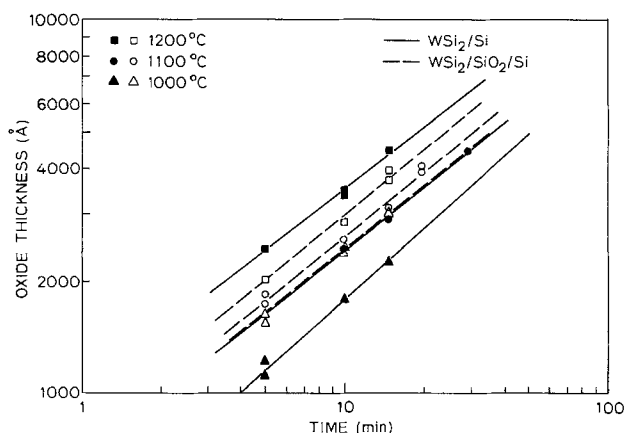


Fig. 6. Oxide thickness as a function of time for steam oxidation of WSi₂ deposited on SiO₂ and single crystal silicon.

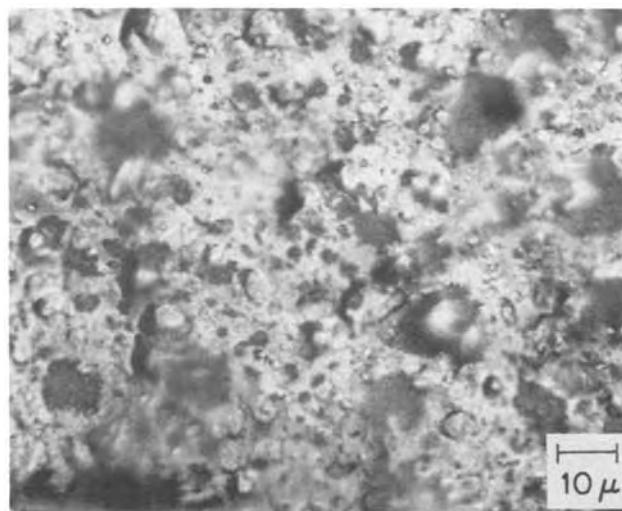


Fig. 7. Optical photomicrograph of Al/WSi₂/SiO₂/Si films annealed above 600°C.

tance was measured as a function of gate voltage at a frequency of 1 MHz. From the C-V plot, flatband voltage, and threshold voltage were measured to be 0 and -0.8V , respectively. From the C-V characteristics the work function of WSi_2 was calculated to be about 4.8 eV (11). Using this value of work function the fixed oxide charge density, Q_{ss} of $8 \times 10^{10} \text{ cm}^{-2}$ was calculated. By doing bias and stress C-V measurements the mobile charge density was found negligible.

Summary

Properties of WSi_2 to form gate electrode and electrical interconnecting material in silicon integrated circuits were examined. The conductivity of WSi_2 was found to be at least an order of magnitude higher than that of poly-Si. The higher conductivity can provide substantial improvement in the resistance of the electrical interconnecting lines used in VLSI structures. After long time annealing at high temperature the grain size of WSi_2 was found to be less than 500Å. This will facilitate etching of submicron lines which is essential for higher packing density. Other physical and chemical properties of WSi_2 are quite comparable to those of poly-Si from the point of view of compatibility with the fabrication technology. MOS devices fabricated with WSi_2 as the gate material showed excellent characteristics. Therefore, in conclusion, the use of WSi_2 as the gate and interconnecting material is feasible and should markedly improve the performance of the integrated circuits.

Acknowledgments

The authors would like to thank Professor J. D. Meindl for his encouragement and suggestions during the course of this work, W. Holmes for depositing the films, M. M. Mandurah for doing the transmission electron microscopy, and J. Rouse for doing the Auger

electron spectroscopy. This work was supported by the DARPA Grant No. MDA 903-79-C-0257.

Manuscript submitted Feb. 27, 1979; revised manuscript received Aug. 30, 1979.

Any discussion of this paper will appear in a Discussion Section to be published in the December 1980 JOURNAL. All discussions for the December 1980 Discussion Section should be submitted by Aug. 1, 1980.

Publication costs of this article were assisted by Stanford University.

REFERENCES

1. T. I. Kamins, M. M. Mandurah, and K. C. Saraswat, *This Journal*, **125**, 927 (1978).
2. T. Mochizuki, K. Shibata, T. Inoue, and K. Ohuchi, *Jpn. J. Appl. Phys.*, **17**, 37 (1977).
3. B. L. Crowder and S. Zirinsky, *IEEE Trans. Electron Devices*, **ed-26**, 369 (1979).
4. L. D. Locker and C. D. Capio, *J. Appl. Phys.*, **44**, 4366 (1973).
5. D. E. R. Kehr, in "Chemical Vapor Deposition, Sixth International Conference," pp. 511-528, The Electrochemical Society Softbound Proceedings Series, Princeton, N.J. (1977).
6. F. Mohammadi, K. C. Saraswat, J. Beaudouin, and J. D. Meindl, Abstract 146, p. 392, The Electrochemical Society Extended Abstracts, Boston, Massachusetts, May 6-11, 1979.
7. S. Zirinsky, W. Hammer, F. d'Heurle, and J. Baglin, *Appl. Phys. Lett.*, **33**, 76 (1978).
8. F. Mohammadi, K. C. Saraswat, and J. D. Meindl, *ibid.*, **35**, 529 (1979).
9. G. J. Van Gorp and W. M. Reukers, Abstract 215, p. 576, The Electrochemical Society Extended Abstracts, Pittsburgh, Pennsylvania, Oct. 15-20, 1978.
10. J. Baglin, F. d'Heurle, and S. Petersson, *Appl. Phys. Lett.*, **33**, 289 (1978).
11. K. C. Saraswat, F. Mohammadi, and J. D. Meindl, Presented at the 1979 IEEE Intl. Electron Devices Meeting, Washington, D.C., Dec. 1979.

An Investigation of Anodically Grown Films on GaAs Using X-Ray Photoelectron Spectroscopy

P. A. Breeze¹ and H. L. Hartnagel²

Department of Electrical and Electronic Engineering, University of Newcastle upon Tyne, England

and P. M. A. Sherwood

The Department of Inorganic Chemistry, University of Newcastle upon Tyne, England

ABSTRACT

Anodic oxides on GaAs have been examined using x-ray photoelectron spectroscopy (ESCA) combined with Ar-ion etching. The ESCA spectra were analyzed using both analog, and in some cases digital techniques. Results showed the films to be composed of As_2O_3 and Ga_2O_3 . The composition at the surface of the films was found to be electrolyte sensitive. At the oxide-semiconductor interface evidence was found suggesting a Ga_2O_3 rich oxide region and a layer adjacent to the semiconductor which appeared to contain elemental As. Anodically grown oxide films on GaAs incorporating Al were also studied and it appeared that the regions of GaAs native oxide above and below an Al_2O_3 region had differing compositions.

The anodic oxidation of GaAs (1) offers a very simple technique for producing barrier-type insulating films on this semiconductor. Such films are of great importance for the fabrication of MOS (metal-oxide-semiconductor) devices and success has already been achieved in producing transistors on GaAs (2, 3) using this technology. However, the oxide and interface

properties obtained still show room for improvement and work in our laboratories is concerned with optimization of the anodization conditions in order to improve device behavior. To do this effectively, detailed structural information is required and of the methods available to obtain this data Auger electron spectroscopy (AES) (4) and x-ray photoelectron spectroscopy (ESCA) (5, 6) are probably the most useful, when combined with a suitable etching technique.

In this paper we present chemical depth profiles of anodically grown films on GaAs, obtained using ESCA combined with Ar-ion etching. We feel that ESCA

¹ Present address: Inorganic Chemistry Laboratory, Oxford, England.

² Present address: Institut für Hochfrequenztechnik, Fachbereich 18, Merckstrasse 25, Germany.

Key words: GaAs, anodic oxidation, ESCA, depth profiles.

offers advantages over AES due to the chemical shift data which is more easily obtained and interpreted with the former (6). However, AES does have the advantage of speed and of being able to examine different parts of a single sample, so that a combination of both techniques where available offers the best solution (5).

Experimental

GaAs samples (Monsanto n-type, carrier concentration 10^{18}) were cleaned in methanol and acetone and dried from acetone. Al (99.995% purity, M.R.C. Limited), where used, was deposited by evaporation under vacuum at about 10^{-6} Torr. GaAs samples were etched for 1 min in 1% HCl solution prior to anodization. Electrolytes were all made up from research grade reagents and deionized water. Two electrolytes were studied. These were: (i) 3% tartaric acid solution mixed in the volume ratio 1:2 with propan 1, 2 diol (AGW) (1) and (ii) 0.02M (NH_4) H_2PO_4 solution mixed in the volume ratio 1:2 with propan 1, 2 diol.

Anodization was carried out under constant current conditions using experimental apparatus and techniques described previously (1). After anodization the samples were rinsed in acetone. Typical sample size was 0.6 cm \times 1.2 cm. The samples were attached to the copper spectrometer sample holder with ELEC-TRODAG 915 conducting paint (Acheson Colloids Company) to minimize sample charging. The sample holder itself was mounted on a UHV rotatable probe to ensure precise repositioning of the sample after rotation for etching.

ESCA spectra were recorded on an A.E.I. E.S. 200B spectrometer at typical chamber pressures of 2×10^{-8} Torr, utilizing Mg $K_{\alpha 1}$ $K_{\alpha 2}$ radiation at 1253.6 eV. They were recorded at 0.1 V sec^{-1} (Ga and As 3d peaks) and 0.05 V sec^{-1} (Al 2p and O 1s regions). Both analog and digital spectra were recorded simultaneously, the sampling rate for the latter being 50 times per minute.

Ar-ion milling was carried out using an ION-TECH saddle field ion source fitted with a scanning facility. The source has a beam of height 1 cm, and this was scanned along the length of the sample, at a mean angle of 45° to the sample surface. Argon was 99.996% purity (B.O.C.). The source was operated at either 8 kV 3 mA or 5 kV 2 mA. Approximate etch rates were 25Å/min in the former and 6Å/min in the latter case. These etch rates were estimated from depth profiles obtained from oxide films of known thickness. The anodic growth constants for oxidation of GaAs have been established previously (1). To obtain depth profiles the samples were etched in a stepwise fashion, spectra being recorded after each period of etching. Some idea of the reproducibility of the etching technique may be obtained from Fig. 6 where etching was continued into the substrate. As may be seen, in this region where constant composition is expected, fluctuations are less than $\pm 5\%$.

Data Processing

Most depth profiles were obtained from the ESCA peak areas of the Ga and As 3d peaks, the Al 2p peak and the O 1s peak in the analog spectra. To calculate these areas a triangular approximation was assumed so that

$$\text{peak area} = \text{peak height} \times \text{width at half height}$$

The intensity of photoelectrons of a given energy observed in a homogeneous material of path length x is given by (7)

$$I = \frac{F\alpha Dk}{\sigma} [1 - \exp(-x\sigma)] \quad [1]$$

if elastic scattering is neglected. I = intensity of photoelectrons emitted; F = x-ray flux; α = cross section for photoionization in a given energy level of a given atom for a given x-ray energy; D = density of the given atom in the material; k = a spectrometer con-

stant; $\sigma = 1/\lambda$, where λ is the mean escape depth of photoelectrons of given kinetic energy.

For two separate core energy levels A and B in the same sample measured under identical conditions [1] may be written

$$\frac{N_A}{N_B} = \frac{D_A}{D_B} = \frac{I_A \alpha_B}{I_B \alpha_A} \quad [2]$$

where N_A and N_B are the number of atoms per unit volume of A and B, if it is assumed that $\lambda_A \approx \lambda_B$. In our case this is true for the Ga and As 3d levels and the Al 2p level to within 3% since $\lambda \propto \sqrt{\text{kinetic energy}}$ (8) and the above-mentioned levels are of very similar kinetic energies. We have used Eq. [2] to give depth profiles that show the relative numbers of atoms per unit volume. The results have been plotted relative

to the Ga 3d intensity I_{Ga} by plotting I_{Ga} , $I_{As} \frac{\alpha_{Ga}}{\alpha_{As}}$ and

$I_{Al} \frac{\alpha_{Ga}}{\alpha_{Al}}$ giving the relative number of atoms per unit

volume in arbitrary units of $\frac{N_A}{N_{Ga}} I_{Ga}$ for atom A.

The cross sections (α) were taken from those calculated by Scofield (9). The O 1s region showed a strong oxide oxygen peak, the intensity of which was only used to obtain interface widths, so no corrections were applied.

Where the Ga 3d peaks due to Ga_2O_3 and GaAs were not clearly resolved the position of the composite peak center at half-height relative to the two extreme positions was used to estimate the amount of each component present, i.e., percentage of peak due to Ga_2O_3

$$\frac{\text{BE}(\text{Ga 3d}) - \text{BE}(\text{GaAs 3d})}{\text{BE}(\text{Ga}_2\text{O}_3 \text{ 3d}) - \text{BE}(\text{GaAs 3d})} \times 100\%$$

In the presence of As_2O_3 , elemental As was always observed after Ar-ion etching. On etching through the oxide film to the GaAs substrate the elemental As peak disappeared. An experiment using a sample of powdered As_2O_3 mounted on double-sided sellotape indicated that some of the oxide was reduced to elemental As by the ion beam. This is illustrated in Fig. 1. A similar experiment showed that Ga_2O_3 was stable towards reduction under the same conditions. It was therefore assumed that the origin of the elemental As peak in the anodic oxide film was from reduction of As_2O_3 . When constructing depth profiles the intensities of the As_2O_3 and elemental As 3d peaks were summed to give the total amount of As originally present as oxide. (Making the approximation that the cross sections and escape depths are the same for the two materials.) Where the elemental As 3d peak was obscured by that due to As in gallium arsenide its peak height was assumed to be one-third of that of the As_2O_3 peak for etching at 8 kV and one-quarter for ion etching at 5 kV. These were the ratios observed experimentally in the bulk of the oxide. Under these circumstances the assumed elemental As intensity was also subtracted from the measured As 3d intensity of GaAs.

In order to assess the errors involved in the above approximations an attempt was made to analyze one complete set of digital spectra by employing a non-linear least squares fitting program which uses a Gaussian Lorentzian product function (10).

In order to obtain meaningful results it was necessary to fix the linewidths of the various 3d peaks of Ga and As in the interface region. The fixed values used were obtained from fits of spectra from the oxide, or from the GaAs substrate. The results are illustrated in Fig. 2, which also includes the profile obtained from the analog spectra. (The dips in the analog profiles after 13 min etching are where the sample was left over night in the spectrometer after having etched for 10 min.)

As a further check of the validity of the approximation used to resolve the Ga 3d peaks of Ga_2O_3 and

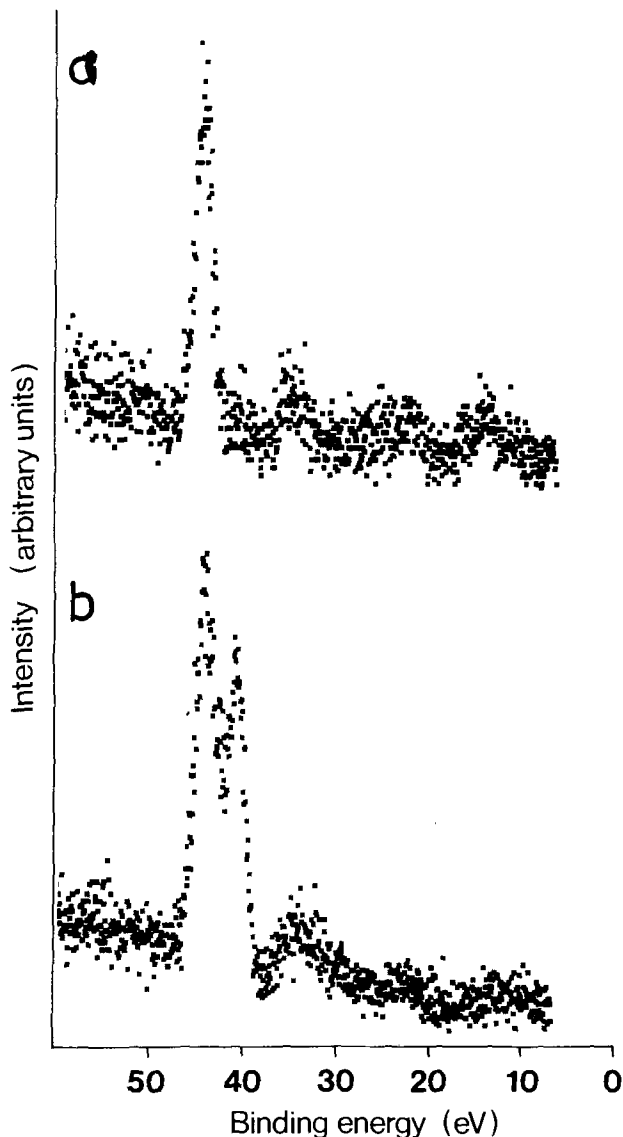


Fig. 1. ESCA spectra of the As 3d peaks for an As_2O_3 powder sample (a) before and (b) Ar-ion etching at 5 kV.

GaAs in the analog spectra the values of the expression

$$\frac{\text{BE}(\text{Ga } 3d) - \text{BE}(\text{GaAs } 3d)}{\text{BE}(\text{Ga}_2\text{O}_3 \text{ } 3d) - \text{BE}(\text{GaAs } 3d)}$$

were compared with values of the expression

$$\frac{I(\text{Ga}_2\text{O}_3)}{I(\text{Ga}_2\text{O}_3) + I(\text{GaAs})}$$

where $I(\text{Ga}_2\text{O}_3)$ is the intensity of the Ga 3d peak of Ga_2O_3 obtained from the digital analysis and similarly $I(\text{GaAs})$ represents the Ga 3d intensity of GaAs. Since both expressions represent the fraction of the Ga 3d peak due to Ga_2O_3 they should be identical. The values agree well ($\pm 5\%$) when the component peaks were of similar intensities but discrepancies appeared where the intensity ratio of the two components was estimated as greater than about 5:1 from the analog data. In these cases the weaker peak appeared relatively stronger from the digital analysis. However only in one case, point 14 in Fig. 2(b), did the difference exceed the $\pm 95\%$ confidence limits (equal to 2 standard deviations) of the digital analysis.

These differences probably arise for two main reasons. First, the approximation used to resolve the analog spectra is not entirely valid under the conditions where the discrepancies occur. Second, the 3d peak shapes are not perfectly fitted to a single peak

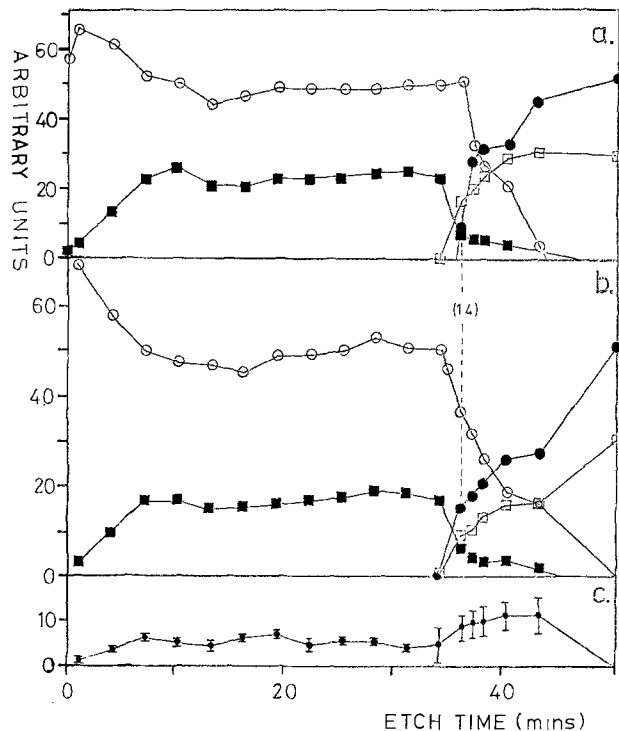


Fig. 2. Depth profiles of Ga and As 3d ESCA intensities from a 1000Å oxide film grown on GaAs in $(\text{NH}_4)\text{H}_2\text{PO}_4/\text{glycol}$ electrolyte at $50 \mu\text{A cm}^{-2}$, Ar ion etching at 8 kV. (a) Profiles from analogue spectra, (b) profiles from digital spectra, and (c) profile of elemental As from digital spectra. For (a) and (b), \circ , Ga in Ga_2O_3 ; \bullet , Ga in GaAs; \blacksquare , As in As_2O_3 ; \square , As in GaAs.

(they are in fact closely overlapping doublets comprising the 3d 5/2 and 3d 3/2 peaks) and so the fitting program may obtain a better statistical fit by modifying the intensity of the weaker peak present. However the good agreement obtained in most cases is encouraging and indicates that the approximation used is a useful one in cases where no other method is available.

The region where the accuracy of the profile becomes most critical is at the interface because here the greatest compositional variations occur. In particular there is the question of whether or not there is any elemental As present at this interface.

In the case of the analog spectra, elemental As could not be resolved out in the presence of gallium arsenide As (i.e., at the interface); rather, a constant ratio of As_2O_3 :As was assured in these cases and only this amount subtracted from the overlapping peak of gallium arsenide (see above). Any additional elemental As over and above this amount will still be included with the gallium arsenide As. Hence, if there were excess elemental As present we might expect to see a profile such as that in Fig. 2(a) where the gallium arsenide As appears before, and is initially more intense than the Ga. (Note that within the substrate the As appears less intense than the Ga due to selective etching. This effect is discussed later.)

From the digital spectra, the computer analysis made it possible to resolve out the As 3d peaks due to As_2O_3 , As, and GaAs as shown in Fig. 3. The As_2O_3 and As intensities have not been summed in Fig. 2(b) but the elemental As plotted separately in Fig. 2(c). (The error bars in the latter figure represent the 95% confidence limits of the digital curve fitting analysis and do not include any other experimental errors.) As may be seen the amount of elemental As appears to increase at the interface even though the amount of As_2O_3 is decreasing. This also suggests the presence of excess elemental As at the interface. However in the digital profile of Fig. 2(b) the gallium arsenide Ga appears earlier than in Fig. 2(a), leading to some

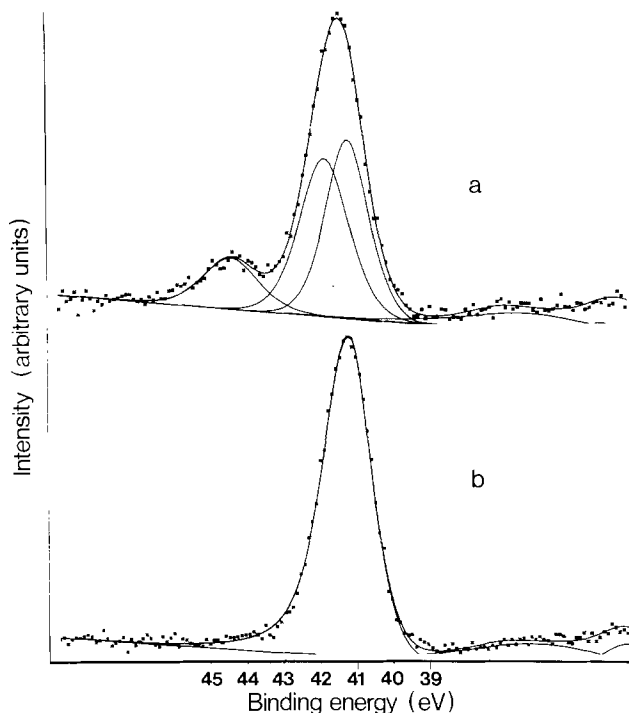


Fig. 3. Expanded spectrum of the As 3d region (a) at the interface showing the digital resolution of the 3d peaks due to As_2O_3 , As, and GaAs; (b) in the GaAs substrate.

uncertainty as to whether the feature in the analog profile can definitely be identified as being due to elemental As and is not merely an artifact of the method of data analysis. Two points should be mentioned in conjunction with this. First, although the Ga profiles do deviate in the interface region the difference between these in Fig. 2(a) and (b) only exceeds the 95% confidence limits of the digital analysis at point 14 (indicated on the figure). Second, the Ga profile of gallium arsenide is iterated to zero arbitrarily at the point shown in Fig. 2(b) since here none was observed. However the profile could be more abrupt than shown.

However better resolution was required in order to clarify this issue. This was achieved for the ESCA spectra by going to the narrowest slit width available. Figure 5 shows spectra at the interface of a sample grown at $10 \mu\text{A cm}^{-2}$ using this maximum resolution. The analog profile for the same sample is shown in Fig. 6. The spectra in Fig. 5 clearly show that significant changes occur in the As 3d spectrum before similar changes occur in the Ga 3d region and we believe that this is due to the presence of elemental As. Subsequently (for the profiles shown in Fig. 7 and 8) improved depth resolution was achieved by using lower Ar-ion etch rates.

With this improved resolution, and since reasonable overall agreement was obtained between the profiles obtained by analog and digital analysis of the same set of data the authors decided to rely exclusively on the analog treatment of the results.

Results

The binding energies of the various 3d peaks of Ga and As and of the Al 2p peak observed in these experiments are listed in Table I and compared with previously reported binding energies. The comparison indicates that the major peaks observed in the anodically grown films on GaAs correspond in position with those of Ga_2O_3 , As_2O_3 , and As within experimental error. In the film incorporating aluminum the Al 2p peak corresponds in position with that of Al_2O_3 . The CIS peak at 284.6 eV (which is the value obtained in this laboratory for a hydrocarbon contamination layer based in $\text{Au } 4f_{7/2}$ at 84.0 eV) was generally used for

Table I. Peak positions

		Binding energy (eV)		
		This work (± 0.2 eV)	Previously reported (11, 12) ^d	F.W.H.M. (This work)
Ga 3d	GaAs	19.4 ^a	19.5	1.6 ^a
	Ga_2O_3	20.5 ^a	20.4	2.0 ^a
As 3d	GaAs	41.2 ^a	41.2	1.6 ^a
	As_2O_3	44.5 ^a	44.4	2.0 ^a
	As	41.8 ^{b,c}	41.8	1.8 ^a
Al 2p	Al_2O_3	74.5 ^b	74.5	1.9

^a Referred to CIS at 284.6 eV.

^b Referred to Ga 3d position of Ga_2O_3 at 20.5 eV.

^c Obtained from the best computer fitted spectra of the anodic oxide.

^d Referred to CIS at 285.0 eV.

^e Obtained from digital spectra.

calibration if possible but in many cases this did not prove reliable. (This may be due to the presence of a carbon-containing species in the anodic films but more work is required to definitely establish this.) Under these circumstances internal calibration against the Ga 3d peak of Ga_2O_3 was used. In all experiments the internal calibration was consistent with the above assignment. Typical ESCA spectra of the Ga and As 3d region for an anodic oxide and the GaAs substrate are illustrated in Fig. 4.

In addition to the ESCA peaks discussed above, several other weaker peaks were also observed in the

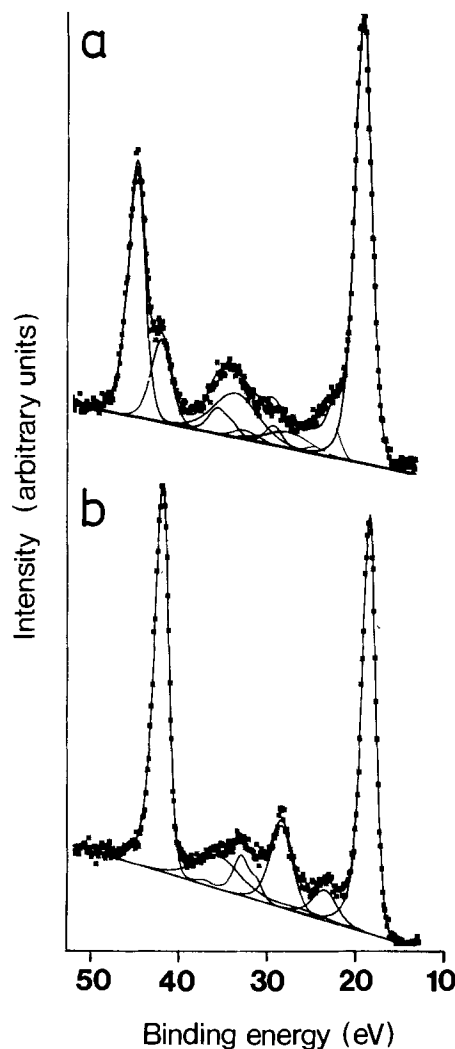


Fig. 4. ESCA spectra of the Ga and As 3d region with computer fit peaks of (a) GaAs native oxide and (b) GaAs substrate after removal of the native oxide by Ar-ion etching at 8 kV.

10-60 eV binding energy region (see Fig. 4). Two pairs of peaks occurred in the anodic oxide spectra between about 26 and 35 eV. These were assigned to the As $L_3M_{45}M_{45}$ Auger transitions (11), there being one pair associated with As_2O_3 and another with elemental As. When GaAs started appearing a third pair of Auger peaks were seen to slightly lower binding energies. Other peaks are the satellite peaks from the nonmonochromated x-radiation used in the spectrometer. Their position and intensity are well known and are taken from x-ray spectroscopy results (13). A broad peak was identified in the computer-analyzed spectra of the anodic oxide at about 39 eV. A similar peak was seen in the GaAs substrate at around 35 eV. The latter peak is a plasmon loss peak associated with GaAs (4, 14) and the lower peak probably has a similar origin. Finally, a new peak was seen at 27.5 (± 1) eV which disappeared on etching through to the substrate. This is probably the oxygen 2s peak (15), the assignment being supported by the fact that the peak correlates quite well with the oxygen 1s intensity which was monitored in most of these experiments.

Oxides grown in the $(NH_4)H_2PO_4$ /glycol electrolyte.—The depth profiles shown in Fig. 2 were obtained from a 1000Å thick native oxide film on GaAs, grown in the $(NH_4)H_2PO_4$ /glycol electrolyte at $50 \mu A cm^{-2}$. As seen in the figure the surface of the oxide grown in this electrolyte is As deficient as compared to the bulk. For a similar sample grown at $500 \mu A cm^{-2}$ the ESCA spectrum showed no As present at the surface. The bulk oxide region is fairly uniform and shows a constant As/Ga ratio of atoms per unit volume of between 0.5 and 0.6, this value appearing to be independent of growth current density over the range $10 \mu A$ - $500 \mu A cm^{-2}$. To what extent this ratio is affected by selective etching has not been established. However it is clear from the Ga and As profiles of gallium arsenide, where the As/Ga ratio is 0.6 instead of unity, that selective etching of As from the substrate definitely occurs.

At the oxide-semiconductor interface the As_2O_3 intensity generally starts to drop before that of Ga_2O_3 . Indeed, in some cases the Ga_2O_3 intensity increases first before dropping off. This leads to a Ga_2O_3 rich oxide next to the substrate. The effect seems to be more pronounced at higher and lower growth current densities than it is at $50 \mu A cm^{-2}$. See for example Fig. 6 for a sample grown at $10 \mu A cm^{-2}$. Similar behavior has been observed for samples grown at $500 \mu A cm^{-2}$.

From the profile in Fig. 2(c) it can be seen that the amount of elemental As observed increases at the oxide-semiconductor interface even though the As_2O_3 intensity is decreasing. This suggests that there is a region adjacent to the GaAs substrate where elemental As was present prior to Ar-ion etching. Alternatively it is possible that very thin films of As_2O_3 may be more readily reduced, leading to a smaller As_2O_3 /As ratio than that observed in the bulk of the film. However, it has been suggested previously (4) that there is an As rich region adjacent to the substrate in anodic films on GaAs. In view of this it seems very probable that what we are seeing here is confirmation of the presence of elemental As at the oxide/semiconductor interface. Figure 5 shows spectra obtained on etching through the interface of a sample grown at $10 \mu A cm^{-2}$. It can be seen that the changes in As 3d spectrum occur earlier than those in the Ga 3d region. The profile from the sample is shown in Fig. 6 and shows a similar region to Fig. 2(c) although in this case the elemental As intensity is included in the As profile of gallium arsenide as discussed earlier. Similar results were also observed for samples grown at $500 \mu A cm^{-2}$.

Interface widths, measured from these profiles, were defined as the distance over which the intensity of the component being measured changed from 20 to 80% of its steady-state value (6). Interface widths

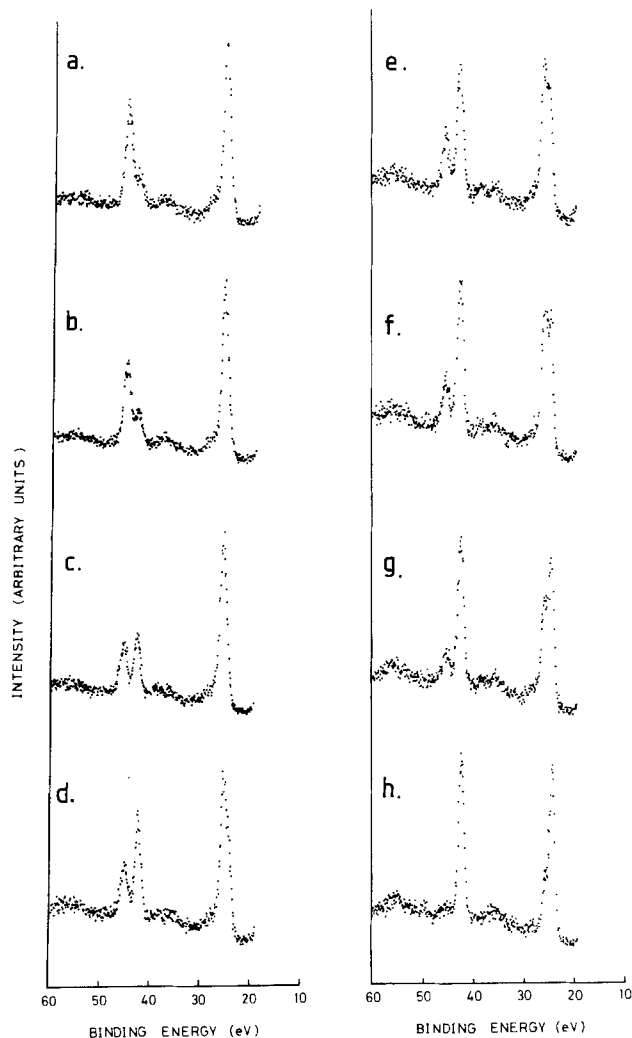


Fig. 5. ESCA spectra of As and Ga 3d region of sample grown at $10 \mu A cm^{-2}$ after Ar-ion etching at 8 kV for (a) 25 min, (b) 28 min, (c) 31 min, (d) 32 min, (e) 33 min, (f) 34 min, (g) 36 min, (h) 39 min.

were measured on both Ga, As, and oxygen profiles. It was found that those measured from the oxygen

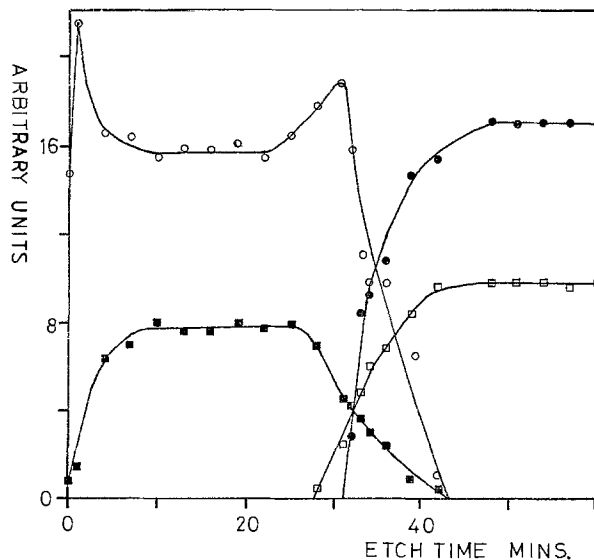


Fig. 6. Depth profiles of Ga and As 3d ESCA intensities from 800Å oxide film grown on GaAs in $(NH_4)H_2PO_4$ /glycol electrolyte at $10 \mu A cm^{-2}$. Ar-ion etching at 8 kV. \circ , Ga in Ga_2O_3 ; \bullet , Ga in GaAs; \blacksquare , As in As_2O_3 ; \square , As in GaAs.

profiles gave the largest widths, as would be expected since they reflect the change in both As_2O_3 and Ga_2O_3 at the interface. The widths from the oxygen profiles are therefore used in discussing the interfaces.

Significantly smaller interface widths were observed when etching at 5 rather than 8 kV. For example the interface width measured for a 1000Å film grown at $500 \mu\text{A cm}^{-2}$ and etched at 8 kV was 210Å whereas the width measured for a similar film etched at 5 kV was about 90Å. This is due to knock-on effects occurring during ion etching which make the interface appear broader than it actually is. The effect is greater for higher energy bombarding ions. Another effect which has not been investigated in a systematic way here is uneven etching. This makes the observed interface width depend on what film thickness has previously been etched away, the broadening increasing for thicker films (6). Because of these effects the measured interface widths represent an upper limit and the actual widths may be expected to be significantly smaller than the measured values.

Oxides grown in the tartaric acid/glycol electrolyte.—Figure 7 shows the profiles obtained from a 500Å native oxide film grown on GaAs in the AGW electrolyte at $200 \mu\text{A cm}^{-2}$. In contrast to oxides grown in the previous electrolyte the surface region is As rich as compared to the bulk. (The first point in all these profiles is unrepresentative due to surface contamination and should be ignored.) The other features of these profiles are very similar to those already discussed. The bulk of the film is uniform with an As/Ga ratio of about 0.5. There is a slightly Ga_2O_3 rich region adjacent to the substrate and the As profile of the GaAs substrate indicates the probable presence of elemental As at the interface. The interface width obtained from the oxygen profile was 60Å. (The sample was etched at 5 kV.)

Using the data shown in Fig. 7 an attempt was made to estimate the amount of elemental As present at the interface over and above that expected due to reduction of As_2O_3 by the ion beam. The gallium arsenide As peak intensities were all corrected for selective etching using the observed Ga/As ratio of the substrate, which is 0.65 instead of unity, and assuming that the effect becomes operative as soon as the substrate appears. Using the corrected values the difference in areas beneath the Ga and As profiles of the gallium arsenide was obtained. From the known etch rate and the known density of As atoms in GaAs the area could be converted into a number of atoms per square centimeter, giving the value 2×10^{15} atoms per cm^2 . It was not possible to assign a realistic value to the errors involved in this estimate.

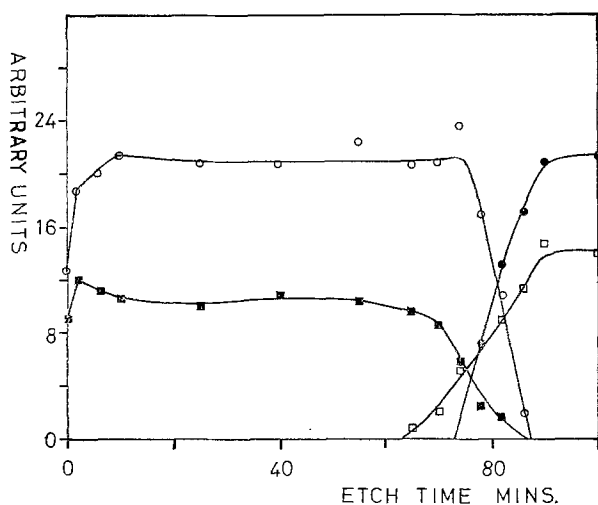


Fig. 7. Depth profiles of Ga and As 3d ESCA intensities from a 500Å oxide film grown on GaAs in tartaric acid/glycol electrolyte at $200 \mu\text{A cm}^{-2}$. Ar-ion etching at 5 kV. ○, Ga in Ga_2O_3 ; ●, Ga in GaAs; ■, As in As_2O_3 ; □, As in GaAs.

Anodic films incorporating aluminum.—Figure 8 shows the profile obtained from an anodic oxide film grown in the AGW electrolyte on a GaAs sample with 200Å of Al deposited onto its surface. ESCA spectra of the Ga and As 3d region taken at points A, B, and C in Fig. 8 are shown in Fig. 9. The total oxide film thickness here is approximately 900Å. As already noted, the Al 2p peak can be assigned to that of Al_2O_3 , (see Table I). This peak was observed all the way through the oxide film and significant amounts were seen at the surface.

From Fig. 8(a) it can be seen that there are two GaAs native oxide regions, one above and one below the Al_2O_3 layer. The native oxide beneath the Al_2O_3 layer is similar in all respects to that observed on GaAs in the absence of Al [compare Fig. 4(a) and Fig. 9(c)] and at the oxide semiconductor interface the probable presence of elemental As is indicated. However the native oxide at the surface of the film [see Fig. 9(a)] shows marked differences when compared to the normal GaAs native oxides grown without Al. First the oxide is very As deficient as compared to the normal anodic oxide. The As/Ga ratio of atoms per unit volume here is about 0.3 rather than 0.5. Second the As_2O_3 :As ratio in this region is almost 1:1, not the 4:1 ratio expected from reduction of As_2O_3 by Ar ions at 5 kV. This situation persists right through the predominantly Al_2O_3 region until the oxide region underneath is reached when the normal ratio is again observed. This seems to suggest that there is some difference between the As_2O_3 in the two regions such that that nearer the surface is more readily reduced. An alternative possibility which cannot be ruled out from the data available here is that there was originally some unoxidized Al present in the film which reacted with As_2O_3 during Ar-ion etching to produce As + Al_2O_3 , since Al_2O_3 is the thermodynamically more stable oxide.

Discussion

The foregoing results indicate that anodic native oxide films on GaAs may be divided into three regions;

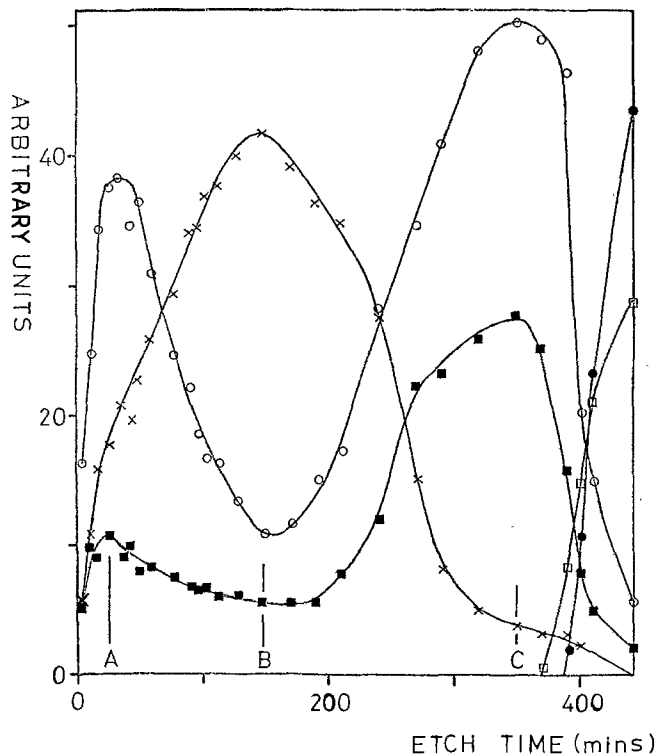


Fig. 8. Depth profiles of Ga and As 3d and Al 2p ESCA intensities from an anodic oxide grown on GaAs + 200Å Al in tartaric acid/glycol electrolyte at 100A cm^{-2} . Ar-ion etching at 5 kV. ○, Ga in Ga_2O_3 ; ●, Ga in GaAs; ■, As in As_2O_3 ; □, As in GaAs; ×, 1/2 of Al 2p intensity in Al_2O_3 .

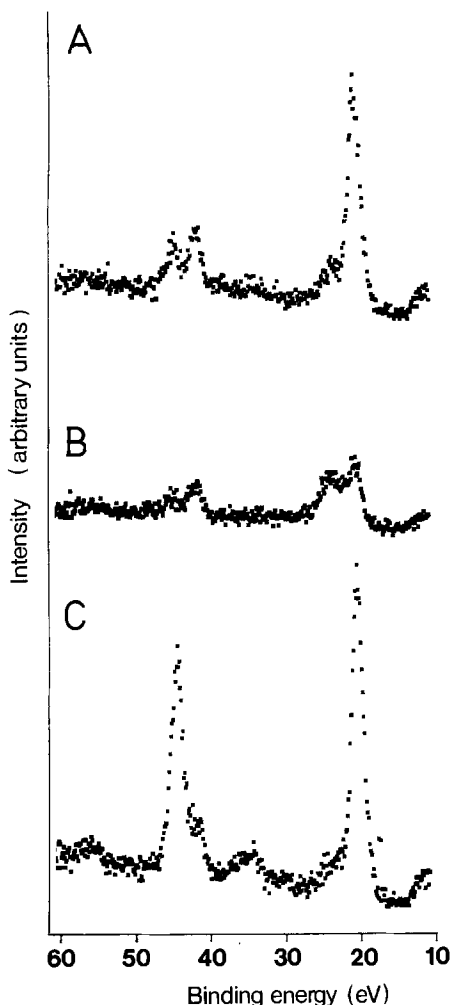


Fig. 9. ESCA spectra of the Ga and As 3d region recorded at points A, B, and C in Fig. 7.

the surface, the oxide bulk, and the oxide/GaAs interface region. In terms of chemical composition the surface region is extensively influenced by the electrolyte whereas the other two regions are not. The factors which control the surface composition are not known but the adsorption behavior of the electrolyte is probably important.

Due to the limited number of samples studied here no definite conclusions have been drawn concerning the influence of growth current density on film structure. However no overall systematic changes were observed over nearly two orders of magnitude ($10\text{--}500 \mu\text{A cm}^{-2}$). The most obvious variation seen was in the extent to which there was a Ga_2O_3 rich region in the oxide near the oxide/semiconductor interface. This seemed much less pronounced for samples grown at $50 \mu\text{A cm}^{-2}$ than for those grown at the extremes of the range studied. It is conceivable that the observed variation was simply an experimental artifact. However a previous report (16) of oriented $\beta\text{-Ga}_2\text{O}_3$ observed at this interface for samples grown at very high current densities ($>2 \text{ mA cm}^{-2}$) may also suggest a more Ga_2O_3 rich oxide at the interface, since As_2O_3 is a primary glass former and its absence could lead to polycrystalline Ga_2O_3 being formed. [Wilmsen and Kee also reported a Ga_2O_3 rich oxide near the interface in anodic oxides grown in both tartaric acid/glycol and H_3PO_4 solutions (5).] There was also some evidence that the surface depletion of As was less severe for samples grown at low current densities in the $(\text{NH}_4)_2\text{H}_2\text{PO}_4$ electrolyte. Similar results have been reported by Croset *et al.* (17) for samples grown in a Na_3PO_4 /glycol electrolyte.

As noted above it is possible that the as-grown anodic oxide films contain elemental As at the oxide/semiconductor interface. The origin of this elemental As is not known, but we have previously suggested (18) that the growth mechanism may be responsible. Whatever the reason for this accumulation, its presence must influence the interface properties and hence device behavior where this technology is employed. Because of this it would be advantageous to be able to control and hopefully eliminate this elemental As buildup. However, at present there is no obvious way in which this might be accomplished.

One further observation of relevance in connection with the oxide film growth mechanism is that in Fig. 8(a) Al_2O_3 is seen throughout the film. Its occurrence deep in the film, below the expected Al_2O_3 region, may be due to knock-on effects during ion etching. However, the spreading towards the oxide surface cannot be explained as an experimental artifact. It may mean that the previously suggested interstitial mechanism for metal ion drift (18) is an oversimplification and that "lattice" and "interstitial" ions can interchange within the film. Further experimental work is required here.

Finally, it is important to consider the effects of ion etching on the sample and how this influences the results. We have observed in these experiments that the Ar-ion beam reduces As_2O_3 . No similar effect was seen with Ga_2O_3 . We have also seen selective etching in the GaAs substrate where the observed Ga:As ratio was not unity. However, we have not yet been able to estimate the extent to which selective etching effects the observed Ga:As ratio in the oxide. Until the extent of this effect is known we cannot make any reliable quantitative measurements from results such as these. Also we have noted that the measured interface width is significantly influenced by the etching conditions, a factor which should be taken into account when using such measurements.

Conclusions

The results presented in this paper illustrate the application of ESCA to the study of anodic oxide films. Using this technique we have been able to obtain chemical depth profiles which provide considerable insight into the structure of such films. They indicate that the oxide/semiconductor interface region is very complex with variations in the $\text{Ga}_2\text{O}_3/\text{As}_2\text{O}_3$ ratio as well as the probable presence of elemental As. Some variation was noted between films grown in two different electrolytes.

Results from an anodic film grown on a GaAs substrate plus 200Å of aluminum also showed complex behavior. Two different native oxide regions were identified, one at the film surface which was relatively As_2O_3 deficient and one below the Al_2O_3 , adjacent to the substrate, which resembled the anodic native oxides seen in the absence of Al.

Much more work is still required, both on anodic native oxides of GaAs and also on multilayer anodic films. It is hoped that progress will be assisted by further applications of ESCA to take advantage of the insight which it allows.

Acknowledgments

Financial support from the European Research Office of the U.S. Army is gratefully acknowledged, and the Science Research Council is thanked for provision of equipment.

Manuscript submitted Oct. 30, 1978; revised manuscript received Aug. 27, 1979.

Any discussion of this paper will appear in a Discussion Section to be published in the December 1980 JOURNAL. All discussions for the December 1980 Discussion Section should be submitted by Aug. 1, 1980.

REFERENCES

1. H. Hasegawa and H. L. Hartnagel, *This Journal*, **123**, 713 (1976).

2. B. Bayraktaroglu, E. Kohn, and H. L. Hartnagel, *Electron. Lett.*, **12**, 53 (1976).
3. E. Kohn, A. Colquhoun, and H. L. Hartnagel, *Solid-State Electron.*, **21**, 877 (1978).
4. C. C. Chang, B. Schwarz, and S. P. Murarka, *This Journal*, **124**, 922 (1977).
5. C. W. Wilmsen and R. W. Kee, *J. Vac. Sci. Technol.*, In press.
6. R. Nishitani, H. Iwasaki, Y. Mizokawa, and S. Nakamura, *Jpn. J. Appl. Phys.*, **17**, 321 (1978).
7. T. A. Carlson and G. E. McGuire, *J. Electron Spectrosc. Relat. Phenom.*, **1**, 161 (1972).
8. M. Klasson, J. Hedman, A. Berndtsson, R. Nilsson, C. Nordling, and P. Melnik, *Physica Scripta*, **5**, 93 (1972).
9. J. H. Scofield, *J. Electron Spectrosc. Relat. Phenom.*, **8**, 129 (1976).
10. R. O. Ansell, T. Dickinson, A. F. Povey, and P. M. A. Sherwood, *J. Electroanal. Chem. Interfacial Electrochem.*, In press.
11. G. Leonhardt, A. Berndtsson, J. Hedman, M. Klasson, R. Nilsson, and C. Nordling, *Phys. Status Solidi B*, **60**, 241 (1973).
12. G. E. McGuire, G. K. Schweitzer, and T. A. Carlson, *Inorg. Chem.*, **12**, 2450 (1973).
13. T. A. Carlson, "Photoelectron and Auger Spectroscopy," p. 24, Plenum Press, New York (1975).
14. J. E. Rowe, J. C. Tracy, and S. B. Christian, *Surf. Sci.*, **52**, 277 (1975).
15. P. Pianetta, I. Lindau, C. Garner, and W. E. Spicer, *Phys. Rev. Lett.*, **35**, 1356 (1975).
16. B. Weiss, E. Kohn, B. Bayraktaroglu, and H. L. Hartnagel, Paper 5.4 presented at 6th Int. Symp. on GaAs & Related Compounds, Edinburgh (U.K.), (1976) Inst. Phys. Conf. Ser. 33a.
17. M. Croset, J. Dias, D. Dieumegard, and L. M. Mercandalli, Paper 192 presented at The Electrochemical Society Meeting, Seattle, Washington, May 21-26, 1978.
18. P. A. Breeze and H. L. Hartnagel, *Thin Solid Films*, **56**, 51 (1979).

Arsenic Ion-Implanted Shallow Junction

Yasuo Wada* and Norikazu Hashimoto

Hitachi, Limited, Central Research Laboratory, Kokubunji, Tokyo 185, Japan

ABSTRACT

Shallow junction formation technology by arsenic ion implantation is evaluated from the viewpoint of practical application to the coming VLSI's. Carrier profile, residual defect profile, and electrical characteristics are examined as functions of acceleration energy, dose, annealing conditions, and surface oxide thickness. The carrier profile is determined mainly by both arsenic ion amount in the substrate layer and annealing conditions. The residual defect profile is determined by implantation energy and surface oxide thickness. It is necessary to implant arsenic ions shallower than the resulting carrier profile, to obtain arsenic ion-implanted junctions with acceptable electrical characteristics. A junction diode, with junction depth as shallow as 0.16 μm is fabricated according to this principle, and is ascertained to have acceptable electrical characteristics.

The increasing demand for higher packing density MOS LSI's has accelerated progress for larger and more densely integrated devices. The integration density has almost tripled every two years, along the trend curve for higher integration (1).

This progress has been achieved mainly through the scale-down theory (2), in which the physical dimensions of the unit device, MOS FET, are reduced $1/k$ times that of original values. This factor k is called the scale-down factor. The resulting circuit speed becomes k times faster, and the resulting power dissipation of the circuit also becomes $1/k^2$ times smaller. According to the scale-down theory, heavily doped shallow junction formation technology is indispensable in addition to fine pattern lithographic technology.

In line with this, heavy arsenic ion implantation technology has attracted attention recently as a means of fabricating shallow and low resistivity MOS LSI source and drain regions (3). The main reasons for this trend are the precise controllability and high flexibility that ion implantation technology provides. The in-process monitoring of ion implantation energy and dose facilitates high accuracy in fabricating very shallow junctions. Moreover, ion implantation technology makes it possible to reduce the lateral spread of impurity as compared with conventional thermal diffusion technology (3). Arsenic ion-implanted emitters of bipolar transistors/LSI's also provide acceptable device characteristics (4).

There, arsenic ion implantation technology will inevitably be used for the formation of shallow and low resistivity source and drain regions of high density MOS LSI's as well as emitters of bipolar devices. However, there still remains the problem of the high density residual defect even after prolonged annealing at high temperatures (5), which might affect the electrical characteristics of junctions.

This paper reports the residual defect penetration depth as well as carrier profile of shallow arsenic ion-implanted layers as functions of implantation energy, dose, annealing conditions, and surface oxide thickness. It also provides information on the electrical characteristics of the shallow junction in relation to carrier and residual defect profile results.

Experimental Procedures

Ion implantation and annealing.—Arsenic ions were implanted through oxide layers into p-type, (100) oriented silicon wafers. The oxide layers were thermally grown to thicknesses of between 0 and 50 nm. The acceleration energy and dose were in the range 40-120 keV and 1×10^{15} cm^{-2} - 2×10^{16} cm^{-2} , respectively. Annealing in a dry nitrogen atmosphere at between 900° and 1100°C for 20-120 min was carried out to activate the implanted ions.

Carrier and defect profile measurements.—Carrier profiles of arsenic ion-implanted layers were measured by the incremental sheet resistivity method (6). Measurement accuracy was better than 20% for carrier number, and better than 5% for depth. Carrier num-

* Electrochemical Society Active Member.

Key words: ion implantation, leakage current, oxygen knock-on, p-n junction.

ber was derived using Irvin's ρ - N relationship (7). Therefore, the clustering effect of heavily arsenic-doped layers (8) was not taken into consideration. Carrier number in the implanted layer was also measured by Hall effect measurements.

The residual defect penetration depth of the arsenic ion-implanted layers was measured using a combination of the layer removal method and thin film transmission electron microscope (TEM) observation technique (9).

Junction diode fabrication and leakage current measurements.—An n^+ - p junction diode with 1 mm^2 area was fabricated by conventional silicon gate MOS LSI processing technologies (14). A $1 \mu\text{m}$ thick oxide layer was thermally grown on a p -type, (100) oriented $10 \Omega\text{-cm}$ silicon wafer. Then, the diode region was delineated by photolithography, followed by thin (20-50 nm thick) thermal oxide growth and arsenic ion implantation. A phosphosilicate glass layer was deposited by the CVD method. Annealing in a dry nitrogen atmosphere was carried out, followed by aluminum metallization and low temperature hydrogen annealing. Phosphorus atoms in the PSG layer do not diffuse into the silicon substrate, because of the thin thermal oxide layers underneath the PSG layer.

Leakage current of the diode was measured using a combination of constant voltage source and picoammeter. Leakage current as low as 10^{-13} A (10^{-11} A/cm^2) could be detected.

Results and Discussion

Dose dependence of carrier profile.—The carrier profiles of arsenic ion-implanted annealed layers were measured as functions of dose, energy, surface oxide thickness, and annealing conditions. Typical results of dose dependence between $1 \times 10^{15} \text{ cm}^{-2}$ and $1 \times 10^{16} \text{ cm}^{-2}$ are shown in Fig. 1. The heavier the ion dose, the deeper the carrier profile becomes. The dose dependence of carrier profile can be explained in terms of concentration dependent arsenic diffusion coefficient in silicon (14). The peak carrier concentration remained at about $2 \times 10^{20} \text{ cm}^{-3}$, regardless of ion dose. Total carrier number measured by Hall effect was less than 50% in the $1 \times 10^{16} \text{ cm}^{-2}$ implanted case, whereas it was about 100% in the $3 \times 10^{15} \text{ cm}^{-2}$ implanted case. These carrier saturation phenomena have been explained in the light of clustering effect in the heavily arsenic ion implanted layers (8). Therefore, in order to form shallow and low resistivity junction, it is better to control the peak arsenic concentration at about $2 \times 10^{20} \text{ cm}^{-3}$, so as to avoid the unnecessary clustering phenomena.

However, it was found that there is a practical limitation for the shallow and low resistivity junction formation. The sheet resistivity and junction depth relationship of the arsenic ion-implanted annealed layer was measured, and the typical results are shown in Fig. 2. In the figure, the low resistivity and shallow junction is on the lower left-hand side, and vice versa. These results clearly show that a practical limitation exists in forming shallow and low resistivity junctions. Taking a $0.2 \mu\text{m}$ depth junction for example, the lowest resistivity achievable by arsenic ion implantation and high temperature annealing is around $35 \Omega/\square$. These limitations are determined by the contribution of temperature dependent solid solubility (8), as well as the concentration dependent arsenic diffusion coefficient in silicon (14).

The influence of initial arsenic profile on the resulting carrier profile was estimated. Typical calculated results assuming Gaussian distribution (12) are shown in Fig. 3, in which the acceleration energy was between 40 and 120 keV. Although the initial profile differed markedly according to the implantation conditions, as shown in Fig. 4 (12), the resulting carrier profiles after high temperature annealing are almost identical. In

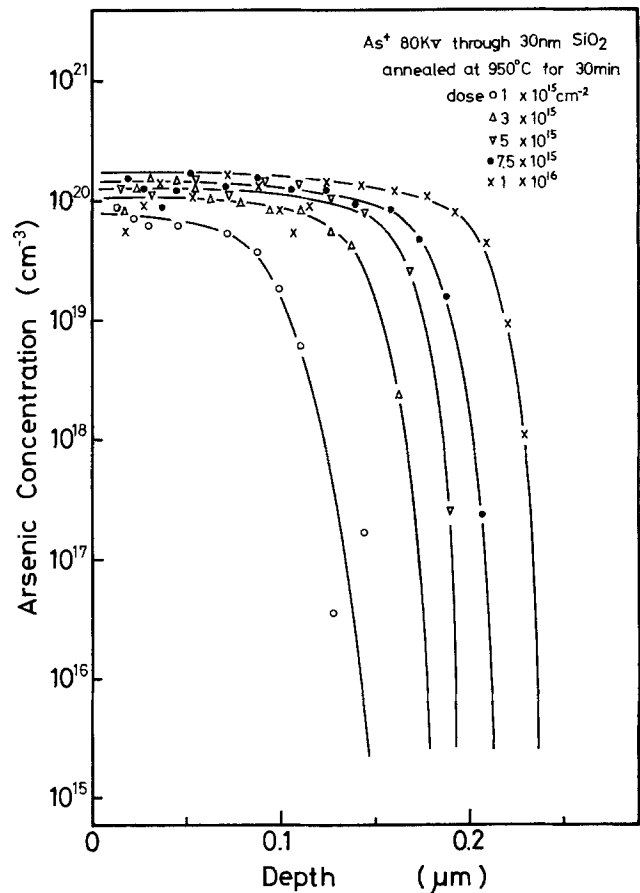


Fig. 1. Dose dependence of carrier profile measured by incremental sheet resistivity method. As^+ ion implantation; 80 keV through 30 nm thick SiO_2 layer. Annealed at 950°C for 30 min in dry N_2 . As^+ dose (10^{15} cm^{-2}); \circ , 1; Δ , 3; ∇ , 5; \bullet , 7.5; \times , 10.

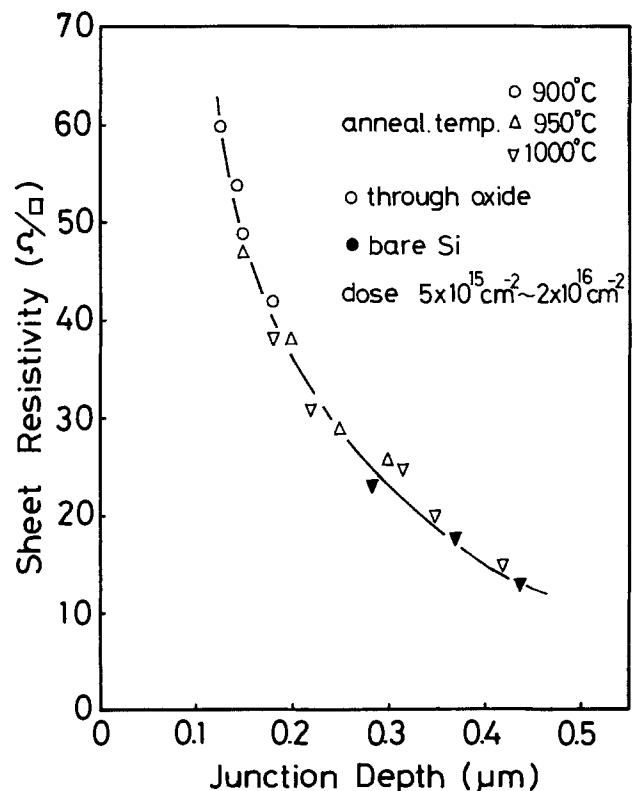


Fig. 2. Junction depth and sheet resistivity relationship measured for As^+ ion-implanted layers.

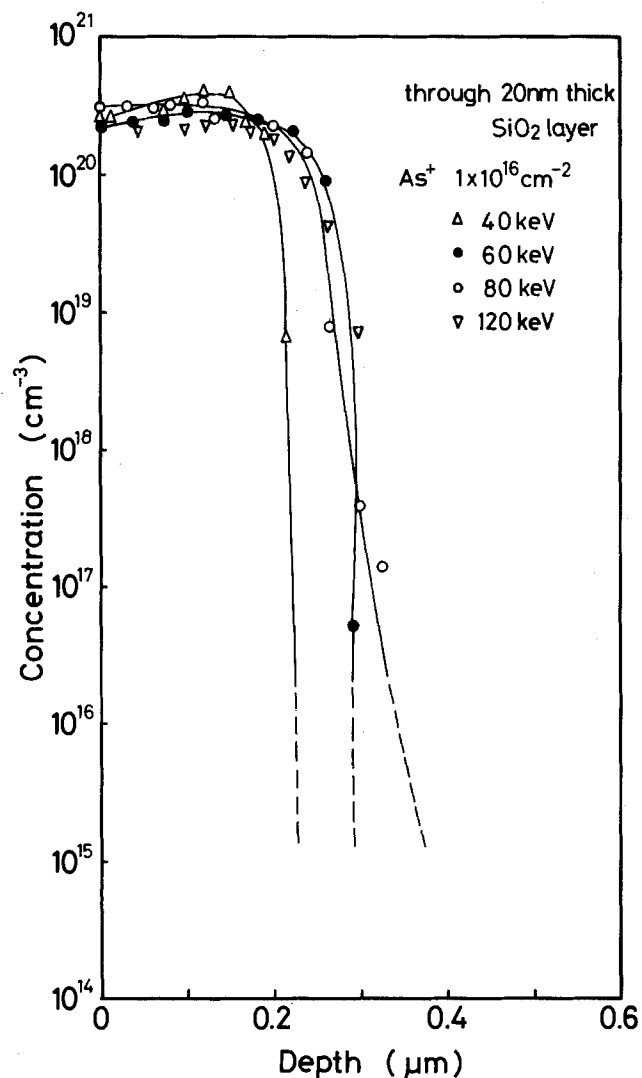


Fig. 3. Acceleration energy dependence of carrier profiles; annealed at 1000°C for 30 min; Δ , 40; \bullet , 60; \circ , 80; ∇ , 120 keV.

comparison with the dose dependence of carrier profile results shown in Fig. 1, it can be concluded that the arsenic ion amounts in the silicon substrate, as well as annealing conditions, almost completely determine the resulting carrier profile in silicon.

Therefore, the resulting carrier profiles after thermal annealing do not depend on the initial arsenic profiles in silicon. It is essential to control the annealing conditions, as well as the arsenic amount in silicon to obtain a suitable carrier profile in the arsenic-implanted layers.

Residual defect penetration depth.—Residual defect penetration depth was measured as functions of acceleration energy and surface oxide thickness. Arsenic ion dose was 1×10^{16} cm⁻². The samples were annealed in a dry nitrogen atmosphere at 1000°C for 30 min. Residual defect differences observed by TEM are depicted in Fig. 5. The result for a 40 keV implanted sample is markedly different from the other TEM micrograph results. The residual defects did not grow to dislocation loops, possibly due to the very shallow residual defect profile. On the other hand, the defects grew to dislocation loops in higher implantation energy cases. If the dose amount was doubled, the residual defect shape changed from dislocation loop to small scattered dislocations. However, prolonged annealing of up to 120 min did not change the residual defect structures. This phenomenon originated from the dislocation pinning effect of knock-on oxygen (3).

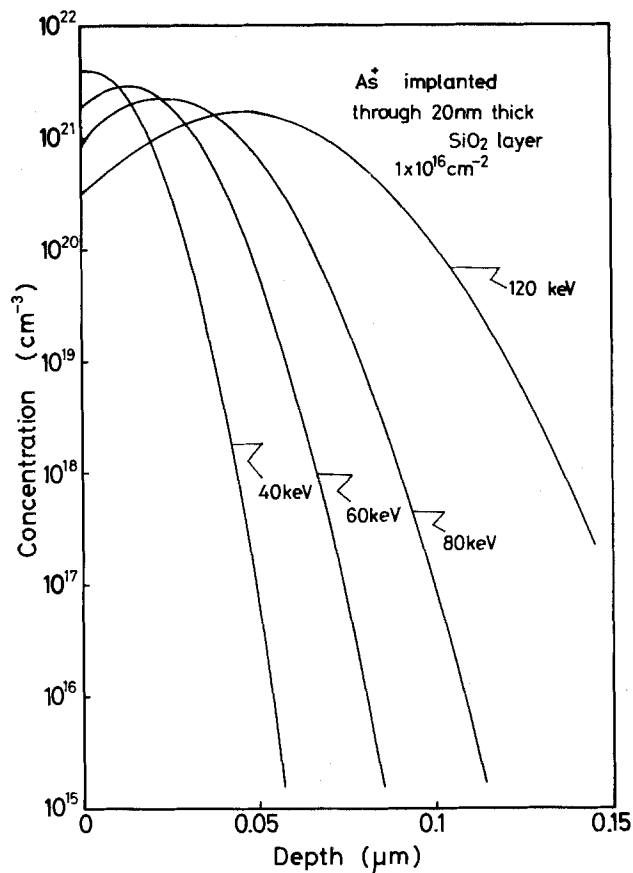


Fig. 4. Calculated as-implanted arsenic profile in silicon As⁺ implantation; 40-120 keV through a 20 nm thick SiO₂ layer.

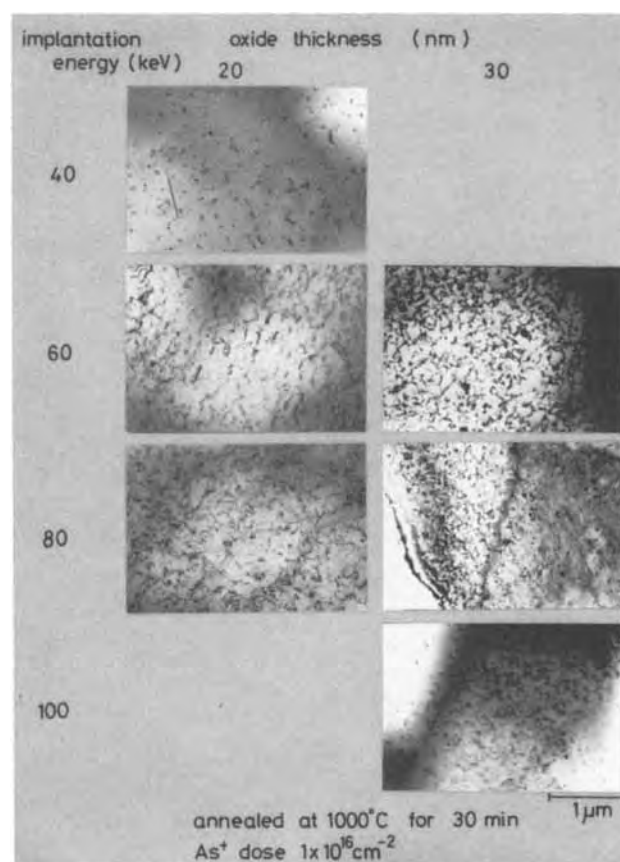
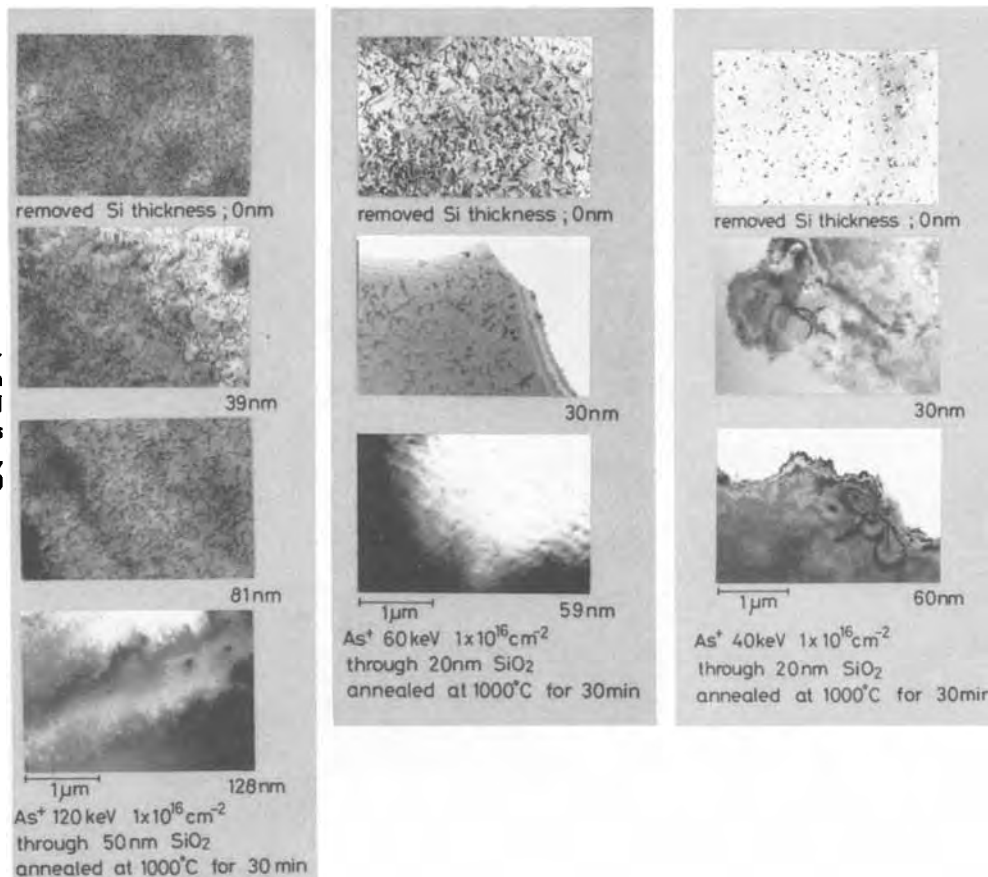


Fig. 5. TEM micrograph of As⁺ ion-implanted layers; As⁺ implantation; 40-120 keV through 20 or 30 nm thick SiO₂ layers; annealed at 1000°C for 30 min.

Fig. 6. TEM micrographs showing residual defect penetration depth measured by layer removal method: acceleration energy, as a parameter; (a, left) 120 keV, (b, center) 60 keV, (c, right) 40 keV.



The defect penetration depths for samples shown in Fig. 5 were measured by the layer removal method, and typical TEM micrographs are shown in Fig. 6(a), (b), and (c). Taking the 40 keV implantation case for example, residual defects remained only within 30 nm of the surface, while the residual defects in samples implanted with a 120 keV acceleration energy penetrated to a depth of around 0.11 μm . Therefore, it can be concluded that the higher the implantation energy, the deeper the residual defect penetration depth becomes in the silicon-silicon dioxide (Si-SiO₂) system.

Defect profile analysis.—The acceleration energy dependence of residual defect penetration depth is analyzed in terms of oxygen knock-on phenomenon (15). A typical knock-on oxygen profile in silicon, measured by secondary ion microanalysis (SIMS) is shown in Fig. 7 by open circles (11). Arsenic ions were implanted through a 102 nm thick surface oxide layer, to a $1 \times 10^{16} \text{ cm}^{-2}$ dose at a 180 keV acceleration energy. In the figure, the calculated arsenic profile in the silicon-silicon dioxide system (Si-SiO₂) is also depicted by a solid line (12).

The distance between the Si-SiO₂ interface and the oxygen profile, normalized by arsenic ion projected range (R_p) in silicon dioxide is derived as a function of surface oxide thickness, that is also normalized by R_p . Typical results are shown in Fig. 8, in which the oxygen concentrations were chosen as 10^{19} and 10^{20} cm^{-3} . The results clearly show that between a normalized surface oxide thickness of 0.5 and 3.0 (e.g., 50-300 nm thick), the thinner the oxide thickness, the deeper the knock-on oxygen profile becomes. If surface oxide thickness is half of R_p , the depth where knock-on oxygen concentration is 10^{20} cm^{-3} becomes about 1.2 times deeper than R_p from the Si-SiO₂ interface, while the depth where the oxygen concentration is 10^{19} cm^{-3} becomes about three times deeper.

The acceleration energy dependence of residual defect penetration depth, shown in Fig. 6, can be analyzed on the basis of normalized knock-on oxygen

penetration depth shown in Fig. 7 and 8. Assuming that the residual defect remains in the region where the knock-on oxygen concentration is above $8 \times 10^{19} \text{ cm}^{-3}$, the experimentally obtained residual defect penetration depth and the calculated penetration depth coincide well, as shown in Fig. 9. In the figure, it is shown that the results for acceleration energy of between 40 and 120 keV fell almost on the same line.

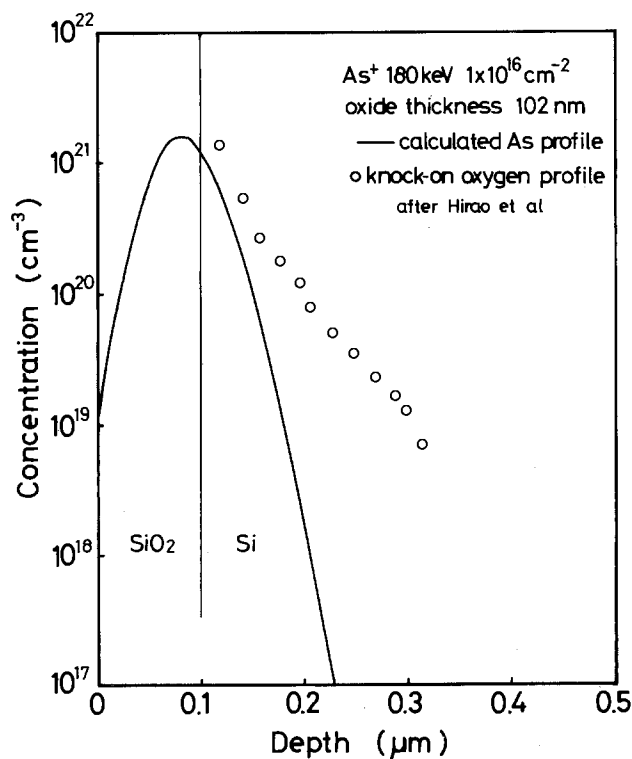


Fig. 7. Knock-on oxygen profile in silicon [after Hirao (10)]

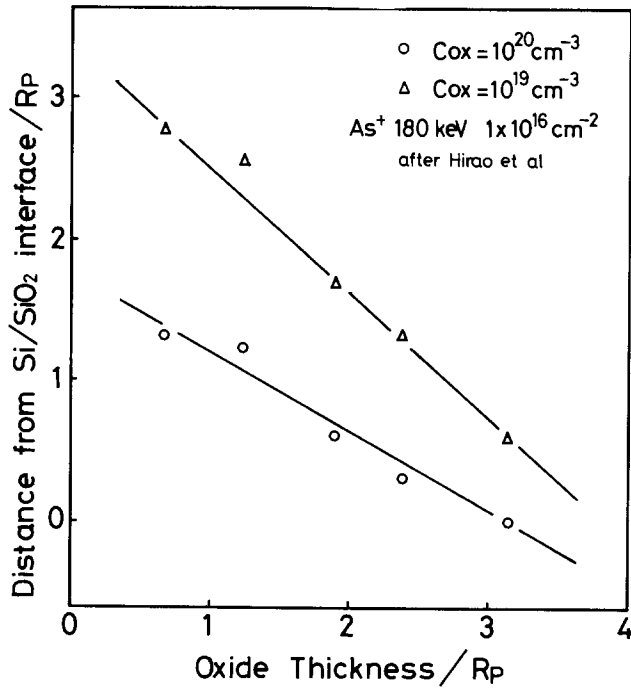


Fig. 8. Normalized relationship between knock-on oxygen penetration depth and surface oxide thickness.

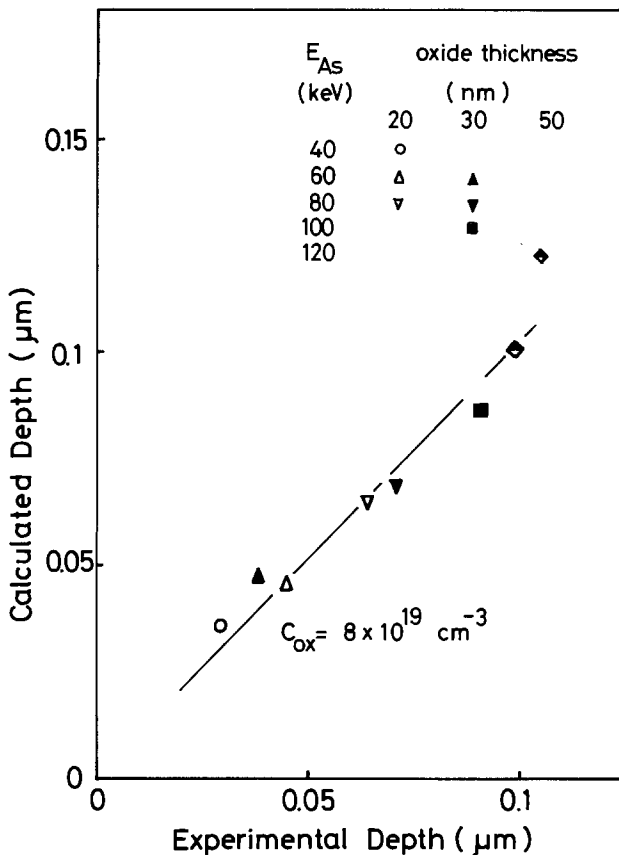


Fig. 9. Comparison of experimental and calculated residual defect penetration depth. Oxygen concentration, $C_{ox} = 8 \times 10^{19} \text{ cm}^{-3}$.

The normalized residual defect penetration depth (X_{defect}/R_p) is expressed as a function of normalized oxide thickness (t_{oxide}/R_p) as follows

$$X_{defect}/R_p = -2/3 (t_{oxide}/R_p) + 2 \quad [1]$$

Therefore, residual defect penetration depth can be predicted from the normalized knock-on oxygen penetration depth and normalized surface oxide thick-

ness relationship shown in Fig. 8. In other words, residual defect penetration depth can be controlled by the suitable choice of implantation energy and surface oxide thickness. These results suggest that low energy ion implantation through thin silicon dioxide layers is recommendable for shallow arsenic ion-implanted junction formation, from the viewpoint of residual defect penetration depth.

Electrical characteristics of junction diode.—If residual defect penetration depth exceeds the junction, the generation-recombination center concentration of the junction would increase markedly. In other words, if arsenic ions were implanted at a high acceleration energy and annealed at low temperature, so that the carrier profile would not move, or would not exceed the residual defect penetration depth, the electrical characteristics of the diodes would become poor. Therefore, practical limitations of shallow junction formation technology were evaluated from the standpoint of diode leakage current characteristics.

The junction leakage current of diodes fabricated by shallow arsenic ion implantation was measured as functions of residual defect penetration depth and carrier profile. The results are shown in Fig. 10. In the figure, junction depths were measured by the bevel-etch staining method (10), as well as by the incremental sheet resistivity method (6). The residual defect penetration depth was derived from the results shown in Fig. 9. As long as the residual defect penetration depth does not exceed the junction depth, the leakage current level is low enough to apply to practical device fabrication (3). Junctions as shallow as $0.16 \mu\text{m}$ depth were shown to have acceptable electrical characteristics.

Annealing temperature dependent leakage current results (13) were also analyzed in view of this defect penetration depth analysis. The relationship of annealing temperature and calculated residual defect penetration depth, as well as junction depth, are shown in Fig. 11. In the figure, arsenic ions were implanted at 100 keV through a 54 nm thick SiO_2 layer to a dose of $4 \times 10^{15} \text{ cm}^{-2}$ (13). The residual defect penetra-

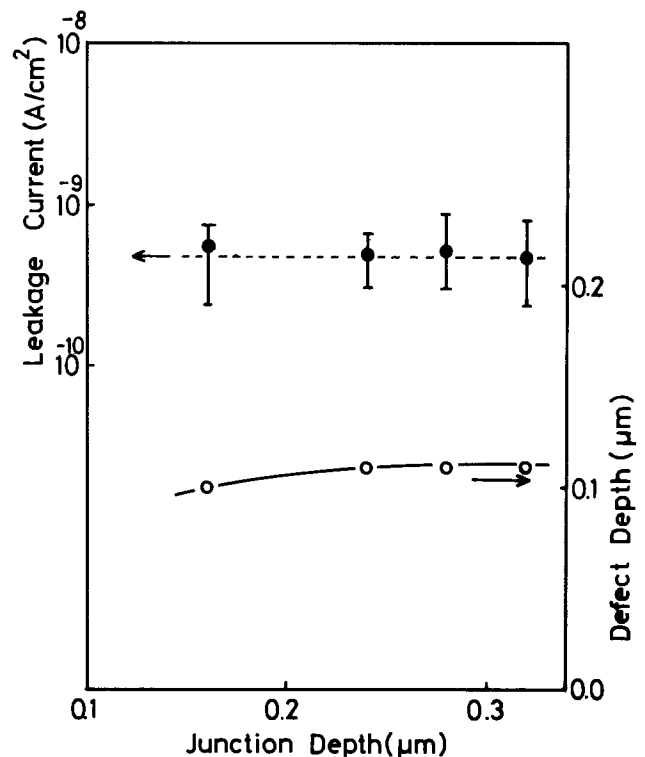


Fig. 10. Junction leakage current of shallow junction diodes fabricated by shallow arsenic ion implantation. Residual defect penetration depth and junction depth, as parameters.

tion depth should be around $0.09 \mu\text{m}$ according to the analysis previously shown. On the other hand, the junction depth increases with annealing temperature. Corresponding leakage current results are also shown in Fig. 11. Leakage current is too high for practical applications, when the difference between junction and defect depth is around $0.02 \mu\text{m}$. These results clearly indicate that junction leakage current is higher when the residual defects penetrate deeper or at least $0.02 \mu\text{m}$ shallower than the carrier profile. Therefore, the guiding principle, i.e., "Junction depth should be deeper than residual defect penetration depth by at least $0.02 \mu\text{m}$," can be derived.

Conclusions

The residual defect penetration depth and the carrier profile of arsenic ion-implanted layers after high temperature annealing were measured as functions of implantation conditions and annealing conditions. The results obtained in this study are summarized as follows.

1. Residual defect penetration depth can be predicted by arsenic ion implantation conditions and surface oxide thickness.

2. Resulting carrier profile after high temperature annealing is determined mostly by arsenic ion amounts

in the substrate region as well as by annealing conditions.

3. Guiding principle, "Junction depth should be deeper than the residual defect penetration depth by at least $0.02 \mu\text{m}$ " can be derived from the device application viewpoint.

4. Shallow arsenic ion implantation technology will be a key tool for the coming VLSI fabrication.

Acknowledgments

The authors wish to express their appreciation to Dr. Takashi Tsuchimoto for valuable discussions. Thanks are also due to Dr. Takashi Tokuyama for his continuous encouragement and valuable discussions. The authors are also grateful to Dr. Fumio Nagata for participating in fruitful discussions on TEM micrographs. The experimental assistance of Mr. Masami Ozawa and Mr. Hiroo Usui are very much appreciated.

Manuscript submitted May 29, 1979; revised manuscript received Aug. 27, 1979. This was Paper 557 presented at the Los Angeles, California, Meeting of the Society, Oct. 14-19, 1979.

Any discussion of this paper will appear in a Discussion Section to be published in the December 1980 JOURNAL. All discussions for the December 1980 Discussion Section should be submitted by Aug. 1, 1980.

Publication costs of this article were assisted by Hitachi, Limited.

REFERENCES

1. G. E. Moor, Paper 1-3 presented at the IEEE International Electron Device Meeting, Washington, D.C., Dec. 1-3, 1975.
2. R. H. Dennard, F. H. Gaensslen, H. N. Yu, V. L. Rideout, E. Bassons, and A. R. LeBlanc, *IEEE J. Solid-State Circuits*, **sc-9**, 256 (1974).
3. Y. Wada and S. Nishimatsu, *Jpn. J. Appl. Phys. Suppl.*, **18**, 255 (1979).
4. R. S. Payne, R. J. Scavuzzo, K. H. Olson, J. M. Nacci, and R. A. Moline, *IEEE Trans. Electron Devices*, **ed-21**, 273 (1974).
5. S. Mader and F. Mishel, *J. Vac. Sci. Technol.*, **13**, 391 (1976).
6. R. B. Fair and J. C. C. Tsai, *This Journal*, **122**, 1689 (1975).
7. J. C. Irvin, *Bell Syst. Tech. J.*, **22**, 265 (1962).
8. R. B. Fair and G. W. Weber, *J. Appl. Phys.*, **44**, 273 (1973).
9. P. B. Hirsch, A. Howie, R. B. Nicholson, D. W. Pashley, and M. J. Whelan, "Electron Microscopy of Thin Crystals," Butterworth, London (1965).
10. R. M. Burger and R. P. Donovan, Editors, "Fundamentals of Silicon Integrated Device Technology," Prentice-Hall, Englewood Cliffs, New Jersey (1967).
11. T. Hirao, K. Inoue, Y. Yaegashi, and S. Takayanagi, *Jpn. J. Appl. Phys.*, **18**, 647 (1979).
12. J. F. Gibbons, W. S. Johnson, and S. W. Myloie, "Projected Range Statistics," Dowder, Hutchinson and Roth, Inc., Stroudsburg, Pennsylvania (1975).
13. A. E. Michel, F. F. Fang, and E. S. Pan, *J. Appl. Phys.*, **45**, 2991 (1974).
14. R. K. Jain and R. J. Van Overstraeten, *This Journal*, **122**, 552 (1975).
15. T. R. Cass and V. D. K. Reddi, *Appl. Phys. Lett.*, **23**, 268 (1973).

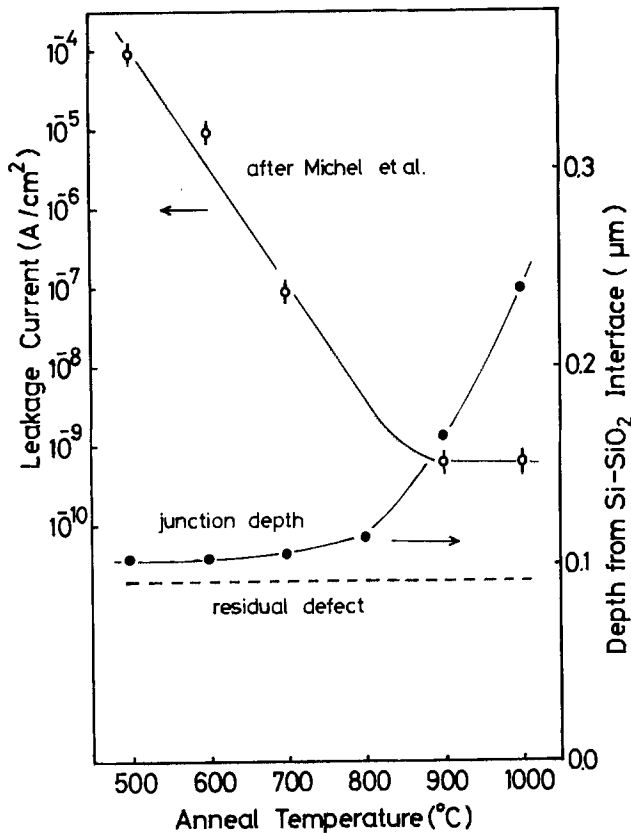


Fig. 11. Annealing temperature dependence of leakage current (after Michel), explained by calculated residual defect penetration depth and junction depth relationship.

The Alloying of Gold and Gold Alloy Ohmic Contact Metallizations with Gallium Arsenide

D. C. Miller

Bell Laboratories, Murray Hill, New Jersey 07974

ABSTRACT

The alloying of gallium arsenide with thin films of pure gold and the gold 12% germanium-silver-gold ohmic contact metallization used for a GaAs FET, has been investigated using optical and scanning electron microscopy. The heating rate and maximum temperature attained during heat-treatment was found to govern the morphology of the pure gold films, and to a lesser extent the ohmic contact metallizations. The alloying cycle commences with decomposition of the underlying GaAs and diffusion of gallium into the metal at about 260°C. Melting commences above about 480°C with pure gold and 360°C with the contact metallization. The final gallium content of the metal increases as the temperature is increased and the solidification temperature of both a pure gold and multicomponent contact heated to 525°C is $343^\circ \pm 2^\circ\text{C}$. The GaAs-metal interface is very irregular consisting of approximately rectangular depressions, often over $1\ \mu\text{m}$ deep, filled with metal.

Gold is used extensively in the fabrication of gallium arsenide devices, both as a component of an alloy in ohmic contacts and as a final metal or conductor. In order to make ohmic contacts of low resistance, the metallization is fused at temperatures often as high as 500°C. This is the temperature at which GaAs itself begins to decompose (1). Furthermore, gold forms low melting point alloys with gallium, so it is not surprising that considerable dissolution of the underlying GaAs takes place during the alloying cycle. The result is a contact with good electrical properties but one which is morphologically very irregular and difficult to reproduce. Even though the contact resistance itself was found not to be directly related to the morphology, morphology may play a significant role in performance and reliability.

Evidence has accumulated which indicates that decomposition of the GaAs accompanies the alloying cycle (2-6). This is confirmed here and further details of the alloying reaction are presented. Some of the parameters which govern the contact morphology are discussed for both pure gold and the alloys used in device manufacturing. Burnout and device performance are specifically not discussed in this paper.

Experimental Details

Transistors in various stages of completion as well as semi-insulating substrates coated with vapor-deposited pure gold were used for the studies reported here. The manufacturing details of the transistors have been presented elsewhere (7), and only certain relevant aspects will be outlined below.

The $0.4\ \mu$ thick active layers are deposited by CVD on chromium-doped semi-insulating substrates oriented about 6° off the (100). Some samples had a semi-insulating CVD layer under the active layer, but this did not affect the alloying or morphology. The standard ohmic contact metallization consists of 400 or 500Å of Au 12 weight percent (w/o) Ge, 1000Å of Ag, and 1000Å of pure Au. It is made by vacuum deposition after 300Å of the GaAs is etched away by an H_2O_2 , NH_4OH solution (8). The samples coated with just pure gold were not etched before deposition, but this did not appear to have any effect on the results. Alloying was accomplished by heating the samples on a resistance heated carbon plate in an H_2 ambient. Alloying was also performed using a hot stage in both an optical

microscope and an SEM. In the optical microscope either a vacuum or various gas ambients could be used. Temperature measurement in all cases was by means of a thermocouple in intimate contact with the underside of the heating strip under the sample, and was accurate to within $\pm 2^\circ\text{C}$ except for very fast heating rates. Calibration was checked by observing the melting points of various metals such as lead, zinc, etc.

Alloying of Pure Gold

Because gold is the major component of the contact metallization, it was decided that the behavior of pure gold on GaAs during heating should first be established as a reference. Consequently, a number of samples of semi-insulating GaAs were coated with 1000Å of Au. A sample given an alloy cycle which can be used to make ohmic contacts is shown in Fig. 1. This cycle consists of raising the temperature at 400°C/min to 490°C then shutting the power off thereby quenching the sample, which cools to below 100°C in a few seconds. This treat-

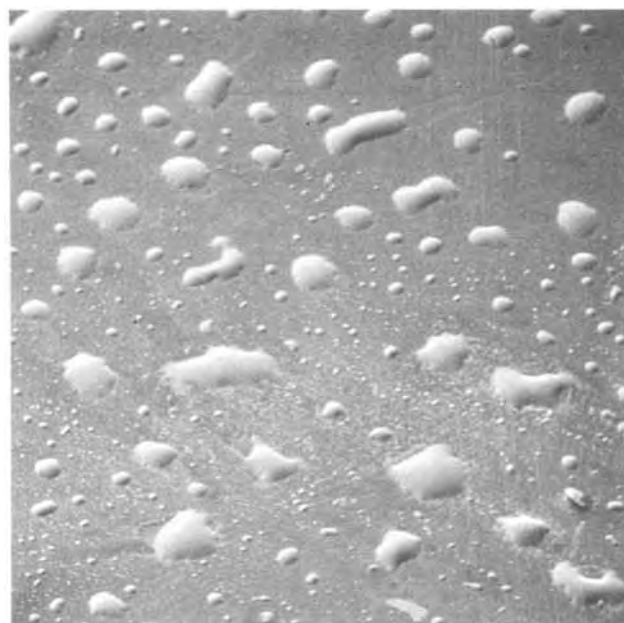


Fig. 1. Pure gold film heated to 500°C at a rate of 400°C/min. 135 \times .

Key words: alloy, films, diffusion.

ment has clearly caused the metal to "ball up" severely.

In an attempt to alter this morphology a number of samples were alloyed under a range of ambients and using various heating rates. The type of gas ambient, or vacuum, had no effect whatever on either the surface or interface morphology, in agreement with the work of Zee and Munir (9). Hence, all subsequent experiments were performed under 1 atm of H_2 , except where otherwise noted. In contrast, the heating sequence used had a significant effect on surface morphology. By reducing the heating rate to below about $100^\circ C/min$ a nonballed, silver colored film of Au-Ga was obtained, with the gallium content increasing as the ultimate temperature attained was increased. This was determined using an energy dispersive x-ray analyzer on the SEM calibrated using various bulk Au-Ga alloys and various thicknesses of unalloyed pure gold to measure the substrate contribution to the Ga signal. The excess As vaporized as evidenced by the presence of an arsenic film on the inside of the cover glass of the heating stage. Heating to $525^\circ C$ over 10 min produced a mirror-like, silver colored film which could not be distinguished from pure Ag by the unaided eye. Its appearance in the SEM is shown in Fig. 2.

During heating, a slight texture change occurred between 260° and $280^\circ C$, but the dramatic color transition from gold to silver began between 480° and $515^\circ C$, normally at the edge of the sample or at an imperfection. As the heating rate was increased, the temperature required to initiate the reaction also increased. Attempts were made to initiate the reaction below $480^\circ C$ by waiting but they were unsuccessful due to equipment overheating problems which developed after about 5 min. This was not sufficient time to initiate the reaction below $480^\circ C$. It was obvious in the microscope that the gold to silver color transition was accompanied by, and probably the result of, the metallization melting. This melting temperature is probably also a function of the thickness of the Au, since the source of Ga is the GaAs decomposition reaction which is temperature-dependent and probably diffusion-limited until the first liquid forms. Once initiated, the rate of advance of the silver colored phase can be controlled by adjusting the temperature of the hot stage and started or stopped by adjusting the temperature above or below $343^\circ \pm 2^\circ C$, respectively. This is very near the

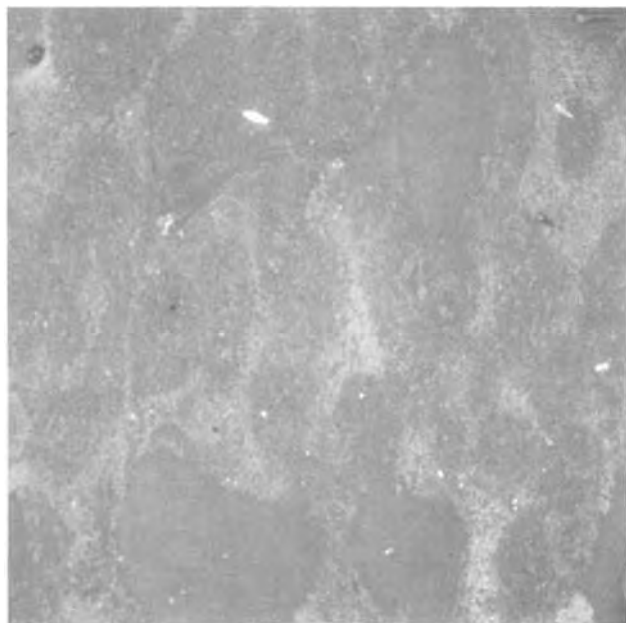


Fig. 2. Pure gold given a reduced heating rate of about $50^\circ C/min$. $135\times$.

eutectic temperature as indicated by the AuGa phase diagram shown in Fig. 3 (10). This phase front on one of the specimens removed to the SEM is shown in Fig. 4. The unmelted gold is to the left and the silver colored gallium alloy is to the right. The small voids in the gold were not quite visible in the optical microscope, but they apparently occur without melting and are not present in the as-deposited gold. The intermediate region between the two regimes puffs up like a soufflé then collapses to form the morphology on the

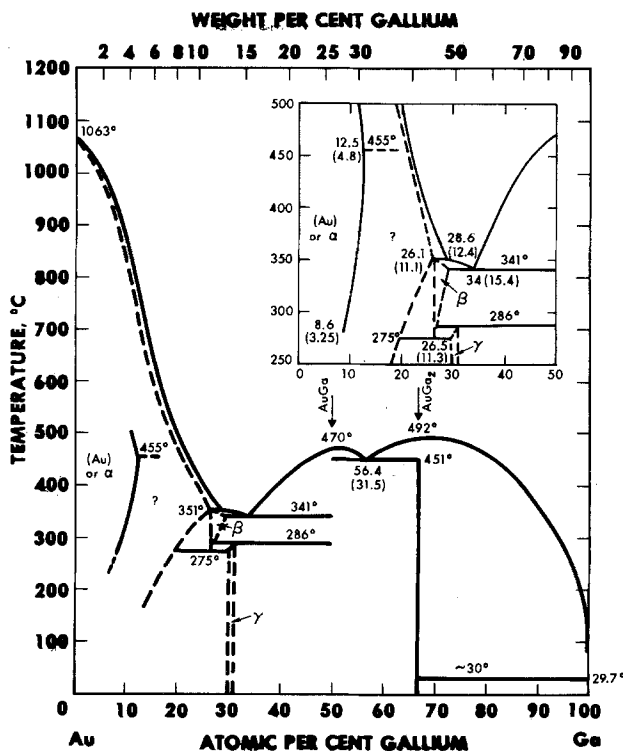


Fig. 3. The gold-gallium phase diagram from Hansen (10)

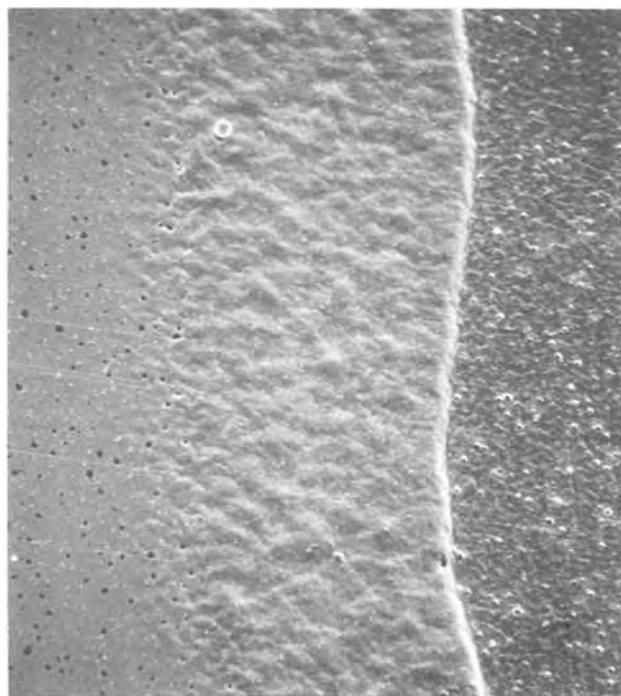


Fig. 4. Gold to silver colored phase boundary. The gold colored region is on the left and the silver colored region is on the right. $1200\times$.

right as the color changes. Arsenic vapor combined with other absorbed gases may cause the puffing up because the Au-GaAs reaction has begun without the topmost layers of the gold having yet melted.

To explore this reaction further, Au-Cr thermocouples were prepared by depositing 2 mm wide stripes 3000Å thick, first of gold then of chromium, orthogonally on semi-insulating GaAs. A Chromel-Alumel thermocouple with 0.002 in. diam. wire was glued to the substrate with silver paste near the thin film thermocouple. The substrate was then heated to 400°C at 36°C/min in a small oven in an N₂ ambient. The potentials of both thermocouples were recorded simultaneously so that the potential of the thin film thermocouple could be determined as a function of temperature and this is shown in Fig. 5. The change in potential at 260°C indicates that at this temperature decomposition of the GaAs has begun and that diffusion of gallium is very rapid at quite low temperatures. The large dip at 340°C correlates well with the Au-Ga eutectic at 341°C. Similar thermocouples made on SiO₂ substrates did not show these changes during similar heating sequences. Upon cooling and subsequent reheating the voltage vs. temperature curves of the thin film thermocouple were smooth and approximately linear, just lower in voltage than before heat-treatment. This experiment indicates that as the alloying sequence is initiated, decomposition of the gallium arsenide and diffusion of gallium into the gold has already begun at low temperatures, and when the first liquid is nucleated significant amounts of gallium are already present in the metal.

Ohmic Contact Metallization

The sequence of events occurring during heating of the ohmic contact metallization should differ markedly from the case of pure gold just discussed. There is the 500Å layer of AuGe of eutectic composition which melts at 356°C, and the 1000Å of Ag between the AuGe and final 1000Å of Au. However, they behave in a remarkably similar fashion except that each event occurs at a somewhat lower temperature with the multi-component contact. The first sign of change occurs at 240°, a modest grain growth resulting in a less yellow appearance. Melting of the AuGe layer begins at about 360° and is accompanied by the development of holes in the metallization without the whole contact melting. This presumably occurs by a diffusion and grain growth process. At 380°C, the gold to silver color transition occurs indicating that the top layer of Au contains enough gallium to almost form the eutectic composition. This was confirmed by physically removing the metallization and measuring the Ga content.

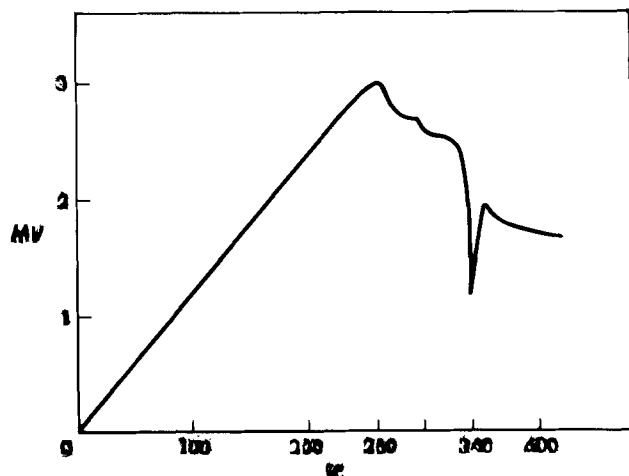


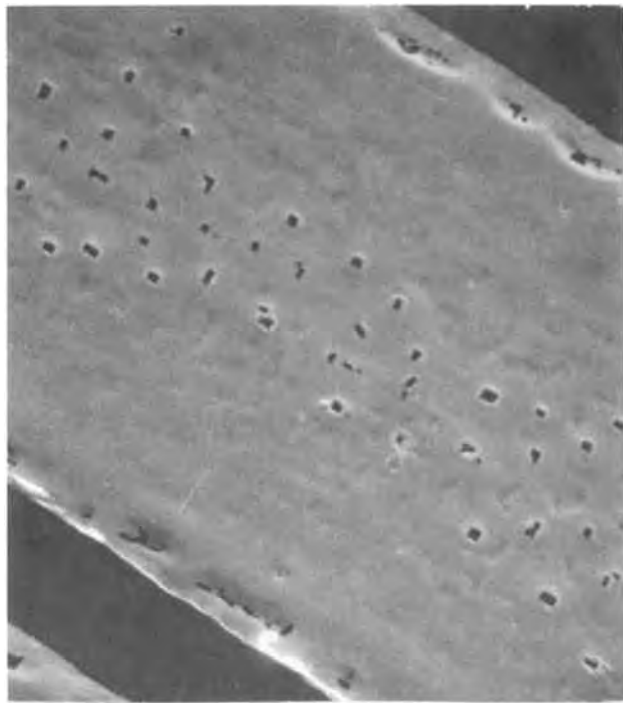
Fig. 5. The mV output vs. temperature of an Au-Cr thin film thermocouple vapor-deposited on semi-insulating GaAs.

This occurs without the Ag layer dissolving. At about 480°C, for reasonable heating times (50-400°C/min), the Ag finally appears to go into solution since the whole contact appears to be liquid. It was, however, not possible to determine reproducibly exactly when or at what temperature this occurs. Melting is clearly complete when balling up begins, but with the lower heating rates there is not enough apparent structural change when the silver dissolves to be obvious in either the optical microscope or SEM when employing hot stages. The gold-silver color transition need involve only gallium, as was indicated by the pure gold results, and the silver does not have to go into solution for the top 1000Å of Au to saturate with Ga and melt. The appearance of a contact during heating is shown in Fig. 6(a-c). Once the contact has melted, it will solidify and remelt at $343^\circ \pm 2^\circ\text{C}$, almost identical to the case of pure Au. Hence, the Au must dominate the AuGeGaAg quaternary (plus whatever As may be present) or else it is just a coincidence that the melting points of the alloyed pure gold and multilayer metallization are so similar. In all cases the total amount of gallium in the metal, whether Au or the contact, increases with an increasing final temperature (see Fig. 7). This was calculated by subtracting the known signal contributed by the gallium in the underlying GaAs from the measured signal using an energy dispersive analyzer in the SEM and by analyzing Au-Ga alloys of known composition.

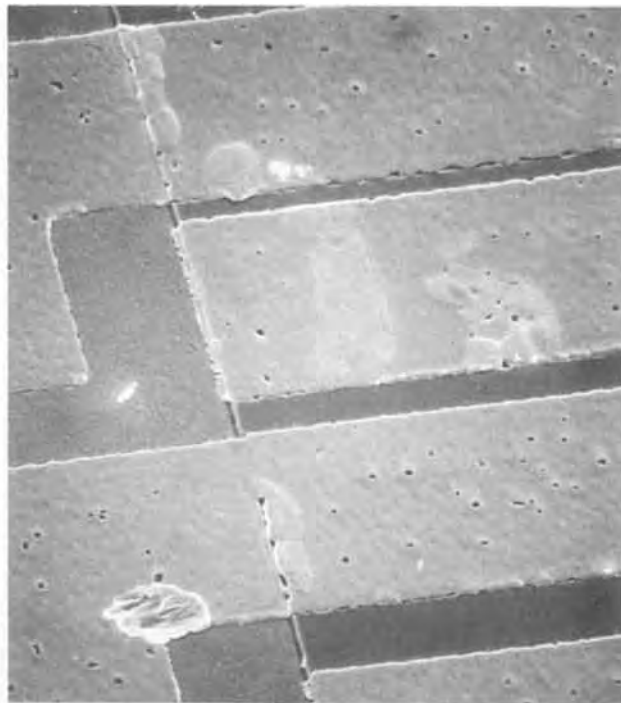
A typical ohmic contact alloying procedure is to increase the temperature at a rate of 400°C/min to about 500°C. Contacts alloyed to temperatures between 480° and 525°C all had adequate contact resistances of about $1 \times 10^{-5} \Omega \text{ cm}^2$ as measured using standard techniques (7), with 490°C appearing to result in the minimum resistance of about $1-2 \times 10^{-6} \Omega \text{ cm}^2$. Two contacts heated to 480° and 525°C are shown in Fig. 8a and 8b, respectively. Contacts heated to 490° showed considerable variation in morphology, varying between that shown in Fig. 8a and b, some times even on the same specimen, despite careful control of the temperature. Apparently, the conversion from the morphology of 8a to b is extremely sensitive to the precise temperature, time, and film thickness combination used. The contact resistance was, however, independent of the morphology in this temperature range. Even heating to 525°C for 40 min or to only 425°C in a minute still resulted in only a factor of four or five higher contact resistances.

Interface Morphology

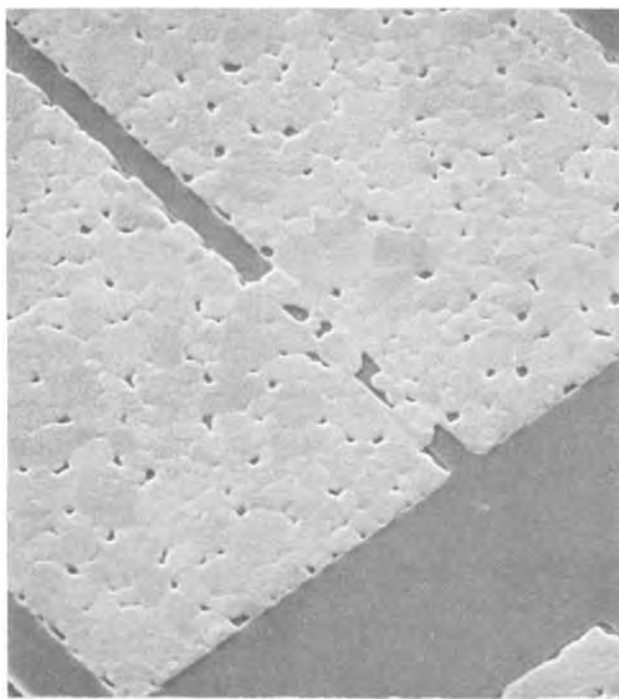
During alloying, a pattern of rectangular depressions forms at the interface which is filled with metal to roughly the level of the GaAs surface. This is true for both pure Au and the metallization, but the metallization is both easier to remove and of greater technical importance so most of the work was performed on the contacts. An example of the interface morphology is shown in Fig. 8b and Fig. 9. The size of the metal patches increases and their density decreases as the maximum temperature attained is increased. The contacts shown in Fig. 9a-d were alloyed at 450°, 480°, 525°, and 560°C, respectively. No patches developed below about 350°C, but none would be expected to develop below 341°C, the Au-Ga eutectic temperature, unless there was some lower melting Au-Ge-Ga ternary. There was no evidence to support this, however. These samples were subjected to a 400°C/min alloying cycle and development of the patches may simply require more time in the 340°-350°C range. If this structure does not form, the contact is not ohmic. However, even at temperatures below 341°C, the GaAs decomposes and gallium transport into the still solid metallization has begun. This is evidenced by the



a



b



c

Fig. 6. A contact at room temperature alloyed on the microscope hot stage, just before (a), stopped in transition (b) and just after (c) the silver has gone into solution. (a) 2600 \times ; (b) 700 \times ; (c) 1600 \times .

thermocouple experiment described earlier, and by the difference in contrast (secondary emission efficiency), apparent under the contact shown in Fig. 10 which was heated to only 280°C. Analysis in the SEM revealed that arsenic was deficient in the region under the contacts.

From the data presented it may safely be concluded that the pattern of rectangular metal patches is the result of melting at the interface. One mechanism of formation may be that GaAs dissolves to saturation in the molten metal mass, which is uniform in composition down to some depth in the GaAs. Then, upon

freezing, two phases form; metal with a little As in solution, and GaAs with a little Au, Ge, and possibly Ag, in solution. Analyses in the SEM do reveal trace concentrations of As in the metal and Au in the GaAs, but the signals could well be generated from the surrounding areas due to scatter, etc. This view is supported by a previous study which indicates that little Au is in the GaAs near the interface (11), and little As could be in solution in alloys in this temperature range (12). Significant amounts of As also vaporize and escape through holes in the layer or from around the edges of the metal.

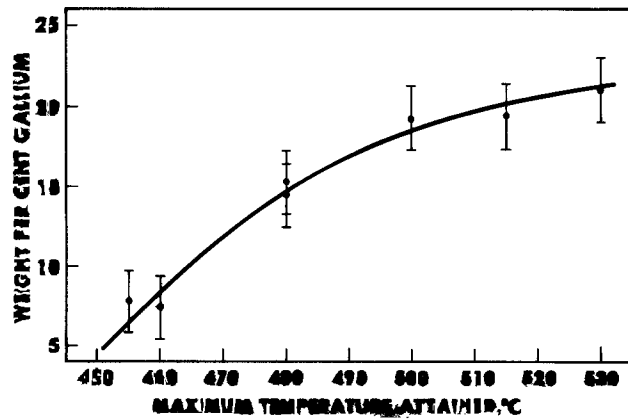


Fig. 7. Relative gallium content of alloyed device contacts vs. final or maximum temperature attained during alloying. This was calculated by subtracting the known signal contributed by the gallium in the underlying GaAs from the measured signal using an energy dispersive analyzer in the SEM.

Another explanation for the reaction is that as heating commences and the GaAs decomposes the gallium permeates the metallization, which is very porous (14), by surface and grain boundary diffusion, and the excess arsenic simply vaporizes. Then the liquid phase "nucleates" in certain spots and these areas expand in a negative crystal growth process which proceeds as long as gallium is required to saturate the metal as the temperature increases. When the temperature is lowered the metal in the rectangular depressions freezes, and a very thin degenerate layer of GaAs grows by LPE between the metal and unaffected GaAs making the contact ohmic. In order to test this hypothesis, a sample was prepared in which a 500Å, sputter-deposited tungsten layer was added between the original 500Å of Au-12% Ge and the silver. Previous evidence suggested that the sputtered tungsten layer was not a gallium diffusion barrier but would prevent liquid flow (13). The results are shown in Fig. 11. The rectangular depressions are

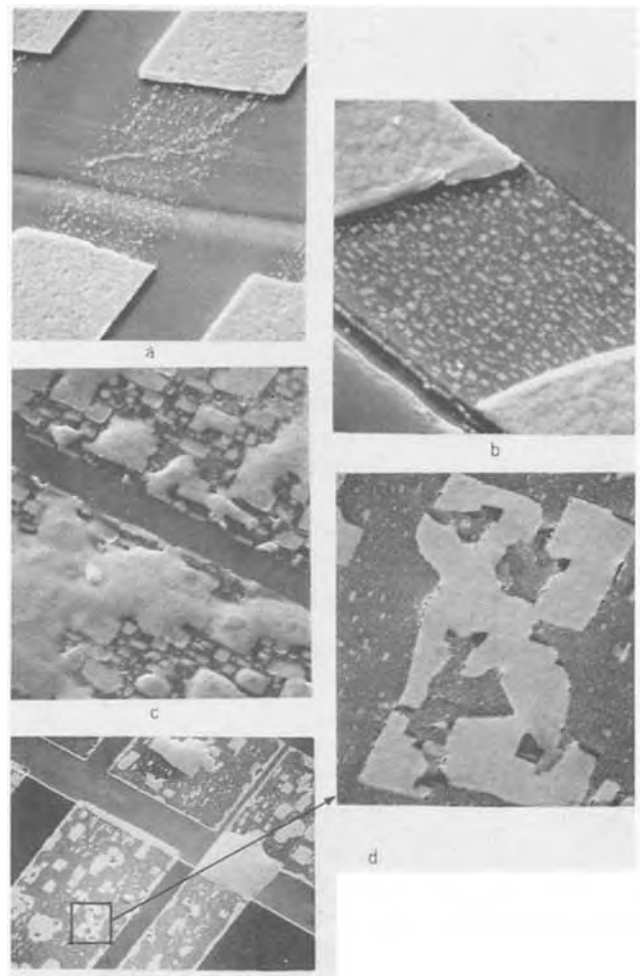


Fig. 9. Contacts with metal removed alloyed to: (a) 450°C 3500X, (b) 480°C, 7200X, (c) 525°C, 5400X, (d) 560°C, 540X inset 5000X.

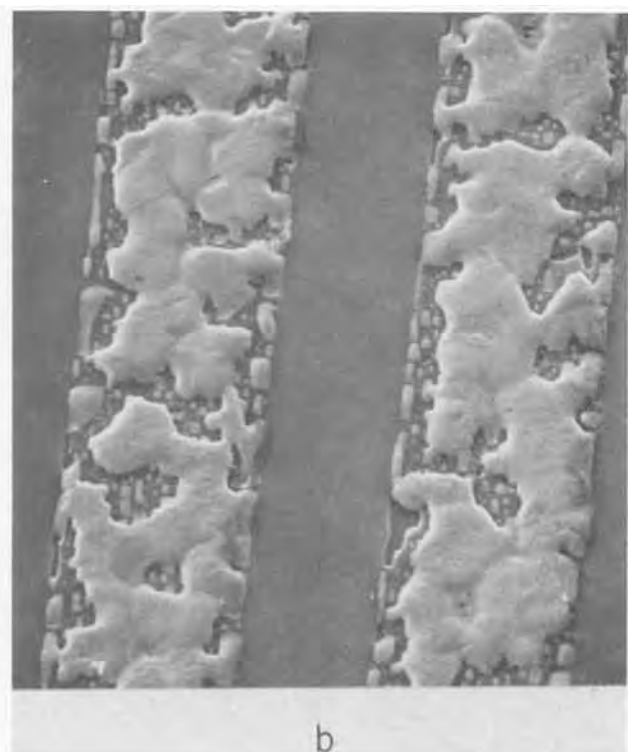
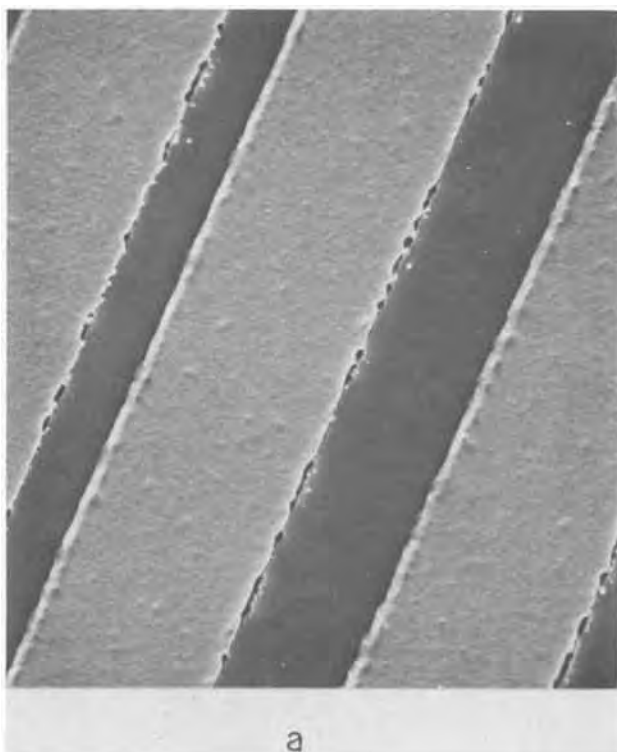


Fig. 8. Two alloyed contacts, (a) 490°C, 3000X, (b) 525°C, 2600X



Fig. 10. A partially removed contact heated to 280°C. The dark regions are deficient in gallium. 1040 \times .

clearly visible under the tungsten and are far too large to have been the result of gallium dissolution in only the 500Å of Au-12% Ge under the W, which has adhered to the underside of the W. Furthermore, the SEM x-ray analysis revealed that the balled metal on top of the tungsten contained as much gallium as when no tungsten was present. Even though this experiment supports the negative crystal growth hypotheses, the mechanism of pattern formation is still not completely clear because the rectangles contain less than 1-2% gallium. This was determined by observing the color of a series of Au-Ga alloys of known composition and then matching their color to that of the rectangular patches. In another experiment, very lightly alloyed contacts (400°C/min heating rate, 425°C final temperature) were analyzed in the SEM. The GaAs was dissolved away with 4H₂SO₄, 2H₂O, 1H₂O₂, leaving only the contact. The GaAs-AuGe interface side of the contact was then analyzed in the SEM and only a trace Ga signal was observed in the protruding

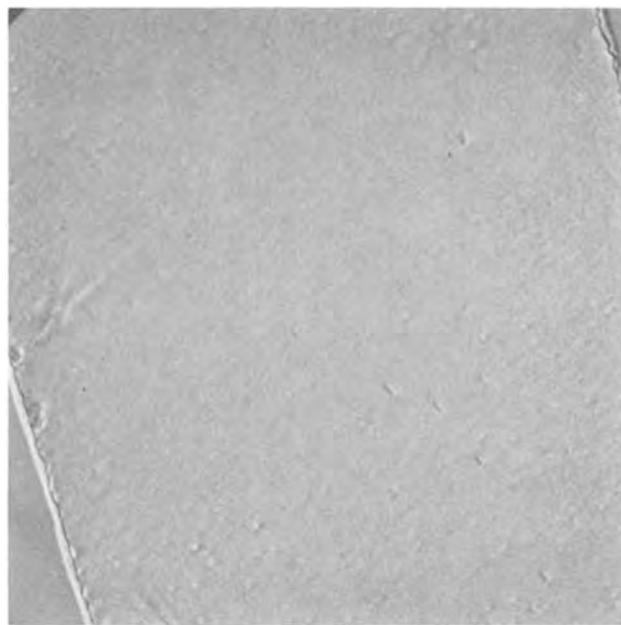
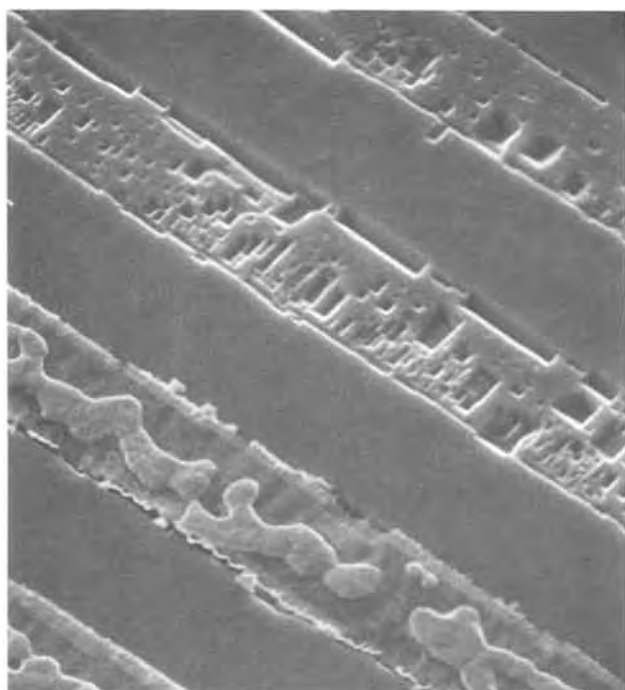


Fig. 12. Device contact heated to 525°C over 65 min in the SEM. 3000 \times .

metal patches, also indicating that if gallium is present in the contact it is near the detection limits of the energy dispersive analyzer, or about 1%. An alloy this low in Ga has a melting point above 700°C! Yet, liquid must have been present to form the islands. The most likely explanation for this paradox is that the second sequence outlined above does occur and the concentration of gallium was high in the thin liquid layer present during alloying and patch formation. Then, upon cooling, or even during alloying, the gallium quickly diffused throughout the remainder of the contact thereby reducing its concentration at



a



b

Fig. 11. The results of placing a sputtered 500Å thick tungsten film between the Au-Ge alloy and the remainder of the contact. (a) 1800 \times , (b) 4800 \times .

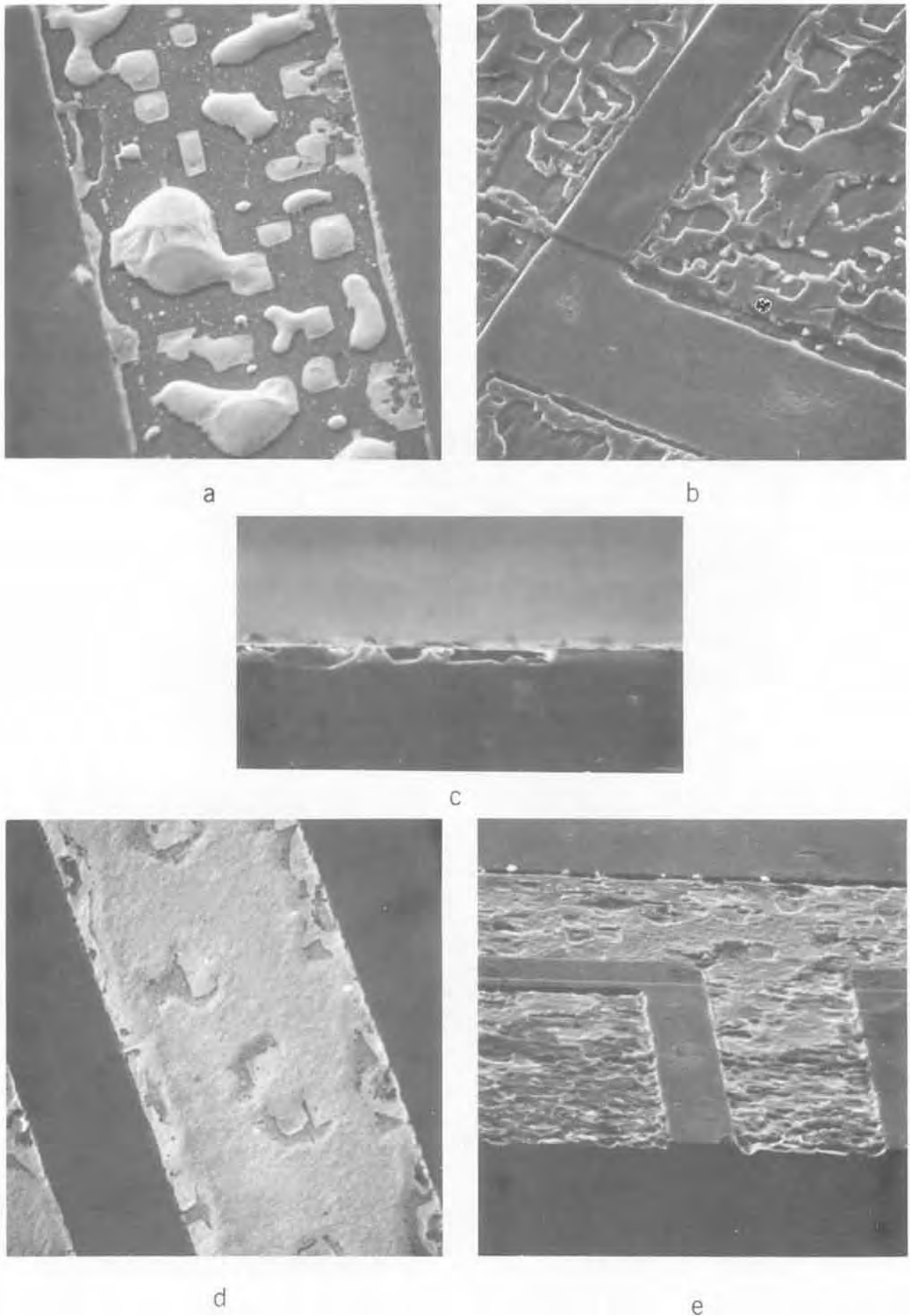


Fig. 13. Contacts alloyed to 540°C at 350°C/min and 30°C/min, (a) and (d), respectively, and with contacts etched away (b), (c), and (e), Fig. 13(c) is a cross section of the sample shown in 13(b). (a) 1440 \times , (b) 1360 \times , (c) 4000 \times , (d) 1360 \times , (e) 1280 \times .

the GaAs-contact interface. Further attempts will be made to detect this gallium.

In spite of the inconsistencies discussed above, the results do indicate clearly that the decomposition of the GaAs is controlled by the Au-Ga reaction. The Ge appears only to change the surface tension and allow the Au-Ga reaction to progress further at lower temperatures because the Au-Ge eutectic melts at 356°C and the liquid metal helps initiate the reaction. The role of Ag is to allow the alloy to melt next to the GaAs without the whole contact melting.

Effect of Different Alloy Cycles

In order to improve both the surface and interface morphology of the contacts, a number of different alloying sequences were tried. Because the slowly alloyed pure gold layer did not "ball," a contact was alloyed to 535°C in the SEM over 65 min and is shown in Fig. 12. It clearly has a superior surface morphology, but contact resistance was up to about $1 \times 10^{-4} \Omega\text{-cm}$. The 8°C/min heating rate could not be duplicated in the microscope hot stage under H₂ because of overheating problems. However, samples heated to 540°C at 350° and 30°C/min are shown in Fig. 13a and d, respectively, and with the contact metal etched away (13b, c, and e). Substantial improvements in surface morphology were achieved, but the metal-GaAs interface remains rough. The depths of the rectangular pits are 1.1 and 1.4 μ , respectively, though with the slower rate they are somewhat more uniform. Modest improvements in surface and interface morphology were achieved with a very fast heating rate of $\sim 1000^\circ\text{C}/\text{min}$ to about 525°C shown before and after contact removal in Fig. 14a and b, respectively. In this case, the Ag layer probably did not have time to melt. Reducing the AuGe layer thickness from 500 to 400Å also helped (Fig. 15). It has not changed the morphology but may have reduced slightly the amount of GaAs which decomposes and the penetration depth. The deepest penetration measured was 0.45 μ , or about the epi thickness (Fig. 16). This is a modest improvement, but the contact between metal and epi remains very irregular and the contact may still penetrate to

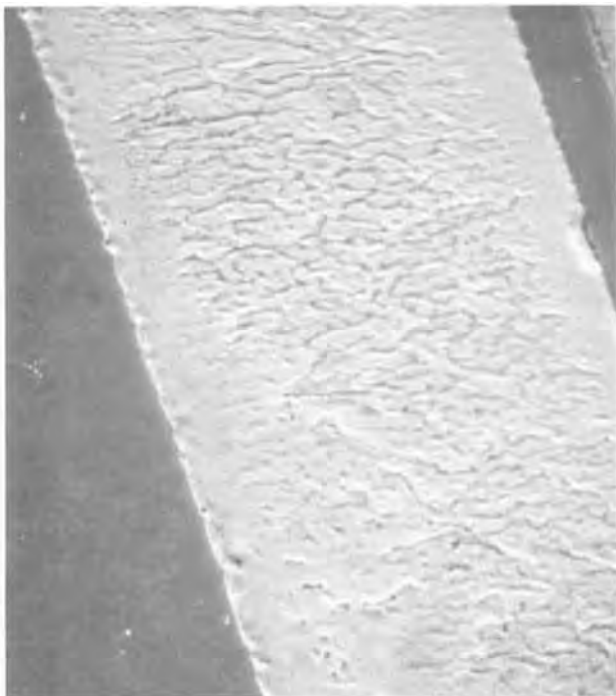
the substrate or buffer layer. As has been shown, this is true even if the contact looks smooth from the top. Hence, an irregular channel width as well as sharp projections of the contact metal into the substrate or buffer layer may still result during alloying. It is important to recognize further that gallium diffusion and further decomposition of the GaAs can proceed involving the final conductor metal if temperatures approach the 250°C range during final processing or operation.

One further test was made. Several samples were annealed in arsenic gas at about 2 atm. Conditions were not the same as reported earlier (15), in that the samples were heated to $500^\circ \pm 10^\circ\text{C}$ over 12 min and some O₂ contamination could also have been present. No improvement in contact resistance or surface morphology was observed. One sample previously alloyed in the normal way was subsequently subjected to the arsenic anneal and the Ga content of the metallization reverted to near its prealloy value suggesting GaAs regrowth had occurred.

Conclusions

From all of the observations and results presented above it must be concluded that gallium arsenide in contact with gold will decompose readily at temperatures as low as 260°C resulting eventually in void formation at the GaAs-metal interface and rapid diffusion of gallium throughout the metallization. This fact should be considered with regard to both the fabrication and long term operation of GaAs devices.

The surface morphology of the alloyed metal can be controlled by adjusting the heating rate. Reducing the AuGe thickness, using faster heating rates, and alloying to lower temperatures improves the interface morphology somewhat without severely increasing contact resistances. However, the rough interface morphology can be modified only in degree, not in its basic character, by changes in the heating cycle. Perhaps a process with better control of the applied heat such as laser alloying (16) is needed to achieve a major improvement.



a



b

Fig. 14. A contact heated to 525°C at a rate of about 1000°C/min before (a) and after (b) contact removal. (a) 1850 \times , (b) 360 \times



a



b

Fig. 15. A contact with 400 Å Au-Ge physically removed, (a) and etched away, (b). (a) 3500×, (b) 3300×



Fig. 16. Cross section of the sample shown in Fig. 15(b). 11,500×

Variations in the irregular morphology of the GaAs-metallization interface do not appear to affect the ohmic properties of the contact, but may play an important role in the reliability of devices using this contact especially in view of the fact that the contact metal may regularly penetrate to the substrate. More work is required to fully understand the mechanism of formation of the rectangular metal patches.

Acknowledgments

The author is indebted to W. C. Niehaus and B. S. Hewitt for generously providing the ohmic contact samples and for many helpful discussions. The aid of J. C. Irvin and B. S. Hewitt in obtaining the metal depositions is gratefully acknowledged. The author

also wishes to thank J. W. Nielsen for reviewing the manuscript, helpful discussions, and support.

Manuscript submitted May 3, 1979; revised manuscript received Aug. 28, 1979. This was Paper 315 presented at the Seattle, Washington, Meeting of the Society, May 21-26, 1978.

Any discussion of this paper will appear in a Discussion Section to be published in the December 1980 JOURNAL. All discussions for the December 1980 Discussion Section should be submitted by Aug. 1, 1980.

Publication costs of this article were assisted by Bell Laboratories.

REFERENCES

1. D. P. Miller, J. G. Harper, and T. R. Perry, *This Journal*, **108**, 1123 (1961).
2. A. K. Shinha and J. M. Poate, *Appl. Phys. Lett.*, **23**, 666 (1973).
3. O. Prakash, *J. Inst. Electron. Telecom. Eng.*, **20**, 153 (1974).
4. G. Y. Robinson, *Solid-State Electron.*, **18**, 331 (1975).
5. C. J. Madams, D. V. Morgan, and M. J. Howes, *Electron. Lett.*, **11**, 574 (1975).
6. S. Guha, B. M. Arora, and V. P. Salvi, *Solid-State Electron.*, **20**, 431 (1977).
7. W. C. Niehaus, H. M. Cox, B. S. Hewitt, S. H. Wemple, J. V. DiLorenzo, W. O. Schlosser, and F. M. Magalhaes, "Gallium Arsenide and Related Compounds," pp. 271-280, Inst. of Physics, St. Louis, Series 33B (1976).
8. J. C. Dymant and G. A. Rozgonyi, *This Journal*, **118**, 1346 (1971).
9. L. Y. Zee and Z. A. Munir, *J. Mater. Sci.*, **10**, 1929 (1975).
10. M. Hansen, "Constitution of Binary Alloys," p. 206, McGraw-Hill, New York (1978).
11. J. Gyulai, J. W. Mayer, V. Rodriguez, A. Y. C. Yu, and H. J. Gopen, *J. Appl. Phys.*, **42**, 3578 (1971).
12. J. C. Irvin, D. C. Miller and A. Loya, Unpublished results.
13. M. P. Panish, *This Journal*, **114**, 516 (1967).
14. O. L. Rehrig, *Plating*, **61**, 43 (1974).
15. T. Sebestyen, H. Hartnagel, and L. H. Herron, *Electron. Lett.*, **10**, 372 (1974).
16. S. Margalit, D. Fekete, D. M. Pepper, C. P. Lee, and A. Yariv, *Appl. Phys. Lett.*, **33**(4), 346 (1978).

Formation Mechanism of Porous Silicon Layer by Anodization in HF Solution

Takashi Unagami

*Nippon Telegraph and Telephone Public Corporation,
Musashino Electrical Communication Laboratory, Musashino-shi, Tokyo, 180, Japan*

ABSTRACT

The mechanism of formation of porous silicon layer (PSL) has been studied according to the following experimental results. PSL is formed by the local dissolution of silicon which occurs only at the base of the pores. The HF concentration of the electrolyte in the pores of PSL is constant during anodization and the anodic reaction in the pores proceeds uniformly in the thickness direction. The dissolution of silicon in the pores is the results of the divalent and the tetravalent reactions of silicon with HF, without the disproportionation reaction. The insoluble surface porous film (SPF) exists at the surface of PSL and the silicic acid is formed in PSL. A model of forming PSL is proposed, with emphasis being placed on the anodic reaction and the local dissolution of silicon which is initiated by SPF and is promoted by the hindrance layers composed of the silicic acid.

The anodization of silicon in hydrofluoric acid solution has been studied by many investigators. These investigations are almost always related to the electropolishing of silicon to process silicon wafers for the electronic device fabrication. On the other hand, Uhlir (1) found in 1936 that anodic film is formed on a silicon wafer by the anodization under certain conditions. This anodic film is the porous silicon layer (PSL) which consists mainly of silicon (2). PSL is oxidized very rapidly at low temperature, so thick oxide layers can be formed by short time oxidation. These thick oxide layers can be applied in the fabrication of integrated circuits (3).

Turner (4), and subsequently Memming and Schwandt (5), investigated the formation condition of PSL and proposed that PSL is formed by the disproportionation reaction of silicon difluoride. On the other hand, in an investigation of the structure of PSL, Arita and Sunohara (6), and Unagami and Seki (7), postulated that the anodic dissolution of silicon occurs at local points on atomic scale to form PSL from the observation that PSL has a single crystal structure. No detailed investigations have been reported with respect to the formation mechanism of PSL, particularly with respect to the mechanism of the progress of the local silicon dissolution.

In this paper the author studied the anode potential-current characteristics for various HF concentration, the HF concentration of the electrolyte in PSL, the dissolution of silicon by the anodization, the structure of PSL, the infrared spectra of PSL, and the electric resistivity of PSL. Based on these results, the formation mechanism of PSL is discussed.

Experimental Procedures

Wafer preparations.—Silicon wafers were (111) p-type single crystals (boron-doped) made by the Czochralski method. Before the anodization, wafers were cleaned by boiling in the solution ($1 \text{ NH}_4\text{OH} + 1 \text{ H}_2\text{O}_2 + 4 \text{ H}_2\text{O}$). After that, the thin oxide layer was removed in dilute HF solution and the wafers were rinsed in deionized water.

PSL formation.—The electrolytic cell for PSL formation by the anodization has been given in a previous paper (7). In the case of high resistivity silicon wafers, aluminum alloy layers were formed before the anodization on the back surface of the silicon wafers in order to make the anodic current distribution uniform.

Key words: porous silicon layer, anodization, formation mechanism.

The silicon wafers were covered with acid-proof wax (Apiezon wax) to perform the anodic reaction selectively in the wafer. Gas bubbles break out from the silicon wafer surface during anodizing, so the ultrasonic oscillator was used to prevent gas bubbles from sticking on the surface. A constant current source was supplied as the electric power.

The measurement of the anode potential-current characteristics.—The anode potential was measured against a saturated calomel electrode (SCE). The anode potential-current characteristics were recorded with a X-Y recorder. The SCE capillary tip end was dipped in HF solution positioned near the silicon wafer surface and the opposite electrode was connected with the anode electrode.

The measurement of weight change.—The weight change was measured with an electric microbalance made by Mettler. After the anodization and immersion in HF solution, the samples were dried by blowing dry N_2 gas on them without rinsing in water.

Infrared spectra measurement.—Infrared transmission spectra were measured with a double beam type infrared spectrometer (a Model IR-27G) made by Shimadzu Seisakusho, Limited. The wafers were $4 \sim 7 \Omega\text{-cm}$ in resistivity. In order to prevent the influence of the absorption of a substrate, a wafer which has the same thickness and the same resistivity was prepared as the reference. The transmission spectra were measured in the wavelength range from 2.5 to $25 \mu\text{m}$.

Experimental Results

The anode potential-current characteristics.—The characteristics of the anodization in various HF concentration solution were measured. The results are shown in Fig. 1. The potentials, obtained at the end of a 30 sec period of supplying the constant anodic current, are plotted. In the region of the low anodic current density, the characteristics obey Tafel's law and the dependence on HF concentration does not appear. On the other hand, in the high current density region, Tafel's law is not satisfied and the characteristics depend strongly on HF concentration. The anode potential becomes high with decreasing HF concentration at the same anodic current density.

The anode potential is shown in Fig. 2 under the condition of the constant current density anodization. HF concentration is 50% in weight percent (w/o). The growth rate of PSL is $8.45 \mu\text{m}/\text{min}$, $4.50 \mu\text{m}/\text{min}$, and $0.95 \mu\text{m}/\text{min}$ at $100 \text{ mA}/\text{cm}^2$, $50 \text{ mA}/\text{cm}^2$, and 10

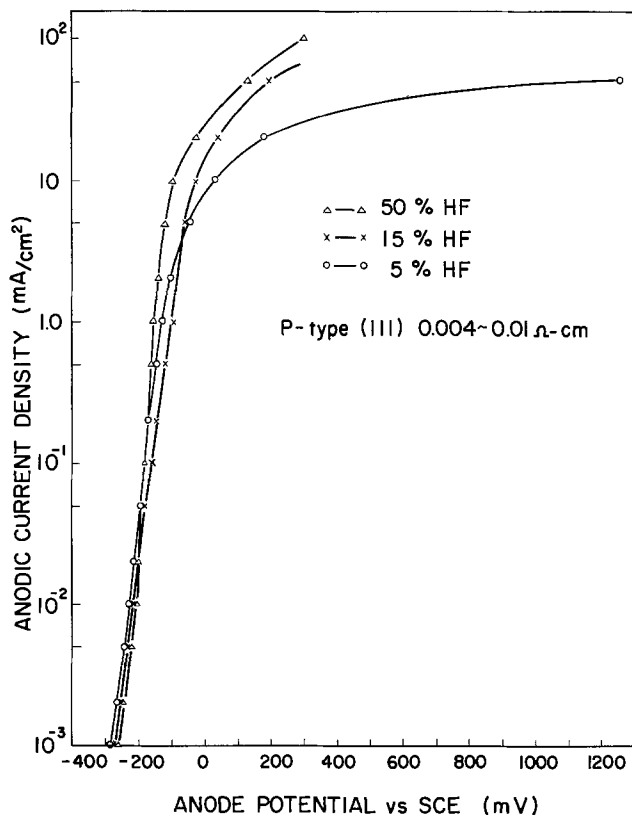


Fig. 1. Anode potential-current characteristics under various HF concentrations.

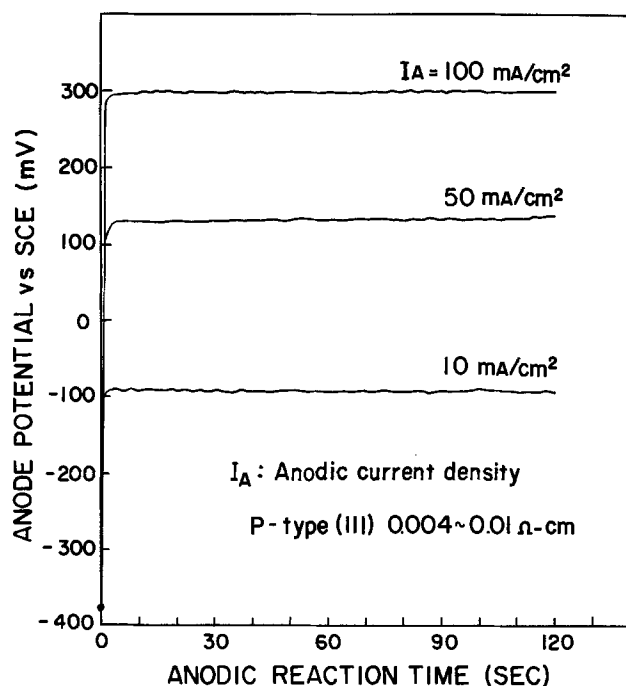


Fig. 2. Relationship between anode potential and anodic reaction time. HF concentration is 50 w/o.

mA/cm² in the anodic current density, respectively. At all anodic current density, the anode potential shows no change, that is, the anode potential is constant in spite of forming thick PSL. From these results, the HF concentration of the electrolyte in PSL is presumed to be constant during the anodization.

Figure 3 shows the relationship between the anode potential and the anodic reaction time under the various HF concentration. The anodic current density is 10 mA/cm². In a highly concentrated HF solution,

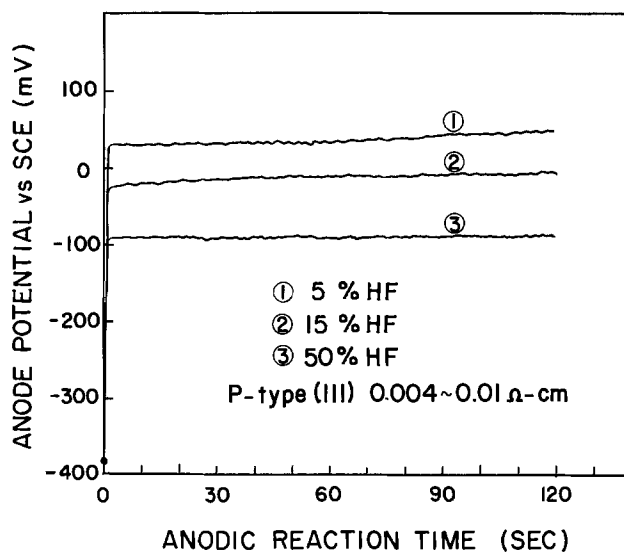


Fig. 3. Relationship between anode potential and anodic reaction time under various HF concentrations. Anodic current density is 10 mA/cm².

the anode potential is constant. However, in a low concentrated (5%, 10%) HF solution, some increase (a few mV) in the anode potential appears after two minutes. When the HF concentration is low, a change in electrolyte concentration appears to occur.

The analysis of the electrolyte in the pores.—The weight and the HF concentration of the electrolyte in the pores were examined by the measurements of the weight change and fluoride ions concentration. The weight was measured before the anodization, just after the anodization, and after the heat-treatment. The weight and fluoride ions concentration just after the anodization were measured without removing the wax, in order to prevent the electrolyte in the pores from coming out into a solvent (trichloroethylene). The heat-treatment was done in dried N₂ gas or a vacuum at 100° ~ 150°C for two hours. The result of the weight change is shown in Fig. 4. ΔW_1 is the change between the weight before and that after the anodization. On the other hand, ΔW_2 is the change between the weight before the anodization and that after the heat-treatment. So, the weight change between these two values, W_E , is the amount of the electrolyte in the pores. The electrolyte in the pores can be released by the heat-treatment. Figure 5 shows this effect. The weight changes, caused by immersing the heat-treated PSL in 50% HF solution and by the heat-treatment of immersed PSL, are shown. The sample has the same weight after the heat-treatment as before immersion in 50% HF solution. That is, the heat-treatment can release all the solution in the pores. From the result shown in Fig. 4, W_E is given in Fig. 6. W_E increases linearly with the anodic reaction time. W_s , given in Fig. 6, is the weight corresponding to the solution with which the volume of the pores in PSL are filled. The total volume of the pores in PSL is calculated from ΔW_2 and the specific gravity of 50% HF solution is 1.12 g/cm³ at the room temperature. As shown in Fig. 6, W_E corresponds to about 57% weight of W_s . That is, about 57% of the pore volume in PSL seems to be filled with HF solution at the time of the anodization. Because of the gas generation at the time of the anodization, the pores are partially filled with the generated gas.

The HF concentration of the electrolyte in the pores was measured with a fluoride electrode. The samples of PSL formed in 50% HF solution were immediately immersed in 10 cm³ deionized water. These experimental solutions were measured after PSL had soaked for two hours. A pH meter was used to measure the

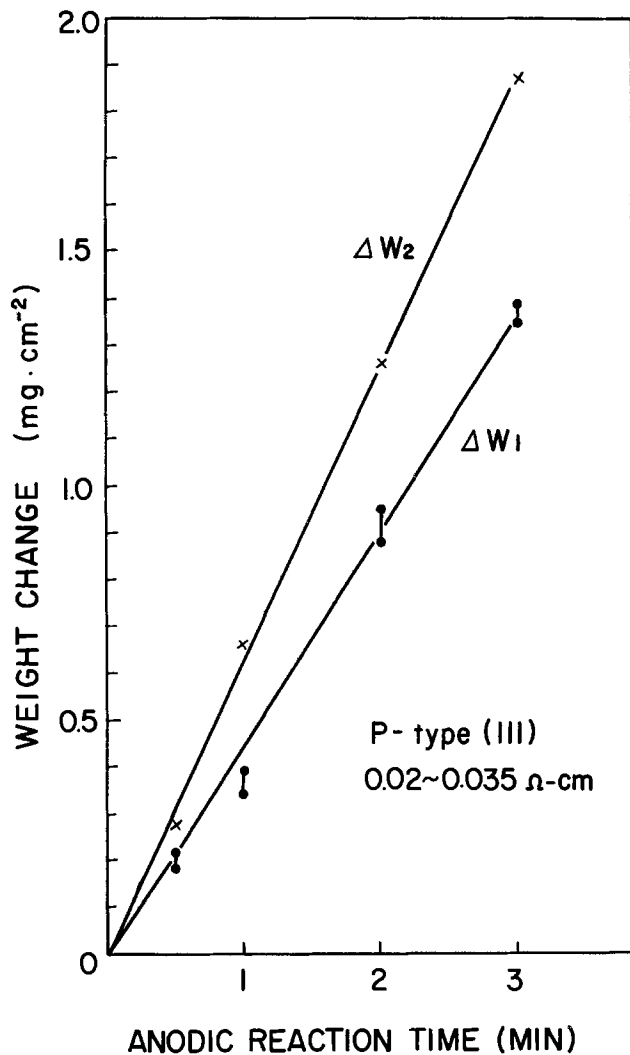


Fig. 4. Relationship between weight change and anodic reaction time. Anodic current density and HF concentration are 100 mA/cm^2 and 50%, respectively.

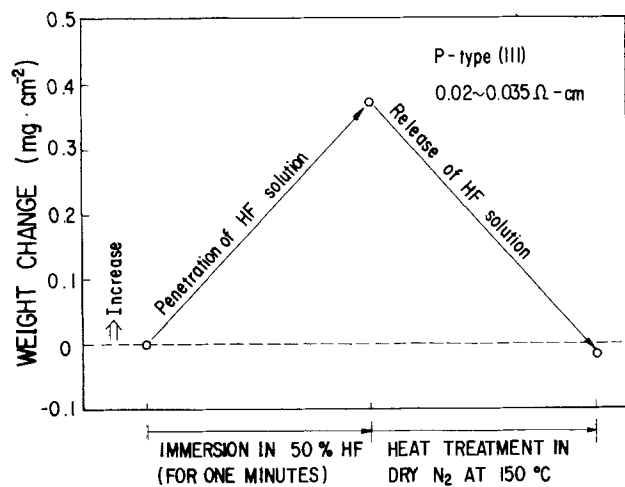


Fig. 5. Weight change by immersion in 50% HF solution and heat-treatment in dry N_2 at 150°C . PSL was formed at 100 mA/cm^2 for 3 min.

potential of the fluoride electrode with respect to SCE connected to the experimental solution in the Teflon beaker. PSL was formed in a p-type silicon substrate ($0.02 \sim 0.035 \Omega\text{-cm}$). The potential of fluoride electrode as a function of HF weight percent is shown in Fig. 7. The HF weight percent of the experimental

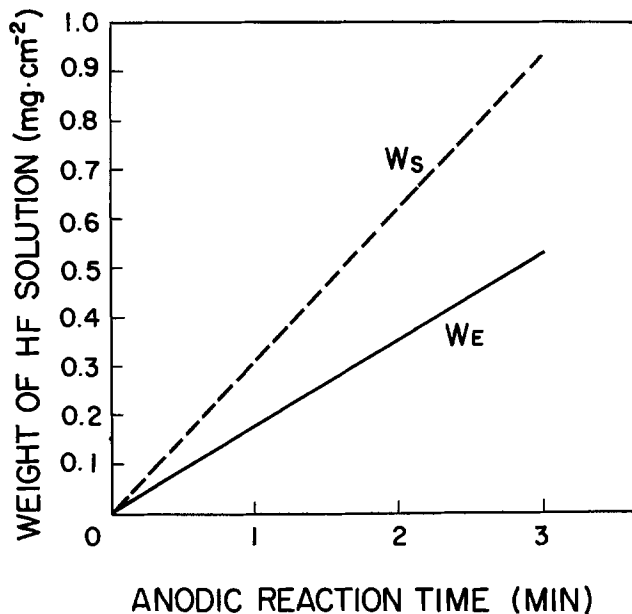


Fig. 6. Relationship between weight of HF solution and anodic reaction time.

solutions is determined according to the result shown in Fig. 7. The results are shown in Table I. The HF weight percent of the electrolyte in the pores is W_t which is obtained from $W_t' \times 10/W_E$. As a result, the HF concentration of the electrolyte in pores is considered to be constant and the same as that of the outer HF solution of the pores. This result is consistent with the result that the anode potential is constant during the constant current anodization, as shown in Fig. 2. Figure 8 shows the weight of HF solution penetrated into the pores when the immersion time in 50% HF solution is changed. The pores in PSL were emptied beforehand by the heat-treatment. It is obvious that HF solution of 50 ~ 60% of W_E can penetrate into the pores within a few seconds. From the results that HF concentration of the electrolyte in the pores is constant and HF solution can penetrate into the pores rapidly, it can be thought that the reactants and the products of the anodic reaction can be supplied and released rapidly in the pores, respectively.

Dissolution of silicon by anodization.—Uhlir (1) and Turner (2) have reported that silicon dissolution is

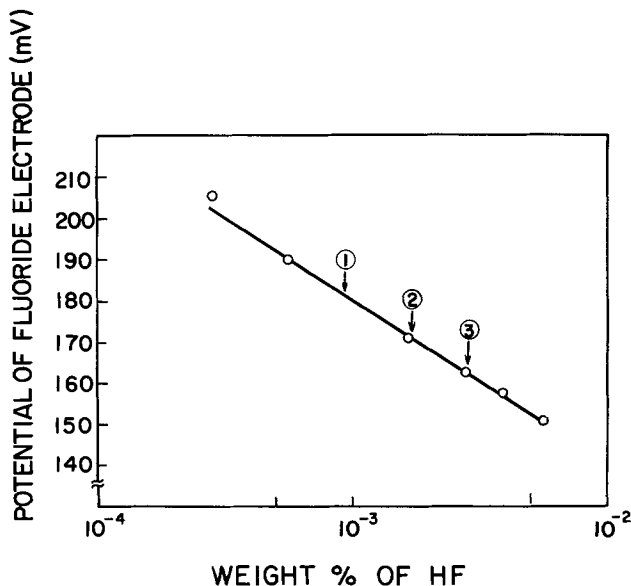


Fig. 7. Relationship between potential of fluoride electrode and HF weight percent.

Table I. Determination of weight percent of HF solution in PSL

Wafer No	Anodization Condition (S = 1 cm ²)	Ex (mV)	Wt' (%)	W _E (g)	W _t (%)
①	100 mA/cm ² 1 min	181.4	9.2 × 10 ⁻⁴	1.8 × 10 ⁻⁴	~51
②	2 min	170.6	1.75 × 10 ⁻³	3.55 × 10 ⁻⁴	~49
③	3 min	161.8	2.8 × 10 ⁻³	5.3 × 10 ⁻⁴	~53

Ex --- Potential of the experimental solution with fluorine electrode
 Wt' --- Weight % of HF in the experimental solution (see Fig.7)
 W_E --- Weight of HF solution in PSL (see Fig.6)
 W_t --- Weight % of HF solution in PSL

divalent in the condition of forming PSL while tetravalent in the condition of electropolishing. In order to study the mechanism of silicon dissolution, the results of the detailed investigation are reported. The substrates of 0.02 Ω-cm in resistivity were used. Figure 9 shows the relationship between the anodic reaction time and both the PSL thickness (T_p) and the amount of dissolved silicon (ΔW). The amount of dissolved silicon per unit area is derived from ΔW₂ as shown in Fig. 4. PSL was formed in 50% HF solution and the anodic current density was 100 mA/cm². T_p and ΔW increase with increasing the anodic reaction time. The silicon density of PSL (ρ) is denoted as the equation

$$\rho = \rho_0 - \frac{\Delta W}{T_p} \quad [1]$$

where ρ₀ is the silicon density of a bulk silicon wafer (2.329 g/cm³). As the values of ΔW and T_p, which are obtained from Fig. 9, are substituted into Eq. [1], ρ is constant to be about 1.5 g/cm³. That is, PSL, which has a uniform silicon density in the thickness direction, is formed. So, it is clear that the dissolution of silicon by the anodization is uniform in the thickness direction.

On the other hand, the effective dissolution valence (Z_i) is given as Z_i = Ne/N_{Si} where N_{Si} is the number of dissolved silicons which is obtained from ΔW and Ne is the number of flowed elementary charges. That is, Z_i corresponds to an average number of elementary charges which is needed for dissolving one atom of silicon. Figure 10 shows the relationship between Z_i and the anodic current density as the HF concentration is varied. Z_i is changed between 2-4 according to the condition of the anodization. It is clear that Z_i

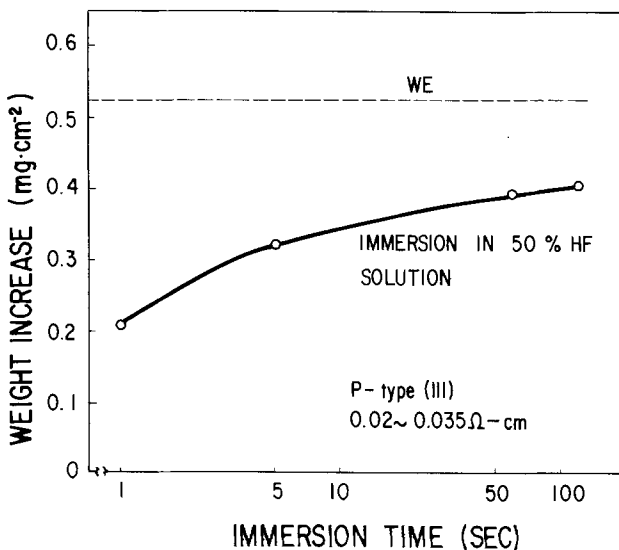


Fig. 8. Weight increase of PSL vs. immersion time. PSL was formed at 100 mA/cm² for 3 min.

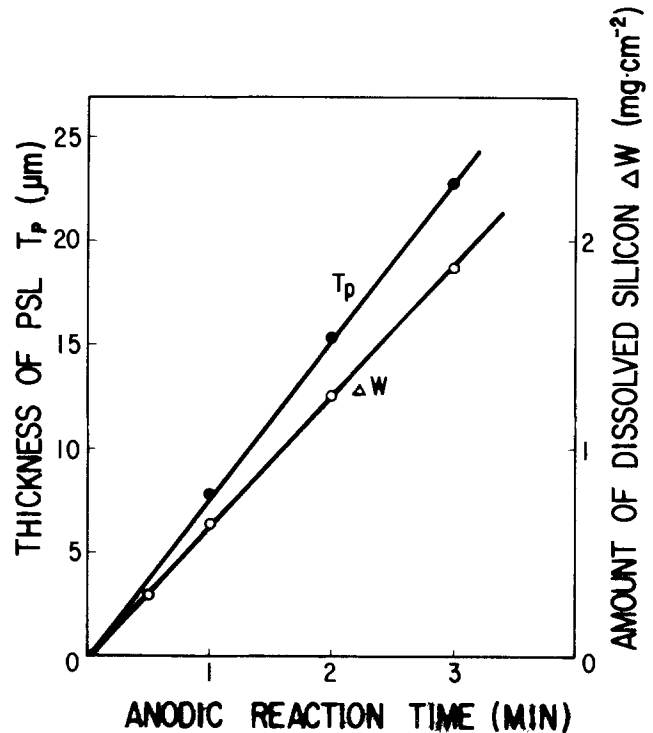


Fig. 9. Thickness of PSL and amount of dissolved silicon vs. anodic reaction time for p-type (0.02 Ω-cm) silicon substrate.

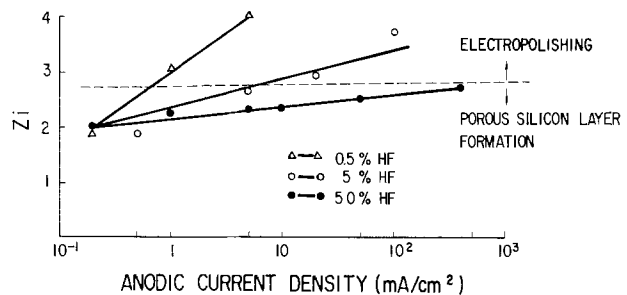


Fig. 10. Relationship between Z_i and anodic current density

has the value from 2 to about 2.8 under the condition of forming PSL.

Structure of PSL.—PSL is a single crystal according to the analysis of x-ray diffraction, but only on the surface of PSL, polycrystalline silicon can be seen by electron diffraction (3, 6, 7). The pores of PSL distribute at random, and the pore diameter at the surface is smaller than some 10Å and that of the inner part of PSL is some 10 ~ 300Å (3). Moreover, the pores are not formed straight; that is, the pores are formed zigzag in the thickness direction of PSL (7).

On the other hand, an insoluble thin porous film in HF solution is formed at the surface of PSL (8). This insoluble thin porous film is left even after PSL is soaked in HF solution for a month while the majority of PSL except this insoluble thin film is active and has dissolved already in HF solution. This insoluble thin film is named as surface porous film (SPF) and is distinguished from the active PSL formed under SPF. That is, PSL can be divided into two layers of SPF and the active PSL, as shown in Fig. 11.

Figure 12 shows the thickness of both SPF (T_s) and PSL (T_p) vs. the anodic reaction time. Substrates of 0.02 Ω-cm in resistivity and 50% HF solution were used to form PSL. T_s is saturated within one minute while T_p increases with increasing the anodic reaction time and grows to be thick (some 10 μm). SPF is formed from the beginning when forming PSL, so the growth of PSL, that is, the dissolution of silicon in a silicon substrate, is done through SPF.

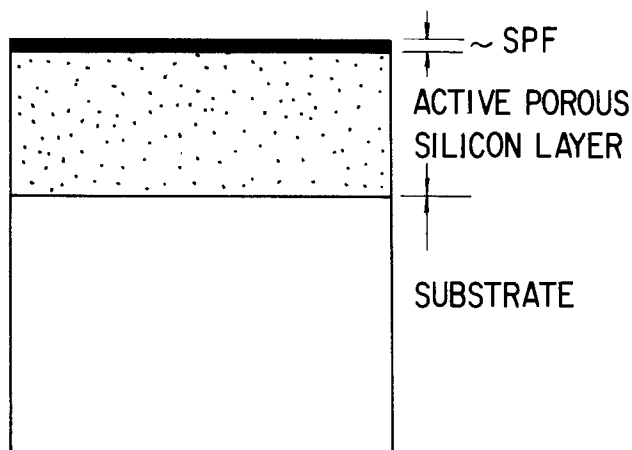


Fig. 11. Structure of PSL

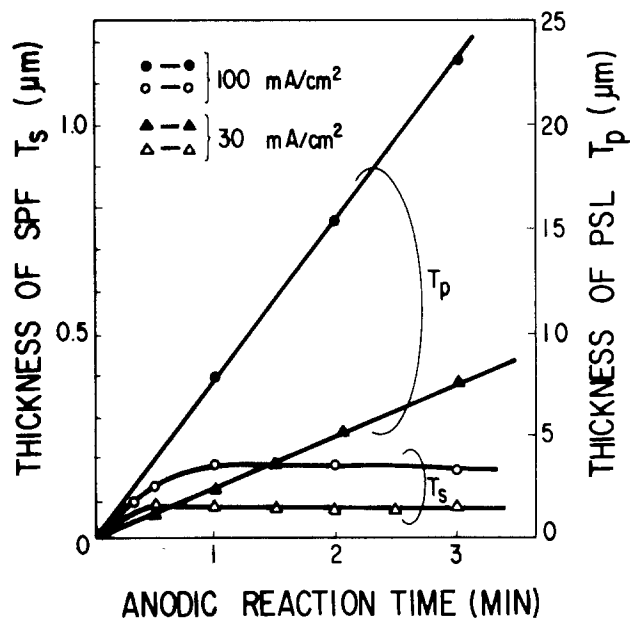


Fig. 12. Thickness of SPF and PSL vs. anodic reaction time, as a function of anodic current density.

The dependence of T_s and T_p on substrate resistivity is shown in Fig. 13. The anodization was performed for two minutes in 50% HF solution and the anodic current density was 100 mA/cm². The amount of dissolved silicon was constant for the various resistivity of substrates. T_s is strongly dependent on substrate resistivity and the maximum of T_s appears at about 0.02 Ω-cm in resistivity. T_p has the same dependence on substrate resistivity as the thickness of the

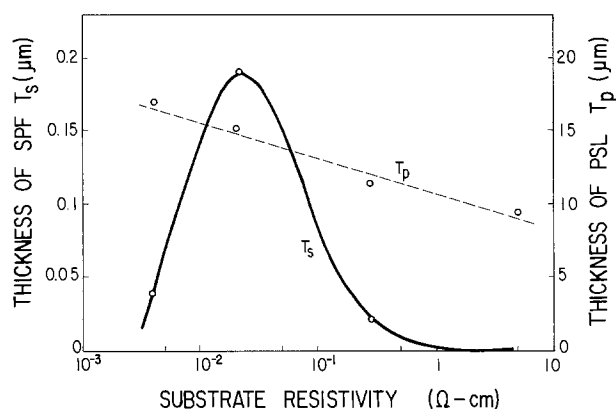
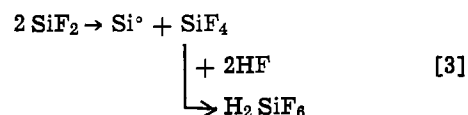
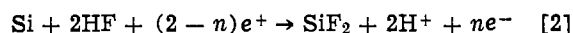


Fig. 13. Dependence of thickness of SPF and PSL on substrate resistivity.

stain film formed in HNO₃-HF solution (9). But the dependence of T_p on substrate resistivity differs from that of T_s and that of the stain film. According to the observation of the PSL surface with electron beam diffraction, there are polycrystalline silicon as well as single-crystalline silicon at the surface of PSL (7). Therefore, SPF consists of polycrystalline and single-crystalline silicon. That is, the crystalline structure of SPF agrees with that of the stain film. Moreover, SPF is insoluble in HF solution but is rapidly dissolved by silicon etches. These chemical properties of SPF agree precisely with those of the stain film.

Considering many similar points between SPF and the stain film, SPF can be thought to be formed by the same anodic reaction as the stain film. As Archer has reported in his paper (9), the disproportionation reaction proposed by Turner occurs at the surface of a substrate. That is



where $n < 2$, e^+ and e^- represent hole and electron. SPF is formed by the deposition of elementary silicon (Si°) produced by the disproportionation reaction [3] on the surface of a substrate. Considering that the growth of SPF can occur only at first as shown in Fig. 12, the disproportionation reaction [3] seems to occur only at the early step of forming PSL and at the surface of PSL. So no disproportionation reaction takes place after the growth of SPF is stopped. The reaction of forming thick PSL under SPF can be thought to differ from that of forming SPF, because of the differences in reactivity to HF solution, the growth progress (Fig. 12) and the dependence on substrate resistivity (Fig. 13).

Infrared spectra of PSL.—The dependence of the absorbance on PSL thickness was examined by infrared spectroscopy. The absorption bands appear at 4.7 μm (ν_1), 9.5 μm (ν_2), 11.1 μm (ν_3), 12.2 μm (ν_4), 16 μm (ν_5), and 21 μm (ν_6) (10). ν_1 and ν_3 are due to the Si-H bond. ν_5 is due to the Si-Si bond, ν_2 , ν_4 , and ν_6 are due to the antisymmetric stretching, symmetric stretching, and bending of the Si-O bond, respectively. The relationship between the absorbance ($\alpha \cdot t$) of these bonds and PSL thickness is shown in Fig. 14. α and t are the extinction coefficient and PSL thickness, respectively. The anodization was done in 50% HF solution at a constant current density of 100 mA/cm². The absorbance increases with increasing PSL thickness. When PSL is etched in a Freon (CF₄) gas plasma, $\alpha \cdot t$ decreases as the PSL thickness decreases. This shows that the Si-H, Si-Si, and Si-O bonds are

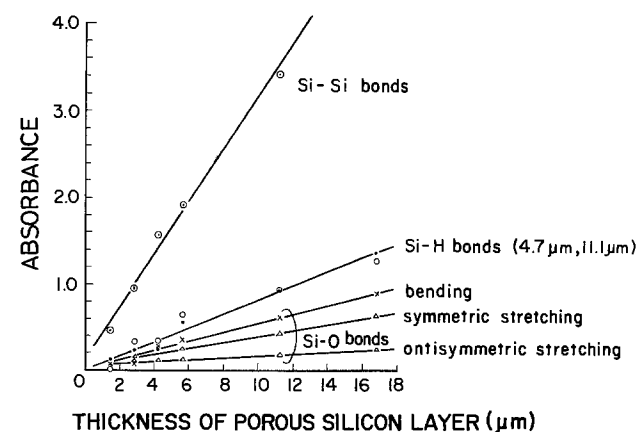


Fig. 14. Relationship between absorbance and thickness of PSL. Resistivity of p-type substrate is 4 ~ 7 Ω-cm.

distributed uniformly in the thickness direction of PSL.

The changes of infrared absorption spectra caused by immersion in 50% HF solution are shown in Fig. 15. The absorption strength of Si-O bonds decreases with increasing the time of immersion. After immersion for about 20 hr, the absorption due to Si-O bonds is still observable. This result means that the product, which is observed as Si-O bonds at 9.5, 12.2, and 21 μm has a small dissolution rate into HF solution. This insoluble product is changed by the heat-treatment above about 300°C in a vacuum as shown in Fig. 16. The absorption at 10.2 μm due to SiO (11), is increased by the heat-treatment. The weight is not increased by the heat-treatment, so oxidation of PSL has not occurred. The increased amount of the absorption at 10.2 μm has vanished immediately by immersion in HF solution. The insoluble product is changed to silicon oxide soluble in HF solution by the heat-treatment. As results, it is clear that the insoluble product formed during anodization has the following three characteristics. (i) The absorbance $(\alpha \cdot t)_{\nu_2}$, $(\alpha \cdot t)_{\nu_4}$, and $(\alpha \cdot t)_{\nu_6}$ at ν_2 , ν_4 , and ν_6 , respectively, are ranked as $(\alpha \cdot t)_{\nu_4} > (\alpha \cdot t)_{\nu_6} > (\alpha \cdot t)_{\nu_2}$ in order

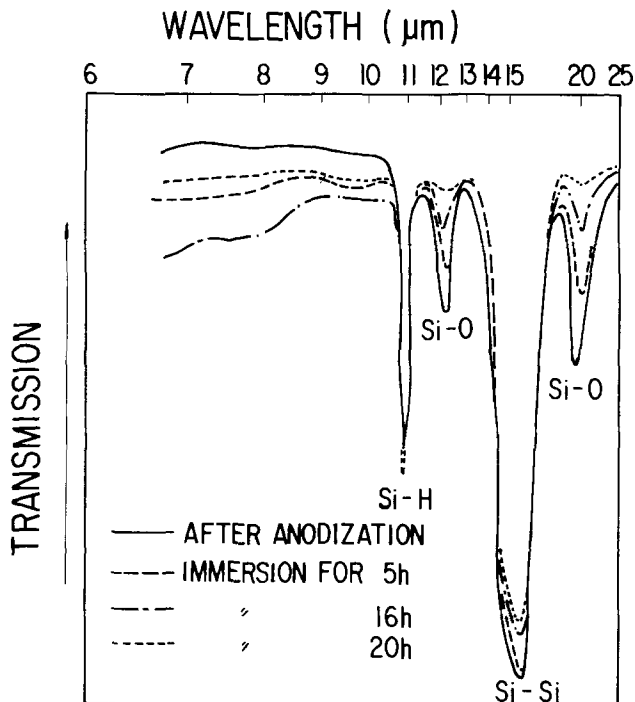


Fig. 15. Change of absorption spectra of PSL by immersion in 50% HF solution.

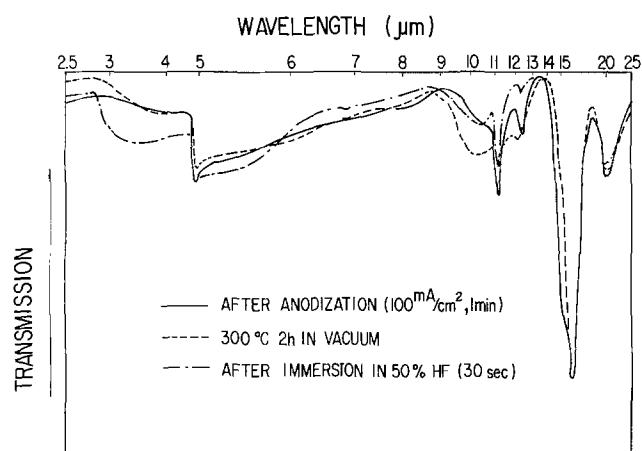


Fig. 16. Absorption spectra of PSL after anodization, heat-treatment at 300°C in a vacuum, and immersion in 50% HF solution.

of magnitude. This order is different from that of silicon dioxide layers formed by high temperature oxidation of bulk silicon. In the case of silicon dioxide layer of bulk silicon, the order is $(\alpha \cdot t)_{\nu_2} > (\alpha \cdot t)_{\nu_6} > (\alpha \cdot t)_{\nu_4}$. (ii) Insolubility in HF solution. (iii) The conversion into SiO occurs by heat-treatment.

On the other hand, SiF_2 or SiF_4 is produced by the anodic reaction, as mentioned later in detail. So it is possible that SiF_2 and SiF_4 react with H_2O in HF solution. When SiF_2 or SiF_4 reacts with H_2O , silicic acid (12) or fluorodisiloxane (13) is considered to be produced. In the infrared spectra of fluorodisiloxane, the strong absorption due to Si-F bonds appears (13). But no absorption due to Si-F bonds appears in the infrared absorption spectra of PSL, so the product observed as Si-O bonds seems to be silicic acid.

The resistivity of PSL.—The resistivity of PSL in the thickness direction was measured by forming an aluminum electrode on the surface of PSL. Aluminum was evaporated in a vacuum. The voltage-current characteristics were measured with a curve tracer without any heat-treatment after forming PSL. A Schottky junction is formed on the surface of PSL. The i - V characteristic gives essentially a straight line in the high current region in the forward direction. The resistivity of PSL in the thickness direction is obtained from the slope of the i - V characteristic. Figure 17 shows the resistivity of PSL formed in the silicon substrates with the various resistivity. PSL was formed in 50% HF solution and the anodic current density was 100 mA/cm^2 . It is clear that the resistivity of PSL has the high resistivity of $10^4 \sim 10^5 \Omega\text{-cm}$.

As shown in Fig. 2, the anode potential is not increased as PSL thickness increases. This means that the anodic current is passed not through the residual silicon layer in PSL but through the pores in PSL. That is, the anodic reaction (the dissolution of silicon) takes place only at the base of the pores in PSL.

Discussion

As already mentioned above, the insoluble surface porous film (SPF) exists at the surface of PSL and is formed by the disproportionation reaction. That is, elementary silicons, which are produced by the disproportionation reaction, deposit on the surface and form SPF. This disproportionation reaction takes place only at the early step of the anodization, because the growth of SPF becomes saturated. Considering that SPF is formed at the surface of PSL from the beginning of the anodization and SPF is insoluble

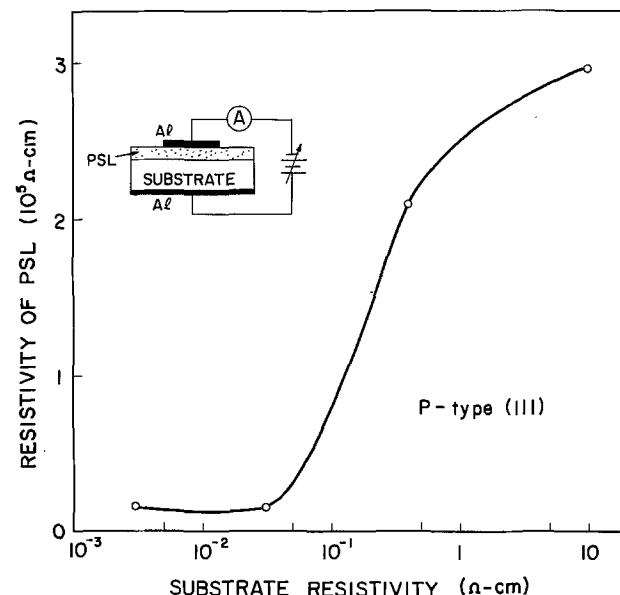
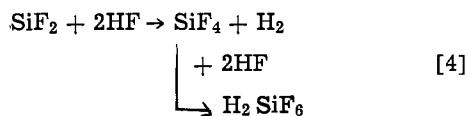


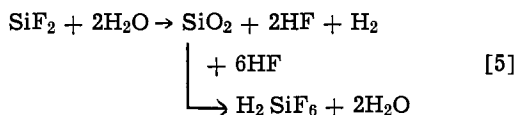
Fig. 17. Resistivity of PSL formed in various resistivity substrates

in HF solution, it can be thought that the place of dissolving silicon in the substrate is restricted by SPF, so that local corrosion occurs.

The anodic reaction of forming thick PSL under SPF differs from that of forming SPF, as discussed above. Therefore, another anodic reaction which does not consist of the disproportionation reaction must be considered in the case of forming PSL under SPF. As for the reaction of dissolving silicon difluoride in HF solution without the disproportionation reaction, two possibilities proposed by Memming and Schwadt are replaced by the disproportionation reaction as follows

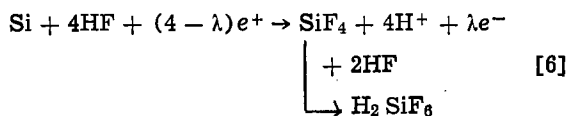


or



The remarkable difference between reaction [4] and [5] is that SiO_2 is formed and dissolved in HF solution in the case of reaction [5], but not in the case of reaction [4]. For the formation of PSL, the dissolution of silicon difluoride is performed by reaction [4] from the following result. As shown in Fig. 10, the growth rate of PSL is $7.5 \mu\text{m}/\text{min}$ at an anodic current density of $100 \text{ mA}/\text{cm}^2$ in 50% HF solution. On the other hand, the dissolution rate of SiO_2 in 50% HF solution is $1.4 \mu\text{m}/\text{min}$. Therefore, in the case of reaction [5], the reaction rate is equal to or smaller than $1.4 \mu\text{m}/\text{cm}^2$. That is, the reaction rate of reaction [5] is much smaller than the growth rate of PSL. Consequently, as the reaction of dissolving silicon difluoride in HF solution occurs, reaction [4] can take place.

According to investigation about the effective dissolution valence (see Fig. 10), the valence has the value between 2 to about 2.8 under the condition of forming PSL. Silicon is thought to be dissolved by the anodization in the divalent state or in the tetravalent state (1, 2, 5), so the effective dissolution valence more than 2 means that the dissolution in the tetravalent state as well as divalent state occurs. From the same reason about the reaction rate as the divalent reaction, the tetravalent dissolution reaction which consists of neither the formation nor the dissolution of SiO_2 must be considered. That is, the reaction between silicon and HF can occur, but that between silicon and H_2O cannot. The following anodic reaction seems to be the most probable for the tetravalent dissolution reaction of silicon



(where $\lambda < 4$)

At the larger value of the effective dissolution valence, the tetravalent reaction [6] seems to increase in ratio between the divalent reaction and the tetravalent reaction.

PSL is formed by the local anodization of generating pores. During anodization, the HF concentration of the electrolyte in the pores is constant and the same as that of the outer HF solution of the pores. HF solution can penetrate into the pores rapidly. Therefore, it can be thought that the reactants and the products of the anodic reaction can be supplied and released rapidly in the pores, respectively. On the other hand, during anodization, the anodic potential is constant in a high concentrated HF solution as

shown in Fig. 2. These results show that the anodic reactions in the pores (reaction [2], [4], and [6]) proceed uniformly in the thickness direction of PSL. This agrees with the result of infrared spectra measurement that Si-H, Si-O, and Si-Si bonds formed by the anodization are distributed uniformly in the thickness direction of PSL.

The resistivity of PSL is very high. So if the anodic current passes through the residual silicon layer in PSL during anodization, the anode potential must increase significantly with increasing PSL thickness. From the fact that the anode potential is constant during the constant current density anodization, it can be considered that the anodic reaction occurs only at the base of pores in PSL.

According to infrared spectra measurement, silicic acid is formed in the process of PSL formation. Moreover, this silicic acid has a small dissolution rate in concentrated HF solution. The silicic acid is thought to be produced by the reaction of H_2O with a part of Si, SiF_2 , or SiF_4 . SiF_2 and SiF_4 are produced by reaction [2], [4], and [6]. The silicic acid is left in PSL during anodization and seems to act as a hindrance layer to the following anodization. That is, the anodization of dissolving silicon can progress only at places where the silicic acid is not formed, and not at places where the silicic acid is formed. It can be said that the local dissolution is promoted by the hindrance layers composed by the silicic acid.

Proposed Formation Mechanism of PSL

The mechanism proposed to form PSL is required to initiate and sustain the local dissolution of silicon in a silicon substrate. At the surface of PSL, the insoluble surface porous film (SPF) is formed from the beginning of the anodization. SPF restricts the place of dissolving silicon, so that the local anodization can be initiated. The following anodic reaction takes place only at the base of the pores in PSL. The silicic acid is produced in PSL during anodization. The local dissolution of silicon is promoted by the hindrance layers composed of the silicic acid. The anodic reaction in the pores is uniform in the thickness direction of PSL and contains no disproportionation reaction. From these results, the mechanism of formation of PSL is proposed as shown in Fig. 18.

Conclusions

From the result of experimental investigations and discussions, the following are obtained.

1. The insoluble surface porous film (SPF) exists at the surface of PSL and is formed by the deposition of elementary silicon. The deposition of elementary silicon takes place only at the early step of the anodization.

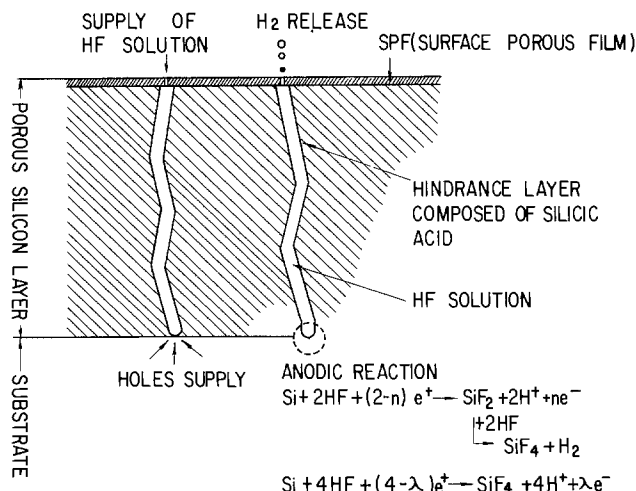
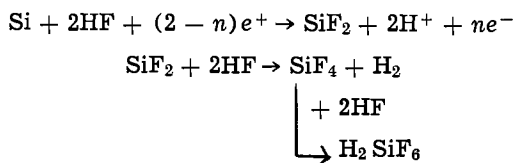
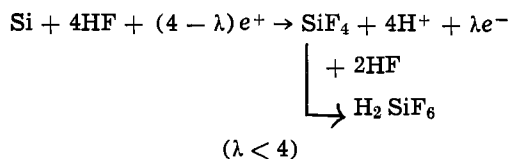


Fig. 18. Proposed formation mechanism of PSL

2. In the pores of PSL, the dissolution of silicon is the result of the divalent and the tetravalent reactions without the disproportionation reaction. The divalent anodic reaction is given as



($n < 2$, e^+ and e^- are hole and electron, respectively). The tetravalent anodic reaction is given as



3. The electrolyte in the pores of PSL has the constant HF concentration during anodization in concentrated HF solution.

4. The anodic reaction in the pores proceeds uniformly in the thickness direction and takes place only at the base of the pores.

5. PSL is formed by the local dissolution of silicon. The local dissolution of silicon is initiated by SPF and is promoted by the hindrance layers composed of the silicic acid.

Acknowledgment

The author would like to thank Mr. H. Ikawa for helpful guidance and discussions.

Manuscript submitted March 27, 1979; revised manuscript received Sept. 20, 1979.

Any discussion of this paper will appear in a Discussion Section to be published in the December 1980 JOURNAL. All discussions for the December 1980 Discussion Section should be submitted by Aug. 1, 1980.

Publication costs of this article were assisted by Nippon Telegraph and Telephone Public Corporation.

REFERENCES

1. A. Uhlir, *Bell Syst. Tech. J.*, **35**, 333 (1956).
2. D. R. Turner, *This Journal*, **105**, 402 (1958).
3. Y. Watanabe, Y. Arita, T. Yokoyama, and Y. Igarashi, *ibid.*, **122**, 1351 (1975).
4. D. R. Turner, in "The Surface Chemistry of Metals and Semiconductors," H. C. Gatos, Editor, p. 285, John Wiley and Sons, New York (1960).
5. R. Memming and G. Schwandt, *Surf. Sci.*, **4**, 109 (1966).
6. Y. Arita and Y. Sunohara, *This Journal*, **124**, 285 (1977).
7. T. Unagami and M. Seki, *ibid.*, **125**, 1339 (1978).
8. T. Unagami and K. Kato, *Trans. IEE Jpn.*, **98-A**, No. 10, 15 (1978).
9. R. J. Archer, *J. Phys. Chem. Solids*, **14**, 104 (1960).
10. K. H. Beckmann, *Surf. Sci.*, **3**, 314 (1965).
11. K. Sato, *This Journal*, **117**, 1065 (1970).
12. For instance: M. Cannon Sneed and Robert C. Brasted, "Comprehensive Inorganic Chemistry," Vol. 7, p. 95, D. Van Nostrand Company, Inc., Princeton, New Jersey.
13. J. L. Margrave, K. G. Sharp, and P. W. Wilson, *J. Am. Chem. Soc.*, **92**, 1530 (1970).

Electronic Properties of As- and P-Implanted Cadmium Telluride

Muren Chu and Richard H. Bube

Department of Materials Science and Engineering, Stanford University, Stanford, California 94305

and James F. Gibbons

Department of Electrical Engineering, Stanford University, Stanford, California 94305

ABSTRACT

Implantation of As and P into preannealed n-type CdTe crystals produced conversion from n- to p-type for the whole range of Cd pressures used for postimplantation annealing. Since Ar-implanted samples showed type conversion only for the lower Cd pressures, it is concluded that As and P cause chemical doping in CdTe. Defect equilibrium behavior and diffusion in the implanted samples as a function of the postimplantation Cd pressure used for annealing were investigated by chemical stripping of the implanted surface. The defect equilibrium behavior is consistent with a model proposed by Selim and Kröger on the basis of their investigation of P impurity in CdTe, in which the shallow acceptors introduced by implantation are compensated by interstitial Cd for higher postimplantation annealing Cd pressures, and by As or P at Cd sites at lower Cd pressures. Two fast diffusion mechanisms were observed in As-implanted samples, but only one of these in P-implanted samples.

Only a few implantation investigations have been carried out with CdTe. Kachurin *et al.* (1) first investigated the implantation of Ag and Ga in CdTe thin films, but the doping effects were unclear. Donnelly (2) implanted As⁺ ions into n-type CdTe crystals and reported conversion to p-type after postimplantation annealing; similar results were reported by Agrinskaya *et al.* (3), who compared the results of implanting Ne and As ions in CdTe and concluded

Key words: implantation, p-n junctions, defects, diffusion.

that As chemically dopes the CdTe. Doping efficiency has been increased by coimplantation of As⁺ and Cd⁺, as well as P⁺ and Cd⁺, to produce p-type CdTe (4).

Gettings and Stephens (5) reported conversion of a p-type CdTe substrate to n-type under implantation of n-type dopants such as Bi and In. An implantation efficiency of 30% was measured for a dose of 10¹⁴ cm⁻² In ions. Although more activity was generated by Bi ions, Te and Ar ions produced no measurable electrical changes. An observed increase in lattice

disorder and sample resistivities for annealing temperatures above 400°C was attributed to thermally generated active defects and to loss of the implanted ion species.

More recently Bean *et al.* (6) have investigated implantation of As, Kr, and Cs in CdTe and suggested that doping due to As implantation appeared to be caused by implantation-induced defects whereas doping due to Cs implantation appeared to be actual chemical doping. The present authors have previously reported successful production of CdTe p-n photo-voltaic junctions by As implantation followed by Cd-pressure controlled postimplantation annealing (7).

Although efforts have been made to improve the doping efficiency in CdTe, the understanding of implantation effects in this material is still quite limited. The factor of defect equilibrium chemistry has been largely neglected during the postimplantation annealing. Figure 1 summarizes the defect equilibrium behavior of CdTe doped with Cu, In, Au, or P, as reported by de Nobel (8) and by Selim and Kröger (9). The conductivity type and the carrier concentration of CdTe are strongly affected by the Cd pressure used in annealing. It is therefore to be expected that the postimplantation annealing Cd pressure can play an important role in controlling the implantation efficiency.

In the research described in this paper, CdTe single crystal samples were implanted with As, P, or Ar. After postimplantation annealing with controlled Cd pressures, these samples were chemically stripped and the experimental results are compared with those of Selim and Kröger (9).

Experimental Procedure

CdTe single crystals without intentional doping were grown by the unidirectional solidification method¹ in Cd and 0.5 atomic percent excess Te solution. The crystal growth conditions and the details of sam-

¹ Crystals were grown by R. Raymakers and Dr. R. S. Feigelson in the Crystal Growth Laboratory of the Center for Materials Research at Stanford University.

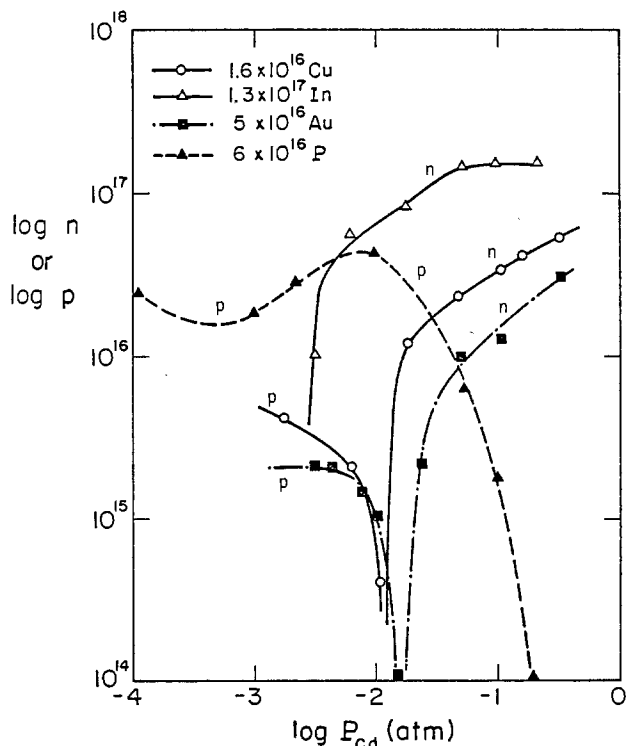


Fig. 1. Carrier concentration of CdTe samples doped with Cu, In, Au, or P as a function of the annealing Cd pressure after the samples were quenched from an annealing temperature of 700°C. P data from Selim and Kröger (9), all other data from de Nobel (8).

ple preparation procedure have been previously reported (7). The samples used here had dimensions of $5 \times 5 \times 1 \text{ mm}^3$.

Preimplantation annealing.—The as-grown CdTe crystals were p-type with a hole concentration of 10^{13} cm^{-3} and a hole mobility of $80 \text{ cm}^2/\text{Vsec}$, as expected due to the generation of Cd vacancies and/or Te interstitials by the growth in excess Te. To obtain n-type substrates for implantation, these crystals were converted to n-type by annealing in a two-zone furnace under Cd pressure for 36 hr in evacuated clean quartz tubes containing Cd. The first zone was used to control the substrate temperature at either 500° or 600°C, and the second zone was used to control the Cd temperature, which determines the Cd pressure in the tube, between 320° and 600°C. After annealing, samples were quickly cooled by quenching the ampul in water.

Implantation.—After preimplantation annealing, samples were etched with bromine-methanol to remove Cd precipitates from the surface. After etching, As, P, or Ar ions were implanted into CdTe substrates held at either 25° or 300°C.

Postimplantation annealing.—The procedure for postimplantation annealing was similar to that for preimplantation annealing except that the annealing time was just 1 hr. The purpose of this annealing was to decrease the crystal damage caused by the implantation and to make the dopant electrically active.

As Implantation

Table I summarizes the seven series of experiments that were carried out in the present investigation of As implantation in n-type CdTe.

Preliminary investigation and reproducibility (series As-1 and control).—Series As-1 was implanted with As for the investigation of type conversion, annealing effects as a function of Cd pressure, and reproducibility of the results. The control samples were processed through all the same procedures as As-1, except that they were not implanted.

After preannealing, all the samples in these two series were n-type with a mobility of $670 \text{ cm}^2/\text{Vsec}$ and an electron density as shown in Fig. 2. For high Cd pressures, the electron density varied as the 0.36 power of the Cd pressure; this value is close to 0.33 which corresponds to determination of the n-type conductivity by doubly ionized native defects, either doubly ionized interstitial Cd or Te vacancies (10-13).

After heating in the implantation system at 300°C, with or without As implantation, the surface of all samples converted to p-type, probably associated with Cd vacancies formed by out-diffusion of Cd, which have a shallow acceptor level with ionization energy of 0.05 eV.

After postimplantation annealing, the control samples were again n-type with identical electrical properties as before processing in the implantation system, provided that the 300°C heating in the implanter was not longer than 1 hr. This indicates that the 500°C postannealing under Cd pressure annihilated the Cd vacancies formed by the 300°C heating in the implanter, unless the 300°C heating was long enough to generate vacancy clusters.

The As-implanted samples, however, showed quite different properties after postimplantation annealing. The substrates of these samples were indeed n-type with the same electrical properties as the control samples, but the As-implanted surfaces were p-type with the sheet hole concentrations shown in Fig. 3 as a function of Cd pressure. Reproducibility for these samples was excellent.

These preliminary experiments confirm that type conversion upon As implantation is due to the As implantation itself, and not to any extraneous processing effects.

Table I. Summary of samples and treatments

Sample series	Preimplantation annealing	Implantation temperature, °C	Dopant and dose, cm ⁻²	Ion energy, keV	Postimplantation annealing
As-1	500°C, p _{ca} varied	300	As, 10 ¹⁵	60	Same as preimplantation annealing
Control	500°C, p _{ca} varied	300	None	None	Same as preimplantation annealing
Ar	500°C, max p _{ca}	300	Ar, 10 ¹⁵	60	500° or 600°C
As-2	500°C, max p _{ca}	300	As, 10 ¹⁵	100	500° or 600°C
As-3	500°C, max p _{ca}	25	As, 10 ¹⁵	100	600°C
As-4	600°C, max p _{ca}	25	As, 10 ¹⁵	100	500° or 600°C
As-5	600°C, max p _{ca}	25	As, 5 × 10 ¹³	100	600°C
P-2	500°C, max p _{ca}	300	P, 10 ¹⁵	100	500° or 600°C
P-3	500°C, max p _{ca}	25	P, 10 ¹⁵	100	500°C
P-4	600°C, max p _{ca}	25	P, 10 ¹⁵	100	500° or 600°C

Implantation damage (Ar series).—Twelve samples comprise the Ar series; these were preannealed, implanted with Ar, and postannealed as described in Table I. After implantation half the samples were annealed at 600°C under different Cd pressures, and half the samples were annealed at 500°C under different Cd pressures.

For a whole range of Cd pressures from 10⁻³ to 10⁻¹ atm at 600°C, and for all Cd pressures greater than 2.5 × 10⁻³ atm at 500°C, no conductivity type conversion is caused by Ar implantation. Only for Cd pressures less than 2.5 × 10⁻³ atm and for annealing at 500°C is conversion to p-type observed, as indicated on Fig. 4. This p-type behavior can be associated with implantation damage (Cd vacancies, Te interstitials, or defect clusters) which is annealed away for all Cd pressures at 600°C, and for all but the lowest Cd pressures at 500°C. These results show that the Cd pressure is an important parameter in annealing the implantation damage, as well as the annealing temperature.

As implantation and electrical properties (series As-2, As-3, As-4, and As-5).—Four series of experiments were carried out to investigate the effects of implantation substrate temperature, preannealing temperature, and postannealing temperature on the electrical properties of As-implanted samples.

Twelve As-2 samples were treated similarly to the Ar samples, except that they were implanted with 100 keV As ions. The implanted surfaces of all samples were converted to p-type, while the substrate remained n-type. The variation of sheet hole concentration mea-

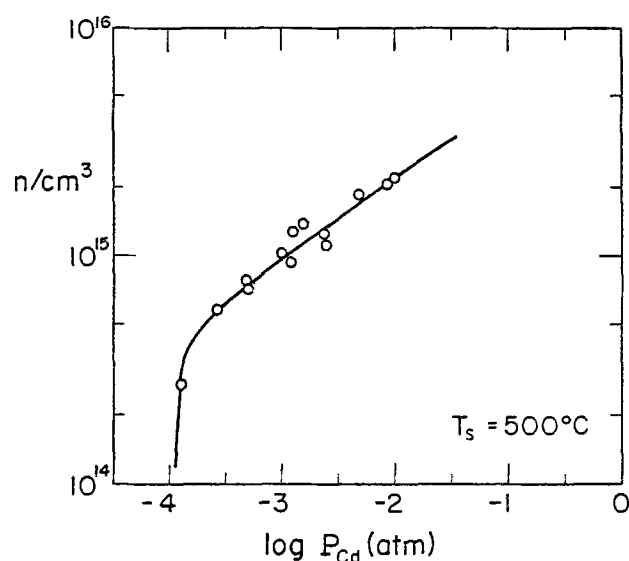


Fig. 2. Electron concentration as a function of annealing Cd pressure for CdTe series As-1 and control in a preimplantation anneal to convert as-grown p-type undoped CdTe to n-type substrates for implantation.

sured on the implanted surface as a function of post-annealing Cd pressure and annealing temperature is given in Fig. 4. The hole mobilities range from 30 to 60 cm²/Vsec for the whole range of pressures and temperatures used. All of these samples were remeasured two months after the initial preparation to check their stability. Only the samples annealed under maximum Cd pressure showed any changes; for them the sheet hole concentration had decreased to half of its initial value.

Six As-3 samples were treated similarly to the As-2 samples, except that they were implanted at 25°C and were postimplantation annealed at 600°C only, to test the effect of implantation substrate temperature. Conductivity type conversion was observed on all these samples with the sheet hole concentration results shown in Fig. 5. The mobilities of these samples decreased from 50 cm²/Vsec at low Cd pressure to 10 cm²/Vsec at maximum Cd pressure. Arkad'eva *et al.* (4) did 25°C-implantation, annealed their samples under maximum Cd pressure, and reported hole mobilities between 9 and 30 cm²/Vsec. Remeasuring these samples after two months again showed no changes ex-

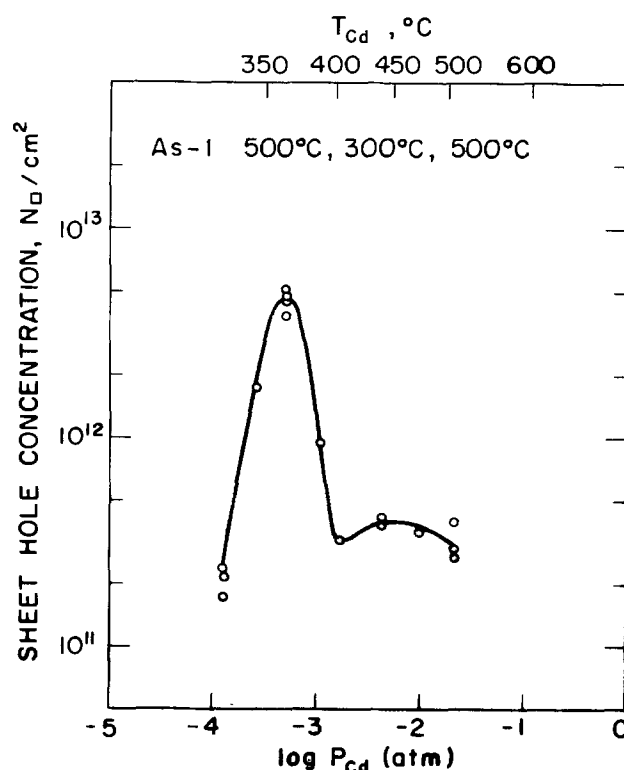


Fig. 3. Sheet hole concentration for As-1 samples as a function of postimplantation Cd pressure. The temperatures given indicate preimplantation annealing, implantation, and postimplantation annealing temperatures.

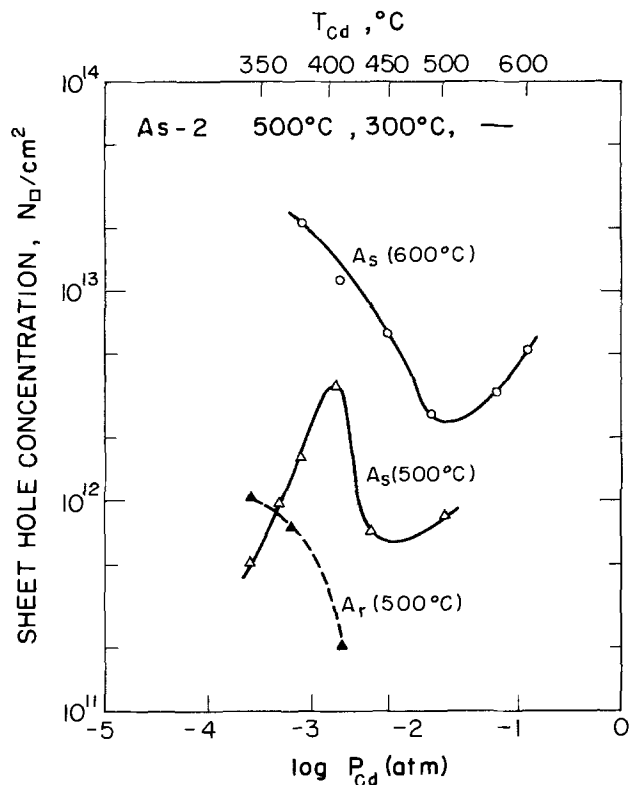


Fig. 4. Sheet hole concentration for As-2 samples as a function of postimplantation Cd pressure at 500° and at 600°C (preimplantation annealing at 500°C and implantation at 300°C), and for Ar samples postimplantation annealed at 500°C. Ar-implanted samples postimplantation annealed at 600°C did not show conductivity type conversion.

cept for the samples annealed under maximum Cd pressure, for which the sheet hole concentration had decreased to half of its initial value.

Ten As-4 samples were used to check the effects of changing the preannealing temperature from 500° to 600°C. The sheet hole concentrations are shown in Fig. 5. Hole mobilities were similar to those found for As-3 samples.

Four As-5 samples were used to check the effects of dose on implantation results. The sheet hole concentrations are also shown in Fig. 5. A decrease in dose by a factor of 20 was accompanied by an increase in the maximum implantation efficiency from 1 to 3%.

Diffusion and defect equilibrium behavior.—Sheet concentrations cannot be used for direct analysis of the detailed doping process because the sheet concentrations are the product of two variables: (i) the hole concentration per unit volume, and (ii) the diffusion distance of As atoms after annealing. These two variables were separated by chemical stripping experiments.

An etching solution was used to etch away a thin layer of the implanted samples. By measuring the sheet hole concentrations before and after etching, and dividing the difference between these two concentrations by the thickness of the etched layer, the hole concentration per unit volume of that layer can be calculated. By a series of such experiments, the profile of the hole density can be obtained for each sample. We used a 0.01% by volume bromine in methanol etchant, which has an etching rate of 2 Å/sec. The profiles of hole density in our samples were calculated by assuming a constant mobility as measured on the surface.²

The hole density profiles for As-2 600°C postimplantation annealed samples are shown in Fig. 6. The theoretical ion distribution in As-implanted samples is also shown in this figure, which was approximated by the following Gaussian distribution (14)

²The difference of the sheet hole concentration between two consecutive measurements was less than 5% of the total sheet hole concentration. Since a 5% error was observed during Hall effect measurements, we did not make Hall measurements after each stripping, but instead assumed an essentially constant mobility and restricted ourselves to conductivity measurement only.

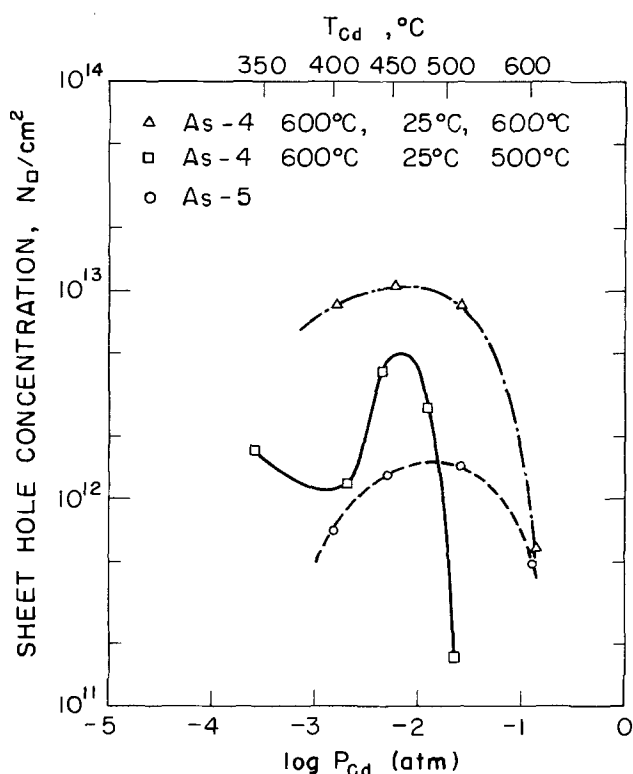
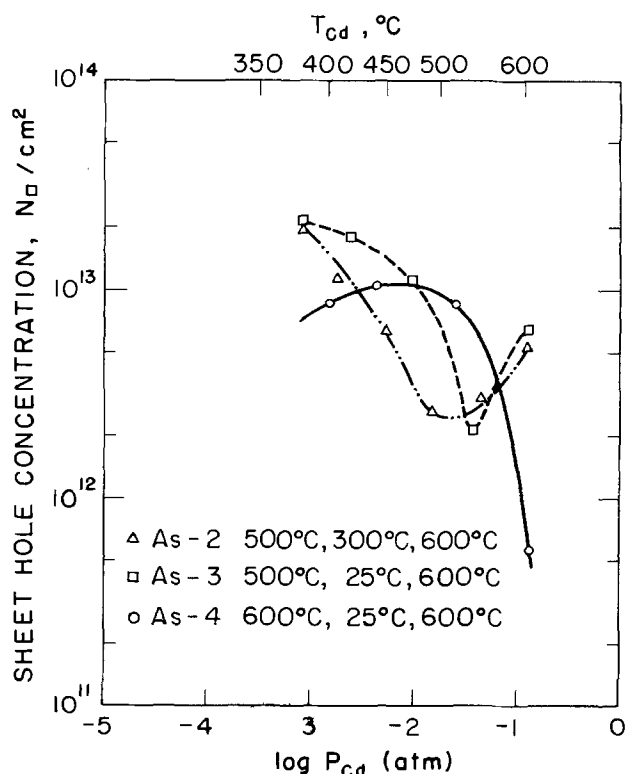


Fig. 5. (a, left) Comparison of the dependence of sheet hole concentration on postimplantation Cd pressure for samples As-2, As-3, and As-4. Temperatures indicated are preimplantation anneal, implantation, and postimplantation anneal. (b, right) Comparison of the dependence of sheet hole concentration on postimplantation Cd pressure for samples As-4 and As-5.

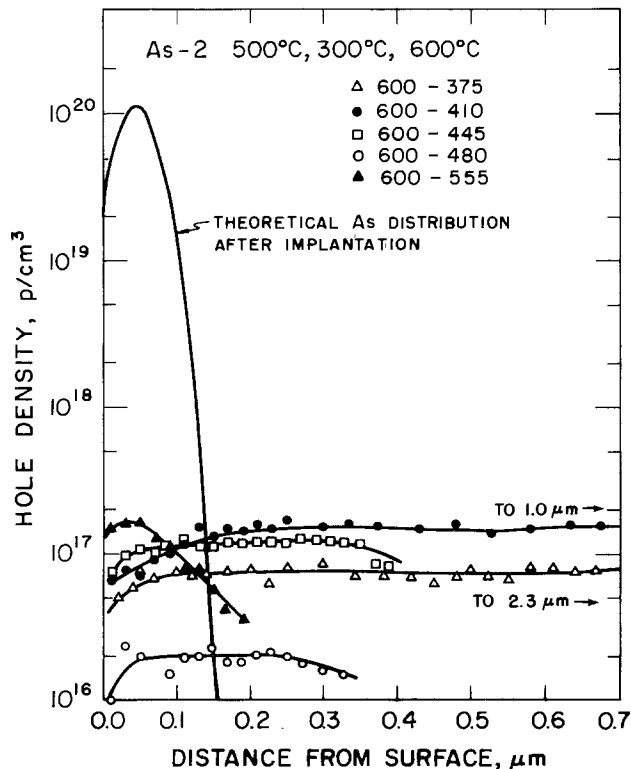


Fig. 6. Hole density profiles in 600°C postimplantation annealed As-2 samples. Each curve is designated with two temperatures; the first, 600, represents the temperature in °C of the postimplantation anneal, while the second gives the temperature in °C of the Cd during the anneal.

$$N(x) = \frac{N_1}{(2\pi)^{2/3}(\Delta R_p)} \exp\left\{-\frac{(x - R_p)^2}{2(\Delta R_p)^2}\right\} \quad [1]$$

where R_p is the projected range, ΔR_p is the standard deviation, x is the perpendicular distance into the substrate, and N_1 is the ion dose. For 100 keV As in CdTe, $R_p = 439\text{Å}$ and $\Delta R_p = 258\text{Å}$ (15). The hole density profiles of the As-2 500°C-annealed samples and the As-4 600°C-annealed samples have also been measured, but are not presented here in the interest of brevity (16).

The curves of Fig. 6 show the dependence of hole density and the effective diffusion distance on annealing Cd pressure. The hole density profiles of most samples, except for two As-2 samples annealed under maximum Cd pressure, were very flat and extended into the samples, indicating that the diffusion of As-associated acceptors was very fast.

The hole densities of these samples (except for those annealed under maximum Cd pressure) are given in Fig. 7 as a function of Cd pressure. There is a close similarity between these curves and those given by Selim and Kröger (9) in Fig. 1.

By using the approximation

$$L \simeq (4D_{\text{eff}}t_d)^{1/2} \quad [2]$$

the effective diffusion coefficients of the samples can be estimated and are plotted in Fig. 8. In Eq. [2], L is the effective diffusion distance, D_{eff} is the electrically active dopant diffusion coefficient, and t_d is the diffusion time (1 hr for our samples).

Shallow acceptor level associated with As implantation.—Low temperature Van der Pauw measurements (a four-point probe measurement) were made on As-implanted samples to determine the energy level of the shallow acceptor levels generated by As implantation. An energy level lying 0.08 eV above the valence band is indicated, which may be associated with As substituted for Te.

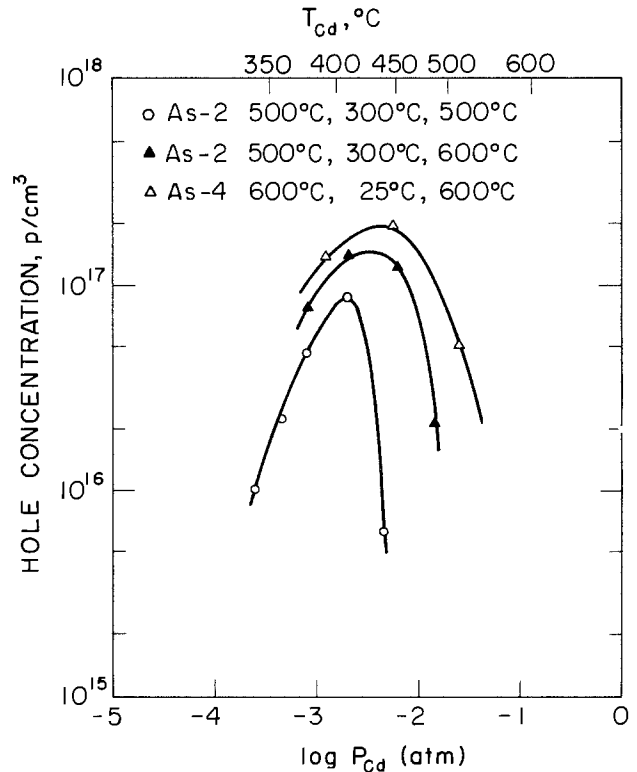


Fig. 7. Hole concentration as a function of postimplantation annealing Cd pressure for As-2 and As-4 samples. Temperatures given correspond to preimplantation annealing, implantation, and postimplantation annealing.

P Implantation

The behavior of P in CdTe has been investigated to a certain extent, providing additional guides for our interpretation of implantation effects. Doping and compensation phenomena of P in CdTe were reported by Lorenz and Segall (17), Morehead and Mandel (18), and Arkad'eva *et al.* (19). Diffusion of P in CdTe at 900° and 950°C has been investigated by Hall and Woodbury (20). We have already mentioned the defect equilibrium chemistry investigation of P-doped CdTe by Selim and Kröger (9).

The procedures used for implanting P in CdTe were similar to those used for implanting As. Three series of experiments were carried out to investigate the effects of implantation substrate temperature, preimplantation conditions, and postimplantation annealing conditions. The samples are summarized in Table I.

Electrical properties (series P-2, P-3, and P-4).—The implanted surfaces of all twelve P-2 samples were converted to p-type while the substrates remained n-type after implantation and postimplantation annealing. Figure 9 shows the sheet hole concentrations of these samples as a function of postimplantation annealing Cd pressure, including also the Ar implantation data for comparison. Although differences in detail are evident, the general behavior after P implantation is quite similar to that after As implantation. Chemical doping by implanted P impurities seems to have occurred.

The hole mobilities in these samples were also measured. An average mobility of 45 cm²/Vsec was found for samples annealed at 500°C, independent of Cd pressure. The mobilities for samples annealed at 600°C decrease from 70 to 33 cm²/Vsec with increasing Cd pressure.

Four P-3 samples were treated similar to P-2 samples except that the implantation was at 25°C. All implanted surfaces were converted to p-type, but van der Pauw measurements in conjunction with chemical stripping experiments showed these samples to be inhomogeneous.

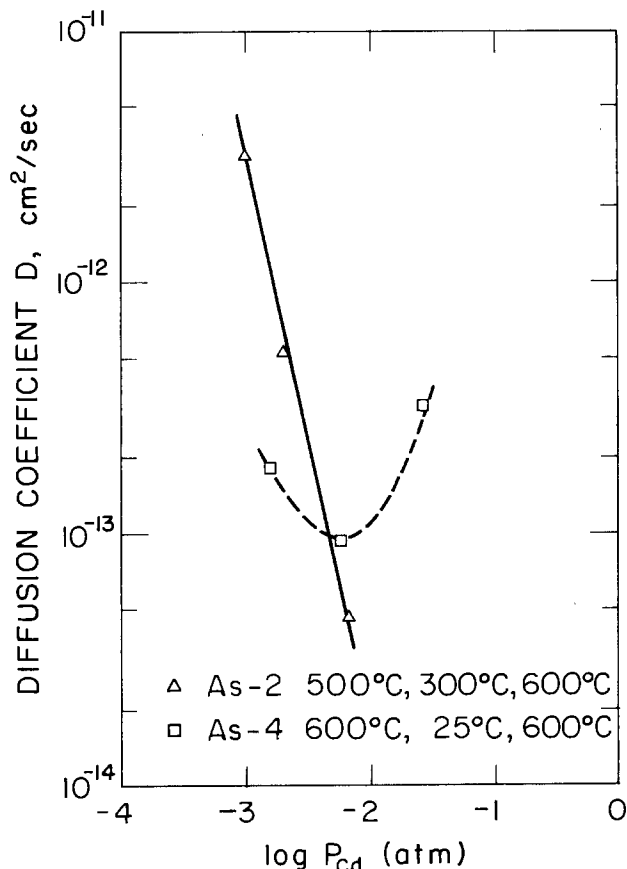


Fig. 8. Effective diffusion coefficients as a function of postimplantation annealing Cd pressure for As-2 and As-4 samples. Temperatures given correspond to preimplantation annealing, implantation, and postimplantation annealing.

Eight P-4 samples were preannealed at 600°C under maximum Cd pressure. All samples showed conversion to p-type on the implanted surface. Those postimplantation annealed at 500°C were again inhomogeneous. The electrical properties of samples annealed at 600°C were measured; the sheet hole concentrations were considerably smaller than those of P-2 samples, while the hole mobilities were comparable to those found for P-2 samples.

Diffusion and defect equilibrium behavior.—Stripping experiments, as described previously for As-implanted samples, were carried out for P-2 samples postimplantation annealed at 500° and 600°C, and for P-4 samples annealed at 600°C. The results for 600°C-annealed P-2 samples are given in Fig. 10, which show that the diffusion coefficient and hole concentrations are a function of the annealing Cd pressure. Figure 10 also includes the theoretical P distribution after implantation calculated using Eq. [1] where $R_p = 875\text{Å}$ and $\Delta R_p = 571\text{Å}$ for a P ion energy of 100 keV (15). The hole concentrations as a function of Cd pressure for the P-2 samples are given in Fig. 11, which includes Selim and Kröger's (9) results for their 600° and 900°C annealed P-doped samples. In their work the P was incorporated during crystal growth and the P concentration was $5 \times 10^{19}\text{ cm}^{-3}$. Higher hole concentrations are apparently achievable by ion implantation.

Stripping experiments also show that P does not have appreciable diffusion in 500°C-annealed P-2 samples or in 600°C-annealed P-4 samples.

Estimates of the diffusion coefficients involved for the 600°C-annealed P-2 samples, according to Eq. [2], are given in Fig. 12.

Shallow acceptor level associated with P implantation.—Low temperature Hall effect measurements were made on P-2 samples to determine the properties of the

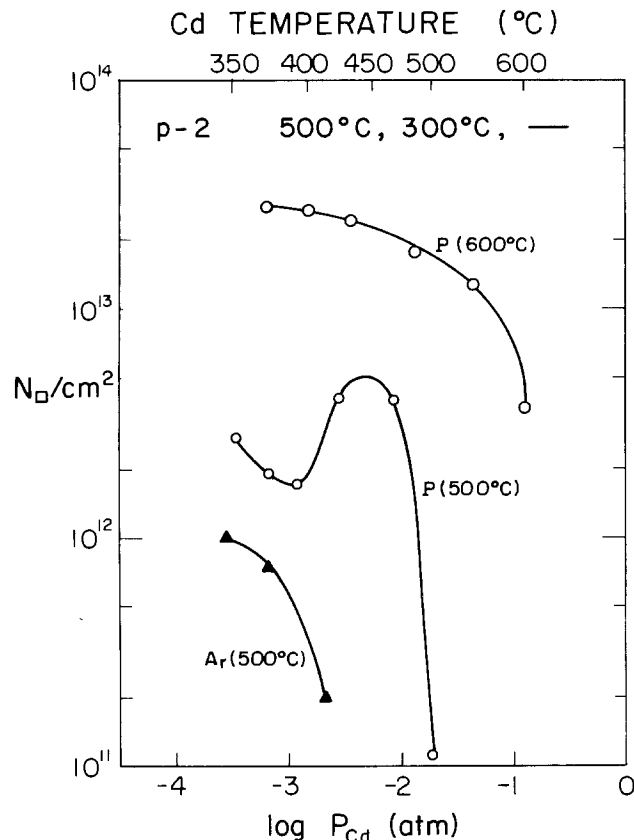


Fig. 9. Sheet hole concentration as a function of postimplantation annealing Cd pressure for P-2 samples compared to Ar samples. P-2 samples were preimplantation annealed at 500°C and implanted at 300°C; postimplantation annealing was carried out at 500°C and at 600°C, yielding the two curves shown.

shallow acceptor level caused by P implantation. An ionization energy of 0.037 eV was found that is in agreement with the published data (9).

Ohmic contacts.—The preparation of ohmic contacts to p-type CdTe is a difficult one. No metal exists with workfunction larger than that of p-type CdTe. Although ohmic contacts to p-type CdTe have been reported (21), the contact resistivities have not been reported. By evaporation of Au on slightly bromine-methanol etched P-implanted p-type CdTe (e.g., a sample of P-2 with postimplantation substrate temperature of 600°C and Cd temperature of 370°C) ohmic contacts were achieved with a contact resistivity of $0.2\ \Omega\text{-cm}^2$.

Discussion: As Implantation

Limitations on quantitative analysis.—Detailed quantitative analysis of our results is limited by two major problems: (i) the effects of implanted As on chemical diffusion in CdTe are unknown, and (ii) the As-related species formed by implantation is unknown.

Since the preimplantation and postimplantation annealing conditions of most samples are not the same (except for the As-1 samples) because of practical limitations on the number of samples to be investigated, there was chemical diffusion in CdTe even without implanted As. This chemical diffusion process has been studied by Zanio (22), Rud' and Sanin (23), and Whelan and Shaw (11). Zanio's experiments covered the temperature range from 500° to 800°C, and he found that the chemical diffusion coefficient could be written as

$$\tilde{D}_{\text{CdTe}} = 4 \exp(-1.15 \text{ eV}/kT) \quad \text{cm}^2 \text{ sec}^{-1} \quad [3]$$

and was independent of the annealing Cd pressure. This result was explained by Chern and Kröger (24) by attributing the chemical diffusion to a combination

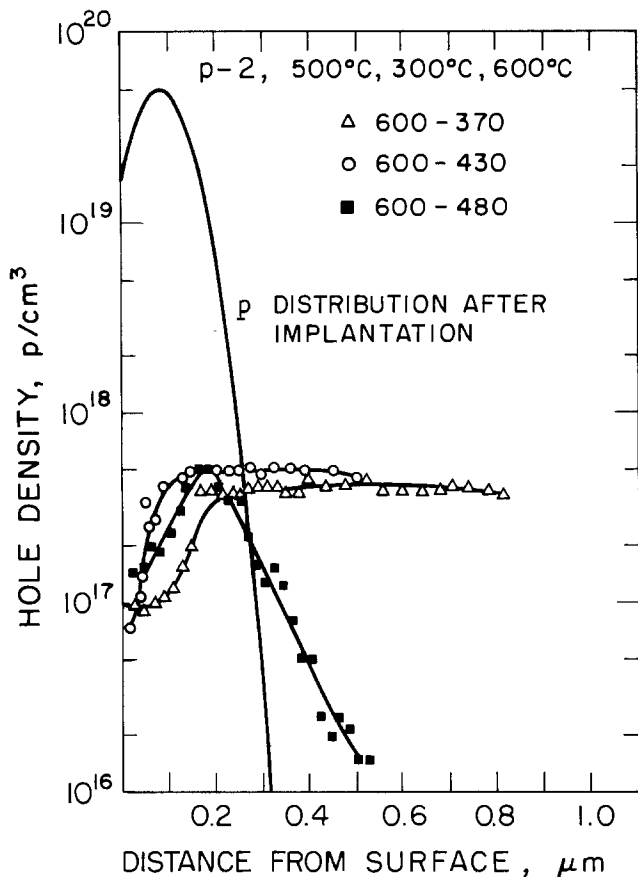


Fig. 10. Hole density profiles for P-2 samples after 600°C post-implantation annealing under Cd pressure. For each curve two figures are given: the first, 600, is the postimplantation annealing temperature in °C, and the second is the Cd temperature during this annealing in °C.

of diffusions of different native defects. In our experiments it is not clear how many diffusion mechanisms the As atoms will have in CdTe, and the interaction between the chemical diffusion of native point defects in CdTe and As is unknown.

In Lidow and Gibbons' work on ion implantation in GaAs (25) they found that $\text{Se}_{\text{As}}\text{-V}_{\text{Ga}}$ complexes formed during implantation above 150°C. Although measurements of photoluminescence that we performed on our samples indicate different photoluminescence responses associated with different As-related species, it is not clear whether these species were formed during implantation or during postimplantation annealing.

In spite of these difficulties, some conclusions can be tentatively drawn from the experimental results described above.

Defect equilibrium chemistry.—Figure 7 is the defect equilibrium diagram for the As-implanted CdTe samples, which is quite similar to the results reported by Selim and Kröger (9) for P-doped CdTe as shown in Fig. 1. Our low temperature Hall measurements indicated only a single acceptor associated with As implantation, which we assigned to As on Te sites. The observed decrease of the hole concentration from the maximum concentration as a function of Cd pressure is apparently caused by compensation; likely defects for such compensation are interstitial Cd at higher Cd pressures, and As on Cd sites at lower Cd pressures. According to Selim and Kröger (9), P can occupy Cd sites and behave as a triple donor during annealing under low Cd pressure; it might be expected that the concentration of As_{Cd} , a triple donor, would be even higher than that of P_{Cd} under the same conditions because the size and electronegativity of As are closer to those of Cd than are those of P. Comparison of Fig. 7 with Fig. 11 does indicate that compensation in As-

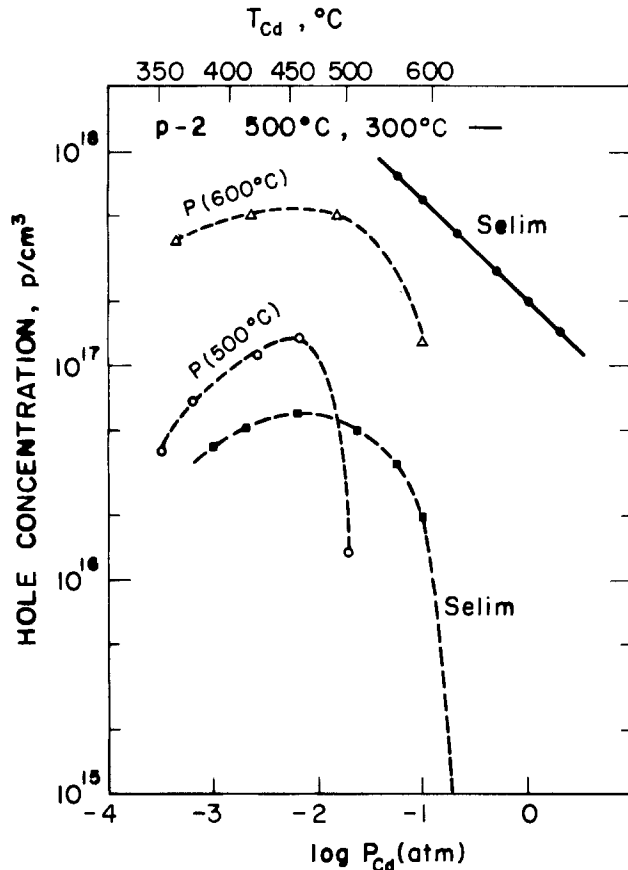


Fig. 11. Hole concentration as a function of postimplantation annealing Cd pressure for P-2 samples, which were preimplantation annealed at 500°C and implanted at 300°C; postimplantation annealing was carried out at 500° and 600°C, yielding the two curves shown. Also shown for comparison are data from Selim and Kröger (9); the lower curve is for 600°C annealing, and the upper curve is for 900°C annealing.

implanted CdTe is stronger than in P-implanted CdTe for low Cd pressures, in agreement with this argument.

Differences indicated in Fig. 7 between the hole concentrations of 600°C-annealed As-2 and As-4 samples might be interpreted as follows. The As-4 samples had a higher density of Te vacancies after higher temperature preimplantation annealing, and since there was no supply of Te atoms during postimplantation annealing, the probability of As going to Te sites and behaving as acceptors was enhanced for the P-4 samples.

Diffusion.—Detailed analysis of the self-diffusion of defects has been carried out by Chern and Kröger (24) who expressed the tracer diffusion coefficients as

$$D^* = D_0^* p_{\text{Cd}}^b \exp(-H^*/kT) \quad \text{cm}^2 \text{sec}^{-1} \quad [4]$$

where b is a number, D_0^* is a constant, and H^* is the activation energy for diffusion. The factor b describes the pressure dependence of the diffusion coefficients for defects and has a different sign for different types of defects; b is positive in CdTe for D_{Cd_i} , and for D_{VTe} , but b is negative for D_{VCd} , D_{VCd} , and D_{Te_i} .

Figure 8 shows that the diffusion coefficients of As-2 samples have a negative b , which indicates that As diffusion is through a mechanism involving Cd vacancy and/or Cd interstitial sites. That As diffusion in Cd interstitial sites should have a negative b follows from the fact that D_{Cd_i} is positive, but an increase in the Cd_i concentration means a decrease in the diffusion rate through interstitial sites.

Figure 8 also suggests that the diffusion coefficients of As-4 samples have components with both positive

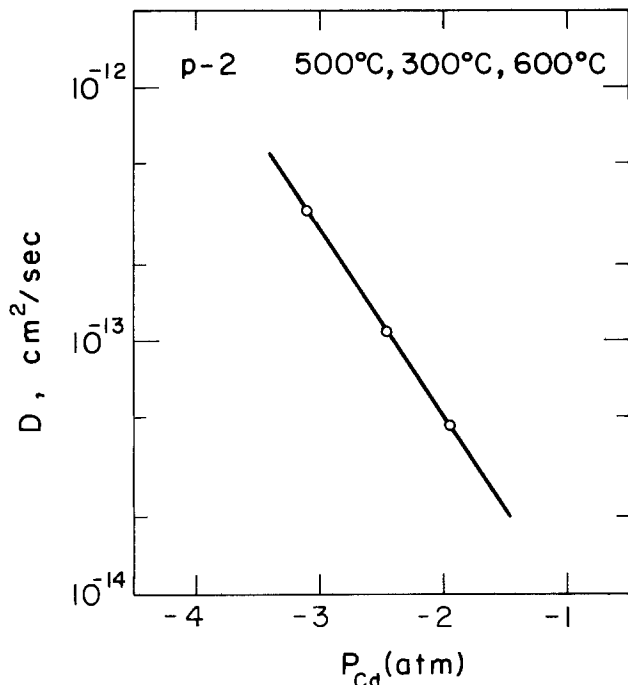


Fig. 12. Effective diffusion coefficients as a function of post-implantation annealing Cd pressure or P-2 samples. The temperatures given correspond to preimplantation annealing, implantation, and postimplantation annealing.

and negative b . Since these samples were preimplantation annealed at a higher temperature than the As-2 samples, under maximum Cd pressure, they will have higher concentrations of Cd_i and V_{Te} and lower concentrations of V_{Cd} than the As-2 samples. The expected result is that the diffusion mechanism with negative b will be suppressed, while that with positive b will be enhanced. This is consistent with the trend of the observations.

Our measurements on the photoluminescence response of these samples support these suggestions. As-2 and As-4 samples with different diffusion characteristics had different photoluminescence responses. In As-2 samples at least one As-associated species is indicated with a photoluminescence peak at 0.77 eV; in As-4 samples, at least three As-associated species are indicated with peaks at 0.77, 0.90, and 1.10 eV, although the intensity of the 0.77 eV peak is much less than that of the other two. Since the preimplantation annealing and implantation conditions for As-2 samples caused many Cd vacancies and a low concentration of Cd interstitials, an identification is reasonable between the 0.77 eV peak and either single As or As complexes, with As at either Cd sites or Cd interstitial sites. The preimplantation annealing of As-4 samples indicates that the concentration of Te vacancies should be greater than in the As-2 samples, and that the concentration of Te interstitials should be less than in As-2 samples. Hence, we might attribute peaks at 0.90 and 1.10 eV to As at Te substitutional or interstitial sites. Although certainly not a tight argument, these assignments are at least consistent with the diffusion data.

Discussion: P Implantation

Defect equilibrium chemistry.—Most of the results of P implantation are quite similar to those of As implantation and can be interpreted within the framework of the interpretation of Selim and Kröger (9). Under higher Cd pressures (Fig. 11) the compensation of P_{Te} acceptors is by interstitial Cd, while at lower Cd pressures, the compensation of P_{Te} is by P_{Cd} , a triple donor. The observation that the hole concentrations reported by Selim and Kröger for 600°C annealing are about ten times smaller than those produced by P

implantation in spite of the high P concentration ($5 \times 10^{19} \text{ cm}^{-3}$) in their samples, cannot be explained without further investigation.

Diffusion.—The effective diffusion coefficients for P-2 samples shown in Fig. 12 are smaller than those of As in As-2 samples treated in a similar way. Only a negative b factor in Eq. [4] is indicated by the results, indicating that electrically active P in these samples diffuses through a mechanism involving P at Cd substitutional or interstitial sites.

The 600°C annealed P-4 samples showed no appreciable diffusion. This result indicates that (i) diffusion through the mechanism involving a negative b factor is suppressed, and (ii) P does not diffuse through a mechanism with a positive b factor.

The inhomogeneity of the 500°C-annealed samples can be attributed to the low P diffusion coefficients.

Summary

A Cd-pressure controlled postimplantation annealing was shown to be a useful method for controlling impurity doping and impurity diffusion. This annealing method is expected to be useful for the studies of ion implantation in a variety of compounds, including II-VI, III-V, and ternaries.

The fact that conductivity-type conversion from n- to p-type was obtained for the whole range of postimplantation annealing Cd pressures after As or P implantation, but only at low annealing temperatures and low Cd pressures after Ar implantation, leads to the interpretation that As and P cause chemical doping in CdTe.

Defect equilibrium behavior is similar in both As- and P-implanted CdTe and can be described in terms of a model proposed by Selim and Kröger (9) on the basis of their investigation of P impurity in CdTe. Under higher postimplantation annealing Cd pressures, the shallow acceptors, (probably As_{Te} or P_{Te}) are compensated by Cd_i , whereas at lower Cd pressures the shallow acceptors are compensated by As_{Cd} or P_{Cd} . The shallow acceptors in As-implanted CdTe have an energy level 0.08 eV above the valence band, and the shallow acceptors in P-implanted CdTe have an energy level 0.037 eV above the valence band.

Two fast diffusion mechanisms were observed in As-implanted samples with different dependence on the annealing Cd pressure: the first is tentatively described in terms of As at Cd or Cd_i sites, and the second in terms of As at Te or Te_i sites. In P-implanted samples, only one fast diffusion mechanism was observed, tentatively, assigned to P at Cd or Cd_i sites.

Ohmic contacts with low resistivity of $0.2 \Omega\text{-cm}^2$ were made on As- and P-implanted CdTe samples.

Acknowledgment

This research was supported by the National Science Foundation through the Center for Materials Research at Stanford University.

Manuscript submitted March 9, 1979; revised manuscript received Aug. 30, 1979.

Any discussion of this paper will appear in a Discussion Section to be published in the December 1980 JOURNAL. All discussions for the December 1980 Discussion Section should be submitted by Aug. 1, 1980.

REFERENCES

- G. A. Kachurin, A. E. Gorodetskii, V. S. Zelevinskaya, and L. S. Smirnov, *Sov. Phys. Semicond.*, **1**, 1187 (1967).
- J. P. Donnelly, A. G. Foyt, E. D. Hinkley, W. T. Lindley, and J. O. Dimmock, *Appl. Phys. Lett.*, **12**, 303 (1968).
- N. V. Agrinskaya, E. N. Arkad'eva, M. I. Guseva, L. V. Maslova, O. A. Matveev, S. M. Ryvkin, V. A. Sladkova, and K. V. Starinin, *Sov. Phys. Semicond.*, **6**, 407 (1972).

4. E. N. Arkad'eva, M. I. Guseva, O. A. Matveev, and V. A. Sladkova, *ibid.*, **9**, 563 (1975).
5. M. Gettings and K. G. Stephens, *Radiat. Eff.*, **22**, 53 (1974).
6. J. C. Bean, Ph.D. Thesis, Stanford University (1976); J. C. Bean, J. F. Gibbons, T. J. Magee, and J. Peng, in "Proc. Fourth International Conference on Implantation in Semiconductors," p. 229, Osaka, Japan (1974).
7. M. Chu, A. L. Fahrenbruch, R. H. Bube, and J. F. Gibbons, *J. Appl. Phys.*, **49**, 322 (1978).
8. D. de Nobel, *Philips Res. Rep.*, **14**, 430 (1959).
9. F. A. Selim and F. A. Kröger, *This Journal*, **124**, 401 (1977).
10. R. C. Whelan and D. Shaw, *Phys. Status Solidi*, **29**, 145 (1968).
11. Yu. V. Rud' and K. V. Sanin, *Sov. Phys. Semicond.*, **5**, 244 (1975).
12. F. A. Selim, V. Swaminathan, and F. A. Kröger, *Phys. Status Solidi A*, **29**, 465 (1975).
13. S. S. Chern, H. R. Vydyanath, and F. A. Kröger, *J. Solid State Chem.*, **14**, 33 (1975).
14. J. Linkhard, M. Sharff, and H. Schiott, *K. Dan. Vidensk. Selsk. Mat. Fys. Medd.*, **33**, 1 (1963).
15. J. F. Gibbons, W. S. Johnson, and S. W. Mylroie, "Projected Range Statistics in Semiconductors and Related Materials," Dowden, Hutchinson, and Ross, Inc., Stroudsburg, Pennsylvania (distributed by Halsted Press, a division of Wiley) (1975).
16. M. Chu, Ph.D. Thesis, Stanford University (1978).
17. M. R. Lorenz and B. Segall, *Phys. Lett.*, **7**, 18 (1963).
18. E. R. Morehead and G. Mandel, *ibid.*, **10**, 5 (1964).
19. E. N. Arkad'eva, O. A. Agrinskaya, and Yu. V. Rud', *Sov. Phys. Solid State*, **8**, 2260 (1967).
20. R. B. Hall and H. H. Woodbury, *J. Appl. Phys.*, **39**, 5361 (1968).
21. J. Gu, T. Kitahara, K. Kawakami, and T. Sagaguchi, *ibid.*, **46**, 1184 (1975).
22. K. Zanio, *J. Appl. Phys.*, **41**, 1935 (1970).
23. Yu. V. Rud' and K. V. Sanin, *Sov. Phys. Semicond.*, **6**, 764 (1972).
24. S. S. Chern and F. A. Kröger, *J. Solid State Chem.*, **14**, 44 (1975).
25. A. Lidow, Ph.D. Thesis, Stanford University (1977).

Additives That Improve Positive Resist Durability for Plasma Etching

Katsuhiko Harada

*Nippon Telegraph and Telephone Public Corporation,
Ibaraki Electrical Communication Laboratory, Tokai, Ibaraki, 319-11, Japan*

ABSTRACT

Additive effects on plasma etching durability for positive resist have been studied. The radical scavenger and plastics antioxidant increase the plasma etching durability of positive resists by reducing thickness loss and pattern deformation after plasma etching (thickness loss decreases about 2 times for 10% additive). The sensitivity, contrast, and development of additive-containing resists, showing slight difference from original resists, are investigated by electron beam exposure.

Dry etching, which has been foreseen as a technique enabling the LSI and other devices manufacture having fine pattern and high accuracy, is performed by the process using active species such as accelerated ion, reactive ion, and radical, which are called sputter etching, reactive ion etching, and plasma etching (1), respectively.

A resist used for the dry etching process requires a dry etching durability in order to achieve the highly accurate process addition to high sensitivity and high resolution which are required mainly by a resist for conventional chemical etching process. The dry etching durability for a resist is defined practically as a minimum of thickness loss and pattern deformation, which are induced by resist decomposition and denaturation as a result of the etching process. However, the resist decomposition and denaturation, under a dry etching atmosphere, have rarely been studied in detail.

The difference between positive and negative resist is apparently an approach to designing high dry etching durability having high sensitivity. Chloromethylated polystyrene (CMS) (2), as a negative resist, makes it possible to have these functions in a homopolymer, owing to designing a polymer which has a benzene-ring as a dry etching durable group and chloromethyl groups as a cross-linking highly sensitive functional group. However, it is not possible to possess these two functions in positive resist, because the main chain decomposition must accelerate for high sensitivity, but it must be inhibited for dry etching

durability. Therefore, positive resist has been a conflicting property between dry etching durability and high sensitivity, e.g., polystyrene sulfone has excellent durability for ion milling, but it has a low sensitivity of 1×10^{-5} C/cm², compared with polyolefin sulfone, which has a high sensitivity of $1 \sim 3 \times 10^{-6}$ C/cm² and low dry etching durability (3, 4). AZ-1350, as a positive photoresist, has high dry etching durability but a low sensitivity of 1.5×10^{-4} C/cm² (4).

Additives, which are expected to have selective reaction with active species and to inhibit positive resist decomposition and denaturation under dry etching atmosphere, have been studied using the plasma etching process in order to avoid this conflicting property on the positive resist.

Experimental

Sample preparation.—Positive resists used in current work are polymethylmethacrylate (PMMA, Elvacite 2041, du Pont), polyhexafluorobutylmethacrylate (FBM, Daikin Kogyo) (5), and polydimethyltetrafluoropropylmethacrylate (FPM) (6). The additives used were commercially available 1,1-diphenyl-2-picrylhydrazyl (DPPH), galvinoxyl (GAL), 2,2-methylene bis(4-methyl-6-tert-butylphenol) (MBP), 2,4,6-tritert-butylphenol (TBP), and 2-mercaptobenzothiazole (MBT).

The about 1 μ m thick resist film samples were prepared on a surface-oxidized silicon wafer using the standard spin-coating technique from the solution which dissolved resist or resist and additive. They were baked in air for 30 min before plasma etching

or electron beam exposure. The baking temperature, considering the glass transition temperature of the resist and the melting point of the additive, was 140°C for original FBM, additive-containing FBM and DPPH, MBP and TBP-containing resist, and 170°C for other resists and additive-containing resists.

Plasma etching.—Plasma etching durability of resists and additive-containing resists were evaluated by thickness loss and pattern deformation after the etching process. Thickness loss is represented with normalized plasma etching selectivity ratio S , defined by

$$S = d_s/d_R$$

where d_s is the etching depth for the SiO_2 substrate and d_R is the thickness loss of the resist after plasma etching. The determination of S is illustrated in Fig. 1. Step heights (a, b, and c) were measured by Talystep (Taylor-Hobson).

The pattern deformation was observed by a scanning electron microscope (SEM).

Plasma etching process was performed by commercially available apparatus (IPC-2005, International Plasma Corporation). Etching gas was tetrafluoromethane, involving 4.2% oxygen. Gas flow rate was 100 cm^3/min and gas pressure was 0.8 ~ 1.1 Torr. Impressed rf power was 200W. All etching processes in the current work were carried out over a 28 min period using an etching tunnel, in which the substrate (SiO_2) was finally etched about 5000Å in depth. The etching atmosphere temperature, measured by a mercury thermometer inserted into the etching chamber, was elevated from room temperature (18° ~ 20°C) to below 100°C.

Electron beam exposure and development.—Thickness-dose curves and pattern delineation for resists and additive-containing resists were obtained by electron beam exposure (accelerating voltage, 20 kV).

The developer used was a solvent mixture consisting of methylisobutylketone (MiBK) and isopropylalcohol (IPA). The mixing ratio was MiBK/IPA = 1/1 for original and additive-containing PMMA, MiBK/IPA = 19/81 for original and additive-containing FPM, and MiBK/IPA = 1/150 for original and additive-containing FBM. The development temperature was controlled at 22.5°C and the development time was 2 min for all resists and additive-containing resists.

Radiation G-value determination and plasma decomposition analysis.—Radiation G-value for resists and

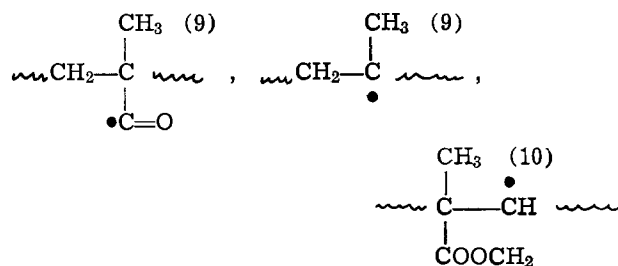
additive-containing resists were determined from the inverse number-average molecular weight $1/M_n$ vs. γ -radiation dosage (7). The film samples were irradiated with γ -rays (Co^{60}) in air at room temperature for 40 days at dosages ranging from 1.5 to 7.1 megarad. The film samples were prepared at first to remove the solvent which dissolved resist or resist and additive, then baked in air for 30 min at 170°C for original and additive-containing PMMA, and at 170°C for original and additive-containing FBM before γ -irradiation.

M_n for radiation G-value and the resist molecular weight variation by plasma etching were measured by gel permeation chromatography (GPC) (HLC-802UR, Toyo Soda Kogyo). The samples for the latter was prepared by dissolving the film on the wafer after plasma etching, which was performed under standard conditions described above.

Results and Discussion

Additive effects on plasma etching durability.—Table I shows plasma etching selectivity ratio S for each resist containing the same amount of additives under the same etching condition. It was recognized that S -value increased by two kinds of additives. One of them was a radical scavenger or free radical, such as DPPH and GAL. The other was a plastics antioxidant such as MBP, TBP, and MBT. S -value also increased according to increasing the additive concentration, as shown in Fig. 2. This behavior was similarly observed in other additives in Table I and additive-containing FPM's and FBM's.

Both radical scavenger and plastics antioxidant have abilities to deactivate an active radical and to decompose a peroxide. Many transient intermediates, such as polymer radical and polymer peroxide, which generate during the polymer decomposition process, are well known in pertinent literature (8). The polymer radicals, indicated as follows, have been proposed for PMMA photolysis (9) and radiolysis (10) as the transient intermediates before main chain scission occurs



Hence, it is considered that the decomposition of the positive resist under plasma etching atmosphere is inhibited by the reaction of the active resist intermediate with the radical scavenger or plastics antioxidant.

Figure 3 shows molecular weight variations resulting from plasma etching. Original PMMA ($M_n = 2.5 \times 10^5$) was highly decomposed and became $M_n = 1.2 \times 10^5$, compared with additive-containing PMMA ($M_n = 2.0 \sim 1.5 \times 10^5$). These results indicate the

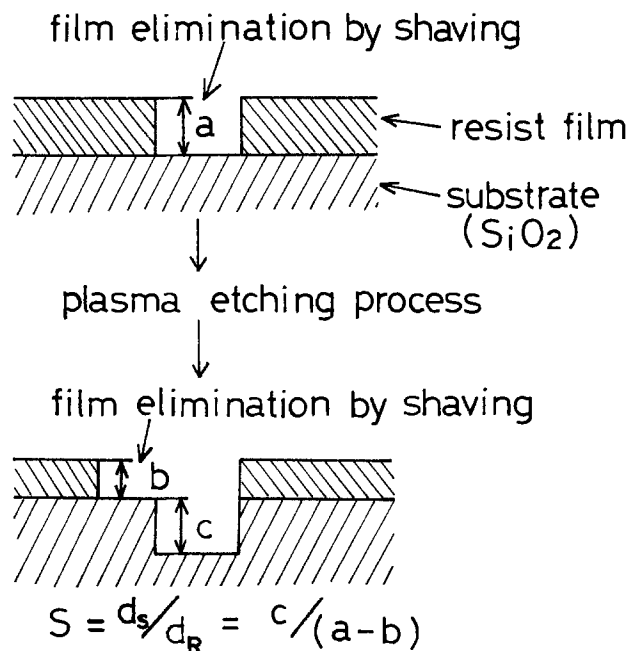


Fig. 1. Determination of plasma etching selectivity ratio S

Table I. Plasma etching selectivity ratio S . Substrate (SiO_2) etching depth, about 5000Å; additive concentration, 9.1 weight percent.

Resist	PMMA	FPM	FBM
None	1.4	2.2	1.1
DPPH	2.5	3.6	2.2
GAL	2.2	3.3	2.5
MBP	2.9	4.0	2.2
TBP	2.6	4.0	1.9
MBT	2.0	—	—

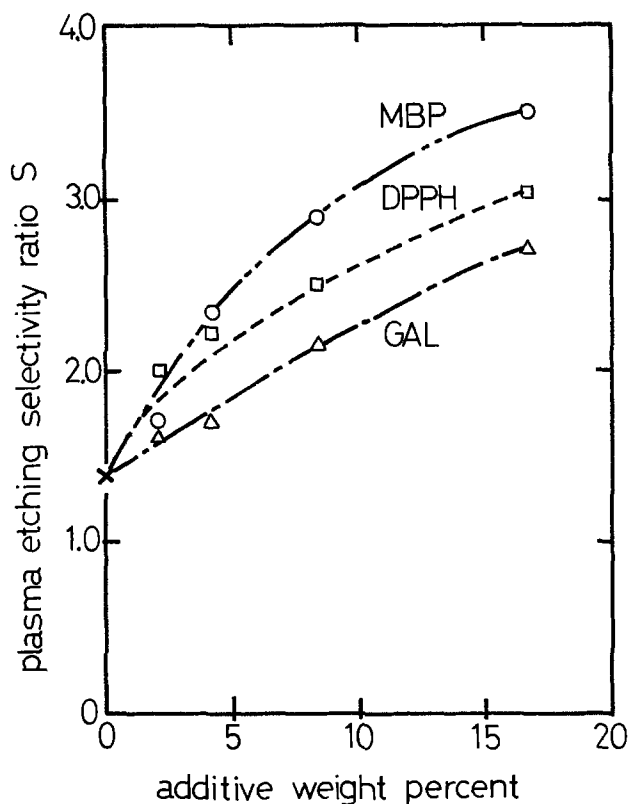


Fig. 2. Additive effects and additive concentrations on plasma etching selectivity ratio S for PMMA. Plasma etching conditions: gas, $\text{CF}_4 + 4.2\% \text{O}_2$; gas flow rate, $100 \text{ cm}^3/\text{min}$; rf power, 200W ; etching time, 28 min.

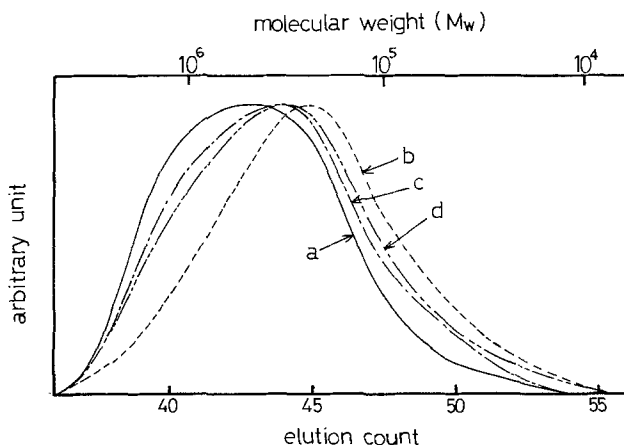


Fig. 3. Variations in PMMA molecular weight distribution by plasma etching. Plasma etching conditions: gas, $\text{CF}_4 + 4.2\% \text{O}_2$; gas flow rate, $100 \text{ cm}^3/\text{min}$; rf power, 200W ; etching time, 28 min. Curve a, original PMMA; curve b, plasma etching PMMA; curve c, plasma etching 9.1% DPPH-containing PMMA; curve d, plasma etching 9.1% MBP-containing PMMA.

effect inhibiting the polymer decomposition by the additive. Two inhibition mechanisms are considered, one of them is a reaction of the additive with the polymer radical described above, the other is a reaction of the additive with active species, such as CF_3 , CF_2 , F, etc. being induced by CF_4 plasma and invading into resist layers.

On the other hand, the additive also inhibited thermal decomposition of the resist. Figure 4 shows a TGA thermogram for original and additive-containing PMMA. The decomposition temperature was heightened about $50^\circ \sim 60^\circ\text{C}$ by the addition. Therefore, this is considered as one of the effects to increase plasma etching durability. It has been proposed that

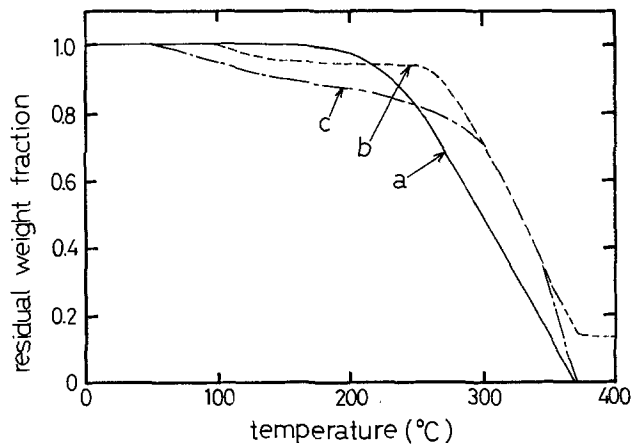


Fig. 4. PMMA TGA thermograms. Atmosphere, N_2 ; heating rate, $5^\circ\text{C}/\text{min}$. Curve a, original PMMA; curve b, 9.1% DPPH-containing PMMA; curve c, 9.1% MBP-containing PMMA.

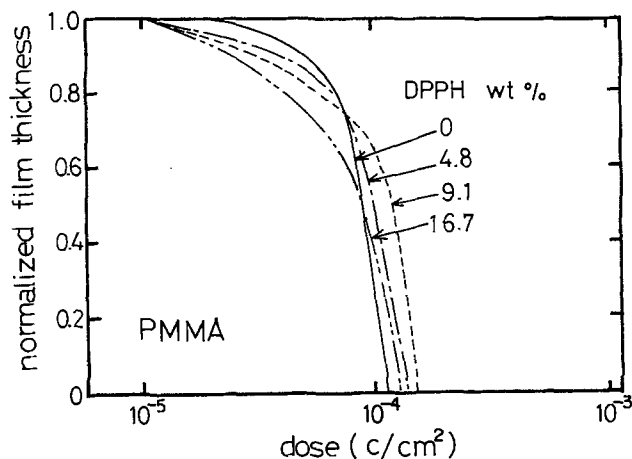


Fig. 5. PMMA sensitivity curves for DPPH concentrations. Development conditions: $\text{MiBK}/\text{IPA} = 1/1$, 22.5°C , 2 min.

the plasma gas temperature is estimated at several hundred degrees centigrade (11), and resist decomposition is possible in such temperature.

Thickness-dose curve and development of an additive-containing resist.—It is presumed that radical scavenger or plastics antioxidant addition to positive resist causes a change in reactivity for high energy rays and physical properties which influence the resist properties. Therefore, several properties of additive-containing resists have been studied.

Table II. Radiation G-value for DPPH concentrations

Resist	DPPH Conc. (wt %)	G-value
PMMA	0	1.09
	4.8	0.38
	9.1	0.27
FBM	0	1.00
	4.8	0.35
	9.1	0.35

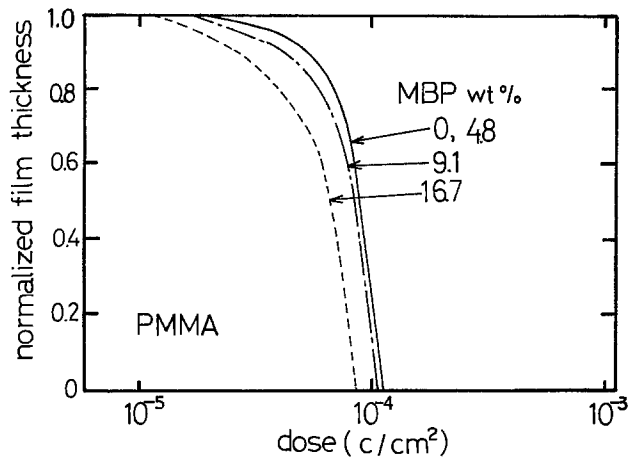


Fig. 6. PMMA sensitivity curves for MBP concentrations. Development conditions: MiBK/IPA = 1/1, 22.5°C, 2 min.

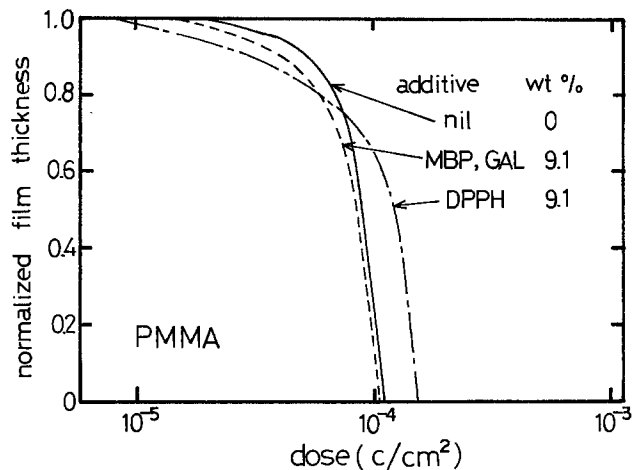


Fig. 8. Sensitivity curves for additive-containing PMMA. Development conditions: MiBK/IPA = 1/1, 22.5°C, 2 min.

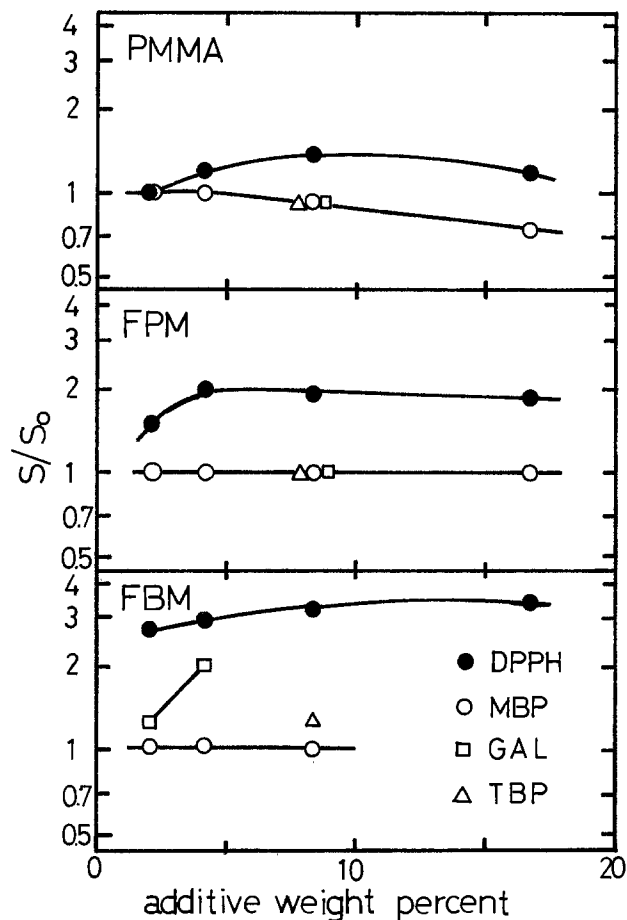


Fig. 7. Resist sensitivity ratios for additive concentrations. Development conditions: 22.5°C, 2 min, developer mixing ratio (MiBK/IPA), PMMA = 1/1, FPM = 19/81, FBM = 1/150. S_0 : original resist sensitivity, S : additive-containing resist sensitivity.

Fundamental important parameters, which influence the properties of positive resists, are radiation G -value and solubility behavior to the developer.

Table II shows radiation G -value for PMMA and FBM with respect to several DPPH concentrations. G -value decreased markedly by DPPH addition and concentration effect was observed on DPPH-containing PMMA.

The representative resist properties are sensitivity and contrast, which are evaluated from the thickness-dose curve. Two behaviors on sensitivity were observed from the thickness-dose curve, with respect to additive addition. One of them was the sensitivity de-

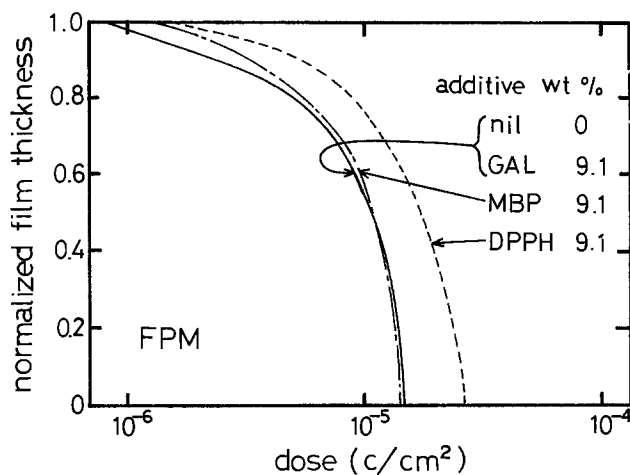


Fig. 9. Sensitivity curves for additive-containing FPM. Development conditions: MiBK/IPA = 19/81, 22.5°C, 2 min.

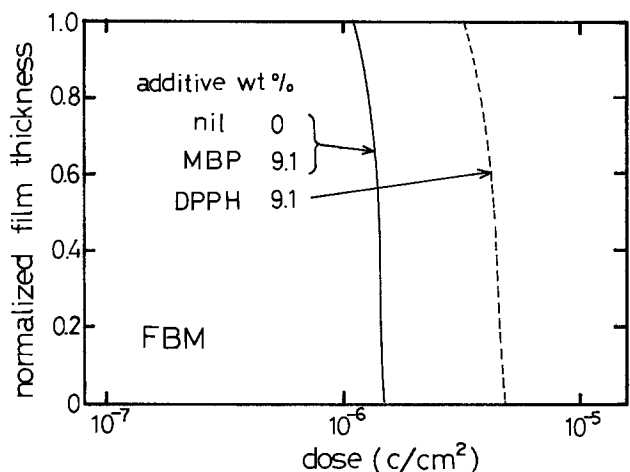


Fig. 10. Sensitivity curves for additive-containing FBM. Development conditions: MiBK/IPA = 1/150, 22.5°C, 2 min.

crease, as shown in Fig. 5. The other was the behavior in which the sensitivity did not change or increased, as shown in Fig. 6. Those behaviors depend on the kind of additive. DPPH and GAL belong to the former and MBP and TBP belong to the latter.

Figure 7 shows the sensitivity ratio with respect to additive concentrations. A similar tendency was observed on sensitivity ratio for DPPH and MBP addi-

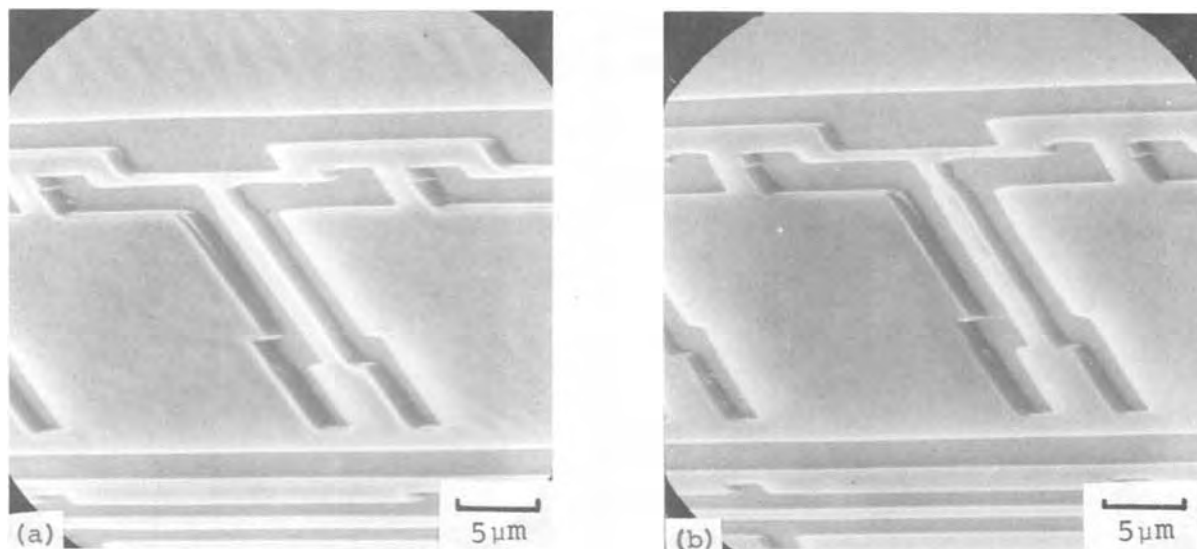


Fig. 11. PMMA patterns after development. Development conditions: MiBK/IPA = 1/1, 22.5°C, 2 min, (a) original PMMA, dosage = 1.2×10^{-4} C/cm²; (b) 16.7% DPPH-containing PMMA, dosage = 1.4×10^{-4} C/cm².

tion. Sensitivity-decreasing magnitudes for DPPH addition are different from resists, in order of PMMA, FPM, and FBM. These results suggest that the most dominant factor for positive resist sensitivity is not radiation G-value. It is considered that one reason for sensitivity decreasing depends on the DPPH solubility to the developer, because DPPH is soluble in MiBK but scarcely in IPA. The MiBK volume percents in the developer are 50, 19, and 0.7 for PMMA, FPM, and FBM, respectively. MBP-containing resist sensitivity did not change, or increase. The reason is also considered to be the MBP solubility to the developer, because MBP is liable to dissolve in both MiBK and IPA.

Figures 8, 9, and 10 show thickness-dose curves for original resists and the same amount of additive-containing resists in order to compare the contrast. The contrasts of additive-containing resists were scarcely changed, compared with that of original resist. However, the contrast of DPPH-containing PMMA decreased somewhat. Figure 11 shows resist patterns for 16.7% DPPH-containing PMMA, compared with original PMMA, after electron beam exposure and development. No difference in pattern accuracy and

surface condition could be detected. This was same as for other additive-containing PMMA's and additive-containing FPM's. On the whole, it is recognized that the contrast of additive-containing positive resists is hardly different from that of original resist in the region of additive concentration, studied in the current work. These facts indicate that an additive in the unexposed resist scarcely effuses to the developer. The reason is considered as being that the additives have a very bulky structure, compared with the side chain of the resist. Therefore, an additive cannot shift among the main chain to effuse.

FBM pattern is obtained under very strict development conditions (5) because FBM solubility changes markedly by little deviation in development conditions. No FBM pattern deformation, containing more than 4.8% additive, was observed. However, FBM's, containing over 9.1% additive, were required to reduce the development time in order to obtain the nondeformed pattern, as shown in Fig. 12.

Resist pattern deformation after plasma etching.—Figure 13 shows sectional views of resist and substrate after plasma etching, with respect to additives and its concentrations. The pattern deformation, uneven

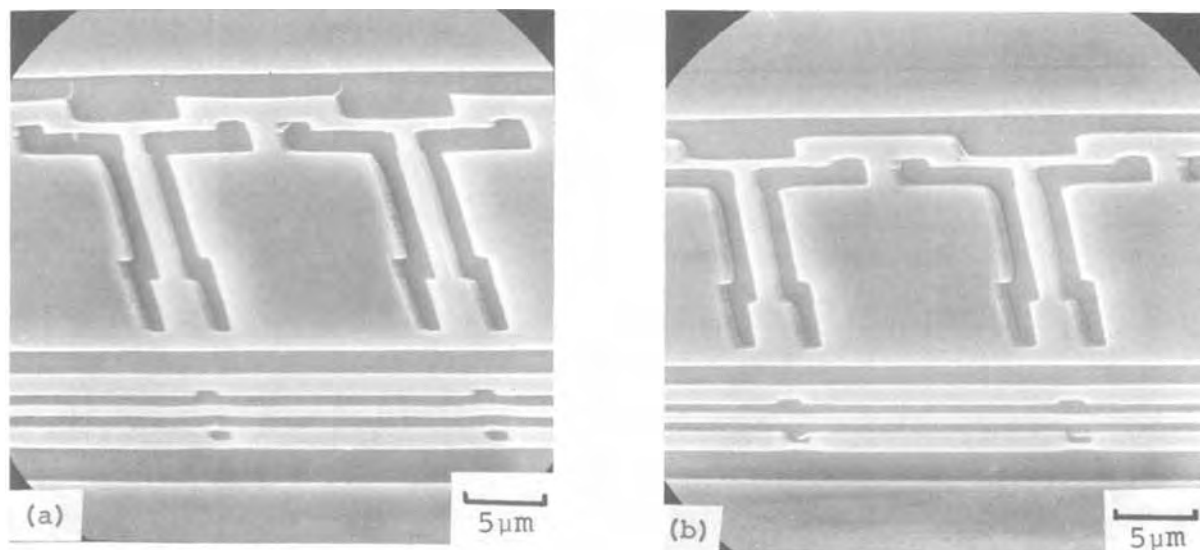


Fig. 12. FBM patterns after development. Development conditions: MiBK/IPA = 1/150, 22.5°C, (a) original FBM, dosage = 2.3×10^{-6} C/cm², development time, 2 min; (b) 9.1% MBP-containing FBM, dosage = 2.5×10^{-6} C/cm², development time, 30 sec.

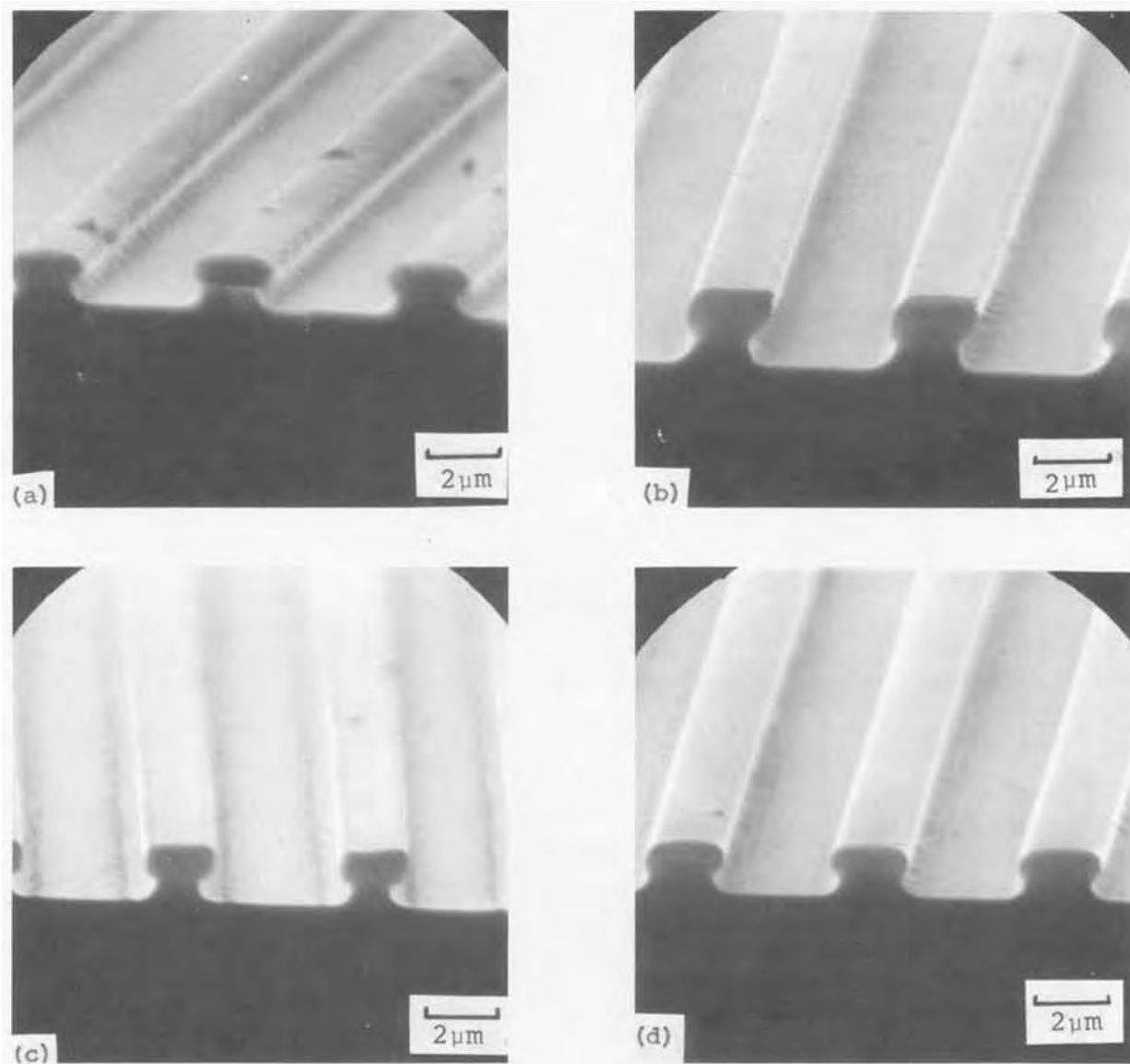


Fig. 13. Sectional views of PMMA pattern and substrate after plasma etching. Plasma etching conditions: gas, $\text{CF}_4 + 4.2\% \text{O}_2$; gas flow rate, $100 \text{ cm}^3/\text{min}$; rf-power, 200W ; etching time, 28 min, substrate (SiO_2) etching depth, about 5000\AA , initial resist thickness, 8000\AA , (a) original PMMA, (b) 9.1% MBP-containing PMMA, (c) 16.7% MBP-containing PMMA, (d) 9.1% DPPH-containing PMMA.

surface, and thickness loss for the resist are observed for original PMMA. But, MBP-containing PMMA indicates the sharp resist pattern and less thickness loss. DPPH-containing PMMA also shows less thickness loss but resist pattern edge rounded slightly. It is revealed that both MBP and DPPH-containing PMMA showed almost the same plasma decomposition behavior (Fig. 3), the same TGA thermograph (Fig. 4), and similar curves for differential scanning calorimeter (DSC). The reason for the difference between plasma etched MBP and DPPH-containing PMMA pattern, in spite of those results, has not been determined experimentally.

FBM has relatively low plasma etching durability. Remarkable pattern deformation and thickness loss were observed on original FBM and even on additive-containing FBM, as shown in Fig. 14(a) and (b). However, when plasma etching was performed at low atmosphere temperature, the pattern deformation decreased and additive effect appeared, as shown in Fig. 14(c) and (d).

Conclusions

It is found that the plasma etching durability of positive resists is increased by addition of additives such as radical scavenger and plastics antioxidant. This effect contributes to the decrease in thickness loss and pattern deformation after plasma etching.

These additives also decrease the radiation G -value of the resist. However, it should be realized that the sensitivity of additive-containing resists is remarkably affected by the solubility of the additive into the developer, rather than the radiation G -value. Consequently, MBP and TBP which do not cause a decrease in sensitivity are obtained. The contrast for additive-containing resists scarcely changes and no pattern deformation occurred after development.

Additives, especially MBP-containing positive resists, show excellent plasma etching durability. These additive effects for plasma etching are to be expected for other dry etching, such as sputter etching and reactive ion etching.

Acknowledgments

The author gratefully acknowledges helpful discussions with Mr. O. Kogure, Dr. S. Sugawara, and Mr. K. Matsuyama.

Manuscript submitted April 11, 1979; revised manuscript received Aug. 15, 1979.

Any discussion of this paper will appear in a Discussion Section to be published in the December 1980 JOURNAL. All discussions for the December 1980 Discussion Section should be submitted by Aug. 1, 1980.

Publication costs of this article were assisted by Nippon Telegraph and Telephone Public Corporation.

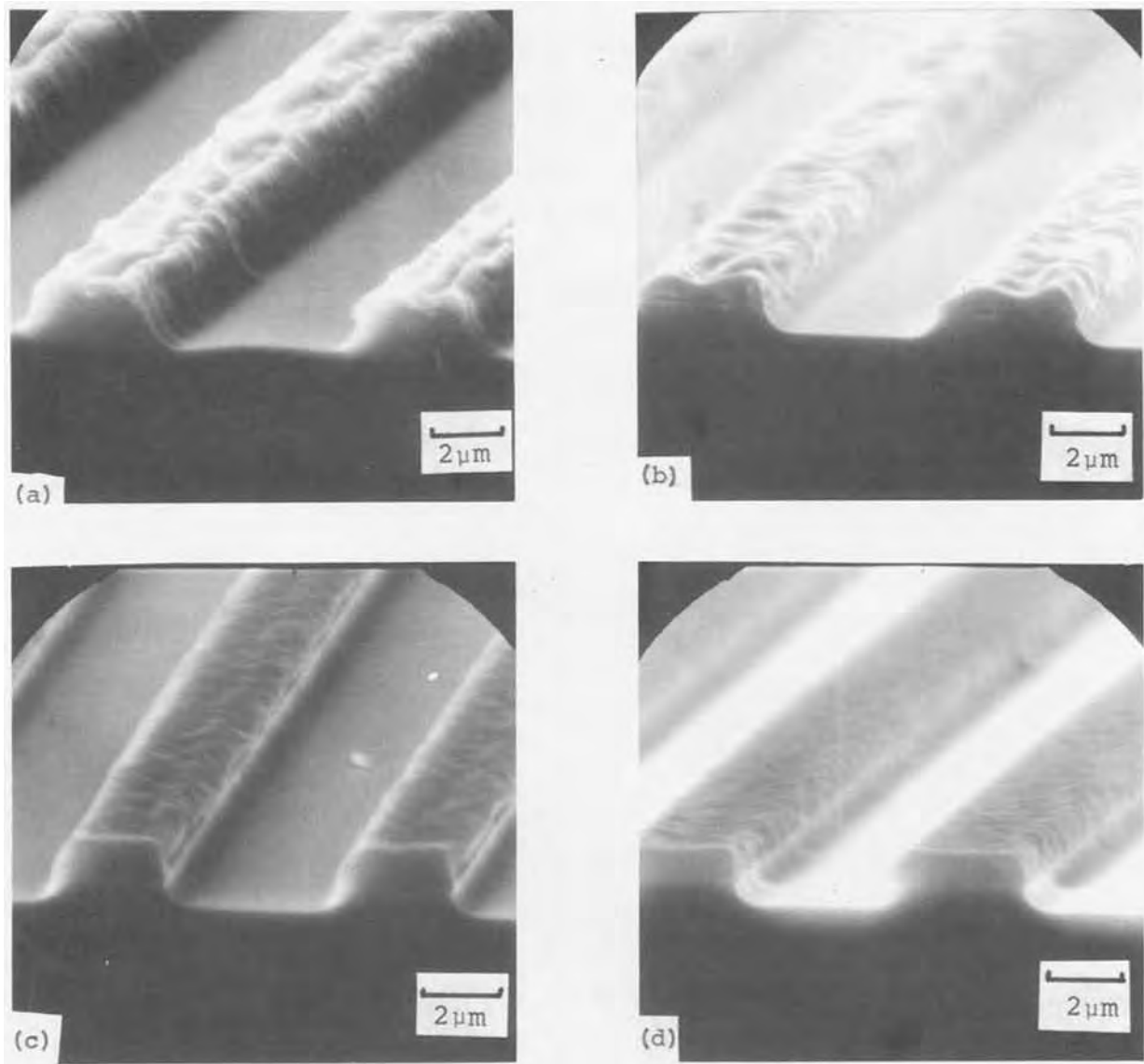


Fig. 14. Sectional views of FBM pattern and substrate after plasma etching. Plasma etching conditions: gas, $\text{CF}_4 + 4.2\% \text{O}_2$; gas flow rate, $100 \text{ cm}^3/\text{min}$; rf-power, 200W, substrate (SiO_2) etching depth, about 5000\AA ; initial resist thickness, $10,000\text{\AA}$; (a) original FBM, etching atm. temp, below 100°C ; (b) 9.1% MBP-containing FBM, etching atm. temp, below 100°C ; (c) original FBM, etching atm. temp, below 50°C ; (d) 4.8% GAL-containing FBM, etching atm. temp, below 50°C .

REFERENCES

1. R. G. Poulsen, *J. Vac. Sci. Technol.*, **14**, 266 (1977).
2. S. Imamura, *This Journal*, **126**, 1628 (1979).
3. M. J. Bowden and L. F. Thompson, *ibid.*, **121**, 1620 (1974).
4. L. F. Thompson, *Solid State Technol.*, **27**, (July 1974).
5. M. Kakuchi, S. Sugawara, K. Murase, and K. Matsuyama, *This Journal*, **124**, 1648 (1977).
6. K. Murase, M. Kakuchi, and S. Sugawara, in "Proc. of the International Conf. on Microlithography," 261-9, Paris (1977).
7. E. Gipstein, A. C. Ouano, D. E. Johnson, and O. U. Need, III, *IBM J. Res. Dev.*, **143** (1977).
8. H. H. G. Jellinek and T. J. Y. Wang, *J. Polym. Sci.*, **11**, 3227 (1973).
9. J. P. Allison, *J. Polym. Sci., Part A-1*, **4**, 1209 (1966).
10. A. Todd, *J. Polym. Sci.*, **22**, 495 (1960).
11. M. Oshima, *Jpn. J. Appl. Phys.*, **17**, 1157 (1978).

Chronopotentiometric Investigation of the Anodic Reaction in Cryolite Melts

Influence of Dissolved Metal Traces

Frédéric Lantelme, Damianos Damianacos, and Marius Chemla*

Laboratoire d'Electrochimie, E.R.A. 310, Université Pierre et Marie Curie, 75230 Paris Cedex 05, France

ABSTRACT

The mechanism of the anodic reaction in cryolite melt is studied in presence and in absence of a layer of aluminum metal in the cell. These two experimental conditions give rise to large differences which are interpreted on the basis of changes in the interfacial properties at the electrode. The chronopotentiometric technique is used to obtain a better insight into these surface variations and on the gas evolution on the graphite anode. The dissolved metal reacts with the graphite to form at its surface aluminum or sodium carbides and gives a better contact between the electrolyte and the electrode. The analysis presented here is illustrated by the generation of three types of anode effects: By depletion of dissolved metal near the electrode which very much changes the wetting properties; by decrease of the pressure in the cell which, in absence of liquid metal, increases the dimension of retained gas bubbles; and by rapid repetition of the galvanostatic pulses which indicates that the gas evolution is a slow process. These observations have the same origin, *i.e.*, the gas covering of the electrode which markedly depends on the presence of dissolved metal.

The industrial preparation of aluminum by electrolysis of alumina dissolved in fused cryolite involves complex electrochemical reactions, especially on the anodic side. In order to improve the working conditions of the electrolytic cells, much research is devoted to the study of these reactions (1); the nature of the ionic associations present in the bath has been studied (2), the diffusion coefficients (3), and the transport numbers of the constituent elements are known (4). From these data different hypotheses have been built up to obtain a better insight into the mechanism of the electrolysis.

However, it has been recently (5, 6) shown that an important part of the observed overvoltage arises from the gas formation on the graphite anode. The kinetic parameters of the electrochemical reaction depend on the pressure in the cell, and the properties of the electrolyte-graphite interface (wetting angle θ and interfacial tension γ) have a considerable influence on the electrode process.

We plan to give here the results of the chronopotentiometric study of these phenomena. Special attention will be paid to the presence of dissolved aluminum in the bath (7) for it has been observed that, when molten cryolite is in contact with liquid aluminum metal, a very large change of the surface tension occurs (8). As a consequence, the results of chronopotentiometry are quite different to those obtained in pure ionic melts.

In industrial cells the electrolyte is in contact with a layer of liquid aluminum; a part of the faradaic loss can be attributed to the oxidation of the dissolved metal (9). Our research indicates also that this presence induces a large change in the interfacial tension at the electrode and influences the gas coverage of the electrode surface.

Experimental

The experiments with liquid aluminum in the bath are carried out in the cell represented in Fig. 1. The graphite crucible is coated with a boron nitride shield; indeed the carbon is unstable in the presence of cryolite saturated with aluminum. The electrical contact between the liquid metal which acts as cathode and the crucible is realized through a disk of titanium

boride. The densities of liquid aluminum and molten cryolite are quite close; to avoid any disturbance we

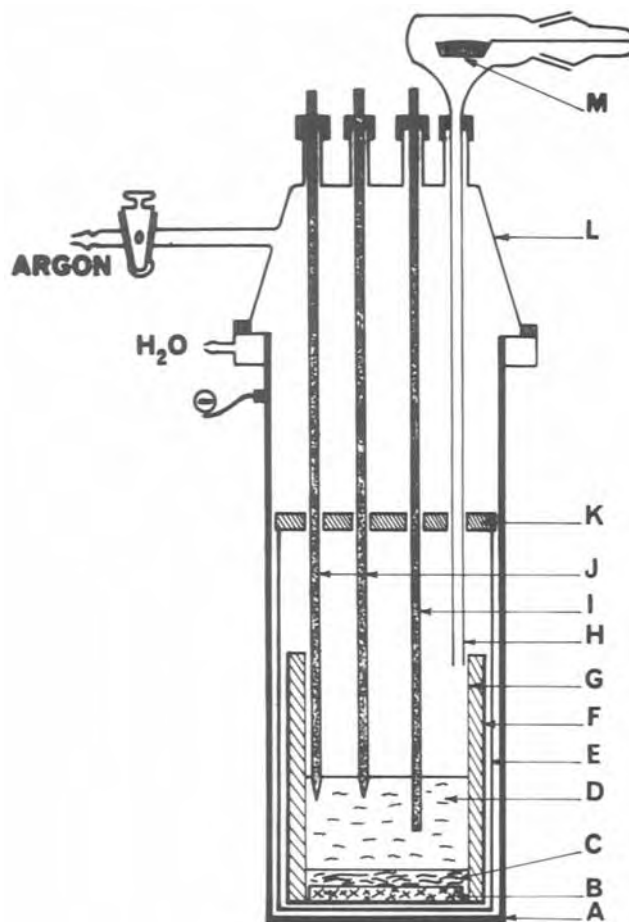


Fig. 1. Electrolytic cell. A, stainless steel vessel; B, titanium boride disk; C, liquid aluminum; D, cryolite bath; E, stainless steel tube; F, graphite crucible; G, boron nitride shield; H, introduction tube; I, reference electrode; J, working electrodes; K, boron nitride disk; L, Pyrex cover; M, alumina.

* Electrochemical Society Active Member.

Key words: adsorption, diffusion, gas, carbon, aluminum.

have used a liquid alloy 40% Al-60% Cu, the activity of which is known (10).

Some experiments were carried out in the absence of liquid aluminum. In this case the bath was directly introduced into a vitreous carbon crucible (11).

Graphite rods (6 mm diam) with a conical extremity (angle: 30°) constitute the working electrodes; the area in contact with the electrolyte (about 1 cm²) is determined from the immersed length. In some experiments the area is determined by shielding the electrode in boron nitride. In general no significant difference appears; however our procedure is more reliable, as it has been observed that when the shield got old penetration of cryolite occurs which leads to random results (12). Different types of graphite supplied by the company "Le Carbone Lorraine" have been used. A reference electrode is formed by electrodeposition of a thin layer of aluminum on a rod of titanium boride (3 mm diam).

The crucible is covered by a disk of boron nitride which also guides the electrode. This assembly is placed in a stainless steel (QA2) container on the top of which is placed a Pyrex cover with torion joints for the electrical conductors. The assembly is vacuum tight, and so a very pure argon atmosphere may be used at different pressures varying from 0.1 to 1 atm.

The melt is prepared from natural cryolite. Definite amounts of alumina are introduced through the tube to study the influence of the alumina content. The nature of the alumina is an important factor in the chronopotentiometric response. Normally α alumina (Patinal Merck) is used; however different tests were also performed with γ alumina.

Procedure for the Galvanostatic Method

Conventional circuitry was used for the chronopotentiometric measurements with pulses delivered by a power galvanostat ($I_{\max} = 60\text{A}$; rise time 10 μsec) built in the laboratory by J. Chevalet. The potential response is recorded on a digital waveform recorder (Biomation, Model 805) and the curve $V(t)$ is drawn on an X-Y plotter. This curve is characterized by a sudden change of potential after a time τ ; this effect corresponds to the complete depletion of the electroactive species at the surface of the electrode. When the transport process is diffusion-controlled, the following expression has been established by Sand (13): $i\tau^{1/2}c^{-1} = 0.5 nF(\pi D)^{1/2}$ where i is the current density, c the concentration, and D the diffusion coefficient of the electroactive species.

As pointed out by Dewing (14) the heterogeneous nature of the graphite creates some difficulties in obtaining reproducible responses. In general the first pulses on a fresh electrode are abnormally long; however with repeated pulses a stationary state is reached. Moreover it is important to avoid the fluoride discharge which strongly perturbs the surface properties of the anode; a special electronic device is used to switch off the current when the potential reaches a predetermined value. The repetition interval between the pulses has to be first determined in order that a change of this time does not affect the value of τ . The influence of this interval depends on the intensity of the current. For short pulses less than 0.1 msec (high current density) a very rapid repetition (5 sec) does not alter τ . In our working conditions we have used repetition intervals ranging from 1 to 3 min in order to obtain reproducible chronopotentiograms.

The results are examined in the frame of Sand's law. The influence of the current density on the product $i\tau^{1/2}$ is first examined and next we try to determine the effect of alumina concentration on this product.

Influence of the Current Density

In general the product $i\tau^{1/2}$ decreases as i increases, but for high values of i a plateau is obtained (Fig. 2). In fact, we have undertaken two sets of determinations according to the experimental conditions.

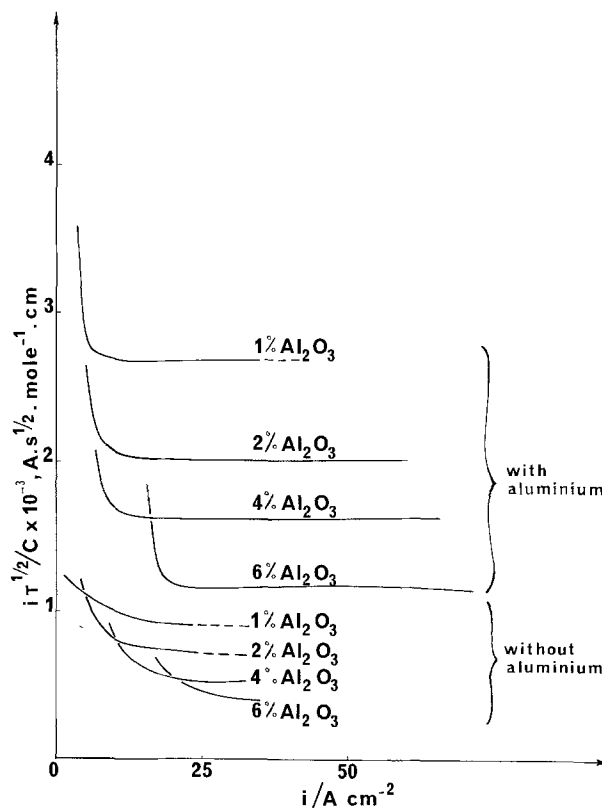


Fig. 2. Plot of $i\tau^{1/2}/c$ vs. i ; graphite electrode (GR 208) at 1036°C.

1. In the absence of aluminum metal in the bath (lower curves on Fig. 2) a continuous change of the quantity $i\tau^{1/2}$ is observed as i is varied; this change becomes important as soon as the transition time is longer than 2 or 3 msec. This effect is attributed to the influence of a convection process (15). The thickness of the diffusion layer corresponds in this case to the mean path $\sqrt{2D\tau}$ of the electroactive species which is about 3 μm . This result is very different from the behavior normally observed in fused salts where the predictions drawn from a diffusion-controlled mechanism are verified up to transition times as long as 5 sec (16). The important contribution of the convection process near the electrode is probably the consequence of the gas evolution. However, as pointed out by Ibl (17), this perturbation depends on the interfacial tension electrolyte-electrode; here, in absence of aluminum, the cryolite does not wet the graphite; the gas bubbles are retained on the electrode surface which is partly covered and their departure induces large turbulences near the surface. The gas evolution seems to be a slow process; indeed for a rapid repetition of the pulse an anode effect is obtained (Fig. 3) which is induced by the total covering of the electrode by the gas phase. A model has been recently proposed to take account of the considerable influence of the retained gases in the aluminum electrolysis (12).

2. In the presence of aluminum metal a strong increase of the duration of the transition time is observed; this duration being amplified by a factor of about 8 as shown in Fig. 2. Using the same working conditions, Grjotheim *et al.* (18) observed the formation of aluminum carbide at the graphite-cryolite interface. During the anodic current, this compound contributes to the oxidation current; on the other hand, in the case of a porous electrode (graphite) the removal of the material could look like a diffusion process (19). However, in our procedure where galvanostatic pulses are repeated at short time intervals, these mechanisms seem to be of little importance, as confirmed by the following two remarks: the oxidation potential is not affected by dissolved metal, and the same be-

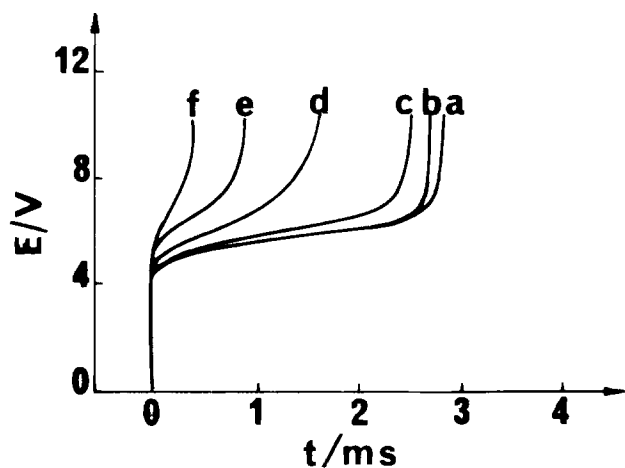


Fig. 3. Chronopotentiograms on a graphite electrode (GR 208). Stationary state; repetition interval: a, 3 mm; b, 1 mm; c, 30 sec; d, 10 sec; e, 5 sec; f, 2 sec. Cryolite bath without dissolved aluminum at 1036°C. $i = 9.0 \text{ A}\cdot\text{cm}^{-2}$.

havior is also observed on a nonporous vitreous carbon electrode.

Moreover, when alumina is introduced in the melt, a corresponding increase of the transition time is observed, which proves the reliability of our method since we do not observe the decrease of carbide pointed out by Grjotheim *et al.* (18). Finally our results lead to the evidence that the main effect of dissolved metal is to change strongly the interfacial properties of the electrode. The presence of aluminum metal in the bath enhances the wetting properties of the electrolyte (8); then the adherence of the gas bubble is less important. As a consequence the active surface of the electrode becomes greater (upper curves on Fig. 2) and the thickness of the diffusion layer increases. The two regions of the curves $i = f(t)$ are more apparent; the plateau corresponding to a constant product $i\tau^{1/2}$ is now well defined. The intervention of the convective regime appears for longer τ (about 40 msec). Moreover, total coverage of the electrode by the gaseous compounds is not obtained, even for very rapidly repeated pulses.

Influence of the Alumina Content

Nature of the alumina.—It must be emphasized that preliminary experiments show a marked effect of the structure of added alumina. As an example when γ alumina (containing about 1.5% of moisture) is introduced in the bath it takes a long time (up to 90 min) to reach a stable value of τ . This is attributed to the chemical desorption of the gases on the electrode. A visual observation shows indeed the presence of numerous small gas bubbles on the graphite. Probably these gases are mainly carbon monoxide and hydrogen, and it is known (20) that they are strongly adsorbed on the graphite. Finally we studied the influence of Al_2O_3 content obtained by successive additions of α alumina (Patinal Merck) which is anhydrous.

Determination of the alumina concentration.—Different attempts have already been made to determine electrochemically the alumina concentration c in the electrolytic cell (21). If the anodic reaction of the oxygenated species was diffusion-controlled the transition time should be proportional to the square of the concentration. In general this relation is not obeyed, except for low values of c , and often a saturation occurs for high c values.

A similar observation has been described by Dewing (22) when noble metals are used as anode; the value of the product $i\tau^{1/2}$ is diffusion-controlled up to 1.6% of Al_2O_3 on platinum electrode and up to 0.7% of Al_2O_3 on gold electrode. This limitation is attributed to the formation of an oxide film on the electrode. With graphite electrode an analogous phenomenon occurs, but now the covering arises from the gases retained at

the electrode surface. This is particularly clear when the influence of the pressure in the cell is studied (12).

1. In the absence of aluminum in the bath a sensible decrease of the transition time is observed when the pressure is lowered (Fig. 4). In some cases (for low current densities) a complete passivation of this electrode is obtained at low pressure; this corresponds to the generation of an anode effect by variation of pressure.

2. In the presence of aluminum this behavior is not observed; a balance occurs between the growing of the gas bubbles at the electrode surface and the improvement of the evolution process which is now possible since the adhesion energy $W_A = \gamma_{LV}(1 + \cos \theta_G)$ is weaker, the angle θ_G being greater than 90° (Fig. 5). This observation may be compared to the process indicated by Jansen at a gas-evolving electrode (23).

Even in this favorable case no linear dependence of $i\tau^{1/2}$ on c is obtained. This may be first attributed to the variation of D vs. c ; as indicated by Desclaux and Rolin (24) a decrease of 25% is observed when c varies from 0 to 6%. This effect is almost sufficient to explain the variation of $i\tau^{1/2}$ when a medium porosity graphite (No. 208 Carbone Lorraine) is used as anode in a cryolite bath in the presence of aluminum. However a partial covering of the electrode surface remains as indicated on the curve of Fig. 6, the higher the

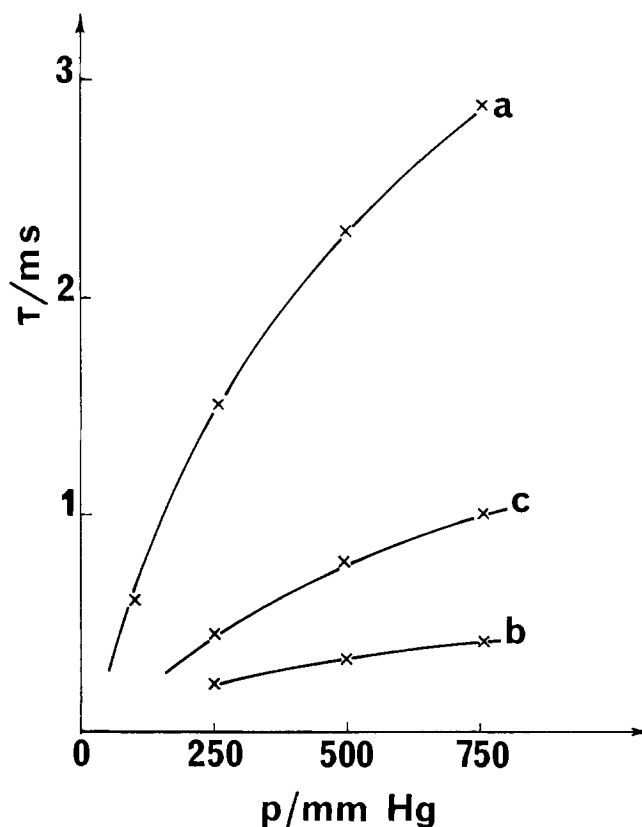


Fig. 4. The effect of the gas pressure on the transition time τ . a, electrode: graphite 235, $i = 10.8 \text{ A}\cdot\text{cm}^{-2}$, 4% Al_2O_3 ; b, electrode: graphite 235, $i = 19.4 \text{ A}\cdot\text{cm}^{-2}$, 4% Al_2O_3 ; c, electrode: graphite 208, $i = 18.0 \text{ A}\cdot\text{cm}^{-2}$, 8% Al_2O_3 . Cryolite bath without dissolved aluminum at 1036°C.

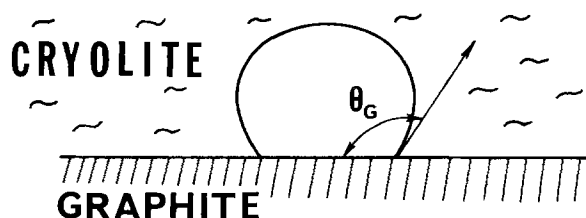


Fig. 5. Gas bubble on a graphite electrode

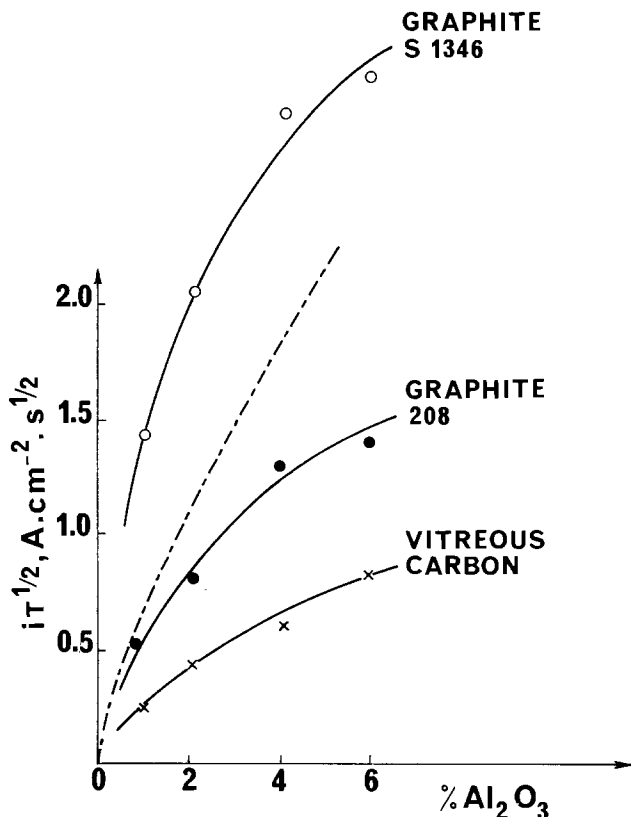


Fig. 6. Plots of $i\tau^{1/2}$ vs. $c_{Al_2O_3}$ in a cryolite bath in presence of dissolved aluminum at 1036°C. Dashed line: theoretical curve corresponding to the Sand's law with the diffusion coefficients indicated by Desclaux and Rolin (24).

alumina concentration the greater this effect. As indicated in a previous paper (5) the chronopotentiometric response may be qualitatively improved by use of an ultrasonic vibration of the electrode.

Hollow-anode.—In the absence of aluminum an efficient method of obtaining a correct chronopotentiometric response is to use a hollow graphite anode [thickness of the wall: 1 mm (11)]. When a depression is created in the central part of the electrode the gas bubbles completely disappear. As a consequence Sand's law is quite well obeyed and chronopotentiometry may be used to determine the variations of alumina concentration with good accuracy (5). However this technique does not work when aluminum metal is present in the bath. As already pointed out the electrolyte wets the graphite and flows through the wall of the electrode.

Influence of dissolved metal.—It appears that the dissolved metal plays an important role in the electrolysis of alumina: (i) it changes the wetting properties of the electrolyte. The preceding study shows (Table I) that this phenomenon very much affects the gas covering of the electrode and the local current density; (ii) it has also a direct influence on the faradaic yield of the cell; the metal may be oxidized either by the carbon dioxide (9) or directly on the anode (25). This last contribution is studied hereafter.

Influence of a Small Oxidation Current

The galvanostatic pulses are now performed on an electrode submitted to a small direct anodic current i_p , the applied voltage is always less than 1V (vs. the Al^{+++}/Al electrode). As indicated in Fig. 7 and Table II, the presence of this current induces shorter transition times. This effect is in agreement with the prediction of the gas wetting model described above; the dissolved metal has a favorable influence on the gas evolution and improves the area of the active surface of the electrode. Since the anodic current i_p creates a depletion of the metal concentration near the elec-

Table I. Coefficient $\nu = S_a/S$ for different experimental conditions: Graphite anode (quality No. 208), $T = 1036^\circ C$, $c = 1\% Al_2O_3$, $D = 2.42 \times 10^{-5} cm^2/sec$ (24), $S_a =$ active surface; $S =$ geometric surface of the electrode

Bath	Anode	$\nu = S_a/S$
Presence of aluminum metal	Hollow, without depression in the central part	8.33
	Graphite rods with a conical extremity	1.036
Absence of aluminum metal (5, 12)	Graphite rods with a conical extremity	0.35
	Ultra-sonic vibration of the electrode	1.18
	Hollow, without depression in the central part	0.35
	Hollow, with depression in the central part	1.25
	Hollow with depression (basic bath)	1.27

Table II. The effect of a small anodic current i_p on the chronopotentiometric response $i\tau^{1/2} c^{-1}$. V_p is the tension of the graphite electrode (vs. Al^{+++}/Al electrode).

i ($A \cdot cm^{-2}$)	τ (msec)	% Al_2O_3	$i\tau^{1/2}/c$ ($A \cdot sec^{1/2} / mole^{-1} cm$)	i_p ($mA \cdot cm^{-2}$)	V_p (mV)
19	2.75	2	2491	0	255
19	0.10	2	475	33.7	1000
49.3	0.80	6	1162	0	305
49.3	0.42	6	842	16.8	390
12.9	12.50	6	1202	16.8	390
12.9	12	6	1178	25.2	430
33.7	0.62	6	700	25.2	430
33.7	0.10	6	281	33.7	630
19	0.20	6	224	33.7	630
12.9	0.55	6	252	33.7	630

trode its influence vanishes progressively. The adhesion energy of the gas bubbles becomes greater, the covering of the electrode increases and thus, for a given galvanostatic pulse i , the transition time is shorter. It happens that for a critical value of this small anodic current $i_{p,c} = 39 mA cm^{-2}$ the electrode becomes completely inactive as shown on the curves of Fig. 7. This phenomenon corresponds to an anode effect obtained by variation of the wetting properties, in agreement with the extensive studies of Mazza, Pedferri, and Re (26).

As a first approximation we consider the preceding critical current density as being equal to the limiting

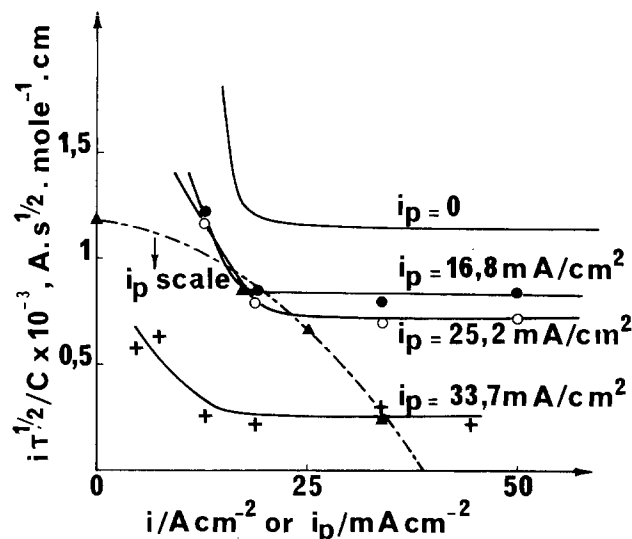


Fig. 7. The effect of the continuous galvanostatic current i_p on the plots $i\tau^{1/2} c^{-1}$ vs. i . Dashed line: evolution of the plateau value of the preceding curves when i_p is varied. Electrode: graphite 208; cryolite bath with dissolved aluminum at 1036°C.

diffusion current of the dissolved metal. According to Vetyukov and Dyblin (27) the aluminum solubility is $C_s = 2.56 \times 10^{-4}$ g-equiv. cm^{-3} at 1036°C ; the same order of magnitude is also given by Yoshida and Dewing (28). The activity a_{Al} of aluminum in the aluminum-copper alloy being known [$a_{\text{Al}} = 0.48$ in the alloy 40% Al-60% Cu (10)], the concentration of dissolved aluminum is proportional to a_{Al}^x (27), with $1/3 < x < 2/3$. The introduction of the x exponent, which is equal to $x = 0.483$, is due to existence of the reactions (27)



In our working conditions, the concentration of dissolved aluminum is then equal to

$$C_{\text{Al}} = C_s \cdot a_{\text{Al}}^x = 6 \times 10^{-5} \text{ g at cm}^{-3}$$

Now, for a thickness of the diffusion layer estimated at $100 \mu\text{m}$ (29) we find for the diffusion coefficient of the dissolved metal $D_{\text{Al}} \approx 2.3 \times 10^{-5} \text{ cm}^2 \text{ sec}^{-1}$. This result agrees quite well with voltamperometric measurements of Saget *et al.* (9) who found $D_{\text{Al}} = 2.10 \times 10^{-5} \text{ cm}^2 \text{ sec}^{-1}$. These values are of the same order of magnitude as the diffusion coefficients of the other components of the melt (3); moreover the observed limiting diffusion current is in good agreement with the value indicated by Thonstad (30). However larger values of D_{Al} have been recently reported by Vetyukov and Dyblin (27), $D_{\text{Al}} = 61.8 \times 10^{-5} \text{ cm}^2 \text{ sec}^{-1}$ as well as by Dewing and Yoshida (31), $D_{\text{Al}} = 28 \times 10^{-5} \text{ cm}^2 \text{ sec}^{-1}$. New investigations are still needed for the precise determination of the content and diffusion constant of dissolved metal in cryolite.

Conclusion

The study of the anodic reaction of alumina in a cryolite bath indicates the considerable influence of the dissolved aluminum metal which changes markedly the interfacial properties of the melt. Indeed the metal may form an aluminum carbide (32) at the surface of the electrode. A detailed study of this reaction has recently been carried out by Grjotheim, Naeumann, and Øye (18), it is shown that the carbide formation is highly dependent on the surface properties of the carbon material.

Moreover, the graphite acts also as a depolarizer for the sodium deposit which forms interstitial compounds (33). In a cryolite bath the aluminum metal reduces the sodium ion in presence of carbon. As an illustration of this process we have observed that in our cell, under a dry argon atmosphere, when aluminum is introduced in the cryolite bath directly placed in a graphite (or vitreous carbon) crucible, drops of sodium metal rapidly appear on the cold parts of the cover of the cell. This may be compared to the primary sodium deposit on graphite which is observed during the starting period of the industrial cell (34). This surface reaction strongly affects the wetting properties of the graphite; in the presence of aluminum the penetration of the electrolyte in the graphite pores becomes important. The chronopotentiometric measurements illustrate this surface variation; they establish also a useful connection between the electrochemical behavior of the system and the important problem of the gas retention at the electrode surface.

Manuscript submitted April 5, 1978; revised manuscript received Aug. 2, 1979.

Any discussion of this paper will appear in a Discussion Section to be published in the December 1980 JOURNAL. All discussions for the December 1980 Discussion Section should be submitted by Aug. 1, 1980.

Publication costs of this article were assisted by the Université Pierre et Marie Curie.

REFERENCES

1. M. Grjotheim, C. Krohn, M. Malinovsky, K. Matiasowśky, and J. Thonstad, "Aluminium Electrolysis," Aluminium Verlag GmbH Düsseldorf, Düsseldorf, Germany (1977).
2. M. Rolin, "Les Equilibres chimiques dans les bains d'Electrolyse de l'aluminium (1973), I.N.S.A., Villeurbanne, France.
3. D. Harari, F. Lantelme, and M. Chemla, *J. Chim. Phys.*, **66**, 1286 (1969) and *C.R. Acad. Sci. Ser. C*, **270**, 653 (1970).
4. A. Tual and M. Rolin, *Electrochim. Acta*, **17**, 1945 and 2277 (1972).
5. F. Lantelme, D. Damianacos, and J. Chevalet, *ibid.*, **23**, 717 (1978).
6. C. Brunet-Lefort, Thesis, Université P. et M. Curie, Paris, France (1977).
7. W. E. Haupin, *This Journal*, **107**, 232 (1960).
8. G. A. Abramov, M. M. Vetyukov, I. P. Gupalo, A. A. Kostyukov, and L. N. Lozhkin, "Theoreticheskie osnovy elektrometallurgii alyuminiya," Metallurgizdat, Moscow (1953).
9. J. P. Saget, V. Plichon, and J. Badoz-Lambling, *Electrochim. Acta*, **20**, 825 (1975).
10. T. S. Wilder, *Trans. Metall. Soc. AIME*, **233**, 1202 (1965).
11. D. Damianacos, Thesis, Université P. et M. Curie, Paris, France (1977).
12. F. Lantelme, D. Damianacos, J. Chevalet, and M. Chemla, *Electrochim. Acta*, **22**, 261 (1977).
13. K. J. Vetter, "Electrochemical Kinetics, Theoretical Aspects," Academic Press, New York (1967).
14. E. W. Dewing, *Can. Metall. Q.*, **13**, 607 (1974).
15. J. Thonstad, *Electrochim. Acta.*, **14**, 127 (1969).
16. J. C. Poinet and M. J. Barbier, *Electrochim. Acta*, **17**, 1227 (1972). F. Lantelme, J. P. Hanselin, and M. Chemla, *ibid.*, **22**, 1113 (1977).
17. N. Ibl, *Oberflaeche Surf.*, **16**, 23 (1975).
18. K. Grjotheim, R. Naeumann, and H. A. Oye, in "Proceeding 106th AIME Meeting Light Metals," **1**, 233 (1977).
19. R. De Levie, "Advances in Electrochemistry and Electrochemical Engineering," Vol. 6, P. Delahay and C. W. Tobias, Editors, p. 329, Interscience, New York (1967).
20. S. S. Barton, G. L. Boulton, and B. H. Harrison, *Carbon*, **10**, 395 (1972).
21. J. Thonstad, *J. Light Metals*, **1**, 137 (1974).
22. E. W. Dewing and E. T. van der Kouwe, *This Journal*, **124**, 58 (1977).
23. L. J. J. Janssen, *Electrochim. Acta*, **23**, 81 (1978).
24. P. Desclaux and M. Rolin, *Rev. Int. Hautes Temp. Refract.*, **8**, 227 (1971).
25. E. W. Dewing and E. T. van der Kouwe, Paper 191 presented at the Electrochemical Society Meeting, New York, N.Y., May 4-9, 1969.
26. B. Mazza, P. Pedferri, and G. Re, *Electrochim. Acta*, **23**, 87 (1978).
27. M. M. Vetyukov and S. S. Dyblin, *Sov. Electrochem.*, **11**, 470 (1975).
28. K. Yoshida and E. W. Dewing, *Metall. Trans.*, **3**, 1817 (1972).
29. M. Rey, "Dissolution de l'alumine dans la cryolithe-Mesure du coefficient de diffusion des ions oxygénés," Internal report, Pechiney-Ugine-Kuhlmann Company, Paris (1974).
30. J. Thonstad and S. Rolseth, in "Proceedings of Internat. Symposium on Molten Salts," J. P. Pemsler, J. Braunstein, K. Nobe, D. R. Morris and N. E. Richards. Editors, p. 393, The Electrochemical Society Softbound Proceedings Series, Princeton, N.J. (1976).
31. E. W. Dewing and K. Yoshida, *Can. Metall. Q.*, **15**, 299 (1976).
32. E. W. Dewing, *Trans. Metall. Soc. AIME*, **227**, 1328 (1963).
33. G. Poupa and M. Rolin, *Electrochim. Met.*, **3**, 301 and 310 (1967).
34. E. Grünert, *Z. Elektroch.*, **48**, 393 (1942).



Cathodoluminescence of $(\text{Zn} + \text{Mg})_3(\text{PO}_4)_2:\text{Mn}^{2+}$

W. Lehmann*

Westinghouse Research and Development Center, Pittsburgh, Pennsylvania 15235

Cathodoluminescent zinc-magnesium phosphate phosphors activated by Mn^{2+} are well-known (1-3). $\text{Zn}_3(\text{PO}_4)_2:\text{Mn}^{2+}$ had been used as red phosphor component in the early days of color television and is still available as P-27. The latter is reported to show, after excitation by short electron beam pulses, near-exponential afterglow requiring approximately 27 msec to 1/10 of the original (4). We observed a substantially longer decay time, also near-exponential, in Mn-activated intermediate zinc-magnesium phosphate of the approximate composition $\text{ZnMgPO}_{4.5}$. According to a published phase diagram (3), a chemical compound of this composition does not exist. A brief investigation was initiated to determine the origin of the long decay time.

The phosphors were prepared by standard techniques. The starting materials (ZnO , MgO , MnCO_3 , and H_3PO_4 -solution) were mixed in aqueous slurries which were then dried and pulverized in a mortar. These powders were fired in open quartz containers in stagnant air for one to several hours. The firing temperatures depended on the material and were in the 900°-1150°C range. Emission spectra were measured under steady excitation by 8 kV electrons of low intensity (about $1 \mu\text{A}/\text{cm}^2$). The spectra given in Fig. 1 are corrected for monochromator transmission and photomultiplier response. Efficiencies were compared, also under 8 kV excitation of low intensity, against NBS-1025 which is a $\text{Zn}_3(\text{PO}_4)_2:\text{Mn}^{2+}$ phosphor reported to have an efficiency of about 6% (5). Decay curves were de-

* Electrochemical Society Active Member.

Key words: cathodoluminescence, luminescence, phosphors phosphorescence, spectra.

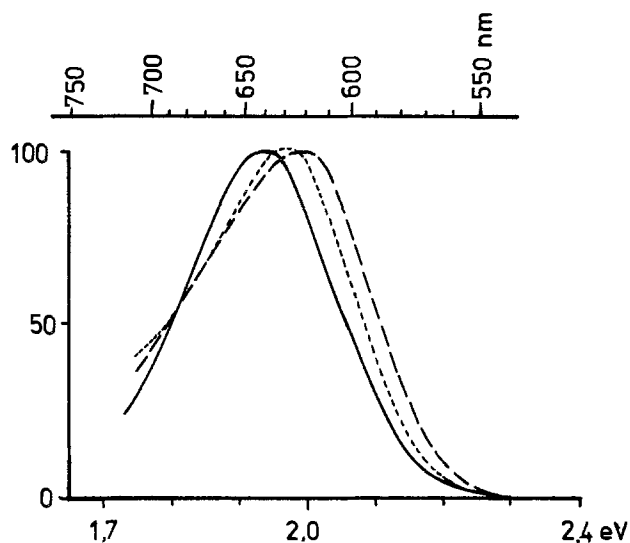


Fig. 1. Typical emission spectra. $\text{Zn}_3(\text{PO}_4)_2:\text{Mn} = \text{—}$, $\text{ZnMgPO}_{4.5}:\text{Mn} = \text{- - -}$, $(\text{Zn}_{1/2} + \text{Mg}_{1/2})_3(\text{PO}_4)_2:\text{Mn} = \text{- · -}$.

termined by exciting the phosphors with 1/10 sec e-beam pulses and by using the photocurrent for vertical deflection of the beam of an oscilloscope with constant horizontal sweep rate. The curves so traced were photographed and evaluated afterwards.

Starting from the original observation on a material of the mole ratio $\text{Zn}:\text{Mg}:\text{P} = 1:1:1$, a series of phosphors was prepared with constant 1:1 ratio of $\text{Zn}:\text{Mg}$ but with different P_2O_5 concentrations. The emission colors of the resulting samples were reddish-orange for the 1:1:1 ratio (that is, $\text{ZnMgPO}_{4.5}$) and less P_2O_5 , and red for 3:3:4 (that is, the *ortho*-phosphate) and higher amounts of P_2O_5 . Typical spectra are shown in Fig. 1. Powder diffraction x-ray spectra of the 1:1:1 and of the 3:3:4 materials both revealed only the *ortho*-phosphate structure with no indication of any undissolved ZnO or MgO . Some decay curves are shown in Fig. 2, and decay times (to 1/10 of the original) and efficiencies in Fig. 3. There is little or no dependence (exceeding the unavoidable scatter) of the added P_2O_5 -concentration on the decay but there is a distinct peak of the efficiency close to the composition of the *ortho*-phosphate. We conclude that the compound responsible for the long decay is the *ortho*-phosphate.

A second series of phosphors, all *ortho*-phosphates, was prepared with varied $\text{Zn}:\text{Mg}$ ratio. Decay curves of these phosphors are shown in Fig. 4. X-ray powder diffraction spectra indicated the sample corresponding to the top curve in Fig. 4 to be $\beta\text{-Zn}_3(\text{PO}_4)_2$, all others had $\text{Mg}_3(\text{PO}_4)_2$ -structure. It is seen that the long decay is restricted to the $\text{Mg}_3(\text{PO}_4)_2$ crystal structure.

A third series was prepared of the 3:3:4 composition ratio (*ortho*-phosphates) with varied Mn -concentrations, the Mn^{2+} substituting for the Zn^{2+} ion. Some

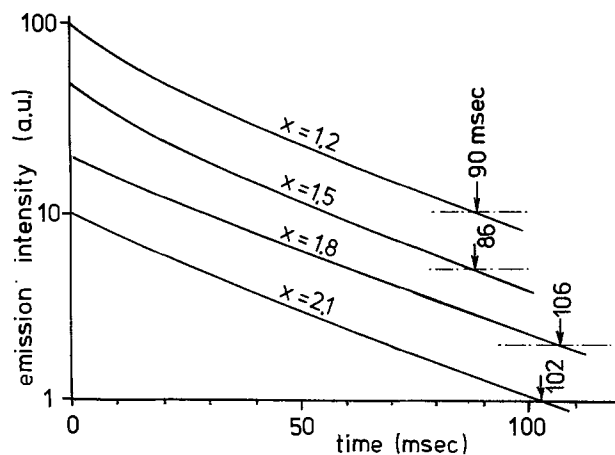


Fig. 2. Decay curves of $(\text{Zn}_{1/2} + \text{Mg}_{1/2})_3(\text{PO}_4)_x:\text{Mn}(0.015)$ for different amounts of added $\text{PO}_{5/2}$. Mn substitutes for Zn. Curves are arbitrarily shifted vertically to provide clarity. Arrows indicate decay times to a 1/10 of original.

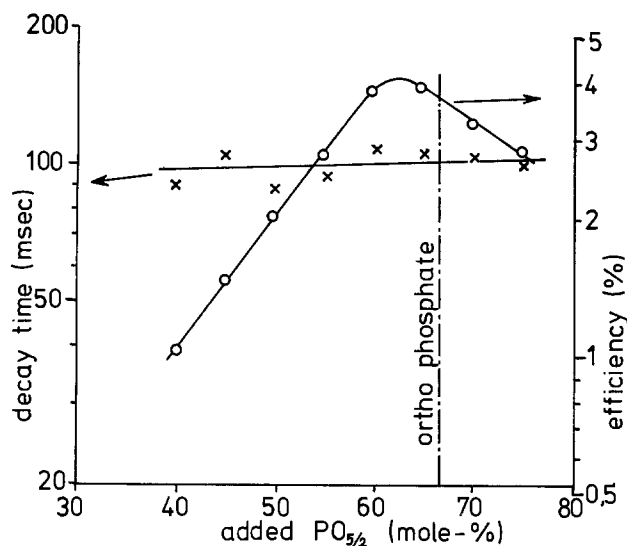


Fig. 3. Efficiency of cathodoluminescence and decay times (to 1/10 of original) of $(Zn_{1/2} + Mg_{1/2})_3(PO_4)_x:Mn(0.015)$ as functions of added concentration of $PO_{5/2}$. Vertical line indicates the ortho-phosphate.

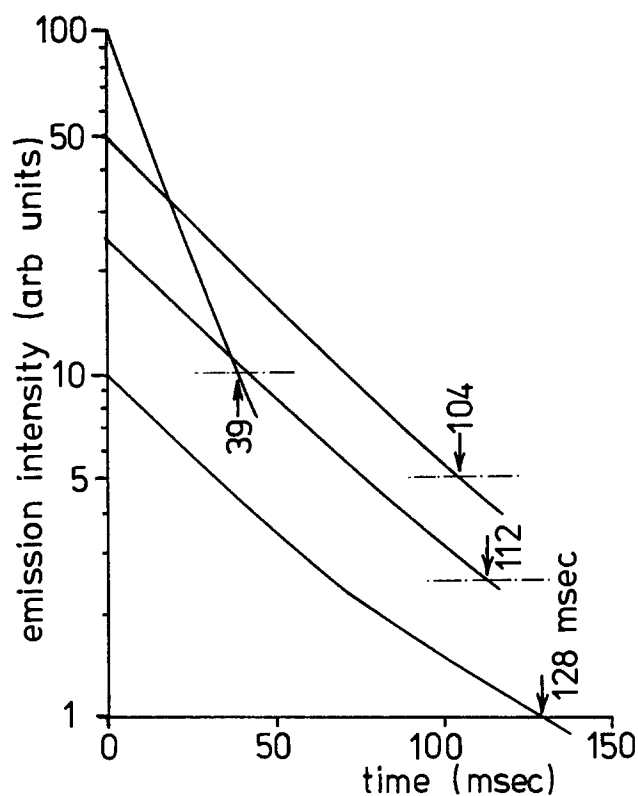


Fig. 4. Decay curves of $N_3(PO_4)_2:Mn(0.015)$. Top to bottom: $N = Zn$; $N = 80\% Zn + 20\% Mg$; $N = 50\% Zn + 50\% Mg$; $N = Mg$. Curves are arbitrarily shifted vertically to provide clarity. Arrows indicate decay times to 1/10 of original.

decay curves are shown in Fig. 5, and decay times and efficiencies in Fig. 6. The decay is near-exponential at low Mn-concentrations requiring slightly more than 100 msec to go to 1/10 of the original. The deviation from the exponential at high Mn-concentrations may be due to a Mn-Mn interaction which also causes the rapidly decreasing efficiency in this range.

While intermediate $(Zn + Mg)_3(PO_4)_2:Mn^{2+}$ phosphors per se are fairly well-known, it seems that their peculiar long times of near-exponential afterglow have not been recognized before. We cannot offer an explanation why these materials do show this long decay while the related $Zn_3(PO_4)_2:Mn^{2+}$ does not. However,

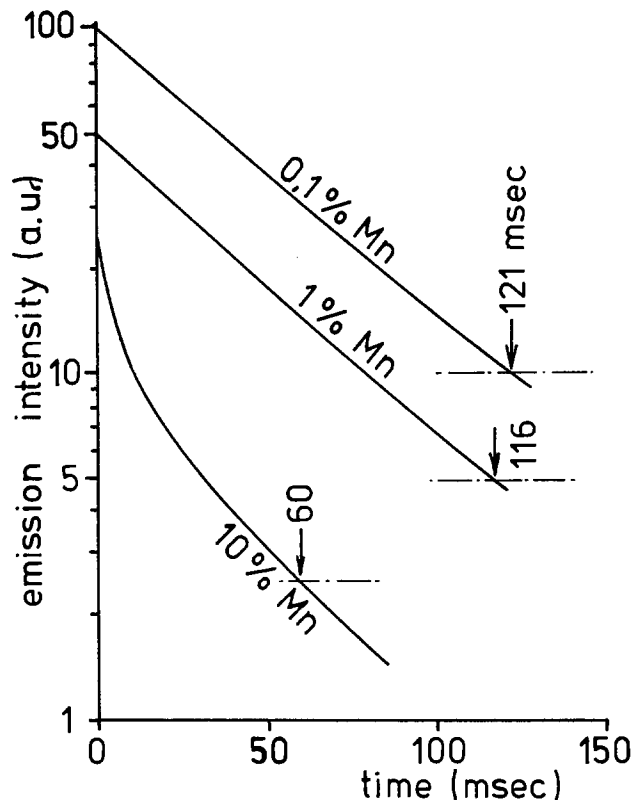


Fig. 5. Decay curves of $(Zn_{1/2} + Mg_{1/2})_3(PO_4)_2:Mn$. The Mn-concentrations are in % of the Zn. Curves are arbitrarily shifted vertically to provide clarity. Arrows indicate decay times to 1/10 of original.

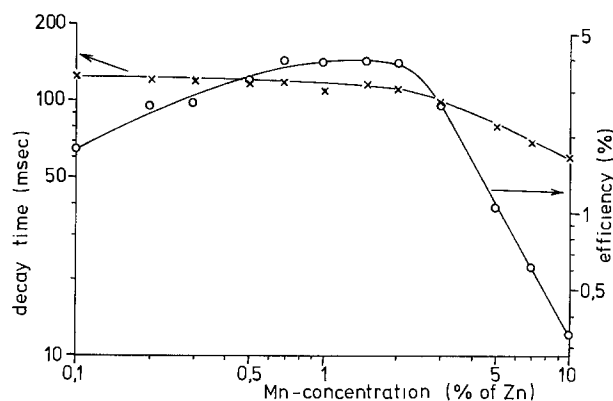


Fig. 6. Efficiency of cathodoluminescence and decay times (to 1/10 of original) of $(Zn_{1/2} + Mg_{1/2})_3(PO_4)_2:Mn$ as functions of the Mn-concentration.

we suggest that orange-to-red emitting $(Zn + Mg)_3(PO_4)_2:Mn^{2+}$ phosphors may be valuable for use in CR-tubes where long decay is desired but where fluoride phosphors (P-12, P-19, P-33, P-38) cannot be tolerated because of their strong tendency to electron burn. Although we have no quantitative data yet on the burn resistance of the phosphates, qualitative observations in this laboratory have shown that they are very much more stable than the fluorides. The decay times of the phosphates (~ 100 - 120 msec to 1/10) are shorter than those of the fluorides (~ 200 msec in P-33) but this appears to be compensated by the higher efficiencies of the phosphates ($\sim 4\%$ so far) over the fluorides ($\sim 2\%$). How much the phosphates can still be improved in long decay and efficiency is not known, but it appears unlikely that the optimum has already been reached.

Manuscript submitted May 22, 1979; revised manuscript received Sept. 3, 1979.

Publication costs of this article were assisted by Westinghouse Electric Corporation.

REFERENCES

1. F. A. Hummel and F. L. Katnack, *This Journal*, **105**, 125, 528 (1958).
2. J. F. Sarver and F. A. Hummel, *ibid.*, **106**, 500 (1959).
3. J. F. Sarver, F. L. Katnack, and F. A. Hummel, *ibid.*, **106**, 960 (1959).
4. "Optical Characteristics of Cathode Ray Tube Phosphors," JEDEC-Publication 16-C, Electronics Industries Association, Washington, D.C. (1975).
5. A. Brill, in "Luminescence in Organic and Inorganic Materials," H. P. Kallman and G. M. Spruch, Editors, p. 479, Wiley Publishing Co., New York (1962).

A Correlation Between Etch Characteristics of GaAs Etch Solutions Containing H₂O₂ and Surface Film Characteristics

E. Kohn

AEG-TELEFUNKEN Serienprodukte AG, Semiconductor Division, D-7100 Heilbronn, West Germany

Several authors have investigated surface contamination of GaAs after chemical treatments (1-5), and surface layers of various compositions and thicknesses have been found, as well as a change in the interfacial stoichiometry of GaAs.

In this note we discuss the influence of such surface layers in respect to the etching behavior of a number of commonly used GaAs etch solutions containing H₂O₂ as listed in Table I. Recently, most attention has been given to very slowly etching solutions, which give a highly polished and flat surface, mainly because such a solution is needed in many device fabrication process steps. However, no systematic investigation has previously been carried out on the influence of a possible surface layer on the etching characteristics of these solutions. These layers being present during the etching process may afterwards be very disadvantageous when the etching step is followed by a Schottky-metal evaporation or ion implantation. In solutions of low H₂O₂ content and high H₂O content, two types of etching behavior are observed apart from preferential anisotropic etching (9): (i) an H₂O₂-diffusion limited type giving enhanced etching at the mask edge, because additional H₂O₂ is provided from the protected area; and (ii) a surface reaction limited type resulting in the desired flat bottomed profile.

Experimental

The etching solutions selected, together with the composition ranges, are listed in Table I. Emphasis is on slow etching rates below 1 μm/min and on solutions leaving a mirror-like surface on polished substrates. The etching experiments were generally carried out in unstirred solutions at a temperature of $\theta = 21^\circ \pm 1^\circ\text{C}$. For the H₃PO₄ solution (F) the temperature was lowered to 15°C because the etched surface may turn rough at higher temperatures (8).

The substrates were (100) oriented and of horizontal boat-grown material with an n-doping concentration in the range of 10¹⁶-10¹⁸ cm⁻³. In some cases Cr-doped semi-insulating material was additionally tested and no difference was observed in the etching behavior or surface layer characteristics within the typical spread of the data. For GaAs, it is well-known that etching characteristics depend strongly on the surface orientation. Thus, etching speed is dependent on the crystal orientation and under certain conditions surface roughening can be expected. However, the etch solutions used here all produced smooth surfaces on the (100) oriented samples at least up to an etched depth of ap-

proximately 1 μm, with some just noticeable roughening, especially due to dislocations, for longer etching times. The protected areas were covered with Pizein wax (Pizein 105 produced by the New York Hamburger Gummi-Waren Compagnie). Starting condition was always a surface cleaned by etching with H₂SO₄-solution C of 8:1:1 composition at 60°C for 3 min followed by a 3 min treatment in HCl, giving a surface layer of 10-15Å. After etching, the samples were rinsed for 3 min in deionized water and then flushed with hot chloroform.

The etched profiles were measured with a Dektak profiler (manufactured by the Sloan Corporation). The surface layer was characterized by ellipsometry at $\lambda = 5461\text{Å}$ and measured immediately after etching. For the calculations of film thickness and refractive index (which was assumed to have no imaginary component), a GaAs reference index of $n_{\text{GaAs}} = 4.065 - j0.304$ was taken (5).

Results

The results are listed in Fig. 1-5. Figure 1 gives two examples to illustrate the surface smoothness and the two types of etching profiles considered here by a depth profile trace. Figure 2a and b shows the surface layer thickness and refractive index vs. rate after 2 min etching time for the various etching solutions. The etching rate Δ_x is determined from an etching depth at an appropriate distance from the mask edge to

Table I. Etching solutions used, with composition ranges.

Type	Etching solution ¹	Composition ²	Ref.
A	NaOH + H ₂ O ₂ + H ₂ O	2 : x : 100 1 < x < 10 →	9
B	NH ₄ OH + H ₂ O ₂ + H ₂ O	1 : 1 : x 16 < x < 50 ←	10
C	H ₂ SO ₄ + H ₂ O ₂ + H ₂ O	x : 1 : 1 10 < x : < 20 ←	11
D	H ₂ SO ₄ + H ₂ O ₂ + H ₂ O	1 : 1 : x 10 < x < 250 ←	11
E	Citric acid + H ₂ O ₂ + H ₂ O	50 : x : 50 1 < x < 10 →	7
F	H ₃ PO ₄ + H ₂ O ₂ + H ₂ O	1 : 1 : x 18 < x < 50 ←	8

¹ H₂O₂: 30% in H₂O. NH₄OH: 25% in NH₃. H₂SO₄: 96% in H₂O. H₃PO₄: 85% in H₂O.

² Arrows indicate direction of increasing etching rate. Components in vol. (cm⁻³), citric acid, and NaOH in weight (g).

Key words: semiconductor topography, contamination, ellipsometry.

Publication costs of this article were assisted by Westinghouse Electric Corporation.

REFERENCES

1. F. A. Hummel and F. L. Katnack, *This Journal*, **105**, 125, 528 (1958).
2. J. F. Sarver and F. A. Hummel, *ibid.*, **106**, 500 (1959).
3. J. F. Sarver, F. L. Katnack, and F. A. Hummel, *ibid.*, **106**, 960 (1959).
4. "Optical Characteristics of Cathode Ray Tube Phosphors," JEDEC-Publication 16-C, Electronics Industries Association, Washington, D.C. (1975).
5. A. Brill, in "Luminescence in Organic and Inorganic Materials," H. P. Kallman and G. M. Spruch, Editors, p. 479, Wiley Publishing Co., New York (1962).

A Correlation Between Etch Characteristics of GaAs Etch Solutions Containing H₂O₂ and Surface Film Characteristics

E. Kohn

AEG-TELEFUNKEN Serienprodukte AG, Semiconductor Division, D-7100 Heilbronn, West Germany

Several authors have investigated surface contamination of GaAs after chemical treatments (1-5), and surface layers of various compositions and thicknesses have been found, as well as a change in the interfacial stoichiometry of GaAs.

In this note we discuss the influence of such surface layers in respect to the etching behavior of a number of commonly used GaAs etch solutions containing H₂O₂ as listed in Table I. Recently, most attention has been given to very slowly etching solutions, which give a highly polished and flat surface, mainly because such a solution is needed in many device fabrication process steps. However, no systematic investigation has previously been carried out on the influence of a possible surface layer on the etching characteristics of these solutions. These layers being present during the etching process may afterwards be very disadvantageous when the etching step is followed by a Schottky-metal evaporation or ion implantation. In solutions of low H₂O₂ content and high H₂O content, two types of etching behavior are observed apart from preferential anisotropic etching (9): (i) an H₂O₂-diffusion limited type giving enhanced etching at the mask edge, because additional H₂O₂ is provided from the protected area; and (ii) a surface reaction limited type resulting in the desired flat bottomed profile.

Experimental

The etching solutions selected, together with the composition ranges, are listed in Table I. Emphasis is on slow etching rates below 1 μm/min and on solutions leaving a mirror-like surface on polished substrates. The etching experiments were generally carried out in unstirred solutions at a temperature of $\theta = 21^\circ \pm 1^\circ\text{C}$. For the H₃PO₄ solution (F) the temperature was lowered to 15°C because the etched surface may turn rough at higher temperatures (8).

The substrates were (100) oriented and of horizontal boat-grown material with an n-doping concentration in the range of 10¹⁶-10¹⁸ cm⁻³. In some cases Cr-doped semi-insulating material was additionally tested and no difference was observed in the etching behavior or surface layer characteristics within the typical spread of the data. For GaAs, it is well-known that etching characteristics depend strongly on the surface orientation. Thus, etching speed is dependent on the crystal orientation and under certain conditions surface roughening can be expected. However, the etch solutions used here all produced smooth surfaces on the (100) oriented samples at least up to an etched depth of ap-

proximately 1 μm, with some just noticeable roughening, especially due to dislocations, for longer etching times. The protected areas were covered with Pizein wax (Pizein 105 produced by the New York Hamburger Gummi-Waren Compagnie). Starting condition was always a surface cleaned by etching with H₂SO₄-solution C of 8:1:1 composition at 60°C for 3 min followed by a 3 min treatment in HCl, giving a surface layer of 10-15Å. After etching, the samples were rinsed for 3 min in deionized water and then flushed with hot chloroform.

The etched profiles were measured with a Dektak profiler (manufactured by the Sloan Corporation). The surface layer was characterized by ellipsometry at $\lambda = 5461\text{Å}$ and measured immediately after etching. For the calculations of film thickness and refractive index (which was assumed to have no imaginary component), a GaAs reference index of $n_{\text{GaAs}} = 4.065 - j0.304$ was taken (5).

Results

The results are listed in Fig. 1-5. Figure 1 gives two examples to illustrate the surface smoothness and the two types of etching profiles considered here by a depth profile trace. Figure 2a and b shows the surface layer thickness and refractive index vs. rate after 2 min etching time for the various etching solutions. The etching rate Δ_x is determined from an etching depth at an appropriate distance from the mask edge to

Table I. Etching solutions used, with composition ranges.

Type	Etching solution ¹	Composition ²	Ref.
A	NaOH + H ₂ O ₂ + H ₂ O	2 : x : 100 1 < x < 10 →	9
B	NH ₄ OH + H ₂ O ₂ + H ₂ O	1 : 1 : x 16 < x < 50 ←	10
C	H ₂ SO ₄ + H ₂ O ₂ + H ₂ O	x : 1 : 1 10 < x : < 20 ←	11
D	H ₂ SO ₄ + H ₂ O ₂ + H ₂ O	1 : 1 : x 10 < x < 250 ←	11
E	Citric acid + H ₂ O ₂ + H ₂ O	50 : x : 50 1 < x < 10 →	7
F	H ₃ PO ₄ + H ₂ O ₂ + H ₂ O	1 : 1 : x 18 < x < 50 ←	8

¹H₂O₂: 30% in H₂O. NH₄OH: 25% in NH₃. H₂SO₄: 96% in H₂O. H₃PO₄: 85% in H₂O.

²Arrows indicate direction of increasing etching rate. Components in vol. (cm⁻³), citric acid, and NaOH in weight (g).

Key words: semiconductor topography, contamination, ellipsometry.

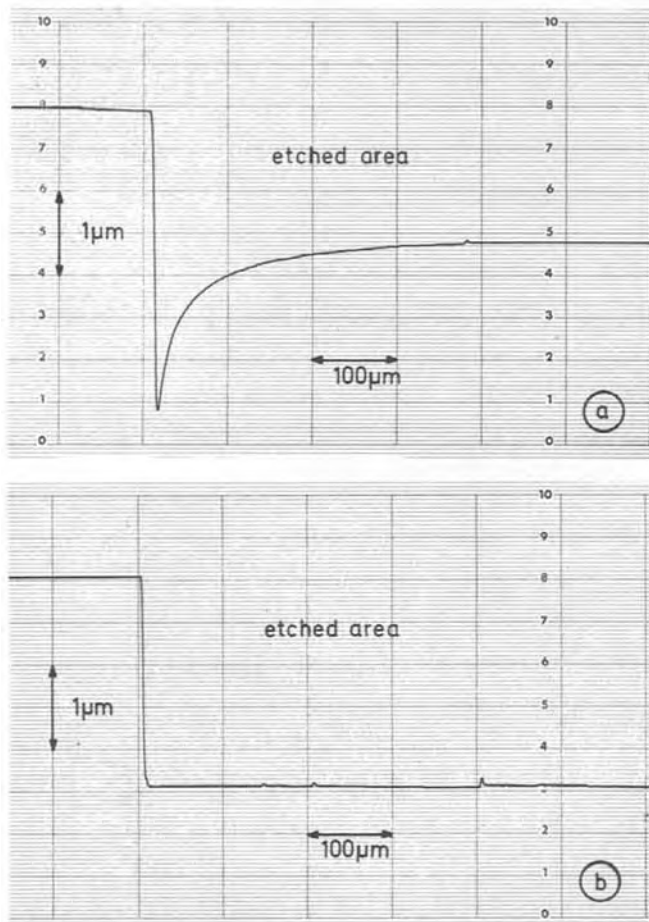


Fig. 1. Dektak etch profile traces for two compositions of the H_2SO_4 etch solutions, showing enhanced etching at the mask edge and flat-bottomed profile, respectively; (a) solution C with composition of 10:1:1; (b) solution D with composition of 1:1:16. Etching time 4 min at 20°C.

exclude the H_2O_2 diffusion effects from the protected area. For each point, at least two independent measurements were taken and the lowest film thickness listed. The spread of the data is typically within 20% for rates $\Delta_\infty > 0.1 \mu\text{m}/\text{min}$, but much higher for lower rates. The corresponding profile topology, i.e., the H_2O_2 diffusion effect is characterized in Fig. 3 by taking the ratio of the enhanced depth at the mask edge to the depth at an appropriate distance from the edge as indicated. Further, the development of the film thickness with increasing etching time is shown in Fig. 4. Figure 4a summarizes the behavior of solutions A, B, E, and F; Fig. 4b shows the behavior for the H_2SO_4 solution D and the influence of an additional HCl treatment. The etching rates are thereby correlated to the H_2O_2 concentration as seen in Fig. 5, all results at $21^\circ \pm 1^\circ\text{C}$.

Taking the various parameters considered as surface contamination, etching rates, etched profiles, and H_2O_2 concentration, it is possible to list a number of general tendencies:

1. A thin surface layer is connected to a pronounced H_2O_2 diffusion effect.
2. No etchant with surface reaction limited behavior is found with a surface layer thickness below 40Å.
3. It takes a few minutes time until the dynamic equilibrium between etching rate and surface layer thickness is established. In most cases the surface layer is built up slowly.
4. In all solutions with low H_2O_2 and high H_2O content the etching rate is roughly proportional to the mole percentage of H_2O_2 content and thus determined by the H_2O_2 -GaAs reaction.

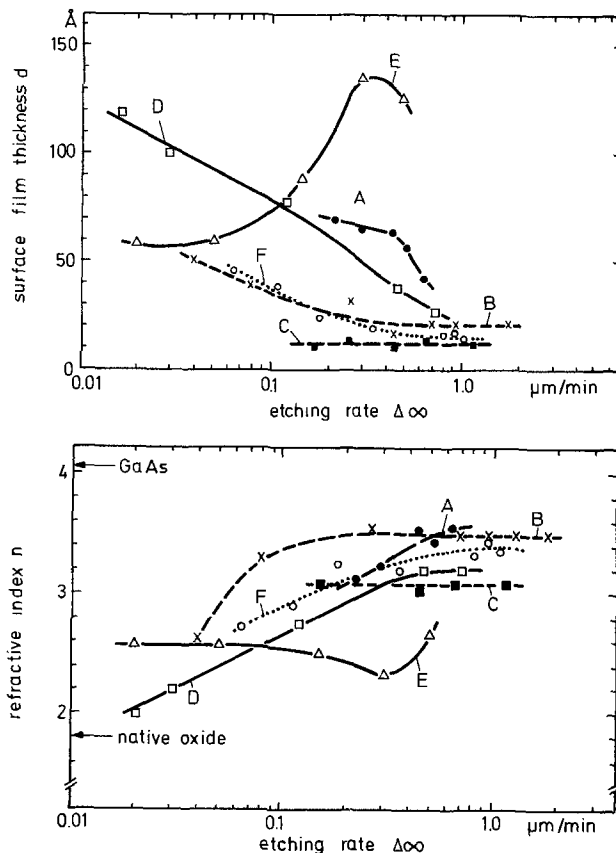


Fig. 2. (a) Film thickness d and (b) refractive index n of the surface film vs. etching rate for various etching solutions. Etching time: 2 min for $\Delta > 0.1 \mu\text{m}/\text{min}$; 4 min for $\Delta < 0.1 \mu\text{m}/\text{min}$. Temperature: 15°C for D, 21°C for A, B, C, E, F.

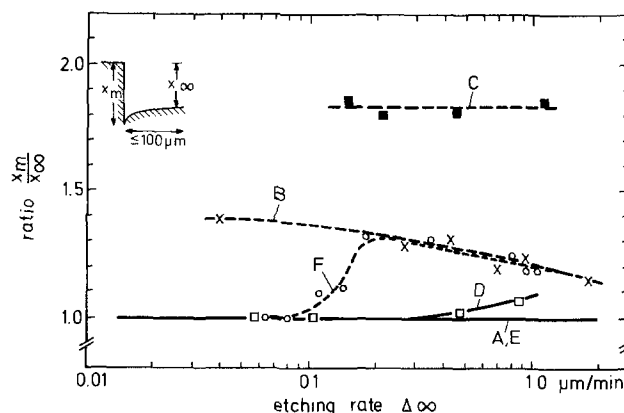


Fig. 3. Effect of enhanced etching at the mask edge vs. etching rates.

5. The overall refractive index stays between that of GaAs (5) and that of native oxide (6), decreasing for thicker films. The high values indicate metal-rich compounds.

The change from the diffusion-limited case to the flat-bottomed profile case corresponding to the build-up of a surface layer can be observed with the H_3PO_4 solution F. The transition occurs at an etching rate of around $0.1 \mu\text{m}/\text{min}$, and no reproducible etching rates were measured in this region. The same tendency is seen for the H_2SO_4 solution when changing from composition C to D. In the case of composition C, the reaction is determined by the H_2SO_4 part, which is bivalent, and the H_2O_2 diffusion in the solution. This gives a subsquare behavior in the etching rate vs. the H_2O_2 concentration relationship. Therefore, the enhanced etching at the mask edge is very pronounced. In contrast to this, changing to the weak H_2O_2 concentration

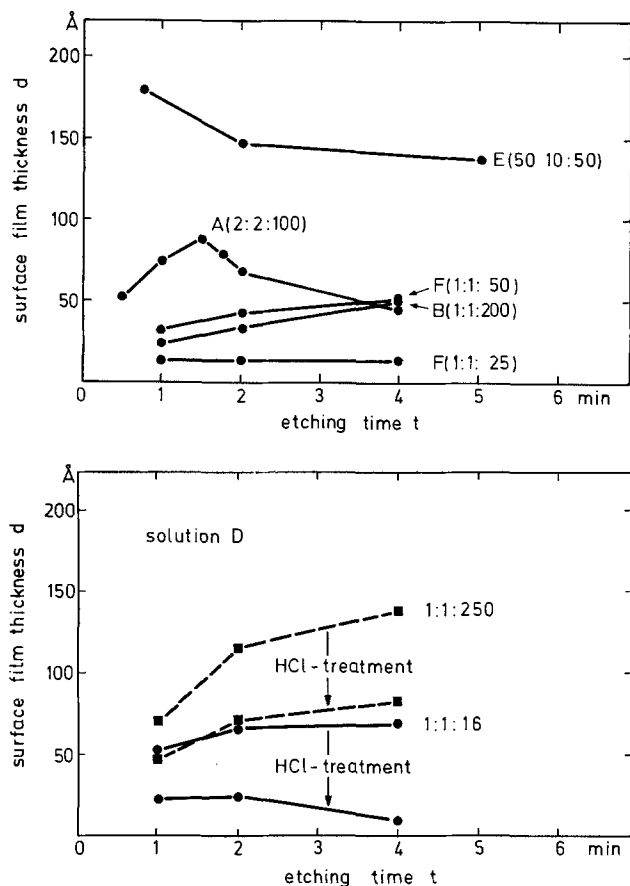


Fig. 4. (a) Evaluation of the film thickness with etching time and (b) the additional influence of an HCl treatment after etching by the H_2SO_4 solution D.

causes the enhanced etching at the mask edge to disappear but at the same time creates a surface layer. The etching rate is now determined by H_2O_2 concentration and diffusion in the surface film.

Etch solution E (citric acid) shows an unusual behavior: the surface film thickness increases with etching rate, but decreases with etching time. However, the film is very porous, and weakly bonded to the surface, and can even be wiped off by a cotton bud.

It was further found that additional treatment in hot HCl, which removes native oxide rapidly, generally does not reduce the film thickness by more than 20% except for the film left by the H_2SO_4 etchant D. This case is additionally indicated in Fig. 3b.

Discussion

In Ref. (8) a general model is given for the etching process of GaAs for mixed solutions containing H_2O_2 and H_2O . The various reaction steps are listed and, for the case of low H_2O_2 and high H_2O contents, the H_2O_2 adsorption to the active centers of the GaAs surface was proposed to be the rate-determining factor.

However, this picture seems to be oversimplified. The etching rate is indeed roughly proportional to the H_2O_2 concentration for all solutions. But by plotting the data carefully, a more or less pronounced sublinearity can be observed [see also Ref. (4)], certainly due to the H_2O_2 diffusion effect, either in the etch solution or in the surface layer. For flat-bottomed profiles, it seems necessary to have a diffusion barrier between etch solution and GaAs surface. Most likely, GaAs is oxidized by the H_2O_2 to form a native oxide, which is highly soluble in the etch solution (all solutions used can etch anodic oxides very quickly). In contrast, the surface layer found cannot be dissolved in HCl or HF. Possibly this layer is formed by a preferential and complex reaction also involving the acidic part of the solution. In some

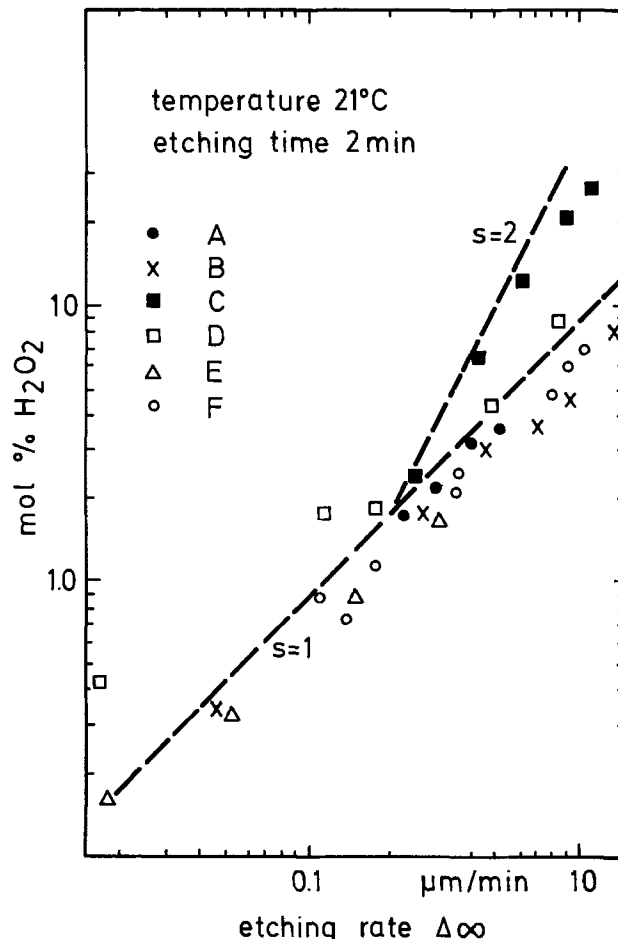


Fig. 5. Correlation between H_2O_2 content and etching rates for the various solutions.

cases, the layer seems to be very porous and unstable. Clearly, a constant etching rate, especially for the first minutes, cannot be expected for these cases, even when starting with a clean surface. This may explain the spread of the data in Fig. 4.

The usefulness of such surfaces for device applications, as for instance Schottky-metal deposition, seems mainly to depend on the composition of this layer and whether or not it can be consumed in an annealing process. Indeed, best Schottky-barrier characteristics are achieved after short forming processes. Further investigations in this direction are being undertaken.

Acknowledgment

This work was financially supported by the German Ministry of Research and Technology, contract No. NT 905.

Manuscript submitted April 17, 1979; revised manuscript received July 28, 1979.

Publication costs of this article were assisted by AEG-TELEFUNKEN Serienprodukte AG.

REFERENCES

1. B. Schwartz, *This Journal*, **118**, 657 (1971).
2. C. C. Chang, P. H. Citrin, and B. Schwartz, Paper presented at 4th Annual Conf. on the Physics of Compound Semiconductor Interfaces, Princeton, N.J., Feb. 1977.
3. J. J. Uebbing, *J. Appl. Phys.*, **41**, 802 (1970).
4. T. Oda and T. Sugano, *Jpn. J. Appl. Phys.*, **15**, 1317 (1976).
5. A. C. Adams and B. R. Pruniaux, *This Journal*,

- 120, 408 (1973).
6. C. J. Dell'Oca, G. Yan, and L. Young, *ibid.*, **118**, 89 (1971).
7. M. Otsubo, T. Oda, H. Kumabe, and H. Miki, *ibid.*, **123**, 676 (1976).
8. Y. Mori and N. Watanabe, *ibid.*, **125**, 1510 (1978).
9. D. W. Shaw, *ibid.*, **113**, 958 (1966).
10. J. J. Gannion and C. J. Nuese, *ibid.*, **121**, 1215 (1974).
11. S. Jida and K. Ito, *ibid.*, **118**, 768 (1971).



Post Field Recombination in the Pulsed Electroluminescence of Zinc Sulfide

M. S. Waite* and A. E. Thomas**

Division of Materials Science, Thames Polytechnic, London, SE18 England

Direct current electroluminescence in ZnS:Mn powder panels (i.e. "Vecht-type") is now an established display technique(1-3). In contrast to the bright yellow-orange luminescence of the Mn doped phosphors, undoped zinc sulphide powder phosphors when prepared as electroluminescent panels in exactly the same way give a very weak, but spectrally broad, emission (Fig. 1, spectrum a-b) (4). The bands stretch from ca. 330nm, the cut-off point of the conducting glass substrate on which the powders are deposited, to ca. 700nm. During the examination of the decay characteristics of undoped zinc sulphide, an additional radiative recombination process was observed, with characteristics as discussed below.

The material used for the preparation of the phosphors was luminescent grade ZnS, from Levy West Ltd., muffle-fired to 950°C and washed with acetic acid before use. The powder was washed in cupric chloride solution, deposited in conducting glass strips, and an Al back electrode was evaporated on exactly as published for ZnS:Mn phosphors (1). The thickness of the powder layer was about 200 microns and the phosphor was formed to 100 V dc before examination of the response to pulsed excitation. The phosphor was not deliberately doped, but contains chlorine and sub ppm traces of Mn.

*Electrochemical Society Active Member

**Present address: Dept. of Applied
Physics & Electronics
Univ. of Durham
Durham, England

Key Words: ZnS, Electroluminescence,
Recombination Process, Self-activated
emission, D-A Recombination

Fig.2(a) illustrates the response of the phosphor to dc pulses of 20 μ sec. length and 230 V peak voltage. With the limited resolution of the equipment, the decay time of the luminescence, following the end of the voltage pulse, could not be reliably estimated, but appears to be less than 100 nano-seconds. There is, however, an additional brightness peak following the main pulse, with a slow rise and decay (peak b in Fig.2).

The rise time, or the delay time between the peak maximum and the end of the voltage pulse is from 5 to 45 μ secs., varying with different samples, and the decay time to 1/10 of peak brightness is at least 300 μ secs. The ratio of the height of the secondary peak to that of the main peak varies with specimen, voltage and the age of the panel. The longer the panel runs, the less prominent the secondary peak, whilst the primary peak increases with voltage at a greater rate than the secondary peak. The ratio of secondary to primary peak heights is also dependent on the length of the excitation pulse. It is difficult to assess for pulse lengths < 40 μ secs., but rises gradually as the pulse length increases (Fig.3). Furthermore, the secondary brightness peak builds up slowly, when the pulsed field is first applied.

By choosing a long pulse length, 200 μ sec., a high duty cycle and a low applied voltage, 80 V, it is possible to obtain emission predominately from the secondary peak (see Fig.2(b)). Thus, the spectral distribution of this secondary emission could be recorded free from interference by the "in-field" emission. It appears as a band with a maximum at 467nm (curve C, Fig. 1) and is identical to the CL spectrum of the original ZnS phosphor. This corresponds to the well-known S-A emission of ZnS, due to

electron-hole recombination at a zinc vacancy-chlorine complex, Fig. 4(5,6). It seems, therefore, that the post-field emission from undoped zinc sulphide arises from the recombination of an electron with a hole bound to a $V_{Zn} - Cl$ site in the lattice. The slow rise in appearance of this emission following the end of the main pulse, may be due to the slow diffusion of electrons as the space charge created by the voltage pulse decays, or the thermal release of electrons from other traps in the phosphor. The secondary emission disappeared when the pulsed field is applied at 77°K and was not observed in ZnS refired in H_2S and lacking the S-A photo or cathodo luminescence. We suggest, therefore, that the self-activated centre is ionised by the field in the formed layer or by collision ionisation, leaving a hole bound to the $V_{Zn} - Cl$ complex and an electron which is trapped elsewhere. The slow rise in appearance, over several minutes, of the secondary peak after the pulsed field is initially applied may be due to the slow creation of trapping centres for the electrons.

By measuring the intensity of the emission in the secondary peak, and assuming each recombination is radiative, with negligible self-absorption, an approximate estimate of the number of ionised centres can be made. For a sample operated at 105 V with a 140 μ sec. pulse width and a frequency of 200 Hz, a recombination rate of 10^{12} sec^{-1} out of phase with the field was estimated, or 5×10^9 recombinations per cycle. The thickness of the formed layer was determined as 3 μ from capacitance measurements, compared with 2 μ found in ZnS / Mn panels (1). This would give an estimated density of ionised centres of ca. $5 \times 10^{19} \text{ m}^{-3}$ in the formed layer following each voltage pulse.

Similar explanations have been proposed for the brightness peak observed during square wave excitation of copper doped zinc sulphide phosphors as the field is turned off, for example Zallen et al(7). In that case, however, the spectral distribution of the "post-field" peak was the same as that of the brightness observed at the start of the pulse. In these undoped zinc sulphide phosphors, the fast decay of the primary emission observed during the pulse and the quenching of the secondary emission as the field is re-applied (see Fig. 2b) suggests that the

recombination process represented by the secondary peak does not also occur whilst the field is on. Thus, doubt is cast on models for dc electroluminescence which involve energy transfer to Mn^{2+} from electron-hole recombination at defect centres, such as the S-A centre. In addition, the difference between the emission spectra arising from continuous dc excitation and the spectra of the recombination process is further evidence that the broad bands, or "avalanche spectra" observed during dc excitation of the undoped ZnS have an intra-band or intervalley origin (8).

Acknowledgement.-- We are grateful to colleagues at Thames for their comments and particularly to Dr D Robbins of R.S.R.E Malvern for his critical reading of the manuscript during preparation.

REFERENCES

1. Vecht, A; Werring, N.J; Ellis, R; Smith P.J.F; J.Phys. D, Appl. Phys. 3 953 (1969).
2. Vecht, A; Werring, N.J; Ellis, R; Smith, P.J.F; This Journal 117 134, (1970).
3. Vecht, A; J.Vac. Sci. Tech. 10, 789, (1973).
4. Smith, R.W; Phys. Review, 100, 760 (1955).
5. Prener, J.S; Williams, F.E; J.Chem.Phys 25, 361, (1956).
6. James, J.R; Nicholls, J.E; Cavenett, B.C; Davies, J.J; Dunstan, D.J; Sol. State Commun. 17, 969 (1975)
7. Zallen, R; Eriksen, W.T; Ahlburg, H; This Journal, 107, 288 (1960).
8. Livingstone, H.W; Allen, J.W; J.Phys.C, 6, 3491 (1973).

Manuscript received Sept. 21, 1979.

Publication costs of this article were assisted by Thames Polytechnic.

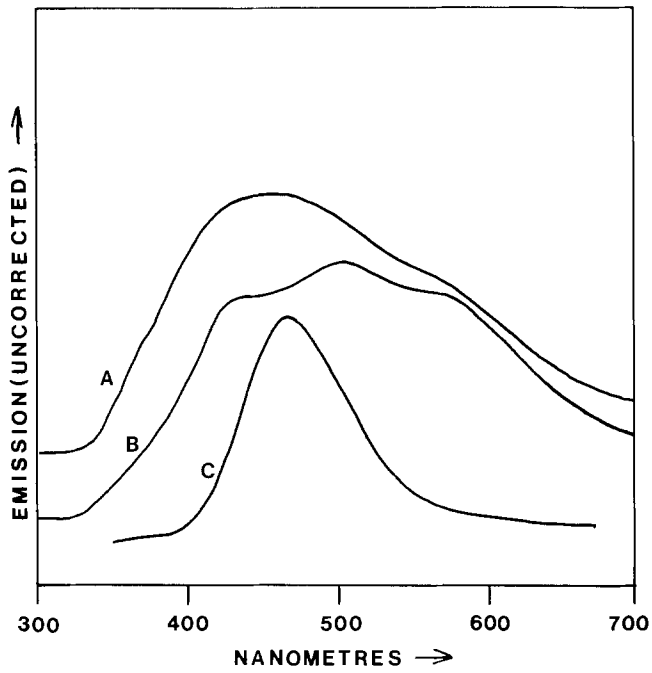


Fig. 1. Spectra with h - c excitation. A: 300°K, B: 77°K and spectrum of "post-field" recombination with square wave excitation (C). The shoulder in the spectra of A and B at 580 nm is presumed to be due to traces of Mn.

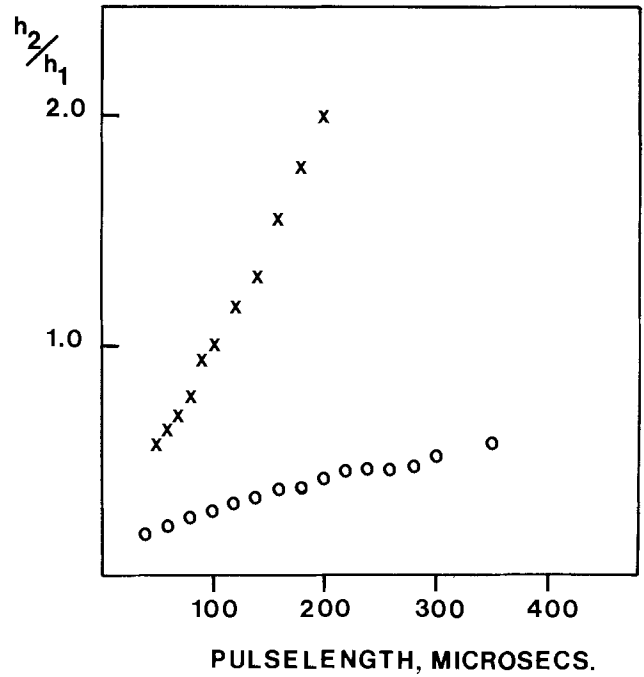


Fig. 3. Ratio of secondary to primary peak heights, $h_2:h_1$ as a function of pulse length. Applied voltage 160V. O: 10^2 Hz, X: 2×10^3 Hz

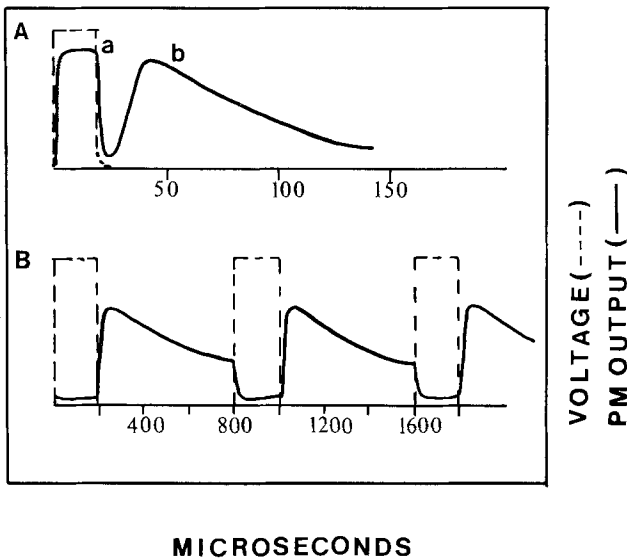


Fig. 2. A: Typical appearance of secondary emission peak with square wave excitation. B: Secondary emission peak with high duty cycle.

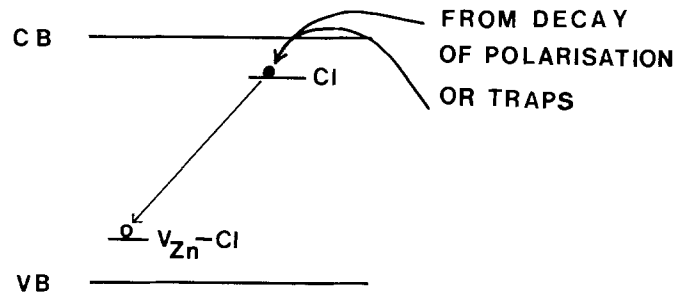


Fig. 4. Possible model for recombination processes in ZnS containing S-A centers.

Silicon Dioxide as Masking Film in Alkaline Etching

Irene Barycka and Helena Teterycz

Instytut Technologii Elektronowej, Politechniki Wrocławskiej, Wrocław, Poland

Anisotropic etching of selected areas of silicon surfaces in alkaline solutions is often applied in technology of silicon semiconductor devices, for example for making grooves, dividing structures, or in production of thin silicon membranes (1-5). In the two last examples, when a large etch depth *ca.* 200 μm is needed, the etch resistance of the masking film is of special importance. The use of SiO_2 films made by silicon wafer oxidation as masking material is well justified for technical reasons. Selected areas of the surface are exposed to etching solution by simple photolithography. It should be emphasized that the shape of hole or groove, especially in the case of deep etching, depends much more on the crystal structure than on the precision of lithography.

The etch resistance of SiO_2 to organic bases is reported by Finne and Klein (6). The rate of this etching is as low as $3.5 \cdot 10^{-4}$ $\mu\text{m}/\text{min}$.

This communication presents the results of investigations on SiO_2 etch resistance to 30 w/o NaOH. Since NaOH is much cheaper and easily handled, its use is fully justified as a substitute for organic bases.

SiO_2 films of 0.5 and 1.3 μm thickness were produced by oxidation of silicon wafers in wet oxygen at 1373°K. It appears that films prepared on smooth, polished, or rough silicon surfaces did not differ in their masking ability.

The wafers under study were mounted on rotating disk (250 rpm) and etched in 30 w/o NaOH in the temperature range 350°-373°K. Etching rate *vs.* reciprocal temperature is plotted in Fig. 1. The calculated activation energy obtained in this same way for silicon is 62-64 kJ/mol. Another interesting result obtained is the ratio of etching rates for slowly etching $\langle 111 \rangle$ and SiO_2 . This is shown in Fig. 2. The results obtained allow one to choose an optimal safe thickness of masking

film for silicon etching to the required depth. In the conditions reported, the ratio of Si $\langle 111 \rangle$ to Si $\langle 100 \rangle$ etching rate is 1:6.6.

The examined SiO_2 films were successfully used as masking material in thin silicon membranes production (7) and in other similar operations

REFERENCES

1. F. E. Holmes, C. A. T. Salama, *Electron. Lett.*, 9, 457 (1973).
2. T. J. Rodgers and Meindl, *IEEE Trans. Electron Devices*, ed-20, 226 (1973).
3. J. C. Greenwood, *This Journal*, 116, 1325 (1969).
4. M. J. Declercq, L. Gerzberg, and J. D. Meindl, *ibid.*, 122, 545 (1975).
5. M. J. Declercq, *IEEE J. Solid-State Circuits*, sc-10, 191 (1975).
6. R. M. Finne and D. L. Klein, *This Journal*, 114, 965 (1967).
7. I. Barycka, H. Teterycz, and Z. Znamirowski, *This Journal*, 126, 345 (1979).

Manuscript submitted June 3, 1979; revised manuscript received Sept. 27, 1979.

Key words: silicon, silicon dioxide, masking film, alkaline etching.

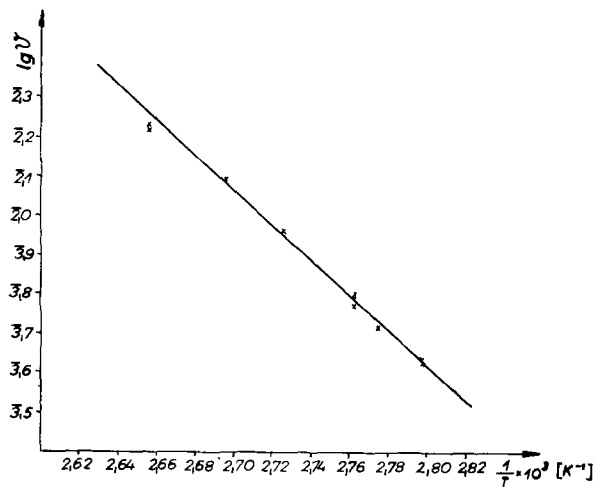


Fig. 1. Etching rate film SiO₂ vs. reciprocal temperature.

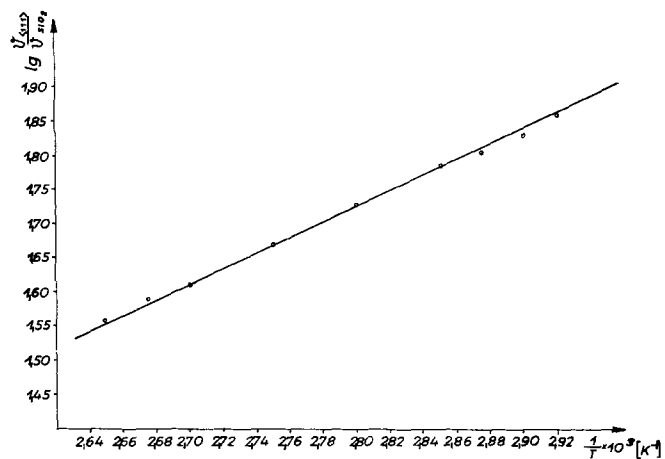


Fig. 2. The ratio of etching velocities for Si <111> and SiO₂ vs. temperature.

Surface Etching by Laser-Generated Free Radicals

J. I. Steinfeld, T. G. Anderson, and C. Reiser

Department of Chemistry, Massachusetts Institute of Technology, Cambridge, Massachusetts 02139

and D. R. Denison, L. D. Hartsough, and J. R. Hollahan*

Perkin-Elmer Corporation, Ultek Division, Mountain View, California 94043

Abstract

We have found that reactive neutral fragments, generated by multiple infrared photon dissociation of various molecules with a CO₂ laser, are capable of etching silicon oxide or nitride surfaces. The laser-generated radical etching process has a potential for major commercial impact, by eliminating ion-bombardment damage in the resulting semiconductor device and by permitting more efficient and selective etching to be performed. In addition, this provides an investigative tool for learning the precise identity of the active species, the extent of their interaction with the substrate surface, and the rates of the key steps in the reactions resulting in net removal of silicon.

Introduction

In the reactive ion etching process, which is in wide current use for processing of semiconductor devices^(1,2) an etch gas such as CF₄ or CHF₃ is dissociated by an rf plasma in a chamber containing the wafers or other workpieces. The resulting fragments then react with the exposed surface of the material. One problem associated with this process is that the charged particles present in the plasma induce radiation damage in the material being etched⁽³⁾; eliminating this damage often requires an additional annealing step in the manufacturing process. Also, the presence of a large number of species in the reactive plasma makes it difficult to establish the mechanism of the etching reactions in any detail⁴.

We have found that etching of SiO₂ surfaces can be accomplished by dissociating a suitable etch gas with a high-power infrared laser, when the beam is focussed near but not directly on the surface. This differs from the usual type of laser-annealing process⁵, in which the sample surface is directly heated by the laser radiation. CF₃Br was chosen as the etch gas, since it is easily dissociated by using a CO₂ laser⁶.

Experimental Results

Initial irradiation was carried out with a Tachisto 215-G TEA CO₂ laser (line-tunable, 0.2-1.5 J/pulse, 45-nsec pulse width, 1 Hz pulse repetition rate). The surface of the substrate in the test chamber was positioned ~ 1 mm away from the focal volume of the laser beam. In a typical result, a sample of silicon dioxide (deposited on a silicon substrate by reaction of SiH₄ + N₂O at 900°C) was etched in an atmosphere of 5.5 Torr CF₃Br. 1200 pulses of the CO₂ laser [R(28), 00°1-02°0 line at 9.23 μm, 0.4 J/pulse] produced an etch depth of 350 Å, as determined by a scanning stylus-probe step-height technique. Silicon nitride samples were also tested, and other etch gases (CF₂Cl₂, CDF₃) were employed; positive evidence of etching was obtained in most cases. Additional surface diagnostics on these samples are being carried out at the present time.

Discussion

The 1200 pulses necessary to achieve an etch depth of 350 Å required 20 minutes irradiation time with a 1-Hz laser. While in absolute terms this appears to be a slow etch rate, some analysis is required to understand the true significance of this result. The 1200 x 45-nsec laser pulses correspond to only 54 μsec of laser "on"-time. A more pertinent time scale is the exposure of the substrate surface to the active species, CF₃. Benson⁽⁷⁾ gives the bimolecular recombination rate for CF₃ radicals as $k = 1.7 \times 10^{10} \text{ liter mole}^{-1} \text{ sec}^{-1}$ at 300°K. Since about 10% of the total CF₃Br (5.5 Torr) was dissociated by each pulse, the mean CF₃ lifetime can be estimated as $t_{1/2}[\text{CF}_3] = 1/[\text{CF}_3]_0 \times k_{\text{recomb}} \approx 1.5 \times 10^{-6} \text{ seconds}$; thus, the total exposure time is $1200 \times 1.5 \mu\text{sec} \approx 1.8 \text{ msec}$. Thus, the true "etch rate" is on the order of $350\text{Å}/1.8 \times 10^{-3} \text{ sec} \approx 200,000 \text{ Å/sec} \approx 12,000,000 \text{ Å/min}$. This is spectacularly greater than the customary plasma etch rate, which at best is about 2000 Å/min.

In practical terms, the 1200 laser pulses could be delivered by a 200 Hz TEA CO₂ laser⁽⁸⁾ in 6 seconds, giving an overall etch rate of 3500 Å/min. This is already quite comparable with current technology in this area, and points up the importance of using a high-repetition-rate laser for further studies of these phenomena. The reaction volume associated with the focussed laser beam can be expanded by suitable optics⁽⁹⁾ to permit exposure of a standard 3-4" wafer to the reactive species, although the extent to which this is feasible will be limited by the threshold fluence requirements for the multiphoton dissociation.

Further development of this laser-generated radical etching technique should lead to a new "dry" processing method which will eliminate compromise of device performance resulting from radiation damage, and also lead to more rapid and selective etching. A possible limitation to this process, which requires further investigation, is the degree of etch anisotropy which can be produced by neutral instead charged species bombarding the surface of the material. Since the laser produces only a single reactive species (e.g., CF₃, CF₂, F, or the like), at a high concentration and also highly localized in time and in proximity to the surface, a detailed mechanistic study of the surface reactions leading to etching can be carried out.

References

- ¹R.L. Bersin, Solid State Technology, May 1976, p. 21.
- ²A.T. Bell, Solid State Technology, April 1978, p. 89.
- ³D.J. DiMaria, L.M. Ephrath, and D.R. Young, J. Appl. Phys. 48, 4973 (1978).
- ⁴H.F. Winters, J.W. Coburn, and E. Kay, J. Appl. Phys. 48, 4973 (1978).
- ⁵C.W. White, J. Narayan, and R.T. Young, Science 204, 461 (1979).
- ⁶E. Würzberg, L.J. Kovalenko, and P.L. Houston, Chem. Phys. 35, 317 (1978).

⁷S.W. Benson, "Fundamentals of Chemical Kinetics", p. 302, McGraw-Hill Book Co., New York (1960).

⁸The operation of such a laser in a ³⁴S enrichment module has been described by V.N. Bagratashvili, Yu.R. Kolomisky, V.S. Letokhov, E.A. Ryabov, V.Yu. Baranov, S.A. Kazakov, V.C. Nizjev, V.D. Pismenny, A.I. Starodubtsev, and E.P. Velikhov, Appl. Phys. 14, 217 (1977). A similar ("mini-TEA") laser is also in operation at the M.I.T. Lincoln Laboratories.

⁹C. Reiser and J.I. Steinfeld, Opt. Eng., to be published.

* Electrochemical Society Active Member.

Manuscript submitted Sept. 28, 1979;
revised manuscript received Nov. 21, 1979.

Publication costs of this article were assisted by the Massachusetts Institute of Technology.

A Different View of the Tafel Equation in Electrode Processes

Akira Doi

Department of Inorganic Materials, Nagoya Institute of Technology, Nagoya 466, Japan

At not too low overvoltages ($|\eta| > RT/zF$), any electrode process satisfies the Tafel equation (1)

$$\eta = a - b \log_{10} i \quad [1]$$

where i is the current density, a and b the Tafel constants, R the universal gas constant, z the valency, and F the Faraday's constant. Although a number of papers deal with Eq. [1] (2), many of them presuppose thermal excitation processes for charge transfer to occur. Even a quantum-mechanical interpretation in terms of electron-tunneling requires thermal rearrangement of solute molecules in the vicinity of relevant electrode (3,4). The purpose of the present note is to suggest an alternative that the Tafel equation can be obtained without reference to thermal equilibrium of the form



where O and R are two oxidation states. For convenience sake, only cathodic polarization ($\eta < 0$) is considered.

Recently, it is inferred(5) that the neutralization process of alkalis in alkali silicate glass is due to tunneling of electrons through the potential barrier in the space charge-cathode double layer, and that the neutralization probability comes close to unity with increasing i , although it depends strongly on the work function of the cathode and perhaps on what the charge carriers are. In alkali silicate glass a potential drop appears in the alkali-depletion layer near the anode(5), whereas in liquid electrolyte having two mobile carriers of the opposite sign, large potential drops are developed on both electrodes and overwhelm a

potential drop across the electrolyte. If the neutralization probability of negative charge carriers on the anode is unity as positive charge carriers on the cathode do, that is, if no space charges are left unneutralized on both electrodes, the polarization potential at the cathode is about $-V/2$, so

$$\eta \approx -\frac{V}{2} + E_e \quad [3]$$

where V is an applied voltage, and E_e is the equilibrium electrode potential. Therefore, for cathodic polarization, η may be equal to an effective potential drop near the cathode. Such a potential drop across the space charge-cathode double layer of an effective thickness d gives an electric field $-\eta/d$ which is sufficient for easy tunneling of electrons to occur.

In these circumstances, since dynamic motion of charge carriers in liquid electrolyte resembles diffusion of constituent ions in solid(6), a theory of ionic conduction in glass(7) can be employed to give the current density as a function of overvoltage, as

$$i = \frac{ne\lambda p}{3} \exp \left[e \left(-\frac{\eta}{d} \right) - \frac{\lambda}{2kT} \right] \quad [4]$$

where

$$p = \nu \exp [-H/kT] \quad [5]$$

is the jumping probability of charge carriers over an energy barrier H , ν the jumping frequency, n the carrier density, and λ the average jumping distance. Rewriting Eq. [4], we obtain the Tafel equation

$$\eta = \frac{2kTd}{e\lambda} \log_e \frac{ne\lambda p}{3} - \frac{2kTd}{e\lambda} \log_e i \quad [6]$$

The Tafel slope b is then

Key words: Tafel equation, charge transfer, tunneling.

$$b = 2.30 \frac{2kTd}{e\lambda}$$
$$\left(= 0.119 \frac{d}{\lambda} \text{ at room temperature} \right) \quad [7]$$

If $d \approx \lambda$, the value of b is in good agreement with the experimental results for e.g. the hydrogen electrode(2). With decreasing η , the polarization curve deviates from Eq. [1] and i becomes proportional to η , in further coincidence with the theory of ionic conduction in solid.

REFERENCES

1. J. Tafel, Z. Phys. Chem. 34, 187 (1900).
2. T. Erdey-Grúz, "Kinetics of Electrode Processes" p.151, Adam Hilger, London (1972).
3. R. R. Dogonadze, A. M. Kuznetsov, and V. G. Levich, Electrochim. Acta 13, 1025 (1968).
4. H. Gerischer, Z. Phys. Chem. 26, 223 (1960).
5. A. Doi, J. Appl. Phys. 50, 1291 (1979).
6. P. A. Egelstaff, "An Introduction to the Liquid State" p.148, Academic, London (1967).
7. A. E. Owen, Progr. Ceram. Sci. 3, 77 (1963).

Manuscript received Oct. 20, 1978.

Publication costs of this article were assisted by Nagoya Institute of Technology.

Semiconductor Electrodes

XXIX. High Efficiency Photoelectrochemical Solar Cells with n-WSe₂ Electrodes in an Aqueous Iodide Medium

Fu-Ren F. Fan, Henry S. White, Bob Wheeler, and Allen J. Bard*

Department of Chemistry, The University of Texas at Austin, Austin, Texas 78712

A number of photoelectrochemical (PEC) photovoltaic (or regenerative) cells based on semiconductor electrodes in aqueous and nonaqueous media have been described; see (1-7) and references therein. High solar energy conversion efficiencies in such cells require a semiconductor band gap energy (E_g) which matches well with the solar spectrum, a semiconductor flat-band potential (V_{fb}) and solution redox couple potential (V_{redox}) which maximizes the output voltage, and conditions which minimize recombination processes in the semiconductor and solution and at the interface. The solution redox couple and solvent are selected to stabilize the semiconductor from photoinduced corrosion processes (8,9). The highest published power efficiency for such cells is the 12% reported for a single crystal n-GaAs electrode in a selenide medium (10). We describe here a PEC cell based on single crystal n-WSe₂ which shows comparable efficiencies.

The applicability of the layer-type compounds based on molybdenum and tungsten dichalcogenides (e.g. MoS₂ and MoSe₂) as semiconductor electrodes was first described and investigated by Tributsch and co-workers (11-15). In more recent work cells based on p-WSe₂ (16,17) and the dependence of the photo-potential on the solution redox couple for n-WSe₂ has been described. These materials appear promising as candidates for practical PEC solar cells because their excitation involves d-d transitions which may provide good stability (12) and because they are relatively cheap and abundant materials. However the performance of cells reported to date have been rather modest. We report here an n-type WSe₂ with a high efficiency.

The n-WSe₂ crystals, grown by chemical vapor transport, were generously donated by Drs. Barry Miller and Frank DiSalvo of Bell Laboratories. They were connected to a copper wire with silver epoxy cement (Allied Products Corp., New Haven, Conn.). Before mounting the crystal, a clean, new crystal surface (\perp c-axis or van-der-Waals surface) was prepared by sticking adhesive tape on the surface, and then pulling it, along with the surface layer of the crystal, off. The crystal was mounted in 7 mm-diameter glass tubing with all sides insulated with silicone rubber sealant (Dow Corning Corp., Midland, Mich.) leaving exposed the van-der-Waals surface with an area of about 0.017 cm². Before use, the electrode surface was etched with 12 M HCl for 5-10 seconds followed by a thorough rinsing with water. The electrochemical measurements followed previous practice (7). The PEC cell consisted of the n-WSe₂ electrode and a Pt foil counter electrode (40 cm²) immersed in a solution of 0.5 M H₂SO₄, 0.5 M Na₂SO₄, 1.0 M NaI and 0.025 M I₂. The path length from the Pyrex window of the cell to the n-WSe₂ electrode was about 1 cm. The n-WSe₂ electrode was irradiated with light from a 450 W xenon lamp which was passed through a 590-nm cut-on and an infrared (water) filter (i.e., only light of wave length longer than 590 nm irradiated the cell). The intensity at the cell window was 150 mW/cm² (which is somewhat higher than the maximum terrestrial solar intensity). Under these conditions I⁻ is photo-oxidized to I₃⁻ at the WSe₂ and I₃⁻ is reduced to I⁻ at the Pt counter electrode with the passage of an external current. The short circuit photocurrent was about 65 mA/cm² and the open-circuit photovoltage was about 0.71 V. The i-V curve for this cell, shown in Figure 1, yields a fill factor of 0.46. The maximum power conversion efficiency under these conditions, without corrections

*Electrochemical Society Active Member. Key words: photovoltaic, energy conversion.

for solution absorbance and electrode and window reflectivities, is about 14%. The short circuit photocurrent was linear with light intensity up to at least 150 mW/cm^2 (Figure 2). Moreover the open circuit photovoltage closely approached its saturation value of 0.7 V at light intensities $\geq 10 \text{ mW/cm}^2$. This latter finding and the high fill factor suggests that recombination processes are relatively unimportant for this material. The cell was operated under roughly maximum power conditions for 8 hours. At this time the current and cell voltage were essentially the same as the initial values and the electrode surface showed no apparent change or signs of degradation. (The total amount of electricity passed in this 8-hour trial, about 32 coulombs, would represent on the order of 113 mg of WSe_2 lost, assuming a one-electron process, if a photodissolution process occurred.)

While the results here are of a preliminary nature and we have found some sample-to-sample variability with WSe_2 , they appear to confirm the earlier predictions of Tributsch, *et. al.* on the potential usefulness of layer-type semiconductors in PEC cells. The nature of the semiconductor surface is also probably of major importance in the attainment of high efficiencies. The investigation of surface pretreatment effects and the application of oriented polycrystalline materials or epitaxial layers of n-WSe_2 in iodide media is currently under investigation.

Acknowledgment.--This work was supported in part by the Office of Naval Research and by the Solar Energy Research Institute (in a cooperative project with SunX Corporation).

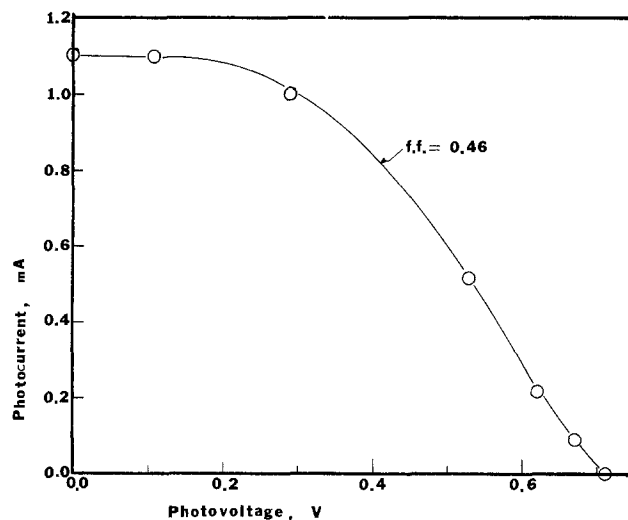


Fig. 1. Photocurrent-photovoltage characteristic of an $\text{n-WSe}_2/0.50 \text{ M Na}_2\text{SO}_4, 0.50 \text{ M H}_2\text{SO}_4, 1.0 \text{ M NaI}, 0.025 \text{ M I}_2/\text{Pt}$ PEC cell. Irradiation was with the output (longer than 590 nm and IR filtered) from a 450 W Xe lamp focused onto the photoelectrode. The optical path through the solution is about 1 cm. (f.f. = fill factor).

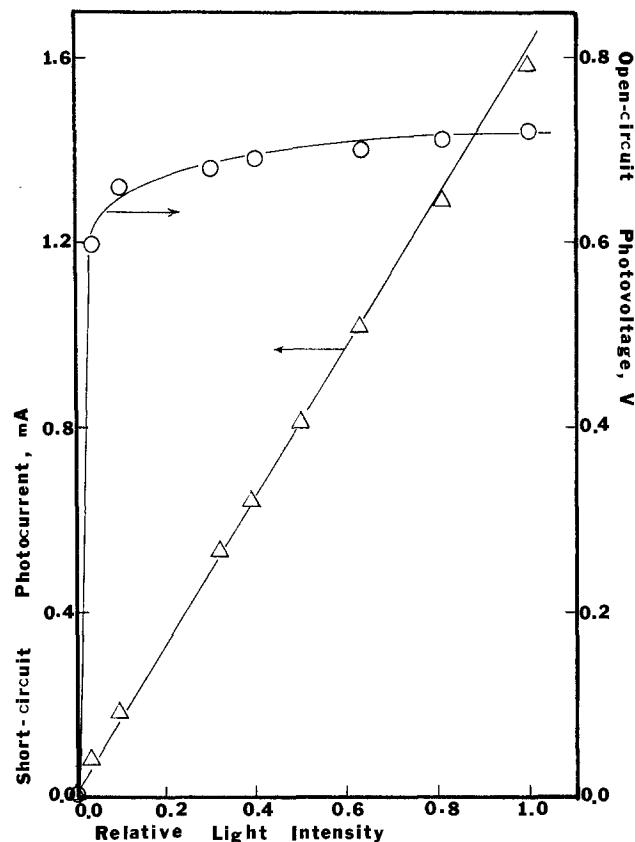


Fig. 2. Open circuit photovoltage and short-circuit photocurrent as functions of light intensity. Conditions as in Fig. 1.

REFERENCES

1. A. J. Nozik, Ann. Rev. Phys. Chem., **29**, 189 (1978).
2. D. Laser and A. J. Bard, This Journal, **123**, 1027 (1976).
3. A. B. Ellis, S. W. Kaiser, and M. S. Wrighton, J. Am. Chem. Soc., **98**, 1635 (1976).
4. T. Inoue, T. Watanabe, A. Fujishima, K. Honda, and K. Kohayaka, This Journal, **124**, 719 (1977).
5. B. Miller, A. Heller, M. Robbins, S. Menezes, K. C. Chang, and J. Thompson, This Journal, **124**, 1019 (1977).
6. A. B. Ellis, J. M. Bolts, and M.S. Wrighton, This Journal, **124**, 1603 (1977).
7. P. A. Kohl and A. J. Bard, This Journal, **126**, 603 (1979).
8. H. Gerischer, J. Electroanal. Chem., **82**, 133 (1977).
9. A. J. Bard and M. S. Wrighton, This Journal, **124**, 1706 (1977).
10. B. A. Parkinson, A. Heller, and B. Miller, This Journal, **126**, 954 (1979).
11. H. Tributsch and J. C. Bennett, J. Electroanal. Chem., **81**, 97 (1977).
12. H. Tributsch, Ber. Bunsenges. Phys. Chem., **81**, 361 (1977).
13. H. Tributsch, ibid., **82**, 169 (1978).
14. H. Tributsch, This Journal, **125**, 1086 (1978).
15. J. Gobrecht, H. Gerischer, and H. Tributsch, This Journal, **125**, 2085 (1978).
16. J. Gobrecht, H. Gerischer, and H. Tributsch, Ber. Bunsenges. Phys. Chem., **82**, 1331 (1978).
17. H. Tributsch, H. Gerischer, C. Clemen, and E. Bucher, ibid., **83**, 655 (1979).

Manuscript received Dec. 18, 1979.

Publication costs of this article were assisted by The University of Texas at Austin.



Anodic Behavior of Lithium in Aqueous Electrolytes

IV. Influence of Temperature

E. L. Littauer* and K. C. Tsai*

Lockheed Palo Alto Research Laboratory,
Lockheed Missiles and Space Company, Incorporated, Palo Alto, California 94304

ABSTRACT

The influence of temperature on the anodic behavior of lithium in LiOH was studied at constant electrolyte flow velocity, concentration, and contact pressure. It was found that the thickness of oxide film decreases significantly with increasing temperature and the active surface area decreases gradually with increase in temperature. A rate equation for the H₂ e.r. at an anodically polarized Li surface serves to predict the current efficiency at various temperatures. By polarizing the anode, the hydrogen evolution reaction is inhibited and this, coupled with a significant decrease of the surface active area with increasing temperature, explains the stability of the lithium electrode in aqueous alkaline electrolytes. Data on the conductivity of 4.5M LiOH at temperatures from 17° to 64°C are reported.

The rapid dissolution of Li in alkaline aqueous solutions can be utilized electrochemically to produce very high rate batteries. In the Li-H₂O system, the rate-limiting process is the oxidation of lithium rather than the reduction of H₂O at the cathode. A critical examination of the corrosion processes has revealed that the H₂ e.r. at the Li surface is rate-determining, not the Li dissolution reaction (1). Thus, unlike conventional battery systems, in Li-H₂O cells the current efficiency is governed by the ratio of two competing processes, namely, the anodic dissolution reaction and the parasitic self-corrosion reaction (2). The current efficiency increases as the electrode is polarized from its OCV, and it decreases at elevated temperatures where the corrosion reaction is stimulated. One of the most important features of the system is the fact that the maximum current (or limiting current) obtained during anodic polarization never exceeds the OCV corrosion rate. This unusual behavior and the impact of elevated temperature on the faradaic efficiency of the cell are examined in this paper.

Experimental

Details of the electrochemical cell and support equipment have been given previously (1). In summary, the test cell housed a circular 11.4-cm² area anode support to which were bonded lithium test specimens. The cathode comprised a wire screen spotwelded to a ribbed iron back plate. Anode-cathode contact pressure was controlled by an air pressure cylinder linked to the anode pushrod. Elimination of the hydraulic pressure component was accomplished by a thrust balance cylinder connected to the inlet and outlet lines of the cell. Electrolyte hydraulic pressure could be varied by a control valve on top of the test cell. A needle point penetrometer was mounted on the cathode compartment such that on activation the

platinum-plated steel needle could pass through the matrix and penetrate the anode surface. The penetrometer was instrumented with an impedance meter and linear motion transducer (2). Accuracy of the probe position was within $\pm 10^{-3}$ cm.

Electrolyte flow through the cathode matrix and across the anode face was provided by a micropump and was monitored with a rotameter. Electrolyte temperature was controlled to $\pm 0.1^\circ\text{C}$ by passing it from a reservoir to a constant temperature heat exchanger, and into the cell.

Real time hydrogen rate measurements were obtained using a wet test meter which was modified with an optical encoder connected to a digital/analog converter.

Lithium hydroxide solutions were prepared using reagent grade chemical and deionized water.

The experimental conditions for the sequence of tests reported here were: LiOH concentration: 4.5M, electrolyte flow rate: 30 cm/sec, anode-cathode contact pressure: 6.2×10^4 Pa, and electrolyte temperature: 18°, 25°, 35°, 45°, 55°C.

Polarizations were performed potentiostatically, using a custom-designed 0-10A, 0-10V instrument. Response time was 60 μsec (from no load), input impedance was $1.5 \times 10^{12} \Omega$, and voltage stability was $\pm 2.5\%$. The duration of each polarization run was less than one minute. Steady-state conditions were actually achieved within a fraction of a second. Runs were repeated three times for each temperature, reproducibility was within $\pm 5\%$. Film thickness measurements were repeated six times by rotating the anode through 60° segments.

Anode potentials were monitored with a cadmium (cadmium hydroxide) reference electrode ($E^\circ = -0.809\text{V vs. NHE}$).

Electrolyte conductivities were measured at 28°, 38°, 45°, 51°, 55°, and 64°C using a conventional conductivity cell of constant 1.07 obtained by reference to 0.1N KCl solution.

* Electrochemical Society Active Member.

Key words: lithium, lithium hydroxide, anodic polarization, corrosion, current efficiency, limiting current.

Results

The influence of temperature on the anodic polarization of Li in 4.5M LiOH at a constant anode-cathode contact pressure, $P = 6.2 \times 10^4$ Pa and electrolyte flow velocity, $v = 30$ cm/sec is shown in Fig. 1. The OCV values measured here at various temperatures are essentially the same (i.e., within 5 mV) of those obtained in an earlier investigation (1). The polarization curves possess two distinct regions, typified by the curve at 55°C. The initial portion of the curve depicted as a-c is linear. It represents IR drop across an essentially invariant protective oxide film layer. The highly polarized curved portion c-l has a configuration which is often characteristic of a limiting current. Over the entire span, a-c-l, it is assumed that the anodic film formation rate is balanced by the film dissolution rate because, as has previously been observed (2), the film thickness is independent of the extent of polarization. Under the experimental conditions specified herein, it was noted that increasing temperature decreased the film's resistance and the maximum current increased markedly with increasing temperature.

From the slopes of the resistive polarization sections of the curves of Fig. 1, a plot of film resistance vs. temperature may be obtained as shown in Fig. 2. Temperature dependence of the limiting current density, i_l , derived from Fig. 1, and of the measured corrosion rate at OCV, i_{cor} , are displayed in Fig. 3. i_{cor} increases significantly at elevated temperatures (i.e., $> 35^\circ\text{C}$) while i_l maintains a linear relationship with temperature over the range of this study.

Figure 4 shows that the relationship between anode film thickness and temperature is nonlinear. The decrease of film thickness x_0 with increasing temperature may be associated with the fact that the solubility of LiOH, which comprises the major portion of the oxide film, increases with increasing temperature (3).

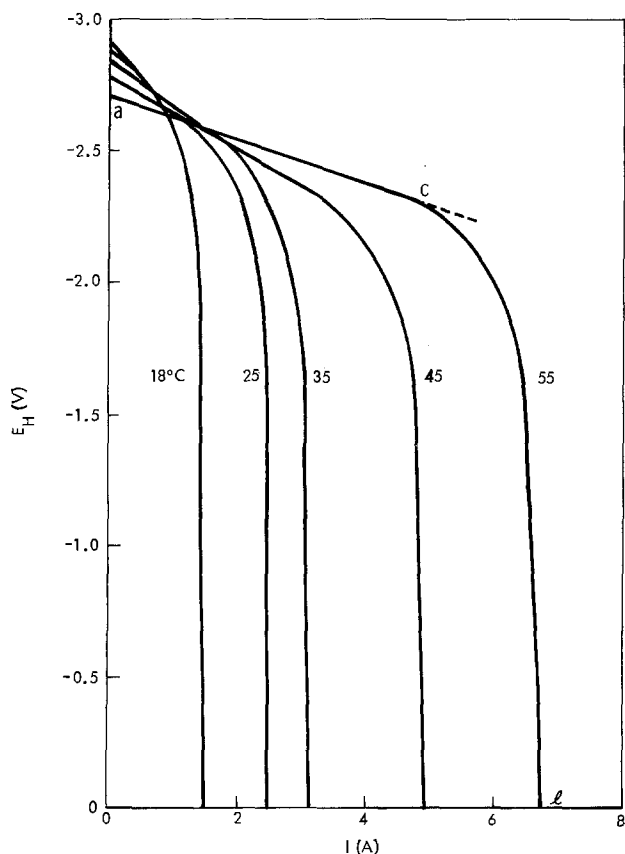


Fig. 1. Anodic polarization of Li in 4.5M LiOH at various temperatures. Anode-cathode contact pressure $P = 6.2 \times 10^4$ Pa, electrolyte flow rate $v = 30$ cm/sec.

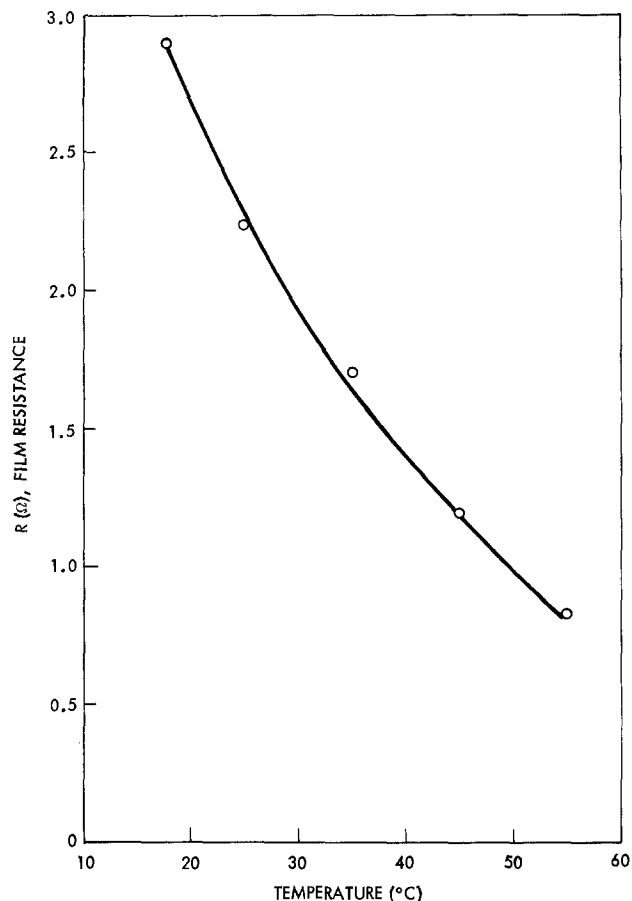


Fig. 2. Influence of electrolyte temperature on anode film resistance in 4.5M LiOH. $P = 6.2 \times 10^4$ Pa, $v = 30$ cm/sec.

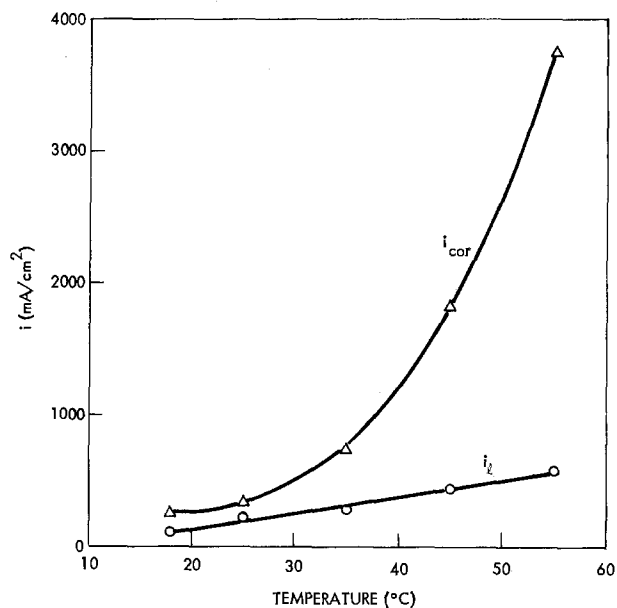


Fig. 3. Li corrosion rate at OCV i_{cor} , and anode limiting current density i_l as function of electrolyte temperature in 4.5M LiOH. $P = 6.2 \times 10^4$ Pa, $v = 30$ cm/sec.

It was found that the variation in film thickness from one 60° segment to the next was somewhat greater at the lower temperatures. Since the film thickness does not change with polarization, it seems reasonable to assume that the solubility of LiOH at various temperatures plays the predominant role in determining the film thickness.

Information on the conductivity of the electrolyte as a function of temperature is required for analysis

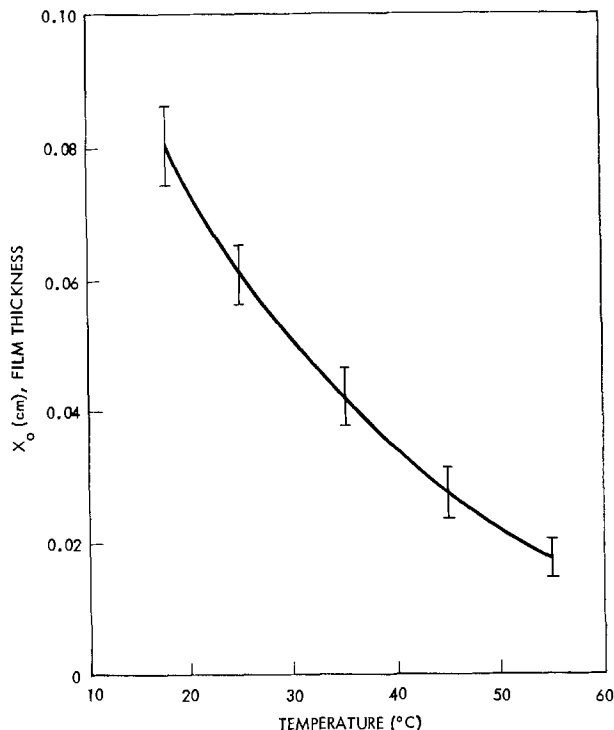
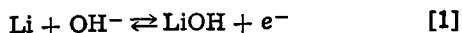


Fig. 4. Influence of electrolyte temperature on the anode film thickness in 4.5M LiOH. $P = 6.2 \times 10^4$ Pa, $v = 30$ cm/sec.

of the experimental data. This data is presented in Fig. 5.

Discussion

In strongly alkaline solution, the dissolution of Li, even when under anodic polarization, consists of two competing processes—an electron-producing electrochemical reaction as described by Eq. [1]



and a direct corrosion (parasitic) reaction as depicted by Eq. [2]



Strictly speaking, the overall corrosion reaction [2] is a coupling of [1] with the cathodic reduction of H_2O at adjacent sites on the anode surface.

Since the competing reactions [1] and [2] can occur at any polarization level at anode sites, one cannot assume that temperature has identical impact on each. Indeed, Fig. 3 clearly illustrates the difference. On one hand, at OCV where there is no external electron-producing reaction, the corrosion rate i_{cor} follows an Arrhenius exponential dependence (1). On the other hand, when the corrosion reaction is suppressed to a negligible amount by polarizing the electrode, the rate of the electron-producing process, i_1 , increases linearly with increasing temperature. Taking a typical polarization curve, such as that at 55°C in Fig. 1, i_{cor} and i_1 represent the rates of Li dissolution at points a and l respectively. During normal operation of the Li- H_2O cell, the Li anode is polarized to a level between a-1 and the current efficiency of the anodic reaction is always somewhat less than 100%. In an earlier paper, a rate equation for the general case of parasitic hy-

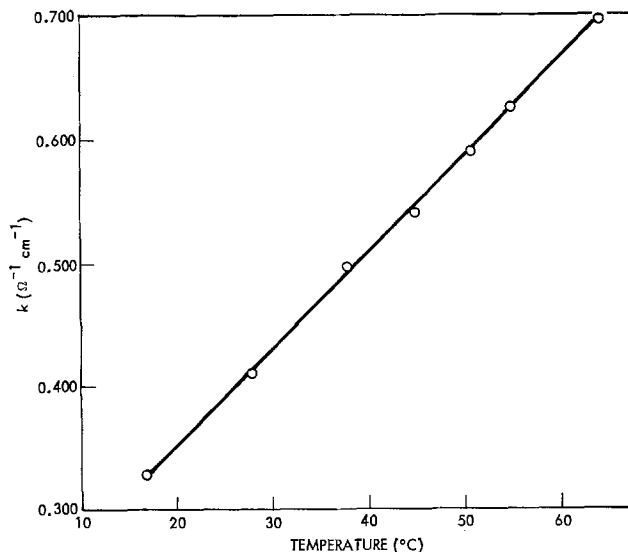


Fig. 5. Temperature dependence of conductivity for 4.5M LiOH

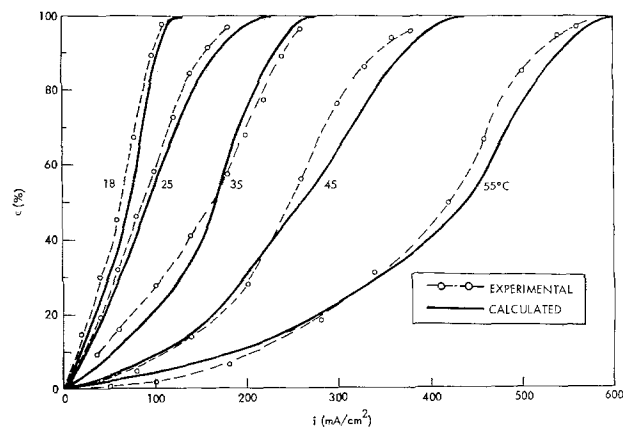


Fig. 6. Current efficiency of a Li anode at various temperatures

drogen evolution reaction at a polarized electrode was derived

$$i_{\text{H}_2} = i_{\text{cor}} \exp\left(\frac{-n\alpha F(E - E_c)}{RT}\right) \quad [3]$$

where E_c is the OCV of the Li at a given temperature; α , the transfer coefficient of H_2 e.r. on the Li surface = 0.14 (1), and the other terms have their usual meaning. The current efficiency for the polarized Li anode is defined as (4)

$$\epsilon(\%) = \frac{i}{i + i_{\text{H}_2}} \quad [4]$$

where i represents the rate of anodic reaction. Using Eq. [3] and the data of Table I, and Fig. 1, $\epsilon(\%)$ at different temperatures have been calculated and are shown in Fig. 6. Figure 6 also includes experimental results obtained from the H_2 rate measurements. Although the two curves are not exactly identical, the similarity in their shapes seems to support the validity of the model which holds that the H_2 e.r. is the rate-determining step in the corrosion reactions of Li. It

Table I. Some basic parameters of the Li- H_2O system in 4.5M LiOH at $P = 6.2 \times 10^4$ Pa and $v = 30$ cm/sec

Temp (°C)	k ($\Omega^{-1} \text{cm}^{-1}$)	i_1 (mA/cm ²)	i_{cor} (mA/cm ²)	x_o (cm)	R (Ω)	$1 - \theta_o$
18	0.332	138	251	0.080	0.290	0.07
25	0.386	219	342	0.061	0.223	0.06
35	0.467	276	762	0.042	0.170	0.05
45	0.540	434	1830	0.027	0.118	0.04
55	0.623	591	3760	0.018	0.082	0.03

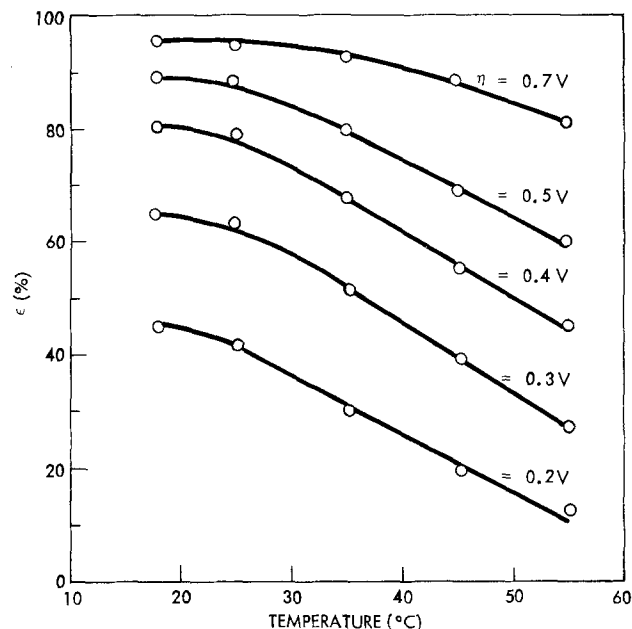


Fig. 7. Effect of anodic polarization on the current efficiency of a Li anode at various temperatures.

should be mentioned that the differences in the curves between the experimental and the calculated results can, with the exception of the 35° data, be eliminated if the value of α is increased from 0.14 to 0.143. In other words, the discrepancy is probably ascribable to errors in the calculation of the H_2 evolution rate using Eq. [3]. It may also be seen from Fig. 6 that by imposing significant polarization, near to 100% current efficiency is obtained. To illustrate the temperature dependence of $\epsilon(\%)$ at various polarization levels, Fig. 7 has been constructed. At elevated temperatures, i.e., $T \cong 55^\circ\text{C}$, $\epsilon(\%)$ is generally degraded due to the very high parasitic reaction rate. Thus, in order to operate the Li- H_2O system efficiently at elevated temperatures, a trade-off has to be taken in the form of additional polarization of the anode to achieve acceptable faradaic efficiency.

Over the span of the active polarization region (curve a-c-1 in Fig. 1), steady-state conditions are observed. It is conceivable that in this region a quasi-equilibrium state exists between active and inactive sites. A simplified model of the system indicates that the fraction of active sites, $1 - \theta_0$, may be related to the film thickness (x_0), the average conductivity of the electrolyte (k), film resistance (R), and the projected surface area (A) by the equation

$$1 - \theta_0 = \frac{x_0}{kAR} \quad [5]$$

where θ_0 is the surface coverage by the oxide film. Coupling this equation with data of Table I enables calculation of $(1 - \theta_0)$ at various temperatures. The results are listed in the last column of Table I. The decreasing trend of $(1 - \theta_0)$ with increasing temperature is an intriguing observation, because earlier investigation on the influence of LiOH concentration on the fraction of the active sites revealed that $(1 - \theta_0)$ decreases markedly with increase in M LiOH, e.g.,

at 25°C, $(1 - \theta_0)$ ranged from 0.34 at 2.96M to 0.05 at 4.84M. However, it should be pointed out that the fraction of active sites calculated in this way only serves to compare changes of the active surface areas as a function of temperature. In the present work, the tortuosity factor has been arbitrarily taken as unity and the bulk electrolyte conductivity has been used directly, the basis for this simplification has been discussed previously (2).

Under steady-state conditions, the solubility of LiOH governs the dynamic balance between oxide film formation and dissolution. There is little doubt that the rapid increase in the dissolution rate of Li (see Fig. 3), and its subsequent crystallization as LiOH on the electrode surface at elevated temperatures, far exceeds the rate of increase of solubility of the salt as the temperature increases (3). This then results in a higher rate of film formation than dissolution. A parallel effect of this imbalance of rates is an increase in surface coverage at higher temperature, and this is reflected by a decrease in $(1 - \theta_0)$. The implication of these observations is the realization that the Li- H_2O system is inherently stable even at elevated temperatures provided sufficient polarization is imposed on the anode.

Conclusions

This study has shed further light on the observation that polarization of the H_2 evolution reaction at the Li surface is the rate-limiting process rather than the anodic dissolution reaction. The rate equation which has not previously been tested for the H_2 e.r. at an anodically polarized Li surface serves successfully to predict the current efficiency at various temperatures. The investigation has also shown that, despite the fact that Li reacts rapidly with H_2O at elevated temperatures, this reaction can be controlled in an electrochemical cell where the H_2 e.r. can be inhibited sufficiently at the anode to permit good current efficiency to be obtained. The decreasing area of surface active sites with increasing temperatures reaffirms the stability of the Li- H_2O system in aqueous alkaline electrolytes.

Acknowledgment

This work was supported by the U.S. Navy, Naval Underwater Systems Center, Newport, Rhode Island, under Contract No. N66604-78-M-8483.

Manuscript submitted April 6, 1979; revised manuscript received Sept. 10, 1979.

Any discussion of this paper will appear in a Discussion Section to be published in the December 1980 JOURNAL. All discussions for the December 1980 Discussion Section should be submitted by Aug. 1, 1980.

Publication costs of this article were assisted by Lockheed Missiles and Space Company, Incorporated.

REFERENCES

1. E. L. Littauer and K. C. Tsai, *This Journal*, **124**, 850 (1977).
2. E. L. Littauer, K. C. Tsai, and R. P. Hollandsworth, *ibid.*, **125**, 845 (1978).
3. E. W. Washburn, Editor, "International Critical Tables of Numerical Data, Physics, Chemistry, and Technology," Vol. 4, p. 233, McGraw-Hill, New York (1926).
4. E. L. Littauer, W. R. Momyer, and K. C. Tsai, *J. Power Sources*, **2**, 163 (1977/78).

Bifunctional Air Electrode for Metal-Air Batteries

Lars Carlsson and Lars Öjefors*

Swedish National Development Company,
Department for Energy and Environmental Technology, 184 00 Akersberga, Sweden

ABSTRACT

In order to fulfill volume and cost requirements on metal-air batteries it is necessary to use bifunctional air electrodes which also serve as counter-electrodes during charge. This twofold duty puts a very high demand on the electrode, especially the structure and catalyst. In the iron-air battery program of SNDC a 0.6 mm porous Ni-electrode with Ag catalyst has been developed for this purpose with a life of more than 1000 charge/discharge cycles. In this paper design, performance, structural changes, mode of failure etc. are discussed.

Secondary metal-air batteries are very attractive from the point of view of energy density because the positive electrochemical reactant, oxygen is supplied from outside the battery. Work on this type of power source started in the middle 1960's in the United States, Japan, and Europe. In most cases these activities were based on know-how from fuel cell development. A short review on these activities is given in Ref. (1).

Swedish National Development Company (SNDC) has been working with an iron-air battery system since 1968. These activities have resulted in full scale batteries tested in vehicles. In 1974 a second generation prototype was tested in a 15 kW-hr-battery in a mine vehicle. Based on experience obtained during these tests a third generation was designed and a 30 kW-hr-battery built and tested during 1974 and 1975. This battery system including auxiliaries is described in Ref. (1).

For primary and mechanically rechargeable metal-air batteries, where zinc dominates the field as negative active electrode material, comparatively simple designs of air electrodes can be used since they only work in discharge mode. Consequently designs used in fuel cells are suitable for these applications. For a secondary metal-air battery the application of the air electrode differs somewhat from its use in fuel cells unless a third auxiliary electrode is used during charge. Since volume is a very critical parameter in a metal-air battery it is necessary to use rechargeable air electrodes which can be used as counterelectrodes during the charge process. This twofold duty puts a very high demand on the electrode, especially the structure and catalyst. The air electrode used in the prototype battery is of a double layer 0.6 mm thick with nickel as the supporting material. In this paper the structure, limiting factors, as well as different possibilities to improve performance and life will be discussed.

Very little has been published on bifunctional air electrodes (2-4). The electrode developed by Siemens is composed of two layers, one of which is a hydrophilic porous nickel sheet adjacent to the electrolyte. The other one bordering the gas phase consists of a hydrophobic carbon layer. During oxygen reduction the carbon layer plays the active part, while the nickel layer catalyzes the electrode process in liberating oxygen. The activity of the carbon powder is increased by addition of silver ($> 9.6 \text{ mg/cm}^2$). These electrodes have a life of slightly more than 100 cycles. Efforts to increase life by providing an additional hydrophobic layer on the gas side were not successful.

Design of the SNDC Air Electrode

The SNDC bifunctional air electrode is built up of a double layer sintered nickel structure where the raw materials are INCO Ni-287-powder and silver for

catalyst. In the production of the electrode, spacer and hydrophobic additives are used. The spacer is mainly used to build up the coarse layer (thickness 0.4 mm) in order to obtain a uniform porosity and pore size. The use of spacers and the technology to vary its form and grain size developed by SNDC (5) has proved to give advantages regarding the utilization of both nickel and silver as well as the adaption of structure to low differential pressure. This technology is based on mixing the prepared spacer, generally a water soluble inorganic salt, with a metal powder and cold pressing it to an electrode. After sintering the electrode plaque the spacer is removed by dissolving it in water, thus forming a porous body. It is also possible to make electrodes consisting of layers with different porosities.

Figure 1, which is a SEM micrograph cross section of an uncycled air-electrode, shows the fine and coarse layer. This electrode has during several years been optimized to fulfill the requirements regarding critical parameters for a full scale metal-air battery. Figure 2 gives the air electrode performance during life test at 40°C and 5M KOH. Each cycle includes 2 hr charge and 1 hr discharge.

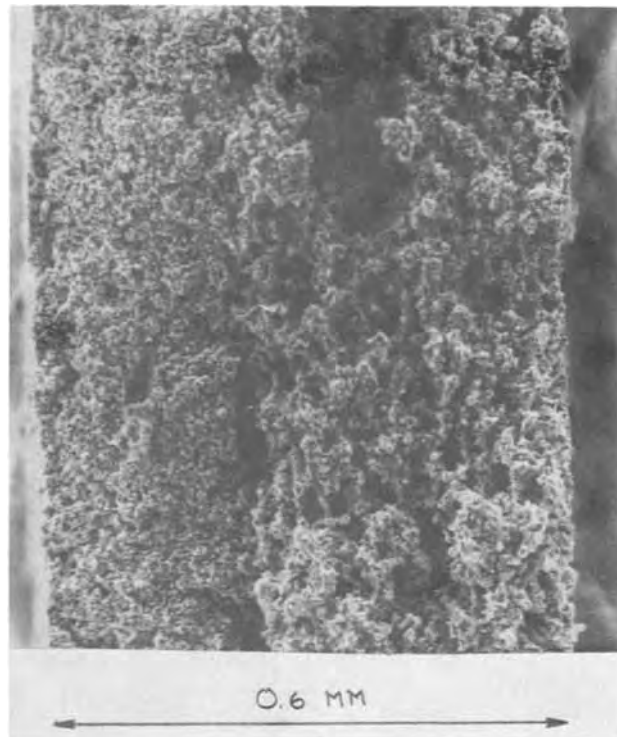


Fig. 1. Scanning electron micrograph of a cross section of an air electrode.

* Electrochemical Society Active Member.
Key words: battery, electrode, air.

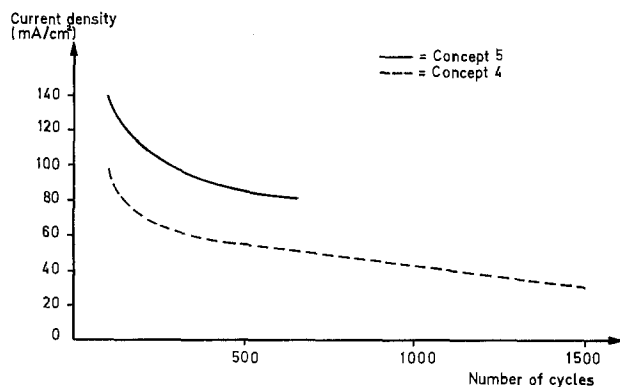


Fig. 2. Air electrode performance during life test. 1 cycle—2 hr charge and 1 hr discharge at 40°C, 5M KOH. Normally 25 mA/cm² is used during the tests.

For a metal-air battery, especially when used in vehicles, the five parameters thickness, differential pressure, working temperature, catalyst contents, and life of the air-electrode are of interest. The thickness is critical since in a metal-air battery the number of air-electrodes is normally twice that of the negatives. This fact together with the fact that volume of the battery stack is more critical than the weight of the battery makes it necessary to develop very thin electrodes. The air-electrodes used in the prototype battery is only 0.6 mm thick.

It is also important to have a low differential pressure in order to minimize the power to pump air through the system as well as the demand on strength and stability on stack design and electrodes. These electrodes are optimized to work at a $\Delta P = 0.02$ bar, a level necessary to keep a steady flow through the system.

Owing to the heat evolved, mainly in the air electrodes, it is necessary to cool the battery. In order to achieve long life for both electrodes and cell stack it is necessary to keep the temperature below 50°C. The electrodes are designed to work at 40°C.

The silver used as catalyst has a tendency to leave its original site in the electrode during cycling and go out into the electrolyte. This phenomenon, which causes decrease in activity and sometimes short-circuiting, depends on the fact that oxygen evolution occurs in the corrosion region of Ag (6). It is important, for economical reasons, to keep the catalyst content at a low level and shield it from dissolving into the electrolyte bulk.

Hydrophobic Treatment

By combining the spacing agent with treatment of hydrophobic agents the active surface of the electrode is increased at the same time as the thickness of the electrolyte layer within the electrode is minimized. This improves the performance of the electrode considerably.

Treatment with hydrophobic agents also decreases the dissolution of silver when going from charge to discharge and vice versa. This depends probably on a thinner electrolyte layer which decreases the possibility for migration of silver ions out into the electrolyte bulk. This effect is shown in Fig. 3 where the silver dissolution is about 10 times lower after treatment with hydrophobic agents. It is evident that hydrophobic additives have a positive influence on the performance and life of the bifunctional air electrode. By optimizing the structure and hydrophobic treatments the performance of the electrode has gradually been improved at the same time as the number of cycles has been increased and the differential pressure has been decreased.

Catalyst Contents

By placing the silver in the active coarse layer zone of the electrode the level can be kept on 2.5

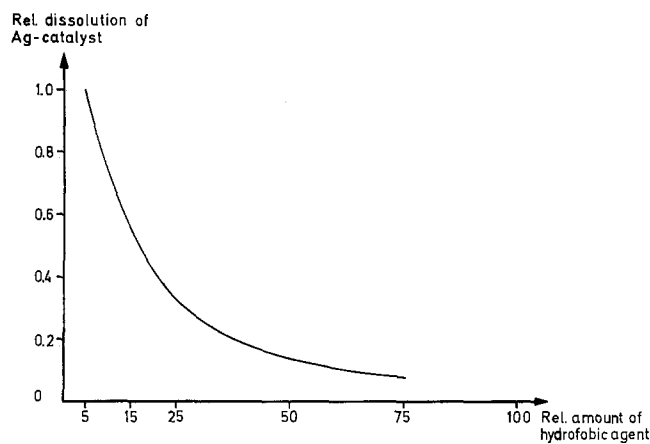


Fig. 3. Influence of hydrophobic treatment on dissolution of Ag-catalyst in SNDC-air electrode. 40°C, 100 cycles.

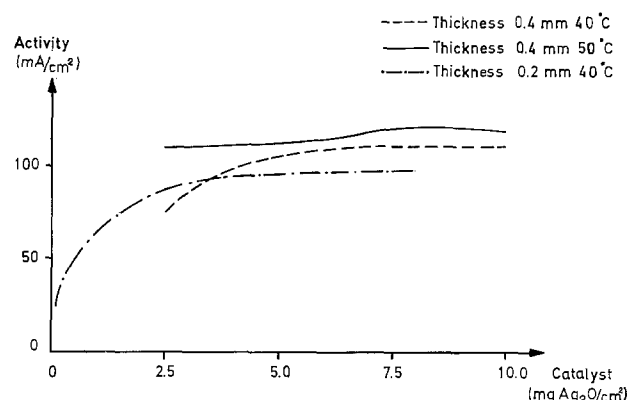


Fig. 4. Influence of catalyst level on air electrode performance. Current density at -300 mV vs. Hg/HgO.

mg/cm² without negative influence on life and performance (Fig. 4).

In this figure results of tests are shown where the catalyst contents have been varied in the interval 10–2.5 mg/cm². It is evident that at 50°C the activity of the electrode is not influenced by the variations in catalyst loading. At 40°C and a coarse layer thickness of 0.4 mm, however, the activity decreases below 5 mg Ag/cm². By decreasing the coarse layer thickness to 0.2 mm the overall activity of the electrode will be lower but with a better utilization of the catalyst. This shows that not only the amount of catalyst is of interest but also the relationship Ni/Ag in the coarse layer. The dissolution of Ag into the electrolyte appears during the first 200 cycles after which the level is almost constant (Fig. 5). The initial loss of Ag is apparently connected to the improvement in capacity during the first 40 cycles (Fig. 6), which also has been observed by Cnobloch *et al.* (4). This depends probably on a redistribution of the catalyst and an increase in the electrochemically active surface of the electrode. The low dissolution rate after 200 cycles de-

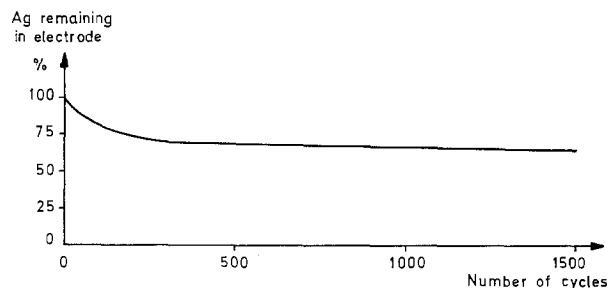


Fig. 5. Dissolution of Ag as a function of cycles

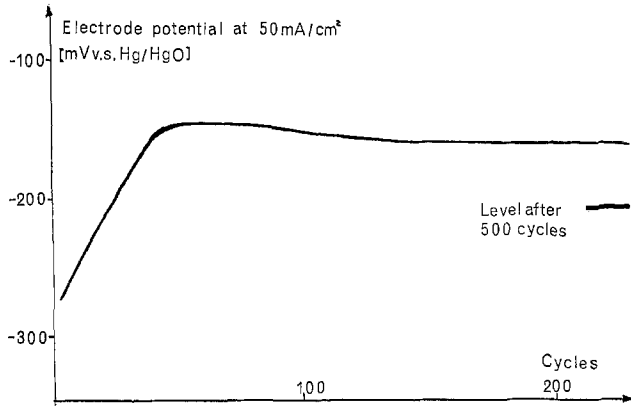


Fig. 6. Performance of air electrodes during cycling. Full cycle 2 hr charge and 1 hr discharge.

depends probably on a decrease in availability of the catalyst partly caused by corrosion products in the Ni-structure.

The relation between catalyst contents and thickness of the coarse layer has also been studied. The tests show that the activity of the electrodes increases from 80 mA/cm² at 0.1 mm coarse layer to the level of 140 mA/cm² at 0.6 mm coarse layer. The catalyst contents were constant as per mg/cm² projected electrode area which means that the highest concentrations of catalyst per volume active material in the thinner layers have not been compensated for the decrease of the specific active surface (Fig. 7).

Life Limiting Factors

After about 150 cycles the performance steadily decreases (Fig. 6). By analyzing electrodes at different stages it has been proved that the main reason for decrease in performance is plugging of the porous structure from corrosion products, mainly Ni(OH)₂. Figure 8 shows how the contents of oxygen which is

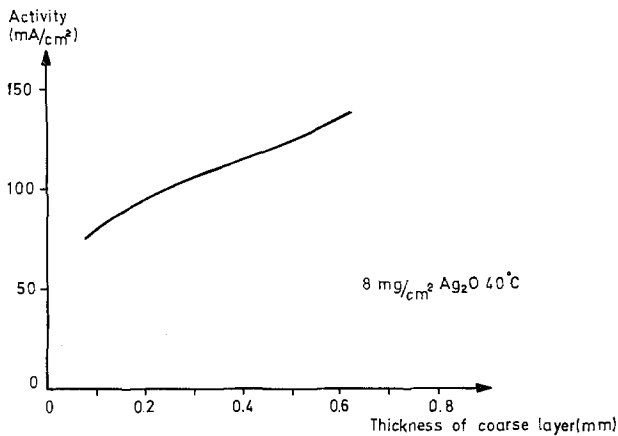


Fig. 7. Influence of coarse layer thickness on air electrode performance. Current density at -300 mV vs. Hg/HgO.

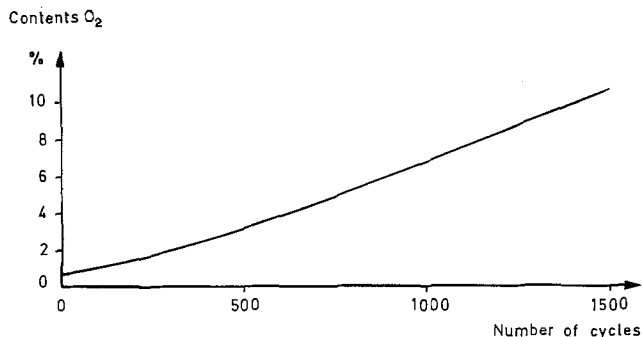


Fig. 8. Development of corrosion products within the air electrode

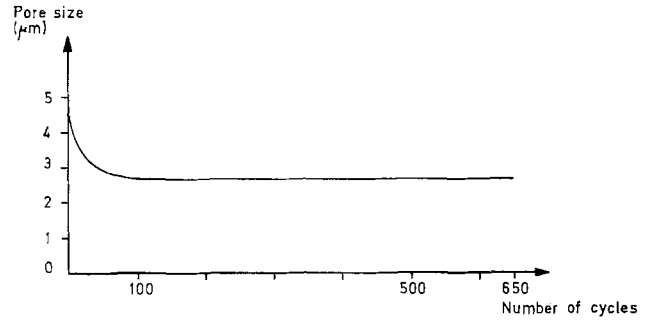


Fig. 9. Mean pore size distribution as a function of cycles

equivalent to corrosion products increase almost linearly when cycling the electrode. This results in a decrease of average pore size according to Fig. 9. The average pore size has been obtained by bubbling air through the electrode. This method is mostly sensitive to changes in the fine pore layer.

The pore size distribution can be determined by mercury porosimetry. Figure 10 gives the distribution for a new electrode, after 650 cycles and after the corrosion products have been dissolved by a special treatment. It is evident that the pore size distribution changes considerably during cycling due to corrosion. The performance of the electrodes at these three stages is given in Fig. 11. After dissolving the corrosion products initial electrode performance is retained. This depends probably not only on the sudden increase in porosity but also on an increase in active catalytic surface. On continued cycling the corrosion process proceeds and performance decreases.

Corrosion of Ni shall normally not occur in the normal working region of a bifunctional air electrode with 5M KOH as electrolyte (7). The corrosion proc-

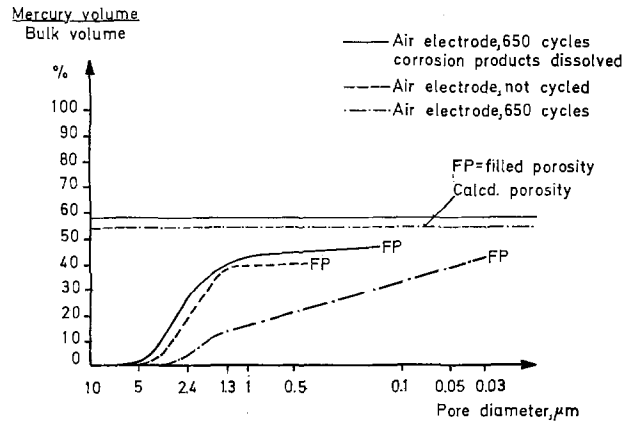


Fig. 10. Pore size distribution of electrodes after different treatments.

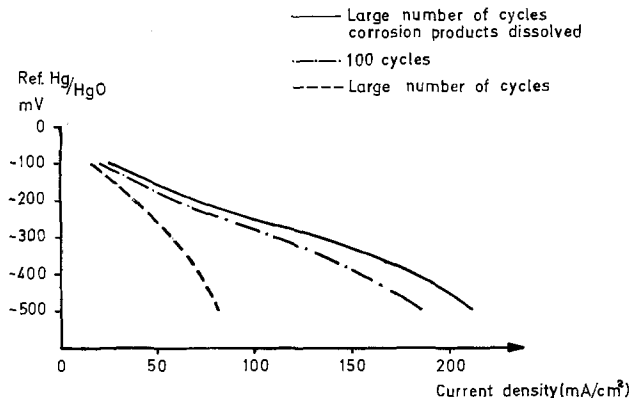


Fig. 11. Polarization curves for air electrodes after different treatments. 40°C ΔP = 0.02 bar.

ess may, however, be catalyzed by traces of chlorine or sulfur which are introduced to the electrode during cycling. Chlorine may emerge from NaCl which is used as spacer and K_2S is sometimes added to the electrolyte to improve the performance of the iron negative electrode. Also the silver catalyst, which is oxidized and reduced during cycling, may have a positive influence on the corrosion process. In order to reduce this life limiting process spacing agents not containing elements with catalytic effect on corrosion of Ni have to be used. Another possibility is to reactivate the electrodes after substantial cycling by dissolving the corrosion products.

Summary

The investigations show that during the first 40-50 cycles of the air electrode an improvement in performance occurs after which the activity is quite stable for about 100 cycles. This means that the electrodes are giving their best performance between 50-150 cycles. This depends probably on an increase in active surface of the nickel electrode at the same time as the catalyst is redistributed. This latter effect means that the dissolution process is comparatively high during this stage of life for the electrode. On continued cycling the catalyst will become less exposed which depends on plugging of the porous electrode by corrosion of the nickel structure. This process presently limits the life of the electrode. The life of

the electrodes can be extended by dissolving the corrosion products. In order to avoid this, spacer materials will be tested not containing elements having catalytic effect on the corrosion.

Manuscript submitted May 22, 1979; revised manuscript received Sept. 28, 1979. This was Paper 31 presented at the Boston, Massachusetts, Meeting of the Society, May 6-11, 1979.

Any discussion of this paper will appear in a Discussion Section to be published in the December 1980 JOURNAL. All discussions for the December 1980 Discussion Section should be submitted by Aug. 1, 1980.

Publication costs of this article were assisted by the Swedish National Development Company.

REFERENCES

1. L. Öjefors and L. Carlsson, *J. Power Sources*, **2**, 287 (1977/78).
2. J. O'M. Bockris, M. Genshaw, E. A. Beer, D. Sepa, and Y. C. Chiu, Final report No. AD 825226, U.S. Army Electronics Command (1967).
3. H. Cnobloch, G. Siemsen, and F. V. Sturm, *Siemens Forsch. Entwicklungsber.*, **2**, 221 (1972).
4. H. Cnobloch, G. Siemsen, and F. V. Sturm, in "Power Sources 4," Academic Press, New York (1973).
5. O. Lindström, U.S. Pat. 3,802,878 (1974).
6. M. Pourbaix, "Atlas of Electrochem. Equilibria in Aqueous Solution," Pergamon Press, Oxford (1966).

Bromine Complexation in Zinc-Bromine Circulating Batteries

Daniel J. Eustace*

Advanced Energy Systems Laboratory, Corporate Applied Research Laboratory,
Exxon Research and Engineering Company, Linden, New Jersey 07036

ABSTRACT

Upon electrolysis of aqueous zinc bromide solutions containing unsymmetrically substituted, cyclic quaternary ammonium bromides, both zinc metal and a bromine-rich liquid are produced. Data, reported for N-ethyl, N-methylmorpholinium (1), N-methoxymethyl, N-methylpiperidinium (2), and N-chloromethyl, N-methylpyrrolidinium (3) bromides suggest that the bromine-rich liquid is a fused salt and separates from the aqueous solution because of insolubility and density differences. The separation process of the bromine fused salt from the aqueous solution is represented as a partitioning of bromine between two phases and is dependent upon electrolysis state-of-charge, quaternary ammonium bromide, bromide ion concentration, and temperature. The bromine-fused salts have properties dependent on composition. Selected examples of densities, specific resistances, viscosities, and polarization are given. Bromine, in the form of a dense, stable, conductive liquid, is useful in circulating zinc-bromine batteries.

The development of zinc-bromine secondary batteries has been impeded by self-discharge, associated with high Br_2 solubility in the aqueous electrolyte, and cell shorting, from dendritic zinc deposition, that limit turn-around efficiency and life.

Recent papers (1) offer a solution to these phenomena by suggesting circulating electrolyte batteries and ion-selective separators that isolate the Br_2 -rich stream from the zinc deposit.

An alternative approach is to complex the Br_2 in a form which lowers its activity in the aqueous phase. The present paper discusses this latter approach and details some of the properties of bromine complexes used in circulating Zn/ Br_2 batteries. A model for

the chemical system where Br_2 is sequestered as an electrochemically active and chemically stable liquid is presented.

Several chemical methods that decrease the solubility of bromine in Zn/ Br_2 aqueous solutions have been reported in context with efforts to reduce the self-discharge of Zn/ Br_2 cells.

The reaction between low molecular weight tetraalkylammonium halides and perchlorates with bromine-containing aqueous solutions to form sparingly soluble polyhalides has been used to reduce bromine solubility in Zn/ Br_2 batteries (2, 3).

Schemes employing bromine extraction as a second liquid phase, coupled with external storage of the cathode-active material, have been employed in circulating electrolyte systems. Bromine extraction that used a miscible organic cosolvent and a quaternary

* Electrochemical Society Active Member.

Key words: battery, electrolyte, energy storage, Br_2 complex, Zn/ Br_2 cell.

ammonium bromide was demonstrated by Walsh and co-workers (4). Br₂ separated from the aqueous electrolyte as a dense liquid, which comprised both the cosolvent and quaternary ammonium polybromide.

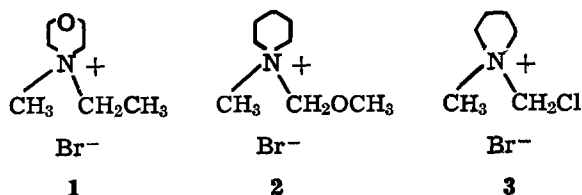
We found that symmetrical quaternary ammonium bromides used as single bromine-separating agents, formed solid polybromide species that were insoluble in aqueous ZnBr₂ solutions. These solids were resistive and formed liquids at higher levels of bromination. Similar results have been reported (2).

A recent paper (5) discusses circulating electrolyte Zn/Br₂ batteries that operated at high turn-around efficiencies (~75%) and to high states-of-charge (>70%). In operation, while Zn is plated, Br₂ is produced, complexed as a dense liquid, and stored in external reservoirs. This paper discusses the chemistry in ZnBr₂ solutions of liquid bromine complexation by unsymmetrically substituted, cyclic quaternary ammonium bromides (QBr).

The nature of the liquid bromine complexes, reported here, is ionic, based on specific resistance measurements. Differential scanning calorimetry indicates that no distinct liquid-solid transitions are observed, yet the product at low temperature is a viscous glass. Spectroscopic and quantitative analyses reveal two major components: the QBr and bromine. Since it is well known that halides and halogens readily combine to form polyhalide species, it is viewed that the liquid complexes are bromine-fused salts.

Experimental

Materials.—The unsymmetrically substituted (*i.e.*, no axis of symmetry) quaternary ammonium salts were synthesized by known synthetic methods. N-ethyl, N-methylmorpholinium bromide **1**, N-methoxy-methyl, N-methylpiperidinium bromide **2**, and N-chloromethyl, N-methylpyrrolidinium bromide **3** gave expected elemental and spectroscopic (ir, NMR) analyses.



Commercial zinc bromide was obtained from American Hoechst Corporation (analysis >98.6%). Fisher Certified ACS grade zinc sulfate, ammonium chloride, ammonium bromide, and potassium chloride were used. Solutions were prepared with doubly distilled water.

Methods of study.—Bromine determinations were made by the indirect iodometric titration method. Zinc ion concentration was measured by EDTA titra-

tion with Eriochrome Black T indicator. Quaternary ammonium salt characterization was accomplished on an A-60 NMR spectrometer. ¹H NMR signal integration was used to quantify mixtures containing the quaternary ammonium salts. Solution conductances were measured on a Beckman Instruments RC-18A Conductivity Bridge and viscosities were measured with Cannon-Fenske viscosimeters.

Electrochemical studies were carried out at constant-current conditions in laboratory cells containing Pt foil electrodes for bromine production and consumption. Spectroscopic carbon rods were the substrates for zinc, and approximately 2.0-4.0 cm³ of electrolyte were used at 23°C, unless otherwise indicated. Constant current electrolysis experiments were terminated at definite intervals and the zinc electrodes removed within 0.25 hr to study the characteristics of the remaining components.

Results

Physical properties of electrolytes.—ZnBr₂ electrolytes can be prepared over a considerable composition range, since the solubility is >10M (1.6 × 10³ W-hr/liter) at ambient temperature. The maximum ZnBr₂ concentration is lower in many multicomponent solutions. Typical compositions and solution physical properties are shown in Table I.

State-of-charge electrolysis studies.—The solutions reported in Table I were studied in constant current electrolysis cells. Passage of current produced zinc metal and a two-phased electrolyte, the composition of which was shown to be dependent upon the initial solution composition, state-of-charge (*i.e.*, percent of ZnBr₂ electrolyzed), temperature, and the presence of supporting electrolytes. The efficiency of Br₂ separation is revealed by the Br₂ concentration of the upper, aqueous phase. The effect of these variables on the Br₂ content of the aqueous phase is shown in Fig. 1-3.

In a similar way, Br₂ can be said to be partitioned between the two phases as expressed by the distribution coefficient, *K*

$$K = \frac{\text{Total Br}_2 \text{ content of Br}_2\text{-rich phase}}{\text{Total Br}_2 \text{ content of aqueous phase}}$$

This parameter is described for the three quaternary salts in Fig. 4, 5, and 6.

The composition of the Br₂-rich phase varies with the state-of-charge of the electrolyte. ¹H NMR integration,¹ and iodometric titration analyses revealed the phase to be exclusively Br₂ and QBr and the Br₂ was greater at higher states-of-charge, as shown in Fig. 7 for **1**.

¹ The ¹H NMR spectrum integration results are reliable with ~5-10% error. Thus, the results in Fig. 7 do not add up to 100% in each case. Also, each experiment produced two phases.

Table I. Compositions and specific resistances of zinc bromine solutions containing quaternary ammonium bromides and supporting electrolytes (23°C)

Solute*	Supporting electrolyte	[ZnBr ₂] (M)	[Solute] (M)	[Supporting electrolyte] (M)	Density (g/cm ³)	Specific resistance (Ω·cm)
1	—	3.0	1.0	—	1.62	22.5
1	—	3.5	1.2	—	1.67	20.9
1	ZnSO ₄	3.0	1.0	0.2	1.61	21.6
1	KCl	3.0	1.0	2.0	1.65	8.5
1	NH ₄ Cl	3.0	1.0	3.0	1.61	8.2
1	NH ₄ Br	3.0	1.0	4.0	1.77	7.8
2	—	3.0	1.0	—	1.59	15.5
2	—	4.0	1.4	—	1.77	30.1
2	—	5.0	1.7	—	1.95	59.7
3	—	3.0	1.0	—	1.60	18.0
3	—	4.0	1.4	—	1.79	26.7
3	—	5.0	1.7	—	1.98	48.6

* The solute refers to the QBr salts in the text.

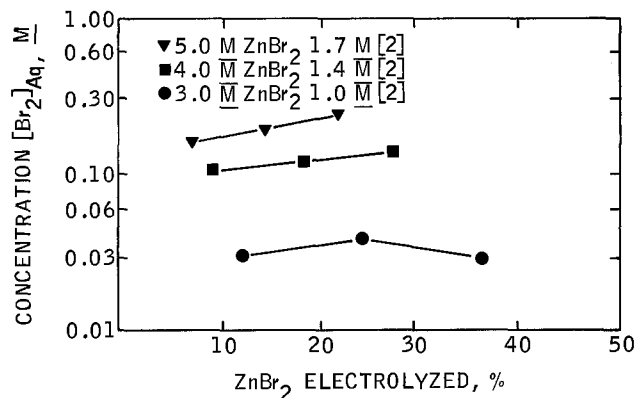


Fig. 1. Effect of N-methoxymethyl, N-methylpiperidinium bromide (2) on aqueous phase bromine concentration at 23°C.

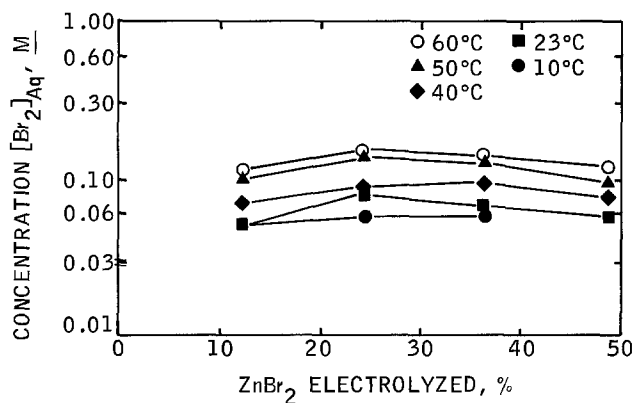


Fig. 2. Effect of temperature on the aqueous concentration of bromine for solutions containing N-ethyl, N-methylmorpholinium bromide (1). Electrolyte: 3.0M ZnBr₂, 1.0M (1), 0.2M ZnSO₄.

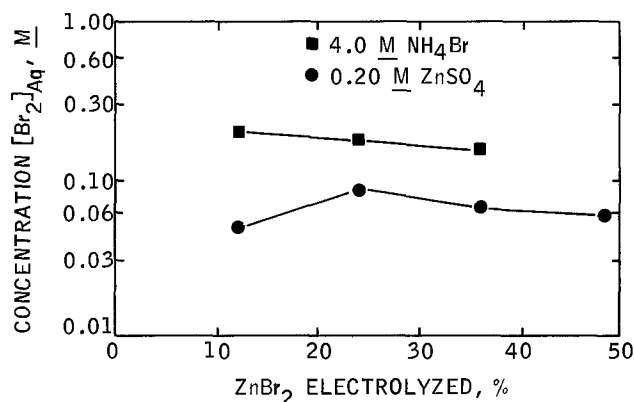


Fig. 3. Effect of supporting electrolytes on aqueous concentration of bromine for solutions containing N-ethyl, N-methylmorpholinium bromide (1.0M) and zinc bromide (3.0M) at 23°C.

Properties of Br₂-rich phase.—Liquid mixtures of Br₂ and QBr produced by electrolysis of ZnBr₂ solutions were in the composition range of 30–80 weight percent (w/o) (x = weight fraction of Br₂). These mixtures are characterized at 23°C by their densities ($\rho \approx 2.0x + 1.1$), specific resistances (for example, Br₂ mixtures with 1 are represented in Fig. 8), and viscosity (for example, for Br₂ complexes of 1, $x = 0.61$, 10.9 c stokes, 25 cp.).

Br₂ liquids of 1 and 3 are stable over the temperature range from 0° to 60°C and for 15 months, as shown by proton NMR. They remain liquids for the same conditions when kept in contact with an aqueous electrolyte. Br₂ complexes of 2 were observed to react at the α -carbon position to the oxygen on stand.

The oxidation-reduction properties of a typical Br₂ complex is shown for 1 ($x = 0.61$) at a Pt electrode in Fig. 9.

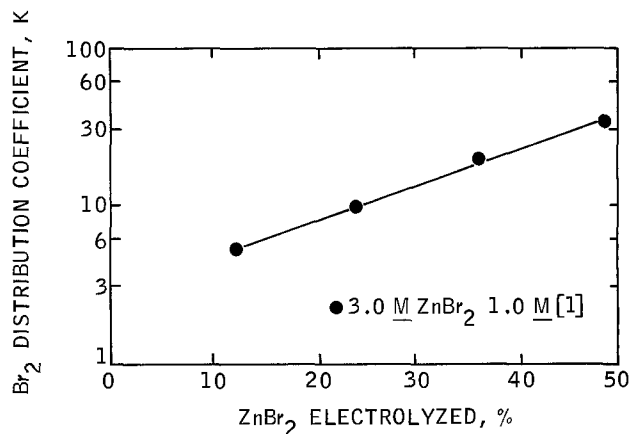


Fig. 4. Bromine distribution coefficient vs. extent of electrolysis for zinc bromide solution with N-ethyl, N-methylmorpholinium bromide (1) at 23°C.

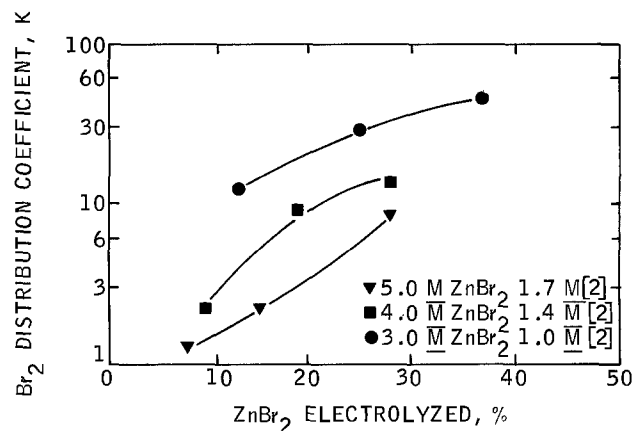


Fig. 5. Bromine distribution coefficient vs. extent of electrolysis for zinc bromide solutions containing N-methoxymethyl, N-methylpiperidinium bromide (2) at 23°C.

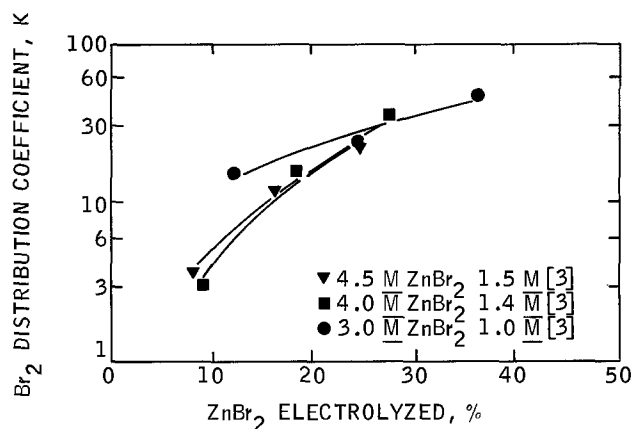


Fig. 6. Bromine distribution coefficient vs. extent of electrolysis for zinc bromide solutions containing N-chloromethyl, N-methylpyrrolidinium bromide (3) at 23°C.

Discussion

System model.—The formation of the bromine-rich phase upon electrolysis of ZnBr₂ solutions containing quaternary ammonium bromides is hypothesized to be a micellar-like separation process where pseudo-microphases coalesce and separate from the aqueous electrolyte by density differences. Parametric studies indicate that the critical



equilibrium is responsive to the bromide ion concen-

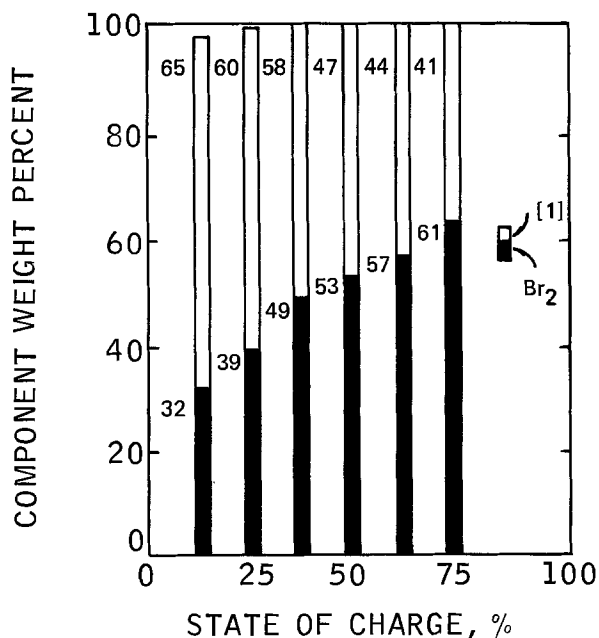


Fig. 7. Bromine-fused salt phase composition as a function of state-of-charge. Starting electrolyte: 3.0M ZnBr₂, 1.0M (1), and 0.2M ZnSO₄.

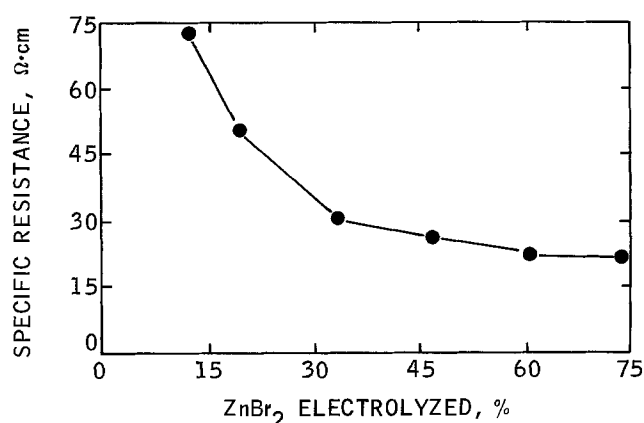


Fig. 8. Specific resistances of bromine-fused salt samples produced by electrolysis 3.0M ZnBr₂, 1.0M (1), and 0.2M ZnSO₄. (Both electrolysis and measurement performed at 23°C.)

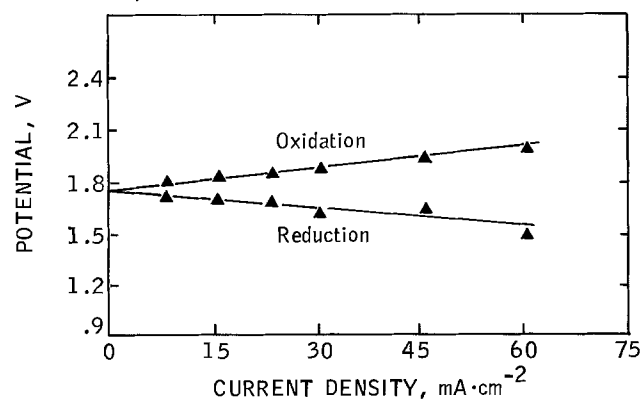
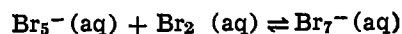
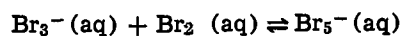
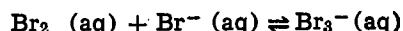


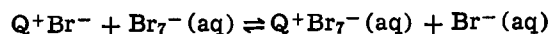
FIGURE 9

Fig. 9. Current-potential performance of bromine-fused salt formed by electrolysis of 3.0M ZnBr₂, 1.0M (1). Experiment: Pt flag, Zn reference, at 23°C.

tration, temperature, and quaternary ammonium salt. This equilibrium is influenced by the multiple ionic equilibria for Br₂ in the aqueous phase of ZnBr₂ solutions, principally polyhalide anion formation; for example



and polyhalide ion pair formation, for example



The second phase is exclusively QBr and Br₂ in a series of polyhalide ion pair mixtures; for example



which is analyzed as a nonstoichiometric mix described simply as a bromine fused salt.

Increasing the concentration of bromide ion is seen to influence the position of the aqueous phase equilibria and, thus, the partitioning of bromine between the aqueous and fused salt phase

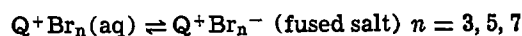


Figure 1 shows the incremental increase of the aqueous phase Br₂ concentration found with incremental increases in the ZnBr₂ concentrations for N-methoxymethyl, N-methylpyrrolidinium bromide 2 solutions. Higher solubility of bromine is shown in Fig. 3 for the 3.0M ZnBr₂ and 1.0M N-methyl, N-methylmorpholinium bromide 1 solution containing 4.0M NH₄Br when compared to the similar ZnBr₂-1 solution with 0.2M ZnSO₄. Indeed, the 0.2M ZnSO₄ has the effect of lowering the aqueous phase bromine concentration by approximately 10% over the similar system without supporting electrolyte.

Increasing the temperature shifts the partitioning equilibria, allowing more bromine to be soluble in the aqueous phase. Although bromine loss by reaction with zinc metal and evaporation affect the values obtained at higher temperatures, 85-90% of the bromine produced in each experiment was accounted for in the analyses. The loss in precision this gives does not affect the trend seen in Fig. 2. Indeed, it is noted that the energy of activation for the partitioning of bromine obtained from the results of the N-ethyl, N-methylmorpholinium bromide system are in the range of -0.6 to -1.4 kcal·mole⁻¹. This activation energy is lower than typical activation energies of ionic diffusion (for example, 3.8-4.6 kcal·mole⁻¹), suggesting a solution ordering effect similar to micellar systems (6).

Differences between the bromine partitioning abilities of the three quaternary salts is obtained by comparing their Br₂ partition coefficients for similar composition solutions. The distribution coefficients are in the decreasing order: 3 ~ 2 > 1.

System analogies.—Systems that are similar to the Br₂-fused salts have been described previously in another context. Kraus and co-workers (7) studied quaternary and tertiary ammonium solutes in the solvent bromine. Typical physical properties for (CH₃)₃NH⁺Br⁻ in bromine, shown in Table II, are quite similar to 1 in bromine at a similar composition.

Br₂ complexation that is used in circulating Zn/Br₂ batteries can also be compared with phase transfer

Table II. Comparison of measured properties of a trimethylammonium polybromide composition with a bromine fused salt composition of (1)

[Data for (CH₃)₃NH⁺Br⁻·nBr₂ taken from P. L. Mercier and C. A. Kraus, *Proc. Natl. Acad. Sci. U.S.A.*, 42, 487 (1956)]

	(CH ₃) ₃ NH ⁺ Br ⁻ ·nBr ₂	Br ₂ fused salt of (1)
Composition Br ₂ w/o	63.4	60.6
Density, g/cm ³	2.243	2.3
Specific resistance Ω·cm	~7	18
Viscosity cp.	~11	25

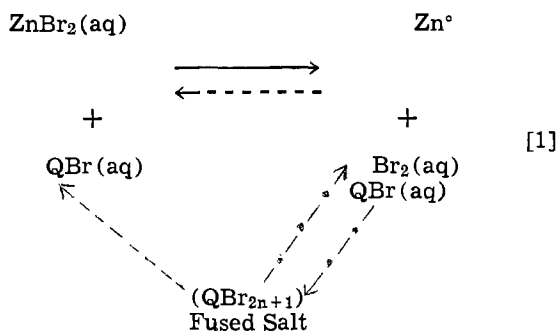
Table III. Comparison of features of Br₂ complexation for circulating batteries with phase transfer catalysis

	Br ₂ complexation for circulating batteries	Phase transfer catalysis
Agents	Unsymmetrically substituted, cyclic quaternary ammonium salts, QBr	Monovalent Cations, i.e., R ₄ N ⁺
Nature of process	Ion pair separation of polyhalides into new phase	Ion pair extraction into second, immiscible phase
Distribution coefficients, K	1-10 ³ QBr dependent	1-10 ⁴ R ₄ N ⁺ and second-phase dependent
Effects of added salts	Enhancing salts: 10% improvement in K (sulfates) Halide salts: 20-50% decline in K	"Salting out" salts: K improved ~10 ³ "Salting in" salts: 20-50% decline in K
Nature of second phase	Stable (0°-60°C) conductive	Promote selected reactions with a turnover of agent

catalysis by quaternary ammonium salts (8) (Table III). Both processes employ monovalent cations that are active ion pair extraction agents. The extraction coefficients for Br₂ separation are typically 1 to 10² and dependent on QBr. Similar distribution coefficients for phase transfer catalysis are from 1 to 10⁴ and both agent- and second-solvent-dependent. Added salts have similar effects on the distribution coefficients. The two systems differ in the fact that a second immiscible phase is required for the catalysis, and that the bromine-fused salt (at least for 1 and 3) is stable and conductive. Also, the catalytic systems promote specific reactions.

System application.—The electrolytic properties of a typical bromine-fused salt are given in Fig. 8 and 9 for compositions generated from 3.0M ZnBr₂ and 1.0M 1. The composition-dependent specific resistance is obtained by using the results shown in Fig. 7 with Fig. 8. In the range where the bromine weight percent falls between 32 and at least 61, the fused salt specific resistances are less than 100 Ω·cm. Taking one composition as an example, Fig. 9 shows that the bromine-fused salt with 61 w/o Br₂ can be charged and discharged with little activation polarization at currents up to approximately 50 mA·cm⁻².

The Zn/Br₂ electrochemical couple can employ the bromine-fused salt in a flowing electrolyte system. Equation [1] schematically represents the chemical processes in the circulating electrolyte Zn/Br₂ battery. On battery charge, ZnBr₂ is electrolyzed to Zn⁰ and Br₂ (→). The Br₂ is consumed by polybromide equilibria partitioning it mostly into a separate bromine-fused salt phase (---→)



Zinc is oxidized and Br₂, both in the fused salt and the aqueous phase, is reduced when the battery is discharged (---→).

System optimization with respect to the quaternary ammonium bromide aims at improving the energy density (increasing the starting ZnBr₂ concentration) without increasing bromine-related self-discharge for

batteries operating at ambient temperature and practical rates.

Summary

The chemistry associated with Br₂ separation in Zn/Br₂ circulating electrolyte batteries has been described. The Br₂-rich liquid phases normally formed in battery operation (Br₂ weight percents are ~30-~80) have been studied and characterized as a bromine-fused salt.

The electrolytic formation of the bromine-fused salt is modeled as a micelle-like process, where the dominant phase separation process is controlled by the polyhalide ion activity in each phase.

This method of Br₂ complexation is useful in energy storage, since it renders Br₂ into a controllable, condensed fluid which is conductive and chemically stable on standing.

Acknowledgments

The author wishes to acknowledge E. L. Stogryn and J. W. Frankenfeld for synthesis of compounds, M. T. Melchior for NMR measurements, and A. W. Groman for laboratory contributions. The author thanks J. A. Shropshire and B. M. L. Rao for fruitful discussions and encouragement during the course of these investigations.

Manuscript submitted May 23, 1979; revised manuscript received Sept. 28, 1979. This was Paper 114 presented at the Los Angeles, California, Meeting of the Society, Oct. 14-19, 1979.

Any discussion of this paper will appear in a Discussion Section to be published in the December 1980 JOURNAL. All discussions for the December 1980 Discussion Section should be submitted by Aug. 1, 1980.

Publication costs of this article were assisted by Exxon Research and Engineering Company.

REFERENCES

- H. S. Lim, A. M. Lackner, and R. C. Knechtli, *This Journal*, **124**, 1154 (1977); F. G. Will, Proc. Int'l. Power Sources Symposium, Brighton, U.K. (1978).
- M. R. Bloch *et al.*, *J. Phys. Chem.*, **53**, 1117 (1949).
- F. Rallo and P. Silvestroni, *This Journal* **119**, 1471 (1972). G. Clerici *et al.*, Proc. 9th Int'l. Power Sources Symposium, pp. 167-181, Brighton, U.K. (1974).
- M. A. Walsh *et al.*, Proc. 10th Intersociety Energy Conversion Eng. Conf., pp. 1141-1142, Chicago, Ill. (1975).
- R. J. Bellows *et al.*, Proc. Int'l. Power Sources Symposium, Brighton, U.K. (1978).
- E. J. Fendler and J. H. Fendler, *Adv. Phys. Org. Chem.*, **8**, 271 (1970).
- P. L. Mercier and C. A. Kraus, *Proc. Nat'l. Acad. Sci. U.S.A.*, **42**, 487 (1956).
- A. Brandstrom, *Adv. Phys. Org. Chem.*, **15**, 267 (1977).

Studies on Pollutants

IV. Electrolytical Recovery of Lead from Battery Scrap

S. Das Gupta, Shahid Abbas Abbasi,¹ R. Raman, and D. L. Roy

Department of Metallurgical Engineering, IIT, Powai, Bombay, India

ABSTRACT

Recovery of lead from waste battery paste has been carried out by an electrolytic method employing paste suspended in sodium hydroxide as electrolyte. Effect of several parameters, viz., current density, temperature, time, lead ion concentration, sodium hydroxide concentration, agitated bath and cathode material on the cathode potential, current efficiency, and nature of deposits, has been studied and possible reasons for the observed effects have been discussed. A mechanism for lead deposition has been elucidated. It is observed that cathodic reaction takes place after the dissolution of lead or lead compounds in sodium hydroxide and the ion responsible for lead deposition is bismuthite (HPbO_2^-) ion. The optimum conditions for conducting the electrolysis are: temperature 60°C, current density 7 A/dm², concentration of sodium hydroxide 600 g/liter, time 120 min.

Used lead acid batteries form an important secondary source of lead, especially in countries which are not otherwise rich in lead resources (1). The treatment of used acid batteries for recovering lead is important from the point of view of lead production as well as pollution abatement as otherwise the battery scrap may lead to disposal problems. The lead in used batteries is in the form of grid plates and pole bridges made up of lead-antimony alloy (5-12% antimony) and paste consisting mainly of antimony-free lead, lead oxide, and lead sulfate.

In an earlier communication (2), a pyrometallurgical method was reported for the recovery of lead from battery scrap using carbon with calcium carbide or calcium carbonate as reducing agents. It was observed that the recovery was not satisfactory because lead sulfate, a constituent of the battery paste, required high temperatures for the reduction causing fume and slag losses. It appeared that the recovery of metal values from the battery scrap will be economical if the battery plates (consisting of antimonial lead) and battery paste (consisting of lead compounds including lead sulfate) are treated separately. An electrochemical method was conceived for the treatment of battery paste in the hope of obtaining high purity lead; detailed studies of which are presented here.

Among the reported electrolytic methods of purification of lead, the conventional type (3-5) makes use of anodes made up of impure lead with suitable leachants for lead as electrolytes. Waheed *et al.* (6) have reported two processes for recovery of lead from battery waste employing a sodium hydroxide bath as electrolyte. The work is confined to feasibility studies and development of process parameters for recovering one pound of lead per hour. In the present work detailed studies have been carried out on the mechanism of lead deposition, and on the cause-effect relationship of several parameters with the lead recovery, nature of deposits, and cathode potential. From the generated data, optimum conditions for lead recovery have been worked out.

Experimental

The electrolytic cell was a 1000 ml glass vessel (Fig. 1) with a cylindrical mild steel rod as cathode. The rod was 12 mm in diameter with an effective length of 7 cm. It was rotated for some experiments by means of a fractional horsepower motor. To investigate the

effect of lower temperatures on the nature of deposits, a chilled cathode was used which was a lower-end-closed cylindrical nickel-plated tube, 2.7 cm diameter by 5 cm long. The cathode was cooled by pouring in ice while water was removed from inside the cathode at regular intervals of 3 min. The anode consisted of two strips of stainless steel 1.2 cm wide by 12 cm long. To investigate the effect of cathode material on cathode potential and current efficiency lead, stainless steel, graphite, and mild steel were used successively as cathodes.

The different baths used for investigations were comprised of sodium hydroxide and one of the following: waste battery paste, lead sulfate, lead monoxide, or powdered lead. The electrolysis in each experiment was conducted with 1000 ml of electrolyte, keeping anode to cathode distance 4.4 cm and anode to anode distance 10 cm. A multispeed stirrer was used to ensure efficient stirring near the cathode. For heating the electrolyte to desired temperatures, an immersion heater, connected to a Variac, was employed.

The cathode and anode were connected to a rectifier through a voltmeter, an ammeter, and a rheostat (to obtain the desired current in the cell).

For measurement of the cathode potential a standard mercury-mercuric oxide (Hg-HgO) electrode was used as a reference electrode. The Luggin tip of the connecting bridge was made to touch the cathode. To record the potential the reference electrode was connected to the positive terminal and the cathode was connected to the negative terminal of a high impedance vacuum tube voltmeter (Heathkit, Model V-7A).

Waste battery paste was analyzed by standard methods (7). Average analysis of battery waste active material was as follows

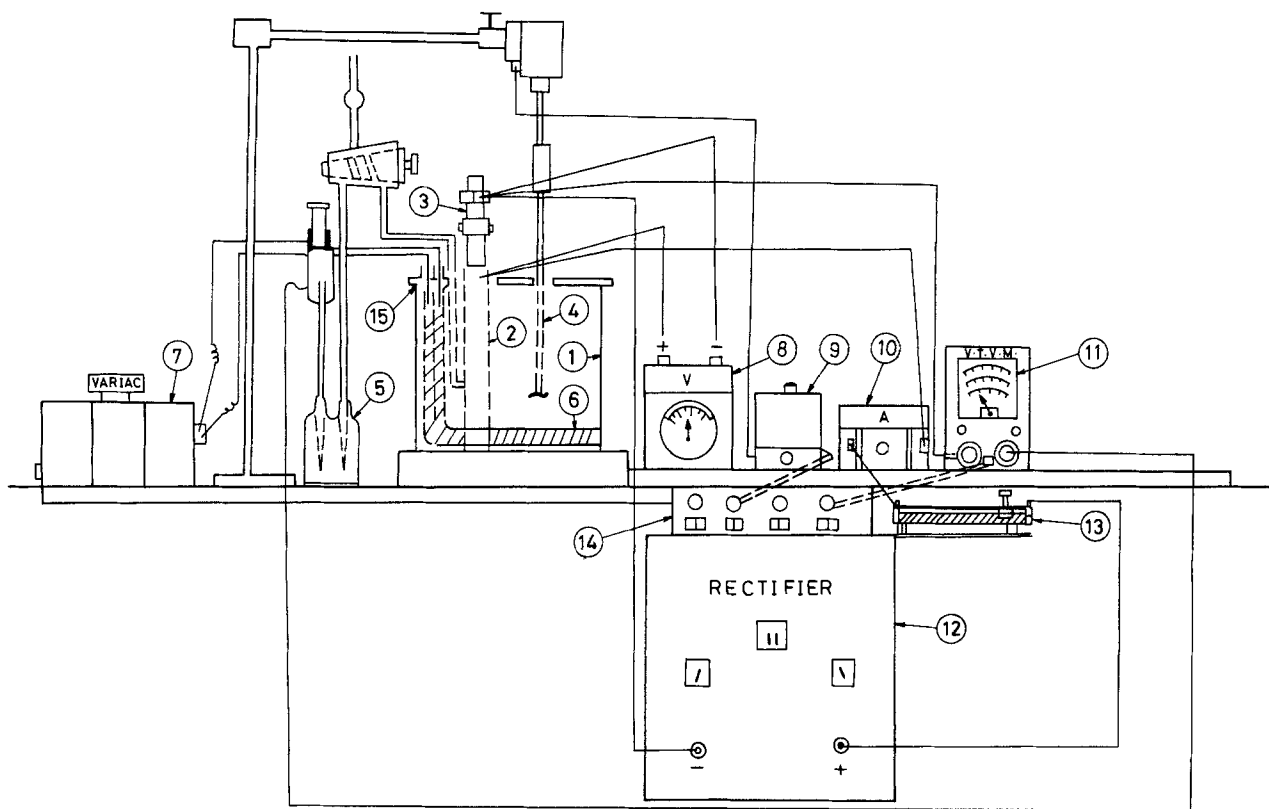
Lead monoxide:	27.77%
Lead sulfate:	63.08%
Free lead:	7.44%
Total lead:	75.42%
Antimony:	2.55%

All the experiments were carried out after stirring the solute (lead sulfate, lead monoxide, lead waste battery paste) in sodium hydroxide at the temperature of 70°-80°C for half an hour. Before each experiment the cathode was cleaned thoroughly with hydrochloric acid and washed.

The lead deposits obtained after each experiment were washed well with water, then with 2% acetic

¹ Present address: Division of Water Quality and Environment, Centre for Water Resources Development and Management, 'Sudha', Old Road, Medical College P.O., Trivandrum 695 011, India.

Key words: mechanism, lead deposition, current efficiency.



- | | | |
|-----------------------|--|--------------------|
| 1 - 1000 ml BEAKER. | 6 - IMMERSION HEATER. | 11 - V. T. V. M. |
| 2 - ANODE. | 7 - VARIAC (FOR CONTROLLING TEMP.) | 12 - RECTIFIER. |
| 3 - CATHODE. | 8 - VOLT METER. | 13 - REHSTAT. |
| 4 - STIRRER. | 9 - REGULATOR (FOR CONTROLLING SPEED OF STIRRER) | 14 - SWITCH BOARD. |
| 5 - Hg/HgO ELECTRODE. | 10 - AMMETER. | 15 - PYREX COVER. |

Fig. 1. Experimental setup for the electrolysis studies

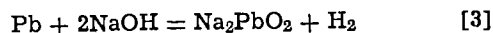
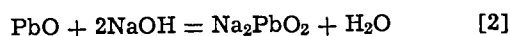
acid, washed again with water, and dried in a vacuum furnace at 100°C for 1 hr.

Results and Discussion

The results of studies on the effects of various parameters, *viz.*, temperature, sodium hydroxide concentration, current density, cathode material, concentration of lead ions, time, etc., on cathode potential, current efficiency, and nature of lead deposits are presented in Tables I-XI. The results of experiments which were carried out with lead sulfate, lead monoxide, or lead powder to elucidate the mechanism of lead deposition are presented in Tables I-IV while results of the experiments carried out with waste battery paste are presented in Tables V-XI.

Reaction mechanism of lead deposition.—The cathodic reaction taking place during electrolysis may involve lead or lead compounds in the solid (suspended) state, or it may proceed after the dissolution of lead or lead compounds.

Results (Tables I-IV) show that the nature of lead deposits changed with the variation of such parameters, *viz.*, sodium hydroxide concentration and temperature, which influenced the dissolution of lead bearing material. This indicates that cathodic reactions were taking place after the dissolution of lead or its compounds in sodium hydroxide. The probable chemical reactions are



All three reactions generate sodium plumbite. The ionization of sodium plumbite during electrolysis may

lead to plumbous ion (Pb^{2+}), biplumbite ion (HPbO_2^-), plumbite ion (PbO_2^{2-}), plumbic ion (Pb^{4+}), acid metaplumbite ion (HPbO_3^-), metaplumbite ion (PbO_3^{2-}), and orthoplumbite ion (PbO_4^{4-}). The potential-pH diagram for the system lead-water (8) indicates that under the highly alkaline condition of the bath ($[\text{NaOH}] > 2\text{M}$, $\text{pH} \approx 14$), the predominant lead-containing ion is biplumbite ion (HPbO_2^-), the concentration of other lead containing ions being insignificant.

The diffusion and hydrodynamic flow force the anions (HPbO_2^-) to move towards the cathode where

Table I. The effect of temperature

Temperature (°C)	Cathode potential (V)	Current efficiency (%)	Purity of lead (%)	Nature of deposits
Sodium hydroxide: 100 g/liter Current density: 5 A/dm ² Time: 30 min				
Material added: lead sulfate: 45 g/liter				
35	-0.80	95.40	90.4	Granular
60	-0.73	91.20	97.3	Powdery
80	-0.72	80.80	97.5	Dendritic
100	-0.72	78.90	95.8	Dendritic
Material added: lead monoxide: 33 g/liter				
35	-0.77	97.01	91.5	Granular
60	-0.70	86.40	94.5	Powdery
80	-0.69	77.03	98.3	Dendritic
100	-0.67	72.30	98.3	Dendritic
Material added: lead: 30 g/liter				
35	-0.75	82.23	91.0	Granular
60	-0.65	84.01	93.7	Dendritic
80	-0.62	79.50	96.5	Dendritic
100	-0.61	78.60	94.7	Dendritic

Table II. The effect of sodium hydroxide concentration

Current density: 5 A/dm²
Temperature: 60°C
Time: 30 min

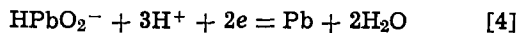
Sodium hydroxide concentration (g/liter)	Cathode potential (V)	Current efficiency (%)	Purity of lead (%)	Nature of deposits
Material added: lead sulfate: 45 g/liter				
100	-0.78	98.60	92.5	Granular
200	-0.78	99.80	98.3	Granular
400	-0.92	98.62	90.3	Black spongy
600	-0.94	99.44	88.3	Black spongy
Material added: lead monoxide: 33 g/liter				
100	-0.70	86.40	97.3	Powdery
200	-0.72	94.10	94.4	Powdery
400	-0.76	98.50	95.8	Powdery
600	-0.77	99.60	97.1	Powdery
Material added: lead: 30 g/liter				
100	-0.66	84.08	95.2	Dendritic
200	-0.68	91.80	97.3	Dendritic
400	-0.74	95.10	95.7	Powdery
600	-0.75	96.80	96.5	Powdery

Table III. The effect of current density

Sodium hydroxide: 40%
Temperature: 60°C
Time: 30 min

Current density (A/dm ²)	Cathode potential (V)	Current efficiency (%)	Purity of lead (%)	Nature of deposits
Material added: lead sulfate: 45 g/liter				
1	-0.76	97.20	97.5	Powdery
2.5	-0.76	99.10	96.4	Powdery
5	-0.77	98.90	92.5	Powdery
10	-0.82	96.03	87.1	Spongy
15	-0.84	90.26	90.1	Spongy
16	-0.84	86.00	92.3	Spongy
Material added: lead monoxide: 33 g/liter				
1	-0.75	97.00	95.8	Powdery
2.55	-0.75	98.70	96.3	Powdery
5	-0.78	98.50	96.9	Powdery
7	-0.77	97.40	97.1	Powdery
10	-0.78	95.60	95.6	Powdery
12.5	-0.81	93.94	92.5	Granular
15	-0.82	89.33	94.0	Granular
16	-0.82	85.00	93.7	Granular

these ions are reduced. High percentage recovery with stirred baths (Table IX) compared to static baths also indicates the importance of convective flow. The probable reaction is



$$E_o = 0.702 - 0.0886 \text{ pH} + 0.0295 \log [\text{HPbO}_2^-] \quad [5]$$

Table V. The effect of current density

Waste battery paste: 20 g/liter
(mesh size -300)
Sodium hydroxide: 200 g/liter
Temperature: 35°C
Time: 60 min

Current density	3 A/dm ²	7 A/dm ²	11 A/dm ²	15 A/dm ²	25 A/dm ²
Time (min)	Cathode potential (V)	Cathode potential (V)	Cathode potential (V)	Cathode potential (V)	Cathode potential (V)
0	-1.24	-1.43	-1.6	-1.46	-1.34
10	-1.08	-1.42	-1.5	-1.41	-1.22
20	-0.94	-1.37	-1.6	-1.38	-1.10
30	-0.89	-1.31	-1.6	-1.30	-1.06
40	-0.87	-1.20	-1.6	-1.12	-1.04
50	-0.85	-1.20	-1.7	-1.06	-1.00
60	-0.82	-1.20	-1.7	-1.02	-0.96
Nature of deposits	Black spongy	Black spongy	Black spongy	Black spongy	Black spongy
Current efficiency (%)	98.3	100.3	94.0	58.8	34.2
Lead (%)	90.0	90.8	93.2	91.0	90.1

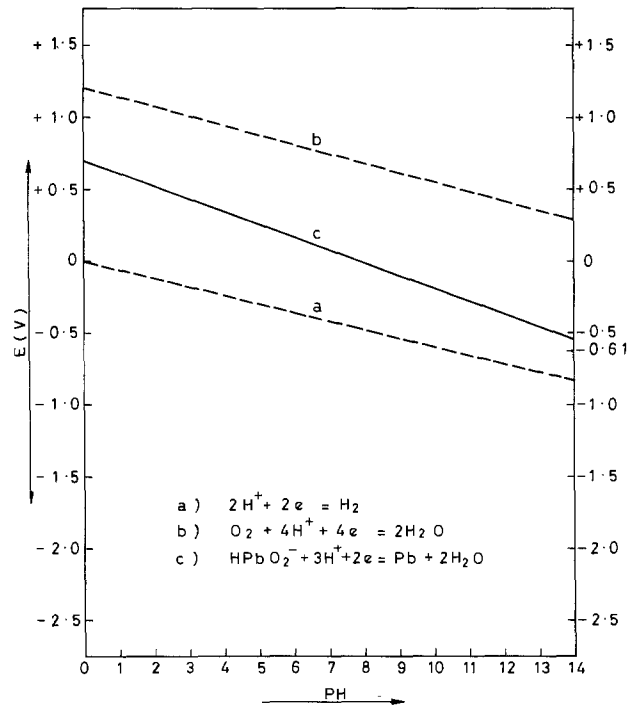


Fig. 2. Proposed potential-pH diagram for the lead-water system, at 298°K.

Assuming activity of biplumbite ion as unity, the above equation has been represented in the E/pH diagram (Fig. 2). At pH = 14 the above reaction is feasible when the cathode potential value is more negative than -0.530. The observed cathode potential values (-0.61 to -1.70V) distinctively show the likelihood of the above reaction.

Table IV. The effect of concentration of lead-containing ions

Current density: 5 A/dm²
Sodium hydroxide: 60%
Temperature: 60°C
Time: 30 min

Concentration of lead sulfate (g/liter)	Cathode potential (V)	Cell voltage (V)	Current efficiency (%)	Nature of deposits
5	-0.89	1.9	71.70	Spongy
10	-0.84	1.7	91.30	Spongy
20	-0.81	1.4	96.8	Granular
30	-0.81	1.4	98.60	Granular

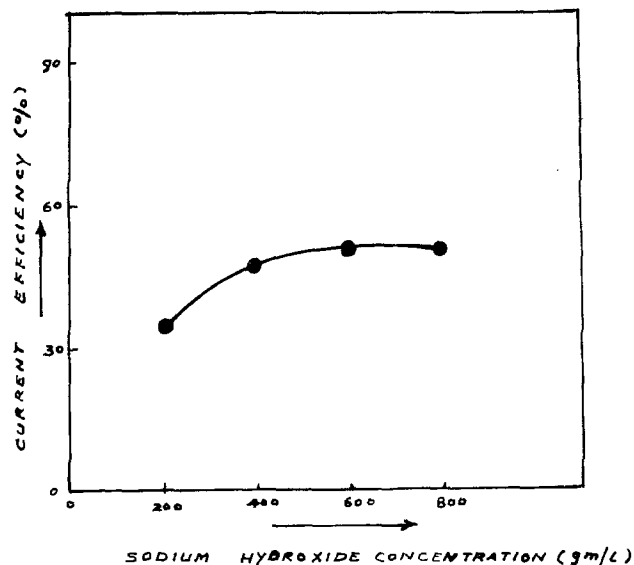


Fig. 3. The effect of sodium hydroxide concentration on the current efficiency. (Waste battery paste 20 g/liter; current density 25 A/dm²; temperature 35°C; time 60 min.)

Effect of various parameters on the electrolysis of waste battery paste.—Effect of current density.—The effects of current density on current efficiency, cathode potential, and nature of lead deposits are represented in Table V (Fig. 3).

The current efficiency did not vary much in the current density range of 2.5–10 A/dm². Above 10 A/dm² the current efficiency decreased rapidly with the increase in current density. With the increase in current density the effective metal ion concentrations in the vicinity of the cathode reduce and hydrogen evolution increases leading to reduced current efficiency. Similar influence of lead-containing ions on current efficiency is observed in the results shown in Table IV. The experiments were carried out keeping the waste battery paste in suspension in the sodium hydroxide solutions and in all likelihood, as detailed during discussion on the mechanism of lead deposition, the electrolysis was preceded by dissolution of paste. The decrease of current efficiency may also be due to the fact that the rate of dissolution of lead compounds and free lead in sodium hydroxide becomes the rate-controlling factor.

The purity of lead obtained was about 90%. This low purity may be due to the presence of lead oxide in the deposits owing to the following reasons:

1. Lead oxide may occur in the lead deposits because of decomposition of mechanically held sodium plum-

bite (in the deposits) during drying. The likely reaction is



The observed value of current efficiency higher than 100% for current density of 7 A/dm² is also probably due to the above mentioned phenomena, i.e., mechanical inclusion.

2. The reactivity of electrolytic powders are in general greater than that of powders prepared by thermal processes. The particles in electrolytic powder consist of clusters of very small crystals (about 0.07 μm in diameter) which are under strained condition (9). This leads to higher reactivity causing oxidation. In the present investigation the oxidation was minimized by using a vacuum furnace during drying.

The nature of deposits was black spongy throughout the current density range studied. The analysis of deposits showed that it contained arsenic (0.056%), antimony (0.55%), copper (0.016%), and iron (0.001%) besides lead oxide.

The effect of temperature.—The effects of temperature on cathode potential, current efficiency, nature of deposits, and purity of lead are represented in Table VI.

With the increase in temperature the cathode potential is seen to decrease (become less negative). It is known that, for overpotential (η)

$$\eta = \eta_c + \eta_a + \eta_R$$

As a rule with the increase in temperature, η_c , the concentration overpotential, η_a , the activation overpotential, and η_R , the resistance overpotential, are all reduced. This may be the reason for the observed lower cathode potential values at higher temperature in the present investigation.

The current efficiency increased with the increase in temperature up to 60°C but beyond this temperature it decreased. This may be due to lower hydrogen overvoltage and higher rate of dissolution of deposited lead at higher temperatures.

At room temperature the nature of deposits was black spongy. In the temperature range 60°–100°C the deposits were black spongy near the cathode while the outer portions were bright and flaky. The bright flaky portion may be due to lower activation polarization and higher concentration polarization. With time of electrolysis the concentration of lead ions in the electrolyte becomes less causing an increase in concentration polarization. The activation polarization is lower with higher temperatures. When concentration polarization dominates over activation polarization, the flakes grow more or less perpendicularly from the electrode surface into the solution.

Table VI. The effect of temperature

Temperature	Waste battery paste: 20 g/liter Sodium hydroxide: 200 g/liter Current density: 25 A/dm ² Time: 60 min			
	35°C	60°C	80°C	100°C
Time (min)	Cathode potential (V)	Cathode potential (V)	Cathode potential (V)	Cathode potential (V)
0	-1.34	-1.30	-1.24	-1.21
10	-1.22	-1.20	-1.14	-1.18
20	-1.10	-1.10	-1.14	-1.15
30	-1.06	-1.10	-1.13	-1.15
40	-1.04	-1.11	-1.12	-1.12
50	-1.00	-1.10	-1.10	-0.98
60	-0.96	-0.94	-1.08	-0.96
Nature of deposits	Black spongy	Spongy, outer layer is bright and flakey	Spongy, outer layer is bright and flakey	Spongy, outer layer is bright and flakey
Current efficiency (%)	34.2	46.5	45.0	42.8
Purity of lead (%)	90.1	93.7	88.8	88.5

Table VII. The effect of sodium hydroxide concentration

Sodium hydroxide concentration	200 g/liter	400 g/liter	600 g/liter	800 g/liter
	Cathode potential (V)	Cathode potential (V)	Cathode potential (V)	Cathode potential (V)
Time (min)				
0	-1.34	-1.41	-1.41	-1.46
10	-1.22	-1.38	-1.44	-1.43
20	-1.10	-1.38	-1.43	-1.44
30	-1.06	-1.38	-1.40	-1.45
40	-1.04	-1.37	-1.40	-1.43
50	-1.00	-1.37	-1.38	-1.43
60	-0.96	-1.37	-1.35	-1.43
Nature of deposits	Black spongy	Black spongy	Black spongy	Black spongy
Current efficiency (%)	34.2	46.8	49.9	50.2
Purity of lead (%)	90.1	88.7	90.3	90.3

The effect of sodium hydroxide concentration.—The results are presented in Table VII (Fig. 4). The change in sodium hydroxide concentration from 200 to 800

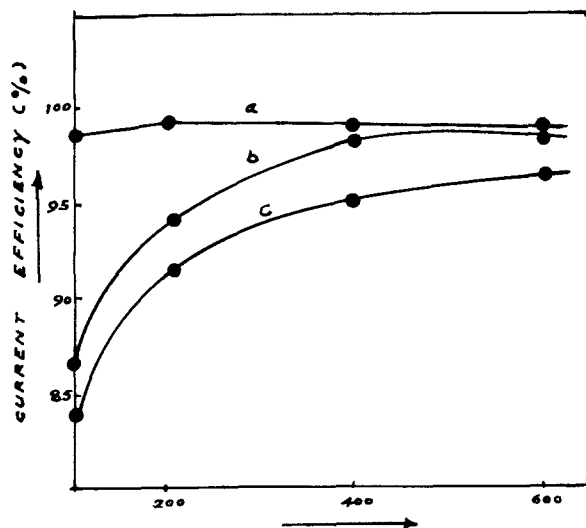


Fig. 4. Variation of current efficiency with the concentration of sodium hydroxide for the different constituents of the battery paste: (a) lead sulfate (b) lead oxide (c) lead. (Current density 5 A/dm²; temperature 60°C; time 30 min.)

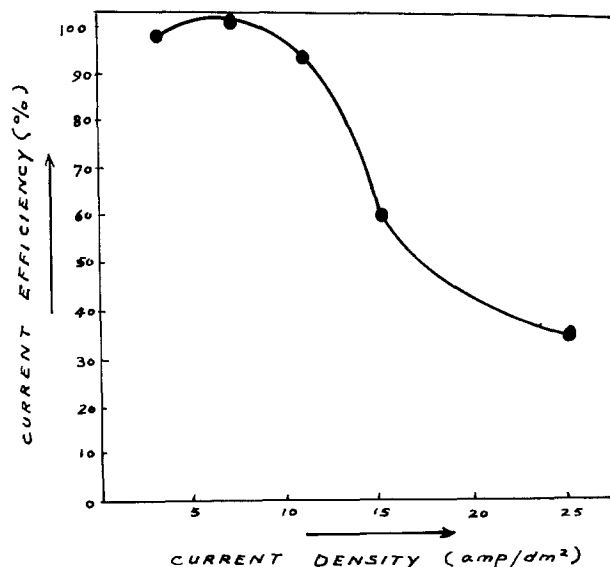


Fig. 5. The effect of current density on current efficiency. (Waste battery paste 20 g/liter; sodium hydroxide 200 g/liter; temperature 35°C; time 60 min.)

g/liter showed an increase in current efficiency from 34.2 to 50.2%. Black spongy deposits were obtained in all cases and the purity of lead was about 90%.

The increase in current efficiency with the concentration of sodium hydroxide is possibly due to the increase in solubility of lead and its compounds. Experiments on different constituents of the paste (Table II Fig. 5) reveal that the current efficiency remained practically constant in case of lead sulfate while it increased with increase in sodium hydroxide concentration when lead or lead monoxide were electrolyzed. The reason for this observation is that the solubility of lead sulfate in sodium hydroxide is high even at low alkali concentrations and the increase in solubility with increase in alkali concentration is not substantial. The dissolution of lead or lead monoxide, on the other hand, increases markedly with the increase in alkali concentrations resulting in a similar trend for current efficiency.

The current efficiency-sodium hydroxide concentration curves level off at, and beyond, the sodium hydroxide concentration of 600 g/liter, and this value is taken as the optimum concentration of sodium hydroxide.

The effect of time.—The results (Table VIII) show that the current efficiency remained practically constant up to 120 min and then decreased slowly up to 210 min. After 210 min the current efficiency fell steeply, probably due to unavailability of lead-containing ions for deposition. The cathode potential increased after 210 min as concentration polarization probably

Table VIII. The effect of time

Time for electrolysis (min)	Lead recovered (g)	Current efficiency (%)	Cathode potential (V)	Nature of deposits	Purity of lead (%)
30	2.44	97.01	0.78	Granular	96.5
30	2.42	96.70	0.78	Granular	94.2
30	2.44	97.01	0.78	Granular	95.5
30	2.44	97.01	0.78	Granular	95.0
30	2.40	95.42	0.78	Granular	97.8
30	2.40	95.42	0.79	Granular	96.1
30	2.35	94.43	0.80	Granular	97.3
30	2.00	80.00	0.98	Spongy	88.3
30	2.00	80.00	1.00	Spongy	86.3
30	1.00	40.00	1.20	Spongy	90.0
30	0.50	20.00	1.50	Spongy	89.5

Total lead recovered in 330 min:

23.9g

No. of A-hr passed: 7.15; avg cell voltage: 1.42

kW-hr/g: 0.000453

Percentage recovery: 93.7%

Table IX. The effect of static bath, agitated bath, and rotation of cathode

Time (min)	Static bath	Agitated bath	Rotation of cathode
	Cathode potential (V)	Cathode potential (V)	Cathode potential (V)
0	-1.43	-1.10	-2.0
10	-1.39	-0.88	-2.0
20	-1.35	-0.89	-2.0
30	-1.29	-0.89	-2.0
40	-1.29	-0.89	-2.0
60	-1.27	-0.91	-2.0
Nature of deposits	Black spongy loosely held on the cathode	Spongy compact and adherent	Spongy compact and adherent
Current efficiency (%)	91.5	98.1	83.7
Purity of lead (%)	91.8	98.4	93.7

arose from insufficient number of lead-containing ions. The weight percent recovery of lead was 91.9%.

Effect of static bath, agitated bath, and rotated cathode.—The results are shown in Table IX.

The deposit of lead on the stationary cathode in the static bath was nonadherent and spongy. It readily peeled off even while the cathode was taken out of the cell. On the other hand the lead deposit in the agitated bath and on the rotating cathode was adherent, spongy, compact, and could be handled easily. It may be due to the fact that rotation of cathode and stirring of the bath reduces the thickness of the electrical double layer, leading to compact and adherent deposits.

The cathode potential in case of the rotated cathode was less than in the case of the static cathode. This unexpected observation may be explained on the basis of contact resistance (electrical contact to the rotating electrode) and/or improper contact of Luggin tip (of reference electrode) with the rotating cathode, which might have developed.

The current efficiency of the static bath-static cathode system (91.5%) was found to be between that of agitated bath-static cathode system (98.1%) and agitated bath-rotated cathode system (83.7%). The higher efficiency in the case of agitated bath-static cathode system compared to that of static bath-static cathode system is expected, but the low value of current

Table XI. The effect of chilled cathode

Time (min)	Cathode potential (V)
0	-1.30
5	-0.92
10	-0.83
15	-0.87
20	-0.89
25	-0.85
30	-1.03
Nature of deposit:	Small amount of fine powder, rest granular
Current efficiency:	93%
Purity of lead:	96%

efficiency in the case of the rotating cathode was probably due to the loss of deposited lead by dissolution and/or peeling off during rotation of the cathode.

Effect of cathode material.—The experiments (Table X) were carried out under similar conditions of electrolysis for all the cathodes. The value of current efficiency for nickel, stainless steel, graphite, and mild steel cathodes were close to each other, about 99%, but the value for the lead cathode was 85.87%. This low value is likely to be due to passivation of the lead cathode.

Effect of chilled cathode.—When the cathode was chilled during electrolysis (Table XI), the lead deposit consisted of fine powder and granules. Electrolytic deposition is a nucleation and growth process. As the cathode is chilled, the growth of the crystals at the cathode surface is hastened resulting in fine powder. Since the heat conductivity of lead is not high, the cooling of the deposited powder is not efficient after a few layers have been deposited. Subsequent deposits are thus granular.

The purity of lead was 96% which was higher than the purity of spongy deposits obtained in earlier experiments. The granular and powdery deposits were easier to wash which possibly reduced the formation of lead oxide during drying and favorably effected the purity of lead.

Conclusion

As discussed earlier (2), the pyrometallurgical method for the recovery of lead from lead battery waste suffers from the drawback that while lead oxide can be efficiently reduced to metallic lead by carbon,

Table X. The effect of cathode materials

Cathode materials	Lead	Nickel	Stainless steel	Graphite	Mild-steel
	Cathode potential (V)	Cathode potential (V)	Cathode potential (V)	Cathode potential (V)	Cathode potential (V)
Time (min)					
0	-1.70	-1.32	-1.70	-1.60	-1.30
10	-1.20	-1.25	-1.50	-1.44	-1.30
20	-1.11	-1.02	-1.35	-1.44	-1.16
30	-1.08	-1.02	-1.33	-1.48	-1.10
40	-1.06	-1.17	-1.31	-1.50	-1.08
50	-1.03	-1.15	-1.38	-1.60	-1.08
60	-1.03	-1.12	-1.50	-1.70	-1.08
Nature of deposits	Black spongy	Black spongy	Black spongy	Black spongy	Black spongy
Current efficiency (%)	85.87	97.94	98.06	98.05	99.20
Purity of lead (%)	90	93	92.7	88.7	91

the reduction of lead sulfate requires high temperature, causing fume and slag losses and reducing the efficiency of lead recovery. If the battery plates, which contain antimonial lead and battery paste, which contains lead compounds including lead sulfate, can be treated separately, the former by pyrometallurgical method and the latter by electrolytic method, the combined "duplex" process may be an economical proposition. In the duplex process the waste paste on the grid plates would be washed thoroughly with a concentrated sodium hydroxide solution, dissolving away all the paste. The grid plates would be then treated pyrometallurgically (2) to recover antimonial lead. The sodium hydroxide solution containing the paste would be electrolyzed to recover pure lead. The present studies prove the feasibility of the electrolytic process though further work is required to evaluate the economics of the process.

The following important conclusions can be drawn from the present work:

1. The deposition of lead takes place at the cathode after the dissolution of lead or lead compounds in sodium hydroxide and the ion responsible for lead deposition is the bismuthite (HPbO_2^-) ion.

2. The optimum values for the various parameters are: current density 7 A/dm², concentration of sodium hydroxide 600 g/liter, temperature 60°C, time of electrolysis 120 min.

3. A current efficiency of 97% is achieved when the electrolysis is carried out under near-optimum conditions (current density 5 A/dm², concentration of

sodium hydroxide 400 g/liter, temperature 60°C, time of electrolysis 120 min).

Manuscript submitted May 19, 1978; revised manuscript received Sept. 14, 1979.

Any discussion of this paper will appear in a Discussion Section to be published in the December 1980 JOURNAL. All discussions for the December 1980 Discussion Section should be submitted by Aug. 1, 1980.

REFERENCES

1. "The Statesman Year Book," Statesman Press, Calcutta, 1977.
2. S. Das Gupta, S. N. Malhotra, S. A. Abbasi, and D. L. Roy, *Indian J. Technol.*, in press.
3. C. G. Fink, *Trans. Electrochem. Soc.*, **58**, 465 (1930).
4. A. G. Arend, *Ind. Chem.*, **58**, 63 (1942).
5. B. B. Dey, V. Aravamuthan, and P. R. Rajagopalan, *Indian Mining J.*, **25**, 100 (1957).
6. A. K. A. Waheed, P. V. Basudeva Rao, S. Ghosh, and H. V. K. Udupa, *J. Ind. Chem. Eng.*, **3**, 168 (1961).
7. A. I. Vogel, "Text Book of Quantitative Inorganic Analysis," Longmans, London (1960).
8. M. Pourbaix, "Atlas of Electrochemical Equilibria in Aqueous Solutions," Pergamon Press, Elmsford Park, N.Y. (1966).
9. W. Eckadt, U.S. Bur. Mines Inform. Circ. No. 7466 (1948); *Chem. Abstr.*, **45**, 6089 (1951).
10. N. T. Kudryavtsev and A. G. Atanasyants, *Zh. Fiz. Kim.*, **29**, 1227 (1955).
11. N. T. Kudryavtsev, *ibid.*, **26**, 270 (1952).
12. N. T. Kudryavtsev, *Electrokhim. Akad. Nauk SSSR*, **37**, 256 (1953).

High Rate Discharge Characteristics of Li/SOCl₂ Cells

K. A. Klinedinst* and M. J. Domeniconi*

GTE Laboratories, Incorporated, Waltham, Massachusetts 02154

ABSTRACT

The performance characteristics of the Li/SOCl₂ cell have been determined as a function of discharge rate, electrolyte composition, cathode thickness, and cell temperature. Cells have been discharged at rates ranging from about 3 to nearly 300 mA/cm². Cathodes with electrolyte solutions have contained either LiAlCl₄ or AlCl₃, with the most efficient discharge characteristics being realized with 1.5M LiAlCl₄ and 4.5M AlCl₃ solutions. The use of pure AlCl₃ dissolved in SOCl₂ as the electrolyte results in substantially higher average discharge voltages and discharge capacities than can be achieved with cells containing the conventional LiAlCl₄ electrolyte. With both electrolytes, however, the discharge capacity per unit cathode volume (the effective cathode utilization) decreases with increasing cathode thickness, the rate of decrease being greater the higher the discharge current density. Increasing cell temperature results in an improvement in cathode utilization and a decrease in overvoltage, again with both LiAlCl₄ and AlCl₃ electrolyte solutions.

The performance characteristics of the lithium/thionyl chloride primary battery system at relatively low rates of discharge ($I \lesssim 10$ mA/cm²) have been frequently described (1-5). However, the characteristics of the battery at high rates of discharge ($I \gtrsim 10$ mA/cm²) are not well known. It has thus been the purpose of this investigation to determine the performance characteristics of the Li/SOCl₂ cell as a function of discharge rate, particularly with respect to current densities greater than about 10 mA/cm². In addition to the discharge rate, the experimental variables explored have included the electrolyte composition, the cathode thickness, and the cell temperature.

In the design of any high rate cell, the anode/cathode interfacial area should be as large as possible

to reduce current density and thus to minimize losses due to polarization or reduced electrode capacity. Since the total cell volume is generally fixed, this usually requires that the electrode thickness be reduced by an amount proportional to the increase in electrode area. For this reason, the cathodes employed in this work were all thinner than 1.0 mm with most being less than 0.1 mm in thickness.

The conventional Li/SOCl₂ cell electrolyte consists of a solution of LiAlCl₄ in SOCl₂. This solution is commonly prepared by first dissolving the required amount of AlCl₃ in purified SOCl₂ followed by the addition of a stoichiometric amount of LiCl (1). On the other hand, we have previously reported that, if the electrolyte solution contains less than the stoichiometric amount of LiCl or even in the complete absence of LiCl, the average discharge voltage and discharge capacity (at a given rate of discharge) assume substantially greater

* Electrochemical Society Active Member.

Key words: battery, cathode, electrolyte, polarization.

values than when the SOCl_2 contains only LiAlCl_4 (6, 7). However, because the excess AlCl_3 will readily remove the passivating film of LiCl which normally is present on the surface of lithium which is in direct contact with SOCl_2 , the Li will continue to be attacked by the SOCl_2 until one of the three reactants (Li, SOCl_2 , or AlCl_3) is exhausted. Thus, Li/ SOCl_2 cells containing excess AlCl_3 must be operated as reserve cells in which the electrolyte is allowed to contact the electrodes shortly before the beginning of discharge. Both LiAlCl_4 and AlCl_3 electrolyte solutions have been used in this work.

Experimental

A schematic diagram of the experimental cell is shown in Fig. 1. The anode was a 0.75 mm thick sheet of lithium pressed onto a nickel metal current collector. The cathode was a layer of carbon black containing 5-10% PTFE (polytetrafluoroethylene) also supported upon a nickel current collector. The cathode was 1 cm² in area and ranged in thickness from 0.025 to 1.0 mm. (Cathode thicknesses were measured by the use of a precision micrometer.) The two electrodes were separated by a 0.13 mm thick sheet of porous glass paper. A PTFE-coated or glass-coated metal weight was used to maintain good interfacial contact between the cell components. Nickel wire current leads were used, and the cell was positioned within an evacuable Pyrex glass container with glass-to-metal seals at the points where the current leads passed through the container.

The cell was assembled in a dry room (relative humidity <2%), and the electrolyte (a solution of either LiAlCl_4 or AlCl_3 in SOCl_2) was placed within the electrolyte reservoir. The sealed Pyrex container was then transferred to the test stand where it was usually allowed to equilibrate at room temperature. In some cases, the glass container was placed within a thermostatically controlled oil bath to equilibrate at either 45° or 65°C. The Pyrex container was evacuated for 30 min. Then, the electrolyte was allowed to enter the evacuated container (through a Teflon stopcock), completely submerging the electrodes. Dry air was added to bring the container to atmospheric pressure, and the constant load or constant current discharge was begun after no more than a ten minute stand on open circuit.

A Fluke datalogger was used to record the cell voltage as a function of time. The average discharge plateau voltages and currents were determined from the resulting discharge curves, and the capacities were calculated by the integration of each discharge curve to a cutoff voltage which was in every case 10% below the average plateau voltage.

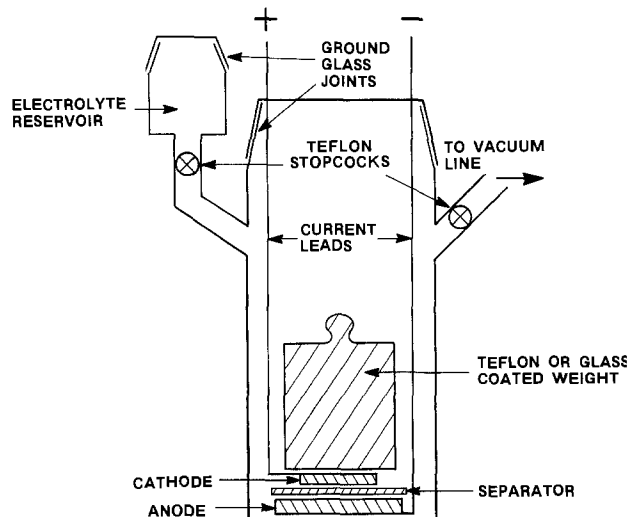


Fig. 1. Schematic diagram of the experimental test cell

The carbon black used in this work was 50% compressed Shawinigan acetylene black, and the PTFE was supplied by du Pont as an aqueous dispersion (TFE-30). The lithium was supplied by Foote Mineral Company. The LiCl was obtained from J. T. Baker and was vacuum dried for 16 hr at 350°C prior to use. The Fluka AlCl_3 (puriss) was obtained from Tridom Chemical Company, and the SOCl_2 from Hooker Chemical Company. Before use, the SOCl_2 was twice distilled over Li. To prepare the electrolyte, an adduct of AlCl_3 and SOCl_2 was first formed. [The preparation of such adducts are described in Ref. (8) and (9)]. Distilled SOCl_2 was added to the adduct to form an AlCl_3 solution of the desired concentration. In order to form the LiAlCl_4 electrolyte, an excess of LiCl was added to the AlCl_3 solution. The undissolved LiCl was subsequently removed by filtration. The extent to which the electrolyte was contaminated by water was determined by infrared spectroscopy (10). The electrolyte was found to be contaminated by less than 0.5 ppm of water, the limit of detection of the infrared spectroscopic method.

Results

In the initial experiments, the concentrations of LiAlCl_4 and AlCl_3 in the electrolyte solutions were varied in order to determine the effect upon discharge capacity. A moderately high discharge current density of about 30 mA/cm² was chosen for these initial experiments. Two cathode thicknesses, 37 and 950 μm, were employed.

The data obtained with the LiAlCl_4 solutions are plotted in Fig. 2. With the 37 μm cathodes, the capacity maximized at a LiAlCl_4 concentration of about 1.5M. However, with the 950 μm cathodes, the capacity maximized at a LiAlCl_4 concentration of about 4.0M. Since most of the succeeding experiments were to be performed with cathodes which were about as thick as the 37 μm cathodes, 1.5M was chosen as the concentration to be used in most of the experiments in which LiAlCl_4 electrolyte solutions were employed.

The data obtained with the AlCl_3 solutions are shown in Fig. 3. With the 37 μm cathodes, the capacity maximized at an AlCl_3 concentration of about 4.5M. With the 950 μm cathodes, on the other hand, the capacity maximized at an AlCl_3 concentration of about 3.0M. As before, since most of the succeeding experiments were to be performed with cathodes which were about as thick as the 37 μm cathodes, 4.5M was chosen as the concentration to be used in most of the experiments in which AlCl_3 electrolyte solutions were employed.

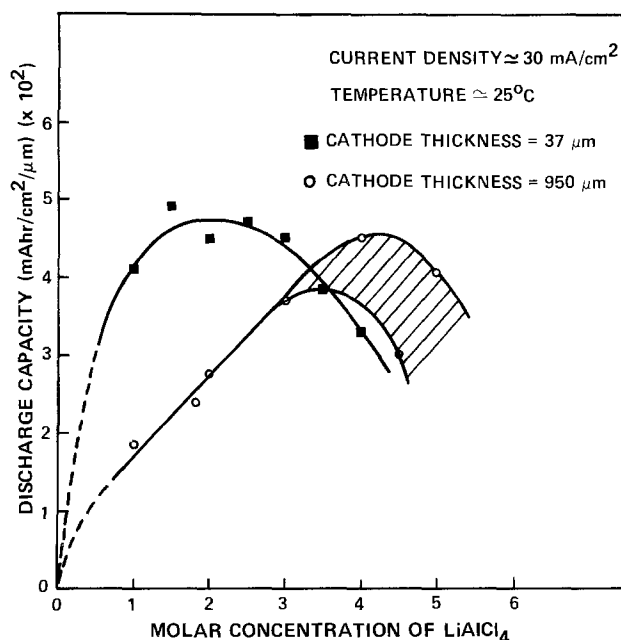


Fig. 2. Discharge capacity vs. LiAlCl_4 concentration

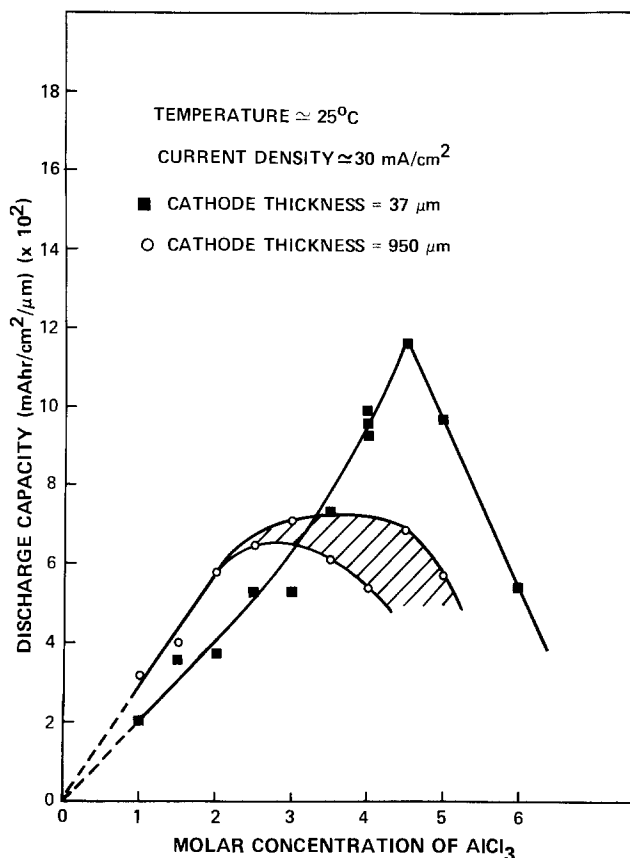


Fig. 3. Discharge capacity vs. AlCl_3 concentration

Typical discharge curves obtained at a current density of 30 mA/cm^2 with 1.5M LiAlCl_4 and 4.5M AlCl_3 electrolyte solutions are compared in Fig. 4. In these experiments, the cathodes were $55 \mu\text{m}$ thick, and the Li/SOCl_2 cells were discharged at room temperature. The increases in both operating voltage and discharge capacity associated with the use of the AlCl_3 -containing electrolyte are apparent.

As shown in Fig. 1 and 2, the discharge capacity (per unit cathode thickness) of the high rate Li/SOCl_2 cell is a function of both electrolyte composition and cathode thickness. Further, with both LiAlCl_4 and AlCl_3 electrolyte solutions, the capacity per unit cathode volume decreases with increasing thickness. This effect is clearly demonstrated by the data in Fig. 5 where the Li/SOCl_2 cell discharge capacity is plotted as a function of thickness for thicknesses ranging from about $20 \mu\text{m}$ to about $950 \mu\text{m}$. Cells were dis-

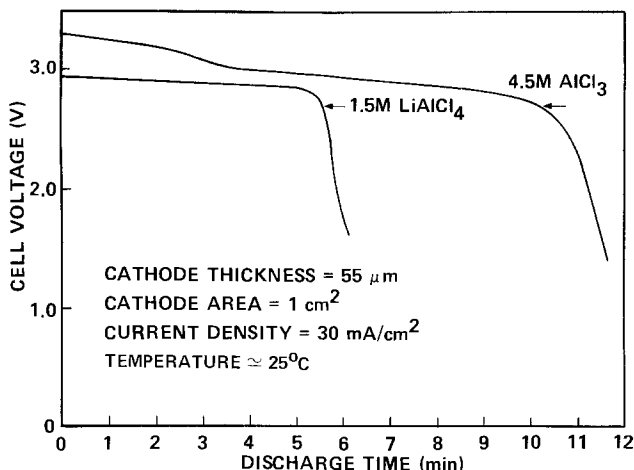


Fig. 4. Discharge curves comparing 1.5M LiAlCl_4 and 4.5M AlCl_3 electrolyte solutions.

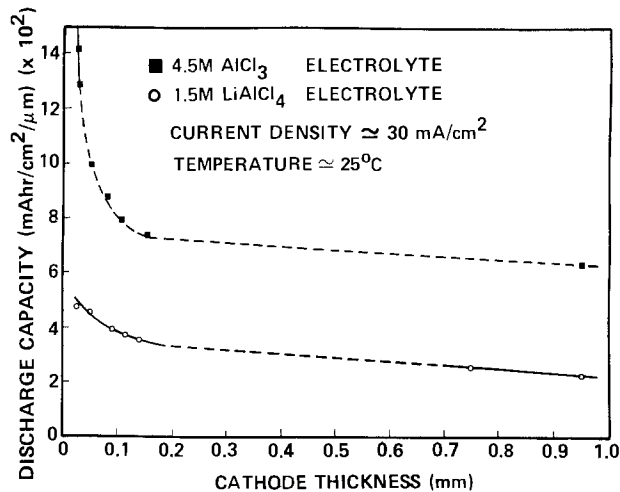


Fig. 5. Discharge capacity vs. cathode thickness.

charged with both 1.5M LiAlCl_4 and 4.5M AlCl_3 electrolyte solutions. (The Li/SOCl_2 cells were all discharged at about 30 mA/cm^2 current density.) It can be seen that, particularly with the 4.5M AlCl_3 solution, the effective cathode utilization increases very significantly as the cathode thickness is decreased below about $150 \mu\text{m}$.

The combined effects of discharge rate, cathode thickness, and electrolyte composition upon the discharge capacities of Li/SOCl_2 cells are shown graphically in Fig. 6 where the average current density is plotted vs. the discharge duration per unit cathode thickness on a log-log scale. Data are shown for both 1.5M LiAlCl_4 and 4.5M AlCl_3 electrolyte solutions and for cathode thicknesses of 55 and $950 \mu\text{m}$. As expected, the discharge capacities obtained with the AlCl_3 electrolyte solution are uniformly larger than those obtained with the LiAlCl_4 electrolyte over the entire range of discharge rates. It can also be seen that, at low current densities, the capacity per unit cathode thickness is approximately independent of thickness. However, at higher discharge rates, the capacity per unit cathode thickness (the apparent cathode utilization) decreases with increasing thickness, the rate of decrease being greater the higher the average current density.

All of the above results were obtained with cells discharged at room temperature. In order to determine what gains in performance might be realized at higher temperatures, Li/SOCl_2 cells were also discharged at 45° and 65°C . The effects of temperature variation are exemplified by the discharge curves shown in Fig. 7 for cells discharged at both room temperature and 65°C . These cells contained $50 \mu\text{m}$ thick cathodes and 1.5M LiAlCl_4 electrolyte solutions and were discharged

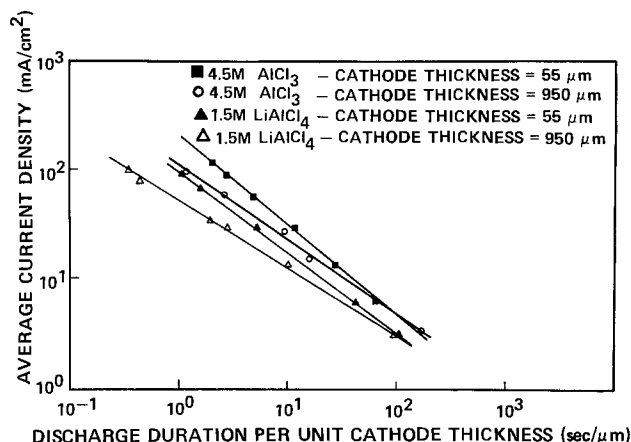


Fig. 6. Average discharge current density vs. discharge duration per unit cathode thickness.

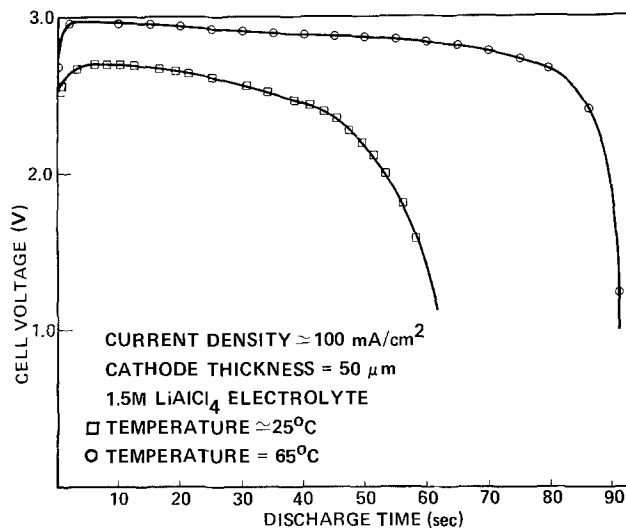


Fig. 7. Discharge curves at room temperature and 65°C

at a current density of about 100 mA/cm². As the figure shows, an increase in temperature causes the cell to discharge for a longer time at a higher operating voltage and with a flatter discharge curve. Thus, operating high rate Li/SOCl₂ cells at elevated temperatures increases cathode utilization and decreases cell polarization.

The current-potential curves (plotted on a semilog scale) derived from the discharge of Li/SOCl₂ cells containing 50 μm cathodes and 1.5M LiAlCl₄ in SOCl₂ as the electrolyte at room temperature, 45°C, and 65°C are compared in Fig. 8. (Each point is determined by the average voltage and average current-density obtained from the plateau portion of the discharge curve of an individual Li/SOCl₂ cell.) The decrease in polarization with increasing temperature is apparent over the entire range of discharge rates.

The discharge duration per unit cathode thickness is plotted as a function of current density on the log-log plot shown in Fig. 9. (Each point corresponds to one of the points in the current-potential curves shown in Fig. 8.) As expected, the discharge capacity increases with increasing temperature and with decreasing discharge rate.

The current-potential curves obtained from the discharge of Li/SOCl₂ cells containing 50 μm cathodes with both 1.5M LiAlCl₄ and 4.5M AlCl₃ electrolyte solutions and at both room temperature and 65°C are compared in Fig. 10. The corresponding discharge rate *vs.* duration data are plotted in Fig. 11. With 4.5M AlCl₃, as with the 1.5M LiAlCl₄ electrolyte, the voltage characteristics improve with increasing temperature, and the discharge capacity increases with increasing tempera-

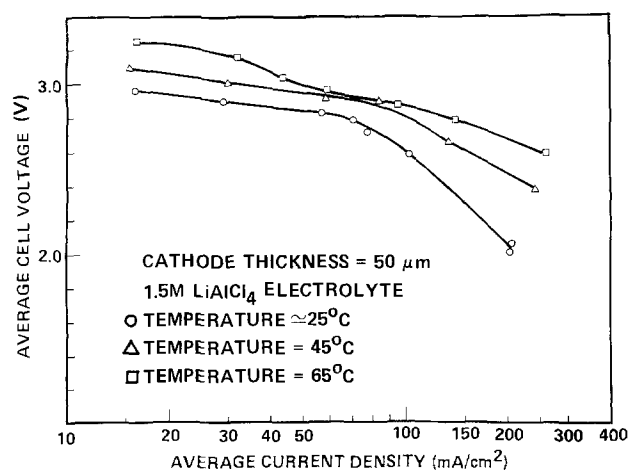


Fig. 8. Average cell voltage vs. average current density

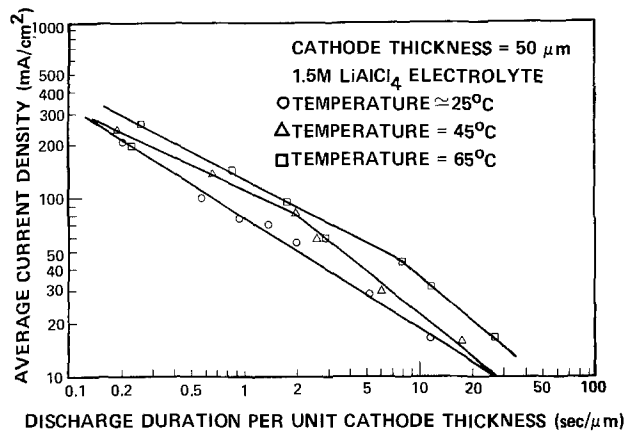


Fig. 9. Average current density vs. discharge duration per unit cathode thickness.

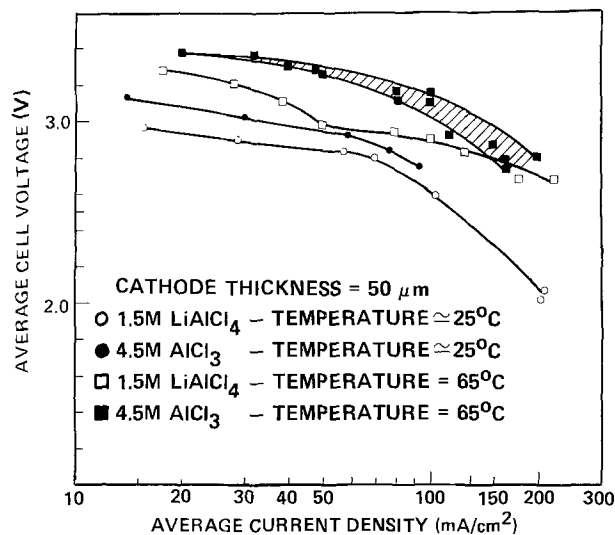


Fig. 10. Average cell voltage vs. average current density

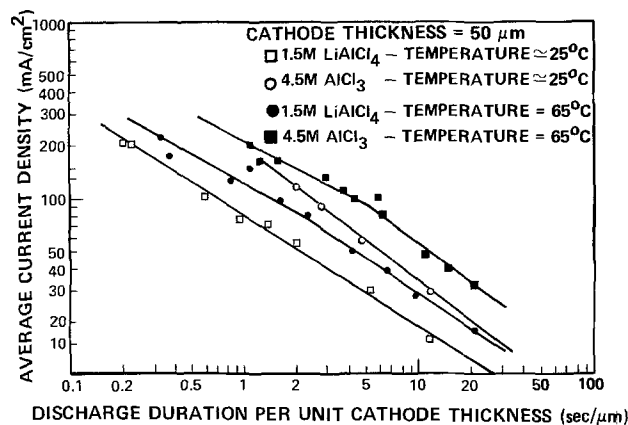


Fig. 11. Average current density vs. discharge duration per unit cathode thickness.

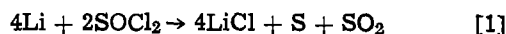
ture and with decreasing discharge rate. As expected, over the entire range of discharge rates and at both temperatures, the use of the 4.5M AlCl₃ electrolyte results in higher voltages on load and larger discharge capacities than are obtained with the conventional 1.5M LiAlCl₄ electrolyte.

Discussion

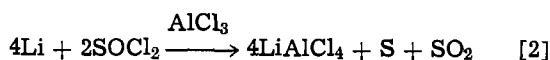
Perhaps the first question to be answered is how a SOCl₂ solution containing only AlCl₃ with no deliberately introduced LiCl can function as a very good electrolyte in Li/SOCl₂ cells, since the room temperature

conductivity of a 3.0M solution of AlCl_3 in SOCl_2 is only about $3 \times 10^{-4} \Omega^{-1} \text{cm}^{-1}$ (11). In such a system, two parallel chemical reactions will be occurring. The Li will be reacting with the SOCl_2 in a direct oxidation-reduction reaction, depositing a protective insoluble LiCl film on the surface of the Li; simultaneously, the AlCl_3 in solution will react with the LiCl film to produce soluble LiAlCl_4 . As this LiCl film is removed from the surface of the Li, more LiCl forms which again reacts with the AlCl_3 . By the continuation of this process, enough LiAlCl_4 is produced to make the solution sufficiently conductive to support the discharge of the cell. The fact that this system is stable to any degree is evidence that the rate of film formation is much more rapid than that of its removal. However as previously noted, if such a cell was allowed to stand indefinitely on open circuit, the Li would continue to be oxidized by the SOCl_2 until one of the three reactants (Li, SOCl_2 , or AlCl_3) was exhausted. Thus, Li/ SOCl_2 cells containing excess AlCl_3 must be discharged soon after the SOCl_2 solution is allowed to contact the electrodes.

The normal overall discharge reaction of the Li/ SOCl_2 cell can be written as (12, 13)



Sulfur crystallizes from the electrolyte once its solubility has been exceeded. The Cl^- produced by the reduction of SOCl_2 reacts with the Li^+ contained within the LiAlCl_4 electrolyte solution to form insoluble LiCl which immediately precipitates within the cathode pores, leading to eventual discharge termination (12, 13). However, if excess AlCl_3 is present, the Cl^- produced during discharge reacts preferentially with the AlCl_3 to produce AlCl_4^- , and the overall discharge reaction now becomes



Since the ΔG for this reaction is greater than that corresponding to Eq. [1], the cell voltages before and during discharge are greater in the presence of excess AlCl_3 than they are in its absence. (The open-circuit voltages of Li/ SOCl_2 cells containing 4.5M AlCl_3 and 1.5M LiAlCl_4 electrolyte solutions are about 4.0V and about 3.6V, respectively.) Later, as the excess AlCl_3 is consumed by reaction with the Cl^- , the primary cell reaction shifts from reaction [2] to reaction [1], giving rise to two distinct discharge plateaus as shown in Fig. 4. Because the discharge of the Li/ SOCl_2 cell terminates when the cathode pores become choked by the precipitating LiCl, such a cell will have a greater discharge capacity when its electrolyte contains excess AlCl_3 than when it does not.

Except for the two-step discharge curve characteristic of the presence of excess AlCl_3 , the general performance characteristics of Li/ SOCl_2 cells with and without excess AlCl_3 are very similar. As shown in Fig. 2 and 3, in both cases the discharge capacity per unit cathode volume maximizes as the AlCl_3 or LiAlCl_4 concentration is increased. The fact that the conductivity of the electrolyte generally increases with increasing AlCl_3 or LiAlCl_4 concentration presumably leads to an increase in capacity with concentration. The subsequent capacity decrease with a further increase in AlCl_3 or LiAlCl_4 concentration is probably the result of the increasing viscosity of the SOCl_2 solution, making it less able to function as an efficient mass and charge transfer medium.

In order to investigate these effects further, the conductivities of a number of solutions containing both AlCl_3 and LiAlCl_4 were measured over the temperature range -20° to $+65^\circ\text{C}$. The introduction of AlCl_3 into the LiAlCl_4 electrolyte was usually found to increase the conductivity at higher temperatures but reduce the conductivity at lower temperatures. For the particular case of a LiAlCl_4 concentration of 0.5M,

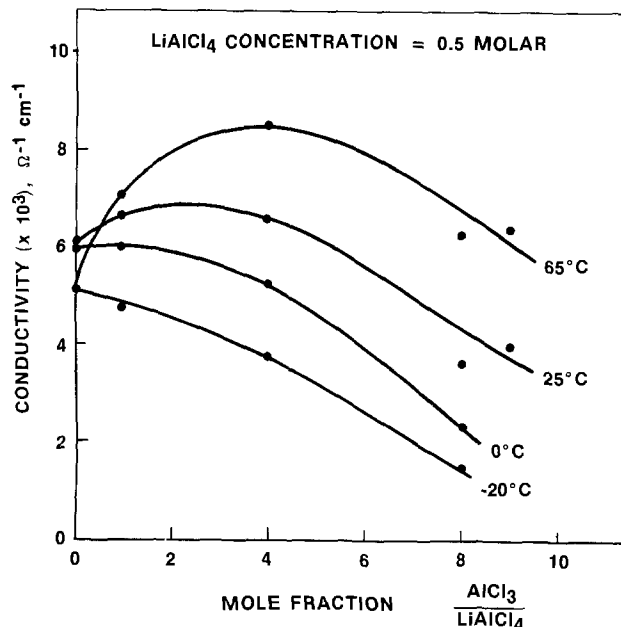


Fig. 12. Conductivity vs. mole fraction $\text{AlCl}_3:\text{LiAlCl}_4$ for a LiAlCl_4 concentration of 0.5M.

Fig. 12 shows the conductivity as a function of the mole ratio $\text{AlCl}_3/\text{LiAlCl}_4$ in solution at four temperatures.

The data suggest that an interaction such as



or perhaps higher complexing is occurring. At low temperatures and at high $\text{AlCl}_3/\text{AlCl}_4^-$ ratios, the equilibrium is displaced to the right, resulting in the formation of the less mobile Al_2Cl_7^- species. Conversely, at high temperatures and low concentrations, the equilibrium is displaced to the left, and the conductivity of the solution is the sum of independent contributions from AlCl_3 and AlCl_4^- .

As shown in Fig. 5, the capacity per unit cathode volume decreases with increasing cathode thickness at constant discharge rate. The depth of discharge in each increment of thickness into the cathode (proportional to the amount of deposited LiCl in that increment) decreases due to the limitations upon mass transport through the rapidly narrowing cathode pores (5). As shown in Fig. 6, the steepness of the cathode utilization vs. thickness curve rapidly increases with increasing discharge rate. The fact that this effect is much more pronounced with the AlCl_3 solution than with the standard LiAlCl_4 electrolyte is a result of the ability of the excess AlCl_3 (contained within the separator as well as within the cathode itself) to act as an effective getter or sink for the LiCl product, thus tripling the effective capacity of the thinnest cathodes.

Finally, as shown by the data in Fig. 7-11, the discharge efficiency of the high rate Li/ SOCl_2 cell can be greatly increased by increasing the cell temperature. There are a number of factors which may combine to result in improved cathode utilization with increasing temperature. The solubilities of the solid reaction products and of the LiAlCl_4 all increase with temperature. Quite probably, the efficiency with which the LiCl is deposited within the porous cathode is also improved at elevated temperatures. The increasing conductivity of the electrolyte with increasing temperature also probably contributes to improved cathode utilization. Which factor may predominate as a function of discharge rate and temperature is, of course, still a matter of conjecture.

Similarly, there are a number of factors which may contribute to a decrease in overvoltage with increasing temperature. In view of the fact that it is not known what physical process primarily determines the over-

voltage of the Li/SOCl₂ cell at room temperature and at relatively low discharge rates, to suggest what factors may result in decreased overvoltage at elevated temperatures and at higher discharge rates is clearly not yet possible. In any case, reduced cell polarization is generally found to accompany an increase in operating temperature.

Summary and Conclusions

The performance characteristics of the Li/SOCl₂ cell have been determined as a function of discharge rate, electrolyte composition, cathode thickness, and cell temperature. Cells have been discharged at rates ranging from about 3 to nearly 300 mA/cm². The SOCl₂ electrolyte solutions have contained either LiAlCl₄ or AlCl₃, with the most efficient discharge characteristics being realized with 1.5M LiAlCl₄ and 4.5M AlCl₃ solutions. Cathodes with thicknesses between 0.025 and 1.0 mm have been utilized.

The discharge curve of a Li/SOCl₂ cell with an electrolyte containing excess AlCl₃ is characterized by two distinct voltage plateaus, resulting from the ability of the AlCl₃ to complex with the Cl⁻ produced by the reduction of the SOCl₂. Moreover, the use of pure AlCl₃ dissolved in SOCl₂ as the electrolyte results in substantially higher average discharge voltages and discharge capacities than can be achieved with cells containing the conventional LiAlCl₄ electrolyte.

With both LiAlCl₄ and AlCl₃ electrolyte solutions, the capacity per unit cathode volume (the effective cathode utilization) decreases with increasing cathode thickness, the rate of decrease being greater the higher the discharge current density. Finally, it has been found that an increase in operating temperature results in an increase in cathode utilization and a decrease in overvoltage, again with both LiAlCl₄ and AlCl₃ electrolyte solutions.

Acknowledgments

The authors wish to thank M. McLaughlin and G. Kadakia for their experimental assistance.

This work was supported in part by a grant from the Office of Naval Research, Arlington, Virginia, under Contract No. N00014-76-C-0524.

Manuscript submitted April 12, 1979; revised manuscript received Sept. 1, 1979.

Any discussion of this paper will appear in a Discussion Section to be published in the December 1980 JOURNAL. All discussions for the December 1980 Discussion Section should be submitted by Aug. 1, 1980.

Publication costs of this article were assisted by GTE Laboratories.

REFERENCES

1. J. J. Auburn, K. W. French, S. I. Lieberman, V. K. Shah, and A. Heller, *This Journal*, **120**, 1613 (1973).
2. W. K. Behl, J. Christopoulos, and S. Gilman, *ibid.*, **120**, 1619 (1973).
3. N. Marincic, J. Epstein, and F. Goebel, in "Proceedings of the 26th Power Sources Symposium," Atlantic City, N.J. (April, 1974).
4. J. P. Gabano, in "Proceedings of the 28th Meeting of the International Society of Electrochemistry," Varna-Druzhba, Bulgaria (September, 1977).
5. A. N. Dey and P. Bro, *This Journal*, **125**, 1574 (1978).
6. M. Domeniconi, K. Klinedinst, N. Marincic, C. Schlaikjer, R. Staniewicz, and L. Swette, Office of Naval Research, Arlington, Va., N00014-76-C-0524 Interim Rep., Dec. 1977.
7. M. J. Domeniconi and K. A. Klinedinst, in "Proceedings of the 28th Power Sources Symposium," Atlantic City, N.J. (June, 1978).
8. H. Hecht, *Z. Anorg. Chem.*, **254**, 37 (1947).
9. D. A. Long and R. T. Bailey, *Trans. Faraday Soc.*, **59**, 594 (1963).
10. K. French, P. Cukor, C. Persiani, and J. Auburn, *This Journal*, **121**, 1045 (1974).
11. J. P. Gabano, Fr. Pat. 1,583,804 (1969).
12. G. L. Holleck, J. R. Driscoll, and D. E. Toland, ECOM-74-0030-6, Grant No. DAAB07-74-C-0030, July, 1975; J. R. Driscoll and G. L. Holleck, Paper 34 presented at The Electrochemical Society Meeting, Dallas, Texas, Oct. 5-9, 1975.
13. C. Schlaikjer, F. Goebel, and N. Marincic, Paper 16 presented at The Electrochemical Society Meeting, Atlanta, Georgia, Oct. 9-14, 1977.

Electrocatalytic Electrodes for the Polysulfide Redox System

Gary Hodes* and Joost Manassen

Plastics Research Department, The Weizmann Institute of Science, Rehovot, Israel

and David Cahen

Structural Chemistry Department, The Weizmann Institute of Science, Rehovot, Israel

ABSTRACT

Porous electrocatalytic electrodes for the polysulfide redox system, containing one of various metallic sulfides (especially of Co, Cu, Pb) are described. Emphasis is placed on their use as counterelectrodes in photoelectrochemical cells employing polysulfide electrolytes. Their activity is measured as a function of electrolyte temperature and composition. The ratio of S to S²⁻, and through it the local redox potential of the solution, is shown to be an important factor controlling electrode activity. The short and long term stability of the electrodes, as cathodes, is discussed, and it is shown that, when used in conjunction with photoanodes, Cu₂S and CoS may poison the photoelectrode surface, thereby reducing total cell efficiency.

Since the discovery that polysulfide electrolytes can stabilize various photoelectrodes against photocorrosion (1-3), in particular CdS and CdSe, the need for

* Electrochemical Society Active Member.
Key words: electrodeposition, sulfidation, photoelectrochemistry, energy conversion.

an efficient counterelectrode has arisen, since electrodes of carbon and platinum, usually used for this purpose, are not very active for the polysulfide redox system [Ref. (4), Fig. 1].

The importance of the counterelectrode in a photoelectrochemical cell (PEC) can be illustrated by Fig.

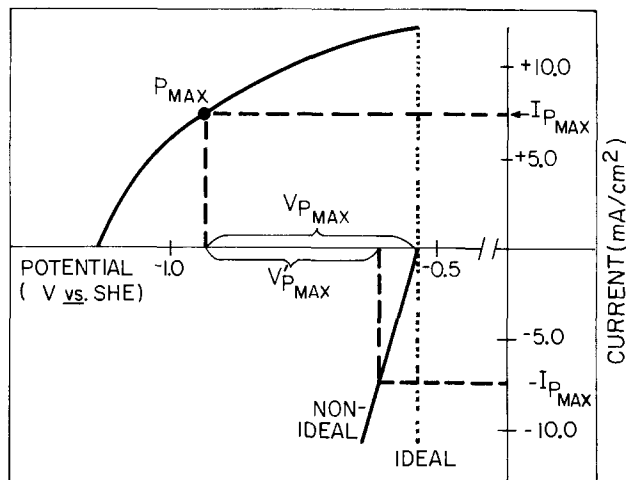


Fig. 1. Potentiostatic current-voltage curve of n-CdSe photoanode together with an ideal and nonideal (polarizable) counter-cathode. P_{\max} represents the maximum power point on the illuminated CdSe I - V curve. The cathodic curves are for an ideal (no polarization broken line) and nonideal counterelectrode.

1, which shows potentiostatic current-voltage curves of both the photo and counterelectrodes. For the purpose of the illustration, the upper curve is that of a typical CdSe electrode [prepared by electroplating (1)] while the lower plot is that of a counterelectrode which is assumed to polarize 100 mV at a cathodic current of 10 mA (solid line) or an ideal counterelectrode which maintains the redox potential of the electrolyte at all current densities (dotted line). Looking first at the CdSe electrode against the ideal counterelectrode, we see that at maximum power the combined system delivers 7.4 mA ($I_{P_{\max}}$) at 400 mV ($V_{P_{\max}}$), i.e., 2.96 mW. If the counterelectrode is the polarizable one, then at $I_{P_{\max}}$, the voltage output of the cell falls to 327 mV ($V'_{P_{\max}}$), and the power delivered is now 2.42 mW. (In fact, the maximum power point will shift slightly, but this will make only a small difference, and will be ignored here.) This represents an 18% drop in power, which is manifested by a drop in fill factor from 0.41 to about 0.34 for the overall cell.

It should be noted that this kind of loss often goes unnoticed or is overlooked when power output of a PEC is derived from potentiostatic I - V plots. Therefore, any influence of the counterelectrode is neutralized and too optimistic a picture of cell performance is obtained.

We reported previously that electrodes of CoS, NiS (4), Cu₂S, and PbS (5) are active for polysulfide reduction (required for n-type photoelectrodes; (poly)sulfide oxidation for p-type photoelectrodes). The purpose of this work is to compare the properties of such electrodes especially those that can be prepared simply (an important consideration for possible practical PEC's), and to find the optimum working conditions for their use, mainly in terms of electrolyte composition.

Experimental

We consider three basic types of electrodes: Cu₂S, CoS, and PbS.

1. Cu₂S electrodes are prepared by immersing a brass gauze (70% Cu, 30% Zn) in a (poly)sulfide solution. The gauze gradually blackens, forming Cu₂S. This process of sulfidization can be accelerated by anodizing the gauze in the (poly)sulfide solution. The presence of zinc in the alloy imparts mechanical coherence to the electrode; copper alone in sulfide solution rapidly disintegrates as Cu₂S forms throughout the bulk of the copper, while sulfidization of zinc is relatively limited to the surface, thereby holding the Cu₂S in a matrix, the bulk of which is zinc metal.

2. Co electrodes are prepared by first electroplating Co(OH)₂ onto a stainless steel cathode. The electroplating solution consists of an aqueous solution of 20g CoSO₄/liter with a potassium biphthalate buffer to maintain the pH between 3 and 6. The anodes are cobalt plates or rods, one on each side of the cathode for an even current distribution. Electrolysis is carried out at room temperature and without stirring. The current density used varies between ~20-60 mA/cm². (In this study, 1 cm² means an electrode of 1 cm² geometric area. Since both sides of all electrodes are exploited, this is really 2 cm². However, assuming a counterelectrode will be, at least, identical in size to the photoelectrode in a PEC, then both sides of the counterelectrode will be available for reaction, unless the counterelectrode is also the back wall of the cell. Since we wish to evaluate a counterelectrode as it will be used in a practical cell, this system of measurement is chosen.) The optimal current density depends mainly on the pH of the electrolyte, the current density increasing as the pH decreases. Thus at a pH of 5, the optimal current density is 30-40 mA/cm². The plating time varies from 3 to 6 min. If plating continues for longer, the layer becomes dendritic, and mechanically unstable. Under these conditions, a black coating is obtained which dries to a blue-green color, and which consists mainly of Co(OH)₂. When immersed in (poly)sulfide solution, this is converted to cobalt sulfide, mainly CoS. A reduction treatment at ~ -1200 mV (*vs.* SCE) in a (poly)sulfide solution for several minutes improves the electrode performance somewhat.

3. PbS electrodes are prepared by electroplating PbO₂ onto a stainless steel anode using a Pt cathode and an aqueous electrolyte of lead nitrate. The conditions for plating (electrolyte composition, current density, plating time) were found to be noncritical; typically the plating was carried out from a 0.3M solution of lead nitrate (or acetate) at a current density of ~50 mA/cm² for 5 min. This layer is then reduced electrolytically in (poly)sulfide solution under the same conditions as those used for CoS. This reduction treatment is essential to obtain active electrodes.

In addition to these three types of electrodes, several other electrode materials were tested, largely for comparison purposes: Platinized platinum (platinum black electroplated on platinum metal); high surface-area carbon in the form of plates ~ 1 mm thick; electroplated brass on steel with a Cu:Zn ratio of 95:5; and RuS₂ prepared by cathodic treatment of a stainless steel substrate in an aqueous solution of 0.5g RuCl₃/liter and subsequent reduction in polysulfide solution as described above for CoS and PbS electrodes.

Potentiostatic current-voltage curves were obtained using either an Elscint CHP-1 or Wenking LT 73 potentiostat. The polysulfide electrolytes contained KOH and S (Frutarom), Na₂S·9H₂O (BDH), and deionized water. A water-jacketed cell, connected to a thermostat was used. Argon was continually passed over the electrolyte to prevent oxidation, but no stirring was employed (unless specifically mentioned). A saturated calomel electrode was used as reference in most cases, though a Pt wire, which takes the potential of the solution, was used in some experiments. The counterelectrode was a 10 cm² Pt gauze.

Results and Discussion

Electrocatalytic activity.—The electrocatalytic activity of the electrodes studied is given directly by the current-potential plots in Fig. 2. Seven types of electrodes are shown here. The three main electrodes studied, CoS, PbS, and sulfided brass (30% Zn), are shown by one plot, since the activities of all three are almost identical, within experimental variations. From Fig. 2, it can be seen that these electrodes outperform all others with the exception of the 95% Cu electrode, which however is not very stable (see under long-term stability of electrodes, below). Platinized Pt, the

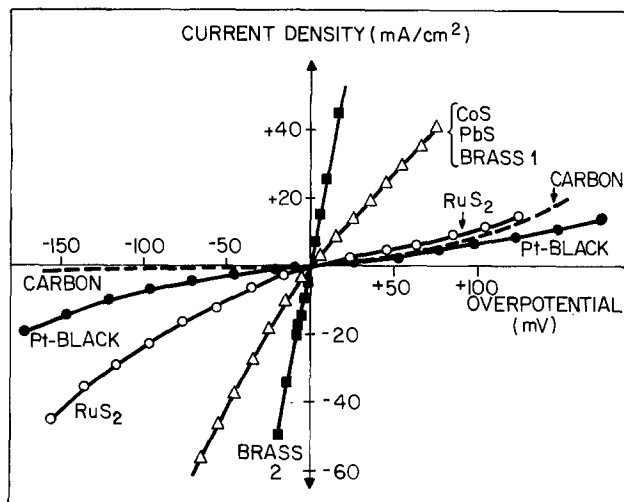


Fig. 2. Anodic and cathodic polarization curves of various electrode materials in $1M[OH^-]$, $1M[S^{2-}]$, and $1M[S]$ electrolyte at $30^\circ C$. Brass (1) contains 70% Cu, 30% Zn. Brass (2) contains 95% Cu, 5% Zn; Pt-black is platinized Pt.

most active electrode studied by Allen and Hickling (6), is much less active, and carbon, even less so. (Smooth Pt is similar, or less active, than carbon.)

The results obtained suggest that other sulfides which are good electrical conductors, i.e., metallic or degenerate semiconductors, may be good electrocatalysts for this system. Preliminary experiments with RuS_2 support this, as can be seen in Fig. 2. These electrodes are intermediate in activity between platinized Pt and the active sulfides in the cathodic direction. At present, we have succeeded in making only very thin layers of RuS_2 by electroplating, much less than the several microns usually plated of the other sulfide electrodes. From this, we may reasonably infer that RuS_2 is intrinsically as active as the other sulfides, and the measured lesser activity is due only to a lower active surface area.

Dependence of activity on electrolyte composition.—The composition of the electrolyte in a photoelectrochemical cell is of crucial importance for cell operation. Even for a redox system which is known to be able to stabilize a certain semiconductor, such as polysulfide/CdSe, the absolute concentrations of the oxidized and reduced forms of the electrolyte can affect such properties as stability of photoelectrode (7, 8), magnitude of photocurrent (9), light absorption in electrolyte, and polarization of the counterelectrode. Since it is the last of these properties which interests us here, we have investigated the effect of the composition of the polysulfide solution on the electrocatalytic activity of the sulfide electrodes.

Normally we would expect an increase in concentration of the electroactive species (for an n-type photoelectrode, the electroactive species at the counterelectrode is the oxidized form) to decrease the polarization at an electrode. If we look at Fig. 3(a), where polarization curves are shown for a CoS electrode in solutions of fixed $[OH^-]$ and $[S^{2-}]$, and varying $[S]$, we see that indeed when $[S] \leq 1M$, this is true for the relevant cathodic direction. The trend to limiting current densities apparent at low $[S]$ concentrations can be explained by normal concentration polarization, where the current is determined by the rate of diffusion of oxidized species to the electrode surface. However, when $[S] > [S^{2-}]$ (1/1/2 and 1/1/3 in Fig. 3), we obtain the unexpected result that the activity again decreases as $[S]$ increases. That the determining factor here is the ratio between $[S]$ and $[S^{2-}]$, rather than the absolute value of $[S]$, is clear from Fig. 3(b), where, for different absolute values of $[OH^-]$ and

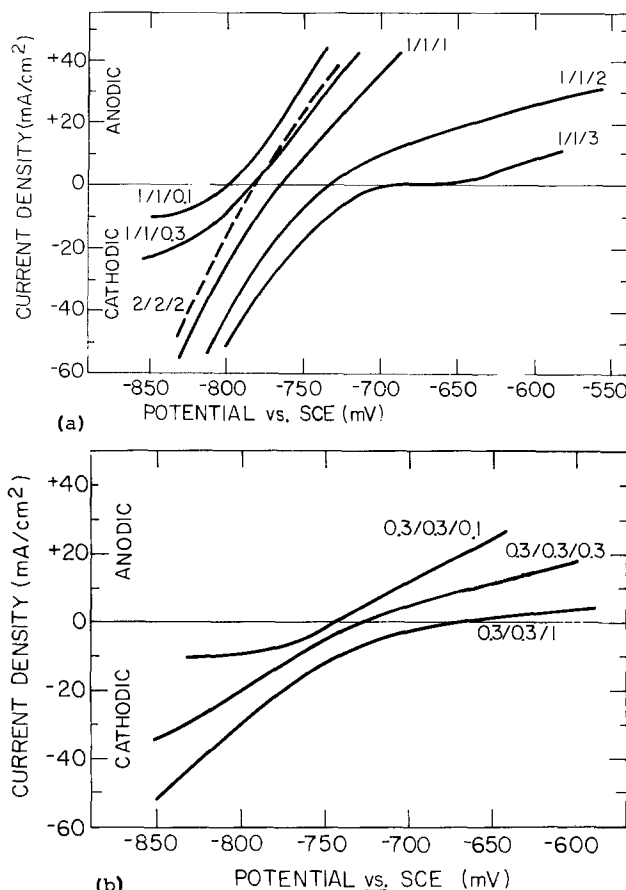


Fig. 3. (a) Polarization curves of a CoS electrode in various polysulfide electrolytes at $30^\circ C$. The number for each curve represent the molar concentrations of $[OH^-]$, $[S^{2-}]$, and $[S]$, respectively. Except for the 2/2/2 electrolyte (broken line), the curves represent a variation of $[S]$ with fixed $[OH^-]$ and $[S^{2-}]$. (b) As Fig. 3(a), but with lower $[OH^-]$ and $[S^{2-}]$ (0.3M each) than in Fig. 3(a).

$[S^{2-}]$, the maximum activity is again obtained when $[S] = [S^{2-}]$, and decreases when $[S]/[S^{2-}] \neq 1$.

This behavior can be rationalized, if we consider the effect of electrolyte composition on the redox potential (potential of zero current in Fig. 3). Figure 4 shows E_{redox} as a function of $[S]$ and the anomalous behavior for $[S] > 1$, which means in this case $[S]/[S^{2-}] > 1$, is obvious. The underlying reason for this steep change in E_{redox} can be found in the rather complicated equilibria involving various higher polysulfides, that enter into the picture under these conditions [as has been explained by Allen and Hickling (10)].

Using Fig. 4 we can now understand the fact that the anodic parts of the curves for 1/1/2 and 1/1/3 [Fig. 3(a)] and 0.3/0.3/1 [Fig. 3(b)] are much flatter than expected. When oxidizing these sulfur-rich solutions more sulfur is formed in and around the pores of the electrode and because of this, the redox potential changes to less negative values, approaching the point of zero current. This is especially obvious in the curve for 1/1/3, where between the voltages -700 and -650 mV vs. SCE the electrode passes practically no current. Because this effect is dependent on the rate by which the S formed is removed from the electrode, one would expect such a phenomena to be strongly influenced by either stirring or temperature. The temperature effect is clearly illustrated in Fig. 5 and the effect of stirring is very similar.

The same reasoning explains the cathodic part of the curve. As long as the polarization is insufficient to shift the electrolyte potential near the electrode out of the non-Nernstian region (where $[S] > [S^{2-}]$) into

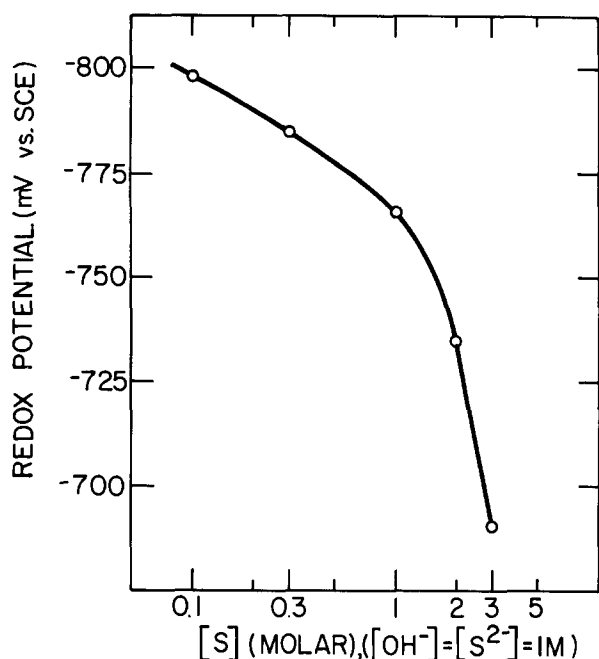


Fig. 4. Effect of $[S]$ on the redox potential of a polysulfide electrolyte at 30°C ; $[\text{OH}^-]$ and $[\text{S}^{2-}]$ fixed at 1M each.

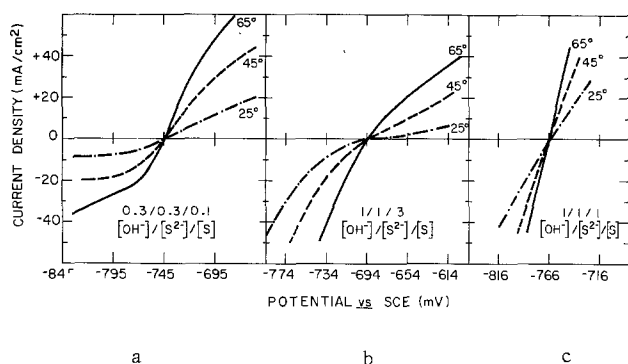


Fig. 5(a). Effect of temperature on the polarization curves of a CoS electrode in a $0.3/0.3/0.1$ polysulfide electrolyte. (b) As Fig. 5(a), but for a $1/1/3$ electrolyte. (c) As Fig. 5(a), but for a $1/1/1$ electrolyte.

the Nernstian region (where $[S] \leq [\text{S}^{2-}]$), a small change in electrolyte composition at the electrode (caused by a small current density) can shift the potential strongly in the cathodic direction (i.e., a large overpotential). When the electrolyte composition near the electrode approaches $[S] = [\text{S}^{2-}]$, it now shows normal Nernstian behavior, and the shift in potential with increasing $[\text{S}^{2-}]$ (i.e., increasing current density) becomes less. At the potential where $[S] = [\text{S}^{2-}]$ [-750 mV in Fig. 3(a)], and $1/1/1$, $1/1/2$, and $1/1/3$ curves all become more or less parallel as is to be expected. This behavior is in contrast with that of a normal concentration overpotential, where the change in overpotential increases with increasing current density, as occurs for example in the cathodic branch of the $1/1/0.1$ and $1/1/0.3$ curves of Fig. 3(a).

Galvanostatic pulse measurements in the S-rich solutions show that the decay of the overpotential after the pulse (and the buildup at the start of the pulse) can take minutes. However, this decay can be shortened considerably by stirring the solution vigorously. Specifically, experiments in a $1/1/1$ electrolyte show that the instantaneous part of the decay (representing a minimum value for IR -losses) accounts for about one third of the measured overpotential. The greater part of the remainder can be eliminated by stirring and therefore any activation overpotential present contributes in a minor way only to the total overpotential.

The diffusion (or concentration) part of the overpotential, which thus makes the largest contribution to the whole, arises in the same way as that described above for electrolytes with $[S]/[\text{S}^{2-}] > 1$.

Figure 3(a) also shows the curve obtained in a $2/2/2$ electrolyte. As expected, since the concentration of electroactive species is higher, yet $[S] = [\text{S}^{2-}]$, this electrolyte gives a somewhat better performance than does the $1/1/1$ electrolyte.

Changing the hydroxide concentration shows no marked effect on the performance of the electrode. Its main effect is to shift E_{redox} to somewhat more negative values with increasing $[\text{OH}^-]$.

Although the results above are illustrated with CoS electrodes, they hold for Cu_2S and PbS electrodes as well.

Temperature dependence of electrolytic activity.— Since the operating temperature of a photoelectrochemical cell may vary over a wide range, from near 0°C to as much as 60°C , the effect of temperature on its operation is of particular importance. Here we are concerned with the effect of temperature on the functioning of the counterelectrode.

Figures 5(a), (b), and (c) show the effect of temperature on the activity of a CoS electrode in three different electrolyte compositions; low concentrations of $[S]$ and $[\text{S}^{2-}]$ ($0.3/0.3/0.1$); high $[S]/[\text{S}^{2-}]$ ratio ($1/1/3$), and the standard electrolyte $1/1/1$. Variation of temperature has a small effect on the redox potential, and for clarity of comparison, it has been neglected here. Since we know from the results described above that a large part of the overpotential is due generally to a diffusion-controlled component, we expect a substantial increase in activity due to increased diffusion at higher temperatures, and this is indeed observed. Of particular interest are the results obtained in Fig. 5(b), where $[S] > [\text{S}^{2-}]$. In the cathodic direction, the polarization in this electrolyte drops from 45 mV at 25°C to 10 mV at 65°C for a current density of 10 mA/cm². Even more striking is the change in the anodic direction, where, for a current density of 5 mA/cm², the polarization varies from 70 mV at 25°C to 8 mV at 65°C . The results from Fig. 5 may be used directly, as shown previously (in Fig. 1) to calculate the losses in a photoelectrochemical cell due to counterelectrode polarization over a certain temperature range. We have found the effect of stirring on electrode activity to be qualitatively similar to that of temperature, as expected from a diffusion-controlled overpotential. Because of the desirability of lack of external stirring in practical PEC's due to external power source and space considerations, we have not given much attention to this effect. However, it may be of importance in combined cells with heat transfer, where the electrolyte is in motion (11).

Stability consideration of the sulfide electrodes.— The most important single characteristic of a counterelectrode for use in a photoelectrochemical cell is, as for the photoelectrode, the long-term stability of the electrode. For the electrodes mainly under consideration in this study, PbS , Cu_2S , and CoS , the stabilities are quite different.

PbS.— PbS is by far the least stable of these three, and therefore it will be dealt with briefly. The activity of a PbS electrode drops slowly to about 10% of its initial activity, over a period of a couple of weeks when used in a cell under normal (day-night) working conditions, and remains constant thereafter. The initial activity may be regenerated by cathodic reduction. Presumably, the deactivation is caused by a surface alteration of the PbS , which itself is probably a surface layer on a substrate of porous PbO_2 .

Cu_2S .—The stability of Cu_2S (in the form of sulfided brass) can be separated into three distinct parts. First of these is the mechanical stability, which we have mentioned briefly already. Pure Cu disintegrates in

polysulfide solutions within a short time. By adding increasing amounts of Zn to the Cu (as brass), the mechanical stability improves. For a 5% Zn, 95% Cu electrode as in Fig. 2, the electrode is stable for a period ranging from hours to a few days. Thus, in spite of the very high activity of such electrodes, they are not practical due to lack of stability. For a brass gauze with a Cu-Zn ratio of $\sim 70:30$ (normal or α -brass) the mechanical disintegration is slowed to such an extent that we have found no visible change in form of the gauze after 1 year in polysulfide solution, although black Cu_2S powder does fall from the electrode very slowly; this is noticeable even after short periods of a few weeks as the Cu_2S settles at the bottom of the cell. This very slow disintegration is open to further reduction by increasing further the Zn content of the brass (which will decrease the electrochemical activity), or possibly by using an alloy metal other than Zn, which itself is not completely stable in these solutions.

The second consideration is the stability of electrochemical activity of the Cu_2S electrode. We have found no change in activity over months of use. This is not unexpected, since the surface of the electrode is subject to a very slow, but continuous, renewal due to the mechanical disintegration.

The third, and less obvious, type of instability to be considered is the effect of the Cu_2S electrode on the photoelectrode. We have noticed during accelerated lifetime experiments (high illumination intensity), using CdSe single crystal photoelectrodes and Cu_2S counterelectrodes, that on some occasions, a bluish-black deposit forms on parts of the surface of the CdSe. Figure 6 shows a scanning electron micrograph of such a deposit, which takes the form of hexagonal platelets of dimensions of several microns, which tend to bunch together into flower petal-like aggregates. Electron microprobe composition measurements, as well as the hexagonal form of the crystallites, show the deposit to be CuS (covellite). Since the composition of the counterelectrode itself has been shown, by x-ray diffraction, to be $\text{Cu}_{>1.75}\text{S}$, it seems that the CuS is formed by photooxidation of Cu_2S at the illuminated CdSe surface. It is unclear whether the copper arrives at the CdSe as Cu^+ ions (although Cu_2S has a very low solubility product, there will be some Cu^+ -containing ions

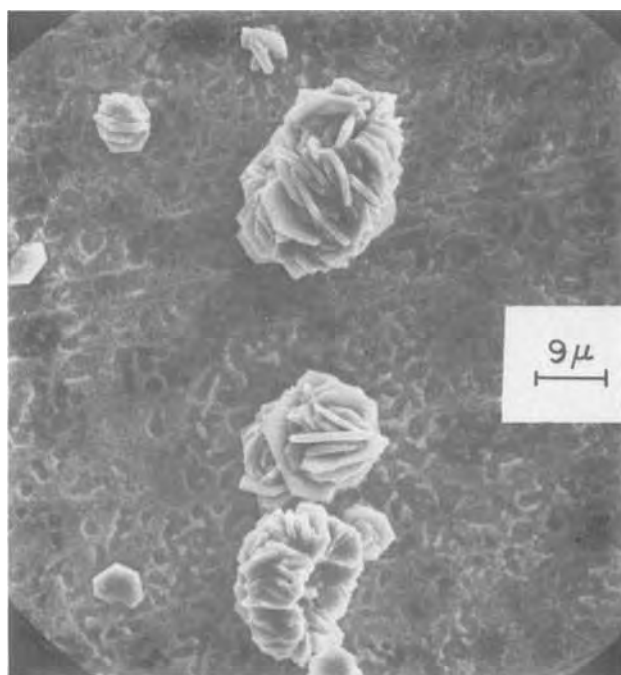


Fig. 6. SEM picture of CuS (covellite) formation on a single crystal n-CdSe photoanode after accelerated test using Cu_2S as a counterelectrode in a photoelectrochemical cell.

in solution) or as Cu_2S particles (colloidal or larger) from the slow disintegration of the sulfided brass. We have carried out some experiments with a Cu_2S and a gold electrode in polysulfide solution. The gold is connected to the negative terminal of a power-supply, to simulate an n-type photoelectrode, and the Cu_2S to the positive terminal. At a voltage between the two electrodes $\approx 0.47\text{V}$, a black deposit is clearly visible on the gold within 24 hr of the start of electrolysis, while at a voltage lower than this, no deposit was visible after two days of electrolysis. This suggests that a field-assisted migration, as well as simple diffusion, may be occurring.

The presence of CuS on the surface of the CdSe can lead to several undesirable effects. One is blocking of the light, incident on the CdSe. Another is a possible local cell action (back-reaction) leading to reduction of polysulfide at the CuS, and loss of current. This is not expected to be serious, as CuS, unlike Cu_2S , is not a very good electrical conductor. A third effect is diffusion of Cu^+ into the CdSe leading to Cu-compensated CdSe. This could lead to a serious deactivation of the CdSe, since CdSe:Cu as used in photoconductors, is a very poor photovoltaic material. We notice some deactivation; in the worst cases $\sim 20\%$ loss in power output for single crystal electrodes. Washing such deactivated electrodes in aqueous KCN (which dissolves CuS) results in a partial restoration of the original activity.

If the Cu_2S deposition is largely due to a field-assisted migration, then use of a Cu_2 electrode with a p-type semiconductor electrode should not be susceptible to this deposition, as the electric field is now in the opposite direction. Furthermore, the mechanical stability of the Cu_2S electrode may conceivably be improved, as Cu^+ which originally came from the electrode may be redeposited on the Cu_2S , which is negative with respect to the photoelectrode.

CoS.—As long as the layer of CoS is not too thick, the electroplated CoS electrode, does not suffer from either mechanical or electrochemical instability over a period of more than four months, which is the longest period over which these electrodes have been tested at present. However, while there is no visible effect on a CdSe photoelectrode, the open-circuit voltage of the cell drops typically from 600–650 mV initially to 500–550 mV within some minutes, which translates to $\sim 15\%$ loss in power conversion efficiency. The photocurrent is not much affected. This suggests that, in a manner, analogous to that observed for Cu_2S , CoS is deposited on the CdSe surface. Since CoS is a good conductor of electricity, we may expect a local cell reaction on the deposited CoS. Due to the shape of the photocurrent-voltage curve of these cells (poor near the open-circuit voltage and good near the short-circuit current), such a local cell action may make a fairly large difference to the open-circuit voltage while the short-circuit current is much less affected, as is indeed observed.

The approximately 100 mV loss in open-circuit voltage due to the CoS does not increase with time, suggesting a limiting layer on the CdSe. If the CdSe is removed from the electrolyte, and placed, without washing, in a new electrolyte with a non-CoS counterelectrode, the drop in photovoltage remains. If, however, the CdSe is washed with water in-between, the original photovoltage is obtained, suggesting a very loose CoS layer is formed on the CdSe. Furthermore, over a period of months, there is often a tendency for the open-circuit voltage to increase somewhat. In analogy with CuS formation on illuminated CdSe, this may be due to oxidation of CoS to a higher, less conducting sulfide.

While we have found this degradation of photovoltage due to the CoS electrode to be a quite general effect, we have noted some cases where such degradation did not occur, while the counterelectrode activity remained high. We have been unable to reproduce

these conditions at will, and do not as yet understand the reason for this effect. However, such exceptions show that the photovoltage deactivation due to the CoS electrode can be overcome. This is an important point for eventual practical use of such electrodes. Clearly, further investigations, especially surface analytical ones, are called for to gain a full understanding of such processes, which, ultimately may play an important role in determining the future of a practical PEC.

Summary

Several metal sulfides have been shown to act as good electrocatalysts for the polysulfide redox reactions. As practical electrodes, only two show sufficient stability for possible practical use—Cu₂S (as sulfided brass) and CoS. The former has the disadvantage that, as presently fabricated, the lifetime will probably be limited to a few years due to mechanical instability, while the latter, due to deactivation of the photoelectrodes lowers the power output of a photoelectrochemical cell in which it is used by 15–20%. Thus, for routine and relatively short-term experiments, Cu₂S is the preferable counterelectrode while for long-term use, CoS becomes preferable.

The effect of electrolyte composition and temperature on the activity of these electrodes has been measured, enabling a choice of electrolyte for polychalcogenide electrochemical cells to be made on the basis of the counterelectrode. In short, for the cathodic direction (which, at the present time, is the more important one), the electrode activity increases as [S] increases, with the important condition that [S] \leq [S²⁻]. Thus, since the maximum solubility of Na₂S in water at normal temperatures is 2–3M, the optimum electrolyte is ~2M S and 2M S²⁻. The concentration of OH⁻ is of secondary importance for the counterelectrode, although there is a slight improvement in performance with higher [OH⁻], particularly at low total ionic concentrations.

At higher temperatures, the necessity for the [S]/[S²⁻] ratio to be <1 becomes less important.

After seven months operation in a PEC, a CoS counterelectrode which did not poison the photoelectrode (CdSe) remained stable, both in electrocatalytic activity and physically, and did not have any adverse effect on the CdSe during the seven months in operation.

Manuscript submitted April 27, 1979; revised manuscript received Sept. 5, 1979.

Any discussion of this paper will appear in a Discussion Section to be published in the December 1980 JOURNAL. All discussions for the December 1980 Discussion Section should be submitted by Aug. 1, 1980.

Publication costs of this article were assisted by The Weizmann Institute of Science.

REFERENCES

1. G. Hodes, J. Manassen, and D. Cahen, *Nature*, **261**, 406 (1976).
2. A. B. Ellis, S. W. Kaiser, and M. S. Wrighton, *J. Am. Chem. Soc.*, **98**, 1635 (1976).
3. B. Miller and A. Heller, *Nature*, **262**, 680 (1976).
4. G. Hodes, J. Manassen, and D. Cahen, *J. Appl. Electrochem.*, **7**, 181 (1977).
5. J. Manassen, G. Hodes, and D. Cahen, in "Semiconductor Liquid-Junction Solar Cells," A. Heller, Editor, p. 34, The Electrochemical Society Softbound Proceedings Series, Princeton, N.J. (1977).
6. P. L. Allen and A. Hickling, *Trans. Faraday Soc.*, **53**, 1626 (1957).
7. B. Miller, A. Heller, M. Robbins, S. Menezes, K. C. Chang, and J. Thomson, Jr., *This Journal*, **124**, 1019 (1977).
8. D. Cahen, G. Hodes, and J. Manassen, *ibid.*, **125**, 1623 (1978).
9. D. Lando, J. Manassen, G. Hodes, and D. Cahen, Submitted for publication.
10. P. L. Allen and A. Hickling, *Chem. Ind.*, **51**, 1558 (1954).
11. Y. Avigal, D. Cahen, G. Hodes, and J. Manassen, *Isr. Patent Appl.* 55477 (1978). Y. Avigal, Abstract No. 8A presented at the Int. Conference on the Application of Solar Energy, Haifa, Israel, Sept. 1978.

A Hydrogen-Bromine Cell for Energy Storage Applications

R. S. Yeo*¹

Brookhaven National Laboratory, Department of Energy and Environment, Upton, New York 11973

and D-T. Chin*

Department of Chemical Engineering, Clarkson College of Technology, Potsdam, New York 13676

ABSTRACT

An experimental and theoretical study has been made to determine the feasibility of a hydrogen-bromine cell for energy storage applications. The laboratory data were collected for the cell performance and the membrane characteristics during the charge and the discharge operations. An unsteady-state heat balance was used to predict the temperature change and the overall electric-to-electric efficiency. The results indicate that the hydrogen-bromine system can achieve an efficiency greater than 70% when the operating cell current density is less than 160 mA/cm².

Electrochemically regenerative hydrogen-halogen cells have been recently proposed for large scale energy storage in weekly cycle load-leveling applications (1–4). The cells can also be coupled with variable and interruptible primary energy sources, such as solar and wind energy, because the cells can be operated at

high current densities and the reactants are stored external to the cell. The system can be independently sized for various energy and power requirements. The operating conditions, and the cell and membrane characteristics of a hydrogen-chlorine system have been previously reported (4, 5). This paper is concerned with the use of a hydrogen-bromine cell for energy storage applications. The laboratory data were collected for the cell performance and membrane characteristics during the charge and discharge operations, and an unsteady-

* Electrochemical Society Active Member.

¹ Present address: The Continental Group, Incorporated, Energy System Laboratory, Cupertino, California 95014.

Key words: battery, conductance, polymers, stoichiometry.

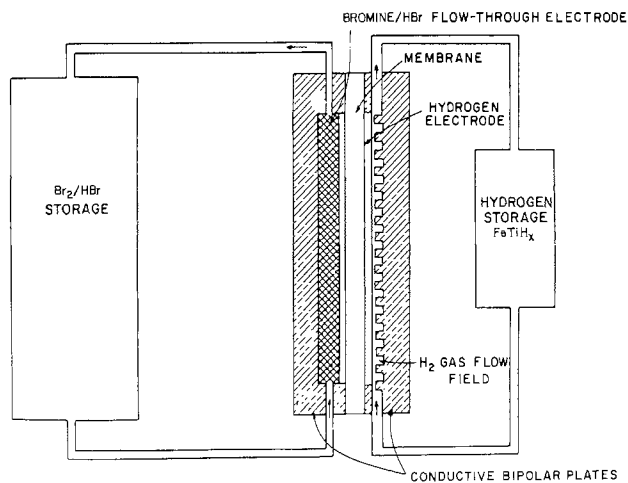
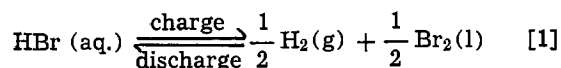


Fig. 1. Schematic of the hydrogen-bromine energy storage system

state mass and heat balance was used to predict the temperature change and the overall electric-to-electric efficiency of the system.

The concept of the hydrogen-bromine system is illustrated schematically in Fig. 1. Off-peak electric energy is used to electrolyze concentrated hydrobromic acid. Cells based on solid polymer electrolyte (SPE) technology can be used (3, 6). The hydrogen and bromine produced are stored external to the cell. During discharge the hydrogen and bromine are fed back to the cell to generate electricity. The overall reaction is



The hydrogen-bromine cell has several advantages: (i) the system has a high electric-to-electric efficiency because of fast electrode kinetics; (ii) the same electrochemical cell can be used for both charge and discharge operations; (iii) it can be operated with shallow discharges, and can tolerate both over charge and over discharge; (iv) the use of the SPE technology allows the anode and the cathode to be operated at different pressures, thus hydrogen can be produced at a pressure high enough for storage as a metal hydride or as compressed gas without further compression; (v) the cell has a high coulombic efficiency because of low self-discharge rate; (vi) there is no mass transfer limitation in the cell operation because of the high solubility of bromine in the hydrobromic acid electrolyte; (vii) the bromine storage unit and the bromine electrode can be operated near the ambient pressure because of the low vapor pressure of bromine; and (viii) since the reactants and products are fluids, the problem of intercell imbalances does not arise.

The General Electric SPE cells use a perfluoro sulfonic acid (Nafion) membrane as the cell separator. The cell usually consists of a bipolar configuration with electrocatalysts bonded on each side of the membrane as shown in Fig. 1. The Nafion membrane possesses excellent corrosion resistance and thermal stability; it is suitable for use in the hydrogen-bromine cell.

Experimental

Nafion membranes.—Unless otherwise specified, all the membrane measurements were performed with a sample having an equivalent weight of 1200. The sample was 0.25 mm thick and was boiled in distilled water for one hour before each experiment.

Laboratory HBr electrolyzer.—The cell components are shown in Fig. 2. A Nafion-115 (equivalent weight of 1100 and thickness of 0.13 mm) was used as the cell separator. Both hydrogen and bromine electrodes were located next to the membrane so that the interelectrode distance was equal to the thickness of the membrane.

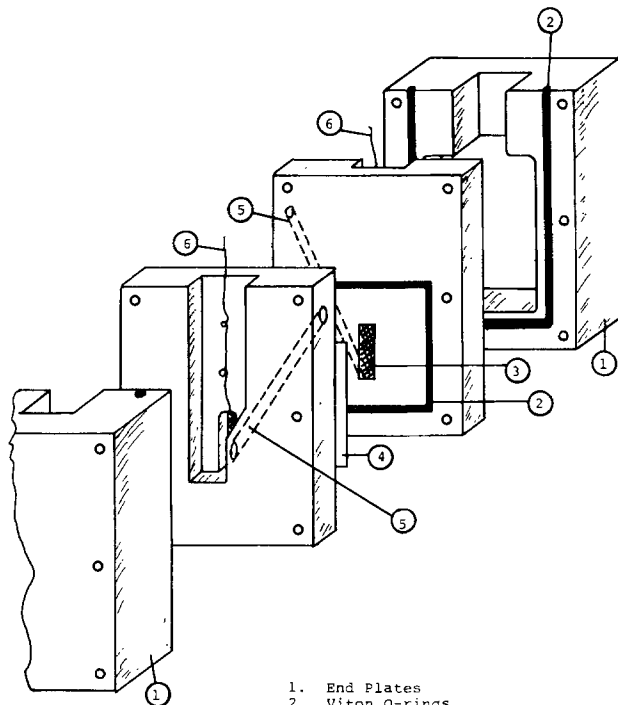


Fig. 2. Construction of a BNL experimental cell

Membrane conductivity studies.—The conductivity measurements were made using the d-c method of Lander and Weaver (7) in a cell described in an earlier report (5). Prior to each measurement, the membrane was boiled in H₂O and then soaked in the HBr electrolyte at 25°C for at least three days.

Electrolyte content in membranes.—The equilibrium electrolyte content of the membrane was determined by a method previously described (8).

Acid concentration in membranes.—The membrane, being on reaching equilibrium in the electrolyte, was removed, surface dried, and then thoroughly leached with water; the extract was titrated for hydrobromic acid. The HBr concentration in the membrane was calculated from the electrolyte content and the amount of acid leached out from the membrane.

Experimental Results

Cell performance.—The experimental cell, shown in Fig. 2, was used to determine the open-circuit cell voltage and the cell polarization for charge at ambient temperature and pressure. The results for the cell voltage vs. charge current densities is shown in Fig. 3. For comparison, the results with the General Electric SPE cells and the results obtained by other investigators (9-11) are also shown in the figure. Figure 4

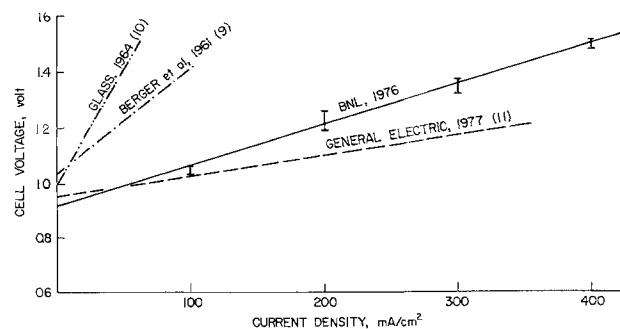


Fig. 3. Charge cell voltage vs. current density for various hydrogen-bromine cells.

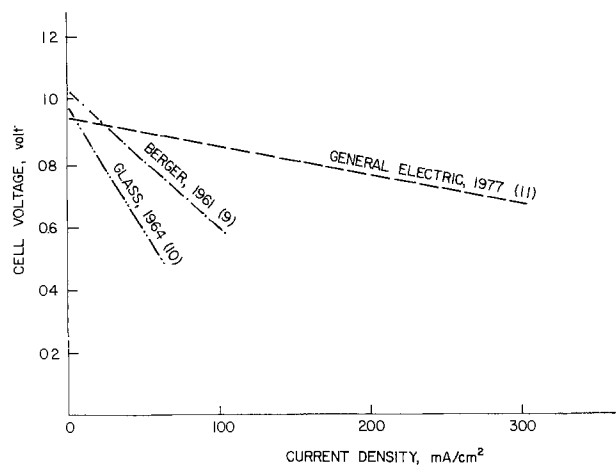


Fig. 4. Discharge cell voltage vs. current density for various hydrogen-bromine cells.

presents the discharge performance of various H_2 - Br_2 cells. It is seen that the General Electric SPE cell and the present cell had very low polarizations; the overvoltage was primarily caused by IR drop across the cell membrane. The results of various HBr concentration and cell temperatures can be summarized by the following empirical equations: For charge

$$E = E_o - 0.681i \quad [2]$$

For discharge

$$E = E_o - 0.589i \exp(2.19X) \quad [3]$$

where i is the charge and discharge current density in A/cm^2 and X is the weight fraction of HBr in the electrolyte. E_o is the open-circuit cell voltage and may be expressed as

$$E_o = \pm \left\{ \phi - (T - 298) \left(4.3 + 1.86 \ln \frac{12.36X}{1-X} \right) \times 10^{-4} + 4.31 \times 10^{-5} T (\ln f_{H_2} + \ln a_{Br_2}) \right\} \quad [4]$$

where

$$\phi = \begin{cases} 1.073 - 0.0567 \ln \frac{12.36X}{1-X} & (0.016 < X < 0.11) \\ 1.095 - 0.1042 \ln \frac{12.36X}{1-X} & (0.11 < X < 0.28) \\ 1.336 - 0.2581 \ln \frac{12.36X}{1-X} & (0.28 < X < 0.58) \end{cases} \quad [5]$$

T = temperature in $^{\circ}K$

f_{H_2} = fugacity of hydrogen gas

a_{Br_2} = activity of Br_2 in the electrolyte, equal to 1.0 for bromine present as a liquid phase.

Equation [4] was obtained for the fuel cell reaction. Consequently, according to the thermodynamical conventions, E_o will have a positive value for discharge and a negative value for charge. These results demonstrate that the General Electric SPE cell can be operated up to $0.3 A/cm^2$ with relatively low overvoltages.

Characterization of membrane.—It was found (5) that the transport properties of the membrane were strongly related to the electrolyte content of the membrane. Figure 5 shows the electrolyte content and the HBr concentration in Nafion membrane as a function of HBr concentration in the electrolyte. It should be mentioned that the membrane was boiled in water for more than two hours before each test. It is seen that the electrolyte content in the membrane decreased with increasing HBr concentration. The relationship can be represented by the following empirical equation

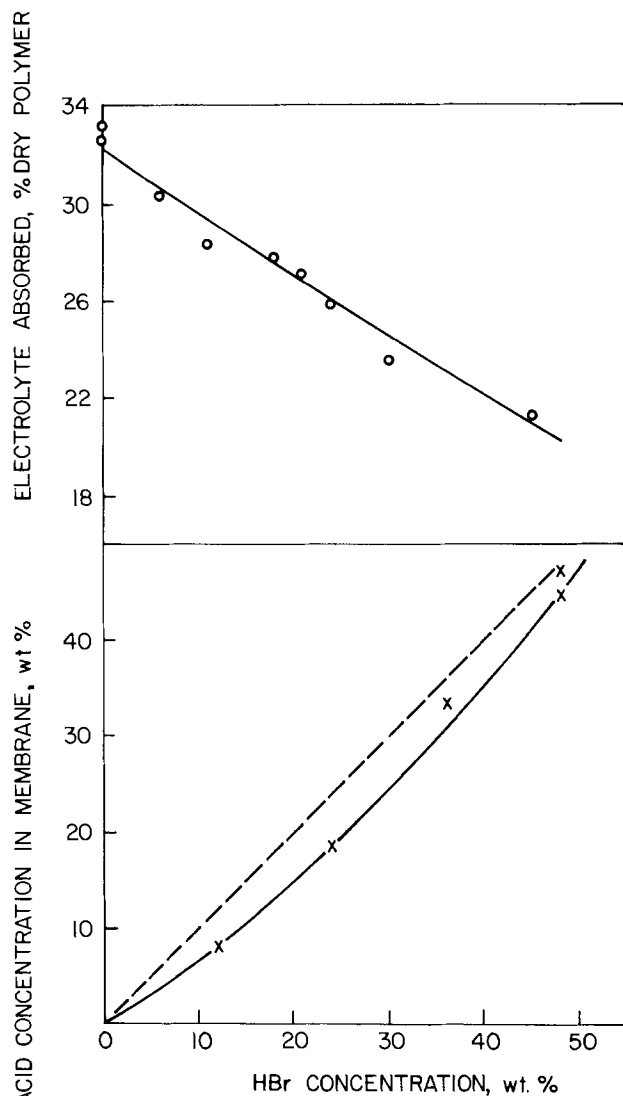


Fig. 5. Electrolyte content and acid concentration in Nafion membrane vs. HBr concentration.

$$W = \frac{0.323}{1 + 0.068M} \quad [6]$$

where W is the electrolyte content in the membrane and M is the molarity of HBr in the electrolyte. Equation [6] is similar to the one previously reported (12), except that the numerical factors are different. The deviation was probably due to the difference in experimental conditions. The HBr concentration in the membrane was less than the acid concentration outside the membrane; however, the difference was not large. When HCl is used as the electrolyte, and the membrane without pretreatment, it has been found that the concentration of HCl in the membrane is only equal to one-half of the acid concentration outside the membrane (13).

Figure 6 presents the membrane conductivity as a function of HBr concentration. The membrane conductivity in H_2O (14) and the conductivity of HBr electrolyte (15) at $25^{\circ}C$ are also included for the sake of comparison. The membrane conductivity is about one order of magnitude less than that of the free electrolyte. The result is similar to those obtained with HCl (5), $ZnBr_2$ (16), and NaBr (16) electrolytes. The solid curve in Fig. 6 can be represented by the following semiempirical equation

$$\sigma = 1.4\sigma_{ex} (1 - V_1)^{2.3} \quad [7]$$

where σ and σ_{ex} are the membrane and the free acid conductivities, respectively, and V_1 is the volume frac-

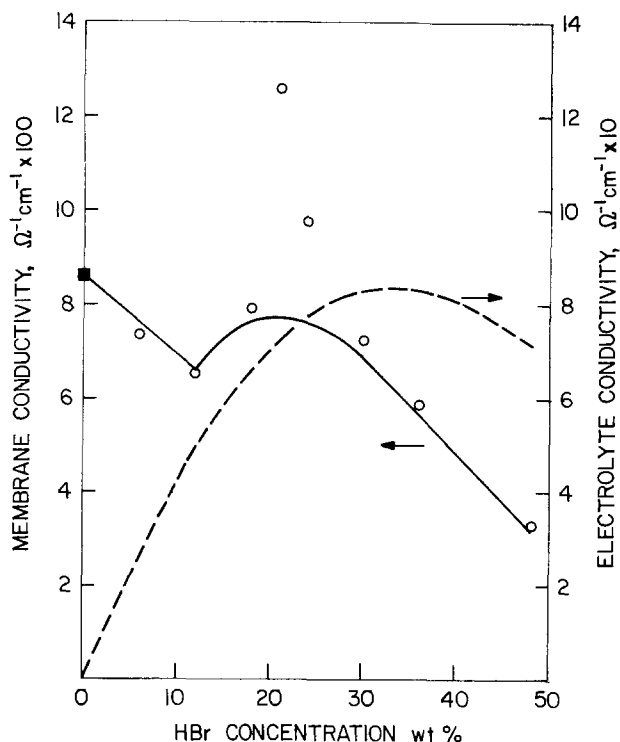


Fig. 6. Membrane and free acid conductivity as a function of HBr concentration. (■) H₂O, after Ref. (14); (○) HBr, present study, (---) free acid conductivity; (—) calculated by Eq. [7].

tion of the polymer matrix in the membrane. V_1 can be calculated from the density of the polymer (2.1 g/cm³) and the electrolyte content estimated by Eq. [6]. For the acid concentrations of less than 12% HBr, $\sigma_{ex} = 0.49 \Omega^{-1} \text{ cm}^{-1}$ should be used for calculations because of the intrinsic conductivity of the membrane.

Table I shows the membrane conductivity under different membrane pretreatments. The membrane conductivity increases with increasing electrolyte content.

Unsteady Heat Balance

For energy storage applications, the operation of the hydrogen-bromine system is of an unsteady nature. Reaction [1] has a large entropy change of 4.4 kcal/g-mole-HBr. This results in a cooling of the electrolyte during charge and an additional heating effect during discharge. The unsteady heat balance can be used to predict the changes in the electrolyte concentration and temperature, and the maximal electric-to-electric efficiency allowed by the thermodynamics and electrokinetics of the cell reactions (4).

A material and energy balance between the time t_0 and t results in the following equations for the system shown in Fig. 1

$$\begin{aligned}
 & -0.8605 \int_{t_0}^t E I dt + Q_{\text{Acid}} \\
 & = \int_{T_0}^{298} \{ W_{\text{HBr},0} C_{\text{P,HBr}}(X_0, T) + W_{\text{Br}_2,0} C_{\text{P,Br}_2(\text{l})}(T) \} dT \\
 & \quad + \Delta n_{\text{HBr}} H^{\circ}_{\text{f,HBr}}(X_0) \\
 & \quad + \frac{W_{\text{HBr}} X}{80.917} \{ H^{\circ}_{\text{f,HBr}}(X) - H^{\circ}_{\text{f,HBr}}(X_0) \} \\
 & \quad + \int_{298}^T \{ W_{\text{HBr}} C_{\text{P,HBr}}(X, T) \\
 & \quad + (W_{\text{Br}_2,0} - 79.91 \Delta n_{\text{HBr}}) C_{\text{P,Br}_2(\text{l})} \\
 & \quad - 1.008 \Delta n_{\text{HBr}} C_{\text{P,H}_2(\text{g})} \} dT \quad [8]
 \end{aligned}$$

$$\Delta n_{\text{HBr}} = \mp 3.7307 \times 10^{-5} \int_{t_0}^t I dt \quad [9]$$

Table I. Effect of thermal history on membrane conductivity

Treatment	Electrolyte content, w/o of dry polymer	Conductivity in 24% HBr, $\Omega^{-1} \text{ cm}^{-1}$
Standard treatment	25.9	0.098
Untreated	17.3	0.076
Dried in vac. at 140°C	11.4	0.035

$$W_{\text{HBr}} = W_{\text{HBr},0} + 80.917 \Delta n_{\text{HBr}} \quad [10]$$

$$X = \frac{W_0 X_0 + 80.917 \Delta n_{\text{HBr}}}{W_0 + 80.917 \Delta n_{\text{HBr}}} \quad [11]$$

$$Q_{\text{Acid}} = 0 \quad \text{for } T_{\text{min}} < T < T_{\text{max}} \quad [12]$$

The symbols in the foregoing equations are explained at the end of the text. The quantities with subscript o are the variables and the physical and thermodynamical properties at the time t_0 ; those without subscript o are the instantaneous values at the time t . The convention used here is that Δn_{HBr} has a negative value when HBr is consumed for electrolysis during charge and a positive value when HBr is produced during discharge. It has been assumed that the temperature of electrolyte in the cell is the same as that in the acid storage tank. This condition is approximately true if the electrolyte is circulating at a high rate. The function of Q_{Acid} is to maintain the electrolyte temperature within a limit specified by T_{min} and T_{max} . At T_{min} , external heat will be needed to maintain the electrolyte temperature, and the values of Q_{Acid} is positive. At T_{max} , cooling will be required and Q_{Acid} will have a negative value. The details of the mathematical modeling have been illustrated elsewhere (4) and will not be discussed here.

Equations [8] and [9] together with the cell voltage data given by Eq. [2]-[5] have been solved numerically on a digital computer for the concentration and the temperature of electrolyte as a function of time at various operating cell current densities. The calculation was made for a 2 MW energy storage module being operated at 10 hr charge and 10 hr discharge cycles. To account for the concentration and temperature variation of the thermodynamical properties, the values of $C_{\text{P,Br}_2(\text{l})}$, $C_{\text{P,H}_2(\text{g})}$, and $H^{\circ}_{\text{f,HBr}}$ published in the literature (18) were used in the computation. Unless otherwise noted, the concentration of HBr electrolyte varied from 7 to 35 weight percent (w/o), and the operating temperature was limited to a maximum of 50°C and a minimum of 15°C. The cell pressure was kept at 10 atm.

Figure 7 shows the change of electrolyte concentration during the charge and the discharge cycles. The change in electrolyte temperature is shown in Fig. 8 for a range of operating current densities from 0 to 350 mA/cm². It is seen that the temperature decreases during charge; the rate of temperature drop decreases with increasing current densities. During discharge, the temperature rises rapidly, and cooling is necessary to maintain the electrolyte at 50°C. This phenomenon is similar to the hydrogen-chlorine cell; however the extent of temperature changes is smaller with the hydrogen-bromine system. Figure 9 shows the magnitude of calculated cell voltages during the charge and the discharge cycles.

The overall electric-to-electric efficiency can be evaluated from the cell voltage changes according to the equation

$$\epsilon\% = - \frac{\left(\int_0^{10} E I dt \right)_{\text{discharge}}}{\left(\int_0^{10} E I dt \right)_{\text{charge}}} \times 100 \quad [13]$$

Figure 10 presents the overall electric-to-electric efficiency as a function of cell current densities. To ex-

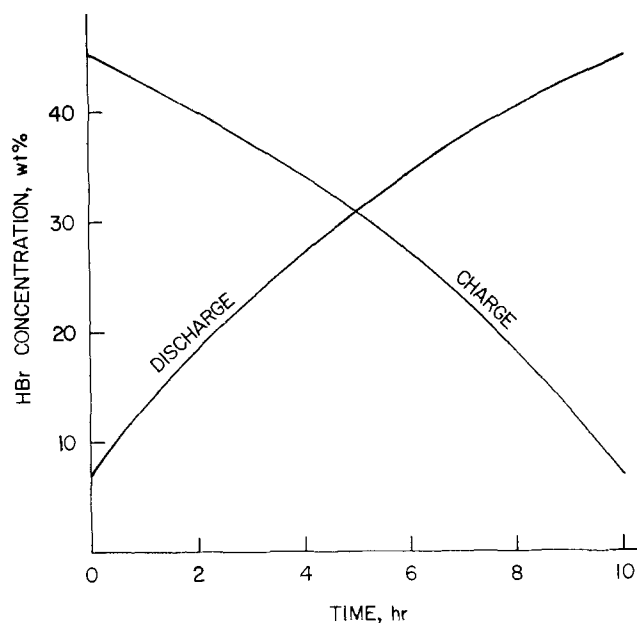


Fig. 7. Changes in HBr concentration during the charge and discharge cycles.

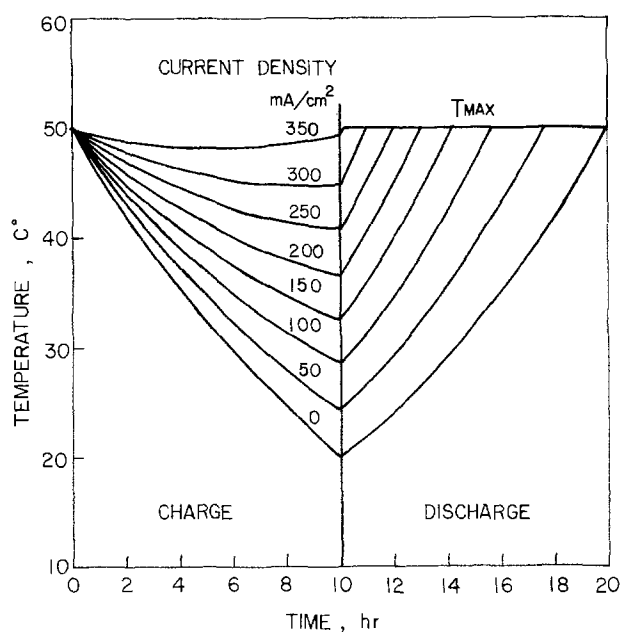


Fig. 8. Changes in the electrolyte temperature during the charge and discharge cycles for various operating cell current densities. The curves were calculated for a range of HBr concentration varying from 7 to 35 w/o during the operation.

amine the effect of electrolyte concentration on the overall efficiency, the unsteady heat balance was also performed for the HBr electrolyte concentration other than 7-35 w/o as shown in the figure. It is seen that the overall efficiency decreases with (i) increasing current densities; and (ii) increasing electrolyte concentration at the onset of charge. These curves were calculated for a cell pressure of 10 atm and a range of operating temperatures between a minimum of 15°C and a maximum of 50°C. Results for different pressures (1 ~ 40 atm) and temperatures (T_{max} between 30°-90°C) indicate that the temperature and the pressure have insignificant effect on the overall efficiency.

Discussion

Efficiency of energy conversion.—The polarization performance of the General Electric SPE cell strongly demonstrates the reversibility of the hydrogen and bromine electrode reactions. Since the electrode ki-

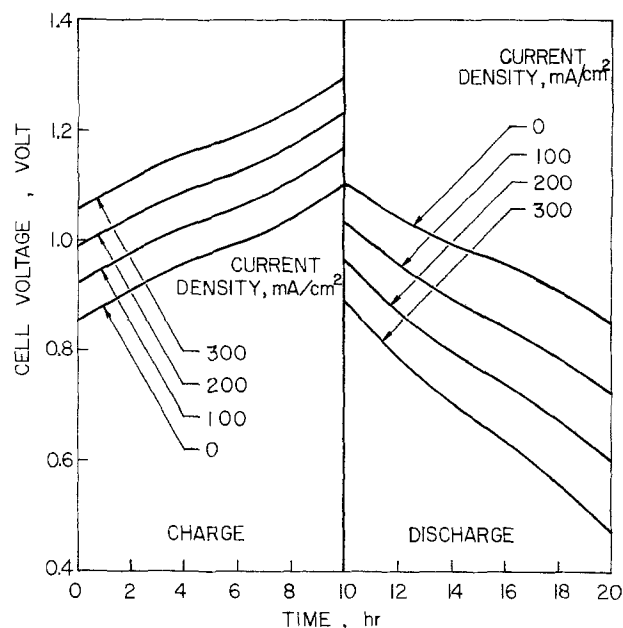


Fig. 9. Charge and discharge cell voltage as a function of time for current densities of 0 mA/cm², 100 mA/cm², 200 mA/cm², and 300 mA/cm². The curves were obtained with 7-35 w/o HBr and a maximum operating temperature of 50°C.

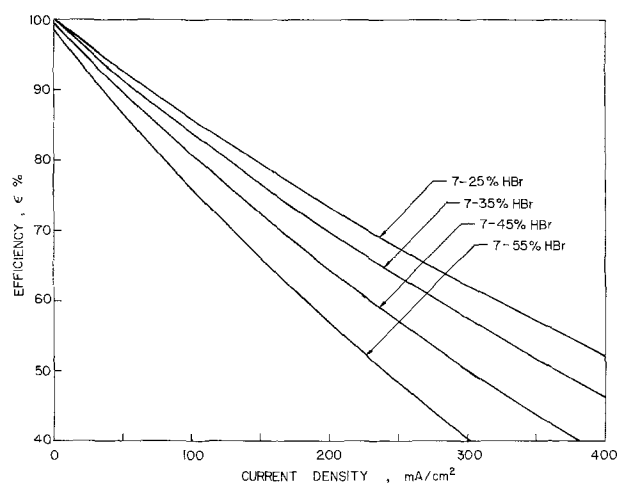


Fig. 10. The electric-to-electric efficiency as a function of cell current density for various acid concentration ranges. The maximum operating temperature was 50°C.

netics is fast, the voltage and coulombic efficiencies are largely determined by the membrane conductivity and the reactant permeation across the membrane. It has been found that because of the formation of negatively charged bromine complex ions (Br_3^- and Br_5^-), the coulombic loss in the hydrogen-bromine cell is less than 2% (5). This suggests that the overall cell efficiency can be simply represented by the voltage efficiency. In the light of this, the improvement in membrane conductivity is vital in the design of efficient cells. The membrane conductivity is strongly related to the electrolyte content of the membrane as well as the method of pretreatment as shown in Table I. There is no doubt that good conductivity can be achieved by boiling the membrane in water to fully swell the polymer matrix prior to installation in the cell. However, the effect of this pretreatment would be destroyed if the membrane is dried, especially at elevated temperatures (12).

Figure 10 demonstrates that the hydrogen-bromine system has an energy conversion efficiency comparable to the hydrogen chlorine system. However, the hydrogen-bromine cell has the advantage of a smaller electrolyte temperature variation during the charge and

discharge cycles. Consequently it can be operated at a lower temperature and pressure to increase the cost effectiveness in the system construction and operation. The space required for the electrolyte storage is comparable to the hydrogen chlorine system because a 45 w/o HBr can be used at the onset of charge. With this concentration, the General Electric SPE cell can be operated up to 160 mA/cm² and yet achieve an electric-to-electric efficiency greater than 70%. The large operating current density also makes the system feasible for use with variable and interruptible loads, such as solar and wind energy generators.

Effect of membrane hysteresis.—The operation of the hydrogen-bromine energy storage system is a time-dependent nonsteady-state process. The electrolyte concentration continuously changes with time as seen in Fig. 7. Accordingly, the electrolyte content of the membrane will decrease with time during discharge and increase during charge. Figure 11 shows the electrolyte content as a function of time. It is clear that the electrolyte content will not reach the equilibrium state. The electrolyte content in the membrane is less than the equilibrium value when the cell is initially started with 45% HBr and then charged to 7% HBr in 10 hr. On the other hand, the membrane would absorb more electrolyte than the equilibrium value if the cell is started with 7% HBr and discharged to 45% HBr in 10 hr. Furthermore, soaking the membrane in H₂O before charge/discharge will result in additional electrolyte uptake, especially during the initial period of charge/discharge operation. Thus, there is a strong hysteresis effect on the cell performance because of the slow diffusion of the electrolyte in the membrane which is about one order of magnitude less than that in the free acid (17). There is the added effect that the diffusion of electrolyte in membrane decreases greatly with increasing electrolyte concentration (13) whereas the diffusion rate in free acid is rather constant (related to the viscosity of the acid) at a given temperature.

The hysteresis is expected to decrease with longer charge/discharge times and with smaller acid concentration range and higher cell temperature. This result indicates that if the cell will become idle for a relatively long period of time, the cell should be filled with water or dilute HBr acid. Also the cell will have a higher efficiency if the plant is started with the discharge rather than the charge cycle.

Acknowledgment

Special thanks are due to Mr. K. L. Hsueh of Clarkson College of Technology for his help in the computer

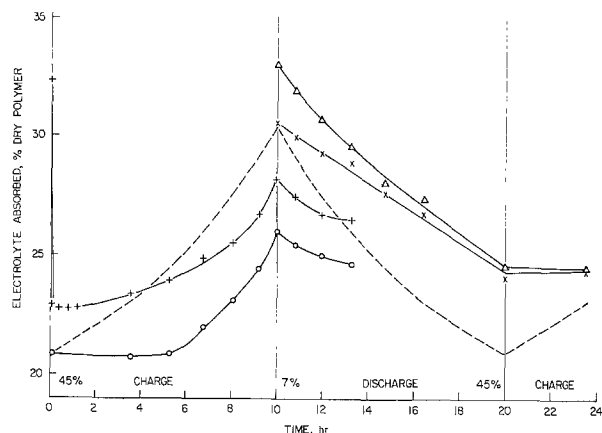


Fig. 11. The electrolyte sorption of Nafion during the charge and discharge cycles under various initial conditions: (+) pre-soaked in H₂O, operation started with charge; (O) pre-soaked in 45% HBr, started with charge; (Δ) pre-soaked in H₂O, started with discharge; (X) pre-soaked in 7% HBr, started with discharge (---) steady-state operation.

work and to Dr. P. Wong of BNL for technical contributions. The authors are also grateful to Drs. J. McBreen and S. Srinivasan, of BNL, and Mr. J. F. McElroy of GE for their helpful discussions. The Nafion membrane samples were kindly supplied by du Pont Company.

This study was carried out under the auspices of the U.S. Department of Energy.

Manuscript submitted April 6, 1979; revised manuscript received Sept. 14, 1979.

Any discussion of this paper will appear in a Discussion Section to be published in the December 1980 JOURNAL. All discussions for the December 1980 Discussion Section should be submitted by Aug. 1, 1980.

Publication costs of this article were assisted by Brookhaven National Laboratory.

LIST OF SYMBOLS

a_{Br_2}	activity of bromine in the electrolyte, dimensionless
$C_{\text{P,Br}_2(\text{l})}$	heat capacity of liquid bromine, kcal/kg/°K
$C_{\text{P,HBr}}$	heat capacity of HBr electrolyte, kcal/kg/°K
$C_{\text{P,H}_2(\text{g})}$	heat capacity of hydrogen gas, kcal/kg/°K
E	cell voltage, V
E_o	open-circuit cell voltage, V
f_{H_2}	fugacity of hydrogen gas, atm
$H^{\circ}_{\text{f,HBr}}$	heat of formation of aqueous HBr solution at 298° and 1 atm kcal/kg-mole HBr
i	operating cell current density, A/cm ²
I	total charge or discharge current, A
M	molarity of HBr in the electrolyte, g-mole/liter
Δn_{HBr}	change in the amount of HBr between the time t_o and t , kg-mole
Q_{Acid}	heat input into the electrolyte storage tank, kcal
t	time, hr
T	temperature of electrolyte, °K or °C
X	weight fraction of HBr in the electrolyte, dimensionless
V_1	volume fraction of polymer matrix in membrane, dimensionless
W	electrolyte content in membrane, kg-electrolyte/kg-dry-polymer
W_{Br_2}	weight of liquid bromine, kg
W_{HBr}	weight of HBr electrolyte, kg

Greek Letters

ϵ	electric-to-electric efficiency, %
σ	conductivity of membrane $\Omega^{-1} \text{cm}^{-1}$
σ_{ex}	conductivity of electrolyte, $\Omega^{-1} \text{cm}^{-1}$
ϕ	a function defined in Eq. [5], V

Subscripts

o	quantities associated with time t_o
-----	---------------------------------------

REFERENCES

1. E. Gileadi, S. Srinivasan, F. J. Salzano, A. Beaufre, S. Gottesfeld, L. J. Nuttall, and A. B. LaConti, *J. Power Sources*, **2**, 191 (1977).
2. S. Srinivasan, R. S. Yeo, and A. Beaufre, in Proceedings of the Second Information Meeting for Hydrogen Contractors in DOE Hydrogen Energy Program, Airlie, Virginia, Nov. 8-9, 1976 (BNL-22164).
3. A. Beaufre, R. S. Yeo, S. Srinivasan, J. McElroy, and G. Hart, in Proceedings of 12th Inter-society Energy Conversion Engineering Conference, Washington, D.C. Aug. 29-Sept. 2, 1977, Paper No. 779148.
4. D-T. Chin, R. S. Yeo, J. McBreen, and S. Srinivasan, *This Journal*, **126**, 713 (1979).
5. R. S. Yeo and J. McBreen, *ibid.*, **126**, 1682 (1979).
6. L. J. Nuttall, J. F. McElroy, S. Srinivasan, and G. Hart, Paper presented at Miami International Conference on Alternative Energy Sources, Miami Beach, Florida, Dec. 5-7, 1977.
7. J. J. Lander and R. D. Weaver, in "Characteristics of Separators for Alkaline Silver Oxide Zinc Secondary Batteries," G. E. Cooper and A. Fleischer, Editors, pp. 53-68, Air Force Aero Propulsion Laboratory, Dayton, Ohio (1965).
8. R. S. C. Yeo, Ph.D. Thesis, McGill University (1976)

9. C. Berger and R. M. Lurie, Paper 28 presented at The Electrochemical Society Meeting, Detroit, Michigan, Oct. 1-5, 1961.
10. W. Glass, "Hydrogen-Bromine Fuel Cell," report on Contract No. AF19(604)-8508. Ionics Inc., Cambridge, Mass. December 11, 1964, Report No. AD616108; W. Glass and G. H. Boyle in "Fuel Cell Systems," R. F. Gould, Editor, *Adv. Chem. Ser.*, **47**, 203 (1965).
11. J. F. McElroy, "Hydrogen/Halogen Energy Storage Systems Development," Phase one summary report, General Electric Company, Wilmington, Mass., Oct. 24, 1977.
12. W. G. Grot, G. E. Munn, and P. N. Walmsley, Paper 154 presented at The Electrochemical Society Meeting, Houston, Texas, May 7-11, 1972.
13. R. S. Yeo, Unpublished data.
14. A. B. LaConti, A. R. Fragala, and J. R. Boyack, Paper 347 presented at The Electrochemical Society Meeting, Philadelphia, Pennsylvania, May 8-13, 1977.
15. R. Haase, P. F. Saueremann, and K. H. Ducker, *Z. Phys. Chem.*, **47**, 224 (1965).
16. F. G. Will and H. S. Spacil, Paper 14 presented at The Electrochemical Society Meeting, Pittsburgh, Pennsylvania, Oct. 15-20, 1978.
17. R. S. Yeo and A. Eisenberg, *J. Appl. Polym. Sci.*, **21**, 875 (1977).
18. R. C. Weast, Editor, "Handbook of Chemistry and Physics," 50th ed. (1970).

Mössbauer Study of the Passive Oxide Film on Iron

William E. O'Grady*

Brookhaven National Laboratory, Department of Energy and Environment, Upton, New York 11973

ABSTRACT

Mössbauer spectroscopy has been used to study the structures of both the *in situ* and dried states of well-passivated iron surfaces. The parameters found in this study correlate only with the parameters found in the literature for iron in amorphous iron (III) oxides and in polymeric chains. The same parameters determined for dried passive films correlate only with those of $\gamma\text{-Fe}_2\text{O}_3$. The effects of drying the film give indications of the important role played by water in the passivation phenomenon.

The role and importance that passive layers play in the protection and strengthening of metals is well documented (1) in the recent Proceedings of the Fourth International Symposium on Passivity. It is interesting to note that one of the main points of discussion was the nature and structure of the protective films formed in aqueous environments on iron surfaces. It appears that the problem of the structure of the passive film is one of the most important problems for corrosion scientists.

In the particular case of the passivation of iron, an extensive effort has been made to work out the structure of the passive film (1, 2). In addition to the many applications of electrochemical techniques (2), ellipsometry (3-6) and electromodulated reflectance spectroscopy (7, 8) have also been utilized in an effort to determine the *in situ* structure of the passive film on iron. *Ex situ* investigations have included the use of electron diffraction (9), Auger electron spectroscopy (1, 10, 11), and photoelectron spectroscopy (12). Despite these efforts, the complete structure of the passive film on iron remains unsolved.

The passivating layer on iron is known to be of the order of 5 nm thick (13). For this layer to make a significant contribution to the Mössbauer spectrum, the volume of the layer must contain a large proportion of the total Mössbauer active iron available. Previously, this has been accomplished by using very small oxidized particles (14) or by supporting the Mössbauer nuclei on high surface-area substrates (15). These two techniques cannot be used in the present study where the iron substrate plays a significant role. Thick oxide films on the surface of nonenriched iron foils have been studied (16) by electroplating enriched ^{57}Fe on the surface and completely oxidizing the ^{57}Fe layer to give a Mössbauer signal which would be large compared to that of the supporting foil. Emission Mössbauer has also been used to study passivated steel and cobalt surfaces (17, 18), but this method is compromised by the possibility of the occurrence of un-

stable oxidation states especially in the presence of water (19). A preliminary report of our *in situ* study of passivated iron has appeared previously (20).

In this investigation we have applied Mössbauer spectroscopy to determine *in situ* the structure of the passive film on iron. Three types of experiments were run in this study. First, the passivated iron was examined *in situ* while the potential was maintained in the passive region. Second, hydration effects in the film were studied by dehydrating and aging the passivation film in dry nitrogen for varying lengths of time. The subsequent rehydration of these same dried samples was also attempted. Third, the temperature dependence of the Mössbauer spectra of both wet and dry samples was obtained.

Experimental Procedures

The electrochemical cell used in this work was designed to allow a 2 mm thick film of solution to lie in the γ -ray beam. The solution causes very little attenuation of the beam as the half thickness at 14 keV is ~ 5 mm (13). The cell consists of two parts as shown in Fig. 1. Both of these parts are machined from Plexiglas, and the cell window is 1.5 mm Plexiglas

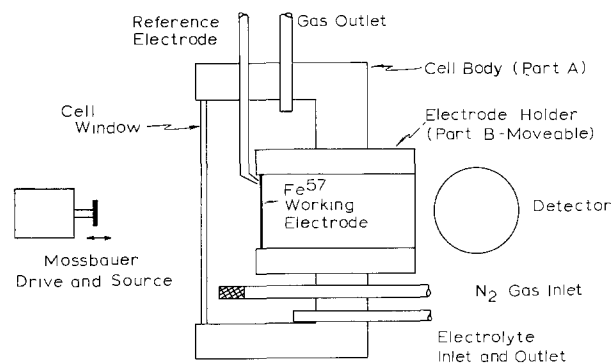


Fig. 1. Schematic diagram of the electrochemical cell used for *in situ* studies of iron passivation.

* Electrochemical Society Active Member.

Key words: oxides, oxy-hydroxides, water passivation.

sheet. The thickness of the solution between the iron working electrode and the window is adjusted to the 2 mm value after the electroplating and washing operations by moving the working electrode holder (B) into the cell body (A) until it contacts the cell window. The radiation passes through the hole in the center of the electrode holder into the shielded detector.

The Mössbauer spectra were recorded with an Elscint AME-30 Mössbauer spectrometer using a 25m Ci $^{57}\text{Co-Cu}$ source (New England Nuclear Corporation). All isomer shift values are reported with respect to a sodium nitroprusside absorber obtained from the National Bureau of Standards. The zero velocity is defined to be half the distance between its two quadrupole split peaks (23). The internal magnetic field was calibrated using a 1 mil iron foil obtained from New England Nuclear Corporation. The minimum line width obtained with the spectrometer was 0.25 mm/sec as determined with an electrochemically plated iron sample containing 2.1×10^{17} atoms of $^{57}\text{Fe}/\text{cm}^2$. The spectrometer was operated at constant acceleration and was driven by a sawtooth function in a flyback mode such that only one spectrum was accumulated in the Victoreen Pip 400A multichannel analyzer (MCA). A Reuter Stokes RSG-61-M, proportional counter tube equipped with aluminized mylar windows was used as the detector to avoid any contribution to the spectrum arising from iron impurities which might be present in beryllium windows. To insure reproducible geometry, the source drive, electrochemical cell, and shielded detector were all centered and aligned on an optical bench.

An Oxford Instrument's continuous flow cryostat (CF-100) was used in the variable temperature experiments. Temperatures were monitored with a calibrated linear resistance thermistor coupled with a bridge. The measured temperatures are believed to be accurate within $\pm 1^\circ\text{K}$.

The Mössbauer spectra were analyzed by computer, fitting the experimental data to a theoretical curve composed of Lorentzian peak shapes superimposed on a parabolic baseline using a least squares fit. The program also evaluated the isomer shift, quadrupole splitting, magnetic hyperfine splitting, and the integrated intensities of the spectrum. The inverse-square-law intensity and background corrections were determined by running a blank sample for the same length of time (24).

Samples were prepared by passivating a thin layer of 90% enriched ^{57}Fe such that the passive layer composed 10-20% of the total available ^{57}Fe , thus giving rise to an easily detectable Mössbauer effect. A layer of ^{57}Fe 25-30 nm thick was electrodeposited (21) onto a 25 nm thick vacuum-deposited gold film supported on 0.04 mm mylar. At the completion of the electrodeposition, the potential of the iron electrode was maintained in the cathodic protection region at -0.740V with respect to the normal hydrogen electrode (NHE), while the plating solution was drained and the electrode and cell washed and filled with 0.15N boric acid-sodium borate buffer solution ($\text{pH} = 8.4$) (22). The sample was then passivated at a potential of 0.6V (NHE) and the *in situ* Mössbauer spectrum was taken. The potential 0.6V (NHE) was chosen because it is well into the passive region and should produce a uniform film.

Dried samples were prepared by passivating as previously described. The solution was then drained from the cell, and the cell and electrode were washed twice with distilled water. The wash solution was drained and dry-purified nitrogen was circulated through the cell at 0.2 liters/min for varying lengths of time. After a prescribed amount of time, circulation of the nitrogen was stopped and the Mössbauer spectrum was taken. After taking the spectrum, circulation of the nitrogen was continued until a total of eight hours of circulation time had accumulated for a given sample. Several samples were stored for six months in a nitrogen-filled vac-

Table I. Mössbauer parameters of *in situ* passive film compared with those of *in situ* frozen samples used for temperature dependent studies and then run at 300°K

Isomer shift (mm/sec)	<i>In Situ</i> Passive Film Quadrupole splitting (mm/sec)	Linewidth (mm/sec)
0.70 ± 0.01	1.02 ± 0.07	0.86 ± 0.08
<i>In Situ</i> Frozen Passive Film		
0.70 ± 0.01	1.05	0.64

uum desiccator to observe if any further changes occurred in the film after the initial drying treatment. Rehydration of a series of these dried samples was attempted. After the sample was dried for a prescribed period, the cell was refilled with fresh borate solution, the electrode potential was held at 0.6V, and the Mössbauer spectrum was taken.

For the cryostatic measurements the samples were prepared by passivating them as described above, but the cell was placed in a nitrogen purged dry box. After the current in the cell reached a value of $0.1 \text{ A}/\text{cm}^2$ the iron electrode was quick frozen with liquid nitrogen, removed from the cell, sealed in a polyethylene sheath, and placed in the precooled (77°K) sample holder of the cryostat. Three individual samples were sandwiched together for each run. The polyethylene sheath was used to prevent dehydration of the samples. The temperature of the cryostat could be brought from 200°K to room temperature in 5 min by flowing dry nitrogen through the Dewar. This technique was used to bring the samples, which were frozen with electrolyte, to room temperature quickly so a spectrum could be run and compared to that obtained from the *in situ* samples. The Mössbauer parameters for these two types of samples are compared in Table I. On the basis of this data it is concluded that quick freezing the passive film does not perturb the structure of the film. Hence, the low temperature spectra are characteristic of the *in situ* passive film.

Experimental Results

The characteristic steady-state current potential behavior for bulk iron (3, 22) is shown in Fig. 2. Superimposed on the bulk iron curves are the points determined for the steady-state behavior of electrodeposited ^{57}Fe . As can be seen in Fig. 2, passivation of the electrodeposited ^{57}Fe closely parallels the characteristic curve for the electrochemical passivation of bulk iron. Also, the value of $+0.6\text{V}$ (NHE) at which the samples were passivated for this study can be seen to be well into the passive region.

The Mössbauer spectrum for a 25 nm ^{57}Fe film held at -0.75V (NHE) in the oxide-free cathodic protection

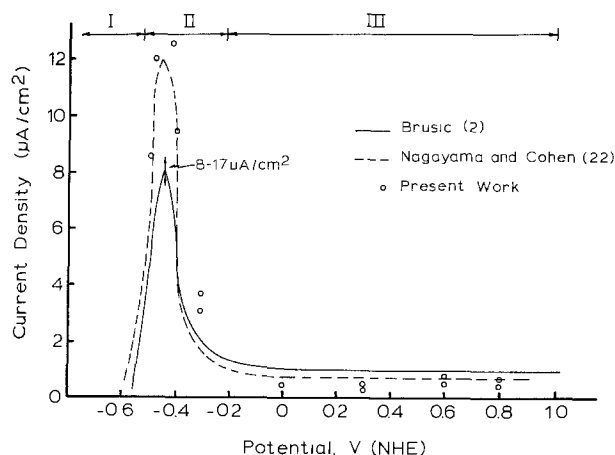


Fig. 2. Current-voltage behavior of electroplated iron films compared to the behavior found in the literature for bulk iron.

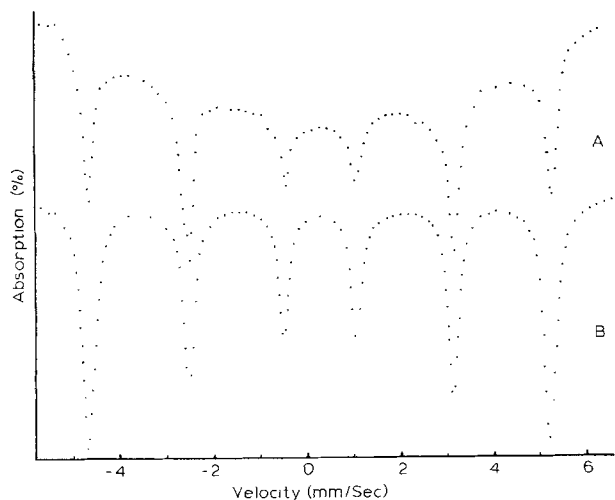


Fig. 3. Mössbauer spectra: A. Electroplated ^{57}Fe film approximately 50 nm in thickness; B. Standard iron foil.

region is shown in Fig. 3A. The spectrum shows the six-line pattern expected for iron. However, the intensity ratios of the electroplated sample lie very near to 3:4:1:1:4:3 whereas the intensity ratios normally found for bulk iron are 3:2:1:1:2:3 as shown in Fig. 3B. The relative intensities of the six-line pattern of iron are a function of the angle θ between the direction of the internal magnetic field and the γ -ray beam. The relative intensities as a function of θ can be written $3:\beta:1:1:\beta:3$ where β is given by $4/(1 + 2 \cot^2\theta)$ (25). In the case of a bulk iron sample, the internal magnetic field is randomly oriented, and an average must be taken over all values of θ which gives rise to the 3:2:1:1:2:3 intensity ratio normally observed. In the case of thin iron films, the internal field is found to be constrained in the plane of the film (26). Therefore $\theta = \pi/2$ and the 3:4:1:1:4:3 intensity ratio is found. This ordering arises in the case of thin films because the particles making up the film are of the same order of size as single domains and the anisotropy constant for the magnetic vector of the particles forces the magnetic vector to lie in the plane of the film. Theoretical calculations (27) indicate that this energetically preferred magnetic domain configuration for thin films breaks down for thicknesses greater than 300 nm and experimental results seem to verify this prediction (28). The isomer shift of the electroplated iron film was 0.00 ± 0.03 mm/sec vs. the standard iron foil. The linewidths, full width at half maximum (Γ), for the outer lines at room temperature were 0.25 and 0.32 mm/sec for the electroplated iron film and the standard iron foil, respectively. Thus, it is concluded that these electroplated iron films behave like bulk iron and will be generally representative of the behavior of iron.

In situ studies.—In Fig. 4 is shown a characteristic spectrum of a passivated iron sample. The spectrum includes the six-line pattern of iron and two new peaks in the center arising from the passive film on the surface of the iron. The center of the spectrum is expanded in Fig. 5 and shows only the contribution of the two inner lines of the iron pattern and the two new peaks which appear with passivation of the iron film and are attributed to the passive oxide film. The computer fitting of the data is shown in Fig. 5; the contributions from both the iron and the oxide film are shown. The analysis in this case was based on the fact that the oxide peaks are a quadrupole split pair. The Mössbauer parameters determined from this analysis with their mean square deviations are 0.70 ± 0.01 mm/sec for the isomer shift, 1.02 ± 0.07 mm/sec for the quadrupole splitting, and 0.86 ± 0.08 mm/sec for the linewidths. These values are the result of the examination of six separate samples. Efforts were also made to fit two quadrupole split sets of peaks to this experimental

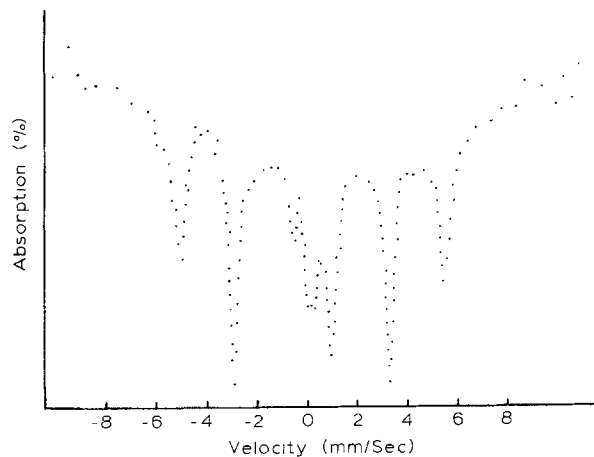


Fig. 4. Mössbauer spectrum of ^{57}Fe film passivated at 0.6V (NHE) showing the characteristic iron spectrum and two new peaks in the center of the spectrum due to the passive film.

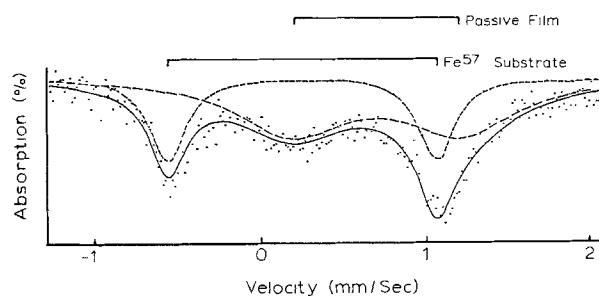


Fig. 5. Expanded Mössbauer spectrum encompassing the two inner lines of the iron spectrum and the two new lines due to the passive oxide film. The dots are the experimental points, the solid line is the computer calculated best fit to the experimental data, the short dashed line is the contribution of the iron substrate, and the long dashed line the contribution of the passive film.

data. However, a much higher χ^2 value was obtained for this fit, and hence the single quadrupole split pair was accepted as the best description of the data.

Dehydration studies.—The dehydration of the passive film gave results which can be divided into two groups. The samples dried for durations of up to five hours gave the values: IS, 0.66 ± 0.01 mm/sec, QS, 1.0 ± 0.1 mm/sec, and Γ , 0.9 ± 0.1 mm/sec. The second group of samples was dried over periods of time between five hours and six months and gave the following values: IS, 0.61 ± 0.01 mm/sec, QS, 0.8 ± 0.1 mm/sec, and Γ , 0.8 ± 0.1 mm/sec. Each group consisted of three separate samples.

Efforts were made to repassivate several samples after they were dehydrated in order to determine the reversibility of the hydration-dehydration process. The results for repassivating the samples dried for times less than five hours are given in Table II. The samples which were dried for longer times could not be successfully repassivated. When the samples dried for longer times were reimmersed in fresh electrolyte the entire sample would curl up and peel off the supporting mylar substrate. This curling suggests that there were strong tensional forces in the film.

Table II. Mössbauer parameters for the repassivated film

Sample	Area	IS (mm/sec)	QS (mm/sec)	Γ (mm/sec)
1— <i>in situ</i>	Film 0.65	0.70	0.99	0.83
1—dried	Film 1.0	0.64	1.03	1.00
1—repassivated	Film 0.64	0.70	0.96	0.86
2— <i>in situ</i>	Film 0.80	0.70	1.03	0.85
2—dried	Film 1.00	0.65	0.96	1.01
2—repassivated	Film 0.75	0.69	1.00	0.82

Low temperature studies.—A series of spectra were run at temperatures down to 3°K in order to further elucidate the structure of the passive film. Many of the iron oxides show magnetic hyperfine splitting resulting from the coupling of the magnetic moment of the nucleus with an external magnetic field usually arising from unpaired d-electrons on the iron atom. This magnetic hyperfine splitting is one of the characteristic features describing a particular oxide material (29).

Figures 6A and 7A show the following spectra: one for a sample that was dried for a period of greater than five hours (Fig. 6A) and one for a sample which was quick frozen in the cell (wet sample) and transferred into the Dewar at 77°K (Fig. 7A). Both spectra exhibit a hyperfine splitting but the dried sample shows much sharper lines than those of the wet sample. A value of ~ 470 kOe is found for the internal magnetic field of both the samples.

The temperature dependence of the hyperfine splitting of a dried sample is shown in Fig. 6. The 4°K spectrum shows hyperfine splitting with a small contribution of unsplit paramagnetic species still remaining in the center of the spectrum. As the temperature is raised, the paramagnetic contribution grows and reaches its maximum at about 45°K.

In the case of the quick frozen samples the temperature dependence is much more complex. At 3°–4°K as seen in Fig. 7 a magnetically split spectrum is observed. The measured internal field is 470 ± 10 kOe and the linewidth (Γ) is 0.96 mm/sec. When the temperature is raised from 4° to 10°K, the outer lines

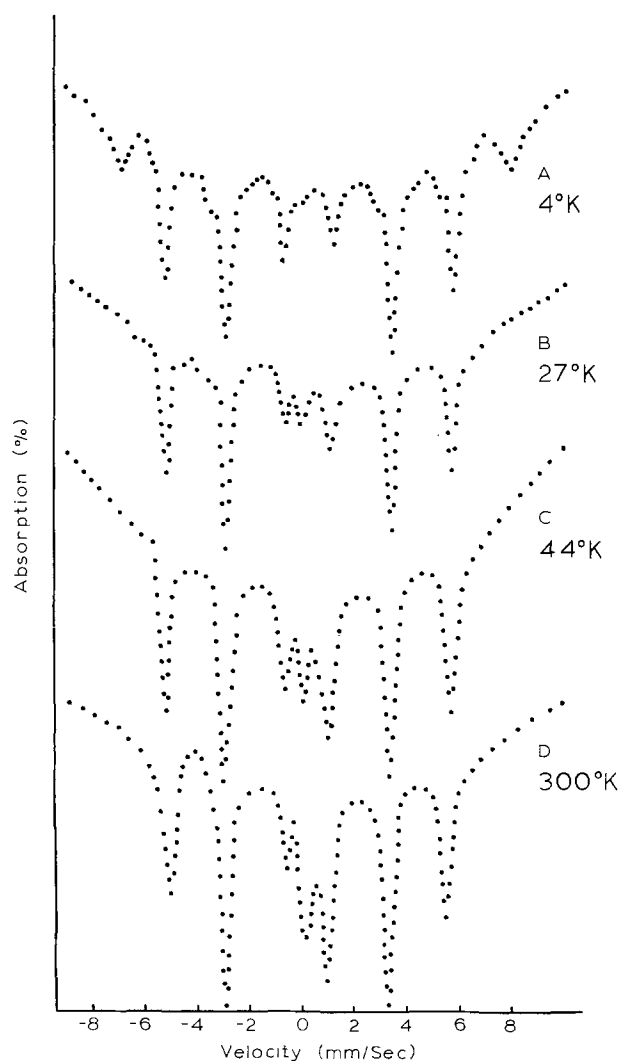


Fig. 6. Temperature dependence of the Mössbauer spectra of dried passive film.

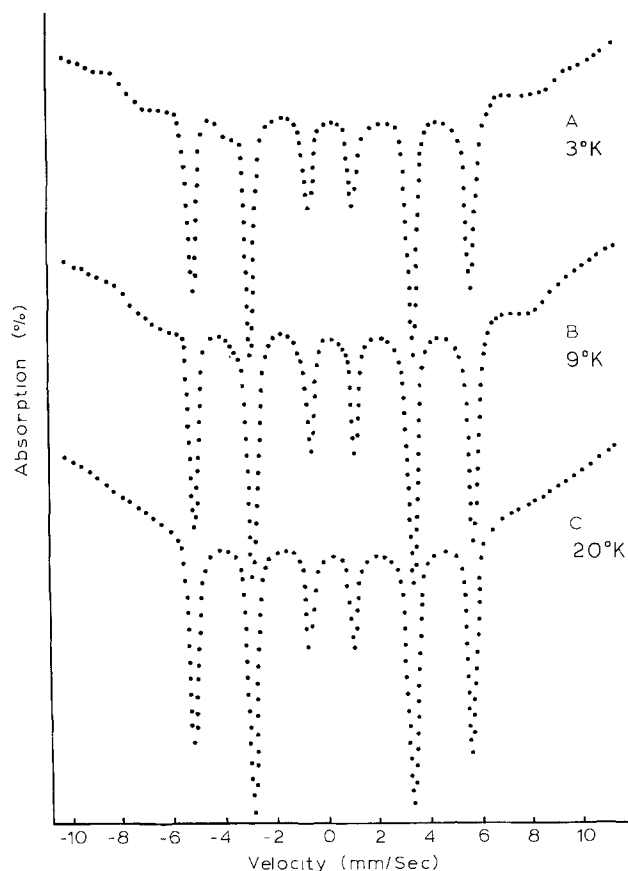


Fig. 7. Temperature dependence of the Mössbauer spectra of a wet passive film.

broadened to 1.8 mm/sec (see Fig. 7B). By 15°K no perceptible structure is visible, only a broad adsorption across the entire spectrum as seen in Fig. 7C. As the temperature is raised, no significant structure appears in the spectrum until a temperature of $\sim 100^\circ\text{K}$ is reached, Fig. 8A. In the temperature range of 100°–160°K two paramagnetic peaks continue to grow until about 70% of the total area under the curve for the passive film is achieved (Fig. 8B). In the temperature range of 160°–170°K, the remaining 30% of the total area for the passive film is obtained under the curve in Fig. 8C.

Discussion

Structure of the *in situ* passive film.—The characteristic parameters which have been derived from the computer fitting of the Mössbauer spectra of the *in situ* passive film are compared with the Mössbauer parameters available in the literature for the well-defined iron oxides and oxy-hydroxides in Table III. Considering only the isomer shift, there are two candidates for the passive film, α -FeOOH and δ -FeOOH. In the case of α -FeOOH no quadrupole splitting is observed while that of the passive film is 1.02 mm/sec. The HFS of α -FeOOH, 515 kOe (77°K) is larger than the 470 kOe (4°K) value of the passive film. For δ -FeOOH the QS is 0.01 mm/sec and the HFS is 505 kOe (80°K) which are also significantly different.

There are no obvious correlations of the Mössbauer parameters determined for the *in situ* passive film with those values collected in Table III. Hence, it is concluded on this basis that the passive film is not any of the well-defined stoichiometric crystalline oxides for oxy-hydroxides.

The isomer shift (0.70 mm/sec) and quadrupole splitting (1.02 mm/sec) found for the passive film tend to be higher than most of those found for the oxides in Table III. However, both values lie well within the range of values found for octahedral high spin ferric iron (30). The HFS value (470 kOe), al-

Table III. Mössbauer parameters of the well-characterized oxides

Compound	Isomer shift ^(a) (mm/sec)	Quadrupole split (mm/sec)	Internal magnetic field (kOe)	Reference
Fe(OH) ₂	1.44	2.92	0	(51)
FeO	1.18	0.8	0	(52)
Fe(OH) ₃	0.59	0.65	480 (5°K)	(53)
α-Fe ₂ O ₃	0.61	0.42	517 (300°K)	(36)
Fe ₂ O ₃ · nH ₂ O	0.64	0.62	470 (4.2°K)	(54)
Fe ₂ O ₃ · 2H ₂ O	0.62	0.64	—	(55)
γ-Fe ₂ O ₃	Td 0.535	0.84	488 (300°K)	(46)
	Oh 0.675	0.68	499 (300°K)	
α-FeOOH	0.70	0	515 (77°K)	(56)
β-FeOOH	0.640 ± 0.006	0.700 ± 0.006	466 (77°K)	(57)
γ-FeOOH	0.648 ± 0.006	0.594 ± 0.006	463 (72°K)	(57)
δFeOOH	0.64 ± 0.06	0.48 ± 0.06	519 (83°K)	(58)
δFeOOH	0.76 ± 0.2	0 ± 0.01	Td 525 (80°K)	(59)
			Oh 505 (80°K)	
Fe ₃ O ₄	Fe ²⁺ 0.61 ± 0.10	0 ± 0.1	Td 500 (300°K)	(29)
			Oh 482 (300°K)	
Amorphous Fe(OH) ₃ · 0.9H ₂ O	Fe ²⁺ 0.96 ± 0.10	0 ± 0.1	450 (300°K)	(61)
			—	
Amorphous iron (III) oxide (thin film)	0.7 ± 0.1	0.96-1.06	460-490 (4.2°K)	(64)
Amorphous iron (III) oxide (thick film)	0.6 ± 0.1	1.01	470 (5°K)	(62)
Passive film (<i>in situ</i>)	0.7 ± 0.01	1.02 ± 0.07	470 (4°K)	

^(a) Isomer shift relative to SNP.

though on the low side for an iron oxide, also indicates the iron in the film is in an octahedral high spin ferric state (30). The values of the HFS for octahedral iron tend to be lower whenever one or more of the coordination sites of the iron is occupied by a hydroxyl ion or by water as seen from the HFS values in Table III for Fe(OH)₃, Fe₂O₃ · nH₂O. However, these species in the coordination sphere do not seem to have any appreciable effect on the isomer shift and quadrupole splitting values found for these compounds.

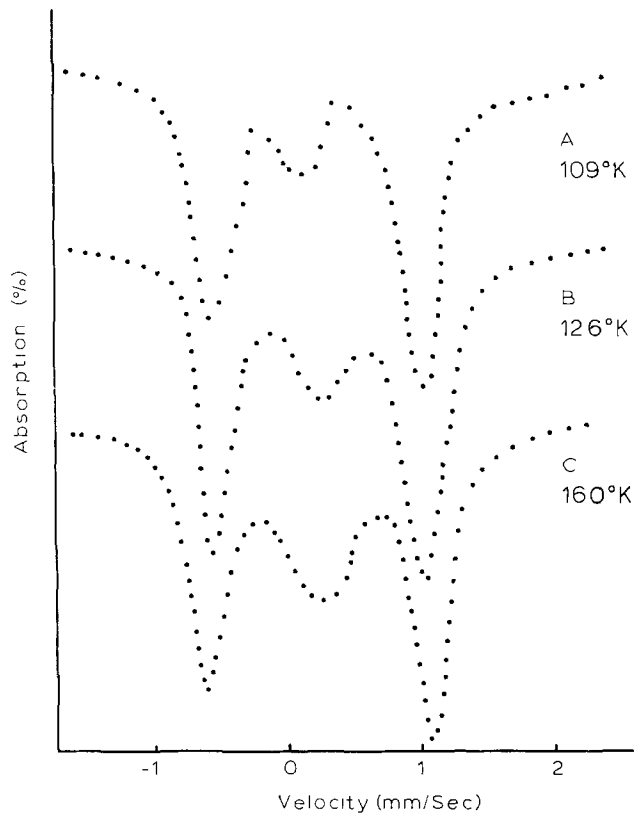


Fig. 8. Temperature dependence of the expanded Mössbauer spectra of a wet passive film.

Considering the amorphous iron (III) oxide also included in Table III, an extremely good correlation of the IS, QS, and HFS with the values found for the passive oxide film is observed. The higher values of the IS and QS are characteristic of amorphous oxides and indicate that the films are composed of FeO₆ octahedra each of which has a different local bonding character. The number of neighboring octahedra may be different as well as the type of bonding to the neighbors, i.e., sharing of corners, edges, or faces. The value of the HFS is also characteristic of the amorphous oxide and this will be discussed in detail later.

Further correlations can be made with literature values of the isomer shift and quadrupole splitting of inorganic compounds of well-defined structure. An extremely good correlation is found with a series of binuclear oxo-bridged iron (III) compounds, as the values in Table IV show (31, 32). Of course no HFS is observed because these dimeric ferric compounds have a dimagnetic ground state, which arises from strong antiferromagnetic coupling.

Also shown in Table IV are a set of values for a trimer of iron atoms connected by dihydroxy-bridge bonds (33, 60). Here again an extremely good correlation is found with the IS and QS values of the passive film. No HFS is seen here due to a very rapid spin-spin relaxation.

Table IV. Mössbauer parameters for binuclear oxo-bridged, trimer, and dimer di-hydroxy-bridged, and polymeric iron compounds

Compound	Isomer shift ^(a) (mm/sec)	Quadrupole splitting (mm/sec)	Reference
(Fe salen) ₂ Opy ₂	0.71	0.92	(31)
{(Fe phensCl) ₂ }Cl ₂ · 5H ₂ O	0.77	1.70	(31, 32)
{(Fe bipy) ₂ O}(SO ₄) ₂ · 5H ₂ O	0.73	1.33	(31, 32)
{(Fe terpy) ₂ O}(NO ₃) ₄ · H ₂ O	0.79	1.93	(31, 32)
{(FeB(H ₂ O) ₂ O)ClO ₄ }	0.81	0.62	(31, 32)
(C ₆ H ₁₆ NH ₃) ₂ FeOH(SO ₄) ₂ (trimer)	0.75	0.89	(33)
Iron dimer	0.77	1.57	(60)
FePO ₃ (glass)	0.75	0.88	(34)

^(a) Isomer shift relative to SNP.

Another comparison can be made with glassy FePO_3 , and the values for its IS and QS (34) are also included in Table IV. The match up of these values with those of the passive film is extremely good. A comparison of crystalline and glassy FePO_3 gives some additional insight into the passive film structure. The IS values 0.77 mm/sec for the crystal and 0.76 mm/sec for the glass indicate that the local environment, coordination number, and type of bonding are essentially the same. The QS values on the other hand, 0.37 mm/sec for the crystal and 0.88 mm/sec for the glass, indicate that the distortion of the sites in the glass is considerably larger than in the crystalline material. The linewidths, 0.53 mm/sec for the crystal and 0.64 mm/sec for the glass, indicate that the distribution of sites is much larger in the glassy material. The structure of the glassy phosphates is generally long chain polymers (35), and this would tend to give rise to the distortions at the iron as seen in the higher QS values.

The low temperature behavior of the samples frozen *in situ* gives further insight into the structure of the passive film. As was demonstrated earlier, this data is characteristic of the hydrated *in situ* passive film. The spectra between 300° and 177°K are essentially equivalent. At temperatures between 170° and 160°K the contribution to the quadrupole split portion of the spectrum decreases by about 30% without developing a magnetically split spectrum. Between 160° and 100°K the remainder of the quadrupole split contribution is lost still without the development of a magnetic split spectrum. Only an increase in the background area is observed. When the temperature reaches values in the region of 10°-15°K, an extremely broad magnetic hyperfine spectrum is observed which sharpens up at 4°K. Behavior of the type demonstrated by the Mössbauer spectra of the passive film at temperatures of 20°K and lower has been observed recently (61-65) in the case of amorphous iron (III) oxides and hydroxides and is the result of a new type of magnetic ordering called sperimagnetism (61). This state is described as a magnetically ordered system at low temperatures with the atomic magnetic moments in a particle randomly oriented and a total moment which does not vanish.

Sperimagnetism is characterized by a very low magnetic ordering temperature 20°-100°K, a large IS (0.5-0.7 mm/sec), and a large QS (0.8-1.2 mm/sec) at room temperature which disappears below the transition temperature. The QS disappears because at low temperatures it is coupled to the hyperfine field which for this type of sample is randomly oriented and hence it is smeared out. A further consequence of this smearing out is the much larger linewidths observed at low temperatures as compared to those at room temperature (64). At 4°K the passive film is magnetically split with the same value for the HFS as is shown by the amorphous oxide materials in Table I. The linewidth of the passive film at 4°K is $\Gamma = 0.96$ mm/sec, while at 300°K $\Gamma = 0.86$ mm/sec. As the temperature increases to 10°K, Γ increases to 1.8 mm/sec, all in agreement with sperimagnetic character observed for the amorphous iron (III) oxides (61-65).

Although the collapse of the magnetic hyperfine splitting at 15°K leads to the unblocking of the superparamagnetic fine particles, the true magnetic ordering temperature is higher, about 100°K. The behavior between 15° and 100°K is undoubtedly due to relaxation effects. This behavior may be accounted for by several explanations, one of which is spin-lattice relaxation. Here, the ions see the fields arising from the splitting of the Kramer's doublets, and the contributions due to the magnetic fields arising from the +5/2, +3/2, +1/2 spin states are unresolved. Thus, the spectrum appears as a continuous broad absorption. It has been shown (37, 38) that when one of the coordinating ligands is water the spin-lattice relaxation is slower. A second explanation suggests that the

FeO_6 octahedra making up the film are more and less strongly bonded to the neighboring octahedra leading to stronger and weaker magnetic interactions, respectively. The distribution of magnetic moments arising from such an ensemble would lead to a general broadening of the entire spectrum. This latter explanation is the more likely one (64).

Above 100°K the Mössbauer spectra show the characteristic behavior of a paramagnetic species.

The structure of the *in situ* passive film which emerges from this discussion is one which is not highly structured but is amorphous and polymeric in nature. It consists of FeO_6 octahedrons in a chainlike structure bonded together by di-oxy and di-hydroxy bridging bonds, and these chains are further linked together by water to form a continuous film covering the iron surface and leading to its protection.

Hydration and dehydration of the in situ passive film.—This set of experiments shows, for the first time, that the passive film undergoes very definite changes when it is removed from the solution, and it demonstrates the necessity to study these films *in situ*.

The reversibility of the hydration of the film as well as the amount of water contained in the film is extremely important information for further understanding the structure of the *in situ* passive film. The samples which were dried for times longer than five hours and which showed irreversible hydration characteristics will be discussed in the next section. The samples, however, that were dried for less than five hours showed reversible hydration behavior. An estimate of the amount of hydration water can be obtained by utilizing the partial isomer shift concept (39). The contribution to the isomer shift due to water is 0.03 mm/sec/ $\text{H}_2\text{O}/\text{Fe}$ atom (40). The isomer shift has changed from 0.70 to 0.64 mm/sec, a total of 0.06 mm/sec. This change in the film is reversible and hence it can be assumed that it arises only from changes in the water content of the film. This results in a loss of two water molecules by each iron atom in the film which agrees with the value obtained from tritium studies (41).

The reversibility of the hydration of the film imposes severe restrictions on the structure of the film. The structure required to allow the water to move in and out of the film must be quite simple to avoid giving rise to condensation reactions or other types of reactions leading to structures prohibiting the reversible exchange of water. It is proposed here that the structure of the passive film is built up of the fundamental units recently suggested for hydrolyzed iron sols (42). This fundamental unit is composed of four octahedrally coordinated iron atoms bonded together by oxy-bridging forming the structure shown in Fig. 9. The passive film would be composed of these tetramer units linked together by water and di-hydroxy bridging bonds forming a continuous film. The water which shows the reversible behavior is the water which links these units together. Furthermore, these units may edge bond to one another as shown in Fig. 10 leading to a face-centered cubic oxygen lattice which is the basis of the iron oxides (35).

The process of dehydration of this structure would involve only those oxygen-containing species which are not involved in the tetramer bonding. With the removal of two water molecules from each unit the final structure will be more compact than the original one, thus leading to the increase in the area found for the dehydrated samples (area values in Table I). This indicates that in the hydrated sample the iron is behaving as though it were solubilized and hence is not as strongly bonded as in the dehydrated case.

Other experimental evidence which supports this model is found in the recent nuclear reaction microanalysis of Agius *et al.* (50). The data presented in this paper gives a value of 1.38 oxygen atoms in the film per electron required to reduce the film. None of

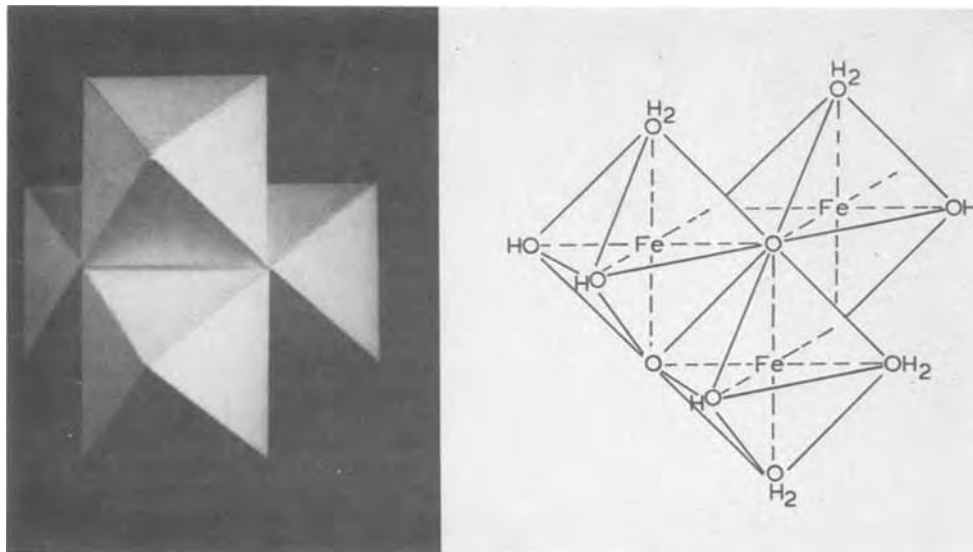


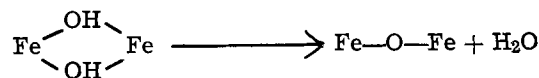
Fig. 9. Model of the basic building unit, the tetramer, suggested for a possible arrangement of the combination of two di-oxy or di-hydroxy chain species to form a tetramer. Inset shows a possible distribution of the oxygen atoms, hydroxyl groups, and water molecules around the iron atoms.

the theoretical values derived for stoichiometric oxides agree with this quantity. However, using the tetramer model suggested here, a value of 1.4 is obtained. This information, combined with the dehydration data obtained in this work, together with the tetramer model leads to a stoichiometry of $\text{Fe}_4\text{O}_4 \cdot (\text{OH})_4 \cdot (\text{H}_2\text{O})_8$. The dehydration of this species would give rise to an unstable form of FeOOH as the intermediate state. The isomer shift (0.66 ± 0.01 mm/sec) value of the intermediate state correlates well with the values given in Table III for several forms of FeOOH . However, the value of the quadrupole splitting (1.0 ± 0.1 mm/sec) and Γ (0.9 ± 0.1 mm/sec) indicate that the structure is highly distorted.

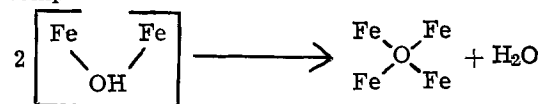
Structure of the dried passive film.—The samples which were shown in Table II to have been dried for periods of longer than five hours will be referred to as the dried film. The Mössbauer parameters, IS, 0.62 mm/sec; QS, 0.88 mm/sec; and HFS, 470 kOe (4°K) match up with those of $\gamma\text{-Fe}_2\text{O}_3$ found in Table III, hence we conclude that the dehydrated film is $\gamma\text{-Fe}_2\text{O}_3$.

Simmons *et al.* (44) made a study of the dried passive film in which they obtained values of 0.62 mm/sec for IS and 0.88 mm/sec for QS in good agreement with this study. Their interpretation of the data is that the film is a hydrated superparamagnetic $\gamma\text{-Fe}_2\text{O}_3$. It is not clear in this reference what the evidence was for considering the sample to be hydrated. In order for the passive film to make the transition from the hydrated to the dried state, two steps are observed. The first

step is the reversible dehydration of the film which lowers the IS from 0.7 to 0.64 mm/sec. The second step is irreversible and involves a change in the bonding in the film. One of the primary steps in the growth of iron oxide from basic solutions has been shown to be the de-oxalation or de-hydroxalation of the di-oxy or di-hydroxy bridging bonds (43, 45). There are several mechanisms whereby this breaking of the bridging bond can occur. One (45) is by a condensation type reaction



with a decrease in the coordination number of the iron. A second (45) is the condensation of two different complexes



with the iron coordination number being conserved.

If it is assumed that the film which has the reversible water removed from it undergoes both of the above condensation reactions resulting in the final distribution of iron atoms being that of $\gamma\text{-Fe}_2\text{O}_3$, it is possible to calculate the final value of the isomer shift. In $\gamma\text{-Fe}_2\text{O}_3$, 61% of the iron atoms occupy octahedral sites (35). The isomer shift for tetrahedral iron in $\gamma\text{-Fe}_2\text{O}_3$ is 0.53 mm/sec and that for octahedral iron is 0.66 mm/sec (46). Using the additivity concept of the isomer shift and calculating the average isomer shift, assuming 61% have a value of 0.66 mm/sec and 39% have a value of 0.53 mm/sec, results in a value of 0.61 mm/sec for the IS. This is in good agreement with the value of 0.62 mm/sec found for the dried passive film.

The mechanism proposed for the growth of the oxide should lead to oxide particles having a characteristic temperature dependence. At 4°K the six-line magnetic hyperfine spectrum is observed (Fig. 7). As the temperature is raised, the hyperfine spectrum is gradually replaced by a paramagnetic quadrupole split doublet. This behavior is quite different from that observed at the Neel point (magnetic ordering temperature) which is very sharp. The behavior observed here for the dried passive film is characteristic of very finely divided particles of magnetic materials and is referred to as superparamagnetism (47). The superparamagnetic state can be represented as a collection of single domain particles, each particle having a simple uniaxial anisotropic energy given by KV where K is the anisotropy energy and V is the volume of the particle.

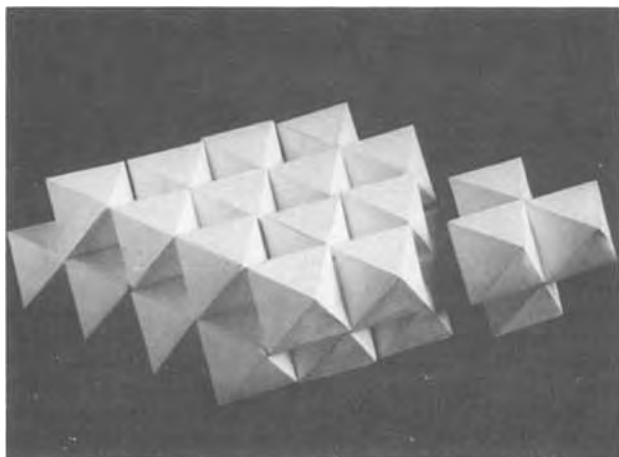


Fig. 10. Condensation of tetramers to form an FCC oxygen lattice.

There is a finite probability that the net magnetization can change its direction due to thermal fluctuations, and this is proportional to $\exp(-KV/kT)$. Hence the net magnetization can fluctuate with a relaxation given by

$$\tau^{-1} = f \exp(-KV/kT)$$

where f is the frequency factor and τ is the rate at which the magnetic vector flips between the easy magnetization directions separated by the energy barrier KV .

The particle size V can be calculated from the prior equation. Substituting the Larmor precession time 2.5×10^{-8} sec for τ and the frequency factor given by Kundig (36) leads to the following equation $\ln(2 \times 10^{-4}K) = KV/kT$, where K is the anisotropy constant, V the volume, k Boltzmann's constant, and T the temperature. The value for the anisotropy constant of γ -Fe₂O₃ given in the literature (48) is 1×10^6 erg/cm³.

The fact that the magnetic transition takes place over a wide temperature span (25°-45°K) indicates that there is a distribution of particle sizes. The temperature at which both states coexist equally is 35°K and this is taken to be the average particle size (36).

The particle size which results from this calculation is a sphere with a diameter of 3.6 nm. This latter value correlates well with the value obtained by Sewell (49) in an electron microscopy study of the growth of oxides on iron single crystals in oxygen.

Summary

In this study the structure of the *in situ* passive film has been determined for the first time using Mössbauer spectroscopy.

The results found here for the *in situ* passive film are not those of any of the stoichiometric, crystalline oxides including γ -Fe₂O₃, Fe₃O₄, and Fe₂O₃ · H₂O. All of the Mössbauer parameters match those of amorphous iron (III) oxides, iron containing polymers, and bi-nuclear iron compounds containing di-oxy and di-hydroxy bridging bonds between the iron atoms. The low temperature studies of the *in situ* frozen samples also show that the film is not highly structured but is amorphous and polymeric in nature. It consists of chains of iron atoms bonded together by di-oxy and di-hydroxy bridging bonds, and these chains are further linked together by water to form a continuous film covering the iron surface and leading to its protection.

Furthermore, it has been shown that γ -Fe₂O₃ results only when extensive drying of the *in situ* passive film has caused irreversible changes.

Acknowledgments

I would like to thank Professor J. O'M. Bockris for the encouragement and direction which he provided during the experimental portion of this work. Also, I would like to thank Professors D. Drazic and R. W. Hoffman for many valuable discussions and Dr. C. R. Anderson for pointing out the papers on sperimagnetism. This work was performed under the auspices of the U.S. Department of Energy.

Manuscript submitted March 7, 1979; revised manuscript received Sept. 12, 1979.

Any discussion of this paper will appear in a Discussion Section to be published in the December 1980 JOURNAL. All discussions for the December 1980 Discussion Section should be submitted by Aug. 1, 1980.

Publication costs of this article were assisted by Brookhaven National Laboratory.

REFERENCES

1. R. P. Frankenthal and J. Kruger, Editors, "Passivity of Metals," Fourth International Symposium on Passivity, The Electrochemical Society, Princeton, N.J. (1978).
2. V. Brusic, in "Oxides and Oxide Films," J. Diggle, Editor, Vol. 1, p. 1, Marcel Dekker, New York (1972).
3. J. O'M. Bockris, M. A. Genshaw, V. Brusic, and H. Wroblowa, *Electrochim. Acta*, **16**, 1859 (1971).
4. H. Wroblowa, V. Brusic, and J. O'M. Bockris, *J. Phys. Chem.*, **75**, 2823 (1971).
5. C. Lukac, J. B. Lumsden, S. Smialowska, and R. W. Staehle, *This Journal*, **122**, 1571 (1975).
6. D. J. Wheeler, B. D. Cahan, C. T. Chen, and E. Yeager, in "Passivity of Metals," R. P. Frankenthal and J. Kruger, Editors, Fourth International Symposium on Passivity, p. 546, The Electrochemical Society, Princeton, N.J. (1978).
7. W. W. Paatsch, *Surf. Sci.*, **37**, 59 (1973).
8. D. J. Wheeler, Ph.D. Thesis, Case Western Reserve University (1978).
9. C. L. Foley, J. Kruger, and C. J. Bechtoldt, *This Journal*, **114**, 994 (1967).
10. M. Seo, J. B. Lunsden, and R. W. Staehle, *Surf. Sci.*, **50**, 541 (1975).
11. R. W. Revie, B. G. Baker, and J. O'M. Bockris, *This Journal*, **122**, 1460 (1975).
12. G. Okamoto, *Corros. Sci.*, **13**, 471 (1973).
13. R. D. Evans, "The Atomic Nucleus," McGraw Hill, New York (1955).
14. A. M. van der Kraan, *Phys. Status Solidi A*, **18**, 215 (1973).
15. W. N. Delgass, R. L. Garten, and M. Boudart, *J. Phys. Chem.*, **73**, 2970 (1969).
16. A. M. Pritchard and C. M. Dobson, *Nature*, **224**, 1295 (1969).
17. A. M. Pritchard and C. M. Dobson, *Chem. Phys. Lett.*, **23**, 514 (1973).
18. G. W. Simmons, E. Kellerman, and H. Leidheiser, Jr., *This Journal*, **123**, 1276 (1976).
19. G. K. Wertheim, *Acc. Chem. Res.*, **4**, 373 (1971).
20. W. E. O'Grady and J. O'M. Bockris, *Surf. Sci.*, **38**, 249 (1973).
21. W. E. O'Grady, Ph.D. Thesis, University of Pennsylvania (1973).
22. M. Nagayama and M. Cohen, *This Journal*, **109**, 670 (1962).
23. *Nat. Bur. Stand. (U.S.) Misc. Publ.*, 260-13 (1967).
24. R. M. Housley, N. E. Erickson, and J. D. Dash, *Nucl. Instrum. Methods*, **27**, 29 (1964).
25. H. Fraunfelder, D. E. Nagle, R. D. Taylor, D. R. F. Cochran, and W. M. Visscher, *Phys. Rev.*, **126**, 1065 (1962).
26. A. Corciovei and D. Vamanu, *J. Appl. Phys.*, **39**, 1381 (1968).
27. C. Kittel, *Phys. Rev.*, **70**, 965 (1946).
28. U. Shimony, K. Rabinovitch, and A. Biran, *J. Appl. Phys.*, **41**, 641 (1970).
29. J. Danon, in "Chemical Application of Mössbauer Spectroscopy," V. I. Goldanskii and R. H. Herber, Editors, p. 159, Academic Press, New York (1968).
30. N. N. Greenwood, in "Physical Chemistry an Advanced Treatise," Vol. 4, H. Eyring, D. Henderson, and W. Yost, Editors, p. 634, Academic Press, New York (1970).
31. W. M. Reiff, G. J. Long, and W. A. Baker, Jr., *J. Am. Chem. Soc.*, **90**, 6347 (1968).
32. W. M. Reiff, *J. Chem. Phys.*, **54**, 4718 (1971).
33. R. Prados and M. L. Good, *J. Inorg. Nucl. Chem.*, **33**, 3733 (1971).
34. C. R. Kurkjian and D. N. E. Buchanan, *Phys. Chem. Glasses*, **5**, 63 (1964).
35. A. F. Wells, "Structural Inorganic Chemistry," Oxford Press, England (1962).
36. W. Kundig, H. Bömmel, G. Constabaris, and R. H. Lindquist, *Phys. Rev.*, **142**, 327 (1966); F. van der Woude and A. J. Dekker, *Phys. Status Solidi*, **9**, 775 (1965).
37. V. I. Goldanskii, I. P. Suzdalev, A. S. Plachinda, and V. P. Korneev, *Dokl. Akad. Nauk SSSR*, **185**, 203 (1969).
38. I. P. Suzdalev, A. M. Afanasev, A. S. Plachinda, V. I. Goldanskii, and E. F. Makarov, *Sov. Phys. JETP*, **28**, 923 (1969).
39. R. H. Herber, R. B. King, and G. K. Wertheim, *Inorg. Chem.*, **3**, 101 (1964).
40. Y. Hazony, R. C. Axtmann, and J. W. Hurley, *Chem. Phys. Lett.*, **2**, 440 (1968).
41. K. Kudo, T. Shibata, G. Okamoto, and N. Sato, *Corros. Sci.*, **8**, 809 (1968).
42. K. Kauffman and F. Hazel, *Inorg. Nucl. Chem.*

- Lett.*, **10**, 595 (1974).
43. G. W. Brady, C. R. Kurkjian, E. F. X. Lyden, M. B. Robin, P. Saltman, J. Spiro, and A. Terzis, *Biochemistry*, **7**, 2185 (1968).
 44. G. W. Simmons, E. Kellerman, and H. Leidheiser, Abstract 150, p. 376, The Electrochemical Society Extended Abstracts, Cleveland, Ohio, Oct. 3-7, 1971.
 45. V. Baran, *Coord. Chem. Rev.*, **6**, 65 (1971).
 46. R. J. Armstrong, A. H. Morrish, and G. A. Sawatzky, *Phys. Lett.*, **23**, 414 (1966).
 47. C. P. Bean and J. D. Livingston, *J. Appl. Phys.*, **30**, 1205 (1959).
 48. D. Khalafalla and A. H. Morrish, *ibid.*, **43**, 624 (1972).
 49. P. B. Sewell, C. D. Stockbridge, and M. Cohen, *This Journal*, **108**, 933 (1961).
 50. B. Agius and J. Siejka, *ibid.*, **122**, 723 (1975).
 51. A. M. Pritchard and B. T. Mould, *Corros. Sci.*, **11**, 1 (1971).
 52. D. P. Johnson, *Solid State Commun.*, **7**, 1785 (1969).
 53. Z. Mathalone, M. Ron, and A. Biran, *ibid.*, **8**, 333 (1970).
 54. A. A. van der Giessen, *Philips Res. Rep. Suppl.*, No. 12 (1968).
 55. D. D. Joye and R. C. Axtmann, *Anal. Chem.*, **40**, 876 (1968).
 56. M. J. Rossiter and A. E. M. Hodgson, *J. Inorg. Nucl. Chem.*, **27**, 63 (1965).
 57. J. H. Terrell and J. J. Spijkerman, *Appl. Phys. Lett.*, **13**, 11 (1968).
 58. A. Ya. Vlasov, G. V. Loseva, E. F. Makarov, N. V. Murashko, and E. P. Povitskii, *Sov.-Phys. Solid State*, **12**, 1177 (1970).
 59. I. Dezzi, L. Keszthelyi, B. Moinar, and N. A. Elissa, *Phys. Status Solidi*, **22**, 617 (1967).
 60. J. L. Mackey and R. L. Collins, *J. Inorg. Nucl. Chem.*, **29**, 655 (1967).
 61. J. M. D. Coey and P. W. Readman, *Nature*, **246**, 476 (1973).
 62. A. M. Van Diepen and Th. J. A. Popma, *J. Phys. Colloq.*, **37**, C6-755 (1976).
 63. A. M. Van Diepen and Th. J. A. Popma, *Solid State Commun.*, **27**, 121 (1978).
 64. S. Okamoto and H. Sekizawa, *J. Phys. Colloq.*, **40**, C2-137 (1979).
 65. T. Shigematsu, Y. Bando, and T. Takada, *ibid.*, **40**, C2-153 (1979).

Atmospheric Corrosion of Nickel

D. W. Rice,* P. B. P. Phipps, and R. Tremoureux

IBM Corporation, General Products Division, San Jose, California 95193

ABSTRACT

Nickel atmospheric corrosion is discussed, ranging from moisture adsorption isotherms to measured indoor corrosion rates. Significant quantities of water are adsorbed on nickel surfaces with a heat of adsorption equal to 10.7 kcal/mole. Corrosion kinetics are linear and exponentially dependent on relative humidity. The partial pressures of SO₂, Cl₂, NO₂, and NH₃ significantly influence nickel corrosion while H₂S and O₃ have little influence. Nickel corrodes in indoor environments at rates significantly less than outdoors and follows log normal statistics over the field site population studied.

The resistance of nickel to atmospheric corrosion is of broad interest because it is a component of many structural materials, as well as an alloying additive in magnetic materials. Nickel is thermodynamically unstable with respect to most practical operating environments. Its stability is therefore controlled by diffusion processes through surface corrosion products and corrosion product dissolution kinetics. Faraday recognized this over a century ago, yet models do not exist today that explain quantitatively the atmospheric behavior of nickel over a broad range of conditions (1).

The mechanism of atmospheric corrosion is a complex combination of dry oxidation and aqueous electrochemistry that depends on temperature, pollutant concentrations, relative humidity, and the material (2, 3). In dry high temperature oxidation, the predominate corrosion product is NiO formed in a multi-stage oxidation mechanism that can be explained by Wagner's defect diffusion theory (4-10). The aqueous electrode kinetics of nickel have been extensively studied (11-24). The dissolution of NiO to form a complex product via a rate-controlling NiOH⁺ step is considered the important mechanism of decay.

Evans states that the main controlling factor in atmospheric corrosion is the moisture content of the air (25). The complexity of the corrosion process on nickel was demonstrated by Vernon four decades ago (26). He showed that the corrosion product on nickel in outdoor industrial atmospheres was not a simple nonstoichiometric oxide but a basic nickel sulfate. Hudson has shown that nickel sheltered from rain

corrodes more rapidly than nonsheltered nickel. He attributed this to the hygroscopic nature of the corrosion products and their ability to accelerate corrosion when left on the surface (27). Campbell and Thomas showed a marked seasonal dependence for nickel indoor corrosion (28).

In this paper we present the results of a study designed to focus attention on the complex process of nickel atmospheric corrosion from water adsorption to observed corrosion in indoor business environments. The quantitative importance of relative humidity and pollutant concentration is presented followed by a discussion of the comparative indoor corrosion of nickel and associated corrosion products. A similar study has been reported for cobalt (2).

Experiment

Materials used in the study were 100 nm (1000Å) nickel films and 12 μm nickel foils. The films were prepared by electron beam evaporation from a 99.99+ purity nickel ingot on AT cut quartz or glass substrates at 0.4 nm/sec. The background pressure during evaporation was less than 10⁻⁶ Torr and the substrate temperature was 200°C. The nickel foils were 99.99+ purity. Both films and foils were cleaned prior to use by a sequence of hot toluene, isopropanol, and DI water immersions.

The cleaned surfaces as measured by XPS (x-ray photoelectron spectroscopy) and Auger electron spectroscopy consisted of significant quantities of hydrocarbon in addition to nickel and oxygen. Traces of sulfur and chlorine were present. The oxide thickness was approximately 0.6 nm. These observations are

* Electrochemical Society Active Member.
Key words: atmosphere, corrosion, nickel.

characteristic of most cleaned air exposed transition metal surfaces. The nonmetallic impurities were easily sputtered away, indicating they were surface not bulk contaminants.

The atmospheric test environments were synthesized from high purity dilute gases, purified air, and water vapor. The reaction chamber and associated gas-handling system was made of Pyrex glass to minimize adsorptive losses. Considerable care was required to purify the air before introducing pollutants. Without this precaution the levels of NO_2 and O_3 were found to fluctuate with the ambient outdoor NO_2 and O_3 levels characteristic of urban California environments. The purified air had concentrations of pollutants equal to or less than $0.1 \mu\text{g}/\text{m}^3$ for NO_2 , $0.05 \mu\text{g}/\text{m}^3$ for Cl^- , $0.006 \mu\text{g}/\text{m}^3$ for H_2S , $0.1 \mu\text{g}/\text{m}^3$ for NH_3 , $1 \mu\text{g}/\text{m}^3$ for O_3 , and $0.9 \mu\text{g}/\text{m}^3$ for SO_2 .

The influence of SO_2 , NO_2 , O_3 , H_2S , Cl_2 , and NH_3 concentrations on the corrosion rate of nickel was studied in a special plexiglass chamber with five reaction regions. Each reaction region was doped with a higher concentration of the pollutant being studied, while the remaining pollutants were held at a fixed reference concentration.

The reference environmental concentrations of the above pollutants, used as the background for the majority of the experiments, the rationale for selection, and the associated analytic procedures are given in Table I. The pollutant levels in the test are estimated to represent the upper 1% of the cumulative distribution function of indoor concentrations, a severe condition for indoor corrosion, but not particularly severe for outdoor urban center. NH_3 was not part of the reference environment, but was evaluated in the kinetic studies because of its "basic" chemical behavior and as a potential indoor pollutant coming from copiers and cleaning agents. The analytic equipment was calibrated using permeation tubes primarily.

The corrosion kinetics of the nickel foils were measured using a microbalance to monitor weight gain. These weighings were not made *in situ* because of the large number of samples tested. The procedure was to place enough 2.54×2.54 cm samples in the chamber to be equivalent to the number of test-time intervals required. Each sample was removed at its appropriate time and weighed, but not returned to the chamber.

The piezoelectric technique was used to measure the H_2O adsorption isotherms. These isotherms were measured in a humidified pure air system on nickel surfaces that had been air exposed (2, 29).

Finally, nickel foils (2.54×2.54 cm) and 100 nm films were placed in eight different indoor environments throughout the United States and the weight gain and reflectivity, respectively, were measured after 6, 12, and 18 months. Benzene soluble organic material was removed before the final weight and reflectivity were measured. The samples were held in a configuration such that the environment flow velocity was 250 cm/sec across the surface. The surface compositions

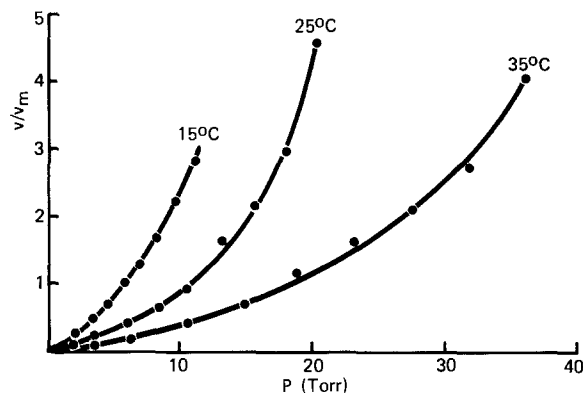


Fig. 1. Nickel thin film (100 nm) moisture adsorption results. Ratio of adsorbed water volume to monolayer volume (v/v_m) vs. water partial pressure (P).

of these returned samples were measured by Auger electron spectroscopy. The resistance increase of the nickel thin films due to corrosion in the field was measured by the four-point probe technique.

Results and Discussion

H_2O adsorption.—The air-formed films on both the evaporated and foil nickel samples showed the presence of hydroxide, oxide, and traces of sulfate and chloride as measured by XPS. This is similar to cobalt surfaces (2) and has been reported by others for nickel (30-32). The adsorption of H_2O on these complex hydroxylated nickel surfaces is characterized by the isotherms measured at three temperatures shown in Fig. 1. These isotherms are typical of those seen on hydroxylated Fe_2O_3 particles (33) and cobalt (2). Figure 2 shows the isotherms plotted vs. p/p_0 , the relative humidity. The isotherms exhibited no hysteresis, suggesting no chemisorption during the H_2O exposures. The surfaces had previously been exposed to enough H_2O , as the surface studies demonstrated, to preclude any further chemisorption during the period of measurements. The amount of adsorbed H_2O could be described by the BET isotherm up to a relative humidity p/p_0 of approximately 0.80 (34). This is characteristic of gas-solid interactions and shown in Fig. 3. The isotherms also show that on nickel many apparent monolayers of water are present at higher RH's. It is not surprising that corrosion should proceed readily via these relatively thick layers of water on the hydroxy surfaces.

Table II summarizes the heat of adsorption (ΔH_{ad}), monolayer volume, and relative humidity at apparent monolayer coverage obtained by fitting the data to a BET isotherm over the interval $p/p_0 = 0-0.5$. The heat of vaporization (ΔH_v) of water was taken as 10.5 kcal/mole in these calculations. The isotheric heat of adsorption was similar to that obtained from the BET isotherm. It was 10.9 kcal/mole at 0.5 monolayer coverage and 8.4 kcal/mole at 3 monolayers coverage.

Table I. Test reference environment (temperature = 25.0°C, gas velocity = 10 cm/sec)

Gas	Concentration ($\mu\text{g}/\text{m}^3$)	Rational for selection and sources	Analytic method
H_2O	70% RH	Known accelerator of galvanic corrosion and present at relatively large P/P_0	Dew point on cooled Au surface (continuous)
SO_2	786	Major pollutant, known to attack iron, nickel, cobalt. Forms acid on metal surface. Fossil fuel source.	Flame photometric (continuous)
NO_2	940	Major pollutant, known to attack Co, Ni, and Fe. Photochemical source.	Chemiluminescence (continuous)
O_3	334	Major pollutant, degrades polymers and accelerates oxidative decay of H_2S , NO_2 , and SO_2 . Photochemical source.	Chemiluminescence (continuous)
H_2S	21	Stress corrosion accelerator. Fossil fuel source.	Pb acetate densitometry (periodic)
Cl_2	8.6	Destabilizes otherwise passive films by lattice impregnation and acid dissolution. Fossil fuel and PVC incineration source.	o-toluidine densitometry (periodic)
NH_3	—	Forms chemically basic surface. Cleaning agent and copier source.	Chemiluminescence (continuous)

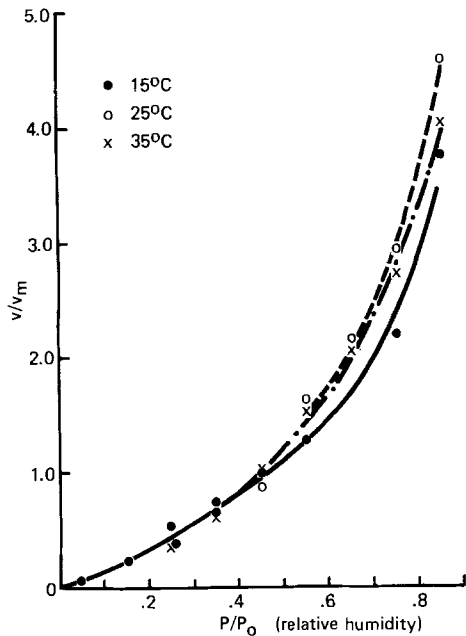


Fig. 2. Nickel thin film moisture adsorption isotherms. Ratio of adsorbed water volume to monolayer volume (v/v_m) vs. the ratio of water partial pressure to equilibrium saturation pressure (P/P_0).

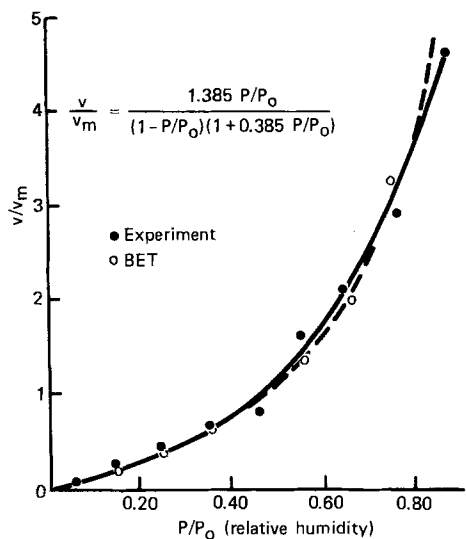


Fig. 3. Nickel thin film (100 nm) moisture adsorption isotherm comparison of experiment and theory ($T = 25^\circ\text{C}$).

The similarity between the ΔH_{ad} and ΔH_v implies that the H_2O molecule shows no great preference for the surface as compared to liquid water. It could just as well combine with a neighboring H_2O molecule to form a local H_2O cluster. The ΔH_{ad} measured in the study of Ni is slightly less than that reported on Fe_2O_3 particles (33), Cu surfaces (35), and Au surfaces (36), but in general agreement. Klier *et al.* have demonstrated that water clusters on surfaces well below apparent monolayer coverage (37). In fact, they found via infrared spectroscopy that silica surfaces at monolayer H_2O coverage consisted of equiv-

Table II. Heats of adsorption (ΔH_{ad}), relative humidity at monolayer coverage, monolayer volume, and C in the BET isotherm for H_2O on air exposed Ni surface

T ($^\circ\text{C}$)	ΔH_{ad} (kcal/ mole)	RH ($v/v_m = 1$)	v_m (cm^3/cm^2)	C
15	10.8	0.45	3.1×10^{-8}	1.71
25	10.7	0.46	3.1×10^{-8}	1.39
35	10.8	0.44	3.1×10^{-8}	1.50

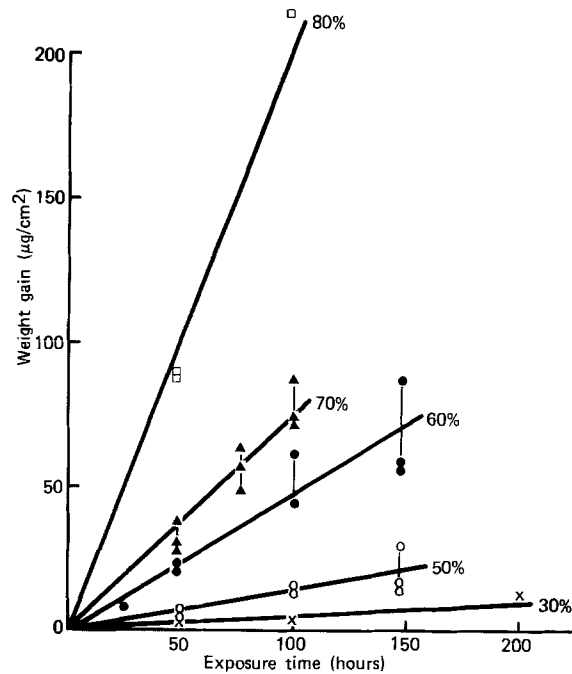


Fig. 4. Weight gain vs. reference environment exposure time for nickel foils at various relative humidities (%).

alent amounts of clustered and surface adsorbed water. These results suggest that the apparent monolayer coverage, as measured in the isotherms for nickel, may significantly underestimate the local surface volume of H_2O due to clustering.

Relative humidity.—Figure 4 shows representative weight gain vs. reference environment exposure time curves for various relative humidities. The corrosion kinetics of nickel in the reference test atmosphere is seen to be linear, exhibiting no tendency to passivate further. Table III summarizes the linear rate constants for the five relative humidities studied at four different SO_2 concentrations with the other pollutants held at the reference test conditions. Figure 5 is a representation of this data. The rate constants were fit to an equation of the form $r = Ae^{bRH}$. The table summarizes the constants obtained from the fit and the correlation coefficient (CC). Relative humidity has a profound influence on nickel corrosion in these atmospheres. No evidence for a critical humidity is seen. In the absence of SO_2 the same influence is observed with a slightly larger dependence of rate on relative humidity.

Cobalt shows similar behavior in these complex environments (2). Nickel in high SO_2 environments has been reported to have a critical humidity at approximately 68% RH determined by the H_2O in equilibrium with hydrated nickel sulfate. Above this relative humidity marked rate increases have been measured (38).

Table III. Nickel corrosion rate ($\mu\text{g}/\text{cm}^2\text{hr}$) vs. relative humidity (RH) at various SO_2 concentrations ($\mu\text{g}/\text{m}^3$)

RH	SO_2			
	0	118	786	1415
0.30	0.011	0.016	0.05	0.045
0.50	0.035	0.05	0.14	0.17
0.60	—	—	0.48	—
0.70	0.35	0.48	0.76	1.16
0.80	—	—	2.82	—
A	0.00068	0.0010	0.0037	0.0037
b	8.65	8.50	7.95	8.12
CC	0.98	0.98	0.984	0.994

Table IV. Nickel corrosion rate r ($\mu\text{g}/\text{cm}^2\text{hr}$) for different pollutant concentrations c ($\mu\text{g}/\text{m}^3$) (70% RH, 25°C)

		n^*					
SO ₂	0.40	c	0	39	118	786	1415
		r	0.36	0.32	0.47	0.88	1.24
NO ₂	0.19	c	0	26	102	376	1316
		r	0.32	0.26	0.30	0.34	0.58
H ₂ S	0.03	c	0	7.9	20	66	328
		r	1.20	0.88	0.87	0.91	0.97
O ₃	0.10	c	0	27	98	333	980
		r	0.72	0.54	0.58	0.54	0.85
Cl ₂	0.28	c	0	8.7	28	116	290
		r	0.9	1.04	1.40	2.01	2.83
NH ₃	-0.37	c	0	2.1	6.7	35	139
		r	0.66	0.57	0.66	0.22	0.15

* Exponent n in rate expression $r = AP_x^n$ where P_x is pollutant concentration.

Pollutants.—The atmospheric corrosion of nickel is dependent on the integrated effects of water vapor, temperature, and pollutants. The simplest form of this dependence is

$$\text{corrosion rate} = A \int_0^1 \int_0^\infty \int_0^\infty P(C_x) [C_x]^{n-1}$$

$$P(T) e^{\frac{\Delta H^{**}}{RT}} P(\text{RH}) e^{b\text{RH}} dC_x dT d\text{RH}$$

where C_x is the pollutant concentration, n and b are constants, ΔH^{**} is the activation energy associated with the atmospheric corrosion mechanism, $P(\text{RH})$, $P(C_x)$, and $P(T)$ are the relative humidity, pollutant, and temperature distribution functions, respectively, and RH is the relative humidity.

The object of this section of the work was to assess the important pollutants from a nickel corrosion point of view and evaluate the constant n for six different pollutants at a fixed RH equal to 70% and at a fixed temperature equal to 25°C. Table IV summarizes the rate data vs. concentration for each pollutant. Recall that all other pollutants were held at the fixed reference level. Figure 6 is a graphical presentation of the results. The range of concentrations is typical of urban environments and considerably lower than most reported laboratory studies.

Four of the pollutants, SO₂, Cl₂, NO₂, and O₃, increased the rate of nickel corrosion with increased concentration, one pollutant, H₂S, showed no marked influence, and NH₃, significantly inhibited nickel corrosion. This is similar to the behavior of cobalt reported earlier (2) except that ammonia did not inhibit cobalt corrosion.

If we assume that the water adsorbed on the corroding metal is similar to bulk water we can provide a qualitative framework for discussing the effect of the various gases. We calculate the concentration of the species derived from the gases from the solubility (39) and ionization constants and the partial pressures of gases in our test atmosphere. Since bisulfite is the dominant anion we can solve for the pH and arrive at the concentrations given in Table V. Direct measurements of the pH of the condensate give values approximately equal to 3.5. A similar value is calculated.

Table V. Species in the gaseous and aqueous phases

Gas	*	CO ₂	NH ₃	NO _x	H ₂ S	SO ₂	O ₂	HCl
p atm		3×10^{-4}	2×10^{-6}	5×10^{-7}	10^{-8}	3×10^{-7}	10^{-1}	3×10^{-9}
Product	H ⁺	H ₂ CO ₃ , HCO ₃ ⁻	NH ₄ OH, NH ₄ ⁺	HNO ₂ , NO ₂ ⁻	H ₂ S, HS ⁻	H ₂ SO ₃ , HSO ₃ ⁻	O ₂	Cl ⁻
log [] moles	-4	-5, -7.5	-6, -0.5	-9, -8.5	-8.8, -12	-6.4, -4.5	-0.36	1

* H⁺ estimate was from pH measurement of the atmosphere chamber condensate as well from these calculations.

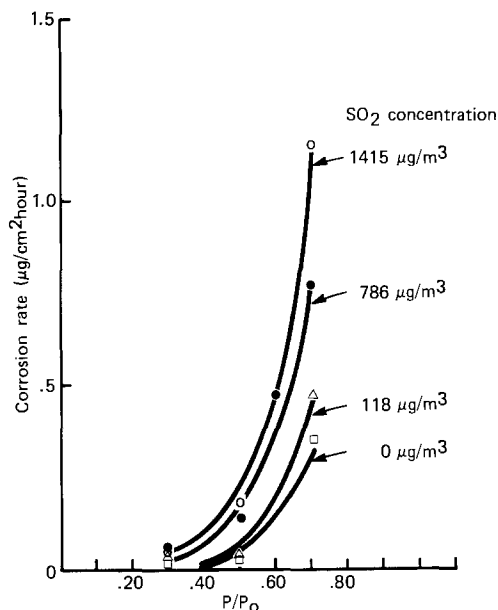


Fig. 5. Nickel corrosion rate vs. relative humidity (P/P_0) for various SO₂ concentrations.

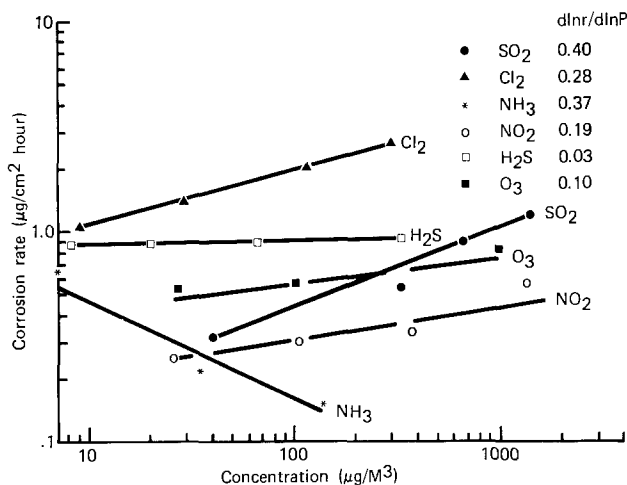


Fig. 6. Nickel corrosion rate vs. pollutant concentration

If we assume a corrosion rate proportional to $[\text{H}^+]$, as has been reported for stainless steel (40-42), we would predict that the corrosion rate of nickel should vary as $(P_{\text{SO}_2})^{0.5}$ from

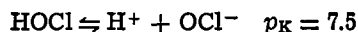
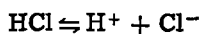
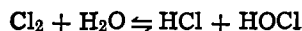


$$[\text{H}^+] \simeq [\text{HSO}_3^-] \text{ (charge neutrality)}$$

Therefore, the corrosion rate $r = k[\text{H}^+] = k(P_{\text{SO}_2})^{0.5}$. The observed dependence is given in Table IV

$$r = A(P_{\text{SO}_2})^{0.4}$$

Similarly, the effect of chlorine on the rate of corrosion might be attributed to



If the pH is less than 8, as predicted from the SO_2 pressure, the HOCl is fully ionized and we could predict $[\text{Cl}^-] = \frac{1}{2}[\text{H}^+] \propto (P_{\text{Cl}_2})^{0.25}$. If the pH is greater than 8, then

$$[\text{Cl}^-] = [\text{H}^+] \propto (P_{\text{Cl}_2})^{0.5}$$

Table IV shows that the corrosion rate is proportional to $(P_{\text{Cl}_2})^{0.28}$. Nickel corrosion has been reported to vary as $[\text{Cl}^-]^{0.28}$ in 0.1N HClO_4 (14). More detailed data is required to discuss this further.

The small effect of NO_2 despite its high concentration can be attributed to its low solubility and the weakness of HNO_2 . Nitrates are not found in our corrosion products from field exposure. The weakness of H_2CO_3 suggests that it too will have very little effect on the surface pH despite the high concentration and solubility of CO_2 .

The sulfide concentration is sufficient to precipitate NiS whose solubility product, K_{sp} , is 10^{-24} mole² liter⁻². The sulfur found is in the form of sulfate. Clearly, the effects of oxidation should be introduced into the simple model.

The effect of NH_3 might be connected with its effect of raising the pH. We would predict

$$[\text{H}^+] \propto (P_{\text{NH}_3})^{-0.5}$$

The corrosion rate reported in Table IV is

$$r \propto (P_{\text{NH}_3})^{-0.37}$$

The reason for the effect on nickel corrosion and not on cobalt corrosion is unknown (2). This simple observation dramatically highlights the complexity of atmospheric corrosion. Metals as similar as nickel and cobalt behave so differently.

Indoor corrosion.—The nickel foils sent to the indoor business environment testing sites showed corrosion rates that ranged from approximately $0-1.18 \times 10^{-2}$ $\mu\text{g}/\text{cm}^2$ hr. Table VI summarizes the data by location and external environmental class. The distribution function for nickel corrosion rates is approximately log normal over the site population as shown on the log probability paper of Fig. 7. The indoor corrosion of nickel measured in this study was slightly

Table VI. Nickel corrosion rate, surface reflectivity, and resistance change ($\Delta R/R_0$) in indoor environments

Location	Environment	Exposure time (hr)	Nickel foil corrosion rate ($\mu\text{g}/\text{cm}^2$ hr $\times 10^4$)	Reflectivity of thin nickel films	Resistance change ($\Delta R/R_0$) of nickel thin films
Texas	Urban	4,380	3.40	14	—
		8,760	0	65	0.01
		13,140	0	42	0.04
Chicago	Urban	4,380	7.08	1494	—
		8,760	5.82	2690	0.39
		13,140	6.01	2230	0.32
New York	Urban	4,380	17.8	30	0.33
		8,760	13.7	170	0.14
		13,140	6.77	170	0.12
Los Angeles	Urban	4,380	36.5	205	0.38
		8,760	23.4	1310	0.74
		13,140	32.4	2640	2.00
South Carolina	Industrial	4,380	16.2	196	0.11
		8,760	5.37	325	0.16
		13,140	7.53	880	0.15
Indiana	Industrial	4,380	41.8	286	0.44
		8,760	24.7	315	0.50
		13,140	21.8	990	0.52
New Jersey	Industrial	4,380	26.9	613	—
		13,140	28.3	2450	3.84
		13,140	29.1	2460	3.50
New Jersey	Industrial	4,380	15.1	459	—
		13,140	118.0	790	∞
		13,140	115.0	850	∞

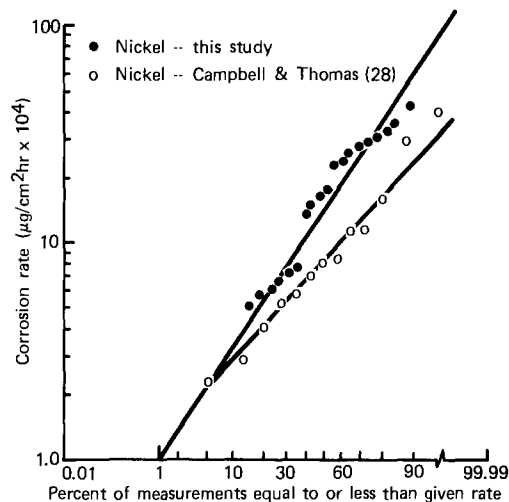


Fig. 7. Nickel corrosion rate distribution in indoor environments

greater than the values measured by Campbell and Thomas (28). Their data is shown for comparison in Fig. 7. Also, Sharma measured the film thickness formed on nickel in a central office in Cleveland (43). This site showed comparatively low rates, 0.6×10^{-4} $\mu\text{g}/\text{cm}^2$ hr, and exhibited parabolic kinetics.

These measured indoor rates are considerably less than values measured by others in outdoor sites. Table VII compares our measured indoor rates with outdoor industrial, sea coast, and rural rates (44). Outdoor industrial environments corrode nickel 600 times greater than indoor urban environments. This is due in large part to the pollutant adsorption losses on internal surface in buildings, coupled with less extreme humidity conditions.

Neither the resistance change nor the surface reflectivity of the thin nickel films correlated well with the weight gain measurements, however, there is a general trend for the more severe corrosion rate sites to show higher reflectivity changes (surface roughening) and resistance increases than the more pristine sites (Fig. 8).

Finally, Auger electron peak-to-peak (P/P) intensities were measured for thin films returned from six of the eight sites after 18 months. The ratio of Cl, S, and O P/P intensities compared to Ni is shown in Fig. 8. No clear picture emerges pointing to one element as the most important indicator of corrosion severity. All samples had varying amounts of S, O, Cl, N, Ni, and C. Limited XPS work showed the oxygen to be associated with hydroxide or more complex anions. The sulfur was present as sulfate, and carbon as hydrocarbon not carbonate. Nitrogen was too low in concentration to make reasonable XPS bonding estimates. The samples returned from Los Angeles showed traces of lead conjectured to result from tetraethyl lead in the urban Los Angeles environment.

Summary

The air-formed surfaces of exposed nickel adsorb significant quantities of water that can be approximated by a BET isotherm. The corrosion rate of nickel in a complex polluted environment is strongly de-

Table VII. Comparison of nickel corrosion rates in indoor and outdoor environments

	Average rate ($\mu\text{g}/\text{cm}^2$ hr)
Indoor urban	0.0013
Indoor industrial	0.0038
Outdoor rural	0.0274
Outdoor sea coast	0.0893
Outdoor industrial	0.7975

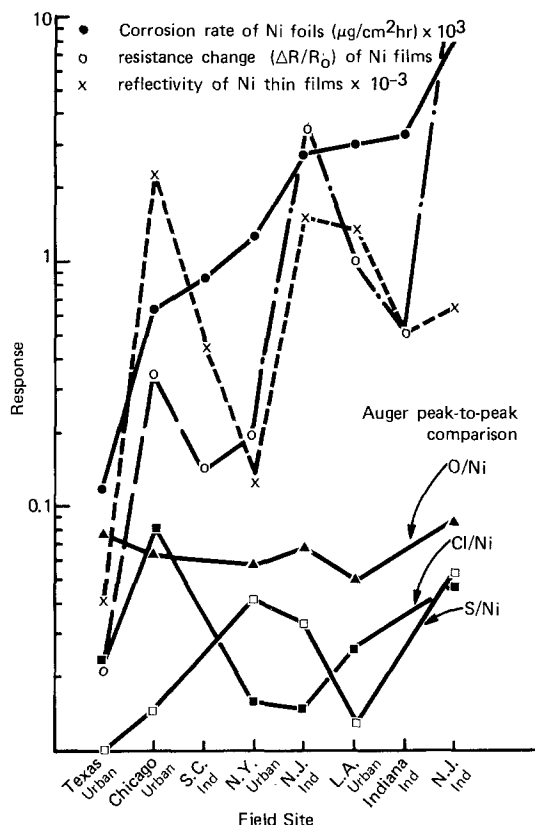


Fig. 8. Comparison of different measurement techniques for samples returned from indoor field locations (Table VI).

pendent on relative humidity. Sulfur dioxide and chlorine both significantly increase the corrosion rate of nickel while ammonia inhibits it. The observed indoor corrosion rates of nickel follow log normal statistics over the site population in this study and are much less than the observed outdoor rates.

Acknowledgments

We thank I. Rodriguez and J. Fazio for taking the rate data, Dr. V. I. Gupta for some of the adsorption data, F. Wagner for his tactical support of the field study, and Dr. H. Anderson for his continued support.

Manuscript submitted April 9, 1979; revised manuscript received May 2, 1979.

Any discussion of this paper will appear in a Discussion Section to be published in the December 1980 JOURNAL. All discussions for the December 1980 Discussion Section should be submitted by Aug. 1, 1980.

Publication costs of this article were assisted by IBM Corporation.

REFERENCES

- U. R. Evans, "An Introduction to Metallic Corrosion," pp. 217-218, Edward Arnold Publishers Ltd., London (1948).
- D. W. Rice, P. B. Phipps, and R. Tremoureux, *This Journal*, **126**, 1459 (1979).
- P. B. Phipps and D. W. Rice, "The Chemistry of Corrosion," ACS Publication (January 1979).
- K. Gupta, J. P. Martan, and J. Schewchun, *This Journal*, **121**, 118 (1974).
- E. A. Gulbranson and K. F. Andrews, *ibid.*, **101**, 128 (1954); *ibid.*, **104**, 451 (1957).
- G. C. Wood, I. G. Wright, and J. M. Ferguson, *Corros. Sci.*, **5**, 645 (1965).
- K. Hauffe, L. Pethe, R. Schmidt, and R. S. Morrison, *This Journal*, **115**, 456 (1968).
- O. Kubaschewski and B. E. Hopkins, "Oxidation of Metals and Alloys," pp. 135-235, 271, Butterworths, London (1967).
- G. Bandel, *Arch. Eisen. Luttenuw.*, **15**, 271 (1941).
- W. Boulkch and P. Funke, *Korros. Metallschutz*, **18**, 126 (1942).
- R. L. Cowan and R. W. Staehle, *This Journal*, **118**, 557 (1971).
- J. O'M. Bockris, A. K. N. Reddy, and B. Rao, *ibid.*, **113**, 1133 (1966).
- K. Arnold and K. J. Vetter, *Z. Electrochem.*, **64**, 407 (1966).
- A. Moon and K. Nobe, *Corrosion*, **22** (8), 300 (1977).
- E. Mikhailova and Z. Iofa, *Sov. Electrochem.*, **1**, 89 (1965).
- L. I. Antropov and L. T. Vakslenko, *Tr. Wkr. Repub. KcnF. Elektrokhim. Ist.*, **1**, 94 (1973).
- X. M. Kolotyrkin, G. Lopovok, and L. Medvedeva, *Prot. Met.*, **2**, 441 (1966).
- H. Feller and M. Kesten, *Electrochim. Acta*, **16**, 763 (1971).
- G. T. Burstein and G. A. Wright, *ibid.*, **20**, 95 (1975).
- G. T. Burstein and G. A. Wright, *ibid.*, **21**, 311 (1976).
- N. Sato and G. Okamoto, *This Journal*, **111**, 897 (1964).
- M. L. Kronenberg, J. C. Banter, E. Yeager, and F. Hovorka, *ibid.*, **110**, 1007 (1962).
- A. K. M. Huq and A. J. Rosenberg, *ibid.*, **111**, 270 (1966).
- R. R. Sanyo and K. Nobe, *Corrosion*, **22**, 81 (1966).
- H. R. Evans, *Br. Corros. J.*, **7**, 11 (1972).
- W. H. J. Vernon, *Trans. Faraday Soc.*, **23**, 113 (1921); **23**, 162 (1927); **27**, 264 (1931); **29**, 35 (1933); **31**, 1668 (1935).
- J. C. Hudson, *ibid.*, **25**, 177 (1929).
- W. E. Campbell and U. B. Thomas, *Holm Conference Proceedings*, pp. 233-265 (1963).
- W. Y. Lee and J. Eldridge, *This Journal*, **124**, 1744 (1977).
- K. S. Kim and N. Winograd, *Surf. Sci.*, **43**, 75 (1974); *Chem. Phys. Lett.*, **19**, 209 (1973).
- T. Robert, M. Bartel, and G. Offergeld, *ibid.*, **33**, 123 (1972).
- K. S. Kim and R. E. Davis, *J. Electron Spectros. Relat. Phenom.*, **1**, 251 (1972/1973).
- E. McCafferty and A. C. Zettlemoyer, *Discuss. Faraday Soc.*, **52**, 239 (1971).
- A. W. Anderson, "Physical Chemistry of Surfaces," pp. 565-644, Interscience (John Wiley & Sons, Inc.), New York (1967).
- W. Hermel and K. Schwabe, *Abb. Beut. Akad. Wiss., Berlin KL. Math. Phys., Tech.*, **1**, 87-92 (1967).
- J. H. Thomas and S. P. Sharma, *J. Vac. Sci. Technol.*, **13**, 549 (1976); **14**, 825 (1977).
- K. Klier, J. H. Shen, and A. Zettlemoyer, *J. Phys. Chem.*, **77**, 1458 (1973).
- P. M. Aziz and H. P. Godard, *Corrosion*, **15**, 529 (1959).
- E. Wilhelm, R. Battino, and R. J. Wilcock, *Chem. Rev.*, **77** (2), 219 (1977).
- H. P. Leckie, *Corrosion*, **24** (3), 71 (1968).
- J. Osterwald and H. H. Uhlig, *This Journal*, **108**, 515 (1961).
- D. A. Vermilyea, *ibid.*, **113**, 1067 (1966).
- S. D. Sharma, *ibid.*, **125**, 2005 (1978).
- Proc. Am. Soc. Testing Mater., **43**, 137-154 (1943).

The Sulfidation of Iron by Carbonyl Sulfide: An Example of Kinetics Involving Parallel Sequences

P. Hadjisavas, M. Caillet, A. Galerie, and J. Besson*

Laboratoire d'Adsorption et Réaction de Gaz sur Solides,
Ecole Nationale Supérieure d'Electrochimie et d'Electrometallurgie,
Domaine Universitaire—BP 44—38401 Saint Martin d'Hères, France

ABSTRACT

The sulfidation of iron by carbonyl sulfide obeys a paralinear rate law in the temperature range from 300° to 700°C, with a linear influence of pressure on the linear rate constant. The morphology of the sulfide scale is complex. Several observations lead to the conclusion that the equilibrium is not reached in the gaseous phase. The proposed mechanism accounting for the kinetic results involves two parallel processes: the decomposition of COS in the gaseous phase and in the adsorbed phase.

The sulfidation of iron by sulfur vapor or by other sulfur-containing gases (H_2S , SO_2 , CS_2) has been extensively studied (1-12), but only few papers describe the behavior of iron in a COS atmosphere (13-14).

Hayen and Steiten (13) showed that COS-CO- CO_2 mixtures react with iron and give only the iron (II) sulfide FeS between 750° and 900°C. The COS partial pressure and the duration of the reaction both influence the form of the rate law: for low pressures and short times, the rate law is linear. According to the same authors, there are two limiting processes: the sorption and the decomposition of COS in the adsorbed phase. When the COS pressure increases, the rate law becomes parabolic.

Rahmel (14) studied the same system but observed the formation of FeO and FeS, the disappearance of one of these products corresponding to a change in the mechanism of the corrosion.

Experimental Procedure

All experiments were carried out with N17 carbonyl sulfide from the Matheson Gas Company. The iron sheets (Feholtzer S, 2N5, from Creusot-Loire) were machined into parallelepiped samples ($15 \times 10 \times 1$ mm). The kinetic experiments were performed with a quartz spring thermobalance in a static COS atmosphere. After evacuating the apparatus down to 10^{-5} Torr ($1.3 \cdot 10^{-3}$ Pa) the iron sample was heated under vacuum in an electric furnace up to the required temperature. The initial time of the reaction corresponds to the introduction of COS in the reaction chamber. The weight gain of the sample was then electronically recorded with an accuracy of about 50 μg . After cooling in the COS atmosphere, the sample was analyzed by x-ray diffraction and observed by scanning electron microscopy.

Results

Product of the reaction.—For all temperatures and COS initial pressures, the x-ray patterns showed only FeS in the corrosion layer.

Influence of the temperature.—For a COS pressure of 100 Torr in the temperature range 300°-700°C, the rate law was paralinear as shown in Fig. 1 and 2. The linear rate constant obeyed the Arrhenius law; the measured activation energy was $76 \text{ kJ} \cdot \text{mole}^{-1}$ (Fig. 3).

Influence of the gas pressure.—The influence of the COS pressure was studied only at 414°C, from 5 to 250 Torr (Fig. 4). The linear rate constant varies with P_{COS} according to a linear law as long as the pressure exceeds 10 Torr (Fig. 5).

Morphological observations.—The cross section of the sulfide scale was studied by scanning electron microscopy. The observed morphology was not different from that of scales prepared by reaction of iron with hydrogen sulfide or sulfur vapor. On the micrographs, three different layers could be identified (Fig. 6a and b): (i) an outer porous layer, often foliated for low values of the temperature or pressure, coarsely crystallized for higher values. Such an observation was already made in the case of the sulfidation of copper by carbonyl sulfide (15): (ii) an intermediate layer, obviously porous, often reduced to scarce iron sulfide bridges; and (iii) an inner layer, finely crystalline the compactness of which is difficult to ascertain. According to many authors we assume that at least a thin layer adjacent to metal is compact.

Composition of the Gas Phase

Thermochemical calculations.—The calculation of the equilibrium partial pressures of the species resulting

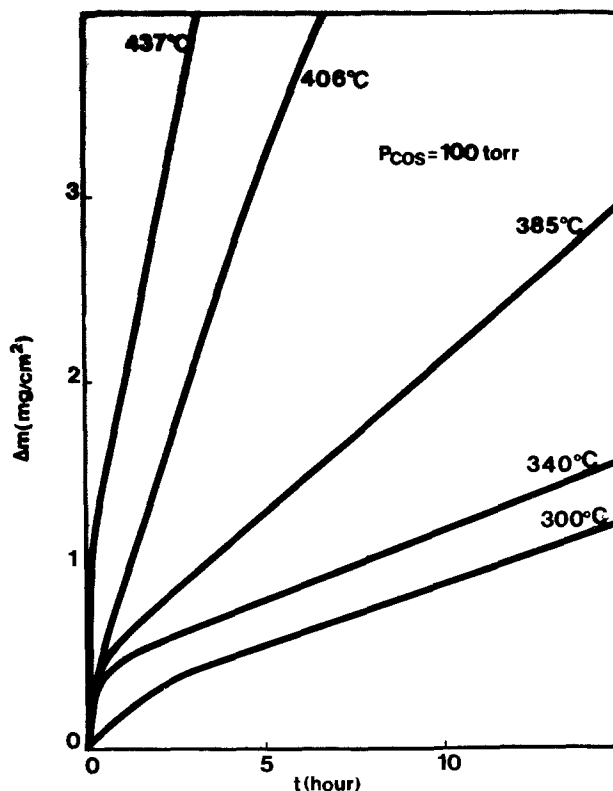


Fig. 1. Kinetic curves for the reaction of COS with iron: influence of temperature.

* Electrochemical Society Active Member.

Key words: heterogeneous kinetics, solid-gas reactions, carbonyl sulfide, iron.

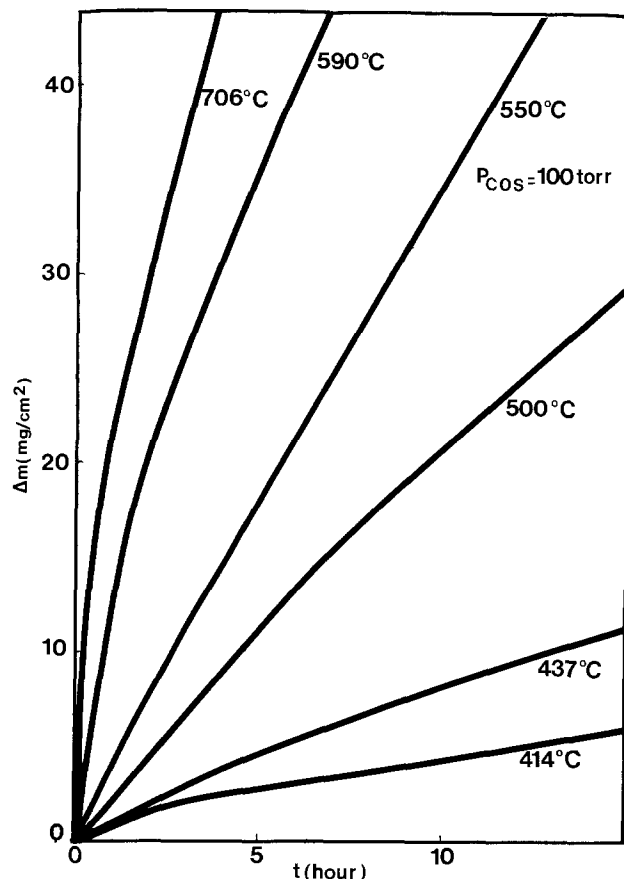


Fig. 2. Kinetic curves for the reaction of COS with iron: influence of temperature.

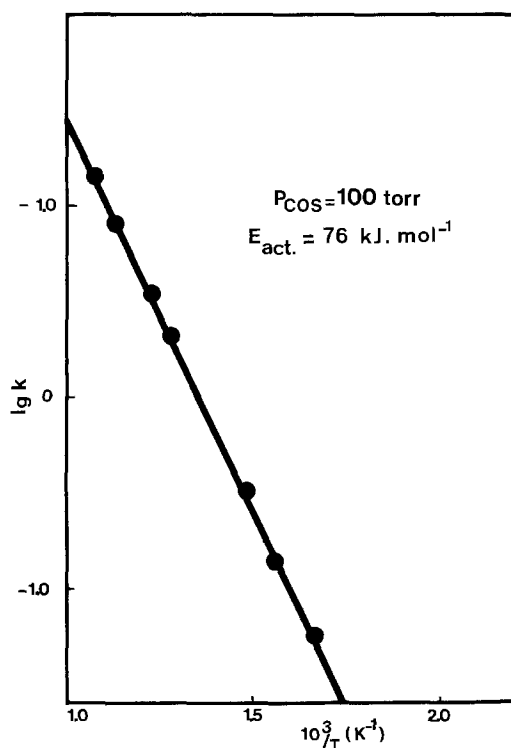


Fig. 3. Arrhenius' plot for the linear rate constant

from the decomposition of COS was carried out in our laboratory by minimizing the total Gibbs free energy of the ternary system C-O-S using the Direct Search Method developed by Hooke and Jeeves (16). In this system, twenty-one different species were considered. Figure 7 shows the results obtained for a COS initial

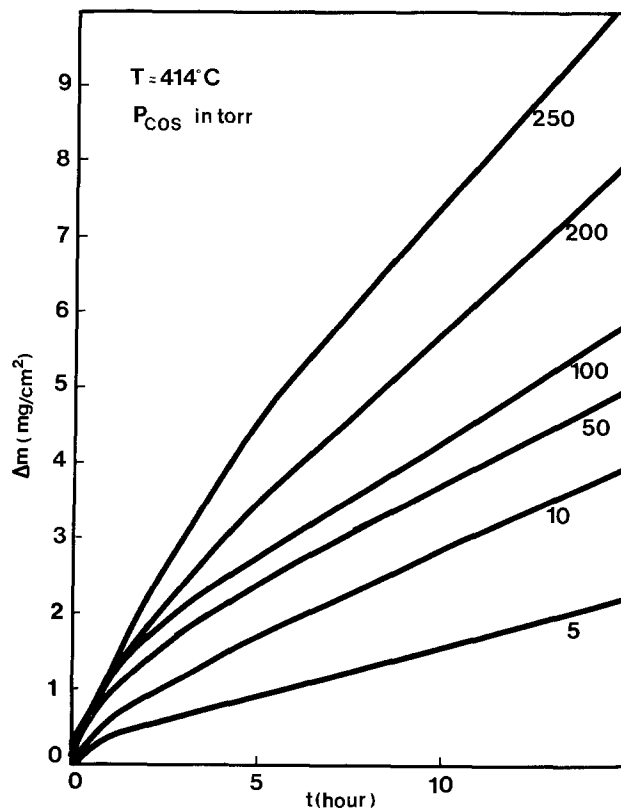


Fig. 4. Influence of pressure

pressure of 100 Torr. From this diagram, it can be seen that: (a) Only eight gaseous species are present in significant amounts at equilibrium between 500° and 1300°K; (b) at equilibrium, the COS pressure never exceeds one-half of its initial value; (c) at high temperatures, the decomposition of this compound is rather complete. As reported in the literature it may be represented approximately by the equation: $\text{COS} \rightleftharpoons \text{CO} + \frac{1}{2} \text{S}_2$; and (d) at low temperatures ($T < 800^\circ\text{K}$) the equation reported in the literature ($2 \text{COS} \rightleftharpoons \text{CO}_2 + \text{CS}_2$) does not agree with our results. In this temperature range, the calculation shows that solid carbon is formed. At 600°K, for example, 45% of the initial carbon is present in the solid phase at equilibrium.

Kinetic observations.—In our experiments, only a small part of the gas is heated. Under such conditions, if sulfur vapor is present in the hot gas phase, solid sulfur is expected to condense on the colder inner wall of the apparatus above the furnace.

In a previous work using carbon disulfide as the sulfidizing agent (11), we have shown that the sulfur condensation takes place with a significant rate for sulfur pressures greater than about 10^{-1} Torr. For lower values, no visible deposit was observed in our apparatus even after 20 hr or more.

In the present case no solid sulfur appeared in the temperature range 300°-700°C. Its partial pressure in the gas phase was therefore very low ($< 10^{-1}$ Torr) so that this phase could not possibly have reached an equilibrium state. The decomposition process of COS in the gas phase is consequently slow and its rate must be taken into account in any interpretation of the kinetics of the overall reaction.

Discussion of the Results

According to Rahmel (14), a linear rate law highly dependent on temperature is an indication of a rate-determining reaction at the scale/gas phase boundary. In this case, FeS and Fe oxides must be formed simultaneously if sulfur and oxygen pressures are greater than the Fe/FeS and Fe/Fe oxide equilibrium pressures.

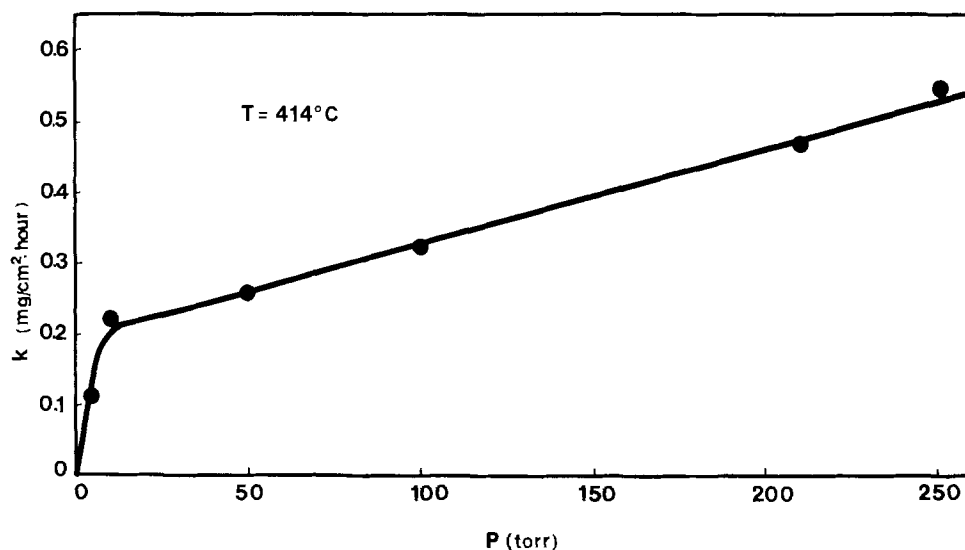


Fig. 5. Influence of pressure

In our experiments, despite the fact that both FeS and FeO (or Fe₃O₄ at lower temperatures) were thermodynamically stable, we never observed any iron oxide. This is another indication of the nonequilibrium state of the gas phase.

In such conditions, it is possible to describe more precisely the elementary steps involved in the gas phase and at the scale/gas phase boundary and to propose a model which can account for our experimental results: linear rate law with linear but nonproportional influence of pressure. This model rests on the following observations: (i) Contrary to the sulfidation of iron by carbon disulfide (11, 12), the reaction of carbonyl sulfide does not liberate carbon. It can therefore be assumed that CS₂ formed by thermal decomposition of COS does not interfere in the reaction. (ii) As the reaction product is pure iron sulfide, the only adsorbed species to be considered are COS and S₂. The species S_x (2 ≤ x ≤ 8) exist also but, due to the observed nonequilibrium state of the gas phase, the partial pressure of sulfur must be very low, thus promoting the diatomic species S₂. (iii) The existence of two different sulfidizing agents in the gas phase (COS and sulfur

vapor) makes it necessary to consider two parallel sequences of elementary steps, both leading to the formation of adsorbed sulfur. (iv) The FeS inner layer (or part of it) is compact so that diffusion through this layer must take place.

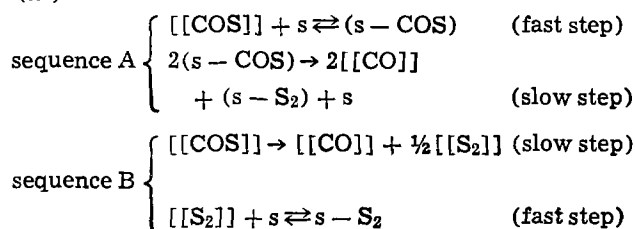
In agreement with these remarks, the successive steps of the reaction can be represented as in Fig. 8. According to this model, the reacting species, consisting of adsorbed S₂ molecules, are formed by two parallel sequences called A and B and two cases are to be distinguished: (a) At least one of the two sequences A and B is fast and consequently these two sequences have no influence on the rate of the overall reaction. Here the limiting step would be either one of the two interfacial half-reactions or the diffusion in the FeS layer, but these processes lead to parabolic or linear rate laws with a nonlinear influence of pressure and must be discarded. (b) The two sequences A and B are slow, therefore not at equilibrium. In this case, the reaction rate is the sum of the rates of each sequence. The overall reaction will obey a simple rate law if only one step of each sequence is slow. If the two steps of at least one sequence are slow, the rate law will be complex.

Considering only simple rate laws, four combinations of rate-determining steps are possible: (i) adsorption of COS/decomposition of COS in the gas phase, (ii) adsorption of COS/adsorption of S₂, (iii) decomposition of COS in the adsorbed phase/decomposition of COS in the gas phase, and (iv) decomposition of COS in the adsorbed phase/adsorption of S₂.

The combinations (ii) and (iv) imply that the decomposition of COS in the gaseous phase reaches its equilibrium state, which is not supported by experiments, so that these combinations may also be discarded.

From the remaining two combinations the first one, already described in the case of the sulfidation of copper (15), leads to a proportionality between the rate constant and the COS pressure and is also in contradiction with experimental evidence (Fig. 5).

There is therefore only one possible combination, (iii)



s is an adsorption site at the surface of the compact part of the FeS layer.

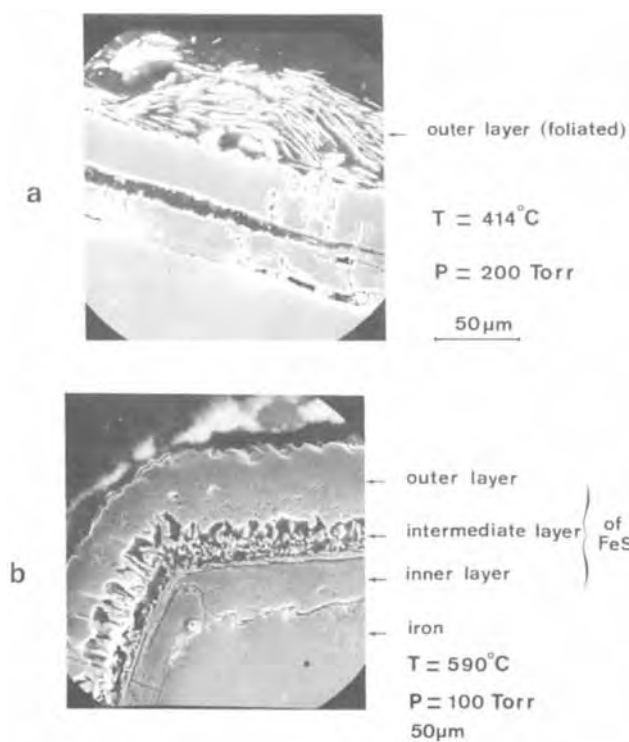
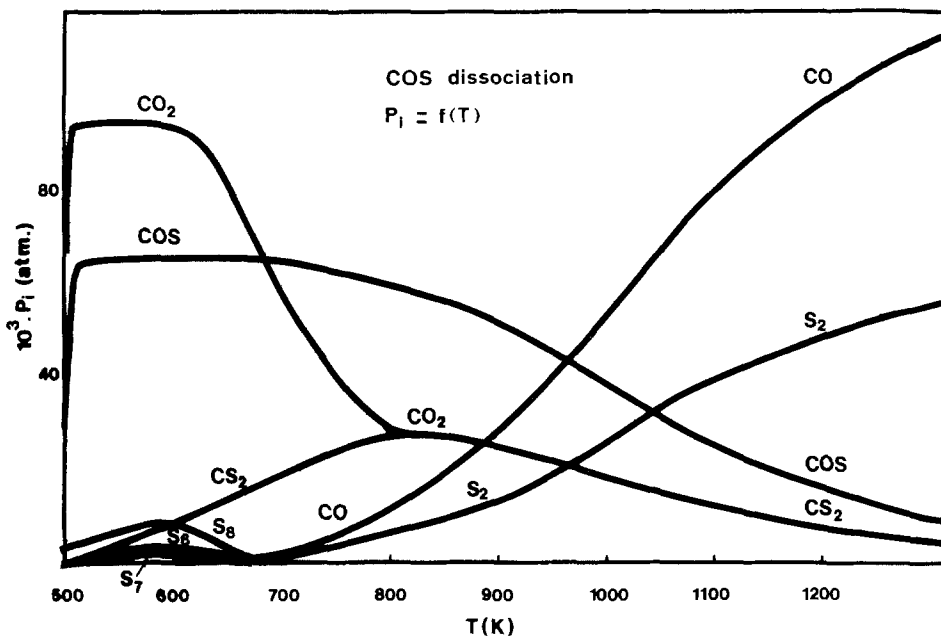


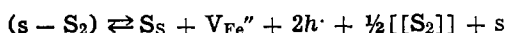
Fig. 6 (a and b). Cross sections of the FeS layer

Fig. 7. Equilibrium partial pressures resulting from the thermal decomposition of carbonyl sulfide.

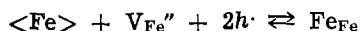


The next steps involve the external and internal half-reactions and are supposed to be fast enough to reach the equilibrium. They can be written

external reaction (equilibrated):



internal reaction (equilibrated):



Let k_{Ad} , k_{Bd} be the elementary rate constants of the slow processes for sequences A and B, respectively and K_{As} , K_{Bs} , the equilibrium constants of the equilibrated processes of sequences A and B. The indexes "s" or "d" refer to the nature of the considered reaction: adsorption or decomposition. P , θ , P_2 , θ_2 are the pressure and the coverage ratio of COS and S_2 , respectively.

If the rate-limiting steps are very far from equilibrium, their rates are given by

$$\begin{cases} v_{Ad} = k_{Ad}\theta^2 \\ \text{(decomposition of COS in the adsorbed phase)} \end{cases} \quad [1]$$

$$\begin{cases} v_{Bd} = k_{Bd}P \\ \text{(decomposition of COS in the gas phase)} \end{cases} \quad [2]$$

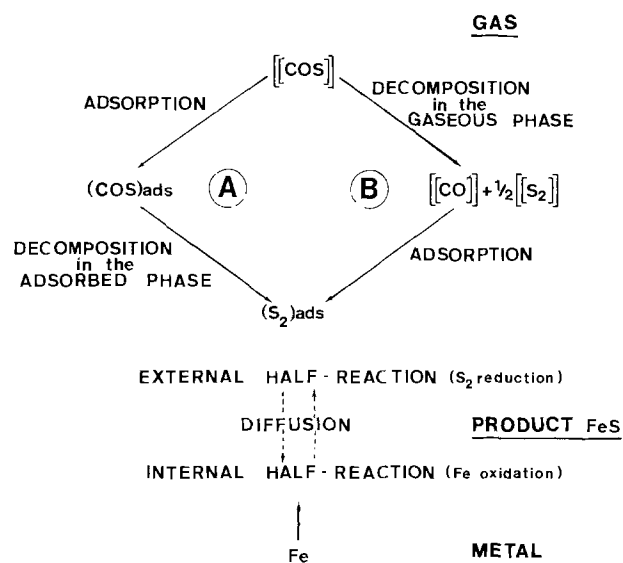


Fig. 8. Schematic diagram illustrating the whole mechanism with parallel sequences.

The coverage ratio θ can be derived from the law of mass action

$$K_{As} = \frac{\theta}{(1 - \theta - \theta_2)P} \quad \text{and} \quad K_{Bs} = \frac{\theta_2}{(1 - \theta - \theta_2)P_2}$$

Therefore

$$\theta = \frac{K_{As}P}{1 + K_{As}P + K_{Bs}P_2} \quad [3]$$

The rate of the overall reaction in $mg \cdot cm^{-2} \cdot hr^{-1}$ is then

$$\frac{d\Delta m/s}{dt} = \frac{M_{COS}k_{Ad}K_{As}^2P^2}{(1 + K_{As}P + K_{Bs}P_2)^2} + M_{COS}k_{Bd}P \quad [4]$$

This equation may account for the observed rate law. As soon as the carbonyl sulfide is introduced into the reaction chamber, a slow dissociation takes place and the sulfur pressure P_2 increases, leading to the observed decreasing speed. After a few hours, a stationary value of P_2 is reached,¹ and the rate law becomes linear. During this second stage of reaction the influence of COS pressure P on the linear rate constant is represented, according to Eq. [4], by

$$k_1 = \frac{aP^2}{(1 + P)^2} + bP$$

where a and b are constants. The corresponding curve agrees with our experimental results (Fig. 5).

Manuscript submitted March 19, 1979; revised manuscript received July 31, 1979.

Any discussion of this paper will appear in a Discussion Section to be published in the December 1980 JOURNAL. All discussions for the December 1980 Discussion Section should be submitted by Aug. 1, 1980.

Publication costs of this article were assisted by A. D. R. Grenoble.

¹ This stationary value is the result of the balance between the slow formation of elementary sulfur S_2 in the gas phase and its condensation on the cold parts of the apparatus.

REFERENCES

1. K. Hauffe and H. Rahmel, *Z. Phys. Chem.*, **199**, 152 (1952).
2. P. V. Geld and A. K. Krasovskaya, *Russ. J. Phys. Chem.*, **34**, 756 (1960); *ibid.*, **34**, 820 (1960).
3. Z. A. Fouroulis, Abstract 266, p. 620, The Electrochemical Society Extended Abstracts, Toronto, Canada, May 11-16, 1975.
4. A. Drawniecks and C. Samans, *This Journal*, **105**,

- 183 (1958).
 5. E. W. Haycock, *ibid.*, **106**, 764 (1959).
 6. C. Mathiron, J. C. Colson, and P. Barret, *Bull. Soc. Chim.*, **2**, 427 (1969).
 7. P. Raynaud, F. Nardou, and M. Billy, *Bull. Soc. Chim.*, **8**, 2799 (1971); *ibid.*, **5**, 1707 (1972).
 8. T. K. Ross, *Corros. Sci.*, **5**, 327 (1965).
 9. T. Flatley and N. Birks, *J. Iron Steel Inst.*, **209**, 523 (1971).
 10. B. Chatterjee and A. J. Dowell, *Corros. Sci.*, **15**, 639 (1975).
 11. A. Galerie, Thesis Grenoble (1977).
 12. A. Galerie, M. Caillet, and J. Besson, "Progress in Vacuum Microbalance Techniques," Vol. 3, Heyden, London (1975).
 13. A. Hayden and S. Steiten, *Oxid. Met.*, **3**, 545 (1971); *ibid.*, **7**, 46 (1973).
 14. A. Rahmel, *Corros. Sci.*, **13**, 125 (1973).
 15. P. Hadjisavas, M. Caillet, A. Galerie, and J. Besson, *Rev. Chim. Miner.*, **14**, 572 (1977).
 16. R. Hooke and T. A. Jeeves, *J. Assoc. Comp. Mach.*, **8**, 212 (1961).

Thin Zinc Films on Aluminum

David Lashmore

Chemical Stability and Corrosion Division, National Bureau of Standards, Washington, D.C. 20234

ABSTRACT

As part of a study of plating on aluminum, the deposition of thin zinc films on aluminum substrates was investigated by transmission electron microscopy and by electron diffraction. Zinc coatings on 99.999% aluminum were formed by immersion in aqueous solutions of sodium zincate. It was found that zinc initially forms epitaxial semicontinuous films on all aluminum principal planes. Subsequent zinc growth continued in the form of separate crystallites (2000Å diam) which grew upon the initial film while continuing to maintain the epitaxial relationship. Using dark field transmission electron microscopy in combination with electron diffraction, it was found that Zn: (0001) $\langle 10\bar{1}0 \rangle //$ Al (100) $\langle 010 \rangle$, Zn: (0001) $\langle 11\bar{2}0 \rangle //$ Al ($\bar{1}10$) $\langle 111 \rangle$, and Zn: (0001) $\langle 11\bar{2}0 \rangle //$ Al (111) $\langle 1\bar{1}0 \rangle$.

The literature covering epitaxial deposits on aluminum is rather limited presumably due to the difficulty in obtaining an oxide-free aluminum surface. Dorey, however, has reported (1) that in high vacuum ($\sim 5 \times 10^{-7}$ Pa), nickel evaporated onto (111) aluminum held at 40°C forms epitaxial islands of AlNi. As the temperature was raised to 250°C, a continuous layer of Al₃Ni was formed with no preferred orientation. At 330°C unstable elongated regions showing a (110) preferred

Key words: films, electron, diffraction.

orientation were observed. These regions tended to form spheres, presumably to minimize their surface area. The aluminum substrate used by Dorey was formed by evaporation of the aluminum onto rock salt, again at high vacuum. Jona (2) has reported good auto-epitaxy of aluminum at room temperature. His specimens were prepared by evaporation of aluminum at similar vacuums onto single crystal aluminum substrates which had undergone elaborate cleaning steps. Substrates of (100), (110), and (111) orientations

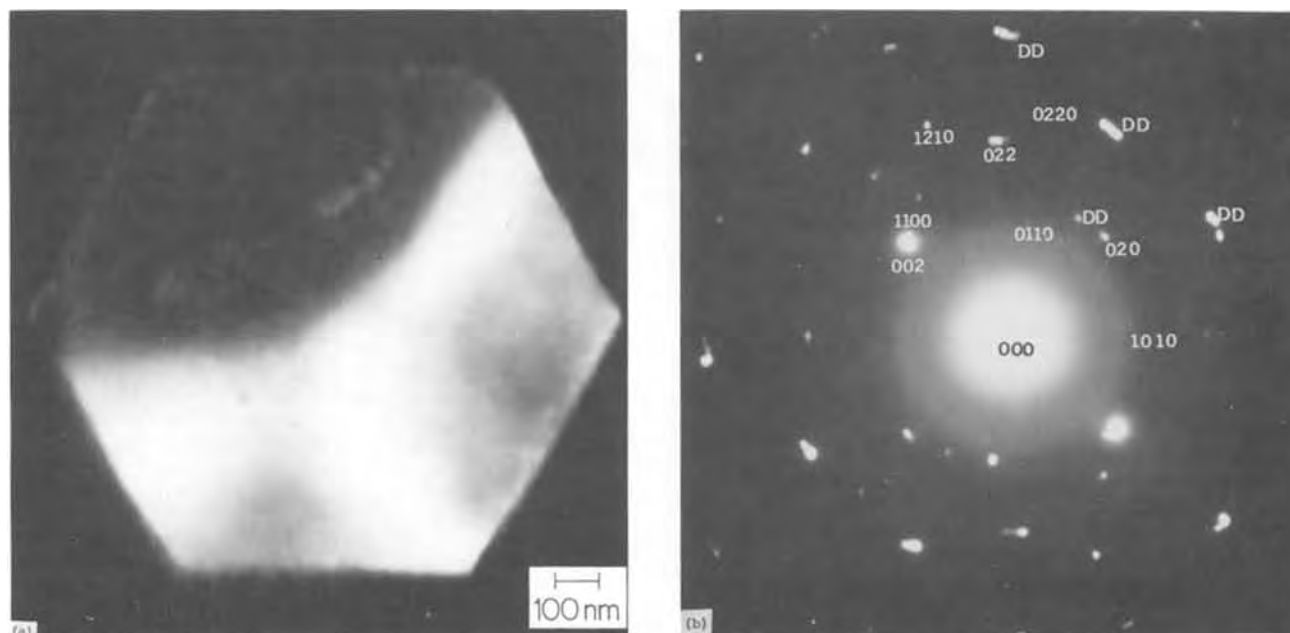


Fig. 1. (a) A dark field TEM micrograph of a single hexagonal crystallite taken with a (002) aluminum reflection. (b) The corresponding selected area diffraction pattern of the (100) zincated aluminum (solution I).

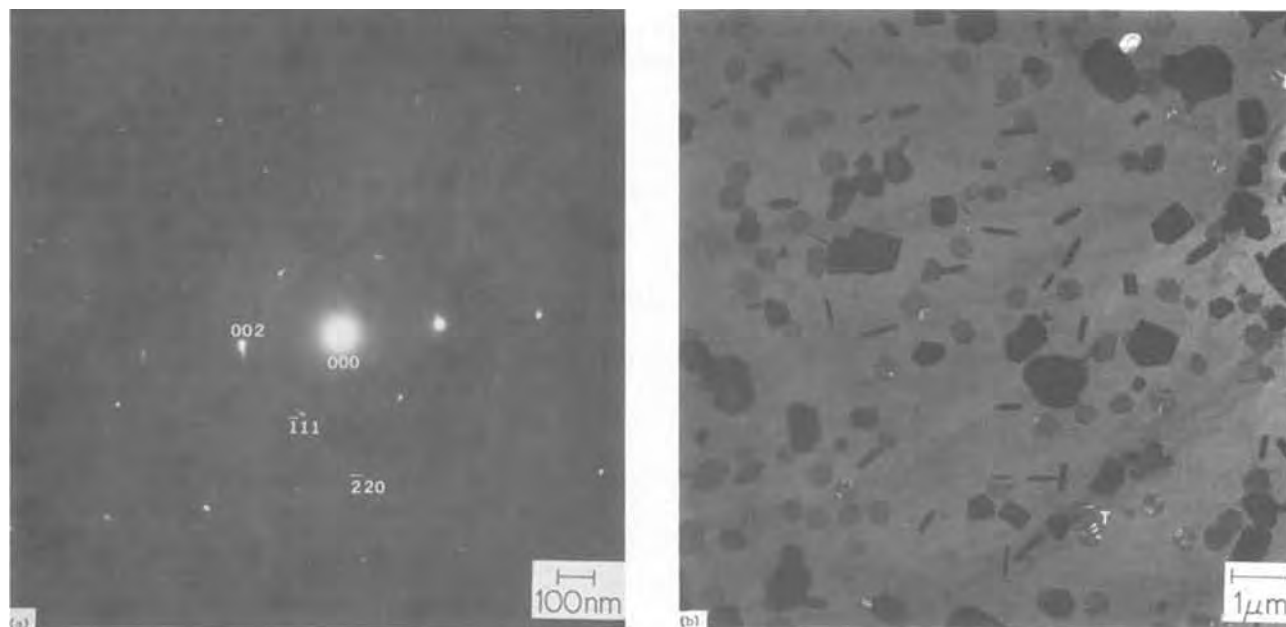


Fig. 2. (a) A single hexagonal zinc crystallite on a (110) aluminum substrate, the selected area diffraction pattern is superimposed. (b) A dark field micrograph of a (110) zincated aluminum substrate taken with a (111) reflection (solution I).

were considered. In all cases epitaxy was found, and on the (110) surfaces Jona found that there were indications of (111) facets present.

In spite of many studies of zinc-coated aluminum (3-9), there have been no reports of zinc epitaxy on aluminum substrates. In an investigation of the zincate process, Bullough and Gardam (4) speculated that adhesion between zinc and aluminum might very well depend on the degree of epitaxy between the deposit

and the substrate, and they gave several examples of orientations of zinc which would be expected on the aluminum principal planes; however, no experimental evidence was presented to support their theory. Bailey (8) published an x-ray and electron diffraction study of zincated aluminum, concluding that the zinc film was covered with separated small single crystallites of zinc. He also offered evidence to support the existence of small amounts of zinc hydroxide on the surface. However, no information on the substrate orientation was presented nor was the morphology described.

The zinc immersion process is used extensively as the first step in electroplating on aluminum (10). Essentially, the process is simply the immersion of a very clean aluminum substrate into an aqueous solution at 23°C of sodium hydroxide and zinc oxide. The aluminum oxide is dissolved in solution and a displacement reaction takes place, where ideally two aluminum atoms pass into solution for every three zinc atoms deposited on the surface. It has been shown (11), however, that the reaction which takes place in solutions containing ferric chloride and Rochelle salt (standard additions) is more complex.

Procedure

Specimens of 99.999% aluminum were electropolished to electron transparency using a twin jet technique. The electrolyte used was a solution of 15% perchloric acid in methanol cooled to 250°K. In most cases it was possible to stop the polishing before the specimens were perforated. After appropriate rinsing, the specimens were zincated for 60 sec on one side using either of two solutions. Solution I consisted of 525 g/dm³ sodium hydroxide and 100 g/dm³ zinc oxide in distilled water. Solution II had, in addition to the above, 1.0 g/dm³ ferric chloride and 10 g/dm³ Rochelle salt. The specimens were examined in transmission electron microscopes at 100 or 200 kV. Both microscopes used in this investigation were equipped with anticontamination stages and double tilt specimen holders.

Results

A dark field micrograph of a single crystallite of threefold symmetry is shown in Fig. 1(a) along with its associated selected area diffraction pattern in 1(b). This micrograph of (100) aluminum was taken with the (002) reflection and, as will be discussed below, indi-

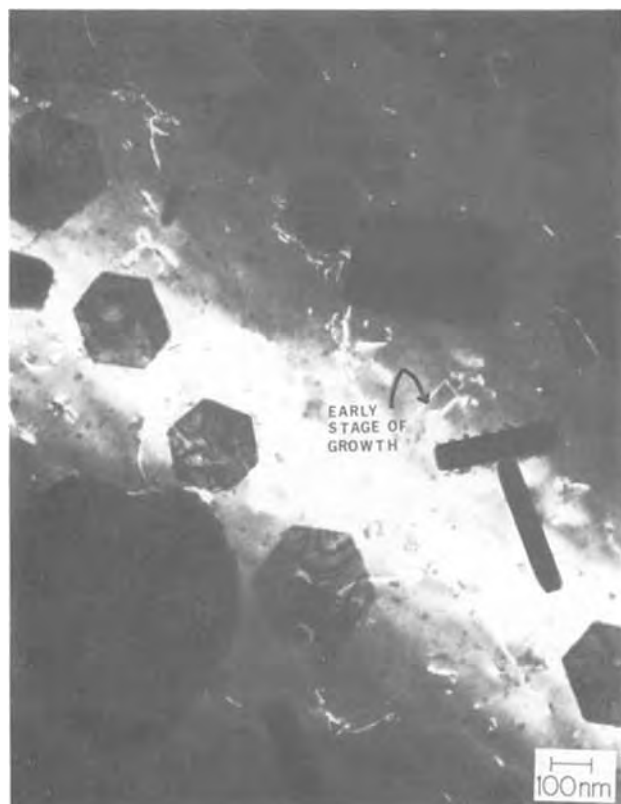


Fig. 3. A dark field micrograph of a (110) zincated specimen taken with a (220) reflection, illustrating the initial growth of a rectangular crystallite. Note the bend contours within the transparent zinc crystallites of hexagonal morphology.

cates that this zinc crystallite is epitaxial on the (100) substrate.

On substrates of the (110) orientation, similar results are observed. A single hexagonal crystallite with its selected area diffraction pattern superimposed upon it is shown in Fig. 2(a). Note that hexagonal crystallites are observed on both (100) and (110) substrates, indicating that (0001) zinc can grow on either orientation. A dark field micrograph taken with a ($\bar{1}\bar{1}\bar{1}$) reflection as shown in Fig. 2(b) indicates that a number of crystallites maintain an epitaxial relationship to the substrate. In Fig. 3 one sees another dark field micrograph of a (110) substrate, taken this time with the (220) reflection which illustrates the initial stages of growth of a rectangular crystallite as well as the general morphology of the zinc on substrates of this orientation (solution I).

Zinc films deposited from solution II show similar epitaxial relationships to the substrate as those formed from solution I. For example, a single hexagonal crystallite is shown in the bright field TEM micrograph of Fig. 4(a) with its corresponding selected area diffraction pattern in Fig. 4(b). A dark field micrograph

taken with the (220) reflection shows the same crystallite in bright contrast in Fig. 4(c).

On {111} grains, the epitaxy between the zinc and the aluminum manifests itself in Moiré fringes, as shown in the bright field-dark field pair in Fig. 5(a) and (b) with the corresponding selected area diffraction pattern in 5(c).

A more or less continuous thin film of zinc formed from the growth and coalescence of numerous nuclei is seen in the bright field micrograph of Fig. 6 of deposits produced from solution II. Note the contrast change from bright to dark across the bend contour. The zinc seems to have been nucleated in discrete areas and eventually grows into connecting regions, many of which exhibit threefold symmetry. Coatings formed from solution I also seem to form noncontinuous zinc films as shown in the bright field TEM micrograph of Fig. 7.

Discussion

Zinc deposits formed from both kinds of solutions considered here can give rise to epitaxial films. Consider first the (100) aluminum plane whose atomic positions are shown in Fig. 8 and upon which the zinc

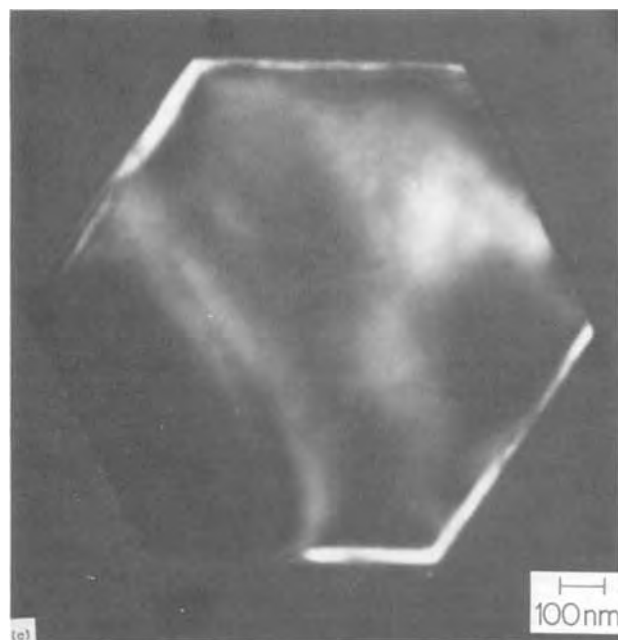
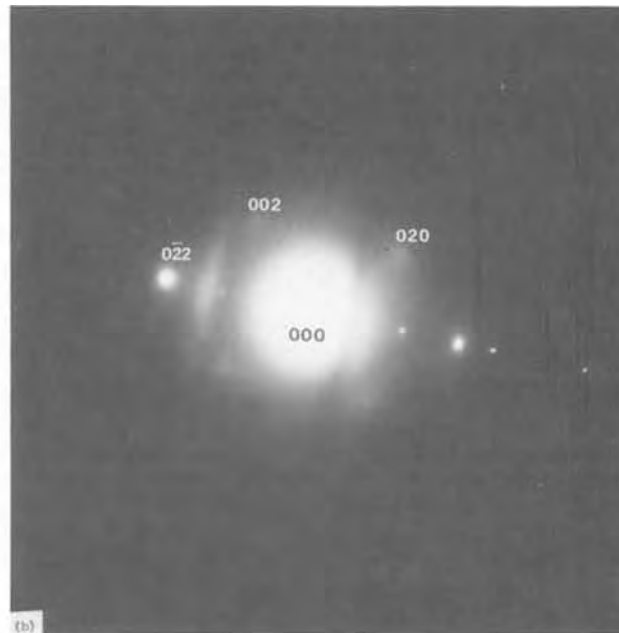
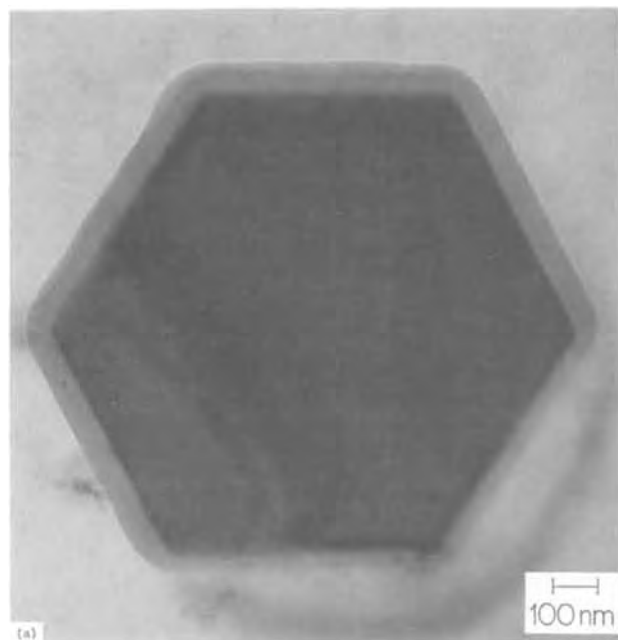


Fig. 4. (a) A single hexagonal crystallite (solution II). (b) The corresponding selected area diffraction pattern. (c) A dark field micrograph of the same crystal taken with a zinc $\langle 10\bar{1}0 \rangle$ reflection.

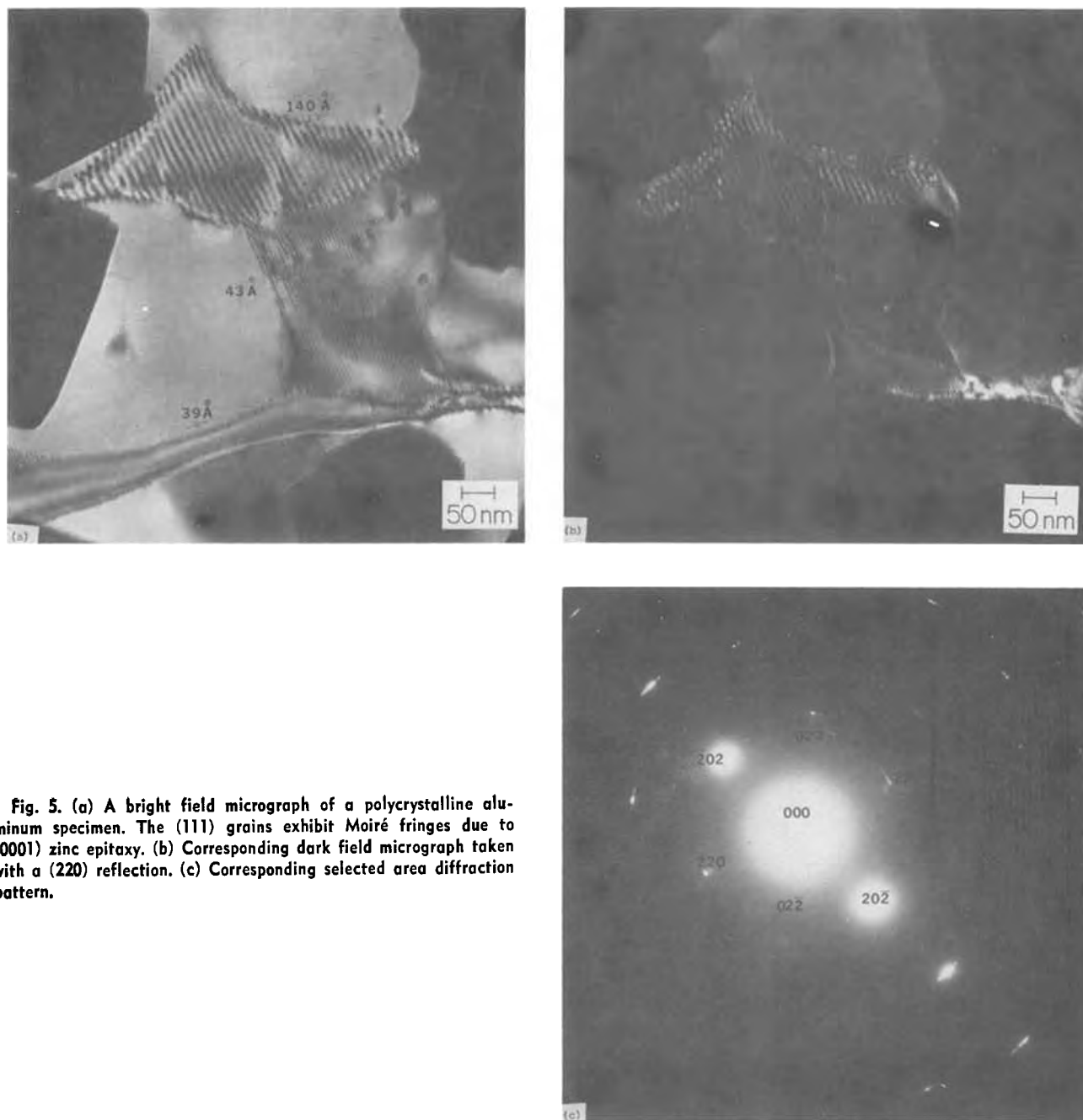


Fig. 5. (a) A bright field micrograph of a polycrystalline aluminum specimen. The (111) grains exhibit Moiré fringes due to (0001) zinc epitaxy. (b) Corresponding dark field micrograph taken with a (220) reflection. (c) Corresponding selected area diffraction pattern.

(0001) plane has been fitted in such a way that the aluminum [010] direction lines up with the $[\bar{1}100]$ directions in the zinc, only one of which is shown in Fig. 8. The zinc misfit in the $\langle 100 \rangle$ direction is given by the zinc spacing $\sim 2.308\text{\AA}$ minus the aluminum spacing $\sim 2.024\text{\AA}$, divided by the zinc spacing, or about 12.3%, which is within the Royer rule of epitaxy ($\sim 15\%$) (12). A diffraction pattern from such an atomic arrangement would be expected to show a distorted pattern in one direction superimposed upon a normal aluminum pattern. The (002) and (002) aluminum spots should coincide approximately with the zinc (1100) and $(\bar{1}100)$ spots. One might, in addition, observe extra spots due to double diffraction. The diffraction pattern seems to correspond quite well with that expected with exception that the $(\bar{1}010)$ and $(10\bar{1}0)$ spots are absent. This is thought to be due to a substrate slightly tilted out of the diffraction condition for these planes. The double diffraction spots are indicated on Fig. 1(b). It can, therefore, be concluded that the (0001) zinc is epitaxial on (100) aluminum.

Consider now (110) aluminum planes. At least three possibilities exist for zinc to be epitaxial on a sub-

strate of this orientation. The first shown in Fig. 9 is a match between the zinc $(0\bar{1}\bar{1}0)$ plane and the aluminum so that the [100] aluminum direction aligns with the zinc [0001] direction. In this situation, for every aluminum atom there exactly corresponds a zinc atom. The misfit between atoms in Al: [100] is about 7.5% while in the other direction, Al [110], the misfit is about 18%. The symmetry of crystallites growing with this orientation would, of course, be twofold. The second possibility for an epitaxial arrangement of the zinc on aluminum is given by a $(01\bar{1}0)$ zinc plane; however, this time consider a rotation of the zinc in such a way that the $\langle 111 \rangle$ aluminum direction is parallel to the zinc [0001] direction. In this case the misfit in the [001] aluminum direction is essentially 0% and in the [110] aluminum direction about 1.5%. This reduction in misfit comes at the expense of two unpaired atoms of the zinc as shown in Fig. 9(b). Lastly, consider the case of the zinc (0001) or basal plane oriented on the (110) aluminum in such a way that the $[11\bar{2}0]$ direction in the zinc coincides with one of the aluminum $\langle 111 \rangle$ directions. In this case, the misfit in the [100] aluminum direction is 12% and

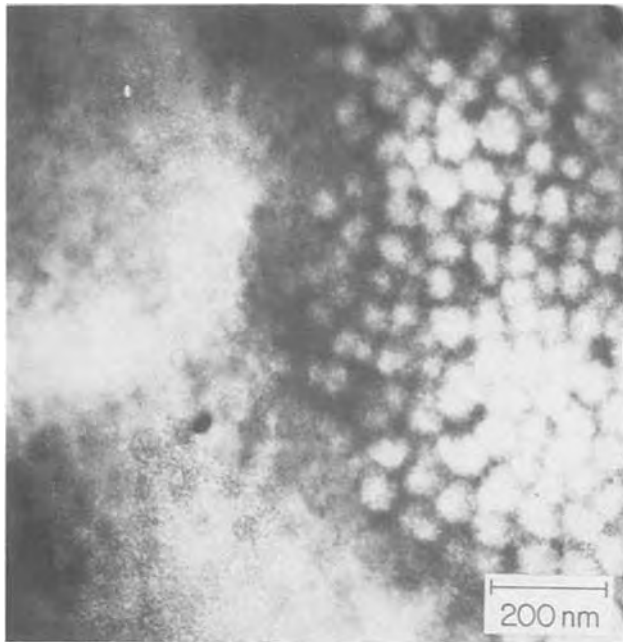


Fig. 6. Bright field micrograph of initial stage of zinc growth from solution I.

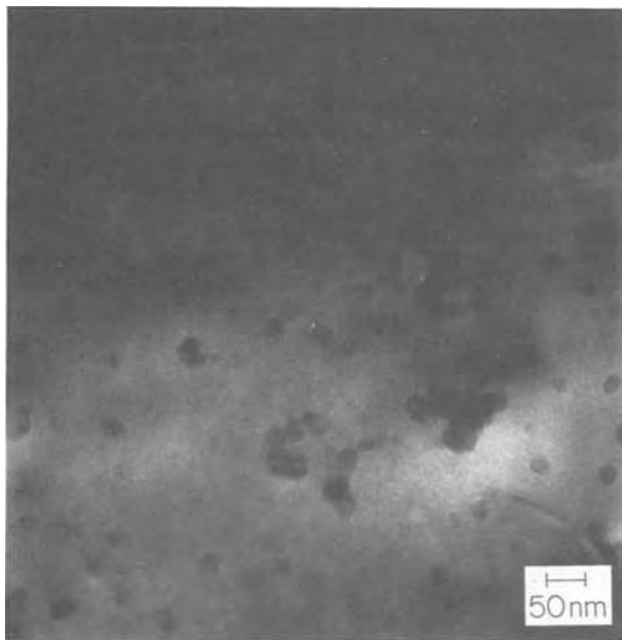


Fig. 7. Bright field micrograph of initial stage of zinc growth from solution II.

in the $[110]$ direction 7.5%. Unpaired zinc atoms do exist as shown in Fig. 9; however, these unpaired zinc atoms would line up with very little misfit with the aluminum atoms on the plane immediately below the surface. In addition, crystallites growing with this orientation would have threefold symmetry. The spots associated with the $(01\bar{1}0)$ zinc orientation have not been observed; see, for example, Fig. 4(b). As the zinc on this orientation has been observed to have both two, three, and sixfold symmetry, and because the diffraction patterns from (0001) zinc would about coincide with that of (110) aluminum, and because the zinc shows up in bright contrast in dark field when one of the aluminum spots is used to form the image, it can be concluded that it is the (0001) zinc orientation, as described in Fig. 9(c), which is epitaxial on the (110) aluminum.

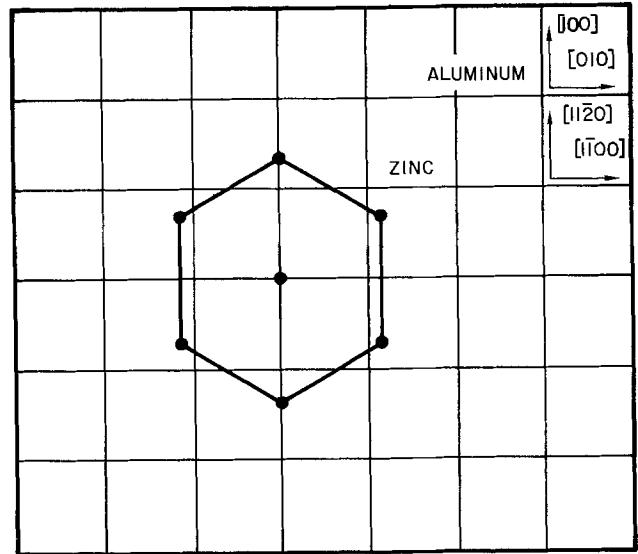


Fig. 8. The atomic positions in the (100) aluminum plane with (0001) zinc oriented such that $\langle 1010 \rangle // \langle 100 \rangle$.

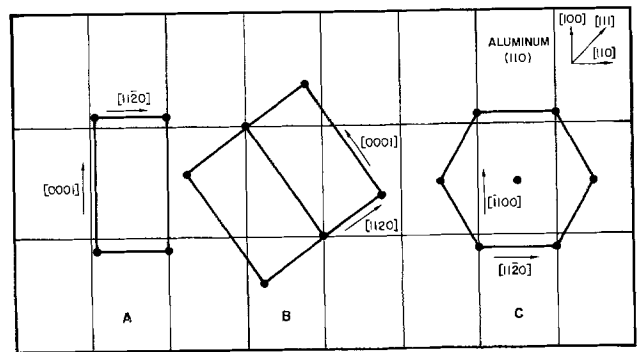


Fig. 9. (a) A (110) aluminum substrate on which a $(01\bar{1}0)$ zinc (prism) plane has been fitted so that the zinc $[0001]$ is parallel to the $[011]$ direction in aluminum. (b) A (110) aluminum substrate on which a $(01\bar{1}0)$ zinc (prism) plane has been fitted so that the zinc $[0001]$ direction is parallel to the aluminum $[111]$ direction. (c) A (111) aluminum substrate on which a (0001) zinc plane has been fitted so that the $[11\bar{2}0]$ direction in zinc aligns with the $[111]$ aluminum direction.

The last aluminum principal plane to consider is the (111) . As shown in Fig. 10, the (0001) zinc plane is quite a good fit. The mismatch of 7.4% is symmetrical.

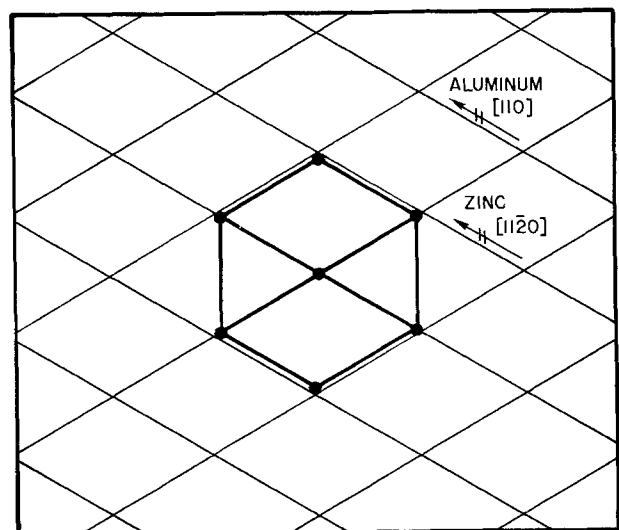


Fig. 10. The atomic positions in the (111) plane with (0001) zinc oriented such that $\langle 11\bar{2}0 \rangle // \langle 110 \rangle$.

Because of this symmetrical mismatch, the Moiré fringes shown in Fig. 5 are not unreasonable. If the fringes are due only to a translational mismatch, the spacing between them is given by

$$D \text{ (fringes spacing in } \text{Å}) = \frac{d_1 d_2}{d_1 d_2} = \frac{(2.8662) \cdot (2.665)}{2.8662 - 2.665} \quad [1]$$

$$\cong 38 \text{Å}$$

As seen in Fig. 5, for the most part the fringe spacing is rather close to this number with the exception of one grain where the spacing is 140Å. Again, because of the symmetry of deposits on grains of this orientation in combination with the above arguments, it seems reasonable that on (111) aluminum that zinc (0001) is epitaxial on the aluminum, and, moreover, zinc on this orientation can be continuous.

The importance of this finding of epitaxy of zinc on aluminum can be understood in terms of the relationship of epitaxy to adhesion of two metals. The adhesion between two surfaces in contact can broadly be understood in terms of their respective surface energies, γ , and the energy of their mutual interface, γ_i . Bonding between these two materials can be characterized by an associated energy of adhesion, E_{Ad} . This energy of adhesion is that energy necessary to take an atom from a distance of approximately one lattice distance to infinity and can be expressed (13) in terms of the surface free energy γ_s for two materials a and b as

$$E_{Ad} = \gamma_{s,a} + \gamma_{s,b} - \gamma_{i,ab} \quad [2]$$

where $\gamma_{i,ab}$ is the interfacial energy of the two metals in contact. If, for example, the two metals are identical then

$$E_{ad} = 2\gamma_s - \gamma_i \quad [3]$$

The adhesion between two materials therefore depends on the interfacial energy. In the case of perfect epitaxy, the adhesive energy reaches a maximum value given by

$$E_{ad} = 2\gamma_a \quad [4]$$

The value of γ_i therefore varies with the nature of the boundary. The lowest values generally are epitaxial interfaces, increasing with twins, stacking faults, low angle boundaries, and grain boundaries.

It has been shown experimentally (14) that the adhesive energy E_{ad} between two dissimilar metals increases with not only the degree of epitaxy but also with the surface energy. This finding is consistent with Eq. [2].

Conclusions

It has been demonstrated that zinc deposited from room temperature (300°K) solutions of sodium zincate forms thin epitaxial films on all the principal planes of aluminum. The morphology of the zinc deposits has been characterized for the first time as a thin semi-continuous film upon which larger epitaxial crystallites grow in such a way that Zn: (0001) $\langle 10\bar{1}0 \rangle$ //Al: (100) $\langle 010 \rangle$, Zn: (0001) $\langle 11\bar{2}0 \rangle$ //Al (110) $\langle 111 \rangle$, and Zn: (0001) $\langle 11\bar{2}0 \rangle$ //Al: (111) $\langle 1\bar{1}0 \rangle$. The adhesion of zinc to aluminum is thought to be aided by the low energy epitaxial boundaries between the zinc and the aluminum.

Acknowledgment

I gratefully acknowledge the financial support of this research through the Aluminum Association and the American Electroplaters' Society. Sincere thanks are due to U. Bertocci for his comments on the manuscript.

Manuscript submitted July 16, 1979; revised manuscript received Oct. 30, 1979.

Any discussion of this paper will appear in a Discussion Section to be published in the December 1980 JOURNAL. All discussions for the December 1980 Discussion Section should be submitted by Aug. 1, 1980.

Publication costs of this article were assisted by the National Bureau of Standards.

REFERENCES

1. G. Dorey, *Thin Solid Films*, **5**, 69 (1970).
2. F. Jona, *J. Phys. Chem. Solids*, **28**, 2155 (1967).
3. M. B. Diggin, *Metal Finishing*, **45**, 67 (1947).
4. W. Bullough and G. E. Gardam, *J. Electrodepositors Tech. Soc.*, **22**, 169 (1947).
5. F. Keller and W. G. Zellely, *Proc. Am. Electroplat. Soc.*, **22**, 149 (1949).
6. S. Heiman, *This Journal*, **95**, 205 (1949).
7. F. Keller and W. G. Zellely, *ibid.*, **97**, 143 (1950).
8. G. L. J. Bailey, *J. Electrodepositors Tech. Soc.*, **27**, 233 (1951).
9. W. G. Zellely, *This Journal*, **100**, 328 (1953).
10. D. S. Lashmore, *Plating and Surface Finishing*, p. 44 (April 1978).
11. D. S. Lashmore, Unpublished.
12. L. Royer, *Bull. Soc. Fr. Mineral.*, **51**:7 (1978) *Compt. Rend.*, 194-1088, 1932.
13. L. Z. Murr, in "Interfacial Phenomena in Metals and Alloys," p. 285, Addison-Wesley, Reading, Massachusetts (1975).
14. D. H. Buckley, in "Physics of Adhesion," Proceedings of the Conference on Physics of Adhesion, Karlsruhe (1969).

The Anodic Sectioning of Beryllium

M. T. Shehata*¹ and Roger Kelly**²

Institute for Materials Research, McMaster University, Hamilton, Ontario, L8S 4M1 Canada

ABSTRACT

The anodic sectioning of a metal permits successive atomically thin layers (2.6-17 nm in the case of Be) to be removed from the surface of macroscopic specimens. The procedure with Be is based on forming an amorphous anodic film in an ethylene-glycol based electrolyte containing sulfate and phosphate ions, followed by dissolving the film in 10% KOH. The inorganic ions replace part of the O²⁻ in the anodic film, the empirical result of this being that P-containing ions reduce the dissolution rate during anodizing whereas S-containing ions increase the dissolution rate of already-grown films in KOH. Thickness calibrations, based on a combination of measuring weight changes and analyzing depth-distribution curves for implanted radioactive ions, may be expressed as follows

$$\text{metal-removal thickness} = -0.18 + 0.066 \times \text{volts } \mu\text{g}/\text{cm}^2$$

$$\text{anodic-film thickness} = -0.7 + 0.23 \times \text{volts } \mu\text{g}/\text{cm}^2$$

The logic used for arriving at the results is developed so that it can in principle be used as a guide for establishing anodic-sectioning procedures with still unstudied systems. Examples of depth distributions of 5, 15, and 30 keV Kr⁺ in both Be and the anodic film on Be are given.

Over the past 20 years, various approaches for the microsectioning of solids have been developed. These include chemical dissolution (1-3), anodic sectioning (4-15), formation and dissolution of films other than oxides (16), vibratory polishing (17), bombardment-induced solubility of surface layers (18, 19), and sputtering (20-22). These techniques have their main applications in measuring depth distributions of implanted ions and radiation damage, and in determining diffusion coefficients at low temperatures (23).

While anodic sectioning is probably the most effective microsectioning technique of all, there is a severe problem in that it is not universally applicable. Not only is it relevant only with metals, but for some time procedures were available only for Al (4), W (5), Si (6-8), Au (9), and, to some extent, Nb and Ta (10). More recently, programs undertaken in our laboratory (11-13) and elsewhere (14, 15) have made possible the anodic sectioning of Mo (11), V (12), Nb, Ta (13), Ag (14), and Cu (15), and have extended the accessible voltages with W from 75 (5) to 140V (13). It is now possible to microsection elements having masses ranging from 27 to 197.

We will consider here the anodic sectioning of Be, which is the lowest mass target that can be conveniently worked with in the field of atomic collisions. The difficulty in the anodic sectioning of Be appeared at first sight to lie in establishing conditions under which a barrier-type, stable, amorphous film could be formed. We showed previously (24), however, that such films were easily obtained by the use of electrolytes based on ethylene glycol which is saturated with Na₂HPO₄ or KH₂PO₄ or both Na₂HPO₄ and Na₂SO₄. As will be seen, these films are readily soluble in KOH and thus permit uniform layers 2.6-17 nm thick to be removed from Be.

An important aspect of what follows is that an attempt will be made to establish a "logic," in so far as one exists, for anodic sectioning. We will, for example, show why in the particular case of Be the electrolyte must contain both sulfate and phosphate ions, and not just one or the other. We will also emphasize that the electrolyte chosen for Be has a pH which corresponds to a passive region in the Pourbaix diagram (25), the same being true for most other anodizable systems (26).

* Electrochemical Society Student Member.

** Electrochemical Society Active Member.

¹ Present address: Department of Energy, Mines, and Resources, Ottawa, Ontario, Canada.

² Present address: IBM Thomas J. Watson Research Center, Yorktown Heights, New York 10598.

Key words: films, electrolyte, anode, oxidation.

Experimental

The Be specimens, obtained from Ventron Corporation (Alpha Products), were polycrystalline foils which were 0.25 mm thick and had a purity claimed to be 99.5%. Most of the experiments involved specimens with dimensions 25 × 12.5 mm. The surfaces were prepared by an initial polishing with SiC papers, further polishing with 6 μm diamond paste using kerosene as a lubricant, and five anodic sectionings at 50V. All polishings were carried out in a special fume hood reserved for this project owing to the toxicity of Be.

Anodizings were carried out at room temperature (~22°C) using a power supply such that limits to both the current and potential could be preset (Hewlett-Packard Model 6186B). The specimens were half submerged in the electrolytes, with the relevant areas determined in hindsight from the interference colors. The electrolytes were neither stirred nor protected from air, and, in view of the possibility of decomposition, were discarded after five anodizings or one hour, whichever came first. For the 25 × 12.5 mm specimens, the cathode consisted of Pt gauze in the form of a cylinder with an inside diameter of 25 mm. Larger specimens were sandwiched between a cathode consisting of two sheets of Pt.

The detection and profiling of impurities in the anodic films was carried out with a secondary-photon spectrometer. This consisted of a mass-separated ion beam (12 keV Kr⁺) striking a target with the target surface viewed, via a quartz lens, by a 0.25m Jarrell-Ash Model 82-410 monochromator. A refrigerated photomultiplier tube (EMI Model 6256 QB) served to detect the photons from atoms sputtered in excited states. Surface oxygen was detected from the enhancement of the Be signal at 235 nm [a similar effect occurs with Al (27)], and S and P were detected from the weak emissions at, respectively, 393 and 215 nm (28). As the beam profile was quite irregular, the results must be regarded as somewhat approximate.

Anodic Sectioning of Be

Choice of electrolyte.—The main requirements of an electrolyte to be used for anodic sectioning are that it should lead to films which are simultaneously barrier-type, stable, and amorphous. Being barrier-type normally assures that a uniform, voltage-dependent, limiting film thickness exists (3); stability assures, in a general sense, that the film does not dissolve extensively in the electrolyte during formation; while amorphicity often plays a role in enabling films to be

chemically stripped without the metal substrate being attacked. We showed previously (24) that the most interesting electrolytes for Be are those consisting of ethylene glycol saturated with Na_2SO_4 , Na_2CO_3 , $\text{Na}_2\text{B}_4\text{O}_7$, Na_2HPO_4 , KH_2PO_4 , or a mixture of Na_2HPO_4 and Na_2SO_4 , the last being designated "electrolyte A."

They were all inferred to lead to barrier-type films, thence uniform, voltage-dependent, limiting film thicknesses, on the basis of the $V-t$ and $I-t$ characteristics [Fig. 5 of Ref. (24)].

Film stability was evaluated in two ways. Approximate current efficiencies were estimated by comparing $\int Idt$, i.e., the area under the $I-t$ curves, with the film weight as determined using electrolyte A and assuming a composition BeO . The results, shown in column 4 of Table I, are subject to the uncertainties that the films were lightly doped with S and P, and that the weights for electrolyte A are not necessarily fully correct. In spite of this, there is little doubt that the phosphate-containing electrolytes yield the highest efficiencies, thence the most stable films.

Stability was also examined in terms of the extent of Be metal dissolution during a full anodizing cycle. Be specimens were implanted with 30 keV ^{85}Kr (beta-active) to a dose of 2×10^{15} ions/cm 2 , and the radioactivity was noted before and after 2 or 4 min anodizings with presettings of 50V and 3.0 mA/cm 2 (column 5 of Table I). If the activity profile is approximated as exponential

$$\text{integral concentration} = \exp(-[x \ln 2]/R_m) \quad [1]$$

where the median range R_m can be taken from Fig. 7 (to follow) as 25 nm, inferred Be losses are obtained as in column 6 of Table I. Minimum losses clearly occurred with the phosphate-containing electrolytes. It is readily seen from Fig. 7 (to follow) that the assumption of exponential profiles underestimates thicknesses in the range 90-100% activity. Specimens which were sectioned to about 50% activity and which should be accurately exponential with $R_m = 25$ nm were therefore used in conjunction with electrolyte A and the Be loss was redetermined to be 2 ± 0.5 nm. Even with this approach there is a major uncertainty in that the inert-gas marker would tend to be buried to an extent which cannot be determined owing to film being formed in part by the outward migration of Be. This causes the Be losses to be underestimated and they are therefore indicated as being lower limits in Table I.

It is worth noting that, however imperfect is the information in Table I, the two approaches as embodied in columns 4 and 6 lead to similar conclusions.

Table I. Approximate current efficiencies and metal losses in ethylene-glycol based electrolytes for 2 or 4 min anodizings of Be with presettings of 50V and 3 mA/cm 2 ^a

Electrolyte (ethylene glycol saturated with indicated compound)	pH	Total anodizing time (min)	Current efficiency ^b	Fraction of Kr implanted which is retained	Inferred loss of Be ^c (nm)
1. Na_2SO_4	6	4	0.18 ± 0.03	0.73 ± 0.04	≈ 11
2. Na_2CO_3	10	4	0.23 ± 0.03	0.88 ± 0.04	≈ 5
3. $\text{Na}_2\text{B}_4\text{O}_7 \cdot 10 \text{H}_2\text{O}$	6	4	—	0.92 ± 0.04	≈ 3
4. Na_2HPO_4	8.5	2	0.90 ± 0.04	0.994 ± 0.008	≈ 0
5. KH_2PO_4	—	2	0.89 ± 0.04	0.994 ± 0.008	≈ 0
6. 1:1 mixture of (1) and (4) ("electrolyte A")	7.5	2	0.67 ± 0.04	0.986 ± 0.006	≈ 1

^a With presettings of (for example) 50V and 3 mA/cm 2 , the anodization proceeds at 3 mA/cm 2 until 50V is reached and then with decreasing current until the process is terminated.

^b Deduced by comparing $\int Idt$ with the film weight as determined using electrolyte A and assuming a composition BeO : see Eq. [3]. The errors do not take into account any associated with the composition of the anodic film.

^c Deduced by substituting the values of Kr retention from preceding column into Eq. [1].

This is that the ordering of the electrolytes in terms of the stability of the films is 1-2-3-6-4/5. (Electrolytes 4 and 5 are equivalent.) Also, the approaches are amenable to a high degree of repeatability and are rapid.

The question of the amorphicity of the films was dealt with previously (24). The films formed with electrolyte A were amorphous in the sense that the reflection electron-diffraction pattern showed halos.

It is interesting to note that the pH's of the electrolytes in Table I range from 6 to 10, for according to the Pourbaix diagram (25) reproduced in Fig. 1 such values all lie within the "passive" region. A similar correlation is also found for other anodizable systems (26). The following electrolytes had pH's lying outside of 6-10 and all showed unacceptably high extents of metal dissolution with Be, the latter being given in the second bracket in nm: a $\text{CrO}_3\text{-HNO}_3$ mixture (29, 30) (≈ 40 nm), 1% H_2SO_4 (≈ 120 nm), 1% HNO_3 (≈ 50 nm), 1% KOH (≈ 60 nm), 0.5M Na_2CO_3 (31) (≈ 50 nm), an acetic-acid based mixture (11, 12) (≈ 60 nm), a $(\text{C}_2\text{H}_5)_2\text{SO}_4\text{-H}_2\text{SO}_4$ mixture (13) (≈ 90 nm), $(\text{C}_2\text{H}_5)_2\text{HPO}_4$ (≈ 90 nm). It is possible that Pourbaix diagrams, although normally used only in low-voltage work, may be an important guide to electrolyte choice in high-voltage applications, as here or in Ref. (26).

Feasibility of doping.—In cases such as Ag, Au, Cu, Mo, Si, V, and W, the anodic films have naturally a high chemical reactivity and are therefore easily dissolved for the purpose of anodic sectioning. In other cases, such as Hf, Nb, Ta, and Zr, the converse is true and one seeks to alter the film chemistry by incorporating ions from the electrolyte. To accomplish this it is essential either that a significant part of the film form by the outward motion of cations, or that the dopant be mobile.

Explicit information on the occurrence of incorporated ions is obtained by sputter profiling. To this end we have anodized Be for 2 min in electrolyte A and have then bombarded the specimens with 12 keV Kr^+ while measuring the secondary-photon emission from Be, S, and P. Results as in Fig. 2 and 3 were obtained. Oxygen was not detected directly but rather was inferred from the enhancement (27) of the Be signal.

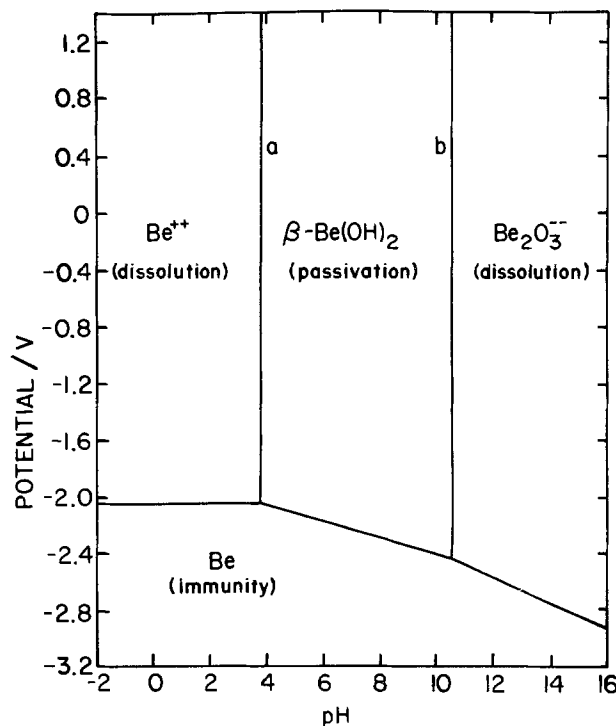


Fig. 1. Potential-pH diagram for the system beryllium-water at 25°C in simplified form after Pourbaix (25). Line a is drawn for $[\text{Be}^{2+}] = 10^{-6}\text{M}$ and line b for $[\text{Be}_2\text{O}_3^{2-}] = 10^{-6}\text{M}$.

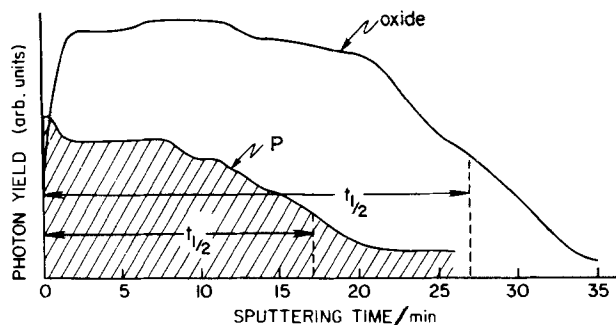


Fig. 2. Composition-depth profiles obtained by measuring secondary-photon yields for P and for Be in the anodic film. Sputtering was undertaken with $15 \mu\text{A}/\text{cm}^2$ of 12 keV Kr^+ , P was detected at $\lambda = 215 \text{ nm}$, and Be in the anodic film was inferred from the oxygen-induced enhancement of the Be signal at $\lambda = 235 \text{ nm}$.

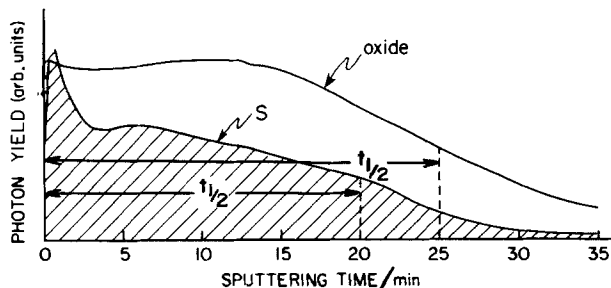


Fig. 3. Like Fig. 2 but for S, which was detected at $\lambda = 393 \text{ nm}$

It is clearly feasible to dope anodic BeO , with the films, in fact, being chemically altered throughout most of their thickness.

The ratio of the half-time, $t_{1/2}$, for S or P to that for oxide, which can be deduced although not with high precision from Fig. 2 and 3, is 0.75 ± 0.07 (total of 8 specimens). If we postulate that S and P are incorporated only at the outer surface and are subsequently immobile, it would follow that the cation transport number (the fraction of the ionic current carried by cations) is also 0.75 ± 0.07 . Given that the cation transport number for Al is 0.33-0.72, for Nb or Ta is 0.28 ± 0.03 , and for Zr or Hf is 0.05 (32, 33), Be would appear to have the highest value amongst systems presently studied. If the S and P were mobile [as with Ta_2O_5 (34)], the cation transport number would be < 0.75 . We would suggest that it is unrealistic to try to obtain transport numbers from information as in the present work owing to the problem of whether the supposed marker is mobile.

Stripping step.—The search for a solvent for an anodic film is largely empirical, though is simplified if the film is labelled with a radioactive tracer. Be specimens were accordingly implanted with $30 \text{ keV } ^{85}\text{Kr}$, anodized for 2 or 4 min with presettings of 50V and $3.0 \text{ mA}/\text{cm}^2$ in each of the six electrolytes of Table I, and exposed to a solvent. By considering the residual activity as in Fig. 4 it was found that 10% KOH had an optimum behavior provided the electrolyte contained Na_2SO_4 . Results are summarized in Table II. Other solvents considered were sulfuric acid, which attacked the metal, and solutions of Be salts, which were too slow. It had been hoped that solutions containing Be^{2+} would remove the anodic film by the formation of complex ions (35).

Since phosphate incorporation minimized the dissolution losses during anodizing and sulfate incorporation optimized the stripping behavior of already-grown films, it follows that a mixture might combine the behavior. The results were favorable (Tables I and II).

The dissolution "end point," e.g., as marked on Fig. 4, was checked from the point of view of its actual representation of complete film stripping. In one series

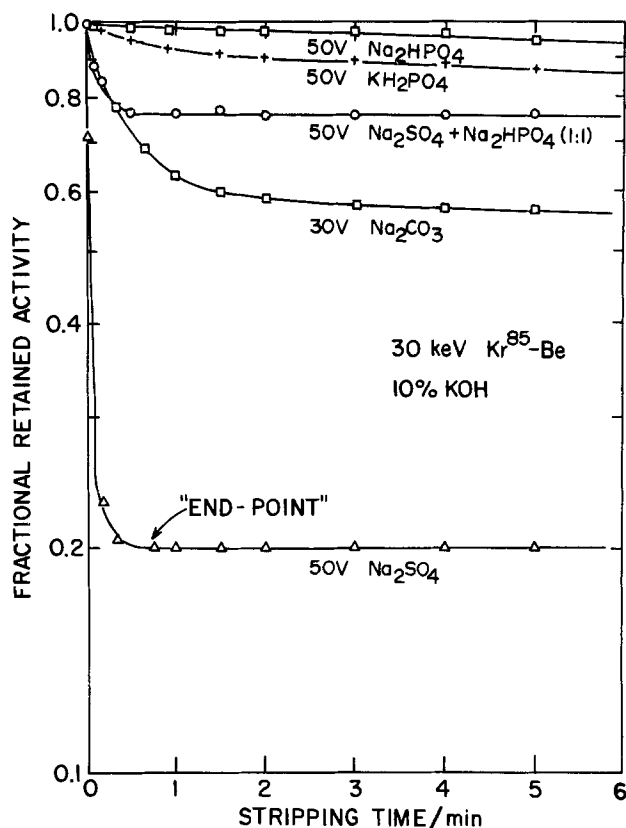


Fig. 4. Dissolution of anodic films on Be as inferred by the loss of radioactivity that was introduced prior to anodization as 2×10^{15} ions/ cm^2 of $30 \text{ keV } ^{85}\text{Kr}$. Films were formed for 2 or 4 min and with a preset current density of $3 \text{ mA}/\text{cm}^2$ at the voltages indicated in ethylene glycol saturated with the indicated compounds. Solvent: 10% KOH at $\sim 20^\circ\text{C}$.

of experiments, specimens were anodically sectioned in electrolyte A at 50V 10-12 times. There was no evidence for accumulated film and the $V-t$ curves were fully reproducible. The second check was done by noting the value of the initial voltage rise in the anodizing cell while applying a very small current density of $30 \mu\text{A}/\text{cm}^2$. The initial voltage rise always lay in the region $< 1\text{V}$, corresponding to roughly $< 2 \text{ nm}$ if one assumes the approximate relation, valid for virtually all anodizable metals, (thickness in nm) $\approx (2.0 \pm 1.0) \times V$.

Summary of anodic-sectioning procedure.—In summary, the films formed by anodizing Be for 2 min with a preset current density of $3 \text{ mA}/\text{cm}^2$ in electrolyte A at up to 50V could be completely stripped within 2 min in 10% KOH solution. Electrolyte A, consisting of a 1:1 mixture of ethylene glycol saturated with Na_2SO_4 and ethylene glycol saturated with Na_2HPO_4 , is chosen as leading to films having simultaneously

Table II. Rates of dissolution of anodic films on Be and of Be metal in aqueous KOH at $\sim 20^\circ\text{C}$. The films were formed as in Table I and the thicknesses are contingent on the film densities being $3.01 \text{ g}/\text{cm}^3$

Electrolyte (ethylene glycol saturated with indicated compound)	Solvent	Rate of anodic-film dissolution (nm/sec)	Rate of Be metal dissolution (nm/sec)
1. Na_2SO_4	10% KOH	2	0.05
2. Na_2CO_3	10% KOH	0.1	0.05
3. Na_2HPO_4	10% KOH	0.05	0.05
4. 1:1 mixture of (1) and (3) ("electrolyte A")	Sat. KOH	Very rapid	2.0
	10% KOH	1.0	0.05
	1% KOH	0.1	0.007

low dissolution losses during anodization and optimum stripping behavior of already-grown films.

Thickness Calibrations

Metal-removal thicknesses.—Two methods were employed to determine metal-removal thicknesses. For larger formation voltages (25–50V), weight-loss was used directly while for smaller voltages (10–20V) the depth-distribution method (12) served to estimate the ratio (thickness)/(thickness at 50V). In the weight-loss method Be specimens were weighed, anodized and stripped 5 to 12 times, and then reweighed. In the depth-distribution method, specimens were bombarded with 30 keV ^{85}Kr to a dose of 2×10^{15} ions/cm² and the residual radioactivities were noted after repeated sectionings at a given low voltage. For example, the residual activity in three specimens after 20 sectionings at 10V was found to be 0.16 ± 0.03 . According to a 30 keV depth-distribution curve constructed from sectionings at higher voltages (Fig. 7, to follow), this activity corresponds to a thickness removed of $9.2 \pm 0.4 \mu\text{g}/\text{cm}^2$. The metal removed in a single sectioning at 10V follows as being $0.46 \pm 0.08 \mu\text{g}/\text{cm}^2$.

Overall results, summarized in Table III and Fig. 5, can be represented to within 10% as follows

$$\begin{aligned} \text{metal-removal thickness} \\ &= -0.18 + 0.066 \times \text{volts } \mu\text{g}/\text{cm}^2 \\ &\approx -1.0 + 0.36 \times \text{volts nm} \quad [2] \end{aligned}$$

the nm form being contingent on the density of Be being $1.85 \text{ g}/\text{cm}^3$. Figure 6 compares metal-removal thicknesses for 8 systems permitting anodic sectioning.

Anodic-film thicknesses.—Anodic-film thicknesses for 20–50V were determined by weight gain, using extra large specimens having a surface area of 20 cm^2 . Thicknesses for 10–15V could, if desired, have been obtained with a modified depth-distribution method (12). The results, included in Table III and Fig. 5, can be represented to within 10% as follows

$$\begin{aligned} \text{anodic-film thickness} &= -0.7 + 0.23 \times \text{volts } \mu\text{g}/\text{cm}^2 \\ &\approx -2.3 + 0.76 \times \text{volts nm} \quad [3] \end{aligned}$$

the nm form being contingent on the density of the film being that of BeO, $3.01 \text{ g}/\text{cm}^3$. The real density would be different as the films are neither crystalline nor pure.

It will be noted that the observed film weights (solid line in Fig. 5) are greater than would be expected for pure BeO based on the metal weights (dashed line). The discrepancy is consistent with the evidence already given in the section "Feasibility of doping" for S and P incorporation and can be understood quantitatively if part of the O^{2-} in the film is replaced by (for example) SO_4^{2-} or HPO_4^{2-} to yield a stoichiometry between $\text{BeO}_{0.92}(\text{SO}_4, \text{HPO}_4)_{0.08}$ and $\text{BeO}_{0.93}(\text{SO}_4, \text{HPO}_4)_{0.07}$. Whether this incorporation arises by the literal replacement of O^{2-} to yield a

Table III. Metal-removal and anodic-film thicknesses for Be anodized in electrolyte A for 2 min with a preset current density of $3 \text{ mA}/\text{cm}^2$

Preset potential (V)	Average metal-removal thickness ($\mu\text{g}/\text{cm}^2$)	Corresponding thickness from Eq. [2] ($\mu\text{g}/\text{cm}^2$)	Average anodic-film thickness ($\mu\text{g}/\text{cm}^2$)	Corresponding thickness from Eq. [3] ($\mu\text{g}/\text{cm}^2$)
10	0.46 ± 0.08	0.48	—	—
15	0.95 ± 0.15	0.81	—	—
20	1.11 ± 0.15	1.14	3.92 ± 0.5	3.90
25	1.42 ± 0.15	1.47	5.06 ± 0.5	5.05
30	1.83 ± 0.26	1.80	6.12 ± 0.5	6.20
35	2.05 ± 0.24	2.13	6.88 ± 0.5	7.35
40	2.56 ± 0.35	2.46	8.14 ± 0.5	8.50
45	2.85 ± 0.25	2.79	10.3 ± 0.5	9.65
50	3.33 ± 0.41	3.12	10.85 ± 0.5	10.8

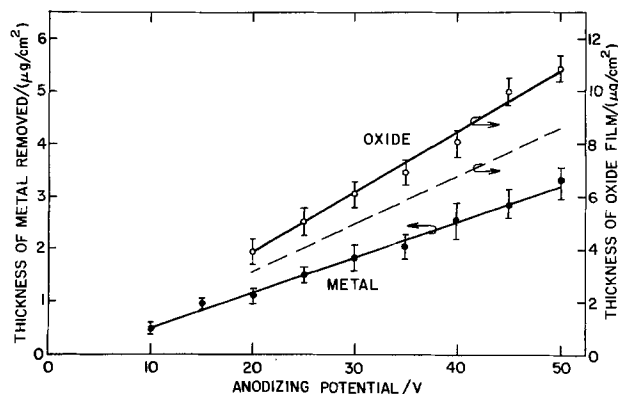


Fig. 5. Calibrations for metal-removal thicknesses (scale at left) and for anodic-film thicknesses (scale at right). The dashed line is calculated for an anodic-film consisting of pure BeO based on the metal-removal results.

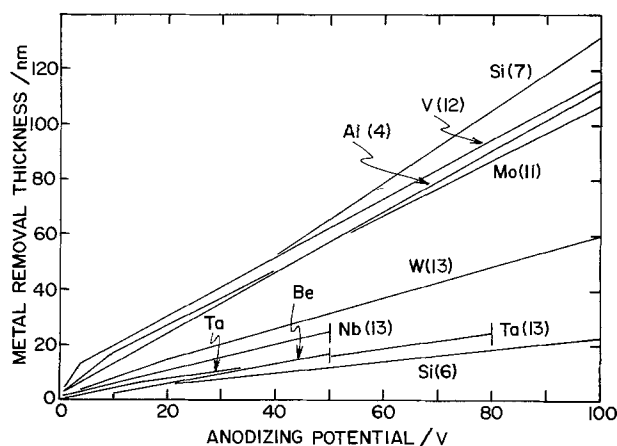


Fig. 6. Comparison of metal-removal thicknesses for 8 systems permitting anodic sectioning. The references are indicated after each symbol. The current-density presettings were as follows: Al (none), Be ($3 \text{ mA}/\text{cm}^2$), Mo, V, and W ($2 \text{ mA}/\text{cm}^2$), Nb and Ta ($5 \text{ mA}/\text{cm}^2$). Si of Ref. (6) ($6 \text{ mA}/\text{cm}^2$), Si of Ref. (7) ($19.41 \text{ mA}/\text{cm}^2$). Si of Ref. (8) was very similar to that of Ref. (6). Ag(14), Au(9), and Cu(15) are not included as the anodic films are not protective, so that the proper representation is rate of metal removal vs. current density.

phase $\text{Be}(\text{O}, \text{SO}_4, \text{HPO}_4)$, or by the physical trapping of Na_2SO_4 or Na_2HPO_4 , cannot be decided. For example, the fact that Na profiles (26) are much nearer the surface than S or P profiles (Fig. 2 and 3) conveys little information owing to the likelihood that the Na could migrate outwards (36, 37). We also see no significance in the result that the films crystallized to a product having the diffraction pattern of BeO alone (24).

Depth Distributions in Be and the Anodic Film on Be

In view of the fact that, as already pointed out, Be is the lowest mass target that can be conveniently worked with in the field of atomic collisions, a limited number of experiments were carried out to determine the integral depth distributions of implanted 5, 15, and 30 keV Kr^+ ions in Be and the anodic film on Be.

With Be, sectioning was accomplished as in the section "Summary of anodic-sectioning procedure," with an anodizing voltage of 20V for 5 keV and 50V for 30 keV. Results based on a total of 48 experimental points are shown in Fig. 7 (solid lines). The reproducibility was such that the median ranges, i.e., depths at 50% activity, could be specified to within about 10% as follows: $1.9 \mu\text{g}/\text{cm}^2$ for 5 keV and $4.7 \mu\text{g}/\text{cm}^2$ for 30 keV.

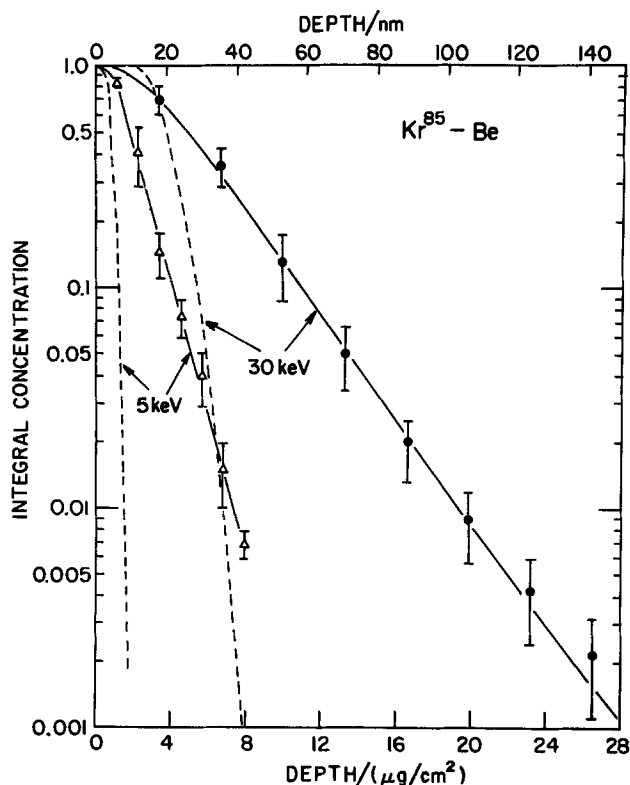


Fig. 7. Integral depth-distribution curves for 5 and 30 keV ^{85}Kr in polycrystalline Be. Dose: 2×10^{15} ions/cm 2 . The dashed lines are the theoretical curves for amorphous Be calculated using Eq. [4] with ranges appropriate to carbon.

With the anodic film on Be the equivalent of sectioning was accomplished with the transmission technique (38). This consisted of forming anodic films, implanting ^{85}Kr ions and counting the radioactivity, stripping the films, and then determining the residual activity in the metal substrate. The results are shown in Fig. 8 (solid lines), with median ranges to within 10% as follows: 1.1 $\mu\text{g}/\text{cm}^2$ for 5 keV, 2.6 $\mu\text{g}/\text{cm}^2$ for 15 keV, and 4.1 $\mu\text{g}/\text{cm}^2$ for 30 keV.

Also shown in Fig. 7 and 8 (dashed lines) are theoretical distributions constructed using an Edgeworth expansion in integral form (39) with the fourth moment ratio β_2 taken as (40)

$$\beta_2 = 3 + \frac{5}{3}\beta_1$$

where β_1 is the third-moment ratio. This expansion is as follows

$$C^{\text{int}} = \frac{1}{2} \operatorname{erfc}(\xi/2^{1/2}) - (2\pi)^{-1/2} \exp(-\xi^2/2) g(\xi) \quad [4]$$

where ξ stands for $(x - \langle x \rangle)/\Delta x$ and $g(\xi)$ stands for

$$\frac{\beta_1^{1/2}}{6} (1 - \xi^2) + \frac{\beta_1}{72} (5\xi^3 - \xi^5) + \dots$$

The various ranges and moments were assigned values appropriate to carbon (40).

The results were in all respects as expected, with Be showing the usual mixture of random and channeled stopping and the anodic film on Be showing stopping in fair agreement with theory, thence mainly random. These results constitute an independent proof that the anodic film is amorphous, the previous evidence being based on electron diffraction (24). The excessive skewness found with the anodic film, confirmed also with WO_3 (19), is possibly due to inadequacies in either the Edgeworth expansion of Eq. [4] or the Thomas-Fermi potential underlying the theoretical

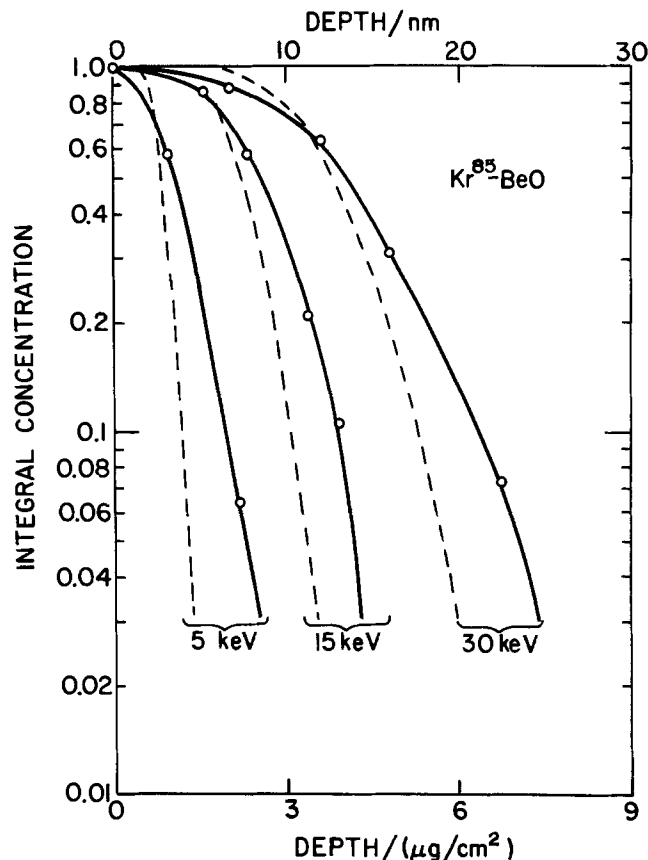


Fig. 8. Integral depth-distribution curves for 5, 15, and 30 keV ^{85}Kr in the anodic film on Be. Dose: 4×10^{14} ions/cm 2 . The dashed lines are the theoretical curves for amorphous BeO calculated using Eq. [4] with ranges appropriate to carbon.

ranges and moments. We regard it as being unlikely that it is due to experimental deficiencies.

Powers and Whaling (41) have given experimental values for the range of Kr in Be using the momentum analysis of elastically scattered protons to accomplish the profiling. Their values for incident energies of 46 to 500 keV may be extrapolated to give $4.6 \pm 0.8 \mu\text{g}/\text{cm}^2$ at 30 keV, the present value being $4.7 \pm 0.3 \mu\text{g}/\text{cm}^2$.

Summary

Electrolytes consisting of ethylene glycol saturated with inorganic salts and having a pH of 6-10 enable protective anodic films to be grown on Be at 10-50V. Those formed in the presence of phosphate showed the least dissolution during anodizing, those formed in the presence of sulfate showed (once grown) the most rapid rate of dissolution in aqueous 10% KOH, while those formed in the presence of both had the expected combined properties.

The pH range 6-10 referred to above lies within the "passive" region of the Pourbaix diagram for Be (Fig. 1). A similar correlation is also found for other anodizable systems (26), suggesting that Pourbaix diagrams may be an important guide to electrolyte choice in high-voltage applications.

Sputter profiling combined with secondary-photon measurement showed that S and P were incorporated into the outer 0.75 ± 0.07 of the anodic films. The films were thus chemically altered throughout most of their thickness, a fact which helps to explain why the composition of the electrolyte referred to above affected the dissolution properties so strongly.

The metal-removal and anodic-film thicknesses were shown to have values as given by Eq. [2] and [3]. The film "thicknesses," in reality weights, were about 20-25% higher than expected from the metal-removal thicknesses. This is understandable in view of the S and P incorporation referred to above.

Depth distributions in Be showed the expected mixture of random and channelled stopping, whereas those in the anodic film on Be were in fair agreement with theory, as if the stopping was mainly random. The latter is of interest in constituting an independent proof that the anodic film is amorphous.

The experiments undertaken here on the anodic sectioning of Be have been described in such a way as to emphasize a "logic," in so far as one exists. For example, a systematic effort was made to establish conditions under which an anodic film could be formed which was simultaneously barrier-type, stable, and amorphous. The Pourbaix diagram turned out to be a useful guide for choosing the pH. The possibility of incorporating foreign atoms into the anodic film in order to alter the film chemistry was confirmed by sputter profiling. Appropriate adjustment of the chemistry then yielded the final film, namely one which was stable enough to be grown (due to P incorporation in the case of Be) but still preserved a high reactivity towards KOH (due to S incorporation in the case of Be).

Acknowledgment

This research was supported by a grant from the National Research Council, Ottawa, Ontario, Canada.

Manuscript submitted April 16, 1979; revised manuscript received Sept. 25, 1979.

Any discussion of this paper will appear in a Discussion Section to be published in the December 1980 JOURNAL. All discussions for the December 1980 Discussion Section should be submitted by Aug. 1, 1980.

Publication costs of this article were assisted by IBM Corporation.

REFERENCES

- J. L. Whitton and H. J. Matzke, *Can. J. Phys.*, **44**, 2905 (1966).
- R. Kelly, *J. Appl. Phys.*, **39**, 5298 (1968).
- J. P. S. Pringle, *This Journal*, **119**, 482 (1972).
- J. A. Davies, J. Friesen, and J. D. McIntyre, *Can. J. Chem.*, **38**, 1526 (1960).
- M. McCargo, J. A. Davies, and F. Brown, *Can. J. Phys.*, **41**, 1231 (1963).
- J. A. Davies, G. C. Ball, F. Brown, and B. Domeij, *ibid.*, **42**, 1070 (1964).
- M. A. Wilkins, Harwell (U.K.) Report AERE R5875 (1968).
- W. Przyborski, J. Roed, J. Lippert, and L. Sarholt-Kristensen, *Radiat. Eff.*, **1**, 33 (1969).
- J. L. Whitton and J. A. Davies, *This Journal*, **111**, 1347 (1964).
- R. E. Pawel, *Rev. Sci. Instrum.*, **35**, 1066 (1964).
- M. R. Arora and R. Kelly, *This Journal*, **119**, 270 (1972).
- M. R. Arora and R. Kelly, *ibid.*, **120**, 128 (1973).
- M. R. Arora and R. Kelly, *Electrochim. Acta*, **19**, 413 (1974).
- N. Q. Lam, S. J. Rothman, and L. J. Nowicki, *This Journal*, **119**, 715 (1972).
- N. Q. Lam, S. J. Rothman, and L. J. Nowicki, *ibid.*, **119**, 1344 (1972).
- T. Andersen and G. Sørensen, *Radiat. Eff.*, **2**, 111 (1969).
- J. L. Whitton, *J. Appl. Phys.*, **36**, 3917 (1965).
- C. Jech, *Phys. Status Solidi*, **27**, 573 (1968).
- N. Q. Lam and R. Kelly, *Can. J. Phys.*, **50**, 1887 (1972).
- H. Lutz and R. Sizmann, *Z. Naturforsch. Teil A*, **19**, 1079 (1964).
- R. Kelly, *Can. J. Phys.*, **46**, 473 (1968).
- D. Gupta and R. T. C. Tsui, *Appl. Phys. Lett.*, **17**, 294 (1970).
- R. E. Pawel and T. S. Lundy, *This Journal*, **115**, 233 (1968).
- M. T. Shehata and R. Kelly, *ibid.*, **122**, 1359 (1975).
- M. Pourbaix, "Atlas of Electrochemical Equilibria in Aqueous Solutions," Nat. Assoc. Corros. Engineers, Houston, Texas (1974).
- M. T. Shehata, Ph.D. Thesis, McMaster University (1978) Chapter II.
- R. Kelly and C. B. Kerkdijk, *Surf. Sci.*, **46**, 537 (1974).
- A. N. Zaidel', V. K. Prokof'ev, S. M. Raikii, V. A. Slavnyi, and E. Ya. Shreider, "Tables of Spectral Lines," IFI/Plenum, New York (1970).
- I. S. Kerr and H. Wilman, *J. Inst. Met.*, **84**, 379 (1955-56).
- M. L. Levin, *Trans. Faraday Soc.*, **54**, 935 (1958).
- K. E. Heusler, *Ber. Bunsenges. Phys. Chem.*, **67**, 943 (1963).
- J. A. Davies, B. Domeij, J. P. S. Pringle, and F. Brown, *This Journal*, **112**, 675 (1965).
- J. P. S. Pringle, *ibid.*, **120**, 398 (1973).
- J. P. S. Pringle, *AECL, Chalk River*, to be published.
- N. V. Sidgwick, "Chemical Elements and Their Compounds," Vol. I, p. 211, Oxford, London (1951).
- W. D. Mackintosh, F. Brown, and H. H. Plattner, *This Journal*, **121**, 1281 (1974).
- D. V. McCaughan, R. A. Kushner, and V. T. Murphy, *Phys. Rev. Lett.*, **30**, 614 (1973).
- B. Domeij, F. Brown, J. A. Davies, and M. McCargo, *Can. J. Phys.*, **42**, 1624 (1964).
- I. Reid and R. Kelly, *Radiat. Eff.*, **17**, 253 (1973).
- J. F. Gibbons, W. S. Johnson, and S. W. Mylroie, "Projected Range Statistics in Semiconductors and Related Materials," 2nd ed., Dowden, Hutchinson, and Ross, Stroudsburg, Pa. (1975).
- D. Powers and W. Whaling, *Phys. Rev.*, **126**, 61 (1962).

The Behavior of Implanted Xenon When Used as a Marker during the Anodic Oxidation of Aluminum

Evidence for an Explanation of a Dose-Dependant Splitting Effect

J. P. Thomas and M. Fallavier

*Institut de Physique Nucléaire et I N2 P3,
Université Claude Bernard—Lyon I, F 69622 Villeurbanne Cedex, France*

and P. Spender and E. Francois

Société Anonyme de Traitements des Métaux et Alliages (SATMA), 38570 Goncelin, France

ABSTRACT

Using 2 MeV lithium ions backscattering and transmission electron microscopy techniques, some of the xenon atoms introduced by implantation in aluminum metal under the initial oxide layer are shown to be transported by the moving metal-oxide interface during anodic oxidation. For specific anodization conditions ($V^{\text{ct}}, T = 90^\circ\text{C}$) this splitting of the initial xenon distribution is interpreted in terms of bubble formation and growth above a given local concentration threshold. A schematic model for this behavior evolution is proposed. This dose dependence is of practical interest in the determination of transport numbers. Although unambiguously measured they may be subject to significant systematic uncertainties which are discussed.

The determination of cationic or anionic transport numbers in the anodic oxidation of metals has widely used implantation of noble gases near the surface of the material. Locating the final position of the marker after anodization and thus extracting transport numbers can be achieved either by using radio emitters (1, 2) or stable isotopes (3). The first case which is often associated with chemical sectioning has the advantage of requiring low implantation doses (typically 10^{13} atoms/cm²) while the second, which is based on Rutherford backscattering analysis (RBS), needs at least a ten times larger value. Neither in the previous work of Brown *et al.* (3) on aluminum, using RBS, nor in the investigations of Pringle (4) on tantalum, using radiotracers, has "anomalous" behavior of the implanted rare gases on anodization been reported. The final location of the marker is unambiguous whatever the transport number values may be. Most of the foregoing investigations dealt with implantation into preformed oxide layers sufficiently thick to contain all the implanted atoms. However, we have observed an anomalous behavior when xenon was implanted into samples covered with only a thin layer of oxide so that some of the Xe atoms were located in the oxide and some in the underlying metal. The amount of xenon implanted was $\sim 10^{15}$ atoms/cm², the energy was 30 keV. After anodization of such samples the distribution of the marker atoms was no longer coherent but split into two distinct agglomerations. This observation was the result of earlier investigations of the possible roles of the initial oxide layers in industrial anodization processes [V constant, high current density (200 mA/cm²) at the start of operation, $T = 90^\circ\text{C}$] (5). In these, the oxide films had been formed during metallurgical elaboration (hardening) annealing or polishing treatments. All were less than 3-4 $\mu\text{g}/\text{cm}^2$ thick.

We report here on the systematic investigations of the parameters responsible for such an unexpected behavior. In addition to the RBS analysis with 2 MeV lithium ions, transmission electron microscopy (TEM) experiments on ultramicrotomed sections have been performed for such a purpose.

Experimental Procedure

In accordance with our interest in the possible effects of the initial oxide layers on the transport, we

used refined aluminum (99.99%) in a sheet form of 90 μm thick, the nature of the oxide layers being determined by the metallurgical treatment (rolling and rough cleaning) for the hardened material or by the thermal treatment for the annealed material. In addition, a chemical polishing treatment identical to the one described by Brown *et al.* (3), has been applied to the hardened material in order to remove the initial layer and to have a more defined air-formed one. In a few cases, we also performed electropolishing of the hardened material and passivation in phosphoric acid (30 g/liter) of the annealed material. A few samples kindly supplied by Mackintosh [disk form, 0.5 mm thick, see Ref (3)] were also used. ¹³¹Xe implantations were performed with the isotope separator of the Institut de Physique Nucléaire de Lyon at various energies but most often at 30 keV and 5 keV for doses ranging from 10^{14} to 10^{16} atoms/cm². Mackintosh's samples were implanted with the isotope separator of Chalk River Nuclear Laboratories at 20 keV for 2×10^{14} and 10^{15} atoms/cm².

Following the industrial procedure of the manufacturer, the samples were anodized after implantation in the following electrolytes: adipic (ammonium adipate) at pH = 5.5, phosphoric (acid) pH = 2.7, boric (ammonium borate) pH = 4.5. The voltage was pre-set at 100V and the typical decrease of the current density was from 200 mA/cm² to 1 mA/cm² after 25 sec, 5 min being allowed for reaching a constant value of the order of 0.04 mA/cm². The temperature was kept at 90°C. For comparison purposes, several samples were treated at a constant current density of 2 mA/cm² in a saturated solution ($\sim 5\%$) of ammonium pentaborate in water at room temperature, and one other in an adipic electrolyte solution.

Rutherford backscattering has been performed with lithium ions instead of alpha particles because of the better depth resolution (about 4.5 $\mu\text{g}/\text{cm}^2$ for aluminum in aluminum oxide) achievable (6) at an incident energy of 2 MeV. Xenon relative displacement can then be followed easily over small thicknesses (typically $\sim 50 \mu\text{g}/\text{cm}^2$ in the present experiments). High yield and consequently good counting statistics can be achieved in about 20 min with the use of a specifically designed pile-up rejection system (5) associated with conventional electronics. In this manner the analyzing beam current can be adjusted for an optimum count rate.

Key words: metals, films, gas, interfaces.

The small thickness of the initial oxide layers was determined by measuring the total oxygen content of these layers with the ^{16}O (d, p) nuclear reaction at 850 keV incident energy (7). For the aluminum matrix the sensitivity of about $0.1 \mu\text{g}/\text{cm}^2$ far exceeds our requirement (the lowest measured concentration is $\sim 1 \mu\text{g}/\text{cm}^2$). One must of course assume an Al_2O_3 stoichiometry to determine the oxide thickness. In view of the shallow depth of Xe implantation (the maximum of the distribution is close to 100\AA) and the need to determine the respective distributions in the initial oxide and in the metal, a grazing angle geometry was used in RBS experiments. Practical considerations such as the roughness and flatness of the samples restricted the detection angle to 177° and the angle between the sample surface and the beam direction (tilt angle) to only 15° . The resulting spectra are shown in the Fig. 1 for two typical samples implanted at $\sim 10^{15}$ atoms/ cm^2 .

Using a technique similar to those of Bethune *et al.* (8) to obtain ultramicrotomed sections of about 1000\AA thick, TEM analysis was performed with the Philips E.M. 300 microscope of the Centre de Recherches de Voreppe (P.U.K. Company). From these measurements structure and linear thickness of the layers as well as marker agglomeration into bubbles were so investigated and confronted to the microanalysis results.

Results and Discussion

For an annealed sample implanted at a preset fluence of 10^{15} atoms/ cm^2 (later determined to be 1.3×10^{15} atoms/ cm^2) the anodization produces a splitting of the initial xenon distribution. This clearly appears in the backscattering spectra of Fig. 2 taken from an anodic layer about $50 \mu\text{g}/\text{cm}^2$ thick (adipic electrolyte - $V_{\text{ct}} = 100\text{V}$). Of course it cannot be stated which peak indicates the transport. On the other hand, no changes in thickness and stoichiometry were detectable from the spectra of the implanted and unimplanted face of the anodized foil. The various surface impurities seen are characteristic of the material and their significance have been discussed elsewhere (9).

The splitting effect cannot be attributed to sample preparation or to the analyzing procedure since most of their possible combinations lead to the same qualitative result (Table I). On the other hand it must be remembered that, as illustrated in Fig. 1, the xenon atoms are in all cases partly located in the initial oxide and partly in the metal. If the implantation is restricted to the oxide layer (*i.e.*, into a preformed oxide film such as at $40\text{V} \approx 20 \mu\text{g}/\text{cm}^2$) only the peak located near the middle of the oxide layer remains. This is in agreement with the results of Brown *et al.* (3). Moreover the xenon fraction introduced in the initial layer depends on its thickness or, for a given layer, can be increased by lowering the implantation

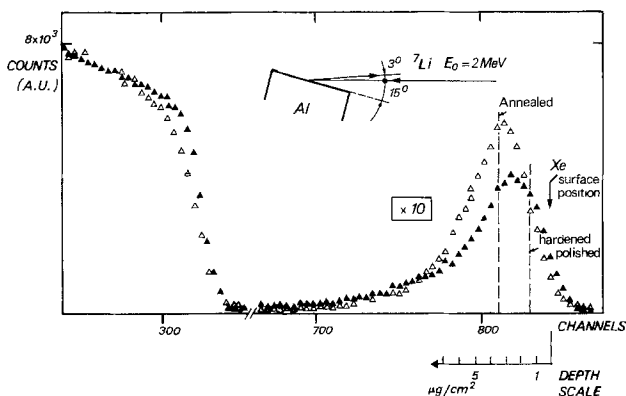


Fig. 1. Grazing angle backscattering spectrum from $\sim 10^{15}$ atoms/ cm^2 Xe atoms implanted in hardened polished $\blacktriangle\blacktriangle$ and annealed $\triangle\triangle\triangle$ samples. Respective initial oxide thicknesses are indicated.

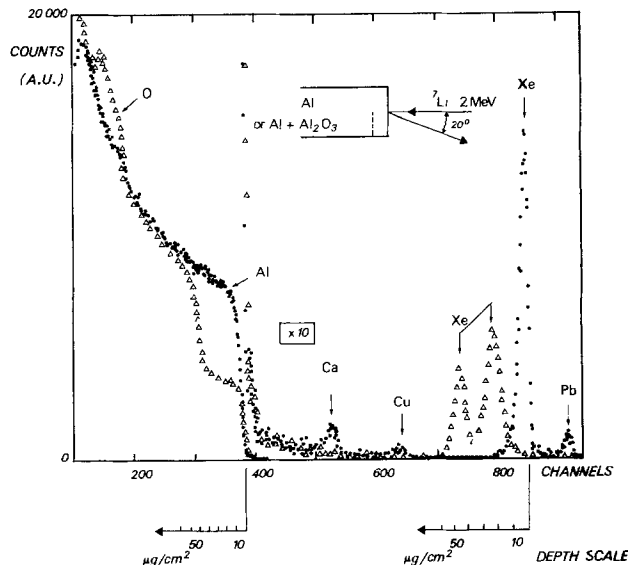


Fig. 2. Backscattering spectrum from 1.3×10^{15} atoms/ cm^2 Xe atoms implanted in annealed sample before . . . and after anodization $\triangle\triangle\triangle\triangle$.

energy (5 keV). As shown in Table I, there is a similar variation of the xenon fraction found near the middle of the anodic oxide layer. Nevertheless the agreement is only qualitative which will be explained later on.

The splitting effect is dose-dependant as evidenced in Fig. 3 which shows the evolution of the xenon peaks after anodization of the most representative samples: annealed and hardened polished. From 10^{14} to 10^{16} atoms/ cm^2 the relative value of the low energy peak increases above a given threshold up to a maximum and then decreases (Fig. 4). Such results point out a "snowplow" effect of the xenon implanted in the metal beneath the initial oxide layer by the moving metal interface during the anodization. The dose dependence can be interpreted in terms of xenon bubbles formation in a two-step process. For a given concentration in the implantation profile, the xenon atoms begin to form bubbles large enough to be trapped at the oxide metal interface and be transported by this moving interface through the defects of the polycrystalline material. When the local concentration increases a critical bubble size is reached. The largest bubbles can no longer be dragged along and are absorbed into the growing oxide layer (see sketches of Fig. 4). The fraction of xenon atoms found near the interface then

Table I. Xenon fraction found near the middle of the layer after 100V anodization. Total fluence 10^{15} atoms/ cm^2 for samples of different initial layer. Layers are obtained for V_{ct} and $T = 90^\circ\text{C}$ except for (*) where $l = C^t$ and $T = 25^\circ\text{C}$

Samples of initial layer thickness range	Implantation energy	Electrolyte			Ammonium pentaborate
		Adipic	Phosphoric	Boric	
Annealed (3.2 → 4.4 $\mu\text{g}/\text{cm}^2$)	30 keV	0.68-0.64	0.61	0.77	
	5 keV	0.87	0.82	0.87	
Hardened (2.7 → 3.5 $\mu\text{g}/\text{cm}^2$)	30 keV	0.34-0.52	0.36	0.36	
	5 keV	0.54	0.7	0.44	
Annealed Passivated (phosphoric) (1.2 → 1.6 $\mu\text{g}/\text{cm}^2$)	30 keV	0.26			
Hardened electro-polished (1.2 → 1.7 $\mu\text{g}/\text{cm}^2$)	30 keV	0.27-0.24*			0.17*
Hardened polished (1 → 1.5 $\mu\text{g}/\text{cm}^2$)	30 keV	0.22			
Polished**	20 keV	0.39			

** Samples supplied by W. D. Mackintosh, A.E.C. Ltd., Chalk River Nuclear Laboratories, Chalk River, Ont., Canada.

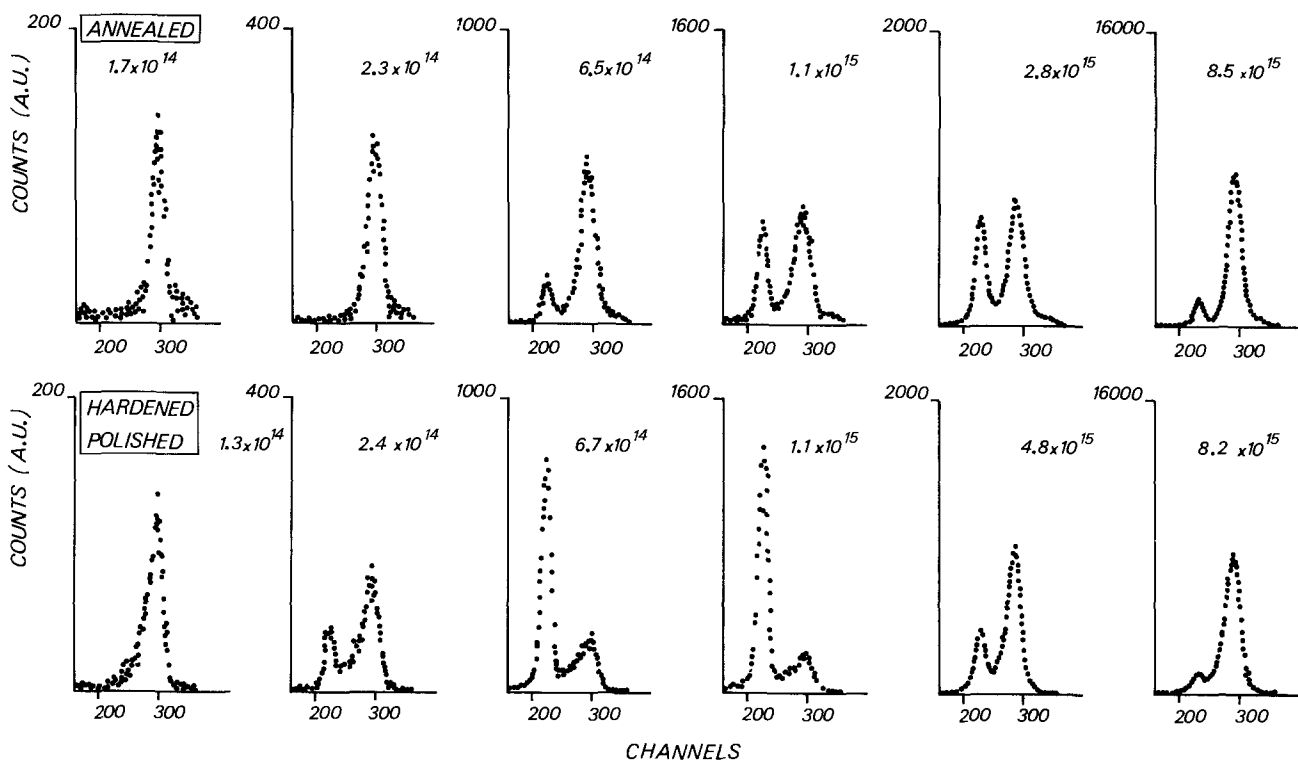


Fig. 3. Evolution of the backscattered xenon peaks after anodization of the hardened polished and annealed samples for doses from 10^{14} to 10^{16} atoms/cm².

decreases. But even at doses as high as 10^{16} atoms/cm² there still remains a large amount of transported bubbles.

Comparison of the number of transported xenon atoms with the number of implanted atoms in the metal beneath the surface layer should provide additional information. As mentioned earlier the fraction of xenon in the metal can be measured but with an uncertainty governed by the oxide thickness determination and the degree with which the interface can be defined. Even with these uncertainties the results shown in Fig. 5 point out some interesting features. First of all, for these two different samples, extrapolated thresholds are very close to each other (between 1 and 1.5×10^{14} for the hardened polished and between 1.5 and 2×10^{14} for the annealed). Next, the increase above the threshold is nearly linear with a slope close to 1 as long as the concentration does not exceed $\sim 10^{15}$ atoms/cm². Further on there is a marked deviation for the two samples which merge again at the higher doses. Thus in the first step, corresponding to the linear rise, all the newly incorporated atoms seem to contribute to the growth of the already formed bubbles more than to create new ones. When a critical size is reached the annealed material seems more

impermeable to the transport than the hardened polished one. This is consistent with the former's lower defect density.

A support for the bubble development and growth model can also be found in the evolution of the xenon peak width corresponding to the "immobile" fraction (Table II). The initial broadening of the peak which appears more clearly in the hardened polished case is due to partial drag towards the interface. When larger bubbles become incorporated into the oxide layer, the peak width decreases significantly due to the variation of the stopping power for the analyzing particles (for a given linear thickness the particles are slowed down into gaseous xenon rather than into aluminum oxide). This is in agreement with the results and interpretation of Liau and Sheng (10) who observed such effects when progressively increasing argon doses were injected into Pt Si.

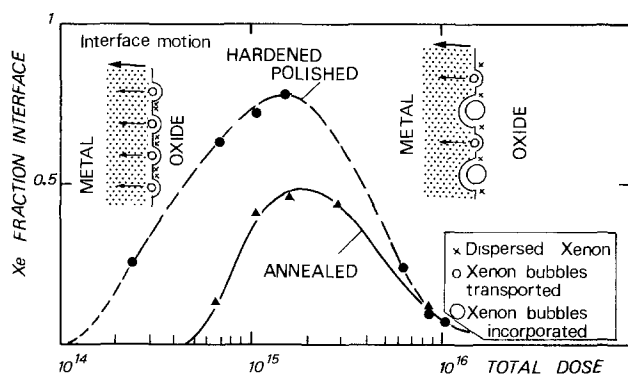


Fig. 4. Variation of the implanted xenon atoms fraction found near the interface vs. the total dose. Inserted are the sketches illustrating the two dominating effects due to the bubble growth.

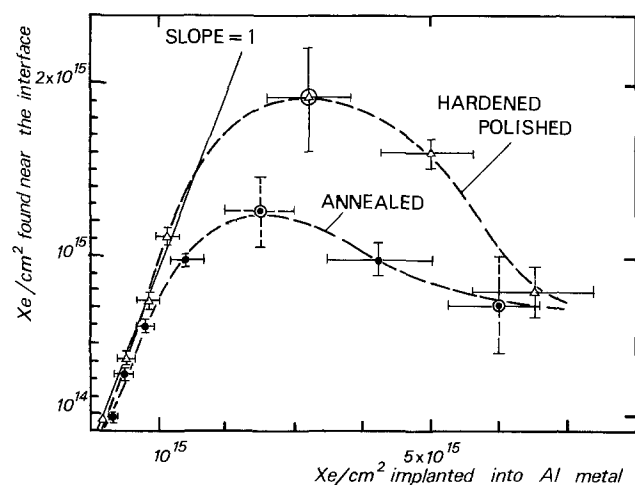


Fig. 5. Number of xenon atoms transported at the interface as a function of the number of xenon atoms implanted in the metal under the initial oxide layer. Circles points have been interpolated from Fig. 4.

Table II. Evolution of the xenon peak width (keV) corresponding to the "immobile" fraction, as a function of the initial total dose at 30 keV (atoms/cm²)

Initial dose	Hardened polished	Annealed
1.5×10^{14}	53	47
2.3×10^{14}	51	43
6.6×10^{14}	60	50
1×10^{15}	58	51
1.5×10^{15}	55	55
2.8×10^{15}		43
6.3×10^{15}	41	
8.3×10^{15}	48	43
1×10^{16}	46	

Such a general evolution must occur for all types of sample preparation but with some quantitative differences arising from the structure of the metal and the definition of the initial oxide layer (for example stoichiometry and structure). This can explain some discrepancies among the values given in Table I for samples of comparable initial oxide layer thickness. Regarding the implantation conditions and especially the energy, a significant parameter for the bubble formation is certainly the xenon distribution. This formation occurs most probably at a given depth corresponding to the maximum of the distribution profile (maximum local concentration of xenon) and, if it is

so, on both side of this maximum there still remains dispersed xenon. Accordingly, only the fraction agglomerated into bubbles will be dragged. Evidence of such a behavior is given in Fig. 6(a) and (b) for implantation at higher energy (150 and 300 keV) into annealed aluminum, showing wider distributions with maximum concentrations deeper in the metal. The interpretation of the peak deformation illustrated by the corresponding sketches is consistent with the previous picture: a large amount of xenon atoms in the metal is not transported because the local concentration is not sufficient for bubbles formation.

The experiments performed with TEM on ultramicrotomed sections were intended to visualize this bubble formation and growth. The micrograph of Fig. 7, taken from an unimplanted face of an annealed sample, clearly shows that the oxide layer is amorphous and has a very well-defined interface. The bubbles agglomeration after implantation and anodization becomes visible for a total dose of 2.8×10^{15} Xe atoms/cm², the distribution being split into $\sim 1.8 \times 10^{15}$ atoms/cm² near the middle of the layer and $\sim 10^{15}$ atoms/cm² at the interface. From Fig. 8 the maximum bubble size appears to be $\sim 30\text{\AA}$ in the central part while there is only a significant shadowing at the interface for attesting to the presence of transported material, compared to the interface of the unimplanted surface. Higher implantation doses reveal more clearly the bubble growth. For 8.5×10^{15} Xe/cm² (split into 7.5×10^{15} and 1×10^{15}), the mean bubble size appears

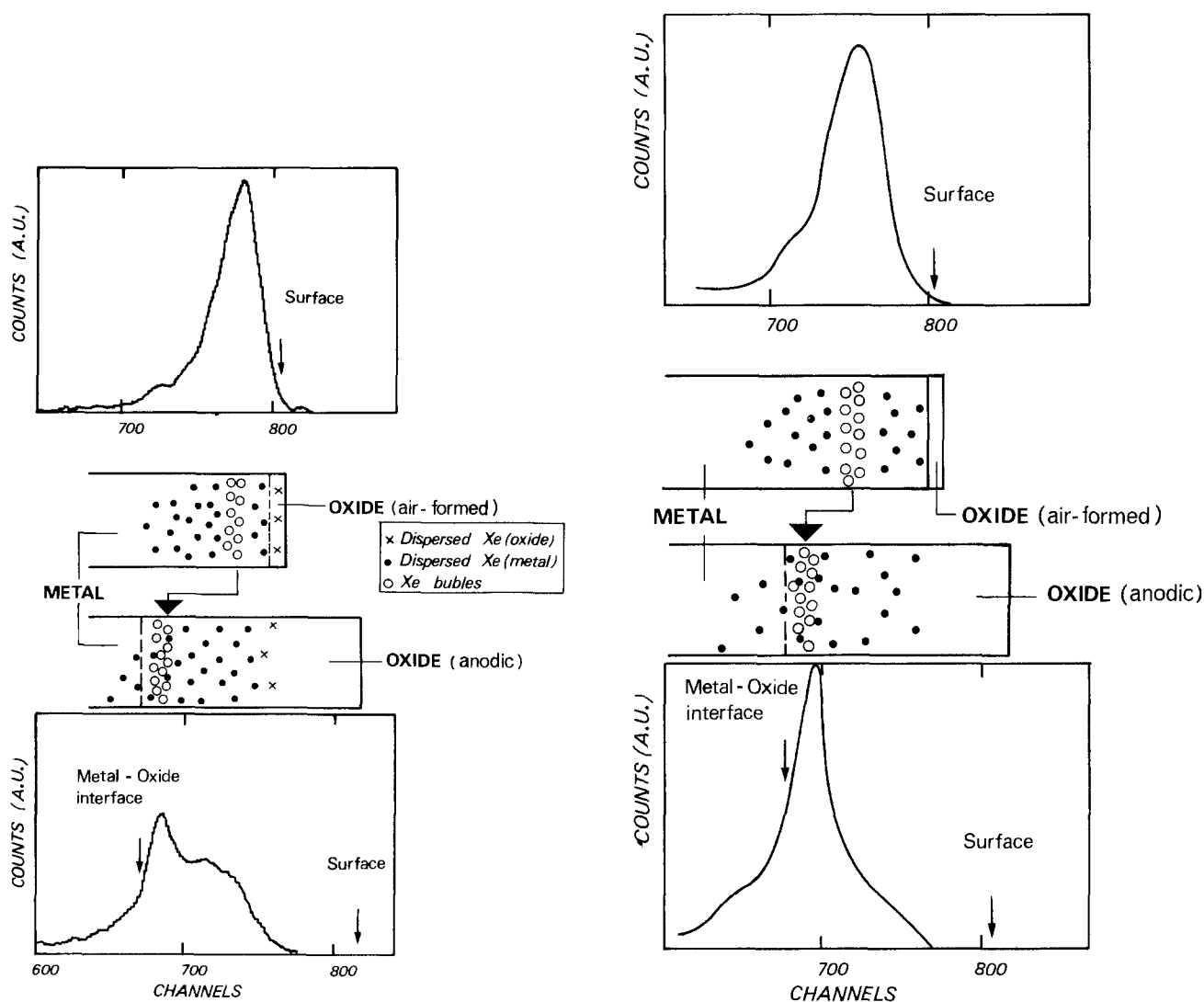


Fig. 6. Backscattered xenon peaks for a 10^{15} atoms/cm² implantation dose at 150 keV (a, left) and 300 keV (b, right) with corresponding model sketches: before (top) and after (bottom) anodization.

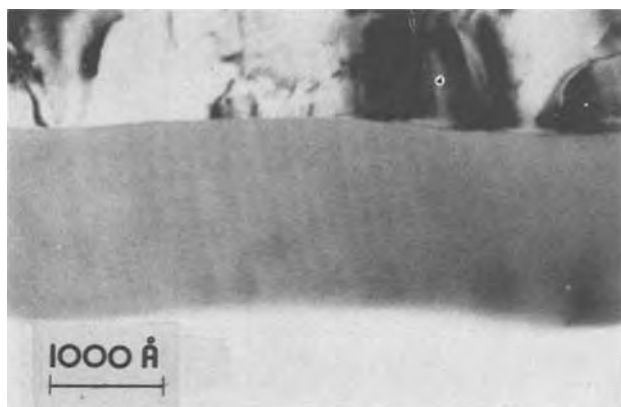


Fig. 7. Ultramicrotomed section of oxide film formed at 100V into adipic electrolyte at 90°C from annealed aluminum (unimplanted face).

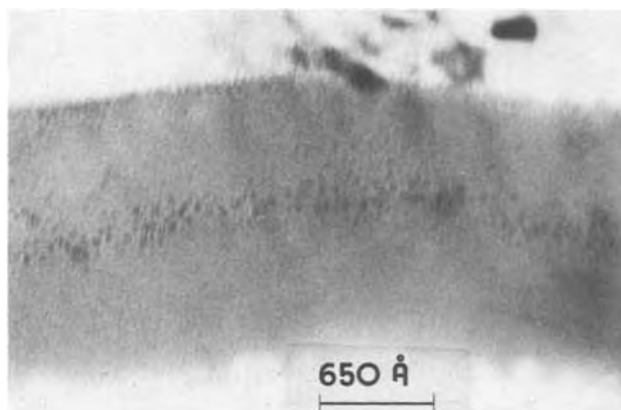


Fig. 8. Ultramicrotomed section of oxide film identically formed as in Fig. 7 but implantation performed at 2.8×10^{15} atoms/cm².

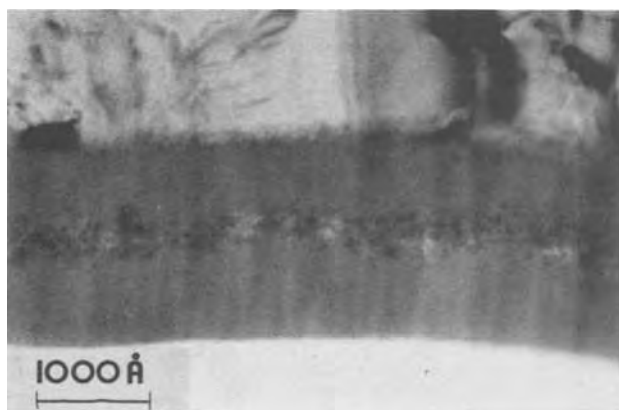


Fig. 9. Ultramicrotomed section of oxide film identically formed as in Fig. 7 but implantation performed at 1.1×10^{16} atoms/cm².

to be $\sim 50\text{Å}$ and on Fig. 9 for 1.1×10^{16} Xe/cm² (split into 9.8×10^{15} and 1.2×10^{15}) it reaches about 100Å. Near the interface, the xenon atom density remains too low for a significant determination of the bubble size, but is still sufficient for attesting, in all cases, to the bubble agglomeration. As additional information these micrographs show that the xenon does not affect the oxidation process since the thickness and the amorphous structure are identical for both implanted and unimplanted side of the foil. The visual determination of the transport number is in very good agreement with the backscattering results ($\pm 5\%$).

One important question remains concerning the confidence one can have on the value of the "right" trans-

port number t_m . We have only done at this time a systematic study for a particular electrolyte (adipic) in very specific anodization conditions (V^{ct} , $T = 90^\circ\text{C}$ see details in experimental procedure). In no case has the maximum deviation exceeded 0.05 for a mean value of 0.49. On the other hand, from the more limited experiments we performed on preanodized samples formed at constant current density in ammonium pentaborate, a significant difference is pointed out ($t_m \leq 0.4$). Such a difference has also been recently reported by Mackintosh *et al.* (11) but using only one anodizing condition. Since the broadening of the marker peak is always very large one cannot exclude a partial transport of the xenon atoms supposed immobile. The xenon part laying in the aluminum phase is the most probable suspect (5 keV implantation gives slightly lower transport numbers) but without further characterization of the initial oxide layer, its role cannot be clarified.

Conclusion

Xenon atoms implanted into aluminum samples beneath their initial oxide layer agglomerate into bubbles when a critical concentration is reached, leading to a "snowplow" effect by the moving oxide-metal interface during anodic oxidation. We found no exceptions to this general behavior for fluences of about 10^{15} atoms/cm² at typical energies of 30 keV. From a more specific study of two differently prepared materials we have pointed out a two-step mechanism by which the growing of the bubbles lead them to be first transported and finally reincorporated into the anodic layer. The first step process has been found to be not only dependant on the total number of implanted atoms into the metal but on the distribution of the species, *i.e.*, of their local concentration.

Although the agglomeration of implanted xenon atoms into bubbles has been recognized in various materials like silicon (12) and its metallic compounds (10, 13) for comparable fluences, such a splitting effect seems to be characteristic of the anodic oxidation of aluminum. Such a behavior is not observed for thermal (13) or anodic (14) oxidation of silicon and for anodic oxidation of tantalum (4). Moreover, in the last case, even higher doses (10^{16} atoms/cm²) do not induce this phenomenon.

In summary we note that partial results have been recently reported by Mackintosh *et al.* (11) confirming the general picture but with some quantitative differences. Our particular conditions may explain the more pronounced splitting effect due to the fast displacement of the moving interface at the beginning of the anodization. Finally there still remains the possibility of partial transport of the xenon atoms which are supposed to be immobile because they are found incorporated into the anodic layer. The remaining discrepancies in the transport numbers determined from implantation into preformed and nonpreformed oxide layers deserves more investigations particularly concerning the role of the initial layer in the whole process.

Acknowledgments

We are very grateful to A. Plantier for his assistance in mass separator operation, B. Payerne and L. Vidal for anodic oxidation, and all the staff of the Van de Graaff accelerators for irradiations. It is a pleasure to acknowledge the help of W. D. Mackintosh for kindly providing samples and unpublished results, and of N. Cue for critical reading of the manuscript. This work was supported by the D.G.R.S.T. (Contracts No. 777 1091 and 1092).

Manuscript submitted April 16, 1979; revised manuscript received Oct. 17, 1979.

Any discussion of this paper will appear in a Discussion Section to be published in the December 1980 JOURNAL. All discussions for the December 1980 Discussion Section should be submitted by Aug. 1, 1980.

Publication costs of this manuscript were assisted by the Université Claude Bernard.

REFERENCES

1. J. A. Davies, B. Domeij, J. P. S. Pringle, and F. Brown, *This Journal*, **112**, 675 (1965).
2. J. P. S. Pringle, *ibid.*, **120**, 398 (1973).
3. F. Brown and W. D. Mackintosh, *ibid.*, **120**, 1096 (1973).
4. J. P. S. Pringle, *ibid.*, **121**, 865 (1974).
5. M. Fallavier, Thesis, University of Lyon, France (1977).
6. J. P. Thomas, A. Cachard, M. Fallavier, J. Tardy, and S. Marsaud, in "Ion Beam Surface Layer Analysis," Vol. 1, O. Meyer, G. Linker, and F. Kappeler, Editors, p. 425 (1976).
7. G. Amsel and D. Samuel, *Anal. Chem.*, **39**, 1689 (1967).
8. B. Bethune, R. C. Furneaux, and G. C. Wood, *J. Mater. Sci.*, **12**, 1764 (1977).
9. M. Fallavier and J. P. Thomas, *Le Vide—Les Couches Minces*, **189**, 17 (1978).
10. Z. L. Llau and T. T. Sheng, *Appl. Phys. Lett.*, **32**, 716 (1978).
11. W. D. Mackintosh, F. Brown, and H. Plattner, A.E.C. Ltd., Chalk River, Progress report, (1978) (Unpublished).
12. S. Mader and K. N. Tu, *J. Vac. Sci. Technol.*, **12**, 501 (1975).
13. W. K. Chu, S. S. Lau, J. W. Mayer, H. Muller, and K. N. Tu, *Thin Solid Films*, **25**, 393 (1975).
14. W. D. Mackintosh and H. H. Plattner, *This Journal*, **124**, 396 (1977).

Studies on Electrodeposition of Nickel-Cobalt-Tungsten Alloys

V. B. Singh, L. C. Singh,¹ and P. K. Tikoo

Department of Chemistry, Banaras Hindu University, Varanasi-221005, India

ABSTRACT

Electrodeposition of nickel-cobalt-tungsten alloys containing 2-51% Ni, 18-79% Co, 5-62% W has been carried out from a citrate bath under different conditions of concentration of electrolyte, current density, pH, and temperature. Tungsten content in the deposit was found to increase with an increase in its content in the bath and also with an increase in pH, temperature, and current density. Surface morphology of the deposits was examined by scanning electron microscopy and crystal structure by x-rays. Microhardness of the deposits increased with an increase in tungsten content in the alloy.

Electrodeposition of tungsten from an aqueous bath has large commercial potentialities. There are, however, many peculiarities observed during the electrodeposition which have attracted the attention of many workers. It would appear that tungsten can only be electrolytically deposited from an aqueous electrolyte as an alloy of metals, the alloying metals being preferably the iron group metals. Electrodeposition of binary alloys of tungsten with iron group metals have been reported by many workers (1-9). The chemical composition of the deposits, their properties, and structures have been studied under different conditions by these investigators. However, work done on the electrodeposition of its ternary alloys with the iron group metals is rather limited. Therefore, it was of interest to study the electrodeposition in such systems.

Preliminary investigations on the electrodeposition of some of its ternary alloys with the iron group metals have been reported earlier (10-12). The present investigation relates to the electrodeposition of ternary nickel-cobalt-tungsten alloys under varied conditions and to some studies on the structure and hardness of the deposits obtained.

Experimental

Experimental setup and working procedures are the same as in the earlier communications (10, 13). Cylindrical platinum electrodes were employed but for qualitative studies copper cathodes were used. Each experiment was carried out in a fresh solution without agitation. The deposits were dissolved in two volumes of fuming nitric acid and one volume of hydrofluoric acid in a polyethylene beaker and evaporated to dryness for chemical analysis. The metal contents in the deposits were determined polarographically (14) using a mixture of ammonia and ammonium oxalate as supporting electrolyte.

¹ Present address: Udai Pratap Postgraduate College, Varanasi, India.

Key words: electrodeposition, cathode potential, scanning electron microscopy, x-rays, microhardness.

Microstructure of the deposits was examined on Phillips 500 scanning electron microscope, and hardness was measured on a microhardness tester (π MT-3).

Results and Discussion

The influence of different variables on composition of the deposit, cathode current efficiency (CCE), structure, and appearance of the deposits is described below.

Concentration of electrolyte.—Variation in composition of the bath by changing the concentration of electrolytes was done as per the guidelines of Brenner (15) and was carried out in three steps. When the concentration of either metal in the bath is increased, the metal content of the respective metal in the deposit also increased [Fig. 1(a), (b), (c)]. Cobalt content in the deposit was found to increase while tungsten content decreased and attained a constant value when citric acid concentration was increased [Fig. 1(d)]. The cathode current efficiency decreased when the metal percentage of tungsten in the bath was kept constant or with increasing concentration of citric acid in the bath [Fig. 1(d)], but it almost attained a constant value or increased after decreasing to some extent in the case when cobalt or nickel percentage in the bath was held constant [Fig. 1(a), (b), (c)]. When the concentration of tungsten in the bath was increased, its content in the deposit was found to be higher than in the bath particularly at low concentrations [Fig. 1(b)], but the curve for tungsten became horizontal towards the right which indicates that tungsten content approaches a limiting value in the deposit [Fig. 1(b)]. At the high tungsten end of the series the deposits tended to flake off the cathode. In most of the cases the deposits were bright and uniform when nickel was added but turned gray by cobalt additions to the bath. Hydrogen evolution was enhanced by increase in tungsten content in the bath. The tungsten content in the deposit which was higher than in the bath particularly in the low concentration range showed preferential deposition of tungsten. The variation in composition of

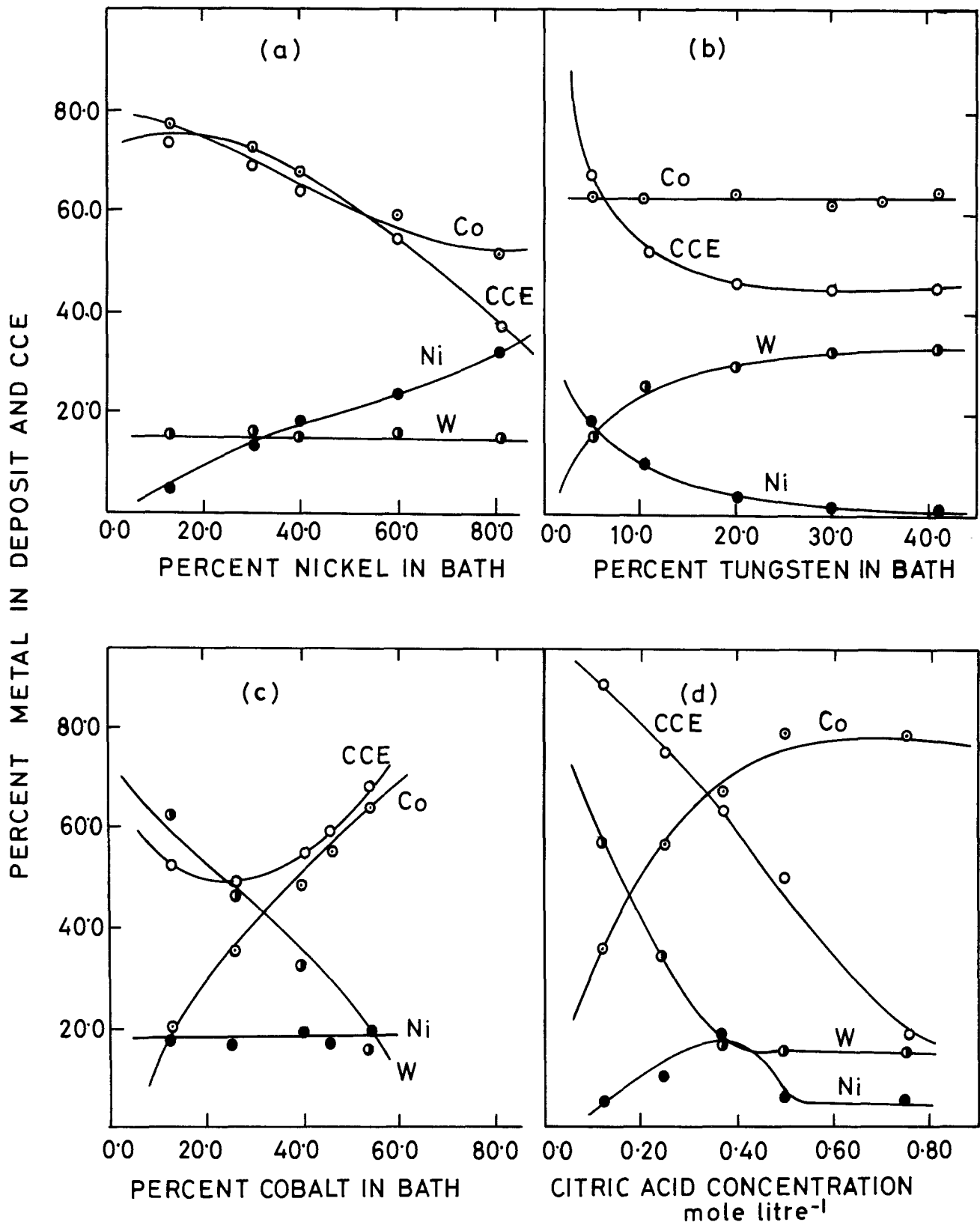


Fig. 1. Represents the effect of bath composition on CCE, and composition of the Ni-Co-W deposits when total metal content (0.2529N) and one of the metal percentages are held constant in the bath (CD 1.0 A/dm², pH 5.2, temp. 35°C). (a), When metal percentage of tungsten (5.1%) is held constant; (b), when metal percentage of cobalt (54.3%) is held constant; (c), when metal percentage of nickel (40.6%) is held constant; and (d), effect of citric acid concentration on CCE and composition of the Ni-Co-W deposit under otherwise optimum conditions.

the deposit and cathode current efficiency with electrolyte concentration is in excellent agreement with that of other workers (11, 16).

The optimum bath composition arrived at by the experiments is as follows: nickel sulfate 0.108M, cobalt sulfate 0.142M, sodium tungstate 0.0045M, citric acid 0.333M, sodium chloride 0.170M.

Current density (CD).—Using a bath of optimum composition, the influence of current density was studied between 0.2–4.0 A/dm². In the lower region of current density the deposits were dull and coarsely crystalline, but with an increase in current density up to 1.5 A/dm² fine grained, bright, and adherent deposits were obtained. As the current density was increased

beyond 1.5 A/dm², it resulted in the formation of relatively inferior deposits which were less bright, cracked, and nodular.

Tungsten content in the deposit initially decreased but increased after 1.5 A/dm². Variation in cobalt content in the deposit with respect to the current density is different from the nature of the tungsten curve. The cathode current efficiency decreased up to 2 A/dm² and became constant afterwards [Fig. 2(a)]. Such variation

in the composition of the deposit with respect to current density has also been reported by Holt *et al.* (11, 17).

pH.—The pH of the bath solution was varied from pH 2-9 and studies were made at optimum current density (1 A/dm²). Unsatisfactory deposits were obtained below pH 4 but bright and adherent deposits were obtained between pH 4.5 and 6. Deposits obtained at lower pH tended to be dull and rough and

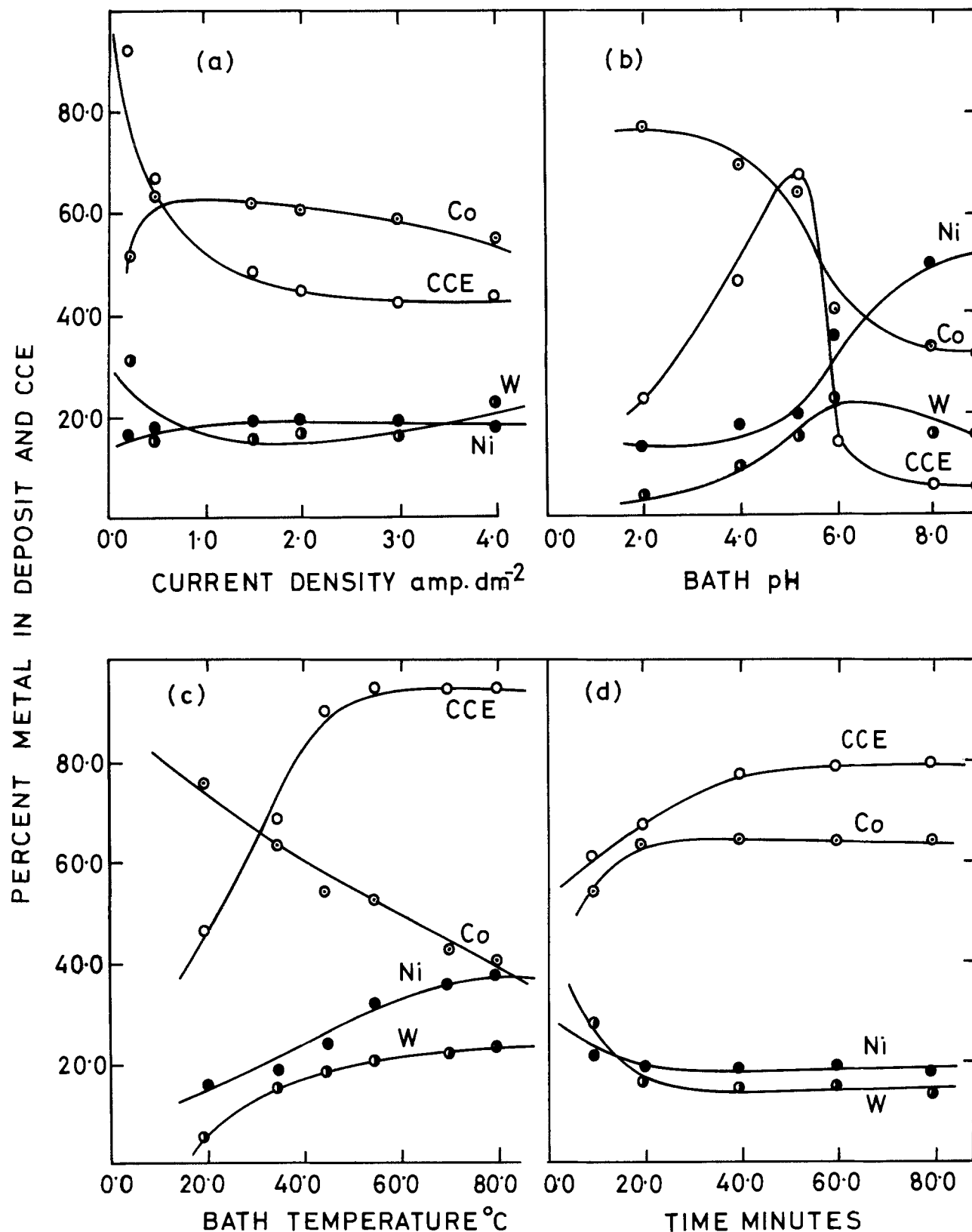


Fig. 2. (a)-(d) represent, respectively, the effect of current density, bath pH, and temperature, and duration of electrolysis on CCE and composition of Ni-Co-W electrodeposits. Bath composition and other conditions at optimum.

ultimately darkened. Tungsten and nickel content in the deposit increased with pH but above pH 6 tungsten content decreased. Cobalt content in the deposit decreased with an increase in pH of the bath. The CCE increased and then decreased after attaining a maximum value at pH 5 [Fig. 2(b)]. However, such a maximum value for tungsten content in the deposit with respect to pH is inconsistent with other findings where a regular increase in tungsten content has been observed (10, 18, 19).

Temperature.—The bath was operated between temperature range 20°–80°C under otherwise optimum conditions (at pH 5.2). Bright, fine grained, and adherent deposits were obtained up to 35°C but the deposit tended to become coarse, rough, and nonuniform beyond this temperature. Deposits at higher temperatures (>55°C) were bright but nodular and contained some dull spots on the surface. Tungsten and nickel content in the deposit increased while cobalt content decreased with an increase in the temperature of the bath. The cathode current efficiency (CCE) improved with temperature and became constant at higher temperatures [Fig. 2(c)]. Such variation in tungsten content in the deposit with respect to the temperature has also been reported by other workers during its codeposition with the iron group metals (4-6, 19-21).

This increase in tungsten content in the deposit and fair improvement in the CCE with temperature of the bath reflects that polarization factor (largely activation type) appears to be predominant.

Electrolysis was carried out (under optimum conditions and for every time in a fresh solution) for varying durations of 10-80 min. The composition of the deposit remained almost unchanged with respect to the different durations of time [Fig. 2(d)] except in the early runs. Sound deposits were obtained up to 20 min,

Table I. Effect of addition agents on metal content and CCE of Ni-Co-W electrodeposit under optimum conditions

Addition agent	Amount (g/liter)	Deposit composition (%)			CCE (%)
		Ni	Co	W	
Tetra-n-butyl ammonium iodide (TnBAI)	0.250	9.3	70.4	19.8	74.0
Tetraethylammonium iodide (TEAI)	0.250	13.9	60.1	25.1	86.2
Tetraethyl ammonium bromide (TEABr)	0.200	23.6	59.1	15.6	58.1
p-Chloraniline	0.300	12.8	65.1	21.6	40.0

but prolonged duration (>40 min) resulted in dull, nodular, and highly cracked deposits.

Some addition agents listed in Table I were separately and singly added to the bath under the optimum conditions. Except tetraethylammonium bromide, other agents used improved the deposits in respect to brightness and grain refinement. These also helped in suppressing the cracks and peeling off to some extent which are seen at higher current densities or during prolonged operation of the bath. The composition of the deposits and CCE also varied to some extent in their presence.

Cathode potential.—Current density vs. cathode potential studies for the metals and alloy (Fig. 3) show that the curve for Ni-Co-W alloy lay at a more noble potential than the curve for nickel and cobalt (curves 4, 1, 2). Curve 3 for tungsten appears due to primarily cathodic hydrogen discharge. The more noble potential for the alloy deposition may be due to the decrease in free energy that occurs in the formation of solid solution; x-ray studies confirmed the formation of solid

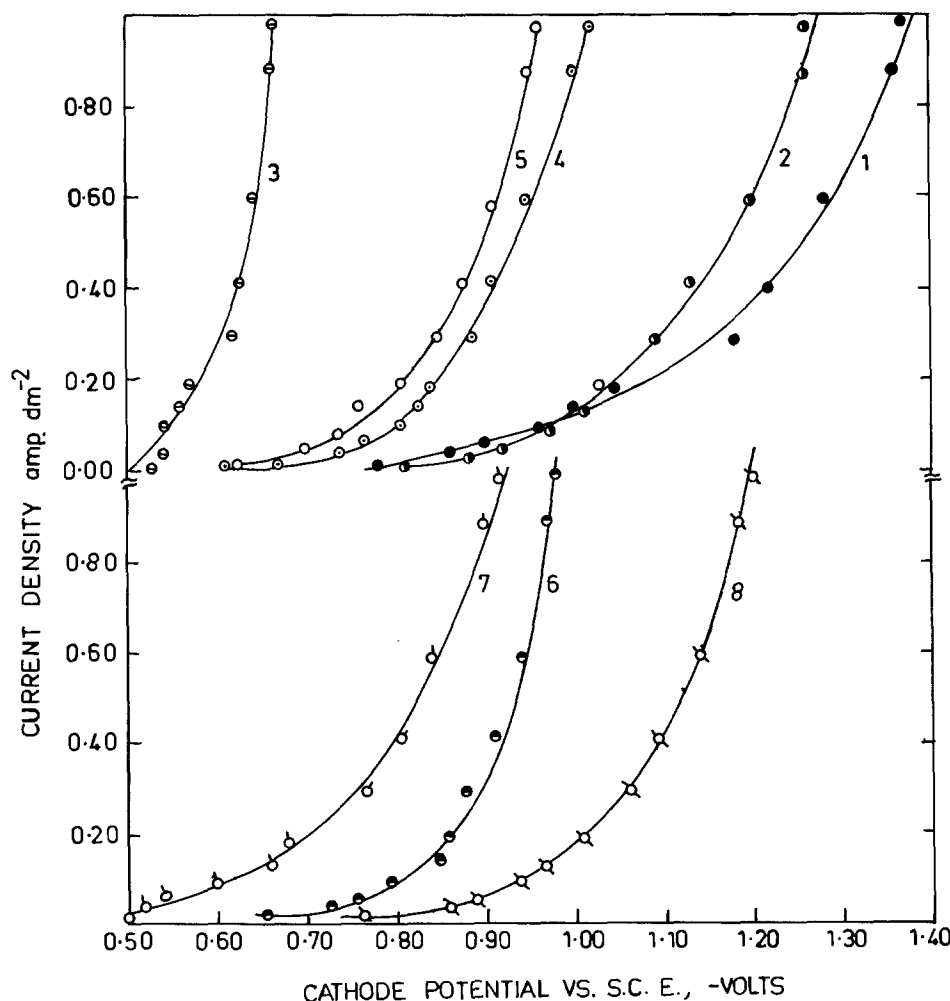


Fig. 3. Current density vs. cathode potential curves for the electrodeposition of Ni-Co-W alloy. Optimum concentration of each electrolyte and citric acid 0.333M has been taken at 35°C. Curve 1, nickel alone; curve 2, cobalt alone; curve 3, tungsten; curve 4, Ni-Co-W alloy; each at pH 5.2. Curve 5, alloy in presence of tetraethyl ammonium iodide (0.250 g/liter); curve 6, alloy in presence of tetra-n-butyl ammonium iodide (0.250 g/liter); curve 7, alloy at pH 3; curve 8, alloy at pH 7.0.

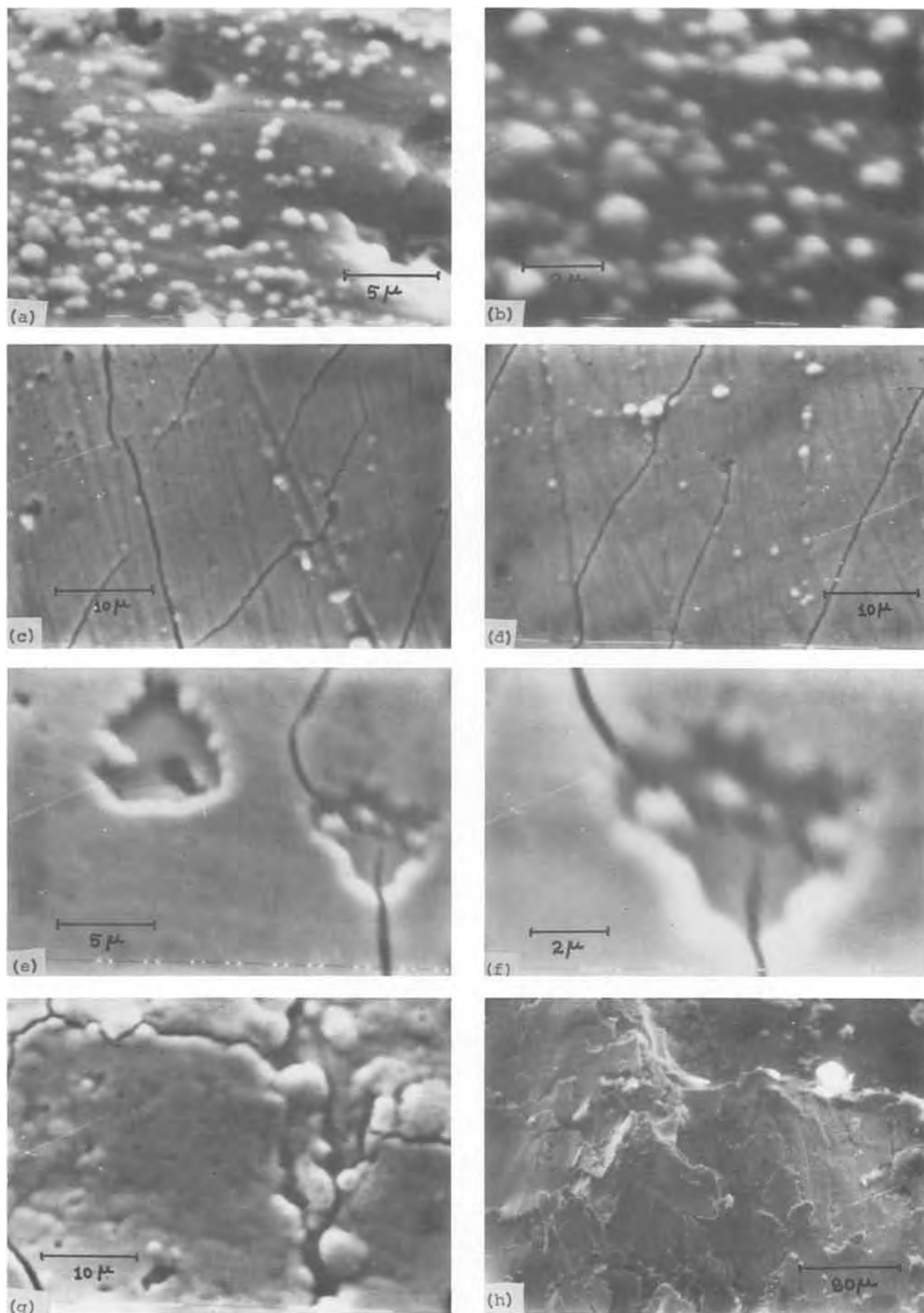


Fig. 4. Scanning electron micrograph of the Ni-Co-W deposits. Plate (a), (5000 \times); (b), (10,000 \times); (c), (2500 \times); (d), (2500 \times); (e), (5000 \times); (f), (10,000 \times); (g), (2500 \times); (h), (320 \times). Composition of the deposits of plates (a), (b), (e), (f) is 13.5% Ni, 60% Co, 26% W. Composition of plates (c), (d), (h) is 20% Ni, 62% Co, 16.5% W. Composition of plate (a) is 26% Ni, 55% Co, 18% W. Conditions of deposition are given in Table II for respective composition of alloy. Original magnification shown for each plate.

Table II. X-ray and hardness studies of the alloy as deposited on copper substrate

Sample No.	Alloy composition (%)			Lattice	Lattice parameter (Å)		Hardness (20g load) (kg/mm ²)	Conditions of deposition
	Ni	Co	W		a	c		
1	13.5	60.0	26.0	hcp	2.523	4.079	185	10.4% W in the bath, CD 2 A/dm ² , other conditions optimum
2	26.0	55.0	18.0	hcp	2.516	4.076	154	Optimum conditions, time 35 min
3	20.0	62.0	16.0	hcp	2.513	4.074	142	Optimum conditions
4	18.6	70.0	10.0	hcp	2.511	4.070	136	pH 4.0, CD 1.5 A/dm ² and other conditions optimum

solution of tungsten with the alloying metals (Table II).

Similar behavior was observed by Goltz and Kharlamov (22). The alloy curve is nearly identical in nature to the curves of pure codepositing metals, Ni and Co.

Tetraethylammonium iodide lowered the polarization of the deposition (Fig. 3, curve 5), while tetra-n butylammonium iodide increased the cathodic polarization (curve 6).

Several attempts have been made to explain the mechanism and characteristics of induced codeposition of tungsten. The hypotheses advanced by various investigators and their shortcomings have been discussed in detail by Brenner (23). It emerges from the results of the present investigation that certain trends observed during the electrodeposition of the ternary nickel-cobalt-tungsten alloys can be explained by the hypothesis of transfer of polarization (23). A large polarization of the activation type, a discharge potential in the vicinity of the equilibrium potential of the reluctant element, and ability to form solid solutions are known to be the effective factors which are mainly responsible for codeposition of the reluctant metal with other metals.

In light of the above discussions, the preferential deposition of tungsten particularly from a bath having a low concentration of tungsten, the increases in tungsten content in the deposit and cathode current efficiency with bath temperature, and the occurrence of alloys as solid solutions (Table II) well agree with the hypothesis of transfer of polarization.

Structure of the deposits.—The alloy deposits were generally bright and silvery to gray in appearance. The low tungsten content alloy deposits were bright, uniform, and adherent while those having high tungsten content contained a few cracks and nonmetallic inclusions and were noncoherent.

An inspection of the deposits by scanning electron microscope showed that deposition was uniform, though some pits and cracks on the surface were also present. The deposits were laminated but also possessed columnar structure with polyhedral grains [Fig. 4(a), (b)]. Polyhedral laminated grains were also present in ternary nickel-iron-tungsten alloys (10), but the deposits were not so adherent and satisfactory as those of nickel-cobalt-tungsten alloys. Hydrogen which evolved during the process of electrodeposition, had a marked effect on the alloy deposits. Possibly it initiated the cracks on the surface which propagated parallel to the surface. Sometimes these cracks initiated from the pits and sometimes terminated at the pits [Fig. 4(c), (d)]. The hydrogen bubbles which might get entrapped in the pits or holes may enlarge them and form a cavity through which the gas diffuses giving rise to multiple minor cracks [Fig. 4(e), (f)]. Such diffusion of hydrogen results in poor internal strength of the deposits leading to embrittlement. Highly cracked and poorly adherent deposits, shown in Fig. 4(g) obtained at high current densities or on prolonged operation of the bath, appear to be due to the adsorbed hydrogen which has caused stress in the deposit. The deposition appears to be in layer form. The alloy coating was examined after bending it and then bringing to the original state; it

was still adherent to the base metal but cleavage facets were seen in the ruptured part of the coating [Fig. 4(h)].

X-ray diffraction studies of the deposits (in as-deposited conditions) containing up to 25% of tungsten showed that the alloy deposits were single phase with expanded lattice of cobalt only (hcp), Table II. Electrodeposited binary alloys of tungsten with the iron group metals (4, 18, 24) have been reported to form solid solutions containing up to 40% of tungsten and the lattice was similar to the codepositing metal but with some expansion.

Microhardness of the deposit was measured at 20g load, the line of application of the load was perpendicular to the surface. The hardness of the deposit was found to increase with tungsten content in the deposit (Table II).

Conclusions

Ternary alloys of nickel-cobalt-tungsten of wide composition range were electrodeposited successfully from a citrate bath. The alloy deposits were sound and satisfactory under most conditions. An explanation has been offered for the various trends observed during the investigation, in light of transfer of polarization hypothesis.

Acknowledgments

Sincere thanks are due to the late Dr. D. Singh, Reader in Chemistry, B.H.U. for suggestions and to Professor B. M. Shukla, Head of the Chemistry Department, Banaras Hindu University for providing necessary facilities.

Manuscript submitted Jan. 23, 1979; revised manuscript received Sept. 4, 1979.

Any discussion of this paper will appear in a Discussion Section to be published in the December 1980 JOURNAL. All discussions for the December 1980 Discussion Section should be submitted by Aug. 1, 1980.

REFERENCES

1. M. L. Holt and L. E. Vaaler, *This Journal*, **94**, 50 (1948).
2. W. E. Clark and M. L. Holt, *ibid.*, **94**, 244 (1948).
3. M. H. Lietzke and M. L. Holt, *ibid.*, **94**, 252 (1948).
4. A. Brenner, P. Burkhead, and E. Seegmiller, *J. Res. Nat. Bur. Stand.*, **29**, 351 (1947).
5. M. L. Holt and R. E. Black, *Trans. Electrochem. Soc.*, **82**, 205 (1942).
6. A. I. Zayats and T. F. Frantsevich-Zabludovskaya, *Ukr. Khim. Zh.*, **24**, 585 (1958).
7. M. Munteanu, A. Schiff, and C. Mareu, *Chem. Abstr.*, **74**, 8917c (1971).
8. G. A. Volyanyuk and R. Kh. Valeeva, *Prom. Obraztsy, Tovarnye Znaki*, **52** (1), 68 (1975); *Chem. Abstr.*, **82**, 177230u (1975).
9. A. N. Yagubets and U. N. Sherstkina, *Elektron. Obrab. Mater.*, **5**, 31 (1975); *Chem. Abstr.*, **82**, 117764m (1975).
10. V. B. Singh, *Surf. Technol.*, **7**, 443 (1978).
11. P. F. Hoglund and M. L. Holt, *Trans. Electrochem. Soc.*, **88**, 359 (1945).
12. M. Sarojamma and T. L. Ramachar, *Met. Finish.*, **7**, 188 (1961).
13. V. B. Singh and P. K. Tikoo, *Electrochim. Acta*, **22**, 1201 (1977); *J. Appl. Electrochem.*, **8**, 41 (1978).
14. L. Meites, "Polarographic Techniques," 2nd ed., p.

- 623, Wiley Interscience, New York (1965).
15. A. Brenner, "Electrodeposition of Alloys," Vol. I, p. 112, Academic Press, New York (1963).
 16. H. J. Seim and M. L. Holt, *Trans. Electrochem. Soc.*, **96**, 205 (1949).
 17. M. L. Holt, *ibid.*, **71**, 301 (1937).
 18. T. P. Hoar and I. A. Bucklow, *Trans. Inst. Met. Finish.*, **32**, 186 (1955).
 19. T. Shimizu and H. Shiio, *Kinzoku Hyomen Gijutsu*, **20**, 101 (1969).
 20. D. W. Ernst, R. F. Amlie, and M. L. Holt, *This Journal*, **102**, 461 (1955).
 21. T. F. Frantsevich-Zabludovskaya, and A. I. Zayats, *Zh. Prikl. Khim.*, **31**, 234 (1958).
 22. L. N. Golt'z and V. N. Kharlamov, *ibid.*, **9**, 640 (1936).
 23. A. Brenner, "Electrodeposition of Alloys," Vol. II, p. 406, Academic Press, New York (1963).
 24. H. Offermanns and M. V. Stackelberg, *Metalloberfläche*, **1**, 142 (1947).

Preparation and Properties of Bismuth Ruthenate Thin Film Electrodes for Chlorine Evolution

P. F. Carcia,* R. B. Flippen, and P. E. Bierstedt

*E. I. du Pont de Nemours and Company,
Central Research and Development Department, Wilmington, Delaware 19898*

ABSTRACT

We have prepared thin film electrodes in a compositional range about $\text{Bi}_2\text{O}_3 \cdot 2\text{RuO}_2$ by rf sputtering directly onto heated titanium substrates. Specifically we prepared $\text{Bi}_2\text{Ru}_2\text{O}_7$ with the pyrochlore structure, $\text{Bi}_3\text{Ru}_3\text{O}_{11}$, and non-crystalline bismuth ruthenate films. The resistivity of all films at 300°K was $<10^{-2}$ Ω -cm. Electrochemical measurements on well-characterized anodes of $\text{Bi}_2\text{Ru}_2\text{O}_7$, and $\text{Bi}_3\text{Ru}_3\text{O}_{11}$ show high activity for chlorine evolution. Examination of the stability of the $\text{Bi}_2\text{Ru}_2\text{O}_7$ electrode shows that some Bi is lost from the surface.

The use of RuO_2 anodes in Cl_2 production is one of the most significant achievements of electrocatalysis. The energy savings to that industry is estimated at several billion kW-hr/yr (1). Appropriately, a number of papers (2-10) have examined the preparation and electrochemical properties of these electrodes. Therefore, the investigation of other Ru oxides as Cl_2 anodes is of great practical interest.

In this paper, we describe the preparation and electrochemical properties of conducting oxides in the compositional range about $\text{Bi}_2\text{O}_3 \cdot \text{RuO}_2$. We prepared electrodes as thin film coatings on heated Ti substrates by rf sputtering (11). Well-characterized electrodes were tested as anodes for Cl_2 evolution from brine. Several had high electrocatalytic activity.

Experimental

Thin films were prepared by rf sputtering in a commercial system (Materials Research Corporation, Model SEM-8620). The target was a 2 in. diam ($\sim 3/4$ in. thick) disk of $\text{Bi}_2\text{Ru}_2\text{O}_7$, fabricated by solid-state sintering of the constituent oxides at 950°C in air overnight.

Substrates were ceramic Al_2O_3 (Alsimag 614, 3M Company) and Ti sheet (Ti-50A obtained from Timet Corporation), degreased and cleaned by standard vacuum cleaning techniques. These substrates could be heated to $\sim 1000^\circ\text{C}$ in the vacuum chamber during deposition. The elevated temperatures were achieved by electrically heating a supporting tungsten ribbon. Temperatures were measured by a Chromel-Alumel thermocouple clamped to the ribbon underside. These are the "substrate temperatures" reported in this paper, and no correction is attempted for actual substrate surface temperature which may differ by as much as 150°C (12).

The sputtering atmosphere was usually 10^{-2} Torr of Ar and 10^{-3} Torr O_2 , established after initial pump-down of the chamber to $\sim 10^{-6}$ Torr. In some experi-

ments the Ar was gettered by passing it over heated Zr and Ti metal filings.

The thin films were routinely characterized by x-ray diffraction. Some were also examined by scanning electron microscopy (SEM) and analyzed for relative chemical composition and valence state by x-ray photoelectron spectroscopy (XPS). Electrical resistivity measurements were made by the standard four-probe method.

Electrochemical measurements were made in a three-compartment glass cell. The cathode (~ 20 cm²) was a Pt screen. The cathode compartment was separated from the main anode reservoir by a fine glass frit or a Nafion® perfluorosulfonic acid membrane. The electrolyte was an aqueous solution of 20 weight percent (w/o) Fisher reagent grade NaCl. The pH remained in the range 3-4 during experiments of several hours duration. All electrode potentials were measured vs. saturated calomel (SCE), at a distance of 2 mm from the electrode surface by a fine capillary tube filled with electrolyte. The entire cell was heated on a standard laboratory hot plate. Temperature control was typically $\pm 3^\circ\text{C}$, determined by measuring temperature before and after an experiment.

The bismuth ruthenate-coated Ti anodes were contacted electrically to a brass screw with silver paste (Dupont 4922). A Cu wire threaded through a glass sleeve was soldered to the screw and the entire configuration potted with a fast-drying epoxy (Adhesive A-36, Armstrong Products Company). Only the bismuth ruthenate surface was exposed to the electrolyte.

Electrochemical measurements were made with a Princeton Applied Research Model 173 Potentiostat/Galvanostat. This unit could be programmed with triangular or pulse waveforms from a PAR Model 175 Universal Programmer. Current densities quoted in this paper were obtained by dividing the measured current by the geometric area of the Ti substrate (typically ~ 1 cm²).

Results and Discussion

Thin films.— Table I summarizes preparation conditions and cubic cell dimensions for bismuth ruthen-

* Electrochemical Society Active Member.

Key words: chloralkali anodes, thin film, pyrochlore, electrodes, electrocatalysis.

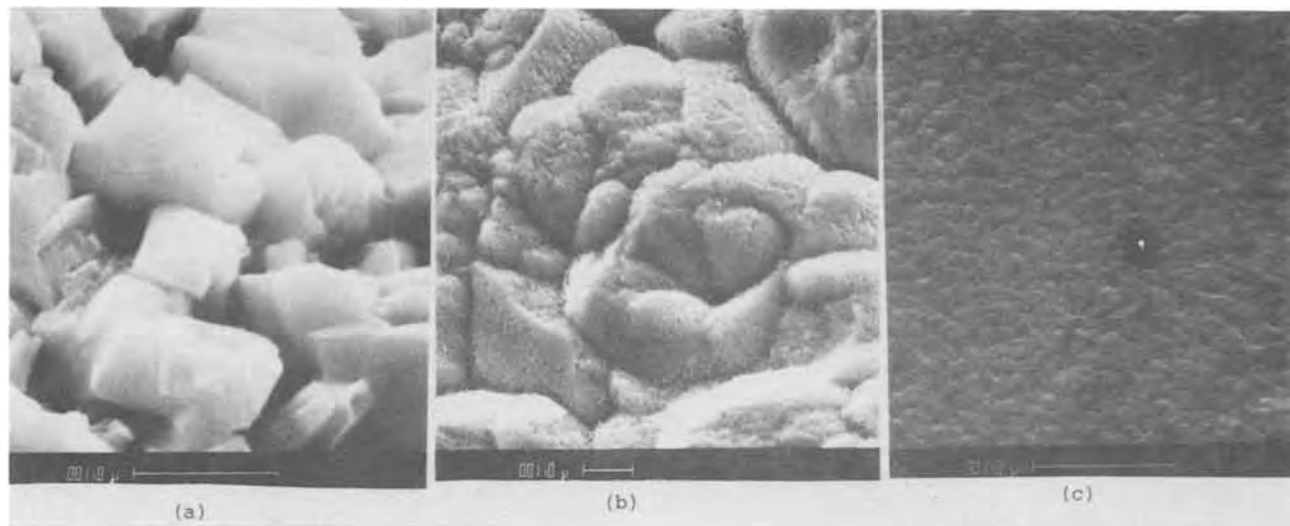


Fig. 1. Scanning electron micrographs of (a) $\text{Bi}_2\text{Ru}_2\text{O}_7$, (b) $\text{Bi}_3\text{Ru}_3\text{O}_{11}$, and (c) amorphous thin films. Scale is $1\ \mu\text{m}$

ate thin films. Films sputtered onto unheated substrates are amorphous to x-rays. At a substrate temperature (T_s) $\sim 725^\circ\text{C}$, the pyrochlore-type $\text{Bi}_2\text{Ru}_2\text{O}_7$ (13) is formed. The KSbO_3 -related $\text{Bi}_3\text{Ru}_3\text{O}_{11}$ (14) crystallizes at $T_s \sim 525^\circ\text{C}$. It could also be prepared by annealing amorphous films on Al_2O_3 substrates in air at $\sim 550^\circ\text{C}$. Film thicknesses were $1\text{--}4\ \mu\text{m}$.

For the pyrochlore-type films on Ti substrates the lattice parameter ranges from 10.35 to $10.43\ \text{\AA}$, or 0.5% to 1.0% larger than air-fired polycrystalline $\text{Bi}_2\text{Ru}_2\text{O}_7$ (13), $a_o = 10.294\ \text{\AA}$. Some of this difference ($\sim 0.5\%$) may be accounted for by differential thermal expansion of the Ti ($\alpha \sim 8 \times 10^{-6}^\circ\text{C}^{-1}$) substrate and the $\text{Bi}_2\text{Ru}_2\text{O}_7$ thin films ($\alpha \sim 11\text{--}12 \times 10^{-6}^\circ\text{C}^{-1}$), putting the film in tension. In fact, the thin film with the smallest measured lattice was slowly cooled to 25°C over two hours to minimize thermal strain.

Another possible explanation for the large lattice parameter is that the pyrochlore-type structure (13) can exist over a wide range of composition and stoichiometry. If one-third of the Ru^{4+} ions are substituted by larger Ru^{3+} ions, the new lattice is calculated to be larger by $\sim 1\%$ (15), i.e., for $\text{Bi}_2^{3+}\text{Ru}_2^{4+}\text{O}_7$, $a_o = 10.30\ \text{\AA}$ and for $\text{Bi}_2^{3+}\text{Ru}_{1.33}^{4+}\text{Ru}_{0.67}^{3+}\text{O}_{6.67}$, $a_o \sim 10.40\ \text{\AA}$. This is reasonable, since the films are prepared in a low O_2 partial pressure. It is also consistent with the observation that the lattice parameter contracts after the film is tested electrochemically under oxidizing conditions as an anode for chlorine evolution.

We characterized surface chemical composition and valence states of one $\text{Bi}_2\text{Ru}_2\text{O}_7$ electrode by XPS. The valence states of the metallic elements were Bi^{3+} and Ru^{4+} . The Ru $3p_{1/2}$ photoelectron peak was used for ruthenium and the Bi $4f_{7/2}$ peak was used for bismuth. The charge corrected binding energies, referenced to the O $1s$ peak, were $160.8\ \text{eV}$ for Bi and $488.4\ \text{eV}$ for Ru. The O/Ru ratio was 3.6 , close to the ideal 3.5 for pyrochlore. We concluded, therefore, that at the surface, the chemical composition of this thin film was close to $\text{Bi}_2^{3+}\text{Ru}_2^{4+}\text{O}_7$.

Table I

Film No.	Substrate temperature T_s ($^\circ\text{C}$)	Gas pressures ($\times 10^{-3}$ Torr)		Phase	Lattice parameter a_o (\AA)
		P_{O_2}	P_{Ar}		
-75	725	1	10	$\text{Bi}_2\text{Ru}_2\text{O}_7$	10.36
-86	525	0.5	10	$\text{Bi}_3\text{Ru}_3\text{O}_{11}$	9.45
-89	725	1	10	$\text{Bi}_2\text{Ru}_2\text{O}_7$	10.43
-15	725	1	10	$\text{Bi}_2\text{Ru}_2\text{O}_7$	10.35
-17	550 (Annealed)	0.5	10	$\text{Bi}_3\text{Ru}_3\text{O}_{11}$	9.31
-87	725	1	10	$\text{Bi}_2\text{Ru}_2\text{O}_7$	10.40
-66	15	1	10	Amorphous	

The lattice parameter for thin films of $\text{Bi}_3\text{Ru}_3\text{O}_{11}$, prepared in the sputtering chamber, is also large, $a_o = 9.45\ \text{\AA}$ compared to the air-fired polycrystalline value, $a_o = 9.30\ \text{\AA}$ (14). However, when this phase was prepared by annealing amorphous thin films in air at $T = 550^\circ\text{--}600^\circ\text{C}$ for 15 to 30 min the lattice parameter was $9.31\ \text{\AA}$. Again, by analogy with the pyrochlore-related bismuth ruthenate films, annealing may relieve strain or decrease an oxygen deficiency.

In Fig. 1 the surface morphologies of $\text{Bi}_3\text{Ru}_3\text{O}_{11}$, $\text{Bi}_2\text{Ru}_2\text{O}_7$, and amorphous thin films are contrasted by SEM. The $\text{Bi}_2\text{Ru}_2\text{O}_7$ surface has sharp, angular crystalline features resembling the octahedral habit of mm-size crystals of $\text{Bi}_2\text{Ru}_2\text{O}_7$ grown in this laboratory. Amorphous and $\text{Bi}_3\text{Ru}_3\text{O}_{11}$ films are less distinctive. $\text{Bi}_3\text{Ru}_3\text{O}_{11}$ films have large ($>1\ \mu\text{m}$) textured grains with a variety of shapes. The amorphous film has a "pebbled" structure with very fine $0.1\text{--}0.2\ \mu\text{m}$ grains. The electrical resistivity of all films at 300°K was $<10^{-2}\ \Omega\text{-cm}$.

Electrochemical properties.—Figures 2 and 3 show equilibrium current density for Cl_2 evolution vs. potential for $\text{Bi}_2\text{Ru}_2\text{O}_7$ and $\text{Bi}_3\text{Ru}_3\text{O}_{11}$ thin film electrodes. Figure 4 shows the polarization behavior of a $\text{Bi}_2\text{Ru}_2\text{O}_7$ electrode obtained by sweeping potential at $20\ \text{mV/sec}$ between 0.7 to $1.2\ \text{V/SCE}$. At 23°C , the current density is $2\ \text{mA/cm}^2$ at $1.10\ \text{V/SCE}$, the same for both electrodes. Above 80°C , this current density increases to nearly $100\ \text{mA/cm}^2$ on a $\text{Bi}_2\text{Ru}_2\text{O}_7$ electrode. This corresponds to an apparent overpotential [measured from the equilibrium potential (16), $E_o = 1.0285\ \text{V/SCE}$] of only $75\ \text{mV}$, an activity comparable to that for $\text{RuO}_2/\text{TiO}_2$ coated Ti anodes (2). The $\text{Bi}_2\text{Ru}_2\text{O}_7$ and $\text{Bi}_3\text{Ru}_3\text{O}_{11}$ thin films are excellent electrocatalysts for

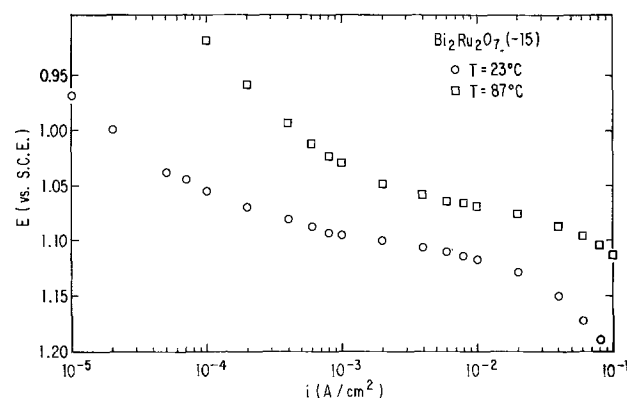


Fig. 2. Anodic polarization behavior of $\text{Bi}_2\text{Ru}_2\text{O}_7$ thin film in $20\ \text{w/o NaCl}$ solution.

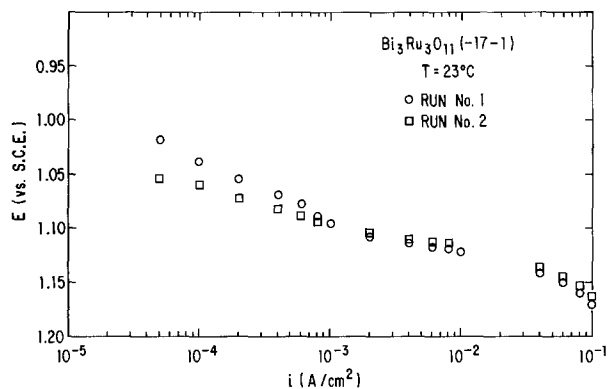


Fig. 3. Anodic polarization behavior of $\text{Bi}_3\text{Ru}_3\text{O}_{11}$ thin film in 20 w/o NaCl solution.

Cl_2 evolution. Of course, as for RuO_2 electrodes, the surface roughness of the bismuth ruthenate electrodes also likely contributes to their low overpotential.

From the linear portion of the $E/\log i$ polarization characteristics (between 10^{-2} and 10^{-3} A/cm^2) in Fig. 2 and 3, we estimate a slope of 30 mV/decade. This is different from the 40 mV/decade Tafel slope (2, 3) observed for $\text{RuO}_2/\text{TiO}_2$ electrodes, perhaps suggesting a different rate-determining step for chlorine evolution on bismuth ruthenate electrodes. However, further detailed investigation is needed to confirm this.

In addition to determining electrocatalytic activity, we have examined the corrosion resistance of a $\text{Bi}_2\text{Ru}_2\text{O}_7$ electrode. Our tests monitored the change in electrode potential vs. the time of Cl_2 evolution. Subsequently, we characterized the electrode by SEM, XPS, and x-ray diffraction.

Only a 1% change in potential ($E = 1.10$ V/SCE) occurred in 6 hr for a $\text{Bi}_2\text{Ru}_2\text{O}_7$ electrode evolving Cl_2 at 90 mA/cm^2 in an aqueous NaCl solution at 85°C . (Much larger changes did occur on $\text{Bi}_3\text{Ru}_3\text{O}_{11}$ and amorphous electrodes.) Scanning electron micrographs in Fig. 5 contrast the surface before and after Cl_2 evolution. The original angular, crystalline features have been replaced by an abraded, less dense surface. Much of the change in morphology is probably caused

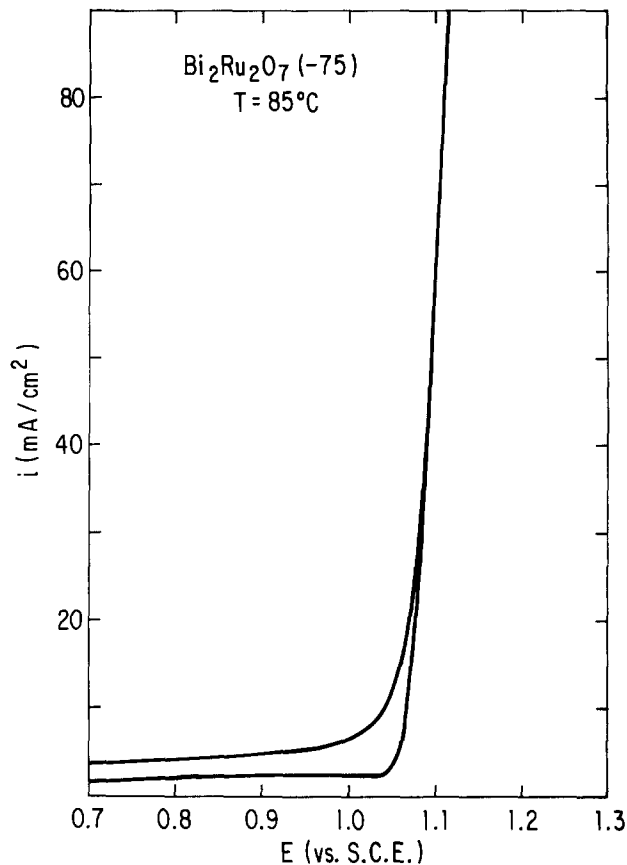


Fig. 4. Polarization characteristic of $\text{Bi}_2\text{Ru}_2\text{O}_7$ thin film obtained by a potential sweep method at 20 mV/sec.

by the frictional forces of Cl_2 gas evolution. Measurement of the surface chemical composition by XPS showed that appreciable ($\sim 50\%$) Bi was lost. X-ray diffraction indicated the presence of some RuO_2 not previously detected. The fact that the activity was not affected indicates that RuO_2 and $\text{Bi}_2\text{Ru}_2\text{O}_7$ have about the same activity. Although these data do suggest some



Fig. 5. Scanning electron micrographs of $\text{Bi}_2\text{Ru}_2\text{O}_7$ electrode (a) before Cl_2 evolution and (b) after Cl_2 evolution. Scale is 1 μm

dissolution of the $\text{Bi}_2\text{Ru}_2\text{O}_7$ electrode, the high activity is encouraging, particularly since no attempt was made to optimize mechanical and chemical characteristics of the electrode, as done by other investigators (2).

In summary, we have prepared bismuth ruthenate electrodes by rf sputtering directly onto heated Ti substrates. These electrodes showed high electrocatalytic activity for Cl_2 evolution. Further studies are required to determine whether these electrodes could be improved by chemical or other modifications.

Acknowledgments

The authors thank A. Biddle for assisting in the x-ray analysis. H. A. Selz prepared the thin films. We also acknowledge helpful discussions with R. J. Bouchard, V. Johnson, J. Pannetier, and D. N. Staikos.

Manuscript submitted June 18, 1979; revised manuscript received Sept. 13, 1979.

Any discussion of this paper will appear in a Discussion Section to be published in the December 1980 JOURNAL. All discussions for the December 1980 Discussion Section should be submitted by Aug. 1, 1980.

Publication costs of this article were assisted by E. I. du Pont de Nemours and Company.

REFERENCES

1. C. J. Harke and J. Renner, *This Journal*, **125**, 455C (1978).

2. F. Hine, M. Yasuda, and T. Yoshida, *ibid.*, **124**, 500 (1977).
3. L. Janssen, L. Starmans, J. Visser, and E. Barendrecht, *Electrochim. Acta.*, **22**, 1093 (1977).
4. A. Kuhn and C. Mortimer, *J. Appl. Electrochem.*, **2**, 283 (1972).
5. T. Loucka, *ibid.*, **7**, 211 (1977).
6. T. Arikado, C. Iwakura, and H. Tamura, *Electrochim. Acta.*, **22**, 513 (1977).
7. C. Iwakura, K. Hiras, and H. Tamura, *ibid.*, **22**, 335 (1977).
8. A. Kuhn and C. Mortimer, *This Journal*, **120**, 231 (1973).
9. L. Burke, O. Murphy, and J. O'Neill, *J. Electroanal. Chem. Interfacial Electrochem.*, **81**, 391 (1977).
10. S. Trassatti and G. Buzzanca, *ibid.*, **29**, app. 1-5 (1971).
11. L. Maissel, in "Handbook of Thin Film Technology," L. Maissel and R. Glang, Editors, pp. 4-31, McGraw-Hill Inc., New York (1970).
12. R. Buitrago, L. Toth, A. Goldman, J. Schwanebeck, and M. Dayan, *Appl. Phys. Lett.*, **32**, 341 (1978).
13. R. J. Bouchard, U.S. Pat. 3,583,931 (1971); R. J. Bouchard and J. Gillson, *Mater. Res. Bull.*, **6**, 669 (1971).
14. F. Abraham, D. Thomas, and G. Nowogrocki, *Bull. Soc. Fr. Mineral. Cristallogr.*, **98**, 25 (1975).
15. J. Pannetier, Private communication.
16. A. Cerquetti, P. Longui, T. Mussini, and G. Natta, *J. Electroanal. Chem. Interfacial Electrochem.*, **20**, 411 (1969).

Chlorine Saturation Levels in the Electrolyte Adjacent to the Anode Surface

Relationship to the Polarization Curves

I. V. Kadija*

Olin Chemicals, Charleston, Tennessee 37310

ABSTRACT

Using a rotating ring electrode, we have simulated chlor-alkali and chlorate anode operation. We have detected considerable supersaturation of molecular chlorine in the electrolyte adjacent to the anode. We have also detected supersaturation in the solution bulk when simulating a chlor-alkali cell. Parts of polarization curves for the anode can be explained in terms of concentration polarization under various operating conditions.

In our earlier work (1-4) with H_2 and O_2 evolution, we used a rotating ring electrode as the operating electrode. The hydrodynamics of the rotating disk and the hydrophobic nature of Teflon (5) caused bubbles to appear at the Teflon insulator adjacent to the outer edge of the ring. Nucleation was not observed at the ring surface and consequently the surface hydrodynamics were undisturbed.

In a rotating double ring electrode combination, the outer ring electrode can be used as the analytical electrode for the species present in the solution near the operating surface. We detected in our previous work (1-4) considerable supersaturation levels of gaseous species (like H_2 and O_2) in the solution adjacent to the operating ring electrode.

The objective of this work was the measurement of steady-state gaseous chlorine concentrations in the electrolyte adjacent to the anode in chlor-alkali cells. From these measurements some reaction characteristics of chlor-alkali cells were deduced.

Experimental Methods

The apparatus is presented in Fig. 1. The ring dimensions are shown in the figure. The rotational speed ranged from 518 to 5525 rpm, with most of our experimental conducted at 2320 rpm.

The two independent electric circuits for two ring electrodes and the rest of the apparatus were previously described (2). In addition, we had air, N_2 , and Cl_2 cylinders for purging the electrolyte as required. Platinizing the platinum ring electrodes has been described elsewhere (1). Electrolytes were made with reagent grade NaCl and the pH was adjusted with HCl and NaOH solutions. The operating temperature was 25°C.

The measurement was conducted in the following manner. The thermostated electrolyte was saturated with one of the gases for several hours while disk rotated at 2320 rpm. After saturation, the limiting current at the outer ring was measured by obtaining a steady-state i - V curve by galvanostatic method. We have used the limiting current at the outer ring at zero current of the operating ring as a measure of the bulk

* Electrochemical Society Active Member.
Key words: electrolyte, anode, polarization.

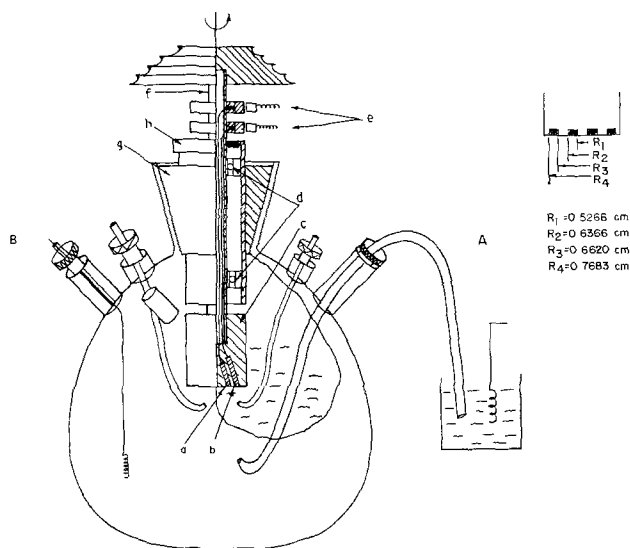


Fig. 1. Experimental cell. A, chlor-alkali cell simulation; B, chlorate cell simulation, a—inner ring, b—outer ring, c—Teflon disk body, d—ball bearings, e—sliding electrical contacts, f—titanium shaft, g—Teflon stopper, h—graphitized asbestos sealing.

saturation level with respective gas. With nitrogen atmosphere only traces of Cl_2 gave a very small limiting current. With Cl_2 we obtained 22 millimoles Cl_2 /liter as chlorine solubility in our solution quite in agreement with literature (6). After establishing the bulk solution limiting current as a reference level for chlorine saturation, we have proceeded with measuring the limiting current at the outer ring at various operating current densities at the inner ring.

Hence, while the inner ring operated with a certain current density G (the range was 0.24–2.76 kA/m^2) we have plotted the i - V curve at the outer ring. In-between each operating current density at the inner ring, we have rechecked the level of chlorine saturation in the bulk by repeating the limiting current measurement $G = 0$ level. In estimating the collecting efficiency of the double ring system we have used previously developed mathematical interpretations (7, 8). For each operating current G we have compared the collecting efficiency at the outer ring with the theoretically predicted value.

We simulated a chlor-alkali cell and a chlorate cell in our experiments. The chlor-alkali cell was simulated by separating the cathode from the anode (inner ring) with an electrolytic bridge (Scheme A, Fig. 1). Thus, the whole content of the reaction flask could be considered as anolyte. The chlorate cell was simulated by operating the cathode and anode in the same reaction flask. Hence, the electrolyte was considered to be chlorate cell liquor (Scheme B, Fig. 1).

Results

Chlor-alkali cell simulation.—In the cell saturated with air and without operation of the inner ring (curve $G = 0$ of Fig. 2) the detection current obtained at the outer ring was very small. As the inner ring started to operate at certain finite anodic currents, the outer ring limiting current increased correspondingly (curves $G = 0.24$ to $G = 2.64$ kA/m^2 of Fig. 2).

In the cell saturated with chlorine from the cylinder the limiting current obtained with the outer ring represented the saturation of chlorine in the bulk. This limiting current (curve $G = 0$ of Fig. 3) depended on the history of the cell. The $G = 0$ curve presented in Fig. 3 was obtained after the shutdown of the inner ring operation at currents higher than 0.2 kA/m^2 .

Figure 4 shows the limiting currents plotted against operating currents for the inner ring in both of the above cases. The lower curve is for the air-purged cell. This curve followed the theoretical prediction until

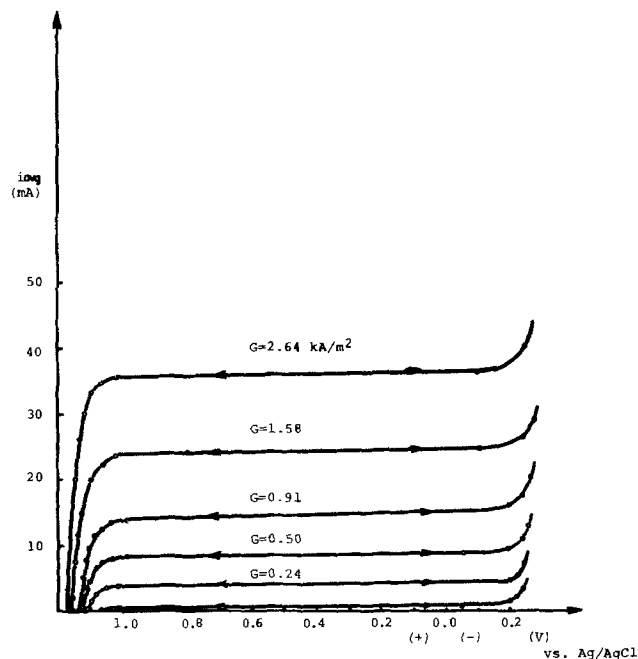


Fig. 2. Outer ring polarograms for Cl_2 reduction, $\text{pH} = 0.45$, 300 g/liter NaCl , 25°C. Air purging through the cell—low Cl_2 in the bulk.

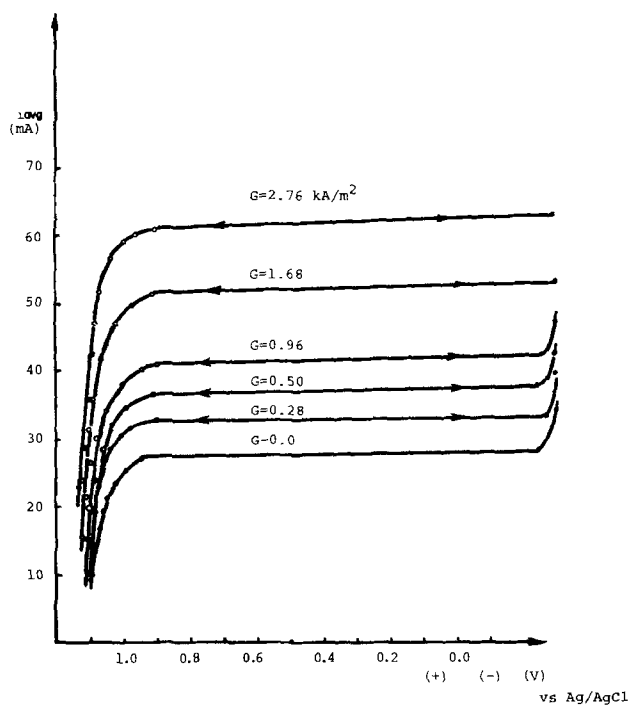


Fig. 3. Outer ring polarograms for Cl_2 reduction, $\text{pH} = 0.5$, 300 g/liter NaCl , 25°C. Cell saturated with Cl_2 under operating conditions.

medium current densities were reached. At current densities above 1 kA/m^2 there was a deviation from the theoretical prediction and the observed limiting current was lower by 20–25%.

A similar shape (upper curve on Fig. 4) was obtained with Cl_2 -saturated solution. At currents lower than 0.2 kA/m^2 , the detection level is considerably smaller than one would predict by extrapolation from the higher current densities. As shown in Fig. 5 and 8, at lower current densities or no current from the inner ring the steady-state $G = 0$ level dropped considerably.

Figure 5 shows the change in Cl_2 concentration after the anode is shutdown with continued stirring. A few seconds after the shutdown at operating currents higher than 0.2 kA/m^2 , the Cl_2 concentration level was much higher and corresponded to a Cl_2 saturation of

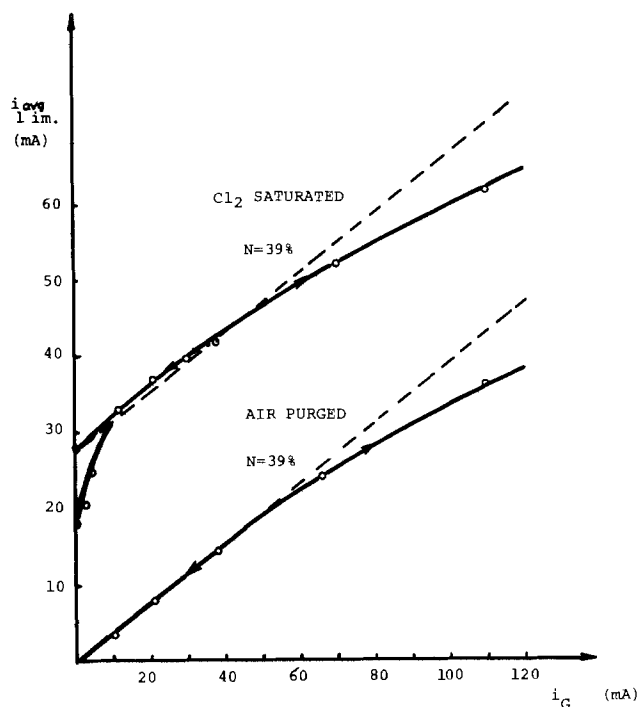


Fig. 4. Outer ring limiting current vs. operating current G on inner ring. $\text{pH} = 0.45$ and 0.50 , 300 g/liter NaCl , 25°C .

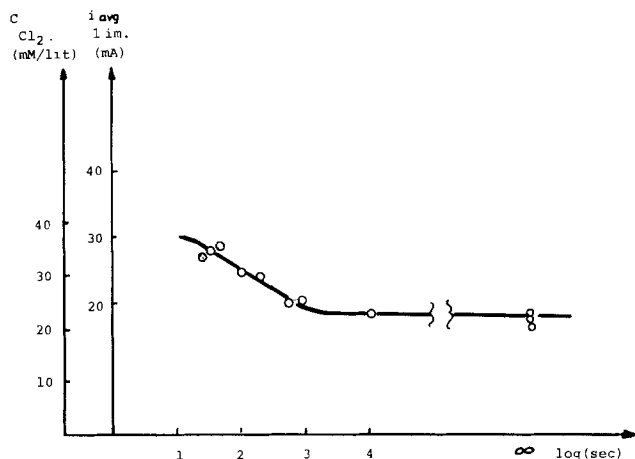


Fig. 5. Bulk Cl_2 reduction limiting current and concentration as a function of time after the anode shutdown.

170-190% compared to equilibrium with a pressure of 1 atm over the solution. The level of Cl_2 in the bulk after a few hours of stirring without current was the same as that obtained by Cl_2 bubbling at 1 atm.

Chlorate cell simulation.—Figure 6 shows the outer ring polarograms obtained at different operating current densities at the inner ring. Four identifiable waves were reproducibly obtained with the outer ring. The first wave from the open circuit corresponds to the chlorine reduction reaction. We suspect that the other three waves correspond to reactions involving ClO^- , ClO_2 radical, or ClO_2^- . We are continuing our investigation in order to positively identify the species as well as the possible interference of platinum oxides reduction.

In order to measure the bulk chlorine saturation we operated our cell for 16 hr at 2.4 kA/m^2 , and immediately after the shutdown obtained the curve $G = 0$ with the outer ring. We could not identify any chlorine in the bulk. The two species identified were probably due to minute amounts of ClO^- and some platinum oxide reduction.

We present the limiting current for chlorine reduction in Fig. 7 as a function of operating current. We

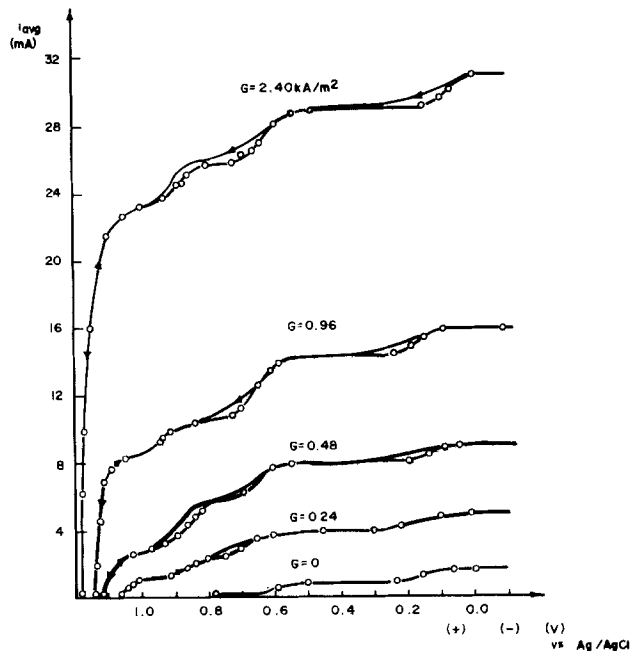


Fig. 6. Reduction polarograms obtained on the outer ring during chlorate cell simulation at different current densities. $\text{pH} = 6.5-7.3$, 200 g/liter NaCl , 25°C . Same hydrodynamic conditions and surface quality as in chlor-alkali cell simulation.

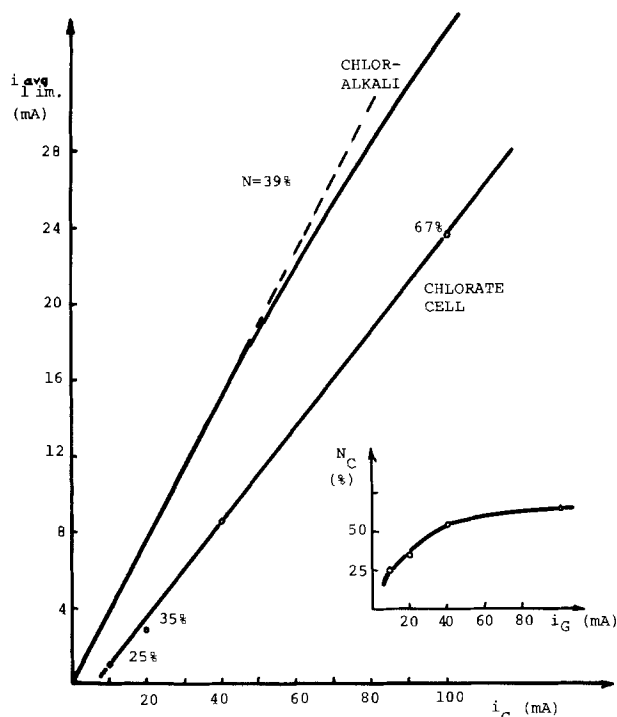


Fig. 7. Outer ring limiting currents for Cl_2 reduction during chlorate cell anode operation. Limiting currents from Fig. 6.

also compare the collection levels for molecular chlorine in two cases: chlor-alkali simulation purged with air, and chlorate cell simulation, both at 2320 rpm. The numbers beside each data point indicate the percentage of detection in the chlorate cell compared to detection at the same operating current in the chlor-alkali cell. The asymptotic approach to the 60-70% detection level is shown in the bottom right graph.

Figure 8 shows the polarization curves for the same anode at the same rotation speed in the three solutions tested above: B_1 = chlor-alkali cell saturated with Cl_2 , B_2 = chlor-alkali cell purged with nitrogen (the air replaced with nitrogen to avoid any influence of

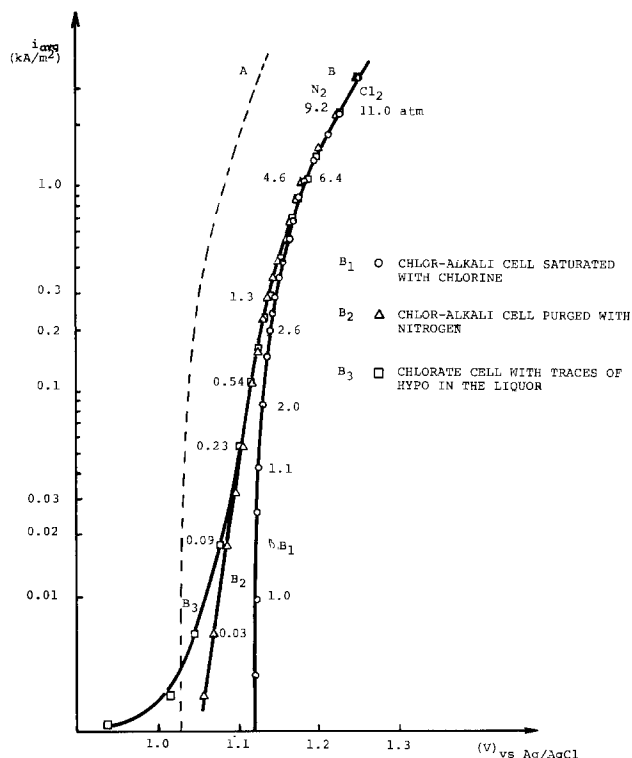


Fig. 8. Inner ring-anode polarization curves in chlor-alkali and chlorate cell simulation. Curve A, theoretical curve, assuming same chlorine concentration at the surface as in the bulk of the chlorate cell. Curve B, experimental curves with calculated actual Cl_2 pressures.

O_2 on potential at low current densities), and B_3 = chlorate cell.

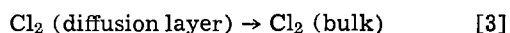
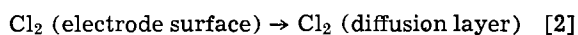
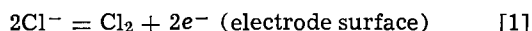
Discussion

Chlor-alkali cell.—The dashed lines in Fig. 4 indicate the limiting currents one should obtain at the outer ring if the species formed on the inner ring is dissolved and can be reduced or oxidized on the outer ring with the same number of electrons per molecule as required for its formation on the inner ring. Since our experimental evidence agrees with the theoretically predicted lines, we can assume that most of the chlorine generated at the inner ring crosses the electrode-liquid interface as a dissolved species.

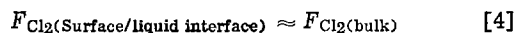
Some deviations are noticeable at higher current densities. We attribute this to the so-called "bubble gate" effect [see Ref. (4)]. At less than 15 mV polarization the bubbles wetting angle is 90° – 110° . Bubbles are attached to the Teflon insulator and penetrate deeper into the solution bulk. As polarization increases, the bubbles wetting angle becomes smaller and so the necks become shorter and bubbles bodies start to interfere with the mass transfer between the two rings. This results in a 20–25% decrease in collecting efficiency at polarizations of 60–80 mV.

The upper curve in Fig. 4 also shows deviations from the predicted line at very low currents but only if the Cl_2 is depleted in the bulk (see Fig. 5). Otherwise, at higher current densities, this curve follows the theoretical predictions, indicating that most of chlorine is produced as dissolved species.

Hence, we suggest the following chlorine production mechanism at the anode surface, regardless of the electrode kinetics phenomena



or



where F_{Cl_2} are the respective fluxes of molecular chlorine.

One finds that it is frequently assumed that the liquid adjacent to the electrode surface can be saturated with gaseous products up to the extent which corresponds to 1 atm pressure of the respective gas. This conclusion is usually based on visual observation of the electrode surface. However, the evidence of extensive bubbling from the electrode surface does not necessarily indicate that saturation stays close or equivalent to 1 atm pressure regardless of the current density. It was already indicated in literature that the saturation can reach far in excess to the one corresponding to 1 atm pressure (9–12). Our findings with O_2 and H_2 have confirmed that also (4). Due to the nature of operation of a ring electrode, we have been able to measure the actual saturation levels at the operating surface which was not covered with bubbles.

The following is our calculation of the surface liquid saturation level as a function of current density and diffusion layer thickness. For a more accurate saturation and equivalent pressure distribution, we have developed the analysis shown in the Appendix of this paper.

In the first approximation for surface concentration calculation one can use the Nernst equation

$$C_{\text{Cl}_2} \text{ (surface)} = C_{\text{Cl}_2} \text{ (bulk)} + \frac{\delta_{\text{avg}} i_{\text{avg}}}{zFD_{\text{Cl}_2}} \quad [5]$$

where δ_{avg} is diffusion layer thickness.

For a ring type electrode δ_{avg} is an average diffusion layer thickness as calculated by the Levich equation

$$\delta_{\text{avg}} = 1.61 D_{\text{Cl}_2}^{1/3} \nu^{1/6} \omega^{-1/2} \left(1 - \frac{r_0^3}{r_1^3} \right)^{1/3} \quad [6]$$

where $D_{\text{Cl}_2} = 1.22 \times 10^{-5}$ cm²/sec, $\nu = 1.75 \times 10^{-2}$ poises, $\omega = 2320$ rpm, $r_0 = 0.5266$ cm, and $r_1 = 0.6398$ cm.

Introducing numerical values in Eq. [5] we obtain the following equation that can be used to estimate the surface Cl_2 concentration in millimole/liter as a function of current density and diffusion layer thickness

$$C_{\text{Cl}_2} \text{ avg (surface)} = 40 + 4.3 \cdot i_{\text{avg}} \cdot \delta_{\text{avg}} \quad [7]$$

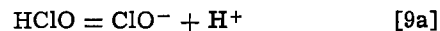
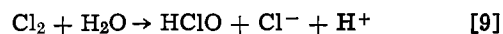
where δ_{avg} is in microns and i_{avg} is in kA/m².

The Cl_2 solubility at 1 atm and 25°C is 22 millimoles/liter atm. Hence, through Henry's constant, one can calculate the equivalent average pressure of gas saturation in the solution adjacent to the operating surface

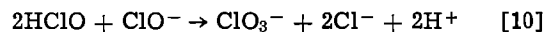
$$P_{\text{Cl}_2} \text{ (surface)} = 1.82 + 0.2 \cdot i_{\text{avg}} \cdot \delta_{\text{avg}} \quad [8]$$

where i_{avg} and δ_{avg} have same units as in Eq. [7].

Chlorate cell.—In a chlorate cell, chlorine hydrolyzes into hypochlorous ions which in turn disproportionate to form chlorate

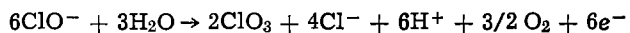


and



Hence, molecular chlorine present in the anode-surface electrolyte converts into chlorate at a certain overall rate. The rate of the reaction, [10] and [11], is a function of pH. The optimum condition for the conversion is pH 6.5–7.5.

During the anode operation chlorate may form electrochemically



This reaction becomes diffusionally limited if the ClO^- concentration in the bulk is too small. Also, reaction [9] causes slightly acidic conditions at the anode

surface; this acidity considerably reduces the rate of the electrochemical reaction (11). We performed our experiments with a dilute hypochlorous ion concentration. Figure 6 shows the $G = 0$ detection curve which indicates only traces of hypochlorous ion or other intermediates in the solution bulk. Under such operating conditions, and especially at higher current densities, one can assume that anode chlorine production efficiency is close to 100%.

The solution layer adjacent to the anode surface became more concentrated with Cl_2 as current increased. The concentration should follow the current density in a manner similar to that observed in the chlor-alkali cells. Our results in Fig. 6 and 7 indicate that the chlorine saturation at the surface increases with the operating current density. However, there appears to be an asymptotic approach to the level of 66% compared to the chlor-alkali cell. Ibl *et al.* [Ref. (13) and (15)], Jakšić (14), and others have indicated that the reaction may occur apart from the electrode surface but still within the limits of the diffusion layer. Our experimental evidence seems to confirm this. A part of the reaction must also take place in the transition region from the inner to the outer ring for the time necessary for transfer of the species from the inner to the outer ring.

In spite of these speculations, there is clear evidence of surface saturation with chlorine. Assuming that transfer and diffusional conditions are similar to a chlor-alkali cell, one can write the following equation

$$C_{\text{Cl}_2 \text{ avg}} (\text{millimole/liter}) = 66 i_{\text{avg}} \quad [12]$$

where i_{avg} is in kA/m^2 and δ_{avg} is taken as $23 \mu\text{m}$ for the 2320 rpm.

In the early 1960's T. Beck proposed the following equation to describe the chlorine concentration at the anode surface as a function of the current density in chlorate cell

$$C_{\text{Cl}_2 \text{ avg}} = \frac{\left(\frac{D_2}{k}\right)^{1/2} \cdot i_{\text{avg}}}{2 \cdot F \cdot D_2} \quad [13]$$

The rate constant k for the reaction is proposed to be about 0.2 sec^{-1} (14).

Instead of $23 \mu\text{m}$ in production, one can have diffusion layer thicknesses of $100\text{--}120 \mu\text{m}$ as proposed and measured by Ibl (13). With this value for δ_{avg} our empirical equation will give concentration levels similar to those predicted by Eq. [13].

Concentration polarization.—We have calculated the equivalent average pressure (8) of molecular chlorine at the anode surface at several polarization data points. These are presented in the graphs in Fig. 8.

Curve B₁.—The anode operating in a chlorine saturated solution did not experience polarization at current densities below $0.05\text{--}0.07 \text{ kA/m}^2$. There was no polarization since the surface chlorine concentration and corresponding pressure was only slightly higher than in the bulk. In addition, the surface was catalytically active (exchange current was higher than operating current at low current densities). At higher current densities, however, both concentration and activation polarization were evident.

Curve B₂.—In nitrogen atmosphere the major source for chlorine at the surface is the Cl^- oxidation current. Hence, as the current increased the chlorine concentration at the surface increased. The dependence was linear and consequently for an order of magnitude of current change we obtained 30 mV of polarization due to a tenfold increase in chlorine saturation at the surface.

At higher current densities the activation polarization adds to the overall polarization and, therefore, curves B₁ and B₂ coincide. However, one has to bear in mind that the 30 mV/dm concentration polarization

is present also at higher current densities. We measured the chlorine saturation gradual increase with current density and this is shown by higher equivalent pressure.

Curve B₃.—The behavior was similar to that observed in the chlor-alkali cell purged with nitrogen (B₂). In the chlorate cell the chlorine concentration in the bulk was very low. Here, Cl_2 was consumed in the hydrolysis reaction. However, the resulting species OCl^- is also electrochemically active at the platinized platinum surface. Therefore, at low current densities and at open circuit, the polarization curve shows potentials which are a result of a mixed reaction where hypochlorous ions were oxidized and chlorine evolved simultaneously.

In the presence of low ClO^- content at moderately low currents 0.02 kA/m^2 or higher) the hypochlorous reaction became diffusion-limited. As the potentials increased, the current generated chlorine under surface conditions similar to that in the nitrogen purged chlor-alkali cell. Consequently, the shapes of the curves became very similar.

The coincidence of the three curves at higher current densities indicates that the surface electrochemical discharge and the chlorine saturation are practically independent of the conditions in the bulk at high reaction rates.

As a hypothetical result, we have plotted Curve A (Fig. 8) assuming no concentration polarization. This allows the initially low Cl_2 concentration in the bulk to be taken as a reference Cl_2 concentration. The resulting curve obviously contradicts the experimental findings. Hence, small bulk concentration of Cl_2 has little bearing on the polarization curves and cannot be used as reference level for the polarization curve.

Conclusions

1. In chlor-alkali simulation, rotating ring electrode operates with considerable supersaturation of molecular chlorine in the adjacent electrolyte. The supersaturation is a linear function of current density.
2. At current densities lower than 0.03 kA/m^2 in chlorate cell simulation, there is no evidence of surface chlorine saturation. At higher current densities, the saturation follows the current density but to a lesser degree than experienced in the chlor-alkali cell.
3. The bulk solution in a chlor-alkali cell can experience chlorine concentrations saturated to the level of 170–190% under operating conditions.
4. Part of the anode polarization curve can be interpreted in terms of concentration polarization in chlor-alkali as well as in chlorate cell operation.
5. We believe that the uneven reactant concentration distribution at the ring surface (see Appendix) has little bearing on our finding. Under our operating conditions, molecular chlorine is primarily produced as dissolved species.
6. Although these findings could be a more general nature, one cannot safely apply our empirical equations on other experimental apparatus without careful study.

Considering the nature of the steady state of gas-producing reactions, we believe that one might obtain similar results with plane electrodes as suggested by Landolt, Mueller, and Tobias (20). However, it appears that ring electrodes are more feasible to build and operate.

Manuscript submitted June 4, 1979; revised manuscript received Sept. 24, 1979. This was Paper 283 presented at the Boston, Massachusetts, Meeting of the Society, May 6–11, 1979.

Any discussion of this paper will appear in a Discussion Section to be published in the December 1980 JOURNAL. All discussions for the December 1980 Discussion Section should be submitted by Aug. 1, 1980.

Publication costs of this article were assisted by Olin Chemicals.

APPENDIX

Current Distribution for Chloride Oxidation

It is generally accepted that a rotating disk electrode is a uniformly accessible surface. This assumption allows the investigation without any particular consideration of possible uneven distribution of reaction rate across its surface. However, one must bear in mind that the so-called uniformity of the rotating disk operation applies only to limiting current conditions as indicated by Newman (16).

Ring electrodes are not uniformly accessible even under limiting current operation. This is true predominantly because of the flow pattern of the solution across the ring surface. Solution flows from the inner towards the outer edge of the ring. This pattern creates considerable differences between the two edges. The inner edge is influenced more by the bulk solution while the outer edge operates in the solution saturated with electrochemical reaction products accumulated in the surface solution. These mechanics of operation require a thorough analysis of the operating conditions to estimate the possible influence on the experimental data.

The recent publications of Pierrini, Parrish, and Newman (17, 18) probably best describe the present understanding of the phenomena involved.

The article (17) which deals with ring electrodes current distribution plots several parameters important for the characterization of the investigated reaction. We have used these parameters to characterize the feasibility of our ring electrode system.

Dimensionless exchange current density (J).—*J* is described by Eq. [9] of the article (17)

$$J = \frac{i_0 r_1 F}{RT\kappa} = 5 \quad [\text{A-1}]$$

where (*i*) is the characteristic exchange current density assumed to be 50 mA/cm², and conductivity of the bulk solution $\kappa = 0.25 \text{ cm}^{-1}$. *J* values are indications of the reaction reversibility. *J* = 1 or close are considered medium rate reversibility reaction and, consequently, *J* = 0 or close are rather irreversible reactions. *J* values above one are considered as fast reactions and above 100 are very fast reactions.

Dimensionless stirring rate (N).—*N* is described by Eq. [10] of the above article

$$N = \frac{r_1^{2\omega/2}}{\nu} \left(\frac{0.51}{3D_{\text{Cl}^-}} \right)^{1/3} \frac{F^2 D_{\text{Cl}^-} C_{\text{Cl}^-}}{RT} = 200 \quad [\text{A-2}]$$

where (ω) is 38.67 sec⁻¹, 1.75×10^{-2} poise, and $D_{\text{Cl}^-} = 1.6 \times 10^{-5} \text{ cm}^2/\text{sec}$. *N* defines the influence of the mass transport on the reaction rate. For finite *N* values there is always a certain influence of the mass transport phenomena on reaction rate and concentration distribution at the surface. For infinite values of *N*, the surface concentration is same as in the bulk.

Our value of 200 indicates that at the 2320 rpm there was still some influence of mass transport on the surface concentration and operating conditions. With our RDRE system, *N* could be varied between 100-300.

Ring radii ratio (r₀/r₁).—The ratio of the ring radii is an important parameter when defining operating conditions for the ring electrode. The values of 0.5-0.7 are considered to be ratios that indicate the ring electrode behavior typical for ring type surfaces. That is, they do not simulate the disk or a plane type electrode. Smaller values indicate that a behavior similar to disk electrode can be expected. Larger values (thin ring electrodes) tend to simulate the current and concentration distributions typical for plane electrodes (18).

Our ratio is

$$\frac{r_0}{r_1} = 0.823 \quad [\text{A-3}]$$

Hence, a typical or close to plane electrode current distribution can be expected when operating with such electrode.

Operating vs. limiting current.—By means of the Levich (19) equation for limiting current, we can estimate

the limiting current for chloride oxidation from the brine

$$i_{\text{avg LIM}} = (0.62 F C_{\text{Cl}^-} D_{\text{Cl}^-}^{-2/3} \nu^{-1/6} \omega^{1/2}) / \left(1 - \frac{r_0^3}{r_1^3} \right)^{1/3} \quad [\text{A-4}]$$

$$i_{\text{avg LIM}} = 2.5 \text{ A/cm}^2$$

In this work, we operated with current densities 1-200 mA/cm². Hence, our operating current vs. limiting current ratio is

$$\frac{i_{\text{avg}}}{i_{\text{avg LIM}}} = 4 \times 10^{-4} - 0.12 \quad [\text{A-5}]$$

Keeping this parameter in mind, we analyzed the information presented by Newman and others (17, 18). It appears that the closest current distribution description is given in Fig. 8 of Ref. (17). We do have a redox couple Cl⁻/Cl₂ with a relatively large exchange current. We are also operating at small $i_{\text{avg}}/i_{\text{avg LIM}}$ ratios. Thus, the curves for ratio = 0.2 best represent our current distribution across the ring electrode width.

Using this information, we plotted our current distribution curve (see on Fig. 9, curve a) and obtained a rather uniform distribution over most of the ring width. However, at the edges, we obtained values equal to 2 to 2.5 times greater than i_{avg} .

Molecular Chlorine Concentration Distribution Across the Ring Electrode Width

Our electrochemical reaction product diffuses into solution. Hence, there is always a concentration gradient between the surface and the bulk. This condition requires the analysis of diffusion layer thickness vs. the ring width and it is described by Levich (19).

Figure 9 (curve b) shows the relative change of diffusion layer thickness against the ring width. At the inner edge it is about 40% of the δ_{avg} and at the outer edge it is about 40% thicker.

By means of curves a and b one can obtain the resulting concentration distribution across the ring width. We used the numerical solutions for several r values using Eq. [7] of this manuscript and obtained curve c, assuming $C_{\text{Cl}_2}(\text{bulk}) = 0$.

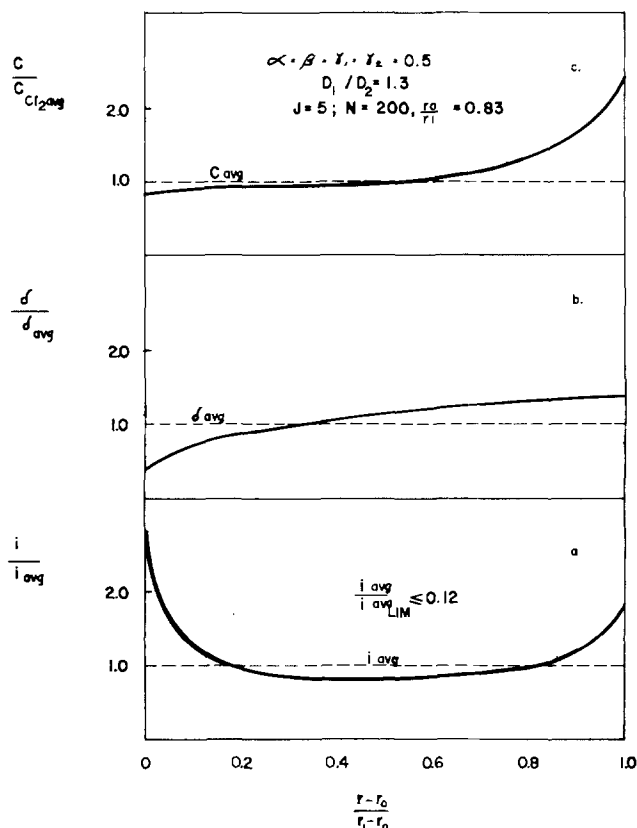


Fig. 9. Distribution of: a, current, b, diffusion layer thickness, and c, molecular chlorine concentration across the operating ring.

One can see that the surface concentration of molecular chlorine appears quite uniform for most of the operating surface. It is interesting, however, that the outer edge of the ring electrode operates with concentrations 2-2.5 times higher than average.

LIST OF SYMBOLS

$C_{Cl_2 \text{ avg}}$	average concentration of molecular chlorine on the operating electrode surface
$C_{Cl_2 \text{ bulk}}$	concentration of molecular chlorine in solution bulk
$D_{1,2}$	chloride ion and molecular chlorine diffusion coefficients, cm^2/sec
F	Faraday constant 96,500 C/equiv.
G	total inner ring current, molecular chlorine generating current. $i_{\text{avg}} = G/\text{surface (cm}^2\text{)}$
i	normal current density at the electrode surface, A/cm^2
i_{avg}	average current density on the ring electrode, A/cm^2
$i_{\text{avg LIM}}$	average limiting current density on the ring electrode, A/cm^2
i_0	characteristic exchange current density, A/cm^2
J	dimensionless exchange current density
r	radial coordinate, cm
r_0	inner ring inner radius, cm
r_1	inner ring outer radius, cm
r_2	outer ring inner radius
r_3	outer ring outer radius
δ	local diffusion layer thickness
δ_{avg}	average diffusion layer thickness on the inner ring electrode
κ	electrical conductivity of the bulk solution, $\Omega^{-1} \text{cm}^{-1}$
ν	kinematic viscosity, cm^2/sec
ω	rotation speed, sec^{-1}

REFERENCES

- I. V. Kadija and V. Nakić, *J. Electroanal. Chem. Interfacial Electrochem.*, **34**, 15 (1972).
- I. V. Kadija and V. Nakić, *ibid.*, **35**, 177 (1972).
- I. V. Kadija, Dissertation, Faculty of Technology, University of Beograd (1973).
- I. V. Kadija, B. Z. Nikolić, and A. R. Despić, *J. Electroanal. Chem. Interfacial Electrochem.*, **577**, 35 (1974).
- I. V. Kadija, *Electrochim. Acta.*, **23**, 149 (1977).
- Olin's Data on Solubility of Cl_2 .
- V. Y. Filinovskiy, I. V. Kadija, and B. Nikolić, *Elektrokhimiya*, **10**, 297 (1974).
- V. Y. Filinovskiy, I. V. Kadija, B. Nikolić, and M. Nakić, *J. Electroanal. Chem. Interfacial Electrochem.*, **54**, 39 (1974).
- V. V. Skorochelletti, "Theory of Metal Corrosion Khimiya," Leningrad (1973), Keter Publishing House, Jerusalem Ltd. (1975). Translated from Russian.
- W. B. Buehl and J. W. Westwater, *AIChE J.*, **12**, 571 (1966).
- B. Kabanov and A. Frumkin, *Z. Phys. Chem.*, **1965**, 433 (1933).
- E. Barendrecht, L. J. J. Janssen, and R. M. de Jonge, Paper 250 presented at The Electrochemical Society Meeting, Boston, Massachusetts, May 6-11, 1979.
- N. Ible and D. Landolt, *This Journal*, **115**, 713 (1968).
- M. M. Jakšić, *Electrochim. Acta.*, **21**, 1127 (1976).
- D. Landolt and N. Ibl, *ibid.*, **15**, 1165 (1970).
- J. Newman, *This Journal*, **113**, 1235 (1966).
- P. Pierini and J. Newman, *ibid.*, **125**, 79 (1978).
- W. R. Parrish and J. Newman, *ibid.*, **116**, 169 (1969).
- V. G. Levich, "Physicochemical Hydrodynamics," p. 108, Prentice-Hall Inc., New York (1962).
- D. Landolt, R. H. Mueller, and C. W. Tobias, *This Journal*, **116**, 1384 (1969).

An Engineering Model for Electro-Organic Synthesis in Continuous Flow-Through Porous Electrodes

Richard C. Alkire* and Ronald M. Gould*¹

Department of Chemical Engineering, University of Illinois, Urbana, Illinois 61801

ABSTRACT

Under controlled experimental conditions, 9-10 diphenylanthracene (DPA) was oxidized in a sectioned flow-through porous electrode in order to study the relation between operating conditions and product yield. The DPA solution contained 0.2N tetraethylammonium perchlorate in acetonitrile. The electrode was fabricated from 100-mesh platinum screens. The reaction rate distribution within the sectioned electrode was measured directly, and the reactor effluent was analyzed to obtain the concentrations of DPA and its cation radical (DPA^+). Experimental data were compared with calculations based on flow-through porous electrode theory with consideration of the multiple reaction sequence (EEC) under study. Literature values, where available, were used without adjustment in making theoretical calculations with use of a mathematical model of the reactor system. The model calculations predicted total currents which were within 4% of experimental data, and gave good agreement with current distribution data at various flow velocities and applied potentials.

Synthesis of organic compounds by electrolysis can usually be carried out with high selectivity provided that the potential along the electrode surface is essentially uniform. In order to achieve large reaction rates per unit volume, a necessary adjunct of large-scale processes, porous electrodes are often used since they possess large internal surfaces on which heterogeneous

charge-transfer reactions may occur. One consequence of using such electrodes is that interior mass transfer and ohmic resistance effects may lead to a nonuniform potential distribution, thereby affecting adversely the selectivity which might otherwise be achieved. Defining the optimal trade-off between high selectivity and high reaction rate is clearly an important engineering design consideration.

The relation between design parameters and reactor performance is particularly complex in the case of most electro-organic processes owing to the interaction

* Electrochemical Society Active Member.

¹ Present address: Mobil Research and Development Corporation, Paulsboro, New Jersey 08066.

Key words: electro-organic, porous electrode, flow, mathematical model.

of multiple reactions which invariably occur. Therefore, it seems reasonable that mathematical models would find use in engineering design, optimization, and scale-up of high rate electro-organic synthesis reactors. In this investigation, the reaction distribution within a flow-through porous electrode was measured experimentally and compared with predictions based on a mathematical model of the electro-organic reaction system.

MacMullin (1) provided a classic discussion of important engineering considerations involved in scale-up of electro-organic processes. Recent vigorous industrial activity has been described in a symposium on electro-organic synthesis technology (2). An indexed bibliography of electro-organic synthesis literature (3) has recently been compiled and utilized as a data base in the evaluation of possible candidates for electrochemical synthesis of high tonnage organic chemicals (4). A variety of high rate electrochemical reactor designs has been critically reviewed by Houghton and Kuhn (5). In particular, past literature on fixed-bed flow-through porous electrode systems has recently been collected and discussed (6).

Electrochemical behavior in the presence of multiple reactions has received considerable attention during recent years. Early electroanalytical investigations successfully analyzed data on EC and ECE sequences by assuming that chemical reaction occurred primarily in the bulk of the solution (7-9). Branching mechanisms in electro-organic systems have been treated in an analogous manner (9, 10). The foregoing analyses generally assumed that the primary reaction occurred under mass transfer control and that the secondary reaction proceeded at a rate characterized by its half-wave potential. Analyses have also been presented for multiple reactions in flow systems in which the presence of a mass transfer boundary layer along a solid electrode was included in the model (8, 11-14); of these theoretical papers, one included experimental verification (12).

Extension of the foregoing principles to porous electrode applications has taken place only recently. The first theoretical treatment (15) evaluated several types of reaction mechanisms, including an electro-organic ECE sequence, and has been the basis for experimental investigations (16), including that reported in the present publication. Other recent studies on two-step reactions evaluated the interaction of convection, axial diffusion, and ohmic resistance (17). Theoretical models have been developed for parasitic reactions where the secondary reaction occurs at a rate characterized either by its half-wave potential (18) or by a linear approximation to the surface polarization equation (19). The importance of feeder plate and counterelectrode placement in minimizing current loss by secondary reactions has also been emphasized (20).

The purpose of the present investigation was to relate the synthesis performance of a flow-through porous electrode reactor to the design parameters which characterized the electrode. The oxidation of 9-10 diphenylanthracene, a reaction sequence which exhibits two successive electrochemical steps followed by a homogeneous chemical reaction, was studied in a porous electrode which was designed to permit measurement of local reaction rates within the cell. Electrolyte flow occurred parallel to the flow of electrical current in the solution phase; the counterelectrode was in the downstream position. A mathematical model of the porous electrode was developed for comparison with the experimental data.

Experimental Apparatus and Procedures

Specific details of cell and electrode design, flow system, and electronic measurements are available elsewhere (21). Therefore, only a brief summary is provided here. The cylindrical anode chamber shown schematically in Fig. 1 was fabricated by drilling out a solid piece of Teflon. The flow-through sectioned anode consisted of a stack of 100-mesh platinum

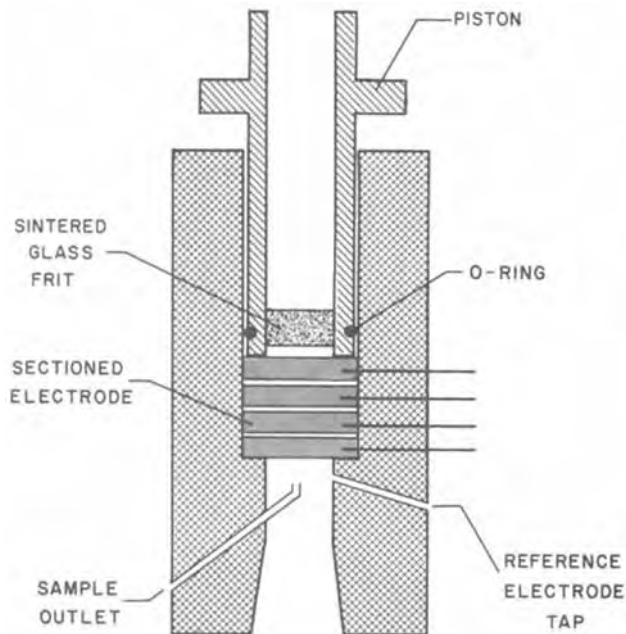


Fig. 1. Cross-sectional diagram of the assembled experimental cell.

screens, 13 mm diam. Electrical contact to each electrode section was made with thin gauge Pt wire fed through the side wall; electrode sections were insulated from each other with Teflon gauze. The counterelectrode (consisting of 80-mesh nickel screen) was positioned in the flow loop downstream from the anode. An aqueous saturated calomel reference electrode (A. H. Thomas Company, No. 4092-F15) was used following procedures recommended elsewhere (22); contamination of the flow system with water was avoided by forming the liquid junction external to the flow circuit. Samples of electrolytic solution were withdrawn through Teflon tubing. A potentiostatic power supply was used to control anode potential with respect to the reference electrode. A multichannel zero-resistance operational amplifier circuit was used to measure individual section currents while maintaining all sections at the same potential.

Electrolyte was freshly prepared under dry nitrogen with the composition 0.0015M 9-10 diphenylanthracene (Aldrich Chemical Company, "Gold Label" No. D20,500-1), 0.2N tetraethylammonium perchlorate (G. F. Smith Chemical Company, polarographic grade) in acetonitrile (Aldrich Chemical Company, "Gold Label" spectrograde No. 15,460-1). Chemicals were used without further purification; the supplier specifications indicated a maximum of 0.03% water in the solvent. The refractive index, viscosity, and conductivity of the acetonitrile solvent were measured and found to be in agreement with literature data (23). Because absorption of atmospheric moisture affects oxidation of the 9-10 diphenylanthracene cation radical (24), the enclosed flow system was purged with copious quantities of dry nitrogen prior to introduction of electrolyte and was maintained under nitrogen atmosphere throughout the course of experimentation.

Prior to conduct of electrolysis, a sample of solution was withdrawn through the upstream sample port. After establishing flow in the system, an anodic potential sweep was carried out at 1 mV/sec over the range 0-2500 mV with respect to SCE. The background current at 900 mV vs. SCE was typically less than 1% of the measured value. The potential was then set to various constant values; at each value, the system was allowed to reach steady state, at which time a 1 ml downstream (outlet) sample of electrolyte was withdrawn. In a like manner, data and solution samples were obtained at various flow rates.

The solution samples were investigated by u.v. absorbance spectrophotometry to measure concentrations of 9-10 diphenylanthracene (DPA) and the cation radical (DPA⁺). Each electrolyte sample was diluted to 10 ml with pure acetonitrile; the blank was pure acetonitrile. Absorbances at 321 and 372.5 nm were recorded and concentrations were calculated based on molar absorptivities as reported elsewhere (25). Analysis of inlet samples was accurate to within $\pm 1.5\%$. Analysis of downstream samples was less certain owing to the half-regeneration reaction of the cation radical with residual water (24, 25). The error inherent in determination of DPA and DPA⁺ in the effluent is $\pm 10\%$.

Since instability of the dication (27) prevented direct quantitative analysis, the DPA⁺² concentration was estimated by a mass balance about the cell with assumption of 100% current efficiency; the error inherent in this procedure is therefore also on the order of 10%.

Theoretical Model

Since the model developed here parallels general procedures that have been outlined previously (15), the following paragraphs are intended only for the purpose of brief description. The geometry of the porous electrode is depicted in Fig. 2(a). Electrolyte flow is in the direction of the y-coordinate, the electrode is of thickness l , and the counterelectrode is downstream from the porous electrode. Other details of cell construction are not taken into account in development of the model. Electrolyte percolates through the porous matrix, supplying reactants to the interior solid surface where electrochemical reaction occurs. The local reaction rate varies with position since the potential and species concentration vary within the electrode owing to ohmic and transport limitations. The following model equations were used to compute the reaction rate distribution throughout the porous electrode and, thereby, to predict the product spectrum in the effluent stream.

Steady-state operation under isothermal conditions is treated. The electrode phase is isopotential, is of uniform porosity, and has pore dimensions which are large with respect to the double layer thickness. The solid surface of the interior region may be of arbitrary configuration since it is accounted for in the following model by a specific area term. Hydrodynamic and mass transport processes occurring within the pore structure are illustrated in Fig. 2(b). Convection through the electrode is assumed to occur by plug flow. Mass transport of reactant species from the cen-

tral region of the pores to the surface is assumed to occur across a mass transfer diffusion layer which occupies a negligible fraction of the pore volume. By this view, homogeneous chemical reactions would occur primarily in the well-mixed core region. Conduction in the solution phase obeys Ohm's law and migration effects are negligible owing to the presence of supporting electrolyte. The foregoing constraints allow the model equations to be written in a one-dimensional form in which the heterogeneous electrochemical reactions appear as pseudohomogeneous source terms.

In the electrolyte there are i reactive solute species which take part in a total of j reactions, which may be either heterogeneous or homogeneous. The stoichiometry of the reactions is defined by

$$\sum_i \nu_{ij} M_i^{+z_i} = n_j e^- \quad [1]$$

In addition to the i reactive solute species, there may be additional inert species which do not take part in the reactions and which are not taken into account in the analysis.

The steady-state one-dimensional species conservation equations are

$$D_i \frac{d^2}{dy^2} [c_i(y)] - v \frac{d}{dy} [c_i(y)] = \sum_j \nu_{ij} S_{ij} \quad [2]$$

Any particular reaction involving species i will be either heterogeneous (electrochemical) or homogeneous (chemical). Heterogeneous reactions take place on the interior surface and obey a rate equation in which the surface concentration appears

$$S_{ij} = \frac{a}{n_j F} f_j^e [c_i^s(y), \phi(y)] \quad [3]$$

Homogeneous reactions take place in the "core" of the flowing electrolyte within the porous electrode and obey rate equations in which the core concentrations appear

$$S_{ij} = f_j^h [c_i(y)] \quad [4]$$

The specific form of the rate equations f_j^e and f_j^h will of course depend on the particular reactions as is illustrated below.

The local concentration difference between surface and core are related to the heterogeneous reaction rate through the mass transfer coefficient

$$f_j^e [c_i^s(y), \phi(y)] = \nu_{ij} n_j k_j F [c_i^s(y) - c_i(y)] \quad [5]$$

The one-dimensional charge balance equation is

$$\frac{d^2}{dy^2} [\phi(y)] = \frac{a}{\kappa} \sum_j f_j^e [c_i^s(y), \phi(y)] \quad [6]$$

Equations [2], [5], and [6] comprise a set of $(2i + 1)$ relations which are sufficient in number to determine the $(2i + 1)$ unknown functions: $c_i(y)$, $c_i^s(y)$, and $\phi(y)$. Whereas Eq. [5] is algebraic, [2] and [6] are differential equations and therefore require boundary conditions.

When the counterelectrode is downstream

$$\begin{aligned} \text{at } y = 0 & \\ c &= c_i^0 \\ \frac{d\phi}{dy} &= 0 \\ \text{at } y = 1 & \\ \frac{dc_i}{dy} &= 0 \\ \phi &= \phi^0 \end{aligned} \quad [7]$$

The following general reaction notation will be used to characterize the anodic E-E-C sequence studied in this investigation

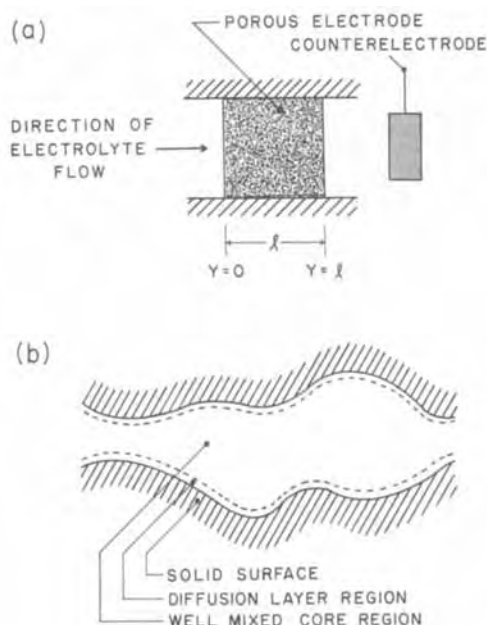
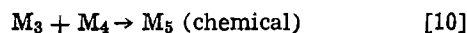
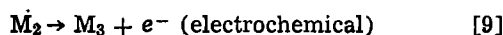
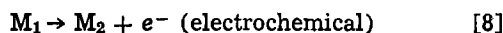


Fig. 2. Schematic diagram of porous electrode



It will be assumed that the two electrochemical reactions proceed with reversible Butler-Volmer rate expressions, while the chemical reaction is first order in each reactant and is irreversible. That is

$$f_1^e = i_{o1} \left\{ \frac{c_1^s}{c_1^o} \exp \left[\frac{\alpha_1 n_1 F \phi}{RT} \right] - \frac{c_2^s}{c_2^o} \exp \left[\frac{-\beta_1 n_1 F \phi}{RT} \right] \right\} \quad [11]$$

$$f_2^e = i_{o2} \left\{ \frac{c_2^s}{c_2^o} \exp \left[\frac{\alpha_2 n_2 F}{RT} (\phi + \phi_r) \right] - \frac{c_3^s}{c_3^o} \exp \left[\frac{-\beta_2 n_2 F}{RT} (\phi + \phi_r) \right] \right\} \quad [12]$$

$$f_3^h = k_c c_3 c_4 \quad [13]$$

In these equations, ϕ is the potential with respect to the rest potential of reaction [8], while ϕ_r is the thermodynamic rest potential of reaction [8] with respect to reaction [9]. The rest potential difference is computed by consideration of the ionic concentration of reactants as they enter the porous electrode. Note that the electrochemical reaction rate depends on the concentration at the surface, c_i^s , while the homogeneous reaction rate depends on the concentrations in the well-mixed core, c_i .

By defining the dimensionless variables

$$C_i = \frac{c_i}{c_i^o}, \quad Y = \frac{y}{l}, \quad \Phi = \frac{F\phi}{RT}, \quad \Phi_r = \frac{F\phi_r}{RT} \quad [14]$$

and by following the manipulations described previously (15), the equations for this coupled system are found to be

$$\begin{aligned} C''_1 - \zeta_1 C'_1 &= +x_1 F_1 \\ C''_2 - \zeta_2 C'_2 &= +x_2 [F_2 - F_1] \\ C''_3 - \zeta_3 C'_3 &= -x_3 F_2 + \Lambda_1 C_3 C_4 \\ C''_4 - \zeta_4 C'_4 &= \Lambda_2 C_3 C_4 \\ C''_5 - \zeta_5 C'_5 &= -\Lambda_3 C_3 C_4 \\ \Phi'' &= \xi_1 F_1 + \xi_2 F_2 \end{aligned} \quad [15]$$

where

$$F_1 = \frac{C_1 \exp[\alpha_1 n_1 \Phi] - C_2 \exp[-\beta_1 n_1 \Phi]}{1 + \frac{\xi_1}{\Gamma_1} [\exp[\alpha_1 n_1 \Phi] + \lambda_1 \exp[-\beta_1 n_1 \Phi]]}$$

$$F_2 = \frac{C_2 \exp[\alpha_2 n_2 (\Phi + \Phi_r)] - C_3 \exp[-\beta_2 n_2 (\Phi + \Phi_r)]}{1 + \frac{\xi_2}{\Gamma_2} [\exp[\alpha_2 n_2 (\Phi + \Phi_r)] + \lambda_2 \exp[-\beta_2 n_2 (\Phi + \Phi_r)]]}$$

$$\zeta_i = \frac{v l}{D_i}$$

$$\Gamma_i = \frac{a k_i n_i F^2 l^2 c_i^o}{\kappa RT}$$

$$\xi_i = \frac{i_{oi} a l^2 F}{\kappa RT}$$

$$x_i = \frac{i_{oi} a l^2}{n_i F D_i c_i^o}$$

$$\Lambda_1 = \frac{k_c l^2 c_4^o}{D_3}$$

$$\Lambda_2 = \frac{k_c l^2 c_3^o}{D_4}$$

$$\Lambda_3 = \frac{k_c l^2 c_3^o c_4^o}{D_5 c_5^o}$$

$$\lambda_1 = \frac{c_1^o}{c_2^o}$$

$$\lambda_2 = \frac{c_2^o}{c_3^o}$$

The dimensionless boundary conditions are

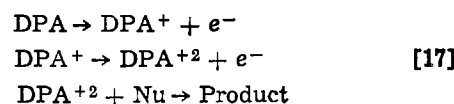
$$\begin{aligned} \text{at } Y = 0 & & C_1 = 1, \quad \Phi' = 0 \\ \text{at } Y = 1 & & C'_i = 0, \quad \Phi = \Phi^o \end{aligned} \quad [16]$$

The dimensionless parameters which arise here are closely related to parameters which arise in other electrochemical analyses and in engineering analyses of chemical reactors. Each of these dimensionless parameters indicates the relative importance of two effects. Usually, however, more than two effects are important in controlling electrode behavior. However, the relative magnitude of the parameters with respect to each other can be employed to estimate intuitively which particular effects would be important for any specific electrode system. Detailed examples of interpretation were given elsewhere describing flow-through porous electrodes with a single electrode reaction and no homogeneous reactions (28), as well as for multiple electrode and homogeneous reactions (15).

The model equations were first linearized about a trial solution, then recast into finite difference form by employing central difference operators. The resulting set of tri-diagonal matrices was inverted by a modified Gauss-Jordan elimination method (29) with the use of a CDC/CYBER-175 computer. Solution of the nonlinear coupled equations was obtained by successive approximation until a convergence of 0.01% was achieved. The number of iterations required for convergence was dependent on the system being modeled, but was usually less than ten. The choice of 101 mesh points gave results which were accurate to within the line width used in graphical representation of the results. At the limiting current, numerical calculations were found to give results which were identical to analytical calculations.

Results and Discussion

In "dry" acetonitrile, the mechanism of the oxidation of 9-10 diphenylanthracene consists of two successive electrochemical reactions followed by a rapid, irreversible reaction of the dication with a nucleophilic species, usually water present in trace amounts in the electrolyte (24)



By comparison of sequence [17] with reactions [8]-[10], it is seen that species 1 through 5 would denote DPA, DPA⁺, DPA⁺², nucleophile, and final product, respectively. Although other reaction paths are available to DPA⁺ when sufficient quantity of nucleophile (such as H₂O) is present (36), the above reaction sequence was used on a tentative basis for the analysis of data. The extent of agreement between theory and data then becomes in part a test of correctness of the assumed reaction sequence.

Table I. Physical properties of 9-10 diphenylanthracene (DPA) solutions

Property	Units	Value	Reference
κ	(Ω -cm) ⁻¹	2.06×10^{-2} *	
μ	g/(cm sec)	$3.67 \pm 0.05 \times 10^{-3}$ *	
ρ	g/cm ³	0.790 ± 0.0005 *	
η	equiv./mole	1.0	
D_1	cm ² /sec	$1.64 \pm 0.12 \times 10^{-1}$ *	(31)
D_2	cm ² /sec	1.64×10^{-2} †	
k	cm/sec	$(1.11 \times 10^{-2}) \text{Re}^{0.364}$	(32)
i_{o_1}	A/cm ²	0.33	(33)
α_1		+0.4	(34)
β_1		+0.6	(34)
ϕ_r	V	0.410 ± 0.025 *	
i_{o_2}	A/cm ²	3.3×10^{-4} †	
α_2		+0.40	
β_2		+0.60	

* Measured in the laboratory.
† Estimated.

Values of the properties of the DPA system are listed in Table I. The effective electrolyte conductivity used in model calculations was calculated according to Bruggemann (30)

$$\kappa_{\text{eff}} = \kappa e^{1.5} \quad [18]$$

Rate constants for oxidation of the cation radical intermediate (DPA⁺) to the dication (DPA²⁺) were neither available in the literature nor readily obtainable by experimental measurement. In order to perform the model calculations in the absence of reliable kinetic and physical property data, the following assumptions were made: (i) the molecular configurational and electronic charge density differences between DPA⁺ and DPA²⁺ were accounted for by the (experimentally measured) thermodynamic rest potential between the two species in solution; (ii) the exchange current densities, i_{o_i} , of the two reactions were directly proportional to the respective inlet concentrations of the anodic reactants; and (iii) the relative values of the inlet concentrations of DPA, DPA⁺, and DPA²⁺ were 1000:1:1. Thus, by the first assumption, the anodic and cathodic transfer coefficients of the second oxidation step are equal to those of the first reaction. The third assumption, although unrealistic, was necessary to avoid computational singularities. Finally, the irreversible nature of the second electrochemical reaction was modeled by equating the cathodic back-reaction to zero.

Electrode geometric properties are listed in Table II. The electrode porosity was found by weighing the electrode and measuring the volume occupied after assembly in the cell. It was found by microscope observation that the wire surface was not smooth, as assumed in correlations of specific surface area (35). Based on auxiliary limiting current data in a single reaction system (16, 21), it was concluded that the value obtained by Ref. (35) should be increased by 15% to account for surface roughness effects. With this procedure, it was found that (a) the adjusted specific surface area was essentially identical to those

Table II. Electrode properties and experimental conditions: 9,10 diphenylanthracene system

Electrode cross-sectional area	0.95 cm ²
Electrode length*	5.4 mm
Number of screens in electrode	30
Number of sections in electrode	5
Electrode porosity	0.731
Specific surface area†	153 cm ² /cm ³
Electrolyte flow rate	0.98-16.7 ml/min

* Includes separator material.

† Based on total length and Ref. (35).

best values found by Alkire and Gracon (28) who used a different procedure of determination; (b) current distribution data agreed well with model predictions as illustrated in this work and elsewhere (16); and (c) the total current agreed to within 3% of model predictions.

Polarization data.—Figure 3 compares the theoretical predictions based on the above parameters to the polarization behavior of the flow-through porous electrode for an electrolyte flow rate of 1.65 ml/min. The experimental curve has not been corrected for the IR drop exterior to the working electrode. Considering the approximations that were made for the kinetic parameters, the agreement is reasonable. The model accurately predicts the limiting current but underestimates the kinetically controlled current attributable to the second electrochemical reaction by about 15%.

Yield data.—Reactant and product conversions defined by the relations

$$\theta_{\text{DPA}} = 1 - \frac{c_{\text{DPA}}^1}{c_{\text{DPA}}^0}$$

$$\theta_{\text{DPA}^+} = \frac{c_{\text{DPA}}^{+1} - c_{\text{DPA}}^{+0}}{c_{\text{DPA}}^{+0} + c_{\text{DPA}}^{+0}}$$

$$\theta_{\text{DPA}^{2+}} = \frac{c_{\text{DPA}}^{2+1} - c_{\text{DPA}}^{2+0}}{c_{\text{DPA}}^{2+0} + c_{\text{DPA}}^{+0} + c_{\text{DPA}}^{2+0}}$$

Figure 4 depicts the influence of electrolyte flow rate on the collection efficiency of the porous electrode at the higher of the applied potentials employed during

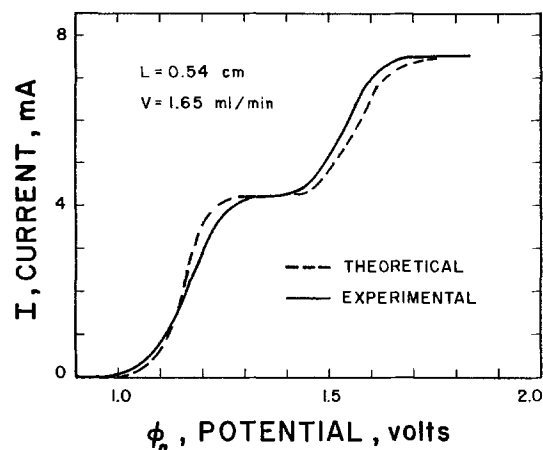


Fig. 3. Comparison of experimental and predicted polarization behavior of 9-10 diphenylanthracene system.

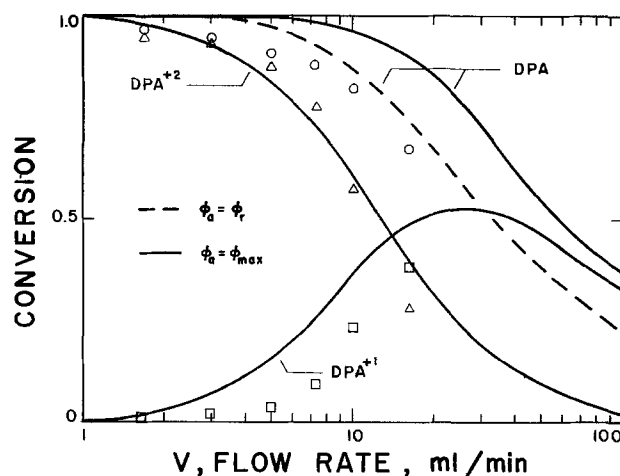


Fig. 4. Collection efficiency vs. flow rate for 9-10 diphenylanthracene system.

each run. All reported applied potentials are *vs.* the downstream SCE and have been corrected for IR drop external to the porous electrode. The DPA conversion efficiency at the lower applied potential value can be determined within experimental error from the DPA conversion curve in Fig. 4. At the lower flow rates, the residence time is sufficiently long to permit nearly quantitative formation of the dication. Decreasing the residence time improves the relative conversion to the radical intermediate since the formation of the final product (DPA²⁺) is affected more adversely by flow rate increases than is the conversion efficiency of DPA to total product.

As mentioned previously, the conversion efficiency of DPA to total product was identical, within experimental error, at both levels of the applied potential employed in this study. The theoretical results for the conversion of DPA to DPA⁺ at an applied potential of $\phi_a = \phi_r$ are indicated by the dotted curve in Fig. 4. The solid lines represent the theoretical calculations for the higher of the two experimentally applied potentials, $\phi_a = \phi_{a,max}$. A summary of the collection efficiencies for the three chemical species is given in Table III. Qualitative agreement with the data is achieved by the model, although the fractional conversion of DPA to DPA⁺ has been underestimated. The predicted total currents are within 3.4% of the observed current levels.

Although experimental limitations prevented investigation of electrode behavior at flow rates in excess of about 20 ml/min, it is apparent from Fig. 4 that the fractional conversion to DPA⁺ for large ϕ_a should eventually reach a maximum value owing to the unabated decrease in the conversion of the starting material to total product as a function of electrolyte flow rate. The anticipated maximum in the outlet concentration of the cation radical supports the contention that a low, single pass conversion at high flow rate is required to maximize the formation of a reaction intermediate (26) for large values of the applied potential. The theoretical calculations indicate that the maximum should occur at 25 ml/min and have a value of 0.53. Therefore, in order to maximize the production efficiency of the reaction intermediate, a low applied potential would be required for flow rates less than 30 ml/min. At higher flow rates, a larger applied potential would result in enhanced DPA⁺ yields at the expense of increased ohmic loss within the electrode and, hence, greater power consumption by the electrochemical reactor.

Current distribution data.—Figures 5 through 10 compare experimental current distribution data with theoretical calculations. All reported applied potentials are *vs.* the downstream SCE and have been corrected for IR drop external to the porous electrode. For the lower of the applied potentials, the multiple reaction sequence is equivalent to a single-electron redox reaction. At the higher of the applied potentials, electrode operation is more complex since the partial current distribution for the second reaction depended on upstream production of DPA⁺ as well as opera-

tional parameters, such as flow rate and electrode length.

The normalized total current distributions for a flow rate of 1.65 ml/min at the two levels of applied potential are shown in Fig. 5. At 1425 mV *vs.* SCE, the oxidation of DPA proceeds at the limiting current throughout the electrode; conversion is quantitative within experimental error. The observed increase in the local current near the electrode outlet is a consequence of fluid channeling along the cell block wall. At 1900 mV *vs.* SCE, reactor performance is also characterized by a highly nonuniform current distribution but with quantitative production of the dication and its nucleophilic addition analog. In Fig. 5, the combination of low flow rate and a uniform potential distribution within the electrode allows both reactions to proceed at their respective mass transfer limited rates.

As the convective supply rate is increased, the second reaction becomes kinetically controlled in the upstream regions of the electrode and the total current distribution becomes more uniform as shown in Fig. 6 and 7. The agreement between theory and experiment indicated by the figures is good.

Figure 8 compares the experimental and theoretical current distributions at two values of the applied potential for a flow rate of 7.25 ml/min. For a low value of the applied potential, ohmic resistance in the solution phase precludes mass transfer control of the initial oxidation step in the upstream region of the electrode. The reaction rate distribution is uniform and the collection efficiency of the cation radical is approximately 87%. The larger ohmic voltage losses

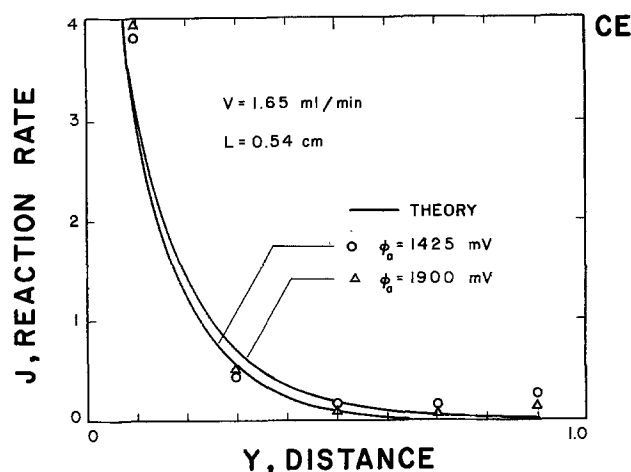


Fig. 5. Total reaction rate distributions for the 9-10 diphenylanthracene system; 1.65 ml/min.

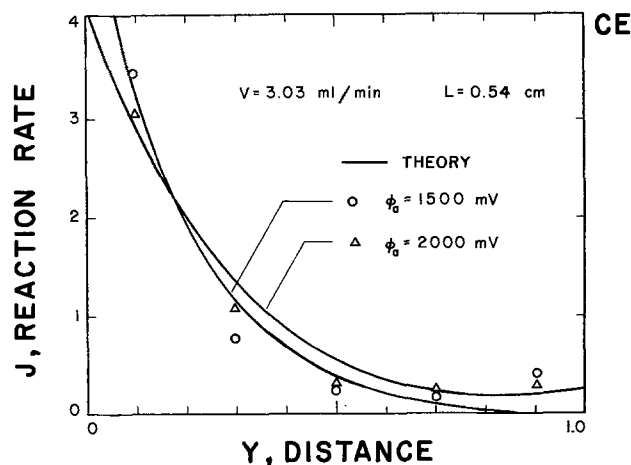


Fig. 6. Total reaction rate distributions for the 9-10 diphenylanthracene system; 3.03 ml/min.

Table III. Collection efficiency measurements: 9-10 diphenylanthracene system

V, ml/min	I _{total} , mA*		θ _{expt}			θ _{calc}		
	Expt	Calc	DPA	DPA ⁺¹	DPA ⁺²	DPA	DPA ⁺	DPA ²⁺
0.94	4.59	4.53	1.00	—	1.00	1.00	—	1.00
1.65	7.55	7.89	0.97	0.01	0.96	1.00	0.02	0.98
3.03	13.73	14.11	0.95	0.01	0.94	1.00	0.06	0.94
4.95	21.75	21.88	0.91	0.02	0.89	1.00	0.15	0.85
7.25	29.90	29.81	0.88	0.11	0.77	0.99	0.26	0.73
9.96	38.50	37.91	0.82	0.25	0.57	0.97	0.37	0.60
16.7	50.83	52.09	0.67	0.39	0.28	0.89	0.49	0.40

* Total current efficiency is 99%+ for each flow rate.

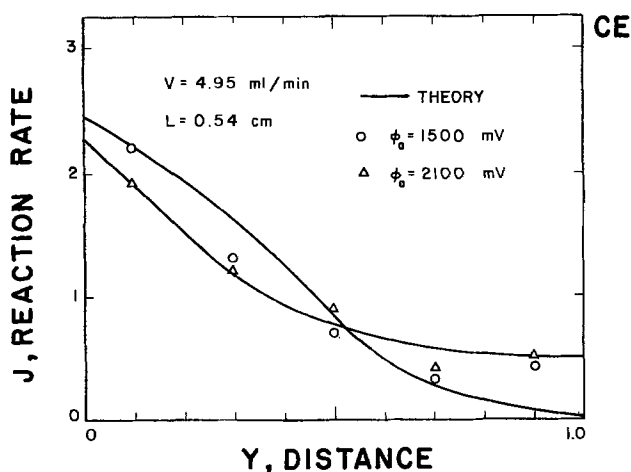


Fig. 7. Total reaction rate distributions for the 9-10 diphenylanthracene system; 4.95 ml/min.

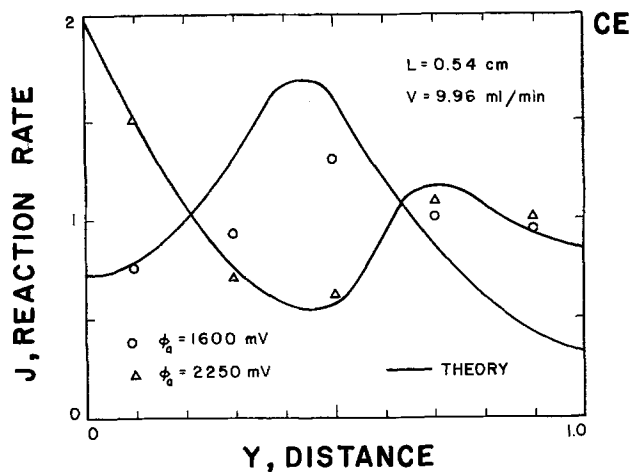


Fig. 9. Total reaction rate distributions for the 9-10 diphenylanthracene system; 9.96 ml/min.

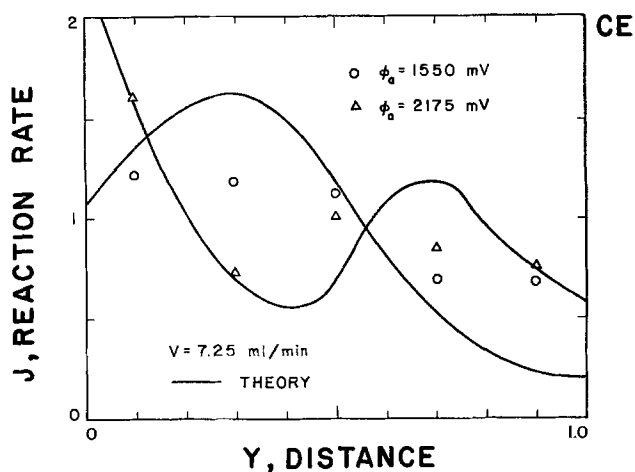


Fig. 8. Total reaction rate distributions for the 9-10 diphenylanthracene system; 7.25 ml/min.

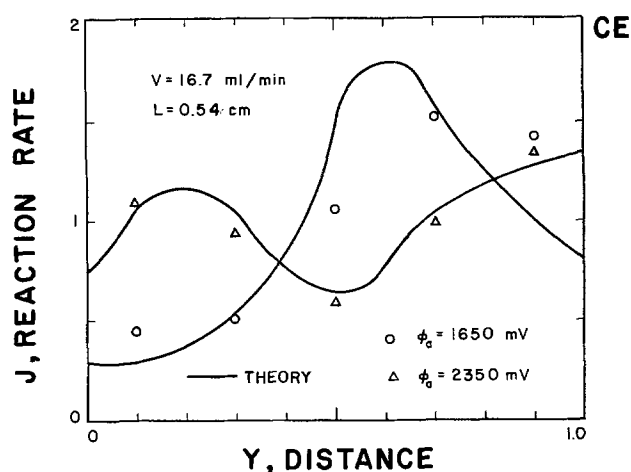


Fig. 10. Total reaction rate distributions for the 9-10 diphenylanthracene system; 16.7 ml/min.

preclude oxidation of DPA^+ in the upstream third of the reactor. At the higher applied potential, the model indicates the DPA consumption occurs at the limiting current in upstream regions and so leads to the observed exponential decrease in total current. As the fluid approaches the counterelectrode, it encounters larger values of the local potential which serve to increase the rate of the second oxidation reaction. The total current proceeds through a maximum owing to reactant depletion in the downstream region. Collection efficiencies for DPA and DPA^+ are 88% and 11%, respectively. Compared to experimental data, the predicted partial current distribution for the second reaction exhibits a greater degree of nonuniformity and is shifted toward the downstream region of the reactor.

Figure 9 shows that, for a large value of the applied potential, an increase in the electrolyte feed rate to 9.96 ml/min yields a more uniform total current distribution and causes a downstream shift in the local maximum owing to the second electrochemical reaction in the sequence. The model tracks the reaction rate distribution with reasonable accuracy and indicates that the oxidation of DPA is kinetically limited for values of the dimensionless distance less than 0.4.

For the highest flow rate investigated, the model predicts a potential drop across the reactor of approximately 1.2V. The large ohmic resistance within the electrolyte is responsible for the local maximum in the partial current distribution of the first oxidation step as illustrated in Fig. 10. In addition, the highly nonuniform potential distribution has restricted the second reaction in the sequence to the down-

stream half of the electrode. The quantitative agreement between theory and experiment at the higher flow rates is an indication that the EEC model can be used to obtain reasonably good estimates of detailed electrode behavior.

Conclusions

In this study, experimental conditions were selected to insure a high level of certainty with respect to reaction chemistry, cell configuration, and theoretical principles for predicting cell behavior. The agreement between experimental data and theoretical calculations reported in this study was particularly noteworthy since it was obtained with use of literature values of system parameters, where known. While still better agreement could have been obtained by further adjustment of parameter values, the purpose of the investigation was to demonstrate the value of engineering models of cell processes in predicting behavior, not to provide an improved data base.

Over the range of conditions studied, a mathematical model of the DPA oxidation reaction was found to provide accurate predictions of cell behavior, even when behavior depends on complex interaction of mass transfer, ohmic, kinetic, and thermodynamic effects. It seems clear that efforts to demonstrate technical feasibility of other electro-organic syntheses might benefit by incorporating mathematical models in the assessment of cell designs. In particular, such models can be used to predict cell behavior and thereby would guide scale-up and optimal specification of design trade-offs. The accuracy of any model is

closely tied to the use of appropriate assumptions and accurate parameter values.

The model used in this study required knowledge of a variety of system characteristics. Included among these were reaction sequence, kinetic rate constants, half-wave potentials, conductivity, mass transfer coefficient, specific surface area, etc. Such detailed knowledge is often not available in practice. Under typical industrial constraints, the act of developing a mathematical model is itself subject to optimal considerations since excessive uncertainty of parameter values can foreshorten the value of any model, no matter how fundamentally sound. Consequently, development of models for specific applications should be guided largely by the availability of information about the process. Improved strategies are needed for constructing engineering models of practical electrochemical systems.

Complications in using mathematical models may be anticipated when cell processes are not understood or easily characterized. Examples which occur frequently in electro-organic syntheses include multiphase flow as with gaseous feedstock, gas evolution reactions, and use of immiscible liquid phases. Additional engineering studies are needed if such processes are to be designed with confidence on a large scale.

Acknowledgments

Research costs were supported by NSF Grant 76-83379 and by fellowship support from E. I. du Pont de Nemours & Company, and the Exxon Education Foundation.

Manuscript submitted April 27, 1979; revised manuscript received Oct. 2, 1979.

Any discussion of this paper will appear in a Discussion Section to be published in the December 1980 JOURNAL. All discussions for the December 1980 Discussion Section should be submitted by Aug. 1, 1980.

Publication costs of this article were assisted by the University of Illinois.

LIST OF SYMBOLS

a	specific surface area, cm^2/cm^3 pore volume
c	concentration, gmole/cm^3
C	concentration, dimensionless
D	axial diffusion coefficient, cm^2/sec
e	symbol of electronic charge
f	intrinsic reaction rate, A/cm^2
F	Faraday's constant, 96,500 C/g equiv.
i_0	exchange current density, A/cm^2
k	mass transfer coefficient, cm/sec
k_c	homogeneous reaction rate constant, liter/gmole-sec
l	electrode length, cm
M_i	symbol for species i participating in reaction
n	number of electrons in a reaction, g equiv./gmole
R	gas constant, 8.314 J/gmole-deg
S	reaction source term, moles/ cm^3 -sec
T	temperature, °K
v	mass average velocity, cm/sec
y	distance along electrode, cm
Y	distance along electrode, dimensionless
z_i	symbol of electronic charge of species i
α	anodic transfer coefficient
β	cathodic transfer coefficient
ϵ	void fraction, cm^3 void space/ cm^3 reactor volume
Γ	mass transfer coefficient, dimensionless
ζ	velocity, dimensionless
κ	electrolyte conductivity, $(\Omega\text{-cm})^{-1}$
λ	species concentration, dimensionless
Λ	heterogeneous rate constant, dimensionless
ν	stoichiometric coefficient
ξ	electrochemical reaction rate constant, dimensionless
ϕ	potential, V
Φ	potential, dimensionless
Φ_a	applied potential, dimensionless
χ	mass transfer resistance parameter, dimensionless.

Superscripts

l	value at reactor outlet
o	value at reactor inlet
s	surface value

Subscripts

i	species i
j	reaction j
r	reference value

REFERENCES

- R. B. MacMullin, *Electrochem. Technol.*, **2**, 106 (1964).
- "Electro-organic Synthesis Technology," E. Weissman, M. Krumpelt and R. Alkire, Editors, A.I.Ch.E. Symp. Ser., New York (1979).
- S. Swann, Jr. and R. Alkire, "Bibliography of Electro-organic Syntheses 1801-1975," The Electrochemical Society, Inc., Princeton, N.J., In press.
- T. R. Beck, R. C. Alkire, and N. L. Weinberg, *This Journal*, **126**, 136C (1979).
- R. W. Houghton and A. T. Kuhn, *J. Appl. Electrochem.*, **4**, 173 (1974).
- J. S. Newman and W. Tiedemann, *Adv. Electrochem. Electrochem. Eng.*, **11**, 353 (1978).
- G. Alberts and I. Shain, *Anal. Chem.*, **35**, 1857 (1963); R. Nicholson and I. Shain, *ibid.*, **36**, 706 (1964); *ibid.*, **37**, 178 (1965).
- J. A. Harrison and D. W. Shoesmith, *J. Electroanal. Chem.*, **28**, 301 (1970).
- A. J. Bard and K. S. V. Santhanam, in "Electroanalytical Chemistry," Vol. 4, A. J. Bard, Editor, p. 215, Marcel Dekker, New York (1970).
- L. N. Klatt, *J. Electroanal. Chem.*, **55**, 161 (1974).
- H. Matsuda, *ibid.*, **15**, 109 (1967).
- R. C. Alkire and A. A. Mirarefi, *This Journal*, **124**, 1214 (1977).
- R. White and J. S. Newman, *J. Electroanal. Chem.*, **82**, 173 (1977).
- R. White, J. A. Trainham, J. S. Newman, and T. W. Chapman, *This Journal*, **124**, 669 (1977).
- R. C. Alkire and R. M. Gould, *ibid.*, **123**, 1842 (1976).
- R. M. Gould and R. C. Alkire, *This Journal*, **126**, 2125 (1979).
- B. G. Ateya and L. G. Austin, *This Journal*, **124**, 1540 (1977); B. G. Ateya, *J. Electroanal. Chem.*, **76**, 315 (1977).
- J. A. Trainham and J. S. Newman, *This Journal*, **124**, 1528 (1977).
- Y. Volkman, *J. Appl. Electrochem.*, **8**, 374 (1978).
- J. A. Trainham and J. S. Newman, *This Journal*, **125**, 58 (1978).
- R. M. Gould, Ph.D. Thesis, University of Illinois (1979).
- M. R. Rifi and R. H. Covitz, "Introduction to Organic Electrochemistry," pp. 96-97, Marcel Dekker, New York (1974).
- J. F. Coetzee, *Pure Appl. Chem.*, **13**, 429 (1966).
- R. E. Sioda, *J. Phys. Chem.*, **72**, 2322 (1968).
- P. T. Kissinger and C. N. Reilley, *Anal. Chem.*, **42**, 12 (1970).
- R. E. Sioda, *Electrochim. Acta*, **20**, 457 (1975).
- C. Madec and J. Courto-Coupez, *J. Electroanal. Chem.*, **84**, 169 (1972).
- R. Alkire and B. Gracon, *This Journal*, **122**, 1594 (1975).
- J. S. Newman, *Ind. Eng. Chem., Fundam.*, **7**, 514 (1968).
- D. A. G. Bruggemann, *Ann. Physic.* **24**, 636 (1935).
- G. Manning, V. D. Parker, and R. N. Adams, *J. Am. Chem. Soc.*, **91**, 4584 (1969).
- C. N. Satterfield and D. H. Cortez, *Ind. Eng. Chem., Fundam.*, **9**, 613 (1970).
- M. E. Peover and B. S. White, *J. Electroanal. Chem.*, **13**, 93 (1967).
- H. Kojima and A. J. Bard, *J. Am. Chem. Soc.*, **97**, 6317 (1975).
- J. C. Armour and J. N. Cannon, *AICHE J.*, **14**, 415 (1968).
- O. Hammerich and V. Parker, *J. Am. Chem. Soc.*, **96**, 4289 (1974).

Determination of Some Physical Properties of N-Type Semiconductor Alloys ($0 \leq x \leq 1$) by Photoelectrochemistry

A. M. Redon* and J. Vigneron

Laboratoire d'Electrochimie Interfaciale, Bellevue, France

and J. Chevallier

Laboratoire de Physique du Solide, Bellevue, France

ABSTRACT

Some physical properties (the bandgap energy, the electronic transition mode, and the diffusion length) are determined on n-type $\text{Ga}_x\text{In}_{1-x}\text{P}$ alloys with ($0 \leq x \leq 1$), using photoelectrochemical techniques. Studies were made in acidic solution ($\text{KCl } 0.5\text{M} + \text{HCl pH} \sim 1$), since the photocurrent is only stable at this pH. The values obtained are in very good agreement with the results of electroreflectance piezotransmission and transmission measurements.

It is well established that the theoretical optimum bandgap energy (E_g) of semiconductors for photo-voltaic conversion of solar energy is about 1.6 eV (1) (Fig. 1). The collecting structure can be a Schottky diode, a p-n junction, or a photoelectrochemical cell (2, 3). Among the different possible materials the $\text{Ga}_x\text{In}_{1-x}\text{P}$ alloys are attractive for this purpose, because for $0 \leq x \leq 0.64$, they have a direct bandgap energy in the range 1.3-2.00 eV.

Due to the direct nature of the electronic transition mode, the absorption coefficient of photons with energy $h\nu > E_g$ is high compared with that for indirect band-gap materials, and the absorption length for such photons is typically a few microns.

In this paper, we study a $\text{Ga}_x\text{In}_{1-x}\text{P}$ photoelectrochemical cell with $0 \leq x \leq 1$, and from the analysis of the photocurrent behavior we deduce several optical and electrical properties of these alloys. All the experiments are made without redox systems. The nature of the photocurrent in this case is developed in this paper. In the future it will clearly be of interest to study these compounds in the presence of redox systems with the aim of improving the quantum yield.

Theoretical Analysis of the Photocurrent

This measurement technique uses the photoeffect across an electrolyte-semiconductor junction. The presence of an electrolyte at the surface of a semiconductor can create either an accumulation or a depletion layer at the surface depending on the nature of the charge distribution of the electrolyte-semiconductor interface. For an n-type semiconductor with a concentration of majority carriers $N_D - N_A \approx 10^{17} \text{ cm}^{-3}$ and an electrolyte concentration 0.5M, a depletion layer is created at the interface. When the semiconductor is illuminated, a photocurrent due to the generation of electron-hole pairs is produced. These pairs are separated by the electric field produced in the space charge region. So, for n-type electrodes, the holes are attracted by the counterelectrode, via the electrolyte, so photoelectrolysis of the water is produced, or anodic dissolution of the electrode depending on the relative position of the free energy of these two reactions, but also, both reactions may take place simultaneously.

If the surface of the cathode is sufficiently large, then the photoresponse of the cell is determined by the oxygen reaction or anodic photodecomposition kinetics, or by the generation-recombination-diffusion

processes of the electron hole pairs generated in the semiconductor. If the variation of the photocurrent is linear with the light intensity, then the carrier generation is the rate-limiting step. So, if the junction electrolyte-semiconductor is considered to be equivalent to a Schottky barrier and if the electron hole recombination at the surface is neglected, as it is possible for polycrystals with large band bending, when there is a linear variation of the photocurrent vs. the incident light energy, it is easy to describe the photocurrent by the theory of Gärtner (4)

$$J = q\Phi[1 - e^{-\alpha W}/(1 + \alpha L_p)] + qp_0D_p/L_p \quad [1]$$

α is the optical absorption coefficient determined with an absorption spectrometer, q is the charge transfer per unit electrochemical reaction, Φ the photon flux density, L_p the diffusion length, D_p the diffusion constant, and p_0 the concentration of holes at equilibrium,

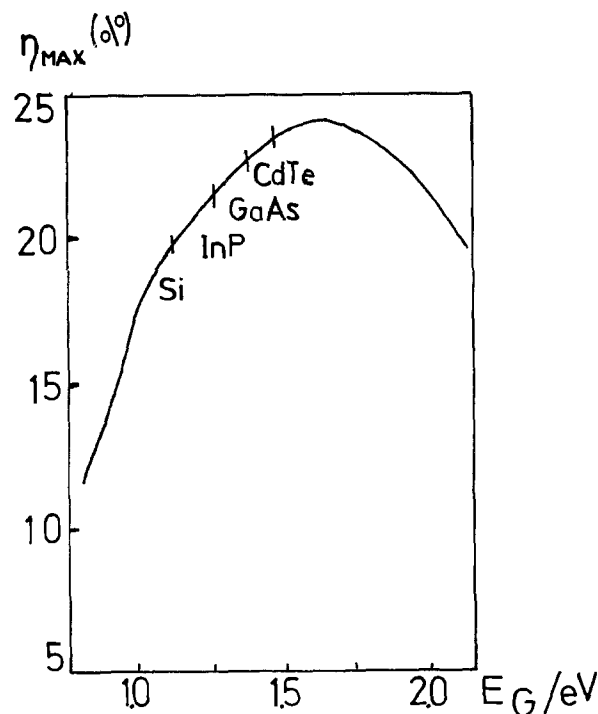


Fig. 1. Theoretical maximum efficiency for solar batteries as a function of the energy gap of the semiconductor (1).

* Electrochemical Society Active Member.

Key words: semiconductors, alloys, photoelectrochemistry, energy conversion.

without illumination. W is the depletion layer width given by the following expression

$$W = K_0(V - V_{fb})^{1/2} \quad [2]$$

V is the applied voltage relative to the reference electrode, V_{fb} the flatband potential measured relatively to the same reference. K_0 is a constant which depends on the permittivities of free space ϵ_0 on the dielectric relative constant in the depletion layer of the semiconductor ϵ_r and on the number of majority carriers ($N_D - N_A$)

$$K_0 = \left(\frac{2\epsilon_r\epsilon_0}{q(N_D - N_A)} \right)^{1/2} \quad [3]$$

The term $qp_0 D_p/L_p$ can be neglected as corresponding to the dark current.

This expression of the current density is also good if the light is chopped with frequencies $\omega < 1/t_0$, t_0 being the carrier transit time through the depletion layer (4). So the quantum efficiency is given by

$$\eta = \frac{J}{q\Phi} = 1 - e^{-\alpha W} / (1 + \alpha L_p) \quad [4]$$

If the potential of the electrode is near the flatband potential so that $\alpha W \ll 1$, then, Eq. [4] can be approximated to

$$\eta = \frac{\alpha}{1 + \alpha L_p} [L_p + K_0(V - V_{fb})^{1/2}] \quad [5]$$

This theory was developed further by Wilson (5) in the case where there is a surface recombination.

Experimental Techniques

For photoelectric measurements, we used a 150W Xenon lamp (Schoeffel) as the light source and a Jobin-Yvon HRS 2 monochromator with a 500 nm blazed grating. The monochromatic light illuminates the electrode through a quartz window situated in the bottom of the electrochemical cell. In order to avoid the dark current contribution, the light is modulated by a chopper (PAR 125 A) and the photocurrent is detected by a lock-in amplifier (PAR Model 121), so that the dark current is eliminated at the detection. However for samples investigated in this work, the dark currents are negligible in front of the photocurrents.

The electrochemical cell is inserted on a plate which can be rotated around three axis and displaced in any of these directions. So, it is easy to position the electrodes very accurately always at the same place and then to compare their efficiencies. The intensity of the light has been determined by a photodiode located behind the cell, so that the contribution of the light absorption in the solution is taken into account.

For linear sweep voltammetry (LSV) measurements, a classical experimental set is used.

Samples and Experimental Conditions

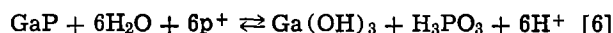
Samples.—The semiconductor electrodes used are polycrystalline $Ga_xIn_{1-x}P$ alloys ($0 \leq x \leq 1$). They were doped with sulfur and the free electron concentration is $(N_D - N_A) \approx 10^{17}/cm^3$ at 300°K for all the alloys. To collect the current, the contact between the semiconductor and the metal must be perfectly ohmic. The decrease of the barrier of the contact is obtained by tin diffusion. The composition of these polycrystals was determined by electron microprobe analysis, and the surface area was measured for all samples by a photographic technique with a precision of about 5%. These polycrystals are mechanically polished. Before studying them the first time, they were etched for a few seconds in a 2% bromine solution in methanol. This etching was not repeated before all experiments, because the photocurrents observed for the compositions with high percentage of In, both in the dark and under the light are unstable. Probably some bromine

remains absorbed on the electrode and can be removed after numerous sweeps, because the I - V curves then become stable.

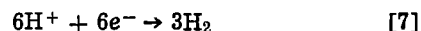
Experimental Conditions and Stability of the Electrodes

The photocurrents observed are stable only in acidic solutions. In solutions of neutral or basic pH, they slowly decrease with the time, except for $x = 0$. This was also observed by Vervaet *et al.* (6) on InP electrodes, and by Gautron and Lemasson (7), on ZnSe. On InP, this result can be explained by the formation of $In(OH)_3$ film which remains on the surface of the electrode in neutral or basic solutions for it is insoluble at this pH (8). In the case of GaP, $Ga(OH)_3$ is formed, which is soluble at all pH because the photocurrent remains always stable. For this reason, all the experiments were done in acidic pH (pH ≈ 1) in 0.5M KCl + HCl electrolyte.

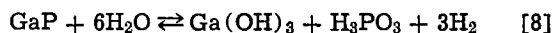
The different decomposition reactions which can be involved are recalled here: for GaP, the anodic dissolution process involves six holes (9-11)



As we have also the following reaction at the counter-electrode



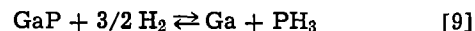
The total reaction is



The calculation of the free energy of this reaction gives, with the free enthalpy of dissociation of GaP: $\Delta G_{GaP} = -24.4$ kcal/mole (12), $E^{\circ}_{1dp GaP} = -\Delta G/nF = -0.29$ eV/NHE at pH = 0 (13). (n is the number of holes ($n = 6$) in the reaction, F is the Faraday constant). As these electrodes have a Nernstian behavior

$$E_{1dp GaP} = -0.35 \text{ V/NHE at pH} = 1$$

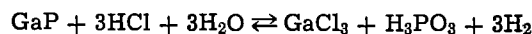
Another reaction of dissolution should be taken into account; the cathodic reaction of dissolution involving hydrogen (14)



that gives as redox potential for this anodic decomposition of GaP $E^{\circ}_{dn} = -0.40$ V at pH = 0 or $E_{dn} = -0.46$ V at pH = 1.

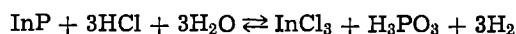
The reactions involved are of the same type for InP, and the free energy of the reactions falls also in the middle of the bandgap. With $\Delta G_{InP} = -11.55$ kcal (15), $E^{\circ}_{1dp InP} = -0.253$ V/NHE at pH = 0 or $E^{\circ}_{1dp InP} = -0.31$ V/NHE at pH = 1. For the cathodic decomposition, $E^{\circ}_{dn} = -0.23$ V/NHE at pH = 0, or $E_{dn} = -0.29$ V/NHE at pH = 1.

Other reactions can be involved in this electrolyte as



The free energy of this reaction is $E^{\circ}_{2dp GaP} = -0.50$ V at pH = 0, or $E_{2dp GaP} = -0.44$ V at pH = 1.

With the InP, the reaction involved is



and the free energies are $E_{2dp InP} = -0.576$ V at pH = 0, or $E_{2dp InP} = -0.516$ V at pH = 1.

Quantum Efficiency of This Photocell Determination of the Bandgap and the Transition Mode of the $Ga_xIn_{1-x}P$ ($0 \leq x \leq 1$)

The main purpose of this work is to obtain the bandgap energy and the electronic transition mode of these compounds by means of a photoelectrochemical technique. With electroreflectance, cathodoluminescence, and transmission measurements, these studies were previously made (Fig. 2-3) (16-18) so the results obtained in this work can be easily compared.

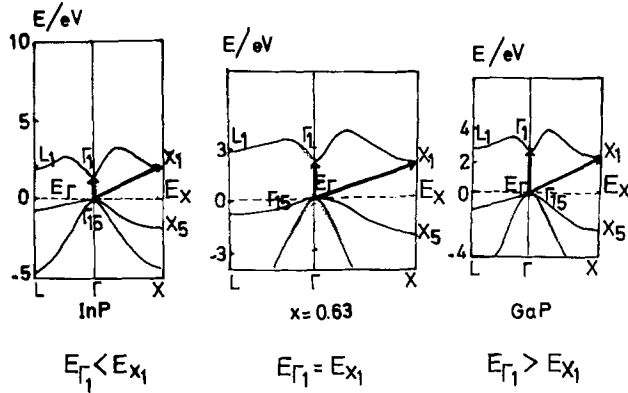


Fig. 2. Band structure for $x = 0$ (InP), $x = 0.63$ ($\text{Ga}_{0.63}\text{In}_{0.37}\text{P}$), $x = 1$ (GaP) (17).

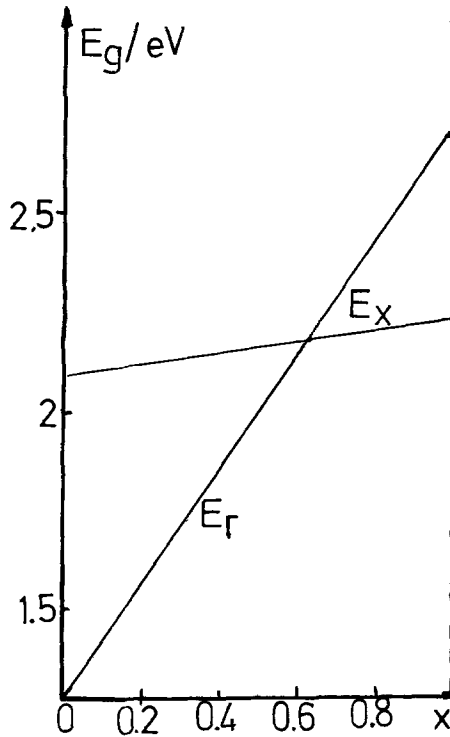


Fig. 3. Variation of the bandgap width as a function of the composition of the alloy (16).

Quantum efficiency vs. the composition of the alloys and the polarization of the electrode.—Determination of L_p .—The electrodes are illuminated and positioned always at the same place corresponding to the maximum of photocurrent. All the intensities are converted to unit area, and the quantum efficiencies are determined and compared for several compositions. Figure 4 shows the quantum efficiency variation obtained with this compound vs. the wavelength of the incident light.

The stationary LSV curves were obtained for different compositions (Fig. 5). The behavior is different, depending on the composition x . This can be easily understood by the difference of diffusion length L_p (Eq. [5]).

After verifying the linearity of the photocurrent vs. the intensity of the incident light so that the limiting rate is the creation of hole pairs, we can estimate the diffusion length L_p of minority carriers using the approximation of Eq. [5], that is to say in the case where $\alpha W \ll 1$. The comparison of our results to those obtained classically using D_p , diffusion constant, and τ_p time recombination of minority carriers, shows that the theory of Gärtner is valid for our compounds.

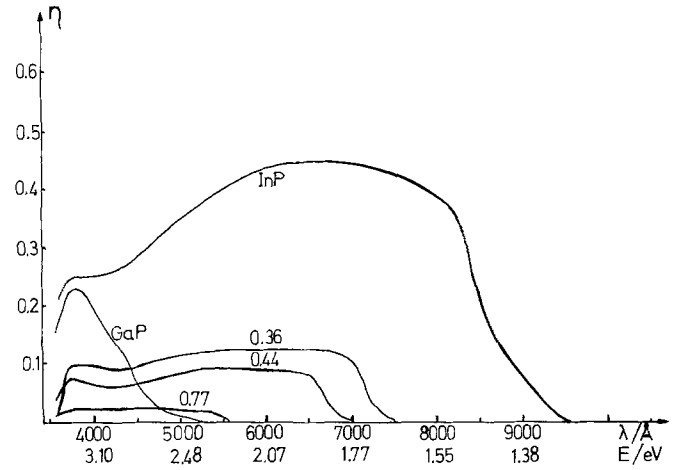


Fig. 4. Variation of the quantum efficiency for the different compositions x of the alloys $\text{Ga}_x\text{In}_{1-x}\text{P}$ vs. the incident photon energy. All the results are corrected from the surface of the sample and the response of the photodiode. Electrolyte, KCl 0.5M + HCl ($\text{pH} \approx 1$). Bias voltage $V = -0.25$ V/NHE.

In the case of GaP, the different constants are $\mu_p = 100$ cm^2/Vsec (mobility of minority carriers), $\tau_p \approx 30$ nsec (time recombination of minority carriers) (19), $\epsilon_r = 11$, $N_D - N_A \approx 10^{23}/\text{m}^3$ and $D_p \approx 2.5$ cm^2/sec . So, as

$$L_p = \sqrt{D_p \tau_p} \quad [10]$$

then the diffusion length is $L_p \approx 2.7$ μm . Studying the photocurrent, as $\alpha \sim 2.25 \cdot 10^2$ cm^{-1} (Fig. 6) for $h\nu = 2.4$ eV, and as $\eta = 0.049$ for the same energy (Fig. 4), with a polarization $V = 1.65$ V/NHE, with $V_{fb} = -1$ V/NHE ($\text{pH} = 1$) (Fig. 11), then the diffusion length obtained is $L_p \approx 2.5$ μm .

For InP compounds, $\mu_p \approx 100$ cm^2/Vsec , $\tau_p \approx 3$ nsec, $\epsilon_r = 12.37$, $N_D - N_A \approx 10^{23}/\text{m}^3$, so that $L_p \approx 0.9$ μm . As $\eta = 0.54$ for $h\nu = 1.35$ eV and $V = 0.7$ V/NHE (Fig. 4), with $\alpha \approx 10^4$ cm^{-1} (Fig. 7) (20), with $V_{fb} = -0.2$ V/NHE ($\text{pH} = 1$) (Fig. 11), the diffusion length of minority carriers obtained is $L_p = 0.9$ μm .

The values obtained are in good agreement.

Determination of the bandgap width and the transition mode.—The absorption coefficient α , directly depends on the photon energy following the expression (21)

$$\alpha = A \frac{(h\nu - E_x)^2}{h\nu} \quad [11]$$

for indirect interband transitions, and

$$\alpha = A \frac{(h\nu - E_\Gamma)^{1/2}}{h\nu} \quad [12]$$

for allowed direct transition.

The quantum efficiency η , in the case of $\alpha L_p \ll 1$ is proportional to α , so, it is easy to determine the bandgap plotting the different values of η^2 or $\eta^{1/2}$ vs. the incident energy $h\nu$, near the bandgap where the variation $h\nu$ is large compared with the difference $(h\nu - E_g)$ (with $E_g = E_\Gamma$ or E_x). Then, E_Γ and E_x being known, the transition mode can be studied plotting $\log(\eta h\nu)$ vs. $(h\nu - E_g)$. So, if the slope is 2, the transition is indirect and if the slope is $1/2$, the transition allowed is direct.

On Fig. 8, the variation of $\sqrt{\eta}$ deduced from Fig. 4, for $x = 0.77$, $x = 0.905$, $x = 1$ is plotted vs. the incident energy $h\nu$. The low energy portion is characteristic of the incident electronic transition, and its extrapolation towards $\eta = 0$ gives the value of the bandgap energy E_x . At higher energy, the dominant absorption comes from the direct electronic transition which arises approximately when the slopes change.

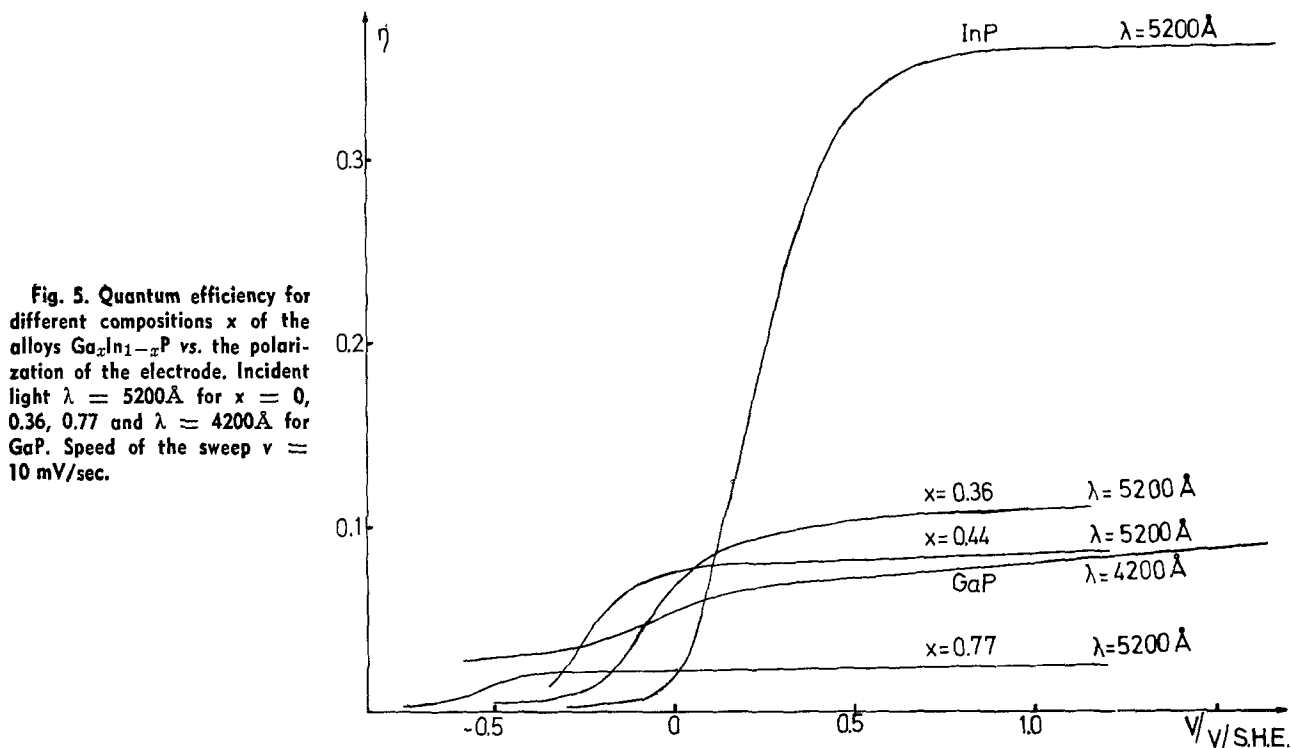


Fig. 5. Quantum efficiency for different compositions x of the alloys $\text{Ga}_x\text{In}_{1-x}\text{P}$ vs. the polarization of the electrode. Incident light $\lambda = 5200\text{\AA}$ for $x = 0, 0.36, 0.77$ and $\lambda = 4200\text{\AA}$ for GaP. Speed of the sweep $v = 10\text{ mV/sec}$.

For $0 \leq x \leq 0.64$, the transition mode is direct, so that η^2 is drawn vs. $h\nu$ (Fig. 9).

These results are also in very good agreement with the results obtained by electroreflectance measurements (17).

Then, drawing $\log(\eta h\nu)$ vs. $(h\nu - E_x)$ or $(h\nu - E_r)$, the optical transition mode can be determined (Fig. 10). The results are also in accordance with the previous works, obtained by transmission, electroreflectance, and piezotransmission (22). For $x = 0, 0.36, 0.44$, the transition is direct, as for $x = 0.77, 0.905, 1$, the transition is indirect.

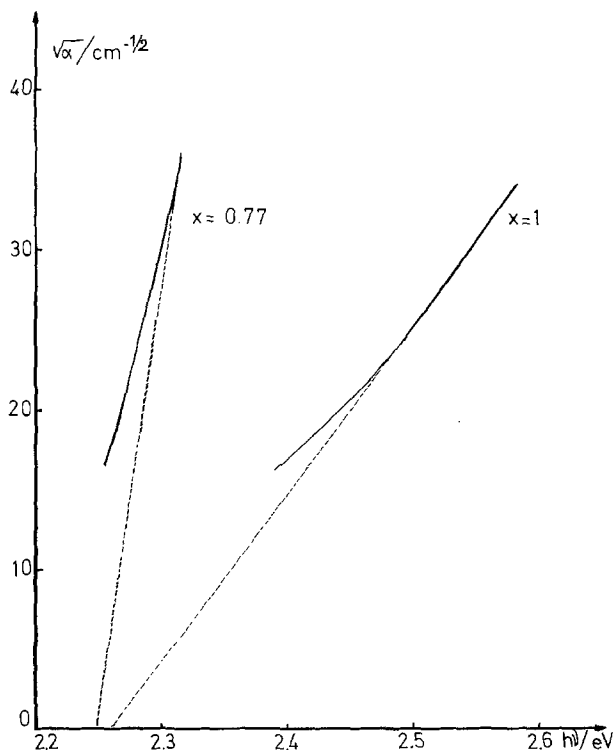


Fig. 6. Variation of the absorption coefficient α for the compositions $x = 0.77$ and $x = 1$ vs. the incident photon energy.

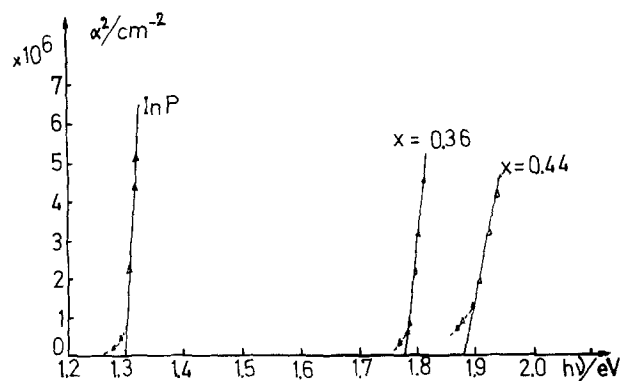


Fig. 7. Variation of the absorption coefficient α for the compositions $0 \leq x \leq 0.64$ vs. the incident photon energy.

Knowing the bandgap energy and the Fermi level from impedance measurement (23, 24), the position of the energy levels are deduced in our experimental conditions ($\text{pH} = 1$) (Fig. 11).

The flatband potential can also be determined studying the variation of the square root of the photocurrent vs. the electrode potential. This study was made by Butler on WO_3 electrodes (25), and by Gautron and Lemasson (7) on ZnSe. If $L_p \ll W$, then Eq. [5] can be approximated by the relation

Table I.

Composition	E_x (eV)	E_r (eV)
GaP ($x = 1$)	2.26	2.7
$x = 0.905$	2.24	2.42
$x = 0.77$	2.22	

Table II.

Composition	E_r (eV)
$x = 0.44$	1.8
$x = 0.36$	1.72
$x = 1$	1.5

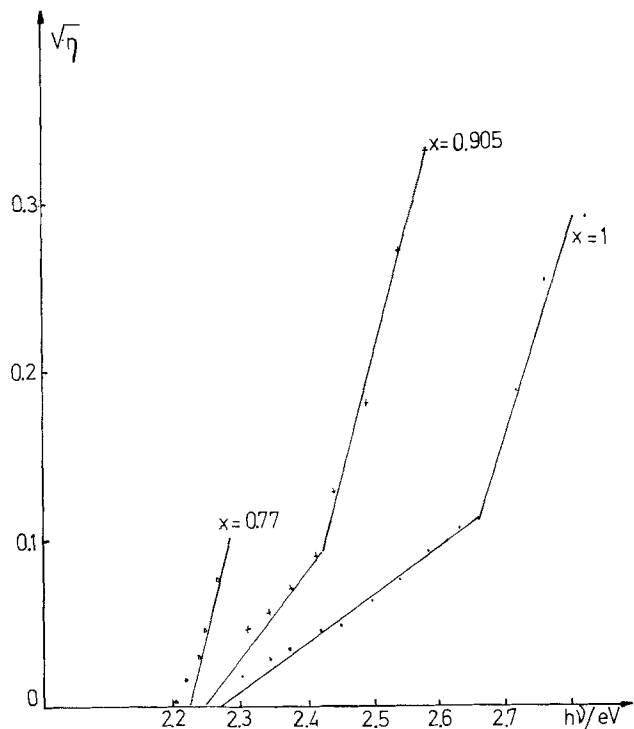


Fig. 8. Variation of $\eta^{1/2}$ for the compositions $0.64 \leq x \leq 1$ vs. the incident photon flux in KCl 0.5M + HCl (pH = 1). Bias voltage $V = -0.25$ V/NHE.

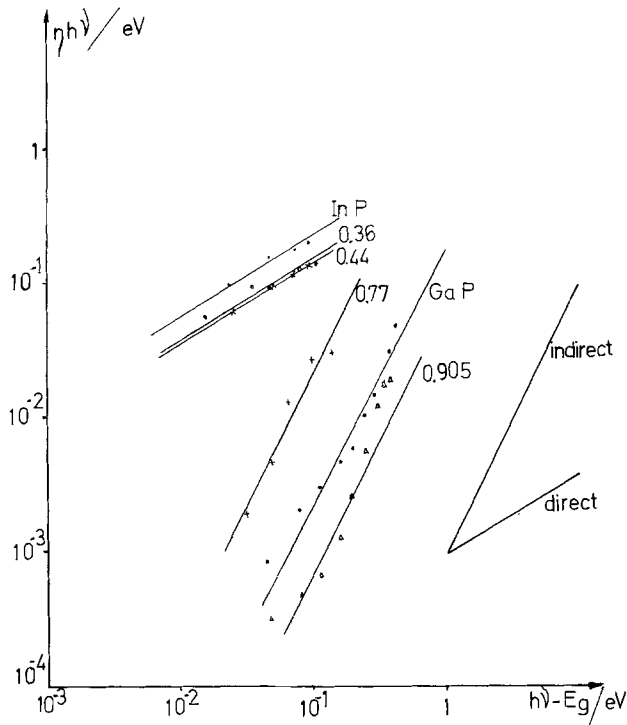


Fig. 10. Behavior of quantum efficiency with incident photon energy for the determination of the electronic transition mode.

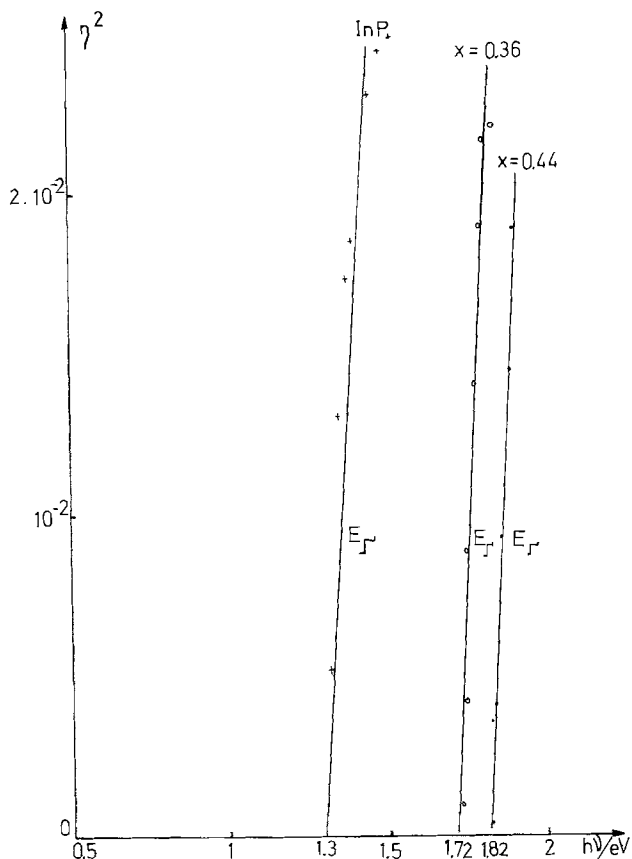


Fig. 9. Variation of η^2 for the compositions $0 \leq x \leq 0.64$ vs. the incident photon flux in KCl 0.5M + HCl (pH = 1). Bias voltage $V = -0.25$ V/NHE.

$$V - V_{fb} = \eta^2(1 + \alpha L_p) / \alpha K_0 \quad [13]$$

The results obtained are approximately the same as those found from impedance measurements (Fig. 11).

Conclusion

The $Ga_xIn_{1-x}P$ alloys ($0 \leq x \leq 1$) are very interesting compounds as for compositions $0 \leq x \leq 0.64$, the transition is direct and the bandgap is included in the range 1.35-2.00 eV the theoretical maximum efficiency being 1.6 eV (1).

By photoelectrochemical measurements, it is easy to determine the bandgap energy, the electronic transition mode, and the diffusion length for new materials, as shown in this work.

But an important disadvantage remains the anodic dissolution of the electrode. First the dark current increases at anodic potentials for compositions with low x , probably due to a dissolution. The potential where the current begins is increasing when x increases. Second, the photocurrents obtained for low x compositions are more important than the photocurrents of $x \approx 1$. As the energy of anodic decomposition is greater than the energy of O_2 formation by photoelectrolysis of the water (E_{1dp}), then this photocurrent, in this experimental condition is due to the reaction of decomposition with the solvent (25). This photo-decomposition is also more important for low x values (Fig. 11). We are working now on the possibility of blocking this dissolution with a suitable redox reaction.

Acknowledgments

The authors wish to thank Dr. Parsons for his helpful discussions, Dr. Ph. Lemasson, Dr. A. M. Baticle, and Dr. J. L. Sculfort for their constant help in the execution of this work. The alloys were made by J. Bourneix and mounted on their support by Mme. de Mende. The construction of the apparatus was executed with aid of a D.G.R.S.T. Contract No. 650.1617.

Manuscript submitted May 24, 1979; revised manuscript received Sept. 24, 1979.

Any discussion of this paper will appear in a Discussion Section to be published in the December 1980 JOURNAL. All discussions for the December 1980 Discussion Section should be submitted by Aug. 1, 1980.

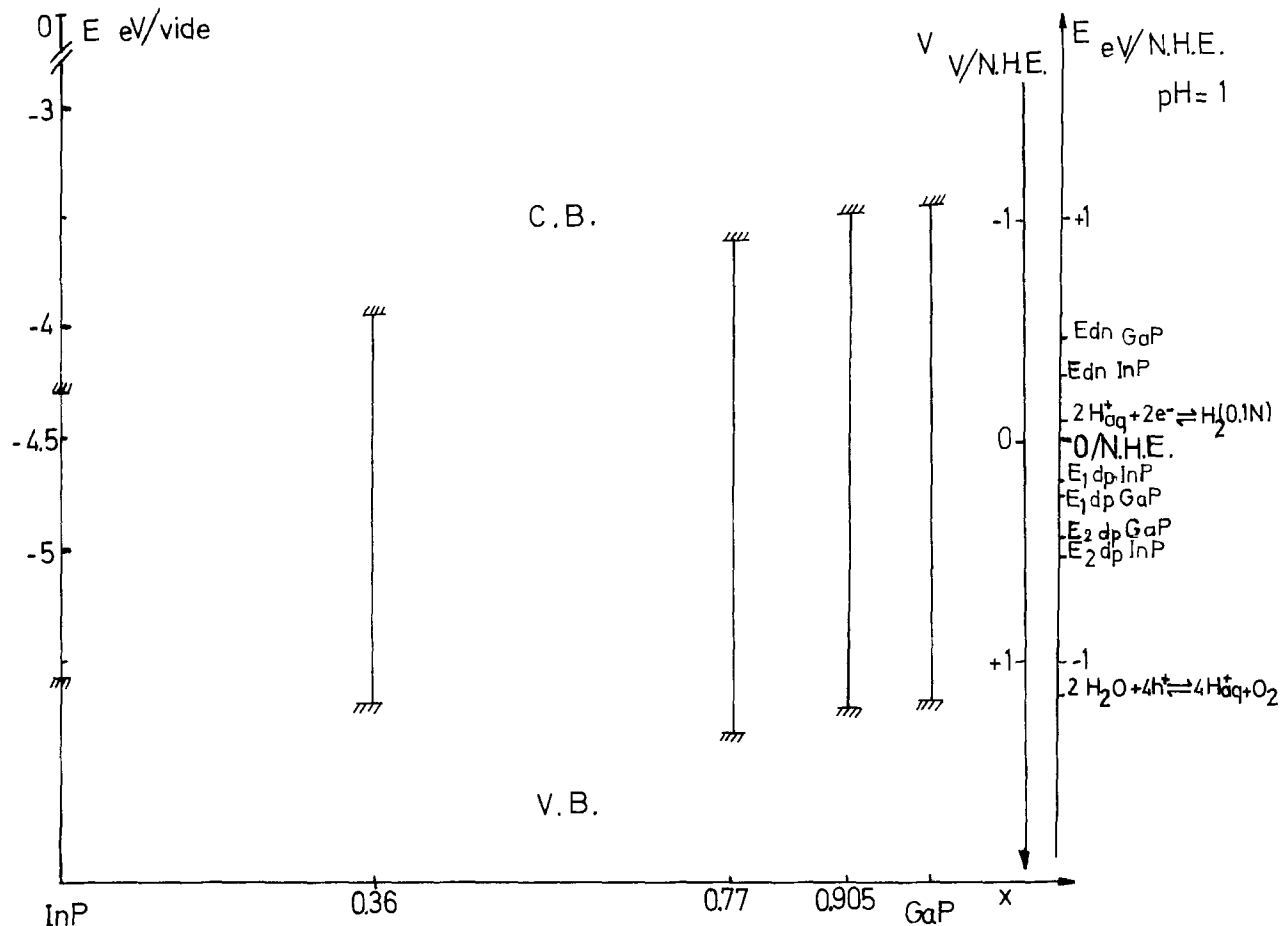


Fig. 11. Characteristic correlations between bandedges of the $Ga_xIn_{1-x}P$ alloys and redox potentials for decomposition ($pH = 1$)

REFERENCES

- J. Loferski, *J. Appl. Phys.*, **27**, 777 (1956).
- F. H. Fischer, in "Festkörperprobleme IV," Pergamon Viewey, Braunschweig (1974).
- H. Gerischer, in "Semiconductor Liquid-Junction Solar Cells," A. Heller, Editor, p. 1, The Electrochemical Society Softbound Proceedings Series, Princeton, N.J. (1977).
- W. W. Gartner, *Phys. Rev.*, **116**, 84 (1959).
- R. H. Wilson, *J. Appl. Phys.*, **48**, 4292 (1977).
- A. A. K. Vervaet and W. P. Gomes, *J. Electroanal. Chem.*, **91**, 133 (1978).
- J. Gautron, P. Lemasson, F. Rabago, and R. Triboulet, *C. R. Acad. Sci.* **C287**, 349 (1978).
- A. J. Busev, "The Analytical Chemistry of Indium," Pergamon, Oxford (1976).
- R. Memming, *Phil. Tech. Rev.* (1978).
- R. Memming, *This Journal*, **125**, 117 (1978).
- R. Memming, in Proceedings of Permanent School on Solar Energy Processes, V. Silvestrini, Editor, Sogesta Urbino, Italy, Nov. 1978.
- C. D. Thurmond, *J. Phys. Chem. Solids*, **26**, 785 (1965).
- W. M. Latimer, "Oxydation Potential," Prentice Hall, Englewood Cliffs, N. J. (1938).
- M. J. Madov, E. Cardon, and W. P. Gomes, *Ber. Bunsenges. Phys. Chem.*, **82**, 819, 823 (1978).
- O. Kubaschewski, E. Li. Evans, and C. B. Alcock, "Metallurgical Thermochemistry," Pergamon Press, Elmsford Park, N.Y. (1967).
- H. Rodot, J. Horak, G. Rouy, and J. Bourneix, *C. R. Acad. Sci. Paris*, **A269**, Série B, 381 (1969).
- J. Chevallier, Thesis of "Doctorat d'Etat," Paris (1975).
- P. Alibert, G. Bordure, A. Laugier, and J. Chevallier, *Phys. Rev. B*, **6**, 1301 (1972).
- P. J. Dean, C. J. Frosch, and C. H. Henry, *J. Appl. Phys.*, **39**, 5631 (1968).
- R. Newman, *Phys. Rev.*, **111**, 1518 (1958).
- J. I. Pankove, in "Optical Processes in Semiconductors," Dover Publication Inc., New York (1971).
- P. Merle, D. Auvergne, H. Mathieu, and J. Chevallier, *Phys. Rev.*, **15**, 2032 (1977).
- J. L. Sculfort and A. M. Baticle, *S.I.E. Budapest*, 465 (1978).
- J. L. Sculfort and A. M. Baticle, *C. R. Acad. Sci. Paris* (1978).
- M. A. Butler, *J. Appl. Phys.*, **48**, 1914 (1977).
- H. Gerischer, in "Electrode Materials and Processes for Solar Energy Conversion and Storage," J. D. E. McIntyre, S. Srinivasan, and F. G. Will, Editors, p. 8, The Electrochemical Society Softbound Proceedings Series, Princeton, N.J. (1977).

On the Kinetics of the Thermal Oxidation of Silicon

I. A Theoretical Perspective

William A. Tiller

Department of Materials Science and Engineering, Stanford University, Stanford, California 94305

ABSTRACT

This paper provides a perspective overview of the partitioning of the total driving force for the oxidation process into the key parallel subprocesses and delineates the boundary value problems needed to quantitatively connect these components. An over-all framework is given for viewing all aspects of this process. This constitutes a new and generalized description of oxidation with specific attention to the oxidation of Si. The free volume supply condition required to sustain such a transformation is explicitly given so that attention is focused on vacancy and interstitial formation in the substrate as well as viscous flow in the oxide. An atomistic level model for the oxidation process is given which appears consistent with much of the earlier data; also five possible paths for influencing the rate and character of the oxidation process are described.

For the past 10-15 years a great debate has occurred over whether or not the Si oxidation process is controlled by the diffusion of charged or neutral species. Jorgensen (1) finds that (i) an applied electric field enhances oxidation when the Si is made positive with respect to the oxide/gas interface and retards it when the Si is made negative, (ii) oxidation under a retarding field ceases when the voltage across the oxide is equivalent to the free energy driving force for the oxidation reaction, and (iii) the dependence of oxidation rate on field indicates that oxygen ions are the predominant diffusing species (otherwise the oxidation reaction could not be completely stopped). Jorgensen and Norton (2) find similar field effects of permeation through SiO₂. On the other hand, Doremus (3) finds that (i) the calculated value of the parabolic rate constant, B , for molecular oxygen in fused silica is within a few percent of that found experimentally for the oxidation of silicon, (ii) the pressure dependence of B is linear with oxygen pressure in the gas which also agrees with experiments for silicon oxidation, and (iii) the activation energy for diffusion of molecular oxygen through fused silica is within 5% of the experimentally determined activation energy for silicon oxidation.

Rayleigh (4) went on to show that, when an electric field is applied to the oxidizing silicon in the manner of Jorgensen, an electrolytic process is superimposed on the normal oxidation process. If an external circuit is provided for the flow of electrons, diffusive transport of oxygen ions requires only ionic conduction through the bulk of the oxide. However, with no such external circuit present, polarization fields would develop to inhibit ionic transport. Collins and Nakayama (5) support Rayleigh's conclusions and suggest that the neutral oxygen species may be in thermodynamic equilibrium with various ionized species. They suggested several possible anodic and cathodic reactions.

More recently, Mills and Kröger (6) measured the electrical conductivity of SiO₂ in the temperature range 0°-700°C and proposed that the species responsible for ionic conduction at elevated temperatures is the doubly negative oxygen ion, O⁼, in interstitial positions. The activation energy, derived from their high temperature data (673°-873°K), for combined defect creation and defect motion is within a few percent of that found for neutral oxygen self-diffusion in silica. Thus, at this point it appears that there is support for both neutral and ionized species diffusion during thermal oxidation.

Key words: thermodynamic model, atomistic model, phase transformation.

Cabrera and Mott (7) showed that it was possible to treat the diffusion of ions in oxides by using an effective diffusion coefficient, $D_{\text{eff}} = 2D_i$, and by neglecting any electric field effects in the analysis of ionic transport during oxidation, provided that the oxide layer thickness was large compared to the space charge thickness. Deal and Grove (8) utilized this approach to provide a simple expression for the oxide layer thickness as a function of time in substantial agreement with oxidation data obtained over a wide range of temperature, partial pressure, and oxide thickness for both oxygen and water oxidants.

The thermal oxidation of heavily doped Si substrates shows that the oxidation rate is substantially faster than that observed on lightly and moderately doped substrates (9). In addition, the incorporation of HCl into the oxidizing ambient substantially influences the oxidation rate (10, 11).

The foregoing seemingly conflicting data on the charged nature of the diffusing oxygen species, plus the need to explain the foreign species effects on the oxidation rate, suggest that perhaps a more basic look at this particular oxidation process may be of value at this point in time. The purpose of this paper is to provide a beginning assessment and it is devoted to both a perspective overview and to a model that qualitatively seems to restore harmony to what might appear to be opposing views.

Review of Unconstrained Crystal Growth from a Melt (12, 13)

In practice, we can distinguish two unique modes of crystallization, constrained and unconstrained. In the unconstrained mode, which occurs in isothermal cooling, crystals nucleate and grow freely in a large bath of liquid of constant temperature which is below the melting temperature of the crystal. Here, the total driving force for the phase change, ΔG , is larger in the liquid far from the interface than it is in the liquid right at the interface because the temperature is lower in the far field than at the interface. In the constrained mode, which occurs in normal crystal pulling, the crystals are grown from a bath of liquid held at a temperature above the melting temperature of the crystal. Here, the total driving force for the phase change, ΔG , is smaller in the liquid far from the interface than it is in the liquid right at the interface.

Let us consider the unconstrained growth of a crystal from a dilute binary alloy melt that is supercooled an amount ΔT ($\Delta G = \Delta S \Delta T$, where ΔS is the entropy of fusion), as illustrated in Fig. 1. Here, $T_L(C_\infty)$ is the equilibrium freezing temperature of the bulk liquid

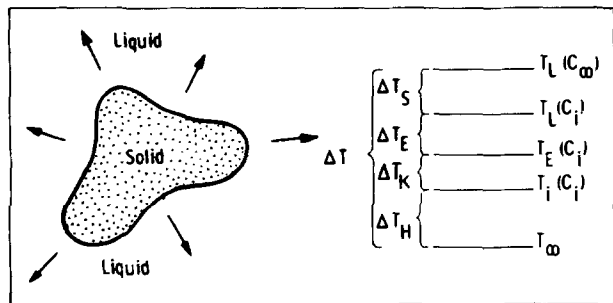


Fig. 1. (Left) A crystal growth from a supercooled binary alloy liquid; (right) the important temperatures in such a growth process. The magnitudes of the temperature differences indicate the degree of solute diffusion, capillarity, attachment kinetics, and heat-transport control.

(the liquidus temperature), and T_∞ is the actual temperature of the liquid far from the growing crystal. Due to the presence of solute atoms in the melt, a partitioning of solute occurs at the moving interface and, because of the slow diffusion of these atoms, the solute concentration changes at the interface from C_∞ to C_i , where C_i depends on the freezing velocity, particle shape, and other factors. This change lowers the liquidus temperature of the crystal surface by ΔT_S to $T_L(C_i)$.

Since the growing crystal is curved, a pressure due to capillarity is imposed on the solid. In addition, the growing crystal may contain nonequilibrium defects. These two effects lower the equilibrium melting temperature of the solid by ΔT_E from $T_L(C_i)$ to $T_E(C_i)$. Further, since the crystal is growing, a certain departure from the equilibrium temperature, ΔT_K , must exist at the interface to drive the molecular transfer from liquid to solid so that the actual interface temperature T_i is below T_E by an amount ΔT_K . Finally, the crystal must be evolving latent heat as it grows and thus T_i must be enough above T_∞ (by the amount ΔT_H) to allow the dissipation of latent heat into the bath.

The foregoing describes the subdivision of the total driving force, ΔG , or the total supercooling, ΔT into its component parts, ΔT_S , ΔT_E , ΔT_K , and ΔT_H , in a simple crystal growth situation wherein no electric fields are applied to the system. All four components are involved in every such growth problem; however, certain ones dominate in different materials. In the growth of large crystals from a relatively pure melt, ΔT_H is approximately equal to ΔT , so this growth is largely controlled by heat flow. During the growth of an oxide crystal from a melt of steel, for example, ΔT_S is approximately equal to ΔT , so the growth is largely matter-transport controlled. During the growth of a polymer crystal from a melt, ΔT_K may be approximately equal to ΔT , and the growth is largely controlled by the kinetics of interface attachment. Finally, during the growth of many lamellar eutectic crystals, ΔT is divided between ΔT_S and ΔT_E and these two factors largely control the growth.

The interplay of these four factors can be simply illustrated by considering the growth velocity of any crystal as a function of time (see Fig. 2). We find that at small times, ΔG_E (or $\Delta T_E = \Delta G_E/\Delta S$) dominates the crystal growth and thus plays an overriding role in its morphology. At zero time, during the nucleation stage, $\Delta G = \Delta G_E$. At large times, ΔG_S and ΔG_H dominate the crystal's growth, which becomes transport limited, and lead to very different morphologies. At intermediate times, all four factors play significant roles in the growth velocity and shape adopted by the crystals.

For these simple cases where the transformation occurs through the variation of one scalar parameter only, the total driving force for crystal growth is given

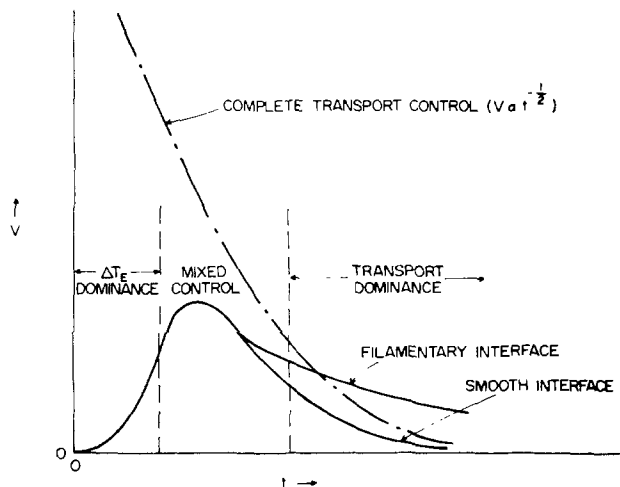


Fig. 2. Schematic representation of a crystal's growth velocity, V , vs. time, t , illustrating the regions where various mechanisms are dominant.

by

melt-solid

$$\Delta G = \Delta S \Delta T \approx H_f [(T - T_0)/T_0]; \quad |\Delta T|/T_0 \ll 1 \quad [1a]$$

solution-solid

$$\Delta G = RT \ln (C/C_0) \approx RT [(C - C_0)/C_0];$$

$$|\Delta C|/C_0 \ll 1 \quad [1b]$$

where T_0 and C_0 are the equilibrium transformation temperature and concentration, respectively, H_f is the heat of fusion, and ΔS is the average entropy of fusion. For the more general case where several scalar parameters vary at the same time, we must use the following relationship

$$\Delta G = A \sum_j [X_j^C \eta_j^C - X_j^N \eta_j^N] \quad [2a]$$

where A is Avogadro's number, C and N refer to crystal and nutrient, respectively, the mole fractions X_j of the j constituents are related by

$$\sum_j X_j^\beta = 1; \quad \beta = C, N \quad [2b]$$

and where the electrochemical potential, η_j , is given by

$$\eta_j = \mu_{j0} + RT \ln a_j + q_j \phi + \sum_n E_n \quad [2c]$$

Here, μ_{j0} is the standard state chemical potential, a_j is the chemical activity, q_j is the charge, ϕ is the electrostatic potential, and E_n is the interaction energy between some additional field n and the species j .

The particular partitioning of the total driving force ΔG into its component parts (ΔG_S , ΔG_K , ΔG_E , and ΔG_H) for the four concurrent interface processes is illustrated in Fig. 3 for a binary alloy system. Here, since we are going from a bulk liquid at point a (C_∞ , T_∞) to an interface liquid at point b (C_i , T_i), the sum of ΔG_S and ΔG_H is given by

$$\Delta G_{SH} = G_L(a) - G_L(b) \quad [3a]$$

in Fig. 3. The maximum available driving force for crystal formation from a liquid of interface concentration C_i occurs for solid of the same chemical potential at point c of concentration C_S and, thus, the sum of ΔG_E and ΔG_K is given by

$$\Delta G_E + \Delta G_K = G_S(c) - G(f) \quad [3b]$$

Since ΔG_E is due purely to an internal energy excess

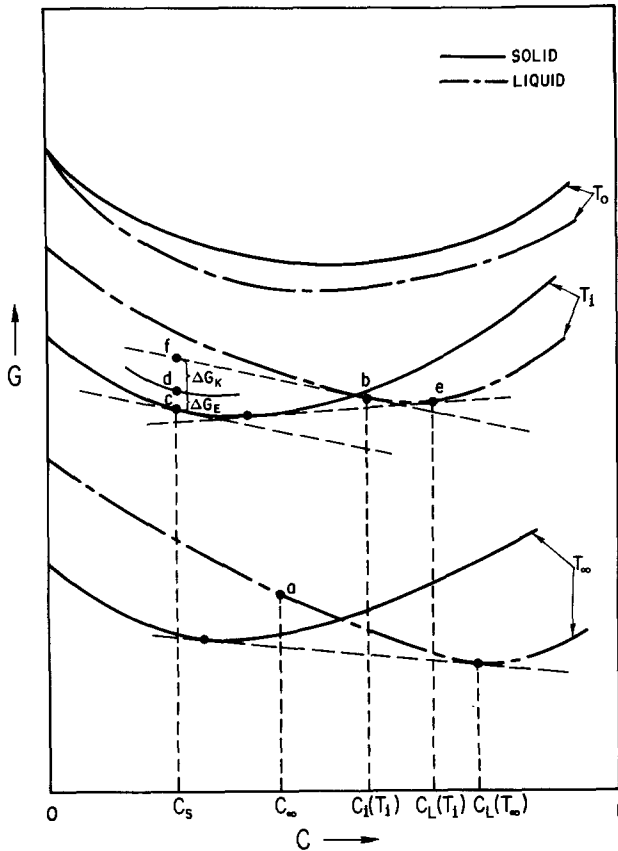


Fig. 3. Free energy, G , curves for solid and liquid as a function of composition, C , of element B for three different temperatures, T_0 (melting temperature of A), T_i (interface temperature), and T_∞ (far-field temperature) needed to evaluate the component ΔG 's in the crystallization process.

of the solid, it can be simply represented as a uniform shift of the G_s curve from point c to point d.

A "coupling" equation can be written for the system in the form

$$\Delta G = \Delta G_{SH} + \Delta G_E + \Delta G_K \quad [4a]$$

It is often operationally much more useful to use a description relation to the subdivision of the total bath undercooling, $\Delta T = \Delta G/\Delta S$, into its four component parts since it is conserved during the growth process; i.e.

$$\Delta T = \Delta T_S + \Delta T_E + \Delta T_K + \Delta T_H \quad [4b]$$

For those who grow crystals mostly from solution and who do not feel comfortable working with a ΔT -coupling equation, one can easily generate a ΔC -coupling equation (or a ΔP -coupling equation for growth from the vapor) since concentration is conserved during the

growth process; e.g., for growth from solution

$$\Delta C = \Delta C_H + \Delta C_E + \Delta C_K + \Delta C_S \quad [4c]$$

Both ΔT -partitioning and ΔC -partitioning are illustrated in Fig. 4, where we note that the phase diagram is being used as our standard reference state. In Eq. [4c], ΔC_H can be readily obtained as $\Delta C_H = (T_i - T_\infty)/m_L$, where m_L is the liquidus slope, ΔC_E is readily obtained as $\Delta G_E/m_L\Delta S$, ΔC_K comes directly from the applicable interface attachment kinetic law, and ΔC_S comes from the solution to the transport equations. As can be readily understood, the only operational temperature and concentration measurements are T_i , T_∞ and C_i , C_∞ , respectively.

If one is growing a crystal from solution containing minor chemical constituents, j , as well as the major host constituent, M , these will be partitioned at the interface and require Eq. [4c] to be altered to become

$$\Delta C = \Delta C_H + \Delta C_E + \Delta C_K + \Delta C_S^M + \Delta C_S^m \quad [4d]$$

where

$$\Delta C_S^m = \sum_j \Delta C_S^j \quad [4e]$$

In addition, it should be recognized that some of these j constituents may strongly interface-adsorb and may either poison or catalyze many of the specific interface sites needed for attachment of the major constituent, M , to the crystal surface. Thus, ΔC_K in Eq. [4d] may be greatly increased or decreased by the presence of the C_∞^j in the bulk solution.

General Overview of Unconstrained Crystallization

When considering the formation of a new crystal from a nutrient phase, the most information we generally have available to us is the bulk free energy driving force, ΔG_∞ . If we are fortunate, we know this function in terms of the important state variables for the reaction; i.e.

$$\Delta G_\infty = G_{N_\infty}(C_\infty, T_\infty, P_\infty, \phi_\infty) - G_{C_\infty}(C_\infty, T_\infty, P_\infty, \phi_\infty) \quad [5a]$$

for the state variables of chemical constitution, temperature, pressure, and electrostatic potential where the subscripts N and C refer to nutrient and crystal, respectively. What we need, to understand the growth process in a fundamental way, is the value of ΔG_i operating at the interface between the two phases; i.e.

$$\Delta G_i = G_{N_i}(C_i, T_i, P_i, \phi_i) - G_{C_i}(C_i, T_i, P_i, \phi_i) \quad [5b]$$

For this, we must obviously gain solutions to the boundary value problems connecting the far-field variables with the interface variables; i.e., we need to evaluate C_i/C_∞ , T_i/T_∞ , P_i/P_∞ , and ϕ_i/ϕ_∞ . Formally, we can express the change in free energy ΔG_{SV} due to the state variable changes in terms of the activity changes at the two locations

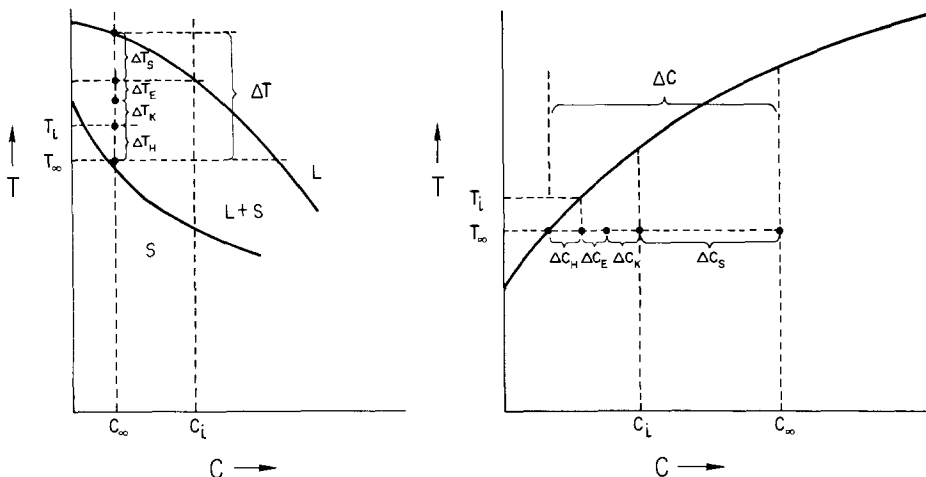
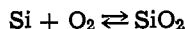


Fig. 4. Phase diagram illustrations of the coupling equations for ΔT and for ΔC during crystal growth from alloy melts. Case a (left) is typical of solvent growth at low alloy concentration while case b (right) is typical of solute crystal growth.

$$\begin{aligned} \Delta G_{SV} &= \Delta G_s - \Delta G_l \\ &= RT[\ln(a_s^{SiO_2}/a_l^{SiO_2}) - \ln(a_s^{Si}/a_l^{Si}) \\ &\quad - \ln(a_s^{O_2}/a_l^{O_2})] \quad [6] \end{aligned}$$

for the reaction example



The driving force, ΔG_i , available at the interface for the transformation, is consumed by two parallel processes. One involves the excess free energy, ΔG_E , generated as a result of the transformation process and stored in both phases as discrete defects and/or strain fields. The other involves the departure from equilibrium, ΔG_K , needed for the molecular transition from the nutrient phase to incorporation in the crystal phase; *i.e.*

$$\Delta G_i = \Delta G_K + \Delta G_E \quad [7]$$

From crystal growth theory, with V = crystallization velocity and μ_i = a material coefficient ($i = 1$ to 4), we find that

$$V = \mu_1 \Delta G_K \quad [8a]$$

$$V = \mu_2 \Delta G_K^2 \quad [8b]$$

or

$$V = \mu_3 \exp(-\mu_4/\Delta G_K) \quad [8c]$$

for either (i) layer edge attachment and uniform attachment limited kinetics (Eq. [8a]), (ii) dislocation source limited kinetics (Eq. [8b]), or (iii) two-dimensional nucleation source limited kinetics (Eq. [8c]), respectively. At low driving forces, layer generation or layer edge attachment operates while at high driving forces, uniform attachment operates. The greater is the difference in binding energy or enthalpy between the two phases, for constant growth temperature, the greater is the value of ΔG_K needed to reach the uniform attachment domain and the smaller are μ_1 , μ_2 , and μ_3 . Likewise, for constant binding energy difference, the lower is the growth temperature, the greater must ΔG_K be to reach the uniform attachment domain and the smaller are μ_1 , μ_2 , and μ_3 .

To obtain the values of C_i , T_i , P_i , and ϕ_i , one must solve some rather complex and coupled boundary value problems in general, so it is best to continue with the specific example of present interest; *i.e.*, the thermal oxidation of Si. For this system, we can assume $T_i/T_s = 1$ and the matter transport constraint yields for the oxidation rate

$$V = \Omega^{SiO_2} [J_{O_2} + \frac{1}{2} J_{O=}] \quad [9a]$$

where J is flux per square centimeter and Ω is the molecular volume. Since

$$J^j = - \frac{D^j C^j}{kT} \frac{\partial \eta^j}{\partial x} \quad [9b]$$

Eq. [9a] becomes

$$V = \Omega_{SiO_2} \sum_j \left\{ - \frac{D^j}{n_j} (\nabla C^j)_i - \left[\frac{D^j}{kT} C^j \nabla (\Delta G^\circ) \right]_i \right\} \quad [9c]$$

where the interface field effect, ΔG° , is given by

$$\Delta G^\circ = Z^j e \phi + \frac{\partial}{\partial C^j} \left[\frac{\epsilon}{2} (\nabla \phi)^2 + \frac{\sigma^2}{2E} \right] + \Delta \mu_{H.M.} + \dots \quad [9d]$$

In Eq. [9], the two diffusing species of greatest interest are $j = O_2$ ($n_j = 1$) and $j = O=$ ($n_j = 2$); D^j is the diffusion coefficient of the j species, Z^j is the valence, ϵ is the permittivity of Si and SiO_2 , which may vary somewhat with position, σ is the stress distribution, E is the modulus, $\Delta \mu_{H.M.}$ is a chemical potential change relating to different bonding energies for solute and solvent species in the interface region, and neglected contributions include activity coefficient effects, etc. To obtain the electrostatic potential in Eq. [9], as a

function of position, we must solve Poisson's equation

$$\nabla^2 \phi = - \frac{4\pi\rho}{\epsilon} \quad [10a]$$

$$\begin{aligned} &= - \frac{4\pi e}{\epsilon} \left\{ (n_p - n_e) + \sum_i (Z_D^i N_D^i - Z_A^i N_A^i) \right. \\ &\quad \left. + \sum_l Z_l N_l + \sum_q Z_{Oq} N_{Oq} \right\} \quad [10b] \end{aligned}$$

and

$$\epsilon_{Si} (\nabla \phi)_{Si} - \epsilon_{SiO_2} (\nabla \phi)_{SiO_2} = \rho_{Si/SiO_2} \quad [10c]$$

In Eq. [10], ρ is the total charge density, n_p and n_e are the density of holes and electrons, respectively, N_D and N_A refer to the densities of donor and acceptor species of un-ionized or ionized variety, respectively, N_l refers to the density of l-type physical defects of valence Z_l created by mechanical or other stress (here, l refers to charged vacancies and charged Si interstitials, etc.), and N_{Oq} refers to the density of oxygen species of un-ionized or ionized nature.

The third group of equations needed to complete Eq. [9] and [10] involves the local pressure and stress distribution created in the interface region as a result of the oxidation process. For the moment, because of the complexity of these equations, we shall content ourselves with a simple functional representation of the interface situation; *i.e.*

$$\frac{P_i}{P_s} = f(\Delta\lambda, E, \sigma, \sigma_Y, V, \rho_i, \eta^*, \dots) \quad [11]$$

Equation [11] is meant to represent that the molecular size mismatch, $\Delta\lambda$, existing at the Si/SiO₂ interface produces a strain which connects to a stress σ through the modulus E . When σ exceeds the yield stress, σ_Y , for the Si and SiO₂, flow begins to occur in these two phases which creates point and line defects of density ρ_i which may be charged. Since the degree of flow depends on the viscosity, η^* , of the materials and the time available, the process also depends on the oxidation rate, V . Eernisse (14) has clearly demonstrated the viability and importance of the viscous flow process during Si oxidation. We shall deal with this complex process at greater length in Part II (15). Here, we are primarily interested in illustrating the coupled nature of the three state variables, C_i , P_i , and ϕ_i .

From the foregoing, we can set up an excess free energy balance for the system and can see that ΔG_E from Eq. [7] is given by

$$\Delta G_E = \frac{1}{V} \frac{\partial}{\partial t} \left[\mathcal{G}_D + \frac{1}{2E} \int \sigma^2 dv \right] \quad [12]$$

where \mathcal{G}_D is the energy stored in defects (planar, line, and nonequilibrium concentrations of point defects) relative to the standard state structure of the Si and the SiO₂ (the equilibrium structures involved in the thermochemical balance under consideration) and the second term in the bracket represents the stored elastic strain energy in the two materials. The final general constraint equation that one wishes to delineate fulfills the requirement that, for the satisfaction of Eq. [9], there must be sufficient free volume available in the interface region for the various incoming oxygen species to occupy and react with the local silicon species. From Rutherford backscattering studies (16), we know that Si does not diffuse to the outer surface of the oxide but that the oxygen diffuses inward. However, a type of viscous flow could occur due to interface stresses wherein SiO₂ units flowed out and free volume flowed in. In addition, the condition might also be satisfied by vacancy influx or interstitial egress from the Si phase. We call this the "free volume supply condition" and express it as

$$V \propto J_V^{Si} + J_V^{SiO_2} \quad [13a]$$

where J_v^i is the flux of free volume from phase i to the interface per unit interfacial area. For example, since the relaxed spacing between the Si atoms in the SiO₂ units is about 1.3 times the Si-Si spacing in the Si lattice, if the Si/SiO₂ interface moves into Si at V cm/sec, the oxide must thicken at $2.25 V$ cm/sec and this requires that free volume flow in at a rate of $1.25 V$ cm/sec to produce an unstrained condition with no Si interstitial flow.

To be more precise, if the Si/SiO₂ interface moves into the Si phase at a velocity V , the number of Si atoms per unit area of interface to be oxidized per unit time, N^* , is equal to the number of SiO₂ molecules formed per unit area per unit time where

$$N^* = \frac{V}{\Omega_{Si}} - (J_I^{Si} - J_{V^*}^{Si}) \quad [13b]$$

Here, Ω is the atomic volume and the bracketed term gives the rate of flow of the Si atoms away from the interface and into the Si via interstitials, I , leaving the interface and vacancies, V^* , approaching the interface. This assumes that those interstitials flowing into the SiO₂ from the interface will all become oxidized to SiO₂, which may not be completely correct. If we assume that either a condition of zero strain exists in the SiO₂ at the interface region or a stationary state strained layer has developed in the SiO₂ at the interface, then the total free volume supply condition becomes

$$N^* (\Omega_{SiO_2} - \Omega_{Si}) = \Omega_{Si} (J_I^{Si} - J_{V^*}^{Si}) + \bar{v}_f^{SiO_2} J_{\bar{v}}^{SiO_2} \quad [13c]$$

Here, $\bar{v}_f^{SiO_2}$ is the average free volume element size for the SiO₂ flow process. If, instead, we assume that an isotropic strain, δ' , develops in the SiO₂ film at the interface, then the free volume supply needed at the interface per unit area time, Δv_f^* , is given by

$$v_f^* \approx N^* [(\Omega_{SiO_2} - \Omega_{Si}) - (\delta' \lambda_{SiO_2}^3)] \quad [13d]$$

where λ is the average SiO₂-SiO₂ distance of equilibrium.

The realistic situation to be considered is the thermal oxidation of Si in the presence of impurities or intentional dopants. The appropriate representation of the driving force is then via the supersaturation, ΔC , so that Eq. [4d] should be used as the governing coupling equation for the SiO₂ as the nutrient phase. This situation is represented pictorially in Fig. 5 where that portion of the driving force needed to maintain the major constituent concentration at the interface, C_I^M , is illustrated as a small portion of the total driving force; i.e., $\Delta C_S^M / \Delta C_\infty \ll 1$. We shall see in Part II (15) that this is probably an appropriate representation of the true state of this system. The component

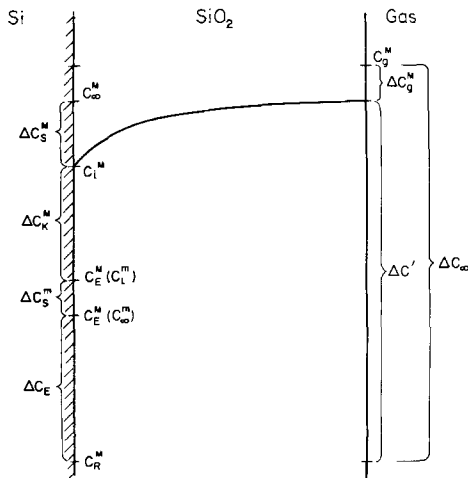


Fig. 5. Schematic representation of the supersaturation coupling equation involved in the thermal oxidation of silicon.

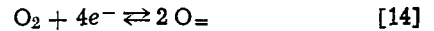
ΔC_S^M may itself be quite small; however, if the j constituents refer to hydrogen or carbon (17), etc., they may either poison or catalyze a sufficiently large fraction of active interface sites for oxygen attachment that ΔC_K^M must be either greatly increased or decreased for the same V . We shall see in Part II that ΔC_E will be very large for a state of completely coherent strain applying at the interface and very small for the state of a completely incoherent interface. Next, C_R^M is the equilibrium concentration of oxygen at the Si/SiO₂ interface and is given in terms of the activities for SiO₂ and Si at the interface and the equilibrium constant for the reaction. Finally, a supersaturation ΔC_g^M is needed to maintain the bulk SiO₂ at an oxygen concentration of C_∞^M . Using the gas as our reference nutrient phase, the applicable coupling equation is

$$\Delta C_\infty = \Delta C_g^M + \Delta C_S^M + \Delta C_K^M + \Delta C_S^M + \Delta C_E \quad [4f]$$

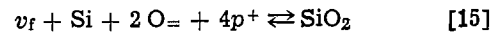
Proposed Oxidation Model for Si

At the initial stages of the oxidation process illustrated in Fig. 6, electrons are thought to transfer from the Si to the SiO₂ in order to equalize the electrochemical potential of the electrons, η_e , throughout both phases. Since the electrons are the most mobile species in the system, they will quickly equilibrate via tunneling and conduction. This charge transfer leads to a positive potential on the Si side and a negative potential on the SiO₂ side of the interface. Electron transfer continues until equilibrium is established for the electrons and a Galvani potential difference $\Delta\phi$ is developed across the three-phase system Si/SiO₂/gas. The magnitude of $e\Delta\phi$ will be given by ΔE_F , the difference in Fermi levels for the Si and the SiO₂ relative to the zero energy state of vacuum. The relative fraction of $\Delta\phi$ developed across each phase requires a solution to Eq. [10] (Poisson's equation).

In the SiO₂ near the gas interface, the following ionization reaction is expected to occur



These O= interstitial ions are formed in the presence of the Si/SiO₂ electrostatic field which attracts them to the interface region. Of course, this loss of negative charge from the SiO₂/gas interface region invites more electron transfer from the Si so that η_e stays constant. At the Si/SiO₂ interface, the O= becomes involved in the reaction



which tends to make the Si more negative so more electron transfer is needed from Si to SiO₂ to restore η_e to a constant value throughout (v_f stands for free

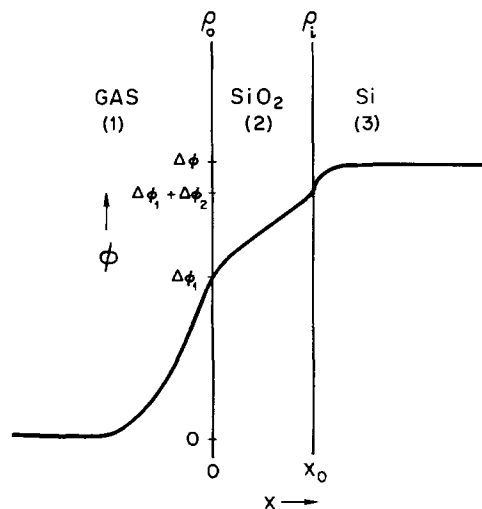


Fig. 6. Illustration of the electrostatic potential variation across the three-phase system, Gas/SiO₂/Si, during the oxidation process.

volume). The O_2 continues to decompose and to pump O_2 to the interface region in order to oxidize the Si. The electron transfer in the reverse direction to equalize η_e completes the electrical circuit and sustains the pumping action so that the interface field, $\nabla\phi_1 \approx \Delta\phi_2/X_0$ in Fig. 6, is maintained.

With this model, one can readily see why Jorgensen (1) was able to stop the oxidation of Si by imposing a sufficiently large negative potential on the Si even if neutral oxygen species were present. One can see that, even with a flow of neutral oxygen toward the Si, if the electric field drives the O_2 away from the Si/SiO₂ interface region, then Eq. [14] will produce ionization of the incoming neutral oxygen to maintain the equilibrium level of O_2 and $\nabla\phi_1$ will move it toward the SiO₂/gas interface. Thus, a conversion of O to O_2 occurs in the interface region and the reverse reaction occurs in the SiO₂/gas region so that no oxygen is available at the interface to react with the Si to form SiO₂.

One can also see why Doremus (3) holds to his viewpoint. The need to satisfy the free volume supply condition of Eq. [13] generally requires either viscous flow, diffusion of oxygen vacancies in the SiO₂, or diffusion of vacancies and interstitials in the Si. The latter of these two SiO₂ processes has an activation energy associated with neutral oxygen diffusion since substitutional oxygen must diffuse outward to the SiO₂/gas interface in order for vacancies to diffuse inward to the Si/SiO₂ interface. However, such a process, already proposed by Fowkes *et al.* (18), does not seem likely to sustain the oxidation reaction. The former SiO₂ process, that of viscous flow, is the more likely one for SiO₂ and, since it involves the breaking of bridging oxygen bonds, the activation energy for the flow process should be similar to that for neutral oxygen transport in SiO₂. By inserting Eq. [14] into Eq. [15], one can also see that the $2O_2$ reaction species is equivalent to the O_2 reaction species so that one expects the driving force for oxidation to be proportional to $[O_2]$ when the system stays close to equilibrium; *i.e.*, to vary linearly with oxygen gas pressure. This may resolve the Doremus objections to O_2 as an oxidizing species.

Specific Pathways for Influencing the Oxidation Velocity

From the two preceding sections, one should realize that any experimental process variation that produces a change in the oxidation rate can do so only via a change in Eq. [4]-[15]. It is via scrutiny of these equations that one may illuminate the factors controlling the oxidation rate in general, and whereby one may discover the possible mechanisms whereby high silicon doping levels can influence V in particular. Let us now consider some of these specific pathways.

1. As mentioned in the text adjoining Eq. [11], and to be discussed more fully in the Part II (15), the strain generated by the molecular size mismatch at the oxidizing interface influences the defect production in the interface region during oxidation. This influences V via the ΔG_E term in Eq. [7] which controls the available ΔG_K , for fixed ΔG_i , and also via the interface charge states to alter $\nabla\phi_1$ in Eq. [9].

2. At sufficiently high doping levels, the Si becomes extrinsic even at the oxidation temperature and the Fermi level shifts from midband. Thus, the electron transfer from the Si to the SiO₂ to produce η_e equal to a constant is shifted. This alters $\nabla\phi_1$ and thus V via Eq. [9]. In addition, the Fermi level shift increases the equilibrium charged vacancy and interstitial concentration in the Si so that $J_{v^{Si}}$ in Eq. [13] may be greatly increased and thus V increased without an increase in ΔG_E . This process path will be discussed at length elsewhere (19).

3. The dopant redistribution at the interface during oxidation will produce a pileup of phosphorus or a depletion of boron at the Si side of the interface because of solute partitioning at the moving interface. This changes the activities of the key species Si and SiO₂ at the interface altering the magnitude of ΔG_i in Eq. [6] and thus altering V via Eq. [7] and [8]. Calculations, to be published elsewhere (20), indicate that the field-determined segregation is much more significant than the segregation due to interface partitioning.

4. The interface pileup of P or depletion of B alters the strength of the Si-Si bonds at the interface. This changes the degree of roughness and interface vacancy states on a molecular scale so that the molecular attachment coefficients μ_j in Eq. [8] are altered. Thus, the oxidation rate will be altered via this change in μ_j . The magnitude of this effect will be assessed at a later date.

5. For completeness, one needs to recognize that, at heavy doping levels, the basic diffusion coefficients D^j in Eq. [9] may be altered as may the thermodynamic activity coefficients entering the complete equation. These would also influence V .

Acknowledgments

Dr. B. E. Deal, Dr. J. D. Plummer, Mr. C. P. Ho, and Mr. H. Z. Massoud provided many helpful discussions of the available thermal oxidation data and of the processes involved. This work was supported by the Defense Advanced Research Projects Agency under Contract No. DAAB07-77-C-2684.

Manuscript submitted Oct. 2, 1978; revised manuscript received Sept. 11, 1979.

Any discussion of this paper will appear in a Discussion Section to be published in the December 1980 JOURNAL. All discussions for the December 1980 Discussion Section should be submitted by Aug 1, 1980.

Publication costs of this article were assisted by Stanford University.

REFERENCES

1. P. J. Jorgensen, *J. Chem. Phys.*, **37**, 874 (1962).
2. P. J. Jorgensen and F. J. Norton, General Electric Research Lab. Rep. No. 65-RL-4003X (July 1965).
3. R. H. Doremus, *J. Chem. Phys.*, **80**, 1773 (1976).
4. D. D. Rayleigh, *This Journal*, **113**, 782 (1966).
5. F. C. Collins and T. Nakayama, *ibid.*, **114**, 162 (1967).
6. T. G. Mills and F. A. Kröger, *ibid.*, **120**, 1582 (1973).
7. N. Cabrera and N. F. Mott, *Rep. Progr. Phys.*, **12**, 163 (1948).
8. B. E. Deal and A. S. Grove, *J. Appl. Phys.*, **36**, 3770 (1965).
9. C. P. Ho, J. D. Plummer, B. E. Deal, and J. D. Meindl, *This Journal*, **125**, 665 (1978).
10. B. E. Deal, D. W. Hess, J. D. Plummer, and C. P. Ho, *ibid.*, **125**, 339 (1978).
11. B. E. Deal, *ibid.*, **125**, 576 (1978).
12. W. A. Tiller, *Science*, **146**, 871 (1964).
13. W. A. Tiller, in "Interfaces," R. C. Gifkins, Editor, p. 257, Australian Institute of Metals, Sydney, Australia (1969).
14. E. P. Eernisse, *Appl. Phys. Lett.*, **30**, 290 (1977).
15. W. A. Tiller, *This Journal*, **127**, 625 (1980).
16. W. D. Mackintosh and H. H. Plattner, *ibid.*, **124**, 396 (1977).
17. A. G. Revesz, To be published in *This Journal*.
18. F. M. Fowkes, D. W. Hess and J. Kiddon, Abstract 76, p. 216, The Electrochemical Society Extended Abstracts, Philadelphia, Pennsylvania, May 8-13, 1977.
19. C. P. Ho and J. D. Plummer, *This Journal*, **126**, 1523 (1979).
20. W. A. Tiller, In preparation.

On the Kinetics of the Thermal Oxidation of Silicon

II. Some Theoretical Evaluations

William A. Tiller

Department of Materials Science and Engineering, Stanford University, Stanford, California 94305

ABSTRACT

A steady-state transport analysis, including electric field effects, leads to orientation-dependent linear and parabolic rate constants. A free energy budget accounting indicates that neutral oxygen diffusion in the SiO₂ cannot alone account for the oxidation reaction. An analysis of the system relaxation associated with the Si/SiO₂ interface disregistry indicates that a network of extra half-planes forms at the interface to reduce the stored strain energy and that movement of the interface requires the influx of vacancies from the Si, egress of Si interstitials from the interface back into the bulk Si, or free volume influx from the SiO₂ to remove the extra half-plane segments. This tends to become a dominant feature of the kinetics of oxidation. An analysis of the proportioning of the total driving force into its component contributions and their relative magnitudes is given. The coordination of a variety of diverse oxidation studies is indicated.

In Part I of this series (1), both a theoretical perspective and a new model of thermal oxidation with specific application to silicon were presented which qualitatively seems to restore harmony to what might appear to be opposing views of the oxidation process. In addition, the various possible process paths available for changes in oxidation rate have been delineated. In the present paper, theoretical consideration is given to (i) a steady-state transport analysis which explicitly delineates interface-field effects, (ii) an analysis of the system relaxation associated with the Si/SiO₂ interface disregistry, and (iii) an analysis of the relative magnitudes of the various parallel driving forces ΔG_{SV} , ΔG_E , and ΔG_K in comparison with ΔG_o for the oxidation process (1). From these considerations, one finds orientation-dependent linear and parabolic rate constants for the oxidation process plus a clear indication that neutral oxygen diffusion alone in the SiO₂ cannot account for the oxidation reaction. In addition, unless the interface relaxes to become partially incoherent, large amounts of strain energy are stored in the SiO₂ and this greatly retards the oxidation process. The relaxation process leaves a network of extra half-plane segments on the Si side with associated dangling bands at the interface. Movement of the interface requires the generation of interstitials and the influx of vacancies to remove these half-plane segments and this becomes a dominant feature in the kinetics of oxidation. From these analyses, the coordination of a variety of diverse Si oxidation studies becomes possible and a number of new experiments are suggested.

Modified Deal-Grove Transport Analysis

Since we cannot unambiguously prove that only one chemical species is migrating in the SiO₂, it seems more useful to consider the presence of two diffusing species, O₂ and O₌, in any transport analysis. Si transport is neglected for the reasons outlined in Part I (1). Even though the concentration ratio of O₌/O₂ may be quite small, the interface field effect may generate comparable fluxes of the two species so that neither should be neglected in the oxidation process. The analysis to follow is carried out in two phases. The first phase deals solely with charged species transport and completely neglects the neutral species diffusion so that we can compare the results with those found by Deal and Grove (2) using the D_{eff} approach (1). The second phase deals with mixed diffusion of the two species, which is the general case.

Key words: field effects, point defects, pseudo-dislocation array.

Some Deal and Grove analysis results.—The steady-state flux, J_2 , of oxygen across an oxide film of thickness X_o and having an SiO₂/gas concentration of C_o and an SiO₂/Si concentration of C_i is given by (2)

$$J_2 = \frac{D_{eff}}{X_o} (C_o - C_i) \quad [1a]$$

$$\frac{C_i}{C^*} = 1 \left| \left[1 + \frac{k^*}{h^*} + \frac{k^* X_o}{D_{eff}} \right] \right. \quad [1b]$$

and

$$\frac{C_o}{C_i} = 1 + \frac{k^* X_o}{D_{eff}} \quad [1c]$$

In Eq. [1], C^* is the equilibrium concentration of the oxidant in the oxide, k^* and h^* are the rate constants for O₂ transfer applying at the SiO₂/Si and the SiO₂/gas interfaces, respectively, and $D_{eff} \approx 2D_i$ if the transport species is ionic. The solution for X_o is found to be

$$X_o^2 + AX_o = B(t + \tau) \quad [2a]$$

where

$$A = 2D_{eff} \left(\frac{1}{k^*} + \frac{1}{h^*} \right) \quad [2b]$$

$$B = 2 \frac{D_{eff} C^*}{N_1} \quad [2c]$$

and

$$\tau = \frac{X_i^2 + AX_i}{B} \quad [2d]$$

In Eq. [2], N_1 is the number of oxidant molecules incorporated into a unit volume of the oxide layer, X_i is the initial layer thickness at $t = 0$, B is the parabolic rate constant for the oxidation regime

$$X_o^2 \approx B(t + \tau) \quad \text{for } t + \tau \gg A^2/4B \quad [3a]$$

while B/A is the linear rate constant for the oxidation regime

$$X_o \approx \frac{B}{A} (t + \tau) \quad \text{for } t + \tau \ll A^2/4B \quad [3b]$$

Modified Deal-Grove analysis for O₌ and a constant field.—We consider the case where the fraction α , of the total macropotential difference, $\Delta\phi$, developed from the gas to Si, is located across the SiO₂ (see Fig. 6 of Part I). We will consider the field to have an approximately constant value $\alpha\Delta\phi/X_o$. Then, equating the ion fluxes at the gas/SiO₂ and the Si/SiO₂ interfaces with J_2 , we find

$$J_2 = D_1 \left[\frac{C_o - C_i}{X_o} + \alpha \left(\frac{2e}{kT} \right) \frac{|\Delta\phi|}{X_o} \left(\frac{C_o + C_i}{2} \right) \right] \quad [4a]$$

$$= \frac{1}{X_o} [C_o a - C_i b] \quad [4b]$$

where

$$a = D_1 \left(1 + \frac{\alpha e |\Delta\phi|}{kT} \right); \quad b = D_1 \left(1 - \frac{\alpha e |\Delta\phi|}{kT} \right) \quad [4c]$$

The solution for the film thickness, X_o is the same as Eq. [2] but with A , B , and τ replaced by A' , B' , and τ' , where

$$A' = 2 \left(\frac{b}{k^*} + \frac{a}{h^*} \right) = 2D_1 \left[\left(1 - \frac{\alpha e |\Delta\phi|}{kT} \right) \frac{1}{k^*} + \left(1 + \frac{\alpha e |\Delta\phi|}{kT} \right) \frac{1}{h^*} \right] \quad [5a]$$

$$B' = \frac{2aC^*}{N_1} = 2D_1 \left(1 + \frac{\alpha e |\Delta\phi|}{kT} \right) \frac{C^*}{N_1} \quad [5b]$$

$$\tau' = (X_1^2 + A'X_1)/B' \quad [5c]$$

$$\frac{B''}{A''} = \frac{C^*}{N_1} \left[\frac{k^* h^*}{k^* + h^* \frac{b}{a}} \right] = \frac{(C^*/N_1)(k^* h^*)}{k^* + h^* \left\{ \frac{1 + (D_{O_2}/2D_{O_2}) \left(1 - \frac{\alpha e |\Delta\phi|}{kT} \right) [p]_1^{-2} \left(\frac{K_1}{K^*} \right)^{1/2} C_i^{-1/2}}{1 + (D_{O_2}/2D_{O_2}) \left(1 + \frac{\alpha e |\Delta\phi|}{kT} \right) [e]_o^2 K_o^{1/2} C_o^{-1/2}} \right\}}$$

$$\alpha = f \left(X_1, \frac{\epsilon_{Si}}{\epsilon_{SiO_2}}, \rho_S \right) \quad [5d]$$

In Eq. [5], ϵ refers to the permittivity, ρ_S to the surface charge density, and $N_1' = 2N_1$. The exact value of α is yet to be determined and it is merely represented here as the function f of the variables involved.

Perhaps the most interesting feature to note about these results is that the electric field effect, which enhances the ionic transport, enters the formal solution as modified kinetic coefficients

$$k^* = D_i k^*/b; \quad h^* = D_i h^*/a \quad [6]$$

as well as an altered parabolic rate constant. Thus, changing the Si doping level, such that the Fermi energy moves away from midband at the oxidizing temperature, should alter the magnitude of α and thus both the linear and the parabolic rate constants. In addition, since $\alpha\Delta\phi$ is expected to depend on the orientation of the Si substrate, both B' and B'/A' will be orientation dependent.

Combined O_2 and O_2 transport with constant field.—We shall define the interface concentrations, C_o and C_i as

$$C_o = C_{O_{O_2}} + C_{O_{O_2}} \approx C_{O_{O_2}} \quad [7a]$$

$$C_i = C_{i_{O_2}} + C_{i_{O_2}} \approx C_{i_{O_2}} \quad [7b]$$

where we have from Eq. [14] and [15] of Part I (1) for the unconstrained case (neglecting v_f)

$$C_{O_{O_2}} = K_o^{1/2} [e]_o^2 C_{O_{O_2}}^{1/2} \quad [8a]$$

$$C_{i_{O_2}} = \frac{K_i^{1/2}}{K^*^{1/2}} [p]_1^{-2} C_{i_{O_2}}^{1/2} \quad [8b]$$

and

$$K^* = [O_2][Si]/[SiO_2] \quad [8c]$$

Following our standard procedure, we obtain

$$J_2 = \frac{D_{O_2}}{X_o} (C_{O_{O_2}} - C_{i_{O_2}}) + \frac{D_{O_2}}{2X_o} \left\{ (C_{O_{O_2}} - C_{i_{O_2}}) + \frac{\alpha e |\Delta\phi|}{kT} (C_{O_{O_2}} - C_{i_{O_2}}) \right\} = \frac{1}{X_o} [C_o a - C_i b] \quad [9a]$$

where

$$a = D_{O_2} + \frac{D_{O_2}}{2} \left(1 + \frac{\alpha e |\Delta\phi|}{kT} \right) [e]_o^2 K_o^{1/2} C_o^{-1/2} \quad [9b]$$

$$b = D_{O_2} + \frac{D_{O_2}}{2} \left(1 - \frac{\alpha e |\Delta\phi|}{kT} \right) [p]_1^{-2} \left(\frac{K_1}{K^*} \right)^{1/2} C_i^{-1/2} \quad [9c]$$

Thus, our solution for X_o is again of the same form as Eq. [2a] with altered A , B , and τ by using Eq. [9b] and [9c] instead of Eq. [4c] in Eq. [5]. In this general case, the modified kinetic coefficients (Eq. [6]) depend on both the Fermi level effect via α and the partial pressure of oxygen in the gas phase.

The parabolic and linear rate constants are given by

$$B'' = \frac{2D_{O_2}C^*}{N_1} \left\{ 1 + \frac{D_{O_2}}{2D_{O_2}} \left(1 + \frac{\alpha e |\Delta\phi|}{kT} \right) [e]_o^2 K_o^{1/2} C_o^{-1/2} \right\} \quad [10a]$$

Although the orientation dependence of these quantities is clearly displayed, the oxygen pressure dependence is not because we do not yet know how α , $[e]_o$, and $[p]_1$ depend on p_{O_2} . For similar reasons, we cannot fully evaluate the heavy doping effects (3) on enhancing the oxide growth velocity, V , even though one expects $\Delta\phi$ to increase for n-type and decrease for p-type dopants.

Consequences of Interface Disregistry

It is relatively easy to discuss the consequences of atomic disregistry at an interface for two crystalline materials but it is much more difficult to do so for a crystalline/amorphous combination. In the latter case, the prevailing opinion is that distorted interface bonds do not produce much strain energy in amorphous material and this is a fair approximation for changes at constant volume. However, for oxidation processes, like that of Si, where large molecular volume differences exist between the two phases, this approximation does not hold. One must visualize extra half-planes in the nutrient crystal phase (Si) terminating at a moving oxide interface where the product phase (SiO_2) has a greater specific volume. The ends of these extra half-planes may not have the same excess energy as they would have if the amorphous phase were crystalline; however, the basic ideas involved should be qualitatively similar. Thus, let us first consider the consequences of disregistry between two crystalline materials and then extend the ideas to the Si/ SiO_2 interface.

In the crystal/crystal disregistry case, it is well known that, for thick crystals, a dislocation net of edge-screw type forms at the interface to satisfy the coherency strains (4). This leads to a predictable spacing between the dislocations with the softer crystal predominantly determining the shear stress level at the interface. For one of the crystals being very thin, the system may adopt a coherent rather than a dislocated interface in order to minimize the free energy of the system and, at some critical film thickness, the system relaxes to provide an interface dislocation net of lower total free energy. Thus, the transition is from a distributed strain energy throughout the film to a localized defect energy at the interface. This same effect is observed as a result of the constitutional strains developed as a result of the diffusion of n-type

or p-type dopant into Si from the surface layer (5, 6). At low doping levels, the strain is not sufficient to cause the transition to dislocation net formation; whereas, above a predictable condition (6), the dislocation net appears.

To illustrate the interface relaxation process more fully, consider taking a single crystal which is sliced along a low index plane and then one-half is rotated with respect to the other by some angle. On the interface, regions will exist where adjacent atoms in the two pieces are within 10-20% of a coincident position. Other regions will exist where adjacent atoms are out of coincidence by more than 20% of a lattice distance. At a temperature suitable for atomic relaxation, those regions wherein only small displacements are needed for coincidence become completely coherent and the adjacent regions become completely incoherent. This situation is illustrated in Fig. 1 for the (110) plane of the body-centered lattice wherein a hexagonal network of dislocations forms at the interface.

Carrying the coincidence net idea a little further, suppose one considered the (111) plane of Si as one surface net of molecules and a random network at the average spacing of SiO_2 as the other surface net of molecules. Placing these two nets in contact would lead to irregular regions of near coincidence separated by domains out of coincidence by a large amount. Thus, relaxation at the interface should lead to irregularly shaped domains of coherence and incoherence at the interface. The relative proportions of these two should be a function of the orientation of the interface. In the incoherent regions, loci of Si surface atoms will exist that do not have a matching SiO_2 molecule associated with them across the interface. This will lead to dangling Si bonds distributed irregularly at the interface. The density of these bonds will be called N_{θ}^b to represent that it will vary with the Si surface orientation, θ .

The importance of these bonds, besides the obvious surface-state connotation, is that they represent the exposed portion of extra half-plane segments of the Si that must be removed by the influx of vacancies or by the egress of interstitials so that the Si/ SiO_2 interface can continue to propagate into the Si during the oxidation process. Thus, N_{θ}^b indirectly controls the oxidation rate in that it determines what the vacancy and interstitial flux must be for a given oxidation velocity V or, assuming a limited and fixed interstitial and vacancy flux, V is determined (see Eq. [19]).

No one has observed a net of dislocations at the Si/ SiO_2 interface, which is not too surprising. Even if the extra half-plane segments were aligned to form a rectangular or triangular grid of macroscopic extent, diffraction would not reveal them as a dislocation net. This is because diffraction contrast is effective only when dealing with small departures from a perfectly regular lattice and, here, one side of the interface rep-

resents only small departures from a perfectly random lattice. Thus, we cannot expect to find the large constructive interference effects against which a dislocation is delineated as a consequence of a line of destructive interference. Although the extra half-plane segments at the Si/ SiO_2 interface might be thought of as dislocation segments, they do not have either the normal strain field associated with a dislocation or the same line energy. In the present case, the line energy of these pseudo-dislocations will be much lower than that for regular dislocations in the Si lattice.

Although it is possible to construct an abrupt transition from a regular Si lattice to a random network of SiO_2 by distortion of interface bonds with a relatively small calculated excess energy storage at the interface for distortions at constant volume, the real distortion condition which involves volume changes should be reflected macroscopically in the modulus of elasticity of the SiO_2 . Thus, the strain energy determined by the use of macroscopic elasticity parameters should specify the excess energy of the interface region. In terms of structural effects in the SiO_2 , one might also expect that, since a regular Si lattice is the starting point for oxidation, some tendency toward a crystalline ordering related to a form of SiO_2 might appear in a narrow transition zone at the interface. The film thickness at which relaxation occurs to the equilibrium configuration of SiO_2 would be of real interest.

If we approximate the situation with the two-crystal analogy where one is a thin film, the minimum free energy of the system will be a compromise between pseudo-dislocation energy, \mathcal{E}_d , and stored strain energy, \mathcal{E}_s . The total energy, \mathcal{E}_T , of the film can be minimized with respect to the degree of strain, δ' , existing at the interface. In the initial stages of oxidation, the oxygen atoms are expected to force themselves between the silicon atoms to form SiO bonds which are highly strained. The initial thin film may be coherent and highly structured in spite of the $\sim 30\%$ compressive strain located in the film. Using $E = 6.6 \times 10^{11}$ dynes/cm² for SiO_2 at 1200°C (7) and $\nu \sim 0.33$, this leads to $\mathcal{E}_s \approx 10^{11}\omega$ dynes/cm² for an SiO_2 film thickness of ω . This reduces to a value of about 60 kcal/mole SiO_2 , which is a very significant energy storage when it is recalled that the free energy of formation, ΔG_o , for SiO_2 from Si and oxygen (1 atm) is -154 kcal/mole at 1000°C ($\Delta G_o = -\Delta G_a$). If we compare this with an interface pseudo-dislocation net of average spacing $\sim 3-4$ Si distances and energy $\mathcal{E}_d \sim 500-1000$ ergs/cm², we find that $\mathcal{E}_s > \mathcal{E}_d$ even when $\omega = 1$ lattice spacing thick. Thus, if it is possible for it to do so, a monolayer of SiO_2 on Si will relax to form a pseudo-dislocation net at the interface. Of course, for such a two-dimensional SiO_2 structure, the equilibrium intermolecular spacing will be somewhat different than for a three-dimensional structure. However, it should be clear that, if the system can rearrange itself to introduce these pseudo-dislocations, it will be energetically favorable to do so and the excess stored energy, ΔG_E , will be reduced to small values characteristic of the residual stored strain energy in the film.

At present, good theoretical and experimental evidence exists for flow via dislocations in glass (8, 9). Silicate glasses tend to flow in a viscous manner, while metallic glasses tend to be plastic, and amorphous polymers fall somewhere in between. In the silicate case, the glass is an open covalently bonded network and the passage of dislocations through it leaves broken bonds (free radicals) in their wake. In addition, density fluctuations, as well as dislocation loops, may be part of the debris left in the wake of a moving dislocation in such a system (9). The shear modulus of amorphous SiO_2 is less than that of crystalline SiO_2 by about 14% (10) and the elastic energy of a dislocated random network is lower than that of the dislocated crystal by the same factor. If the plastic deformation of a glass is not absolutely uniform, dislocation-like defects with

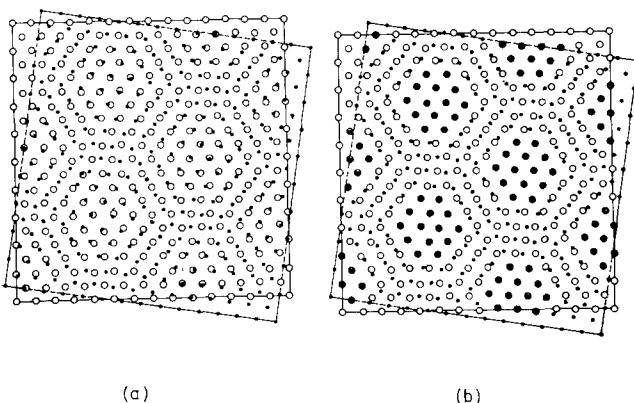


Fig. 1. Formation of a hexagonal network in the (110) plane of the body-centered lattice: (a) after rotation of the two nets of atoms and (b) after relaxation of the atoms.

long-range stress fields separate regions that have suffered different shears. Given sufficient time, the long-range stress field will relax by a kinematic process involving the uncorrelated motion of pairs, or small groups, of atoms, a process not possible in a crystal because its translational symmetry permits only correlated motion. These relaxed defects have been named "disjunctions" and they, rather than dislocations, will be found in well-annealed glass (10).

Disjunctions are expected to influence electrical and optical properties by introducing new electronic energy levels into the network. They will also act as high diffusivity paths for mass-transport in network glasses. Because they have low energy (roughly equal to the core energy of a dislocation) and do not interact strongly, it may be possible to introduce a very high density of disjunctions into a glass.

For the total energy associated with the film-forming process, we must include the nonequilibrium vacancy and interstitial effects in the silicon; *i.e.*, we must use, per unit area of interface

$$E_T = \mathcal{E}_d + \mathcal{E}_s + \int_0^\infty [(C_V - C_{V \text{ equil.}})\eta_V + (C_I - C_{I \text{ equil.}})\eta_I] dx \quad [11]$$

where \mathcal{E}_d is the pseudo-dislocation net energy and \mathcal{E}_s is the stored strain energy, while the equilibrium concentrations, $C_{j \text{ equil.}}$, and the electrochemical potentials, η_j , for the vacancies and interstitials will be a function of the Fermi energy, the local electrostatic potential, and the state of stress. For the moment, we shall neglect the V and I effects and will return to them later. Let us first consider the macroscopic flow of the SiO_2 to determine how easily that process can influence pseudo-dislocation network formation and propagation at the Si/SiO_2 interface.

The viscoelastic process.—Ernisse (11) has clearly demonstrated the viability and importance of the viscous flow process during Si oxidation at high temperatures, so let us consider the kinetics of this flow at normal oxidation temperatures. The general viscoelastic expression relating applied stress, τ , to strain rate, $\dot{\gamma}$, is

$$\dot{\gamma} = A \left(\frac{\tau}{\tau_y} \right)^n \quad [12]$$

where τ_y is the yield stress, A is a constant, and $n = 1$ for linear elasticity, $1 < n < 10$ for nonlinear elasticity, and $n > 10$ for ideal plasticity. Let us first consider the simple approximation that our SiO_2 film yields in the same fashion as the simple "Maxwell element" shown in Fig. 2. For this case, $n = 1$ and the load τ acting on the spring leads to an initial strain γ_{sp} given by

$$\gamma_{sp} = 3\tau/E \quad [13a]$$

and the dashpot begins to relax at a strain rate $\dot{\gamma}_{dp}$ given by

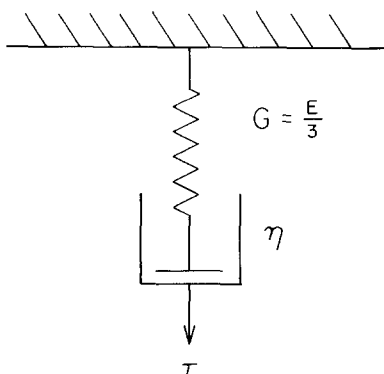


Fig. 2. A simple Maxwell viscoelastic element as a mechanical analogue to the SiO_2 stress relaxation.

$$\dot{\gamma}_{dp} = \tau/\eta^* \quad [13b]$$

Solving the differential equation for the stress as a function of time, utilizing the condition $\dot{\gamma}_{sp} + \dot{\gamma}_{dp} = 0$, leads to

$$\tau(t) = \tau_0 \exp\left(-\frac{Et}{3\eta^*}\right) \quad [14]$$

Thus, the stress relaxation rate depends on the viscosity of the material. Using Eq. [14], we can ask how far into the oxide, $m^*\lambda_0$, where m^* is a number and λ_0 is the intermolecular distance, we must go before the stress has relaxed by an order of magnitude. This distance would give us the effective size of a nonequilibrium structured layer of SiO_2 at the Si interface. Allowing $t^* = m^*\lambda_0/\bar{V}$, where \bar{V} is the average oxidation velocity, the width of the structured layer, $m^*\lambda_0$, is given by

$$m^*\lambda_0 \approx 9\eta^*\bar{V}/E \quad [15]$$

Using $T = 1000^\circ\text{C}$, $\bar{V} \sim 10^{-9}$ cm/sec, $E \sim 10^{12}$ dynes/cm², $\eta_{\text{equil.}}^* = 6.3 \times 10^{16}$ poise for dry O_2 (I.R. Vitreosil) (11), and $\eta_{\text{equil.}}^* = 5.6 \times 10^{14}$ poise for wet O_2 (O.G. Vitreosil + 0.4% OH) (11), we find $m^*\lambda_0 \sim 5 \times 10^{-4}$ cm and 5×10^{-6} cm, respectively, for dry O_2 and wet O_2 . This number seems to be a factor $\sim 10^3$ too large which suggests that the value of n to be used in Eq. [12] should be at least 2. Thus, although we cannot proceed effectively to evaluate the application of Eq. [12] with higher values of n because of uncertainties with respect to A and τ_y , we can see that (i) the flow process does not readily generate the minimum free energy condition and (ii) the flow process will yield a nonequilibrium structured SiO_2 layer of some thickness X^* at the Si/SiO_2 interface, X^* for dry oxygen will be greater than X^* for wet oxygen, and X^* for each will increase as the temperature is decreased. If we had used $\tau_y = \beta\eta^{*1/p}$ in Eq. [12], where β and p are fitting parameters for a given material, we would have found for $n/p = 2/3$, that $m^*\lambda_0 \sim 55\text{\AA}$ for dry O_2 at 1000°C when $m^*\lambda_0 \sim 3.5\text{\AA}$ for wet O_2 at the same temperature.

Investigators working in the area of the mechanical properties of crystalline materials (12, 13) have shown how many of these properties may be explained in terms of dislocation dynamical modeling. One usually invokes the Taylor-Orowan equation as the basic description for plastic flow; *i.e.*

$$\dot{\gamma} = \alpha'\rho_m Vb \quad [16]$$

where $\dot{\gamma}$ is the plastic strain rate, α' is a geometrical constant, ρ_m is the mobile dislocation density, \bar{V} is the average dislocation velocity, and b is the Burger's vector. In addition, one uses an equation analogous to Eq. [12] to represent the strain rate sensitivity n as

$$n^{-1} = \frac{d \ln \tau}{d \ln \dot{\gamma}} \quad [17]$$

and assumes a power law stress-velocity relationship of the form

$$V = (\tau/\tau_0)^m \quad [18]$$

where τ_0 and m are constants. Such a relationship has been experimentally verified for many fcc and bcc metals (14-16). Recently (17) it has been shown that, if proper account is taken of the fraction of mobile dislocations and the internal back stresses due to work hardening, the dislocation dynamical modeling which worked so well for bcc metals can be extended to fcc metals.

The application of this approach to the SiO_2 flow problem at the Si/SiO_2 interface is beyond the scope of this paper. However, it has been introduced here both to set the stage for further work and to reveal the importance of the dislocation velocity to the overall process. The reason for introducing this latter aspect is to indicate another important electrical feature that

will enter the SiO_2 flow considerations. It has been shown (18) that the dislocation mobility in the vicinity of a surface is strongly dependent on the charged nature of the surface. If the surface is at its isoelectric point (uncharged), the dislocation mobility is least. If the surface is strongly charged, either positively or negatively, the dislocation mobility is highest. Such a change in basic dislocation mobility for crystals, glasses, polymers, rocks, etc., transforms a basically brittle material into a plastic one as ϕ_i increases to large positive or negative values and vice versa as ϕ_i decreases toward a zero value.

Interface pseudo-dislocation grid propagation.—Since the formation of the interface pseudo-dislocation grid lower the free energy of the system quite significantly and, since the flow properties of the SiO_2 do not easily allow the grid to form, the maintenance and propagation of the grid is likely to be a key consideration in the oxidation process. Thus, how is it to propagate at

$$C_{I\text{equil.}}(x) = \sqrt{2} N \exp \left\{ - \left[\frac{(\Delta G_I + \Delta G_V) + 2Z_I e(\phi(x) - \phi_0)}{2kT} \right] \right\} \quad [20a]$$

$$C_{V\text{equil.}}(x) = \sqrt{2} N \exp \left\{ - \left[\frac{(\Delta G_I + \Delta G_V) + 2Z_V e(\phi(x) - \phi_0)}{2kT} \right] \right\} \quad [20b]$$

the oxidation rate V ? If the edge pseudo-dislocation forming the array were lying on the $\{111\}$ planes making an angle to the Si/SiO_2 interface, then the film stress might possibly cause dislocation glide in the proper direction and at the proper rate to move the entire grid at velocity V perpendicular to the interface. A more likely alternative is that the pseudo-dislocations could climb in a direction toward the Si at the necessary rate to allow the grid to move at velocity V . If only climb could operate (see Fig. 3), at low temperatures (no viscous flow in SiO_2), the average spacing, D , of the propagating pseudo-dislocation grid would assume that value allowed by the vacancy plus interstitial flux in the Si and the remainder of the molecular mismatch would be retained as stress in the film; i.e., the oxidation reaction requires an interface front velocity of V but the vacancy influx process and the interstitial outflux process may only allow a grid of spacing $D > D^*$ to propagate at V (D^* is the optimum spacing for minimum free energy).

To gain a deeper perspective of the low temperature situation, let us assume that the interface contains a perpendicularly crossed grid of pseudo-dislocations, of spacing D , so that the interface can only advance by

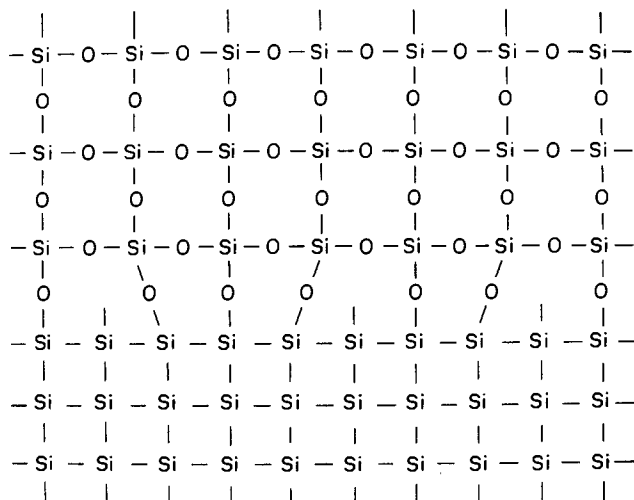


Fig. 3. Representation of pseudo-dislocation net (extra half-planes) and dangling bonds at the Si/SiO_2 interface for an idealized ordered SiO_2 .

pure climb driven by the free volume flux from the Si. For this case, the number of vacant sites needed per unit area of interface per second is $2V/D\lambda_{\text{Si}}^2$ where λ_{Si} is the unit cell spacing at the interface. Since the supply is just $J_I^{\text{Si}} - J_V^{\text{Si}}$, we have the allowed spacing, D , given by

$$D = 2V/\lambda_{\text{Si}}^2(J_I^{\text{Si}} - J_V^{\text{Si}}) \quad [19]$$

The vacancy and interstitial distributions are illustrated in Fig. 4. Since C_{II} and C_{VI} are functions of the level of strain, δ' , existing at the interface, Eq. [19] is coupled to Eq. [11] via the film strain level δ' . Thus, the allowable dislocation grid spacing, and thus the film stored energy, is determined by the point defect flux. For an alloyed system where impurity-vacancy and impurity-interstitial complexes must be considered, the description of the equilibrium distributions of various species is beyond the scope of this paper. However, for a relatively pure system where such complexes can be neglected, we find

where N is the number of lattice sites per unit volume and Z_I and Z_V are the valencies of the interstitials and vacancies, respectively.

Relative Magnitude of the Component Driving Forces

A perspective can be gained on the relative importance of the previous sections to the oxidation process by considering a free energy balance equation for the overall process; i.e.

$$\Delta G = \Delta G_{\text{SV}} + \Delta G_{\text{E}} + \Delta G_{\text{K}} \quad [21]$$

We know that $\Delta G_{\text{S}} = 154$ kcal/mole at 1000°C and that $\Delta G_{\text{E}} \gtrsim 60$ kcal/mole (it may be higher if our chosen modulus value is too small). We have not yet explored ΔG_{K} in this paper but will estimate its order of magnitude from other work. However, let us first consider the magnitude of ΔG_{SV} .

First, if we consider the work of Deal and Grove (2) and use the D_{eff} approach, so that the electric field dependence is neglected, and also assume that we have primarily neutral O_2 diffusion so that ΔG_{SV} arises only from the difference between C_0 and C_i , then we have

$$\Delta G_{\text{SV}} = \Delta G_{\text{S}} = RT \ln C_0/C_i \quad [22]$$

This can be evaluated by equating the transport flux through the oxide, F_2 , with the interface flux at the Si/SiO_2 interface, F_3 ; i.e.

$$F_3 = kC_i = \frac{D_{\text{eff}}}{X_0} C_i \left(\frac{C_0}{C_i} - 1 \right) = F_2 \quad [23]$$

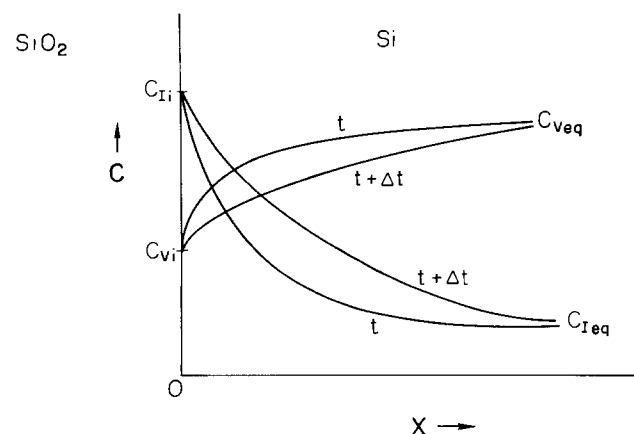


Fig. 4. Schematic illustration of interstitial and vacancy distributions on the Si side of the Si/SiO_2 interface for times t and $t + \Delta t$.

Using $k = 3.6 \times 10^4 \mu\text{m/hr}$ for dry O_2 at 1000°C (2) and $D_{\text{eff}} \approx 2.8 \times 10^8 \mu\text{m}^2/\text{hr}$ for oxygen in fused silica at 1000°C (19), we find that $C_o/C_i \approx 1.26$ – 13.9 for X_o from 0.2 to $1.0 \mu\text{m}$. Thus, in this range of X_o , ΔG_S is 0.58 – 6.6 kcal/mole. These are very small values indeed and the range is so small compared to ΔG_o that one begins to question the meaning of a "transport limited" reaction for this case.

Next, if we consider $\text{O}_=$ transport as being the prime diffusing species in the process, then we have

$$\Delta G_{\text{SV}} = \Delta G_{\text{S},\phi} = RT \ln \frac{C_o}{C_i} - 2F(\phi_o - \phi_i) \quad [24]$$

where F is the Faraday ($96,484\text{C}$). Thus, for $(\phi_o - \phi_i) \sim -1\text{V}$, the electrostatic term would be ~ 46 kcal/mole, a much more respectable range for a process that has a transport-controlling regime as the Si oxidation reaction appears to have. To more fully evaluate $\Delta G_{\text{S},\phi}$, let us look at the linear rate constant B'/A' from Eq. [5]; i.e.

$$B'/A' = \left(\frac{C^*}{N_i} \right) \frac{k^* h^*}{k^* + h^*} \frac{1 - \alpha e^{|\Delta\phi|/kT}}{1 + \alpha e^{|\Delta\phi|/kT}} \quad [25]$$

From Eq. [25], if $\alpha e^{|\Delta\phi|/kT} \ll 1$, then B'/A' equals B/A from Eq. [2] and $\Delta G_{\text{S},\phi} \approx \Delta G_S \gtrsim 7$ kcal/mole. If $\alpha e^{|\Delta\phi|/kT} \gg 1$, then B'/A' becomes negative and $k^* = 3.6 \times 10^4 \mu\text{m/hr}$ from the Deal and Grove analysis. If $\alpha e^{|\Delta\phi|/kT} \approx 1$, then k^* can be larger by several orders of magnitude and it can be positive or negative. This would increase C_o/C_i in proportion so that ΔG_S might increase to ~ 20 kcal/mole but the electrostatic contribution would decrease to about 5 kcal/mole leading to $\Delta G_{\text{S},\phi} \sim 25$ kcal/mole, which is of respectable magnitude.

To estimate ΔG_K , we can slightly modify the simple rate theory as applied to the liquid/crystal transformation (20). There, a molecule in the liquid at the interface must transcend an activation barrier and join the crystal lattice at selected sites on the interface so that μ_1 in Eq. [8a] of Part I (1) is given by

$$\mu_1 = \frac{\beta^* \alpha^* D}{\lambda RT} \quad [26]$$

where D is the diffusion coefficient for transport across the interface (generally assumed to be the same as diffusion in the liquid), α^* is the fraction of interface sites available for molecular attachment (generally only those at layer edges and sometimes only a fraction of them), and β^* is the number of liquid molecular sites within one jump distance of an attachment site ($\beta^* \sim 3$ – 4). When one is dealing with a network liquid so that intermolecular bonds must be broken before the interface attachment jump can occur, another factor must be included in D to account for the probability that the bond-breaking event will occur.

In our case, the situation is not too dissimilar. We can think of the oxygen species as diffusing interstitially in the SiO_2 up to the Si/SiO₂ interface. The critical activation barrier at the interface involves both a normal diffusion-type jump plus the breaking of Si-Si bonds. Thus, Eq. [26] should be altered to

$$\mu_1 = \frac{\beta^* \alpha^* D_{\text{O}_2}}{\lambda RT} e^{-\Delta G^*/RT} \quad [27]$$

where ΔG^* is the energy required to break a Si-Si bond (~ 42 kcal/mole when the silicon is unstrained). Evaluating Eq. [27] leads to $\mu_1 \sim 2.5 \times 10^{-8} \alpha^* \text{ cm/sec/kcal/mole}$. For a (111) interface, one would expect $10^{-4} < \alpha^* < 10^{-2}$ and, picking the intermediate value, we predict that $\Delta G_K \sim 40$ kcal/mole for $V \sim 10^{-9} \text{ cm/sec}$. Since the value of α^* will depend on

the source of layer edges (dislocations or two-dimensional nucleation), it will vary with interface temperature and interface supersaturation so that ΔG_K will vary accordingly. In addition, α^* may be sensitively dependent on the presence of certain impurities like H or C, etc. (21).

From the foregoing, we have found that $\Delta G_E \gtrsim 60$ kcal/mole, $\Delta G_{\text{S},\phi} \sim 25$ kcal/mole, and $\Delta G_K \sim 40$ kcal/mole. Since an error of a factor of 2 could reasonably be ascribed to any or all of these, we may allow that all of the ΔG_o has been accounted for. It is interesting to note that the recent modeling of Blanc (22) focuses totally on the ΔG_K contribution, that of Svensson (23) is involved with the structural aspects of the ΔG_E contribution, while that of Fowkes *et al.* (24) brings to light the importance of possible defect equilibria such as enter the $\Delta G_{\text{S},\phi}$ contribution. It should also be noted that no real attention has been given to the magnitude of the driving force, ΔC_g^M , needed for the transfer of gaseous species across the gas/SiO₂ interface. This is expected to be small (2) but, for completeness, it needs to be considered more carefully in the future.

Discussion

From the use of Eq. [22] and [23], it is clearly seen that the diffusion of neutral oxygen through SiO₂ to oxidize the Si cannot be responsible for the parabolic rate constant represented by Eq. [2c]. This would indicate that the position held by Doremus (25) is untenable, provided that the data on k^* generated from the Deal and Grove analysis (2) is correct. The diffusion of ionized oxygen is a more likely candidate for the oxidation process based on the use of Eq. [24] and [25]. However, it is difficult to see how it could become totally rate controlling and lead to a diffusion-limited regime where the parabolic rate constant B' dominates the process because this would require that ΔG_{SV} approach ΔG_o in magnitude. Such a situation would require a large value of $\phi_i - \phi_o$ in Eq. [24], which would lead to a negative value for k^* unless the assumption that $h^* \gg k^*$ (2) is in error (if ΔC_g^M is not negligible in magnitude). Perhaps it is necessary to look elsewhere for the source of the diffusion-limited regime.

One heretofore overlooked possibility is that the parabolic term arises as a consequence of vacancy and interstitial transport in the Si as a response to the free volume supply condition (see Part I (1), Eq. [13]). Certainly, from Eq. [19], the average grid spacing of the pseudo-dislocation net at the interface is determined by the flux of interstitials and vacancies in the Si. From Eq. [11], ΔG_E may be strongly determined by the nonequilibrium vacancy and interstitial concentration levels needed to provide this flux of Si atoms away from the interface. The ΔG_E contribution is of sufficient magnitude to completely dominate the oxidation process; thus, if the pseudo-dislocation net forms and the residual strain stored in the film is negligible, as much as -50 kcal/mole could be pumped into the Si vacancy-interstitial diffusion mechanism, which would definitely yield a significant parabolic term in the thermal oxidation process. This possibility certainly shifts the focus of one's attention to a new direction.

From Eq. [27], the molecular attachment kinetic coefficient μ_1 will be a strong function of temperature through ΔH^* and the activation energy for D_{O_2} . However, for the vacancy flux mechanism, the term $\exp(-\Delta H^*/RT)$ will be replaced by a term proportional to the vacancy concentration at the interface and this will very likely be a nonequilibrium value. Some support for this possibility comes from the work of Ho and Plummer (26) who have provided a quantitative explanation of the enhanced oxidation rate via heavy doping of Si with n-type or p-type solutes.

In Eq. [27], α^* is a key parameter and it may be reduced or increased by the presence of specific interfacial impurities. Both Revesz (21) and Gunthner and Maserjian (27) have shown that the presence of H and C in an initial surface film prior to oxidation reduces the oxidation rate and that these impurities migrate with the interface. Thus, these impurities appear to reduce the fraction of active sites for oxidation, α^* , at the interface. Perhaps this is the reason for the initially rapid oxidation rate in dry O_2 which results in a value of $X_i \sim 200\text{\AA}$ for Eq. [2]. We might speculate that it takes a short time of oxidation until the interface builds up to a stationary state hydrogen concentration with α^* reduced to some stationary state value. On the other hand, oxidation with wet O_2 is faster than with dry O_2 and $X_i \approx 0$ in this case. This would seem to require that either α^* is increased or that the reduced viscosity of the SiO_2 , with the H_2O content, allows flow to occur in the film to provide the excess free volume needed for the interface process to proceed. To resolve these issues, a close look at the geometrical aspects of the oxidation process will be needed. In addition, the value of n in Eq. [12] needs to be determined experimentally for SiO_2 in both dry and wet O_2 for the temperature ranges of interest.

Such a strain rate experiment would apply to bulk vitreous SiO_2 but might not completely apply to the interfacial SiO_2 which may have some crystalline characteristics added to it and which may really be of stoichiometry SiO_x . In this regard, it is of interest to note that the lattice parameters of low temperature cristobalite are $a \approx 5.1\text{\AA}$ and $c \approx 7.4\text{\AA}$ if extrapolated to $\approx 1000^\circ\text{C}$ (28). Further, the volume change from high cristobalite to low cristobalite at 218°C is a decrease of 3.7% (29). Thus, the a-plane of low cristobalite has a size registration that is close to that of the Si so that a trace of this type of ordering might be found in the Si/ SiO_2 interface layer material. Such an ordering would undoubtedly influence the flow properties.

From the foregoing, one can project a variety of processing alterations that should lead to enhanced oxidation rates:

1. Apply a negative surface charge to the SiO_2 /gas interface to enhance the oxide electric field and thus V (similar to plasma anodization if just O_2 used).

2. Produce dissociation in the gas phase so that the surface sees O rather than O_2 which should lead to a higher population of O_2 in the oxide if there is a kinetic barrier to its formation from O_2 .

3. Irradiate the growing oxide with u.v. at a photon energy beyond the bandgap to break Si/Si bonds at the interfaces and thus reduce ΔG_K (in addition, Fermi energy changes occur which should be beneficial for highly doped p-type Si).

4. Enhance the available vacancy source strength in the Si by annealing Si slices at very high temperatures prior to oxidation and quenching to the oxidation temperature.

5. Enhance the available vacancy source strength in the Si at the oxidizing interface by the application of an electric field to the Si prior to oxidation so that excess vacancies migrate to the appropriate side of the slice.

6. Use heavy doping of the Si and anneal at a high temperature prior to oxidation so that excess vacancies will be generated due to the Fermi level shift away from midband.

7. Add network terminators to the oxidizing gas so that the SiO_2 will have a lower viscosity and less strain energy will be stored in the SiO_2 film and ΔG_E will be reduced.

It is very likely that the oxidation studies of Ligenza (28) utilizing a microwave excited oxygen plasma is an example of 1 and 2 combined from the above list. The O^- ion is generated in large popula-

tions, which will both charge the surface and enhance the ion flux to the interface. The work of Oren and Ghandhi (30) is an example of item 3 above. The work of Ho *et al.* (3) is an example of item 6 and Cl additions to the gas stream (31) may be beneficial in part via item 7 above.

A final comment should perhaps be made concerning the accuracy of using the Cabrera and Mott (32) D_{eff} procedure. In their treatment, they neglected any displacement current effects associated with moving space charges and this is not appropriate for the type of moving interface situation we are dealing with here. A much more accurate procedure is to deal with the electric field directly, as was done in the section on Modified Deal-Grove Transport Analysis. As one goes toward treating much thinner films, or when one wants to say something about surface charge and volume charge which relates to detailed solute distributions, and when one wants to deal with more subtle film properties like interface instability and solute redistribution, one should not use the D_{eff} approximation.

Acknowledgments

Dr. B. E. Deal, Dr. J. D. Plummer, Mr. C. P. Ho, and Mr. H. Z. Massoud provided many helpful discussions of the available thermal oxidation data and of the processes involved. Discussions with Dr. E. Eernisse on viscous flow of SiO_2 were also helpful. This work was supported by the Defense Advanced Research Projects Agency under Contract No. DAAB07-77-C-2684.

Manuscript submitted Oct. 2, 1978; revised manuscript received Sept. 11, 1979.

Any discussion of this paper will appear in a Discussion Section to be published in the December 1980 JOURNAL. All discussions for the December 1980 Discussion Section should be submitted by Aug. 1, 1980.

Publication costs of this article were assisted by Stanford University.

REFERENCES

1. W. A. Tiller, *This Journal*, **127**, 619 (1980).
2. B. E. Deal and A. S. Grove, *J. Appl. Phys.*, **36**, 3770 (1965).
3. C. P. Ho, J. D. Plummer, B. E. Deal, and J. D. Meindl, *This Journal*, **125**, 665 (1978).
4. H. Brooks, in "Metal Interfaces," R. M. Brick, Editor, chap. 2, ASM, Cleveland (1952).
5. J. Washburn, G. Thomas, and H. J. Queisser, *J. Appl. Phys.*, **35**, 1909 (1964).
6. R. B. Fair, *This Journal*, **125**, 923 (1978).
7. R. J. Jaccodine and W. A. Schlegel, *J. Appl. Phys.*, **37**, 2429 (1966).
8. D. M. March, in "Fracture of Solids," D. C. Drucker and J. J. Gilman, Editors, p. 143, Interscience, New York (1963).
9. J. J. Gilman, *J. Appl. Phys.*, **44**, 675 (1973).
10. M. F. Ashby and J. Logan, *Scr. Metall.*, **7**, 513 (1973).
11. E. P. Eernisse, *Appl. Phys. Lett.*, **30**, 290 (1977).
12. W. G. Johnston and J. J. Gilman, *J. Appl. Phys.*, **30**, 129 (1959).
13. G. T. Hahn, *Acta Metall.*, **10**, 727 (1962).
14. T. Vreeland, Jr., "Dislocation Dynamics," p. 529, McGraw Hill Book Co., New York (1968).
15. D. F. Stein and J. R. Low, Jr., *J. Appl. Phys.*, **31**, 362 (1960).
16. H. W. Schadler, *Acta Metall.*, **12**, 861 (1964).
17. G. M. Pharr and W. D. Nix, *ibid.*, **27**, 433 (1979).
18. R. M. Latanision and J. T. Fourie, Editors, "Surface Effects in Crystal Plasticity," chap. 1, 2, Noordhoff, Leyden (1977).
19. F. J. Norton, *Nature*, **171**, 701 (1961).
20. W. B. Hillig, in "Kinetics of High Temperature Process," W. B. Kingery, Editor, p. 142, John Wiley & Sons, Inc., New York (1959).
21. A. Revesz, To be published in *This Journal*.
22. J. Blanc, *Appl. Phys. Lett.*, **33**, 424 (1978).
23. C. M. Svensson, in "The Physics of SiO_2 and its Interfaces," S. T. Pantelides, Editor, p. 328, Pergamon, New York (1979).

24. F. M. Fowkes and D. W. Hess, Paper 76 presented at The Electrochemical Society Meeting, Philadelphia, Pennsylvania, May 8-13, 1977.
25. R. H. Doremus, *J. Chem. Phys.*, **80**, 1773 (1976).
26. C. P. Ho and J. D. Plummer, *This Journal*, **126**, 1516 and 1523 (1979).
27. F. J. Gunthamer and J. Maserjian, in "The Physics of SiO₂ and its Interfaces," S. T. Pantelides, Editor, p. 389, Pergamon, New York (1979).
28. J. R. Ligenza, *J. Appl. Phys.*, **36**, 2703 (1965).
29. W. Johnson and K. W. Andrews, *Trans. Br. Ceram. Soc.*, **55**, 227 (1956).
30. R. Oren and S. K. Ghandhi, *J. Appl. Phys.*, **42**, 752 (1971).
31. B. E. Deal, D. W. Hess, J. D. Plummer, and C. P. Ho, *This Journal*, **125**, 339 (1978).
32. N. Cabrera and N. F. Mott, *Rep. Progr. Phys.*, **12**, 163 (1948).

The Rotating Cylinder-Collector Electrode (RCCE)

Michael C. H. McKubre* and Digby D. Macdonald*¹

SRI International, Materials Research Laboratory, Menlo Park, California 94025

ABSTRACT

A rotating cylinder-collector electrode (RCCE) for the study of electrochemical processes that involve electroactive intermediates and/or products is described. Calibrations of the collector efficiencies (N) for both major and minor sectors have been performed using the ferri/ferrocyanide redox couple over a wide range of rotational velocity (225-3060 rpm). With the minor sector as the collector, a collection efficiency of $\sim 7.2\%$ was observed, and N was found to be independent of rotational velocity over the range considered. However, the collection efficiency increased to $\sim 67\%$ when the major sector was used as the collector, thereby indicating that the RCCE is a sensitive device for the detection of dissolved electroactive species. The utility of this electrode is illustrated by investigating the anodic behavior of copper and nickel in hydroxide solution at various temperatures between 0° and 80°C.

The rotating disk (RDE) and rotating ring-disk electrodes (RRDE) have proved to be powerful tools in the study of electrochemical process (1-5). In the latter case, electroactive intermediates formed at the disk electrode are detected at the ring by oxidation or reduction under potentiostatic or potentiodynamic control. Thus, the ratio of the ring to disk currents for the removal and generation of the active species, respectively, defines the collection efficiency (N) for the electrode. Ideally, the collection efficiency is a function of geometry only; in practice, however, it is found to depend on the state of the collector surface and the hydrodynamic properties of the system (5). Typically, N varies between 0.1 and 0.5 depending on the relative dimensions of the disk and the ring (5). It is important to note, however, that the theories developed to date apply only to the case of complete mass transfer control.

In spite of its popularity, the rotating disk and rotating ring-disk electrodes suffer a number of disadvantages when not operating under complete mass transfer control or when being used for the study of surface controlled processes. Thus, in the absence of complete mass transfer control, the current density is not uniform across the disk radius due to the ohmic potential drop in solution. Newman (6) and Nanis (7) have elaborated on this problem and Newman (6) has shown that the current density at the center can vary between 50 and 100% of the average current density. The distribution in current density under these conditions implies a distribution in potential across the disk radius, and consequently a distribution in electrochemical state. While this property does not pose a limitation on the validity of the RDE or the RRDE for most of the application reported so far (mass transfer controlled systems), it does so for the study of technologically important phenomena, such as corrosion, where frequently complete mass transfer control is not observed.

A second problem with both the RDE and the RRDE is that a distribution in Reynolds number

$$Re_r = r^2\omega/\nu \quad [1]$$

where ν is the kinematic viscosity and ω is the rotational velocity (rad/sec) also exists across the surface. This Re varies from zero at the rotation axis to a maximum at the outer edge of the disk. Since the shear stress at the interface increases with the velocity gradient (and hence with Re), it is clear that the mechanical stresses to which surface films are subjected are dependent on the distance from the axis of rotation. It is expected that this property could have an important effect on film growth processes occurring at the surface of RDE.

In this paper we describe a rotating cylinder-collector electrode (RCCE) that exhibits certain characteristics that we believe are superior to those for the RRDE. For example, the roles of both the "source" and "collector" are interchangeable which can result in an advantageously large change in the collection efficiency. Also, the system is characterized by a single value for Re , and the distribution in current density across the surface is thought to be more uniform than that for a RDE or RRDE operating below the mass transfer limit. It is worth mentioning, however, that the observation of a steady-state current clearly demonstrates the existence of a flow pattern that is not a property of a perfect rotating cylinder. The existence of such a flow may well impose a considerable degree of nonuniformity under mass transport controlled conditions.

The collection efficiency for the system is evaluated empirically and the application of the RCCE to the study of electrochemical processes is illustrated by considering the anodic behavior of copper and nickel in hydroxide solution.

Experimental

Construction of electrode.—The RCCE was fabricated from 99.999% Cu rod machined to produce two approximately hemi-cylindrical sections of the desired length, and from 99.998% Ni sheet 1 mm thick. These three components plus two Mylar insulating spacers 0.011 cm thick are shown in Fig. 1. Machining of the parts does not present any practical difficulties, provided these are made oversized and the electrode turned, once final assembly is completed, to a circular cross section of the desired radius.

* Electrochemical Society Active Member.

¹ Present address: Department of Metallurgical Engineering, The Ohio State University, Columbus, Ohio 43210.

Key words: electrochemistry, corrosion, rotating cylinder electrode, collection electrode.

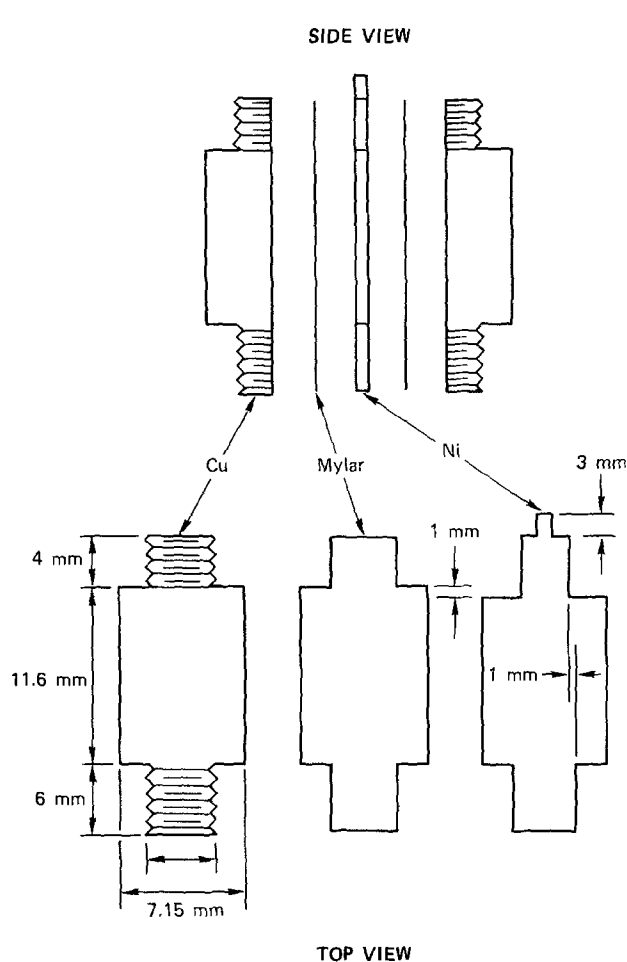


Fig. 1. Exploded view of RCC electrode components

The electrode and supporting shaft are shown in Fig. 2. After loose assembly the electrode was screwed into a threaded Delrin² end cap previously filled with unset epoxy which ensures that there are no voids for electrolyte penetration, and provides mechanical strength upon setting. The top of the electrode assembly was screwed into an internally threaded 0.953 cm ($\frac{3}{8}$ in.) stainless steel tube which makes electrical contact to and between the two hemi-cylindrical Cu electrode sections. Electrical contact to the Ni key was accomplished by an insulated Cu wire soft soldered to the protruding key shown in Fig. 1.

Electrolyte contact with the supporting stainless steel cylinder was prevented by the use of heat shrinkable FEP tubing (8).

The cell was constructed entirely of Teflon (both FEP and PTFE) incorporating an internal 0.5 mm diam Pt wire counterelectrode and having the form of a circle coaxial with the RCCE assembly, and coplanar with the midpoint of the working electrode and the tip of the Luggin probe (see Fig. 3).

Variable rotation speed was accomplished using a side mounted d-c motor and pulley assembly with a variable voltage supply. Conventional bearings were employed and quadrature mounted amalgamated copper brushes were used to make reliable electrical contact with the Cu and Ni section of the RCCE.

The completed electrode assembly had the following dimensions. Overall electrode length 1.150 cm, electrode diameter 0.775 cm, working electrode area 2.800 cm², thickness of Mylar 0.011 cm, thickness of Ni 0.095 cm, exposed area of Ni 0.219 cm², exposed area of Cu 2.556 cm². The area ratio Cu:Ni was 11.69:1.

Electrode surface preparation.—Before experimentation the RCCE was polished with various grades of

² Trade name.

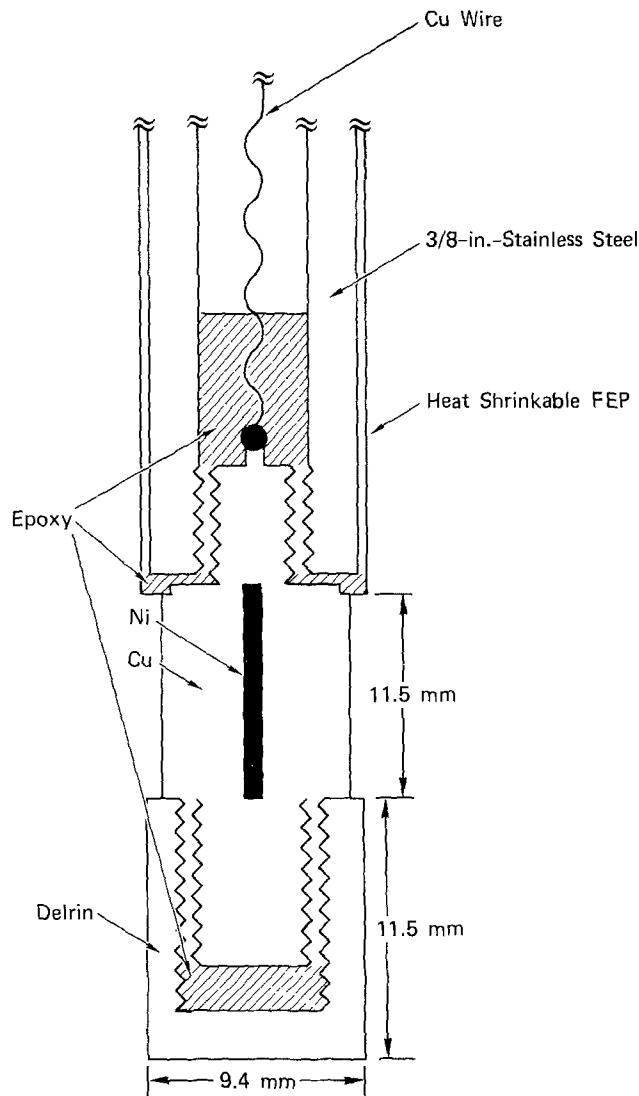


Fig. 2. Mounted RCC electrode

emery paper, finishing with 600 grit (25 micron particle size) while rotating the assembly in air. This technique was found to produce a good polished finish, and reproducible electrochemical properties.

For some experiments utilizing the copper electrode as a collector (see later), the surface was previously amalgamated to reduce cathodic competition from the reductive evolution of H₂ gas. Such amalgamation must necessarily be accomplished without contamination of the exposed Ni surface with Hg metal, since the electrode cannot subsequently be polished. A very simple procedure proved to be effective. A freshly polished RCCE was wet with dilute HCl to remove the surface copper oxide and a very small drop of mercury transferred to the surface with a copper wire. The contact angle is very small and the mercury immediately wetted one hemi-cylindrical copper electrode section, up to the insulating Mylar spacer, which is not wetted by mercury. This process was repeated for the remaining copper hemi-cylinder, and a lustrous silver colored amalgamated surface was achieved.

Reagents.—Electrolytes were prepared from AnalaR reagents using doubly distilled deionized water, with the second distillation under N₂ to exclude CO₂. High purity (99.999%) nitrogen was used to sparge the cell.

Electronics.—Two potentiostatic circuits with common reference (SCE or Hg/HgO) and counterelectrodes were used to control the Ni and Cu electrodes in a variety of experiments. During initial experiments a PAR Model 173 potentiostat was used to control the working electrode, and a specially con-

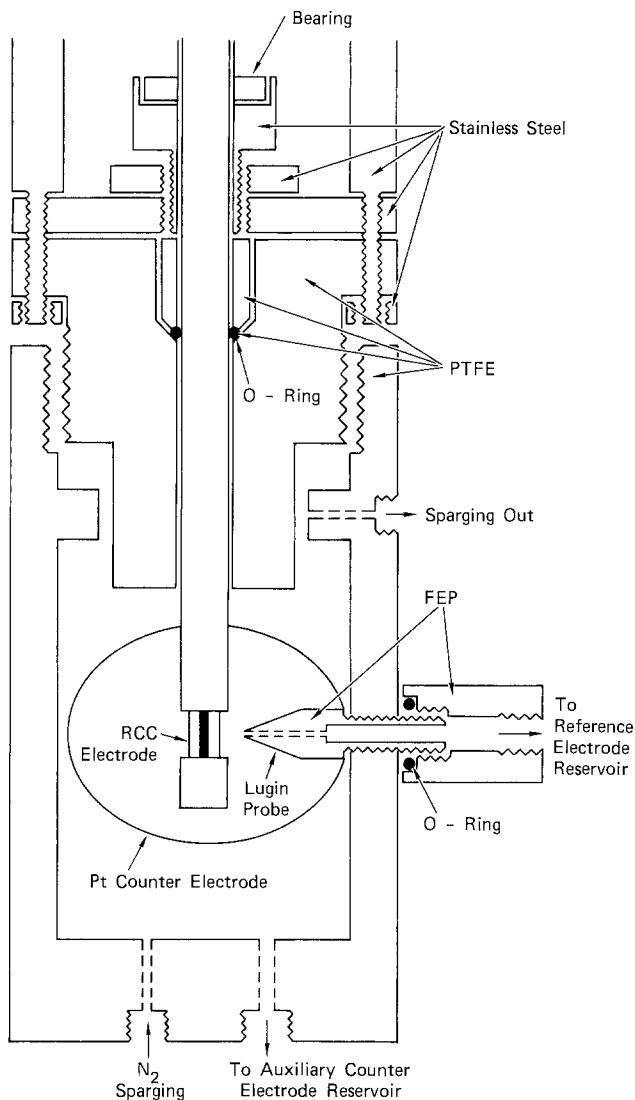


Fig. 3. RCC electrode and cell assembly

structed (9) fast potentiostat with a high degree of electrical isolation was used to control the collector. In subsequent experiments two PAR 173's were used; one connected to mains ground, and the other isolated at a high resistance from ground using an isolating transformer. Leakage across this transformer did not appear to result in spurious collector currents, and this latter combination allowed greater flexibility of current and voltage output.

All experiments described in this paper were performed under potentiostatic control and in a temperature controlled bath thermostated to within $\pm 0.1\text{K}$.

Results and Discussion

Collection efficiency.—Experiments were designed to reproduce those of Miller (10) for the calibration of a ring disk electrode in $0.1\text{M K}_3\text{Fe}(\text{CN})_6$ with 1.0M NaOH supporting electrolyte, at 20°C .

Collection efficiency is defined here as the percentage of the mobile dissolved species produced at the working electrode, that react electrochemically at the collector. Since there almost always exists a background current on both electrodes, this definition requires some elucidation.

As mentioned in above, unlike rotating ring disk systems, the RCC sections are complementary, and either may be used as the working or collector electrodes. Consequently, the electrode was calibrated in both configurations; first with the copper functioning as the working electrode reducing $\text{Fe}(\text{CN})_6^{3-}$ to $\text{Fe}(\text{CN})_6^{4-}$, and the nickel electrode as the collector,

performing the converse reaction, and secondly vice versa.

Before the results of these calibrations are presented, it is necessary to comment on the use of a swept potential for this purpose, and the separation of collection currents from the observed and unobserved background currents.

It is certainly not necessary, here, to propound the advantages of potentiodynamic experiments, but for ring disk, RCC, and other electrodes with collectors, it is possible to sweep either the working or the collector electrodes separately, or both simultaneously. While the latter course has certain theoretical advantages, these are complex, and the practical difficulties are extreme, and this alternative will not be discussed further in this paper.

Figure 4 shows the observed potentiodynamic response for the Cu and Ni sections of the stationary RCCE separately swept at 100 mV sec^{-1} , in the calibrating electrolyte. Potentials are with respect to a saturated calomel electrode, and the current density scales are identical but are displaced for clarity.

From Fig. 4 it is clear that peaks associated with the formation and reduction of higher nickel oxides occur at potentials similar to those of the ferri/ferro-cyanide couple. Thus, it is not possible to sweep the nickel electrode either as a working or collector electrode without incurring serious errors in the measured collection efficiency. For Cu however, the only significant potentiodynamic features between hydrogen evolution and oxygen evolution occur well cathodic of the ferri/ferro-cyanide peaks. Thus, this electrode can be swept either as a working or collector electrode, and having a stable and reproducible base current, the collection efficiency can be measured accurately.

A considerable source of error in the calculated collection efficiency for a system having either the working of collector electrode reactions not completely under mass transport control, can be introduced by an apparent coupling of the working and collector electrode currents in their shared IR drop. This has been separately treated by the present authors (11) and will be invoked to explain some of the results in this work. However, for a swept electrode system it is usually sufficient to observe the collected current in the presence and absence of rotation, or as a function of rotation, in order to eliminate the effects of coupled IR drops. Dissolved working electrode reaction products cannot reasonably be expected to be transported to the collector electrode in short times in a quiescent system. Thus, the collector current observed (as a function of voltage sweep) can be considered as a base

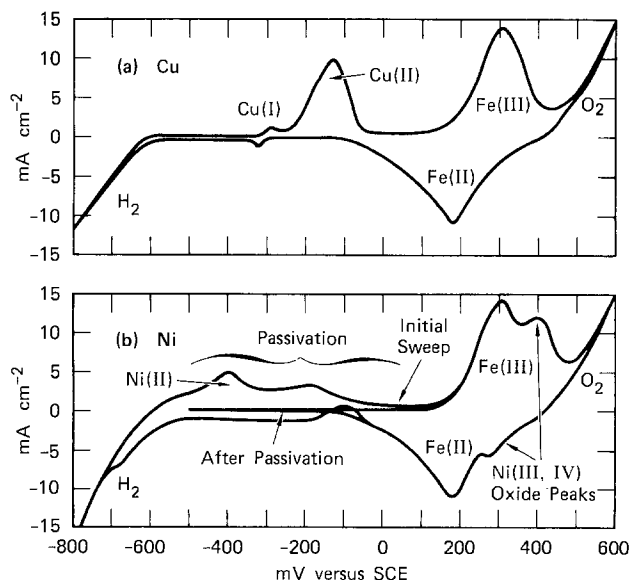


Fig. 4. Typical cyclic voltammograms for Cu and Ni electrodes in $0.1\text{M K}_3\text{Fe}(\text{CN})_6/1.0\text{M NaOH}$.

line, and be subtracted from the current observed at the rotating electrode, in order to calculate the electrode collection efficiency.

Calibration case 1: Ni collector.—Figure 5 shows the influence of electrode rotation on the working (Cu) and collector (Ni) electrode currents. The collector was held at +500 mV vs. SCE to oxidize Fe(II), and the working electrode was swept from -700 to +600 mV vs. SCE at 100 mV sec⁻¹. Assuming that at -500 mV (for example) all the working electrode current goes to produce Fe(II), and that the collector oxidation of this species may be equated with the difference between the rotating and quiescent Ni electrode currents, then the collection efficiency may be calculated as

$$N = 100 \times \frac{(7.05 - 0.7)}{69} = 9.20\%$$

A better estimate of the collection efficiency can be obtained by holding the working and collector electrodes at constant potentials, and measuring the two reaction currents as a function of electrode rotation speed, ω .

Figure 6 shows the results of three separate experiments with the working electrode (Cu) potentiostated at -500 mV and the collector electrode at +500 mV vs. SCE. From Fig. 6a we see that the working electrode current I_w varies with the square root of rotation velocity, with the regression line for all data given by

$$I_w = -13.3 + 2.98 \omega^{-1/2}$$

and having a regression coefficient (12)

$$r^2 = 0.993$$

Figure 6b shows values of collector current, I_c , plotted against I_w for all data between 225 and 3060 rpm. These data were transcribed from X-Y recorder plots of the two currents, and show a clear linearity, the slope of which being the collection efficiency. The regression line for the data in Fig. 6 is

$$I_c = 0.763 + 0.072 I_w$$

with a regression coefficient

$$r^2 = 0.994$$

A linear dependence of I_c on I_w is thus well obeyed, and the measured collection efficiency is 7.2%.

The upper limit of rotation speed was imposed by the motor, but at speeds lower than 225 rpm, significant

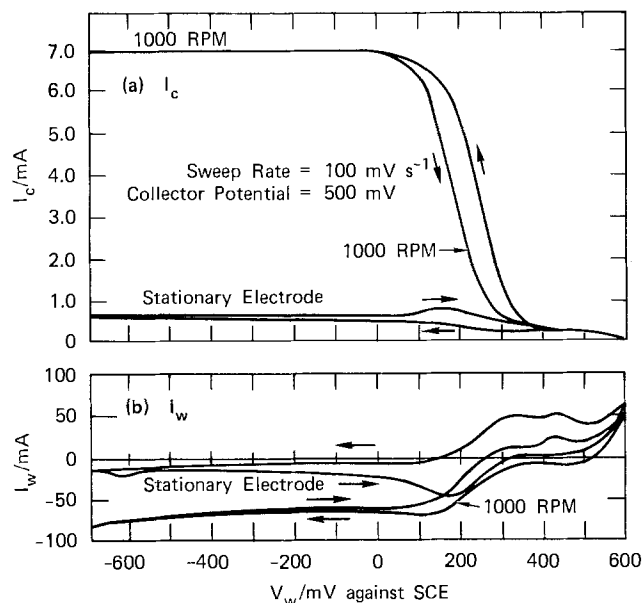
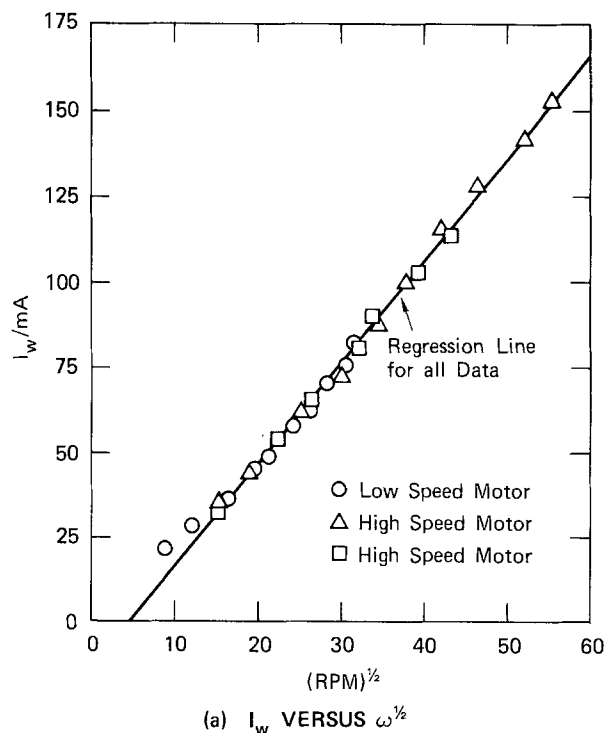
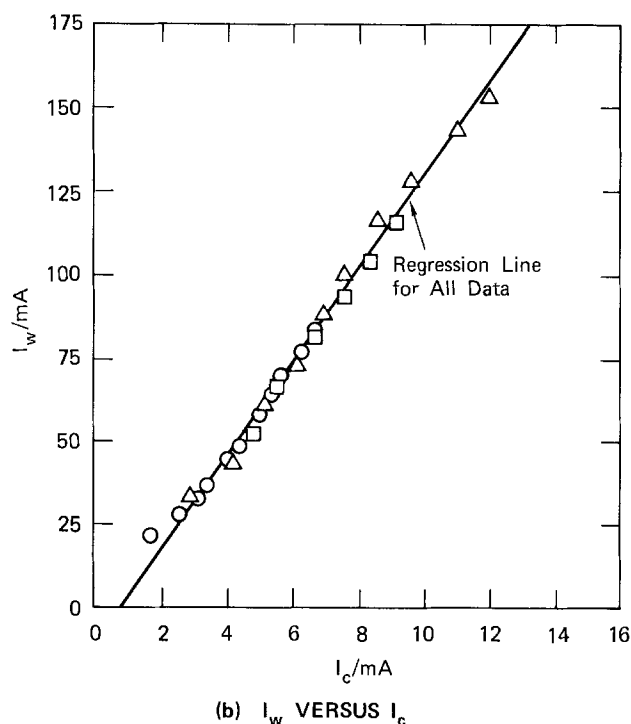


Fig. 5. Copper working and nickel collector electrode currents at 20°C in 0.1M K₃Fe(CN)₆/1.0M NaOH.



(a) I_w VERSUS $\omega^{1/2}$



(b) I_w VERSUS I_c

Fig. 6. Calibration of Cu working, Ni collector, RCC electrode in 0.1M K₃Fe(CN)₆/1.0M NaOH.

curvature was observed in a plot of I_c vs. I_w , presumably due to the increasing influence of radial diffusion with decreasing rotation speed.

At this point it is worth noting that while a collection efficiency of 7.2% represents a rather small value compared with those possible for a rotating ring-disk system, (5, 10, 13-15), the working electrode in a RCCE may have a relatively much greater area for this particular configuration. The collector currents may thus be very large compared with likely ring currents. Since the cylinder collector area is not significantly larger than the collector ring in a ring disk assembly, the RCCE affords the advantage of a larger collected current without a substantial increase in collector background current.

Calibration case 2: Cu collector.—A significant improvement in collection efficiency at the expense of decreased collector current and increased background current, can be achieved by using the smaller area nickel electrode as the working electrode, and the larger area copper electrode as the collector.

Calibration was accomplished precisely as described in the previous section, but with the Ni electrode potentiostated at -500 mV to reduce Fe (III), and the Cu collector held at $+500$ mV vs. SCE to reoxidize Fe (II) to Fe (III).

Figure 7a shows the influence of rotation speed on I_w , and Fig. 7b is a plot of I_c vs. I_w for rotation speeds up to 3140 rpm. The regression line for I_w vs. $\omega^{-1/2}$ is

$$I_w = 0.418 + 0.228 \omega^{-1/2}$$

with the regression coefficient

$$r^2 = 0.998$$

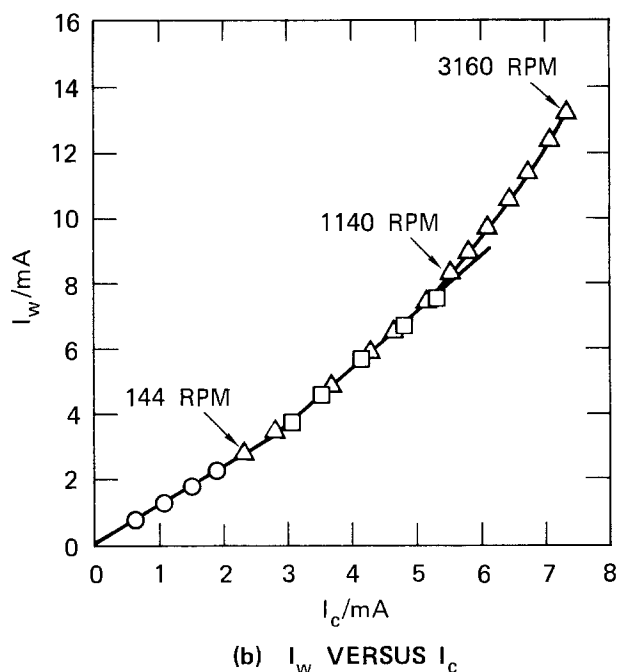
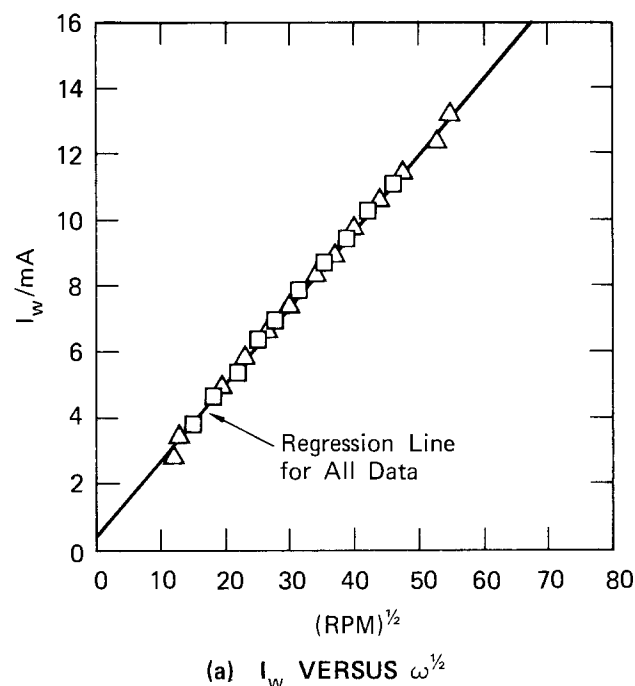


Fig. 7. Calibration of Ni working, Cu collector, RCC electrode in $0.1M$ $K_3Fe(CN)_6/0.1M$ NaOH.

Figure 7b shows three distinct regions of collection efficiency. For the uncalibrated rotation speeds below 100 rpm (the rotation speed is not an explicit parameter in this plot), the slope of I_c vs. I_w approaches unity, and thus the collection efficiency approaches 100%. Between 100 and 1000 rpm, I_c vs. I_w has a well-behaved linear form, with regression line

$$I_c = 0.623 + 0.670 I_w$$

and

$$r^2 = 0.999$$

indicating a collection efficiency of 67.0%. The large collector background current of 0.623 mA ($= 0.243$ mA \cdot cm $^{-2}$) is due either to the dissolution of the incompletely passivated Cu electrode surface, or to background oxygen evolution. Both processes are effectively uninfluenced by electrode rotation.

At rotation speeds greater than 1000 rpm, the I_w vs. I_c correlation Fig. 7b shows some curvature, and the collection efficiency (dI_c/dI_w) declines to below 50% at 3140 rpm. The reason for this decline is not immediately apparent but may be due to the occurrence of stable hydrodynamic vortices with radial components of convection (16).

These results indicate that, provided a relatively high background current can be tolerated, a substantial rotation "window" exists for this electrode configuration, having a constant and large (67%) collection efficiency.

The anodic dissolution of Cu in alkaline solution.—Having calibrated the RCCE collection frequency, two further experiments were planned to demonstrate the utility of this system in each configuration of working and collector electrodes.

In the first, an attempt was made to reproduce and extend the elegant experiments of Miller (17) in which evidence from a split ring disk study was used to infer the presence of Cu (I), Cu (II), and Cu (III) dissolved species.

With the exception that an RCCE was used with Cu working and Ni collector electrodes, experimental conditions were as far as possible identical with those described by Miller (17). Briefly, experiments were performed in sparged 1M NaOH thermostated at three temperatures, 0° , 25° , and 50° C. An Hg/HgO reference electrode was used instead of the SCE employed by Miller.

Experiments were performed in the following manner. Prior to measurement, the Cu electrode was held in hydrogen evolution and the system sparged for at least 5 min to ensure a reproducible and oxide-free surface. With the Ni potentiostated at the desired value, the Cu electrode was subjected to a single potentiodynamic sweep well into oxygen evolution and back into hydrogen evolution. Since some of the chosen collector (Ni) electrode potentials coincided with those of nickel oxide growth or reduction, this electrode was held at constant potential prior to a measurement for a sufficient time such that I_c in the quiescent system declined to a steady value. I_w and I_c were recorded simultaneously against working electrode potential, first with the RCCE electrodes rotating (at 1000 rpm), then the experiment was repeated with a stationary electrode. Values of I_c presented in Fig. 9 represent the difference between the rotating and stationary collector currents. I_w was not significantly influenced by electrode rotation. A constant potentiodynamic sweep rate of 20 mV sec $^{-1}$ was used.

25° C.—Figure 8 shows the results of potentiodynamic sweeps for a stationary and rotating Cu working electrode at 25° C. The three transitions of interest are labeled I, II, and III and are associated by Miller (17) with these Cu species.

Direct evidence for a Cu (II)/Cu (III) transition is difficult to obtain from Fig. 8. Any oxidation peak is overwhelmed by oxygen evolution and the reductive

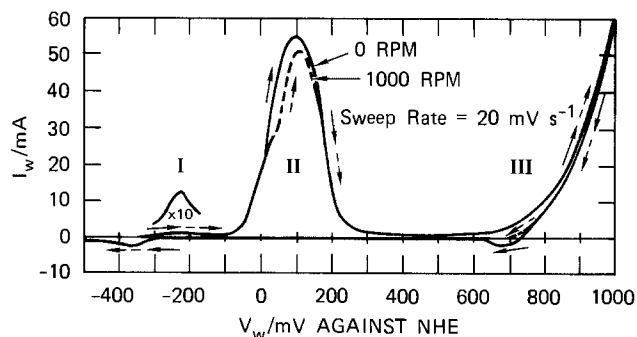


Fig. 8. Single potentiodynamic sweeps of copper electrode at 25°C for stationary and rotating electrode.

peak is not well defined for the stationary electrode, and apparently absent at a rotating electrode. However, by holding the collector electrode at appropriate potentials we can reduce any dissolved Cu (III) species and possibly oxidize or reduce dissolved Cu (I) and Cu (II), in order to demonstrate the existence of these species.

Figure 9a shows the results of experiments at 25°C with collector held at four different potentials. The top trace shows a typical working (Cu) electrode current trace to define the potential scale. The second trace shows collector currents with the collector held at +100 and +375 mV against an NHE. In contrast with the observations of Miller (17), no oxidative collector processes (specifically, associated with $\text{Cu (I)} \rightarrow \text{Cu (II)}$) were observed, but the appearance of a reductive collector peak at 660 mV is strong evidence for the presence of a dissolved Cu (III) species.

The potential at which this collector peak occurs is well into the region of oxygen evolution on the working electrode. Figure 9b shows the magnitude of Cu dissolution current required to cause the observed collector peak, calculated using the measured value of collection efficiency, and compared to the observed total current from this, it is possible to deconvolve the measured working electrode current into currents associated with oxygen evolution and Cu dissolution.

Despite the considerable extent of oxygen evolution on the working electrode, it is unlikely that a significant component of the observed collector current can be ascribed to the presence of dissolved oxygen since, (i) a potential of +375 mV is barely sufficient to reduce oxygen to hydroxyl ions $E_{\text{O}_2/\text{OH}^-}^e = 0.40\text{V}$ for $\text{O}_2 = 1\text{ atm}$ at 25°C in 1M NaOH), and (ii) the rate of oxygen evolution on the working electrode must increase exponentially with anodic potential (18). Collector reduction current associated with the presence of dissolved O_2 may be expected to parallel this, attaining a limiting value, but not passing through a maximum.

The third trace in Fig. 9a shows the current observed with the collector held at +800 mV, a potential assumed to be sufficient to oxidize any dissolved species. This is similar to the comparable trace observed by Miller (17). However, we do not believe that this current profile provides unequivocal proof of the existence of dissolved Cu (I) or Cu (II) species. For this case alone, the background collector current at the stationary electrode showed considerable "coloration" with swept working electrode potential. Figure 10 shows the collector current at +800 mV, vs. working electrode potential for the electrode rotating at 1000 rpm and stationary, together with the collected current defined as the difference between these. The major features of the rotating and stationary current traces are similar, and conform almost exactly with the shape of the derivative of the working electrode cyclic voltammogram. The current determined as the difference between these is probably associated more with a small change in the reference potential than a real collected current.

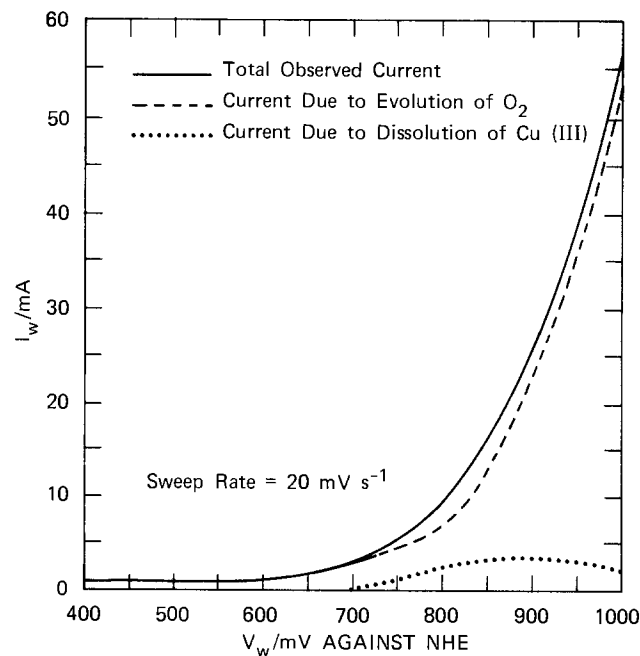
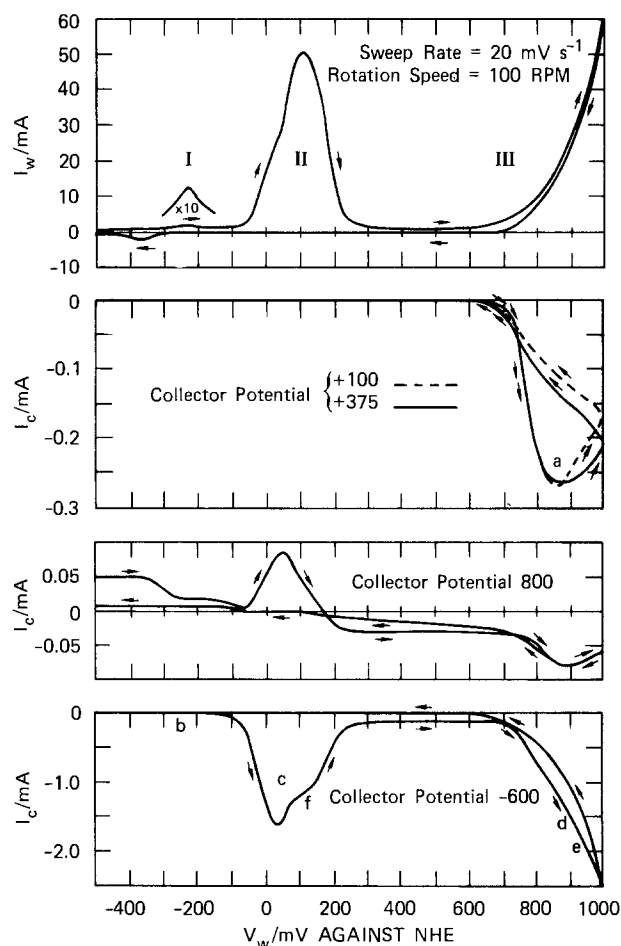


Fig. 9. Copper dissolution data at 25°C. (a, top) Copper working and nickel collector electrode currents for a single potentiodynamic sweep at 25°C. (b, bottom) Measured copper working electrode current for a single anodic potentiodynamic sweep, deconvolved into its component currents at high potentials.

The features described above conform precisely with those predicted and observed to be associated with a coupling of the IR drops due to working and collector electrode currents (11).

For the bottom trace in Fig. 9a, the collector was held at -600 mV. This potential is sufficient to reduce

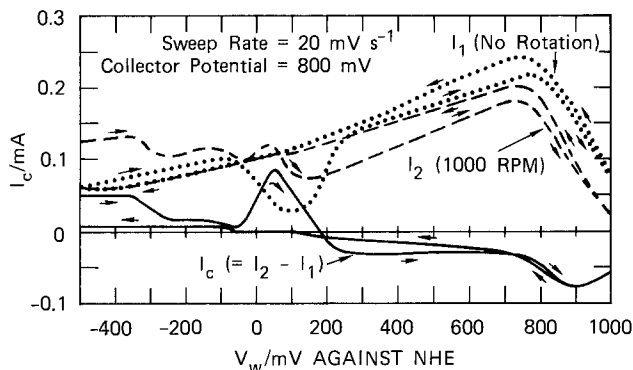


Fig. 10. Collector current at 800 mV at stationary and rotating electrode.

all copper ions back to metal, and oxygen to hydroxyl ions (17). For this case our observations and interpretation conform exactly with those of Miller (17). In confirmation of this previous work, the processes we believe to be associated with the labeled features of the collector currents are as follows.

- a. $\text{Cu (III)} \rightarrow \text{Cu (II)}$
- b. $\text{Cu (I)} \rightarrow \text{Cu (O)}$
- c. $\text{Cu (II)} \rightarrow \text{Cu (O)}$
- d. $\text{Cu (III)} \rightarrow \text{Cu (O)}$
- e. $\text{O}_2 \rightarrow \text{OH}^-$

Using the measured collection efficiency of 7.2%, we calculate that the charge associated with dissolved Cu (I) accounts for approximately $\frac{1}{4}$ of the total charge in peak I. The remainder of the charge presumably goes to form a passivating Cu (I) oxide on the electrode.

Interestingly, the features of the working electrode current in peak II are reflected more strongly in collector current peak c, with the order of peak and shoulder reversed. We can speculate that these peaks indeed disguise two surface reactions and different dissolved species.

The shoulder labeled f, associated with the reduction of Cu (II), was apparently not observed by Miller.

0° and 50°C.—Figure 11 shows the results of potentiodynamic sweeps of the Cu electrode as a function of temperature. At 0°C, the reduction of oxygen evolution at potentials greater than +700 mV vs. NHE, resolves a peak, presumably associated with Cu (II) \rightarrow Cu (III), in Fig. 11a. Figure 11b shows the current collected at a potential of +375 mV increases abruptly at a working electrode potential coinciding with this observed I_w peak (approximately +750 mV).

The combined observation of a working electrode oxidation current peak associated with a dissolved species reducible at +375 mV leaves little room for doubt that a Cu (III) species is indeed involved.

Because of the increased rate of oxygen evolution at 50°C and the apparently negligible shift in the Cu (II)/Cu(III) redox potential with temperature, there is no direct evidence for such a transition at 50°C in Fig. 11a. However, Fig. 11b shows that an appreciable dissolution of Cu (III) occurs at working electrode potentials more positive than +700 mV vs. NHE.

Unlike the data at 25°C, the dissolution currents at 0° and 50°C do not display a maximum, but appear to approach a plateau; suggesting that no surface Cu(II) oxide, or an imperfectly passivating oxide film is formed.

Dissolution of Ni in concentrated alkali.—Over a limited potential range in highly concentrated alkali solutions, the thermodynamically most stable nickel species (19, 20) is in the monovalent ion HNiO_2^- or possibly NiO_2^{2-} . To our knowledge this ion has not

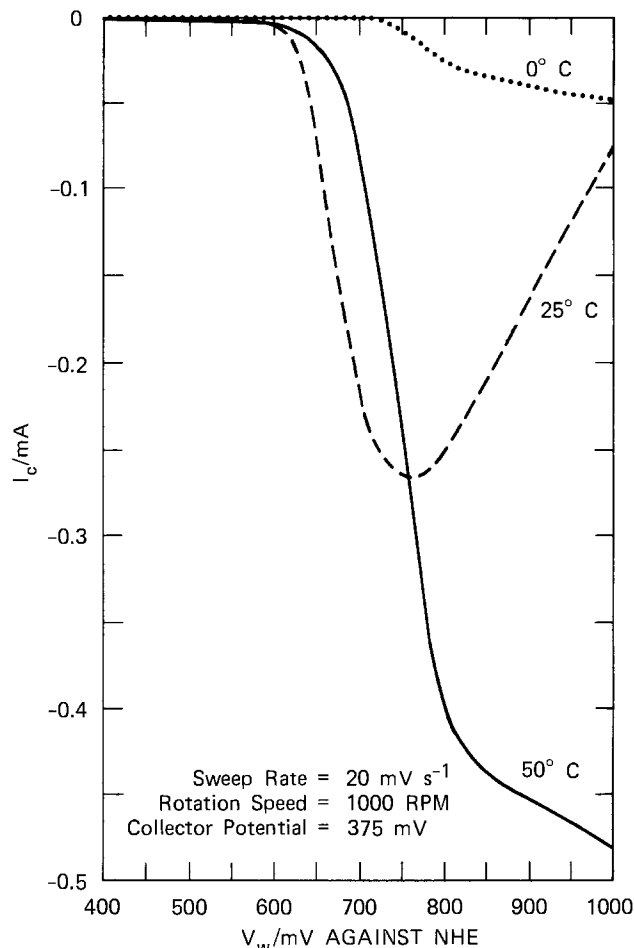
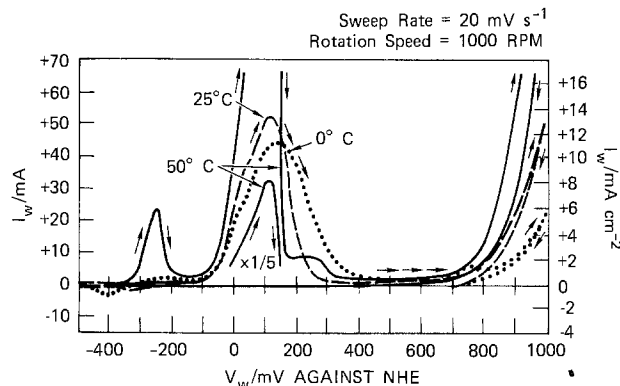


Fig. 11. (a, top) Potentiodynamic response of copper electrode in 1M NaOH, as a function of temperature. (b, bottom) Cu(III) dissolution current as a function of temperature.

been observed directly, but the possibility of Ni dissolution products at high potentials has serious implications for many industrial processes, particularly those involving Ni battery electrodes.

We have attempted to observe this species employing a conventional rotating Pt ring/Ni disk electrode and for a variety of reasons (20), have failed to identify it unambiguously.

By using a working electrode and the copper (amalgamated as described in the section Electrode surface preparation) as a collector, the RCCE described here offers a number of advantages over a rotation ring-disk electrode. Paramount amongst these are the advantages of a defined potential distribution described in the introduction, and the very large (approximately 70%) collection efficiencies that can be attained.

Experiments were performed at 40° and 80°C in 6M NaOH. With the amalgamated Cu collector held

at the desired potential, the Ni electrode was subjected to a single potentiodynamic sweep at 20 mV sec^{-1} , well into oxygen evolution and back. I_w and I_c were recorded simultaneously against V_w with the electrode rotating and in a quiescent system. Working electrode currents were insignificantly influenced by electrode rotation, and values of I_c are reported as the difference between the measured rotating and stationary electrode currents.

The only features observable at the collector appear with the collector at large negative potentials and with the Ni working electrode well into oxygen evolution. This has two important experimental consequences: (i) the reduction of a dissolved species at the collector occurs at such a large negative potential that it is necessary to amalgamate the collector in order to increase the hydrogen evolution overvoltage sufficiently to resolve the collector current, and (ii) with substantial oxygen evolution at the working electrode and the collector at a potential sufficiently cathodic to reduce O_2 it is necessary to distinguish between collector current due to dissolved Ni ions, and dissolved oxygen.

Figure 12a shows working and collector electrode currents against working electrode potential, for dif-

ferent values of collector potential. At 40°C the forward sweep shows a well-defined peak in I_c at collector potentials more negative than -1100 mV vs. NHE . Beyond this peak and on the retrace, the collector current increases again marginally, and then returns to the background at $+1100 \text{ mV}$. This peak we associate with dissolution of nickel. The second process, and the collector current at collection potentials more anodic than -1100 mV , we attribute to the presence of dissolved oxygen.

At 80°C the collector current peak on the forward sweep increases roughly by a factor of two. However, the current due to reduction of oxygen on the collector increases markedly, consistent with the greatly increased working electrode oxygen evolution current.

The collector current goes through a peak on the cathodic sweep. This peak appears over a wide range of collector potentials and regardless of whether a peak appears on the forward anodic sweep, and presumably signifies that the near surface O_2 concentration goes through a maximum shortly after reversal of potential.

Summary and Conclusions

1. The RCCE is an effective device for the detection of electroactive dissolved intermediates. This system has the advantage over the rotating ring-disk electrode (RRDE) that the working and collector electrodes are complementary. Thus, interchanging the roles of the two electrodes affords a wide range of collection efficiency. Calibration of the RCCE using the ferri-ferrocyanide redox couple demonstrates that, for the electrode used in this study, collection efficiencies of 7.2 and 67% are attainable.

2. The RCCE system has an additional advantage over the RRDE in that the current distribution due to uncompensated resistance is significantly reduced, and there is no distribution of Reynolds number over the working electrode surface.

3. Experiments on the anodization of copper in 1M sodium hydroxide solution at 0° , 25° , and 50°C provides confirmatory evidence for the formation of soluble Cu (III) species at potentials close to oxygen evolution as previously reported by Miller (17).

4. Using a RCCE we have also detected the formation of soluble species on anodization of nickel in 6M NaOH at 40°C at potentials close to massive oxygen evolution. We were unable to detect these dissolved species using a RDDE, partly because of the lower collector current and collector efficiencies. The formation of soluble species on the nickel anode in strong alkaline systems possibly has important implications for the performance of nickel-based alkaline battery systems.

Acknowledgments

The authors wish to thank SRI International for an Internal R and D grant for support of this work.

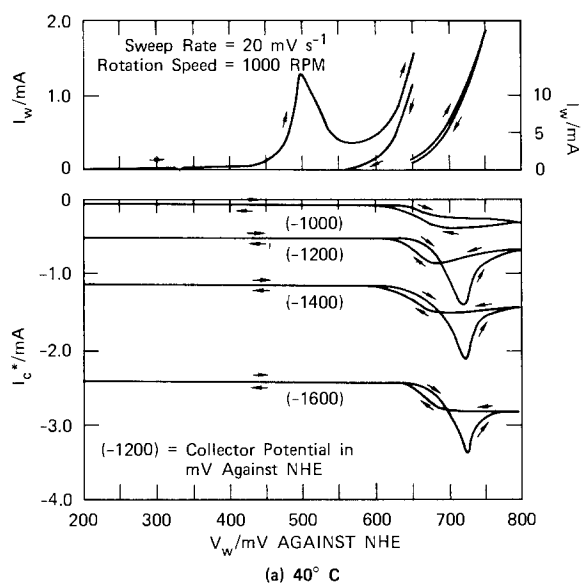
Manuscript submitted July 5, 1979; revised manuscript received Oct. 19, 1979.

Any discussion of this paper will appear in a Discussion Section to be published in the December 1980 JOURNAL. All discussions for the December 1980 Discussion Section should be submitted by Aug. 1, 1980.

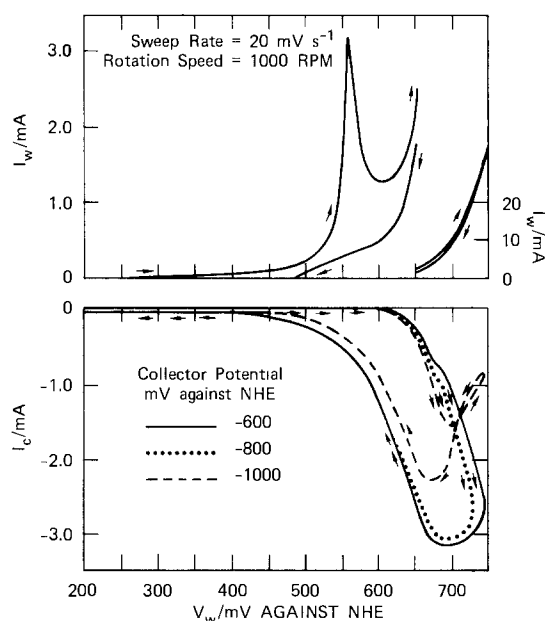
Publication costs of this article were assisted by SRI International.

REFERENCES

1. V. G. Levich, "Physicochemical Hydrodynamics," Chap. VI, N. J. (1962).
2. A. N. Frumkin and L. N. Nekrasov, *Dokl. Akad. Nauk SSSR*, **126**, 115 (1959).
3. A. N. Frumkin, L. N. Nekrasov, V. G. Levich, and Ju. Ivanov, *J. Electroanal. Chem.*, **1**, 84 (1959).
4. L. N. Nekrasov and N. P. Berezina, *Dokl. Akad. Nauk SSR*, **142**, 855 (1962).
5. W. J. Albery and S. Bruckenstein, *Trans. Faraday Soc.*, **62**, 1920, 1946 (1966).
6. J. Newman, *This Journal*, **113**, 1235 (1966).
7. L. Nanis and W. Kesselman, *ibid.*, **118**, 454 (1971).



(a) 40°C



(b) 80°C

*These data are presented without the subtraction of the collector background current to emphasize the extent of Hydrogen evolution.

Fig. 12. Nickel dissolution current in 5M NaOH

8. Penntube Plastics Product Guide, Clifton Heights, Pa., 19018 (1970).
9. M. C. H. McKubre and D. D. Macdonald, Final Report, U.S. Dept. of Energy Report, Contract EM-78-C-01-5159, Feb. 1980.
10. B. Miller, *This Journal*, **116**, 1117 (1969).
11. M. C. H. McKubre and D. D. Macdonald, Submitted to *This Journal*.
12. Y. Beers, "The Theory of Error," Addison-Wesley, Reading, Mass. (1962).
13. W. J. Albery and S. Bruckenstein, *Trans. Faraday Soc.*, **62**, 1946 (1966).
14. B. Miller, *This Journal*, **117**, 491 (1970).
15. B. Miller and R. E. Visco, *ibid.*, **115**, 251 (1968).
16. H. Schlichting, "Boundary Layer Theory," McGraw Hill, New York (1960).
17. B. Miller, *This Journal*, **116**, 1675 (1969).
18. J. O'M. Bockris and A. K. N. Reddy, "Modern Electrochemistry," Plenum, New York (1970).
19. D. D. Macdonald, Atomic Energy of Canada Limited Report 4139 (1972).
20. D. D. Macdonald and M. C. H. McKubre, To be published.

Factors Affecting the Electrochemical Responses of Metal Complexes at Pyrolytic Graphite Electrodes Coated with Films of Poly(4-Vinylpyridine)

Noboru Oyama* and Fred C. Anson*

Arthur Amos Noyes Laboratory, California Institute of Technology, Pasadena, California 91125

ABSTRACT

Electrochemical responses from the reduction of Ru^{III} (edta) coordinated to films of high molecular weight poly(4-vinylpyridine) on pyrolytic graphite electrodes were studied as functions of film thickness, temperature, supporting electrolyte composition, and solvent. Responses at filmed electrodes from metal complexes that do not coordinate to the films were also examined. With films thicker than ca. 1000Å, the current responses are limited by the rates of molecular motions within the films. Penetration of counterions, segmental motion of sections of the polymer chains, and juxtapositioning of pairs of attached metal complexes to facilitate intercomplex electron transfer within the film or combinations of the three are suggested as likely current limiting processes.

There has been considerable current interest in the preparation and properties of polymer-coated electrode surfaces (1-12). Examples of polymer coatings that have been described include nonelectroactive polymers (1, 6), polymers bearing repeating electroactive groups (2, 3, 7, 8, 11), and electroinactive polymeric coatings that become electroactive when metal complexes are attached to them (4, 5, 7, 9). Among the questions that await definitive answers for such coatings is how electron transfer is accomplished between the electrode surface and electroactive sites present in the polymeric films.

Kaufman and Engler (8) have recently proposed that electrons are conducted through rather thick films of a polymeric pyrazoline by electron transfer between the electroactive groups within the polymer. They proposed that such transfer required that the sites of electroactivity be mobile enough to achieve appropriate juxtapositions of neighboring sites in order for electron transfer to occur. In addition, the polymer film must be porous enough to allow penetration by ions of the supporting electrolyte to maintain electroneutrality within the film.

In the present report we address this and related issues for films of poly(4-vinylpyridine) (PVP) attached to pyrolytic graphite electrodes. The versatility of this polymeric ligand in anchoring transition metal complexes to electrode surfaces was described recently (9) and it seemed desirable to obtain more information on the electron transfer properties of these films which have electroactive groups (metal complexes) introduced into them after they have been attached to the graphite surface.

Experimental

Pyrolytic graphite electrodes with the graphitic basal planes exposed to the solutions were prepared and treated as previously described (9). Glassy carbon electrodes were prepared by cutting disks from

cylindrical stock (Tokai Electrode Manufacturing Company, Limited, Tokyo). The disks were sealed to the ends of glass tubing with heat-shrinkable polyolefin tubing (Alfa Wire Company) to produce an electrode area of 0.2 cm. The glassy carbon surface was polished with silicon carbide paper of successively finer grain and finally with 0.3 μ alumina. The polished surface was washed with excess water and methanol.

Poly(4-vinylpyridine) (Borden Incorporated, Philadelphia, Pennsylvania) was recrystallized twice from methanol-diethyl ether. Its average molecular weight was determined viscometrically (13) to be 7.4×10^5 . This was the polymer utilized in all experiments except those associated with Fig. 2. Aquoethylenediaminetetraacetatoruthenium (III) was prepared and purified as previously described (9). Other chemicals were reagent grade and were used as received. Aqueous solutions were prepared with triply distilled water. The supporting electrolyte for most electrochemical measurements in aqueous media was 0.2M CF₃COONa adjusted to the desired pH with CF₃COOH. Potentials are quoted with respect to a sodium chloride saturated calomel reference electrode (SSCE).

The electrochemical instrumentation and procedures utilized have been described previously (9). With electrodes bearing heavy coatings of PVP and Ru^{III} (edta) the quantity of electrochemically active attached complex could not be determined reliably by electronic integration of voltammograms. Figure 1 shows an example of a voltammogram for a coated electrode and its area as measured by electronic integration of the current during the potential scan. Note that the slope of the integrated current curve does not drop to background levels even at potentials well negative of the peak potential. Significant contributions to the current integral continue to accumulate at potentials far removed from the peak. For this reason the quantities of reactants attached to polymer layers were evaluated by integration of the current that passed when the electrode potential was stepped and held at a value well beyond the voltammetric

* Electrochemical Society Active Member.

Key words: polymers, modified electrode, surfaces.

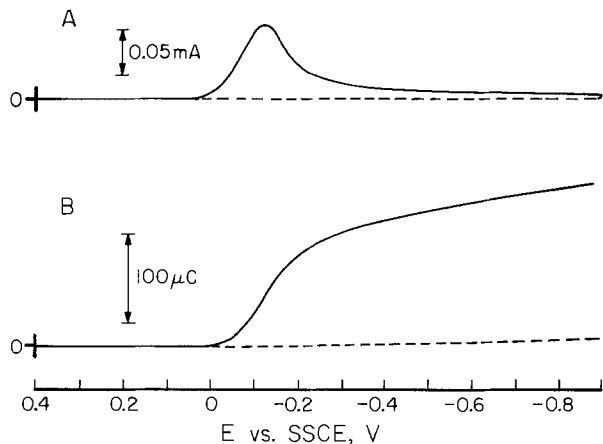


Fig. 1. A, voltammogram for the reduction of Ru^{III} (edta) attached to a coating of 2.3×10^{-7} moles cm^{-2} of pyridine as PVP on a pyrolytic graphite electrode. Ru^{III} (edta) attachment was that resulting when the PVP-coated electrode was exposed to a 5 mmole solution of Ru^{III} (edta) at pH 3.9 for 15 min. Supporting electrolyte: 0.2M CF_3COONa (pH = 2.85). Scan rate: 100 mV sec^{-1} . B, area under the voltammogram in A obtained by electronic integration of the current as the voltammogram was recorded. Background current and its integral are shown by the dashed lines.

peak potential until the rate of charge accumulation decreased to background levels.

To provide electrode surfaces containing known quantities of attached PVP, measured aliquots of a stock solution of the polymer in methanol were carefully transferred to the surface of a horizontally mounted electrode with a microliter syringe. 1-4 microliters of the solution spread uniformly on pyrolytic graphite and well-polished glassy carbon surfaces without overflowing, to produce a visibly uniform film upon evaporation of the solvent. To introduce Ru^{III} (edta) onto the electrode surfaces the resulting polymer-coated electrodes were immersed in a 5 mmole aqueous solution of Ru^{III} (edta) at pH 3.9 for 15 min. After attachment of the complex by coordination to the pendant pyridine ligands in the polymer coating (9), the electrodes were washed repeatedly with water, dried, and stored. This procedure is not well calculated to ensure a uniform distribution of coordinated Ru^{III} (edta) throughout the PVP layer. None of the electrochemical experiments performed with these coatings of PVP- $\text{Ru}(\text{edta})$ gave indications of highly anisotropic film compositions but it would not be surprising to find that more of the attached complex resided near the electrolyte/film interface than the electrode/film interface.

Scanning electron micrographs were obtained with an ETEC Corporation Autoscan U-1 (Hayward, California) instrument. Electrodes were coated by the procedure just described. Cross-sectional views of coatings applied to polished glassy carbon electrodes were obtained by appropriate mounting of the electrode specimens in the microscope. In this way the thickness of the polymeric layers could be estimated.

Results and Discussion

Effects of molecular weight on the adsorption of PVP on graphite.—To assess the dependence of the molecular weight of the PVP on the extent of its attachment to pyrolytic graphite, a set of PVP samples fractionated by successive crystallization from methanol solutions to which increasing amounts of diethyl ether were added was prepared and the average molecular weight of each fraction was determined viscometrically (13). Freshly cleaved pyrolytic graphite electrodes were exposed to 0.5% solutions of each fraction in methanol for 15 min followed by washing with methanol (for 15 min) and exposure of the resulting PVP coated electrodes to a 5 mmole solution of Ru^{III} (edta) for 15 min. The amount of Ru^{III} (edta) that coordinated

to the PVP coating was then determined electrochemically in 0.2M CF_3COONa (pH 2.7) supporting electrolyte by the methods described in the Experimental section. The extent of Ru^{III} (edta) coordination depended on the average molecular weight of the PVP used to coat the electrode as shown in Fig. 2. The first two points correspond to the use of 4-ethylpyridine and 1,2-bis(4-pyridyl)-ethane to coat the electrode. Neither produced a surface with measurable affinity for Ru^{III} (edta). With polymers of higher average molecular weight the extent of binding of Ru^{III} (edta) is assumed to reflect an increase in the quantity of PVP that is present on the graphite surface. PVP samples with average molecular weights in excess of 2×10^5 are clearly the most potent for preparing electrode coatings that accept the largest quantities of Ru^{III} (edta).

Film morphology.—Scanning electron micrographs of films of PVP on glassy carbon show the polymer to be distributed somewhat unevenly with islands of polymer surrounded by bare or lightly covered areas. The unevenness appears to increase when Ru^{III} (edta) is coordinated to the polymer. A cross-sectional view of the layer produced when a methanolic solution containing 6×10^{-7} moles cm^{-2} of monomeric pyridine units was allowed to evaporate on a glassy carbon surface is shown in Fig. 3. The apparent thickness of the layer is $(8 \pm 2) \times 10^4 \text{ \AA}$ which corresponds to an effective density of only ca. 0.08 g/cm^{-3} . Since the density of bulk poly(4-vinylpyridine) is 1.1 this could indicate that the polypyridine layer is quite porous. However, the apparent film thickness observed in the SEM may not be an accurate reflection of that prevailing on the electrodes used in the electrochemical experiments. For example, several of the experiments to be described in what follows indicate clearly that PVP films deposited on graphite under some conditions behave electrochemically as if they presented a dense, impervious domain to reactants seeking the electrode surface. Thus, exposure of films deposited from methanol to the low pressures within the SEM may cause a large expansion of the film as residual trapped solvent escapes from the film, causing them to appear less dense. For this reason we do not regard the film densities estimated from SEM measurements as representative of electrode surfaces that are never exposed to high vacuum.

Coatings of PVP on glassy carbon that exceed ca. 5×10^{-8} moles cm^{-2} (expressed as monomeric pyridine units) are clearly visible without magnification. The originally black surface becomes gray and the glassy carbon loses its luster. When Ru^{III} (edta) is coordinated to such heavy PVP coatings, a distinct and persistent golden color develops on the electrode surface when the $\text{Ru}(\text{III})$ is reduced to $\text{Ru}(\text{II})$. The electrode can be cycled repeatedly between potentials that cause reduction and oxidation of the ruthenium

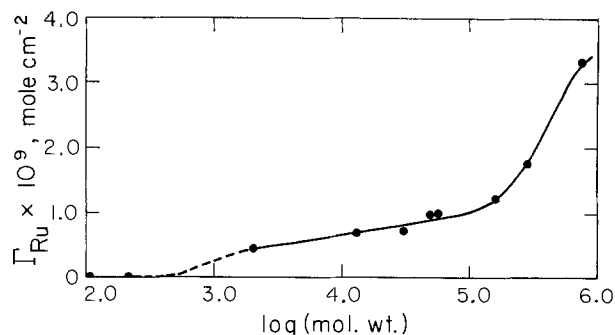


Fig. 2. Effect of the average molecular weight of PVP on its attachment to graphite electrodes as reflected in the coordination of Ru^{III} (edta) to the polymer coatings under standard conditions (see text for details).

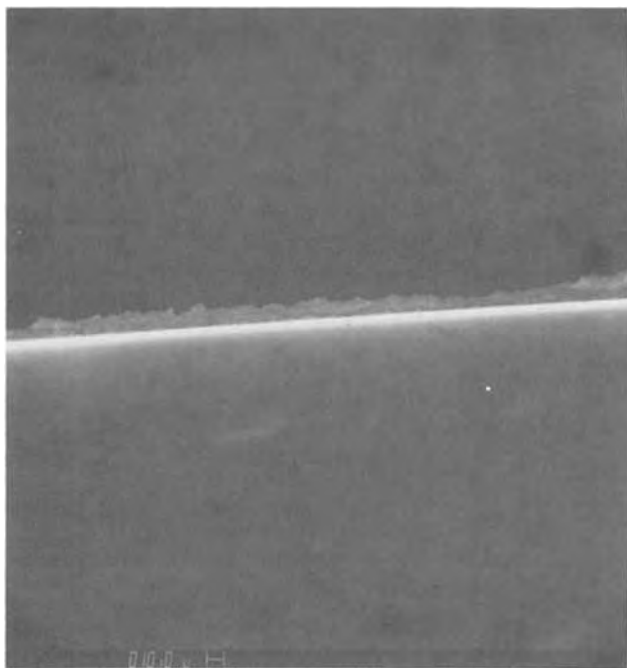


Fig. 3. Scanning electron micrograph of a PVP coating on a glassy carbon electrode. 6×10^{-7} moles cm^{-2} of pyridine as PVP was placed on the surface by evaporation of an aliquot of a methanolic solution. The calibration mark at the bottom of the micrograph corresponds to 10 microns.

centers and the golden color fades and reappears correspondingly. Similar observations have been made with polypyrazoline films (8).

Cyclic voltammetry and chronocoulometry.—Cyclic voltammograms obtained with electrodes coated with PVP to the extent of no more than $\text{ca. } 10^{-8}$ moles cm^{-2} (of pyridine units) and then with Ru^{III} (edta), by exposure to a 5 mmole solution for 15 min, exhibit the symmetrical shapes and linear dependence of peak currents on scan rate expected for reactants that are attached to electrode surfaces (14). In addition, the area under voltammograms for such coatings shows almost no dependence on scan rate. However, as shown in Fig. 4, increasing the quantity of PVP applied to the electrode surface causes the shapes and peak currents of the resulting voltammograms to change: at first, increasing the quantity of PVP on the electrode surface causes the peak current to increase but still heavier coatings produce diminished peak currents. At the same time the shape of the voltammograms becomes less symmetric and they come to resemble voltammograms for unattached reactants that diffuse to the electrode surface. There is a corresponding change in the scan rate-dependence of the peak currents. With light polymer coatings the peak currents are proportional to the scan rate (Fig. 5) as expected for attached reactants (14) but with sufficiently heavy coatings, the peak currents exhibit the proportionality to the square root of scan rate typical of diffusing reactants (Fig. 5). The apparent areas under the voltammograms obtained with heavy polymer coatings show a strong inverse dependence on scan rate and the integral of the current that passes in response to a potential step from 0.7 to -0.7V grows rapidly at first and then continues to increase slowly for periods as long as 30 or 40 min. Figure 6 compares the charge consumed one minute after a potential step was applied with the charge required to reduce all of the attached complex. With sufficiently heavy coatings of PVP the charge consumed in a fixed time interval is smaller than with lighter coatings even though the actual quantity of Ru^{III} (edta) coordinated to the coating continues to increase as heavier PVP coatings are applied. [This assertion was

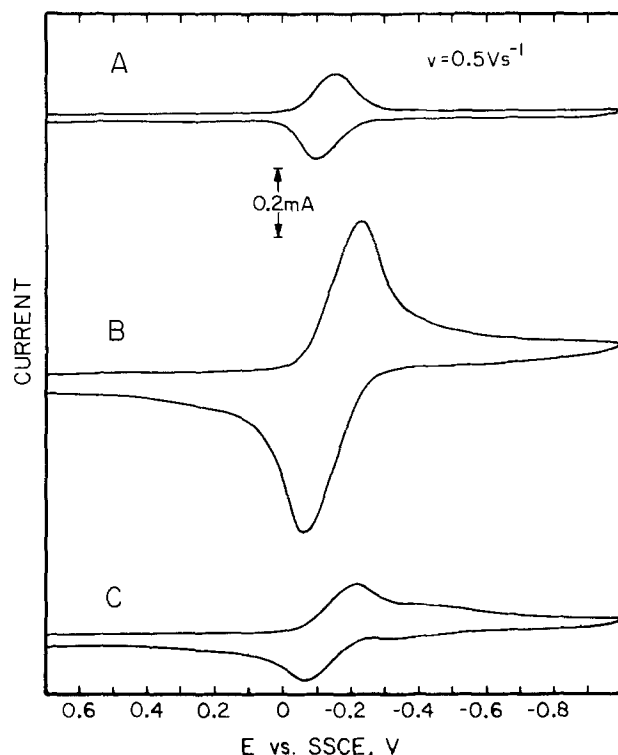


Fig. 4. Cyclic voltammograms for Ru^{III} (edta) attached to pyrolytic graphite electrodes coated with increasing quantities of PVP. PVP coatings were prepared by evaporation of measured aliquots of solutions of the polymer in methanol. Ru^{III} (edta) attachment procedure as in Fig. 1. Quantity of pyridine introduced on surface as PVP, moles cm^{-2} : A, 2.3×10^{-8} ; B, 4.6×10^{-7} ; C, 2.3×10^{-6} . Quantity of Ru^{III} (edta) attached, moles cm^{-2} : A, 2.4×10^{-9} ; B, 1.5×10^{-7} ; C, $>3 \times 10^{-7}$. Supporting electrolyte: $0.2\text{M CF}_3\text{COONa}$ ($\text{pH} = 4.2$). Scan rate: 500 mV sec^{-1} .

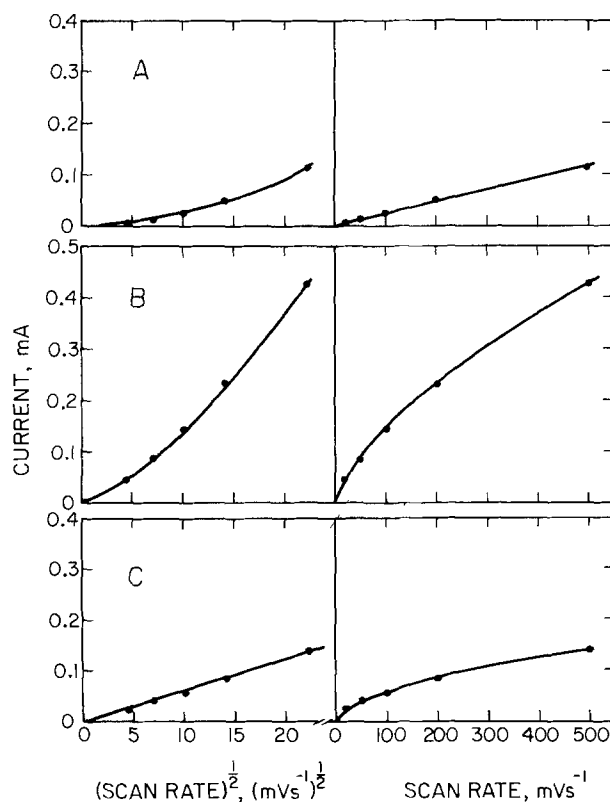


Fig. 5. Peak currents for the three electrodes of Fig. 3 as a function of scan rate and $(\text{scan rate})^{1/2}$.

confirmed by spectroelectrochemical measurements using optically transparent graphite electrodes (15, 16).]

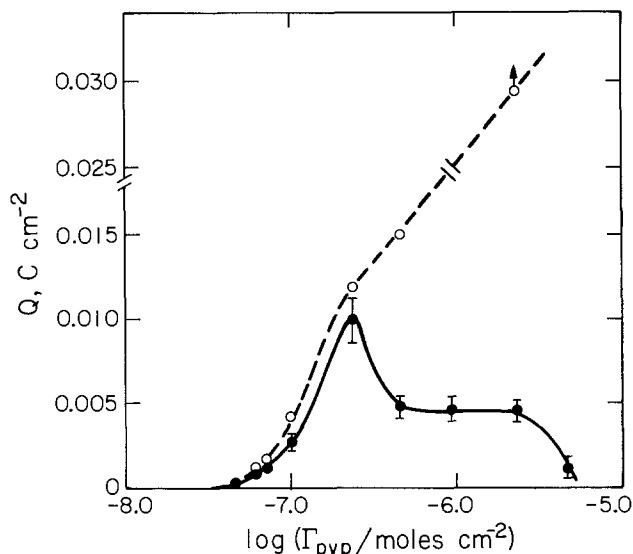


Fig. 6. Charge consumed by the reduction of Ru^{III} (edta) attached to PVP-coated electrodes. (\bullet) Charge consumed during the first 60 sec following the application of a potential step from +0.7 to -0.7V. (\circ) Charge required for complete reduction of the attached complex at -0.7V. Supporting electrolyte: 0.2M CF_3COONa (pH = 4.2). Ru^{III} (edta) attachment procedure as in Fig. 1. The charges required for complete reduction were obtained by continuing the current integration until the rate of increase of charge matched background levels.

Straight lines were obtained for chronocoulometric plots of the charge passed in response to the potential step against the square root of time. This behavior suggests diffusive transport as the current-limiting factor. In line with the proposals of Kaufman and Engler (8), both the motions of the anchored metal complexes to achieve the proper juxtaposition for inter-complex electron transfer as well as diffusive supply of counterions to the sites where the attached complex is to be reduced could be responsible for the observed behavior. Both the attached Ru^{III} (edta) and Ru^{II} (edta) complexes are likely to be anionic at the pH of the supporting electrolyte, 4.2 (17). Upon reduction, the negative charge on the complex doubles so that a cation must be supplied to each attachment site before the reduction of the attached Ru^{III} (edta) can

occur. The current may be limited by the rate at which segments of the polymer chains within the attached layer can move out of the pathway of counterions entering the film (18). (Note that such motion is required even if the polymer layer contains an abundance of supporting electrolyte because an additional counterion must still be transported from the bulk of the solution to each site where an additional charge is generated.)

Temperature dependence of the electrochemical response.—The diffusion of small molecules (and ions) through polymeric matrices has received considerable study (19-21). Apparent diffusion coefficients that have been measured typically exhibit an Arrhenius type of temperature dependence and the corresponding activation process has been identified with segmental motions within the polymer (20). To evaluate diffusional activation energies for the reduction of the Ru^{III} (edta) complex attached to the polymeric layer the temperature dependence of cyclic voltammetric peak currents and chronocoulometric slopes were measured. Figure 7B shows the cyclic voltammograms for Ru^{III} (edta) coordinated to a PVP layer on the electrode surface at 5° and 45°C. The temperature dependence of the peak currents is comparable to that observed with freely diffusing Ru^{III} (edta). However, since significant quantities of the attached complex can remain unreduced under cyclic voltammetric conditions (Fig. 4), the magnitude of the peak current does not provide a reliable measure of the apparent diffusion coefficient. For this reason we used the slopes of the linear chronocoulometric charge-(time)^{1/2} plots shown in Fig. 7A as measures of the product of the (square root of the) apparent diffusion coefficient and the concentration of the diffusing species. It is not straightforward to obtain numerical values of the apparent diffusion coefficients from the slopes of the plots such as those in Fig. 5C and 7A because the concentration of the "diffusing" species is not known. The concentration of counterions in the bulk of the solution is not the appropriate concentration to use because we observed no change in the magnitude of voltammetric peak currents when the concentration of the supporting electrolyte was varied between 0.02 and 2.0M at constant pH.

Figure 8 shows the Arrhenius plot of the slopes of the chronocoulometric plots in Fig. 6A from which an apparent diffusional activation energy of 4.6 kcal per

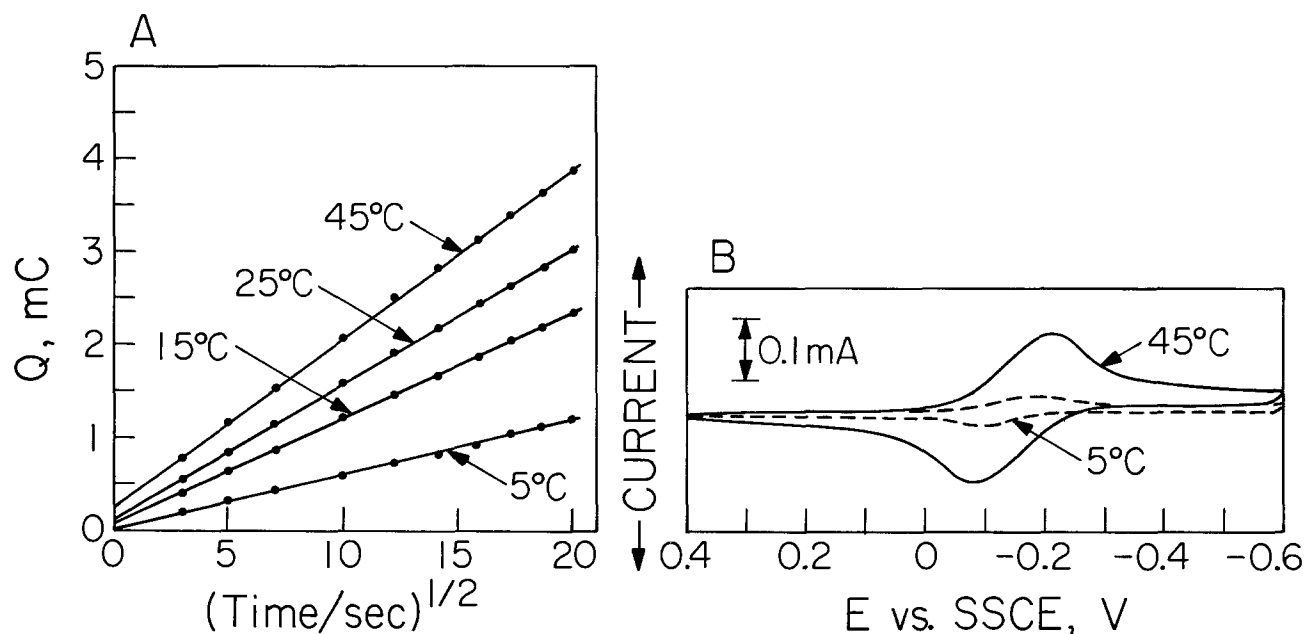


Fig. 7. Temperature dependence of (A), charge-(time)^{1/2} plots and (B), cyclic voltammograms (scan rate: 200 mV sec⁻¹) for Ru^{III} (edta) attached to electrodes coated with 2.3×10^{-6} moles cm⁻² of pyridine as PVP. Ru^{III} (edta) attachment procedure and supporting electrolyte as in Fig. 2 except pH was 3.4.

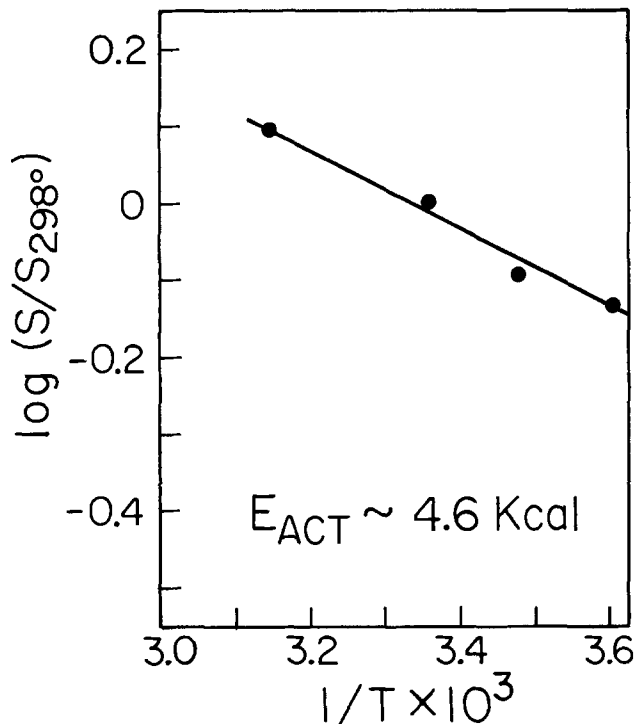


Fig. 8. Arrhenius plot of the slopes of the charge-(time)^{1/2} lines in Fig. 7 relative to the slope at 298°K.

mole was calculated. This is a somewhat smaller value than those reported for the diffusion of small molecules within solid polymer films (20) but it is similar to values observed for such films in the presence of plasticizing agents that facilitate segmental motions of molecular chains within polymeric matrices (20). It does not seem unreasonable that acidic, aqueous solu-

tions could serve to "plasticize" the coatings of PVP on graphite surfaces. The activation energy evaluated in Fig. 8 could then be regarded as a measure of the barrier faced by small segments of the PVP chains as they reorient to juxtapose pairs of anchored Ru(edta) complexes and to permit counterions to reach (or depart from) the sites where the electrode reaction causes an increase (or decrease) in ionic charge.

Effect of solvent on the electrochemical response.—Changes in the solvent employed to conduct electrochemical measurements on Ru^{III}(edta) coordinated to PVP coatings can produce dramatic differences in the responses obtained. Figure 8 shows the responses obtained from the same coating in five different solvents. The Ru^{III}(edta) is rendered virtually electroinactive in acetonitrile and dimethyl sulfoxide. The effect is not the result of removal of the complex from the surface because transfer of electrodes that give very small responses to an aqueous electrolyte immediately restores the electrochemical activity of the attached complex.

In separate experiments with optically transparent graphite electrodes (15) we have found that essentially all of the Ru^{III}(edta) attached to PVP coatings is electroactive in aqueous supporting electrolytes with polymer coatings similar to those employed in Fig. 9. Thus, these results show that changes in solvent can cause a fully electroactive film to become largely inactive.

Solvents that diminish the electroactivity of complexes attached to polymer coatings produce similar effects on electrode process involving unattached reactants: Fig. 10A shows a cyclic voltammogram for ferrocene at an uncoated pyrolyte graphite electrode in acetonitrile. Coating the electrode with a moderately heavy layer of PVP (10⁻⁷ to 10⁻⁶ moles cm⁻² of pyridine) somewhat inhibits the ferrocene wave. If

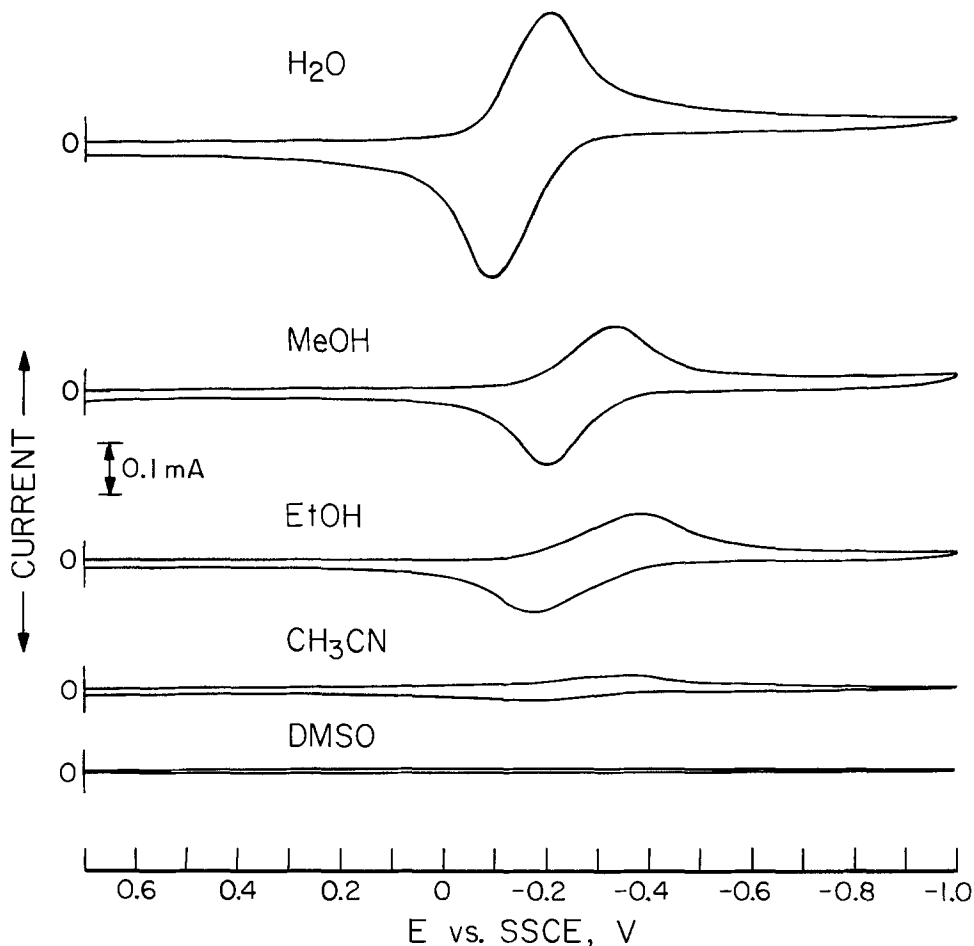


Fig. 9. Solvent dependence of steady-state cyclic voltammograms for Ru^{III}(edta) attached to electrodes coated with 4.6×10^{-7} moles cm⁻² of pyridine as PVP. Supporting electrolytes: H₂O, 0.2M CF₃COONa (pH = 4.2); other solvents, 0.2M NaClO₄. Scan rate: 200 mV sec⁻¹. Ru^{III}(edta) attachment procedure as in Fig. 2. A freshly coated electrode was used in each solvent.

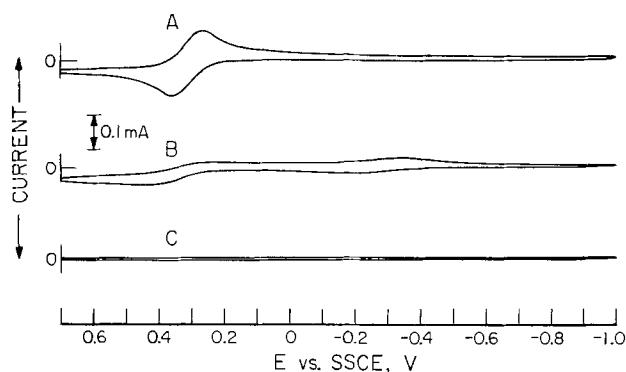


Fig. 10. Steady-state cyclic voltammograms for 1.3 mmole ferrocene at pyrolytic graphite electrodes in acetonitrile. Electrode treatments: A, freshly cleaved; B, coated with 4.6×10^{-7} moles cm^{-2} of pyridine as PVP, soaked in 5 mmole $\text{Ru}^{\text{III}}(\text{edta})$ for 15 min, washed with H_2O and acetonitrile. C, coated with 2.3×10^{-6} moles cm^{-2} of pyridine as PVP then as in B. Scan rate: 200 mV sec^{-1} . Supporting electrolyte: 0.2M NaClO_4 .

$\text{Ru}^{\text{III}}(\text{edta})$ is attached to the coating, inhibited responses are observed for both the attached complex and ferrocene in the solution (Fig. 10B). With heavier coatings of PVP, the responses from both the attached and the dissolved reactant are severely inhibited (Fig. 10C). That the wave for the dissolved ferrocene can be almost eliminated with sufficiently heavy coatings of PVP indicates that the PVP films produced by exposure to this solvent are relatively free of holes or other defects that would allow the ferrocene to reach the graphite surface. Since the supporting electrolyte would presumably also be unable to penetrate the film, it is not surprising that reactants attached to such films should also exhibit little or no electroactivity. Structures of polymeric films that are compact enough to impede the motion of supporting electrolytes through them might also lack adequate flexibility for the needed positioning of the redox centers to accomplish electron transfer through the film.

The swelling of polymeric matrices bearing ionic groups, e.g., ion exchange resins, by exposure to aqueous media (22) provides a familiar example of the ability of solvents to influence the density and texture of polymeric materials (20). It seems likely that the differences among the voltammograms in Fig. 9 can be attributed in large measure to variations in the swelling tendencies among the solvents tested.

Effects of changes in supporting electrolyte.—Change in the nature of the aqueous supporting electrolytes in which the electrochemistry of attached $\text{Ru}^{\text{III}}(\text{edta})$ is observed produce quantitative differences in the responses obtained rather than the qualitative differences arising from changes in the solvent. Figure 11

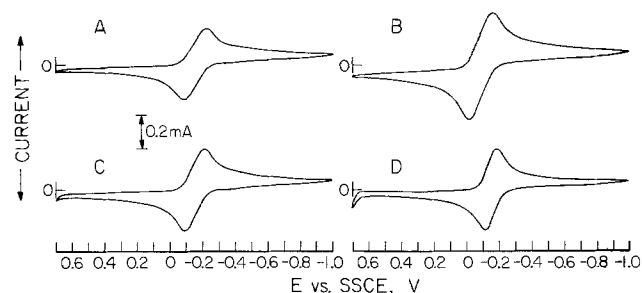


Fig. 11. Effects of supporting electrolyte on steady-state cyclic voltammograms for $\text{Ru}^{\text{III}}(\text{edta})$ attached to electrodes coated with 2.3×10^{-6} moles cm^{-2} of pyridine as PVP. A, $0.2\text{M CF}_3\text{COONa}$ ($\text{pH} = 4.2$). B, $0.2\text{M CF}_3\text{COONa}$ plus $0.025\text{M CF}_3\text{COOH}$ ($\text{pH} = 1.6$). C, 0.2M NaBr ($\text{pH} = 4.2$). D, $0.2\text{M (CH}_3)_4\text{NBr}$ ($\text{pH} = 4.2$). Scan rate: 200 mV sec^{-1} . $\text{Ru}^{\text{III}}(\text{edta})$ attachment procedure as in Fig. 2.

compares cyclic voltammograms recorded in four different supporting electrolytes with identically prepared electrode surfaces. The peak current in the electrolyte at $\text{pH} 1.6$ (curve B) is about twice as large as those in the other electrolytes indicating that charge transfer through the film is facilitated by protonation of the pyridine groups. Protonated PVP chains no doubt tend to stretch apart to minimize coulombic repulsions (23) and this would lead to a film through which ions could move more readily. As a result, segmental motions within the polymer layer may also be facilitated because the penetration of macromolecular solids by low molecular weight species is known to produce such effects (24).

Curves A and C in Fig. 11 have rather similar shapes indicating that changing the anion of the supporting electrolyte from trifluoroacetate to bromide produces only small effects. The change of supporting electrolyte cation from sodium to tetramethylammonium (curves C and D) yields a more symmetrical voltammogram. This might be the result of less hydration of the latter cation with a corresponding decrease in the extent of segmental motion within the polymer required for its penetration.

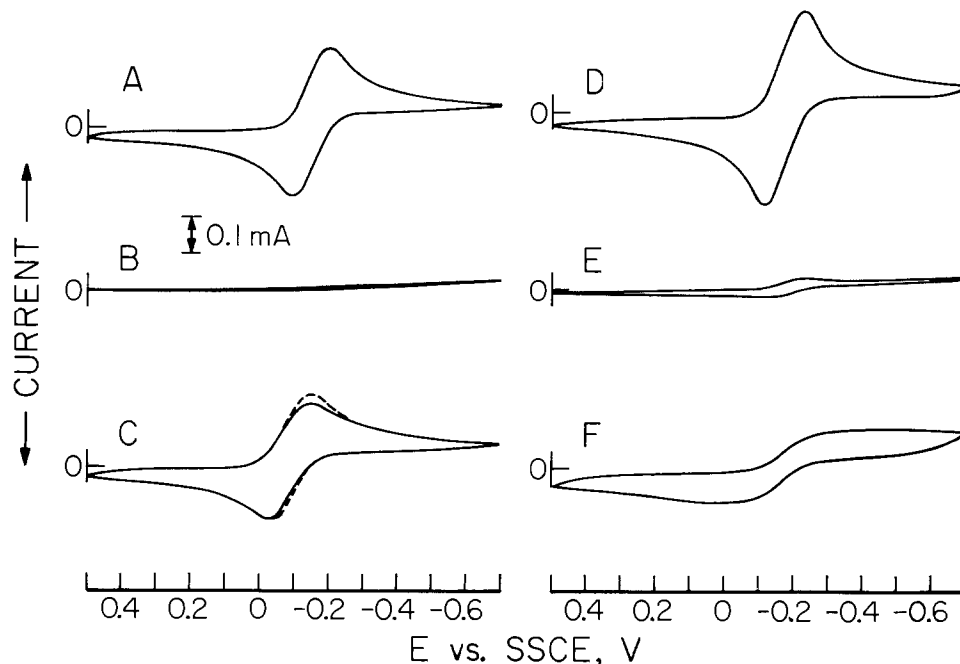
The suggestion that the current enhancement in curve B of Fig. 11 results from an "opening up" of the polymeric structure because of repulsive interactions among protonated sites along the polymer chains receives added support from the voltammograms in Fig. 12. Curve A in Fig. 12 is a cyclic voltammogram for $\text{Fe}^{\text{III}}(\text{edta})$ at an uncoated electrode. Curve B results when the electrode is coated with PVP and used in the solution of $\text{Fe}^{\text{III}}(\text{edta})$ at a pH where the PVP is not significantly protonated (25). The polymer layer apparently cannot be penetrated by the $\text{Fe}^{\text{III}}(\text{edta})$ complex. However, when the pH is lowered to a value where the PVP layer is protonated, the electroreduction of $\text{Fe}^{\text{III}}(\text{edta})$ is immediately restored (curve C). When $\text{Ru}(\text{NH}_3)_6^{3+}$ is substituted for the anionic $\text{Fe}^{\text{III}}(\text{edta})$ complex and the experiments repeated, curves D, E, and F in Fig. 12 are obtained. Protonation of the PVP film restores only partially the electrochemical response from the reduction of $\text{Ru}(\text{NH}_3)_6^{3+}$ (curve F). Protonation of the polymer produces a more porous film but it is also highly positively charged so that the tri-positive reactant evidently can traverse it only with difficulty. This would account for the drawn-out shape of voltammogram F compared with that for the anionic $\text{Fe}^{\text{III}}(\text{edta})$ complex in voltammogram C.

An additional factor that could influence the ionic conductivity of PVP layers is the increase in the quantity of counterions within the polymeric matrix that must accompany the introduction of charged sites. Thus, the quantity of anions that are electrostatically held within a protonated PVP layer will be relatively insensitive to the ionic strength of the supporting electrolyte but highly sensitive to its pH . The magnitudes of voltammetric peak currents and chronocoulometric slopes for anchored reactants exhibit similar sensitivities which might be an indication that the counterionic content of the polymer coatings controls the magnitude of the currents that can traverse them.

One is left with two possible rationalizations for the increased currents that result when charged sites are introduced into PVP films: increased permeability arising from stretching of the polymer chains by repulsive electrostatic interactions among sites and/or increased conductivity within the polymeric matrix resulting from a higher salt content. The data presently available do not allow a clear choice to be made between these two rationalizations or rule out the possibility that both mechanisms are operative.

If protonation of PVP films produces a more open texture the introduction of other charged ions into the polymer might be expected to produce similar effects. Figure 13 demonstrates that the attachment of $\text{Ru}^{\text{III}}(\text{edta})$ to a PVP film does indeed convert a

Fig. 12. Steady-state cyclic voltammograms for 5 mmole solutions of Fe^{III} (edta) or $\text{Ru}(\text{NH}_3)_6^{3+}$ at pyrolytic graphite electrodes under following conditions: A, D, freshly cleaved electrode; supporting electrolyte, 0.2M CF_3COONa at pH 5.4 (Fe) or 6.0 (Ru). B, E, coated with 4.6×10^{-7} moles of pyridine as PVP; supporting electrolyte as in A, D. C, F, supporting electrolyte adjusted to pH 2.2 with CF_3COOH . The dashed line in curve C is the response at a freshly cleaved electrode at pH 2.2. The response for $\text{Ru}(\text{NH}_3)_6^{3+}$ showed no significant pH dependence. Scan rate: 200 mV sec^{-1} .



blocking layer into one at which the $\text{Fe}(\text{CN})_6^{3-/4-}$ redox reaction can proceed. The cyclic voltammogram obtained at an uncoated electrode (curve A) is annihilated by the presence of an unprotonated PVP coating (curve B) but it reappears, in a slightly distorted form, when Ru^{III} (edta) [a monoanion at pH 5.4 (17)] is coordinated to the polymer (curve C). In this case the density of bound (anionic) charge is not as high as that resulting from protonation of the polymer at low pH but the restored response is almost as great as that obtained at the uncoated electrode. The coated electrode can also be unblocked by protonation, as in Fig. 12.

The response observed for the $\text{Fe}(\text{CN})_6^{3-/4-}$ couple in curve C of Fig. 13 can be understood simply in terms of an increase in the porosity of the film which allows the reactant to pass into the film much more readily than was true under the conditions of curve B. However, a second possible origin of the increased film conductance in this case (as contrasted with curves C and F in Fig. 12) is the transmission of electrons through the film via the attached Ru^{III} (edta) centers. That is, electron transfer from the graphite to the $\text{Fe}(\text{CN})_6^{3-/4-}$ couple may be mediated by electron transfer among the anchored redox centers in the film. Distinguishing between these two mechanisms of

charge transfer may be possible by suitable manipulation of mass transfer and charge transfer rates and we have such experiments underway. However, it may be worth emphasizing two points in conclusion. (i) The presence of electroactive redox centers within polymer films is no assurance that the films will support charge transfer either to the attached redox centers or to reactants dissolved in solution: PVP coatings containing large quantities of coordinated Ru^{III} (edta) nevertheless behave as insulating layers in certain nonaqueous solvents (Fig. 10). (ii) Charge transfer between dissolved reactants and electrode surfaces covered with thick (1-10 μm) PVP films can occur rapidly even when the films do not have redox centers attached to them: protonation converts an insulating PVP film to one that does not impede the reduction of dissolved reactants (Fig. 12).

Acknowledgments

The assistance of Prof. J. P. Revel and Pat Cohen in obtaining electron micrographs is acknowledged gratefully. Drs. Alan Rembaum and Roger Williams kindly provided the samples of fractionated PVP that were used to obtain the data for Fig. 2. Several perceptive comments and criticisms by the reviewers of an earlier version of this manuscript helped us to formulate our speculations more clearly.

This work was supported by the National Science Foundation and the U.S. Army Research Office.

Manuscript submitted July 23, 1979; revised manuscript received Oct. 15, 1979.

Any discussion of this paper will appear in a Discussion Section to be published in the December 1980 JOURNAL. All discussions for the December 1980 Discussion Section should be submitted by Aug. 1, 1980.

Publication costs of this article were assisted by the California Institute of Technology.

REFERENCES

1. L. L. Miller and M. R. Van de Mark, *J. Am. Chem. Soc.*, **100**, 639 (1978); *J. Electroanal. Chem. Interfacial Electrochem.*, **88**, 437 (1978).
2. M. R. Van de Mark and L. L. Miller, *J. Am. Chem. Soc.*, **100**, 3225 (1978).
3. A. Merz and A. J. Bard, *ibid.*, **100**, 3222 (1978).
4. K. Itaya and A. J. Bard, *J. Anal. Chem.*, **51**, 1487 (1978).
5. N. Oyama and F. C. Anson, *J. Am. Chem. Soc.*, **101**, 739 (1979).
6. K. Döbelhofer, D. Noete, and J. Ulstrup, *Ber. Bunsenges. Phys. Chem.*, **82**, 403 (1978).

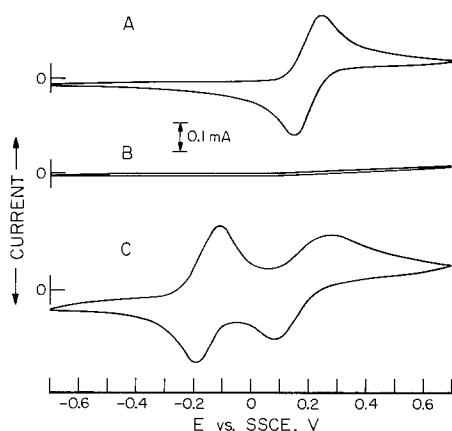


Fig. 13. Steady-state cyclic voltammograms for a 5 mmole solution of $\text{Fe}(\text{CN})_6^{4-}$ in 0.2M CF_3COONa at pH 6.0. Pyrolytic graphite electrode pretreatments: A, freshly cleaved; B, coated with 4.6×10^{-7} moles cm^{-2} of pyridine as PVP; C, after the electrode used to record curve B was soaked for 15 min in 5 mmole Ru^{III} (edta) and rinsed. Scan rate: 200 mV sec^{-1} .

7. R. Nowak, F. A. Schultz, M. Umana, H. Abruna, and R. W. Murray, *J. Electroanal. Chem., Interfacial Electrochem.*, **94**, 219 (1978).
8. F. B. Kaufman and E. M. Engler, *J. Am. Chem. Soc.*, **101**, 547 (1979).
9. N. Oyama and F. C. Anson, *ibid.*, **101**, 3450 (1979).
10. F. B. Kaufman, A. H. Schroeder, E. M. Engler, S. R. Kramer, and J. Q. Chambers, *ibid.*, In press.
11. F. B. Kaufman, A. H. Schroeder, E. M. Engler, J. Q. Chambers, and S. R. Kramer, Abstract 301, p. 778, The Electrochemical Society Extended Abstracts, Boston, Massachusetts, May 6-11, 1979.
12. P. Peerce and A. J. Bard, Abstract 302, p. 781, The Electrochemical Society Extended Abstracts, Boston, Massachusetts, May 6-11, 1979.
13. S. R. Rafikov, S. A. Pavlova, and I. I. Tverdokhlebova, "Determination of Molecular Weights and Polydispersity of High Polymers," Ch. IX, Daniel Davey and Co., Inc., New York (1964).
14. E. Laviron, *J. Electroanal. Chem. Interfacial Electrochem.*, **39**, 1 (1972).
15. N. Scott, N. Oyama, and F. C. Anson, *J. Electroanal. Chem. Interfacial Electrochem.*, In press.
16. T. P. DeAngelis, R. W. Hurst, A. M. Yacynck, H. B. Mark, Jr., W. R. Heineman, and J. S. Mattson, *Anal. Chem.*, **49**, 1395 (1977).
17. K. Shimizu, T. Matsubara, and G. P. Sato, *Bull. Chem. Soc. Jpn.*, **47**, 1651 (1974).
18. J. Frank and G. S. Park, Editors, "Diffusion in Polymers," Chap. 10, Academic Press, New York (1968).
19. J. Frank and G. S. Park, Editors, "Diffusion in Polymers," Chap. 2-10, Academic Press, New York (1968).
20. L. Rebenfeld, P. J. Makarewicz, H. Weigmann, and G. L. Wilkes, *J. Macromol. Sci. Rev. Macromol. Chem.*, Chap. 15, p. 279 (1976).
21. R. McGregor, "Diffusion and Sorption in Fibers and Films," Chap. 15, Academic Press, New York (1974).
22. W. Rieman and H. F. Walton, "Ion Exchange in Analytical Chemistry," Pergamon, New York (1970).
23. H. Morawetz, "Macromolecules in Solution," 2nd ed., Chap. VII, John Wiley and Sons, Inc., New York (1975).
24. R. Kosfeld and L. Zumkley, *Ber. Bunsenges, Phys. Chem.*, **83**, 392 (1979).
25. H. Nishikawa and E. Tsuchida, *J. Phys. Chem.*, **79**, 2072 (1975).

A Digital Simulation Model for Electrochromic Processes at WO₃ Electrodes

Benjamin Reichman and Allen J. Bard*

Department of Chemistry, The University of Texas at Austin, Austin, Texas 78712

and Daniel Laser

Department of Chemistry, Tel Aviv University, Ramat-Aviv, Israel

ABSTRACT

Current-potential (*i-E*) curves for the electrochromic process at WO₃ electrodes were calculated with a digital simulation model which assigns the rate of charge transfer at the oxide/solution interface and the rate of diffusion of hydrogen into the bulk of the film as major variables. The simulated *i-E* curves agreed well with experimental ones for different types of WO₃ films and predicted the observed dependency of current on scan rate. The simulation required knowledge of the form of the electrochemical isotherm, which was obtained experimentally, and adjustment of a charge transfer rate constant, k_t , and the hydrogen atom diffusion coefficient within the film, D_H . The best fit was obtained with $k_t = 9 \times 10^{-3} \text{ sec}^{-1} (\text{mole/cm}^3)^{-2}$ and $D_H = 1 \times 10^{-9}$ to $2 \times 10^{-10} \text{ cm}^2/\text{sec}$ for the WO₃ films prepared by vacuum evaporation and $k_t = 7.2 \text{ sec}^{-1} (\text{mole/cm}^3)^{-2}$ and $D_H = 5 \times 10^{-8} \text{ cm}^2/\text{sec}$ for WO₃ anodic films. Simulated potential step results, which are similar to the experimental curves at longer times but show some discrepancy in the short time region, and concentration profiles are also reported.

Recently a great effort has been made to understand the electrochromic process which occurs at WO₃ electrodes during reduction and reoxidation and to construct display devices based on this process (1-5). While it appears clear that the process involves formation and oxidation of hydrogen tungsten bronzes, the detailed mechanism and a quantitative model of the electrochromic process and the steps which govern the rate of the color-bleach (CB) process have not been resolved. Different WO₃ films produced by vacuum evaporation exhibit different response times for coloring and bleaching, even when they are prepared by similar techniques (5). Moreover different types of WO₃ electrodes (e.g., anodic vs. evaporated films) show significant differences in response time and electrochemical characteristics in the electrochromic region (6-8). The existence of water in the WO₃ film

(7-9) and film porosity (7-8) appear to play important roles in determining the response time of the WO₃ electrodes. Crandall and Faughnan (10) discussed the factors entering into the dynamics of the CB process at WO₃ and compared values for the composition of the film with time, obtained during potential-step experiments, with calculated values. Their model assumed that mass transfer within the film was very large and that the rate-limiting steps involved proton transfer at the WO₃/liquid interface and the buildup of a "back emf" as the hydrogen bronze formed. Good agreement between the experimental and calculated values was obtained in the short time region after the start of the coloring step or when the coloring step was made at low potentials within the electrochromic region. With this model (5) the bleaching process is limited by the "space charge" which is created by accumulation of H⁺ in the film. Arnoldussen (11) measured exchange currents and transfer coefficients for

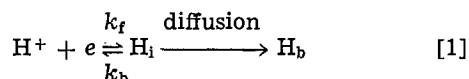
* Electrochemical Society Active Member.
Key words: electrode, interfaces, films.

the electrochromic process but did not relate these values to any particular mechanism for the process. In the model previously suggested for the coloration process (10), diffusion of hydrogen atoms within the WO_3 film was not taken into consideration nor were fits to potential sweeps for different films attempted. These were thus restricted to descriptions of processes occurring at very short times after the start of the coloration process, at low coloration levels, or for very thin WO_3 films.

In this paper we present a digital simulation model of the WO_3 systems and report calculated current-potential (i - E) and current-time (i - t) curves which compare well to those obtained with WO_3 evaporated and anodic film electrodes in the electrochromic region (7, 8). This model includes the effects of charge-transfer from the electrode to the hydrogen ion in solution and diffusion of hydrogen atoms in the film. The differences in the electrochromic behavior between the evaporated and anodic film electrodes, which was attributed (7, 8) to a significant difference in the charge transfer rate constants and the diffusion coefficient of the hydrogen atom in both these films is demonstrated by the simulation. The model proposed here may also be relevant to the thin layer behavior found in electrodes prepared by coating with films of polymers or other electrodes with multilayer surface modification.

Models

Theoretical model.—The model we propose for the CB process at the WO_3 electrode is shown in Fig. 1. We assume that mass transfer of protons in solution and transport of electrons through the semiconducting films are not rate-limiting and that there is no barrier to electron injection at the metal/ WO_3 contact (10). The rate-determining processes are then (i) charge transfer to protons at the WO_3 /solution interface to form hydrogen atoms (H); (ii) diffusion of H-atoms within the film; (iii) build up of the H-atom concentration within the film towards the saturation level, y , determined by the ultimate film composition, H_yWO_3 . This is represented by the equation



where H_i and H_b represent H-atoms at the interface and in the bulk film, and k_f and k_b are charge transfer rate constants. The concentration of H-atoms within the film, which is a function of x and t , is represented as $[\text{H}]$ and the relative saturation or occupancy of H-atoms, θ , is given by

$$\theta = [\text{H}]/C_{\text{max}} \quad [2]$$

where C_{max} represents the maximum concentration of hydrogen within the film. At the interface $[\text{H}] = [\text{H}]_i$ and $\theta = \theta_i$. The rate of formation of H-atoms at the interface can be related to the current density, j , and

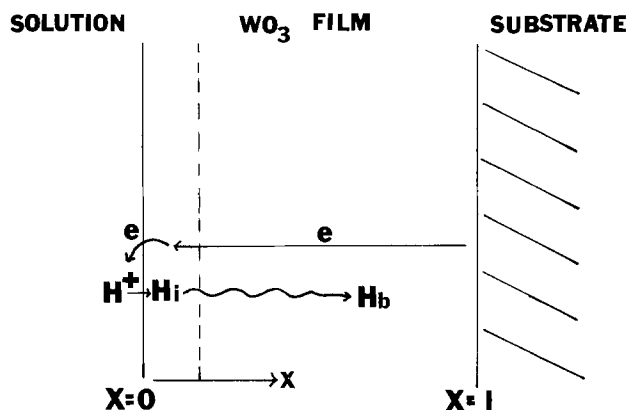


Fig. 1. Model for the electrochromic process at WO_3 electrodes

the potential drop across the interface, V , by the following equation

$$\begin{aligned} \frac{d[\text{H}]_i}{dt} &= \frac{j}{nF} - D \left(\frac{\partial^2 [\text{H}]_i}{\partial x^2} \right) \\ &= k_f [\text{H}^+] C_{\text{max}}^q (1 - \theta_i)^q \exp \left[\frac{-\beta nF}{RT} V \right] \\ &\quad - k_r C_{\text{max}}^m \theta_i^m \exp \left[\frac{(1 - \beta) nF}{RT} V \right] \exp[-r\theta_i] \\ &\quad - D \left(\frac{\partial^2 [\text{H}]_i}{\partial x^2} \right) \quad [3] \end{aligned}$$

This equation is of the usual form for interfacial charge transfer with a transfer coefficient, β . The empirical coefficients, q , m , and r , which must be determined experimentally, take account of the fact that: (i) the forward reaction is attenuated by a factor representing the availability of free sites on the WO_3 for H-atoms, $(1 - \theta_i)$; (ii) the backward reaction is governed by the activity of the dissolved hydrogen, rather than by its concentration [expressed by the term $\exp(-r\theta_i)$, which is equivalent to the interaction term in the Frumkin isotherm (12), where r is the factor expressing the extent of interaction between the absorbed hydrogen atoms, with a negative value of r implying a repulsive interaction].

We assume that the motion of hydrogen atoms in the film is governed by diffusion processes, governed by Fick's law (Eq. [4]), and that at the

$$\partial[\text{H}]/\partial t = D_H (\partial^2 [\text{H}]/\partial x^2) \quad [4]$$

boundaries of the film $x = 0$ (the oxide-electrolyte interface) and $x = l$ (the oxide-conductor interface) the conditions are always

$$\frac{j}{nF} = D_H (\partial[\text{H}]/\partial x)_{x=0} \quad (x = 0) \quad [5]$$

$$D_H (\partial[\text{H}]/\partial x) = 0 \quad (x = l) \quad [6]$$

where D_H is the diffusion coefficient of hydrogen atom in the film. These boundary conditions express the assumptions that there is no accumulation of H-atoms at the oxide-electrolyte interface, and that there is no transfer of hydrogen across the oxide-conductor

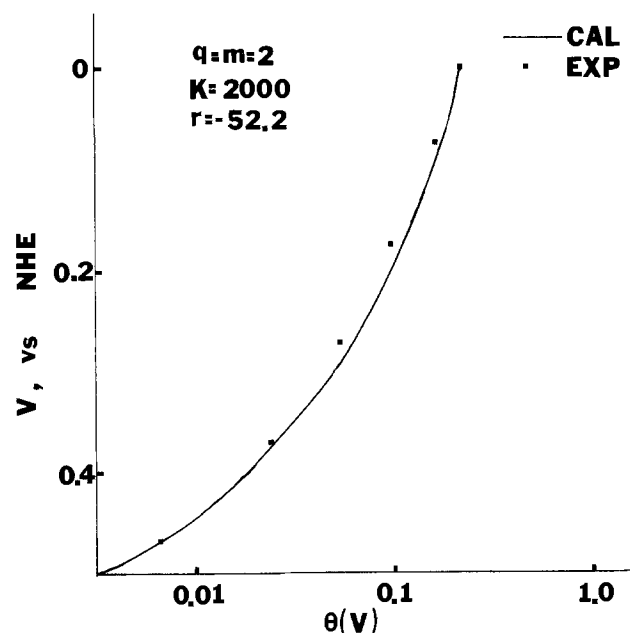


Fig. 2. Electrochemical isotherm for hydrogen in WO_3 electrodes. The line represents Eq. [9] with $q = m = 2$, $r = -52.2$, and $k = 2000$. The points are experimental data.

interface. The initial condition is

$$[H] = 0 \quad (t = 0, \text{ at all } x) \quad [7]$$

Digital simulation model.—The digital simulation followed the usual finite difference approach to the solution of electrochemical problems (13-16), where the film was divided into increments of thickness, Δx , and $[H]$ and θ are calculated for different times, divided into increments, Δt . The $[H]$ (and θ) in the first space element (*i.e.*, at the surface) is obtained from its rate of production, Eq. [3], corrected for the loss into the film by diffusion. Within the film, $[H]$ and θ are controlled only by diffusion, subject to the constraints of finite thickness and saturation of $[H]$ at its maximum value at a given potential.

Results and Discussion

Hydrogen isotherm.—To carry out the simulation, values of the parameters q , m , and r must be obtained.

These are available from the equilibrium isotherm. At a given potential, V , equilibrium is achieved when the distribution of H throughout the film is uniform (*i.e.*, $\partial\theta/\partial x = 0$) and θ attains its maximum value for that potential, $\theta_{eq}(V)$. At equilibrium, $j = 0$, so from Eq. [3]

$$k_f[H^+][1 - \theta_{eq}(V)]^q \exp\left[\frac{-\beta nF}{RT}V\right] = k_r\theta_{eq}(V)^m \exp\left[\frac{(1 - \beta)nFV}{RT}\right] C_{max}^{m-q} e^{-r\theta_{eq}(V)} \quad [8]$$

$$\frac{\theta_{eq}(V)^m}{[1 - \theta_{eq}(V)]^q} e^{-r\theta_{eq}(V)} = K[H^+] e^{-(nF/RT)V} C_{max}^{m-q} \quad [9]$$

where $K = k_f/k_r$. C_{max} was evaluated by assuming a formula of HWO_3 , for the oxide saturated with hydrogen (17). The parameters q , m , and r were estimated by fitting Eq. [9] to the experimental electrochromic isotherm. The isotherm was determined

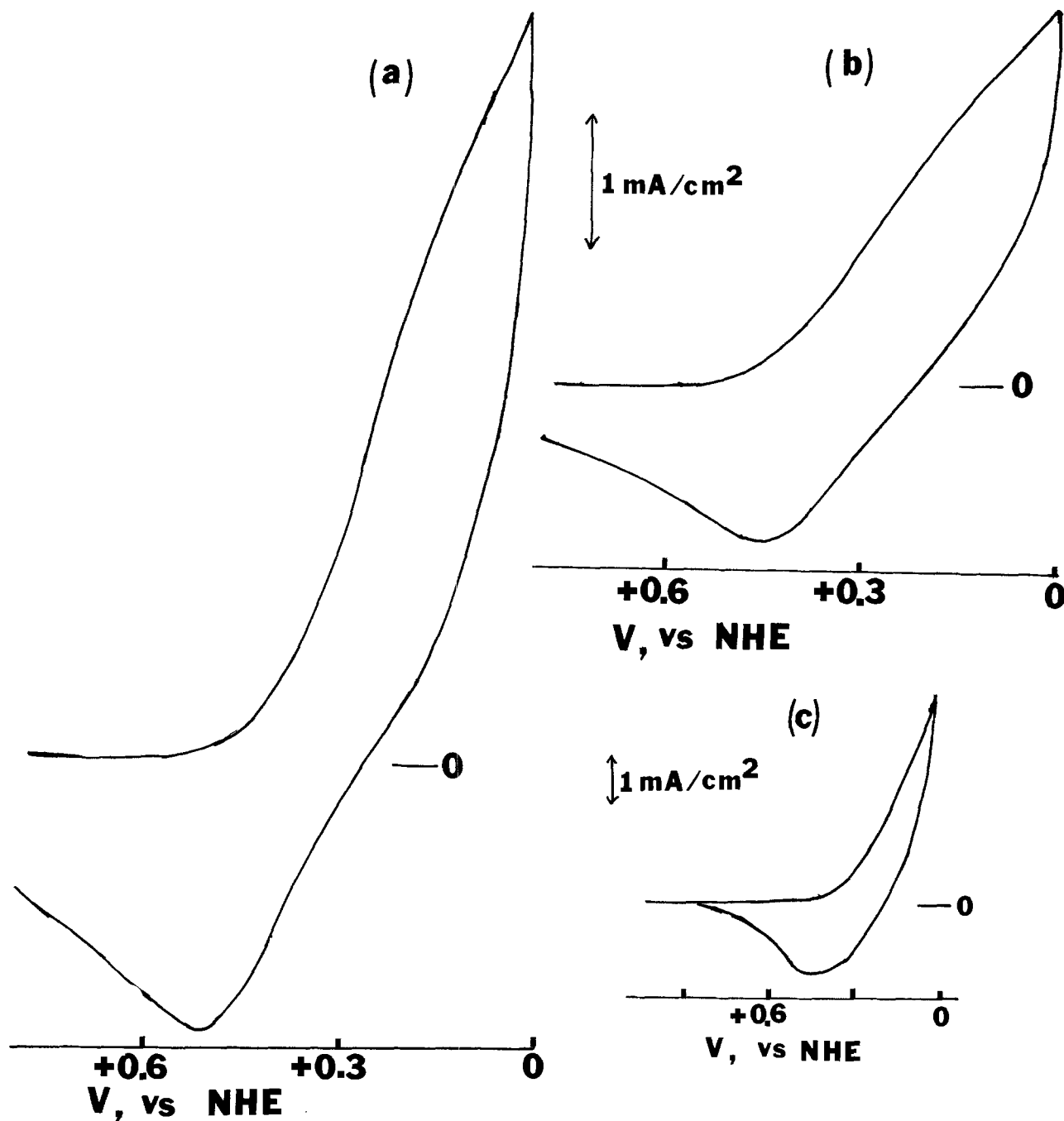


Fig. 3. Simulated current-potential curves for the electrochromic process at WO_3 . Film thickness, $1.8 \mu\text{m}$; scan rate, 100 mV/sec ; k_f , $9 \times 10^{-3} \text{ sec}^{-1} (\text{mole/cm}^3)^{-2}$; and (a) $D_H = 1 \times 10^{-9} \text{ cm}^2/\text{sec}$, (b) $D_H = 2 \times 10^{-10} \text{ cm}^2/\text{sec}$. (c) Typical experimental current-potential curve for WO_3 evaporated film electrode $1.8 \mu\text{m}$ thick at scan rate of 100 mV/sec .

by stepping the WO_3 electrode potential to a certain value, V , with respect to the reference electrode ($\text{Hg}/\text{Hg}_2\text{SO}_4/1\text{M H}_2\text{SO}_4$), within the electrochromic region. After stepping the potential, the amount of charge involved in coloration was determined coulometrically by integrating the current until it decayed to zero and equilibrium was attained. This procedure was repeated with various potentials within the coloration region. A similar isotherm was obtained by Faughnan *et al.* (17). The experimental isotherm and the calculated one are shown in Fig. 2. The best fit was obtained with $q = m = 2$, $K = 2000 \text{ cm}^3/\text{mole}$, and $r = -52.2$. A similar conclusion regarding the values of q and m was reached by Faughnan *et al.* (17). Since $K = k_f/k_r$, the assignment of a numerical value to K requires that only the magnitude of either k_f or k_r is needed in the simulation.

Evaporated film electrodes.—The digital simulation was carried out by taking $\beta = 0.5$ and assuming different values for k_f and D_H . Typical simulated curves (illustrated with a 1 cm^2 electrode area, $1.8 \mu\text{m}$ thick film, and scan rate, v , of $100 \text{ mV}/\text{sec}$) with $k_f = 9 \times 10^{-3} \text{ sec}^{-1} (\text{mole}/\text{cm}^3)^{-2}$ and D_H of (a) 1×10^{-9} and (b) $2 \times 10^{-10} \text{ cm}^2/\text{sec}$ are shown in Fig. 3. These are of the same shape as experimental i - E curves found for evaporated film WO_3 electrodes (7) [Fig. 3(c)]. Thus the cathodic current, which begins at $\sim 0.5\text{V}$, increases monotonically upon scanning to more negative potentials and upon reversal of the scan direction, the current remains cathodic only becoming anodic at potentials 0.2 - 0.3V more positive than the reversal potential for $1.8 \mu\text{m}$ films. The anodic current peak is typically 2-3 times smaller than the cathodic current at 0V . The magnitudes of currents shown in the simulated curves are also similar to those obtained experimentally. The dependence

of the simulated electrochromic i - E curves on scan rate is shown in Fig. 4. The simulation shows that the coloration current at more negative potentials is linearly dependent on $v^{1/2}$ as observed experimentally with the evaporated WO_3 film electrodes (7) [see Fig. 4(c)].

The k_f and D_H values both affect the rate of the electrochromic process, the shape of the i - E curves, and the scan rate dependence. For a film with a given thickness, l , the potential at which the simulated electrochromic current changes its sign from cathodic to anodic following the change in the direction of the potential scan, is very sensitive to the charge transfer rate constant, k_f . This is illustrated in Fig. 5. Typically the experiments with $1.8 \mu\text{m}$ WO_3 evaporated film electrodes produced i - V curves which crossed the X-axis about 200 - 300 mV after the potential of scan reversal. This behavior, shown in Fig. 3, puts k_f at a value of $\sim 9 \times 10^{-3} \text{ sec}^{-1} (\text{mole}/\text{cm}^3)^{-2}$. For a typical evaporated WO_3 film, this choice of k_f value produces a ratio of the cathodic to the anodic peak current similar to the experimental values. For some evaporated films the experimental anodic current started to appear at more positive potentials. The simulation results suggest that in these cases k_f was smaller, perhaps because of some change in the nature of the surface of the film. In other extreme cases the experimental anodic current started to appear at a more negative potential, indicating a larger k_f value for these. The value of D_H also affects the potential at which the anodic current begins on scan reversal but its effect on this value is smaller than that of k_f . However the magnitude of D_H strongly affects the size of the electrochromic current, as shown in Fig. 3. For two films with the same k_f an increase in D_H by a factor of five causes an increase

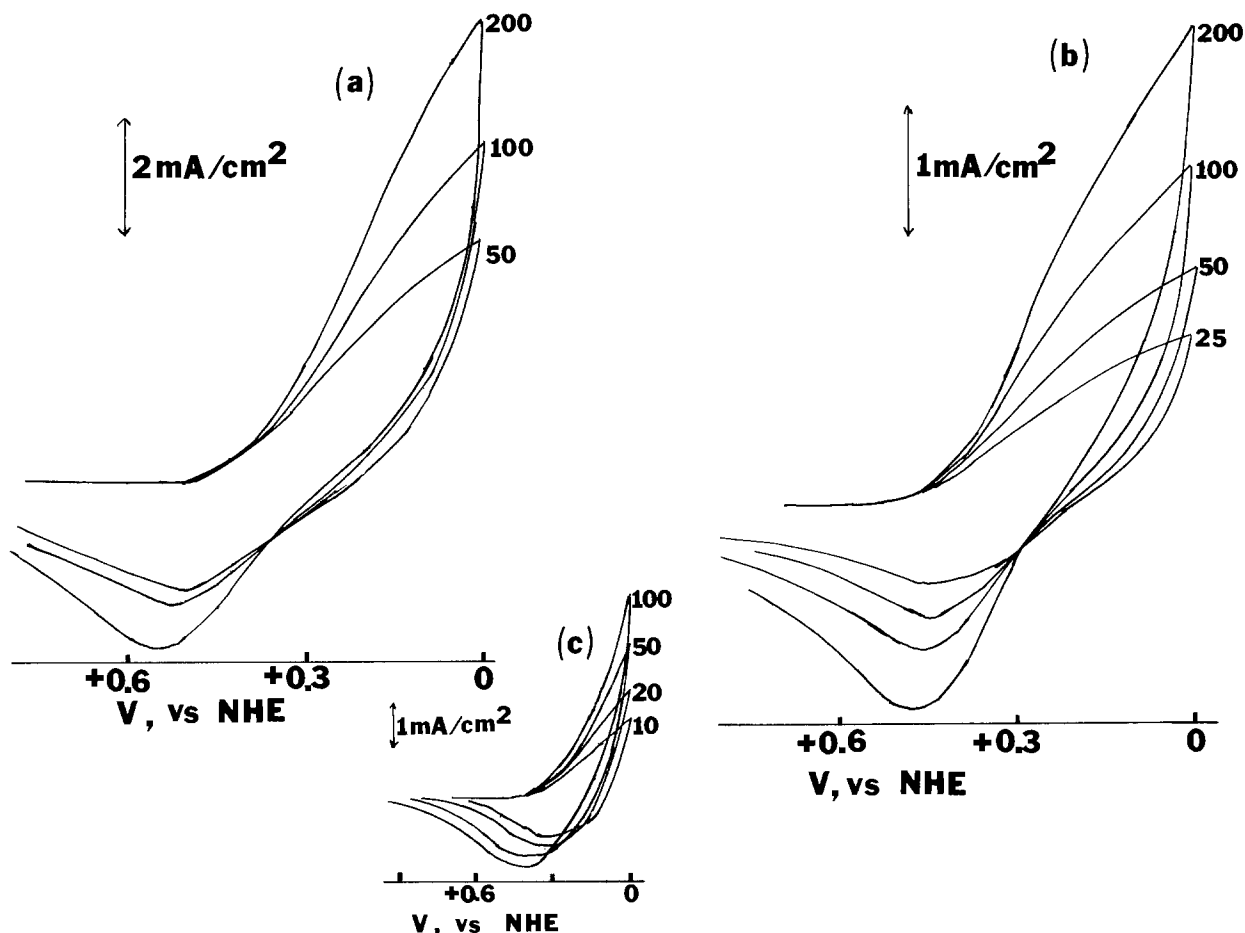


Fig. 4. (a), (b) Simulated electrochromic current-potential curves, as in Fig. 3, for different scan rates. (c) Experimental current-potential curve of the evaporated film shown in Fig. 3(c) at different scan rates. The numbers are the scan rates in mV/sec .

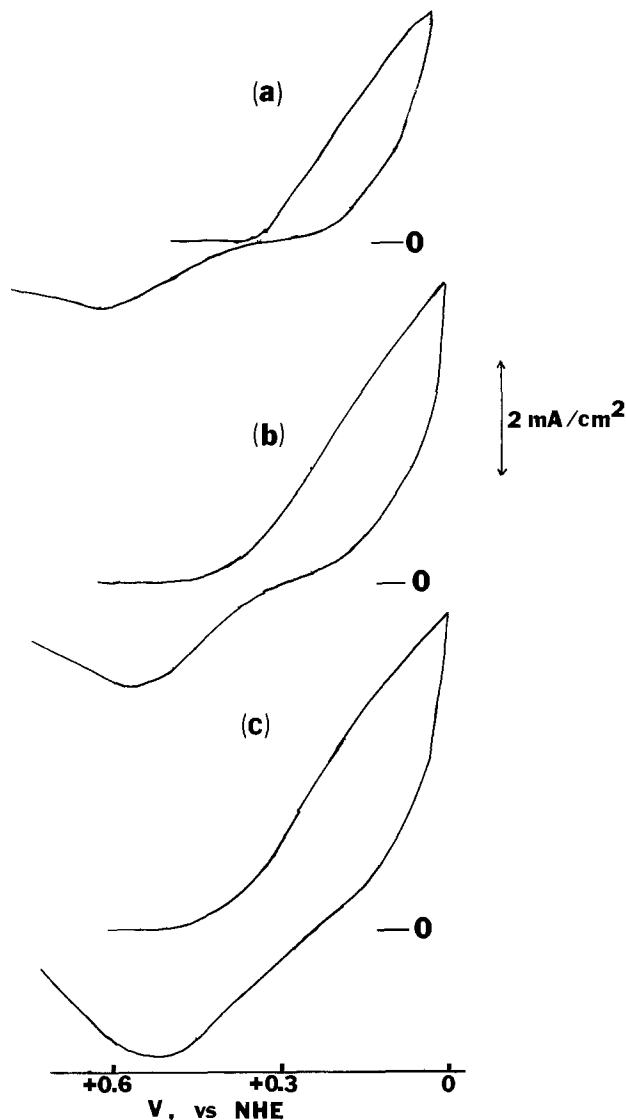


Fig. 5. Simulated current-potential curves for the electrochromic process at a WO_3 film, $1.8 \mu\text{m}$ thick with $D_{\text{H}} = 1 \times 10^{-9} \text{ cm}^2/\text{sec}$ and with k_{f} values of (a) 1.8×10^{-3} , (b) 4.5×10^{-3} , (c) $9 \times 10^{-3} \text{ sec}^{-1} (\text{mole}/\text{cm}^3)^{-2}$.

in the electrochromic current by a factor of about 2. The values of D_{H} which produced simulated i - E curves with currents similar in magnitude to typical experimental ones with evaporated WO_3 films were 1×10^{-9} - $2 \times 10^{-10} \text{ cm}^2/\text{sec}$. Mainly l and D_{H} determine the dependence of the current on the scan rate. The calculated concentration profile of the hydrogen atom within the evaporated film at the negative potential limit (0V vs. NHE) is shown in Fig. 6(a) and (b) for different scan rates and two different film thicknesses. As expected the concentration profile shows a sharp slope at the surface, which is caused by slow diffusion into the film. It is this behavior which results in the $v^{1/2}$ dependence observed in the i - E curves. We have observed similar i - E curves and scan rate dependences for WO_3 layers obtained by thermal oxidation of W (18), which suggests that these films have k_{f} and D_{H} values similar to those of the evaporated film electrodes.

Anodic film electrodes.—The shape of the i - E curves and the scan rate dependence were different for the WO_3 anodic film electrodes (7, 8) [Fig. 7(a) and (b)]. These i - E curves appear more reversible than those for the WO_3 evaporated film electrodes discussed above. Thus, the electrochromic current changes sign from cathodic (coloring) to anodic (bleaching) almost immediately after the direction of the potential scan

is reversed. The anodic current magnitude is similar to that of the cathodic current and generally the curves look more symmetrical. Moreover, the electrochromic current in this case depends directly on v [Fig. 7(b)] as opposed to the $v^{1/2}$ dependence found with the evaporated or thermally oxidized films. This difference in behavior can be ascribed to large differences in k_{f} and D_{H} . Indeed to obtain simulated i - E curves which resembled those obtained experimentally with the WO_3 anodic film electrodes, much larger values of k_{f} and D_{H} had to be used [Fig. 7(c) and (d)]. To obtain an i - E curve of this shape, k_{f} must be taken as about $7.2 \text{ sec}^{-1} (\text{mole}/\text{cm}^3)^{-2}$. D_{H} values of about $5 \times 10^{-8} \text{ cm}^2/\text{sec}$ then yield current magnitudes in the simulated i - E curves similar to those obtained experimentally. With these k_{f} and D_{H} values, the current in the simulated i - E curves is linearly dependent on v [compare curves (b) and (d) in Fig. 7]. The H-concentration profile within the film, calculated for $E = 0\text{V}$ vs. NHE, with the same thickness (l), k_{f} , and D_{H} values as in Fig. 7 is shown for several scan rates in Fig. 6(c). These concentration profiles are almost flat, so that the concentration of hydrogen atoms is essentially uniform throughout the film. This concentration is also near the equilibrium value at this potential (compare with the data in Fig. 2). This type of response is typical of "thin film" behavior as found for thin electrochemical cells (19) and as well as for adsorbed layers, modified electrodes, etc., and results in a dependency of current directly on v .

Current-time curves.—Simulated current-time (i - t) curves for the electrochromic process can be calculated with the same digital simulation model and parameters. Simulated i - t curves for the coloration process at two different potentials are compared to an experimental one obtained with the WO_3 evaporated films in Fig. 8. The values of k_{f} and D_{H} used for the calculation of the simulated curves are those which were used for calculated i - E curves of Fig. 3. While these values give simulated i - t curves which are similar to the experimental ones, there is some discrepancy between the simulated and the experimental curves in the shorter time region. In general the experimental i - t curves show a bump or irregularity in the short time region, while the simulated curves are smooth at all times. The source of this irregularity in the short time region has not yet been established, and we could not simulate it by any minor variations in the model (such as attempts to incorporate a proton source, like water, within the film). The H-concentration profiles during a coloration potential step, which are directly related to the intensity, were calculated for several times (Fig. 9). Such curves are useful for predicting what degree of coloration will be obtained at a given time after the onset of a potential step into the coloration region. For the evaporated film electrodes, $1.8 \mu\text{m}$ thick, 50% of the maximum coloration occurs at about 15 sec. This is similar to what is found experimentally.

Conclusions

The model suggested here describes in a satisfactory way the experimental results obtained for the electrochromic processes at different types of WO_3 electrodes. The model proposes as major factors both the rate of diffusion of hydrogen atoms within the WO_3 films and the rate of charge transfer at the WO_3 /solution interface along with the saturation effect which occurs as the hydrogen tungsten bronze forms. The scan rate dependence of the current and rate of coloration of the films is mainly a function of D_{H} and l and the behavior can be roughly classified according to the dimensionless parameter $S = (RT/F)D_{\text{H}}/v l^2$. When S is greater than ~ 1 , i varies with v and "thin layer" behavior is observed. For S less than ~ 0.1 , a $v^{1/2}$ dependency is found. This model also describes in a generally satisfactory

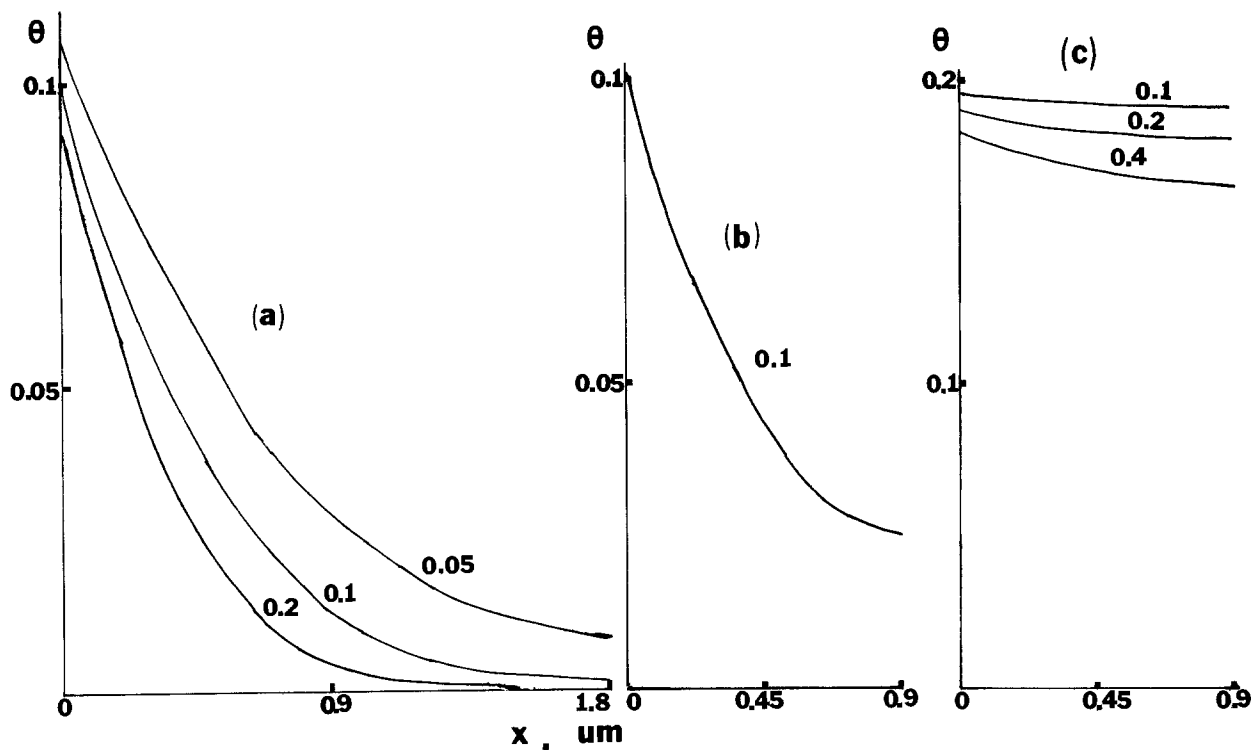


Fig. 6. Simulated concentration profiles of hydrogen atoms within the WO_3 evaporated film. (a) $k_f = 9 \times 10^{-3} \text{ sec}^{-1} (\text{mole}/\text{cm}^3)^{-2}$, $D_{\text{H}} = 1 \times 10^{-9} \text{ cm}^2/\text{sec}$, $l = 1.8 \mu\text{m}$; (b) as (a) with $l = 0.9 \mu\text{m}$; (c) $k_f = 7.2 \text{ sec}^{-1} (\text{mole}/\text{cm}^3)^{-2}$, $D_{\text{H}} = 5 \times 10^{-8} \text{ cm}^2/\text{sec}$, $l = 0.9 \mu\text{m}$. All curves are for an electrode potential of 0V, at the scan rates indicated on the curves (mV/sec).

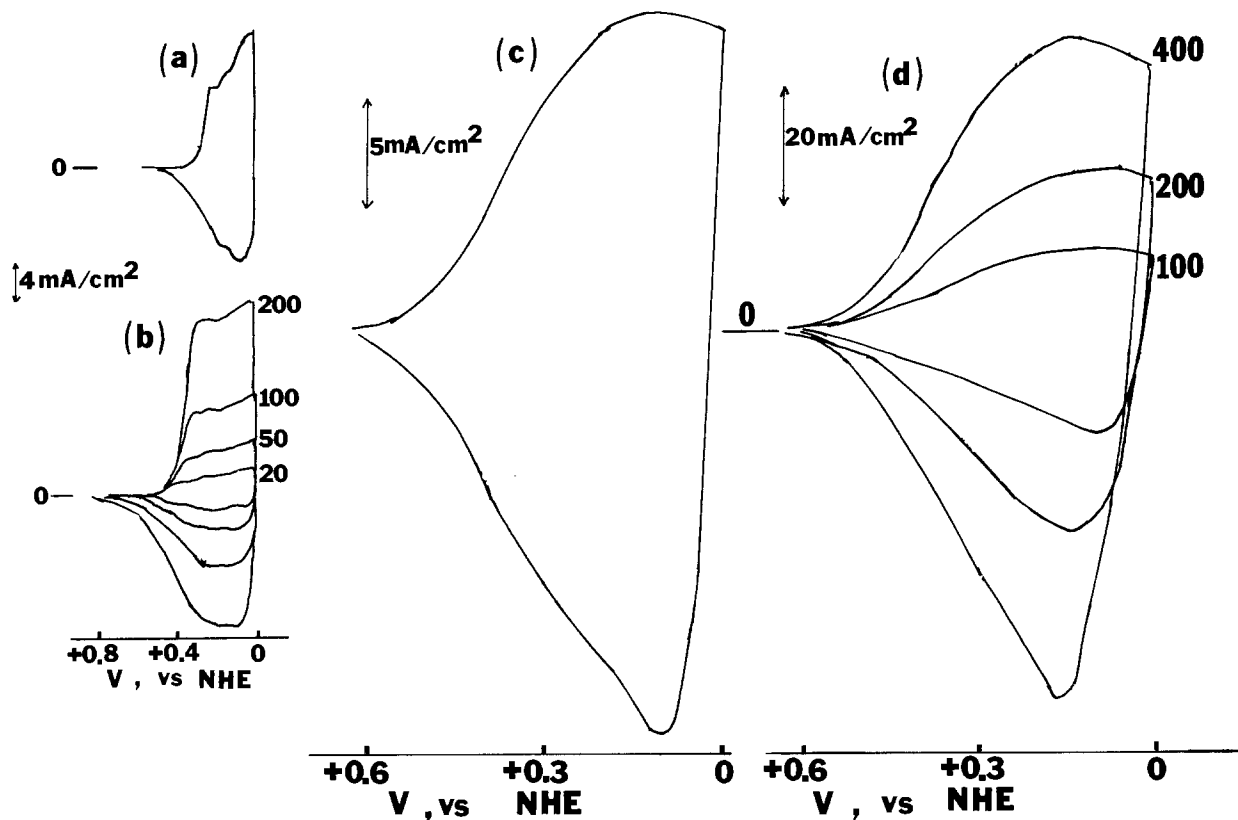


Fig. 7. (a) Experimental current-potential curves recorded at 100 mV/sec for $0.9 \mu\text{m}$ thick anodic film electrodes in $1\text{M H}_2\text{SO}_4$ solution; (b) as (a) for different scan rates indicated on the curves (mV/sec); (c) simulated current-potential curve with $l = 0.9 \mu\text{m}$, $k_f = 7.2 \text{ sec}^{-1} (\text{mole}/\text{cm}^3)^{-2}$, $D_{\text{H}} = 5 \times 10^{-8} \text{ cm}^2/\text{sec}$, scan rate = 100 mV/sec; (d) simulated current-potential curve as in (c), for different scan rates.

way the i - E behavior of WO_3 electrodes as well as i - t transients at longer times. The discrepancies between the experimental data and the simulated i - t curves in the short time region remain to be explained and

modifications of the model which can simulate this behavior may lead to further insight into the nature of the electrochromic process and changes which occur in the films during coloration and bleaching.

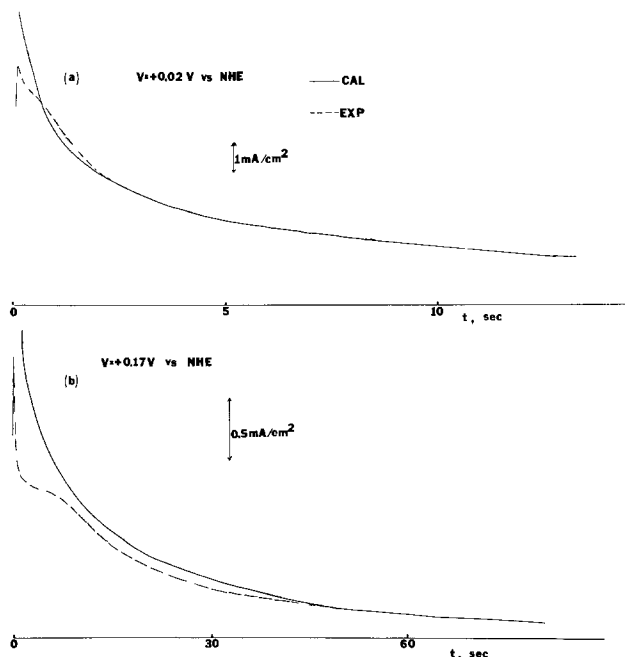


Fig. 8. Simulated (—) and experimental (---) current-time curves during the coloration process at WO_3 evaporated film electrode, $1.8 \mu\text{m}$ thick at two different potentials (a) $+0.02\text{V}$, (b) $+0.17\text{V}$ vs. NHE. The values of k_f and D_H used for the calculation were the same as those which were used to calculate the current-potential curves of Fig. 3(a).

Acknowledgment

The support of this research by Texas Instruments is gratefully acknowledged.

Manuscript submitted July 25, 1979; revised manuscript received Aug. 29, 1979.

Any discussion of this paper will appear in a Discussion Section to be published in the December 1980 JOURNAL. All discussions for the December 1980 Discussion Section should be submitted by Aug. 1, 1980.

Publication costs of this article were assisted by The University of Texas at Austin.

REFERENCES

1. S. K. Deb, *Philos. Mag.*, **27**, 807 (1973).
2. B. W. Faughnan, R. S. Crandall, and P. M. Heyman, *RCA Rev.*, **36**, 177 (1975).
3. H. N. Hersh, W. E. Kramer, and J. H. McGee, *Appl. Phys. Lett.*, **27**, 646 (1975).
4. I. F. Chang, B. L. Gilbert, and T. I. Sun, *This Journal*, **122**, 955 (1975).
5. B. W. Faughnan, R. S. Crandall, and M. A. Lampert, *Appl. Phys. Lett.*, **27**, 275 (1975).
6. H. R. Zeller and H. U. Beyeler, *Appl. Phys.*, **13**, 231 (1977).
7. B. Reichman and A. J. Bard, *This Journal*, **126**, 583 (1979).
8. B. Reichman and A. J. Bard, Abstract B-9, The 20th Conference on Electronic Materials, University of California, Santa Barbara, Calif., June, 1978.
9. J. Hurditch, *Electron. Lett.*, **11**, 142 (1975).
10. R. S. Crandall and B. W. Faughnan, *Appl. Phys.*

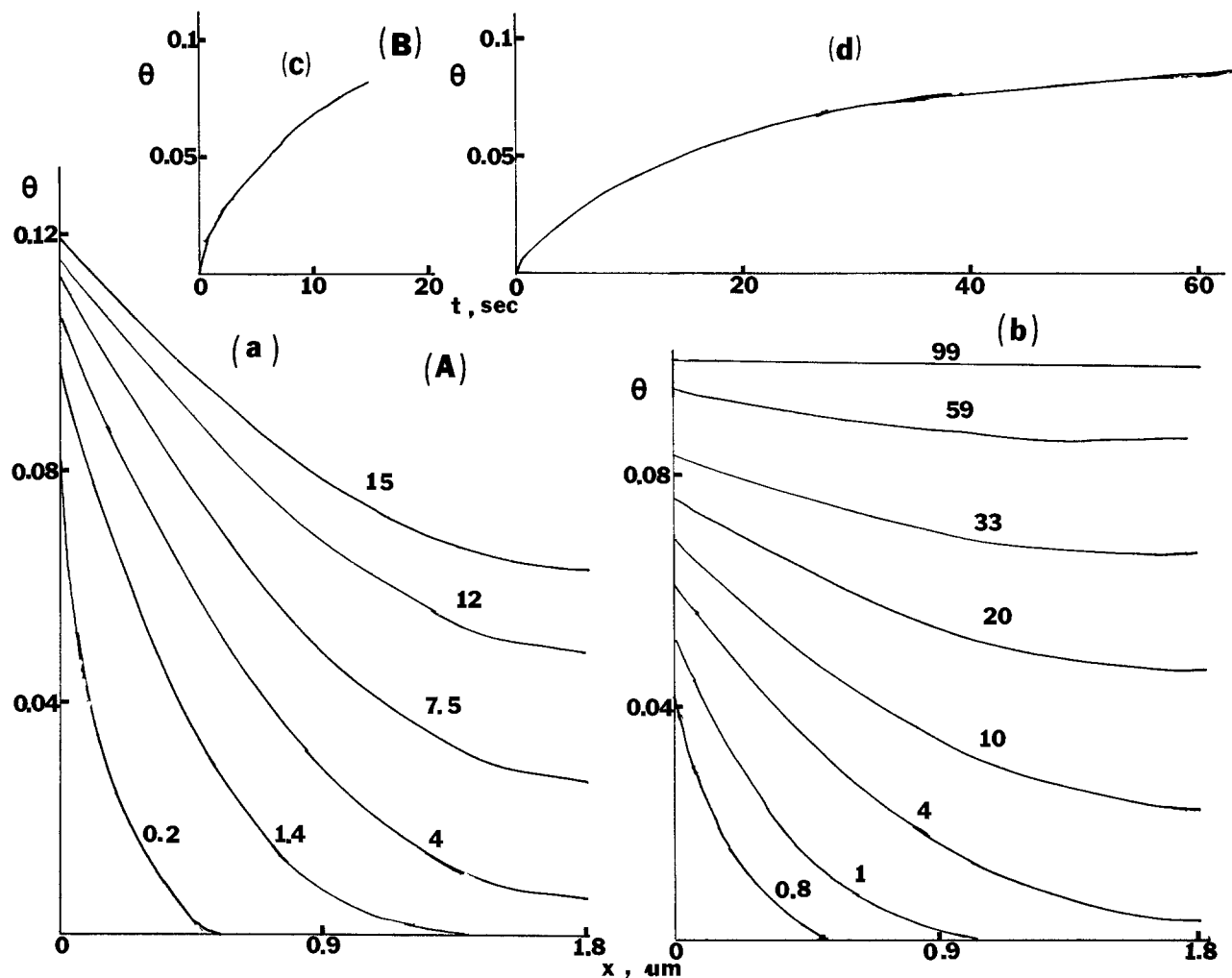


Fig. 9. (A) Calculated hydrogen concentration profiles at different times (sec) shown on curves during the coloration process at (a) $V = +0.02\text{V}$ and (b) $+0.17\text{V}$ (vs. NHE). (B) Calculated total hydrogen concentration inside the WO_3 film, as a function of time during the coloration process at (c) $V = +0.02\text{V}$ (d) $V = +0.17\text{V}$ (vs. NHE). The parameters k_f and D_H are those of Fig. 3(a).

- Lett.*, **28**, 95 (1976).
- T. C. Arnoldussen, Paper 199 presented at The Electrochemical Society Meeting, Las Vegas, Nevada, October 17-22, 1976.
 - E. Gileadi, E. Kirowa-Eisner, and J. Penciner, "Interfacial Electrochemistry," p. 83, Addison-Wesley, Reading, Mass. (1975).
 - S. W. Feldberg, in "Electroanalytical Chemistry," Vol. 3, A. J. Bard, Editor, Chap. 4, Marcel Dekker, Inc., New York (1965).
 - S. W. Feldberg, in "Computers in Chemistry and Instrumentation," Vol. 2, J. S. Mattson, H. B. Mark, Jr., and H. C. MacDonald, Jr., Editors, Chap. 7, Marcel Dekker, New York (1972).
 - A. J. Bard and L. R. Faulkner, "Electrochemical Methods," Appendix B, Wiley, New York (1980).
 - I. B. Goldberg, A. J. Bard, and S. W. Feldberg, *J. Phys. Chem.*, **76**, 2250 (1972).
 - R. S. Crandall, P. J. Wajtoneicz, and B. W. Faughnan, *Solid State Commun.*, **18**, 1409 (1976).
 - B. Reichman and A. J. Bard, *This Journal*, In press.
 - A. T. Hubbard and F. C. Anson, in "Electroanalytical Chemistry," Vol. 4, A. J. Bard, Editor, Chap. 2, Marcel Dekker, Inc., New York (1966).

The Thionine-Coated Electrode for Photogalvanic Cells

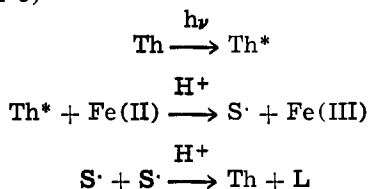
W. John Albery, Andrew W. Foulds, Keith J. Hall, and A. Robert Hillman

Department of Chemistry, Imperial College, London SW7 2AY, England

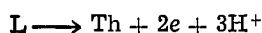
ABSTRACT

The successful operation of a photogalvanic cell for solar energy conversion requires that the illuminated electrode should discriminate between the two redox couples in solution. In the case of the iron-thionine system the electrode must oxidize photogenerated leucothionine but not reduce the photogenerated Fe(III). Modified electrodes with coatings of thionine of up to 20 monolayers can be prepared on Pt and SnO₂. These electrodes have been investigated using ring disk, cyclic voltammetry, XPES, and spectroelectrochemical measurements. Results for the modified electrode kinetics are presented for the following systems: thionine, disulfonated thionine, Fe(II), Fe(CN)₆⁴⁻, Ru(bpy)₃³⁺, Ce(IV), quinone, and N,N,N',N'-tetramethyl-p-phenylenediamine. The results for the Fe(III) and thionine systems show that this modified electrode is suitable for the iron-thionine photogalvanic cell.

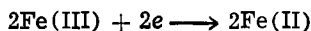
A typical photogalvanic cell for solar energy conversion is shown in Fig. 1. The iron-thionine system for such a cell works according to the following reaction scheme (1-3)



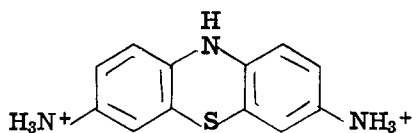
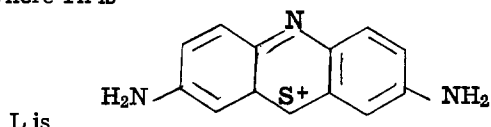
Illuminated electrode



Dark electrode



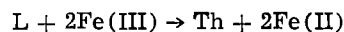
where Th is



and S[·] is the semithionine radical.

In order to obtain power from the cell it is essential that the illuminated electrode should discriminate between the photogenerated leucothionine (L) and Fe(III) (4). If the electrode does not so discriminate, then addition of the electrode reactions in the reaction scheme shows that the electrode merely catalyzes the back-reaction of photogenerated products into the original reactants

Key words: photogalvanic cells, modified electrodes, thionine.



The illuminated electrode must remove one of the photogenerated products, in this case L, and force the other, Fe(III), to diffuse across the cell and react on

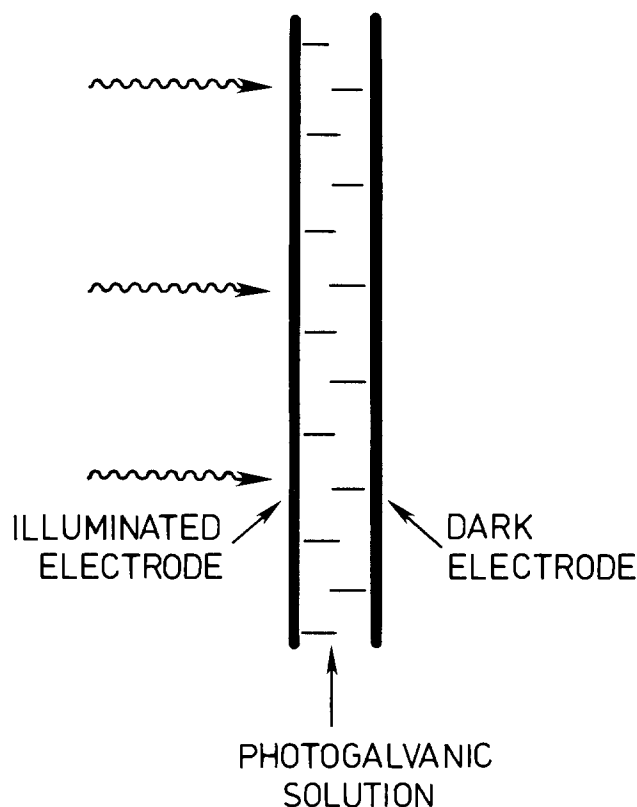
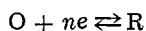


Fig. 1. Typical photogalvanic cell

the dark electrode. It should be noted that for an efficient photogalvanic cell the electrode kinetics of the two electrodes must be different (5). If the Fe(III) reaction is blocked on the dark electrode as well as the illuminated electrode then the cell operates only as a concentration cell and produces insufficient voltage of $\sim RT/F$ (6). In this paper we describe how to modify the illuminated electrode by coating it with thionine itself. The modified electrode then discriminates between the photogenerated L and Fe(III). A photogalvanic cell with a modified and an unmodified SnO₂ electrode will then possess the necessary differential electrode kinetics (7).

Theory

The kinetics of the electrode processes were measured on the rotating disk electrode. For the reaction



we can derive the general equation

$$\ln \left\{ \frac{i_o}{i} - 1 + \left(\frac{i_R}{i} + 1 \right) \left(\frac{D_O}{D_R} \right)^{2/3} \exp \left[\frac{n(E - E')F}{RT} \right] \right\} = y = \ln \left(\frac{k_{D,O'}}{k_o'} \right) + \frac{\alpha(E - E')F}{RT} \quad [1]$$

where i_o and i_R are the limiting currents for the reduction of O and oxidation of R, respectively, E' is the formal potential for the O, R couple in the particular medium, $k_{D,O'}$ is the mass transfer rate constant for O, and k_o' is the standard electrochemical rate constant for the O, R couple at $E = E'$.

At a rotating disk electrode (11, 12)

$$k_{D,O'} = 1.55D_O^{2/3}\nu^{-1/6}W^{1/2} \quad [2]$$

$$i_o = nAFk_{D,O'}[O] \quad [3]$$

ν is the kinematic viscosity and W is the rotation speed in Hz.

For the irreversible reduction of O the current voltage curve is observed when $(E - E')$ is fairly negative and hence the exponential term in [1] may be neglected leading to the usual Tafel equation corrected for mass transport

$$\ln \left(\frac{i_o}{i} - 1 \right) = y = \ln \left(\frac{k_{D,O'}}{k_o'} \right) + \alpha \frac{(E - E')F}{RT} \quad [4]$$

In this work we observe limiting currents that are not entirely transport controlled. There is a two-step reaction at the electrode where the rate constant, k_2' , of one of the steps does not depend on potential. For such a scheme with two consecutive steps we replaced $k_{D,O'}$ in [1] or [3] with

$$k_{D,O'}^{-1} = k_{D,O'}^{-1} + k_2'^{-1} \quad [5]$$

where $k_{D,O}'$ will be determined by the smaller of the two rate constants $k_{D,O}'$ and k_2' . At reducing potentials we then obtain from [3] and [2] the usual Koutecky Levich equation (13) for the limiting current

$$\frac{nAF[O]}{i_o} = \frac{1}{k_{D,O'}} + \frac{1}{k_2'} = \frac{0.65D_O^{-2/3}\nu^{1/6}}{W^{1/2}} + \frac{1}{k_2'} \quad [6]$$

Experimental

All the electrochemical experiments were carried out at 25°C and all potentials reported with respect to the saturated calomel electrode. Rotating disk and ring disk studies were performed using an Oxford Electrodes motor controller, rotating assembly, and control electronics. Antimony-doped SnO₂ electrodes were prepared by spraying a solution of 10 ml SnCl₄ and 0.6 ml SbCl₅ added to 20 ml ethyl acetate for 3 sec

onto the end of a quartz rod heated to 1000°C and rotating at 5 Hz. Spectra were recorded on a Unicam SP 600 recording spectrophotometer. XPS spectra were measured on an AEI ES 200 B photoelectron spectrometer using Mg K α exciting radiation; the base pressure was $\sim 10^{-9}$ Torr. The conductance of the thionine coating was measured in the d-c mode after vapor deposition of an Au contact.

Results and Discussion

Preparation and properties of modified electrodes.— Both Pt and SnO₂ electrodes can be coated with a stable layer of thionine by holding the electrode at 1.1–1.5V for a period of several minutes in a solution containing thionine. Figure 2 shows a ring disk experiment which monitors the consumption of thionine during the coating process. From the decrease in the transport limited current for thionine at the ring electrode we can calculate from $N^{-1} \int \Delta i_R dt$ the amount of thionine consumed on the disk where N is the collection efficiency (8, 9). When the modified electrode is removed from the thionine solution, washed and placed in background electrolyte (e.g., 50 mmole H₂SO₄) containing no thionine, cyclic voltammograms as shown in Fig. 3 are

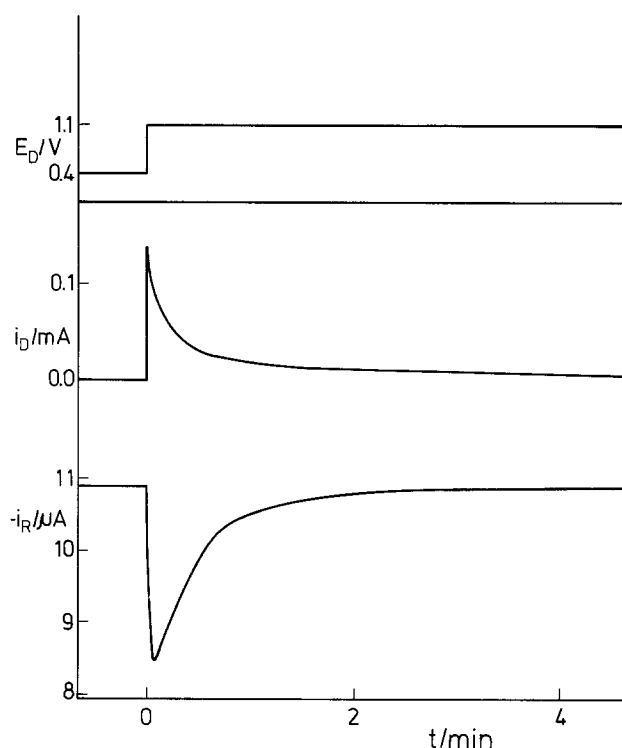


Fig. 2. Ring disk study of coating process; E_D , disk potential; i_D , disk current; i_R ring current. Amount of thionine coated on disk found from $N^{-1} \int \Delta i_R dt$.

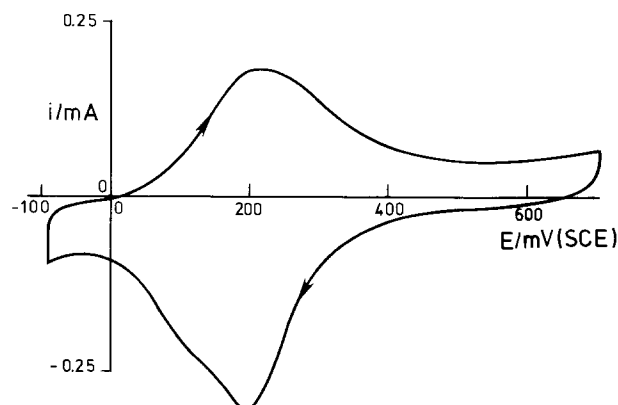


Fig. 3. Cyclic voltammogram of thionine-coated Pt electrode in 0.05M H₂SO₄ containing no thionine.

obtained. The peak height of these voltammograms varies linearly with sweep rate as expected for surface bound species. From the charge passed per cycle we can also calculate the amount of thionine in the layer. The coverages found from cyclic voltammetry agree with those from the ring disk experiment but are usually about 20% lower. Coatings of up to 20 monolayers can be obtained and these coatings are stable in background electrolyte for at least several months. XPES studies, see Fig. 4, of a coated electrode show identical peaks to those of thionine and the Pt 4f peak is completely absent (10).

The cyclic voltammograms before and after the XPES experiment show that exposure to high vacuum for several hours only reduces the coverage by about 10%.

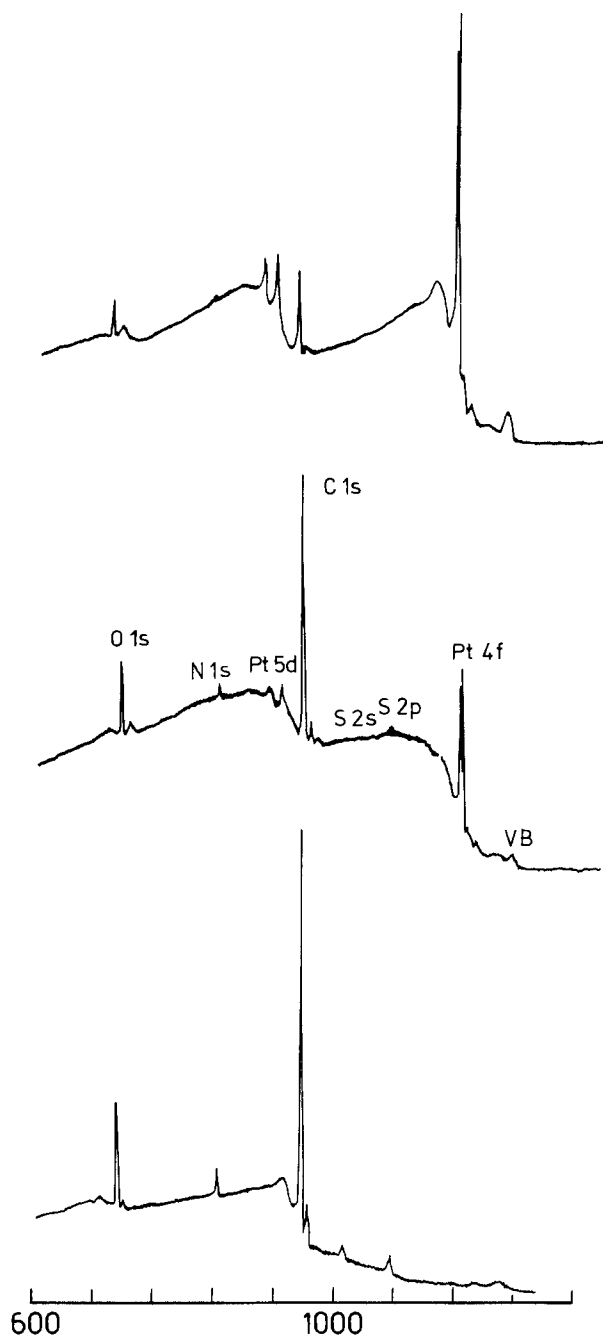


Fig. 4. Typical XPE spectra. The top trace shows a Pt electrode that has been exposed to thionine solution at 0.4V. The principal feature is the Pt 4f signal. The second and third traces show Pt electrodes coated at 1.0 and 1.1V, respectively. The Pt signal becomes progressively suppressed; C, N, and S peaks corresponding to thionine are found. x-axis, KE/eV.

Compared to thionine in solution the visible spectrum of a coated SnO₂ electrode on a quartz plate shows a broadened peak at much the same wavelength ($\lambda_{\text{max}}/\text{nm} \approx 600$) (10). At reducing potentials this peak disappears. As shown in Fig. 5 the proportion of thionine, f , and leucothionine in the layer obeys the Nernst equation

$$\frac{RT}{nF} \ln \left(\frac{f}{1-f} \right) = E - E_c' \quad [7]$$

We find $n = 2$ and $E_c'/\text{mV} = 180$. This value is similar to that of thionine in our solution ($E'/\text{mV} = 208$). The resistance of 1 cm² of a layer coated at 1.1V containing 6 nmole cm⁻² was found to be 60Ω. From these results we conclude firstly that the layer consists of thionine or leucothionine depending on the electrode potential. Secondly, the layer is remarkably stable and coherent; it cannot be washed off and the disappearance of the Pt signal in the XPE spectrum is particularly noteworthy. Thirdly, for current densities less than 150 μA cm⁻² the voltage drop across the layer is less than 10 mV and can be neglected.

Thionine.—We now examine the electrode kinetics of various redox couples on the thionine-coated electrode starting with thionine itself. Figure 6 shows typical current voltage curves for the reduction of thionine on a clean and a thionine-coated Pt electrode. On the clean electrode the system is reversible. On the coated electrode the system is nearly reversible. Figure 7 shows the current voltage data plotted according to [1]. Kinetic parameters for different electrodes are collected in Table I. We conclude firstly that on the coated electrode there is little difference between Pt and SnO₂ as the substrate surface. Secondly the electrochemical rate constant is decreased for electrodes coated at higher voltages and for longer times. In particular there is a significant reduction in rate constant for electrodes coated at 1.4V or above for periods longer than one hour. It should be noted from Fig. 2 that after the initial coating process lasting two min-

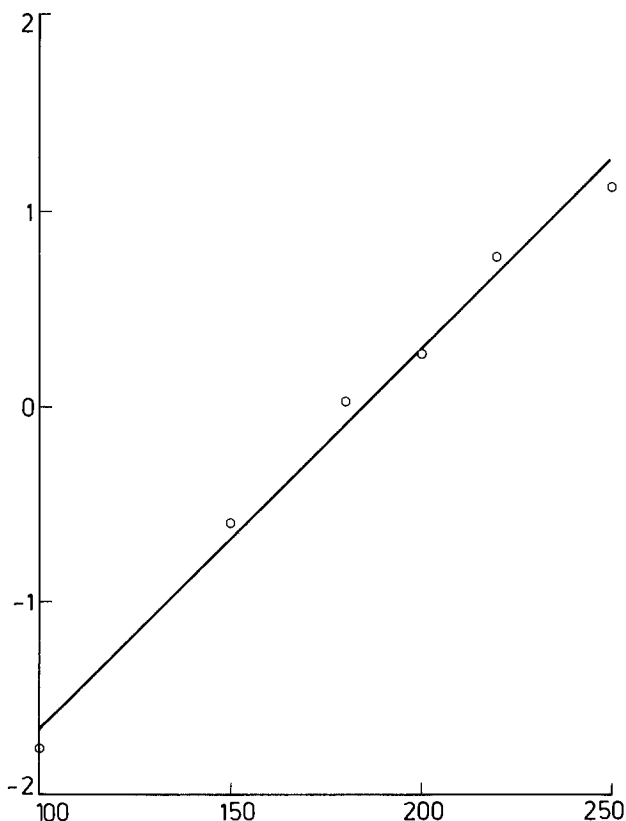


Fig. 5. Plot of Nernst Eq. [7] describing the bleaching of the thionine layer. x-axis, E/mV(SCE); y-axis, $\ln(f/1-f)$.

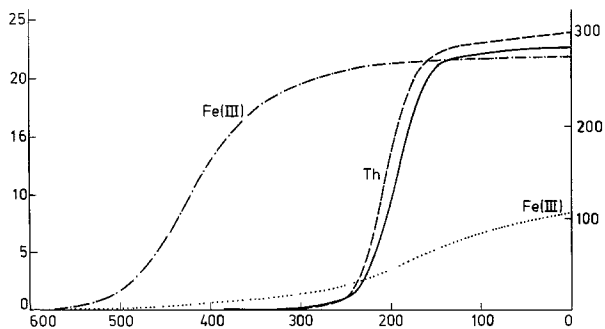
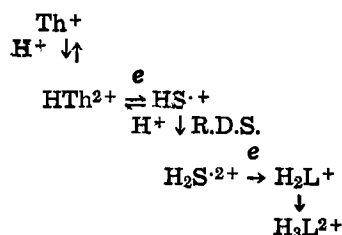


Fig. 6. Typical current voltage curves for thionine (Th) and Fe(III) on an uncoated (- - - and - · - ·) and thionine-coated Pt electrode (— and . . .). x-axis, $E/mV(SCE)$; left-hand y-axis, $i_{Th}/\mu A$; right-hand y-axis, $i_{Fe(III)}/\mu A$.

utes, the ring electrode does not detect any further consumption of thionine on the disk electrode. From cyclic voltammetry (see Fig. 3) the amount of adsorbed thionine does not change significantly after the initial coating process.

The value of $\alpha \simeq 1.0$ is interesting. It suggests that the rate-determining step in the reduction of thionine involves a reaction of a semithionine species which is in equilibrium with the thionine. On a clean Pt electrode as the pH is increased the value of k_o' decreases. Preliminary results are consistent with the following scheme of squares (14, 15) mechanism



In this scheme we have included the added protons explicitly. We have estimated the pK's of the transition states from the pK's of the thionine, semithionine, and leucothionine species (16-20). In order to explain the variation of k_o' with coating conditions (see Table I) the thionine species must be adsorbed on the electrode.

Disulfonated thionine.—Photogalvanic cells have so far been extremely inefficient for the conversion of solar energy (21) because thionine is not sufficiently soluble to absorb the solar radiation close enough to the illuminated electrode (3). We have recently synthesized disulfonated thionine. The solubility is increased so that solutions $\sim 10^{-2}M$ can be prepared and furthermore from the visible spectrum there is no evidence for dimer formation. The disulfonated thionine cannot be coated onto the electrode in the same way as thionine. However the electrode kinetics of disulfonated thionine are very similar to those of thionine. Results are given in Table II.

Table I. Kinetic parameters for the reduction of thionine

Electrode	Coating voltage, V	Coating time, hr	α	k_o' , cm ksec ⁻¹
Pt	Clean	—	—	>30
SnO ₂	Clean	—	0.8	9.0
Pt	1.1	¼	0.9	9.3
SnO ₂	1.1	¼	1.2	9.0
Pt	1.4	¼	1.0	2.8
SnO ₂	1.4	¼	0.9	6.1
Pt	1.5	¼	1.2	2.9
SnO ₂	1.5	¼	0.9	5.1
SnO ₂	1.1	1	0.9	5.5
SnO ₂	1.4	1	0.9	0.86
SnO ₂	1.5	1	0.9	0.66
SnO ₂	1.1	2	1.0	3.6
SnO ₂	1.5	3	1.0	0.70

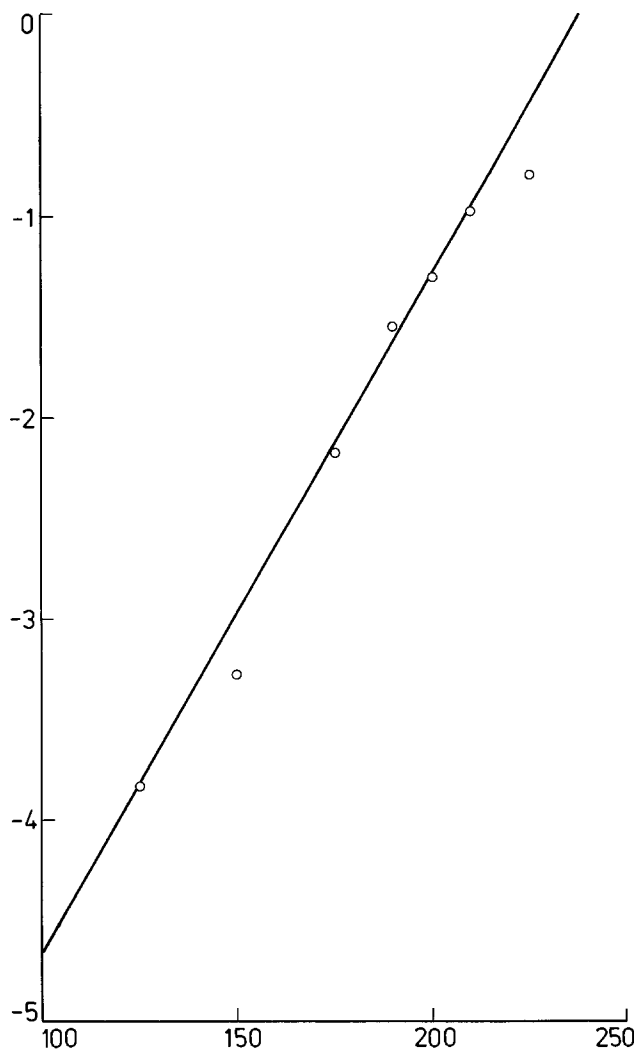
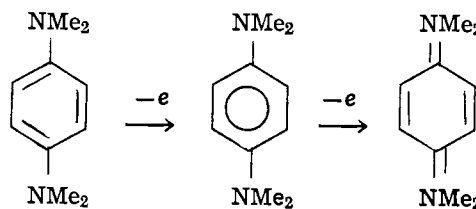


Fig. 7. Tafel plot from Eq. [1] for reduction of thionine at a thionine-coated Pt electrode. x-axis, $E/mV(SCE)$; y-axis, y .

Quinone.—Results for the reduction of quinone are given in Table III. In these experiments a Pt electrode was used throughout and the coating time was ¼ hr. The reduction was carried out in 0.1M H₂SO₄. It can be seen that the thionine coating has practically no effect on the electrode kinetics of the quinone reduction.

N,N,N',N'-tetramethyl-p-phenylenediamine.—The normal reaction scheme for the oxidation of N,N,N',N'-tetramethyl-p-phenylenediamine is as follows



Wurster's Blue +

As shown in Fig. 8 at pH 7 on a clean electrode two separate waves corresponding to the two steps in the

Table II. Kinetic parameters for disulfonated thionine

Electrode	Coating voltage, V	Coating time, hr	α	k_o' , cm ksec ⁻¹
Pt	—	—	0.8	6.2
Pt	1.1	¼	0.8	2.7
Pt	1.5	¼	0.9	1.5

Table III. Kinetic parameters for reduction of quinone

Coating voltage, V	α	k_o' , cm ksec ⁻¹
Clean	0.6	0.18
1.1	0.6	0.24
1.4	0.6	0.20
1.5	0.7	0.15

reaction are observed. On an electrode coated with thionine at 1.1V for ¼ hr while the rate constant for the first wave is somewhat reduced, the second electron transfer is completely blocked. At present we can offer no explanation for this complete blocking. It is true that Wurster's blue is positively charged but then the positively charged thionine reacts rapidly as shown in Fig. 6.

Apart from the complication of Wurster's blue and the small variations in Table I, we find that for these organic species the thionine coating does not produce a drastic change in the electrode kinetics. This is to be contrasted with the inorganic systems that we now consider.

Fe(III).—Typical current voltage curves for the reduction of Fe(III) are shown in Fig. 6. It can be seen at once that the coating produces firstly a shift of some 200 mV in the half-wave potential and secondly that the limiting current of the shifted wave is very much less than that on the untreated electrode. The variation of the limiting currents of the shifted waves with rotation speed are plotted in Fig. 9 according to the Koutecky Levich equation Eq. [6]. From the intercept, which corresponds to infinite rotation speed, we can find values of k_o' . For the rising part of the current voltage curve we can use the simple irreversible Eq. [4] with i_o being the observed limiting current. A typical plot is shown in Fig. 10. Results for the Fe(III) system are collected in Table IV. Instead of extrapolating the results for k_o' for the coated electrodes a long way to the E' for the Fe(III)/Fe(II) couple, we have reported the results at E' for thionine.

The first point to note is that for this reaction α is close to 0.5. This suggests that the potential dependent rate constant is still describing an electron transfer, even though the rate is much slower on a coated electrode compared to a clean electrode. The conductivity of the thionine film means that there cannot be large potential differences within the film and hence the

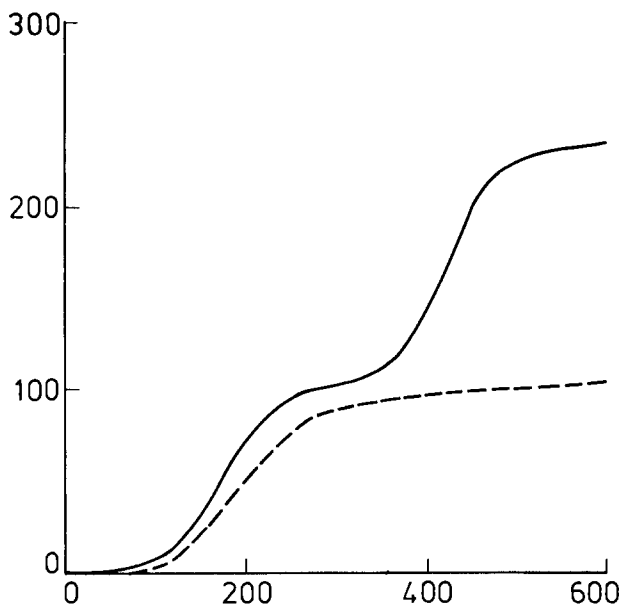


Fig. 8. Current voltage curves for oxidation of N,N,N',N'-tetramethyl-p-phenylenediamine on a clean (—) and coated (---) Pt electrode. x-axis, $E/mV(SCE)$; y-axis, $i/\mu A$.

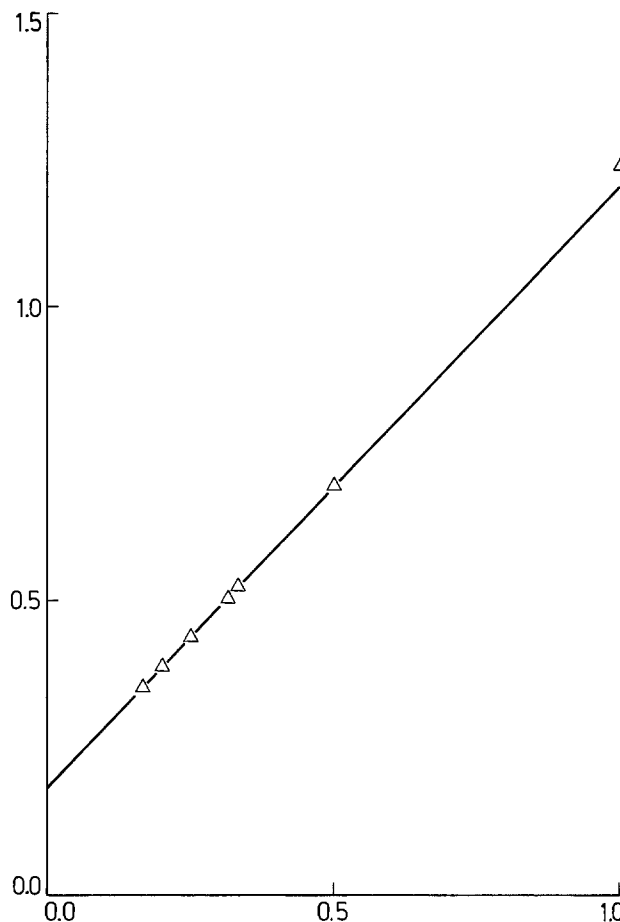


Fig. 9. Koutecky Levich plot, Eq. [6], for reduction of Fe(III) on a coated Pt electrode. x-axis, $(W/Hz)^{-1/2}$; y-axis, $(i_L/\mu A)^{-1}$.

main potential drop occurs at the thionine/water interface. The second point to note is that, like thionine, although Fe(III) has different electrode kinetics on clean Pt and clean SnO₂, there is not much difference once the electrodes are coated. Thirdly, the existence of k_o' means that there must be a second step in the mechanism, the rate constant of which is not greatly affected by potential. These results will be further discussed below.

Fe(CN)₆⁴⁻.—Results for the oxidation of Fe(CN)₆⁴⁻ in 0.4M K₂SO₄ at pH 7 are similar to those for Fe(III). Typical results are shown in Fig. 11. On a clean Pt electrode as expected the couple is reversible but on a coated electrode the wave is irreversible and again there is a second step. For an electrode coated at 1.1V for ¼ hr we find $k_o'/cm\ ksec^{-1} \approx 0.6$ and $k_2'/cm\ ksec^{-1} \approx 2.2$. It is very striking how the thionine coat has blocked this normally rapid electron transfer.

Table IV. Kinetic parameters for the reduction of Fe(III)

Electrode material	Coating voltage, V	Coating time, hr	$E_{1/2}$, V	α	k_o' ^(a) , cm ksec ⁻¹	k_2' , cm ksec ⁻¹
Pt	Clean	—	0.42	0.4	100	—
SnO ₂	Clean	—	0.28	0.5	15.2	—
Pt	1.1	¼	0.23	0.4	3.5	9.4
SnO ₂	1.1	¼	0.23	0.5	5.0	14
SnO ₂	1.1	1	0.20	0.6	1.4	3.6
SnO ₂	1.1	2	0.19	0.6	0.79	2.1
Pt	1.3	¼	0.22	0.4	2.0	6.3
Pt	1.4	¼	0.22	0.4	2.1	3.1
SnO ₂	1.4	¼	0.23	0.5	3.7	9.5
Pt	1.5	¼	0.17	0.4	0.88	2.8
SnO ₂	1.5	¼	0.20	0.5	2.0	6.2
SnO ₂	1.5	3	0.11	0.3	0.072	0.30

^(a) Value of k' at E' for thionine where $E'/V = 0.208$.

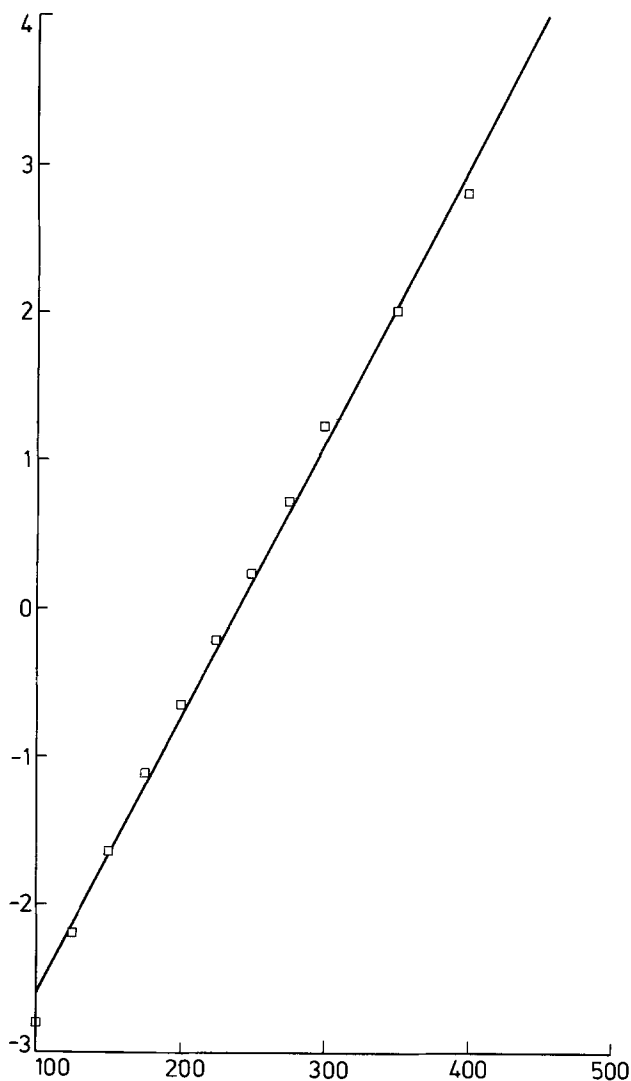


Fig. 10. Typical Tafel plot, Eq. [4], for reduction of Fe(III) on a coated Pt electrode. Label x-axis, $E/\text{mV}(\text{SCE})$; y-axis, y .

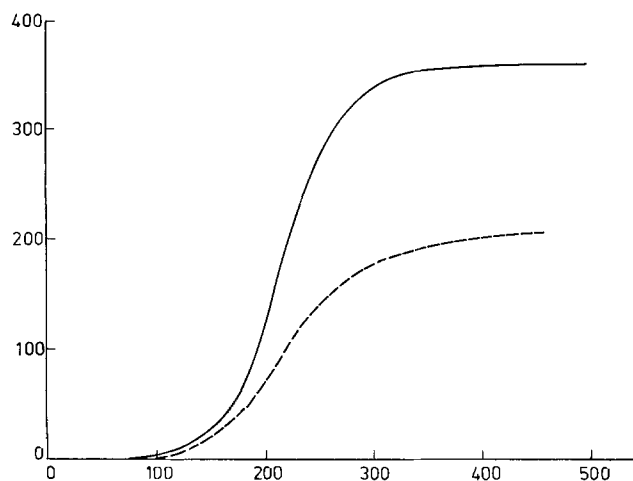


Fig. 11. Typical current voltage curves for oxidation of $\text{Fe}(\text{CN})_6^{4-}$ on a clean (—) and a coated (---) Pt electrode. Label x-axis, $E/\text{mV}(\text{SCE})$; y-axis, $i/\mu\text{A}$.

$\text{Ru}(\text{bpy})_3^{3+}$.—Even more dramatic are the results for the reduction of $\text{Ru}(\text{bpy})_3^{3+}$ in $0.5\text{M H}_2\text{SO}_4$ where *bpy* is 2,2' bipyridine. Results on a coated electrode are shown in Fig. 12. On a clean electrode $\text{Ru}(\text{bpy})_3^{3+}$ is reduced at potentials less than 1.0V , in a reversible wave. The thermodynamics for the reduction are favorable and the kinetics are rapid. However on the coated electrode the transport limited current is not

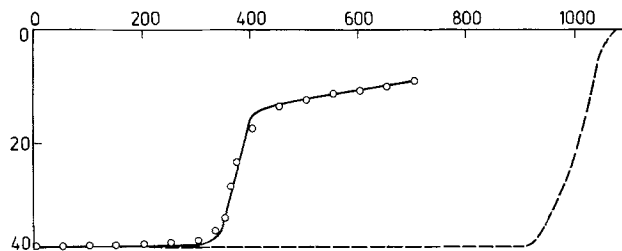
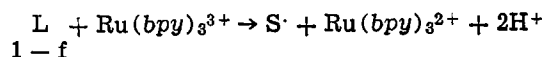
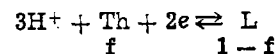


Fig. 12. Current voltage curves for reduction of $\text{Ru}(\text{bpy})_3^{3+}$ on a clean (---) and a coated (○) Pt electrode. The solid line is the calculated curve for the two parallel processes discussed in the text. Label x-axis, $E/\text{mV}(\text{SCE})$; y-axis, $i/\mu\text{A}$.

reached until 0.30V . Inspection of the current voltage curve shows that there are two parallel processes. For potentials greater than 0.40V we find a small current which increases gradually as the potential decreases. Figure 13 shows a Tafel plot of this current according to Eq. [4]. A reasonable straight line is obtained with a low value of $\alpha = 0.05$. At 0.4V a second process takes over and the current rises rapidly to its transport limited value. To allow for the two parallel processes we use a modified form of [4]

$$\ln y = \ln \left(\frac{i_0 - i}{i - i_1} \cdot \frac{i_0 - i_1}{i_0} \right) = \ln \frac{k_{D,O'}}{k_2'} + \alpha \frac{(E - E_{\text{Ru}'})F}{RT} \quad [8]$$

where i_1 is the current due to the process plotted in Fig. 13 at $E \approx 0.4\text{V}$. When $i_1 = 0$, [8] reduced to [4]. The data for the steep part of the wave are plotted in Fig. 14. A reasonable straight line is found with α close to 2. This high value of α cannot be caused by driving the electron transfer for the reduction of Ru(III). For that reaction we would expect [as was found for Fe(III)] that $\alpha \approx 1/2$, and in any case α must be less than unity. Returning to the data in Fig. 5 where $n = 2$ we propose that the second process is the reaction of Ru(III) with L formed on the outside of the layer



The very small fraction of L ($\sim 2 \times 10^{-3}$) present when the second process takes over can be estimated from the Nernst Eq. [7] and the value of E_c' for $0.5\text{M H}_2\text{SO}_4$ where $E_c'/V = 0.270$. Combining [7] and [8] we obtain

$$k_2' \exp \left[\frac{-2(E - E_{\text{Ru}'})F}{RT} \right] = k'(1-f) \approx k' \exp \left[\frac{-2(E - E_c')F}{RT} \right]$$

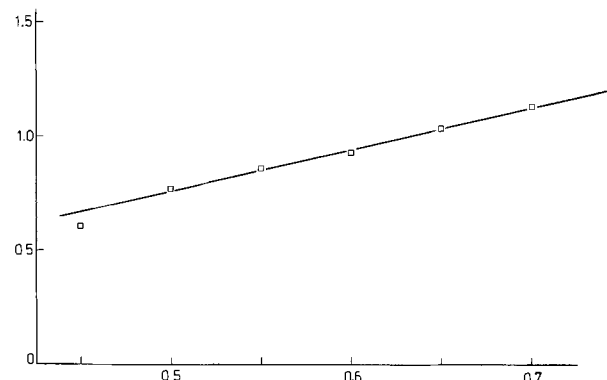


Fig. 13. Tafel plot [4] for points in Fig. 12 for $E/\text{mV} > 400$. Label x-axis, $E/\text{V}(\text{SCE})$; y-axis, y .

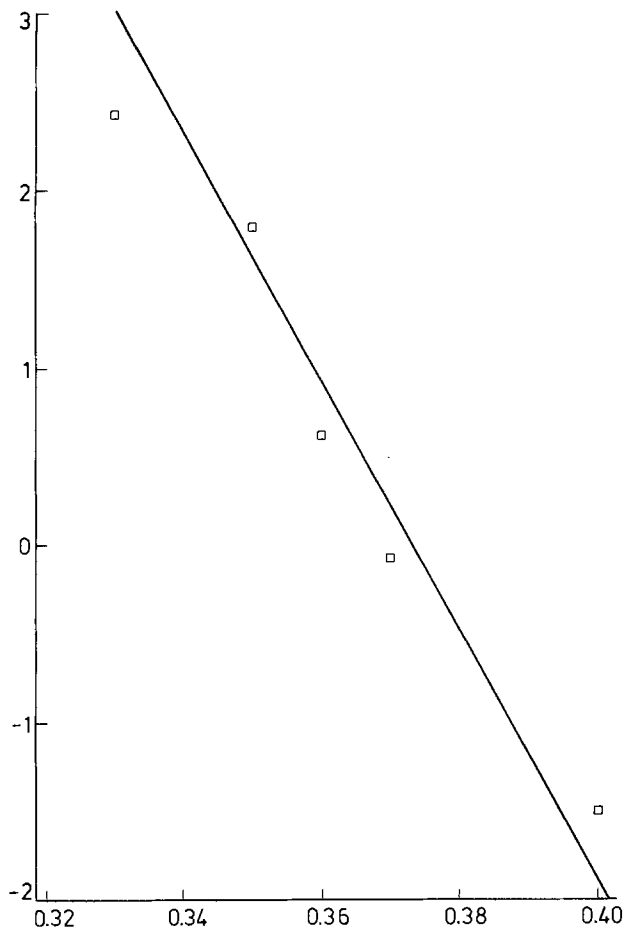


Fig. 14. Plot of Eq. [8] for steep part of current voltage curve for reduction of $\text{Ru}(\text{bpy})_3^{3+}$ shown in Fig. 12. Label x-axis, $E/\text{V}(\text{SCE})$; y-axis, y .

From the data for k_2' in Fig. 13 we find

$$k'/\text{cm sec}^{-1} = 9 \quad [9]$$

It is interesting that this fast rate constant can be measured in the steady state by the dilution of the active species on the surface of the electrode; Fig. 5 shows that the oxidation state of the thionine layer obeys the Nernst equation.

We have also measured the homogeneous rate constant, k_2 , for the reaction between $\text{Ru}(\text{bpy})_3^{3+}$ and leucothionine in 0.5M H_2SO_4 using stopped flow. We find

$$k_2/M^{-1} \text{sec}^{-1} = 1 \times 10^8$$

This rate constant and the heterogeneous rate constant in [9] are each some two to three orders of magnitude below the respective encounter rates (22) for neutral species. This may be because of the coulombic interaction between $\text{Ru}(\text{bpy})_3^{3+}$ and the doubly charged leucothionine, or there may be a small free energy barrier of much the same size in both processes.

Finally we return to Fig. 12 and calculate the current voltage curve using the parameters derived from the analysis in Fig. 13 and 14. A good fit is found. The fact that in this treatment we use $\alpha = 2$ confirms the conclusion from the conductance measurements the IR losses in the coat are negligible.

While our model for the second process fits the data very well, we do not as yet have a detailed model for the slow process occurring at potentials greater than 0.4V. The very low value of α means that the process is not a straightforward electron transfer. It may be that this process is similar to the k_2' step in the reduction of $\text{Fe}(\text{III})$. The potential range over which we can observe the k_2' process for $\text{Fe}(\text{III})$ is too restricted to be certain if k_2' depends slightly on potential or not.

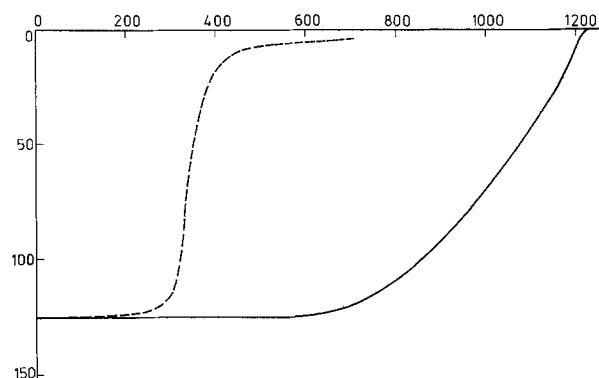


Fig. 15. Current voltage curves for reduction of $\text{Ce}(\text{IV})$ on a clean (—) and a coated (---) Pt electrode. Label x-axis, $E/\text{mV}(\text{SCE})$; y-axis, $i/\mu\text{A}$.

$\text{Ce}(\text{IV})$.—The reduction of $\text{Ce}(\text{IV})$ resembles that of $\text{Ru}(\text{bpy})_3^{3+}$. A typical current voltage curve is shown in Fig. 15. Again two processes are evident. Following the same analysis as for $\text{Ru}(\text{bpy})_3^{3+}$ we find that the steep part gives a somewhat curved Tafel plot with α varying between 1.4 and 2.0. The fact that these values are greater than unity suggests that we must again be seeing a reaction between L in the coat and $\text{Ce}(\text{IV})$.

Effects of coating voltages and coating times.—Because of our interest in photogalvanic cells we have investigated the thionine and $\text{Fe}(\text{III})$ systems in more detail. For these systems we find that there is some reduction in the kinetic parameters the higher the coating voltage and the longer the coating time. This effect can be seen in k_0' in Table I and k_0' and k_2' in Table IV. In Fig. 16 and 17 we show that there is a correlation between the different sets of rate constants; there is a particularly good correlation with a gradient of unity between k_0' and k_2' for the $\text{Fe}(\text{III})$ system. Since these rate constants describe different processes we assume that the correlations arise through a general effect of the higher voltage or coating time on the coat itself. This affects all three processes, the reduction of thionine, the electrochemical step, and the k_2' step in the reduction of $\text{Fe}(\text{III})$, to much the same extent. The higher coating voltages and coating times may cause this, for instance, by blocking off active sites on the surface.

Inorganic electron transfers.—While as discussed above the coat seems to have no drastic effect on the reduction of thionines or of quinone, single electron transfers to inorganic ions which normally proceed by outer sphere mechanisms are in all cases blocked by the coat. This is probably because the thickness of the

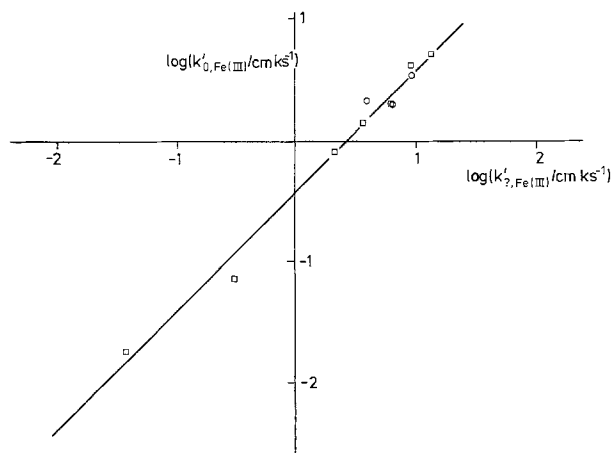


Fig. 16. Correlation between k_0' and k_2' from Table IV for reduction of $\text{Fe}(\text{III})$ at coated electrodes: Pt, \circ ; SnO_2 \square .

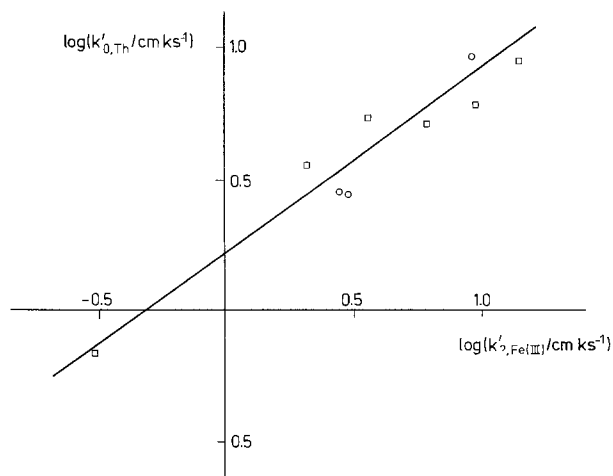


Fig. 17. Correlation between k'_0 for thionine from Table I and k'_0 for Fe(III) from Table IV at coated electrodes: Pt, \circ ; SnO_2 \square .

coat prevents the direct tunnelling of electrons from the metal or SnO_2 to the solvated inorganic ion. For strong oxidizing agents like Ru(III) and Ce(IV) it appears that the main path for reaction is the oxidation of leucothionine on the outside of the coat. For Fe(III), because there is not such a strong thermodynamic driving force, the reaction between Fe(III) and L is 7 orders of magnitude slower than diffusion control. Hence it appears that we have a two-step mechanism of which one step is an electron transfer and we suggest that the other is the formation of a "complex" between Fe(III) and leucothionine at the surface. Such complexes have been found in homogeneous reactions between Fe(III) and L (23). It is interesting that the half-wave potential for the reduction of Fe(III) is close to that of E' for thionine suggesting that the conversion of thionine to leucothionine in the coat may well be necessary for the reaction.

Implications for photogalvanic cells.—Finally we return to the question of the selectivity of these electrodes for use in photogalvanic cells. Inspection of Fig. 6 shows that the thionine-coated electrode does have the required selectivity. The coating leaves the electrode kinetics of the thionine couple sufficiently rapid to handle the photogenerated thionine (3) but it blocks the reduction of Fe(III). Thus an illuminated electrode working at a potential where it is oxidizing leucothionine will only have a small current caused by the simultaneous reduction of Fe(III). Hence we conclude that the thionine coated electrode is an ideal illuminated electrode for the iron-thionine photogalvanic cell. The fact that it can be made so easily and that it is relatively stable are added advantages.

Acknowledgments

We thank Mr. A. F. Orchard and Dr. R. G. Egdell for making the XPES measurements reported in this

paper. We thank Dr. R. Whiteside for making the disulfonated thionine. We thank the SRC for equipment grants and for studentships for ARH and AWF. This is a contribution from the Oxford Imperial Energy Group.

Manuscript received Aug. 13, 1979. This was Paper 331 presented at the Boston, Massachusetts, Meeting of the Society, May 6-11, 1979.

Any discussion of this paper will appear in a Discussion Section to be published in the December 1980 JOURNAL. All discussions for the December 1980 Discussion Section should be submitted by Aug. 1, 1980.

REFERENCES

1. N. N. Lichtin, "Solar Power and Fuels," J. R. Bolton, Editor, p. 119 *et seq.*, Academic Press, New York (1977).
2. M. I. C. Ferreira and A. Harriman, *J. Chem. Soc. Faraday Trans. 1*, **73**, 1085 (1977).
3. W. J. Albery and A. W. Foulds, *J. Photochem.*, **10**, 41 (1979).
4. W. J. Albery and M. D. Archer, *This Journal*, **124**, 688 (1977).
5. W. J. Albery and M. D. Archer, *Nature*, **270**, 399 (1977).
6. W. J. Albery and M. D. Archer, *J. Electroanal. Chem. Interfacial Electrochem.*, **86**, 1 (1978).
7. W. J. Albery and M. D. Archer, *ibid.*, **86**, 19 (1978).
8. W. J. Albery and S. Bruckenstein, *Trans. Faraday Soc.*, **62**, 1920 (1966).
9. W. J. Albery, *ibid.*, **67**, 153 (1971).
10. W. J. Albery, W. R. Bowen, F. S. Fisher, A. W. Foulds, K. J. Hall, A. R. Hillman, R. G. Egdell, and A. F. Orchard, *J. Electroanal. Chem. Interfacial Electrochem.*, To be published.
11. W. J. Albery, "Electrode Kinetics," p. 58, Clarendon Press, Oxford (1975).
12. V. G. Levich, "Physicochemical Hydrodynamics," p. 68, Prentice Hall, Englewood Cliffs, N.J. (1962).
13. J. Koutecky and V. G. Levich, *Zh. Fiz. Khim.*, **32**, 1565 (1956).
14. J. Jacq, *Electrochim. Acta*, **12**, 1345 (1967).
15. W. J. Albery and M. L. Hitchman, "Ring Disc Electrodes," p. 38 *et seq.*, Clarendon Press, Oxford (1971).
16. W. M. Clark, H. D. Gibbs, and B. Cohen, *Public Health Rep.*, **40**, 1160 (1935).
17. S. Granick, L. Michealis, and M. P. Schubert, *J. Am. Chem. Soc.*, **62**, 1802 (1940).
18. J. Faure, R. Bonneau, and J. Joussot-Dubien, *J. Chim. Phys.*, **65**, 369 (1968).
19. L. F. Epstein, F. Karush, and E. Rabinowitch, *J. Opt. Soc. Am.*, **31**, 77 (1941).
20. I. Ferreira, Ph.D. Thesis, London University (1978).
21. D. E. Hall, W. D. K. Clark, J. A. Eckert, N. N. Lichtin, and P. D. Wildes, *Ceram. Bull.*, **56**, 408 (1977).
22. R. A. Marcus, *J. Phys. Chem.*, **67**, 853 (1963).
23. T. L. Osif, N. N. Lichtin, and M. Z. Hoffman, *ibid.*, **82**, 1778 (1978).



The Effect of Anion Activity on Electrochemical Equilibria: Three-Dimensional Potential-pH Diagram for Pb/H₂SO₄/H₂O System

Kathryn R. Bullock*

Globe-Union Incorporated, Corporate Applied Research Group, Milwaukee, Wisconsin 53201

Potential-pH diagrams have been widely applied to electrochemical problems in corrosion, electrodeposition, and batteries. They summarize a large volume of data in a single graph and thereby provide a quick visual means of identifying the influence of potential and pH on the principal products of the reaction (1, 2).

One disadvantage of such a representation is that it is necessary to assume either that the metal ion does not complex with anions in the solution or that the activity of the anion remains fixed as the pH varies. Frequently, neither assumption is valid. A well-known example is the lead-acid battery in which the positive lead grid corrodes to form PbSO₄, basic lead-sulfates, and lead oxides (3). The relative predominance of these species is dependent on both the hydrogen ion activity and the sulfate ion activity, and these values vary as the battery charges and discharges. Furthermore, the PbSO₄ film produced when the grid corrodes inhibits diffusion of hydrogen and sulfate ions to the corroding lead interface, creating a concentration gradient across the corrosion film (4).

Potential-pH diagrams have been published assuming the log of the total sulfate ion activity to be 0 (5, 6), -4 (7), or -7 (6). Such assumptions are unnecessary if modern computer graphics methods are used to plot potential-pH diagrams in which the anion activity is represented as a third dimension. DISSPLA software (Integrated Software Systems Corporation), a Honeywell 6640 computer, and a Tektronix 4014 terminal were used to plot the three-dimensional diagram shown in Fig. 1 for the Pb/H₂SO₄/H₂O system. The pH is plotted on the x-axis, the negative log of the sulfate ion activity, pS, is plotted on the y-axis, and the standard hydrogen potential, E_h, is plotted on the z-axis. The stability region of each species is separately depicted as a solid figure in the three-dimensional box. By fitting these solid figures together much like the pieces in a three-dimensional puzzle, the complete diagram (Fig. 1g) is formed.

The electrochemical equilibria among all the compounds shown in Table I were considered. The diagram was then simplified by determining which compound forms at the lowest potential under each set of conditions and at what potential this compound oxidizes further. Table II shows the equations used to generate the lines in the simplified diagram. Below pH = 1.9, the equilibria involving HSO₄⁻ were used and above this pH the equilibria involving SO₄⁼ were used.

In all potential-pH diagrams, a region of immunity exists at low potentials where the metal does not corrode. The immunity region for Pb, defined by Eq. [1]-[5], is shown in Fig. 1h.

* Electrochemical Society Active Member.

Key words: acid, battery, thermodynamics, corrosion.

Above this region, the lead (II) species, Pb(OH)₂, 3PbO · PbSO₄ · H₂O, PbO · PbSO₄, and PbSO₄, can form (Fig. 1c, 1d, 1e, 1f, respectively). The tetrabasic lead sulfate, 4PbO · PbSO₄, is not stable with respect to the lead oxides at room temperature. Experimental uncertainties in the free energies of formation of the lead (II) oxides have produced conflicting opinions as to which is actually the most stable species [see for example Ref. (2), (5), and (8)]. Pb(OH)₂, which is most stable according to the equations in Table II, was chosen to represent all three lead (II) oxides shown in Table I.

Two lead (II) species, Pb(OH)₂ and 3PbO · PbSO₄ · H₂O will oxidize under basic conditions to Pb₃O₄ at a

Table I. Compounds in Pb/H₂SO₄/H₂O system

Pb
PbSO₄
PbO · PbSO₄
3PbO · PbSO₄ · H₂O
4PbO · PbSO₄
Pb(OH)₂
PbO (red)
5PbO · 2H₂O
Pb₂O₃
Pb₃O₄
PbO₂

Table II. Equations used in three-dimensional diagram

	Ref.
Eq. [1]. PbSO ₄ + H ⁺ + 2e ⁻ ⇌ Pb + HSO ₄ ⁻ E _h = -0.302 - 0.025 pH + 0.0295 pS	(6)
Eq. [2]. PbSO ₄ + 2e ⁻ ⇌ Pb + SO ₄ ⁼ E _h = -0.356 + 0.0295 pS	(6)
Eq. [3]. PbO · PbSO ₄ + 2H ⁺ + 4e ⁻ ⇌ 2Pb + SO ₄ ⁼ + H ₂ O E _h = -0.099 - 0.0295 pH + 0.0148 pS	(6)
Eq. [4]. 3PbO · PbSO ₄ · H ₂ O + 6H ⁺ + 8e ⁻ ⇌ 4Pb + SO ₄ ⁼ + 4H ₂ O E _h = 0.037 - 0.0443 pH + 0.0074 pS	(6)
Eq. [5]. Pb(OH) ₂ + 2H ⁺ + 2e ⁻ ⇌ Pb + 2H ₂ O E _h = 0.242 - 0.0591 pH	(5)
Eq. [6]. 4Pb ₃ O ₄ + 3SO ₄ ⁼ + 14H ⁺ + 8e ⁻ ⇌ 3[3PbO · PbSO ₄ · H ₂ O] + 4H ₂ O E _h = 1.605 - 0.1035 pH - 0.0222 pS	(6)
Eq. [7]. Pb ₃ O ₄ + 2H ₂ O + 2H ⁺ + 2e ⁻ ⇌ 3Pb(OH) ₂ E _h = 1.101 - 0.0591 pH	(5)
Eq. [8]. PbO ₂ + HSO ₄ ⁻ + 3H ⁺ + 2e ⁻ ⇌ PbSO ₄ + 2H ₂ O E _h = 1.628 - 0.0886 pH - 0.025 pS	(6)
Eq. [9]. PbO ₂ + SO ₄ ⁼ + 4H ⁺ + 2e ⁻ ⇌ PbSO ₄ + 2H ₂ O E _h = 1.685 - 0.1182 pH - 0.0295 pS	(6)
Eq. [10]. 2PbO ₂ + SO ₄ ⁼ + 6H ⁺ + 4e ⁻ ⇌ PbO · PbSO ₄ + 3H ₂ O E _h = 1.436 - 0.0886 pH - 0.0147 pS	(7)
Eq. [11]. 4PbO ₂ + SO ₄ ⁼ + 10 H ⁺ + 8e ⁻ ⇌ 3PbO · PbSO ₄ · H ₂ O + 4H ₂ O E _h = 1.285 - 0.0739 pH - 0.0074 pS	(6)
Eq. [12]. PbO ₂ + 2H ⁺ + 2e ⁻ ⇌ Pb(OH) ₂ E _h = 1.113 - 0.0591 pH	(5)

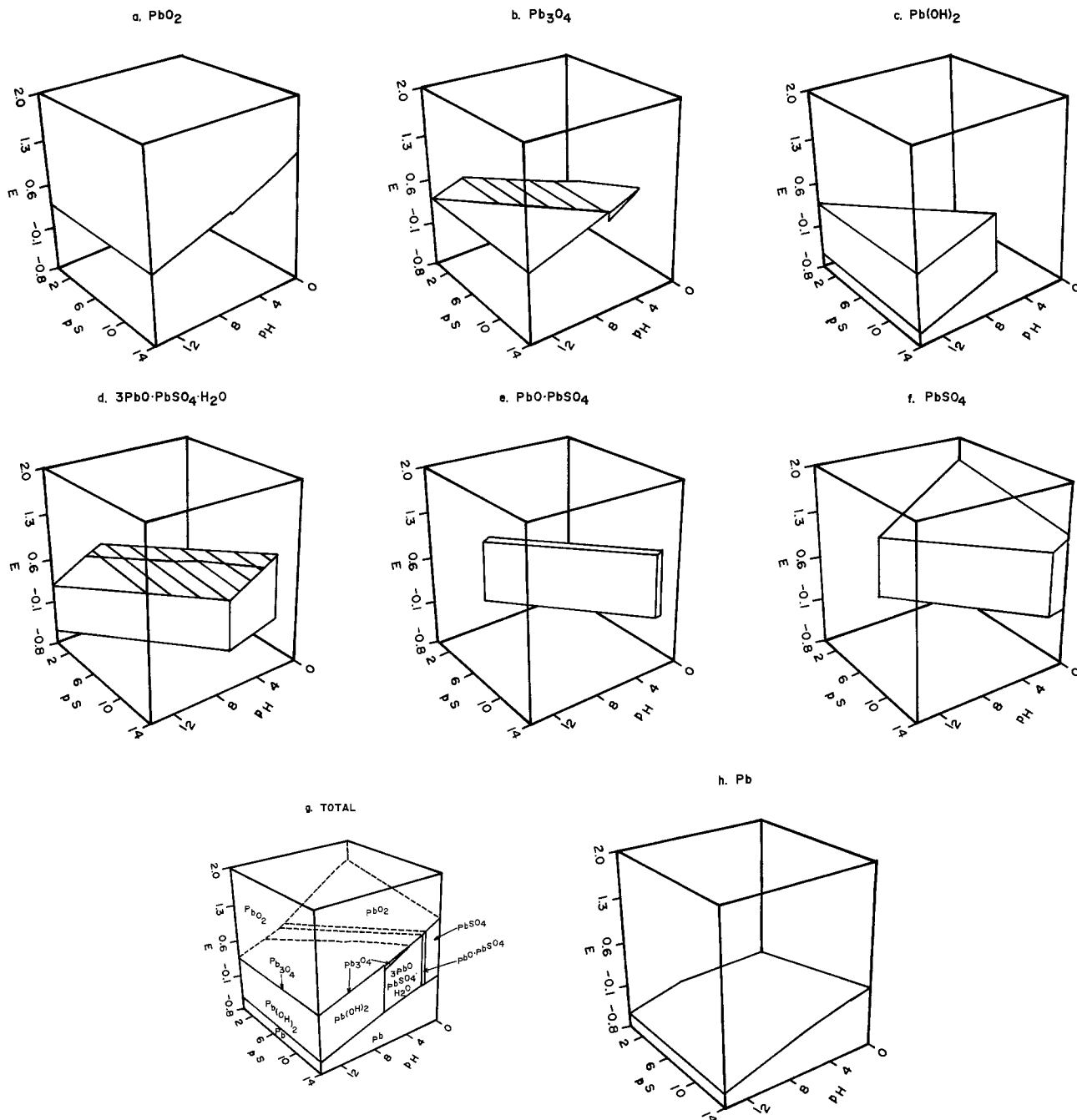


Fig. 1. Three-Dimensional diagram of $\text{Pb}/\text{H}_2\text{SO}_4/\text{H}_2\text{O}$ system with observer viewpoint at $\text{pH} = +19$, $\text{pS} = +25$, $E = +15$

slightly lower potential than they will oxidize to PbO_2 . This leads to the thin stability region for Pb_3O_4 shown in Fig. 1b, which is defined by Eq. [6], [7], [11], and [12]. The uncertainties in Eq. [6], [7], and [11] are larger than in the other equations in Table II and give rise to slight mismatches of the lines. This occurs because the experimental errors in the determination of the free energies of formation are multiplied by 3 for $3\text{PbO} \cdot \text{PbSO}_4 \cdot \text{H}_2\text{O}$ and by 4 for Pb_3O_4 in deriving Eq. [6], by 3 for $\text{Pb}(\text{OH})_2$ in deriving Eq. [7], and by 4 for PbO_2 in deriving Eq. [11]. The most obvious mismatch in the Pb_3O_4 diagram is between Eq. [6] and [7], evidenced by the sudden increase in the thickness of the figure at pS of 14 and pH of about 7. At higher pH values the figure is so thin that the bottom line (from Eq. [7]) and the top line (from Eq. [12]) are nearly indistinguishable.

Pb_2O_3 has a very small stability region within the Pb_3O_4 region. This is not shown in the figure because the equilibrium properties of Pb_2O_3 are not well known (5) and the uncertainties in the data are larger than the calculated stability region.

The PbO_2 stability region occurs at the top of the box (Fig. 1a) where the potentials are highest. No attempt has been made to differentiate between α - and β - PbO_2 , since at 25°C the free energies of these two polymorphs differ by only 4 kcal/mole (9). α - PbO_2 will form under basic conditions and β - PbO_2 under acidic conditions (6).

The competition among lead (II) species is strongly influenced by both the hydrogen and the sulfate ion activities. At low values of pS and pH , PbSO_4 predominates. As pS and pH increase, first $\text{PbO} \cdot \text{PbSO}_4$, then $3\text{PbO} \cdot \text{PbSO}_4 \cdot \text{H}_2\text{O}$, and finally $\text{Pb}(\text{OH})_2$ and PbO will form. In a lead-acid battery, the corrosion film consists of successive layers of these compounds as the pH and pS increase from the film/solution interface to the grid/film interface (6). This same conclusion can be reached by considering the effect of sulfate and hydrogen ion activities on the solubilities of the lead (II) compounds and assuming that the least soluble compound is the most stable in the corrosion film (10).

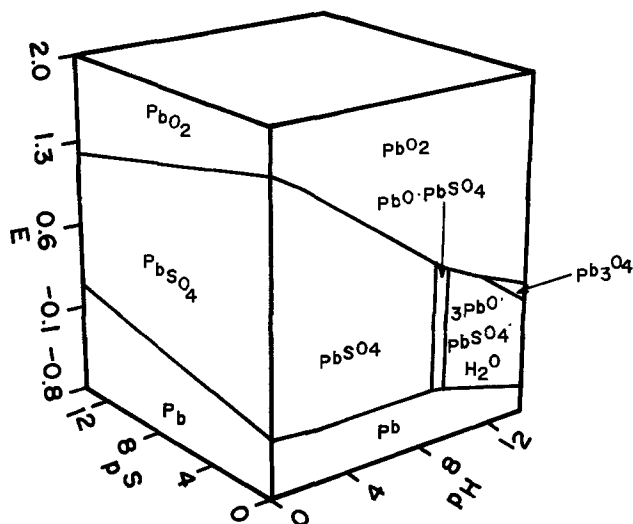


Fig. 2. Three-dimensional diagram of Pb/H₂SO₄/H₂O system with observer viewpoint at pH = -19, pS = -25, E = +15.

Figure 1g shows the stability regions from a viewpoint which emphasizes the conditions at the grid/film interface (high pH and pS). The left front wall, which is a potential-pS diagram at a pH of 14, shows that oxidation of lead will give Pb(OH)₂ and PbO at the grid/film interface. Further oxidation will give Pb₃O₄ and then α-PbO₂. These processes are independent of sulfate ion activity.

The right front wall is a conventional potential-pH diagram at a pS of 14. It is similar to previously published diagrams (5, 6) with pS values of 0 and 7. The principal effect of decreasing sulfate ion activity (increasing pS) is to shift the regions of predominance to lower pH values, thus favoring formation of the basic lead sulfates and lead oxides. For example, the pH at which Pb(OH)₂ can form changes from 14 when pS = 0 to 6.9 when pS = 14.

One advantage of computer graphics is that the viewpoint from which a three-dimensional diagram is observed can easily be changed. Thus, Fig. 2 shows the complete diagram turned around so that the conditions at the film/solution interface are emphasized. In this figure the potential-pH diagram for pS of 0 can be seen on the right front wall and compared to previously

published results (5, 6). The potential-pS diagram on the left front wall shows that at the corrosion film/solution interface at pH of 0, only Pb, PbSO₄, and PbO₂ can form and the product will depend on the potential. This is in agreement with the double sulfate mechanism for charge and discharge in a lead-acid battery (3, 7). The battery potential will decrease as pS increases.

No additional experimental data are required to derive a three-dimensional diagram of this type from a conventional potential-pH diagram. The computer programs used to plot these diagrams are short and easily understood. Thus the effect of the anion concentration on electrochemical equilibria need not be ignored.

Acknowledgments

The author is indebted to Globe-Union Incorporated for the support of this work and to W. Tiedemann for helpful discussions.

Manuscript submitted May 31, 1979; revised manuscript received Sept. 14, 1979.

Any discussion of this paper will appear in a Discussion Section to be published in the December 1980 JOURNAL. All discussions for the December 1980 Discussion Section should be submitted by Aug. 1, 1980.

Publication costs of this article were assisted by Globe-Union, Incorporated.

REFERENCES

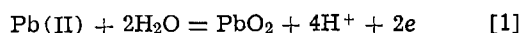
1. M. Pourbaix, "Lectures on Electrochemical Corrosion," Plenum Press, New York (1973).
2. M. Pourbaix, "Atlas of Electrochemical Equilibria," Pergamon Press, Oxford (1966).
3. J. Burbank, A. C. Simon, and E. Willihnganz, in "Advances in Electrochemistry and Electrochemical Engineering," C. W. Tobias, Editor, p. 157, Wiley-Interscience, New York (1971).
4. P. Ruetschi, *This Journal*, **120**, 331 (1973).
5. P. Delahay, M. Pourbaix, and P. Van Rysselberghe, *ibid.*, **98**, 57 (1951).
6. P. Ruetschi and R. T. Angstadt, *ibid.*, **111**, 1323 (1964).
7. H. Bode, "Lead-Acid Batteries," John Wiley, New York (1977).
8. W. M. Latimer, "Oxidation Potentials," Prentice-Hall, Englewood Cliffs, N.J. (1952).
9. R. T. Angstadt, C. J. Venuto, and P. Ruetschi, *This Journal*, **109**, 177 (1962).
10. K. R. Bullock, *ibid.*, **126**, 1848 (1979).

Pore Volumes and Densities of Lead Dioxide of Lead Acid Positive Plates

C. W. Fleischmann*

Eltra Corporation, C&D Batteries Division, Plymouth Meeting, Pennsylvania 19462

Previous reports (1, 2) discussed the porosity and density of unformed active material of positive plates for use in lead-acid batteries. The type of positive plate which had been studied used flat, cast, lead-alloy grids, into which the active material precursor was pressed as a paste. The pastes were made from acidified lead oxides (1, 3-5), or from tetrabasic lead sulfate (2, 6-7). After a curing step, the precursor was electrochemically oxidized to lead dioxide, the positive active material, according to Eq. [1]



* Electrochemical Society Active Member.

Key words: battery plates, electrode porosity, electrode density, lead-acid battery.

The porosity of the positive active material ultimately affects the battery performance (3, 5, 6, 8), and, therefore, is an important parameter of battery production. In the previous studies (1, 2), the pore volumes and dry paste densities were measured for unformed, cured pastes by a simple method. In the present study, the same experimental method was used to obtain values of the porosity and apparent densities of formed plates and of cycled plates.

Experimental

Acidified lead oxide plates were prepared variously from three commercial oxides and cured by different methods. The characteristics of the precursor oxides

(1, 9) and the compositions of the pastes after various cures (9) were given in earlier reports for duplicate plates of this same series. The apparent densities of the dry, unformed pastes varied from 3.4 to 4.8 g/cm³, and the specific void volumes ranged from 0.08 to 0.15 cm³/g. The symbol "D" will be used for the apparent density of the formed active material and the symbol "v" for the specific void volume. Percentage porosity is given by 100 Dv. The measured density of the active material (PbO₂) in the plate is represented by "d."

The plates were electrochemically formed to lead dioxide overnight at a sufficient charging rate to provide 80% more coulombs than required by Eq. [1]. After formation, the plates were cycled. Some plates were removed after formation and some after different numbers of cycles up to and including ten. Individual positive plates were cycled against two negatives in excess acid of 1.210 specific gravity. No separators were employed. Each positive was discharged to a polarization of 250 mV from the open-circuit value, measured using a positive lead-acid reference electrode (10, 11). Since the plates employed were of four different thicknesses, 0.18, 0.41, 0.68, and 0.79 cm, and since a range of paste densities were used, different currents were required to provide for discharge in approximately five hours. The plates were recharged at a constant current for 16-18 hr at a rate sufficient to provide a nominal 10% overcharge. The data are not identified in this report according to variations in plate thickness, cure, oxide type, or number of cycles, because correlations to these parameters could not be identified. On the other hand, the data are discussed in terms of apparent density of the active material and the void volumes as these parameters were found to be relevant.

Pore volumes were determined for all plates by the amount of water the plate absorbed under vacuum. The water absorbed was determined gravimetrically. The apparent density of the soaked plates was then determined by weighing in air and then submerged in water and applying Archimedes' Principle. The process was repeated after removing a determined mass of active material from the plate. From the measured values for the mass and volume of the material removed, it was possible to determine the apparent density of that active material. [The procedure was similar to that previously used to determine the pore volumes and densities of unformed positive material (1, 2).] Measurements were made on 63 plates including 11 of 0.18 cm thickness, 24 of 0.41 cm thickness, 9 of 0.68 cm thickness, and 19 of 0.79 cm thickness.

The active materials of four of the thinnest (automotive type) plates and of three of each of the plates of the other thicknesses were subsequently evaluated for density of the solids by the method of gas (helium) pycnometry using a Quantachrome Model PY-5. Eight of these samples were subsequently purified to remove sulfates and then reexamined by gas pycnometry. Sulfates were removed by boiling for 20 min in a solution 4.4M in ammonium acetate and 2.5M in acetic acid. The active material was analyzed for PbO₂ using an iodine titration. The pycnometry determinations and the PbO₂ analyses were performed as services by the Materials Testing Laboratory of C&D Batteries of Eltra Corporation.

Identification of the crystal form of PbO₂ by x-ray analysis was a service from the Materials Laboratory of the Prestolite Electrical Division of Eltra Corporation.

Evaluation of the data of Fig. 1 for a linear fit was developed by a curve-fitting program in the Standard Pac of the Hewlett Packard HP-97 desk calculator.

Results and Discussion

The apparent density, *D*, of the active material of each plate is plotted in Fig. 1 against the specific void volume, *v*. The curve drawn through the data points

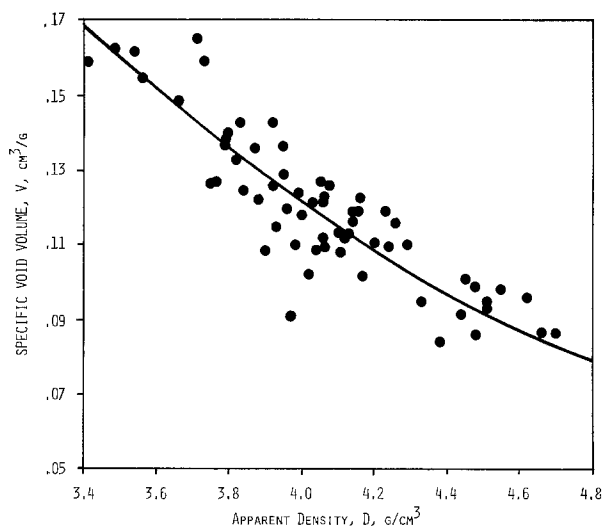


Fig. 1. The specific pore volumes of various formed or formed and cycled plates plotted against the apparent densities of the active material of the plates.

corresponds to a visual fit of these data to the curve obeying a constant value of 7.8 g/cm³ for the density, *d*, of the active material (PbO₂) of the positive plate. For a constant value of *d*, the values of *D* and *v* are fixed according to Eq. [2], which simply states that the total plate volume, *D*⁻¹, is the sum of the volume of the active material, *d*⁻¹, and the void volume, *v*

$$D^{-1} = d^{-1} + v \quad [2]$$

The standard deviation of *v* for a given *D* was estimated to be ±0.01 cm³/g which corresponds to a deviation of ±0.6 g/cm³ for *d*.

Analyses of these and other plates in the same series always showed that the PbO₂ was of the β-PbO₂ (rutile) structure and that the active material contained at most 10%, usually about 5%, of lead compounds in the lower oxidation state.

The literature gives a value of 9.63 g/cm³ for the density of β-PbO₂ (12). The most probable, and least dense, impurity found in cycled positive active material is the unconverted discharge product, PbSO₄, with a density of 6.323 g/cm³ (12). The expected density range for the PbO₂ in the plate, considering up to 10% PbSO₄ as an impurity, would be 9.30-9.63 g/cm³.

The evaluation of the solids' density of the 13 plates examined by gas pycnometry gave an independent and direct value of the active material density of 8.5 ± 0.4 g/cm³ (standard deviation). This value is in fair agreement with the value 7.8 ± 0.6 g/cm³ that conforms to the data of Fig. 1. Furthermore, when eight of the thirteen samples were subsequently chemically leached to remove sulfates, the mean density for these samples was essentially unchanged (8.6 ± 0.4 g/cm³). This result suggests that the estimate of sulfation by chemical analysis was, if anything, too high.

Since the low experimental values for the solids' density compared to the theoretical value could not be attributed to sulfate impurities, it is assumed that the PbO₂ in the electrochemically charged plates was of sufficiently poor crystalline perfection to provide the measured values.

Acknowledgments

This work was supported, in part, by Eltra Corporation's Prestolite Battery Division. Most of the experimental work was conducted by T. A. Bavaria, a co-op student from Drexel University, and by D. K. Bauman. K. Centrella is also acknowledged for the services of the C&D Materials Testing Laboratory.

Any discussion of this paper will appear in a Discussion Section to be published in the December 1980 JOURNAL. All discussions for the December 1980 Discussion Section should be submitted by Aug. 1, 1980.

Publication costs of this article were assisted by Eltra Corporation.

LIST OF SYMBOLS

- D apparent density of formed, or formed and cycled positive active material, in g/cm^3
 d measured density for the solids' portion of the positive active material, essentially PbO_2 , in g/cm^3
 v specific void volume of the positive active material, in cm^3/g

REFERENCES

1. C. W. Fleischmann and W. J. Schlotter, *This Journal*, **123**, 969 (1976).
2. W. J. Schlotter and C. W. Fleischmann, *ibid.*, **124**, 1487 (1977).
3. G. W. Vinal, "Storage Batteries," 4th. ed., John Wiley & Sons, Inc., New York (1967).
4. H. B. Stephensen, C. L. Hixon, H. S. Long, J. S.

5. H. Bode, "Lead-Acid Batteries," translated by R. J. Brodd and K. V. Kordes, John Wiley and Sons, Inc., N.Y. (1977).
6. R. V. Biagetti and M. C. Weeks, *Bell Syst. Tech. J.*, **49**, 1305 (1970).
7. C. F. Yarnell, Papers 31 and 32 presented at The Electrochemical Society Meeting, New York, N.Y., October 13-17, 1974.
8. H. R. Harner and M. F. Chubb, "Data for Storage Battery Design, Starting and Lighting Batteries, Number 6 in a Series," Eagle-Picher Co., Cincinnati, Ohio (1946).
9. B. P. Varma and C. W. Fleischmann, *This Journal*, **124**, 718 (1977).
10. E. Willihnganz, A. Howard, G. Mayer, and L. D. Zachau, Jr., Paper No. C75-193-8 presented at the IEEE Power Engineering Society Winter Meeting, New York, N.Y., January 26-31, 1975.
11. E. A. Willihnganz, U.S. Pat. 3,657,639 (1972).
12. J. Burbank, *This Journal*, **113**, 10 (1966).

A Technique for the Study of Flow Patterns in Electrolysis

M. S. Quraishi and T. Z. Fahidy*

Department of Chemical Engineering, University of Waterloo, Waterloo, Ontario, Canada

Flow patterns in liquid media have been widely studied by indirect methods, e.g., by suspended particles, interferometry, and Schlieren photographs; these methods have certain advantages but their major drawback, two-dimensional and/or abstract nature, renders the visualization of three-dimensional flow patterns rather difficult. For electrolysis, where three-dimensional flow patterns are usual, the electrolytic visualization technique, presented in this communication, is better suited for the study of flow-profile development and for the understanding of the dynamics of electrolytic flow phenomena. The proposed technique is illustrated by the specific case of natural convection in magnetically enhanced electrolysis where it has been found (1) that flow patterns differ appreciably from those observed in the absence of a magnetic field. Notably, some velocity components of electrolyte flow have a major effect on the dynamics of an electrolytic system (2) while in conventional electrolysis the effect of such components may be negligible. Proper understanding of flow behavior both in the bulk and in the vicinity of the electrodes, required for the study of the dynamics of the governing transport phenomena, makes the utilization of a nonabstract three-dimensional flow visualization technique imperative.

The essential advantage of the presented technique is that clear visual contrast due to color change is obtained via the passage of the same electric current used for electrolysis; moreover, the change in color is accompanied by a change in darkness and opaqueness. The bulk fluid is clear-light-yellow and the marked fluid flowing away from the cathode in the cell is opaque-dark-blue; thus, the boundary between the two fluid phases is continuously well defined. The color contrast is caused by strongly different local hydronium ion concentrations (the pH range for the Thymol-blue indicator is 1.2-2.8; $pK_{in} = 1.6$). The approach is a modification of the method of Baker (3) which has more than fifty different applications in heat transfer and fluid mechanics. The authors are not aware of any

major previous modification of the electrolyte solution used originally by Baker except for the alteration proposed by Gerrard (4) via the addition of a minute amount of NaCl to increase the intensity of the electrolytically produced dye. The color change due to locally different hydronium-ion concentrations has apparently

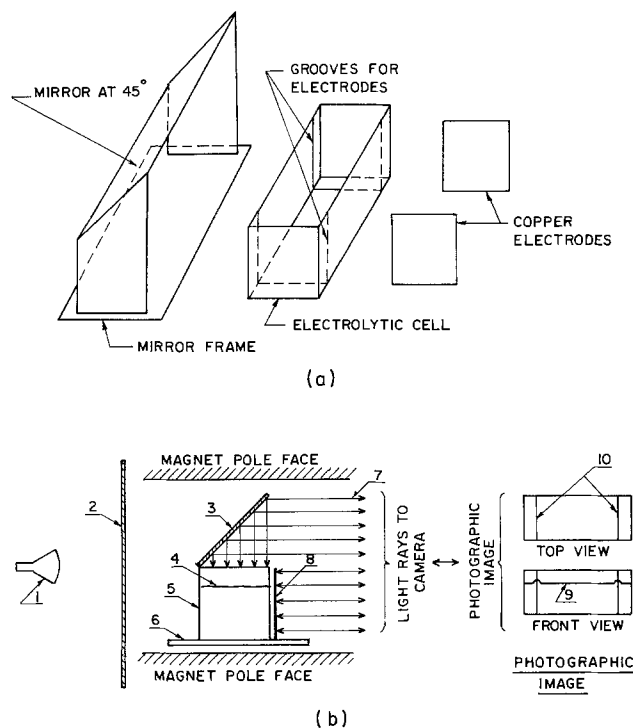


Fig. 1. Schematic diagram of the electrolytic cell assembly and the experimental setup. (a) parts of the electrolytic cell assembly; (b) experimental layout: 1. photo floodlight, 2. white light-diffusion screen, 3. mirror, 4. electrolyte surface, 5. electrolytic cell, 6. white light-diffusion card, 7. light rays to camera, 8. gray photographic filter, 9. electrolyte level, 10. electrode positions.

* Electrochemical Society Active Member.

not been employed for the study of fluid motion generated by electrolysis until the current investigation, although electrolytically induced color changes in voltammetric studies (5) have been observed.

Amongst various *a priori* possibilities considered, aqueous solutions containing Thymol blue, NaCl, and HCl were found best suited for this study, where high electric conductivity and low pH must simultaneously be maintained. Adding a small amount of concentrated Thymol-blue solution to a large volume of NaCl-HCl solution avoids difficulties during the preparation of electrolyte, such as precipitation due to low pH and common ion effects.

Figure 1 shows a schematic diagram of the experimental setup. The electrolytic cell is a five-sided rectangular box with an open top in which two vertical copper electrodes are fitted in parallel position against opposite walls. The cell assembly is placed inside a frame on whose top a mirror inclined at 45° toward the electrolyte surface is mounted. The entire assembly is placed between the pole faces of a regulated d-c electromagnet. Diffused photo-floodlight is provided from the back and photographic filters are used to match the exposure required for the top view through the mirror and for the direct front view of the electrolyte in the cell. Photographs were taken in a predetermined time sequence throughout each experiment, where the voltage drop across the cell and the magnetic field strength imposed transversely to the electric field are set to desired values. Figures 2-4, chosen out of about 2500 photographs, illustrate typical flow patterns in natural convection at vertical plates. At zero time a voltage drop of 2.5V was set between the pure copper electrodes. The electrolyte solution was made up of 0.1 g dm^{-3} Thymol blue, $0.998 \text{ mole dm}^{-3}$ NaCl, and $0.0025 \text{ mole dm}^{-3}$ HCl. The photographs show instantaneous flow patterns existing at 5, 30, and 120 sec, after start of electrolysis; each time instant is illustrated by one figure showing the effect of the imposed magnetic field

at the flux density of 0.004, 0.100, 0.285, and 0.540 Tesla. The upper part of each photograph gives the view of the electrolyte surface (top view) as seen through the mirror, and the lower part gives the front view of the electrolyte in the cell.

Since it is rather difficult to represent three-dimensional flow by two-dimensional images, the best recording via photographic means is by taking at the same time instantaneous pictures of the flow pattern at mutually perpendicular directions. In this manner three-dimensional structure may be visualized.

In discussing the complex nature of the flow pattern of the marked fluid leaving the cathode, reference is made to Fig. 5. The coordinate system is defined in the following manner: x -direction from cathode towards anode, z -direction from free surface toward bottom, and y -direction mutually perpendicular to both x and z .

Due to the physical nature of the cathode process under these operating conditions (current density at 5 sec about $120 \text{ A}\cdot\text{m}^{-2}$) the marked fluid rises at the cathode ($V_z < 0$) and reaches the free surface as seen in Fig. 2. At very low magnetic flux densities (residual field of 0.04T) the marked fluid travels on the free surface (xy plane) toward the cathode but with a V_y velocity component in the direction pointing away from the cell wall, thus creating two flows at the surface whose momentum exchange generates a flow in the z -direction (xz plane) as shown by the dark line in the upper view in Fig. 3a. The xz plane corresponding to this line may be denoted as the central plane. In this flow pattern V_z near the central plane is positive and near the walls negative. Motion in the y -direction extends from walls to the central plane near the free surface, and from central plane to walls in the vicinity of the cell bottom. V_x reaches a positive maximum at the free surface, then becomes progressively smaller as z increases; it finally becomes negative in the neighborhood of the bottom. As time progresses, this

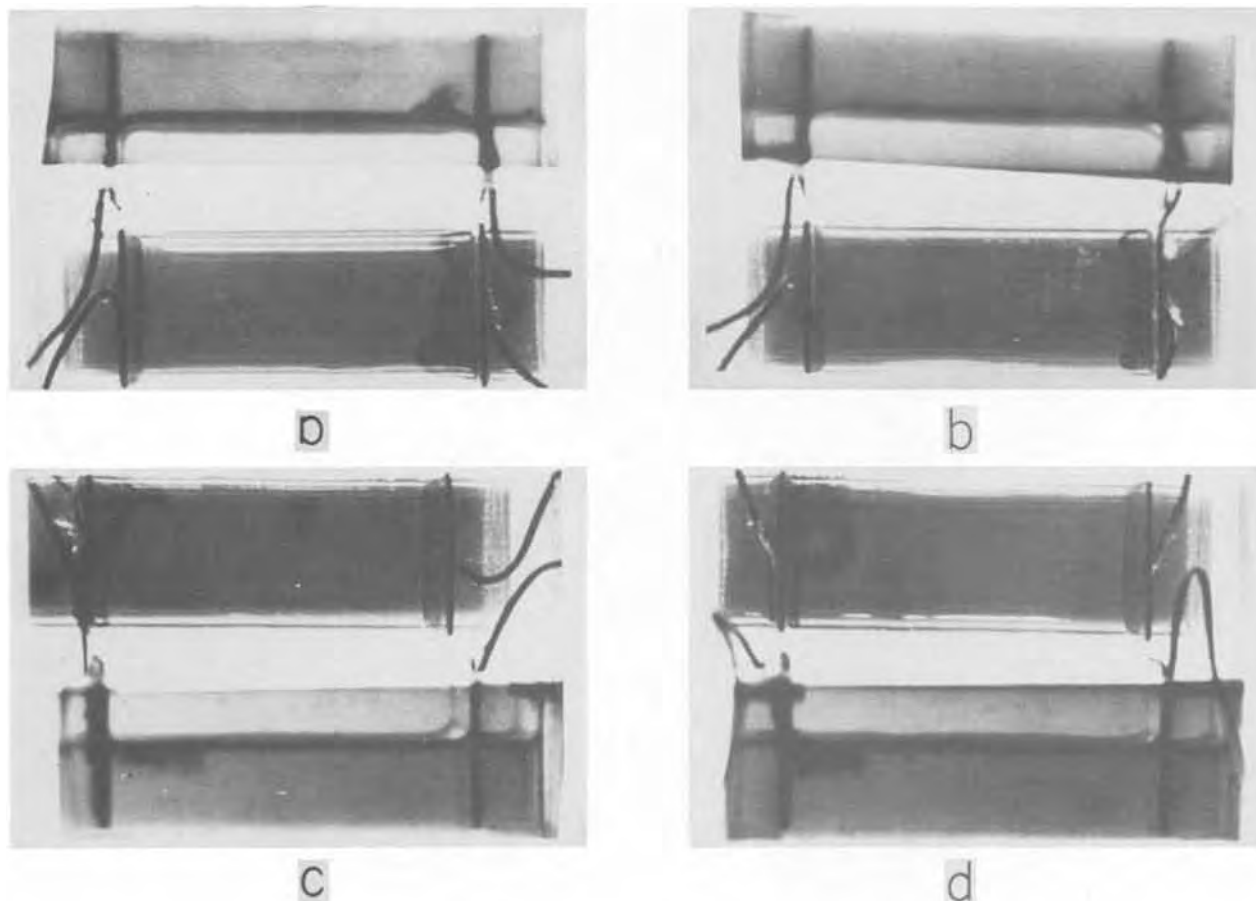


Fig. 2. Flow patterns in the electrolytic cell at various magnetic flux densities at 5 sec after the start of electrolysis. (a) 4 mT, (b) 100 mT, (c) 285 mT, (d) 540 mT.

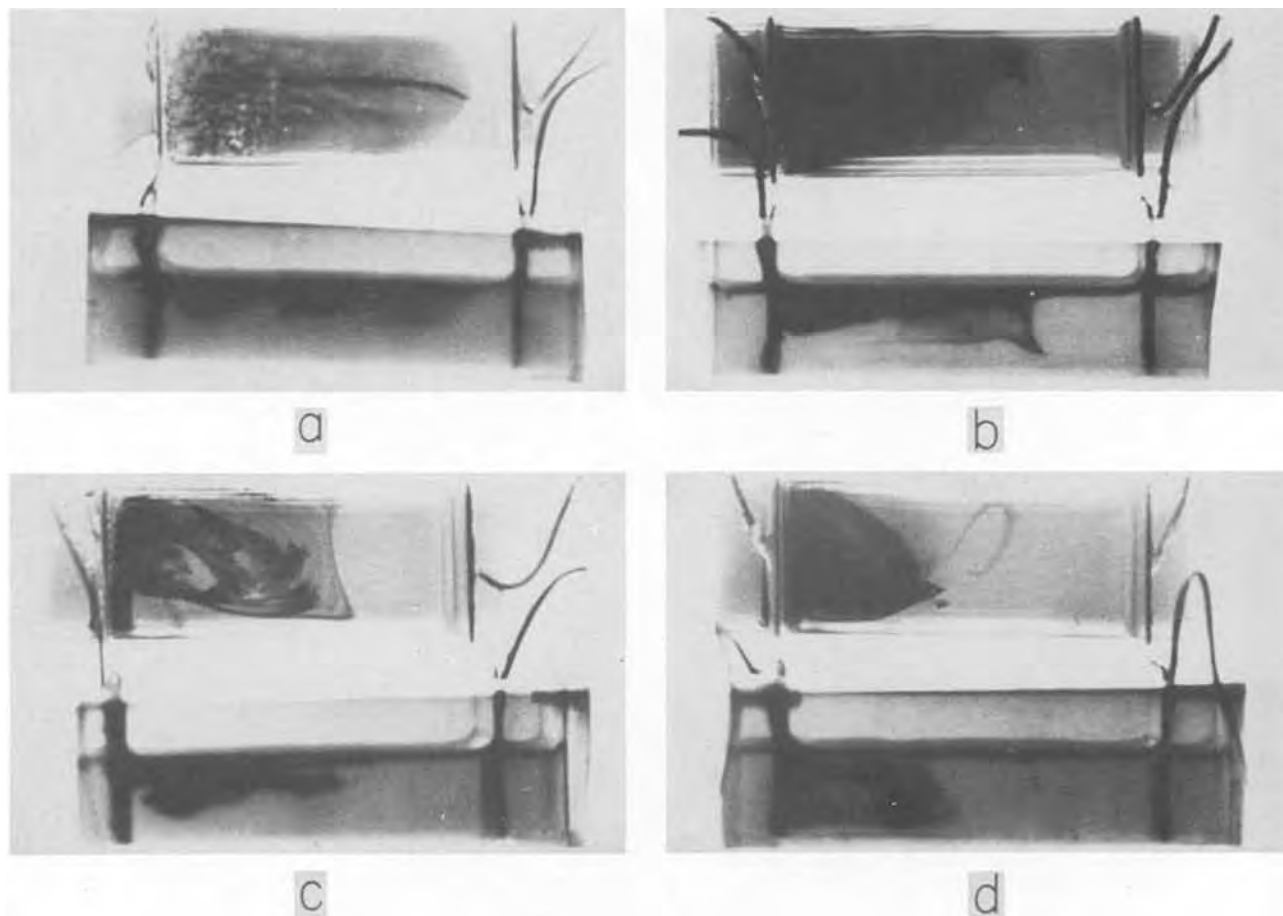


Fig. 3. Flow patterns in the electrolytic cell at various magnetic flux densities at 30 sec after the start of electrolysis. (a) 4 mT, (b) 100 mT, (c) 285 mT, (d) 540 mT.

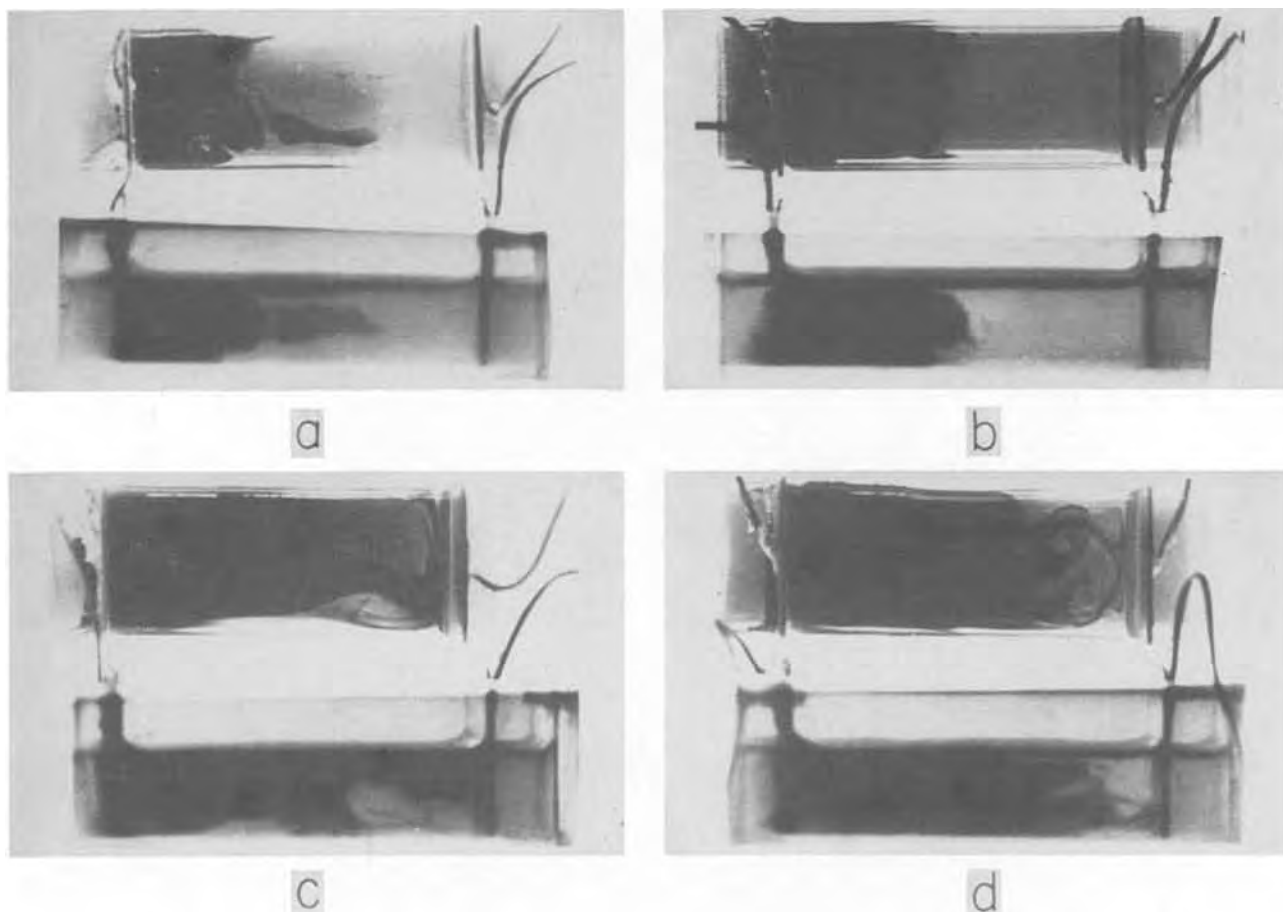


Fig. 4. Flow patterns in the electrolytic cell at various magnetic flux densities at 120 sec after the start of electrolysis. (a) 4 mT, (b) 100 mT, (c) 285 mT, (d) 540 mT.

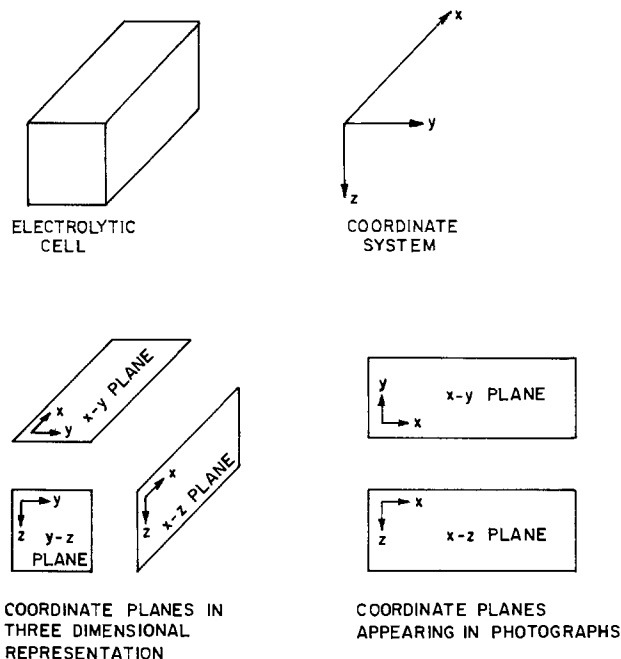


Fig. 5. Definition of the coordinate system and coordinate planes

development results in a typical pattern shown in Fig. 4a; the freshly marked fluid is confined to the cathode area. In the meantime, the "old" marked fluid becomes very faint and finally disappears due to diffusion of H ions from the bulk.

The imposition of a magnetic field will increase V_y in one direction and decrease it in the opposite direction, the net result being the displacement of the central plane towards one of the walls. Even at as weak a field as 0.1T, this distortion of V_y can be strong enough to suppress this velocity component in the opposite direction and the central plane essentially coincides with one wall. The stronger the magnetic field, the larger the magnitude of V_y as clearly seen in Fig. 2. The marked fluid no longer covers the entire free surface but it is confined to a triangle whose outer edge is defined by the marked fluid leaving the opposite edge of the cathode. As the magnetic field strength is in-

creased this triangle is formed increasingly faster but its size becomes smaller. The flow developed in this case is similar to the flow observed in very weak magnetic fields, with one cell wall virtually "replaced" by the central plane. Magnetohydrodynamic forces, due to combined electric/magnetic fields, generate faster motion and result in the expansion of the marked fluid confined to the cathode areas, as shown in Fig. 4.

The potential usefulness of this flow visualization technique is by no means restricted to magnetically enhanced natural convection, although this particular example is a very good illustration of its value. Fresh marking of the fluid is done continuously by the electrolytic process at the cathode and the coexistence of marked and unmarked fluids, and their travelling boundary can easily be observed. No "abstract" visualization is required and the possibility of motion misjudgment is minimized. The technique is equally promising for the study of flow patterns generated by different shapes and orientations of two-dimensional and three-dimensional electrodes and, in general, for various investigations of transport phenomena where the surface under study can be made cathodic for continuous marking of the fluid leaving the surface.

Acknowledgment

This research has been supported by a Natural Sciences and Engineering Research Council of Canada Grant and Postdoctoral Fellowship.

Manuscript submitted Aug. 7, 1979; revised manuscript received Oct. 5, 1979.

Any discussion of this paper will appear in a Discussion Section to be published in the December 1980 JOURNAL. All discussions for the December 1980 Discussion Section should be submitted by Aug. 1, 1980.

Publication costs of this article were assisted by the University of Waterloo.

REFERENCES

1. M. S. Quraishi, Ph.D. Thesis, University of Waterloo (1978).
2. M. S. Quraishi and T. Z. Fahidy, *Electrochim. Acta.*, In press.
3. D. J. Baker, *J. Fluid Mech.*, **26**, 573 (1966).
4. J. H. Gerrard, *ibid.*, **46**, 43 (1971).
5. K. S. V. Santhanam and A. J. Bard, *J. Am. Chem. Soc.*, **88**, 2669 (1966).



The Effect of Zirconium on the Isothermal Oxidation of Nominal Ni-14Cr-24Al Alloys

A. S. Kahn,¹ C. E. Lowell, and C. A. Barrett

National Aeronautics and Space Administration, Lewis Research Center, Cleveland, Ohio 44135

ABSTRACT

The isothermal oxidation of Ni-14Cr-24Al- x Zr, typical $\gamma/\gamma' + \beta$ alloys, was performed in still air at 1100°, 1150°, and 1200°C for times up to 200 hr. The zirconium content of the alloys varied from 0-0.63 atom percent (a/o). The oxidized surfaces were studied by optical microscopy, x-ray diffraction, and scanning electron microscopy. The base alloy was an alumina former with the zirconium-containing alloys also developing some ZrO₂. The addition of zirconium above 0.066 a/o increased the rate of weight gain relative to the base alloy. Due to oxide penetration, the weight gain increased with Zr content, however, the scale thickness did not increase. The Zr did increase the adherence of the oxide, particularly at 1200°C. The $\Delta W/A$ vs. time data fit the parabolic model of oxidation. The specific diffusion mechanism operative could not be identified by analysis of the calculated activation energies. Measurements of the Al₂O₃ scale lattice constants yielded the same values for all alloys.

The extent of adhesion of oxide scales to a substrate is one of the most important indicators of high temperature cyclic oxidation resistance of an alloy. Poor adhesion may result in spalling of the oxide to bare metal on cooling to room temperature. Good adhesion does not necessarily eliminate spalling, but restricts it to within the oxide layer and, in general, results in substantially lower metal consumption rates in cyclic tests.

A small addition of rare earth elements or reactive elements such as Si (1-6) has often resulted in a significant improvement of the cyclic oxidation resistance of alloys primarily by increasing scale adhesion. The mechanism(s) by which these tramp elements can improve oxide adhesion is not clearly understood. Several mechanisms have been proposed. In the mechanical pegging model (2, 4, 6) it has been proposed that oxide pegs are developed at the oxide-alloy interface which prevent oxide spallation during cycling. On the other hand, in the vacancy sink model (7) it has been proposed that formation of voids at the oxide-alloy interface leads to poor oxide adhesion. The added tramp elements are purported to prevent void formation and, therefore, enhance oxide adhesion. It has also been suggested that the added element might form stronger chemical bonds across the alloy-oxide interface (8). The subject of oxide adhesion has been treated by Wright (9) and by Giggins and Pettit (10) who included references up to 1975.

Recently Golightly *et al.* (11) proposed that in the absence of rare earth additions, oxide growth occurs within the existing layer and the lateral stresses resulting from this growth cause oxide detachment at the oxidation temperature which results in extensive spalling during cooling. Oxide growth within the existing layer was also assumed to be responsible for the

observed convoluted oxide configuration. Additions of yttrium may prevent oxide formation within the layer and thus cause the oxide growth to occur at the alloy-oxide interface. This would result in an adherent scale. Despite various models proposed to explain the enhanced oxide adhesion by tramp additions, it has not been possible as yet to rationalize all the observed oxidation characteristics of tramp-element containing alloys by any of these models.

Previous publications from NASA Lewis Research Center on the oxidation of Ni-Cr-Al alloys (12, 13) indicated that alloys melted in zirconia crucibles have significantly improved cyclic oxidation and hot corrosion resistance compared to comparable alloys with no significant zirconium. In view of these results it was decided to critically examine the role of zirconium in the high temperature oxidation resistance of Ni-Cr-Al alloys. As a first step, this paper describes the effect of small amounts of zirconium on the isothermal oxidation on a Ni-Cr-Al alloy. This composition was chosen as representative of a wide range of alumina-forming alloys with good cyclic oxidation resistances as was demonstrated in Ref. (12). In this paper the effects of zirconium on the isothermal oxidation of these alloys is described in terms of scale growth and adhesion. A detailed cyclic oxidation study is in preparation.

Materials

Chemical compositions and thermal histories of the alloys prepared for this investigation are presented in Table I. Compositions of the alloys were determined both by standard wet chemical methods and by atomic absorption spectroscopy. In Table I, compositions are expressed in both weight percent (w/o) and atom percent (a/o). The concentration of chromium varied from 12-19 a/o while that of aluminum varied from 22-26 a/o. The concentration of zirconium varied between 0 and 0.63 a/o. For the sake of simplicity in identification in this report and also to emphasize the

¹ Present address: Pratt & Whitney Aircraft, West Palm Beach, Florida 33402.

Key words: scale adhesion, scale spalling, aluminum oxide, nickel aluminum oxide.

Table I. Alloy designation, heat number, composition, and melt history of the Ni-Cr-Al test alloys with Zr additions

Alloy No.	Heat No.	Composition, (a/o)				Composition, (w/o)				Melt history	As-cast phases
		Ni	Cr	Al	Zr	Ni	Cr	Al	Zr		
I-(0)	5C	Bal.	13.89	25.74	0	Bal.	14.56	14.00	0	Certified Alloy master ingot	$\alpha, \beta, \gamma, \gamma'$
II-(0)	570-IN.	Bal.	12.22	22.07	0	Bal.*	12.49	11.70	0	Cannon Muskegon master ingot	$\alpha, \beta, \gamma, \gamma'$
II-(0)A	570-IN.	Bal.	12.22	22.07	0	Bal.*	12.49	11.70	0	Induction melted from II-(0) master ingot in alumina crucible and poured into zirconia leaf mold	$\alpha, \beta, \gamma, \gamma'$
III-(0.038)	6B	Bal.	19.17	24.40	0.038	Bal.	20.06	13.25	0.07	Induction melted from elemental constituents in zirconia crucible and poured into zirconia leaf mold	$\alpha, \beta, \gamma, \gamma'$
IV-(0.066)	5A-orig.	Bal.	14.35	23.65	0.066	Bal.	14.85	12.70	0.12	Same procedure as III-(0.038)	$\alpha, \beta, \gamma, \gamma'$
V-(0.33)	570-M-3	Bal.	12.30	23.17	0.33	Bal.	12.63	12.35	0.60	Induction melted from II-(0) master ingot in alumina crucible with 0.33 a/o Zr added and poured into zirconia leaf mold	$\alpha, \beta, \gamma, \gamma'$
VI-(0.63)	5A-HI-Z	Bal.	14.01	22.34	0.63	Bal.	14.32	11.85	1.13	Same procedure as III-(0.038) but held longer in crucible to pick up additional Zr	$\alpha, \beta, \gamma, \gamma'$

* Contains 1.5 w/o Fe picked up from steel mold.

variation of oxidation properties with zirconium content, the alloys studied have been represented by a general composition, Ni-14Cr-24Al-xZr, while the actual compositions are shown in Table I. The alloys will be referred to by the Roman numerals from Table I with the zirconium atom percent in parentheses. The Zr-free alloys were machined directly from vacuum induction melted master heat ingots or from these master ingots induction remelted in alumina crucibles. The alloys III-(0.038), IV-(0.066), and VI-(0.63) were vacuum induction melted using individual elements in zirconia crucibles and poured into zirconia leaf molds. These three alloys picked up Zr from the zirconia crucible. Alloy VI-(0.63) was held molten in the crucible for a longer time than usual which accounts for the higher pickup. An additional alloy V-(0.33) was induction vacuum remelted from a master ingot in an alumina crucible with 0.33 a/o Zr added to the melt and poured into a zirconia leaf mold. The phase diagram of the Ni-Cr-Al system is presented in Fig. 1 (14). The alloys tested are plotted on this ternary at their specific Cr and Al levels. The Zr composition is also listed.

Metallographic analysis on the alloys showed that they have similar structures. A typical photomicrograph is presented in Fig. 2. The structure is charac-

terized by γ (nickel solid solution), γ' (Ni_3Al type), and β (NiAl) phases with small particles of αCr (chromium solid solution) in the β phase. The presence of α , β , γ , and γ' and a possible segregation of zirconium in the matrix were investigated by SEM, EDS, and elemental x-ray scan. These procedures were performed on the alloy with the maximum Zr content in the series, i.e., VI-(0.63). The SEM micrograph of the alloy VI-(0.63) presented in Fig. 3 shows the cubic γ' phase in the matrix of γ and that αCr is randomly distributed in the β phase. The EDS spectra shown in Fig. 3 give the peak intensity for the wave lengths of the elements. These peaks are qualitative indication of relative abundance only. The elemental x-ray micrograph for zirconium did not show any zirconium enriched area (Fig. 3), although the spectrum trace showed that zirconium was present. It is therefore concluded that the tramp zirconium in the alloys studied is uniformly distributed and the solubility of zirconium in this class of alloys is in excess of 0.63 a/o.

Procedure

The isothermal oxidation of the Ni-14Cr-24Al-xZr type alloys was performed in static air. Oxidation coupons were $22 \times 10 \times 2$ mm with a hole drilled in one end for suspension in the ceramic tube furnace. Prior to testing, specimens were ultrasonically cleaned in alcohol. Isothermal oxidation experiments were carried out at several temperatures in the range 1000°-1200°C for periods of up to 200 hr. The specimens were suspended with a platinum hanger from a Mettler H-2

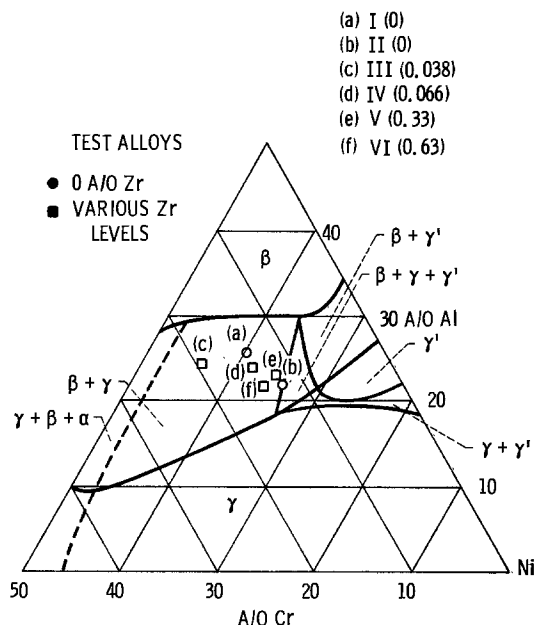


Fig. 1. The phase diagram of the Ni-Cr-Al system at 1150°C after Floyd and Taylor (14).

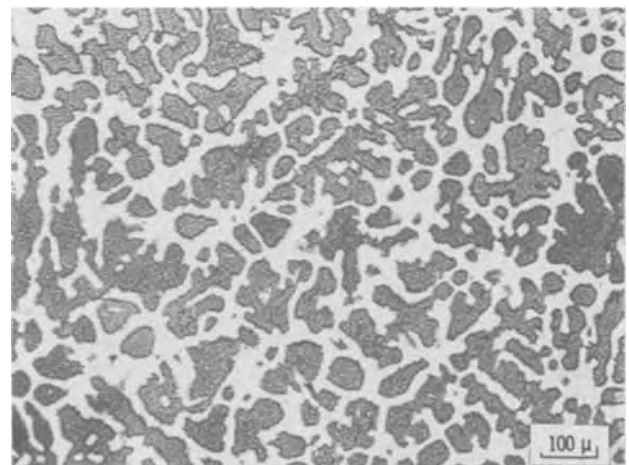


Fig. 2. Representative microstructure of Ni-14Cr-24Al-xZr. Here the concentration of zirconium is 0.066 a/o; alloy IV-(0.066).

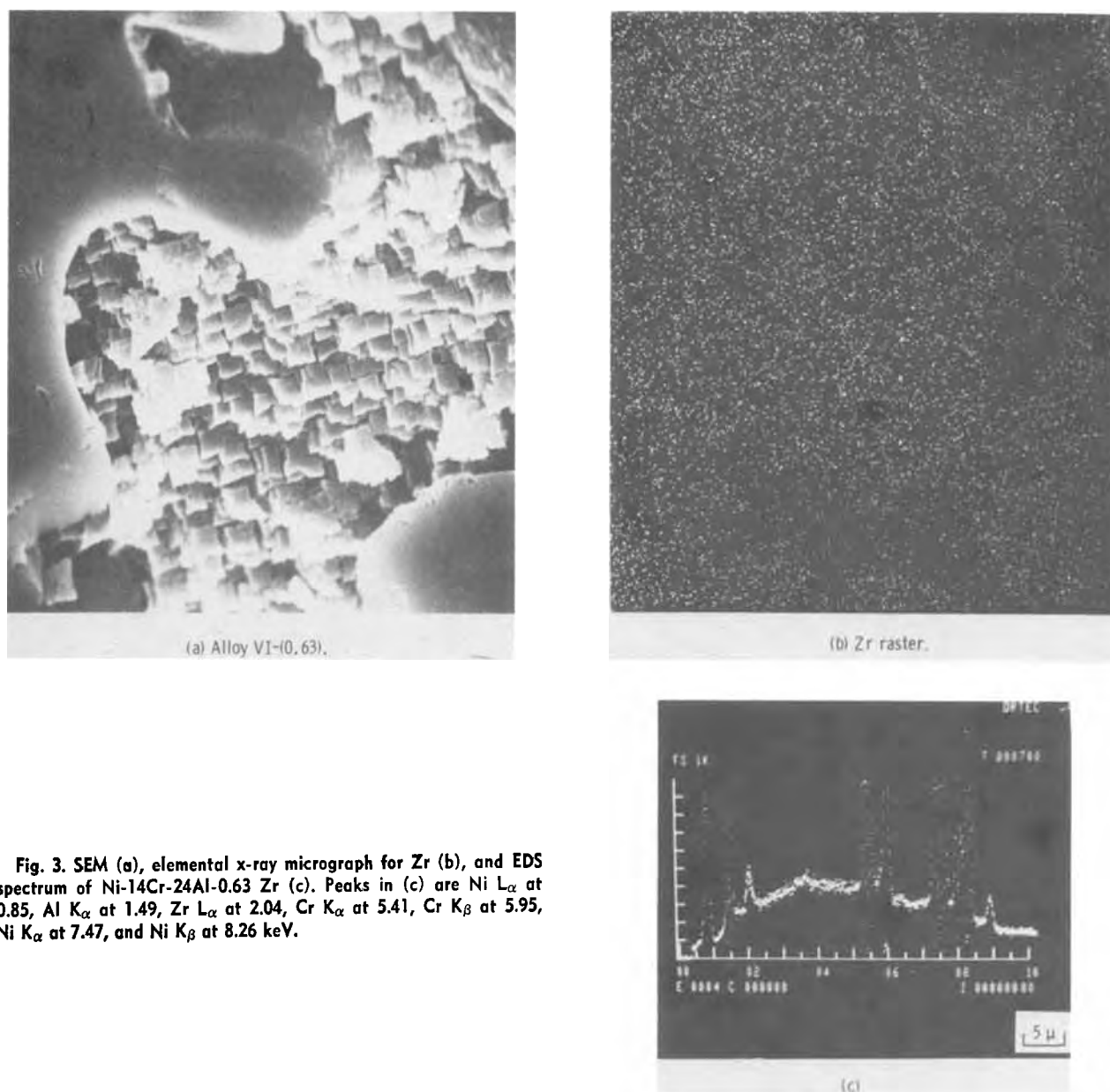


Fig. 3. SEM (a), elemental x-ray micrograph for Zr (b), and EDS spectrum of Ni-14Cr-24Al-0.63 Zr (c). Peaks in (c) are Ni L_{α} at 0.85, Al K_{α} at 1.49, Zr L_{α} at 2.04, Cr K_{α} at 5.41, Cr K_{β} at 5.95, Ni K_{α} at 7.47, and Ni K_{β} at 8.26 keV.

recording balance. At the start of the test the furnace was heated to the test temperature and oxidation was initiated by raising the furnace. The temperature of the furnace was controlled to within $\pm 2^{\circ}\text{C}$. At various time intervals, the weights of the specimens were obtained as a digital millivolt (mV) printout. The weight data were also recorded continuously on a strip chart recorder. Data were simultaneously printed on two channels and the weights obtained were generally within ± 0.1 mg of each other, but occasional variation of as much as 0.5 mg in the weight was observed between them. The maximum scatter in $\Delta W/A$ was about ± 0.1 mg/cm². In addition to this, there was a loss of platinum from the hanger due to volatilization at temperature. It was necessary to correct each weight change value for this loss. Blank experiments were performed with Pt-13Rh suspension rod at 1100°, 1150°, and 1200°C for 200 hr. The weight loss of the hanger was found to be nearly linear. The total weight loss of the hanger for 200 hr at 1100° and 1150°C was below 5 mg, but at 1200°C the weight loss was close to 10 mg. The loss of the suspension rod will depend on the quantity of material, test temperature, the temperature gradient to which it is exposed, and the subsequent condensation of the vaporizing species on the cooler part of the suspension rod. Therefore, the weight of the hanger rod was recorded at the beginning and at

the end of every experiment and with correction for the weight loss applied assuming a linear weight loss. From such corrected data, the parabolic scaling constants were calculated for 30.5 hr oxidation times. Weights at $t = 0$ hr were determined by back extrapolation.

At the completion of the test the furnace was rapidly lowered and the sample was surrounded by a Pyrex beaker to catch any spall as the sample cooled. This spall was subsequently analyzed by x-ray diffraction. To retain the scale formed at temperature, several samples were potted in a low melting point alloy (Cerrobend). These oxidized specimens were rapidly removed from the furnace and held in a cavity made from an aluminum block and potted by pouring molten metal around the hot sample. After cooling, the alloy mount was removed from the aluminum block and sectioned for examination.

Treatment of Data

Kinetic data obtained for the isothermal oxidation of the nominal Ni-14Cr-24Al-Zr alloys at 1100°, 1150°, and 1200°C were fitted to a parabolic model of oxidation. This model assumes the oxidation to be diffusion controlled. Mathematically, the expression is given by $\Delta W/A = k_p^{1/2} t^{1/2}$, where ΔW is the weight change at any time, t ; A is the area of the specimen; and k_p is

Table II. Summary of phases observed after isothermal oxidation of Ni-14Cr-24Al(Zr) in air for 200 hr

Alloy	Zr (a/o)	Temp, °C	Surface phases	Spall
VI-(0.63)	0.63	1200	Al ₂ O ₃ , NiAl ₂ O ₄ , ZrO ₂ *	Al ₂ O ₃ , NiO, NiAl ₂ O ₄ , ZrO ₂ *
VI-(0.63)	0.63	1150	Al ₂ O ₃ , NiAl ₂ O ₄ , ZrO ₂ *	Al ₂ O ₃ , NiO, NiAl ₂ O ₄ , ZrO ₂ *
VI-(0.63)	0.63	1100	Al ₂ O ₃ , NiAl ₂ O ₄ , ZrO ₂ *	Al ₂ O ₃ , NiO, NiAl ₂ O ₄ , ZrO ₂ *
V-(0.33)	0.33	1200	Al ₂ O ₃ , NiAl ₂ O ₄ , ZrO ₂ *	Al ₂ O ₃ , NiO, NiAl ₂ O ₄ , ZrO ₂ *
V-(0.33)	0.33	1100	Al ₂ O ₃ , NiAl ₂ O ₄ , ZrO ₂ *	Al ₂ O ₃ , NiO, NiAl ₂ O ₄ , ZrO ₂ *
IV-(0.066)	0.066	1200	Al ₂ O ₃ , Ni S.S. †, ZrO ₂ *	None detected
IV-(0.066)	0.066	1150	Al ₂ O ₃ , Ni S.S. †, ZrO ₂ *	None detected
IV-(0.066)	0.066	1100	Al ₂ O ₃ , Ni S.S. †, ZrO ₂ *	None detected
III-(0.038)	0.038	1200	Al ₂ O ₃ , Ni S.S.	None detected
III-(0.038)	0.038	1150	Al ₂ O ₃ , ZrO ₂ , Ni S.S.	None detected
III-(0.038)	0.038	1100	Al ₂ O ₃ , NiAl ₂ O ₄ , Ni S.S.	None detected
I-(0)	0	1200	Al ₂ O ₃ , Ni S.S.	Al ₂ O ₃
I-(0)	0	1100	Al ₂ O ₃ , Ni S.S.	Al ₂ O ₃

* ZrO₂: cubic and monoclinic.
† Ni S.S.: nickel solid solution.

the parabolic constant. The $\Delta W/A$ vs. time data were treated by a regression analysis which yielded $k_p^{1/2}$; standard error of estimate, σ ; and the coefficient of determination, R^2 . The regression equations and the computer programs for the calculation have been described by Barrett *et al.* (15). In most cases the fit was excellent with R^2 values over 0.90. At all temperatures the $k_p^{1/2}$ (and therefore k_p) values were evaluated using all the data up to 30.5 hr.

The $k_p^{1/2}$ estimates derived from the shorter time data were used to compute the expected $\Delta W/A$ values at both 30.5 and 200 hr. These values ($\Delta W/A_{calc.}$) are listed along with the actual observed values ($\Delta W/A_{obs.}$) where available for comparison.

Results and Discussion

Metallographic and x-ray analyses.—The surface and the spalled oxides were analyzed by x-ray diffraction (XRD). Oxidized surfaces were also characterized by metallography and SEM. The results of XRD are shown in Table II, from which it is seen that alumina was the primary oxide formed in the temperature range 1100°–1200°C. In addition to Al₂O₃, some ZrO₂ (cubic and monoclinic) and the spinel NiAl₂O₄ ($a_0 = 8.10\text{\AA}$) were also formed on the alloys containing Zr. Photomicrographs obtained from alloys IV-(0.066) and V-(0.33) tested at 1150°C, and which were cooled in air, are shown in Fig. 4. The structure shown in Fig. 4 is characterized by the presence of oxide penetration and is typical of the alloys containing Zr. Oxide penetration increased considerably with the Zr content of the alloy and with temperature. The zero zirconium alloy did not show any oxide penetration. Metallography to obtain the total oxide scale along with oxide penetration was difficult due to external scale spalling during cooling. In order to observe the total scale, certain samples containing 0, 0.066, and 0.63 a/o Zr were potted in a low melting point alloy (Cerrobend) which prevented the scale from spalling during cooling. A cross section of the scales in the Cerrobend mount is shown in Fig. 5 for alloys containing 0, 0.036, and 0.63 a/o Zr. An examination of Fig. 5 shows that the oxide scales of all the alloys appeared to have been retained by this procedure. It may also be seen that the alloys exhibit an oxide penetration which increases with Zr content, while the outer scale thickness was nearly independent of Zr content. This would indicate that the increase in oxidation kinetics (see below) is due primarily to increases in oxide penetration rather than scale growth.

SEM and elemental x-ray micrographs of the V-(0.33) alloy at 1200°C are presented in Fig. 6. An examination of Fig. 6 reveals that no Zr is concentrated near the surface. Al₂O₃ penetrates from the surface to a depth of about 50 μm . Zr concentration away from the surface appears to be associated with the alumina

penetration. This microstructure is typical of all Zr-containing alloys.

Kinetic data.—The specific weight change ($\Delta W/A$) data are plotted in Fig. 7. The test temperatures represented are 1100°, 1150°, and 1200°C and times are to 200 hr. Duplicate runs were plotted in several cases



Fig. 4. Oxide penetration in Ni-14Cr-24Al-xZr. Zr contents for (a) and (b) are 0.066 and 0.33 a/o, respectively. Specimens were isothermally oxidized for 200 hr at 1150°C.

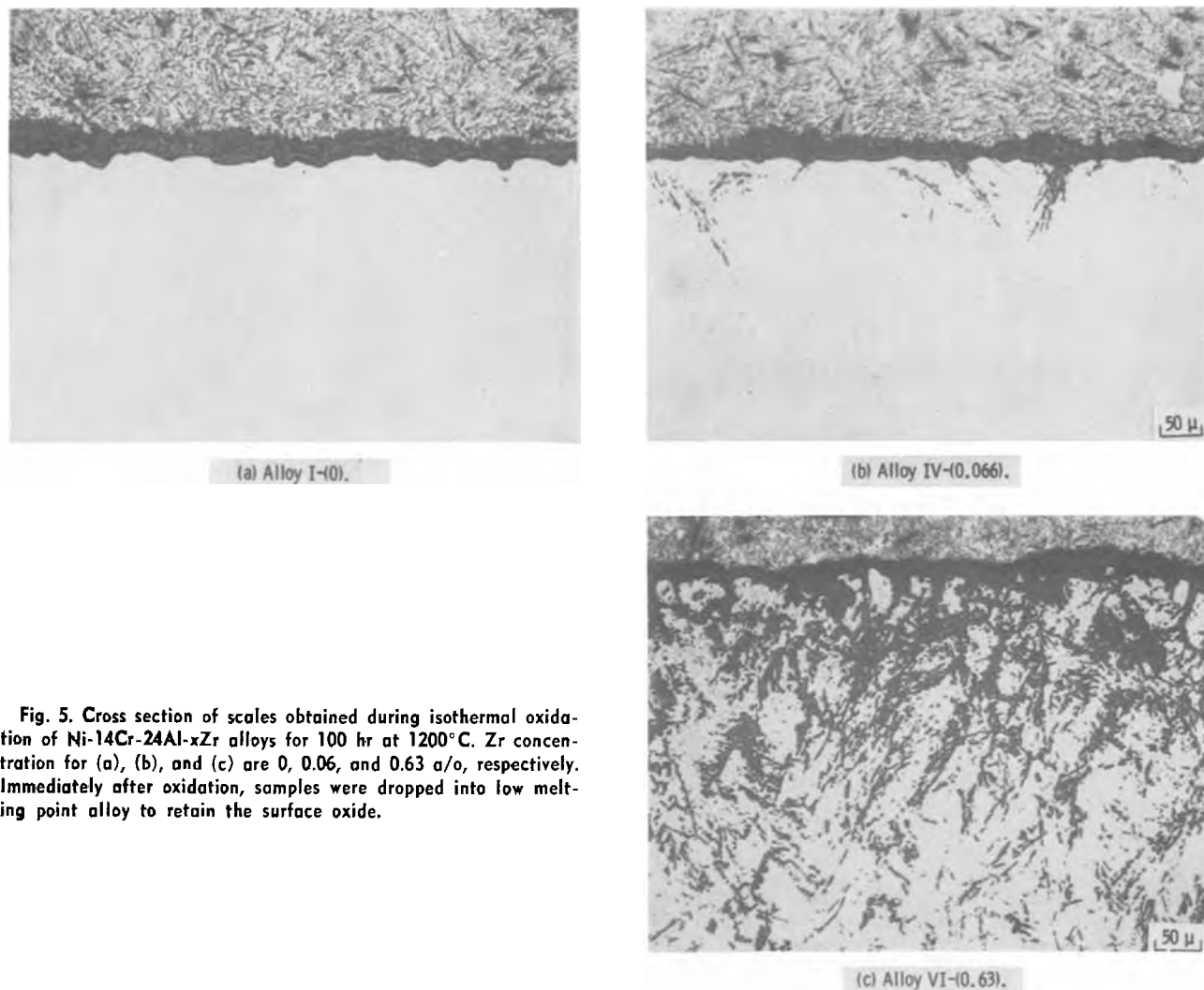


Fig. 5. Cross section of scales obtained during isothermal oxidation of Ni-14Cr-24Al-xZr alloys for 100 hr at 1200°C. Zr concentration for (a), (b), and (c) are 0, 0.06, and 0.63 a/o, respectively. Immediately after oxidation, samples were dropped into low melting point alloy to retain the surface oxide.

to allow an evaluation of over-all variability. The derived parabolic kinetic constants are listed in Table III and the average k_p 's are plotted in Fig. 8. At 1150° and 1200°C, k_p became slightly smaller as Zr increased to 0.038 a/o. Further increases in Zr content resulted in large increases in the calculated k_p . As noted above, this increase in weight gain is primarily associated with

increasing oxide penetration rather than with an increased scale growth. Since such oxide penetration represents a major portion of the total change in weight, the parabolic scaling constants derived from alloys with substantial oxide penetration cannot be used to calculate scale thickness. However, they can be used to determine total metal consumption.

Table III. Parabolic fit of Ni-14Cr-24Al alloys with various Zr levels based on 0-30.5 hr isothermal data (weight change corrected for Pt hanger loss)

Alloy	n	Temp, °C	$k_p^{1/2}$	k_p	R^2	S.e.e. (σ)	30.5 hr values		200 hr values	
							$\Delta W/A_{obs.}$	$\Delta W/A_{calc.}$	$\Delta W/A_{obs.}$	$\Delta W/A_{calc.}$
VI-(0.63)	28	1200	1.23048	1.51408	0.999	0.16	6.96	6.80	21.87	17.40
VI-(0.63)	28	1200	1.14138	1.30275	0.999	0.14	6.51	6.30	—	16.14
V-(0.33)	28	1200	0.685079	0.46933	0.999	0.06	3.89	3.78	11.86	9.69
V-(0.33)	28	1200	0.679313	0.461461	0.998	0.10	3.85	3.75	12.36	9.61
IV-(0.066)	28	1200	0.103860	0.010787	0.885	0.14	0.83	0.57	1.89	1.47
IV-(0.066)	28	1200	0.109357	0.011959	0.993	0.03	0.56	0.57	1.99	1.55
III-(0.038)	28	1200	0.0862657	0.0074418	0.960	0.06	0.50	0.48	1.53*	1.22
II-(0)	28	1200	0.185208	0.0343020	0.998	0.03	1.05	1.02	2.12	2.62
II-(0)a	28	1200	0.157356	0.0247609	0.988	0.06	0.87	0.87	—	2.23
II-(0)a	28	1200	0.135513	0.0183638	0.978	0.07	0.75	0.75	1.67	1.92
I-(0)	28	1200	0.134886	0.0181942	0.981	0.07	0.84	0.74	1.89	1.91
I-(0)	28	1200	0.244586	0.0598223	0.995	0.06	1.37	1.35	2.99	3.46
VI-(0.63)	28	1150	0.544536	0.296519	0.999	0.05	3.03	3.01	7.99	7.70
V-(0.33)	28	1150	0.349995	0.122496	0.999	0.04	2.02	1.93	5.09	4.95
IV-(0.066)	28	1150	0.120840	0.0146023	0.977	0.07	0.62	0.67	1.63	1.71
III-(0.038)	28	1150	0.0434558	0.0018884	0.979	0.02	0.26	0.24	0.84	0.61
II-(0)	28	1150	0.087964	0.0077377	0.973	0.05	0.48	0.49	1.43	1.24
VI-(0.63)	28	1100	0.271039	0.0734621	0.986	0.12	1.41	1.50	2.98	3.83
V-(0.33)	28	1100	0.119832	0.0143597	0.983	0.06	0.74	0.66	1.94	1.69
IV-(0.066)	28	1100	0.103906	0.0120793	0.969	0.07	0.61	0.61	1.35	1.55
III-(0.038)	28	1100	0.0486002	0.0023620	0.973	0.03	0.24	0.27	0.53	0.69
II-(0)a	28	1100	0.0295981	0.00087604	0.896	0.04	0.16	0.16	0.68	0.42
I-(0)	28	1100	0.0465930	0.0021709	0.968	0.03	0.25	0.26	—	0.66

* 190.5 hr.

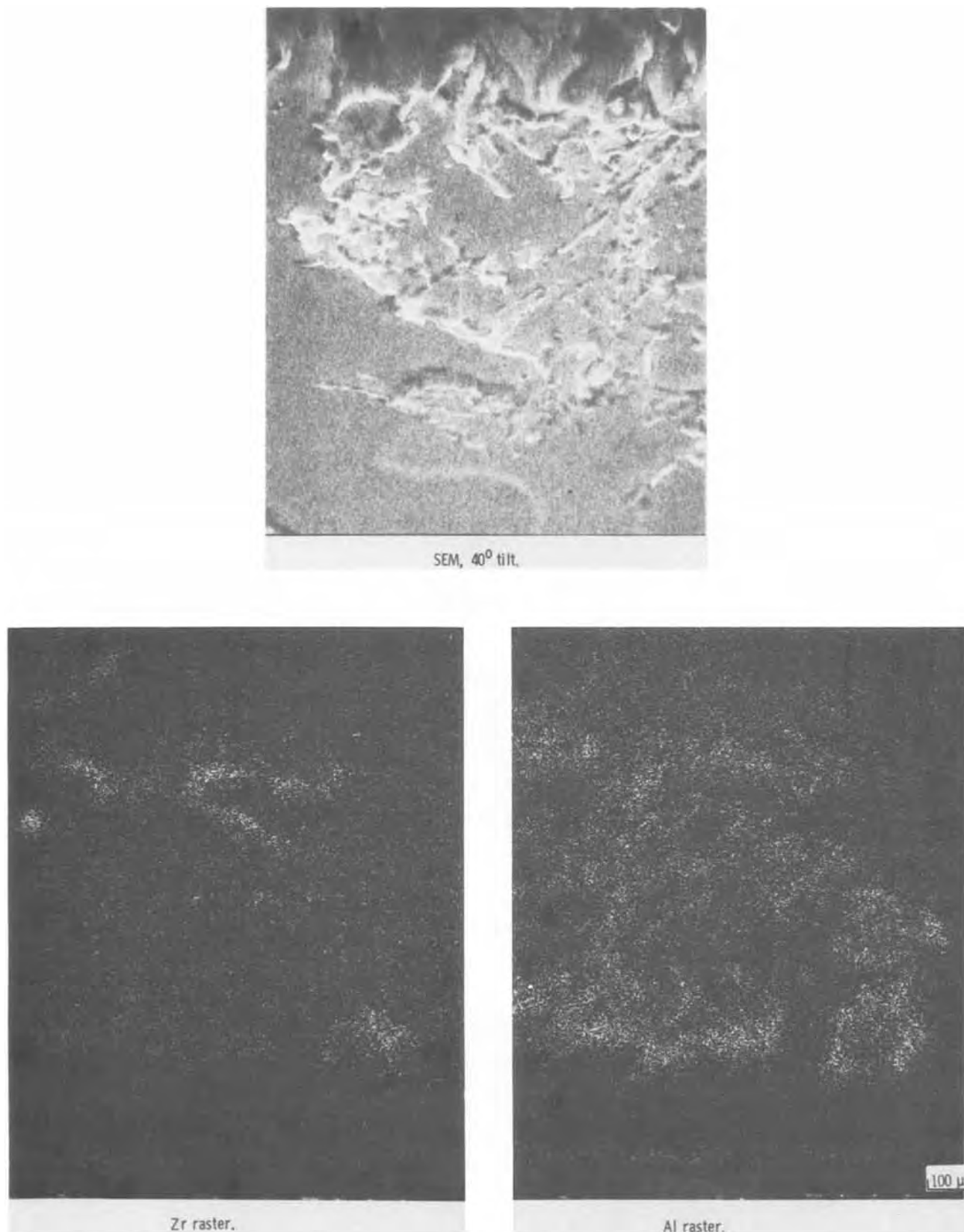


Fig. 6. Distribution of Al and Zr on Ni-14Cr-24Al cross section after 200 hr at 1200°C (0.33 a/o Zr); 1500×

In an attempt to evaluate the temperature dependence of the short time (30.5 hr) k_p values in light of the diffusion of Al and O in Al_2O_3 , the data were plotted as k_p vs. $1/T$ in Fig. 9 and activation energies computed. For comparison, diffusion data of Paladino and Kingery (16, 17) and Oishi and Kingery (18) are also plotted on Fig. 9. In addition, data up to 48 hr for the oxidation of a pure NiCrAl alloy reported by Giggins and Pettit (19) are plotted. Except for alloy

IV-(0.066) the activation energies derived from the present study are remarkably consistent (see Table IV). The activation energies range from -114 to -123 kcal/mole [except for alloy IV-(0.066)] and are consistent with the data of Giggins and Pettit (19). Unfortunately, little insight can be gained from these data in regard to which diffusing species is controlling oxidation as the activation energies calculated are similar to those for both Al and O in polycrystalline

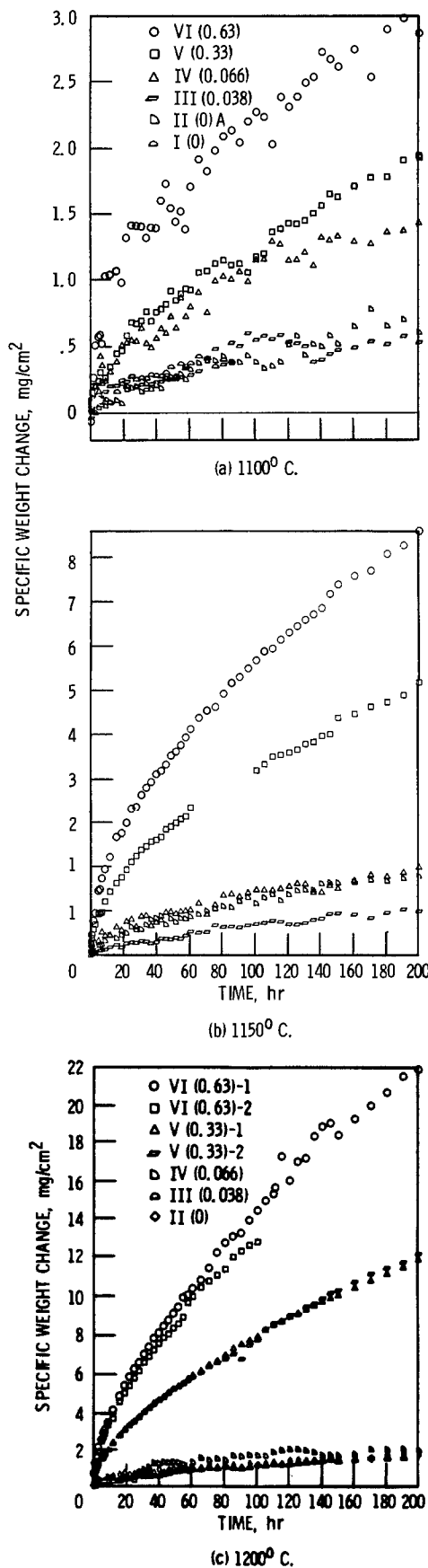


Fig. 7. Selected specific weight change vs. time plots for Ni-14Cr-24Al alloys with various Zr levels at (a) 1100°C, (b) 1150°C, and (c) 1200°C in still air.

Al_2O_3 at high temperatures (17, 18). The data for alloy IV-(0.066) are anomalous. The k_p is nearly independent of temperature which could indicate a change in oxidation or diffusion mechanism. How-

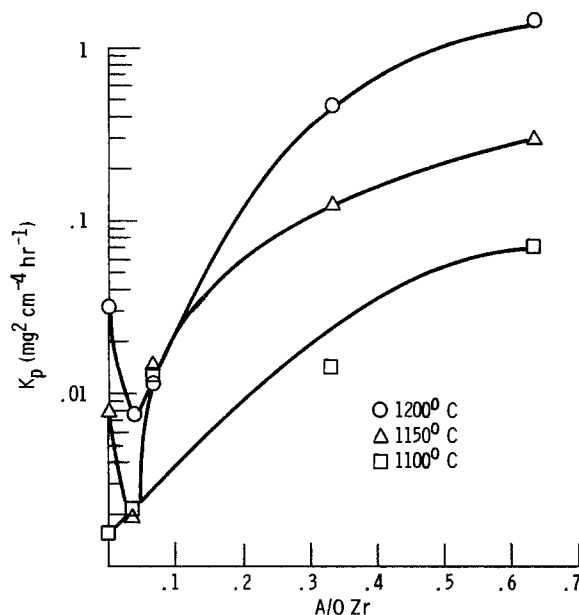


Fig. 8. Average parabolic scaling constants of nominal Ni-14Cr-24Al alloys as a function of Zr content. The k_p values are computed from data up to 30.5 hr.

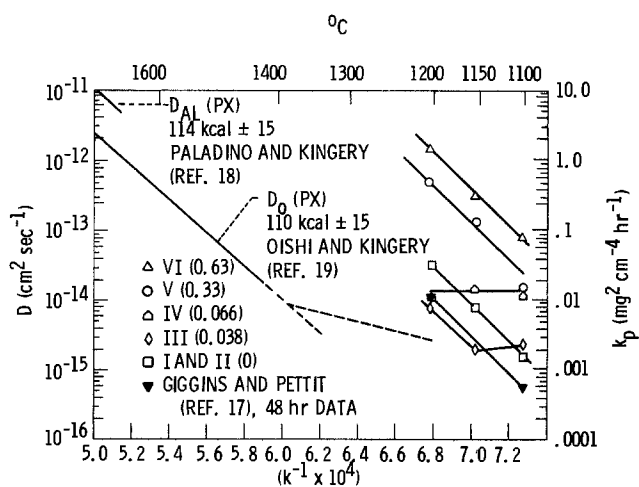


Fig. 9. Comparison of the average parabolic scaling constant of NiCrAl alloys with Al and O diffusion rate constants in Al_2O_3 . NASA k_p values are computed from data up to 30.5 hr.

ever, at this Zr concentration, the oxides formed were essentially the same based on the analyses performed for all temperatures. In addition, microstructural examination of this alloy revealed substantially the same oxide penetration regardless of temperature (see Fig. 10). This effect deserves further attention.

Oxide adhesion.—The kinetics of scale formation are an important part of the oxidation process. Equally important, however, in cyclic oxidation is the role of

Table IV. Calculated oxidation activation energies in the 1100°-1200°C range for some NiCrAl(Zr) alloys 30.5 hr data

Alloy	-E (kcal/mole)
I and II-(0)	121.7
III-(0.038)*	114.0
IV-(0.066)	~0
V-(0.33)	117.8
VI-(0.63)	118.7
Giggins and Pettit†	122.9

* 1100°C point not included.

† 48 hr data obtained on Ni14Cr13Al alloy (17).

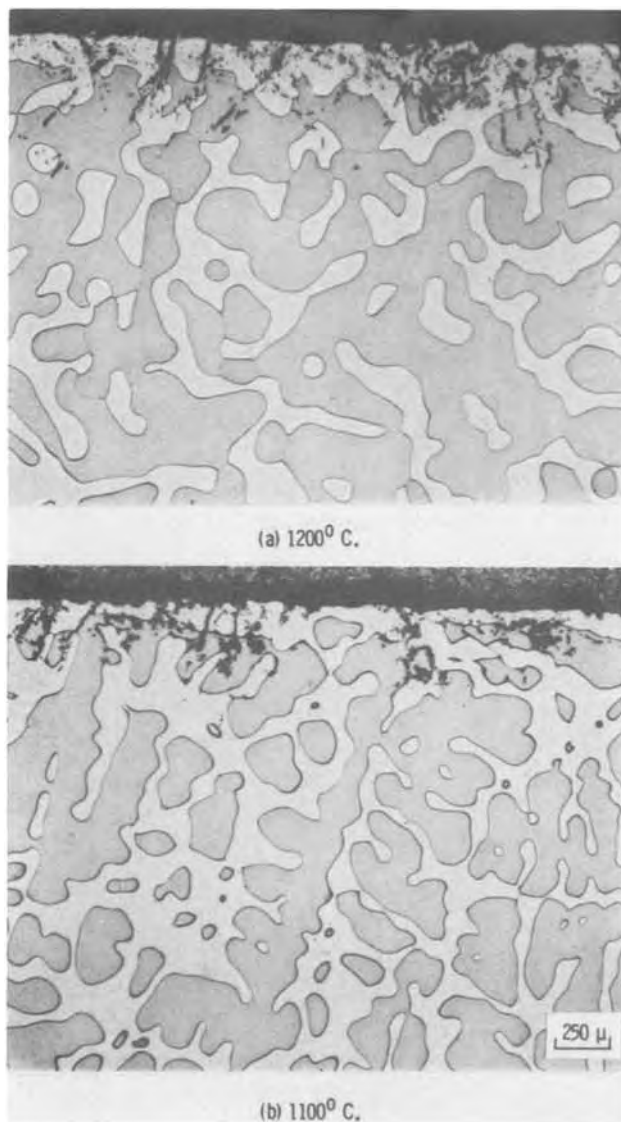


Fig. 10. Microstructure of IV-(0.066) after 200 hr in air oxidation

oxide adhesion and spalling. While these tests were not aimed specifically at the latter phenomena, the changes in oxide adhesion with zirconium were dramatic. Figures 11(a) through (f) show SEM photographs of the surface of I-(9), IV-(0.066), and V-(0.33) after 200 hr in air at 1200°C. The I-(0) sample shows spalling to bare metal over major portions of the surface. The remaining oxide is convoluted and is only in partial contact with the metal. This Al_2O_3 scale morphology is quite similar to that found by Golightly (11) and perhaps is an indication of his lateral growth stress mechanism.

The SEM photographs of IV-(0.066) and V-(0.33) show that what spalling has taken place is all within the oxide, i.e., no bare metal spalling. These two alloys appear to spall as small platelets of sheets of oxide resembling mica. This behavior is most strikingly observed on the surface of the V-(0.33). Of all

the alloy levels of Zr tested, the minimum amount of spall collected was for the alloys III-(0.038) and IV-(0.066) where not enough could be collected after any temperature test to run a diffraction pattern. These results are consistent with those found by Allam *et al.* (20) in their examination of the effects of hafnium additions on the oxidation of cobalt-chromium-aluminum. They demonstrated that hafnium increased oxide adhesion and prevented spalling to bare metal. They also found that hafnium additions led to Al_2O_3 oxide penetration and attributed the increased scale adhesion to such penetrations or "pegs."

The pegging explanation is consistent with the microstructural observations both in Ref. (20) and the current work. However, it does not account for either the elimination of oxide-metal interface voids or the evident reduction of lateral growth stresses in the oxide which are present in the pure alloys. It appears, therefore, that the hafnium effect on cobalt-chromium-aluminum alloys is the same as that of zirconium on nickel-chromium-aluminum, but the mechanism remains unclear.

It seems likely that Zr is present in the oxide and is the cause for the increased diffusion of oxygen through the scale which is evidenced by the increases in k_p and the formation of oxide penetration. However, no direct evidence for Zr solution in the Al_2O_3 scale was found. Lattice constant measurements of the Al_2O_3 formed during selected tests were made. These data are tabulated in Table V along with lattice constants from a pure Al_2O_3 powder. No significant differences were found. Therefore, any solutioning effects which occur must be quite small, i.e., below the levels of x-ray detectability. More detailed investigations of the structure of adherent and nonadherent Al_2O_3 must be made to clarify the situation.

Conclusions

As a result of the isothermal oxidation of nominal Ni-14Cr-24Al-*x*Zr alloys, containing from 0 to 0.63 a/o Zr, at 1100°, 1150°, and 1200°C, the following conclusions were reached:

1. Up to some critical, but low value near 0.06 a/o, small additions of zirconium lead to increased scale adhesion on cooling and to minimal oxide spalling. The spalling that does take place occurs within the scale while the absence of Zr leads to much poorer adherence and localized oxide spalling to bare metal on cooling.

2. Over the range studied, increased Zr does not lead to measurably increased Zr solution in the Al_2O_3 lattice, nor does it lead to any significant change in the rate of external scale growth. The controlling oxide is still $\alpha-Al_2O_3$.

3. The Zr does tend to increase the rate of oxygen uptake after an initial drop at very low Zr concentrations, thereby increasing the amount of Al_2O_3 oxide penetration. Scale growth is still nearly parabolic.

Manuscript submitted July 30, 1979; revised manuscript received Oct. 5, 1979.

Any discussion of this paper will appear in a Discussion Section to be published in the December 1980 JOURNAL. All discussions for the December 1980 Discussion Section should be submitted by Aug. 1, 1980.

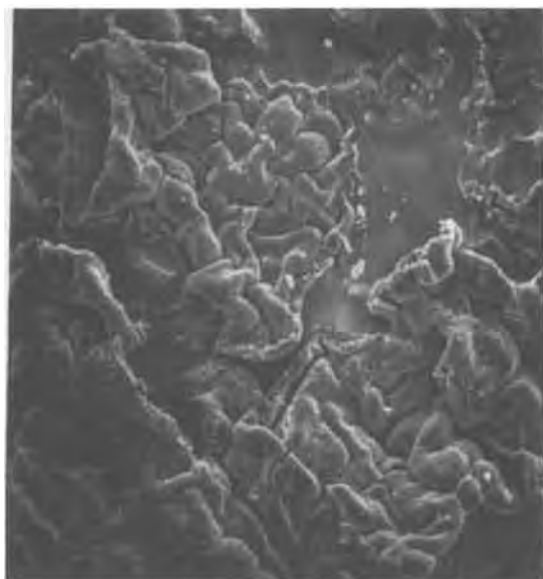
Publication costs of this article were assisted by NASA Lewis Research Center.

REFERENCES

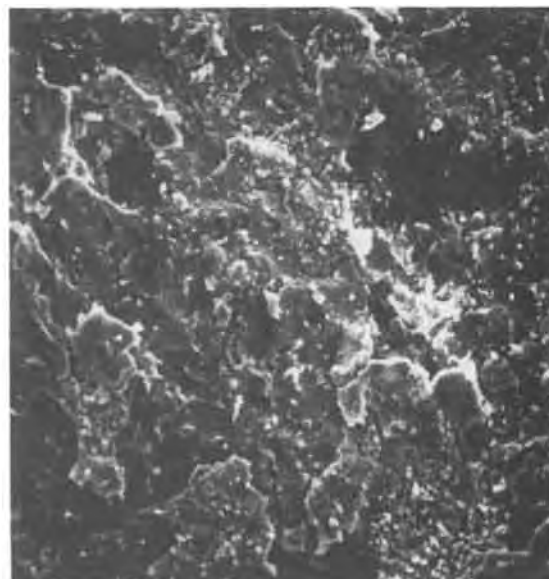
1. W. Hessenbruck, "Metalle und Legierungen für Hoch Temperaturen," Part I, J. Springer, Berlin (1940).
2. B. Lustman, *J. Metals*, **188**, 995 (1950).
3. E. J. Felten, *This Journal*, **108**, 490 (1961).
4. C. S. Wukusick and J. F. Collins, *Mater. Res. Stand.*, **4**, 637 (1964).
5. J. K. Tien and F. S. Pettit, *Metall. Trans.*, **3**, 1587 (1972).
6. C. S. Giggins, B. H. Kear, F. S. Pettit, and J. K.

Table V. Lattice constants of Al_2O_3 formed on NiCrAl alloys after 150 hr at 1200°C. Debye Scherer powder pattern

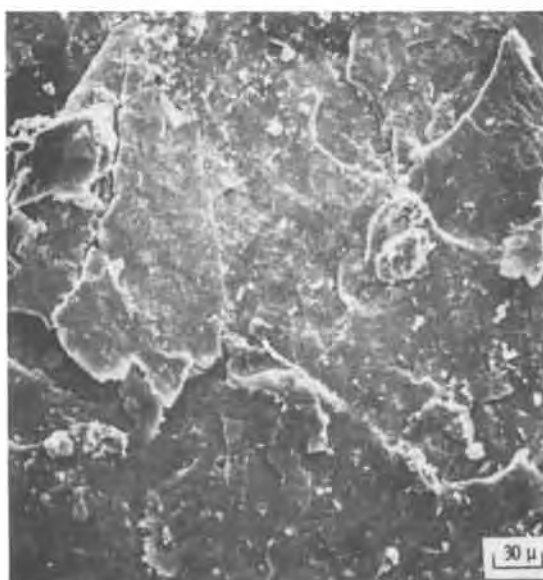
Alloy	a/o Zr	a_0	c_0
I	0	4.759 ± 0.001	13.002 ± 0.005
V	0.33	4.756 ± 0.002	13.005 ± 0.004
VI	0.63	4.758 ± 0.002	13.001 ± 0.007
3 μm Al_2O_3 std	0	4.761 ± 0.001	13.001 ± 0.003



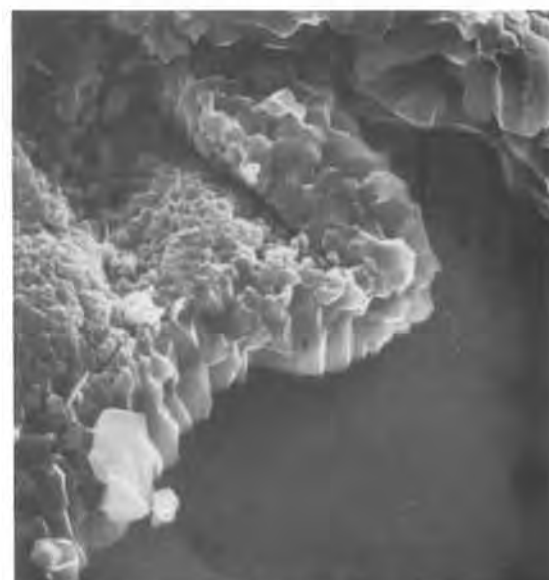
(a) Alloy I-0, tilt 15°.



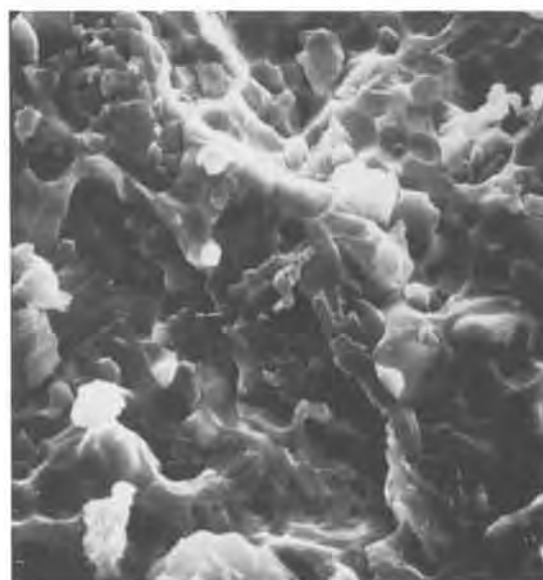
(b) Alloy IV-0.066, tilt 15°.



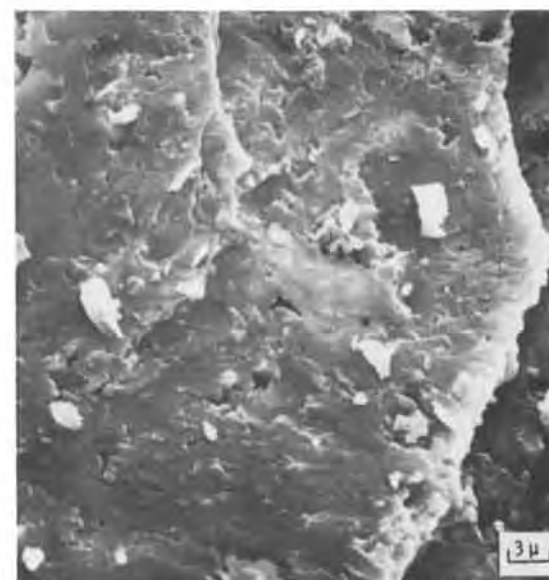
(c) Alloy V-0.33, tilt 15°.



(d) Alloy I-0, tilt 30°.



(e) Alloy IV-0.066, tilt 30°.



(f) Alloy V-0.33, tilt 30°.

Fig. 11. Oxide spalling from selected Ni-14Cr-24Al-xZr alloys after 200 hr oxidation at 1200°C

- Tien, *ibid.*, **5**, 1685 (1974).
7. J. Stringer, *Metall. Rev.*, **11**, 113 (1966).
 8. J. E. McDonald and J. G. Eberhart, *Trans. AIME*, **233**, 512 (1965).
 9. I. G. Wright, Metals and Ceramic Information Center, Battelle Columbus Labs., Ohio, MCIC-72-07 (1972).
 10. C. S. Giggins and F. S. Pettit, Pratt & Whitney Aircraft, East Hartford, Conn., PWA-5364 (1975), (ARL-TR-75-0234, AD-A024104).
 11. F. A. Golightly, F. H. Stott, and G. C. Wood, *Oxid. Met.*, **10**, 163 (1976).
 12. C. A. Barrett and C. E. Lowell, *ibid.*, **12**, 293 (1978).
 13. G. J. Santoro and C. A. Barrett, *This Journal*, **125**, 271 (1978).
 14. A. Taylor and R. W. Floyd, *J. Inst. Metals.*, **81**, 451 (1952-1953).
 15. C. A. Barrett and A. F. Presler, National Aeronautics and Space Admin., Washington, D.C., NASA TN D-8132 (1976).
 16. P. Kofstad, "High Temperature Oxidation of Materials," p. 103, John Wiley & Sons, Ltd., Chichester, Sussex, England (1966).
 17. A. E. Paladino and W. D. Kingery, *J. Chem. Phys.*, **37**, 957 (1962).
 18. Y. Oishi and W. D. Kingery, *ibid.*, **33**, 480 (1960).
 19. G. S. Giggins and F. S. Pettit, Pratt & Whitney Aircraft, East Hartford, Conn., PWA-4786 (1973).
 20. I. M. Allam, D. P. Whittle, and J. Stringer, *Oxid. Met.*, **12**, 35 (1978).

Diffusional Analysis for Growth of the Monosulfide Scale on Cobalt-Iron Alloys

D. J. Young,^{*1} T. Narita,^{*2} and W. W. Smeltzer*

Department of Metallurgy and Materials Science, McMaster University, Hamilton, Ontario, Canada, L8S 4M1

ABSTRACT

A ternary diffusion model is invoked to interpret growth of the (CoFe)S scale on Co-Fe alloys containing greater than 40 atomic percent (a/o) Fe in H₂S-H₂ atmospheres, $3.4 \times 10^{-7} \leq P_{S_2} \leq 1 \times 10^{-5}$ atm, at temperatures 533°-980°C. Concentration profiles in the solid phases were determined from electron probe microanalyses; the iron concentration across a scale continuously decreased from its highest value at the scale/alloy interface. Computations demonstrated that the relative self-diffusivity of cobalt to iron in (CoFe)S was dependent on concentration increasing asymptotically from a value of 1.3 in essentially pure FeS to a value of 2.4 at 60 a/o FeS. A numerical computing method capable of determining sulfidation rates of a binary alloy from diffusional and thermodynamic data was used to demonstrate that calculated metal composition profiles in the (CoFe)S scales and values of the parabolic sulfidation rate constants were in good agreement with the experimental determinations.

Kinetics and morphological development of sulfide scales formed on Co-Fe alloys (1, 2) and iron (3, 4) in H₂S-H₂ atmospheres of various sulfur activities at temperatures 533°-980°C were determined in earlier investigations. A reaction mechanism based on metal diffusion through the scales was advanced to account for the parabolic sulfidation kinetics. Ternary diffusion theory has been recently applied to interpret high temperature sulfidation kinetics and cation profiles in monosulfide scales formed on several iron-base binary alloys (5, 6). The purpose of this investigation is to interpret by diffusion theory measurements of metal concentration profiles in (CoFe)S scales formed on Co-Fe alloys and to obtain the most reliable computing method for predicting sulfidation rates of these alloys when scaling data are not available.

Experimental

Co-Fe alloys containing 38.6, 49.9, 60.0, 80.1, and 90.0 weight percent Fe were sulfidized in H₂S-H₂ atmospheres, $3.4 \times 10^{-7} \leq P_{S_2} \leq 1 \times 10^{-5}$ atm, at 533°, 600°, and 700°C. Methods, materials, and the scaling kinetics were presented previously (1, 2). Linear regression fit of the parabolic rate constant values for growth of (CoFe)S scales on the alloys at 700°C to the relationship

$$\log k_p = \frac{1}{n} \log P_{S_2} + \text{constant} \quad [1]$$

yielded $n = 5.6 \pm 0.5$.

Sulfidized specimens were cross sectioned and metallographically polished finishing with 0.25 μm diamond paste. The large columnar grained scales were compact and adherent to the metal substrate. Electron probe microanalysis (EPMA) was used to measure compositions as a function of position in these scales. Identical results were obtained using two different instruments with different take-off angles for the emergent x-rays when Co, Fe, and S were measured simultaneously to negate any instrumental drift. X-ray counts were converted to composition by comparison to standards of FeS₂, a Fe-FeS two-phase mixture, and a series of Co-Fe alloys. Results were corrected for atomic number and absorption effects; fluorescence corrections were negligible and they were ignored. An example of the columnar (CoFe)S scale and its compositional profile determined by EPMA is illustrated in Fig. 1.

Compositions at several positions in each scale normalized to $y = x/x_s$, where x_s is scale thickness, were evaluated as FeS mole fraction knowing atom fractions of Co, Fe, and S and by considering (CoFe)_{1-δ}S as a pseudo-binary solution of the pure metal sulfides. Compositions were often determined over two and three different regions of a scale cross section. Concentration profiles in the scales formed on the series of alloys at 700°C and $P_{S_2} = 2 \times 10^{-6}$ atm are shown in Fig. 2. Figure 3 shows these profiles in scales formed on Co-60 Fe at 700°C and sulfur pressures in range 1×10^{-5} - 3.4×10^{-7} atm while Fig. 4 shows these scale profiles for $P_{S_2} = 2 \times 10^{-6}$ atm and temperatures of 700°, 600°, and 533°C. In all scales, iron contents of (CoFe)S were largest at the alloy/scale interface and continuously decreased to smaller values at the scale/gas interface. Values are given in

* Electrochemical Society Active Member.

¹ Present address: School of Chemical Technology, The University of New South Wales, Kensington, N.S.W., Australia, 2033.

² Present address: Metals Research Institute, Faculty of Engineering, Hokkaido University, Sapporo 060, Japan.

Key words: sulfidation, Co-Fe alloys, diffusion model, alloy.

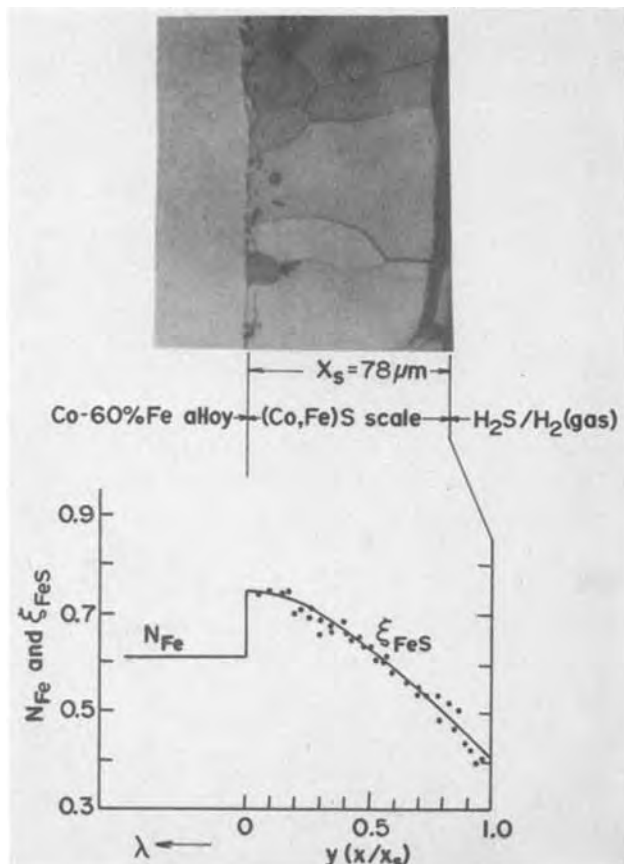


Fig. 1. (CoFe)S scale formed on Co-60% Fe alloy at 600°C and $P_{S_2} = 2 \times 10^{-6}$ atm in 1 hr. Compositions of the solid phases were determined from EPMA of Co, Fe, and S concentrations.

Table I of the FeS content in (CoFe)S at the alloy and gas interfaces, ξ' and ξ'' , respectively, and its average composition in scales formed on the various alloys at 700°C and $P_{S_2} = 2 \times 10^{-6}$ atm.

Diffusion Model for Growth of (CoFe)S Scales

Wagner (7) has presented a theory for binary alloy oxidation and sulfidation which applies to growth by

ambipolar metal diffusion of a solid solution scale. Before considering this diffusion model, it is necessary to establish features of the defect structure and cation diffusivities of the metal sulfides. $Fe_{1-\delta}S$ exhibits a broad range of nonstoichiometry arising from the presence of iron vacancies; the iron self-diffusion coefficient D_{Fe} is related to the chemical diffusivity \tilde{D} and nonstoichiometry δ by the following expression (3)

$$D_{Fe} = \frac{\tilde{D}_0 \delta}{1 + \left[\frac{8}{R} \delta(1-\delta) \right] \left[\frac{7900}{T} + 4 \right]} \exp - \tilde{E}/RT \quad [2]$$

where $\tilde{D}_0 = (6.7 \pm 2) \times 10^{-2}$ cm²/sec, $\tilde{E} = 20,900 \pm 600$ cal/g atom, R is the gas constant, and T is the absolute temperature. D_{Fe} can be regarded as linearly related to δ only at extremely low sulfur pressures. At sulfur pressures of scale growth in this investigation, D_{Fe} is related to sulfur activity $a_s = (P_{S_2})^{1/2}$ as a good first approximation (3) by

$$D_{Fe} = D_{Fe}^0 a_s^{2/n} \quad [3]$$

where $n = 5$ and D_{Fe}^0 at $P_{S_2} = 2 \times 10^{-6}$ atm is taken as the standard reference value at each temperature (3, 8). Cobalt diffusivity D_{Co} in $Co_{1-\delta}S$ is not known.

Cobalt and iron monosulfides exhibit similar defect structures. The ratio of cation vacancy concentrations in CoS and FeS is estimated to be 0.60 at 700°C and $P_{S_2} = 2 \times 10^{-6}$ atm (9, 10). We therefore express cation self-diffusivities of (CoFe)S in the manner used for describing diffusional properties of (CoNi)O (11). That is

$$D_{Fe} = D_{Fe}^0 \beta^{1-\xi} a_s^{2/n} \quad [4a]$$

$$D_{Co} = D_{Co}^0 \beta^{1-\xi} a_s^{2/n} \quad [4b]$$

where ξ is the FeS mole fraction in (CoFe)S and β signifies the ratio of vacancy concentrations for the pure binary sulfides. For example, $\beta = 0.60$ at 700°C and $n = 5$.

Equations [11] and [19] from Wagner's original paper (7), which describe the metal flux in a (CoFe)S scale normalized to fractional thickness y in terms of the parabolic rate constant k and the metal gradient in the scale, can be expressed as follows

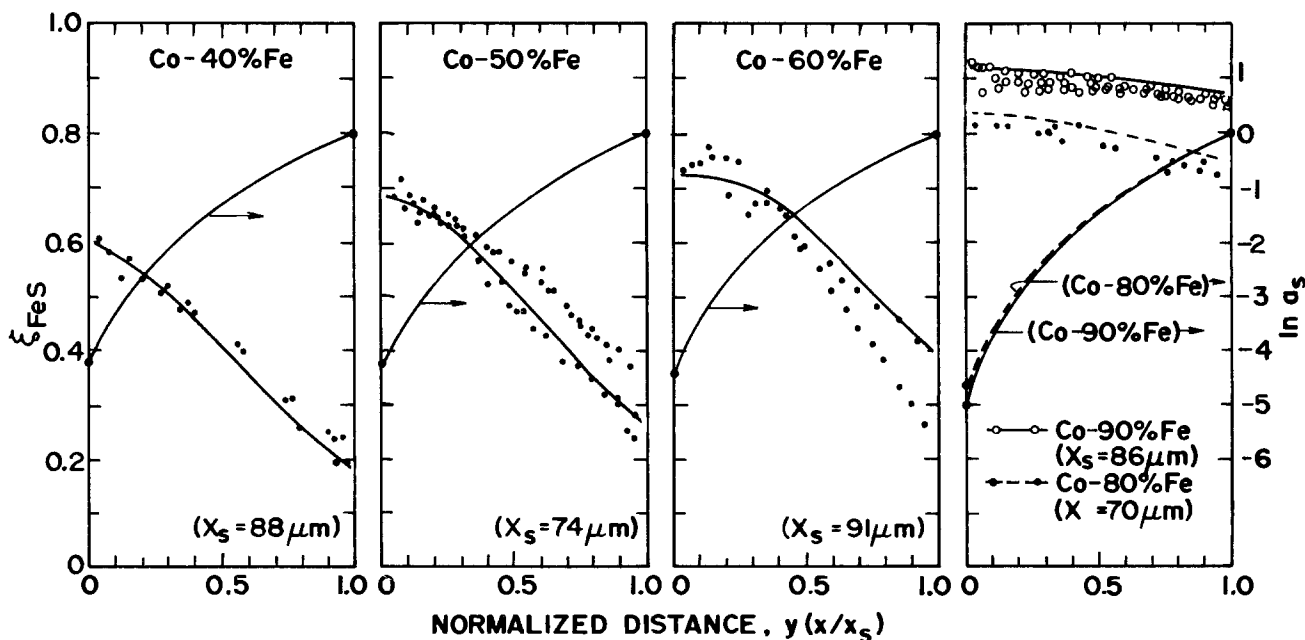


Fig. 2. FeS composition of (CoFe)S scales grown on Co-Fe alloys at 700°C and $P_{S_2} = 2 \times 10^{-6}$ atm. The plots represent calculated FeS composition and sulfur activity profiles.

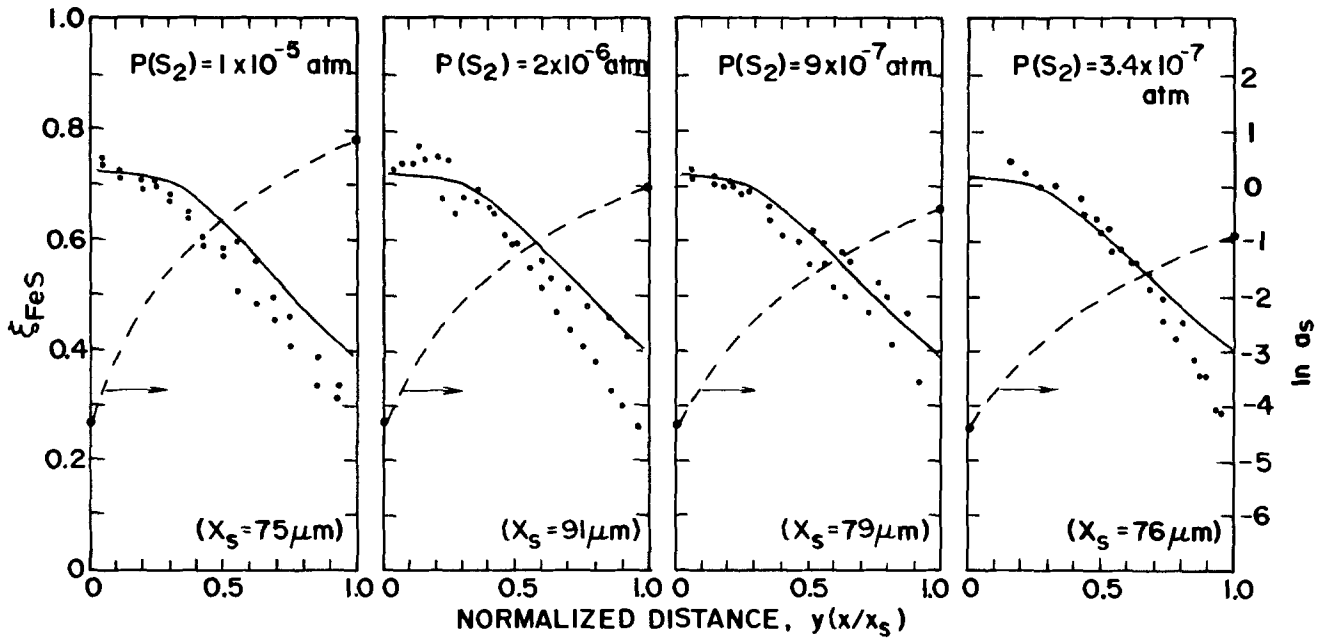


Fig. 3. FeS compositions of (CoFe)S scales grown on Co-60% Fe alloy at 700°C and $3.4 \times 10^{-7} \leq P_{S_2} \leq 1 \times 10^{-5}$ atm. The plots represent calculated profiles.

$$D_{Co}(1-\xi) \left(\frac{-d \ln a_{CoS}}{d\xi} \frac{d\xi}{dy} + \frac{Z_{Co}}{Z_s} \frac{d \ln a_s}{dy} \right) + D_{Fe}\xi \left(\frac{-d \ln a_{FeS}}{d\xi} \frac{d\xi}{dy} + \frac{Z_{Fe}}{Z_s} \frac{d \ln a_s}{dy} \right) = k \quad [5]$$

$$yk \frac{d\xi}{dy} = \frac{-d}{dy} \left[D_{Fe}\xi \left(\frac{d \ln a_{FeS}}{d\xi} \frac{d\xi}{dy} - \frac{d \ln a_s}{dy} \right) \right] \quad [6]$$

The symbols D , a , and ξ refer to the appropriate metal self-diffusion coefficient, activity, and iron composition, respectively. These two equations are placed in the following forms for computational purposes assuming ideal solution of the binary sulfides and $Z_{Co} = Z_{Fe} = |Z_s| = 2$

$$\frac{d \ln a_s}{dy} = \left[\frac{k}{D_{Fe}} - (p-1) \frac{d\xi}{dy} \right] / W \quad [5a]$$

$$\frac{D_{Fe}p}{W} \frac{d^2\xi}{dy^2} + \left[\frac{d\xi}{dy} - \xi \frac{d \ln a_s}{dy} + \frac{k\xi}{D_{Fe}W} \right] \frac{d}{dy} (D_{Fe}) + \left\{ \left[\frac{k\xi}{W^2} - D_{Fe} \frac{(p-1)\xi}{W^2} \frac{d\xi}{dy} \right] (1-\xi) + D_{Fe} \frac{\xi}{W} \frac{d\xi}{dy} \right\} \frac{d}{dy} (p) + \left\{ yk - D_{Fe} \frac{d \ln a_s}{dy} - \left[k - (p-1) \frac{d\xi}{dy} \right] \frac{(p-1)\xi}{W^2} \right\} \frac{d\xi}{dy} = 0 \quad [6a]$$

where $p = D_{Co}/D_{Fe}$, $W = p - (p-1)\xi$, and

$$\frac{d}{dy} (D_{Fe}) = D_{Fe} \left(\frac{2}{n} \frac{d \ln a_s}{dy} - \ln \beta \frac{d\xi}{dy} \right)$$

The parabolic rate constant k (cm²/sec) in these equations is related to the experimental k_p (g²/cm⁴/sec)

by

$$k = \frac{1}{2} \left(\frac{M_{(CoFe)S}}{\rho_{(CoFe)S} M_s} \right)^2 k_p \quad [7]$$

where M_s is the atomic weight of sulfur, $M_{(CoFe)S}$ is the average molecular weight of (CoFe)S of metal ratio equal to that in the specific alloy, and $\rho_{(CoFe)S}$ is the (CoFe)S density (g/cm³) calculated from room temperature densities of pure metal sulfides assuming a linear dependence between these sulfides with composition and a temperature expansion coefficient of $2 \times 10^{-5}/^\circ\text{C}$ equal to that for FeS (3).

Several auxiliary equations may be used in this numerical analysis. Values for $(d\xi/dy)_{y=1}$ are estimated from a mass balance at the scale/gas interface (Eq. [39] in Ref. (7))

$$\left(\frac{d\xi}{dy} \right)_{y=1} = - \frac{k^*}{\beta^{(1-\xi'')}(a''_s)^{2/n}} \cdot \frac{(p''-1)(1-\xi'')\xi''}{p''} \quad [8]$$

where $k^* = k/D_{Fe}$ and double primes refer to this interface. Also, the ratio of cobalt to iron flux into a scale at its inner interface is equivalent to metal ratio in bulk alloy. Equation [35] in Ref. (7) gives

$$\left(\frac{d\xi}{dy} \right)_{y=0} = - \frac{k^*}{\beta^{(1-\xi')}(a'_s)^{2/n}} \left\{ \frac{N_{Fe}[p' - (p'-1)\xi'] - \xi'}{p'} \right\} \quad [9]$$

where N_{Fe} is iron mole fraction in bulk alloy and a single prime refers to metal interface. This latter expression is applicable when significant depletion of the alloying element does not exist in the metal substrate.

Sulfur activity, a''_s , at a scale surface is established by its atmospheric activity. The displacement reaction

Table I. Alloy compositions and experimental results of sulfide compositions in the (Co, Fe)S scales and the values of parabolic sulfidation rate constant at 700°C and $P_{S_2} = 2 \times 10^{-6}$ atm

Nominal alloy composition (a/o)	40	50	60	80	90
Actual alloy composition (a/o)	39.9	51.3	61.3	81.0	90.5
$\xi_{y=0}$ (FeS m/o)	54 ~ 61	66 ~ 73	73 ~ 80	79 ~ 86	87 ~ 94
$\xi_{y=1}$ (FeS m/o)	16 ~ 24	20 ~ 35	25 ~ 38	72 ~ 75	84 ~ 88
k_p (g ² /cm ⁴ ·sec)	3.01×10^{-7}	2.28×10^{-7}	2.55×10^{-7}	2.69×10^{-7}	2.51×10^{-7}
Average measured sulfide composition (FeS m/o)	40 ± 2	50 ± 3	59 ± 3	79 ± 3	89 ± 2

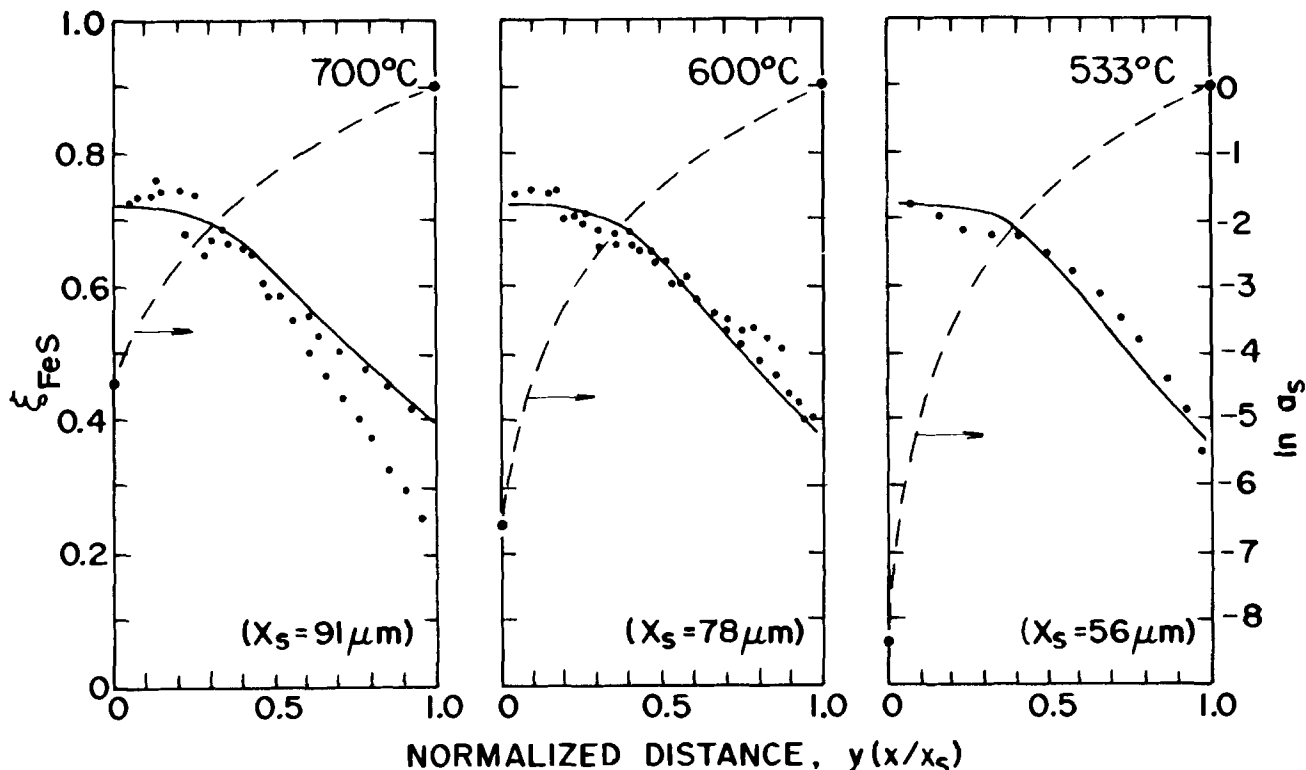


Fig. 4. FeS compositions of (CoFe)S scales grown on Co-60% Fe alloy at 533°, 600°, and 700° and $P_{S_2} = 2 \times 10^{-6}$ atm. The plots represent calculated profiles.

between pure sulfides and alloy components defines the sulfur activity at inner interface, a'_s , as a function of interfacial composition ξ'

$$a'_s = [\gamma - (\gamma - 1)\xi'] \exp \Delta G^\circ_{FeS}/RT \quad [10]$$

where $\gamma = \exp[(\Delta G^\circ_{CoS} - \Delta G^\circ_{FeS})/RT]$ and ΔG° is a standard free energy change for formation of a pure binary sulfide.

Computer Simulation of (CoFe)S Scale Growth

Preliminary calculations.—Equations [5a] and [6a], which are simultaneous nonlinear differential equations in dependent variables ξ and a_s , were numerically solved using the modified predictor-corrector Hamming method containing automatic changes of step width (12). Four boundary values ξ' , a'_s , ξ'' , and a''_s and also the first derivative of concentration at the scale/gas interface $(d\xi/dy)_{y=1}$ were used for numerical integration of the above equations from this interface to its inner interface.

$(d\xi/dy)_{y=1}$ is obtained in terms of k^* and p'' from Eq. [8] and in preliminary calculation methods p was assumed to be constant independent of composition for the scale formed on a specific alloy. In the first method, k was chosen equal to the experimental value and values of n and p obtained by computation to obtain best fit to the FeS concentration profile using Eq. [5a] and [6a] with maximum and minimum boundary estimates of ξ'' and ξ' , respectively. This method was discarded as the fits were not good and the value of $n = 3.2$ was not in agreement with $n = 5.6 \pm 0.5$ determined from the experimental sulfur dependence on k . This type of fit to the concentration profile in a scale formed on the Co-60 Fe alloy involving $p = 2.15$ and $n = 3.16$ is shown in Fig. 5. The second method involved selecting a value $n = 5$; values of p and k were obtained by numerically integrating Eq. [5a] and [6a] to obtain best fit to a concentration profile commencing with the outer minimum or maximum estimated ξ'' and ending with inner maximum or minimum estimated ξ' , respectively. These two types of fit are also illustrated for the concentration profile in Fig. 5. It was apparent from these

preliminary calculations that assumption of a constant value of p was unwarranted because best fits for concentration profiles in scales on the various alloys demonstrated that p actually exhibited a compositional

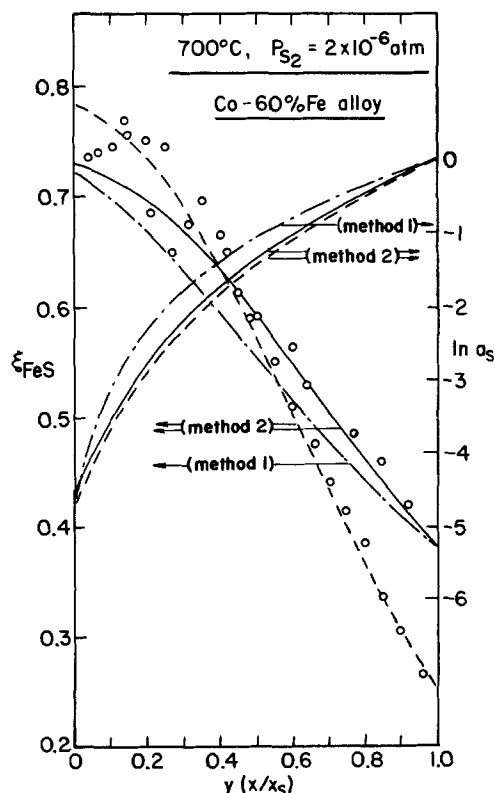


Fig. 5. Fits of calculated profiles to determinations of FeS compositions in the (CoFe)S scale formed on Co-60% Fe alloy. Computation methods given in text. Method 1: $k_p^* = 1.66$, $\xi' = 0.72$, $\xi'' = 0.38$. Method 2: $n = 5$, for $\xi' = 0.73$ and $\xi'' = 0.38$, and for $\xi' = 0.79$ and $\xi'' = 0.25$.

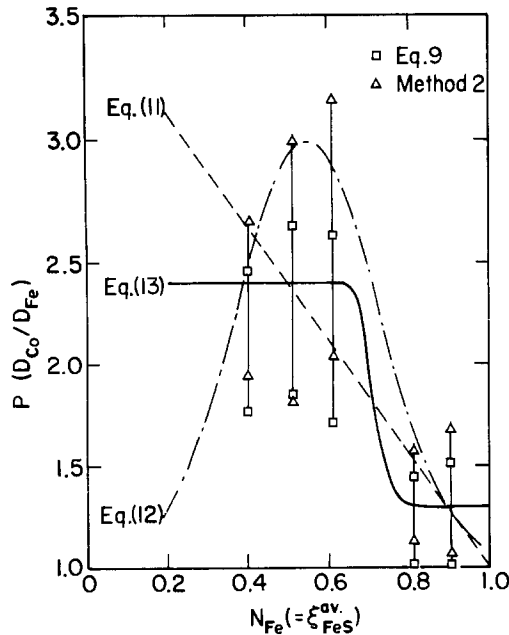


Fig. 6. Values of $p = D_{Co}/D_{Fe}$ as a function of the average scale composition calculated by method 2 and Eq. [9] as described in text. Plots represent calculations of the dependences of p on average scale composition using Eq. [11], [12], and [13] of text.

variation and the values of p calculated by the second method are shown in Fig. 6. There is also included here minimum and maximum estimates of p obtained from Eq. [9] by assuming $(d\xi/dy)_{y=0} = 0$ (Fig. 2-4) which arises if the metal diffusivities are much less in the alloy than in the reaction product scale. This condition applied because $\tilde{D}_{alloy} (13) \sim 10^{-5} D_{Fe}$ in FeS (3, 8).

Complete calculations.—Since preliminary calculations demonstrated that the ratio of metal diffusivities in a sulfide scale exhibited a compositional variation, a complete computer simulation program was established to gain a description for parabolic growth of the scale using only diffusional and thermodynamic data for the alloy and scale compound. In principle, it is necessary in the general case for growth of a solid solution scale on a binary alloy to solve the flux and continuity equations for the scale and alloy using metal diffusivities and appropriate boundary conditions at the gas/scale and scale/alloy interfaces knowing the original alloy composition, ambient sulfur pressure, and temperature. The input data, therefore, are the self-diffusivity of iron and $p = D_{Co}/D_{Fe}$ for

the sulfide scale, the interdiffusion coefficient \tilde{D}_{all} for the alloy, and the free energy change ΔG for the displacement reaction between the pure metal sulfides with the alloy components. Sulfur activities at the gas/scale and scale/alloy interfaces are defined by the atmospheric sulfur pressure and the thermodynamic relationship given by Eq. [10], respectively. Auxiliary equations [8] and [9], which include the parabolic scale growth parameter $k^* = k/D_{Fe}$, were derived from interfacial mass balances to obtain expressions for the metal concentrations and gradients at the inner and outer scale interfaces.

A flowchart for the computer simulation is given in Fig. 7. D_{Fe} in (CoFe)S is related to the self-diffusivity of iron in pure FeS (3, 8), scale composition, and sulfur activity by Eq. [4a]. Since $p = D_{Co}/D_{Fe}$ was previously shown to be dependent on the scale composition, the preliminary calculated values of this parameter were empirically represented by functions representing linear, probability, and asymptotic type compositional dependences using the average FeS content of a (CoFe)S scale. The appropriate equations

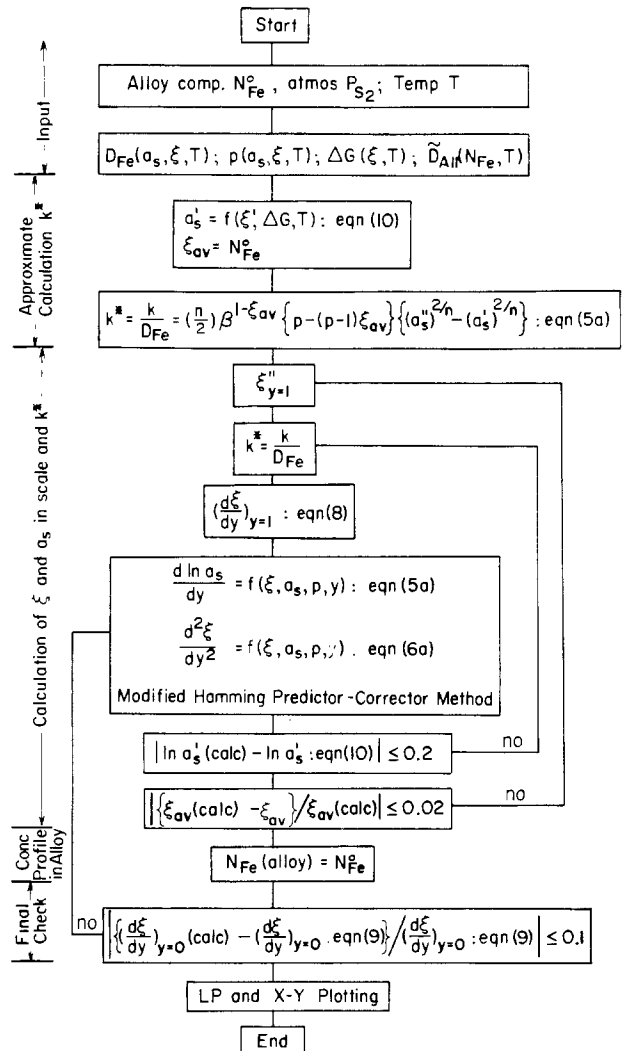


Fig. 7. Flowchart for computer simulation of the sulfidation of Co-Fe alloys to (CoFe)S scales.

were

$$p = 3.7 - 2.7\xi \quad [11]$$

$$p = 1.0 + 2.0 \exp - \{(\xi - 0.55)/0.25\}^2 \quad [12]$$

$$p = 2.4 \text{ for } \xi \leq 0.65 \quad [13]$$

$$= 1.3 + 1.1 \exp - \{(\xi - 0.65)/0.07\}^2 \text{ for } \xi \geq 0.65$$

These three dependences were chosen because no results are available of diffusion in (CoFe)S and each equation represented the preliminary evaluations of p as shown by the plots in Fig. 6.

It was not necessary to consider diffusion in the alloy in the calculations because $D_M(\text{CoFe})S/\tilde{D}_{all} \gg 1$; hence, the iron alloy concentration was equal to the average FeS content of a (CoFe)S scale (7). As illustrated in the flow sheet, a first estimate of $k^* = k/D_{Fe}$ was made by solving Eq. [5a] under the approximation that $d\xi/dy = 0$ and $\xi = \xi_{av} = N_{Fe}^o$. This value of k^* , an arbitrarily chosen value of $\xi''_{y=1}$, $(d\xi/dy)_{y=1}$ given by Eq. [8], was then utilized to initiate integration of Eq. [5a] and [6a] from the outer to inner scale interface using the modified Hamming predictor-corrector method (12) to obtain values of ξ and a_s across a scale and the most reliable value of k^* . Two do loops were employed with prescribed absolute error limits to a_s and ξ_{av} and integration step intervals were adjusted automatically to satisfy $< 10^{-8}$ truncation error. A final check of the calculations was carried out by comparing the calculated $(d\xi/dy)_{y=0}$ to that given by Eq. [9] assuming

that the alloy composition remained equal to its initial value.

Calculations were first carried out to determine which equation for p (Eq. [11], [12], or [13]) led to best representation of the measured iron contents of the (CoFe)S scales. A comparison of the fits obtained for the composition profiles in scales formed on the 40% and 60% Fe alloys at $T = 700^\circ\text{C}$ and $P_{\text{S}_2} = 2 \times 10^{-6}$ atm is shown in Fig. 8 for illustrative purposes. Best fits were obtained using Eq. [13] which describes p as asymptotically approaching a high from low value with decreasing iron content of (CoFe)S as shown in Fig. 6. The calculated ξ and a_s profiles across scales formed on exposing the alloys at several temperatures and sulfur pressures using Eq. [13] for p , Eq. [4a] for D_{Fe} , and Eq. [10] for ΔG as input data into the computer program are depicted by the plots in Fig. 2-4.

A comparison of values for the sulfidation rate constants obtained by computation to those determined experimentally for alloys containing $\geq 40\%$ Fe at $T = 533^\circ$ and 700°C and $P_{\text{S}_2} = 2 \times 10^{-6}$ atm is given in Fig. 9. Predicted and experimental values agree within the uncertainty of the determinations. The variation of the parabolic rate constant with sulfur pressure is also accurately predicted as illustrated in Fig. 10. At $P_{\text{S}_2} \geq 10^{-7}$ atm, the pressure dependence approaches k vs. $P_{\text{S}_2}^{1/5}$ as given by the model. Calculations for the temperature dependence of the rate constant gave an interesting prediction in that this coefficient attained a maximum at intermediate temperature (14). The plots in Fig. 11 illustrate this behavior for the calculated rate constants of alloys containing 99% and 60% Fe sulfidized at $P_{\text{S}_2} = 2 \times 10^{-6}$ and $533^\circ \leq T \leq 980^\circ\text{C}$: maxima are obtained at $\sim 900^\circ$ and 850°C , respectively. A maximum value of the parabolic sulfidation rate constant at an intermediate temperature is determined by two factors: First, the temperature coefficients of the metal dif-

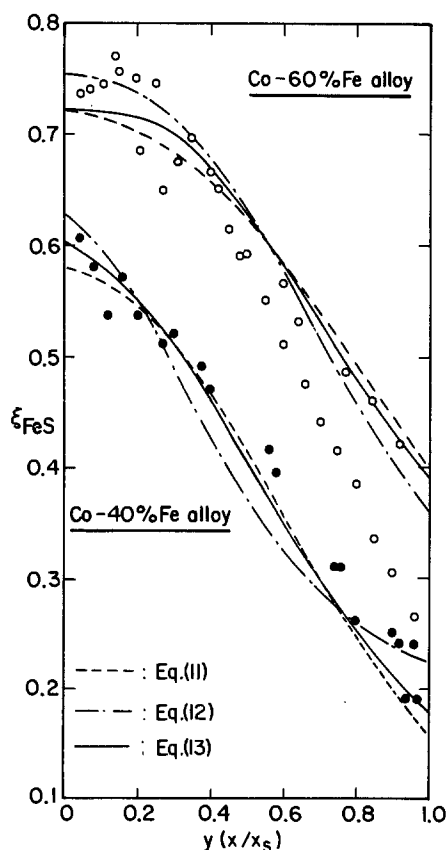


Fig. 8. Calculated fits to composition profiles in (CoFe)S scales on Co-40% and 60% Fe alloys at $T = 700^\circ\text{C}$ and $P_{\text{S}_2} = 2 \times 10^{-6}$ atm as discussed in text.

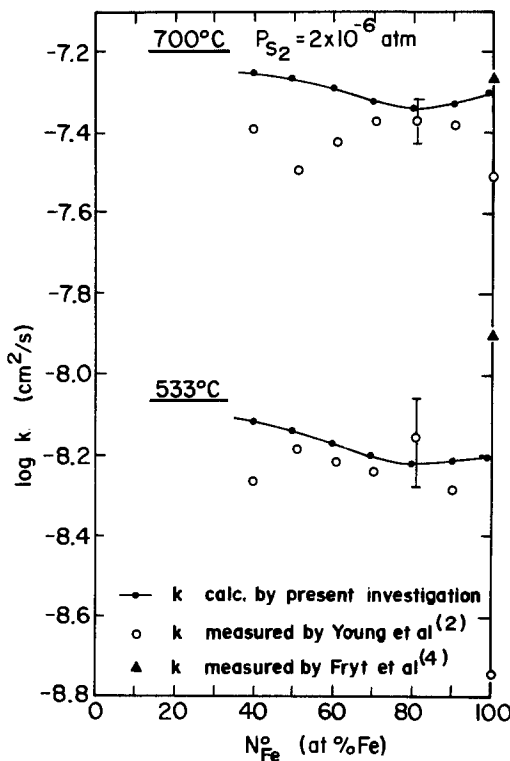


Fig. 9. A comparison of values for the parabolic sulfidation rate constants obtained by computation to those determined experimentally.

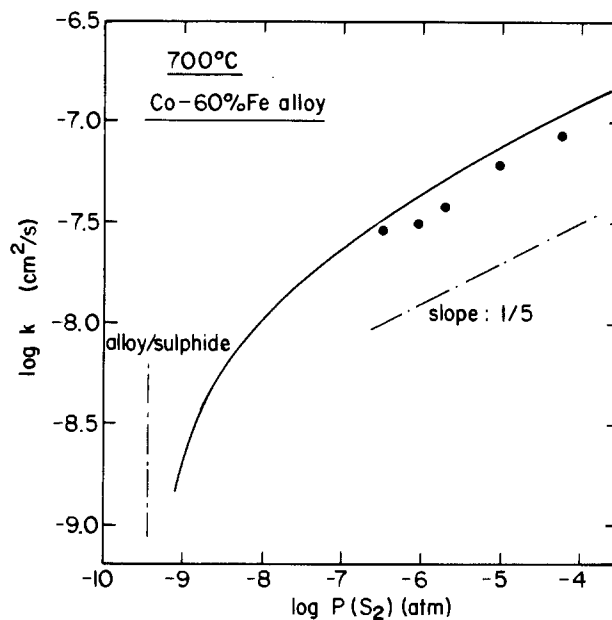


Fig. 10. Calculated and experimentally determined values for the parabolic sulfidation rate constants as a function of sulfur pressure.

fusivities (plot of D^*_{Fe} vs. $1/T$ in Fig. 11) increase less significantly with increasing temperature due to a regular Arrhenius-type increase in the mobility of cation vacancies but with a decreasing vacancy concentration at constant sulfur pressure (4); and, second, the sulfur activity gradient across a scale decreased with increasing temperature due to larger sulfur activities given by Eq. [10] governing equilibria at the scale/alloy interface.

The computation program using the above estimated relations for D_{Fe} , p , and ΔG was used to evaluate master plots of the FeS composition and sulfur activity profiles across the scales formed on Co-60% Fe at 700°C and sulfur pressures $1 \times 10^{-9} \leq P_{\text{S}_2} \leq$

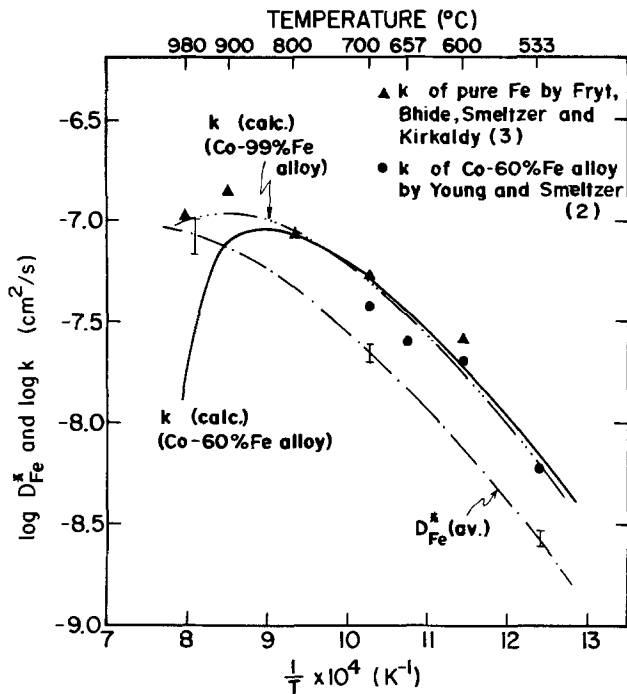


Fig. 11. Temperature dependences of calculated and experimentally determined parabolic sulfidation rate constants.

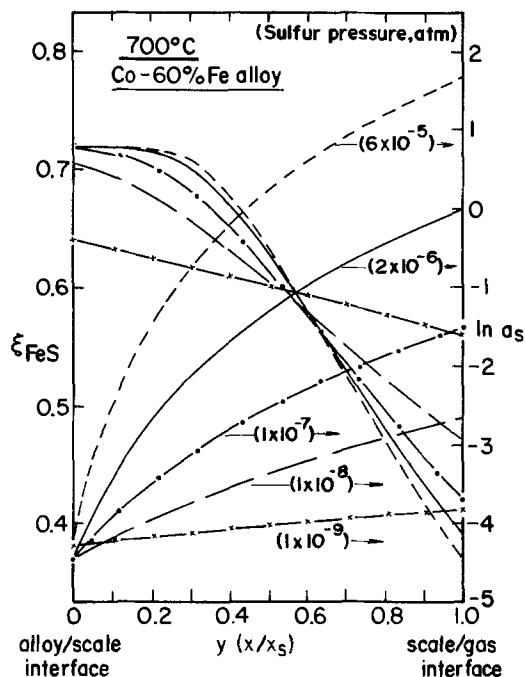


Fig. 12. Master plots of the FeS composition of (CoFe)S scale on Co-60% Fe alloy at $T = 700^\circ\text{C}$ and $1 \times 10^{-9} \leq P_{S_2} \leq 6 \times 10^{-5}$ atm.

6×10^{-5} atm, Fig. 12, and at various temperatures $600^\circ \leq T \leq 980^\circ\text{C}$ and $P_{S_2} = 2 \times 10^{-6}$ atm as shown in Fig. 13. The corresponding calculated parabolic rate constants under these conditions are those given in Fig. 10 and 11. It is seen that the FeS profiles in the scales formed isothermally become flatter and approach the average composition equal to N_{Fe} because of the decrease in sulfidation rate with decreasing sulfur pressure. A similar effect on the composition profile is shown by increasing temperature especially above 900°C at constant sulfur pressure because the parabolic rate constant attained a maximum at this temperature due to the influence of temperature

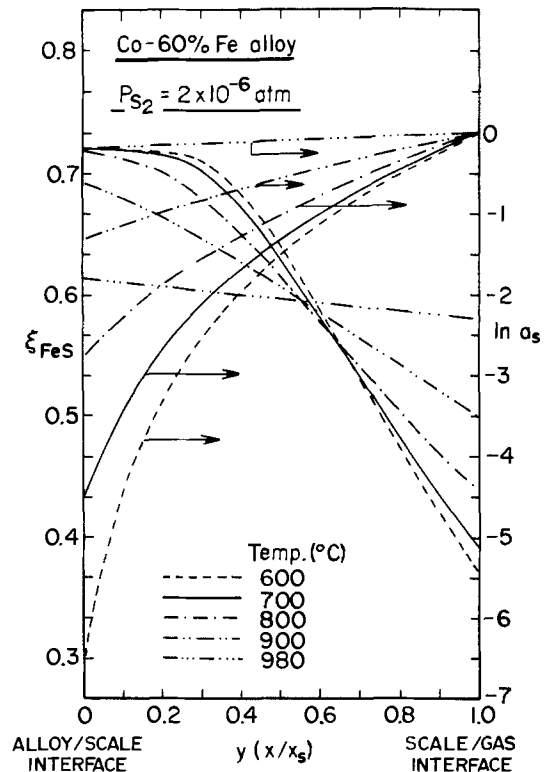


Fig. 13. Master plots of the FeS composition of (CoFe)S scale on Co-60% Fe alloy at $P_{S_2} = 2 \times 10^{-6}$ atm and $600^\circ \leq T \leq 980^\circ\text{C}$.

on the metal diffusivities and on the sulfur activity gradient across the scale as previously discussed.

This analysis has demonstrated that a reliable computation method was obtained for predicting parabolic sulfidation rates and concentration profiles in the solid phases when scale growth is controlled by metal diffusion. Scaling data are not required in these calculations since the problem is defined knowing the influence of the dependent variables, composition, and sulfur activity on the diffusivities and thermodynamic equilibria. These latter properties are not completely known for any binary alloy-sulfur system. A dearth of such information is exemplified by the present analysis which demonstrated that calculations had to be carried out assuming relationships for the diffusivities and thermodynamics of (CoFe)S using sulfidation scaling data to define the dependence of the metal diffusivities on composition and sulfur activity.

Acknowledgments

The authors gratefully acknowledge financial support for this research by the Natural Sciences and Engineering Research Council of Canada.

Manuscript received Aug. 22, 1979.

Any discussion of this paper will appear in a Discussion Section to be published in the December 1980 JOURNAL. All discussions for the December 1980 Discussion Section should be submitted by Aug. 1, 1980.

Publication costs of this article were assisted by McMaster University.

REFERENCES

1. D. J. Young, P. Mayer, and W. W. Smeltzer, *This Journal*, **121**, 889 (1974).
2. D. J. Young and W. W. Smeltzer, *ibid.*, **123**, 229 (1976).
3. E. M. Fryt, W. W. Smeltzer, and J. S. Kirkaldy, *ibid.*, **126**, 673 (1979).
4. E. M. Fryt, V. S. Bhide, W. W. Smeltzer, and J. S. Kirkaldy, *ibid.*, **126**, 683 (1979).
5. T. Narita and K. Nishida, *Denki Kagaku*, **43**, 443 (1975).

6. T. Narita and K. Nishida, *ibid.*, **44**, 159 (1976).
7. C. Wagner, *Corros. Sci.*, **9**, 91 (1969).
8. R. H. Condit, R. R. Hobbins, and C. E. Birchenall, *Oxid. Met.*, **8**, 409 (1974).
9. Y. O. Chen and Y. A. Chang, *Metall. Trans.*, **9B**, 61 (1978).
10. T. Rosenqvist, *J. Iron Steel Inst.*, **176**, 37 (1954).
11. A. D. Dalvi and D. E. Coates, *Oxid. Met.*, **3**, 203 (1971).
12. International Business Machine Inc., New York, Scientific Subroutine Package, System 360, Version III.
13. K. Hirano, Y. Iijima, K. Araki, and H. Homma, *Trans. ISIJ*, **17**, 194 (1977).
14. G. Simkovich and S. Kertoatmodjo, *Scr. Metall.*, **7**, 573 (1973).

Structure and Properties of LPCVD Silicon Films

T. I. Kamins*

Hewlett-Packard Laboratories, Palo Alto, California 94304

ABSTRACT

Silicon films deposited by low pressure chemical-vapor deposition over the temperature range from 525° to 725°C were investigated. It was found that polycrystalline films are formed above 600°C and are more stable than the amorphous films deposited at lower temperatures. Their crystal structure is a strong function of the deposition temperature and a weaker function of the deposition rate. Either the {110} or the {100} texture may dominate the structure, depending primarily on the deposition temperature. The electrical resistance obtained on doping the LPCVD films that are polycrystalline as deposited is maximum for films deposited at the lower temperatures (near 600°C), although this dependence on deposition temperature decreases after annealing at higher temperatures. Dopant atoms reversibly segregate to the grain boundaries during lower temperature heat-treatments subsequent to doping and are dispersed at higher temperatures, with corresponding changes in resistivity. The oxidation rate is only a weak function of the deposition temperature, although the initially amorphous films may oxidize somewhat more rapidly. The index of refraction of amorphous films is significantly higher than that of polycrystalline films.

The deposition of polycrystalline silicon at reduced pressures has recently become widespread throughout the semiconductor industry, primarily because of its compatibility with high volume wafer fabrication (1). Since this type of polysilicon is replacing material deposited at atmospheric pressure and several hundred degrees higher temperature, an understanding of its properties and their sensitivity to variations in the deposition conditions is needed.

A previous study (2) showed that LPCVD films deposited at 580°C were amorphous, while those deposited above 600°C were polycrystalline immediately after the deposition. By contrast, at atmospheric pressure, temperatures even higher than the 625°C normally used for LPCVD polysilicon deposition can also produce amorphous films (3). Since amorphous films are unstable upon further heat cycling, their compatibility with integrated circuits must be carefully considered, or deposition conditions must be chosen to avoid obtaining such films.

Because the normally used LPCVD silicon deposition temperature (625°C) is near the amorphous-to-polycrystalline transition, a more detailed investigation of the dependence of the structure and other properties of LPCVD silicon films on the deposition temperature was undertaken. The LPCVD system used in the present study was completely independent of that employed in the previous investigation (2) so system-to-system variations could be observed.

The structure of the films was examined by both transmission electron microscopy and x-ray diffraction. The dependence of the sheet resistance on film deposition temperature was considered both for a gaseous predeposition from a POCl₃ source and for implanted phosphorus, and the oxidation rate of both undoped and phosphorus-doped films was investigated. For the latter studies, dopant concentrations

were chosen to maximize the resistivity differences between the various films; the differences expected in practical cases may be less.

Film Deposition

A series of films was deposited every 25°C over the temperature range from 525° to 725°C, and the films were compared to polysilicon deposited at atmospheric pressure and a temperature of approximately 960°C, the temperature often used for deposition of atmospheric pressure polysilicon.

All films were deposited onto lightly doped, 7.6 cm diam silicon wafers covered with 100 nm of thermally grown silicon dioxide. The wafers were not cleaned between the oxidation and the silicon deposition. The LPCVD films were deposited in a resistance-heated reactor (4) with a uniform temperature profile measured at atmospheric pressure just outside the evacuated deposition chamber. A single thermocouple within the vacuum indicated a temperature there within 4°C of that measured outside the chamber.

Wafers were loaded vertically, with their faces perpendicular to the axis of the tube. The wafers were spaced 0.48 cm apart and were inserted into the chamber at the desired deposition temperature. A constant silane gas flow of 53 cm³/min was used in all depositions, and the deposition rate consequently varied with temperature; it was approximately 10 nm/min at 625°C. The target film thickness was 0.5 μm, and films deposited at all except the lowest temperatures were reasonably close to this value. The films deposited at 525°C (denoted LP525) were only about half the desired thickness. The thicknesses of the polycrystalline silicon films were usually measured with an automated spectrophotometer, and selected measurements were confirmed with a manual spectrophotometer and a mechanical surface profilometer. The latter was also used to determine the thicknesses of the amorphous films, which are highly absorbing and have a different

* Electrochemical Society Active Member.
Key words: films, LPCVD, silicon.

Table I. Average grain size as a function of deposition temperature

Temperature (°C)	Grain size (nm)
600	55
625	87
650	72
675	74
700	73
725	86

index of refraction from single crystal or polycrystalline silicon.

Transmission Electron Microscopy

Films deposited at each temperature were analyzed by transmission electron microscopy and diffraction.¹ The samples were prepared using a jet thinning technique. Diffraction patterns of films deposited at 525°, 550°, and 575°C exhibited the diffuse halos characteristic of amorphous samples [Ref. (4), Fig. 6a]. The micrographs also exhibited no structure over the majority of the area. However, small inclusions were seen within the structureless background. The density of these inclusions appears to increase with increasing deposition temperature, and one might speculate that they represent incipient crystallites, suggesting that the amorphous film is unstable. The inclusions are probably not an artifact of the sample preparation technique.

Micrographs of the film deposited at 600°C exhibited a very fine grain polycrystalline structure, with an average grain size of 55 nm, as indicated in Table I. The diffraction pattern was also characteristic of polycrystalline material; the second halo of the amorphous samples deposited at lower temperatures split into two rings, and some spots appeared superposed on the rings.

Films deposited over the temperature range 625°-725°C appeared qualitatively different from those deposited at lower temperatures, but generally similar to each other [Ref. (4), Fig. 6b]. Larger grain polycrystalline material was observed in the micrographs, with a much more ordered structure than at 600°C. The average grain size was in the range 72-87 nm for all of these films (Table I). Diffraction patterns showed the ring-dot structure characteristic of polycrystalline material, with the dots much better defined than in the film deposited at 600°C.

From this portion of the study, we may conclude that silicon films deposited in the LPCVD system at temperatures of 575°C and below are amorphous while those deposited above 600°C are polycrystalline, with the transition temperature close to 600°C. The proximity of the transition to 600°C suggests that this temperature should be avoided in order to obtain the same structure repeatably.

X-ray Diffraction

The preferred orientation of the crystallites was examined by x-ray diffraction on samples from the same wafers used for the transmission electron microscopy study. The intensities of the {111}, {220}, {311}, {400}, and {331} peaks were measured to indicate the amounts of {111}, {110}, {311}, {100}, and {331} texture present in the films. The relative amounts are plotted in Fig. 1 as a function of deposition temperature for the low pressure films and for a sample deposited at atmospheric pressure (AP) and a higher temperature (960°C). Neither the {311} or the {331} texture was dominant in any film investigated. All data are normalized for the strength of the signal expected from a randomly oriented film (5) and corrected for the film thickness (6).

No structure was seen in the 525° or 550°C films, but some was observed in the films deposited at 575°C,

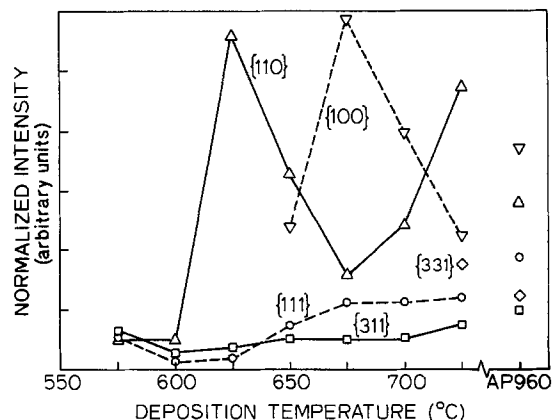


Fig. 1. X-ray texture as a function of deposition temperature for LPCVD silicon films and for an atmospheric pressure film.

which had been found to be basically amorphous by transmission electron microscopy. This x-ray texture can perhaps be related to the inclusions visible in the amorphous background of these films. The {110} texture shows a distinct peak at a deposition temperature of 625°C followed by a minimum at a higher deposition temperature and then a subsequent increase. The {100} texture has a maximum coincident with the {110} minimum. Except at the lower temperatures, the {111} texture shows a monotonic increase with increasing deposition temperature. The average grain size shown in Table I correlates with the amount of {110} texture, although this may be an artifact of the method of determining the grain size.

The structure seen in these low pressure films may be compared to that observed in films deposited in an rf-heated reactor at atmospheric pressure over a wide temperature range. Figure 2 shows previously reported data measured on films deposited elsewhere at atmospheric pressure (7). Each film was about 0.6 μm thick, and at all except the lowest temperatures, the deposition rate was held constant at about 0.12 $\mu\text{m}/\text{min}$.

As in the low pressure films, the {110} texture in these atmospheric pressure films shows a maximum at intermediate temperatures, followed by a minimum and then a subsequent increase. While this behavior is qualitatively similar to that observed in the low pressure films, the temperature range over which it is seen is markedly different. The {111} texture also shows similar trends in the two cases, with a monotonic increase with increasing deposition temperature at all except the lowest temperatures. In both cases the x-ray signal seen at the lowest temperatures may arise from inclusions in basically amorphous films. [The transition temperature between polycrystalline and amorphous deposits is generally

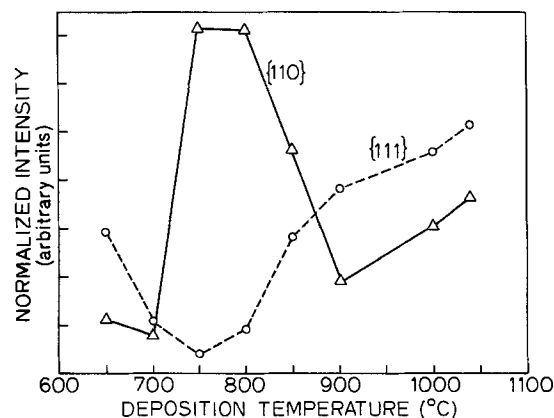


Fig. 2. X-ray texture as a function of deposition temperature for submicron atmospheric pressure films studied previously (7).

¹The analysis was performed by Advanced Research and Applications Corporation, Sunnyvale, California.

felt to be in the high 600°C temperature range for typical atmospheric pressure deposition conditions (3)].

Although the sensitivity of the x-ray diffraction measurements in the previous study of atmospheric pressure films was not adequate to reveal {100} texture in the submicron films, in thicker films the {100} texture was dominant in the temperature range where the {110} texture was minimum (7). This behavior is consistent with the {100} maximum seen in the low pressure films (Fig. 1).

The markedly different temperature range over which similar behavior is observed in the low pressure and atmospheric pressure films may be related either to the different deposition pressures or to the different deposition rates. It is known that large quantities of hydrogen may be adsorbed on the silicon surface during deposition of silicon from silane at atmospheric pressure in a hydrogen ambient (8). Not only does the presence of this hydrogen retard the silane decomposition reaction, but the adsorbed hydrogen also appears to impede surface migration of the silicon atoms which must move on the surface to form a given structure. Thus, with deposition rate held constant, a higher deposition temperature is needed to form a similar structure at atmospheric pressure than at low pressure, since additional energy is required to allow the same amount of surface migration.

More detailed comparison of the experimental data is complicated by the different deposition rates and the fact that the deposition rate was constant in the atmospheric pressure depositions while it varied with deposition temperature in the present experiment. A higher deposition rate R_D is expected to affect the structure in a similar manner to a lower deposition temperature, with the structure determined by the ratio R_D/D (9), where D is the diffusivity representing the motion of the silicon atoms on the surface before they are covered by subsequently arriving silicon atoms. Since D is strongly temperature dependent, a large change in deposition rate is needed to compensate for a small change in temperature in order to retain a given structure. A brief x-ray diffraction study of the structure formed at 625°C at several different deposition rates ranging from 5.6 to 14.7 nm/min in the low pressure system suggests that a factor of two change in deposition rate is approximately equivalent to a change of 30°C in deposition temperature near 625°C.

Where corresponding data are available, the temperature dependence of the dominant {110} texture in films in this study was similar to that of the previous investigation of LPCVD films (2). Except for an apparent 12°C temperature calibration difference, the two independent deposition systems produced similar films, lending support to the basic nature of the behavior seen. (Only a small portion of this apparent difference may be related to the slightly different deposition rates.) Of particular importance, the transition between the deposition of amorphous and polycrystalline films occurred at nearly the same temperature in both LPCVD systems and at a temperature markedly lower than that seen in atmospheric pressure systems.

Sheet Resistance

Since circuit speed may be critically dependent on the resistance of long polysilicon lines, the dependence of the sheet resistance on the deposition temperature of the silicon films was investigated. In one set of samples, phosphorus was added from a POCl_3 gaseous predeposition. In order to maximize any differences in resistance between the different samples (10), the predeposition was performed at a low temperature (900°C) with a relatively small amount of POCl_3 . The gaseous ambient during the predeposition consisted of 3800 cm^3/min of N_2 diluent, 1000 cm^3/min of O_2 , and

200 cm^3/min of N_2 saturated with POCl_3 by passing it through liquid POCl_3 at 22°C. The POCl_3 source was on for 30 min, and this portion of the cycle was followed by 5 min of N_2 before the wafers were slowly pulled from the furnace in 10 min. After removing the phosphorus glass in dilute HF, the sheet resistance was measured at five locations on each wafer with the results shown in Fig. 3 (solid lines). The sheet resistances on <111>- and <100>-oriented, single crystal wafers (with no deposited films) doped at the same time, averaged 44.3 Ω/\square ($\pm 5\%$).

The wafers were then protected with a low temperature deposited oxide to prevent surface damage and dopant loss and annealed for 80 min at 1000°C in a dry N_2 ambient. The sheet resistances measured after removing the deposited oxide are shown by the dashed lines in Fig. 3. The films deposited at the three lowest deposition temperatures have an unstable, amorphous structure, which crystallizes at annealing temperatures below 800°C, forming grains which may be even larger than those found in initially polycrystalline films (2). Consequently, the temperature of the POCl_3 predeposition will itself be adequate to form large crystallites in these films, leading to a low resistance since fewer grain boundary and other trapping sites are available to remove dopant atoms and carriers from the conduction process. The small change during the subsequent 1000°C anneal in these films indicates that the recrystallized structure in the initially amorphous films is reasonably stable.

At deposition temperatures of 600°C and above, a polycrystalline structure is formed during the film deposition. The decrease in resistance with increasing deposition temperature seen in Fig. 3 indicates a decreasing trap density, even though the average grain size in the as-deposited films does not vary greatly with deposition temperature.

The marked decrease in the resistance seen after the 1000°C anneal may be attributed to a decrease in the defect density or to an increase in the grain size with this additional heat-treatment, as well as to movement of dopant atoms out of the grain boundaries. This decrease in resistance is especially significant in the polycrystalline films deposited between 600° and 650°C, consistent with a less stable structure in these films.

Phosphorus was added to other samples by ion implantation of 5×10^{15} ions/ cm^2 at an energy of 50 keV. The films were then annealed at 550°C in dry N_2 for 75 min. High sheet resistances (greater than 10 $\text{k}\Omega/\square$) were measured on the films deposited at 525° and 550°C, probably reflecting their amorphous structure, while the sheet resistances of the initially polycrystalline films decreased with increasing deposition temperature from 3 $\text{k}\Omega/\square$ to 300 Ω/\square for dep-

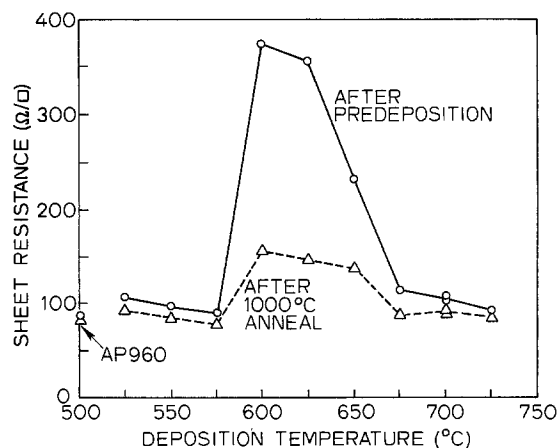


Fig. 3. Sheet resistance as a function of deposition temperature after a 900°C POCl_3 predeposition (solid lines) and after a subsequent 80 min anneal at 1000°C in dry N_2 (dashed lines).

osition temperatures varying from 600° to 725°C. The film deposited at 575°C showed intermediate results, with some conduction observed after the 550°C anneal, suggesting that this film is very unstable. After a subsequent 1000°C anneal the resistances of the initially amorphous films were lowest (approximately 40 Ω/\square), reflecting the influence of the large grain size in these films after annealing. The sheet resistances of the initially polycrystalline films ranged from 74 to 60 Ω/\square , again with the highest resistances for films deposited at the lowest temperatures.

It should be noted that the conditions of this experiment were chosen to maximize the differences in resistance between the various samples, especially in those doped from a POCl_3 source. At higher dopant concentrations, the trapping sites become saturated so that the effective carrier concentration becomes much less strongly dependent on the grain size (11). Impurity-assisted grain growth (12) may also become as important as the structure of the initial film so that the resistivity differences between samples are less. For practical implant doses, however, significant differences may still be seen.

In a related experiment reversible changes in the sheet resistance of polysilicon samples were briefly investigated as the annealing temperature was varied. Low pressure films deposited at 625°C were doped with POCl_3 at 950°C to produce a sheet resistance of 12.5 Ω/\square after the predeposition cycle. The samples were then sequentially annealed at different temperatures in the range from 400° to 1000°C for 80 min in a dry N_2 ambient, with the same samples receiving all annealing cycles. The samples were not protected by deposited oxide during these heat-treatments. After each anneal, the sheet resistance was measured, with the results shown in Fig. 4 for a sample which received 15 successive annealing cycles.

The resistance generally returns to a similar value as the annealing sequence is repeated, suggesting that dopant atoms segregate to grain boundaries at lower temperatures and are dispersed into the grains at higher temperatures (13, 14). As the dopant atoms are dispersed, they become active, lowering the resistance. This behavior indicates that dopant segregation at grain boundaries, as well as carrier trapping there, is important in determining the resistivity of polycrystalline-silicon films. The slightly higher resistance seen after the second sequence of annealing cycles may be attributed to the slightly different temperatures used in the two sequences or to a small loss of phosphorus since the wafer surfaces were not protected during the heat-treatment.

It is relevant for practical applications of polysilicon to note that the resistance is maximum after an intermediate temperature anneal and decreases at higher temperatures. At the lowest temperatures, the equilibrium value of the resistance is probably much higher than shown in Fig. 4, but the anneal time is

not adequate for equilibrium to be reached. Consequently, only a limited amount of dopant is able to segregate at the grain boundaries during the anneal, and the resistance only increases slightly from its high temperature value. It follows from this reasoning that the resistance would be much higher than indicated in Fig. 4 after a low temperature anneal if this low temperature anneal followed an anneal at an intermediate temperature, rather than one at a high temperature. Thus, the resistance of the polysilicon in an integrated circuit depends on the sequence of thermal processes after the polysilicon is doped.

Oxidation

In order to reveal further differences between the various types of polysilicon, the oxidation rate was briefly considered. Both the POCl_3 -doped and the implanted samples described in the previous section were oxidized along with undoped samples which did not receive any further heat-treatment after they were deposited. The films were oxidized at 850°C in a steam ambient to emphasize the surface reactions which dominate the oxidation kinetics in this region. In order to obtain oxide thicknesses that were convenient to measure with a u.v. spectrophotometer (15), the undoped samples were oxidized for 150 min while the doped samples were oxidized for only 75 min.

The oxide thickness measured on the undoped samples are shown in Fig. 5 along with oxide thicknesses measured on $\langle 111 \rangle$ - and $\langle 100 \rangle$ -oriented single crystal control wafers which were not covered with silicon films. The oxide thicknesses on the undoped films are close to that on lightly doped, $\langle 111 \rangle$ -oriented, single crystal silicon. The oxide thicknesses on all initially polycrystalline low pressure films (deposited at 600°-725°C) were within 8% and were slightly less than that on $\langle 111 \rangle$ silicon, probably indicative of the slower oxidation of other crystal orientations within the polycrystalline structure. Within the group of polycrystalline films there appears to be some correlation of the oxide thickness with the detailed orientation of the crystallites seen in Fig. 1. The thickest oxide is obtained on films with dominant $\{110\}$ texture (625° and 725°C) while the minimum occurs in the intermediate range where the $\{100\}$ texture is dominant. The oxide thickness on the initially amorphous films appears to be somewhat greater than that on $\langle 111 \rangle$ silicon. This thicker oxide may be related to the less stable structure in these films and the change in the structure during the oxidation cycle, since an 850°C heat cycle is sufficient to convert the amorphous structure to a polycrystalline one.

The oxide thicknesses on the doped samples appear to be dominated by the average dopant concentration in the film (dopant atoms/cm² divided by film thickness) so that thinner films oxidize more rapidly than

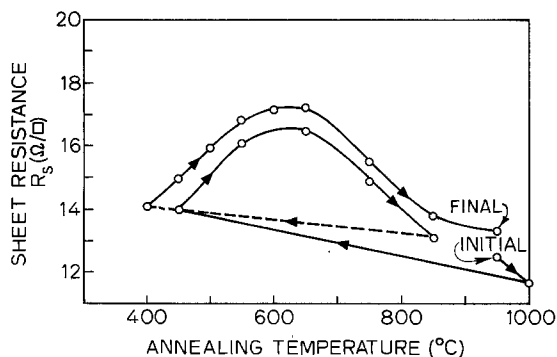


Fig. 4. Sheet resistance as a function of annealing temperature as the same phosphorus-doped sample is sequentially annealed. The film was deposited at 625°C.

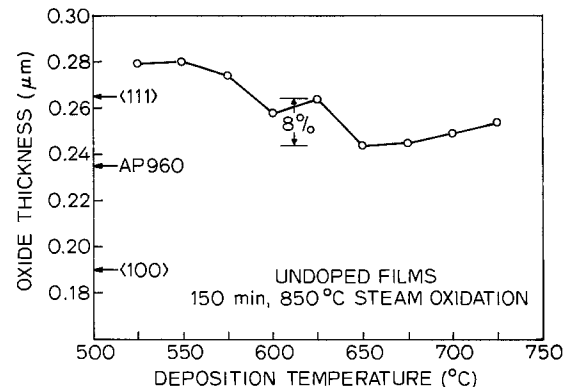


Fig. 5. Oxide thickness as a function of deposition temperature for undoped films after a 150 min steam oxidation at 850°C.

thicker films even if the structure is the same (15). While some similar dependence on film deposition temperature was seen for the implanted and annealed films as for the undoped films, the trends were less pronounced. No clear trends were seen for the POCl_3 -doped films that were subjected to a 1000°C anneal before oxidation, suggesting that grain-growth effects preceding oxidation may have dominated the oxidation kinetics.

Index of Refraction

The thickness of a deposited polysilicon film is usually measured by optical interference with either manual or automated spectrophotometers. Since the index of refraction of a polycrystalline-silicon film is close to that of single crystal silicon in the wavelength range of interest (16), analysis of the measurements is straightforward. Application of this technique to an amorphous silicon film is complicated by the different index of refraction and the large absorption, which decreases the reflected intensity available and shifts the apparent location of interference extrema.

To investigate the refractive index of amorphous silicon films, steps were etched in some amorphous and polycrystalline silicon films, and the films were measured with a surface profilometer and a spectrophotometer. From the thickness determined by step-height measurements and the wavelengths of the interference extrema measured with the spectrophotometer, the real part of the index of refraction of the amorphous films deposited at 525° and 550°C was determined as a function of wavelength, as shown in the upper curve of Fig. 6. The same films were then annealed at 900°C in N_2 for 40 min to crystallize the amorphous films, and the measurements were repeated. The index of refraction of the crystallized, initially amorphous films is shown by the lower curve of Fig. 6 and is now similar to that of crystalline silicon. Similar changes in the refractive index have recently been reported when amorphous films formed by atmospheric pressure CVD were crystallized (17). In the present experiment the properties of similarly treated, initially polycrystalline films did not change during the anneal.

Since the optical properties may depend on the detailed nature of the amorphous films, and consequently their deposition conditions, data obtained for amorphous films deposited at 525° or 550°C cannot be used with confidence for amorphous films obtained under markedly different deposition conditions.

Summary

Silicon films deposited by low pressure chemical-vapor deposition may be either amorphous or polycrystalline immediately after deposition, depending primarily on their deposition temperature. The amor-

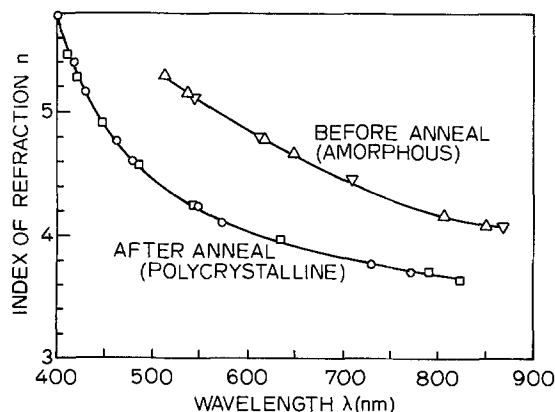


Fig. 6. Index of refraction as a function of wavelength for amorphous silicon films deposited at 525° and 550°C (upper curve) and for the same samples after annealing to crystallize the films (lower curve).

phous films are unstable and crystallize readily on further heat-treatment, such as those seen in integrated circuit processing. The properties of the amorphous films may differ significantly from those of crystalline silicon. The polycrystalline films, which are deposited above 600°C , are more stable. Their crystal structure is a strong function of the deposition temperature.

The resistance obtained on doping LPCVD silicon films depends on the film deposition temperature, although this dependence decreases after annealing the films at high temperatures. The resistance also changes reversibly as dopant atoms segregate at grain boundaries at lower temperatures and are dispersed into the grains at higher temperatures.

The oxidation rate is only a weak function of the deposition temperature for undoped films, although the initially amorphous films appear to oxidize somewhat more rapidly. The oxidation rate of heavily doped films is dominated by the dopant concentration, and the effect of deposition temperature is secondary. The index of refraction of the amorphous films is significantly larger than that of the polycrystalline films. Because of the marked differences between the properties of amorphous and polycrystalline films, deposition near the transition temperature should be avoided.

Acknowledgment

The author would like to thank W. A. Brown for depositing the films, F. Perlaki for assistance in securing the electron micrographs, R. Smith for the x-ray diffraction measurements, and Drs. C. J. Dell'Oca, J. L. Moll, and F. N. Schwettmann for encouragement during the course of this study.

Manuscript submitted July 9, 1979; revised manuscript received Oct. 12, 1979.

Any discussion of this paper will appear in a Discussion Section to be published in the December 1980 JOURNAL. All discussions for the December 1980 Discussion Section should be submitted by Aug. 1, 1980.

Publication costs of this article were assisted by Hewlett-Packard Laboratories.

REFERENCES

- R. S. Rosler, *Solid State Technol.*, **20**, 63 (April, 1977).
- T. I. Kamins, M. M. Mandurah, and K. C. Saraswat, *This Journal*, **125**, 927 (1978).
- N. Nagasima and N. Kubota, *Jpn. J. Appl. Phys.*, **14**, 1105 (1975).
- W. A. Brown and T. I. Kamins, *Solid State Technol.*, **22**, 51 (July, 1979).
- J. V. Smith, Editor, "X-Ray Power Data File," Card 5-0565, American Society for Testing and Materials, Philadelphia (1960).
- B. D. Cullity, "Elements of X-Ray Diffraction," p. 270, Addison-Wesley, Reading, Mass. (1956).
- T. I. Kamins and T. R. Cass, *Thin Solid Films*, **16**, 147 (1973).
- M. J.-P. Duchemin, M. M. Bonnet, and M. F. Koelsch, *This Journal*, **125**, 637 (1978).
- J. Bloem and L. J. Giling, in "Current Topics in Materials Science," Vol. 1, E. Kaldis, Editor, p. 163, North-Holland (1978).
- T. I. Kamins, *This Journal*, **126**, 833 (1979).
- T. I. Kamins, *IEEE Trans. Parts, Hybrids and Packaging*, **php-10**, 221 (1974).
- Y. Wada and S. Nishimatsu, *This Journal*, **125**, 1499 (1978).
- M. M. Mandurah, K. C. Saraswat, and T. I. Kamins, Abstract 571, p. 1433, The Electrochemical Society Extended Abstracts, Los Angeles, California, Oct. 14-19, 1979.
- J. C. North, A. C. Adams, and G. F. Richards, Abstract 202, p. 540, The Electrochemical Society Extended Abstracts, Pittsburgh, Pennsylvania, Oct. 15-20, 1978.
- T. I. Kamins, *This Journal*, **126**, 838 (1979).
- C. J. Dell'Oca, *ibid.*, **119**, 108 (1972).
- M. Hirose, M. Taniguchi, and Y. Osaka, *J. Appl. Phys.*, **50**, 377 (1979).

Effect of Chemical Structure on Thermal Depolarization of Phenolic Electrets

Padma Vasudevan

Center for Biomedical Engineering, Indian Institute of Technology, New Delhi-110029, India

and P. S. Viswanathan and K. L. Taneja

Department of Chemistry, Indian Institute of Technology, New Delhi-110029, India

ABSTRACT

Thermally stimulated depolarization (TSD) of novolac and novolac allyl ether electrets prepared at different polarizing temperatures of 36°, 56°, and 66°C with field strength of 1-3 kV/cm is compared with that of resols. Effects of the differences in chemical structure on the position of the TSD peaks and amount of stored charge are discussed. A correlation exists between these peak positions and chemical transformations occurring in the resin as indicated by infrared and differential thermal analytical studies.

Although electret formation in many of the common thermoplastic materials is known, very few papers are available on thermosetting resins like the phenolics (1), epoxy resins (2), polyimides (3), and synthetic melanins (4). Electrets of such resins are of interest since they are likely to be more thermally stable than those of thermoplastics and also because they are used in the electrical industry. The exact nature of the chemical phenomena occurring during the process of curing in thermosets is not fully understood. In recent years differential thermal analysis (DTA) and infrared spectral studies have been successfully applied (5, 6) for studying the curing phenomena. While it is well established that in the thermal depolarization of polar dielectrics, peaks corresponding to various relaxation processes can be identified, no report is available on the possibility of correlating the position of such peaks with chemical changes occurring on the polar groups.

Preliminary work (1) done on electret formation in semicured resols was encouraging. The present work is an extension of these studies to novolacs and novolac allyl ether and aims at a correlation between structural effects and electret behavior.

Experimental

As described earlier (1), resols were prepared by the standard method, and cast on an aluminum electrode by filling a square shaped mica cavity placed on it, followed by curing at the desired temperature to get sample I.

Novolacs and novolac allyl ether were prepared by the method described by Hui and Yip (7). These novolacs could not be cast on the aluminum electrode as described in Ref. (1), because during curing of novolacs excessive gas formation occurred and some of the gas was generally trapped. However, a few samples could be prepared without porosity by mixing novolac with hexamethylene tetramine (HMT) at ratios of 3:1 and 2:1 in methanol and pouring the solution in a mica cavity as above. These samples were cured at 70°C for 12 hr and dried in a vacuum dessicator to get samples II(a) and II(b).

A further set of samples was prepared by mixing novolac with HMT in the ratio 5:1 in methanol. The excess of methanol was removed by heating at 60°C for 30 min. These samples were then dried under vacuum, powdered, and made into pellets in vacuum under a load of 9 tons to get samples III.

As an alternative method of sample preparation, filter paper (Whatman 41) was dipped in a methanolic

solution of novolac and novolac allyl ether and cured in an oven for 24 hr at 60°C. The weight increase of the paper after curing was a measure of the sample taken. These were dried in a vacuum dessicator to get samples IV and V, respectively. After preparation, all the samples (I to V) were stored under vacuum to avoid interference of adsorbed moisture in the experiments. The samples were characterized by infrared and DTA techniques and the conductivities were measured as a function of temperature.

For electret formation samples I to V were sandwiched between aluminum electrodes and polarized at different temperatures as shown in Table I, in a specially designed oven at a field strength of 1-3 kV/cm for 1 hr. Without removing the voltage source, the samples were cooled to room temperature over a period of 1 hr and thereafter the voltage source was disconnected. The depolarization current from the samples was measured as a function of time and temperature for a linear rate of heating of 4°C/min. Similar experiments were carried out with the filter paper alone, to confirm that there was no electret effect in the blank paper.

Results

As already reported (1) resols I show depolarization peaks with T_m at 110°-160°C. The position of the peaks varied to some extent with the sample preparation, including conditions of curing. At high fields the presence of more than one overlapping peaks was noted. Since the resins are thermosetting, it was not possible to completely separate out the two peaks by peak cleaning as described by Perlman (8). Once the sample is heated to higher temperatures, changes in chemical structure would have occurred and the sample cannot again be polarized and studied by TSD. However, it was possible to locate the position of the second peak alone by heating the polarized samples to 110°C, cooling, and reheating. A sharper peak was thus obtained at about 130°C, for resols polarized at 76°C with a field of 1 kV/cm.

In the case of novolacs the results were very much dependent on the conditions of preparation. Table I summarizes the depolarization data of novolacs cured with and without HMT. Figure 1 is a TSD plot for novolacs cured without HMT (sample IV). In this case only one peak is observed at 110°C. This peak is fairly sharp and does not shift with temperature of polarization (T_p). When cured with HMT [samples II(a), II(b), and III] the TSD spectra became more complicated.

In the case of novolac allyl ether (sample V) the T_m appears at 130°C as seen from Fig. 2. At higher

Key words: electret, infrared, dielectrics.

Table I. Thermal depolarization data

Compound	T_p , °C	Field strength, kV/cm	T_{max} obtained, °C	i_{max} obtained, nA	Activation energy (E_a)	
					Initial rise method, eV/molecule	From conductivity data, eV/molecule
Resol (I)	56	1	110	30	0.62 ± 0.1	0.85-
	66	1	140	60		
	76	1	110, 160	300-700		
Novolac (III(a)) with HMT	56	1	106, 162	28, 23	—	—
	56	1	110-158	43		
	66	1	90-162	6, 36		
Novolac (III(b)) with HMT	50	1	94, 132-140, 200	22, 16, 29	—	—
	60	1	95-100, 200	74, 30		
Novolac with (III) HMT	60	1	106	0.64	—	—
	80	1	110	8.8		
Novolac without HMT (paper laminate) (IV)	36	3	112	120	0.87 ± 0.08	—
	56	3	106	255		
	66	3	103	255		
Novolac allyl ether (V)	36	3	126	60	0.96 ± 0.1	0.60
	56	3	130	140		
	66	3	132	275		

T_p , additional broad peaks occur at 150°-180°C. However at these temperatures the samples tend to melt and more detailed analysis could not be made and no further attempt was made towards the peak assignments.

The activation energy (E_a) was calculated for some samples by the initial rise method as well as from semi-log plots of resistance (R) of the unpolarized samples as a function of temperature. A representative plot is shown in Fig. 3.

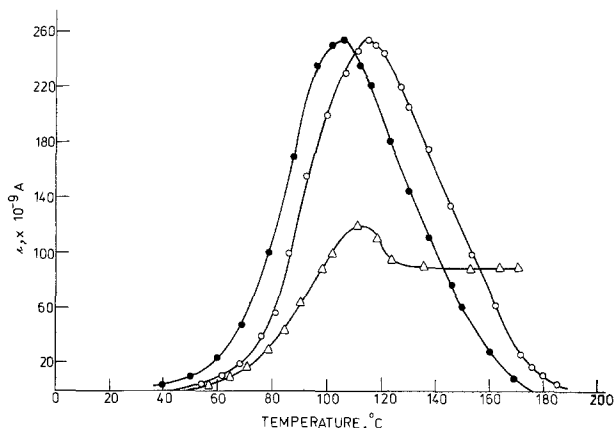


Fig. 1. Thermal depolarization spectra of novolacs. $T_p = 0$, 66°C; ●, 56°C; △, 36°C.

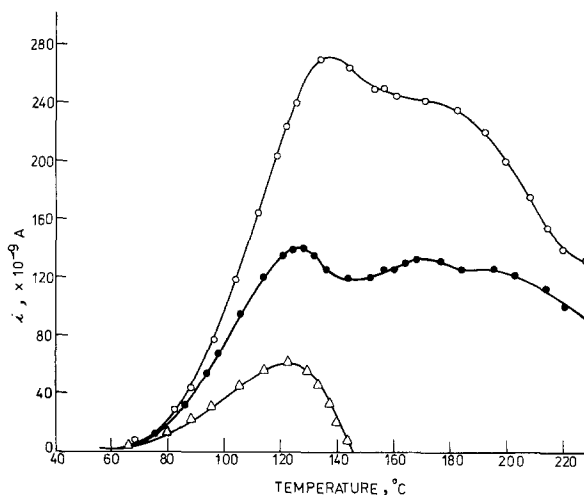


Fig. 2. Thermal depolarization spectra of novolac allyl ether. $T_p = 0$, 66°C; ●, 56°C; △, 36°C.

Discussion

In the absence of charge injection, the two basic mechanisms by which charge storage is expected to occur are by dipole orientation and space charge effects. In the semicured phenolics the dipoles available are the phenolic-OH and $-\text{CH}_2\text{OH}$ substituents on the phenol ring. The bridging of the rings are basically through methylene units and a few ether bridges may also be present. The nature and number of the various groups would depend on the initial phenol:formaldehyde ratio, conditions of condensation including pH, temperature, and presence of curing agents.

DTA studies on novolac formation (5) have indicated only one peak at 90°-110°C, attributed to condensation through formation of simple methylene linkages. Thus plain novolacs are normally expected to have only the phenolic $-\text{OH}$, and methylol groups would not be present to any significant extent. The

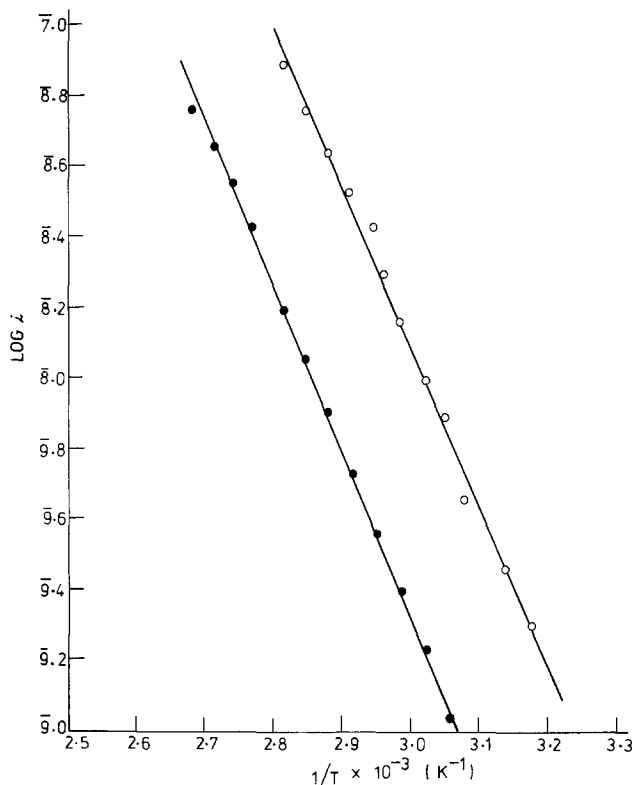


Fig. 3. Activation energy (E_a) by initial rise method. ○—novolac; ●—novolac allyl ether.

Table II. Principal infrared absorption peaks

Group	Wave number of peaks, cm^{-1} (Ref. (7), (9))	Novolac without HMT	Novolac allyl ether	Resol
—OH	3350	Present	Almost absent	Present
Benzene ring	1450-1600	Present	Present	Present
Allyl double bond	990, 920	Absent	Present	Absent
CH ₂ —OH	1010	Almost absent	Almost absent	Present
—CH ₂ —O—CH ₂ —	1075	Absent	Absent	—
—CH ₂ —	1445, 910	Present	Present	Present

infrared absorption of our semicured novolac samples are shown in Table II. Absence of a band at 1075 cm^{-1} indicates the absence of dimethylene ether bridges. The peak due to the phenolic —OH at 3400 cm^{-1} is quite prominent. The band at 1010 cm^{-1} corresponding to —CH₂OH is not significant. In our TSD experiments on novolac paper laminates (sample IV), we observe only one peak at about 105° – 110°C , in agreement with DTA results. Possibly this peak is associated with the phenomenon of curing. In fact sample III which is a mixture of novolac and HMT in the pellet form, also gives only one peak around 110°C . This indicates that cellulose-novolac interface or possible air trapping, is not responsible for this peak because these are present in sample IV but not in III.

In preparing sample III, time was not allowed for curing, and the HMT only served to lightly cross-link the matrix to enable pellet formation. However, novolac samples II(a) and II(b) containing HMT and resol (sample I) were allowed to cure. In such cases additional peaks are observed at 150° – 160°C and may be attributed to the depolarization of —CH₂OH groups with simultaneous condensation to form ether linkages. In fact, the DTA and infrared studies on resol formation (6) have indicated that phenols condense, with —CH₂ bridge formation, at 110°C , and monosubstituted phenols condense at 148°C . At 160°C , substituent methylol groups come together to form the dimethyl ether and at 200° – 210°C these may cleave. Thus the peaks at 200° – 210°C observed in samples II(a) and II(b) possibly correspond to charge

storage in the —CH₂—O—CH₂— linkages which cleave at this temperature.

Generally, under comparable conditions the i_{max} and stored charge are in the order novolac > allyl novolac > novolac cured with HMT. The addition of HMT enables novolacs to cross-link extensively and makes the orientation of dipoles difficult during the polarization process. However, resols store more charge as compared to novolac cured with HMT, probably through the increased number of —CH₂OH groups present.

The E_a values obtained by the initial rise method for the first peaks in the types of samples are of the same order (Table I). These match fairly well with the values obtained by conductivity measurement in the same temperature range.

Acknowledgment

One of the authors (K.L.T.) thanks the Indian Space Research Organization (ISRO), Department of Space, Government of India for financial support. We wish to thank Prof. P. K. C. Pillai for his valuable suggestions.

Manuscript submitted June 27, 1978; revised manuscript received Oct. 19, 1979.

Any discussion of this paper will appear in a Discussion Section to be published in the December 1980 JOURNAL. All discussions for the December 1980 Discussion Section should be submitted by Aug. 1, 1980.

Publication costs of this article were assisted by the Indian Institute of Technology.

REFERENCES

1. M. Goel, P. S. Viswanathan, and P. Vasudevan, *Polymer*, **19**, 905 (1978).
2. P. K. C. Pillai, and M. Goel, *This Journal*, **120**, 395 (1973).
3. E. Sacher, *IEEE Trans. Electr. Insul.*, **ei-14**, 85 (1979).
4. P. Baraldi, R. Capelletti, P. R. Crippa, and N. Romeo, *This Journal*, **126**, 1207 (1979).
5. V. A. Era, J. J. Linderg, and A. Malitia, *Angew. Makromol. Chem.*, **46**, 187 (1967).
6. Z. Katovic, *J. Appl., Polym. Sci.*, **11**, 85 (1967).
7. K. M. Hui and L. C. Yip, *J. Polym. Sci., Polym. Chem. Ed.*, **14**, 2323 (1976).
8. M. M. Perlman, *J. Appl. Phys.*, **42**, 2645 (1971).
9. D. O. Hummel, "IR Analysis of Polymers, Resins and Additives," Vol. 1, Wiley Interscience, New York (1971).

Thermal Quenching of Luminescence in a Disordered Compound: $\text{EuNa}_2\text{Mg}_2(\text{VO}_4)_3$

Hajime Yamamoto,* Setsuko Seki, Jean-Pierre Jeser,¹ and Tsutomu Ishiba

Hitachi Limited, Central Research Laboratory, Kokubunji, Tokyo 185, Japan

ABSTRACT

Luminescence of $\text{EuNa}_2\text{Mg}_2(\text{VO}_4)_3$ is six times as bright as that of $\text{YVO}_4:\text{Eu}$ under 365 nm light excitation at room temperature, but it suffers from thermal quenching at higher temperatures. The quenching is mainly caused by non-radiative relaxation from the emitting states. Energy diffusion among the lowest excited states, $^5\text{D}_0$, to sinks is a main reason of relatively weak quenching below 500°K. At higher temperatures, drastic quenching due to nonradiative relaxation within each Eu^{3+} ion is observed. Disordered distribution of Eu^{3+} and Na^+ revealed by optical and powder x-ray diffraction measurements is considered to induce the thermal quenching. Similar strong quenching beginning at around 500°-600°K is observed also for other disordered compounds, $\text{EuK}_5(\text{MoO}_4)_4$ and $\text{EuA}(\text{MoO}_4)_2$ ($A = \text{Na}, \text{K}, \text{and Rb}$).

Since Danielmeyer and his colleagues (1, 2) found that $\text{NdP}_5\text{O}_{14}$ is useful as a miniature laser material in 1972, various concentrated rare earth compounds called "stoichiometric"² materials have been studied extensively. These compounds are characterized by separations as great as 5-6Å between nearest neighbor rare earth ions, and consequently, by small interionic interaction even at high concentrations such as 10^{22} ions/cm³. Later, this characteristic naturally attracted attention to phosphor applications as well (3, 4).

The present work was also initiated with the aim of finding efficient "stoichiometric" Eu^{3+} phosphors. During the course of investigations, it was found that $\text{EuNa}_2\text{Mg}_2(\text{VO}_4)_3$ and its modifications with garnet structure show bright luminescence under 365 nm light excitation at room temperature. However, it was also found that luminescence efficiency and lifetime of the lowest emitting state $^5\text{D}_0$ greatly decrease at higher temperatures.

It is known that Eu^{3+} and Na^+ occupy equivalent sites in the garnet structure (5). If their distribution is ordered, the shortest distance between Eu^{3+} ions is 6.2Å, so that $\text{EuNa}_2\text{Mg}_2(\text{VO}_4)_3$ would be a "stoichiometric" material. Meanwhile, it was found that in several known "stoichiometric" Eu compounds, lifetimes of $^5\text{D}_0$ are independent of temperature. This is not consistent with the result for $\text{EuNa}_2\text{Mg}_2(\text{VO}_4)_3$ and raises doubts that this material is not "stoichiometric." This observation motivated the present work to find the reasons for thermal quenching. Analysis of the crystal structure and optical properties has revealed that Eu and Na are distributed in a disordered way. Therefore, the material is actually not a "stoichiometric" compound. The shortest distance between Eu ions is 3.8Å. Mechanism of the thermal quenching and its relationship with disordered distribution is discussed in the Discussion Section. Thermal quenching as measured by an increase in decay rates of the $^5\text{D}_0$ state was also found for other compounds, $\text{EuK}_5(\text{MoO}_4)_4$ and $\text{EuA}(\text{MoO}_4)_2$ ($A = \text{Na}, \text{K}, \text{Rb}, \text{and Cs}$). All of these compounds, except for $\text{EuCs}(\text{MoO}_4)_2$, show an indication of disordered distribution of Eu and alkali ions.

Experimental

Sample preparation.— $\text{Eu}_x\text{R}_{1-x}\text{Na}_2\text{Mg}_2(\text{VO}_4)_3$, ($R = \text{Y or La}, 0.1 \leq x \leq 1.0$).—The method used to prepare

* Electrochemical Society Active Member.

¹ Present address: Standard Elektrik Lorenz AG, D7000 Stuttgart 40, Germany.

Key words: luminescence, thermal quenching, nonradiative processes.

² Use of the word "stoichiometric" is not correct in this case, because it usually refers to the ratio between cations and anions and not to the ratio between two kinds of cations. So in this work, we use this word always with quotation marks.

the series of materials can be described by taking $\text{EuNa}_2\text{Mg}_2(\text{VO}_4)_3$, ($x = 1$) as an example. Essentially, the material is prepared by firing mixtures of high purity Na_2CO_3 , Eu_2O_3 , MgCO_3 , and NH_4VO_3 at 850°C in air for 24 hr. However, the preparation conditions had to be refined, because fired products did not have single phase garnet structure due to formation of a zircon structure, EuVO_4 . Thermogravimetric and differential thermal analysis as well as x-ray diffraction measurements showed that EuVO_4 is formed at a temperature lower than the formation temperature of $\text{EuNa}_2\text{Mg}_2(\text{VO}_4)_3$ and that EuVO_4 formation proceeds more rapidly at a fast (20 deg/min) heating rate than at a slow (5 deg/min) heating rate. It was also confirmed that EuVO_4 once fired at 850°C can be converted to $\text{EuNa}_2\text{Mg}_2(\text{VO}_4)_3$ by refiring with Na_2CO_3 , MgCO_3 , and NH_4VO_3 at 850°C. Therefore, the quantity of EuVO_4 can be minimized by repeating that refiring process two or three times. The x-ray powder pattern of samples prepared in this way showed that the intensity of the strongest diffraction line of EuVO_4 was less than 5% that of $\text{EuNa}_2\text{Mg}_2(\text{VO}_4)_3$.

Other materials.—Europium alkali molybdates and tungstates were prepared by firing stoichiometric mixtures of Eu_2O_3 , alkali carbonates, and MoO_3 or H_2WO_4 in air at 620°C. X-ray diffraction analysis showed that samples prepared this way are single phase.

More usual compounds were prepared in conventional ways: EuPO_4 by firing a mixture of Eu_2O_3 , $(\text{NH}_4)_2\text{HPO}_4$, and Na_2CO_3 in O_2 at 1160°C for 3 hr; EuVO_4 by firing a mixture of Eu_2O_3 and NH_4VO_3 in air at 1200°C for 2 hr. The last material, $\text{EuP}_5\text{O}_{14}$, was prepared by one of the authors (J-P. J.) at the Max Planck Institut, Stuttgart.

Optical measurements.—Luminescence spectra were measured in two different ways. Low resolution spectra covering the whole visible region were measured by a Nikon P-250 monochromator which has a dispersion of 6 nm/mm. A photomultiplier signal was processed by a data acquisition system, Hewlett-Packard 9825A, to obtain corrected spectra. Peak wavelengths and shapes of emission lines were obtained from high resolution spectra measured with a Spex 1400 monochromator with a dispersion of 1 nm/mm. In both cases, the excitation source employed was a high pressure Hg lamp combined with a CuSO_4 solution filter and a glass filter, Toshiba UV-D1A, which cuts off visible light.

Excitation spectra were measured by the conventional method with a Hitachi MPF-4 spectrometer. For measurements of decay characteristics, an Avco-

Everett Model 1000 tunable dye-laser system was used as an excitation source.

The laser was operated at 464 nm, which corresponds to the ${}^7F_0 \rightarrow {}^5D_2$ transition of Eu^{3+} . Pulsed duration was 6 μsec , and spectral width was about 6 nm. Luminescence from a sample was focused on a slit of a Nikon P-250 monochromator. Usually, the wavelength of the monochromator was set at the position of the main peak of $(\text{Eu}, \text{Y})\text{Na}_2\text{Mg}_2(\text{VO}_4)_3$, which is 609.7 nm, in order to eliminate emission from the by-product $(\text{Eu}, \text{Y})\text{VO}_4$. The luminescence was detected with an HTV R 666S photomultiplier. The photomultiplier signal was stored by a Biomation Model 1010 waveform recorder and averaged by a signal averager, Toyo Model 1010S. The average of 50 or 100 decay curves was converted to a semilogarithmic plot by the data acquisition system 9825A.

Raman spectra of powder samples were measured at room temperature by using a Cary 82 Raman spectrometer. Powder was charged in a quartz capillary and mounted parallel to the entrance slit of the spectrometer. The incident laser light came into the bottom of the capillary and propagated along the wall of the capillary. Scattered light was collected by a condenser lens and focused on the slit efficiently.

Results

Luminescence spectra.—The luminescence spectrum of $\text{EuNa}_2\text{Mg}_2(\text{VO}_4)_3$ is quite similar to the reported spectra of $\text{NaCa}_{1.9}\text{Eu}_{0.1}\text{Li}_{0.1}\text{Mg}_{1.9}(\text{VO}_4)_3$ (6) and of $\text{Ca}_{2-2x}\text{Na}_{1-x}\text{Eu}_x\text{Mg}_2(\text{VO}_4)_3$, ($0 < x \leq 1.0$) (7), which have garnet structure. In the systems $(\text{Eu}_x\text{R}_{1-x})\text{Na}_2\text{Mg}_2(\text{VO}_4)_3$, ($\text{R} = \text{Y}$ or La , $0.1 \leq x \leq 1.0$), luminescence spectra have essentially the same features irrespective of x , except for the widths of the lines. This result agrees with x-ray diffraction data which show that these systems form perfect solid solutions. It was also found that temperature changes in the range of $77^\circ\text{--}570^\circ\text{K}$ do not cause any significant changes in low resolution spectra.

Local site symmetry around Eu^{3+} ions was examined by observation of crystal-field structures in the luminescence spectrum of $\text{EuNa}_2\text{Mg}_2(\text{VO}_4)_3$. The dodecahedral site in the garnet structure has site symmetry D_2 . The numbers of the crystal-field components of the 7F_J states expected from group theory agree well with the observed numbers except for 7F_3 , in which three lines are missing. It can be safely concluded that Eu^{3+} occupies the dodecahedral site, since the missing lines were quite possibly not detected because of their low intensities.

Relative luminescence intensities vs. Eu concentration and temperature.—The relative intensities of the 5D_0 emission of $\text{Eu}_x\text{Y}_{1-x}\text{Na}_2\text{Mg}_2(\text{VO}_4)_3$ under 365 nm excitation at room temperature as a function of the Eu concentration are shown in Fig. 1. The broad maximum light output is found at around 70%, or 3×10^{21} Eu ions/ cm^3 . This density is relatively large compared with typical doped phosphors and is closer to the values found in "stoichiometric" phosphors. For example, the density of Eu ions is 5×10^{20} ions/ cm^3 in $\text{YVO}_4:\text{Eu}(4\%)$, and 4×10^{21} ions/ cm^3 in $\text{EuP}_5\text{O}_{14}$. The fact is that $\text{Eu}_x\text{Y}_{1-x}\text{Na}_2\text{Mg}_2(\text{VO}_4)_3$ is not a "stoichiometric" material, as is discussed later. The high optimum concentration is commented on in a later section.

At room temperature, $\text{Eu}_x\text{Y}_{1-x}\text{Na}_2\text{Mg}_2(\text{VO}_4)_3$, ($0.1 \leq x \leq 1$), is a more efficient phosphor than the commercial phosphor $\text{YVO}_4:\text{Eu}$.³ At $x = 0.7$, the former is 8.4 times as bright as the latter. An investigation of compounds with modified chemical composition led to the finding that $\text{Eu}_{0.7}\text{La}_{0.3}\text{Na}_2\text{Mg}_2(\text{VO}_4)_3$ is 14.6 times as bright as $\text{YVO}_4:\text{Eu}$. In Fig. 2 are shown the brightness data of $\text{EuNa}_2\text{Mg}_2(\text{VO}_4)_3$, $\text{Eu}_{0.7}\text{La}_{0.3}\text{Na}_2\text{Mg}_2(\text{VO}_4)_3$, and $\text{YVO}_4:\text{Eu}$ under 365 nm excitation as a function of temperature. As is well known (8), $\text{YVO}_4:\text{Eu}$ shows a steep increase in efficiency with increasing temperature. In contrast, $(\text{Eu}, \text{R})\text{Na}_2\text{Mg}_2(\text{VO}_4)_3$, ($\text{R} = \text{Y}$ or La), suffers from a drastic thermal quenching. In this way, the two kinds of vanadates show quite contrary temperature dependence. The thermal quenching of $(\text{Eu}, \text{R})\text{Na}_2\text{Mg}_2(\text{VO}_4)_3$ can also be observed by means of excitation spectra at varying temperatures: Fig. 3 shows the result for $\text{EuNa}_2\text{Mg}_2(\text{VO}_4)_3$. The 4f-4f excitation lines of Eu^{3+} as well as the broad band due to host absorption lose intensity with increasing temperature. The intensity of the ${}^7F_0 \rightarrow {}^5D_2$ excitation line at 464 nm is plotted against temperature in Fig. 4. Its temperature dependence is nearly the same as that of the intensity under 365 nm excitation, which indicates that the main loss processes occur at 5D_2 and/or the lower states, 5D_1 , 5D_0 .

Excitation and diffuse reflection spectra were measured at room temperature for a series of $\text{Eu}_x\text{Y}_{1-x}\text{Na}_2\text{Mg}_2(\text{VO}_4)_3$ in the region of 290-600 nm. Changes due to variation in x were not found near the host absorption region. In other words, the charge transfer band from O^{2-} to Eu^{3+} was not detected.

Decay characteristics.—The temperature dependence of the decay characteristics of 5D_0 emission was mea-

³ Exactly speaking, PO_4^{3-} ions substitute 6 mole percent of VO_4^{3-} in this phosphor. The Eu concentration is 4 atom percent.

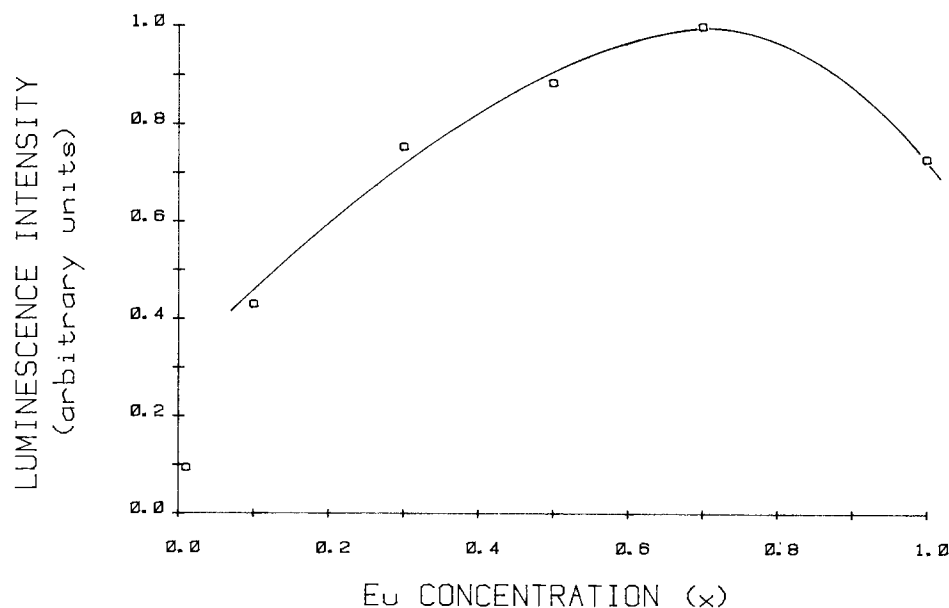
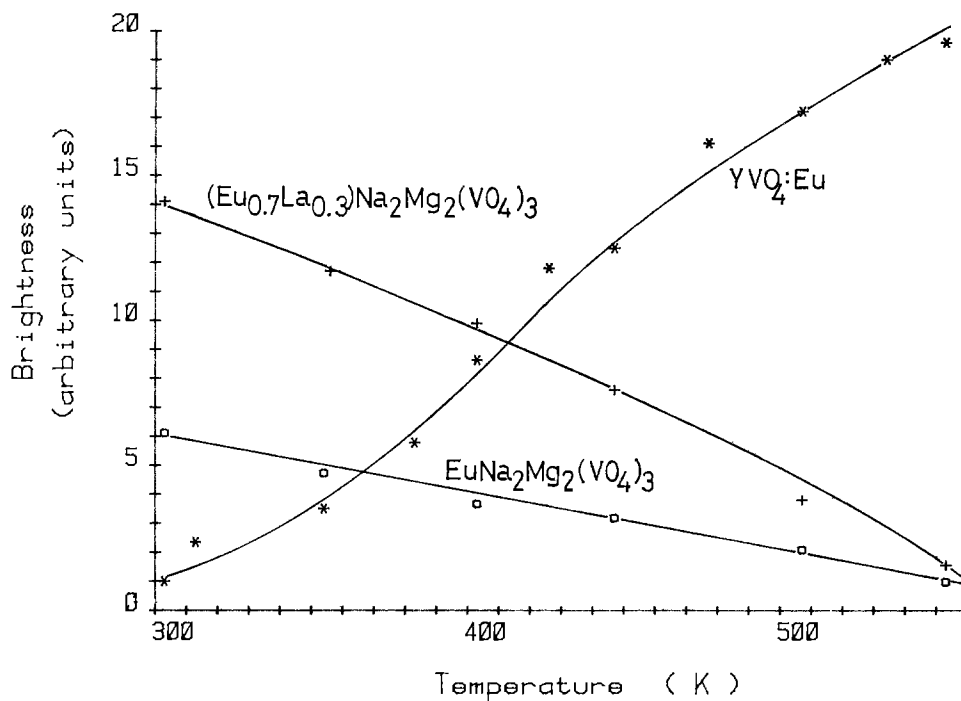


Fig. 1. Dependence of the luminescence intensity of $\text{Eu}_x\text{Y}_{1-x}\text{Na}_2\text{Mg}_2(\text{VO}_4)_3$ on Eu concentration ($0.1 \leq x \leq 1.0$) at room temperature. Excitation was made with a high pressure Hg lamp and the luminescence from the 5D_0 state was monitored.

Fig. 2. Temperature dependence of brightness under 365 nm light excitation at room temperature. (\square) $\text{EuNa}_2\text{Mg}_2(\text{VO}_4)_3$, (+) $\text{Eu}_{0.7}\text{La}_{0.3}\text{Na}_2\text{Mg}_2(\text{VO}_4)_3$, and (*) $\text{YVO}_4:\text{Eu}$. Brightness is normalized at the value of $\text{YVO}_4:\text{Eu}$ at room temperature.



sured for $\text{Eu}_x\text{Y}_{1-x}\text{Na}_2\text{Mg}_2(\text{VO}_4)_3$ ($x = 1, 0.5$, and 0.1) from 77°K to 600°K .

The decay characteristics depend on both the Eu concentration and temperature. Some examples are shown in Fig. 5. The decay curves are nearly exponential when the Eu concentration and temperature are both sufficiently low or high. In other regions [for example, at a low Eu concentration ($x = 0.1$) and a high temperature (above 650°K), or at a high Eu concentration ($x = 1.0$) and an intermediate temperature (near 500°K)] decay curves are strongly nonexponential. However, at long times after the excitation pulse, an exponential component is observed. This component probably originates in diffusion-limited relaxation and its rate is written as

$$1/\tau = 1/\tau_0 + 1/\tau_D \quad [1]$$

where $1/\tau_0$ is the radiative decay rate and $1/\tau_D$ is the decay rate due to diffusion. The exponential decay

rate, $1/\tau$, is plotted against temperature in Fig. 6. It increases with increasing temperature as indicated by a decrease in the excitation-line intensity at 464 nm (Fig. 4). The temperature dependence of the decay rates differs greatly in the two regions. Below 500°K , the decay rate shows relatively small changes with temperature. At 77°K the decay rates are nearly the same for the three Eu concentrations. This value should be the intrinsic radiative transition probability. Above 500°K the decay rate increases greatly. The nonradiative decay added to the lower temperature rate is insensitive to the Eu concentration. The activation energy is $(9 \pm 1) \times 10^3\text{ cm}^{-1}$ for the three concentrations. This behavior forms a sharp contrast with that in the lower temperature region, where nonradiative decay increases greatly with the Eu concentration. The result given in Fig. 4 shows that the most important factor on thermal quenching is energy loss within Eu^{3+} ions. The loss processes take place

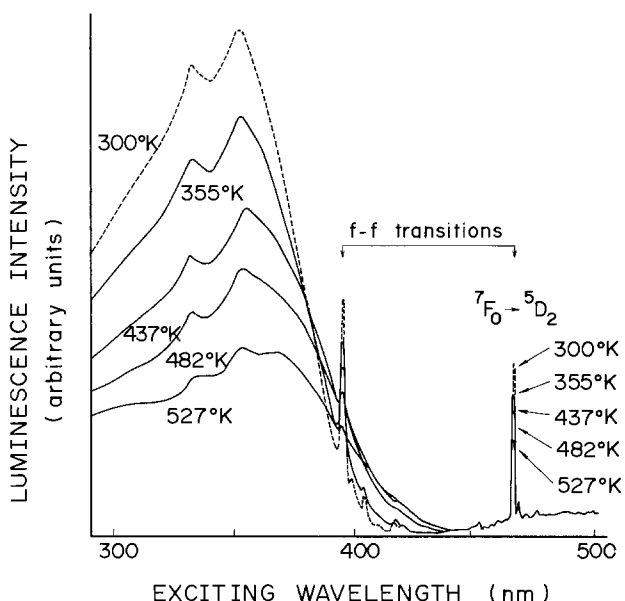


Fig. 3. Excitation spectra of $\text{EuNa}_2\text{Mg}_2(\text{VO}_4)_3$ at various temperatures. Luminescence intensity was monitored at 610 nm with a bandwidth of 1 nm .

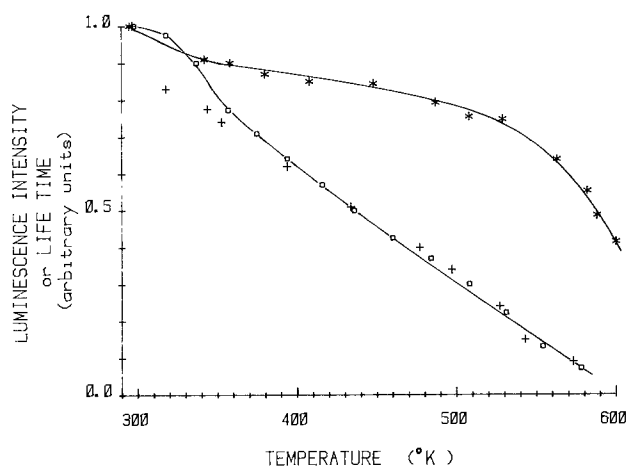


Fig. 4. Temperature dependence of the $^5\text{D}_0$ lifetime (*); the $^5\text{D}_0$ luminescence intensity excited by 464 nm light, which corresponds to the $^7\text{F}_0 \rightarrow ^5\text{D}_2$ transition (\square); and the $^5\text{D}_0$ luminescence intensity under 365 nm excitation corresponding to the VO_4^{3-} absorption (+). The data are normalized to room temperature values. The $^5\text{D}_0$ luminescence intensity under 464 nm excitation was obtained by an integration of excitation peak in Fig. 3. The intensity under 365 nm excitation was obtained independently by using a high pressure Hg lamp.

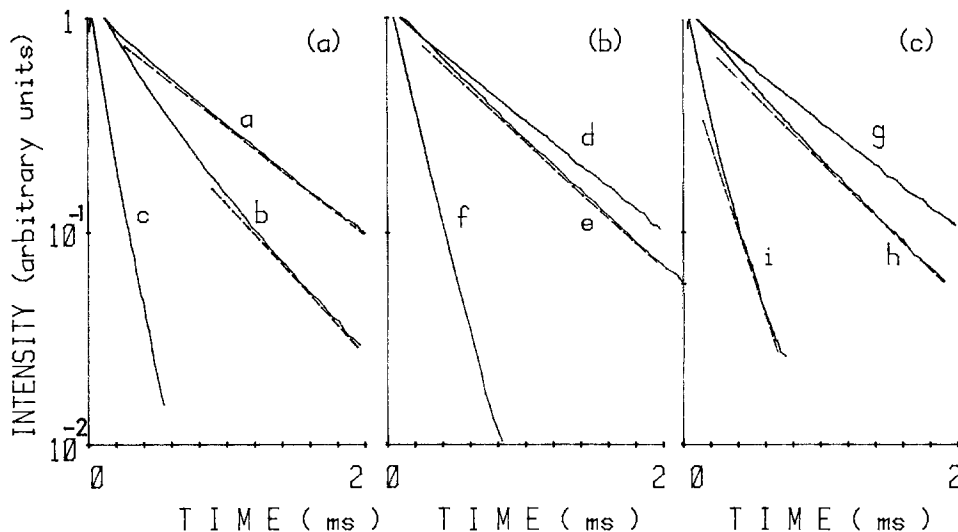


Fig. 5. Examples of decay curves of 5D_0 luminescence from $\text{Eu}_x\text{Y}_{1-x}\text{Na}_2\text{Mg}_2(\text{VO}_4)_3$. (a) $x = 1.0$; curve a, 77°K; curve b, 448°K; and curve c, 653°K. (b) $x = 0.5$; curve d, 77°K; curve e, 443°K; and curve f, 645°K. (c) $x = 0.1$; curve g, 77°K; curve h, 385°K; and curve i, 680°K. Note how decay curves deviate from exponential forms indicated by broken straight lines.

mainly at the 5D_0 state, as shown in Fig. 6. In general, the energy-level structure of Eu^{3+} is unfavorable for quenching of 5D_0 emission by multiphonon emission, since 5D_0 is widely separated from the highest metastable state 7F_6 . In fact, it is rather unusual that the lifetime of 5D_0 gets shorter with increasing temperature. As a comparison, the 5D_0 lifetimes of various compounds including Eu^{3+} were measured as functions of temperature. The studied materials are (i) "stoichiometric" materials, $\text{EuP}_5\text{O}_{14}$, $\text{EuNa}_5(\text{MoO}_4)_4$,

and $\text{EuNa}_5(\text{WO}_4)_4$; (ii) Eu compounds with a normal distance (3-4Å) between the nearest Eu ions, EuPO_4 , EuVO_4 , $\text{EuA}(\text{MoO}_4)_2$ with $A = \text{Na, K, Rb, or Cs}$, and $\text{EuK}_5(\text{MoO}_4)_4$; and (iii) a doped material, $\text{YVO}_4:\text{Eu}$ (4%). The decay rates of $\text{YVO}_4:\text{Eu}$, EuPO_4 , and the "stoichiometric" materials are nearly independent of temperature from room temperature to 680°K. The decay rate of EuVO_4 decreases from room temperature to 450°K, but at higher temperatures stays constant (Fig. 7). On the other hand, $\text{EuA}(\text{MoO}_4)_2$ and $\text{EuK}_5(\text{MoO}_4)_4$ show drastic increases in the decay rate with increasing temperature above 500°K, just as $(\text{Eu, Y})\text{Na}_2\text{Mg}_2(\text{VO}_4)_3$ does (see Fig. 8).

Here we add a brief description of decay characteristics. The "stoichiometric" compounds and the doped phosphor, $\text{YVO}_4:\text{Eu}$, show nearly single exponential decays. Other compounds show more or less non-exponential decays. Since in most cases, the tail of a decay curve can be reasonably approximated as exponential, its decay rate was taken as the representative value and plotted in Fig. 7 and 8. The decay curve of EuPO_4 is composed of two exponential parts with comparable intensities. For convenience, the smaller rate is given in Fig. 7. The compounds, $\text{EuNa}(\text{MoO}_4)_2$,

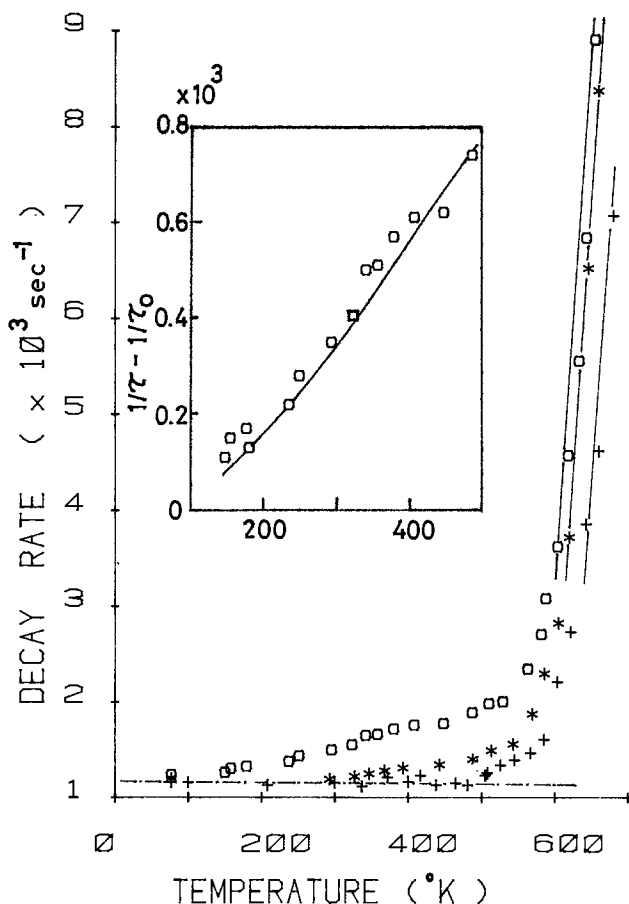


Fig. 6. Temperature dependence of decay rates for $\text{Eu}_x\text{Y}_{1-x}\text{Na}_2\text{Mg}_2(\text{VO}_4)_3$. (\square) $x = 1.0$, ($*$) $x = 0.5$, and ($+$) $x = 0.1$. In the inset, the lower temperature region for $x = 1.0$ is magnified. The ordinate of the inset figure is the nonradiative decay rate, $1/\tau - 1/\tau_0$, where $1/\tau$ is the observed decay rate and $1/\tau_0$ is the radiative decay rate, $1.15 \times 10^3 \text{ cm}^{-1}$, indicated by the dash-dot line at the bottom of the main figure. The solid curve in the inset was calculated according to Weber's formula (see text).

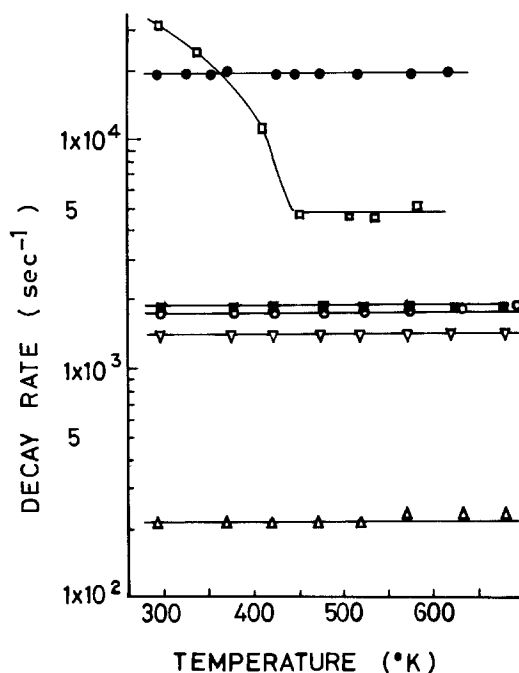


Fig. 7. Temperature dependence of decay rates. (Δ) $\text{EuP}_5\text{O}_{14}$, (∇) $\text{EuNa}_5(\text{WO}_4)_4$, (\circ) $\text{EuNa}_5(\text{MoO}_4)_4$, (\blacksquare) $\text{YVO}_4:\text{Eu}$, (\bullet) EuPO_4 , and (\square) EuVO_4 .

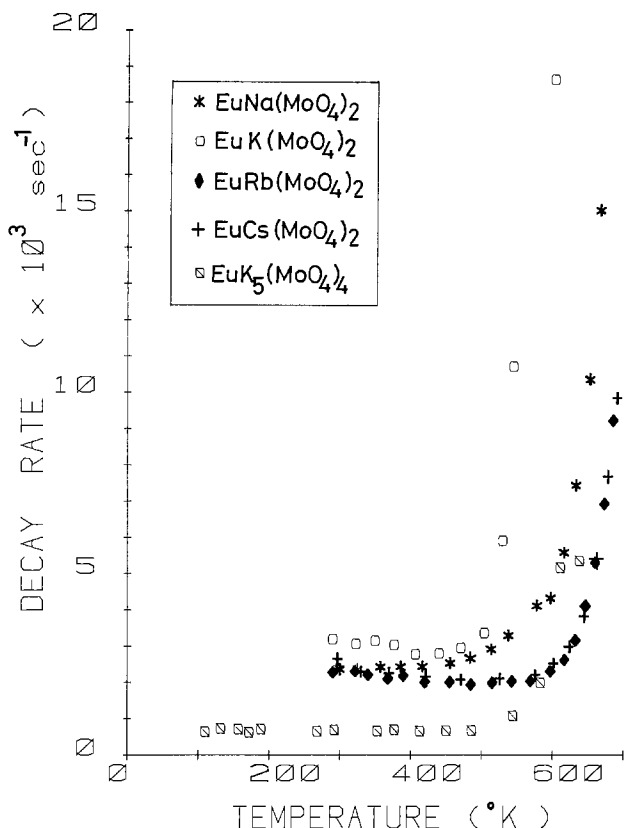


Fig. 8. Temperature dependence of decay rates. (*) $\text{EuNa}(\text{MoO}_4)_2$, (\square) $\text{EuK}(\text{MoO}_4)_2$, (\blacklozenge) $\text{EuRb}(\text{MoO}_4)_2$, (+) $\text{EuCs}(\text{MoO}_4)_2$, and (\boxtimes) $\text{EuK}_5(\text{MoO}_4)_4$.

$\text{EuK}(\text{MoO}_4)_2$, and $\text{EuK}_5(\text{MoO}_4)_4$ have fast components in the initial period of decay. The decay rate was determined at the tails of the curves. This is good approximation below about 400°K since the intensity of the fast component is not large. However, as the thermal quenching occurs, the whole decay curve looks like the sum of two or more components of comparable intensity. Fitting with an exponential form is only moderately good. In Fig. 8, the slowest component within the measured time span (0.2-1 msec) is plotted. In their initial periods, $\text{EuRb}(\text{MoO}_4)_2$, $\text{EuCs}(\text{MoO}_4)_2$, and EuVO_4 also show fairly strong fast components. The slower components, however, can be fitted with exponential forms even above 500°K.

These characteristics suggest that there are complicated factors controlling decay curves in these materials.

Luminescence line widths.—The widths of Eu^{3+} luminescence lines were measured at 77°K for $\text{EuNa}_2\text{Mg}_2(\text{VO}_4)_3$ and the compounds shown in Fig. 7 and 8 as a means of checking the regularity of the crystal field around Eu^{3+} ions. A convenient probe is the strongly forbidden ${}^5\text{D}_0 \rightarrow {}^7\text{F}_0$ line, which usually has a width of less than a few cm^{-1} . The results are given in Table I. The compounds $\text{EuNa}_2\text{Mg}_2(\text{VO}_4)_3$, $\text{EuNa}(\text{MoO}_4)_2$, $\text{EuK}(\text{MoO}_4)_2$, $\text{EuRb}(\text{MoO}_4)_2$, and $\text{EuK}_5(\text{MoO}_4)_4$ show inhomogeneous broadening, while the other compounds have normal narrow lines. It has been reported that $\text{EuK}_5(\text{MoO}_4)_4$ has a disordered lattice, in which Eu^{3+} and K^+ are randomly distributed at equivalent sites (9). Therefore, it is most straightforward to assume that $\text{EuNa}_2\text{Mg}_2(\text{VO}_4)_3$ is also a disordered compound. These compounds show a decrease in the ${}^5\text{D}_0$ lifetime with temperature (Fig. 6 and 8). An exception is $\text{EuCs}(\text{MoO}_4)_2$, which shows a decrease in the ${}^5\text{D}_0$ lifetime in spite of normal narrow widths at 77°K. So far, no phase transition has been found on this compound (10).

Table I. Half-widths of ${}^5\text{D}_0 \rightarrow {}^7\text{F}_0$ emission lines at 77°K. For materials marked with (*), half-widths of ${}^5\text{D}_0 \rightarrow {}^7\text{F}_1$ lines are given, since ${}^5\text{D}_0 \rightarrow {}^7\text{F}_0$ lines were not found.

Materials	Line width (cm^{-1})
$\text{YVO}_4:\text{Eu}$	2.3
$\text{EuP}_5\text{O}_{14}$	3.5
$\text{EuNa}(\text{MoO}_4)_2$	14.3
$\text{EuK}(\text{MoO}_4)_2$	11.8
$\text{EuRb}(\text{MoO}_4)_2$	13.3
$\text{EuCs}(\text{MoO}_4)_2$	4.1*
$\text{EuNa}_2(\text{VO}_4)_3$	4.0*
$\text{EuK}_5(\text{VO}_4)_4$	16.7
$\text{EuNa}_2\text{Mg}_2(\text{VO}_4)_3$	14.7

Raman spectra.—Raman spectra of powder samples were measured at room temperature as another means of observing lattice irregularity. In this experiment, $\text{YNa}_2\text{Mg}_2(\text{VO}_4)_3$ and YVO_4 were compared with each other. The Raman spectrum of single crystal YVO_4 has been measured and its assignment is well established (11). Our powder Raman data agree well with the crystal data.

The spectrum of $\text{YNa}_2\text{Mg}_2(\text{VO}_4)_3$ is similar to the published spectrum of Na_3VO_4 (12) in the number and energies of the lines. As the symmetry of VO_4^{3-} in Na_3VO_4 is T_d , that of VO_4^{3-} in $\text{YNa}_2\text{Mg}_2(\text{VO}_4)_3$ is also T_d in the first approximation. The half-widths of the YVO_4 lines are 2-3 cm^{-1} ; the lines of $\text{YNa}_2\text{Mg}_2(\text{VO}_4)_3$ are much broader, with the half-widths of 10-15 cm^{-1} . This result suggests that the structure of VO_4^{3-} in $\text{YNa}_2\text{Mg}_2(\text{VO}_4)_3$ fluctuates statistically around the average configuration with the T_d symmetry. If Y^{3+} and Na^+ ions randomly occupy the dodecahedral site, their disordered arrangement will cause a weak distortion from T_d . In this sense, the Raman spectrum is not inconsistent with the disordered arrangement.

Calculation of x-ray powder diffraction intensities.—In the previous sections, a disordered distribution of Eu^{3+} and Na^+ was assumed based on spectroscopic data. To confirm this assumption, x-ray powder diffraction intensities were calculated for both ordered and disordered distributions. Calculation was performed by a computer program which outputs diffraction angles, interplanar spacings, Miller indexes, and intensities. Input data were obtained by the following procedures. Atomic positions of lattice points were cited from the work of Wyckoff (12). The positions of the Eu sites in the ordered distribution were uniquely determined by the two conditions: (i) eight Eu ions are positioned in 24 dodecahedral sites in a unit cell in such a way that each ion is separated from the others as far as possible, and (ii) translational symmetry is reserved.

In the disordered distribution, Eu^{3+} and Na^+ ions randomly occupy 24 sites with occupation probability of 1:2. Therefore, the atomic scattering factor, f , of the site was assumed to be a weighted average of the scattering factors of Eu and Na

$$f = (1/3)f_{\text{Eu}} + (2/3)f_{\text{Na}} \quad [2]$$

The calculated diffraction intensities are plotted against the Miller indexes in Fig. 9. When normalized at the strongest line, line intensities in the disordered distribution are, in general, smaller than those in the ordered distribution. In addition, one finds some vanishing lines in the disordered distribution. They are (101) to (211) at small angles, (321), (631), (721), and (732).

The observed diffraction pattern (open circles in Fig. 9) resembles the disordered distribution pattern (filled triangles) more than the ordered distribution (open triangles). Therefore, the assumed disordered distribution seems plausible.

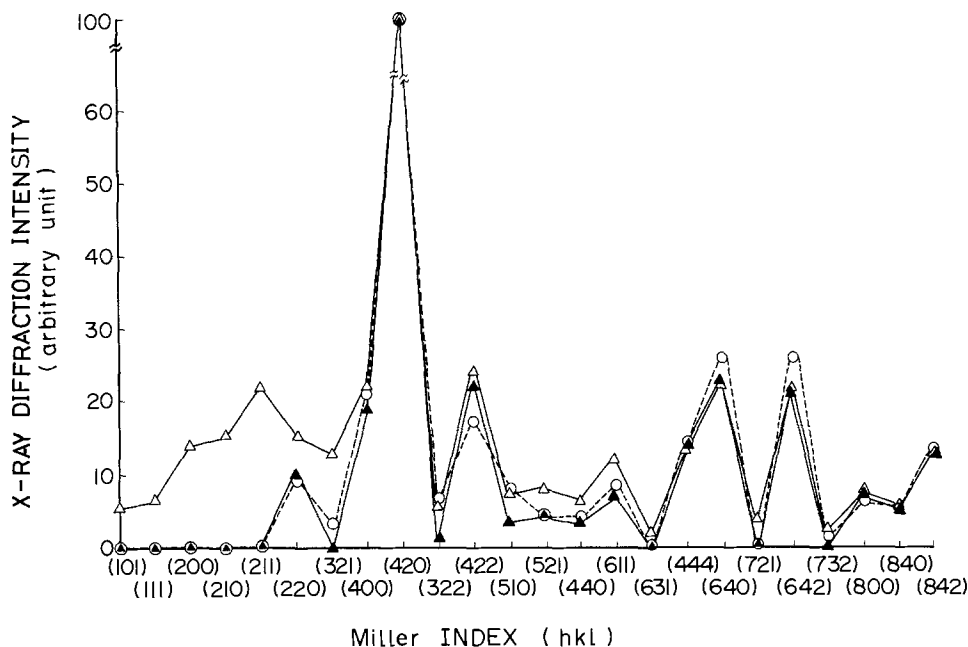


Fig. 9. Powder x-ray diffraction intensities. (○) Observed, (△) calculated for the ordered distribution, and (▲) calculated for the disordered distribution.

According to this result, the shortest distance between Eu ions is not 6.2Å as expected for the ordered "stoichiometric" compound, but only 3.8Å. With such a short minimum separation, the characteristics typical of a "stoichiometric" compound should no longer be retained.

This statement does not seem consistent with the fact that the optimum Eu concentration is nearly as high as that in "stoichiometric" compounds. A picture which may help understanding this point was proposed by Sommerdijk, Brill, and Hoex-Strix (13). They found that, in $\text{NaCa}_2\text{Mg}_2(\text{VO}_4)_3:\text{Dy}^{3+}$ which also has garnet structure, the optimum Dy concentration is about 20%. The high concentration was explained as resulting from inefficient energy transfer from host lattice to Dy^{3+} . In $(\text{Eu}, \text{Y})\text{Na}_2\text{Mg}_2(\text{VO}_4)_3$ as well, energy transfer from VO_4^{3-} to Eu^{3+} is not efficient. This is shown by an observation that green emission from the VO_4^{3-} group is seen at high Eu concentrations such as 50%. Therefore, the above picture will work also in this case.

Discussion

The increase in the ${}^5\text{D}_0$ decay rate with increasing temperature is presumably caused by an increase in nonradiative decay rate, because the luminescence intensity decreases with temperature. In this section, possible mechanisms for these nonradiative processes are discussed.

As previously stated, the ${}^5\text{D}_0$ decay rate of $(\text{Eu}, \text{Y})\text{Na}_2\text{Mg}_2(\text{VO}_4)_3$ depends on the temperature and Eu concentration in different ways in two temperature regions. Below 500°K, the decay rate depends strongly on the Eu concentration, and is, therefore, caused by interionic interaction. Above 500°K, the nonradiative decay rate added to the lower temperature rate is insensitive to the Eu concentration, which indicates that the nonradiative decay takes place within each ion.

Several processes have been proposed as candidates for the thermal quenching mechanism of ${}^5\text{D}_0$ luminescence. These include (i) nonradiative decay via a charge-transfer state which has a crossover point with the ${}^5\text{D}_0$ and ${}^7\text{F}_j$ states (14), and (ii) temperature-dependent diffusion of the ${}^5\text{D}_0$ states to quenching centers.

Multiphonon emission from ${}^5\text{D}_0$ can be neglected because the lattice vibration frequencies in $\text{YNa}_2\text{Mg}_2(\text{VO}_4)_3$ are not particularly high (section on Raman spectra). It is tempting to think that a phase transition might occur at the temperature dividing the two re-

gions, since the decay rate builds up very steeply at around 500°K. We checked this possibility by measuring powder x-ray diffraction patterns and thermal differential analysis. However, no evidence was found to support that there is a phase transition.

After these possibilities are ruled out, the quenching characteristics above and below 500°K can be most reasonably ascribed to the above-mentioned (i) and (ii), respectively.

In the following, the temperature dependences in the two regions are discussed separately in more detail.

The lower temperature region.—Temperature-dependent decay of ${}^5\text{D}_0$ has been well studied in glasses containing Eu^{3+} ions. It is useful to recall here the mechanisms proposed for energy migration in glasses. In 1971 Weber (15) proposed a model in which energy migrates efficiently only between the transitions ${}^5\text{D}_0 \rightarrow {}^7\text{F}_1, {}^7\text{F}_2$ and ${}^7\text{F}_1, {}^7\text{F}_2 \rightarrow {}^5\text{D}_0$ because the ${}^5\text{D}_0 \rightarrow {}^7\text{F}_0$ transition is strongly forbidden. This mechanism requires thermal population of the metastable states ${}^7\text{F}_1$ and ${}^7\text{F}_2$ and gives rise to strong temperature dependence of the ${}^5\text{D}_0$ decay rate. Essentially the same mechanism was considered by Takushi and Kushida (16) in their work on a $\text{Ca}(\text{PO}_3)_2:\text{Eu}$ glass.

We tested this model following the procedure shown by Weber. The nonradiative decay rate by diffusion, $1/\tau_D$, is given by

$$1/\tau_D = 4\pi D \cdot q \cdot \rho \quad [3]$$

where D is a diffusion constant, q the concentration of sinks, and ρ the interaction distance between an energy donor and a sink. When energy transfers from a donor to a sink by dipole-dipole interaction, ρ can be expressed as

$$\rho = 0.68(C/D)^{1/4} \quad [4]$$

where C is an interaction constant.

The temperature dependence of D was calculated according to an approximation which considers only the thermal population of ${}^7\text{F}_j$ states

$$D \propto \sum_i g_i \cdot \exp(-E_i/kT) (g_i/g_1) (f_{ij}^2/\nu_{ij}^2 \cdot \Delta\nu_{ij}) / \sum_i g_i \cdot \exp(-E_i/kT) \quad [5]$$

where E is the energy of a level, f_{ij} the oscillator strength, ν_{ij} the frequency, and $\Delta\nu_{ij}$ the line width, all of the transition between an i th and j th levels, and g the degeneracy of a level. Among the ground states, ${}^7\text{F}_0$, ${}^7\text{F}_1$, and ${}^7\text{F}_2$ become significantly populated near or above room temperature. The right-hand side of Eq. [5] was calculated by using f_{ij} 's obtained from

the observed radiative decay rate ($1/\tau_0$), $1.15 \times 10^3 \text{ sec}^{-1}$, and branching ratios. From Eq. [3] and [4], one finds $1/\tau_D \propto D^{3/4}$. Accordingly, the $3/4$ power of D is compared with the observed ($1/\tau - 1/\tau_0$) in the inset of Fig. 6. Thermal broadening of homogeneous line width was neglected. The agreement between the predicted temperature dependence and the measured variation of $1/\tau_D = (1/\tau - 1/\tau_0)$ is satisfactory. Therefore, it can be concluded that the above model essentially accounts for the observed result in the lower temperature region. Phonon-assisted energy transfer no doubt occurs between mismatched energy levels. However, it does not seem necessary to take into account this mechanism to explain the measured variation of the decay rates.

Energy migration via thermally populated 7F_1 and 7F_2 states could occur in any concentrated Eu compounds if the separation between Eu ions is small enough. The fact is that the increase in the decay rates with temperature observed for $\text{EuNa}_2\text{Mg}_2(\text{VO}_4)_3$ was not found for other disordered compounds, such as $\text{EuK}_5(\text{MoO}_4)_4$, or for EuPO_4 and EuVO_4 . All these compounds show strongly nonexponential decay curves and these decay characteristics do not change with temperatures below 500°K . This is an indication of little energy migration among 5D_0 states in these compounds. It seems that a high Eu concentration and a small distance between nearest neighbor ions are necessary but not sufficient conditions for energy migration.

The higher temperature region.—As stated before, the drastic nonradiative process above 500°K proceeds through a thermally populated charge-transfer state (CTS). The activation energy of the decay rate observed for $\text{EuNa}_2\text{Mg}_2(\text{VO}_4)_3$ ($9 \times 10^3 \text{ cm}^{-1}$) is within a reasonable region to be explained by the configurational coordinate model. It is comparable to the activation energy in $\text{LaAlO}_3:\text{Eu}$ ($1.4 \times 10^4 \text{ cm}^{-1}$) (17) or in $\text{La}_2\text{O}_2\text{S}:\text{Eu}$ ($1 \times 10^4 \text{ cm}^{-1}$) (18). The higher excited states, 5D_1 and 5D_2 , are deactivated at lower temperatures by the same mechanism, which explains a trend that the 5D_0 luminescence intensity excited at the ${}^7F_0 \rightarrow {}^5D_2$ transition decreases more than the 5D_0 lifetime does (see Fig. 4).

There is, however, a difficulty that the CTS is not found in excitation and reflection spectra up to 300 nm (section on relative luminescence intensities). Within the framework of the configurational coordinate model, the only way to avoid this difficulty is to assume that the CTS has large Franck-Condon offset. An example of the effect of offset on thermal quenching is given by the recent work of de Hair and Blasse (19). Large offset is realized, when the CTS can spatially expand or, specifically in this case, when a cation sharing an oxygen with Eu^{3+} is loosely bonded with the oxygen. All the materials which show the thermal quenching under consideration contain alkali ions. As is well known, alkali ions become mobile in many compounds through vacancies, dislocations, or interstitial sites at sufficiently high temperatures. Even if they do not really jump from one site to another, they will have large amplitude of oscillation. In other words, an alkali-oxygen bond is weakened at high temperatures.

As a preliminary check of ionic conductivity, a-c conductivity was measured on sintered $\text{EuNa}_2\text{Mg}_2(\text{VO}_4)_3$ and $\text{EuK}(\text{MoO}_4)_2$, and on a single crystal $\text{EuCs}(\text{MoO}_4)_2$. The conductivity was measured by a conventional method at 1V peak-to-peak voltage with a frequency of 1 kHz . When the temperature is varied from 670° to 770°K , the conductivity of $\text{EuNa}_2\text{Mg}_2(\text{VO}_4)_3$ changes from 2×10^{-7} to $8 \times 10^{-6} (\Omega \text{ cm})^{-1}$, and that of $\text{EuK}(\text{MoO}_4)_2$ changes from 4×10^{-7} to $3 \times 10^{-6} (\Omega \text{ cm})^{-1}$. The conductivity of $\text{EuCs}(\text{MoO}_4)_2$ changes from 1×10^{-7} to $5 \times 10^{-7} (\Omega \text{ cm})^{-1}$ in the range of 520° - 670°K . These values are of the same

order of magnitude as the conductivity of a regular ionic conductor, LiF (20). This fact indicates that a small fraction of alkali ions actually moves in the lattices. In this respect, there is some reason to propose the above hypothesis.

Among the compounds studied here, the disordered materials seem to favor the characteristic thermal quenching. A reason one can speculate is that strain caused by expansion of an Eu-O bond is more easily accommodated in disordered lattices than in ordered lattices.

The most straightforward way to test this hypothesis is to measure luminescence quenching in an ordered phase. Attempts were made to prepare the ordered phase of $\text{EuNa}_2\text{Mg}_2(\text{VO}_4)_3$ by annealing. Modification of chemical composition was also tried to search for ordered vanadates with garnet structure. However, these experiments were unsuccessful.

Conclusions

The dominant factor of the thermal quenching of luminescence from $\text{EuNa}_2\text{Mg}_2(\text{VO}_4)_3$ is nonradiative processes working on the emitting states of Eu^{3+} . Dependence of the decay rate on temperature and Eu^{3+} concentration differs very much in the two temperature regions: below and above 500°K . Below 500°K energy diffusion among Eu^{3+} ions increases the decay rate. Optical and powder x-ray diffraction data show that Eu^{3+} and Na^+ ions are randomly distributed on the dodecahedral sites in the garnet structure. The shortest distance between Eu^{3+} ions has a normal value of 3.8\AA , which is not as large as would be expected in an ordered state. The short minimum distance between Eu^{3+} ions makes energy diffusion possible. Above 500°K nonradiative relaxation occurs inside single Eu^{3+} ions. This is tentatively explained by a model in which the 5D_0 state is deactivated through a thermally populated charge transfer state. The most reasonable explanation of the nonradiative process above 500°K is that the adiabatic potential curve of the Eu^{3+} charge transfer state has large offset, because of soft surrounding of Eu^{3+} . A similar thermal quenching characterized by a drastic increase in 5D_0 decay rates is also found for several disordered Eu alkali molybdates. The result suggests that the charge transfer state can expand easily in Eu alkali compounds, particularly when ions are randomly distributed.

Acknowledgments

Possible correlation between luminescence quenching and ionic conductivity was suggested by Dr. Hidehito Ohbayashi. He also measured electrical conductivity on the authors' samples. His inspiring suggestion and cooperation in experiments are very much appreciated. The authors are indebted to Mr. Hideji Fujii who developed the computer program to calculate powder x-ray diffraction intensities, and to Dr. Toshikazu Shimada who built a setup for powder Raman spectroscopy. In the initial stage of this work, Dr. Atsushi Suzuki, Dr. Tadashi Fukuzawa, and Mr. Osamu Kanehisa contributed to optical measurements and discussions. Helpful discussions with Dr. Koichi Urabe and Mr. Yasutoshi Kashiwada are also acknowledged.

Manuscript submitted July 27, 1979; revised manuscript received Oct. 1, 1979.

Any discussion of this paper will appear in a Discussion Section to be published in the December 1980 JOURNAL. All discussions for the December 1980 Discussion Section should be submitted by Aug. 1, 1980.

Publication costs of this article were assisted by Hitachi Limited.

REFERENCES

1. H. G. Danielmeyer and H. P. Weber, *IEEE J. Quantum Electron.*, **qe-8**, 805 (1972).
2. H. G. Danielmeyer, *Festkoerperproblem*, **XV**, 253 (1975).

3. D. Bimberg, D. J. Robbins, D. R. Wigth, and J-P. Jeser, *Appl. Phys. Lett.*, **27**, 67 (1975).
4. Y. Tsujimoto, Y. Fukuda, and M. Fukai, *This Journal*, **124**, 553 (1977).
5. G. Ronniger and B. V. Mill', *Sov. Phys. Crystallogr.*, **16**, 902 (1972).
6. G. Blasse and A. Bril, *This Journal*, **114**, 250 (1967).
7. B. Blanzat and J. Loriers, *C. R. Acad. Sci., Ser. B*, **276**, 95 (1973).
8. R. K. Datta, *Trans. Metall. Soc. AIME*, **239**, 365 (1967).
9. G. Huber, W. Lenth, J. Liberts, and F. Lutz, *J. Lumin.*, **16**, 353 (1978).
10. V. A. Vinokurov and P. V. Klevtsov, *Sov. Phys. Crystallogr.*, **17**, 102 (1971).
11. H. Siebert, *Z. Anorg. Allg. Chem.*, **275**, 225 (1954).
12. S. A. Miller, H. H. Caspers, and H. E. Rast, *Phys. Rev.*, **168**, 964 (1968).
13. J. L. Sommerdijk, A. Bril, and F. M. J. H. Hoex-Strik, *Philips Res. Rep.*, **32**, 149 (1977).
14. For example, C. W. Struck and W. H. Fonger, *J. Lumin.*, **10**, 1 (1975).
15. M. J. Weber, *Phys. Rev. B*, **4**, 2932 (1971).
16. E. Takushi and T. Kushida, *J. Lumin.*, **18/19**, 661 (1979).
17. G. Blasse, A. Bril, and J. A. dePoorter, *J. Chem. Phys.*, **53**, 4450 (1970).
18. C. W. Struck and W. H. Fonger, *J. Lumin.*, **1/2**, 456 (1970).
19. J. Th. W. de Hair and G. Blasse, *J. Solid State Chem.*, **19**, 263 (1976).
20. For example, M. S. Whittingham, *Electrochim. Acta*, **20**, 575 (1975).

The D-C MOSFET Dopant Profile Method

M. G. Buehler

National Bureau of Standards, Electron Devices Division, Washington, D.C. 20234

ABSTRACT

Dopant profiles can be determined from d-c measurements on a four-terminal surface-channel MOSFET. The region from about three Debye lengths from the oxide-silicon interface to a maximum depth, limited by the avalanche breakdown in silicon, can be profiled by this method. Within three Debye lengths of the surface, the depletion approximation fails, and in this region the profile has a characteristic dip which is easily recognized. Other limitations include effects due to the field dependence of the channel mobility, short channel effects, and the lack of parallelism of the depletion edge with the interface. The method is illustrated by dopant profiles of bulk wafers, implanted layers, and a diffused layer. The dopant densities covered by these profiles vary from $6 \times 10^{14} \text{ cm}^{-3}$ to $2 \times 10^{18} \text{ cm}^{-3}$.

The feasibility of measuring dopant profiles by analyzing the d-c characteristics of a MOSFET was reported previously (1, 2). Because the measurement requires the use of direct currents, it is easily implemented with automated data acquisition equipment that is normally used to measure the traditional MOSFET electrical characteristics. In this paper the method is applied to the measurement of dopant profiles that cover the range from $6 \times 10^{14} \text{ cm}^{-3}$ to $2 \times 10^{18} \text{ cm}^{-3}$. Examples of measurements on homogeneous, diffused, and implanted layers are given. This paper explores the various factors that influence the measurement of the dopant profiles.

The MOSFET d-c profiler utilizes a four-terminal surface-channel MOSFET for evaluating the dopant density in the silicon under the gate (1, 2). The dopant profile is obtained by sequentially moving the depletion region through the silicon by using the back-gate bias effect. As the gate-source voltage, V_{GS} , is changed, the drain-source current, I_{DS} , is held constant by adjusting the source-body voltage, V_{SB} . These voltages plus the silicon and oxide dielectric constants and the oxide thickness are sufficient to compute the dopant profile.

Dopant Profile Equations

The profile equations can be derived for the case of uniformly doped silicon by assuming that the depletion approximation (3) is valid and by ignoring charge in the oxide, interface states, and work function differences between the metal and silicon. These are unimportant factors as long as they are stable quantities. Consider a surface-channel MOSFET operated with a negligibly small drain-source voltage, V_{DS} . For this condition, the following derivation as-

sumes that the gate-channel and channel-body voltages are equivalent to the gate-source voltage, V_{GS} , and the source-body voltage, V_{SB} , respectively.

At the oxide-silicon interface the solution to Poisson's equation using Gauss' law yields

$$Q_o = qn_s + Q_b \quad [1]$$

where n_s is the inversion-layer charge density per unit area, Q_o is the charge per unit area on the gate, Q_b is the charge per unit area induced at the interface by the charge in the depletion region, and q is the electronic charge. If the charge in the inversion layer is held constant as V_{GS} is varied, Eq. [1] becomes

$$dQ_o/dV_{GS} = dQ_b/dV_{GS} \quad [2]$$

because $dn_s/dV_{GS} = 0$. This reveals the essence of the measurement; that is, the change in the charge on the gate balanced by the change in the charge induced at the interface due to the charge in the depletion region of the silicon. This is achieved by adjusting V_{SB} at each new V_{GS} value so that n_s is constant.

The additional relationships needed in the derivation are given next. In the oxide

$$Q_o = \epsilon_o E_o = \epsilon_o (V_{GS} - 2\psi_b)/X_o \quad [3]$$

where ϵ_o is the oxide dielectric constant, E_o is the oxide electric field, X_o is the oxide thickness, and ψ_b is the bulk potential difference between the Fermi level and intrinsic Fermi level. For a one-dimensional model, Poisson's equation and Gauss' law yield

$$Q_b = qNW \quad [4]$$

where N is the dopant density and W is the width of the depletion region in the silicon. Assuming the inversion layer approximates a one-sided step junc-

tion (3), one obtains

$$V_{SB} + 2\psi_b = (qN/2\epsilon_s)W^2 \quad [5]$$

where ϵ_s is the silicon dielectric constant.

The combination of Eq. [2]-[5] can be manipulated to obtain the dopant profile equations

$$W_m = (\epsilon_s X_o / \epsilon_o) (dV_{SB} / dV_{GS}) \quad [6]$$

and

$$N_m(W_m) = (\epsilon_o^2 / q\epsilon_s X_o^2) / (d^2 V_{SB} / dV_{GS}^2) \quad [7]$$

where the subscript m refers to quantities derived from the measured voltages, V_{SB} and V_{GS} . Although these equations were derived for a uniform dopant density, it has also been shown that they are valid for an arbitrary dopant density (1).

In the actual measurement of a dopant profile the inversion layer charge, n_s , is presumed to be held constant by maintaining a constant drain-source current, I_{DS} . The success of this assumption and others can be judged from the current expression for the MOSFET operated in the linear range ($V_{DS} < 2\psi_b$)

$$I_{DS} = qn_s\mu(Z/L)V_{DS} \quad [8]$$

where μ is the channel mobility, Z is the channel width, and L is the channel length. In order for the profile equations to be valid, certain assumptions must be maintained. These are listed in Table I. Also listed is the effect on the dopant profile of violating an assumption. If these assumptions hold, then the channel current is proportional to n_s and holding I_{DS} constant holds n_s at a fixed value.

Channel Mobility Effect

The measured dopant profiles are influenced by the field dependence of the channel mobility. A model for this effect follows from the measurement constraint that $dI_{DS}/dV_{GS} = 0$. The combination of this constraint with Eq. [1], [3]-[8] leads to the expressions for the true depletion width

$$W = W_m / (1 - F_1) \quad [9a]$$

where

$$F_1 = G_{DS}(X_o/\epsilon_o)(L/Z)(d\mu^{-1}/dV_{GS}) \quad [9b]$$

and for the true dopant density

$$N = N_m(1 - F_1)^2 / (1 + F_2) \quad [10a]$$

where

$$F_2 = G_{DS}(qN_m W X_o^2 / \epsilon_o^2)(L/Z)(d^2\mu^{-1}/dV_{GS}^2) \quad [10b]$$

In these expressions G_{DS} is the channel conductance given by $G_{DS} = I_{DS}/V_{DS}$.

The magnitude of the effect on the measured dopant density can be estimated from an empirical expression (4) for the channel mobility in a MOSFET operated in the linear range

$$\mu = \mu_o / [1 + \theta(V_{GS} - V_T)] \quad [11]$$

where μ_o is the zero-field channel mobility, θ is a coefficient, and V_T is the threshold voltage. The combination of Eq. [10] and [11] yields

$$N = N_m(1 - RG_{DS})^2 \quad [12a]$$

where

Table I. Effect of the violation of the ideal assumptions on dopant profiles

Parameter	Ideal assumption	Effect
Channel mobility, μ	$\mu \neq \mu(V_{GS})$	Increase in N_m
Channel charge density, n_s	Sheet of charge	Dip in N_m near interface
Channel length, L	$Q_b = qNW$	Negative slope of profile
Channel width, Z	No fringing fields	No effect for circular MOSFET
Drain-source voltage, V_{DS}	Depletion edge parallel to interface	Fall-off of profile near interface

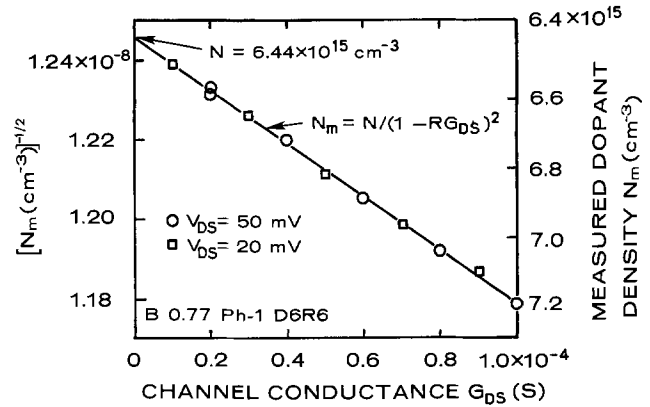


Fig. 1. Influence of the channel conductance on the measured dopant density. The intercept at $G_{DS} = 0$ is the true bulk dopant density for this p-channel MOSFET fabricated in phosphorus-doped $0.77 \Omega \cdot \text{cm}$ silicon. For $G_{DS} = 0.2 \times 10^{-4} \text{S}$, the N_m value was taken from the flat portion of profile like the one shown in Fig. 4).

$$R = (X_o/\epsilon_o)(L/Z)(\theta/\mu_o) \quad [12b]$$

Notice that for the above mobility expression, $F_2 = 0$.

Experimental results for an n-type wafer are shown in Fig. 1 where N_m is plotted against G_{DS} for two values of V_{DS} . The fit of the data to the model is adequate which indicates that the expression in Eq. [11] is satisfactory. The true dopant density, N , is obtained from the zero-conductance intercept and the R -value is obtained from the slope. For this sample the effect is small; that is, a ten-fold change in G_{DS} caused only an 11% change in N_m . For other MOSFET's, the magnitude of this effect can be estimated from the resistance parameter, R , as given in Eq. [12b].

The effect of the electric field on the channel mobility was studied in other samples; the results are listed in Table II. The μ_o/θ ratio is also listed and was calculated from the R -values using the appropriate values for X_o , ϵ_o , and L/Z in Eq. [12b]. For the circular MOSFET's used in this study, $Z/L = 18.22$.

Depletion Approximation Limit

In deriving the profile equations, it is assumed that the depletion approximation is valid. This approximation assumes that the depletion layer is free of holes and electrons. For reverse bias values of V_{SB} , the inversion layer charge can be modeled effectively as a sheet of charge at the interface. For forward bias values of V_{SB} , the depletion width becomes smaller and the inversion layer charge spreads to take up a larger fraction of the depletion layer. As this happens, the depletion approximation no longer holds.

This effect was studied using a theoretical model (5) which assumes that p-type silicon is uniformly doped, that there is no work function difference, no interface states, no oxide charge, and negligible leakage currents. Under these conditions, the electric field in the oxide at the interface is

$$E_o = V_{GS}/X_o = (\epsilon_s/\epsilon_o)E_s(\psi_s) \quad [13]$$

where E_s is the electric field in the silicon at the interface for a surface potential ψ_s . The channel charge per unit area is given by

$$n_s = \int_0^{X_o} n(x) dx = \int_{\psi_o}^{\psi_s} [n(\psi)/E_s(\psi)] d\psi \quad [14]$$

Table II. Channel conductance parameters

Wafer	Type	Resistivity ($\Omega \cdot \text{cm}$)	N (cm^{-3})	R (Ω)	μ_o/θ (cm^2/sec)
B3.0B-3	p	3.0	4.80×10^{15}	217	3.12×10^4
C21B-3	p	21	6.68×10^{14}	404	1.65×10^4
B0.77Ph-1	n	0.77	6.44×10^{15}	536	1.16×10^4

where X_c is the effective channel thickness, ψ_0 is the potential near the edge of the depletion region ($\psi_0 = 0.1 \psi_b$), and ψ is the potential difference between the bulk and depletion layer intrinsic Fermi levels. The channel charge per unit volume is given by

$$n(\psi) = (n_i^2/N_A) \exp[\beta(\psi - V_{SB})] \quad [15]$$

where n_i is the intrinsic charge density, N_A is the acceptor density, and $\beta = q/kT$ where k is the Boltzmann constant and T is the temperature. The electric field in the silicon at the interface is given by

$$E_s(\psi) = (2qN_A/\epsilon_s\beta)^{1/2}F(\psi) \quad [16a]$$

where

$$F(\psi) = [e^{-\beta\psi} + \beta\psi - 1 + (n_i/N_A)^2(e^{\beta(\psi - V_{SB})} - \beta\psi - e^{-\beta V_{SB}})]^{1/2} \quad [16b]$$

For $T = 300\text{K}$ and a particular value of N_A , the above equations were solved to obtain V_{SB} as a function of V_{GS} at a fixed value of n_s . The computations required double-precision arithmetic and proceeded as follows. At a given value of V_{GS} and an estimated value of V_{SB} , Eq. [13] and [16] were solved for ψ_s by an iteration procedure. Then Eq. [14] was integrated and the resulting value of n_s was compared to a target value. From this comparison, a new value of V_{SB} was derived and the procedure repeated until n_s reached the target value.

Dopant profiles were obtained from Eq. [6] and [7] by numerically differentiating the $V_{SB} - V_{GS}$ table established by the above procedure. The results are shown in Fig. 2. The distance was normalized by the Debye length $\lambda = (2\epsilon_s/qN_A\beta)^{1/2}$. The results indicate that the failure of the depletion approximation causes a dip in the profile at a distance near 3λ from the interface. This dip is observed experimentally.

The profiles shown in Fig. 2 are different from the profiles determined from the pulsed capacitance technique for measuring dopant profiles using MOS capacitors (6). With this technique, the profiles simply rise within 2λ to 3λ of the interface (7).

Other Limitations

The MOSFET d-c profile measurements are influenced by a variety of other effects also indicated in Table I. A sloping depletion edge, fringing fields found at the ends of a linear MOSFET, and short channel effects (8) can distort the profiles. However, for the large circular MOSFET used in this study, these effects are negligible. As shown in the previous sec-

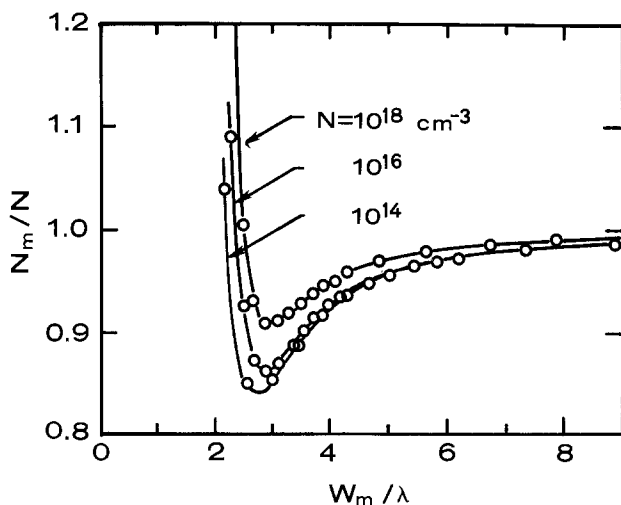


Fig. 2. Normalized dopant density profile showing the dip in the profile which is characteristic of the failure of the depletion approximation. This data was derived from a theoretical model where the dopant density was assumed to have a constant value, $N = 10^{14}$, 10^{16} , or 10^{18} cm^{-3} .

tion, profiles are limited to distances greater than 3λ from the interface. The maximum depth is limited by avalanche breakdown of the channel to body, source to body, or drain to body junctions.

Experimental Results

The MOSFET used in this study has a circular geometry with a source radius of $216 \mu\text{m}$ (8.5 mil) and a drain radius of $305 \mu\text{m}$ (12.0 mil); the effective Z/L ratio is 18.22 (9). The oxide thickness was determined from 1 MHz capacitance measurements using a MOS capacitor located near the MOSFET. The experimental dopant profiles were obtained using the operational amplifier circuit described elsewhere (1). In this circuit V_{SB} is automatically adjusted as V_{GS} is incremented so that I_{DS} is held constant. The data acquisition is computer controlled as is the data reduction and presentation.

Two profiles are presented to illustrate the application of this method. The first profile, shown in Fig. 3, was obtained on a (111)-oriented $0.81 \Omega \cdot \text{cm}$ boron-doped silicon wafer. The initial $0.35 \mu\text{m}$ thick pyrogenic oxide was grown at 1100°C for 50 min. Then a phosphorus source-drain was deposited at 950°C for 20 min which was followed by an 80 min diffusion-oxidation cycle at 1100°C . Finally, a boron channel stop was deposited at 1050°C for 15 min which was followed by a 35 min diffusion at 925°C . The total gate oxide thickness was $0.42 \mu\text{m}$.

The boron redistribution effect (3) is clearly shown in Fig. 3 as is the dip in the profile near the surface. The dip in the profile near the surface is in qualitative agreement with the theoretical predictions shown in Fig. 2. Also shown in Fig. 3 is the 3λ limit curve and the zero-bias point for the profile. The profile begins to deviate from the expected profile (indicated by the solid line) near the zero-bias point. The profile is especially inaccurate for distances within 3λ of the interface.

The second profile, shown in Fig. 4, was obtained from a (111)-oriented $0.77 \Omega \cdot \text{cm}$ phosphorus-doped silicon wafer. The initial $0.35 \mu\text{m}$ -thick pyrogenic oxide was grown at 1100°C for 30 min. Then a boron source-drain was deposited at 935°C for 35 min which was followed by an 85 min diffusion-oxidation cycle at 1100°C . Finally, a phosphorus channel stop was deposited at 1025°C for 15 min which was followed by a 35 min diffusion at 925°C .

The phosphorus pile-up effect (3) is quite apparent in Fig. 4 as is the dip in the profile near the surface. The expected profile is shown by the solid line. As with the previous example, this profile is reliable up to the zero-bias point and inaccurate for distances within 3λ of the interface.

A summary of various profiles is shown in Fig. 5 along with the 3λ , zero-bias, and breakdown (5) limits. The dip portion of a profile is shown by a dashed line. The boron profile (Fig. 3) is repeated as curve (d), and the phosphorus profile (Fig. 4) is

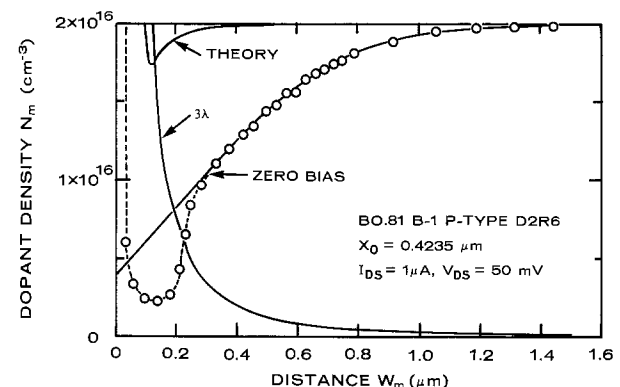


Fig. 3. Dopant profile of boron-doped $0.81 \Omega \cdot \text{cm}$ silicon showing boron redistribution due to thermal oxidation.

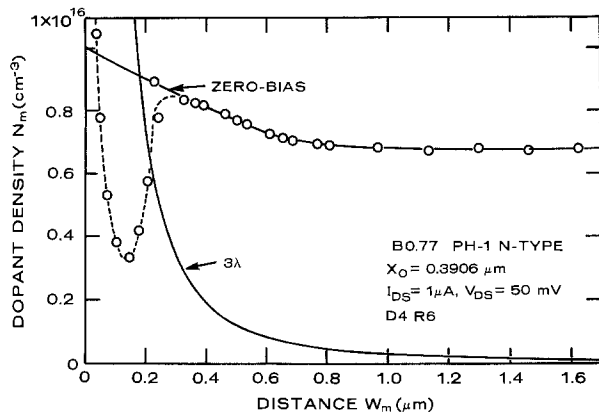


Fig. 4. Dopant profile of phosphorus-doped $0.77 \Omega \cdot \text{cm}$ silicon showing phosphorus pile-up due to thermal oxidation.

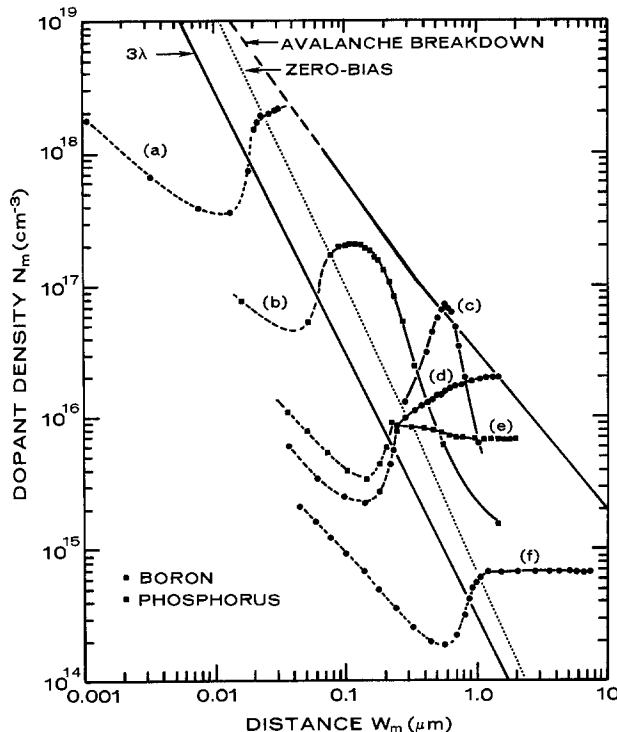


Fig. 5. Dopant profiles of curve (a) boron diffusion; curve (b) phosphorus implant; curve (c) boron implant; curve (d) boron-doped bulk (see Fig. 3); curve (e) phosphorus-doped bulk (see Fig. 4); and curve (f) boron-doped bulk.

repeated as curve (e). Curve (f) was obtained on a lightly doped boron wafer that was fabricated in a manner similar to the wafer whose profile is shown in Fig. 3. Curve (b) is a phosphorus layer implanted at 180 keV through a $0.1\text{-}\mu\text{m}$ -thick oxide layer to a dose of $4 \times 10^{12} \text{ cm}^{-2}$ and annealed at 900°C for 30 min in dry nitrogen. The starting wafer has a phosphorus density of $1 \times 10^{15} \text{ cm}^{-3}$. Curve (c) is a boron layer implanted at 280 keV through a $0.1 \mu\text{m}$ -thick oxide layer to a dose of $2.6 \times 10^{12} \text{ cm}^{-2}$ and annealed at 900°C for 30 min in nitrogen. The starting wafer had a boron density of $3 \times 10^{15} \text{ cm}^{-3}$. Both layers were implanted 7 degrees off the (111) axis of the silicon wafer. Curve (a) is the profile of a boron diffusion

with a sheet resistance of $273 \Omega/\square$ and a junction depth of $1.8 \mu\text{m}$. A phosphorus source-drain was diffused into the boron layer to form the MOSFET. Only a small fraction of the entire diffusion profile is revealed and it lies between 0.02 and $0.03 \mu\text{m}$ from the interface.

Discussion

The profiles presented in this paper cover the dopant density range from 6×10^{14} to $2 \times 10^{18} \text{ cm}^{-3}$. Of the various limitations discussed, the most important is the failure of the depletion approximation which prevents accurate profiles near the oxide-silicon interface. A unique dip in the profile identifies the region of erroneous data. A theoretical model explains the shape of the experimental observations but underestimates the magnitude of the effect.

The field dependence of the channel mobility can also influence the measurement of the dopant profile. This effect can be minimized by proper MOSFET design ($R \approx 0$) and by proper measurement conditions ($G_{DS} \approx 0$) as seen in Eq. [12]. The empirical mobility expression, Eq. [11], adequately describes the observed effect.

Future work involves the comparison of this method with other methods (for example, the diode C-V method). In addition, the short channel effect on the measure profiles is being studied with the use of MOSFET that are linear and more compact than those used in this study.

Acknowledgment

The author wishes to thank Y. M. Liu for the MOSFET fabrication, L. W. Linholm for the diffused layer profile, D. R. Myers and H. Dietrich of the Naval Research Laboratories for the boron implantation, and D. McCarthy of the Westinghouse Advanced Technology Laboratories for the phosphorus implantation. This work was conducted as part of the Semiconductor Technology Program at the National Bureau of Standards. This work was supported by the Defense Advanced Research Projects Agency (Order No. 2397, Program Code 7D10) and the Defense Nuclear Agency (Subtask Z99QAZTDO72, Work Unit 66).

Manuscript submitted March 5, 1979; revised manuscript received Aug. 1, 1979. This was Paper 248 presented at the Seattle, Washington, Meeting of the Society, May 21-26, 1978.

Any discussion of this paper will appear in a Discussion Section to be published in the December 1980 JOURNAL. All discussions for the December 1980 Discussion Section should be submitted by Aug. 1, 1980.

Publication costs of this article were assisted by the National Bureau of Standards.

REFERENCES

1. M. G. Buehler, *Appl. Phys. Lett.*, **31**, 848 (1977).
2. J. M. Shannon, *Solid-State Electron.*, **14**, 1099 (1971).
3. A. S. Grove, "Physics and Technology of Semiconductor Devices," Wiley, New York (1967).
4. P. P. Wang, *IEEE Trans. Electron Devices*, **ED-24**, 196 (1977).
5. S. M. Sze, "Physics of Semiconductor Devices," Wiley-Interscience, New York (1969).
6. A. R. LeBlanc, D. Dale Kleppinger, and J. P. Walsh, *This Journal*, **119**, 1068 (1972).
7. K. Zeigler, E. Klausmann, and S. Kar, *Solid-State Electron.*, **18**, 189 (1975).
8. L. D. Yau, *ibid.*, **17**, 1059 (1974).
9. M. G. Buehler, *Natl. Bur. Stand. Spec. Publ.*, **400**, 22 (1976).

Silicon Oxidation Studies: Morphological Aspects of the Oxidation of Polycrystalline Silicon

E. A. Irene,* E. Tierney, and D. W. Dong

IBM Thomas J. Watson Research Center, Yorktown Heights, New York 10598

ABSTRACT

Previous studies have shown that the oxide grown from polycrystalline silicon displays degraded reliability in terms of higher leakage current and premature dielectric breakdown as compared with the oxide grown from single crystal silicon. Present transmission electron microscope studies of the morphology of polycrystalline silicon films and the oxide grown therefrom show several novel features. The polycrystalline silicon becomes rougher after oxidation, the oxide displays thickness undulations which replicate the previous grain boundaries with thinner oxide over grain boundaries, and the oxide forms intergranularly as well as on the free silicon surface. Despite the intergranular oxide formation, the film skin of oxidized polycrystalline silicon does not become significantly more compressive. The surface roughness features of the polycrystalline silicon and oxide and the film stress values are explained by a Si creep mechanism. From these studies some aspects of the reliability of polycrystalline silicon and oxide are understood.

The thermal oxidation of polycrystalline silicon (poly-Si) is technologically important because the SiO₂ film produced from this oxidation, (from here on referred to as poly-OX), is needed to provide electrical isolation for conducting poly-Si lines and therefore the poly-OX must be a reliable, low conductivity, dielectric.

Kamins and MacKenna (1) have reported that at lower oxidation temperatures where the oxidation mechanism is predominantly surface reaction controlled, the rate of oxidation of poly-Si is characteristic of the random orientations of the poly-Si grains. The different oxidation rates across the surface would cause roughening. At higher oxidation temperatures where the oxidation is predominantly diffusion controlled, a smoother poly-Si surface is produced. Andersen and Kerr (2) have reported that the higher than expected electrical conductivity found for poly-OX films (3, 4) is due to Si asperities which they observed on the poly-Si surface and which can cause local electric field enhancement. It was also reported (2, 4) that higher temperature oxidation produces a lower conductivity poly-OX.

Based on these apparently concordant studies (1-4), it appears that the morphological and electrical characteristics of poly-OX are reasonably well understood. However, our recent transmission electron microscope (TEM) observations on poly-OX (5, 6) to be detailed in this paper, strongly suggest that the morphology of the poly-OX itself (rather than, or in addition to, the poly-Si morphology) can cause the observed high conductivities of poly-OX. Furthermore the origin of poly-Si surface irregularities is elucidated from the TEM observations. A better understanding of poly-Si and poly-OX evolves which is based on the growth of a morphologically complex oxide film, poly-OX.

The present study is essentially a morphological characterization of the oxide films grown as a result of thermal oxidation of poly-Si. As a first step, the poly-Si itself is characterized by TEM and our results are compared with some of the relevant literature. Doped and undoped poly-Si films are oxidized from 800° to 1200°C for short and long times and the morphological results compared. In addition film stress measurements were performed on the poly-Si and poly-OX films, since these measurements were needed to confirm the mechanisms deduced from the morphological observations.

* Electrochemical Society Active Member.
Key words: oxidation, films, dielectric.

Experimental Procedures

Sample preparation.—Poly-Si films were deposited on thermally oxidized Si wafers by chemical vapor deposition, CVD, using gaseous SiH₄ diluted in N₂. The CVD reactor temperature was either at 650°C to prepare initially amorphous silicon films or at 800°C to prepare initially polycrystalline films. In this study TEM observations were made on undoped and POCl₃ doped films, prior to and after oxidation.

TEM.—For TEM observations on poly-Si and poly-OX films, the Si substrates and oxide on Si were removed by chemical etching using HF-HNO₃ mixtures by a previously outlined procedure (7) or by first prethinning using HF-HNO₃ then using pyrocatechol-ethylenediamine-H₂O mixtures at elevated temperatures (8) to remove single crystal and polycrystalline silicon but leaving oxide for observations, and thirdly ion milling was occasionally used as an additional method to insure that the TEM observations were independent of the sample preparation procedures.

In some cases the poly-Si samples were oxidized and then thinned for TEM observation, however we found it useful to first thin a poly-Si specimen for TEM observation and then to oxidize the specimen and reobserve the same specimen for oxidation effects. In this case oxidation occurred from both sides of the poly-Si samples. We found no essential differences between these procedures except for the extent of oxidation.

Film stress.—The film stress of poly-Si films on oxidized Si substrate wafers was measured before and after oxidation of the poly-Si so as to observe any sintering and oxidation effects on the residual film stress. The method was to observe substrate bending by means of counting the Newton rings which are produced by optical interference between an optical flat and the curved substrates. The exact method used was previously discussed (9).

Experimental Results

Morphology of poly-Si.—For chemically vapor deposited silicon films, the temperature for the deposition is important in determining whether the silicon film is amorphous or crystalline. Figure 1 shows as-deposited silicon films prepared at 650°C on an oxidized silicon surface in a resistance heated CVD system in 1(a) and in a radiant heated system in 1(b). In both cases the material is composed of small Si crystals imbedded in an amorphous Si matrix. The silicon deposited below 600°C appears to be totally

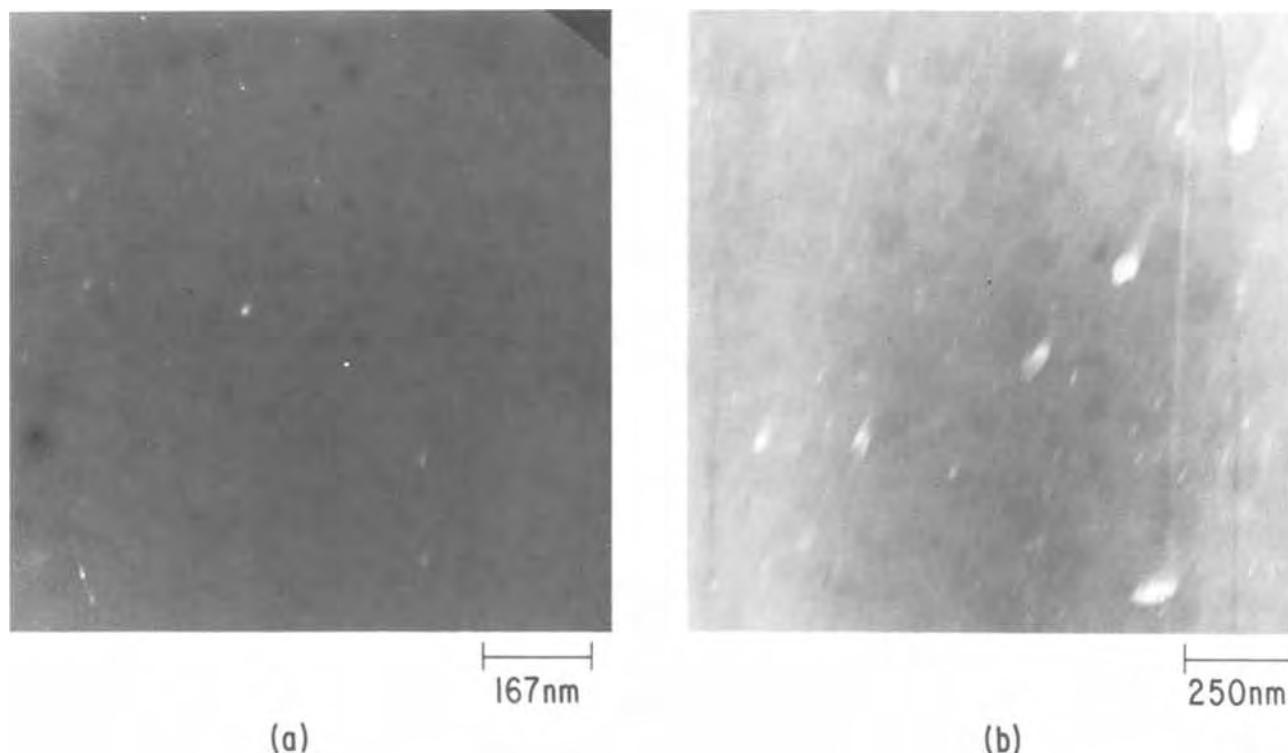


Fig. 1. Deflected aperture dark field TEM micrographs of poly-Si deposited onto an oxidized silicon substrate at 650°C by the decomposition of SiH_4 in (a) a resistance heated furnace and (b) a radiant heated system.

amorphous by TEM while at CVD temperatures above about 700°C the films are entirely polycrystalline. These results are similar to published TEM studies on Si films [see for example Ref. (10)]. The specific polycrystalline morphology is dependent upon the temperature and time of annealing and on doping (10, 11).

The changes which occur in poly-Si films as a result of oxidation heat-treatments are of particular importance in the present study. Figure 2 compares the poly-Si morphology for films prepared at 650°C in 2(a), (b), and (c) to films prepared identically but doped by POCl_3 deposition and drive-in at 900°C in 2(d), (e), and (f). All the samples were oxidized in dry O_2 to produce about 30 nm SiO_2 at 800°C for (a) and (d), 1000°C for (b) and (e), and 1100°C for (c) and (f). From this comparison it is seen that the undoped samples all possess a more dendritic morphology which is characteristic of rapid crystallization but little grain growth. As the temperature exposure increases the number and size of equiaxed grains increase. Grain growth to equiaxed grain morphologies occurs readily for the doped samples and this is probably due to the increased mobility of Si atoms in the presence of P in Si (12).

Replicas of the surfaces of as-deposited and doped samples are shown in Fig. 3. It is seen that for the samples which received either an 800° or 1100°C heat-treatment, the surfaces are rougher for the undoped samples, i.e., there are more and sharper protuberances. Figure 2 has shown that the lateral dimensions of the grains are larger for the doped material. Therefore, it appears that due to the increased mobility of Si in the presence of P (12) lateral grain growth is possible for the doped samples but more difficult for the undoped poly-Si grains which extend upward rather than laterally.

As apparent from Fig. 3(d), ridges on the replica outline the poly-Si grain boundaries. Since the replica is a negative impression of the poly-Si surface, the ridges represent depressions at the grain boundaries. Rather than being grain boundary grooves associated with the attainment of minimum radius of curvature, we believe that these features are due to intergranular

oxidation. Evidence that these grooves widen and deepen with oxidation will be shown later.

The TEM observations show that doping and temperature determine the grain structure. P doping yields larger grains with smoother surfaces. Nearly dendritic morphologies are observed for undoped samples.

Morphology of poly-OX.—As was shown in Fig. 2 there are basically two poly-Si grain morphologies: one is primarily dendritic and the other equiaxed. The tendency toward the equiaxed morphology increases as the mobility of Si atoms increases as a result of a higher processing temperature and/or phosphorous dopant concentration. The heavily doped poly-Si is more representative of an industrially useful case while the oxidation of the undoped material is of scientific interest. Figure 4 shows a comparison of the oxide grown on single crystal Si in 4(a), undoped poly-Si in 4(b), doped poly-Si in 4(c), and in 4(d) doped poly-Si but thinned for TEM by ion milling rather than chemical etching so as to obviate any possible chemical etching artifacts. It is seen that the SiO_2 grown on single crystal Si is comparatively featureless. The poly-OX, however, clearly shows thickness undulations. The thin regions of the poly-OX outline the previous grain boundaries as is especially apparent in Fig. 4(c) and (d) where the grain boundaries of the poly-Si are well defined. For the more complex poly-Si grain morphology, i.e., smaller grains and mixed dendritic and equiaxed morphologies, the thickness undulation patterns are also more complex as seen in 4(b). The use of chemical etching and ion milling yielded essentially the same morphologies. Chemical etching, being more rapid and equally reliable, will be used throughout this study.

In order to clarify the magnitude of the intergranular oxidation effect and to further confirm the above thickness undulation observations in the absence of possible etching effects, the following experiment was performed. A poly-Si film on SiO_2 on Si was prepared for TEM examination in the usual way (7) leaving

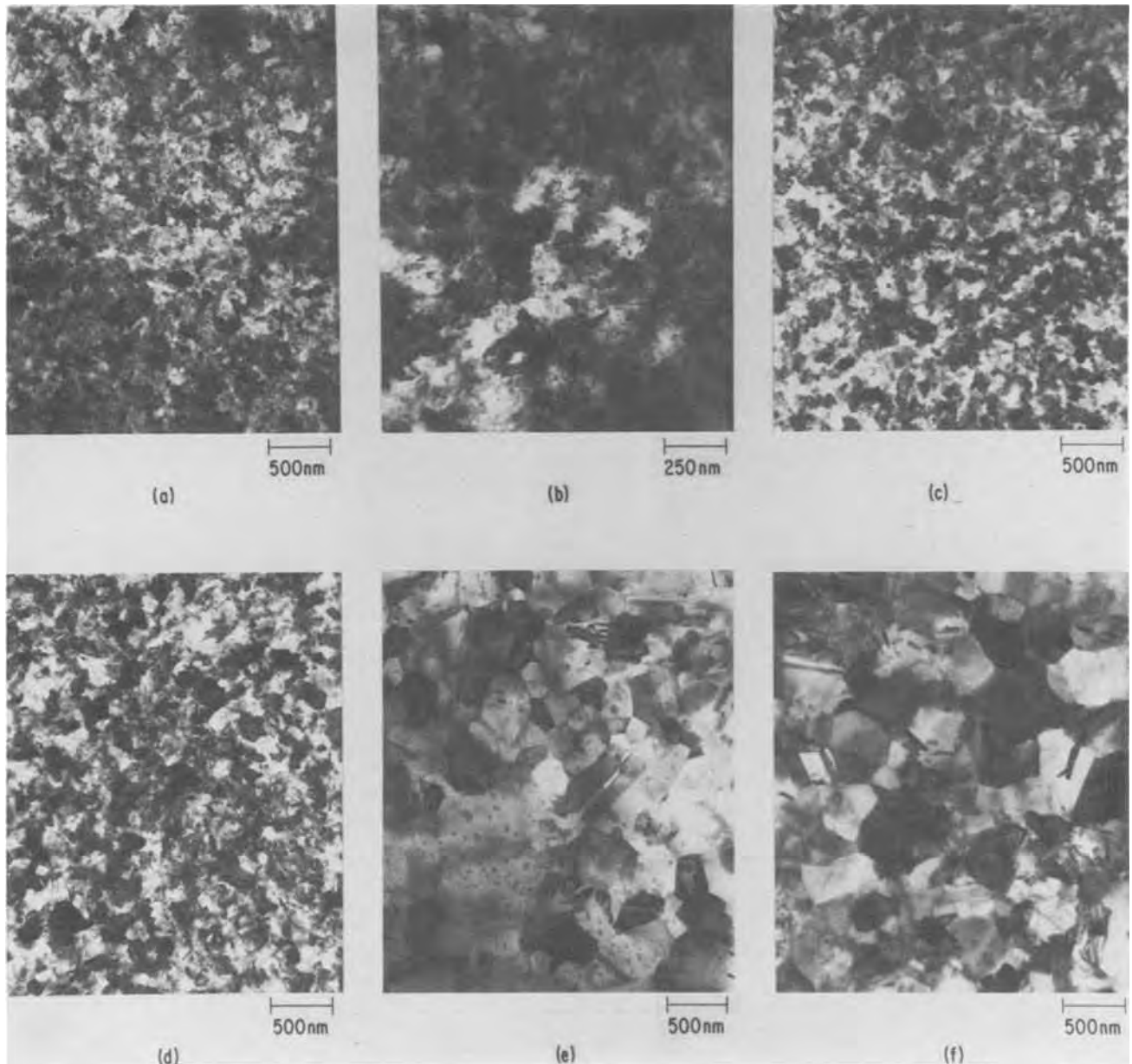


Fig. 2. Comparison of poly-Si deposited at 650°C oxidized (a) at 800°C, (b) 1000°C, and (c) 1100°C to produce 30 nm SiO₂. For (d), (e), and (f) the samples are the same as (a), (b), and (c), respectively, with the exception that (d), (e), and (f) have received POC₁₃ doping. The SiO₂ was removed in HF prior to TEM.

an area of poly-Si thin enough for examination as shown in Fig. 5(a). This sample was then oxidized repeatedly and examined after each oxidation to determine the effects of further oxidation treatments: the results are shown in Fig. 5. In 5(b) the sharply outlined relatively darker areas which have broad slip bands; bending contours and thickness fringes are the remnants of partially oxidized poly-Si grains. Surrounding these grains is poly-OX which has a graded thickness. The thinnest regions are nearest the previous grain boundaries. In some areas actual separation of the poly-OX occurs at the thinnest poly-OX regions. For illustration purposes Fig. 5(b) shows an area with a higher incidence of separation than is usual. Figure 5(c) is a more representative one with further advanced oxidation. We believe that the separation phenomena in 5(b) is due to the contraction of the silicon grain remnants upon cooling from the oxidation temperature. The silicon grain remnants contract more than the oxide causing tensile forces to be exerted at the already thinned oxide regions. Figure 5(c) shows the smaller crystalline remnants of the grains at the dark-

est hence thickest regions of the films. After the initial thinning to produce 5(a) the sample was not chemically or otherwise treated in any way after oxidation, except to make the TEM observations, and therefore the sample is coated with an oxide film parallel to the plane of the micrographs. This oxide film forms as a result of the oxidation of the free surface of the poly-Si grains as with the oxidation of single crystal Si. As oxidation progresses the oxide on the free surface grows thicker and thereby reduces the total electron transmission through the sample. This effect plus the fact that diffuse scattering occurs because the oxide is amorphous causes the micrograph images to become less sharp for samples with thick oxides. Figure 5(d) shows the sample oxidized completely for ~ 18 hr. The very thick regions represent the grain centers which are consumed last but because of the greater oxide thickness the features of these regions are not discernable.

During oxidation the poly-Si surface becomes roughened more than the oxide although even the poly-OX surface is rough relative to the oxide grown on single

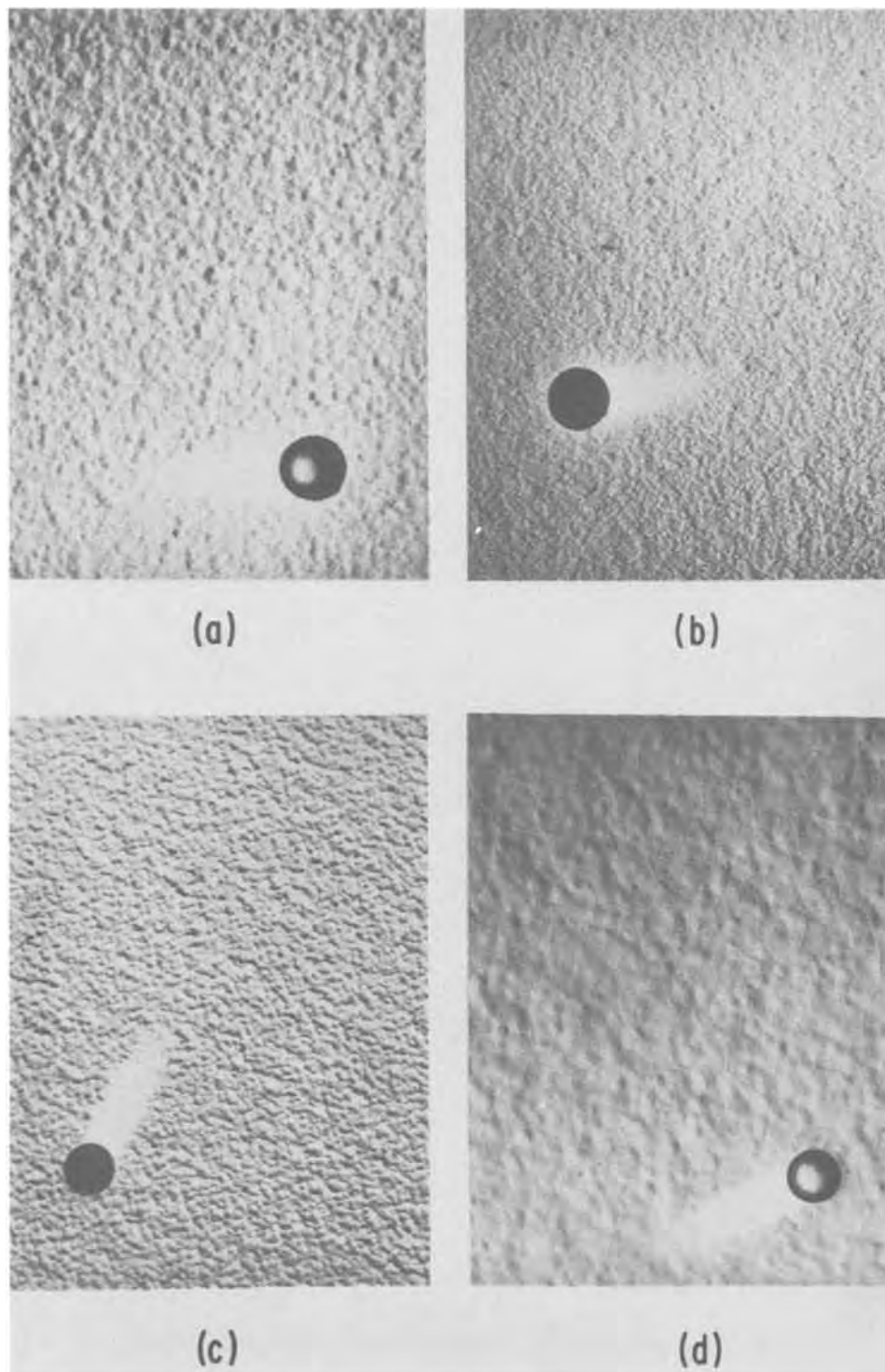


Fig. 3. Replicas (negative) of CVD silicon films (a) deposited at 650°C, undoped, 800°C oxidation, (b) deposited 650°C, POCl₃ doped, 800°C oxidation, (c) deposited at 800°C, undoped, 1100°C oxidation, (d) deposited at 800°C, POCl₃ doped, 1100°C oxidation. The oxide was ~30 nm and removed prior to replication.

crystal silicon. This is seen in Fig. 6(a) and (c) which show oxidized poly-Si and 6(b) and (d) which show the same samples with the oxide removed.

From these TEM observations several conclusions can be made. Firstly, the poly-OX is not uniformly thick, i.e., it has thickness undulations which replicate the previous grain boundaries with the thinnest poly-OX being near previous grain boundaries. Secondly, oxidation occurs intergranularly as well as on the free surface. The poly-Si surface, although initially rough, becomes further roughened as a result of oxidation. These characteristic features of the oxidation of poly-Si will enable a mechanism to be proposed.

Stress in poly-Si films.—When Si is converted to SiO₂ there is more than a twofold (2.2) increase in volume. For the oxidation of single crystal Si this volume is obtained by the outward expansion of the

oxide film from the single crystal surface that is being oxidized. However, for the case of poly-Si oxidation in which oxidation occurs not only on the free surface but also intergranularly, the volume required for oxidation is not as readily available. The intergranular mode of oxidation could lead to the buildup of a large compressive stress in the plane of the poly-Si film. Experience has shown that even for total oxidation of poly-Si, the films do not show any mechanical failure due to stress buildup. Thick poly-Si films (10³ nm) have been reported (13) to impart a substantial tensile stress to silicon substrates. It was also reported (13) that this tensile stress could be reduced by adding oxygen to the CVD ambient. In a recent detailed study of the wafer deformation caused by poly-Si films (14), a tensile poly-Si film stress was also reported. This tensile stress increased during

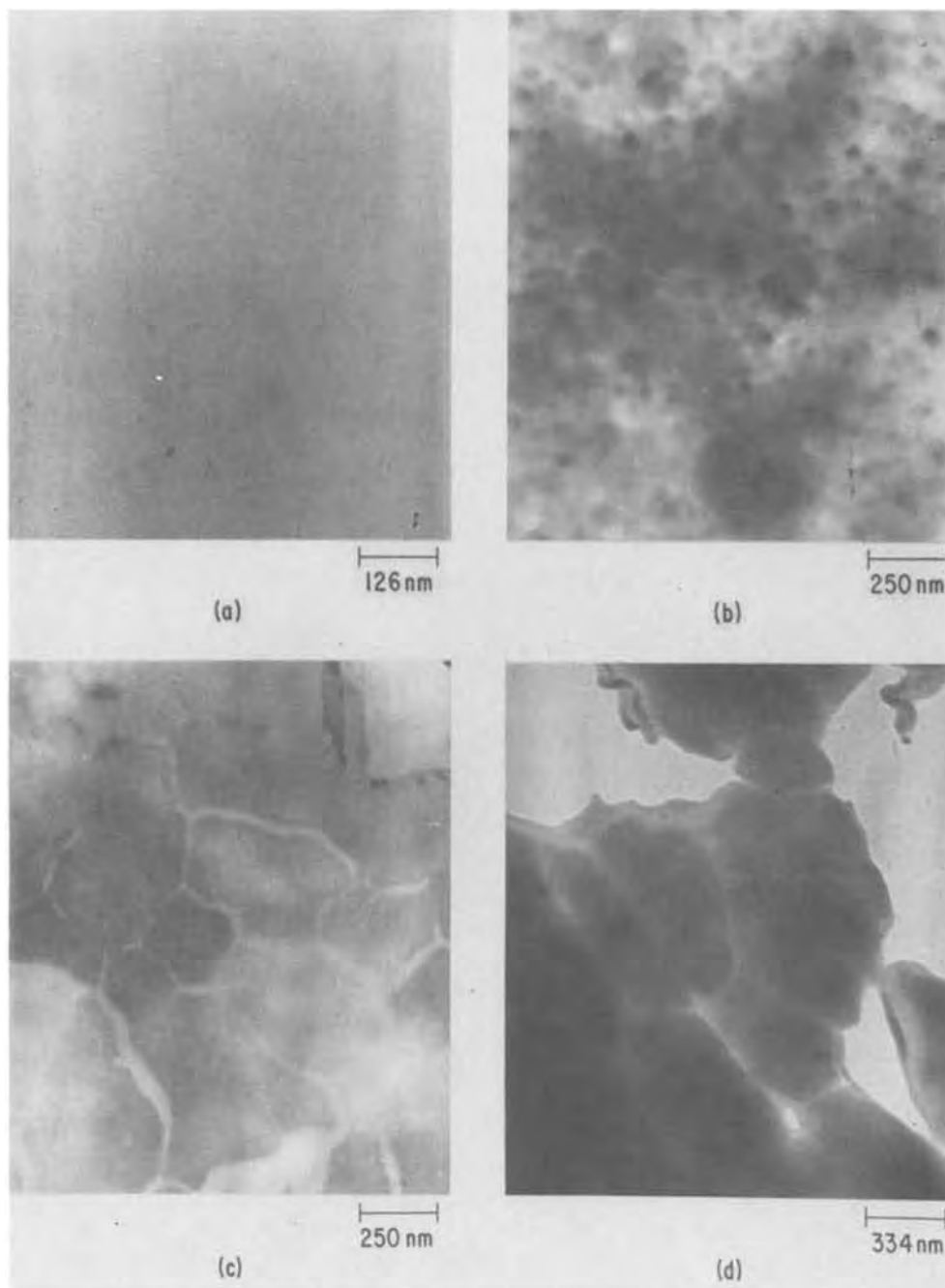


Fig. 4. Comparison of oxide grown at 1000°C in dry O₂ on (a) single crystal Si, (b) undoped poly-Si, (c) doped poly-Si and, (d) doped poly-Si but prepared for TEM by ion milling.

inert ambient (N₂ or Ar) anneals due to sintering but decreased if O₂ was added to the annealing ambient. These studies (13, 14) strongly support the contention that intergranular oxidation can lead to a compressive stress.

In order to determine the change in film stress before and after oxidation of poly-Si, several poly-Si samples both undoped and POCl₃ doped were measured before and after oxidation. It is seen in Table I that for all samples the total change in stress after oxidation is small. The doped samples all became more compressive (–) while the undoped became more tensile (+) after oxidation. We believe that the scatter in the data is primarily due to the smallness of measured changes. These stress results can be understood by considering that the grain morphology of the undoped poly-Si samples is immature with respect to further high temperature heat-treatments. As shown in Fig. 2 the undoped samples undergo grain growth during oxidation. Grain growth causes a reduction in volume by eliminating grain boundaries and with the volume decrease of the film,

a more tensile stress is expected. Therefore, for the undoped material there are two opposing processes occurring during oxidation: intergranular oxidation causing a more compressive film stress and grain growth causing a more tensile stress. Apparently

Table I. The change in residual stress in polycrystalline silicon films after oxidation

Sample ID	Change in number of Newton rings	Change in stress ($\Delta\tau \cdot 10^{-8}$ dynes/cm ²)
Doped:		
30	–1.5	–7
33	–2	–9
34	–2	–9
38	–2.5	–11
Undoped:		
39	+6	+27
40	+7	+31
41	+5	+22
42	+5	+22
43	+5	+22
44	+5	+22

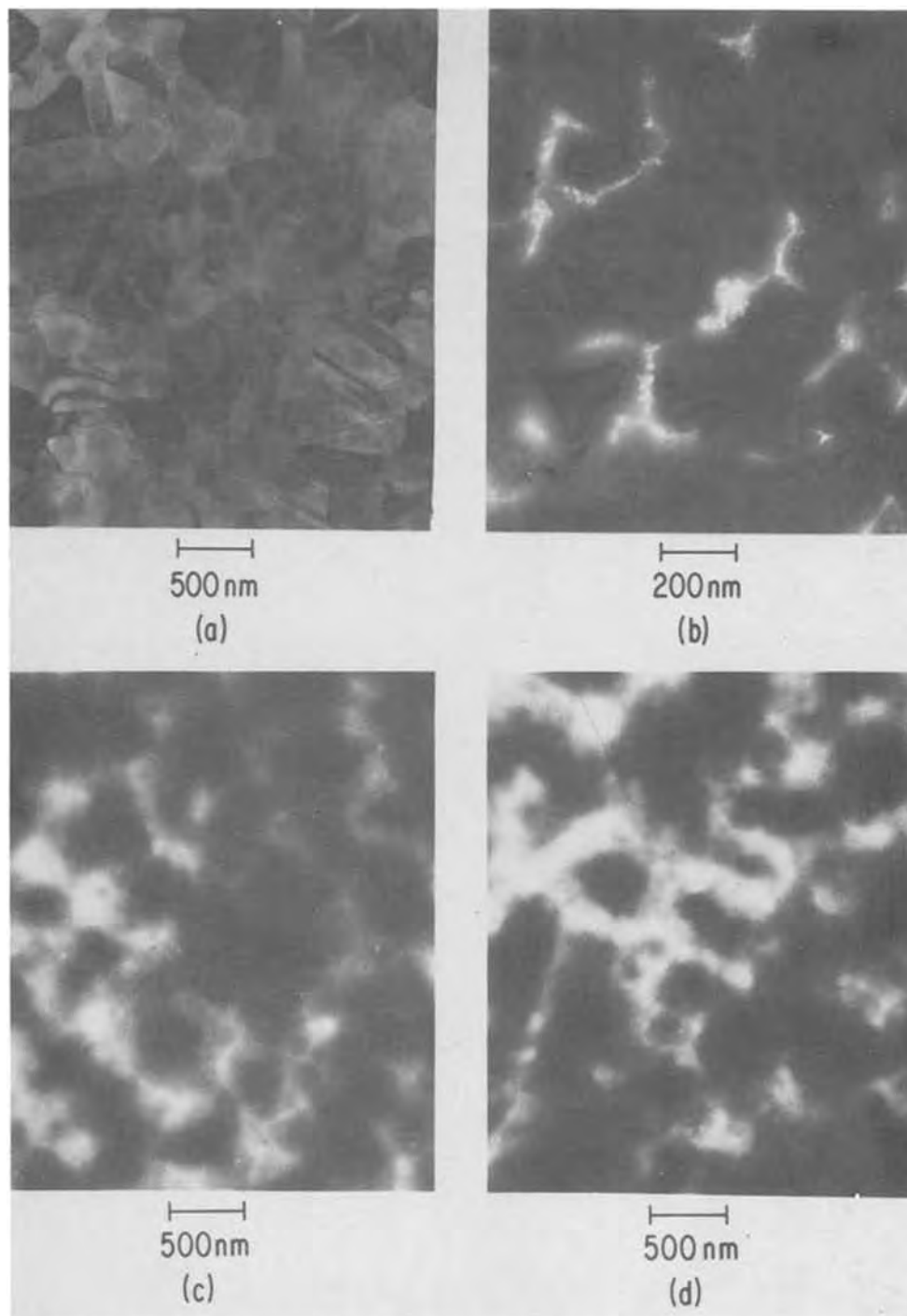


Fig. 5. Progressive stages of oxidation of poly-Si, (a) unoxidized, (b) oxidized to produce ~ 50 nm SiO_2 , (c) oxidized to produce ~ 150 nm SiO_2 , (d) completely oxidized ~ 300 nm SiO_2 .

grain growth is more dominant. For the doped material, the grain morphology is more mature hence the dominant effect during oxidation is due to intergranular oxidation which results in a compressive stress.

Intuitively a large compressive stress is anticipated due to intergranular oxidation. The magnitude of this stress can be estimated by considering ~ 50 nm diam grains with 1 nm intergranular oxide formed (from Fig. 4 and 5, only 1 nm intergranular oxide is a very conservative value). From these values a film stress of more than 10^{11} dynes/cm² is calculated which yields more than 10^2 more Newtons rings than is observed. It is clear that such a large stress would be easy to measure. The large discrepancy between the anticipated stress attributed to intergranular oxidation and measured stress strongly suggests that matter flows to create the necessary volume to accommodate intergranular oxidation and preclude the buildup of a large compressive stress.

Model for the oxidation of poly-Si.—The low stress values for poly-Si oxidation means that either Si and/or SiO_2 plastically deforms or creeps to relieve the stress and preclude film failure. If SiO_2 flows under oxidation conditions, then each oxidizing grain boundary acts as a source of SiO_2 and from each boundary SiO_2 would flow. The net result would be a thicker poly-OX at previous grain boundaries. Since negative thickness undulations are observed, it is concluded that Si creeps from the grain boundaries in order to relieve the strain.

A Nabarro-Herring type creep mechanism (15, 16) closely describes the situation at hand. In this mechanism a compressive stress is exerted in the grain boundaries by the growing oxide in a direction parallel to the plane of the poly-Si film. To relieve the strain vacancies flow toward the oxidizing boundary, thereby supplying the volume necessary to relieve the compression. Si atoms flow in the opposite direction thereby causing the grains to elongate in a direction

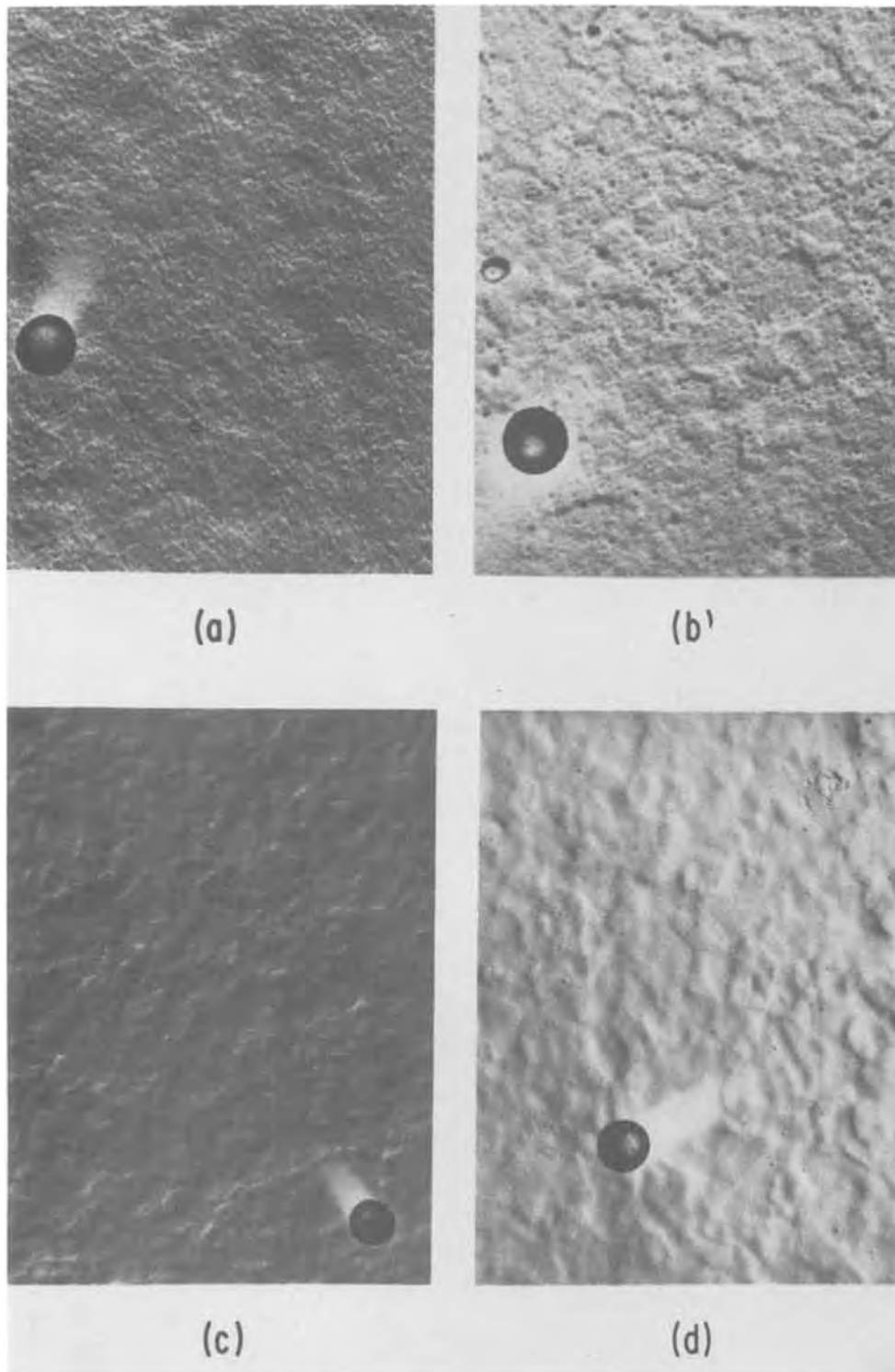


Fig. 6. Replicas of the surface of oxidized poly-Si and poly-Si with the poly-OX removed, (a) 650°C prepared, doped, oxidized to ~50 nm at 1000°C, (b) same as (a) but oxide removed, (c) 800°C prepared, doped, oxidized to ~50 nm at 1000°C, (d) same as (c) but oxide removed.

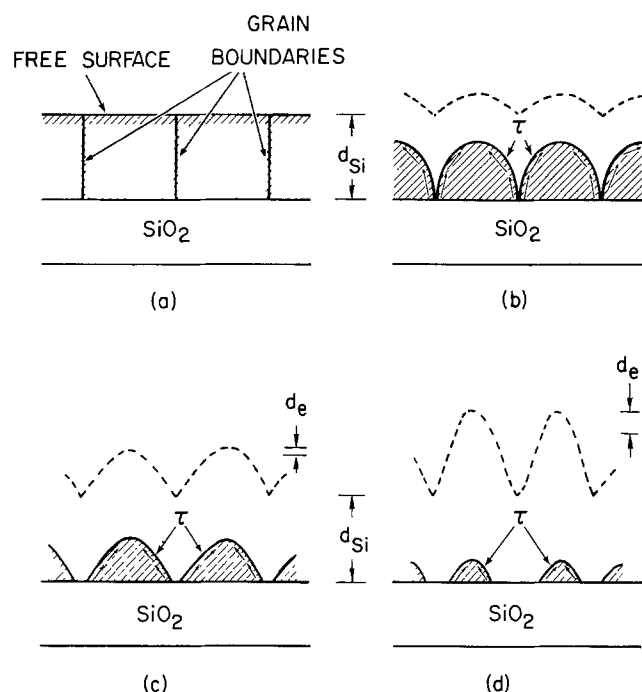
normal to the stress. This type of mechanism has been observed to occur at high temperatures and under low stress which are the conditions where intergranular silicon oxidation commences.

The operation of this mechanism is clarified by consideration of Fig. 7. Figure 7(a) shows the idealized grain morphology for poly-Si showing the free and grain boundary surfaces. As oxidation ensues a stress, τ , builds up in the grain boundaries as a result of the volume increase resulting from intergranular oxide formation. The small arrows show the direction of motion of Si atoms away from the source of the strain and towards the midgrain regions so as to relieve the strain. This motion of Si depletes the amount of Si at the grain boundaries and enhances the amount at the midgrain regions thereby elongating

the grains normal to the stress. Simultaneous with the Si motion, oxidation also occurs and hence there is consumption of Si both in the grain boundaries and at midgrain regions. Therefore, the net result is a thinner oxide formed at previous grain boundaries due to Si depletion and a thicker oxide of midgrain regions that receive the excess Si. This flow of Si and the growth of the oxide is seen in 7(c) and (d) where d_e is the extra growth of oxide due to the Si which flowed to the midgrain regions.

At higher oxidation temperatures it may be expected that SiO_2 as well as Si flows. This would result in less severe poly-OX thickness undulations for higher temperature oxidations and more severe for lower temperature oxidation. Figure 8 shows a comparison of the same sample as used in Fig. 5 oxidized

OXIDATION OF POLYCRYSTALLINE Si



d_{Si} = ORIGINAL Si GRAIN THICKNESS

d_e = SiO_2 PRODUCED DUE TO Si CREEP

Fig. 7. Model for the intergranular oxidation of poly-Si (a) unoxidized, idealized grain structure, (b), (c), (d) progressive stages of oxidation.

nearly completely and to the same extent at 800°C [8(a)] and 1150°C [8(b)]. Less severe thickness undulations are seen for the higher temperature case.

In summary, a consistent explanation is realized by considering an Si creep mechanism as the predominant factor in determining the overall poly-Si and poly-OX morphology after oxidation.

Implications of the model.—From a comparison of dark and photo currents in poly-OX (4), a uniform barrier lowering effect was ruled out as the cause of higher than expected currents in poly-OX. Localized field enhancement effects due to protuberances on the poly-Si surface were deemed causative of the observed high conductivity of poly-OX (2-4). The present study has shown that surface roughness of poly-Si is a direct result of intergranular oxidation of poly-Si. Also the original poly-Si grain morphology while being a function of preparation temperature and doping does not greatly affect the surface roughness of poly-Si after oxidation. This explains why higher than normal poly-OX currents are seen for poly-OX grown on doped and undoped poly-Si even though the original grain sizes and morphologies are vastly different.

In addition to poly-Si surface roughness effects, the present study also showed that the poly-OX has thickness undulations. The TEM micrographs show that the thin regions of poly-OX over previous grain boundaries represent a smaller area than the thick poly-OX over midgrain regions. As estimated from the micrographs, the poly-OX is more than 25% thinner near previous grain boundaries. The usual film thickness measuring techniques used to measure poly-OX thicknesses such as interference, ellipsometry, or mechanical step height techniques will yield poly-OX thicknesses representative of the larger areas, i.e., the thicker regions. However, the electronic currents in poly-OX are determined by the thinnest regions which yield the maximum field for an applied voltage. Therefore, the reported electric fields for poly-OX based on the conventionally measured poly-OX thicknesses could be erroneously low. It is interesting to note that a 30-35% decrease in film thickness will yield ~ 1.5 increase in field which is sufficient to

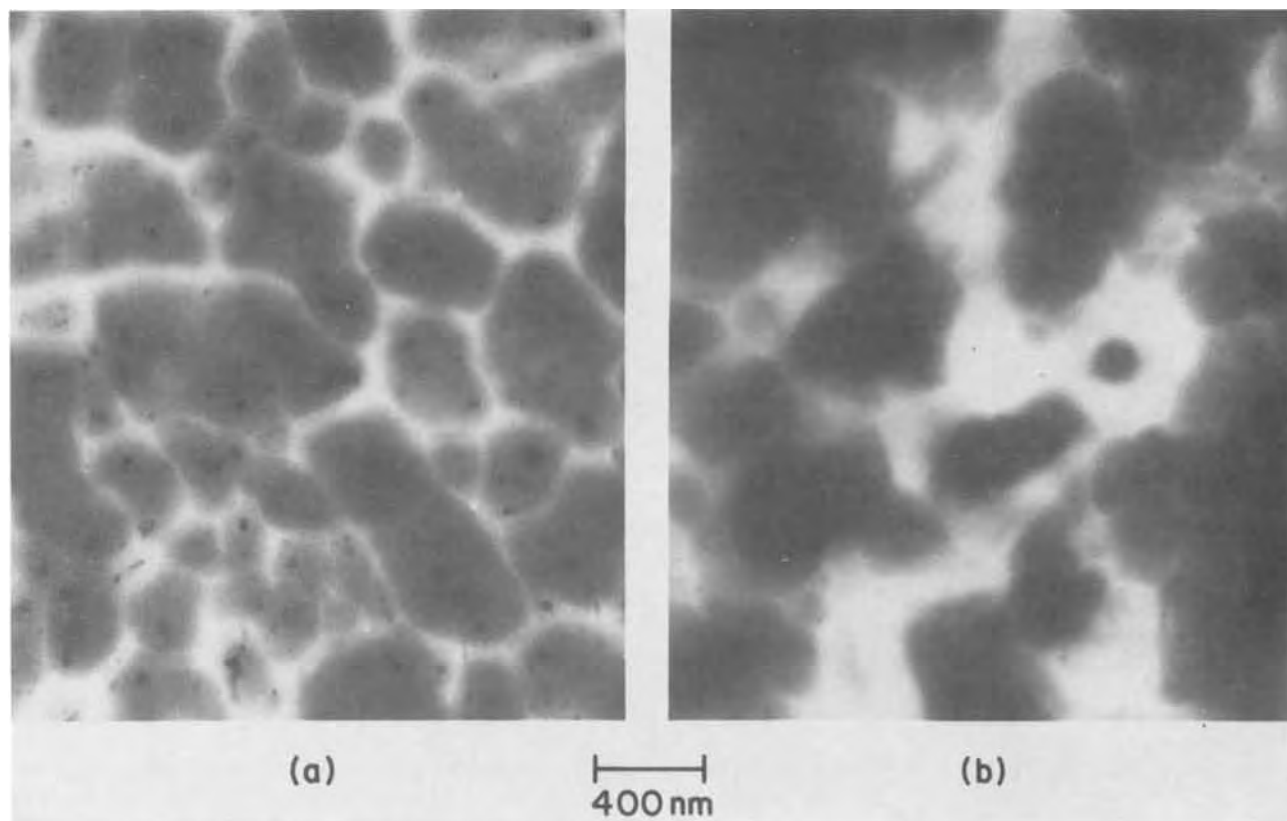


Fig. 8. Poly-Si samples as in Fig. 5, oxidized to the same extent in dry O_2 (a) 800°C and (b) 1150°C

explain some of the reported field enhancement effects in poly-OX (4).

We have found initial electrical shorts in some devices which utilize poly-Si lines. The shorts extend through the poly-Si lines and through an underlying oxide to the substrate or another line. The shorts occur as a result of removing the poly-OX on a line using an HF based chemical etchant so that metal can be evaporated for the contact to the poly-Si line. This shorting problem is understood by considering that due to intergranular oxidation of poly-Si, poly-OX forms in the grain boundaries of the poly-Si lines. When the surface poly-OX is removed by chemical etching, the etchant penetrates into the intergranular poly-OX and in some places where intergranular oxidation is extensive, through the underlying oxide. Evaporated Al will fill these holes thereby causing the electrical shorts. These reliability implications are treated in more depth in a separate publication (17).

Conclusions

TEM studies of the oxidation mechanism of poly-Si has revealed the following: (i) there is intergranular oxidation as well as oxide forming on the free silicon surface; and (ii) the intergranular oxidation of poly-Si leads to poly-Si roughness and thickness undulations in poly-OX.

A Si creep mechanism describes the oxidation behavior and the morphological features that develop as a result of oxidation help to explain some electrical reliability aspects of poly-OX.

Acknowledgment

This research was partially supported by the Defense Advanced Research Projects Agency and monitored by the Deputy for Electronic Technology, RADC, under Contract F19628-76-C-0249.

Manuscript received Aug. 20, 1979.

Any discussion of this paper will appear in a Discussion Section to be published in the December 1980

JOURNAL. All discussions for the December 1980 Discussion Section should be submitted by Aug. 1, 1980.

Publication costs of this article were assisted by IBM Thomas J. Watson Research Center.

REFERENCES

1. T. I. Kamins and E. L. MacKenna, *Metall. Trans.*, **2**, 2292 (1971).
2. R. M. Anderson and D. R. Kerr, *J. Appl. Phys.*, **48**, 4834 (1977).
3. S. A. Abbas and C. A. Barile, in 13th Annual Proceedings, Reliability Physics Symposium, IEEE, Las Vegas, 1975.
4. D. J. DiMaria and D. R. Kerr, *Appl. Phys. Lett.*, **27**, 507 (1975).
5. E. A. Irene, in "Proceedings of the International Topical Conference on The Physics of SiO₂ and its Interfaces," S. T. Pantelides, Editor, Pergamon Press, New York (1978).
6. E. A. Irene, Paper 186 presented at The Electrochemical Society Meeting, Pittsburgh, Pennsylvania, Oct. 15-20, 1978.
7. E. A. Irene, V. J. Silvestri, and G. R. Woolhouse, *J. Electron. Mater.*, **4**, 409 (1975).
8. R. M. Finne and D. L. Klein, *This Journal*, **114**, 965 (1967).
9. E. A. Irene, *J. Electron. Mater.*, **5**, 287 (1976).
10. R. M. Anderson, *This Journal*, **120**, 1540 (1973).
11. Y. Wada and S. Nishimatsu, *ibid.*, **125**, 1499 (1978).
12. J. M. Fairfield and B. J. Masters, *J. Appl. Phys.*, **38**, 3148 (1967).
13. Y. Sumitomo, K. Niwa, H. Sawazaki, and K. Sakai, in "Semiconductor Silicon 1973," H. R. Huff and R. R. Burgess, Editors, p. 893, The Electrochemical Society Softbound Proceedings Series, Princeton, N.J. (1973).
14. T. Suzuki, A. Minura, and T. Ogawa, *This Journal*, **124**, 1776 (1977).
15. F. R. N. Nabarro, in Bristol Conference on Strength of Solids, Physical Society, London, p. 75 (1948).
16. C. Herring, *J. Appl. Phys.*, **21**, 437 (1950).
17. E. Irene and E. Tierney, "Some Relationships Between the Oxidation Mechanism and the Electrical Reliability of Polycrystalline Silicon Films," presented at the Twelfth Annual International Metallographic Society Meeting, Tamiment, Penn., July 1979.

Evaluation of Ultrathin Native Oxide on GaAs Surface

I. Sakai, M. Hirose, and Y. Osaka

Department of Electrical Engineering, Hiroshima University, Hiroshima 730, Japan

ABSTRACT

This paper describes a new method to determine the thickness of the interfacial oxide layer of metal/n-GaAs Schottky barriers from their capacitance-voltage characteristics and photoresponse. It is found that the thickness of the native oxide formed on an etched n-GaAs surface appreciably increases with decreasing carrier concentration. This is interpreted in terms of the chemical activity of the GaAs surface which is remarkably enhanced with the presence of holes at the surface.

Oxygen atoms adsorbed on a chemically cleaned semiconductor surface produce a very thin oxide layer even at room temperature. The thickness of such native oxide on an etched GaAs surface has been estimated to be 10-30Å from ellipsometry (1). Shiota *et al.* (2) have investigated oxide layers formed on GaAs cleaned by different kinds of etchants by Auger electron spectroscopy, and found an etching procedure best suited to the preparation of GaAs(100) surface with the least amount of residual oxide thickness (~10Å). GaAs MESFET's (3) and GaAs

Schottky-type solar cells (4) should have thin interfacial oxide layers between metal and GaAs. At present, there is no straightforward technique to evaluate electrical properties or thickness of the residual oxide layer for a metal/GaAs system.

In this paper, we describe a new method to determine the thickness of the interfacial oxide layer of a metal/GaAs Schottky barrier from its capacitance-voltage characteristics and photoresponse. It was found that the oxide thickness at a metal/etched GaAs interface decreases with increasing bulk carrier concentration.

Key words: gallium arsenide, native oxide, Schottky barrier.

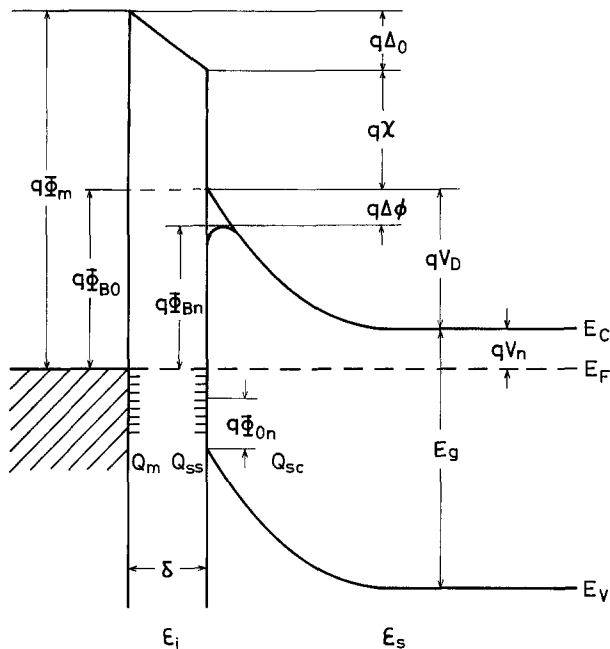


Fig. 1. Energy band diagram of metal/GaAs Schottky barrier. Φ_m : metal work function, Φ_{Bn} : barrier height, χ : electron affinity of GaAs, $\Delta\phi$: image force barrier lowering, Φ_{0n} : energy level determined by distribution of GaAs surface state charge, δ : thickness of interfacial layer, Δ_0 : potential difference across oxide layer, Q_m : surface charge density on metal, Q_{ss} : surface state charge density on GaAs, Q_{sc} : space charge density in GaAs, V_D : diffusion voltage, V_n : Fermi energy, ϵ_i : permittivity of interfacial layer, ϵ_s : permittivity of GaAs.

Theory

Figure 1 illustrates the energy band diagram of a Schottky barrier diode including an interfacial oxide layer and surface states on GaAs. From this figure, the differential capacitance of a GaAs Schottky barrier is given by (5)

$$\frac{1}{C^2} = \frac{\delta^2}{\epsilon_i^2} + \frac{2}{qN_D\epsilon_s} \left(V_D - V - \frac{kT}{q} + \Delta_0 - \frac{\delta Q_{ss}}{\epsilon_i} \right) \quad [1]$$

Using the relation $\Delta_0 = (\delta/\epsilon_i)(Q_{ss} + Q_{sc})$, one obtains (6)

$$\frac{1}{C^2} = \frac{2}{qN_D\epsilon_s} \left\{ -V + \left(V_D - \frac{kT}{q} + \alpha \right) \right\} \quad [2]$$

$$\alpha = \frac{\delta}{\epsilon_s} qN_D W_0 \quad [3]$$

Here, W_0 is the thickness of the depletion layer at zero bias. Then

$$\delta = \frac{\epsilon_i}{2\epsilon_s} \cdot \frac{\alpha}{V_D - \frac{kT}{q} + \alpha} W_0 \quad [4]$$

Since the barrier height $\Phi_{Bn}(C-V)$ measured by the capacitance-voltage ($C-V$) characteristic involves the effect of the interfacial layer, $\Phi_{Bn}(C-V)$ is described by

$$\Phi_{Bn}(C-V) = (V_D + V_n - \Delta\phi) + \alpha \quad [5]$$

The effective barrier height is directly obtained from the photoresponse of a Schottky barrier because all of photoelectrons emitted from metal to GaAs are able to tunnel through the very thin oxide layer. The Fowler plot of the photoresponse provides the barrier height $\Phi_{Bn}(\text{photo}) = V_D + V_n - \Delta\phi$.

Therefore, the thickness of the interfacial oxide layer δ is given by the following equation

$$\delta = \frac{\epsilon_i}{2\epsilon_s} \cdot \frac{\alpha}{V_1} W_0 \quad [6]$$

Here, $\alpha = \Phi_{Bn}(C-V) - \Phi_{Bn}(\text{photo})$, and V_1 is the intercept voltage in $1/C^2$ vs. V plot.

Experimental

A boat grown n -GaAs(100) wafer was mechano-chemically polished and then cleaned by $H_2SO_4:H_2O_2:H_2O = 3:1:1$ solution for 40 ~ 60 sec, or by $Br_2 + CH_3OH$ mixture for 1 min followed by rinse in $HCl:H_2O = 1:2$. Immediately after this cleaning, the wafer was transferred into an oil-free vacuum system and Au dots as thick as $\sim 1000\text{\AA}$ were evaporated onto the top surface since Au film should not react with native oxide around room temperature. Some of the GaAs wafers were annealed in H_2 or O_2 atmosphere, and then cleaned by $Br_2 + CH_3OH$ mixture and successive rinse in $HCl:H_2O = 1:2$, or by rinse in $HCl:H_2O = 1:2$ only, prior to fabrication of Schottky barriers.

Results

Figure 2 shows representative $C-V$ characteristics for Au/ n -GaAs Schottky barriers. $1/C^2$ vs. V plot in high bias range is nonlinear only for a wafer with a low carrier concentration ($\sim 10^{16} \text{ cm}^{-3}$) on account of deep traps in the GaAs substrate. In such case, $1/C^2$ vs. V plot could be corrected by the method of Vasudev *et al.* (7) (see curves b-1 and b-2 in Fig. 2). This obtained intercept voltage is only by 8% smaller than that determined from the straight line portion of the $1/C^2$ vs. V plot at low biases.

Figure 3 represents the Fowler plots of photoresponse for Au/ n -GaAs Schottky barriers. Using Eq.

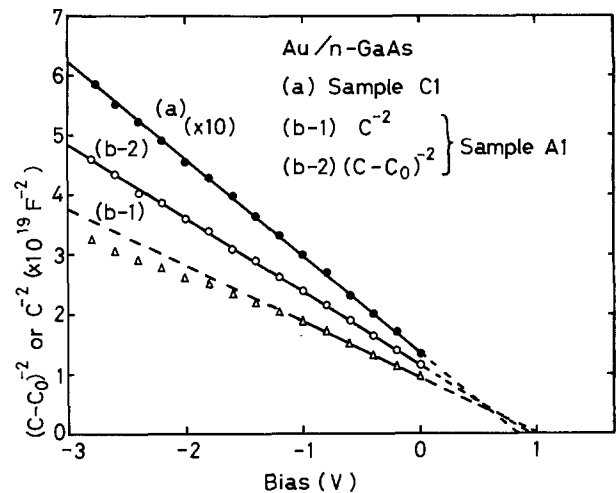


Fig. 2. Capacitance-voltage characteristics of Au/ n -GaAs Schottky barriers.

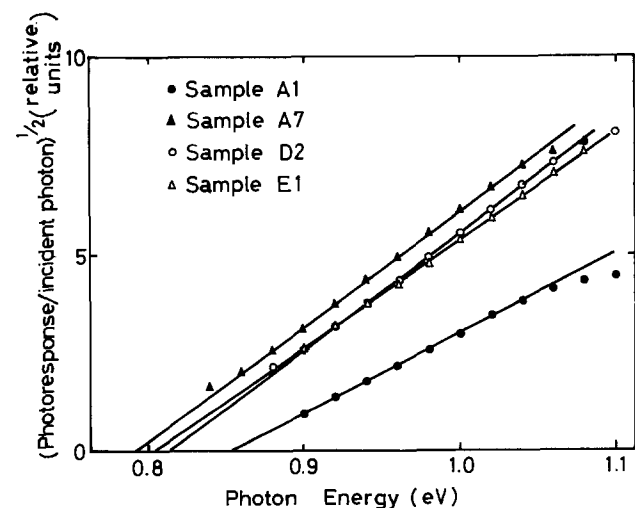


Fig. 3. Photoresponse of Au/ n -GaAs Schottky barriers with different thickness of interfacial layer.

[6], we can determine the oxide thickness δ . The small photocurrent for sample A1 is attributable to a thick native oxide layer (65Å) grown at room temperature. For all the thickest oxide (114Å) of sample A7, the photoresponse is larger than that of sample A1. Note that the oxide of sample A7 was grown in O_2 atmosphere at 500°C. From ellipsometry at 5460Å, the refractive index of the thermal oxide grown at 500°C was found to be 1.56 which is close to the value of Ga_2O_3 (8). This indicates that the amount of As atoms in the thermal oxide (sample A7) should be much less than that in the native oxide (sample A1), leading to a smaller barrier height of the oxide for sample A7. Table I summarizes calculated oxide thicknesses for unannealed samples. Here, permittivity of the oxide was assumed to be 5.4 (9). The oxide thickness tends to increase with decreasing carrier concentration. The minimum thickness of oxide for sample E1 is compatible with result of ellipsometry (1). The accuracy of a calculated oxide thickness is estimated to be better than 10%, if one takes an ambiguity of the intercept in the $1/C^2$ vs. V plot and the Fowler plot into account.

The oxide thicknesses for the samples chemically cleaned after annealing in H_2 or O_2 atmosphere are given in Table II. Some of these oxide thicknesses might be a little smaller than those indicated in Table II, because the permittivity of the oxide for samples in this table was again assumed to be 5.4. Actually, the permittivity for the thermal oxide grown at a high temperature is smaller than that for the oxide grown at room temperature, as suggested by ellipsometry which provides a refractive index of 1.85 at 5460Å for the native oxide grown at room temperature (1, 10) and of 1.56 for the thermal oxide grown at 500°C. The result of Table II shows that etching in $Br_2 + CH_3OH$ mixture for more than 1 min can remove most of the thermal oxide layer on a substrate with a high carrier concentration. On the contrary, aqueous HCl solution appears to be less

Table I. Oxide thickness for unannealed samples

Sample	Gate metal	$n = N_D - N_A$ (cm^{-3})	Etchant*	δ (Å)
A1	Au	1.71×10^{16}	A	65
2	Au	2.12×10^{16}	A	58
3	Au	2.32×10^{16}	B	39
B1	Au	3.42×10^{16}	A	35
C1	Au Cu	1.11×10^{17}	A	11 18
D1**	Au	2.31×10^{17}	A	20
2	Au	2.36×10^{17}	B	26
E1	Au	6.83×10^{17}	A	7
2	Au	8.46×10^{17}	A	16

* A and B refer to $H_2SO_4:H_2O_2:H_2O = 3:1:1$ and $Br_2 + CH_3OH$ mixture, respectively.

** Crystal orientation of sample D is exceptionally (111) direction.

Table II. Oxide thickness for annealed samples

Sample	$n = N_D - N_A$ (cm^{-3})	Annealing	Etchant after annealing*	δ (Å)
A1	1.71×10^{16}	Unannealed		65
4	1.73×10^{16}	$H_2, 500^\circ C, 1$ hr		24
5	2.21×10^{16}	$O_2, 500^\circ C, 1$ hr	B, 1 min	40
6	1.85×10^{16}	$O_2, 500^\circ C, 1$ hr	C, 2.5 min	120
7	1.87×10^{16}	$O_2, 340^\circ C, 1$ hr	C, 2 min	114
D1	2.31×10^{17}	Unannealed		20
3	1.76×10^{17}	$H_2, 500^\circ C, 1$ hr	B, 1 min	30
4	1.95×10^{17}	$O_2, 500^\circ C, 1$ hr	B, 1 min	20
5	1.69×10^{17}	$O_2, 500^\circ C, 1$ hr	B, 0.5 min	101
6	1.11×10^{17}	$O_2, 500^\circ C, 1$ hr	C, 3 min	75

* B and C refer to $Br_2 + CH_3OH$ mixture and $HCl:H_2O = 1:2$, respectively.

efficient to dissolve the thermal oxide. This is inconsistent with the result of Murarka (11) who showed that thermal oxide grown in air was insoluble in a $Br_2 + CH_3OH$ mixture.

Discussion

In Fig. 4 the thickness of native oxide δ at Au/GaAs interfacial region is plotted against the carrier concentration n for unannealed samples. The slope of the straight line yields the empirical relation

$$\delta \propto n^{-1/2} \quad [7]$$

The effective barrier height Φ_{Bn} which is obtained from the Fowler plot is shown as a function of carrier concentration in Fig. 5. The value of Φ_{Bn} is fitted to the equation

$$\Phi_{Bn} = -\frac{kT}{q} \ln n + \Phi_0 \quad [8-a]$$

or

$$n \propto \exp\left(-\frac{q\Phi_{Bn}}{kT}\right) \quad [8-b]$$

The electron concentration at the GaAs surface n_s for a metal/GaAs system is written by

$$n_s \propto \exp\left(-\frac{q\Phi_{Bn}}{kT}\right) \quad [9]$$

Using Eq. [7]-[9], the oxide thickness is related to

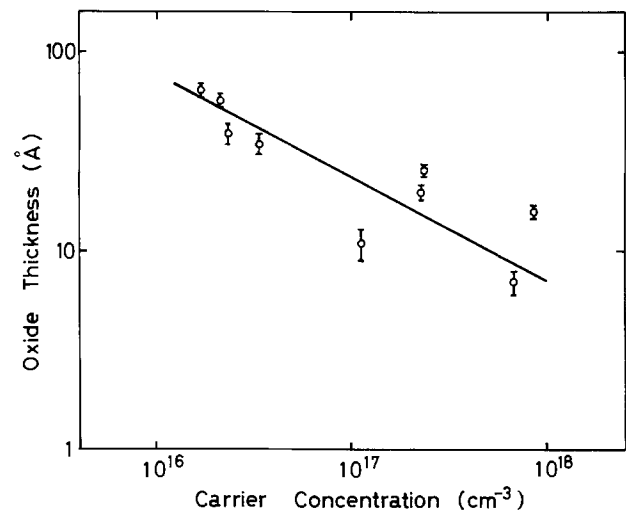


Fig. 4. Thickness of native oxide at Au/GaAs interface as a function of carrier concentration.

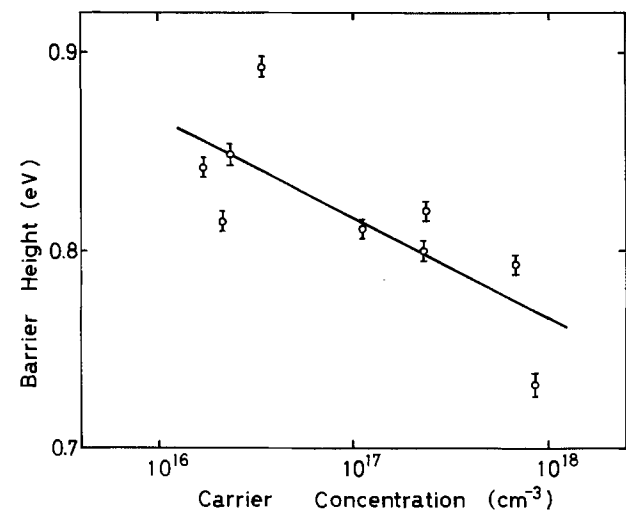


Fig. 5. Barrier height of Au/n-GaAs Schottky diodes as a function of carrier concentration.

the hole concentration at the GaAs surface p_s as

$$\delta \propto p_s^{1/2} \quad [10]$$

If the native oxide layer is sufficiently thin, the oxidation process is controlled by reaction rate at the GaAs surface (12). Note that holes at the GaAs surface produce broken bonds of GaAs which can react with oxygen atoms, resulting in oxidation of GaAs. Therefore the thickness could be related to the hole concentration at the GaAs surface.

The permittivity of the native oxide layer on GaAs, which is dependent on oxidation processes, was regarded as a parameter in the present analysis. The optical refractive indexes are 1.56 for the thermal oxide of GaAs at 5460Å and $1.8 \sim 1.9$ (1, 10) for the native oxide. The electrostatic permittivity for both the oxides should be correspondingly different in the similar range. In the present study, an electrostatic permittivity of 5.4 (9) for the thick anodic oxide film was employed for calculating the oxide thickness. The validity of this permittivity is supported by the fact that the optical refractive index for thin native oxide is almost identical to that for thick anodic oxide (1, 10). The relationship $\delta \propto n^{-1/2}$ is well satisfied, even if the actual permittivity is slightly different from 5.4.

In conclusion, it has been clarified that the chemical activity of n-GaAs surface for oxidizing agent is remarkably enhanced with lowering of the bulk electron concentration.

Manuscript submitted July 20, 1979; revised manuscript received Oct. 2, 1979.

Any discussion of this paper will appear in a Discussion Section to be published in the December 1980 JOURNAL. All discussions for the December 1980 Discussion Section should be submitted by Aug. 1, 1980.

Publication costs of this article were assisted by Hiroshima University.

REFERENCES

1. A. C. Adams and B. R. Pruniaux, *This Journal*, **120**, 408 (1973).
2. I. Shiota, K. Motoya, T. Ohmi, N. Miyamoto, and J. Nishizawa, *ibid.*, **124**, 155 (1977).
3. C. A. Liechti and R. L. Tillman, *IEEE Trans. Microwave Theory Tech.*, **22**, 510 (1974).
4. R. J. Stirn and Y. C. M. Yeh, *Appl. Phys. Lett.*, **27**, 95 (1975).
5. R. J. Archer and M. M. Atalla, *Ann. N.Y. Acad. Sci.*, **101**, 697 (1963).
6. M. Hirose, S. Kurinobu, T. Nakashita, and M. Kido, *Oyo Butsuri*, **43**, 798 (1974) (in Japanese).
7. P. K. Vasudev, B. L. Mattes, E. Pietras, and R. H. Bube, *Solid-State Electron.*, **19**, 557 (1976).
8. T. Hariu, S. Sasaki, H. Adachi, and Y. Shibata, *Jpn. J. Appl. Phys.*, **16**, 841 (1977).
9. R. A. Logan, B. Schwartz, and W. J. Sundburg, *This Journal*, **120**, 1385 (1973).
10. A. Shimano, A. Moritani, and J. Nakai, *Solid-State Electron.*, **21**, 1149 (1978).
11. S. P. Murarka, *Appl. Phys. Lett.*, **26**, 180 (1975).
12. A. S. Grove, "Physics and Technology of Semiconductor Devices," Chap. 2, John Wiley and Sons, New York (1967).

A Study of Stacking Faults during CMOS Processing: Origin, Elimination and Contribution to Leakage

S. P. Murarka,* T. E. Seidel, J. V. Dalton, J. M. Dishman, and M. H. Read

Bell Laboratories, Murray Hill, New Jersey 07974

ABSTRACT

An investigation of the generation of the stacking faults in silicon during the CMOS processing has been carried out using n-type 2-5 Ω -cm 7.5 cm diam (100) silicon wafers obtained from different manufacturers. Various thermal oxidation steps and the etching or cleaning steps preceding such oxidations were evaluated. It has been found: (a) Stacking faults were produced in densities of less than 1000/cm² in 1050°C wet oxidations; (b) the p-tub drive-in (1200°C/15.5 hr/10% O₂-90% N₂) generated stacking fault nuclei which grew into stacking faults (in densities of $\geq 10^4$ /cm²) during subsequent oxidations; (c) all stacking fault nucleation centers of type (b) and most of type (a) could be gettered by the presence of mechanical damage (such as the saw damage) on the back side of wafers, and densities $\sim 10^2$ /cm² (a), and ~ 0 /cm² (b) were found; (d) stacking faults thus formed contributed to leakage currents even when they appear not to be decorated with impurities. Various experiments leading to the above conclusions have been described and the results have been discussed. It is highly recommended that wafers with damaged back sides be used during processing in order to minimize the generation and growth of stacking faults and the leakage associated with such faults.

The presence of oxidation-induced stacking faults (OISF) in the silicon near the oxide-silicon boundary is detrimental to the electrical performance of devices (1-13). In a recent paper, Dishman *et al.* (2) have reported the results of their investigation of the excess leakage in CMOS integrated circuits. Evidence was presented that the anomalous component of the junction leakage in devices was due to the occurrence of decorated stacking faults at the intersection of the silicon surface with the p-n junction boundary. We have investigated the role of process-

ing in producing stacking faults in silicon at the oxide-silicon boundary. In the early part of the study it became apparent that the large density ($\geq 10^4$ cm²) of OISF was very commonly but not always associated with the wet oxidation following the 1200°C boron drive-in, which is carried out to create the so-called p-tub (for CMOS circuits) in the n-type wafers. It will be shown that such generation of stacking fault nuclei (which grow into faults during subsequent oxidation) was completely suppressed in 2-5 Ω -cm wafers with intentionally (or unintentionally) created back side mechanical damage. The data

* Electrochemical Society Active Member.
Key words: gettering, oxidation, SiC.

relating the density of faults with the measured leakage on finished devices are also presented.

Experimental Procedure and Results

Unless otherwise mentioned, only n-type, 7.5 cm diam (100) wafers were used in these investigations. The experimental technique consisted mainly of Secco etching the wafers after a given oxidation and examining the stacking faults on such wafers. Oxidation was always carried out at 1050°C in the stream of oxygen bubbling through water maintained at 98°C. Stacking faults were then revealed by the removal of the oxide and etching in Secco etch.

In the early stages of the CMOS processing silicon wafers went through the following processing steps:

1. Clean and wet oxidation at 1050°C.
2. Photolithography and etching to open window in oxide.
3. Boron implant $1 \times 10^{13} \text{ cm}^{-2}$ at 30 keV, resist strip, clean.
4. Boron drive-in, 1200°C/15.5 hr in 10% O₂-90% N₂.
5. Etch oxide off, clean, wet reoxidation at 1050°C.

In preliminary experiments we examined a large number of the wafers pulled out at various steps. The conclusions of these first examinations were:

(a) Wafers pulled after step 1, to determine the density of OISF produced during wet oxidation alone, eliminated the possibility that this oxidation alone produced OISF in densities greater than $10^3/\text{cm}^2$. (Only float zone crystal produced large densities of stacking faults, see Table I.)

(b) Following step 5, some wafers had a very large density of OISF (10^5 - 10^7 cm^{-2}). On the other hand, others which were processed with those above at the same time had a low density of similar OISF ($< 10^3 \text{ cm}^{-2}$). As shown in Fig. 1 faults in the density of 10^4 cm^{-2} or more were usually distributed in such a way that they formed circular striations which appeared similar to swirl patterns (14).

(c) The boron drive-in step played a role as a source of OISF in densities greater than $10^3/\text{cm}^2$. Initially the results appeared highly nonreproducible from run-to-run (each run containing several wafers from various manufacturers).

These observations also led to the further investigations. It was rather easy to visibly distinguish between the wafers with OISF density $\geq 10^4 \text{ cm}^{-2}$ and those with a lesser number of faults, as a large density of faults caused the front surface to appear blotchy. Wafers with lesser number of faults were shiny. Blotchiness could be due to a "dirt" effect or a nonuniform (not striated) distribution of oxygen.

P-tub implant eliminated as a cause.—Ion implantation of low boron doses ($1 \times 10^{13} \text{ cm}^{-2}$) followed by oxidation has been shown not to produce stacking nuclei in any appreciable numbers (15). We confirmed

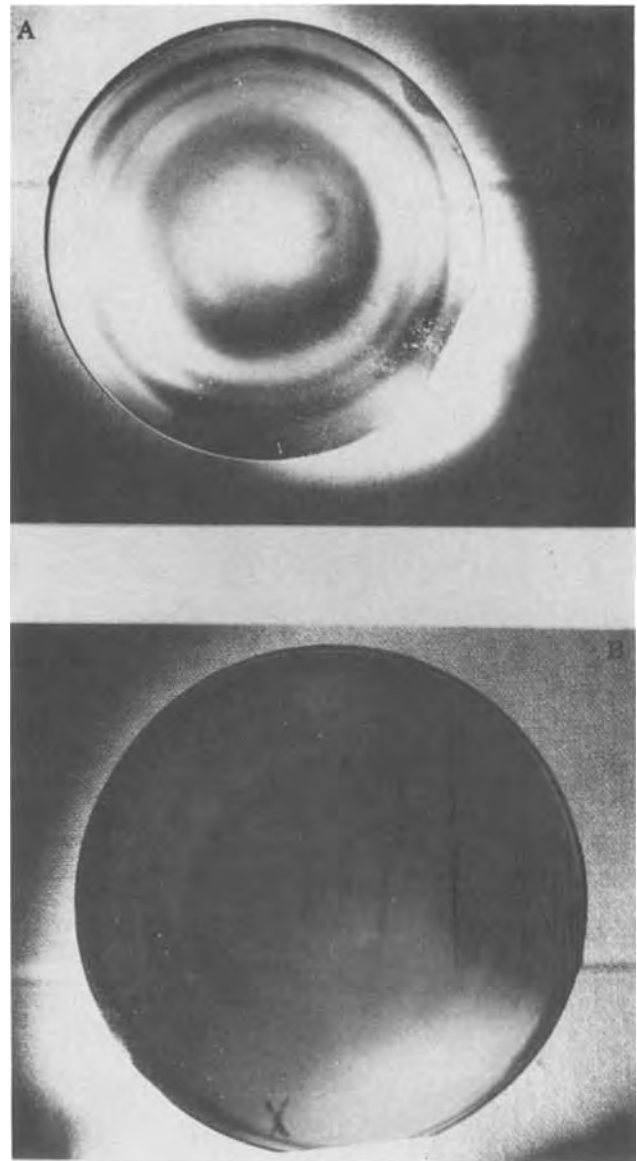


Fig. 1. Low magnification photomicrographs showing striations due to stacking faults formed in wafers after p-tub drive-in, oxide etch, and reoxidation. (a) $0.96\times$ (b) $1.11\times$.

this by carrying out experiments with boron-implanted wafers (which did not go through drive-in) and did not observe any high density stacking fault blotchiness after a 1050°C wet oxidation. (Implantation-sputter related effects have been observed to cause stacking fault nuclei near the rim of the sample holder, see Appendix).

Boron drive-in and back side damage play a role.—Wafers (from different manufacturers) with no implantations were driven-in (annealed) at 1200°C for 15.5 hr in 10% O₂-90% N₂. The oxide was etched off and the wafers were reoxidized in oxygen bubbled through 98°C water for 47 min at 1050°C. Stacking faults were then revealed by removing oxide and by a Secco etch of 30 sec. The results are summarized in Table II. If the results of manufacturer Z are excluded, a comparison of Table II with Table I indicated that the boron drive-in and not the wet gas oxidation was responsible for blotchiness. Wafers from manufacturers of Table II were also given a one-step wet oxidation, as those in Table I, and the stacking fault densities were low. These results lead to two important conclusions: (i) High density stacking fault blotchiness was never observed on the wafers from manufacturer Z and (ii) wafers from all other

Table I. Density of stacking faults on wafers oxidized at 1050°C for 2 hr in wet oxygen (water temperature 98°C)

Manufacturer	Wafer		Type (dopant)	Resistivity, ($\Omega\text{-cm}$)	Fault density* (cm^{-2})
	Diameter (cm)	Thickness (μm)			
A	5	250-350	n(P)	1.5-2.5	163
B	5	250-350	n(P)	5-10	331
C**	5	350-490	n(P)	5-10	$10,000 \dagger + 10 \ddagger$
D	7.5	425-500	n(P)	5-10	948
E	7.5	425-500	n(P)	5-10	339
F	7.5	425-500	n(P)	2.5-5.0	497§
G	7.5	425-500	p(B)	8-20	33

* Average of measurements on at least 5 wafers.

** Float zone silicon; all others Czochralski grown.

† Large density of very small faults.

‡ A few faults of size equal to that observed on others.

§ One area had blotchiness which contributed most.

Table II. Density of stacking faults on wafers subjected to p-tub drive-in and reoxidation*

Manufacturer	Faulty density† (cm ⁻²)
M	~10 ⁵ -10 ⁶
W	>10 ⁵
RE	~10 ⁵
Y	>10 ⁵
Z	~10 ²

* All wafers were n-type phosphorus doped in the resistivity range of 2.5-10 Ω-cm, 7.5 cm diam, 450-500 μm thick.

† Average of measurements on several wafers. Occasionally, a few wafers in the lot will have stacking fault density less than 10²/cm². Other times only part of the wafer will have very high density faults. In latter case, usually the part having faults will have circular striations.

manufacturers usually showed high OSIF for 1200°C drive-in plus reoxidation at 1050°C, but not for a 1050°C oxidation alone.

In order to understand the observed results, we carefully examined wafers from all manufacturers. It was found that the wafers obtained from manufacturer Z had a rough back surface due to saw damage which was not entirely removed during back side etching. Cross sectioning showed the depth of the saw damage to be about 15 μm. Wafers from all other manufacturers (including float zone wafers) had a comparatively smoother back surface (as a result of the longer etching by the supplier). Figure 2 shows

the back surfaces of the wafers from manufacturers Z and RE in two magnifications. The difference in the degree of the surface roughness is evident. The rougher surface had scattered the light at all angles and thus appeared bright (Fig. 2b). The more polished surface (Fig. 2a) (examined in exactly the same light conditions) reflected the light away from the camera except at the scratched identification marks near the flat of the water. The roughness of the back of wafers Z was probably responsible for gettering the fault nuclei during the oxidation process. Mechanical damage gettering has been advocated in the past (16-19) to getter undesirable impurities in a way phenomenologically similar to the commonly used phosphorus diffusion gettering (20). It has not been documented that mechanical damage prevents the formation of OISF through the CMOS process. To evaluate the role of mechanical damage the following experiments were carried out.

Removal and addition of back side damage.—Part of the back surface and all of the front surface of the wafers from the manufacturer Z (rough back side) were masked. The exposed back surface was then etched in a silicon etch to remove ~25 to 74 μm of silicon. The back surface that had been etched was then smoother and appeared similar to the back surfaces of the wafers from other manufacturers. After etching, the mask material was removed and the wafers were cleaned. These wafers together with unetched wafers from manufacturer Z and all others, were then processed with a 1200°C oxidizing drive-in and 1050°C wet oxidation.

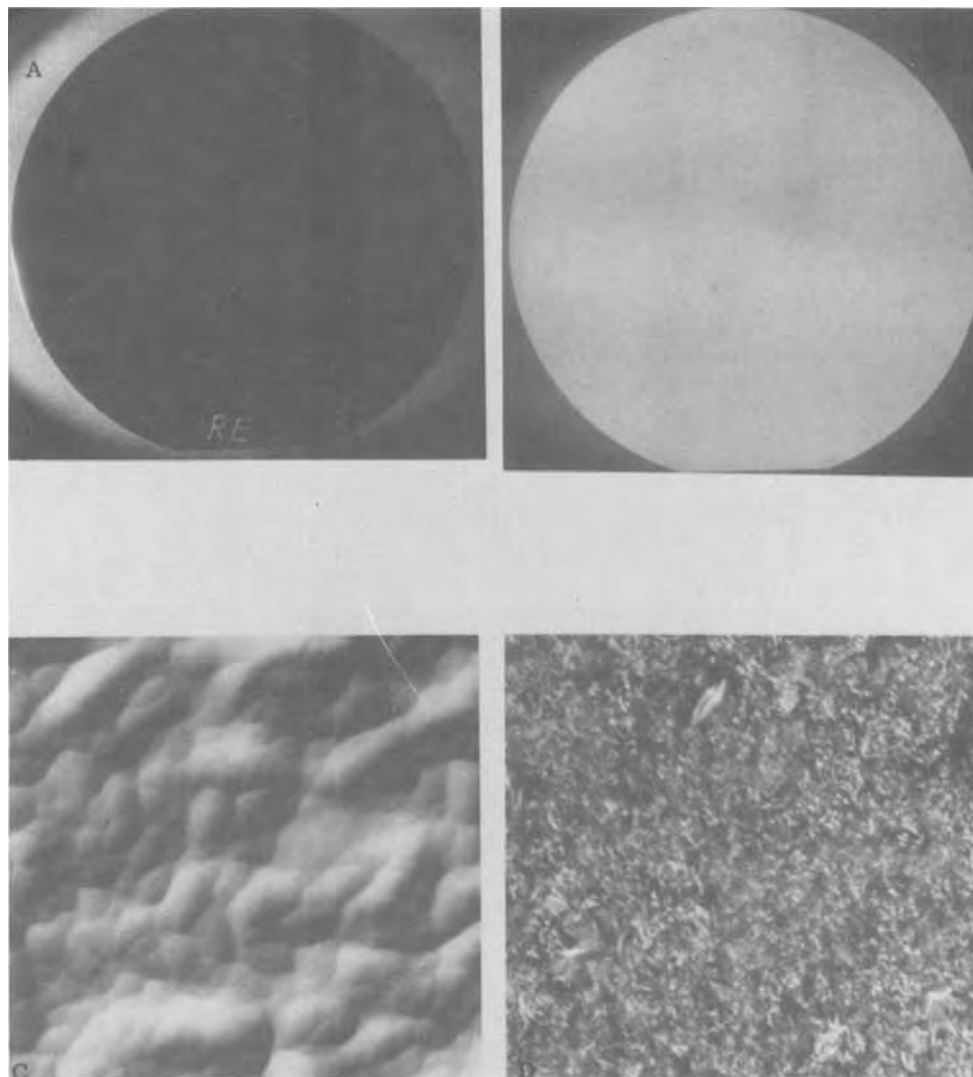


Fig. 2. Micrographs showing the comparative roughness on the back of a wafer with blotchiness (on front) due to stacking faults (a) 1.12× and (c) 1000×, and the wafer with no blotchiness (on front) (b) 1.17× and (d) 1000×.

In a reverse experiment back surfaces of the wafers, from all manufacturers with the exception of Z, were ground on a 180 grit polishing paper to produce mechanical damage. Such wafers, together with as-received wafers from all manufacturers were processed through drive-in and wet oxidation.

Figure 3 shows the front surface of a Z-wafer after removal of the back side damage in the "cross" region. (Ignore the narrow uneven vertical white band across the wafer surface. This band is a result of loss of adherence of the mask material protecting the front surface of the wafer during the back surface etching.) The dark triangular regions had stacking fault density of less than $100/\text{cm}^2$ and replicate the protected, unetched back surface. The blotchy "cross" area in the middle had a density of faults $\geq 10^5/\text{cm}^2$, where back surface damage had been etched away. High magnification photomicrographs showing the boundary between the gettered and ungettered regions, and the stacking faults in the ungettered regions, are shown in Fig. 4. The optical examination of the wafers from the addition of damage experiment confirmed the findings of the removal of damage. All wafers which had been subjected to the mechanical damage on the back surfaces, irrespective of who manufactured them, were clean of stacking faults. All other control wafers in both experiments showed exactly the behavior as described earlier. The results clearly demonstrated the gettering by the residual mechanical damage on the back side of the wafers.

Repeated drive-in experiment.—In this experiment only wafers from the manufacturer Z were used. Figure 5 describes a step-by-step scheme of this experiment. The wafers were cleaned and (oxidized) annealed at 1200°C for 15.5 hr in 10% O_2 -90% N_2 ambient. The front surfaces of some (group I) of these

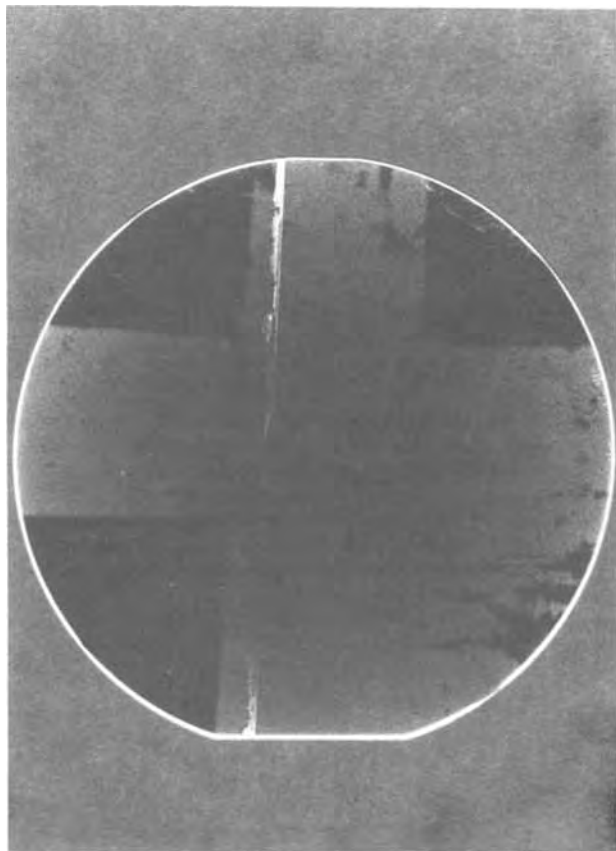


Fig. 3. Micrograph of the front of the wafer with black areas and blotchy surface areas. The blotchiness on the front is due to very large density of stacking faults. Black areas do not have stacking faults in such numbers. The back of the wafer was etched in the regions where blotchiness occurred.

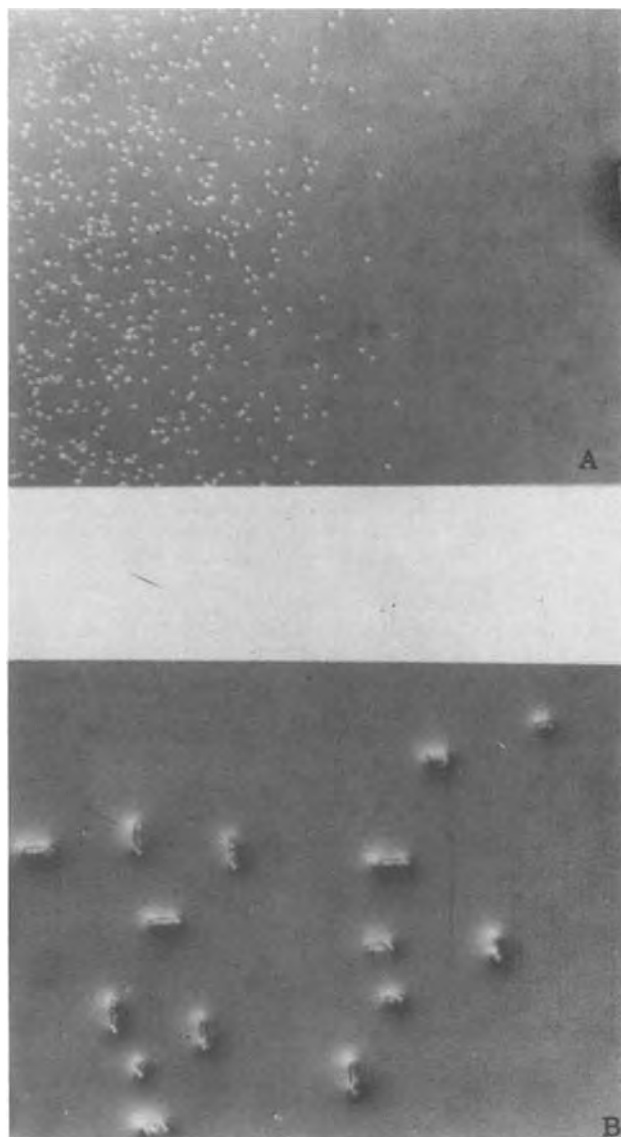


Fig. 4. High magnification photomicrographs of (a) the boundary between blotchy and black areas of the wafer shown in Fig. 4 and of (b) the stacking faults in the blotchy area. (a) $60\times$, (b) $1000\times$.

wafers were then protected by use of electroplaters tape and the backs were etched in a silicon etch to remove the mechanical roughness. After tape removal, degreasing, and cleaning, the oxide was etched off these and off a few of the remaining (group II controls) unetched wafers. All group I and II were then subjected to second 1200°C , 15.5 hr drive-in 10% O_2 -90% N_2 . After the second drive-in, all wafers (including the rest (group III control) of those held after the first drive-in) were placed in BHF to remove the oxide. They all were then reoxidized in wet oxygen at 1050°C for 50 min and etched in Secco etch (following an oxide removal etch) for a 30 sec etch. Blotchiness due to OISF was present only on the wafers subjected to the second 1200°C drive-in after the back surface etch. All other wafers, with undisturbed back surface and with the first or second drive-in, had no blotchiness. These results thus established that, to effectively getter nucleation centers, the damage on the back surface of the wafers should be present during all subsequent oxidizing heat-treatments. This also means that nucleation centers were continuously introduced or formed during the drive-in. These nuclei are getterable, through repeated drive-in cycles, as long as sufficient mechanical damage is present on the back surface.

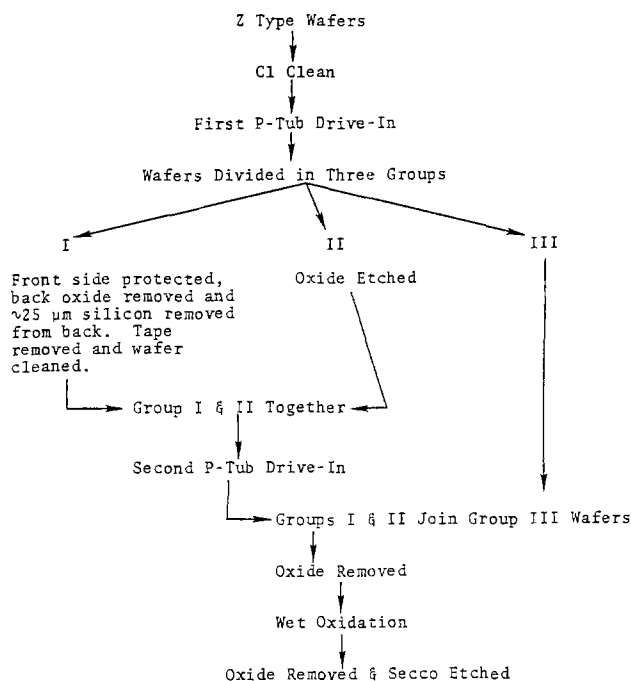


Fig. 5. Step-by-step scheme of the repeated drive-in experiment

Depth distribution of stacking fault density.—In this experiment, the depth distribution of the stacking fault density due to the boron drive-in and reoxidation was determined for samples with polished backs. Sequential front side etching and density count revealed a slight increase in the OISF density up to $\sim 4\text{--}5\ \mu\text{m}$ in silicon. Beyond this depth no new stacking faults appeared. The front surfaces of such wafers (with blotchiness) were Syton polished to remove an additional $10\text{--}15\ \mu\text{m}$ (a total of $15\text{--}20\ \mu\text{m}$). After cleaning, wafers were reoxidized in wet oxygen at 1050°C and were examined after Secco etch. If a blotchiness appeared on the wafer, the above polishing and oxidation steps were repeated until no blotchiness was observed. In all cases, blotchiness was gone after removal of $\sim 25\text{--}30\ \mu\text{m}$ of silicon. Blotchiness was never observed below $30\ \mu\text{m}$ no matter how many low temperature oxidations were carried out. If, however, such wafers were subjected to a second boron 1200°C drive-in and 1050°C reoxidation, the blotchiness (not necessarily exactly similar to one before polishing) would reappear. These experiments clearly indicated that the boron drive-in created stacking fault nuclei in silicon close to the $\text{SiO}_2\text{--Si}$ surface (within $25\text{--}30\ \mu\text{m}$ of surface).

Relation of stacking faults and leakage.—The contribution of undecorated stacking faults to leakage is determined here.

Dishman *et al.* (2) have presented evidence showing that the anomalous component of the junction leakage in devices made on $7.5\ \text{cm}$ diam wafers was due to the occurrence of decorated stacking faults at the intersection of the silicon surface with the p-n junction boundary. Following the suggestion of Seidel (2), reduction in the leakage current to an acceptable level on devices was achieved by stripping the back surface oxide before phosphorus diffusion gettering near the end of the processing sequence. This gettering process removed impurities from the decorated faults and improved device performance. A defect evaluation of such device wafers was carried out.

In this experiment, we examined fully processed wafers after their device evaluation. Wafers with a spectrum of leakage currents were collected. Junction leakage currents had been measured at special test features on the whole wafer, depending on the particular device there were 5 to 11 such test patterns

on a wafer. After physically locating such test features, all the top layers (e.g., Al, dielectric, etc.) were removed by etching. The test features under investigation were clearly visible, usually free of any etch artifacts. Finally, wafers were given Secco etch of 30 sec to reveal stacking fault features if any.

Wafers with both high and low density of faults were found. In all these wafers, the faults appeared undecorated (2). Since there was a wafer-to-wafer variation in the leakage currents we sought to obtain a correlation between the density of stacking faults near the test features and the leakage current. We, therefore, computed the density of faults on and near the test features. We also counted the number of stacking faults which intersected the boundaries of these test features such that a leakage path could develop from the test structure to the substrate. Figure 6 shows a typical test pattern and the large density of faults crowding the pattern.

A plot of the leakage as a function of the stacking fault density is shown as Fig. 7. A reasonably good straight line can be drawn through the data points indicating a monotonic dependence of the leakage on the stacking fault density. The straight line thus obtained could be curve fitted to an equation

$$I = 1.5 \times 10^{-8} d^{0.3} \text{ A/cm}^2 + I_0 \quad [1]$$

where I is the leakage current in A/cm^2 , d is the density of stacking faults per cm^2 , and I_0 is $\sim 1 \times 10^{-9} \text{ A/cm}^2$.

We have also computed the number of stacking faults which intersect the boundaries of the test features such that a leakage path could form between test features and the surrounding material. (It is thus assumed that the faults present within the boundaries of the test features and those close to such boundaries are not contributing to leakage.) Figure 8a shows a plot of the leakage current as a function of the number of stacking faults that intersect the boundaries of the test features. In the absence of a stacking fault intersecting the device boundaries, the leakage is $\sim 2 \times 10^{-10} \text{ A}$. By subtracting this number from the total leakage current and then plotting the leakage current as a function of the number of faults which intersect the boundaries, we obtain a straight line fit as shown in Fig. 8b. The leakage in this case is thus given by

$$I = 1.5 \times 10^{-12} N_1^{2.2} + 2 \times 10^{-10} \text{ A} \quad [2]$$

Where N_1 is the number of faults intersecting the boundaries of the devices for which leakage current was measured.

Discussion

In the preceding, evidence has been presented to establish the following:

1. Stacking faults were produced in densities of less than $1000/\text{cm}^2$ in low temperature oxidations such as a 1050°C wet initial oxidation.

2. With the exception of the back side damaged wafers, the boron drive-in (i.e., $1200^\circ\text{C}/15.5\ \text{hr}$ anneal in $10\% \text{ O}_2\text{--}90\% \text{ N}_2$) generates stacking fault nuclei near the exposed surface of the silicon wafer. Such nuclei are not produced at low temperature wet oxidations and are not produced in bulk (about $\sim 25\ \mu\text{m}$ away from the surface) silicon. The nuclei once formed grow into stacking faults on subsequent wet gas or steam oxidation.

3. All such stacking fault nucleation centers can be gettered by introducing mechanical damage on the back surface of the wafers.

4. Stacking faults thus formed contribute measurable leakage currents even when they appear not to be decorated with impurities.

Finally fully processed wafers taken from split lots (Z-type *vs.* M-type wafers and Z-type *vs.* X-type) were stripped and examined for stacking faults. Only

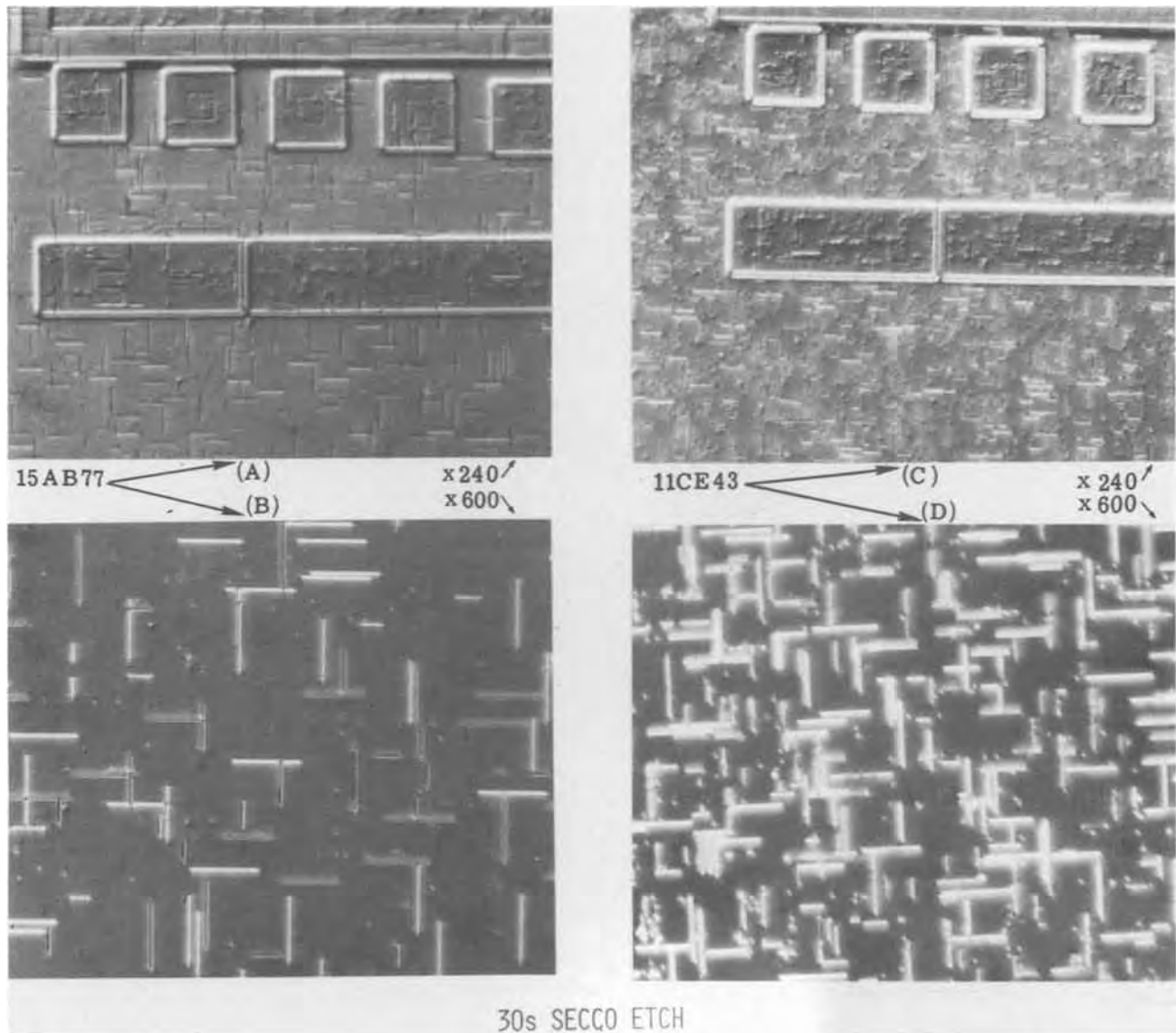


Fig. 6. Photomicrographs of the full processed, electrically characterized and etched wafers showing the test pads and high density of faults surrounding such pads. Note that faults seem to be undecorated (2).

the wafers with a high degree of back side polish exhibited significant stacking fault densities. Z- and X-type wafers, both having residual saw back side damage, were essentially free of stacking faults. Thus, in the presence of the back side damage, stacking fault formation is suppressed throughout the processing. It must, however, be noted that the ex-

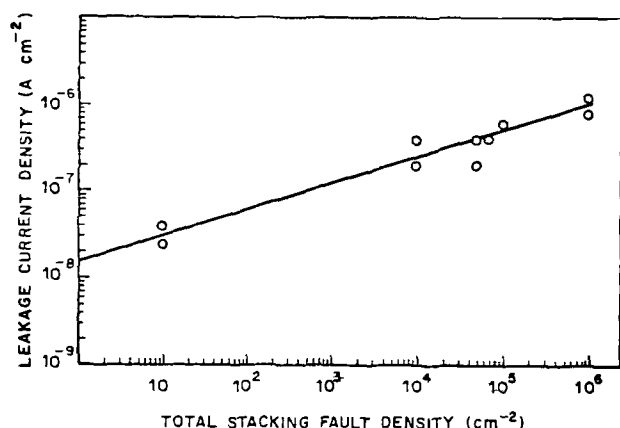


Fig. 7. Leakage current measured on the test pads as function of total stacking fault density around these pads.

periments of the first type (on wafers with back side damage) show that the back side saw damage does not suppress all stacking fault formation, when very strong stacking fault nuclei are present with wet oxidation ambients. Such nuclei are very less in number, usually, $\lesssim 10^2/\text{cm}^2$ and occasionally up to $10^3/\text{cm}^2$. Therefore, it cannot be concluded that remnant saw damage will always guarantee zero stacking fault density. It may, however, be concluded that most stacking faults, which would otherwise form, are gettered. It is highly recommended that wafers with mechanical damage on the back surface (such as Z wafers) be used in the device processing line.

Defect nucleation and growth.—One may attribute the formation of stacking fault nuclei, during the boron drive-in, to the bulk nuclei near the surface and/or high temperature annealing, especially in oxygen. From Fig. 1 it would appear that the stacking faults are distributed in a manner similar to as-grown microdefects in the so-called Swirl pattern (14) or in the striated distribution observed in dislocation-free float zone and Czochralski materials. One is thus tempted to suggest that the high density stacking fault blotchiness observed after the heat-treatment in our experiments, could be due to the nucleation and growth of faults at the microdefects in as-grown material. Working with both float zone and Czochralski wafers, Ravi

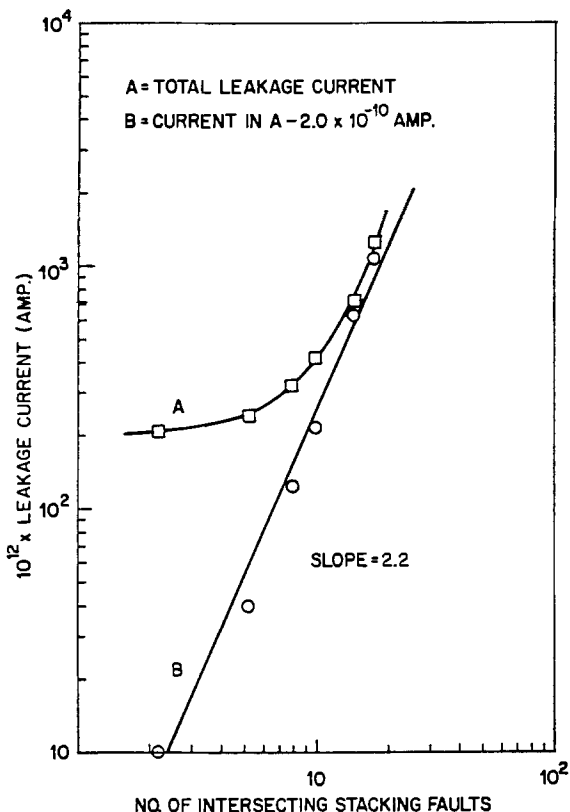


Fig. 8. Leakage current measured on the test pads as a function of the number of the stacking faults which intersect the test pad boundaries.

(22) has shown that long oxidation at temperatures as high as 1200°C resulted in the formation of discrete precipitates. Ravi (22) attributed the formation of striations (such as those shown in Fig. 2) to inhomogeneous distribution of vacancy clusters where the precipitates form during annealing. Maher *et al.* (23) have found that extrinsic stacking faults formed during heat-treatment of silicon contained colonies of coherent microprecipitates at their center. Mahajan *et al.* (24) proposed that the first stage in the evolution of stacking faults can be envisaged to be a localized oxidation leading to the formation of silicon-oxygen clusters. It would appear from our results that the boron drive-in was necessary for the formation of OISF during subsequent oxidations. The role of the boron drive-in is, therefore, to generate defects along the growth striations. Abe *et al.* (25) have recently shown that the presence of growth striations in Czochralski material is mainly due to heterogeneous distribution of oxygen and that a 1200°C/16 hr anneal in oxygen is required to generate defects along those striations. It may be noted that the occasional absence of blotchiness on the wafers (even with polished surface, *i.e.*, without any damage to getter) after drive-in and re-oxidation was observed only in Czochralski materials. This absence of formation of faults could be attributed to the absence of the growth striations in these wafers or the presence of bulk gettering oxygen precipitates.

The role of oxygen during anneal becomes very apparent when one considers the depth distribution of stacking faults. It was found that the stacking fault nuclei formation during the boron drive-in was limited to ~20-30 μm of silicon from the SiO_2 -Si interface. Mahajan *et al.* (24) have proposed a model in which a localized oxidation of silicon is assumed to occur in the vicinity of existing heterogeneities in the silicon. Nucleation of faults then occurs due to generation of silicon interstitials in large enough concentration to plate out into an extrinsic fault. If the concentration of Si interstitials (and hence that of oxygen to cause

localized oxidation) is not large enough, nucleation of fault will not take place. During a 1200°C (or a high temperature) drive-in, oxygen can diffuse to an approximate depth of $\sqrt{4DT} \sim 42 \mu\text{m}$ (26). Thus, it may be assumed that beyond a certain depth in silicon, the concentration of oxygen falls below a concentration required to nucleate faults at the bulk defect centers. Thus, the results of experiment could be attributed to oxygen diffusion depth limited nucleation. The presence of both the heterogeneities and oxygen is necessary to nucleate faults. In absence of one or the other (for example due to mechanical damage gettering) faults do not form.

It may be pointed out that although OISF up to 70 μm in length have been observed on the samples annealed in 100% oxygen for 15.5 hr at 1200°C, stacking faults were not visible in our optical examinations of the Secco-etched wafers after boron drive-in. It has been shown recently by Murarka (27,28) that the growth of the faults is considerably retarded in reduced oxygen partial pressures such as 10% used during the high temperature drive-in. It has also been shown that the stacking fault retrogrowth temperature is considerably lower in such an ambient. Both of these effects could reduce the size of OISF's so that they are too small to be detected optically. These faults could form nucleation centers for the growth during low temperature wet oxygen or steam oxidation following a boron drive-in.

Gettering of the defect nuclei.—It has been shown that no matter what is the source of nucleation of OISF during boron drive-in, the defect nucleation can be completely suppressed by the gettering action of the mechanical damage on the back of the wafer. Gettering induced by back surface damage is not new. Pomerantz (16) had suggested the same technique to get rid of process-induced defects. Strain generated due to mechanical damage could lead to the precipitation of the impurities in the damaged region or enhance their diffusivities in the bulk silicon. This results in the entrapment of the impurities and point defects which are responsible for nucleation of faults, into the damaged back layer of the silicon. In addition, it is possible that the back side damage competes for silicon interstitials with stacking fault nuclei (or less likely is a source of vacancies for the stacking fault suppression).

Contribution of the faults to leakage in the devices.—The presence of the faults in the silicon provides a strained region of interest for impurities which could be entrapped in such regions. These impurities may have ionization levels in the bandgap of the silicon and thus provide charged generation levels. If the fault lies in or across a space charge region the levels will generate leakage.

For the present we do not have any model to explain the relationships of types described by Eq. [1] and [2]. It is hard to synthesize an argument (similar to one given for impurity decorated faults) for a fault which is free of any impurities. A fault in the lattice produces a strained region. If the strain is large enough, it could affect the nature of the semiconductor energy levels. A large number of faults, when present together in a small area, could perhaps cause such an effect leading to unexpected leakage. The role of such a large number of stacking faults in causing leakage is apparent in Fig. 7 and 8. The results may be compared to leakages measured on emitter base junction with stacking faults (29), where the electric fields are larger than those shown for the MOS leakage test junction.

Acknowledgments

Authors would like to thank H. J. Levinstein for many useful discussions and T. T. Sheng for polishing of the wafers.

Manuscript submitted March 5, 1979; revised manuscript received Sept. 24, 1979.

Any discussion of this paper will appear in a Discussion Section to be published in the December 1980 JOURNAL. All discussions for the December 1980 Discussion Section should be submitted by Aug. 1, 1980.

Publication costs of this article were assisted by Bell Laboratories.

APPENDIX

The Effect of Wafer Holders in the Ion Implanters

During our investigations with boron-implanted, driven-in, and reoxidized wafers, we had always without exception observed a large density of stacking faults in an area within approximately 1 mm from the edge of the wafers. At low magnifications faults appeared to form a circular ring around the wafer as shown in Fig. A-1. Figures A-1b-d clearly show these faults. Such an effect was never observed in nonimplanted wafers. In the present series of experiments, an as-implanted (but not heat-treated) wafer was Secco etched. A differential etching near the edge of the wafer resulted in a ring about 1 mm away from the edge. The differential etching occurred due to different etch rates of n (near the edge) and p (rest of the wafer, due to B-implant) type material. No stacking faults were present on the wafer. The presence of this ring could be associated with a rim of aluminum in

the wafer holder for the implantation. Wafers are held against this rim during ion implantation. As shown in Fig. A-2a, the rim which is about a millimeter wide thus shields the wafer edge from the ion beam. Thus, no implantation occurs on the wafer under the rim (hence, the differential etching effect). The ion beam, however, can cause sputtering from the aluminum rim and leads to implantation of the species (near the edge of the wafers) which are probably the nucleating centers for the stacking faults. The contamination resulting from the contact of the wafer with the metallic rim could also introduce impurities responsible for stacking fault nucleation. We shall call this effect a rim effect. Such preferential nucleation at the edge of the wafer cannot be associated with damage from p-tub implants. The ion implanted dose is small compared to the doses required to produce centers for stacking faults as reported by Rozgonyi and Seidel (15). Appearances of blotchiness could never be associated with the p-tub boron implants. In order to verify this rim effect, we implanted a few wafers in a different commercial ion implanter. In this machine, the wafers are loaded in cassettes in such a way that they rest against a plate with an angular cutout as shown in Fig. A-2b. The wafers were subsequently processed and Secco etched in the same manner as described earlier. Microscopic examination of these wafers showed the rim effect in exactly the same geometry as shown in Fig. A-1; thus, confirming our explanation given above to

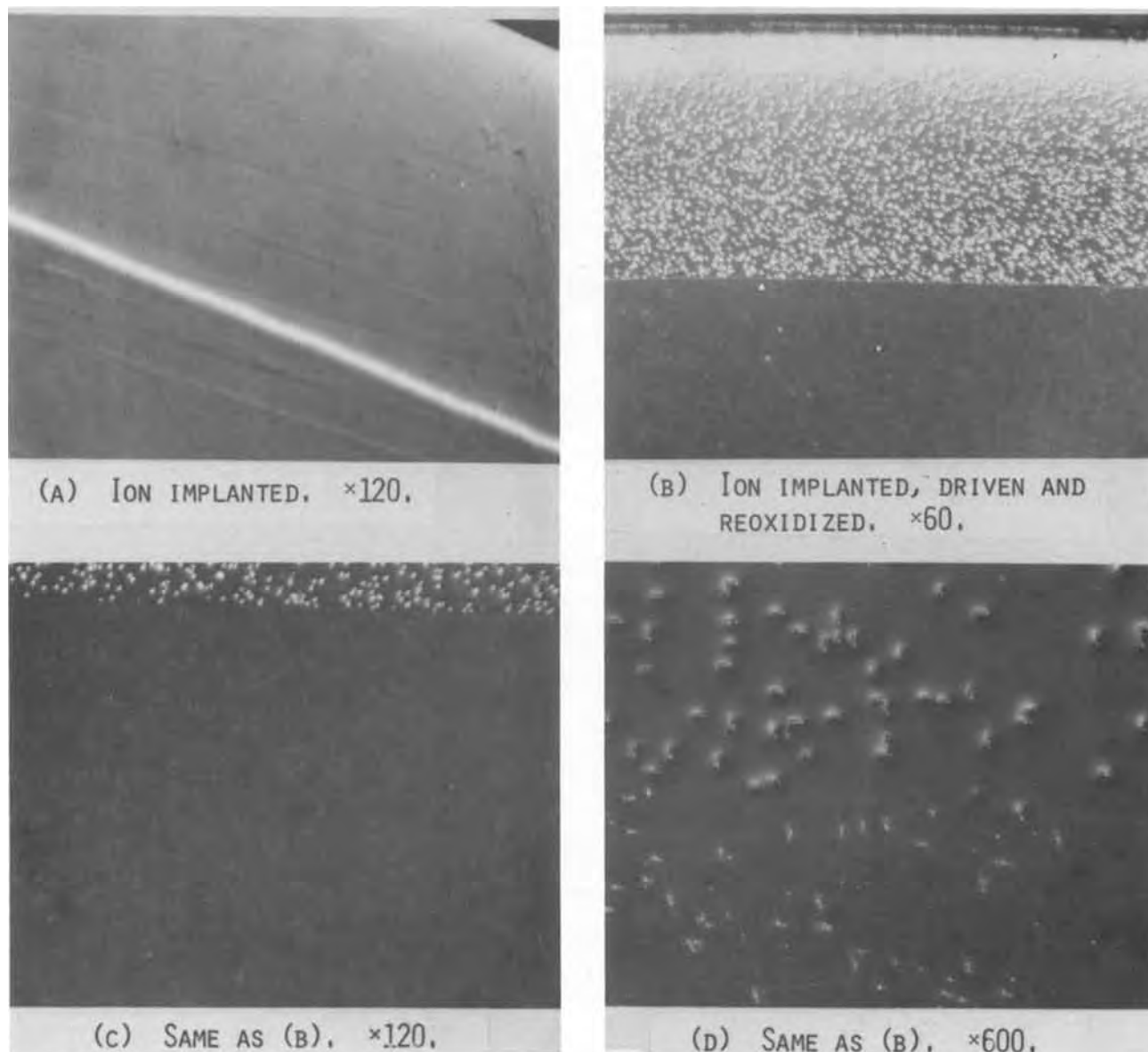


Fig. A-1. Photomicrographs showing the rim effect (see text) presumably due to backspattering, which leads to formation of stacking fault nuclei, from the wafer holder during the ion implantation.

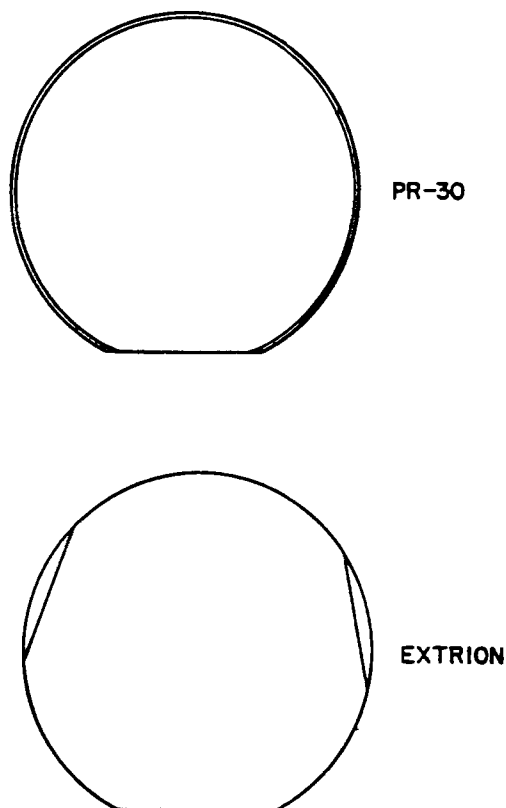


Fig. A-2. Schematic drawings of the metallic holders in PR-30 and Extrion ion implanters. Wafers are held against the metal at the outer edges as shown. (Not to scale.)

account for the rim effect. It may be recalled here that Katz and Moller (21) have reported that sputtering of nickel and other impurities in the same commercial implanter had led to the generation of a high density of stacking faults during later oxidations. All the results mentioned in the above paragraphs were obtained on wafers with back surfaces free of saw damage. To check the effect of mechanical damage gettering on the nucleation centers apparently caused by impurities associated with the rim of the metal holding the wafer (the rim effect), we used wafers with rough back surfaces, those manufactured by Z. These wafers were implanted with boron in a different implanter, driven-in, and reoxidized. Secco etch of these wafers revealed a p-n etch rate associated ring similar to that observed on just implanted wafers (Fig. A-1a). Only a few stacking faults in the rim area or in the rest of the wafer were observed. This indicated that mechanical damage on the back of the wafer was able to getter the nucleation centers due to the rim effect.

REFERENCES

1. F. Barson, M. S. Hess, and M. M. Roy, *This Journal*, **116**, 304 (1969).
2. J. M. Dishman, S. E. Haszko, R. B. Marcus, S. P. Murarka, and T. T. Sheng, *J. Appl. Phys.*, **50**, 2689 (1979).
3. T. Kato, H. Koyata, T. Matsukawa, and K. Fujikawa, *Solid State Electron.*, **19**, 955 (1976).
4. T. Kato, T. Matsukawa, and R. Shimizu, *Appl. Phys. Lett.*, **26**, 415 (1975).
5. S. P. Murarka, G. Quintana, S. E. Haszko, and R. B. Marcus, Unpublished work.
6. C. M. Osburn and D. W. Ormond, *This Journal*, **121**, 1229 (1974).
7. K. V. Ravi, C. J. Varker, and C. E. Volk, *ibid.*, **120**, 533 (1973).
8. D. W. Small and R. F. Pirret, *Appl. Phys. Lett.*, **27**, 148 (1975).
9. C. J. Varker and K. V. Ravi, *J. Appl. Phys.*, **45**, 272 (1974).
10. C. L. Claeys, E. E. Laes, G. J. Declerck, and R. J. Van Overstraeten, in "Semiconductor Silicon 1977," H. R. Huff and E. Sirtl, Editors, p. 774, The Electrochemical Society Softbound Proceedings Series, Princeton, New Jersey (1977).
11. K. Tanikawa, Y. Ito, and H. Sei, *Appl. Phys. Lett.*, **28**, 285 (1976).
12. S. P. Murarka and G. Quintana, *J. Appl. Phys.*, **48**, 46 (1977).
13. G. A. Rozgonyi, S. Mahajan, M. H. Read, and D. Brasen, *Appl. Phys. Lett.*, **29**, 531 (1976).
14. A. J. R. DeKock, *ibid.*, **16**, 100 (1970).
15. G. A. Rozgonyi and T. E. Seidel, in "Semiconductor Silicon 1977," H. R. Huff and E. Sirtl, Editors, p. 616, The Electrochemical Society Softbound Proceedings Series, Princeton, New Jersey (1977).
16. D. Pomerantz, *J. Appl. Phys.*, **38**, 5020 (1967).
17. M. Nakamura, T. Kato, and N. Oi, *Jpn. J. Appl. Phys.*, **7**, 512 (1968).
18. E. J. Mets, *This Journal*, **112**, 420 (1965).
19. M. Kikuchi and S. Iijima, *J. Phys. Soc. Jpn.*, **12**, 824 (1957).
20. S. P. Murarka, *This Journal*, **123**, 765 (1976). For a list of references on this subject see this paper.
21. L. E. Katz and W. M. Moller, Unpublished work.
22. K. V. Ravi, *This Journal*, **121**, 1090 (1974).
23. D. M. Maher, A. Staudinger, and J. R. Patel, *J. Appl. Phys.*, **47**, 3813 (1976).
24. S. Mahajan, G. A. Rozgonyi, and D. Brasen, *Appl. Phys. Lett.*, **30**, 73 (1977).
25. T. Abe, K. Kikuchi, and S. Shiraki, in "Semiconductor Silicon 1977," H. R. Huff and E. Sirtl, Editors, The Electrochemical Society Softbound Proceedings Series, Princeton, New Jersey (1977).
26. R. A. Kushner, Abstract 260, p. 643, The Electrochemical Society Extended Abstracts, Electrochemical Society 1972 Fall Meeting, Miami Beach, Florida, Oct. 8-13, 1972.
27. S. P. Murarka, *J. Appl. Phys.*, **48**, 5020 (1977).
28. S. P. Murarka, *ibid.*, **49**, 2513 (1978).
29. T. E. Seidel, R. S. Payne, R. A. Moline, W. R. Costello, J. C. C. Tsai, and K. R. Gardner, *IEEE Trans. Electron Devices*, **ed-24**, 717 (1977).

Thin Film CdSe Photoanodes for Electrochemical Photovoltaic Cells

Michael A. Russak and Joseph Reichman*

Grumman Aerospace Corporation, Research Department, Bethpage, New York 11714

and Horst Witzke,¹ S. K. Deb,^{*,2} and S. N. Chen^{*,3}

Optel Corporation, Princeton, New Jersey 08540

ABSTRACT

Electrochemical photovoltaic cells rely on the junction formed between a semiconductor and electrolyte to accomplish photovoltaic conversion. As a result, they offer certain technical features that make them an attractive alternative to all solid-state solar cells, especially if thin film photoelectrodes are used. This paper describes the fabrication and evaluation of thin film CdSe electrodes for use with sulfide/polysulfide electrolyte in these cells. The effects of electrode preparation and electrolyte concentration on efficiency and stability are presented. *I-V* curves and action spectra are also discussed. Simple depletion layer theory is applied to monochromatic photocurrent curves and a correlation between efficiency and minority carrier diffusion length is shown. Conversion efficiencies (AM1) as high as 5% are reported.

The photoelectrochemical effect has been known for many years (1); only recently, however, has a significant effort been directed toward the practical application of this effect to photovoltaic energy conversion (2-8). Electrochemical photovoltaic cells, which utilize the junction formed at the interface between a semiconductor and an electrolyte for photoconversion, have several technical features that make them an attractive alternative to solid-state solar cells for low cost photovoltaic conversion: (i) the photovoltaic junction is formed spontaneously on immersion of a semiconductor of one carrier type in a suitable electrolyte; (ii) the geometry of the junction is such that radiation can impinge directly on the space charge region, minimizing surface recombination losses; (iii) the most promising materials investigated are direct bandgap materials, which promote the use of thin film electrodes which are an important factor in ultimately producing low cost devices (9). This paper presents some of our results on making thin film n-CdSe photoelectrodes and their photoelectrochemical characterization. CdSe used in conjunction with sulfide-polysulfide containing electrolytes is a system capable of achieving AM1 conversion efficiency of 10% or greater (8, 10). Therefore, it can be considered as a candidate system for future practical application.

Experimental

Thin films of polycrystalline CdSe were deposited on commercially pure (99.9%) titanium substrates (0.254 mm thick), which were cleaned in a chromic-sulfuric acid mixture and degreased in isopropyl alcohol. Films were made by evaporation of CdSe as well as co-evaporation of Cd and Se. In both cases materials of 99.999% purity (Ventron Corporation, Danvers, Massachusetts) were evaporated from Ta or W boats with a background pressure $\sim 10^{-6}$ Torr. Substrate temperatures were held at $\sim 100^\circ\text{C}$ during deposition; film thicknesses were varied from ~ 0.5 - $2 \mu\text{m}$ and deposition rates varied from ~ 5 - $50 \text{ \AA}/\text{sec}$. Film thickness was determined with a quartz crystal thickness monitor (Sloan Technology, Santa Barbara, California)

* Electrochemical Society Active Member.

¹ Present address: Exxon Research and Engineering, Linden, New Jersey 07036.

² Present address: SERI, Golden, Colorado 80401.

³ Present address: Chronar Corporation, Princeton, New Jersey 08540.

Key words: photoelectrochemical energy conversion, thin film electrodes, thermal vacuum evaporation, solar cells, sulfide/polysulfide electrolytes.

and in some cases confirmed from SEM micrographs. Some co-evaporations were done using an automated rate controller (INFICON, Syracuse, New York) for the Se source, which was found more difficult to control manually than the Cd source. After deposition, the electrodes were heat-treated in air at temperatures from 300° to 500°C for 5-60 min. A copper wire was attached to the back of the electrodes with silver-filled epoxy or indium solder. Common epoxy was used to cover the back and sides of the electrodes. The exposed area was $\sim 1 \text{ cm}^2$. In some cases the electrodes were etched from 5-30 sec in 50% HCl:50% H_2O before use.

For photoelectrochemical evaluation, the semiconductor electrode was the working electrode in a conventional three-electrode cell with a platinum foil counterelectrode ($\sim 15 \text{ cm}^2$) and a calomel reference electrode (SCE). The semiconductor electrodes were illuminated through an optically flat Pyrex or quartz window that had been epoxied into a Pyrex beaker modified for this purpose. The CdSe electrodes were positioned $\sim 1 \text{ mm}$ from the window to minimize electrolyte absorption without limiting mass transport in the cell. Photoelectrochemical experiments were done at room temperature ($\sim 22^\circ\text{C}$). Baseline data for comparison with experiments done on thin film electrodes were obtained using CdSe single crystal electrodes (Cleveland Crystal Corporation, Cleveland, Ohio), which were prepared for photoelectrochemical evaluation according to procedures found in the literature (5).

Selected electrolytes in the composition range of 1F-2.5F Na_2S and 0.1F-2.5F S in 1F NaOH were used for specific experiments. Most high light intensity ($>10 \text{ mW}/\text{cm}^2$) *I-V* curves were measured using 2.5F Na_2S , 1.0F S, 1F NaOH electrolyte, while most spectral response curves ($<1 \text{ mW}/\text{cm}^2$) were measured using 2.5F Na_2S , 0.01F S, 1F NaOH electrolyte. All solutions were made from reagent grade chemicals under an Ar atmosphere. Ar was bubbled through the test cell during electrochemical experiments.

Voltammetric measurements were made with a PAR (Princeton Applied Research, Princeton, New Jersey) Model 173 potentiostat and Model 175 universal programmer using a scan rate of 2 mV/sec and recorded directly on an HP 7040A X-Y recorder (Hewlett Packard, San Diego, California).

The cell was illuminated with the output of a 1 kW filtered (AM1) Xe light source (Schoeffel Instruments, Westwood, New Jersey) for determination of white light *I-V* curves. The same source was used with a

monochromator (Jarrell-Ash, Waltham, Massachusetts) or a series of narrow band pass filters (Ditric Optical, Marlboro, Massachusetts) for spectral response curves. The radiant power was measured using a thermopile detector (Epply Laboratory, Providence, Rhode Island).

Capacitance-voltage measurements were done using a GR 1657 Digibridge (Gen Rad, Concord, Massachusetts) and a Harrison 6112A power supply. The CdSe electrode potential vs. SCE was monitored using a DVM (Fluke Manufacturing Company, Seattle, Washington).

An x-ray diffractometer (Picker Inst., Cleveland, Ohio) was used to determine crystalline phase and orientation and a scanning electron microscope (AMR Corporation, Bedford, Massachusetts) was used for microstructural observations and chemical analysis of the thin films with an Edax attachment (Edax International Inc., Prairie View, Illinois). Transmission spectra of various electrolytes and CdSe films deposited on glass substrates were obtained using a Carey 14 spectrophotometer (Applied Physics Corporation, Monrovia, California).

Results

Compound evaporation produced n-type films irrespective of deposition conditions and conversion efficiencies (η) obtained with these films (regardless of postdeposition heat-treatment) were $<1\%$. Compound evaporation was abandoned in favor of co-evaporation of Cd and Se, which afforded better control of film stoichiometry. The as-deposited co-evaporated films were polycrystalline and predominantly single phase hexagonal CdSe with a (0001) growth texture. Some x-ray patterns indicated the presence of a small amount of cubic CdSe in which case a (111) growth texture was observed. The films adhered fairly well to the Ti substrate and were quite uniform and monolithic. Figure 1 shows a scanning electron micrograph of a typical as-deposited film. Crystallite sizes are small ($<1000\text{\AA}$), and there is a suggestion of a columnar growth structure, which is consistent with the observed growth texture. The as-deposited films showed little or no photoresponse when tested potentiostatically and peeled from the substrate after a short period of time in the electrolyte. Postdeposition heat-treatments in air were found to improve the I - V performance and adherence of the thin film electrodes dramatically.

Figure 2 shows representative data indicating the effect of several heat-treatment temperatures (all for 15 min) on I - V performance. It can be seen that the best performance is obtained at 400°C . At temperatures greater than 400°C film thinning due to evaporation became significant and the I - V performance is not as good as at 400°C . The effect of heat-treatment time was also investigated. Heat-treatment for more than 15 min at 400°C did not improve performance further. As a result of this evaluation, a heat-treatment of 400°C for 15 min was adopted as a "standard" so that the effect of variation of deposition parameters and resultant electrode efficiency could be investigated systematically. I - V traces of thin film sandwich structures (i.e., In/CdSe/Ti substrate) before and after the standard heat-treatment indicated that it improves the ohmicity of the CdSe/Ti contact and reduces the resistivity of the films from $\sim 10^8$ to $\sim 10^4$ - $10^5 \Omega\text{-cm}$. Scanning electron micrographs indicated a slight increase in crystallite size with heat-treatment.

The I - V performance of heat-treated electrodes was found to depend on electrolyte concentration at light intensities typical of terrestrial solar fluxes. Figure 3 shows the effect of increasing the electrolyte concentration from 1F to 2.5F Na₂S and S on I - V performance of a thin film electrode. The drop-off in efficiency with increasing light intensity in the 1F electrolyte is due to reductions in short-circuit current density (J_{sc}) and fill factor (FF). The open-circuit voltages (V_{oc}) were comparable for both solutions owing to the

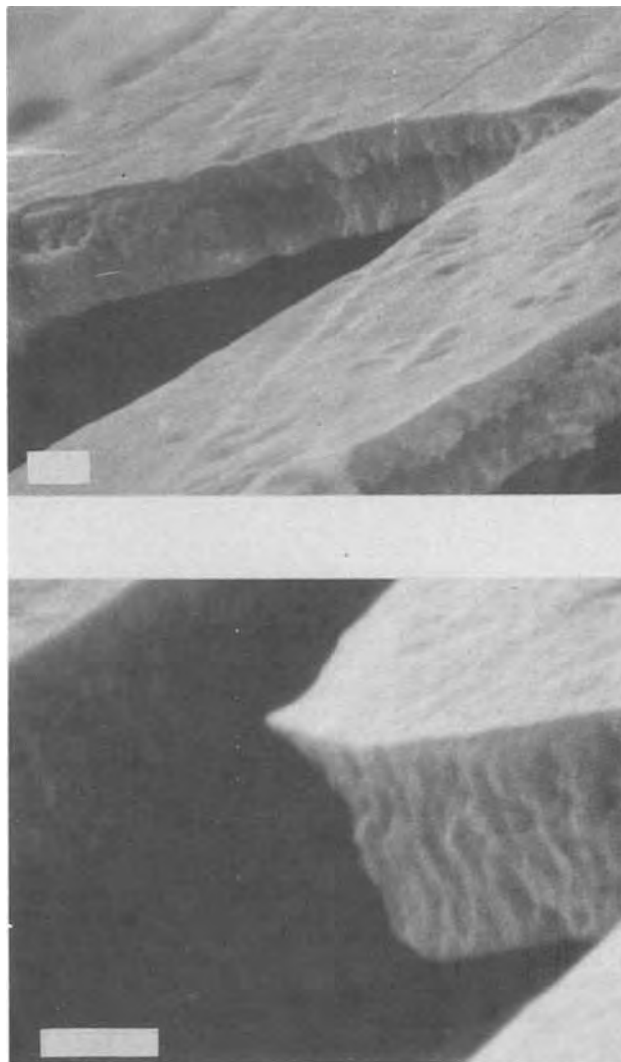


Fig. 1. SEM micrographs of co-evaporated CdSe film

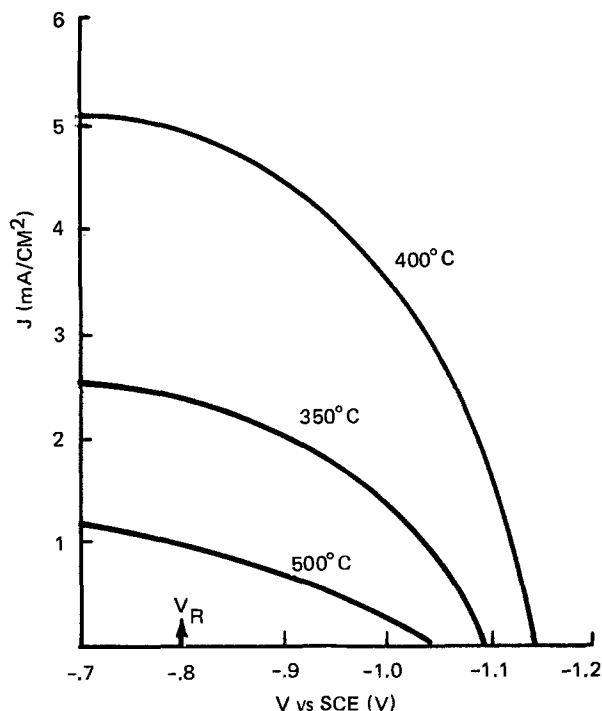


Fig. 2. The effect of heat-treatment temperature on I - V performance of a thin film CdSe electrode. V_R shows the electrolyte rest potential in the dark.

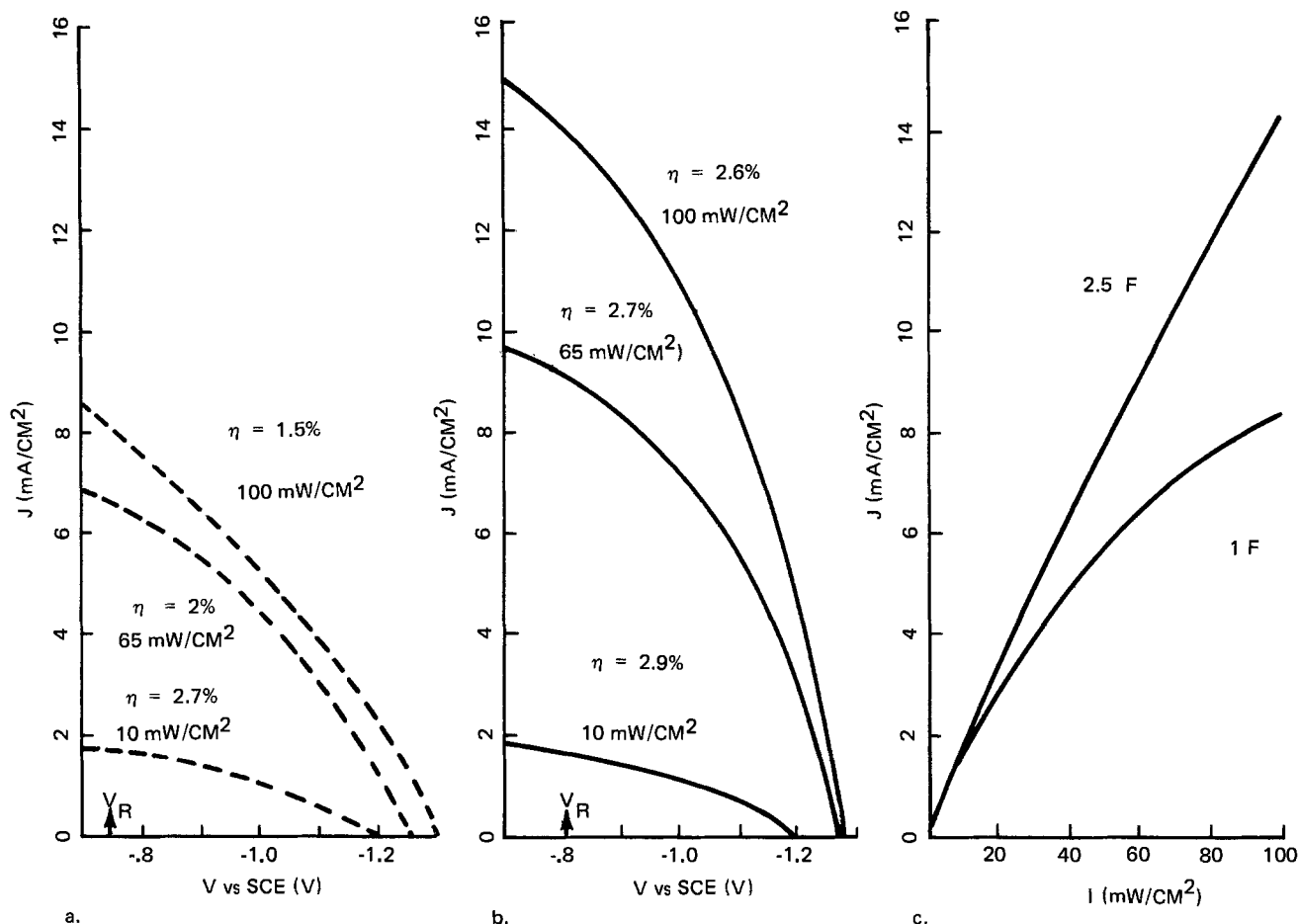


Fig. 3. The effect of electrolyte concentration on I - V performance at various light intensities: (a) 1F Na_2S , 1F S; (b) 2.5F Na_2S , 2.5F S. V_R indicates the electrolyte rest potential in the dark.

minimal change in redox potential (-0.76V vs. SCE for 1F and -0.79V vs. SCE for 2.5F) and therefore the amount of band bending in a given electrode. As shown in Fig. 3a and b, the maximum photopotential in each solution is comparable at similar intensities so that the difference between the redox potential and maximum photopotential (*i.e.*, V_{oc}) does not vary significantly. However, J_{sc} was strongly affected by concentration variation (Fig. 3c). The J_{sc} in 1F electrolyte at 100 mW/cm^2 light intensity is less than 60% of the value in the 2.5F electrolyte at the same intensity. The FF also changes significantly: in going from 10 to 100 mW/cm^2 in 1F electrolyte, the FF drops from 0.42 to 0.31; in 2.5F electrolyte, it drops from 0.46 to 0.40. The combination of these factors gives rise to the observed efficiency saturation in the 1F electrolyte. Subsequent experiments indicated that the S concentration, which also changes the visible absorption of the electrolyte considerably, could be reduced to $\sim 1\text{F}$ without adversely affecting η at 100 mW/cm^2 . In view of these results the electrolyte composition was standardized at 2.5F Na_2S , 1F S, 1F NaOH for all white light I - V curves at 10 mW/cm^2 intensity or greater.

The I - V performance of thin film CdSe electrodes varied from deposition to deposition and was found to depend primarily on how constant the individual elemental deposition rates could be controlled. Table I summarizes the variation in photovoltaic performance data recorded for 12 sequential co-evaporations with only slight variation in deposition control parameters. All samples were subjected to the standard heat-treatment, and I - V data were taken in 2.5F Na_2S , 1F S, 1F NaOH electrolyte at 50 mW/cm^2 . The variation of properties in Table I is consistent with that previously reported for co-evaporated semiconductor thin films (11, 12) and can be attributed to slight differences in film stoichiometry, defect structure, and crystallite

size that result from the deposition method and subsequent heat-treatment. These electrodes were fabricated using manual control of the evaporation sources, with good reproducibility.

Analysis of Edax spectra indicated that nominally stoichiometric CdSe films resulted after the standard heat-treatment; no systematic variation in Cd/Se ratio however, could be correlated with the I - V performance variation observed in Table I, most likely because of the limits of detectability of Edax ($\pm 0.2\%$); this should not be taken to indicate that the films do not differ on a microchemical basis.

The variation of performance of sample 2 with light intensity is shown in Fig. 4. It can be seen from these data the V_{oc} follows a logarithmic relation with increasing intensity, while J_{sc} varies nearly linearly, as expected. The fill factor, however, and thus the efficiency fall off slightly. The variation of solar cell parameters with light intensity found with

Table I. Variation of I - V performance of co-evaporated CdSe thin film electrodes

$V_R = -0.8\text{V vs. SCE}$, $I = 50\text{ mW/cm}^2$

Run	V_{oc} (V)	J_{sc} (mA/cm^2)	FF	η (%)
1	0.56	5.28	0.48	2.9
2	0.48	7.95	0.60	4.5
3	0.51	8.24	0.61	5.1
4	0.45	7.23	0.52	3.5
5	0.49	7.64	0.54	4.0
6	0.45	3.76	0.44	1.5
7	0.55	7.45	0.47	3.9
8	0.41	7.25	0.48	2.8
9	0.50	6.38	0.51	3.2
10	0.44	7.08	0.44	2.7
11	0.43	6.26	0.49	2.6
12	0.48	5.94	0.53	3.1

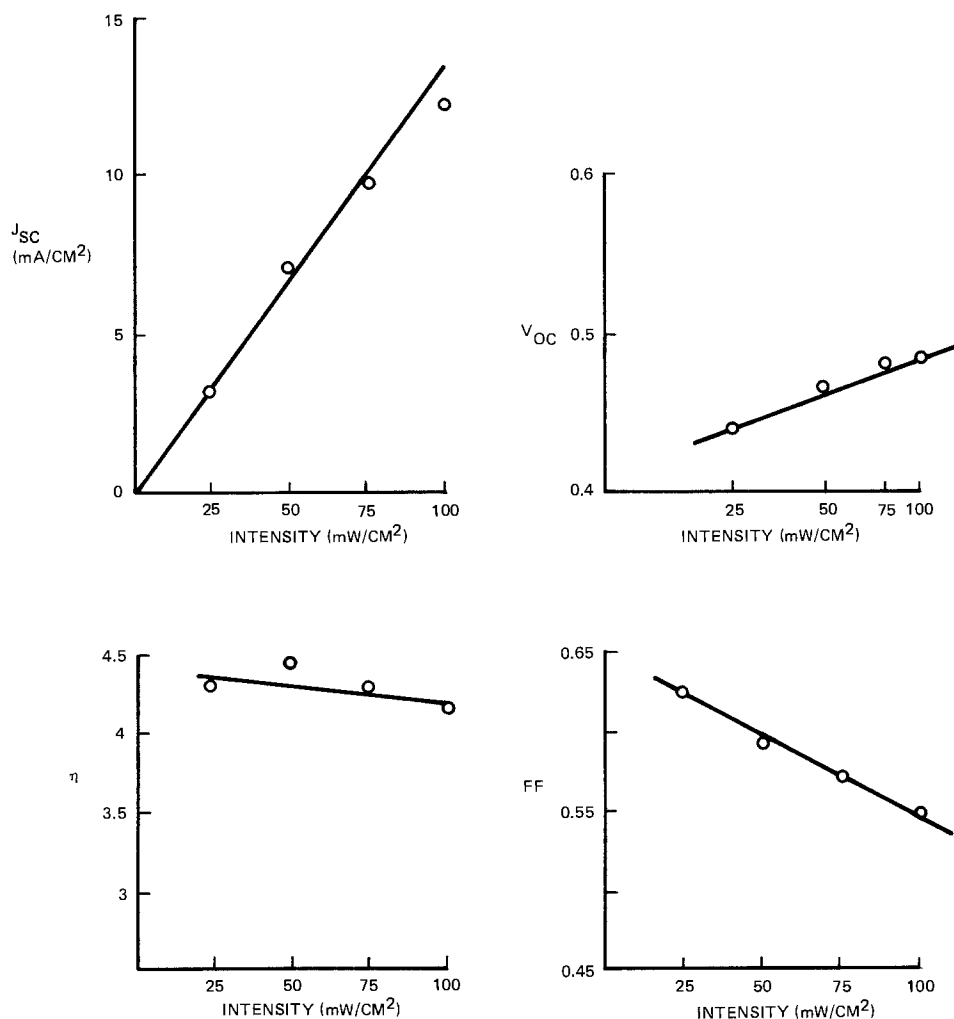


Fig. 4. I - V curves and solar cell parameters of a co-evaporated CdSe electrode at various light intensities.

sample 2 is typical of samples with higher efficiencies; whereas films with efficiencies less than 1% showed more pronounced saturation effects in short-circuit current and fill factor.

Figure 5 presents a typical transmission spectrum of a fired film (glass substrate). It can be seen that there is absorption beyond the bandgap energy (720 nm). This type of behavior has been reported for thin films of CdSe processed in the same temperature regime and attributed to the large number of crystallite defects that give rise to the observed bandtailing (13). A film thickness of 0.8 μm was calculated from the interference fringes.

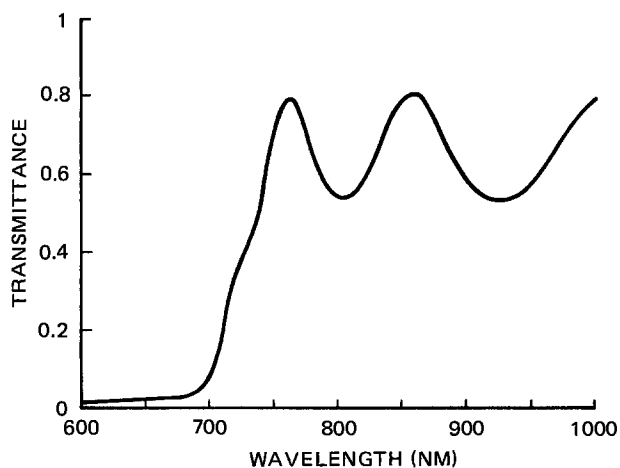


Fig. 5. Transmission spectrum of a fired CdSe film $\sim 0.8 \mu\text{m}$ thick.

Attempts were made to quantify the differences in electronic properties of various films so that correlations among processing parameters, electronic properties, and I - V performance could be established. A study of the change in space charge layer capacitance, as a function of applied potential was undertaken to determine the donor density and flatband potential using the well-known Mott-Schottky relation (14)

$$C_s^{-2} = \frac{2}{q\epsilon\epsilon_0 N_D} \left(V_A - V_B - \frac{kT}{q} \right) \quad [1]$$

where C_s is the space charge capacitance per unit area, q the electronic charge, ϵ the semiconductor dielectric constant [10 for CdSe (15)], $\epsilon_0 = 8.86 \times 10^{-14} \text{ F/cm}$, V_A and V_B are the applied potential and the flatband potential (*vs.* SCE) respectively, N_D the donor density, k Boltzmann's constant, and T the absolute temperature (kT/q can be neglected at room temperature).

Figure 6 shows representative C_s^{-2} *vs.* V_A plots for a single crystal sample, a thin film electrode, and a bare heat-treated Ti substrate. Linear, single slope plots of C_s^{-2} *vs.* V_A were obtained for single crystal samples (Fig. 6a) from which reasonable values of N_D and V_B could be obtained; for example, $N_D = 1.2 \times 10^{17}/\text{cm}^3$ and $V_B = -1.4 \text{ V vs. SCE}$. However, most thin film electrodes exhibited linear plots with two slopes (Fig. 6b). This type of behavior has been observed previously with polycrystalline samples in electrochemical cells and attributed to the presence of both shallow and deep donor levels in the samples studied (16). In our case the measured capacitance values were large (in some cases $>10 \mu\text{F}/\text{cm}^2$), which results in anomalously high calculated donor densities for both slopes ($>10^{20}/\text{cm}^3$). C_s and N_D values of this order yield de-

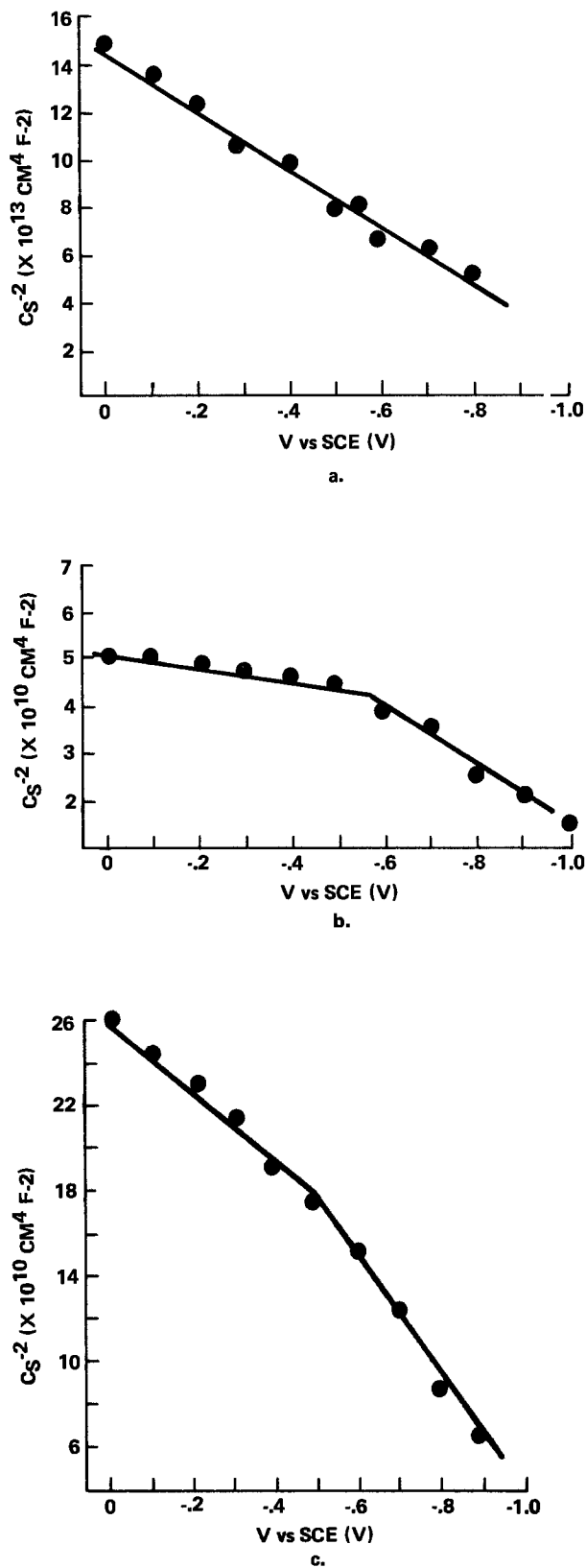


Fig. 6. C_s^{-2} vs. V plots for (a) CdSe single crystal, (b) CdSe thin film, and (c) heat-treated Ti substrate.

pletion layer widths of less than 100Å calculated from the depletion layer relation (17)

$$d = \left(\frac{2\epsilon\epsilon_0\psi_s}{qN_D} \right)^{1/2} \quad [2]$$

where ψ_s is the voltage drop across the space charge layer, taken here to be ~ 0.7 V, the difference between V_B and the reversible redox potential for the electro-

Table II. Zero bias capacitance, calculated donor densities, and AM1 power efficiencies of several thin film electrodes

Sample	C_s ($\mu\text{F}/\text{cm}^2$)	N_D (cm^{-3})	η (%)
1	6.0	9.6×10^{20}	0.15
2	6.4	7.8×10^{20}	3.1
3	8.7	1.1×10^{21}	2.7
4	11.6	9.3×10^{20}	1.8
5	7.6	8.8×10^{20}	0.05

lyte. Table II presents C_s at zero bias, N_D , and η for several thin film electrodes. There is no apparent correlation between N_D values and η . Electrode efficiency varies by an order of magnitude, yet the C_s and N_D values are almost constant. This observation and the fact that the good I - V performance of the thin film electrodes would not be expected with very narrow depletion layer widths led us to investigate the C - V performance of the Ti substrate alone. Figure 6c shows a typical result for an uncoated Ti substrate after the standard heat-treatment. It can be seen that the characteristic break in the curve is present. X-ray diffraction analysis of the heat-treated substrate indicated the presence of TiO_2 (rutile). Calculations using Eq. [1] and $\epsilon = 120$ for TiO_2 (18) result in $N_D \sim 10^{19}/\text{cm}^2$ and $d \sim 200\text{\AA}$, which are reasonable values in view of the growth conditions of such a thin film.

An explanation of the CdSe thin film C - V results is found by noting that Eq. [1] is based on the assumption that the semiconductor-electrolyte interface can be treated as three capacitances in series: the semiconductor depletion region, the Helmholtz layer, and the Gouy layer. At high ionic concentration in the electrolyte the capacitance of the Gouy layer can be neglected. The capacitance of the Helmholtz layer is much larger than that of the depletion region and can also be neglected so that Eq. [1] results and can be used to investigate the semiconductor depletion layer. However, the data presented here are complicated by the existence of pinholes and cracks in the CdSe thin film resulting from heat-treatment, which allow contact between the electrolyte and substrate. We interpret the observed C_s^{-2} vs. V_A behavior as an indication that the measured C_s represents contributions from the CdSe, as well as the oxidized Ti substrate. Therefore, Eq. [1] is not applicable to analysis of these data, and the lack of correlation shown in Table II is attributed to the effect of exposed substrate area. These results suggest that analysis of C_s^{-2} vs. V data is not useful for thin film electrodes unless complete substrate coverage is assured.

Analysis of monochromatic and white light I - V curves and action spectra proved to be the most useful in quantifying the performance of various thin film electrodes. Figure 7 compares the normalized spectral response curves of a single crystal sample ($\eta = 6.5\%$) and a thin film electrode ($\eta = 3.9\%$) taken in 2.5F Na_2S , 0.01F S, 1F NaOH electrolyte. This electrolyte minimizes the absorption correction necessary at the blue end of the spectrum (transmittance of 1 mm thickness of this electrolyte at 400 nm is 0.975). Peak external quantum efficiencies were 75% for the single crystal and 60% for the thin film electrode. Both curves show a fall off of response at shorter wavelengths, but it is more pronounced in the thin film sample. The thin film action spectrum also exhibits a greater response beyond 720 nm than the single crystal curve. Thin film electrodes generally showed significant photoresponse at wavelengths with energies less than the bandgap energy of CdSe, as in Fig. 7, curve b. This is consistent with the thin film transmission spectra, which show absorption >720 nm. Sub-bandgap photocurrents have been reported previously (5, 19) and attributed to defect states at energy levels within the bandgap that are responsible for the optical transitions (or band tailing) stimulated by light of less than bandgap en-

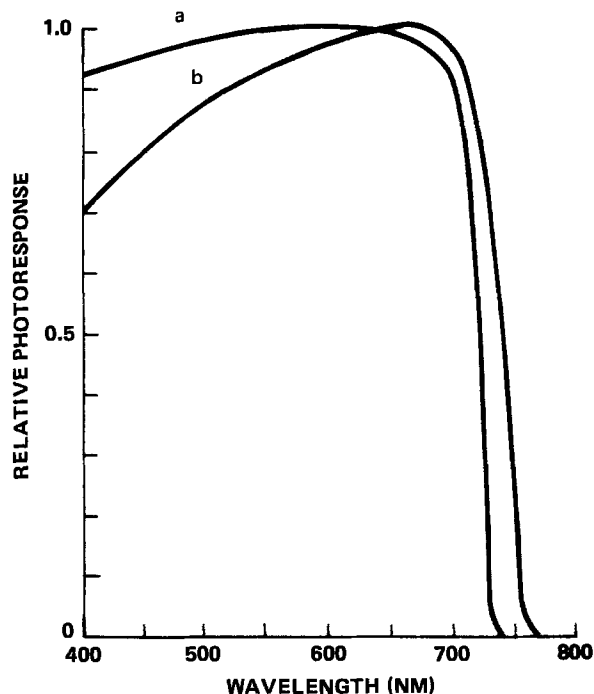


Fig. 7. Action spectra for single crystal CdSe (a) and thin film CdSe (b) electrodes.

ergy. These sub-bandgap photocurrents in effect extend the spectral response of the CdSe so that a greater portion of the solar spectrum can be utilized.

Etching these electrodes does not result in a significant increase in *I-V* performance as reported for single crystal and large grained polycrystalline hot pressed pellet electrodes (5, 19). This indicates that, although surface layer recombination losses are present in the thin film samples as evidenced by the drop off of spectral response in the blue, recombination centers resulting from the defect structure of the thin film electrodes are not restricted to the surface layer, but extend into the film.

Direct comparison of the *I-V* curves (50 mW/cm²) for these two samples (Fig. 8) shows that the fill factors are comparable (~0.60), but the thin film has a lower *J_{sc}* (6.3 mA/cm² vs. 7.8 mA/cm²) and *V_{oc}* (0.5V vs. 0.68V), which results in a lower over-all efficiency (3.9% vs. 6.5%). The lower *J_{sc}* is due to the defective nature of the thin film while the lower *V_{oc}* results from the higher dark currents observed for thin film electrodes under forward bias compared to single crystal samples. This difference in *V_{oc}* is attributed to the defective nature of the thin film

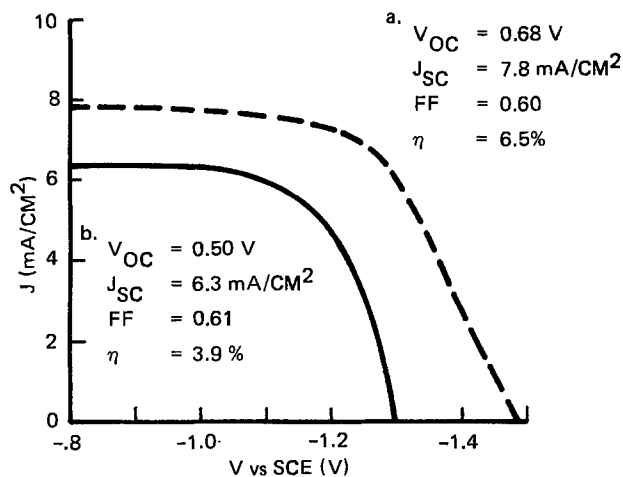


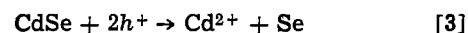
Fig. 8. Light *I-V* curves for single crystal CdSe (a) and thin film CdSe (b) electrodes at 50 mW/cm² (simulated AM1).

electrodes as well as to areas where the substrate and the electrolyte are in contact directly. The lower *V_{oc}* for the thin film electrode is also consistent with the interdependence of *V_{oc}* and *J_{sc}* predicted from simple solar cell theory (i.e., $V_{oc} \propto \ln J_{sc}/J_{dark}$).

The difference in the performance of various electrodes could be quantified by analysis of their monochromatic *I-V* curves. Figure 9 shows photocurrent efficiency (*N_p*) vs. potential curves at 700 nm for the same single crystal and thin film samples used to obtain Fig. 7 and 8 as well as two other thin film electrodes. These curves were obtained by taking the difference between the light and dark current densities and dividing by the calculated photon current at 700 nm, which was ~0.35 mA/cm². The variation in photocurrent efficiency and curve shape with over-all power efficiency can readily be seen in these curves.

Discussion

Recently, the dependence of the output stability of CdSe photoelectrodes on electrolyte composition has been studied in some detail (5, 20-23); however, the dependence of η on electrolyte composition has only been noted briefly. Our results show that the electrolyte composition has a significant effect on η at light intensities that would be encountered in normal solar cell applications. The *V_{oc}* is not significantly affected by the change in concentration from 1F to 2.5F Na₂S and S, but the observed saturation of *J_{sc}* and decrease of FF in 1F electrolyte with increasing light intensity indicate that the transfer kinetics are not sufficiently rapid to accommodate the higher photon fluxes. Apparently, the 1F electrolyte cannot provide sufficient reduced polysulfide species to the interface rapidly enough to react with the hole flux being swept to the CdSe surface. This unfavorable kinetic situation should, in principle, result in destabilization of the semiconductor because of incomplete scavenging of holes by the electrolyte, allowing dissolution reactions [3] and [4] to proceed



The net effect of this dissolution process has been shown to be a decrease of photocurrent output with time (6, 20, 23). We have observed a decrease in photocurrent output (i.e., *J_{sc}*) in 1F electrolyte from 10 to 1.5 mA/cm² after passage of 1500 C/cm².

This situation is improved greatly as the electrolyte concentration is increased so that with a concentration of 2.5F Na₂S and 1F S in 1F NaOH, *J_{sc}* and FF do not decrease significantly with increasing light intensity. Output stability is also improved and the output of an electrode operating at *J_{sc}* of 10 mA/cm² remains constant (within $\pm 5\%$) with passage of 1500 C/cm². However, longer term experiments do indicate a slight drop off in output with time. Although short term stability and *I-V* performance are enhanced by increasing the polysulfide concentration, the long term stability (i.e., several years) required for device applications remains to be established. We have observed Se/S substitution in some electrodes using Auger spectroscopy and are continuing longer term stability studies.

Optical transmission spectra and action spectra of the CdSe thin films indicate the presence of defect states that give rise to photoabsorption at energies less than that required for a band-to-band transition. For example, action spectra show a significant response at 750 nm. This band tailing could result from grain boundaries as well as impurities or lattice defects within the crystallites themselves. It has been shown that in semiconductor thin films with small crystallite size grain boundary recombinations are the current-limiting mechanism because the grain boundaries act as "sinks" for minority carriers as

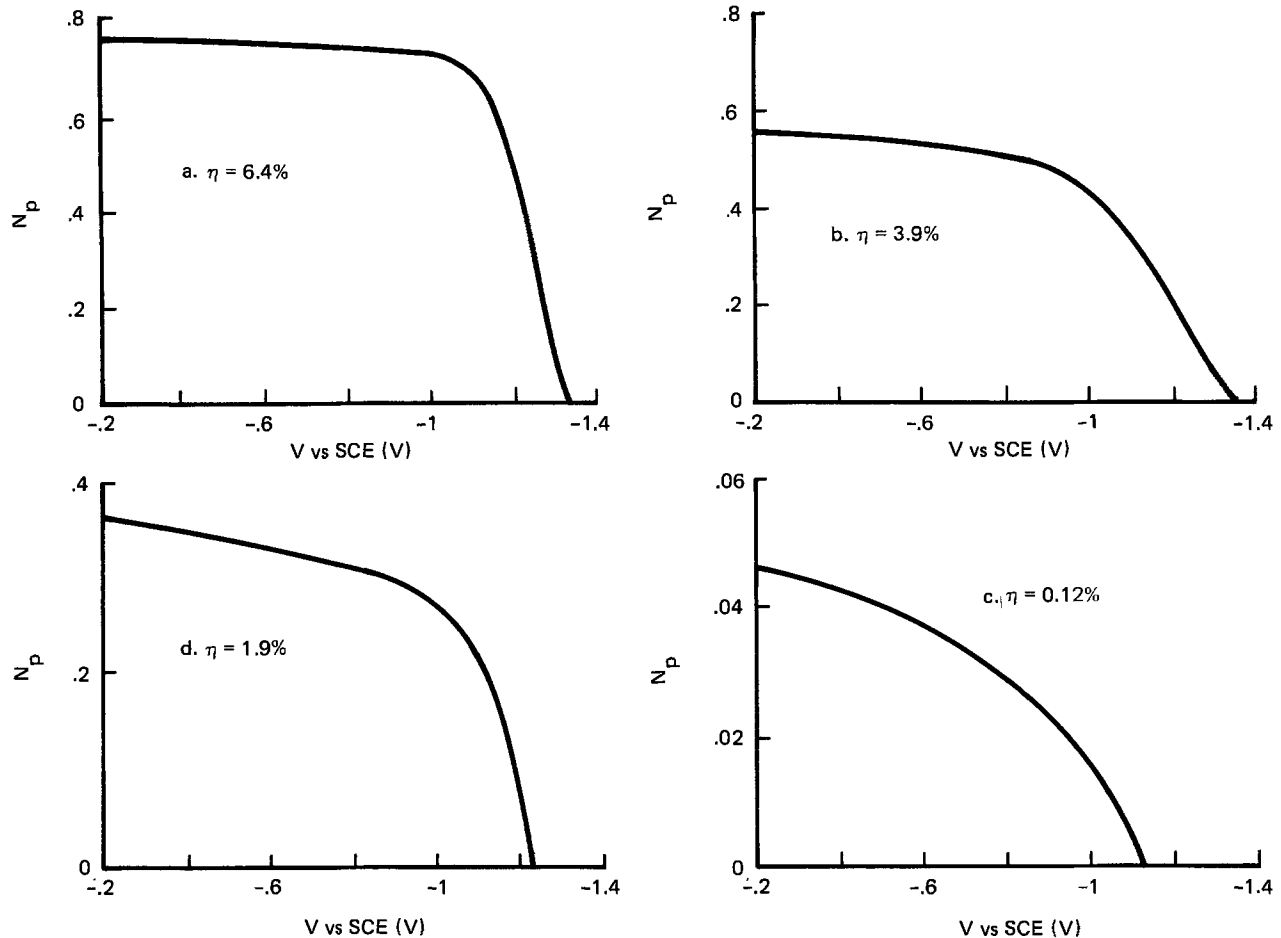


Fig. 9. Monochromatic photocurrent efficiency vs. applied potential curves at 700 nm: (a) single crystal, (b) thin film 1, (c) thin film 2, (d) thin film 3.

well as barriers to majority carrier flow (24). We suggest that this is the cause of the I - V behavior with intensity variation of reasonably efficient thin film electrodes (Fig. 4). The reduction in fill factor with increasing photon flux can be attributed to recombinations due to grain boundaries or defect sites in the space charge layer that become more pronounced with higher photon flux under forward bias (near the maximum power point). Yet, we find power efficiencies just slightly less than those reported for large grained (10-20 μm) hot pressed CdSe electrodes (25). The large grained CdSe electrodes have higher V_{oc} values (0.72 compared to 0.5), presumably due to lower dark currents, lower fill factors (0.5 compared to 0.6), and comparable J_{sc} values.

As noted earlier, analysis of C - V data did not prove to be useful for calculating thin film donor densities and flatband potentials. Thus, an alternate technique was necessary to begin to quantify the relationship between electrode I - V performance, semiconductor properties, and processing conditions. Analysis of photocurrent efficiency vs. electrode potential curves was quite useful in this regard.

N_D values as well as minority carrier diffusion lengths, L_p , could be calculated for various thin film electrodes by application of depletion layer theory to these curves in the reverse bias direction (*i.e.*, potential positive of -0.8V vs. SCE). The internal photocurrent efficiency, N_p , for negligible recombination losses can be approximated by (17)

$$N_p = 1 - e^{-\alpha d / 1 + \alpha L_p} \quad [5]$$

where α is the absorption coefficient at a chosen wavelength, d is the depletion layer width, and L_p is the minority carrier diffusion length. This relationship can be combined with Eq. [2] to yield (26)

$$\ln(1 - N_p) = -\alpha \left(\frac{2\epsilon\epsilon_0}{qN_D} \right)^{1/2} V_d^{1/2} - \ln(1 + \alpha L_p) \quad [6]$$

Applying this relation to a plot of $\ln(1 - N_p)$ vs. $V_d^{1/2}$, N_D can be calculated from the slope and L_p from the intercept. In using this analysis on the data of Fig. 9 it was assumed that all the voltage drop in the semiconductor electrolyte interface is across the depletion region and that V_d is given by the difference between the applied potential and the potential of zero anodic photocurrent, which is fairly close to the flatband potential. Figure 10 presents the replotted data, and Table III summarizes the calculated values of N_D and L_p (α at 700 nm $\equiv 3 \times 10^4 \text{ cm}^{-1}$). It can be seen from these data that the conversion efficiency is more sensitive to L_p than N_D , which is expected for defective polycrystalline semiconductors such as these (24, 27). L_p is a function of lifetime and mobility, which in turn are related to scattering centers and recombination centers within the crystallite itself or at grain boundaries. In these films it is likely that grain boundaries as well as defects within the crystallites themselves are limiting L_p .

Table III. Comparison of N_D and L_p values obtained from photocurrent analysis and power conversion efficiency

Sample	Power efficiency, η (%)	N_D (cm^{-3})	L_p (μm)
Single crystal	6.5	8×10^{16}	1.46
Thin film 1	3.9	6×10^{16}	0.40
Thin film 2	1.9	5×10^{16}	0.13
Thin film 3	0.12	1×10^{16}	0.006

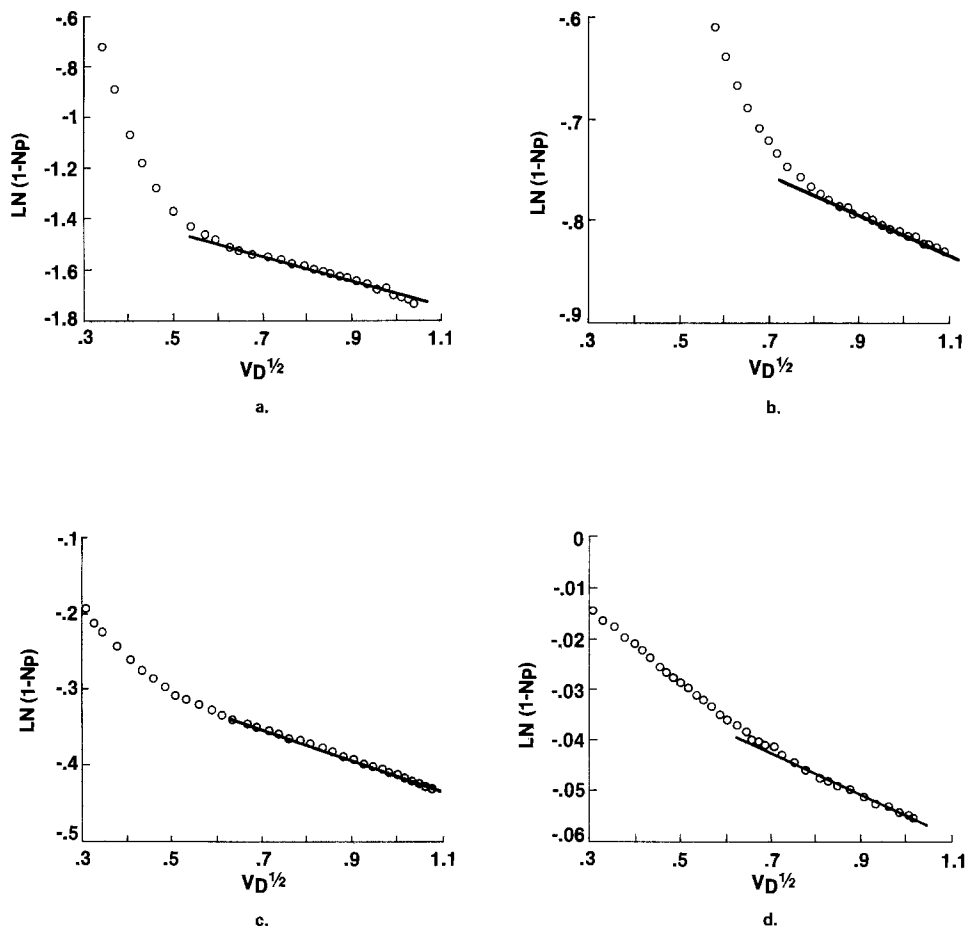


Fig. 10. Data of Fig. 9 replotted for determination of N_D and L_p : (a) single crystal, (b) thin film 1, (c) thin film 2, (d) thin film 3.

The model used in this analysis is not adequate to predict completely the I - V behavior of semiconductor liquid junction devices, particularly under forward bias, due to the inherent assumption that recombinations within the space charge region can be neglected. However, within the limits defined here (*i.e.*, reverse bias and a wavelength that minimizes surface recombination effects), this depletion layer model does yield very useful information in terms of sample-to-sample variation for the thin film electrodes and can be used to correlate I - V performance with donor density and minority carrier diffusion length. We have developed a more comprehensive model that will be presented in a future publication (28).

Summary

Thermal vacuum evaporation of Cd and Se has been used to produce CdSe thin film electrodes for use as photoanodes in electrochemical photovoltaic cells. Postdeposition heat-treatment of these electrodes in air has been found to greatly improve their I - V performance under illumination. In addition, polysulfide electrolyte concentration has been shown to have a significant effect on the I - V behavior of the CdSe thin films at light intensities typical of solar fluxes. Selection of deposition conditions, heat-treatment schedule, and electrolyte composition has resulted in conversion efficiencies in excess of 5%.

The use of C-V data to determine doping densities and flatband potentials of the CdSe films was hindered by substrate effects, which were due to pinholes and cracks in the heat-treated films. Analysis of action spectra indicated the films were defective, evidenced by the drop off of photoresponse at shorter wavelengths, as well as the presence of sub-bandgap energy photocurrents. Finally, by applying simple depletion layer theory to monochromatic photocurrent curves, N_D and L_p were determined and a correlation between η and L_p found.

Acknowledgment

The authors wish to acknowledge the very capable technical assistance of C. Creter, R. J. Axton, and J. Vicari in performing various phases of this work.

Manuscript submitted July 2, 1979; revised manuscript received Oct. 3, 1979.

Any discussion of this paper will appear in a Discussion Section to be published in the December 1980 JOURNAL. All discussions for the December 1980 Discussion Section should be submitted by Aug. 1, 1980.

Publication costs of this article were assisted by Grumman Aerospace Corporation.

REFERENCES

1. E. Becquerel, *Hebd. Seanc. C. R. Acad. Sci. Paris*, **9**, 561 (1839).
2. A. B. Ellis, S. W. Kaiser, and M. S. Wrighton, *J. Am. Chem. Soc.*, **98**, 1635 (1976).
3. A. B. Ellis, S. W. Kaiser, J. M. Botts, and M. S. Wrighton, *ibid.*, **99**, 2839 (1977).
4. J. Manassen, G. Hodes, and D. Cahen, *This Journal*, **124**, 532 (1977).
5. B. Miller and A. Heller, *ibid.*, **124**, 697 (1977).
6. A. Heller, G. Schwartz, R. Vadimsky, S. Menezes, and B. Miller, *ibid.*, **125**, 1156 (1978).
7. W. A. Gerrard and J. R. Owen, *Mater. Res. Bull.*, **12**, 677 (1977).
8. R. Noufi, P. Kohl, and A. Bard, *This Journal*, **125**, 375 (1978).
9. R. M. Moore, *Solar Energy*, **18**, 225 (1976).
10. J. Reichman and M. Russak, Unpublished data.
11. L. L. Kazmerski, M. S. Ayyagari, and G. A. Sanborn, *J. Appl. Phys.*, **46**, 4865 (1975).
12. L. L. Kazmerski, W. B. Berry, and C. W. Allen, *ibid.*, **43**, 3515 (1972).
13. R. Rentzsch and H. Berger, *Thin Solid Films*, **37**, 235 (1976).
14. J. F. Dewald, *Bell Syst. Tech. J.*, **39**, 615 (1960).
15. D. Berlincourt, H. Jaffee, and L. R. Schiozawa, *Phys. Rev.*, **129**, 1009 (1963).
16. J. H. Kennedy and K. W. Freese, Jr., *This Journal*, **125**, 723 (1978).

17. W. W. Gartner, *Phys. Rev.*, **116**, 84 (1959).
18. W. D. Kingery, "Introduction to Ceramics," John Wiley & Sons, Inc., New York (1960).
19. A. Heller, K. C. Chang, and B. Miller, in "Semiconductor Liquid-Junction Solar Cells," A. Heller, Editor, p. 54, The Electrochemical Society Softbound Proceedings Series, Princeton, N.J. (1977).
20. D. Cahen, G. Hodes, and J. Manassen, *This Journal*, **125**, 1623 (1978).
21. A. J. Bard and M. S. Wrighton, *ibid.*, **124**, 1706 (1977).
22. H. Gerischer, *J. Electroanal. Chem. Interfacial Electrochem.*, **58**, 263 (1975).
23. H. Gerischer and J. Gobrecht, *Ber. Bunsenges. Phys. Chem.*, **82**, 520 (1978).
24. H. J. Hovel, "Semiconductors and Semimetals," Vol. 11, "Solar Cells," Academic Press, New York (1975).
25. B. Miller, A. Heller, M. Robbins, S. Menezes, K. C. Chang, and J. Thomson, Jr., *This Journal*, **125**, 1019 (1977).
26. J. H. Kennedy and K. W. Freese, Jr., *ibid.*, **123**, 1683 (1976).
27. P. Rai-Choudhuri and P. L. Hower, *ibid.*, **120**, 1761 (1973).
28. J. Reichman, Paper 243, presented at The Electrochemical Society Meeting, Boston, Massachusetts, May 6-11, 1979.

VPE Growth of InGaP/InGaAs Structures for Transferred-Electron Photocathodes

R. R. Saxena,* S. B. Hyder,* P. E. Gregory, and J. S. Escher

Varian Associates, Incorporated, Corporate Solid State Laboratory, Palo Alto, California 94303

ABSTRACT

Vapor phase epitaxial growth has been used to prepare InGaP/InGaAs structures for use as a transferred-electron photocathode. Growth parameters have been established for InGaP growth using equal size metal sources with the hydride process. Field-assisted photoemission has been demonstrated and better than 1.0% overall efficiency at 1.06 μm was obtained.

In 1974, Bell, James and Moon (1) demonstrated a bias-assisted p-InP cathode using for the first time the mechanism of transferred-electron (TE) photoemission. TE photoemission is based on the fact that for certain III-V semiconductors such as InP, InGaAsP alloys, and GaAs, electrons can be promoted to the upper conduction band valleys with reasonable efficiency by applying modest electric fields. Photogenerated electrons which successfully transfer to the upper valleys have a good probability of being emitted over the surface energy barriers into vacuum.

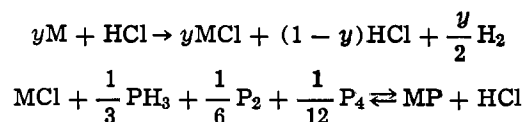
A cathode design which potentially offers high 1.06 micron sensitivity, is a p-InGaP/p-InGaAs heterojunction TE cathode. The electron emitting layer p-InGaP has higher X and L levels than that of p-InP; therefore it is anticipated (based on experimental NEA work) that the surface escape probability from a p-InGaP emitter would be superior to that of p-InP, and hence offer improved performance over that of either the p-InGaAsP direct emitter cathode or the p-InP/p-InGaAsP heterojunction cathode (2, 3). The InGaAs is the optical absorbing layer, which dictates that it have a 1.15 eV or lower bandgap at 300°K. Thus the InGaAs composition should be approximately 18% In, i.e., $\text{In}_{0.18}\text{Ga}_{0.82}\text{As}$. The InGaP composition lattice matched to $\text{In}_{0.18}\text{Ga}_{0.82}\text{As}$ is approximately 60% In, i.e., $\text{In}_{0.60}\text{Ga}_{0.40}\text{P}$.

The vapor phase epitaxial (VPE) growth of the InGaP/InGaAs heterojunction structures is presented here. The main emphasis is on establishing the growth conditions for InGaP layers lattice matched to InGaAs. Although various InGaP/InGaAs heterojunction devices have been reported in the literature, the growth conditions have not been discussed (4-6). The growth of InGaAs graded layers on GaAs substrates has been reported and is used in our work (7-9). InGaP lattice matched to GaAs has been reported and forms the basis for the heterojunction growth conditions established in this study (10-12). A brief summary of the pre-

vious work on the VPE growth of InGaP is given first. This is followed by a description of the experimental setup and the procedures used. The growth parameters and the characterization of the grown layers are discussed in the next section followed by a short conclusion.

Previous Work on InGaP/GaAs

The basic equations governing the growth of InGaP can be written as follows



where M represents either of the In and Ga metals and P_2 , P_4 are the products formed by the decomposition of PH_3 at high temperatures (10).

The growth of InGaP ternary alloys is complicated by the need for precise control of a number of parameters. Due to the large difference in their free energies of formation, the GaP component is much more readily deposited than InP (10). This makes it necessary to have a large $\text{In}(\text{HCl})/\text{Ga}(\text{HCl})$ ratio for growing InGaP lattice matched to GaAs. For a fixed set of other conditions the In/Ga ratio needed for growing a particular composition increases with the deposition temperature. With increasing deposition temperature, larger changes in the In/Ga ratio are therefore needed to effect small changes in the composition. It is essential that a steady temperature be maintained because the composition is a strong function of the deposition temperature. The change in the composition is of the order of 0.3 mole percent (m/o) per degree centigrade (11).

The growth of InGaP can be accomplished with either stoichiometric (i.e., $\sum \text{MCl} = \sum \text{P}$) or off-stoichiometric conditions. A surplus of P tends to promote InP deposition while a surplus of HCl lowers the InP content (12). At higher source temperatures the conversion of HCl to MCl is more efficient, and this effects

* Electrochemical Society Active Member.
Key words: electron, growth, cathode.

the composition by changing the total HCl present in the deposition zone. The decomposition of PH_3 also increases with temperature. The extent of PH_3 dissociation is important since InP deposition is more favorable through a reaction of InCl with PH_3 rather than with P_2 or P_4 (12). It is also important to ensure adequate mixing of gases for good homogeneity of composition. Finally, it is imperative that a clean, leak-free system be maintained.

Although thermodynamic calculations for InGaP growth have been performed, the results cannot be directly used for growing desired compositions since the study concluded that the experimental conditions deviate from equilibrium (10). Also, the growth parameters used in other studies usually are not directly applicable because of the differences in reactor design, furnace profile, etc. Hence for each new reactor system, it is necessary to go through an initial stage of experimentation to determine the optimum conditions for the desired growth.

Experimental Set-up

A schematic diagram of the reactor used for vapor phase epitaxial (VPE) growth of InGaP is shown in Fig. 1. The growth system can be divided into three zones. In the first zone, In and Ga metal sources are placed in two separate chambers and a mixture of HCl and H_2 is passed over each. The HCl reacts with the metal sources to form volatile metal chlorides which are swept downstream. The system has a provision for using either electronic grade HCl/ H_2 gas mixture or higher purity HCl from cracking AsCl_3 at high temperatures. Since under typical growth conditions the HCl flow over the Ga source is much smaller than that over the In source, extra H_2 is added to the HCl(Ga) so that equal total flow of gases over both the sources can be maintained. This ensures equal residence time of gases on the sources. A baffle is placed in each of the source chambers to enhance mixing and residence time and to avoid back-diffusion of gases toward the sources.

In the central zone various gases are introduced. Bypass H_2 and HCl for etching the deposits on the reactor walls and the substrate are also brought in. For p-type doping, an H_2 stream passing over a heated Zn pellet is used. Electronic grade gas mixtures of 10% PH_3/H_2 and 10% AsH_3/H_2 are also introduced in this zone. All the gas flows are controlled by Tylan mass flow controllers. In the third zone deposition takes place.

Procedures

The temperature profile of the three-zone resistance heated furnace is shown in the reactor schematic diagram. All the results discussed below were obtained with this profile. The optimum position for growth has been experimentally determined to be about 8 cm downstream from the PH_3 and AsH_3 entry position, as shown in Fig. 1. Thus, the growth takes place at 720°C on a temperature slope of $5^\circ\text{C}/\text{cm}$. The bypass H_2 flow is adjusted to obtain maximum deposits at the substrate position.

A typical growth experiment consists of 15 min of thermal equilibration, followed by 10 min of MCl saturation, and then 5 min for stabilization of growth conditions with AsH_3 and/or PH_3 flows. Growth is allowed after this 30 min period. The MCl saturation step is important and if omitted results in poor growth. To ensure MCl saturation when the HCl flow for growth is small (e.g., only $2\text{ cm}^3/\text{min}$ HCl flow over the Ga source for the InGaP growth), about $50\text{ cm}^3/\text{min}$ HCl is passed for 2 min before reducing it to the appropriate value.

The reactor wall deposits are etched away in a separate run after each growth. This eliminates any possibility of contaminating the InGaP growth with As or the InGaAs growth P. It also ensures the same starting conditions for each growth and the reproducibility of the results is assured.

A few attempts were made to grow the complete heterojunction structure in one run. This was difficult since the InGaAs growth produces excessive wall deposits which require etching of the reactor for about the same time duration as the growth itself. Attempts to do this without taking out the sample were not reproducibly successful since uncontrolled etching does take place causing poor InGaP growth. Hence InGaAs and InGaP layers are grown in separate runs.

To prepare the GaAs substrate for InGaAs growth, the first step is pad polishing with $\text{Br}_2\text{-CH}_3\text{OH}$ solution. Just before putting in the reactor, the polished substrates are ultrasonically solvent cleaned (TCE, ACE, Alconox) and a 4:1:1 etch ($\text{H}_2\text{SO}_4:\text{H}_2\text{O}_2:\text{H}_2\text{O}$) is used followed by IPA rinse. For InGaP growth the graded InGaAs layers are lightly polished in $<1\%$ $\text{Br}_2\text{-CH}_3\text{OH}$ solution and then solvent cleaned before putting in the reactor. No 4:1:1 etch is used since it could remove too much of the grown layer.

The grown layers were characterized using x-ray diffraction for lattice constant determination, 77°K photoluminescence (PL) measurements, and vacuum

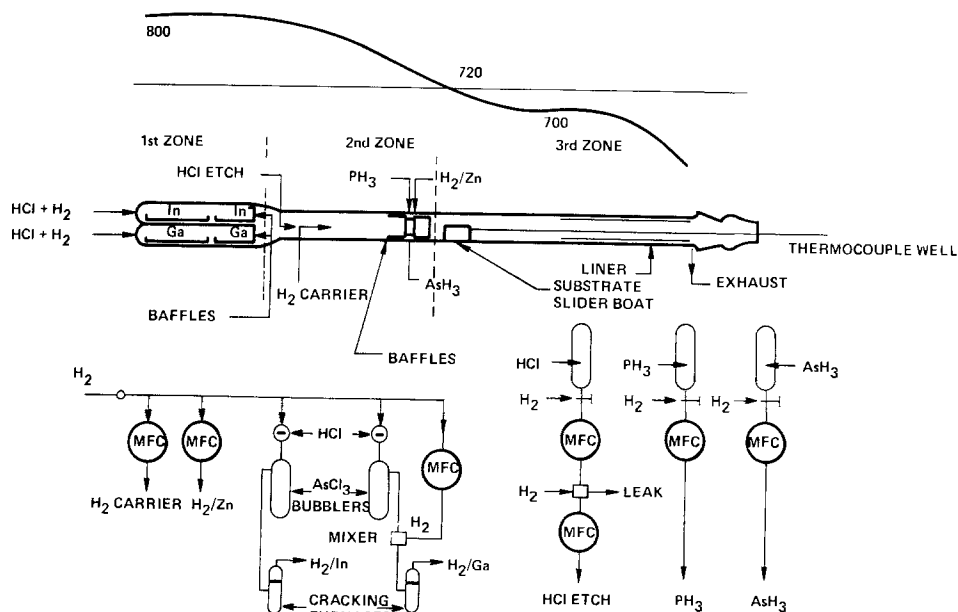


Fig. 1. Schematic diagram of the InGaP/InGaAs VPE growth system.

photoemission studies. The composition values are calculated from the equations developed by Moon *et al.* (13). The difference between bandgap (E_g) at 77° and 300°K is taken to be 0.07 eV for both InGaAs and InGaP. The composition values determined from these techniques are in reasonable agreement with each other. The background doping of this reactor has been found to be about 10^{15} cm^{-3} for InGaP layers grown on GaAs (Cr).

VPE Growth

InGaAs growth.—For InGaAs growth on GaAs, equal flow of AsH_3 and total MCl ($50 \text{ cm}^3/\text{min}$) are used. Under typical growth conditions a thin layer of GaAs is grown first, followed by a graded region, and finally a constant composition layer of desired thickness. Step grading is used in our experiments since it results in reduced overall dislocation density (6). A digital Data Trak programmer, Model 6610, is used to change the HCl flows over the sources in a specified manner for step grading. The step grading program is based upon InGaAs growth parameters experimentally established in this lab and published data (7-9). The grading rate is about $5 \text{ m}/\mu\text{m}$.

The InGaAs layers are shiny in appearance with a fine cross-hatch pattern. This arises from the dislocation network generated in the graded region (9). Sharp PL spectra are obtained from these layers. Van der Pauw measurements on p-type $\text{In}_{0.18}\text{Ga}_{0.82}\text{As}$ grown on GaAs (Cr) gave mobility values of $944 \text{ cm}^2/\text{V}\cdot\text{sec}$ at 77°K and $146 \text{ cm}^2/\text{V}\cdot\text{sec}$ at 300°K. The corresponding doping levels were $1.9 \cdot 10^{16} \text{ cm}^{-3}$ and $7.4 \cdot 10^{16} \text{ cm}^{-3}$. Typical growth rates are $0.15\text{-}0.2 \mu/\text{min}$.

InGaP growth.—To establish appropriate conditions for growing InGaP, two experimental approaches were used. First, the ratio of $\text{In}(\text{HCl})/\text{Ga}(\text{HCl})$ was changed and second, the PH_3 flow compared to MCl was changed. Since excess PH_3 compared to MCl tended to produce a poor quality surface, it was decided to grow InGaP under conditions of $\text{PH}_3 < \text{MCl}$. This finds support in a study of GaAs grown by the hydride process where improved lifetime and diffusion length of minority carriers are obtained when $\text{AsH}_3 < \text{GaCl}$ (14).

To grow InGaP layers lattice matched to InGaAs substrates, the HCl flow over the In source is adjusted. The HCl flow over the Ga source and the PH_3 flow are kept fixed at $2 \text{ cm}^3/\text{min}$ and $50 \text{ cm}^3/\text{min}$, respectively. Since 77°K photoluminescence is routinely used to characterize the grown layers, a relationship between the $\text{In}(\text{HCl})$ flow needed to grow lattice-matched InGaP layers and the InGaAs bandgap (E_g) at 77°K has been established and is shown in Fig. 2. The same program was always used for growing InGaAs; the variations in the composition grown are

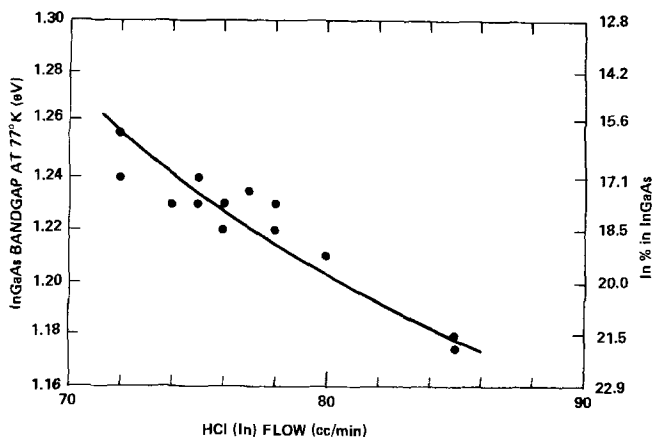


Fig. 2. Relationship between the InGaAs bandgap at 77°K and the $\text{In}(\text{HCl})$ flow required for lattice-matched InGaP/InGaAs growth.

believed due to minor changes in the system, *e.g.*, the source surface areas which change as the sources are used up, change in the source and substrate temperatures from run to run. Also, each time the reactor is taken down for cleaning and reinstalled, the positioning is not identical and the temperature profile can be slightly shifted. The scatter in the $\text{In}(\text{HCl})$ flows needed to grow lattice-matched InGaP is also due to the same reasons. The $\text{In}(\text{HCl})$ flow used for growing InGaP lattice matched to GaAs is $54 \text{ cm}^3/\text{min}$.

It must be emphasized that very critical control of parameters is needed to grow good quality InGaP layers. A $2 \text{ cm}^3/\text{min}$ change in the $\text{In}(\text{HCl})$ flow can easily ruin the growth. It has been found that when the grown layer is shiny in the middle and dark around the edges the $\text{In}(\text{HCl})$ needs to be reduced for lattice-matched conditions. When the $\text{In}(\text{HCl})$ flow is less than required the growth is patchy and dull in appearance. From Auger studies As has often been seen on the surface of such wafers. However, a certain amount of lattice latching has also been observed while growing InGaP on graded InGaAs. Two such layers of differing E_g at 77°K (1.18 and 1.21 eV) were placed next to each other and lattice-matched growth of InGaP was obtained on both of them. The $\text{In}(\text{HCl})$ flow used was intermediate between the flows needed for lattice-matched growth separately.

These growth conditions have been established for equal source boats, each of which has a surface area of 15 cm^2 . For unequal sources these conditions are not appropriate and lattice-matched growth is not obtained. Also, for equal sources but with substantially different surface area, the conditions would have to be adjusted slightly.

The relationship between the InGaAs bandgap at 77°K and that of InGaP is shown in Fig. 3. No attempt has been made to draw the expected relationship since a wide variation exists in the reported InGaP bandgap *vs.* composition in the literature (15). These data points are for the best heterojunctions grown. The best growths are characterized by sharp PL spectra, uniform coverage, specularly reflective surfaces, and good cleaving characteristics. For the few samples where x-ray diffraction was performed, the layers were found to be lattice matched.

The InGaP layers lattice matched to InGaAs substrates are shiny in appearance and the surface has a characteristic cross-hatch pattern as shown in Fig. 4. The asymmetry in the pattern follows from the asym-

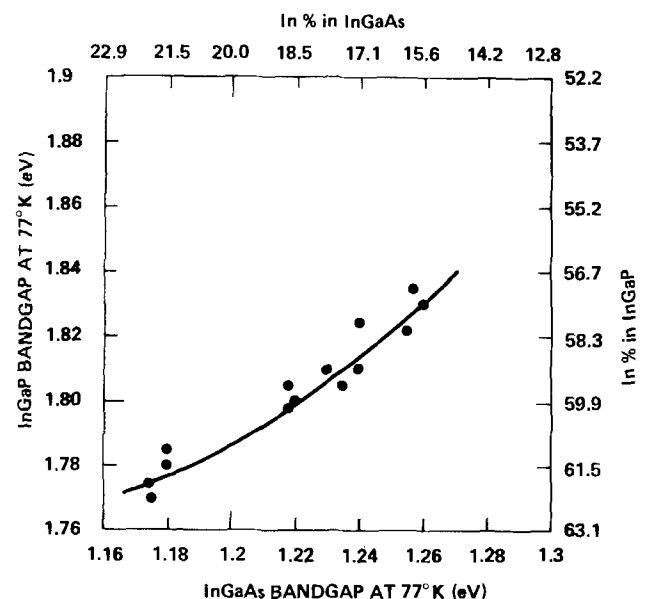


Fig. 3. Relationship between the InGaAs and InGaP bandgaps at 77°K for lattice-matched layers.

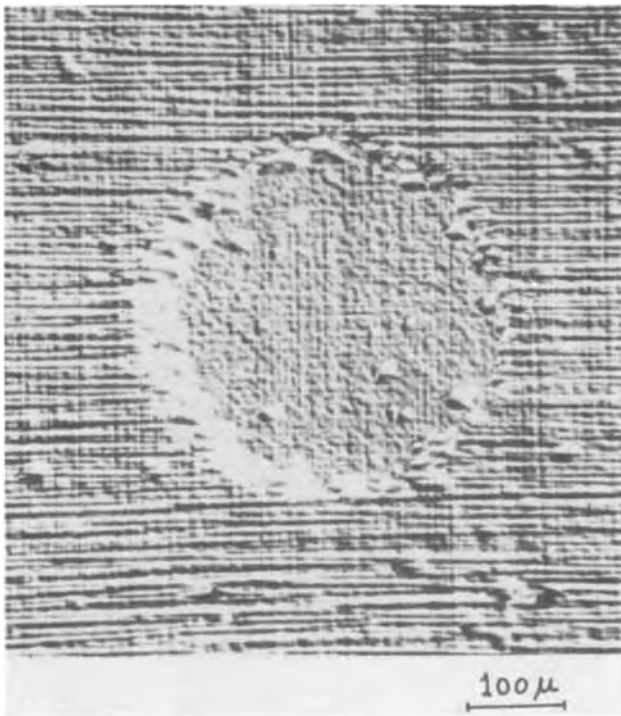


Fig. 4. Crosshatch patterns on InGaP and InGaAs layers. InGaP did not grow in the circular region.

metry in the zinc blend structure as discussed by Olsen *et al.* (16). It is found that the surface of the InGaP lattice matched to GaAs has no cross-hatch. Similar findings have been reported earlier when InGaP graded on GaP was found to have a cross-hatch pattern on the surface while InGaP grown directly on GaAs showed no cross-hatch (17). Thus, the cross-hatch seen on the InGaP surface grown on graded InGaAs substrate is due to the substrate itself. This is clearly seen in Fig. 4, which shows the cross-hatch pattern on a wafer where the InGaP did not grow in a few localized regions.

Lattice-matched InGaP/InGaAs growths are found to cleave easily without cracking and show a sharp interface, whereas mismatched layers are difficult to cleave; cracking on cleavage of imperfect layers has been reported earlier (5). A cleaved picture of the InGaP/InGaAs/GaAs structure is shown in Fig. 5.

Sharp PL spectra of FWHM of <50 meV are obtained from lattice-matched InGaP/InGaAs layers; for mismatched layers the PL spectrum is very broad. A sharp PL spectrum is also indicative of compositional homogeneity (18).

To obtain different p-type doping levels the Zn heater temperature is varied while the H_2 flow is kept fixed at 50 cm^3/min . The doping levels have usually been determined by C-V measurements. The doping levels achieved in the InGaP layers for various Zn pellet temperatures are shown in Fig. 6. The PL spectra for p-InGaP have a distinct Zn peak and the

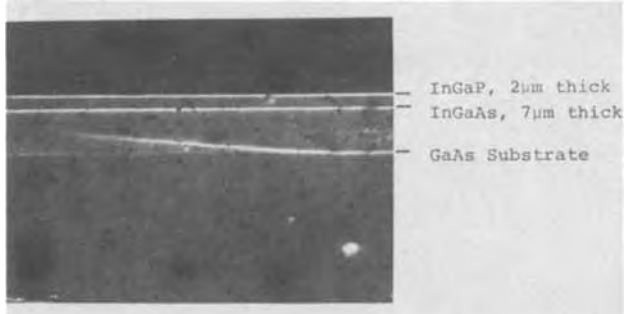


Fig. 5. Cleaved picture of the InGaP/InGaAs/GaAs structure

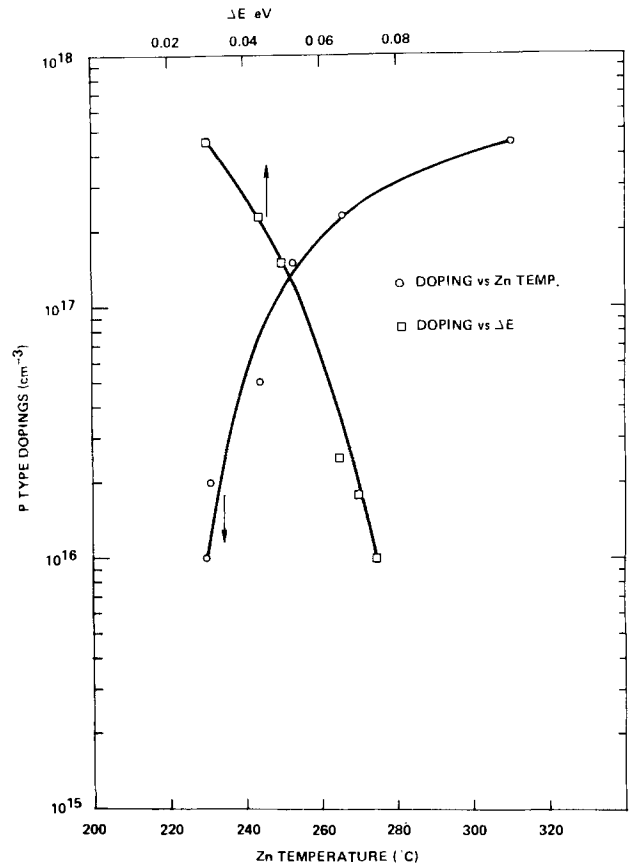


Fig. 6. Doping level in the InGaP layer as a function of the Zn temperature and the ionization energy as measured from the photoluminescence spectrum.

ionization energy measured is a function of doping itself (12). The established relationship is also shown in Fig. 6. The ionization energy is a slow function of the In% as well (19), but the doping level effects dominate in Fig. 6 since the data are for $In_xGa_{1-x}P$ layers with $x = 0.60 \pm 0.03$ only.

Van der Pauw measurements have been somewhat difficult due to contacting problems associated with a high bandgap material. For InGaP lattice matched to GaAs, a hole mobility of 104 $cm^2/Vsec$ was measured at room temperature for a carrier concentration of $8.4 \cdot 10^{15}$ cm^{-3} . Typical growth rate for InGaP is 0.1 μ/min .

Conclusion

Growth parameters have been established for growing InGaP lattice matched to InGaAs. To improve the reproducibility of the results, it would be beneficial to design a source region such that the surface area exposed and the residence time of gases over the sources are kept as nearly constant as possible. For better resolution in controlling the InGaP composition, the flows should all be increased since with 2 cm^3/min flow over the Ga source even 1 cm^3/min change in the In(HCl) flow makes a difference. Field-assisted photoemission from InGaP/InGaAs cathodes has been demonstrated and better than 1% overall efficiency at 1.06 micron has been obtained with this structure.

Acknowledgments

The authors wish to thank Dr. R. L. Bell for his continued support and useful discussions and Dr. G. A. Antypas for supplying the GaAs substrates. Thanks are also due to Mr. L. Garbini, Mrs. C. E. Hooper, and Miss S. Fonte for x-ray analyses, C-V measurements, and Van der Pauw measurements, respectively. This work was supported by the Air Force Avionics Laboratory under Contract F33615-76-C-1351, Wright-Patterson AFB, Ohio 45433.

Manuscript received June 11, 1979. This was Paper 184 presented at the Boston, Massachusetts, Meeting of the Society, May 6-11, 1979.

Any discussion of this paper will appear in a Discussion Section to be published in the December 1980 JOURNAL. All discussions for the December 1980 Discussion Section should be submitted by Aug. 1, 1980.

Publication costs of this article were assisted by Varian Associates.

REFERENCES

1. R. L. Bell, L. W. James, and R. L. Moon, *Appl. Phys. Lett.*, **25**, 645 (1974).
2. J. S. Escher, P. E. Gregory, S. B. Hyder, and R. R. Saxena, Air Force Avionics Laboratory Report No. AFA1-TR-78-78, May 1978, for Contract F33615-76-C-1351.
3. J. S. Escher, G. A. Antypas, and J. Edgecumbe, *Appl. Phys. Lett.*, **28**, 153 (1976).
4. H. Kressel, *J. Electron. Mater.*, **4**, 1081 (1975).
5. C. J. Nuese and G. H. Olsen, *Appl. Phys. Lett.*, **26**, 528 (1975).
6. C. J. Nuese, G. H. Olsen, M. Ettenberg, J. J. Gannon, and T. J. Zamerowski, *ibid.*, **28**, 807 (1976).
7. S. B. Hyder, *This Journal*, **123**, 1503 (1976).
8. V. S. Ban and M. Ettenberg, in "Chemical Vapor Deposition, Fourth International Conference," G. F. Wakefield and J. M. Blocher, Jr., Editors, p. 31, The Electrochemical Society Softbound Proceeding Series, Princeton, N.J. (1973).
9. R. E. Enstrom, D. Richman, M. S. Abrahams, J. R. Apert, D. G. Fisher, A. H. Sommer, and B. F. Williams, in "Proceedings of the Third International Symposium on Gallium Arsenide and Related Compounds," Institute of Physics and the Physics Society, London (1970).
10. V. S. Ban and M. Ettenberg, *J. Phys. Chem. Solids*, **34**, 1119 (1973).
11. A. G. Sigai, C. J. Nuese, R. E. Enstrom, and T. Zamerowski, *This Journal*, **120**, 947 (1973).
12. R. E. Enstrom, C. J. Nuese, V. S. Ban, and J. R. Apert, "Gallium Arsenide and Related Compounds," Conf. Ser. No. 17, The Institute of Physics, London, p. 37 (1973).
13. R. L. Moon, G. A. Antypas, and L. W. James, *J. Electron. Mater.*, **3**, 635 (1974).
14. M. Ettenberg, G. H. Olsen, and C. J. Nuese, *Appl. Phys. Lett.*, **29**, 141 (1976).
15. G. B. Stringfellow, P. F. Lindquist, and R. A. Burmeister, *J. Electron. Mater.*, **1**, 437 (1972).
16. G. H. Olsen, M. S. Abrahams, and T. J. Zamerowski, *This Journal*, **121**, 1650 (1974).
17. C. J. Nuese, A. G. Sigai, J. J. Gannon, and T. Zamerowski, *J. Electron. Mater.*, **3**, 51 (1974).
18. O. N. Ermakov, R. S. Ignatkina, V. P. Sushkov, and M. V. Chukichev, *Sov. Phys. Semicond.*, **11**, 651 (1977).
19. T. Kato, T. Matsumoto, and T. Ishida, *Jpn. J. Appl. Phys.*, **15**, 2265 (1976).

Advances in Transmission Electron Microscope Techniques Applied to Device Failure Analysis

T. T. Sheng and R. B. Marcus

Bell Laboratories, Murray Hill, New Jersey 07974

ABSTRACT

Special techniques have been developed for routine preparation of transmission electron microscope samples from integrated circuit devices. These methods, which are described and illustrated in this paper, are the preparation of replicas of fractured multilayer structures, vertical cross sections, horizontal cross sections, and feature enhancement on cross-section samples through the use of special staining and etching treatments.

Transmission electron microscopy (TEM) has played an active role in materials studies related to the processing and fabrication of microelectronic devices. TEM has been an important research tool in providing essential information in generic studies of oxidation, interdiffusion, implant damage, and annealing and propagation of defects. In a device processing and failure analysis environment, however, problems continuously appear on the scene which demand fast analysis and solution. TEM has traditionally been of little use in this type of environment because of difficulties of sample preparation. Although there is some published information on the application of TEM to processing problems in real device structures (1, 2), most published TEM work on processing problems has been done on special samples with geometries more suitable for TEM analysis and which are made to simulate the real device (2).

For a number of years we have used TEM in a device processing and failure analysis working environment. TEM has been used to solve a large number of processing problems related to vertical and horizontal shorts, junction leakages and voltage breakdowns, poor contacts, and variations in resistivity and oxidation

kinetics. We are able to use TEM on these problems mainly because procedures have been developed for preparing samples so that regions of interest in real device structures can be studied and information obtained within a short time period. TEM is thus made an equal partner along with other in-process testing procedures towards the analysis and solution of processing-related problems as they arise.

TEM is often used in conjunction with other analytical approaches for device failure analysis studies. Cooperative work with optical microscopy, scanning electron microscopy (in the secondary electron, voltage contrast, and EBIC modes), Rutherford scattering, and Auger electron spectroscopy have been particularly useful. Although cooperative analysis of this type lengthens the time of the analysis, the information obtained from these studies is usually well worth the extra time.

The main purpose of this paper is to describe the procedures which have been developed for preparing device samples for TEM studies. Electron micrographs of typical samples are used to illustrate the type of information obtained from these studies. Most of our interaction has been with silicon semiconductor device processing and most of the illustrations reflect this bias. Samples for TEM analysis are prepared from any

Key words: electron microscopy, failure analysis, integrated circuits.

point in the processing sequence, including finished and tested devices.

Four main sample preparation techniques will be described: edge fracture replica, horizontal section, vertical section, and feature enhancement. The first technique is a method for preparing a replica of a fractured surface of a device; the second and third techniques are methods for preparing device material for direct study in the electron microscope; the last technique is a means of enhancing the contrast of device features (in horizontal or vertical sections) that would otherwise be difficult to see in the electron microscope.

A major aid in TEM failure analysis studies is the use of a TEM test pattern which is incorporated at a number of sites on each device wafer. This test pattern contains all the morphological features of interest compressed into a small area so that a sample can be made with nearly 100% certainty of capturing the region of interest for TEM study using any of the four sample preparation techniques.

Sample Preparation Technique-Edge Fracture Replica

Multilayer device structures can be examined by fracturing in a direction normal to the surface and studying a shadowed replica made from that surface. The replica technique is a very old one for the study of surface texture (3). In the usual variation of the method a small amount of a heavy metal is deposited at an oblique angle to a surface, resulting in thickness variations that depend on the angle of inclination of the local surface. Shadows are cast by surface protuberances whose far side (away from the metal source) form an angle with the surface greater than the inclination of the metal source to the surface. A carbon film is deposited over the surface and is then withdrawn, extracting the deposits of heavy metal. The replica with regions of varying heavy metal deposit is then examined in the electron microscope, and local variations in metal thickness produce variations in electron absorption which result in an image that is closely related to the texture of the original surface.

In the method to be described, advantage is taken of the fact that multilayer structures generally do not fracture cleanly through all layers, but one of the layer edges at an interface is usually set back slightly. A shadowed replica can be made simultaneously of the exposed interfacial surfaces and of the fracture surfaces. The technique for preparing such a replica from a 0.020 in. wafer is illustrated in Fig. 1 and is described below; the fractured surface is assumed normal to the device surface. (i) Scribe two co-linear marks on opposite sides of the region of interest. (ii) Fracture. Sandwich the wafer between glass slides with scribe marks lining up along the slide edges. Ap-

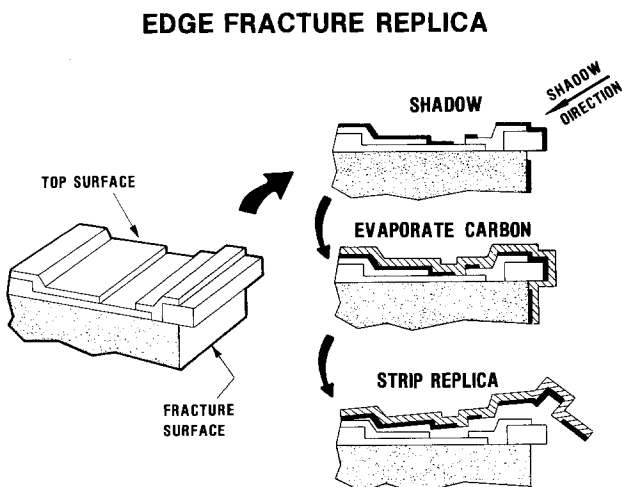


Fig. 1. Edge fracture replica technique

ply a downward force so that the working surface (containing the scribe marks) is the first to break. (iii) Shadow and replicate. The shadow angle is 15° to both surfaces (sample surface and fracture surface). The carbon angle is 45° to both surfaces. (iv) Strip the shadowed replica by dissolving the underlying material. The chemical etchant must act slowly. Violent dissolution with bubble formation will break up the replica. For samples of oxide and poly layers on silicon a convenient etch is: HOAc:HF:HNO₃ = 6:6:10 diluted 1 part to 10 parts HOAc.

Electron micrographs of edge fracture replicas are shown in Fig. 2 and 3. Note that in Fig. 2 the surface textures of the substrate, gate oxide, poly, and top SiO₂ can be seen, and the edges of the three top oxide layers can be distinguished. The texture of the top surface of the gate oxide is related to the poly grain structure, which can be determined from studying both the fractured and top surfaces of the poly. The three top oxides can be distinguished because of differences in the microtexture of these layers.

In Fig. 3, the B-glass, polysilicon, and field oxide layers are easily distinguished. An important piece

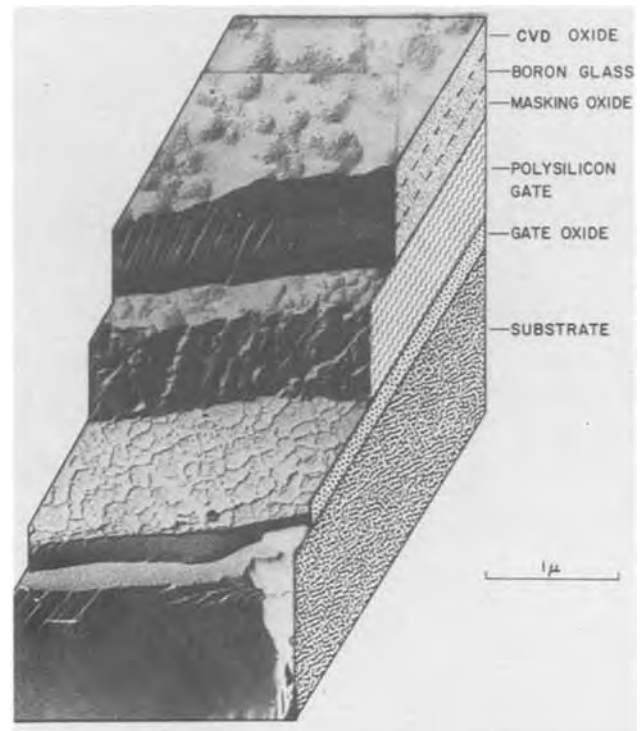


Fig. 2. TEM photo of fracture replica of multilayer structure on a silicon substrate. The fractured edges of the three top oxide layers are distinguished, and the surface textures of three layers plus the substrate can be seen.



Fig. 3. TEM photo of edge fracture replica through a sample of B-glass on poly over oxide on a silicon substrate.

of information is contained in the region at the edge of the poly runner. After patterning the poly and treating with BHF, an undercut was produced (arrow) which filled up with B-glass. The B-glass flows sufficiently so that the oxide undercut is unimportant as a failure mode.

Sample Preparation Technique-Horizontal Section

When a sample is to be examined directly in the transmission electron microscope at 100-200 keV, it first must be thinned to $\sim 1000\text{\AA}$. Thin film samples which are prepared parallel to the wafer surface are referred to in this paper as "horizontal sections." These can be made in such a way that the original surface remains as one surface of the sample, or a section can be prepared from a region below the surface in cases where an interface needs to be examined.

Chemical thinning of silicon and SiO_2 is faster than ion milling and for this reason is preferred as the final thinning process for preparing horizontal sections. In cases where multilayer structures are present and chemical attack of different layers occurs at widely different rates, ion milling must be used. The main steps in preparing horizontal sections are illustrated in Fig. 4 and described below: (i) Mechanically lap the sample to $< 100\ \mu\text{m}$ using No. 400 grit paper. (ii) Cut a disk using an ultrasonic cutter with the area of interest approximately at the center. The disk should be of a size appropriate for the sample holder of the electron microscope. (iii) Using wax, mount the disk face down on a clear sapphire plate. Wax should protect the front surface and edge of the disk but the back surface of the disk should be exposed. The transparency of the sapphire aids in determining the end point during thinning. (iv) Chemically etch the sample until a small hole is formed. This is accomplished for a silicon sample by ~ 5 min immersion in 6:6:10 HF:HOAc:HNO₃. Etching is stopped by flooding the sample with DI water. (v) Dissolve the wax in a solvent and remove the sample. The taper at the edge of the hole is usually sufficiently small so that a sample transparent to 100 keV electrons can be produced which extends back from the hole $\sim 10\text{-}40\ \mu\text{m}$. (vi) If a region say $0.5\ \mu\text{m}$ depth below the surface is to be examined, the front surface must be ion milled. Using an IMMI ion milling machine with Ar gas at $10\ \mu\text{m}$ chamber pressure, and an ion beam from one gun operating at 6 kV and $100\ \mu\text{A}$ beam current striking a sample at 15° angle rotating at 15 rpm, the thinning rate for Si is $\sim 1.0\ \mu\text{m/hr}$.

An example of the application of the horizontal section technique to the solution of processing problems is illustrated in Fig. 5. High leakage at pn junctions on van der Pauw testers was localized to specific sites [2 in Fig. 5(A)] by SEM EBIC analysis. The site was marked with polymerized hydrocarbon from SEM study [Fig. 5(B)] and a horizontal section pre-

pared and examined in the TEM. The leakage site was found to be coincident with a stacking fault crossing the junction [Fig. 5(C)] and further TEM study [Fig. 5(D-F)] showed the fault to contain a copper-rich precipitate. More extreme gettering procedures were then used to remove precipitates, and although stacking faults were still produced during processing, junction leakage was lowered drastically (4).

Sample Preparation Technique-Vertical Section

The preparation of a section normal to the device surface requires somewhat more labor than does the preparation of a horizontal section. The method is illustrated in Fig. 6 and is now described: (i) Lap the sample to $< 100\ \mu\text{m}$ using No. 400 grit paper. (ii) Scribe and cleave a small number of pieces $\sim 1.5\ \text{mm} \times 3\ \text{mm}$, so that the region of interest is near the center of each piece. (iii) Bond a stack of the cleaved pieces face-to-face or face-to-back using epoxy. The epoxy should be squeezed out between the pieces so that only thin epoxy films of approximately uniform thickness separate the pieces. (iv) Imbed the stack in an epoxy "button" using a round silicone rubber mold such as Model No. 23650 from Ladd Research Industries. (v) Lap and polish both sides of the button to a final thickness of $< 100\ \mu\text{m}$. No. 400 grit paper followed by ~ 5 min of No. 600 paper followed by polishing with $3\ \mu\text{m}$ grit works well for silicon device samples. (vi) Cut a disk ultrasonically with the area of interest approximately at the center. Because of the fragile nature of this assembly, it is useful at this point to epoxy bond the disk to a small molybdenum ring whose OD corresponds to the sample holder size of the electron microscope. (vii) Ion mill both surfaces simultaneously until a small hole develops in the sample. Regions from the edge of the hole extending back $\sim 50\ \mu\text{m}$ are usually thin enough for TEM study.

Two important points should be noted regarding use of this technique. Because of uncertainties regarding the exact site at which a hole appears in the sample, and because the hole is sometimes larger than $100\ \mu\text{m}$ diameter, [the sample thickness after step (i)], it is useful to have 4-5 pieces comprise one sample button. A second point regards the different speed at which materials are ion milled. Epoxy mills faster than most other materials. If the epoxy between (face-to-back) pieces is milled away, the outer edge of the surface of the face will also tend to suffer some erosion from ion milling, and this material will be lost to TEM study. This loss can be prevented by coating the wafer with a sacrificial layer of $\sim 0.5\ \mu\text{m}$ poly, SiO_2 , or Si_3N_4 just before TEM sample preparation.

Examples of the application of the vertical section technique to failure analysis problems are shown in Fig. 7, 8, and 9. Figure 7 shows three stages in processing using a selective oxidation technique for growing the isolation oxide (a-c), with severely thinned gate oxide at the "bird's beak" edge as shown in 7(c). After a change in processing, gate oxidation no longer produced the thinning (5) as shown in Fig. 7(d). Figure 8 shows a TEM of a vertical section through a two-level poly structure showing the extreme one-sided thinning of poly I, and the narrow gap at the "cat's paw" separating poly II from the substrate; this latter morphological feature was the cause of a low breakdown voltage in these devices (6). Figure 9 shows two P-glass contact window sites in an MOS device; an aluminum to poly contact is shown in Fig. 9(a) and an aluminum to substrate contact is shown in Fig. 9(b). The disturbance of the silicon due to pitting can be seen in both figures.

Sample Preparation Technique-Image Enhancement

Electron micrograph image contrast from single crystal silicon, poly, or various metallization is pri-

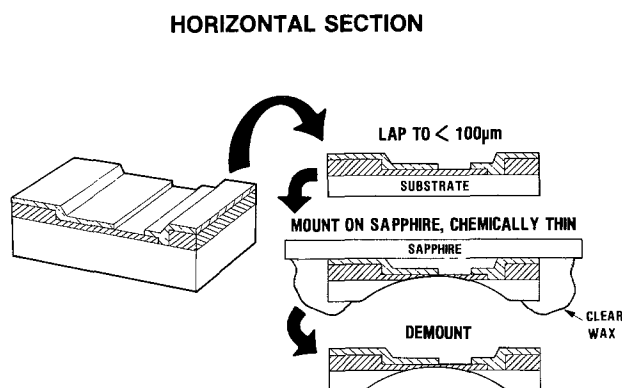


Fig. 4. Steps in preparing a horizontal section for TEM study. The wafer is lapped to $< 100\ \mu\text{m}$ thickness, mounted on clean sapphire and chemically etched until a small hole appears.

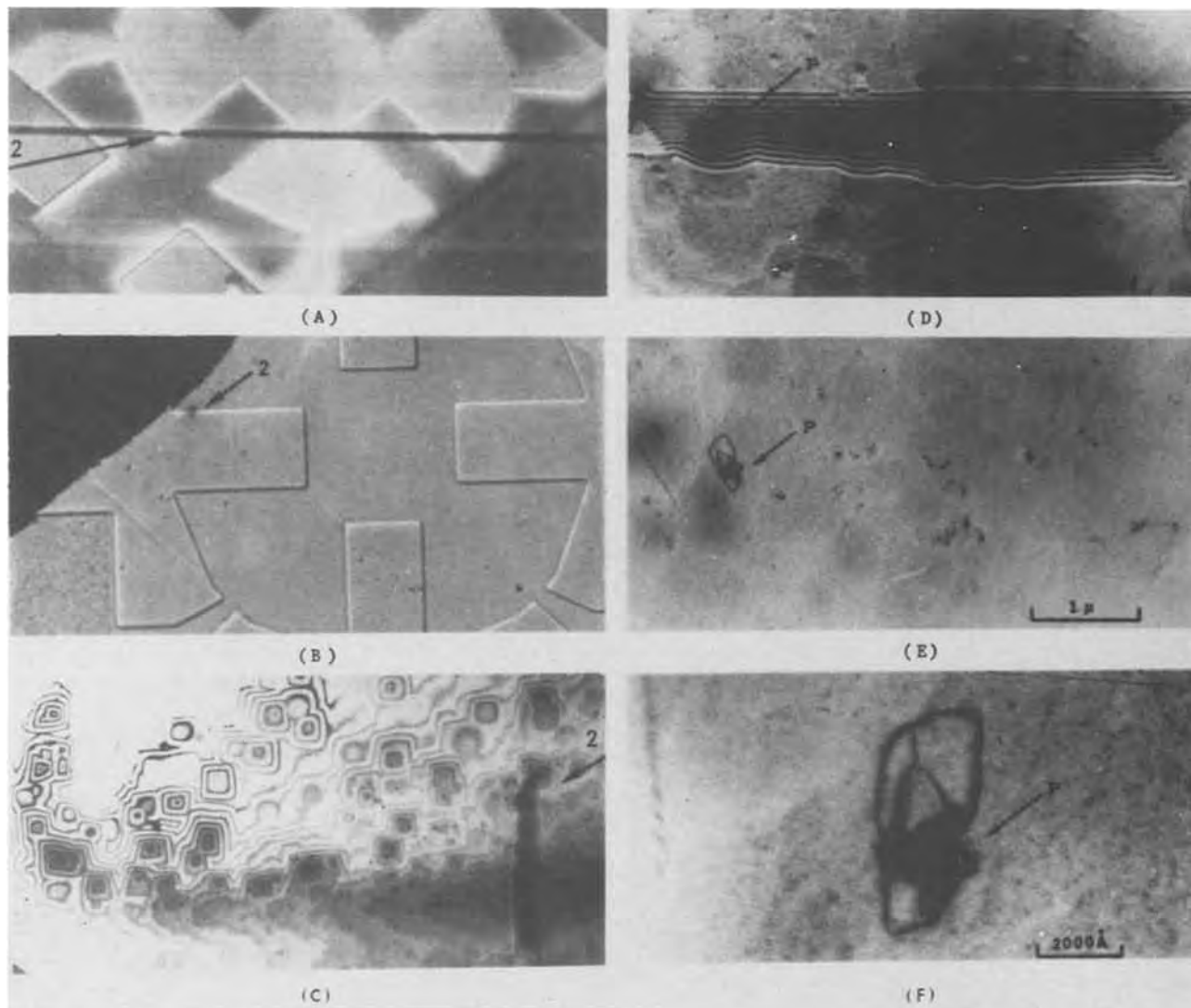


Fig. 5. Study of origin of pn junction leakage sites: (A) shows an SEM photograph of a test pattern with the leakage site, 2, marked by EBIC study. (B) is an optical photo showing the leakage site marked by polymerized hydrocarbon. (C-F) are TEM photos of a stacking fault containing a precipitate which intersects the pn junction. Viewing conditions were adjusted for extinction of the stacking fault contrast in (E) and (F).

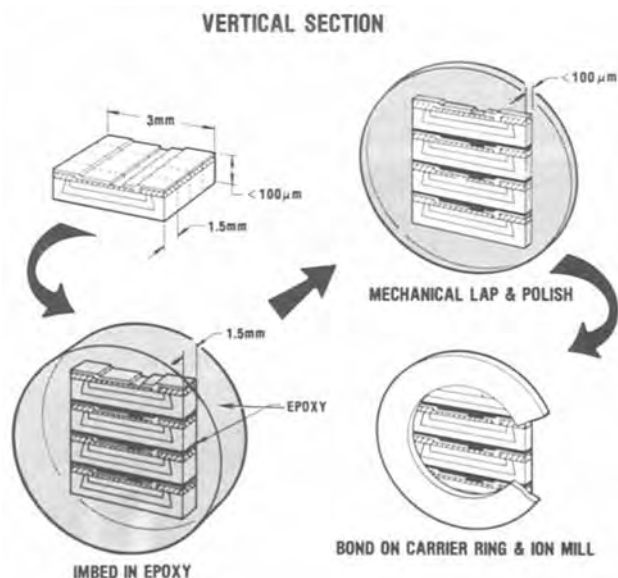


Fig. 6. Steps in preparing vertical section for TEM study. The wafer is lapped to $<100 \mu\text{m}$, diced into small pieces and bonded face-to-face or face-to-back in an epoxy button. After further lapping and polishing to $<100 \mu\text{m}$ thickness and bonding to a carrier ring, the sample is further thinned using ion milling.

marily controlled by diffraction effects which are determined by crystal orientation, thickness, and defect structure. The ability to resolve small features in these materials, including the definition of layer edges is usually not a problem and is mainly limited by the condition of the electron microscope. The material on opposite sides of a pn junction in silicon does not differ in any of the essential properties just mentioned, however, and in order to make the junction visible, methods must be used for enhancing contrast by changing the thickness of either the n or p region by selectively removing material. We have delineated p+n and n+p junctions by dipping both horizontal and vertical cross-section samples into 0.25% HNO_3 in HF for 2-4 sec under strong light. Figure 10 shows a vertical cross-section sample through a "stained" p+n junction at the edge of a poly gate (which has been removed). The p+ region was made with boron and the Si substrate contains phosphorus. The curvature of the stained region under the gate can be seen and accurately measured. It is not known if the transition seen in the micrograph corresponds exactly to the p+n junction, but it is safe to assume, as in more typical cases of angle lap-staining on larger samples, that the transition lies parallel to the junction. Figure 11 shows micrographs of another n+p junction made by implanting and diffusing As into p-type silicon. The junction is not delineated in the two face-to-face

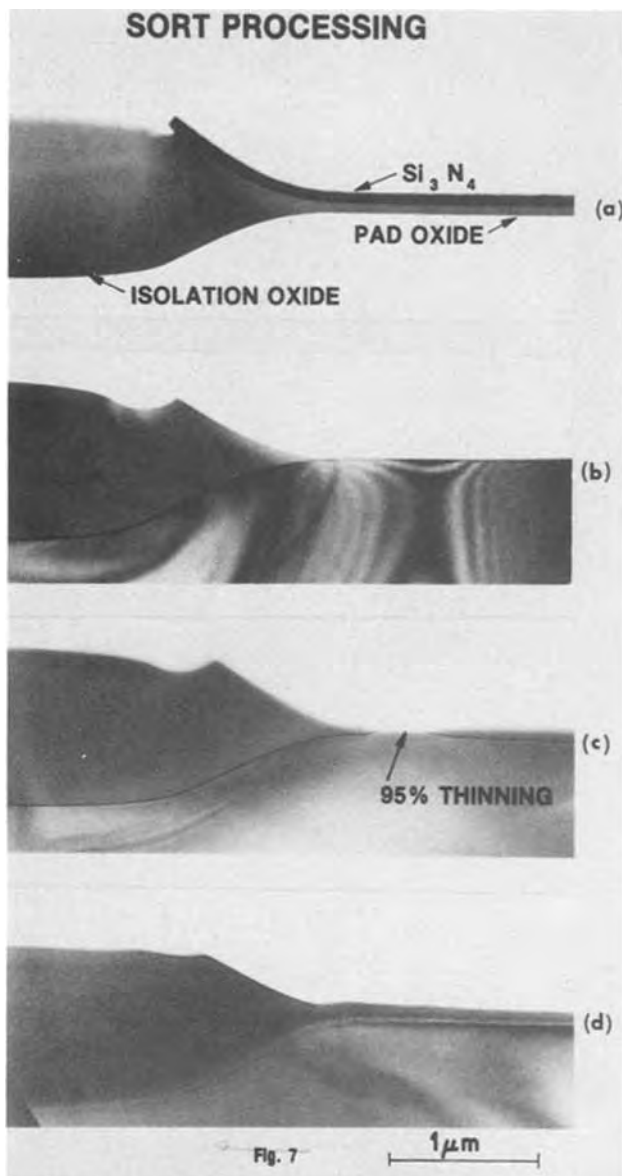


Fig. 7. TEM photos of vertical cross sections through samples at various stages in processing (a)-(c) leading to a gate oxide thinning (c), and a sample after a processing change was introduced to eliminate thinning (d). The Si_3N_4 and pad SiO_2 layers shown in (a) have been removed in (b), and gate oxide has been grown in (c) and (d).

samples prepared by ion milling (a), but appears after 4 sec etch (b) and 8 sec etch (c). The n^+ region is preferentially etched and converted to an amorphous layer, probably an oxide, after 8 sec etch.

Image contrast from amorphous or nearly amorphous layers such as SiO_2 or Si_3N_4 is primarily controlled by variations in thickness in a given phase or differences in scattering power when going across a phase boundary. The change in scattering power across a thermal SiO_2 -CVD SiO_2 interface is usually too weak to give useful contrast changes, but can be enhanced by light treatment with buffered HF which etches CVD SiO_2 significantly faster than thermal SiO_2 . Very small voids in amorphous material can be made visible by adding a heavy metal "stain" to these regions, or by opening the void to a convenient size for study by additional etching. Figure 12 shows micrographs of a vertical cross section (a) at the edge of a poly gate and the corresponding horizontal cross section (b) from a generically identical region. The sample shown in (b) corresponds to the region bounded by the dashed lines in (a). After source-drain implant and diffusion, a phosphorus-containing

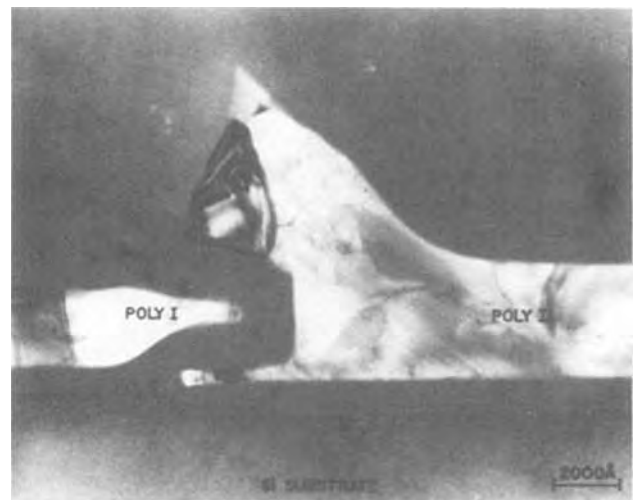


Fig. 8. TEM photo of a vertical cross section through a two-level poly device. The narrow gap separating poly II and the substrate at the "cat's paw" was the cause of low breakdown voltages in these devices.

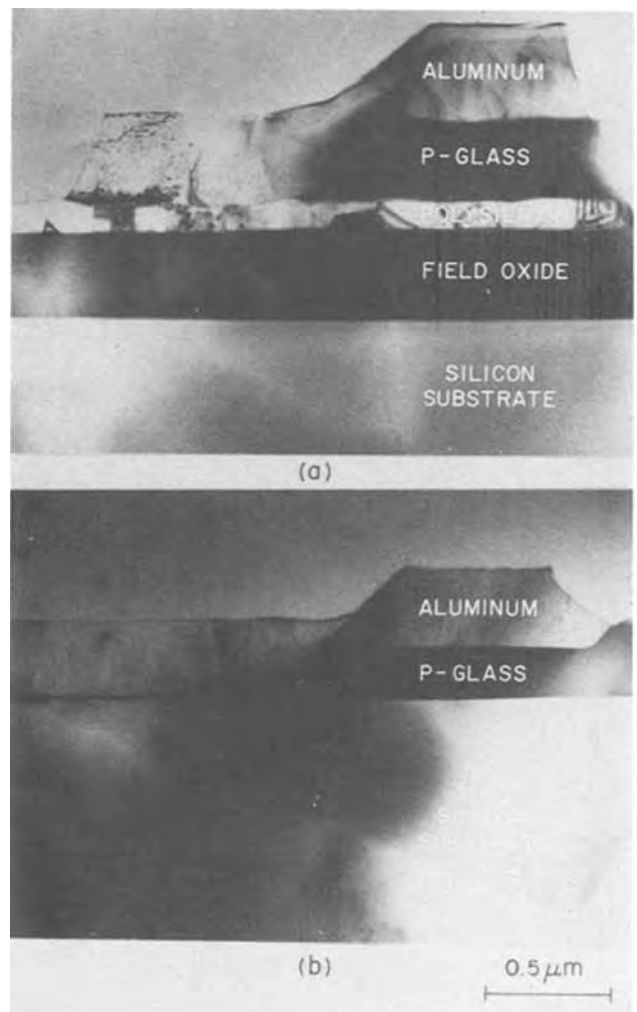


Fig. 9. TEM photos of vertical cross section through n-channel MOS device showing aluminum to poly contact (a) and aluminum to substrate contact (b).

P-glass had been deposited over the device, leaving a small void under the edge of the poly gate due to severe etch-back of oxide when the source-drain regions were etched to expose the silicon. OsO_4 stain was applied to the horizontal section, and capillary action drew the stain into the void region, enhancing

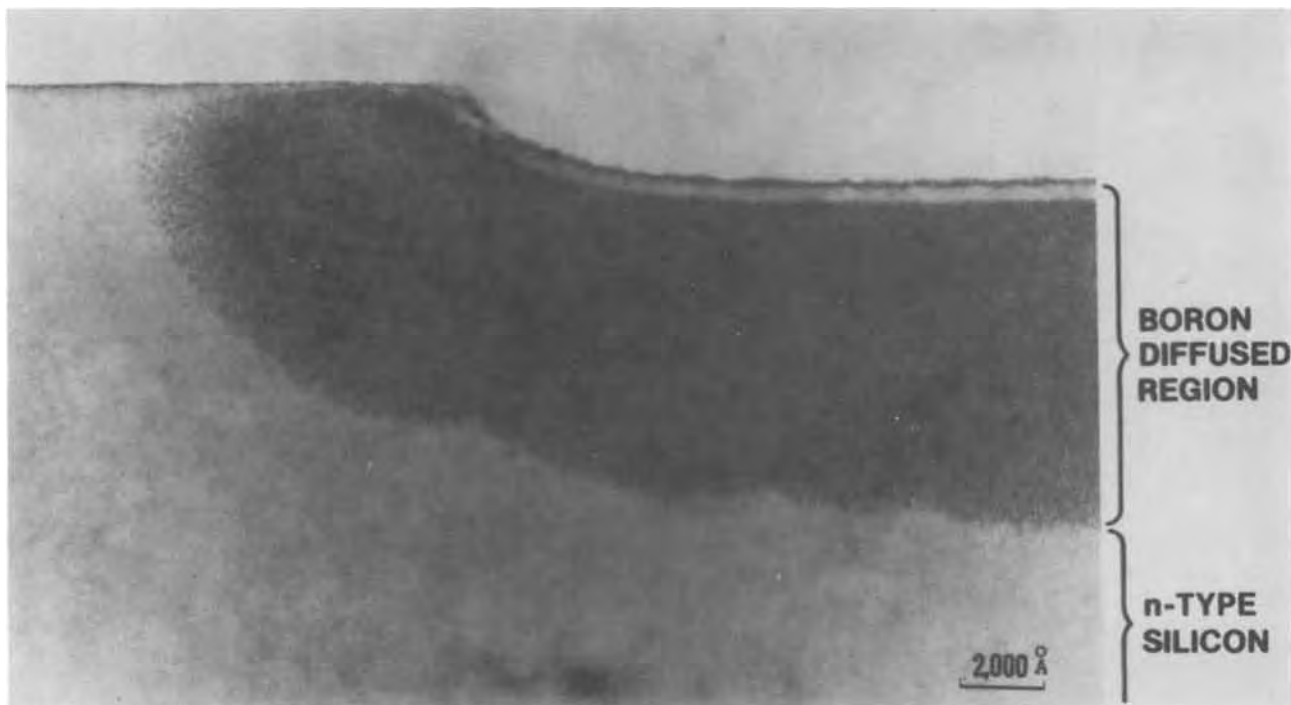


Fig. 10. TEM photo of a vertical cross section through a "stained" $p + n$ junction in the region of the gate

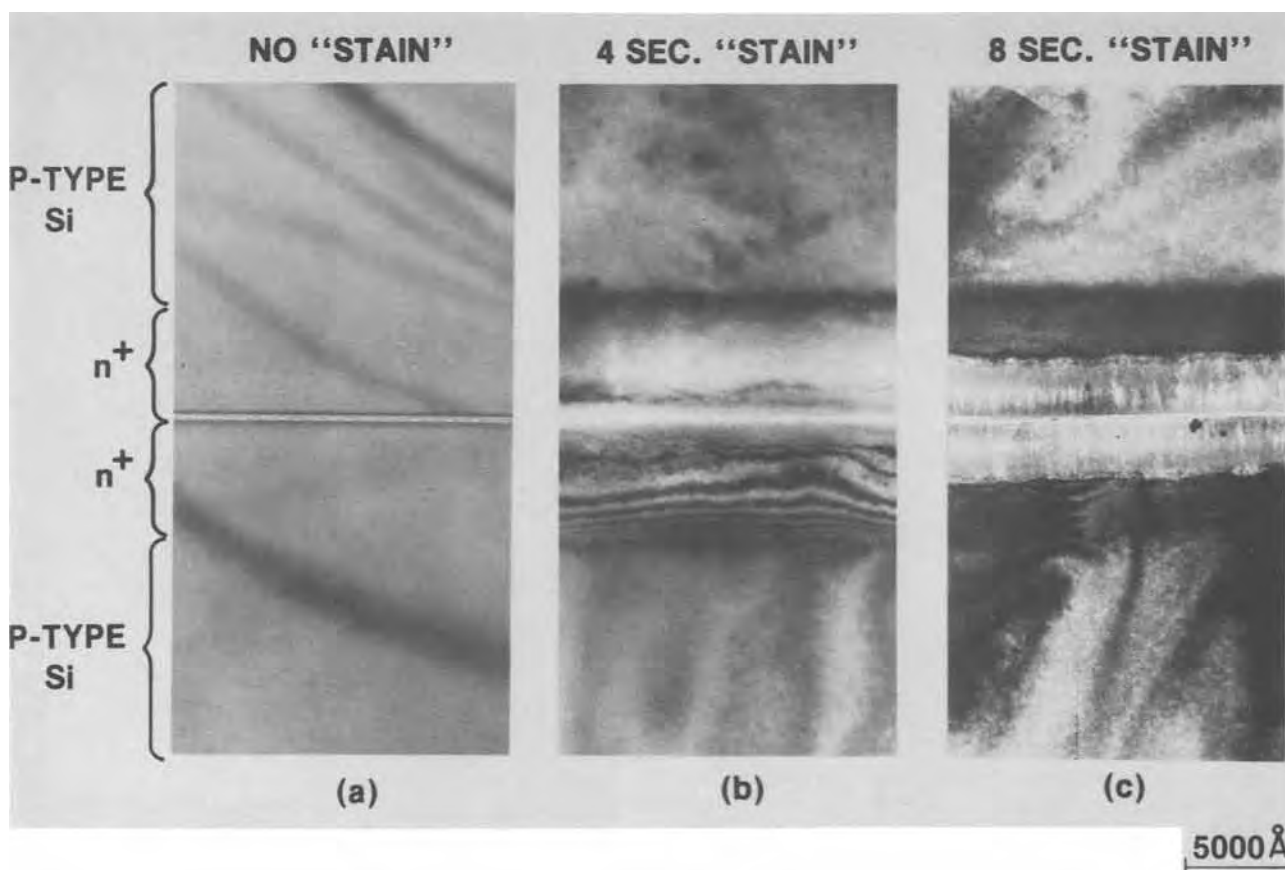


Fig. 11. TEM photos of vertical cross sections through n^+p samples after sample preparation by ion milling (a), after 4 sec "stain" (b), and after 8 sec stain (c).

the TEM contrast in this region due to the large scattering of electrons by osmium.

TEM Test Pattern

Horizontal and vertical section samples usually contain regions thin enough for TEM study over a distance less than $\sim 40 \mu\text{m}$ from the edge of the hole. The probability that a sample contains a specific feature of interest in the electron transparent region is

increased to nearly 100% when a special test pattern is incorporated in the wafer, and the TEM sample is prepared from this test pattern. The test pattern contains all the essential morphological features (contacts, steps, gate oxide, etc.) compressed in a region less than $40 \mu\text{m}$ along the surface and extending 1 mm in the orthogonal surface direction. The $40 \mu\text{m}$ (or smaller) unit is repeated a sufficient number of times to cover a total distance of 2 mm. An example

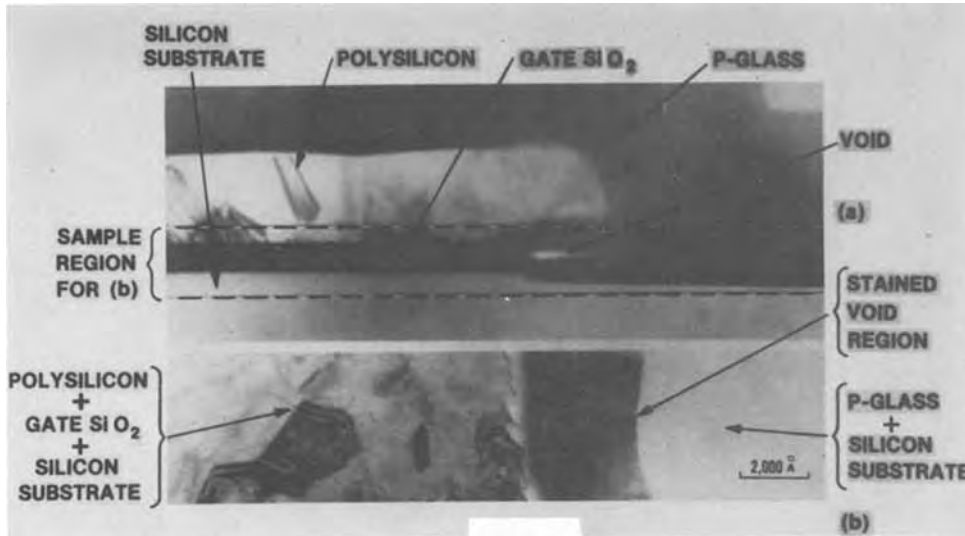


Fig. 12. TEM photos at the edge of a poly gate. A vertical cross section (a) shows a void under the edge of the poly, and a horizontal cross section (b) shows the void region in enhanced contrast because of the addition of OsO_4 stain.

of a test pattern incorporated in an n-channel device code which uses selective oxidation is shown in Fig. 13. The lower illustration shows the position of four test chips on the wafer (not drawn to scale) and the upper illustration shows the composition of the $27\ \mu\text{m}$ unit which is repeated 74 times. The test chips are small and are inserted adjacent to alignment features so that no active device space is used.

The main requirements in designing such a test chip (other than incorporating all the essential processing features) are that (i) the total area be similar to that described in Fig. 13, e.g., $1\ \text{mm} \times 2\ \text{mm}$ with the repeat unit running parallel to the $2\ \text{mm}$ axis, (ii) the direction parallel to the $2\ \text{mm}$ axis be a cleavage direction, (iii) the repeat unit be less than $\sim 40\ \mu\text{m}$, (iv) at least 3 test chips appear on a wafer, and (v) the test chips not be bunched together but rather separated; each one needs to be separately cleaved from the wafer.

Summary

Four techniques for preparing SIC device samples for TEM study have been described. Of these methods, vertical and horizontal sections have provided the most useful information on a nearly routine basis.

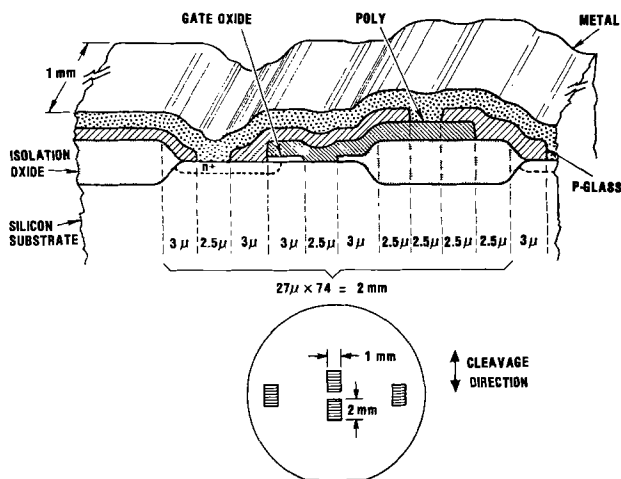


Fig. 13. Schematic illustrations of a TEM test pattern for n-channel device code using selective oxidation showing composition of repeat unit (upper) and position of pattern on wafer (lower).

Edge fracture replica and image enhancement techniques are used in special cases. All of these techniques are used from time to time in conjunction with other analytical methods in providing in depth studies when the occasion demands, and the literature contains many such examples of such cooperative efforts. Examples of cooperative efforts from this laboratory are the correlation of TEM studies with optical microscopy for the revealing of laser annealing (7), with Rutherford scattering for the revealing of Ar bubble in Si (8), and laser-induced reactions of metal films with Si (9), with Auger electron spectroscopy for determination of depth profiles of phases and elements in oxidized GaAlAs (10), and with SEM in the EBIC mode for revealing the role of decorated stacking faults in causing pn junction leakage in CMOS devices (4).

Manuscript submitted Aug. 6, 1979; revised manuscript received Sept. 21, 1979.

Any discussion of this paper will appear in a Discussion Section to be published in the December 1980 JOURNAL. All discussions for the December 1980 Discussion Section should be submitted by Aug. 1, 1980.

Publication costs of this article were assisted by Bell Laboratories.

REFERENCES

1. W. E. Ham, M. S. Abrahams, J. Blanc, and C. J. Buicocchi, *RCA Rev.*, **38**, 351 (1977).
2. T. T. Sheng and C. C. Chang, *IEEE Trans. Electron Devices*, ed-23, 531 (1976).
3. R. B. Marcus, in "Physical Measurement and Analysis of Thin Films," E. M. Murt and W. G. Guldner Editors, p. 105, Plenum, New York (1969).
4. J. Dishman, S. E. Haszko, R. B. Marcus, S. P. Murarka, and T. T. Sheng, *J. Appl. Phys.*, **50**, 2689 (1979).
5. T. Shankoff, T. T. Sheng, S. E. Haszko, R. B. Marcus, and T. E. Smith, *This Journal*, **127**, 216 (1980).
6. A. K. Sinha, T. T. Sheng, T. A. Shankoff, W. S. Lindenberger, E. N. Fuls, and C. C. Chang, in 17th Annual Proceedings Reliability Physics, 1979.
7. H. J. Leamy, G. A. Rozgonyi, T. T. Sheng, and G. K. Celler, *Appl. Phys. Lett.*, **32**, 535 (1968).
8. Z. L. Liau and T. T. Sheng, *ibid.*, **32**, 716 (1978).
9. J. M. Poate, H. J. Leamy, T. T. Sheng, and G. K. Celler, *ibid.*, **33**, 918 (1978).
10. R. P. H. Chang, C. C. Chang, and T. T. Sheng, *ibid.*, **30**, 657 (1977).

Silicon Deposition on a Rotating Disk

Richard Pollard*¹ and John Newman*

Materials and Molecular Research Division, Lawrence Berkeley Laboratory
and Department of Chemical Engineering, University of California, Berkeley, California 94720

ABSTRACT

A one-dimensional model has been developed which describes the interactions among hydrodynamics, multicomponent heat and mass transfer, and reaction kinetics for the rotating disk system. The analysis includes variable physical properties and finite interfacial velocity and has provision for an arbitrary number of simultaneous homogeneous and heterogeneous reactions. The model has been applied to the chemical vapor deposition of silicon from silicon tetrachloride in excess hydrogen. Predictions for the dependence of silicon production rate on disk temperature and rotation rate are compared with available experimental data.

Many chemical syntheses with important industrial applications involve simultaneous homogeneous and heterogeneous reactions. In the semiconductor industry there is considerable interest in chemical vapor deposition of high quality silicon and germanium. Tubular reactors, where reactant gases pass across the growing surface, have been used for silicon deposition from SiCl_4 (alternatively, SiHCl_3 or SiCl_2) in excess hydrogen. Experimental studies in these systems have included spectroscopic identification of gas phase species and measurement of composition, temperature, and velocity profiles in the diffusion layer adjacent to the susceptor surface (1-4).

A theoretical analysis of silicon deposition in a tubular flow reactor has considered the effects of heat, mass, and momentum transfer (5). However, the complex nature of the transport processes necessitated incorporation of certain assumptions, such as constant physical properties and fully developed flow profiles, into the model.

The rotating disk has been used to study chemical vapor deposition because the hydrodynamics and mass transfer characteristics of this system are relatively well understood. A one-dimensional model has been developed for the transport-limited reaction of iodine and germanium (6). This analysis includes the effects of density variations in the boundary layer, multicomponent diffusion, and finite interfacial velocity. However, it is assumed that the system is isothermal and that the axial velocity depends linearly on the distance from the disk surface. Epitaxial growth of silicon has also been studied by the rotating disk method (7). The model includes natural convection and temperature variations but it assumes constant physical properties and equilibrium in the gas phase, and it is not able to account fully for the experimentally observed temperature dependence of silicon growth rate.

This paper presents a general approach to the analysis of silicon deposition on a rotating disk. The model considers multicomponent heat and mass transfer, coupled with laminar fluid flow, and simultaneous homogeneous and heterogeneous reactions with finite reaction rates. Variable physical properties are included, as well as a finite interfacial velocity at the disk surface. The analysis can be used to investigate the influence of disk temperature and rotation rate on the deposition process and to consider the rate-limiting factors in the system. The formulation of the silicon deposition problem has been developed in

a general manner so that it can be readily applied to a wide variety of different physical situations.

Transport Phenomena

Momentum, heat, and mass transfer for a rotating disk are modeled subject to the following restrictions: (i) steady-state operation, (ii) laminar flow of Newtonian fluid, (iii) no viscous dissipation of energy, (iv) radiation and natural convection neglected, (v) no end effects, and (vi) ideal gas mixture. These assumptions simplify the calculational procedure significantly. The ideal gas condition is necessary in the absence of information required to justify a more sophisticated equation of state. The validity of assumptions (iv) and (v) is discussed below.

With these restrictions, it can be shown that the velocity component normal to the disk, and the gas composition, depend only on the axial coordinate, so that the surface is uniformly accessible from a mass transfer standpoint. Consequently, the transport properties are also independent of radial position, and the problem becomes one-dimensional.

The transformation of von Kármán (8) suggests that, with cylindrical coordinates, the velocity components and the pressure can be expressed as (9)

$$\left. \begin{aligned} v_r &= r\Omega F(\zeta), & v_\theta &= r\Omega G(\zeta), & v_z &= \sqrt{\nu_\infty \Omega} H(\zeta) \\ p &= \mu_\infty \Omega P(\zeta) + g_z \int_0^z \rho dz \end{aligned} \right\} \quad [1]$$

where

$$\zeta = z\sqrt{\Omega/\nu_\infty} \quad [2]$$

and where the direction of gravitational acceleration is taken to be perpendicular to the disk surface. Equation [1] defines dimensionless functions F , G , H , and P and shows how velocity components and pressure depend on disk rotation speed and on the coordinates for radial and axial position, r and ζ .

The steady-state equations of motion and continuity of the fluid are

$$\rho \underline{v} \cdot \nabla \underline{v} = -\nabla p - \nabla \cdot \underline{\tau} + \rho \underline{g} \quad [3]$$

$$\nabla \cdot (\rho \underline{v}) = 0 \quad [4]$$

where the viscous stress for a Newtonian fluid is

$$\underline{\tau} = -\mu[\nabla \underline{v} + (\nabla \underline{v})^T] + \frac{2}{3}\mu I \nabla \cdot \underline{v} \quad [5]$$

Substitution of Eq. [1] into Eq. [3] and [4], gives

$$2F + H' = -H \frac{d \ln \rho}{d\zeta} \quad [6]$$

* Electrochemical Society Active Member.

¹ Present address: Department of Chemical Engineering, University of Houston, Houston, Texas 77004.

Key words: silicon deposition, rotating disk, chemical vapor deposition of silicon, modeling.

for the continuity equation and, with Eq. [5]

$$\left. \begin{aligned} F^2 - G^2 + HF' &= -\frac{\rho_\infty}{\rho} \frac{d}{d\zeta} \left(\frac{\mu F'}{\mu_\infty} \right) \\ 2FG + HG' &= \frac{\rho_\infty}{\rho} \frac{d}{d\zeta} \left(\frac{\mu G'}{\mu_\infty} \right) \end{aligned} \right\} \quad [7]$$

$$\frac{\rho}{\rho_\infty} HH' + P' = \frac{4}{3} \frac{d}{d\zeta} \left[\frac{\mu}{\mu_\infty} (H' - F) \right] + \frac{2\mu F'}{\mu_\infty} \quad [8]$$

for the equations of motion (10). The boundary conditions include

$$\left. \begin{aligned} F = 0, \quad G = 1 & \quad \text{at } \zeta = 0 \\ F = G = 0 & \quad \text{at } \zeta = \infty \end{aligned} \right\} \quad [9]$$

In addition, the normal velocity component is related to the mass transfer rate at the surface by the definition for the mass average velocity

$$\underline{v} = \frac{1}{\rho} \sum_i M_i \underline{N}_i \quad [10]$$

where N_i is the molar flux of species i .

The fluid density ρ , used in the equations above, is directly related to total gas concentration by

$$\rho = \bar{M}c \quad [11]$$

where $\bar{M} = \sum_i x_i M_i$. The concentration is, in turn, related to pressure with the ideal gas law

$$p = cRT \quad [12]$$

A steady-state, thermal energy equation for an ideal gas mixture can be rewritten as (11)

$$c\tilde{C}_p \underline{v} \cdot \nabla T = \nabla \cdot (k\nabla T) + \underline{v} \cdot \nabla p - \sum_i (\underline{J}_i \cdot \nabla \bar{H}_i + \bar{H}_i R_i) \quad [13]$$

provided that viscous energy dissipation and the Dufour energy flux can be neglected. The last term on the right represents thermal effects due to interdiffusion of species and homogeneous chemical reactions, \underline{J}_i is the flux of species i relative to the mass average velocity, given by

$$\underline{J}_i = \underline{N}_i - c_i \underline{v} \quad [14]$$

and \tilde{C}_p is the mean specific heat of the mixture, defined as

$$\tilde{C}_p = \sum_i x_i \tilde{C}_{pi} \quad [15]$$

Equation [13] can be expressed in dimensionless form as

$$\frac{\tilde{C}_p}{\tilde{C}_{p\infty}} HT' = \frac{T}{Pr_\infty T_\infty} \left[\frac{k}{\kappa_\infty} T'' + T' \frac{d(k/k_\infty)}{d\zeta} \right] + \frac{RTH}{\tilde{C}_{p\infty}} \frac{d \ln p}{d\zeta} + \frac{sTT'}{T_\infty} + UT \quad [16]$$

The dimensionless quantities Pr_∞ , s , and U are defined by

$$Pr = \frac{p\mu_\infty \tilde{C}_{p\infty}}{p_\infty \kappa_\infty \bar{M}_\infty} \quad [17]$$

$$s = \frac{-p_\infty \sum_i J_i \tilde{C}_{pi}}{p \tilde{C}_{p\infty}} \quad [18]$$

and

$$U = -\frac{p_\infty \sum_i \tilde{H}_i^* R_i}{p T_\infty \tilde{C}_{p\infty}} \quad [19]$$

respectively, where $J_i = \underline{J}_i/c_\infty \sqrt{\nu_\infty \Omega}$, $R_i = R_i/c_\infty \Omega$, and $\tilde{H}_i = \tilde{H}_i^*$ for an ideal gas. The temperatures of the disk and the bulk fluid are specified as boundary conditions for Eq. [16].

The multicomponent diffusion equation (11)

$$c_i \left(\nabla \mu_i + \bar{S}_i \nabla T - \frac{M_i \nabla p}{\rho} \right) = RT \sum_{k \neq i} \frac{c_i c_k}{c D_{ik}} \left[\underline{v}_k - \underline{v}_i + \left(\frac{D_k T}{\rho_k} - \frac{D_i T}{\rho_i} \right) \nabla \ln T \right] \quad [20]$$

describes the motion of species i relative to the surrounding fluid. If thermal diffusion is assumed to be negligible, and if the gas mixture behaves ideally, Eq. [20] may be written in dimensionless form as

$$\nabla x_i + x_i \left(1 - \frac{M_i}{\bar{M}} \right) \nabla \ln p = \sum_{k \neq i} \frac{x_i J_k - x_k J_i}{D_{ik}} \quad [21]$$

where D_{ik} is a dimensionless transport property for binary interactions, defined as $D_{ik} = c D_{ik}/c_\infty \nu_\infty$. For a mixture of n species, there are $(n - 1)$ independent force balances in the form of Eq. [21], and there are $\frac{1}{2} n(n - 1)$ independent transport properties because D_{ii} is not defined and, by Newton's third law of motion, $D_{ik} = D_{ki}$.

A steady-state material balance in the gas phase is

$$\nabla \cdot \underline{N}_i = R_i \quad [22]$$

where R_i is the net homogeneous rate of production of species i .

Equation [21] can be inverted numerically to give explicit expressions for the fluxes, which can then be substituted into Eq. [22] to give a dimensionless material balance

$$\frac{d^2 x_i}{d\zeta^2} = \sum_{k \neq i} \left[\frac{x_i R_k - x_k R_i}{D_{ik}} - \frac{cH}{c_\infty D_{ik}} \left(x_i \frac{dx_k}{d\zeta} - x_k \frac{dx_i}{d\zeta} \right) + J_k \frac{d}{d\zeta} \left(\frac{x_i}{D_{ik}} \right) - J_i \frac{d}{d\zeta} \left(\frac{x_k}{D_{ik}} \right) \right] \quad [23]$$

for the one-dimensional problem considered here. There are $n - 1$ independent force balances with the form of Eq. [23] which can be used, in conjunction with the relationship between the fluxes

$$\sum_i M_i J_i = 0 \quad [24]$$

to describe mass transfer in a multicomponent system.

In this way, it is possible to incorporate the conservation conditions while still leaving the overall continuity Eq. [4] to be counted as one of the hydrodynamic equations. Furthermore, arbitrary selection of one component is not required in order to replace a species material balance with Eq. [24] or to invert the Stefan-Maxwell relations [21].

At the disk surface, $n - 1$ Stefan-Maxwell relations, Eq. [21], are used, together with the relationship between mole fractions, $\sum_i x_i = 1$. Far from the disk, the compositions approach their equilibrium values at the bulk fluid temperature.

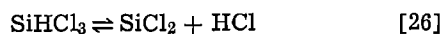
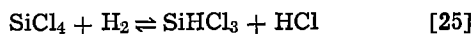
Chemical Reactions

The equations derived above, which describe the transfer of heat, mass, and momentum for a disk ro-

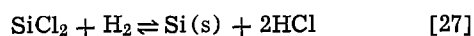
tating in an infinite medium, can be used to predict the behavior of systems with an arbitrary number of homogeneous and heterogeneous reactions.

To illustrate the use of this technique, epitaxial deposition of silicon from an input mixture of SiCl_4 in excess hydrogen is analyzed. Thermodynamic studies indicate that, for the temperature range of interest, five principal species are present in the gas phase: H_2 , HCl , SiCl_4 , SiHCl_3 , and SiCl_2 (12). Dichlorosilane (SiH_2Cl_2) has also been detected under some experimental conditions, but this species is not considered explicitly in the present study.

Several mechanisms have been proposed for the formation of silicon from SiCl_4 (2, 13, 14). Here, it is assumed that SiCl_4 can be reduced either homogeneously or heterogeneously by the following reversible reactions



On the surface, the deposition reaction



can also take place. This mechanism may need to be refined subsequently to match experimentally observed behavior.

The net rate of each reaction is regarded as the difference between the rates of forward and backward reactions and can be represented as

$$r_i = k_{if} \prod_i x_i^{\nu_{i1}} - k_{ib} \prod_i x_i^{-\nu_{i1}} \quad [28]$$

$\nu_{i1} > 0 \quad \nu_{i1} < 0$

where k_{if} and k_{ib} are rate constants for forward and backward reactions, respectively. The exponent ν_{i1} is the stoichiometric coefficient for species i in reaction 1. It is positive for reactants and negative for products and may be obtained from Eq. [25]-[27], which are assumed to be elementary reaction steps.

The temperature dependence of the rate constants in Eq. [28] is assumed to be given by

$$k_{ib} = A_i e^{-E_i/T} \quad [29]$$

where E_i can be regarded as an activation energy for reaction 1.

In the model, five independent parameters are used to describe the kinetic behavior: E_a ; $\theta_1 = k_{3b}/k_{1b}$; $\theta_2 = k'_{2b}/k'_{1b}$; $\theta_3 = k_{1b}^2 e^{E_a/T_s}/c_{\infty} \nu_2 k'_{1b}$; $\theta_4 = 10^2 e^{-E_a/T_s} c_{\infty} \Omega/k'_{2b}$. The term E_a represents an activation energy for the deposition process. Different activation energies could be chosen for each reaction but it is assumed that the temperature dependence of the deposition rate will be influenced more by the activation energy for the rate-limiting step than by the activation energies for the other reactions. The parameters θ_1 and θ_2 describe the relative rates of the two heterogeneous and the two homogeneous reactions, respectively. θ_3 is a ratio of the rates of the heterogeneous and homogeneous reactions and θ_4 specifies the rate of homogeneous production of SiCl_2 , as described by Eq. [26], relative to the mass transfer rate characterized by the disk speed, Ω .

The forward and backward rate constants are related by an equilibrium constant $K_1 = k_{1b}/k_{1f}$, which is defined in terms of equilibrium reactant and product compositions as

$$K_1 = p^m \prod_i x_{ie}^{-\nu_{i1}} \quad [30]$$

In Eq. [30], the activity of any solid phase is taken to be unity, and m represents the net number of molecules produced by reaction 1. The temperature dependence of k_{1f} is predicted from standard heats of reaction $\Delta H(T)$, with

$$\left[\frac{\partial \ln K_1}{\partial (1/T)} \right]_p = -\Delta H(T)/R \quad [31]$$

and from free energy data at 25°C (15), to give expressions of the form

$$\ln K_1 = \alpha_1 + \beta_1/T + \gamma_1 \ln T \quad [32]$$

The coefficients α_1 , β_1 , γ_1 , used for the reactions are summarized in Table I.

In the gas phase, the net rate of production of species i is given as

$$R_i = \sum_j \nu_{ij} r_j \quad [33]$$

At the surface, a similar summation for the heterogeneous reactions represents the molar flux N_i from the surface relative to the interface. The variables N_i and R_i link the rates of the individual reactions to the equations that describe heat, mass, and momentum transfer for the rotating disk.

Interactions among the governing differential equations are caused directly by the inclusion of a finite interfacial velocity (see Eq. [10]) and variable physical properties in the analysis. Relationships for the temperature and composition dependences of physical parameters needed in the model are summarized in the Appendix.

For the example of chemical vapor deposition of silicon, with five species in the gas phase, the steady-state behavior is described by a set of 15 coupled, nonlinear, ordinary differential equations. These equations, subject to specified boundary conditions, can be solved numerically by a finite difference technique accurate to $0(h^2)$ (11, 16, 17). The model can be used to study the influence of process variables on the rate of silicon deposition and on the profiles for compositions, velocities, and temperature in the diffusion layer. Parameters that must be specified in the model include surface and bulk temperatures, inlet gas composition, disk rotation rate, and operating pressure.

Results and Discussion

Preliminary computer simulations indicated that pressure variations through the diffusion layer are small and that they do not affect the overall behavior significantly. Consequently, results are presented for a constant operating pressure, which is taken to be 1.013 bar. In addition, the influence of bulk gas composition is not considered explicitly in this study, and results are for an inlet gas mixture of 1 mole percent SiCl_4 in hydrogen. The values chosen for pressure and composition correspond to standard operating conditions for chemical vapor deposition of silicon (5).

A typical composition profile, with the disk temperature controlled at 1473°K and a bulk gas temperature of 293°K, is shown in Fig. 1. The gas mixture is assumed to be at equilibrium at the bulk temperature, far from the disk. Closer to the surface, the mole fractions alter in response to the specified homogeneous and heterogeneous reactions.

Spectroscopic methods have been used to measure composition profiles in the diffusion layer for silicon deposition in a horizontal channel reactor, where reactant gases flow over the susceptor surface (3, 4). These measurements indicate the presence of a maximum in SiCl_2 concentration approximately 2 mm from the surface. The magnitude of the maximum mole

Table I. Equilibrium constants for silicon deposition reactions: coefficients for Eq. [32]

	α_1	β_1	γ_1
K_1	16.2412	-6730.9	-1.7004
K_2 (atm)	14.9848	-30520.7	0.5032
K_3	-1.0685	2229.3	-0.1756

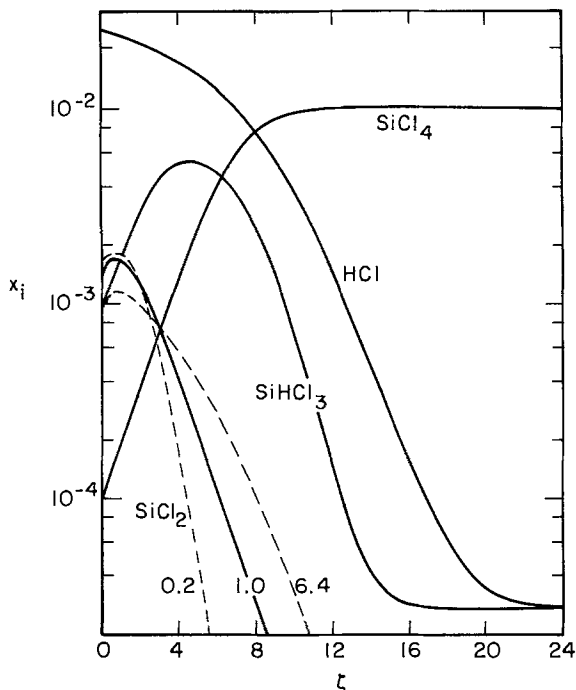


Fig. 1. Typical composition profiles in diffusion layer adjacent to rotating disk. Parameter values: $T_s = 1473^\circ\text{K}$; $T_\infty = 293^\circ\text{K}$; $\Omega_b = 12.57 \text{ rad/sec}$; $p_\infty = 1.013 \times 10^5 \text{ N/m}^2$; $(x_{\text{H}_2})_\infty = 0.99$; $\theta_1 = 25.0$; $\theta_2 = 10.0$; $\theta_3 = 1.25$; $\theta_4 = 5/6$; $E_a = 1258.18^\circ\text{K}$. Dashed lines represent x_{SiCl_2} profiles for different disk speeds, Ω/Ω_b .

fraction becomes larger further from the leading edge of the crystal. Analogous behavior is expected with the rotating disk system since smaller rotation rates, and hence larger diffusion layers, should correspond, at least qualitatively, to positions further downstream in the channel flow reactor. This is exemplified by the dashed lines in Fig. 1 which show the position dependence of SiCl_2 mole fraction calculated at rotation rates larger and smaller than the base value. In addition, the model predicts a maximum in the SiHCl_3 composition profile, at greater distances from the disk surface than the SiCl_2 maximum.

Figure 1 is calculated for a particular set of kinetic parameters that give a qualitative match between theoretical and experimental composition profiles. The relative importance of each parameter is discussed below in the context of rotation rate and surface temperature effects. However, it is noted here that in order to obtain a maximum in SiCl_2 composition it is necessary to eliminate the possibility for heterogeneous SiCl_2 production. This is in keeping with some mechanisms that have been postulated for the deposition process.

An approximate estimate of the diffusion layer thickness can be obtained from the composition profiles, even though some species reach their bulk compositions closer to the surface than others. For the example in Fig. 1, an approximate thickness is 5 cm, which is considerably larger than values of 10^{-2} - 10^{-3} cm often encountered with electrolyte solutions.

If the size of the disk and the diffusion layer are comparable, it is necessary to consider the influence of radial effects on observed deposition rates. A singular perturbation analysis of the elliptic region at the edge of a rotating disk that results from radial diffusion has been developed previously for fluids with high Schmidt numbers (18). This approach can be generalized to give the ratio λ of overall mass transfer rates, with and without radial diffusion effects, as

$$\lambda = 1 + 1.9193\text{Re}^{-3/4}\text{Sc}^{-1/4} \quad [34]$$

for any fluid but for large values of $\text{ScRe}^{3/2}$. With average values for physical properties and with $\Omega =$

12.57 rad/sec and $r_0 = 2.5 \text{ cm}$, it may be shown that $\lambda \approx 1.1$. This analysis indicates that radial effects can contribute to an increase in overall silicon deposition rate under these conditions, although at higher rotation rates the influence of edge effects will be reduced, in accordance with Eq. [34].

For the operating conditions used in Fig. 1, the variations of some physical properties are shown in Fig. 2. The density changes by a factor of 6 across the diffusion layer in direct association with changes in T and \bar{M} . Viscosity and thermal conductivity both vary by factors of about 3. This leads to a maximum in the axial velocity profile in the boundary layer, as illustrated in Fig. 3. In this example, the magnitude of the interfacial velocity, which arises from chemical reactions at the disk surface, is -2.0 mm/sec . An assumption of zero interfacial velocity can lead to errors of approximately 1-6% in deposition rate, dependent on the process conditions.

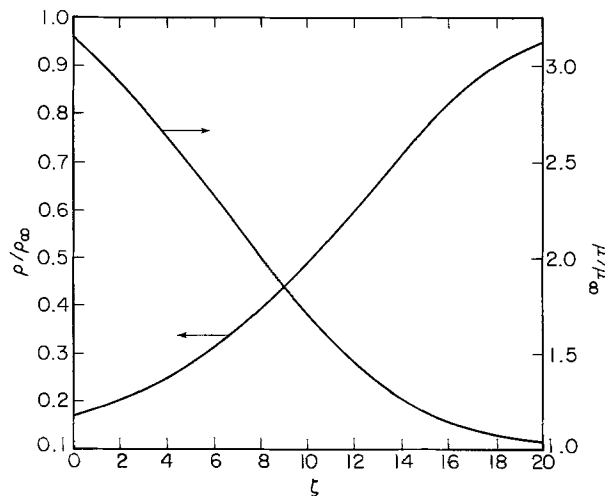


Fig. 2. Dependence of viscosity and density on distance from surface of rotating disk. Parameter values as for Fig. 1. $\rho_\infty = 0.1536 \text{ kg/m}^3$; $\mu_\infty = 9.602 \times 10^{-6} \text{ kg/m} \cdot \text{sec}$.

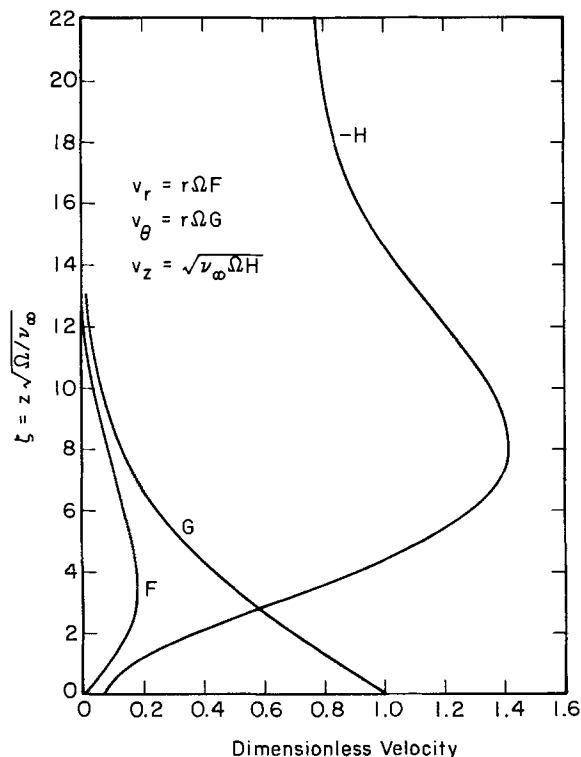


Fig. 3. Velocity profiles for silicon deposition on a rotating disk. Parameter values as for Fig. 1 and 2.

Measurements of silicon deposition rates at various susceptor temperatures and for a fixed rotation speed show that there are two regimes of temperature behavior in the range 1273°–1523°K. At higher temperatures an apparent activation energy for deposition lies in the range 4–13 kJ/mole, whereas at lower temperatures it is reported as 90–125 kJ/mole (7). This change in temperature dependence is attributed to a shift from reaction rate control to mass transfer control as the disk temperature is raised.

An experimental curve, obtained with a rotation rate of 12.5 rad/sec, is given in Fig. 4, where the parameter S represents the actual deposition rate, made dimensionless with the quantity $c_x \sqrt{\nu_s \Omega}$. The dashed line is the locus of maximum deposition rates calculated with the mathematical model. It can be regarded as a combined thermodynamic-mass transfer limit since, for this curve, the reactions are locally at equilibrium but the finite mass transfer rate through the diffusion layer limits the fraction of the bulk fluid that can reach the disk surface.

There are several possible explanations for the discrepancy between the thermodynamic-mass transfer limit and experimental results at high temperatures. First, errors in estimates of collision diameters and interaction energies for some combinations of species could lead to incorrect predictions of physical properties such as diffusion coefficients and viscosity (see Appendix). Errors may also arise from incorrect predictions of equilibrium constants (see Table I). A thermodynamic evaluation of the Si-H-Cl system shows that the parameters K_1 are particularly sensitive to the standard heat of formation of SiHCl_3 (12).

Radial effects can lead to enhanced mass transfer rates. However, it has been shown (see below Eq. [34]) that the magnitude of this effect is insufficient to account fully for the differences between experiment and theory. Nevertheless, it should be noted that the analysis of radial dependences does not consider the influence of hydrodynamic disturbances that could arise from axial motion at the disk edge.

Even though inlet gases are at 293°K, the wall temperature in the experiment is recorded as 673°K (7) and heat transfer between the disk and walls and the

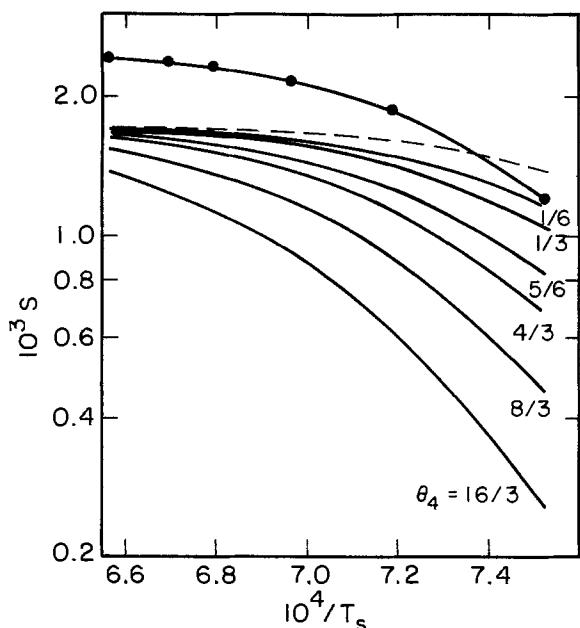


Fig. 4. Dependence of dimensionless silicon deposition rate on disk temperature. S = actual deposition rate/ $c_x \sqrt{\nu_s \Omega}$. Dotted line: experimental data (7), $\Omega = 12.57$ rad/s-c. Dashed curve: thermodynamic-mass transfer limit for deposition rate. Full curves: theoretical predictions for different values of θ_4 , with other parameters as in Fig. 1-3.

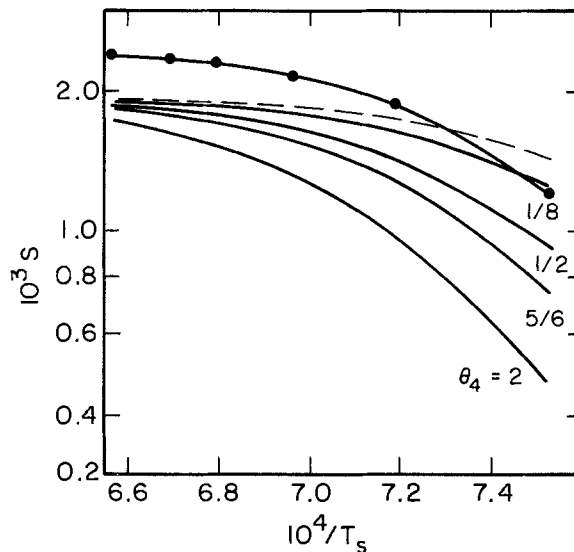


Fig. 5. Dependence of dimensionless silicon deposition rate on disk temperature. As Fig. 4, but $T_w = 673^\circ\text{K}$.

inlet gas (e.g., by radiation) could raise the bulk gas temperature substantially. Figure 5 shows the temperature dependence of dimensionless deposition rate with $T_w = 673^\circ\text{K}$. The discrepancy between experimental results and the thermodynamic-mass transfer limit is reduced with this new boundary condition, but significant differences still exist.

Another possible explanation for the enhanced mass transfer rate is natural convection. The ratio

$$\frac{\text{Gr}}{\text{Re}^2} = \frac{(T_s - T_w)g}{T_{\text{av}}\Omega^2 r_0} \quad [35]$$

can be used to represent the ratio of buoyancy forces to viscous forces in the system. With $T_s - T_w = 1200^\circ\text{K}$, $T_{\text{av}} = 1000^\circ\text{K}$, $r_0 = 2.5$ cm, and $\Omega = 12.57$ rad/sec, this ratio is approximately 3.0. For an upward-facing disk, it has been shown (1) that natural convection is the dominant heat transfer mechanism for $\text{Gr}/\text{Re}^2 > 4.1$ and that forced convection dominates when $\text{Gr}/\text{Re}^2 < 0.4$. Consequently, for the disk considered in the example, there will be a transition region for $10.72 < \Omega$ (rad/sec) < 34.31 . Unfortunately, experimental information for silicon deposition on a rotating disk is only available for conditions where natural convection could be important. Therefore an exact match between experimental results and theoretical predictions based on forced convection should not be expected. Nevertheless, under different conditions, such as larger disks and higher rotation rates, the model presented will have greater quantitative significance.

Despite the uncertainty in the absolute magnitude of the deposition rate, Fig. 4 and 5 both show that the thermodynamic-mass transfer limit does not adequately explain the temperature dependence of the deposition rate over the whole temperature range considered. With finite kinetic parameters it is possible to obtain a satisfactory match between the shapes of the theoretical and experimental curves. In Fig. 4 and 5, the kinetic parameters θ_1 , θ_2 , θ_3 , and E_a are fixed, and θ_4 is varied. The sets of curves can be interpreted as showing the effect of variations either in rotation rate at fixed k_2 or in k_2 at fixed Ω . Inspection of Fig. 4 ($T_w = 293^\circ\text{K}$) shows that a value of $\theta_4 = 5/6$ provides a reasonable fit between the shapes of the experimental and theoretical curves. As the surface temperature is decreased, the $\theta_4 = 5/6$ curve moves away from the thermodynamic-mass transfer limit and the deposition rate becomes more dependent on kinetic factors. However, as T_s is reduced further, equilibrium limitations are expected to become important again and eventually, below a surface temperature of approximately

1108°K, silicon deposition will no longer be thermodynamically feasible.

It is necessary to consider the sensitivity of the results to the values chosen for the kinetic parameters. Figures 6 and 7 show predicted temperature dependences for different values of E_a , with fixed values of θ_1 and θ_2 and with the value of θ_3 matched at 1473°K for the different activation energies. The diagrams show that the overall shapes of the curves do not depend noticeably on E_a for $0 \leq E_a \leq 6290.90$.

Variations in θ_1 and θ_3 cause relatively small changes in calculated temperature profiles, for fixed values of θ_2 , θ_4 , and E_a . Changes in θ_2 have a more noticeable effect but, as with alterations in E_a , it merely shifts the value of θ_4 which best fits the shape of the experimental curve. From these results it is evident that the dependence of silicon deposition rate on temperature alone is insufficient to be able to predict the most appropriate values for the kinetic parameters.

Information is also available on the dependence of deposition rate on disk speed (7). Figure 8 shows experimental results and theoretical predictions with the same kinetic parameters (θ_1 , θ_2 , θ_3 , E_a) that were used in Fig. 4. The deposition rate S_b is made dimensionless with a specified rotation rate Ω_b which is taken as 26.18 rad/sec, close to the midpoint in the range of experi-

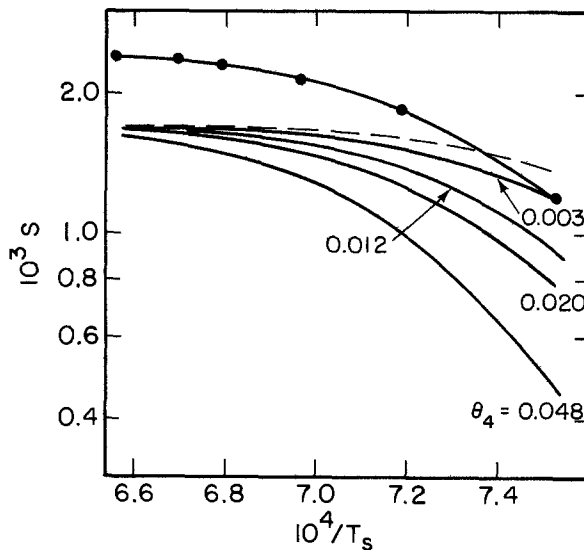


Fig. 6. Dependence of dimensionless silicon deposition rate on disk temperature. As Fig. 4, but $E_a = 6290.90^\circ\text{K}$ and $\theta_3 = 38.071$.

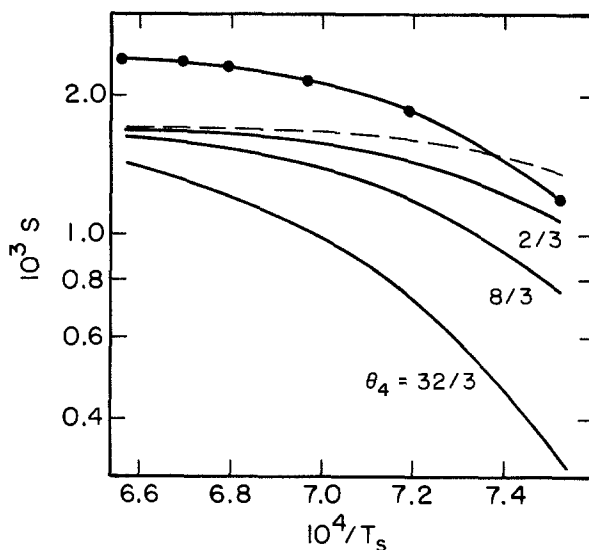


Fig. 7. Dependence of dimensionless silicon deposition rate on disk temperature. As Fig. 4, but $E_a = 0$ and $\theta_3 = 0.5321$.

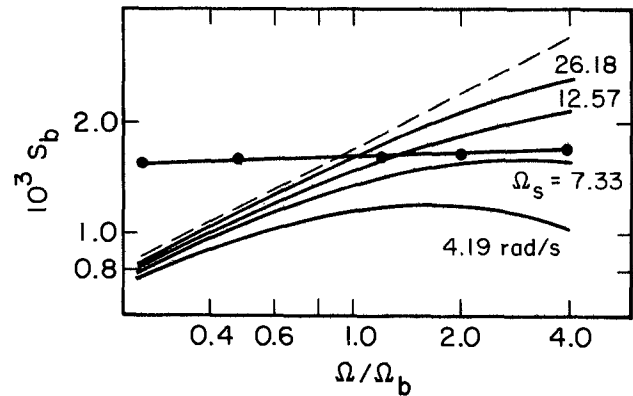


Fig. 8. Dependence of dimensionless silicon deposition rate on disk speed. $S_b = 5 \sqrt{\Omega/\Omega_b}$. Dotted line: experimental data $T_s = 1473^\circ\text{K}$. Dashed curve: thermodynamic-mass transfer limit for deposition rate. Full curves: theoretical predictions for different values of Ω_s (equivalent to θ_4). Parameter values: $T_s = 1473^\circ\text{K}$; $T_\infty = 293^\circ\text{K}$; $\Omega_b = 26.18$ rad/sec; $p_\infty = 1.013 \times 10^5$ N/m²; $(x_{\text{H}_2})_\infty = 0.99$; $\theta_1 = 25.0$; $\theta_2 = 10.0$; $\theta_3 = 1.25$; $E_a = 1258.18^\circ\text{K}$.

mental data. The parameter Ω_s , which equivalent to θ_4 , represents the rotation rate which corresponds to the curve that best fits the shape of the data in Fig. 4. (For example, a stipulation that the best curve in Fig. 4 has a rotation rate of 12.57 rad/sec yields the curve $\Omega_s = 12.57$ rad/sec on Fig. 8.) From the standpoint of temperature dependence, it would seem most acceptable to choose $\Omega_s = 12.57$, since this is the rotation rate at which the experiments were performed. However, this curve follows the thermodynamic-mass transfer limit too closely in Fig. 8 and does not match the experimental data, which are almost independent of rotation rate.

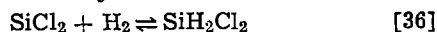
At low speeds, mass transfer control might be expected, as illustrated by the thermodynamic-mass transfer limit ($S_b \propto \sqrt{\Omega}$), whereas at higher speeds the rotation rate dependence could change markedly as reaction rate control is approached. A higher disk speed not only raises the rate at which reactants can reach the disk surface, but it also affects the rate at which intermediate species in the reaction sequence can be convected away from the disk. In addition, the relative importance of the homogeneous and heterogeneous reactions can shift as Ω is changed. Consequently, it is conceivable that, under some circumstances, an increase in Ω could lead to a reduction in deposition rate.

These effects become apparent as the parameter is reduced below $\Omega_s = 12.57$ rad/sec. At $\Omega_s = 7.33$ rad/sec, the theoretical curve rises from the thermodynamic-mass transfer limit to the experimental line as the rotation rate is increased. Below 26.18 rad/sec, the experimentally observed behavior cannot be matched because the results lie above the predicted limit. This may be due to error in the assessment of the thermodynamic-mass transfer curve as discussed earlier and, in particular, it might result from natural convection which would be expected to be more important at low disk speeds. Therefore, it is possible that, for these experimental conditions, there is no range of rotation rates for which forced convection mass transfer controls the system behavior. Furthermore, Fig. 8 is practically unchanged for modest changes in kinetic parameters, and it is not possible to choose different values for θ_1 to θ_4 or E_a which would provide a substantially better fit of the experimental data. It should also be noted that natural convection could alter the shapes of the temperature curves in Fig. 4, as well as the absolute value of the thermodynamic-mass transfer limit.

Notwithstanding the possible influence of natural convection, prediction of a consistent set of kinetic

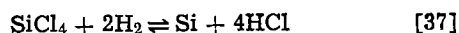
parameters, which fit the observations, is hampered by the relatively short ranges of T_s and Ω for which data are available. Also the surface temperature in Fig. 8 lies, ostensibly, in a mass transfer controlled region, and therefore one should not expect to be able to use this information to obtain well-defined kinetic information. In principle, it should be possible to use experimental data in the reaction controlled regime to obtain better estimates of the kinetic constants.

It is also necessary to assess the extent to which the predicted behavior is influenced by the assumed reaction mechanism. The mechanism proposed includes homogeneous and heterogeneous production of SiHCl_3 , homogeneous decomposition of SiHCl_3 to give SiCl_2 , and reduction of SiCl_2 on the disk surface to yield silicon. Under some circumstances, significant quantities of SiH_2Cl_2 can be present in the gas phase (12). This could be produced by

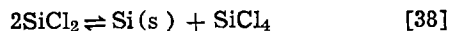


and it could decompose on the surface to give silicon directly. Consequently, it might be regarded as an intermediate in the overall conversion of SiCl_2 to silicon so that inclusion of SiH_2Cl_2 in the model would not be expected to alter the predictions significantly. Incorporation of SiH_2Cl_2 as an additional species would not cause operational difficulties with the model but it would necessitate additional equilibrium data and consideration of another independent kinetic parameter.

Direct reactions of the form



have not been included because they are kinetically less favorable than the elementary processes used in the analysis. An additional reaction which could be included in more sophisticated studies of reaction mechanisms involves disproportionation of SiCl_2 according to



Again, an additional kinetic parameter would be needed in the model.

The rate-determining step for the reaction sequence considered (Eq. [25]-[27]) is thought to be homogeneous production of SiHCl_3 (Eq. [25]). Heterogeneous formation of SiHCl_3 becomes more important when the bulk gas temperature is higher. The basis for this postulate is that, for the range of T_s and Ω considered, the relative rate of the backward and forward reaction was consistently smallest for this step. This theory is supported by observations of higher deposition rates from SiHCl_3 , rather than SiCl_4 , under parallel experimental conditions (19).

Conclusions

A model has been developed which describes the interactions among hydrodynamics, multicomponent heat and mass transport, and reaction kinetics for the rotating disk system. The analysis includes variable physical properties, finite interfacial velocity, and simultaneous homogeneous and heterogeneous reactions.

This model has been used to study chemical vapor deposition of silicon from SiCl_4 in excess hydrogen. The effects of disk speed and temperature on the silicon deposition rate have been investigated, and several features of the process have been elucidated:

1. The diffusion layer thickness is 1-10 cm, which is considerably larger than values commonly encountered for liquid systems. Nevertheless, radial diffusion does not affect predicted mass transfer rates markedly.

2. Physical properties, such as density and viscosity, vary by factors of between 3 and 6, through the diffusion layer. This distorts the fluid flow profile and gives a maximum in the axial velocity.

3. With five gas-phase species and a set of five independent kinetic parameters, the shape of the pre-

dicted temperature dependence of deposition rate matches experimental results. At high surface temperatures, a combined mass transfer and thermodynamic limit controls the deposition rate, but as the disk temperature is lowered kinetic limitations gradually became more important. At much lower temperatures, thermodynamic considerations again dominate, and deposition is no longer feasible below approximately 1108°K. However, effects not included in the model, such as natural convection, could be responsible for discrepancies in absolute magnitudes of predicted and observed deposition rates and in the influence of disk speed on the system behavior. Furthermore, the kinetic parameters cannot be specified uniquely from the limited experimental data available.

4. Homogeneous and heterogeneous reactions are both important in chemical vapor deposition of silicon. For the range of conditions studied, the rate-limiting step is found to be formation of the intermediate species SiHCl_3 , by reduction of SiCl_4 .

Acknowledgment

This work was supported by the Division of Solar, Geothermal, Electric and Storage Systems, Office of the Assistant Secretary for Energy Technology, U.S. Department of Energy.

Manuscript received June 29, 1979.

Any discussion of this paper will appear in a Discussion Section to be published in the December 1980 JOURNAL. All discussions for the December 1980 Discussion Section should be submitted by Aug. 1, 1980.

Publication costs of this article were assisted by The University of California.

APPENDIX

Physical Properties

Viscosity.—The temperature dependence of the viscosity of each species in the gas phase is predicted from the Chapman-Enskog kinetic theory (10)

$$\mu_i = \frac{2.6693 \times 10^{-5} \sqrt{M_i T}}{\sigma_i^2 \Omega_{\mu i}} \quad [A-1]$$

The parameter σ_i is the collision diameter, and $\Omega_{\mu i}$ is a dimensionless function which depends on kT/ϵ_i , where ϵ_i is a characteristic energy of interaction between molecules and k is Boltzmann's constant. For each species, Eq. [A-1] is rewritten in the simplified form

$$\mu_i = \delta_{1i} T^{\psi_{1i}} \quad [A-2]$$

and values for δ_{1i} and ψ_{1i} are given in Table II. The viscosity of the gas mixture is calculated with the Wilke correlation (20)

$$\mu_{\text{mix}} = \sum_{i=1}^n \left(x_i \mu_i \right) / \sum_{i=1}^n x_i \Phi_{ij} \quad [A-3]$$

where

$$\Phi_{ij} = [1 + (\mu_i/\mu_j)^{1/2} (M_j/M_i)^{1/4}]^2 / [8 + 8 M_i/M_j]^{1/2}$$

Diffusivity.—Diffusion coefficients for binary interactions are estimated from (10)

$$\frac{c D_{ij}}{\sqrt{T}} = \frac{2.2646 \times 10^{-5} \left(\frac{1}{M_i} + \frac{1}{M_j} \right)^{1/2}}{\sigma_{ij}^2 \Omega_{D,ij}} \quad [A-4]$$

where σ_{ij} is a mean collision diameter which is taken as $(\sigma_i + \sigma_j)/2$. The dimensionless quantity $\Omega_{D,ij}$ is

Table II. Values for parameters in Eq. [A-2] and [A-8]

Species, i	μ_i (Nsec/m ²)		k_i (W/m · °K)	
	$10^7 \delta_{1i}$	ψ_{1i}	δ_{2i}	ψ_{2i}
H ₂	2.05	0.66	2.64×10^{-9}	0.725
HCl	1.06	0.87	7.36×10^{-5}	0.941
SiCl ₄	0.75	0.87	4.10×10^{-5}	0.900
SiHCl ₃	0.70	0.87	1.30×10^{-5}	1.070
SiCl ₂	1.20	0.82	4.10×10^{-5}	0.900

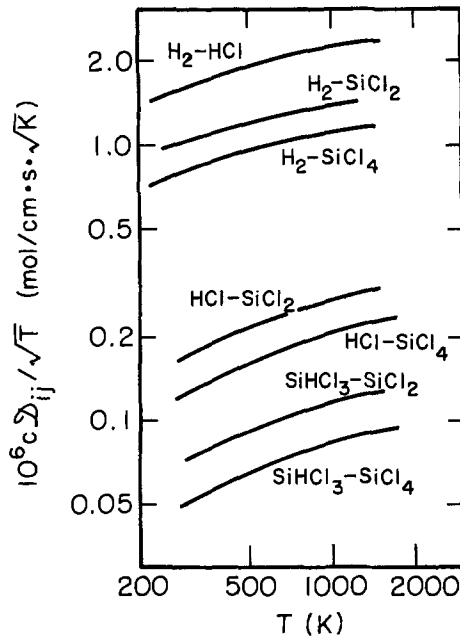


Fig. 9. Temperature dependence of binary diffusion coefficients

analogous to $\Omega_{\mu i}$ used for the viscosity calculations, but the characteristic of the intermolecular potential field should now represent both species i and j , and is assumed to be given by $\epsilon_{ij} = \sqrt{\epsilon_i \epsilon_j}$. Figure 9 shows the temperature dependence of diffusion coefficients obtained from Eq. [A-4]. In the analysis, a simplified form

$$cD_{ij} = B_{ij}T^{1.1} \quad [A-5]$$

is chosen with parameters which best fit the curves in Eq. [9] over the temperature range of interest (see Table III).

Specific heat.—The temperature dependence of the heat capacity of each species is obtained from

$$\tilde{C}_{pi} = \alpha_i + \beta_i T + \gamma_i T^2 \quad [A-6]$$

where the coefficients are summarized in Table IV.

Thermal conductivity.—Eucken's equation for polyatomic gases (10)

$$k_i = (\tilde{C}_{pi} + 5R/4) \frac{\mu_i}{M_i} \quad [A-7]$$

is used to relate the thermal conductivity and viscosity

Table III. Values for parameters in Eq. [A-5] for diffusion coefficients

Species		B_{ij}	l_{ij}
i	j		
H ₂	HCl	4.376×10^{-7}	0.732
H ₂	SiCl ₄	2.190×10^{-7}	0.732
H ₂	SiHCl ₃	2.263×10^{-7}	0.732
H ₂	SiCl ₂	3.117×10^{-7}	0.714
HCl	SiCl ₄	1.523×10^{-8}	0.873
HCl	SiHCl ₃	1.601×10^{-8}	0.873
HCl	SiCl ₂	2.491×10^{-8}	0.845
SiCl ₄	SiHCl ₃	6.109×10^{-9}	0.873
SiCl ₄	SiCl ₂	9.704×10^{-9}	0.845
SiHCl ₃	SiCl ₂	1.039×10^{-8}	0.845

Table IV. Values for parameters in Eq. [A-6] for heat capacities (J/mole · °K)

Species, i	α_i	β_i	γ_i
H ₂	29.086	-8.110×10^{-4}	1.970×10^{-6}
HCl	28.219	1.756×10^{-3}	1.543×10^{-6}
SiCl ₄	81.626	4.346×10^{-2}	-1.817×10^{-5}
SiHCl ₃	61.035	6.477×10^{-2}	-2.472×10^{-5}
SiCl ₂	48.056	1.684×10^{-2}	-7.084×10^{-6}

of each species at a given temperature. An approximate relationship

$$k_i = \delta_{21} T^{0.91} \quad [A-8]$$

is then used to describe the temperature dependence of k_i (see Table II). The thermal conductivity of the mixture is given by an expression analogous to Eq. [A-3]

$$k_{\text{mix}} = \sum_{i=1}^n \left(x_i k_i \left/ \sum_{j=1}^n x_j \Phi_{ij} \right. \right) \quad [A-9]$$

where

$$\Phi_{ij} = [1 + (k_i/k_j)^{1/2} (M_j/M_i)^{1/4}]^2 / [8 + 8 M_i/M_j]^{1/2}$$

LIST OF SYMBOLS

- A_1 preexponential factor for backward rate constant
- c total concentration (mole/cm³)
- c_i concentration of species i (mole/cm³)
- C dimensionless total concentration, c/c_∞
- \tilde{C}_p molar heat capacity of mixture (J/mole · °K)
- \tilde{C}_{pi} molar heat capacity of species i (J/mole · °K)
- D_{ik} diffusion coefficient for binary interactions (cm²/sec)
- D_{ik} dimensionless diffusion coefficient for binary interactions
- D_{kT} thermal diffusivity for species k (kg/m · sec)
- E_a kinetic parameter representing activation energy of rate-limiting step (°K)
- E_l activation energy for reaction l (°K)
- F dimensionless radial velocity defined in Eq. [1]
- g_z gravitational acceleration in z direction (m/sec²)
- G dimensionless angular velocity defined in Eq. [1]
- Gr Grashof number
- h mesh size (m)
- H dimensionless axial velocity defined by Eq. [1]
- \bar{H}_i partial molar enthalpy of species i (J/mole)
- \bar{H}^*_i molar enthalpy of ideal gas (J/mole)
- I unit matrix
- \bar{J}_i flux of species i relative to mass average velocity (mole/m² · sec)
- \tilde{J}_i dimensionless J_i
- k Boltzmann constant (1.3806×10^{-23} J/°K)
- k_i thermal conductivity of species i (W/m · °K)
- k_{1f} forward rate constant for reaction 1
- k_{1b} backward rate constant for reaction 1
- k'_{1b} backward rate constant for homogeneous reaction 1
- K_1 equilibrium constant for reaction 1
- m exponent in Eq. [5]
- \bar{M}_i molecular weight of species i
- \bar{M} average molecular weight
- \bar{N}_i flux of species i (mole/m² · sec)
- \bar{p} gas pressure (N/m²)
- P dimensionless gas pressure
- Pr Prandtl number
- r radial coordinate (m)
- r_1 rate of reaction 1
- r_o disk radius (m)
- R universal gas constant (8.3143 J/mole · °K)
- Re Reynolds number
- R_i rate of homogeneous production of species i (mole/m³ · sec)
- \bar{R}_i dimensionless R_i
- s dimensionless parameter defined by Eq. [18]
- S dimensionless silicon deposition rate
- Sc Schmidt number
- \bar{S}_i partial molar entropy (J/mole · °K)
- T temperature (°K)
- U dimensionless parameter defined by Eq. [19]
- \bar{v} mass average velocity (m/sec)
- \bar{v}_r radial velocity (m/sec)
- \bar{v}_θ angular velocity (m/sec)
- \bar{v}_z axial velocity (m/sec)
- x_i mole fraction of species i
- z axial distance from disk surface (m)

Greek symbols

- ϵ_{ij} maximum energy of attraction between molecules i and j (J)
- ζ dimensionless axial distance coordinate defined by Eq. [2]

θ_k dimensionless kinetic parameter ($k = 1-4$)
 λ parameter defined by Eq. [34]
 μ fluid viscosity (kg/m·sec)
 ν_{ii} stoichiometric coefficient for species i in reaction l
 ν_{∞} bulk kinematic viscosity (m²/sec)
 ρ fluid density (kg/m³)
 σ collision diameter for Lennard-Jones potential (m)
 τ viscous stress tensor (N/m²)
 Ω rotation speed of disk (rad/sec)
 Ω_s shape parameter (rad/sec)

Superscripts

* ideal gas
 — partial molar quantity
 T transpose

Subscripts

l reaction l
 s at surface
 ∞ in bulk

REFERENCES

1. R. Takahashi, Y. Koga, and K. Sugawara, *This Journal*, **119**, 1406 (1972).
2. V. S. Ban and S. L. Gilbert, *ibid.*, **122**, 1382 (1975).
3. V. S. Ban, in "Chemical Vapor Deposition, Sixth International Conference," L. F. Donaghey, P. Rai-Choudhury, and R. N. Tauber, Editors, pp. 66-77, The Electrochemical Society Softbound Proceedings Series, Princeton, N.J. (1977).
4. T. O. Sedgwick, G. V. Arbach, and R. Ghez, *ibid.*, pp. 78-89 (1977).
5. C. W. Manke and L. F. Donaghey, *This Journal*, **124**, 561 (1977).
6. D. R. Olander, *Ind. Eng. Chem. Fundam.*, **6**, 188 (1967).
7. K. Sugawara, *This Journal*, **119**, 1749 (1972).
8. Th. v. Kármán, *Z. Angew. Math. Mech.*, **1**, 233 (1921).
9. J. Newman and L. Hsueh, *Electrochim. Acta*, **12**, 417 (1967).
10. R. B. Bird, W. E. Stewart, and E. N. Lightfoot, "Transport Phenomena," John Wiley & Sons, Inc., New York (1960).
11. J. S. Newman, "Electrochemical Systems," Prentice-Hall, Inc., Englewood Cliffs, N.J. (1973).
12. L. P. Hunt and E. Sirtl, *This Journal*, **119**, 1741 (1972).
13. E. Sirtl, L. P. Hunt, and D. H. Sawyer, *ibid.*, **121**, 919 (1975).
14. J. Nishizawa and N. Nihira, *J. Cryst. Growth*, **45**, 82 (1978).
15. D. R. Stull and H. Prophet, Editors, "JANAF Thermochemical Tables," National Bureau of Standards, Washington, D.C. NSRDS-NBS 37 (1971).
16. J. Newman, *Ind. Eng. Chem. Fundam.*, **7**, 514 (1968).
17. R. E. White, *ibid.*, **17**, 367 (1978).
18. W. H. Smryl and J. Newman, *This Journal*, **118**, 1079 (1971).
19. V. S. Ban, *ibid.*, **122**, 1389 (1975).
20. C. R. Wilke, *J. Chem. Phys.*, **18**, 517 (1950).

Technical Notes



Changes in Thickness and Infrared Spectrum of Phosphosilicate Glass Film with Heat-Treatment in H₂ Gas

Hideaki Takeuchi and Junichi Murota

*Nippon Telegraph and Telephone Public Corporation,
 Musashino Electrical Communication Laboratory, Musashino, Tokyo, 180 Japan*

Phosphosilicate glass (PSG) films deposited by chemical vapor deposition (CVD) techniques are important materials for insulation layers in MOS LSI's (1). Structural changes in PSG films with heat-treatment in atmospheres of N₂ gas, Ar gas, and steam have been studied (2-5). However, little is known about structural changes in PSG film with heat-treatment in H₂ gas. In the present work, the changes in thickness and infrared (IR) spectrum of a PSG film with heat-treatment in H₂ gas were investigated. It was found that voids are formed in the film and the integrated absorbance of P = O band near 1330 cm⁻¹ is reduced by high temperature heat-treatment in H₂ gas.

Experimental

PSG films were deposited at 420°C in a horizontal reactor using an SiH₄-PH₃-O₂-N₂ gas system. The thickness of the as-deposited film was about 6300Å. The substrates used were p-type Si wafers of 30-50 Ω-cm with mirror polished (100) surface. The Si substrates were thermally oxidized before PSG film

deposition in order to prevent phosphorus diffusion into the substrates from the PSG films (4). The PSG films were heat-treated in atmospheres of H₂ and N₂ gas. In some cases, films heat-treated in H₂ gas were subsequently heat-treated in O₂ gas or N₂ gas. Film thicknesses (T_{PSG}) were measured with a Taylor Hobson Talystep. Cross sections of the heat-treated films were observed by a scanning electron microscope. The total phosphorus weight (W_P) per square centimeter of the film was determined by x-ray fluorescence techniques and neutron activation analysis. The IR spectrum of the film was measured with a double beam IR spectrophotometer. The integrated absorbance of the P = O band ($A_{P=O}$) was estimated from the product of the absorbance and the half-width of the P = O absorption band (6).

Results

Figure 1 shows the T_{PSG} change of film containing 9 weight percent (w/o) phosphorus (as-deposited) as a function of heat-treatment temperature in H₂ and N₂ gas. In H₂ gas, the T_{PSG} increases drastically above 1000°C but not below 950°C. In N₂ gas, no increase in the T_{PSG} takes place under the present con-

Key words: voids formation, phosphosilicate glass, chemical vapor deposition, P=O absorption band.

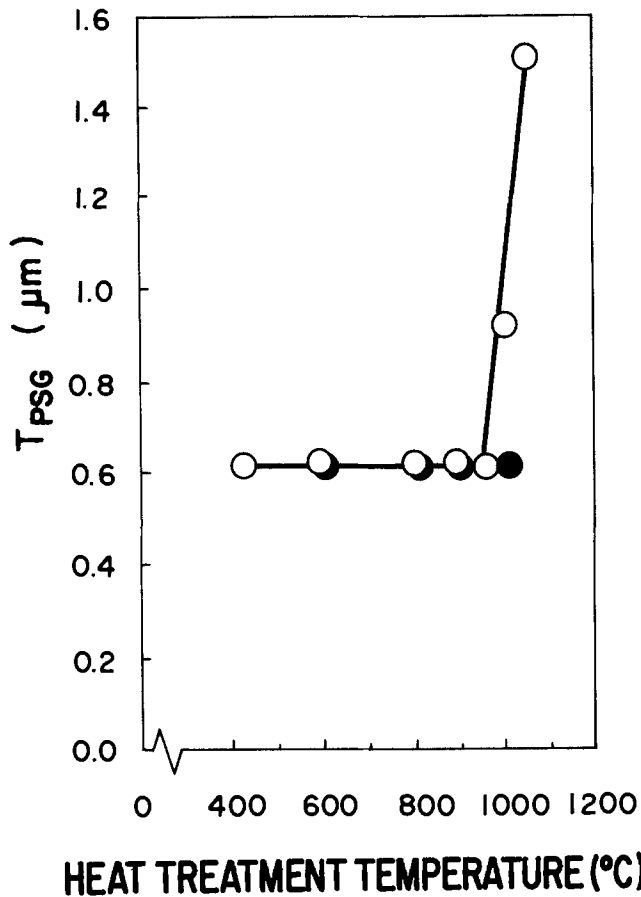


Fig. 1. Dependence of T_{PSG} on heat-treatment temperature with H_2 or N_2 gas for 20 min. Open circles are results in H_2 and closed circles are results in N_2 . Phosphorus concentration and T_{PSG} of as-deposited film are 9 w/o and 6300Å, respectively.

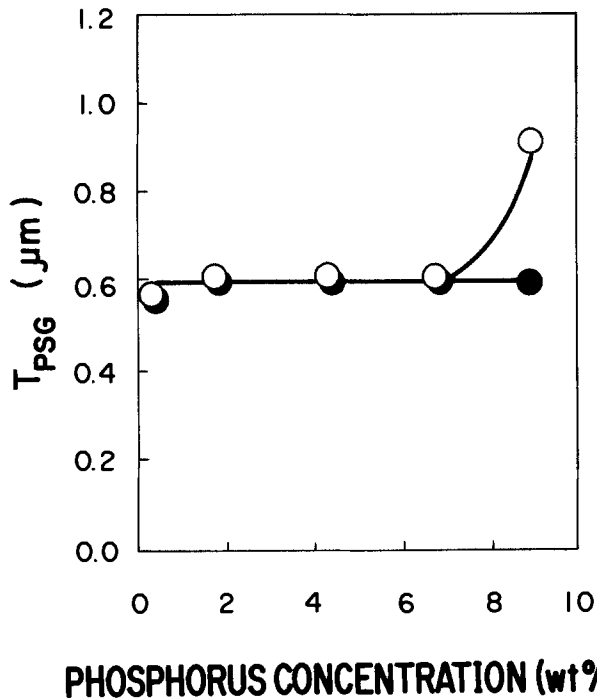


Fig. 2. Relationship between T_{PSG} and phosphorus concentration (as-deposited) with heat-treatment in H_2 or N_2 gas at 1000°C for 20 min. Open circles are results in H_2 and closed circles are results in N_2 . The T_{PSG} of as-deposited film is 6300Å.

ditions. Figure 2 shows the T_{PSG} change as a function of phosphorus concentration in the film with heat-

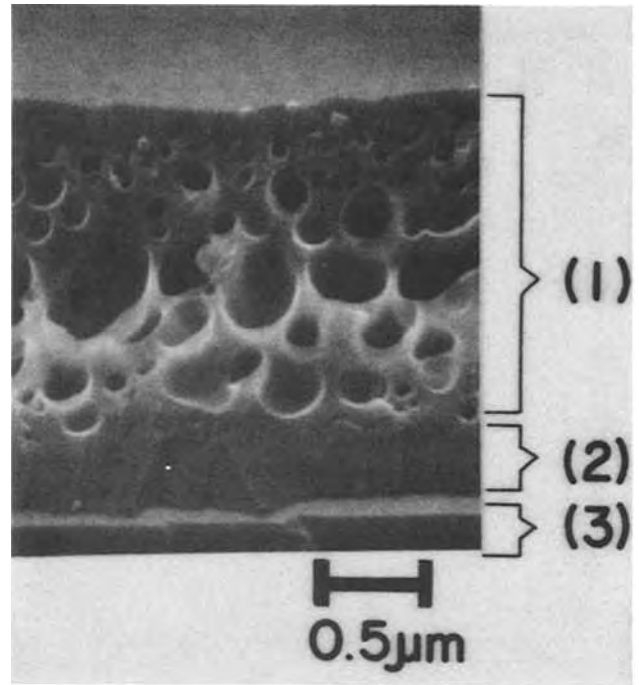


Fig. 3. Scanning electron micrograph of a cross section of PSG film of which T_{PSG} expanded with heat-treatment in H_2 gas at 1000°C for 20 min. Phosphorus concentration of as-deposited film is 9 w/o: (1) PSG film; (2) thermally grown SiO_2 film; (3) Si substrate.

treatment at 1000°C. For lower phosphorus concentration (below 7 w/o) films, no increase in the T_{PSG} takes place in H_2 gas. A cross section of a film which became thicker with heat-treatment in H_2 at 1000°C is shown in Fig. 3. Many voids, with sizes ranging from 0.1 to 0.3 μm , are distributed in the film. The total volume of the voids is in good agreement with the PSG film volume increment, where the total volume of the voids was estimated from the number and the sizes of the voids on the assumption that the voids are spherical. PSG films which expanded in thickness with heat-treatment in H_2 gas were subsequently heat-treated in O_2 or N_2 gas at 1000°C. The results are shown in Table I. With heat-treatment in O_2 gas, the T_{PSG} decreases to that of the as-deposited film and the voids are diminished. With heat-treatment in N_2 gas, the T_{PSG} does not change, i.e., the voids are not diminished. From these results, it is supposed that voids are formed in the PSG film by reduction in H_2 gas and are diminished by oxidation in O_2 gas.

To elucidate the reaction in the PSG film, IR spectra of PSG films heat-treated in H_2 or N_2 gas were studied. It was found that the changes in $A_{\text{P=O}}$ were different between H_2 and N_2 gas. In Fig. 4, the changes in $A_{\text{P=O}}$ and W_{P} of PSG film containing 9 w/o phosphorus (as-deposited) are shown as a function of heat-treatment temperature. In N_2 gas, the $A_{\text{P=O}}$ increases initially with increasing temperature and is saturated above 800°C. This increment of $A_{\text{P=O}}$ agrees with the results reported by Kern *et al.* (2, 3). In

Table I. Changes in T_{PSG} with heat-treatment under various conditions

Heat-treatment conditions	T_{PSG} (Å)
As-deposited	6300
H_2 gas 1000°C 20 min	9300
H_2 gas 1000°C 20 min + O_2 gas 1000°C 60 min	6300
H_2 gas 1000°C 20 min + N_2 gas 1000°C 60 min	9400

Phosphorus concentration of as-deposited film is 9 w/o.

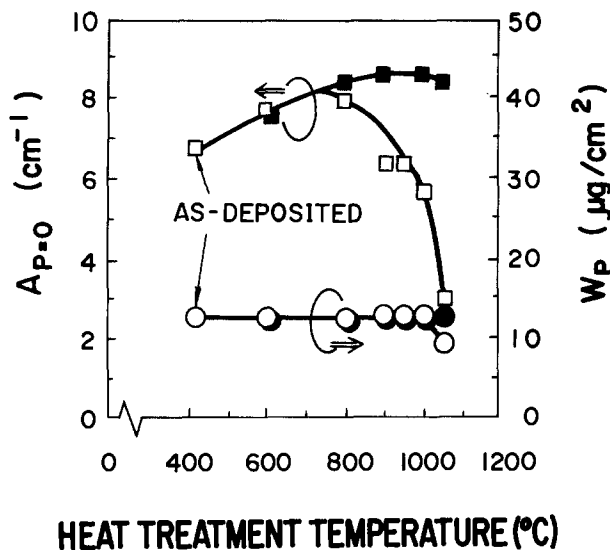


Fig. 4. Dependence of $A_{P=O}$ and W_P upon heat-treatment temperature with heat-treatment in H_2 or N_2 gas for 20 min. Open squares and circles are results in H_2 ; closed squares and circles are results in N_2 ; phosphorus concentration of as-deposited film is 9 w/o.

H_2 gas, the $A_{P=O}$ increases initially with heat-treatment temperature and decreases above $800^\circ C$. The decrease of the $A_{P=O}$ above $800^\circ C$ cannot be explained by phosphorus loss during the heat-treatment because the W_P does not decrease with heat-treatment, except for the heat-treatment at $1050^\circ C$ in H_2 gas. From this result, it is suggested that $P=O$ bonds dissociate with heat-treatment in H_2 gas. Assuming that some volatile gases such as phosphorus species or H_2O are generated by the reduction of the $P=O$ bonds, voids are expected to be formed because of the com-

ination of the increased volatile gas pressure and the low viscosity of the PSG film due to higher heat-treatment temperature and higher phosphorus concentration. More work on the behavior of phosphorus in PSG film under heat-treatment in H_2 gas is needed to understand the void formation mechanism.

In conclusion, the structural changes of PSG film with heat-treatment in H_2 gas are different from those in N_2 gas. In H_2 gas voids are formed in the PSG film in association with the film thickness increment, and the integrated absorbance of the $P=O$ band near 1330 cm^{-1} decreases with high temperature heat-treatment.

Acknowledgments

The authors wish to express their gratitude for encouragement to Mr. M. Kondo, and to Mr. F. Yanagawa for executing the study. They also would like to thank Dr. E. Arai for his useful discussions and valuable advice, and Mr. I. Kawashima for x-ray fluorescence analysis.

Manuscript submitted Aug. 20, 1979.

Any discussion of this paper will appear in a Discussion Section to be published in the December 1980 JOURNAL. All discussions for the December 1980 Discussion Section should be submitted by Aug. 1, 1980.

Publication costs of this article were assisted by Nippon Telegraph and Telephone Public Corporation.

REFERENCES

1. W. Kern and R. S. Rosler, *J. Vac. Sci. Technol.*, **14**, 1082 (1977).
2. W. Kern and R. C. Heim, *This Journal*, **177**, 568 (1970).
3. W. Kern, *RCA Rev.*, **37**, 55 (1976).
4. J. Wong, *J. Non-Cryst. Solids*, **20**, 83 (1976).
5. N. Nagasima, H. Suzuki, K. Tanaka, and S. Nishida, *This Journal*, **121**, 424 (1974).
6. J. Wong, *This Journal*, **120**, 122 (1973).

Oxygen Precipitation in Silicon at $650^\circ C$

P. E. Freeland

Bell Laboratories, Murray Hill, New Jersey 07974

A great deal of attention has focused on the precipitation of oxygen (1) in silicon in the temperature range $1000^\circ\text{--}1200^\circ C$ because of the relevance to device processing, there has been relatively little work (2) at lower temperatures around $600^\circ C$. [In some recent work associated with laser annealing studies it was desirable to produce a large number of small defects by heat-treating silicon at as low a temperature as possible consistent with a reasonable time (3).] In this study, we follow the oxygen precipitation behavior of a crystal heated at $650^\circ C$ for 10 days by infrared absorption, x-ray anomalous transmission, and x-ray Pendellösung fringes. In previous precipitation studies (4) at higher temperature ($1000^\circ C$) the above three diagnostic techniques have supplemented each other and have been valuable aids in determining the degree and nature of precipitation in bulk crystals.

Experimental

The Czochralski crystals used had been especially grown to contain a high oxygen concentration (5). The 3 in. diameter crystals were oriented, sliced, and polished to a thickness of 2.5 mm. They were chemically cleaned and then heated at $650^\circ C$ in an H_2 atmosphere for 10 days. The heat-treatment was done in a quartz-lined furnace and the sample was supported on a silicon substrate. Following this treatment the sample and

Key words: silicon, oxygen precipitation.

its as-grown control were subjected to the tests described below.

Results

Infrared absorption.—The infrared absorption spectra of the heat-treated and as-grown samples are shown in Fig. 1. Curve A for the as-grown sample shows a large

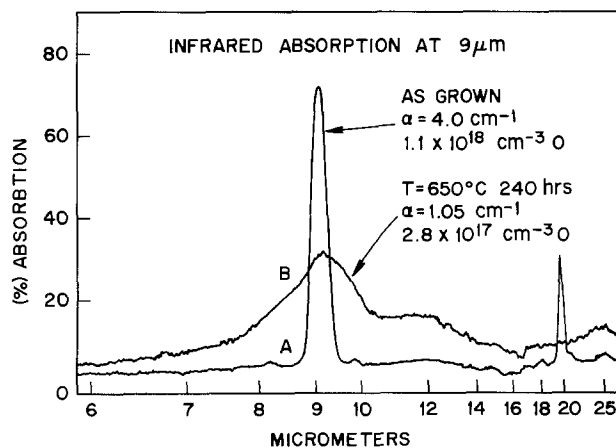


Fig. 1. Infrared absorption spectra of as-grown (curve A) and heat-treated silicon (curve B).

absorption peak at $9 \mu\text{m}$ which is a measure of the dissolved oxygen. The peak value of the absorption coefficient is $\alpha = 4.0 \text{ cm}^{-1}$ which corresponds to an oxygen concentration of $1.1 \times 10^{18} \text{ cm}^{-3}$ according to the calibration determined by Kaiser *et al.* (6). [See recent review (7).] This value is high compared to the values of about $7-8 \times 10^{17} \text{ cm}^{-3}$ found in crystals of similar diameter at the seed end. For the as-grown spectra, there is also an absorption peak at $19.4 \mu\text{m}$ which corresponds to the ν_2 symmetry bending vibration mode of the Si_2O configuration, according to Hrostowski and Kaiser (8). These curves were obtained with a low oxygen, low carbon floating zone high purity crystal as

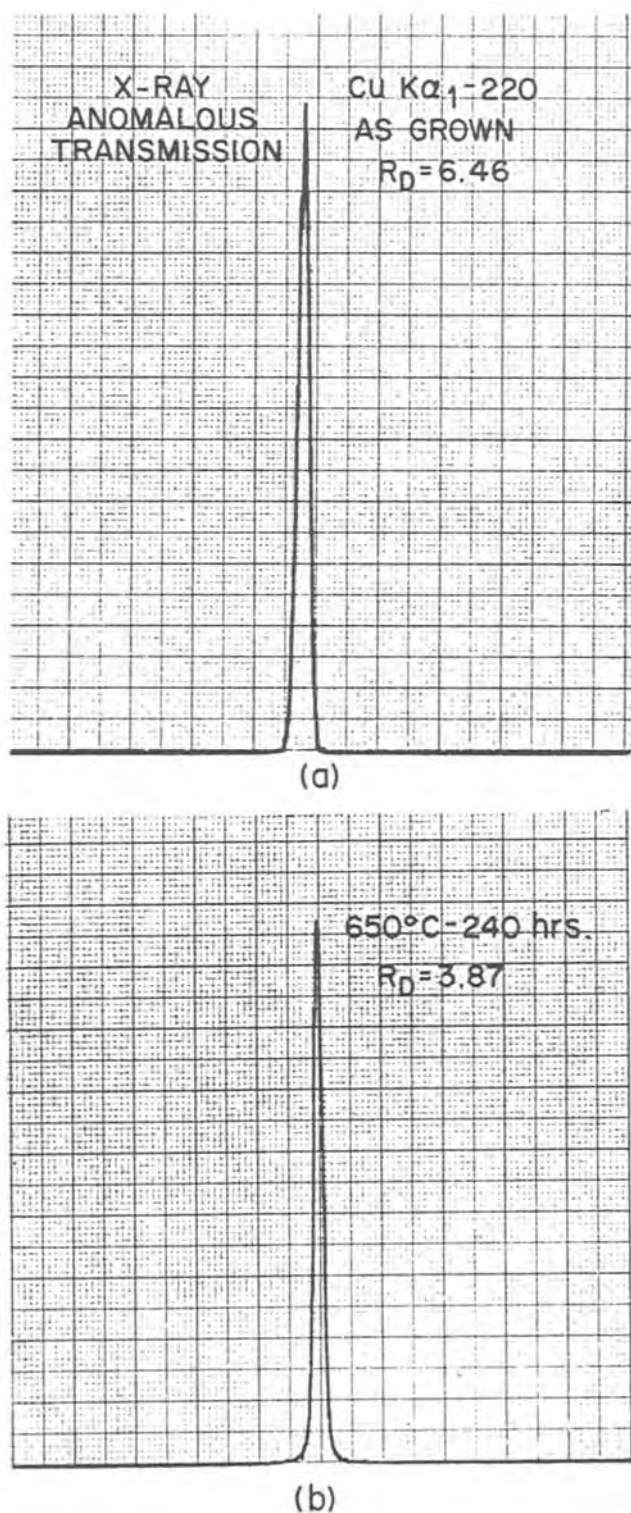


Fig. 2. X-ray anomalous transmission spectra of as-grown (curve a) and heat-treated silicon (curve b).

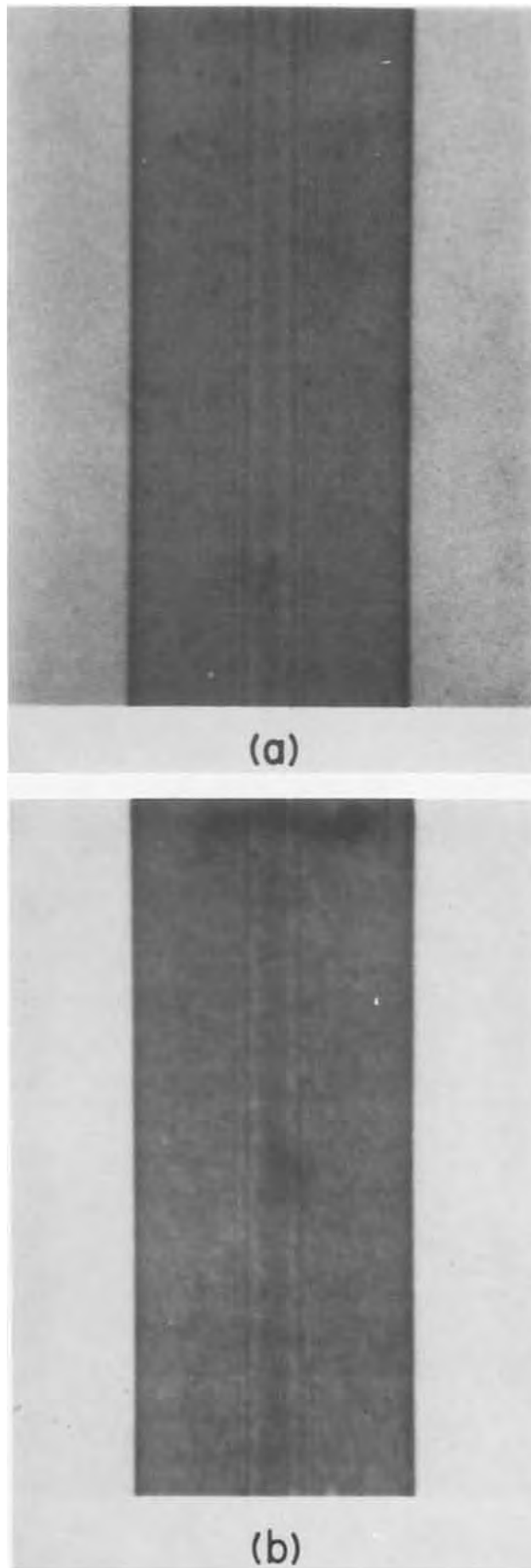


Fig. 3. (a) X-ray section topograph of as-grown high oxygen silicon ($1.1 \times 10^{18} \text{ cm}^{-3}$) using $\text{AgK}\alpha_1$ radiation; (b) x-ray section topograph of silicon with high oxygen content after heat-treatment (650°C -240 hr).

a reference in a dual beam spectrometer. No trace of carbon is observed in the spectra for the Czochralski silicon at 16.5 μm . After heat-treatment, spectra curve B shows a much lower absorption at 9 μm , $\alpha = 1.05 \text{ cm}^{-1}$ which corresponds to an oxygen concentration of $2.8 \times 10^{17} \text{ cm}^{-3}$. Note that the peak at 19.4 μm has disappeared entirely. This suggests that this peak might be a more sensitive indicator of the precipitation process. Note also that the 9 μm peak in curve B is considerably broadened probably due to contributions from the precipitated oxygen. From the 9 μm data one would conclude that a large amount of precipitation has occurred even at the relatively low temperature of 650°C.

X-ray anomalous transmission.—This method was shown to be a very sensitive indicator of the precipitation of oxygen in silicon heated for varying times at 1000°C (9). The results of x-ray anomalous transmission integrated intensity measurements are shown in Fig. 2. In the as-grown sample (Fig. 2a) the integrated intensity was $R_d = 6.46$ (arbitrary scale). The beam size was 1 mm² and no variation in integrated intensity was observed in different regions of the sample before or after heat-treatment. After heat-treatment at 650°C, $R_d = 3.87$, a decrease of only about 40%. Clearly the x-ray method is less sensitive than the infrared method where the intensity has decreased by a factor of 4. This result is diametrically opposed to the findings in previous experiments on silicon heated at 1000°C where the x-ray intensity R_d changes by 2 orders of magnitude before any change is observed in infrared at 9 μm .

Pendellösung fringe section topographs.—Section topographs were taken of samples before heat-treatment (Fig. 3a) and after heat-treatment (Fig. 3b). Although the samples were not ideal thickness for $\text{AgK}\alpha$ radiation ($\mu t > 1$ where μ is the absorption coefficient and t the specimen thickness); fringes are evident in the as-grown sample and are only slightly less clear in the heated sample. However, the heat-treated sample topograph does have a mottled background appearance and edges which are not as dark as the as-grown sample topograph. This is an indication of a decrease in crystal perfection. In contrast, samples heated at 1000°C for only 1 hr show the presence of precipitate in section topographs (4). After 6 hr at 1000°C, the fringes have completely disappeared and are replaced by bands of defects (4).

Conclusion

It is well known that because of the large volume expansion accompanying oxygen precipitation in sili-

con ($\text{Si} + 2\text{O} \rightarrow \text{SiO}_2$; $V_{\text{SiO}_2}/V_{\text{Si}} \approx 2$) the crystal is highly strained (9). The high sensitivity of the x-ray method in earlier experiments (9) is due to the large precipitate size which is of the order of or larger than the Pendellösung length ($\sim 18 \mu\text{m}$). At low temperatures where the precipitate size is expected to be small, probably much smaller than the Pendellösung distance, the x-ray anomalous transmission method is no longer as sensitive to these precipitates. Another x-ray technique such as diffuse scattering of x-rays in the vicinity of the Bragg peaks would be more relevant. Previous experiments at 1000°C had led to the conclusion that the x-ray dynamical diffraction method was more sensitive than infrared absorption to oxygen precipitation in silicon. This is no longer true at low temperatures where the x-ray dynamical diffraction method is not very sensitive to the small precipitate size. In this temperature range, the infrared measurement is a better indicator of oxygen precipitation.

Acknowledgment

The author wishes to acknowledge the support and encouragement of J. R. Patel in this work.

Manuscript submitted July 20, 1979; revised manuscript received Oct. 1, 1979.

Any discussion of this paper will appear in a Discussion Section to be published in the December 1980 JOURNAL. All discussions for the December 1980 Discussion Section should be submitted by Aug. 1, 1980.

Publication costs of this article were assisted by Bell Laboratories.

REFERENCES

1. J. R. Patel, K. A. Jackson, and H. Reiss, *J. Appl. Phys.*, **48**, 5279 (1977).
2. K. Tempelhoff and F. Spiegelberg, in "Semiconductor Silicon," H. R. Huff and E. Sirtl, Editors, p. 585, The Electrochemical Society Softbound Proceedings Series, Princeton, N.J. (1977).
3. P. Petroff, Device Research Conference, Boulder, Colorado, June 1979, To be published.
4. J. R. Patel, *J. Appl. Phys.*, **44**, 3903 (1973).
5. L. E. Katz and D. W. Hill, *This Journal*, **125**, 1151 (1978).
6. W. Kaiser, P. H. Keck, and C. F. Lange, *J. Appl. Phys.*, **28**, 882 (1957).
7. J. R. Patel, in "Semiconductor Silicon," H. R. Huff and E. Sirtl, Editors, p. 521, The Electrochemical Society Softbound Proceedings Series, Princeton, N.J. (1977).
8. H. J. Hrostowski and R. H. Kaiser, *Phys. Rev.*, **107**, 966 (1957).
9. J. R. Patel and B. W. Batterman, *J. Appl. Phys.*, **34**, 2716 (1963).



Chlorine Evolution Reaction on Tin Oxide Anodes in an $\text{AlCl}_3\text{-NaCl}$ Melt at 175°C

I. Uchida,* H. Urushibata, and S. Toshima

Department of Applied Chemistry, Faculty of Engineering, Tohoku University, Sendai 980, Japan

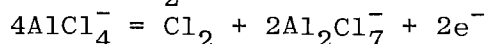
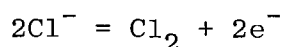
Sodium tetrachloroaluminate melts are of special interest from the viewpoint of molten salt batteries and metal winning processes. One of the problems relating to them is developing suitable anode materials workable for chlorine evolution reaction. The previous investigations on chlorine electrode in the melts have been done by employing glassy carbon (1-3) and graphite and platinum (4). Carbon is the most popular with regard to chemical durability and economic accessibility. However, it is noted that carbon electrodes except glassy carbon show considerable swelling and disintegration in the melts. Recently, we reported on the chlorine evolution on tin oxide electrodes in LiCl-KCl eutectic at 450°C (5) and characterization of the interface between tin oxide and the chloroaluminate melts of different $p\text{Cl}$ at 175°C (6), noting that Sb-doped tin oxide is a versatile electrode material stable in the melts.

In the present paper we show current-potential curves of chlorine evolution on the tin oxide electrodes with different doping levels, comparing them with the kinetic behavior of glassy carbon electrodes (GCE).

Experimental.--Sb-doped tin oxide electrodes were polycrystalline films prepared on Pyrex substrates in rectangular shape by a spray method. Electrode surfaces were held vertically in the melt. Details of the film preparation and the electrode construction are given elsewhere (6). A rod of GC was sealed into Pyrex tubing with a technique described previously (7) and cut off at 45° . Purification of the melt and experimen-

tal procedures were described previously (5,6). Measurements were carried out at $175\pm 2^\circ\text{C}$ and electrode potentials were given with respect to the potential of an Al electrode in the melt saturated with NaCl.

Results and discussion.--Fig. 1 shows the steady-state current vs. potential curves of chlorine evolution measured in the melt of $p\text{Cl}=1.1$. The Tafel slope observed on GCE was close to RT/F . According to Letisse et al. (2), the Tafel region corresponds to the oxidation of free Cl^- ions and the plateau is the limiting current of Cl^- , while the further increase of current beyond the diffusion limit is due to the oxidation of AlCl_4^- . Thus we have two chlorine evolution reactions at the different potential regions,



Arvia et al. reported that the Tafel slope on graphite at 190°C is $RT/2F$ (4), suggesting that the rate-determining step is a combination process expressed as $\text{Cl}(\text{ad})+\text{Cl}(\text{ad})\rightarrow\text{Cl}_2$. Our result on GCE was larger than that of Arvia et al., being rather close to the Tafel slope on GCE obtained by reconstructing the data in ref. (2).

The polarization behavior on semiconducting tin oxide electrodes was different from that on GCE, showing the notable dependence on electron concentration of the oxides as seen in the curve (b) and (c). The shoulder observed on a low-doped tin oxide electrode ($N_d = 7\times 10^{19} \text{ cm}^{-3}$) at lower current densities is not due to the diffusion of Cl^- , and the difference between the low-doped and high-doped ($N_d = 3\times 10^{20} \text{ cm}^{-3}$) specimens in the polarization behavior is too large to

*Electrochemical Society Active Member.
Key words: semiconductor, electrode, Tafel slope.

be explained in terms of the effect of ohmic drop. The cell resistances measured between the reference and the tin oxide electrodes (area = 0.5 cm^2) were about 15 ohm and there was no considerable difference between the two specimens. Thus it was demonstrated that the high-doped electrode shows fairly improved polarization similar to the behavior of GCE. However, a well-defined Tafel slope was not obtained in this case. As described in aqueous systems (8) and in melt systems (5,9), highly doped tin oxide electrodes are metal-like electrodes, indicating the reversible behavior for simple charge transfer reactions, because the space charge barrier present at the semiconductor surface is highly transparent to electrons due to tunneling.

It has been reported that the differential capacity measured at the SnO_2 -melt interface obeys the Mott-Schottky relationship (6). The carrier densities given in this work and flat band potentials were determined from the Mott-Schottky plots. The flat band potential in the melt of $\text{pCl}=1.1$ was found to be 1.49 V for the high-doped SnO_2 and 1.68 V for the low-doped one. Obviously, the chlorine evolution takes place at potentials more positive to the flat band potentials where the space charge barrier is extremely thin particularly for the high-doped SnO_2 . The electron tunneling through the space charge barrier is much easier at the high-doped SnO_2 electrode than at the low-doped one. The presence of the shoulder in the polarization behavior at the low-doped one suggests that the tunneling process may involve two mechanisms, tunneling via surface states in the band gap and direct elastic tunneling.

Since the preparation of SnO_2 having much higher carrier densities ($\sim 10^{21} \text{ cm}^{-3}$) is technically possible as obtained by Elliott et al. (8), more improved polarization than the curve (b) would be expected with such highly doped specimens. It is of interest to develop SnO_2 -based electrocatalyzers usable in melt systems by applying the oxide-coating technology used in the production of DSA.

REFERENCES

1. T. Sato, T. Ishikawa and R. Midorikawa, *Denki-Kagaku*, **41**, 123 (1973).
2. G. Letisse and B. Tremillon, *J. Electroanal. Chem.*, **17**, 387 (1968).
3. G. L. Holleck, *This Journal*, **119**, 1158 (1972).
4. H. J. Vandenbroele and A. J. Arvia, *An. Asoc. Quim. Argent.*, **55**, 21 (1967). C. A. 68-65146a.
5. I. Uchida and S. Toshima, *J. Appl. Electrochem.*, in press.
6. I. Uchida, H. Urushibata and S. Toshima, *J. Electroanal. Chem.*, **96**, 45 (1979).
7. H. A. Laitinen, Y. Yamamura and I. Uchida, *This Journal*, **125**, 1450 (1978).
8. D. Elliott, D. L. Zellmer and H. A. Laitinen, *ibid.*, **117**, 1343 (1970).
9. I. Uchida, K. Niki and H. A. Laitinen, *ibid.*, **125**, 1759 (1978).

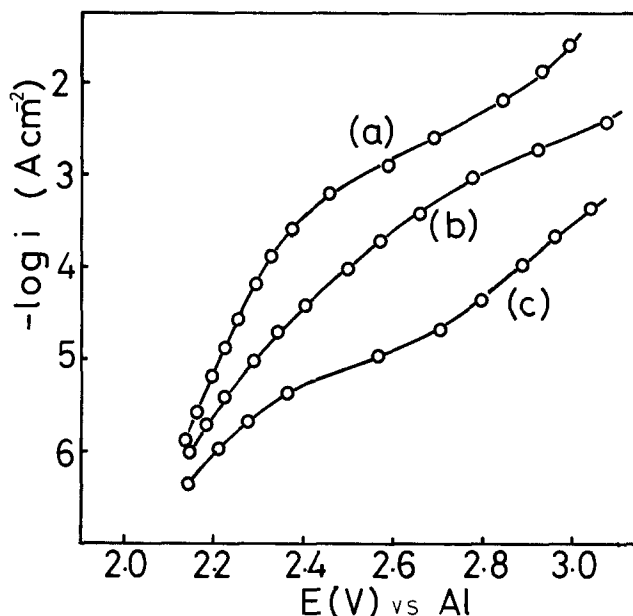


Fig. 1. Steady-state current vs. potential curves for chlorine evolution in the AlCl_3 - NaCl melt of $\text{pCl}=1.1$ at 175°C . (a) glassy carbon, (b) SnO_2 , $N_d=3 \times 10^{20} \text{ cm}^{-3}$, (c) SnO_2 , $N_d=7 \times 10^{19} \text{ cm}^{-3}$.

Manuscript received March 7, 1979.

Publication costs of this article were assisted by Tohoku University.

Reduction of Oxygen on Silver Electrodes in Ternary Alkali Carbonate Eutectic Melt

A. J. Appleby*

Electric Power Research Institute, Palo Alto, California 95303

S. B. Nicholson

Institute of Gas Technology, Chicago, Illinois 60616

Tyurikov et al.⁽¹⁾ have described results obtained for reduction of oxygen on various substrates in a number of carbonate melts. They show that on smooth silver electrodes currents were greater than those on gold. Unless their observation can be explained by geometric factors, this result is inconsistent with the supposition of an essentially diffusion-controlled mechanism involving initial chemical formation of peroxide and superoxide ions from O_2 and CO_3^{2-} , as described in previous work (2,3).

Accordingly, a study of oxygen reduction on immersed silver electrode, with a polished 0.5 cm^2 surface was conducted. Apparatus and experimental procedure were as in previous work (2,3). Potentials are given on the $0.33 \text{ atm } O_2/0.66 \text{ atm } CO_2$ scale. Potentiostatic results obtained at $650^\circ C$ under steady-state conditions in a $10\% O_2$ - $10\% CO_2$ atmosphere may be summarized as follows:

1. Extremely high current densities (> 10 times those on gold) were obtained on silver electrodes that had been dipped in H_2O_2 or nitric acid before being inserted into the carbonate cell. These electrodes had rest potentials of about -250 mV (well below the theoretical value of -101 mV) and the cathodic currents slowly decayed over a period of days when the electrodes were polarized at -900 mV .

2. Electrodes that had been untreated with oxidizing agents, or that had been hydrogen-reduced, showed lower current densities, which decayed more quickly, and somewhat lower rest potentials.
3. After 2-3 days for oxidized electrodes and after a few hours for reduced or untreated electrodes, currents had decayed to the same order of magnitude as those on gold at -900 mV . The high initial currents were stirring-independent; the final currents were stirring-dependent, as observed on gold⁽³⁾. Rest potentials on these electrodes fell to about -775 to -800 mV .

Figure 1 shows a comparison of oxygen reduction on an unoxidized electrode a short time after being placed in the cell and on the same electrode after 8 hours exposure to the melt. The very large current density, which was independent of stirring, indicates that the oxygen being reduced is present in or on the metal. As silver normally contains large quantities of dissolved oxygen that occlude at high temperatures, the current observed is clearly due to the reduction of this material. The high rest potentials under these conditions indicate the occurrence of an oxide passivation phenomenon.

* Electrochemical Society Member

Key Words: molten carbonate fuel cell, cathode, silver

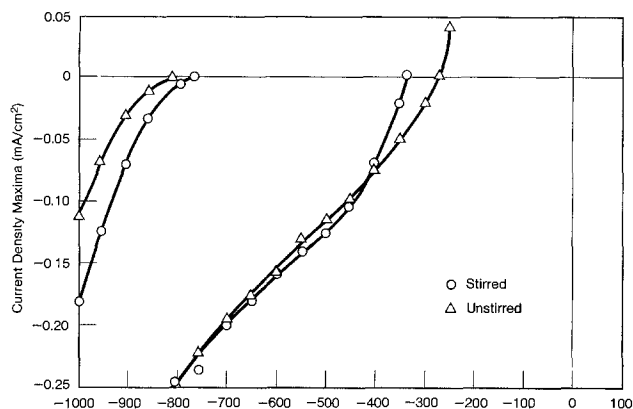


Figure 1. CATHODIC REDUCTION OF OXYGEN ON SILVER: COMPARISON OF ELECTRODE IN FRESH CONDITION AND AFTER 8 HOURS EXPOSURE TO MELT AT -800 mV. POTENTIALS ON 0.33 atm $O_2/0.66$ atm CO_2 SCALE.

In a molten carbonate fuel cell, it therefore appears that silver cathodes act as oxygen transfer agents, for which the bulk of the oxygen diffuses through the metal. Corrosion is slowed by a combination of passivation due to oxide formation and concentration polarization due to dissolved silver ions. The effect of this type of polarization is evident in the stirring-dependence of the rest potential in Figure 1.

Figure 2 shows the effect of an 8-minute exposure of the silver electrode to the atmosphere above the melt at 650°C. In this case, the amount of oxygen adsorbed after this short exposure is considerable, and it is not entirely reduced after one polarization cycle.

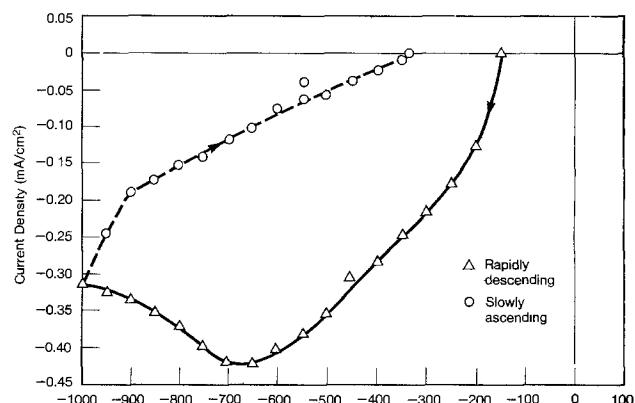


Figure 2. UNSTIRRED CATHODIC PLOTS ON SILVER ELECTRODE AFTER 8 MINUTE EXPOSURE TO ATMOSPHERE ABOVE MELT. POTENTIALS AS ON FIGURE 1.

Acknowledgements

This paper is published with the permission of the sponsors of the TARGET Fuel Cell Program and the Power Systems Division of United Technologies Corporation.

REFERENCES

- (1) G. S. Tyurikov, N. P. Vasilistov, A. V. Silakov and Yu. M. Pashkov, *Elektrokhimiya* **5**, 308 (1969)
- (2) A. J. Appleby and S. B. Nicholson, *J. Electroanal. Chem.* **53**, 105 (1974)
- (3) A. J. Appleby and S. B. Nicholson, *J. Electroanal. Chem.* **83**, 309 (1977)

Manuscript received Dec. 3, 1979.

Li/TiS₂ Cell with Solvate Melt

B. M. L. Rao* and L. P. Klemann*

Exxon Research and Engineering Company, Advanced Energy Systems Laboratory, Linden, New Jersey 07036

Li/TiS₂ solid electrolyte cells with solvate complexes of lithium salts have been recently disclosed (1). In this paper, we present the behavior of Li/TiS₂ cells in a low-temperature melt consisting of LiI:glyme solvate.

Lithium iodide forms solvate adducts with glyme(s) (mono-, di-, tri-glyme) which result in crystalline solids and ultraconcentrated solutions in 1-4 mole ratio of the solvent per mole of the solute. The solid adducts may be generated by mixing, melting, (~70°C), and cooling the ingredients in a 1:1 to 1:2 mole ratio of LiI:glyme(s). At a higher solvent ratio (~2.5-3), solid compositions co-exist with ultra-concentrated solutions, and compositions with >4 moles of solvent per mole of solute are liquids, at room temperature.

Fig. 1 illustrates the specific resistivity composition data for the LiI:glyme(s) melts at 95°C. The data indicate that the solvate adduct melts are ionic liquids, which may be of interest in the development of high energy density lithium cells, based on low temperature (<100°C) fused salts.

The LiI:glyme (1,2-dimethoxyethane, b.p. 85°C) adduct is a light yellow solid (m.p. 60-65°C) in the composition range 1.75-2.85 moles of solvent per mole of solute. A Li/TiS₂ cell was tested in this electrolyte at 75°C.

The test cell consisted of a lithium anode ~90 mAh/cm² (1"x1"x0.02" foil on nickel grid), a pressed powder, 45 mAh/cm² TiS₂ cathode (1"x1"x(0.04"-0.05"), 10 w/o teflon, 40-50% porous), a fiber glass separator (0.015" thick, 75% porous), and was held together with a fiber glass strap. The cell was assembled in a helium dry box and was contained in a suitable glass jar with provision for external electrical connections. The cell was operated at 75°C after adding LiI:glyme molten electrolyte of composition 1.75-2.25 moles of glyme per mole of LiI.

First discharge data for Li/TiS₂ cells at 10-20 mA/cm² is given in Fig. 2. It is noted that the material utilization (% M.U.)

of the cathode-limiting cell is ~90% of the theoretical capacity to 1.5 V. The cells were not rechargeable under the ambient temperature conditions of this work. We note the recent report wherein a sodium-TiS₂ cell has been operated at 130°C in an electrolyte of NaI-triglyme[2].

The following experiments were carried out to understand the lack of rechargeability of the cells.

1. Lithium electroplating and anodic stripping experiments were done in the electrolyte in half-cell mode using a lithium reference and a nickel grid working electrode. The electrodeposition resulted in plating of a black, non-adherent deposit, which yielded 30% anodic stripping efficiency, and gassing was noted at the working electrode during the electrodeposition and stripping experiments. In the pre-lithium deposition potential region, a background current of ~1 mA/cm², probably associated with the gassing reaction, was noted.

2. TiS₂ half-cell studies indicated that the cathode is inherently rechargeable.

3. Examination of the spent cell revealed a blue-grey film on the lithium anode; also, a yellow discoloration was seen on the cathode side of the separator. Finally, a TiS₂ cathode had expanded ~100% in thickness.

4. X-ray diffraction studies on the discharged TiS₂ cathode indicated intercalation of the glyme, in addition to the expected formation of Li/TiS₂.

Analysis of the experimental results suggested that the lack of rechargeability may be associated with very strong complexing of Li⁺ ions by glyme. Strong complexation of Li⁺ by multidentate chelating ethers might be expected to inhibit the molecular process of cation release required for adatom formation during electrodeposition. Inhibition of the desolvation process might, in turn, make alternate reaction pathways preferable energetically, and such an alternate pathway seems to be the gassing (reductive degradation of glyme) reaction at the polarized electrode. If the strong complexation of Li⁺ ion inhibits the

release of the cation, additional effects would be expected at the TiS_2 cathode during the discharge of the cell. In this case, intercalation of lithium occurs, but not without substantial co-intercalation of the strongly coordinated polyether ligand, as witnessed by the excessive expansion of the cathode and the X-ray diffraction data. The co-intercalation of the polyether offers one plausible mechanistic interpretation for the point of inflection observed in the discharge curve (Fig. 2), although this offering is speculative. Discharge performance did not appear to be severely affected by the polyether co-intercalation.

Other points worth highlighting are as follows:

(a) The cells may be discharged at high rates in the low temperature melt, and

(b) the cells may be stored in solid electrolyte mode to favor long storage life.

These features render the solvate adduct an attractive candidate for a low-temperature Li/TiS_2 thermal cell.

ACKNOWLEDGMENTS

The authors wish to acknowledge the skilled experimental assistance of Mr. M. T. Vidnansky during the course of this work.

REFERENCES

- (1) R. W. Francis and G. H. Newman, U.S. Patent 4,075,397, Feb. 21, 1978.
- (2) K. M. Abraham, R. Schiff, and S. B. Brummer, ECS Fall Meeting, Oct. 1979, Abs. 154.

*Electrochemical Society Active Member.

Key Words: Li/TiS_2 Cell, Solvate Melt, $LiI:Glyme(s)$ Complexes.

Manuscript received Dec. 3, 1979.

Publication costs of this article were assisted by Exxon Research & Engineering Company.

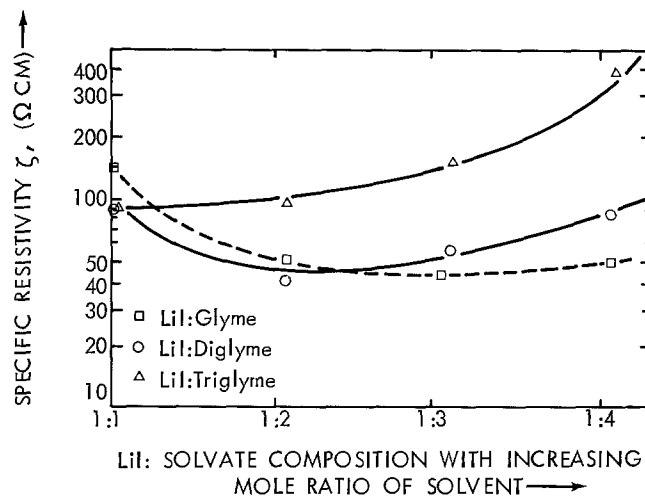


Fig. 1. Specific resistivity of $LiI:Glyme(s)$ at $95^\circ C$

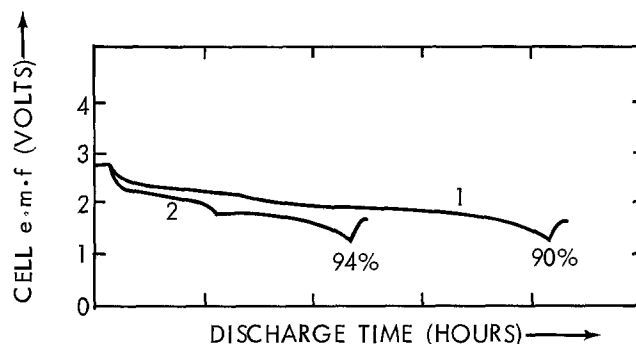


Fig. 2. Discharge behavior of Li/TiS_2 cells in $LiI:Glyme$ melt at $75^\circ C$

- (1) 10 mA/cm^2 discharge. Cathode 45 mAh/cm^2
- (2) 20 mA/cm^2 discharge. Cathode 45 mAh/cm^2

Auger Electron Spectroscopy Depth Profile of Thin Oxide on a Ti-Mo Alloy

Daniel Laser

Department of Chemistry, Tel-Aviv University, Ramat Aviv, Israel

Harris L. Marcus

Department of Mechanical Engineering/Material Science and Engineering,
University of Texas at Austin, Austin, Texas 78712

Recently we investigated⁽¹⁾ the growth and properties of thin oxide films which were grown on a titanium electrode. It is the aim of this communication to describe some properties of an anodic oxide which were grown on a Ti-Mo alloy.

For the formation of a controlled oxide thickness on a bare substrate to be used as an AES sample, the previously described⁽¹⁾ method was employed which consists of polishing the electrode surface (3 μ diamond dust embedded in a polishing cloth) while holding it at a cathodic bias (-0.95V vs SCE) and then applying to it a positive linear potential scan.

The alloy studied was the β -III, a Ti based metastable alloy (Ti, 11.5 Mo, 4.5 Sn, 6 Zr) the stress-corrosion behaviour of which was studied by Hickman et al⁽²⁾ and which was used as received without any heat treatment.

The current/potential curve during the anodic potential scan of the alloy electrode in slightly acidic solution is shown in fig. 1, where it is compared to the voltammogram of pure Ti and pure Mo under the same conditions.

As in the case of pure Ti, the voltammogram is distinguished by an extended potential interval ($\sim 2V$) in which the anodic current which is attributed to oxide formation remains constant. Such a mode of oxide growth results in the formation of a homogeneous film the

thickness of which varies linearly with the applied potential at full current efficiency.⁽¹⁾ However, the "dissolution peak" which is observed at pure Ti ($\sim -0.65V$) is missing. This is in agreement with the finding of Tomashov et al⁽³⁾ who find a suppression in the dissolution rate of Ti at the prepassive state when alloyed with Mo in the β phase and will be discussed later.

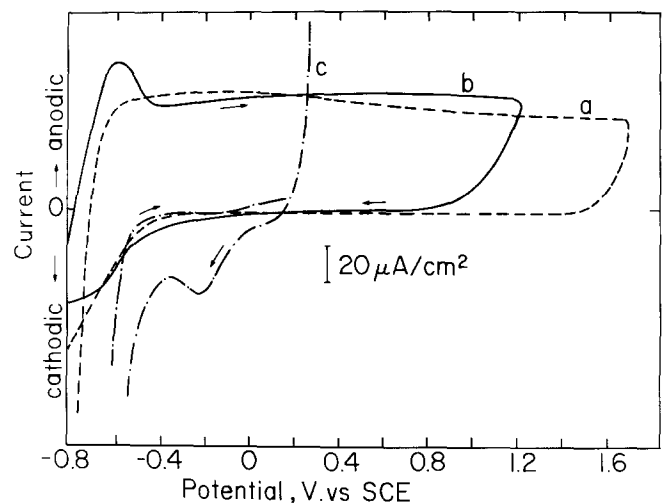


Fig. 1. Current voltage curve for a - β III alloy, b - Ti and c - Mo in 1N Na₂SO₄, PH 2.3.

Little is known about the composition of anodic oxides of alloyed Ti. Recently Paleolog et al⁽⁴⁾ assumed that the anodic oxide of a Ti-Ni alloy consists mainly of TiO₂ with Ni doping at the metal/oxide interface.

We adopt a similar picture with regard to the distribution of Mo within the oxide of the β -III and in order to probe it the oxides were subjected to Auger Electron Spectroscopy (AES)

Key Words: Alloy, Electrode, AES, sputtering

depth profiling immediately after their formation with the use of a PHI Model 590A Scanning Auger system equipped with sputtering, multiplexing and in situ fracturing facilities.

The difficulties in quantitative AES application to very thin (<100Å) TiO₂ films and to Mo oxides have been described before^(5,6). However, our aim was to locate the Mo distribution within the oxide. The appearance of the Mo major peaks (186,221 eV in the $\frac{dN}{dE}$ mode) in the absence of the 27 eV peak which is characteristic of metallic Ti, proves the existence of Mo within the oxide if the escape depth of the 27 and 221(186) eV Auger electrons are assumed to be about equal. The depth profile of the oxide is shown in fig. 2. The outer layer of the oxide (oxide/solution interface) consists exclusively of TiO₂ and the Mo concentration increases toward the metal oxide interface. The increase in the carbon concentration increases toward the metal oxide interface. The increase in the carbon concentration in this region is attributed to the polishing procedure prior to film formation (polishing with diamond dust). It should be noted that a similar apparent distribution of Mo can result if: (a) There is a preferential sputtering of Ti over Mo⁽⁷⁾ which leads to the surface accumulation of Mo during the sputtering, or (b) Mo is gradually reduced by the ion beam,⁽⁶⁾ or continuously changes its oxidation state while penetrating the film in such a way that its Auger peak shape is changed and enhanced even without any increase in its concentration.

Possibility (a) should also be manifested after the film is completely sputtered through; however the Mo signal then reaches a steady state. Also the Auger peak of Mo oxide grown at 1V did not change during the sputtering which eliminates the second possibility. We

believe the chemical state of Mo within the oxide to be that of Mo ion (Mo⁺³ or Mo⁺⁵), which because of its size, does not fit the TiO₂ phase and thus exhibits in it a much slower mobility than the Ti ion. It probably does not reach the solution/oxide interface except in the very early stages of film growth.

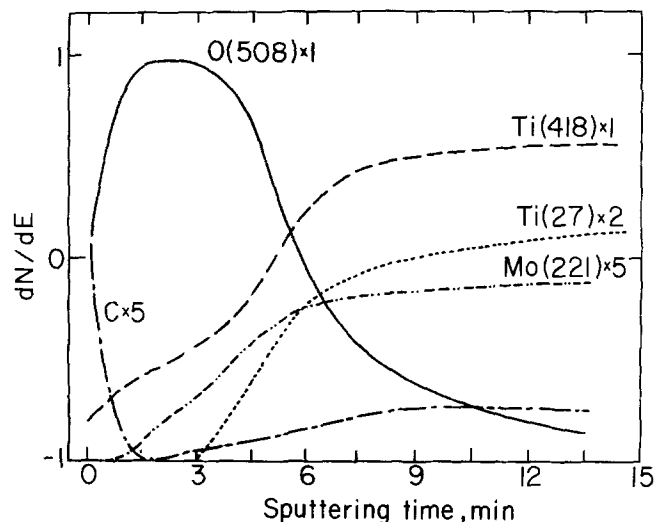


Fig. 2. AES depth profile of oxide formed at β III alloy at 2V vs SCE, solution as in fig. 1. Sputtering by 3 keV Kr⁺ ions.

The absence of the Ti dissolution peak (fig. 1) may be relevant to the superior behaviour of this alloy in corrosive media^(2,3) when the bare substrate might be exposed to solution. Two explanations, which are supported by the AES findings, can be provided for this observation. Firstly: In the AES of pure Mo or of its oxide the 221 eV Auger peak is smaller than the 186 eV peak, but the 221 eV peak of Mo in the alloy is bigger than the 186 eV one (in the $\frac{dN}{dE}$ mode, fig. 3). This reflects some specific interaction between Ti and Mo in alloyed state, which may possibly stabilize the Ti atom in the solid compared to its state in pure Ti. Secondly: At -0.95V while polishing, Ti dissolves into solution⁽¹⁾, but

this electrode potential is too negative for the Mo dissolution⁽⁸⁾ and it seems, therefore, feasible that the substrate surface prior to film formation is enriched with Mo which provides a barrier for the Ti dissolution. Indeed, the concentration of Mo which is found by AES after the oxide is removed by sputtering and which represents its quantity at the surface prior to anodization, is much higher than its concentration at the surface which was obtained by the in situ fracturing of the alloy (fig.4)

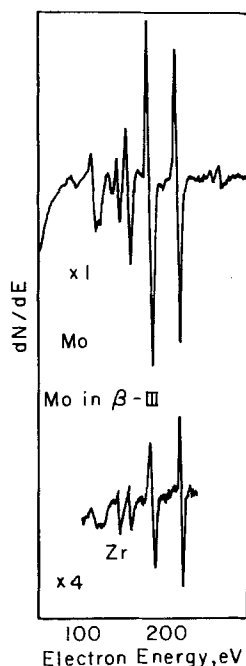


Fig. 3. AES of Mo in its pure state and in β III alloy.

References:

1. D. Laser, M. Yaniv and S. Gottesfeld, L. Electrochem. Soc., 125, 358 (1978).
2. B.S. Hickman, H.L. Marcus and Y.L. Williams, "Stress corrosion cracking of Titanium Alloys in Methanolic and Aqueous Environments". Presented at an International symposium on Stress Corrosion Mechanisms in Titanium Alloy, Atlanta, Georgia, January 1971.

3. N.D. Tomashov, G.P. Chernova, Y.S. Rusca and G.A. Ayuyan, Electrochim. Acta, 19, 159 (1974).
4. E.N. Paleolog, A.Z. Fedotova, O.G. Derjagina and N.D. Tomashov, J. Electrochem. Soc., 125, 1410 (1978).
5. H.J. Mathieu, D.E. McClure and D. Landolt, J. Vac. Sci. Technol. 14, 1023 (1977).
6. T.T. Lin and D. Lichtman, J. Vac. Sci. Technol., 15, 1689 (1978).
7. M.L. Tarn and G.K. Wehner, J. Appl., 43, 2268 (1972).
8. A.A. Pozdeeva, E.I. Antonovskaya and A.M. Sukhotin, Corros. Sci., 6, 149 (1966).

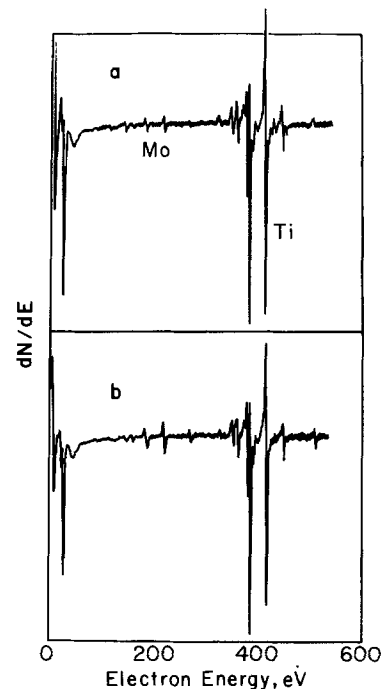


Fig. 4. AES of β alloy; a - fractured in UHV, b- after sputtering through the anodic oxide.

Acknowledgement: This work was supported by the office of Naval Research under contract number N00014-78-C-0094.

Manuscript submitted Sept. 28, 1979; revised manuscript received Dec. 21, 1979.

The Electrodeposition of Metal Chalcogenides

A. S. Baranski and W. R. Fawcett*

*Guelph-Waterloo Centre for Graduate Work in Chemistry,
Department of Chemistry, University of Guelph, Guelph, Ontario, Canada N1G 2W1*

Although metal chalcogenides can be grown on the parent metal by anodic oxidation in a sulphide containing electrolyte (1,2,3), and by cathodic reduction from aqueous solutions containing soluble metal and chalcogen compounds (4,5), no effective method of growing smooth coherent films of these compounds from non-aqueous solutions in a cathodic process has been reported in the literature. Recently, a general method of cathodic electrodeposition of metal chalcogenides on a variety of conducting substrates has been developed in this laboratory. The principle of the technique involves dissolving a salt containing the desired metal ion and the elemental chalcogen in a suitable non-aqueous solvent and depositing the metal ion at a suitable cathode under current control; the metal chalcogenide is formed by rapid reaction of a freshly deposited metal monolayer with the dissolved chalcogen. The technique has proven successful in depositing thin films of CdS, HgS, PbS, Tl₂S, Bi₂S₃, Cu₂S, NiS, CoS and CdSe. The substrate conductors have included Pt, Au, stainless steel, Ni, Zn and glass covered with a conducting film of SnO₂. The non-aqueous solvent was usually dimethylsulphoxide (DMSO) but deposits of good quality were also obtained from dimethylformamide (DMF) and ethylene glycol.

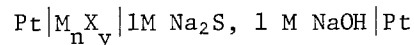
In the case of CdS, good quality deposits were obtained from DMSO solutions containing 6 g litre⁻¹ sulphur and 10 g litre⁻¹ CdCl₂ where electrolysis was carried out between Pt electrodes with a current density $\leq 2.5 \text{ mA cm}^{-2}$ at 110°C. The quality of the deposit was independent of sulphur and CdCl₂ concentration; moreover, addition of up to ten percent water to the solution had no significant effect on deposit quality. In this case there was no need to separate anolyte and catholyte compartments. Deposit characteristics depended on temperature, highly non-stoichiometric deposits being obtained below 90°C. This result undoubtedly reflects the need for the chemical reactions accompanying electron transfer to proceed at a rate sufficiently high to maintain an almost stoichiometric electrodeposit.

The properties of the electrodeposited CdS films are very interesting with respect to

their potential use in photovoltaic devices. X-ray examination of the films has shown that the crystallites are all oriented with their [111] planes parallel to the electrode surface. Although their specific resistivity is rather high ($\sim 10^6 \Omega \text{ cm}$), it may be considerably reduced by adding NaI to the catholyte compartment of a cell in which the anolyte and catholyte are separated by a barrier such as a fritted glass disc.

The technique for producing films of PbS, Bi₂S₃, NiS, CoS and Tl₂S was the same as that for CdS, CdCl₂ being replaced by PbCl₂, BiCl₃, NiCl₂, CoCl₂ and TlCNS, respectively. Slightly modified procedures were used in other cases. Cu₂S was electrodeposited from a solution containing 5 g litre⁻¹ CuCN, 5 g litre⁻¹ CsCl and 6 g litre⁻¹ S. The cuprous cyanide salt was used to prevent the formation of undesirable intermediates which arise when other copper salts are used; the CsCl was added to increase solution conductivity. In the case of HgS, the solution contained 23 g litre⁻¹ HgI₂ and 8 g litre⁻¹ KI together with the usual amount of sulphur. In the presence of iodide ion, the reduction potential of Hg⁺⁺ is shifted into a more negative region where complications due to oxidation processes are not present. CdSe was most conveniently deposited from a DMF solution saturated with selenium and containing 10 g litre⁻¹ CdCl₂ and 10 g litre⁻¹ KI. A lower current density ($\sim 0.5 \text{ mA cm}^{-2}$) was employed because of the reduced chalcogen concentration.

The semiconductor properties of the electrodeposited films have been examined in cells of the configuration



where M_nX_y represents a metal chalcogenide with metallic cation M^{+a} and chalcogenide anion X^{-b} (an=by). Illumination of a Pt electrode covered with metallic chalcogenide resulted in an anodic photocurrent in the cases of CdS and Bi₂S₃ indicating that the film had the properties of a n-type semiconductor. On the other hand, Tl₂S in the same configuration behaved as a photocathode, that is, as a p-type semiconductor (6). NiS and CoS had metallic conduc-

tivity and showed good catalytic properties for electrode processes involving sulphur compounds in which the sulphur is in a low oxidation state (7).

A detailed study of the properties of the electrodeposited films by scanning electron microscopy is currently in progress. The results of this investigation as well as an investigation of the mechanism of the process will be reported in future papers.

References

1. B. Miller and A. Heller, *Nature*, 262, 680 (1976).
2. L.M. Peter, *Electrochim. Acta*, 23, 165 (1978).
3. L.M. Peter, *J. Electroanal. Chem.*, 98, 49 (1979).
4. G. Hodes, J. Manassen and D. Cahan, *Nature*, 261, 403 (1976).
5. M.P.R. Panicker, M. Knaster and F.A. Kroger, *J. Electrochem. Soc.*, 125, 566 (1978).
6. H. Gerischer in *Physical Chemistry, An Advanced Treatise*, H. Eyring editor, Academic Press, New York, 1970, Volume IXA, Chapter 5.
7. G. Hodes, J. Manassen and D. Cahan, *J. Appl. Electrochem.*, 7, 181 (1977).

***Electrochemical Society Active Member.**

Manuscript submitted Sept. 27, 1979;
revised manuscript received Dec. 24, 1979.

Publication costs of this article were
assisted by the University of Guelph.

On the Limiting of Minimum Size of SOS/MOS Devices by the Microtwins in the Silicon

W. E. Ham,* M. S. Abrahams, and C. J. Buicchi
RCA Laboratories, Princeton, New Jersey 08540

Abstract

Plan view TEM micrographs of operating SOS/MOS transistors clearly show the extent and distribution of the silicon microtwins throughout the junction and channel regions. Numerous microtwins are found in the junctions without causing any detectable electrical problems. It is suggested that these defects will probably not be a fundamental limitation to geometrical reduction of SOS/MOS devices. The twins cause a dependence of field effect mobility on current flow direction.

There has been concern expressed that crystal imperfections in epitaxial silicon (100) on sapphire (1102) films in the thickness range usually used for MOS devices (0.4-0.7 μm) may limit the size reductions possible in the devices. Size reduction is generally considered to be critical to the successful implementation of devices in VLSI (Very Large Scale Integration) and VHSI (Very High Speed Integration) applications. We show in this note TEM micrographs which give a clear indication of the extent, distribution, and physical size of the most common defects in the SOS epi films, namely the microtwins, in an operating MOS transistor. It is shown that one can expect a population of these microtwins in any size device that might reasonably be considered for VLSI or VHSI applications.

We have shown previously that four systems of microtwins exist in typical SOS films used for devices using TEM methods [1-6]. X-Ray data has also indicated the presence of these systems [7]. This previous TEM work all used cross sectional samples which are only 1000 - 2000 \AA thick in a direction parallel to the Si-sapphire interfacial plane (The X-Y plane). Typical VHSI devices might have minimum X-Y plane geometries ten or more times this size. The cross sectional views show that many of the microtwins intersect the top surface of the film where the surface channel exists. It is usually found that the top surface density

of two of the four [111] twin systems is much greater than that of the others.

Information on the distribution of the defects in the X-Y plane is also necessary to determine their probable impact on very small geometry devices and on P-N junctions. In order to determine this distribution, MOS devices which were fabricated by conventional processes in the factory were examined using a vertical (or plan) view for the TEM specimen. The micrographs to be shown are from a transistor which was carefully measured for electrical performance before it was formed into a TEM compatible form. The transistor was typical of thousands of similar well behaved devices which were also measured.

The TEM specimens have had the polysilicon gate removed from the top of the epi island but the polysilicon remains on the adjacent sapphire as shown in Figure 1. The polysilicon remaining on the sapphire clearly indicates the approximate position of the source and drain p-n junctions since a self-aligned process was used for their formation. The device chosen for this micrograph has nominal channel dimensions which would be considered large for most VHSI applications. However the relatively large size coupled with a clear picture of the junction regions allows one to construct any size device that is desired on the micrograph.

Figure 2 shows a bright field TEM image obtained by thinning the specimen entirely from the sapphire side to a point where a very small amount of sapphire remains under the silicon. The entire channel region is visible in the low magnification micrograph (Fig. 2B) and the distribution of the microtwins is evident. It is especially relevant that there is no noticeable boundary present between the heavily doped source and drain regions and the lightly doped silicon in the channel region. There are numerous twins present in the junctions.

Since normal device operation is found in this transistor, it is reasonable to project that these microtwins will not be an obstacle to geometrical reduction of SOS devices to the micron and sub-micron range. Of course, traditional small device effects should be expected, but this data clearly shows that microtwins in the junction will not cause significantly inferior performance.

It has been found, however, that a maximum in the field effect mobility exists when the current flow direction is parallel to only one of the two vectors shown in Fig. 2D. For the device shown in Figure 2, a mobility degradation exists since the current flow direction is at $\sim 45^\circ$ to the vectors. The magnitude of this effect depends on the twin density on the respective [111] planes but is not strongly dependent on the type of surface channel (N or P). As the current flow direction is rotated through 360° in the plane of the sapphire surface (using test structures previously described [8]) maxima and minima occur with 180° symmetry. A typical ratio of maximum to minimum mobility for films with twin densities similar to that shown in Fig. 2 is 1.4 for both electrons and holes. This bipolar effect would not be expected if a simple stress mechanism were responsible for the anisotropy. A cooperative effect between the two twin systems which intersect the top surface is probably responsible. For very high twin densities [9] ratios as high as 10 have been observed. A more detailed discussion of these orientation effects is in preparation.

*Electrochemical Society Active Member.

Manuscript received Sept. 21, 1979.

Publication costs of this article were assisted by RCA Laboratories.

Acknowledgement

The authors thank E. M. Strouse and A. Buchholtz for preparing the samples for TEM thinning and A. T. O'Toole for performing the electrical measurements. Thanks are also due to R. T. Smith for useful discussions of the crystallography of the microtwins.

References

1. M. S. Abrahams and C. J. Buiocchi, "Cross Sectional Electron Microscopy of Silicon on Sapphire", *Appl. Phys. Lett.*, 27, 325 (1975).
2. M. S. Abrahams, "The Microstructure of Silicon on Sapphire by Transmission Electron Microscopy", *Proceedings of the Sixth European Congress on Electron Microscopy*, Jerusalem, p. 212 (1976).
3. W. E. Ham, "The Measurement and Interpretation of the Electrical Properties of SOS", *Extended Abstracts of the Electrochemical Society*, Vol. 76-2, Abstract No. 172, p. 462, Las Vegas (1976).
4. W. E. Ham, M. S. Abrahams, C. J. Buiocchi, and J. Blanc, "Direct Observation of the Structure of Thin, Commercially Useful Silicon on Sapphire Films by Cross Sectional Electron Microscopy", *J. Electrochem. Soc.* 124, 634 (1977).
5. M. S. Abrahams, J. Blanc, C. J. Buiocchi, and W. E. Ham, "Cross Sectional TEM Studies of Silicon on Sapphire", *IEEE SOS Workshop*, Vail, CO (1977), unpublished.
6. W. E. Ham, M. S. Abrahams, J. Blanc, and C. J. Buiocchi, "The Study of Microcircuits by Transmission Electron Microscopy", *RCA Rev.* 38, 351 (1977).
7. R. T. Smith and C. E. Weitzel, "Influence of Sapphire Substrate Orientation on SOS Crystalline Quality and SOS/MOS Transistor Mobility", *IEEE SOS Workshop*, Vail Co. (1978), unpublished.
8. W. E. Ham, "Test Pattern Design and Analysis for SOS/LSI", *Interim Report No. 1*, Contract No. 5-35916, National Bureau of Standards, Gaithersburg, MD (1977). (NBS Special Publication 400-56).
9. M. S. Abrahams and W. E. Ham, "Some Effects of Planar Defects near the Si/SiO₂ Interface on the Electrical Properties of Silicon on Sapphire Devices", *Appl. Phys. Lett.* 33 (8), 773 (1978).

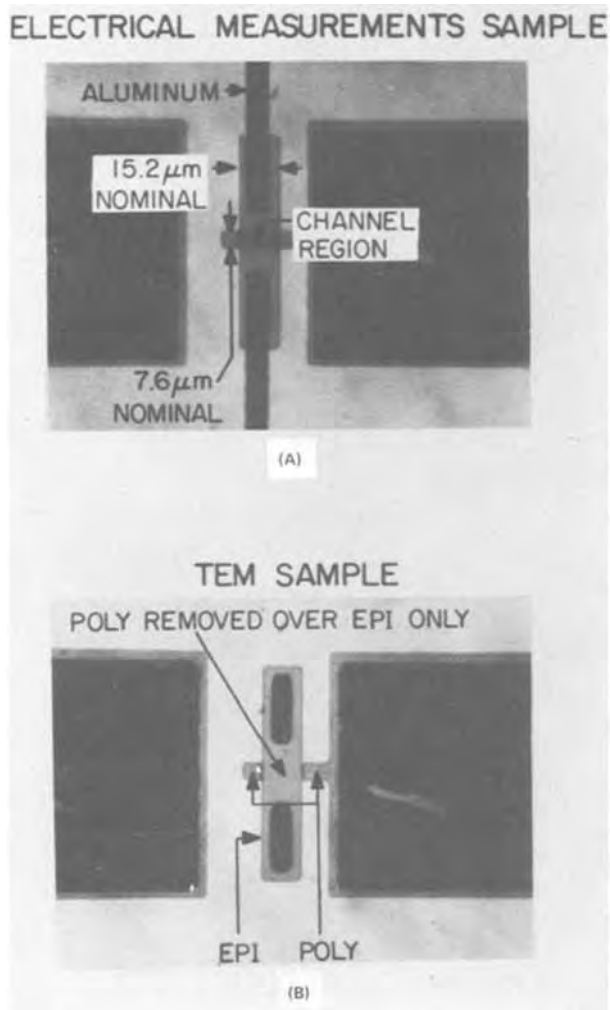


Figure 1.

Optical micrographs of transistors similar to those used for the TEM samples. Top view with light transmitted through the sapphire.

- (A) Configuration used during electrical measurements.
- (B) TEM sample before ion thinning. The poly over the epi island only was selectively removed. The aluminum remains only in the contact holes.

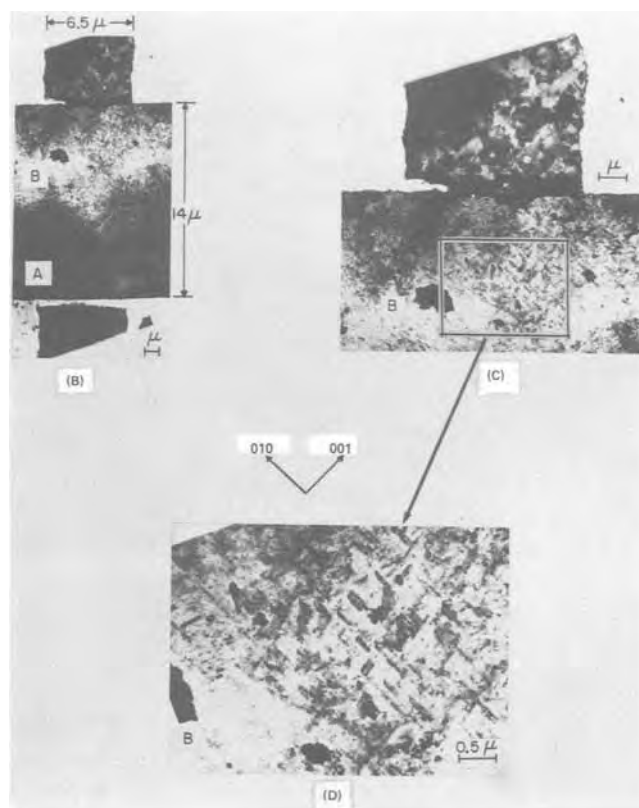
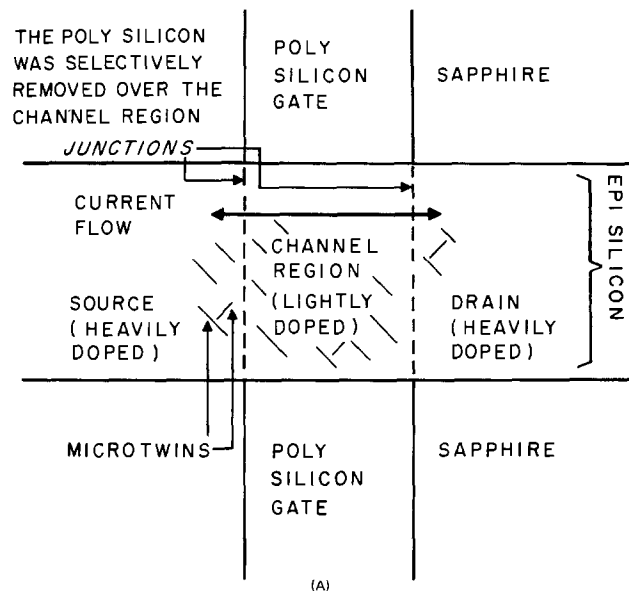


Figure 2.

Plan views of the same SOS/MOS transistor at different magnifications.

- (A) Schematic
- (B) Transmission electron micrograph showing overall view of transistor structure. Dark region at A is thick region of sapphire.
- (C) TEM showing grain structure of poly silicon at top and microtwins in the epi silicon at bottom. Dark regions at B are artifacts.
- (D) TEM showing microtwins in epi silicon.

B, C, and D were taken in bright field, many beam condition with $B = 100$.

Effect of Carbon on the Dissolution of Fused Silica in Liquid Silicon

B. Bathey, H. E. Bates,* and M. Cretella**

Mobil Tyco Solar Energy Corporation, Waltham, Massachusetts 02154

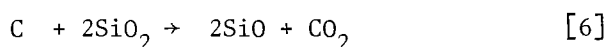
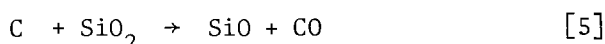
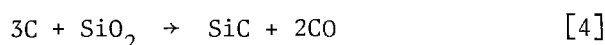
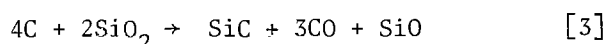
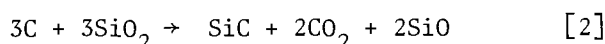
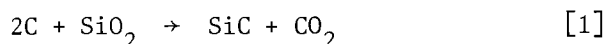
Dissolution of industrial silica in molten silicon was studied by Chaney and Varker (1). For EFG silicon ribbon growth (2), graphite is generally used as a die material with either a graphite or quartz crucible to contain the melt. Since various reactions are possible between oxygen, silicon, and carbon (3,4,5), an effort was made to measure the dissolution rate of silica in the presence of carbonaceous atmosphere.

The experimental procedure consisted of inserting a GE-204 quartz rod into liquid silicon at a given temperature. After four hours exposure at temperature, the rod was removed from the melt and the change in the diameter of the rod was measured to calculate the dissolution rate. It was found that the addition of carbon into the melt increased the dissolution rate of quartz. Fig. 1 shows the effect of adding various amounts of carbon to the melt on the dissolution rate. It was also found that the dissolution was slightly higher for radio frequency stirred melts compared with resistance heated melts. Fig. 2 shows the dissolution rates with and without carbon in the melts as a function of temperature on Arrhenius plots. For melts with carbon, a SiO₂/C surface area ratio of about 10.5 was selected. This is a typical ratio for an EFG ribbon production unit. However, it is possible to estimate approximately the results at other ratios from these two graphs.

The depth of the groove developed in the liquid-solid-ambient (argon) interface meniscus due to surface tension driven convective flow was very irregular and no correlation with exposure time could be established.

After exposure to liquid silicon, quartz samples were examined by X-ray diffraction. In

addition to α -cristobolite, β -SiC was detected. The following reactions are possible between quartz and carbon depending upon the melt temperature and the partial pressure of the gas species.



Among these reactions [4] and [5] are thermodynamically favorable. Schmid et al. (3) have made a complete thermodynamic analysis of these reactions and established the regions of stability of these reactions as a function of pressure and temperature. On the basis of the experimental evidence and thermodynamic analysis, we conclude that the presence of carbon in the melt enhances the dissolution of silica.

REFERENCES

- (1) R. E. Chaney and C. J. Varker, "The Dissolution of Fused Silica in Molten Silicon," *J. Crystal Growth* **33**, 188 (1976).
- (2) J. C. Swartz, T. Surek, and B. Chalmers, "The EFG Process Applied to the Growth of Silicon Ribbons," *J. Electronic Materials* **4**, 255 (1975).
- (3) F. Schmid, C. P. Khattak, T. G. Digges, and L. Kaufman, "Origin of SiC Impurities in Silicon Crystals Grown From the Melt in Vacuum," *This Journal*, **126**, 935 (1979).
- (4) N. Klinger, E. L. Strauss, and K. L. Komaneck, "Reactions Between Silica and Graphite," *J. American Ceramic Soc.* **49**, 369 (1966).

* Now with Energy Materials Corp., Harvard, Massachusetts, U.S.A.

** Electrochemical Society Active Member.

Key Words: dissolution, silicon, silica, carbon.

- (5) R. A. Roques and D. M. Coldwell, "Silicon Material Task, Part III, Low-Cost Silicon Solar Array Project," Texas Instruments, Inc., Report No. 03-76-36, JPL Contract No. 954412, June 1976.

Manuscript received Nov. 5, 1979.

Publication costs of this article were assisted by Mobil Tyco Solar Energy Corporation.

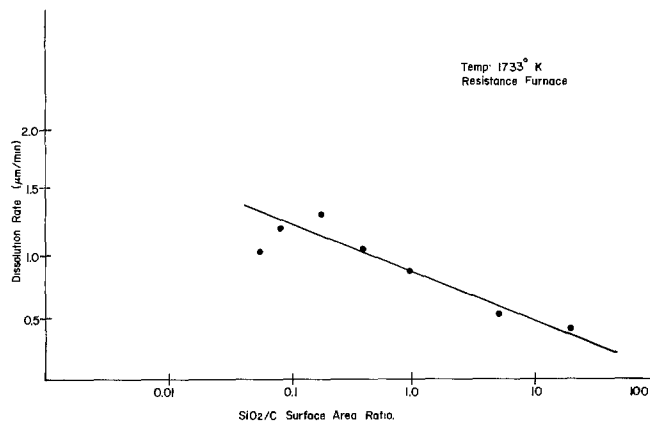


Fig. 1. The Dissolution Rate of Quartz As A Function of SiO_2 Surface Area Ratio in the Liquid Silicon.

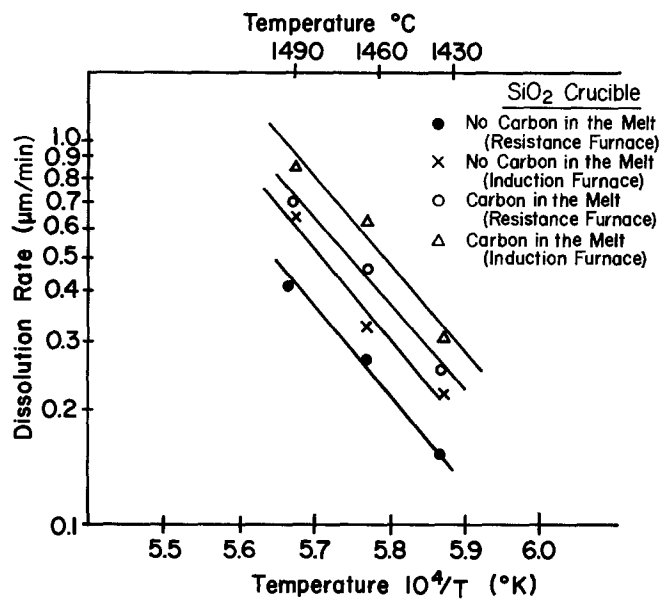


Fig. 2. The Dissolution Rate of Quartz in Liquid Silicon as a Function of Temperature.

A Cyclable Lithium Organic Electrolyte Cell Based on Two Intercalation Electrodes

M. Lazzari

Centro Studio Processi Elettrodici del C.N.R., Polytechnic of Milan, Milan, Italy

and B. Scrosati*

Istituto di Chimica Fisica, University of Rome, Rome, Italy

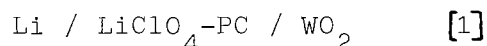
Lithium organic electrolyte batteries based on intercalation or topochemical reactions are currently considered of great interest as high energy, secondary power sources. However, while the complete reversibility of the intercalation electrodes has been extensively proved(1-3), still remain some problems in overall cell rechargeability, mainly related to the lithium electrode, which presents a very poor plating-stripping efficiency in organic electrolytes(4-6). This problem has been largely emphasized and various solutions, especially directed to the selection of improved electrolyte media(7), have been proposed.

In alternative, we have considered the possibility of replacing the lithium electrode with another intercalation electrode, in order to realize a cell with two intercalation electrodes having a different lithium activity. With **respect** to systems using lithium negatives, such a combination should result in lower potential values but in higher rechargeability characteristics.

Indeed, the beneficial effect of this combination has been already proved in our laboratories for the cyclability of copper solid-state cells(8).

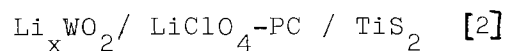
To test its validity also in lithium organic electrolyte cells, we have considered the $\text{Li}_x\text{WO}_2/\text{Li}_y\text{TiS}_2$ system. The choice has been motivated by the fact that both Li_xWO_2 (9) and Li_xTiS_2 (1,2) are reversible electrodes and have e.m.f. values vs Li which range from 1.1V to 0.5V and from 2.6V to 1.9V, respectively, for $0 < x < 1$. Consequently, the e.m.f. range of the $\text{Li}_x\text{WO}_2/\text{Li}_y\text{TiS}_2$ system should fall between 2.1V ($x=1, y=0$) and 0.8V ($x=0, y=1$), a range which may be considered of practical interest.

As preliminary test of the above considerations, we have first assembled a small cell of the type



by subsequently contacting in a teflon container having nickel terminals, a lithium disc, three glass wool separator discs soaked with 1M LiClO_4 solution in propylene carbonate(PC) and a small amount (typically around 20 mg) of powdered WO_2 .

After discharge at 0.1 mAcm^{-2} to 0.5 V cut-off, the cell was disconnected and the lithium disc replaced with powdered TiS_2 , in order to form the cell



*Electrochemical Society Active Member

Key words: cyclable lithium batteries,
intercalation electrodes.

Cell [2] had an open circuit voltage (OCV) of 2.0V at 25 °C.

A typical example of 'charge-discharge'

cycles, which practically involve the reversible transference of lithium across the cell, is shown in figure 1.

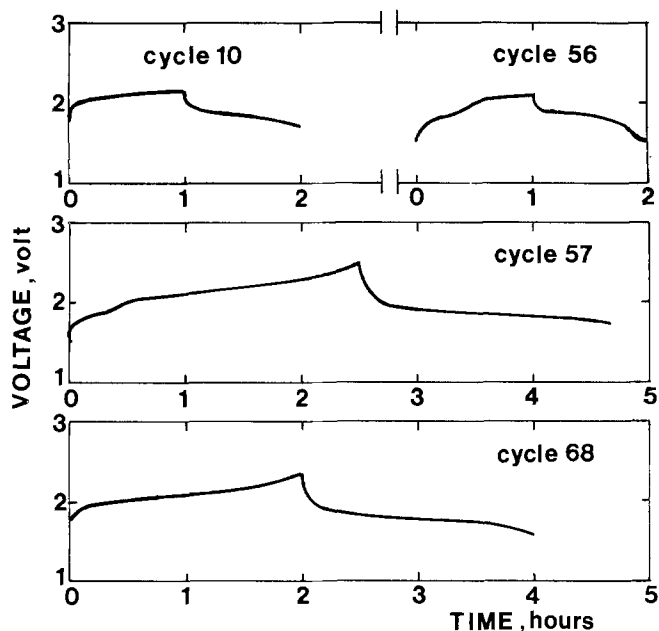


Figure 1. Typical 'charge-discharge' cycles of cell [2] at 0.1 mAcm^{-2} and at room temperature.

Upon prolonged cycling, no massive indications of cell deterioration, such as progressive increase of internal resistance and substantial lack of 'charge-discharge' efficiency were noticed.

The results appear encouraging for expanding in more details the preliminary study here reported as well as for extending the investigation of lithium 'concentration' cells to other electrodic systems.

This research activity is presently in progress in our laboratories.

ACKNOWLEDGMENTS

This work has been carried out with financial support from the Consiglio Nazionale delle Ricerche (C.N.R.).

REFERENCES

1. M.S. Whittingham, *Prog. Solid St. Chem.* **12**, 41 (1978).
2. G.L. Holleck and J.R. Driscoll, *Electrochim. Acta*, **22**, 647 (1977).
3. D.W. Murphy and P.A. Christian, *Science*, **205**, 651 (1979).
4. J.O. Basenhard, *J. Electroanal. Chem.*, **94**, 77 (1978).
5. R.D. Rauh, T.F. Reise and S.B. Brummer, *This Journal*, **125**, 186 (1978).
6. R.D. Rauh and S.B. Brummer, *Electrochim. Acta*, **22**, 75 (1977).
7. V.R. Koch and J.H. Young, *Science*, **204**, 499 (1979).
8. B. Scrosati, M.A. Voso and M. Lazzari, *This Journal*, **126**, 699 (1979).
9. D.W. Murphy, F.J. Di Salvo, J.N. Carides and J.V. Waszczak, *Mat. Res. Bull.*, **13**, 1395 (1978).

Manuscript received Dec. 19, 1979.

Publication costs of this article were assisted by the University of Rome.



Safety Studies on Li/SO₂ Cells

II. Kinetics of Lithium-Organic Solvent Exothermic Reactions

A. N. Dey* and R. W. Holmes

P. R. Mallory & Company, Incorporated, Laboratory for Physical Science, Burlington, Massachusetts 01803

ABSTRACT

An isothermal DTA technique was developed for studying the kinetics of the heterogeneous exothermic reactions involving lithium metal and organic solvents used in the Li/SO₂ batteries. The results showed that while film forming agents such as SO₂ and PC retard the Li + AN exothermic reaction (the crucial reaction for Li/SO₂ cell safety), the organic solvents such as MF, DME, DG, and THF enhance the Li + AN exothermic reaction most probably due to an enhanced solubilizing effect on the Li film. The above solvents by themselves were found to be quite stable with Li.

Li/SO₂ organic electrolyte system is one of the most advanced high energy density systems (1-4) known to date and is available from several manufacturers. Although these batteries are quite abuse resistant for a variety of applications, it was attempted to explore the feasibility of improving the abuse resistance of these cells even further so that these are safe under all user conditions. We carried out DTA (differential thermal analysis) of individual cell components (5) as well as the cells (6) in an effort to identify the reactive cell constituents which could initiate and/or propagate a thermal runaway. The commercially available Li/SO₂ cells contain an Li anode, porous carbon cathode pasted on expanded aluminum grid, and an organic electrolyte containing LiBr, acetonitrile (AN), and liquid SO₂. SO₂ acts as the cathode active material.

From the DTA studies we have shown that the reactions most likely to initiate a thermal runaway are the Li-organic solvent reactions, particularly the exothermic Li-acetonitrile reaction which occurs at room temperature. For this reason, we chose to concentrate on the study of the kinetics of this reaction in an effort to find ways and means of quenching it. We also carried out kinetic study of several other organic solvents in an effort to find suitable candidates for replacing acetonitrile in the electrolyte of the Li/SO₂ cells or adding to it, if possible. The extent of the reaction is proportional to the heat evolved and the rate of the reactions is proportional to the rate of the heat evolution at a constant temperature and at a constant surface area of the Li. Therefore, an isothermal DTA technique was used to study these reactions. The experimental details and the results are reported here.

Experimental

The Mettler TA2000 Differential Thermal Analysis System with the high pressure hermetic crucibles, described elsewhere (5), was used for the isothermal DTA runs. A 0.098 in. diam piece of 0.005 in. thick Li foil weighing 0.00029g was placed in the DTA sample crucible in an argon filled dry box. 20 μl of the

appropriate organic solvent was injected into the crucible and the crucible sealed. The Li disk size, weight, and the location inside the sample container as well as the volume of the organic solvent were kept as constant as possible from run to run. The mixtures were then heated very quickly to various temperatures in the DTA furnace and maintained at those temperatures while the differential temperatures were recorded as a function of time yielding isothermal DTA thermograms at the various temperatures.

All the organic solvents used were of the highest purity available from Eastman Kodak and were used as received except for PC which was vacuum distilled over Li foil prior to use.

The Li foils were used as received from the Foote Mineral Company and contained 1% Na as impurity. The foils were shiny in appearance and all the experiments were carried out using freshly punched Li from one roll except for some preliminary experiments with AN for which the Li disks were punched several days prior to the experiments. Although the Li foil was shiny in appearance it is reasonable to assume that it has a thin protective film and the freshly punched areas of the disks are probably most active towards the organic solvents. Therefore, the duration between the punching of a Li disk and the isothermal run was kept constant in order to reduce any variation of the activity of the Li surface from run to run.

Results and Discussion

Some typical isothermal DTA thermograms at various temperatures for the Li + AN system are shown in Fig. 1. It can be shown that the slopes of the rising portion of the DTA thermogram at the point of inflection of the temperature-time curve can be expressed as

$$\frac{d\Delta T}{dt} = k \left(\frac{\Delta H}{L + S} \right) \quad [1]$$

where ΔH = heat of the reaction, k = zeroth order rate constant, L = heat capacity of reaction mixture, and S = heat capacity of container, when the DTA furnace is maintained at a constant temperature and the chemical reaction obeys zeroth order kinetics,

* Electrochemical Society Active Member.
 Key words: DTA, kinetics, battery, organic.

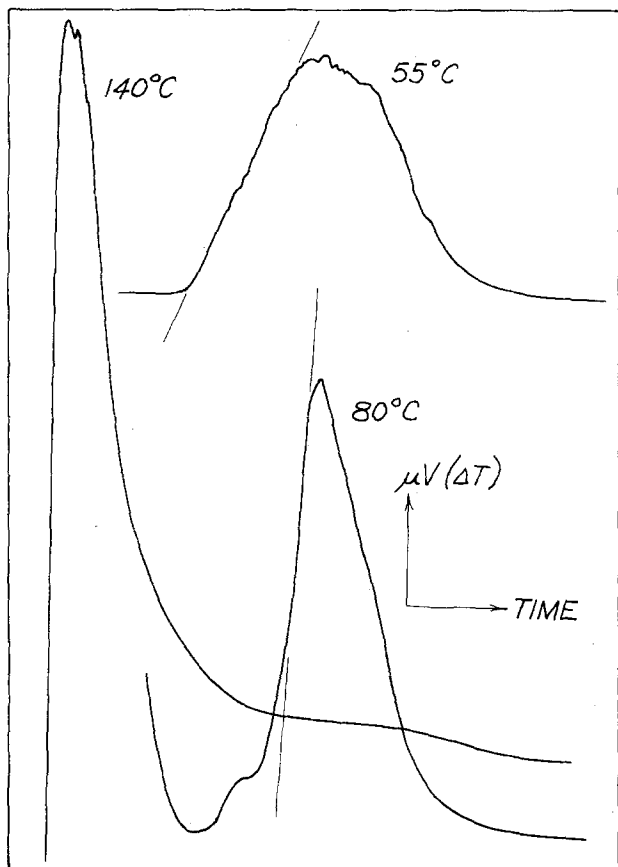


Fig. 1. Typical isothermal DTA thermograms of Li + AN system at various temperatures.

Since ΔH , L , and S are constants, the slope is proportional to the rate constant of the Li^+ solvent reaction which is controlled by the reaction temperature and the surface area of the Li disk which was kept constant for all the runs.

An Arrhenius plot of the above slopes as a function of the reaction temperature for the Li + AN system with Li disks cut several days prior to the experiment is shown in Fig. 2. The plot is linear and the energy of activation as determined from the least squares slope (excluding the point at the lowest temperature) was $13 \text{ kcal mole}^{-1}$ with a frequency factor of 8. A similar plot of the same system with freshly cut Li disks as shown in Fig. 2 was also linear and had a higher reaction rate and a slightly lower activation energy; $10 \text{ kcal mole}^{-1}$. This probably reflects the effect of the Li film (formed during storage in the dry box) on the kinetics of the Li + AN reaction.

The effect of LiBr on the kinetics of the Li + AN reaction was studied and the Arrhenius plot is also shown in Fig. 2. The activation energy of the reaction was reduced further to 6 kcal mole^{-1} possibly indicating the catalytic effect of Li^+ (7) on the Li + AN reaction.

Although PC was found to be rather inert towards Li at room temperature, it reacted with Li at higher temperatures. The energy of activation as determined from the linear Arrhenius plot, shown in Fig. 3, was $22 \text{ kcal mole}^{-1}$.

The effect of addition of PC on the Li and AN reactivity was studied. The results are shown in Fig. 3. The addition of PC, up to 20%, resulted in a lowering of the reaction rates without altering the energy of activation significantly. This probably indicates that the Li + AN reaction is occurring through a film which only lowers the reaction rates without altering the activation energy. PC is known (8) to form an insoluble film of Li_2CO_3 on Li thus protecting it from further attack. With 50% PC, the reaction rates were

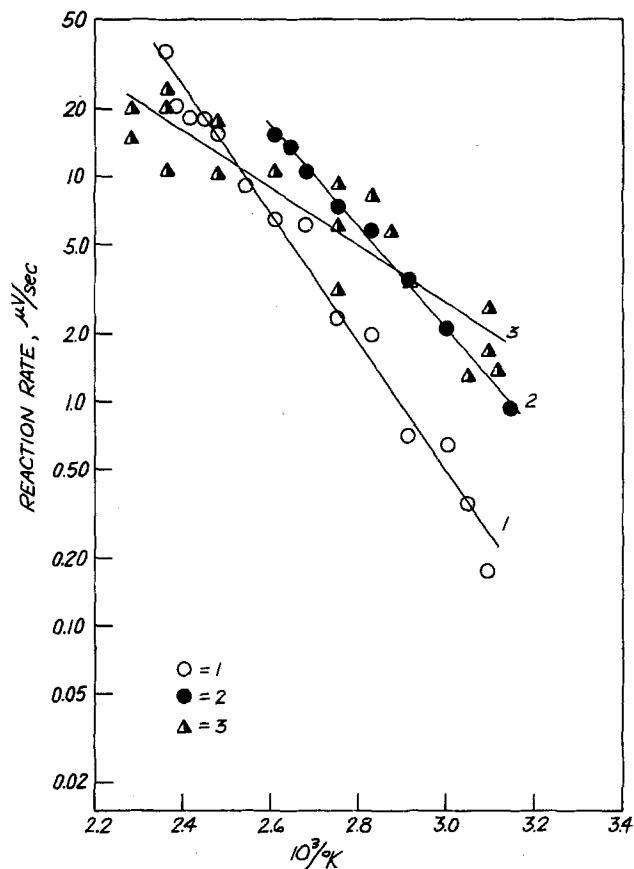


Fig. 2. Arrhenius plots of the Li + AN system; curve 1, with Li disks aged in dry box; curve 2, freshly cut Li disks; curve 3, with 0.32M LiBr in AN.

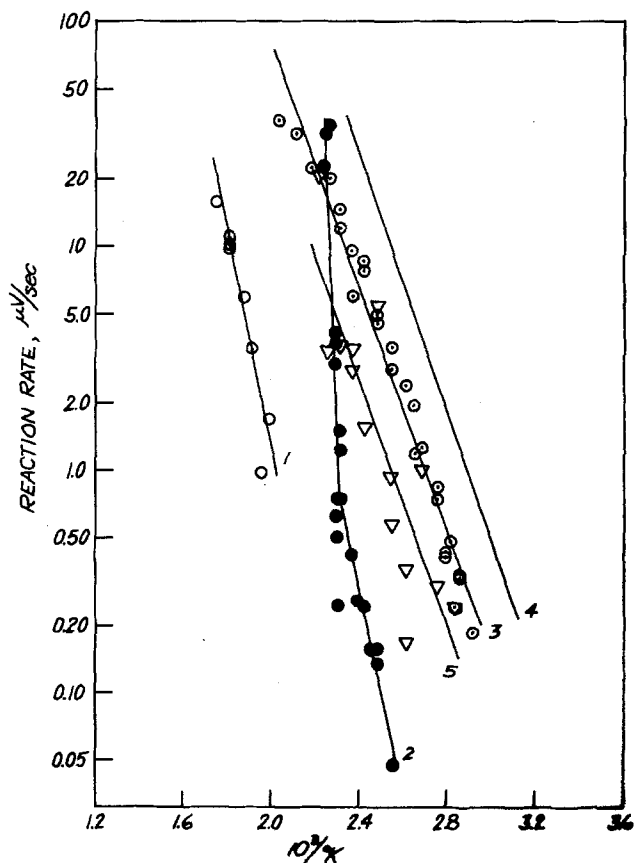


Fig. 3. Arrhenius plots of the Li + AN + PC system; curve 1, 0% AN; curve 2, 50% AN; curve 3, 80% and 95% AN; curve 4, 100% AN; and curve 5, 0% PC and 3% SO_2 .

reduced drastically, and the Arrhenius plots showed two linear regions corresponding to activation energies of 22 and 113 kcal mole⁻¹ for the lower and the upper region, respectively. In this mixture, the reaction temperatures are very high, and as such, complex reactions may occur to give rise to this type of behavior.

The addition of small amounts of SO₂ (3%) to the AN resulted in a sharp reduction of the reaction rates, as shown in Fig. 3, without altering the energy of activation. This demonstrates the excellent film forming ability of small amounts of SO₂ and its efficacy in reducing the Li + AN reactivity, the key element in the safety of the Li/SO₂ cells.

Li was found to be stable in MF (methyl formate) at ambient temperature and reacted only at very high temperatures. Surprisingly, the reaction rates were found to be considerably lower than those of the Li + PC. Also the energy of activation, as determined from the Arrhenius plot shown in Fig. 4, was almost twice that of the Li + PC, viz. 43 kcal mole⁻¹.

The effect of MF on the Li + AN reaction was studied. The reaction rates increased significantly with 5% MF present giving rise to a nonlinear plot as shown in Fig. 4. At higher concentration of MF, the reaction was too rapid, particularly at the higher temperature, so that it was not possible to measure the rates by the isothermal DTA method. A substantial part of the reaction was completed during the heating period so that the slopes were not representative of the reaction rates. The Arrhenius plots with 20% MF were found to be meaningless as shown in Fig. 4. In a normal isothermal DTA run, as shown in Fig. 5(a), the first short peak represents the difference in temperature between the sample and the reference during the short heating period. Note that the differential temperature reached the base line before it shot up as a result of the exothermic reaction. Also the area under this major peak, representing the heat released, is very similar for all the runs at various temperatures

for a particular system, indicating the correctness of our assumptions regarding reasonable adiabaticity. The abnormal isothermal runs with the Li + AN + MF system, is shown in Fig. 5(b). Note that the differential temperature does not reach the base line after the first short peak (corresponding to the heating of the sample) prior to the reaction exotherm, indicating that the reaction was already initiated during the heating up period. Also, the areas under these exothermic peaks are different from run to run. These results demonstrate the limitation of this technique which is applicable to only those heterogeneous reactions which have a sufficiently long induction period during which the samples may be heated without any substantial reactions. In systems such as Li + AN + MF, the induction periods are too short, most likely due to the increased solubility of the reaction products in the mixed solvents. Thus, although MF by itself is less reactive to Li, addition of it to AN increased the Li solvent reactivity to a greater extent than the reactivity with the individual solvents. The above results indicate that although pure MF may be used by itself in Li/SO₂ cells, the mixture of MF and AN may be deleterious from a safety standpoint. The reported (9) unsafe behavior of Li/SO₂ cells with MF in the electrolyte may be due to the presence of other impurities which may act as cosolvents with MF to dissolve the protective lithium film.

The Li + DME (dimethoxyethane) reaction was found to be extremely slow at the moderate to high temperatures used in our studies. However, the reactivities of AN + DME mixtures of Li were examined successfully. The Arrhenius plots, shown in Fig. 6, were found to be linear. The reaction rates were increased significantly by the addition of DME to AN and the activation energies were reduced. The results again point to a solubilizing effect of the AN + DME mixed solvents towards the lithium film formed as a result of the Li-solvent reaction.

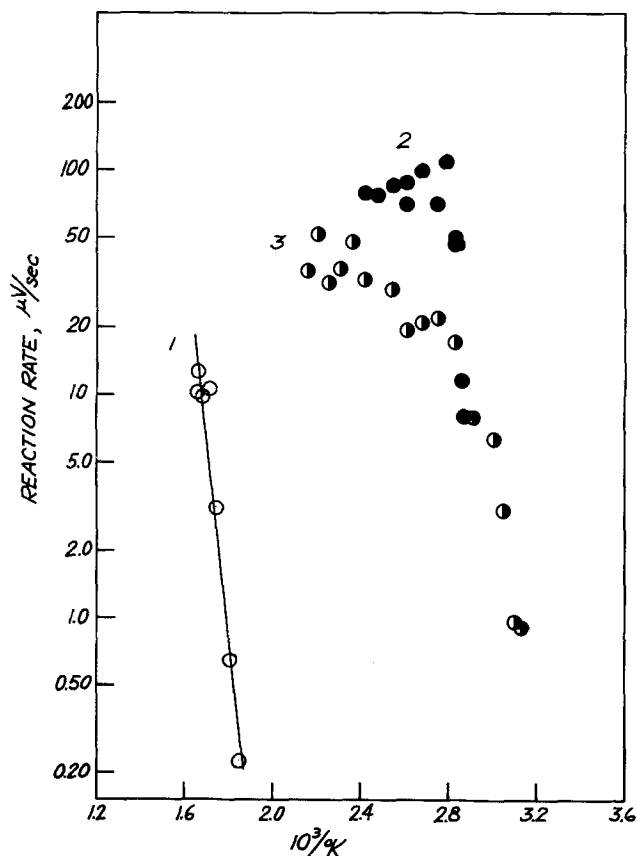


Fig. 4. Arrhenius plots of Li + AN + MF system; curve 1, 0% AN; curve 2, 80% AN; and curve 3, 95% AN.

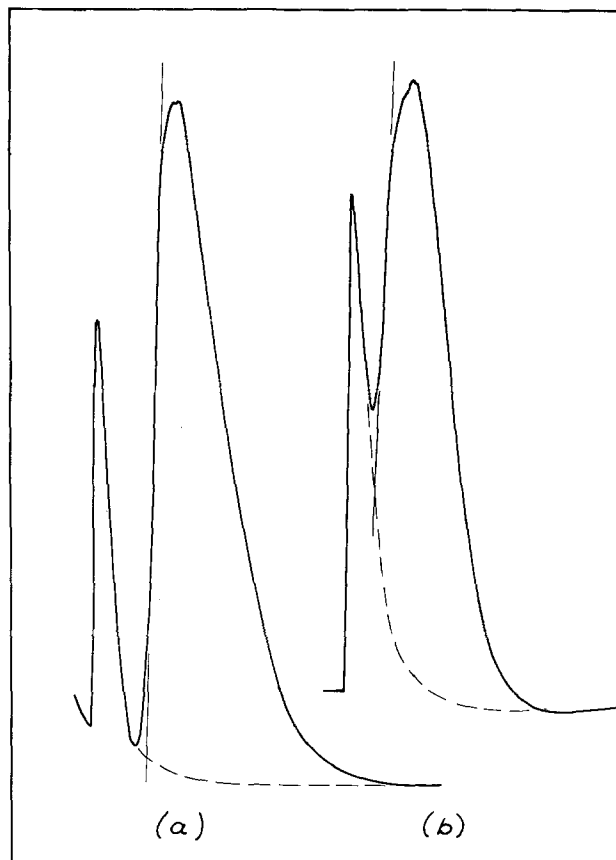


Fig. 5. Isothermal DTA thermograms; (a) normal runs, (b) for reactions with short induction periods as with Li + AN/MF (80/20).

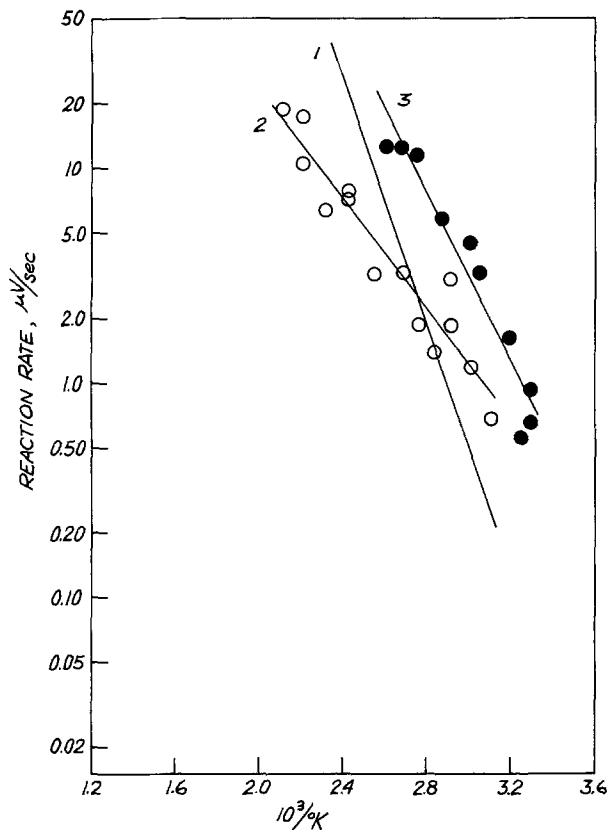


Fig. 6. Arrhenius plots of Li + AN + DME system; curve 1, 0% DME; curve 2, 5% DME; and curve 3, 20% DME.

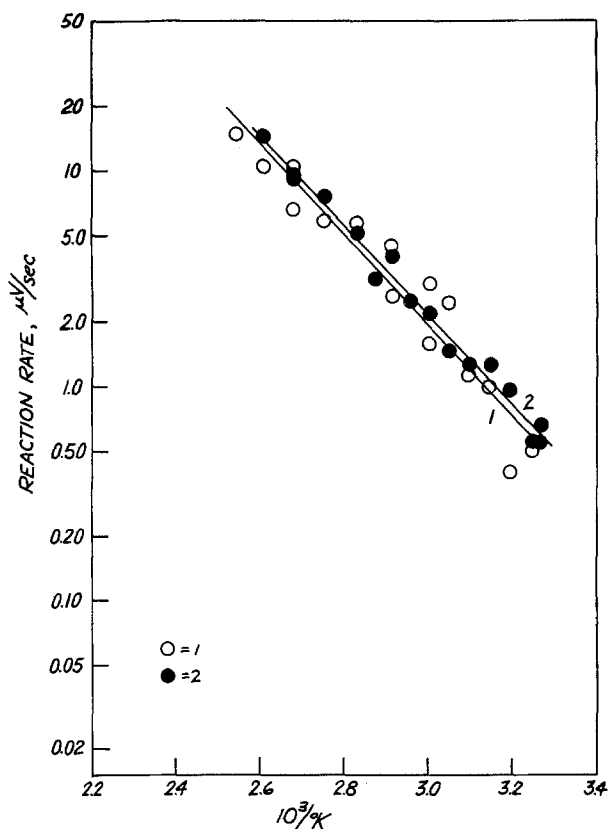


Fig. 7. Arrhenius plots of curve 1, Li + AN/THF (95/5); and curve 2, Li + AN/DG (95/5) systems.

Table I. The activation energy and the frequency factor of various Li-organic solvent heterogeneous reactions determined by isothermal DTA method

Reactions	Activation energy (kcal mole ⁻¹)	Frequency factor
1. Li + AN	13.1 ± 0.5	8.3
2. Li (freshly cut) + AN	10.3 ± 0.3	7.1
3. Li + 0.32M LiBr, AN	5.9 ± 0.6	4.3
4. Li + PC	22.3 ± 3.2	9.8
5. Li + AN/PC (95/5)	15.0 ± 0.6	8.8
6. Li + AN/PC (80/20)	11.1 ± 0.6	6.6
7. Li + AN/PC (50/50)	21.7 ± 2.5	10.8
	112.9 ± 22.6	56.8
8. Li + AN/SO ₂ (97/3)	12.5 ± 2.1	7.0
9. Li + MF	42.7 ± 5.2	16.7
10. Li + AN/DME (95/5)	5.9 ± 0.5	3.9
11. Li + AN/DME (80/20)	9.1 ± 0.9	6.4
12. Li + AN/DG (95/5)	9.5 ± 0.3	6.6
13. Li + AN/THF (95/5)	9.6 ± 0.8	6.6

Similar runs with AN + DG (diglyme) and AN + THF (tetrahydrofuran) systems (Fig. 7) also showed enhanced reactivity.

The energy of activation and the frequency factors of all the above reactions are presented in Table I.

Conclusions

The isothermal DTA technique developed for studying the kinetics of the heterogeneous reactions involving Li and organic solvents at various temperatures provided an effective tool to assess the usefulness of solvent additives to the Li/SO₂ electrolyte in improving the safety of the Li/SO₂ cells. The results show that whereas SO₂ and PC are effective in reducing the Li + AN reactivity, organic solvents such as MF, DME, THF, and DG enhance the Li + AN reactivity and are unsuitable electrolyte additives for safety, although these may be used in place of AN in the electrolyte.

Acknowledgment

The authors wish to thank Dr. Sol Gilman and Dr. Per Bro for helpful discussions. The work was carried out under a contract from U.S. Army ERADCOM, Contract No. DAAB07-78-C-0563.

Manuscript received Dec. 27, 1978.

Any discussion of this paper will appear in a Discussion Section to be published in the December 1980 JOURNAL. All discussions for the December 1980 Discussion Section should be submitted by Aug. 1, 1980.

Publication costs of this article were assisted by P. R. Mallory & Company, Incorporated.

REFERENCES

1. P. Bro, R. Holmes, N. Marincic, and H. Taylor, Paper No. 45, "Proc. Intl. Power Sources Symposium," Brighton, England (1974).
2. P. Bro, H. Y. Kang, C. Schlaikjer, and H. Taylor, "Tenth Intersociety Energy Conversion Engineering Conference," Newark, Delaware, p. 432 (1975).
3. H. Taylor and B. McDonald, "Proc. 27th Power Sources Symposium," p. 66, Atlantic City, N.J. (1976).
4. E. S. Brooks, "Proc. 26th Power Sources Symposium," p. 42, Atlantic City, N.J. (1974).
5. A. N. Dey and R. W. Holmes, *This Journal*, **126**, 1637 (1979).
6. A. N. Dey, *This Journal*, To be published (May, 1980).
7. A. Soffer and E. Yeager, Paper 547 presented at The Electrochemical Society Meeting, Seattle, Washington, May 21-26, 1978.
8. A. N. Dey, *Thin Solid Films*, **43**, 131 (1977).
9. H. F. Hunger and J. A. Christopoulos, R&D Technical Report ECOM-4292, February 1975.

Electrochemistry of Amorphous V_2S_5 in Lithium Cells

A. J. Jacobson and S. M. Rich

Exxon Research and Engineering Company, Corporate Research, Linden, New Jersey 07036

ABSTRACT

Amorphous V_2S_5 , prepared by thermal decomposition of $(NH_4)_3VS_4$, has been found to react readily with n-butyl lithium to give amorphous compositions $Li_xV_2S_5$ ($x \leq 6.0$). In lithium electrochemical cells, V_2S_5 cathodes react with 2.5 Li per vanadium above 1.40V on primary discharge at 0.5 mA/cm². Eighty-five percent of this capacity is recovered on the first recharge to 2.8V also at 0.5 mA/cm². On subsequent cycling the capacity eventually falls to 30% of the initial value with an accompanying change in the voltage composition profile.

Interest in ambient temperature secondary lithium batteries has focused recently on the use of crystalline compounds as cathode materials (1). In particular the layered dichalcogenide, TiS_2 , has been found to possess many of the desirable characteristics for a lithium battery cathode (2). The Li_xTiS_2 system exists as a continuous nonstoichiometric phase for $0 \leq x \leq 1$ and has a high free energy of formation (3). Reaction with lithium produces only a small volume expansion of the TiS_2 lattice which together with high lithium diffusivity results in a highly reversible cathode system. Several other layered and chain structure compounds have also been investigated, including the trichalcogenides (4, 5), $KFeS_2$ (6, 7), $NbSe_4$ (8), MPS_3 ($M = Ni, Fe$) (9, 10), and MoO_3 (11-14). Many of these systems have, in principle, increased capacity over TiS_2 for reaction with lithium in that they contain either high oxidation state transition metal ions, e.g., $Mo(VI)O_3$, or polyanion bonds in addition to a reducible transition metal. However, for most of these compounds and also for many of the dichalcogenides reactions with lithium result in structure changes of the host lattice which limit reversibility (3). In addition to the layer and chain structure compounds, the reaction of lithium with a number of three-dimensionally connected oxide structures including V_6O_{13} (15), Cr_3O_8 (1, 16, 17), TiO_2 (anatase) (18), and a number of MO_2 oxides with the rutile structure (19) have been studied. Of these, V_6O_{13} when prepared by thermal decomposition of ammonium metavanadate has recently been reported to have high energy density (800 W-hr/kg) and good secondary characteristics.

We recently reported that amorphous MoS_2 (a- MoS_2) prepared by a low temperature precipitation technique exhibits superior characteristics to crystalline MoS_2 in lithium cells (20). Higher coulombic capacities were obtained and the lithium a- MoS_2 reaction was found to be highly reversible. While the Li/a- MoS_2 system itself does not possess high energy density, the electrochemical results have led us to explore more generally the reactions of alkali metals with amorphous materials, and in this paper we describe results obtained for a- V_2S_5 which formally contains vanadium in its highest oxidation state (V).

Amorphous V_2S_5 (a- V_2S_5) is prepared by the thermal decomposition of $(NH_4)_3VS_4$ in vacuum or in an inert atmosphere and is stable over only a limited temperature range (21-23). For example, Prasad and Müller (23) reported the formation of V_2S_5 from $(NH_4)_3VS_4$ in 1 atm N_2 at 190°C and its decomposition above 290°C with loss of sulfur and the formation of crystalline V_2S_3 . a- V_2S_5 is considered to be a definite composition and not a mixture of a lower sulfide and noncrystalline sulfur. No sulfur can be extracted with CS_2 and V_2S_5 dissolves in aqueous alkalis to form thiovanadates (VS_4^{3-}). A model for

the structure of V_2S_5 has been determined from an analysis of the x-ray diffuse scattering (24). From the radial distribution function, six V-S distances at 2.34Å and six V-V distances at 3.42Å were obtained compatible with a microcrystalline model based on a distorted CdI_2 layer structure. The excess sulfur is accommodated at the edges of small (20Å) particles containing approximately 15 vanadium atoms.

In this report we describe our results for the synthesis of amorphous V_2S_5 and its chemical and electrochemical reactions with lithium.

Experimental

Ammonium thiovanadate was prepared by a modification of previously described procedures (20, 21). Sodium pyrovanadate ($Na_4V_2O_7$, 28g) was dissolved in 100 ml water and 300 ml of 55% $(NH_4)_2S$ added. The solution was cooled to 0°C. Pure H_2S was bubbled through the solution for a total of 5 hr. After this time dark violet crystals were precipitated in the reaction flask. The apparatus was purged with nitrogen and the crystals removed by vacuum filtration, washed with $(NH_4)_2S$ and ethanol and dried under nitrogen. The dry crystals were transferred to a helium filled glove box. The composition was confirmed by elemental analysis which gave 5.27% H, 17.71% N, 22.02% V, 54.84% S (calc 5.15% H, 18.02% N, 21.84% V, and 55.00% S). Thermogravimetric analysis data for the decomposition of $(NH_4)_3VS_4$ were obtained using a du Pont thermal analyzer. Data were obtained in argon at a heating rate of 10°C/min and are shown in Fig. 1. The results are in good agreement with those obtained previously (22, 23). The first weight loss corresponds to the formation of V_2S_5 (obs 44.5%, calc 43.8%) which is stable between 200° and 350°C. The second weight loss is due to the formation of $VS_{1.53}$ and an x-ray powder pattern of the TGA residue confirmed this to be crystalline V_2S_3 . Large samples of V_2S_5 were prepared by decomposition of $(NH_4)_3VS_4$ at 275°C in flowing helium. After reaction the reaction tube was sealed and transferred to a helium filled glove box. V_2S_5 is sensitive to atmospheric oxidation at room temperature and must be handled under inert conditions. In some circumstances, particularly when the initial $(NH_4)_3VS_4$ particle size is small, we have obtained V_2S_5 samples which were pyrophoric.

Samples of V_2S_5 were reacted with n-butyl lithium in (Foote Mineral Company) hexane (24). After reaction the solid products were removed by filtration and washed with hexane. The unreacted butyl lithium was determined by addition of standard HCl and back titration with standard NaOH. When a 1.6M solution of butyl lithium was used, the reactions were extremely vigorous, sufficient heat being evolved to boil the hexane. The reaction could, however, be moderated by initially adding to the solid sample dry hexane to reduce the butyl lithium concentration. The titration

Key words: cathode, amorphous vanadium sulfide, lithium, nonaqueous cell.

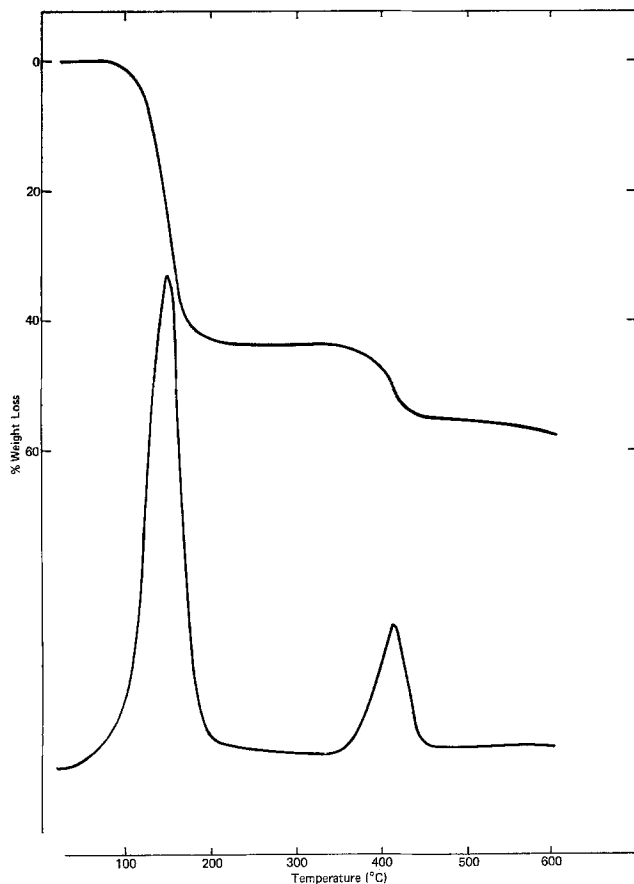


Fig. 1. Thermogravimetric analysis data for $(\text{NH}_4)_3\text{VS}_4$ in argon

results indicated a limiting composition of $\text{Li}_6\text{V}_2\text{S}_5$, but in some cases especially when the reaction was allowed to proceed rapidly or when a large excess of n-butyl lithium was added, a milky white solid was observed suspended in the supernatant hexane, indicative of side reactions. X-ray powder patterns of V_2S_5 and lithiated products of different compositions were recorded with samples protected from atmospheric oxidation and hydrolysis by Kapton films. All powder patterns were broad and contained no sharp Bragg peaks.

For electrochemical measurements, cathodes were prepared by hot pressing at 300°C a mixture of cathode material mixed with 14-16 weight percent (w/o) Teflon into expanded stainless steel mesh. The cathode area was 2 cm^2 . In some cases, 40 w/o graphite was added to the cathode mix. Cells were constructed by surrounding the cathodes with polypropylene separators and lithium sheet anodes. The assembled cells were immersed in a 2.0 molar solution of LiClO_4 in dioxolane¹ as the electrolyte contained in a polypropylene bag. Electrochemical measurements were made with PAR potentiostats equipped with voltage limiting devices under constant current conditions.

Electrochemical Results

First discharge data for four cells tested under different conditions are given in Table I. The voltage composition profile for cell No. 1 is shown in Fig. 2 for the first discharge and first recharge to 2.8V at 0.5 mA/cm^2 . The discharge data are smoothly varying over the whole composition range and there is a definite though broad down turn (end point) towards the end of the discharge. The mean discharge voltage is 1.96V which together with the capacity of 1743 C/g of V_2S_5 or 484 mA-hr/g of V_2S_5 gives a gravimetric energy density of 949 W-hr/kg. On recharge, 84% of the discharge capacity is recovered and a definite re-

Table I. First discharge data for $\text{Li}/\text{V}_2\text{S}_5$ cells

Cell	w/o graphite	i (mA/cm ²)	Lower cutoff voltage	Capacity (C/g V_2S_5)	e/vanadium
1	0	0.5	1.65	1743	2.37
2	40	0.5	1.60	1697	2.30
3	0	0.5	1.40	1871	2.54
4	0	2.5	1.40	1562	2.12

charge end point is observed. The first cycle data for cell No. 2 are closely similar even though the cathode contained 40 w/o graphite added to improve current collection, indicating that V_2S_5 itself is probably a good electronic conductor. Cell No. 3 was discharged to a lower cut off voltage of 1.40V with increases in both capacity (1743 C/g or 520 mA-hr/g) and energy density (1004 W-hr/kg, at a mean voltage of 1.93V). Cell No. 4 was discharged at a higher rate, 2.5 mA/cm^2 , with a corresponding reduction in capacity.

The second cycle data are shown for cell No. 1 in Fig. 2. Apart from a small increase in the mean discharge voltage (1.96 to 2.05V) the voltage composition profile for the second cycle closely resembles the first cycle data in overall shape. There is, however, a significant further loss in capacity. The capacity continues to decrease with repeated cycling under the same conditions. Thus on cycles 10, 20, and 30 the capacities are 41, 35, and 33% of the initial capacity, respectively. The capacity on cycle 30 corresponds to 0.77 Li/V. The losses in capacity on cycling as a percentage of first discharge capacity for all four cells are nearly identical. The fall in cycling capacity is also accompanied by pronounced changes in the voltage composition profiles. Data for cycles 12 and 30 are shown in Fig. 3. On cycle 12 the mean discharge voltage is 2.12V and on cycle 30, 2.28V, to be compared with values of 1.96 and 2.05V, respectively, for cycles 1 and 2. The voltage efficiency also improves on cycling; the voltage difference between the discharge and recharge profiles at half discharge capacity are 340, 250, 130, and 100 mV for cycles 1, 2, 12, and 30. Normally on cycling cells, decreased charging efficiency is expected due to increasing IR effects. The V_2S_5 data, however, strongly suggest that the initial V_2S_5 is being converted into another phase. The new phase reacts with less lithium but does so in a highly reversible manner. After cycle 30 a series of polarization curves to 1.60V were obtained at different discharge current densities (Fig. 4) all with a 0.5 mA/cm^2 recharge rate. The successive loss in capacity on increasing discharge rate up to 8 mA/cm^2 can almost entirely be accounted for by cell IR; again showing the high reversibility of the system at this point.

X-ray diffraction patterns of the spent cathodes were taken under Kapton films. No evidence was found for the formation of any crystalline phases just as found

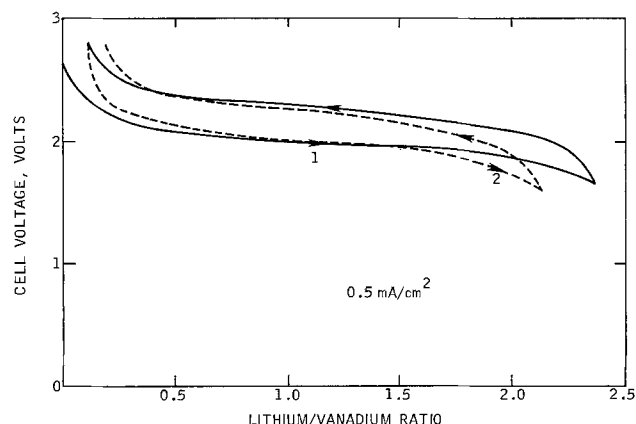


Fig. 2. First and second cycle data for $\text{Li}/\text{LiClO}_4\text{-dioxolane}/\text{V}_2\text{S}_5$

¹ Such solutions are potentially explosive.

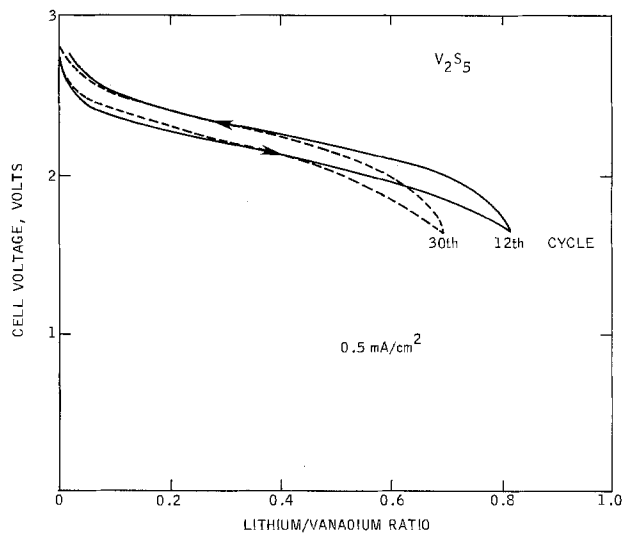


Fig. 3. Cycle 12 and cycle 30 data for Li/LiClO₄-dioxolane/V₂S₅

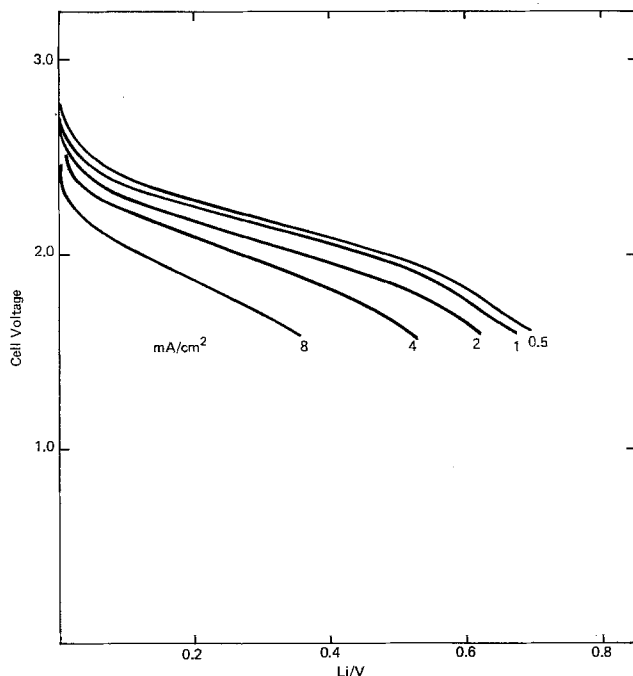


Fig. 4. Polarization data for Li/V₂S₅

for Li₂V₂S₅ compositions prepared by reaction with *n* butyl lithium.

Conclusions

Amorphous V₂S₅ has been found to react readily with *n*-butyl lithium and electrochemically to give amorphous Li₂V₂S₅ compositions. On primary discharge electrochemically to 1.40V V₂S₅ reacts with five lithiums at a mean voltage of 1.93V to give a gravimetric energy density of 1 kW-hr/kg. On cycling the capacity initially drops and subsequently levels out at approximately 30% of the initial discharge capacity; 300 W-hr/kg. During the initial capacity fading, the mean discharge voltage increases as does the voltage efficiency suggesting the formation of a second amorphous phase which is highly reversible towards reaction with lithium. Diemann's microcrystalline model (25) for the structure of V₂S₅ suggests that a possible explanation for the observed behavior might be the removal of edge sulfur atoms as lithium sulfide with polymerization to form amorphous VS₂. Some preliminary results for amorphous VS₂ prepared by low temperature precipitation have been reported (26)

and a more detailed comparison with the V₂S₅ data is in progress (27). It is interesting to note that *a*-V₂S₅ behaves quite differently to crystalline VS₂ (28). In the latter system the electrochemical capacity at ambient temperature is limited to 0.5 Li/VS₂ by the occurrence of distorted intermediate phases. In contrast, capacity faded V₂S₅ cells cycle 0.7-0.8 Li per vanadium at comparable voltages with little polarization and no evidence for discontinuities in the voltage composition profile.

Acknowledgments

We would like to thank R. R. Chianelli, M. S. Whittingham, and A. H. Thompson for helpful discussions and J. A. Panella for experimental assistance.

Manuscript submitted July 27, 1979; revised manuscript received Oct. 31, 1979.

Any discussion of this paper will appear in a Discussion Section to be published in the December 1980 JOURNAL. All discussions for the December 1980 Discussion Section should be submitted by Aug. 1, 1980.

Publication costs of this article were assisted by Exxon Research and Engineering Company.

REFERENCES

1. M. S. Whittingham, *Prog. Solid State Chem.*, **12**, 41 (1978).
2. M. S. Whittingham, *Science*, **192**, 1126 (1976).
3. M. S. Whittingham, *This Journal*, **123**, 315 (1976).
4. D. W. Murphy and F. A. Trumbore, *ibid.*, **123**, 960 (1976).
5. R. R. Chianelli and M. B. Dines, *Inorg. Chem.*, **14**, 2417 (1975).
6. A. J. Jacobson, M. S. Whittingham, and S. M. Rich, *This Journal*, **126**, 887 (1979).
7. A. J. Jacobson and L. E. McCandlish, *J. Solid State Chem.*, **29**, 355 (1979).
8. D. W. Murphy, F. A. Trumbore, and J. N. Carides, *This Journal*, **124**, 325 (1977).
9. A. H. Thompson and M. S. Whittingham, *Mater. Res. Bull.*, **12**, 741 (1977).
10. A. Le Mehaute, G. Ouvrard, R. Brec, and J. Rouxel, *ibid.*, **12**, 1191 (1977).
11. L. Campanella and G. Pistora, *This Journal*, **118**, 1905 (1971).
12. F. W. Dampier, *ibid.*, **121**, 658 (1974).
13. N. Margalit, *ibid.*, **121**, 1460 (1974).
14. J. O. Besenhard and R. Schollhorn, *J. Power Sources*, **1**, 267 (1977).
15. D. W. Murphy, P. A. Christian, F. J. DiSalvo, and J. N. Carides, *This Journal*, **126**, 497 (1979).
16. M. Armand, in "Fast Ion Transport in Solids," W. Van Gool, Editor, p. 665, North Holland Publishing Co., Amsterdam (1973).
17. J. O. Besenhard and R. Schollhorn, *This Journal*, **124**, 968 (1977).
18. T. Ohzuku, Z. Takehara, and S. Yoshizawa, *Electrochim Acta*, **24**, 219 (1979).
19. D. W. Murphy, F. J. DiSalvo, J. N. Carides, and J. V. Waszczak, *Mater. Res. Bull.*, **13**, 1395 (1978).
20. A. J. Jacobson, R. R. Chianelli, and M. S. Whittingham, Third International Conference on the Chemistry and Use of Molybdenum, Ann Arbor, Michigan, 1979.
21. A. Buisine and G. Tridot, *Bull. Soc. Chim. Fr.*, 1383 (1961).
22. A. Buisine and G. Tridot, *Comptes Rendus*, **251**, 2729 (1960).
23. T. P. Prasad and A. Müller, *J. Therm. Anal.*, **10**, 369 (1976).
24. M. S. Whittingham and M. B. Dines, *This Journal*, **124**, 1387 (1977).
25. E. Diemann and A. Müller, *Z. Anorg. Allg. Chem.*, **444**, 181 (1978).
26. R. R. Chianelli and M. B. Dines, *Inorg. Chem.*, **17**, 2758 (1978).
27. R. R. Chianelli, A. J. Jacobson, and K. S. Liang, *This Journal*, To be submitted.
28. D. W. Murphy, J. N. Carides, F. J. DiSalvo, C. Cros, and J. V. Waszczak, *Mater. Res. Bull.*, **12**, 825 (1977).

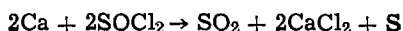
A Study of the Calcium-Thionyl Chloride Electrochemical System

Robert J. Staniewicz*¹

GTE Laboratories, Incorporated, Power Sources Center, Waltham, Massachusetts 02154

ABSTRACT

The use of calcium metal as an anode in SOCl_2 electrolytes was investigated. Calcium showed an open-circuit potential (OCP) of 3.22V vs. a carbon cathode in 1M $\text{Ca}(\text{AlCl}_4)_2\text{-SOCl}_2$ electrolyte. Hermetically sealed D cells, when discharged at 1 mA/cm², displayed level discharge plateaus of 2.8V. SEM photographs indicated the rapid formation of a crystalline layer on the anode; the composition of this film was established as CaCl_2 . Storage of calcium samples in $\text{Ca}(\text{AlCl}_4)_2\text{-SOCl}_2$ electrolyte resulted in corrosion of the metal. This corrosion was particularly pronounced at 55°C and it appeared to be a fundamental behavior which was not eliminated by rigid control of electrolyte purity. The following cell chemistry was suggested by chemical analysis of discharged electrolytes and cathodes



Electrodeposition experiments indicated no evidence for the plating of Ca onto a nickel substrate.

One of the principal incentives for investigating the Ca/SOCl_2 system is that calcium anodes have the prospect for higher temperature operation when compared with lithium anodes. The higher melting point of calcium (839°C) compared to lithium (180°C) would obviate the possibility of anode melting under high temperature stress, e.g., as a result of large short-circuit currents generated in a high power cell configuration. A comparison of the calculated theoretical energy densities of lithium and calcium/ SOCl_2 cells is presented below assuming reaction products of SO_2 , S, and either LiCl or CaCl_2 . These values indicate that

	Cell potential (V)	Energy density (W-hr/cm ²)	Specific energy density (W-hr/kg)
Li	3.65	2.00 (32.8 W-hr/in. ²)	1474 (667.9 W-hr/lb)
Ca	3.64	1.97 (32.3 W-hr/in. ²)	1230 (557.0 W-hr/lb)

the energy densities of the Ca/SOCl_2 system compare favorably with Li/SOCl_2 and therefore provided another encouragement for investigating calcium as an anode in SOCl_2 . Furthermore, calcium is also more abundant than lithium and has the propitious physical property of higher electronic conductivity.

The work reported here is an investigation and evaluation of the Ca/SOCl_2 system as an alternative to the Li/SOCl_2 system and coincidentally provides insight into the discharge and deposition behavior of metal/inorganic electrolyte systems.

Experimental

Electrolytes and solvents.—The thionyl chloride was obtained from Mobay and was fractionally distilled from lithium chips in a dry room of less than 3% relative humidity. The AlCl_3 , puriss grade, was used as obtained from Fluka.

The Alfa-Ventron SbCl_5 was vacuum distilled at 17 Torr and a light yellow fraction was collected between 70° to 72°C. Anhydrous FeCl_3 was prepared by refluxing Baker-Analyzed $\text{FeCl}_3 \cdot 6\text{H}_2\text{O}$ with SOCl_2 . The Anachemia reagent $\text{CaCl}_2 \cdot 2\text{H}_2\text{O}$ was dehydrated by incrementally vacuum drying to 300°C. All other chemicals and solvents used were of reagent grade quality.

* Electrochemical Society Active Member.

¹ Present address: ARAMCO, Laboratories Department, Dhahran, Saudi Arabia.

Key words: inorganic, battery, electrodeposition, corrosion.

Several procedures were explored to prepare $\text{Ca}(\text{AlCl}_4)_2$ electrolyte. The preferred procedure for preparation involved addition of AlCl_3 to SOCl_2 followed by CaCl_2 (5% excess). This mixture was refluxed in a dry room overnight and subsequently filtered in a dry box. By this procedure, a 2M $\text{Ca}(\text{AlCl}_4)_2$ solution could be prepared although they were quite viscous and displayed lowered conductivity (*vide infra*). The average stoichiometric ratio of Al:Ca in the electrolyte was 2.02 to 1. The $\text{Ca}(\text{SbCl}_6)_2$ and $\text{Ca}(\text{FeCl}_4)_2$ electrolyte solutions were prepared similarly to the above procedure for $\text{Ca}(\text{AlCl}_4)_2$. The tetraethylammonium tetrachloroaluminate electrolyte was made by addition of a SOCl_2 solution of tetraethylammonium chloride to a lithium tetrachloroaluminate solution. The lithium chloride which precipitated was filtered, yielding the $(\text{Et}_4\text{N})(\text{AlCl}_4)$ solution.

Calcium.—The rolled calcium metal (0.050 cm) was obtained from Kaweckiberyleo Industries, Reading, Pennsylvania and was mechanically abraded of the oxide coating in an argon atmosphere dry box and washed with anhydrous ethyl ether. An alternative and more convenient method of cleaning the calcium surface has been reported (1) and was used for the calcium samples which were vacuum annealed (500°C, 6×10^{-5} Torr). Despite the fact that the annealed calcium was quite smooth and flexible, the rate of corrosion (*vide infra*) in the electrolytes was not significantly reduced. Thus, all the reported work was accomplished with the abraded unannealed calcium. Analysis of the Ca metal by atomic absorption indicated the following composition, 0.265% Mg, 0.234% Al, 0.077% Sr, 0.003% Fe, 0.0028% Na, and 0.0005% Li. A sample of vapor-deposited Ca on (0.020 in.) steel was obtained from Catalyst Research Corporation, Baltimore Maryland and also evaluated.

Instrumental methods.—Conductivity measurements were obtained using a glass conductivity cell consisting of two heavy gauge parallel platinized platinum electrodes fixed in a glass holder. The cell constant was experimentally determined using standard KCl aqueous solutions (2, 3). Resistance measurements were made at room temperature ($25^\circ \pm 1^\circ\text{C}$) using a General Radio Model 1656 impedance bridge coupled with an external signal generator, PAR Model 175 Universal Programmer. The solutions were prepared by appropriate dilution of a 2.00M standard $\text{Ca}(\text{AlCl}_4)_2$ solution.

The infrared spectra were obtained using a Beckman Model IR-10 recording spectrophotometer. For electrolyte evaluation, the infrared cells were either Infrasil quartz cells or Barnes Engineering NaCl cavity cells.

For the plating experiments, a PAR Model 173 Potentiostat/Galvanostat was coupled with an HP X-Y recorder set in the time mode. Cell discharges were generally through a constant load consisting of a precision resistor and monitored by means of a Fluke 2240 B Datalogger.

Scanning electron micrographs of calcium samples were obtained using a JSM-U3 Scanning Electron Microscope equipped with a PAR x-ray energy analyzer. Calcium samples exposed to anhydrous $\text{Ca}(\text{AlCl}_4)_2$ electrolyte under varying durations and temperatures were withdrawn from the sealed glass ampuls, washed three times with anhydrous SOCl_2 , and vacuum dried. All operations were conducted in a dry box. The calcium samples were mounted on brass holders with silver paint and transferred to the microscope under anhydrous conditions by means of a specially designed argon transfer chamber. The micrographs were obtained at an accelerating voltage of 20 kV in the secondary electron mode at a goniometer tilt of 42° .

Experimental cell assembly.—The initial survey of electrolytes was accomplished using the flooded three electrode configurations shown in Fig. 1. Two methods were utilized for assembly of the 1×2 cm calcium electrodes; the early procedure for maintaining mechanical and electrical contact to the Ni lead was by means of a stainless steel fastener while the latter and more effective method involved welding the Ca in a dry room to a Ni substrate (0.005 cm Ni shim stock). The cathodes ($1 \times 2 \times 0.1$ cm) consisted of a carbon-Teflon mixture supported on Ni Exmet. The cells were assembled in a dry room and filled in a dry argon glove box (2-3 ppm H_2O). For the chemical analyses of discharged cathodes and electrolytes, larger cathodes and calcium anodes were utilized. For calcium deposition experiments, the geometry was maintained by use of a Teflon holder in which planar rectangular electrodes were situated 1 cm apart. The effective area of the Ca anode and the Ni cathode was

1.6 cm^2 . The reference calcium electrode was positioned 2 mm from the working Ni surface. A limited number of investigations were also carried out with thin cathodes of $\sim 50 \mu\text{m}$. These experiments were designed to evaluate cathode capacity for lithium and calcium cells.

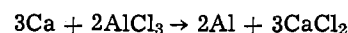
The hermetic "D" cell's cross section is presented in Fig. 2. The point of interest is the treatment of the calcium for use as a cylindrical anode. Calcium metal was welded to 0.005 cm Ni shim stock which acted as a current collector. The Ni foil in turn was welded to the stainless steel "D" can as depicted.

Results and Discussion

Electrolyte preparations.—A survey of possible calcium electrolyte salts revealed that solutions of $\text{Ca}(\text{AlCl}_4)_2$ in SOCl_2 could be made by appropriately refluxing excess CaCl_2 with an AlCl_3 - SOCl_2 solution. The reflux served a twofold purpose. First, it allowed sufficient time for the dissolution of the solid CaCl_2 to insure a 1:2 stoichiometric ratio of Ca:Al. Second, the reflux provided an avenue for the SOCl_2 to act as a desiccant for OH groups present. These products of hydrolysis are minor contaminants introduced by the CaCl_2 and AlCl_3 solids, both of which are hygroscopic.

The presence of excess AlCl_3 in SOCl_2 would manifest itself by a corrosive effect on the calcium metal; the initial effect is reaction of the CaCl_2 film on the calcium with the Lewis acid followed by reaction of the bare metal with the solvent.

It may also be possible that AlCl_3 reacts directly with the Ca metal



The net result is an undesirable corrosion of the metallic calcium. The determination of calcium and aluminum in the electrolyte solutions demonstrated a stoichiometric ratio of Ca:Al of 1:2 with the concomitant conclusion that no excess AlCl_3 was present and therefore any possibility of corrosion by AlCl_3 was eliminated at the outset of the study.

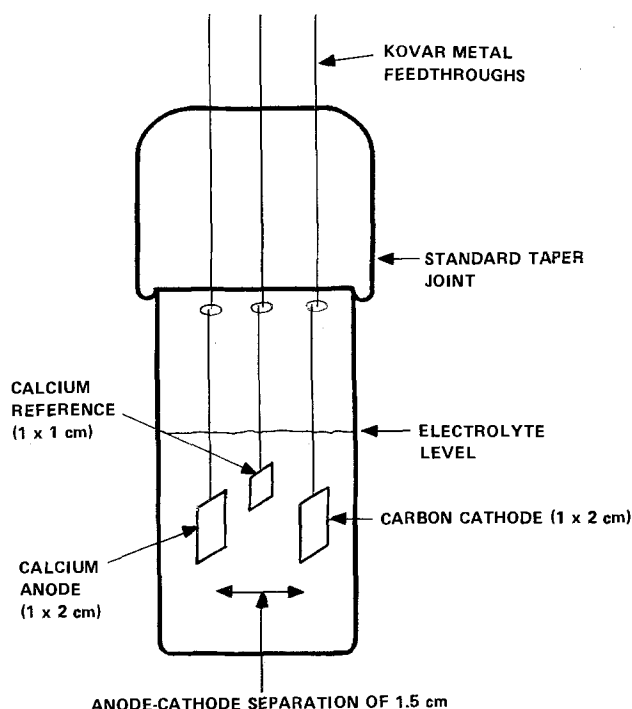
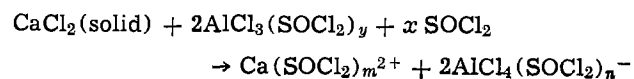


Fig. 1. Flooded three electrode cells used to survey the various electrolytes.

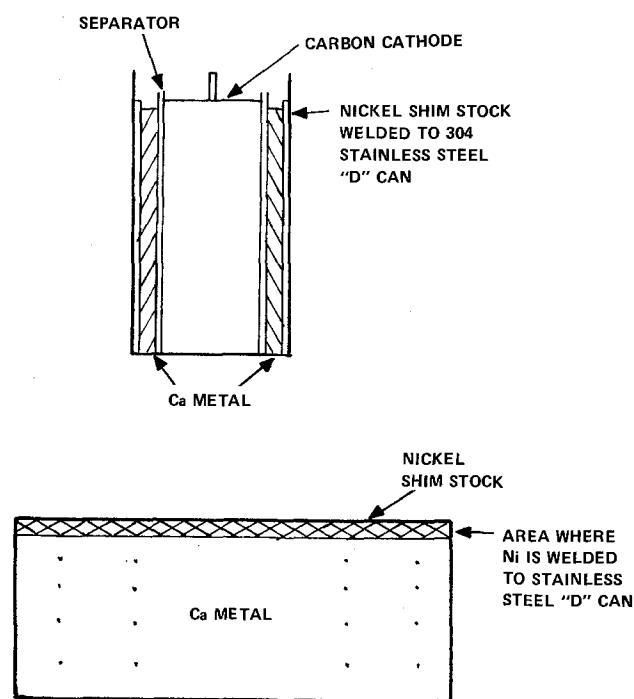
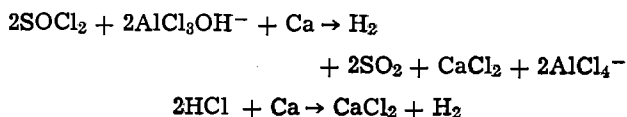
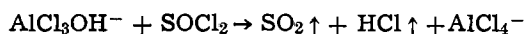


Fig. 2. Cross section of a calcium "D" cell

The contamination of SOCl_2 electrolyte with hydrolysis materials such as AlCl_3OH^- and HCl has been suggested to be deleterious to the lithium anode performance and by analogy would be harmful to the Ca electrode



The AlCl_3OH^- species shows an infrared absorption at 3400 cm^{-1} while the HCl molecule absorbs at 2800 cm^{-1} in SOCl_2 (4) and thus an infrared scan of the electrolyte is diagnostic of the purity of the solution. An infrared spectrum of the refluxed electrolyte showed no absorption for HCl , AlCl_3OH^- , or SO_2 (symmetrical vibration at 1330 cm^{-1}). Therefore, the products of the desiccation reaction, SO_2 and HCl , are expelled at reflux temperature as evidenced by the absence of their infrared maxima



A conductivity study (uncorrected for viscosity) of the electrolyte solutions (Fig. 3) showed a maximum specific conductivity of $0.6 \times 10^{-2}\ \Omega^{-1}\text{ cm}^{-1}$ at $\sim 1\text{M}$ $\text{Ca}(\text{AlCl}_4)_2$. The concentrated solutions, 1.6 and 2.0M $\text{Ca}(\text{AlCl}_4)_2$ appeared significantly more viscous. Thus, the shape of the conductivity curve may arise from several influences: (i) viscosity effects, (ii) significant solute-solvent interactions, and (iii) solute-solute interactions as a result of the polarizing ability of the doubly charged Ca^{2+} ion. It should be noted that the maximum conductivity of the $\text{Ca}(\text{AlCl}_4)_2$ electrolyte is only approximately 30% of that observed for LiAlCl_4 ($2.04 \times 10^{-2}\ \Omega^{-1}\text{ cm}^{-1}$) at the same temperature (5).

A survey of $\text{Ca}(\text{FeCl}_4)_2$, $\text{Ca}(\text{SbCl}_6)_2$, and $(\text{Et}_4\text{N})(\text{AlCl}_4)$ as suitable electrolyte salts was also undertaken. Solutions of composition 0.5M $\text{Ca}(\text{FeCl}_4)_2$, 0.75M $\text{Ca}(\text{SbCl}_6)_2$, and 1M $(\text{Et}_4\text{N})(\text{AlCl}_4)$ were prepared as discussed in the Experimental section, and were also evaluated in terms of calcium corrosion and cell performance.

Compatibility studies.—To ascertain the corrosion rate of calcium metal in the various electrolytes, sealed glass ampuls were prepared containing the metal and the appropriate electrolyte. Table I summarizes those tests.

It should be noted that it was not possible to monitor weight changes of calcium metal exposed to SOCl_2 electrolyte because the CaCl_2 formed was not adherent.

Upon immersion of shiny calcium metal into 1M $\text{Ca}(\text{AlCl}_4)_2$ the following immediate observations were

Table I. Relative corrosion of calcium metal stored with various electrolytes

Electrolyte	Relative corrosion at room temperature	Relative corrosion at 55°C
$\text{Ca}(\text{AlCl}_4)_2$	Moderate	Rapid
$\text{Ca}(\text{SbCl}_6)_2$	Rapid	Very rapid
$\text{Ca}(\text{FeCl}_4)_2$	Rapid	Very rapid
$\text{Li}(\text{AlCl}_4)$	Moderate	Rapid
$\text{Et}_4\text{N}(\text{AlCl}_4)$	Very rapid	—
Solvent only (SOCl_2)	Slow	Slow

noted: (i) small dark areas appeared randomly over the surface and especially at the cut edges of the metal; (ii) these areas transformed to gray areas within several days; and (iii) long-term storage resulted in samples which appear dull gray and which have distinct corroded or etched areas. Removal of the samples from the electrolyte followed by washing with SOCl_2 resulted in samples which had a significant film of white crystals covering the Ca surface. The Ca samples exposed to distilled SOCl_2 did not initially display the corrosion exhibited by Ca in electrolyte, however, after 10 months of storage at room temperature, crystalline CaCl_2 deposits appeared in these Ca/SOCl_2 ampuls. The calcium samples stored 3 months at 55°C in SOCl_2 did not show significant corrosion deposits.

The rate of calcium degradation in $\text{Ca}(\text{AlCl}_4)_2$ electrolyte at room temperature appeared to diminish after 1 month as ascertained by observing the CaCl_2 deposits at the ampul bottom. Sample storage at 55°C in electrolyte indicated progressive corrosion with substantial disintegration of the metal after 6 months of storage. The corrosion was not uniform, but instead specific sites underwent more rapid reaction as evidenced by the mechanical breakup of some pieces and relative integrity of others.

The composition of the solid film on the Ca was determined both by x-ray emission and x-ray diffraction to be CaCl_2 . The scanning electron micrographs (Fig. 4-7) depict the transformation of the calcium surface with varied time and temperature storage in electrolyte and SOCl_2 . Some comments on these photographs appear in order. The samples exposed to electrolyte at room temperature showed a crystal growth pattern which did not change dramatically with the duration of exposure to electrolyte; only the quantity and thickness of the CaCl_2 are indicated as variables. The CaCl_2 layer did not appear especially well-formed under $1000\times$ magnification and manifested an aggrega-

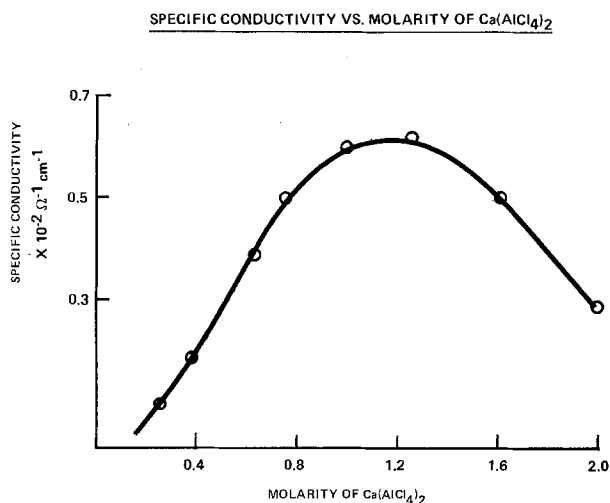


Fig. 3. Variation of specific conductivity with molarity of $\text{Ca}(\text{AlCl}_4)_2$.

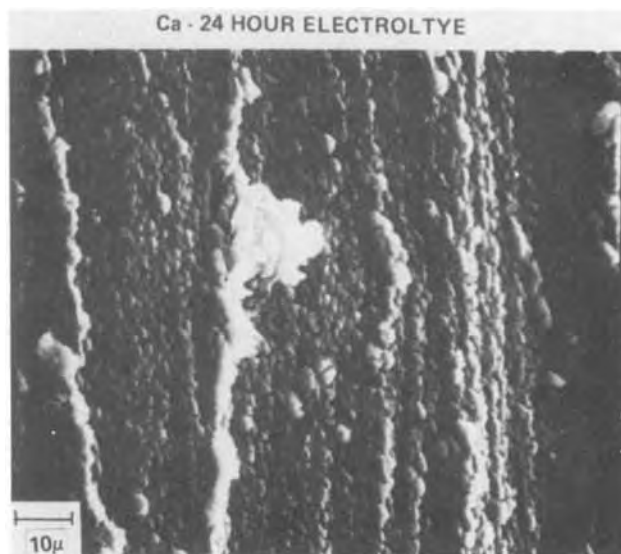


Fig. 4. Micrograph of Ca exposed 1 day to electrolyte ($1000\times$)

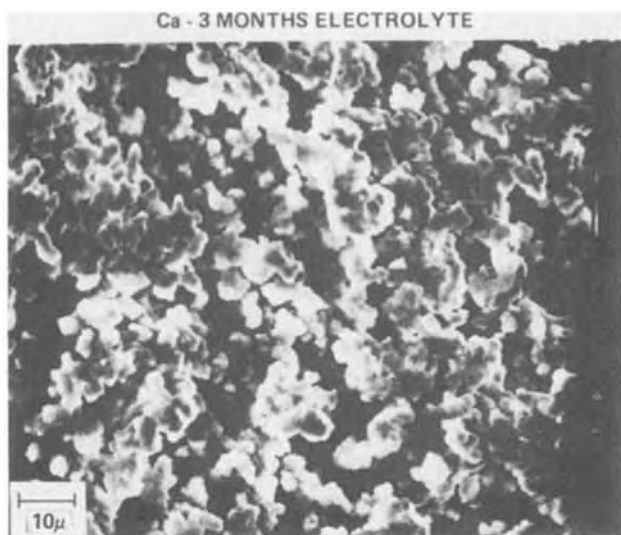


Fig. 5. Micrograph of Ca exposed 3 months to electrolyte (1000 \times)

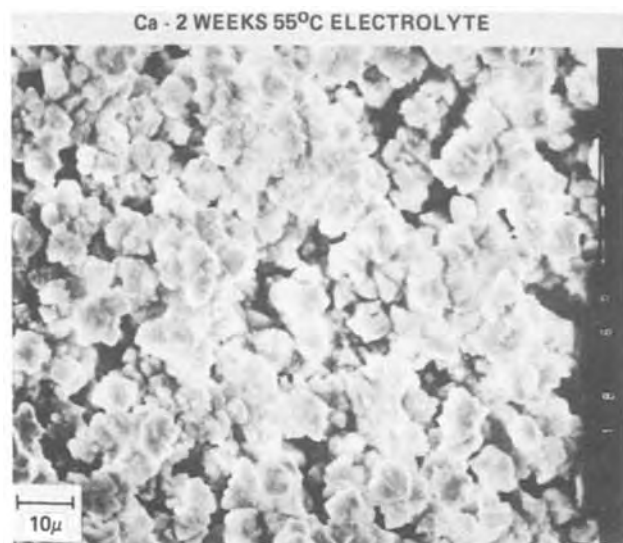


Fig. 6. Micrograph of Ca exposed 2 weeks at 55°C to electrolyte (1000 \times).

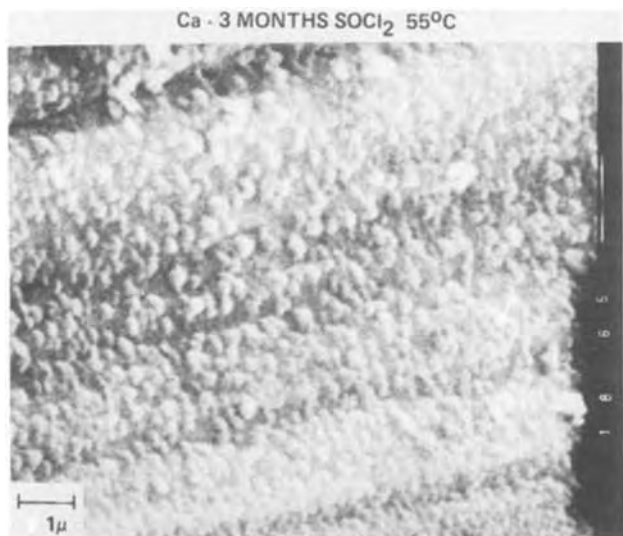


Fig. 7. Micrograph of Ca exposed 3 months at 55°C to SOCl_2 (10,000 \times).

tion of small crystallites. This CaCl_2 morphology differs from the independent observations of Dey and Peled regarding the crystal growth of lithium and lithium

alloys stored in LiAlCl_4 electrolyte at room temperature (6-8). They reported well-defined crystals of considerably larger size. Storage of Ca at 55°C resulted in transformation of the crystallites into larger crystals, a result also affirmed by Peled (7) with lithium alloys. The calcium metal stored 3 months at 55°C in SOCl_2 (Fig. 7) showed at 10,000 \times magnification a compact layer of CaCl_2 and significantly reduced corrosion when compared to the electrolyte storage tests.

The compatibility tests of Ca metal with $\text{Ca}(\text{FeCl}_4)_2$, $\text{Ca}(\text{SbCl}_6)_2$, and $(\text{Et}_4\text{N})(\text{AlCl}_4)$ electrolytes all showed accelerated corrosion when compared with the $\text{Ca}(\text{AlCl}_4)_2$ standard. The solutions are not considered viable alternatives and therefore were the subject of limited further evaluation. The interest with the tetraethylammonium tetrachloroaluminate salt arose from the supposition that the presence of metallic cations, Ca^{2+} or Li^+ , in solution contributes to a catalytic corrosion of the bulk calcium metal and that replacement with a nonmetallic cation would reduce corrosion. In fact, the opposite was observed, in that complete disintegration of the Ca metal occurred after 1 week storage in the $\text{Et}_4\text{N}(\text{AlCl}_4)\text{-SOCl}_2$.

Electrolyte compatibility tests were also conducted with annealed calcium in which the CaO coating was removed by chemical means, but no significant decrease in corrosion was observed. It has been anticipated that reduction of the work hardening and surface roughness would result in lowered contact between the current collector and the anode. The projected consequence of this better contact may be higher anode utilization.

Experimental cell discharge.—The initial survey of calcium discharge was conducted in flooded cells. Newly prepared cells showed initial open-circuit potentials between 2.9-3.0V which slowly increased and stabilized at 3.22V after 12 hr. Figure 8 shows the discharge data for a typical $\text{Ca}/\text{Ca}(\text{AlCl}_4)_2\text{-SOCl}_2$ flooded cell when a 2000 Ω load (0.7 mA/cm² Ca) was imposed. Of note is the fairly level cathode discharge and increasing anode polarization as discharge continued. The anode discharge was not uniform as evidenced by the pitting which was particularly pronounced on the edges. The Ca reference suffered similar though less severe corrosion during the cell discharge. The increasing anode polarization is probably the result of increased thickness of the passivating layer as discharge continued. The white corrosion material which appeared on the anode was identified by x-ray diffraction as CaCl_2 . It is believed that this material was formed by the continued reaction of calcium with the SOCl_2 , possibly the result of the morphology of the porous CaCl_2 film which may be characteristic for the electrolyte. Failure of these flooded cells typically resulted from corrosion and the subsequent mechanical disintegration of the anode.

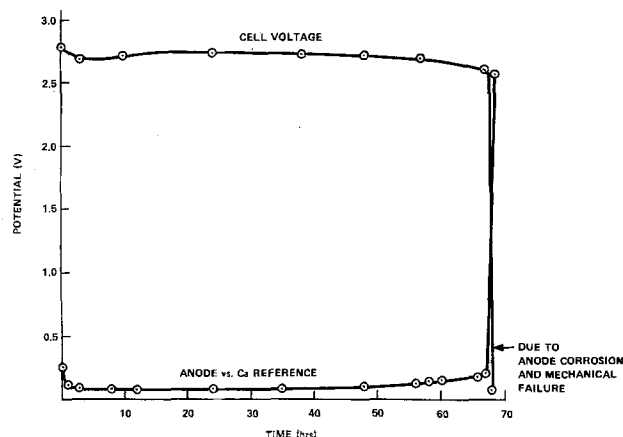


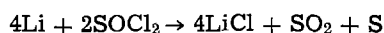
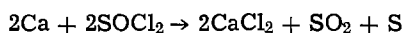
Fig. 8. Discharge profile for a $\text{Ca}/\text{Ca}(\text{AlCl}_4)_2\text{-SOCl}_2$ cell through a 2000 Ω load. The OCP of the cell is not shown.

Based on the coulombs passed during discharge, only 50% utilization of the anode was realized. The remaining calcium either suffered corrosion or became mechanically detached from the Ni lead.

Calcium was also surveyed using $\text{Ca}(\text{FeCl}_4)_2$, $\text{Ca}(\text{SbCl}_6)_2$, and LiAlCl_4 electrolytes. In general the Fe and Sb based anions showed poor performance in terms of lower discharge voltage and lower anode utilization, while the LiAlCl_4 electrolyte compared favorably with the $\text{Ca}(\text{AlCl}_4)_2$ electrolyte.

Hermetically sealed "D" cells were assembled containing 1.0M $\text{Ca}(\text{AlCl}_4)_2$ electrolyte which had a theoretical capacity based on the calcium anode mass of 4.1 A-hr ($4.5 \times 9.7 \text{ cm}$; 3.0-3.1g). Typically, the freshly filled cells showed open-circuit potentials of 3.00-3.05V which rose after 6 hr to 3.15-3.20V. The cells were discharged through a 70Ω precision resistor which simulated a 1 mA/cm^2 (Ca surface area $\sim 44 \text{ cm}^2$) discharge rate. The cells were divided into several groups for storage at ambient room temperature and 55°C . This data is summarized in Table II and Fig. 9 shows the discharge curves for three representative fresh "D" cells discharged at room temperature. It should be noted that the experimental capacity of freshly filled cells and the cells stored 1 month at room temperature was $\sim 50\%$ of the capacity based upon the mass of the calcium. Elevated temperature and longer storage time at room temperature both seriously reduce the cell capacity to $\sim 40\%$ of the rated value, presumably a result of continued parasitic reaction between the SOCl_2 and the Ca metal. The discharged cells were opened and the interior was inspected. A grayish salt existed between the Ni substrate and glass separator, where the anode had been, indicative of anode corrosion. The cathode capacity had not been exceeded as evidenced by continued cell discharge when a new Ca anode was inserted into the cell.

The capacity of cathodes as a function of the electrochemical system, $\text{Li/LiAlCl}_4\text{-SOCl}_2$ and $\text{Ca/Ca}(\text{AlCl}_4)_2\text{-SOCl}_2$ was also investigated. The failure of the cathodes in Li/SOCl_2 cells has been suggested to result from accumulation of LiCl in the pores of the cathode (9). In fact, a comprehensive study of the reaction profiles and composition of cathodes for Li/SOCl_2 has been reported (10). The capacity of the cathodes as a first order model should be related to the molar volume of the deposited salt, LiCl or CaCl_2 per equivalent of charge passed. The equivalent volume of LiCl is 20.5 cm^3 and that of CaCl_2 is 25.8 cm^3 . The model assumes the following reaction mechanisms (*vide infra*)



Relatively thin carbon cathodes ($40\text{-}60 \mu\text{m}$) were discharged in the study at various current densities with both Ca and Li anodes and the appropriate electrolyte. A plot of the logarithm of the rate *vs.* the normalized cathode capacity for both Li and Ca cells is shown in Fig. 10. Based on the comparison of the equivalent volumes, a calcium cell's cathode capacity is calculated to be $\sim 80\%$ of a similarly constructed

Table II. Discharge data for hermetic Ca/SOCl_2 "D" cells

Cell	Number of cells	Capacity (A-hr)	Average life above 2V (hr)
Fresh	10	2.0	52.3
1 month at $25^\circ \pm 2^\circ\text{C}$	2	2.0	51.5
1 month at 55°C	3	1.7	43
$2\frac{1}{2}$ months $25^\circ \pm 2^\circ\text{C}$	3	1.6	44

Capacity based on anode mass = 4.1 A-hr.

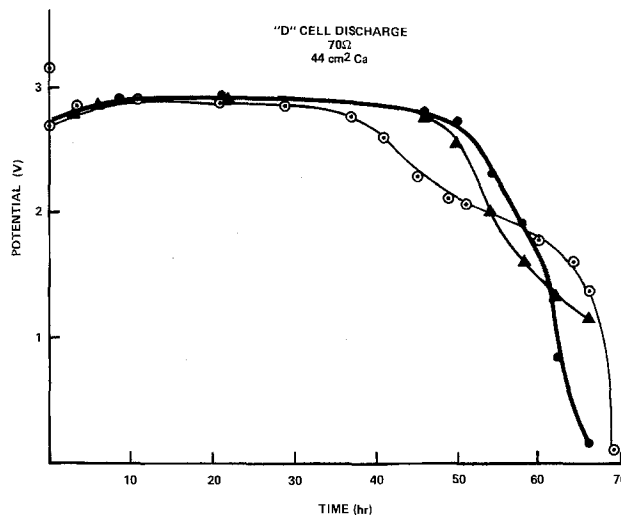


Fig. 9. Discharge curves for 3 freshly filled "D" cells through a 70Ω load (1 mA/cm^2 Ca). The circled point above the discharge curve shows the OCP of the cells.

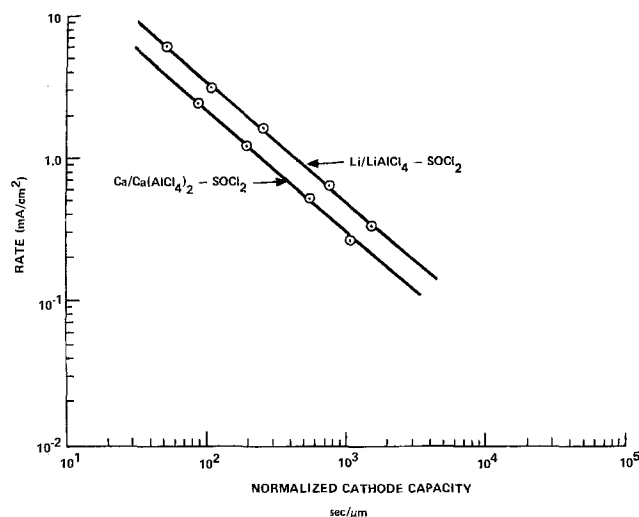


Fig. 10. Logarithm of the rate *vs.* logarithm of the cathode capacity for Ca/SOCl_2 and LiSOCl_2 cells.

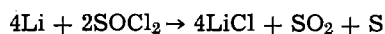
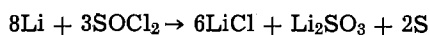
lithium cell. From the data in the graph, the calcium cell's capacity is $\sim 58\%$ of the Li cell. Thus, the proposed model (based solely on the molar volume of the deposited salt) is too simplistic and other factors, *e.g.*, the mobility of Ca^{2+} and Li^+ ions in SOCl_2 and diffusion of Ca^{2+} and Li^+ into the cathode pores should be considered. It may well be that, despite the use of thin cathodes, the interior of cathodes is particularly underutilized as the result of the lower mobility of Ca^{2+} relative to Li^+ . The results of this particular study do indicate however that the cathode capacity for a calcium cell will be lower than for a similarly constructed lithium cell.

We have also investigated whether leaving the oxide coating intact is beneficial to the Ca/SOCl_2 system. A relatively large piece of oxide-coated calcium (20 cm^2) was exposed to 1M $\text{Ca}(\text{AlCl}_4)_2$ electrolyte at 55°C and initially showed significantly reduced corrosion, although the cut edges showed some corrosion. At a specific site along one edge, pitting commenced and a circular corroded area of $\sim 1 \text{ cm}^2$ was apparent after 2 months storage at 55°C . The corrosion at this site continued progressively throughout the duration of the test. It should be stressed that corrosion was initiated at this singular site with the other edges having small areas where white crystalline deposits appeared and which apparently self-healed. Electrodes were also constructed from the oxide-coated calcium and evaluated. This calcium could not

effectively be welded to nickel substrate and thus the calcium was mechanically fixed to a nickel lead. Flooded cells using oxide-coated anodes and references showed initial open-circuit potential (OCP) of $\sim 3.10V$ and were discharged through a 2000Ω load. The A-hr capacity of such cells was ~ 0.075 A-hr (40% of that expected based on the anode mass) and the discharged anode remained relatively intact but showed a 3V polarization *vs.* the reference. These anodes were collected, intentionally hydrolyzed, and the resulting solutions titrated for $Ca(OH)_2$ to assess the available Ca metal. The analysis showed that approximately 40% of the original Ca remained entrapped within a CaO and $CaCl_2$ coating and that approximately 20% corrosion had occurred. This is a significant improvement in the corrosion rate and indicates that the oxide coating does provide a protective film through which the Ca can discharge but eventually the remaining Ca metal is electronically isolated.

Vapor-deposited Ca on steel was also evaluated in the $Ca(AlCl_4)_2-SOCl_2$ electrolyte. This material was obtained from Catalyst Research Corporation of Baltimore, Maryland and was 0.020 cm thick with an average Ca density of 1.51 g/cm³. A flooded cell was constructed which showed an OCP of 3.25V and when discharged showed only a 25% utilization of the Ca with the remainder of the Ca apparently suffering parasitic corrosion. The reference electrode was also inspected after discharge and this inspection revealed that the steel substrate was devoid of calcium metal. Significant deposits of $CaCl_2$ were observed at the bottom of the cell as a result of the anode and reference corrosion.

Cell chemistry.—There are many possible overall cell reactions for the Li/SOCl₂ system (11), among these the following two reactions



have been mentioned frequently for room temperature discharge. The second reaction is now considered the probable overall reaction, although some specific unanswered questions still remain (11). It was therefore considered beneficial and informative, by comparison, to identify qualitatively the products of the Ca/SOCl₂ cell reaction at room temperature.

Before discharge, no SO₂ was detected in the infrared spectrum of the electrolyte. After discharge, a large infrared absorption appeared at 1330 cm⁻¹ which is diagnostic of SO₂ dissolved in SOCl₂ and as the electrolyte was protected from H₂O contamination, the SO₂ resulted from the reduction of SOCl₂.

A discharged carbon cathode was first washed with SOCl₂ to remove LiAlCl₄ then leached with distilled water to remove water soluble products. A portion of the solution was immediately withdrawn and tested for sulfite by addition of an acidified KMnO₄ solution. The solution did not decolorize and thus no reducing agents such as SO₃²⁻ were present. Addition of an aqueous Ba²⁺ solution to a portion of the leached cathode solution did not result in precipitation of solid, thus SO₄²⁻ was not present. A white solid recovered from the leach solution was shown to be a single phase of CaCl₂ by x-ray diffraction techniques. Although the discharged electrolyte was not specifically tested for the presence of dissolved sulfur, the conclusive evidence presented for SO₂ and CaCl₂ suggests the following overall cell reaction at room temperature



It should be stressed that the overall products of this electrochemical reaction do not necessarily imply a specific mechanistic pathway and, in fact, significant temperature changes may favor another pathway and concomitantly different products. The Li/SOCl₂ cell is a good example of where the relation of temperature

and mechanism have yet to be definitively elucidated (11, 11a).

The lower capacity for thin cathodes in Ca/SOCl₂ (*vide supra*) should also be emphasized in light of finding CaCl₂ in the cathode. Per equivalent of charge passed, the CaCl₂ precipitated in the cathode matrix would occupy a larger molar volume than LiCl and hence a lower cathode capacity.

Electrodeposition of calcium.—The experimental assembly used for deposition experiments contained 1.0M $Ca(AlCl_4)_2-SOCl_2$, a Ca reference, Ca anode, and nickel substrate or cathode. The open-circuit potential between the planar nickel electrode and the calcium electrode was about 3V. When a constant current of 0.125 mA/cm² was applied to the nickel working electrode, the potential of the nickel (measured against the Ca reference) decreased very slowly from 3 to 2V after 70 min. On turning off the current, the nickel potential rose quickly to near 3V. When a larger constant current of 1.25 mA/cm² was applied to the nickel electrode, the potential of the nickel decreased rapidly from 3 to $-10V$ and remained at that potential until the current was turned off, whereupon, the potential rose immediately to anodic values and was near 3V within 20 min (Fig. 11).

There is little evidence for calcium deposition on the Ni substrate. When the nickel is made cathodic, the surface can directly transfer electrons to the SOCl₂, thus, solvent reduction can occur. The products of the reaction may be SO₂ and S, which are soluble in SOCl₂, and CaCl₂, which precipitates on the Ni surface, inhibiting electron transfer (voltage driven to $-10V$). Considering the model of the solid electrolyte interphase (SEI) advanced by Peled (12, 12a), the Ni is now covered by a CaCl₂ SEI layer. Calcium chloride is essentially an electronic insulator, thus the current must now depend on the migration of ions through the passivating film (ionic current) to the Ni surface (Fig. 12). However, the cation transport numbers of alkaline earth halides is low (13), with the anion transport number likely close to unity. Thus, the current will predominately be carried by the anion defect sites as shown in Fig. 12. By this hypothetical mechanism, Cl⁻ must move outward through defect sites to precipitate as CaCl₂ on the surface and leave Ca as a deposit on the Ni substrate. Apparently this process does not function efficiently. This mechanism would require destruction of CaCl₂ at the nickel surface, and the growing of CaCl₂ crystals at the interface with the solution, at a rate commensurate with the current being drawn. These crystals, almost certainly dendritic, could offer no protection to the calcium, and so the deposit would be corroded as fast as it was plated.

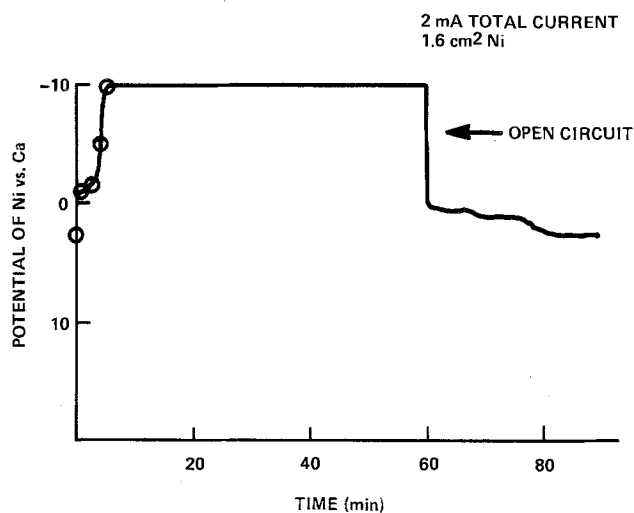


Fig. 11. Calcium deposition to Ni substrate in 1M $Ca(AlCl_4)_2-SOCl_2$.

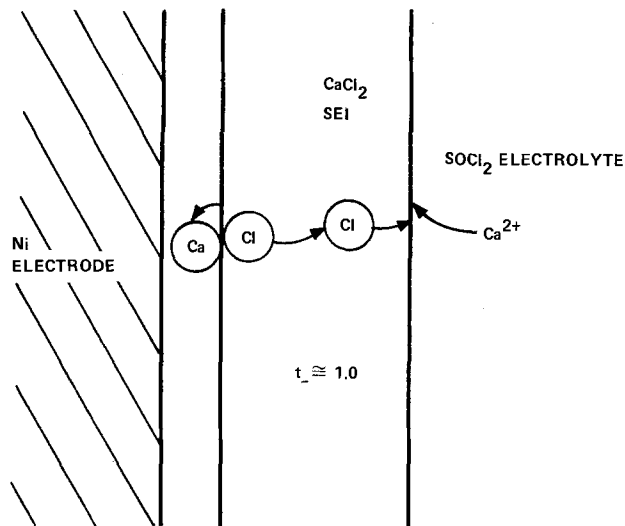


Fig. 12. Model for calcium deposition through a solid electrolyte interphase layer of CaCl_2 . Ionic current is carried by anion as a result of the low transport number of the calcium cation.

In contrast, the plating or dissolution of lithium through a lithium salt SEI would not require the growth or the demise of crystals of the lithium salt, since lithium ions could simply pass through this layer. With lithium, the process either of plating or particularly of anodic oxidation would require only that the SEI be physically transported, intact, as the metal was plated or stripped.

Calcium corrosion.—The accelerated corrosion of abraded Ca metal in the thionyl chloride electrolytes as compared to SOCl_2 alone is puzzling at first glance.

The extensive investigations with lithium and the LiCl film in SOCl_2 are available for contrast and comparison. Lithium appears far less reactive both in SOCl_2 and the various suitable electrolytes which is evidenced by discharge of cells at efficiencies approaching 100% utilization of the lithium anode. Peled and Dey independently have proposed compatible explanations of the nature of the film growth and morphology (6-8). In particular, Dey (8) has considered the Pilling-Bedworth ratio (14) which relates the molar volume of the coating or film to the molar volume of the metal. This use of this ratio was originally confined to explanations of protective and nonprotective metal oxides. The effectiveness of the coating was judged according to the ratio R

$$R = \frac{V_s}{nV}$$

where V_s is the molar volume of a Li or Ca compound, n is the number of gram atoms of Li or Ca in one mole of the compound, and V the gram atomic volume of Li or Ca. When this ratio is greater than 1, the compound forms a protective film. The following examples are included for comparison

Compound	R
Li ₂ O	0.57
Li ₂ N	0.64
Li ₂ CO ₃	1.34
LiCl	1.58
CaO	0.66
CaCl ₂	1.98

It is obvious from these considerations that LiCl would be expected to be protective and in fact has been shown to be kinetically protective for lithium in SOCl_2 . The same conclusion would be drawn for CaCl_2 on Ca, yet we have not found this to be the case. The discrepancy lies in the relative simplicity of the Pilling-Bedworth ratio, and corrosion treatises (15,

16) indicate that only a qualitative agreement is expected. Other considerations such as a coefficient of expansion equal to the metal substrate, good adherence, and low electrical conductivity are equally important (16). In addition to these factors, the intrinsic qualities such as mechanical film breakdown, chemical breakdown of the film, and breakdown by undermining at any fortuitous imperfection, provide a more complete view of film protection or nonprotection (16).

The presence of dissolved salts aggravates the calcium corrosion, a result not unexpected when considering the Li/ SOCl_2 system where the nature of the dissolved salt apparently changes or influences the LiCl film growth rate and morphology (17, 18). Finally, the calcium corrosion may also result from the presence of relatively high amounts of magnesium and aluminum which would be expected to be present at the grain interfaces and which may give rise to galvanic corrosion cells within the anode.

The open-circuit potential of the calcium- SOCl_2 cell differs considerably from the value calculated from thermodynamic functions (see the introduction). This discrepancy may arise from two considerations: first, the thickness of the SEI may affect the potential (6) and second, active corrosion implies a corrosion current and a consequent lower potential through polarization of the anode.

Summary and Conclusions

In addition to the above generalized discussion of calcium corrosion, the salient results of this investigation were:

1. Suitable electrolytes such as $\text{Ca}(\text{AlCl}_4)_2$ can be prepared if attention is paid to the purity of materials and water is painstakingly excluded.

2. Corrosion of the calcium metal in electrolytes is a significant problem under the conditions studied. The corrosion occurs during storage, and apparently, more rapidly under anode discharge when the SEI or CaCl_2 film may be thinner and more susceptible to continued reaction with the SOCl_2 .

3. Cathode capacities when compared to Li/ SOCl_2 cells are lower, a probable result of the larger molar volume occupied by CaCl_2 and lowered mobility of calcium ions relative to lithium ions in the electrolyte.

4. Both SO_2 and CaCl_2 were confirmed as products of cell discharge intimating that the electroreduction of SOCl_2 proceeds to S, SO_2 , and Cl^-



5. The calcium plating experiments in SOCl_2 suggested that calcium metal was not electrodeposited on the nickel substrate. This behavior may result from a rapid corrosion rate or fundamental transport problems through the CaCl_2 film formed on the substrate.

6. Vacuum annealing of the calcium reduces the work hardening and results in better anode utilization, although corrosion is not eliminated.

Acknowledgments

Research costs associated with this investigation were supported in part by the Office of Naval Research Contract No. N00014-76-0524. The author would like to acknowledge the laboratory assistance of Mr. Richard Gary and the SEM work of Mr. Kim Ostreicher. In addition, helpful discussions and the encouragement of Dr. Carl Schlaikjer are appreciated.

Manuscript submitted July 11, 1979; revised manuscript received Oct. 29, 1979. This was Paper 57 presented at the Pittsburgh, Pennsylvania, Meeting of the Society, Oct. 15-20, 1978.

Any discussion of this paper will appear in a Discussion Section to be published in the December 1980 JOURNAL. All discussions for the December 1980 Discussion Section should be submitted by Aug. 1, 1980.

Publication costs of this article were assisted by GTE Laboratories.

REFERENCES

1. M. H. Miles, D. A. Fine, and A. N. Fletcher, *This Journal*, **125**, 1209 (1978).
2. G. J. Janz and R. P. T. Tomkins, *ibid.*, **124**, 55C (1977).
3. D. T. Sawyer and J. L. Roberts, "Experimental Electrochemistry for Chemists," p. 224, John Wiley & Sons, New York (1974).
4. R. J. Staniewicz and R. Gary, *This Journal*, **126**, 981 (1979).
5. J. J. Auborn, K. W. French, S. I. Lieberman, V. K. Shah, and A. Heller, *ibid.*, **120**, 1613 (1973).
6. E. Peled, Paper 4 presented at The Electrochemical Society Meeting, Atlanta, Georgia, Oct. 9-14, 1977.
7. E. Peled, Proceedings of the 28th Power Sources Symposium, Atlantic City, N.J., June 1978.
8. A. N. Dey, *Thin Solid Films*, **43**, 131 (1977).
9. J. J. Auborn, R. D. Bezman, K. W. Heller, S. I. Lieberman, Proceedings of the 26th Power Sources Conference, Atlantic City, N.J., May 1974.
10. A. N. Dey and P. Bro, *This Journal*, **125**, 1574 (1978).
11. C. R. Schlaikjer, F. Goebel, and N. Marincic, *ibid.*, **126**, 513 (1979).
- 11a. W. K. Behl, *J. Electroanal. Chem. Interfacial Electrochem.*, **101**, 367 (1979).
12. E. Peled and H. Stranze, *This Journal*, **124**, 1030 (1977).
- 12a. E. Peled, *This Journal*, **126**, 2047 (1979).
13. C. E. Derrington, A. Lindner, and M. O'Keeffe, *J. Solid State Chem.*, **15**, 171 (1975).
14. N. B. Pilling and R. E. Bedworth, *J. Inst. Met.*, **29**, 529 (1923).
15. L. L. Shreir, "Corrosion," Vol. 1, p. 254, Newnes-Butterworths, Boston (1976).
16. M. G. Fontana and N. D. Green, "Corrosion Engineering," pp. 347-349, McGraw-Hill Co., New York (1978).
17. C. R. Schlaikjer, U.S. Pat. 4,020,240.
18. J. P. Gabano and P. Lenfant, Paper 27 presented at The Electrochemical Society Meeting, Pittsburgh, Pennsylvania, Oct. 15-20, 1978.

Role of Oxide Defects in the Anodic Oxidation of Nickel

B. MacDougall*

National Research Council of Canada, Ottawa, Ontario, Canada K1A 0R9

ABSTRACT

The galvanostatic oxidation of nickel electrodes in pH 2.8 Na₂SO₄ requires the presence of a prior oxide film in order to avoid the active nickel dissolution region. Either the 6-8Å NiO film on electropolished nickel or that formed during the early stages of anodic passivation can serve as an appropriate starting surface for galvanostatic experiments. Anodic charging of such electrodes gives a distinct transition region over a potential range of almost 1V. The current efficiency for nickel dissolution during the potential transient is high (>80%) with only a small portion of the charge contributing to oxide growth. This situation persists even at high charging rates and/or high solution pH's where it appears that chemical dissolution of the oxide is not playing an important role. The results suggest that the standard high field oxide growth mechanism is not operative during galvanostatic oxidation of nickel. The results are best explained in terms of a defective oxide film where the change of potential during the transient is associated with an increase in the state of film perfection. Anodic charge consumption would be mainly due to a continuous breakdown and repair of the oxide film at defect sites, most of the charge going towards Ni → Ni²⁺ + 2e during inefficient film repair. The increase in anodic potential with increasing perfection of the film is interpreted in terms of an overvoltage effect, i.e., the area over which breakdown and repair is occurring decreases with increasing film perfection and therefore the anodic current density increases. At potentials > +0.4V, the rate of increase in oxide film perfection decreases and an eventual steady state is reached. The influence of potential of anodization and solution pH on nickel dissolution, oxide repair, and oxide perfection is discussed. The defect model of oxide film development is shown to apply equally well during potentiostatic oxidation of nickel, the NiO film reaching an almost steady thickness very soon after the potential step anodization with the continual long-term decrease of anodic current with time of anodization being due to a localized increase in oxide film perfection.

The anodic oxidation of nickel in acid or neutral electrolytes has been extensively studied by workers using potentiostatic (1-7), potentiodynamic (8, 9), and galvanostatic charging techniques (10-13). It is generally accepted that a surface oxide film on the nickel electrode is responsible for retardation of the nickel dissolution reaction and that, on a previously oxide-free nickel surface which is polarized into the passive potential region, the oxide composition is NiO as opposed to Ni(OH)₂ or higher oxides of nickel. On the other hand, there is still controversy concerning the mechanism of film growth with regard to changes in oxide thickness and/or electronic conduc-

tivity with time and/or potential of anodization, with several models having been presented in the literature. In previous work, MacDougall and Cohen found no substantial change in oxide thickness with time or potential of anodization, a film of 9-12Å of NiO forming very rapidly on the electrode surface after polarization in the passive potential region (1, 2, 4, 14, 15). Correspondingly large changes in the stability of the oxide towards open-circuit breakdown were explained in terms of a defect model of the NiO film, film stability being determined by the character of the oxide at localized weak points in the film. Since the total surface coverage by these defects is quite small (≤2%) and the surface analysis measurements are averages representative of the entire oxide, the

* Electrochemical Society Active Member.

Key words: defects, electrode, passivity, oxidation.

measured film thicknesses and stoichiometries are essentially independent of film perfection. This model was substantiated by: (i) electron microscopic examination of single crystal nickel electrodes following open-circuit oxide breakdown; (ii) solution analysis for Ni^{2+} at various stages during film breakdown; and (iii) both anodic and cathodic polarization experiments (16, 17).

A model for passive oxide film formation on nickel has been presented by Ord *et al.* (12) to explain an ellipsometrically determined increase in oxide film thickness during galvanostatic anodic charging in both neutral sulfate and borate solutions. The oxide thickness appeared to increase from 2 to 18 Å during anodic charging, this increase paralleling an increase in anodic potential. This suggested a high field oxide growth mechanism similar to that proposed by other workers for oxide growth on nickel under potentiostatic conditions in acid solutions (18, 19). The oxide film was believed to be a poor electronic conductor and thus able to sustain a substantial potential drop across it. The oxide giving rise to the potential transient was believed to be NiO while that formed in the plateau potential region was probably βNiOOH with a higher electronic conductivity than NiO (12).

An important issue in the anodic oxidation of nickel under both potentiostatic (18) and galvanostatic (19) conditions concerns the current efficiency for oxide growth in the passive potential region, *i.e.*, what portion of the overall anodic current goes towards an increase in film thickness? It is recognized that corrections must be made for chemical dissolution of the oxide, *i.e.*, $\text{NiO} + 2\text{H}^+ \rightarrow \text{Ni}^{2+} + \text{H}_2\text{O}$, because an electron-transfer reaction occurs to replace the dissolved oxide, *i.e.*, $\text{Ni} + \text{H}_2\text{O} \rightarrow \text{NiO} + 2\text{H}^+ + 2e$. The problem is that the charge associated with this coupled reaction may represent a large part of the measured anodic charge but it does not contribute to an actual increase in the amount of oxide on the surface. The usually accepted method of correction is to assume a constant rate of chemical dissolution, and thus a constant anodic current contribution, which depends only on solution pH (18-20). The dissolution current can then be subtracted from the overall anodic current to give the rate of oxide growth. It appears, however, that this method may be too simplistic in that the anodic currents may be associated with other processes besides oxide growth and chemical dissolution. In particular, work on the anodic oxidation of iron and nickel (21, 22) indicates that chemical dissolution of the oxide may only be responsible for a small portion of the anodic current not contributing to oxide growth. The majority of the nonoxide growth anodic current is believed to be due to metal dissolution ($\text{M} \rightarrow \text{M}^{2+} + 2e$) under the influence of a high electric field within the oxide. Other work would seem to indicate that the rate of oxide chemical dissolution is dependent on the anodic potential (7, 23), *i.e.*, the rate of $\text{MO} + 2\text{H}^+ \rightarrow \text{M}^{2+} + \text{H}_2\text{O}$ is determined by the potential across the oxide-electrolyte interface as well as the solution pH. This means that during oxide growth, (i) oxide chemical dissolution, (ii) electrochemical oxide dissolution, and (iii) field assisted metal dissolution may be contributing to the measured anodic current, in which case the correction term could depend on time and potential of anodization as well as solution pH. Interpretation of current efficiency data for growth of thin oxide films is therefore a complicated matter.

In the present paper, the mechanism of the anodic passivation of nickel under galvanostatic and potentiostatic conditions will be investigated by directly measuring the current efficiency for oxide growth on preoxidized electrodes. The roles of the various reactions responsible for lowering the oxide current efficiency will be studied by working at different anodic charging rates and solution pH's. An alternative to

the high-field oxide growth model will be presented to explain the results, this model involving changes in the defect character of the oxide during anodization. The role of breakdown and repair of oxide at the defect sites will be discussed and it will be shown how localized reactions may be responsible for a large part of the charge consumption during both galvanostatic and potentiostatic polarization.

Experimental

Polycrystalline specimens, 1×2.5 cm, were prepared from zone-refined nickel sheet of 99.996% purity as described elsewhere (1). They were degreased with benzene, chemically polished (1), electropolished for 2 min at 23°C in a 57 volume percent (v/o) sulfuric acid solution at 0.5 $\text{A}\cdot\text{cm}^{-2}$, and then annealed at 800°C in a vacuum of 10^{-8} Torr. The specimens were electropolished again immediately before use in an experiment. Potentials quoted in this paper are referred to the $\text{Hg}/\text{Hg}_2\text{SO}_4$ reference electrode in 0.15N Na_2SO_4 (+0.665V with respect to the standard reversible hydrogen electrode). Deaerated solutions of 0.15N Na_2SO_4 were adjusted to pH 2.8. Experiments were conducted at 25°C. Electropolished electrodes were either potentiostatically or galvanostatically anodized both with and without cathodic reduction of the prior oxide film. Solutions were analyzed for Ni^{2+} by carbon rod atomic absorption spectroscopy, the lower limit of detection by this method being 0.2 $\mu\text{g cm}^{-2}$ (sample area = 5 cm^2 ; cell volume = 50 ml). X-ray emission spectroscopy was used to determine oxide film thickness (1).

Results

Transient Results

Galvanostatic oxidation of nickel.—Figure 1 shows the anodic galvanostatic charging profiles for nickel electrodes in pH 2.8 Na_2SO_4 at 4, 20, and 200 $\mu\text{A cm}^{-2}$. The electrode pretreatment consisted of electropolishing and immersion in the pH 2.8 electrolyte with an applied cathodic current of 20 $\mu\text{A cm}^{-2}$ to remove the prior 6-8 Å NiO film (1). The potential is then stepped to -0.3V for 30 sec to avoid the potential region of active metal dissolution. The starting surfaces are thus covered by an anodically formed oxide film. A constant potential plateau is observed at potentials more anodic than the reversible potential for oxygen evolution in the present system, *i.e.*, +0.4V. The plateau potential, and thus the reaction over-

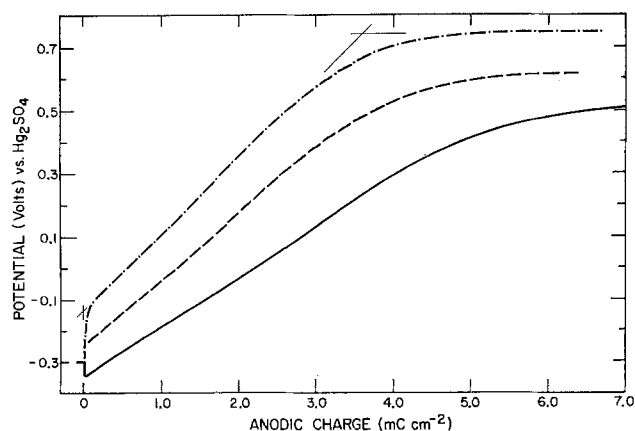


Fig. 1. Anodic charging curves for nickel electrodes in pH 2.8 Na_2SO_4 at 4 $\mu\text{A cm}^{-2}$ (—), 20 $\mu\text{A cm}^{-2}$ (---), and 80 $\mu\text{A cm}^{-2}$ (-·-). Electrode pretreatment consisted of electropolishing, cathodic reduction, and stepping the potential to -0.3V for 30 sec. The standard method was used for determining the transition time of the anodic arrest and is illustrated for the 80 $\mu\text{A cm}^{-2}$ charging profile. The points of intersection of the extrapolated lines for the various charging processes are taken as defining the beginning and end of the change transient.

voltage, is dependent on the anodic charging rate with a Tafel slope of ca. 0.13V. Between the initial potential and that of the plateau, the potential increases steadily at an almost constant rate (i.e., $dV_a/dQ_a = \text{constant}$) giving rise to what will be defined as an anodic transient.

The transient charge is plotted as a function of anodic charging current in Fig. 2. The transient charge is almost independent of anodic charging current above ca. $50 \mu\text{A cm}^{-2}$. At lower charging rates, Q_a^t increases with decreasing i_a^s , an observation that can be explained in terms of an increased amount of chemical dissolution of the oxide at the longer transition times. The value of the anodic charging current at which Q_a^t becomes independent of i_a^s increases with decreasing pH and decreases with increasing pH, in agreement with a chemical dissolution model. At pH 2.8, an anodic charging rate of $80 \mu\text{A cm}^{-2}$ is used to study the transient oxidation of nickel in order to avoid the region of large changes of Q_a^t with i_a^s (Fig. 2).

Role of the air-formed oxide film.—It is known (1) that nickel electrodes which have been electropolished in 57 v/o H_2SO_4 and subsequently exposed to the air are covered with a 6-8Å "air-formed" NiO film. The possibility of using this previously characterized film as a means of avoiding the active potential region was investigated. When electropolished nickel is immersed in pH 2.8 Na_2SO_4 at $80 \mu\text{A cm}^{-2}$, the potential rapidly adjusts to -0.14V and then increases almost linearly with Q_a until $+0.7\text{V}$ (Fig. 3). Shown for comparison in Fig. 3 is the result obtained with an initially oxide-free electrode which was given a 30 sec anodization at -0.3V prior to anodic charging. After this treatment, initiation of galvanostatic charging with $80 \mu\text{A cm}^{-2}$ results in an immediate potential increase to -0.18V , i.e., close to the -0.14V observed with electropolished nickel, followed by an anodic transient almost identical to that obtained with electropolished nickel. The results suggest that this anodic oxide film is similar in character to the air-formed film. Also shown in Fig. 3 is the anodic charging profile obtained with an electropolished nickel electrode which was anodized at -0.3V for 30 sec without prior reduction of the air-formed oxide film, i.e., it was immersed in the electrolyte under polarization at -0.3V . The presence of the 6-8Å NiO film reduces the transient charge by only a small amount. The fact that the presence of the oxide film on electropolished nickel does not alter the overall transient oxidation

¹ In the text, V_a and t_a refer to the potential and time of anodization; i_a is the anodic current; Q_a is the anodic charge passed; i_a^s is the anodic galvanostatic charging current, and Q_a^t is the anodic transient charge.

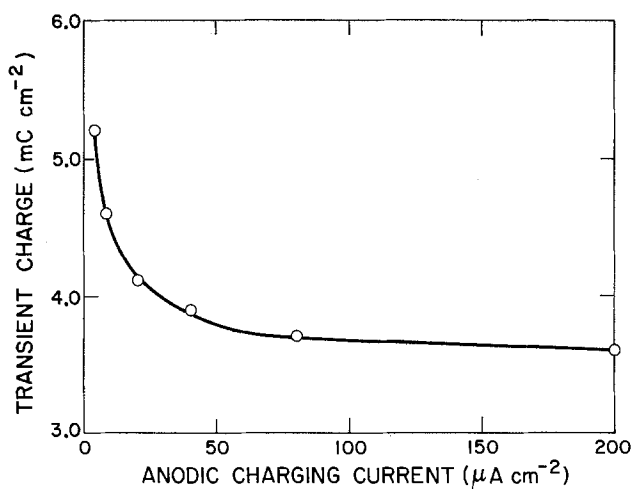


Fig. 2. Variation of the transient charge with anodic charging current, in pH 2.8 Na_2SO_4 , for nickel electrodes electropolished, cathodically reduced, and anodized at -0.3V for 30 sec.

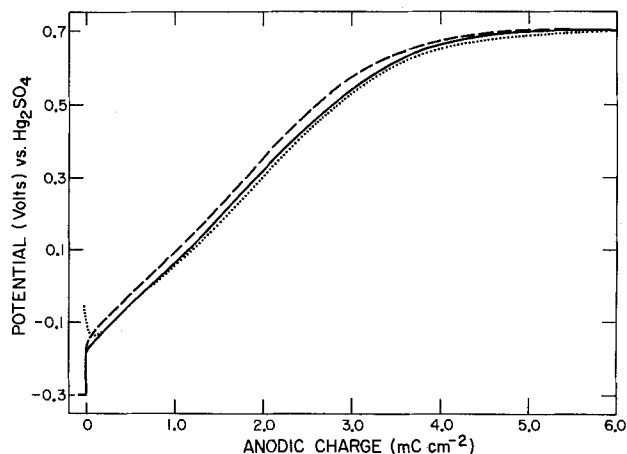


Fig. 3. Anodic charging curves for electropolished nickel electrodes in pH 2.8 Na_2SO_4 at $80 \mu\text{A cm}^{-2}$ after different pretreatments: (···) immersion in solution at $80 \mu\text{A cm}^{-2}$; (—) cathodically reduced with the potential stepped to -0.3V for 30 sec; (---) immersion in solution at -0.3V for 30 sec without prior cathodic reduction.

characteristics means that it can serve as a "partially passivated" surface from which to start oxidation studies.

Role of pH and temperature.—Figure 4 shows the anodic galvanostatic charging profiles, at $80 \mu\text{A cm}^{-2}$, for electropolished nickel electrodes at pH 2.0, 2.8, and 6.0. The anodic transient charge decreases by ca. 20% in going from pH 2.0 to pH 6.0. The plateau potential is independent of pH; also the immersion potential does not vary substantially with pH. (Changes in the reference electrode potential do not account for this result since the $\text{Hg}/\text{Hg}_2\text{SO}_4$ reaction is independent of pH.) Also shown in Fig. 4 is the effect on the anodic charge of a decrease in temperature from 25° to 6°C at pH 2.8. The anodic charging profile is similar to that obtained at 25°C except that the entire curve is shifted to more positive potentials.

Solution analysis for Ni^{2+} .—The solution was analyzed for Ni^{2+} at various times during anodic charging of electropolished surfaces. The amount of Ni^{2+} in solution increased with the quantity of charge passed and accounted for $>80\%$ of the anodic charge over the entire transient region at both pH 2.8 and 6.0 (Table I). This situation continued into the plateau potential region.

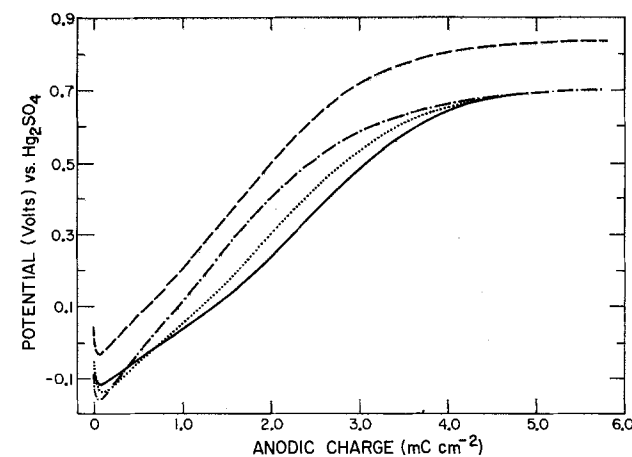


Fig. 4. Anodic charging curves for electropolished nickel electrodes at $80 \mu\text{A cm}^{-2}$ in $0.15\text{N Na}_2\text{SO}_4$ solutions of different pH's: (—) pH 2.0; (···) pH 2.8; (---) pH 6.0. Solution temperature is 25°C . Also shown is the result obtained in pH 2.8 Na_2SO_4 at 6°C (-·-·-).

Table I. Quantity of Ni^{2+} in solution as a function of amount of anodic charge passed during the galvanostatic oxidation of electropolished nickel at $80 \mu\text{A cm}^{-2}$. The transient charge has been converted to $\mu\text{g Ni}^{2+} \text{ cm}^{-2}$ by assuming a current efficiency of 100%

Solution pH	Transient time (sec)	Anodic charge ($\mu\text{g Ni}^{2+} \text{ cm}^{-2}$) $\pm 2\%$	$[\text{Ni}^{2+}]$ in solution ($\mu\text{g cm}^{-2}$) $\pm 10\%$
2.8	4.5	0.1	<0.2
2.8	22.0	0.54	0.48
2.8	29.3	0.71	0.72
2.8	38.8	0.95	0.80
2.8	55.0	1.34	1.10
2.8	125.0	3.05	2.90
6.0	36.0	0.88	0.84

Surface analysis of oxide films.—X-ray emission spectroscopy was used to determine the thickness of NiO films formed during galvanostatic charging. For both the air-formed or anodic prior oxide films, the NiO film thickness obtained by galvanostatic charging in pH 2.8 at $80 \mu\text{A cm}^{-2}$ (to +0.6V) was 9–12Å, i.e., an increase of $\sim 50\%$ over the 6–8Å of air-formed NiO originally present on electropolished nickel.

The structure the oxide film formed on nickel by galvanostatic charging was studied by reflection electron diffraction using a Ni (111) single crystal. (The single crystal gave anodic charging profiles which were almost identical to those obtained with polycrystalline nickel.) The oxide formed by anodic charging at $80 \mu\text{A cm}^{-2}$ (to +0.6V) is a highly epitaxed NiO whose character appears to be independent of prior removal of the air-formed oxide.

Long-Term Potentiostatic Results

The role of the air-formed oxide film in the potentiostatic oxidation of nickel was investigated by immersing an electropolished nickel electrode into the solution at 0 volts and comparing the i_a/t_a decay with the case where the air-formed oxide film was previously reduced before the potential was stepped to 0 volts. The results are shown in Table II. The presence of the air-formed oxide film reduces the initial i_a by a factor of 100 times, i.e., active nickel dissolution is greatly inhibited by the film. However, after ca. 3 sec of anodization at 0 volts, the currents are the same in both cases. Figure 5 shows the long term decay of anodic current with time (from 15 min to 160 hr) at 0 volts.

The nature of the long term anodic currents in Fig. 5 was investigated by analyzing the solution for Ni^{2+} at various times. An electrode was anodized at 0 volts for 1 hr and then removed to the air for 15 min. Upon reimmersion in a fresh pH 2.8 solution at 0 volts, a very small anodic charge flowed and the original current (corresponding to 1 hr at 0 volts) is reached within 60 sec. This indicates that the oxide film had changed very little during the 15 min air

Table II. Anodic currents as a function of time of anodization at 0.0V in pH 2.8 Na_2SO_4 for electropolished nickel electrodes with (A) and without (B) cathodic reduction of the air-formed oxide film

Time of anodization, t_a (sec)	Anodic currents, i_a (mA cm^{-2})	
	A	B
0	60	0.6
1	0.36	0.20
2	0.18	0.13
3	0.09	0.09
4	0.068	0.070
5	0.054	0.056
10	0.028	0.030
15	0.019	0.020
30	0.010	0.011
60	0.0054	0.0056
120	0.0028	0.0028
300	0.0014	0.0014

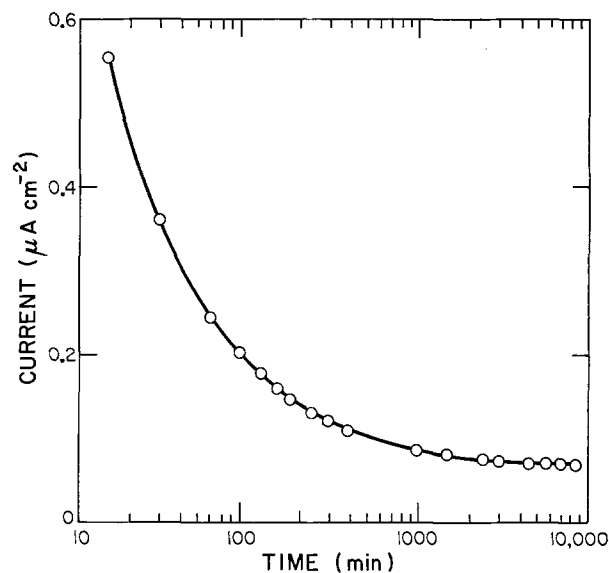


Fig. 5. Decay of the anodic current with time of anodization at an anodic step potential of 0 volts for an initially oxide-free nickel electrode. Solution is pH 2.8 Na_2SO_4 .

exposure [cf. Ref. (4)]. During this 60 sec reanodization, solution analysis indicated $<0.2 \mu\text{g cm}^{-2}$ of Ni^{2+} in solution. The same experiment was repeated but this time the reimmersed electrode was left in the solution at 0 volts for 24 hr. During this time, 8.8 mC cm^{-2} of anodic charge passed and $2.9 \mu\text{g cm}^{-2}$ ($\pm 10\%$) of nickel dissolved as Ni^{2+} . This amount of Ni^{2+} corresponds to 9.5 mC cm^{-2} , i.e., within experimental error all the long term anodic charge can be accounted for by the dissolution reaction $\text{Ni} \rightarrow \text{Ni}^{2+} + 2e$. This is in agreement with previous x-ray observations (1–4) that the overall thickness of nickel oxide films is almost independent of time of anodization.

To determine the influence of V_a on i_a , a nickel electrode was anodized at 0 volts for 1 hr, the anodic current falling to $0.24 \mu\text{A cm}^{-2}$. The potential was then rapidly adjusted to -0.2V and the current initially decreased to $0.03 \mu\text{A cm}^{-2}$ and began to increase very slowly. Open-circuit decay experiments indicate that the character of the oxide formed at 0 volts ($t_a = 1 \text{ hr}$) is not affected by the potential step to -0.2V for at least the first half hour, i.e., the character of the oxide is frozen for a substantial period of time after the potential step to a less anodic potential. If the anodization had been at -0.2V from the start, the anodic current would have been $0.25 \mu\text{A cm}^{-2}$ after 1 hr of anodization. In the present case, i_a continues to increase from $0.03 \mu\text{A cm}^{-2}$ for up to 10 hr after the potential step from 0 volts indicating that the film is taking a very long time to adjust to the form associated with anodization at -0.2V .

The effect of potentiostatic holding at -0.3V and 0 volts, for various periods of time, on the anodic charging profiles is shown in Fig. 6. Potentiostatic holding increases the anodic value to which the potential abruptly jumps with application of the constant anodic charging current and this results in a decrease of the anodic transient charge. The potential jump to the higher anodic value indicates that the character of the oxide film is dependent on the time as well as the potential of anodization, in agreement with previous observations from open-circuit work (4). With increasing time at -0.3V or 0 volts the film is converting to a higher potential form through changes in the character of the oxide.

Discussion

Distinct transients are observed over a potential range of almost 1V during anodic galvanostatic charg-

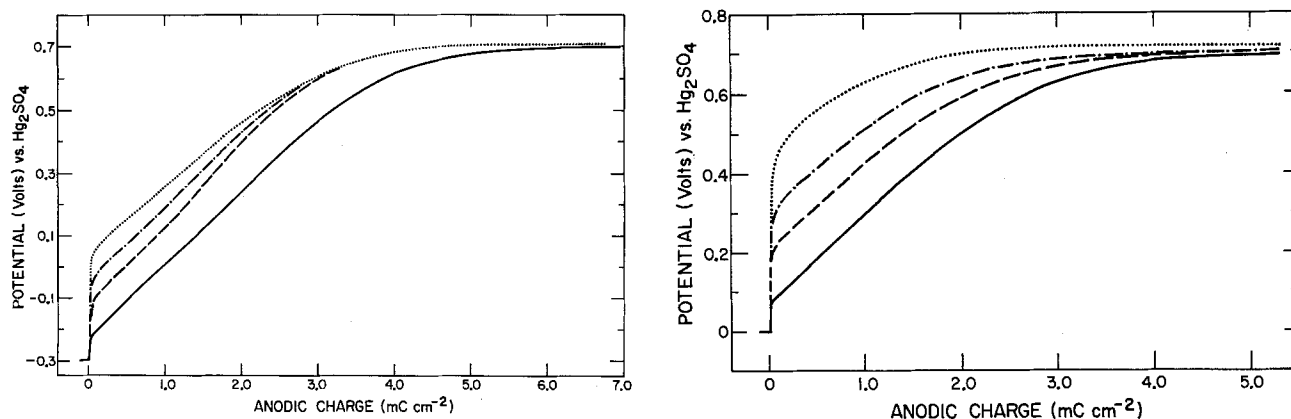


Fig. 6. (a, left) Anodic charging curves for previously oxide-free nickel electrodes in pH 2.8 Na_2SO_4 at $80 \mu\text{A cm}^{-2}$ as a function of time of anodization at -0.3V : (—) 10 sec; (---) 2 min; (-·-) 15 min; (···) 20 hr. (b, right) As in (a) but with an anodization potential of 0 volts.

ing of either electropolished or anodically pretreated nickel electrodes (Fig. 1 and 3). Similar results have been obtained by other workers (12, 19) which have been interpreted in terms of a high field oxide growth mechanism where the transient increase in anodic potential is due solely to an increase in thickness of the nickel oxide film. In the present work, the transient charge (up to $+0.6\text{V}$ at a charging rate of $80 \mu\text{A cm}^{-2}$ and assuming a 100% current efficiency for oxide growth) is equivalent to 20\AA of NiO so that the total NiO thickness (including the prior oxide) should be $\sim 27\text{\AA}$ after galvanostatic charging. X-ray emission measurements indicate, however, that the majority of the transient charge does not contribute to an increase in oxide thickness since the oxide is $\sim 9\text{-}12\text{\AA}$ thick after anodic charging and the prior oxide itself was $6\text{-}8\text{\AA}$. In agreement with this, solution analysis for Ni^{2+} indicates that the current efficiency for nickel dissolution is $>80\%$ throughout the transient region (Table I), i.e., the transient charge is mainly associated with nickel dissolution rather than oxide film growth. It could be argued that a high field mechanism with a very low oxide formation current efficiency is responsible for the apparent increase in oxide thickness from ~ 7 to $\sim 10\text{\AA}$, chemical dissolution of the oxide being responsible for the low current efficiency. However, this seems unlikely since the transient charge does not vary substantially with pH (Fig. 4) or with i_{a^s} above ca. $80 \mu\text{A cm}^{-2}$ (Fig. 2), the oxide formation current efficiency remaining very low ($<20\%$) throughout (Table I). Thus the standard high field oxide growth mechanism does not seem to apply and an alternative model is required to explain the existence of the distinct anodic transient during galvanostatic charging of preanodized nickel electrodes.

Three possible interpretations of the results will now be presented. The first involves a potential dependent rate of oxide dissolution with the rate increasing with anodic potential, i.e., electrochemical oxide dissolution (7, 23). The argument would be that the resistance of the oxide to dissolution increases throughout the transient region and consequently the anodic potential must increase in order that the constant anodic current can be consumed. In this model, a high electric field does not have to be present across the oxide since the potential responsible for dissolution is across the oxide-solution interface. The second interpretation involves a modified high field oxide growth mechanism whereby the field across the oxide is responsible for nickel dissolution. In this model, nickel ions diffusing across the oxide film can either incorporate into the oxide film or dissolve in solution (cf. 21, 22) and the majority would thus appear to dissolve. The increase in anodic potential in the transient region would be a monitor of either

an increase in oxide thickness or a change in its electronic properties (e.g., conductivity) so that higher anodic potentials are required to maintain the same anodic reaction rate. Both of the above models assume that the dissolution process is uniform with all sites over the surface of the oxide being essentially equivalent. The third and preferred interpretation is one which considers a defective oxide film and this will now be presented in some detail.

The defect model of the oxide film evolved from previous constant potential work where it was found that the thicknesses of anodically formed nickel oxide films were $9\text{-}12\text{\AA}$, independent of V_a and t_a in both acid and neutral solutions (1-4, 14-17). At the same time, however, the stability of these anodic oxide films towards open-circuit dissolution was highly dependent on the conditions of anodization. These earlier results were explained in terms of a defect model of the oxide film in which a small coverage of defective oxide determines the stability of the film, the number and/or stability of these defect oxide sites being dependent on the anodic treatment. With increasing time or potential of anodization in the passive region, the stability of the oxide at the defect sites increases and the oxide film becomes more perfect. Since the majority of the film is nondefective, the overall character of the film (e.g., thickness, stoichiometry) does not vary substantially with anodic treatment and changes in the oxide at the defect areas would be difficult to observe. It may also be that small changes in the overall character of the oxide have a drastic influence on the number and/or stability of defect areas. The present results show that anodic holding at any V_a leads to a decrease of the subsequent transient charge (Fig. 6), i.e., the processes occurring during potentiostatic holding and anodic charging through the transient region appear to be similar. Therefore, the defect model will now be used in an attempt to explain the anodic galvanostatic charging results.

When electropolished nickel is immersed in a pH 2.8 Na_2SO_4 solution with an anodic charging current of $80 \mu\text{A cm}^{-2}$, the potential adopted by the electrode is determined by the number and stability of oxide defect sites, these being the areas where electrochemical reactions can occur and where the anodic charge can thus be consumed. The most probable mechanism for charge consumption is localized oxide breakdown (e.g., $\text{NiO} + 2\text{H}^+ \rightarrow \text{Ni}^{2+} + \text{H}_2\text{O}$) followed by inefficient film repair involving competition between $\text{Ni} \rightarrow \text{Ni}^{2+} + 2e$ and $\text{Ni} + \text{H}_2\text{O} \rightarrow \text{NiO} + 2\text{H}^+ + 2e$. The kinetics of breakdown and repair of the oxide will determine the extent of the nickel dissolution reaction. It is known that the $6\text{-}8\text{\AA}$ NiO film on electropolished nickel is extremely defective, breaking down on open circuit in <90 sec in pH 2.8 Na_2SO_4 (4) and there

are thus many defect sites which will be breaking down (and repairing) upon immersion in the solution at $80 \mu\text{A cm}^{-2}$. During anodization at $80 \mu\text{A cm}^{-2}$, the perfection of this oxide film increases, *i.e.*, the number and/or stability of oxide defect sites changes so that fewer sites are breaking down and/or the sites are breaking down less frequently (16). The increase in potential throughout the transient region could therefore be due to a decrease in the effective active area, with corresponding increase in anodic overvoltage, as the film perfects. Although the effective active area decreases during the transient, the rate of change of V_a with Q_a does not change dramatically. Since dV_a/dQ_a is a measure of the rate of perfection of the oxide, the current efficiency for oxide perfection must decrease with increasing V_a . The fact that the $80 \mu\text{A cm}^{-2}$ can be consumed by the reduced active area with no change in the rate of perfection means that the current efficiency for repair of the oxide must also decrease with increasing V_a and this can be related to more of the anodic current going towards nickel dissolution. There is probably some connection between repair and perfection of the oxide² so that their current efficiencies move hand in hand, *i.e.*, any decrease in the current efficiency for film repair probably results in a corresponding decrease in that for film perfection.

During galvanostatic oxidation, the rate of increase in film perfection (*i.e.*, dV_a/dQ_a) begins to diminish at *ca.* $+0.4\text{V}$ (Fig. 4). Eventually, a steady state of perfection is reached and a potential plateau results, the higher anodic potentials leading to rather high rates of nickel dissolution (Table I). This region is often referred to as the transpassive region of nickel dissolution (5, 7, 8, 18, 24, 25). It is known from previous work (4) that the stability of NiO films, potentiostatically formed for a constant t_a , towards open-circuit dissolution decreases with increasing anodic potential when $V_a > 0.4\text{V}$, *i.e.*, at approximately the same potential where the anodic transient begins to flatten out. This increase in breakdown susceptibility of the film at the higher anodic potentials may be associated with oxidation of Ni^{2+} to Ni^{3+} within the oxide, the occurrence of elements of the oxygen evolution reaction, or a change in the structure and epitaxy of the oxide film.

The lack of influence of solution pH on both the potential of immersion of electropolished nickel and the plateau potential (Fig. 4) is somewhat unexpected in terms of the present model. When electropolished nickel is immersed in a solution of higher pH, it is expected that the amount of effective active area should be less than with a more aggressive (*i.e.*, lower pH) solution and this should result in an increased anodic overvoltage for nickel dissolution. However, a surface intermediate such as NiOH_{ads} may be playing a role in both nickel dissolution and oxide formation (6), in which case a change in solution pH will not only change the reversible potential of oxide formation and the rate of film breakdown but may also alter the kinetics of the nickel dissolution reaction. If the exchange current density for nickel dissolution increases with increasing pH, as has been suggested by other workers, this could compensate for the decrease in active area and leave the immersion potential almost constant. A similar explanation can be advanced for the lack of influence of pH on the plateau region at $+0.7\text{V}$. The influence of temperature in shifting the entire charging profile in the positive direction is quite dramatic (Fig. 4) and may be associated with a decrease in the rate of film breakdown and a corresponding increase in the anodic overvoltage for oxide formation and nickel dissolution.

As was mentioned earlier, the increase in perfection of the oxide film can be associated with either an actual decrease in the number of active defect sites or an increase in the stability of the active sites without any great change in their total number. In either case, the effective active area decreases. It has been found that the nickel surface roughens in a general way when the potential is maintained in the plateau region or potentiostatically in the passive region for long periods of time. This observation suggests that there is not a small static number of active defect sites undergoing breakdown and repair since such a situation should give rise to heavy localized attack. It may thus be that the more appropriate model is one where the total number of defect sites does not change substantially during film perfection. However, the frequency of any particular site breaking down does decrease with increasing film perfection so that, during any particular time period, fewer sites are active the more perfect is the film. Over a long period of time, all of the defect sites originally present on the surface break down and thereby give rise to the general surface attack. It may also be that breakdown is a random process, in terms of where it will occur on the electrode surface, and that all surface sites are susceptible to breakdown at some point in time. The exact nature of the defective oxide areas and their relationship to the overall character of the film is still open to speculation.

The results obtained during the potentiostatic oxidation of nickel can also be interpreted in terms of the defect model of the oxide film. It appears that, after a potential step to 0 volts, the oxide film reaches an almost steady-state thickness within the first five seconds (Table II). However, it is known that the stability of the film towards open-circuit breakdown increases (and the i_a decreases) with increasing t_a over a period of several days (2, 4, 14-17). This can be interpreted in terms of a perfecting of the film with a corresponding decrease in the effective active defect area, the oxide film formed during the first 5 sec at 0 volts being extremely defective. The results indicate that this film is initially similar to the air-formed film on electropolished nickel, *i.e.*, very defective, and this explains previous observations that the open-circuit breakdown characteristics of the anodically formed oxide film is the same, independent of prior removal of the air-formed film. The i_a , which is a measure of the active defect area at any V_a , is dependent on V_a and t_a . When the potential is rapidly shifted to -0.2V , after a 1 hr anodization at 0 volts, the defect area associated with the anodization at 0 volts is initially frozen, *i.e.*, the defect state of the oxide does not change. As mentioned previously, it is known that oxide film stability increases with increasing potential of anodization (4) (in the passive region for a constant time), *i.e.*, the film formed at 0 volts is more stable than that formed at -0.2V . The decrease in i_a from 0.24 to $0.03 \mu\text{A cm}^{-2}$, upon stepping the potential from 0 volts to -0.2V , is due to the influence of the lower V_a on the nickel dissolution reaction ($\text{Ni} \rightarrow \text{Ni}^{2+} + 2e$) the defect area of the oxide being initially constant at that established by the anodization at 0 volts. If the 1 hr anodization had been at -0.2V from the start, the i_a would have been $>0.03 \mu\text{A cm}^{-2}$ since the defect area of the oxide would have been higher, *i.e.*, V_a controls both the rate of stabilization (and therefore the defect area) of the film as well as the rate of anodic reactions at the defect sites. The proposal that most of the long-term i_a is not directly accounted for by chemical dissolution of the oxide is supported by the substantial decrease in i_a upon stepping the potential from 0 volts to -0.2V . The $0.21 \mu\text{A cm}^{-2}$ difference in current would be equivalent to a thinning rate of 8\AA of NiO hr^{-1} and since the oxide is only 10\AA thick and the i_a at -0.2V continues to

² Repair occurs whenever the oxide film breaks down locally and reforms; perfection occurs when a repair event leads to an increase in the local film stability so that either the oxide is more resistant to breakdown or subsequent repair occurs more rapidly.

increase for up to 10 hr after the potential step, the majority of the anodic current cannot simply be due to $\text{NiO} + 2\text{H}^+ \rightarrow \text{Ni}^{2+} + \text{H}_2\text{O}$. Very inefficient film repair is the most probable explanation with most of the measured i_a associated with nickel dissolution. The extremely slow increase of i_a with t_a at -0.2V is probably due to slow, local dissolution of the film formed at 0 volts with replacement by the less stable film now being formed at -0.2V .

Summary

1. The current efficiency for oxide film formation during galvanostatic oxidation of preanodized nickel electrodes is less than 20%. The majority of the change is associated with nickel dissolution.

2. The low current efficiency for oxide growth is mainly due to nickel dissolution, $\text{Ni} \rightarrow \text{Ni}^{2+} + 2e$, during inefficient film repair, $\text{Ni} + \text{H}_2\text{O} \rightarrow \text{NiO} + 2\text{H}^+ + 2e$, after film breakdown, $\text{NiO} + 2\text{H}^+ \rightarrow \text{Ni}^{2+} + \text{H}_2\text{O}$. Chemical dissolution of the oxide cannot, by itself, explain the results.

3. The results are consistent with a model in which defects in the oxide film are perfected by both increased potential and time of anodization up to $\approx 0.4\text{V}$. At a constant changing current, the potential increases with increasing state of the film perfection since the effective breakdown area is decreasing.

4. The majority of the long-term anodic current observed during constant potential polarization is due to inefficient film repair, the potential controlling both the rate of $\text{Ni} \rightarrow \text{Ni}^{2+} + 2e$ and the rate of change of film perfection.

Acknowledgment

The author wishes to thank Dr. D. F. Mitchell for the x-ray measurements of NiO thicknesses, Mr. A. Desaulniers for the A.A. analysis of Ni^{2+} , and Drs. M. J. Graham and M. Cohen for helpful discussions and suggestions.

Manuscript submitted June 11, 1979; revised manuscript received Nov. 6, 1979.

Any discussion of this paper will appear in a Discussion Section to be published in the December 1980 JOURNAL. All discussions for the December 1980 Discussion Section should be submitted by Aug. 1, 1980.

Publication costs of this article were assisted by the National Research Council of Canada.

REFERENCES

1. B. MacDougall and M. Cohen, *This Journal*, **121**, 1152 (1974).
2. B. MacDougall and M. Cohen, *ibid.*, **123**, 191 (1976).
3. B. MacDougall and M. Cohen, *ibid.*, **123**, 1783 (1976).
4. B. MacDougall and M. Cohen, *ibid.*, **124**, 1185 (1977).
5. I. A. Ammar and S. Darwish, *Electrochim. Acta*, **11**, 1541 (1966).
6. N. Sato and G. Okamoto, *This Journal*, **111**, 897 (1964).
7. N. Sato and G. Okamoto, *ibid.*, **110**, 605 (1963).
8. A. B. Ijzermans, *Corros. Sci.*, **10**, 113 (1970).
9. G. T. Burstein and G. A. Wright, *Electrochim. Acta*, **20**, 95 (1975).
10. M. Okuyama and S. Haruyama, *Corros. Sci.*, **14**, 1 (1974).
11. M. Okuyama, S. Haruyama, and K. Nagasaki, "Proc. 5th Inter. Congr. Met. Corr." p. 197, Houston, Texas (1974).
12. J. L. Ord, J. C. Clayton, and D. J. DeSmet, *This Journal*, **124**, 1714 (1977).
13. K. Arnold and K. J. Vetter, *Z. Elektrochem.*, **64**, 407 (1960).
14. B. MacDougall and M. Cohen, *Electrochim. Acta*, **23**, 145 (1978).
15. B. MacDougall, *This Journal*, **125**, 1883 (1978).
16. B. MacDougall and M. Cohen, Paper presented at the Fourth International Symposium on Passivity, Airlie, Virginia, Oct. 17-21, 1977.
17. B. MacDougall, *Is. J. Chem.*, **18**, 125 (1979).
18. G. Okamoto, H. Kobayashi, M. Nagayama, and N. Sato, *Z. Elektrochem.*, **62**, 775 (1958).
19. M. Zamin and M. B. Iues, *This Journal*, **126**, 470 (1979).
20. G. Okamoto and N. Sato, *J. Electrochem. Soc. Jpn.*, (overseas ed.) **27**, E125 (1959).
21. V. M. Novarousky, *Electrochim. Acta*, **10**, 353 (1965); also V. M. Novarousky and M. A. Likhachev, *ibid.*, **12**, 267 (1967).
22. J. Siejka, C. Cherki, and J. Yahalom, *This Journal*, **119**, 991 (1972).
23. H. J. Engell, *Z. Phys. Chem.*, **7**, 158 (1956), see also *Z. Elektrochem.*, **60**, 905 (1956).
24. K. J. Vetter and K. Arnold, *Z. Elektrochem.*, **64**, 244 (1960).
25. N. Sato and G. Okamoto, *Electrochim. Acta.*, **10**, 495 (1965).

Noncatalytic Electrodes for Solid-Electrolyte Oxygen Sensors

David M. Haaland

Sandia Laboratories, Albuquerque, New Mexico 87185

ABSTRACT

The catalytic effects of various electrode materials on nonequilibrium oxygen measurements using solid-electrolyte oxygen sensors have been investigated. Catalytically active electrodes can perturb the measurement of oxygen in nonequilibrium mixtures of oxygen and combustible gases. This paper reports the development of noncatalytic electrodes for accurate measurement of the free oxygen content in nonequilibrium gas mixtures containing O_2 and CH_4 , C_3H_6 , CO , or H_2 . The effects of Pt, Au, Ag, Ag deposited on Pt, and S- or Pb-poisoned Pt electrodes on the measurement of oxygen in nonequilibrium gas mixtures were determined. These studies were made using solid-electrolyte oxygen sensors of a new internal-reference design as well as with traditional air-reference sensors. Pt electrodes are catalytic in all of the gas mixtures studied. Both Ag electrodes and Ag vapor deposited on Pt were found to be noncatalytic to CH_4 oxidation while Au electrodes were only slightly catalytic. Pt electrodes poisoned by S introduced as H_2S were also noncatalytic to CH_4 oxidation until the sulfur desorbed at $\sim 800^\circ C$. The above electrodes were sufficiently catalytic to CO oxidation that they could not be used for quantitative nonequilibrium oxygen measurements when CO is present. Pt electrodes poisoned by Pb (introduced as PbS) produced the least perturbation of the nonequilibrium mixtures of oxygen with CH_4 , C_3H_6 , CO , or H_2 . The Pb-poisoned Pt electrodes allow quantitative measurement of the bulk nonequilibrium oxygen concentrations at temperatures above 500° - $550^\circ C$, depending on the combustible gas present. At lower temperatures, even the Pb-poisoned electrodes are catalytic. This suggests that Pb may poison the platinum activity by decreasing the heat of adsorption of adsorbed reaction species. Sulfur- or Pb-poisoned Pt or Pt with a thin layer ($< 200\text{\AA}$) of Ag had no adverse effect on the electrochemical O_2 pumping capabilities of Pt. Ag and Au electrodes performed poorly as electrochemical O_2 pump electrodes. The capability of solid-electrolyte oxygen sensors to measure the partial pressure of gas phase oxygen at the electrode surface was used to investigate the catalytic reaction mechanism of CO oxidation on Pt electrodes partially poisoned by Pb. The results are best fit by an Eley-Rideal mechanism where adsorbed O_2 reacts with gas phase CO . However, the data are not sufficiently definitive to rule out the Langmuir-Hinshelwood mechanism where adsorbed O and CO react on the surface. The methods used demonstrate that solid-electrolyte oxygen sensors can be useful experimental tools for identifying catalytic mechanisms.

Solid-electrolyte oxygen sensors have been used in a variety of applications for over two decades (1, 2). Almost all applications have either involved the monitoring of oxygen in inert environments or the measurement of equilibrium oxygen in reactive environments. For these purposes, platinum is the electrode material of choice due to its excellent oxygen electrode capabilities (e.g., low polarization) as well as its high catalytic activity for driving oxidation reactions to equilibrium. In applications such as oxygen monitoring of automobile exhaust, any degradation of the platinum electrode catalytic activity is severely detrimental to the desired equilibrium measurement since oxygen is often present in thermodynamic nonequilibrium with reactive gases (3). However, in those applications where nonequilibrium oxygen content in the presence of combustible gases is the desired quantity to be measured, platinum electrodes are not appropriate. Noncatalytic electrodes for solid-electrolyte oxygen sensors would be necessary in these cases [e.g., oxygen monitoring during air-fired *in situ* oil shale retorting (4) or coal gasification, control of air-fired furnaces for decreased pollution and maximized efficiency, or monitoring the presence of combustible gases (5)]. Reduction or elimination of the catalytic activity of the electrodes must be accomplished without diminishing the characteristics of electrodes which allow them to perform

Key words: oxygen sensors, noncatalytic electrodes, catalytic mechanisms, catalyst poisons.

as good oxygen electrodes. Both nonplatinum electrode materials and poisoned platinum were tested for the purpose of making nonequilibrium oxygen measurements, and the results are presented in this paper.

Much of the data were collected with a new design of solid-electrolyte oxygen sensor which was developed for our primary application of *in situ* oil shale retorting. This sensor, which has been described elsewhere (4, 6), does not use a flowing gas reference or a fixed metal/metal oxide buffer reference. Rather, it uses electrochemical transfer of oxygen in and out of the internal volume of the sensor as a technique to generate its own internal reference. This self-contained sensor is ideal for remote oxygen sensing at temperatures too low for rapid equilibration of the normal internal metal/metal oxide references.

Some of the less catalytic oxygen electrodes were investigated in greater detail, and experiments were designed to elucidate the reaction mechanisms occurring on these electrodes. These experiments demonstrate the potential power of using solid-electrolyte oxygen sensors for investigating catalytic reaction mechanisms and determining the role poisons play in reducing catalytic activity.

Experimental Procedures

Initial studies were conducted using air-reference solid-electrolyte oxygen sensors of various electrolyte compositions. These were constructed of tubes of sta-

bilized zirconia closed on one end with a flowing air reference inside and platinum paste electrodes on the end tip of the tube [see Ref. (2) for a general description of these sensors]. However, in order to reach the constant temperature zone of the furnace, the tubes were required to be 50 cm long. At temperatures above $\sim 600^\circ\text{C}$, the thermal gradients in the furnace beyond the constant temperature zone resulted in repeated fracture of the tubes of the high conductivity stabilized zirconias [i.e., $(\text{ZrO}_2)_{0.90} \cdot (\text{Y}_2\text{O}_3)_{0.10}$ or $(\text{ZrO}_2)_{0.85} \cdot (\text{CaO})_{0.15}$]. The thermal shock resistant electrolyte materials of $(\text{ZrO}_2)_{0.95} \cdot (\text{Y}_2\text{O}_3)_{0.05}$ had too high an impedance to be fully useful at the lower temperatures investigated.

Because of the problem outlined above, much of this work was completed using solid-electrolyte oxygen sensors of a design which has been described in detail elsewhere (4, 6). These oxygen sensors are composed of two independent electrochemical oxygen concentration cells separated by a ring of stabilized zirconia (see Fig. 1). The sealed internal volume serves as a fixed volume in forming an internal reference. Each cell is a thin disk of stabilized zirconia to which porous electrodes have been applied. One cell is an electrochemical pumping cell (Faraday cell) used to quantitatively pump oxygen into or out of the internal volume of the sensor. This oxygen transport is accomplished with an applied potential of the appropriate magnitude and polarity (generally 0.1V). The integrated pumping current is used to calculate the amount of oxygen transported (4 electrons/molecule of O_2). The second zirconia disk is used directly as an oxygen monitoring cell to measure the ratio of oxygen partial pressures inside and outside the sensor. The potential (E) developed across the cell is related to these partial pressures through the Nernst equation

$$E = \frac{RT}{4F} \ln \left(\frac{P_{\text{O}_2}''}{P_{\text{O}_2}'} \right) \quad [1]$$

where P_{O_2}'' and P_{O_2}' are the partial pressures of oxygen outside and inside the sensor, respectively, R is the ideal gas constant, F the Faraday constant, and T is the temperature in Kelvins. The absolute oxygen partial pressure outside the cell is determined in the following manner. First, oxygen is electrochemically pumped out of the sealed internal volume of the sensor in order to provide a zero point reference. Oxygen from the surrounding gas is then electrochemically pumped back into the sensor by reversing the applied potential. Oxygen pumping is continued until the potential of the monitoring cell is zero (i.e., partial pressures of O_2 inside and outside the sensor are equal). The integrated current (i.e., moles of oxygen, n_{O_2}) required to achieve this condition is used along with the known internal volume (V) and the measured temperature to calculate the oxygen partial pressure (P_{O_2}) by application of the ideal gas law

$$P_{\text{O}_2} = \frac{n_{\text{O}_2}RT}{V} \quad [2]$$

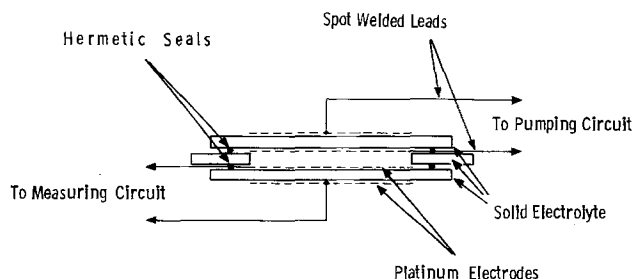


Fig. 1. Schematic diagram of the internal-reference solid-electrolyte oxygen sensor.

(For the temperatures and pressures used in this study, the accuracy of Eq. [2] is better than 1%.) In this manner, the need for a fixed or external reference is eliminated. The fraction of O_2 in the gas being monitored can be calculated if the total gas pressure is known. If there are no leaks or diffusion of oxygen into or out of the sensor, then once the pumping procedure is performed changes in external oxygen content can be continuously monitored by determining the potential of the measuring cell. $(\text{ZrO}_2)_{0.90} \cdot (\text{Y}_2\text{O}_3)_{0.10}$ was the solid electrolyte used because of its high ionic conductivity (i.e., low temperature of operation). This material suffers poor thermal shock resistance, but the small size of the internal-reference sensor makes this property unimportant in these experiments since the sensor sees only a small temperature gradient.

For the most part, the sensor parts were sealed together with a glass-ceramic material which formed hermetic seals up to $\sim 950^\circ\text{C}$ (4). A few sensors, however, were prepared with zirconia-metal thermal compression seals (4). Electrodes were primarily prepared by air-firing metal pastes, although other preparation methods were used in specific cases which are detailed later. Electrode materials used included platinum, silver, gold, and poisoned platinum.

The experiments were performed within a 4 cm ID quartz tube located inside a two-zone Lindberg furnace. Ultrahigh purity Matheson nitrogen (99.999%) along with dry air, CH_4 , CO , C_3H_8 , and H_2 were metered through calibrated Matheson flow tubes to form gas mixtures of various compositions. The accuracy and repeatability of the flow tubes were generally found to be $\sim \pm 5\%$. The normal total flow rate was 2500 standard cubic centimeters per minute (scm) corresponding to a gas velocity of 200 cm/min. This is a typical value of the gas flows encountered in oil shale retorting applications. Input oxygen concentrations were of the order of 0.5% corresponding to the nonequilibrium oxygen content often encountered in a number of applications.

Catalytic mechanisms for the oxidation of CO on poisoned platinum electrodes were investigated and required a number of gas composition measurements. The partial pressure of oxygen gas at the surface of the electrode was measured by the internal-reference oxygen sensor while bulk gas phase oxygen concentrations were obtained with the use of a Taylor Servomex OA-137 paramagnetic oxygen analyzer. Since the paramagnetic oxygen analyzer examined the exhaust gases from the furnace, the possibility of continued homogeneous gas phase reaction beyond the location of the sensor existed in a few cases. This reaction, however, was found to be small except at temperatures above 700°C , and these cases will be noted. CO concentrations were determined from calibrated flow tube settings (using an individually calibrated flow tube with $\pm 1\%$ accuracy).

In addition, air-reference solid-electrolyte oxygen sensors with platinum paste electrodes were often used to simultaneously monitor catalyzed oxygen concentrations. Noticeable contamination of these electrodes by vaporization of nonplatinum electrodes or transport of the poison from the poisoned platinum electrodes was observed. Thus the oxygen partial pressures determined by this method are only upper bounds for the oxygen which would be measured by pure, catalytic platinum electrodes. However, the results do give an indication of the extent of catalytic reaction with platinum electrodes. The necessary use of thermal shock resistant $(\text{ZrO}_2)_{0.95} \cdot (\text{Y}_2\text{O}_3)_{0.05}$ in these air-reference sensors limited data to $\geq 600^\circ\text{C}$ for oxygen contents of $> 0.1\%$.

Results

Platinum electrodes.—As many as four combustible gases were studied separately in the presence of oxygen. These included methane (CH_4), propene (C_3H_6),

carbon monoxide (CO), and hydrogen (H₂). CH₄ and CO were used to screen the catalytic activity of the various electrode materials. Only the platinum and Pt/Pb electrodes were studied in all four gases.

The ease of homogeneous reaction of combustible gases with oxygen, as well as ease of heterogeneous catalytic reactivity, was found to increase in the order given above. This is illustrated in Table I for a 50% stoichiometric excess of each gas in the presence of oxygen and nitrogen. These data were obtained with platinum paste electrodes on an air-reference solid-electrolyte oxygen sensor at a temperature of 700°C and a flow rate of 200 cm/min. The amount of oxygen introduced into the furnace in each case was ~0.5%. At slower flow rates or under stagnant conditions, the results more closely approach equilibrium oxygen values. The results do, however, illustrate qualitatively the relative extent of catalytic reaction on the platinum electrodes at these flow rates. Thus platinum electrodes are not useful for nonequilibrium oxygen measurements.

Silver electrodes.—Except at stagnant flow conditions, silver electrodes exhibit essentially no catalytic activity to CH₄ oxidation. Sandler has reported similar results for silver electrodes and has demonstrated that this property of silver electrodes makes possible a methane sensor when used in conjunction with a catalytic platinum electrode oxygen sensor (5, 7). A direct comparison of the oxygen levels measured by both silver and platinum paste electrodes on air-reference solid-electrolyte oxygen sensors is given in Table II at different temperatures for a large stoichiometric excess of methane. The same lack of reaction on the silver electrode surface was found over a wide range of flow rates and variations in oxygen and methane concentrations in the N₂ diluent. (The actual flow rates and concentration ranges investigated in this study were 2500–250 sccm, oxygen concentrations from 0.5 to 5%, and CH₄ concentrations from 0 to 10%.) The apparent decrease in catalytic activity with the platinum electrodes at higher temperatures is discussed later.

Unfortunately, the catalytic activity of silver electrodes to CO oxidation, although reduced from that of platinum, is still too high even for qualitative oxygen

measurements. For example, a 0.5% oxygen level in the presence of a stoichiometric excess of CO resulted in an oxygen content at the silver electrode of $4 \times 10^{-3}\%$ compared with $1 \times 10^{-5}\%$ with platinum electrodes under the same conditions. In addition, the high solubility of oxygen in silver (8) can create some further complications, e.g., the large hysteresis effects found in the current-voltage curves of these electrodes (4). In the present study, the problem with oxygen solubility was evident during the use of internal-reference oxygen sensors prepared with silver paste electrodes. The high oxygen solubility in silver resulted in a very slow release of oxygen from the inner pump electrode. This caused extreme overshoot errors in oxygen monitoring which rendered this silver-electrode internal-reference sensor useless.

Electrodes of silver vapor deposited on platinum.—An excellent oxygen pumping electrode that was noncatalytic to CH₄ oxidation was prepared by vapor deposition of a thin layer of Ag over a platinum electrode. The silver appeared to remain primarily on the surface as might be expected from the predicted strong Ag surface segregation of Pt-Ag alloys at high temperature (9). The layer of silver was adequate to eliminate catalytic surface reaction with CH₄ yet was sufficiently thin to prevent the problems associated with oxygen solubility in the Ag. It was found that the Ag layer on platinum could be formed by the construction of the internal-reference sensor with a silver-zirconia thermal compression seal (4), i.e., the preparation of the seal resulted in a silver vapor deposit on the platinum electrodes. The silver layer was found to be <200Å as determined by Auger and sputter analyses. A sensor with this silver seal kept its noncatalytic silver layer even at prolonged periods of operation at 700° and 800°C. The results from this sensor closely paralleled those of an air-reference oxygen sensor with pure silver electrodes in that it was inactive to CH₄ oxidation but exhibited reduced (compared to pure Pt electrodes) but still significant catalytic activity to CO oxidation.

Gold electrodes.—Gold paste electrodes were investigated since oxygen is neither soluble in nor adsorbed on gold (10), and gold is less catalytic to oxidation reactions than Pt (11). Although significantly less reactive than platinum, gold electrodes were found to be slightly more catalytic than silver electrodes. The results of side-by-side air-reference solid-electrolyte oxygen sensors of (ZrO₂)_{0.90}·(Y₂O₃)_{0.10} with silver and gold electrodes are compared in Table III. Assuming no catalytic activity to methane oxidation with silver electrode, the percent of methane oxidation on gold is calculated and shown in the final column of the table. The low value for oxygen measured by the Au electrode sensor at 500°C is probably due to the poor oxygen electrode properties of gold at low temperatures since the measurement of O₂ and N₂ mixtures also resulted in low oxygen values at 500°C as with the electrodes previously examined, gold electrodes catalyzed the reaction of CO and oxygen. In addition, it

Table I. Catalytic activity of platinum electrodes in a variety of combustible gases at 700°C

Combustible gas present in stoichiometric excess	%O ₂ in bulk gas phase	%O ₂ measured by Pt electrode sensor
CH ₄	0.5	2×10^{-3}
C ₂ H ₆	0.5	1×10^{-3}
CO	0.45	1×10^{-5}
H ₂	~0.03*	$1 \times 10^{-10}\dagger$

* Hydrogen is reacting in the gas phase at 700°C.

† Equilibrium oxygen content for this mixture of gases is calculated to be $\sim 1 \times 10^{-20}\%$.

Table II. Comparison of catalytic behavior of silver and platinum electrodes in the presence of nonequilibrium CH₄ and O₂ mixtures

Temp (°C)	%CH ₄ in	%O ₂ in	%O ₂ measured* (Ag electrodes)	%O ₂ measured* (Pt electrodes)
500	6.5	1.33	1.36	—
600	6.5	1.33	1.35	2.1×10^{-4}
700	6.5	1.33	1.33	9×10^{-3}
800	6.5	1.33	1.33	0.11

* Measurements using air-reference oxygen sensors constructed with (ZrO₂)_{0.90}·(Y₂O₃)_{0.10} solid electrolyte.

Table III. Catalytic activity of Au relative to noncatalytic Ag electrodes for oxidation of CH₄*

Temp (°C)	%O ₂ measured (Ag electrodes)	%O ₂ measured (Au electrodes)	% Reaction on Au electrodes
500	1.42	0.62	56
600	1.44	1.35	6
700	1.52	1.33	12
800	1.45	1.16	20
850	2.04	0.49	76

* CH₄ concentration was held constant at 7% during these experiments. Input oxygen concentrations were the same as measured by the Ag electrode sensor to within experimental error.

was found that gold performed poorly as an electrochemical oxygen pump electrode below 700°C. The oxygen pump rate below 700°C was so slow as to render the internal-reference solid-electrolyte oxygen sensors inoperative below this temperature when gold electrodes were used.

H₂S-poisoned platinum electrodes.—The success of Ag and Au electrodes for use in the measurement of nonequilibrium oxygen concentrations was limited primarily to CH₄-containing gas mixtures. Available non-metal electrode materials have been found generally useful for oxygen sensor applications only at temperatures exceeding those for which nonequilibrium oxygen gas mixtures are found to exist (12). Therefore, effort was concentrated on poisoning the catalytic activity of platinum electrodes while retaining their excellent oxygen electrode capabilities. Since those properties which make platinum a good catalyst are often properties which make good oxygen electrodes (e.g., adsorption and/or dissociation of oxygen), the use of catalytic poisons on oxygen sensor electrodes was expected to be of marginal success. This was not the case and may aid in defining the role platinum plays in both catalytic and oxygen sensor applications.

Sulfur is known to be an efficient poison of Pt catalytic activity (13, 14) and was introduced onto the electrode surface in the form of H₂S. Recent Auger and low energy electron diffraction studies on H₂S-poisoned Pt show that H₂S dissociates on Pt leaving only adsorbed elemental sulfur poison (13). In this study, the electrodes were found to be effectively poisoned to CH₄ oxidation after the addition of ~0.5% H₂S to the flowing gas mixture for several minutes at 600°C. The sensor was then capable of accurately monitoring oxygen content in a nonequilibrium mixture of oxygen and methane. Poisoning with sulfur caused no reduction in the efficiency of electrochemical oxygen pumping. The poisoning effects of the sulfur were found to continue at 700°C. Even with air flowing over the electrodes for 24 hr the poisoning persisted. However, after treatment of the catalyst at 800°C, the catalytic activity of the platinum was restored for all reaction temperatures. This is probably due to rapid desorption of sulfur and is consistent with results obtained on sulfur poisoning of platinum-based catalytic converters used for automobile emission control (15). Further studies showed these H₂S-poisoned electrodes to be relatively ineffective in reducing the catalytic activity of platinum to CO oxidation. This along with the rapid desorption of sulfur at 800°C limits the usefulness of H₂S-poisoned sensors for many applications.

Pb-poisoned Pt electrodes.—A recent patent by Takao *et al.* (16) has suggested that lead sulfide (PbS) can be used as a catalytic poison for Pt electrodes, but the limited results presented indicated that PbS/Pt electrodes were more catalytic than gold electrodes. However, since no detailed results were presented by Takao *et al.*, these electrodes were investigated further. Platinum electrodes containing 1 and 50 weight percent PbS were prepared by adding -400 mesh PbS powder to the du Pont 7919 platinum paste. This mixture was applied over a ~1.5 μm layer of sputtered platinum and fired in air at 700°C for several hours. These electrodes exhibited oxygen pumping capabilities which were similar to those of sputtered platinum electrodes. Since sputtered platinum has been found not to exhibit polarization characteristics at the temperatures employed here (6, 17), the PbS does not appear to introduce any new polarization which would reduce oxygen pumping rates. The air-fired electrodes were initially catalytic until they were reduced in a flowing mixture of 2% CO in N₂ at 700°C. The resulting electrodes from 50% PbS were quite effectively poisoned whether in oxidizing or reducing environments. The electrodes containing 1% PbS were not sufficiently poisoned for quantitative work.

The 700°C air firing results in lead oxide formation (18) while the reduction step with CO should cause the formation of elemental lead. Lead oxide is insoluble in platinum (19) and the physical mixture of PbO and Pt has no significant effect on the catalytic activity of Pt. However, the lead formed during the reduction rapidly forms an alloy with the Pt (20) which is apparently relatively inactive. Oxidizing environments may cause the formation of insoluble PbO on the Pt/Pb electrode surface but PbO is also noncatalytic (19).

Oxygen measurements using poisoned Pt/Pb electrode sensors of the internal-reference type were compared with measurements obtained using catalytic platinum electrode air-reference sensors and with data from the paramagnetic oxygen analyzer. These results are presented in Tables IV-VIII. In those cases where reactive gases were present, the combustible gas was added with at least a 50% stoichiometric excess. Differences between the platinum electrode sensor and the poisoned electrode sensors indicate how effectively the catalytic activity of the electrode has been reduced by the lead. However, the presence of the poisoned electrodes in the vicinity of the pure Pt electrodes did result in reduced Pt activity probably due to a transfer of either Pb or S to the platinum. This is especially noticeable with the CH₄ mixture since only a small degree of contamination is effective in poisoning this reaction. The monitoring of the free oxygen content of exit gases with the paramagnetic oxygen analyzer was necessary to distinguish between the occurrence of catalytic surface reaction and gas phase reaction caused simply by thermal excitation. The percent difference column in each table is the percent difference between the poisoned electrode sensor results and those of the paramagnetic oxygen analyzer which was used as the reference.

Table IV shows the results of tests with ~0.5% oxygen in flowing nitrogen, i.e., no combustible gas present. At temperatures of ~600°C and lower, the low ionic conductivity of the air-reference sensor causes it to respond extremely slowly at these relatively high oxygen concentrations, and equilibrium is not achieved during the measurement period. Although electrode polarization of the Pt paste electrodes may contribute to the slow equilibration experienced at these low temperatures, the fact that sensors made from high conductivity (ZrO₂)_{0.90}·(Y₂O₃)_{0.10} did not experience these problems until temperatures below 500°C indicates that ionic conductivity limitations are the dominant factor. Unfortunately, high conductivity (ZrO₂)_{0.90}·(Y₂O₃)_{0.10} did not survive the thermal gradients in the furnace and could not be used on a routine basis. The data in Table IV show good agreement between the poisoned electrode sensor and the paramagnetic analyzer.

Table V shows data obtained in mixtures of oxygen and nitrogen containing a stoichiometric excess of CH₄. Again the air-reference sensor results below 700°C

Table IV. Oxygen analyses in oxygen and nitrogen gas mixtures

Temp (°C)	%O ₂ Pt electrode air-reference sensor	%O ₂ Pt/Pb electrode internal-reference sensor	%O ₂ bulk gas phase at exit	% Difference*
800	0.39†	0.55	0.51	+8
700	0.52	0.53	0.51	+4
600	‡	0.53	0.52	+2
500	‡	0.51	0.51	0

* Percent difference between paramagnetic oxygen analyzer results and Pt/Pb electrode sensor results using the paramagnetic oxygen analyzer for the reference value.

† This low value may be a result of cooling of the solid electrolyte by the flowing air reference at 800°C.

‡ Temperatures were too low for reliable O₂ measurements with this (ZrO₂)_{0.95}·(Y₂O₃)_{0.05} solid-electrolyte sensor.

Table V. Oxygen analyses in oxygen, nitrogen, and methane gas mixtures

Temp (°C)	%O ₂ Pt electrode air-reference sensor	%O ₂ Pt/Pb electrode internal-reference sensor	%O ₂ bulk gas phase at exit	% Difference*
800	0.49 (0.1)‡	0.55	0.49	+12
700	0.52 (9 × 10 ⁻³)‡	0.52	0.51	+2
600	† (2 × 10 ⁻⁴)‡	0.53	0.51	+4
500	†	0.51	0.51	0

* Percent difference between paramagnetic oxygen analyzer results and Pt/Pb electrode sensor results using the paramagnetic oxygen analyzer for the reference value.

† Temperatures were too low for reliable O₂ measurements with this (ZrO₂)_{0.85} · (Y₂O₃)_{0.05} solid-electrolyte sensor.

‡ Results from earlier experiments with clean platinum electrode oxygen sensors.

were in error due to the high resistivity of these cells. Note that the close proximity of the PbS-poisoned electrode to the platinum electrode has introduced some poisoning into the platinum. This is confirmed by the data for platinum electrode sensors in the absence of PbS (see results in parentheses in Table V) which show the significant catalytic activity of pure platinum electrodes. The most important point to note in Table V is the lack of catalytic activity obtained with the Pt/Pb electrodes. The oxygen concentration at the electrode surface is in excellent agreement with the bulk gas phase oxygen concentration measured by the paramagnetic oxygen analyzer.

Table VI presents results for a stoichiometric excess of C₃H₆ in oxygen and nitrogen mixtures. C₃H₆ has been used previously as a molecule which most closely represents the average oxidation characteristics of combustible hydrocarbon molecules for predicting the behavior of catalysts in automotive catalytic converters (21). The gases are beginning to react spontaneously in the gas phase at 800°C. Agreement between the bulk oxygen content and the O₂ sensor results is good except at 500°C. At this temperature, there is surface reaction even on this poisoned electrode. This is observed even more dramatically for CO and H₂ oxidation. Thus at lower temperatures, reactants (O₂ and/or CO) still adsorb on the poisoned electrode surface and react, while at the higher temperatures the amounts of adsorbed reactants are small and, therefore, surface reaction is minimal. The net result is that catalytic efficiency on the poisoned electrode goes through a maximum at some temperature below 600°C. Decreased adsorption and reaction as temperatures increase is also seen with the pure platinum electrode results in Table II. Catalytic activity actually appears to decrease slightly with these electrodes as the temperature increases.

Table VI. Oxygen analyses in oxygen, nitrogen, and propene (C₃H₆) gas mixtures

Temp (°C)	%O Pt electrode air-reference sensor	%O ₂ Pt/Pb electrode internal-reference sensor	%O ₂ bulk gas phase at exit	% Difference*
800	†	0.12	0.14	-14
700	0.008	0.42	0.45	-7
600	‡	0.47	0.48	-2
500	‡	0.32	0.49	-35

* Percent difference between paramagnetic oxygen analyzer results and Pt/Pb electrode sensor results using the paramagnetic oxygen analyzer for the reference value.

† Air-reference sensor did not survive the temperature gradients encountered at 800°C.

‡ Temperatures were too low for reliable O₂ measurements with this (ZrO₂)_{0.85} · (Y₂O₃)_{0.05} solid-electrolyte sensor.

Table VII gives similar results for a stoichiometric excess of CO in oxygen and nitrogen mixtures. Here the platinum electrode sensor shows extensive catalytic action at all temperatures. Full interpretation of the data in Table VII required some careful gas analyses by the paramagnetic oxygen analyzer over a continuous range of temperatures. At the flow rates of this experiment, it was found that CO and O₂ start to react spontaneously in the gas phase at ~700°C and reaction is nearly complete above 800°C. Therefore, the Pt/Pb electrode sensor results are higher than the paramagnetic analyzer results at 800°C because of the different measurement locations. The sensor is measuring the oxygen concentration at its location in the furnace while the paramagnetic analyzer is measuring oxygen contents of the gases after they exhaust the furnace. At 800°C, there is continued reaction in the gas phase in the high temperature zone beyond the location of the oxygen sensor. At 500°C, catalytic surface reaction is becoming significant.

Finally, Table VIII shows results for a stoichiometric excess of hydrogen in oxygen and nitrogen mixtures. Since homogeneous gas phase reaction was significant even at 600°C with 200 cm/min flow rate, flows were increased ~50% to reduce the extent of reaction for meaningful results to be obtained. At the flow rate used here, there is little gas phase reaction at 500° and 600°C while the reaction is nearly complete at 700°C. At 600°C, there is some reaction at the electrode but semi-quantitative results are possible. This is in contrast to the platinum electrode sensor which records nearly equilibrium oxygen values. As in the case of CO and C₃H₆, reaction on the Pt/Pb electrode surface again becomes significant at the lower 500°C temperature. It should be noted that both the catalytic surface reaction at low temperatures and the homogeneous gas phase reaction at high temperatures observed in Table VI-VIII were independent of whether each temperature was approached from initially high or low temperatures. Although the data presented in these tables were obtained after equilibration at each temperature,

Table VII. Oxygen analyses in oxygen, nitrogen, and carbon monoxide gas mixtures

Temp (°C)	%O ₂ Pt electrode air-reference sensor	%O ₂ Pt/Pb electrode internal-reference sensor	%O ₂ bulk gas phase at exit	% Difference*
800	2 × 10 ⁻⁵	0.25	0.06†	+316
700	1 × 10 ⁻⁵	0.47	0.50	-6
600	1 × 10 ⁻⁶	0.37	0.42	-12
500	5 × 10 ⁻⁷	0.028	0.44	-94

* Percent difference between paramagnetic oxygen analyzer results and Pt/Pb electrode sensor results using the paramagnetic oxygen analyzer for the reference value.

† There was some homogeneous reaction in the gas phase at 800°C which continued beyond the location of the sensor.

Table VIII. Oxygen analyses in oxygen, nitrogen, and hydrogen gas mixtures

Temp (°C)	%O ₂ Pt electrode air-reference sensor	%O ₂ Pt/Pb electrode internal-reference sensor	%O ₂ bulk gas phase at exit	% Difference*
700	1 × 10 ⁻¹⁹	0.03	0.00	—
600	8 × 10 ⁻²²	0.30	0.46	-35
500	1 × 10 ⁻²⁵	0.05	0.43	-88

* Percent difference between paramagnetic oxygen analyzer results and Pt/Pb electrode sensor results using the paramagnetic oxygen analyzer for the reference value.

similar results were obtained during temperature ramping at 10°C/min.

Reaction mechanism studies using solid-electrolyte oxygen sensors.—Solid-electrolyte oxygen sensors are a valuable tool for the catalytic chemist since they allow the measurement of the partial pressure of oxygen at the surface of catalytic electrodes during catalytic oxidation. This can be accomplished at high temperature and pressure, and kinetic studies can be performed even under mass transport controlled conditions. Already oxygen sensors have been used in studying the oscillation reactions encountered during CO oxidation on platinum (22). In this study, they are used as an aid in examining the reaction mechanisms of CO oxidation on partially poisoned platinum electrodes.

The mechanisms of the catalytic oxidation of combustible gases in general and CO in particular have been investigated and reported numerous times [e.g., see Ref. (15, 21)]. The primary mechanisms for CO oxidation on metallic catalyst surfaces include: (i) the Langmuir-Hinshelwood mechanism where both CO and oxygen adsorb on the surface before reacting and (ii) the Eley-Rideal mechanism where CO in the gas phase reacts with oxygen adsorbed on the surface. Both reaction mechanisms have been found to be operative at low pressure; the dominant one depending on the initial experimental surface conditions (23). We will show that it is possible to use solid-electrolyte oxygen sensors to identify catalytic mechanisms of oxidation reactions on reactive surfaces, especially if flow rates are sufficiently high to reduce the extent of reaction or if the catalytic rate is relatively slow. The latter is the case with the poisoned platinum electrodes used in this study.

The oxygen content of a flowing mixture of O₂, CO, and nitrogen over an isothermal electrode surface at high temperature was monitored by several methods during these experiments. An internal-reference solid-electrolyte oxygen sensor which was not completely poisoned by the PbS treatment was used to measure directly the partial pressure of gas phase oxygen at the surface of the partially catalytic electrode. It should be noted, however, that all Pt/Pb electrodes exhibited some surface reaction with a large stoichiometric excess of CO or H₂. The bulk gas phase composition of the oxygen away from the sensor electrodes was monitored by the paramagnetic oxygen analyzer. Finally the CO content at the surface of the electrode was determined from the input CO concentration and the extent of surface reaction as detailed later in the report. This information, if sufficiently accurate, is adequate to distinguish between reaction mechanisms if relative concentrations of the reactants are varied.

Under the experimental conditions studied, the reactants CO and O₂ are dilute relative to the nitrogen carrier gas, and it can be assumed that the reaction has no effect on the physical properties of the mixture. Also, the extent of reaction is kept relatively small, and therefore the temperatures are constant and the concentration of gases at the electrode surface are approximately constant over the area of the electrode. Under these conditions and at steady state, the consumption of oxygen at the electrode surface must be equal to the flux of oxygen to the surface by mass transport (convection and diffusion). Since the concentration of the reactants differ significantly from the bulk values only in a thin region near the electrode surface and the convection velocity is small in this region, we assume that diffusion is the important transport process. The diffusion of oxygen from the bulk gas phase to the surface at steady state is given by

$$J_{O_2} = -\frac{D}{RT} \frac{dP_{O_2}}{dx} \quad [3]$$

where J_{O_2} is the molar flux of oxygen per unit time and area, D is the diffusion coefficient for O₂ diffusing

through the gas, R is the gas constant, and T the absolute temperature. The time rate of change of oxygen concentration per unit area (r_{O_2}) due to reaction at the surface of the electrode is given by

$$r_{O_2} = \left(\frac{dn_{O_2}}{dt} \right) / A \quad [4]$$

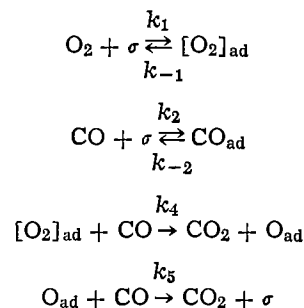
The form of r_{O_2} depends on the detailed surface reaction mechanism for O₂ reacting with CO. At steady state where the rate of reaction is balanced by the flux due to diffusion, we have

$$r_{O_2} + J_{O_2} = 0$$

or

$$r_{O_2} = \frac{D}{RT} \frac{dP_{O_2}}{dx} \quad [5]$$

In order to distinguish between Langmuir-Hinshelwood and Eley-Rideal reaction mechanisms for the experimental conditions chosen, it is required to investigate the detailed reaction mechanism of each and determine the corresponding overall rate laws. The reaction mechanism which best describes the wide range of data presented by Sklyarov *et al.* (24), Bonzel and Ku (25), and others (26, 27) is the Eley-Rideal mechanism. They assume that the rate of dissociation of adsorbed O₂ is negligible compared to its reaction rate with CO. The reactions they consider include the following (σ = adsorption site)



Thus the reaction takes place between gas phase CO and both adsorbed molecular and atomic oxygen. The rate of CO₂ formation at steady state is given by Sklyarov *et al.* by

$$r_{CO_2} = -2r_{O_2} = 2k_4K_1P_{O_2}P_{CO} \left[1 + K_1 \left(1 + \frac{k_4}{k_5} \right) P_{O_2} + \left(K_2 + \frac{k_4}{k_{-1}} \right) P_{CO} + K_2 \frac{k_4}{k_{-1}} P_{CO}^2 \right]^{-1} \quad [6]$$

where K_1 and K_2 are the equilibrium constants for the first two reactions ($K_1 = k_1/k_{-1}$, $K_2 = k_2/k_{-2}$). Bonzel and Ku as well as Sklyarov *et al.* show that this expression fits their data over a wide range of temperatures and partial pressures of O₂ and CO. As described by Bonzel and Ku, Eq. [6] reduces to

$$r_{O_2} = -k_4K_1P_{CO}P_{O_2} \quad [7]$$

at high temperatures (i.e., where K_1 and K_2 are very small or alternatively the fractional surface coverages of adsorbed species are small compared to unity). These are reasonable assumptions at 700°C as indicated by lower temperature infrared data (28) and thermal desorption experiments (29, 30). It should be noted that the partial pressures P_{CO} and P_{O_2} in Eq. [7] are the partial pressures of the gases at the surface of the electrode [$P_i(\text{surf.})$]. At steady state $P_{O_2}(\text{surf.})$ and $P_{CO}(\text{surf.})$ are constant and different from the bulk partial pressures [$P_i(\text{bulk})$]. Therefore Eq. [7] becomes

$$r_{O_2} = -k_4K_1P_{CO}(\text{surf.})P_{O_2}(\text{surf.}) \quad [8]$$

$P_{O_2}(\text{surf.})$ is reasonably assumed to be the partial pressure of O₂ measured by the oxygen sensors.

$P_{\text{CO}}(\text{surf.})$ is determined from the known input partial pressure of CO minus the amount reacted as calculated by the difference of the bulk and surface O_2 partial pressures, *i.e.*

$$P_{\text{CO}}(\text{surf.}) = P_{\text{CO}}(\text{bulk}) - 2[P_{\text{O}_2}(\text{bulk}) - P_{\text{O}_2}(\text{surf.})] \quad [9]$$

Substituting Eq. [8] into Eq. [5] yields

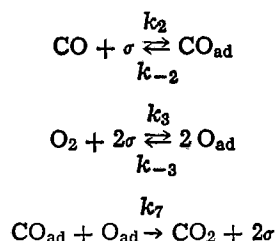
$$-k_4K_1P_{\text{CO}}(\text{surf.})P_{\text{O}_2}(\text{surf.}) = \frac{D}{RT} \frac{dP_{\text{O}_2}}{dx} \quad [10]$$

Separating variables and integrating yields

$$P_{\text{CO}}(\text{surf.}) = \frac{D}{k_4K_1\delta RT} \left[\frac{P_{\text{O}_2}(\text{bulk}) - P_{\text{O}_2}(\text{surf.})}{P_{\text{O}_2}(\text{surf.})} \right] \quad [11]$$

where δ is the thickness of the diffusion layer. Thus a plot of $P_{\text{CO}}(\text{surf.})$ vs. $[P_{\text{O}_2}(\text{bulk}) - P_{\text{O}_2}(\text{surf.})]/P_{\text{O}_2}(\text{surf.})$ should be linear if the above Eley-Rideal mechanism holds for our partially poisoned electrodes.

The Langmuir-Hinshelwood mechanism assumes the primary reaction mechanism is between adsorbed oxygen atoms and adsorbed CO (15, 21, 23, 31). Under these conditions, the reactions to be considered are



Assuming again low coverage of surface species at high temperatures (700°C) and the equilibration of reactions [2] and [3], the following high temperature Langmuir-Hinshelwood rate law is obtained

$$r_{\text{O}_2} = -k_7K_2K_3^{1/2}P_{\text{CO}}(\text{surf.})[P_{\text{O}_2}(\text{surf.})]^{1/2} \quad [12]$$

The linear dependence on CO partial pressure in Eq. [8] and [12] is a result of low surface coverage at high temperatures. This is in contrast to the inverse dependence on CO partial pressure observed by others at low temperatures (23-26) due to inhibition effects at high CO surface coverages. At steady state under diffusion-controlled conditions, the rate law for Langmuir-Hinshelwood kinetics from Eq. [12] takes the form

$$P_{\text{CO}}(\text{surf.}) = \frac{D}{k_7K_2K_3^{1/2}\delta RT} \left[\frac{P_{\text{O}_2}(\text{bulk}) - P_{\text{O}_2}(\text{surf.})}{[P_{\text{O}_2}(\text{surf.})]^{1/2}} \right] \quad [13]$$

A plot of $P_{\text{CO}}(\text{surf.})$ vs. the quantity in brackets in Eq. [13] will therefore be linear if this reaction mechanism is operative.

Plots in the form of Eq. [11] and Eq. [13] are presented in Fig. 2 and 3, respectively, for data taken at 700°C with Pt/Pb electrode sensors. A linear least squares fit of the data shows a better fit to the Eley-Rideal mechanism (the coefficient of determination for the Eley-Rideal mechanism is 0.999 while that for the Langmuir-Hinshelwood plot is 0.991). In addition, the least squares Eley-Rideal plot intersects the origin while that of the Langmuir-Hinshelwood intersects above the origin and the latter data show a slight systematic curvature about the least squares fit. However, while a better fit to the data is obtained for the Eley-Rideal mechanism, the data are not significantly accurate to exclude the Langmuir-Hinshelwood mechanism as indicated by the error bars in Fig. 2 and 3. More precise monitoring of the bulk CO and O_2 partial pressures would be required to definitely distinguish be-

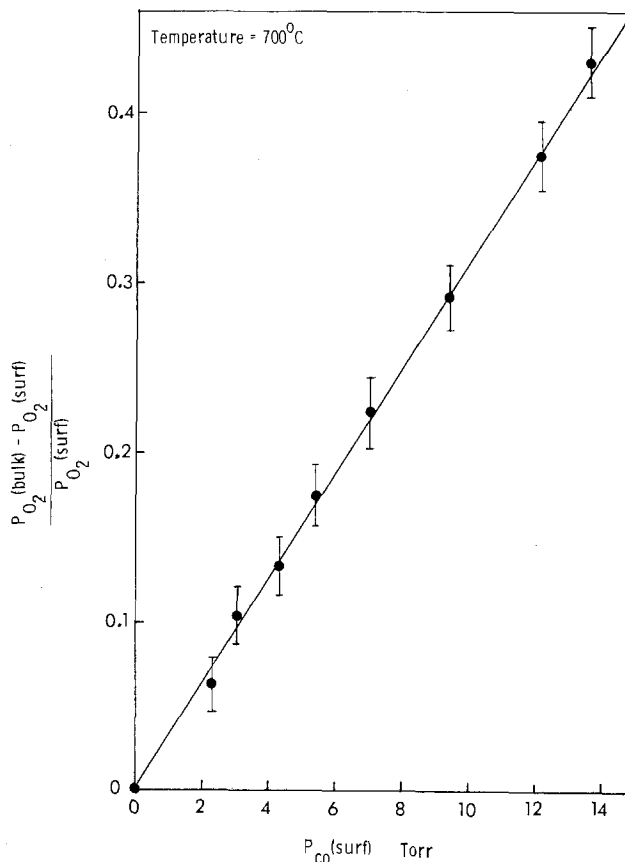


Fig. 2. Plot of data assuming that the catalytic oxidation of CO on a partially poisoned Pt/Pb electrode follows the Eley-Rideal mechanism, Eq. [11]. A linear least squares fit to the data is also shown.

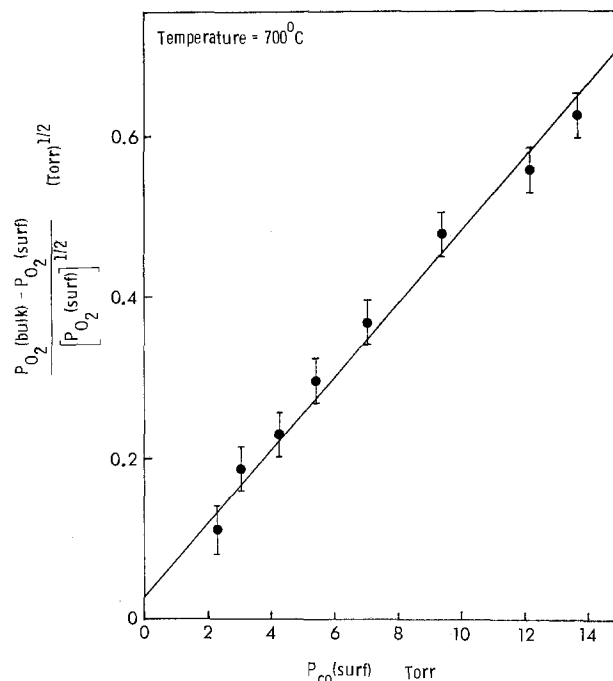


Fig. 3. Plot of data assuming that the catalytic oxidation of CO on a partially poisoned Pt/Pb electrode follows the Langmuir-Hinshelwood mechanism, Eq. [13]. A linear least squares fit to the data is also shown.

tween these two mechanisms with such similar rate laws. Of course, if both reaction mechanisms are operative, then the rate law would be of an intermediate form between Eq. [11] and [13].

Information about the nature of the electrode poisoning by lead can be obtained from the fact that the Pt/Pb electrodes are relatively noncatalytic to CO oxidation at 700°C yet are fairly catalytic at 500°C. Thus the role of lead is not solely due to pore mouth blocking observed by others (32). Assuming the Eley-Rideal mechanism to be operative, the Pb may be decreasing the strength of the bond of adsorbed O₂ to the surface (or the adsorbed O and CO bonds if the Langmuir-Hinshelwood mechanism is important). Thus, the catalytic reaction rate would be affected to a greater extent at high temperatures than at low. Since Pb forms a solid solution with Pt, it may be assumed that as in other alloy systems (33), the role of the alloying with Pb is to decrease the heat of adsorption of the reaction species thereby decreasing the range of temperature at which catalytic activity is important. However, the possibility of changing surface composition or surface segregation of the Pt/Pb alloy with temperature cannot be ruled out.

The fact that neither sulfur nor lead decreases the rate of electrochemical oxygen pumping for electrodes which exhibit no polarization yields insight into the role of these species as catalytic poisons. Thus, these poisons reduce catalytic activity without greatly affecting any of the steps involved in the electrochemical pumping of oxygen. Although the dominant sources of electrode polarization are dependent on operating parameters (34), it would appear that Pb and S do not significantly impede dissociation and diffusion of atomic O through Pt, or O₂ diffusion through the electrode pores.

Summary

Both air-reference and the new internal-reference solid-electrolyte oxygen sensors were used in the search for noncatalytic electrodes for free oxygen measurement in nonequilibrium environments. Platinum electrodes catalyze oxidation reactions of combustible gases with the ease of reaction increasing in the order CH₄, C₃H₆, CO, and H₂. Gold and silver show limited or no catalytic oxidation with CH₄ but still exhibit significant catalysis of CO oxidation. Both silver and gold have limitations where the electrochemical pumping of oxygen is required. A thin layer of silver over platinum has the same catalytic characteristics of pure silver but exhibits oxygen pumping properties similar to platinum.

Poisoning of the platinum electrode with H₂S was effective in eliminating catalytic oxidation of CH₄, but the sulfur desorbs at ~800°C. H₂S-poisoned platinum is still somewhat catalytic to CO oxidation. Lead poisoning of platinum (introduced initially in the form of PbS) is significant in certain temperature ranges for CH₄, C₃H₆, CO, and H₂ at the flow rates studied. At the lower temperature ranges of operation of the solid-electrolyte oxygen sensors (500°-550°C), the catalytic activity of these poisoned electrodes is evident. These data support the theory that lead acts to decrease the heat of adsorption of oxygen on the surface of platinum. Oxygen sensors using these lead-poisoned platinum electrodes have been successfully tested in aboveground oil shale retorting experiments where the monitoring of nonequilibrium oxygen concentrations is desirable (4).

The use of poisoned electrodes, coupled with the solid-electrolyte oxygen sensor capability of measuring the partial pressure of gaseous oxygen at the surface of the electrode, allows the direct measurement of surface catalytic mechanisms. The data for the oxidation of CO on partially poisoned Pt electrodes is best fit by the Eley-Rideal mechanism where gas phase CO reacts with adsorbed molecular oxygen. However, the data are not sufficiently accurate to definitely exclude the Langmuir-Hinshelwood mechanism. The results demonstrate the possible use of the surface information obtained with solid-electrolyte oxygen sensors for obtaining reaction mechanism in-

formation. The information about oxygen partial pressures at the electrode surface may also aid in understanding the mechanisms by which poisons decrease catalytic activity.

Acknowledgments

The author would like to acknowledge the very valuable assistance of J. M. Freese and G. E. Rivord in the acquisition of some of the experimental data. C. D. Tuthill prepared the majority of seals for the sensors and along with R. D. Bland developed the successful glass-ceramic seals. D. K. Kramer completed the Auger analysis of the Ag-covered Pt electrodes. This work was supported by the U.S. Department of Energy under Contract No. DE-AC04-76-DP000789.

Manuscript submitted May 21, 1979; revised manuscript received Sept. 28, 1979.

Any discussion of this paper will appear in a Discussion Section to be published in the December 1980 JOURNAL. All discussions for the December 1980 Discussion Section should be submitted by Aug. 1, 1980.

Publication costs of this article were assisted by Sandia Laboratories.

REFERENCES

1. K. Kiukkola and C. Wagner, *This Journal*, **104**, 379 (1957).
2. M. Sato, in "Research Techniques for High Pressure and High Temperature," G. C. Ulmer, Editor, Chap. 3, Springer Verlag, Berlin, New York (1971).
3. W. J. Fleming, *This Journal*, **124**, 21 (1977).
4. D. M. Haaland, Final Report, SAND78-0319, March 1978.
5. Y. L. Sandler, *This Journal*, **118**, 1378 (1971).
6. D. M. Haaland, *Anal. Chem.*, **49**, 1813 (1977).
7. Y. L. Sandler, Abstract 328, p. 732, The Electrochemical Society Extended Abstracts, Spring Meeting, Los Angeles, Calif., May 10-15, 1970.
8. J. Fouletier, H. Seiner, and M. Kleitz, *J. Appl. Electrochem.*, **5**, 177 (1975).
9. F. L. Williams and D. Nason, *Surf. Sci.*, **45**, 377 (1974).
10. G. Wedler and D. F. Klemperer, "Chemisorption: An Experimental Approach," p. 199, Butterworths and Co., London (1976).
11. J. O'M. Bockris and A. K. N. Reddy, "Modern Electrochemistry," Vol. 2, p. 1161, Plenum Press, New York (1973).
12. J. T. Brown *et al.*, 1970 Final Report Project Fuel Cell Research Development Report No. 57, Prepared for Office of Coal Research, August 1970, Contract No. 14-01-0001-303.
13. T. E. Fischer and S. R. Kelemen, *J. Catal.*, **53**, 24 (1978).
14. H. P. Bonzel and R. Ku, *J. Chem. Phys.*, **59**, 1641 (1973).
15. J. Wei, in "Advances in Catalysis," Vol. 24, D. D. Eley, H. Pines, and P. B. Weisz, Editors, p. 57, Academic Press, New York (1975).
16. H. Takao, K. Togawa, K. Mato, and Y. Hata, U.S. Pat. 3,941,673 (1976).
17. R. J. Brook, W. L. Pelzmann, and F. A. Kröger, *This Journal*, **118**, 185 (1971).
18. D. R. Stull and H. Prophet, Project Directors, JANAF Thermochemical Tables, National Bureau of Standards, Washington, D.C. (June 1971).
19. F. L. Williams and K. Baron, *J. Catal.*, **40**, 108 (1975).
20. M. Hansen, "Constitution of Binary Alloys," p. 1096, McGraw-Hill Book Co., New York (1958).
21. F. G. Dwyer, in "Catalysis Reviews," Vol. 6, H. Heinemann, Editor, p. 261, Marcel Dekker, Inc., New York (1972).
22. R. E. Hetrick and E. M. Logothetis, *Appl. Phys. Lett.*, **34**, 117 (1979).
23. H. P. Bonzel and R. Ku, *Surf. Sci.*, **33**, 91 (1972).
24. A. V. Sklyarov, I. I. Tret'yakov, B. R. Shub, and S. Z. Roginskii, *Dokl. Akad. Nauk SSSR*, **189**, 1302 (1969).
25. H. P. Bonzel and R. Ku, *J. Vac. Sci. Technol.*, **9**, 663 (1972).

26. G. M. Schwab and K. Gosaner, *Z. Phys. Chem. (Frankfurt)*, **16**, 89 (1958).
27. G. C. Bond, "Catalysis by Metals," p. 460, Academic Press Inc., New York (1962).
28. R. F. Baddour, M. Modell, and U. K. Heusser, *J. Phys. Chem.*, **79**, 3621 (1968).
29. G. Ertl and J. Koch, in Proceedings of the 5th International Congress on Catalysis, Miami Beach, Fla., Aug. 20-26, 1972, Paper 67, p. 969.
30. D. M. Collins and W. E. Spicer, *Surf. Sci.*, **69**, 85 (1977).
31. H. P. Bonzel and J. J. Burton, *ibid.*, **52**, 223 (1975).
32. R. E. Polomski and E. E. Wolf, *J. Catal.*, **52**, 272 (1978).
33. J. H. Sinfelt and J. A. Cusumano, in "Advances in Materials in Catalysis," J. J. Burton and R. L. Gorton, Editors, p. 1, Academic Press, New York (1977).
34. R. E. W. Casselton, *J. Appl. Electrochem.*, **4**, 25 (1974).

Cermet Cathodes for High Temperature Water Electrolysis with Zirconia Cells

R. Accorsi

SA Automobiles Citroën, Service recherches, 92000 Nanterre, France

and E. Bergmann*¹

Battelle Memorial Institute, Geneva Research Center, 1227 Carouge/GE, Switzerland

ABSTRACT

The steam electrolysis between 800° and 950°C has been investigated with a cell consisting of the following elements: electrolyte, 400 μ of ytterbia stabilized zirconia; anode, 100 μ of vacuum deposited tin doped india; cathode, a sputter deposited cermet of nickel and urania doped ytterbia stabilized zirconia. These cells can be operated below 1.5V at 1 A/cm² over 1000 hr.

High temperature water vapor electrolysis with solid electrolyte cells offers two advantages over the low temperature process currently in use, a thermodynamic and a kinetic one. The negative entropy of reaction of the water decomposition reaction causes a lower open-circuit voltage. Since the heat necessary to bring the water vapor up to the temperature of operation would be available from heat exchangers with the product gas, cell losses, and eventually the exhaust of the electricity generating plant, high temperature water electrolysis should lead to important savings of scarce free energy and lower costs of hydrogen production (1, 2). Furthermore, the rate of reaction of water decomposition becomes relatively fast at high temperatures and this leads to lower cathode polarizations at high current densities. However, these two advantages are partly compensated by severe stability problems of all cell components: e.g., alkaline earth stabilized zirconia can be used in all applications except high temperature fuel cells and electrolyzers where only rare earth stabilization of zirconia has given stable conductivities so far. The particular problems with an electrode structure are illustrated in the paper. Because of these materials problems we did limit most of our experiments to 900°C which we believe represents a good compromise between performance and stability.

Thermodynamic Considerations

At room temperature the open-circuit voltage is determined by the standard free enthalpy of the reaction, since both hydrogen and oxygen are released to atmospheric pressure. For steam electrolysis the situation differs: Oxygen is not released but at 0.21 atm and therefore

$$\Delta G(900^\circ\text{C}) = \Delta G^\circ(900^\circ\text{C}) - \frac{RT}{2} \ln 0.21 \\ = -41.84 \text{ kcal/mole} \quad [1]$$

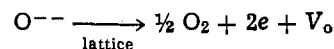
At the same time the open-circuit voltage will vary with the degree of decomposition of the steam at the cathode, α , defined as

$$\alpha = \frac{p(\text{H}_2)}{p(\text{H}_2\text{O})}$$

Therefore, if we assume a simple Nernstian relation, the theoretical open-circuit voltage will be

$$E_{\text{th}}(\alpha) = \frac{RT}{4F} \ln \frac{p_{\text{anode}}(\text{O}_2)}{p_{\text{cathode}}(\text{O}_2)} = 0.906\text{V} + 0.05053 \ln \frac{\alpha}{1-\alpha} \\ 4.76 \cdot 10^{-6} < \alpha < 0.999999 \quad [3] \\ = E_{\text{th}}^\circ + 0.05053 \ln \frac{\alpha}{1-\alpha}$$

The lower limit of validity is given by the equilibrium pressure of hydrogen in steam at 900°C and the upper limit by the onset of electronic conduction with the shift in stoichiometry in the zirconia electrolyte



V_{O} oxygen lattice vacancy, for which we take an equilibrium voltage of $E_{\text{th}}(900^\circ\text{C}) = 1.66\text{V}$ which corresponds to an oxygen partial pressure of 10^{-15} atm (3, 4).

One sees from Eq. [3] that the measurements with a mixture of 50% volume hydrogen in steam correspond to the theoretical decomposition voltage. It is also worthwhile noting that the shape of the curve $E_{\text{th}}(\alpha)$ ensures that the decomposition voltage of 70% of all possible compositions lies within $\pm 10\%$ of E_{th}° . In Fig. 1 we compare some values measured with a specific feed gas flow of 1.7 cm/sec with Eq. [3].

Experimental

Setup (5).—Figures 2 and 3 show the cell structure which we have used in most of the measurements. The electrochemical cell is a flat hat of sintered sta-

* Electrochemical Society Active Member.

¹ Present address: ASUAG, Coordination R & D, 6, Faubourg du Lac, 2500 Bienne, Switzerland.

Key words: zirconia cells, water electrolysis, fuel cells, sputtered cermets.

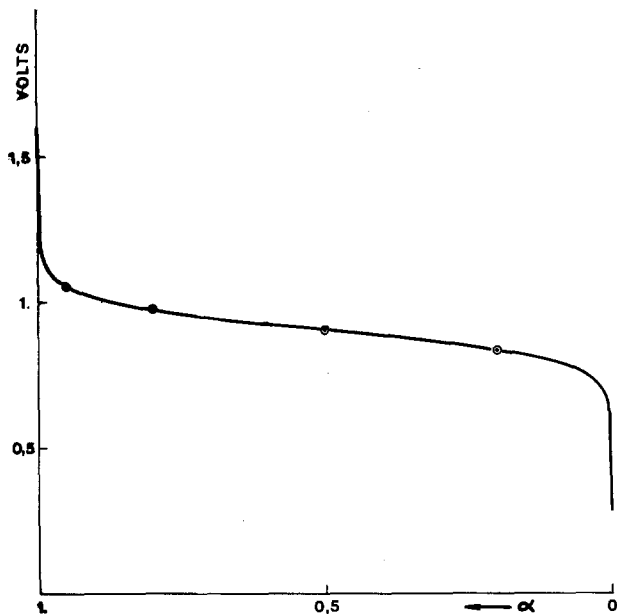


Fig. 1. Comparison of the theoretical open-circuit voltage as a function of steam decomposition with the measured open-circuit voltages at 900°C under 1.7 cm/sec of specific feed gas flow.

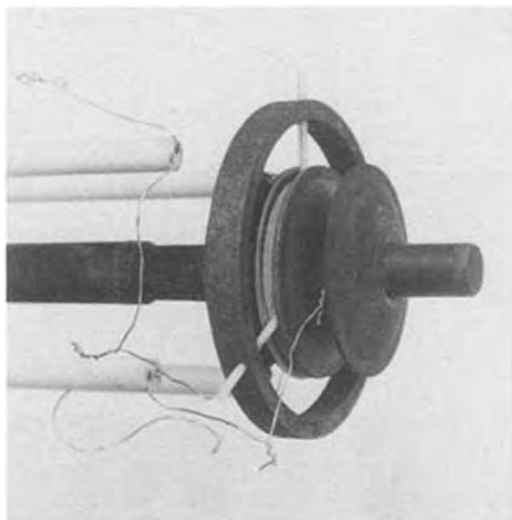


Fig. 2. The electrolysis cell with the various connections

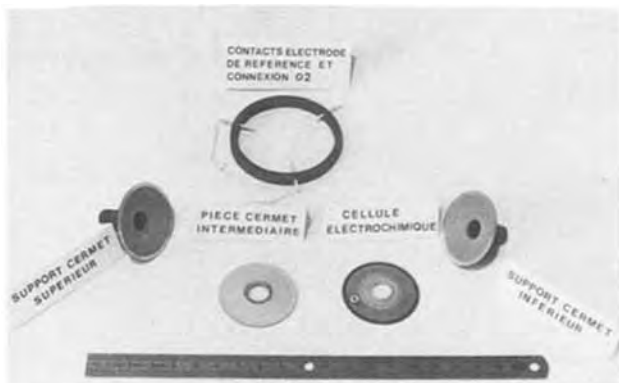


Fig. 3. The components of a measurement cell. On top the support ring with contacts for the reference electrode and the anodic rim sensor. From left to right: the upper cermet support, the intermediary cermet connecting element, the electrochemical cell, and the lower support cermet.

bilized zirconia contacted on both sides by cermet disks of identical shape. Gas tightness is achieved by mechanical pressure. The cell shown in Fig. 3 has an active surface area of 5 cm². The anodic top cermet is contacted by another cermet hat, brazed to a steel

mug. The cathodic cermet is brazed to a steel tube fitted into the exhaust tube. The whole is mounted onto two concentric gas feed/exhaust tubes. These feed tubes serve at the same time as connections for the electrical load. All measurements were made in "open" electrical furnaces against ambient air. The cell potentials are picked up by two platinum wires. Replacing a wire by a thermocouple allows one to compare the effective cell temperature with the value usually measured at 1 cm from the cathode rim. The cell temperature was found not to exceed the furnace temperature by more than 10°-15°C under fuel cell operation of 1 A/cm². The support ring serves for the addition of two more measurement points, namely, a platinum contact to the flat rim (border) of the anode and a "reference electrode" in the middle of the anode whose signal is discussed later.

Components.—The electrolyte is a membrane of ytterbia stabilized zirconia [nominal composition (ZrO₂)_{0.92}(Yb₂O₃)_{0.08}] of 0.4 mm thickness fired at 1850°C. Its electrical conductivity measured in air with 4 kHz (Tacussel CD 6N) as a function of temperature is given in Fig. 4. The anode is essentially made of 0.1 mm electron beam deposited tin oxide doped india (6) [nominal composition (In₂O₃)_{0.96}(SnO₂)_{0.4}] on a sublayer of urania doped ytterbia stabilized zirconia [(ZrO₂)_{0.82}(Yb₂O₃)_{0.1}(UO₂)_{0.08}]. Its electrical conductivity is shown in Fig. 5.

The cathode, a sputtered nickel zirconia cermet was the only component varied systematically in this phase of the program. Details are given in the next section.

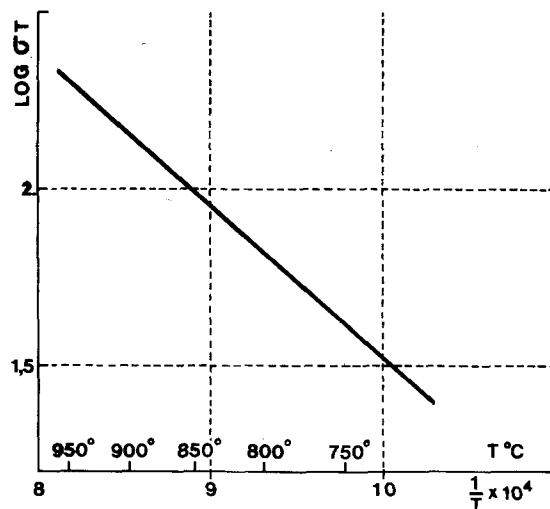


Fig. 4. Electrical conductivity of the electrolyte, (ZrO₂)_{0.92}(Yb₂O₃)_{0.08}, as a function of temperature.

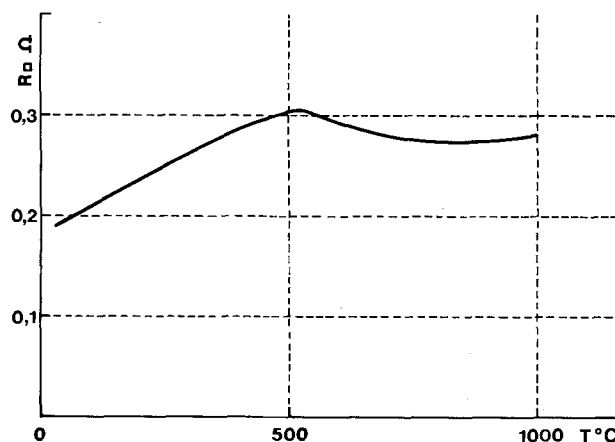
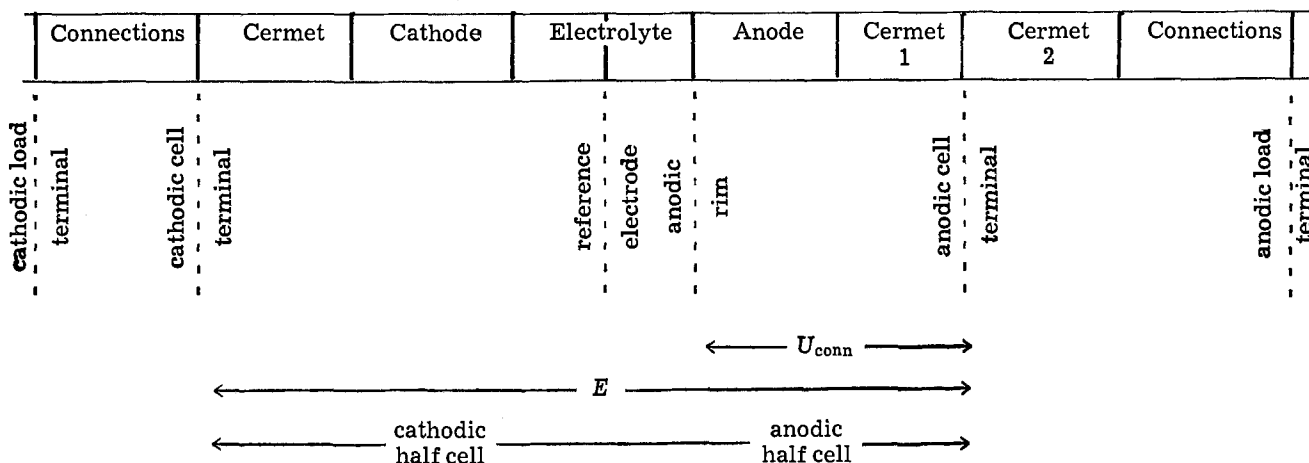


Fig. 5. Lateral resistance of the anode, (In₂O₃)_{0.96}(SnO₂)_{0.4}, as a function of temperature. Thickness 85 μ . Density: 31.6 mg/cm³. Measurements taken on an alumina substrate after 960 hr at 900°C in air with the Van der Pauw method.

Connectors.—These cermet hats are produced by firing a mixture of 70% Cr + 20% MgO + 10% Al₂O₃ at 1600°C under an argon pressure of 200 Torr. They introduce an electrical resistance of $5 \cdot 10^{-3} \Omega$, which was not corrected for in the measurements.

The mug and the support tubes are made of suitable ferritic chrome steel.

Electrical measurements.—In most of the experiments we did use a "reference electrode" formed by the dissection of two small (ϕ : 2 mm) opposing circles in the cathode and anode (gap widths: 1 mm). In principle such a contact should measure the halfway potential between the two electrodes. Since we can only contact the anodic spot, we were not able to verify the assumptions underlying the scheme of Fig. 6. Our "6-point" measurement can be summarized in the following way:



U_{conn} , the potential drop between the anodic rim and the anodic cell terminal consists of: (i) the lateral resistance of the anode which can be related straightforwardly to its specific resistance (e.g., 60 mV at 1 A/cm² for 0.3 Ω /square), (ii) the potential drop in the anode/cermet contact, and (iii) the potential drop in the cermet connection.

The difference between the load terminal voltages and cell terminal voltages was not systematically recorded.

For the cell measurements we used a galvanostatic pulse technique. Measurements were made with the automatic pilot shown in Fig. 7, constructed at CITROEN which fulfills the following functions: (i) checking of the furnace temperatures, (ii) galvanostatic feeding of up to 12 electrolysis cells, (iii) continuous recording and printing of temperature, current, and 3 voltages, and (iv) logical command for routine measurements all 10 hr for the long-time experiments and the manually triggered measurement of the polarization curves.

The sequence of a measurement is shown in Table I.

Table I. Sequence of measurement

Time	Load	Quantity measured at the terminals
0	j (A)	E : stationary electrolysis voltage
5 μ sec	0	$E - U_R$
50 μ sec	0	E_{th} : open-circuit voltage
30 sec	0	

These sequences need some explanation. Usually galvanostatic current pulses would be applied incrementally, but then one is more limited by the performance of the electronic equipment. It is the rise time of the functional amplifier of the galvanostat for the large currents needed, which leads to the notion of

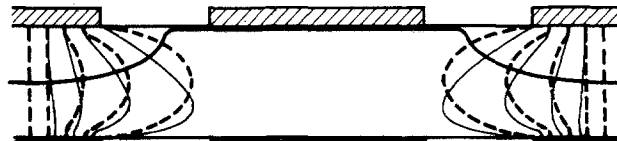


Fig. 6. Schematic representation of current lines and the equipotential surface around our "reference electrode." In principle both contacts should measure the same potential, corresponding to the half-plane of the disk. Thin lines indicate the electrolysis of very hydrogen-rich mixtures.

5 μ sec, which was indeed the time necessary to raise the current in the incremental experiment. An additional advantage of the decremental procedure is that it introduces an empirically well-defined open-circuit voltage. In previous experiments with other electrodes

we had often observed "long term polarizations," i.e., open-circuit voltages that did stay below their original theoretical value after long periods of load for many minutes. In this case, 30 sec can be considered as much longer than the relaxation times of the electrode processes.

U_R will be referred to as the rapid part of the polarization. It was always found to behave ohmically as expected. $U_R = E - E_{\text{th}} - U_R$, the slow part of the polarization, can be associated with the diffusional and kinetic impedances of the electrode processes. If we are aware of the limits of this separation it can prove very useful in the development of the components (e.g., a change in U_L (O_2) would imply a failure of the kinetic function of the anode, caused by sintering). In the same way we find the rapid and slow contributions to the half-cell potential from values recorded at the "reference electrode," so that we are left with the following observed quantities: U_R , rapid contribution to the cell polarization; U_L , slow contribution to the cell polarization; U_R (H_2), rapid contribution to the cathodic cell polarization; U_L (H_2), slow contribution to the cathodic cell polarization; U_R (O_2), rapid contribution to the anodic cell polarization; U_L (O_2), slow contribution to the anodic cell polarization. These data allow us in principle to distinguish the component which has failed.

Fabrication and Structure of the Cermet Cathodes

Process.—We use magnetron sputtering for the cathodes (7). While it is usual to employ rf power for the sputtering of cermets, we did use d-c because of its essentially better deposition rates. While the details of the process cannot be revealed at the moment, we can give the following summary (8): (i) multiple targets which can be activated and controlled separately; (ii) reactive gas sputtering or inert gas sputtering, depending, on the state of oxidation

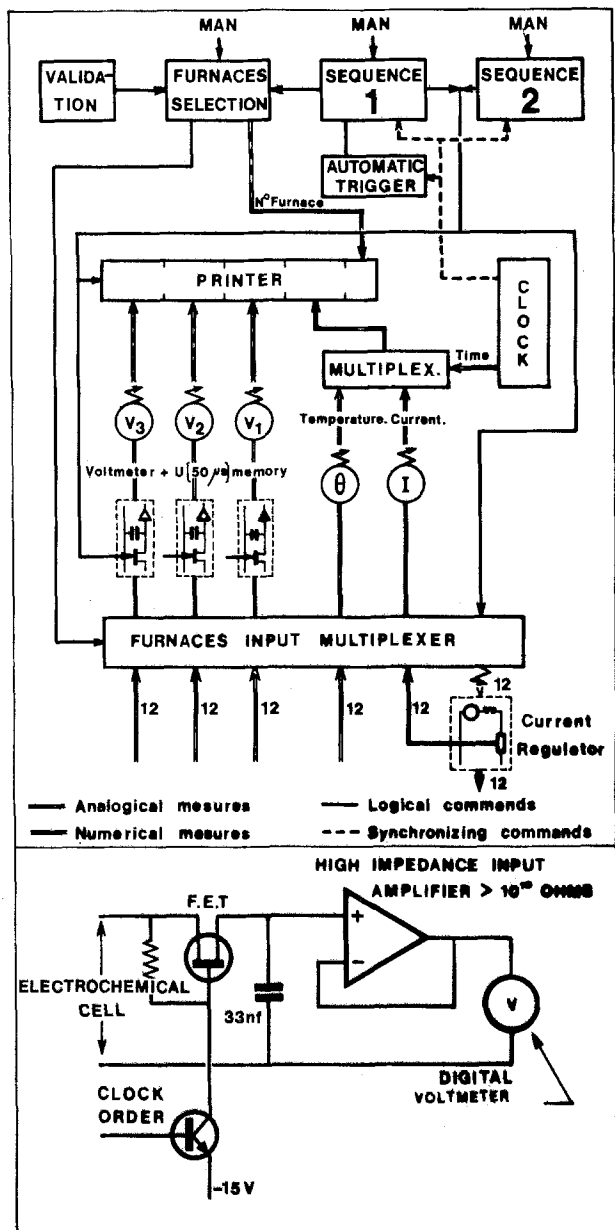


Fig. 7. Schematic representation of the measurement pilot. The insert shows the element used for the pulse measurements.

one wants to achieve for the deposit; and (iii) deposition rate of the order of $0.1 \mu/\text{min}$.

Composition.—We have used mixtures of ZrO_2 , Yb_2O_3 , UO_2 , Ni , Ti , and Ag . The ceramic components correspond to a composition of $(\text{ZrO}_2)_{0.82}(\text{Yb}_2\text{O}_3)_{0.1}(\text{UO}_2)_{0.08}$. The nickel content was varied. The process also allows the manufacture of layered structures as well as a grading of the cermets. The additions of titanium and silver were abandoned when they did not lead to the expected benefits.

Structure.—The initial structure of the deposit is almost amorphous (grain size $< 30\text{\AA}$). Upon heating to the operating temperature of the electrolysis cell, the deposit crystallizes to a fine layer of completely stabilized zirconia, mixed with nickel (x-ray and SEM observations).

Electrical properties.—We have measured the electrical conductivity of various cermet compositions deposited on stabilized zirconia under hydrogen as a function of temperature up to 900°C . These measurements did reveal a critical composition of 40 volume percent (v/o) nickel (9). Below 40% the cermets reach a very high resistivity once heated. In agreement with Hill's theory (10) the temperature de-

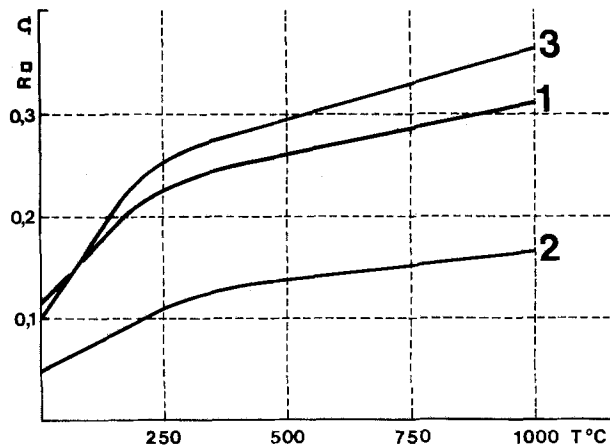


Fig. 8. Lateral resistance of three cermets layers as a function of temperature. Van der Pauw measurements on alumina in $\text{H}_2 + 3\% \text{H}_2\text{O}$ after sintering at 900°C . Curve 1. $(\text{ZrO}_2)_{0.82}(\text{Yb}_2\text{O}_3)_{0.1}(\text{UO}_2)_{0.08}$ 44.6 w/o + nickel 5μ . Curve 2. $(\text{ZrO}_2)_{0.82}(\text{Yb}_2\text{O}_3)_{0.1}(\text{UO}_2)_{0.08}$ 30.8 w/o + nickel 5μ . Curve 3. $5 \times [(\text{ZrO}_2)_{0.82}(\text{Yb}_2\text{O}_3)_{0.1}(\text{UO}_2)_{0.08}$ 30.8 w/o + nickel 0.5μ + $(\text{ZrO}_2) \cdot 0.82(\text{Yb}_2\text{O}_3)_{0.1}(\text{UO}_2)_{0.08}$ 76.4 w/o + nickel 0.05μ] + $(\text{ZrO}_2)_{0.82}(\text{Yb}_2\text{O}_3)_{0.1}(\text{UO}_2)_{0.08}$ 30.8 w/o + nickel 0.5μ .

pendence of the resistance is exponential. This is even observed for the first irreversible rise. Above 40 v/o nickel, the cermets show a completely metallic behavior as shown in Fig. 8.

Results

We think the results one can obtain with the structure described are best illustrated with one example, a simple cermet cathode, 55.4 weight percent (w/o) of nickel with urania doped ytterbia stabilized zirconia of 6μ thickness. Figures 9-12 give the measurements of this cell at different water decomposition levels. We have combined in one figure the stationary current-

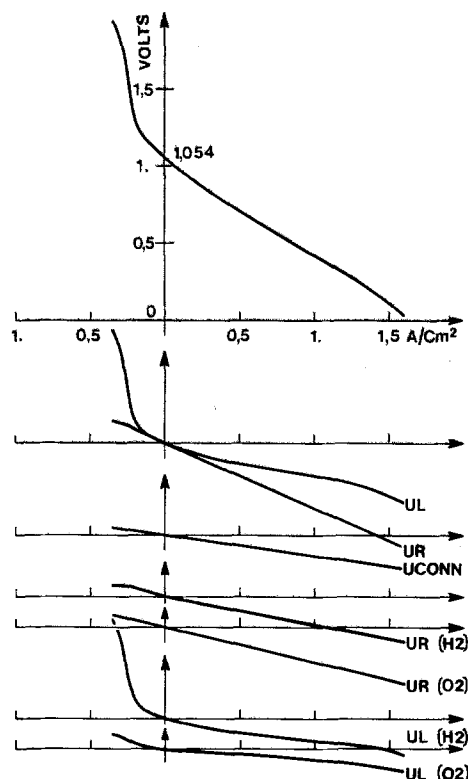


Fig. 9. Characteristic of a cell with components as described and a cathode of 6μ of cermet with 50% volume of nickel. Feed gas: 95% $\text{H}_2 + 5\% \text{H}_2\text{O}$ at a specific flow rate of $1.7 \text{ cm}^3/\text{sec}$ at 900°C after 643 hr of operation with an $\alpha = 1/2$ mixture at 900°C . The lower half gives the various contributions to the cell polarization.

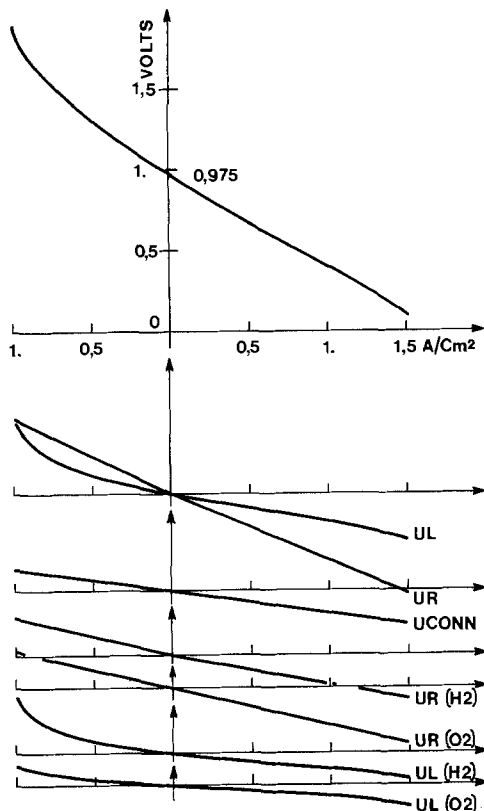


Fig. 10. Same as Fig. 9, but with 80% H₂ + 20% H₂O

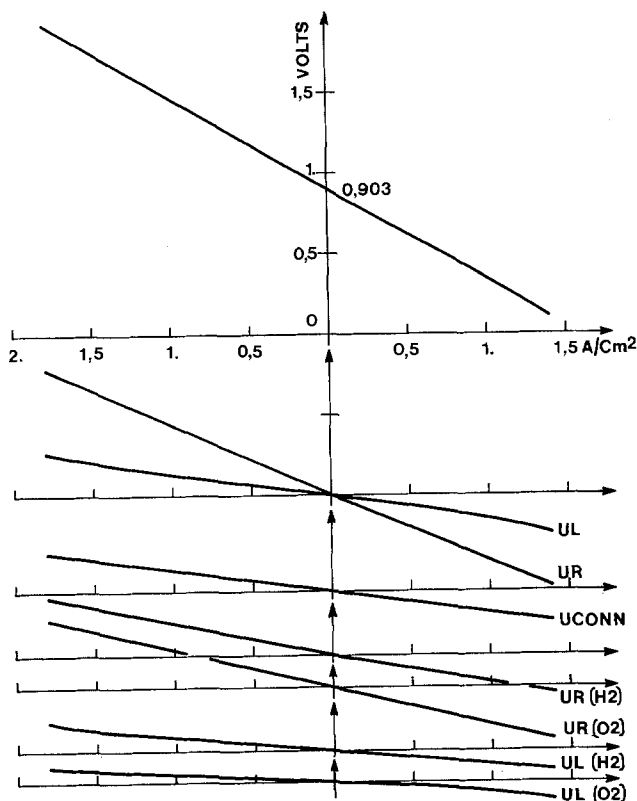


Fig. 11. Same as Fig. 9, but with 50% H₂ + 50% H₂O feed gas

voltage plot and the contributions of the different polarization mechanisms to the total polarization for fuel cell and electrolysis operation. The measurements were taken at 900°C after 694-713 hr of operation, under an electrolysis load of 1 A/cm² in a mixture with $\alpha = \frac{1}{2}$.

Figure 9 shows that for the very low concentration of water vapor of 5%, diffusion limitation sets in

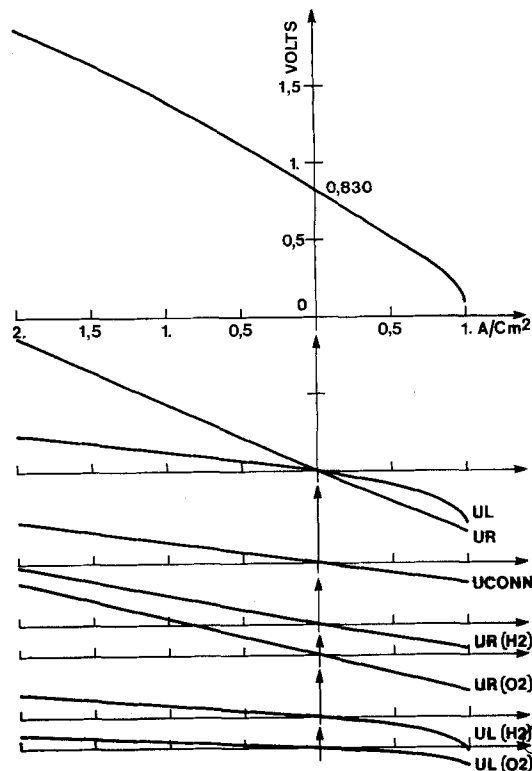


Fig. 12. Same as Fig. 9, but with 20% H₂ + 80% H₂O

below 0.2 A/cm². As it should be, almost all this polarization shows up as a slow polarization of the cathodic half-cell. Let us mention that this characteristic gives a maximum power density for fuel cell operation of 430 mW/cm². Furthermore one sees from these figures that the main contribution to the polarization of the oxygen half-cell comes from U_{CONN} , i.e., the limited lateral conductivity of the oxygen electrode; this pertains to fuel cell operation where the kinetic impedance of the oxygen dissociation reaction causes a larger slow polarization of the oxygen half-cell than the one observed in electrolysis for oxygen rejection.

Evidently the water dissociation reaction does not represent a problem with these nickel cermets. However, anodes where the last layer contains only 23.6 w/o of nickel initially have an additional slow cathode polarization of the order of 100-150 mV at 1 A/cm², which decreases with time. As long as they are nickel rich, the optimum anode thickness will be determined by a compromise between slow and fast polarization, i.e., lateral collection resistance and oxygen diffusive resistance.

The rise in the slow polarization of the oxygen half-cell in Fig. 9 is an interesting example of the breakdown of our assumptions concerning the reference electrode. Indeed, as steam diffusion limitation sets in we must take electrode border effects into account, notably that the diffusion limiting current will be larger at the cathode edge facing the "reference electrode." In this situation, an electrode with uniform current density faces an electrode with nonuniform current density and this leads to a distortion of the current lines shown as additional thin lines in Fig. 6. This distortion displaces the equipotential line on which our "reference" sits at the cathode, increasing the size of the oxygen half-cell and therefore its potential drop. The inverse happens of course in Fig. 11 for the fuel cell operation under high water content. An interesting detail of this analysis is the flat portion of $U_R(\text{H}_2)$ for cell voltages larger than 1.7V under 95% H₂ which indicates the onset of electronic conductivity in the zirconia under these large

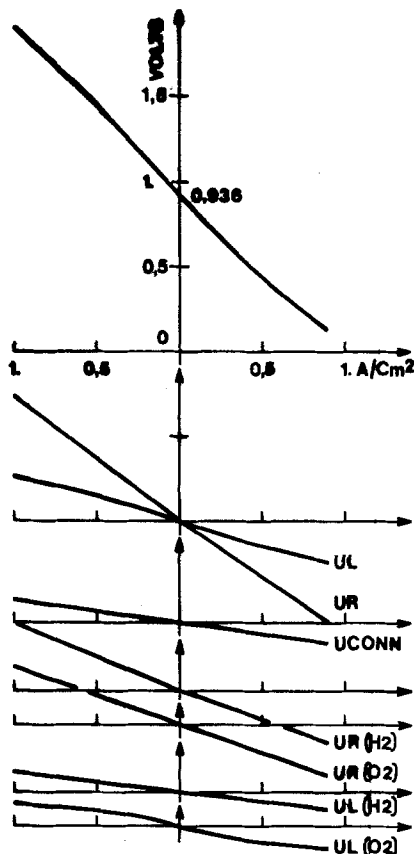


Fig. 13. Same as Fig 11, but at 800°C and after 813 hr of operation

polarizations. The value agrees roughly with previous observations (3, 4).

This onset of electronic conduction was observed in fact with a large number of cells of varying performance and cathode structure. In Fig. 13-16, we give the measurements at different temperatures: 800°, 850°, 900°, and 950°C made after 813-817 hr of operation in an $\alpha = \frac{1}{2}$ mixture. One sees that above 850° there is no important slow (reaction) polarization with our electrodes. The sharp drop in performance at low temperatures is due to the use of a thick electrolyte. Table II compares the various calculated contributions to the polarization with the measured values. Since we compare values measured previously on other virgin cell components, the agreement is better than one could expect.

Long-term stability.—We had limited our long-term tests to 1000 hr for practical reasons. As a matter of fact most experiments were terminated before 1000 hr because of various accidents, since the cells used at that stage of the program did not support thermal cycling. Twenty five cells were tested. The result of the cell discussed in the previous section is given in Fig. 17 which again gives the various contributions to the polarization.

Over the period of 930 hr, the cell voltage under a load of 1 A/cm² only increased from 1.45 to 1.49V. All this deterioration can be traced to the cathode. After 930 hr the water supply of the saturator was

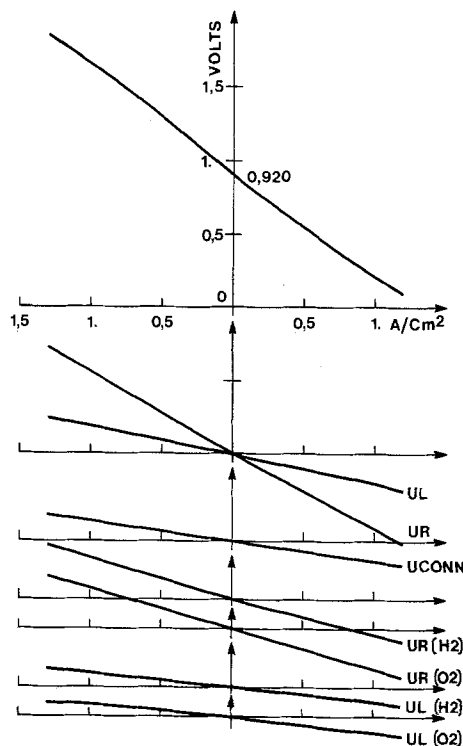


Fig. 14. Same as Fig. 13 at 850°C

interrupted over a weekend. The electrical load was maintained with a flow of pure hydrogen probably causing zirconia electrolysis. After repair, the cell started again but at a higher polarization.

Anode and electrolyte show no measurable or visible degradation. The behavior of the cathodes is less satisfactory. Under water electrolysis conditions, they show a large tendency to demix. This can easily be explained by the known: (i) weak interfacial tension of nickel on zirconia and (ii) hydrophilic nature of nickel, which leads, e.g., to the decomposition of copper-nickel alloys in water vapor (10). This can lead to a complete segregation of nickel and within 100 hr. A complete nickel layer forms at the surface and can be stripped off by hand, leaving behind an insulating powdery layer of zirconia (Fig. 18).

Additions of titanium are known to stabilize nickel-zirconia cermets by increasing the wetting angle (11). But this is achieved in bulk cermets, where titanium concentrates in the surface of the nickel grains. We did not find any influence on the demixing, maybe because in the failing electrodes demixing is faster than titanium precipitation in the grain boundary.

The problem can only be overcome by a careful adjustment of the nickel content and/or layered structures. A further problem at the high end of the temperature is the evaporation of nickel, which theoretically reaches 2.5 μ /1000 hr at 950°C. Indeed one cathode has been observed to be superficially insulating after 980 hr.

Conclusion

Steam electrolysis with thick zirconia cells can be achieved at 900°C with a cell voltage below 1.5V at 1 A/cm². Stability of the electrolyte and the vacuum-

Table II. Comparison of calculated contributions to polarization with measured values

Temp (°C)	R electrolyte (Ω cm)	R (anode) (Ω)	R (cathode) (Ω)	Ohmic loss calculated (V)	U _R (V)	U _L (V)
800	16.2	0.4	0.58	0.790	0.740	0.270
850	11.5	0.4	0.59	0.603	0.560	0.185
900	8.2	0.4	0.60	0.472	0.450	0.140
950	6.0	0.4	0.61	0.385	0.380	0.120

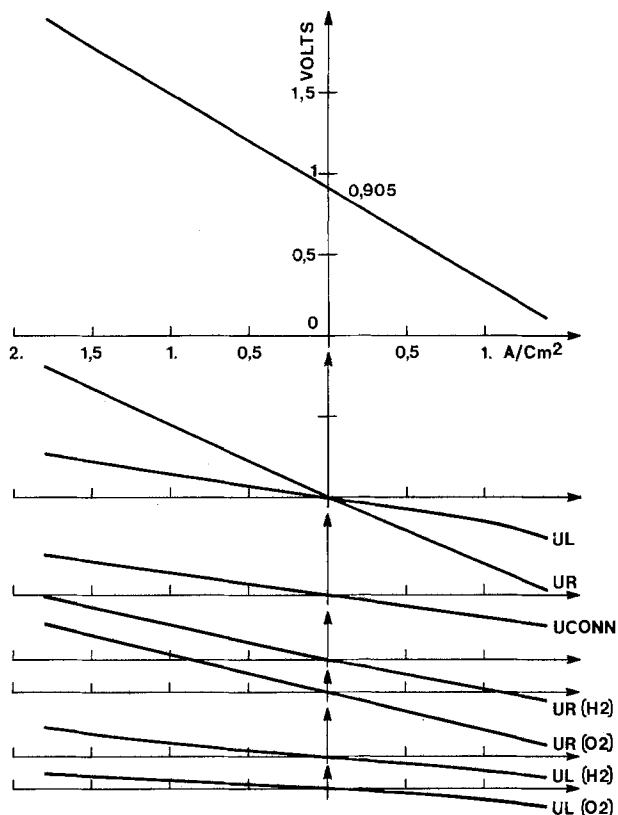


Fig. 15. Same as Fig. 13 at 900°C

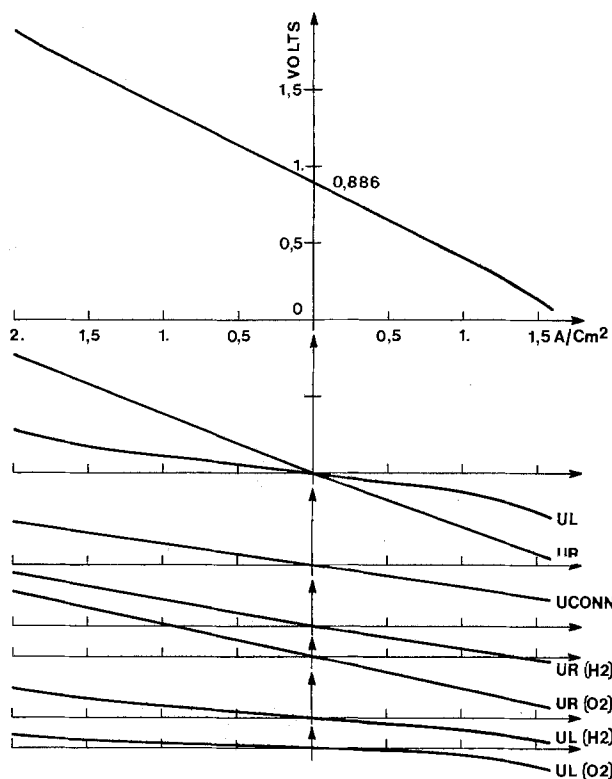


Fig. 16. Same as Fig. 13 at 950°C

deposited india anode does not represent a problem over 1000 hr of operation. Sputtered nickel/zirconia cermet electrodes are limited by demixing and nickel evaporation. Operation with a feed gas containing less than 20% of steam does not appear feasible. This will limit the decomposition level that can be achieved with a battery of cells in series.

Acknowledgment

We would like to thank Messrs. G. Horlville and J. Stauchmann for their assistance in the experiments,

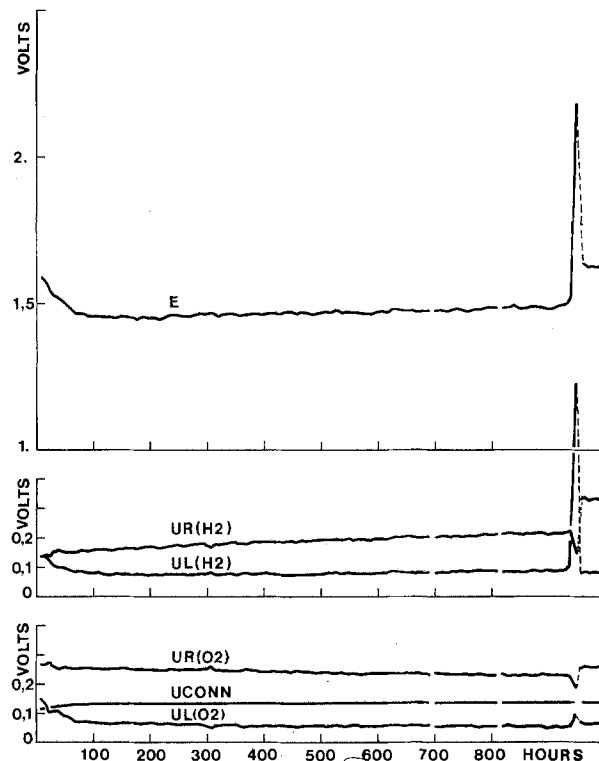


Fig. 17. Evolution of the cell voltage and the various contributions to the cell polarization for a cell with cermet cathode containing 55.4 w/o of nickel over 930 hr under an electrolysis of 1 A/cm² in a mixture of 50% H₂ + 50% H₂O at 900°C.



Fig. 18. A demixed cathode, after long term operation under 50% H₂O + 50% H₂ at 900°C.

Mr. G. Ducrot for the design of the measuring pilot, and Mr. J. Nougrou, Director of Research of CITROEN, for his continuous support and encouragement.

Manuscript submitted July 23, 1979; revised manuscript received Oct. 27, 1979.

Any discussion of this paper will appear in a Discussion Section to be published in the December 1980 JOURNAL. All discussions for the December 1980 Discussion Section should be submitted by Aug. 1, 1980.

Publication costs of this article were assisted by Battelle Memorial Institute.

REFERENCES

1. M. Warshay, NASA TM-X-71855 (1976).
2. H. Tannenberger, Abstract 48 presented at the 27th meeting ISE, Zürich, 1976.
3. J. Fouletier, Thesis No. A.O. 12.210, University of Grenoble, France.
4. T. H. Etsell and S. N. Flengas, *Chem. Rev.*, **70**, 341 (1970).
5. French Pat. 2,182,650.
6. P. van den Berghe and H. Tannenberger, U.S. Pat. 4,124,024.
7. F. M. Penning, U.S. Pat. 2,146,025; P. S. McLeod, U.S. Pat. 3,956,093 or S. Schiller, U. Heisig, and K. Goedicke, *Thin Solid Films*, **54**, 33 (1978).
8. E. Bergmann and G. Horlville, French Pat. application 79.09.199.
9. T. L. Hill and T. G. Coutts, *Thin Solid Films*, **42**, 201 (1977).
10. P. W. Selwood, *J. Catal.*, **42**, 148 (1976).
11. C. R. Kurkjian and W. D. Kingery, *J. Phys. Chem.*, **60**, 961 (1956).

Oxygen Evolution on $\text{La}_{1-x}\text{Sr}_x\text{CoO}_3$ Electrodes in Alkaline Solutions

Y. Matsumoto, H. Manabe, and E. Sato

Department of Industrial Chemistry, Faculty of Engineering, Utsunomiya University, Utsunomiya, Japan

ABSTRACT

Anodic characteristics of $\text{La}_{1-x}\text{Sr}_x\text{CoO}_3$ (with $x = 0.2$ and 0.4) electrodes were investigated in alkaline solutions. It was found that the catalytic activities for the oxygen evolution reaction are relatively high and that the activity of the electrode with $x = 0.4$ is higher than that of $x = 0.2$. The secondary chemical step, i.e., $\text{CoOH} + \text{OH}^- \rightarrow \text{CoO}^- + \text{H}_2\text{O}$, is rate-controlling in the oxygen evolution reaction. Therefore, it is concluded that the rate of the secondary chemical step is more rapid at the electrode with the higher value of x because of the beneficial effect of the higher positive charge on the Co cation on this step. $\text{La}_{1-x}\text{Sr}_x\text{CoO}_3$ electrodes are suitable for the anode material in alkaline solutions, because anodic dissolution scarcely occurs.

The anodic evolution of oxygen is of special importance in water electrolysis, because the activation overpotential at the electrode is the chief cause of efficiency loss in this process. Recently, low cost transition metal oxides such as MnO_2 (1-3), NiCo_2O_4 (4), $\text{La}_{1-x}\text{M}_x\text{CoO}_3$ (5), $\text{La}_{1-x}\text{Sr}_x\text{MnO}_3$ (6), and SrFeO_3 (7) have been reported to be good electrocatalysts for the anodic evolution of oxygen, and the catalysis of the latter two oxides is explained by applying the theory of σ^* band formation in the oxide to the oxide surface (6, 7). This concept predicts the catalytic activity of the oxide having the σ^* band to be high.

$\text{La}_{1-x}\text{Sr}_x\text{CoO}_3$ series oxides with perovskite-type structure such as $\text{La}_{1-x}\text{Sr}_x\text{MnO}_3$ and SrFeO_3 have also shown interesting electrocatalytic properties for electrochemical oxygen reduction (8-13). $\text{La}_{1-x}\text{Sr}_x\text{CoO}_3$, with the value of x over 0.2, exhibits high electrical conductivity because of the partially filled σ^* band in the oxide (14, 15), which also produces high catalytic activity according to the above concept. The properties of these oxides, which are resistive to anodic oxidation in alkaline solutions (11), make them extremely useful as the anode material in alkaline solutions. However, no details of the anodic characteristics are clear. Therefore, in this paper, the anodic characteristics of $\text{La}_{1-x}\text{Sr}_x\text{CoO}_3$ with $x = 0.2$ and 0.4 electrodes as well as the catalytic properties for the anodic evolution of oxygen are studied in detail in alkaline solutions.

Experimental

$\text{La}_{1-x}\text{Sr}_x\text{CoO}_3$ with $x = 0.2$ and 0.4 were prepared by using La_2O_3 , SrCO_3 , and CoO as the starting materials. These materials were mixed in stoichiometric quantities with an agate mortar and then heated at 1200°C for 6 hr in air. The prepared perovskite oxides, whose compositions were checked by x-ray analysis, were pressed into tablet form with 100 kg/cm^2 , then sintered at 1350°C for 2 ~ 3 hr. The porosity of the sintered disk was determined by filling the pores with water. The

Key words: oxygen evolution, perovskite type oxide, electrocatalysis.

porosities of these sintered disk samples were about 20% for both samples with $x = 0.2$ and 0.4 . The specific resistivities measured by four probe method were $7 \times 10^{-4} \Omega \cdot \text{cm}$ and $2 \times 10^{-4} \Omega \cdot \text{cm}$ for $\text{La}_{0.8}\text{Sr}_{0.2}\text{CoO}_3$ and $\text{La}_{0.6}\text{Sr}_{0.4}\text{CoO}_3$, respectively. These specimens were waterproofed with polystyrene in order to obtain good reproducible results. Both end surfaces of these specimens were polished with No. 2000 emery paper, and an electrical lead was connected via silver paste on one side of the surface. The specimens were then mounted in glass tubes with epoxy resin. The real areas of the prepared electrodes were, of course, larger than the apparent areas.

The electrodes prepared by this manner were immersed in $0.5\text{M H}_2\text{SO}_4$ for 10 sec as a pretreatment, followed by washing with distilled water. The solutions were pre-electrolyzed 1M KOH and various concentrations of K_2SO_4 which were of constant ionic strength but various pH values by adding a few drops of dilute KOH . An Hg/HgO electrode was used as the reference electrode and electrode potentials cited in this paper are referred to this electrode, unless otherwise stated. IR-free current/potential curves at steady state were obtained by correcting for the ohmic drops. The ohmic drops were observed by a synchroscope (SS-5057V, Iwatsu), using a current interruption technique.

The small amount of Co ion dissolved in the electrolyte was determined colorimetrically by the method using β -nitroso- α -naphthol as the color-producing reagent (16).

Results and Discussion

Figure 1 shows a typical voltammogram for a $\text{La}_{0.6}\text{Sr}_{0.4}\text{CoO}_3$ electrode in alkaline solution in the anodic potential region. A voltammogram similar to this figure was also obtained in the case of the $\text{La}_{0.8}\text{Sr}_{0.2}\text{CoO}_3$ electrode. In the anodic potential region, no electrochemical reaction at the electrode itself, except for the anodic evolution of oxygen, was observed. Therefore, in the potential region covered, the electrode surface will still exist as the near stoichio-

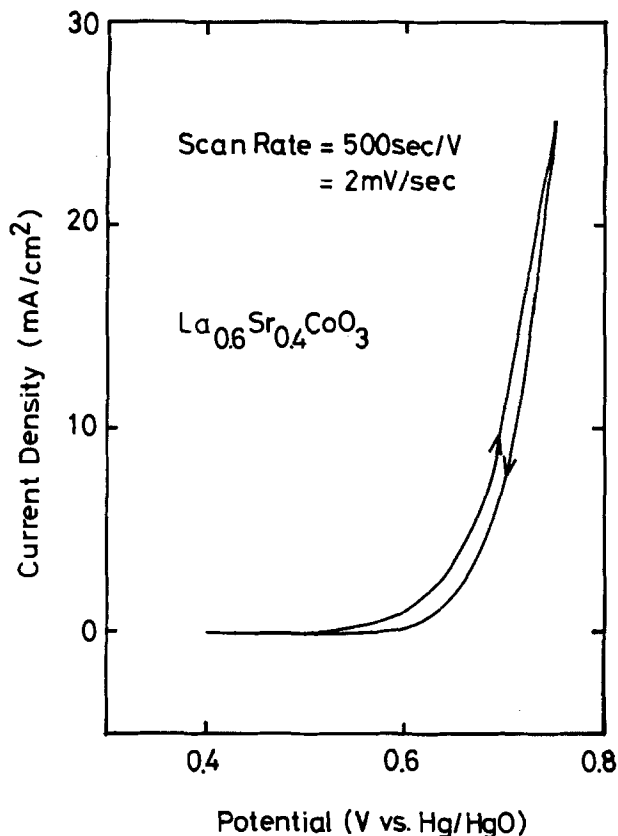


Fig. 1. Potential sweep voltammogram of $\text{La}_{0.6}\text{Sr}_{0.4}\text{CoO}_3$ in 1M KOH at 25°C.

metric compound, $\text{La}_{1-x}\text{Sr}_x\text{CoO}_3$, unaffected by the oxygen evolution. The above result shows that $\text{La}_{1-x}\text{Sr}_x\text{CoO}_3$ is preferable as the anode material in alkaline solution, although very slight anodic dissolution of the electrodes occurs in the high overpotential region (at 50 mA/cm^2) as described in a later section.

The IR-free polarization curves for the anodic evolution of oxygen are shown in Fig. 2. The standard potential of an oxygen electrode, which is the potential at zero overvoltage, is +0.303V (*vs.* Hg/HgO) in basic solution. Therefore, the overvoltages of $\text{La}_{0.8}\text{Sr}_{0.2}\text{CoO}_3$ and $\text{La}_{0.6}\text{Sr}_{0.4}\text{CoO}_3$ electrodes at 10 mA/cm^2 are 0.44 and 0.40V, respectively. The overvoltage in the case of $\text{La}_{0.6}\text{Sr}_{0.4}\text{CoO}_3$ electrode is almost same as those of SrFeO_3 (7) and $\text{Ti}/\text{RuO}_x/\text{MnO}_3$ electrodes (17) but is larger than that of DSA(RuO_x) (18), therefore, the catalytic activities of the $\text{La}_{1-x}\text{Sr}_x\text{CoO}_3$ series oxides for the oxygen evolution reaction are judged to be relatively high. The catalytic activity of the $\text{La}_{0.6}\text{Sr}_{0.4}\text{CoO}_3$ electrode is higher than that of the $\text{La}_{0.8}\text{Sr}_{0.2}\text{CoO}_3$ electrode. This fact suggests that the increase of the positive charge on the Co cation driven by the substitution of Sr^{2+} ion in the oxide has a favorable effect on the rate of the oxygen evolution reaction. The Tafel slopes, b , for the oxygen evolution reaction were 0.065V per decade, or near 2.303 (RT/F) in both cases.

The dependence of the current density on pH for the anodic evolution of oxygen at constant E is shown in Fig. 3 for the $\text{La}_{1-x}\text{Sr}_x\text{CoO}_3$ electrodes. The slopes obtained from the linear relationships were about 1.8, or near 2 in the both cases. We can, therefore, conclude that the reaction order of OH^- ion in the mechanism of the oxygen evolution reaction at $\text{La}_{1-x}\text{Sr}_x\text{CoO}_3$ electrodes is 2. The obtained kinetic parameters are summarized in Table I.

Consequently, the experimental results over all current densities for the anodic evolutions of oxygen at $\text{La}_{1-x}\text{Sr}_x\text{CoO}_3$ with $x = 0.2$ and $x = 0.4$ electrodes can be formulated as follows

$$i = nFka^2_{\text{OH}^-} \exp(FE/RT) \quad [1]$$

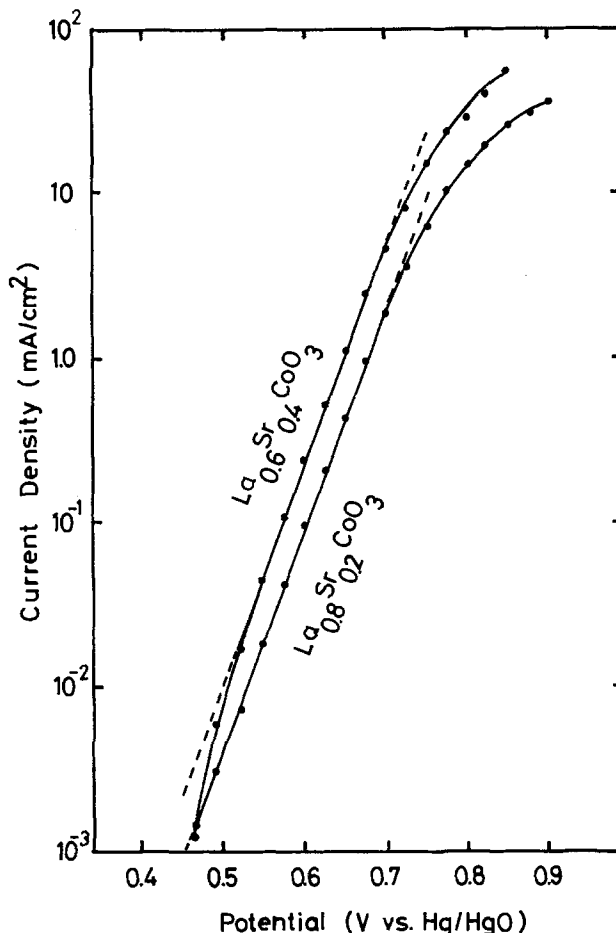
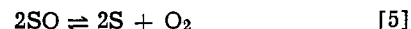
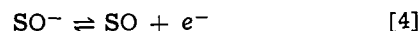
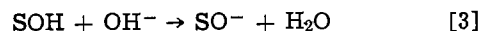
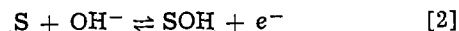


Fig. 2. Anodic polarization curves for oxygen evolution on $\text{La}_{1-x}\text{Sr}_x\text{CoO}_3$ electrodes in 1M KOH at 25°C.

in alkaline solution, where k is the rate constant and other symbols have their usual meanings.

In alkaline solutions the following oxygen evolution mechanism



seems probable for oxide electrodes (6, 7, 19), where S stands for a site at the electrode surface and is presumed to be Co cation in the present case. In any case, any one of the O_2 reaction paths already proposed by Bockris (20) and Damjanovic *et al.* (21), will satisfy the present data with the assumption of Langmuirian adsorption conditions in alkaline solution if the 2nd step [3] is rate-determining. With this assumption the current expression in the Tafel region can be written as

$$i = nF(k_1k_2/k_{-1}) a^2_{\text{OH}^-} \exp(FE/RT) \quad [6]$$

where k_1 , k_{-1} , and k_2 are the rate constants for the 1st [2] and the 2nd [3] steps. The theoretically deduced rate equation [6] is consistent with the experimentally obtained expression [1]. The above proposed mechanism

Table I. Kinetic parameters for the oxygen evolution reaction on $\text{La}_{1-x}\text{Sr}_x\text{CoO}_3$ electrodes at 25°C

Electrode	Tafel slope (V)	i_0 (A/cm^2) (in 1M KOH)	$\left(\frac{\partial \log i}{\partial \log a_{\text{OH}^-}}\right)_E$
$\text{La}_{0.8}\text{Sr}_{0.2}\text{CoO}_3$	0.065	3.0×10^{-9}	1.8
$\text{La}_{0.6}\text{Sr}_{0.4}\text{CoO}_3$	0.065	7.4×10^{-9}	1.8

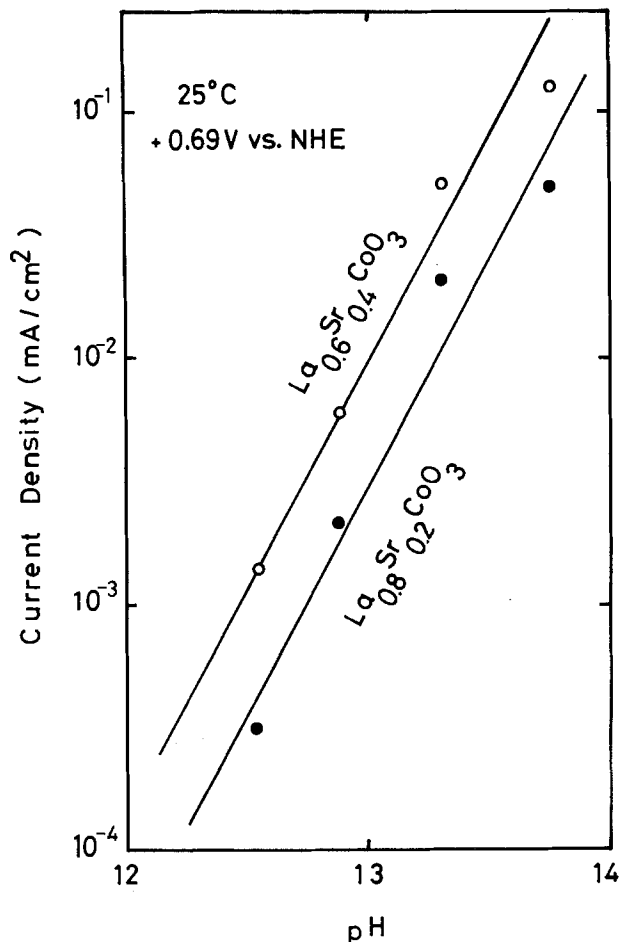


Fig. 3. pH dependences of current density of oxygen evolution reaction on $\text{La}_{1-x}\text{Sr}_x\text{CoO}_3$ electrodes at 0.69V vs. NHE (0.59V vs. Hg/HgO) at 25°C.

ism on the $\text{La}_{1-x}\text{Sr}_x\text{CoO}_3$ electrodes is same as that on SrFeO_3 electrode (7). The σ^* band is formed in the $\text{La}_{1-x}\text{Sr}_x\text{CoO}_3$ with $x = 0.2$ and 0.4 (15), therefore, the rate of the electron transfer in the 1st step must be rapid at the surfaces of these oxides. This leads the other chemical step, i.e., the 2nd step, to become the rate-controlling in analogy with the case of SrFeO_3 electrode (7).

Figures 4 and 5 show the typical Arrhenius plots at constant overvoltage for the oxygen evolution reaction in 1M KOH at $\text{La}_{0.8}\text{Sr}_{0.2}\text{CoO}_3$ and $\text{La}_{0.6}\text{Sr}_{0.4}\text{CoO}_3$ electrodes, respectively. An apparent activation energy can be calculated from the gradient of each straight line by using Eq. [7]

$$\Delta \tilde{H}^\ddagger(\eta) = -2.303R(\partial \log i / \partial (1/T))_\eta + \alpha n F \eta [\text{cal/mole}] \quad [7]$$

where $\alpha n = 2.303RT/bF$, α is the formal value of charge transfer coefficient, and F is the Faraday constant. Activation energies for the oxygen evolution reaction at $\text{La}_{0.8}\text{Sr}_{0.2}\text{CoO}_3$ and $\text{La}_{0.6}\text{Sr}_{0.4}\text{CoO}_3$ electrodes are summarized in Table II.

The dependence of current density i on the apparent activation energy at constant pressure p , overpotential η on polarization, and activity of reactant a can be expressed by the equation (2, 21, 22)

$$i = nFA a^2_{\text{OH}^-} \exp(-\Delta \tilde{H}^\ddagger(\eta)/RT) \quad [8]$$

where A is the pre-exponential factor at given overpotential. From the comparison of this equation with Eq. [6], $\Delta \tilde{H}^\ddagger(\eta)$ will be expressed as follows

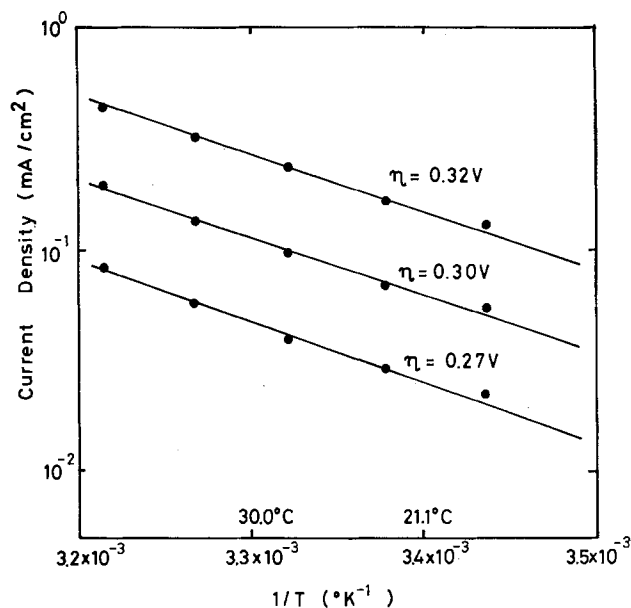


Fig. 4. Temperature dependences of current density of oxygen evolution reaction on $\text{La}_{0.8}\text{Sr}_{0.2}\text{CoO}_3$ electrode in 1M KOH at various overpotentials.

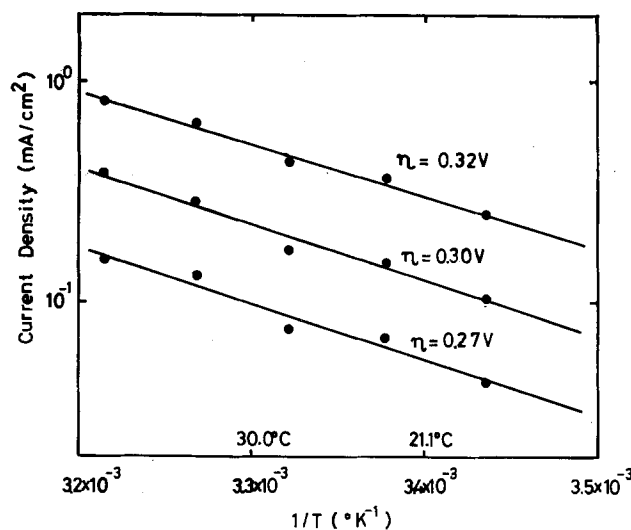


Fig. 5. Temperature dependences of current density of oxygen evolution reaction on $\text{La}_{0.6}\text{Sr}_{0.4}\text{CoO}_3$ electrode in 1M KOH at various overpotentials.

$$\Delta \tilde{H}^\ddagger(\eta) = \Delta H_1^\ddagger + \Delta H_2^\ddagger - \Delta H_{-1}^\ddagger - FE(\eta) \quad [9]$$

where ΔH_1^\ddagger , ΔH_2^\ddagger , and ΔH_{-1}^\ddagger are the chemical activation energies for 1st and 2nd steps, respectively. From Eq. [8] the ratio of the current density for the oxygen evolution reaction at $\text{La}_{0.6}\text{Sr}_{0.4}\text{CoO}_3$ electrode to that at $\text{La}_{0.8}\text{Sr}_{0.2}\text{CoO}_3$ electrode is expressed by Eq. [10], if the pre-exponential factors A are supposed to be the same for both electrodes

Table II. Apparent activation energies on $\text{La}_{1-x}\text{Sr}_x\text{CoO}_3$ with $x = 0.2$ and 0.4 electrodes and their differences in 1M KOH

Over-voltage η (V)	$\Delta \tilde{H}^\ddagger$ (kcal/mole)		Energy difference $(\Delta \tilde{H}_{x=0.2}^\ddagger - \Delta \tilde{H}_{x=0.4}^\ddagger)$ (kcal/mole)
	$\text{La}_{0.8}\text{Sr}_{0.2}\text{CoO}_3$	$\text{La}_{0.6}\text{Sr}_{0.4}\text{CoO}_3$	
0.27	18.1	17.3	0.8
0.30	18.2	17.7	0.5
0.32	18.2	17.5	0.7
			0.67 (Average)

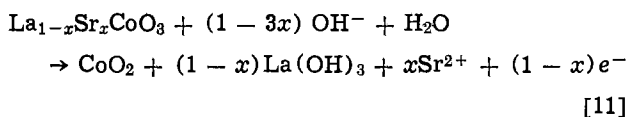
$$i_{x=0.4}/i_{x=0.2} = \exp [(\Delta\tilde{H}^\ddagger(\eta)_{x=0.2} - \Delta\tilde{H}^\ddagger(\eta)_{x=0.4})/RT] \quad [10]$$

The current ratio obtained from Fig. 2 at 25°C is about 2.5 in all potential regions covering the Tafel relation. From Eq. [10], the difference between the apparent activation energies for $\text{La}_{1-x}\text{Sr}_x\text{CoO}_3$ with $x = 0.2$ and 0.4 electrodes is calculated to be about 0.54 kcal/mole. This is almost consistent with the average difference, 0.67 kcal/mole, in the apparent activation energies measured by Arrhenius plots as shown in Table II. This result confirms that the oxygen evolution reaction at $\text{La}_{1-x}\text{Sr}_x\text{CoO}_3$ electrodes proceeds with the activation control stated already. Since ΔH_{1^\ddagger} and ΔH_{-1^\ddagger} are negligible in comparison with ΔH_{2^\ddagger} in Eq. [9] because

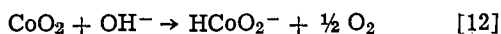
of the rate control of the 2nd step, $\Delta\tilde{H}^\ddagger(\eta) \approx \Delta H_{2^\ddagger}(\eta) - FE(\eta)$ is derived in the present case.

At this stage, we can discuss the catalysis of the Co cation in the $\text{La}_{1-x}\text{Sr}_x\text{CoO}_3$ in the 2nd step shown by Eq. [3], in which S stands for the Co cation on the surface. The 2nd step implies that the rate of capture of the hydrogen atom in the CoOH by OH^- ion increases, when the density of the positive charge on this hydrogen atom increases. The increase of the positive charge density on the hydrogen atom in the CoOH will be brought about by the increase of the positive charge density on the Co cation. Since the positive charge density on the Co cation increases with the increase of x as a result of charge delocalization, it is concluded that the catalytic activity for the oxygen evolution reaction increases with the increases of x in the $\text{La}_{1-x}\text{Sr}_x\text{CoO}_3$ electrodes. This theory satisfies the experimental result very well.

Figure 6 shows the variations of the potentials with time during the anodic polarization at 50 mA/cm² in 1M KOH at 25°C. The potentials were virtually invariant for both the electrodes except for a small variation (less than 50 mV) in the initial stage. After electrolyzing for 72 hr at 50 mA/cm², the amount of the very slightly dissolved Co ion which exists as HCoO_2^- ion in alkaline solution was determined by the manner described in the experimental section. From consideration of a Pourbaix diagram the anodic dissolution of the $\text{La}_{1-x}\text{Sr}_x\text{CoO}_3$ is proposed to be as follows



Then the CoO_2 produced on the electrode surface will decompose to HCoO_2^- ion as follows



The current efficiencies of the dissolutions of the $\text{La}_{1-x}\text{Sr}_x\text{CoO}_3$ electrodes calculated by using the above

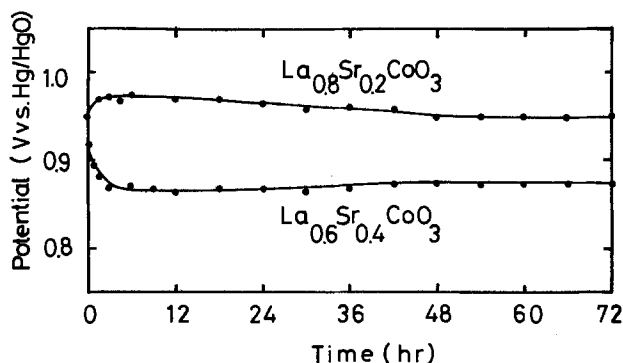


Fig. 6. Potential-time curves under anodic polarization of $\text{La}_{1-x}\text{Sr}_x\text{CoO}_3$ electrodes in 1M KOH at 50 mA/cm² at 25°C.

Table III. Current efficiencies of the anodic dissolution of $\text{La}_{1-x}\text{Sr}_x\text{CoO}_3$ electrodes at 50 mA/cm² in 1M KOH at 25°C

Electrode	Current efficiency (%)
$\text{La}_{0.6}\text{Sr}_{0.4}\text{CoO}_3$	6.8×10^{-3}
$\text{La}_{0.8}\text{Sr}_{0.2}\text{CoO}_3$	1.5×10^{-3}

Eq. [11] and [12] are shown in Table III. The efficiencies for both $\text{La}_{0.6}\text{Sr}_{0.4}\text{CoO}_3$ and $\text{La}_{0.8}\text{Sr}_{0.2}\text{CoO}_3$ electrodes are quite small. The smaller value of the efficiency in the case of $\text{La}_{0.6}\text{Sr}_{0.4}\text{CoO}_3$, compared to $\text{La}_{0.8}\text{Sr}_{0.2}\text{CoO}_3$, is believed to be caused by the smaller amount of Co^{3+} ion in the former oxide, when the Co cation in the oxide is expressed as Co^{3+} or Co^{4+} ion for convenience. The results in Figure 6 and Table III show that $\text{La}_{1-x}\text{Sr}_x\text{CoO}_3$ electrode is excellent for use as an anode material for long periods in alkaline solution. In conclusion, $\text{La}_{0.6}\text{Sr}_{0.4}\text{CoO}_3$ has good catalytic activity and appears to be a promising material for the anode in electrolysis of alkaline solutions.

Manuscript submitted June 4, 1979; revised manuscript received Sept. 12, 1979.

Any discussion of this paper will appear in a Discussion Section to be published in the December 1980 JOURNAL. All discussions for the December 1980 Discussion Section should be submitted by Aug. 1, 1980.

Publication costs of this article were assisted by Utsunomiya University.

REFERENCES

- G. N. Kokhanov, R. A. Anganova, and N. G. Milova, *Elektrokhimya*, **8**, 862 (1972).
- R. Mráz, V. Srb, and S. Tichý, *Electrochim. Acta*, **18**, 551 (1973).
- M. Morita, C. Iwakura, and H. Tamura, *ibid.*, **22**, 325 (1977).
- A. C. C. Tseung and S. Jasem, *ibid.*, **22**, 31 (1977).
- A. G. C. Kobussen, F. R. van Buren, T. G. M. van den Belt, and H. J. A. van Wees, *J. Electroanal. Chem. Interfacial Electrochem.*, **96**, 123 (1979).
- Y. Matsumoto and E. Sato, *Electrochim. Acta*, **22**, 421 (1979).
- Y. Matsumoto, J. Kurimoto, and E. Sato, *J. Electroanal. Chem. Interfacial Electrochem.*, In press.
- D. B. Meadowcroft, *Nature*, **226**, 847 (1970).
- A. C. C. Tseung and H. L. Bevan, *J. Electroanal. Chem. Interfacial Electrochem.*, **45**, 429 (1973).
- T. Kudo, H. Obayashi, and T. Gejo, *This Journal*, **122**, 159 (1975).
- T. Kudo, H. Obayashi, and M. Yoshida, *ibid.*, **124**, 321 (1977).
- K. L. K. Yeung and A. C. C. Tseung, *ibid.*, **125**, 878 (1978).
- F. R. van Buren, G. H. J. Broers, C. Boesveld, and A. J. Bouman, *J. Electroanal. Chem. Interfacial Electrochem.*, **87**, 381 (1978).
- H. Obayashi, T. Kudo, and T. Gejo, *J. Appl. Phys.*, **13**, 1 (1974).
- J. B. Goodenough, "Progress in Solid-state Chemistry," Vol. 5, pp. 145-399, Pergamon, Oxford (1971).
- E. B. Sandell, "Colorimetric Determination of Traces of Metals," 3rd ed., p. 409, Interscience, New York (1959).
- M. Morita, C. Iwakura, and H. Tamura, *Electrochim. Acta*, **23**, 331 (1978).
- W. O'Grady, C. Iwakura, J. Huang, and E. Yeager, "Proceedings of the Symposium on Electrocatalysis," M. W. Breiter, Editor, p. 286, The Electrochemical Society Softbound Proceedings Series, Princeton, N.J. (1974).
- C. Iwakura, K. Fukuda, and H. Tamura, *Electrochim. Acta*, **21**, 501 (1976).
- J. O'M. Bockris, *J. Chem. Phys.*, **24**, 817 (1956).
- A. Damjanovic, A. Dey, and J. O'M. Bockris, *Electrochim. Acta*, **11**, 791 (1966).
- Y. Yoneda, *J. Electrochem. Soc. Jpn.*, **22**, 226 (1949).

The Electrochemical Oxidation of I⁻ in a Nonpolar Solvent Consisting of Al₂Br₆ and KBr in an Aromatic Hydrocarbon

M. Elam and E. Gileadi*

Institute of Chemistry, Tel-Aviv University, Ramat Aviv, Israel

ABSTRACT

The mechanism of oxidation of I⁻ in a nonpolar solvent consisting of 1.0M Al₂Br₆ and 0.80M KBr in an aromatic hydrocarbon was studied. A chemical step following charge transfer, in which I⁻ is regenerated, was observed. It was postulated that bromination of the solvent occurred. Oxidation of Br⁻ by I₂ to IBr or Br₂ is possible in this system since the standard potentials for different redox couples are much closer than in aqueous solutions. Qualitative mechanistic information obtained from analysis of cyclic voltammograms was consistent with the mechanism derived on the basis of steady-state current/potential measurements. It was observed that iodine is reduced rapidly in this system if mesitylene is used as the solvent and much more slowly in benzene. The half-wave potential for the oxidation of I⁻ is about 1.10V vs. RAIE, compared to about 2.2V in aqueous solutions.

The chemical and electrochemical properties of a solvent system consisting of Al₂Br₆ and an alkali metal bromide (MBr) in an aromatic hydrocarbon (ArH) have been studied by Plotnikov and co-workers (1-9). In recent years there has been renewed interest in this system as a possible bath for the electroplating of aluminum (10-15). Apart from its practical importance this bath may be expected to exhibit unusual electrochemical behavior, due to the unique combination of its low dielectric constant and relatively high conductivity.

Some of the chemical and electrochemical properties of this system have been studied recently in our laboratory (16-22). A review of earlier work was given in Ref. (18), and a summary of work done in this laboratory was presented very recently (23).

In a previous study (21) surface phenomena occurring on different electrode materials in this solvent system were investigated. Glassy carbon was found to be inactive. On platinum a well-defined adsorption pseudocapacitance peak was observed, associated with the adsorption of bromine atoms on the surface. On gold electrodes several adsorption and desorption peaks could be discerned, yielding a rather complex pattern. The initial potential for oxidation of bromine was found to depend significantly on the type of hydrocarbon used as the solvent; decreasing from benzene to mesitylene with increasing chemical rate constant for the bromination of the hydrocarbon (24).

In the present work the kinetics of electrooxidation of I⁻ on platinum electrodes and the subsequent chemical reactions of the I₂ produced in this solvent system were investigated.

Experimental

The cell, electrodes, and electrochemical equipment employed for measurements of cyclic voltammograms were described in a previous publication (21). Steady-state Tafel plots were measured with the same setup, in which the function generator was replaced by a "first drop" polarographic unit (homemade), triggered by a Radiometer Type DLT-1 drop-life timer. This unit provides potential steps of increasing amplitude (6 mV increments) and adjustable length. The pulse width was set to 30 sec. This was found to be long enough for the current to reach its steady-state value in all ranges of potential and concentration studied. Between pulses the potential was held for an equal

length of time at its initial value, where no Faradaic reaction took place. The solutions were stirred gently with a magnetic stirrer during these measurements.

For the determination of *n*, the number of electrons taking part in the over-all reaction, a large platinum gauze working electrode was used in order to decrease the time required for electrolysis.

All experiments were performed in rigorously dried and purified solutions, inside a glove box filled with purified argon. Details were given in earlier publications (16, 19, 21).

Results

Cyclic voltammetry.—A typical set of voltammograms taken at different concentrations of KI, employing benzene as the solvent, is shown in Fig. 1. The function *i*/*C*⁰ is plotted in this figure against the potential to eliminate the trivial effect of concentration. The influence of the solvent on the shape of the voltammogram is seen in Fig. 2. The peak potentials on the anodic and the cathodic sweeps are plotted as a function of log *v* (*v* ≡ *dE*/*dt*) in Fig. 3 and 4, respectively. Simple behavior is observed in Fig. 3 when benzene or mesitylene are used as the solvent, while ethyl benzene and *o*-xylene exhibit anomalous behavior, particularly at low concentrations of KI. On the cathodic sweep no reduction peak occurred when

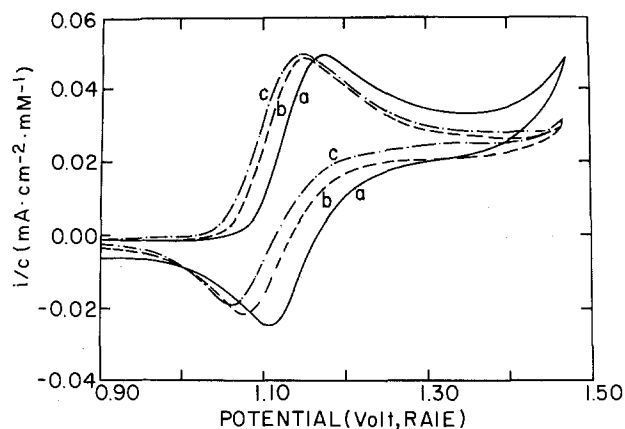


Fig. 1. Cyclic voltammograms for different concentrations of KI in a solution of 1.0M Al₂Br₆ and 0.8M KBr in benzene, taken at *v* = 12.5 mV/sec. Curve a, 2.0 mmoles; curve b, 11.8 mmoles; curve c, 37.5 mmoles.

* Electrochemical Society Active Member.

Key words: oxidation, bromination, voltammograms.

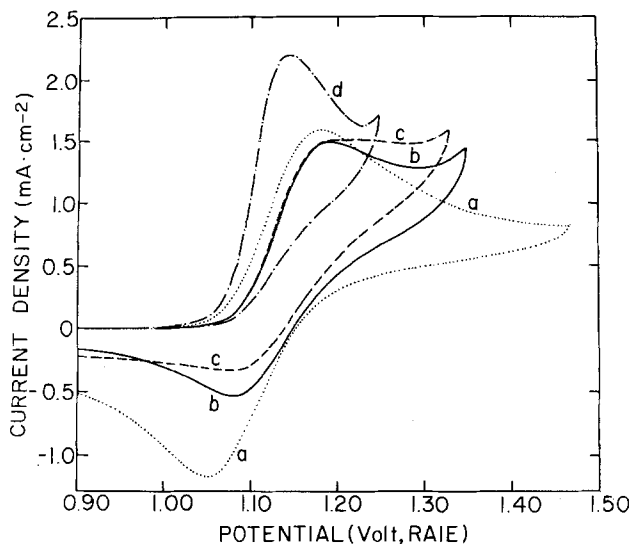


Fig. 2. The influence of the solvent on the shape of the voltammogram. $C_{KI} = 11.8$ mmoles, $v = 120$ mV/sec. a, Benzene; b, ethyl benzene; c, o-xylene; d, mesitylene.

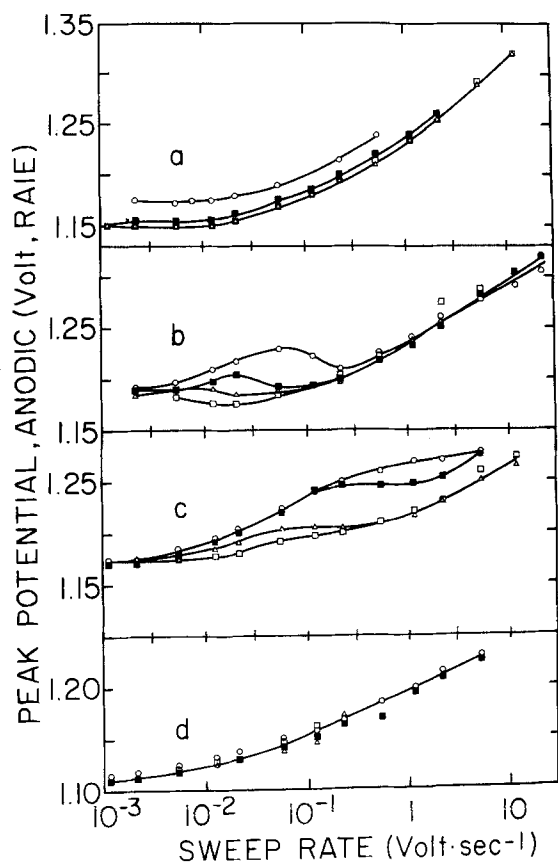


Fig. 3. The peak potential on the anodic sweep, E_p (a), as a function of $\log v$ for: a, benzene; b, ethyl benzene; c, o-xylene; d, mesitylene. C_{KI} : $\circ\circ\circ$, 2.0 mmoles; $\blacksquare\blacksquare\blacksquare$, 5.9 mmoles; $\triangle\triangle\triangle$, 11.8 mmoles; $\square\square\square$, 26.8 mmoles.

mesitylene was employed as the solvent even at the highest sweep rates studied, showing that the iodine formed during the anodic sweep disappeared rapidly due to a chemical reaction. The anodic peak current i_p (a) was proportional to the concentration of KI in all four solvents.

The unusual behavior of o-xylene can be seen further in Fig. 5 in which the cathodic peak current i_p (c) is plotted against the sweep rate on a log-log scale for different concentrations of KI. As the concentration of KI increases the plots resemble more and more those obtained in benzene or ethyl benzene,

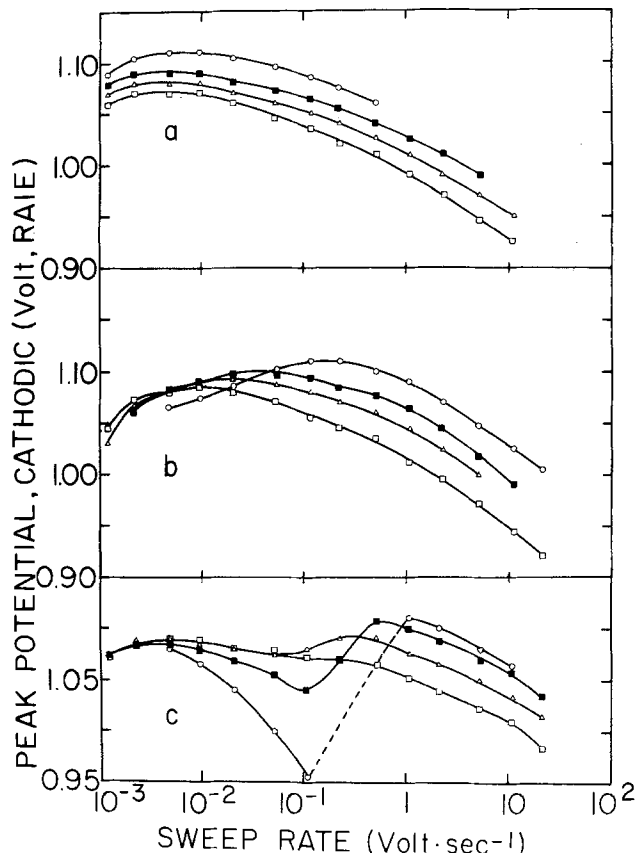


Fig. 4. The peak potential on the cathodic sweep, E_p (c), as a function of $\log v$ for: a, benzene; b, ethyl benzene; c, o-xylene. Concentrations of KI as in Fig. 3.

which are also given in the same figure for comparison.

Steady-state measurements.—Tafel plots determined at different concentrations of KI in ethyl benzene are shown in Fig. 6.¹ It can be seen that the lines are very closely parallel. The average value of the Tafel slope (based on measurements at eight concentrations of KI in ethyl benzene) was 34 ± 1 mV. The effect of the solvent on the slope is shown in Fig. 7. The Tafel slopes and reaction orders obtained in three solvents are given in Table I. All kinetic parameters were determined in the range of $i \leq 0.05i_L$ under essentially pure activation control. In the limiting current region the reaction order was unity in all the solvents studied.

The over-all reaction.—Early experiments in cyclic voltammetry have already indicated that only part of the iodine produced during the anodic sweep was available for reduction in the following cathodic sweep, the rest being consumed in a chemical reaction. If this chemical reaction leads to regeneration of I^- ,² one should observe an increase in the apparent value of n , the number of electrons taking part in the over-all reaction. This quantity was determined by setting the potential to a value in the limiting current region and following the decrease of current with time. Since the limiting current is proportional to the concentration, it is easy to show (25) that the current will decrease with time following the equation

$$I(t) = I^\circ \exp(-I^\circ/nFC^\circ V)t \quad [1]$$

where V is the volume of the solution, C° the initial concentration, and I° the total current extrapolated back to zero time. The parameter n is determined from the slope of a plot of $\log I$ vs. t . Such plots are shown in Fig. 8 for benzene and ethyl benzene as the

¹ For the sake of clarity only one out of three experimental points are shown in this figure.

² It will be shown below that this is indeed the case.

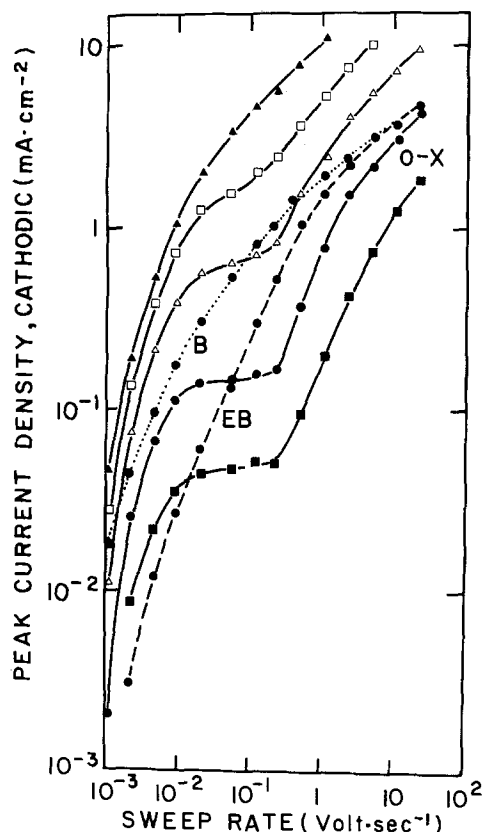


Fig. 5. Plots of $\log i_p$ (c) vs. $\log v$ in o-xylene. C_{KI} : ■■■, 4.0 mmoles; ●●●, 7.9 mmoles; △△△, 19.4 mmoles; □□□, 37.5 mmoles; ▲▲▲, 80 mmoles. Broken lines are for 7.9 mmoles KI in: ··· benzene; --- ethyl benzene.

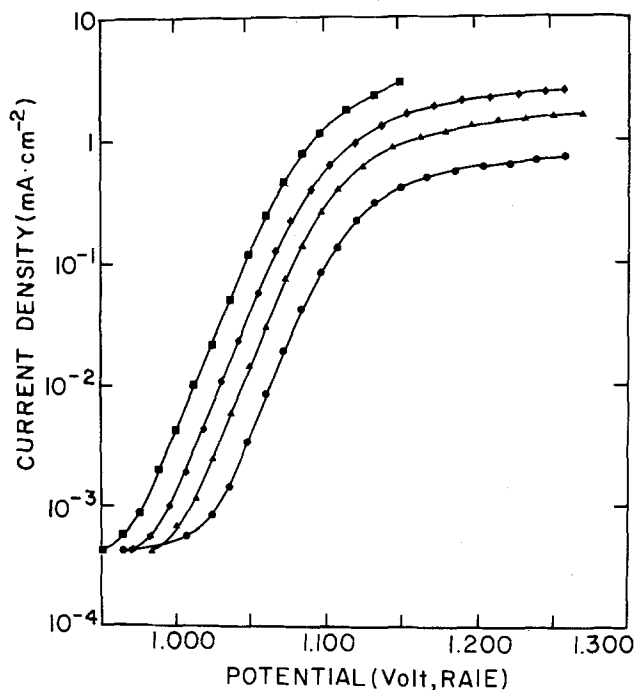


Fig. 6. Steady-state Tafel plots in ethyl benzene. C_{KI} : ●●●, 11.8 mmoles; ▲▲▲, 26.8 mmoles; ◆◆◆, 54.5 mmoles; ■■■, 120 mmoles.

solvent. In both solvents $n > 1$ and increases with time, as would be expected for a catalytic process following charge transfer, in which the reactant is regenerated. The calculated values of n at different intervals of time after electrolysis was started are shown in Table II. When mesitylene was employed as the solvent, the apparent value of n approached infinity, i.e., the current did not decrease with time.

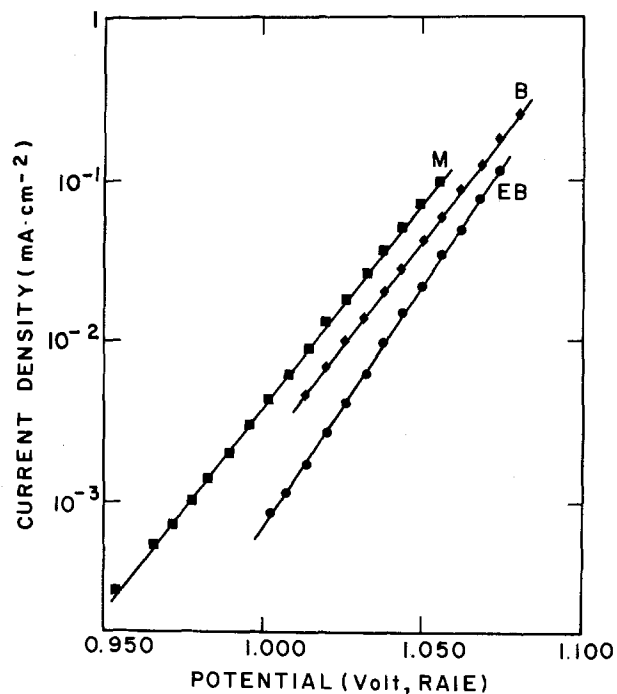


Fig. 7. The effect of the solvent on the steady-state Tafel plots $C_{KI} = 37.5$ mmoles.

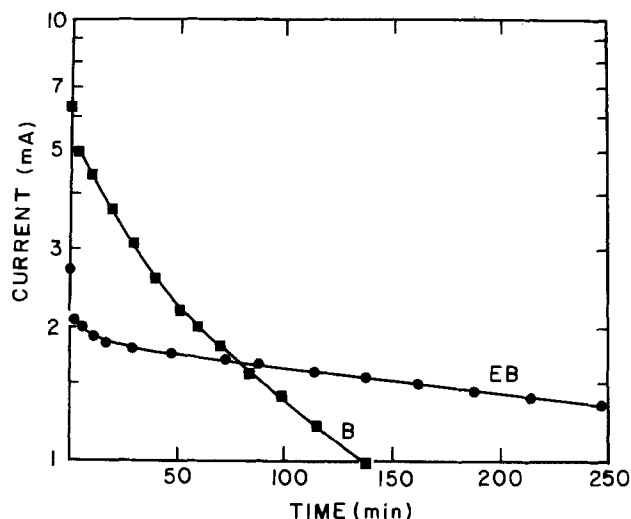


Fig. 8. Plots of $\log I$ vs. t during constant potential electrolysis $C_{KI} = 20.5$ mmoles; $E = 1.12V$, (RAIE).

The reaction of molecular iodine.—Following the experiments described above it was of interest to determine whether the chemical step following electro-

Table I. Kinetic parameters from steady-state measurements

Solvent	Tafel slope (mV)	Reaction order
Benzene	39 ± 3	1.6 ± 0.1
Ethyl benzene	34 ± 1	1.4 ± 0.1
Mesitylene	40 ± 1	1.1 ± 0.1

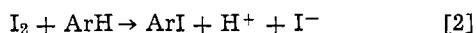
Table II. The apparent value of n in two solvents

Time interval (min)	% of initial current	Solvent	Apparent n
4-40	77-41	Benzene	1.3
55-140	33-16	Benzene	2.9
2-17	77-69	Ethyl benzene	1.6
25-250	67-50	Ethyl benzene	8.1

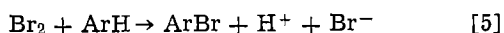
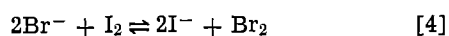
chemical oxidation of I^- was a bulk reaction in which molecular iodine took place or a reaction requiring an electrochemically formed intermediate, which could only occur at the electrode surface. For this purpose a solution of I_2 in the pure solvent was added to another solution containing 1.0M Al_2Br_6 and 0.80M KBr in the same solvent, and the change of concentration of iodine with time was followed by standard analytical methods. In a typical experiment the initial concentration of I_2 was 28 mmoles. After four days at room temperature it decreased to 19 mmoles in benzene and to 5 mmoles in mesitylene. These experiments were performed in a cell which had no electrodes in it, confirming that the chemical reaction in which iodine is consumed can occur in the bulk. The possibility that it can occur faster on the electrode surface in the presence of electrochemically formed intermediate cannot be excluded, however.

Discussion

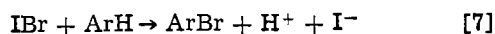
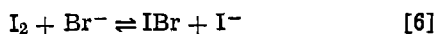
General.—The results presented above show that iodine formed electrochemically or introduced into a solution containing Al_2Br_6 and KBr in an aromatic hydrocarbon undergoes a chemical reaction. The rate of this reaction increases with increasing rate of bromination of the hydrocarbon (21, 24). This is best seen in Fig. 2, where the ratio of cathodic to anodic peak currents decreases as the initial potential for bromine evolution becomes less anodic.³ The fact that the apparent value of n , the number of electrons taking part in the over-all reaction, is larger than unity shows that I^- is regenerated in this chemical reaction. Direct iodination of the aromatic hydrocarbon in a reaction of the type



could fit these experimental observations. However, it is well known that iodination of aromatic hydrocarbons does not occur under the conditions of the present experiment. It is more likely that bromination will take place in a reaction sequence such as



In aqueous solutions this reaction sequence could not proceed since it implies that Br^- is oxidized by I_2 although the oxidation potential for the Br^-/Br_2 couple is about half a volt higher than that of the I^-/I_2 couple. In the present system, however, the reversible potentials for different redox couples were shown to be much closer (17, 18, 23). Thus the initial potentials of I_2 and Br_2 evolution⁴ are 1.15 and 1.45V (RAIE), respectively, if benzene is used as the solvent. In mesitylene the corresponding values are 1.11 and 1.21V (RAIE). Moreover, the reaction sequence given above could be substituted by

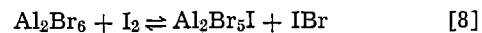


Iodobromine is formed at a potential lower than that required for the formation of Br_2 (26, 27). Thus steps [4] and [6] will not be shifted completely to the left in the present system and bromination of the hydrocarbon may be expected to occur at a significant rate. It may be noted that free Br^- and I^- ions do not exist

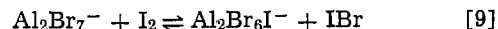
³ It was shown in a previous publication (21) that the initial potential for bromine evolution decreases with increasing rate constant for bromination of the hydrocarbon.

⁴ The initial potentials are used here instead of the half-wave potentials or the formal potentials which were not determined. It is reasonable to assume that the difference in the initial potentials of the two redox couples is close enough to the difference in their half-wave potentials for the purpose of the qualitative argument given above.

in this system (22, 23) and more complex equilibria of the type



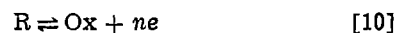
or



are probably involved. Since the exact nature of the negative ion is not important for the subsequent arguments, nor is it exactly known, the simple ions will be written in all further equations for brevity.

It may be concluded that electrochemical oxidation of iodide in the presence of a large excess of bromide is followed by formation of IBr or Br_2 and regeneration of I^- , along with bromination of the hydrocarbon. If mesitylene is used as the solvent the bromination reaction is so fast that all of the iodine formed is rapidly reduced back to I^- . As a result a cathodic peak cannot be observed on the voltammogram even at high sweep rates, and the apparent value of n tends to infinity. The bromination of benzene occurs several orders of magnitude more slowly. Therefore, the ratio of cathodic to anodic peak currents approaches unity at high sweep rates and n is only slightly higher than unity at short electrolysis times. The behavior of other hydrocarbons such as ethyl benzene and *o*-xylene falls between these two extremes.

Analysis of the cyclic voltammograms.—A detailed mathematical analysis of the shape of the voltammograms for reversible and irreversible electrochemical reactions, preceded or followed by chemical reactions, was given by Nicholson and Shain (28). One of the diagnostic criteria proposed by these authors is a plot of the "current function" $i_p(a)/C^0v^{1/2}$ against the sweep rate v .⁵ This is shown in Fig. 9 for the four solvents studied. For a simple charge transfer process this function should be independent of sweep rate. The behavior shown in Fig. 9 is consistent, according to Nicholson and Shain (28), with either reversible or irreversible charge transfer followed by an irreversible chemical reaction which regenerated the reactant, according to the formal scheme



⁵ In the original paper the current function is defined as $i_p/nFC^0v^{1/2}D^{1/2}$. For a given system this only differs from the function employed here by a constant factor.

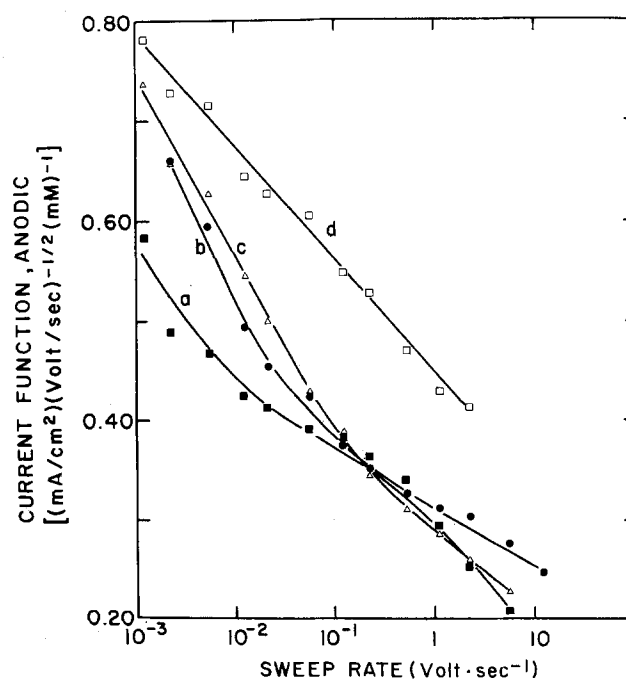


Fig. 9. Plots of the "current function," $i_p(a)/v^{1/2} C^0$, against $\log v$ in four solvents at $C_{KI} = 7.9$ mmoles. Curve a, benzene; curve b, ethyl benzene; curve c, *o*-xylene; curve d, mesitylene.



In the present system this would correspond to step [3] followed by steps [4] and [5] (or [6] and [7]) combined.⁶

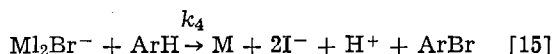
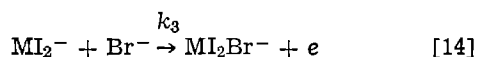
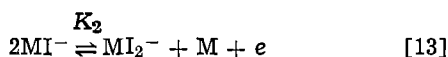
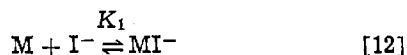
A similar case in which charge transfer is preceded by adsorption of the reactant was also treated mathematically (29). It was shown that the "current function" should increase with increasing rate constant of the chemical step following charge transfer. It can be seen in Fig. 9 that the "current function" is highest for mesitylene and lowest for benzene, which is to be expected if bromination of the solvent is involved in the chemical step following charge transfer.

It may be noted (cf. Fig. 2) that the anodic peak current for mesitylene is significantly higher and occurs at a less anodic potential than for the other three solvents. This shows that the chemical reaction following charge transfer is too slow to effect significantly the concentration of I₂ and regenerate a noticeable amount of I⁻ during the anodic sweep in all cases except when mesitylene is used as the solvent.

In conclusion it can be seen that the oxidation of iodide and subsequent bromination of the solvent in the present system is a complex process, and only qualitative conclusions can be drawn from cyclic voltammetry. It appears that: (i) the reactant (I⁻) is adsorbed on the surface, (ii) the product (I₂) reacts further chemically, (iii) the reactant is regenerated in this chemical reaction, and (iv) the rate of the chemical reaction depends strongly on the solvent in the order: mesitylene >> o-xylene > ethyl benzene > benzene.

Steady-state measurements.—Tafel plots obtained under steady-state conditions are shown in Fig. 6 and 7. The Tafel slopes and reaction orders (with respect to KI) are given in Table I. Several closely related mechanisms can give rise to the observed kinetic parameters and are also consistent with other experimental findings, namely the regeneration of I⁻ in the chemical reaction following charge transfer and the order of reactivity of the solvent molecules. One of these mechanisms will be treated in detail below.

The reaction pathway.—Consider the reaction sequence given in the following equations



where M represents a site of the surface, and from the condition of quasi-equilibrium in step [12] one has

$$\frac{\theta_{\text{MI}^-}}{1 - \theta} = K_1 C_{\text{I}^-} \exp - g(\theta) \quad [16]$$

in which the function $g(\theta)$ is the rate of change of the apparent standard free energy of adsorption with coverage

$$g(\theta) \equiv \partial \Delta G^\circ_{\text{ads}} / \partial \theta \quad [17]$$

and θ without a subscript is the sum of the fractional coverage by all adsorbed species. At intermediate values of the coverage, where the Temkin isotherm applies, Eq. [16] can be written approximately (30, 31) as

$$\exp g(\theta) = K_1 C_{\text{I}^-} \quad [18]$$

similarly for quasi-equilibrium in step [13] one has

$$\frac{\theta_{\text{MI}_2^-}}{\theta_{\text{MI}^-}^2} = K_2 \exp (\Delta \phi F / RT) \exp g(\theta) \quad [19]$$

Note that the sign of the function $g(\theta)$ in the exponent is negative in Eq. [16] and positive in Eq. [19]. This arises because step [12] is an adsorption step, which is slowed down as the surface coverage increases while step [13] is a desorption step which is enhanced by increasing the coverage.

The mechanism in mesitylene.—Assume that step [14] in the above reaction sequence is the rate-determining step. The rate equation will be

$$v_3 = k_3 \theta_{\text{MI}_2^-} C_{\text{Br}^-} \exp (\beta \Delta \phi F / RT) \quad [20]$$

If coverage is mainly by I⁻, i.e., $\theta_{\text{MI}^-} \sim \theta$ and $\theta_{\text{MI}_2^-} \ll \theta_{\text{MI}^-}$, we can rewrite the rate equation combining Eq. [18]–[20] as

$$v_3 = k'_3 C_{\text{Br}^-} C_{\text{I}^-} \exp [(1 + \beta) \Delta \phi F / RT] \quad [21]$$

where k'_3 is a combined constant and the change of the pre-exponential term in θ_{MI^-} has been neglected compared to the change in $\exp g(\theta)$ over the potential region where a linear Tafel plot is observed (30, 31). Equation [21] corresponds to a reaction order (ρ_{I^-}) of unity with respect to KI and a Tafel slope of

$$b = 2.3RT / (1 + \beta) F \sim 40 \text{ mV} \quad [22]$$

in excellent agreement with the observed values of $b = 40 \pm 1 \text{ mV}$ and $\rho_{\text{I}^-} = 1.1 \pm 0.1$ given in Table I. Bromination of mesitylene occurs very rapidly (21, 24) and thus step [15] could not be rate determining when this solvent is employed.

The mechanism in ethyl benzene.—The rate of bromination of ethyl benzene is much slower than that of mesitylene and this process (i.e., step [15]) may reasonably be expected to become rate determining. The resulting rate equation will be

$$v_4 = k_4 \theta_{\text{MI}_2\text{Br}^-} C_{\text{ArH}} \exp [ag(\theta)] \quad [23]$$

In this case step [14] can be regarded at quasi-equilibrium, yielding

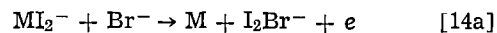
$$\frac{\theta_{\text{MI}_2\text{Br}^-}}{\theta_{\text{MI}_2^-}} = K_3 C_{\text{Br}^-} \exp (\Delta \phi F / RT) \quad [24]$$

substituting $\theta_{\text{MI}_2\text{Br}^-}$ in Eq. [23] from Eq. [24] and combining with Eq. [18] and [19]; assuming that I⁻ is still the main species on the surface and its adsorption follows the Temkin isotherm at intermediate values of coverage; lead to

$$v_4 = k'_4 C_{\text{Br}^-} C_{\text{I}^-}^{(1+\alpha)} \exp (2\Delta \phi F / RT) \quad [25]$$

Equation [25] leads to a Tafel slope of 30 mV and a reaction order of 1.5 in good agreement with the values of $b = 34 \pm 1 \text{ mV}$ and $\rho_{\text{I}^-} = 1.4 \pm 0.1$ found experimentally (cf. Table I).

The mechanism in benzene.—In this solvent the rate of bromination is very slow and step [15] does not occur to a sufficient extent to effect the observed kinetic parameters. If the species I₂Br⁻ (which is stable in solution) is not removed from the surface by subsequent reaction with the solvent (as in the previous two cases) it may be expected to leave the surface in the oxidation step itself, leading to a slightly modified form of step [14],⁷ namely



If this step is assumed to be rate determining, the rate equation will take the form

$$v'_3 = k_3 \theta_{\text{MI}_2^-} C_{\text{Br}^-} \exp (\beta \Delta \phi F / RT) \exp [ag(\theta)] \quad [26]$$

⁷This step may occur to some extent in the case of ethyl benzene leading to a slightly increased Tafel slope.

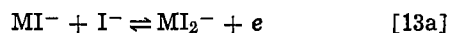
⁶A scheme in which the irreversible chemical reaction following charge transfer does not regenerate the reactant would also lead to a similar dependence of the "current function" on sweep rate, but this is excluded on the basis of the other experimental evidence discussed above.

Combining Eq. [26] with Eq. [18] and [19] and making the same assumptions with respect to coverage by the different intermediates as in the above two cases we have

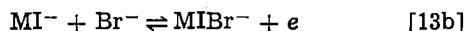
$$v_3 = k_3 C_{Br} - C_{I^{-(1+\alpha)}} \exp [(1 + \beta) \Delta \phi F / RT] \quad [27]$$

This leads to a Tafel slope of $2.3 RT / (1 + \beta) F \sim 40$ mV and a reaction order of $(1 + \alpha) \sim 1.5$ in excellent agreement with the experimentally observed values of $b = 39 \pm 3$ mV and $\rho_{I^-} = 1.6 \pm 0.1$ shown in Table I.

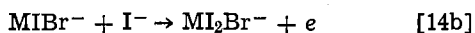
Alternative mechanisms.—Small variations in the above reaction sequence can lead to the same kinetic parameters and hence cannot be distinguished on the basis of the experimental results available. These include replacement of step [13] by



all other steps being unchanged. Similarly, replacing step [13a] by



followed by



does not affect the kinetic parameters. These, however, are only minor variations of the basic reaction sequence which involves: (i) adsorption of I^- , (ii) oxidation to MI_2^- or $MIBr^-$, (iii) further oxidation to MI_2Br^- , and (iv) bromination of the hydrocarbon and regeneration of I^- . The first two steps are fast and the third or fourth steps are rate determining, depending on the ease of bromination of the aromatic solvent.

Conclusions

The oxidation of iodide in a solution of Al_2Br_6 and KBr in aromatic hydrocarbons proceeds with initial adsorption of I^- on the electrode surface. The iodine formed reacts partially with Br^- or other bromide-containing species such as $Al_2Br_7^-$ to form Br_2 or IBr which react with the aromatic solvent to brominate it. This unusual process of oxidation of Br^- by iodine is possible because of the small differences in the standard potentials of different redox couples in this solvent system, as discussed earlier (17, 18, 23). Iodide is regenerated in the chemical reaction following its electrochemical oxidation to iodine. Reduction of iodine and bromination of the solvent can occur also as a chemical bulk reaction, although it is probably catalyzed by the electrochemical pathway. The qualitative mechanistic information obtained from analysis of the cyclic voltammograms is confirmed by considering the Tafel slopes and reaction orders measured under steady-state conditions.

Manuscript submitted June 27, 1979; revised manuscript received Nov. 1, 1979.

Any discussion of this paper will appear in a Discussion Section to be published in the December 1980 JOURNAL. All discussions for the December 1980 Discussion Section should be submitted by Aug. 1, 1980.

REFERENCES

- V. A. Plotnikov, I. A. Sheka, and V. A. Yankelevich, *J. Gen. Chem. USSR*, **3**, 481 (1933).
- E. Ya. Gorenbein, *Univ. Etat. Kiev, Bull. Sci. Rec. Chim.*, **1**, 101 (1935).
- V. A. Plotnikov and S. I. Yakubson, *J. Gen. Chem. USSR*, **6**, 1690 (1936).
- V. A. Plotnikov and E. Ya. Gorenbein, *ibid.*, **7**, 372 (1937).
- V. A. Plotnikov, I. B. Barmashenko, and E. B. Gitman, *Mem. Inst. Chem. Acad. Sci. Ukr. SSR*, **5**, 3 (1938).
- E. Ya. Gorenbein, *J. Gen. Chem. USSR*, **9**, 2041 (1939).
- V. A. Plotnikov and S. I. Yakubson, *Z. Physik. Chem. Lit.*, **A147**, 227 (1930).
- V. A. Yankelevich and I. A. Sheka, *Mem. Inst. Chem. Acad. Sci. Ukr. SSR*, **5**, 59 (1938).
- V. A. Plotnikov and A. T. Dibrova, *Zapiski Inst. Khim. Acad. Sci. USSR*, **7**, 337 (1940).
- L. Simanavicius and A. Karpavichyus, *Lietuvos TSR Mokslu Akad. Darbai, Ser. B*, **83**, 1 (1971).
- L. Simanavicius, A. Karpavichyus, and P. Dobrovolskis, in "Electrodeposition of Metals," Proceedings of IVth Lithuanian Conference on Electrochemistry, Israel Program for Scientific Translations (1970).
- G. A. Capuano and W. G. Davenport, *This Journal*, **118**, 1688 (1971).
- G. A. Capuano and W. G. Davenport, *Plating*, **60**, 251 (1973).
- E. Peled and E. Gileadi, *ibid.*, **62**, 342 (1975).
- E. Peled and E. Gileadi, *This Journal*, **123**, 15 (1976).
- A. Reger, E. Peled, and E. Gileadi, *ibid.*, **123**, 638 (1976).
- E. Peled, A. Mitavski, and E. Gileadi, *Z. Phys. Chem.*, **96**, 111 (1976).
- E. Peled, A. Mitavski, A. Reger, and E. Gileadi, *J. Electroanal. Chem. Interfacial Electrochem.*, **75**, 677 (1977).
- S. Ziegel, E. Peled, and E. Gileadi, *Electrochim. Acta*, **23**, 363 (1978).
- S. Ziegel, E. Peled, and E. Gileadi, *ibid.*, **24**, 513 (1979).
- M. Elam and E. Gileadi, *This Journal*, **126**, 1474 (1979).
- A. Reger, E. Peled, and E. Gileadi, *J. Phys. Chem.*, **83**, 869, 873 (1979).
- E. Gileadi, in "Proceedings of 3rd Symposium on Electrode Processes," E. B. Yeager, Editor, The Electrochemical Society Softbound Proceedings Series, To be published.
- L. J. Andrews and R. M. Keefer, *J. Am. Chem. Soc.*, **78**, 4540 (1956).
- E. Gileadi, E. Kirowa-Eisner, and J. Penciner, "Interfacial Electrochemistry—An Experimental Approach," pp. 60-62, Addison-Wesley Publishing Co., Reading, Mass. (1975).
- A. I. Popov and D. H. Geske, *J. Am. Chem. Soc.*, **80**, 5346 (1958).
- G. Dryhurst and P. J. Elving, *Anal. Chem.*, **39**, 606 (1967).
- R. S. Nicholson and I. Shain, *ibid.*, **36** 706 (1964).
- R. H. Wopschall and I. Shain, *ibid.*, **39**, 1535 (1967).
- B. E. Conway and E. Gileadi, *Trans. Faraday Soc.*, **58**, 2493 (1962).
- E. Gileadi and B. E. Conway, in "Modern Aspects of Electrochemistry," Vol. III, J. O'M. Bockris and B. E. Conway, Editors, chap. 5, Butterworths, London (1964).

Galvanostatic Transients in Lutetium Diphthalocyanine Films

M. M. Nicholson* and F. A. Pizzarello

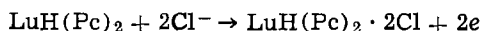
Rockwell International, Electronics Research Center, Anaheim, California 92803

ABSTRACT

The anodic oxidation of lutetium diphthalocyanine films on tin oxide in 1M KCl was investigated by a galvanostatic transient technique. The reaction was monitored by simultaneous measurement of the optical transmission. At current densities of 0.3-6 mA/cm², the kinetics was controlled by an ionic space charge in the red oxidation product. A dielectric constant of 10 was estimated for this material, using the solid-state mobility of the chloride ion determined in a previous moving-boundary study.

A rare earth diphthalocyanine film in contact with an aqueous electrolyte undergoes a series of faradaic reactions that cause pronounced color changes. The dependence of color on potential was first reported by Moskalev and Kirin, who examined a film of lutetium diphthalocyanine [LuH(Pc)₂] on a tin oxide electrode of unspecified resistance (1, 2). The electrolyte was 0.1M KCl. We subsequently investigated this system for electrochromic display applications (3, 4). It was found that the color changes could occur in milliseconds under potentiostatic pulses when the substrate resistivity was approximately 10 Ω/square. This is a fast response for an electrode process converting one insoluble organic material to another as a layer about 50 molecules thick.

A lutetium diphthalocyanine film is initially green. It can assume four or five discrete color forms, depending on the oxidation state of the complex. To account for the fast electrode kinetics, we proposed that all of these forms were electrically conductive in the solid state. NdH(Pc)₂ was already known to be an electronic conductor (5). In a recent study by a moving-boundary technique, we showed that the red oxidation product of LuH(Pc)₂ prepared with a potassium chloride or a sodium sulfate electrolyte was also conductive (6). Those experiments were performed with the dye film on an insulating alumina substrate instead of tin oxide. Only the end of the film was immersed in the electrolyte. Under constant applied current, a red/green boundary generated at the electrolyte contact travelled upward along the dry film a distance of several millimeters. The experiments took about two hours because the film resistance was high in the direction of current flow. The charges used in the coloring process corresponded approximately to a 2-electron oxidation of LuH(Pc)₂ in both electrolytes. Carrier concentrations and mobilities determined in the oxidation products suggested that the red materials were solid anion conductors. For a chloride solution contact, the proposed reaction was



The chloride ions which entered the solid to compensate the lost electrons then remained as charge carriers with a room temperature mobility of 4×10^{-6} cm²/Vsec. A later investigation with radioactive chloride confirmed the presence of the anion in the red film at a ratio of approximately 1.5 anions to one molecule of dye (7). Thus the proposed oxidation mechanism was verified.

This paper reports a kinetic investigation of the same electrode process on tin oxide in 1M KCl by a galvanostatic pulse technique. The electrode potential and the optical transmittance of the film were monitored simultaneously during the pulse. Since the film was completely immersed in the electrolyte and the

direction of current flow was perpendicular to the film surface, the color conversion was completed in times ranging from milliseconds to seconds. The transients are discussed in relation to several physical models for the rate-controlling process. It will be seen that the data for current densities up to 6 mA/cm² conform to equations based on control by an ionic space charge in the dye film.

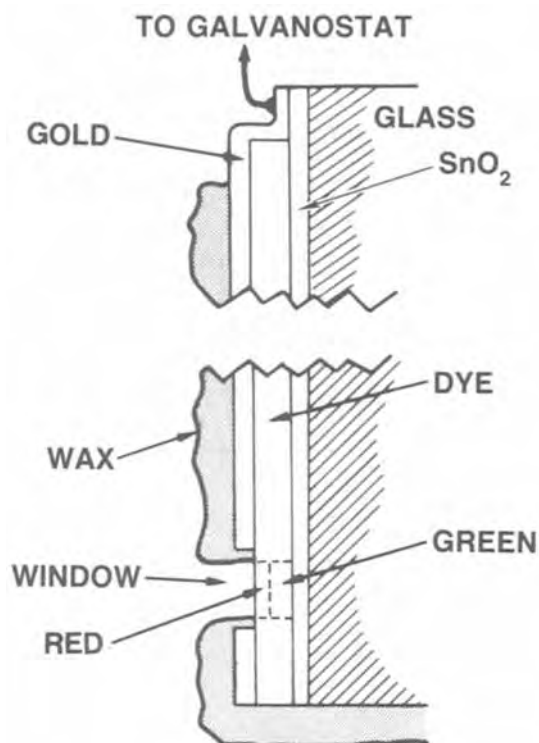
Experimental

Working electrodes were prepared by vacuum sublimation of lutetium diphthalocyanine dye onto a Corning tin oxide-glass substrate (6). The tin oxide layer, which was produced chemically by a fog process, had a sheet resistivity of 10-15 Ω/square. The weight of dye per unit area and the approximate film thickness were determined from the optical density in the initial green state at the absorption maximum near 670 nm (3). The dye was deposited over the entire front surface of a 1.25 × 5 cm tin oxide plate. An active electrode area within this plate was defined and electrically contacted in two different ways. For initial experiments, a metal contact was made at the top of the plate, and most of the area below was insulated from the electrolyte by Apiezon W wax applied directly over the dye. A window of dye about 1.5 cm² in area remained exposed near the lower end. This electrode is designated as one with an upper SnO₂ contact. A lower resistance working electrode was needed for more detailed transient studies. Its structure is shown in Fig. 1(a). In this case, a gold film was sputtered over the dye surface, leaving only a window approximately 0.6 × 1.0 cm for the active area. Apiezon W was applied on top of the gold, except for a strip at the upper end of the plate, which served as the electrical contact. This electrode is identified as one with a peripheral Au contact. The estimated series resistance in the tin oxide was 3-6Ω with the peripheral contact and 25-35Ω with the upper SnO₂ contact.

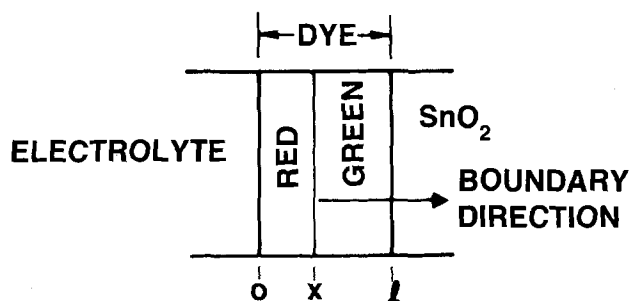
The reference and counterelectrodes were both Ag/AgCl strips prepared by anodizing porous silver in 1M KCl. The porous silver was obtained by thermally decomposing a layer of Ag₂O that had been spread on a silver ribbon approximately 0.5 cm wide.

For the electro-optical measurements, the electrodes were assembled in a flat-sided glass Klett colorimeter cell containing air-saturated 1M KCl. The cell and instrumentation were arranged as shown in Fig. 2. The light source was a tungsten-filament microscope lamp operated with a regulated d-c power supply. Between the source and the cell was a Bausch and Lomb high-intensity monochromator, Kaelite Corporation Model 7400PR, set at 670 nm. The transmitted light was monitored with an EG&G silicon photodetector having a rise and decay time of 100 nsec. To minimize extraneous electrode processes, the PAR 173 galvanostat was programmed to provide a single current pulse only slightly longer than the time required to complete the green-to-red transformation. The potential of the working electrode and the output of the photodetector

* Electrochemical Society Active Member.
Key words: diphthalocyanines, kinetics, space charge, mobility, electrochromism.



(a) SCHEMATIC CROSS SECTION



(b) ENLARGED VIEW OF WINDOW REGION

Fig. 1. Working electrode

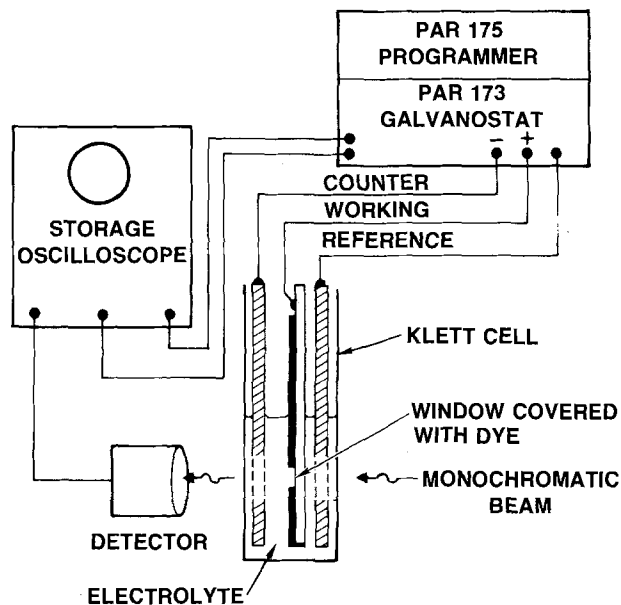


Fig. 2. Apparatus

were recorded simultaneously during the pulse on a Tektronix 564B dual-trace storage oscilloscope equipped with a Polaroid camera. After each pulse, the working electrode was returned to the Ag/AgCl potential in 1M KCl by manually shorting it to the counterelectrode. The color thereupon returned to a green shade.

Results and Discussion

The data and results are summarized in Table I. Transients recorded for both types of electrode structures are shown in Fig. 3. At current densities up to 66 mA/cm², the voltage curve had a transition typical of a material depletion process. Since the optical transmission reached a maximum level at about the same time, it can be surmised that the transition marked the end of the dye reaction. Curves of the type shown in Fig. 3(a), for a peripheral-contact electrode at relatively low current density, were amenable to detailed interpretation. The electrical transition time τ_{elec} was measured from the beginning of the stored oscilloscope trace to the intersection point of tangents drawn to the sloping and final plateau portions of the curve. Under conditions of Fig. 3(b), the ohmic effect in the tin oxide was much larger and probably time-dependent due to nonuniformity of the current density

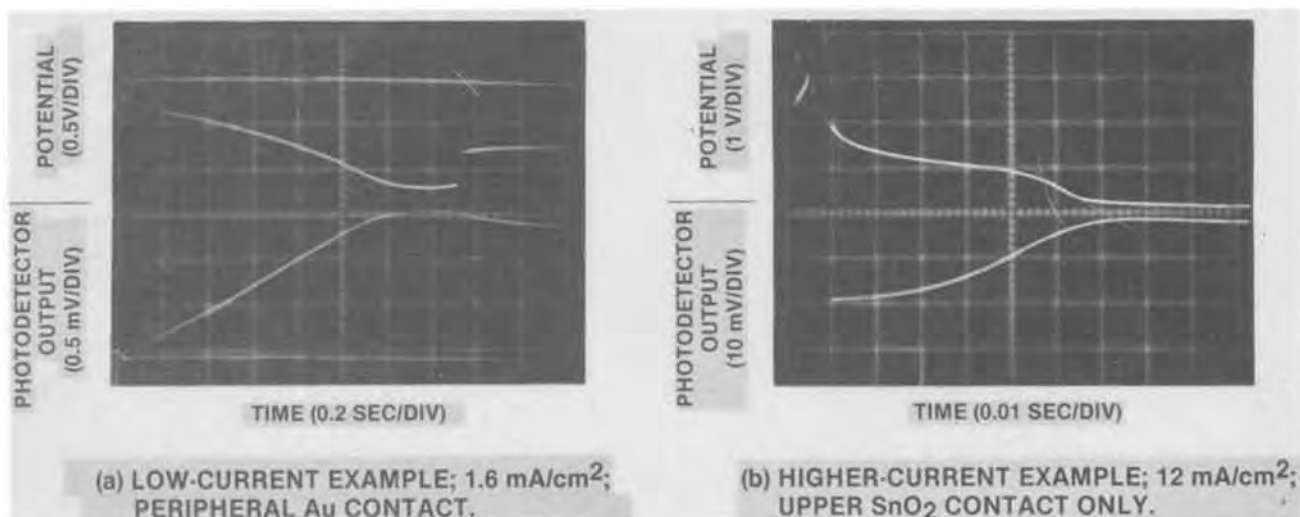


Fig. 3. Oscilloscope traces of electrical and optical transients at constant current densities

Table I. Galvanostatic transient data for LuH(Pc)₂ in 1M KCl

Electrode	Area (cm ²)	D _{init}	I (A/cm ²) × 10 ³	τ _{opt} (sec)	τ _{elec} (sec)	n _{eff} ^a	Slope of (ΔE/I ²) vs. t ^{3/2} (V · cm ⁴ /A ² · sec ^{3/2}) × 10 ⁻⁶	κ μ ₁ (cm ² /Vsec) × 10 ⁵
1 ^b	0.65	1.20	0.31	3.8	4.2	0.84	0.63	3.9
			0.46	2.2	2.5	0.74		
			0.77	1.2	1.5	0.70		
			1.54	0.70	0.75	0.67		
			6.2	0.17	0.16	0.80		
						0.78		
			Avg 0.77	Avg 0.58				
2 ^b	0.63	1.34	0.32	9.6	9.8	2.0	0.17	4.3
			0.64	4.1	4.7	1.3	0.18	
			0.95	2.2	2.4	1.4	0.22	
			1.27	1.75	2.0	1.5	0.18	
			1.59	1.04	1.20	1.7	0.27	
			3.2	0.75	0.75	1.6	0.14	
			Avg 1.5	Avg 0.19				
3 ^c	1.51	0.94	2.65	0.54	0.48	1.4	4.3	
			3.31	0.52	0.47	1.6		
			6.62	0.24	0.24	1.5		
			66.2	0.027	0.020	1.6		
			132	0.014	— ^d	1.7		
			199	0.009	—	1.6		
265	0.007	—	1.7					
			Avg 1.6					

^a From optical transition time.

^b Peripheral Au contact.

^c Upper SnO₂ contact only.

^d Electrical transition not discernible at very high current densities.

over the electrode surface (8). Although the transition time should have had its usual significance in such cases, the voltage curve was subject to distortion, and the optical curve may also have been influenced. In the following discussion, the optical response is first analyzed to determine the transition time, independent of that found electrically. The kinetics of the dye electrode process is then considered.

The optical transient.—The optical transient, represented by the lower curve in Fig. 3(a), was converted to linear form by application of Beer's law. Two models of the reacting film may be considered for this purpose.

In the first case, the reactant and product molecules are assumed to be uniformly mixed at the respective volume concentrations c_1 and c_2 in a film of constant thickness l . Then

$$c_1 + c_2 = c_0 \quad [1]$$

where c_0 is the initial concentration of dye in the film. If the corresponding molar extinction coefficients at the selected wavelength are e_1 and e_2 , the total optical density D of the film at a time t following application of the current is given by

$$D = (e_1 c_1 + e_2 c_2) l \quad [2]$$

From Eq. [1] and [2]

$$dD/dt = (e_2 - e_1) l \cdot dc_2/dt \quad [3]$$

Since dc_2/dt is constant at constant current density, dD/dt is also constant, and the optical density at time t may be expressed as the linear function

$$D = e_1 c_0 l + (dD/dt) t \quad [4]$$

where $e_1 c_0 l$ is the optical density of the film before the current is applied.

The second model is that of two optical filters in series. This corresponds to the case in which a sharp reaction boundary moves through the film in the direction of current flow, as depicted in Fig. 1(b). Then the optical density of the film is given by

$$D = e_2 c_0 x + e_1 c_0 (l - x) \quad [5]$$

where x is the thickness of the converted layer. Hence

$$dD/dt = (e_2 - e_1) c_0 dx/dt \quad [6]$$

In the mixture model, the amount of dye converted in a time dt is expressed as $l dc_2$. In the moving-

boundary model, the same quantity of material is converted, but it is given by $c_0 dx$. Therefore, Eq. [3] and [6] can be reduced to the common form

$$dD/dt = 10^{-3} (e_2 - e_1) I / (nF) \quad [7]$$

where I is the magnitude of the current density in A/cm², n is the number of electrons transferred per molecule of dye, and F is the faraday. The uniform-mixture and moving-boundary cases therefore could not be distinguished on the basis of the optical data. The optical transient was used, however, to confirm the constancy of the color-conversion rate and to obtain an independent value of the transition time. The analysis is as follows.

It can be shown that the change in optical density of the cell at time t due to the dye reaction is given by

$$\log (T_\tau / T_t) = (t - \tau) dD/dt \quad [8]$$

where T_τ is the measured limiting intensity of transmitted light following the color transition at time τ , and T_t is the intensity in the interval $0 \leq t \leq \tau$. A plot of $\log (T_\tau / T_t)$ vs. t should therefore be a straight line with a slope equal to dD/dt in Eq. [7] and an intercept on the t -axis equal to the transition time.

An experimental plot of this type is shown in Fig. 4. The optical transition time τ_{opt} of 1.2 sec found by extrapolation is comparable to the electrical transition time τ_{elec} of 1.5 sec for the same experiment.

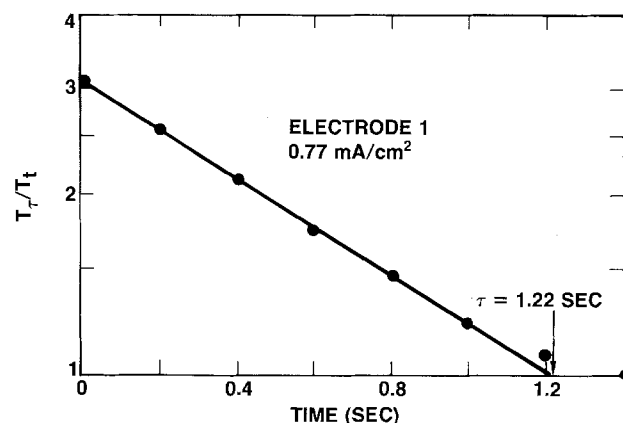


Fig. 4. Determination of optical transition time

The electrical transient.—Each potential-time curve began with a sharp rise that included terms due to the ohmic resistance of the electrode, any significant faradaic resistance, and any fast-charging capacitance in the electrode system. A thermodynamic potential arising from creation of a new red/green boundary within the organic solid would also be established at the outset of the conversion process. We shall not attempt to analyze the earliest part of the transient in this discussion. The primary objective is to account for the time dependence of potential as the reaction proceeds to completion. Five models are considered for the rate-controlling mechanism: concentration polarization in the liquid electrolyte, ionic charge transfer at the electrolyte/dye interface, a solid-solution film acting as a reversible couple, a two-layer film behaving as variable ohmic resistors in series, and a two-layer space-charge model.

Concentration change in electrolyte.—Since chloride ion is utilized in the faradaic reaction of the dye, the possibility of a significant voltage shift due to depletion of the anion in the liquid phase must be examined. This effect may be calculated from equations developed by Morris and Lingane for chronopotentiometry in the absence of a supporting electrolyte (9). In KCl, the concentration of chloride ion at an electrode surface where it is consumed is given by

$$C_{\text{Cl}^-}(0, t) = C_{\text{KCl}}^0 - \frac{I}{FD_{\text{Cl}^-}} \left(\frac{D_{\text{KCl}}}{\pi} \right)^{1/2} \cdot t^{1/2} \quad [9]$$

in which C_{KCl}^0 is the bulk concentration of the salt and D_{Cl^-} and D_{KCl} are diffusion coefficients with the respective values of 2.03×10^{-5} and 2.00×10^{-5} cm²/sec (at infinite dilution) (10).

At the highest current density used in the present work (265 mA/cm²), the transition time for the dye reaction was 7 msec. For those conditions, Eq. [9] indicates that the ratio of surface to bulk concentration of chloride ion was 0.97. The corresponding shift in equilibrium potential at the interface between the red film and the electrolyte should have been only 0.86 mV. Since the observed change was > 1V in most cases, it is evident that mass-transfer overvoltage at the liquid interface made no appreciable contribution to the potential-time curve.

Ionic charge transfer at the electrolyte interface.—If the transfer of chloride ion across a potential barrier at the dye/solution interface were controlling, the current density might be expressed, at moderate to large overvoltages, by the equation

$$I = FC_{\text{Cl}^-} \cdot k_f \quad [10]$$

in which k_f is a potential-dependent heterogeneous rate constant for the forward reaction, and C_{Cl^-} is the constant chloride ion concentration on the liquid side of the interface. For this case, the potential shift ΔE should be a linear function of $\log I$, with a Tafel slope of the order of 50 mV. Moreover, the value of ΔE should remain fixed during a given pulse, once a steady-state condition is established at the electrolyte interface. The observed transients in the lower current series (Electrodes 1 and 2) had quite different characteristics. The potential was almost independent of current density near the beginning of the pulse, and it rose continuously during the color conversion.

Solid-solution film acting as reversible couple.—It was shown above that a two-layer dye film could not be distinguished from a solid-solution film by means of the optical transient. Such a distinction is feasible, however, with the electrical transient. For the solid-solution case, the red component may be defined as the organic cation plus a stoichiometric quantity of chloride ion. The chloride concentration in the liquid phase will again be denoted by C_{Cl^-} , while c_g and c_r will represent the concentrations of the green and

red components in the solid film. Since C_{Cl^-} is almost constant during the current pulse, the time dependence of the electrode potential arises from the variations of c_g and c_r .

If the faradaic process is reversible, and activities are assumed equal to concentrations, the electrode potential $E_{g/r}$ should be given by the Nernst equation

$$E_{g/r} = E_{g/r}^0 + (RT/nF) \ln [c_r / (c_g \cdot C_{\text{Cl}^-}^n)] \quad [11]$$

in which $E_{g/r}^0$ is a standard potential of the green/red dye couple with respect to the Ag/AgCl electrode. Since

$$c_r = c_0(t/\tau) \text{ and } c_g = c_0[(1 - t/\tau)] \quad [12]$$

a potential-time curve may be calculated from Eq. [11], taking $n = 2$. The predicted potential change in the interval $0.1 \leq t/\tau \leq 0.9$ is 0.056V, regardless of the current density. From Fig. 3(a), it is obvious that this model does not fit the experimental data; the actual potential change was about 20 times larger.

Two variable ohmic resistors in series.—In the moving-boundary study of lutetium diphthalocyanine, the red and green films on alumina had lengths of the order of 1 cm. They were treated as two ohmic resistors in series (6). Approximate bulk resistivities of both phases and the carrier concentration in the red phase are known from that work. Since the current path in the present experiments was about five orders of magnitude shorter, a departure from ohmic behavior due to higher fields would not be surprising. However, it is essential to know the time-dependent voltage drop that would occur in such a thin film if it conformed to a two-layer ohmic model represented by Fig. 1(b). This drop, ΔE_{ohmic} , is given by

$$\Delta E_{\text{ohmic}} = Il [\rho_g + (\rho_r - \rho_g)(t/\tau)] \quad [13]$$

where ρ_r and ρ_g are bulk resistivities with the respective values of 1300 and 370 Ω -cm (6). A film with a thickness l of 1×10^{-5} cm and a current density of 6 mA/cm² may be taken as an example. Equation [13] predicts for this case an initial potential jump of 0.02 mV at $t = 0$, while the film is all green, and a final ohmic drop of 0.08 mV at $t = \tau$, when it is all red. The difference between these values is insignificant compared to the potential increase of $\sim 1V$ observed for Electrode 1 under such conditions.

Two-layer space-charge system.—Referring again to Fig. 1(b), we may envision two space-charge layers, rather than two ohmic resistors, in series. A related model was used by Faughnan, Crandall, and Lampert to describe the bleaching of a tungsten oxide electrochromic film (11). They developed equations for a single predominant space-charge layer with a thickness that increased continuously under constant applied voltage. Here, we consider two space-charge layers as a more general case and assume the condition of constant applied current density.

The time-dependent part ΔE_t of the total potential change is given by

$$\Delta E_t = \Delta E_1 + \Delta E_2 \quad [14]$$

where ΔE_1 is the potential drop across the reactant layer (green) and ΔE_2 is the drop across the product layer (red). As in the resistance model, the time dependence arises from variation of the layer thicknesses as the boundary propagation distance x increases.

At a constant current density I , the boundary velocity is given by

$$\frac{dx}{dt} = \frac{I}{z_1 c_1 F} \quad [15]$$

where c_1 is the volume concentration of the ion incorporated in the solid reaction product and z_1 is the magnitude of its valence.

It will be assumed, as an approximation, that each layer has a square-law current-voltage characteristic.

If the reactant layer is a one-carrier material conforming to Child's law

$$\Delta E_1^2 = \frac{I}{\kappa_1 \epsilon_0 \mu_1} \cdot (l - x)^3 \quad [16]$$

A similar equation for the product layer is

$$\Delta E_2^2 = \frac{I}{\kappa_2 \epsilon_0 \mu_2} \cdot x^3 \quad [17]$$

In Eq. [16] and [17], μ_1 and μ_2 are carrier mobilities; κ_1 and κ_2 represent dimensionless dielectric constants, and ϵ_0 is the permittivity of space (8.85×10^{-14} f/cm).

Equation [16] should apply to a simple one-carrier electronic conductor. The rationale for using Eq. [17] in this instance is more complex, since the red layer is a special type of double-injection system. Anions are injected at the solution interface, while positive charges are generated at the red/green reaction boundary. We may regard the latter process as injection of holes that are immediately trapped to form organic cations. The injected anions are mobile, however. A double-injection system in which one of the carriers is strongly trapped can behave in accordance with Child's law (12). For that model, Eq. [17] should be applicable to the red layer, and μ_2 should closely approximate the mobility of the chloride ion.

Noting from Eq. [15] that the propagation distance and the transition time are related by

$$x/l = t/\tau \quad [18]$$

we find from Eq. [14]-[17] that

$$\Delta E_t = \left(\frac{z_i c_i F}{\kappa_2 \epsilon_0 \mu_2 \tau} \right)^{1/2} l^2 \left[(t/\tau)^{3/2} + (1 - t/\tau)^{3/2} \cdot \left(\frac{\kappa_2 \mu_2}{\kappa_1 \mu_1} \right)^{1/2} \right] \quad [19]$$

For convenience, a dimensionless potential Φ may be defined by

$$\Phi = \frac{\Delta E_t}{\Delta E_\tau} = \frac{\Delta E_t}{\left(\frac{z_i c_i F}{\kappa_2 \epsilon_0 \mu_2 \tau} \right)^{1/2} \cdot l^2} \quad [20]$$

Then, with Eq. [19]

$$\Phi = (t/\tau)^{3/2} + (1 - t/\tau)^{3/2} \cdot \left(\frac{\kappa_2 \mu_2}{\kappa_1 \mu_1} \right)^{1/2} \quad [21]$$

Equation [21] predicts the shape of the galvanostatic transient for different values of the mobility parameter $(\kappa_2 \mu_2)/(\kappa_1 \mu_1)$. Figure 5 shows a family of these curves, which have several distinctive features. All are concave away from the time axis, and all converge, by definition, at $\Phi = 1$ when $t = \tau$. The function

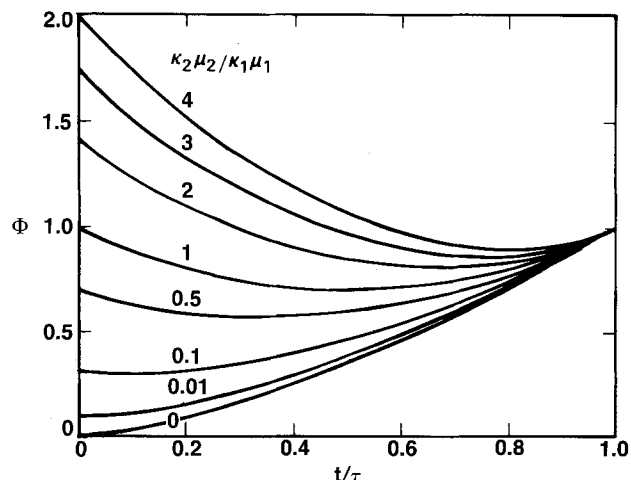


Fig. 5. Dimensionless potential function for different values of the mobility parameter.

Φ reaches a minimum at a time t_{\min} given by

$$\frac{t_{\min}}{\tau} = \left(\frac{\kappa_2 \mu_2}{\kappa_1 \mu_1 + \kappa_2 \mu_2} \right) \quad [22]$$

or, if $\kappa_1 = \kappa_2$, by

$$\frac{t_{\min}}{\tau} = \left(\frac{\mu_2}{\mu_1 + \mu_2} \right) \quad (\kappa_1 = \kappa_2) \quad [23]$$

Hence, when $(\kappa_2 \mu_2)/(\kappa_1 \mu_1)$ is zero, the voltage transient starts from the origin, with zero initial slope. If this ratio is larger than zero, the potential rises at $t = 0$ when the current is applied, then decreases and passes through a minimum. When $(\kappa_2 \mu_2)/(\kappa_1 \mu_1)$ is unity, the minimum potential occurs at $t/\tau = 0.5$.

The potential transient in Fig. 3(a) is typical of the low-current data for lutetium diphthalocyanine. Concavity away from the time axis is evident through most of the reaction period, and no decrease in potential occurs. This shape is characteristic of a space-charge system with a much higher $\kappa \mu$ in the reactant phase than in the product.

The data may be presented in other forms for quantitative comparisons with the space-charge model. It is known from previous work that the red product is an ionic conductor with a carrier mobility of 4×10^{-6} cm²/Vsec, and the green reactant is an electronic conductor. To a good approximation, therefore

$$\frac{\mu_i}{\mu_e} = 0 = \frac{\kappa_2 \mu_2}{\kappa_1 \mu_1} \quad [24]$$

where μ_i and μ_e are the ionic and electronic mobilities. Equation [19] then reduces to Eq. [17], which is Child's law for the red layer. According to that relationship, a plot of $\log I$ vs. $\log \Delta E_t$ at a given time should be a straight line with a slope of 2. Figure 6 shows this plot for Electrodes 1 and 2 in terms of the total current i and the potential change ΔE evaluated at the optical transition time. Although the data for both films lie on the same straight line, the experimental slope is 2.7 rather than 2.0. The higher slope is actually consistent with a double-injection system in which neither charged species is fully immobilized (12).

A more detailed test of the square-law model is based on the relationship

$$\frac{\Delta E_t}{I^2} = \left(\frac{1}{\kappa \epsilon_0 \mu_i} \right)^{1/2} \left(\frac{1}{z_i c_i F} \right)^{3/2} \cdot t^{3/2} \quad [25]$$

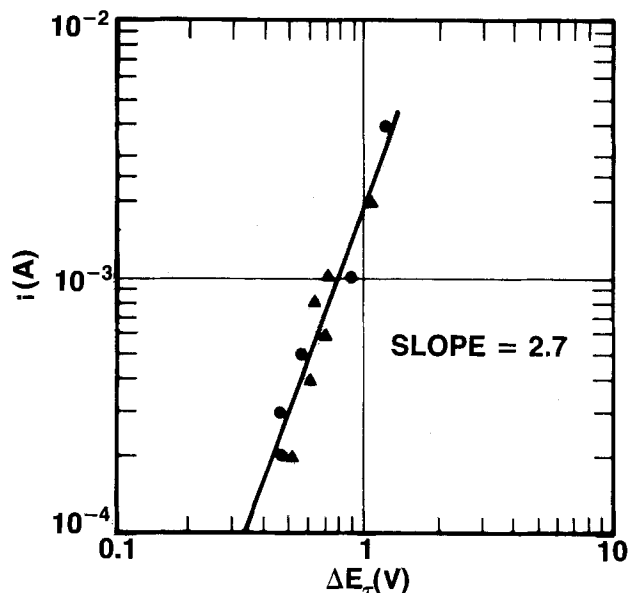


Fig. 6. Current-potential relationship at the optical transition time. Circles, Electrode 1; triangles, Electrode 2; ΔE_τ evaluated at t_{opt} from type of plot shown in Fig. 7.

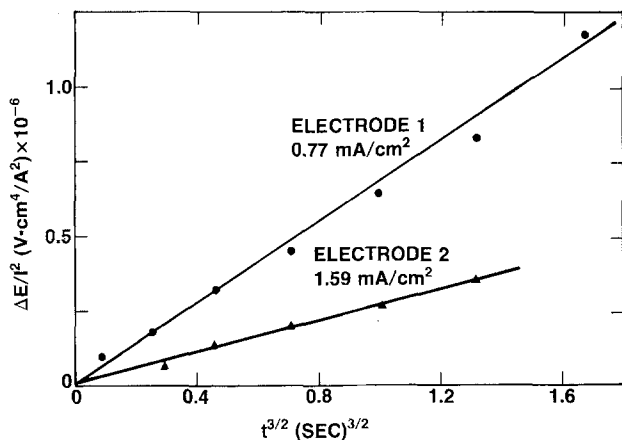


Fig. 7. Space-charge plots for determination of $\kappa\mu_i$ in the oxidation product.

or its equivalent

$$\frac{\Delta E_t}{I^2} = \left(\frac{1}{\kappa\epsilon_0\mu_i} \right)^{1/2} \left(\frac{l}{z_i I \tau_{opt}} \right)^{3/2} \cdot t^{3/2} \quad [26]$$

A plot of $\Delta E_t/I^2$ vs. $t^{3/2}$ should be a straight line passing through the origin, with a slope from which the product $\kappa\mu_i$ for the red material may be evaluated. Figure 7 shows this plot for Electrodes 1 and 2. Potentials here and in Fig. 6 are referred to a zero level found by extrapolating the main transient¹ back to $t = 0$, thus neglecting the early part of the curve. The values of $\kappa\mu_i$ from the slopes at different current densities are 3.9×10^{-5} and 4.3×10^{-5} cm²/Vsec. A chloride ion mobility of 4×10^{-6} cm²/Vsec was found for the red oxidation product in the moving-boundary study on alumina (6). Hence, a dielectric constant of 10 is estimated for the red film. This value is quite acceptable in comparison with 4.85, which has been reported for copper phthalocyanine in pressed-powder form (13). The ionic character of the red material should impart additional polarizability, which would result in a higher dielectric constant.

A lower limit of the electron mobility in the green material can be estimated by means of Eq. [23]. Although no minimum was actually observed in the potential-time curves, a minimum would have been detectable, generally, if it had occurred after the first 5% of the reaction time. Then with $t_{min} < 0.05\tau$ and $\mu_i = 4 \times 10^{-6}$ cm²/Vsec, Eq. [23] indicates $\mu_e > 8 \times 10^{-5}$ cm²/Vsec.

Faradaic n values and transients at high current densities.—The number of electrons lost per molecule of dye, based on the optical transition time, is given as the effective n value n_{eff} in Table I. Average n 's of 2.5 and 1.5 had been found in prior studies with 1M KCl (6, 7). While none of these n determinations was very precise, Electrode 1 in the present work yielded a significantly lower n_{eff} of 0.77. It was evident visually and from the optical transmission measurements that this film did not fully return to the normal green color when the cell was shorted. To minimize such an effect in the transient analysis, the ion concentration c_i for Eq. [15], [19], and [20] was based on the optical transition time, or the effective n , rather than the assumption that $n = 2$. The geometric film thickness l was calculated, however, from the optical density determined in the dry state before the film was used in the electrochemical cell.

The high current-density data for Electrode 3 led to several interesting observations. At 265 mA/cm², the green-to-red transformation occurred in only 7 msec, with no decrease in the current efficiency as indicated by n_{eff} . This conversion rate is faster than required for

¹ Concave downward in Fig. 3(a).

most electronic display applications. The high current efficiency suggested that the product layer, next to the electrolyte, had essentially no electronic conductivity. Anodic decomposition of the electrolyte simultaneously with the dye oxidation should be blocked in such a system, but consecutive oxidation of Cl⁻ after the red film reaches the tin oxide interface should be permitted, since the converted film acts as a solid chloride ion conductor.

In the highest current-density range explored (132–265 mA/cm²), the electrical transition was no longer discernible, although the optical transition was still defined. This may signify a change from space-charge control to another control mechanism such as ionic charge transfer across the solution/red-film interface. This concept has a precedent in the tungsten oxide electrochromic system, for which proton transfer across the liquid/solid boundary is believed to govern the coloring kinetics (11).

Conclusions

The anodic oxidation of a lutetium diphthalocyanine film on tin oxide in 1M KCl occurs by propagation of a reaction front from the electrolyte interface, through the film, to the tin oxide boundary. The results of this study confirm our previous observations that electrons lost by the dye are compensated by anions migrating into the organic material under an electric field.

In films approximately 10^{-5} cm thick, the electrode process is space-charge-limited at current densities from 0.3 to at least 6 mA/cm². On comparing the shape of the experimental voltage transient with those predicted for a two-layer space-charge model, it is concluded that a predominant space charge resides in the red oxidation product, which is an ionic conductor. No space charge is observed in the green reactant layer under these conditions, since it is an electronic conductor of higher carrier mobility.

The dielectric constant-mobility product $\kappa\mu_i$ in the red phase, evaluated by means of the space-charge theory, is 4×10^{-5} cm²/Vsec. The corresponding product estimated for the electronic carrier in the green phase is at least 8×10^{-4} cm²/Vsec. With the chloride ion mobility of 4×10^{-6} cm²/Vsec from previous work, a dielectric constant of 10 is found for the red material.

Details of the voltage transient at higher current densities can be obscured by ohmic drop in the tin oxide. However, the optical transient shows that the color transformation still proceeds with high current efficiency, even at 265 mA/cm². Ionic transfer at the electrolyte interface, rather than space-charge conduction, may then control the electrode kinetics.

Acknowledgments

This research was sponsored by the Air Force Office of Scientific Research (AFSC), United States Air Force, under Contract F49620-77-C-0074.

R. V. Galiardi assisted in part of the experimental work.

Manuscript submitted July 10, 1979; revised manuscript received Nov. 8, 1979.

Any discussion of this paper will appear in a Discussion Section to be published in the December 1980 JOURNAL. All discussions for the December 1980 Discussion Section should be submitted by Aug. 1, 1980.

Publication costs of this article were assisted by Rockwell International.

LIST OF SYMBOLS

C_{Cl^-}	concentration of Cl ⁻ in liquid electrolyte, moles/cm ³ or moles/liter
$C^{\circ}_{Cl^-}$ and C°_{KCl}	concentrations of Cl ⁻ and KCl in liquid electrolyte at the dye surface, moles/cm ³
c_0	initial concentration of reactant in film, moles/liter
c_1	concentration of reactant in film, moles/liter
c_2	concentration of product in film, moles/liter
c_g	concentration of green material in film, moles/liter

c_i	concentration of ionic charge carrier in film, moles/cm ³	ϵ_0	dielectric permittivity of space, 8.85×10^{-14} f/cm
c_r	concentration of red material in film, moles/liter	κ_1	dielectric constant of reactant film, dimensionless
D	optical density of dye film, dimensionless	κ_2	dielectric constant of product film, dimensionless
D_{init}	initial optical density of dye film, dimensionless	μ_1	carrier mobility in reactant film, cm ² /Vsec
D_{Cl^-} and D_{KCl}	diffusion coefficients of Cl ⁻ and KCl in liquid electrolyte, cm ² /sec	μ_2	carrier mobility in product film, cm ² /Vsec
$E_{g/r}$	potential of dye electrode in reversible-couple model, V vs. Ag/AgCl, Cl ⁻	μ_i	ion mobility, cm ² /Vsec
$E_{g/r}^\circ$	standard potential of dye electrode in reversible-couple model, V vs. Ag/AgCl, Cl ⁻	μ_e	electron mobility, cm ² /Vsec
ΔE_1	potential drop across reactant layer in space-charge model, V	ρ_r	resistivity of red film, Ω -cm
ΔE_2	potential drop across product layer in space-charge model, V	ρ_g	resistivity of green film, Ω -cm
ΔE_{ohmic}	ohmic potential drop across dye film in resistance model, V	τ	transition time, sec
ΔE_t and ΔE_τ	potential changes at times t and τ , following application of current, V	τ_{elec}	electrical transition time, sec
e_1	molar extinction coefficient of reactant, liters/mole-cm	τ_{opt}	optical transition time, sec
e_2	molar extinction coefficient of product, liters/mole-cm	Φ	dimensionless potential change in space-charge model
F	faraday constant, 96,494 C/g-equiv.		
I	current density, A/cm ²		
i	current, A		
k_f	heterogeneous rate constant of electrochemical reaction in ionic charge-transfer model, cm/sec		
l	thickness of dye film, cm		
n	number of electrons lost per molecule of dye in anodic reaction		
n_{eff}	effective number of electrons lost per molecule of dye, based on optical transition time		
R	gas constant, 8.314 J/deg-mole		
T	absolute temperature, °K		
T_t and T_τ	intensities of transmitted light at times t and τ , arbitrary units proportional to photo-detector response		
t	time, sec		
t_{min}	time of minimum potential in two-layer space-charge model, sec		
x	distance, cm		
z_i	magnitude of anion valence		

REFERENCES

- P. N. Moskalev and I. S. Kirin, *Opt. Spectrosc.*, **29**, 220 (1970).
- P. N. Moskalev and I. S. Kirin, *Russ. J. Phys. Chem.*, **46**, 1019 (1972).
- M. M. Nicholson and R. V. Galiardi, Final Report, Contract N62269-76-C-0574, AD-A039596, May 1977; Chem Abstr. 87:144073v.
- M. M. Nicholson and R. V. Galiardi, *SID Int. Symp. Dig.*, **IX**, 24 (1978).
- I. S. Kirin and P. N. Moskalev, *Russ. J. Phys. Chem.*, **41**, 251 (1967).
- M. M. Nicholson and F. A. Pizzarello, *This Journal*, **126**, 1490 (1979).
- F. A. Pizzarello and M. M. Nicholson, Abstr. B-1 presented at the 21st Electronic Materials Conf., Boulder, Colorado, 1979.
- I. B. Goldberg and A. J. Bard, *J. Electroanal. Chem. Interfacial Electrochem.*, **38**, 313 (1972).
- M. D. Morris and J. J. Lingane, *ibid.*, **6**, 300 (1963).
- B. E. Conway, "Electrochemical Data," p. 144, Greenwood Press, Westport, Connecticut (1952).
- B. W. Faughnan, R. S. Crandall, and M. A. Lampert, *Appl. Phys. Lett.*, **27**, 275 (1975).
- M. A. Lampert and P. Mark, "Current Injection in Solids," p. 224, Academic Press, New York (1970).
- A. Voet and L. R. Suriani, *J. Colloid Sci.*, **7**, 1 (1952).

The Electrocatalytic Oxidation of Ethylene on Platinized Platinum at Different Saturation Pressures

W. E. Triaca, A. M. Castro Luna, and A. J. Arvía*

Instituto de Investigaciones Fisicoquímicas Teóricas y Aplicadas, División Electroquímica, 1900 La Plata, Argentina

ABSTRACT

The influence of the hydrocarbon partial pressure ($10^{-3} \text{ atm} \leq P_E \leq 1 \text{ atm}$) in the electrooxidation of ethylene on platinized platinum in 1N H₂SO₄ was investigated from potentiodynamic and stationary state data. A positive effect of the ethylene saturation pressure on the electrochemical reaction rate has been observed over the whole pressure range. At $P_E > 5 \times 10^{-2} \text{ atm}$, the electrochemical reaction rate tends to become pressure independent. The characteristics of the electrochemical reaction can be explained through a reaction pathway involving the electrosorption of ethylene followed by an electron transfer step as rate determining. The present results confirm the recently proposed reaction mechanism for the ethylene potentiodynamic electrooxidation on platinum.

The electrooxidation of ethylene on platinized platinum in acid electrolytes in the 40°-80°C range yields CO₂ and hydrogen ions in solution with an efficiency close to 100%. The electrochemical reaction has been investigated by both stationary-state and relaxation

techniques (1-22). The overall ethylene electrooxidation process was earlier interpreted through a reaction mechanism involving the adsorption of the hydrocarbon molecule on the electrode surface followed by the discharge of water on bare platinum sites, the latter stage being the rate-determining step (1). Then, the hydrocarbon oxidation is accomplished through fast reactions involving the adsorbed hydrocarbon and the

* Electrochemical Society Active Member.

Key words: electrocatalysis, ethylene electrooxidation, platinized platinum, ethylene electrosorption.

adsorbed OH species. This reaction model, derived principally from quasistationary kinetic data, yields a negative ethylene pressure influence on the rate of the overall reaction, which apparently explained the trend of the experimental results in the $1\text{-}10^{-4}$ atm ethylene pressure range.

On the other hand, the results obtained under non-stationary conditions furnish a distinction of the various types of processes involved in the overall electrode reaction. Thus, the reaction implies a diffusion and an electroadsorption of the reacting species prior to actual electrochemical reaction. The latter involves the electrooxidation of the electroadsorbed species through the participation of water and finally, at sufficiently high anodic potentials, the electrooxidation of the platinum surface. Recent potentiodynamic results obtained, avoiding any hydrocarbon readsorption, have shown that the earlier accepted mechanism for the ethylene electrooxidation is unsatisfactory (23). The new reaction mechanism was based on the initial deprotonation of the electroadsorbed species on the electrocatalyst surface as the rate-determining step. Consequently, the influence of the ethylene partial pressure on the reaction should correspond to two limiting cases: (i) Under saturation coverage, a pressure independent reaction rate should be reached and (ii) when the degree of surface coverage depends on the equilibrium pressure according to the corresponding adsorption isotherm, a positive pressure influence should be observed.

The present paper deals with the influence of the ethylene partial pressure on the hydrocarbon electrooxidation rate both under potentiodynamic and under steady-state conditions. A positive influence of the ethylene saturation pressure on the potentiodynamic electrooxidation rate is clearly observed, particularly below 0.1 atm. The effect appreciably decreases as the ethylene saturation pressure increases and the reaction rate tends to become pressure independent.

Experimental

The experimental setup, materials, and techniques used, were the same as those described in a recent publication (23). Two procedures were used for the working electrode preparation, namely, using either a platinized plating bath without lead acetate addition (23) or a plating bath containing up to a maximum of 0.02% of lead acetate according to the procedure reported elsewhere (1, 2). The electrochemical response of the different electrodes was independent of the preparation procedure. The real area of the platinized-platinum surface was determined from the charge transferred during the adsorption of a monolayer of hydrogen adatoms. The potential of the working electrode was measured against a reversible hydrogen electrode in contact with the electrolyte (1N H_2SO_4).

Saturation of the electrolyte with the hydrocarbon (10^{-3} atm $\leq P_E \leq 1$ atm) was achieved by bubbling ethylene (CP grade Matheson), either pure or diluted with purified nitrogen. A.R. H_2SO_4 (Merck) and triply distilled water, which satisfied the purity standards recently referred in the literature (24), were employed. Experiments were carried out at 60°C.

The following measurements were performed: (i) potentiodynamic E/I curves at 0.4 V/sec to avoid the hydrocarbon readsorption (23) and (ii) stationary current/potential curves.

Results

Potentiodynamic runs.—The potentiodynamic runs were made with triangular potential sweeps initiated from the potential range related to the maximum adsorption ($E_{ad} \approx 0.25\text{-}0.30\text{V}$) up to 1.5V, immediately after the electrode pretreatment indicated in Fig. 1. The rationale behind the various potential steps has been discussed in detail elsewhere (23). Experiments were performed either in the absence (blanks) or in the presence of ethylene under exactly the same per-

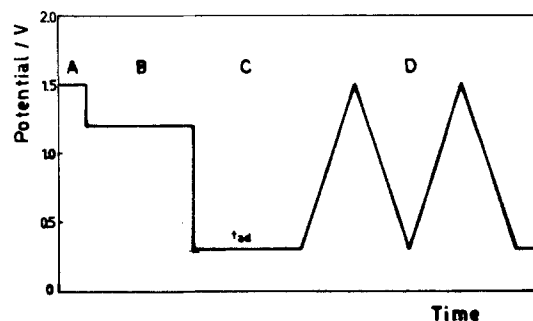


Fig. 1. Potential perturbation program. Time axis arbitrary scale. Step width: A = 15 sec; B = 120 sec (gas bubbling) or 60 sec (gas bubbling) + 120 sec (quiescent solution); C = t_{ad} . D = triangular potential sweep.

turbation conditions. In the $1\text{-}10^{-2}$ atm ethylene partial pressure range, the E/I profiles exhibit (Fig. 2), in principle, the same features previously described (23), namely, the initiation of the hydrocarbon electrooxidation at ca. 0.4V and its characteristic net anodic current peak at ca. 0.90V. The hydrocarbon electrooxidation is apparently completed at ca. 1.5V as deduced from the second positive-going potential scan (23). The total anodic charge includes that corresponding to the electrooxidation of the platinum surface. The negative-going potential scan exhibits the characteristic current peak corresponding to the electroreduction of the oxygen-containing layer formed on platinum.

The charge related to the electrooxidation of the electroadsorbed ethylene species, Q_E , was evaluated by subtracting from the total anodic charge, previously corrected for the double layer effect, the cathodic charge pertaining to the electrodesorption of the oxygen-containing layer formed during the anodic scan. In this sense blank experiments served as reference (23).

At each ethylene partial pressure, the adsorption time (t_{ad}) at E_{ad} was chosen to reach the maximum stationary surface coverage by the electroadsorbed species. The time required to attain it decreased as the ethylene saturation pressure increased (Table I). During the ethylene electroadsorption process a net dehydrogenation charge, Q_H , was evaluated through the current transient recorded after applying to the interface a potentiostatic step at the maximum adsorption potential (23). This charge is related to the electrooxidation of hydrogen adatoms produced during the electroadsorption process. The Q_E value is determined through a potentiodynamic scan immediately after the relaxing current reached the constant value of the blank ($I \approx 0$). The Q_H/Q_E charge ratio at 80°C and 1 atm hydrocarbon saturation pressure is in good correspondence with the formation of a C_2H_2 residual electroadsorbed species (23).

In the $1\text{-}0.1$ atm pressure range, the charge required to electrooxidize the electroadsorbed ethylene species at 0.3V decreases slightly on decreasing the ethylene saturation pressure; but at pressures lower than 0.1 atm,

Table I. Stationary ethylene surface coverage at 0.3V for different hydrocarbon saturation pressures in quiescent solution

P_E (atm)	t_{ad} (min)	Q_E (mC cm^{-2})	θ_E^*
1	5	0.91	0.96
0.5	15	0.88	0.93
0.1	30	0.83	0.88
0.05	40	0.80	0.84
0.01	60	0.65	0.69
0.001	90	0.42	0.44

* $\theta_a = Q_E/Q_{E,M}$; $Q_{E,M}$ corresponds to the maximum charge related to the electrooxidation of the adsorbed ethylene species. The average $Q_{E,M}$ value is 0.947 ± 0.010 mC/ cm^2 real electrode area (23).

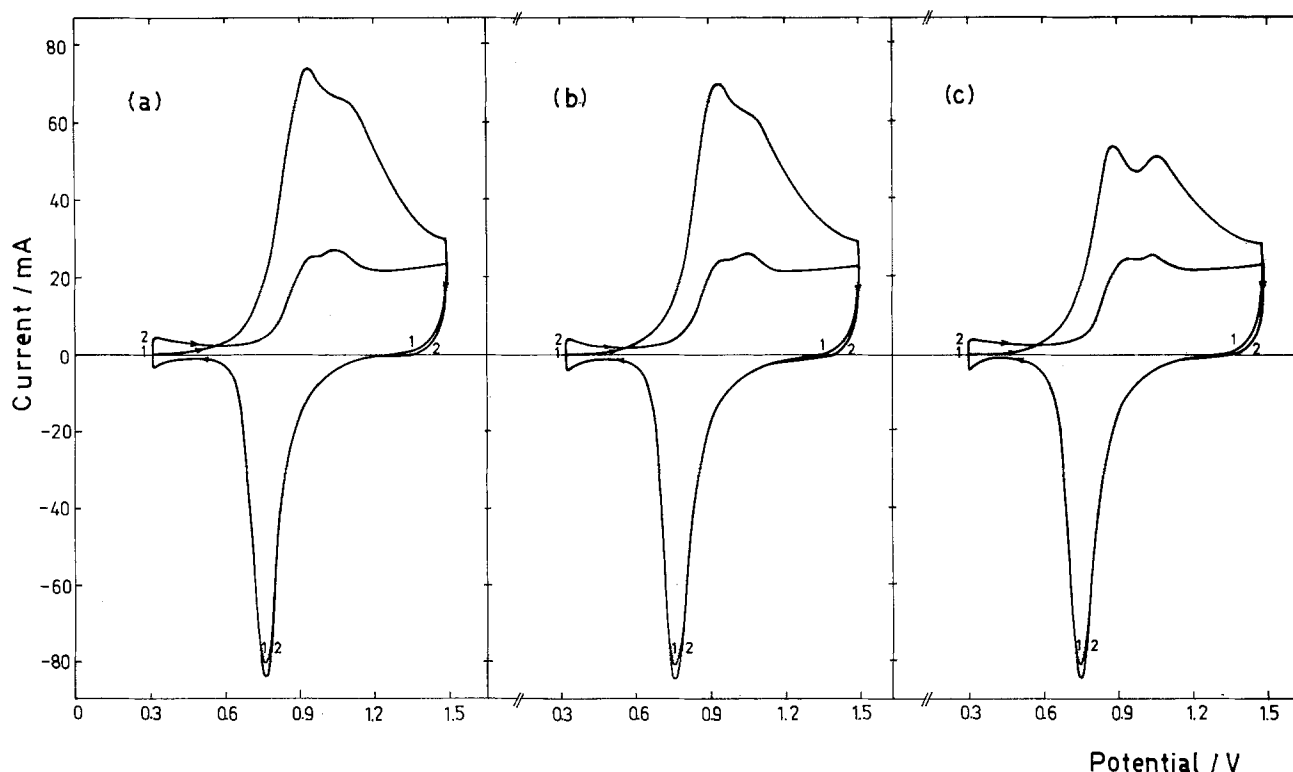


Fig. 2. Potentiodynamic E/I profiles run at 0.4 V/sec after adsorption at $E_{ad} = 0.3V$ during t_{ad} . (a) $P_E = 1$ atm, $t_{ad} = 5$ min; (b) $P_E = 0.1$ atm, $t_{ad} = 30$ min; (c) $P_E = 0.01$ atm, $t_{ad} = 60$ min. Real electrode area = 78.3 cm². Full lines correspond to successive E/I profiles 1 and 2 run with the ethylene-saturated electrolyte at P_E . Profile 2 approaches the blank contour (nitrogen-saturated electrolyte).

a faster decrease of that charge is observed (Table I). However, at the lowest ethylene saturation pressure the results are probably influenced by traces of impurities present in the system because large adsorption times are required to attain the corresponding stationary surface coverage at E_{ad} .

In the 1-0.1 atm ethylene saturation pressure range, the height of the current peak assigned to the hydrocarbon electrooxidation decreases slightly on decreasing the pressure, while at saturation pressures lower than 0.1 atm, the anodic current peak height approaches a linear dependence with the logarithm of the ethylene saturation pressure (Fig. 3). The same influence of the ethylene partial pressure is observed on the current read at a constant potential in the 0.55-0.75V range from the E/I profiles at 0.4 V/sec (Table II).

After equilibration at ethylene partial pressures larger than 10^{-2} atm the first positive-going potential scan shows that in the 0.25-0.40V range the hydrogen adatoms electrooxidation current is practically suppressed (Fig. 2). Contrarily, the hydrogen desorption

current progressively contributes at ethylene saturation pressures lower than 10^{-2} atm. As a matter of fact, during the repetitive potential scans at potential sweep rates fast enough to avoid any appreciable ethylene readsorption, the electrooxidation current related to the hydrogen adatoms progressively increases during the successive potential scans. These results indicate that for values of the degree of ethylene surface coverage (θ_E) larger than ca. 0.5, the electroadsorption of hydrogen adatoms on the electrocatalyst surface is appreciably hindered.

In the $1-10^{-2}$ atm ethylene partial pressure range, the anodic $E/\log I$ plots made with data taken from the initial portion of the E/I profiles recorded at 0.4 V/sec yield reasonably straight lines with slopes slightly larger than the $2.303(2RT/F)$ ratio. After the proper ethylene surface coverage correction described elsewhere (23), e.g., when the currents are referred to the unit coverage of the ethylene surface species, Tafel lines with slopes equal to the $2.303(2RT/F)$ ratio are obtained (Fig. 4).

Steady-state E/I measurements.—The steady-state E/I measurements were made after perturbing the electrochemical interface with the E /time programs indicated in Fig. 5. The two perturbation programs involve initially the electrooxidation at 1.5V for a few seconds of any residual organic species existing on the electrocatalyst surface. Then, the potential is stepped down to 1.2V for 2 min to electroform an oxygen monolayer on platinum which prevents the electroadsorption

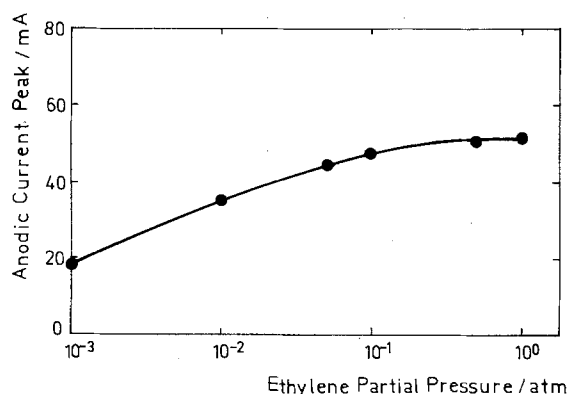


Fig. 3. Dependence of the anodic current peak height related to the electrooxidation of the adsorbed hydrocarbon species on the ethylene partial pressure. $E_{ad} = 0.3V$, t_{ad} at each P_E is indicated in Table I. Real electrode area = 78.3 cm².

Table II. Current densities from the E/I profiles at 0.4 V sec⁻¹ at different potentials and ethylene partial pressures

E (V)	i (0.01 atm) (mA cm ⁻²)	i (0.05 atm) (mA cm ⁻²)	i (0.1 atm) (mA cm ⁻²)	i (1 atm) (mA cm ⁻²)
0.55	0.014	0.018	0.019	0.021
0.60	0.031	0.038	0.039	0.041
0.65	0.069	0.084	0.088	0.091
0.70	0.153	0.175	0.181	0.187
0.75	0.275	0.325	0.325	0.340

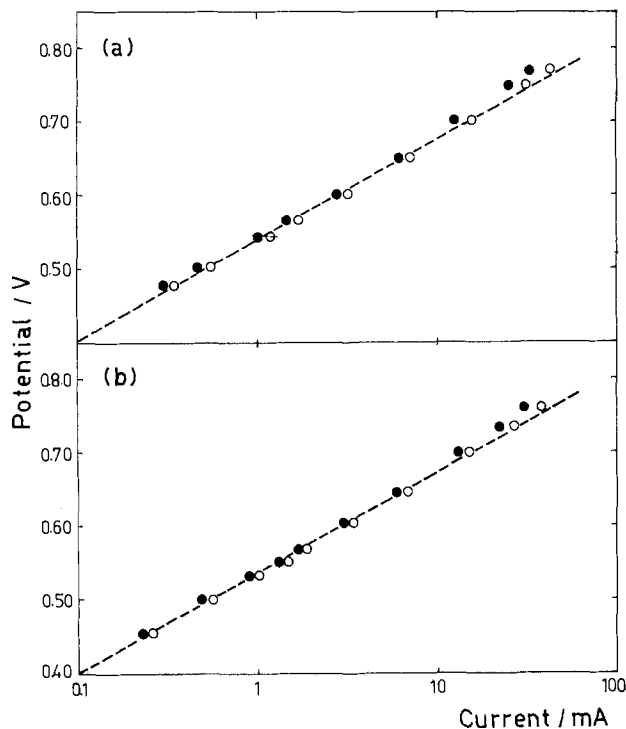


Fig. 4. $E/\log I$ plots derived from potentiodynamic runs. $E_{ad} = 0.3V$. Real electrode area = 78.3 cm^2 . (a) $P_E = 0.05 \text{ atm}$, $t_{ad} = 40 \text{ min}$. (b) $P_E = 0.1 \text{ atm}$, $t_{ad} = 30 \text{ min}$. With (○) and without (●) ethylene surface coverage correction. The dashed lines correspond to the $2.303 (2RT/F)$ slope.

of ethylene from solution. Afterward, in the first case, the potential is stepped down from 1.2V to a preset potential in the 0.40-0.75V range where the oxygen-containing layer is electroreduced simultaneously with the initiation of the hydrocarbon electrosorption and its further electrooxidation. A steady current value at the preset potential is attained after a lapse comprised between 3 and 6 hr, depending on the preset potential value and the hydrocarbon saturation pressure.

In the second case, the potential is stepped down from 1.2 to 0.25V and the system is held at this potential value a time long enough to completely electro-reduce the oxygen-containing surface species and to attain a maximum surface coverage by the ethylene electrosorbed species. The time required for the latter process depends on the ethylene saturation pressure. Then, the potential is brought to a preset value in the 0.40-0.80V range where the corresponding steady current is recorded. In this second case, a longer time is required to achieve the steady state current at constant potential and ethylene partial pressure than in the former case. However, the steady current at any preset potential and at a constant hydrocarbon satura-

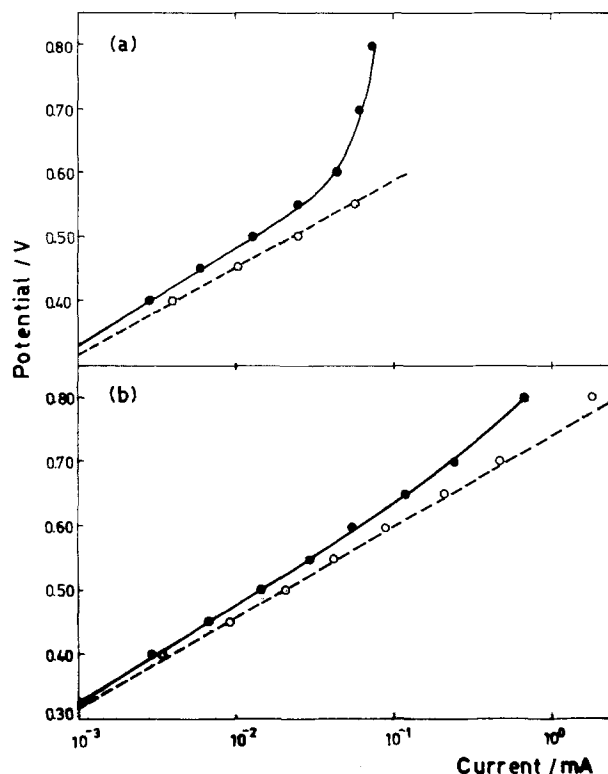


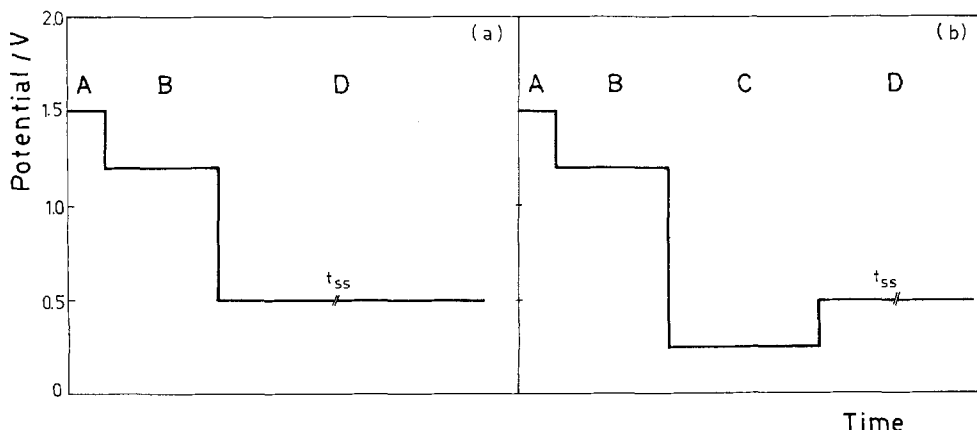
Fig. 6. $E/\log I$ plots derived from stationary measurements. Real electrode area = 78.3 cm^2 . (a) $P_E = 0.01 \text{ atm}$; (b) $P_E = 1 \text{ atm}$. With (○) and without (●) ethylene surface coverage correction. The dashed lines correspond to the $2.303 (2RT/F)$ slope.

tion pressure is always independent of the potential program used.

From the steady-state measurements, reasonable linear Tafel regions are observed in the $E/\log I$ plots, which cover a smaller range as the ethylene partial pressure decreases (Fig. 6). Actually, the $E/\log I$ plots exhibit on the average a very slight curvature. This effect is due to the change of the ethylene surface coverage with the applied potential. Tafel lines with the slope equal to the $2.303 (2RT/F)$ ratio are obtained after the proper ethylene surface coverage correction described elsewhere (23) (Fig. 6). At potentials higher than ca. 0.6V the data deviate from the Tafel line due to mass transport contributions. From the $E/\log I$ plots, such as those depicted in Fig. 6, it is also concluded that at a constant potential in the $1-10^{-2} \text{ atm}$ ethylene partial pressure range the rate of the electrooxidation process under stationary conditions is slightly lower as the ethylene saturation pressure decreases.

Tafel relationships can also be obtained with current values read by holding the system at a constant potential during a fixed time. In this case, however, the

Fig. 5. Potential perturbation programs used for the stationary E/I measurements. Time axis arbitrary scale. Step width: A = 15 sec; B = 120 sec (gas bubbling); C = t_{ad} ; D = time required to reach the stationary current.



Tafel slopes change appreciably with the lapse of time implied in the current reading (Fig. 7). The higher the slope the shorter the reading time. From the data of Fig. 7, it can be seen that Tafel slopes equal to the 2.303 ($2RT/F$) ratio are approached after a 3 hr waiting time for the current reading at a constant potential. Therefore, any reaction order derived from experiments made either under slow potential sweeps or by reading the current at a fixed potential and at a constant preset time is unsatisfactory for mechanistic conclusions.

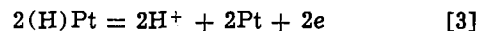
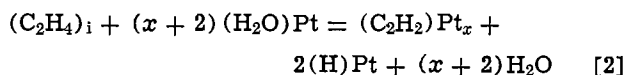
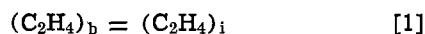
Discussion

The present results show that the electrooxidation of ethylene on platinized platinum under either stationary-state or potentiodynamic conditions involve a common Tafel slope when the data are referred to the unit coverage of the ethylene surface species. The coincidence of the Tafel slopes suggests that the electrooxidation process in both cases likely proceeds through the same basic reaction mechanism. Furthermore, both in the steady-state and in the potentiodynamic measurements and within the ethylene saturation pressure range investigated, a positive influence of the hydrocarbon pressure on the reaction rate is noticed. Under stationary conditions, at potentials more positive than the maximum adsorption potential where the hydrocarbon electrooxidation takes place and the Tafel line is approached, a decrease of θ_E with the increasing potential is observed in the $0.4 \leq \theta_E \leq 0.9$ range at 1 atm ethylene partial pressure (23). The stationary E/I plot at potentials exceeding the Tafel line range exhibits a limiting anodic current which corresponds to a mass transfer rate control of dissolved ethylene toward a partially electrochemically oxidized electrocatalyst surface. These contributions are more clearly seen at the lowest ethylene saturation pressures (Fig. 6).

The interpretation of the kinetic results over the whole pressure range investigated can be given by extending the reaction mechanism previously postulated for the potentiodynamic electrooxidation of ethylene on platinized platinum in the absence of hydrocarbon readsorption (23) to the reaction under stationary-state conditions.

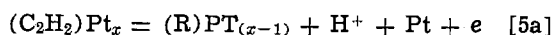
As has been established earlier (23), the proper electrooxidation reaction implies the preceding electrosorption yielding protons and an adsorbed residual ethylene species. The electrosorption process is obviously preceded by the ethylene diffusion from the bulk of the electrolyte toward the reaction interface. The latter, in principle, exists as a surface which is covered either with H, OH, H₂O, or ions, depending on the electrode potential. Thus, the electrosorption of the hydrogen should imply a potential-dependent complex electrochemical reaction. Nevertheless, for the sake of

simplicity any ionic adsorption is regarded as a constant contribution in the mechanistic interpretation of the reaction. It should be noted, however, that both sulfate and bisulfate ions particularly influence the reactions occurring at potentials which are more positive than the potential of zero charge of the electrochemical interface (25, 26). The latter is close to the potential where the maximum hydrocarbon adsorption takes place. Therefore, the simplest formalism to explain the electrooxidation of ethylene on platinum can be put forward in terms of the following sequence of partial stages

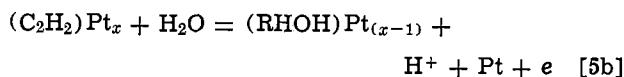


Step [1] corresponds to the diffusion of ethylene from the bulk of the solution to the electrochemical interface. Step [2] represents the dissociative electrosorption of ethylene on the platinum surface covered by water molecules in direct contact with the metal yielding the adsorbed residual ethylene species and hydrogen adatoms. The value of x , the average number of Pt sites occupied by the adsorbed radical, is ca. 2.3 (23). Step [3] is the electrooxidation of hydrogen adatoms. At potentials higher than 0.4V the rate of this reaction becomes so fast that steps [2] and [3] are then actually undistinguishable. Reaction [4] indicates that any available free platinum surface is immediately covered to a large extent by water molecules.

Steps [1] to [4] are followed by a deprotonation process. The latter may occur either through the following reaction

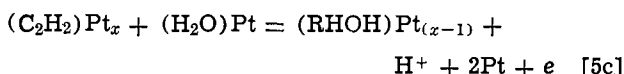


or through the solvent participation as follows



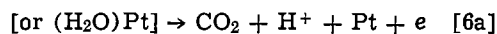
R and RHOH denote intermediates produced in the course of the electrochemical reaction. At this stage, the average number of Pt sites related to these new intermediates is certainly unknown although it is likely that it decreases along the course of the reaction.

Another possible equivalent reaction which may contribute at ethylene surface coverages lower than the saturation coverage is



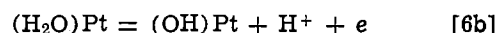
After either reaction [5a], [5b], or [5c] the water or the $(H_2O)Pt$ species react with the surface organic intermediates yielding finally CO₂ and H⁺ through a sequence of undetermined fast reactions. These reactions can be expressed by the overall anodic process

Surface organic intermediates + H₂O



The postulated reaction pathway involves the participation of water in the ethylene electrooxidation process at anodic potentials lower than those corresponding to the initiation of the oxygen monolayer formation.

Alternatively, the direct discharge of water



may contribute particularly at higher positive potentials. In the absence of organic adsorbates, there is evidence that step [6b] corresponds to a reversible fast electron transfer reaction over a relatively large potential range preceding the monolayer formation (27-

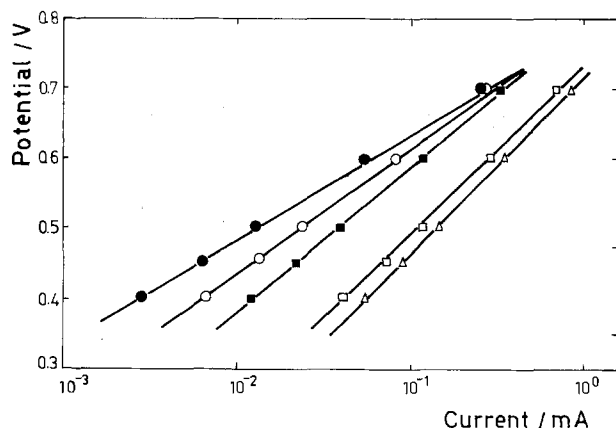
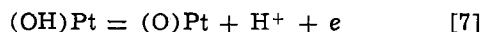


Fig. 7. Dependence of the Tafel plot at $P_E = 1$ atm on the waiting time for the current reading at constant potential. (Δ) 75 sec; (\square) 120 sec; (\blacksquare) 20 min; (\circ) 1 hr; (\bullet) 6 hr. Real electrode area = 78.3 cm².

29). The (OH)Pt species reacts either with the surface organic intermediates yielding finally CO_2 and H^+ through a series of fast surface radical reactions or, as the surface organic intermediate concentration is depleted, it undergoes the oxygen monolayer formation according to a complex reaction pathway (29, 30), which can be formally put forward as follows



Under potentiodynamic conditions and in the absence of ethylene readsorption, either step [5a] or [5b] and the following ones describe the electrooxidation process occurring on platinum. As discussed earlier (23) the kinetic parameters sustain that the initial deprotonation of the adsorbed radical, either through reaction [5a] or [5b], is the likely rate-determining step. Similarly, for the stationary electrooxidation, both the Tafel slope and the pressure dependence of the reaction rate sustain, as in the potentiodynamic case, that any form of step [5] is the rate-determining step.

At intermediate electrode surface coverages by the adsorbed hydrocarbon species, the kinetics of the process is better represented by a Temkin-type isotherm. This conclusion is based on the approximate $\theta_E/\log P_E$ linear relationship obtained at 0.3V, particularly at low ethylene saturation pressure (Table I and Fig. 8). The same relationship comes out from the linear dependence of the potentiodynamic anodic current peak with $\log P_E$ at ethylene saturation pressures lower than 0.1 atm. Then, the rate equation of the rds in terms of current density, i , is given by

$$i = k'\theta_E \exp(\alpha FE/RT) \exp(f\theta_T) \quad [8]$$

where k' is the formal rate constant in electrical units, θ_E refers to the electrode surface coverage by C_2H_2 species, α is the transfer coefficient assisting the reaction in the anodic direction, f is a Temkin-type coefficient, and θ_T refers to the total surface coverage by the adsorbed radicals. When the effects of coverage by the adsorbed species on the activation energy of the reaction exactly compensate each other as one adsorbed species is progressively replaced by another one, the f value is zero. Taking into account the type of adsorbed species involved in reaction [5] it seems reasonable that the latter situation is actually approached. Then, Eq. [8] becomes

$$i = k'\theta_E \exp(\alpha FE/RT) \quad [9]$$

so that an apparent Langmuir adsorption behavior of the intermediates results. Equation [9] involves a linear E vs. $\log(i/\theta_E)$ relationship with the slope equal to the $2.303(RT/\alpha F)$ ratio. Therefore, the experimental Tafel slope obtained either from potentiodynamic or steady-state measurements agrees with the latter for $\alpha = 0.5$.

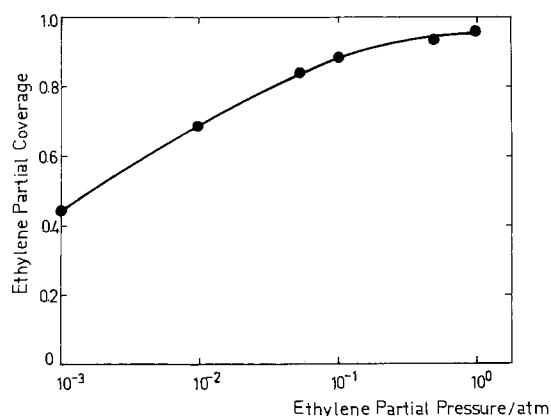


Fig. 8. Dependence of the degree of ethylene surface coverage at 0.3V on the ethylene partial pressure.

When step [5] is rate determining and the ethylene surface coverage degree is in the 0.2-0.8 range, the preceding steps can be regarded as in quasi equilibrium. The electrode surface is then significantly covered only by C_2H_2 species (and water) and therefore $\theta_T \approx \theta_E$. Hence, using an overall reaction for the preceding steps, under Temkin conditions, the rates in the forward (v_f) and in the backward (v_b) directions are given by

$$v_f = k'_f P_E (1 - \theta_E)^x \exp(2\alpha FE/RT) \exp(-\gamma r_E \theta_E/RT) \quad [10]$$

$$v_b = k'_b C_{\text{H}^+}^{\theta_E} \exp[-2(1 - \alpha) FE/RT] \exp[(1 - \gamma) r_E \theta_E/RT] \quad [11]$$

where k'_f and k'_b are the corresponding formal rate constants; γ is a symmetry factor, and r_E is a coefficient which denotes the variation of the apparent standard free energy of adsorption with the coverage. Under quasi-equilibrium conditions ($v_f \approx v_b$) and for $\alpha = \gamma = 0.5$, it results

$$\theta_E = K + K' \log P_E + K'' EF \quad [12]$$

where the term K depends on the solution pH and temperature and K' and K'' are constants at constant temperature. This equation, under the present circumstances, is approached at the maximum adsorption potential where practically no steady-state ethylene electrooxidation occurs. Thus, at 0.3V, for $0.2 \leq \theta_E \leq 0.8$, the linear $\theta_E/\log P_E$ relationship is justified. At potentials more positive than 0.35V the ethylene partial pressure at the interface decreases due to various contributions which are potential dependent such as the slow diffusion of ethylene from the bulk of the electrolyte toward the reaction interface and the duration of ethylene at the interface because of CO_2 generation. All these effects in addition to the electroadsorption of oxygen which competes with the hydrocarbon for surface sites and to the oxidation of the adsorbed ethylene species reflect in the decreasing part of the already known θ_E vs. E plot at values of E more positive than 0.35V (23).

A further detail of the reaction concerning the activity of the electrocatalyst is given by the different times required to attain a stationary current when the potential is either stepped up from 0.25V to E or stepped down from 1.2V to E . This should be related to the reactivity enhancement of the surface produced in the second case during the electroreduction of the oxygen monolayer formed on Pt (30).

The explanation of the present results is given through the participation of (C_2H_2) as the main organic radical in the ethylene electrooxidation process. Other types of dehydrogenated chemisorbed particles (11-13, 21) which probably become important at higher temperatures are not discarded, but under the present circumstances they appear without appreciable kinetic relevance.

Finally, the present results indicate that the previously postulated mechanism (1), which was mainly based on the negative pressure influence on the reaction rate, is unsatisfactory. As a matter of fact, the negative ethylene pressure effect was reproduced in this laboratory when, for instance, the E/I records were obtained at a low potential sweep rate (e.g., 0.01 mV/sec) and they were arbitrarily assigned to stationary E/I profiles. Under these circumstances, the fact that different times are required to attain steady currents at different potentials and hydrocarbon saturation pressures is overlooked.

Acknowledgment

INIFTA is sponsored by the Consejo Nacional de Investigaciones Científicas y Técnicas, the Universidad Nacional de La Plata, and the Comisión de Investigaciones Científicas (Provincia de Buenos Aires). This

work was partially supported by the Regional Program for the Scientific and Technological Development of the Organization of American States.

Manuscript submitted April 11, 1979; revised manuscript received Nov. 1, 1979.

Any discussion of this paper will appear in a Discussion Section to be published in the December 1980 JOURNAL. All discussions for the December 1980 Discussion Section should be submitted by Aug. 1, 1980.

Publication costs of this article were assisted by the Instituto de Investigaciones Fisicoquímicas Teóricas y Aplicadas.

REFERENCES

- H. Wroblowa, B. J. Piersma, and J. O'M. Bockris, *J. Electroanal. Chem.*, **6**, 401 (1963).
- M. Green, J. Weber, and V. Drazic, *This Journal*, **111**, 721 (1964).
- H. Dahms and J. O'M. Bockris, *ibid.*, **111**, 728 (1964).
- J. O'M. Bockris, H. Wroblowa, E. Gileadi, and B. J. Piersma, *Trans. Faraday Soc.*, **61**, 2531 (1965).
- A. T. Kuhn, H. Wroblowa, and J. O'M. Bockris, *ibid.*, **63**, 1458 (1967).
- L. W. Niedrach, *This Journal*, **111**, 1309 (1964).
- S. Gilman, *Trans. Faraday Soc.*, **62**, 466 (1966).
- S. Gilman, *ibid.*, **62**, 481 (1966).
- S. Gilman, *This Journal*, **113**, 1036 (1966).
- V. S. Tyurin, A. G. Pshenichnikov, and R. Kh. Burshtein, *Elektrokhimiya*, **2**, 948 (1966).
- V. S. Tyurin, A. G. Pshenichnikov, and R. Kh. Burshtein, *ibid.*, **5**, 1165 (1969).
- V. S. Tyurin, A. G. Pshenichnikov, and R. Kh. Burshtein, *ibid.*, **5**, 1441 (1969).
- A. A. Michri, A. G. Pshenichnikov, and R. Kh. Burshtein, *ibid.*, **8**, 276 (1972).
- B. J. Piersma and E. Gileadi, in "Modern Aspects of Electrochemistry," Vol. 4, J. O'M. Bockris, Editor, Plenum Press, New York (1966).
- B. J. Piersma, in "Electrosorption," E. Gileadi, Editor, Plenum Press, New York (1967).
- J. O'M. Bockris and S. Srinivasan, "Fuel Cells: Their Electrochemistry," McGraw-Hill, Inc., New York (1969).
- M. W. Breiter, "Electrochemical Processes in Fuel Cells," Springer-Verlag, New York (1969).
- B. Damaskin, O. A. Petrii, and V. V. Batrakov, "Adsorption of Organic Compounds on Electrodes," Plenum Press, New York (1971).
- E. J. Cairns, in "Advances in Electrochemistry and Electrochemical Engineering," Vol. 8, Wiley-Interscience, New York (1971).
- O. A. Petrii, in "Progress in Electrochemistry of Organic Compounds," A. N. Frumkin and A. B. Ershler, Editors, Plenum Press, London (1971).
- A. A. Michri and A. G. Pshenichnikov, *Elektrokhimiya*, **10**, 137 (1974).
- M. W. Breiter, in "Modern Aspects of Electrochemistry," Vol. 10, J. O'M. Bockris and B. E. Conway, Editors, Plenum Press, New York (1975).
- W. E. Triaca, T. Rabockai, and A. J. Arvia, *This Journal*, **126**, 218 (1979).
- B. E. Conway, H. Angerstein-Kozlowska, W. B. A. Sharp, and E. E. Criddle, *Anal. Chem.*, **45**, 1331 (1973).
- V. S. Bagotzkii, Yu. B. Vassiliev, J. Weber, and J. N. Pirtskhalava, *J. Electroanal. Chem. Interfacial Electrochem.*, **27**, 31 (1970).
- R. O. Lezna, N. R. de Tacconi, and A. J. Arvia, *This Journal*, **126**, 2140 (1979).
- A. N. Frumkin, O. A. Petrii, and A. M. Kossaya, *Elektrokhimiya*, **4**, 475 (1968).
- O. A. Petrii, A. N. Frumkin, and V. V. Topolev, *ibid.*, **4**, 1104 (1968).
- G. Bélanger and A. K. Vijh, in "Oxides and Oxide Films," Vol. 5, A. K. Vijh, Editor, chap. 1, M. Dekker, New York (1977).
- M. E. Folger, J. O. Zerbino, N. R. de Tacconi, and A. J. Arvia, *This Journal*, **126**, 592 (1979).

Electrochemical Oxidation of H₂ and CO in Fused Alkali Metal Carbonates

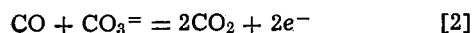
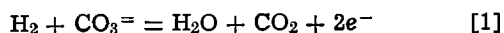
W. M. Vogel,* L. J. Bregoli, and S. W. Smith*

United Technologies Corporation, Fuel Cell Operations, Power Systems Division, South Windsor, Connecticut 06074

ABSTRACT

By using meniscus electrodes and shift gases of relatively low CO content, it was possible to study the electrochemical oxidation of H₂ in molten carbonate with little interference by CO. Data are presented which indicate that the H₂ reaction proceeds with negligible activation polarization on Ni, Au, Pt, and Pt-Rh alloy. The observed overvoltages are explained as diffusion overvoltages for H₂, H₂O, and CO₂. Hydrogen diffusion through metal was appreciable for thin Ni membranes and very fast for Pd wires. The CO oxidation is far more complex and proceeds in stages. At low polarizations the rates are very small but increase greatly above approximately 200 mV. Applied to fuel cell anodes, the results suggest that, in order to utilize large CO content gases efficiently, internal shifting is required.

The H₂/H₂O and CO/CO₂ electrode reactions in molten carbonate can be written as



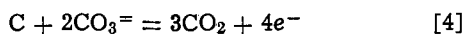
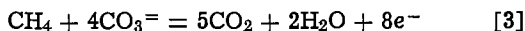
The study of the hydrogen reaction is hampered by the fact that the four gas pressures are interrelated by the shift reaction which is the electrically neutral sum of reactions [1] and [2]. It is not possible, therefore,

to vary the pressures of H₂, H₂O, and CO₂ independently of each other, nor can we investigate reaction [1] without any interference by reaction [2]. In order to obtain meaningful results it is necessary to control the gas composition rather closely, and some seemingly obvious experiments cannot be done at all. For instance, it is not possible to obtain useful voltammograms in the absence/presence of H₂, CO, H₂O, and CO₂. In the absence of CO₂ the melt turns solid (oxide formation). In the absence of CO the polarization curves reflect CO₂ reduction. Presence of H₂O automatically produces H₂, and vice versa. It is not neces-

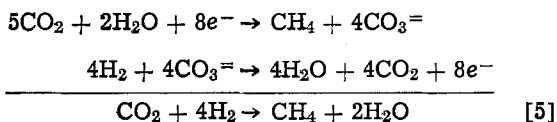
* Electrochemical Society Active Member.
Key words: molten carbonate, fuel cell anode.

sary to start an experiment with a dry melt. The melt comes to equilibrium rather quickly with respect to H_2O (or OH^-). (Vacuum drying of the melt would in any event produce a solid mass of oxides rather than a dry carbonate melt.)

More complications arise from the methane and carbon reactions. We have, in addition to [1] and [2]



In an electrochemical experiment, where an electrode is supplied with a nonequilibrated gas containing H, O, and C atoms, it is difficult to predict where the chemical reactions will take place. For instance, methane may be formed during preheating the gas, or electrochemically¹ at the electrode as product of a local cell with the partial reactions [1] and [3], *i.e.*



Since the equilibrium constants of the chemical reactions vary with temperature, it is sometimes impossible to calculate the equilibrium potential from the composition of the initial feed gas. During preheating, carbon or methane may be formed even though neither reaction is possible at the operating temperature. Carbon formation would be irreversible under such conditions and methane reforming at the higher temperature may be too slow to reach equilibrium.

Many of these complexities can be avoided by using gas mixtures which cannot form carbon at any of the temperatures encountered, *i.e.*, usually between room temperature and operating temperature. In addition, it is prudent to preheat the gas in a manner which ensures equilibrium prior to entering the cell. When these precautions are taken, the open-circuit potential (ocp) agrees accurately with the (equal) equilibrium potentials of reactions [1]-[3] (1). Without these precautions, very large differences may be observed between ocp and the value calculated for the composition of the feed gas (1-3) even if the (cold) feed gas was mixed in the proportions corresponding to equilibrium at operating temperature. Recently, the present work and that of Ref. (1) were criticized (4) as erroneous. The basis for this criticism is a certain characteristic of molten carbonate systems.

Carbonate melts have very small buffer capacities. The acid is a gas (CO_2) of low solubility. It is not possible, therefore, to study the present reactions at constant melt acidity, the latter being expressed as $p\text{CO}_2 \equiv -\log P_{\text{CO}_2}$ (5), nor is it practical to use a reference electrode (RE) "in the same medium." The latter expression normally indicates that the RE and the working electrode (WE) are in the same ionic medium, including the same acidity. We do not mean that the media are truly identical, even with respect to small concentrations of, *e.g.*, dissolved gases. Identical media would, of course, result in a zero potential difference between the working and reference electrodes.

Different media imply liquid junction potentials and/or acidity differences with the effects of the two impossible to separate accurately in many cases. For example, we cannot change the pH of an acid very much and still measure it (against a constant reference electrode) because we simultaneously change the liquid junction between indicator and reference electrodes. However, we can vary the CO_2 pressure above a carbonate melt, and thereby the melt acidity, by

¹ The possible electrochemical formation of CH_4 was not investigated. This would require use of gases which are (thermodynamically) capable of producing CH_4 at cell temperature. This falls outside the scope of the present studies for H_2 where the gases used were incapable of significant CH_4 formation at cell conditions.

many orders of magnitude without introducing or changing any liquid junction potentials. The same is true for changes in H_2O pressure. The concentrations of O^- and OH^- ions in the melt are very small over a wide range of these pressures.

We can, therefore, separate the various electrodes from each other and supply each with a different gas without introducing junction potential errors. The only requirements are that each compartment be supplied with at least a few hundred parts per million of CO_2 , and that the H_2O pressure not exceed a few atmospheres. Of course, rapid exchange of melt between compartments must be prevented.

It was the purpose of this study to obtain more information about the roles of reactions [1] and [2] in the overall process of oxidizing H_2 -containing gases, to obtain information about the complex diffusion overvoltage, and to confirm previous findings (2, 6-8) that reaction [1] proceeds with negligible activation polarization at a variety of different metals.

Experiments

The cell is shown schematically in Fig. 1. The alumina parts consisted of COORS AD-998 grade alumina. The outer container was made from Incoloy 800.

The RE and WE (wires, tubes) were enclosed in alumina tubes. The lower ends of these tubes were closed except for 1×3 mm slits. To prevent convective melt exchange through these slits, inert powder (LiAlO_2) was pressed into the tube bottoms so that the powder/melt paste covered the slits. The gold wire of the RE was immersed a few millimeters into the melt within the alumina tube. The wire or metal tube WE was positioned in the alumina tube so that it barely touched the melt surface. In order to aid in centering the WE wires within the alumina tubes, and to prevent formation of erratic menisci between the wires and tube wall, these wires were sheathed in tightly fitting alumina tubes which extended to within 3 cm of the lower wire end. The melt compositions at the RE and this type of WE were governed by the respective feed gases supplied via tight fittings at the upper ends of the alumina tubes. The WE and RE assemblies were immersed in the bulk melt which also contained a gold counterelectrode.

In some experiments Ni membrane electrodes were used. These electrodes were constructed by welding circular Ni foils into gas housing. Gases were passed through the latter by means of two tubes welded onto the housing. The entire electrode assembly consisted of Ni. Two kinds of Ni foils were used: a nonporous foil and a foil containing regularly spaced tapered holes, perpendicular to the foil surface (supplied by Buckby-Mears, St. Paul, Minnesota). There were 2890 holes per 1 cm^2 of foil. The large hole diameter was approximately 5×10^{-3} cm. The tapered shape of the holes made it easy to maintain menisci in the holes without either flooding the pores or bubbling gas through

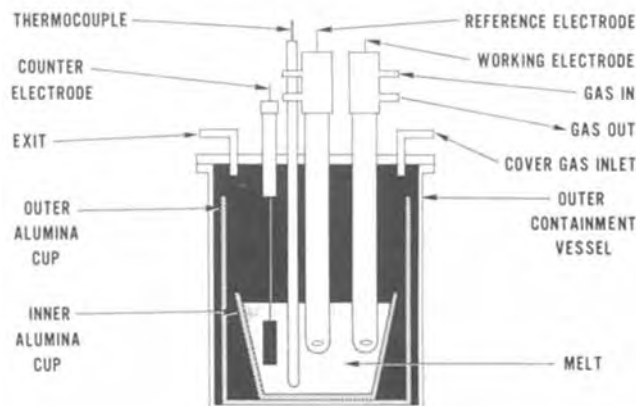


Fig. 1. Cell used with wire or tube electrodes

them. Both kinds of foils were 7.6×10^{-3} cm thick. These membrane electrodes, being rather bulky, were immersed directly into the bulk melt.

A blanket gas of 0.25 atm CO₂ and 0.75 atm N₂ was flowed slowly over the bulk melt. This gas, rather than the CO- or H₂-containing gas at the WE, was used for safety reasons and for convenience sake. It allowed the use of cells which were not completely gas tight between blanket gas and environment. The difference in gas composition above the bulk melt and at RE and WE was of no consequence for those experiments in which separated WE's were used (wires, tubes) as has been explained above. However, the Ni membrane electrodes were somewhat influenced by this difference. Thus, the ocp's of the two types of membranes were within 5 mV of each other but they were 10-20 mV higher than the equilibrium potential calculated for the feed gas to the WE. This difference presumably reflects formation of a mixed potential between the hydrogen reaction at the membrane and the CO/CO₂ reaction at the other more massive metal parts of these electrode assemblies. (If pure CO₂ rather than diluted CO₂ was used as blanket gas, all metal parts except the membrane surfaces evolved gas bubbles, presumably CO.) For the present purpose, the divergence of the ocp of the membrane electrodes was of minor importance since the primary interest was to determine the effect of pores on the polarization of an H₂(Ni) membrane electrode.

All gases were of CP grade. The dry gas mixture was analyzed in each case. The Au reference electrode was supplied with a mixture of 0.33 atm O₂ and 0.67 atm CO₂. The water pressures for the reactant gases were established by means of saturators and were verified by analysis. The gases were preheated prior to entering the cell.

The gases chosen for this study were such that carbon formation was impossible at all temperatures encountered, and such that the equilibrium methane pressure at operating temperature was negligible. The ocp of all but the membrane electrodes agreed within ± 2 mV with the thermodynamic potentials calculated with the gas compositions at equilibrium at 650°C. This close agreement indicated that methane formation at lower temperatures during preheating either did not occur or was reversed at the higher temperature.

The melt was prepared by fusing 62 mole percent (m/o) Li₂CO₃ and 38 m/o K₂CO₃, both of analytical grade.

The cell was heated in a Lindberg crucible furnace. All experiments were done at $650^\circ \pm 5^\circ\text{C}$, measured inside the WE and RE holders. Electrode potentials were controlled using either a PARTM Potentiostat Model 173 or a solid-state programmable voltage generator designed and built in-house. Voltammograms were recorded with a Hewlett-Packard X-Y Recorder, Model 7044A.

The quoted potentials are referred to the O₂ (0.33 atm)/CO₂ (0.67 atm) reference electrode and are corrected for ohmic losses between WE and RE. Corrections were also applied for thermovoltages if dissimilar metals were at different temperatures. Since a gold wire was used as RE, this correction was necessary for all WE's other than gold. In some tests gold lead wires were welded to the WE, so that the drop from 650°C to the environmental temperature occurred on gold wires. In these experiments no correction for thermovoltage was applied. The thermovoltages were measured using the respective dissimilar metals under identical gases (usually shift gas). The measured values agreed well with those calculated from tabulated published data.

Results and Discussion

With the exception of the membrane electrodes, our electrodes were essentially meniscus electrodes. Such electrodes normally present very complex transport

conditions associated with thin liquid films extending above the visible meniscus. We chose this configuration for the following reasons.

We were primarily interested in obtaining information about the H₂ and CO oxidation in the very complex porous gas diffusion electrodes used in fuel cells. To apply data obtained with simple immersed electrodes (wires, sheets, etc.) to such porous structures requires using models, the physical realism of which is difficult to prove. The uncertainties introduced by these models can easily lead to erroneous conclusions about the nature of the polarization. This is particularly true for molten carbonate electrodes. Thus, the observation of essentially linear polarization curves (*i* vs. *E*), or of long and linear Tafel lines ($\log i$ vs. *E*) might be interpreted as indications for ohmic or transfer polarizations even though these types of polarization curves can result from pure diffusion overvoltage under certain conditions.

To demonstrate the latter case of a long linear Tafel line assume identical and one-dimensional diffusion paths for H₂, H₂O, and CO₂. The diffusion overvoltage of reaction [1] is now²

$$\eta_d = \frac{RT}{2F} \ln \frac{(1 - i/i_{\text{H}_2\text{O}})(1 - i/i_{\text{CO}_2})}{1 - i/i_{\text{H}_2}} \quad [6]$$

The limiting currents (*i_j*) for species (*j*) are negative (cathodic) for CO₂ and H₂O, and positive for H₂. The latter is equal to the experimental anodic limiting current. Assume now that $-i_{\text{H}_2\text{O}}$ and i_{H_2} are much larger than i_{CO_2} . Then

$$i = i_{\text{CO}_2} (\exp \eta/b' - 1), \quad b' \equiv \frac{RT}{2F} \quad [7]$$

The shape of a polarization curve following Eq. [7] is practically indistinguishable from that for pure one-electron transfer polarization which is given by

$$i = i_0 [\exp \eta/b - \exp(-\eta/b)], \quad b: \text{Tafel slope} \quad [8]$$

Curves of this general shape were observed with dipping Pd wires (Fig. 3). Without being able to change i_{CO_2} by changing the diffusion path length, it is very difficult to analytically distinguish between the two kinds of polarization. A distinction would be possible if a limiting current were observed. However, in Eq. [7] the limiting current would be seen only under cathodic polarization. In the case of porous gas diffusion electrodes, we have the additional problem that even limiting currents for the reactant rarely allow one to calculate the diffusion overvoltage at lower currents (9).

These difficulties in applying data obtained with immersed electrodes to porous electrodes are to a degree avoided by using meniscus electrode data which are more directly transferable, i.e., without need for a model.

A second reason for using meniscus electrodes was the following. Accelerating the diffusional transport of the gases to and from the metal surface should diminish the effects of homogenous reactions such as the shift reaction which takes place between these gases in the liquid boundary adjacent to the metal surface. A meniscus is particularly effective in this respect. Most of the very large currents are generated in a narrow zone of the meniscus.

The third reason will become apparent from a study of Fig. 2 which reproduces the stationary polarization curve for a dipping Ni wire under a mixture of 0.512 H₂, 0.285 H₂O, 0.106 CO₂, and 0.097 CO (gas I, all in atm). The solid line was calculated from Eq. [6] with

² For this equation see, e.g., K. Vetter, "Electrochemical Kinetics," eq. 2.93, p. 163, Academic Press, New York (1967). It would be incorrect only if the reaction product is H⁺ (not OH⁻), and if such H⁺ could diffuse some distance into the surrounding melt. In such a case one could not use Fick's first law. This problem arises at the O₂ cathode. No problems arise from using Fick's law for the anode.

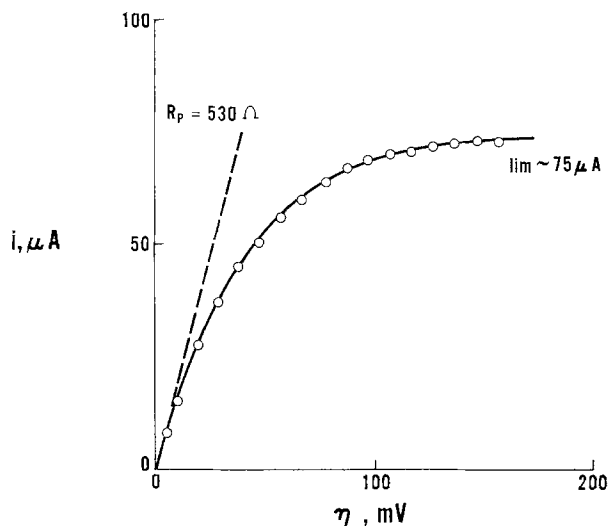


Fig. 2. Stationary polarization curve for dipping Ni wire on gas I $P_{H_2} = 0.512$, $P_{H_2O} = 0.285$, $P_{CO_2} = 0.106$, $P_{CO} = 0.097$ (all in atmospheres).

the fitting parameters $-i_{H_2O}$, $-i_{CO_2} \gg i_{H_2} = 75 \mu A$.³ The data fit this curve surprisingly well considering the fact that Eq. [6] applies to linear diffusion. The polarization resistance (R_p) in Fig. 2, calculated from the limiting current and Eq. [6], also agreed very well with the observed value.

The explanation of this agreement, we believe, is that the metal wires were poorly wetted by the melt, and that, therefore, liquid films above the visible meniscus should be of the nature of adsorption films. At extremely thin films no significant currents would be generated. Nearly all of the current would be produced in a narrow zone at the three-phase boundary where the diffusion path can be approximated by an average value. We assume that these conditions are somewhat analogous to a rotating wire which also can be frequently described with an average limiting current even though the exact transport conditions are very complex. Preliminary measurements yielded a value of $50^\circ \pm 10^\circ$ for the contact angle with Ni at these potentials. We also noticed an abrupt change in appearance of the metal at the visible meniscus line. We assume that this change in appearance was caused by minute rearrangements in the metal surface in contact with melt which did not show up under the microscope but which were easily visible with the naked eye.

Data such as those in Fig. 2 were generally well reproducible in shape but not in i_{lim} which tended to vary within a range of $\pm 20\%$. This variation presumably reflected difficulties in reproducing the meniscus shape. The best reproducibility was achieved by lowering the electrode end into the melt surface. Lowering it and then retracting it to the just touching position gave generally erratic results.

Other metal wires (Au, Pt, Pt-Rh-alloy) yielded results nearly identical with Fig. 2. By repeatedly oxidizing and reducing the Ni wire surface, the metal roughness was varied by a factor of about 3 which had no effect on the results. The relative roughness was estimated from the area change under the NiO peaks in voltammograms.

Figure 3 presents the results for a dipping Ni wire under a different gas, i.e., 0.799 H_2 , 0.140 H_2O , 0.014 CO_2 and 0.047 CO (gas II, all in atmospheres). The solid

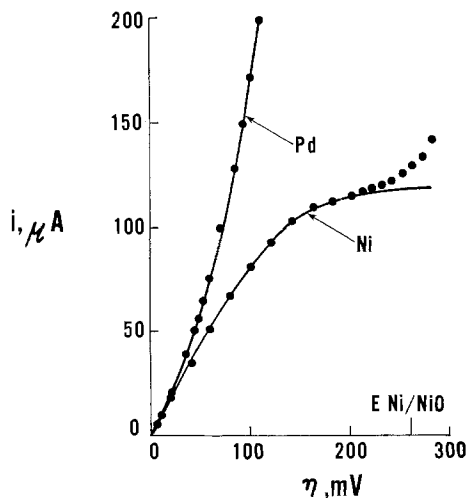


Fig. 3. Stationary polarization curves for dipping Ni and Pd wires on gas II $P_{H_2} = 0.799$, $P_{H_2O} = 0.140$, $P_{CO_2} = 0.014$, $P_{CO} = 0.047$ (all in atmospheres).

line was calculated using Eq. [6] with $i_{H_2} = 120 \mu A$. The two cathodic limiting currents were -65 and $-100 \mu A$. (These cathodic limiting currents are curve fitting parameters. They were not actually observed. In fact, it is impossible to observe them in the present case because carbon formation begins at quite small cathodic overvoltages.) We see that, at low η , the currents on gas II were smaller than on gas I despite the higher H_2 pressure on gas II. The upturn in current at $\eta > 200$ mV in Fig. 3 was due to onset of NiO formation which in this case prevented the observation of a well-defined limiting current. (The Ni/NiO potential against our reference is $-758 + 91.6 \log P_{CO_2}$).⁴

We cannot tell which one of the two cathodic limiting currents, required to fit the data in Fig. 3, is to be assigned to H_2O and which to CO_2 . They are of similar magnitude. Because of this, and because the H_2O pressure was ten times the CO_2 pressure, it appears that the product (solubility \times diffusion coefficient) for CO_2 is much larger than that for H_2O . It should also be mentioned that the data in Fig. 3 could not be fitted with Eq. [6] and only one cathodic limiting current in addition to i_{H_2} .

The values for i_{H_2} , required to fit the data in Fig. 2 and 3, show the expected proportionality to P_{H_2} , i.e., $i_{H_2}/P_{H_2} = 148 \pm 2 \mu A/atm$. For the cathodic currents we obtain, using the average of the two fitting parameters, $i_{H_2O}/P_{H_2O} \sim 600$ and $i_{CO_2}/P_{CO_2} \sim 6000 \mu A/atm$. Applying these values to gas I, we obtain for the data in Fig. 2 $i_{H_2O} \sim -170$ and $i_{CO_2} \sim -640 \mu A$. This agrees fairly well with the assumption made in fitting the data in Fig. 2, i.e., that the H_2O and CO_2 limiting currents were large compared with that for H_2 .

A more accurate determination of i_{H_2O}/P_{H_2O} and i_{CO_2}/P_{CO_2} was difficult and not attempted. In the case of H_2O , such a measurement would require large H_2 and CO_2 pressures, combined with a small H_2O pressure. Because of the shift reaction, such a gas would have a high CO pressure and interference by CO would be expected.

Included in Fig. 3 are the results for a dipping Pd wire under the same gas II. The solid line was calculated from Eq. [6] with $i_{H_2} \rightarrow \infty$ and the same values for i_{CO_2} and i_{H_2O} as were used to fit the Ni wire data. The anodic limiting current for the Pd electrode was very large. This is shown in Fig. 4 which extends the scale to higher overvoltages. The solid line in Fig. 4 is the calculated one.

Despite the very different shapes of the curves in Fig. 2, 3, and 4, they all follow Eq. [6] with approxi-

³ The relative order of the three limiting currents follows from the curve shape. From the observation of a limiting current follows a predictable concentration overvoltage at lower currents. In the present case this overvoltage left no room for any other polarization form. (The fact that in this case P_{H_2O} , $P_{CO_2} < P_{H_2}$ does not contradict this assumption if it is understood that it is the concentrations of H_2 , CO , CO_2 in the melt rather than the partial pressures which count. The Henry law constants can be very different for different gases.)

⁴ The NiO formation has been carefully investigated (unpublished work). The results clearly demonstrate that in the present work the results relate to Ni electrodes, except in those cases mentioned elsewhere in this paper.

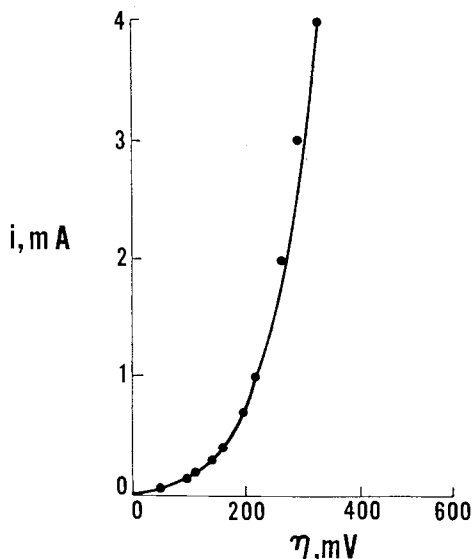


Fig. 4. Stationary polarization curve for dipping Pd wire. Extended range of polarization, same conditions as in Fig. 3.

mately the same values for the limiting currents for the gases, adjusting them for the particular gas pressures. The only exception is the H₂ limiting current on Pd which is hardly surprising.

The absence of an effect of metal nature (Au, Pt, Ni, Pt-Rh) on the results indicates that Pd is the exception and not Ni. The possibility that the low H₂ oxidation current on Ni, *vs.* that on Pd, is due to the influence of a NiO film is not supported. The similarity of the polarization curves for various metals (except Pd) also suggests that our data for Ni were not noticeably influenced by metallic H diffusion. This mode of hydrogen transport was of interest in applying wire data to porous Ni electrodes where the metallic diffusion may be much faster. For this reason, we studied this question in more detail.

Figure 5 shows results for a dipping Ni tube (0.225 cm ID, 0.318 cm OD). At this tube the inner meniscus was located above the outer one and significant hydrogen diffusion through the thin tube wall should have increased i_{H_2} relative to i_{H_2O} and i_{CO_2} . The data in Fig. 5 could be fitted reasonably well with Eq. [6] (solid line) and $i_{H_2} = 1550$, $i_{H_2O} = -840$, $i_{CO_2} = -1290$ μ A. The ratio of these values is the same as that for the corresponding currents for the Ni wire under the same gas (Fig. 3, *i.e.*, $i_{H_2} : (-i_{H_2O}) : (-i_{CO_2}) = 1.85 : 1.54 : 1$). This result suggests that the Ni wire

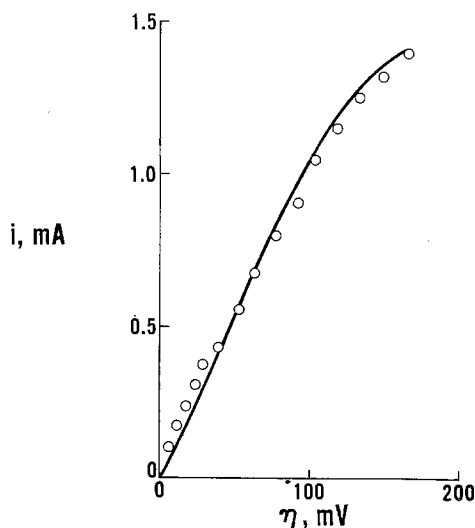


Fig. 5. Stationary polarization curve for dipping Ni tube. Same conditions as in Fig. 3.

data in Fig. 2 and 3 were not significantly affected by metallic hydrogen diffusion.

Figure 6 reproduces results for a solid Ni membrane and for a perforated foil of the same thickness and size. The perforated foil can serve, as does the dipping wire, as a simple model for a porous fuel cell anode. The data for the nonporous membrane cannot be related directly to wire data because of the very different transport paths for H₂ and for H₂O, CO₂. The perforated foil should show the current generated at numerous menisci added to the current from the nonporous foil. Significant supply of hydrogen through the metal to the menisci in the pores should have been noticeable because this supply would be more pronounced than with a dipping wire.

We estimated the contribution of the holes to the current by adjusting the wire data for the difference in (total) length of the three-phase boundary. The length of this line for a single pore was determined from photomicrographs of frozen and cross-sectioned electrodes withdrawn from the melt under operating conditions. We assumed that the meniscus had the same shape when liquid. The total length of the three-phase boundary was obtained by multiplying that of a single pore by the total number of pores in the foil. The sum of this estimated meniscus current and that for the nonporous foil matched fairly well the actual data (see Fig. 6). (In passing, it may be remarked that a similar adjustment of the wire data for total length of the three-phase line in porous Ni fuel cell anodes, estimated from the mean pore size, also agreed well with actual data for the latter. In this comparison metallic hydrogen diffusion was neglected.) The efficiency of a meniscus as a gas electrode can be appreciated from the fact that the total cross section of holes was only $\sim 3\%$ of the foil area.

One of the reasons why no interference by CO was noticed was that the CO pressures used were much smaller than the H₂ pressures. An equally important reason will become clear from the following.

At higher polarization (> 200 mV) the Ni oxidation obscured the anodic gas reaction on this metal. On more inert metals (Au, Pt, Pt-Rh), the current increased beyond the H₂ limiting current. These currents at > 200 mV were poorly reproducible. Closer investigation, using wires, suggested a strong dependency on time of exposure of the melt to gas, and some effect of H₂O pressure. We assumed that this reaction at larger η was due to the CO content of the gas and proceeded accordingly.

Figure 7 reproduces the data for the oxidation of dry CO/CO₂ mixtures at dipping wires of Ni, Au, and Pt. The data on Ni at > 200 mV were obscured by NiO formation. On Au and Pt, the current increased strongly above 200 mV, but was similarly unreproducible as that under H₂-containing gases in this potential region.

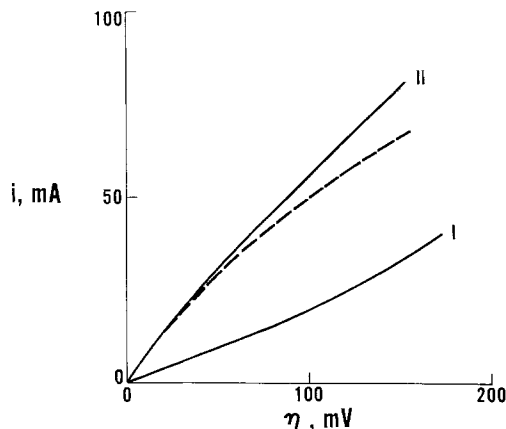


Fig. 6. Stationary polarization curves for a nonporous I and a perforated Ni foil II. Dashed curve: Sum of curve I and Ni-wire data, adjusted for meniscus length in pores of perforated membrane.

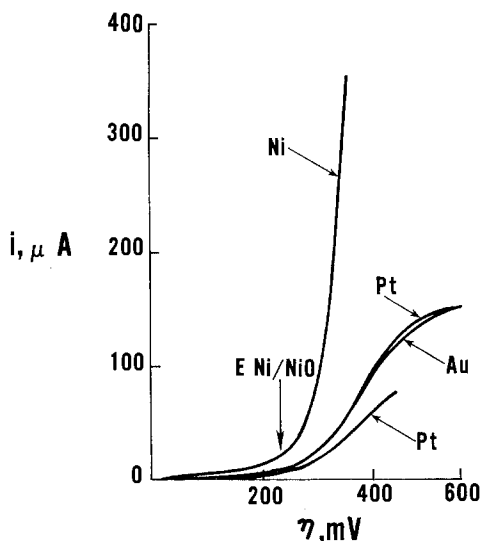


Fig. 7. Polarization curves for dipping wires of different metals on a mixture of 0.67 atm CO_2 and 0.33 atm CO.

Figures 8 and 9 show the changes in the voltammograms with elapsed time after replacing a CO/CO_2 mixture with an He/CO_2 mixture of the same CO_2 content (Fig. 8), and for the reverse process of reintroducing CO (Fig. 9). The slow changes evident in these figures could not be accelerated by agitating the melt. In contrast to the very slow changes in the main current wave at > 200 mV, the ocp responded very fast (seconds) to changes in CO pressure without, however, quite reaching for some time the equilibrium value on switching from He to CO. This behavior was in marked contrast to the H_2 reaction which responded very much faster to changes in the pressures of H_2 , H_2O , and CO_2 .

The results suggest that the oxidation of CO is a complex process. The first wave appears to be due to

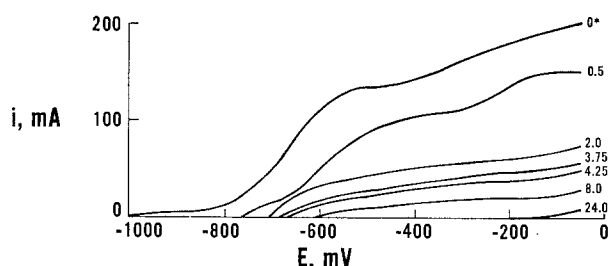


Fig. 8. Polarization curves for dipping Au wire. Parameters indicating time elapsed (hours) after replacing CO/CO_2 (1:2) mixture with an He/CO_2 (1:2) mixture.

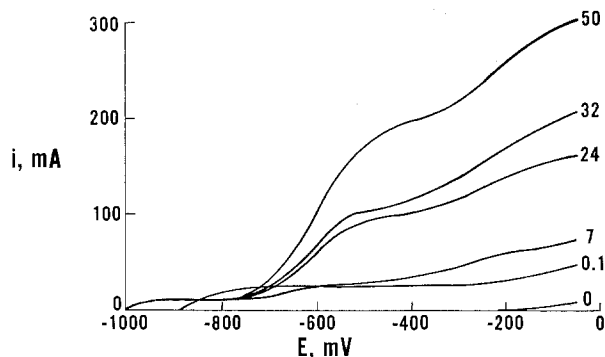
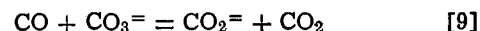


Fig. 9. Polarization curves for dipping Au wire. Parameters indicating time elapsed (hours) after replacing an He/CO_2 (1:2) mixture with a CO/CO_2 (1:2) mixture.

the direct oxidation of dissolved molecular CO. The much larger subsequent waves, of which there are at least two, apparently are not due to such dissolved CO molecules. It is difficult to reconcile the very slow increase of these waves with a simple dissolution process. The rapid response of the ocp to change in P_{CO} also contradicts such assumptions. Rather, these subsequent waves suggest oxidation of products formed by chemical reaction between CO and melt as has been suggested by Borucka and Appleby (10).

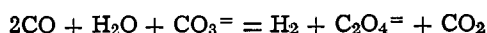
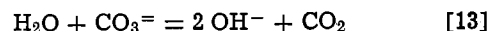
We analyzed a melt which had been exposed to CO for many hours. The frozen melt was dissolved in water. The solution was acidified and the remaining CO expelled by bubbling N_2 . Titration with permanganate revealed substantial quantities of oxidizable substance which was not, however, identified qualitatively. (It seems likely that whatever had been present in the melt would have been altered by our analytical procedure.) A blank test with melt not subjected to CO did not show such oxidizable substance.

Borucka and Appleby, who made similar observations with submersed electrodes at 800°C in ternary Li, Na, K-carbonate melt, suggested formation of CO_2^- ions



This substance, containing the highly reactive carbanion, would be expected to produce, e.g., formate in the course of our chemical analysis. Our analysis, therefore, would not have distinguished between CO_2^- and other possible compounds such as oxalate and/or formate in the melt. Borucka and Appleby based their conclusion of CO_2^- formation on the proportionality of the second wave to $1/P_{\text{CO}_2}$ according to reaction [9]. These authors did not report any difficulties in achieving equilibrium between melt and gas such as are exemplified by the data in Fig. 8 and 9. Because of these difficulties we have been unable to determine the effect of CO_2 pressure on the second current wave. Borucka and Appleby also apparently did not observe the third wave in Fig. 8 and 9.

Generally, one should not expect CO_2^- ions to be stable in the presence of CO_2 and/or H_2O . If this ion behaves similarly to other substances containing carbanion with a free electron pair at the carbon, we should expect formation of oxalate and/or formate (in the presence of H_2O). Formates decompose at high temperature to oxalate and H_2 . Thus the following reactions, which are analogous to well-known industrial processes, cannot be excluded at present

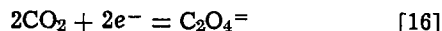
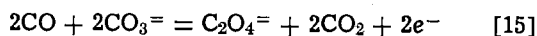


$$[14] = [11] + [12] + [13]$$

These reactions can serve to explain several of our observations, some of which cannot be rationalized with the assumption of CO_2^- ions. Intermediate formation of formate would explain the apparent accelerating effect of H_2O . Waves similar to those in Fig. 8 and 9 were also observed with shift gases but the waves at large η usually appeared much faster than with dry CO/CO_2 .

In formate, as in CO_2^- , the formal oxidation state of carbon is the same as in CO. In fact, CO is the anhydride of formic acid not only formally but also exhibited in organic reactions. In oxalate, the oxidation state of carbon lies between those in CO and CO_2 . The oxidation of CO to C_2O_4^- can therefore also proceed electrochemically, and chemical formation of oxalate can occur by an electrochemical mechanism.

Instead of reaction [10] we then have



Reactions [15] and [16] represent the two-step oxidation of CO to CO₂ if both run anodically.

In order to explain our observations, we would assume that reaction [16] has a smaller rate constant than reaction [15]. Now, at a given overall anodic polarization, the polarization of [15] decreases because of accumulation of oxalate produced by the current. The steady-state current is small and not much larger than the equivalent rate of oxalate diffusion into the bulk melt. This may be the reason why the polarization resistance for the gold meniscus electrode in Fig. 7 is so much larger than those for immersed electrodes (10). A meniscus electrode may accumulate ionic intermediates more rapidly than an immersed one.

At higher polarization C₂O₄⁼ would be oxidized and the current would increase accordingly. This current could be larger than the equivalent diffusion rate of CO because it would be the sum of the oxidation of CO and of accumulated oxalate. Removing or resupplying CO would have little effect on the large wave at η > 200 mV which would decay, or reappear slowly as oxalate is decomposed, or formed in the bulk melt (primarily by reaction [10]). However, the ocp would respond almost immediately to changes in P_{CO}. These intermediate ocp's although being mixed potentials, would be dictated by the CO/C₂O₄⁼ electrode rather than by the CO/CO₂ reaction

$$\text{ocp} \sim E_o + \frac{RT}{2F} \ln (\text{C}_2\text{O}_4 =) P_{\text{CO}_2} / P_{\text{CO}}^2 \quad [17]$$

At very slowly changing oxalate activity, and P_{CO₂} = const., this potential would change rapidly with CO pressure.

Finally, the discussed reactions can also serve as rationalization for the fact that one frequently finds, with H₂-containing gases, ocp's which lie substantially (60-100 mV) below the equilibrium potential for gas (11). Initially, with very little oxalate present, the potential of reaction [15] would be strongly negative and the ocp can be explained as the mixed potential between the H₂/H₂O and CO₂/C₂O₄⁼ reactions, both running cathodically, and the CO/C₂O₄⁼ electrode running anodically. Formation of CO₂⁼ could not be used as an explanation since any explanation requires an anodic partial reaction proceeding fast and at potentials below that of the H₂/H₂O electrode. CO₂⁼ would be produced from CO without change in state of oxidation.

Conclusions

The data in Fig. 2-6 suggest that the polarization of the H₂/H₂O electrode is essentially diffusion overvoltage. This conclusion is supported by the absence of effects of metal roughness and the kind of metal, and it is in full agreement with previous findings (2, 6-8).

In the presence of very fast hydrogen transport, the diffusion overvoltage due to the products (H₂O, CO₂) bore a striking resemblance with activation polarization, particularly because no limiting current was observed. Under certain conditions, the polarization curve (I vs. E) can be approximately linear over a fairly wide range of currents. Small concentrations of CO had no noticeable effect on the H₂ reaction.

The electrochemical oxidation of CO is far more complex. For meniscus electrodes, and at polarizations

smaller than 200 mV, this reaction is very slow. This reaction presumably is the oxidation of molecular CO (10). The nature of the reaction product(s) between CO and melt which gives rise to much larger current waves at η > 200 mV is not clear. It probably would require optical measurements in order to identify this product.

Applied to molten carbonate fuel cell anodes operating at around 650°C, the results suggest that H₂ is the fuel of choice. The utilization of CO as fuel is hindered by the very slow reaction rate at low overvoltages on meniscus electrodes which porous electrodes essentially are. The products of the direct reaction of CO with the melt are formed too slowly to sustain the cell current under steady operating conditions. Furthermore, the saturation concentration of molecular CO in the melt appears to be very small, much smaller than that of H₂. It seems questionable, therefore, that better catalysts would suffice to make efficient CO anodes.

As a consequence, we conclude that efficient CO utilization requires anode structures capable of functioning as internal shift reactors. Such a dual function implies long gas pores with walls which are catalytically active for the shift reaction. This shift reactor would be in series with the electrochemically active meniscus region at the end of the gas pore. Since long gas pores increase diffusional losses, it would appear necessary to use structures designed to optimize both functions. Such optimization, however, would become necessary only below a certain H₂/CO ratio for a given thickness.

Manuscript submitted May 1, 1979; revised manuscript received Nov. 7, 1979. This was Paper 376 presented at the Pittsburgh, Pennsylvania, Meeting of the Society, Oct. 15-20, 1978.

Any discussion of this paper will appear in a Discussion Section to be published in the December 1980 JOURNAL. All discussions for the December 1980 Discussion Section should be submitted by Aug. 1, 1980.

Publication costs of this article were assisted by United Technologies Corporation.

REFERENCES

1. W. M. Vogel and C. D. Iacovangelo, *This Journal*, **124**, 1305 (1977).
2. G. G. Arkhipov and G. K. Stepanov, in "Electrochemistry of Molten and Solid Electrolytes," Vol. 3, A. N. Baraboshkin, Editor, p. 73, New York Consultants Bureau (1964).
3. N. Busson, S. Palous, J. Millet, and R. Buvet, *Electrochim. Acta*, **12**, 1609 (1967).
4. A. Borucka, Abstract 369, p. 989, The Electrochemical Society Extended Abstracts, Fall Meeting, Pittsburgh, Pennsylvania, Oct. 15-20, 1978.
5. M. D. Ingram and G. J. Janz, *Electrochim. Acta*, **10**, 783 (1965).
6. G. H. J. Broers and M. Schenke, in "Fuel Cells," Vol. 2, G. J. Young, Editor, p. 6, Reinhold Publishing Corp., New York (1963).
7. I. Trachtenberg, "Fuel Cell Systems," Advances in Chemistry Series, No. 47, p. 232, American Chemical Society, Washington, D.C. (1965).
8. A. D. S. Tantram, A. C. C. Tseung, and B. S. Harris, in "Hydrocarbon Fuel Cell Technology," B. S. Baker, Editor, p. 187, Academic Press, New York (1965).
9. W. M. Vogel and J. T. Lundquist, *This Journal*, **117**, 1512 (1970).
10. A. Borucka and A. J. Appleby, *J. Chem. Soc., Faraday Trans. 1*, **73**, 1420 (1977).
11. See also, G. G. Arkhipov and G. K. Stepanov, in "Electrochemistry of Molten and Solid Electrolytes," Vol. 3, A. N. Baraboshkin, Editor, p. 67, New York Consultants Bureau (1964).

Simultaneous Determination of Quantum Efficiency and Energy Efficiency of Semiconductor Photoelectrochemical Cells by Photothermal Spectroscopy

Akira Fujishima,* Yasuhisa Maeda, and Kenichi Honda

Department of Synthetic Chemistry, Faculty of Engineering, The University of Tokyo, Hongo, Tokyo 113, Japan

and George H. Brilmyer** and Allen J. Bard*

Department of Chemistry, The University of Texas at Austin, Austin, Texas 78712

ABSTRACT

During a photoelectrochemical reaction only a portion of the light energy absorbed by the semiconductor (CdS or TiO₂ single crystal) is utilized in the electrode reaction. The unused portion of energy is expended through various mechanisms as heat. Therefore by monitoring temperature changes within the photoanode as a function of electrode potential and light intensity, information concerning the efficiency of the process can be obtained. Experimental results are presented and interpreted using a model for the energy balance within the system. This permits the determination of the quantum and energy efficiencies simultaneously without the need to calibrate the light source.

A number of photoelectrochemical cells based on semiconductor electrodes for photoelectrosynthesis (e.g., the photodecomposition of water) and the conversion of solar energy to electricity have been reported (1-15). The major factors determining the efficacy of these semiconductor electrode cells are the quantum efficiency for electron flow (i.e., number of electrons flowing/number of photons absorbed), and the power conversion efficiency (i.e., chemical or electrical power output/input radiant power). It is not uncommon to find near unity quantum yields for electron flow at a sufficiently high bias (positive for the case of n-type semiconductors) during irradiation with greater than bandgap energy light for many semiconductors. However, even when high quantum efficiencies have been obtained, the power efficiencies were much lower (10-15). For example, for photo-oxidation at a CdS single crystal anode, Wrighton *et al.* (15) reported that with an Se²⁻ solution the maximum monochromatic power efficiency obtained was 3.4% with a maximum quantum efficiency of 49%. Such findings demonstrate that the major part of the light energy absorbed by the semiconductor is not used for the photo-assisted oxidation but rather is converted to heat energy probably via radiationless transitions within the conduction band of the semiconductor (i.e., when the photon energy is in excess of the bandgap energy) or electron-hole recombination processes. Consequently, thermal measurements of the semiconductor electrode during electrolysis can aid in the determination of the efficiencies and perhaps in the elucidation of the mechanism of the cell processes.

We recently described a new spectroscopic method called Photothermal Spectroscopy (PTS) (16). This technique involves placing a thermistor on or in close proximity to a sample and measuring temperature changes (i.e., thermistor resistance changes) during sample irradiation with monochromatic light. This technique can be easily adapted to cases when the sample is a semiconductor electrode (17). Cahen (18) has also shown that similar measurements with photoacoustic spectroscopy can be used to determine the efficiency of solid-state photovoltaic devices. We report in this paper measurements of the conversion of light energy to chemical and/or electrical energy at

CdS and TiO₂ photoanodes by direct determination of the temperature changes of semiconductor electrodes. The results were interpreted using a theoretical equation for the energy balance within the system. In this manner the quantum efficiency and power efficiency could be determined without calibration of the irradiation source.

Experimental

Procedure.—The basic photothermal experiment was essentially carried out as previously described with slight modifications (16, 17). In these experiments the photoanodes studied were CdS and TiO₂ single crystals. The results reported here are for monochromatic radiation at wavelengths corresponding to energies greater than the bandgap energy (for example, for CdS, 490 nm). The photothermal responses were obtained for the photoanodes during both anodic polarization and under open-circuit conditions in the electrolyte solutions. The corresponding current and temperature changes were then plotted as a function of potential. Experiments were carried out in two laboratories with two different experimental setups (referred to as A and B).

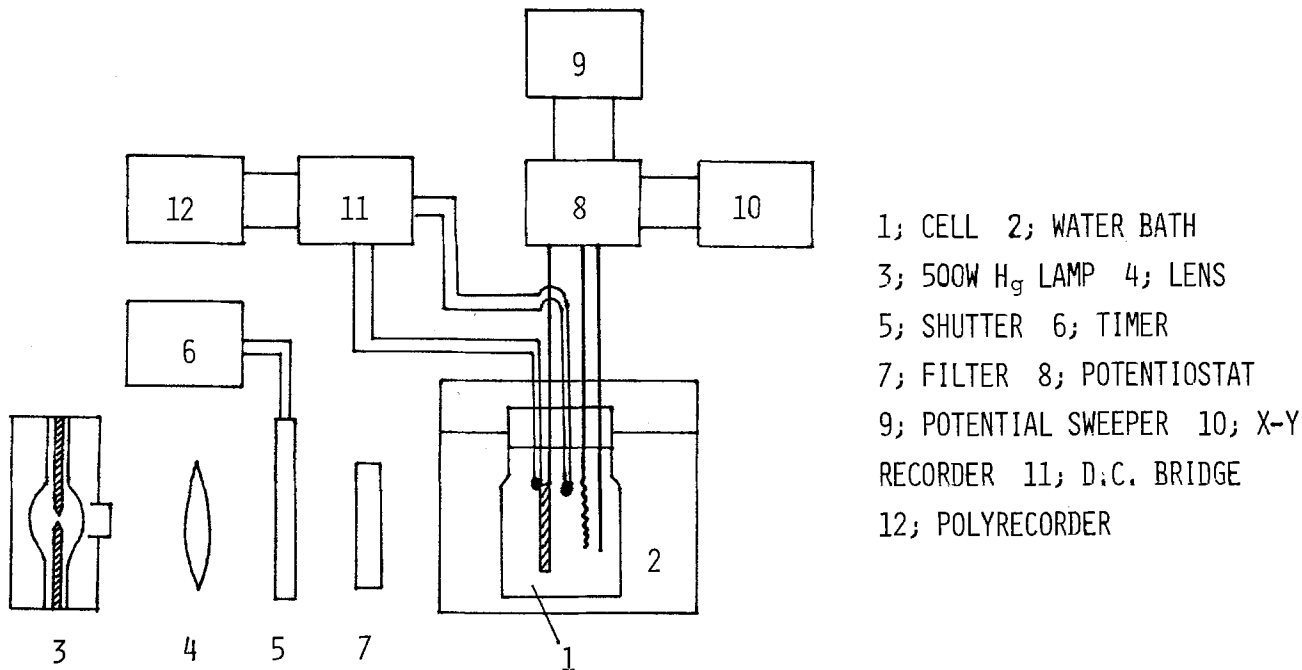
Instrumental.—Block diagrams of these are shown in Fig. 1 and 2. The apparatus (A) in Fig. 1 employed a 500W high pressure mercury lamp (Ushio Electric Company Limited) housed in an Ushio Model UI-501C housing. A lens was used to focus the light beam and interference filters (Koshin Kogaku Company Limited) were employed to select the wavelength of exciting light. A shutter with two timers, made by special order for this experiment (Ishikawa Seisakusho Company Limited) was used to fix precisely the irradiation period. System B is shown in Fig. 2. The light source was a 2500W short arc xenon lamp housed in an Oriel Model LH-152N housing. The output of the lamp was first chopped mechanically (on 20 sec; off 40 sec) and then focused using f/1 quartz optics on the entrance slit of a Jarrell-Ash Monochromator (Model 82-410). The resulting monochromatic light (10 nm bandpass) was then filtered of second order and finally focused on the photoanode within the electrochemical cell.

All cells were equipped with platinum counter-electrodes and saturated calomel reference electrodes (SCE). Irradiation was accomplished through optically flat windows both in the water baths and in the cells. The working electrodes were placed a sufficient distance from the cell window (~2 cm) to avoid any

* Electrochemical Society Active Member.

** Electrochemical Society Student Member.

Key words: photoelectrochemical, semiconductor electrode, quantum efficiency, energy efficiency, temperature changes.



- 1; CELL 2; WATER BATH
- 3; 500W H_g LAMP 4; LENS
- 5; SHUTTER 6; TIMER
- 7; FILTER 8; POTENTIOSTAT
- 9; POTENTIAL SWEEPER 10; X-Y RECORDER
- 11; D.C. BRIDGE
- 12; POLYRECORDER

Fig. 1. Measurement assembly, A

heating effects due to window heating. A nitrogen bubbler was employed for deoxygenating the solutions. The cell temperature was maintained by a water bath which in System A was thermostatted.

The working electrodes were cadmium sulfide single crystals [(001) surface] (Teikoku Tsushin Company Limited) which had dimensions $10 \times 10 \times 1$ mm and a carrier density of $4.8 \times 10^{16} \text{ cm}^{-3}$, and titanium dioxide single crystals [(001) surface] (Nakazumi Crystal Company Limited) each having dimensions about $10 \times 10 \times 1.5$ mm and treated by reduction to increase carrier density. The ohmic contacts were made by electroplating indium on one side of each crystal and then attaching a copper wire to the contact with conducting silver epoxy [Seisin Shoji Company Limited, No. 4992 (A), or Allied Products Corporation, New Haven, Connecticut (B)]. The back and sides of the crystal were insulated and mounted on a flat piece of glass attached to a glass rod with epoxy resin [Semedian Company Limited (A), or Devcon Incorporated, Danvers, Massachusetts (B)]. The semiconductor surfaces were polished with $0.3 \mu\text{m}$ polishing alumina prior to use. Then, in the case of CdS they were etched just before use in concentrated hydrochloric acid for 10 sec.

The structure of the semiconductor electrode (with a thermistor in place) is shown in Fig. 3. Matched pairs of thermistors were used: (A) Shibaura Elec-

tronics Model BSB4-41A; nominal resistance $4 \text{ k}\Omega$ sensitivity, $0.052^\circ\text{C}/\Omega$ or (B) Victory Engineering Incorporated, Model 32A223; nominal resistance, $2 \text{ k}\Omega$, sensitivity, $0.013^\circ\text{C}/\Omega$. Both had time constants of 0.4 sec when immersed in unstirred water. The thermistors were used in a differential arrangement with one thermistor held against the front surface of the electrode and the other positioned behind the electrode while not touching it. The cell was carefully positioned so that the monochromatic light beam struck the whole exposed surface of the electrode but neither of the thermistors. Thus a change in temperature of the electrode caused a resistive change in the thermistor and produced a voltage imbalance in (A) the d-c or (B) the a-c bridges. This small voltage was amplified and then displayed on strip chart re-

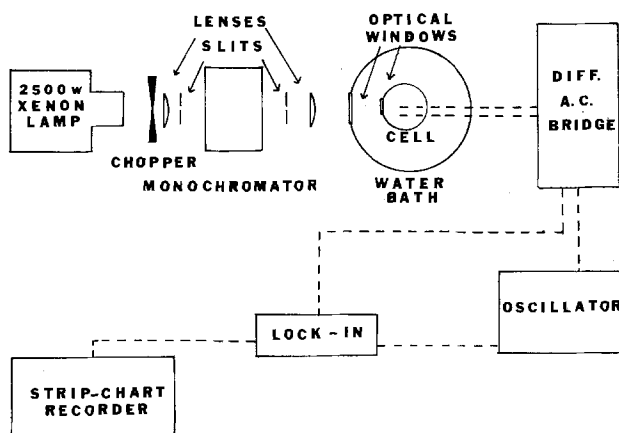
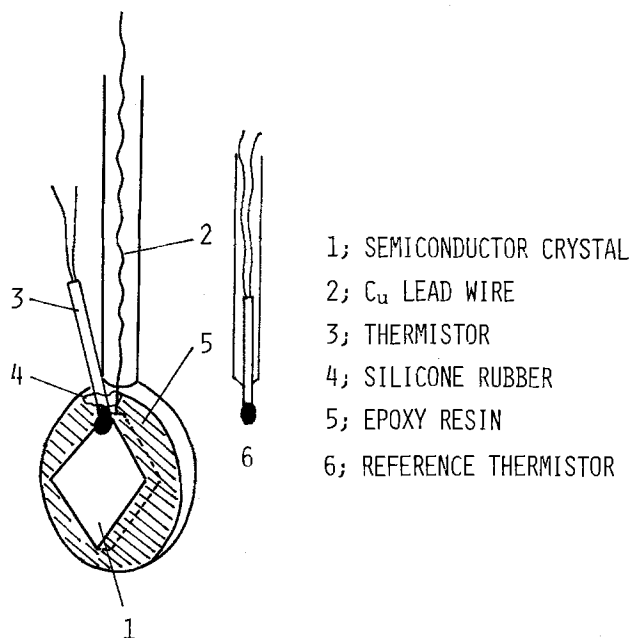


Fig. 2. Measurement assembly, B



- 1; SEMICONDUCTOR CRYSTAL
- 2; Cu LEAD WIRE
- 3; THERMISTOR
- 4; SILICONE RUBBER
- 5; EPOXY RESIN
- 6; REFERENCE THERMISTOR

Fig. 3. Structure of semiconductor electrode. Light irradiates only the semiconductor surface and not the thermistors. The contact to the electrode and the thermistor is insulated from the solution by a thin layer of epoxy cement.

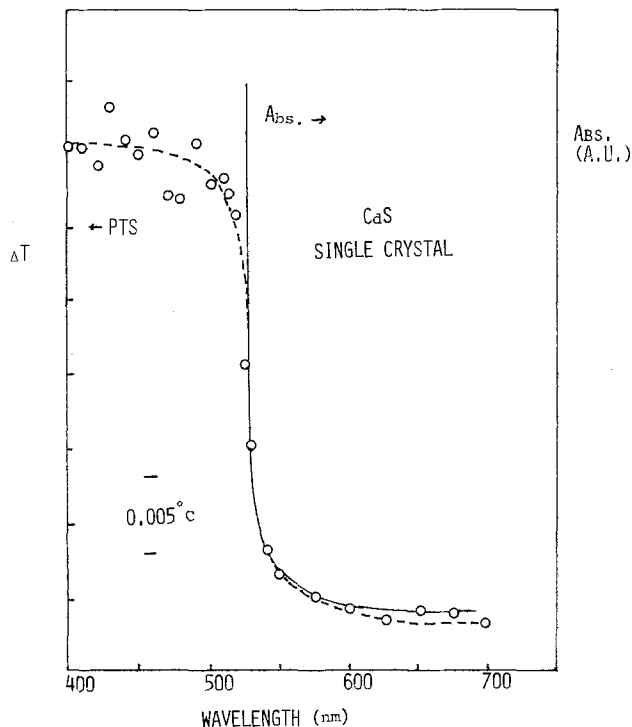


Fig. 4. Photothermal spectrum (PTS) of CdS single crystal. The solid line shows the absorption spectrum of the same crystal.

orders (A) Tao Electronics Model ERP-2T or (B) Tosely Model 7100B.

The current-potential and current-time curves were measured under potentiostatic conditions using potentiostats and potential programmers: (A) Nikko Keisoky Company Limited (Models NRG-301 and NPS-2) and (B) Princeton Applied Research (Models 173 and 175). Cyclic voltammograms and current-time curves were displayed on an X-Y recorder [(A) Yokokawa Type 3078 or (B) Houston Instruments Model 2000].

The monochromatic lamp intensity was measured precisely using either (A) a chemical actinometric method (potassium ferrous oxalate) or (B) an EG&G radiometer/photometer Model 550-1. All chemicals were of reagent grade and were used without further purification.

Results

Previous studies with photothermal spectroscopy (PTS) have shown that the temperature changes which occur upon light absorption correlate well with the results of optical absorption spectroscopy. This is demonstrated in the PTS of single crystal CdS (Fig. 4) where irradiation with light of energy greater than the bandgap produces electron-hole pairs which, if

the semiconductor is not a fluorescent, phosphorescent, or photochemically active material, recombine through radiationless transitions to produce heat. Although the spectrum shown in this figure was observed for the sample in air, similar PTS spectra of smaller magnitude were measured in water. The magnitude of the observed signal depends on the thermal conductivity and the heat capacity of the sample and its environment.

When an n-type semiconductor is used as a photoanode of a photoelectrochemical cell, that portion of the impinging radiant energy which is not converted to electrical energy or stored as chemical energy is dissipated as heat. One source of this heat is the difference between the photon energy, $E (=h\nu)$, and the bandgap energy, E_g ; this represents radiationless processes within the conduction band after light absorption. Other factors leading to heat dissipation are the difference between the valence band energy level and the solution redox level, $|E_{VB} - E_{redox}|$ and the difference (usually small) between the Fermi level and conduction band level, $|E_{F, flatband} - E_{CB}|$. Note that even when the quantum efficiency is unity, dissipation caused by these factors will cause heating at the electrode surface.

CdS/Fe(CN)₆³⁻, Fe(CN)₆⁴⁻ system.—The photothermal experiment was applied to the photo-oxidation of $K_4Fe(CN)_6$ at the CdS photoanode. The solution used was 0.1M $K_4Fe(CN)_6$, 0.001M $K_3Fe(CN)_6$, and 0.2M Na_2SO_4 as the electrolyte. Current-potential curves using the CdS electrode showed typical behavior of an n-type semiconductor electrode ($V_{FB} = -1.0V$ vs. SCE). The quantum efficiency of the CdS crystal was calculated to be nearly 100%, when the crystal was irradiated with greater than bandgap light (490 nm) (which was not absorbed by the electrolyte solution) and the electrode maintained at 2.0V vs. SCE. When the crystal was used as a photoanode in the solution, there was no change in photocurrent with time and no sulfur was detected on the surface after prolonged use. Therefore, we conclude that the $K_4Fe(CN)_6$ was the species oxidized and that the photoanode was stable in this solution.

The changes in temperature vs. time were measured at each applied potential while the photocurrent was recorded simultaneously. In the dark, no change in temperature was observed either at open circuit or at potentials positive of V_{FB} , where the observed currents were less than 10^{-9} A/cm². Figure 5 illustrates typical changes in temperature with time upon irradiation with greater than bandgap light (490 nm) at open-circuit condition and with various applied potentials. The temperature increased almost linearly when the light pulse was initiated. When the light pulse was terminated (after 20 sec irradiation) the temperature decreased quickly. We have already dis-

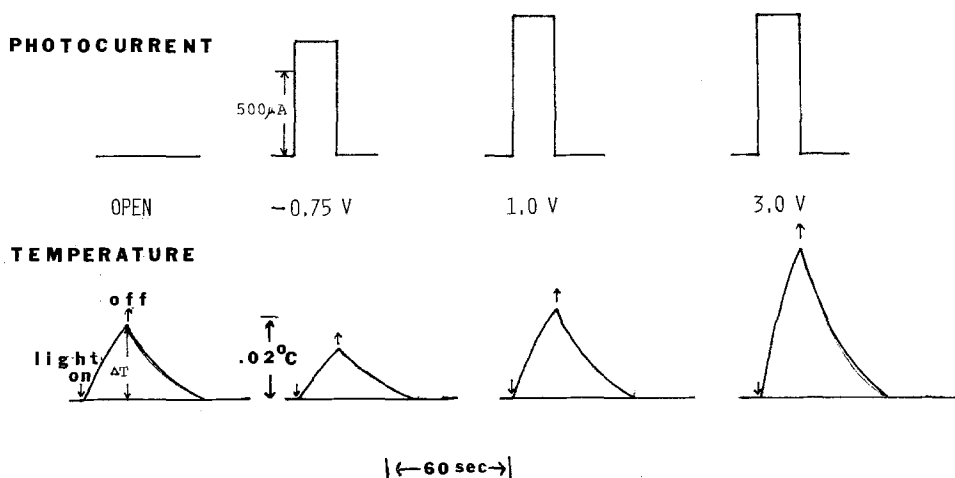


Fig. 5. The change in temperature vs. time for the CdS anode in 0.1M $K_4Fe(CN)_6$, 0.001M $K_3Fe(CN)_6$, and 0.2M Na_2SO_4 . Upper curves show the anodic photocurrent vs. time.

cussed this behavior in the simplified theory of PTS (16).

In Fig. 6 the temperature change *vs.* potential and the corresponding photocurrent-potential curves are experimentally plotted. These results are representative of those obtained with both systems. Compared with the heating observed at open circuit, the temperature increase was smaller at $-0.5V$ and larger at $2.0V$ and $4.0V$, respectively.

TiO₂/H₂SO₄ system.—As the TiO₂ photoanode, three different TiO₂ single crystals were used. Each was reductively treated under vacuum at various temperatures and for different lengths of time: (i) 3 hr at 650°C; (ii) 3 hr at 550°C; (iii) 4 hr at 800°C. The experiments were conducted using each TiO₂ single crystal electrode in a 1M sulfuric acid solution. Since the bandgap of TiO₂ is 3.0 eV, the wavelength of the light chosen for irradiation was 370 nm. The irradiation period was fixed at 20 sec in each case. The results of a typical experiment using the first (and most efficient) TiO₂ electrode are shown in Fig. 7. The three different crystals showed quite different slopes for the temperature increase *vs.* potential curves. The semiconductor electrode which produced the largest photocurrent showed the steepest slope.

Theoretical Treatment

The experimental results can be interpreted by considering the energy balance within the photoelectrochemical cell. The first aspect of this formulation will be to examine a simple electrochemical reaction from a thermodynamic point of view to determine what information concerning the system can be obtained via thermal measurements. This model will then be modified to fit the constraints of the photoelectrochemical system which is slightly more complex yet very similar. The resulting thermal relationships will then be used to investigate the quantitative aspects of various photoelectrochemical devices.

Calorimetry has been used by previous investigators to measure the enthalpy change (ΔH_c) which occurs during an electrochemical reaction (19). Such a system can be described by the equation

$$\Delta H_c = Q - W_e \quad [1]$$

where W_e is the electrical work into (or out of) the system and Q is the heat evolved in the system from reversible and irreversible work. The electrical work can be expressed in terms of current, voltage, and

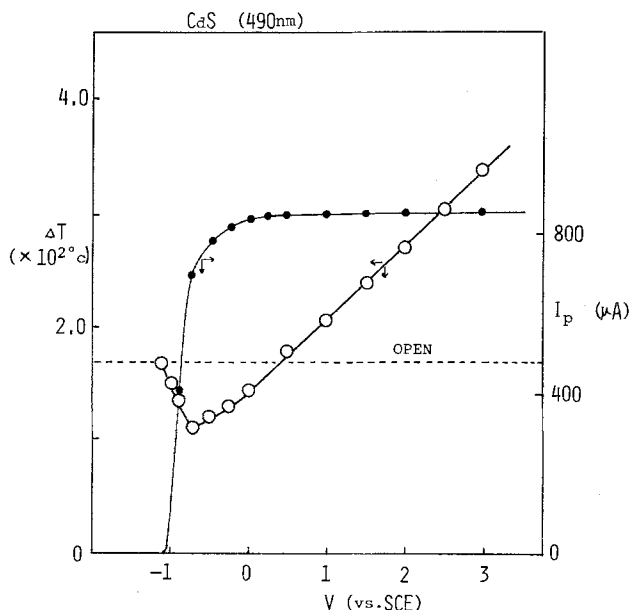


Fig. 6. Temperature change *vs.* potential (○) and photocurrent *vs.* potential (●) of the CdS single crystal electrode.

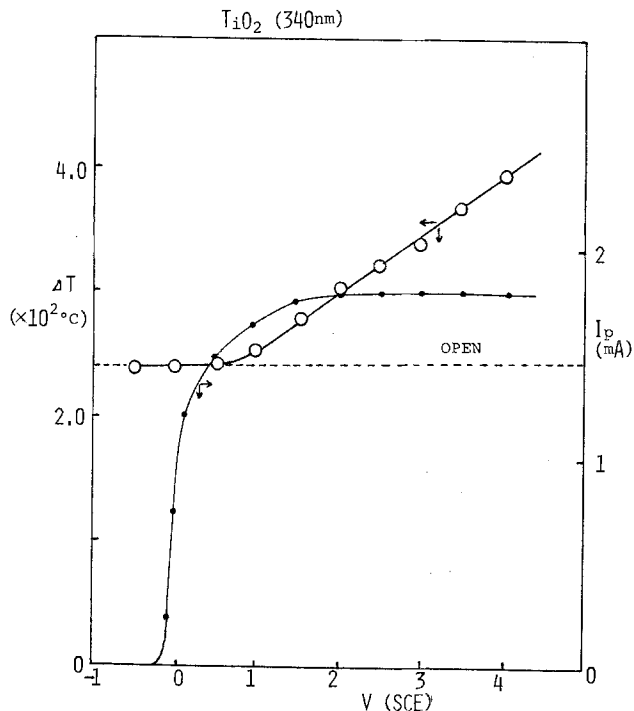


Fig. 7. Temperature change *vs.* potential (○) and photocurrent *vs.* potential (●) of the TiO₂ single crystal electrode. TiO₂ single crystal was treated in the vacuum for 3 hr at 650°C.

time (Vit) and the heat evolved in terms of an entropy change for the whole cell reaction ($T\Delta S$), activation energy, in terms of overpotential, η , (ηit) and the contribution from electrode and solution resistance, R , (i^2Rt). The total expression for the enthalpy is thus

$$\Delta H_c = T\Delta S + \eta it + i^2Rt - Vit \quad [2]$$

This equation is directly applicable to the photoelectrochemical situation by considering two additional energy terms and by reevaluating the electrochemical cell in terms of energy in and out.

For the case of a photoelectrochemical device one must now consider that the electrode is illuminated with a monochromatic light pulse having an energy E (eV/photon), with an average absorbed intensity I (photon/sec) for a time t (sec). Therefore the total energy put into the system per light pulse is EIt (eV). This energy can then either be used by the semiconductor to promote the electrode reaction with production of electrical work (Vit) or evolved as heat in the semiconductor (Q_{sc}) via recombination and other radiationless processes. The resulting equation for the overall photoelectrochemical reaction is

$$\Delta H_c = Q_T - W_T \quad [3]$$

where

$$Q_T = T\Delta S + \eta it + i^2Rt + Q_{sc} \quad [4]$$

$$W_T = EIt + Vit \quad [5]$$

therefore

$$\Delta H_c = T\Delta S + \eta it + i^2RT + Q_{sc} - EIt - Vit \quad [6]$$

Upon rearrangement the relationship between the measured quantity, Q_T , and the rest of the variables we obtain

$$Q_T = Q_{sc} + T\Delta S + \eta it + i^2RT = EIt + Vit + \Delta H_c \quad [7]$$

This final equation can now be related to the actual photoelectrochemical experiment. Although determination of Q_T by calorimetric means is possible, in the photothermal experiments relative temperature changes are measured and these are used to extract the desired information. This is done by comparing Q_T

measured during current flow in the photoelectrochemical experiment to that measured when the cell is at open circuit. In the open circuit case no net electrochemical reaction occurs and all the absorbed light energy is converted to heat, Q_{OT} , within the semiconductor, so that

$$Q_{\text{OT}} = Q_{\text{sc}} = EIt \quad [8]$$

This condition shows that the heat absorbed by the system is directly proportional to the light energy put into this system. Therefore

$$\frac{Q_{\text{T}}}{Q_{\text{OT}}} = \frac{Q_{\text{sc}} + T\Delta S + \eta it + i^2 RT}{EIt} \quad [9]$$

The corresponding relative change in temperature at the semiconductor surface can be represented by

$$\frac{\Delta T}{\Delta T^{\circ}} = \Delta T_{\text{rel}} = \frac{Q_{\text{sc}} + T\Delta S + \eta it + i^2 RT - k\Delta T}{EIt - k\Delta T^{\circ}} \quad [10]$$

where $k\Delta T$ is the heat lost by conduction from the electrode. Several assumptions must be made at this point concerning these temperature measurements. The first and most important is that temperature changes occurring on the electrode surface both in the semiconductor (Q_{sc}) and in solution ($T\Delta S + \eta it + i^2 Rt$) are equally detectable. This is a good assumption because in general, the thermal conductivity of the electrode is at least an order of magnitude greater than that of the solvent. Other assumptions which must be made to simplify the treatment are that the terms $k\Delta T$ and $i^2 RT$ are very small and can therefore be neglected. This is acceptable because the temperature changes measured are typically on the order of millidegrees and the total resistance is usually very low. Note that if the $k\Delta T$ terms are not negligible, corrected values of ΔT can be obtained by extrapolation of the initial linear portion of the temperature rise with time to the value ΔT_{corr} at the time when the temperature begins to fall. In the activation term the overpotential, η , is actually $V - V_{\text{FB}}$ (where V_{FB} is the flatband potential of the semiconductor) so that Eq. [10] can be written as

$$\frac{\Delta T}{\Delta T^{\circ}} = \frac{Q_{\text{sc}} + T\Delta S}{EIt} + \frac{i(V - V_{\text{FB}})}{EI} \quad [11]$$

The left side of the equation can be given specific energy units to facilitate the mathematical treatment to finally yield

$$E \frac{\Delta T}{\Delta T^{\circ}} = \frac{Q_{\text{sc}} + T\Delta S}{It} + \eta_{\text{q}}(V - V_{\text{FB}}) \quad [12]$$

where $\eta_{\text{q}} = i/I =$ quantum efficiency of the photooxidation and $(Q_{\text{sc}} + T\Delta S)/It$ is the total heat change (usually evolved) in the system (at the photoanode). Therefore under constant illumination conditions (i.e., EIt held constant) a plot of $E \frac{\Delta T}{\Delta T^{\circ}}$ against $(V - V_{\text{FB}})$ yields the quantum efficiency, η_{q} , from the slope of the straight line and the loss term, $(Q_{\text{sc}} + T\Delta S)/It$, is obtained from the intercept of the $E \frac{\Delta T}{\Delta T^{\circ}}$ axis at $V = V_{\text{FB}}$ as shown in Fig. 8. We define the single electrode, monochromatic energy efficiency of the system as

$$\eta_{\text{e}} = \frac{EIt - Q_{\text{sc}}}{EIt} \times 100 \quad [13]$$

The efficiency as defined above can then be obtained by making the appropriate correction for the entropy change associated with the electrode reaction. The details associated with this correction are described in the following discussion.

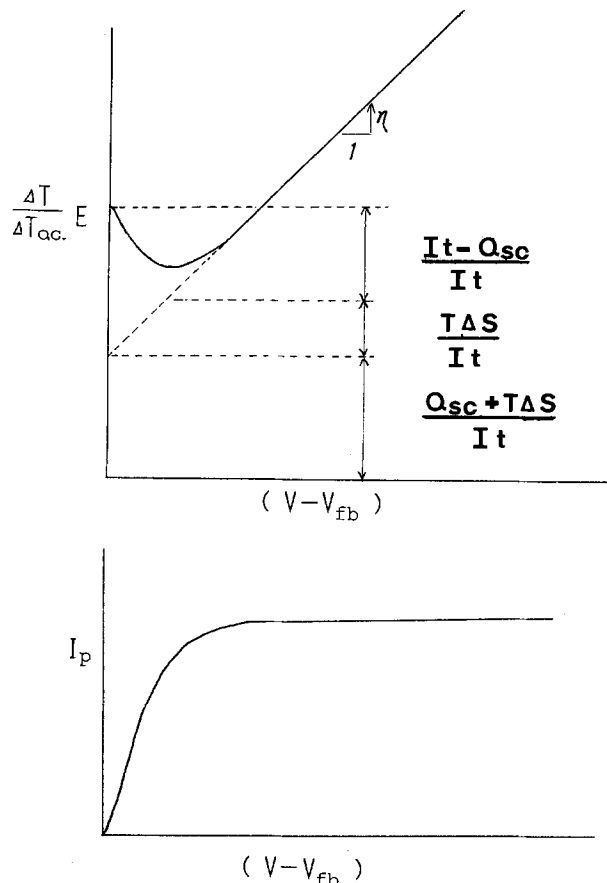


Fig. 8. (Top) Theoretical behavior of the photothermal signal vs. potential according to Eq. [12]. (Bottom) Photocurrent vs. potential.

Discussion

To illustrate the use of the Eq. [12] in obtaining the quantum and energy efficiencies, the results shown in Fig. 6 and 7 are replotted in Fig. 9 and 10, in which the ordinate is $E \frac{\Delta T}{\Delta T_{\text{oc}}}$ and the abscissa is $(V - V_{\text{FB}})$.

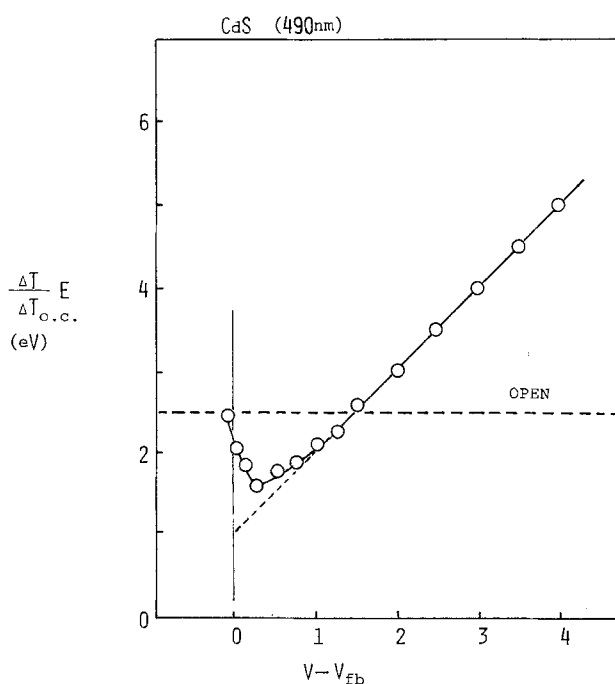


Fig. 9. Normalized photothermal signal vs. potential from the flatband potential of the CdS electrode.

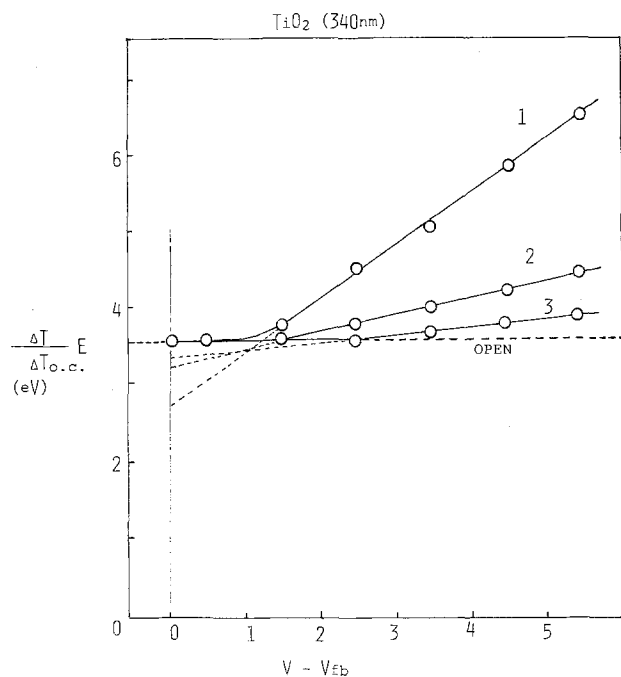


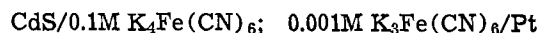
Fig. 10. Normalized photothermal signal vs. potential from the flatband potential of the TiO_2 electrodes. TiO_2 single crystals were treated in the vacuum atmosphere, No. 1: for 3 hr at 650°C ; No. 2: for 3 hr at 550°C ; No. 3: for 4 hr at 800°C .

For the $\text{CdS}/\text{Fe}(\text{CN})_6^{3-}$, $\text{Fe}(\text{CN})_6^{4-}$ system the temperature increase of $1.7 \times 10^{-2}^\circ\text{C}$ which was measured at open circuit corresponds to $E = 2.5$ eV because 490 nm monochromatic light was used to excite the CdS electrode (Fig. 9). In the limiting photocurrent region, we find a straight line with a slope equal to 1.0. This means that the quantum efficiency of the photoreaction on the CdS electrode is unity, which is similar to the value found from the photocurrent and the calibrated light intensity (number of photons striking the electrode). From the intercept of the Y-axis obtained by extrapolating the linear portion of the curve to the flatband potential, we can calculate the energy efficiency of the photoconductor reaction, if entropic heat attributable to the electrode reaction ($T\Delta S$ or the Peltier heat) can be obtained. The behavior known as the electrochemical Peltier effect (i.e., the entropy change at the electrode surface) has been investigated by Tamamushi (20). This effect can be attributed to three contributions: the entropy of the electrode reaction, the entropy attributed to the migration of ions and electrons, and the entropy caused by electrochemical polarization. Tamamushi investigated this effect during a study of the electrochemistry of the $\text{K}_4\text{Fe}(\text{CN})_6/\text{K}_3\text{Fe}(\text{CN})_6$ redox couple at a gold electrode. Cooling was observed during the oxidation step and heating occurred during reduction at potentials near the equilibrium potential; this can be attributed primarily to an entropy effect of the electrode reaction. This same effect must also be included in the photochemical reaction on the CdS surface.

To obtain the appropriate corrections in our thermal measurements, the electrochemistry of the $\text{K}_4\text{Fe}(\text{CN})_6/\text{K}_3\text{Fe}(\text{CN})_6$ couple at a platinum electrode was studied. The entropy effect was similar to that found by Tamamushi in which cooling occurred under the anodic polarization and an equal amount of heating occurred under the cathodic polarization. It is only necessary to make this further correction for the electrochemical reaction entropy near the equilibrium potential, because the polarization effect was already included in the $\eta_q(V - V_{\text{FB}})$ term in Eq. [8] and the migration effect would be negligible (the solution and the CdS electrode, resistivity = 1-2 Ω/cm , were both highly conductive).

In this same solution, heating was also observed during the dark cathodic reaction on the CdS electrode under nitrogen bubbling. The amount of heating was $3.4 \times 10^{-3}^\circ\text{C}$ (which corresponds to 0.5 eV in this case), when a cathodic current of 850 μA (which was the same as the saturated photoanodic current) was passed for 20 sec. Therefore, assuming that the photoanodic reaction entropy is equal but opposite to this entropy (from the results on the platinum electrode), the endothermic entropy change on the CdS photoanode for a 20 sec light pulse was determined to be 0.5 eV.

The value of the intercept in Fig. 9, $(Q_{\text{sc}} + T\Delta S)/It$, was 1.0 eV. So, taking $T\Delta S/It = 0.5$ eV (endothermic), we find $Q_{\text{sc}}/It = 1.5$ eV. In this case (490 nm irradiation), the monochromatic energy conversion efficiency is $100 \times EIt - Q_{\text{sc}}/EIt = 100 \times 1.0/2.5 = 40\%$. This result is also consistent with the fact that only a fraction of the energy is being utilized for the oxidation of $\text{Fe}(\text{CN})_6^{4-}$ to $\text{Fe}(\text{CN})_6^{3-}$; i.e., for the whole cell

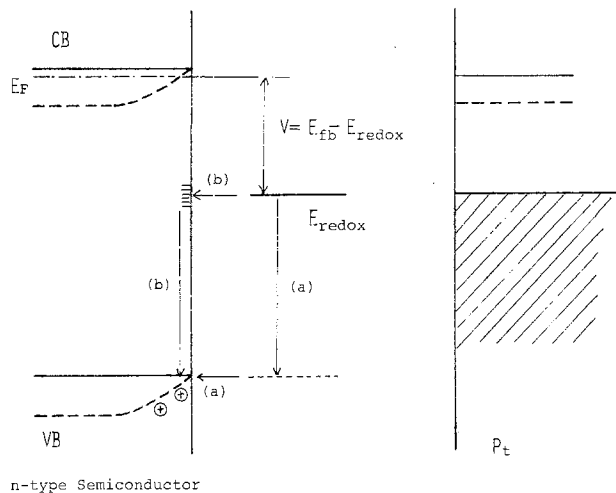


the maximum cell voltage obtainable is $|V_{\text{FB}} - V_{\text{redox}}| \approx 1.0\text{V}$, while the energy of the incoming radiation is 2.5 eV (490 nm).

As shown in Fig. 10 for the $\text{TiO}_2/\text{H}_2\text{SO}_4$ system, three different lines were obtained, with slopes of 0.7, 0.3, and 0.1. These correspond to the quantum efficiencies of the different TiO_2 photoanodes. Again, as in the case of CdS, calculations using the intercepts of these lines can yield the various energy efficiencies. As is obvious from the results in Fig. 10, the photoanode which shows the smallest quantum efficiency (i.e., smaller slope) has the largest intercept (i.e., the lowest energy conversion efficiency). To get the actual energy conversion efficiency, we must again correct for the Peltier entropy effect, which is proportional to the magnitude of the photocurrent. The oxidation on the TiO_2 photoanode was oxygen evolution based on water decomposition. Contrary to the oxidation of $\text{Fe}(\text{CN})_6^{4-}$ as mentioned above, oxygen evolution on the electrode showed exothermic heating behavior, mainly due to the entropy of the electrochemical reaction. To make the appropriate corrections for this entropy effect the reduction of $\text{K}_3\text{Fe}(\text{CN})_6$ was examined at TiO_2 and platinum and the results compared to those observed during the oxidation of water at platinum. In this manner the magnitude of the entropy effect occurring during the photo-oxidation at TiO_2 could be estimated. When the anodic photocurrent was 1.8 mA (No. 1 in Fig. 10), it was found that the entropy effect corresponded to 0.5 eV. Therefore for electrode 1, since $E = 3.5$ eV (340 nm), $Q_{\text{sc}} + T\Delta S/It = 2.7$ eV (from the intercept), and $T\Delta S/It = -0.5$ eV (the entropy effect). Therefore, $Q_{\text{sc}}/It = 2.2$ eV. The energy conversion efficiency can be determined as

$$100 \times \frac{EIt - Q_{\text{sc}}}{EIt} = 100 \times 1.3/3.5 = 37\%$$

The fraction of the photon energy that is not used in the oxidation of the redox species is dissipated as heat via two possible mechanisms as shown in Fig. 11. The first mechanism, (a), represents the filling of a valence band hole by the reduced species in solution to produce a vibrationally excited species. This energy is quickly dissipated in the solution as heat. The second mechanism, (b), represents the isoenergetic electron transfer from the reduced species in solution to a surface state which then recombines with a hole in the valence band of the semiconductor, with the heat dissipated in the semiconductor itself. However, at this time we can not distinguish the difference between heat produced in solution or heat on the electrode itself. Therefore neither mechanism can be verified using only the temperature measurement.



n-type Semiconductor

Fig. 11. Maximum open-circuit photopotential and heat dissipation mechanism.

Conclusion

By *in situ* temperature measurements of the semiconductor electrode, the quantum and energy efficiency of the electrode reaction could be obtained. The advantage of this type of measurement lies in the fact that it is a relative measurement and therefore does not depend upon knowing the light intensity. This eliminates the need for calibration of the excitation source and establishes a method by which results in different laboratories can be compared more easily. A disadvantage of the technique is that the precision of the measurements ($\sim \pm 1\%$) limits its use to the more efficient systems.

In considering the efficiencies obtained in this manner one should note that the results presented refer to the efficiency of the electrode reaction and not to the entire photoelectrochemical cell. In this work no attention was given to the reaction occurring at the counterelectrode or to whether the cell was photovoltaic or photosynthetic. In order to treat the entire system thermal measurements during the cell reaction would be necessary. Such measurements could be carried out in a manner similar to that described above or by placing the entire photoelectrochemical cell in a photocalorimeter and measuring the overall thermal change of the cell resulting from illumination. By using the former method both the electrode and cell efficiencies could be determined while calorimetric techniques would only yield the cell efficiency.

Acknowledgment

The support of this research by the National Science Foundation and the U.S. Army Research Office—Durham is gratefully acknowledged.

Manuscript submitted June 18, 1979; revised manuscript received Oct. 19, 1979.

Any discussion of this paper will appear in a Discussion Section to be published in the December 1980 JOURNAL. All discussions for the December 1980 Discussion Section should be submitted by Aug. 1, 1980.

Publication costs of this article were assisted by The University of Texas at Austin.

REFERENCES

1. A. Fujishima and K. Honda, *Nature*, **238**, 37 (1972).
2. A. Fujishima, K. Kohayakawa, and K. Honda, *This Journal*, **122**, 1487 (1975).
3. H. Yoneyama, H. Sakamoto, and H. Tamura, *Electrochim. Acta*, **20**, 341 (1975).
4. K. L. Hardee and A. J. Bard, *This Journal*, **123**, 1027 (1976).
5. A. J. Nozik, *Nature*, **257**, 383 (1975).
6. G. Hodes, D. Cahen, and J. Manassen, *ibid.*, **260**, 312 (1976).
7. H. Gerischer and J. Gobrecht, *Ber. Bunsenges. Phys. Chem.*, **80**, 327 (1976).
8. B. Miller and A. Heller, *Nature*, **262**, 680 (1976).
9. A. B. Ellis, S. W. Kaiser, J. M. Bolts, and M. S. Wrighton, *J. Am. Chem. Soc.*, **99**, 2839 (1977).
10. H. Gerischer, *J. Electroanal. Chem. Interfacial Electrochem.*, **58**, 263 (1975).
11. M. S. Wrighton, A. B. Ellis, P. T. Wolczanski, D. L. Morse, H. B. Abrahamson, and D. S. Ginley, *J. Am. Chem. Soc.*, **98**, 2774 (1976).
12. J. G. Mavroides, D. I. Tchernev, J. A. Kafalas, and D. F. Kolesar, *Mater. Res. Bull.*, **10**, 1023 (1975).
13. Y. G. Chai and W. W. Anderson, *Appl. Phys. Lett.*, **27**, 183 (1975).
14. M. S. Wrighton, D. S. Ginley, P. T. Wolczanski, A. B. Ellis, D. L. Morse, and A. Linz, *Proc. Natl. Acad. Sci. U.S.A.*, **72**, 1518 (1976).
15. A. B. Ellis, S. W. Kaiser, and M. S. Wrighton, *J. Am. Chem. Soc.*, **98**, 6855 (1976).
16. G. H. Brilmyer, A. Fujishima, K. S. V. Santhanam, and A. J. Bard, *Anal. Chem.*, **49**, 2057 (1977).
17. A. Fujishima, G. H. Brilmyer, and A. J. Bard, in "Semiconductor Liquid-Junction Solar Cells," A. Heller, Editor, p. 172, The Electrochemical Society Softbound Proceedings Series, Princeton, N.J. (1977).
18. D. Cahen, *Appl. Phys. Lett.*, **33**, 810 (1978).
19. J. M. Sherfey and A. Brenner, *This Journal*, **105**, 665 (1958).
20. R. Tamamushi, *J. Electroanal. Chem. Interfacial Electrochem.*, **45**, 500 (1973); **65**, 263 (1975).

Electrochemical Surface Reactions on PbTe

H. H. Strehblow^{*,1}

Institut für Physikalische Chemie der Freien Universität Berlin, D-1000 Berlin 33, Germany

and M. Bettini

Fraunhofer-Institut für Angewandte Festkörperphysik, D-7800 Freiburg, Germany

ABSTRACT

The electrochemical reactions of PbTe in acetate buffer of pH 4.9 were compared with those in strongly acidic and alkaline solutions. Rotating ring-disk studies provided information on the nature of soluble products, while the composition of the surface layers was analyzed by XPS. In the potential range of 0–0.4 V_H a Te-layer of only $\sim 3\text{\AA}$ thickness is formed and an equivalent amount of Pb^{2+} is dissolved, this Te-layer being too thin for coating or passivation purposes. At $>0.4 V_H$ an oxide layer is formed which contains mostly TeO_2 (H_2TeO_3) and $\sim 30\%$ PbO on the surface. There is a competing process between oxide film growth and dissolution of approximately 50% of these oxides. The reduction of TeO_2 and PbO to elemental Te and PbTe occurs at $<0 V_H$ and the reduction of Te to soluble tellurides at $<-0.5 V_H$. By appropriate cyclic oxidation and reduction the Pb concentration in the anodic oxide and the reduced layer can be further decreased to $\sim 15\%$. The oxide layers are not good insulators ($\sim 1000\text{\AA}$ film, anodic current $\geq 10 \text{ mA/cm}^2$ at $1.5 V_H$). The use of electrochemical processes on PbTe for forming well passivating or insulating surface layers is limited.

The best qualities of infrared photovoltaic detectors on PbTe and $\text{Pb}_{0.8}\text{Sn}_{0.2}\text{Te}$ materials can only be obtained by a surface passivation which minimizes surface leakage with respect to bulk leakage. Investigations of $\text{PbTe-Pb}_{0.8}\text{Sn}_{0.2}\text{Te}$ heterodiodes have shown that the reverse currents of diodes with Te-coated surfaces are more than an order of magnitude lower than those with surfaces oxidized in air (1). The Te coating has been prepared by preferential etching of the PbTe and $\text{Pb}_{0.8}\text{Sn}_{0.2}\text{Te}$ surfaces. A previous paper (2) has demonstrated that PbTe surfaces etched with HBr-Br_2 or HNO_3 yield thin elemental Te layers ($\sim 600\text{\AA}$ thick) which, however, may be quite porous. They only partially prevent oxidation at the underlying PbTe interface and are insufficiently passivating. Therefore, new processes producing thin protective Te layers on PbTe and $\text{Pb}_{0.8}\text{Sn}_{0.2}\text{Te}$ surfaces are still desirable.

Electrochemically controlled etching gives decisive advantages with respect to pure chemical processes. The surface reactions can be controlled using an electronic potentiostat. Formation, reduction, and thickness of surface layers are determined by the fixed electrode potential and are measured by the electrical charges related to the corresponding reactions. The semiconductor surface can be prepared with identical starting conditions and can be cleaned of any initial surface layers by dissolution processes at appropriate potentials. Even electronically insulating continuous and poreless surface layers may be formed because the redox process at the oxide/electrolyte interface is replaced by the potentiostatic circuit. One may envisage the direct anodic oxidation of PbTe to Te and dissolution of Pb^{2+} into the electrolyte similar to the preferential etching by oxidizing solutions. A different possibility for forming a Te layer exists in the anodic oxidation of the PbTe surface preferentially into a TeO_2 film and its subsequent reduction to elemental Te. The latter process would also yield information on oxide layers which may be useful for CCD device fabrication similar to the case of $\text{Hg}_{0.7}\text{Cd}_{0.3}\text{Te}$ (3). In general MIS devices and CCD operation on PbTe are limited by the high dielectric constant of PbTe.

For the preparation of Te and TeO_2 layers on PbTe and $\text{Pb}_{0.8}\text{Sn}_{0.2}\text{Te}$ the conditions for the different oxida-

tion and reduction processes must be known. The electrochemical reactions become more complex with an increasing number of elements in the semiconductor compound. Therefore, the electrochemical behavior of the simpler binary compound PbTe is presented in this paper and is compared with the properties of pure Pb and Te.

Like PbTe, Te is a semiconductor with a low bandgap of about 0.3 eV (4). The Fermi levels for n and p doping are close to each other and no rectification is observed in diode structures at 300°K . Therefore, the electrochemical behavior of these materials should be similar to those of metals and alloys. Usual potentiodynamic and potentiostatic experiments were performed and the soluble products were determined with a rotating ring-disk arrangement. The composition of the surface after the different electrochemical treatments was examined by XPS analysis. The value of XPS for the surface analysis of electrochemically treated semiconductors has been demonstrated by depth profiling of anodic oxide films (5).

Experimental

The samples were mostly PbTe films freshly prepared by evaporation with a modified hot wall technique (6) on cleaved $\langle 111 \rangle$ BaF_2 platelets. The epitaxially grown films were single crystalline, 5–10 μm thick with a surface of $\langle 111 \rangle$ orientation and 0.3 cm^2 area. The sample surface was covered by native oxide during air exposure before the electrochemical experiments (7). Depending on the partial pressure of Te p- and n-type films were grown with typical electrical properties of $n, p = 10^{17}\text{--}10^{18} \text{ cm}^{-3}$ and μ (300°K) = $1000\text{--}2000 \text{ cm}^2\text{V}^{-1} \text{ sec}^{-1}$. However, the doping was irrelevant, because we did not observe differences in the electrochemical behavior between n and p samples, in agreement with the low bandgap. For test experiments and the ring-disk arrangement large sized poly and single crystalline bulk material was used. The disk front surface was oriented to $\langle 111 \rangle$ within 10 degrees and the doping was $p \sim 10^{18} \text{ cm}^{-3}$.

The Te experiments were performed with large sized polycrystalline platelets and disks with front surface parallel to the $\{110\}$ cleavage planes (4). The electrical properties are $p \sim 10^{16} \text{ cm}^{-3}$ and μ (77°K) $\sim 10^3 \text{ cm}^2\text{V}^{-1} \text{ sec}^{-1}$.

The specimens were welded with indium to a copper wire for good ohmic contact. The contact area was covered with epoxy resin and fixed to a glass tube for good

* Electrochemical Society Active Member.

¹ Present address: Institut für Physikalische Chemie II, Universität Düsseldorf, D-4000 Düsseldorf, Germany.

Key words: rotating ring disk, film growth, passivation, XPS analysis.

mechanical stability of the electrodes. No resin was used for the XPS measurements so as to achieve a rapid sample transfer from the electrolyte into the UHV chamber. Electrochemical reactions at the unprotected contact area do not interfere with the processes at the clean parts of the samples and therefore no contamination is observed. A potentiostat, Tektronix pulse generators of Type 26 G3, and a function generator for linear potential variations were used for the electrochemical measurements. The pulse program was directly fed into the adder of the potentiostat.

The formation of soluble products during the electrochemical reactions was measured with a rotating Pt ring-PbTe(Te) disk electrode. A cylindrical PbTe specimen was drilled ultrasonically from a single crystal and covered with a 0.025 cm epoxy film. Two half Pt cylinders were fixed to the specimen and the whole assembly was inserted into a Plexiglas cylinder filled with epoxy resin. The front plane was mechanically polished with a final 1 μm graded diamond paste. The tellurium ring-disk electrode was prepared in the same way. A modified ASR 2 Pine disk rotator with rotating mercury contacts was used. Two coupled potentiostats built with differential amplifiers provided independent variation of the potential for the disk and the analytical Pt ring. The two potentiostatic circuits worked with a common grounded Pt counterelectrode and one reference electrode.

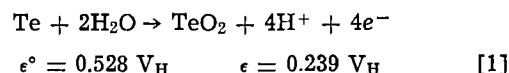
Hg/Hg₂SO₄/1N H₂SO₄ served as reference electrode. In this paper all potentials are given relative to the standard hydrogen electrode and are corrected for liquid junction potentials. Most experiments were performed in acetate buffer pH 4.9 with 0.073M Na acetate and 0.029M acetic acid providing good solubility for Pb²⁺ and low solubility for TeO₂, as desired. In Ref. (8) a similar slightly acidic electrolyte was used for anodic oxide film preparation on Pb_{1-x}Sn_xTe. Some experiments were performed in strongly acidic pH = 1.1 (0.1M HClO₄, HBr, and HNO₃) and alkaline solutions pH = 12.9 (0.1M KOH). All solutions were prepared with analytically pure substances and triply distilled water.

The surface composition was measured with x-ray photoelectron spectroscopy (XPS) in a Leybold-Heraeus system equipped with a sample interlock, a spherical sector analyzer, and a MgK α x-ray source (1253.6 eV). The resolution was ~ 1 eV and the detection depth $\sim 20\text{\AA}$. Before introduction into the UHV chamber the electrochemically prepared samples were rinsed with triply distilled water.

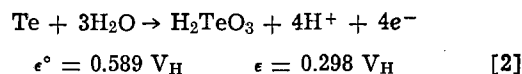
Results and Discussion

Investigation of tellurium.—Electrochemical studies.
—Potentiodynamic polarization curves of tellurium in

acetate buffer pH 4.9 show a current increase at $\epsilon > 0.4$ V_H, a peak of 1.3 mA/cm² at 0.65 V_H, and a current plateau of 0.8 mA/cm² up to several volts (Fig. 1). No oxygen evolution is observed despite the high electrode potentials. An electronically insulating tellurium oxide layer may explain the suppression of oxygen evolution. At ≤ 0 V_H the reduction of the covering oxide to elemental tellurium is shown by a cathodic current peak with its maximum at -0.10 to -0.20 V_H. A second cathodic peak appears at more negative potentials especially when the anodic oxide film is grown at high potentials. The onset of the anodic current density fits reasonably well to the thermodynamic value of the formation of TeO₂ or H₂TeO₃ from

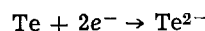


and



ϵ° is calculated with the values for the standard free enthalpy ΔG° of the compounds involved in the processes of Ref. (9). ϵ refers to pH 4.9. The cathodic reduction of the oxide occurs at more negative potentials as expected. Apparently this process is not reversible enough. The cathodic peak appears only if anodic polarization to > 0.40 V_H is performed. The height and area of the cathodic peak increase with the maximum potential reached during the anodic scan (Fig. 1). This demonstrates qualitatively the formation and thickening of the oxide layer on Te with increasing electrode potential.

At < -0.50 V_H the reduction of Te to Te²⁻ or Te₂²⁻ leads to a strong increase of the cathodic current from



$$\epsilon^\circ = -0.92 \text{ V}_H \quad \epsilon = -0.77 \text{ V}_H \quad [3]$$

ϵ refers to a solution with 10⁻⁵M of Te²⁻ to simulate a bulk electrolyte virtually free of soluble tellurium compounds.

Ring-disk voltammetry.—Examination with the rotating ring-disk electrode reveals that the oxidation product at the disk is quite soluble (Fig. 2). At a ring potential of $\epsilon_R = -0.25$ V_H a cathodic ring current I_R is observed, corresponding to the anodic disk current I_D , at $\epsilon_D > 0.4$ V_H. With potentiodynamically decreasing disk potential (10 mV/sec) the value of the cathodic ring current is unchanged even for $\epsilon_D < 0.40$ V_H when no corresponding anodic oxidation at the disk takes place, indicating that the oxide layer is still dissolving

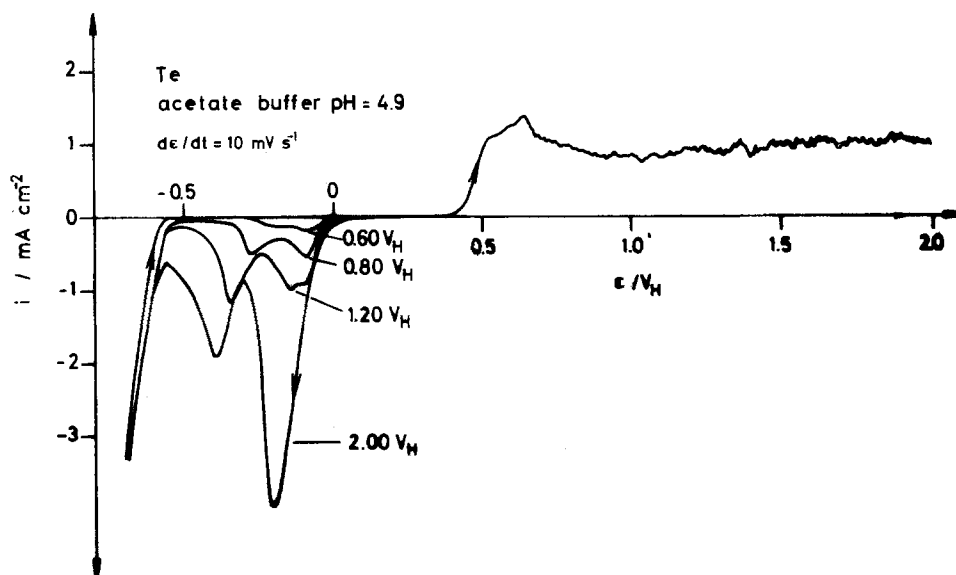


Fig. 1. Potentiodynamic polarization curve of tellurium in acetate buffer pH 4.9 with $dc/dt = \pm 10$ mV/sec. The scan to positive voltages is performed up to the indicated values.

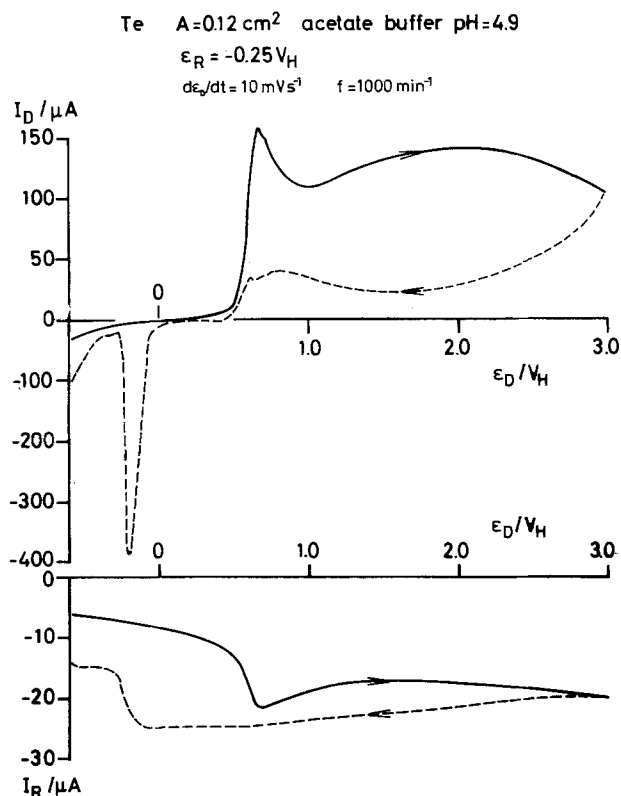


Fig. 2. Potentiodynamic polarization curve with a rotating Pt ring-Te disk electrode in acetate buffer pH 4.9 with variable disk potential $d\epsilon_D/dt = 10 \text{ mV/sec}$, fixed ring potential $\epsilon_R = -0.25 V_H$, disk current I_D , ring current I_R , $f = 1000 \text{ min}^{-1}$, disk area $A = 0.12 \text{ cm}^2$.

until it is reduced at $\epsilon_D = -0.1 V_H$. Consequently, the cathodic ring current becomes less negative for $\epsilon_D < -0.1 V_H$. For quasistationary current conditions, 2 min after a potential in the current plateau is established, the collection efficiency for the ring is 17%. This is $\sim 66\%$ of the value expected theoretically for the geometry of the ring-disk electrode used if all anodic products at the disk would be soluble. Therefore only $\sim 34\%$ of the disk current has to be attributed to the formation of a stable $\text{TeO}_2(\text{H}_2\text{TeO}_3)$ layer on the Te surface.

In the plateau region the quasistationary current densities I_D and I_R increase with the square root of the rotation frequency. The anodic current is therefore determined by a diffusion-controlled process as given by the Levich equation. The TeO_2 layer is continuously dissolved as tellurite and its transport into the bulk solution by diffusion is the rate-determining step.

Thickness of the tellurium oxide layer.—The partial consumption of the anodic current density for the oxide film growth is seen more directly by the determination of the film thickness. The oxide was formed at sufficiently positive potentials ($\geq 0.50 V_H$) for a definite period of time and reduced potentiodynamically (10 mV/sec) in the potential range of 0.10 to $-0.60 V_H$. The charge of the integrated cathodic current peaks Q is used to obtain a value of the layer thickness of TeO_2 or H_2TeO_3 applying Faraday's law to reactions [1] and [2] for oxide reduction.

Molar volumes of 27.5 and $58.23 \text{ cm}^3/\text{mole}$ are used for TeO_2 and H_2TeO_3 , respectively.

The increasing layer thickness with the time of oxidation for four different electrode potentials is given in Fig. 3. A constant layer thickness of $\sim 100 \text{ \AA}$ TeO_2 is obtained within about 1 min for 0.5 - $0.6 V_H$ while a linear increase of the oxide thickness with the square root of time up to several hundred angstroms is obtained for higher potentials. No growth saturation is observed. The increase of oxide thickness with the

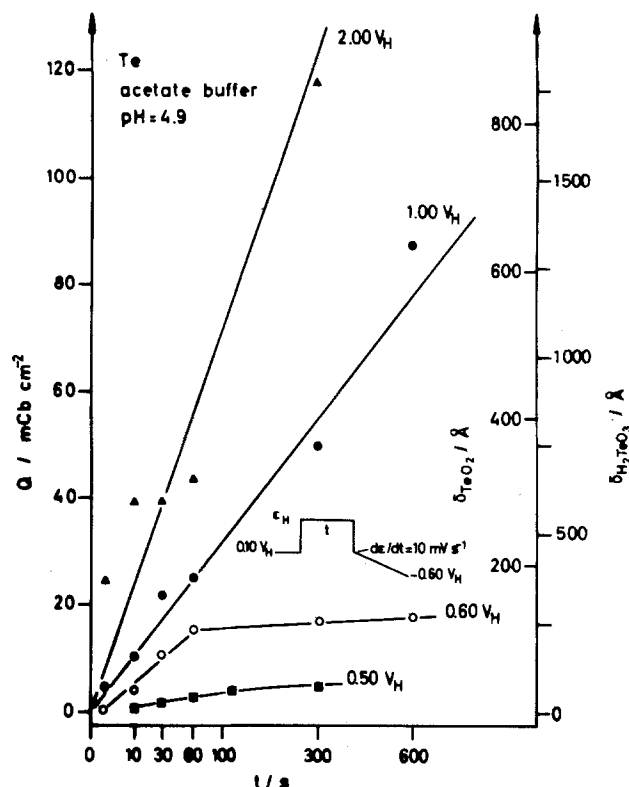


Fig. 3. Increase of the cathodic charge Q and the related oxide thicknesses δTeO_2 and $\delta\text{H}_2\text{TeO}_3$ with oxidation time of tellurium in acetate buffer pH 4.9 for four fixed potentials. Charge Q is determined by the indicated potentiodynamic reduction with $d\epsilon_D/dt = -10 \text{ mV/sec}$.

electrode potential for a fixed time of anodic oxidation is nearly linear (300 \AA at $4.0 V_H$ after 10 sec). These values, however, cannot be related to a constant layer thickness because it is still increasing with time.

It seems reasonable to assume a double structure of the covering oxide. A dense inner layer prevents the direct contact of the tellurium surface to the electrolyte. Therefore, no oxygen evolution takes place. An outer part is presumably porous or has a good ionic conductivity. The oxide thickness obtained is relatively high for the small electrode potentials. The layer does not effectively block the further anodic oxidation. The double structure of the cathodic current peak for high oxidation potentials (Fig. 1) might be an indication for a double structure of the anodic oxide. The oxide thickness decreases by dissolution in the electrolyte for open-circuit conditions or at $0.10 V_H$ when neither oxide formation nor reduction occurs. Approximately 60% of the oxide is dissolved during the first 50 sec whereas the rest is not removed within 200 sec, another hint for a double structure of the oxide.

Investigation of lead telluride.—*Electrochemical studies.*—The potentiodynamic polarization curve of PbTe-films at pH 4.9 has two distinct anodic peaks AI and AII (Fig. 4). At potentials more positive than peak AII the current density shows a weak plateau and then increases again at $>0.9 V_H$. The scan in negative direction reveals two cathodic peaks CI and CII (Fig. 4), the latter being observed only if the potential has been more positive than peak AII, while peak CI is closely related to peak AI. AI is only observed if the potential has crossed the CI position and vice versa. The close relation between the anodic and cathodic peaks demonstrates, therefore, that stable anodic oxidation products on the surface are reduced during the cathodic scan.

The potentiodynamic curve of PbTe can be compared directly to that of elemental Te. The increase of the anodic current at $0.40 V_H$ and the AII peak occur at the

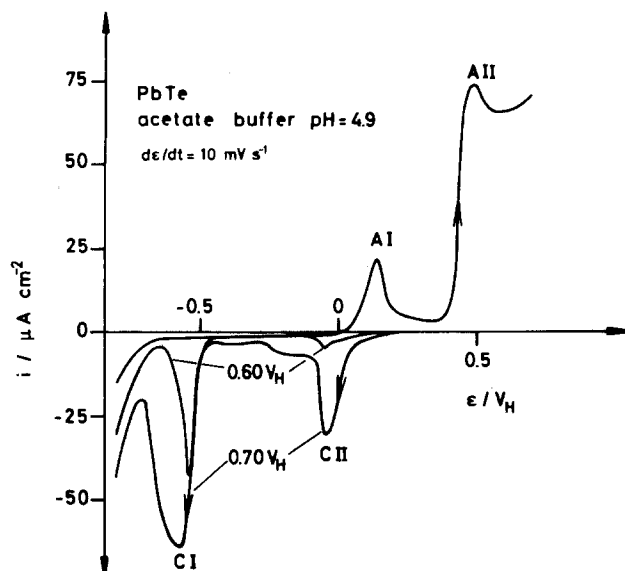
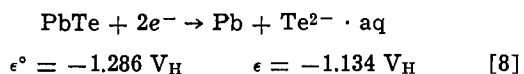
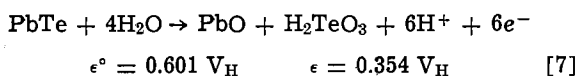
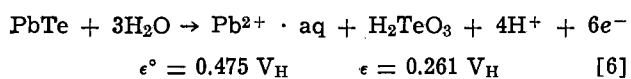
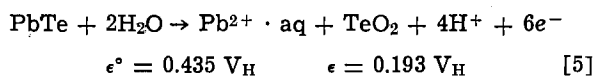
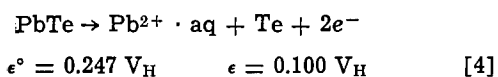


Fig. 4. Potentiodynamic polarization curves of PbTe in acetate buffer pH 4.9 with $d\epsilon/dt = \pm 10$ mV/sec and scans up to 0.6 and 0.7 V_H .

same potential as the anodic structure for the pure Te specimen. Peak CI is in the position of the increasing cathodic current for Te at $-0.55 V_H$ and CII for the PbTe film is observed at about the same position as the cathodic peak of Te. Its position shifts in negative direction with increasing scan rate of the potential. A shoulder at negative potentials is obtained similar to Te. Only the AI peak is a new feature of PbTe.

For freshly deposited PbTe films, the current plateau at potentials more positive than $0.5 V_H$ (peak AII) reaches values in the range of $60 \mu A/cm^2$. Higher current densities of some $100 \mu A/cm^2$ are observed in subsequent experiments which is a consequence of surface roughening during anodic oxidation. This current plateau ends at $0.9 V_H$ where a further steep current increase is obtained. In contrast to the behavior of pure tellurium no limiting current is achieved, with the current density rising to more than $10 mA/cm^2$ at potentials of $\approx 1.5 V_H$.

The relevant electrochemical reactions occurring at the PbTe surface in the potential range of interest (-0.8 to $1.3 V_H$) are given below with the standard potentials ϵ° , which are calculated from the standard free enthalpy of formation of the compounds involved in the processes (9). The ΔG° value for PbTe is obtained from the standard enthalpy of formation and the standard entropy of Ref. (10). The electrode potentials ϵ refer to a solution of pH 4.9 and to a concentration of $10^{-5}M$ for all soluble substances which are not part of the composition of the bulk electrolyte



The anodic oxidation in the potential range of 0 – $0.4 V_H$ and the current peak AI at $0.140 V_H$ correspond to

reaction [4], this being in agreement with the calculated potential value of $\epsilon = 0.10 V_H$. Te remains at the surface and blocks a further oxidation leading to small stationary current densities of $\sim 0.5 \mu A/cm^2$ (Fig. 4 and 8). The reduction of the Te layer to soluble Te^{2-} according to reaction [3] $\epsilon = -0.77 V_H$ starts at $-0.5 V_H$ with the CI minimum at $-0.55 V_H$ (Fig. 4), analogous to the reduction of elemental Te in the same electrolyte (Fig. 1). The reduction of PbTe to Pb and soluble Te^{2-} at $\leq -0.5 V_H$ according to reaction [8] can be excluded because of the very negative value $\epsilon = -1.13 V_H$.

The anodic oxidation of Te and PbTe according to the reactions [1], [2], and [5] to [7] is expected in the potential range of 0.20 – $0.35 V_H$ after the thermodynamical values. These values are in fair agreement with $\sim 0.40 V_H$ and the AII peak found experimentally for both materials. In the range of peak CII from -0.10 to $-0.40 V_H$ the oxide layer is reduced to elemental Te and PbTe which is supported by the XPS measurements described later.

Some characteristic differences are observed for the polarization curves in strongly acidic solutions like $0.1M \text{HClO}_4$, HNO_3 , and HBr ($\text{pH} = 1.1$) (Fig. 5). Peak AI remains unchanged at $0.2 V_H$. The independence of pH is expected because no H^+ ions are involved in reaction [4] occurring in this potential range. In the range of the AII peak, at $>0.5 V_H$, a pronounced current increase is obtained. No second plateau is reached as in acetate buffer pH = 4.9. Soluble oxidation products are apparently forming and no stable surface films. Consequently, no pronounced cathodic current peaks are obtained with potentiodynamic investigations for negative potential scans. These results agree with those of tellurium in the same strongly acidic solutions (not shown in this work). An oxide layer is detected by a small cathodic peak only when its reduction is performed immediately after its formation by a rapid cathodic potential scan. TeO_2 (H_2TeO_3) dissolves too fast and no protective layer remains on the semiconductor surface for a longer period of time. The shift of the current increase at $0.40 V_H$ for pH 4.9 to $0.60 V_H$ at pH 1.1 can be explained by the usual change of the potential of oxide formation with the pH value (40 mV/pH , Eq. [5] and [6]). At $-0.3 V_H$ a small anodic peak is superimposed for positive scans. The peak is related to the oxidation of Pb to soluble Pb^{2+} , the Pb having been deposited by reduction of Pb^{2+} in solution, dissolved during a previous experiment.

Results in strongly alkaline solution of $0.1M \text{KOH}$ ($\text{pH} 12.9$) are similar to those in acidic solutions. The steep anodic current increase (AII range) is shifted to $-0.2 V_H$ (Fig. 5), this change corresponding to a pH shift of 8 and 12 units compared to the acidic solutions pH 4.9 and pH 1.1, respectively. The anodic peak at $-0.5 V_H$ is due to oxidation of Pb to PbO deposited cathodically during a previous run. However no anodic peak related to AI is observed because the potential shift of the AII reaction conceals it. No pronounced cathodic peaks are detected, this indicating unstable anodic surface film formation.

Etching solutions like HBr/Br_2 or HNO_3 were used successfully to obtain Te surface layers of some 100\AA thickness. The electrode potential depends on the kinetics of the partial reactions of PbTe, the oxidant, and the thermodynamic conditions. In the case of the chemical etchants above this has not been measured, however, it should be in the range of 0.1 – $0.6 V_H$ when Te is formed at the surface but no TeO_2 . The polarization curve of PbTe in $0.1M \text{HNO}_3$ (Fig. 5) shows a pronounced current plateau of $\sim 20 \mu A/cm^2$ in this potential range. The relatively thick Te layers have to be porous to enable the Pb^{2+} transport into the solution. This apparently results in the poor coating properties of the films against oxidation in air for longer exposure (2). Similar results were obtained for Te-rich films produced by cyclic electrochemical oxidation and reduction (see section on XPS investigation).

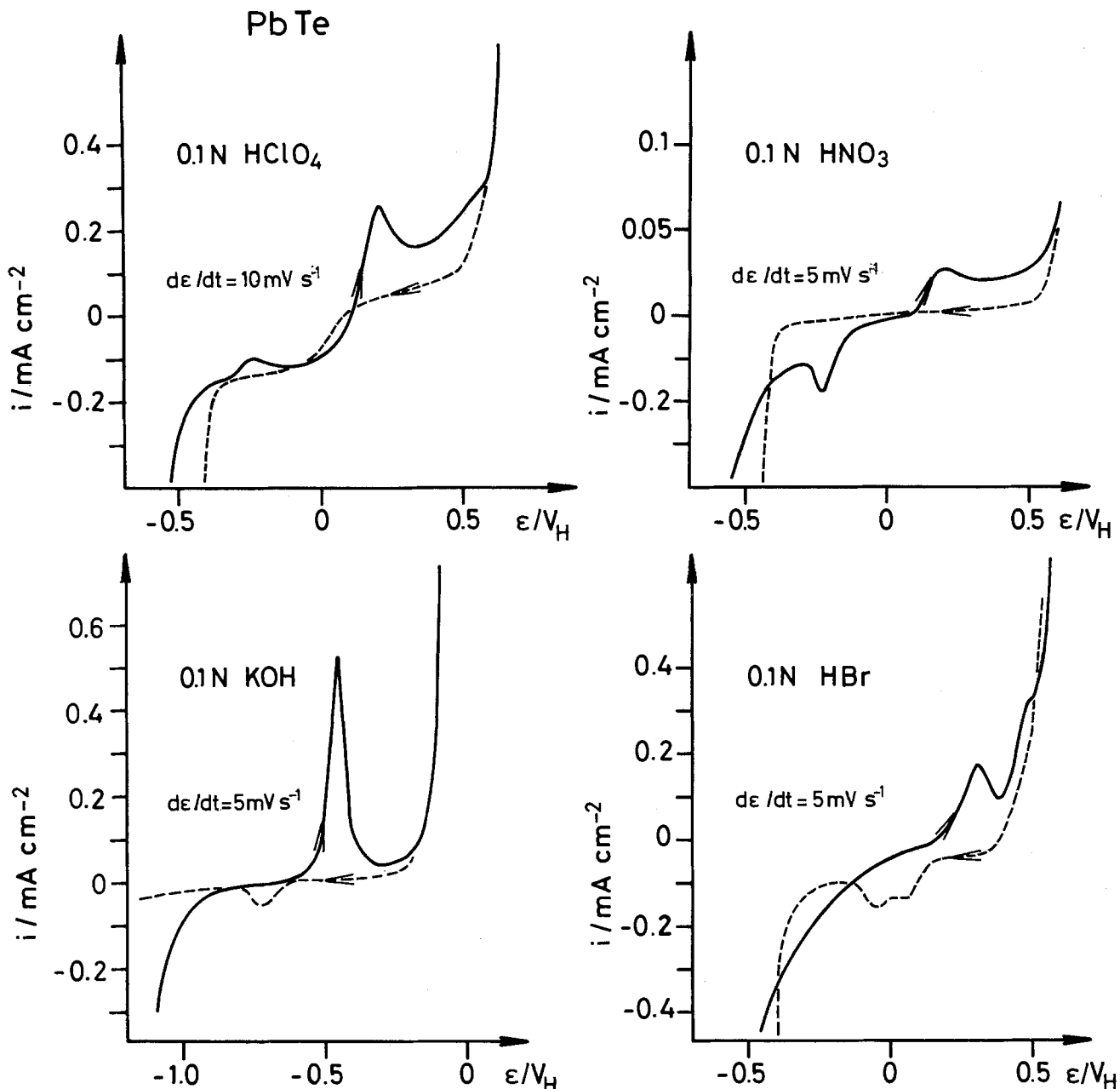


Fig. 5. Potentiodynamic polarization curves of PbTe in 0.1M solutions of HClO₄, HNO₃, HBr (pH 1.1), and KOH (pH 12.9)

During the electrochemical examination of PbTe films in acetate buffer pH 4.9 in the potential range -0.80 to 0.80 V_H, no change of the surface smoothness is observed. If, however, the potential is increased above 0.9 V_H the steep current increase is accompanied by a local attack of the surface and the formation of black deposits (Fig. 6), which grow and finally coalesce into a continuous surface film. The presence of some irregular pits again demonstrates the local attack of the semiconductor surface.

Ring-disk voltammetry.—To examine whether the rotating ring-disk arrangement is suitable for the determination of the soluble oxidation products of PbTe in acetate buffer pH 4.9 the potentiodynamic polarization curve of the Pt ring was examined (Fig. 7a). For disk potentials $\epsilon_D \geq 0.40$ V_H the dissolution of tellurite is indicated by a cathodic step of I_R at $\epsilon_R = -0.1$ V_H (reaction [1] and [2]) for negative potential scans. At $\epsilon_R \leq -0.30$ V_H the reduction of Pb²⁺ is superimposed. For disk potentials $\epsilon_D \leq 0.30$ V_H this step is not observed because no oxidation products are formed. The steeper current increase at $\epsilon_D < -0.3$ V_H and $\epsilon_R > 1.40$

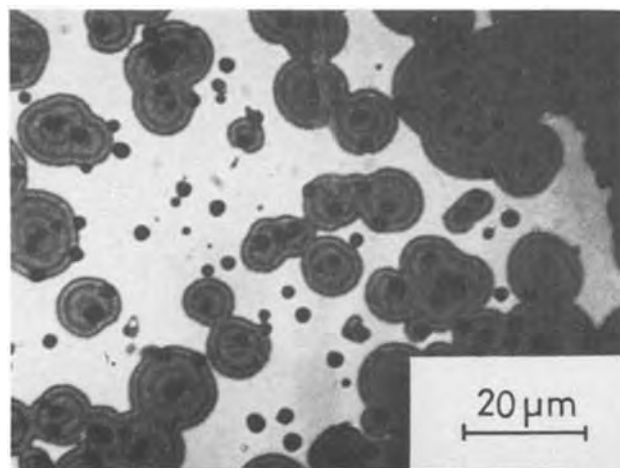
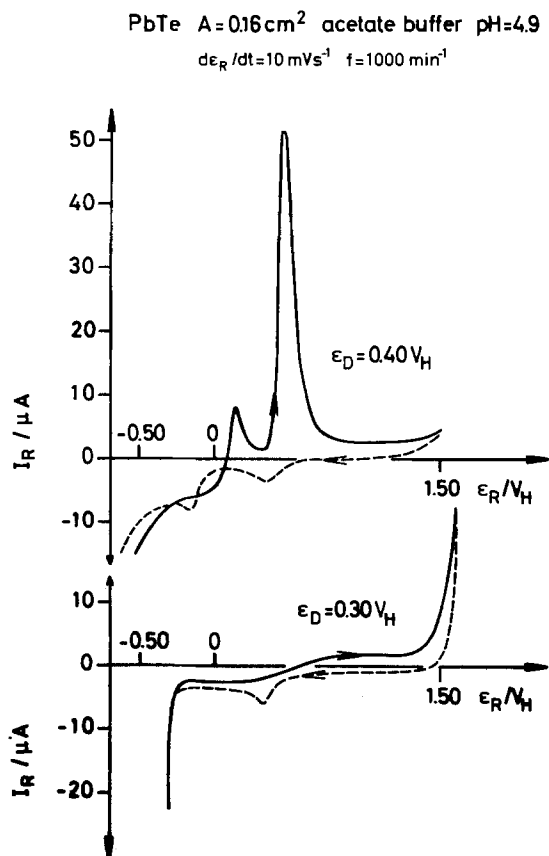
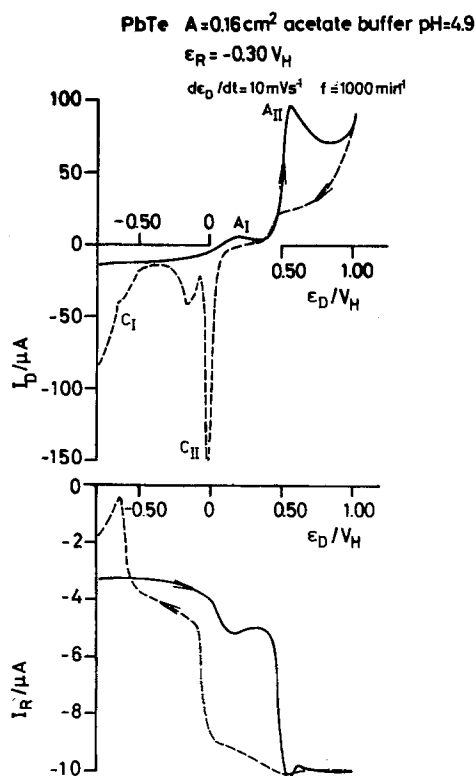


Fig. 6. Photomicrograph of local attack and formation of deposits on a PbTe film after electrochemical treatment at 1.00 V_H for 5 min in acetate buffer pH 4.9.



(a) Ring current I_R vs. ring potential ϵ_R with $d\epsilon_R/dt = \pm 10$ mV/sec and two fixed disk potentials $\epsilon_D = 0.30 V_H$ ($i_D = 0$) and $\epsilon_D = 0.40 V_H$ ($i_D = 0.22 \text{ mA/cm}^2$).



(b) Ring I_R and disk I_D current vs. disk potential ϵ_D with $d\epsilon_D/dt = \pm 10$ mV/sec and fixed ring potential $\epsilon_R = -0.30 V_H$.

Fig. 7. Potentiodynamic polarization curve of a rotating Pt ring-PbTe disk electrode in acetate buffer pH 4.9 with $f = 1000 \text{ min}^{-1}$, disk area $A = 0.16 \text{ cm}^2$.

V_H is caused by an enhanced hydrogen or oxygen evolution on the clean platinum ring not covered by any oxidation or reduction products of PbTe. The cathodic peak at $0.40 V_H$ for both disk potentials is correlated to the reduction of platinum oxide formed at potentials $\epsilon_R > 0.7 V_H$. The products deposited by cathodic reduction on the ring cause anodic peaks at $\epsilon_R = 0.10$ and $0.50 V_H$ for positive scans. Apparently similar reactions are occurring as on PbTe suggesting the formation of PbTe and Te during cathodic reduction of the dissolution products of the disk.

Analogous to Fig. 2 for Te, Fig. 7b shows the close correlation of the ring and disk current for a potentiodynamic variation of the disk potential. The anodic disk current I_D of $6 \mu\text{A}$ around peak AI gives rise to a cathodic ring current I_R of $\Delta I_R = 1.5 \mu\text{A}$, the current values agreeing with the theoretical collection efficiency of $\sim 20\%$. These observations may be explained by reaction [4]. A Te film is produced on the disk, while Pb^{2+} is completely dissolved in the electrolyte and is reduced to Pb at the ring with the same number of electrons.

The current increase at $\epsilon_D > 0.4 V_H$ is accompanied by a higher cathodic ring current, and the collection efficiency of about 10% indicates better oxide formation and less dissolution than for the case of elemental Te (theoretical efficiency 20%). Again I_R becomes less negative when the surface oxide is reduced in the range of 0 to $-0.10 V_H$, and presumably some PbO in the oxide layer is reduced between -0.10 and $-0.50 V_H$ (see XPS results in later section). At $\epsilon_D < -0.50 V_H$ and $\epsilon_R = -0.30 V_H$ a superimposed anodic current peak at the ring results from the oxidation of Te^{2-} which is produced and dissolved at the disk. The cathodic disk current at $\epsilon_D < -0.50 V_H$ corresponds to peak CI when the tellurium at the surface is reduced to soluble telluride.

Thickness of the surface layers on PbTe.—The close relation between the peaks AI and CI has been pointed out already. If a PbTe film is anodically oxidized for a sufficiently long time at $0.20 V_H$ ($> AI = 0.15 V_H$) the anodic current density almost vanishes ($< 1 \mu\text{A/cm}^2$) (Fig. 8). However, after the cathodic reduction at peak CI $< -0.50 V_H$, AI regains its original height, indicating that the anodic reaction AI leads to a reproducible passivation film on the semiconductor surface. The reduction of the anodic product at peak CI reestablishes the original surface, peak CI being observed only after an anodic oxidation in the range of AI. The cathodic charge increases with the anodic potential and with the time of AI oxidation for a constant potential (Fig. 9). The structure and area of CI does not change with the scan rate, only the peak position is slightly shifted to more positive values with decreasing scan rates. At potentials between the CI and AI peak and at open-circuit conditions the area of CI is maintained for at least 2 min, thus demonstrating no dissolution of the anodic film. Its position, however, is slightly shifted to more negative values. The cathodic charge Q_{CI} amounts to 0.33 mC/cm^2 for 10^3 sec oxidation at $0.2 V_H$, approximately the same charge obtained for peak AI. With a surface roughness factor of one for a freshly deposited PbTe film and with the interpretation of peak AI by reaction [4] (see sections on Electrochemical studies, Ring-disk voltammetry, and Fig. 7b) a maximum Te layer of 3.4 \AA is obtained ($V_{M,Te} = 20.4 \text{ cm}^3$).

The one to two monolayer thick Te layer, produced by direct oxidation, is too thin to provide a sufficient surface coating or passivation for devices. Thicker layers ($\sim 100 \text{ \AA}$) would require transport of Pb^{2+} ions through a continuous poreless Te film into the electrolyte. Normally such processes involve migration in high electric fields, however the appropriate field strength cannot be built up because of the anodic oxidation of Te and PbTe which occurs at $\geq 0.4 V_H$.

The thickness of the oxide layer, formed at the AII peak $> 0.4 V_H$, is estimated assuming a complete TeO_2

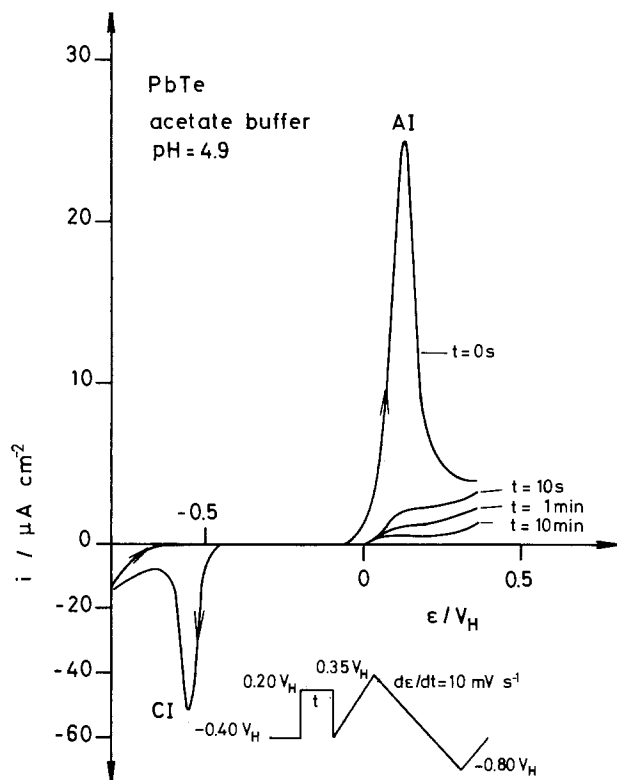


Fig. 8. Decrease of the potentiodynamic anodic current peak AI by prepassivation at $0.20 V_H$ for different times and the related cathodic reduction peak CI in acetate buffer pH 4.9.

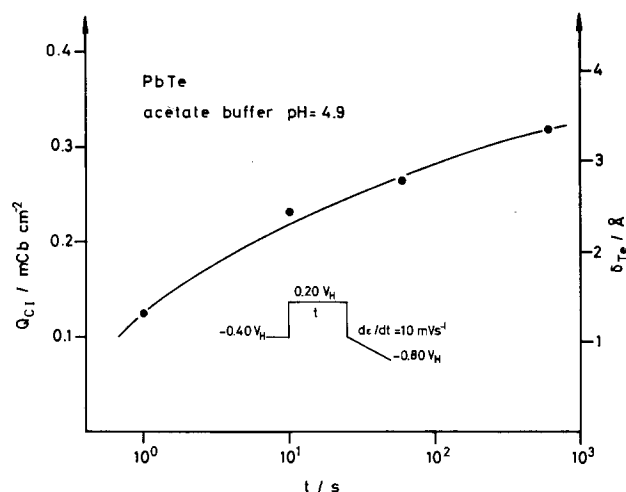


Fig. 9. Cathodic charge Q_{CII} and thickness of Te layer formed by anodic oxidation at $0.20 V_H$ for different times t .

or H_2TeO_3 composition. XPS measurements discussed later however will show that this assumption is not quite correct. The thickness is determined by the charge corresponding to the cathodic peak CII which is essentially the reduction of the AII oxide film to the element. The interpretation and calculation is the same as for the pure Te sample discussed in an earlier section. In the plateau range from 0.5 to 0.9 V_H the oxide film thickness increases linearly with the logarithm of the oxidation time so that after 100 sec at 0.8 V_H 8 mC/cm² are transferred, corresponding to $\sim 60 \text{ \AA}$ TeO_2 or $\sim 120 \text{ \AA}$ H_2TeO_3 . No growth saturation within this time and voltage range is observed.

XPS investigation.—After the different oxidation and reduction processes, the specimens were analyzed by XPS. The relative transition intensities provide in-

formation about the composition of the surface within the detection depth of $\sim 20 \text{ \AA}$, while the different chemical bonds give rise to chemical shifts. Figure 10 shows the expanded spectra of the core level transitions Pb 4f⁷ and Te 3d⁵ from samples which have undergone the indicated electrochemical treatments. The positions of the peaks for the elements and the compounds of interest are in agreement with other authors (11-14): Te^{4+} in TeO_2 —576.3 eV, Te^0 in elemental Te —573.0 eV, Te^{2-} in PbTe —572.3 eV, PbO final oxidation stage —138.8 eV, Pb^{2+} in PbTe —137.8 eV, Pb^0 in metallic Pb —136.9 eV. The difference in chemical shift between Te^0 and Te^{2-} is at our resolution (~ 1 eV) too small for a clear separation. We would like to note that no sputter profiling of the surface layers was attempted, therefore, the XPS results only represent the actual surface in contact with the electrolyte.

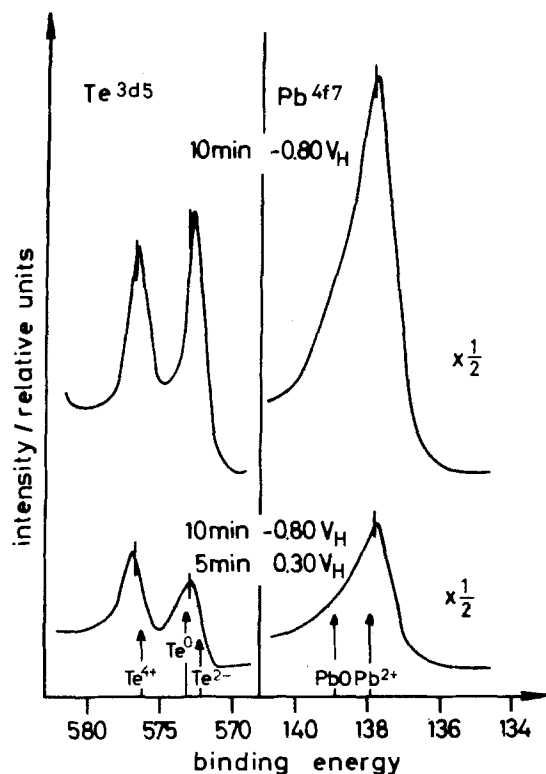
After reduction of PbTe for 10 min at -0.80 eV ($< CI$ peak, Fig. 10a) the first Te-peak has a binding energy of 572.6 eV as expected for Te^{2-} . Oxidation at $0.30 V_H$ ($> AI$ peak) for 5 min shifts this peak to 573.1 eV. This slight shift might be attributed to contributions from elemental Te which supports the interpretation of the electrochemical results. In both cases a second peak at 576.9 eV shows TeO_2 on the surface. The wet PbTe surface oxidizes in air during sample transfer from the electrolyte to the UHV chamber and therefore complicates the interpretation. The Pb 4f⁷ transition remains the same after each treatment with the prominent peak at the position of Pb^{2+} of PbTe and a PbO shoulder at higher binding energies resulting from oxidation during sample transfer.

The anodic AII oxidation starts at $0.45 V_H$ and leads gradually to an oxidation of the surface to TeO_2 and PbO within the detection depth (Fig. 10b), an appreciable PbO concentration being incorporated into the TeO_2 layer. The peaks of Pb^{2+} and Te^{2-} are still observed after 5 min indicating that the oxide formation does not exceed $\sim 20 \text{ \AA}$.

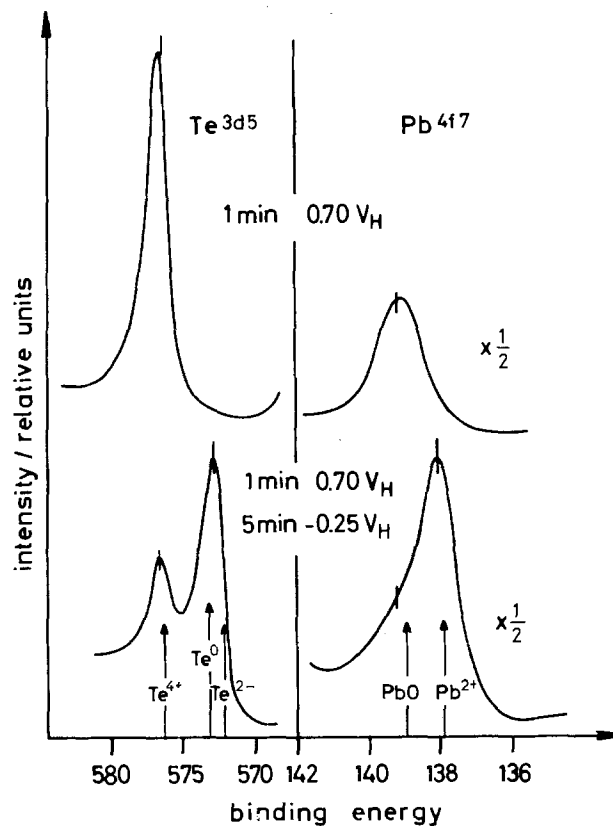
Anodic oxidation within the current plateau at potentials $> 0.5 V_H$ leads to a rapid and complete coverage of the surface by TeO_2 and PbO (Fig. 10c). The intensity ratio of Pb 4f⁷/Te 3d⁵ is smaller by a factor of $\sim 1/3$ compared to peaks on a clean PbTe surface (7) and this change is used for an estimate of the Pb concentration within the oxide surface at 30%. At $-0.25 V_H$ ($< CII$ peak) the oxides are reduced to elemental Te (Te^0) and PbTe (Pb^{2+} and Te^{2-}), the oxide peaks (TeO_2 and PbO) resulting from oxidation during sample transfer. A shorter reduction period of 1 min increases the PbO shoulder and the TeO_2 peak demonstrating that the reduction of such a $\sim 70 \text{ \AA}$ thick oxide layer takes more than 1 min. After the CII reduction no change of the Pb/Te ratio is observed with no preferential dissolution of one of the elements. Oxide layers grown $> 0.9 V_H$ show a similar Pb/Te ratio in the film as described above.

In order to reduce the Pb concentration in the oxide layer, a cyclic oxidation and reduction was carried out the oxidation being performed at $0.70 V_H$ and the reduction at -0.25 or $-0.40 V_H$. After two or four cycles no appreciable decrease of the Pb concentration is observed for equal oxidation periods. If, however, the second oxidation is only half as long as the first one the Pb/Te ratio decreases by another factor ~ 0.5 . In the second oxidation less TeO_2 should be formed than in the first one to prevent the oxidation of the bulk PbTe which produces new PbO and compensates, therefore, the Pb losses of the surface film during oxidation.

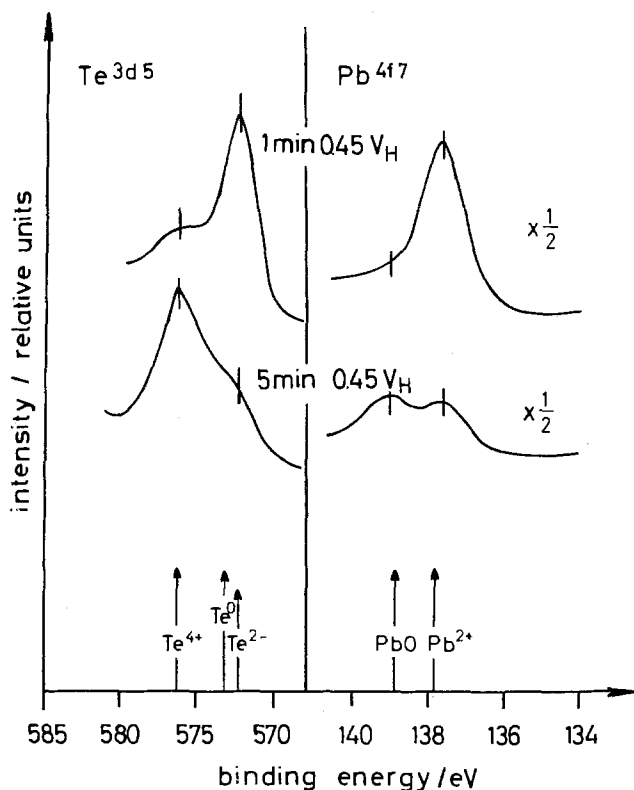
The formation of a continuous, poreless, Pb-free layer of TeO_2 or Te^0 by AII oxidation or CII reduction cannot be expected in principle. In any case the Pb^{2+} ions have to pass through a dense oxide film which automatically leads to its Pb content. A 50% Pb-bulk material does not allow an appreciable accumulation at its interface to the oxide layer. The preferential dissolution of Pb^{2+} requires the presence of a porous layer as mentioned above.



(a) Reduction 10 min at $-0.80 V_H$ (Cl peak) and additional oxidation 5 min at $0.30 V_H$ (Al peak).



(c) Complete anodic oxidation 1 min at $0.70 V_H$ (All peak) and reduction 5 min at $-0.25 V_H$ (CII peak).



(b) Beginning of anodic oxide growth at $0.45 V_H$ (All peak)

Summary and Conclusions

The goal of a thin protective Te layer on PbTe could not be achieved in this study since the direct oxidation (AI oxidation) yields too thin a Te film for coating and passivation purposes. A cyclic oxidation (AII) and reduction (CII) process does not yield Pb free films although its concentration can be reduced appreciably.

The AII oxidation shows that in a competing growth and dissolution process TeO₂ (H₂TeO₃) rich surface

layers can be produced. After a cyclic process they contain at least ~15% PbO on the surface which is in contact with the electrolyte. This value is, therefore, a lower limit of the Pb concentration within the whole oxide film. Thus claims of anodic oxide films on PbTe, Pb_{1-x}Sn_xTe consisting mostly of TeO₂ (8), must be checked by a critical evaluation of the preparation process. If the sample is chemically etched, in HBr-Br₂ for instance, before anodic oxidation the surface is al-

ready covered by a Te layer (1, 2). Therefore, the Te enrichment may be not only due to the anodic oxidation but essentially due to the previous chemical etching. The oxide films are quite conductive and porous because of the high current densities at high anodic potentials.

Similar results to those reported in this paper are expected for $\text{Pb}_{0.8}\text{Sn}_{0.2}\text{Te}$. Although Sn and especially SnO_2 behave differently than Pb, Te, and their oxides in chemical solutions, the Sn concentration is still low. Preferential oxidation, reduction, and dissolution processes and growth of thick surface layers have to deal, therefore, with similar diffusion and migration problems of one of the elements in the surface layer as was encountered in PbTe.

Acknowledgment

We are indebted to H. Maier of AEG-Telefunken, Heilbronn (FRG), for supplying single crystalline PbTe bulk material and T. Jakobus for the epitaxial PbTe films. The critical reading of the manuscript by K. Eisele is appreciated. We acknowledge the technical assistance of B. Titze.

Manuscript submitted July 27, 1979; revised manuscript received Oct. 18, 1979.

Any discussion of this paper will appear in a Discussion Section to be published in the December 1980 JOURNAL. All discussions for the December 1980 Discussion Section should be submitted by Aug. 1, 1980.

Publication costs of this article were assisted by the Fraunhofer-Institut für Angewandte Festkörperphysik.

REFERENCES

1. R. W. Grant, J. G. Pasko, J. T. Longo, and A. M. Andrews, *J. Vac. Sci. Technol.*, **13**, 940 (1976).
2. M. Bettini, G. Brandt, and Sh. Rotter, *J. Vac. Sci. Technol.*, **16**, 1548 (1979).
3. R. A. Chapman, M. A. Kinch, S. R. Borrello, H. Simmons, and D. D. Buss, International Conference on Application of CCD's, Naval Ocean Systems Center, San Diego, California (1978).
4. P. Grosse, "Springer Tracts in Modern Physics," Vol. 48, Springer-Verlag, Berlin (1969).
5. P. A. Breeze and H. C. Hartnagel, *Thin Solid Films*, **56**, 51 (1978).
6. J. Kasai, D. W. Bassett, and J. Hornung, *J. Appl. Phys.*, **47**, 3167 (1976).
7. M. Bettini and H. J. Richter, *Surf. Sci.*, **80**, 334 (1979).
8. T. Jimbo, M. Umeno, H. Shimizu, and J. Ameniya, International Conference on Vapor Growth and Epitaxy, ICVGE-4, Nagoya, Japan (1978).
9. Handbook of Chemistry and Physics, Vol. 52 (1971-1972).
10. Landolt-Börnstein, **4**, 258, Springer-Verlag (1961).
11. M. K. Bahl, R. L. Watson, and J. J. Irgalic, *J. Chem. Phys.*, **66**, 5526 (1977).
12. St. Evans and J. M. Thomas, *J. Chem. Soc. Faraday Trans. 2*, **71**, 313 (1975).
13. J. M. Thomas and M. J. Tricker, *ibid.*, **71**, 329 (1975).
14. W. E. Morgan and J. R. van Wazer, *Phys. Chem.*, **77**, 964 (1973).

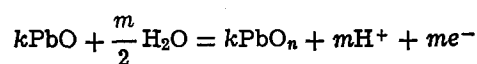
Mechanism of the Electrochemical Oxidation of Lead to Lead Dioxide Electrode in H_2SO_4 Solution

D. Pavlov* and Z. Dinev

Central Laboratory of Electrochemical Power Sources, Bulgarian Academy of Sciences, Sofia 1040, Bulgaria

ABSTRACT

The electrode system Pb/PbO layer/PbSO₄ membrane/H₂SO₄ solution forms when a lead electrode immersed in an H₂SO₄ solution is in the potential range between -400 and +960 mV (vs. the Hg/HgSO₄ electrode). When the electrode potential is raised above +960 mV the PbO and PbSO₄ layers are oxidized to PbO₂. The mechanism of this oxidation is determined by the electric properties and the crystal structure of PbO and PbSO₄. The paper deals with the electrochemical behavior of the electrode during potential sweeps from the PbO into the PbO₂ potential ranges. It was found that first PbO is oxidized via solid-phase reactions to nonstoichiometric PbO_n, without a change of its crystal structure. This takes place via the electrochemical reaction



which proceeds at the PbO/solution interface. Since PbO_n is a semiconductor, the oxidation of the Pb²⁺ ions in its crystal lattice probably takes place through a mechanism in which surface states and mobile acceptors take part. Such are O⁻ and O, evolved during the reaction of oxygen evolution. When *n* reaches a critical value $n = d$, α-PbO₂ nucleation commences in the pores of the PbSO₄ membrane. When this phase reaches the H₂SO₄ solution the oxidation of PbSO₄ crystals to β-PbO₂ begins. This takes place according to the mechanism

dissolution of PbSO₄ → diffusion of Pb²⁺ ions → oxidation of Pb²⁺

at the PbO₂ surface → precipitation of β-PbO₂

The dissolution of PbSO₄ crystals begins at the apexes of the crystals and continues at their edges and faces.

The processes occurring during electrochemical oxidation of the Pb electrode to PbO₂ in H₂SO₄ solution

* Electrochemical Society Active Member.

Key words: LSV (linear sweep voltammetry), lead dioxide electrode, oxidation of PbO, oxidation of PbSO₄, solid-state reactions, electrochemical reactions in anodic multilayer deposit.

depend on the structure and composition of the anodic layer (1-4). They all are determined by the electrode potential (3, 4). There are three potential regions, according to the anodic layer phase composition (3, 4). Upon oxidation of Pb from -970 to -400 mV (vs.

Hg/Hg₂SO₄ electrode), the anodic layer consists of PbSO₄ crystals, so this is the lead sulfate region. From -400 to +960 mV (lead oxide region), the anodic layer acquires the following structure

Pb/tet-PbO layer/PbSO₄ membrane/H₂SO₄ solution

Above +960 mV (lead dioxide region) the anodic layer contains α - and β -PbO₂ and tet-PbO. The method of oxidation (potentiostatic or galvanostatic) affects only the ratio of the phases, but not their presence in the anodic layer.

During the last decade linear sweep voltammetry was used to study the anodic layer oxidation to PbO₂ layer (5-11). These papers contain considerable information concerning the behavior of the lead electrode both on anodic polarization and cathodic reduction of the PbO₂ layer. Valeriotte and Gallop (12) recently carried out a potentiostatic study of the anodic layer oxidation, taking into account the existence of PbO and PbSO₄ phases. They treat the aspects of ion diffusion in the anodic layer solution and of PbO₂ nucleation.

The present paper aims to determine the mechanism of electrochemical oxidation of the Pb/PbO/PbSO₄ electrode system to the Pb/PbO₂ electrode.

Experimental Methods

The electrode was a 99.999% Pb cylinder, pressed into a Teflon holder, so that only its base with an area of 0.5 cm² is oxidized. Before every series of experiments a thin layer was cut off from the electrode so that a fresh surface was formed. Then the electrode was rinsed in triply distilled water and inserted into the cell. A 5 min reduction at -1200 mV followed and then the potential was set to the desired value.

A one-compartment glass cell was used. The window wall facing the electrode was optically flat. The counterelectrode was of platinum. An electrolyte of 1N H₂SO₄ was used for both the cell and the reference Hg/Hg₂SO₄ electrode. All potentials in this paper are presented against the Hg/Hg₂SO₄ electrode. The temperature of the cell and the reference electrode was maintained at 25°C by means of a thermostat. The potentiostat was Radelkis, Type OH-405.

To obtain a Pb/PbO/PbSO₄/H₂SO₄ electrode system the electrode was oxidized initially for 4 hr at +600 mV in the dark.

The Pb/PbO_n/PbSO₄/H₂SO₄ system was formed by means of photoactivation. During the oxidation at +600 mV the electrode was recurrently illuminated with white light. Experimental details concerning photoactivation are given in Ref. (13).

Both systems were oxidized by potentiodynamic polarization from +700 mV to a potential of the PbO₂ region in the dark. A cathodic potential sweep followed to indicate the formation of PbO₂. Various scanning rates and upper potential limits were tried in order to separate the different chemical and electrochemical reactions.

Experiments and Discussion

Nature of the overvoltage at the oxidation of Pb/PbO/PbSO₄/H₂SO₄ to Pb/PbO_n/PbSO₄/H₂SO₄ system in the dark.—The structure of the anodic layer (Fig. 1), formed in the PbO region, was determined by x-ray diffraction analysis and electron microscope observations (4).

The PbSO₄ crystals form a membrane. The processes in the solution during its formation were elucidated in Ref. (14) Pavlov and Popova (15) established and determined the electrochemical properties of the membrane. Later Ruetschi (16) has confirmed these properties on chemically precipitated BaSO₄ and PbSO₄ membranes. The dense layer of tet-PbO is obviously situated between the PbSO₄ sublayer and the metal.

Sometimes during anodic polarization small quantities of basic lead sulfates are formed. However, these

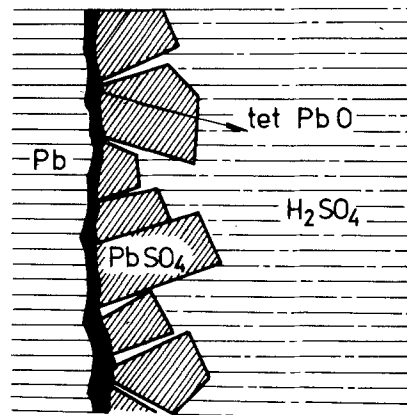
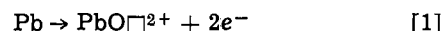


Fig. 1. Structure of the anodic layer formed in the PbO potential region.

compounds are not of a primary importance and are omitted here.

In two previous studies (13, 17) we have shown that when the electrode is not illuminated, the rate of Pb oxidation is limited by the tet-PbO layer ionic conductivity. It was suggested that the conductivity is realized by migration of oxygen vacancies from the metal/oxide interface to the oxide/solution one. A possible model of this process was given in Ref. (17) and is presented in Fig. 2. Let us assume for simplicity that the PbO crystal lattice is built up of PbO molecules. At the Pb/PbO interface Pb is oxidized to PbO by the reaction



PbO \square^{2+} marks a PbO molecule containing an oxygen vacancy ($\text{O} \square^{2+}$). Under the action of the electric field the $\text{O} \square^{2+}$ vacancies migrate into the oxide layer and reach the oxide/solution interface. Here they react with water, whereby PbO and H⁺ ions are formed



The H⁺ ions migrate through the PbSO₄ membrane into the bulk of the solution.

Such a system was subjected to potentiodynamic polarization at a scanning rate of 10 mV/sec. Figure 3

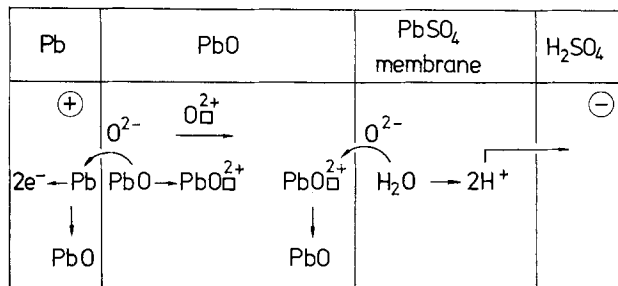


Fig. 2. Scheme of the elementary reactions at current flow through the anodic layer during oxidation of Pb in the PbO potential region.

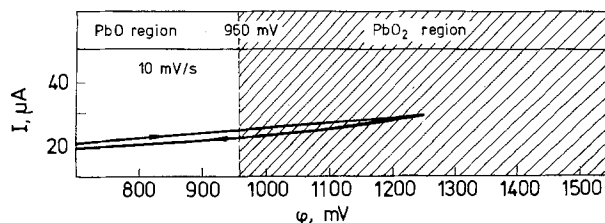


Fig. 3. Voltammogram of a sweep to 1250 mV

present the voltammogram of a potential sweep to 1260 mV. Except oxidation of Pb to PbO, no new electrochemical reaction takes place, although the potential reaches 300 mV deep into the PbO₂ region. The positive-going sweep follows Ohm's law.

Figure 4 presents the voltammograms of five successive potential sweeps to 1450 mV. When 1325 mV is reached, a new electrochemical reaction occurs, causing a rise of the anodic current (first sweep). At the first three sweeps no minimum is observed during the negative-going sweep. This means that the product of the new reaction is not reduced and remains in the anodic layer. Thus the nature of the electrode is changed and the electrochemical reaction begins at more negative potentials at the post-coming sweeps.

A minimum only appears at the fifth sweep. It may be related to PbO₂ reduction. Some changes occur, therefore, in the anodic layer before PbO₂ formation.

We may assume that it is only the stoichiometric composition of the oxide that is changed. The over-all reaction of nonstoichiometric oxide PbO_n formation may be presented by the equation



where

$$n = \frac{k + m/2}{k}$$

PbO_n can be formed in the tet-PbO lattice by solid-state reactions without the formation of a new phase (17).

The comparison of Fig. 3 and 4 suggests that initially there is a potential barrier in the PbO layer, hindering reaction [3]. When PbO is oxidized to PbO_n, this barrier decreases and reaction [3] begins at more negative potentials.

The nature of this barrier may be understood by comparing the electric conductivity of PbO and PbO_n. Lappe (18) has studied the dependence of PbO_n conductivity on its stoichiometric coefficient. Figure 5 presents this relationship, based on Lappe's experimental data. Tet-PbO has very low conductivity. It is

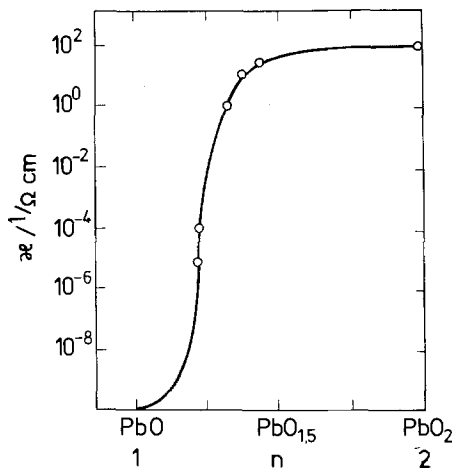


Fig. 5. Dependence of PbO_n specific electric conductivity on its stoichiometric coefficient *n*.

an ionic conductor (19). Such an oxide is formed during potentiostatic oxidation at +600 mV in the dark. With the increase of *n*, electric conductivity rises too. PbO_n is a semiconductor (20). When *n* becomes equal to about 1.4 the oxide acquires electronic conductivity.

Reaction [3] proceeds at the PbO/solution interface. Its rate depends on the interface potential, which in its turn depends for a given electrode potential on the oxide layer thickness and specific conductivity. Let us for simplicity assume that the potential drops linearly across the PbO layer and is marked by φ₀, the potential at which reaction [3] commences.

On the basis of the experimental data, presented in Fig. 4, we suggest that the following changes take place on the electrode as a result of the sweeps (Fig. 6):

The oxide has the initial composition of PbO. Let us mark the oxide/solution interface potential prior to the first sweep by φ₁. Its value is unknown, but it is obviously negative of φ₀, since no electrochemical reaction except oxidation of Pb to PbO takes place. When at the first sweep the oxide/solution potential reaches φ₀, reaction [3] begins. This corresponds to 1325 mV. PbO_n piles up. Before the second sweep the potential at the oxide/solution interface φ₂ is more positive than φ₁ because the PbO_n layer has higher conductivity than the PbO layer. Hence reaction [3] at the second sweep begins earlier (at 1275 mV). Thus the transformation of PbO into PbO_n results in in-

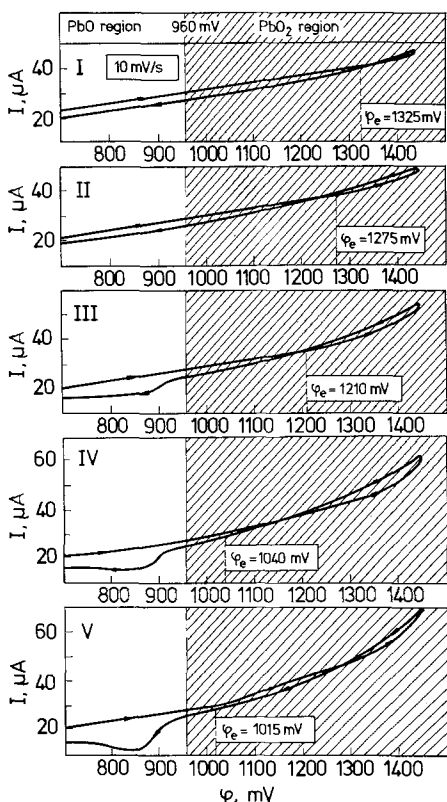


Fig. 4. Voltammograms of a series of successive sweeps to 1450 mV at 10 mV/sec.

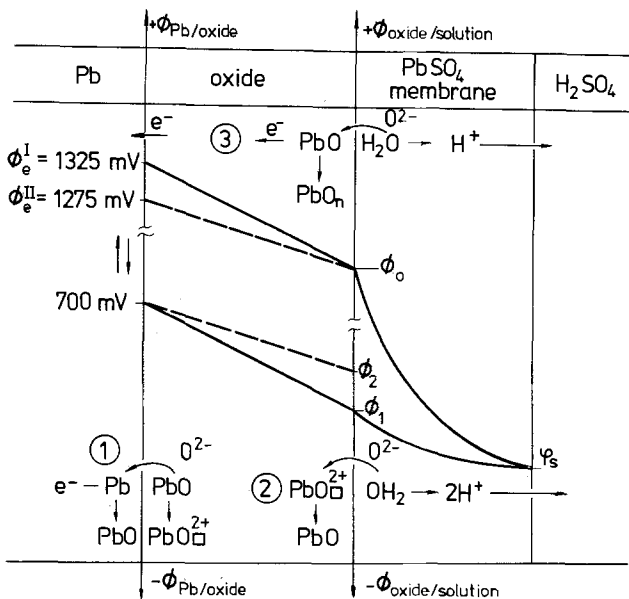


Fig. 6. Scheme of potential distribution across the anodic layer and the reactions at the PbO interfaces.

creasing the oxide layer conductivity and lowering the barrier to reaction [3].

The value of n is potential dependent. Reactions [1] and [2] tend to decrease it and reaction [3] to increase it.

Elementary reactions during oxidation of the PbO_n layer.—Electrochemical behavior of the electrode at the increase of n in PbO_n .—To study these reactions it is necessary to keep the $PbSO_4$ membrane structure unchanged. So the potential was swept to values just entering the PbO_2 region.

Some information about the elementary reactions may be obtained from the voltammogram shape. The reactions can be separated by varying the sweep rate and the upper potential of the sweep.

To obtain reproducible voltammograms we should eliminate the initial influence of the potential barrier, discussed previously. To this aim the oxidation of PbO to PbO_n was effected by means of photoelectrochemical reactions. The processes during photoactivation were discussed in Ref. (13). The electrode was oxidized at +600 mV for 4 hr, being illuminated every 30 min with white light for 3 min. Then three sweeps were carried out from +700 to +1100 mV and backward at a rate of 1 mV/sec in the dark. This electrode was subjected to oxidation by sweeps at three rates (10, 5, and 1 mV/sec) from +700 mV to various upper potentials. After each sweep the electrode was polarized at +600 mV for 10 min.

Figure 7 presents voltammograms to +960 mV. Three interesting features can be observed on them. First, the reaction begins at more positive potentials when the sweep rate increases. Second, at the negative-going sweep the current rises for some time, passes through a maximum and only then decreases. Third, the current due to reaction [3] is higher when the sweep rate is lower.

We believe that this behavior is due to the electrode system structure. The potential sweep produced by the potentiostat is applied to the Pb/PbO_n interface. Then begins a rearrangement of the ionic charges in the PbO_n layer. As this process is slow, the sweep arrives with a delay at the PbO_n /solution interface where reaction [3] takes place. For this reason elec-

trochemical reaction [3] begins at more positive potentials when the sweep rate is high (first feature). When the sweep rate is low, the potential at the PbO_n /solution interface follows more closely the potential at the Pb/PbO_n interface. For this reason the rate of reaction [3] increases when the sweep rate is low (third feature).

When at +960 mV the potential sweep is switched over to negative direction, because of the delay of the sweep through the PbO layer, the potential at the PbO_n /solution interface continues to rise. From Fig. 7 it follows that the sweep of the potentiostat arrives at the PbO_n /solution interface for a period of 5-20 sec. During this period the rate of reaction [3] increases although that of the potential at the Pb/PbO_n interface decreases. The current maximum, corresponding to the highest positive potential which is reached at the PbO_n /solution interface, appears at a more negative potential than the upper potential limit of the sweep (second feature).

Figure 8 presents voltammograms of sweeps to 990 mV. The anodic maximum on Fig. 8c is due to the formation of PbO_2 . At the negative-going sweep a minimum appears at 935 mV due to the reduction of PbO_2 .

Figure 9 shows sweeps to 1020 mV and Fig. 10 to 1080 mV. At 10 mV/sec (Fig. 10) the electrode is still not passivated although the anodic current reaches 1.5 mA. The current in the negative-going sweep becomes negative and almost constant. No minimum is observed to +700 mV.

Figure 10b shows that the anodic current passes through a maximum in the sweep to 1080 mV at a rate of 5 mV/sec. The value of the maximum is 750 μA . A PbO_2 reduction minimum appears at 910 mV in the negative-going sweep.

Figure 11 presents sweeps at a rate of 10 and 5 mV/sec to 1140 mV and at a rate of 10 mV/sec to 1200 mV. At the sweep rate of 10 mV/sec a maximum is seen at about 1075 mV.

Figures 8 to 11 show that PbO_2 formation, expressed through an anodic maximum, depends on the sweep rate. Table I shows the potentials and currents, corresponding to the anodic maximum. It is seen from

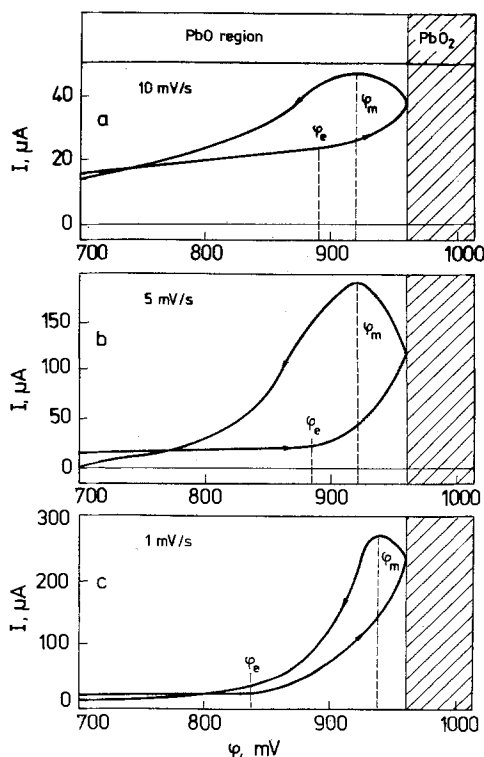


Fig. 7. Sweeps to 960 mV

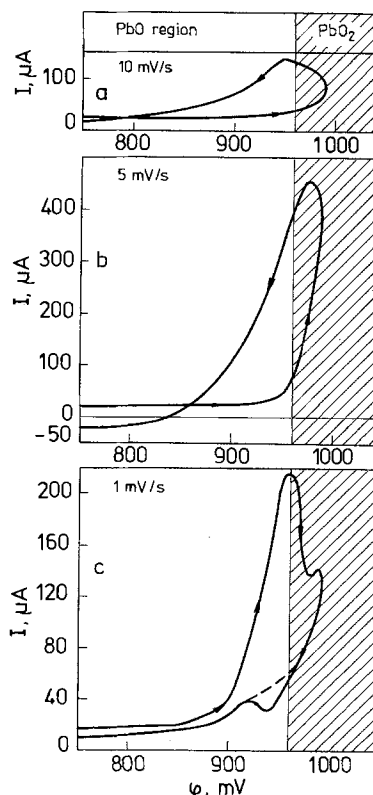


Fig. 8. Sweeps to 990 mV

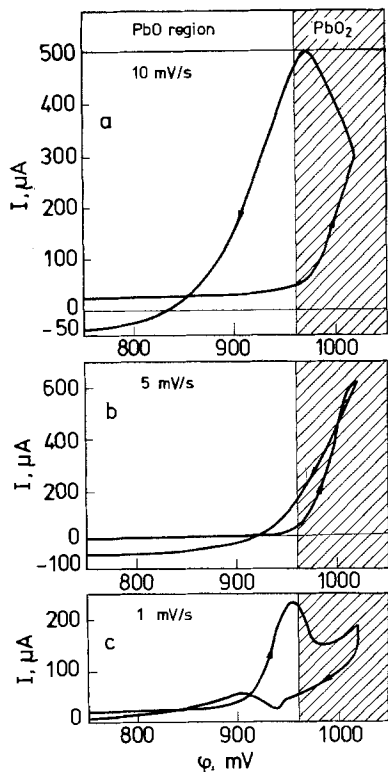


Fig. 9. Sweeps to 1020 mV

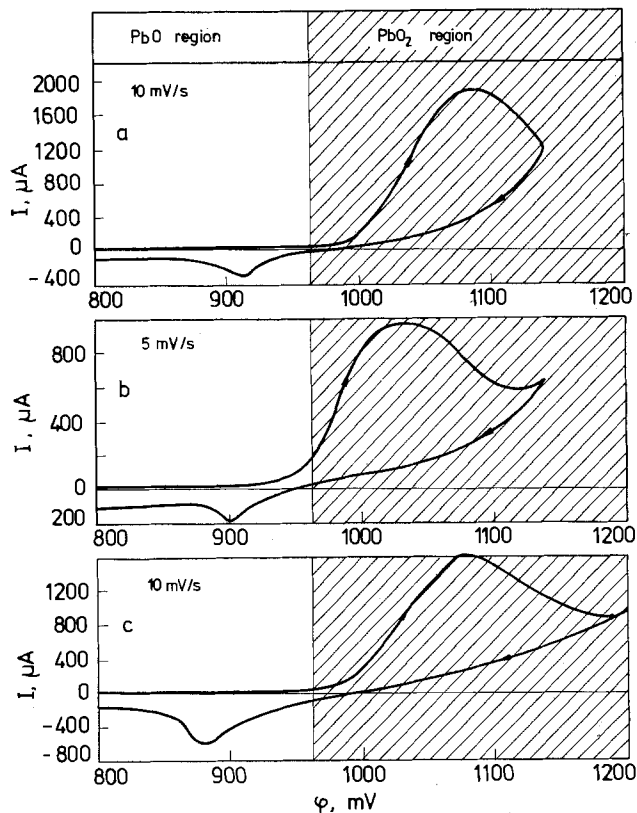


Fig. 11. Sweeps to 1140 and 1200 mV

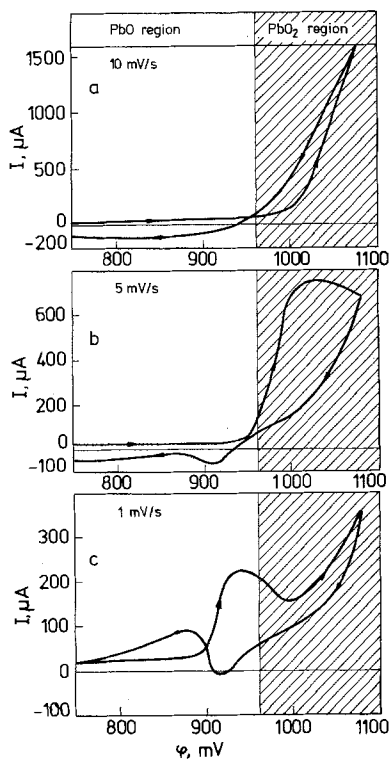


Fig. 10. Sweeps to 1080 mV

the table that when the sweep rate increases 10 times, i_{max} also increases about 10 times.

Table II shows the quantity of electricity flown until the maximum at each sweep. The values of Q vary between $1.02 \cdot 10^{-2}$ and $1.44 \cdot 10^{-2} C$. We assume that this is one single value with its errors. Obviously PbO_2 formation begins after a certain quantity of electricity (Q_d) has flown through the electrode, regardless of the sweep rate in the PbO_2 potential region.

We can generalize our interpretation of the experimental data as follows. Reaction [3] causes an in-

crease of the value of n in the PbO_n layer. When a certain quantity of electricity Q_d has flown, n reaches a critical value. A crystal lattice of the new phase, PbO_2 , begins to be formed.

Model of the elementary reactions at the anodic oxidation of PbO_n .—As PbO_n is a semiconductor, the mechanism of the elementary processes of PbO_n oxidation should be based on the energy band scheme (17). Two electrons have to jump over the bandgap (1.9 eV) for the oxidation of each Pb^{2+} ion of the crystal lattice to a Pb^{4+} ion. In the dark a possible way to overcome the bandgap is through surface states. This is a process of electron exchange between species, chemisorbed on the PbO_n /solution interface and the PbO_n conduction and valence bands. A possible model of this process was given in (17). We shall use this model to explain the experiments of this study. A simplified scheme of the processes is presented in Fig. 12.

The chemisorbed OH^- ions, OH and O^- radicals, and O atoms may serve as surface states. Let us simplify the model by eliminating the voltage drop across the PbO layer, though it influences the starting potential of electrochemical reaction [3].

OH^- ions are adsorbed on the PbO_n /solution interface. They have an electron energy level, which at

Table I

mV/sec	ϕ_{max} (mV)	i_{max} (μA)	Figure
1	960	220	9c, 10c
5	1030	780-980	10b, 11b
10	1075	1900	11a

Table II

mV/sec	990 mV Q (C)	1020 mV Q (C)	1080 mV Q (C)	1140 mV Q (C)	1200 mV Q (C)
1	$1.28 \cdot 10^{-2}$	$1.36 \cdot 10^{-2}$	$1.44 \cdot 10^{-2}$		
5			$1.02 \cdot 10^{-2}$	$1.34 \cdot 10^{-2}$	
10				$1.20 \cdot 10^{-2}$	$1.25 \cdot 10^{-2}$

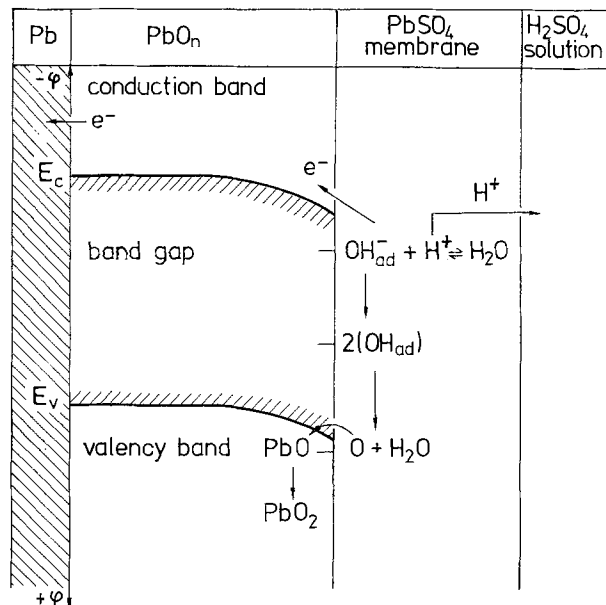


Fig. 12. Energy band scheme of PbO_n

+700 mV is at the PbO_n bandgap. When the potential is increased, the conduction band gets closer to this level. Electrons are injected from the OH^- ions into the conduction band and the following reaction takes place



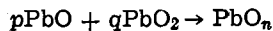
The chemisorbed OH_{ad} radicals are unstable and they recombined



The oxygen atom is a strong acceptor. Its electron energy level lies in the valency band or near it in the bandgap. The O atom may attract electrons from the Pb^{2+} ions whereby a PbO_2 molecule is formed



The tet- PbO unit cell is built up of 4 molecules (21). As they are not oxidized simultaneously, non-stoichiometric PbO_n is formed within the tet- PbO crystal lattice



The chemisorbed OH_{ad} radicals may recombine with OH^- ions too, giving O^- radicals. They are electron acceptors too, capable of partially oxidizing PbO molecules.

Tet- PbO has a layer structure (21, 22). Its crystal structure is given in Fig. 13. The O^{2-} ions are arranged in one layer and there is an empty layer between 2 layers of Pb^{2+} ions. The OH^- ions have a radius of 1.52 Å, the O^{2-} ion 1.32 Å, and the O atom 0.66 Å. The O^- radical has a radius intermediate between that of the O atom and the O^{2-} ion. Obviously the O atom and the O^- radical have a smaller diameter than the width of the tet- PbO lattice free layer (Fig. 13). So they may penetrate into it and oxidize PbO molecules within the PbO_n layer. They behave thus as mobile acceptor levels. As a result of these processes the value of n is highest at the PbO_n /solution interface, decreases in the layer, and is lowest at the Pb/PbO_n interface.

Formation of α - PbO_2 phase during PbO_n oxidation.—The formation of PbO_2 crystal lattice may take place either through rearrangement of the tet- PbO lattice or by destruction of the tet- PbO crystal structure and building up of a new one. To determine the mechanism of PbO_2 crystal lattice formation electron microscope observation of the anodic layer was made after a potential sweep to 1050 mV at a rate of 1 mV/sec.

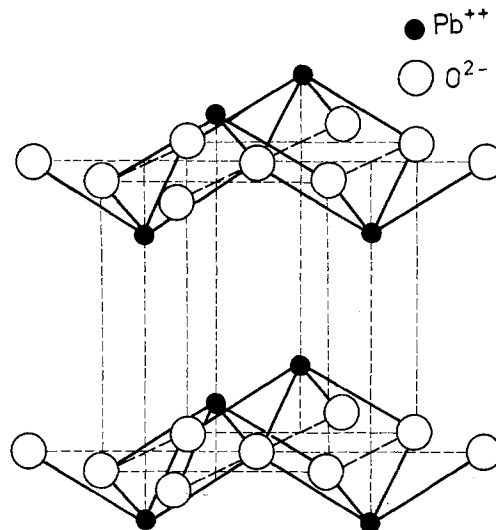
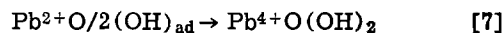


Fig. 13. Crystal structure of tet- PbO

Figure 14 presents three electron micrographs. A carbon-platinum replica was made. It was separated from the electrode in NH_4CH_3COO solution, which dissolves PbO and $PbSO_4$. PbO_2 remains on the replica and can be observed.

The $PbSO_4$ membrane is built up by well-shaped crystals. The PbO_2 phase (black spots) is a shapeless mass, streaming out of some of the pores (Fig. 14c). We can assume on this basis that PbO_2 is formed as a new phase on the PbO_n /solution interface. The PbO_2 phase nucleates in the pores. The newly formed nuclei of PbO_2 push out of the pores the nuclei formed before.

The following elementary reactions may occur along this model of the mechanism: The OH_{ad} radical concentration at the PbO_n /solution interface becomes so high that the bond between the surface PbO molecules, at which 2 OH radicals are chemisorbed, and the PbO_n lattice is weakened and broken. Some of the molecules undergo oxidation



Nucleation takes place after dehydration



One PbO_2 nucleus is formed by $pPbO_2$ molecules. The concentration of $PbO(OH)_2$ is highest on the PbO_n /solution interface so nucleation probably begins here. The solution in the pores is alkaline, so α - PbO_2 is formed. The new phase fills partially or entirely the $PbSO_4$ membrane pores. The access of water to the PbO_n surface is hindered and the rate of electrochemical reaction [4] decreases. The current passes through a maximum and begins to decrease (Fig. 8-11). The water, which is evolved in reaction [8], supplies for some time reaction [4] with OH^- ions. The H^+ ions migrate into the H_2SO_4 solution. The PbO_2 nuclei, formed at this stage, ensure electron contact between PbO_n and PbO_2 .

As a result of reactions [7] and [8], the PbO_n layer becomes thinner. The PbO_n /solution interface turns into a PbO_n/PbO_2 interface. The pores are relatively short and the PbO_2 phase goes out of them, coming into contact with the H_2SO_4 solution.

According to Lappe (18) (Fig. 5), the conductivity increases until n reaches 1.4. On the other hand, Ljamina, Korolkova, and Gorbunova (23) established that on reduction of α - PbO_2 in solid state, the stoichiometric coefficient decreases from 1.9 to 1.4 and lattice defects increase, but the α - PbO_2 crystal lattice remains unchanged. Aguf (24) studied the change of the PbO_2 electrode thermodynamic performance when the oxygen content in it decreases. We can assume, therefore, that the critical value of $n = d$ is about 1.4.

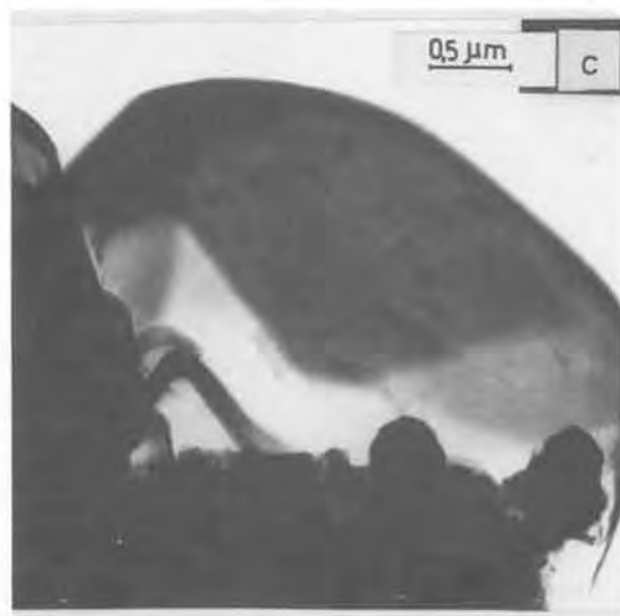
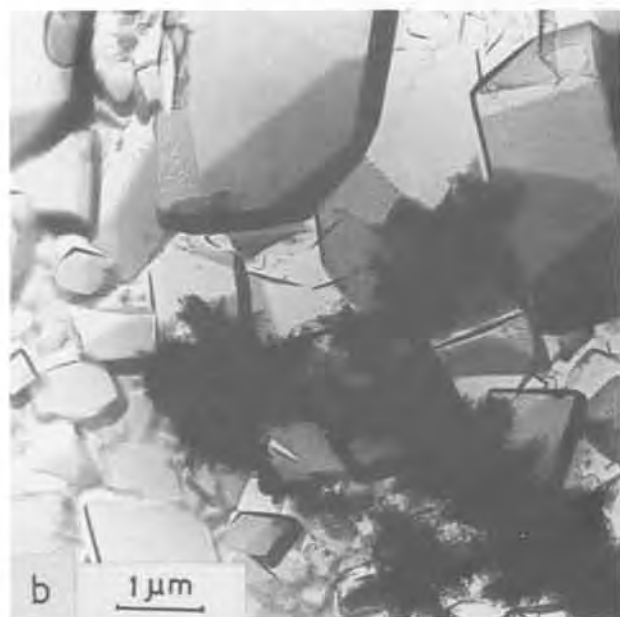
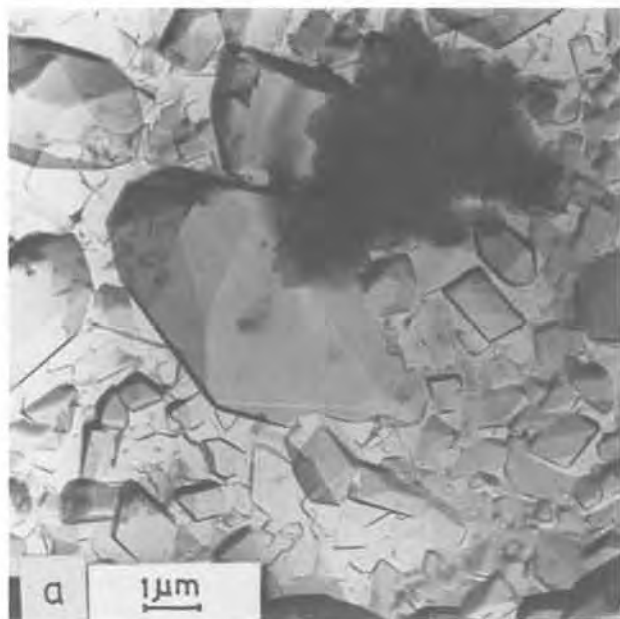


Fig. 14. Electron micrographs of the initial stage of PbO_2 formation.

It is seen from the micrographs (Fig. 14) that PbO_2 phase is formed only in some of the $PbSO_4$ membrane pores. They are probably the largest ones, where there is easy ion exchange between the PbO_n surface and the bulk of the solution. The ion exchange is hindered in the narrower pores and impossible in the third kind of pores, which are entirely blocked.

We can generalize the tet- PbO layer oxidation to α - PbO_2 as follows. Tet- PbO is first oxidized to PbO_n through solid-state reactions. During the oxidation tet- PbO crystal lattice remains unchanged, because the Pb^{2+} ion sublattice is stable and does not change significantly at low values of n . This is why no new phase

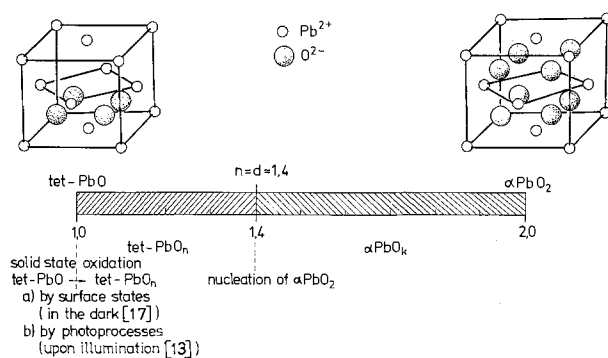


Fig. 15. Model of tet- PbO oxidation to α - PbO_2

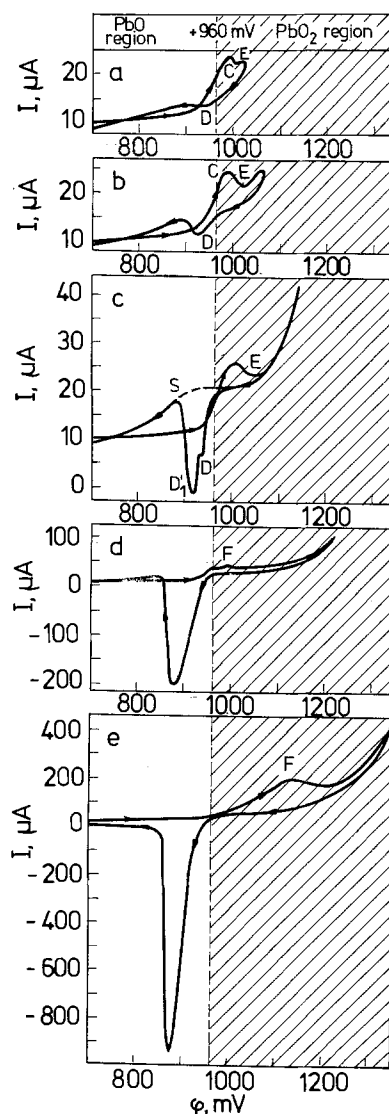


Fig. 16. Sweeps to potentials of $PbSO_4$ membrane destruction

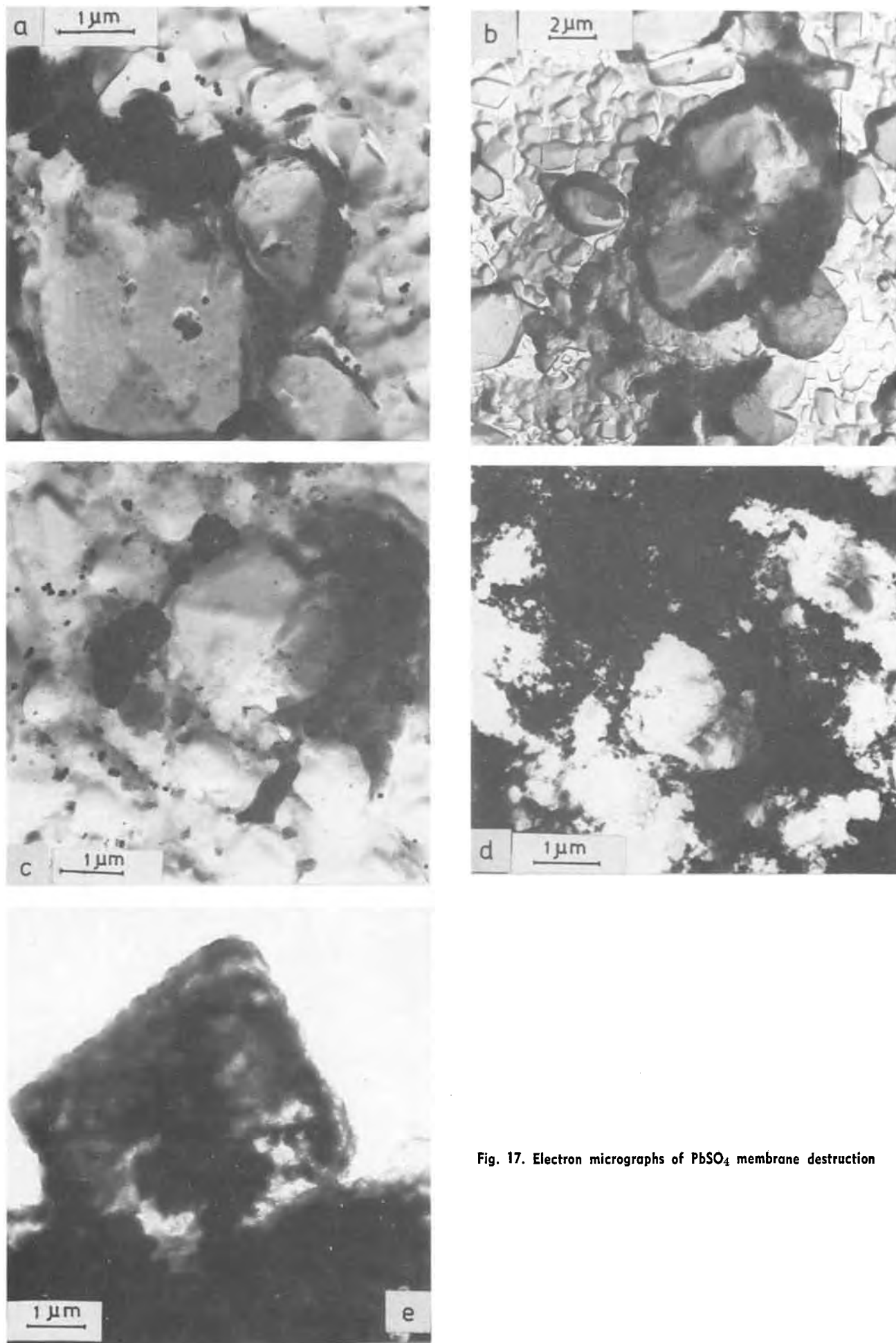


Fig. 17. Electron micrographs of PbSO_4 membrane destruction

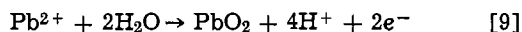
nucleation occurs during the oxidation of tet-PbO to PbO_n. The O²⁻ ion sublattice is rather mobile due to the presence of empty layers and oxygen vacancies in it. The O²⁻ ion sublattice determines the solid electrolyte properties of PbO_n.

The Pb²⁺ ion sublattice determines the semiconductor properties of PbO_n. As the width of the bandgap is 1.9 eV, the oxidation of Pb²⁺ to Pb⁴⁺ is possible if the valency electrons receive energy higher than 1.9 eV. The oxidation of Pb²⁺ ions may take place through the mechanism of surface states. Such surface states are O atoms and O⁻ radicals, evolved during the reaction of oxygen evolution (Fig. 15).

When *n* rises to a critical value of $n = d \approx 1.4$, the defect concentration in the PbO_n crystal lattice becomes so high that rearrangement of the lattice begins through α-PbO₂ nucleation. This process is facilitated by the similarity of tet-PbO and α-PbO₂ crystal lattice (21). The newly formed α-PbO₂ phase is probably also nonstoichiometric, with values of the oxygen coefficient *k* from 1.4 to 2.0 (Fig. 15).

Oxidation of the PbSO₄ layer to PbO₂.—These processes were studied on an electrode, prepared as in the case of PbO_n oxidation. The potential was, however, swept to more positive potentials at which the PbSO₄ membrane is destroyed. Figure 16 shows voltammograms of this series.

At the first sweep a maximum C appears, which we attribute to α-PbO₂ formation in the PbSO₄ membrane pores. When the α-PbO₂ phase comes into contact with the H₂SO₄ solution, a new electrochemical process begins on its surface. The Pb²⁺ ions of the solution (obtained as a result of the dissolution of PbSO₄) are oxidized



Due to this process, the current rises after the minimum E (Fig. 16a, b, c). β-PbO₂ is formed, because the process takes place in the H₂SO₄ solution.

During the negative-going sweep a second minimum appears at a more negative potential than the first one. It is probably due to β-PbO₂ reduction (Fig. 16c) Further on the shape of the voltammogram may depend on the processes of the membrane destruction. One or more maxima F appear at the anodic sweep. As the destruction of the membrane progresses, the two cathodic minima D and D' merge into one and the latter shifts to more negative potentials (Fig. 16d, e).

A maximum S is observed after the minima D and D₁ (Fig. 15c). Sharpe (8) relates it to the increased rate of Pb oxidation. The PbO_n layer becomes thinner as PbO₂ is formed. When PbO₂ is reduced at the cathodic sweep, the PbO_n surface comes into contact with the solution and the rate of Pb oxidation (reactions [1] and [2]) increases. The dotted line presents the rate of oxidation as given by Sharpe (8).

After the PbSO₄ membrane destruction the current passes through a minimum and increases again. This increase is related to the reaction of oxygen evolution on the PbO₂ surface. The slowest stage of this process, according to Kabanov (25), is recombination of O atoms into a molecule. This stage sustains a certain concentration of O atoms at the PbO₂ surface.

Figure 17 shows electron micrographs of the PbSO₄ layer destruction. PbO₂ is seen predominantly among the biggest PbSO₄ crystals (Fig. 17a). During the oxidation of PbSO₄ to PbO₂ the pores widen and the access of H₂SO₄ into them becomes possible.

It is seen from Fig. 17a, b, c that the PbSO₄ crystals dissolve initially at the apexes and the edges and only

later at the faces. The crystals become round and the membrane turns into a shapeless layer (Fig. 17c), partially covered with a PbO₂ layer (Fig. 17d). A possible interpretation of these observations is that PbSO₄ is oxidized along the following mechanism: dissolution of Pb²⁺ ions → diffusion of Pb²⁺ ions → oxidation of Pb²⁺ ions on the PbO₂ surface → precipitation of PbO₂.

The growth of PbO₂ is determined by the flow of Pb²⁺ ions. Figure 17e shows the profile of a PbSO₄ crystal surface. The Pb²⁺ ions move by surface diffusion along the PbSO₄ crystal surface toward the PbO₂ phase, where they are oxidized.

The PbO₂ phase looks like an amorphous deposit (Fig. 17). Fine crystals of one or both PbO₂ modifications are detected by x-ray analysis (3-4). There is probably an amorphous mass too (26). The fine structure of PbO₂ indicates that the rate of nucleation exceeds many times the rate of PbO₂ crystal growth.

Manuscript submitted Dec. 1, 1978; revised manuscript received Oct. 8, 1979.

Any discussion of this paper will appear in a Discussion Section to be published in the December 1980 JOURNAL. All discussions for the December 1980 Discussion Section should be submitted by Aug. 1, 1980.

REFERENCES

1. J. J. Lander, *This Journal*, **98**, 213 (1951); *ibid.*, **103**, 1 (1956).
2. J. Burbank, *ibid.*, **106**, 369 (1959).
3. D. Pavlov, C. N. Poulieff, E. Klaja, and N. Jordanov, *ibid.*, **116**, 316 (1969).
4. D. Pavlov and N. Jordanov, *ibid.*, **117**, 1103 (1970).
5. H. S. Panesar, in "Power Sources," Vol. 3, D. H. Collins, Editor, p. 79, Oriel Press, Newcastle upon Tyne (1970).
6. J. P. Carr, N. A. Hampson, and R. Taylor, *J. Electroanal. Chem. Interfacial Electrochem.*, **33**, 109 (1971).
7. M. P. Brenuan, B. N. Stirrup, and N. A. Hampson, *J. Appl. Electrochem.*, **4**, 49 (1974).
8. T. F. Sharpe, *This Journal*, **122**, 845 (1975); *ibid.*, **124**, 168 (1977).
9. W. Visscher, *J. Power Sources*, **1**, 257 (1976/1977).
10. S. G. Canagaratna, P. Casson, N. A. Hampson, and K. Peters, *J. Electroanal. Chem. Interfacial Electrochem.*, **79**, 273, 281 (1977).
11. R. W. Garrad and D. B. Matthews, Flinders Institute Energy Studies, FIES 7801 (1978).
12. E. M. Valerjote and L. D. Gallop, *This Journal*, **124**, 370, 380 (1977).
13. D. Pavlov, S. Zanova, and G. Papazov, *ibid.*, **124**, 1522 (1977).
14. D. Pavlov, *Electrochim. Acta*, **13**, 2051 (1968).
15. D. Pavlov and R. Popova, *ibid.*, **15**, 1483 (1970).
16. P. Ruetschi, *This Journal*, **120**, 331 (1973).
17. D. Pavlov, *Electrochim. Acta*, **23**, 845 (1978).
18. F. Lappe, *J. Phys. Chem. Solids*, **23**, 1563 (1962).
19. B. A. Thompson and R. L. Strong, *J. Phys. Chem.*, **67**, 594 (1963).
20. V. A. Izvozhicov, *Phys. Status Solidi*, **5**, 2060, 3229 (1961).
21. H. Bode and E. Voss, *Ber. Bunsenges., Phys. Chem.*, **60**, 1053 (1953).
22. D. Greniger, V. Kollonitsch, and Ch. Kline, "Lead Chemicals," p. 50, International Lead Zinc Research Organization Inc., New York.
23. L. I. Ljamina, N. I. Korol'kova, and K. M. Gorbunova, *Elektrochimia*, **10**, 394 (1972).
24. I. A. Aguf, *J. Phys. Chem.*, **39**, 1127 (1965).
25. N. B. Kabanov, in Transactions of the Fourth Meeting on Electrochemistry, 1956, p. 252 ANSSSR, Moscow (1959).
26. K. Kordesh, *Chem. Ing. Technik*, **39**, 639 (1966).

Effect of the Distribution of Current Within a Pit on the Variation in Potential in the Vicinity of the Pit

P. H. Melville

Central Electricity Research Laboratories, Materials Division, Leatherhead, Surrey, England

ABSTRACT

A technique using integrals of Bessel functions has been used to calculate the effect of an anodic current distribution of the form $j_a = j_m(\beta_0 + \beta_1 r^2/a^2 + \beta_2 r^4/a^4)$ within the pit on the potential distribution in the plane of the electrode surface, and analytic solutions have been obtained for situations where linear polarization kinetics may be assumed. If the radius of the pit is small compared to the Wagner polarization parameter L_c for the unpitted electrode, the potential distribution is independent of the polarization parameter, and thus insensitive to the assumption of linear kinetics. The potential within the pit depends mainly on the value of the total current flowing from the pit, and is less sensitive to the form of the current distribution. The potential outside the pit on the surface of the electrode depends on the mean current density and is virtually unaffected by the form of the current distribution.

In a recent paper (1) a Fourier integral technique has been used to calculate the distribution of potential around a scratch in a passive film. This has been extended (2) to cylindrical coordinates to calculate the variation in potential around a pit, assuming that the current density flowing from the pit is uniform across the pit. Here this method of solution is extended to allow for a variation in the current density across the pit. As in Ref. (2) it is assumed that the pit (the anode) is very small compared with the rest of the electrode, which may be treated as infinite, so that integration may be used as in Ref. (2-4) instead of summation, which is necessary for finite systems with this geometry (5-7).

Mathematical Model

As in Ref. (2) the problem considered is that of an infinite plate perpendicular to the z -axis at $z = 0$ with a small pit of radius a at the origin $r = 0$. The general solution for the distribution of the electrostatic potential P is given from the Laplace equation with the boundary conditions that P is a constant at $z = \infty$, and that the solutions are symmetric about $r = 0$. This requires that $P(r, z)$ is of the form

$$P(r, z) = B_0 + \int_0^\infty B(t) J_0(rt) e^{-zt} dt \quad [1]$$

where $J_0(\)$ is a Bessel function of the first kind of order zero, and where the constant B_0 and the function $B(t)$ have to be determined from the boundary conditions at the electrode surface. If the change in potential is small, linear polarization kinetics may be assumed as in Ref. (1) and (2) and as in the solutions of Waber and his associates (8-13) for strip geometry and by Gal-Or *et al.* (5) and McCafferty (6, 7) for circular geometry. The current density at the electrode surface is given by

$$j(r) = -\sigma \left. \frac{\partial P}{\partial z} \right|_{z=0} \quad [2]$$

where σ is the conductivity of the electrolyte.

This has to satisfy the electrochemical relations for the electrode, which if linear polarization kinetics are assumed is of the form

$$j^* = \frac{\sigma}{L_c} (E^* - E_c) \quad [3]$$

where E_c is the free corrosion potential and L_c the Wagner polarization parameter (14) for the unpitted area (the cathode), and E^* , the electrode potential, is related to the electrostatic potential by

$$E^*(r) = V - P(r, 0) \quad [4]$$

where V is some constant. At $z = 0$ this then gives

$$j(r) = \frac{\sigma}{L_c} [P + (E_c - V)] [1 - \phi(r/a)] + j_a(r) \quad [5]$$

where $\phi(r/a)$ is the step function

$$\begin{aligned} \phi(r/a) &= 0, & r < a \\ &= 1, & r > a \end{aligned} \quad [6]$$

The terms in $j_a(r)$ describe the current density flowing from the pit, so that $j_a(r) = 0$ for $r > a$. Within the pit ($r < a$), $j_a(r)$ is equal to the current density flowing from the pit, provided that this current density is much larger than that flowing in the unpitted region. If, as in Ref. (1) and (2), it may be assumed that the current density over the anode is very much greater than the current density elsewhere, Eq. [5] reduces to

$$\sigma \frac{\partial P}{\partial z} = \frac{\sigma}{L_c} [P + (E_c - V)] - j_a(r) \quad [7]$$

This equation is most readily solved, if $j_a(r)$, like $P(r, z)$ (see Eq. [1]) may be expressed as an integral of Bessel functions. This may be achieved by using the relation

$$\begin{aligned} \int_0^\infty J_{2n+1}(at) J_0(rt) dt &= \frac{1}{a} P_n \left(1 - 2 \frac{r^2}{a^2} \right) & r < a \\ &= 0 & r > a \end{aligned} \quad [8]$$

which is a special result of an integral given by Erdélyi *et al.* (15) [see also (16)]. Here $J_{2n+1}(\)$ is a Bessel function of the first kind of order $2n + 1$ where $n = 0, 1, 2, \dots$ and where $P_n(\)$ is a Legendre polynomial of order n , where

$$P_0(x) = 1 \quad [9]$$

Key words: anodic current distribution, pitting, integral of Bessel functions.

$$P_1(x) = x \tag{10}$$

$$P_2(x) = \frac{1}{2}(3x^2 - 1) \tag{11}$$

In the analysis presented here only terms as far as $n = 2$ will be considered, but further terms may be included, if necessary. The current density $j_a(r)$ may thus be expressed as

$$j_a(r) = aj_m \int_0^\infty [J_1(at) + \alpha_1 J_3(at) + \alpha_2 J_5(at)] J_0(rt) dt \tag{12}$$

which gives

$$j_a(r) = j_m \left[(1 + \alpha_1 + \alpha_2) - (2\sigma_1 + 6\alpha_2) \frac{r^2}{a^2} + 6\alpha_2 \frac{r^4}{a^4} \right], \quad r < a$$

$$= 0, \quad r > a \tag{13}$$

where j_m , α_1 , and α_2 are constants, and where integration of Eq. [13] over the area of the pit gives

$$I = \int_0^a j_a(r) 2\pi r dr = \pi a^2 j_m \tag{14}$$

so that j_m may be identified as the mean value of $j_a(r)$. Substitution for the integral representations for $P(r, 0)$, dP/dz , and $j_a(r)$ into Eq. [7] then gives

$$\sigma \int_0^\infty tB(t) J_0(rt) dt = -\frac{\sigma}{L_c} [B_0 + (E_c - V)]$$

$$-\frac{\sigma}{L_c} \int_0^\infty B(t) J_0(rt) dt + j_m a \int_0^\infty [J_1(at) + \alpha_1 J_3(at) + \alpha_2 J_5(at)] J_0(rt) dt = 0 \tag{15}$$

from which the constant B_0 and the function $B(t)$ are given by

$$B_0 = - (E_c - V) \tag{16}$$

$$B(t) = \frac{j_m a}{\sigma} \left[\frac{J_1(at) + \alpha_1 J_3(at) + \alpha_2 J_5(at)}{t + 1/L_c} \right] \tag{17}$$

The potential distribution may then be found by substitution for B_0 and $B(t)$ in Eq. [1] and integration.

Potential at Center of Pit

At the center of the pit ($r = 0, z = 0$) $J_0(rt) = e^{-zt} = 1$, so that from Eq. [1], [16], and [17] the potential may be expressed as

$$P(0, 0) = - (E_c - V) + \frac{j_m a}{\sigma} \int_0^\infty \frac{J_1(x) + \alpha_1 J_3(x) + \alpha_2 J_5(x) dx}{x + \delta} \tag{18}$$

where at has been replaced by x and where $\delta = a/L_c$. The third and fifth order Bessel functions may be expressed in terms of Bessel functions of order zero and one by use of the identities

$$J_3(x) = \left(\frac{8}{x^2} - 1 \right) J_1(x) - \frac{4}{x} J_0(x) \tag{19}$$

$$J_5(x) = \frac{12}{x} \left(1 - \frac{16}{x^2} \right) J_0(x) + \left(\frac{384}{x^4} - \frac{72}{x^2} + 1 \right) J_1(x) \tag{20}$$

Repeated application of the identity

$$\frac{1}{x^n(x + \delta)} = \frac{1}{x^{n-1}\delta} \left[\frac{1}{x} - \frac{1}{x + \delta} \right] \tag{21}$$

may then be used to reduce Eq. [18] to the known integrals

$$\int_0^\infty \frac{xJ_0(x)}{x + \delta} dx = \frac{\pi}{2} [H_0(\delta) - N_0(\delta)] = f_0(\delta) \tag{22}$$

$$\int_0^\infty \frac{xJ_1(x)}{x + \delta} dx = \delta \left\{ \frac{\pi}{2} [H_1(\delta) - N_1(\delta)] - 1 \right\} = \delta f_1(\delta) \tag{23}$$

(16, 17) [see also (2)] and integrals in terms of $x^{-n}J_0(x)$ and $x^{-n}J_1(x)$, where $n = 0, 1, 2, 3, \dots$, $H_0(\delta)$ and $H_1(\delta)$ are Struve functions of order zero and one, respectively, and $N_0(\delta)$ and $N_1(\delta)$ are Bessel functions of the second kind of order zero and one. The functions $f_0(\delta)$ and $f_1(\delta)$ are defined by these equations. The terms in $x^{-n}J_0(x)$ and $x^{-n}J_1(x)$ may be grouped together and identified with the standard relations

$$\frac{d}{dx} J_1(x) = J_0(x) - \frac{J_1(x)}{x} \tag{24}$$

$$\frac{d}{dx} J_2(x) = \frac{2J_0(x)}{x} + \left(1 - \frac{4}{x^2} \right) J_1(x) \tag{25}$$

$$\frac{d}{dx} J_3(x) = \left(\frac{12}{x^2} - 1 \right) J_0(x) + \left(5 - \frac{24}{x^2} \right) \frac{J_1(x)}{x} \tag{26}$$

$$\frac{d}{dx} J_4(x) = \frac{8}{x} \left(\frac{12}{x^2} - 1 \right) J_0(x) - \left(\frac{192}{x^4} - \frac{40}{x^2} + 1 \right) J_1(x) \tag{27}$$

$$\frac{d}{dx} J_5(x) = \left(\frac{960}{x^4} - \frac{84}{x^2} + 1 \right) J_0(x) - \left(\frac{1920}{x^4} - \frac{408}{x^2} + 13 \right) \frac{J_1(x)}{x} \tag{28}$$

where since $J_m(0) = J_m(\infty) = 0$ where $m = 1, 2, 3 \dots$ integrals of these groups of terms are zero. Integrals of the remaining terms in $J_0(x)$ and $J_1(x)$ are obtained from

$$\int_0^\infty J_0(x) dx = \int_0^\infty J_1(x) dx = 1 \tag{29}$$

The integral of Eq. [18] is then given by

$$P(0, 0) = - (E_c - V) + \frac{j_m a}{\sigma} [g_0(\delta) + 1/3 \alpha_1 g_1(\delta) + 1/5 \alpha_2 g_2(\delta)] \tag{30}$$

where

$$g_0(\delta) = 1/\delta - f_1(\delta) \tag{31}$$

$$\frac{1}{3} g_1(\delta) = \left(\frac{8}{\delta^3} - \frac{8}{\delta^2} + \frac{1}{\delta} \right) + \frac{4}{\delta} f_0(\delta) - \left(\frac{8}{\delta^2} - 1 \right) f_1(\delta) \tag{32}$$

$$\frac{1}{5} g_2(\delta) = \left(\frac{384}{\delta^5} - \frac{384}{\delta^4} + \frac{24}{\delta^3} + \frac{8}{\delta^2} + \frac{1}{\delta} \right) + \frac{12}{\delta} \left(\frac{16}{\delta^2} - 1 \right) f_0(\delta) - \left(\frac{384}{\delta^4} - \frac{72}{\delta^2} + 1 \right) f_1(\delta) \tag{33}$$

where the functions $f_0(\delta)$ and $f_1(\delta)$ are defined in Eq. [22] and [23]. The functions $g_0(\delta)$, $g_1(\delta)$, and $g_2(\delta)$ are shown in Fig. 1. In the limit of small δ (i.e., $a \ll L_c$) $g_0 = g_1 = g_2 = 1$. As shown in Fig. 1, the error made, if δ is set equal to zero is small ($\lesssim 10\%$), provided $\delta \gtrsim 0.05$, i.e., if the pit radius $a \gtrsim L_c/20$.

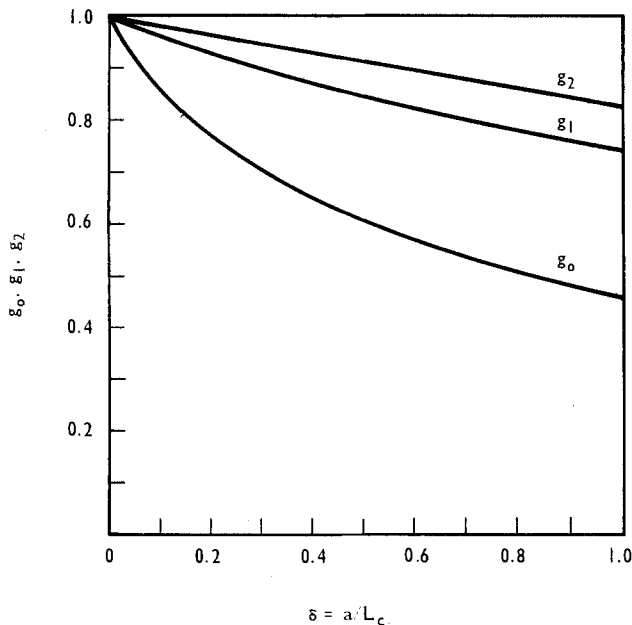


Fig. 1. $g_0(\delta)$, $g_1(\delta)$, and $g_2(\delta)$ (see Eq. [31]-[33]), giving the effect of the relative magnitudes of the size of the pit a and the Wagner polarization parameter L_c .

Distribution of Potential on the Electrode Surface

If the pit is much smaller than the Wagner polarization parameter, so that $\delta = a/L_c$ may be set equal to zero, the potential along the surface of the electrode is given by

$$P(r, 0) = - (E_c - V) + \frac{j_m a}{\sigma} \int_0^\infty \frac{[J_1(at) + \alpha_1 J_3(at) + \alpha_2 J_5(at)] J_0(rt)}{t} J_0(rt) dt \quad [34]$$

This is the zeroth order term in an expansion in δ , and is valid provided both a and r are small compared with L_c , i.e., it is restricted to positions close to the pit. Expansion of the integral in terms of δ is discussed in Ref. (2). The first term in the integral [see (2, 4)] is given by Erdélyi *et al.* (15) as

$$\int_0^\infty \frac{J_1(at) J_0(rt) dt}{t} = \frac{2}{\pi} E\left(\frac{r}{a}\right), \quad r < a$$

$$= \frac{2}{\pi} \frac{r}{a} \left[E\left(\frac{a}{r}\right) - \left(1 - \frac{a^2}{r^2}\right) K\left(\frac{a}{r}\right) \right], \quad r > a \quad [35]$$

where $K(\)$ and $E(\)$ are complete elliptic integrals of the first and second kinds, respectively. The other terms are obtained as a special result of an integral by Watson (17) and Magnus and Oberhettinger (18) [see also (14)] which in this case gives

$$\int_0^\infty \frac{J_{2n+1}(at) J_0(rt)}{t} dt = \frac{1}{(2n+1)} F\left(n + \frac{1}{2}, -(n + \frac{1}{2}); 1; \frac{r^2}{a^2}\right), \quad r < a$$

$$= \frac{(-2)^n}{\pi n (2n+1)^2} F\left(n + \frac{1}{2}, n + \frac{1}{2}; 2n+2; \frac{a^2}{r^2}\right), \quad r > a \quad [36]$$

for $n = 1, 2, 3, \dots$, where $F(\ ; \ ; \ ; \)$ are hypergeometric

functions. In this case for integer n these hypergeometric functions are related to complete elliptic integrals of the first and second kinds, which may be expressed in terms of hypergeometric functions as

$$K(k) = \frac{\pi}{2} F\left(\frac{1}{2}, \frac{1}{2}; 1; k^2\right) \quad [37]$$

$$E(k) = \frac{\pi}{2} F\left(-\frac{1}{2}, \frac{1}{2}; 1; k^2\right) \quad [38]$$

respectively. The hypergeometric functions of Eq. [36] may thus be reduced to complete elliptic integrals by repeated use of the Gauss recursion relations. After some algebra this eventually gives

$$\int_0^\infty \frac{J_3(at) J_0(rt)}{t} dt = \frac{2}{9\pi} \left[\left(7 - 8 \frac{r^2}{a^2}\right) E\left(\frac{r}{a}\right) - 4 \left(1 - \frac{r^2}{a^2}\right) K\left(\frac{r}{a}\right) \right], \quad r < a$$

$$= \frac{2}{9\pi} \frac{r^3}{a^3} \left[- \left(8 - 7 \frac{a^2}{r^2}\right) E\left(\frac{a}{r}\right) + \left(8 - 3 \frac{a^2}{r^2}\right) \left(1 - \frac{a^2}{r^2}\right) K\left(\frac{a}{r}\right) \right], \quad r > a \quad [39]$$

$$\int_0^\infty \frac{J_5(at) J_0(rt)}{t} dt = \frac{2}{75\pi} \left[\left(43 - 168 \frac{r^2}{a^2} + 128 \frac{r^4}{a^4}\right) E\left(\frac{r}{a}\right) - 4 \left(7 - 16 \frac{r^2}{a^2}\right) \left(1 - \frac{r^2}{a^2}\right) K\left(\frac{r}{a}\right) \right], \quad r < a$$

$$= \frac{2}{75\pi} \frac{r^5}{a^5} \left[\left(128 - 168 \frac{a^2}{r^2} + 43 \frac{r^4}{a^4}\right) E\left(\frac{a}{r}\right) - \left(128 - 104 \frac{a^2}{r^2} + 15 \frac{a^4}{r^4}\right) \left(1 - \frac{a^2}{r^2}\right) K\left(\frac{a}{r}\right) \right], \quad r > a \quad [40]$$

The potential distributions are thus found by substituting for these integrals (Eq. [35], [39], and [40]) into Eq. [34]. The solutions obtained in this way for the variation of potential along the electrode surface are valid for zero order in r/L_c , and the current density flowing from the electrode outside the pit is effectively ignored (since L_c is large). The situation is thus similar to that for a disk electrode embedded in an insulating layer, and the solution obtained for constant current density from the pit, i.e., $\alpha_1 = \alpha_2 = 0$ gives a potential distribution identical to that obtained by Nannis and Kesselman (4) for the disk electrode problem. Potential distributions predicted by these equations are shown in Fig. 2 for a number of different values of α_1 and α_2 but for the same value of the mean current density j_m . The corresponding current density distributions are shown in Fig. 3. Current density distributions of the form $j_a = j_m (\beta_0 + \beta_1 r^2/a^2)$ are considered in Fig. 2a and 3a, $j_a = j_m (\beta_0 + \beta_2 r^4/a^4)$ in Fig. 2b and 3b, and $j_a = j_m (\beta_0 + \beta_1 r^2/a^2 + \beta_2 r^4/a^4)$ in Fig. 2c and 3c. The potentials shown here are in the plane of the electrode surface. Despite the wide variation in the form of the current density distributions, the curves for the potential distribution are not as dissimilar in the region of the pit and are virtually identical outside the pit. The potential generally has a single maximum at the center of the pit, but there is a dip in the potential at the center, if the current density

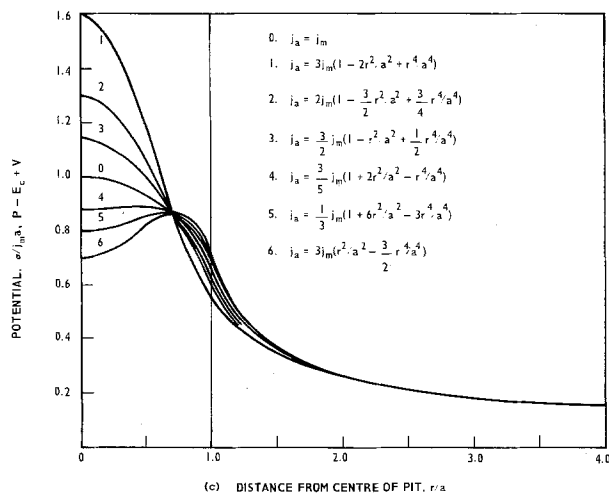
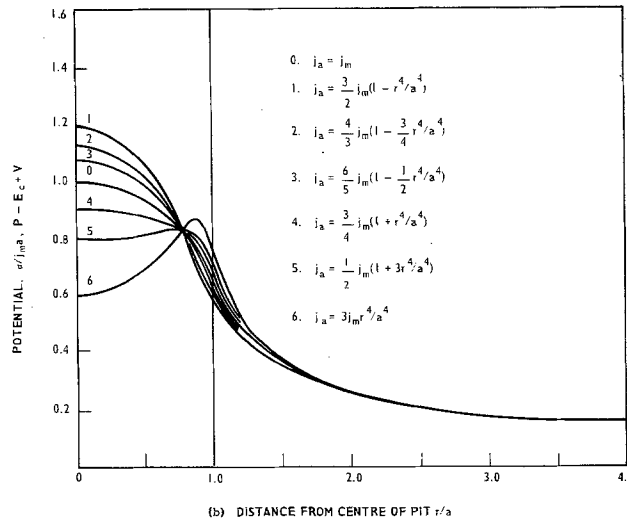
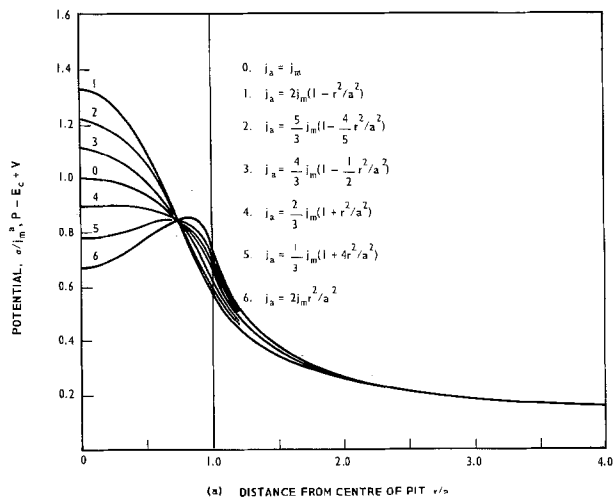


Fig. 2. Variation in potential for different current distributions

here is less than about half the mean value. Values of the potential that are of particular interest are the potential at the center of the pit

$$P(0,0) = -(E_c - V) + \frac{j_m a}{\sigma} \left[1 + \frac{1}{3} \alpha_1 + \frac{1}{3} \alpha_2 \right] \quad [41]$$

(see also Eq. [30]) and the potential at the edge of the pit given by

$$P(a,0) = -(E_c - V) + \frac{j_m a}{\sigma} \left(\frac{2}{\pi} \right) \left[1 - \frac{1}{9} \alpha_1 + \frac{1}{25} \alpha_2 \right] \quad [42]$$

When compared with the expressions for the current density at the center and edge of the pit

$$j_a(0) = j_m [1 + \alpha_1 + \alpha_2] \quad [43]$$

$$j_a(a) = j_m [1 - \alpha_1 + \alpha_2] \quad [44]$$

it may be seen that the potential at the center of the pit is less sensitive to the values of α_1 and α_2 than is the current density ($1/3\alpha_1$ and $1/5\alpha_2$ instead of α_1 and α_2) and that the potential at the edge of the pit is still less sensitive ($1/9\alpha_1$ and $1/25\alpha_2$), in agreement with the observations made above.

Conclusions

1. A technique using integral of Bessel functions has been used to calculate the effect of an anodic current distribution of the form $j_a = j_m(\beta_0 + \beta_1 r^2/a^2 + \beta_2 r^4/a^4)$ within the pit on the potential distribution in the plane of the electrode surface.

2. Analytic solutions have been obtained for situations where linear polarization kinetics may be as-

sumed, e.g., where the pit is small so that the change in potential $\sim j_m a/\sigma$ is small.

3. If the radius of the pit a is small compared to the Wagner polarization parameter L_c for the unpitted electrode, i.e., $a \lesssim L_c/20$, the potential distribution is independent of the polarization parameter, and thus insensitive to the assumption of linear kinetics.

4. The potential depends mainly on the mean value of the current density flowing from the pit, and is less sensitive to the form of the current distribution.

5. Quite large changes in the form of the current distribution are required to produce changes in the potential at the center of the pit for the same mean current density, and the potential at the edge of the pit is still less sensitive to the form of the current distribution.

6. The potential outside the pit on the surface of the electrode depends on the mean current density and is virtually unaffected by the form of the current distribution.

Acknowledgments

This work was carried out at the Central Electricity Research Laboratories, and is published by permission of the Central Electricity Generating Board.

Manuscript submitted April 10, 1979; revised manuscript received Sept. 18, 1979.

Any discussion of this paper will appear in a Discussion Section to be published in the December 1980 JOURNAL. All discussions for the December 1980 Discussion Section should be submitted by Aug. 1, 1980.

LIST OF SYMBOLS

a radius of pit
 $B(t)$ function determined by boundary conditions

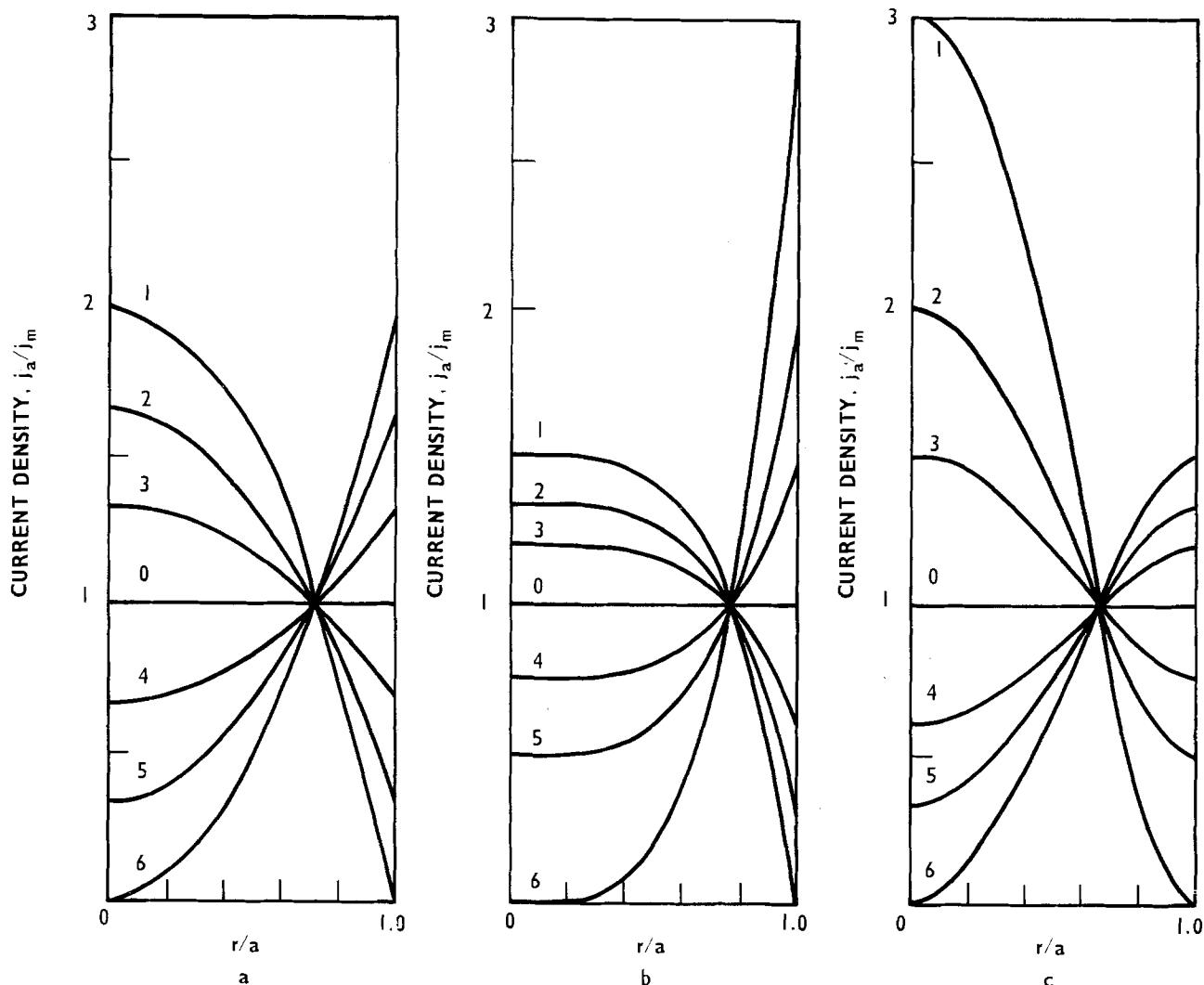


Fig. 3. Current distributions giving the potential variations shown in Fig. 2

B_0	constant determined by boundary conditions
$E(\)$	complete elliptic integral of second kind
E^*	electrode potential
E_c	free corrosion potential for unpitted part of electrode
$F(\ , \ ; \)$	hypergeometric function
$f_0(\), f_1(\)$	function defined in Eq. [22], [23]
$g_0(\), g_1(\), g_2(\)$	function defined in Eq. [31], [32], [33]
$H_0(\), H_1(\)$	Struve functions
\tilde{I}	total current flowing from pit
$J_0(\), J_1(\), J_2(\), J_3(\), J_4(\), J_5(\), J_m(\), J_{2n+1}(\)$	Bessel functions of first kind
j	current density at electrode surface
j_a	current density flowing from pit
$K(\)$	complete elliptic integral of first kind
L_c	Wagner polarization parameter for unpitted part of electrode
m	integer
$N_0(\), N_1(\)$	Bessel functions of second kind
n	integer
P	electrostatic potential
$P_0(\), P_1(\), P_2(\), P_n(\)$	Legendre polynomials
r	coordinate
t	dummy variable
V	constant potential
x	dummy variable
z	coordinate
α_1, α_2	constants
$\beta_0, \beta_1, \beta_2$	constants
δ	$= a/L_c$
σ	conductivity
$\phi(\)$	step function

REFERENCES

1. P. H. Melville, *This Journal*, **126**, 2081 (1979).
2. P. H. Melville, *Corros. Sci.*, To be published.
3. B. Levich and A. Frumkin, *Acta Physicochim., U.R.S.S.*, **18**, 1 (1943).
4. L. Nanis and W. Kesselman, *This Journal*, **118**, 454 (1971).
5. L. Gal-Or, Y. Raz, and J. Yahalom, *ibid.*, **120**, 589 (1973).
6. E. McCafferty, *Corros. Sci.*, **16**, 283 (1976).
7. E. McCafferty, *This Journal*, **124**, 1869 (1977).
8. J. T. Waber, *ibid.*, **101**, 271 (1954).
9. J. T. Waber and M. Rosenbluth, *ibid.*, **102**, 344 (1955).
10. J. T. Waber, *ibid.*, **102**, 420 (1955).
11. J. T. Waber and B. Fagan, *ibid.*, **103**, 64 (1956).
12. E. Kennard and J. T. Waber, *ibid.*, **117**, 880 (1970).
13. J. T. Waber, in "Localized Corrosion," R. W. Staehle *et al.*, Editors, p. 221, NACE, Houston (1974).
14. C. Wagner, *ibid.*, **98**, 116 (1951).
15. A. Erdélyi, W. Magnus, F. Oberhettinger, and F. G. Tricomi, "Bateman Manuscript Project—Tables of Integral Transforms," Vol. II, McGraw-Hill, New York (1954).
16. I. S. Gradshteyn and I. M. Ryzhik, "Tables of Integrals, Series, and Products" 4th ed., Academic Press, New York (English Edition) (1965).
17. G. N. Watson, "A Treatise on the Theory of Bessel Functions," 2nd ed., Cambridge University Press (1944).
18. W. Magnus and F. Oberhettinger, "Formeln und Sätze für die speziellen Funktionen der mathematischen Physik," Springer Verlag, Berlin (1948).

Studies in Selenious Acid Reduction and CdSe Film Deposition

M. Skyllas Kazacos* and B. Miller*

Bell Laboratories, Murray Hill, New Jersey 07974

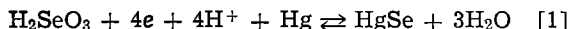
ABSTRACT

The reaction sequence for the reduction of H_2SeO_3 in 1M H_2SO_4 at various surfaces and the formation of selenide films in this medium with and without metal ions present have been investigated by rotating disk and ring-disk electrode techniques. The system is complicated by competitive paths leading to selenium formation from $\text{Se}(-2)$ - $\text{Se}(+4)$ chemical reactions and the result is sensitive both to the nature of the substrate with the possibility of metal selenide formation and to the concentration of solution species. The implications for cathodic deposition of semiconductors like CdSe, from voltammetric and photospectral data, are discussed.

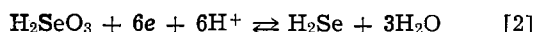
n-CdSe single crystals have been used as photoanodes in semiconductor liquid junction solar cells to give overall power conversion efficiencies of 7.5% (1). Pressure sintered CdSe polycrystalline electrodes have shown 70% of the single crystal efficiency (2). Films anodically generated from cadmium metal in selenide solution exhibit the spectral properties of the single crystal form, but much lower power conversion efficiencies (3). A number of problems are recognized with the anodic films grown for photovoltaic purposes, including limited thickness, uncertain composition, defects, unknown doping, and small crystallite size (3, 4).

Deposition of CdSe by cathodization in a selenious acid-cadmium ion solution has been accomplished by the Weizmann Institute group (5), and layers up to several microns have been achieved on a Ti substrate. Although the problem of limited thickness can be overcome by this technique, codeposition of excess selenium is difficult to control, and poor crystallinity gives rise to reduced photoresponse in the as-deposited material. These can be offset to some extent by a subsequent annealing process which increases the crystallinity and stoichiometry of the films. A mechanistic understanding of the deposition process is presently lacking and is an object of this study. Insights into the reaction sequence may lead to improving the quality of the films.

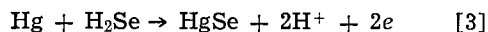
Considerable work has already been done on the kinetics of $\text{Se}(IV)$ reduction and a number of mechanisms have been proposed. From a detailed study of the polarographic behavior of tetravalent selenium, Lingane and Niedrach (6) suggested the following overall equation to describe the initial main wave



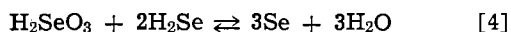
This actually results from the superimposed partial processes of



and the anodic dissolution of mercury by



In acidic and alkaline solutions, a second cathodic wave is observed and corresponds to the six-electron reduction of $\text{Se}(+4)$ species to $\text{Se}(-2)$. In the intermediate pH range, however, a net four-electron process is observed because H_2Se reacts sufficiently rapidly with $\text{Se}(+4)$ by



Jónás (7) investigated the polarographic behavior of $\text{Se}(+4)$ in a large number of buffer and nonbuffer

solutions and observed up to four different cathodic waves depending on the pH value. She concluded, however, that reaction [4] does not take place during the reduction of $\text{Se}(+4)$, attributing the presence of the first wave to reaction [1], and the second wave to reaction [2]. The further waves were ascribed to HSeO_3^- and SeO_3^{2-} reduction, depending on pH.

A number of workers (8-10) have asserted that the second wave of $\text{Se}(+4)$ in acidic solutions might represent catalytic hydrogen evolution in addition to reaction [2]. Thus, the reduction in acidic solutions could end with elemental selenium via reaction [4].

Several other polarographic studies (11-14) show a similar disagreement concerning the mechanism of $\text{Se}(IV)$ reduction, in particular, with regard to the nature of the final product. This is especially of importance in the cathodic CdSe deposition since the concurrent formation of elemental selenium at the electrode surface is one of the major problems associated with this technique.

Rotating disk (RDE) and ring-disk electrode (RRDE) studies were initiated to investigate selenious acid reduction in 1M H_2SO_4 at various metal surfaces and the mechanism of the CdSe film deposition in solutions also containing Cd(II) ions. In addition, sinusoidal hydrodynamic modulation (SHM) of rotation speed, which is useful in discriminating between surface and mass transfer controlled reactions, was also applied where appropriate. The results are examined with respect to electrochemical preparation of photoactive II-VI semiconductor substrates.

Experimental

The construction and electronics of the RRDE have previously been described (15), as has the apparatus for the sinusoidal speed modulation (16). The RRDE's used were either gold disk-gold ring, or silver disk-carbon ring electrodes. RDE studies were also carried out on platinum, copper, amalgamated gold, and wax impregnated carbon surfaces.

The electrodes were rotated in a three compartment cell equipped with a bottom optical flat window to enable illumination of the disk surface. Solutions were prepared with triply distilled water and reagent grades of Na_2SeO_3 , CdSO_4 , and 95% H_2SO_4 . A saturated calomel electrode served as reference and unless otherwise specified, a rotation speed of 1600 rpm was used in all experiments.

Results and Discussion

Reduction of $\text{Se}(IV)$ in 1M H_2SO_4 .—The cathodic behavior of H_2SeO_3 in sulfuric acid was found to be strongly influenced by the nature of the disk electrode used. In general, however, these could be grouped into two different categories depending on how "noble"

* Electrochemical Society Active Member
Key words: electrodeposition, voltammetry, semiconductor.

these electrodes behaved with respect to the electroactive reactants or intermediates.

Rotating disk voltammograms in 5 mM H_2SeO_3 for Group I electrodes (gold, platinum, and carbon) in the potential range 0 to -1.2V vs. SCE, are shown in Fig. 1-3 as curve 1, for scans first positive to negative, then reverse. In each case, a single reduction wave can be observed before the current increases rapidly with H_2 evolution. The reduction wave is decidedly better defined on the reverse, although there is some

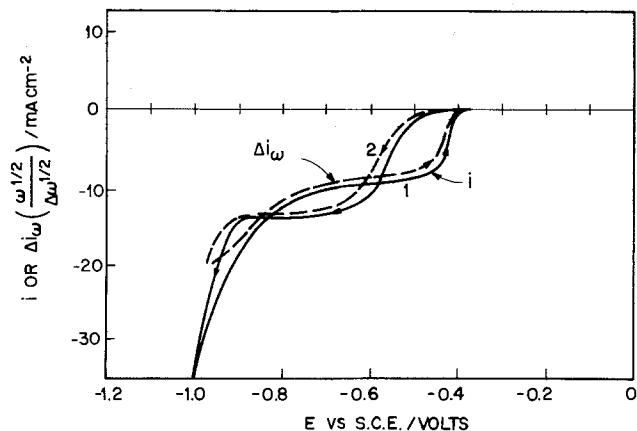


Fig. 1. Curve 1, Controlled potential sweep cycle of 0.175 cm^2 gold disk in 5 mM H_2SeO_3 -1M H_2SO_4 at 10 mV sec^{-1} scan rate. Curve 2, Modulated component of disk current for potential scan of curve 1. Central rotation speed, $\omega = 1600\text{ rpm}$; modulation amplitude, $\Delta\omega^{1/2} = 2\text{ rpm}^{1/2}$; modulation frequency, $f = 1\text{ Hz}$.

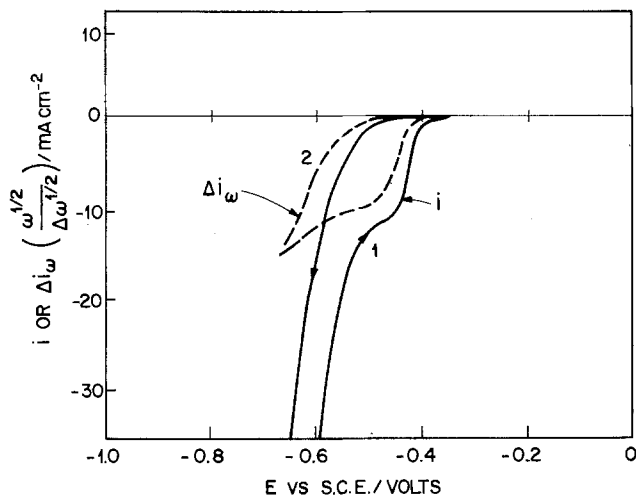


Fig. 2. Curves 1 and 2 as Fig. 1 but with platinum disk

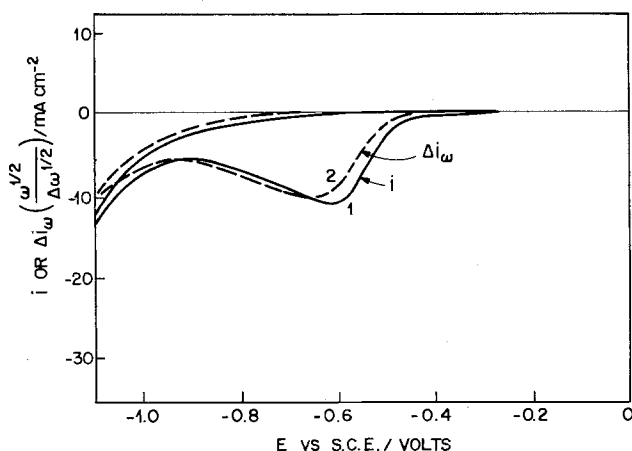


Fig. 3. Curves 1 and 2 as Fig. 1 but with carbon disk

limiting current loss on the step. With each successive full cycle of the potential (not shown) the limiting current decreases due to the formation of a passivating red selenium film on the electrode surface. The carbon electrode is seen to passivate more rapidly than the others so that already on the reverse (positive-going) scan of the first cycle no reduction wave can be observed.

If the potential is scanned and held at a value corresponding to copious hydrogen evolution, the red film gradually disappears. This can be accounted for by either a further reduction of Se to H_2Se or to a mechanical removal of the Se by the action of the hydrogen bubbles.

The $i/\omega^{1/2}$ values at the first step, curve 1, for the limiting currents (or the maximum current for carbon which passivates more rapidly) are equal for all three electrodes. In order to confirm a mass transfer limited process for the cathodic step and to see whether a second reduction wave is present and hidden by H_2 evolution, sinusoidal hydrodynamic modulation experiments were performed and shown as curve 2 in Fig. 1-3. (Curves 1 and 2 of these figures were actually obtained in the same experiment where i is the average total current. The results for curve 1 are independent of the superimposed SHM). The corresponding Δi_ω values are in accord with Levich equation expectation, as shown by the near superposition of the $\Delta i_\omega \times \omega^{1/2}/\Delta\omega^{1/2}$ and i curves in these regions.

Using this technique, it should be possible to differentiate between a convective diffusion controlled process such as H_2SeO_3 reduction, for which SHM response is expected, and a process which is not kinetically reversible and not limited by the rate of diffusion of an electroactive species to the electrode surface (i.e., H_2 evolution at gold in 1M H_2SO_4 at these currents). The latter is thus insensitive to ω variation. The curves for gold show the best evidence for the presence of a second wave for a further reduction of Se to H_2Se beyond the hydrogen potential. However, because of the interference both of the sharply rising hydrogen current and bubble evolution, a quantitative ratio of limiting currents for the two processes cannot be established.

The reduction of H_2SeO_3 on Au-Hg and Ag (Group II) disk electrodes is shown in Fig. 4 and 5, respectively. Both electrodes exhibit a different behavior from the Group I electrodes with the most significant common feature being a more positive first wave potential suggestive of some interaction between the electrode surface and the solution species. The appearance of a black film, if the potential is held at a value more positive than -0.4V , implies HgSe and Ag_2Se formation in the respective cases. At more negative potentials, the red selenium deposit appears. In the case of Au-Hg, the presence of several small peaks during the initial scan from -0.2V is probably the result of HgSe formation [initiating at -0.35V , in agreement with other work (6, 7)]. The inhibition of

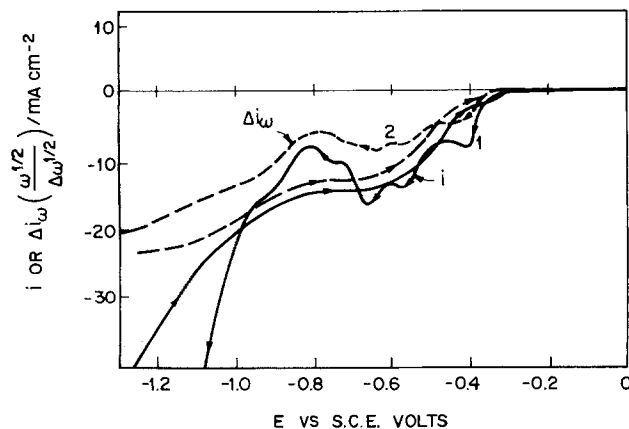


Fig. 4. Curves 1 and 2 as Fig. 1 but with amalgamated gold disk

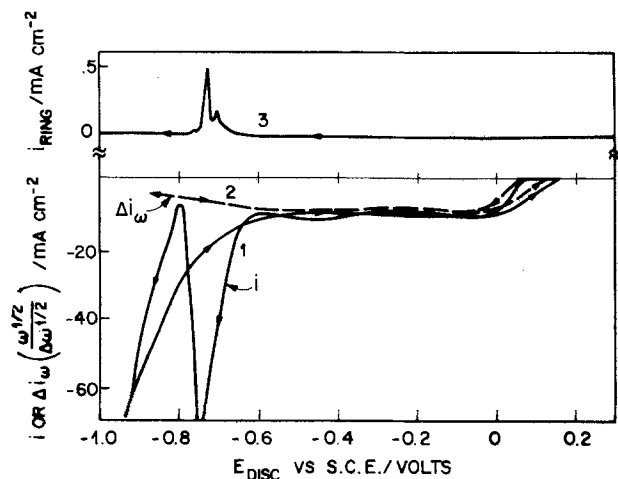
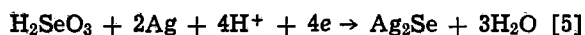


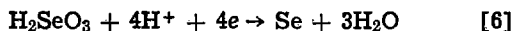
Fig. 5. Curves 1 and 2 as Fig. 1 but with silver disk. Curve 3, Ring current response to silver disk scan of curve 1. $E_R = 0.2V$ vs. SCE.

current by this film is followed by a subsequent reduction of the $HgSe$ to Hg and H_2Se , not separated from hydrogen evolution. Reversal of the scan gives rise to a single smooth wave corresponding to Se deposition on Hg , then on $HgSe$. The initial $HgSe$ peak is absent since the Hg electrode is now isolated from the solution by the $Se-HgSe$ film.

On the silver electrode Ag_2Se is deposited until the rate of diffusion of Ag to the electrode surface is limited by the thickness of the film. Then, through electronic conduction in the film, Se deposition takes place. Since four electrons are involved in each reaction, i.e.



and



only one reduction wave is observed for the two reactions. At potentials more negative than $-0.6V$, a large cathodic peak can be seen, together with the appearance of a black deposit of Ag . Thus, at these potentials, Ag_2Se is reduced to Ag with the release of H_2Se . It should therefore be possible to detect at a ring electrode, any H_2Se released into solution. Using a silver disk-carbon ring electrode and potentiostating the ring at $0.2V$, the disk potential was scanned negative from $0.2V$. Curve 3 of Fig. 5 shows the anodic ring peak which appears as the Ag_2Se is reduced at the disk. Thus, as Ag_2Se is reduced, Ag deposits on the disk electrode, and as the H_2Se that is not reacted by H_2SeO_3 in transit is swept across the ring electrode, it is oxidized to Se .

From the above, although it is apparent from the visual evidence that elemental selenium is the product of the reduction of selenious acid, it remains necessary to distinguish between two different mechanisms; either a four electron reduction as given by Eq. [6], or a six electron reduction to H_2Se followed by a fast chemical reaction as given by Eq. [2] and [4]. If the latter is true and the rate of the subsequent chemical reaction is dependent on the rate of diffusion of the species H_2SeO_3 to the electrode surface, the rate of reaction [4] should be influenced by the concentration of H_2SeO_3 in solution.

Using a 0.5 mM solution of H_2SeO_3 in $1M$ H_2SO_4 , the voltammograms shown in Fig. 6-8 were obtained for Au , Ag , and Cu (Cu is a Group II type) electrodes, respectively. The most significant feature here is the presence of two reduction waves on silver and copper. Figure 9 shows Levich plots for both waves in each of the limiting current regions (i.e., at -0.3 and $-0.6V$). The results for both metals essentially superimpose, yielding two straight lines with a slope ratio of approximately 2:3 for each system. Thus, if four electrons

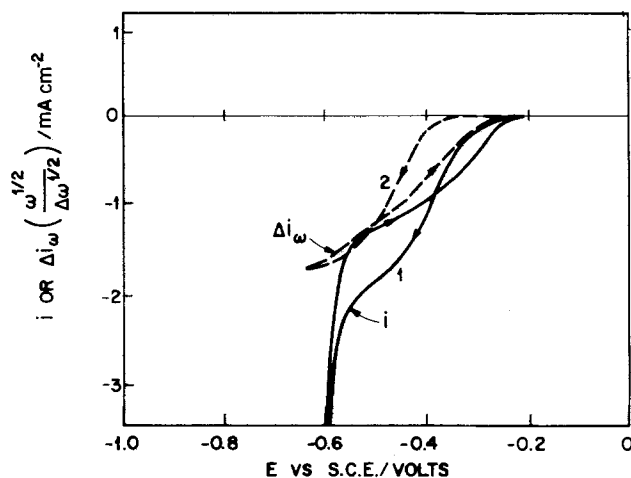


Fig. 6. Curves 1 and 2, conditions of Fig. 1 at gold disk, except solution is 0.5 mM H_2SeO_3-1M H_2SO_4 .

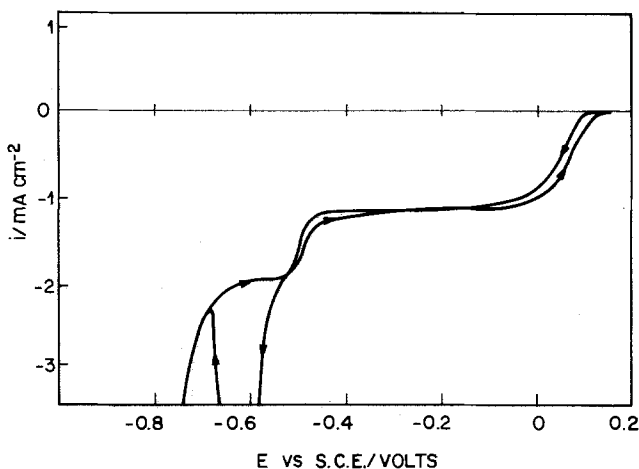


Fig. 7. Conditions of Fig. 5 at silver disk, without modulation, except solution is 0.5 mM H_2SeO_3-1M H_2SO_4 .

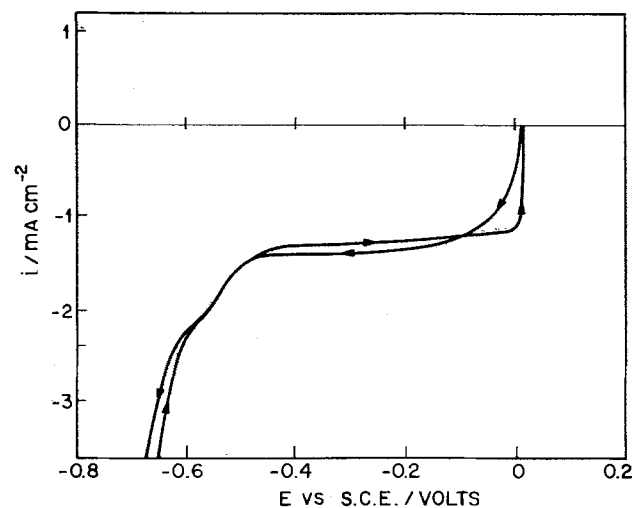


Fig. 8. Conditions of Fig. 7 at copper disk.

are involved in the first reduction step, with the formation of Ag_2Se and Cu_2Se , respectively, the second cathodic wave corresponds to the six electron reduction of H_2SeO_3 to H_2Se .

The Levich plots of wave height/concentration vs. $\omega^{1/2}$ for 0.5 mM H_2SeO_3 solutions (Fig. 10) at a gold disk also give a slope 50% higher for the more dilute solution, consistent with an apparent change from 4 to 6 in electrons transferred. Furthermore, holding the potential of the disk electrodes in the region of H_2Se

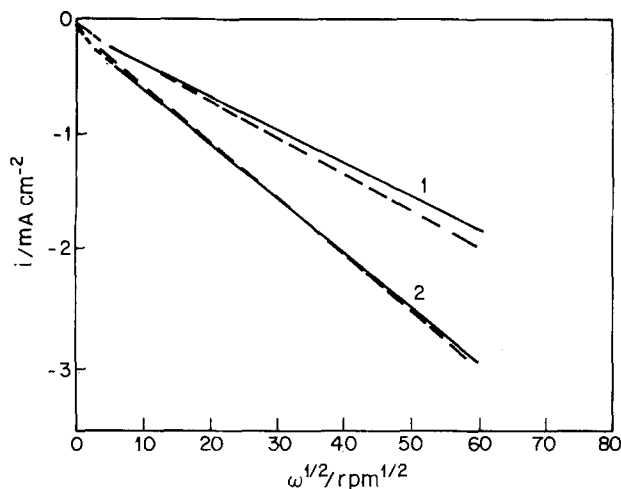
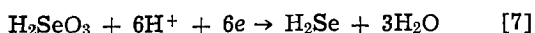
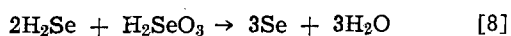


Fig. 9. Levich plots for silver and copper rotating disks in 0.5 mM H_2SeO_3 -1M H_2SO_4 . Curve 1, currents at $E = -0.2\text{V}$ vs. SCE; Curve 2, currents at $E = -0.6\text{V}$ vs. SCE. — Ag; --- Cu.

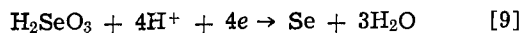
formation for several minutes in the 0.5 mM H_2SeO_3 solution does not lead to the deposition of any observable amount of red selenium at the disk. A red film is, however, formed outward from the periphery of the electrode, again showing that Se formation does result from a chemical interaction between H_2Se and H_2SeO_3 . Thus, the following sequence is proposed for the reduction of H_2SeO_3 in 1M H_2SO_4 at a "noble" electrode



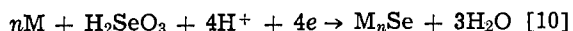
followed by the chemical reaction



The rate of the chemical reaction is dependent on the concentration of H_2SeO_3 , so that at high H_2SeO_3 concentrations, reaction [8] is fast and the overall process taking place at the electrode surface appears to be



For the Group II electrodes however, an interaction takes place between the metal surface and the electroactive species. The following reaction occurs at these electrodes



where M stands for Hg, Ag, or Cu, respectively, with $n = 1$ for Hg, 2 for Ag and Cu. These reactions take

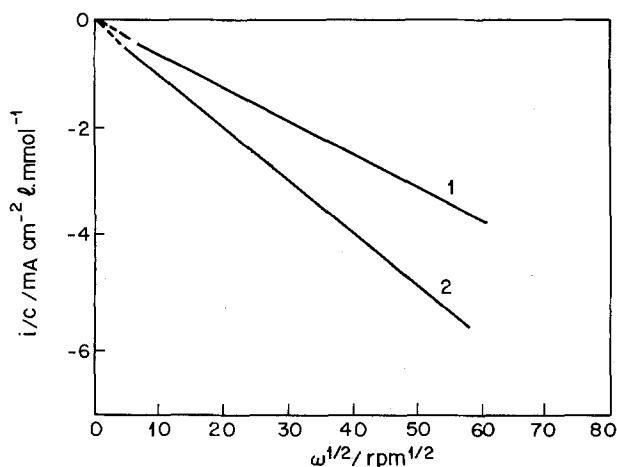


Fig. 10. Levich plots for gold rotating disk on limiting current steps of H_2SeO_3 reduction wave in 1M H_2SO_4 . Curve 1, 4 mM H_2SeO_3 , $E = -0.65\text{V}$ vs. SCE; Curve 2, 0.5 mM H_2SeO_3 , $E = -0.5\text{V}$ vs. SCE; (see curves of Fig. 1 and 6).

place more readily, i.e., at more positive potentials, because of the additional driving force of the insoluble metal-selenide formation, than does H_2Se formation by reaction [2]. However, as the flux of the species M by diffusion through the also electronically conducting selenide film decreases, reaction [7] or [9] takes over.

A further feature of the selenious acid reduction is the irreversibility of the reaction, with no reoxidation wave appearing after selenium deposition. It is also to be noted that Se(IV) cannot be oxidized to Se(VI) in this system and such a ring reaction is not available to determine the number of electrons transferred in disk reaction consuming Se(IV).

Deposition of CdSe.—The technique developed by the Weizmann Institute group (5) for the cathodic deposition of CdSe, involves the use of millimolar SeO_2 solutions in 1M H_2SO_4 in the presence of relatively high concentrations of CdSO_4 . Using a Cd stick as anode and a Ti plate as substrate, no external voltage is required when the two electrodes are shorted together. Solution stirring and concentration of SeO_2 are adjusted so as to maintain a current of 5-10 mA cm^{-2} of Ti. Higher SeO_2 concentrations result in the formation of a red insulating layer of Se which prevents further deposition.

From the results presented in the section "Reduction of Se(IV) in 1M H_2SO_4 ," the reduction of selenite in 1M H_2SO_4 gives rise to H_2Se which undergoes a rapid chemical reaction with the solution to yield elemental selenium at the electrode surface. In solutions of high H_2SeO_3 concentrations, i.e., $\cong 5$ mM H_2SeO_3 , the post chemical reaction is so fast that the overall process appears as a four electron reduction to Se. Under such conditions, the precipitation of Cd^{2+} at the surface of the electrode would not be able to compete favorably, even at high Cd^{2+} concentrations with Se deposition. Decreasing the concentration of H_2SeO_3 however, slows down the subsequent chemical reaction of H_2Se so that a six electron reduction results at the surface of the electrode. Under such circumstances, it should be possible to deposit CdSe more efficiently, although excess Se could still be expected if the chemical reaction [8] is fast enough.

Figure 11 shows a voltammogram obtained for a gold electrode in a 1M H_2SO_4 solution containing 0.5 mM Na_2SeO_3 and 0.1M CdSO_4 . A reduction wave, corresponding to the six electron reduction of H_2SeO_3 , appears at approximately -0.5V vs. SCE. At potentials more negative than -0.7V , the current increases rapidly due to the reduction of Cd^{2+} . Reversal of the scan from that point gives rise to an anodic peak cor-

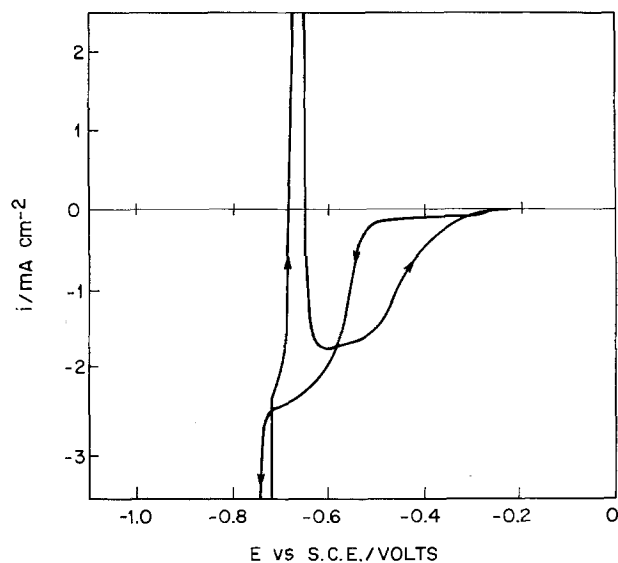


Fig. 11. Controlled potential sweep cycle at Au disk in 0.5 mM $\text{H}_2\text{SeO}_3 + 0.1\text{M CdSO}_4$ in 1M H_2SO_4 . Conditions as for Fig. 1.

responding to the reoxidation of Cd, superimposed on the H_2SeO_3 reduction wave. The hysteresis observed in the region of -0.4V indicates that once sufficient CdSe has been deposited, the reduction of H_2SeO_3 can occur at less negative potentials.

These results thus illustrate the relatively high nucleation overpotential associated with the deposition of CdSe on a gold surface. A similar effect was also observed on a carbon electrode. Ti surfaces (5) have not been investigated here.

Using 0.1M CdSO_4 solutions in 1M H_2SO_4 , containing H_2SeO_3 in concentrations ranging from 1 to 3 mM, CdSe films were deposited on both carbon and gold surfaces. This was accomplished by stepping the potential to -0.6V vs. SCE and plating for 1/2 hr or until the electrode passivated. Electrode passivation was quite rapid in solutions containing 2 mmoles per liter or higher H_2SeO_3 , showing that selenium deposition is still relatively fast under these conditions. On illuminating the electrodes with white light, p-type behavior was observed, this also being indicative of excess Se present in the CdSe films.

Figure 12 shows a typical open-circuit photovoltage spectral response curve which was obtained for a CdSe electrode prepared by the above method. For this spectrum, "d-c" monochromatic incident radiation from a 100W quartz halogen (filament) lamp was used. The electrode was immersed in 1M H_2SO_4 and the open-circuit potential was measured vs. SCE. The main feature of such spectra is wavelength regions with net p- or n-type behavior. The photoresponse extends to about 720 nm, equivalent to the known approximately 1.7 eV bandgaps of either CdSe or Se. Presumably since the higher wavelength region is dominated by the direct gap, n-type CdSe, it represents the CdSe band-edge. We ascribe no further significance to the compensation point at 550 nm or to the shapes of these spectra other than the particular composition produced by a given electrodeposition run.

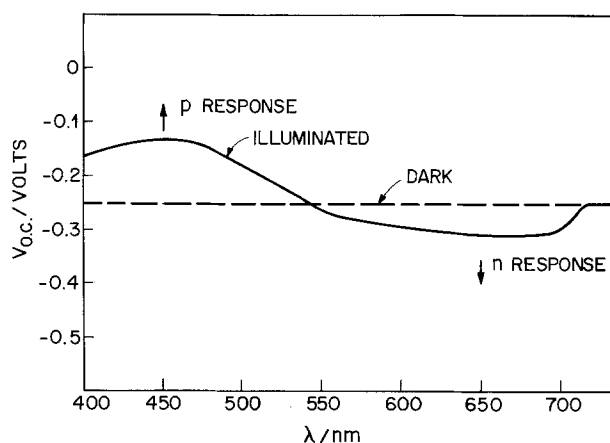


Fig. 12. Photovoltage spectral response curve for CdSe film electrode prepared by cathodic deposition. Open-circuit potential of CdSe measured vs. SCE in 1M H_2SO_4 .

In solutions containing less than 2 mM H_2SeO_3 , or for current densities below 5 mA cm^{-2} , electrode passivation was much slower by the above technique, and in some cases slight n-type behavior could be observed when illuminating the films with white light. The very low photovoltages with monochromatic light, however, were inadequate to obtain reliable photovoltage spectra.

A lower plating rate in dilute H_2SeO_3 solutions thus appears to minimize the level of excess selenium incorporated in the CdSe films prepared cathodically. However, the low photoresponse of these films, probably due to poor crystallinity, means that a final annealing process is still unavoidable if these electrodes are to be used as photoanodes in liquid junction solar cells. Finally, we note that a slower plating rate also resulted in improved adherence of the deposited films on the substrate. This is a major problem with the films prepared from more concentrated solutions.

Acknowledgment

M. S. Kazacos is indebted to the Australian Commonwealth Scientific and Industrial Research Organization for a post-doctoral fellowship grant.

Manuscript submitted Sept. 21, 1979; revised manuscript received Nov. 7, 1979.

Any discussion of this paper will appear in a Discussion Section to be published in the December 1980 JOURNAL. All discussions for the December 1980 Discussion Section should be submitted by Aug. 1, 1980.

Publication costs of this article were assisted by Bell Laboratories.

REFERENCES

1. A. Heller, G. P. Schwartz, R. G. Vadimsky, S. Menezes, and B. Miller, *This Journal*, **125**, 1156 (1978).
2. B. Miller, A. Heller, M. Robbins, S. Menezes, K. C. Chang, and J. Thomson, Jr., *ibid.*, **124**, 1019 (1977).
3. B. Miller and A. Heller, *Nature*, **262**, 680 (1976).
4. L. M. Peter, *Electrochim. Acta*, **23**, 165 (1978).
5. G. Hodes, J. Manassen, and D. Cahen, *Nature*, **261**, 403 (1976).
6. J. J. Lingane and L. W. Niedrach, *J. Am. Chem. Soc.*, **71**, 196 (1949).
7. K. Jónás, *Acta Chem. Acad. Sci. Hung.*, **25**, 379 (1960).
8. E. F. Speranskaya, *Zh. Anal. Khim.*, **17**, 347 (1962).
9. A. I. Alekperov, *Azerb. Khim. Zh.*, **1**, 73 (1963).
10. V. P. Gladyshev and Z. B. Rozhdestvenskaya, *Chem. Zvesti*, **17**, 586 (1963).
11. G. D. Christian, E. C. Knoblock, and W. C. Purdy, *Anal. Chem.*, **37**, 425 (1965).
12. V. V. Kuznetsov and G. A. Sadakov, *Zh. Anal. Khim.*, **18**, 1486 (1963).
13. G. D. Christian, E. C. Knoblock, and W. C. Purdy, *Anal. Chem.*, **35**, 1128 (1963).
14. W. Hans and M. von Stackelberg, *Ber. Bunsenges. Phys. Chem.*, **54**, 62 (1950).
15. B. Miller, *This Journal*, **116**, 1117 (1969).
16. B. Miller and S. Bruckenstein, *Anal. Chem.*, **46**, 2026 (1974).

Temperature Study of Oxide Film Growth at Platinum Anodes in H₂SO₄ Solutions

A. Damjanovic,* L.-S. R. Yeh,* and J. F. Wolf

Allied Chemical Corporation, Corporate Research Center, Morristown, New Jersey 07960

ABSTRACT

The growth of anodic oxide films at platinum in sulfuric acid solution was studied at different temperatures using galvanostatic transients. The activation energy and preexponential factor for the rate of growth were evaluated. In the plane in which the rate-determining step occurs the surface density of ions, or ion pairs participating in the growth process, is about 10^{15} cm⁻². This is close to the density of atoms in the surface of the metal. The analysis appears to support the process at the metal/oxide interface being the rate-determining step. However, the same value for N is compatible with the field-assisted place exchange process as the rate-determining step at the metal/oxide interface or within the oxide phase. Because the growth follows the same rate equation from the very early stages of oxide formation, the process at the metal/oxide interface seems to be the rate-determining step.

It has recently been reported that the kinetics of oxide growth at platinum anodes in acid solutions from about 1.0V vs. RHE to the potential at which O₂ evolution becomes the predominant reaction is represented by the equation (1, 2)

$$i_{og} = i_{og,0} \exp \frac{\alpha(V - V_0)}{d} \quad [1]$$

Apparently, the growth process follows (1-4) the well-known formalism of the Cabrera-Mott model (5) for the high field-assisted formation of "very-thin" oxide films. If the growth indeed proceeds according to this model, then the rate of growth given as the change of the average thickness of the oxide film, d , with time satisfies the equation [cf. Ref. (5, 6)]

$$\frac{d(d)}{dt} = ri_{og} = 2N\nu\lambda\omega \exp \left[\frac{-W}{kT} \right] \exp \left[\frac{ze\lambda\Delta V_{of}}{kTd} \right] \quad [2]$$

In this equation ze is the charge and λ is the half-jump length of the migrating ions, ν is their mean vibration frequency, W is the activation energy, and ω is the area of the oxide layer per single metal ion in the oxide phase. Factor r ($= 9 \times 10^3$ Åcm²/C) converts experimentally determined charge density q (in C cm⁻²) into thickness in angstroms (1), i.e., $d = r q$. ΔV_{of} ($= V - V_0$) is the potential difference across the oxide film. N is the surface density of the ions participating in the growth process for the plane in which the rate-determining step occurs (5, 6).

In the original Cabrera-Mott theory, it was assumed that only cations migrate in the process of growth. Further, it was assumed that a process at the metal/solution interface in the very early stage of growth, or a process at the metal/oxide film interface in subsequent stages of growth, is the rate-determining step. With this assumption, N should closely be equal to the surface density of atoms in the metal itself, i.e., about 1.5×10^{15} cm⁻². This may be contrasted with the migration of interstitial cations within the oxide phase being the rate-determining step [the Verwey model (7)]. In this case N should be equal to the surface density of interstitial cations in the reaction plane, i.e., should be much less than 1.5×10^{15} cm⁻².

Parameter α was found to be 160 ÅV⁻¹. This value checks favorably with the theoretically predicted value for $\alpha = ze\lambda/kT$ when $z\lambda = 4$ Å (1). It implies that $z = 2$ and $\lambda = 2$ Å and that Pt⁺⁺ ions are the migrating species in the oxide phase. The phase itself was identified by ellipsometry as Pt(OH)₂ (8, 9). The agreement

evidently provided support, if not confirmation, for the proposed model of growth. It was further suggested (1) that the process at the metal/oxide film interface was the rate-determining step. This is because the rate equation describes the growth from the very early stages when the film is perhaps only one atomic layer thick [cf. Ref. (10)]. The exchange current density, $i_{og,0}$ ($= 1.8 \times 10^{-10}$ Acm⁻²), was found (11) to be independent of pH, as expected for the model (cf. Eq. [1] and [2]).

Though much has been learned in recent years about oxide growth at Pt anodes [cf. Ref. (1-4, 8-15)], the question concerning the over-all path and rate-determining step remains open. For instance, is the process at the metal/oxide film interface or the process within the oxide phase the rate-determining step? Could the process at the oxide/solution be the rate-determining step? The latter process has not been considered to be rate determining. An analysis of the exchange current density

$$\begin{aligned} i_{og,0} &= 2N\nu\lambda\omega r^{-1} \exp \left[\frac{-W}{kT} \right] \\ &= i_0 \exp \left[\frac{-W}{kT} \right] \end{aligned} \quad [3]$$

can provide information concerning the rate-determining step if i_0 is known so that the product $N\nu$, and hence N , can be evaluated. For, if the process of ion migration in interstitial positions within the oxide phase is the rate-determining step, N is expected to be a few orders of magnitude less than N for the process of ion formation at the metal/oxide film interface. Here, we report kinetic data on anodic oxide growth at Pt anodes in 2N H₂SO₄ solution at different temperatures and correlate the factor N to the rate-determining step.

Experimental

An all-glass cell was used in this work. The working and reference electrode compartments of the cell were jacketed so that the solutions in both compartments could be maintained at a given temperature by circulating a thermostated liquid through the jackets around both compartments. The working platinum wire electrode was "sealed" in a soft glass tube. The stated purity of platinum was better than 99.99%. The roughness factor ($R = 1.7$) was determined from capacitance measurements in the polarizable region and used to correct all data reported here. To ensure uniform field distribution at the working electrode, three Pt gauze counterelectrodes were symmetrically placed around the working electrode at a distance of about 1

* Electrochemical Society Active Member.
Key words: metals, electrode, kinetics.

cm. The solution in the working electrode compartment was saturated with high purity grade O₂. A hydrogen electrode in the same solution and temperature was used as the reference electrode.

The constant current charging technique was used in this study. Details of the experimental procedures and instrumentation were the same as previously described (1, 2, 11).

Results and Discussion

When a constant current is applied to a prereduced electrode initially at the rest potential, the potential after an initial sharp and nonlinear rise increases linearly with time, or charge density *q*, until a point is reached when O₂ starts evolving (1, 11). As previously shown, in the linear region the charge is used almost entirely for oxide film formation (1, 11). From the experiments at room temperature, these linear *V-q* traces at different constant current densities are shown to follow Eq. [1].

In Fig. 1, *V-q* traces are shown for 1.5 × 10⁻⁵, 1.5 × 10⁻⁴, 1.5 × 10⁻³, and 1.5 × 10⁻² Acm⁻² in 2N H₂SO₄ solution at 50°C. As expected, the general forms of these traces are similar to the charging curves at room temperature [cf. Fig. 1 and 2 in Ref. (11)]. However, for the same current density, *dV/dq* slopes of the *V-q* traces at 50°C are significantly lower than the slopes at room temperature. In Fig. 2, the *dV/dq* slopes are plotted against the logarithm of the applied current density at 0°, 23°, 50°, 65°, and 75°C. Slopes of these *dV/dq vs. log i* traces increase as temperature increases. This is shown in Fig. 3. Before proceeding with the

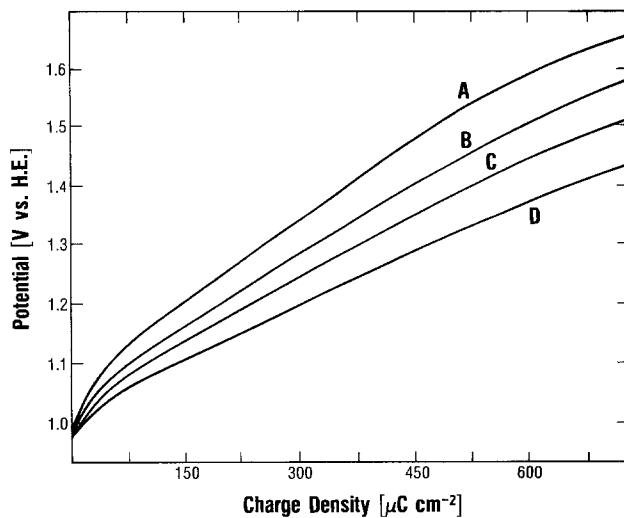


Fig. 1. *V-q* transients at: A, 1.5 × 10⁻²; B, 1.5 × 10⁻³; C, 1.5 × 10⁻⁴; and D, 1.5 × 10⁻⁵ Acm⁻² at 50°C.

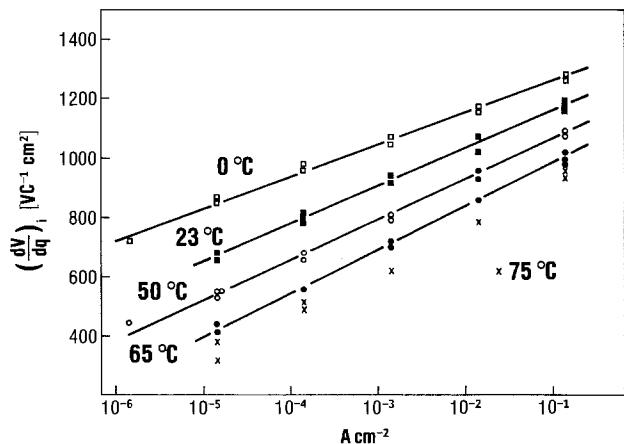


Fig. 2. *dV/dq* dependence on log *i* for 0°, 23°, 50°, 65°, and 75°C.

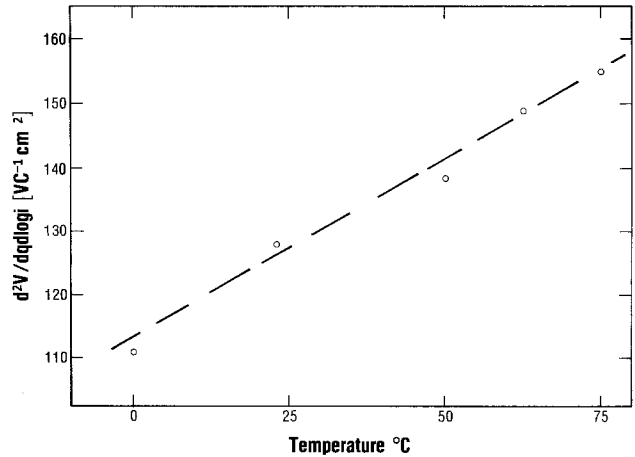


Fig. 3. Slopes of the *dV/dq vs. log i* traces as function of temperature.

analysis of data in Fig. 2 and 3, it is helpful to examine Eq. [2]. From this equation by differentiation one obtains

$$\left[\frac{dV}{d(d)} \right]_{i,T} = \frac{kT}{ze\lambda} \ln \frac{i_{og}}{i_o} + \frac{W}{ze\lambda} + \frac{d}{ze\lambda} \frac{dW}{d(d)} \quad [4]$$

As previously shown (1, 15) and confirmed in this work, for a constant temperature and a given *i*_{og}, *dV/d(d)* is constant and independent of *d*. It follows that *W* ≠ *f(d)* and the last term in Eq. [4] can be dropped. Other parameters in the equation do not depend on *d* either. Since *d* = *rq*, the observed linear dependence of *dV/dq* on log *i*_{og} for over five decades of current densities (cf. Fig. 2) is accounted for by the model of "thin oxide film growth." The linear increase of the slopes of *dV/dq vs. log i*_{og}, i.e., of *d²V/dq d* in *i*_{og}, with temperature is also in accordance with the model (cf. Eq. [4]). From such a slope at room temperature, the *zλ* product was previously calculated and *z* (= 2) and *λ* (= 2Å) analyzed (1, 11). It follows from Fig. 2 and 3 that *z* and *λ* are independent of temperature as expected for the model. (In this narrow temperature range the change in the unit cell dimensions, and hence in *λ*, is insignificant.)

Parameter *i*_o, and hence *N*, can readily be obtained from Eq. [4] using the relationship

$$\left[\frac{\Delta \frac{dV}{dq}}{\Delta T} \right]_1 = \frac{kr}{ze\lambda} \ln \frac{i}{i_o} \quad [5]$$

For *i* = 1 Acm⁻², this relationship simplifies to

$$\left[\frac{\Delta \frac{dV}{dq}}{\Delta T} \right]_{1 \text{ Acm}^{-2}} = \frac{-kr}{ze\lambda} \ln i_o \quad [6]$$

with *i*_o given in Acm⁻².

In these equations it is taken that *W* ≠ *f(T)*. This is certainly true for a narrow range of temperature as in the present experiments.

Now, returning to the experimental data of Fig. 2, the separation of the *dV/dq vs. log i* lines at 1 Acm⁻² for the temperature difference of 75°C is -280 VC⁻¹ cm². This is shown in Fig. 4 in which *dV/dq* extrapolated to 1 Acm⁻² are plotted vs. temperature. It follows from Eq. [6] that *i*_o is 6 × 10⁸ Acm⁻². It should be noted that *i*_o is not the exchange current density but the preexponential term in the exchange current density *i*_{og,0} (cf. Eq. [3]). In this calculation, the factor *r* (= 9 × 10³ Åcm²/C⁻¹) is used to convert coulombs/square centimeter into thickness in angstroms. An error in *r*, however, does not affect this numerical evaluation of *i*_o since the product *zλ*, used for this evaluation, was determined using the same factor and any error that

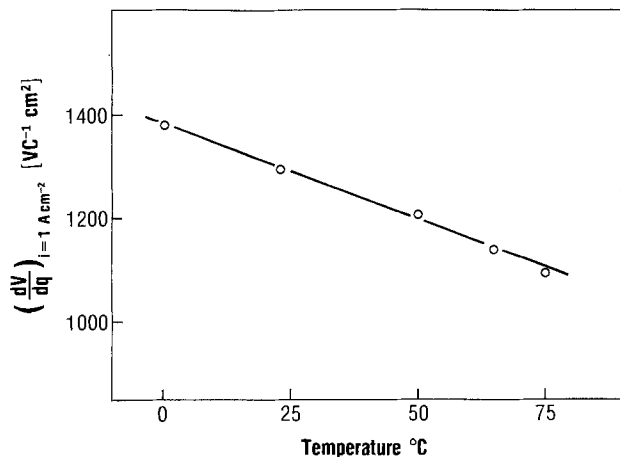


Fig. 4. The values of dV/dq extrapolated to $i = 1 \text{ A cm}^{-2}$ at different temperatures.

might be introduced with r cancels out. With $i_0 = 6 \times 10^8 \text{ A cm}^{-2}$, the $N\nu$ product can be calculated from

$$N = \frac{i_0 r}{2\nu\lambda\omega} \quad [7]$$

if ω is known. From the definitions of various parameters it follows that $2\lambda\omega$ is the volume of the oxide film per single migrating cation (of charge z). Consequently, the product $2\lambda\omega r^{-1}$ is the number of coulombs per single cation. This, however, is nothing else but ze , so that N in Eq. [7] is given by

$$N = \frac{i_0}{ze\nu} = \frac{6 \times 10^{23} i_0}{zF\nu} \quad [8]$$

With $z = 2$, $N\nu = 1.9 \times 10^{27} \sim 2 \times 10^{27} \text{ cm}^{-2} \text{ sec}^{-1}$. Now, with $\nu = 3k\theta/(4h)$, where θ , k , and h are Debye temperature [= 225°K for Pt (16)], Boltzmann's constant, and Planck's constant, respectively, the mean vibrational frequency is calculated as $\nu = 3.5 \times 10^{12} \text{ sec}^{-1}$. With $\nu = 10^{12} \text{ sec}^{-1}$, as usually taken, the surface density of sites, N , that are active in the rate-determining reaction plane is $2 \times 10^{15} \text{ cm}^{-2}$. Even if $\nu = 3.5 \times 10^{12} \text{ sec}^{-1}$, N is surprisingly close to the density of atom sites in the surface of the metal ($\sim 1.5 \times 10^{15} \text{ cm}^{-2}$). This close agreement appears to provide strong evidence for the ion formation at the metal/oxide interface as the rate-determining step in the over-all reaction path.

Finally, the activation energy can be determined from i_0 and the exchange current density, $i_{0g,0}$, according to Eq. [3]. An easy way to obtain $i_{0g,0}$ is to read from Fig. 2 the value of dV/dq as $i = 1 \text{ A cm}^{-2}$ and a given temperature and apply this value to

$$\left(\frac{dV}{dq}\right)_{T,i=1 \text{ A cm}^{-2}} = \frac{-rkT}{ze\lambda} \ln i_{0g,0} \quad [9]$$

This relationship follows directly from Eq. [4]. Again, $i_{0g,0}$ is not affected by the conversion factor r . The exchange current density at 23°C is $2 \times 10^{-10} \text{ A cm}^{-2}$. This value compares well with that previously reported (1) for room temperature ($1.8 \times 10^{-10} \text{ A cm}^{-2}$). The exchange current density increases with temperature as expected from Eq. [3]. With $i_{0g,0}$ for a given temperature and with i_0 as determined above, the activation energy is 1.08 eV or close to 25 kcal-mole. This value, though on a high side, compares well with the activation energies reported for growths of oxide films at valve metals and Al.

The present study, therefore, confirms the view that the oxide films at platinum anodes grow according to the simple model of high field-assisted formation of metal ions at the metal/oxide interface and their migration in the field from one presumable interstitial position to another. Further, it appears that the rate-

determining step is the process at the metal/oxide film interface.

A conclusion regarding the rate-determining step that is based on the numerical value of N may, however, be subject to an uncertainty due to a possible amorphous character of the oxide film. In an amorphous oxide all sites could be regarded as "interstitial" and active in the process of growth. In this case N cannot differentiate between the two rate-determining steps. Electron diffraction indicates (17), however, that, even in these very thin oxide films, there is a degree of ordering and perhaps the uncertainty is limited.

The process of growth may, however, be more complex than it is pictured by the simple model discussed above. First of all, anions too may participate in the growth process as in the case of Ta (18). There is no way to distinguish with the present experimental data between the anionic and cationic transport in the platinum oxide films. With OH^- as the charge transporting anions, and with $z\lambda = 4\text{\AA}$, the half-jump distance would become too large, i.e., 4\AA . This calculation, however, only indicates, but it does not prove, that OH^- is not the charge-carrying species. It is in general possible that both anions and cations participate in the charge transport. However, if these two processes are independent of each other, it is unlikely that their rates will be comparable. This is because the activation energies for these two so widely different ions are expected to be different. If indeed both anions and cations independently participate in the charge transport with comparable rates, it is unlikely that a linear dV/dq vs. $\log i$ dependence would be observed for five decades of current density, as in the present study. This is because the slope of this dependence would in this case vary with the field and hence with applied current density.

The place-exchange mechanism is another process for oxide growth that is, however, usually reserved for the direct logarithmic growth. This process too may be field assisted and, if it is nonsimultaneous [cf. Ref. (19)], it could easily account for the observed kinetics. In this mechanism, both anions and cations participate with equal or comparable rates in the charge transport. In Fig. 5, simultaneous rotation of one Pt^{++} and two OH^- ions illustrates in a simple way such a place-exchange process. For the place-exchange mechanism, N will be the same both for the process at the interface(s) and for the process within the oxide phase as rate-determining steps. Therefore, if one accepts the place-exchange mechanism as a possible process, the value of

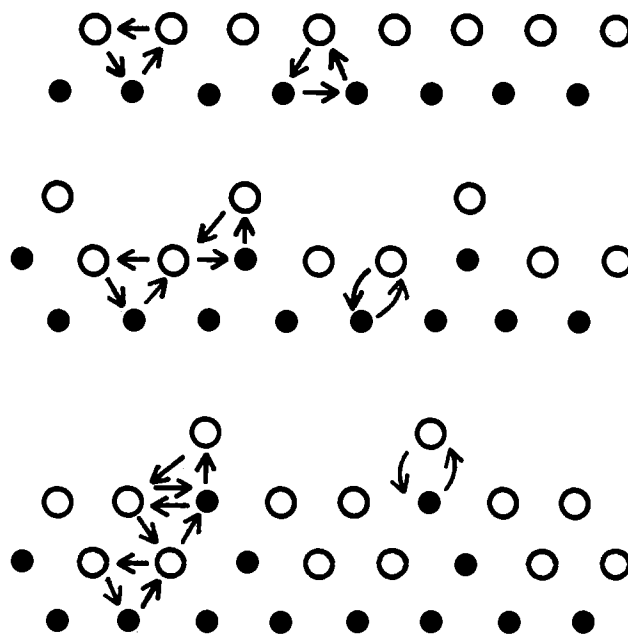


Fig. 5. Representations of the field assisted place-exchange process. Open circles, OH^- ; full circles, M^{++} .

N alone cannot serve as a criterion for the choice of the rate-determining step. Then, only the fact that the observed kinetics is described by Eq. [2] from the earliest stages of growth supports the process at the metal/oxide interface as the rate-determining step. Further studies, not necessarily electrochemical ones, are still needed to elucidate the over-all mechanism and rate-determining step. It should be noted that the initial growth is followed by an extended growth which is known (14) to proceed according to the direct logarithmic growth law (i.e., $i = i_0 \exp(\alpha V - \delta d)$). The transition from the initial stages of growth, which proceeds according to Eq. [1], to the extended growth is not clear, and an analysis of the transition itself may help in elucidating the growth processes in both regions of growth. We shall discuss these problems in subsequent papers.

Manuscript submitted Oct. 9, 1978; revised manuscript received Sept. 19, 1979.

Any discussion of this paper will appear in a Discussion Section to be published in the December 1980 JOURNAL. All discussions for the December 1980 Discussion Section should be submitted by Aug. 1, 1980.

Publication costs of this article were assisted by Allied Chemical Corporation.

REFERENCES

1. A. Damjanovic, A. T. Ward, B. Ulrick, and M. O'Jea, *This Journal*, **122**, 471 (1975).

2. L. B. Harris and A. Damjanovic, *ibid.*, **122**, 593 (1976).
3. J. L. Ord and F. C. Ho, *ibid.*, **118**, 46 (1971).
4. K. J. Vetter and J. W. Schultze, *J. Electroanal. Chem. Interfacial Electrochem.*, **34**, 141 (1972).
5. N. Cabrera and N. F. Mott, *Rep. Prog. Phys.*, **12**, 163 (1949).
6. A. Damjanovic and A. T. Ward, "International Review of Science: Physical Chemistry," Series II, Vol. 6, Butterworths (1976).
7. E. J. W. Verwey, *Physica*, **2**, 1059 (1935).
8. R. Parsons and W. Visscher, *J. Electroanal. Chem. Interfacial Electrochem.*, **36**, 329 (1972).
9. S. H. Kim, W. Paik, and J. O'M. Brockis, *Surf. Sci.*, **33**, 617 (1972).
10. K. J. Vetter and J. W. Schultze, *J. Electroanal. Chem. Interfacial Electrochem.*, **34**, 131 (1972).
11. A. Damjanovic and L.-S. R. Yeh, *This Journal*, **126**, 555 (1979).
12. H. Angerstein-Kozłowska, B. E. Conway, and W. B. A. Sharp, *J. Electroanal. Chem. Interfacial Electrochem.*, **43**, 9 (1973).
13. B. E. Conway and S. Gottesfeld, *J. Chem. Soc. Faraday Trans. 1*, **69**, 1090 (1973).
14. A. Ward, A. Damjanovic, E. Gray, and M. O'Jea, *This Journal*, **123**, 1599 (1976).
15. D. Gilroy, *J. Electroanal. Chem. Interfacial Electrochem.*, **71**, 257 (1976).
16. Ch. Kittel, "Introduction to Solid State Physics," p. 77, John Wiley & Sons, Inc., New York (1954).
17. S. Shibata, *Electrochim. Acta*, **17**, 345 (1972).
18. J. P. S. Pringle, *This Journal*, **120**, 398 (1973).
19. N. Sato and M. Cohen, *ibid.*, **111**, 512 (1964).

Technical Notes



Mixed Electrolyte Solutions of Propylene Carbonate and Dimethoxyethane for High Energy Density Batteries

Y. Matsuda* and H. Satake

Department of Industrial Chemistry, Faculty of Engineering,
Yamaguchi University, Tokiwadai, Ube, Yamaguchi, Japan

Interest in high energy batteries has increased in recent years and some kinds of Li batteries with organic electrolytes have been developed (1-10). During the course of the investigations in this field, some workers reported on the mixing effect of the organic electrolytes (11-14). One of the authors (15) has reported on the improvement of anodic performance of Mg in mixed PC and 1,2-dimethoxyethane (DME) system, and in formamide and tetrahydrofuran (THF) system, and the mixing effect of solvents on cathodic performance of some metal sulfides (16). Recently, Koch and co-workers (17) have reported on THF-based electrolytes for secondary Li electrodes, and Ikeda and co-workers (4) have adopted PC-DME electrolytes in the Li/MnO₂ batteries. However, the reason for the synergistic effect of mixed organic electrolytes has not been clarified in these investigations. In this study, the effects of mixing the organic solvents, PC-DME, containing some perchlorates were investigated in connection with the electric conductance, dielectric constant, and viscosity.

Experimental

PC and DME were purified by the methods described in previous papers (15, 18). The water content was measured, using Karl Fisher reagent, and it was below 80 ppm in PC and 50 ppm in DME. Lithium perchlorate was an extra pure reagent by Kanto Kagaku Company Limited, and the other perchlorates were the same grade reagents by Wako Pure Chemical Industries, Limited. They were used after drying under reduced pressure at 160°-170°C for 24 hr. The dielectric constant of solvents was measured with a bridge method using 1 kHz a.c., and viscosity was measured with a modified Ostwald viscometer. The electric conductance of the electrolytes was measured with an impedance bridge using 1 kHz a.c.

Results and Discussion

The viscosities of PC-DME with and without 1M NaClO₄ as a function of the composition of the solvents are shown in Fig. 1. The viscosity of the mixed solvent increased with addition of PC into DME and the experimental value was lower than that expected according to the assumption that the theory of the ideal solution would be applied on the viscosities of the mixed solvents.

* Electrochemical Society Active Member.

Key words: mixed organic electrolyte solution, propylene carbonate-1,2-dimethoxyethane system, electric conductance of organic electrolyte solution.

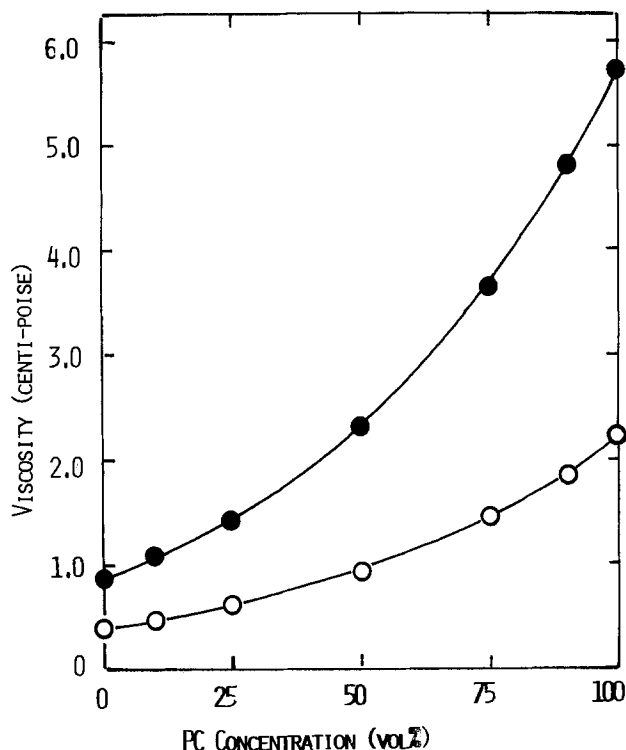


Fig. 1. Correlations between the composition of PC-DME system and the viscosity. ○: solvent only, ●: the solution containing 1M NaClO₄ 30°C.

The dielectric constants of the mixed solvents were then measured, and the results are shown in Fig. 2. The values increased by adding PC into DME. The

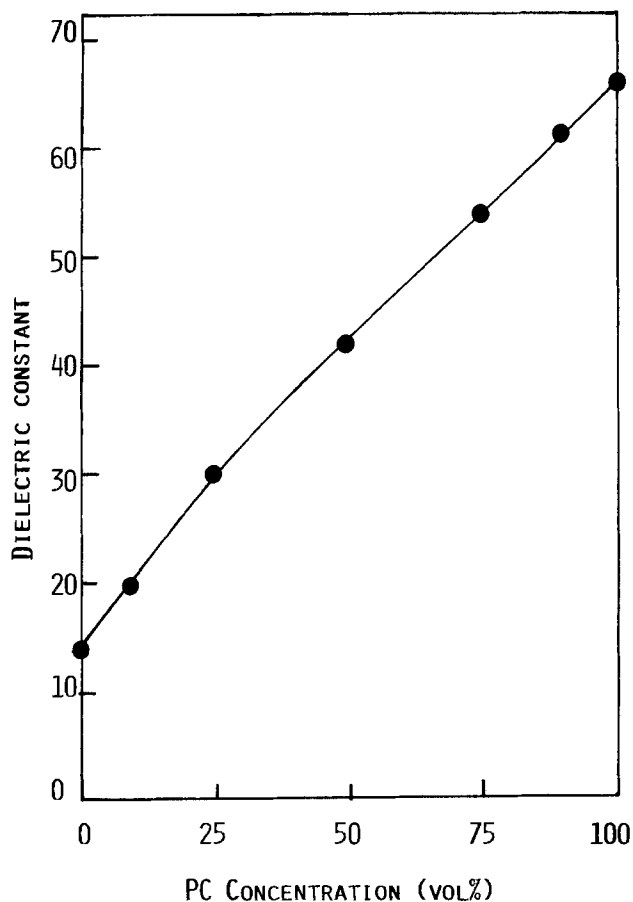


Fig. 2. Correlation between the composition of PC-DME and the dielectric constant, 20°C.

measured values were almost linear, but a small deviation was observed between the experimental values and those expected from the additive properties of each component. Also, the densities of PC-DME system were measured, and these increased linearly with addition of PC into DME though the increase was small.

In Fig. 3, the equivalent conductance of PC-DME containing 1M NaClO₄ is shown as a function of the mixed ratio. The conductance of the mixed electrolytes was higher than that of each single solvent with NaClO₄ and the maximum value of the equivalent conductance was obtained at the mixing ratio of about one to one. The very significant factors affecting the conductance of ionic solutions would be the dielectric constant and the viscosity in connection with the solvation of the ions and the solvent-solvent interaction. The increase of equivalent conductance of the solution due to addition of DME into PC in Fig. 3 is probably caused by low viscosities of DME. However, the conductance decreased again in DME-rich solutions. This phenomenon might be caused by some variation of solvation of the cation and the anion, and the Stokes' radii, and these would be concerned with the specific solvation (19-21) and the low ionization of the solute due to the decrease of the dielectric constants of the solvents (22-24).

The equivalent conductances (Λ) of NaClO₄ in PC, DME, and these 1:1 mixture are shown in Fig. 4 as a function of the solute concentration. In the case of the PC and PC-DME (1:1), the relation between Λ and concentration of NaClO₄ was found to be almost linear in the region of diluted concentration though the mechanism of the conductance has not been clarified. The equivalent conductance of the mixed organic electrolyte (PC-DME, 1:1) was higher than that of each single system (PC or DME). Among those, the behavior of the DME system was entirely different from that of the others. But a similar phenomenon has been observed in THF containing NaClO₄ (25).

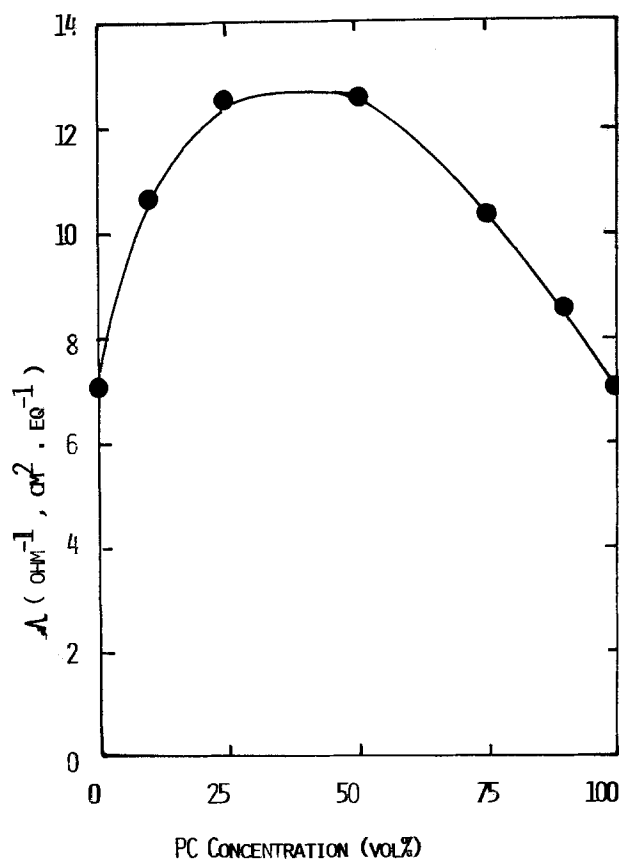


Fig. 3. Correlation between the composition of PC-DME containing 1M NaClO₄ and the equivalent conductance of NaClO₄, 30°C.

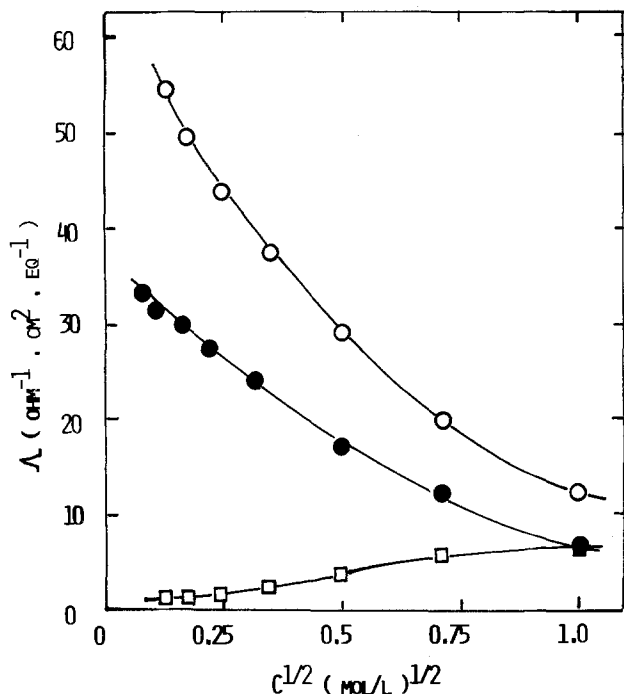


Fig. 4. Correlations between concentration of NaClO_4 and the equivalent conductances of NaClO_4 in PC, DME, and PC-DME (1:1). ●: in PC, ○: in PC-DME (1:1), □: in DME, 30°C.

Manuscript submitted Jan. 5, 1979; revised manuscript received Nov. 8, 1979.

Any discussion of this paper will appear in a Discussion Section to be published in the December 1980 JOURNAL. All discussions for the December 1980 Discussion Section should be submitted by Aug. 1, 1980.

Publication costs of this article were assisted by Yamaguchi University.

REFERENCES

1. R. J. Brodd, A. Kozawa, and K. V. Kordesch, *This Journal*, **125**, 271C (1978).

2. M. Fukuda and T. Iijima, in "Power Sources 5," D. H. Collins, Editor, p. 713, Academic Press, New York (1975).
3. M. Fukuda and T. Iijima, *Denki Kagaku*, **44**, 543 (1976).
4. H. Ikeda, T. Saito, and H. Tamura, *ibid.*, **45**, 314 (1977).
5. H. Ikeda, S. Ueno, T. Saito, S. Nakaido, and H. Tamura, *ibid.*, **45**, 391 (1977).
6. G. H. Lehmann, T. Rassinoux, G. Gerbier, and J. P. Gabano, in "Power Sources 4," D. H. Collins, Editor, p. 493, Oriel Press Ltd., Newcastle upon Tyne, England (1973).
7. G. Lehmann, G. Gerbier, A. Brych, and J. P. Gabano, in "Power Sources 5," D. H. Collins, Editor, p. 695, Academic Press, New York (1975).
8. J. P. Gabano, V. Dechenaux, G. Gerbier, and J. Jammet, *This Journal*, **119**, 459 (1972).
9. D. Linden, N. Wilburn, and E. Brooks, in "Power Sources 4," D. H. Collins, Editor, p. 483, Oriel Press Ltd., Newcastle upon Tyne, England (1973).
10. S. C. Levy, "Proceedings of 27th Power Sources Conf.," p. 52, Atlantic City, June 21-24, 1976.
11. R. Jasinski, *Electrochem. Technol.*, **6**, 28 (1968).
12. H. Bauman, J. Chilton, W. Connor, and G. Cook, Tech. Report No. RTD-TDR 63-4083 (Oct. 1963).
13. M. Fisenberg and J. Pavlovic, Final Report, Contract No. 63-0618-c (May 1965).
14. W. Elliott, S. Hsu, and W. Towle, First Quarterly Report, Contract NAS 3-6015 (Sept. 1964).
15. T. Saito, H. Ikeda, Y. Matsuda, and H. Tamura, *J. Appl. Electrochem.*, **6**, 85 (1976).
16. Y. Matsuda, K. Teraji, and Y. Takasu, Unpublished.
17. V. R. Koch and J. H. Young, *This Journal*, **125**, 1371 (1978).
18. Y. Matsuda, Y. Ouchi, and H. Tamura, *J. Appl. Electrochem.*, **4**, 53 (1974).
19. J. B. Hyen, *J. Am. Chem. Soc.*, **82**, 5129 (1960).
20. J. B. Hyen, R. Wills, and R. E. Wonkka, *ibid.*, **84**, 2914 (1962).
21. J. B. Hyen and R. Wills, *ibid.*, **85**, 3650 (1963).
22. F. Accascina, R. De. Lisi, and M. Goffredi, *Electrochim. Acta*, **15**, 1209 (1970).
23. G. P. Johari, *J. Phys. Chem.*, **74**, 934 (1970).
24. J. Thomas and D. F. Evans, *ibid.*, **74**, 3812 (1970).
25. Y. Matsuda and H. Satake, *Denki Kagaku*, **47**, 743 (1979).

Cathodic Deposition of a Trivalent Chromium Film as a Bonding Interface Between Copper and Polyethylene

F. Simchock, K. Ramachandran, R. Haynes,* and F. J. Jannett

Western Electric Company, The Engineering Research Center, Princeton, New Jersey 08540

Many studies are available concerning the use of various surface treatments of copper for bonding to various dielectrics (1). Most of these studies are performed on simple geometries and may not be comparable directly to the present system. Few studies (2) have been done on the specific application to millimeter waveguide systems such as that recently investigated for the Bell System's (3) WT4.

The purpose of this study was to test the durability of copper oxide and chromate as bonding interface between copper and polyethylene in copper plated steel tubes, 51 and 60 mm ID, to be used for dielectric lined millimeter waveguides.

Experimental Procedure

Steel tubes, 51 and 60 mm ID, were copper plated from a copper cyanide solution at 20 A/ft² to a thickness of 12 μm . Copper was either oxidized or chromated depending on the bonding interface to be bonded. Copper was oxidized electrochemically from a 2N NaOH solution saturated with copper oxides at 160°F at 3.5, 7.1, and 13.6 mA/cm² to obtain oxide thicknesses of 4000, 10,000, and 14,000Å. Ratios of cuprous to cupric oxides were determined by chronopotentiometric technique from 0.2N NH_4Cl at 1 mA/cm². Cuprous oxide was maintained in the range of 20 to 40% of the total oxide thickness. Chromate was deposited on copper by cathodic polarization at 25°C from 3% aqueous solution of sodium citrate, chromate, and carbonate. The thick-

* Electrochemical Society Active Member.
Key words: films, interfaces, bonding.

ness of the chromium-containing film is approximately $1.0 \mu\text{g}/\text{cm}^2$. ESCA studies (4) indicate the film is not a simple uniform monolayer structure. Low density polyethylene was hot melt bonded to either the oxidized or chromated copper interface. A tubular film of electrical grade low density polyethylene (such as Union Carbide—DFDA 0166), $150 \mu\text{m}$ thick was sealed at one end. A pressurizing cap was applied at the other end and the liner inflated with nitrogen. The exterior surface (bonding surface) of such an inflated liner was cleaned by wiping with Freon TF solvent and dried. The liner was then inserted into the pipe and end caps applied at both ends. Interior of the liner and the interface was next evacuated. The liner was then inflated with oxygen-free nitrogen at a pressure of 1200 mm Hg to press against the treated copper surface. Such an assembly was next heated to bonding temperatures by passing through an induction coil. The pipe was allowed to cool down slowly. A typical heating cycle is shown in Fig. 1. It is to be noted here that temperatures referred to in the following sections are the peak temperatures attained at copper surface in such a heating cycle. When the pipe has cooled down to room temperature, sections were cut off for testing. To prepare samples for 180° peel tests, a second layer of polyethylene ($150 \mu\text{m}$ thick) was bonded at a temperature of 135°C with induction heating and allowed to cool under ambient conditions.

Peel lips for fitting into the Instron jaws were obtained by two techniques: (i) Dipping one end of a section in HCl, a small length (approximately 2.5 cm) was delaminated; or (ii) A ring was cut from the pipe. The interior of the ring was machined off of all polyethylene to expose steel to a length of about 2.5 cm from one end. 180° peel tests were done at room temperature on an Instron machine with a jaw separation rate of 50.8 mm/min.

Results

The results of this study are shown in Table I and Fig. 1-3. Table I shows results after sections were left in a humid environment of 35°C and 90% RH. As seen, thinner oxides show a decrease of about 40% in peel

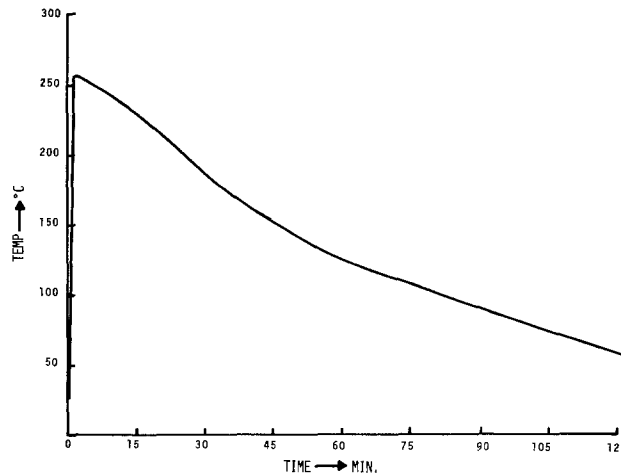


Fig. 1. Temperature rise and cool down of test sections

strengths while thicker oxides show no appreciable change.

With cathodic chromate as an interface, a sharp rise in bond strength was observed when inductively heated to temperatures above 265°C . As seen from Fig. 3, at a temperature of about 300°C , a $150 \mu\text{m}$ thick polyethylene can be bonded to the surface such that failures occur through the thickness of polyethylene when peeled.

Section of chromated samples were tested for 180° peel-creep under humid conditions of 35°C and 90% RH by applying a constant load of 400 g/cm for 24 hr. When bonded at 300°C , no peeling was observed.

Scanning electron micrographs of oxidized and monolayer surfaces of copper show chromated copper yields a smooth interface.

Conclusion

It has been shown that cathodic chromate can be used as a bonding interface between polyethylene and copper. Such an interface is smooth and yields bonds of

Table I. Effect of humidity on oxidized samples

THICKNESS		OXIDE COMPOSITION		PRESSURE	PEAK TEMP.	180° PEEL STRENGTH	
LINER	OXIDE	CUPROUS	CUPRIC			INITIAL	AFTER 24hrs @35°C&90%RH
300μ	3750 Å	1150 Å	2600 Å	1200 MM HG	204°C	1.5 KG/CM	0.6 KG/CM
300μ	3350 Å	1100 Å	2250 Å	1200	232°C	1.8	1.0
300μ	3350 Å	1100 Å	2250 Å	1200	260°C	1.9	1.4
300μ	9300 Å	3500 Å	5800 Å	1200	204°C	1.7	1.4
300μ	9300 Å	3500 Å	5800 Å	1200	260°C	2.7	2.2
300μ	15300 Å	5500 Å	9800 Å	1200	232°C	2.4	2.4

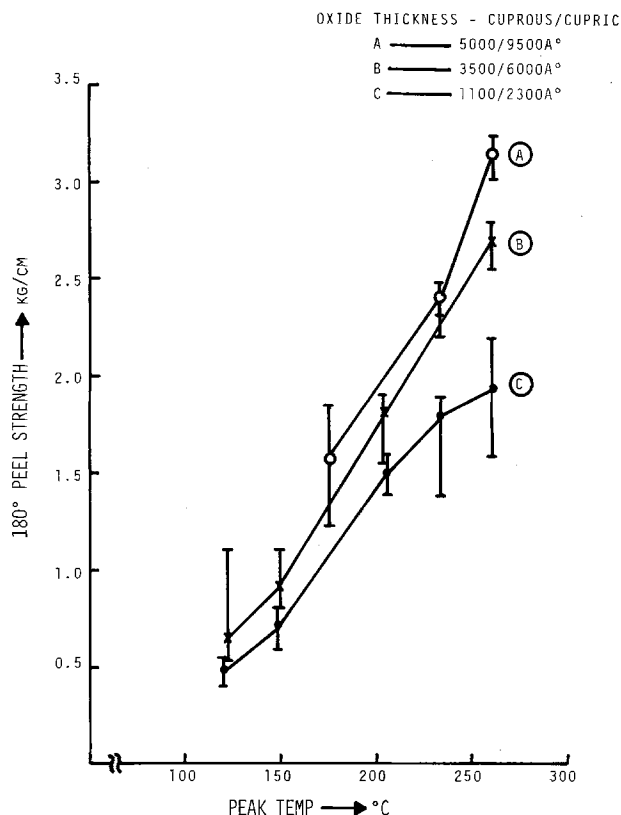


Fig. 2. 180°C peel strengths of polyethylene over oxidized copper

quality comparable to those obtained with thicker oxides in the range 10,000-14,000Å. Hence, when smoothness and electrical characteristics of interface are considered crucial, cathodic chromate may be investigated as an alternate. Both these interfacial processes were scaled up to pilot plant capability. High frequency loss measurements were made (in the millimeter waveguide range) on both systems. The chromate interface was chosen because of less electrical loss and approximately 13 miles of waveguide tubes were processed (3).

Manuscript submitted June 8, 1979; revised manuscript received Oct. 11, 1979. This was Paper 367 presented at the Atlanta, Georgia, Meeting of the Society, Oct. 9-14, 1977.

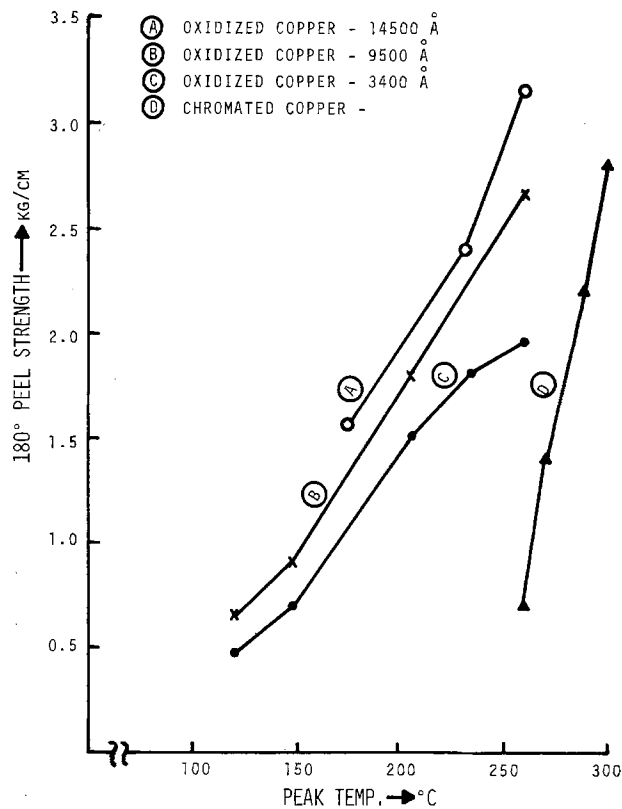


Fig. 3. 180°C peel strengths of polyethylene oxidized copper vs. chromated copper: a comparison of bonding temperatures.

Any discussion of this paper will appear in a Discussion Section to be published in the December 1980 JOURNAL. All discussions for the December 1980 Discussion Section should be submitted by Aug. 1, 1980.

Publication costs of this article were assisted by Western Electric.

REFERENCES

1. H. V. Varzirani, *J. Adhes.*, **1**, 208 (1969); R. G. Baker and A. T. Spencer, *Ind. Eng. Chem.*, **52**, 1015 (1960); L. Sharpe and S. Seeger, Private communication.
2. T. Nakahara *et al.*, Sumitomo Electric, Technical Review No. 10, p. 82 (1967).
3. *Bell Syst. Tech. J.*, **56** (1977).
4. R. Roberts, Private communication.

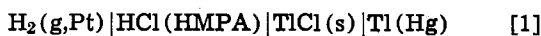
Electrochemistry in Hexamethylphosphorotriamide (HMPA)

I. The $H_2(g, Pt) | HCl(HMPA) | TlCl(s) | Tl(Hg)$ Cell

Carlos H. Contreras-Ortega¹ and Peter A. Rock*

Department of Chemistry, University of California, Davis, California 95616

We have investigated the cell



where HMPA is the solvent hexamethylphosphorotriamide $[(CH_3)_2N]_3PO$, as part of an electrochemical study of the thermodynamics of hydrogen-isotope-exchange reactions (1). At the outset of this work HMPA looked promising as an aprotic solvent for use in electrochemical cells. HMPA has a wide liquid range (7° to

235°C at 1 atm), the vapor pressure at 25°C is less than 0.1 Torr, and the dielectric constant of 30 is high enough to permit the dissolution of electrolytes. However, HMPA is difficult to prepare in a high purity anhydrous state, and as was found in this study, HMPA slowly decomposes in the presence of HCl. However we were able to obtain an estimate of the standard cell potential for cell [1] by extrapolating the measured cell voltage to zero time. The value of \mathcal{G}° obtained is compared with \mathcal{G}° values for cells of the type [1] involving other solvents.

Because of the need to exclude oxygen and water from the cell, the entire cell was set up and studied as an automatically controlled closed system on the vac-

* Electrochemical Society Active Member.

¹ Present address: Departamento de Química, Centro de Investigación y de Estudios Avanzados del Instituto Politécnico Nacional, A.P. 14-740, Mexico 14 D.F., Mexico.

Key words: hexamethylphosphorotriamide, HMPA, hydrogen electrode, thallium electrode.

uum line. The details of the cell construction, hydrogen and Tl(Hg)|TlCl(s) electrode preparations, HCl(g) and HCl (solution) preparation, and the measurement system have already been described (2, 3). The HMPA (Dow Chemical Company, Dorcol, Practical Grade) used was purified by the method of Gal and Yvernault (4) which involves three successive vacuum distillations; the first over a Na mirror, the second over CaH₂(s), followed by storage for 48 hr over molecular sieves in a helium atmosphere, and the third vacuum distillation utilizes a 50 cm adiabatic column with a larger inner surface (head temperature 60°-80°C, pressures less than 1 Torr). The final collected middle fraction (about one third of the initial volume) was stored under vacuum in a black container. Tests for primary and secondary amines were negative.

The molalities of the HCl(HMPA) cell solutions were determined by potentiometric titration of weighted samples obtained from the solution preparation flask on the vacuum line. The analyses were carried out on the solutions immediately after preparation. The HCl(HMPA) sample was added to 10 ml of 0.1M NaClO₄(aq) diluted to 50 ml and then titrated with carbonate-free NaOH(aq) (Beckman E-2 glass electrode vs. a saturated calomel). The end point was not affected by addition of pure HMPA to the solution.

The results of our measurements on cells of the type [1] are given in Table I. The emf, pressure, and temperature readings were taken at 1 hr intervals over approximately an 80 hr period for each cell. The observed emf values increased in an approximately linear manner over the life of the cell at a rate of less than 0.3 mV/hr. The rate of increase was roughly proportional to the concentration of HCl in the cell solution. The concentration of HCl in the cell solution as determined potentiometrically also decreased linearly with time. After about 80 hr the cell solutions were noticeably brownish yellow. The emf values reported in Table I were obtained from least squares zero-time intercept of an emf vs. time plot, where time zero was defined as the time that the cell solutions were prepared.

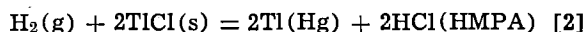
Other electrochemical studies (conductivity and potentiometry) involving HCl(HMPA) solutions (4, 6, 7) had not reported the decomposition of HCl(HMPA) solutions with time possibly because the time required for the experiments was much less than in the present study. The decomposition of the HCl(HMPA) solutions with time is also evidenced in the potentiometric titration curves. Fresh HCl(HMPA) + H₂O solutions yield [on titration with NaOH(aq)] a titration curve with a single inflection point, whereas older solutions yield titration curves with two inflection points. The appearance of a second inflection point occurs more rapidly if the HCl(HMPA) solution is heated. The second inflection point is presumably due to the production of (CH₃)₂NP(O)(OH)₂ (6).

Table I. Results of measurements on the cell
H₂(g,Pt)|HCl(m,HMPA)|TlCl(s)|Tl(Hg,X_{Tl} = 0.0376)
(T = 297° ± 1°K)

M _{HCl} (mole · kg ⁻¹)	P _{H₂} (Torr)	ℰ (expt) ^a (mV)	ℰ° (calc) (mV)
0.0276	736	-383	-546
0.00828	731	-369	-563
0.00610	724	-360	-561
0.00111	727	-305	-549
0.0320	723	-396	-554
0.0131	725	-363	-544
0.00659	724	-353	-552
0.00546	732	-337	-542

^a The last four cells in this table were run with 99.5% D₂, 99.9% DCl(HMPA) rather than with H₂ and HCl(HMPA). The reported emf values for the deuterium cells were converted to hydrogen cells by subtracting 8 mV from the measured emf values (5). Because of the instability of the HCl(HMPA) solution the values of ℰ (expt) are uncertain by about ±5 mV (see text).

The postulated cell reaction for [1] is



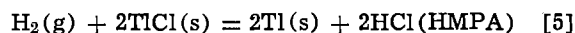
Application of the Nernst equation to this reaction yields ($\omega = RT/F$)

$$\mathcal{E} = \mathcal{E}^\circ - \frac{\omega}{2} \ln \left\{ \frac{\alpha_{\text{Tl}(\text{Hg})}^2 \alpha_{\text{HCl}(\text{HMPA})}}{\alpha_{\text{H}_2(\text{g})} \alpha_{\text{TlCl}(\text{s})}^2} \right\} \quad [3]$$

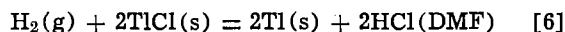
If we take $\alpha_{\text{H}_2(\text{g})} = (P_{\text{H}_2}/760)$, $\alpha_{\text{Tl}(\text{Hg})} = X_{\text{Tl}} \gamma_{\text{Tl}}$, $\alpha_{\text{TlCl}(\text{s})} = 1$, and $\alpha_{\text{HCl}} \approx m_{\text{HCl}}$ [HCl in HMPA has been shown by conductance measurements (6) to be a weak electrolyte], then

$$\mathcal{E}^\circ = \mathcal{E} + \omega \ln X_{\text{Tl}} \gamma_{\text{Tl}} + \omega \ln m_{\text{HCl}} - (\omega/2) \ln (P_{\text{H}_2}/760) \quad [4]$$

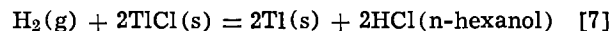
The thallium amalgam used had $X_{\text{Tl}} = 0.0376$ for which $\ln \gamma_{\text{Tl}} = 0.456$ (8, 3). Application of Eq. [4] to the data in the first three columns in Table I ($\omega = 25.56$) yields the values of \mathcal{E}° (calc) given in the last column of Table I. The average of these values is $\mathcal{E}^\circ_{\text{m}} = -551 \pm 6$ mV which is standard potential (on the molality scale) at 297°K for the reaction



The value of the standard potential on the mole fraction scale [$\mathcal{E}^\circ_{\text{x}} = \mathcal{E}^\circ_{\text{m}} - \omega \ln (1000/179.2)$] is $\mathcal{E}^\circ_{\text{x}} = -594 \pm 6$ mV. Based on our previously reported cell data (2, 3) the value of $\mathcal{E}^\circ_{\text{x}}$ at 297°K for the reaction



(where DMF represents N,N-dimethylformamide) is -744 ± 3 mV (undissociated HCl, mole fraction composition scale), whereas for the reaction



$\mathcal{E}^\circ_{\text{x}} = -809 \pm 2$ mV (undissociated HCl, mole fraction composition scale).

The data for the three solvents DMF, HMPA, and n-hexanol can be combined to calculate the Gibbs energy of transfer of HCl (undissociated, mole fraction scale)

$$\text{HCl}(\text{DMF}) = \text{HCl}(\text{HMPA}) \quad \Delta G^\circ = -14.4 \text{ kJ}$$

$$\text{HCl}(\text{n-hexanol}) = \text{HCl}(\text{HMPA}) \quad \Delta G^\circ = -20.7 \text{ kJ}$$

The dipole moments for the three solvents are HMPA (5.37), DMF (3.82), and n-hexanol (1.60), whereas the dipole moment of HCl is 1.03. The negative ΔG° values for the solute transfer reactions reflect the stronger dipole-dipole interaction between HCl and the HMPA solvent dipoles than that between HCl and the DMF or n-hexanol solvent dipoles. In the mean-spherical model of solutions for which dipolar interactions are dominant (9), the Gibbs energy of transfer is approximately equal to $-k(\hat{\mu}_2^2 - \hat{\mu}_1^2)$ where $2\hat{\mu}_1^2 = \mu^2_{\text{solvent}} + \mu^2_{\text{solute}}$ (10) and k is a constant characteristic of the solute. The above data yield a value of k for HCl of 1.7 ± 0.1 kJ/Debye².

Manuscript submitted Sept. 24, 1979; revised manuscript received Nov. 7, 1979.

Any discussion of this paper will appear in a Discussion Section to be published in the December 1980 JOURNAL. All discussions for the December 1980 Discussion Section should be submitted by Aug. 1, 1980.

Publication costs of this article were assisted by the University of California.

REFERENCES

- C. H. Contreras-Ortega, C. P. Nash, and P. A. Rock, *J. Solution Chem.*, **5**, 133 (1975).
- C. H. Contreras-Ortega and P. A. Rock, *This Journal*, **121**, 1048 (1974).
- L. F. Silvester and P. A. Rock, *ibid.*, **121**, 251 (1974).
- J.-Y. Gal and Th. Yvernault, *Bull. Soc. Chim. Fr.*, **2770** (1971).

5. P. A. Rock, ACS Symposium Series No. 11, "Isotopes and Chemical Principles," American Chemical Society, pp. 131-162, 1975.
 6. J. F. Normant and H. Deshayet, *Bull. Soc. Chim. Fr.*, 1001 (1969).
 7. A. P. Kreshkov, *Zh. Obshch. Khim.*, **40**, 2364 (1970).
 8. T. W. Richards and F. Daniels, *J. Am. Chem. Soc.*, **41**, 1732 (1919).
 9. J. W. H. Sutherland, G. Niehuis, and J. M. Deutch, *Mol. Phys.*, **27**, 721 (1974).
 10. D. A. McQuarrie and P. A. Rock, *J. Solution Chem.*, To be submitted.
-

Errata

In the paper "Atmospheric Corrosion of Cobalt" by D. W. Rice, P. B. P. Phipps, and R. Tremoureux that appeared on pp. 1459-1466 in the September 1979 JOURNAL, Vol. 126, No. 9, the concentration legend in the upper middle of Figure 9 on page 1463 should read:

- × 1415 $\mu\text{g}/\text{m}^3$
- 810 $\mu\text{g}/\text{m}^3$
- ▲ 136 $\mu\text{g}/\text{m}^3$
- 0 $\mu\text{g}/\text{m}^3$

Also, the first row of data, fourth column of Table IV should read 0.32 not 0.82.

Editor's Note: It is of interest to note that this was called to our attention by Ulick R. Evans who is well known to all who have worked in the field of Corrosion.

In the paper "A Finite Difference Numerical Analysis of Galvanic Corrosion for Semi-Infinite Linear Coplanar Electrodes" by P. Doig and P. E. J. Flewitt which appeared on pp. 2057-2063 in the December 1979 JOURNAL, Vol. 126, No. 12, in the Discussion Section on page 2063, the last sentence of the first paragraph should read: "Clearly, for fixed values of i_0 and C , the earlier approximation of unidirectional current flow becomes more accurate as the value of this parameter increases."



The Stability of Tellurium Films in Moist Air; A Model for Atmospheric Corrosion

Alfred Milch and Pedro Tasaico¹

Philips Laboratories, Briarcliff Manor, New York 10510

ABSTRACT

The effect of extended shelf life on the information storage capability of tellurium films on polymethylmethacrylate (PMMA) was investigated. Aging tests were performed for as long as fourteen months under various temperature and humidity conditions. The rate of change of sensitivity to the writing of information (hole formation by laser machining) was chosen as the basis on which to estimate stability quantitatively. It is suggested that aging is caused by oxidation, and a theoretical model for film oxidation as a function of temperature and relative humidity is proposed. Preliminary experimental support for the model is presented, based on the comparison of predicted and observed accelerated decay.

The primary objective of this work was to assess the suitability of tellurium films on polymethylmethacrylate (PMMA) as an information storage medium after extended periods of shelf life. Information is impressed in the Te films as a series of micron-sized holes which are formed by the absorption of energy from a properly modulated and focused laser beam (1, 2). If the films are stored in air, the efficiency of the hole forming process decreases. It is also observed that the films oxidize in air. When the air is sufficiently moist, it is possible to convert the tellurium film entirely to the white TeO₂ in a short time. The oxide is almost completely transparent to the employed laser radiation. Since the incident radiation is only partially absorbed in the Te, with a portion being transmitted, less energy is absorbed in a thinner film. Hence the decay of hole forming efficiency, which is the criterion by which film stability was judged, is ascribed to a thinning of the metallic portion of the film via atmospheric corrosion.

A widely used method of studying corrosion is by accelerated aging. The processes that are operative in normal decay are artificially intensified so as to accelerate the aging process and hence make available quickly results that would develop more slowly under normal conditions. An important assumption here is that the acceleration does not significantly distort natural aging. This assumption is frequently not entirely justified, and it is therefore very important to validate, independently if possible, the results of aging experiments. In the present work, the atmospheric corrosion of tellurium films vacuum-deposited on PMMA substrates was studied as a function of temperature and relative humidity (T/H) within the range 2-70% relative humidity and 25°-90°C. If the oxidation is of the simple Arrhenius type, a straight line relationship between the logarithm of the rate and reciprocal temperature should be observed. In this case, however, highly non-linear Arrhenius plots were obtained when the ab-

solute ambient humidity was left constant while the temperature was varied.

A model was constructed which reproduces the distorted Arrhenius plots. Theoretical parametric curves are displayed which predict rates of accelerated corrosion over the entire T/H field. Isolated experimental points are in reasonable agreement with these predictions. The well-known phenomenon of critical humidity appears as part of the model.

Experiment

Sample substrates were made from PMMA slips 1 mm thick by 18 mm square which were cleaned with ultrasonic agitation in hot aqueous detergent followed by hot running tap water and running deionized water. Immediately thereafter, substrates were placed eight at a time in a conventional vacuum coater where they received a tellurium deposit 300Å thick by 16 mm diam. Substrates were held at ambient temperature during deposition. It is assumed that the films were microcrystalline and nonoriented. After deposition, sets of samples identified by evaporation number and mask position symbol were stored vertically in slotted polypropylene carriers (Fluoroware Type PA-45) designed for maximum circulation of ambient around each sample. The carriers themselves were tested for exposure to the most severe conditions anticipated. They proved quite satisfactory during testing and later in service. During T/H aging, the loaded carriers were stored unenclosed in their respective environmental chambers. Upon periodic removal for testing, they were held in clean plastic boxes to protect them against accidental damage.

Initially, aging experiments were carried out at 25°, 55°, 75°, and 90°C, all at ambient humidity. Normal lab ambient humidity was approximately 50%. The laboratory environment is air conditioned and relatively constant and uncontaminated. Hence the presence of pollutants was assumed to produce negligible bias. The humidities experienced at the other test temperatures are displayed in Table I. Subsequent higher humidity experiments were performed in a Blue-M Model AC temperature/humidity cabinet.

¹ Present address: Macbeth Division of Kollmorgen Corporation, Newburgh, New York 12550.

Key words: aging, accelerated corrosion, humidity, metals.

Table I. Environmental test conditions

Temperature, °C	Relative humidity (fractional)
25 (ambient)	0.50 (ambient; $P_{H_2O} = 12 \text{ mm}$)
55	0.10
75	0.041
90	0.023

The apparatus for producing holes is sketched in Fig. 1. It consists of three major parts: a Lexel Model 85 argon ion laser emitting at 4881Å, a Coherent Radiation Model 3025 electrooptic modulator, and a focusing arrangement containing a 0.85 N.A. Olympus objective lens. Desirable operating conditions are constant power density at focus, high extinction ratio in the modulator, a square pulse, and a focused spot that is circular, has a Gaussian energy distribution, and is about one micron in diameter. The hole diameter of interest is one micron. The system was operated in the out-of-focus, static model (1), which allowed large numbers of observations to be made in a relatively short time. The beam was incident on the film side of the sample. For testing, a sample was caused to pass through the pulsed laser beam several times at different beam power levels producing tracks of holes in the metal film. For each track, the largest hole corresponds to optimum matching between beam power level, out-of-focus spot size, pulse duration, and the thermal properties of the metal film substrate. The samples were then photographed at 400× and 2000× magnification in order to record and measure the resulting tracks. Typical examples are shown in Fig. 2. A disadvantage of this method is that the holes are formed by laser beams whose degree of focus and hence energy distributions change from moment to moment as the sample traverses the beam. Thus, while the total power which forms the hole is known, the energy distribution is not. In particular, that portion of the out-of-focus beam which is effective in hole formation is unknown, hence the measured power constitutes an upper limit on that required to form a hole.

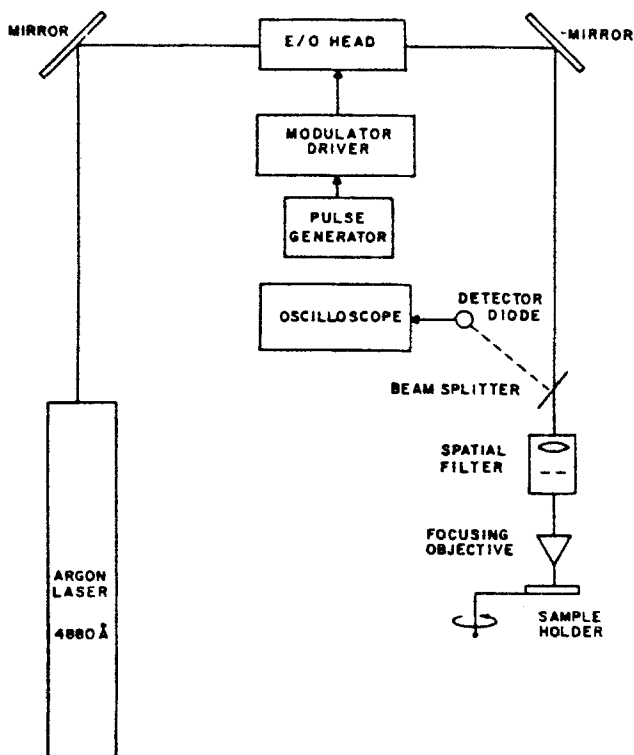


Fig. 1. Hole forming apparatus

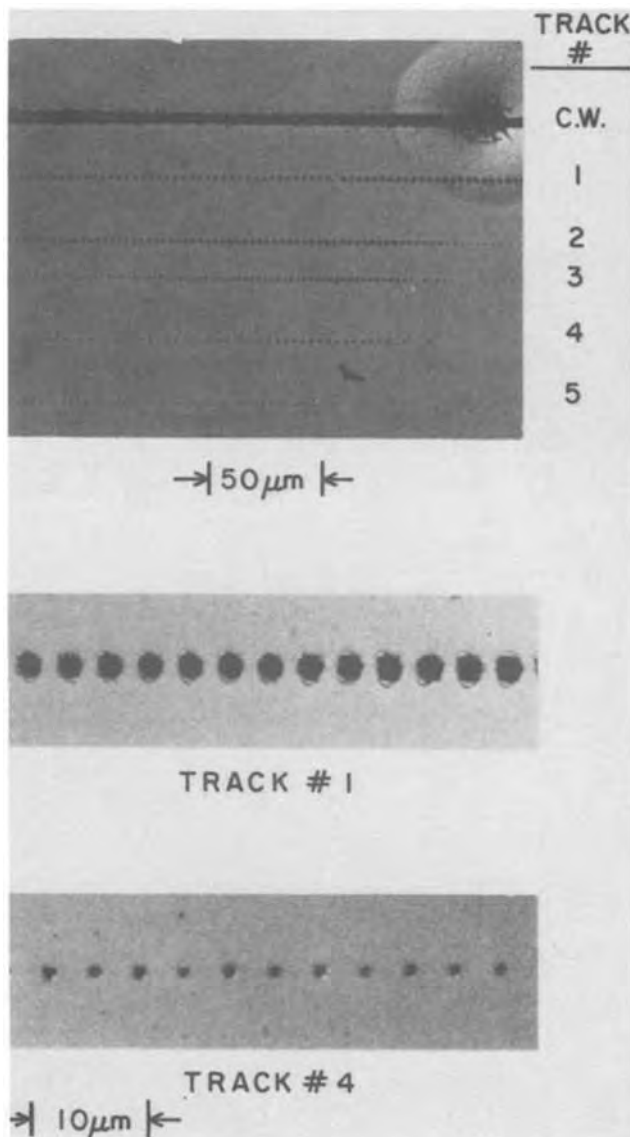


Fig. 2. Typical static hole burning in Te on PMMA. $\lambda = 4881 \text{ \AA}$ (Ar ion laser); pulse width = 750 nsec; pulse separation = 100 μsec.

Track No.	Power mW	Hole diam μm	S mJ/cm ²
C.W.	—	—	—
1	12.5	2.6	177
2	6.7	1.3	351
3	5.0	1.1	361
4	4.0	1.0	382
5	3.1	0.6	701

From a 2000× photograph of each track, a measurement was made of the hole diameter, d (cm), of the largest hole produced by a laser burst of known power, P (mW), and duration τ (sec). Sensitivity in mJ/cm² is defined as the energy per unit hole area required to form a hole of diameter d (cm)

$$S_d = 4P\tau/\pi d^2 \quad [1]$$

Pulse durations of 750 nsec were employed. The very high magnification and high speed, grainy film employed led to relatively large errors in measuring hole diameters. Consequently, errors of about 50% were encountered in estimating the areas of one micron holes (2 mm image). The importance of statistically averaging large amounts of data is obvious.

Analysis of Results

In order to reveal certain important properties of the hole forming process, results are plotted in terms

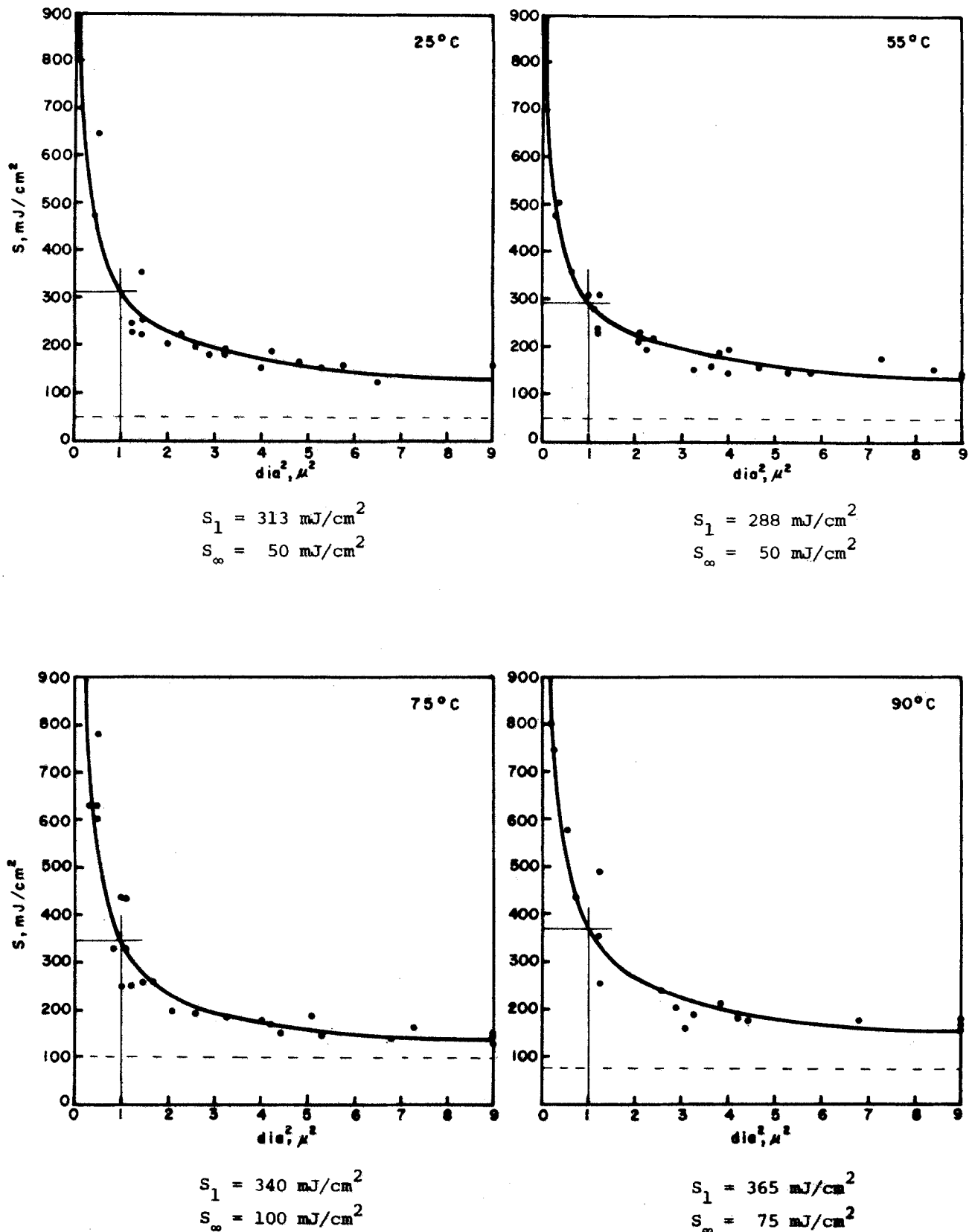


Fig. 3. Typical result of hole forming experiment (aged 4728 hr)

of sensitivity *vs.* relative hole area. A typical plot is displayed in Fig. 3. Vertical and horizontal asymptotes appear. We have found empirically that the hyperbolic dependence of S_d on d^2 required by Eq. [1] takes the functional form

$$\frac{\pi d^{2m}}{4} \cdot (S_d - S_\infty) = E_c \quad [2a]$$

where m is close to unity but is included for generality. The $\pi/4$ term maintains consistency with Eq. [1]. The constant, S_∞ is the value of the horizontal asymptote, *i.e.*, it is the sensitivity for the formation of very large holes. Comparison with Eq. [1] (assuming $m = 1$) in the form $(P\tau)_\infty = S_\infty \cdot \pi d_\infty^2/4$ shows that the energy required to form large holes is directly proportional to the area of the holes for a given film thickness; that is,

to the amount of material removed. Hence, S_{∞} may be viewed as the sensitivity for moving material from within the hole area.

The constant, E_c , is an energy term. If the indicated multiplication in Eq. [2a] is performed, one may write

$$E_d - E_{d,\infty} = E_c \quad [2b]$$

where $E_d = \pi d^2 S_d / 4$ (see Eq. [1]) is the total energy required to form a hole. $E_{d,\infty} = \pi d^2 S_{\infty} / 4$ is, according to Eq. [1] and the above interpretation of S_{∞} , the energy required to move material from the hole area. It follows, then, that E_c is that portion of the energy in the hole forming process that initiates the hole and enlarges the perimeter. Since it is a constant, the energy required to enlarge the perimeter must essentially be zero. As hole size decreases, E_d approaches E_c , and the vertical asymptote follows from the nearly constant E_d for any hole, no matter how small.

A statistical estimate for one micron holes may be arrived at by putting Eq. [2a] into linear form

$$\ln(S_d - S_{\infty}) = m \ln d^2 + \ln C \quad [3]$$

where

$$C = 4E_c / \pi$$

Equation [3] was treated by a least squares analysis for the case in which errors were expected in both S_d and d^2 . This yielded values for m , C , and the correlation coefficient, r . The method was applied repeatedly to a given set of data, varying the value of S_{∞} as an adjustable parameter, until r^2 was maximized. The lines drawn in Fig. 3 are a result of this type of analysis. Thirty-eight samples were followed for over 10,000 hr, during which time over 1000 pairs of S vs. d measurements were made. The results are gathered in Table II.

To a first approximation, the rate of decay in sensitivity, R , given in terms of sensitivity units per 1000 hr (s.u./1000 hr) should be initially linear with time

$$S = S_0 + Rt \quad [4]$$

where the unsubscripted "S" henceforth refers to sensitivity for one micron holes. A linear least squares analysis was applied to the data in Table II assuming no errors in the measurement of time. The method yielded the rate, R , the zero-time sensitivity, S_0 , the one standard deviation errors on the rate, ϵ_r , on S_0 , ϵ_b , and the standard deviation of fit, σ . The results are shown in Table III. Also shown are shelf lives based upon an initial sensitivity of 340 sensitivity units/1000 hr and a criterion of 20% maximum allowable decay during use. It is clear that tellurium has only a limited useful shelf life at ordinary lab ambient and that the combined effects of temperature and humidity on this important property are not straightforward.

Equation [4] is plotted in Fig. 4 for a typical case. Also plotted is the one standard deviation error envelope for predicting the location of the line within a

Table II. Sensitivity for formation of 1 μ m holes in 300Å Te films on PMMA

Age (thousands of hours)	25°C (mJ/cm ²)	55°C (mJ/cm ²)	75°C (mJ/cm ²)	90°C (mJ/cm ²)	Brand of PMMA
0	350	416	348	396	Sixteen samples; Glasflex-Electroglas
1.00	346	345	362	352	
1.90	316	320	358	332	
2.90	373	311	385	337	
4.73	313	288	340	365	
8.90	547	408	435	510	
0	368	308	326	283	Six samples; Glasflex-Electroglas
0.36	274	360	350	306	
1.66	200	328	270	325	
3.22	480	362	289	552	
10.20	391	482	456	517	
0	408	417	424	428	Sixteen samples; Rohm No. 218 brand
0.96	475	365	383	321	
5.52	419	412	477	454	

Table III. Decay rates for 1 μ m hole formation in Te on PMMA as a function of temperature

	Temperature			
	25°C	55°C	75°C	90°C
$R(\Delta S/1000 \text{ hr})$	14.0 ± 6.6	7.8 ± 4.2	10.0 ± 4.4	18.1 ± 5.6
S_0	320 ± 21	343 ± 14	342 ± 14	338 ± 18
Standard deviation of fit, σ	78	50	53	67
Relative humidity	50%	10%	4.1%	2.3%
Useful life	6 months	1 year	9 months	5 months

confidence interval of 50%

$$\epsilon_{\text{line}} = \pm \sqrt{\epsilon_b^2 + \epsilon_r^2 t^2} \quad [5]$$

An Arrhenius plot of the information contained in Table III is shown in Fig. 5.

Discussion

Interpretation of data.—By the law of mass action, the oxidation rate of tellurium in the chemical change: $\text{Te} + \text{O}_2 \rightarrow \text{TeO}_2$, at a fixed temperature is given by

$$r = K \cdot C_{\text{Te}} \cdot C_{\text{O}_2} \quad [6]$$

where K is the reaction rate constant and C 's are concentrations. In its initial stages, the oxidation rate in air is constant at constant temperature since the con-

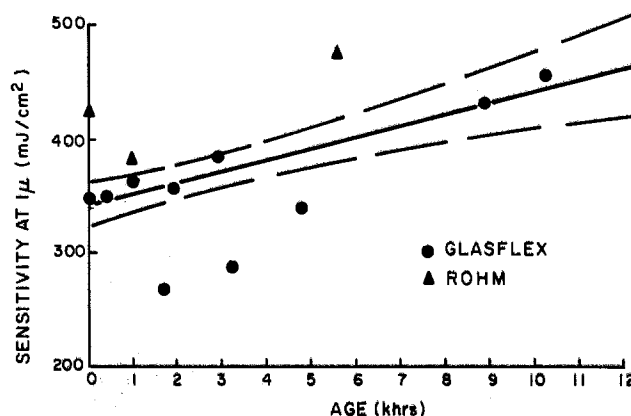


Fig. 4. Typical aging characteristic (storage temperature: 75°C)

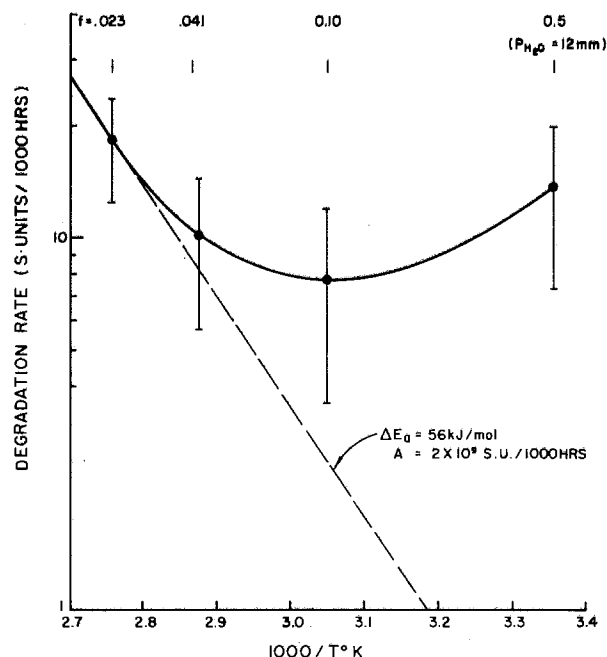


Fig. 5. Experimental Arrhenius plot

centration terms are effectively constant. Hence, we may equate the rate constant to the observed rate, R , as

$$K = r/C_{Te} \cdot C_{O_2} = \alpha R \quad [7]$$

where α is the constant of proportionality.

As transparent TeO_2 forms and metallic Te disappears, the hole forming efficiency diminishes. Hence, the oxidation rate is identified with the sensitivity decay rate, R , appearing in Table III. Because of the restriction embodied in Eq. [7], the Arrhenius equation expressing the temperature dependence of the rate constant may thus be stated in terms of the observed rate

$$R = A \exp(-\Delta E_a/kT) \quad [8]$$

where A is the Arrhenius constant, ΔE_a is the activation energy, k is Boltzmann's constant, and T is the absolute temperature.

Very often in aging experiments, the accelerated rate at an elevated temperature is compared to the normal rate at ambient temperatures via Eq. [8] as follows

$$\frac{\text{time at ambient}}{\text{time under acceleration}} = \frac{R_{\text{accel}}}{R_{\text{amb}}} \\ = \exp \left[\frac{\Delta E_a}{k} (T_{\text{amb}}^{-1} - T_{\text{accel}}^{-1}) \right] \quad [9]$$

where the first equality implies equal chemical action at the two conditions. This ratio, the acceleration factor, F , specifies the time at normal temperature required to produce the same oxidation observed at the aging temperature. This factor may be plotted against activation energy for a given T_{ambient} such as 25°C. Predicted oxidation aging time at 25°C may be obtained from this figure by multiplying the time under acceleration by the factor, F , corresponding to the appropriate activation energy and aging temperature. Such a plot is valid as far as it goes; that is, in a dry environment. But it fails in conditions of significant air humidity owing to the unavailability of a unique value of the activation energy as is demonstrated in Fig. 5.

According to Eq. [8], the experimental data should yield a straight line with a negative slope, $-\Delta E_a/k$. The very strong "U"-shaped curvature in Fig. 5 is attributed to the effect of relative humidity based on the following qualitative argument.

All aging was performed in ordinary air ovens at ambient humidity (average 50% at 25°C); that is, the partial pressure of water vapor at all temperatures was 12 mm Hg, approximately. Hence the (fractional) relative humidity, f , varied strongly with temperature as shown across the top of Fig. 5. At high humidity, moisture tends to condense on sample surfaces. Hence the normal effect of decreasing temperature on corrosion rate is overcome by the increasing chemical reactivity in the adsorbed water layer. In principle, at still lower temperatures, the slope must again go negative with an activation energy characteristic of a corrosion mechanism in a liquid water medium.

At low humidity, the reverse is true and dry environmental conditions are approached. The straight line extrapolation in Fig. 5 of the high temperature tangent portion of the "U" curve is an expression of this conclusion. It is employed to yield limiting "dry" values of the Arrhenius parameters.

A model for atmospheric corrosion.—There exists a vast literature on corrosion (3), both in book and periodical form. In the older literature, atmospheric corrosion received relatively little attention, and most of that was devoted to empirical descriptions of the effects of chemically active contaminants, such as sulfur oxides and nitrogen oxides. One significant concept, that of critical humidity in the onset of enhanced, or "accelerated" atmospheric corrosion (4, 5), has been de-

scribed. This important principle states that atmospheric corrosion is significantly accelerated only when the relative humidity exceeds a certain value. Only recently, in connection with microelectronic circuits, has detailed work begun to appear on the effect of relative humidity alone on atmospheric corrosion (6-14).

A model is here proposed in which the Arrhenius equation is modified so as to yield the quantitative functional dependency of atmospheric corrosion rate on temperature and relative humidity. An essential feature of this model is the well-known concept that the initial water adsorbed from the atmosphere on a clean metal surface is chemically bound to form a "hydroxylated" surface (8); i.e., an oxidized monolayer of more or less unspecified stoichiometry. Since this first monolayer is strongly bound (13, 14) to the underlying metal it provides for little or no ionic motion and therefore does not contribute to electrolyte activity. Subsequent adsorption of atmospheric water forms the adphase in which ion motion and consequently accelerated corrosion takes place. It is assumed that the ionic population of the adlayer is drawn from the ionization of the water itself, from dissolved air, and from mobile species of tellurium formed by detachment of ions which have diffused through the immobile oxidized layer (12). We suggest that the formation of the first, immobile, hydroxylated monolayer may be associated with the critical humidity, below which accelerated corrosion does not occur. Hence, the value of critical humidity should be very much a function of the reactivity of the metal under consideration.

A knowledge of how the adlayer thickness varies with humidity and temperature is crucial to an understanding of the corrosion process. This dependence is described adequately by the Frenkel-Halsey-Hill (FHH) adsorption isotherm (15), which is valid in the relative humidity range 10-90%

$$\theta = \left(\frac{-q}{kT \ln f} \right)^{1/s} \quad [10]$$

where θ is the adlayer thickness in monolayers, q is the heat of adsorption of the mobile admolecules, f is the (fractional) relative humidity, and s is a measure of the rate of decay of the adsorption potential on moving far from the surface.

In the present state of knowledge, the value of q , and possibly of s , are little more than parameters to be adjusted in order to obtain a reasonable fit to a particular set of data. Thus if estimates of material constants are taken from Ref. (8) ($q = 5.5$ kJ/mole, $s = 2.33$), then Eq. [10] calls for $\theta < 1$ over most of the range of interest, while the experimental Arrhenius plot (Fig. 5) indicates significant corrosion acceleration ($\theta > 1$) in most of the same range. This contradiction implies that Cerofolini's value for q is not appropriate for the system being studied here. That is, the heat of adsorption of the mobile portion of the adphase on tellurium may be significantly different from that given for the hypothetical metal described in Ref. (8).

At a sufficiently low relative humidity, linear Arrhenius behavior is expected. The deviation from linear Arrhenius behavior with decreasing temperature in Fig. 5 appears to occur at about 90°C/2.3% RH. This signals the critical humidity condition below which corrosion acceleration does not occur, and according to our model, coincides with the (hydroxylated) monolayer state: $\theta = 1$. We therefore insert the above values of T , f , and θ into Eq. [10] to determine that the heat of adsorption of the mobile water adphase on tellurium is $q = 11$ kJ/mole. The rate of atmospheric corrosion in the absence of water vapor is determined solely by the Arrhenius equation as described above. When water vapor is introduced and after an aqueous adlayer forms, the rate is accelerated

by a factor which depends on the number of dissolved ions in the vicinity of the surface and on their thermal diffusivity. For very thin adlayers and dilute solutions, the number of ions is proportional to the thickness of the adlayer. Hence the accelerated rate may be represented by a modified Arrhenius equation as follows

$$R(\text{acc}) = \text{const} \cdot \theta D \cdot A \exp(-\Delta E_a/kT) \quad [11]$$

D is the ionic diffusivity according to Einstein's equation

$$D = kT\mu/e \quad [12]$$

where μ is the ionic mobility and e is the electronic charge.

We adopt now a simplified version of the scheme presented in Ref. (8). Ionic mobility in the adphase is assumed to be a thermally activated process with an activation energy that is linearly dependent on the thickness of the layer

$$E(\theta) = E_o \left(\frac{\theta_c - \theta}{\theta_c} \right) \quad [13]$$

where E_o = activation energy for mobility for zero coverage and θ_c = critical coverage in monolayers at which bulk water properties appear.

This expression has the properties that $E(\theta)$ is at a maximum for very small coverages, decrease linearly with increasing θ , and vanishes in liquid water where $\theta = \theta_c$. If an activation energy for mobility persists in liquid water, it is assumed to be small compared to E_o . Ionic mobility in the adphase then becomes

$$\mu = \mu_o \exp \left[-E_o \left(\frac{\theta_c - \theta}{\theta_c} \right) / kT \right] \quad [14]$$

where μ_o is the temperature independent part of ionic mobility. Defining the term θD in Eq. [11] as the "sheet diffusivity" D_{\square} , we arrive at

$$D_{\square} = \frac{kT\mu_o\theta}{e} \exp \left[-E_o \left(\frac{\theta_c - \theta}{\theta_c} \right) / kT \right] \quad [15]$$

Equations [10] and [15], taken together, give the explicit dependence of the adlayer sheet diffusivity on the environmental factors temperature and relative humidity. Since failure is a result of accelerated corrosion via ionic diffusion in the presence of the adlayer electrolyte, D_{\square} may be taken as a measure of risk of failure. Recalling that at the critical coverage, $\theta = 1$, little, if any, corrosion acceleration is to be expected

$$D_{\square, \theta=1} = \frac{kT\mu_o}{e} \exp \left[-E_o \left(\frac{\theta_c - 1}{\theta_c} \right) / kT \right] \quad [16]$$

This expression defines the critical sheet diffusivity below which no corrosion acceleration is to be expected. We normalize Eq. [15] to this limiting condition to yield

$$\frac{D_{\square, \theta}}{D_{\square, \theta=1}} = \theta \exp \left[E_o \left(\frac{\theta - 1}{\theta_c} \right) / kT \right] \quad [17]$$

in order to obtain the factor by which corrosion is enhanced at any temperature and humidity above critical humidity.

Equation [17], then, complements Eq. [9] as the acceleration factor by which a corrosion rate is enhanced. But while Eq. [9] is merely the Arrhenius equation rewritten, Eq. [17] is the factor which modifies the Arrhenius equation so as to take both temperature and relative humidity explicitly into account

$$\text{Rate}(T, f) = A \theta \exp \left[\left(E_o \left(\frac{\theta - 1}{\theta_c} \right) - \Delta E_a \right) / kT \right] \quad [18]$$

In other words, the constant of proportionality for Eq. [11] is $1/D_{\square, \theta=1}$. Somewhat similar equations have appeared elsewhere (6, 7), but they are empirical modifications of the Arrhenius equation, they do not show the important phenomenon of critical humidity, and they do not revert to the Arrhenius equation at low humidity. Perhaps their chief drawback is that they tacitly assume that corrosion acceleration is absent in the absence of metallic electrodes and applied electric fields.

It is now possible to construct an Arrhenius plot for the experimental data in Table III with the help of Eq. [18]. Material constants employed are: $\Delta E_a = 56$ kJ/mole (from Fig. 5, extrapolated "dry" value); $A = 2 \times 10^9$ (from Fig. 5, extrapolated "dry" value); $E_o = 43$ kJ/mole [Ref. (8)]; and $\theta_c = 7$ (a curve fitting parameter).

Equation [18] and the experimental rate data are plotted in Fig. 6. During the plotting, a point is reached at which $\theta = 1$ and Eq. [18] reverts to the normal Arrhenius relation (Eq. [8]). For the small segment where $\theta < 1$ ($T > 90^\circ\text{C}$), Eq. [8] was employed. This may be justified if we assume that for $\theta < 1$ the adphase exists as a patchwork of $\theta = 0$ and $\theta = 1$ areas. For $\theta = 0$, Eq. [8] is valid by construct, and for $\theta = 1$, Eq. [18] is valid as a limiting case and reduces to Eq. [8]. Hence the model includes the concept of critical humidity described above. The cutoff at low relative humidity is in recognition of the fact that for $\theta \leq 1$ the admolecules are immobile and the electrolyte-diffusivity approach is invalid.

Equation [18] is mapped onto a temperature/humidity field as lines of constant accelerated Arrhenius rates in Fig. 7. Rates are normalized to unity at a laboratory ambient of 25°C and 50% relative humidity. Predicted aging at lab ambient is obtainable by multiplying time under test by the acceleration factor (relative rate) corresponding to the appropriate test temperature and relative humidity. For example, suppose samples exposed to 40°C and 80% relative humidity degraded to failure in four weeks. According to Fig. 7, these conditions would produce an accelerated rate of 100 relative to lab ambient. Therefore the model predicts a life to failure of 400 weeks at 25°C and 50% relative humidity.

A more precise validation of the model is highly desirable. An experiment was designed to meet this

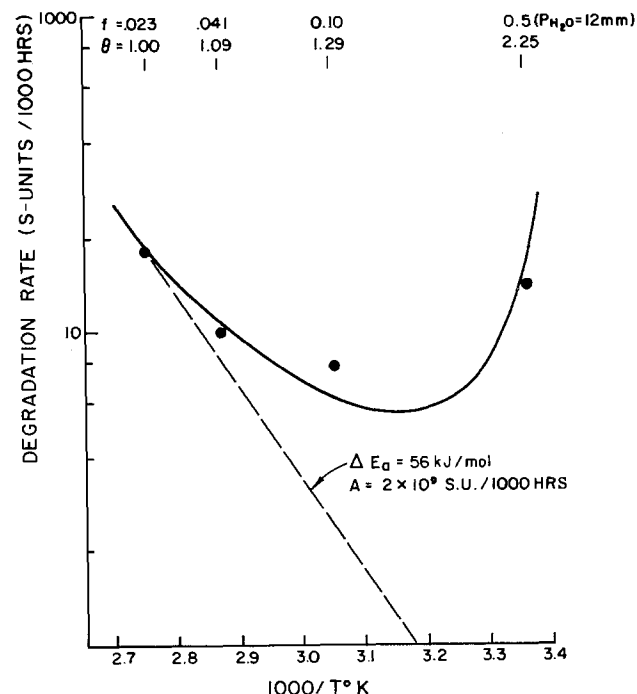


Fig. 6. Arrhenius plot, theoretical curve

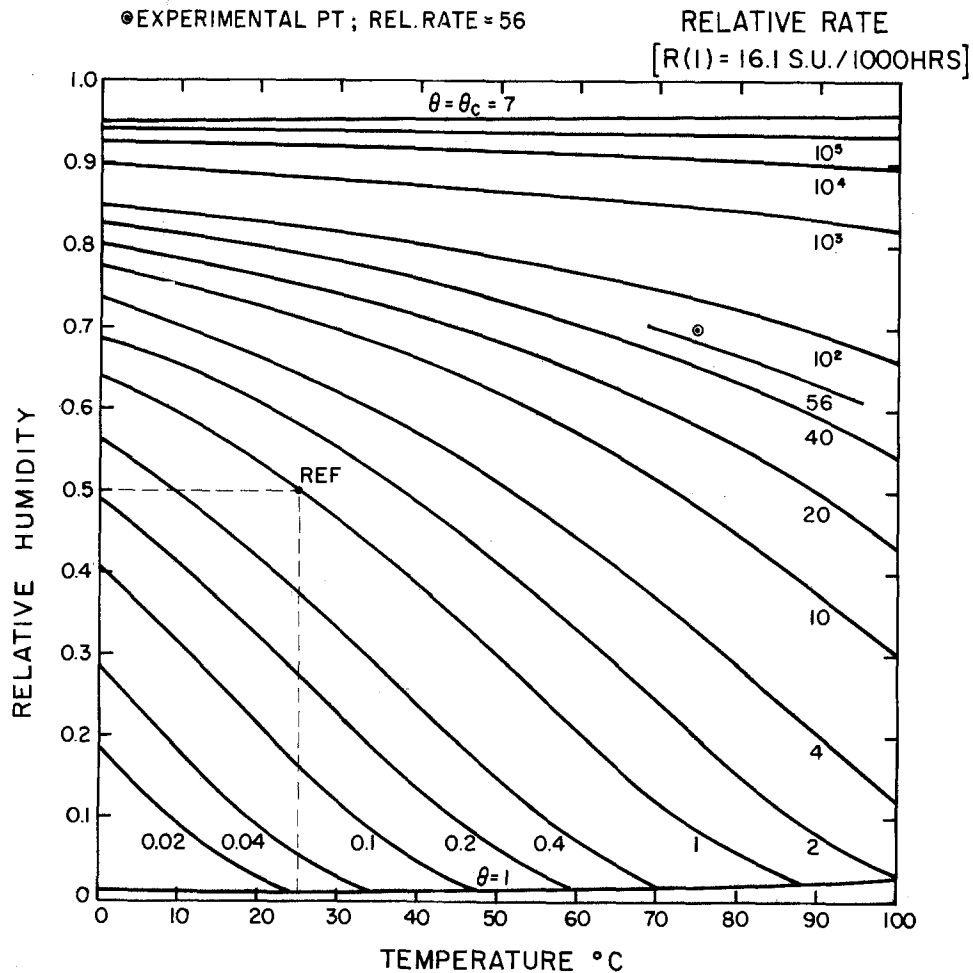


Fig. 7. Lines of constant accelerated Arrhenius rates (Eq. [18]).

requirement. A set of isobarically accelerated Arrhenius curves are plotted in Fig. 8 from which the 75°C/70% relative humidity point ($P_{H_2O} = 203$ mm) was chosen. One set of eight samples of tellurium on PMMA was aged for about 300 hr at 75°C and 70% relative humidity. The results are plotted in Fig. 9. By best estimate, the initial degradation rate was ap-

proximately 900 sensitivity units per one thousand hours. This single experimental point is plotted onto Fig. 7 and 8.

An additional interesting example of the usefulness of the Arrhenius rate mapping in Fig. 7 is presented in Table IV. In it, the data from Table III are converted to conditions of 25°C ambient for each of the relative humidity conditions encountered. The results demonstrate the overriding importance of relative humidity in determining the useful shelf life of tellurium films on PMMA when used as an optical disk storage medium.

Conclusions

Tellurium, as a medium for information storage via laser machining, suffers from a drawback of signifi-

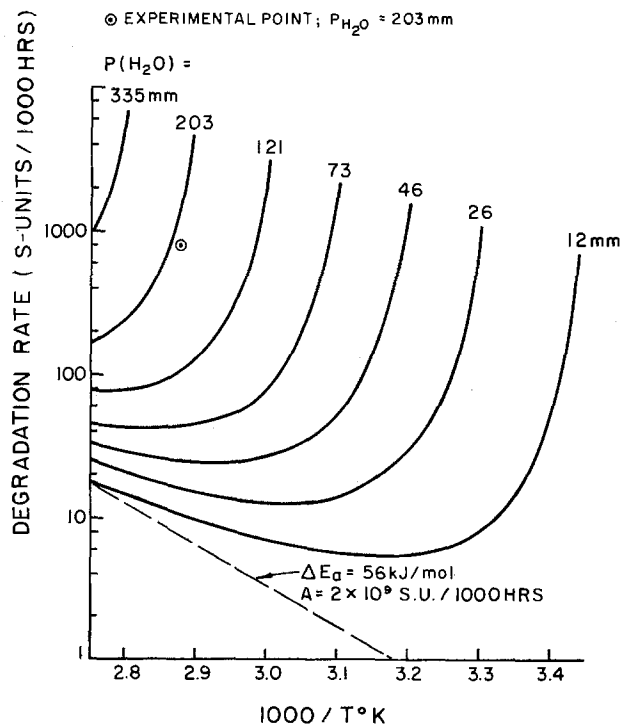


Fig. 8. Isobarically accelerated Arrhenius rates (Eq. [18])

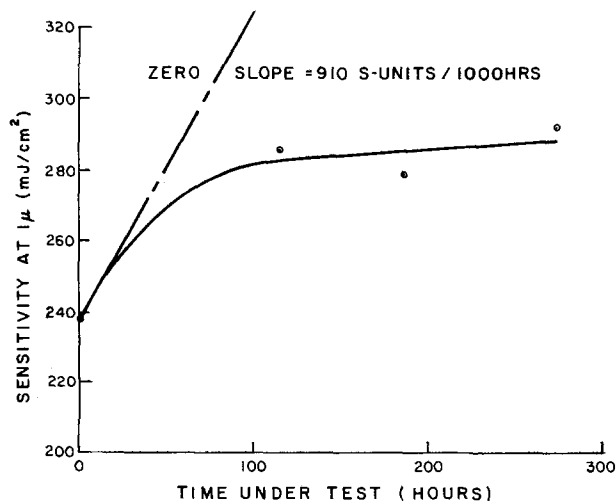


Fig. 9. Aging characteristics at 75°C and 70% relative humidity

Table IV. Decay rates for Table III data assuming 25°C throughout

Relative humidity (%)	Relative rate from Fig. 9	Useful life
50	1	6 months (observed)
10	0.06	8 years
4	0.03	17 years
3	0.02	25 years

cant atmospheric corrosion within a period of one or two years. Rates of decay are somewhat reduced by storing the films at a slightly elevated temperature (approximately 55°C) when the normal laboratory ambient is 25°C and 50% relative humidity. Significant improvement could be obtained by reducing the ambient humidity to 10% or lower.

A model for atmospheric corrosion is presented. It is based on a version of the Arrhenius equation modified to express the effects of both temperature and relative humidity explicitly via an adsorbed layer of water which accelerates corrosion. The concept of critical humidity appears in terms of monolayer coverage below which corrosion acceleration does not occur. Under this condition, the rate equation reduces to the normal Arrhenius relationship. Limits of validity are from monolayer coverage ($\theta = 1$) to the appearance of bulk water behavior ($\theta = \theta_c$). Experimental evidence in support of the model is presented.

Acknowledgments

The authors extend their appreciation to George Kenney for his enthusiastic encouragement and support in all phases of this work. We are grateful to Gertrude Neumark for her very generous theoretical assistance. David Lou provided helpful discussions and assistance in the experimental design, and Gertrude Neumark and Gerard Blom assisted in critically reading the manuscript.

Manuscript submitted Aug. 3, 1979; revised manuscript received Nov. 13, 1979.

Any discussion of this paper will appear in a Discussion Section to be published in the December 1980 JOURNAL. All discussions for the December 1980 Discussion Section should be submitted by Aug. 1, 1980.

Publication costs of this article were assisted by Philips Laboratories.

REFERENCES

1. D. Maydan, *Bell Syst. Tech. J.*, **50**, 1761 (1971).
2. R. Bartolini, H. Weakleim, and B. Williams, *Opt. Eng.*, **15**, 99 (1976).
3. H. H. Uhlig, *This Journal*, **125**, 58C (1978).
4. W. H. J. Vernon, *Trans. Faraday Soc.*, **27**, 255 (1931).
5. Von K. Barton and Z. Bartonova, *Z. Werskt. Korros.*, **21**(2), 85 (1970).
6. A. Hornung, *Annu. Conf. Reliab. Phys.*, **10**, 149 (1972).
7. G. F. Piacentini and G. Minelli, *Microelectron. Reliab.*, **15**, 451 (1976).
8. G. F. Cerofolini and C. Rovere, *Thin Solid Films*, **47**, 83 (1977).
9. S. P. Sharma, *This Journal*, **125**, 2005 (1978).
10. S. H. Kulpa and R. P. Frankenthal, *ibid.*, **124**, 1588 (1978).
11. W. Lee, G. Scherer, J. M. Eldridge, M. H. Lee, and R. H. Geiss, *ibid.*, **126**, 547 (1979).
12. C. R. A. Catlow, W. C. Mackrodt, M. J. Norgett, and A. M. Stoneham, *Philos. Mag. A*, **40**, 161 (1979).
13. D. M. Young and A. D. Crowell, "Physical Adsorption of Gases," pp. 2, 3, Butterworth and Co., London (1962).
14. A. D. Adamson, "Physical Chemistry of Surfaces," pp. 652, 653, John Wiley & Sons, New York (1976).
15. Y. I. Frenkel, "Kinetic Theory of Liquids," Oxford University Press, London (1946); G. D. Halsey, *J. Chem. Phys.*, **16**, 931 (1948); T. L. Hill, *Adv. Catal.*, **4**, 211 (1952).

Indoor Corrosion of Metals

D. W. Rice,* R. J. Cappell, W. Kinsolving, and J. J. Laskowski

IBM Corporation, General Products Division, San Jose, California 95193

ABSTRACT

The indoor corrosion rates of copper, silver, nickel, cobalt, and iron were measured at eight locations in the United States. Concurrent pollutant and relative humidity measurements were also made at six sites. The rates are shown to be lognormally distributed over the sample population. A statistical comparison of outdoor and indoor rates shows that Ag corrodes approximately the same both indoors and outdoors. Cu and Ni corrode 100 times faster outdoors, and Fe corrodes 2000 times faster outdoors. The corrosion rate sensitivity to relative humidity is speculated to explain these differences. Pollutant concentrations are shown to be generally attenuated indoors except for NH₃ and reduced forms of sulfur. The indoor corrosion rates of copper and silver are reasonably well correlated to the measured reduced sulfur concentrations. Nickel rates correlate best to the acid chlorine containing gases.

The atmospheric stability of copper, silver, nickel, cobalt, and iron is determined to a large extent by the chemistry and integrity of surface reaction products. These metals and the alloys prepared from them are thermodynamically unstable with respect to most practical operating environments. Faraday recognized this over a century ago (1). A significant effort has been expended to understand the factors that influence outdoor marine and urban atmospheric corrosion (2-4). Relative humidity, temperature, pollutant concen-

tration, particle concentration, and sample orientation are among the more important ones. Only limited success has been achieved in relating outdoor corrosion rates to these atmospheric parameters (5, 6).

It is well recognized that outdoor atmospheric parameters may be significantly changed inside structures (7-10). Pollutant adsorption and particle deposition on internal surfaces, humidification and dehumidification, temperature control, filtration, air flow design, and internal pollutant sources all modify the internal environment with respect to outdoor conditions. The purpose of this paper is to discuss the indoor corrosion of copper, silver, nickel, cobalt, and iron at a limited num-

* Electrochemical Society Active Member.

Key words: environment, pollution, reliability, copper, cobalt, iron, nickel, silver.

ber of test sites in the United States. Particular emphasis is given to the magnitude of indoor corrosion, indoor corrosion products, statistical aspects of indoor corrosion, indoor atmospheric parameters, and indoor-outdoor comparisons of rates and pollutant levels. This is the first published indoor study that measures both rates and atmospheric parameters concurrently. Insight is gained on the important pollutants for certain metals as well as the buffering capability of buildings.

Experiment

Metallic foils, 2.54 cm squared, were sent to eight indoor locations in the United States. The suppliers specified purities of the five metals tested are given in Table I. The geographical location, local outdoor environment, and the nature of the internal air conditioning for the eight sites is given in Table II. The metal foils were cleaned by a sequence of hot xylene, ethanol, and D.I. water immersions and weighed to the nearest one microgram. The samples were then clamped along two opposite edges in a flow control tunnel that pulled air from the indoor environment over them at 2.5 M/sec. Samples were retrieved from the sites at 6 (4380 hr), 12 (8760 hr), and 18 (13,140 hr) month intervals.

The test began in December, 1973 and ended in May, 1975. The returned samples were rinsed in benzene to remove organic deposits, then reweighed. The change in wt/cm² of metal divided by the test time interval is the reported rate of weight gain.

High resolution x-ray photoelectron spectroscopy (XPS) was used in the majority of cases to analyze the corrosion products (11). Auger electron spectroscopy was used for nickel (12). Corrosion product analysis was made only on the 18 month samples. Both AES and XPS spectroscopy sample the uppermost 1.0 nm (10Å)-5.0 nm (50Å). XPS yields some limited bonding information about the elements, while Auger yields only atomic composition. Neither method is particularly quantitative for a complex problem like atmospheric corrosion product identification. The hydrocarbon contribution to the XPS C(1s) spectra was not used in the surface composition calculation. XPS sensitivity factors, published by C. D. Wagner (13), were used to convert the integrated peak intensities to the percentage atomic compositions given in the tables. Auger sensitivity factors, published by Palmberg *et al.* (14), were used to convert the peak-to-peak intensities of the surface products on nickel to the atomic compositions.

The pollutant concentrations were measured at six of the eight sites. Sulfur dioxide (SO₂), nitrogen dioxide (NO₂), ammonia (NH₃), reduced sulfur gases (H₂S,

S₈, CH₃SH), inorganic (or acidic) chlorine gases (Cl₂, HCl), and airborne dust were monitored by pulling a known volume of site air through a series of filters designed to trap specific pollutants. The procedure required a month of sampling because of the low concentration of most pollutants indoors. The reported data are, therefore, approximately one-month integrated averages. The reported standard deviations would be significantly greater for shorter sampling intervals. The filters were returned to the laboratory after each sampling period and analyzed by specially developed wet chemical procedures. Relative humidity was measured using calibrated human hair bundles as the sensing element (15). Calibration at 6 month intervals was necessary to assure an accuracy of ±5% RH.

Results

Table III summarizes the corrosion rates at the eight sites for the three test exposure intervals. All the rates were used to fit to a lognormal distribution. Table IV summarizes these fits with the 10-99% cumulative percentage of measurement data points, the standard deviation of the logs, and the correlation coefficient that relates the fit to the data. Lognormal statistics are obeyed by many naturally occurring processes (16). It is not surprising that the corrosion rates should obey this distribution. Table IV also summarizes the composite indoor distribution function, which includes the data in this study plus other reported literature for indoor corrosion, and an estimate of the outdoor lognormal distribution function. The data are also given on lognormal probability coordinates in Fig. 1, 3, 4, 6, and 7.

Table V is a statistical summary of the pollutant data at each site. The arithmetic mean values, M_a , are the most reliable because they are determined directly from the pollutant data and are weighted to account for the length of each sampling period. The lognormal functions which include the geometric mean, M_g , and the standard geometric deviation, S_g , were calculated from the equations shown and are based on the assumption that the data are lognormal distributed. Table VI is a summary of the relative humidity distribution and mean relative humidity for each site, as well as a composite humidity distribution using all humidity data obtained in this study.

Specific monthly pollutant concentration variability will be presented in the body of the discussion sections as will the corrosion product summary. The measured

Table I. Metal foil purity and thickness as specified by the supplier

Metal	Purity	Thickness (mm)
Copper	99.999+ OFHC	0.13
Silver	99.999+	0.13
Nickel	99.99	0.25
Cobalt	99	0.13
Iron	99.56	0.511

Table II. Field site physical characteristics

Site	Location	Outdoor environment	Air-conditioned
1	Los Angeles	Urban	Yes
2	Chicago	Urban	Yes
3	Manhattan, New York City	Urban	Yes
4	Texas	Industrial/rural	Yes
5	Indiana	Industrial	Yes
6	South Carolina	Industrial	Yes
7	New Jersey	Industrial	No
8	New Jersey	Industrial	No

Table III. Summary of indoor corrosion rates*

Site	Exposure time (hr)	Corrosion rate (μg/cm ² hr × 10 ⁴)				
		Copper	Silver	Nickel	Cobalt	Iron
Los Angeles	4380	14.1	34.2	36.5	7.99	1.10
	8760	13.8	33.9	23.4	27.5	21.0
	13140	13.7	23.9	32.4	28.6	19.9
Chicago	4380	19.6	32.9	7.08	13.5	31.9
	8760	13.8	20.7	5.82	11.8	23.9
	13140	12.4	18.1	6.01	7.34	16.6
New York City	4380	24.4	39.0	17.8	13.3	9.73
	8760	23.8	39.6	13.7	18.2	9.82
	13140	12.7	31.1	6.77	13.3	9.91
Texas	4380	10.5	28.3	3.40	8.3	4.78
	8760	4.22	32.0	0.00	0.80	2.01
	13140	1.75	29.6	0.00	0.00	1.83
Indiana	4380	65.8	33.8	41.8	61.9	—
	8760	25.5	31.3	24.7	39.3	109.8
	13140	36.5	47.4	31.8	32.9	60.5
S. Carolina	4380	139	90.6	16.2	31.9	54.0
	8760	—	65.8	5.37	7.2	8.5
	13140	49.2	64.1	7.53	10.7	26.0
New Jersey (7)	4380	35.6	38.1	15.1	18.7	66.7
	8760	25.7	22.7	118.0	62.1	539.4
	13140	26.3	23.1	115.0	54.9	67.0
New Jersey (8)	4380	60.8	67.8	26.9	25.8	21.0
	8760	70.5	57.2	28.3	21.3	567.0
	13140	56.9	35.5	29.1	26.3	476.0

* Rates are in μg/cm² hr × 10⁴.

Table IV. Lognormal distribution summary of indoor and outdoor corrosion rates of metals

Cumulative percent of measurements	Copper			Silver			Nickel			Cobalt	Iron	
	Indoor*		Out-door**	Indoor		Out-door	Indoor		Out-door	Indoor	Indoor	Out-door
	This study	Composite (10, 17)	(18-23)	This study	Composite (10)	(31)	This study	Composite (10)	(33)	This study	This study	(39-41)
10	6.4	5.86	0.08	21.2	20.6	10.4	2.02	2.18	0.01	3.71	2.56	2.50
30	13.5	10.5	0.13	29.0	28.0	12.7	6.0	6.0	0.054	8.50	10.0	3.81
50	22.5	15.7	0.19	36.1	34.9	14.6	13.1	11.4	0.14	15.4	25.2	5.12
70	37.6	23.6	0.28	44.9	43.0	16.8	26.5	21.5	0.36	27.0	62.0	6.87
90	80.0	42.4	0.49	61.6	58.2	20.7	80.0	56.0	1.58	61.0	231.6	10.5
99	219.0	95.1	0.96	95.2	90.0	27.4	380.0	200.0	10.0	190.0	1850.0	18.9
$\ln r_{84.1\%} - \ln r_{15.9\%}$												
$\sigma = \frac{2}{\text{Correlation coefficient}}$	0.98	0.77	0.69	0.42	0.41	0.27	1.45	1.29	1.95	1.11	1.79	0.56
Correlation coefficient	0.97	0.97	0.99	0.98	0.97	0.94	0.94	0.96	0.97	0.93	0.98	0.98

* Indoor rates = $\mu\text{g}/\text{cm}^2 \text{ hr} \times 10^4$.

** Outdoor rates = $\mu\text{g}/\text{cm}^2 \text{ hr}$ except for silver outdoor rates which have the same magnitude as indoor rates.

Table V. Indoor atmospheric pollutant, dust, and relative humidity statistical summary

Site	Sulfur* dioxide			Nitrogen* dioxide			Reduced* sulfur (H ₂ S, S ₈ , CH ₃ SH)			Ammonia*			Chlorine* gases (HCl, Cl ₂ , HOCl)			Airborne* dust			RH
	M _a	M _g	S _g	M _a	M _g	S _g	M _a	M _g	S _g	M _a	M _g	S _g	M _a	M _g	S _g	M _a	M _g	S _g	%
Los Angeles	2.62	1.83	2.34	55.8	52.1	1.62	0.20	0.18	1.72	12.7	12.2	1.29	0.29	0.27	1.61	17.7	17.3	1.25	30
Chicago	13.6	11.8	2.20	23.3	23.5	1.36	0.45	0.43	1.37	15.3	13.5	1.40	0.12	0.11	1.89	3.9	3.7	1.22	49
New York City	39.6	17.6	3.70	35.0	35.7	1.81	0.46	0.43	1.23	11.3	11.3	1.30	0.28	0.26	1.36	11.1	10.9	1.21	44
Texas	1.57	1.31	2.08	4.50	4.32	1.38	0.47	0.43	1.49	159.0	155.0	1.23	0.08	0.06	2.22	6.8	6.7	1.19	59
Indiana	12.8	9.17	2.53	25.6	25.4	1.21	0.82	0.74	1.59	18.4	15.8	1.62	0.26	0.24	1.62	22.2	21.4	1.32	55
S. Carolina	2.10	1.57	2.52	3.01	2.63	1.68	4.24	3.31	2.07	24.7	24.4	1.21	0.16	0.14	1.74	33.0	32.5	1.19	50

* $\mu\text{g}/\text{m}^3$; $M_a = \frac{\sum X}{N}$ = arithmetic mean; $M_g = e^{\frac{\sum \ln X}{N}}$ = geometric mean; $S_g = e^{\left[\frac{\sum \ln^2 X - N(\ln M_g)^2}{N-1} \right]^{1/2}}$ = standard deviation.

Table VI. Summary of indoor relative humidity data

Relative humidity range	Percentage of time						
	Los Angeles	New York City	Chicago	Indiana	Texas	S. Carolina	All sites
0-5	0.00	0.00	0.00	0.00	0.00	0.00	0.00
6-10	0.00	0.92	0.00	0.00	0.00	0.00	0.13
11-15	0.53	2.64	0.36	0.14	0.00	0.00	0.52
16-20	1.61	5.03	1.51	1.19	0.03	0.00	1.41
21-25	5.13	7.29	3.08	3.80	0.53	0.19	2.94
26-30	5.38	11.15	6.95	6.36	1.89	3.19	5.30
31-35	11.36	10.82	10.62	8.74	2.64	4.91	7.53
36-40	8.31	9.87	11.43	10.10	5.48	11.52	9.57
41-45	6.10	3.36	9.33	7.30	6.59	9.52	8.18
46-50	7.23	5.73	8.32	5.50	6.84	21.98	10.41
51-55	7.40	6.48	6.92	6.47	12.10	29.09	12.69
56-60	12.05	9.82	6.44	5.30	19.22	14.68	13.00
61-65	15.13	10.57	5.97	7.44	26.18	4.33	10.79
66-70	10.81	9.93	9.53	10.05	14.33	0.58	8.01
71-75	6.65	4.23	5.18	9.77	3.78	0.00	4.23
76-80	1.94	2.03	6.39	8.10	0.31	0.00	2.68
81-85	0.39	0.14	5.24	6.91	0.08	0.00	1.82
86-90	0.00	0.00	2.24	2.61	0.00	0.00	0.69
91-95	0.00	0.00	0.11	0.11	0.00	0.00	0.03
96-100	0.00	0.00	0.36	0.11	0.00	0.07	
Mean RH (%)	50	44	49	55	59	50	50

concentration is shown numerically either within or above the vertical bars. Note that when a vertical bar in Fig. 9-14 does not exist no data (ND) were obtained.

Discussion

Metallic corrosion.—The indoor environment can significantly influence the level of each atmospheric parameter as well as its distribution. Pollutant concentrations are generally reduced indoors except when internal sources are present (9). Shair *et al.* have developed a theoretical mass balance model that relates indoor pollutant levels to outdoor levels for the case without internal sources (7). The corrosion rates inside buildings would be expected to be less than outside, but the magnitude of reduction is not clear because of

the complexity of the rate expression. We will focus our attention on each metal followed by a discussion of the indoor atmospheric parameters.

Copper.—The corrosion rate of copper at the eight indoor sites shows a general decrease with time particularly for the less corrosive sites. This is characteristic of parabolic or higher order kinetics. The corrosion products inhibit further copper oxidation by limiting cation and/or anion flux. Campbell and Thomas (10) observed a similar behavior for copper in telephone switching rooms in the U.S.

The corrosion products on the 18 month exposure samples, as measured by high resolution XPS, are complex combinations of copper hydroxide, chloride, sulfate (sulfit), carbonate, and nitrate. Table VII

Table VII. Surface corrosion products on 18 month exposed copper samples measured by XPS

Site	Atomic percentage					
	Cu (2p _{3/2}) (934.4 eV)	O (1s) (531.4 eV)	C (1s) (288 eV)	Cl (2p) (197.8 eV)	S (2p) (167.6 eV)	N (1s) (399.5 eV)
Los Angeles	25	50	17	5.9	0.0	2.5
Chicago	25	47	14	7.5	1.8	4.3
New York City	—	—	—	—	—	—
Texas	52	31	7.6	3.0	1.4	5.1
Indiana	10	53	13	6.2	1.9	11
S. Carolina	25	50	13	4.4	0.0	8.2

summarizes the atomic percentage (a/o) of each element at each site as well as the associated binding energy (BE) of the photoelectrons. The dominant copper binding energy at 934.3 eV is characteristic of oxidized copper 2p_{3/2} photoelectrons. The oxygen 1s BE is 531.6 eV and typical of oxygen in OH⁻, SO₄⁼, CO₃⁼, and NO₃⁻, but not in oxide O⁼. Carbonate, adsorbed CO₂, and adsorbed CO could account for the observed carbon 1s spectra at 288 eV. The chlorine 2p doublet at 198.1 and 199.5 eV, respectively, is characteristic of chlorides. The sulfur 2p BE was 168 eV and characteristic of sulfate or sulfite, not sulfide. The sulfide 2p BE would occur at 162 eV. Finally, the nitrogen 1s BE at 399.4 eV is typical of nitrite or nitrate.

The indoor copper corrosion rate distribution for the 23 measurements in this study was a lognormal function with an excellent correlation coefficient, 0.97. Furthermore, the indoor work of Campbell and Thomas (10), and Sharma (17) was combined with this study to produce a composite indoor distribution function. A lognormal approximation was again an appropriate fit. Figure 1 compares the data of this study with the composite data. Table IV summarizes the geometric means

$$r_{50\%} = e^{\Sigma \ln r/n}$$

the standard deviation

$$\sigma = \frac{\ln r_{84.1} - \ln r_{15.9}}{2}$$

and the correlation coefficients. The fact that the indoor corrosion rate of copper over a range of times and sites is lognormally distributed can help assess failure rates of copper materials, the cost associated with field repairs, and field maintenance plans.

The outdoor corrosion rate distribution function for copper corrosion was generated from data reported by others (18-23). The lognormal distribution is an excellent approximation. Figure 1 and Table IV summarize the fitting parameters. Indoor corrosion is two orders of magnitude less than outdoor corrosion. For example, comparison of the geometric means, $r_{50\%}$, shows outdoor corrosion to be 119 times greater than indoor corrosion. Corrosion products on outdoor ex-

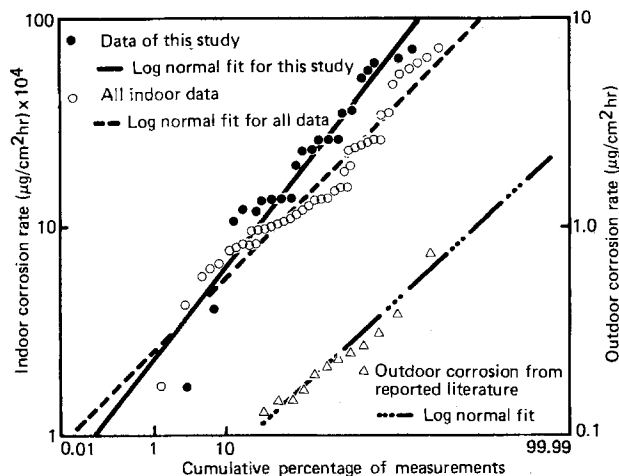


Fig. 1. Copper corrosion rate distribution

posed samples have been reported to be complex copper hydroxides, sulfates, carbonates, and chlorides (24). These are similar to our indoor results.

The fact that the indoor corrosion of copper is orders of magnitude less than outdoors is not surprising. The indoor environment is less severe from an atmospheric parameter point of view. Copper has been reported to be sensitive to relative humidity, sulfur dioxide, sulfur gases, and chloride contaminants since the pioneering work of Vernon (25, 26). Rice *et al.* have shown that the functional dependence of corrosion rate, r , on relative humidity, RH, is of the form $r = ae^{4.6RH}$ with little evidence for a critical humidity in a complex environment. Sulfur dioxide, H₂S, and O₃ were also shown to have a significant influence while NO₂, Cl₂, and NH₃ have little influence (27). Leidheiser (24) has reviewed much of the current understanding of copper corrosion.

Examination of pollutant data, Table V, measured at the sites in this study during the same interval as the copper exposure indicates the reduced sulfur content, S_x , of the indoor environment is the best pollutant indicator of copper corrosion. Figure 2 is a presentation of the fit and actual rate *vs.* reduced sulfur concentration data. The form of the numerical fit is $r = 30 \times 10^{-4} (S_x)^{0.76}$ with a correlation coefficient equal to 0.8. It would be naive to presume that reduced sulfur is the only operative in the polluted environment; however, it may be an effective guide to indoor environmental severity with respect to copper.

Silver.—The corrosion rate of silver, like copper, decreased with time for most of the sites. Silver has been used as a classic example of a material that corrodes parabolically; in particular, the kinetics of iodization (28) and sulfidation (29) are parabolic. The corrosion products were silver sulfide, chloride, hydroxide, and nitrate (nitrite). The binding energies of electrons as-

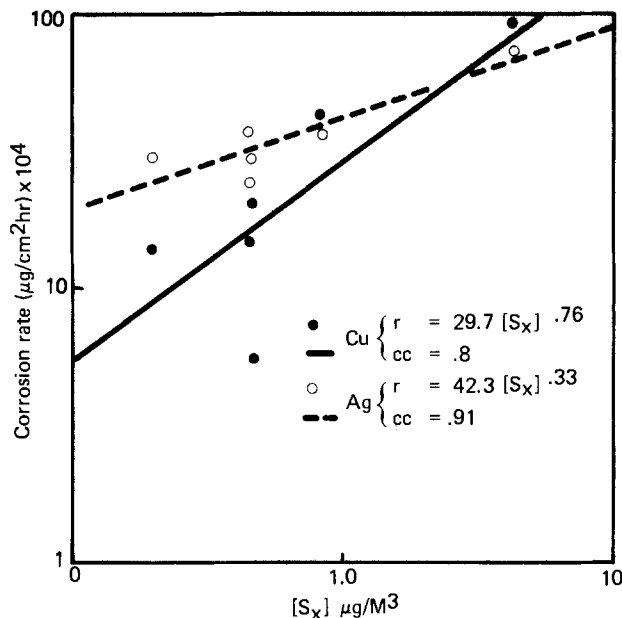


Fig. 2. Field corrosion rate of copper and silver vs. mean reduced sulfur concentration at each site.

Table VIII. Surface corrosion products on 18 month exposed silver samples measured by XPS

Site	Atomic percentage				
	Ag (3d _{5/2}) (368.4 eV)	O (1s) (531.8 eV)	Cl (2p) (198.3 eV)	S (2p) (161.6 eV)	N (1s) (399.5 eV)
Los Angeles	49	29	5.8	9.3	6.6
Chicago	52	24	6.2	11	7.1
New York City	33	50	5.2	5.8	5.6
Texas	60	20	1.5	15	4.6
Indiana	66	23	1.3	2.3	7.9
S. Carolina	61	15	3.9	16.4	3.6

sociated with all anions, except sulfur, were similar to those observed on copper. The sulfur was present as a sulfide not sulfate on these returned samples. This is in general agreement with the work of others (30). However, the presence of significant chlorides, hydroxides, and nitrates/nitrites complicates the picture somewhat. Table VIII summarizes the corrosion product results.

The indoor corrosion rate distribution for this study and for the composite of reported indoor data (10) both fit lognormal statistics with a correlation coefficient equal to or greater than 0.97. Figure 3 compares the results. The standard deviation for silver is significantly less than copper, while the mean corrosion rate is greater.

The outdoor corrosion of silver, a recognized problem, is not well documented. The limited data that the authors could find (31) fit a lognormal distribution well, as shown in Fig. 3. Unlike copper and the other metals in this study, silver corrodes indoors at approximately equivalent rates to outdoors. In fact, the geometric mean of the outdoor data is only 43% of the indoor geometric mean. The reason for this similarity between outdoor and indoor rates is speculated to be the independence of silver corrosion rate on relative humidity (27). Extremes in outdoor humidity will not accelerate silver corrosion, while the corrosion rate of the other metals in this study will be markedly accelerated. Subtle influences such as flow velocity and reduced sulfur gas concentrations will then account for the comparative differences between indoor and outdoor rates. Silver corrosion rate is dependent on the reduced sulfur pollutant concentration which can often be greater indoors than outdoors.

As with copper, the total reduced sulfur in the indoor atmosphere correlates better than the other measured pollutants with the observed indoor corrosion of silver. Figure 2 plots the observed rate vs. the reduced sulfur content of the environment. The equation is $r = 42.3 \times 10^{-4} (S_x)^{0.33}$ where r is the mean site corrosion rate and S_x is the reduced sulfur arithmetic mean over the test interval. This is even more

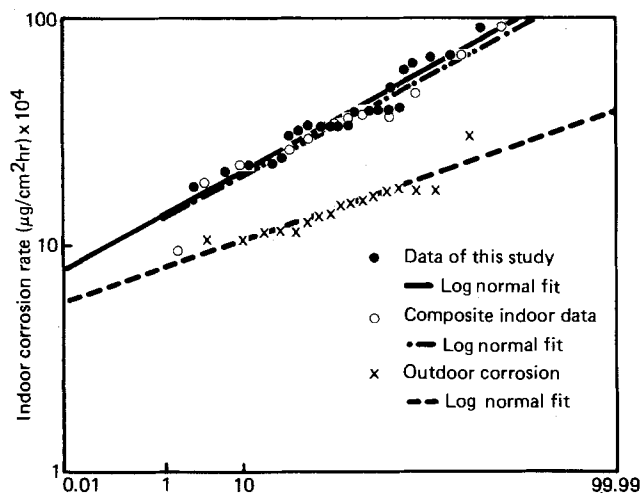


Fig. 3. Silver corrosion rate distribution. x — 9 × 15 = cumulative percentage of measurements.

plausible for silver because it is less sensitive to SO₂ and RH than copper (27).

Nickel.—The corrosion rate of nickel showed linear kinetics for most of the indoor locations, unlike copper and silver. Campbell and Thomas (10) showed a marked seasonal dependence for nickel indoor corrosion in switching rooms. Winter corrosion was often only 10-20% of the summer value. The fact that we observed linear kinetics over the 1.5 year interval may indicate that the air conditioned facilities buffer the humidity extremes and average the corrosiveness of the environment.

The corrosion products on nickel were only measured by AES, Table IX summarizes the results. Suffice it to say that in addition to nickel, sulfur, chlorine, oxygen, carbon, and nitrogen were present in the corrosion product. The corrosion product on nickel exposed to outdoor environments is a complex combination of basic nickel hydroxy chloro sulfate as summarized by Aziz and Goddard (32).

The indoor and outdoor corrosion rates were fit to the lognormal distributions summarized in Table IV and shown in Fig. 4. The lognormal fit was good. The composite indoor distribution agreed with this study. The geometric mean of the outdoor rates (33) is 100 times that of the indoor rates. This again demonstrates the significant positive influence buildings have on reducing materials corrosion.

The corrosion rate of nickel has been shown in laboratory studies to be strongly influenced by relative humidity, SO₂, NO₂, Cl₂, and hygroscopic salts (34-37). The field mean site indoor corrosion rates correlated best with the chloride content, Cl_x, of the environment yielding an equation of the form $r = 0.0448 (Cl_x)^{2.24}$

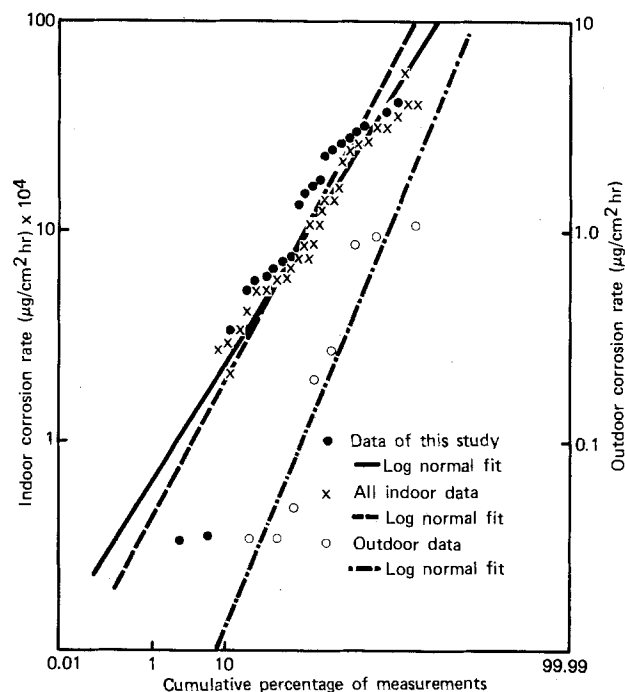


Fig. 4. Nickel corrosion rate distribution

Table IX. Surface corrosion products on 18 month exposed nickel samples measured by AES

Site	Atomic percentages					
	Ni (845 eV)	O (510 eV)	C (270 eV)	Cl (180 eV)	S (150 eV)	N (380 eV)
Los Angeles	25	13	47	6	3	6
Chicago	28	18	22	24	4	3
New York City	18	11	56	3	8	6
Texas	40	31	15	9	3	1
New Jersey (1)	26	23	23	12	14	2
New Jersey (2)	44	30	5	7	14	1

Table X. Surface corrosion products on 18 month exposed cobalt samples measured by XPS

Site	Atomic percentage					
	Co (2p _{3/2}) (780.7 eV)	O (1s) (531.3 eV)	C (1s) (288 eV)	Cl (2p) (198.4 eV)	S (2p) (168.5 eV)	N (1s) (399.3 eV)
Los Angeles	13	72	17	6.4	1.9	5.9
Chicago	11	61	13	8.6	1.6	4.9
New York City	12	57	17	3.2	6.4	4.6
Texas	9.4	65	16	2.4	1.1	6.6
Indiana	8.4	64	16	3.4	1.9	7.1
S. Carolina	6.8	66	16	2.1	1.9	7.9

with a correlation coefficient equal to 0.93. Unlike copper and silver, nickel shows little correlation with the reduced sulfur levels in the environment. Figure 5 shows the data and fit comparison.

Cobalt.—Cobalt's chemistry is very similar to nickel and we would expect its atmospheric corrosion to be similar. Very little has been published on the atmospheric corrosion of cobalt, although it is a significant alloying additive in many corrosion resistant materials (38). Cobalt's indoor corrosion rate was very similar to nickel in this study. The kinetics were closer to linear except for the very clean Texas site. The mean indoor corrosion rate was less than both copper and silver.

The corrosion product summary is given in Table X. The cobalt was present in an oxidized bonding state at concentrations ranging from 6.8 to 13 a/o. A large quantity of oxygen was present ranging from 57 to 72

a/o. Chlorides were present between 2.1-8.6 a/o. Sulfur was in the form of sulfate or sulfite, not sulfide.

Figure 6 summarizes the lognormal fit of the cobalt indoor corrosion rates. There has been neither indoor nor outdoor data published on cobalt for comparison to this study.

Like nickel, cobalt corrosion is significantly influenced by relative humidity, sulfur dioxide, and chlorine (38). The correlations of any one pollutant to the observed field corrosion rate were not good for cobalt.

Iron.—The indoor corrosion of iron showed a range of kinetics from parabolic at the less corrosive sites to linear at the more corrosive sites. The nonair-conditioned sites exhibited the highest rates. The indoor data were fit to a lognormal distribution with a correlation coefficient equal to 0.98. The iron indoor corrosion rates showed the largest standard deviation of the metals tested. A comparison of the indoor data to an outdoor distribution created from some of the published data (39-41), Fig. 7, shows that the indoor environment reduces iron corrosion by a factor of 1/2000, significantly more than for the other metals tested. The corrosion products (Table XI) show the presence of oxidized iron, sulfate, nitrite, hydroxide, oxide, and carbonate. Only one site showed chlorides. There is no simple correlation of pollutant concentration with the observed iron corrosion rates.

Metallic corrosion summary.—A summary of the metallic corrosion results is given in Table XII. The

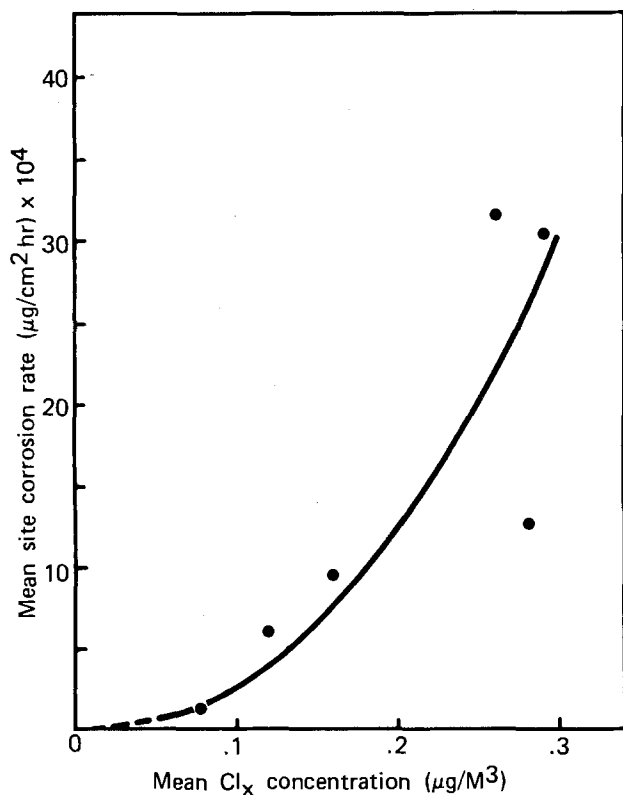


Fig. 5. Nickel corrosion rate vs. chlorine gas concentration

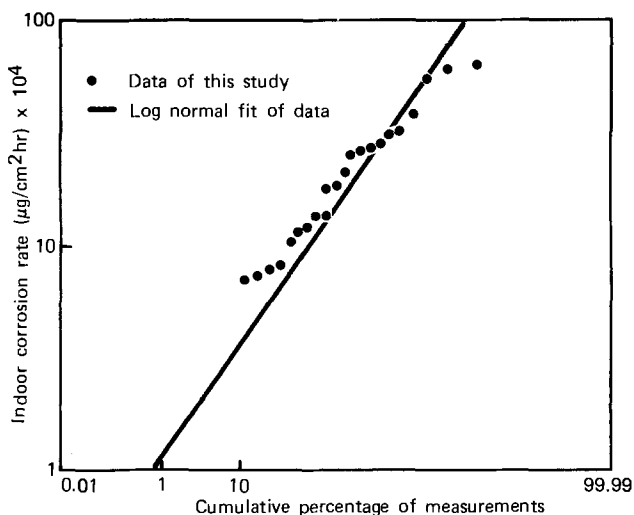


Fig. 6. Cobalt corrosion rate distribution

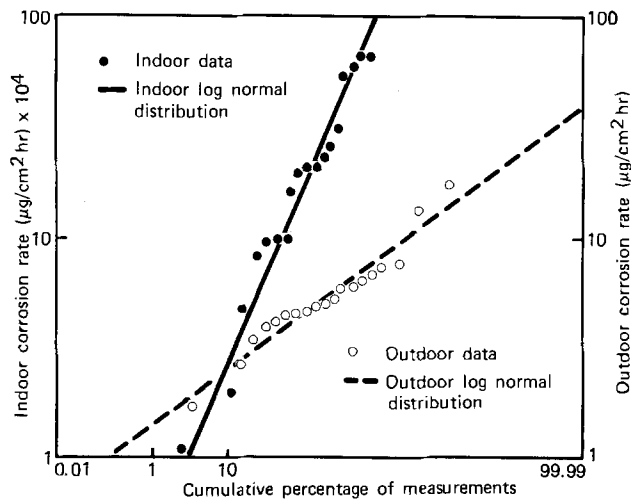


Fig. 7. Iron corrosion rate distribution

corrosion kinetics range from linear to parabolic. Corrosion products are complex consisting of sulfates (sulfites), chlorides, carbonates, nitrates (nitrites), and hydroxides. Silver showed the presence of sulfide instead of sulfate.

The indoor corrosion rate geometric means, obtained from the lognormal distributions for each metal, differed by only a factor of 3, with silver being the most corrosive and nickel the least. Lognormal statistics were obeyed by all corrosion rates both indoors and outdoors over the site populations studied. A comparison of outdoor to indoor rates shows silver to corrode similarly indoors and outdoors, copper and nickel to corrode 100 times greater outdoors, and iron 2000 times greater. We propose that the reason for this marked difference in the indoor/outdoor ratio for these metals is in their corrosion rate sensitivity to relative humidity. Iron is markedly accelerated by outdoor high humidity excursions, while silver is not at all. The corrosion rate, r , dependence on relative humidity, RH, for each metal can be expressed by an equation of the form $r = ae^{bRH}$ where b is the measure of the corrosion rate sensitivity to RH. Table XII summarizes the constant b for each metal and shows iron to be comparatively sensitive, silver insensitive, and Cu, Ni, Co to be sensitive and about the same. In outdoor environments where higher humidities are more probable, iron will be most affected and silver least. Iron had the largest sigma, while silver had the

lowest sigma for indoor corrosion. This may result from the same sensitivity to RH as shown above.

Atmospheric Parameters

Pollutants.—The environmental factors that influence metallic corrosion are as varied as the types of metals. Some of those factors that are clearly established include water vapor, sulfur dioxide, sulfur gases, chlorides, and salt particles (2-6). These factors may be significantly influenced inside buildings by loss mechanisms on internal surfaces (42), air filters, and air conditioning systems (7, 8). Models that relate outdoor to indoor pollutant levels have been proposed with some demonstrated success for ozone (7).

Relative humidity.—The relative humidity mean for the air-conditioned sites ranged from a low of 44% at New York to a high of 59% at the Texas site. While a normal distribution, Fig. 8, was found to fit the composite data, it did not at all represent each of the individual sites. Multimodal distributions were observed at some of the sites. These could be related to seasonal variations. Generally, the summer months were the biggest contributor to the high humidity peaks and the winter months to the low humidity peaks. One clearly cannot account for the relative severity of sites on the basis of RH alone. The Texas site was generally the least corrosive but exhibited the highest mean RH. Furthermore, the site severity did not correlate very well with high humidity excursions alone.

Sulfur dioxide.—Sulfur dioxide is the most studied pollutant with respect to atmospheric corrosion. It is highly soluble in aqueous phases, can profoundly influence metallic corrosion, and is present at comparatively high concentrations in urban environments. Burning of fossil fuels is the predominant anthropogenic source. The indoor SO₂ measurements made in this study are shown in Fig. 9. Significant seasonal trends were observed for the eastern U.S. sites. This is typical of the trends of outdoor levels in the high fossil fuel use regions of the U.S. In New York, the indoor concentrations range from 106 in the winter to less than 2 µg/m³ in the summer. Indiana and Chicago sites exhibited similar seasonal fluctuations. The mean indoor SO₂ concentration in the New York City site, 39.6 µg/m³, was approximately 50% of the outdoor level reported at stations in Manhattan in 1974 (43). Furthermore, the mean indoor site SO₂ average concentration from this study, 12.2 µg/m³, is 69% of the mean outdoor site average, 17.6 µg/m³, for 840 monitoring stations reported by the U.S. Environmental Protection Agency in 1975 (44).

Table XI. Surface corrosion products on 18 month exposed iron samples measured by XPS

Site	Atomic percentage					
	Fe (2p _{3/2}) (711 eV)	O (1s) (531.5 eV)	C (1s) (288.3 eV)	Cl (2p) (200 eV)	S (2p) (168.3 eV)	N (1s) (399.8 eV)
Los Angeles	4.5	66	18	0	3.7	7.8
Chicago	14.0	68*	11	0	2.1	4.6
New York City	4.8	65	17	0	3.6	9.6
Texas	9.5	66*	17	0	2.1	5.8
Indiana	4.4	65	13	0	3.3	14
S. Carolina	28	68	17	0.8	2.8	11

* A 530.0 eV peak was observed.

Table XII. Summary of field metallic corrosion rate results

Metal	Kinetics	Corrosion products	Indoor distribution	Indoor rate (r _{50%})	Outdoor rate (r _{50%})	r _{50%} out-door/r _{50%} indoor	b (r = ae ^{bRH})	σ Field indoor
Ag	Parabolic	Ag ₂ S, OH ⁻ , Cl ⁻ , NO ₂ ⁻ , CO ₃ ⁼	Lognormal	0.0035	0.0015	0.4	0.13	0.41
Cu	Parabolic	CuSO ₄ (SO ₃ ⁼), OH ⁻ , Cl ⁻ , NO ₂ ⁻ , CO ₃ ⁼	Lognormal	0.0016	0.19	119.0	4.6	0.77
Ni	Linear	NiSO ₄ , OH ⁻ , Cl ⁻ , NO ₂ ⁻ , CO ₃ ⁼	Lognormal	0.0011	0.14	127.0	7.95	1.29
Co	Linear	CoSO ₄ , OH ⁻ , Cl ⁻ , NO ₂ ⁻ , CO ₃ ⁼	Lognormal	0.0015	—	—	6.6	1.11
Fe	Linear parabolic	FeSO ₄ , OH ⁻ , CO ₃ ⁼ , NO ₂ ⁻ , O ⁼	Lognormal	0.0025	5.12	2045.0	12.6	1.79

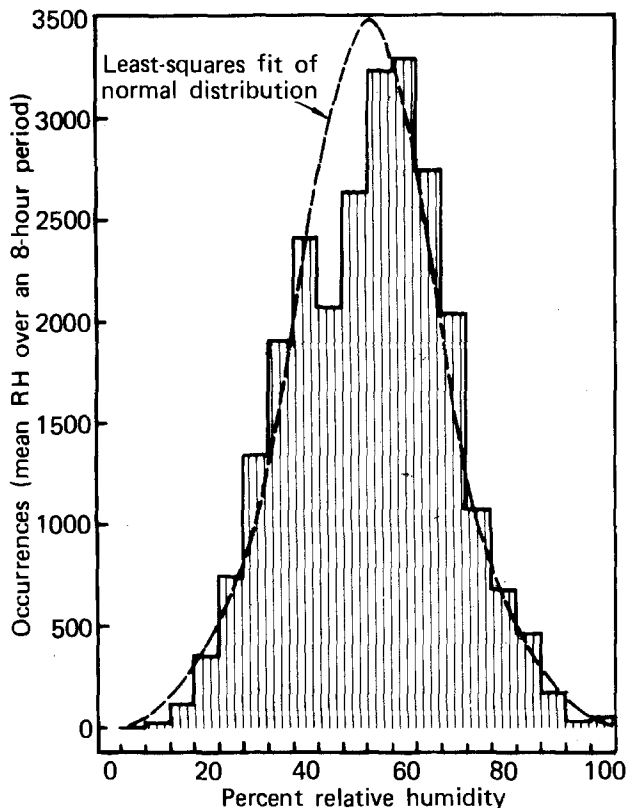


Fig. 8. Composite relative humidity indoor histogram for 6 sites and least squares fit to a normal distribution.

Nitrogen dioxide.—Nitrogen dioxide's influence on metallic corrosion has not been studied extensively. It is a precursor to nitrous and nitric acid. Its urban concentrations are comparatively high. Urban anthropogenic NO_2 is a secondary pollutant resulting from the oxidation of NO. It shows regional highs in the western U.S. Figure 10 shows the indoor results for the six sites monitored in this study. Los Angeles has the highest NO_2 level and the seasonal fluctuations are typical of outdoor Los Angeles. The indoor Los Angeles NO_2 concentration, 55.8, is approximately 80% of the outdoor levels of $69 \mu\text{g}/\text{m}^3$ in major California urban areas (45). The mean NO_2 indoor site average is $26 \mu\text{g}/\text{m}^3$. This indoor mean is 60% of the outdoor average of $43.5 \mu\text{g}/\text{m}^3$ for 701 U.S. monitoring stations for 1975 (46).

Reduced sulfur.—The reduced sulfur gases, which include H_2S , sulfur vapor, and mercaptans, significantly influence copper and silver corrosion (27), as well as accelerate stress corrosion cracking of steel (47). The source is predominantly organic decay processes, fossil fuel combustion, and refining. There is a paucity of published data for H_2S or reduced sulfur gas levels. This is due to the extremely low levels normally encountered in the atmosphere and the lack of sensitive, reliable measurement methods. The best reported estimates of the H_2S background levels in unpolluted air are from 0.2 to $0.5 \mu\text{g}/\text{cm}^3$ (48). Urban levels around $34 \mu\text{g}/\text{m}^3$ have been reported, but these were probably near localized sources of H_2S (49, 50). Our limited measurements in four cities (Chicago, Los Angeles, New York, and San Jose) indicate that the average outdoor total reduced sulfur levels are below $1 \mu\text{g}/\text{m}^3$.

The monthly average measurements for each of the indoor sites are summarized in Fig. 11. A slight seasonal dependence is seen for all sites. The winter levels are higher, probably resulting from enhanced fossil fuel use. The indoor levels, except for South Carolina, are only slightly higher than reported background levels; however, they are quite near the expected outdoor levels as indicated above. In an independent

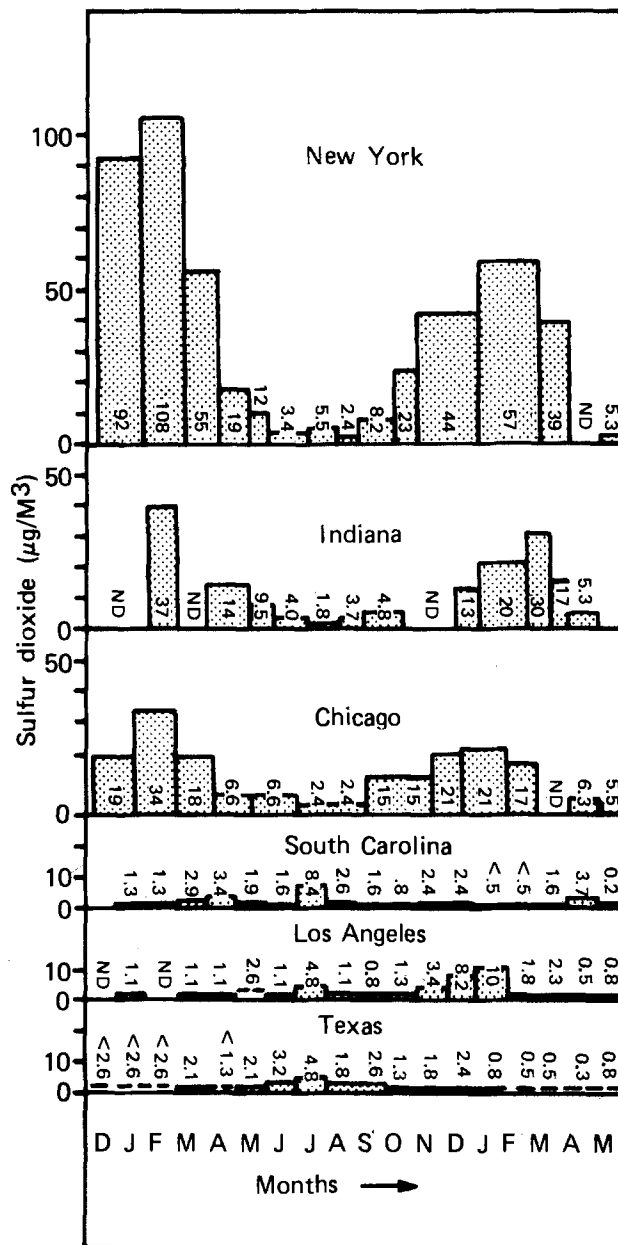


Fig. 9. Indoor concentration of sulfur dioxide at 6 sites for 18 months.

study, using the measurement techniques outlined here, indoor and outdoor reduced sulfur levels were monitored continuously for one to two years at sites in Los Angeles and San Jose, California. In both cases the indoor measurements were made in modern, air-conditioned office buildings. The results for San Jose showed an average outdoor level of 0.25 and an indoor level of $0.19 \mu\text{g}/\text{m}^3$. For Los Angeles the average outdoor level was 0.32 and the indoor level was $0.35 \mu\text{g}/\text{m}^3$. There was obviously little attenuation of reduced sulfur gas levels from outdoor to indoor environments. In fact, the higher indoor level in Los Angeles indicates some internal source of this gas. The silver corrosion data tend to confirm the similar indoor and outdoor levels, in that the corrosion rates are also similar, and the reduced sulfur gases are known to be primarily responsible for silver corrosion.

Ammonia.—Ammonia accelerates the corrosion of cobalt and silver, but not nickel and copper, degrades organics, dissolves readily in water, and originates from many anthropogenic and natural sources (50).

The ammonia in the indoor environments showed the monthly average concentrations shown in Fig. 12. Five of the sites had geometric means between 10-22

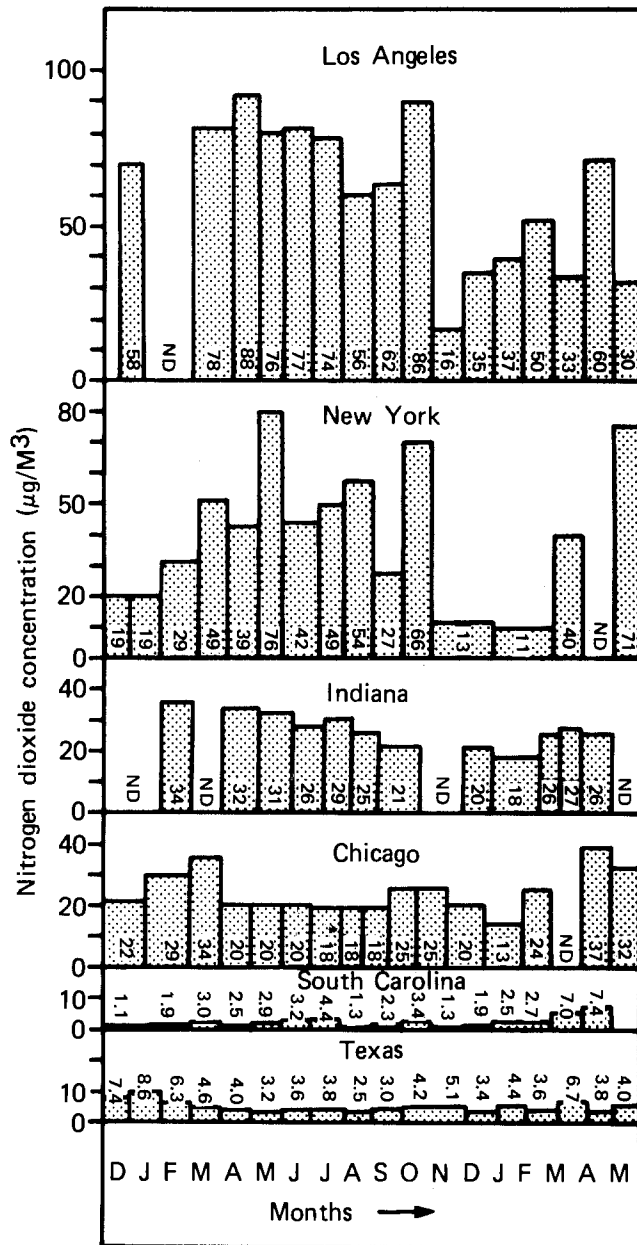


Fig. 10. Indoor concentration of nitrogen dioxide at 6 sites for 18 months.

µg/m³. These values are equal to or slightly greater than reported outdoor urban concentrations of 10 µg/m³ (51). Furthermore, no seasonal variations are apparent in the indoor data. Internal generation of ammonia is expected to be a significant source unlike most of the other pollutants. The air-conditioned industrial Texas site showed NH₃ concentrations at least an order of magnitude greater than the others, which is suspected to result from a reproduction system using anhydrous ammonia in an adjacent room.

Chlorine gases.—Chlorine gases, which include Cl₂ and HCl, accelerate the corrosion of nickel, cobalt, and silver, enhance pinhole corrosion of many materials, and degrade insulator surfaces. The critical role of chlorides in aqueous electrochemical decay of metals is well recognized. The anthropogenic nonindustrial sources of the chlorine gases are incineration of synthetics, burning of fossil fuels, water treatment, and insecticides. Interaction of NO₂ with chloride containing salts from ocean spray is thought to be an important natural source of HCl (52).

The indoor measurements are shown in Fig. 13. The geometric mean ranged from 0.08 to 0.29 µg/m³. No

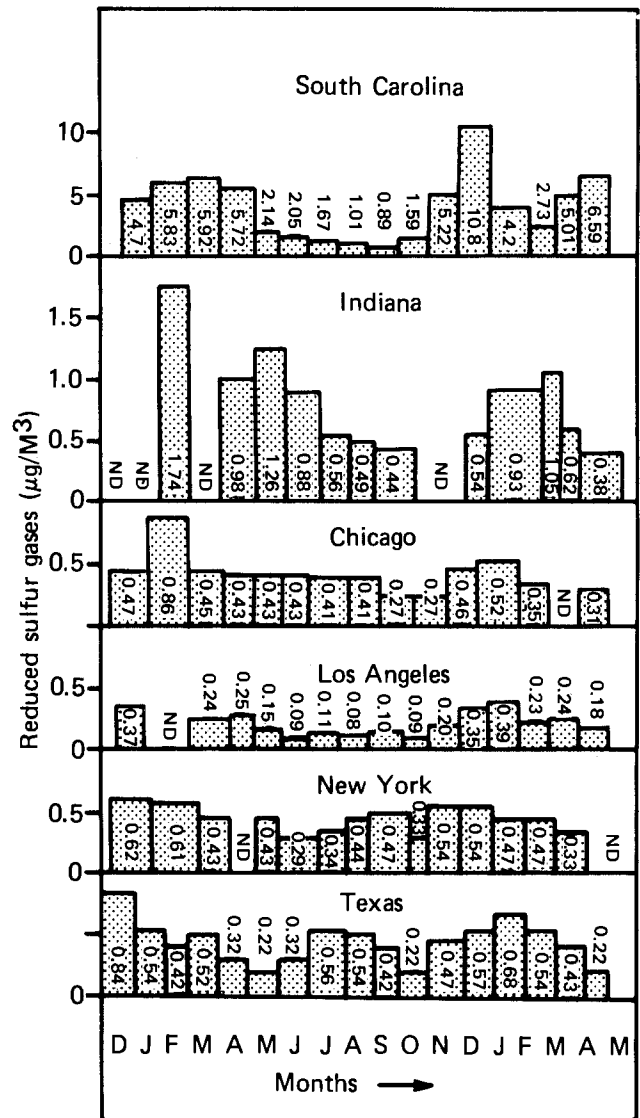


Fig. 11. Indoor concentration of reduced sulfur gases at 6 sites for 18 months.

significant seasonal variation was observed. These indoor values are 20% or less of the values estimated for outdoor urban areas, 1.52 µg/m³ (53, 54). Indoor chlorine gas concentration correlated reasonably well with nickel corrosion.

Airborne dust.—Airborne dust can settle on materials which may increase the amount of local water as well as result in mechanical failures. Particles come from industrial sources, fuel combustion, fires, and natural processes. The median outdoor level is 61 µg/m³ from 3760 sites (55). The dust levels in our study show a site mean between 3-33 µg/m³, Fig. 14. The mean site average is 16 µg/m³ which is 26% of the outdoor mean. No significant seasonal variation was observed for the indoor data. It seems obvious that the indoor dust level is greatly influenced by the quality of the air conditioning and air handling systems.

Pollutant summary.—The measured indoor pollutant mean site concentrations are generally less than mean outdoor values in the United States except for NH₃ and reduced sulfur. Table XIII summarizes the mean indoor and outdoor levels as well as the ratio of indoor to outdoor concentrations.

Conclusions

The indoor corrosion rates of Cu, Ag, Ni, Co, and Fe are lognormally distributed with respect to the sam-

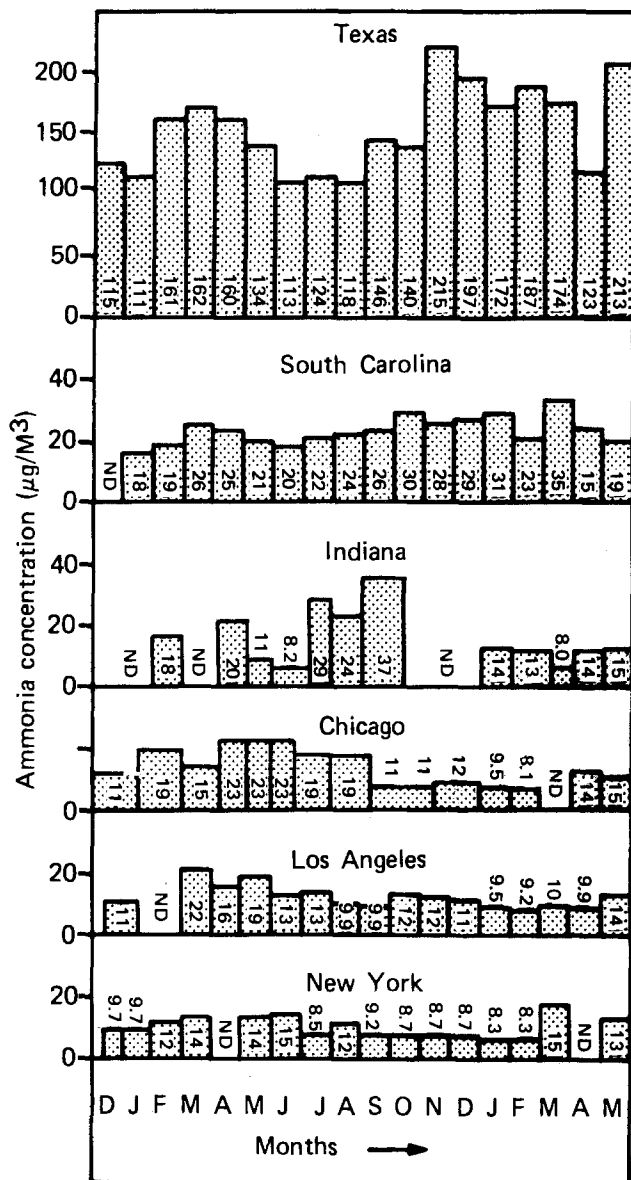


Fig. 12. Indoor concentration of ammonia at 6 sites for 18 months

ple population in this study. The rates are significantly less than outdoor values except for silver. The corrosion products on all of these metals are complex hydroxides, carbonates, sulfates or sulfides, nitrates, and chlorides. Indoor pollutant concentrations of reduced sulfur and chlorine gases are reasonable indicators of

Table XIII. Comparison of indoor and outdoor pollutant concentrations ($\mu\text{g}/\text{m}^3$)

Pollutant	Indoor* (Ci)	Outdoor** (Co)	$\frac{C_i}{C_o} \times 100$ (%)
SO ₂	12.2	17.6	69
NO ₂	26.0	43.5	60
NH ₃	14.9	10.0	149
Reduced sulfur	0.48	0.48***	100
Chlorine gases	0.2	1.5	13
Airborne dust	16.0	61.0	26

* Average of site means.
 ** See text for references and discussion.
 *** This number is based upon two California sites where indoor and outdoor levels are approximately equivalent.

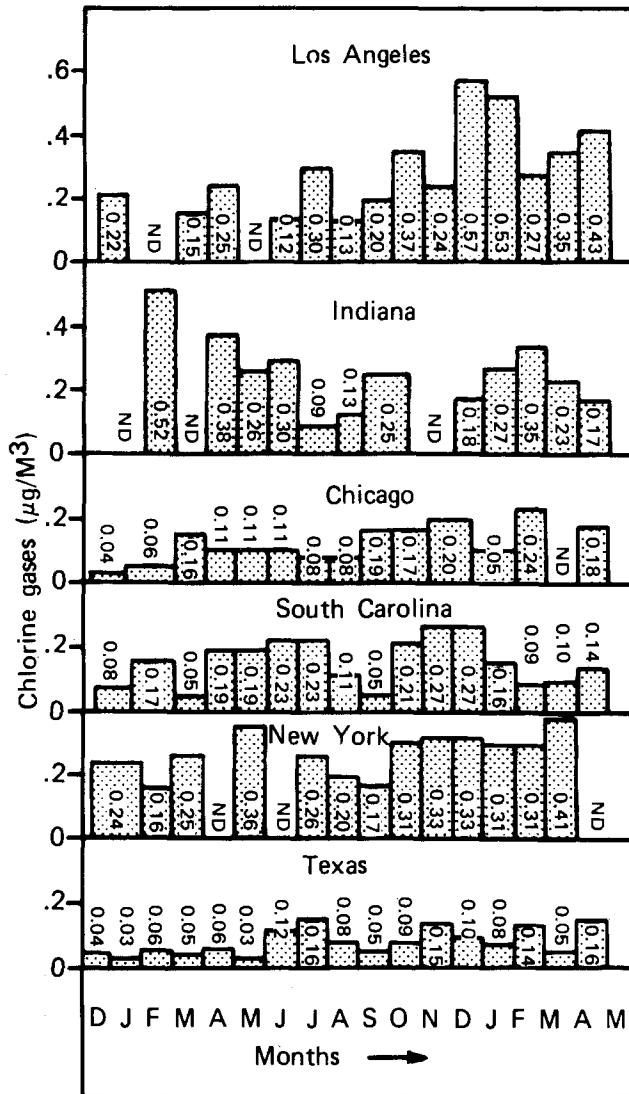


Fig. 13. Indoor concentration of chlorine gases at 6 sites for 18 months.

the atmospheric corrosive severity toward Cu/Ag and Ni, respectively. The indoor pollutant levels, except for NH₃, and possibly reduced sulfur gases, are less than mean outdoor levels. The marked reduction in indoor metallic corrosion must be accounted for by both a reduction in high humidity occurrences and a reduction in pollutant level. The fact that silver corrosion is about the same indoors and outdoors is accounted for by the similarity of reduced sulfur gas levels and the lack of a corrosion rate dependence on relative humidity.

Acknowledgments

We thank R. Tremoureux and I. Rodrigues for the field sample analysis, W. McChesney for the XPS measurements, F. Wagner for the field site logistics, and Dr. H. Andersen for his continued support.

Manuscript submitted Aug. 23, 1979; revised manuscript received Nov. 8, 1979.

Any discussion of this paper will appear in a Discussion Section to be published in the December 1980 JOURNAL. All discussions for the December 1980 Discussion Section should be submitted by Aug. 1, 1980.

Publication costs of this article were assisted by IBM Corporation.

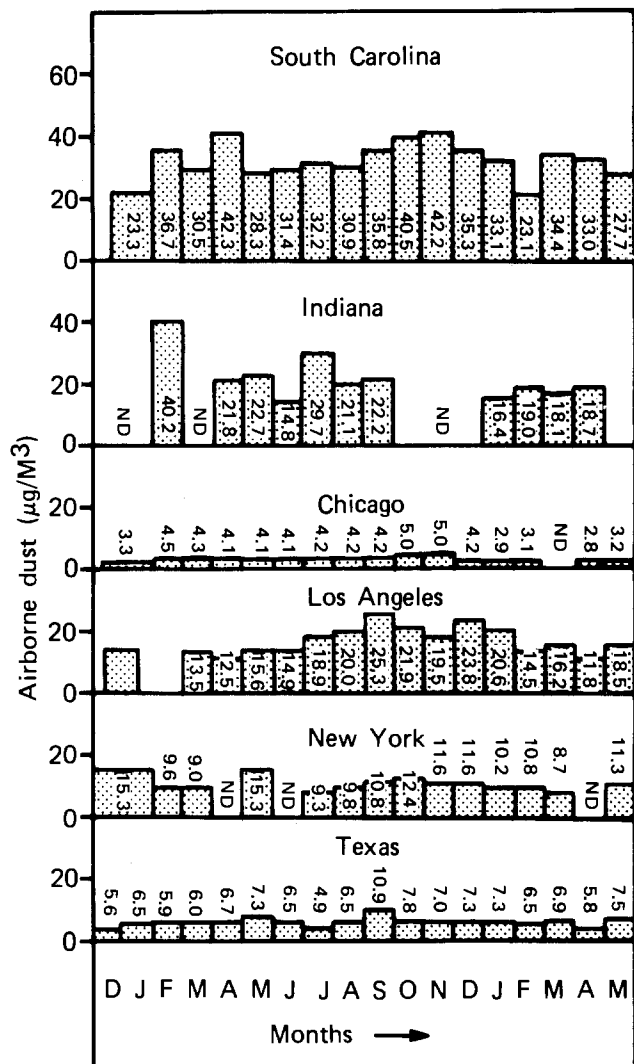


Fig. 14. Indoor concentration of airborne dust at 6 sites for 18 months.

REFERENCES

- J. O'M. Bockris and A. K. N. Reddy, "Modern Electrochemistry," Vol. 1, pp. 13-19, Plenum Press, New York (1970).
- I. L. Rozenfeld, "Atmospheric Corrosion of Metals," National Association of Corrosion Engineers, Houston, Texas (1972).
- S. K. Coburn, Editor, *Am. Soc. Test. Mater. Spec. Tech. Publ.* 646, (1978).
- P. J. Sereda, *ibid.*, 558, 7-22 (1974).
- P. J. Sereda, *Ind. Eng. Chem.*, 52, 157 (1960).
- F. H. Haynie and J. B. Upham, *Am. Soc. Test. Mater. Spec. Tech. Publ.* 558, 33-43 (1974).
- F. H. Shair and K. L. Heitner, *Environ. Sci. Technol.*, 8, 444 (1974).
- R. H. Saberskey, D. A. Sinema, and F. H. Shair, *ibid.*, 7, 347 (1973).
- F. B. Benson, J. S. Henderson, and D. E. Caldwell, "Indoor-Outdoor Air Pollution Relationships: A Literature Review," **EDA-NERC 27709** (1972).
- W. E. Campbell and U. B. Thomas, in "Holm Conference Proceedings," pp. 233-265 (1968).
- K. Seigbahn, C. Nordling, and A. Fahlman, "Electron Spectroscopy for Chemical Analysis," **AFML-TR-189** (1968).
- J. C. Tracy, in "Electron Emission Spectroscopy," W. Dekeyser, Editor, pp. 372-395, D. Reidel Publishing Co., Dordrecht, Holland (1973).
- C. D. Wagner, *Anal. Chem.*, 44, 1050 (1972).
- P. W. Palmberg, L. E. Davis, N. C. MacDonald, G. E. Riach, and R. E. Weber, "Handbook of Auger Electron Spectroscopy," Physical Electronics Ind. Inc., Eden Prairie, Minnesota (1976).
- "Weather Measure Corporation Manual for H311 Hygrothermograph," Sacramento, California (1961).
- C. Lipson and N. Sheth, "Statistical Design and

- Analysis of Engineering Experiments," p. 29, McGraw-Hill, New York (1973).
- S. D. Sharma, *This Journal*, 125, 2005 (1978).
- H. Guttman and P. J. Sereda, *Am. Soc. Test. Mater. Spec. Tech. Publ.* 435, 326-359 (1968).
- A. W. Tracy, *ibid.*, 175, 67 (1955).
- W. Wiederhold, *Werkst. Korros.*, 15, 633 (1964).
- K. S. Rajagopalan, M. Sundaram, and P. L. Annamalai, *Corrosion*, 15 (1959).
- D. Knotkova-Cermakova, B. Bosek, and J. Vlckova, *Am. Soc. Test. Mater. Spec. Tech. Publ.* 558, 52-72 (1974).
- R. S. Herman and A. P. Castillo, *ibid.* 558, 82-96 (1974).
- H. Leidheiser, "The Corrosion of Copper, Tin, and Their Alloys," John Wiley and Sons, Inc., New York (1974).
- W. H. J. Vernon, *Trans. Faraday Soc.*, 23, 113 (1921); 23, 162 (1927); 27, 264 (1931).
- W. H. J. Vernon, *ibid.*, 29, 35 (1933); 31, 1668 (1935).
- D. W. Rice, P. B. P. Phipps, P. Peterson, and B. Rigby, To be published.
- C. Ilscher-Gensch and C. Wagner, *This Journal*, 105, 198, 635 (1958).
- S. Mrowec, in "High Temperature Metallic Corrosion of Sulfur and Its Compounds," Z. A. Foroulis, Editor, pp. 55-109, The Electrochemical Society Softbound Proceedings Series, Princeton, N.J. (1970).
- S. Miner, NTIS Document PB 188-068 (1969).
- F. Mansfield, Regional Air Pollution Study, AMC 7010, 112 AR, p. 32 (May, 1977).
- P. M. Aziz and H. P. Godard, *Corrosion*, 529 (1959).
- H. H. Uhlig, "The Corrosion Handbook," p. 266, John Wiley & Sons, Inc., New York (1948).
- D. W. Rice, P. B. P. Phipps, and R. Tremoureux, *This Journal*, 127, 534 (1980).
- J. C. Hudson, *Trans. Faraday Soc.*, 25, 177 (1929).
- U. Frank, *Sb. Korroziya Metallov, I. M. Goskhimizdat*, 254 (1952).
- G. Tamman and W. Koster, *Z. Anorg. Chem.*, 123, 196 (1922).
- D. W. Rice, P. B. P. Phipps, and R. Tremoureux, *This Journal*, 126, 1459 (1979).
- D. Knotkova-Cermakova, B. Bosek, and J. Vlckova, *Am. Soc. Test. Mater. Spec. Tech. Publ.* 558, 60-61 (1974).
- R. Franks, *Trans. Am. Soc. Met.*, 35, 616 (1945).
- H. Copson, *Corrosion*, 15, 533t (1959).
- J. G. Wilson, *Proc. R. Soc. London Ser. A*, 300, 215-221 (1968).
- City of New York, Dept. of Air Resources, Bureau of Technical Services, *Data Report Aerometric Network-Calendar Year 1973* (1974).
- Environmental Protection Agency, "Air Quality Data, 1975 Statistics," EPA-450-2-77-002, 109 (May 1977).
- ibid.*, p. 143.
- ibid.*, p. 155.
- J. Gerhard and F. H. Haynie, Environmental Protection Agency, NTIS Document PB238-290 (1974).
- R. J. Breeding, J. P. Lodge, J. B. Pate, D. C. Sheesley, H. B. Klonis, B. Fogle, J. A. Anderson, T. R. Englert, P. L. Haagensen, R. B. McBeth, A. L. Morris, R. Pogue, and A. F. Wartburg, *J. Geophys. Res.*, 78, 7057 (1971).
- T. E. Graedel, B. Kleiner, and C. C. Patterson, *ibid.*, 79, 4467 (1974).
- T. E. Graedel and N. Schwartz, *Mater. Perform.*, 17 (August 1977).
- J. C. Mollen and M. J. Trzeciak, "Electrical Contacts-1070," p. 37, ITT Research Institute, Chicago (1970).
- R. C. Robbins, R. D. Cadle, and D. L. Eckhardt, *J. Meteorol.*, 16, 53 (1959); C. S. Martins, J. J. Wesolowski, R. C. Harris, and R. Kafir, *J. Geophys. Res.*, 78, 8778 (1973).
- R. A. Duce, *J. Geophys. Res.*, 74, 4597 (1969).
- M. Ackerman, D. Frimout, A. Girard, M. Gottignies, and C. Muller, *Geophys. Res. Lett.*, 3, 81 (1976).
- Environmental Protection Agency, "Air Quality Data, 1973, Annual Statistics," EPA 450/2-74-015, Research Triangle Park, N.C. (1974).

Steam Oxidation of Fe-32% Ni-23% Cr Alloys with Manganese and Carbon

H. F. Bittner,^{*1} J. T. Bell, and J. F. Land

Oak Ridge National Laboratory, Oak Ridge, Tennessee 37830

ABSTRACT

Effects of manganese and carbon on oxidation properties of simulated Incoloy 800 were determined. Iron-base alloys containing 32% nickel and 23% chromium were prepared with 0, 1, or 2% manganese and residual (0.002%) or 0.1% carbon. Samples were exposed at 660°C to 0.94 atm steam for 2, 48, 528 hr, and resulting oxides were examined by optical microscopy and analyzed using Secondary Ion Mass Spectrometry (SIMS) as well as x-ray diffraction techniques. Carbon additions in all cases led to thicker oxides with higher $\alpha\text{Fe}_2\text{O}_3$ to Cr_2O_3 ratios. Manganese was incorporated into the spinel phase, forming $\text{Mn}(\text{Fe}_{1-x}\text{Cr}_x)_2\text{O}_4$. Manganese additions to alloys containing carbon tended to mitigate the effects of carbon additions, leading to thinner oxides with lower $\alpha\text{Fe}_2\text{O}_3$ to Cr_2O_3 ratios.

This work is part of an effort to characterize high temperature oxidation properties of structural materials important to energy systems. Within this study, *in situ* formed oxide coatings on steam generator materials have been proposed as tritium permeation barriers, and tritium permeation through oxide coatings on Incoloy 800 has been measured (1). These *in situ* formed oxides have been chemically analyzed (2), and it was found that manganese, which comprised less than 1% of the bulk Incoloy 800, became greatly enriched in the oxide, to more than 80% in one case. It also became apparent that carbon played an important role in determining the nature of the oxidation products. In order to understand the effects of these two constituents on the oxidation properties of Incoloy 800, iron-chromium-nickel alloys with various amounts of manganese and carbon were prepared with concentrations approximating those of Incoloy 800 (commercial Incoloy 800 contains, in weight percent, 30.0-35.0 Ni, 19.0-23.0 Cr, 37.0-47.0 Fe, 1.5 max Mn, 0.1 max C, 1.0 max Si, 0.15-0.60 Al, 0.15-0.60 Ti). Tab samples of these alloys were oxidized under the same conditions employed in the earlier studies involving Incoloy 800 (1, 2), and resulting oxides were analyzed using SIMS, x-ray diffraction, and optical microscopy.

Effects of manganese on the oxidation properties of several different alloys have been investigated by other researchers. Caplan *et al.* (3) studied the effect of 1% manganese addition to Fe-26Cr, exposing the alloys to 1 atm pure oxygen at 870°C for 98 hr or 1090°C for 20 hr. Analysis of resulting oxides showed that manganese addition promoted formation of a spinel structure, probably MnCr_2O_4 . Under the experimental conditions of that study, the alloy containing manganese showed a greater weight gain. Francis (4) studied 20Cr-25Ni-Nb stabilized steels with and without 0.7% manganese. Oxidation was performed in carbon dioxide at 750° or 850°C for 100 hr. At the higher temperature, manganese promoted formation of the spinel $\text{Mn}_2\text{Fe}_{3-x}\text{O}_4$. At both temperatures, manganese led to a greater weight gain, and decreased the amount of Fe_2O_3 in the surface film. Douglas and Armijo (5) studied the effect of manganese addition to Ni-20 Cr alloys. Oxidation conditions were 0.21 atm oxygen at 600°, 1100°, and 1200°C for times up to 3 weeks. Three percent addition of manganese promoted formation of an inner layer of MnCr_2O_4 , whereas 1% manganese addition did not. It was concluded that

3% manganese resulted in a reduced oxidation rate; however, as these authors point out, if spalling occurred at short oxidation times, this conclusion based on weight gain measurements might not be valid.

The effect of carbon on oxidation properties of stainless steels has been recognized for some time; Bain *et al.* (6) stated that austenitic stainless steels, after exposure to moderately elevated temperatures, became susceptible to intergranular corrosion. These authors developed a phenomenological model which attributed this sensitization to formation of chromium carbides at grain boundaries with concomitant depletion of chromium in adjacent regions. A detailed review of research performed concerning the role of carbon in sensitization of stainless steels has appeared (7). In that review, the chromium depletion theory is supported as the most widely accepted model to account for intergranular corrosion as a result of sensitization. Factors promoting sensitization are increased carbon content, decreased chromium content, and heat-treatments high enough to promote carbide precipitation at grain boundaries, but sufficiently low so as not to allow chromium diffusion into the chromium depleted regions. Carbon-gettering materials are added to some steels to preferentially tie up the carbon, such as titanium in the case of Incoloy 800, and thereby minimize sensitization. The temperature range for sensitization of Incoloy 800 is 540°-760°C (8). Generally, sensitization studies have been associated with passivation *vs.* nonpassivation; to our knowledge no studies have been carried out associated with effects of carbon on the chemical species of oxide produced.

Comparison of oxidation studies must be done carefully because the number of variable parameters is large, and includes oxidizing atmosphere, pressure, temperature, time, alloy composition, and sample pretreatment. Our previous work (2) has shown that sample pretreatment can be especially important to oxidation characteristics. For this reason, fabrication of the alloys was carried out under strictly prescribed conditions, based on findings of our earlier studies. Other parameters involved in the oxidation process were comparable to those in our previous work (1, 2).

Experimental

Samples were prepared from high purity materials using induction melting techniques. Ingots were subsequently hot-rolled at 1100°C to 0.403 cm, then cold-rolled to 0.315 ± 0.008 cm. The materials were then stress relieved at 900°C for 30 min. Coupons approximately 1.5×0.5 cm were cut from the sheets, degreased, and then electropolished. Samples were tested for susceptibility to intergranular corrosion using the

* Electrochemical Society Active Member.

¹ Present address: The Aerospace Corporation, P.O. Box 52957, Los Angeles, California 90009.

Key words: metals, surfaces, corrosion, diffraction.

Table I. Compositions of alloys

Sample number	Metal composition (weight percent)				Carbon content (weight ppm)
	Fe	Cr	Ni	Mn	
1	45.2	22.6	31.9	—	986
2	45.1	22.6	32.2	—	17
3	45.9	22.6	31.4	1.04	916
4	44.8	22.4	31.0	1.05	17
5	46.1	21.3	31.4	2.17	948
6	44.8	21.4	30.8	2.15	16

acid ferric sulfate test (ASTM Designation G28-71). Samples which contained added carbon sustained a significant weight loss, indicating sensitization, while those samples which contained only residual carbon showed virtually no weight loss. Therefore, without consideration for the effects of manganese, it was expected that samples containing added carbon would undergo a greater degree of oxidation due to intergranular corrosion.

Coupons were oxidized for 2, 48, and 528 hr at 660°C in 0.94 atm steam carried by an argon-hydrogen mixture yielding a hydrogen to water ratio of 2.2×10^{-5} , simulating the environment of previous tritium permeation experiments (1). Intact oxide coatings on samples exposed 528 hr were analyzed by x-ray diffraction techniques. Cross sections of all samples were mounted in epoxy, polished, and then analyzed by secondary ion mass spectrometry (SIMS) and optical microscopy. Relative amounts of phases identified by x-ray diffraction were calculated by integrating the area under the most intense reflection for each phase. Lattice parameters were obtained by standard techniques.

Results and Discussion

Samples oxidized for 528 hr were characterized in some detail, using SIMS, x-ray diffraction, and optical microscopy. The bulk of this section will be devoted to a discussion of these results. Samples oxidized for 2 and 48 hr were analyzed in a more cursory fashion with SIMS and optical microscopy, and will be briefly discussed towards the end of this section; results from these samples help elucidate the mechanism for formation of the oxides.

Compositions of alloys based on chemical analyses are given in Table I. X-ray diffraction results are presented in Table II for the oxides on samples oxidized 528 hr, along with oxide thicknesses measured by optical microscopy. In general, oxides formed after 528 hr exposure were relatively uniform in thickness and adherent to the base metal, with the exception of sample 1. This sample, which contained 0.1% carbon and no manganese, had a thick oxide which showed evidence of spalling and was less uniform than oxides on other samples; the micrograph for the cross section of this sample is presented in Fig. 1(a). Micrographs for cross sections of sample 2, which contained no manganese and residual carbon, and sample 3, which contained 1% manganese and 0.1% carbon, are presented in Fig. 1(b) and (c), respectively.

The effect of carbon with no manganese was best seen by comparison of ion microprobe profiles for samples 1 and 2, exposed for 528 hr, containing 0.1% and residual carbon, respectively (see Fig. 2 and 3). The oxide on the sample with added carbon was considerably thicker (see Table II), and enriched in iron at the surface with an enrichment of chromium beneath the iron. SIMS results, Fig. 2, indicated a greater total amount of chromium than iron in the oxide, but x-ray diffraction results indicated a ratio of $\alpha\text{Fe}_2\text{O}_3$ to Cr_2O_3 of 1.3; therefore, the bulk of the chromium must have been incorporated in the spinel phase. The lattice parameter measured for the spinel phase, $a_0 = 8.35\text{\AA}$, is in agreement with a stoichiometry $(\text{Ni}_{1-x}\text{Fe}_x)\text{Cr}_2\text{O}_4$, according to Yearian *et al.* (9). The nickel enrichment towards the surface of the oxide, Fig. 2, likely was in the form $(\text{Ni}_{1-x}\text{Fe}_x)\text{Fe}_2\text{O}_4$, which has a lattice parameter very similar to that of the $(\text{Ni}_{1-x}\text{Fe}_x)\text{Cr}_2\text{O}_4$ system (9), and could therefore not be distinguished by x-ray diffraction. The specimen with no added carbon, sample 2 shown in Fig. 3, had a much thinner oxide; the ratio of spinel phase to hexagonal phases ($\alpha\text{Fe}_2\text{O}_3$ and Cr_2O_3) was about the same; however, the ratio of $\alpha\text{Fe}_2\text{O}_3$ to Cr_2O_3 was about 0.5, much lower than the sample with 0.1% carbon. The lattice parameter for the spinel phase on the sample with residual carbon was only slightly smaller than the one for that phase on the sample with added carbon; therefore, the composition of this spinel phase also was expected to be $(\text{Ni}_{1-x}\text{Fe}_x)\text{Cr}_2\text{O}_4$. The major difference in these two samples, then, is that the sample with no added carbon had a much thinner oxide with a smaller $\alpha\text{Fe}_2\text{O}_3$ to Cr_2O_3 ratio.

The effect of manganese in the absence of added carbon was apparent from comparison of samples 2 and 4 oxidized for 528 hr containing 0 and 1% manganese, respectively. SIMS results for sample 2 are shown in Fig. 3, and indicate that the oxide is rich in chromium. SIMS results for sample 4, containing 1% manganese, showed that the oxide was rich in chromium and manganese. The oxide on this sample was approximately half as thick as that observed on sample 2 which contained no manganese; however, relative amounts of $\alpha\text{Fe}_2\text{O}_3$, Cr_2O_3 , and spinel phase were similar for each sample. Lattice parameters for the spinel phases were different; the larger lattice parameter for sample 4, $a_0 = 8.41\text{\AA}$, is consistent with a spinel containing manganese (10), and similar to that for MnCr_2O_4 , $a_0 = 8.426\text{\AA}$ (11). (Diffraction peaks for the spinel phase on samples which contained manganese were broader relative to reflections for spinels on samples without manganese. This indicated a strained structure or the presence of several spinel phases of similar lattice parameter.)

Effects of manganese were most apparent in comparison of samples 1 and 3, exposed for 528 hr, the former containing no manganese and the latter 1%, and both containing 0.1% added carbon; SIMS results are shown in Fig. 2 and 4, respectively. The oxide on the sample containing manganese was almost a factor of ten thinner, and was rich in chromium and manganese, whereas the oxide in the sample with no manganese

Table II. Compositions of untreated alloys and data for oxides of samples exposed for 528 hr to 0.94 atm steam at 660°C

Sample	Approximate manganese and carbon content of alloys (weight percent)		Average oxide thickness (in microns)	Relative intensities of diffraction peaks of oxide phases, normalized to 1.00			Average lattice parameter of spinel phase (in Å)
	Mn	C		Cr_2O_3	$\alpha\text{Fe}_2\text{O}_3$	Spinel	
1	0	0.1	11	0.14	0.19	0.67	8.35
2	0	0.0	2.5	0.25	0.14	0.61	8.34
3	1	0.1	1.4	0.11	0.11	0.78	8.46
4	1	0.0	1.3	0.19	0.12	0.69	8.41
5	2	0.1	2.1	0.07	0.08	0.85	8.44
6	2	0.0	1.4	0.08	0.11	0.81	8.42

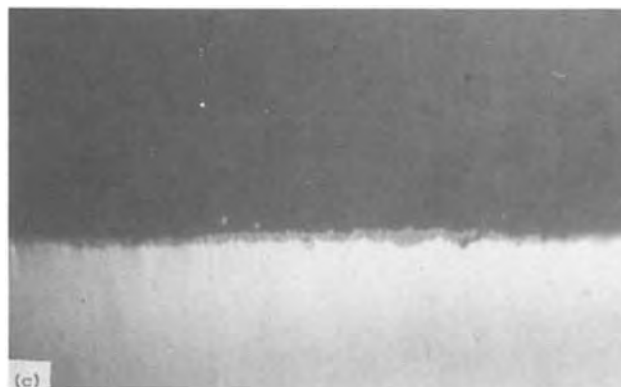
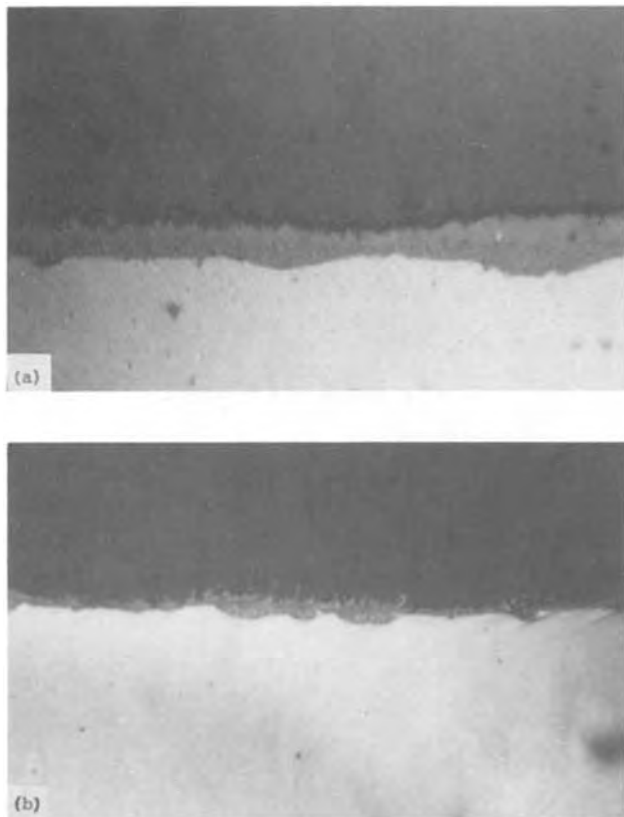


Fig. 1. Micrographs for cross sections of oxides (528 hr oxidation) on samples containing (a) 0.1% carbon, 0% manganese; (b) 0.0% carbon, 0% manganese; and (c) 0.1% carbon, 1% manganese. Magnification is 1000X.

was rich in iron at the surface. X-ray diffraction results, Table II, show that the sample containing manganese had a lower $\alpha\text{Fe}_2\text{O}_3$ to Cr_2O_3 ratio, and that the spinel phase comprised a greater percentage of the total oxide. The spinel lattice parameter for the sample containing manganese, $a_0 = 8.46\text{\AA}$, probably

corresponded to $\text{Mn}(\text{Fe}_{1-x}\text{Cr}_x)_2\text{O}_4$ (11), while the primary spinel phase on the sample with no manganese was $(\text{Ni}_{1-x}\text{Fe}_x)\text{Cr}_2\text{O}_4$, as discussed previously.

Results for the specimens containing 2% manganese, with 0.1 and 0.0% carbon (samples 5 and 6, respectively) oxidized for 528 hr, are not greatly different

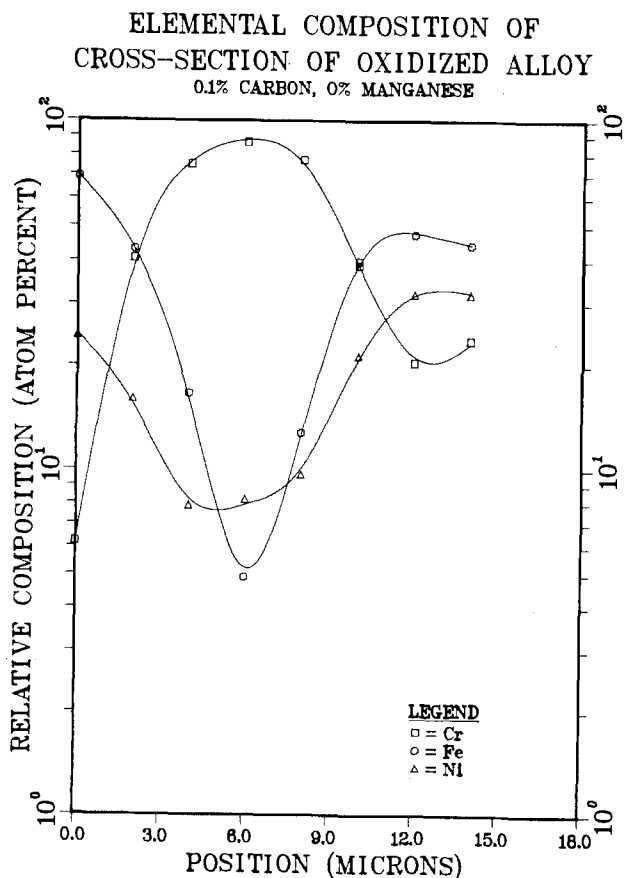


Fig. 2. Ion microprobe profile for sample 1, oxidized for 528 hr. Steam-oxide interface is at zero microns.

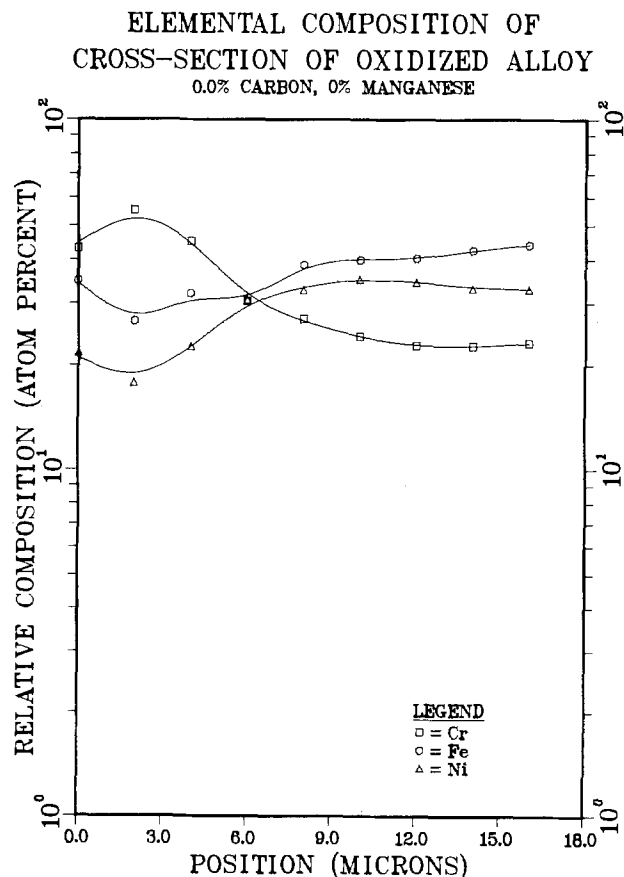


Fig. 3. Ion microprobe profile for sample 2, oxidized for 528 hr. Steam-oxide interface is at zero microns.

ELEMENTAL COMPOSITION OF
CROSS-SECTION OF OXIDIZED ALLOY
0.1% CARBON, 1% MANGANESE

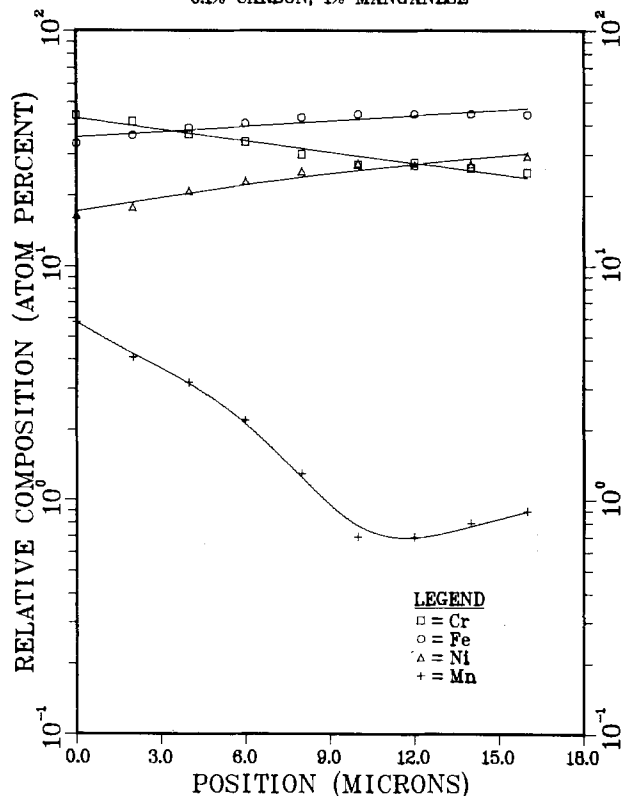


Fig. 4. Ion microprobe profile for sample 3, oxidized for 528 hr. Steam-oxide interface is at zero microns.

than those for specimens containing 1% manganese, samples 3 and 4. The higher manganese content led to a somewhat larger percentage of spinel phase in the oxide and to a slightly larger $\alpha\text{Fe}_2\text{O}_3$ to Cr_2O_3 ratio. The oxide thickness was virtually identical for specimens containing 1 and 2% manganese and no added carbon, samples 4 and 6. However, in the presence of added carbon, 2% manganese led to a somewhat thicker and less uniform oxide than the sample containing 1% manganese. The difference in thickness was not large, 2.1 vs. 1.4 microns, particularly in comparison with the 11 microns thick oxide on the sample containing added carbon and no manganese. It may be that approximately 1% manganese substitution is the optimum content for producing a thin protective oxide coating. It is noted here that Caplan *et al.* (3) and Francis (4) found greater weight gains after 100 hr oxidation for samples containing manganese. However, spalling might have occurred with longer oxidation times, as was observed in the present work, discussed below.

Ion microprobe analyses were performed for samples exposed 2 and 48 hr; results are summarized here, and give an indication of the mechanism for formation of the oxides after 528 hr exposure. Sample 1, containing 0.1% carbon and no manganese, formed a very thick, scaly iron oxide at the surface for all exposure times studied. Regions of chromium-rich oxide, which formed beneath the iron oxide layer, grew with longer exposure times; chromium was not observed at the surface of the oxide. Sample 2, which contained no added carbon or manganese, showed regions of chromium oxide at the surface interspersed with regions of iron oxide after 2 hr oxidation; further exposure resulted in a more uniform oxide comprised primarily of chromium. Apparently the iron oxide, which formed initially, spalled with further oxidation; this characteristic was found for other samples. The general trend

was that those samples which contained carbon required a longer exposure time to effect formation of a uniform chromium oxide layer, with concomitant spalling of the outer iron oxide; manganese showed the opposite effect, tending to promote formation of the uniform chromium oxide layer at the surface. The two extremes are sample 1, containing no manganese and 0.1% carbon, which never formed a chromium oxide layer at the surface, and sample 6, containing 2% manganese and only residual carbon, which formed a nearly complete chromium oxide layer after 48 hr. This mechanism for formation of a chromium oxide layer, via initial iron oxide formation which subsequently spalls, was also found for commercial Incoloy 800 in our earlier work (2).

These results clearly indicate that carbon stimulates a greater degree of oxidation after 528 hr steam exposure, with the oxide containing a large amount of iron. This may be due to formation of chromium carbide precipitates along grain boundaries, which could deplete chromium in these regions and inhibit formation of a protective Cr_2O_3 layer (7). The greater iron content of the oxides on samples containing added carbon would be consistent with chromium depletion at the grain boundaries. Manganese substitution, however, seemingly reversed the effects of added carbon. The reasons for this are not clear; however, Glen (12) reported that manganese reduced the diffusion of carbon in carbon steel, and Austin (13) found that manganese in carbon steel caused a re-resolution of iron carbide and subsequent precipitation of manganese carbide. It is unlikely, though, that manganese would cause a re-resolution of chromium carbide, since the latter is more stable (14). From the present study it is apparent that manganese subsequently led to formation of a manganese-containing spinel, in agreement with the findings of Caplan *et al.* (6); the formation of this phase may account for the different oxidation characteristics of carbon-containing samples with and without manganese substitution.

Summary

The following observations have been made regarding the 660°C steam oxidation for 528 hr of Fe-32 Ni-23 Cr alloys with manganese substitutions and carbon additions:

1. In the absence of manganese, addition of 0.1% carbon led to a much thicker oxide with a higher $\alpha\text{Fe}_2\text{O}_3$ to Cr_2O_3 ratio.
2. In the absence of added carbon, substitution of 1% manganese led to a somewhat thinner oxide, but did not greatly change the $\alpha\text{Fe}_2\text{O}_3$ to Cr_2O_3 ratio.
3. For samples containing 0.1% carbon, substitution of 1% manganese led to an oxide one-tenth the thickness with a lower $\alpha\text{Fe}_2\text{O}_3$ to Cr_2O_3 ratio.
4. Higher manganese substitutions led to a greater percentage of spinel phase in the oxides.
5. In the absence of manganese, the predominant spinel phase was probably $(\text{Ni}_{1-x}\text{Fe}_x)\text{Cr}_2\text{O}_4$, whereas for samples containing manganese, the spinel lattice parameters were in close agreement with $\text{Mn}(\text{Fe}_{1-x}\text{Cr}_x)_2\text{O}_4$.

Acknowledgments

The assistance of O. B. Cavin, who obtained the x-ray diffraction diagrams, R. E. Eby, who performed the SIMS analyses, and R. L. Heestand, who fabricated the materials, is gratefully acknowledged. This research was sponsored by the Division of Materials Sciences, U.S. Department of Energy under Contract W-7405-eng-26 with the Union Carbide Corporation.

Manuscript received July 30, 1979. This was Paper 234 presented at the Los Angeles, California, Meeting of the Society, Oct. 14-19, 1979.

Any discussion of this paper will appear in a Discussion Section to be published in the December 1980

JOURNAL. All discussions for the December 1980 Discussion Section should be submitted by Aug. 1, 1980.

Publication costs of this article were assisted by Oak Ridge National Laboratory.

REFERENCES

1. J. T. Bell, J. D. Redman, H. F. Bittner, and W. H. Christie, in "Proceedings of the Third Topical Meeting on the Technology of Controlled Nuclear Fusion," Vol. 2, p. 757, Sante Fe, New Mexico, May 1978.
2. H. F. Bittner, J. T. Bell, J. D. Redman, and W. H. Christie, Abstract 49, p. 130, The Electrochemical Society Extended Abstracts, Boston, Massachusetts, May 6-11, 1979.
3. D. Caplan, P. E. Beaubien, and M. Cohen, *Trans. Metall. Soc. AIME*, **233**, 766 (1965).
4. J. M. Francis, *J. Iron Steel Inst.*, **204**, 910 (1966).
5. D. L. Douglas and J. S. Armijo, *Oxid. Met.*, **2**, 207 (1970).
6. E. C. Bain, R. H. Aborn, and J. J. B. Rutherford, *Trans. Am. Soc. Steel Treat.*, **21**, 481 (1933).
7. R. L. Cowan, II and C. S. Tedman, Jr., "Advances in Corrosion Science and Technology," Vol. 3, pp. 293-400, Plenum Press, New York (1973).
8. "Incoloy Alloy 800," Huntington Alloy Products Division, The International Nickel Company, Inc., Huntington, West Virginia 25720.
9. H. J. Yearian, H. E. Boren, Jr., and R. E. Warr, *Corrosion (Houston)*, **12**, 45 (1956).
10. H. J. Yearian, E. C. Randell, and T. A. Longo, *ibid.*, **12**, 55 (1956).
11. A. J. C. Wilson, Editor, "Structure Reports," Vol. 18, p. 454, N.V.A. Oosthoek's Uitgevers MIJ, Utrecht (1961).
12. J. Glen, *J. Iron Steel Inst.*, **186**, 21 (1957).
13. J. B. Austin, *Trans. Am. Soc. Met.*, **38**, 28 (1947).
14. S. R. Shatynski, *Oxid. Met.*, **13**, 105 (1979).

A Microstructure Study of Corrosion in Ag-Cu Flex Leads

K. Kumar

The Charles Stark Draper Laboratory, Incorporated, Cambridge, Massachusetts 02139

ABSTRACT

85 Ag-15 Cu flex leads, used as current-carrying conductors in inertial instruments, corrode in a BTFE (bromotrifluoroethylene) fluid environment. The corrosion scale has a nodular appearance similar to that of the Ag-rich particles which are present in the flex lead matrix. The Ag-rich phase is the predominant phase in the material and exists as discrete particles surrounded by the Cu-rich phase located at what appears as a quasi-continuous network of grain boundaries. Corrosion proceeds along the Cu-rich phase resulting in separation of the Ag-rich metallic particles from the matrix and incorporation into the corrosion debris. After buildup of a certain thickness, the corrosion layer detaches from the flex lead (contaminating the fluid) and exposes fresh metal surface for more attack. When the chemical etching behavior of a good lead (one that showed negligible corrosion) was compared to that of a poor lead (where substantial corrosion effects were observed), the good lead was found to etch more slowly, by at least a factor of six. The differences in etching behavior have been attributed mainly to differences in prior thermal history, and partly to possible local variations in overall composition. The observed corrosion has been explained by mechanisms involving chemical reaction between the metallic phases and the fluid, and those involving the formation of an electrochemical corrosion cell.

Current-carrying conductors (flex leads) are used in inertial instruments for transferring power from externally located sources to electromechanical assemblies contained in sealed metal containers which are floated in a fluid medium. Bromotrifluoroethylene (BTFE) fluid is commonly used for suspending the float in a buoyant state. The material selected for flex lead fabrication needs to be solderable (for easy installation and disassembly), have high resistance to deformation from cyclic mechanical loading (to retain its properties with small movements of the float), and have a high electrical conductivity (to reduce energy losses in the form of heat). All of these constraints severely limit the number of materials that can be considered for application.

85 Ag-15 Cu ribbons produced by alternating drawing and annealing processes¹ have been used as flex leads in a BTFE environment. Many of these flex leads have corroded with extended use. The extent of damage introduced has varied from negligible to severe, in some instances even resulting in failure in the current-carrying capability of the flex lead through fracture

occurring in the corrosion environment. In addition to the observed deterioration of the flex lead, degradation of fluid properties has also occurred from the chemical reactions that accompany the corrosion processes and from the contamination that is introduced when the corrosion scale separates from the flex lead. Since all of this affects instrument life and reliability, this study was initiated to develop a correspondence between the observed corrosion and the microstructure of the samples. It was hoped that such an approach would aid in the understanding of the causes of the observed failures. This paper reports on the results of these investigations.

Experimental

About 0.5 cm long, 0.0009 cm thick, and 0.025 cm wide 85 Ag-15 Cu ribbons (at different stages of corrosion) were mounted in a resin-containing cast and polished for metallographic examination using standard techniques. The samples were mounted such that the viewing direction was perpendicular to the direction of drawing. The lateral (thin) side of the sample was examined after appropriate chemical etching of the exposed polished surface. The etching solution consisted of 50 ml H₂O, 42 ml HCl, and 8 ml HNO₃. Etching was accomplished by immersing the samples into the

Key words: etch behavior, heat-treatment, phase separation.

¹ Manufactured by Sigmund Cohn Corporation, Mount Vernon, New York.

etching solution at room temperature. The bath was manually agitated during the entire etching procedure. The etched surfaces were photographed using optical and scanning electron microscopy. Chemical analysis was performed using the EDAX (energy dispersive analysis of x-rays) technique.

Results and Discussion

Figure 1 represents an as-polished view of a poor flex lead (one that showed substantial corrosion). The corrosion scale consisted of several submicron size, equidimensional, shiny, metallic-looking particles individually surrounded by a dull-gray exterior. The corrosion scale was about $2\ \mu\text{m}$ thick and appeared to extend fairly uniformly (over its surface) into the ribbon interior. When this sample was etched for 1 min to determine its bulk microstructure, small, submicron size, equidimensional, grain-like features (similar in appearance to the particles found in the corrosion scale) were observed. (See Fig. 2a). The contrast developed upon etching this sample was considered an indication of a two-phase microstructure which was expected for this composition from the binary Ag-Cu phase diagram (1).

The etching response of this poor lead was quite different from that observed for a good lead (one that had shown negligible corrosion). Figure 2b was obtained on the good lead after etching for 1 min. In contrast to the quick response to etching of the poor lead, the good lead showed a fairly featureless interior. Upon increasing the time of etching, however, the contrast was observed to improve and after 6 min of etching, the good lead appeared to assume a level of contrast similar to that observed in Fig. 2a for the poor lead (see Fig. 2c). This slow response to etching of the good lead was interpreted as resulting mainly from differences in second phase composition and distribution (because of differences in prior thermal history,) and from possible slight differences in overall chemical composition

(which could give rise to a somewhat lesser amount of the second phase, resulting in an apparently lower level of observed contrast). In any event, it was considered significant that the lead that etched more rapidly was also the one that corroded more severely than the lead that showed a slow response to the etching treatment.

The effects of thermal treatment on etching behavior were investigated by subjecting as-received samples, for different time, to temperatures of 590° and 950°K in hydrogen. Exposure at temperature was followed by rapid removal of the muffle from the furnace resulting in quick cooling of the samples. Subsequent studies were then directly related to the time and temperature of exposure without regard for effects resulting from slow cooling of the material. The heat-treated samples were mounted and polished, and examined for etching response. It was found that increased thermal exposure resulted in a decreased resistance to development of contrast. The micrographs in Fig. 3 show that even a 48-hr exposure to a reasonably low, 590°K , temperature resulted in an enhanced contrast (compared to the as-received material). This thermally activated, enhanced-contrast behavior must have resulted from separation and agglomeration of the second (Cu-rich) phase. The phase agglomeration process is more dramatically illustrated in Fig. 4 which was obtained on a sample that was exposed to 950°K for 24 hr. The Cu-rich phase, in this sample, appears as discrete second phase particles of about $2\ \mu\text{m}$ size, possibly representing a close-to-equilibrium microstructure. 950° and 590°K were selected for sample exposure mainly because the ribbons are subjected to these temperatures during manufacturing and subsequent processing stages. 950°K is used by the manufacturer for annealing (in between drawing operations) and 590°K is used for forming the ribbon into flex lead geometry by conforming the shape of the flex lead ribbon to the curved surface of a preselected metal mandrel. The lack of a

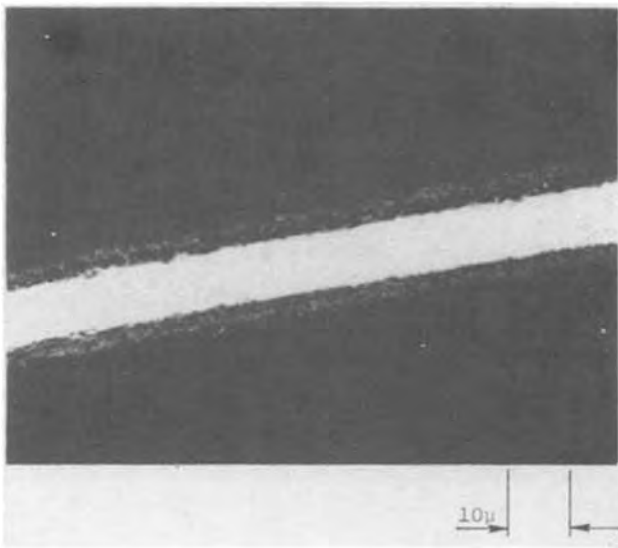


Fig. 1. Poor flex lead. As-polished. Corrosion scale contains nodular, metallic particles surrounded by dull gray exterior.

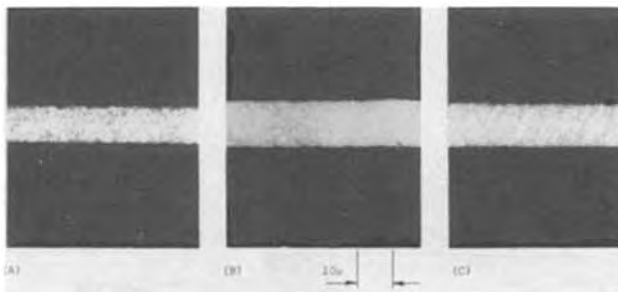


Fig. 2. Development of contrast with etching time: (a) poor lead, 1 min; (b) good lead, 1 min; (c) good lead, 6 min.

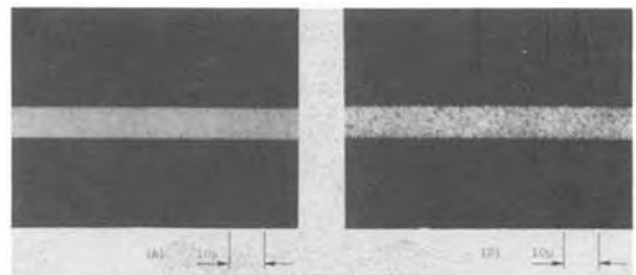


Fig. 3. Contrast development in (a) as-received, (b) 590°K , 48 hr treated Ag-Cu ribbons. 1 min etch time.

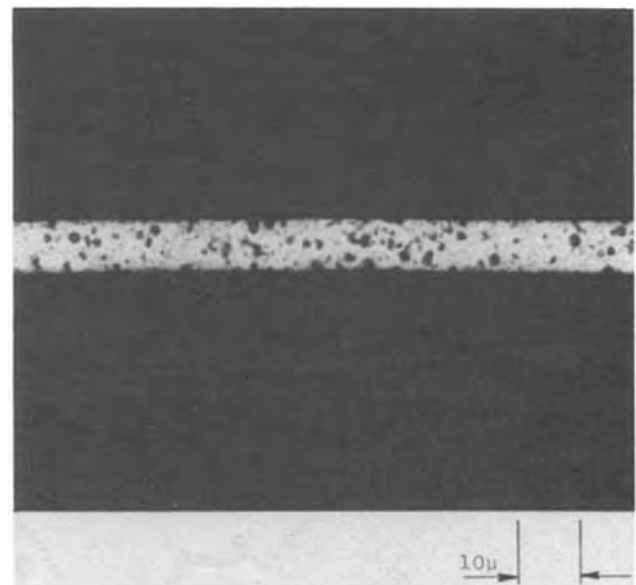


Fig. 4. Phase agglomeration from 950°K , 24 hr treatment

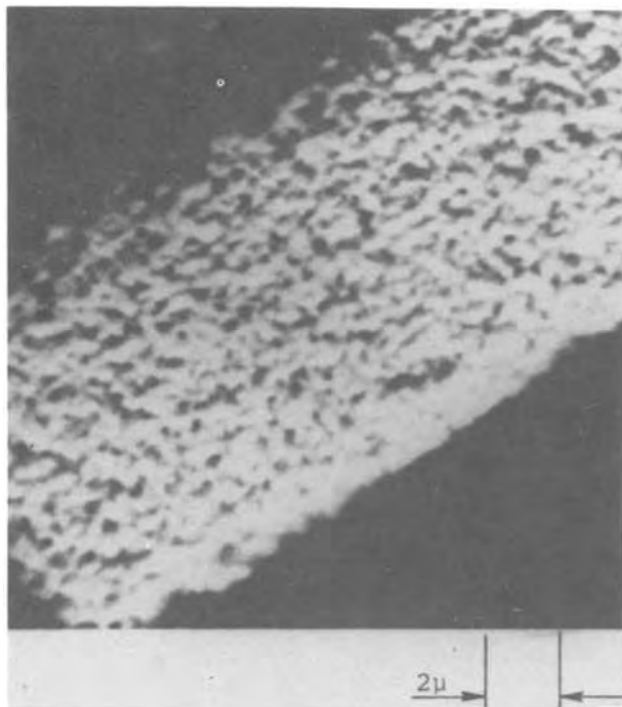


Fig. 5. SEM photograph of 1 min etch poor lead surface showing nodular features.

fibrous texture in the microstructure of these ribbons is attributed to the annealing treatment used by the manufacturer. It is evident that the length of exposure to 950°K during the annealing treatment used by the manufacturer must be considerably shorter than the 24 hr used in this study. This is consistent with the very fine segregation of the Cu-rich phase (at what appears as grain boundaries) present in the as-received material, as opposed to the large discrete Cu-rich particles observed in this study after a 24-hr exposure at 950°K.

The etched sample surfaces were examined in the scanning electron microscope. Nodular-shaped features shown in Fig. 5 were observed in both (the good and poor) flex lead samples. An EDAX analysis of the etched surface showed a deficiency of copper compared to the amount of copper observed for the bulk on the as-polished surface. The copper deficiency was more pronounced in the 1 min etch poor lead sample than in the 6 min etch good lead sample. This is consistent with the slower etching behavior of the good lead sample, and may well indicate that the Ag-rich phase in this sample contains more copper (and, therefore, the Cu-rich phase contains more silver) than in the poor lead sample. The difference in the response of these two samples, as indicated earlier, could then have resulted from the heat-treatment that these leads were subjected to before use in the BTFE fluid. Alternatively, as stated earlier, it could also be argued that the differences in the etching behavior of these samples may have resulted from differences in the relative amounts of the second (Cu-rich phase) present in the samples. But this fails to explain the higher amount of copper measured

in the Ag-rich phase of the 6 min etched good lead sample compared to the 1 min etched poor lead sample. In a two-phase alloy, such as this, the composition of the individual phases is determined solely by the heat-treatment that is employed. Changes in overall alloy composition will only affect the relative amounts of the two phases and not their individual compositions. It is, however, clearly possible that both the above mechanisms might have contributed, to some degree, to the differences in the etching behavior of these samples.

The EDAX scans obtained on these samples are shown in Fig. 6. Figure 6 also contains an EDAX scan obtained on the surface of an unattacked region of a flex lead and is, therefore, an indication of the overall composition of this material. These EDAX analyses clearly demonstrate that the chemical etching treatment resulted in preferential dissolution of the Cu-rich phase leaving the Ag-rich nodular phase exposed at the surface. The SEM micrograph of Fig. 5 also suggests that the dissolved (Cu-rich) phase must have been located all around the nodular Ag-rich particles at what appears as a quasi-continuous network of grain boundaries. The as-received microstructure of the ribbons, therefore, essentially consisted of the major, nodular Ag-rich phase dispersed in the minor, quasi-continuous Cu-rich matrix.

The nodular morphology of the Ag-rich particles is quite similar to that found for the corrosion scale. Figure 7 shows SEM photographs obtained on corroded flex lead samples where in one instance part of the scale had separated from the underlying alloy ribbon exposing fresh surface for more attack. This sample, shown in Fig. 7a, had also failed in its current-carrying ability through fracture occurring in the corrosion environment. The exact mode of fracture in these materials is not clear. However, since the flex leads are subjected to very low levels of stress at relatively low frequencies (with small movements of the float), it is possible that fracture resulted from corrosion fatigue of the material. The presence of corrosion products over the entire area of the fracture surface and the absence of the appearance of a region indicative of a shiny brittle-type fracture is attributed to the subsequent corrosion of the freshly formed surface in the fluid environment. Corrosion was found to have occurred at the tip of the flex lead, where fracture had probably taken place, as also on the newly exposed surface, which resulted from separation of the corrosion scale. Even more interesting, however, was the close similarity in appearance of the etched alloy surface (Fig. 5) and the corrosion scale surface (Fig. 7b), thereby clearly indicating a close correspondence between the observed corrosion and the microstructure of the sample.

Corrosion is mostly observed to take place along the Cu-rich phase. This contention is supported by the micrograph of Fig. 1 which shows that the corrosion scale consists of shiny, metallic-looking equidimensional particles surrounded by a dull-gray exterior. These particles exist through the entire thickness of the corrosion scale. Since the thickness of the corrosion layer is considerably more than the size of these particles, it is clear that the corrosion reaction proceeds

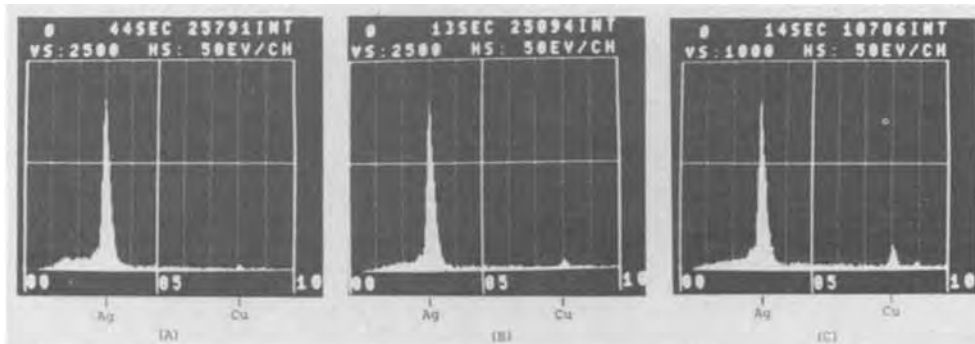


Fig. 6. EDAX scans on (a) poor lead, 1 min etch, (b) good lead, 6 min etch, and (c) unattacked flex lead samples.

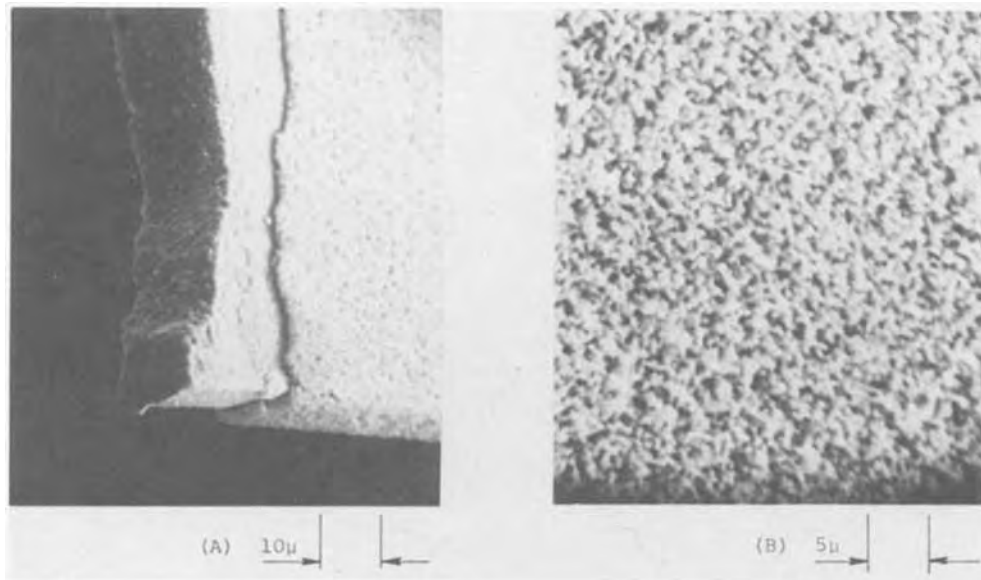


Fig. 7. SEM photographs of (a) corroded flex lead showing area where scale had separated and tip where fracture occurred, and (b) the corrosion scale.

much more rapidly through the (Cu-rich) layer that surrounds the particles than it does into any given (Ag-rich) particle. This results in separation of the Ag-rich particles from the alloy matrix and incorporation into the corrosion debris. The Ag-rich particles in the debris are separated from each other and from the alloy matrix by the dull-gray phase which is believed to be the product of the corrosion reaction. The corrosion scale, therefore, consists of small Ag-rich, single-phase, nodular particles surrounded by a corrosion product which contains bromine (as verified by an EDAX scan) in addition to Cu and Ag. The corrosion layer increases in thickness with continued exposure to the fluid. Detachment of the corrosion scale from the surface, as is found in some instances, is believed to result from an increased interfacial stress buildup with increasing corrosion layer thickness. The presence of bromine in the corrosion scale is a firm indication of fluid degradation. This degradation, in addition to fluid contamination resulting from detachment of the corrosion layer from the ribbon surface, leads to a gradual deterioration in fluid properties, and all of this severely affects satisfactory performance of the inertial instruments.

Chemical reactions between the alloy phases and the fluid, and galvanic-type corrosion of the less-noble, Cu-rich phase (accelerated in instances where air and moisture were trapped during handling) are believed to be the dominant mechanisms in the observed corrosion (2). Both these mechanisms are consistent with past experiences which show that flex lead corrosion effects vary from negligible, to moderate, to severe from one inertial instrument to another. All leads, in any given instrument, usually show a similar level of corrosion. Since all of the leads that are mounted in any one instrument are subjected to the same heat-treatment (for forming purposes), and since all of them are in contact with the same fluid (during instrument operation), the sources of corrosion must originate either from microstructure changes induced in the flex lead, as a result of heat-treatment, or from environmental (air and moisture) contamination of the fluid. The presence of bromine in the corrosion product can be explained by the formation of bromides as a consequence of these two corrosion processes. The metal ions formed from galvanically promoted dissolution of the less-noble, Cu-rich phase are free to combine with bromine ions, which are also believed to be present in the fluid through chemical interaction between the BTFE fluid and the epoxy materials that are used for instrument fabrication. Alternatively, direct chemical reaction between the metals and the fluid can also account for the formation of metal bromides. Either way, it is interesting to note that the Cu-rich phase that contains a higher amount of Ag (as was indicated for the

good lead sample) will be less reactive chemically (because Ag-bromides possess higher free energy of formation values than do Cu-bromides) and will also be less susceptible to galvanic-type corrosion (because of a reduced potential difference between the two phases resulting from a higher Ag-content in the Cu-rich phase and a higher Cu-content in the Ag-rich phase). Differences in the relative amounts of the two phases, as mentioned earlier, will also play a role in determining the extent of the corrosion in the material.

The foregoing suggests that it is important to exercise good control over the 590°K heat-treatment that the flex leads are subjected to during the shape-forming stages, and over the avoidance of environment-related contaminants in the BTFE fluid during instrument filling and handling operations. While it is recognized that some diffusion-related phenomenon must occur for the flex leads to assume the shape of the metal mandrel, it is important to note that this treatment should be confined to the minimum that is required. Excessive thermal activation leads to excessive second-phase separation and agglomeration, and this has an adverse effect on the corrosion-resisting properties of the 85 Ag-15 Cu flex lead material.

Summary and Conclusions

1. The as-received microstructure of the 85 Ag-15 Cu flex lead ribbons consisted of the major, nodular sub-micron size Ag-rich phase dispersed in the minor, quasi-continuous Cu-rich matrix. The Cu-rich phase was located at what appeared as grain boundaries.
2. A close correspondence was found between the etching characteristics of the samples (which are an indication of the microstructure) and the observed corrosion. It is suggested that differences in etching behavior resulted from differences in prior thermal treatment and overall composition. The sample that etched slowly was also the one that showed very few signs of corrosion.
3. Corrosion is found to proceed along the Cu-rich phase resulting in separation of the Ag-rich particles from the metal matrix and incorporation into the corrosion layer. After build-up of a certain thickness, the corrosion layer detaches from the surface (possibly because of an increased interfacial stress), and exposes fresh metal surface for more attack.
4. The morphology found for the Ag-rich particles (which were exposed at the surface by a chemical etching treatment) was quite similar to that observed for the corrosion scale. The processes believed to be responsible for giving rise to the observed corrosion are those resulting from chemical interaction of the metallic phases with the fluid and those related to an existing electrochemical corrosion cell.

Acknowledgment

The author wishes to thank Dr. A. Moscaritolo and Dr. D. Das for reading this manuscript. The support and cooperation of D. Keaney, and Dr. J. Stemmiski, and J. McCarthy is deeply appreciated. This work was performed under funding provided by the Strategic Systems Project Office, Department of the U.S. Navy.

Manuscript submitted June 25, 1979; revised manuscript received Nov. 11, 1979.

Any discussion of this paper will appear in a Discussion Section to be published in the December 1980

JOURNAL. All discussions for the December 1980 Discussion Section should be submitted by Aug. 1, 1980.

Publication costs of this article were assisted by The Charles Stark Draper Laboratory, Incorporated.

REFERENCES

1. Metals Reference Book, 5th Edition, C. J. Smithells, Editor, Butterworths, London and Boston (1976).
2. J. M. West, "Electrodeposition and Corrosion Processes," D. Van Nostrand Company Ltd., London (1965).

TEM Observations of Pyramidal Hillocks Formed on (001) Silicon Wafers during Chemical Etching

Fumio Shimura

NEC-TOSHIBA Information Systems Incorporated, Research Laboratories, Miyazaki, Takatsu-ku, Kawasaki, 213 Japan

ABSTRACT

The pyramidal hillocks bounded by four convergent {111} planes have appeared on annealed (001) silicon wafers. Observations by TEM (transmission electron microscope) of an annealed (001) wafer with oxidation-induced stacking faults show that the pyramidal hillock is not an extraneous substance such as SiO₂ precipitate but an intrinsic part of the substrate silicon crystal. A possible mechanism of hillock formation discussed in detail verifies the formation of pyramidal hillocks on annealed (001) silicon wafers. By using the ultrasonic agitating etching technique, a flat (001) surface without pyramidal hillocks can be obtained.

It is well known that various types of microdefects are generated when bulk dislocation-free silicon crystals containing oxygen are annealed at high temperature (1, 2). Recently, surface- and inner-microdefects in annealed (111) silicon wafers examined after a two-step annealing process have been compared and related to the intrinsic gettering phenomenon (3). The result showed that all such microdefects resulted from "precipitates" generated in an annealed wafer. The type of Si-O complex precipitate generated strongly depended on annealing temperatures. The Si-O complex precipitate generation is also strongly dependent on the oxygen concentration in as-grown silicon crystals. In the case that the oxygen concentration of silicon crystal is low, Si-O complex precipitates are difficult to generate even after high temperature annealing (4).

Pyramidal hillocks, which seem to be Si-O complex "precipitates," with a micro substance at their apexes were easily observed by TEM in (001) wafers. However, this phenomenon was quite different from that in the annealed (111) wafers mentioned above.

This study takes a detailed look at these pyramidal hillocks in annealed (001) silicon wafers by means of TEM. The essence of pyramidal hillock is revealed from TEM observation results and a possible mechanism of hillock formation is discussed in detail.

Experimental

The wafers used in this study were grown by Czochralski technique and (001) oriented with the backs chemically etched and the fronts mirror polished. The n-type (P-doped) wafers, 75 mm in diameter and 400 μm in thickness, had a resistivity of 4-7 Ω·cm. The oxygen content of as-grown wafers measured by the infrared absorption (at 1106 cm⁻¹) method was 11 × 10¹⁷

cm⁻³ using the calibration given by ASTM F-121 (5). According to our sorting, this oxygen concentration is included in "low concentration" mentioned above. The wafers were annealed at temperatures from 900° to 1200°C for 16 hr in a dry O₂ atmosphere.

Surface- and inner-parts (about 30 μm chemically etched off from the front surface of a wafer) were examined using TEM. For the preparation of TEM samples, 3 mm diam disks were cut with an ultrasonic cutter. These disks were mechanically polished to a thickness of about 60 μm, then chemically thinned to electron transparency (< 2 μm) with an etchant of 3 parts concentrated HNO₃ and 1 part 49% HF. The TEM observations were carried out at an accelerating voltage of 200 kV and goniometer stage was used.

All the electron micrographs presented are bright-field images printed emulsion up and indexed assuming a (001) crystal normal. Moreover, the image plane normal (*z*), diffraction vector (*g*), and crystal tilt sense were defined in the usual way from the Kikuchi pattern.

Results and Discussion

As shown in Fig. 1, various sizes of pyramidal hillocks were observed in both surface and inner parts of (001) wafers annealed at all temperatures from 900° to 1200°C. Using stereo TEM techniques, it was found that the pyramidal hillock is bounded by four convergent {111} planes or their approximation. The shape seems to be exactly the same form as the half of a regular octahedral precipitate generated in (111) silicon wafers annealed at temperatures above 1100°C (3). This octahedral precipitate was identified as silicon oxide directly by the analysis of electron energy loss spectra (6). Furthermore, an octahedral precipitate is most likely amorphous SiO₂ from the infrared absorption data (7).

Key words: chemical etching, oxidation-induced stacking fault, ultrasonic agitation, extraneous substance.

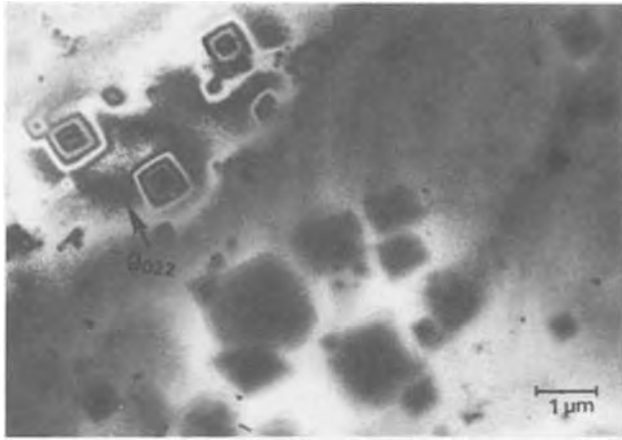


Fig. 1. TEM image of pyramidal hillocks in (001) wafer annealed at 1100°C. $g = [022]$, $z = [001]$, $s \sim 0$.

However, if these pyramidal hillocks are SiO_2 precipitates, certain discrepancies would have to be resolved:

1. The total volume of pyramidal " SiO_2 precipitates" observed here seems to be in excess of the amount of the oxygen concentration of wafers ($\sim 10^{18} \text{ cm}^{-3}$).
2. In the annealing experiments of (111) silicon wafers, octahedral precipitates were generated only at temperatures higher than 1100°C (3). On the contrary, the pyramidal hillocks were observed in (001) wafers annealed at all temperatures from 900° to 1200°C.
3. The size of octahedral precipitates generated in annealed (111) wafers were around 0.3 μm in diameter (3), however, the size of pyramidal hillocks generated in (001) wafers ranged from 0.1 μm to a few microns.
4. In spite of such large "precipitates," no prismatic punched-out dislocations were observed around the "precipitates."

Such discrepancies would seem to preclude the idea that the pyramidal hillocks shown in Fig. 1 are Si-O complex precipitates. Instead, they support the conception that the hillocks are part of the silicon substrate crystal itself.

To verify this, TEM observations were carried out on an annealed (001) wafer with oxidation-induced stacking faults (OSF). The OSF shown in Fig. 2 intersects a pyramidal hillock in a (001) wafer annealed at 1100°C for 16 hr in a dry O_2 atmosphere. In this case, dynamical theory of image contrast proves that the breadth of the stacking fault TEM image is proportional to the thickness of the TEM sample. That is, the variation in the breadth of OSF fringes represents the shape of the sample where OSF is intersecting as schematically

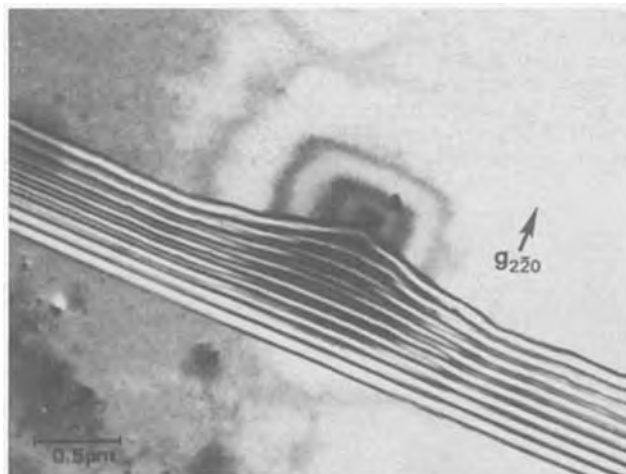


Fig. 2. TEM image of stacking fault intersecting pyramidal hillock in (001) wafer annealed at 1100°C. $g = [220]$, $z = [001]$, $s = 0$.

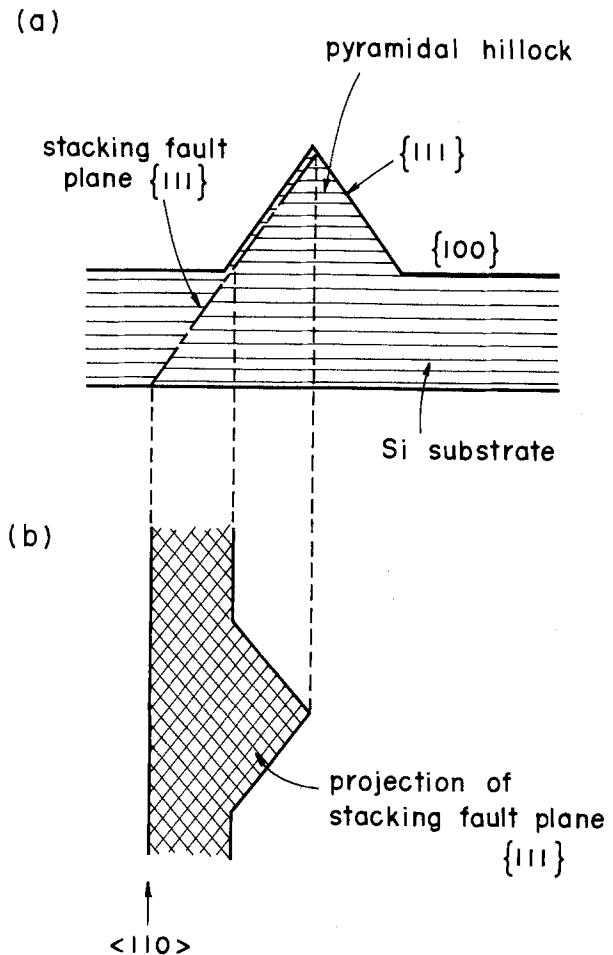


Fig. 3. Schematic illustration of stacking fault intersecting pyramidal hillock; (a) cross section of stacking fault plane and pyramidal hillock viewed from $\langle 110 \rangle$ direction, (b) projection of stacking fault plane.

shown in Fig. 3. It must be emphasized that continuous stacking fault fringes at the part of the pyramidal hillock shown in Fig. 2 can only verify that the pyramidal hillock is not an extraneous substance such as SiO_2 but an intrinsic part of the substrate, namely the silicon crystal itself. Moreover, the thickness of the TEM sample and the height of the pyramidal hillock shown in Fig. 2 were estimated at 0.85 and 1.17 μm , respectively. The triangular projections of the stacking fault plane shown in Fig. 2 and 3 are somewhat different from each other. That is, the convergent planes of the pyramidal hillock which are observable in Fig. 2 are $\sim \{113\}$ deviating slightly from $\{111\}$ planes shown in Fig. 3.

In addition, the TEM image of a stacking fault intersecting an octahedral precipitate generated in a (111) wafer annealed at 1100°C for 16 hr in a dry O_2 atmosphere (see Fig. 4) is completely different from the previous TEM image as is the correlation between a precipitate and stacking fault projection (Fig. 5). Stacking fault fringes as definitely shown in Fig. 4 and 5 cannot be produced with a precipitate.

Consequently, pyramidal hillocks shown in Fig. 1 and 2 are not an extraneous substance such as amorphous SiO_2 but hillocks of an intrinsic part of the silicon substrate crystal itself. The pyramidal hillocks seem to be formed by chemical thinning when a thin foil for TEM observation was prepared.

Using stereo TEM techniques, a micro substance, a few nm in size, was observed at the apex of some pyramidal hillocks as shown in Fig. 6. This micro substance must have participated when the pyramidal hillock was formed by chemical thinning. A model for the formation of pyramidal hillocks by chemical thinning is presented schematically in Fig. 7. When the polished sample is chemically thinned to electron transparency,

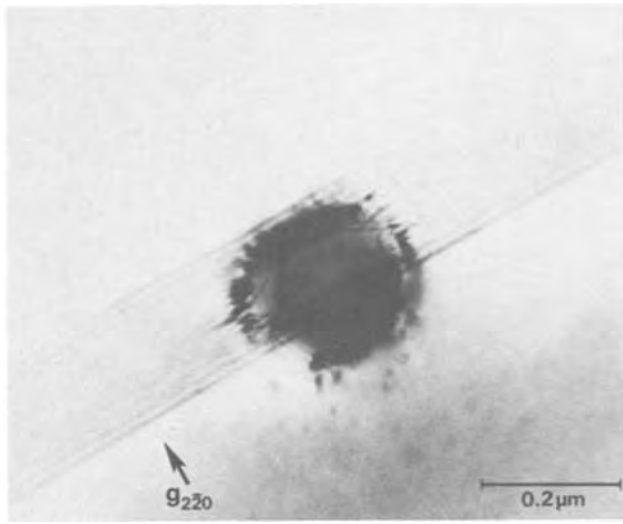
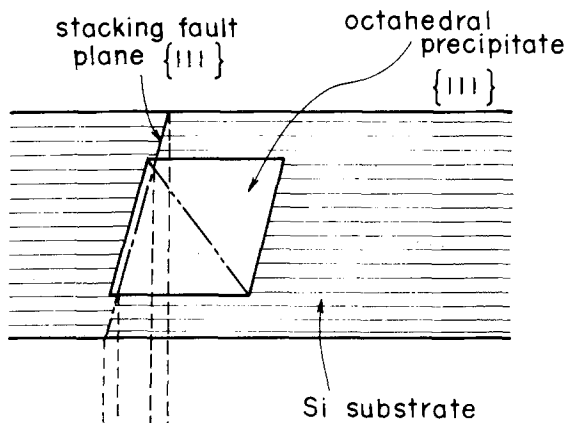


Fig. 4. TEM image of stacking fault intersecting octahedral precipitate generated in (111) silicon wafer annealed at 1100°C. $g = [2\bar{2}0]$, $z = [111]$, $s = 0$.

(a)



(b)

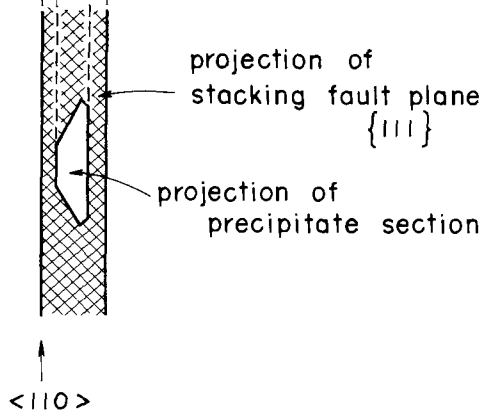


Fig. 5. Schematic illustration of stacking fault intersecting octahedral precipitate; (a) cross section of stacking fault plane and octahedral precipitate viewed from $\langle 110 \rangle$ direction, (b) projection of octahedral precipitate and stacking fault plane.

the etching rate depresses where the extraneous substance exists. No anisotropic etching occurs on a (111) silicon surface on which the etching rate is the minimum, however, in the case of a (001) surface, pyramidal hillocks bounded by four convergent {111} planes or their approximation are formed as a consequence as the chemical etching proceeds leaving {111} planes. Bassous *et al.* (8) reported square pyramidal cavities bounded by convergent {111} planes that were formed by chemical jet etching with an orifice. Both

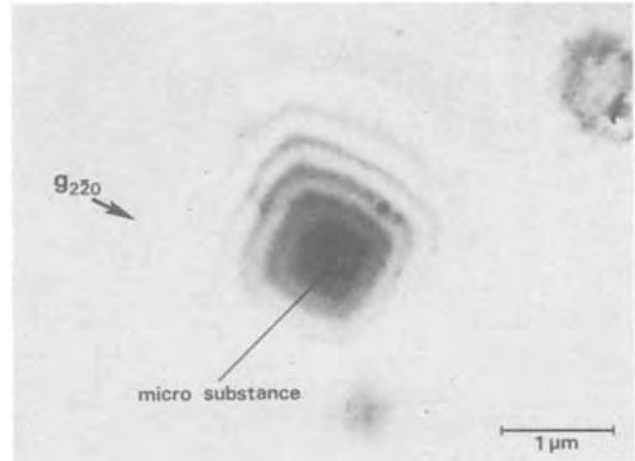


Fig. 6. TEM image of micro substance located at pyramidal hillock apex. $g = [220]$, $z = [001]$, $s = 0$.

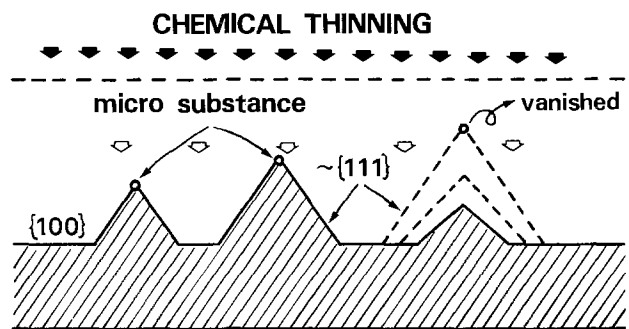


Fig. 7. Schematic illustration of pyramidal hillock formation model by chemical etching with micro substance.

the pyramidal cavity and hillock bounded by convergent {111} planes are caused from the anisotropy of the etching rate among crystal planes. As shown in Fig. 7, some micro substances vanish in the middle of the chemical thinning and some remain at the apex of pyramidal hillocks. Pyramidal hillock size depends on the position of the micro substance in a wafer and/or the substance disappearance time.

The micro substance mentioned above seems to be a micro precipitate and/or adsorbed impurities. The exact identification of the micro substance located at the apex of a pyramidal hillock has not yet been accomplished at present. However, it is very important in the silicon industry to identify the substance that results in pyramidal hillocks.

Annealed (001) wafers were chemically etched by various techniques to obtain a flat etched surface without such hillocks and to verify the pyramidal hillock formation model presented here. Optical microscope images of surfaces chemically etched by both a usual manner and an ultrasonic agitating technique using a 1HF:3HNO₃ mixture as an etchant mentioned before are shown in Fig. 8. With ultrasonic agitation, far fewer

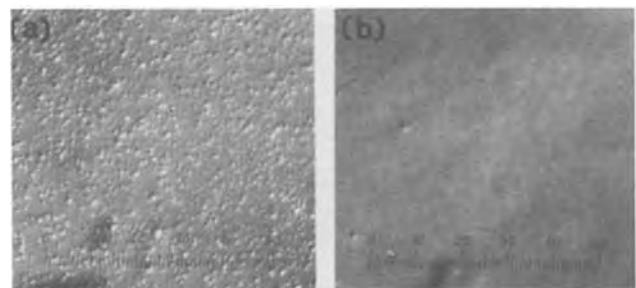


Fig. 8. Etched surfaces of annealed (001) silicon wafer with 1 HF: 3 HNO₃ mixture; (a) usual manner, (b) with ultrasonic agitation.

pyramidal hillocks were formed on the surface than the usual manner. The difference between the surface shapes etched in different manners verifies the model mentioned above, that is, these pyramidal hillocks are formed as a result of chemical etching and a micro substance at the apex of pyramidal hillock. Ultrasonic agitation should sweep away micro substances which affect the formation of pyramidal hillocks. Furthermore, ultrasonic agitation is also required to minimize etching artifacts due to gas bubble formation during etching (9), and to minimize the etching time necessary to achieve the required thickness of electron transparency.

Summary

Pyramidal hillocks bounded by four convergent {111} planes or their approximation on the (001) silicon surface are not extraneous substances such as octahedral amorphous SiO₂ precipitates but an intrinsic part of the silicon substrate crystal. They are formed by chemical etching. By using ultrasonic agitation, the formation of these pyramidal hillocks can be avoided.

Acknowledgment

The author wishes to acknowledge Drs. T. Kawamura and H. Tsuya for their continued interest and encouragement in the course of this work. He also wishes to express his thanks to Dr. J. Matsui for his helpful dis-

cussions and M. Mito for his help in TEM sample preparation.

Manuscript submitted Aug. 1, 1979; revised manuscript received Oct. 22, 1979.

Any discussion of this paper will appear in a Discussion Section to be published in the December 1980 JOURNAL. All discussions for the December 1980 Discussion Section should be submitted by Aug. 1, 1980.

Publication costs of this article were assisted by NEC-TOSHIBA Information Systems, Incorporated.

REFERENCES

1. D. M. Maher, A. Staudinger, and J. R. Patel, *J. Appl. Phys.*, **42**, 3813 (1976).
2. A. Staudinger, *ibid.*, **49**, 3870 (1978).
3. F. Shimura, H. Tsuya, and T. Kawamura, *ibid.*, **51**, 269 (1980).
4. F. Shimura, Unpublished.
5. Annual Book of ASTM Standards (1977), F-121.
6. K. H. Yang, R. Anderson, and H. F. Kappert, *Appl. Phys. Lett.*, **33**, 225 (1978).
7. K. Tempelhoff, F. Spiegelberg, and R. Gleichmann, in "Semiconductor Silicon 1977," H. R. Huff and E. Sirtl, Editors, p. 585, The Electrochemical Society Softbound Proceedings Series, Princeton, N.J. (1977).
8. E. Bassous and E. F. Baran, *This Journal*, **125**, 1321 (1978).
9. D. G. Schimmel, *ibid.*, **126**, 479 (1979).

Analysis of the Main Factors Influencing the Thickness Uniformity of VPE GaAs Thin Layers

Jean-Paul Chané

Laboratoires d'Electronique et de Physique Appliquée, 94450 Limeil-Brevannes, France

ABSTRACT

It is shown that the homogeneity in thickness of a large area GaAs thin layer obtained by VPE is a function of the composition of the gaseous phase, its homogeneity, and the hydrodynamics of its flow in the vicinity of the substrate. The influence of each of these factors has been investigated. Modifications have consequently been introduced into the low temperature growth technique using AsCl₃/H₂/GaAs which lead to very uniform layers with a pinch-off voltage variation of $\pm 5\%$ for FET.

State of the art GaAs microwave devices use widely epitaxial material. A great deal of attention is devoted to the field effect transistor and GaAs IC's which are currently entering into industrial development. In order to assure high production efficiency the material should not only be of high quality but should also be homogeneous, particularly in its essential parameters of thickness and doping.

In the field of GaAs integrated circuits, it would even seem, at the present time, that an increase of area with uniform thickness is an essential condition for the use of epitaxial layers. Usually, the observed dispersions were attributed to the hydrodynamics of the gas flow for which it was possible to have only an intuitive idea. Although certain publications (1-4) have detailed the CVD growth of Si in a cold wall reactor, little has been published concerning hydrodynamics in hot wall reactors using the AsCl₃ method. Fairman and Solomon (5) found a variation of the epitaxial layer thickness along the flow axis; this variation depends on the thermal gradient in the deposition zone. Komeno *et al.* (6) derived a growth rate equation on the basis of a model (7) which assumes a laminar boundary layer. The use of this equation permits the

description of the growth rate variation along the substrate with different conditions of flow and temperature. However the authors used a few microns thick epitaxial layers and a growth method with inert gas.

In this work, the problem was investigated by systematic measurements of velocity by mean of an anemometric probe. For low temperature growth, using the AsCl₃/H₂/GaAs method (8), it appears that the phenomena responsible for the inhomogeneities in a thin layer are located at three different positions: (i) at the sample, where the flow of gas is concerned; (ii) at the entrance to the deposition zone, where the chemical homogeneity of the gas phase is involved; and (iii) finally at the GaAs source, where the pseudo-equilibrium of the gas is concerned.

Experimental Technique

The influence of the composition of the gas phase at the source on the homogeneity of the growth has been studied in a conventional epitaxial reactor (Fig. 1). The source consists of GaAs polycrystals inside a quartz tube T ($\phi = 28$ mm) with a 10 mm exit aperture. A small tube feeds the source with hydrogen saturated with AsCl₃. Downstream from the source is a baffle C. The substrate is placed on a rectangular sample holder

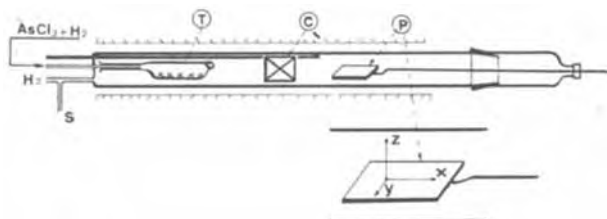


Fig. 1. Schema of the epitaxial reactor

P which can be inclined with respect to the axis of the reactor.

The temperature of the source is 660°C and that of the substrate 630°C. Flow rates are, respectively, 200 and 650 cm³/min for source and carrier gases. AsCl₃ mole fraction after dilution is 3·10⁻³. The doping is obtained by a sulfur circuit which is connected to the hydrogen carrier gas.

Epitaxial growths on Cr-doped substrates were performed in these conditions. The thickness of the layers are evaluated using C-V measurements with the double mercury Schottky probe described earlier (9).

The homogeneity of the gas phase at the entrance to the growth zone has been studied by simulating the flow with TiO₂ fumes. The reactor used is of identical geometry to that described above (Fig. 2). A flow of hydrogen saturated with TiCl₄ is introduced into the source; at its exit it meets a flow of humid hydrogen coming from upstream of the reactor. The mixture of the two gases then passes into a homogenization chamber. The degree of homogenization is easily controlled by observing the white TiO₂ fumes at the exit of the chamber. Experiments have been performed at room temperature, however the conclusions can also be applied to the effective operating conditions as it corresponds to a constant temperature region of the reactor.

The gas flow in the region of the sample holder has been experimentally determined by measuring the velocity throughout the stream of gas. In order to effect these measurements the preceding reactor was equipped with a sliding trolley which supported an anemometric probe that had been specially adapted for small velocities (0-30 cm/sec) (Fig. 3 and 4). The probe consists of a hot oscillating wire (250 Hz) whose output voltage is a linear function of the gas velocity. Its sensitivity is 0.1 cm/sec. The fine construction of the probe causes no detectable perturbation in the measurements.

Measurements were performed at room temperature using nitrogen carrier gas in order to keep the Reynold number close to the practical values in the epitaxy reactor ($2 < Re < 10$).

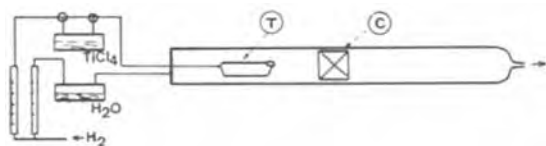


Fig. 2. Schema of the reactor used in the study of the homogeneity of the gas. T: source, C: baffle.

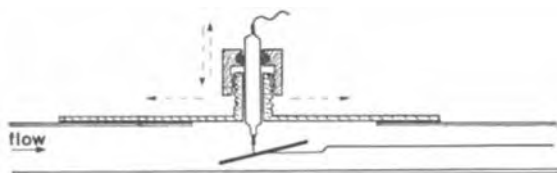


Fig. 3. Anemometric equipment used in the study of the gas flow around the substrate.

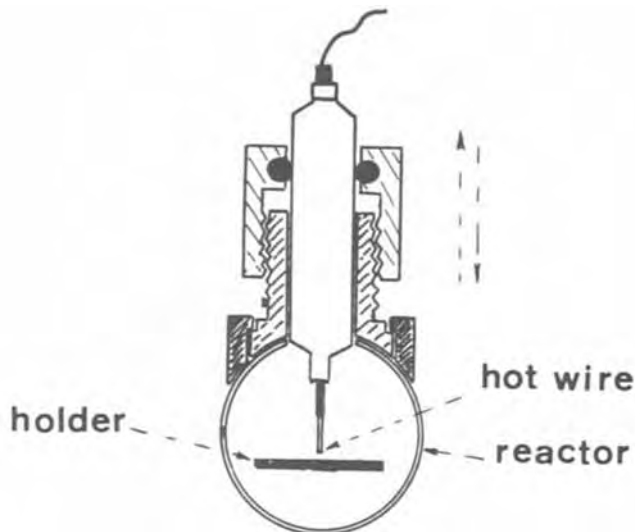


Fig. 4. Diagram of the probe and the carrier (in the axis of the reactor).

Results and Discussion

Influence of the source geometry.—Some short growths (a few minutes, leading to around 0.3 μm of deposit) have been carried out in the reactor described above. It has been found for consecutive growths that the growth rate, determined on the thin layer, and the dispersion in thickness were very sensitive to: (i) the granulation of the polycrystalline GaAs introduced in the tube T: an increase of the granulation increases the growth rate while the dispersion in thickness tends to decrease; and (ii) the filling of tube T. By filling only the bottom of the tube, the average thickness increases progressively, from one run to the next one.

The experimental conditions used were such that the control of the gas flow (10, 11), could not be held responsible for these fluctuations. Possible explanations are related to the residence time of the gas, the total surface available for reaction and the surface faceting (12). All these effects induce variations of the supersaturation in the gas phase and the effect of this on the growth rate is even more serious for submicronic layers as steady-state conditions may not be reached. Optimum source loading has been empirically determined in order to obtain reproducible growth rate over several dozen successive growths.

Homogeneity of the gases after dilution.—The source gases meet the hydrogen stream at the exit of the tube T (Fig. 1), and the problem is to get a homogeneous gas phase before its arrival at the growth zone.

The TiO₂ visualization technique reveals the difference of velocity between the gas at the source exit (V_s) and the hydrogen carrier gas V_H . It also shows that a period of several minutes is necessary to reach a fully developed phase when the flow corresponding to V_s is established in the already existing carrier flow (for $V_s/V_H \sim 10$, a typical time is about 10 min). The practical consequence of this is that the solid/gas interface at the sample surface is not under uniform partial pressure conditions, which is particularly detrimental for short growth times.

In fact, the gases must be well mixed together before reaching the neighborhood of the sample. One way of ensuring this is to interpose a baffle between the source exit and the growth zone (11).

Hydrodynamics of the flow in the growth zone.—Anemometric measurements, carried out in the vertical plane above the sample holder every cm, along Ox, and every mm, along Oz (Fig. 1) have confirmed the existence of a boundary layer at the surface of the sample.

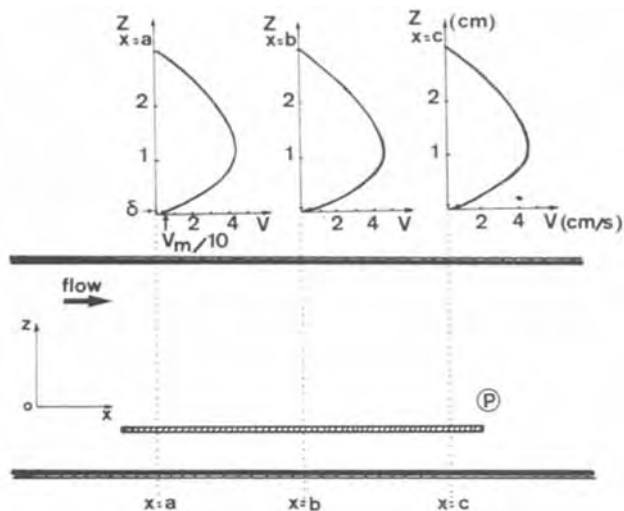


Fig. 5. Velocity profile along Oz above the sample holder and parallel to the flow axis.

The boundary layer is defined as being the height of the fluid below which the velocity is 10% of the input velocity. Its thickness (δ) is directly measurable using the anemometer. However, it appears that it is very small. So, in order to increase the accuracy of the measurements, attention was in fact focused on the gas layer where $V = V_m/2$ whose behavior above the substrate is similar to that of the boundary layer since the velocity profile in this region is linear.

In the case of a horizontal reactor, the velocity profile above the sample holder does not have the same form along the flow axis Ox , and the perpendicular axis Oy .

Along the flow axis.—If the sample holder is parallel to Ox , the vertical velocity profile is of a parabolic nature and remains the same across the holder. It depends only on the input velocity of the gases (Fig. 5). Slight deviation from the parabolic shape is due to the misalignment of the input pipe.

This situation is changed should the sample holder be inclined with respect to Ox . The velocity profile becomes deformed across the holder and the flattening effect of the parabola becomes more accentuated with increasing tilt angle (Fig. 6a, 6b). Under these circumstances, the boundary layer is no longer of uniform thickness. $\delta(x)$ becomes a decreasing function of x and its derivative $d\delta(x)/dx$ is a function of: (i) the

input velocity of the gas. $\delta(x)$ decreases less quickly when the velocity increases; (ii) the tilt angle of the sample holder. A total variation of δ of 100%, for $V_m = 8$ cm/sec and a holder length of 7 cm (along Ox) was measured for a tilt of 8° , and 250% for an angle of 16° (Fig. 7).

These results are similar to those obtained by Eversteyn (2) with the exception that our hydrodynamic approach is essentially experimental and does not necessitate the knowledge of the growth rate for the determination of δ .

Along the direction perpendicular to the flow.—The anemometric measurements have shown that the velocity profile depends on the ratio R of the width of the sample holder to the diameter of the reactor. Figure 8 shows the forms of three profiles for a width practically equal to the diameter, $R = 100\%$; R equal to 75% (which is usually the case in our reactors). The presence of a very mobile stream of gas either side of the sample holder is observed; finally R equal to 90%. This is an optimum value, empirically determined.

It may be deduced that the thickness, $\delta(y)$, of the boundary layer also depends on R . $\delta(y)$ is constant for $R = 90\%$ but in the case where $R = 75\%$ it decreases in value at the edges of the sample holder.

Influence of the thickness of the boundary layer on the homogeneity of the epitaxial growth.—In this section, it is supposed that the problems associated with the source have been solved and that the composition of the gas arriving in the growth zone is constant. Growths have been carried out under these conditions on samples of the same area and the velocity of the gas flow was identical throughout. The experiment revealed two factors: the supersaturation γ and the growth rate τ , influence the homogeneity of the growth thickness. Figure 9 summarizes the following observations: (I) the supersaturation γ is low: the thickness of the epitaxial layer decreases regularly along the flow direction; and (II) the supersaturation is high: two possibilities exist: (i) the growth rate is small and the thickness of the epitaxial layer is practically constant along Ox . (ii) τ is large in which case a gradient in thickness reappears along Ox . In both cases, the presence of such a gradient signifies a decrease in the supersaturation ($\Delta\gamma$), along the substrate which produces a corresponding reduction in growth rate ($\Delta\tau$).

These results (I and II) agree with those of Hollan *et al.* (13), concerning the influence of the supersaturation on the growth rate even though their results in-

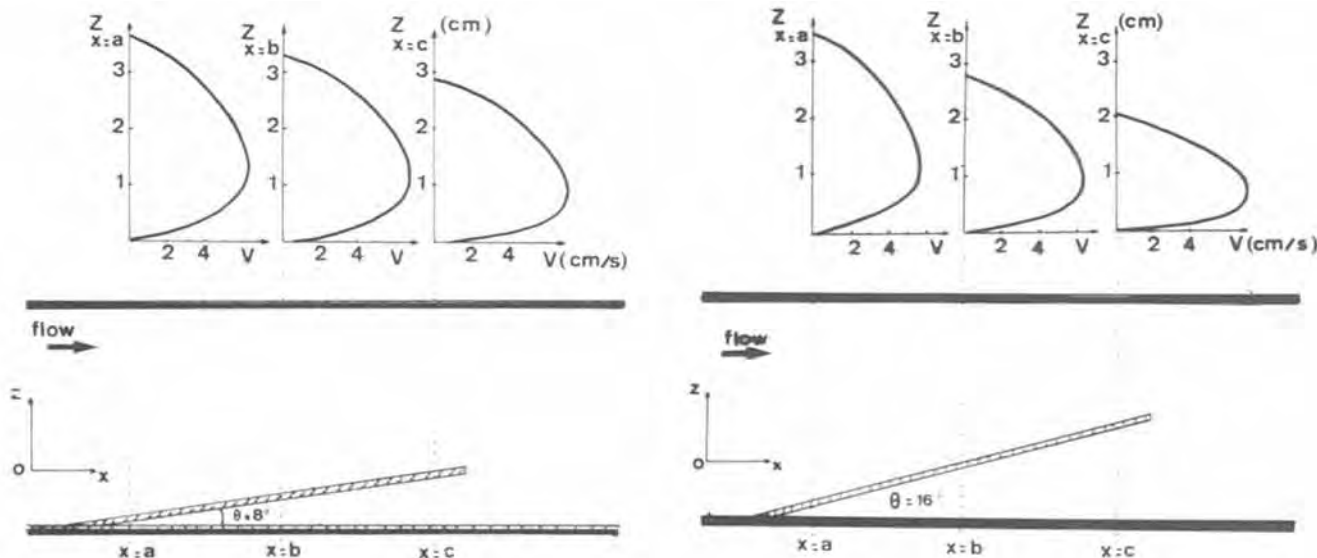


Fig. 6. (a, left) Velocity profile along Oz above the sample holder tilted at $\theta = 8^\circ$ with respect to the flow axis Ox . (b, right) Same profile with $\theta = 16^\circ$.

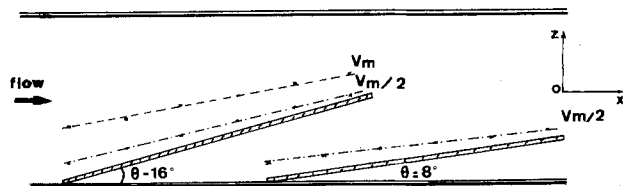


Fig. 7. Thickness profile of the gas layer corresponding to $V_m/2$ measured above the sample holder which is tilted at 8° and 16° .

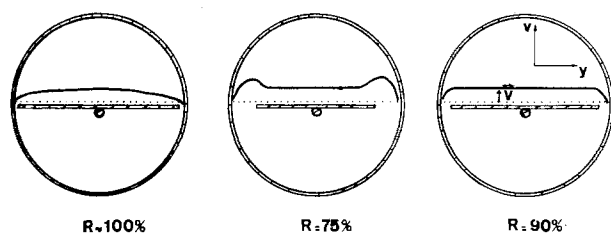


Fig. 8. Velocity profile at 1 mm from the surface of the sample holder in the perpendicular axis Oy for different ratios

$$R = \frac{\text{width of the sample holder}}{\text{diameter of the reactor}}$$

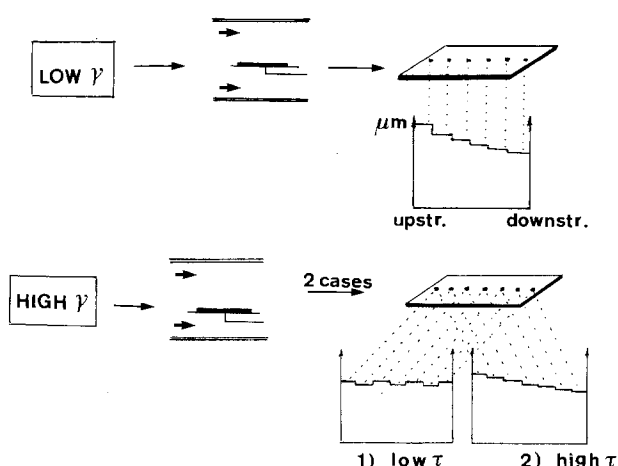


Fig. 9. Table showing the respective influences of the thermodynamics, the surface kinetics, and the hydrodynamics on the homogeneity of the growth.

involved average growth rates calculated from growths of several microns.

Figure 10, which summarizes their results, shows: (i) that at low γ the curves always present a steep slope irrespective of the growth temperature. This slope $\Delta\tau/\Delta\gamma$ explains the gradient of the thickness which is always observed on thin layers at low γ (Fig. 9, low γ). (ii) it also shows that, at high γ ($\gamma \geq 3$), the slope of the curves varies as a function of T_D . At $T_D \leq 680^\circ\text{C}$ $\Delta\tau/\Delta\gamma \sim 0$ which corresponds to case 1, high γ in Fig. 9; the thickness of the epitaxial layer is uniform. Above 700°C $\Delta\tau/\Delta\gamma$ is no longer zero, this corresponds to case 2, high γ in Fig. 9 where a gradient in the epitaxial layer thickness reappears.

The dispersion can be explained by the mass transfer limitation of the growth: the boundary layer plays the role of a screen through which the gas molecules must diffuse in order to reach the crystal (2, 6). This is a mass transfer by diffusion; the substrate is under isothermal conditions and consequently the flux of matter, J (expressed in mole \cdot cm $^{-2}$ \cdot sec $^{-1}$) which reaches the crystal is given by

$$J = D \frac{C_G - C_i}{\delta} \quad \text{for each element}$$

where δ = thickness of the boundary layer in x , D = diffusion coefficient, C_G = concentration of the element in the gas, and C_i = concentration of the element at the solid/gas interface.

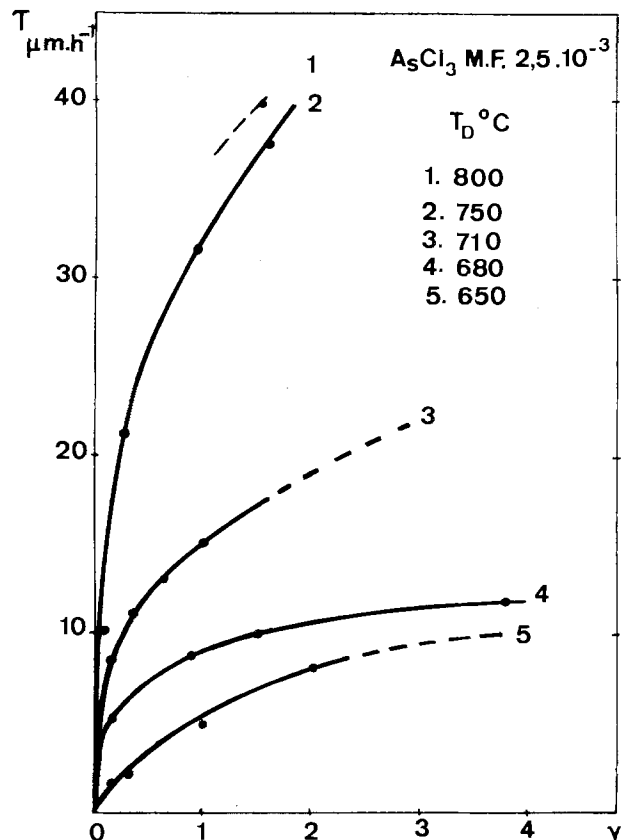


Fig. 10. GaAs deposition rates τ as a function of the supersaturation γ [after (13)].

At the limit

$$C_i = 0 \quad \text{then} \quad J = D \frac{C_G}{\delta}$$

The growth thickness would be homogeneous if substrate were exposed to the same flux at its extremities x_1 and x_2 . Then

$$\frac{DC_G(x_1)}{\delta(x_1)} = \frac{DC_G(x_2)}{\delta(x_2)}$$

and hence

$$\frac{\delta(x_1)}{\delta(x_2)} = \frac{C_G(x_1)}{C_G(x_2)}$$

In other words, the homogeneity of the growth requires that the boundary layer should decrease in thickness across the layer in the same proportions as the concentration in the gas stream.

It would be possible to calculate the tilt angle of the sample holder which would satisfy the above condition. But the calculation is not straightforward because it would be necessary to consider each individual gaseous component and take them into account. Furthermore, all concentrations are not known. Thus, the tilt angle was obtained experimentally. Another method to obtain a thickness uniformity consists in establishing a thermal gradient along the substrate (5). But this is more difficult to control.

Application.—In the following, the tilt angle of the substrate holder with respect to $0x$ is 15° .

Epitaxial layers of $0.25 \mu\text{m}$ in thickness, with a doping level of about $1 \cdot 10^{17} \text{ cm}^{-3}$ in order to give a pinch-off voltage $V_p \sim 4.5\text{V}$ are grown. Figure 11 shows the dispersion in thickness, and Fig. 12 displays the V_p variation along $0x$ and $0y$.

The variation in V_p is less than 25% along the largest dimension of the sample (oriented parallel to the axis of the gas flow). This variation decreases to as little as 10% if the first and last two millimeters of the samples are neglected (edge effects).

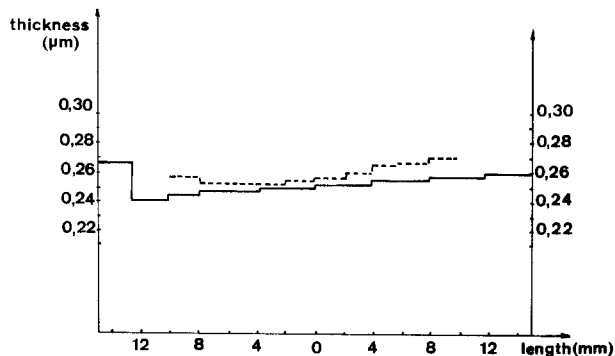


Fig. 11. Dispersion of the layer thickness along the flow axis (full line) and the perpendicular axis (dashed line) (accuracy $\pm 50\text{\AA}$).

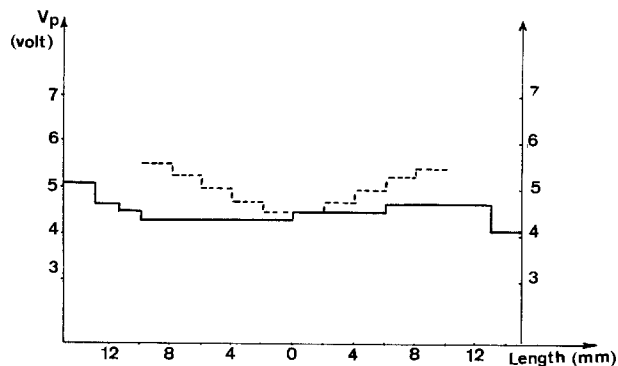


Fig. 12. Dispersion in the pinch-off voltage, V_p , of a FET epitaxial layer along the flow axis (full line) and the perpendicular axis (dashed line) accuracy = $\pm 0.05\text{V}$.

The dispersion is bigger along the perpendicular axis. This is explained by the width of the sample holder which only represents 75% for the reactor diameter.

Conclusion

The uniformity in thickness of a thin layer of GaAs grown by vapor phase epitaxy (trichloride method) is essentially determined by three factors: (i) the composition of the gas phase at the exit of the source; (ii) the homogeneity after dilution; and (iii) the hydrodynamics of the flow.

The second factor may be considered separately. A solution has been proposed which has given satisfactory results (interposition of a baffle between the source exit and the growth zone).

The other two factors, however, cannot be considered separately.

It is necessary that the progressive exhaustion of the gas phase resulting from the growth along the axis of the gas flow, be compensated by a continuous reduction thickness of the boundary layer which screens the crystal.

The determination of the best compromise resulted from experimental measurements of the thickness of the boundary layer using an anemometric probe in relation with the supersaturation of the vapor phase.

This work has been applied to the growth of thin epitaxial layers for FET's. Considerable improvement in their uniformity of pinch-off voltage has been observed, particularly in the direction of the gas flow, where it has been reduced to $\pm 5\%$.

However, the dispersion along the perpendicular axis is slightly larger. The optimization of the ratio:

$$\frac{\text{width of the holder}}{\text{diameter of the reactor}} \text{ should reduce it.}$$

Acknowledgments

The author would like to express his gratitude to Mme J. Baelde for her technical assistance, to Mr. Lyot for his help with the anemometric measurements, and finally to Dr. Hallais for many helpful discussions.

Manuscript submitted Dec. 28, 1978; revised manuscript received Oct. 24, 1979.

Any discussion of this paper will appear in a Discussion Section to be published in the December 1980 JOURNAL. All discussions for the December 1980 Discussion Section should be submitted by Aug. 1, 1980.

REFERENCES

1. W. H. Shepherd, *This Journal*, **112**, 988 (1965).
2. F. C. Eversteijn, P. J. W. Severin, C. H. J. v. d. Brekel, and H. L. Peck, *ibid.*, **117**, 925 (1970).
3. R. Takahashi, Y. Koga, and K. Sugawara, *ibid.*, **119**, 1406 (1972).
4. V. S. Ban, *ibid.*, **125**, 317 (1978).
5. R. D. Fairman and R. Solomon, *ibid.*, **120**, 54 (1973).
6. J. Komeno, S. Ohkawa, A. Miura, K. Dazai, and O. Ruyan, *ibid.*, **124**, 1440 (1977).
7. A. S. Grove, "Physics and Technology of Semiconductor Devices," John Wiley and Sons, Inc., New York (1967).
8. J. Hallais, D. Boccon-Gibod, J. P. Chane, J. M. Durand, and L. Hollan, *This Journal*, **124**, 1290 (1977).
9. M. Binet, *Electron. Lett.*, **24**, 11 (1975).
10. H. Watanabe, *Jpn. J. Appl. Phys.*, **14**, 1451 (1975).
11. J. P. Chane, and J. Hallais, Final Report of D.G.R.S.T., Contract 75.7.1489, Dec. 1976.
12. J. P. Chane, Patent No. 78.33.831 (1978).
13. J. Hollan, J. M. Durand, and R. Cadoret, *This Journal*, **124**, 135 (1977).

Transparent Conducting Cadmium-Tin Oxide Films Deposited by RF Sputtering from a CdO-SnO₂ Target

N. Miyata, K. Miyake, K. Koga, and T. Fukushima

Faculty of Engineering, Yamaguchi University, Ube, Japan

ABSTRACT

Transparent conducting films of cadmium-tin oxide (CTO) were prepared by rf sputtering from a sintered CdO-SnO₂ target in an Ar or an Ar-O₂ atmosphere. The electrical and optical properties of the films were found to depend upon the oxygen concentration in the gas mixture. The films with the lowest resistivity of $4.82 \times 10^{-4} \Omega\text{-cm}$ and high optical transmission of 85% over the visible region were obtained without post-heat-treatment.

The films of cadmium-tin oxide (CTO) are attractive materials as transparent electrodes on optoelectronics devices. Nozik (1) and Haacke (2, 3) have reported the physical properties of CTO films deposited by rf sputtering from a hot-pressed polycrystalline Cd₂SnO₄ target. The films were annealed in an H₂ or an Ar-CdS atmosphere after the deposition in order to obtain high transparency and high conductivity, respectively. We have reported that CTO films were deposited by d-c reactive sputtering from a Cd-Sn alloy target (4-6), and that films with high transparency and high conductivity were obtained without post-heat-treatment; the properties of as-sputtered films were almost equivalent to those of post-annealed films in an H₂ or an Ar-CdS atmosphere. We suggested that it is possible to adjust the electrical and optical properties of films by varying the oxygen concentration in an Ar-O₂ atmosphere (4).

This paper describes a method to prepare transparent, conducting CTO films by rf sputtering from a sintered CdO-SnO₂ target without post-heat-treatment.

Experimental

Films of cadmium-tin oxide (CTO) were deposited by rf sputtering from a CdO-SnO₂ target. The experimental apparatus is an rf sputtering system which is capable of achieving an ultimate pressure of 1×10^{-6} Torr. Sintered CdO-SnO₂ targets (CdO/SnO₂ mole ratio of 2/1, 58 mm in diam) were utilized. The rf power was in the range of 100-360W. The sputtering atmosphere used was an Ar or Ar-O₂ mixture. The pressure of pure Ar or Ar-O₂ mixtures was in the range of 2.0×10^{-2} - 8.0×10^{-2} Torr. The water-cooled target to substrate spacing was kept at 66 mm in all experiments. The sputtering chamber was equipped with a stainless shutter that was placed between the target and substrate during evacuation and predeposition.

The chamber was initially evacuated to 1×10^{-6} Torr and then Ar gas or Ar-O₂ mixtures were introduced through a variable leak valve, by which the total pressure was controlled to maintain at a given constant value. The time of presputtering was 15 min. The deposition rate was in the range of 5-30 Å/min. Borosilicate glass plates (26 × 12 × 1.0 mm) used as substrates to measure the optical transmission and electrical resistance were cleaned chemically prior to mounting on the substrate holder. The thickness of deposited films was in the range of 0.1-1.5 μm. The substrate temperature was measured with a Chromel-Alumel thermocouple attached to the substrate.

Resistivity measurements were made using the four-point probe method or the Van der Pauw technique which is also used for Hall coefficient measurements.

Key words: transparent electrodes, cadmium-tin oxide films, electrical sheet resistance, optical transmission.

The spectral transmission was measured over the visible and near infrared regions (from 0.34 to 2.6 μm) with a Hitachi 323-type double beam spectrophotometer. A 9 kG electromagnet was used in the Hall coefficient measurements. The sign of the charge carriers was determined from the Hall effect measurement and the thermoelectric hot probe technique. The structure of the deposited films was examined by x-ray diffraction.

Results

The deposition rate of the films depends upon the rf power in a pure Ar or an Ar-8%O₂ atmosphere, and the rate increases linearly with increasing rf power. At 300W rf power, the deposition rate of films in a pure Ar atmosphere was about 30 Å/min and that of films in an Ar-8%O₂ atmosphere was about 20 Å/min.

Figure 1 shows the relations between sheet resistance and thickness of CTO films deposited in a pure Ar gas, Ar-2%O₂, and Ar-13%O₂ mixture, respectively.

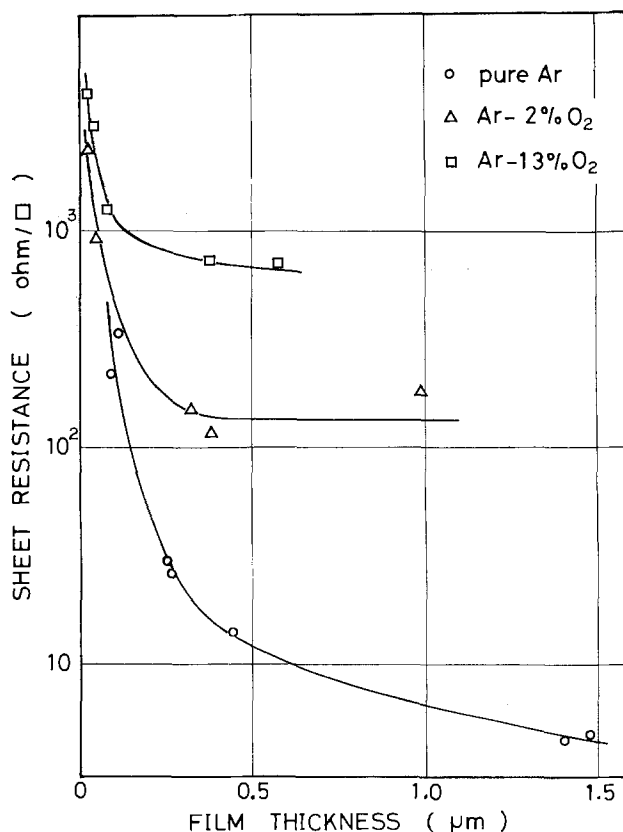


Fig. 1. The relations between sheet resistance and thickness of CTO films deposited in an Ar or Ar-O₂ mixtures.

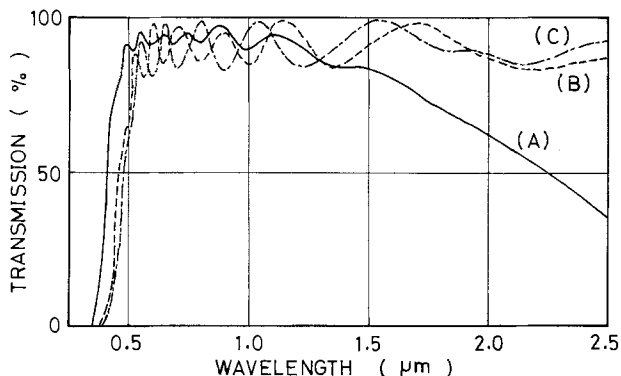


Fig. 2. The visible and near-infrared transmission of CTO films formed in Ar or Ar-O₂ mixtures (blank substrate in the reference beam).

The sheet resistance of thick films (more than 0.6 μm) deposited in a pure Ar atmosphere was below 10 Ω/square, and the lowest resistivity achieved was 4.82×10^{-4} Ω-cm, the visible transmission being approximately 85%. The sheet resistance of films deposited in an Ar-O₂ atmosphere increases with increasing oxygen concentration in gas mixtures.

Figure 2 shows spectral transmission of three CTO films (approximately 0.4 μm thick) in the visible and infrared region. Curve (A) is for the film formed in a pure Ar with resistivity 6.2×10^{-4} Ω-cm, sheet resistance 14 Ω/square, curve (B) for the film formed in an Ar-2%O₂ with resistivity 4.4×10^{-3} Ω-cm, sheet resistance 120 Ω/square, and curve (C) for the film formed in an Ar-13%O₂ with resistivity 1.8×10^{-2} Ω-cm, sheet resistance 460 Ω/square. The average optical transmission of these films was more than 85% in the wavelength range of 0.5-0.7 μm. As shown in the figure, the transmission of the films deposited in a pure Ar atmosphere drops rapidly in the near infrared region (36% transmission at 2.5 μm wavelength).

Figure 3 shows that the optical bandgap of CTO films derived from a plot of $(\alpha h\nu)^{1/2}$ vs. $h\nu$ varies with the oxygen concentration in the sputtering atmosphere, where α is the absorption coefficient. The absorption edge shifts toward shorter wavelength with decreasing oxygen concentration. From the figure, the bandgap of the film formed in a pure Ar was determined to be 2.71 eV and that of the film formed in an Ar-2%O₂ and Ar-13%O₂ determined to be 2.45 eV and 2.39 eV, respectively.

Thus, the electrical and optical properties of CTO films depend upon the sputtering conditions, especially oxygen concentration in the Ar-O₂ atmosphere. Physical properties of typical samples are summarized in Table I. It is apparent that oxygen concentration is an important factor in determining the electrical and optical properties of films.

Furthermore, from conductivity measurement as a function of temperature in the range of 110°-295°K, it was found that the films with carrier concentration more than 4×10^{19} cm⁻³ were n-type degenerate semiconductors. For the CTO films deposited in

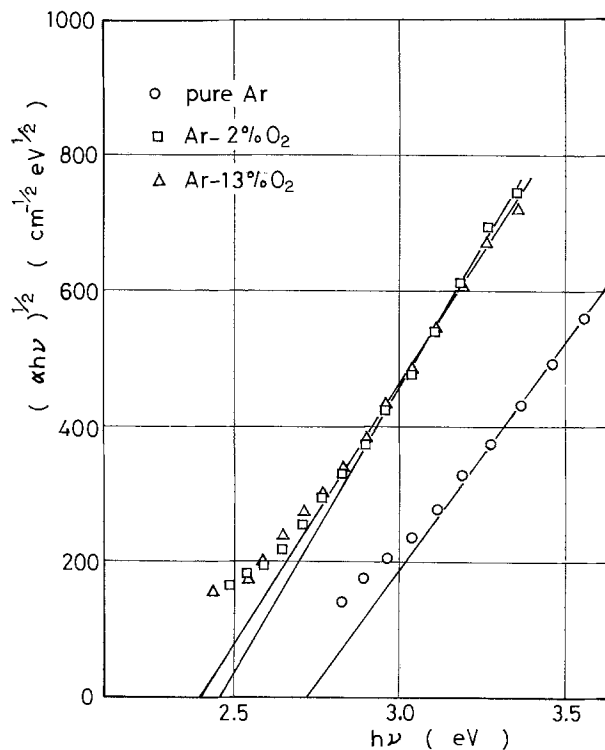


Fig. 3. $(\alpha h\nu)^{1/2}$ vs. $h\nu$ for CTO films

a pure Ar or an Ar-O₂ atmosphere, x-ray diffraction patterns exhibit a broad Cd₂SnO₄(130) peak (7).

Conclusions

Transparent, conducting CTO films were prepared by rf sputtering from a sintered CdO-SnO₂ target in an Ar or Ar-O₂ atmosphere. For the sputtered films in a pure Ar atmosphere, the lowest sheet resistance achieved was 4 Ω/square (1.5 μm thick), the lowest resistivity obtained was 4.8×10^{-4} Ω-cm and the 80% average optical transmission of the films was obtained in the visible region.

For the sputtered films in an Ar-O₂ atmosphere, it is apparent that the resistivity increases with increasing oxygen concentration in a gas mixture and the absorption edge shifts toward longer wavelength. The resistivity of the films deposited in an Ar-2%O₂, and in an Ar-13%O₂ was 4.4×10^{-3} Ω-cm (0.37 μm thick), and 1.8×10^{-2} Ω-cm (0.4 μm thick), respectively. The absorption edge energy of these films was 2.45 and 2.39 eV, respectively. The carrier concentration (8.2×10^{17} - 5.0×10^{20} cm⁻³), Hall mobility (8-73 cm²/Vsec), and optical bandgap of the films have almost the same values as those of films prepared by Nozik and Haacke.

Acknowledgment

The authors wish to thank the Narumi China Corporation for their preparing CdO-SnO₂ targets. They want to thank Mr. M. Nakao for his technical assistance in this study.

Manuscript submitted July 20, 1979; revised manuscript received Oct. 18, 1979.

Table I. The physical properties of CTO films

Sample	Sputtering conditions (atmosphere, power)	Thickness (Å)	Sheet resistance (Ω/□)	Resistivity (Ω-cm)	Average transmission (%)	Carrier concentration (cm ⁻³)	Hall mobility (cm ² /Vsec)	Optical bandgap (eV)
A	Ar 100% 290W	4400	14	6.2×10^{-4}	93	5.0×10^{20}	22	2.71
B	Ar-2% O ₂ 195W	3700	120	4.4×10^{-3}	87	1.5×10^{20}	11	2.45
C	Ar-13% O ₂ 195W	4000	460	1.8×10^{-2}	86	8.8×10^{18}	73	2.39

Any discussion of this paper will appear in a Discussion Section to be published in the December 1980 JOURNAL. All discussions for the December 1980 Discussion Section should be submitted by Aug. 1, 1980.

Publication costs of this article were assisted by Yamaguchi University.

REFERENCES

1. A. J. Nozik, *Phys. Rev.*, **B6**, 453 (1972).
2. G. Haacke, *Appl. Phys. Lett.*, **28**, 622 (1976).
3. G. Haacke, W. E. Mealmaker, and L. A. Siegel, *Thin Solid Films*, **55**, 67 (1978).
4. N. Miyata and K. Miyake, *Jpn. J. Appl. Phys.*, **17**, 1693 (1978).
5. N. Miyata, K. Miyake, and S. Nao, *Thin Solid Films*, **58**, 385 (1979).
6. N. Miyata and K. Miyake, *Surf. Sci.*, **86**, 384 (1979).
7. N. Miyata, K. Miyake, T. Fukushima, and K. Koga, *Appl. Phys. Lett.*, **35**, 542 (1979).

Thermally Stimulated Discharge Current Studies in Photoresist KTFR

V. K. Jain, C. L. Gupta, R. K. Jain, and Prem Swarup

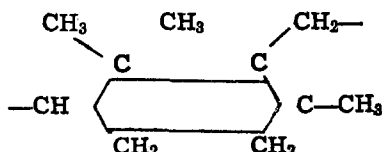
Solidstate Physics Laboratory, Delhi-110007, India

ABSTRACT

Efforts have been made to study the electret and photoelectret effects in pure and doped negative photoresist KTFR. In KTFR, dipoles are available to form electret and photoelectret effect due to the photopolymerization. This term can be applied to cross-linking of polymers. Details are not available regarding the initial steps of the photoreaction but it is clear that N_2 is split off and nitrene is formed as a highly reactive intermediate, which can subsequently add to double bonds or insert into labile-CH or -NH groups in polymeric materials. Doping of impurities created certain new energy levels or molecular states. More investigations are required for the optimization to change the sensitivity of this material on other wavelengths without changing its basic properties.

The experimental investigations of electrets (1-4) have so far mainly been confined to the nature of the charge developed in different types of dielectric materials. But very little work has been done in complex dielectric systems. Here, the efforts have been made to study the electret and photoelectret (5, 6) effects in photoresist (7) material. These are the organic compounds whose structure and solubility change on exposure to ultraviolet light. The use of photoresist materials in semiconductor technology (8) is well known. Photoresists, in liquid state, are less sensitive to light, but sensitivity increases rapidly as they become dry, as the solvent retention interferes with cross-linking by exposure. During the exposure of these materials to light, photocrosslinking takes place. The cross-linking (9) process involves a chain reaction in which a considerable number of molecules interact to form a high molecular weight material.

A negative photoresist, KTFR (10) made by Kodak Company, has been selected for study. It contains a photocrosslinking agent along with a synthetic polymer in a solvent-based solution. The polymer has been established as a partially cyclized cis-polyisoprene with a double bond content of the polymer of 17% which corresponds to one double bond per ten carbon atoms. A proposed structure for this polymer is (10)



A diazide is used as the photoinitiator to promote photocrosslinking in this solution. This material has an advantage that it can be used to make electrets as

Key words: discharge, current, electret.

well as photoelectrets. The photoelectret behavior is different in this material from that in regular photoelectrets. Once a photoelectret of this material is made, the material cannot be used again and depolarization current cannot be observed with the help of exposure to light.

This paper presents the thermally stimulated discharge current studies of KTFR material and calculations for trap depth, relaxation time, and charge, etc. These parameters are very helpful in understanding the nature of the material. Efforts are also made to dope this material with impurities like iodine and rhodamine to study their effect in changing the basic properties of the material.

Experimental

Thin films of KTFR were made on glass slides (8). To achieve coatings of controlled and uniform thickness, xylene was used to lower the viscosity of the resist solution. For making the thin films, glass substrates were kept on a motor driven rotary vacuum chuck mounted in a bowl. The surface is then flooded with the liquid resist through a syringe with a filter membrane and the motor is turned on. The centrifugal forces distribute the viscous liquid evenly before much solvent evaporation takes place, and the excess material thrown off at the substrate edges. The platform was rotated with a speed of 1000 rpm. The film thickness of these deposited films varied from 5 to 8 μm . Doped films of this resist were also made by mixing the known quantity of I_2 and rhodamine in benzene and alcohol with resist solution (11). These films were then baked in a thermostat at 80°C for half an hour to remove the solvent from the films.

Aluminum electrodes were vacuum-evaporated onto these films leaving a parallel gap of 1 mm between the electrodes for the TSC measurements. The films were subjected to a high d-c field for polarization, at temperature T_p for a fixed period of time, and then cooled to room temperature under the same electric stress.

Ten minutes after the removal of the electrical field the films were placed in a shielded chamber to measure TSC in which the temperature increased at a constant rate, i.e., 5°C min⁻¹ from room temperature to 200°C. The temperature of the sample was measured with a copper-constantan thermocouple. An X-Y (Varian F-80) recorder and a Keithley 610C electrometer were used for the measurements (11).

Theory (12, 13)

The discharge current associated with the change of polarization due to heating is given by

$$i = \frac{p_0}{\tau} \exp\left(-\int_0^t \frac{dt}{\tau}\right) \quad [1]$$

where p_0 is the initial polarization of the sample and τ is the relaxation time. The total charge thermally released is given by

$$Q = \int_0^\infty i dt \quad [2]$$

The temperature dependence of the relaxation time can be written as

$$\tau = \tau_0 \exp\left(\frac{u}{kT}\right) \quad [3]$$

where τ_0 is a constant, u is the activation energy, k is the Boltzmann constant, and T is the temperature. Equation [1] can be written as

$$i(T) = \frac{p_0}{\tau_0} \exp\left[-\frac{u}{kT} - \frac{1}{\beta\tau_0} \int_{T_0}^T \exp\left(-\frac{u}{kT'}\right) dT'\right] \quad [4]$$

where β is the heating rate.

The temperature T_m for the maximum current is now given by

$$\tau_0 = \frac{kT_m^2}{\beta u \exp\left(\frac{u}{kT_m}\right)} \quad [5]$$

while the low temperature distribution in Eq. [4] can be written as

$$\ln i(T) = \text{const.} - \frac{u}{kT} \quad [6]$$

The activation energy u can now be determined from a semilog plot of the temperature dependence of the current. τ_0 can be calculated from Eq. [5]. The TSC peaks have been analyzed by other workers in the case of semiconductors and dielectrics. Grossweiner (14) has extended the TSC technique to find the capture cross section and also the detrapping frequency. The expressions used are

$$\sigma_n = \frac{\nu}{2.9 \times 10^{24} T_m^2} \quad (m^2)$$

$$\nu = \frac{3T_m\beta}{2T_m(T_m - T')} \exp\left(\frac{u}{kT_m}\right) \quad [5']$$

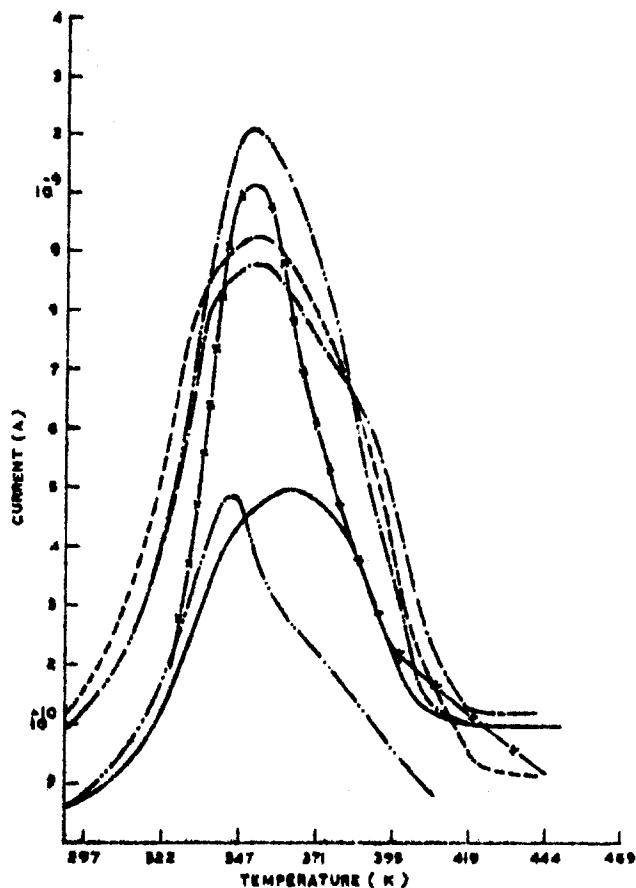


Fig. 1. TSC spectra of pure KTRF films polarized at various temperatures ($E_p = 1.5$ kV/cm; $t_p = 45$ min). — 333°K, --- 353°K, -x-x- 373°K, 396°K, - - - - - 423°K, - - - - - u.v. light.

where σ_n is the capture cross section, ν is the attempt to escape frequency, β the heating rate, and T' the temperature at half maximum intensity on the low temperature side.

Results

The TSC spectra of pure and doped KTRF is shown in Fig. 1-4. Figure 1 shows the spectra of pure KTRF films polarized at different temperatures under the electric field of 1.5 kV/cm. These curves show that the charge retaining capacity increases with the increase of the polarizing temperature. The various parameters were calculated from these curves and are shown in Table I. Relaxation time (τ_0) decreases with the increase of polarizing temperature. As the material is sensitive to u.v. light, the samples having a polarizing field of 1.5 kV/cm were exposed to it at room temperature and for the same polarizing time. It was found that the energy of u.v. light is sufficient in KTRF sample to polarize it and give the photoelectret effect. The results can be seen in Fig. 1. The sample was exposed for 30 min by a 100W mercury lamp, for u.v. irradiation.

Table I

Temperature of polarization T_p (°K)	Maximum temperature (T_m) (°K)	Activation energy u (eV)	Relaxation time τ (sec)	Relaxation time corresponding to T_m sec ($\times 10^2$)	Attempt to escape frequency ν (sec ⁻¹)	Capture cross section σ (m ²)	Charge Q (C) $\times 10^{-9}$
333	3625	0.49	4.2×10^{-5}	2.8	2.4×10^4	6.3×10^{-26}	5.2
353	353	0.48	3.7×10^{-5}	2.7	2.7×10^4	7.6×10^{-26}	7.8
	389	1.74	2.3×10^{-21}	0.9	4.3×10^{20}	9.8×10^{-10}	0.6
373	350	0.87	4.3×10^{-11}	1.5	2.4×10^{10}	6.6×10^{-20}	6.0
	395	1.64	1.1×10^{-10}	0.98	9.4×10^{18}	2.1×10^{-11}	2.5
396	350	0.59	6.8×10^{-7}	2.2	1.5×10^6	4.1×10^{-24}	6.4
	391	1.32	1.1×10^{-15}	1.2	8.9×10^{14}	2.0×10^{-15}	1.4
423	350	0.70	1.5×10^{-8}	1.8	6.7×10^7	1.9×10^{-22}	8.1
u.v.	344	0.77	8.3×10^{-10}	1.6	1.2×10^9	3.5×10^{-21}	2.6
radiation	371	1.44	2.5×10^{-18}	0.99	4.0×10^{17}	1.0×10^{-20}	1.2

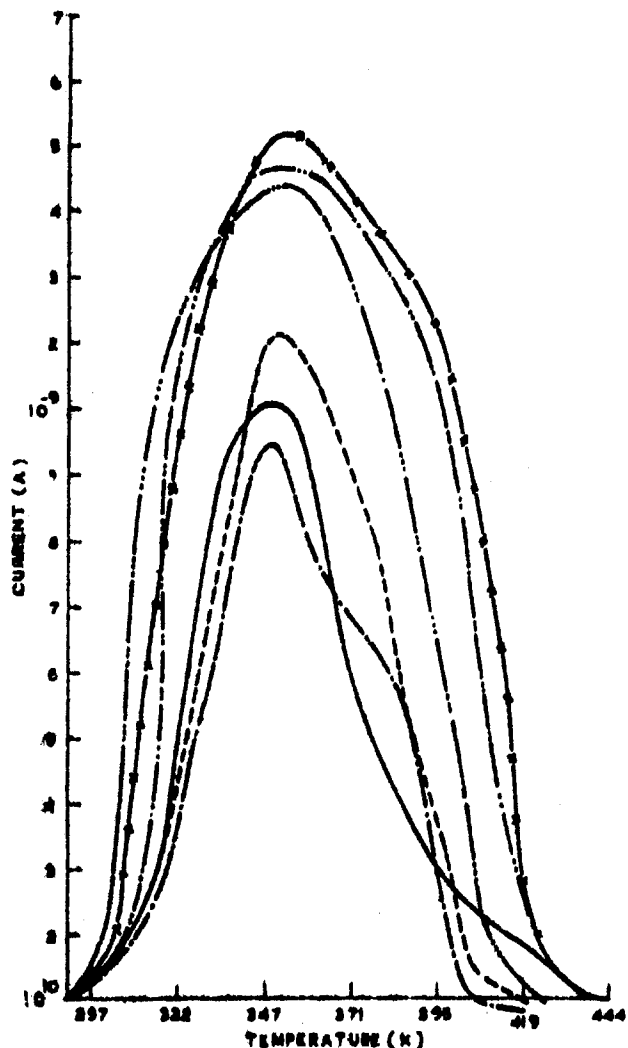


Fig. 2. TSC spectra of pure KTFR films polarized at various fields, 431°K for 40 min. - · - · - 1 kV/cm, — 1.25 kV/cm, - - - - 1.5 kV/cm, - · - · - 2.0 kV/cm, - - - - 3.0 kV/cm, -x-x- 4.5 kV/cm.

tion, kept at a distance of 8 cm. The sample was maintained at room temperature in the presence of air. This exposure produces charge in the sample at room temperature comparable to the result obtained with the thermo-electrets prepared at 60°C with the same polarizing field.

Figure 2 shows the results obtained with the samples of KTFR polarized at different polarizing fields and at 431°K for 40 min. The samples attained more charge with the increase of polarizing field. The calculated parameters are shown in Table II. It is observed that the relaxation time increases with the increase of polarizing field. Figure 3 shows the TSC spectra of 5% rhodamine-doped KTFR films polarized with 1.5 kV/cm for 40 min at different polarizing temperatures.

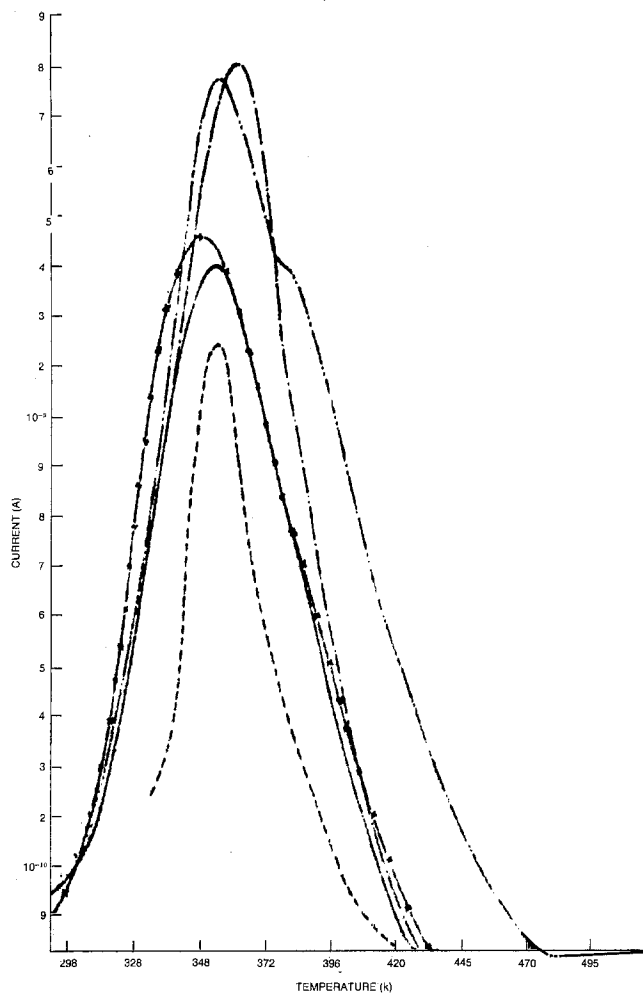


Fig. 3. TSC spectra of rhodamine-doped KTFR films polarized at various temperatures ($E_p = 1.5$ kV/cm; $t_p = 40$ min). - · - · - 353°K, — 377°K, - - - - 397°K, -x-x- 423°K, - · - · - 457°K.

The first intense peak occurs around 350°K, while the second peak was observed with the samples polarized at higher temperatures and disappeared at lower temperatures. Figure 4 shows the TSC spectra of 5% iodine-doped KTFR films polarized at various polarizing temperatures. The current increases with the increasing polarizing temperature in a similar way to that observed in the case of KTFR films. Two peaks were observed in this case. Calculated parameters are shown in Tables III and IV.

KTFR films doped with rhodamine were polarized under u.v. radiation at different polarizing voltages, and at room temperature. The results are shown in Fig. 5. One sample was polarized at zero field which did not show any significant polarization effect. Other samples polarized with polarizing fields show the presence of two TSC peaks. It clearly shows that during the polymerization, if there is a d-c field applied, exposure

Table II

Polarizing voltage variation (V_p) (volts)	Maximum temperature T_m (°K)	Activation energy u (eV)	Relaxation time τ (sec)	Relaxation time corresponding to T_m (sec) $\times 10^2$	Attempt to escape frequency ν (sec ⁻¹)	Capture cross section σ (m ²)	Charge Q (C) $\times 10^{-8}$
100	350	0.69	2×10^{-8}	1.8	5.1×10^7	1.4×10^{-22}	0.6
	383	1.14	1.2×10^{-28}	1.3	8.1×10^{12}	1.9×10^{-17}	0.8
125	347	0.61	2.7×10^{-7}	2.0	3.7×10^9	1.0×10^{-23}	6.4
	389	0.93	1.4×10^{-10}	1.7	7.0×10^9	1.6×10^{-20}	1.1
150	350	0.69	1.5×10^{-8}	1.8	6.7×10^7	1.9×10^{-22}	7.4
	377	1.49	1.1×10^{-18}	1.0	9.2×10^{17}	2.2×10^{-12}	1.6
200	353	0.38	1.2×10^{-8}	3.4	8.0×10^2	2.2×10^{-27}	56.4
	353	0.42	3.0×10^{-4}	3.0	3.3×10^8	9.1×10^{-27}	63.6
450	353	0.40	6.1×10^{-4}	3.2	1.6×10^8	4.5×10^{-27}	45.0
	400	0.94	2.4×10^{-10}	1.8	4.2×10^9	9.0×10^{-21}	36.0

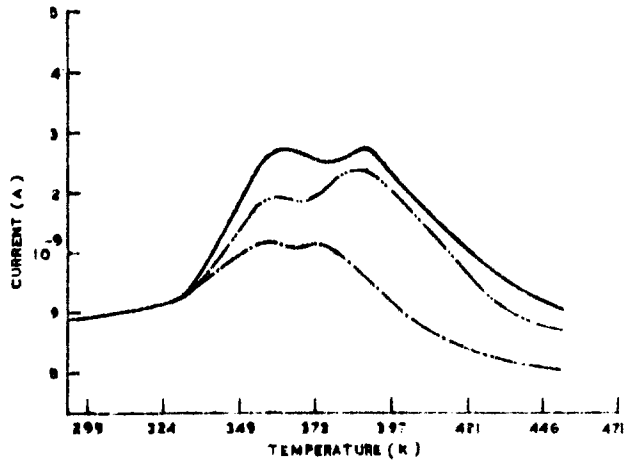


Fig. 4. TSC spectra of 5% iodine-doped KTFR films polarized at various temperatures ($E_p = 1.5$ kV/cm, $t_p = 40$ min). - - - - 353°K, ——— 373°K, - · - · - 393°K.

can produce electrets at room temperature. Figure 6 shows the variation of peak currents of TSC spectra with their respective temperatures.

Discussion

The decay of an electret proceeds slowly at room temperature, therefore, it is advisable to stimulate the discharge by heating. Bucci and Fieshi (12) have put forward a theory of ITC. This theory has been generalized by Gross (15), Perlman (16), and Thurnhout (17) for electret effect (18). The permanent polarization in electrets has been attributed mainly to the orientation of dipoles, but no observation in this respect has been recorded so far. The electric polarization of these dielectrics can be produced by dipole alignment, migration of ions within the material, or charge injection from the electrodes. The trapping center originates in the transition of the crystalline state into amorphous regions, in the rearrangement of molecules in the polymer chain, and from the presence of impurities and defects in the material. The various defects, in addition to giving rise to their own characteristic trapping levels, can also combine with other trapping centers present around them, and thus they can modify qualitatively as well as quantitatively the TSC spectra observed under different conditions. It is, therefore, difficult to correlate a peak with a particular configuration of defects in the material. Since this material has a special property of its sensitivity to

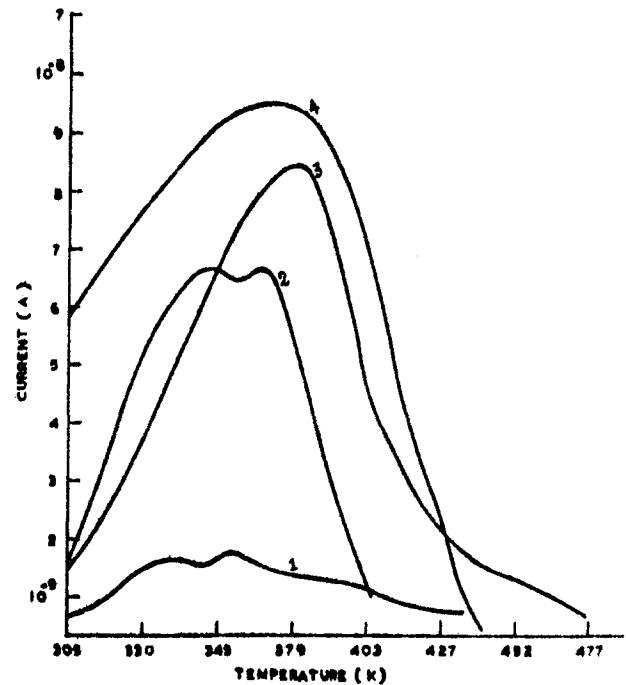


Fig. 5. TSC spectra of rhodamine-doped KTFR films polarized at various fields, 431°K for 45 min. Curve 1, 0 kV/cm; curve 2, 0.5 kV/cm; curve 3, 1.0 kV/cm; curve 4, 2.0 kV/cm.

ultraviolet radiation, it can be used to give a photoelectret also (5).

Photopolymerization of monomers involves a chain reaction in which a considerable number of molecules interact to form a high molecular weight material. When insolubility is required a poly-functional monomer is added to the monomer mixture in order to promote cross-linking. Photoinitiated polymerization requires the generation of an initiating species under the influence of light. Therefore, the photopolymerization process is restricted to monomers subject to free radical initiation and propagation. The generation of free radicals at room temperature occurs when this material is exposed to light. Photocrosslinking of a polymer may be achieved by several different methods. However, in all cases preformed polymers are converted into higher molecular weight. Cross-linking may result when polymers containing functional groups subject to photosensitized dimerization are exposed to

Table III. KTFR:rhodamine 5% (temperature variation)

Temperature of polarization T_p (°K)	Maximum temperature T_m (°K)	Activation energy u (eV)	Relaxation time τ (sec)	Relaxation time corresponding to T_m (sec) $\times 10^2$	Attempt to escape frequency ν (sec ⁻¹)	Capture cross section σ (m ²)	Charge Q (C) $\times 10^{-5}$
353	354	1.12	1.8×10^{-10}	1.4	5.5×10^9	1.9×10^{-20}	6.7
377	353	0.54	4.5×10^{-6}	2.4	2.2×10^6	6.1×10^{-25}	11.4
397	360	0.54	6.6×10^{-6}	2.5	1.5×10^5	4.0×10^{-26}	14.0
423	348	0.53	4.8×10^{-6}	2.4	2.1×10^6	5.9×10^{-25}	10.0
	390	0.68	3.6×10^{-7}	2.3	2.8×10^6	6.2×10^{-24}	7.7
457	354	0.60	6.0×10^{-7}	2.1	1.7×10^6	4.6×10^{-24}	12.9
	402	0.86	3.1×10^{-9}	1.9	3.3×10^8	6.9×10^{-22}	7.5

Table IV. KTFR:5% iodine, temperature variation

Temperature of polarization T_p (°K)	Maximum temperature T_m (°K)	Activation energy u (eV)	Relaxation time τ (sec)	Relaxation time corresponding to T_m (sec) $\times 10^2$	Attempt to escape frequency ν (sec ⁻¹)	Capture cross section σ (m ²)	Charge Q (C) $\times 10^{-8}$
353	355	0.61	8.9×10^{-7}	1.5	1.1×10^{10}	3.1×10^{-20}	5.0
	385	0.96	4.1×10^{-11}	1.6	2.4×10^{10}	5.7×10^{-20}	6.0
373	355	0.48	4.0×10^{-5}	2.7	2.5×10^4	6.8×10^{-26}	9.4
	400	1.38	4.3×10^{-16}	1.2	2.3×10^{15}	5.0×10^{-16}	1.7
397	358	0.58	2.9×10^{-5}	2.4	3.4×10^6	9.3×10^{-26}	42.0
	403	1.06	8.3×10^{-12}	1.6	1.2×10^{12}	2.6×10^{-19}	12.6

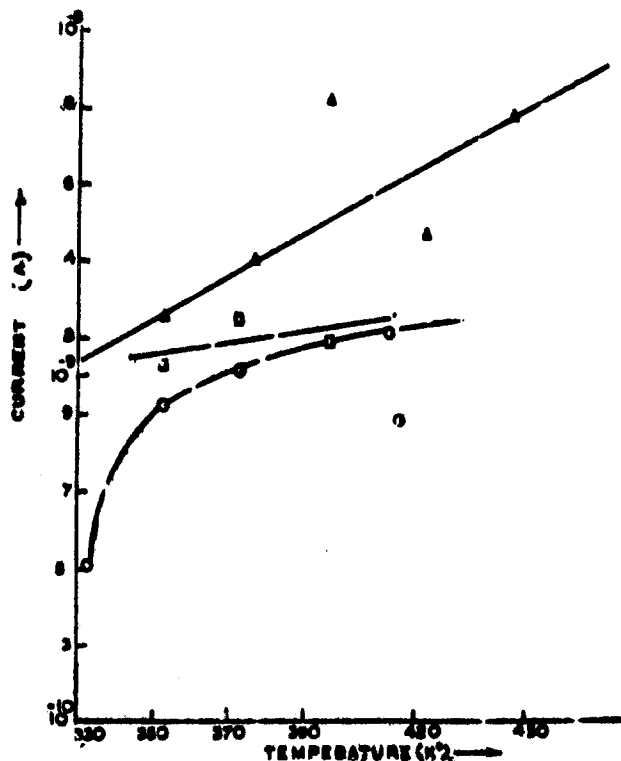
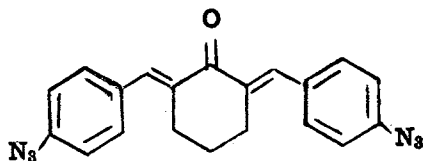


Fig. 6. Variation of peak currents of TSC spectra at their respective temperatures. \circ — pure KTFR, \square — KTFR doped with 5% I_2 , \triangle — KTFR doped with 5% rhodamine.

light or upon photolysis of polymers containing groups which are photolabile.

The negative photoresist (KTFR) was made by dissolving bis(4-azidobenzal)-cyclohexanone



and cyclized polyisoprene in Kodak KTFR thinner (19, 20), cyclized polyisoprene was prepared by refluxing a solution of toluene, cis-1,4-polyisoprene, and p-toluenesulfonic acid. Cyclized rubber was dissolved in KTFR thinner and bisazide was added based on polymer. The available information is ambiguous regarding the initial step in the photoreaction of a variety of bisazides. But it is clear that N_2 is split off and nitrene formed as a highly reactive intermediate which can subsequently add to double bonds or insert labile $-CH$ or $-NH$ groups in polymeric materials. Bisazide derivatives can be used as cross-linking additives to polymers containing residual unsaturation, e.g., cis-1,4-polyisoprene, cyclized rubber, or cyclized polyisoprene and chlorinated rubber. When the azide groups are attached to a polymer, backbone photocrosslinking occurs.

The first photoelectret was formed with u.v. irradiation of ordinary KTFR and then with rhodamine-doped KTFR. In this case, unlike an ordinary photoelectret, a discharge current is not possible by reilluminating the sample with the u.v. light since the u.v.

absorbing bisazide is photodecomposed and hence TSC measurements have been made by increasing the temperature at a linear rate. These results are not sufficient to give a conclusion about the effect of the rhodamine dopings on the basic properties of the material. Efforts are in progress to see whether the photosensitivity of this material can be changed to some other wavelength without changing the basic photocrosslinking property of the material.

Similar type of behavior, i.e., of thermoelectret phenomenon was observed with ordinary and I_2 -doped KTFR. It cannot be confirmed until the material doped with I_2 is studied with conductivity, EPR, infrared spectroscopy, etc. measurements, that I_2 will be able to link the polymer molecules by forming donor-acceptor complexes at appropriate sites on the chain. Electron transfer from a polymer chain to iodine then allows easy movement of charge along with the molecule.

Conclusion

It is possible to form thermoelectrets and photoelectrets using KTFR. Doping of impurities created certain new molecular states. Further detailed measurements are required to optimize the sensitivity of this material to other wavelengths without changing its basic properties. With this change, utility of this material in semiconductor technology will increase.

Acknowledgment

We are grateful to Prof. S. C. Jain for his encouragement and permission to publish this work.

Manuscript submitted April 18, 1979; revised manuscript received Sept. 24, 1979.

Any discussion of this paper will appear in a Discussion Section to be published in the December 1980 JOURNAL. All discussions for the December 1980 Discussion Section should be submitted by Aug. 1, 1980.

REFERENCES

1. B. Gross, *J. Chem. Phys.*, **17**, 866 (1949); *Phys. Rev.*, **66**, 26 (1944); **57**, 57 (1940).
2. P. K. C. Pillai, K. Jain, and V. K. Jain, *Phys. Status Solidi A*, **13**, 341 (1972); **4**, 29 (1971); *J. Phys. D*, **3**, 829 (1970).
3. D. E. Tilly, *This Journal*, **115**, 40 (1968).
4. M. M. Perlman, *J. Appl. Phys.*, **42**, 2645 (1971).
5. V. M. Fridkin and I. S. Zheludev, "Photoelectrets and Electrophotographic Process," Consultants Bureau, New York (1960).
6. P. K. C. Pillai, K. G. Balakrishnan, and V. K. Jain, *J. Appl. Phys.*, **42**, 525 (1971).
7. K. G. Clark, *Electron. Comp.*, **13**, 869 (1972); **14**, 553 (1973).
8. K. G. Clark, *ibid.*, **14**, No. 14, 711 (1973); *Microelectron.*, **3**, 25 (1971).
9. K. G. Clark, *Microelectron.*, **3**, 23 (1971).
10. K. G. Clark, *Electron. Comp.*, **14**, 621 (1973).
11. V. K. Jain, C. L. Gupta, R. K. Jain, and R. C. Tyagi, *Thin Solid Films*, **48**, 175 (1978).
12. C. Bucci and R. Fieschi, *Phys. Rev. Lett.*, **12**, 16 (1964).
13. G. F. J. Garlick and A. F. Gibson, *Proc. Phys. Soc. London*, **60**, 574 (1948).
14. L. I. Grossweiner, *J. Appl. Phys.*, **24**, 1306 (1953).
15. B. Gross, *This Journal*, **115**, 376 (1968).
16. M. M. Perlman, *J. Appl. Phys.*, **42**, 2465 (1971).
17. J. V. Turnhout, *Polym. J.*, **2**, 173 (1971).
18. P. K. C. Pillai, K. Jain, and V. K. Jain, *Phys. Lett. A*, **35**, 403 (1971).
19. S. Shimizu and G. R. Bird, *This Journal*, **124**, 1394 (1977).
20. S. Shimizu, *ibid.*, **125**, 1127 (1978).

Capless Annealing of Ion-Implanted Gallium Arsenide by a Melt-Controlled Ambient Technique

C. Lawrence Anderson,* K. V. Vaidyanathan,* H. L. Dunlap, and G. S. Kamath

Hughes Research Laboratories, Malibu, California 90265

ABSTRACT

A novel capless technique for the annealing of ion-implanted GaAs is described. The apparatus employed consists of a large solution of GaAs in Ga, into which is immersed a suitable sample holder containing the wafer to be annealed. Se-implanted layers annealed using this technique behave electrically in the manner expected for well-annealed group VI dopant implants into GaAs. The electrical activity of implanted Si, however, decreases with increasing anneal temperature in the range from 800° to 900°C. Possible explanations for the behavior of the implanted Si are discussed.

Dielectric encapsulants such as SiO_2 (1), Si_3N_4 (2, 3, 4), and AlN (5) are commonly used to prevent dissociation of GaAs during the annealing cycles required to electrically activate ion-implanted impurities. In such "capped" annealing cycles, the dielectric encapsulant must perform a number of partially contradictory functions if the implanted layer is to exhibit good electrical properties. The encapsulant must possess sufficient mechanical integrity and adherence to GaAs to remain intact during the annealing cycle, yet it must be sufficiently plastic that it will not stress the GaAs severely as a result of thermal expansion mismatch. It must be chemically stable and inert to prevent it from reacting with and/or doping the GaAs, yet it must be readily removable by chemical means. To maintain surface stoichiometry, it must also be impermeable to the outdiffusion of Ga and As.

Considering the diverse demands on the dielectric encapsulants during "capped" annealing, it is not surprising that there has been considerable interest recently in encapsulant-free or "capless" annealing techniques. Previously reported successful techniques include performing the anneals in flowing ambients with controlled arsenic vapor pressure (6), embedding the sample in powdered graphite previously saturated with Ga and As (7), and placing the implanted sample in close proximity to an unimplanted GaAs sample (8). In this paper we discuss a novel approach to capless annealing of GaAs (9). In this technique, a highly stable controlled ambient is provided by a solution of Ga saturated with GaAs. The sample, contained in a specially designed sample holder, never comes into physical contact with the solution, but vapor phase contact is maintained between the solution and the sample. Thus, the solution acts as a large thermodynamic reservoir which provides a highly reproducible arsenic vapor pressure in the vicinity of the sample. For this reason, we have termed this annealing concept the melt-controlled ambient technique, or MCAT.

Description of Apparatus and Experimental Procedure

The apparatus used in MCAT annealing was originally developed for liquid phase epitaxial growth of III-V compound semiconductors employing a large solution (10-12). This system, illustrated schematically in Fig. 1, consists of a crucible which contains the required solution, which typically has a mass of a few kilograms. This crucible is contained in an all-quartz annealing chamber which is connected to a stainless steel entry chamber through a high vacuum valve. The interior annealing chamber is continuously maintained in an ambient of palladium-diffused hydrogen. If desired, it could be maintained easily with other ambients. The entry chamber can be independently evacu-

ated and purged. By use of a linear motion feedthrough mounted in the top cap of the entry chamber and by employing adequate purging procedures, it is possible to introduce samples into the annealing chamber without introducing significant amounts of gaseous contaminants into the system.

Samples to be annealed are held in a specially designed graphite sample holder. The chamber which contains the sample is enclosed by a sliding cover. This design does not allow the melt to come into contact with the samples being annealed. The sample holder, while liquid tight, is not vapor tight. Annealing is performed by immersing the samples in the melt maintained at the required temperature. Using this technique, samples of ion-implanted GaAs have been annealed at temperature up to 900°C. The surface morphology of MCAT annealed samples is generally indis-

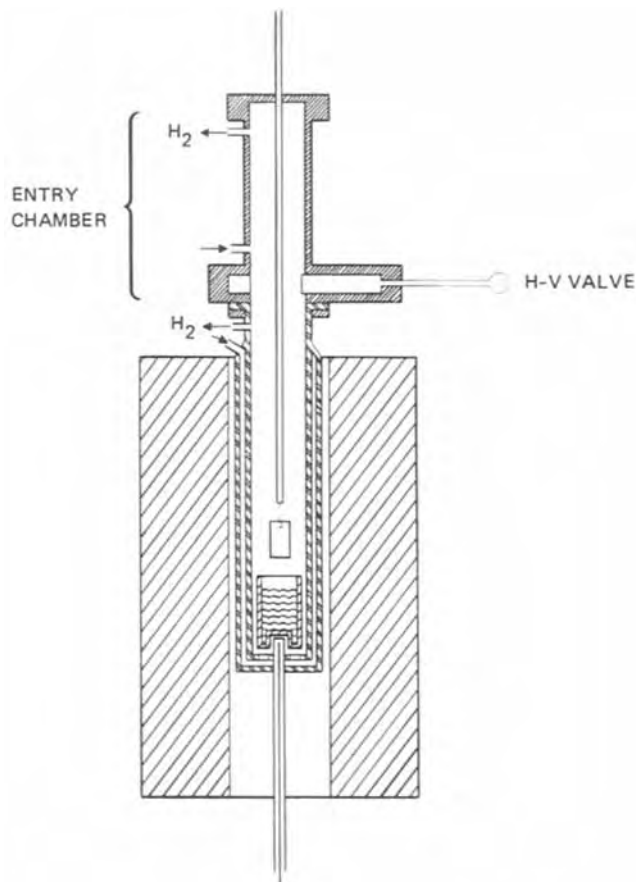


Fig. 1. Schematic of the MCAT annealing apparatus

* Electrochemical Society Active Member.

Key words: gallium arsenide, ion implantation, capless annealing, electrical properties.

Table I. Electrical properties of room temperature Se-implanted, MCAT-annealed GaAs

Dose/energy	Anneal temperature (°C)	Sheet resistivity (Ω/\square)	Hall electron mobility ($\text{cm}^2 \text{V}^{-1} \text{s}^{-1}$)	Sheet electron concentration (cm^{-2})
$1 \times 10^{13} \text{ cm}^{-2}$ 260 keV	800	2720 ± 730	2200 ± 230	$(1.1 \pm 0.2) \times 10^{12}$
$5 \times 10^{13} \text{ cm}^{-2}$ 260 keV	850	600 ± 125	2870 ± 270	$(3.7 \pm 0.6) \times 10^{12}$
$1 \times 10^{14} \text{ cm}^{-2}$ 260 keV	850	1420 ± 470	1970 ± 530	$(2.4 \pm 0.3) \times 10^{12}$
$1 \times 10^{14} \text{ cm}^{-2}$ 260 keV	875	620 ± 40	2470 ± 50	$(4.1 \pm 0.2) \times 10^{12}$
$1 \times 10^{14} \text{ cm}^{-2}$ 260 keV	850	1170 ± 120	2280 ± 160	$(2.4 \pm 0.1) \times 10^{12}$
$1 \times 10^{14} \text{ cm}^{-2}$ 260 keV	875	630 ± 70	2070 ± 170	$(4.8 \pm 0.3) \times 10^{12}$

* Se corner contact implants, $5 \times 10^{13} \text{ cm}^{-2}$ at 220 keV; all control samples had $R_s > 7 \times 10^4 \Omega/\square$.

tinguishable from that of unannealed samples under electron microscopic examination.

Experimental Results

Samples from (100) Cr-doped semi-insulating ingots obtained from Crystal Specialties, Incorporated were implanted with either 260 keV Se or 100 keV Si. The Si implants were performed at room temperature. Se implants were performed at either 250°C or at room temperature. The samples were tilted at $\sim 7^\circ$ relative to the incident ion beam to avoid channeling effects. The samples were then MCAT annealed at the required temperature. Square ($\sim 4 \times 4 \text{ mm}$) Hall specimens cleaved from the implanted wafers were prepared by making ohmic contacts at the corners using an In:Ag:Ge alloy.

Results from Hall effect measurements performed on room temperature Se-implanted samples are presented in Table I. A range of doses from $1 \times 10^{13} \text{ cm}^{-2}$ to $1 \times 10^{14} \text{ cm}^{-2}$ was covered and the samples were MCAT annealed at the temperatures shown. The electrical activation in all cases studied is rather poor. This result is consistent with previous studies which show that high activation from the moderate fluence Se implants is generally obtained only from samples implanted at elevated temperatures ($> 150^\circ\text{C}$) (13-15). Since con-

siderable surface dissociation can take place at implant temperatures in excess of 400°C (16-17), elevated temperature Se implants were performed at 250°C . These samples were MCAT annealed at temperatures between 800° and 900°C for 30 min. The electrical properties of these layers are presented in Fig. 2. This figure shows the variation of sheet electron concentration (cm^{-2}) and sheet electron mobility ($\text{cm}^2 \text{V}^{-1} \text{s}^{-1}$) as a function of anneal temperature for samples implanted to fluences ranging from $1 \times 10^{13} \text{ cm}^{-2}$ to $1 \times 10^{14} \text{ cm}^{-2}$. The electrical activation at all doses increases with anneal temperature. In the case of low fluence implants ($1 \times 10^{13} \text{ cm}^{-2}$ and less), over 90% of the implanted ions become electrically active when annealed at 900°C for 30 min. The mobilities in these layers were $> 3200 \text{ cm}^2 \text{V}^{-1} \text{s}^{-1}$. In the case of high fluence implants ($1 \times 10^{14} \text{ cm}^{-2}$), sheet carrier concentrations of $6 \times 10^{13} \text{ cm}^{-2}$ with mobilities of $\sim 1800 \text{ cm}^2 \text{V}^{-1} \text{s}^{-1}$ were measured following an anneal at 900°C . These results are in excellent agreement with the highest activation reported for Se-implanted GaAs annealed with an encapsulant.

Figure 3 shows the measured sheet carrier concentration for samples annealed at 900°C as a function of the implant dose. The dashed line represents the case of 100% apparent electrical activation. At low fluences ($< 10^{13} \text{ cm}^{-2}$), almost all the implanted ions are electrically active. Approximately 80% apparent electrical activation is obtained at a fluence of $5 \times 10^{13} \text{ cm}^{-2}$. At high doses, the measured carrier concentration saturates at $\sim 7 \times 10^{13} \text{ cm}^{-2}$. These results are in excellent agreement with the earlier results of Donnelly et al. (15).

Figure 4 illustrates the variation of sheet electron concentration and electron mobility as functions of an-

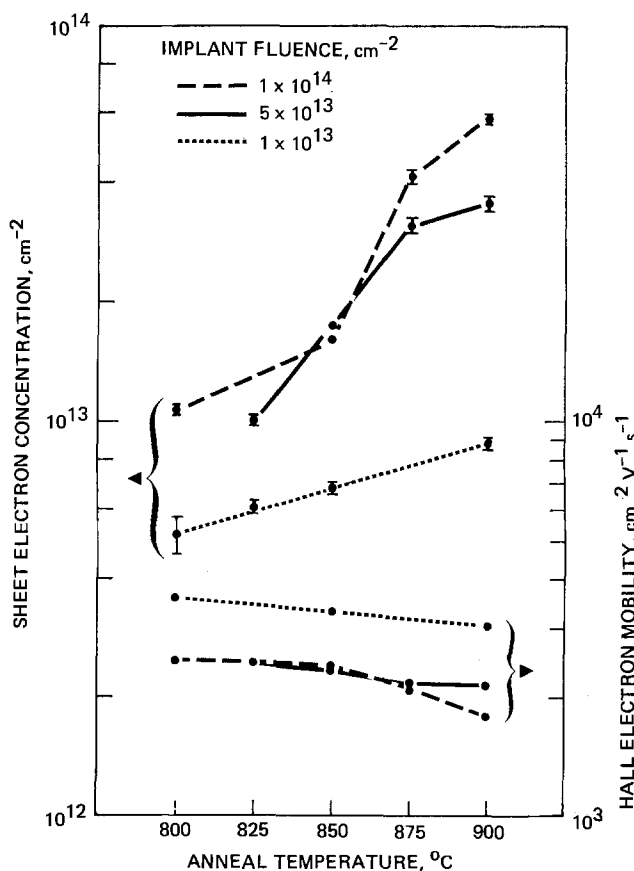


Fig. 2. Variation of sheet carrier concentration and mobility of 260 keV Se-implanted samples as a function of anneal temperature. The samples were implanted at 250°C to fluences indicated.

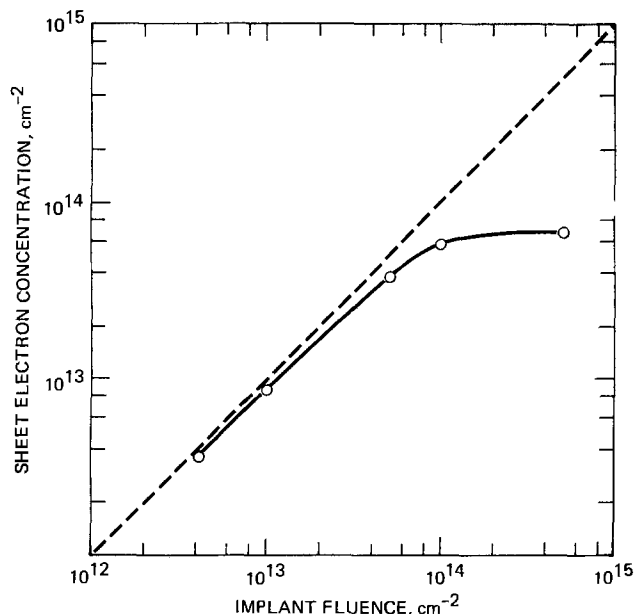


Fig. 3. Sheet carrier concentration vs. dose for 260 keV Se-implanted GaAs. The implants were performed at 250°C and post-annealed using MCAT at 900°C for 30 min.

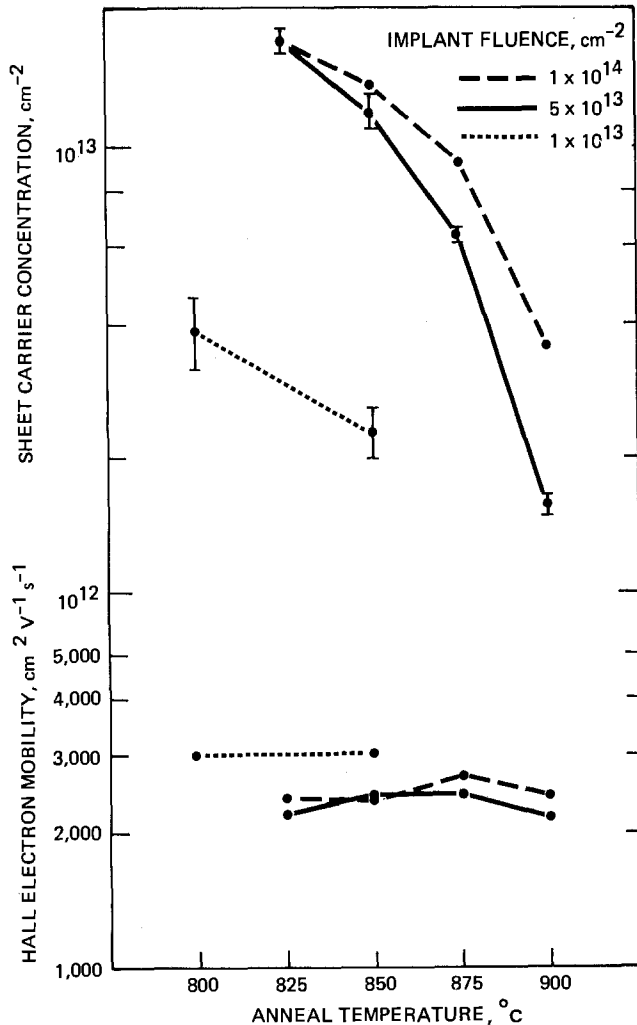


Fig. 4. Sheet carrier concentration and mobility as a function of anneal temperature for 100 keV Si-implanted GaAs.

neal temperature for samples implanted at room temperature to different fluences with 100 keV Si⁺. In contrast to the behavior of the Se-implanted samples, the measured sheet carrier concentration in the Si-implanted samples decreases as the anneal temperature is increased in all cases studied. The mobility stays essentially constant. These results are contrary to the normal encapsulated annealing behavior of Si-implanted GaAs.

Two possible explanations for the anomalous annealing behavior of silicon-implanted MCAT annealed GaAs are as follows: first, drastic redistribution of implanted silicon during annealing with concurrent loss of silicon due to outdiffusion would explain the observed results. Preliminary secondary ion mass spectrometry (SIMS) studies of the annealed sample indicate that the silicon distribution remains roughly gaussian following MCAT annealing. Second, the implanted silicon may be exhibiting amphoteric doping behavior. If the solution is not completely saturated at the anneal temperature, or if the vapor exchange between the sample and the solution is insufficient, As vacancies may be generated in the sample. In the presence of these vacancies, the implanted silicon will tend to occupy As sites and thus act as an acceptor. Recently, Walukiewicz *et al.* (18) have studied the effect of compensation on electron mobility in GaAs. Using their data in conjunction with the measured mobility, we estimate the compensation ratio in these samples to be greater than 0.5. We believe that the poor activation observed in Si-implanted MCAT annealed samples can be explained at least in part on the basis of the amphoteric doping behavior of silicon in GaAs. Techniques to alter the vapor pressure of As within the

sample holder, and the effect of these techniques on the electrical behavior of implanted Si, are presently under investigation and should help clarify the situation. In addition, extension of this technique to other semiconductors (e.g., InP) and to other dopants in GaAs is in progress.

Conclusions

The melt-controlled ambient technique (MCAT), which employs the vapors of a solution of GaAs in Ga as a source of As overpressure for capless annealing, has been used to anneal Si- and Se-implanted GaAs. Excellent electrical activation and high electron mobilities have been achieved in Se-implanted samples. In the case of Si-implanted samples, however, low electrical activation and mobilities consistent with moderately high compensation have been observed. This behavior has been attributed to amphoteric behavior of Si under As-deficient conditions.

Acknowledgment

This work was supported in part by the Air Force Office of Scientific Research.

Manuscript submitted Sept. 17, 1979; revised manuscript received Nov. 13, 1979. This was Paper 107 presented at the Boston, Massachusetts, Meeting of the Society, May 6-11, 1979.

Any discussion of this paper will appear in a Discussion Section to be published in the December 1980 JOURNAL. All discussions for the December 1980 Discussion Section should be submitted by Aug. 1, 1980.

Publication costs of this article were assisted by Hughes Research Laboratories.

REFERENCES

1. A. G. Foyt, J. P. Donnelly, and W. T. Lindley, *Appl. Phys. Lett.*, **14**, 73 (1969).
2. J. P. Donnelly, W. T. Lindley, and C. E. Hurwitz, *ibid.*, **27**, 41 (1975); J. P. Donnelly, F. J. Leonberger, and C. O. Bozler, *ibid.*, **28**, 706 (1976).
3. K. V. Vaidyanathan, M. J. Helix, D. J. Wolford, B. G. Streetman, R. J. Blattner, and C. A. Evans, Jr., *This Journal*, **124**, 1781 (1977).
4. F. H. Eisen, B. M. Welch, K. Gamo, T. Inada, H. Muller, M. A. Nicolet, and J. W. Mayer, in "Applications of Ion Beams to Materials," G. Carter, J. S. Colligan, and W. A. Grant, Editors, Conf. Series 28, Institute of Physics, Bristol, London (1976).
5. K. Gamo, T. Inada, S. Krekeler, J. W. Mayer, F. H. Eisen, and B. M. Welch, *Solid State Electron.*, **20**, 213 (1977).
6. R. M. Malbon, D. H. Lee, and J. M. Whelan, *This Journal*, **123**, 1413 (1976).
7. A. A. Immerlica and F. H. Eisen, *Appl. Phys. Lett.*, **29**, 94 (1976).
8. R. P. Mandal and W. R. Scoble, in "Gallium Arsenide and Related Compounds," Conference Series 45, Institute of Physics, Bristol, London (1978).
9. C. L. Anderson and H. L. Dunlap, U.S. Pat. 4,135,952 (1979).
10. G. S. Kamath, J. Ewan, and R. C. Knechtli, *IEEE Trans. Electron Devices*, ed-24, 473 (1977).
11. G. S. Kamath and H. P. Mitchell, U.S. Pat. 4,026,735 (1977).
12. G. S. Kamath and B. W. Smith, "U.S. Pat. 3,994,755 (1976).
13. A. G. Foyt, W. T. Lindley, C. M. Wolfe, and J. P. Donnelly, *Solid State Electron.*, **12**, 209 (1969).
14. J. M. Woodcock, J. M. Shannon, and D. J. Clark, *ibid.*, **18**, 267 (1975).
15. J. P. Donnelly, in "Gallium Arsenide and Related Compounds," Conference Series 336, Institute of Physics, Bristol, London (1976) and references therein.
16. S. T. Picraux, in "Ion Implantation in Semiconductors and Other Materials," B. Crowder, Editor, Plenum Press, New York (1973).
17. D. J. Mazey and R. S. Nelson, *Radiat. Eff.*, **1**, 229 (1969).
18. W. Walukiewicz, L. Lagowski, L. Jastrezebski, M. Lichtensteiger, and H. C. Gatos, *J. Appl. Phys.*, **50**, 899 (1979).

Aluminum Etching in Carbon Tetrachloride Plasmas

K. Tokunaga* and D. W. Hess**

Department of Chemical Engineering, University of California, Berkeley, California 94720

ABSTRACT

Etch rates of aluminum and native aluminum oxide films in carbon tetrachloride plasmas were investigated as functions of substrate temperature and electrode material in a parallel plate plasma etching system. Use of stainless steel electrodes resulted in the formation of a carbon-chlorine polymer which precluded aluminum etching. Anodized aluminum electrodes minimized polymer formation and etching was achieved. Several inherent differences in the electrode materials were considered to account for this effect. Analysis of the effluent from the reactor suggested possible chemical reactions occurring in the carbon tetrachloride plasma, as well as a precursor to polymer formation.

Although liquid etching techniques abound in current integrated circuit fabrication processes, the intense interest in micron and submicron geometries has recently kindled extensive efforts in plasma-assisted etching (1). Much of this effort has centered around plasma (or reactive ion) etching of silicon-based materials, e.g., polysilicon, silicon nitride, and silicon dioxide. Somewhat less information is available on plasma etching of aluminum or aluminum alloys, which are the most common metallization layers in silicon IC's.

Several investigators have reported the successful etching of aluminum films in a parallel plate plasma etcher using chlorine- or bromine-containing gases (2-7). In particular, aluminum and aluminum alloys have been plasma-etched in boron trichloride (3, 4) and in carbon tetrachloride vapor containing argon (3, 6) or helium (5, 6). Less success has been achieved using hydrogen chloride or chlorine plasmas, presumably due to the inability of these gases to etch through the native aluminum oxide layer on the aluminum surface (3). Reactive ion etching (RIE), however, has demonstrated the ability to etch aluminum and its silicon- and copper-containing alloys in gas mixtures of argon with either chlorine, bromine, hydrogen chloride, or hydrogen bromide, although these processes were not always reproducible (7). Excellent results were obtained with RIE (7) using carbon tetrachloride/argon mixtures.

Information concerning the plasma etching of aluminum films in pure carbon tetrachloride vapor is absent in most studies. Mention has been made of the fact that etching in carbon tetrachloride is possible, at least in RIE (7) or under conditions of very high power densities (6). In this paper, we describe the results of plasma etching aluminum films in carbon tetrachloride vapor using a parallel plate plasma etcher. Successful etching of these films is shown to be dependent upon minimization of a carbon-based polymer resulting from the decomposition of carbon tetrachloride.

Experimental Procedure

The parallel plate plasma etcher used in this investigation is shown in Fig. 1. The substrates were laid on a 20.4 cm diam lower electrode, which was resistance-heated by a coil of stainless steel encased Nichrome wire, and was cooled by circulation of a cooled fluid through 1/8 in. stainless steel tubing, also coiled beneath the electrode. Power from a 13.56 MHz rf generator was supplied to the top electrode, which was separated from the grounded lower electrode by a distance of 2.5 cm. The temperature was monitored by an iron-constantan thermocouple attached to the bottom electrode.

* Electrochemical Society Student Member.

** Electrochemical Society Active Member.

Key words: plasma etching, aluminum, electrode effects, carbon tetrachloride.

Etch gases were metered through needle valves and rotameters, and entered the plasma region through holes in the hollow upper electrode. The ideal gas flow rate at standard conditions was determined for the CCl_4 rotameter by measuring the rate of weight loss of the CCl_4 container at 20°C. The pressure was monitored by a capacitance manometer, and could be changed by varying the setting of a throttle valve on the pump and/or by changing the etch gas flow rate. A liquid nitrogen cold trap between the pump and the vacuum system prevented oil back-diffusion and protected the pump from corrosive gases.

Etch samples were prepared by evaporating aluminum from a tungsten filament on to 2.2 cm diam Pyrex cover slips or onto oxidized silicon wafers. The film thicknesses studied ranged from 30 to 1000 nm, but were usually 400 nm.

A test run was generally performed to establish the etch gas flow rate and the rf power and impedance matching. Etch runs were typically carried out at

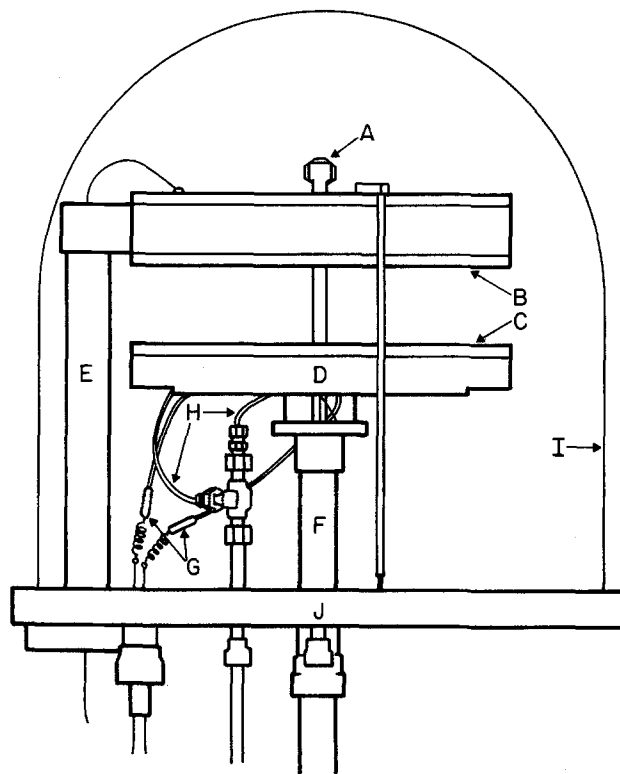


Fig. 1. Parallel plate plasma etcher. (A) gas input; (B), (C), upper and lower electrode plates; (D) heating and cooling plate; (E) rf power feedthrough column; (F) pumping port and lower electrode support; (G) heating coil; (H) cooling coil; (I) Pyrex bell jar; (J) stainless steel base plate.

100W rf power (0.3 W/cm^2), and 67 Pa (0.5 Torr) pressure, which corresponds to $\sim 30 \text{ sccm CCl}_4$ for the above system. Since etching commenced on the edge of the samples and proceeded toward the center of the substrates, the etch time was taken as the time necessary to completely clear the aluminum film.

Results and Discussion

It is well known that aluminum films have on their surface a native oxide film, that presents a low etch rate barrier to chlorinated etch gases (3-7). In an attempt to determine both the aluminum and the native oxide etch rates, data were taken simultaneously on both thin (30-40 nm) and thick ($>300 \text{ nm}$) aluminum films. The total etch time for these two films can then be expressed by

$$t_1 = \frac{(T_{\text{ox}})_1}{r_{\text{ox}}} + \frac{(T_{\text{Al}})_1}{r_{\text{Al}}} \quad [1]$$

$$t_2 = \frac{(T_{\text{ox}})_2}{r_{\text{ox}}} + \frac{(T_{\text{Al}})_2}{r_{\text{Al}}} \quad [2]$$

where t_1, t_2 = etch times for samples 1 and 2, T_{ox} = the thickness of the native aluminum oxide film, T_{Al} = the thickness of aluminum film, r_{ox} = the etch rate of native aluminum oxide film, and r_{Al} = the etch rate of aluminum film. However, since $(T_{\text{ox}})_1 = (T_{\text{ox}})_2 \cong 3 \text{ nm}$ (11), etch time measurements allow the calculation of etch rates for both aluminum and the native aluminum oxide films. It should be mentioned that the etch rates determined for the native oxide films by this method assume that the inhibition of aluminum etching by chlorinated gases is due solely to the slow etching aluminum oxide coating. Since water oxidation of several aluminum samples (8) has shown large increases in oxide etch time, this is in part a reasonable assumption. However, another factor which contributes to the etching inhibition is the presence of moisture adsorbed on the system walls, possibly resulting from hygroscopic aluminum chloride (9). In our experiments, effects of aluminum chloride are minimized, because our chamber and electrodes are cleaned between etch runs. Despite such drawbacks for the exact determination of native aluminum oxide etch rates, these considerations have little effect on the aluminum etch rate.

Stainless steel electrodes.—Initial experiments utilizing stainless steel electrodes, pressures up to 100 Pa CCl_4 , substrate temperatures up to 150°C , and rf power levels to 120W, resulted in no aluminum etching for plasma exposure times in excess of 40 min. Subsequent experiments demonstrated that argon addition did not significantly improve the etching ability of CCl_4 under the above conditions. Further, in all cases, a brown deposit (Fig. 2) was observed on the electrodes and substrates. Since etching was easily accomplished under identical conditions using a BCl_3 plasma, and this procedure yielded no deposit, a carbonaceous residue was suspected. Indeed, an Auger spectrum (Fig. 3) indicated that a carbon-chlorine compound was present on the surface of the aluminum samples. In addition, Fig. 3 shows that little aluminum oxide could be detected, suggesting that the polymer-type deposit was thicker than 2 nm. Subsequent Auger analyses using a Physical Electronics Model 590 Scanning Auger Electron Microprobe demonstrated that the micron-sized particles shown in Fig. 2 had the same composition as the regions adjacent to them. Thus it would appear that either these particles formed as a result of polymer nucleation or contamination present on the sample surface, or that the particles arose directly from the polymer coating, perhaps by sputtering. Presently, it is not clear whether the polymer immediately coats the aluminum surface, or whether the polymerization rate is simply greater than the native oxide etch rate in CCl_4 . Nevertheless, the final result



Fig. 2. Deposit observed on aluminum film exposed to a CCl_4 plasma using stainless steel electrodes. Plasma conditions were 67 Pa CCl_4 , 100W, 100°C , and 2.5 cm electrode spacing.

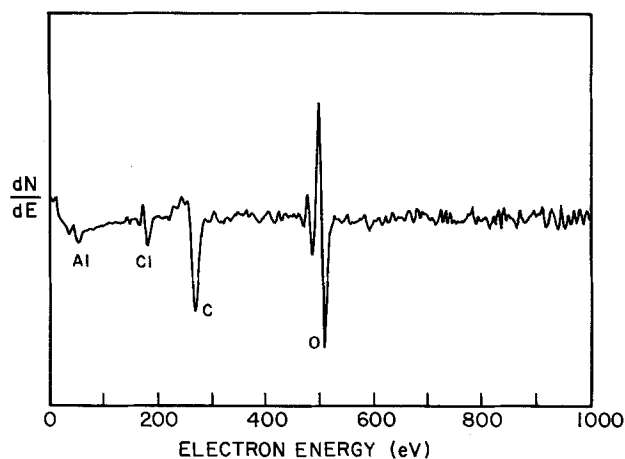


Fig. 3. Scanning Auger spectrum of aluminum film exposed to a CCl_4 plasma using stainless steel electrodes. Electron beam energy was 5 keV. Plasma parameters are the same as noted for Fig. 2.

is the same—inhibition of aluminum etching due to a carbon-chlorine film.

Anodized aluminum electrodes.—Preliminary results indicated that aluminum films could be plasma-etched in CCl_4 using aluminum electrodes without significant polymer formation, although the reproducibility of this procedure is questionable. In order to minimize attack of the electrode material, aluminum electrodes were oxidized in hot ($60^\circ\text{--}80^\circ\text{C}$) DI water (8) to increase the surface oxide thickness. Since this process greatly improved the reproducibility of the etch rate data, and little or no polymer was observed on the electrode surfaces, aluminum electrodes were anodized in an aqueous sulfuric acid solution (15% by volume) under constant current conditions to a thickness of $\sim 10 \mu\text{m}$.

The results of etching aluminum films at 100W rf power and 67 Pa CCl_4 pressure using anodized aluminum electrodes are given in Fig. 4. The change in etch rate due to a change in electrode material is dramatic—from an etch rate of zero to ~ 130 nm/min at an electrode temperature of 100°C .

The Arrhenius plot shown in Fig. 4 yields an activation energy for the etching of aluminum and native aluminum oxide films in pure CCl_4 plasmas of 0.3 eV/mole, which is similar to activation energies for the plasma etching of other thin film materials (10). It is curious that the activation energies for the etching of native aluminum oxide and aluminum films are essentially the same, since the primary etchant species for these two materials are probably different (3).

Preliminary results obtained with BCl_3 plasmas have shown that the etch rates of aluminum films are more reproducible with anodized aluminum electrodes than with stainless steel electrodes (11). Since Auger spectroscopy did not detect iron contamination on samples etched in CCl_4 on stainless steel electrodes, it is unlikely that the difference in etch reproducibility cited above is a result of iron chlorides in the case of stainless steel electrodes and BCl_3 . Also, aluminum etch rates using BCl_3 displayed no temperature dependence on anodized electrodes (11), which is consistent with previous BCl_3 studies on stainless steel electrodes (3). These data suggest that under the above plasma conditions, the rate-limiting step in BCl_3 etching is the gas-phase generation of "active" chlorine species.

Comparison between stainless steel and anodized aluminum electrodes.—It is interesting to speculate about the reasons for the gross inconsistencies in aluminum etching results observed with CCl_4 on stainless steel vs. anodized aluminum electrodes. Oxygen has been shown to play an important role in the etching of silicon in fluorinated hydrocarbon gases (12-15). In particular, surface studies (13) have demonstrated the participation of lattice oxygen in removing carbon

films deposited by CF_3^+ bombardment of a silicon surface.

Figure 5 shows the effect of oxygen addition to a CCl_4 plasma on the etch time of a 540 nm aluminum film. Additional data with oxygen additions up to 14% (by volume) indicated that the etch rate decreased up to 12% oxygen, after which no etching was observed, even on anodized aluminum electrodes. Further, an etch run utilizing 50 ppm oxygen (by dilution in argon) in CCl_4 also diminished the etch rate on anodized aluminum electrodes, and failed to produce etching on stainless steel electrodes. Such results suggest that the etchant species responsible for aluminum oxide (and possibly aluminum) etching is consumed by oxygen, thereby slowing or ultimately precluding etching. Since carbon compounds should react readily with oxygen, these data lend support to the proposal that CCl_3 or CCl_2 groups are responsible for aluminum oxide etching (3).

An additional concern with oxygen inclusion during plasma etching of aluminum is that aluminum oxidation could occur, thus increasing further the etch time for the aluminum film. Plasma oxidation of metals is well known (16), but under the present plasma and substrate bias conditions, it is unlikely that significant aluminum oxide growth will take place, although the differences in etch rate between aluminum oxide and aluminum suggest that a small amount of oxide would increase the overall etch time considerably.

A second consideration with regard to the observed differences between anodized aluminum and stainless steel electrodes relates to the differences in secondary electron emission from the electrode material. It has been demonstrated that insulators display greater secondary electron emission than do metals (17). In fact, this observation has been invoked to explain the increase in etch rate of silicon in CF_4 when silicon dioxide, rather than aluminum, serves as a cathode material (18). For the present investigation, however, it is felt that the changes in etch rates on the two electrode

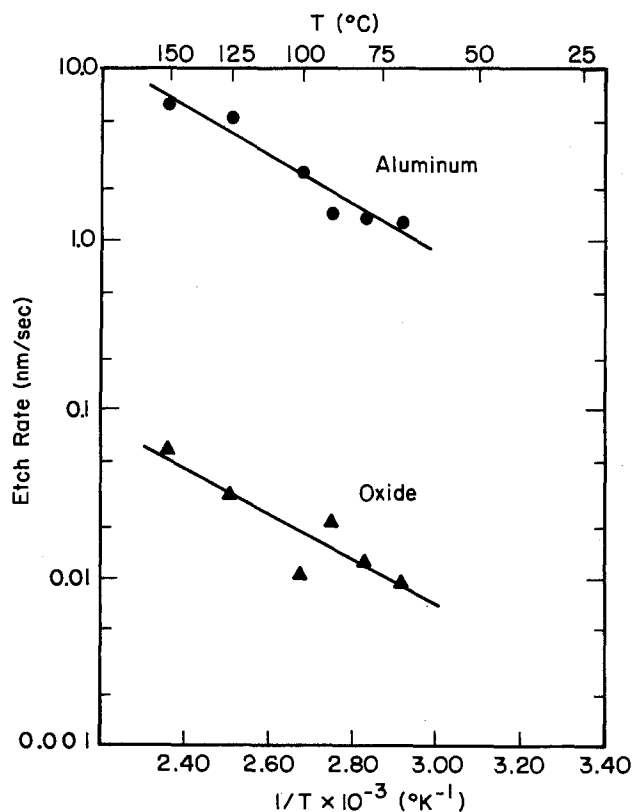


Fig. 4. Arrhenius plot of the etch rates of aluminum and native aluminum oxide films in CCl_4 plasmas. Plasma conditions were 67 Pa CCl_4 , 100W, and 2.5 cm electrode spacing.

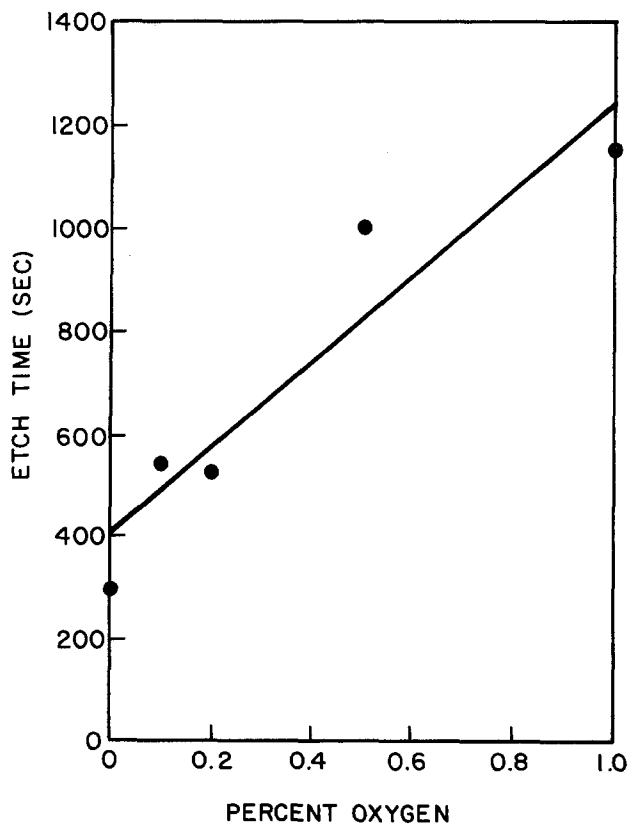


Fig. 5. Effect of oxygen addition (volume percent) to a CCl_4 plasma on the total etch time of a 540 nm aluminum film. Plasma parameters were 67 Pa CCl_4 , 100W, 100°C , and 2.5 cm electrode spacing.

materials are too large to be accounted for by an increase of a factor of 2-5 in secondary electron emission.

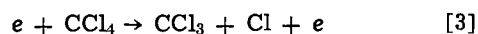
A third difference between anodized aluminum and stainless steel electrodes involves the fact that alumina is an insulator, and stainless steel is a metal. It is well known that surfaces exposed to a plasma and not externally grounded or biased assume a floating potential which is negative with respect to the plasma potential (19). Since anodized aluminum is an insulator, the high negative potential generated on this surface can cause an increase in positive ion bombardment relative to that experienced by the stainless steel (metal) electrode, thereby enhancing the etch rate under similar plasma conditions (20). This possibility was investigated by placing a sheet of Teflon between the stainless steel lower electrode and the heating and cooling assembly (which was grounded) to electrically isolate the electrode. However, aluminum etching was still not successful using CCl_4 , indicating that the insulating character of the electrode is not the controlling factor in aluminum etching on these two electrode materials.

A final consideration in the use of stainless steel *vs.* anodized aluminum electrodes involves the surface chemistry of chlorocarbons on these two materials. Although stainless steel was found to be a good recombination surface for fluorine atoms (15), extension of this model to chlorine is not obvious, since BCl_3 showed significant etch rates of aluminum oxide and aluminum using stainless steel electrodes. Recombination of carbon-containing species is a possibility, however, since polymer deposits were always found with CCl_4 plasmas using stainless steel electrodes. Indeed, iron and nickel are both Fischer-Tropsch catalysts (21), and are thus used to generate long chain hydrocarbons (C_5 - C_{30}) from carbon monoxide and hydrogen. Such a mechanism could be operative on stainless steel electrodes when chlorocarbon fragments are present, thereby generating polymer-type films.

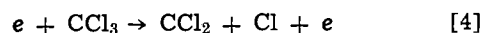
Further indication of a surface controlled reaction on stainless steel electrodes using CCl_4 arises from two additional sets of experiments. First, in at least one experiment it was observed that if the carbon-chlorine coating is not removed after an initial CCl_4 plasma, and virgin aluminum samples are subsequently exposed to a CCl_4 plasma, etching can be achieved. Second, aluminum etching has been attempted with an upper stainless steel and a lower anodized aluminum electrode, with the result that etching proceeded at approximately the same rate as it would have if both electrodes were anodized aluminum. However, the reverse electrode configuration (SS bottom, anodized aluminum top) again precluded etching.

Plasma chemistry of CCl_4 .—In an attempt to elucidate the chemistry occurring in CCl_4 plasmas, the effluent from the reactor shown in Fig. 1 was collected by means of a series of cold traps between the system and the vacuum pump. Combustion analysis of a white powder which was routinely observed whether stainless steel or anodized aluminum electrodes were used, proved the compound to be hexachloroethane (C_2Cl_6). Chlorine gas was also found in the effluent, and was quantitatively analyzed by titration techniques (22). Gas chromatographic studies (Hewlett Packard Model No. 5840A) of the liquid portion of the effluent identified tetrachloroethylene (C_2Cl_4) and CCl_4 as reaction products.

The above data suggest possible mechanisms for the breakdown of CCl_4 in a plasma environment. First, the CCl_4 undergoes decomposition upon electron bombardment



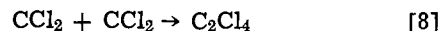
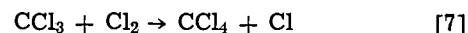
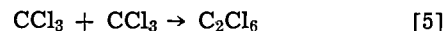
although ionization to CCl_3^+ and Cl^- probably occurs to some extent. Further breakdown of the CCl_3 can also take place



Indeed, these species have been observed by other in-

vestigators (3, 24) and in addition, CCl has been reported from optical emission (23) and mass spectroscopic studies of CCl_4 plasmas and vapors (24). Finally, one can envision other more complicated reactions occurring, stemming from the breakdown of C_2Cl_6 , as has been shown for the case of C_2F_6 (14).

Recombination on the wall or in the gas phase of the various fragments indicated in Eq. [3] and [4] then generate the observed products in the cold traps (along with unreacted CCl_4)



The chlorine radical, as generated by Eq. [3], [4], and [7], is probably responsible for aluminum etching, as proposed previously (3, 6, 7). Finally, aluminum reacts with Cl to form AlCl , AlCl_2 , or AlCl_3 (ultimately) as noted by other investigators (3, 23). By way of comparison, species such as CCl_3 , CCl_2 , CCl_3^+ and CCl_2^+ are most likely the etchants for Al_2O_3 (3, 7). It should be mentioned that the proposed chemical reaction mechanisms for aluminum etching in CCl_4 plasmas reported in this paper are consistent with results reported for the gas phase photolysis of CCl_4 (25), as well as with Si and SiO_2 etch studies using CF_4 (15).

Still another indication of the importance of surface effects in the plasma environment arises from comparison of the yield of reaction products on stainless steel *vs.* anodized aluminum electrodes. Table I gives the weight percent of the observed products (relative to the weight of CCl_4 input) from a CCl_4 plasma created using the two electrode materials. The factor of 10 increase in C_2Cl_4 yield with stainless steel electrodes suggests that this compound is in part responsible for polymer formation (note that the material balance is incomplete for the stainless steel electrodes, due in large part to polymer formation within the reactor). To be sure, a C_2Cl_4 plasma resulted in polymer formation under the above plasma conditions, even on anodized aluminum electrodes.

Table I. Effluent composition from CCl_4 plasma at 100W, 67 Pa, 100°C substrate temperature, and 2.5 cm electrode spacing using anodized aluminum and stainless steel electrodes

	Weight percent			
	CCl_4	C_2Cl_6	Cl_2	C_2Cl_4
Anodized Al	73.8	14.3	8.6	0.8
Stainless steel	57.1	13.9	6.8	8.3

The chemical mechanism responsible for the increase in C_2Cl_4 content for stainless steel electrodes is not clear at the present time. As discussed earlier, a surface effect involving either the stainless steel surface or the resulting carbon-chlorine polymer surface is probably operative, but other possibilities exist. For instance, if stainless steel does not permit the generation of large amounts of free chlorine radicals, due to recombination, then a mechanism similar to that described by Flamm for the observation of C_2F_4 from C_2F_6 discharges might occur (15).

Summary

The etch rates of aluminum and native aluminum oxide films in CCl_4 plasmas were studied as functions of substrate temperature and electrode material in a parallel plate plasma etcher. Formation of a carbon-chlorine polymer precluded aluminum and aluminum oxide etching when stainless steel electrodes were used. Anodized aluminum electrodes permitted aluminum and aluminum oxide etching with an activation energy of 0.3 eV/mole. The etch rate of aluminum was found to be 100 times greater than that of aluminum oxide. Several possible differences between the two electrode

materials were considered including oxygen effects, electric potential, and secondary electron emission. However, the most probable cause of the electrode effects involves the surface chemistry of chlorocarbon fragments.

Analysis of the effluent vapors from the parallel plate reactor demonstrated the presence of CCl_4 , C_2Cl_6 , Cl_2 , and C_2Cl_4 . These constituents suggest possible chemical reactions taking place in the CCl_4 plasma. Little difference between stainless steel and anodized aluminum electrodes was observed in the quantities of CCl_4 , C_2Cl_6 , and Cl_2 obtained from the CCl_4 plasma. However, a factor of ten increase in C_2Cl_4 was noted for stainless steel relative to anodized aluminum electrodes, indicating that dimers and possibly higher homologues of CCl_2 are formed when stainless steel electrodes are used. Aluminum etching is thus inhibited by C_2Cl_4 polymerization along with the formation of higher molecular weight polymers via surface recombination of many chlorocarbon fragments.

Acknowledgment

This material is based upon work supported by the National Science Foundation under Grant ENG-7812236.

Manuscript submitted Sept. 10, 1979; revised manuscript received Oct. 30, 1979. This was Paper 609 presented at the Los Angeles, California, Meeting of the Society, Oct. 14-19, 1979.

Any discussion of this paper will appear in a Discussion Section to be published in the December 1980 JOURNAL. All discussions for the December 1980 Discussion Section should be submitted by Aug. 1, 1980.

Publication costs of this article were assisted by the University of California.

REFERENCES

1. C. M. Melliar-Smith and C. J. Mogab, in "Thin Film Processes," J. L. Vossen and W. Kern, Editors, p. 497, Academic Press, New York (1978).
2. A. R. Reinberg, in "Etching for Pattern Definition," H. G. Hughes and M. J. Rand, Editors, p. 91, The Electrochemical Society Softbound Proceedings Series, Princeton, N.J. (1976).
3. R. G. Poulsen, H. Nentwich, and S. Ingre, in "Proceedings of the International Electron Devices Meeting," IEEE, p. 205, Washington, D.C. (1976).
4. T. O. Herndon and R. L. Burke, Interface '77 Kodak Microelectronics Symposium, Monterey, California, 1977.
5. R. Reichelderfer, D. Vogel, and R. L. Bersin, Abstract 151, p. 414, The Electrochemical Society Extended Abstracts, Atlanta, Georgia, Oct. 9-14, 1977.
6. A. Yasuoka, H. Nagata, H. Harada, and T. Enomoto, IPC Technical Report, 1977.
7. P. M. Schaible, W. C. Metzger, and J. P. Anderson, *J. Vac. Sci. Technol.*, **15**, 334 (1978).
8. C. C. Chang, D. B. Fraser, M. J. Grieco, J. T. Sheng, S. E. Haszko, R. E. Kerwin, R. B. Marcus, and A. K. Sinha, *This Journal*, **125**, 787 (1978).
9. R. LeClaire, *Solid State Technol.*, 139 (April, 1979).
10. C. M. Melliar-Smith and C. J. Mogab, in "Thin Film Processes," J. L. Vossen and W. Kern, Editors, p. 535, Academic Press, New York (1978).
11. K. Tokunaga and D. W. Hess, To be published.
12. W. R. Harshbarger, T. A. Miller, P. Norton, and R. A. Porter, *Appl. Spectrosc.*, **31**, 201 (1977).
13. J. W. Coburn, H. F. Winters, and T. J. Chuang, *J. Appl. Phys.*, **48**, 3532 (1977).
14. C. J. Mogab, A. C. Adams, and D. L. Flamm, *ibid.*, **49**, 3796 (1978).
15. D. L. Flamm, *Solid State Technol.*, 109 (April, 1979).
16. C. J. Dell'Oca, D. L. Pulfrey, and L. Young, "Physics of Thin Films," Vol. 6, p. 1 (1971).
17. O. Hachenberg, and W. Brauer, in "Advances in Electronics and Electron Physics," L. Marton, Editor, Vol. XI, p. 413 (1959).
18. L. M. Ephrath, *J. Electron. Mater.*, **7**, 415 (1978).
19. J. L. Vossen, *This Journal*, **126**, 319 (1979).
20. J. W. Coburn and H. F. Winters, *J. Appl. Phys.*, **50**, 3189 (1979).
21. J. M. Thomas and W. J. Thomas, "Introduction to the Principles of Heterogeneous Catalysis," p. 401, Academic Press, New York (1967).
22. J. M. Koltoff, E. B. Sandell, E. J. Meekam, and S. Bruckenstein, "Quantitative Chemical Analysis," MacMillan Co., New York (1969).
23. B. J. Curtis and H. J. Brunner, *This Journal*, **125**, 829 (1978).
24. C. M. Melliar-Smith and C. J. Mogab, in "Thin Film Processes," J. L. Vossen and W. Kern, Editors, p. 527, Academic Press, New York (1978).
25. D. D. Davis, J. F. Schmidt, C. M. Neeley, and R. J. Hanrahan, *J. Phys. Chem.*, **79**, 11 (1975).

Time Dependent MOS Gate Oxide Defects Using Liquid Crystals

A. K. M. Zakzouk*

Electrical Engineering Department, Riyadh University, Riyadh, Saudi Arabia

ABSTRACT

Localized conducting regions of silicon dioxide are a major source of failure of integrated circuits. By using nematic liquid crystals in contact with the oxide, and simultaneously applying an electric field across such a sandwich structure, defective regions can be nondestructively identified. By examining the number of defects as a function of the magnitude and polarity of the applied voltage, time, and oxide thickness, it is possible to obtain information on the cause and nature of these localized regions of high conduction. Measurements have been performed on oxide conduction in thin layers (1000-2000Å) of silicon dioxide, similar to those commonly employed as gate dielectrics in MOS devices, grown in dry oxygen. The liquid crystal technique has been shown to be a valuable nondestructive technique for studying the behavior of oxide defects as a function of the magnitude and polarity of the applied voltage, time, and oxide thickness.

A major source of loss of yield and/or reliability of integrated circuits is caused by the presence, or forma-

tion during life, of defects in the silicon dioxide layer on the surface of the silicon. These defects have been the subject of studies by a number of investigators (1-3). For this reason also, fundamental studies of oxide conduction (4, 5) and breakdown (6) have been under-

* Electrochemical Society Active Member.

Key words: integrated circuit testing, dielectric, liquid crystals, oxide defects, field, time dependence.

taken. The study of defective oxide was, until recently, hampered by the lack of a reproducible nondestructive technique for locating the defects. A review of the available techniques has been presented by Kern (7).

Di Stefano (8) has used photoemission measurements to show that a highly localized reduction of the silicon dioxide barrier can occur, particularly after contamination of the oxide by impurity ions such as sodium. The barrier is lower after applying an electric field across the oxide which drives the impurity ions to the silicon surface. Williams *et al.* (9) have suggested that the cause of the localized barrier lowering is a condensation of sodium ions at particular points on the silicon surface. The potential energy of a particular ion is shown to be lower when it is situated near to a metallic-like surface. An accumulated silicon surface approximates such a surface and the positive sodium ions will induce such a surface condition. The effect promotes the condensation and would be expected to produce the highly localized barrier lowering described by Di Stefano (8).

Raider (10) has demonstrated that sodium drift can be responsible for time-dependent breakdowns, presumably due to electron injection into the film at localized regions where the barrier is lowered. Fritzsche (11) found that the primary mode of breakdown in silicon dioxide was electronic in nature, thus exhibiting no dependence on the duration of the applied field. In contrast, Worthing (12) found that when a constant, positive voltage was applied to the metal for the time required to cause breakdown, the breakdown field of silicon dioxide films on n-type, degenerate silicon was proportional to (time)^{-1/4}. This particular time dependence has been frequently observed for bulk insulators where it is known as Peek's law (13). This has the effect of lowering the dielectric strength of the silicon dioxide film from 6.7 MV/cm for fast stressing rates to approximately 3 MV/cm for a testing voltage applied at an infinitely slow rate. However, no time dependence was observed by Worthing when the silicon was positively biased.

Inconsistent with Fritzsche's breakdown model (11), which implies that processing steps promoting local crystallization of the oxide will result in an increase in defect-related breakdown, Chou and Eldridge (2) have demonstrated that: (i) while a lowering of the concentration of mobile impurities reduces the occurrence of defect-related breakdown, it does not change the magnitude of the primary (intrinsic) breakdown strength (7-9 MV/cm) of silicon dioxide; (ii) under identical silicon dioxide growth conditions, reduction of film thickness is accompanied by an increase in the density of oxide faults. Excessively high defect density in the oxide gives rise to a time dependence of the breakdown characteristics and can therefore lower the magnitude of the primary breakdown strength under certain testing conditions; and (iii) sodium contamination can result in severe oxide deterioration, especially during film growth at temperatures in the 1000°-1200°C range. This has been followed by a large amount of work on the effect of sodium on conduction and breakdown (14, 15), all of which must ultimately be fitted into any general theory of oxide conduction and breakdown.

Conduction has been studied in oxides with, presumably, minimal amounts of barrier lowering by Lenzlinger and Snow (4). Their results, obtained on MOS capacitor structures, indicate that conduction is primarily limited by Fowler-Nordheim tunneling either from the metal or silicon into the oxide. Osburn and Weitzman (5) have arrived at similar conclusions, but also indicate the importance of mobile ions and trapping phenomena in the conduction process. The tunneling distance and barrier height can be reduced by the presence of positive charge, a short distance from the interface (8), within the oxide, or by a large applied electric field. The effect of the electric field may be enhanced by the presence of physical irregu-

larities (16-18) at the silicon surface causing field intensification. Only when one of these effects is present will the conduction process be limited by the silicon dioxide bulk properties. When this is the case, we have a defective region and relatively high currents will flow, a premature breakdown is then possible. This is particularly important in integrated circuits containing thin oxides (*e.g.*, MOS and CCD devices). Breakdown may occur by a self-healing (19) process whereby the metal is blown clear of the hole after melting. Frequently, however, device failure will result when the oxide becomes short-circuited. This process is not well understood, but statistical evidence would suggest that it becomes increasingly probable with thicker metal layers (>1 μm), or with passivated structures, and is presumably associated with the inability of the metal to evaporate.

The Liquid Crystal Technique

In order to study oxide defects it is desirable to have a nondestructive technique for locating them. On the basis of the evidence currently available, the liquid crystal technique (1) (LCT) is such a method. The negative nematic liquid crystal used in the present work was contained between the plane parallel electrodes (16), the lower of which is the oxidized silicon slice, the upper a glass plate coated on its underside with a conducting, but transparent, layer (*e.g.*, tin oxide).

With a voltage difference between this conducting layer and the silicon slice, defects can be seen through the glass plate, with an optical microscope, as areas of turbulence. The thickness of the liquid crystal layer, under the weight of the glass slice was in the 10-25 μm range. When the required test voltage is applied between the tin oxide layer and the silicon slice, turbulence is seen in the liquid crystal, wherever there is a current leakage path to the substrate and a field greater than the threshold of approximately 5 kV/cm across the liquid crystal. Typically, 7 or 8V were required for a display on uninsulated parts of the substrate, but higher voltages were required before there was sufficient leakage current to give a display on other parts of the substrate. The current density required to produce a display is extremely small, approximately 30 mA/m². The highly resistive liquid crystal is in series with the sample under test, therefore, even if the breakdown voltage of the dielectric is exceeded, the current is limited and no permanent damage occurs, although there is sufficient current to produce a display. Breakdown of the defective region of the film is prevented by an increasing fraction of the applied voltage being taken up by the liquid crystal, as the current increased. Displays can be reproduced many times. The turbulence at the location of a defect is caused by molecules in the liquid crystal absorbing electrons from the oxide. The passage of these charged molecules causes a hydrodynamic torque on the rod-like molecules of the liquid crystal.

Preparation of Samples

All the results described here, unless otherwise stated were obtained on (111) orientation 5 Ω-cm n-type polished silicon substrates. The silicon was initially degreased and was then boiled in nitric acid, followed by treatment in hydrofluoric acid, before washing in deionized water. The oxidation was carried out in dry oxygen at 1000°C for sufficient lengths of time to produce 1000-2000Å thick films. The furnace was resistance heated and the silicon slices were contained on a quartz boat in a single wall quartz tube. All the oxidations were carried out with the slices horizontal, fully supported by the quartz boat. This minimizes the stress on the silicon during oxidation and cooling. In many cases this procedure was preceded by steam oxidation of the silicon. Using conventional photolithography small windows were etched in the steam oxide (≈1 μm) and the thin dry oxide was

grown in the windows. This procedure was carried out to facilitate precise location of a particular region of oxide during the experiments and to simulate typical processing steps of MOS and charge coupled device (CCD) oxides. The oxide was removed from the back of the slice and this was placed in contact with an aluminum plate. A small amount of the nematic liquid crystal (MBBA) was then placed on the top of the oxidized surface of the slice, and the apparatus was set up as shown in Fig. 1.

Experimental Results and Discussion

Measurements on (111) orientation, n-type silicon, with the liquid crystal technique (LCT) and the arithmetic mean of the numbers of defects in a large number of small areas, were used.

Using LCT a range of phenomena becomes apparent (16, 18, 20-23):

1. The density of turbulent areas is considerably greater with the silicon negative rather than positive. Those defects occurring only when the silicon negative are termed type II. Type I occurs under both polarities.

2. Type II defects grow in number with time, reaching apparent saturation densities in approximately 15 min for effective applied oxide field ≈ 1 MV/cm.

3. By photoengraving windows in thick oxide followed by the production of thin oxide in these windows, it is found that type II defects cluster around the edge of the windows at the ledge of the silicon.

These phenomena, together with work (8) on the study of impurity ion migration and clustering, lead to a relatively simple model (16) for a defect. Impurity ions, such as sodium, migrate through the film and form clusters at the interface. The resulting enhanced Fowler-Nordheim, or Schottky emission, gives rise to increased electron currents in the oxide, from the silicon when the latter is negative. Physical irregularities at the silicon surface cause field intensification and enhance electron currents both directly and by promoting the ion clusters as shown in Fig. 2. The model developed depends on the cooperative effects of impurity ions and slow trapping. The purpose of this publication is to present experimental results of time-dependent thin (1000-2000Å) oxide defects.

Voltages of both polarity were applied to the silicon and the samples were observed for long periods of time. With positive bias on the silicon, very few turbulent regions were seen. The oxide itself showed faults in these regions when viewed without liquid crystal, and it is believed that these regions are pinholes presumably caused by contamination during the oxidation process. We shall, henceforth, refer to these as type I defects. Figure 3a shows a type I defect.

With negative bias applied to the silicon, many more defects were seen, although type I defects are still present. We shall refer to those defects occurring under negative bias only as type II defects. Figure 3b shows the appearance of a sample after applying negative bias to the silicon. Figure 3c shows the same region of oxide sometime later. Both Fig. 3b and 3c show the type I defect present in Fig. 3a. There is also, clearly, an increase in the number of type II defects with time.

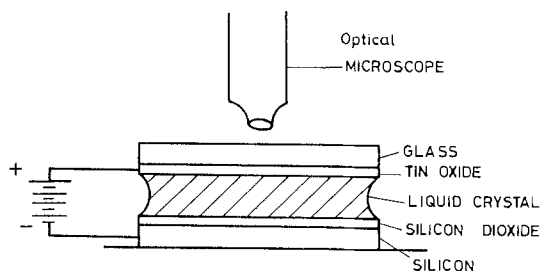


Fig. 1. The apparatus used for the study of oxide defects using liquid crystal. No spacers are necessary since the tin oxide coated glass plate is supported by the liquid crystal film.

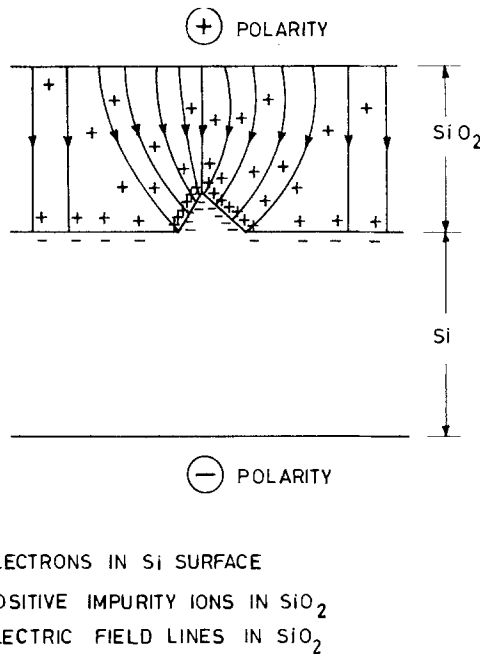


Fig. 2. Shows a point of field intensification and positive impurity ions in the silicon dioxide film condensed at that point.

Figure 4 shows the way in which the log of the defect density increases with the fourth root of time for two films of thickness $0.10 \mu\text{m}$ (curves A and B) and $0.2 \mu\text{m}$ (curves C and D) at different conditions. For both films the defect density (D), with negative bias on the silicon substrate, was found to increase exponentially with the fourth root of time as follows

$$D = D_0 \exp\left(\frac{t}{\tau}\right)^{1/4}$$

in the time range of $0 \leq t \leq T_s$. Where D_0 and τ are constants dependent on the applied field, oxide thickness, and the history of the oxide. T_s is the saturation time dependent on the oxide thickness, the history of the oxide, and the applied field. The wafer-to-wafer variability is within $\pm 10\%$ for similar oxides. The defect density saturates with time after approximately 5 min for $0.1 \mu\text{m}$ thick film (curve A) and approximately 15 min for $0.2 \mu\text{m}$ thick film (curve C). If positive bias is applied to the silicon substrate for certain time, only type I defects are visible, but on subsequent negative biasing the density of type II defects is initially reduced (curve B). However, after a further time has elapsed the defect density rises above its earlier value and ultimately saturates after longer saturation time.

The tendency for type II defects to be distributed along ledges in the silicon (Fig. 5) indicates the importance of silicon imperfections in these phenomena. During the application of the negative voltage to the silicon substrate as shown in Fig. 2 any scratches or similar discontinuities act as points of field intensification and positive impurity ions in the film condense at these points. This, together with the field intensification due to the geometry of irregularities (18), causes barrier lowering. Since the height of the barrier primarily controls the current, the current increases. Because of the relatively high mobility of electrons in the silicon dioxide, the barrier can be reduced by a large amount before the conduction becomes bulk limited. Presumably, the current ultimately becomes limited by some form of Poole-Frenkel conduction. As positive charge enters the region of field intensification by diffusion from other parts of the film, one would expect the current and, hence, size of the turbulence to increase. Ultimately the total number of defects seen will saturate, either due to the number of available im-

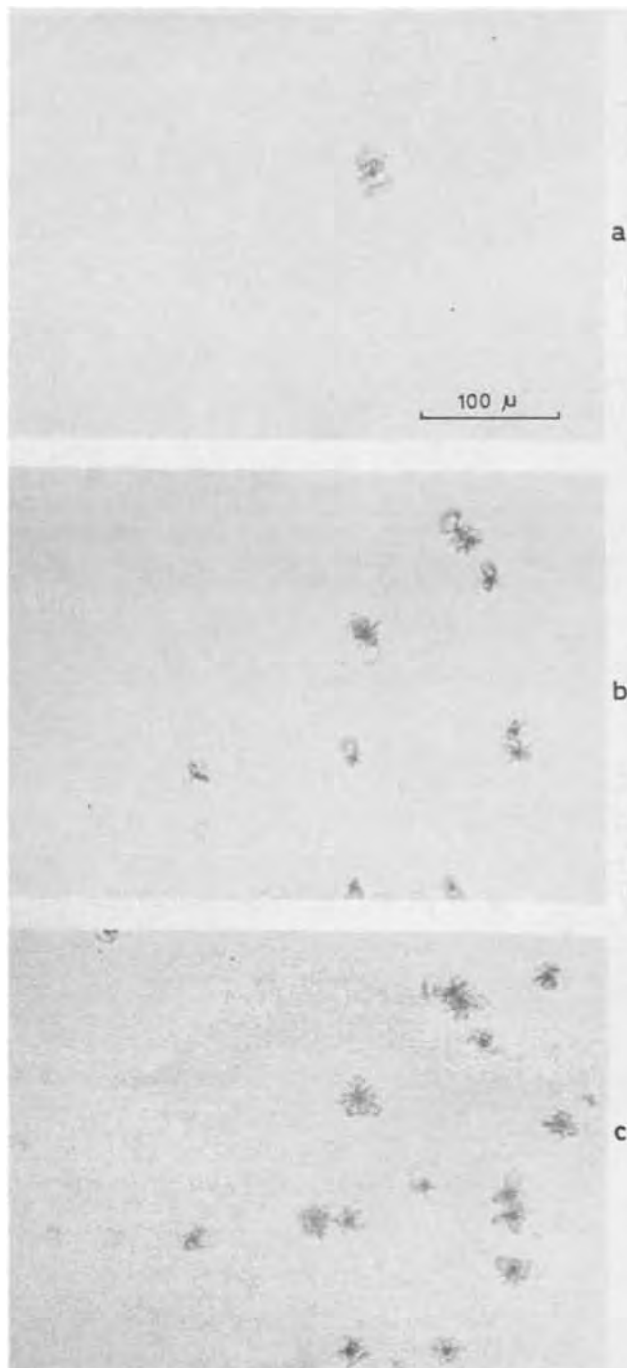


Fig. 3. The appearance of a region of $0.1 \mu\text{m}$ thick oxide using liquid crystal technique. (a) With a positive voltage applied to the silicon substrate. A type I defect is present (applied voltage = 40V). (b) After reversal of the applied voltage polarity, more defects are seen (type II defects), but type I defect still present (applied voltage = -40V). (c) After 10 min the density of type II defects has increased considerably.

purity ions becoming exhausted, or when all the available silicon sites are producing turbulence.

On applying positive voltage to the silicon substrate, the positive ions are removed from the region of the silicon surface and geometrical effects cause the positive ions to spread out into the oxide. No turbulence is now present in the liquid crystal indicating that all the voltage is now falling across the oxide. It is well documented that such a high field causes the release, by tunneling, of electrons from traps in the oxide. The tunneling process involves no change of electron energy and the traps must therefore have energies coincident with the conduction band in the presence of the applied field for charge to transfer to the conduction

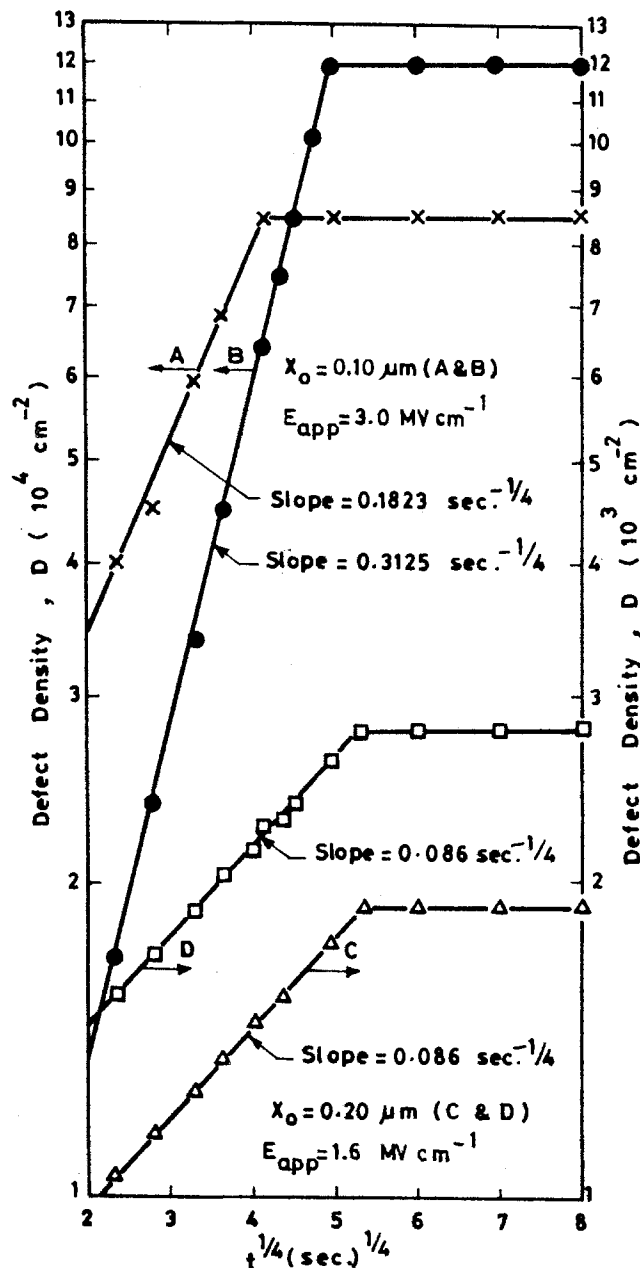


Fig. 4. Time dependent silicon dioxide defect density, with the silicon substrate is negatively biased. Curves A and B for a $0.1 \mu\text{m}$ thick film and an applied field of 3.0 MV cm^{-1} , but curve B was obtained after biasing the silicon substrate positively for 35 min with a field of 3.0 MV cm^{-1} . Curves C and D for a $0.2 \mu\text{m}$ thick film and an applied field of 1.6 MV cm^{-1} , but curve D was obtained after biasing the substrate positively for 35 min with a field of 5.3 MV cm^{-1} .



Fig. 5. After opening windows in the thick (steam) oxide, the thin (dry oxygen) oxide was grown. This thin oxide is contained within the circular area. It can be clearly seen that type II defects occur preferentially at the intersection of thin and thick oxides where a ledge in the silicon is situated (circle diameter = $168 \mu\text{m}$).

band. Positive charge is created in the oxide. On returning to negative voltage on the silicon substrate, the number of turbulences would be expected to be initially small. Impurity ions condense with the lapse of time and gradually the number of defects increases. The total positive charge is now due to not only impurity but also the ionized traps obtained through the previous application of positive bias to the silicon substrate. It is not surprising that curves B and D of Fig. 4 show an increased number of turbulences since some smaller defects may now have sufficient positive charge surrounding them to produce large enough electron currents for them to become visible.

Since curves A and C of Fig. 4 show quite definite saturation, we are forced to deduce that we are primarily limited by the concentration of impurity ions in the oxide. Curves B and D of Fig. 4 indicate that more silicon imperfections are present in the sample than are shown in A and C.

In view of the comparatively large amount of liquid crystals in contact with the oxide, it was decided to check the effect of liquid crystals on the oxide films. The capacitance-voltage technique was used to show that the liquid crystal is not a source of contamination. The oxidized silicon wafer was divided into two pieces. The first one was examined by the liquid crystal technique for long time (about 1 hr) under negative bias on the silicon substrate condition. After washing the liquid crystal, the two pieces were cleaned and metallized at the same time with the same pattern of aluminum dots. The C_g - V_g curves were plotted for the similar MOS diodes of both pieces. The results are shown in Fig. 6 where curve a for the second piece (which was not examined by liquid crystals) and curve b for the first piece (which was examined by liquid crystals). The small reduction in the magnitude of the flatband voltage, after applying the liquid crystals to the oxide film, is due to the expected variation in the flatband voltage throughout the film surface and the measurement errors. Over several measurements for several oxide films the change in flatband voltage after applying the liquid crystals was within the limits of -0.5 to $+0.5$ V due to the mentioned reasons. This very small change in flatband voltage corresponds to $\Delta N_a = \pm 5.4 \times 10^{10}$ ions cm^{-2} which represent a variation in the mobile ions density of $\pm 2.25\%$ for these oxides.

Conclusions

Measurements have been performed on oxide conduction in thin (1000-2000Å) layers of silicon dioxide grown in dry oxygen. The liquid crystal technique has been shown to be a valuable nondestructive technique

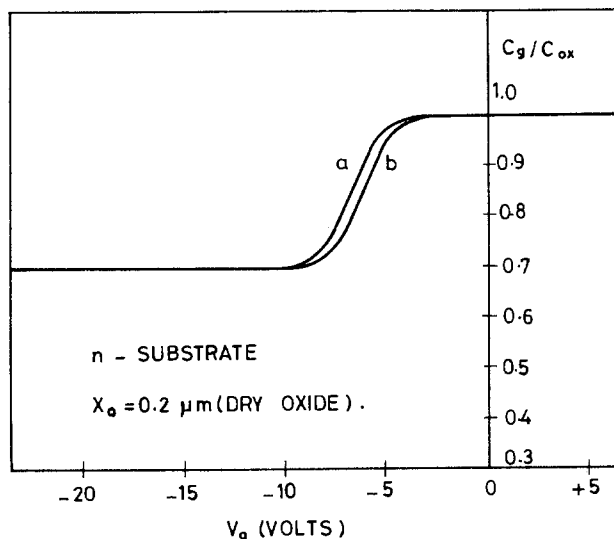


Fig. 6. Capacitance-voltage characteristics of a silicon dioxide film: (a) before and (b) after applying the liquid crystals.

for studying the behavior of oxide defects as a function of both magnitude and polarity of applied voltage, time, and oxide thickness. The liquid crystal is not a source of contamination to the oxide. Two types of defect have been found. Type I defects are probably pinholes and have a very low density. Type II defects occur only under negative bias (on the silicon substrate) and show a strong dependence of density on time.

The defect density (D), with negative bias on the silicon substrate, was found to exponentially increase with the fourth root of time, in the time range $0 \leq t \leq T_s$, where T_s is the saturation time dependent on the applied field, the oxide thickness, and the history of the oxide. The defect density saturates with time after approximately 5 and 15 min for 0.1 and 0.2 μm thick films, respectively. By cycling the voltage between positive and negative, it has been possible to suggest a simple qualitative model for the behavior of defects which would seem to be associated with physical irregularities in the silicon. The model developed depends on the cooperative effects of impurity ions and slow trapping. It suggests that devices will be subject to failure from oxide defects for either type of polarity. Further experimental and theoretical studies for the time dependence on SiO_2 defects are in progress and will be published later.

Acknowledgments

The author wishes to thank Dr. W. Eccleston and Dr. R. A. Stuart of the Department of Electrical Engineering and Electronics, Liverpool University, for useful discussions. The author would like to thank the JOURNAL referees for their useful comments and suggestions.

Manuscript submitted July 23, 1979; revised manuscript received ca. Oct. 25, 1979.

Any discussion of this paper will appear in a Discussion Section to be published in the December 1980 JOURNAL. All discussions for the December 1980 Discussion Section should be submitted by Aug. 1, 1980.

REFERENCES

1. J. M. Keen, *Electron. Lett.*, **7**, 432 (1971).
2. N. J. Chou and J. M. Eldridge, *This Journal*, **117**, 1287 (1970).
3. F. W. Ainger, *J. Mater. Sci.*, **1**, 1 (1966).
4. M. Lenzlinger and E. H. Snow, *J. Appl. Phys.*, **40**, 278 (1969).
5. C. M. Osburn and E. J. Weitzman, *This Journal*, **119**, 603 (1972).
6. N. Klein, *IEEE Trans. Electron Devices*, **ed-13**, 788 (1966).
7. W. Kern, *RCA Rev.*, **34**, 655 (1973).
8. T. H. Di Stefano, *Appl. Phys. Lett.*, **19**, 280 (1971).
9. R. Williams and M. H. Woods, *ibid.*, **22**, 458 (1973).
10. S. I. Raider, *ibid.*, **23**, 34 (1973).
11. C. Fritzsche, *Z. Angew.-Phys.*, **24**, 48 (1968).
12. F. L. Worthing, *This Journal*, **115**, 88 (1968).
13. D. F. Miner, "Insulation of Electrical Apparatus," p. 40, McGraw-Hill Book Co., New York (1941).
14. C. M. Osburn and S. I. Raider, *This Journal*, **120**, 1369 (1973).
15. C. M. Osburn and D. W. Ormond, *ibid.*, **121**, 1195 (1974).
16. A. K. Zakzouk, R. A. Stuart, and W. Eccleston, *ibid.*, **123**, 1551 (1976).
17. R. M. Anderson and D. R. Kerr, *J. Appl. Phys.*, **48**, 4834 (1977).
18. A. K. M. Zakzouk, *This Journal*, **126**, 1771 (1979).
19. N. Klein and H. Gafni, *IEEE Trans. Electron Devices*, **ed-13**, 281 (1966).
20. A. K. Zakzouk, W. Eccleston, and R. A. Stuart, *Solid-State Electron.*, **19**, 133 (1976).
21. D. Baglee, A. K. Zakzouk, W. Eccleston, and R. A. Stuart, *ibid.*, **21**, 763 (1978).
22. W. Eccleston, D. A. Baglee, A. K. Zakzouk, R. S. Gill, and R. A. Stuart, Abstract 265, p. 659, The Electrochemical Society Extended Abstracts, Seattle, Wash., May 21-26, 1978.
23. A. K. M. Zakzouk, Abstract 205, p. 536, The Electrochemical Society Extended Abstracts, Boston, Mass., May 6-11, 1979.

Molecular Beam Epitaxial Growth of ZnTe and ZnSe

Fumitaka Kitagawa, Tomoyoshi Mishima, and Kiyoshi Takahashi

Department of Physical Electronics, Tokyo Institute of Technology, Meguro-ku, Tokyo, Japan 152

ABSTRACT

The electrical and optical properties of ZnTe and ZnSe prepared by molecular beam epitaxy have been studied. Epitaxial growth was found to take place at $\geq 250^\circ\text{C}$ for ZnTe on GaAs and ZnTe and at $\geq 300^\circ\text{C}$ for ZnSe on GaAs; the epitaxial growth ceased at $430^\circ \sim 470^\circ\text{C}$ for ZnTe and at $450^\circ \sim 500^\circ\text{C}$ for ZnSe because of the reevaporation of compound and/or impinging molecules. The observed growth rate dependence on substrate temperature and on impinging rate ratio has been explained on the basis of a model in which the number of incorporated and reevaporated molecules are strongly coverage dependent. ZnSe on GaAs, and ZnTe on GaAs and ZnTe had good mirror smooth surfaces. ZnTe on InAs and ZnS, however, had a rather rough surface. Ga was found to diffuse, due to a large number of misfit defects at GaAs-ZnTe interface, from the GaAs substrate into ZnTe influencing the electrical and optical properties of grown layers considerably. The resistivities of undoped layers were $\sim 5 \Omega\text{-cm}$ for ZnTe on ZnTe and $\sim 10^4 \Omega\text{-cm}$ for ZnSe on GaAs. Sb was used to increase the hole concentration of ZnTe on ZnTe up to $\sim 10^{18} \text{cm}^{-3}$. The resistivities of ZnSe on GaAs were found to decrease to $\sim 0.07 \Omega\text{-cm}$ by Ga doping. The results of photoluminescence measurement suggest that the higher substrate temperature makes the better quality layers.

Zn- and Cd-chalcogenides have the wide and direct forbidden bandgaps and high electro-optic coefficients which are attractive for opto-electronic devices and acousto-optic waveguide modulators etc. Furthermore, ZnTe and CdTe have large effective atomic numbers making them promising materials for γ -ray detectors. However, II-VI compound solid-state devices with good device performance have not been fabricated yet. This is partly due to the lack of crystal growth techniques to obtain epitaxial layers and bulk crystals with good optical and electrical properties, and partly due to the difficulty of carrier concentration control because of self-compensation effects.

Most of II-VI compound materials for electronic devices, e.g., EL displays, CRT, etc., are at present used in powder or polycrystalline forms. High quality epitaxial layers, however, are desirable for aforementioned solid-state devices and heterojunction devices in particular. In the present work, epitaxial growth of ZnTe and ZnSe was tried by molecular beam epitaxy (MBE) (1) due to lower growth temperature as compared to other growth methods (this permits low growth rates for achieving good thickness control and reduces the interdiffusion in multilayer structures). MBE method also allows the easy choice of growth environment for the better control of stoichiometry. Although many epitaxial II-VI compound layers grown by MBE (2-5) and vacuum evaporation (6) have been reported, very little of the electrical and optical properties has been mentioned. The present paper discusses the molecular beam epitaxial growth of ZnTe and ZnSe, and their electrical and optical properties.

Experimental

Crystal growth.—The high vacuum growth chamber is pumped by a 110 liter/sec noble-ion pump and by titanium sublimation pumps which are backed with two sorption pumps. A four-positioned substrate holder in growth chamber allows four samples to be prepared in one growth run. The high purity carbon effusion cells are surrounded with a liquid-nitrogen-cooled shroud. Source materials are evaporated from these effusion cells heated by tungsten wire wound around them. The temperatures were held within $\pm 2^\circ\text{C}$ at set temperature. One of the effusion cells, i.e., the Zn effusion cell, has an ionizer to ionize part of Zn atoms evaporated from the effusion cell. The details

of this ionizing system have been previously reported (7) and the results will be reported elsewhere. The base pressure of growth chamber was $\sim 10^{-7}$ Pa before growth and $\lesssim 10^{-6}$ Pa during growth (the increase in pressure occurs mainly because of evaporant vapors). All of the source materials used, i.e., Zn, Se, Te, Ga, As, Sb (the latter three materials were used as dopants) have 6-nines purity.

The substrates used were $\{100\}$, $(\bar{1}\bar{1}\bar{1})$ GaAs for ZnSe, $(\bar{1}\bar{1}\bar{1})$ InAs, $\{100\}$ GaAs, $(\bar{1}\bar{1}\bar{1})$ ZnS, $\{100\}$, $\{110\}$, $\{111\}$ ZnTe for ZnTe. However $\{100\}$ GaAs for ZnSe and $\{100\}$ GaAs, $\{111\}$ ZnTe for ZnTe were most frequently used. GaAs substrates were etched in H_2SO_4 : H_2O_2 : H_2O (3:1:1 by volume) for 1 min at 80°C . ZnTe substrates, which were cut from ingots grown by Bridgman method (8) in our laboratory, were oriented to $\{100\}$, $\{110\}$, or $\{111\}$ plane within $\pm 5^\circ$, and were etched in $\text{K}_2\text{Cr}_2\text{O}_7$ (1g) + H_2O (40 ml) + H_2SO_4 (5 ml) for 30 sec at 80°C and/or in Br-methanol for a few minutes at room temperature. Deteriorative Cr compounds, probably Cr oxide, were sometimes found to be deposited on the substrate surface when the former etchant was used. Therefore, subsequent etching by the other etchant such as Br-methanol was necessary. Both etchants were found to be excellent for obtaining a mirror smooth surface. As-grown undoped ZnTe substrates were p-type with hole concentration $p \sim 10^{14} \text{cm}^{-3}$ and hole mobility $\mu_h = 70 \sim 100 \text{cm}^2 \text{V}^{-1} \text{sec}^{-1}$ at room temperature. After chemical etching, these were thermally etched in the ultrahigh vacuum growth chamber for 20 \sim 30 min at $450^\circ \sim 500^\circ\text{C}$ for ZnTe substrates and at 600°C for GaAs substrates just before growth.

Films were deposited at substrate temperature $T_{\text{sub}} = 200^\circ \sim 450^\circ\text{C}$ with various group-II/VI impingement rate ratio F_1/F_2 , where F_1 and F_2 are impingement rates of group II and VI molecules, respectively. The values of F [$\text{cm}^{-2} \text{sec}^{-1}$] were estimated using Eq. [1]

$$F = K\sqrt{P/MT}/r^2 \quad [1]$$

where K is the form factor determined by the shape of effusion cell etc., P (Pa) vapor pressure (9), T ($^\circ\text{K}$) the cell temperature, M the molecular weight and r [cm] is the distance between the effusion cell and the substrate. The discrepancy between the values calculated from Eq. [1] and the actual values are estimated to be within $\pm 20\%$ in consideration of the shape of effusion cell, which was not Knudsen-type, and the

Key words: semiconductor, resistivity, photoluminescence, epitaxy.

strong dependence of source material vapor pressure on the material surface temperature which did not always coincide with the measured effusion cell temperature. The thickness of the epitaxial films was about 10 μm for resistivity measurements and 2 ~ 3 μm for other purposes. The typical deposition rate was ~1 $\mu\text{m/hr}$.

Characterization.—The resistivities of grown layers were measured using In-doped ZnTe and Cr-doped GaAs substrates with resistivities $\sim 10^8 \Omega\text{-cm}$ or more. The influence of substrate resistivity on the layer resistivity measurement (due to shunt effects) can be ignored for low resistivity layers ($\lesssim 10^3 \Omega\text{-cm}$), however, cannot be ignored for high resistivity layers ($\gtrsim 10^5 \Omega\text{-cm}$) because these sheet resistances are comparable to or more than those of substrates. Therefore, the following method was used for calculation of resistivity of high resistivity layers. The apparent conductivity σ_{ex} obtained from measured resistance $R_{\text{ex}} = L/\sigma_{\text{ex}}t_f W$ of a composite layer (as shown in Fig. 1a) can be represented by

$$\sigma_{\text{ex}} = \sigma_f + (\sigma_s t_s/t_f) \quad [2]$$

where σ_f and σ_s are conductivities, t_f and t_s are thicknesses of the layer and of the substrate, respectively. σ_{ex} was extrapolated to $t_s/t_f = 0$ by etching step by step as shown in Fig. 1b and assuming a uniform layer with no lattice defects and no influence of the interface

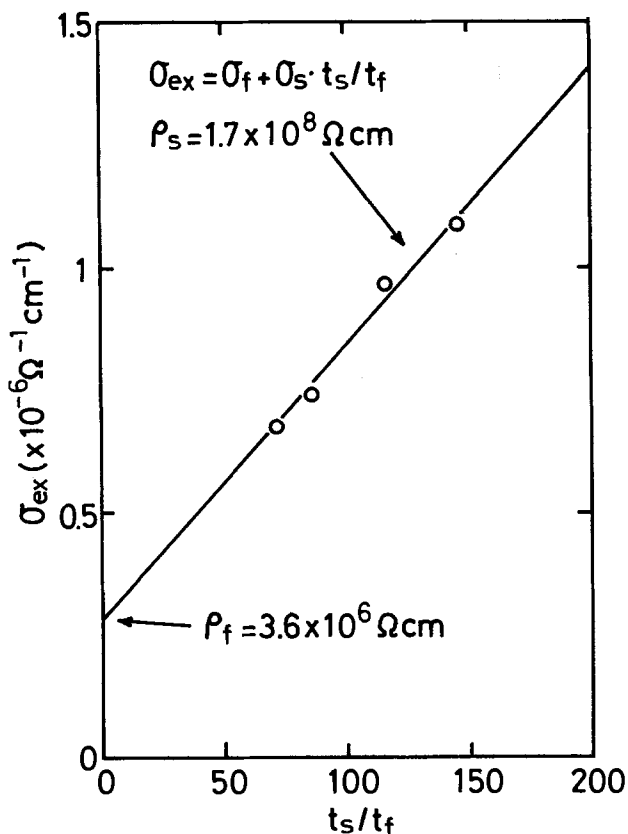
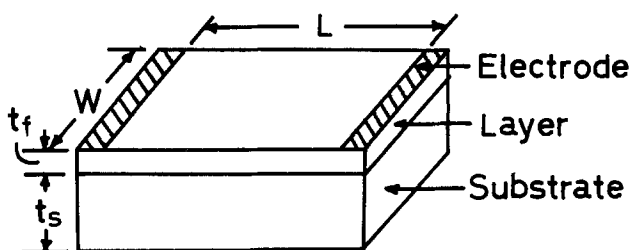


Fig. 1. Resistivity measurement method for high resistive layers: (a, top) shape of samples, (b, bottom) σ_{ex} vs. t_s/t_f used for extrapolation to calculate resistivities.

between the layer and the substrate. Hall measurements were made by the van der Pauw method. Contacts were made with electroless plated Ag for ZnTe and by evaporated In-Ga (2:1 by weight) with subsequent heating in N_2 for 3 min at 300°C for ZnSe.

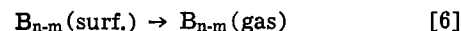
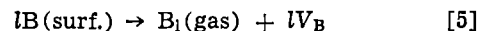
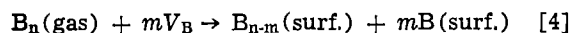
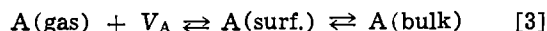
ZnS and GaAs substrates were used for optical transmittance measurements of grown layers. ZnS substrates are nearly transparent in the measured wavelength region of 450 ~ 800 nm for ZnTe and of 400 ~ 800 nm for ZnSe, the influence of the substrate on the measured transmittance was, however, subtracted with the aid of refractive index of ZnS substrate $n = 2.37$, and product of the absorption coefficient α and substrate thickness d , i.e., $\alpha d = 0.1$ (these values were confirmed by transmittance measurement of the substrate before growth). GaAs substrates were etched off in $\text{H}_2\text{O}_2:\text{NH}_4\text{OH}$ (20:1 by volume) at room temperature to obtain very thin layers (1 ~ 3 μm) for transmittance measurements. Etching rate of ZnTe was negligibly small and very small for ZnSe in the aforementioned etchant.

Photoluminescence was measured for estimation of crystallographic quality using Ar laser (488 nm, 100 mW) for ZnTe and Hg lamp for ZnSe as excitation source.

Results and Discussion

Crystal growth.—The growth rate was found to depend on F_1 and F_2 for lower value of impingement rate as shown in Fig. 2 for ZnTe and the substrate temperature as shown in Fig. 3. This is consistent with the results reported by Smith and Pickhardt (2) and can be explained as follows.

Since the vapor pressure of AB (10) is much lower than that of A and B, it seems reasonable to assume that the lifetime τ_{11} of an impinging A atom adsorbed into A atom on AB surface is much smaller than the lifetime τ_{12} of an impinging A atom adsorbed into B atom on AB surface, i.e., $\tau_{11} \ll \tau_{12}$, at the growth temperature. The vaporization kinetics of element A and compound AB have been considered similar, where A and B are the group II- and VI-atom and subscripts 1 and 2 pertain to A and B, respectively. A similar assumption holds for the case of impinging B molecules, i.e., $\tau_{22} \ll \tau_{21}$. Dissociation reaction of B molecules is also assumed. Based on these assumptions, the following reaction sequences can be considered



where subscripts (gas), (surf.), and (bulk) denote an impinging molecule, a surface species, and an atom incorporated into bulk crystal, and V_A and V_B mean adsorbed sites for A and B atom, respectively. Since S and Se generate a series of polyatomic molecule, several dissociation reactions as shown in Eq. [4] occur simultaneously. For simplicity, however, only one reaction will be taken into consideration. Assuming $n = m = l$, the above reaction sequence leads to following steady-state equations

$$R \propto \frac{dn_1}{dt} = \frac{dn_2}{dt} \quad [8]$$

$$\frac{dn_1}{dt} = [k_1 F_1 \theta_2 - (\theta_1/\tau_{12})] N_s \quad [9]$$

$$\frac{dn_2}{dt} = [k_2 F_2^{1/n} \theta_1 - (\theta_2/\tau_{21})] N_s \quad [10]$$

where R is the growth rate, n_1 and n_2 the number of A and B atom per unit area in the grown layer, N_s the total number of adsorbed sites, F_1 and F_2 the impingement

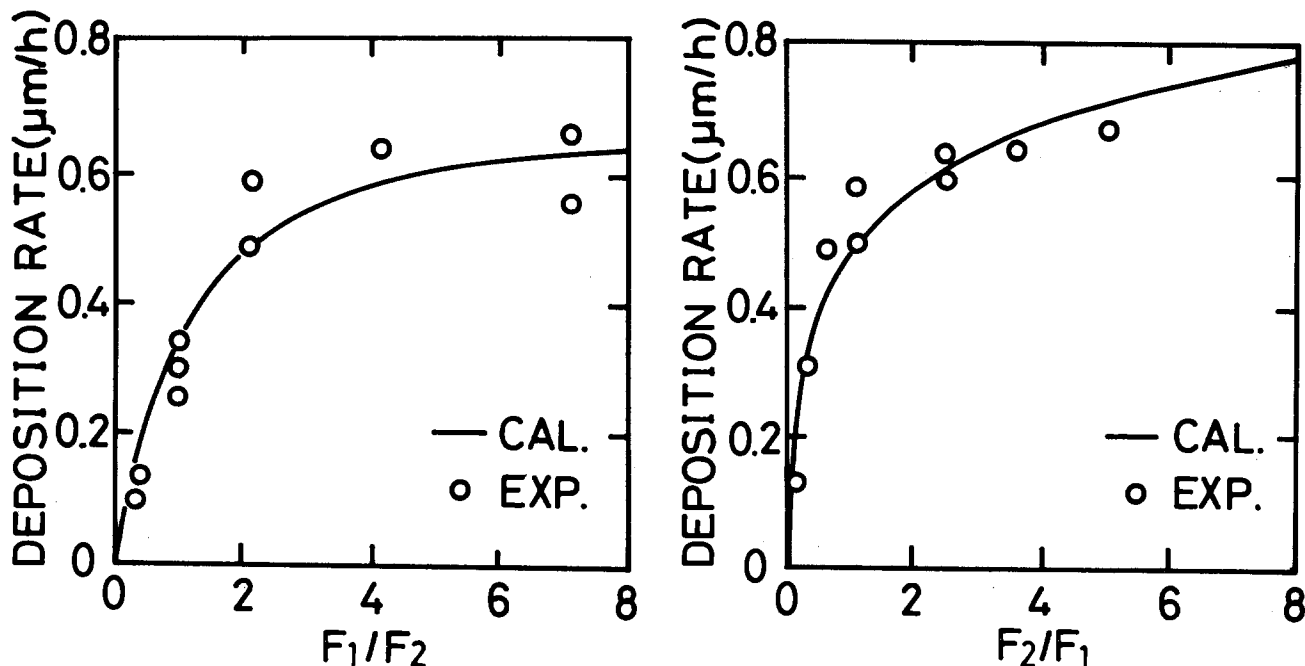


Fig. 2. Dependence of ZnTe growth rate on impingement rate ratio (a, left) for constant Te cell temperature ($T_{Te} = 285^\circ\text{C}$, $F_2 = 1.75 \times 10^{14} \text{ cm}^{-2} \text{ sec}^{-1}$, $k_1/k_2 = 2.13 F_2^{-1/2}$) and (b, right) for constant Zn cell temperature ($T_{Zn} = 240^\circ\text{C}$, $F_1 = 5.86 \times 10^{14} \text{ cm}^{-2} \text{ sec}^{-1}$, $k_1/k_2 = 1.51 F_1^{-1/2}$).

ing molecule fluxes of A and B, and θ_1 and θ_2 the fraction of N_s adsorbed by A and B (then $\theta_1 + \theta_2 = 1$). From Eq. [8] \sim [10]

$$R \propto \frac{k_1 F_1 k_2 F_2^{1/n} - (1/\tau_{12}\tau_{21})}{k_1 F_1 + k_2 F_2^{1/n} + (1/\tau_{12}) + (1/\tau_{21})} \quad [11]$$

Equation [11] is a very simplified form derived from the above assumptions. It, however, expresses well the actual growth kinetics of II-VI compounds and suggests that the growth of II-VI compounds should cease at high substrate temperatures due to increasing value of $1/\tau_{12}\tau_{21}$ in numerator and/or decreasing k_1 and k_2 . The growth rate depends on $k_1 F_1$ and/or $k_2 F_2^{1/n}$ in the optimum substrate temperature region for epitaxial growth. The increase of $1/\tau_{12}\tau_{21}$ means the reevaporation of constituent elements. The decrease of k_1 and k_2 means the reevaporation of impinging molecules before compound formation. The substrate temperatures for which growth of ZnSe and ZnTe were found to cease under the typical growth condition (the growth rate $R \sim 1 \mu\text{m/hr}$) were $450^\circ \sim 500^\circ\text{C}$ and $430^\circ \sim 470^\circ\text{C}$, respectively, and it slightly depended on im-

pinging molecular fluxes. The evaporation rates of ZnSe and ZnTe reached $1 \mu\text{m/hr}$ at 560° and 470°C , respectively, as calculated from the equilibrium vapor pressure of compounds (14, 15). These results suggest that the upper limit of the epitaxial growth temperature depends on reevaporation of compound for ZnTe and of impinging molecules for ZnSe. Solid lines in Fig. 2 show the calculated values of deposition rates as functions of F_1/F_2 from Eq. [11]; sticking coefficients of Zn and Te for $F_1/2F_2 = 1/10$ and 10, respectively, are $S_{Zn} = 0.8 \pm 0.2$, $S_{Te} = 0.6 \pm 0.2$. Experimental results are in good agreement with calculated values within experimental fluctuation. At lower substrate temperatures, Eq. [11] is invalid because the assumptions of $\tau_{11} \ll \tau_{12}$ and $\tau_{22} \ll \tau_{21}$ no longer hold true, i.e., unreacted impinging molecules are incompletely reevaporated and remain on the substrate surface. Therefore, the precipitation of constituent elements is expected to occur. However, no precipitation was observed above 250°C for growth rate $1 \mu\text{m/hr}$ with various molecular flux ratios for ZnTe and ZnSe. On the analogy of the Ueda's results for CdTe (19), this expectation will be realized at $<200^\circ\text{C}$. Sticking coefficient and consequently growth rate also depended on substrate orientation, and increased in the following order: $\{100\} \lesssim \{110\} < \{111\}$ for ZnTe on ZnTe substrate and $\{100\} < \{\bar{1}\bar{1}\bar{1}\}$ for ZnSe on GaAs. The ratio of growth rate on $\{111\}$ and $\{100\}$ $R_{\{111\}}/R_{\{100\}}$ is about 1.6 for both of ZnTe and ZnSe.

Epitaxial growth temperature is $\geq 250^\circ\text{C}$ for ZnTe and $\geq 300^\circ\text{C}$ for ZnSe. Figure 4 shows the RHEED pattern of ZnTe film grown at 250°C with $F_1/2F_2 = 1/2$. The lower limit of the epitaxial growth temperature strongly depends on the ratio of impingement rate F_1/F_2 . In the case of ZnTe, epitaxial growth occurred only around $F_1/2F_2 = 1/2$ at 250°C . In addition, the results of x-ray analysis suggest that films deposited under excess Te condition have better crystallographic quality than those under excess Zn condition, even if these are polycrystalline in structure.

ZnSe and ZnTe on GaAs substrates had good mirror-smooth surfaces independent of substrate orientation. However, rough surfaces were obtained for most of ZnTe films on InAs and ZnS, and for a few of ZnTe on

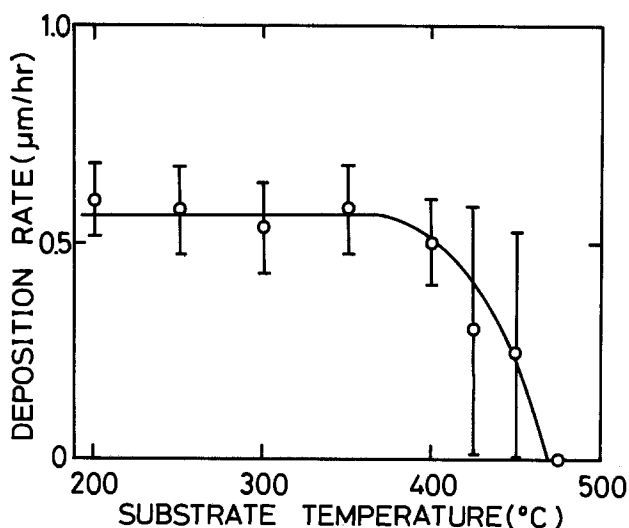


Fig. 3. Dependence of growth rate on substrate temperature



Fig. 4. RHEED pattern of ZnTe on GaAs grown at 250°C, $F_1/2F_2 = 1/2$.

ZnTe. In former case, RHEED patterns showed that rough surface samples always had a twin structure and smooth surface samples did not. In addition, results of RHEED analysis suggest that these twin structures are derived from the defect structures of substrates. It is, therefore, necessary that good quality substrates without twins should be used to obtain the films with good mirror-smooth surfaces. In the latter case, SEM photographs of rough surface showed pyramid-like structures as shown in Fig. 5. The shape of these pyramids was very sensitive to substrate orientation. It is found that the occurrence of grown layers with rough surfaces increased in the following order: $\{111\} < \{110\} < \{100\}$. The origin of this tendency is not yet well understood. It is, however, expected that the substrate orientation dependence of growth rate and the occurrence of rough surface layer are due to the reactivity of substrate surface.

No impurity other than surface contaminants was detected in undoped layers by ion microprobe analysis (IMA) except for ZnTe layers on GaAs. IMA results of ZnTe layers on GaAs suggest that a large amount of Ga ($10^{18} \sim 10^{19} \text{ cm}^{-3}$ at the surface of grown layers) diffuses from the GaAs substrate. This large Ga diffusion is supposed to be attributed to lattice defects, e.g., misfit dislocations, caused by a large lattice misfit (7.6%), i.e., defect-induced diffusion. Another evidence of misfit defects in ZnTe on GaAs is the poor cleavage faces of grown layers compared with mirror cleavage faces of substrates and grown layers on ZnTe and InAs.

Electrical properties.—Electrical resistivity of undoped ZnTe layers on GaAs was $\approx 10^4 \Omega\text{-cm}$ and a little sensitive to impingement rate ratio F_1/F_2 ; the

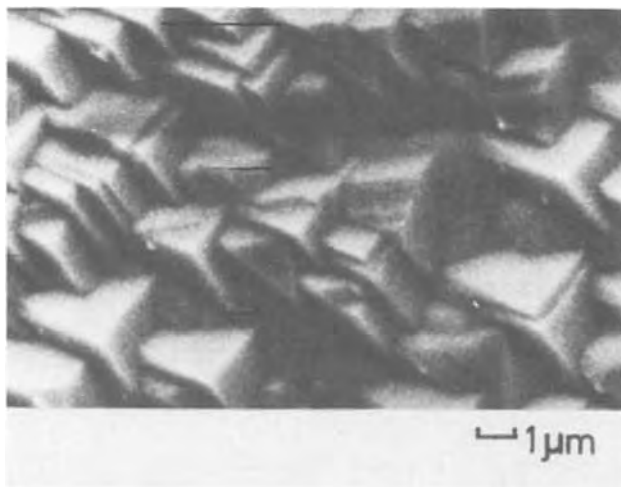


Fig. 5. SEM photographs of pyramid-like surface of ZnTe on $\{110\}$ ZnTe.

resistivity of the ZnTe layer grown under Te excess was a little lower than that of layer grown under Zn excess. On the other hand, the resistivities of undoped ZnTe layers on ZnTe were about $5 \Omega\text{-cm}$ with no dependence of impingement rate ratio. High resistivity of the former is attributed to a large amount of lattice defects and Ga diffusion from the GaAs substrate. The dependence on impingement rate ratio is probably due to the variation of native defect concentration. No observation of such dependence for ZnTe on ZnTe is supposed by small variation of native defect concentration compared with a large amount of unintentionally doped acceptor. The hole mobility of undoped ZnTe on ZnTe was $47 \sim 70 \text{ cm}^2 \text{ V}^{-1} \text{ sec}^{-1}$. This is lower than that of bulk ZnTe [$120 \text{ cm}^2 \text{ V}^{-1} \text{ sec}^{-1}$ (11)] and implies the existence of scattering centers which result in reduced mobility.

Arsenic and antimony were used as dopants for ZnTe. Arsenic was not effective in increasing the hole concentration even if the As impinging rate was more than ten times that of Zn or Te. The sticking coefficient of As was estimated to be ~ 0 on the assumption that the whole of incorporated As atoms were ionized and contributed to hole concentration without any other effects on electrical properties. In contrast, the increase of hole concentration up to 10^{18} cm^{-3} was achieved with Sb doping as shown in Fig. 6. Though the hole mobility decreased significantly with increasing hole concentration (Fig. 6), the resistivity decreased only by two orders of magnitude; the minimum value was $0.3 \Omega\text{-cm}$. On the basis of the same assumptions as for the As case, the sticking coefficients of Sb was estimated to be $10^{-2} \sim 10^{-3}$ from measured hole concentration and Sb impinging rate. It is expected that for this case the significant decrease of mobility with the increase of hole concentration occurs partly due to the disturbance of epitaxial growth by a large amount of impinging Sb molecules. The impinging Sb flux was more than those of Zn and Te during growth to obtain a hole concentration of $\sim 10^{18} \text{ cm}^{-3}$.

Undoped ZnSe layers on GaAs had the resistivity of $\sim 10^4 \Omega\text{-cm}$. Simultaneous Ga doping in the ZnSe layer was attempted during the growth to reduce the resistivity. The resistivity of ZnSe layers decreased to $0.07 \Omega\text{-cm}$ with increasing temperature of Ga effusion cell up to $\sim 380^\circ\text{C}$ above which it increased as shown in Fig. 7. The increase of the resistivity at higher temperatures is attributed to the reduction of crystallographic quality judging from the fact that $K_{\alpha 1}$ x-ray diffraction intensity of ZnSe decreased with increasing

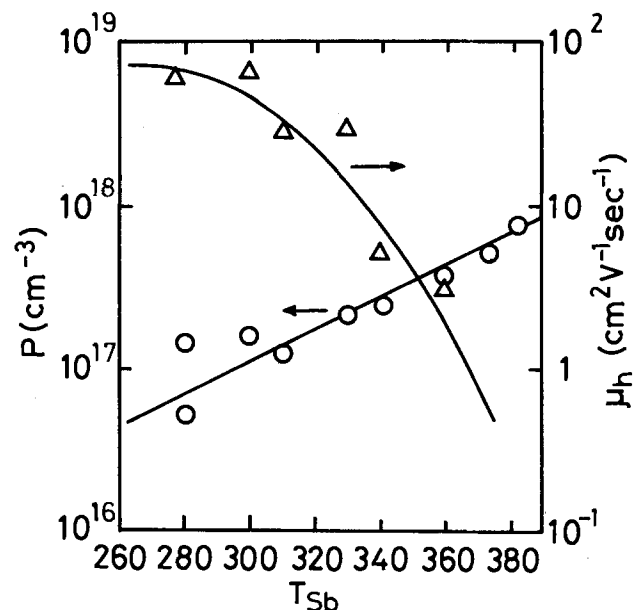


Fig. 6. Dependence of hole concentration and hole mobility of ZnTe on ZnTe on Sb cell temperature.

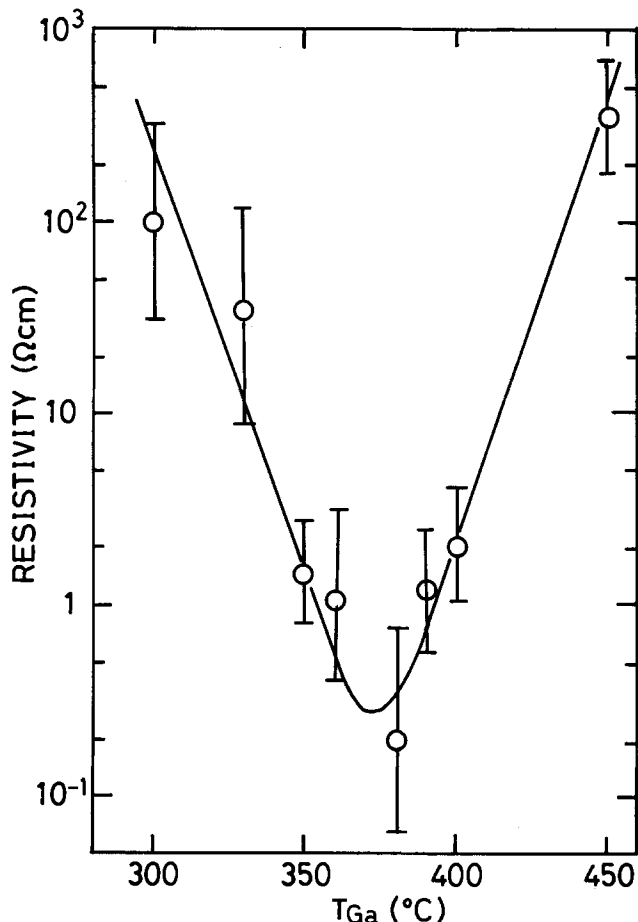


Fig. 7. Dependence of resistivity of ZnSe on Ga cell temperature

Ga effusion cell temperature, while that of GaAs substrate remained nearly unchanged as shown in Fig. 8. Electron mobility in low resistive ZnSe layers was $200 \sim 250 \text{ cm}^2 \text{ V}^{-1} \text{ sec}^{-1}$ with no temperature dependence.

Optical properties.—Transmittance of ZnSe and ZnTe and their temperature dependence were measured in the wavelength range of $400 \sim 800 \text{ nm}$ and $450 \sim 800 \text{ nm}$, respectively. Figure 9 shows transmittance spectra of ZnSe and ZnTe layers at room temperature. Relatively low values in the transparent region for ZnSe and ZnTe on GaAs substrate are due to a surface roughening caused during the selective etching of the substrate. More desirable results in the transparent region were obtained from ZnTe layers on ZnS as shown in Fig. 9. The fringes of the spectra are due to interference effects. No temperature dependence of transmittance spectra was observed except for the absorption edge shift as shown in Fig. 10, and no absorption band due to lattice defects was observed.

Figure 11 shows photoluminescence spectra of undoped ZnTe on ZnTe and GaAs at 4.2°K (listed in Table I). All emission lines and bands from ZnTe on ZnTe were stronger and sharper than those from ZnTe on GaAs, which implies that the former layer had better quality than the latter. Two broad emission bands observed in the spectra of ZnTe on GaAs (centered at 578 and 765 nm) were absent in the spectra of ZnTe on ZnTe. These two emission bands are reported to be absent in the spectra of ZnTe on Ge (5). These, therefore, cannot be attributed to misfit defects, but arise due to Ga diffusion from GaAs substrate into ZnTe layer. The diffused Ga is expected to form Ga center and the complex centers with misfit or native defects giving rise to emission bands centered at 578 and 765 nm. Photon energies of these two emission bands were 2.15 and 1.62 eV. Reported values of the

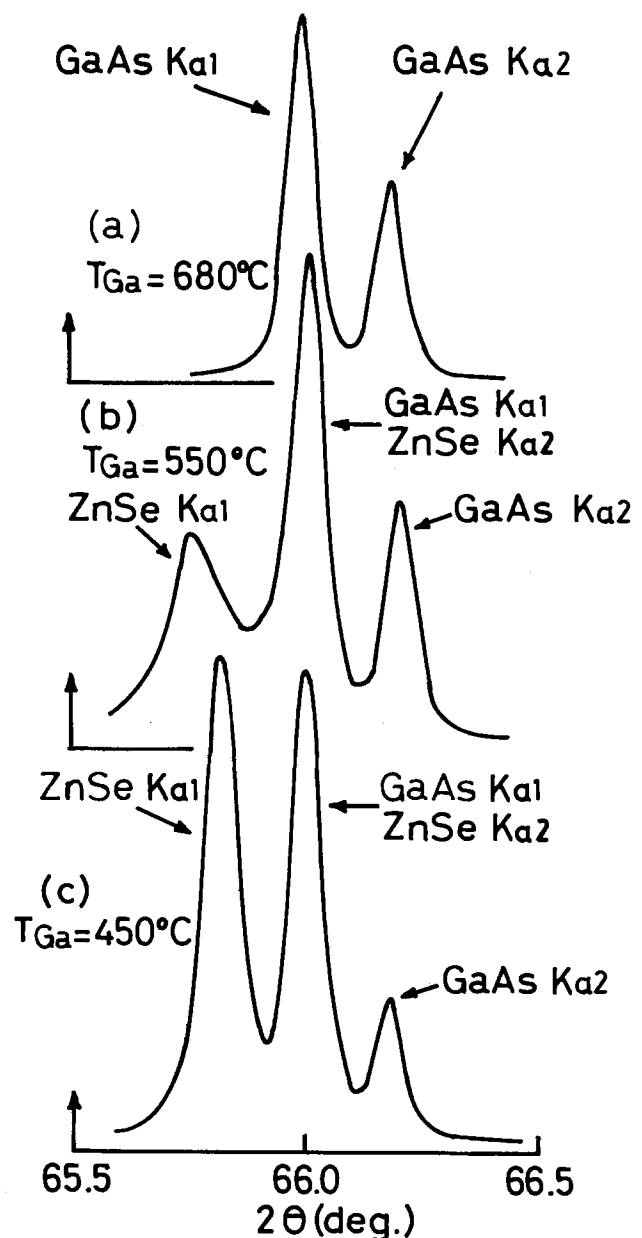


Fig. 8. X-ray patterns of ZnSe on GaAs {100}: (a) Ga cell temperature $T_{Ga} = 680^\circ\text{C}$, (b) $T_{Ga} = 550^\circ\text{C}$, (c) $T_{Ga} = 450^\circ\text{C}$.

second level of Zn vacancy, Ga donor level, and Ga complex level are 0.14, 0.24, and 0.6 eV, respectively (12). Therefore, the observed bands are expected to be due to the radiative transitions between valence band and Ga donor level (0.24 eV) and between Ga complex level (0.62 eV) and the second level of Zn vacancy (0.14 eV). Haynes rule (13) has suggested that I_A (5218.5Å) and I_B (5220.7Å) lines in the spectra of ZnTe on ZnTe are due to excitons bound to shallow acceptor corresponding to A (5303Å) and B (5322Å) lines, respectively. I_1 line in the spectra of ZnTe on GaAs are probably due to the similar excitons. A series of emission lines between 625 and 700 nm are attributed to be due to oxygen isoelectronic traps (16). The intensity of all emission lines increased with increasing substrate temperature suggesting that the higher substrate temperature makes the better quality layer.

Figure 12 shows the photoluminescence spectrum of Ga-doped ZnSe on GaAs at 77°K . These emission lines and bands remained even at room temperature though with reduced intensity. Since the intensity of broad emission bands increased with increasing Ga effusion cell temperature, these bands are, therefore, attributed to Ga doping and/or its associated mechanism.

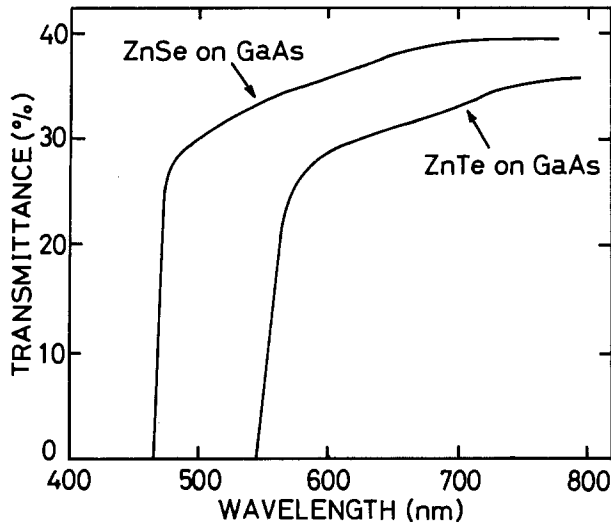


Fig. 9. Transmittance spectra of ZnSe and ZnTe on GaAs {100}

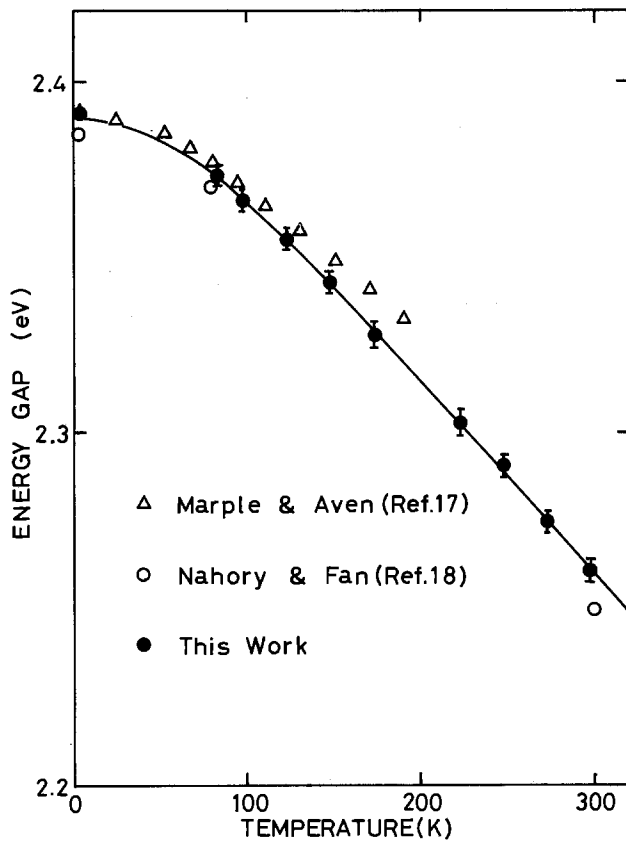


Fig. 10. Temperature dependence of absorption edge of ZnTe

Conclusion

The epitaxial growth by molecular beam epitaxy of ZnTe and ZnSe was found to occur at $\approx 250^\circ$ and at

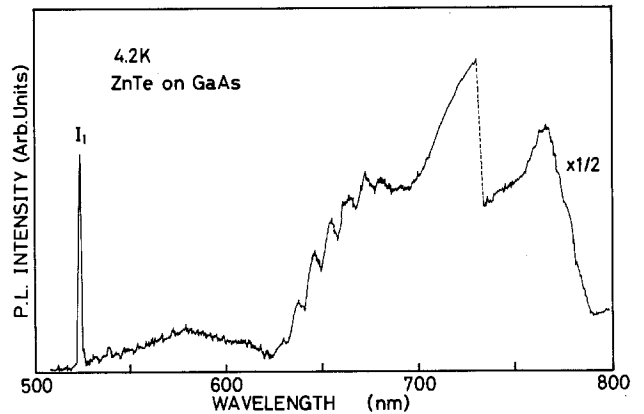
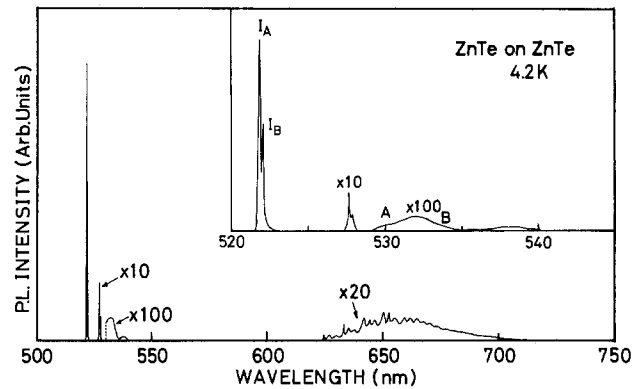


Fig. 11. Photoluminescence spectra of ZnTe on ZnTe (a, top) (along with the details in the region of 520 ~ 545 nm) and of ZnTe on GaAs (b, bottom) at 4.2°K.

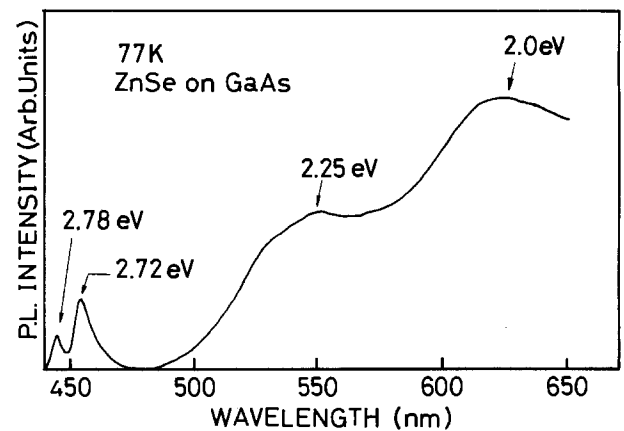


Fig. 12. Photoluminescence spectra of Ga-doped ZnSe on GaAs at 77°K.

$\approx 300^\circ\text{C}$, respectively, and to cease at $450^\circ \sim 500^\circ\text{C}$ for ZnSe and at $430^\circ \sim 470^\circ\text{C}$ for ZnTe with small impinging rate dependence. It was possible to explain the observed dependence of growth rate on substrate temperature and impinging rate ratio on the basis of a model in which the number of incorporated and re-

Table I. Emission lines and bands in photoluminescence spectra of ZnTe layers at 4.2°K

	Wavelength	Photon energy (eV)	Half-width (Å)	Origin	Remarks
ZnTe on ZnTe	5218.5Å	2.3758	~ 1	Bound exciton	} With phonon replica
	5220.7Å	2.3748	~ 1		
	5303Å	2.338	~ 20	} Shallow acceptor	
	5322Å	2.330	~ 20		
	625 ~700 nm				
ZnTe on GaAs	5245Å	2.364	~ 20	Bound exciton	
	~578 nm	2.15		Ga donor?	
	625 ~700 nm			Oxygen isoelectronic traps	
	~765 nm	1.62		Ga complex to 2nd Zn vacancy level?	

evaporated molecules, and consequently the sticking coefficients of group II- and VI-molecules, are strongly coverage dependent: e.g., the sticking coefficient of group II-molecules depends on group VI atom coverage and vice versa. ZnSe and ZnTe on GaAs and ZnTe on ZnTe had good enough mirror-smooth surfaces for the preparation of solid-state devices. Most of ZnTe layers on InAs and ZnS, however, had rather rough surfaces. The rough surface is probably due to a poor substrate surface preparation as judged from the results of RHEED analysis. The growth rate of ZnSe on GaAs and ZnTe on ZnTe depended on the substrate orientation, e.g., the {111} face had faster growth rate than the {100} face.

The resistivity of undoped ZnTe on GaAs and on ZnTe was $\geq 10^4$ and ~ 5 Ω -cm, respectively. The high resistivity for the former case is attributed to a large amount of lattice defects and the outdiffusion of Ga from the GaAs substrate into the ZnTe layer. The hole mobility of undoped ZnTe on ZnTe was $47 \sim 70$ $\text{cm}^2 \text{V}^{-1} \text{sec}^{-1}$. It was found that As is not effective for simultaneous doping of a ZnTe layer, i.e., the sticking coefficient of As is ~ 0 . Antimony is, however, used to increase the hole concentration up to $\sim 10^{18} \text{cm}^{-3}$ and to decrease the resistivity to ~ 0.3 Ω -cm. The sticking coefficient of Sb is estimated to be $10^{-2} \sim 10^{-3}$.

The resistivity of undoped ZnSe on GaAs was $\sim 10^4$ Ω -cm and could be decreased to ~ 0.07 Ω -cm by simultaneous doping of Ga. The electron mobility of Ga-doped ZnSe was typically $200 \sim 250$ $\text{cm}^2 \text{V}^{-1} \text{sec}^{-1}$. Their temperature independence implies the existence of such a scattering center as neutral impurities.

In the photoluminescence spectra of ZnTe on ZnTe at 4.2°K, two emission lines due to shallow acceptors and two exciton lines bound to them with their phonon replicas and a broad emission band due to oxygen isoelectronic traps were observed. In addition to these lines and band, two additional broad bands were observed in ZnTe on GaAs. These bands are attributed to the diffused Ga and their complex center with lattice defects. The results of photoluminescence measurement suggest that the higher substrate temperature makes the better quality layer. However, the ceasing of the epitaxial growth over a certain substrate temperature requires a suitable compromise

between its single crystalline nature and overall quality.

In the photoluminescence spectrum of Ga-doped ZnSe on GaAs, an emission line and two broad emission bands were observed. These broad bands are attributed to Ga doping.

Manuscript submitted Aug. 3, 1979; revised manuscript received Nov. 6, 1979.

Any discussion of this paper will appear in a Discussion Section to be published in the December 1980 JOURNAL. All discussions for the December 1980 Discussion Section should be submitted by Aug. 1, 1980.

Publication costs of this article were assisted by the Tokyo Institute of Technology.

REFERENCES

1. A. Y. Cho and J. R. Arthur, *Prog. Solid State Chem.*, **10**, 157 (1975).
2. D. L. Smith and V. Y. Pickhardt, *J. Appl. Phys.*, **46**, 2366 (1975).
3. T. Yao *et al.*, *Jpn. J. Appl. Phys.*, **16**, Suppl. 16-1, 451 (1977).
4. T. Yao *et al.*, *J. Cryst. Growth*, **45**, 309 (1978).
5. T. Yao *et al.*, *Jpn. J. Appl. Phys.*, **15**, 1001 (1976).
6. D. B. Holt, *Thin Solid Films*, **24**, 1 (1974).
7. N. Matsunaga *et al.*, *J. Appl. Phys.*, **49**, 5710 (1978).
8. R. S. Title *et al.*, *Phys. Rev. A*, **136**, 300 (1964).
9. R. E. Honig and D. A. Kramer, *RCA Rev.*, **30**, 285 (1969).
10. K. C. Mills, "Thermodynamic Data for Inorganic Sulfides, Selenides and Tellurides," Butterworth, London (1974).
11. M. Aven, *J. Appl. Phys.*, **38**, 4421 (1967).
12. J. R. Fischer, *J. Appl. Phys.*, **44**, 1708 (1973).
13. R. E. Halsted and M. Aven, *Phys. Rev. Lett.*, **14**, 64 (1965).
14. R. F. Brebrick, *This Journal*, **116**, 1274 (1969).
15. W. J. Wösten and M. G. Geers, *J. Chem. Phys.*, **66**, 1252 (1962).
16. R. E. Dietz *et al.*, *Phys. Rev. Lett.*, **8**, 391 (1962).
17. D. T. F. Marple and M. Aven, "Proc. Intern. Conf. on II-VI Semiconducting Compounds," D. G. Thomas, Editor, p. 315, Benjamin, New York (1967).
18. R. E. Nahory and H. Fan, *Phys. Rev.*, **156**, 825 (1967).
19. R. Ueda, *J. Cryst. Growth*, **31**, 333 (1975).

Growth Kinetics and Polymorphism of Chemically Deposited CdS Films

Inderjeet Kaur, D. K. Pandya, and K. L. Chopra

Department of Physics, Indian Institute of Technology, Delhi, New Delhi 110029, India

ABSTRACT

The kinetics of growth for chemical deposition of CdS films from alkaline solutions of cadmium salts has been studied with respect to temperature of deposition and the relative concentrations of the various reactants in the solution. It has been established that the growth of the film takes place either by ion-by-ion condensation of Cd^{+2} and S^{-2} ions or by adsorption of colloidal particles of CdS formed in the solution, depending on the various deposition parameters and the method of preparation. The former process of growth results in thin, hard, adherent and specularly reflecting films, whereas the latter results in thick, powdery and diffusely reflecting films. Occurrence of different polymorphic phases of CdS (hexagonal and cubic) has been observed under different growth conditions. A model for growth mechanism has also been proposed.

Multicomponent materials like compound semiconductors and their alloys are of considerable technical

Key words: CdS, chemical deposition, growth kinetics, thin films.

interest in the field of electronic and electrooptical devices. In general, it is difficult to prepare these materials in bulk form over a wide range of compositions because of limited solubility of materials in each other.

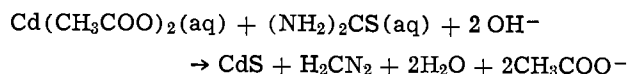
However, synthesis can be readily achieved in case of thin films, where the solubility conditions are known (1) to relax. The commonly used methods of preparation of thin films of these materials are vacuum evaporation, sputtering, and spray pyrolysis.

A relatively less common but inexpensive and convenient method for large area preparation of thin films at low temperatures is a chemical solution growth technique, which has been known (2-6) for some time for thin film deposition of such compound semiconductors as CdS, PbS, PbSe, CdSe, and ZnSe. In this method, thin films of sulfide can be prepared by decomposition of thiourea (or thioacetamide) in alkaline solutions of the salts of the corresponding cation. In general, the process involves the application of a controllable chemical reaction which proceeds at a low rate in an aqueous solution containing the various reactants. The substrates are immersed in this solution. The reaction rate can be controlled by adjustment of pH, temperature, and the relative concentrations of the various reactants in the solution. Since the solution growth technique is a low temperature (less than 90°C) deposition method, it does not limit the choice of the substrate material. By contrast, in spray pyrolysis only a limited number of substrate materials which can withstand high temperature and chemical corrosion during pyrolysis can be used. Further, in a solution growth technique, since the deposition is from ions in aqueous solution, which are slowly being generated, the solubility product helps to maintain the stoichiometry constant for any ratio of cations and anions. As a result of these processes homogeneous phases of compounds are obtained. It must be emphasized that formation of homogeneous and stoichiometric compound films by vacuum evaporation requires a critical adjustment of the substrate and various source temperatures, as well as the adjustment of the concentrations of the various components. Note that homogeneous precipitation by *in situ* generation of the precipitating anion is well known in chemistry for improving the stoichiometry of the precipitates.

In spite of considerable interest, the solution growth technique (2-13) has remained recipe-oriented and little is known about the kinetics of the process. It is essential to understand the kinetics and mechanism of the growth of films formed by this technique so that it may be extended to other semiconducting materials. CdS is an important material for application in large area solar cells. Therefore, we have undertaken a study of the process of deposition of CdS films by the solution growth technique. This paper reports on the kinetics of growth of CdS films and the occurrence of different conditions in the solution. A model for the growth mechanism has been proposed.

Experimental

Thin films of sulfides of Cd/Zn/Pb can be prepared by decomposition of thiourea in an alkaline solution containing a salt of Cd/Zn/Pb. The chemical reaction involved for a typical case of formation of CdS films from Cd(CH₃COO)₂ is as follows



CdSO₄, Cd(NO₃)₂, CdCl₂, etc. can also be used in a similar way. Reaction mixtures can be prepared in two ways. Different types of films are obtained from solution depending on whether the solution is being stirred or not during the deposition of the films.

(i) Appropriate volumes of 1M Cd(CH₃COO)₂, 14M NH₃ solution and distilled water are mixed slowly at room temperature with continuous stirring. Substrates are then immersed in the beaker containing the reaction mixture. The beaker is placed in a water bath having automatic temperature control. The solution is

stirred with the help of a magnetic stirrer, as shown in Fig. 1. The solution is heated with continuous stirring to the required temperature of deposition, and the temperature is controlled to within ±1°C. An appropriate amount of 1M thiourea solution is then added with continuous stirring. Thereafter, the stirring is stopped in one case and continued in the other. Substrates are then taken out after a suitable time, washed with distilled water, and dried.

(ii) A reaction mixture of composition: 0.1M Cd(CH₃COO)₂, 6M NH₃, and 0.2M thiourea is prepared at room temperature. Substrates are then immersed in the solution and the solution is slowly heated to about 75°C, with continuous vigorous stirring. After about half an hour, substrates are taken out, washed with distilled water, and dried.

The substrates used in our study are ultrasonically cleaned glass slides, freshly etched single crystal silicon slices, and Sb-doped SnO₂-coated conducting glass slides. These were chosen with a view to studying the kinetics on different types of substrate materials, *viz.*, insulating, semiconducting, and conducting; the last one being used for making solar cells.

The film thickness was measured by a mechanical stylus arrangement (Talystep). Electron diffraction studies were done using an AEI-EM 802 electron microscope. The lattice constants were calculated by routine methods.

Results

The qualitative nature of the growth kinetics is the same on all the three substrate materials. Detailed studies were carried out on glass substrates. The quantitative differences arise due to differences in the nature of the substrate surface. Figures 2-5 show the growth kinetics on glass substrates.

We have found that different qualities of films can be obtained under different conditions in the working solution. Previous results of Kitaev *et al.* (2, 11-13) on kinetics show that film formation is possible only in the presence of Cd(OH)₂ in the working solution, but we have found that this is not always true. NH₃ plays a major role in determining the quality of the films. For convenience we have divided the whole NH₃ concentration range covered in the present study into three regions:

(i) The region in which (a) the amount of NH₃ is not sufficient (less than 1.8M) to redissolve completely the white precipitate of Cd(OH)₂ formed by the addition of NH₃ solution to the salt solution. (b) Although the amount of NH₃ is sufficient to completely

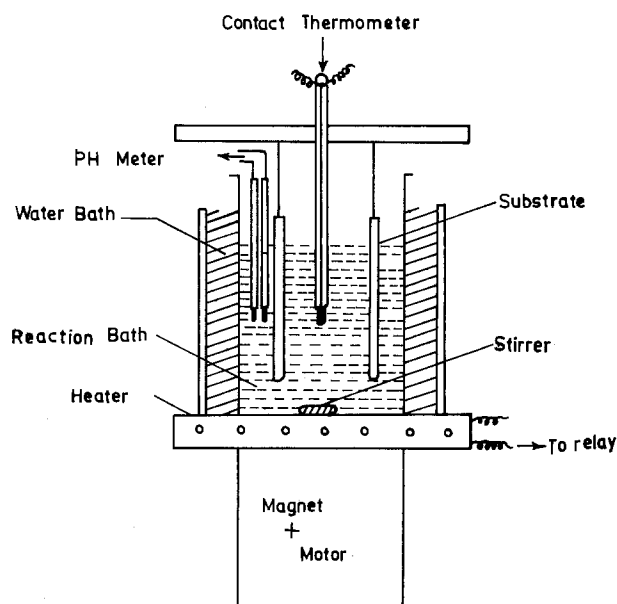


Fig. 1. Experimental setup for preparation of films

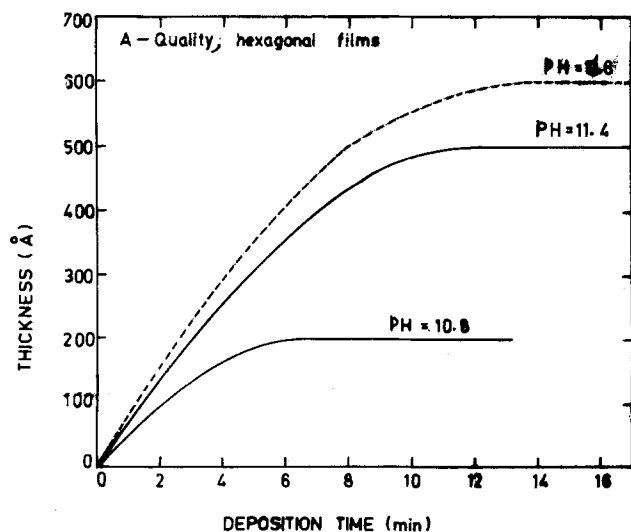


Fig. 2a. Thickness as a function of time for a reaction mixture at 65°C and of composition: 0.1M $\text{Cd}(\text{CH}_3\text{COO})_2$, 0.2M $(\text{NH}_2)_2\text{CS}$, and various NH_3 concentrations in region A_I (solid curves) and A_{II} (dashed curve).

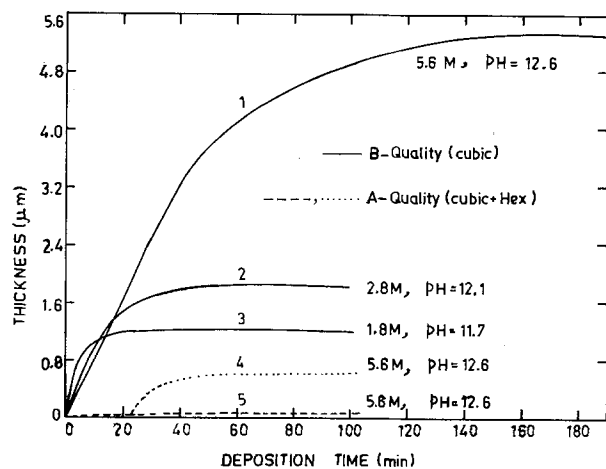


Fig. 2b. Thickness as a function of time for a reaction mixture at 65°C and of composition: 0.1M $\text{Cd}(\text{CH}_3\text{COO})_2$, 0.2M $(\text{NH}_2)_2\text{CS}$, and different NH_3 concentrations. (—) Unstirred solutions in region B_{II} , --- stirred method (a); method (b).

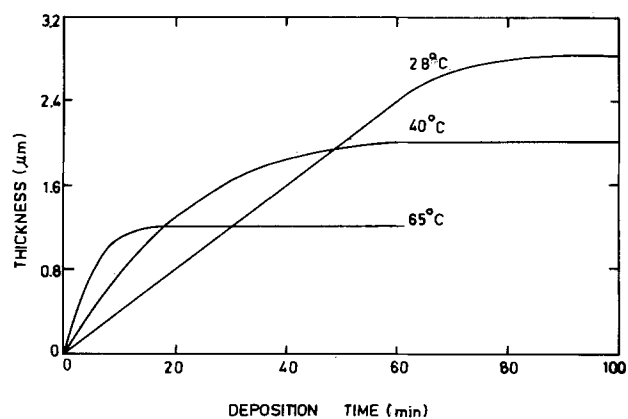


Fig. 3. Thickness as a function of time for a reaction mixture (unstirred) of composition: 0.1M $\text{Cd}(\text{CH}_3\text{COO})_2$, 1.8M NH_3 , 0.2M $(\text{NH}_2)_2\text{CS}$ at different temperatures.

redissolve $\text{Cd}(\text{OH})_2$ precipitate, additional alkali is added to the solution for the formation of $\text{Cd}(\text{OH})_2$. The solutions, in this case, are turbid before the addition of thiourea.

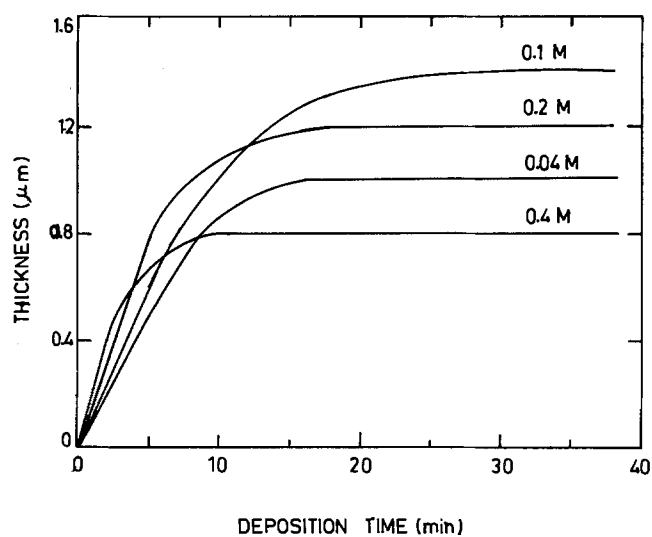


Fig. 4. Thickness as a function of time for a reaction mixture (at 65°C, unstirred) and of composition: 0.1M $\text{Cd}(\text{CH}_3\text{COO})_2$, 1.8M NH_3 , and different $(\text{NH}_2)_2\text{CS}$ concentrations.

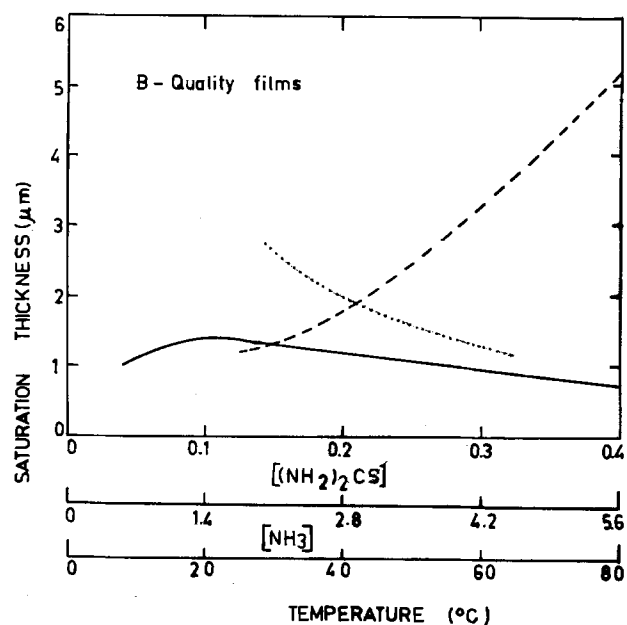


Fig. 5. Saturation thickness for B-type films as a function of (i) $(\text{NH}_2)_2\text{CS}$ as derived from Fig. 4 (—); (ii) NH_3 as derived from Fig. 2b (---); (iii) temperature as derived from Fig. 3 (.....).

(ii) The region in which the amount of NH_3 is just sufficient to completely redissolve the white precipitate of $\text{Cd}(\text{OH})_2$.

(iii) The region in which the amount of NH_3 is in much excess, 3-4 times as much as in region ii. The solutions in regions ii and iii are clear before the addition of thiourea.

Turbid solutions containing a thin suspension of $\text{Cd}(\text{OH})_2$ give rise to thin (thickness $\sim 600\text{Å}$), adherent, physically coherent, and specularly reflecting films. These we refer to as A-quality films. The kinetics of growth for such films is shown in Fig. 2a. The dotted curve corresponds to films formed in region i(b) and the continuous curves in region i(a). These have wurtzite (hexagonal) structure when the solutions are vigorously stirred during the deposition. The films prepared under the same conditions but without stirring have wurtzite (hexagonal) structure with a large fraction of sphalerite (cubic) phase also, as shown in Table I, showing the d values of the various phases. Also, these films are less reflecting than the ones obtained by stirring.

Table I.

Hexagonal			Cubic			Mixed (hexagonal + cubic)		
dA		hkl	dA		hkl	dA measured	Hexagonal hkl	Cubic hkl
Measured	Standard		Measured	Standard				
3.615	3.580	100	—	—	—	—	—	—
3.337	3.360	002	3.363	3.360	111	3.395	002	111
3.155	3.160	101	—	—	—	—	—	—
2.444	2.450	102	—	—	—	—	—	—
2.075	2.060	110	2.056	2.058	220	2.136	110	220
2.075	2.060	110	—	—	—	1.916	103	—
1.902	1.898	103	—	—	—	1.788	112	—
1.770	1.761	112	1.752	1.753	311	1.788	—	311
—	—	—	1.325	1.337	331	1.359	—	331
—	—	—	1.290	1.298	420	—	—	—

Unstirred clear solutions in region *ii* give rise to thick (thickness $\sim 1-3 \mu\text{m}$ depending on the various deposition parameters), less adherent and powdery films having sphalerite (cubic) structure (Table I). These we refer to as B-quality films. Films obtained by stirring the solutions in this region are not very different from those obtained without stirring. Curve 3 in Fig. 2b shows the kinetics of growth for one of such films.

Unstirred solutions in region *iii* give rise to thick (thickness $\sim 5 \mu\text{m}$) adherent B-quality films having cubic structure. Curves 1 and 2 in Fig. 2b show the kinetics of growth for films prepared from unstirred solutions with different ammonia concentrations in this region. When the solutions are vigorously stirred during deposition, thin (thickness $\sim 500\text{\AA}$) A-quality films (curve 5 in Fig. 2b) are obtained, with a structure corresponding to mixed hexagonal and cubic phases.

In procedure (b) the solution is slowly heated to about 75°C with continuous stirring, in the presence of thiourea [in contrast to method (a) where thiourea is added to the reaction mixture only after bringing it to the required temperature of deposition and maintaining it]. Films prepared by this procedure were $\sim 6000\text{\AA}$ thick, of A-quality with a structure corresponding to mixed hexagonal and cubic phases (curve 4 in Fig. 2b).

The lattice constants of the hexagonal and cubic phases, as calculated are: hexagonal, $a = 4.16\text{\AA}$ and $c = 6.67\text{\AA}$; cubic, $a = 5.82\text{\AA}$. These values are very close to the known values of the bulk material as given in ASTM cards. Standard values: hexagonal, $a = 4.138\text{\AA}$ and $c = 6.713\text{\AA}$; cubic, $a = 5.818\text{\AA}$.

Discussion

The main results of our study are: (i) the films prepared in presence of $\text{Cd}(\text{OH})_2$ in the solution are very adherent, physically coherent, and specularly reflecting; (ii) vigorous stirring of the solution decreases the powdery nature and increases adhesion, physical coherence, and specular reflectance of the films; (iii) in general, the higher the deposition rate, the lower is the saturation thickness; and (iv) A-quality films are formed more readily on smooth surfaces while B-quality films are formed more readily on rough surfaces.

Based on the experimentally observed facts, we have proposed a model for the mechanism of growth of these films, which explains all the above features of growth. Similar to formation of precipitate in the solution, formation of film on the substrate takes place by nucleation and growth processes. It is well known that nucleation of a precipitate in the solution starts at some local inhomogeneities present in the solution (e.g., due to some solid impurities), where the ionic product exceeds the solubility product. Growth of these nuclei by addition of more ions from the solution results in formation of stable nuclei of size greater than the critical size. Further growth, up to a particle size of $10 \mu\text{m}$, results in formation of a colloidal dispersion. Nucleation on the substrate, according to Kitaev *et al.* (2) takes place by adsorption of these primary colloids. Growth takes place as a result of surface coagulation of

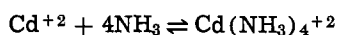
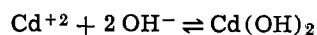
these particles, resulting in thin, adherent, and specularly reflecting A-quality films. An important result of our previous studies, which completely rules out the possibility of nucleation of A-quality films by adsorption of colloidal particles and cluster-by-cluster growth model, is the possibility of occurrence of epitaxial growth in some of the cases (14) on suitably chosen single crystal substrates. This strongly suggests the atomistic (that is, ion-by-ion) nature of nucleation and growth. Other evidence in favor of the ion-by-ion growth model (and against the cluster-by-cluster growth model) is the strong adhesion and specular reflectance of A-quality films. Note that electrophoretic deposits, which grow cluster-by-cluster from a colloidal dispersion, are known (15) to be loose and powdery. The fact that the structure of A-quality films is either pure hexagonal or a mixture of hexagonal and cubic phases, whereas the precipitate is always cubic, again suggests ion-by-ion growth of A-quality films. Cluster-by-cluster growth of B-quality films is supported by the fact that they have a structure similar to that of the precipitate (cubic). Cluster-by-cluster growth of B-quality films explains the experimentally observed fact that they are more readily formed on rough surfaces.

Formation of CdS nuclei by the combination of ions on the substrate surface requires preferential adsorption of at least one type of the reacting ions on the substrate. Preferential adsorption of either Cd^{+2} or S^{-2} on glass surfaces from aqueous solutions is not known; so that formation of CdS nuclei on the substrate requires some catalytic solid phase on the substrate which can preferentially adsorb Cd^{+2} or S^{-2} ions. We have seen that a glass slide dipped in a suspension of $\text{Cd}(\text{OH})_2$ has a layer of $\text{Cd}(\text{OH})_2$ on it, which is known (13) to stimulate the decomposition of thiourea. This suggests that in solutions containing a suspension of $\text{Cd}(\text{OH})_2$, this layer is converted to CdS by adsorption of S^{-2} ions formed by decomposition of thiourea on the catalytic surface of $\text{Cd}(\text{OH})_2$. Further growth takes place on CdS by addition of more Cd^{+2} and S^{-2} ions. Vigorous stirring of the solution increases the rate of arrival of Cd^{+2} and S^{-2} ions on the substrate and also the rate of coagulation of colloidal CdS particles in the solution. This results in precipitation of the colloidal CdS particles which now cannot be adsorbed on the substrate leaving the films to grow by only ion-by-ion growth. This also explains, why, if solutions are not stirred, films contain a large fraction of cubic CdS also. The colloidal CdS particles which are adsorbed if solution is not stirred give rise to scattering in the films, thus decreasing their specular reflectance.

In case of clear solutions containing no $\text{Cd}(\text{OH})_2$ in the bulk of the solution, accumulation of CdS in the solution takes place homogeneously by slow hydrolysis of thiourea and decomposition of the complex $\text{Cd}(\text{NH}_3)_4^{+2}$. The colloidal CdS solution is stable in this case for a long time when the solution is not being stirred, so that nucleation and growth of film take place by colloidal particles resulting in B-quality films. But when the clear solution is vigorously stirred, the colloid becomes unstable due to enhanced coagulation,

forming larger particles of CdS which cannot be adsorbed to start nucleation. In unstirred solutions very few Cd^{+2} and S^{-2} ions reach the substrate, since most of them condense on colloidal CdS formed in the solution. But during stirring the substrate surface is bombarded with a large number of Cd^{+2} and S^{-2} ions. This, coupled with the fact that a hydrophilic surface preferentially adsorbs OH^- ions from aqueous alkaline solutions, results in formation of $\text{Cd}(\text{OH})_2$ nuclei on the substrate, although there is no $\text{Cd}(\text{OH})_2$ in the solution due to high NH_3 concentration. (We have seen that on hydrophobic surfaces like Teflon, greasy glass slides, A-quality films are not formed. B-quality powdery films can be obtained on any surface, including hydrophobic, if the surface is not smooth). These $\text{Cd}(\text{OH})_2$ nuclei act as nucleation centers for CdS. These nuclei grow ion-by-ion and coalesce to form a continuous CdS film. This ion-by-ion growth of film proceeds until some large precipitate particles of CdS collect on the substrate surface.

The various other features of growth kinetics (Fig. 2-5) can be explained on the basis of a diagram (Fig. 6) which represents a graphical solution of equations representing the equilibria



This diagram has been drawn on a basis similar to that of Kitaev *et al.* (13). The analysis is as follows.

From standard tables, the solubility product constant of $\text{Cd}(\text{OH})_2$ and the instability constant of $\text{Cd}(\text{NH}_3)_4^{+2}$ are given, respectively, by

$$SP = 2.2 \times 10^{-14} \quad (pSP = 13.66)$$

$$K = 7.56 \times 10^{-8} \quad (pK = 7.12)$$

That is

$$[\text{Cd}^{+2}][\text{OH}^-]^2 = 2.2 \times 10^{-14}$$

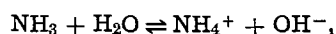
$$\frac{[\text{Cd}^{+2}][\text{NH}_3]^4}{[\text{Cd}(\text{NH}_3)_4^{+2}]} = 7.56 \times 10^{-8}$$

Converting to logarithmic concentrations

$$pH = 0.5p[\text{Cd}^{+2}] + 7.17 \quad [1]$$

$$p[\text{Cd}^{+2}] + 4p[\text{NH}_3] - p[\text{Cd}(\text{NH}_3)_4^{+2}] = 7.12 \quad [2]$$

Using base hydrolysis of NH_3



$$K_b = 1.8 \times 10^{-5} \quad (pK_b = 4.76)$$

$$2p[\text{OH}] = 4.76 + p[\text{NH}_3]$$

$$p[\text{NH}_3] = 23.24 - 2pH \quad [3]$$

Substituting $p[\text{NH}_3]$ from [3] into [2] and assuming that NH_3 is present in excess so that $[\text{Cd}(\text{NH}_3)_4^{+2}] \approx [\text{salt}]$, we obtain for 0.1M $\text{Cd}(\text{CH}_3\text{COO})_2$

$$pH = \frac{1}{8} p[\text{Cd}^{+2}] + 10.6 \quad [4]$$

This is true only for $[\text{NH}_3] \gg 4 [\text{salt}]$, so that the approximation $[\text{Cd}(\text{NH}_3)_4^{+2}] \gg [\text{Cd}^{+2}]$ is valid. Equations [1] and [4] when plotted as pH vs. $p[\text{Cd}^{+2}]$ are called hydroxide line and complex line, respectively. $\text{Cd}(\text{OH})_2$ is formed in the solution only for pH values above the hydroxide line, and the complex $\text{Cd}(\text{NH}_3)_4^{+2}$ is stable only for pH values below the complex line. For pH values above complex line, the complex is hydrolyzed to $\text{Cd}(\text{OH})_2$. The $p[\text{Cd}^{+2}]$ scale has been converted to $p[\text{NH}_3]$ scale using Eq. [2] (with $[\text{Cd}(\text{NH}_3)_4^{+2}] \approx [\text{salt}] = 0.1$). The pH value of the solution for a given $[\text{NH}_3]$ can be calculated from the solution of Eq. [1] and [2]. From [1] and [2], eliminating $p[\text{Cd}^{+2}]$, we obtain

$$pH = 11.23 - 2p[\text{NH}_3] \quad \text{for } 0.1\text{M } \text{Cd}(\text{CH}_3\text{COO})_2$$

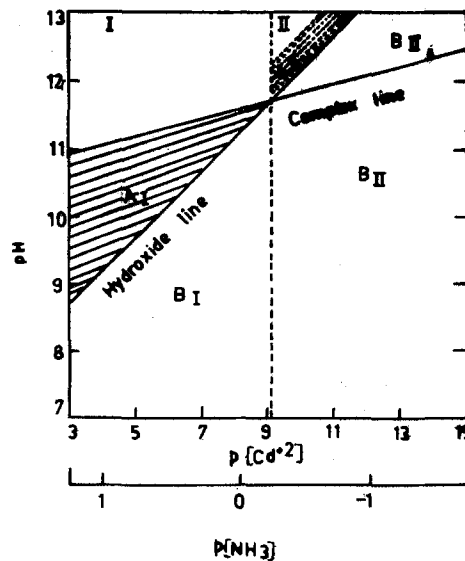


Fig. 6. A plot of Eq. [1] and [4]

pH values of different solutions as calculated by this equation are in close agreement with the experimentally measured values, shown in Fig. 2b.

The whole diagram can be divided by a vertical line, into two regions I and II. In region I, the complex line lies above the hydroxide line, implying that $\text{Cd}(\text{OH})_2$ and $\text{Cd}(\text{NH}_3)_4^{+2}$ inevitably exist in the solution in the region between the hydroxide and the complex line. The true equilibrium of the system $\text{Cd}(\text{CH}_3\text{COO})_2\text{-NH}_3$ in water is represented by some curve lying in A_I in region I and by the complex line in region II. Working at other points in the diagram requires additional introduction of an acid or alkali. Region A_I is, thus, the theoretically predicted region for coexistence of $\text{Cd}(\text{OH})_2$ and $\text{Cd}(\text{NH}_3)_4^{+2}$. For very small amounts of $\text{Cd}(\text{OH})_2$ in the solution, A-quality films are formed in this region. Larger amounts of $\text{Cd}(\text{OH})_2$ lead to precipitation only and no film formation. Kinetics of growth for these films is shown by solid curves in Fig. 2a. Since below the hydroxide line, there is no $\text{Cd}(\text{OH})_2$ present in the solution, A-quality films are not expected in the region B_I . Experimentally this has also been found to be true.

In region II, the hydroxide line lies above the complex line. The solutions are clear in the region below the hydroxide line, and to form $\text{Cd}(\text{OH})_2$ in the working solution, an alkali must be introduced into the solution. Thus, A-quality films are expected in the region A_{II} . The film thickness decreases rapidly as higher pH values are approached where, due to rapid reaction, only precipitation will occur. The dotted portion shows the experimental values for obtaining A-quality films of measurable thickness, thus verifying the theoretically predicted results. The kinetics of film growth in this region is shown in Fig. 2a, dotted curve. Thus, A_I and A_{II} correspond to region i mentioned earlier in the text under Results. In region B_{II} below the hydroxide line, no $\text{Cd}(\text{OH})_2$ can exist in the solution and B-quality films are expected with no stirring (solid curves 1, 2, and 3 in Fig. 2b) and A-quality with vigorous stirring (dashed curve 5 in Fig. 2b). In this region, most of the Cd^{+2} ions are bound in the complex form and only a very small fraction ($\sim 10^{-13}$) is present as free Cd^{+2} . Moreover, there is no solid phase of $\text{Cd}(\text{OH})_2$ present to enhance the decomposition of thiourea. It is, therefore, expected that film formation will take place only above a certain temperature for each concentration of NH_3 . This arises from the fact that below this temperature, the product $[\text{Cd}^{+2}][\text{S}^{-2}]$ is less than the solubility product of CdS. Heating of the solution helps the decomposition of thiourea and also provides kinetic energy to the ions, resulting in increased number of collisions and hence their combination to form

CdS. This is in conformity with the experimental observations. For example, solutions containing 5.6M NH_3 must be heated to temperatures greater than 45°C to obtain films.

The saturation behavior of the film thickness in kinetics curves (Fig. 2a, 2b, 3, and 4) is because of eventual reduction of the ionic product of CdS in the solution to values below the solubility product and coagulation of colloidal particles of CdS to form larger particles which cannot be adsorbed.

Figure 6 shows that as the NH_3 concentration increases, the Cd^{+2} concentration decreases, resulting in slow rates of deposition at high NH_3 concentrations. Also since Cd^{+2} ions are being generated very slowly, the rate of precipitation is very much reduced, giving more time for film formation, thus accounting for the general observed feature that the lower the deposition rate, the higher the ultimate film thickness obtained (Fig. 5).

As mentioned earlier, the increase of deposition rate with increase of temperature is because of the increased number of collisions between Cd^{+2} and S^{-2} ions and thermal decomposition of thiourea to give more S^{-2} ions. The increase of deposition rate with increasing thiourea is very obvious, as the rate of any chemical reaction is proportional to the concentration of the reacting species. The saturation thickness vs. $[(\text{NH}_2)_2\text{CS}]$ shows a maximum because at lower concentrations of thiourea, the number of S^{-2} ions is insufficient to combine with all the available Cd^{+2} ions. At high concentrations of thiourea, the rate of reaction becomes very high, resulting in lower film thicknesses.

Conclusions

1. According to our growth model, the growth of the chemically deposited CdS films takes place either by ion-by-ion condensation of Cd^{+2} and S^{-2} ions or by adsorption of colloidal CdS particles formed in the solution.

2. The former process of growth results in thin, adherent, and physically coherent films whereas the latter results in thick and powdery films. The growth in the first case being ion-by-ion suggests the possibility of mixing various materials in the film, revealing a novel technique for making multicomponent materials, such as semiconductor alloys, in thin film form.

3. The thickness, adhesion, and physical coherence of films are determined by the temperature of deposition, relative concentration of the various reactants in the solution, and method of preparation.

4. Different polymorphic phases (cubic and hexagonal) of CdS and their mixtures can be stabilized in films under different growth conditions.

Acknowledgments

It is a pleasure to acknowledge Mr. R. C. Kainthla for helpful discussions. Research fellowship awarded by National Council of Educational Research and Training is gratefully acknowledged by one of the authors (I.K.).

Manuscript submitted July 20, 1979; revised manuscript received Sept. 25, 1979.

Any discussion of this paper will appear in a Discussion Section to be published in the December 1980 JOURNAL. All discussions for the December 1980 Discussion Section should be submitted by Aug. 1, 1980.

REFERENCES

1. K. L. Chopra, "Thin Film Phenomena," McGraw-Hill Book Co., New York (1969).
2. G. A. Kitaev, S. G. Mokrushin, and A. A. Uritskaya, *Colloid J. USSR*, **27**, 38 (1965).
3. G. A. Kitaev, G. M. Fofanov, and A. P. Lundin, *Neorg. Materialy (USA)*, **3**, 473 (1967).
4. R. A. Zingaro and D. O. Skovlin, *This Journal*, **111**, 42 (1965).
5. G. A. Kitaev and T. S. Terekhova, *Russian J. Inorg. Chem.*, **15**, 25 (1970).
6. G. A. Kitaev and T. P. Sokolova, *ibid.*, **15**, 167 (1970).
7. N. C. Sharma, D. K. Pandya, A. K. Mukherjee, H. K. Sehgal, and K. L. Chopra, *Appl. Opt.*, **16**, 2945 (1977).
8. M. Nagao and S. Watanabe, *Jpn. J. App. Phys.*, **7**, 684 (1968).
9. N. R. Pavaskar, C. A. Menezes, and A. P. B. Sinha, *This Journal*, **124**, 743 (1977).
10. V. B. Bogdanovich, A. A. Velikanov, B. B. Kaganoich, I. K. Ostrovskaya, and S. V. Svechnikov, *Inorg. Mater.*, **7**, 1847 (1971).
11. G. A. Kitaev, S. G. Mokrushin, and A. A. Uritskaya, *Colloid J. USSR*, **27**, 317 (1965).
12. G. A. Kitaev, S. G. Mokrushin, and A. A. Uritskaya, *ibid.*, **27**, 654 (1965).
13. G. A. Kitaev, A. A. Uritskaya, and S. G. Mokrushin, *Russian J. Phys. Chem.*, **39**, 1101 (1965).
14. N. C. Sharma, D. K. Pandya, H. K. Sehgal, and K. L. Chopra, *Thin Solid Films*, **59**, 157 (1979).
15. "The Encyclopedia of Electrochemistry." A. Hampe, Editor, Reinhold Publishing Corp., New York, Chapman and Hall Ltd., London (1964).

Reduction of the Dislocation Density in GaAs_{1-x}Sb_x Layer on GaAs Grown by an Improved LPE Method

Yorimitsu Nishitani, Kenzo Akita, Akio Yamaguchi, and Tsuyoshi Kotani

Fujitsu Laboratories, Limited, Nakahara-ku, Kawasaki, Japan

ABSTRACT

An improved LPE method in which the solid surface is always covered by a solution during step-graded growth of GaAs_{1-x}Sb_x on GaAs substrates produces etch pit densities of $3-6 \times 10^5 \text{ cm}^{-2}$. In contrast, layers grown by conventional step or continuously graded LPE have EPD of $6 \times 10^6-2 \times 10^7 \text{ cm}^{-2}$. The composition of the top layer is approximately GaAs_{0.9}Sb_{0.1} in all cases. The reduction of EPD by the improved LPE method is attributed to limiting the nucleation of small islands to the first buffer layer, under the conditions that the grown surface is always covered by the solution subsequent to the growth of the first buffer layer.

GaAs_{1-x}Sb_x is a useful material for the optoelectronic devices (1-4). However, it is difficult to directly grow device quality GaAs_{1-x}Sb_x crystals with $x > 0.05$ on the GaAs substrates by liquid phase epitaxy (LPE) because of the large mismatch in lattice constants between the epitaxial layer and the substrate. Usually, the buffer layers are inserted between the layer and the substrate to reduce the lattice mismatch.

Two types of the buffer layers, stepwise and continuously graded buffer layers, have been reported (5-8). Nagai and Noguchi (6), reported that the dislocation density of GaAs_{0.86}Sb_{0.14} on GaAs decreased from 1×10^7 to $2 \times 10^6 \text{ cm}^{-2}$ by changing the buffer layer from stepwise to continuous grading. This continuously graded buffer layer of about $30 \mu\text{m}$ thick was realized by utilizing the high distribution coefficient of phosphorus in the Ga-rich solution. Nahory *et al.* (4) reported that the GaAsSb crystalline quality of stepwise graded buffer layer was better than the continuously graded buffer layer, but they did not report the dislocation density.

In this paper, we report the reduction of the dislocation density in the GaAsSb layer grown by an improved LPE method in which the substrate is always covered with the solution during the growth of multilayers (9, 10). We also discussed the comparison of the dislocation density among the three kinds of buffer layers.

Experimental

A horizontal LPE growth system was used for the growth of GaAs_{1-x}Sb_x layers. Two types of boats were employed. One type is a conventional sliding boat and another type is an improved sliding boat in which the partition between the compartments for the solution lifts by $500 \mu\text{m}$ when the container is moved and the piston on the solution is pushed mechanically by the piston-pusher to eliminate the melt mixing. Figure 1 shows a cross section of this new boat. A (100) oriented GaAs crystal was used for the substrate. The thickness was $300 \mu\text{m}$ and etch pit density (EPD) was less than 5000 cm^{-2} . The substrate was etched in $5\text{H}_2\text{SO}_4-1\text{H}_2\text{O}_2-1\text{H}_2\text{O}$ solution before the growth. The starting growth temperature and the cooling rate were 850° and $0.4^\circ\text{C}/\text{min}$, respectively.

Three kinds of buffer layers were grown. (i) A stepwise graded buffer layer consisting of 3-5 layers of GaAs_{1-x}Sb_x using the conventional sliding boat; the x value of each layer was increased ~ 0.03 .

(ii) A continuously graded GaAs_{1-x}Sb_x buffer layer grown using the conventional sliding boat. Phosphorus was added to the solution as GaP for lattice matching at the interface between the epitaxial layer and the

substrate. The lattice constant of GaAs_{1-x-y}Sb_xP_y increases along the growth direction because of depletion of phosphorus in the solution. The optimum GaP content was determined by x-ray diffraction measurement on about $1 \mu\text{m}$ thick layers. Various amounts of GaP were added to the solution for the growth of a final layer with a composition of $x = 0.1$. The lattice constant of initial growth matched that of the GaAs substrate when the GaP content in the solution was 0.36 weight percent (w/o), as shown in Fig. 2. Using this solution containing 0.36 w/o GaP, when the interface layer thickness reaches about $35 \mu\text{m}$, the GaP mole fraction in the solid was almost zero.

(iii) A stepwise graded buffer layer grown by using the improved boat. The layer structure was the same as (i).

The GaSb mole fraction was determined by the band-edge peak of photoluminescence and electron probe microanalyzer (EPMA) measurement. Etch pits were revealed by immersing the sample in the molten KOH

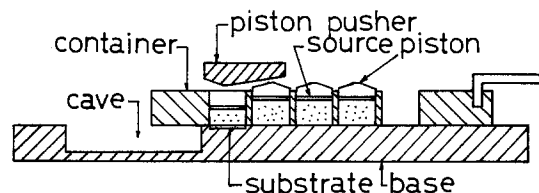


Fig. 1. Cross section of the improved boat

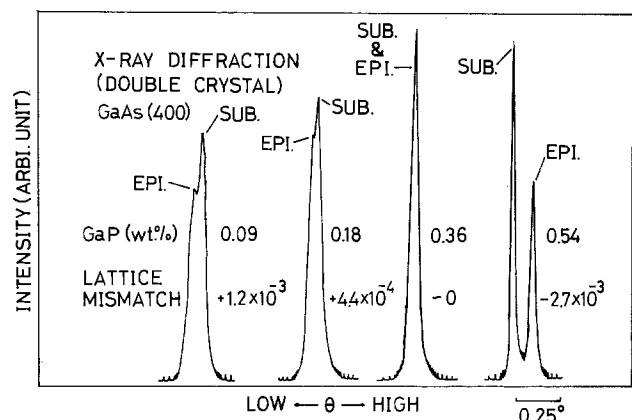


Fig. 2. X-ray diffraction peaks of continuously graded GaAs_{1-x}Sb_x buffer layers with various amounts of GaP added to the solution.

Key words: LPE, GaAsSb, etch pit, dislocation, buffer layer.

contained in a SiC crucible for 5 min at 340°C. All the $\text{GaAs}_{1-x}\text{Sb}_x$ layers were 10–20 μm thick. To reveal etch pits 3–5 μm were removed by the KOH. The etch pit density was calculated from the number of etch pits in a $200 \times 200 \mu\text{m}$ area of the photograph.

Results and Discussion

Shapes of the etch pits.—Figure 3 shows a typical shape of the etch pits revealed on the $\text{GaAs}_{1-x}\text{Sb}_x$ layers after etching with molten KOH. They were hexagonal, independent of the GaSb mole fraction (x), and always contained centers. It is impossible to associate these pits with dislocations by x-ray topography because of high density (more than 10^4 cm^{-3}). However, these pits have certain shapes and centers. They are thought to show dislocations (11). In the case of the stepwise graded buffer layer, these etch pits were observed, independent of the growth method. In the case of the continuous graded buffer layer, small etch pits of a different shape, as shown in Fig. 4, were observed.

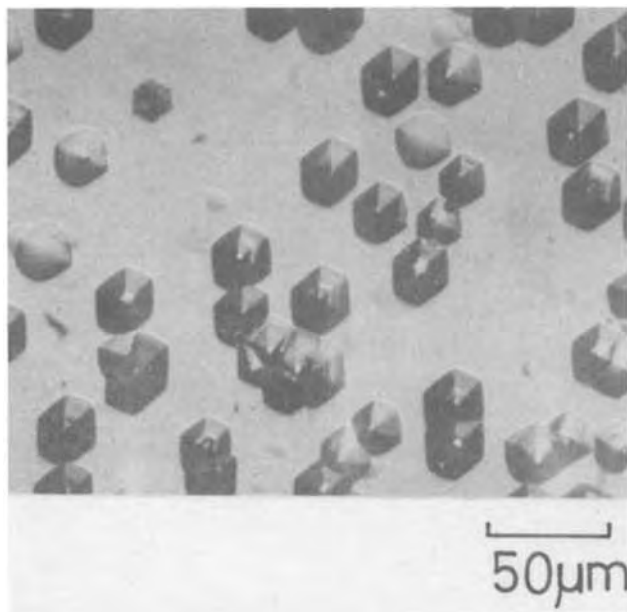


Fig. 3. Typical etch pits of $\text{GaAs}_{1-x}\text{Sb}_x$ layer revealed by molten KOH for 5 min at 340°C.

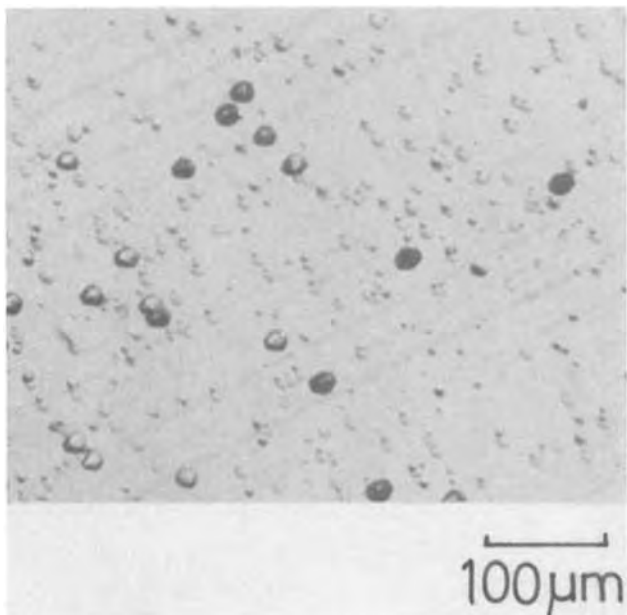


Fig. 4. Another shape of etch pits revealed on the surface of 10 μm thick $\text{GaAs}_{1-x}\text{Sb}_x$ layer with phosphorus added for the lattice matching.

These small etch pits were thought to show dislocations also, because they have centers. These etch pits were revealed on the surfaces of layers more than 5 μm in thickness and were not observed on the stepwise graded buffer layers. These extra pits are like "pair pits," but each pair pit has a center. Only the center was counted as an etch pit. This type of etch pit is thought to be produced on the $\text{GaAs}_{1-x-y}\text{Sb}_x\text{P}_y$ layer.

Etch pit distribution.—Figure 5a shows the etch pit distribution on the surface of the stepwise graded $\text{GaAs}_{1-x}\text{Sb}_x$ buffer layer grown by the conventional growth method. The clusters of the etch pits lie along the $\langle 110 \rangle$ and $\langle 1\bar{1}0 \rangle$ directions. Most of the pits indicate misfit dislocations due to the lattice mismatch. Figure 5b shows an enlarged photograph of the pattern shown in Fig. 5a. The etch pit densities were as high as 10^7 – 10^9 cm^{-2} in the areas of the clusters. These clusters may generate at the early stage of the growth. Figure 6 shows the etch pit distribution on the surface of the stepwise graded $\text{GaAs}_{0.9}\text{Sb}_{0.1}$ buffer layer grown by the improved method. These rectangularly shaped pits were produced by etching at a temperature of more

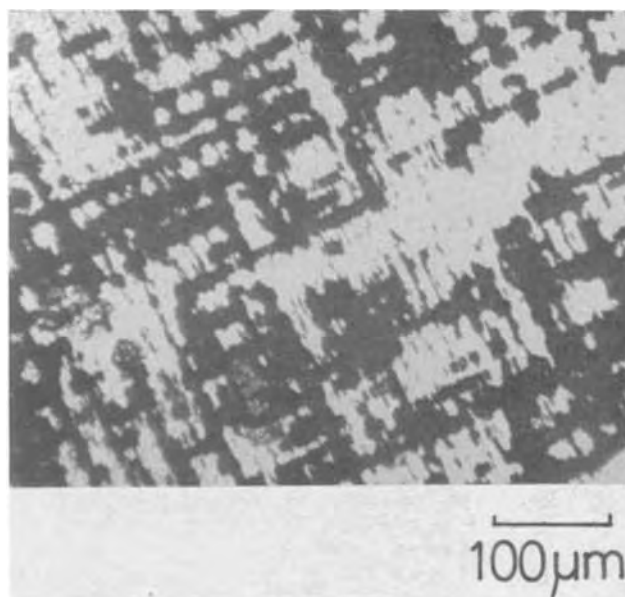


Fig. 5a. Etch pit distribution on a $\text{GaAs}_{0.9}\text{Sb}_{0.1}$ layer surface grown by the conventional method.

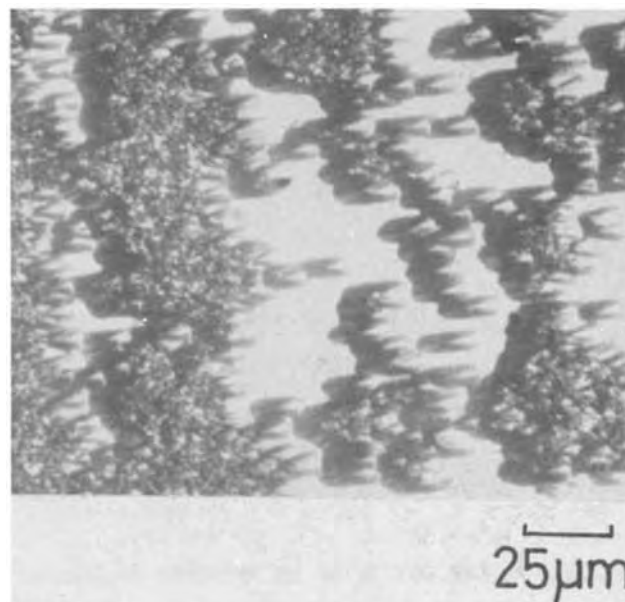


Fig. 5b. Clusters of etch pits enlarged from Fig. 5a

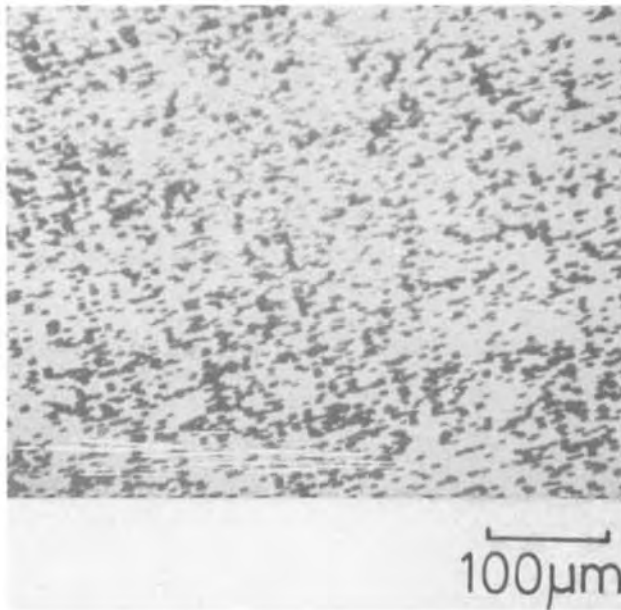


Fig. 6. Etch pit distribution on a $\text{GaAs}_{1-x}\text{Sb}_x$ layer surface grown by the improved method.

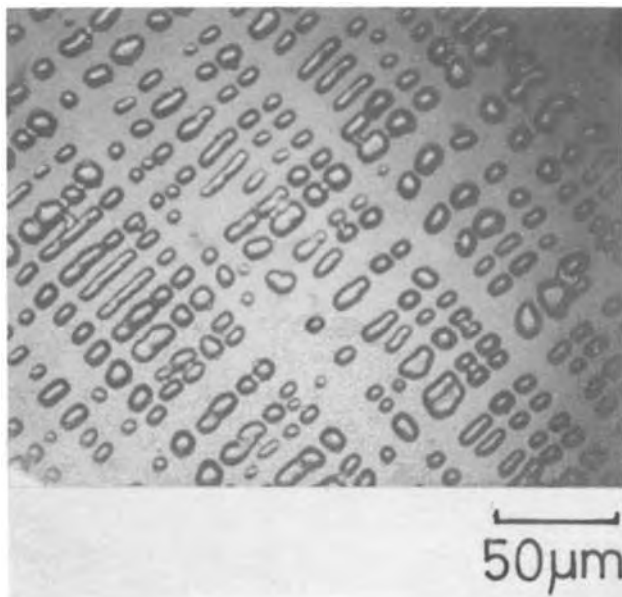


Fig. 7a. Initial stage surface of the second layer growth (x was 0.03 and 0.06 for the first and second layer, respectively).

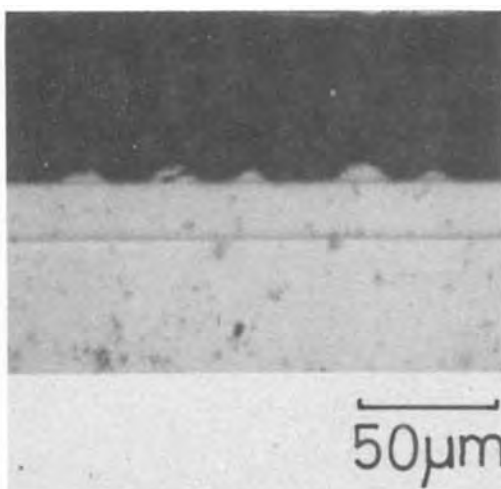


Fig. 7b. Cross section of the initial stage of the second layer growth.

Table I. Etch pit density under various growth conditions

Growth method	Layer structure	Layer thickness (μm)	Dislocation density (cm^{-2})
Improved	Stepwise	15	3.6×10^5
Conventional	Stepwise	15	$3 \times 10^6 - 5 \times 10^7$
Conventional	Continuously	38	2.6×10^6

than 340°C . The highest etch pit density observed on layers grown by the improved method was $5 \times 10^5 \text{ cm}^{-2}$. The centers of the etch pits are separated so clearly that it is possible to count the number of pits easily in the photographic enlargements for densities less than 10^6 cm^{-2} . The etch pits shown in Fig. 6 are observed at random in comparison with the layer grown by the conventional method. Figure 7a shows the initial stage surface of the second layer grown by the conventional growth method, in which x is 0.06, and Fig. 7b shows the cross section of the same sample. Small nucleation sites lie in the $\langle 110 \rangle$ and $\langle \bar{1}\bar{1}0 \rangle$ directions with the separation distance of $10 \mu\text{m}$ or less. On the next stage of the coalescence, the misfit dislocations are introduced. On the other hand, such nucleation did not occur for the layer grown by the new method because the solution always covered the substrate.

Etch pit density.—Figure 8 shows the dependence of the etch pit density introduced in the continuously graded buffer layer on the layer thickness. It increases with increasing the layer thickness. The density was $2-7 \times 10^6 \text{ cm}^{-2}$ on the sample of $38 \mu\text{m}$ thick. Figure 9 shows the etch pit density on the stepwise graded buffer layer for various GaSb mole fractions (x) using two types of the growth boats. The etch pit density increased with increasing x in both cases. However, when the x was more than 0.03, the etch pit density in the case of the conventional boat increased more rapidly than in the case of the improved boat. This fact indicates that the improved growth method is not different from the conventional one in the first layer, but it is effective in reducing the introduction of dislocations in subsequent layers. The etch pits densities seem to be saturated at $3-6 \times 10^5 \text{ cm}^{-2}$ in the case of using this type of boat. These values are the lowest reported for $\text{GaAs}_{0.9}\text{Sb}_{0.1}$ layers grown on GaAs.

For the growth of $\text{In}_x\text{Ga}_{1-x}\text{As}$ on GaAs substrates, the tetragonal distortions were usually observed. For example, 0.3% distortion has been observed in vapor phase epitaxial (VPE) $\text{In}_{0.1}\text{Ga}_{0.9}\text{As}$ on GaAs (12).

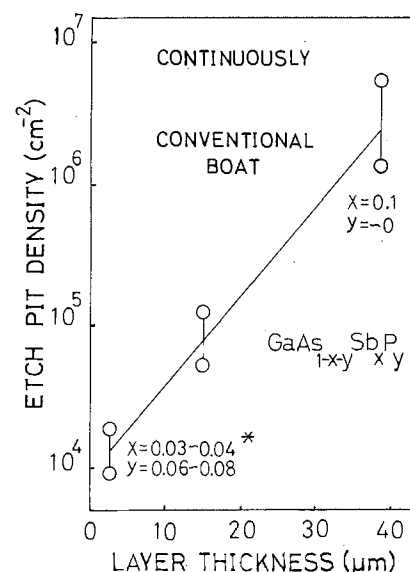


Fig. 8. Etch pit density of a continuously graded buffer layer as a function of the layer thickness [* values estimated from Ref. (6-7)].

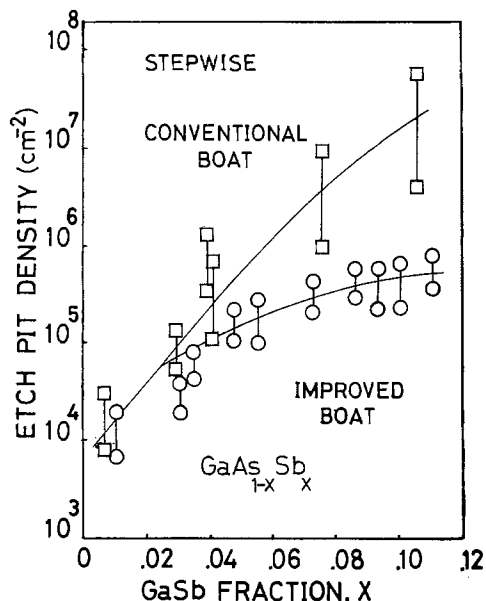


Fig. 9. Etch pit density of stepwise graded buffer layer for GaSb mole fraction, x .

Moreover, concave bending is usually observed in LPE $\text{In}_{1-x}\text{Ga}_x\text{As}$ on GaAs (13). These facts indicate that $\text{In}_{1-x}\text{Ga}_x\text{As}$ crystals tend to be deformed from cubic to tetragonal. On the other hand, $\text{GaAs}_{1-x}\text{Sb}_x$ crystals do not indicate large bending and suggest the release of the lattice stress by introduction of the misfit dislocations rather than by tetragonal distortions.

In the stepwise graded $\text{GaAs}_{1-x}\text{Sb}_x$ buffer layer grown by the conventional growth method, many etch pits were generated from a large number of the dislocation clusters lying along to the $\langle 110 \rangle$ and $\langle \bar{1}\bar{1}0 \rangle$ directions in the early stage of the growth.

In the case of a continuously graded buffer layer, the dislocations are introduced when the layer thickness exceeds the critical thickness. The largest dislocation density is estimated to be

$$\left[\frac{10^8}{a \times \frac{\Delta a}{a}} \right]^2$$

cm^{-2} , where a and Δa are the lattice constant of the substrate and the difference of the lattice constant (in angstroms) between the epitaxial layer and the substrate, respectively. For $\text{GaAs}_{0.9}\text{Sb}_{0.1}$ on GaAs ($a = 5.653\text{\AA}$, $\Delta a/a = 0.008$), the dislocation density is estimated to be 10^{10} cm^{-2} . In the actual crystals, the dislocation density of 10^6 cm^{-2} was observed. This indicates the existence of much interaction between dislocations in the continuously graded buffer layer as reported by Olsen (12).

In the case of stepwise graded buffer layer grown by the improved method, the etch pits were distributed at random on the surface, in contrast with usual stepwise graded buffer layers. It is considered that the nucleation of small islands is suppressed at the interfaces, with the exception of the interface between the first

layer and the substrate, and the islands buffer may not be produced in the growth of successive buffer layers because the grown surface is always wetted with the solution. This suggests that the crystal bonds are continuous in contrast to the usual buffer layer in which the crystal bonds are closed by exposure to the H_2 atmosphere. The suppression of the island nucleation provides the possibility of a large amount of interaction between dislocations at the interfaces. The abrupt change of lattice constant introduces many dislocations with different direction of Burgers vector in the limited thickness of the epitaxial layer.

Conclusion

The etch pit density of $\text{GaAs}_{0.9}\text{Sb}_{0.1}$ was reduced from $5 \times 10^6 \text{ cm}^{-2}$ to $3.6 \times 10^5 \text{ cm}^{-2}$ by using an improved growth method in which stepwise buffer layers were grown consecutively without exposure of the grown surface, except for the final layer, to the ambient gas. The reduction of the etch pit density is attributed to limiting the nucleation of small islands to the first buffer layer, because the grown surface is always covered with solution.

Acknowledgments

The authors are indebted to O. Ryuzan and T. Yamaoka for helpful discussion and would like to express their thanks to S. Nakai for technical assistance.

Manuscript submitted Sept. 25, 1978; revised manuscript received Oct. 11, 1979.

Any discussion of this paper will appear in a Discussion Section to be published in the December 1980 JOURNAL. All discussions for the December 1980 Discussion Section should be submitted by Aug. 1, 1980.

Publication costs of this article were assisted by Fujitsu Laboratories, Limited.

REFERENCES

1. R. C. Eden, *Proc. IEEE*, **63**, 32 (1975).
2. S. K. Brierly and C. G. Fonstad, *J. Appl. Phys.*, **46**, 36 (1975).
3. A. P. Bogatov, L. M. Dolginov, L. V. Druzhinina, P. G. Eliseev, B. N. Sverdlov, and E. G. Shevchenko, *Sov. J. Quantum Electron.*, **4**, 1281 (1975).
4. R. E. Nahory, M. A. Pollack, E. D. Beebe, and J. C. DeWinter, *Appl. Phys. Lett.*, **28**, 19 (1976).
5. L. M. Dolginov, L. V. Druzhinina, M. G. Milvidski, V. B. Osvenski, and T. G. Yugova, *Kristallografiya*, **21**, 184 (1976).
6. H. Nagai and Y. Noguchi, IEEE International Semiconductor Laser Conference, LV-5 (1976).
7. M. A. Pollack, R. E. Nahory, and L. C. DeWinter, *Inst. Phys. Conf. Ser.* 33b, chap. 2, p. 60 (1977).
8. R. E. Nahory, M. A. Pollack, J. C. DeWinter, and K. M. Williams, *J. Appl. Phys.*, **48**, 1607 (1977).
9. Y. Nishitani, K. Akita, S. Komiya, K. Nakajima, A. Yamaguchi, O. Ueda, and T. Kotani, *J. Cryst. Growth*, **35**, 279 (1976).
10. K. Akita, Y. Nishitani, K. Nakajima, A. Yamaguchi, T. Kusunoki, T. Kotani, H. Imai, M. Takusagawa, and O. Ryuzan, *IEEE J. Quantum. Electron.*, **qe-13**, 585 (1977).
11. S. Komiya and T. Kotani, *This Journal*, **125**, 2019 (1978).
12. G. H. Olsen, *J. Cryst. Growth*, **31**, 223 (1925).
13. T. Kotani, A. Yamaguchi, K. Akita, and S. Nakai, *ibid.*, **44**, 543 (1978).

Optical Constants of Silicon by Unpolarized Incident Radiation

O. L. Russo

Department of Physics, New Jersey Institute of Technology, Newark, New Jersey 07102

ABSTRACT

It is shown that the reflectance of modulated unpolarized incident radiation at the pseudo-polarizing angle can be used to accurately determine the optical constants of absorbing media in the visible region. The approximation that the principal angle of incidence occurs at the pseudo-polarizing angle is assumed to contribute negligible error. Expressions for the refractive index, n , and the extinction coefficient, K , are given in terms of the pseudo-polarizing angle and the reflectance ratio of the parallel (to the plane of incidence) reflected wave vector intensity to the normal reflected wave vector intensity. The experimental values for n and K are determined at wavelengths in the visible spectrum between 4250 and 5750 Å, for boron-doped p-type highly polished silicon of 0.01 and 95 Ω -cm resistivity. These values correspond to impurity concentrations of about 10^{-3} - $10^{-6}\%$, respectively. The 0.01 Ω -cm K curve indicates the possibility that direct optical transitions between acceptor levels and the conduction band can be resolved and that this occurs at about 5250 Å (≈ 2.4 eV).

Various methods of transmission or reflection of electromagnetic waves have been used by numerous investigators to determine the optical constants of solids. Transmission of a beam of radiation through a very thin layer (1) or by various modified reflectance methods (2-8) have been used to obtain the optical constants for semiconductors in the infrared and visible region of the spectrum. The transmission method although valuable because it permits the absorption centers to be easily identified has several disadvantages. There are difficulties in the measurement of the thickness and uniformity of the thin layer which causes errors in the determined optical constant values, and there are further inaccuracies caused by improper correction due to the reflection of the incident radiation from the two surfaces. The reflectance method has been by far the most successful and more commonly employed of the two methods, perhaps because of its versatility. There are numerous reflectance methods and most are variations of using normal reflectance, oblique reflectance, or reflectance at the polarizing angle. The reflectance method at normal incidence while being easy to implement, consequently extensively employed, can result in considerable inaccuracy for the refractive index, n , and the extinction coefficient, K , in the range of values for which n and K both vary between 1.0 and 4.0 (9).

The method in which the reflectance is measured for oblique incident radiation requires that, in general, the measurements be made at two or more incident angles. The data, notably the angles and reflectances are then used to determine the optical constants by graphical methods. The method has been applied to absorbing isotropic media using unpolarized (10) and polarized (11) incident light.

A graphical analysis in which the ratio of reflectances is measured at two or more incident angles has been shown to have the advantages of increased accuracy and independence of the sample surface size (12). Other methods using the reflectance ratio have been used to obtain the optical constants by geometric means (13, 14). It has been shown that the minimum in the ratio of the reflectance at its corresponding incident angle can be used to yield the optical constants (15).

The reflectance method in which the data is obtained at the polarizing angle is simpler and as

Key words: reflectance, visible, doping, refractive index, extinction coefficient.

accurate as the oblique method and certainly more accurate than the normal method. Determination of the optical constants n and K by this method requires that the ratio, ρ , of the reflected wave vector, R_p (parallel to the plane of incidence), to the reflected wave vector, R_s (perpendicular to the plane of incidence), be measured at the polarizing angle. The pseudo-Brewster or pseudo-polarizing angle, θ_p , however, for absorbing materials occurs when the value of R_p is a minimum, but not zero as is true in non-absorbing media. The incident radiation is polarized and the azimuth of restored polarization which determines ρ must then be measured along with the pseudo-polarizing angle. The method although straightforward requires that the angle of restored polarization be measured with sufficient accuracy in order that errors in the optical constants be minimized. This measurement is critical especially if small values of the extinction coefficient K are to be accurately determined.

When the polarizer is positioned between the specimen and the detector, as in this study, the quantity ρ is determined simply by the ratio of two reflectances. Provided the incident radiation is unpolarized, one reflectance is always in the vertical plane and the other in the horizontal plane. There is the disadvantage, that in positioning the polarizer between the unpolarized source and specimen (incident light polarized), that either ρ be determined by measurement of the: (i) angle of restored polarization or (ii) reflectances, but, in which the plane of polarization is now rotated because of reflection. As a consequence, some systematic experimental error is introduced because the reflectances are no longer in their respective vertical and horizontal planes. The values thus are obtained by a search for a minimum and maximum value.

In this paper, measurement of the reflectance ratio at the polarizing angle is made using unpolarized incident modulated radiation. This facilitates the experimental procedure and eliminates the need for the measurement of the angle of restored polarization, which results in improved accuracy. Measurements made on highly polished doped silicon surfaces show that it is possible to resolve samples of differing conductivities. Expressions for the refractive index, n , and the extinction coefficient, K are given in terms of the pseudo-polarizing angle, θ_p , and the reflectance, ρ_p , measured at the angle, θ_p . The expressions are

based on the assumption that θ_p occurs at the principal angle of incidence.

Experimental Arrangement

The diagram in Fig. 1 shows a positionally fixed monochromatic light source which consists of a tungsten bulb and a grating monochromator capable of wavelengths from 4000 to 7000Å with monochromaticity to within $\pm 1\text{Å}$ at the 50% intensity points. The experimental values, however, were measured with the 50% bandwidth fixed at 50Å in order to keep the light intensity at reasonable levels in comparison to the system noise. A mechanical chopper wheel is used to modulate the light beam at a frequency of 2010 Hz while supplying a reference signal to the lock-in amplifier. After the modulated light beam is collimated, it reflects from the highly polished silicon wafer supported by a holder mounted on a turntable. The light beam then passes through an analyzer which has a permissible total integrated transmission to two crossed polarizers of 0.0005% over the wavelength region of the measurements. A photomultiplier used to measure the light intensity is equipped with a slotted mask (to reduce spurious light) over the face of the tube (RCA 6342A) which has a peak response in the visible range. When the photomultiplier and analyzer assembly is rotated, it is arranged to rotate through twice the angle of rotation of the turntable, consequently requiring that it always be at the angle of reflection.

The lock-in amplifier synchronized by the reference signal so as to have a peak response at the modulating frequency is then used to measure the intensities of the normal, R_s , and parallel, R_p , wave vectors of the reflected wave. These intensity measurements are made with the transmission axes of the analyzer parallel (for R_p) and then normal (for R_s) to the plane of incidence. The value of the normal reflected intensity is measured at the pseudo-polarizing angle which is determined as the angle where the measured parallel reflected intensity is a minimum.

Care was taken to minimize errors by insuring adequate linearity of the system over the range of intensities required for the measurements. Accuracy in the measurement of the modulated reflected intensity was achieved because of the relative independence of the a-c photomultiplier on small power supply fluctuations. The small amount of polarization in the incident beam was measured by directing the beam so as to be incident directly on the slot of the masked photomultiplier tube. Corrections for the amount of incident polarization were accounted for in the calculation of ρ .

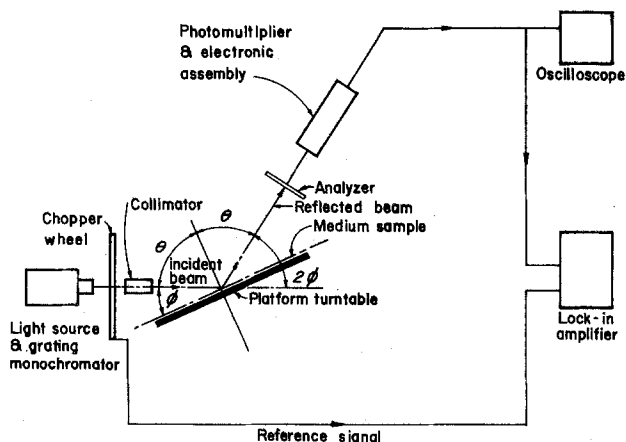


Fig. 1. Schematic diagram of the apparatus described in the text used for the measurement of the pseudo-polarizing angle and the reflectance ratio.

Theory

The Fresnel reflection equations as determined using the boundary conditions demand that the tangential components of the electric field vector, E , and the magnetic vector, H (no surface current density) be continuous and also that the normal components of the magnetic induction, B , and the displacement, D (no surface charge density), be continuous at an interface. These equations which are given in terms of the incident and refracted angles can be expressed in complex form as

$$\hat{R}_p = A_p \frac{\tan(\theta - \beta)}{\tan(\theta + \beta)} \quad [1]$$

and

$$\hat{R}_s = -A_s \frac{\sin(\theta - \beta)}{\sin(\theta + \beta)} \quad [2]$$

The complex quantities \hat{R}_p and \hat{R}_s are complex reflected wave vectors, respectively parallel and normal to the plane of incidence and the real quantities A_p and A_s , respectively incident wave vectors parallel and normal to the plane of incidence. The quantity θ is the angle of incidence in air and β is the complex refracted quantity which for a medium which is absorbing, is given by

$$\sin \beta = \frac{\sin \theta}{\hat{n}} \quad [3]$$

where \hat{n} , the complex refractive index of the medium

$$\hat{n} = n(1 - iq) \quad [4]$$

is given in terms of the real refractive index, n , and an attenuation constant, q .

The electric wave vectors, A , of unpolarized light, occupying planes intersecting concurrently with but randomly oriented in the plane of incidence, can be resolved into parallel, A_p , and normal, A_s , components. Each of these components undergoes upon reflection a phase shift between it and its associated reflected component. Then the complex reflected vectors which are given by

$$\hat{R}_p = R_p e^{i\delta_p} \quad \text{and} \quad \hat{R}_s = R_s e^{i\delta_s}$$

can be used with [1] and [2] to yield

$$\rho e^{i\delta} = - \frac{\cos(\theta + \beta)}{\cos(\theta - \beta)} \quad [5]$$

where $\rho = (R_p/R_s)/(A_s/A_p)$ and the relative difference of phase $\delta = \delta_p - \delta_s$. From [3] and [5], it can be shown that

$$\frac{1 + \rho e^{i\delta}}{1 - \rho e^{i\delta}} = \frac{\sin \theta \tan \theta}{(\hat{n}^2 - \sin^2 \theta)^{1/2}} \quad [6]$$

As the angle of incidence θ changes from grazing incidence to normal incidence ($\pi/2$ to zero), the angle δ changes from zero to π . For some angle θ in this range, the angle $\delta = \pi/2$ which occurs at the angle θ which is the principal angle of incidence θ_1 . It can be seen that when $\delta = \pi/2$ and using [4] in [6], then the expressions for n and q are given by

$$\frac{1 - q^2}{q} = \frac{1 - (4\rho_1 \cos^2 \theta_1 (\tan \theta_1^2 - 1))}{2\rho_1 \sin^2 \theta_1} \quad [7]$$

and

$$n^2 q = \frac{2z \sin^2 \theta_1 \tan^2 \theta_1}{1 + 4z^2} \quad [8]$$

where

$$z = \frac{\rho_1}{1 - \rho_1^2}$$

and ρ_1 is the value of ρ measured at θ_1 .

The assumption is usually made that the pseudo-Brewster angle, θ_p , for visible light nearly occurs at the principal angle of incidence for metals whenever $n^2 + K^2 \gg 1$ (16). The fact that the minimum in the ratio of R_p/R_s does not occur exactly at the principal angle of incidence, θ_i , has been examined carefully for opaque materials (17). Here it is shown that the error which may be important in the infrared is small for the visible region.

It is therefore assumed for silicon, in the visible region, where the refractive index is between 3 and 5 and K greater than zero, that, $\theta = \theta_i = \theta_p$ and $\rho_i = \rho_p$ where ρ_p is the minimum value of ρ (which occurs at θ_p). Then, for these conditions, Eq. [7] and [8] become

$$\frac{1 - q^2}{q} = \frac{1 - 4\rho_p \cos^2 \theta_p (\tan^2 \theta_p - 1)}{2\rho_p \sin^2 \theta_p} \quad [9]$$

and

$$n^2 q = \frac{2z_p \sin^2 \theta_p \tan^2 \theta_p}{1 + 4z_p^2} \quad [10]$$

where

$$z_p = \frac{\rho_p}{1 - \rho_p^2}$$

The value of the extinction coefficient is known from the relationship

$$K = nq \quad [11]$$

The value of ρ as given by Eq. [5] can be measured as a ratio of intensities or voltages. This is evident when it is considered that for a plane electromagnetic wave propagating in an absorbing medium, given by

$$E(x, t) = E_0 e^{i(\omega t - kx)} \quad [12]$$

that the intensity of the electromagnetic field, I , which can be expressed as the product of the velocity of the wave and the time averaged electric energy density, is given by

$$I \propto E_0^2(x) \quad [13]$$

for observation times which are large compared to a period of oscillation of the wave.

Then, it follows that

$$\rho = \left[\frac{I_{Rp} I_{As}}{I_{Rs} I_{Ap}} \right]^{1/2} \quad [14]$$

where I_{Rp} , I_{Rs} , I_{Ap} , and I_{As} are the intensities corresponding to the reflected parallel, reflected normal, incident parallel, and incident normal waves, respectively.

Results and Discussion

The experimental values of the refractive index, n , and the extinction coefficient, K , for the semiconductor silicon were determined at room temperature by the reflectance of modulated unpolarized incident light at the pseudo-polarizing angle. The resistivity values for the silicon samples used in this study were 95 and 0.01 Ω -cm. These boron-doped p-type (111) orientation wafers correspond to impurity concentrations of from about 10^{-3} to $10^{-6}\%$ of the host. A comparison of the refractive indexes for the two resistivity samples is given by Fig. 2 and of the extinction coefficients by Fig. 3. The results for the refractive index of 95 Ω -cm silicon is in agreement with those reported elsewhere for single crystal silicon (4, 18).

Inspection of Fig. 3 indicates that there is some peaking in the K curve for the 0.01 Ω -cm material which occurs near 5250 \AA (≈ 2.4 eV). This pronounced hump does not appear to be caused by any obvious anomaly in either the experimental arrangement or the procedure. The condition may be the result of direct transitions between the acceptor levels in the p-doped silicon to the conduction band. It is reasonable to expect that this will occur at energies just below

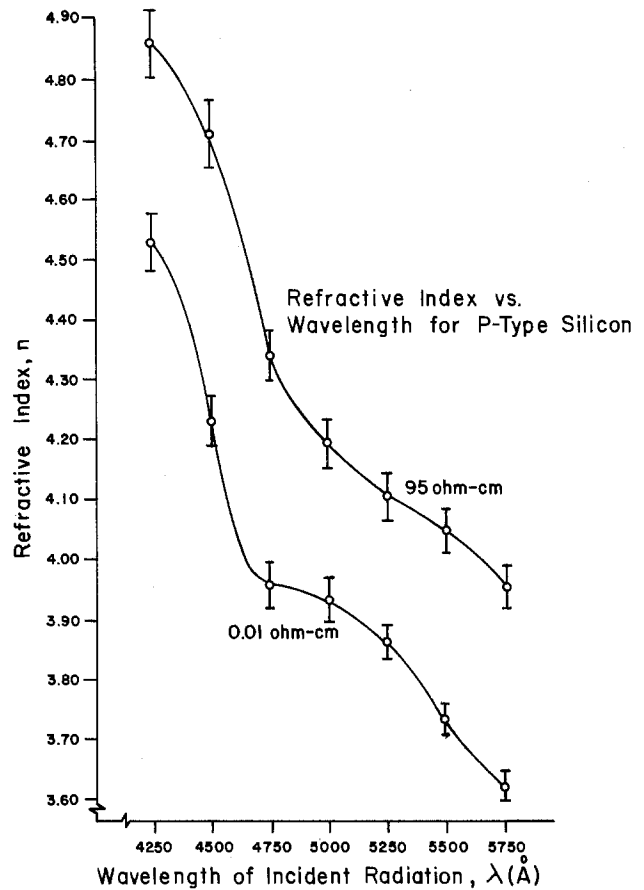


Fig. 2. Experimental curves for the refractive index as a function of wavelength at room temperature for polished p-type silicon of 0.01 and 95 Ω -cm resistivity.

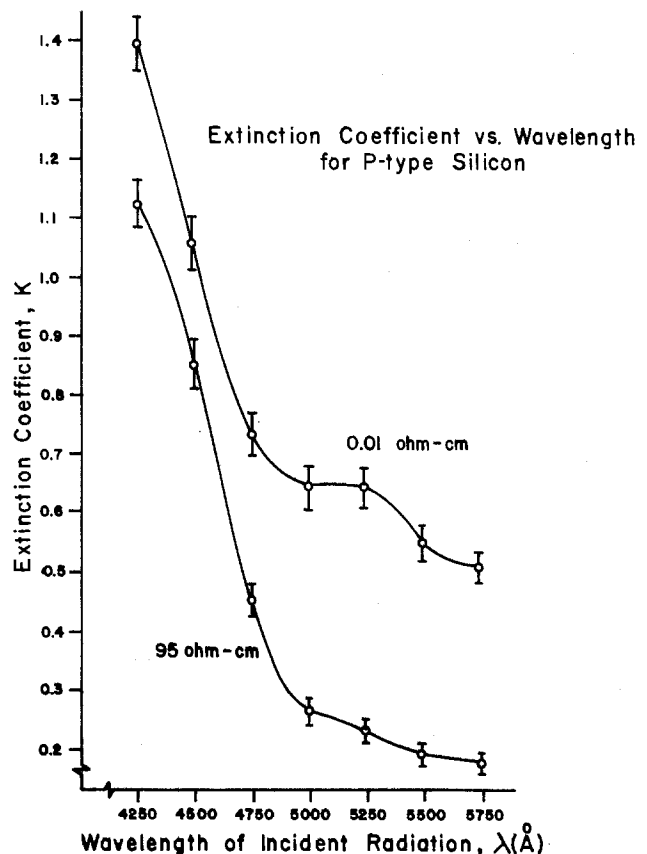


Fig. 3. Experimental curves for the extinction coefficient as a function of wavelength at room temperature for polished p-type silicon of 0.01 and 95 Ω -cm resistivity.

Table I. Optical constants of p-type silicon (boron doped) as a function of wavelength

Wave-length, λ (Å)	Resistivity			
	0.01 Ω -cm		95 Ω -cm	
	Refractive index, n	Extinction coefficient, K	Refractive index, n	Extinction coefficient, K
4250	4.52	1.39	4.86	1.12
4500	4.22	1.05	4.71	0.851
4750	3.95	0.730	4.34	0.463
5000	3.93	0.644	4.19	0.274
5250	3.87	0.639	4.11	0.240
5500	3.74	0.567	4.06	0.202
5750	3.61	0.520	3.95	0.191

the optical (valence-conduction) gap. The valence-conduction direct transitions can be seen from the curve to occur in the vicinity of 5000Å (≈ 2.5 eV). This hump is not manifest in the 95 Ω -cm curve, probably because of the relatively low impurity density.

Care was taken to prevent the formation of an oxide layer on the highly specular silicon surface. The surface preparation process consisted of cleansing the wafers in an alconox detergent solution, and after rinsing, etching in a 15 to 1 water to hydrofluoric acid bath for 10 min. Reflectance measurements were then made immediately after the samples were rinsed and dried. This procedure insures that an oxide formation while not completely eliminated will be minimized.

The accuracies of the measured parameters which consisted of the pseudo-polarizing angle (measured to \pm one minute of arc) and the reflectance (to about 0.1%) were well within the range of the experimental error as shown in Fig. 2 and 3. The average for five independent trials is plotted and the error bars represent the statistical variations over the five trials taken within a time duration of 3 hr after etching. There was no conclusive evidence that an oxide layer was formed (increasing K with time) during the time interval of the experiment. It is reasonable to assume that some oxide layer (probably between 5-10Å) exists immediately after etching, however, it appears that the thickness of one layer may not be very different from the other.

Signal to noise considerations and the photomultiplier gain limitations demanded that a minimum bandwidth of 50Å be used for the incident radiation. This lack of monochromaticity, by itself, introduces some systematic error, because the intensity of the parallel, R_p , vector at the pseudo-polarizing angle is larger than that obtained by more monochromatic incident radiation of the same intensity.

The values of the attenuation constant, q , and the refractive index, n , requires that the pseudo-polarizing angle θ_p , and the ratio of the modulated reflected parallel to normal intensities, ρ_p , be measured. The ratio, ρ_p , is independent of the photomultiplier frequency response and to variations in the intensity of the incident beam. Also, the modulated beam when used with the lock-in amplifier results in a significant enhancement of the signal to noise ratio and a consequent improvement in accuracy and resolution over that which can be obtained by an unmodulated signal. This results in the apparent advantages of increased accuracy and repeatability when compared to measurements made as a reflectance ratio when the incident beam is not modulated, and also when compared to measurements of the azimuth of restored polarization (to determine q when the incident radiation is polarized). It is unlikely that measurements in which the

azimuth of polarization as determined by the method of Drude (19) and subsequently by numerous authors can be resolved with the same precision.

The limiting factor in determining the value of the intensity I_{Rp} is the noise in the system, which can be minimized by lowering the temperature of the photomultiplier tube if necessary. It is essential that this be done when the medium under investigation has low values of q such as materials which can be classified as nonabsorbing (e.g., glass). For the materials studied and reported here, the noise level was considerably less than the lowest I_{Rp} values so that the errors introduced were negligible.

Conclusion

It has been shown that the refractive indexes and extinction coefficients can be obtained for polished materials by measuring the reflectances at the pseudo-polarizing angle for incident unpolarized radiation. The ratio of the reflectances determines n and K more accurately than can be obtained by measurement of the azimuth of restored polarization (incident radiation polarized) especially when the media is such that the attenuation constant, q , is small. It is also significant that it is feasible to resolve the optical constants for host materials in which the impurity concentrations are different, and, further to discern variations caused by changing the impurity concentration. Although the boron-doped p-silicon material used had impurity concentrations which differ by about three orders of magnitude, the accuracy and resolution could be improved by careful attention to the signal to noise ratio and the monochromaticity of the radiation.

Manuscript submitted March 7, 1978; revised manuscript received July 3, 1979.

Any discussion of this paper will appear in a Discussion Section to be published in the December 1980 JOURNAL. All discussions for the December 1980 Discussion Section should be submitted by Aug. 1, 1980.

Publication costs of this article were assisted by the New Jersey Institute of Technology.

REFERENCES

1. W. H. Brattain and H. B. Briggs, *Phys. Rev.*, **75**, 1705 (1949).
2. R. J. Archer, *ibid.*, **110**, 354 (1958).
3. H. R. Philipp and E. A. Taft, *ibid.*, **113**, 1002 (1959).
4. H. R. Philipp and E. A. Taft, *ibid.*, **120**, 37 (1960).
5. R. F. Potter, *ibid.*, **150**, 562 (1966).
6. P. A. Schumann, Jr., W. A. Keenan, A. H. Tong, H. H. Gegenworth, and C. P. Schneider, *This Journal*, **118**, 145 (1971).
7. G. Jungk, *Phys. Status Solidi*, **46**, 603 (June, 1971).
8. W. A. Keenan and P. A. Schumann, Jr., *This Journal*, **118**, 2010 (1971).
9. R. F. Miller, L. S. Julien, and A. J. Taylor, *J. Phys. D.: Appl. Phys.*, **4**, (1971).
10. R. Tousey, *J. Opt. Soc. Am.*, **29**, 235 (1939).
11. I. Simon, *ibid.*, **41**, 336 (1951).
12. D. G. Avery, *Proc. Phys. Soc. (London)*, **B65**, 425 (1952).
13. R. E. Lindquist and A. W. Ewald, *J. Opt. Soc. Am.*, **53**, 247 (1963).
14. H. Damany, *ibid.*, **55**, 1558 (1965).
15. R. F. Potter, *ibid.*, **54**, 904 (1964).
16. M. Born and E. Wolf, "Principles of Optics," p. 615, Pergamon Press (1959).
17. G. K. T. Conn and G. K. Eaton, *J. Opt. Soc. Am.*, **44**, 477 (1954).
18. E. Schmidt, *Appl. Opt.*, **8**, 1905 (1969).
19. P. Drude, "Theory of Optics," p. 363, (English Translation by G. R. Mann and R. A. Millikan), Longmans, Green and Company, New York (1902).

Optimization of the Deposition Conditions for Epitaxial Silicon Films on Czochralski Sapphire in the Silane-Hydrogen System

M. Druminski

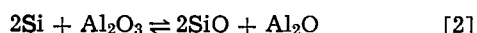
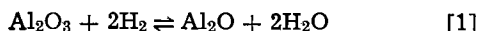
Siemens AG, Research Laboratories, D-8000 München, Otto-Hahn-Ring 6, Germany

ABSTRACT

The deposition of epitaxial silicon films on $(\bar{1}012)$ Czochralski sapphire from the silane/hydrogen system was investigated for growth temperatures from 880° to 980°C and for growth rates from 0.2 to 6.0 $\mu\text{m}/\text{min}$. The film quality was evaluated by optical absorption measurements. The temperature range, in which epitaxial film quality was obtained, shifts with increasing growth rates to higher deposition temperatures. This epitaxial temperature range is rather broad, e.g., 915°-965°C for 0.2-0.5 $\mu\text{m}/\text{min}$ and 935°-985°C for 5.3-6.0 $\mu\text{m}/\text{min}$. A region for the optimum epitaxial deposition conditions, very suitable for MOS applications, is defined by the minimum values obtained from the optical absorption measurements. At temperatures below 915°C, decreasing crystalline quality was observed due to an increasing fraction of polycrystalline silicon. In addition the influence of the H_2O content on the crystalline quality of the silicon films was investigated; for the production of a good epitaxial silicon film the H_2O impurity fraction must be smaller than 1 ppm, especially in the low temperature region.

Thin epitaxial silicon films on insulators (ESFI), especially silicon on sapphire (SOS), have reached increasing importance in recent years (1, 2). Up to now distinct ways were chosen for the deposition of silicon on insulators with the goal of the production of good epitaxial film quality. First experiments by Manasevit and Simpson (3) and by Seiter and Zamminer (4) with SiCl_4 as silicon source showed that this system has the disadvantage of unwanted reaction products, especially due to the hydrogen chloride, which is evolved at higher temperatures. The use of silane, which decomposes irreversibly, became, therefore, the common way for the deposition of epitaxial silicon films on insulators. The advantages of this silicon source are: first; no unwanted reaction products such as chlorides are evolved and, second; a lower deposition temperature can be chosen than in the case of silicon tetrachloride.

Nevertheless the quality of such epitaxial silicon films is mainly limited by Eq. [1] (5) and [2] (6)



The influence of these reactions rises with increasing temperature, resulting in partial etching and autodoping effects:

Partial etching can more or less deteriorate the single crystal surface and may result in either polycrystalline growth or in the production of a layer with a high density of crystal imperfections. This can be prevented by lowering the deposition temperature which is possible according to Richman and Arlett (7) with silane in the SiH_4/He system for homoepitaxial silicon. Studies for heteroepitaxial silicon on sapphire and spinel from this system were published by several authors (8-10) and modified to the $\text{SiH}_4/\text{He}/\text{H}_2$ system by Manasevit for silicon on spinel (11).

Autodoping effects can occur due to reverse reactions which cause aluminum to be incorporated in the silicon film to be deposited. They can be reduced by using a low deposition temperature and a high growth rate simultaneously, in order to completely cover the surface of the substrate with a closed silicon film as quickly as possible. Once the surface and the sides of

the wafers are completely covered no more reactions such as [1] and [2] can occur because there is no further formation or transport of volatile suboxides. Different two-step growth techniques with a first high growth rate (for quickly covering the substrate) followed by a lower growth rate were established by several authors (12-15).

All these methods are of interest for growing epitaxial films of good quality, but it seems rather difficult to control two different growth rates especially for thin ($< 1 \mu\text{m}$) films.

Therefore, we endeavored to optimize the growing conditions by a more "conventional" method in order to have a deposition process that should be as simple as possible. After having studied the influence of the substrate preparation in an earlier work (16), we tried to establish optimum temperatures and corresponding growth rates for silicon films grown on $(\bar{1}012)$ sapphire.

Experimental

Substrate preparation.—Since the (100) orientation is preferred for MOS applications, sapphire slices with the $(\bar{1}012)$ orientation were used.¹ The slices were chemically-mechanically polished by the supplier or in our laboratories using colloidal silica;² they must be free of direct surface damage and of subsurface damage (16). This was confirmed before use by a pre-inspection of a representative number of slices from one polishing lot. These slices were etched at 275°C in KOH for 5 min. In Fig. 1 a comparison is made between two different surfaces: (a) with and (b) without subsurface damage. Only surfaces free of subsurface damage can be expected to provide good films. The small etch figures are due to dislocations, present in this case in Czochralski material (dislocation density of $2 \times 10^5 \text{ cm}^{-2}$). The slices were first scrubbed to remove mechanical polishing compound residues; then a cleaning procedure similar to that described by Union Carbide (17) was followed. After the last rinsing step in water up to 18M Ωcm at 25°C, the slices were spin dried under hot filtered nitrogen of high purity (H_2O , $\text{O}_2 < 1 \text{ ppm}$). This was always done immediately before deposition; because storage produced statically held particles on the substrate sur-

Key words: optical absorption, crystalline quality, quality evaluation, substrate preparation.

¹ Union Carbide Corporation, San Diego, California.

² Syton of Monsanto Chemical Corporation, St. Louis, Missouri.

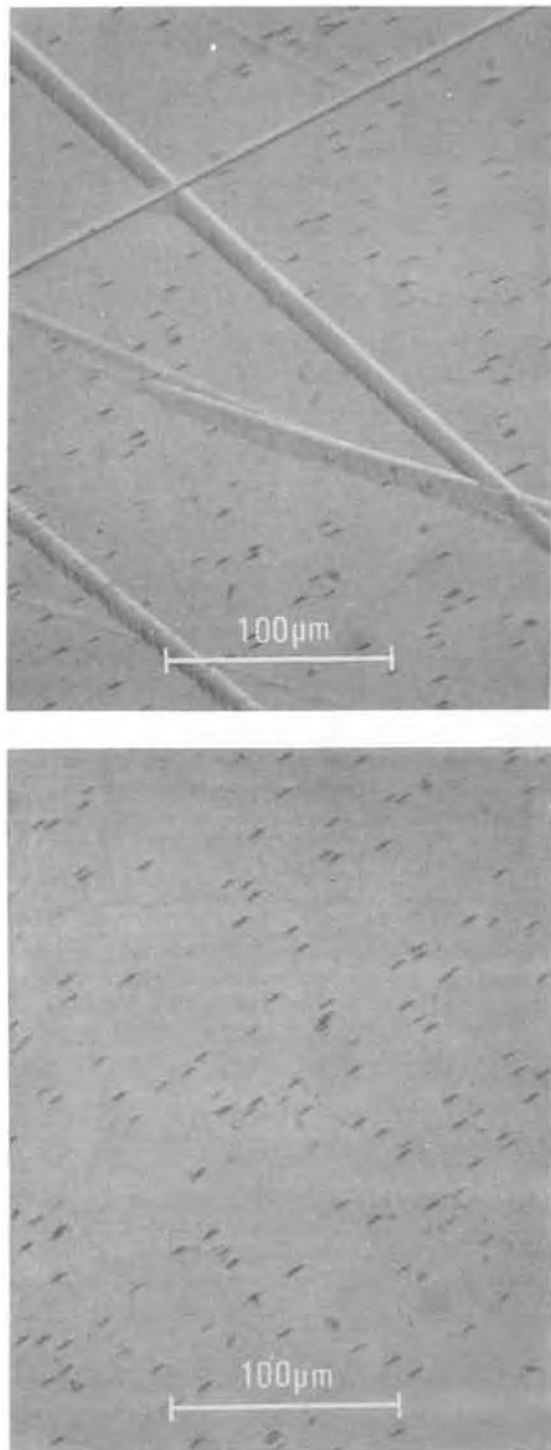


Fig. 1. Interference contrast micrographs of sapphire surfaces etched with KOH at 275°C (5 min), with (a) and without (b) sub-surface damage.

face, and this resulted in a deterioration of the film quality.

Reactor system and deposition.—The deposition was performed in a water-cooled reaction cell with rectangular cross section (80 × 35 mm) as previously described (15). The rf heated graphite susceptor³ was coated with silicon (thickness about 20 μm) prior to film deposition on sapphire. The susceptor was tilted about 1.7° in the direction of the gas inlet and could be loaded with four 2 in. diam substrates. A timer was used to switch the required electromagnetic valves on and off thus enabling reproducible runs and results.

³ Schunk and Ebe Company, Giessen, Germany (quality term FP 499).

The gas velocity in the reactor was about 100 cm/sec. The temperatures were measured by means of an optical pyrometer operating in the wavelength range around 0.65 μm. All temperatures given in this paper are uncorrected pyrometric temperatures. The lowest investigated temperature (880°C) corresponds to an actual temperature of 914°C, the highest investigated temperature (980°C) corresponds to a true temperature of 1020°C. The emissivity correction was taken from Allen's work (18).

Electronic grade silane (3% in hydrogen)⁴ was used for the experiments. Hydrogen from the main gas line was purified by a hydrogen purifier.⁵ The oxygen and water content in all gases, including hydrogen and nitrogen (for purging), were less than 1 ppm, controlled by a Shaw hygrometer⁶ and an oxygen monitor.⁷

Substrate heating in hydrogen at 980°C for 10 min was followed by the film growth in the region from 880° to 980°C at a growth rate of 0.2–6.0 μm/min. The final thickness of the films was in all cases 0.8 μm.

Quality evaluation.—The quality of the silicon films was investigated by visual inspection, light microscopy, and optical absorption measurements.

For visual inspection a focused grazing light beam in an otherwise dark area was used. By this method major imperfections could easily be observed.

The investigation using the light microscope was made in the Nomarski interference contrast mode. In this way smaller particles (e.g., polycrystalline crystals) could be detected.

The optical absorption measurements, described elsewhere in the literature (19), result in the absorption factor F_A describing the spectral dependence of the absorption constant α . F_A is defined as a product of the slope of the absorption edge and the absorption constant at a definite wave number: $F_A = (\alpha_{22} - \alpha_{16}) \cdot \alpha_{17} \cdot 10^6 \text{ cm}^{-2}$ (the subscripts denote the wave number in 10^6 cm^{-2}).

The absorption factor F_A agrees well with other methods, e.g., electron diffraction and ion backscattering measurements. In addition, F_A is in good correlation with transistor parameters, as for example the channel mobility (20, 21). Therefore, F_A was used in this present work as a tool to define the epitaxial film quality. The closer the value for F_A approaches the value for single crystal silicon ($F_A = 90 \cdot 10^6 \text{ cm}^{-2}$) the better the quality of the film. According to earlier investigation, F_A values of $140 \cdot 10^6 \text{ cm}^{-2}$ or less are acceptable for silicon on (1012) sapphire (16).

Results and Discussion

If the F_A values for the different growth rates r_g are plotted against the growth temperature T_g , curves as shown in Fig. 2 are obtained, their curvatures being rather similar. (The different signs in Fig. 2 are the average values of all F_A measurements made for a distinct growth rate or growth temperature, respectively. The vertical bars indicate the range in which all corresponding values were obtained. In the following considerations concerning the F_A curves these bars are included.) The curve for the lowest growth rate region (0.2–0.5 μm/min), investigated in this series, will be taken as an example: between 920° and 940°C a rather flat minimum of the curve with $F_A = 125\text{--}130 \times 10^6 \text{ cm}^{-2}$ exists. The F_A values increase both with decreasing and with increasing growth temperatures but remain smaller than $140 \cdot 10^6 \text{ cm}^{-2}$ between about 915° and 965°C, indicating an epitaxial film quality. The very obvious rise at the lower temperature region ($T_g < 900^\circ\text{C}$) indicates poor film quality due to an increasing fraction of polycrystalline silicon. According to Fig. 2, at growth temperatures above 950°C the rise of

⁴ Messer Griesheim Company, Duisburg, Germany.

⁵ Advanced Semiconductor Materials, Bilthoven, The Netherlands.

⁶ Zimmer and Williams, Rheydt, Germany.

⁷ Research Incorporated, Minneapolis, Minnesota.

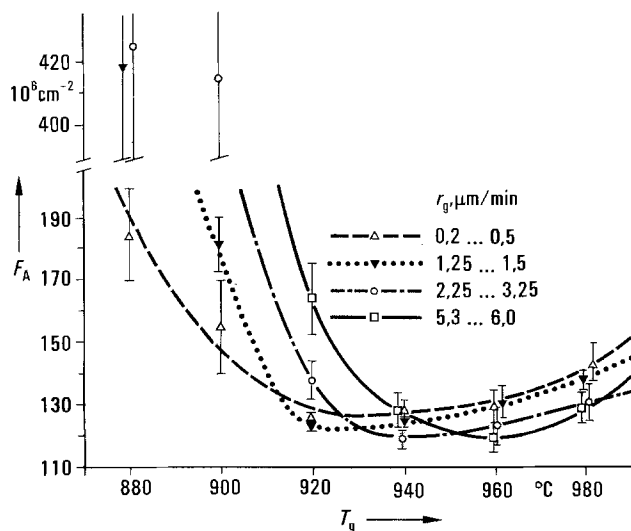


Fig. 2. Absorption factor F_A as a function of the growth temperature T_g for different growth rates.

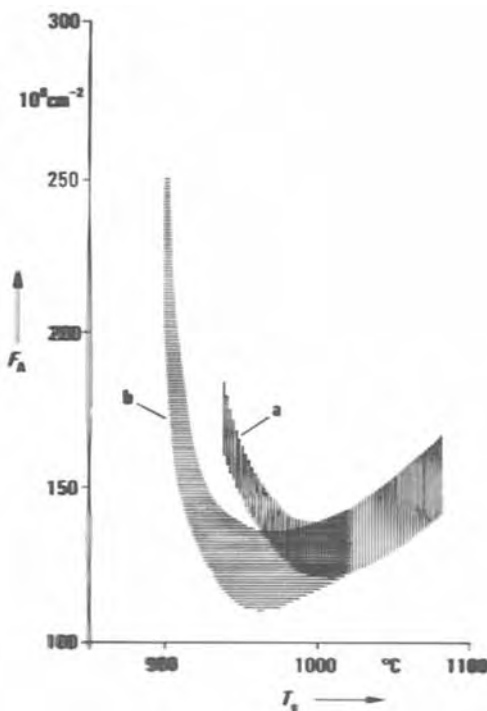


Fig. 3. Quality survey of epitaxial silicon films on sapphire represented by the absorption factor F_A as a function of the growth temperature T_g . (a) Results up to 1974, (b) results in 1976.

the F_A values is only small. At higher growth temperatures than 980°C, which were not investigated in this present series, the rise of F_A is much more obvious. This is demonstrated by Fig. 3 which is taken from an earlier investigation series for a growth rate of 2.5 $\mu\text{m}/\text{min}$ (16). The F_A value rises remarkably with higher temperatures, indicating the increasing influence of the above-mentioned etching reactions (1, 2). The curves represent the epitaxial quality of silicon films on chemically-mechanically polished sapphire: *a* is for results up to 1974, *b* shows the results in 1976. The better results in 1976 are due to the improved quality of the gases and an improvement in the polishing art. (The polishing of the slices from Fig. 3 was done exclusively in our laboratories, using colloidal silica.⁸)

In addition to the growth rate range 0.2-0.5 $\mu\text{m}/\text{min}$ as discussed above, in Fig. 2 further growth rate ranges

are shown, e.g., 1.25-1.5 $\mu\text{m}/\text{min}$, 2.25-3.25 $\mu\text{m}/\text{min}$, and 5.3-6.0 $\mu\text{m}/\text{min}$. As already mentioned, the F_A curves for these different growth rate ranges are similar. It can be seen, especially in the very low temperature range (880°-920°C): the higher the growth rate, the more the corresponding curve for the F_A values is shifted to a higher growth temperature range. With the exception of the lowest rate, this applies also to the flat minima of the F_A curves. These minima lie between 920° and 940°C for 1.25-1.5 $\mu\text{m}/\text{min}$, between 930° and 955°C for 2.25-3.25 $\mu\text{m}/\text{min}$, and between 950° and 970°C for 5.3-6.0 $\mu\text{m}/\text{min}$. It is obvious that the higher the deposition rate, the higher the deposition temperature must be for the production of a good epitaxial film and vice versa. It further can be seen that for the 0.2-0.5 $\mu\text{m}/\text{min}$ range the slope of the curve is not as steep as for the other growth rate ranges, indicating that in this growth rate range the deposition conditions of epitaxial silicon are not so critical as for higher growth rates. On the other hand, the F_A minimum values for the lowest growth rate range are at a slightly higher level ($F_A = 125\text{-}130 \cdot 10^6 \text{ cm}^{-2}$) than for all other investigated rates ($F_A = 115\text{-}120 \cdot 10^6 \text{ cm}^{-2}$). This may be due to the slower coverage of the sapphire surface with silicon at the lower growth rates, thus allowing slightly increased etching reactions ([1] and [2]) and therefore a slight deterioration of the film. Nevertheless even with the lowest growth rates epitaxial films with $F_A < 140 \cdot 10^6 \text{ cm}^{-2}$ can be obtained.

If the curves of Fig. 2 are considered in direction to higher growth temperatures, a slight increase for all curves can be seen. The curves for the growth rate ranges 0.2-0.5 $\mu\text{m}/\text{min}$ and 1.25-1.5 $\mu\text{m}/\text{min}$ exceed the F_A value of $140 \cdot 10^6 \text{ cm}^{-2}$ at approximately 965°-970°C. The curve for the highest investigated growth rate range 5.3-6.0 $\mu\text{m}/\text{min}$ exceeds this F_A value at about 985°C. Only the curve for the growth rate range 2.25-3.25 $\mu\text{m}/\text{min}$ reaches the F_A value of $140 \cdot 10^6 \text{ cm}^{-2}$ at a higher temperature (approximately at 995°C), this being the most independent growth rate range concerning the choice of the deposition parameters. Growth rates smaller than 2.25-3.25 $\mu\text{m}/\text{min}$ may be slightly too low so that the above-mentioned etching reactions ([1] and [2]) play an increasing role with rising temperature. The marked increase of the curve for the high growth rate range 5.3-6.0 $\mu\text{m}/\text{min}$ could be attributed to the fact that nucleation in the gas phase with SiH_4 may occur resulting in the deterioration of the films, too.

As mentioned above, for every investigated growth rate range a certain corresponding growth temperature range exists, in which the F_A values are smaller than $140 \cdot 10^6 \text{ cm}^{-2}$. If these "epitaxial temperature ranges" and the corresponding growth rate ranges are plotted against each other, an epitaxial deposition region is obtained concerning T_g and r_g , respectively. This epitaxial region is shown in Fig. 4 as the hatched area. Here again it can be seen, that for the growth rate range 2.25-3.25 $\mu\text{m}/\text{min}$ a very large deposition temperature range can be chosen (930°-995°C) without deteriorating the film quality remarkably. Within the hatched area of Fig. 4 a crosshatched additional region is shown. The horizontal bars in this region represent the deposition temperature ranges, in which the flat minima of the F_A curves for the different growth rate ranges were obtained (see Fig. 2). From the crosshatched region in Fig. 4 the optimum deposition parameters for different growth temperatures and different growth rates can be determined. The "optimum epitaxial region" can be extended to even higher growth rates. This was verified experimentally by growing films at the very high growth rate of 7.5 $\mu\text{m}/\text{min}$. A growth temperature of 975°C was chosen simply by extrapolation from the optimum deposition conditions for the lower growth rate ranges (i.e., 2.25-3.25 $\mu\text{m}/\text{min}$ and 5.3-6.0 $\mu\text{m}/\text{min}$). The corresponding F_A values were found to be about $120 \cdot 10^6 \text{ cm}^{-2}$, which

⁸Besides the above-mentioned Syton of Monsanto Chemical Corporation, Spectrolite and Mirrolux of Materials Development Corporation, Santa Monica, California were used in these earlier experiments.

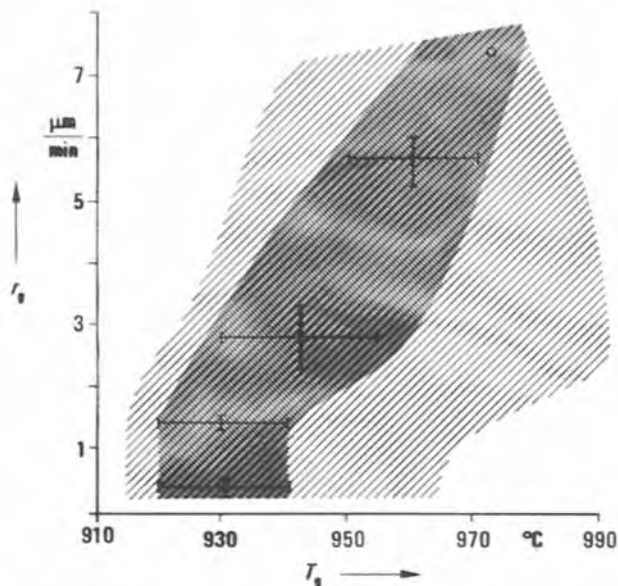


Fig. 4. Growth rate r_g as function of the growth temperature T_g for epitaxial silicon films on (1012) sapphire with $F_A \leq 140 \cdot 10^6 \text{ cm}^{-2}$ (hatched area). The crosshatched region indicates the optimum deposition conditions ($F_A = 125\text{-}130 \cdot 10^6 \text{ cm}^{-2}$ for the 0.2-0.5 $\mu\text{m}/\text{min}$ growth rate range and $F_A = 115\text{-}120 \cdot 10^6 \text{ cm}^{-2}$ for all other investigated growth rate ranges). The circle is from an additional experiment with $r_g = 7.5 \mu\text{m}/\text{min}$ and $T_g = 975^\circ\text{C}$ (resulting in an F_A value of about $120 \cdot 10^6 \text{ cm}^{-2}$; see text).

is in the lower part of the above-mentioned F_A value region (this is not represented in Fig. 2, because only one growth temperature was verified experimentally; in Fig. 4 this additional experiment is included as a circle).

For the growth rate regions 0.2-0.5 $\mu\text{m}/\text{min}$ and 1.25-1.5 $\mu\text{m}/\text{min}$ the optimum epitaxial deposition range is nearly the same (920°-940°C). This indicates that below this temperature range further optimization was not possible. Growth temperatures of 900°C or less resulted in polycrystalline silicon in our case, indicating that these deposition temperatures are too low for a good arrangement of the silicon atoms in the silicon lattice and, therefore, for growth of an epitaxial film. From the viewpoint of autodoping due to the above-mentioned etching reactions [1] and [2], the growth temperature range $T_g = 920^\circ\text{-}940^\circ\text{C}$ is most favorable in our system.

The lowest optimum growth temperature is not a constant based on physical or chemical principles, but depends very substantially on the surface quality of the substrate and consequently on the existing state of the polishing art. It can be assumed today that the art of polishing is rather advanced, because damage-free (including subsurface damage free) substrate surfaces can be produced (16).

The optimum deposition temperature depends additionally on the purity of the gases used, e.g., H_2O or O_2 impurities, the geometry of the reactor cell, and the flow conditions. In Fig. 5 the influence of H_2O impurities on the epitaxial quality of the silicon films (growth temperature 980°C, growth rate 2.5 $\mu\text{m}/\text{min}$), represented again by the absorption factor F_A , is shown. These experiments were done with hydrogen with a known H_2O impurity fraction. (This hydrogen was taken from different cylinders without use of the gas purifier; the H_2O impurity fractions were measured before deposition with the Shaw hygrometer.) It can be seen that as the H_2O impurity level increases the quality of the films drops drastically. The rise in F_A at higher impurity concentrations may be attributed to the increasing fraction of silicon oxides, which are incorporated into the film. For the production of a good epitaxial film on sapphire the H_2O impurity fraction

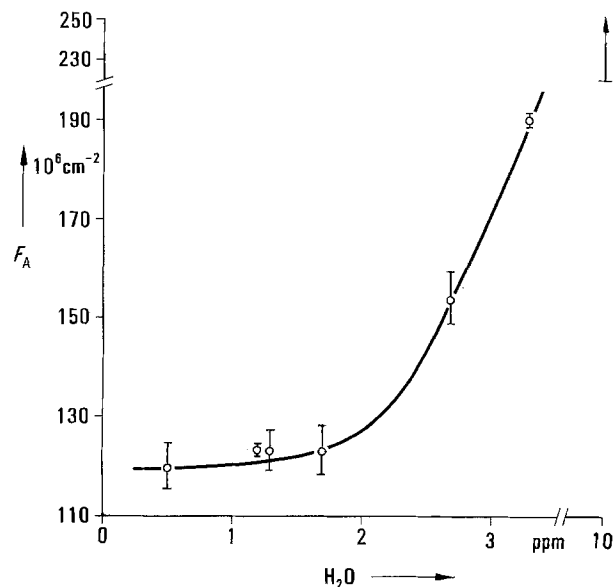


Fig. 5. Absorption factor F_A as a function of H_2O content added to the hydrogen. Deposition temperature 980°C, growth rate 2.5 $\mu\text{m}/\text{min}$.

must be below 2 ppm for a growth temperature of 980°C. Further experiments showed that the H_2O impurity fraction at lower growth temperatures (e.g., 930°C) must be even less (e.g., < 1 ppm). Similar curves are expected, if traces of oxygen are introduced into the gas system.

Conclusion

For an optimization of the deposition conditions for epitaxial silicon on sapphire in the SiH_4/H_2 system, the following requisites must be supplied.

In addition to a suitable substrate material, i.e., free of crystal imperfections due to the crystal growth: (i) the polishing of the substrate must be excellent (free of damage and subsurface damage) and the cleaning process (for the removal of polishing impurities) must be excellent; (ii) the purity of the gases is very important (e.g., H_2O impurity fraction < 1 ppm required for low growth temperatures); and (iii) during the growth, etching reactions between the sapphire surface and the deposited silicon can deteriorate the crystal film quality. This can be reduced to a minimum if the growth temperature is as low as possible, and if the growth rate is as high as possible, thus decreasing both the amount of and the time for the etching reactions. The growth temperature and the growth rate cannot be chosen independently but must be fitted, because for each growth rate range there exists an optimum deposition temperature range which can be determined with the data presented in this paper. By this method high quality epitaxial films were produced, e.g., with 5.3-6.0 $\mu\text{m}/\text{min}$ at 950°-970°C, with 2.25-3.25 $\mu\text{m}/\text{min}$ at 930°-955°C, and with 1.25-1.5 $\mu\text{m}/\text{min}$ at 920°-940°C.

Acknowledgment

This work has been supported by the technological program of the Federal Department for Research and Technology of the FRG. The author alone is responsible for the contents. The author further wishes to thank Mrs. E. Harbeck and Mrs. S. Rheinboldt for the preparing of the silicon films, Mr. R. Gessner for the gas measurements, and Mrs. B. Spindler for the absorption measurements.

Manuscript submitted Sept. 23, 1977; revised manuscript received Sept. 25, 1979. This was Paper 183 presented at the Las Vegas, Nevada, Meeting of the Society, Oct. 17-22, 1976.

Any discussion of this paper will appear in a Discussion Section to be published in the December 1980

JOURNAL. All discussions for the December 1980 Discussion Section should be submitted by Aug. 1, 1980.

Publication costs of this article were assisted by Siemens AG.

REFERENCES

1. E. Preuss, M. Pomper, Ch. Raetzl, and H. Splittgerber, *Siemens Forsch. Entwicklungsber.*, **5**, 338 (1976).
2. E. Preuss and H. Schlötterer, ESSDERC 1977, Brighton, England, Inst. Phys. Conf. Ser. No. 40, p. 7 (1978).
3. H. M. Manasevit and W. I. Simpson, *J. Appl. Phys.*, **35**, 1349 (1964).
4. H. Seiter and C. Zamminer, *Z. Angew. Phys.*, **20**, 158 (1965).
5. R. C. DeVries and G. W. Sears, *J. Chem. Phys.*, **31**, 1256 (1959).
6. G. von Grube, A. Schneider, U. Esch, and M. Flad, *Z. Anorg. Chem.*, **260**, 120 (1949).
7. D. Richman and R. H. Arlett, *This Journal*, **116**, 872 (1969).
8. D. J. Dumin, P. H. Robinson, G. W. Cullen, and G. E. Gottlieb, *RCA Rev.*, **31**, 620 (1970).
9. J. Mercier, *This Journal*, **118**, 962 (1971).
10. Y. S. Chiang and G. W. Looney, *ibid.*, **120**, 550 (1973).
11. H. M. Manasevit, Paper 182 presented at the Electrochemical Society Meeting, Las Vegas, Nevada, Oct. 17-22, 1976.
12. H. M. Manasevit, R. L. Nolder, and L. A. Moudy, *Trans. Met. Soc. AIME*, **242**, 465 (1968).
13. G. E. Gottlieb and J. F. Corboy, *J. Cryst. Growth*, **17**, 261 (1972).
14. G. W. Cullen, J. F. Corboy, and R. T. Smith, *ibid.*, **31**, 274 (1975).
15. M. Druminski and H. Schlötterer, *ibid.*, **17**, 249 (1972).
16. M. Druminski and Ch. Kühl, *Siemens Forsch. Entwicklungsber.*, **5**, 139 (1976).
17. J. E. A. Maurits, Paper 169 presented at the Electrochemical Society Meeting, Las Vegas, Nevada, Oct. 17-22, 1976.
18. F. G. Allen, *J. Appl. Phys.*, **28**, 1510 (1957).
19. Ch. Kühl, H. Schlötterer, and F. Schwidofsky, *This Journal*, **121**, 1496 (1974).
20. M. Druminski, Ch. Kühl, E. Preuss, F. Schwidofsky, J. Tihanyi, and K. Schmid, Paper 139 presented at The Electrochemical Society Meeting, New York, Oct. 13-17, 1974.
21. M. Druminski, Ch. Kühl, E. Preuss, F. Schwidofsky, H. Splittgerber, and D. Takacs, *Suppl. Jpn. J. Appl. Phys.*, **15**, 217 (1976).

Warpage of Silicon Wafers

B. Leroy* and C. Plougonven

Compagnie IBM France, 91102 Corbeil-Essonnes, France

ABSTRACT

High temperature processing of Czochralski grown silicon wafers can create temperature gradients high enough to generate slip. The generation of slip and the slip patterns have been found to depend on three factors: the temperature and the temperature gradient, the amount and form of the precipitated oxygen, and the direction of the initial bow and the wafer diameter over thickness ratio. A model is presented to fit experimental data of critical stress in silicon, temperature gradients, and wafer curvature to predict the critical temperature above which warpage will occur. An important result is that increased wafer diameter over thickness ratio makes the wafers more sensitive to warpage. When this is the case the difference in stresses on both sides of the wafer, because of the bending, makes the area affected by slip on the concave side much larger than on the convex side.

High temperature processing of silicon wafers often produces sufficient thermal stresses to generate slip and dislocations (1-3). The stresses arise during temperature transient because in order to enhance productivity the wafers are stacked vertically in diffusion or oxidation boats. When such a boat is inserted or pulled out of a high temperature furnace a temperature gradient arises between the center and edges of the wafers and the resulting stresses can be sufficient to generate dislocations which propagate in (111) type planes and form slip bands (4). The dislocations are generated where the resolved shear stress in a (111) slip plane along a (110) direction exceeds the critical shear stress. Patterns of slip lines can be different depending on temperature, wafer dimensions (thickness and diameter), and amount and form of oxygen precipitation inside the wafer. Generally the slip damage occurs at the periphery for small wafers and temperatures in the 1000°C range whereas larger wafers and lower temperatures (900°C range) result in slip in the center.

The experiments described here relate the critical stress dependence on oxygen precipitation, wafer dimension and shape, and temperature to the resulting slip patterns.

* Electrochemical Society Active Member.

Key words: critical shear stress, oxygen precipitation, plastic deformation, thermal gradient, warpage.

Experimental Procedure and Results

Experimental procedure.—<001> wafers sliced from Czochralski grown crystals have been used throughout the experiments. The wafers were chemically polished on both sides, 400 μm thick, and the diameter was 82.5 mm in most cases, with a few experiments on 57 mm wafers to evaluate the impact of the thickness over diameter ratio on the wafer deformation ability.

The first series of experiments were aimed at determining the pattern of slips observed when varying (i) the amount of precipitated oxygen, (ii) the cooling environment: open tube or capsule, (iii) the temperature of the furnace, and (iv) the diameter over thickness ratio.

For these experiments the wafers received an oxygen precipitation heat-treatment at temperatures between 900° and 1100°C for various durations. They were stacked in the vertical position in a boat with 2.5 mm distance between wafers and at least seven dummy wafers at the end to insure the same cooling kinetics of all the test wafers. At the end of the thermal treatment, the boat was quickly hand-pulled (about 1 sec), and as a result of the temperature difference between the edges and the center of the wafers, slips lines could be generated (1, 4). Typical slip distribution around the wafer has been described by Longo (5) and Hu *et al.* (6).

Slip pattern.—The wafers were then observed by x-ray topography using the (220) reflection in most cases. Figure 1 shows the slip pattern thus obtained on 82.5 mm wafers in the case of an open-tube processing, at two different temperatures 970° and 1050°C, and for high oxygen precipitation and no oxygen precipitation. For Czochralski grown crystals the oxygen precipitates along rings which correspond to the frozen-in microdefects formed during the crystal pulling operation. On x-ray topographs, two types of features can be observed: (i) dark rings concentric to the wafers which correspond to areas with a high density of oxide precipitates, and (ii) sharp lines in the $\langle 110 \rangle$ type direction, at the center or at the edge of the wafer which correspond to slip bands.

From the patterns of dislocations observed on Fig. 1 it can be stated that in the case of cooling from 1050°C slip occurs at the edge only when there is little oxide precipitation and slip occurs at the edge and in the center when the precipitation of oxygen is high, and in the case of cooling from 970°C slip has occurred only in the center of the wafers with a high oxygen precipitation.

Figure 2 shows the results of a similar experiment carried out with 57 mm wafers. The top row of topographs corresponds to wafers in a capsule quickly pulled out of a furnace at 1100°C. It shows that slip occurs only at the edge of the wafers even in the case of high oxygen precipitation. The bottom row shows topographs of wafers quickly pulled out of a furnace at 1050°C in an open tube. Here slip has occurred both at the edge and in the center, for the case of high oxygen precipitation as well as low oxygen precipitation. The same pattern was found on 82.5 mm wafers pulled out of the furnace at 1050°C in an open tube.

However, x-ray topographs show a picture of slip through the wafer. To look at the slip pattern emerging at the surface, wafers were Jenkins-Wright etched for 20 mn. Figure 3 shows a typical result on a 82.5 mm wafer: the center slip portion is much more extended on the concave side than on the convex side. To understand this interesting observation, high resolution x-ray topographs were performed on a wafer with little slip in the center. Figure 4 shows prismatic loops of dislocations generated around a center defect, which is assumed to be an oxide precipitate as such

loops exist only in the dark rings corresponding to oxygen precipitation. This is similar to Matsui's observations (7). The wafer was then etched from the concave side and the same x-ray topograph was taken again (Fig. 4b). The size of the loops has decreased indicating that the loops extended toward the concave side, in (111) family planes. The emergence of such loops on the concave side forms the slip pattern visible after the Jenkins-Wright etch. The loops generated in the bulk extend to the concave side because it is the most compressed region, and it is where stresses have to be relieved first. This will be demonstrated later following the model of Dyer *et al.* (8). From contrast extinction analysis of x-ray topographs of such loops using (220), ($\bar{2}20$), (111), ($\bar{1}\bar{1}\bar{1}$), ($\bar{1}\bar{1}\bar{1}$), ($\bar{1}\bar{1}\bar{1}$), (400), and (040) reflections the Burgers vector associated with the dislocation loops is always $\langle 101 \rangle$ or $\langle 011 \rangle$ type and never $\langle 110 \rangle$ type. Slip associated with these loops in the center of the wafer will therefore be accompanied by a movement perpendicular to the surface, and the bow of the wafer is increased. This is generally called warpage (9, 10).

To summarize these observations, slip patterns are at the wafer edge only for capsule cooling and in case of little oxygen precipitation, and at the center of the wafer only for larger diameter wafers and with some oxygen precipitation. When plastic deformation occurs in the center of the wafer, the initial bow is increased. As the result of this plastic bending, slip lines will concentrate on the concave side, as is fully developed in the Discussion section.

Experimental determination of a critical temperature.—We define a critical temperature as the temperature above which the quick withdrawal of a boat of wafers will result in formation of slip. This critical temperature T_c is a function of: (i) the wafer loading geometry which imposes the temperature gradient and therefore the stress distribution on a wafer, (ii) the critical stress of silicon which is a function of oxygen precipitation, and (iii) the shape of the wafer at the furnace temperature, *i.e.*, the initial bow (9).

The experiments aimed at the determination of T_c were carried out on 82.5 mm diam wafers in the temperature range 800°-1000°C such as to be in the case of center slip, *i.e.*, where the presence or absence of

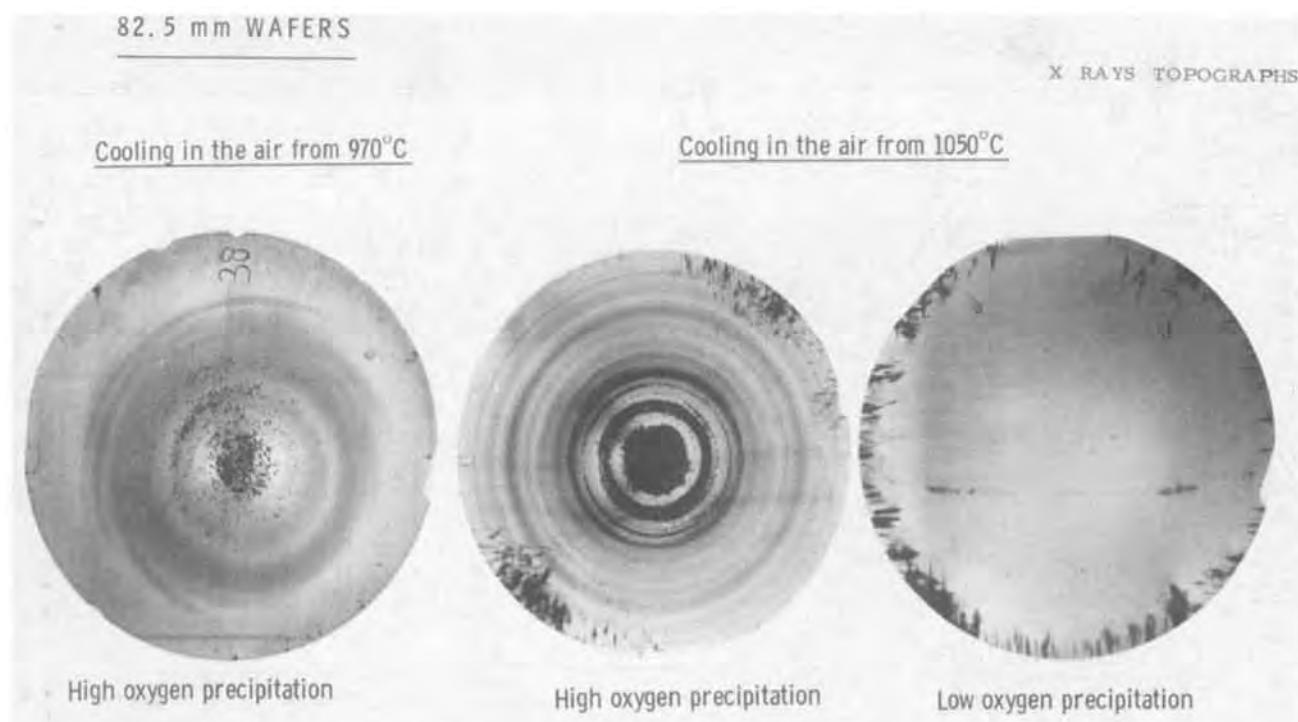


Fig. 1. X-ray topographs of 82.5 mm diam wafers after a thermal treatment which induced an oxygen precipitation

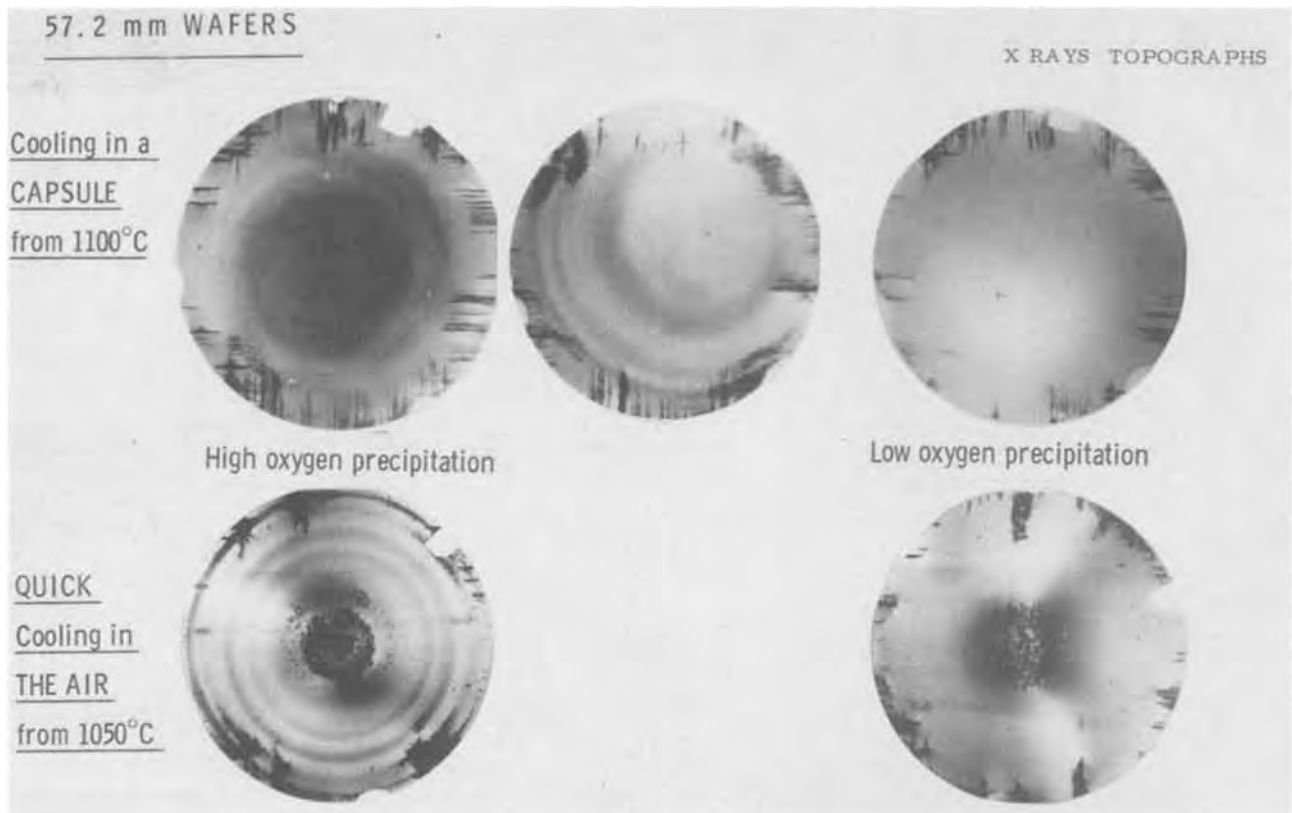


Fig. 2. X-ray topographs of 57 mm diam wafers after a thermal treatment which induced an oxygen precipitation

slip can simply be determined by a measurement of the bow increase before and after each heat-treatment. The wafer loading geometry was kept constant throughout the experiment with the following loading scheme: 2.5 mm spacing between wafers and at least seven dummy wafers on each end of the batch of experimental wafers.

The design of the boat was such that its heat mass was very small, which insures a nearly concentric temperature distribution during cooling.

The amount of precipitated oxygen was determined as the difference between the concentration of interstitial oxygen before and after a precipitation heat-treatment. This amount of precipitated oxygen was varied by choosing wafers with different initial oxygen content and by varying the precipitation heat-treatment or sequence of heat-treatment. The interstitial oxygen content was measured from infrared absorption peak at $9 \mu\text{m}$ using Patrick's (11) relationship $[O] = 2.8 \cdot 10^{17} x$, where x is the absorption coefficient in centimeters. The range of oxygen concentration was found to be $5 \cdot 10^{17} < [O] < 13 \cdot 10^{17}$ at./cm³. The actual wafer measurements were corrected using a calibration curve to account for the thin slice instead of the thick slugs measurements.

Finally in order to vary the initial bow of the wafers a layer of 1000 or 1600Å of silicon nitride was deposited on one side of some wafers. The nitride layer induces a tensile stress which bends the substrate (12). The bow of the wafers was measured by a standard Solex pressure gauge instrument. The extra deformation induced by the 1000 and 1600Å thick nitride film is, respectively, 16 and 25 μm at room temperature and is expected to be 30 and 50 μm , respectively, at 1000°C (12).

Table I summarizes the precipitation heat-treatments and the nitride deposition treatments.

The warpage experiments were carried out by quickly withdrawing the boat of wafers from an idling temperature T . In the case of wafers from groups A and B (Fig. 5) the furnace temperature was slowly lowered from the precipitation temperature (1000°C) to 900° or 950°C or it was left at 1000°C, and the boat was quickly hand-pulled out of the furnace (in about 2 sec). In the case of groups C or D wafers (Fig. 6) the wafers were reinserted in a furnace at a temperature $T_0 = 780^\circ\text{C}$ after the precipitation heat-treatments and, after about 30 min to allow for temperature equilibrium, the wafers were quickly hand-pulled. The bow of every wafer was then remeasured and the

Table I. Summary of heat-treatments for each group of wafers

Wafer group	First-heat-treatment	Nitride film	Second heat-treatment	Warpage experiment
A	None	None	1000°C 3 hr Dry oxygen	Withdrawal at 900°, 950°, and 1000°C
B	None	None	1000°C 18 hr Dry oxygen	Withdrawal at 900°, 950°, and 1000°C
C	1000°C 20 hr Dry oxygen	Group C1: None Group C2: 1000Å	None	Started at 780°C and incremented by 20°C at each experiment
D	925°C 100 mn Dry oxygen	Group D1: None Group D2: 1000Å Group D3: 1600Å	1050°C 20 hr Argon atmosphere	Started at 780°C and incremented by 20°C at each experiment



Fig. 3. Slip patterns on both sides of a plastically warped wafer delineated by Jenkins-Wright etch.

plastically deformed wafers were sorted out. The same experiment was then rerun at a temperature $T_0 + 20^\circ\text{C}$ and subsequently by 20°C increments each time until all wafers were plastically warped (Fig. 6). Therefore for groups A and B wafers, for a given furnace temperature, a critical amount of precipitated oxygen was determined as the boundary above which plastic deformation occurs. The role of different initial oxygen content was only to vary the amount of precipitated oxygen for a given heat-treatment. In the case of groups C and D wafers, a critical temperature was determined for each wafer. In this set of experiments no difference could be found between the groups of wafers with different initial bow and the first-order parameter on which T depends seems to be the oxygen precipitation.

To summarize the results from both groups of experiments a temperature vs. amount of oxygen precipitation diagram has been drawn (Fig. 7) showing the domain free of plastic deformation.

Theory

The main factors determining the dislocation pattern are: (i) the critical shear stress of the silicon which is a function of the oxygen precipitation, (ii) the wafer loading geometry which imposes the temperature gradient and therefore the stress distribution on a wafer, and (iii) the shape of the wafer at the furnace temperature, i.e., the initial bow (9).

We will now determine the role of each factor and show how the experimental data illustrate this behavior.

Critical shear stress.—When a boat of closely spaced wafers is pulled out of a furnace, stresses build up across a wafer as a result of the temperature gradient. The stresses are compressive in the center and tensile at the edges. When the temperature gradient is large enough, dislocations are generated in the areas where the shear stresses exceed the critical shear stress τ_c in the (111) family plane in a [101] direction. Then the dislocations can glide from their source under the thermal stresses.

Experimental values of the yield point of silicon, i.e., the critical stress σ_c , has been reported by Patel *et al.* (13, 14) as a function of oxygen precipitation, dislocation density, temperature, and strain rate. Figure 8 shows his data converted into resolved shear stress in a (111) glide plane by the relationship $\tau_c = \frac{1}{2} \sigma_c$ taking into account his crystal orientation. From Patel's tensile experiments it was established that a maximum applied stress τ_m had to be reached before plastic deformation could occur. Once τ_m has been reached, plastic deformation will continue under a smaller applied stress τ_f . τ_m decreases with increasing temperature, dislocation densities, precipitated oxygen, and with slower strain rates.

In order to take his critical stress measurements as the basis for our quantitative model to understand and predict occurrence of slip on silicon wafers, it must be verified that the conditions are the same. Patel's measurements were carried out at 800°C for the oxygen dependence and between 700° and 1000°C for the temperature dependence, compared with 800° - 1000°C furnace temperatures in our warpage experiments. The oxygen precipitation heat-treatments were conducted at 1000°C both in Patel's experiments and for most of our wafers. The last parameter to be compared is the strain rate.

Patel's measurements of τ_m as a function of the strain rate were made with high strain rates ($\dot{\gamma} \geq 2 \cdot 10^{-3} \text{ mn}^{-1}$) and for the case of no precipitated oxygen. The strain rates in the case of cooling of a wafer are lower. Therefore, his results must be interpolated somewhere between the τ_m plot corresponding to $\dot{\gamma} = 2 \cdot 10^{-3} \text{ mn}^{-1}$ ($5 \cdot 10^{-3} \text{ cm/mn}$) and the τ_f plot. This is done on Fig. 8, which shows τ_m as a function of temperature for different strain rates. It will be verified by superimposing this plot on the wafer applied stress during cooling that these values are consistent.

The influence of a $7 \cdot 10^{17} \text{ at./cm}^3$ oxygen precipitation is shown by Patel to reduce the critical shear stress by a factor of 5 at 800°C . We suppose that this factor is independent of the temperature and the strain rate. This reduction of the critical resolved shear stress is due to the compressive stress fields around the precipitates (15). As the thermal stresses are compressive in the center of the wafer and tensile at the edge, the critical resolved shear stress may not be reduced by the same amount in these two cases, depending on the precipitate shape (globuli, platelet, etc.) and on the temperature.

As a result high oxygen precipitation favors defects in the center of the wafer because of the effect of the oxygen precipitates and the stress field surrounding them, and the low oxygen precipitation, favors defects at the edge because there is no lowering of τ_c in the center of the wafer due to the lack of oxygen precipitates (Fig. 1 and 2). Based on these remarks we take

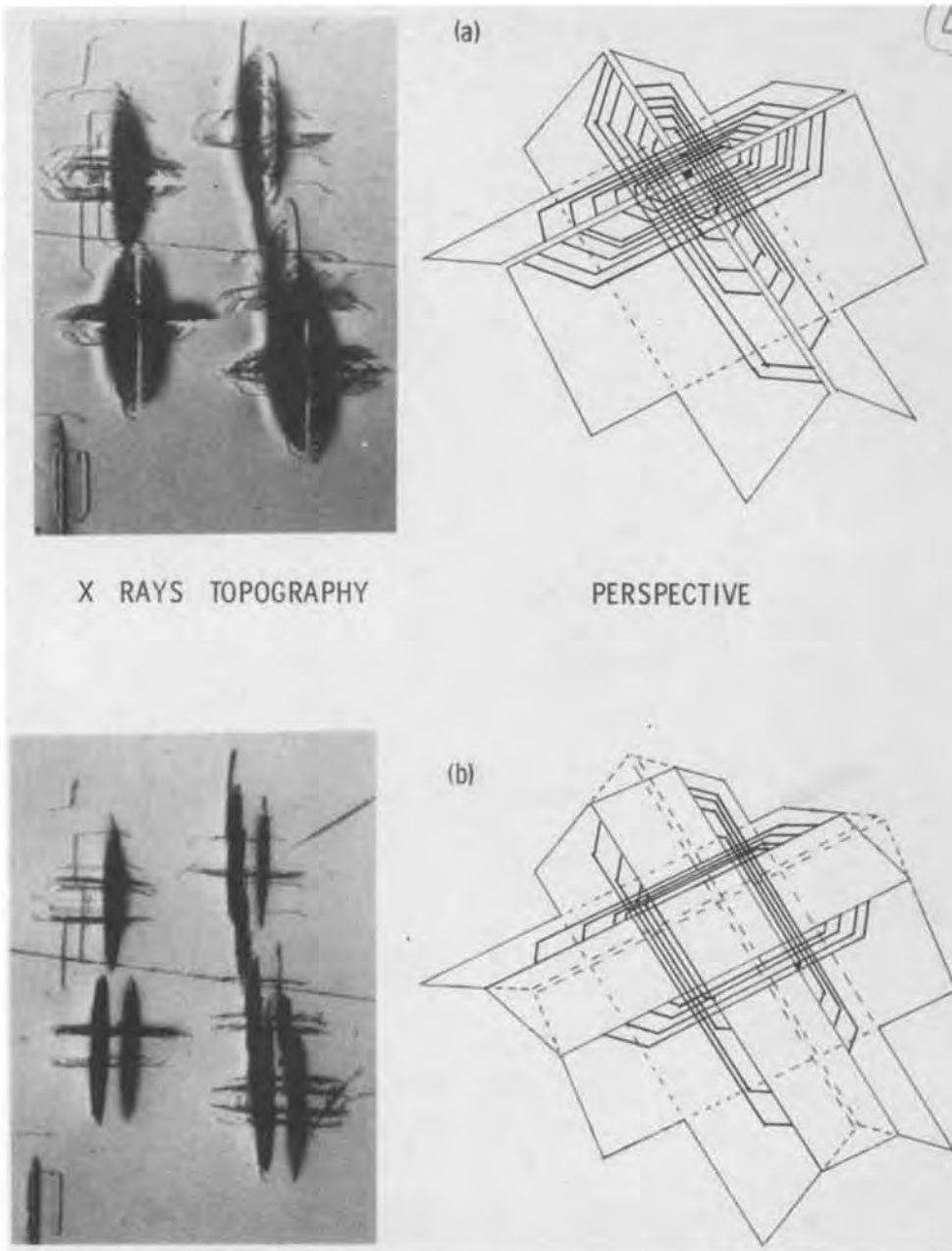


Fig. 4. Magnification of x-ray topographs of dislocation loops generated in a region in the center of the wafer where oxygen is precipitated (a) before etching, (b) after etching 80 μm on the concave side. The right-hand side drawing shows a perspective of the loops in their (111) type glide plane.

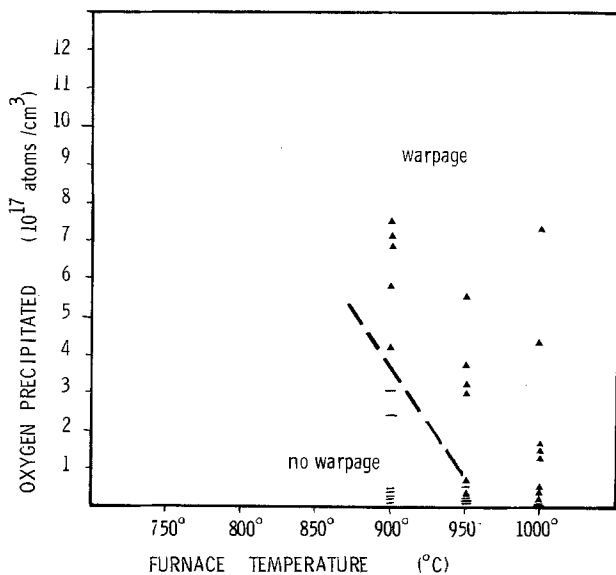


Fig. 5. Warpage of wafers from groups A and B: \blacktriangle warped wafers; — not warped wafers.

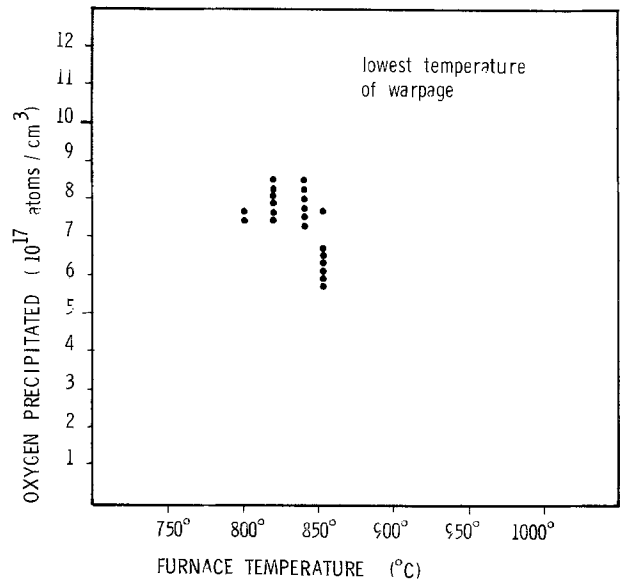


Fig. 6. Critical temperature for the warpage of the wafers from groups C and D.

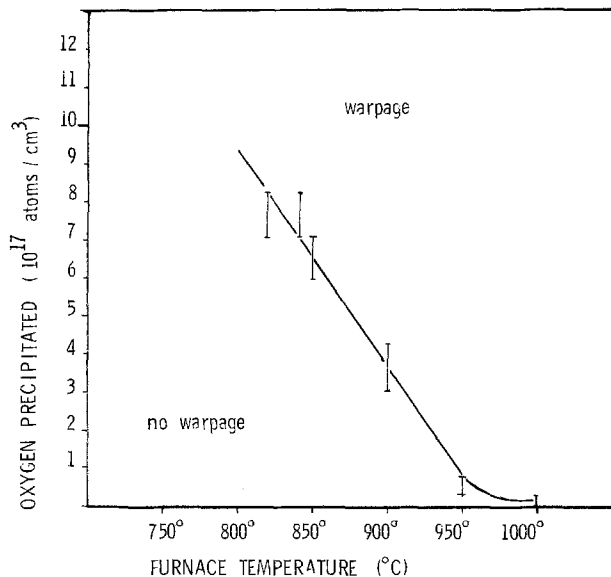


Fig. 7. Critical furnace temperature as a function of oxygen precipitation for generation of warpage. Solid line: curve calculated in text, section on Complete calculation.

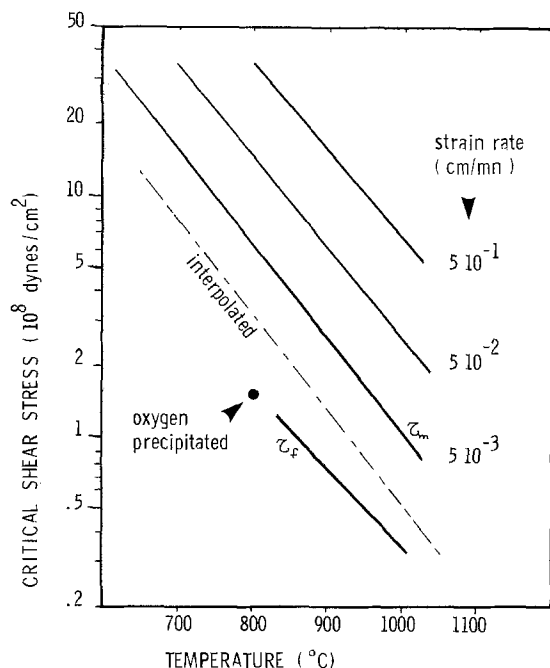


Fig. 8. Critical shear stress from Patel's data (13, 14) and interpolated values.

Patel's measurements as corresponding to τ_{ce} , i.e., τ_c at the edge of the wafer, and so we have from Patel τ_{ce} for the case of no oxygen precipitation and for $7 \cdot 10^{17}$ at./cm³ of oxygen precipitated.

In the center τ_{cc} is the same as τ_{ce} when there is no oxygen precipitation and a little smaller for high oxygen precipitation. To be consistent with the experimental data of Fig. 7, we suppose that the τ_{cc} varies linearly with the amount of oxygen precipitated when it is larger than 10^{17} at./cm³. The resulting network of τ_{cc} vs. T is shown in Fig. 9. Now, to explain the results in capsule, i.e., lower temperature gradient, higher temperature, and no center slip, we must suppose that the difference $\tau_{ce} - \tau_{cc}$ decreases when the temperature increases. Such values of τ_{ce} are illustrated in Fig. 9.

Temperature distribution during nonuniform cooling.—Morizane and Gleim (1) reported temperature gradients between the center and edge of a row of

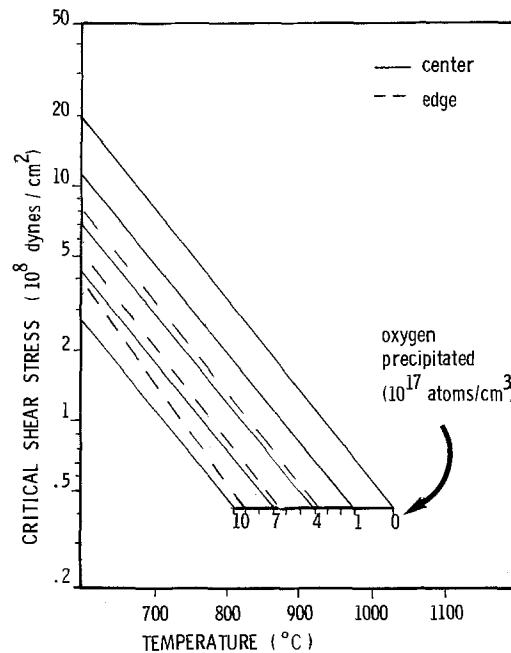


Fig. 9. Critical shear stress at the center (—) and at the edge (---) of the wafer as a function of the temperature and the oxygen precipitated.

seven wafers, when inserted in or pulled out of a furnace, but their measurement was influenced by the large heat mass of the boat, which was not the case in our experiments. More recent measurements by Hearn *et al.* (16) on 57 mm diam wafers reported a ΔT of 170°C during cooling from 1000°C and of 120°C during cooling from 800°C. During heating to 1000°C ΔT was only 120°C. We will assume ΔT values close to Hearn's measurements. Other measurements by Kasper and Clauss (17) in the case of a 1200°C furnace show a ΔT of 150°C for heating and 300°C for cooling. The main difference between heating and cooling comes from the temperature at which the gradient is maximum: in the case of heating the larger ΔT occurs at a lower temperature than for cooling. As the critical stress increases rapidly with decreasing temperatures, only large ΔT at high temperatures will cause slip. Therefore, the model developed here will be for the case of cooling wafers rather than heating.

Calculations of the temperature distribution across wafers for ideal cooling conditions of a row of closely spaced wafers have been carried out by Hu (4) taking into account the heat losses by radiation and conduction.

Note that in this case, Hu (4) found a temperature distribution nearly independent of the wafer diameter, so we can extend his values as well as Hearn's actual measurements from 57 to 82 mm diam wafers.

Table II shows the maximum temperature gradient across the wafer for several starting temperatures as calculated from Hu's model and as measured in Hearn's experiments. There is good agreement for high temperature (1000°C and higher) but for lower temperatures the calculated ΔT becomes significantly higher than the measured one. The reason for this discrepancy is thought to be that the cooling by radiative process is overestimated at lower temperatures, i.e., below 900°C. In this case heat losses by conduction become predominant and the temperature distribution is parabolic resulting in lower maximum ΔT . In real experimental conditions, two variations from this ideal cooling case exist.

First, open-tube processes are where the boat is withdrawn in a quartz tube outside of the furnace. In this case the proximity of the cooler quartz walls leads to slightly greater heat losses at the wafer edges by convection. Hearn's measurements were carried out in

Table II. Maximum temperature gradient across wafer

T (°C)	T (°K)	ΔT (max) [Hu (4)]	T (max) [Hearn (16)]	τ_{max} [Hu (4)] (10^8 dynes/cm ²)		Parabolic app. [Hearn (16)] (10^8 dynes/cm ²)	
				Center	Edge	Center	Edge
1100	1373	192	195	1.55	5.6		
1000	1273	178	170	1.43	5.2		
900	1173	164	145	1.31	4.8		
800	1073	150	120	1.2	4.4	1.6	3.9
700	973	136	95	1.1	4.0	1.26	3.0

these conditions and therefore his results reflect this effect which is probably negligible at high temperatures ($T > 900^\circ\text{C}$) but not at lower temperatures.

Second is the case of a capsule process. When the boat inside the capsule is withdrawn from the furnace, the hot capsule quartz walls irradiate back at the wafers edge and hence reduce the cooling rate of the edges. These conditions are similar to the closed boat approach of Hearn where he measured a temperature difference of 65°C between the center and the edge of a wafer cooled from 900°C . It is, however, likely that the maximum ΔT is reached quickly in the case of the open tube and later when there is a compensation between the radiation of the quartz walls and the wafers.

Figure 10 shows the temperature drop calculated from Hu's model and for our experimental conditions. The capsule cooling temperature plot is adjusted to fit Hearn's measured ΔT .

Stresses distribution.—Timoshenko *et al.* (18) calculated the radial distribution of stresses induced by the thermal gradient, when the bending moment of the wafer can be neglected (flat wafer).

The ratio of the thermal stresses to the maximum of shear stress was taken from Hu (4) to be 2 at the edge and $\sqrt{6}$ in the center.

So by assuming the temperature distribution across the wafer discussed previously, the maximum shear stress can be calculated in the center of the wafer and at the edge as a function of the center and the edge temperature, respectively. Figure 11 shows such plots for different starting temperatures: 800° , 900° , 1000° , and 1100°C . τ_m has been plotted as a function of the temperature T instead of time in order to later compare τ_m with τ_c which also varies with temperature but not with time.

In order to determine when plastic deformation will start τ_m must be compared to τ_c at any given time.

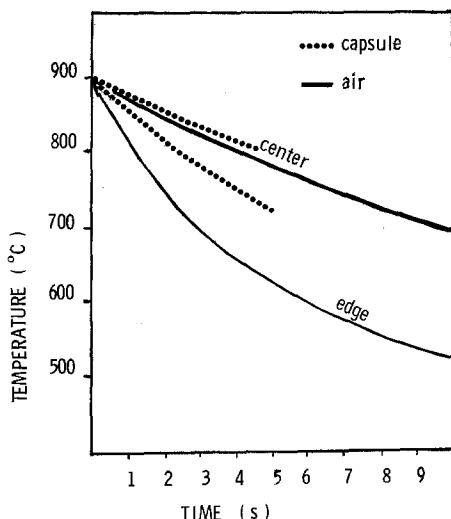


Fig. 10. Cooling kinetics at the center and at the edge of the wafers during cooling in the air (—) and cooling in a capsule (....).

τ_m and τ_c vary with temperature and therefore it is convenient to represent on the same figure the plots of τ_m vs. T and τ_c vs. T . Plastic deformation will occur when the two plots intersect and for a given wafer, *i.e.*, where τ_c is determined, the critical ΔT admissible is determined by making τ_m vs. T become tangent to τ_c vs. T .

Figures 12 and 13 show, respectively, for air cooling and capsule cooling two cases of τ_m vs. T compared to τ_c vs. T for different starting temperatures. The stress curves in the open-tube case (Fig. 12) are taken from Fig. 11 and in the capsule case they are derived from the cooling curves of Fig. 10.

Note that the center stress curve has to be compared to τ_{ce} , *i.e.*, τ_c corresponding to the center whereas the edge stress curve must be compared to τ_{ce} , *i.e.*, τ_c corresponding to the edge. Let us consider each case separately.

Open-tube case.—Cooling from high temperature ($T > 1000^\circ\text{C}$), the critical shear stress is reached first at the edge. Three types of slip time patterns can therefore result: (a) little oxygen precipitation, *i.e.*, high τ_c ; no slip lines will form; (b) moderate oxygen precipitation; slip lines are generated first at the edges of the wafer thereby relieving the thermal stresses and preventing slip in the center, and (c) high oxygen precipitation; slip occurs both at the center (lower τ_c) and at the edge of the wafers. Such patterns are shown on Fig. 1 and 2. Note that the reduction of the cooling rate has the same effect as a reduction of precipitated oxygen. Cooling from lower temperatures: cases (a) and (c) described above remain the same but case (b) leads to slip in the center only due to

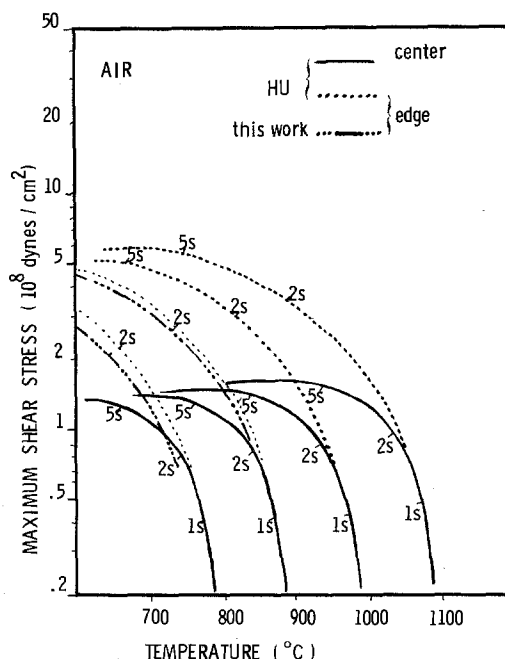


Fig. 11. Maximum shear stress at the center and at the edge of the wafers during cooling in the air from different temperatures. The numbers beside the curves are the time in seconds.

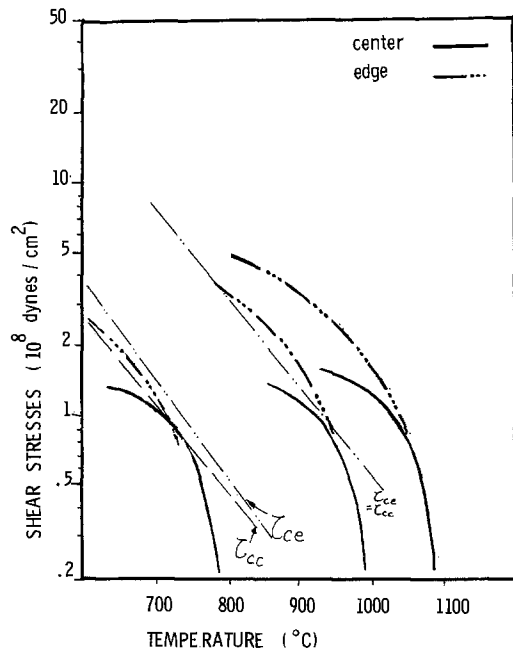


Fig. 12. Plot of the calculated maximum shear stress and the critical shear stress at the center and at the edge of the wafers during cooling in the air from 800°, 1000°, and 1100°C.

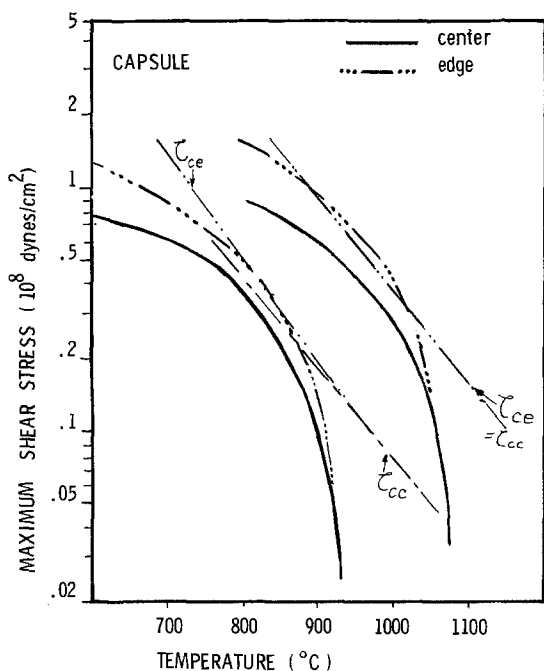


Fig. 13. Plot of the calculated maximum shear stress and the critical shear stress at the center and at the edge of the wafers during cooling in a capsule from 950° and 1100°C.

the smaller critical stress of the edges as discussed previously. When slip occurs in the center the wafers warpage increases.

Cooling in a capsule.—Due to the reduced radial temperature differential in a capsule compared to an open tube, the generation of dislocations in a capsule requires a starting temperature of the order of 100°C greater than the tube case. At this temperature, the critical shear stress is nearly the same at the center and at the edge and is always reached first at the edges (Fig. 13). This is consistent with the slip pattern shown in Fig. 2.

Bending.—The radial temperature distributions, therefore, can be such that peripheral and/or center

slip can take place. However, the thin membrane flat disk approach is a good approximation only for flat wafers with a not too large diameter over thickness ratio. For larger wafers two variations from the membrane case must be taken into account: (a) the wafer can no longer be accurately approximated as a flat disk. Its equilibrium shape can be described as a circular disk with a finite initial curvature, and (b) when the ratio of diameter over thickness increases, as a result the resistance to bending decreases. When such a wafer is submitted to a radial temperature differential ΔT during cooling a hot central portion is trapped within a cold annular zone. The compressive stresses in the center will tend to increase the curvature of the wafer.

The complete stress analysis taking into account the effects of this increased elastic curvature of the wafer has been carried out by Dyer *et al.* (8). The total radial and tangential stresses are composed of membrane stresses plus bending stresses. The effect of the elastic bending due to the compressive stresses in the center of the wafer is to increase the stresses on the concave side and to reduce them on the convex side (8) compared to the membrane case.

Using Dyer's (8) solutions the deflection w and the tangential ($\sigma_{\phi\phi}$) and radial (σ_{rr}) stresses have been calculated as a function of the initial deflection w_0 for small ΔT , with the geometrical parameters of the wafers used in our experiment, *i.e.*, a radius $R = 4.12$ cm and a thickness $h = 385 \mu\text{m}$. Figure 14 shows the radial distribution of $\sigma_{\phi\phi}$ and σ_{rr} calculated for $\Delta T = 120^\circ\text{C}$ and $w_0 = 20 \mu\text{m}$ and for the concave side, the convex side, and for the membrane case. It shows that the compressive stress in the center on the con-

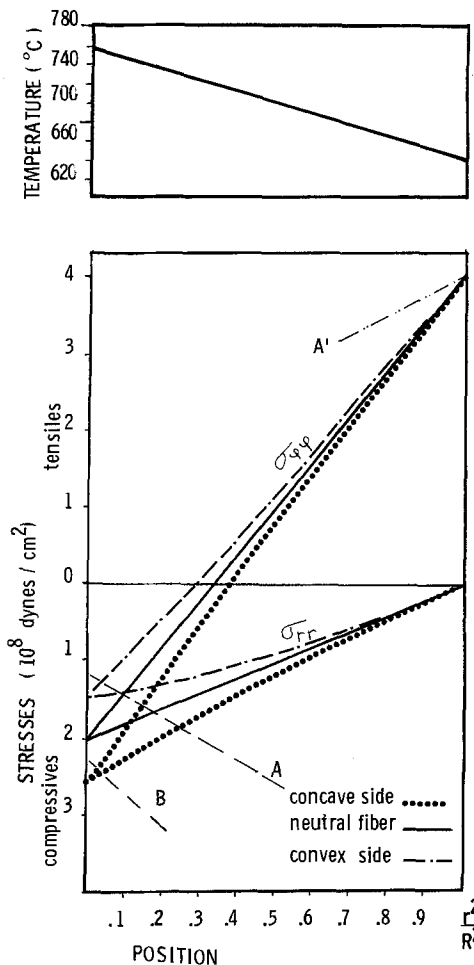


Fig. 14. Distribution of the temperature and of the stresses along a radius of a wafer on the convex and on the concave sides and on the neutral fiber, calculated for an initial bow of 20 μm .

cave side can be increased almost by a factor of 1.5 compared to the convex side whereas at the edge the difference between both sides is negligible. In the center of the wafer the stress on the concave side will always be greater than on the convex side and therefore the dislocation pattern can be expected to be dissymmetric. For instance on Fig. 14 we can superimpose a plot of σ_c which is $\sqrt{6}\tau_c$ in the center and $2\tau_c$ at the edge. Also the radial variation of τ_c shown takes into account the temperature distribution assumed for the calculation of the σ 's. The AA' τ_c plot corresponds to an oxygen precipitation of 10^{17} at./cm³. In this case, no slip line will be generated at the edge of the wafer and in the center, the radius of the defective area will be $0.2R$ on the convex side and $0.5R$ on the concave side, i.e., an area 6 times larger. If there is no oxygen precipitation (curve B) dislocations will be generated only on the concave side of the wafer. This result is illustrated by the dislocation pattern of Fig. 3 where the dislocation pattern is larger in the central area on the concave side than on the convex side, and the dislocations are generated in the oxide precipitate rings (see also Fig. 4).

Therefore the stress difference between both sides of the wafer imposed by the elastic bending when the center of the wafer is under compression is also a determining factor to explain the slip patterns. Intuitively the stress enhancement on the concave side compared to the membrane case will depend on the magnitude of the elastic bending which is a function of the temperature differential, the radius, and the thickness of the wafer. From Dyer's equations, this stress enhancement can be calculated as a function of these parameters. If we choose the z axis perpendicular to the wafer surface with its origin in the middle of the wafer thickness, the total stress along the z direction can be written

$$\sigma(z) = \sigma(0) + \Delta\sigma(z)$$

where $\sigma(0)$ is the membrane stress and $\Delta\sigma(z)$ is the stress enhancement due to the bending.

Carrying out the calculations of $\sigma(z)$ and $\Delta\sigma(z)$ from Dyer's solutions shows that these two parameters are a function of z , the radial distance to the center of the wafer r , the initial deflection w_0 and a parameter $\Delta T(R^2/h^2)$. It is important to note that σ and $\Delta\sigma$ do not vary with ΔT , R , and h independently but with the product $\Delta T(R^2/h^2)$.

Let us call stress enhancement factor the ratio $Se_{(z)} = \Delta\sigma(z)/\sigma(0)$. The numerical calculations of this factor have been performed as a function of the parameter

$\Delta T(R^2/h^2)$ and for different values of w_0 and the results are shown in Fig. 15. The development of Dyer is correct if ΔT is not too large (solid line on Fig. 15) and the calculation has been interpolated for larger ΔT values (dashed lines). According to these plots, for our experimental conditions which correspond to $\Delta T(R^2/h^2)$ of the order of $1.3 \cdot 10^6$ one expects to see an impact of the initial deflection on the occurrence of slip for values greater than $40 \mu\text{m}$, i.e., a $\Delta\sigma$ due to the bending larger than 20% compared to the case of wafers with initial deflection between 10 and $20 \mu\text{m}$. In our experiments the initial deflection was varied by depositing a layer of silicon nitride but the deflection increase thus obtained was probably insufficient to induce a large enough stress enhancement such as to have an effect on the warpage temperature measurement (T_c was measured at $\pm 10^\circ\text{C}$). In addition, another factor must be taken into account: the distribution of oxide precipitates in the wafer thickness. The density of precipitates is very high in the middle of the wafer thickness but close to the surface a layer 50-100 μm thick is almost free of precipitates. The result is a higher σ_c close to the surface where the stress enhancement is the largest. The dislocations are generated around oxide precipitates, i.e., at some distance from the surface and therefore only the stress enhancement up to that distance should be considered. The calculation of the stress enhancement factor assuming that the precipitation is uniform only in half of the wafer thickness, i.e., for $-h/4 < z < +h/4$. The stress enhancement at $h/4$ is half its value at $h/2$. In our experiments, ΔT is $\approx 70^\circ\text{-}130^\circ$ when dislocations are emitted, w_0 is between 0 and $60 \mu\text{m}$ and the oxide precipitates are only in the half of the wafer thickness. The stress enhancement is then between 0 and 0.3. When the initial bow varies from 0 to $60 \mu\text{m}$, the impact on the critical warpage temperature is the same as an increase of the oxygen precipitation from $3 \cdot 10^{17}$ to $5 \cdot 10^{17}$ at./cm³. Also one can see that the stress enhancement is larger for larger diameter wafers if we keep ΔT and h constant. This explains why center slip is observed on 57 mm wafers only in cases of very high oxygen precipitation in the center but for smaller oxygen precipitation for the 82.5 mm wafers.

Because of this stress enhancement factor, on Fig. 11, 12, and 13 the stresses on both sides of the wafers should be plotted separately, i.e., higher on the concave side and lower on the convex side at the center of the wafer.

Complete calculation.—Now the experimental plot of Fig. 7 can be calculated from the three factors just described: (i) Stresses in the wafers during cooling

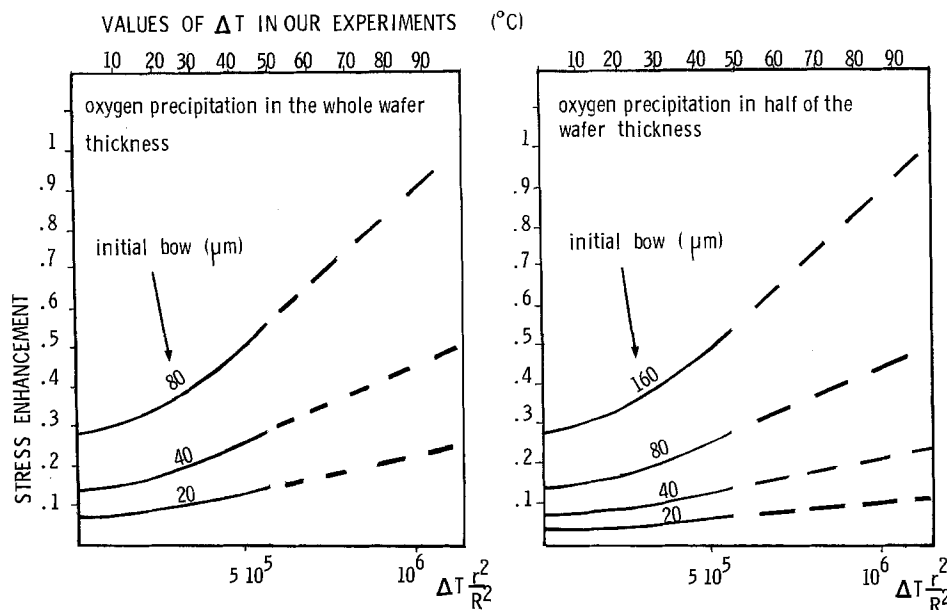


Fig. 15. Stress enhancement in the central area of the wafer, in the part of the thickness where the dislocations are generated.

from different temperatures as shown in Fig. 11 and 12; (ii) the relationship between the critical stress, the temperature, and the amount of oxygen precipitated given in Fig. 9; and (iii) a stress enhancement at the center of the concave side calculated from Fig. 15 assuming an initial bow between 20 and 30 μm .

Under these conditions the critical temperature is calculated for different amounts of precipitated oxygen and the line joining these points separates two domains: one where the warpage occurs and one without warpage.

This result corresponds to a critical stress obtained in our oxygen precipitation experiments. But for other heat-treatments, where another process of precipitation is involved, σ_c will differ from values of Fig. 9 (19).

Conclusion

Experimental slip patterns have been explained by a model fitting stresses calculated from a temperature distribution across a wafer induced by nonuniform cooling and variations of the critical stress of silicon as a function of the temperature and the amount of precipitated oxygen. The effect of bending explains that for larger diameter over thickness ratio, wafers become more sensitive to warpage, and also that warped wafers show a much larger area affected by slip on the concave side than on the convex side. The model also predicts the critical temperature above which warpage will occur as a function of amount of oxygen precipitated.

Acknowledgments

The authors wish to thank A. Gorry, A. Rousseau, and J. Arhan for providing the x-rays topographs.

Manuscript submitted June 4, 1979; revised manuscript received Nov. 1, 1979.

Any discussion of this paper will appear in a Discussion Section to be published in the December 1980 JOURNAL. All discussions for the December 1980 Discussion Section should be submitted by Aug. 1, 1980.

Publication costs of this article were assisted by Compagnie IBM France.

REFERENCES

1. K. Morizane and P. S. Gleim, *J. Appl. Phys.*, **40**, 4104 (1969).
2. S. M. Hu, *Appl. Phys. Lett.*, **22**, 261 (1973).
3. W. A. Porter, D. D. Drew, and J. S. Linder, *J. Appl. Phys.*, **43**, 1477 (1972).
4. S. M. Hu, *ibid.*, **40**, 4413 (1969).
5. S. Longo, Thesis, University of Paris (1972).
6. S. M. Hu, S. P. Klepner, R. O. Schwenker, and D. K. Seto, *J. Appl. Phys.*, **47**, 4098 (1976).
7. J. Matsui, *This Journal*, **122**, 977 (1975).
8. L. D. Dyer, H. R. Huff, and W. W. Boyd, *J. Appl. Phys.*, **42**, 5680 (1971).
9. K. G. Moerschel, C. W. Pearce, and R. E. Reusser, in "Semiconductor Silicon 1977," H. R. Huff and E. Sirtl, Editors, p. 170, The Electrochemical Society Softbound Proceedings Series, Princeton, N.J. (1977).
10. B. Leroy and C. Plougonven, Abstract 68, p. 193, The Electrochemical Society Extended Abstracts, Spring Meeting, Philadelphia, Pa., May 8-13, 1977.
11. W. J. Patrick, Silicon Device Processing, Maryland Symposium, Feb. 6, 1970, NBS Special Pub. 337, p. 442.
12. M. Tamura and H. Sunami, *Jpn. J. Appl. Phys.*, **8**, 1097 (1972).
13. J. R. Patel and A. R. Chaudhury, *J. Appl. Phys.*, **34**, 2788 (1963).
14. J. R. Patel, *Discuss. Faraday Soc.*, **38**, 201 (1964).
15. W. K. Tice and T. Y. Tan, *Appl. Phys. Lett.*, **28**, 564 (1976).
16. E. Hearn, E. H. Te Kaat, and G. H. Schwuttke, *Microelectron. Reliability*, **15**, 61 (1976).
17. E. Kaspers and H. Clauss, *Wiss. Ber. AEG Telefunken*, **48**, 183 (1975).
18. S. Timoshenko and J. N. Goodier, "Theory of Elasticity," McGraw-Hill Book Co., New York (1970).
19. B. Leroy and C. Plougonven, To be published.

Thermodynamic Properties and Subphases of Wustite Field Determined by Means of Thermogravimetric Method in the Temperature Range of 1100°-1300°C

Eiji Takayama and Noboru Kimizuka

National Institute for Researches in Inorganic Materials, Sakuramura, Niiharigun, Ibaraki, Japan 305

ABSTRACT

The composition of the wustite phase field under various oxygen fugacities was determined in great detail by means of the thermogravimetric method in the temperature range of 1100°-1300°C. There is a breaking point, which means a second or possibly higher order transition in the wustite phase, in every isothermal line of oxygen fugacity vs. composition of wustite. The phase diagram containing the subphase boundary was obtained. Some thermodynamic functions were also determined and compared with the previously published data.

Darken and Gurry (1, 2) established the equilibrium phase diagram of the Fe-O system in detail at higher temperatures by using controlled oxygen fugacities, and they determined the important thermodynamic values. Since their work, thermogravimetry and the solid-state galvanic cell method have been intensively

Key words: solids, thermodynamics, stoichiometry, phase transitions.

applied to the study of wustite in order to determine the thermodynamic properties more precisely (the references are listed in the review of Giddings and Gordon (3) and Spencer and Kubaschewsky (4), for instance).

Vallet and Raccach (5, 6) and Kleman (7) suggested that there are three subphases in the wustite phase field on the basis of thermogravimetry. Their sugges-

tion was supported by Fender and Riley (8) and Carel and Gavarri (9) on the basis of emf measurements, x-ray study, and dilatometry. However, Giddings and Gordon (3, 10) and Hayakawa *et al.* (11) asserted that no positive evidence indicating such subphases could be observed in the available data published so far and concluded that the experimental errors in the data of Vallet and Racciah or Fender and Riley were too large to suggest the existence of subphases.

On the other hand, defect structure analyses of quenched samples of the wustite phase have been made by means of x-ray, neutron, and electron diffraction and they suggest that defect ordering in the wustite phase may be complex (the references are listed in the review of Gavarri *et al.* (12), for instance). But there are gaps and discrepancies among the available data and none support clearly the presence of subphases. These discrepancies may be owing to the fact that perfect quenching of the wustite phase is very difficult because the atoms in wustite, having large amounts of defects, can move too rapidly to be quenched in the process of normal rapid cooling.

A few studies of high temperature x-ray and neutron diffraction of the wustite phase have also been reported (13-15). In these studies, Cheetham *et al.* (13) support the presence of subphases. On the other hand, Hayakawa *et al.* (14, 15) found no evidence for it.

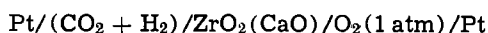
The objective of our present study is to test whether the subphases are present or not. For this purpose, we determined the detailed relationships between equilibrium oxygen fugacity and composition of the wustite phase on the basis of thermogravimetry in the temperature range of 1100°-1300°C. We also determined the thermodynamic functions, relative partial entropies and enthalpies of oxygen, and partial molar free energies, entropies, and enthalpies of formation of the wustite phase.

Experimental

Apparatus.—The experimental apparatus used in this work was made up mainly of three parts; (i) a platinum (40% rhodium alloyed) wire wound tubular-type furnace in which a galvanic cell of a stabilized ZrO₂ tube was set up to determine directly the oxygen fugacity around a sample; (ii) a gas mixer designed to continuously supply a mixture of hydrogen and carbon dioxide gas in a definite constant proportion; and (iii) Mettler H54AR-type balance for measuring the weight of a sample.

The furnace had three independently controllable heating zones and had a central region of about 8 cm in length, where the temperature was distributed within $\pm 0.5^\circ\text{C}$. In this region, the temperature distribution in the radial direction was also flat in the inner reaction tube, more than 5 mm away from the tube wall. The temperature of the furnace was controlled to be maintained within $\pm 0.5^\circ\text{C}$ at any point for extended periods with a temperature controller (Eurotherm Company Limited, Type 090) and was measured with a Pt-Pt-13%Rh thermocouple which was regularly calibrated at the gold point.

Two kinds of calcia-stabilized zirconia tubes were employed for the galvanic cell (Zr-23 of Degussa Company and Zr-11 of Nippon Kagaku Tokyo Company) and the value of the emf did not depend on the kind of tube. Before composing a cell, every tube was evacuated to check for gas tightness. The construction of the galvanic cell was as follows



No paste was used for fixing Pt wire to the tube. Oxygen fugacity of the mixture of CO₂-H₂ in the furnace was evaluated from the emf according to the Nernst equation

$$\text{emf} = RT/4F \ln [P_{\text{O}_2}(1 \text{ atm O}_2)/P_{\text{O}_2}(\text{CO}_2 + \text{H}_2)]$$

where R , T , and F are the gas constant, absolute temperature, and the Faraday constant, respectively, and $P_{\text{O}_2}(\text{CO}_2 + \text{H}_2)$ and $P_{\text{O}_2}(1 \text{ atm O}_2)$ are oxygen fugacities in both electrodes. The transference number of oxygen ion(II) in the solid electrolyte was reasonably assumed to be unity in the present experimental conditions (16). A potentiometer (Yokogawa Company, Type 2722) was employed for emf measurement.

The gas mixer was similar to that described by Johnston and Walker (17) and Darken and Gurry (1). Two capillaries for CO₂ and H₂ were both calibrated at 0°C in the water-ice system and were maintained all through the experiment at the same temperature in order to avoid any fluctuation of mixing ratio caused by variation of the room temperature.

The oxygen fugacity calculated from thermochemical data for the gases (18) was compared with the one determined by the galvanic cell described above, and the two values were in agreement with each other within ± 0.02 (about $\pm 0.2\%$) above 1100°C and ± 0.03 (about $\pm 0.25\%$) at 1100°C in terms of long P_{O_2} over the whole range of the mixing ratio.

Between the furnace and the balance, there were a marble plate (about 40 mm in thickness) and a water-cooled brass plate in order to shield the heat from the furnace and inhibit convection of air which caused experimental error in weight measurement.

Materials.—High purity grade of Fe₂O₃ powder (99.9%, Kojundo Kagaku Kenkyusho Company) was employed for all starting materials. In addition, Specpure grade of Fe₂O₃ powder (Johnson Matthey Chemicals Limited, detected impurity Mg: 1 ppm) was employed at 1200° and 1300°C. The results obtained from these two materials, however, were in agreement with each other within experimental error.

Commercial high purity grade of hydrogen and carbon dioxide gas (99.99%) which had been purified by passing it over a copper-containing catalyst at 180°C were employed to control the oxygen fugacity in the furnace. Both gases were mixed to the desired ratios by using the gas mixer. After drying over phosphorus pentoxide powder, the mixture was supplied to the furnace.

Procedure.—About 6g of Fe₂O₃ were sintered around a high purity grade thin alumina rod (30 mm in length, 2 mm in diameter, Degussa Company) in a Pt crucible at 1200°C in air. Instead of using a crucible, every sample was suspended in the furnace together with the galvanic cell and the thermocouple so that they might be situated in the even temperature region as close as possible but not in contact with each other, as illustrated in Fig. 1. Since the contact area of iron oxide and the alumina rod was very small, the chemical reaction between two materials could be ignored. Actually, no detectable change was observed in the weight of the alumina rod measured before and after the experimental run. The sample weight was measured immediately after the gas flow in the furnace was stopped, before the oxygen fugacity in the furnace was affected by the effect of thermal diffusion (1).

The experiment was performed in the temperature range of 1100°-1300°C. Since vaporization of the sample could not be ignored at these higher temperatures, correction for the vaporization was indispensable for determining the composition of the wustite phase. For this correction, the weight of the sample under a fixed atmosphere (we selected the CO₂/H₂ mixing ratio of 2.0 at every temperature) was measured every 100 min in the course of each run. Total weight loss by vaporization went up to about 0.12% of the sample weight, at 1250°C for instance. An approximately linear relationship between the weight of the sample at CO₂/H₂ = 2.0 and the time was obtained as shown in Fig. 2. From this experimental relationship, we could correct the composition of the

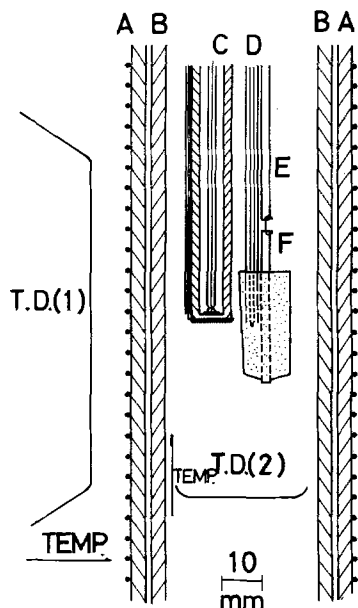


Fig. 1. The schematic diagram of the furnace. A, Al_2O_3 outer tube (Degussa Company, Al-23); B, Al_2O_3 inner tube (Al-23); C, the galvanic cell; D, the thermocouple; E, Al_2O_3 rod (Al-23); F, the sample. "T.D. (1)" and "T.D. (2)" mean the temperature distribution of vertical and radial direction of the furnace, respectively.

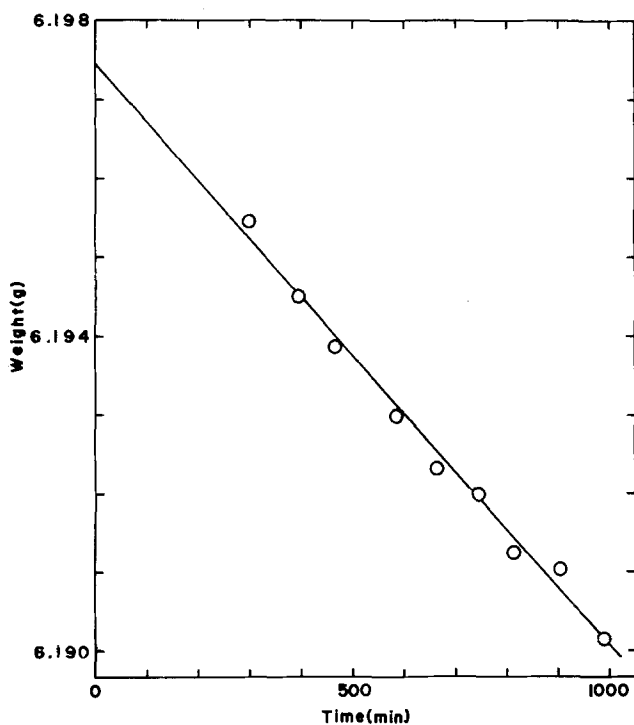


Fig. 2. The decrease in the weight of the sample at $\text{CO}_2/\text{H}_2 = 2.0$ by vaporization in the course of the experimental run at 1250°C .

wustite phase for vaporization by recording the time at which the weight of the sample was measured. The correction for the buoyancy with the mixed gas in the furnace was also performed but was not so large.

At 1200°C , the experiment was performed three times (twice with 99.9% starting material and once with Specpure material) and the standard deviation was less than 0.0006 for every x value in FeO_x .

Results and Discussion

The relationships between $\log P_{\text{O}_2}$ and x in FeO_x .—The relationships between $\log P_{\text{O}_2}$ and x in FeO_x in the temperature range of 1100°C – 1300°C are shown in Fig. 3. Each set of isothermal data was at first

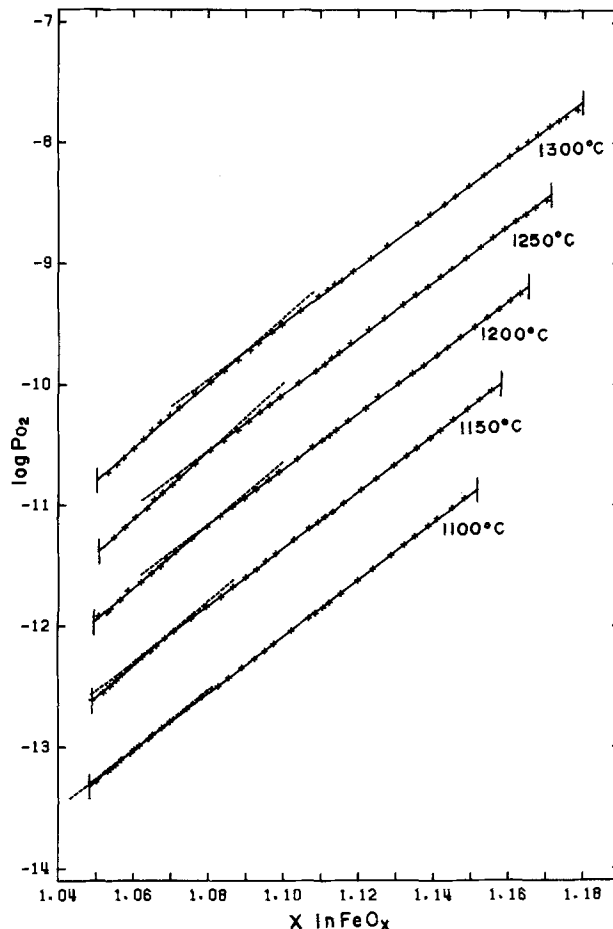


Fig. 3. The relationship between the $\log P_{\text{O}_2}$ and x in FeO_x . The intersecting lines indicate Eq. [2] and [3] in the text.

approximated by following one linear function

$$\log P_{\text{O}_2} = Mx + B \quad [1]$$

where M and B are constants. However, the difference plots, one of which is shown in Fig. 4, reveal that

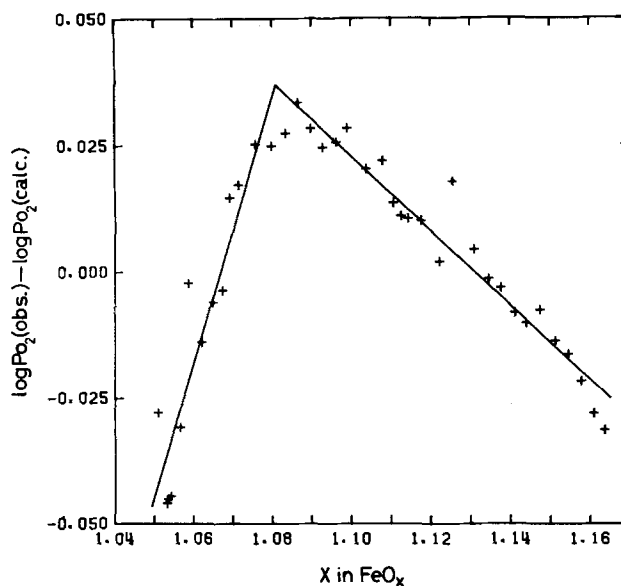


Fig. 4. The difference plot for the data obtained at 1200°C . Calculated oxygen fugacity is based on the following one linear equation (Eq. [1] in the text)

$$\log P_{\text{O}_2} = 23.875x - 36.998$$

The lines indicate the difference value of [$\log P_{\text{O}_2}$ (from Eq. [2] or [3]) – $\log P_{\text{O}_2}$ (from Eq. [1])].

Table I. Analysis of data for $\log P_{O_2}$ vs. x in FeO_x

T (°C)	M_1	B_1	M_2	B_2	X_1^*	$\sigma^\dagger \times 10^3$	M^\ddagger	B^\ddagger
1100	25.327	-39.897	23.656	-38.121	1.0629	4.9	23.772	-38.242
1150	26.792	-40.744	23.659	-37.397	1.0684	4.7	—	—
1200	26.528	-39.829	23.133	-36.158	1.0814	6.8	24.155	-37.298
1250	28.512	-41.366	23.288	-35.715	1.0818	7.0	—	—
1300	27.106	-39.284	23.028	-34.839	1.0898	10.5	24.491	-36.437

* x at intersecting point.† Mean standard deviation of $\log P_{O_2}$.

‡ The values of Giddings and Gordon (3).

this approximation is not appropriate except for the data obtained at 1100°C. The values of $[\log P_{O_2}(\text{obs.}) - \log P_{O_2}(\text{calc.})]$ are not distributed randomly around zero, but vary with a certain tendency indicating that the slope of $\log P_{O_2}$ vs. x changes abruptly near $x = 1.08$. The following two intersecting straight lines were therefore adopted to fit the data in the more oxygen-rich and the less oxygen-rich regions, respectively

$$\log P_{O_2} = M_1x + B_1 \quad [2]$$

$$\log P_{O_2} = M_2x + B_2 \quad [3]$$

where M_1 , M_2 , B_1 , and B_2 are constants. These four values were calculated simultaneously by the least squares method, so that the lines might be the best fit for the whole isothermal data. The intersecting lines are drawn in Fig. 3 and 4, and the values of the parameters are listed in Table I. One of the difference plots from the intersecting lines is shown in Fig. 5. These figures indicate clearly that two intersecting straight lines are a better fit than one straight line.

The most important conclusion derived from the facts described above is that the first derivative of the thermodynamic function, namely, $d(\log P_{O_2})/dx$ or $d\Delta\bar{G}_o/dx$ ($\Delta\bar{G}_o$ represents the relative free energy of oxygen in wustite phase), is not a smooth function of x ; there is an abrupt change of it near the intersecting point calculated above. This suggests the existence of a second or possibly higher order transition in the wustite phase.

Giddings and Gordon (3) presented a review of the available data on the wustite phase obtained by thermogravimetry and the galvanic cell method and

concluded that the relation between $\log P_{O_2}$ and x was linear with no breaking point to suggest any phase transitions. Their M and B values are intermediate between M_1 and M_2 or B_1 and B_2 values of the present work as shown in Table I. In order to test their assertion, a few data at 1200°C (6, 19, 20) are replotted together with our own data in Fig. 6. (Since almost all the relationships between $\log P_{O_2}$ and x were illustrated in the figures instead of being tabulated, we could not explicitly refer to the data, except a few.) The composite data scatter so widely around the present ones, that it is impossible to conclude definitely whether the relation is linear or not. In the difference plot for the composite data (Fig. 7), however, the data of Bransky and Hed (20) show, though not clearly because of wide scattering, a tendency similar to that shown in Fig. 4. The other two sets of data (6, 19) have too few experimental points to discuss in this respect.

It seems that the data quoted by Giddings and Gordon are in themselves not adequate to conclude definitely whether a breaking point is present or not.

Some physical properties of the wustite phase such as electrical conductivity, Seebeck coefficient (21-24), and work function (25) have been reported and in these physical properties, the change in the sign of the Seebeck coefficient, which means p-to-n transition, is remarkable. This p-to-n transition is situated in the middle of the wustite phase field where the subphase boundary determined in the present work exists at higher temperature (see Fig. 8).

Phase diagram of the wustite region.—The phase boundaries of iron and wustite and wustite and magnetite are in good agreement with those of Darken and Gurry (1) as shown in Fig. 8. The subphase

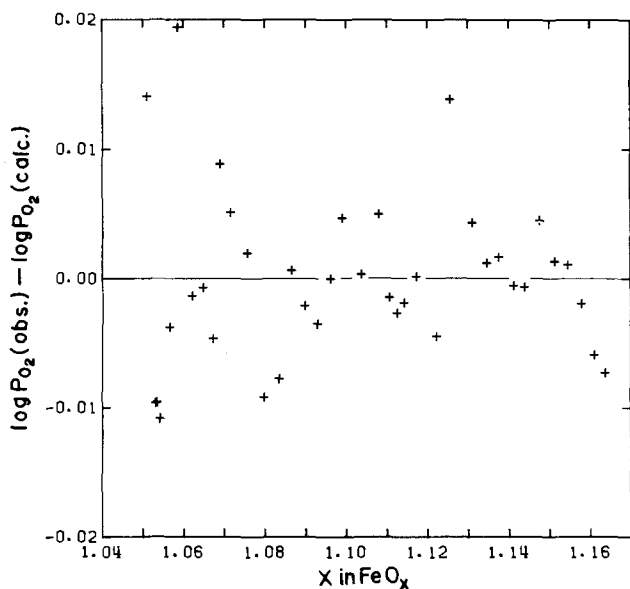


Fig. 5. The difference plot for the data obtained at 1200°C. Calculated oxygen fugacity is based on Eq. [2] and [3] in the text.

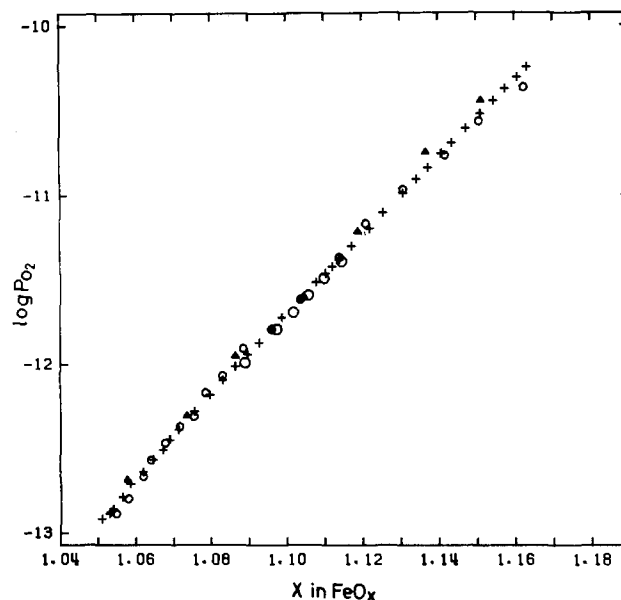


Fig. 6. The replotted data of $\log P_{O_2}$ vs. x in FeO_x at 1200°C. +, Present work; ▲, Ref. (6); ○, Ref. (19); ○, Ref. (20).

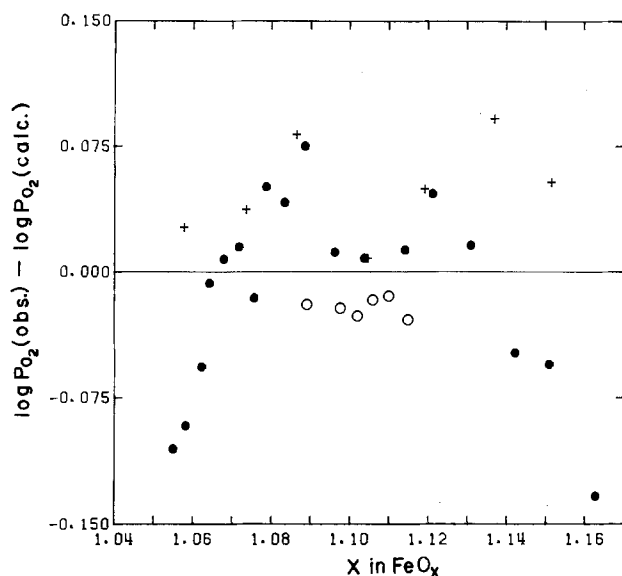


Fig. 7. The difference plot for the composite data at 1200°C. Calculated oxygen fugacity is based on the following linear equation

$$\log P_{O_2} = 23.793x - 36.895$$

which was fitted for the three sets of data by least squares method. +, Ref. (6); O, Ref. (19); ●, Ref. (20).

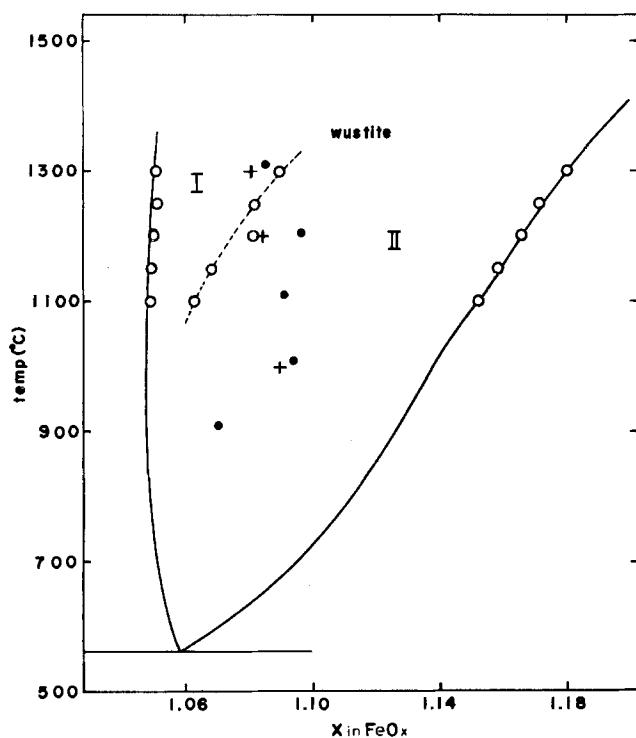


Fig. 8. The phase diagram of wustite. —, After Darken and Gurry (1); - - - - and O, subphase boundary and experimental points in the present work; + and ●, p-to-n transition after Ref. (23) and Ref. (24), respectively.

boundary obtained in this work is shown with a dotted line and apparently disagrees with that of Vallet and Raccach (5, 6) and Kleman (7) or Fender and Riley (8) (see Fig. 9).

The basis of Vallet and Raccach and Kleman for suggesting the three subphases is abrupt changes of the average slopes of $\log P_{O_2}$ vs. x with reciprocal of the absolute temperature. Their "semiempirical" analysis, however, does not seem to be appropriate. They detected no breaking point in the isothermal line of $\log P_{O_2}$ vs. x above 900°C. In spite of this, they calculated x values of the subphase boundaries

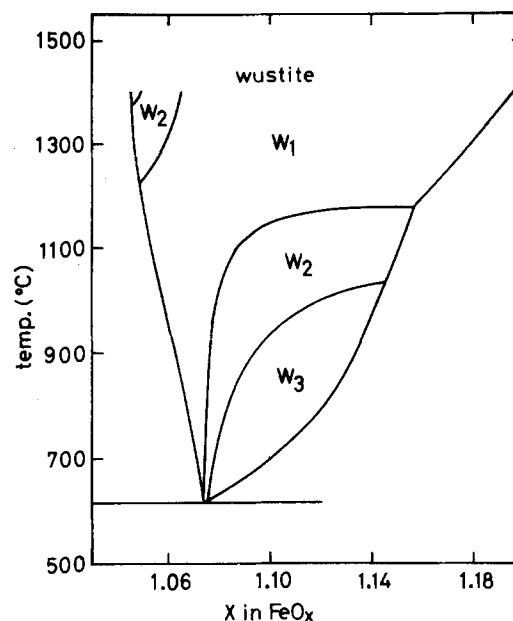


Fig. 9. The phase diagram of wustite after Vallet and Raccach (5)

by using the average slopes of $\log P_{O_2}$ vs. x , spanning a range of compositions across the subphase boundaries which would be determined as a result of their calculation. Similarly, the data of Fender and Riley do not seem to be reasonable because of experimental errors, mainly oxygen permeation through the electrolyte as already pointed out by Giddings and Gordon (10). Actually, the phase boundary between wustite and magnetite reported by them (8) is greatly different from that of the present work or Darken and Gurry (1).

Thermodynamic functions.—The relative partial entropies ($\Delta\bar{S}_o$) and enthalpies ($\Delta\bar{H}_o$) of oxygen in the wustite phase were calculated from the following equations

$$\Delta\bar{G}_o = 1/2 RT \ln P_{O_2} = (2.3026/2)$$

$$RT[M_1(M_2)x + B_1(B_2)]$$

$$\Delta\bar{G}_o = \Delta\bar{H}_o - T\Delta\bar{S}_o$$

by using the least squares method. The calculated values are indicated in Table II in which three values of $\Delta\bar{S}_o$ and $\Delta\bar{H}_o$ are given for $x = 1.07$ and 1.08 at which the isocomposition line traverses the subphase boundary, that is, the mean value spanning the two

Table II. Relative partial molar entropy and enthalpy of oxygen in wustite phase

x	$\Delta\bar{H}_o$ (cal/mole)	$\Delta\bar{S}_o$ (cal/mole · deg)
1.06	-61,330 ± 556*	-14.83 ± 0.38
1.07	-62,120 ± 479	-15.97 ± 0.32
	(-61,842 ± 437) ‡	(-15.79 ± 0.30)
	[-64,335 ± 252] ‡	[-17.56 ± 0.17]
1.08	-63,272 ± 405	-17.35 ± 0.27
	(-62,353 ± 487)	(-16.75 ± 0.33)
	[-64,173 ± 228]	[-17.99 ± 0.15]
1.09	-64,013 ± 213	-18.41 ± 0.14
1.10	-63,853 ± 210	-18.84 ± 0.14
1.11	-63,690 ± 218	-19.26 ± 0.15
1.12	-63,531 ± 238	-19.69 ± 0.16
1.13	-63,369 ± 265	-20.11 ± 0.18
1.14	-63,211 ± 299	-20.54 ± 0.20

* Errors are indicated by mean standard deviation.

‡ At $x = 1.07$ and 1.08 , the values parenthesized with () and [] were calculated from Eq. [2] and Eq. [3], respectively, and the other was the mean value spanning the subphases (see the explanation in the text).

subphases obtained from Eq. [2] and [3], the value from only Eq. [2], and the value from only Eq. [3].

Since oxygen atoms in the wustite phase form an almost perfect anion sublattice (26), the change of $\Delta\bar{S}_0$ with x is mainly contributed from the change of the vibrational state of the oxygen sublattice. Moreover, since the lattice parameter of the wustite diminishes linearly with increasing x (15), the vibrational entropy of the oxygen sublattice is thought to have a tendency to decrease with increasing x .

In the present data, the $\Delta\bar{S}_0$ value decreases not smoothly with increasing x , but in the oxygen richer region, the slope of $\Delta\bar{S}_0$ vs. x becomes smaller than that in the iron richer region. This seems to suggest a structural change of the oxygen sublattice near the breaking point. Similarly, the $\Delta\bar{H}_0$ value does not decrease monotonically with x but has a minimum point. This tendency is in agreement with the data of Darken and Gurry (1), but not in agreement with that of Giddings and Gordon (3). All these facts support the presence of a second or possibly higher order transition in the wustite phase field.

The partial molar free energies ($\Delta\bar{G}_f^\circ$), entropies ($\Delta\bar{S}_f^\circ$), and enthalpies ($\Delta\bar{H}_f^\circ$) of formation of the wustite phase were calculated from the following equations

$$\Delta\bar{G}_f^\circ(\text{FeO}_x) = \Delta\bar{G}_f^\circ(\text{FeO}_{x_0}) + 1/2 RT \int_{x_0}^x \ln P_{\text{O}_2} dx$$

$$\Delta\bar{G}_f^\circ = \Delta\bar{H}_f^\circ - T\Delta\bar{S}_f^\circ$$

where $\Delta\bar{G}_f^\circ(\text{FeO}_{x_0})$ represents the formation free energy of the wustite in equilibrium with iron which was calculated from the equilibrium oxygen fugacity at the phase boundary of wustite and iron. The $\Delta\bar{G}_f^\circ$ values are shown in Fig. 10, and the $\Delta\bar{S}_f^\circ$ and $\Delta\bar{H}_f^\circ$ values are shown in Table III.

Since these values are integrated ones, no abrupt changes with x are detected. The values are in good agreement with those of Darken and Gurry (1) and Giddings and Gordon (3).

Summary

The detailed relationships between the oxygen fugacity and the composition of wustite phase were determined on the basis of thermogravimetry in the temperature range of 1100°-1300°C. There exists a breaking point in every isothermal line of $\log P_{\text{O}_2}$ vs. x in FeO_x , and each side of this point, the relation-

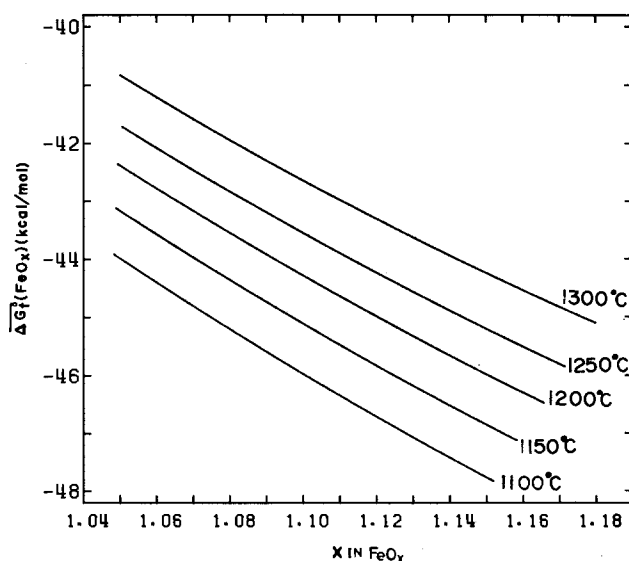


Fig. 10. Formation free energy of wustite

Table III. Partial molar entropy and enthalpy of formation of wustite phase

x	$\Delta\bar{H}_f^\circ$ (cal/mole-FeO _x)	$\Delta\bar{S}_f^\circ$ (cal/mole-FeO _x · deg)
1.06	-65,925 ± 408*	-15.72 ± 0.28
1.07	-66,541 ± 412	-15.87 ± 0.28
1.08	-67,169 ± 415	-16.04 ± 0.28
1.09	-67,804 ± 415	-16.22 ± 0.28
1.10	-68,446 ± 417	-16.40 ± 0.28
1.11	-69,083 ± 419	-16.59 ± 0.28
1.12	-69,719 ± 420	-16.79 ± 0.29
1.13	-70,353 ± 422	-16.99 ± 0.29
1.14	-70,986 ± 423	-17.19 ± 0.29

* Errors are indicated by the mean standard deviation.

ship can be represented by a linear equation. The existence of the breaking point indicates a second or possibly higher order transition in the wustite phase. Some thermodynamic functions were determined and in these functions, the relative partial entropies and enthalpies of oxygen in wustite phase do not change smoothly with the composition, supporting the transition described above.

Acknowledgment

The present authors express their sincere thanks to Mr. K. Hirota for his technical advice and Dr. K. Kato for his helpful encouragement through this study.

Manuscript submitted April 10, 1979; revised manuscript received Nov. 5, 1979.

Any discussion of this paper will appear in a Discussion Section to be published in the December 1980 JOURNAL. All discussions for the December 1980 Discussion Section should be submitted by Aug. 1, 1980.

Publication costs of this article were assisted by the National Institute for Researchers in Inorganic Materials.

REFERENCES

1. L. S. Darken and R. W. Gurry, *J. Am. Chem. Soc.*, **67**, 1398 (1945).
2. L. S. Darken and R. W. Gurry, *ibid.*, **68**, 798 (1946).
3. R. A. Giddings and R. S. Gordon, *J. Am. Ceram. Soc.*, **56**, 111 (1973).
4. P. J. Spencer and O. Kubaschewski, *CALPHAD*, **2**, 147 (1978).
5. P. Vallet and P. Raccach, *Compt. Rend.*, **258**, 3679 (1964).
6. P. Vallet and P. Raccach, *Mem. Sci. Rev. Met.*, **62**, 1 (1965).
7. M. Kleman, *ibid.*, **62**, 457 (1965).
8. B. E. F. Fender and F. D. Riley, *J. Phys. Chem. Solids*, **30**, 793 (1969).
9. C. Carel and J. R. Gavarri, *Mater. Res. Bull.*, **11**, 745 (1976).
10. R. A. Giddings and R. S. Gordon, *This Journal*, **121**, 793 (1974).
11. M. Hayakawa, J. B. Wagner, Jr., and J. B. Cohen, *Mater. Res. Bull.*, **12**, 429 (1977).
12. J. R. Gavarri, D. Weigel, and C. Carel, *ibid.*, **11**, 917 (1976).
13. A. K. Cheetham, B. E. F. Fender, and R. I. Taylor, *J. Phys. C*, **4**, 2160 (1971).
14. M. Hayakawa, M. Morinaga, and J. B. Cohen, in "Defects and Transport in Oxides," M. S. Seltzer and R. I. Jaffee, Editors, p. 177, Plenum Press, New York (1974).
15. M. Hayakawa, J. B. Cohen, and T. B. Reed, *J. Am. Ceram. Soc.*, **55**, 160 (1972).
16. M. Sato, in "Research Techniques for High Pressure and High Temperature," G. C. Ulmer, Editor, p. 43, Springer Verlag, New York (1971).
17. J. Johnston and A. C. Walker, *J. Am. Chem. Soc.*, **47**, 1807 (1925).
18. D. R. Stull and H. Prophet, JANAF Thermochemical Tables, 2nd ed., NSRDS-NBS 37, U. S. Govt. Printing Office, Washington, D. C. (1971).
19. B. Swaroop and J. B. Wagner, Jr., *Trans. AIME*, **239**, 1215 (1967).
20. I. Bransky and A. Z. Hed, *J. Am. Ceram. Soc.*, **51**, 231 (1968).

21. D. S. Tannhauser, *J. Phys. Chem. Solids*, **23**, 25 (1962).
 22. G. H. Geiger, R. L. Levin, and J. B. Wagner, Jr., *ibid.*, **27**, 947 (1966).
 23. W. J. Hillegas, Jr. and J. B. Wagner, Jr., *Phys. Lett.*, **25A**, 742 (1967).
 24. I. Bransky and D. S. Tannhauser, *Trans. AIME*, **239**, 75 (1967).
 25. J. Nowotny and I. Sikora, *This Journal*, **125**, 781 (1978).
 26. E. R. Jette and F. Foote, *J. Chem. Phys.*, **1**, 29 (1933).

Technical Notes



Electrical Transport Properties of In and Cu-Doped n-Type Epitaxial Thin PbTe Films

A. L. Dawar,¹ O. P. Taneja,² K. V. Krishna, and P. C. Mathur

Department of Physics and Astrophysics, University of Delhi, Delhi, 110 007, India

The investigation of transport phenomenon in bulk crystalline materials having low resistivity is often difficult because the resistance of the ohmic contacts may be comparable to or even greater than, the resistance of the bulk material. In such cases, thin films are more suitable for studying the electrical properties due to the higher resistance of the films as compared to that of ohmic contacts. The main drawbacks of using thin films for the study of transport phenomenon are a large number of dislocations present in the films, scattering due to intercrystalline grain boundary barrier potential, and the variation of the charge carrier concentration in the film as it grows. The information about these effects can best be obtained by electrical measurements rather than by optical studies.

Lead telluride is a semiconductor in which the mobility of the charge carriers at low temperatures is mainly limited by phonon scattering rather than by impurity scattering (1). The reason that the ionized impurity scattering is very weak in PbTe is that its static dielectric constant is very high (2, 3) and optical phonon frequency is quite low (4, 5).

Considerable work has been done on the nucleation and growth of epitaxial films of lead telluride (6, 7). While the primary tools in these studies have been electron transmission microscopy and diffraction (8, 9), some workers have also used galvanomagnetic properties of the films (10, 11). The galvanomagnetic properties are very sensitive to the degree of perfection of the films and the concentration of the charge carriers. While high mobility epitaxial films of PbTe have been obtained by many of these workers, not much effort has been made to investigate the variation of grain boundary barrier potential and dislocation density as a function of extrinsic carrier concentration and growth conditions.

In the present work, the results of conductivity and Hall mobility measurements on a few n-type epitaxial films of PbTe have been presented. The effect of In and Cu doping on dislocations and grain boundary scattering have been investigated.

Experimental Details

Films, rectangular in shape (22 × 5 mm), were grown by evaporating stoichiometric (99.999%) PbTe

¹ Present address: Defence Science Laboratory, Metcalfe House, Delhi, 110 054, India.

² Present address: Government College, Gurgaon, Haryana, 122 001, India.

Key words: lead telluride, thin film, Hall coefficient, grain boundary.

under a high vacuum better than 5×10^{-6} Torr. Film thicknesses are shown in Table I. Freshly cleaved mica was used as substrate, which was kept at 280°C. The rate of growth of the films was controlled by a quartz crystal thickness monitor (12). After growth the films were cooled to room temperature in about 4 hr. Indium and copper were added to the films by coevaporating through a separate boat. Electron micrographs of the films showed the existence of some voids and cracks and the average grain diameter was found to be ~300Å in all the films. High purity silver was evaporated on the films under a high vacuum for making ohmic contacts. The current contacts were spread over the entire width, while the voltage contacts were only dots ~0.5 mm in diameter. Five probe technique, as described by Putley (13), was used to measure the Hall coefficient R_H and d-c conductivity σ . The ohmic nature of the contacts was verified, throughout the temperature range, by the linearity of the I-V characteristics. The directions of the current and the magnetic fields ($B \approx 5$ kg) were reversed so as to eliminate the errors due to the thermomagnetic effects. Geometrical influence of the films on Hall measurements was avoided as the length to width ratio was greater than four. The sign of the Hall voltage showed that all the films were n-type.

Measurement of the Hall coefficient as a function of temperature was found to be reproducible for three to four runs. The Hall coefficient was found to be independent of the magnetic field and the sample current. The overall maximum error in the Hall mobility ($R_H \times \sigma$) is estimated to be about 5%. A copper block with electrical insulation was used to mount the sample which was further kept in a Dewar flask containing liquid nitrogen. A copper constantan thermocouple,

Table I.

Film	Dopant concentration (atom percent)	Thickness (μm)	μ_c (cm^2/Vsec)	N_D ($10^{19}/\text{cm}^3$) at 300°K
a. Undoped	—	1.2	2725	2.80
b. Undoped	—	0.6	2330	3.31
c. Undoped	—	0.4	1500	4.53
d. Excess of Pb	—	0.4	1200	6.03
e. In-doped	1.0	0.4	600	3.96
f. Cu-doped	1.0	0.4	1150	4.28

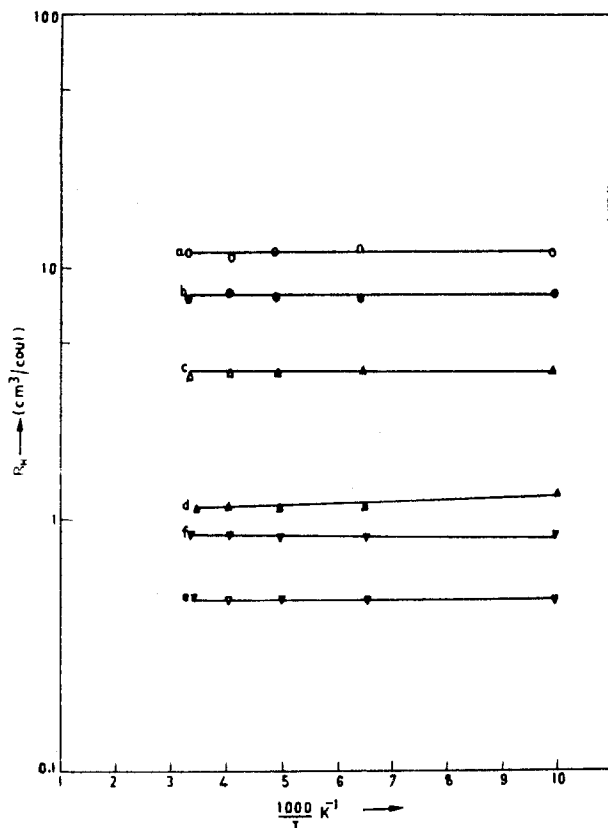


Fig. 1. Variation of Hall coefficient with temperature for PbTe films; (a), 1.2 μm ; (b), 0.6 μm ; (c), 0.4 μm ; (d), 0.4 μm , excess of Pb; (e), 0.4 μm , In-doped; (f), 0.4 μm , Cu-doped.

soldered to the copper block, was used to record the temperature.

Results and Discussion

The observed variation of R_H with temperature ($\log R_H$ vs. $1/T$) for all the films is shown in Fig. 1. It is evident that R_H is practically independent of temperature, which is characteristic of an extrinsic degenerate semiconductor. It is observed that R_H increases with the thickness of the film. The reason for this effect can be formation of an accumulation layer on the surface of the films due to surface states caused by atmospheric oxygen as has been explained by Zemel *et al.* (10). The effect of an accumulation layer, which seems to act as a donor source, will be relatively more significant for thinner films which further explains the observed increase of R_H with the thickness of the films. The value of R_H is found to decrease with the addition of In and Cu but the decrease in R_H is more significant in the case of In. This shows that In impurities in PbTe act as donors. It may be mentioned here that In in PbTe is known to form deep impurity states (14). However, it is also an observed fact that irrespective of the concentration of In, the Hall density of electrons in bulk does not exceed a few units of 10^{18} cm^{-3} (15, 16).

As explained by Rosenberg *et al.* (17), this is due to the fact that a substantial fraction of indium atoms in PbTe enter the octahedral and tetrahedral interstitials of the Te atom sublattice. The observed decrease of R_H in Cu-doped films can either be as a result of the electrostatic shorting of the Hall field due to Cu filaments incorporated between the PbTe crystallites or due to the donor action of Cu. However the Hall field shorting should also be followed by an increase in the mobility, which has been observed in the present case. Cu has less donor electrons per atom than In and therefore the relative effect of In and Cu on R_H is understandable.

The variation of the observed Hall mobility ($R_H \times \sigma$) with temperature for all the films is shown in

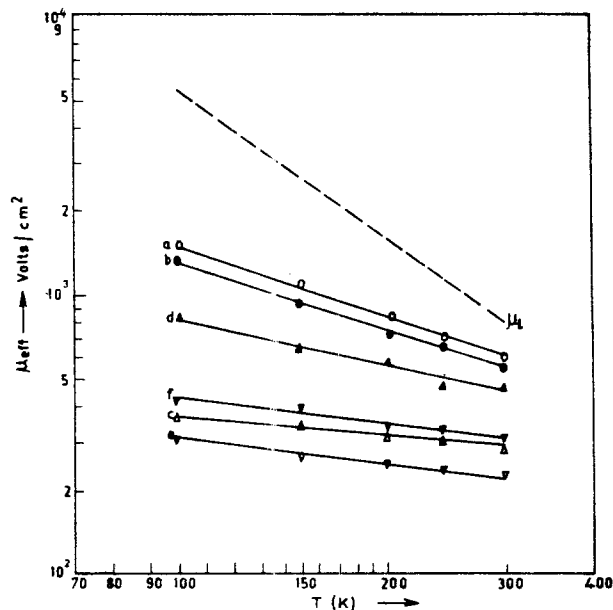


Fig. 2. Variation of observed Hall mobility, with temperature. The dotted line shows the bulk mobility. (a), 1.2 μm ; (b), 0.6 μm ; (c), 0.4 μm ; (d), 0.4 μm , excess of Pb; (e), 0.4 μm , In-doped; (f), 0.4 μm , Cu-doped.

Fig. 2. The mobility for all the films is found to decrease with the increase of temperature but the rate of decrease of mobility with temperature becomes weaker with increase of carrier concentration in the films. This shows the predominance of some scattering mechanism in which the mobility increases with the temperature as the carrier concentration in the film increases. These scatterings can be due to the presence of intercrystalline grain boundaries, which are well founded for lead chalcogenides films (10). The contribution of grain boundary scattering is independent of temperature for a degenerate material and the corresponding mobility μ_c for the process is given by

$$\mu_c = \frac{2q}{h} X_c \left(\frac{3n}{\pi} \right)^{-1/3} \quad [1]$$

where X_c is the mean crystallite size, n is the carrier concentration, q is the electronic charge, and h is Planck's constant. In the present work X_c has been determined by electron diffraction micrographs and the calculated values of μ_c using Eq. [1] are shown in Table I.

Using these values of μ_c , the values of μ_D , the mobility (caused by point defects such as vacancies and interstitials) limited by dislocation scattering has been calculated by the well-known relation

$$\frac{1}{\mu_B} = \frac{1}{\mu_i} + \frac{1}{\mu_D} + \frac{1}{\mu_c} \quad [2]$$

where μ_B is the observed mobility and μ_i is the mobility for the bulk material. The data for μ_i has been taken from Zemel *et al.* (10). The calculated values of μ_D as a function of temperature are shown in Fig. 3 for all the films. It is observed that the contribution due to dislocation scattering increases with decrease of the film thickness. It is further observed that the contribution of dislocation scattering also increases with increase of the charge concentration in PbTe films. On the other hand, the addition of In results in significant decrease in the dislocation density. This shows that the dislocation density is very sensitive to the clusters of Pb vacancies, which are filled up by In. While addition of Cu also results in a decrease in the dislocation density, the effect is not as significant as it is in the case of In. A probable reason for this effect is that since the atomic radius of Cu is much less than that of Pb,

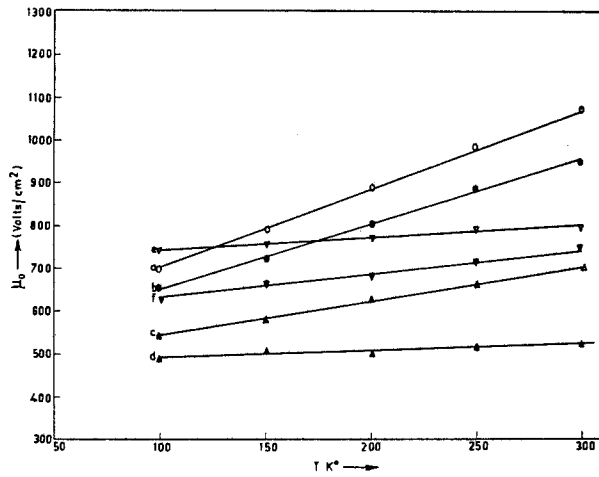


Fig. 3. Calculated values of μ_D as a function of temperature. (a), 1.2 μm ; (b), 0.6 μm ; (c), 0.4 μm ; (d), 0.4 μm , excess of Pb; (e), 0.4 μm ; In-doped; (f), 0.4 μm , Cu-doped.

the probability of a Cu atom filling the Pb vacancy is comparatively smaller.

The dislocation density N_D , calculated from the mobility data at 300°K is shown in Table I. The calculations for N_D have been made as follows.

The mobility μ_D due to dislocation scattering is expressed as

$$\mu_D = (q/m^*)\tau_D \quad [3]$$

where τ_D is the relaxation time and m^* is the effective mass of the charge carriers. The value of τ_D is given by (19)

$$\tau_D = \frac{32}{3\pi} \left(\frac{1-\nu}{1-2\nu} \right)^2 \frac{KT/q}{\epsilon^2 \lambda^2 N_D} \quad [4]$$

where ϵ is the energy (20) associated with the dislocations and its value is calculated from the temperature dependence of the effective mass bandgap and volume expansion coefficient of PbTe (21); n is the electron density, λ is the unit crystallographic slip distance (22), and ν is the Poisson's ratio.

Using Eq. [3] and [4], the value of N_D is given by

$$N_D = \frac{32}{3\pi} \left(\frac{1-\nu}{1-2\nu} \right)^2 \frac{KT/q}{\epsilon^2 \lambda^2 \mu_D m^*} \quad [5]$$

The values of μ_D obtained from Fig. 3 were used to calculate the values of N_D . It is observed from Table I that the value of N_D increases as the carrier concentra-

tion in pure PbTe films increases with the addition of In or Cu into the films. The effect of In in reducing the dislocations density is far more pronounced than the effect of Cu. This suggests that the main cause of dislocations in the PbTe lattice is the defect aggregation of Pb vacancies developed during the growth of the films.

Manuscript submitted May 3, 1979; revised manuscript received Sept. 6, 1979.

Any discussion of this paper will appear in a Discussion Section to be published in the December 1980 JOURNAL. All discussions for the December 1980 Discussion Section should be submitted by Aug. 1, 1980.

REFERENCES

- R. S. Allgaier and W. W. Scanlar, *Phys. Rev.*, **111**, 1029 (1958).
- A. K. Walton and T. S. Moss, *Proc. Phys. Soc. (London)* **81**, 509 (1963).
- Y. Kanai and K. Schohno, *J. Appl. Phys. Jpn.*, **2**, 6 (1964).
- R. N. Hall and J. H. Racette, *J. Appl. Phys.*, **32**, 2078 (1961).
- W. Cochran, *Phys. Lett.*, **13**, 193 (1964).
- S. A. Semile and I. P. Voronia, *Sov. Phys. Dokl.*, (Engl. Transl.), **8**, 960 (1964).
- J. W. Matthews, *Philos. Mag.*, **8**, 711 (1963).
- R. B. Schoolar and J. N. Zemel, *J. Appl. Phys.*, **35**, 1848 (1964).
- L. S. Palatnik, V. K. Sorokin, and M. V. Lebedeva, *Sov. Phys. Solid State* (Engl. Transl.), **7**, 1374 (1965).
- J. N. Zemel, J. D. Jenson, and R. B. Schoolar, *Phys. Rev. A*, **140**, 330 (1965).
- H. Gobrecht, K. E. Boeters, and H. J. Fleischer, *Z. Phys.*, **187**, 232 (1965).
- J. I. Lee, *J. Phys. E*, **10**, 161 (1977).
- E. H. Putley, "The Hall Coefficient and Semiconductor Physics," p. 42, Dover Publications Inc., New York (1968).
- A. A. Averkin, V. I. Kaidanov, and R. B. Mel'nik, *Sov. Phys. Semicond.*, **5**, 175 (1971).
- A. J. Rosenberg and G. Wald, *J. Phys. Chem. Solids*, **26**, 1079 (1961).
- E. Niehus and H. Nieke, *Ann. Phys. (Leipzig)*, **17**, 77 (1966).
- A. J. Rosenberg, R. Grierson, J. C. Wooley, and P. Nicolic, *Trans. AIME*, **230**, 342 (1964).
- M. Green, "Solid State Surface Science," Vol. I, p. 358, Marcel Dekker Inc., New York (1969).
- H. H. Wieder, *Solid State Electron.*, **9**, 3737 (1966).
- H. Ehrnreich, *Phys. Chem. Solids*, **2**, 131 (1957).
- L. J. Gaicoletto, "Electronic Designers Handbook," McGraw-Hill Co., New York (1977).
- W. B. Pearson, "Handbook of Lattice Spacings and Structure of Metals and Alloys," Pergamon Press, New York (1977).

A Simple Luminescence Experiment Suggesting Rare Earth Ion Pairing in the Fluorite Structure

G. Blasse and G. J. Dirksen

Physical Laboratory, State University, 3508 TA Utrecht, The Netherlands

It is well known that the luminescence of the Sm^{3+} ion is quenched by cross relaxation in Sm^{3+} pairs ($^4\text{G}_{5/2} \rightarrow ^6\text{F}_{9/2}$ and $^6\text{H}_{5/2} \rightarrow ^6\text{F}_{9/2}$) (1). It has been shown that the maximum intensity of the $^4\text{G}_{5/2}$ luminescence occurs at roughly the same Sm^{3+} concentration in a large number of oxide host lattices, viz., one Sm^{3+} ion per 4600A^3 . We have used this property to demonstrate trivalent rare earth ion clustering in the fluorite lattice (2).

Key words: inorganic, ultraviolet, photoluminescence.

We prepared two series of samples, viz., $\text{NaY}_{1-x}\text{Sm}_x\text{F}_4$ and $\text{Ca}_{1-x}\text{Sm}_x\text{F}_{2+x}$ with $0.01 \leq x \leq 0.08$. In the former the Sm^{3+} ion replaces the Y^{3+} ion substitutionally. We assume that this occurs statistically, since there is not any reason for the opposite in view of the similarity between both ions. These samples show the red Sm^{3+} luminescence from the $^4\text{G}_{5/2}$ level with a maximum intensity at about $x = 0.02$. The compound NaYF_4 has a hexagonal crystal structure (3). From the crystallographic parameters ($a = 5.967$ and $c = 3.523\text{A}$

and $Z = 3/2$) it is found that $x = 0.02$ corresponds roughly with one Sm^{3+} ion per 4000\AA^3 . This is reasonably in line with the results of Van Uitert and Johnson. Our results are not accurate enough to conclude that the Sm^{3+} - Sm^{3+} interaction in fluorides is somewhat weaker than in oxides which were used in the earlier work. These results are consistent with our assumption that the Sm^{3+} ions are randomly distributed among the Y^{3+} sublattice. The value of x was obtained at room temperature, but is not strikingly different at lower temperatures.

Let us now turn to the fluorite samples $\text{Ca}_{1-x}\text{Sm}_x\text{F}_{2+x}$. In view of the sample preparation we may exclude the presence of considerable amounts of oxygen in the lattice. None of these samples showed any Sm^{3+} luminescence at all, independent of the sample temperature. In view of the model developed by Van Uitert and Johnson this suggests that the Sm^{3+} ions occur for the greater part as pairs or even more complicated clusters. There is no obvious reason why an isolated Sm^{3+} ion should not luminescence in this lattice. The absence of luminescence is, therefore, ascribed to cross relaxation in the Sm^{3+} pairs.

Clustering of trivalent rare earth ions in the fluorite lattice has been demonstrated earlier by spectroscopical techniques (4, 5); but none of these was so simple as the present one. Finally it is interesting to note that Andeen *et al.* (6) have found from complex dielectric constant measurements that in Sm^{3+} -doped fluorite samples with x as low as 0.001 cluster formation already occurs.

Experimental

Samples $\text{NaY}_{1-x}\text{Sm}_x\text{F}_4$ were prepared by heating NaF and (Y, Sm) F_3 together with NH_4F . The mixed trifluoride was precipitated from aqueous solution with HF and dried thoroughly. Samples $\text{Ca}_{1-x}\text{Sm}_x\text{F}_{2+x}$ were

prepared by heating mixtures of CaCO_3 and Sm_2O_3 together with a large excess of NH_4F . All samples were checked by x-ray analysis. If the fluorite samples were heated in air without excess of NH_4F , they showed bright yellowish luminescence under short wavelength ultraviolet excitation. This emission reminds one of that emission in BaFCl which was ascribed to oxygen on fluorine sites (7).

Acknowledgment

The authors are indebted to Dr. J. Schoonman for instructive discussions on the rare earth ion clusters in the fluorite-lattice.

Manuscript submitted Oct. 3, 1979; revised manuscript received Nov. 5, 1979.

Any discussion of this paper will appear in a Discussion Section to be published in the December 1980 JOURNAL. All discussions for the December 1980 Discussion Section should be submitted by Aug. 1, 1980.

Publication costs of this article were assisted by State University.

REFERENCES

1. L. G. van Uitert and L. F. Johnson, *J. Chem. Phys.*, **44**, 3514 (1966).
2. See, *e.g.*, K. E. D. Wapenaar and J. Schoonman, *This Journal*, **126**, 667 (1979).
3. O. Muller and R. Roy, "The Major Ternary Structural Families," Springer Verlag, Berlin (1974).
4. D. R. Talland, D. S. Moore, and J. C. Wright, *J. Chem. Phys.*, **67**, 2897 (1977).
5. J. Kliava, P. Evesque, and J. Duran, *J. Phys. C.*, **11**, 3357 (1978).
6. C. Andeen, D. Link, and J. Fontanella, *Phys. Rev. B*, **16**, 3762 (1977).
7. G. P. M. van den Heuvel, G. Blasse, and J. Schoonman, *Solid State Commun.*, **28**, 689 (1978).

Standardized Terminology for Oxide Charges Associated with Thermally Oxidized Silicon

Bruce E. Deal*

Fairchild Camera and Instrument Corporation, Research and Development Laboratory, Palo Alto, California 94304

MOS transistors were first produced on a commercial basis in the 1963-1964 time period. At the same time various charges associated with the thermally oxidized silicon structure were observed to cause serious yield and reliability problems. Subsequently a number of investigations concerned with oxide charges were started in various laboratories and many have continued to the present time (1). Initially most of the studies were designed to determine the dependence of charge densities on processing parameters so that their adverse effects on device properties could be minimized. More recently efforts have focused on a quantitative understanding of the densities, cross sections, and the nature of oxide charges and traps so that ultimate device performance might be achieved.

During the past 15 years or so, it has been generally established that four general types of charges are associated with the Si-SiO₂ system (2, 3). However, no common set of symbols has been used to designate these four types of charges. This has caused substantial confusion and disagreement during discussions at technical meetings and in interpretation of the large number of publications in the area of semiconductor passivation. This was emphasized by a survey undertaken by the author in 1976 (4).

Because of the lack of a common terminology for oxide charges, a committee was established in January 1978 by the Electronics Division of the Electrochemical Society and the IEEE-sponsored Semiconductor Interface Specialists Conference. The names and affiliations of the committee members along with those representing the sponsoring groups are listed below:

Bruce E. Deal (Committee Chairman)	Fairchild Camera and Instrument Corporation Palo Alto, California
W. Murray Bullis	National Bureau of Standards Washington, DC
Sidney R. Butler	Lehigh University Bethlehem, Pennsylvania
Edward H. Nicollian	Bell Laboratories Murray Hill, New Jersey
Donald R. Young	IBM Corporation Yorktown Heights, New York
Arnold Reisman (ECS Electronics Division)	IBM Corporation Yorktown Heights, New York
Al Tasch (IEEE SISC)	Texas Instruments Dallas, Texas

* Electrochemical Society Active Member.
Key words: charge, semiconductor, interface.

Pieter Balk
(Europe representative)

Technischen Hochschule
Aachen
Aachen, West Germany

Takuo Sugano
(Japan representative)

University of Tokyo
Tokyo, Japan

The committee met over a one and one-half year period, during which time a number of specialists in silicon passivation were solicited for opinions and guidance. This was done by personal contact, discussions at technical meetings, and a detailed survey. Several general preferences regarding a standard terminology for oxide charges were evident. These were:

1. Standardization of oxide charge terminology is highly desirable;
2. Such a terminology system should be as simple as possible, i.e., subscripts for symbols should be one letter if possible;
3. The symbols and subscripts should indicate or suggest the nature of the charge type;
4. A symbol representing a given charge should not be easily confused with any of those representing the other charge types;
5. If possible, the symbols selected should not be the same as those used previously by any appreciable segment of semiconductor technologists.

These and other considerations were discussed in considerable detail by the committee. Various sets of symbols were proposed and problems associated with each set were noted. For instance, a symbol subscript which might give rise to confusion would be "i" which stands for both "interface" and "ion." Thus, the single letter "i" should probably not be used as a subscript. Likewise, the use of only "o" or "ox" as subscripts could represent any or all of the charge types and also should not be used.

Finally, at a meeting of the committee in May, 1979, (Spring Meeting of The Electrochemical Society, Boston, Massachusetts) a final terminology was agreed upon. Insofar as practical, the general preferences were observed. Where this turned out not to be possible because of mutually conflicting requirements, the compromise thought to result in the least confusion and ambiguity was selected.

The recommended names for the four types of oxide charges illustrated in Fig. 1 are:

1. Fixed Oxide Charge—Positive charge, due primarily to structural defects (ionized silicon) in the oxide layer less than 25Å from the Si-SiO₂ interface. The density of this charge, whose origin is related to the oxidation process, depends on oxidation ambient and temperature, cooling conditions, and on silicon orientation. Since fixed oxide charge density cannot be

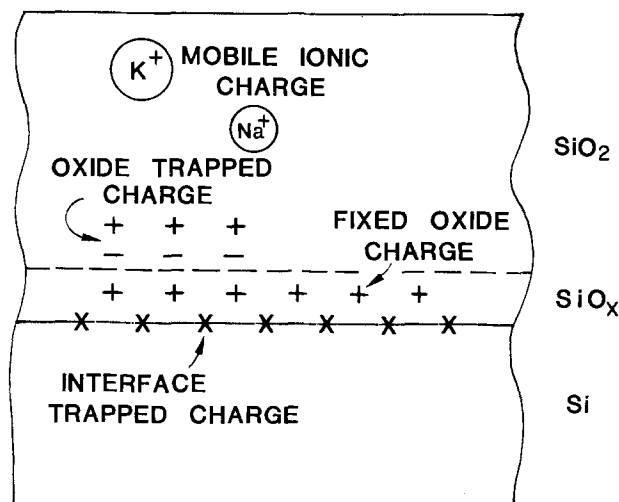


Fig. 1. Names and location of charges in thermally oxidized silicon.

determined unambiguously in the presence of moderate densities of interface trapped charge, it is only measured after a low temperature ($\sim 450^\circ\text{C}$) hydrogen treatment which minimizes interface trap density. Fixed oxide charge is not in electrical communication with the underlying silicon.

2. Mobile Ionic Charge—Primarily due to ionic impurities such as Li⁺, Na⁺, K⁺, and possibly H⁺. Negative ions and heavy metals may contribute to this charge even though they are not mobile below 500°C.

3. Interface Trapped Charge—Positive or negative charges, due to (i) structural, oxidation-induced defects, (ii) metal impurities, or (iii) other defects caused by radiation or similar bond breaking processes. They are located at the Si-SiO₂ interface. Unlike fixed charge or trapped charge, interface trapped charge is in electrical communication with the underlying silicon and can thus be charged or discharged, depending on the surface potential. Most of the interface trapped charge can be neutralized by low temperature (450°C) hydrogen annealing. This charge type in the past has been called surface states, fast states, interface states, etc.

4. Oxide Trapped Charge—May be positive or negative due to holes or electrons trapped in the bulk of the oxide. Trapping may result from ionizing radiation, avalanche injection, or other similar processes. Unlike fixed charge, oxide trapped charge is generally annealed out by low temperature (<500°C) treatment, although neutral traps may remain.

In general, the densities of all of the charges except interface trapped charge may be determined using the high frequency capacitance-voltage (C-V) technique. More elaborate measurement procedures such as "quasistatic C-V analysis" are required for interface trap charge.

The symbols selected to denote the oxide charges were based on the following assumptions:

Q = Net effective charge per unit area at the Si-SiO₂ interface (C/cm²).

N = Net number of charges per unit area at the Si-SiO₂ interface (no/cm²).

Thus, $|Q/q| = N$ where q = electronic charge.

The sign of Q is either positive or negative depending on whether the majority of charge is positive or negative. By definition, however, N is always positive. Also, it should be kept in mind that Q and N are defined as effective net charge at the Si-SiO₂ interface, even though the actual charge density may be considerably larger if the charge is located some distance from that interface. Uncharged trapping centers are not covered by this proposed terminology.

Following are the recommended symbols for the four types of oxide charge:

Fixed Oxide Charge	Q_f, N_f
Mobile Ionic Charge	Q_m, N_m
Interface Trapped Charge	Q_{it}, N_{it}
Oxide Trapped Charge	Q_{ot}, N_{ot}

As indicated above, the charges represented by the above symbols are expressed in terms of density per unit area. In one particular case, that of interface trapped charge, it is common to express its density in terms of unit area and energy in the silicon bandgap. Therefore, a special symbol is recommended:

Interface Trap Density D_{it} (no./cm²-eV)

The committee strongly urges all scientists and engineers active in silicon oxide work to use the above terminology in oral presentations or written publications. It is recognized that after 15 years of using a particular system, some emotional attachment to some particular nomenclature may exist. However, those persons "brought up" on designating fixed oxide charge as Q_{ss} should remember that others have used, just as diligently, the same symbol for interface traps

(or fast states, or surface states, or interface traps, etc.). Likewise, other groups refer to fixed charge as Q_{ox} (or Q_{fc} or N_o or Q_s , etc.). The only way to resolve the difficulties and confusion regarding oxide charge terminology which have persisted for 15 or more years is for everyone to decide that one system should be used and that some compromise in personal feeling on everyone's part will be required.

The author wishes to thank the above named committee members for their valuable assistance during the course of these efforts. Also, considerable thanks are due to many individuals who contributed opinions and suggestions to the committee.

Manuscript received Oct. 26, 1979.

Any discussion of this paper will appear in a Discussion Section to be published in the December 1980

JOURNAL. All discussions for the December 1980 Discussion Section should be submitted by Aug. 1, 1980.

Publication costs of this article were assisted by Fairchild Camera and Instrument Corporation.

REFERENCES

1. A. H. Agajanian, "Semiconductor Devices. A Bibliography of Fabrication Technology, Properties, and Applications," pp. 547-619, Plenum Publishing Corporation, New York (1976).
2. B. E. Deal, *This Journal*, **121**, 188C (1974).
3. Y. C. Cheng, *Prog. Surf. Sci.*, **8**, 181 (1977).
4. B. E. Deal in "Semiconductor Silicon 1977," H. R. Huff and E. Sirtl, Editors, pp. 276-296, The Electrochemical Society Softbound Proceedings Series, Princeton, N.J. (1977).

Anomalous Boron Profiles Produced by BF_2 Implantation into Silicon

T. W. Sigmon*

Stanford Electronics Laboratories, Stanford, California 94305

and V. R. Deline and C. A. Evans, Jr.

Charles Evans and Associates, San Mateo, California 94402

and W. M. Katz

Department of Chemistry and Materials Research Laboratory, University of Illinois, Urbana, Illinois 61801

It is common practice in the production of low sheet resistance, shallow p-type contacts, such as those used for high frequency Si bipolar transistors, to use BF_2 as the implant species. There are several reasons for this approach: (i) to produce a low-energy boron implant distribution while operating at a reasonably high accelerator voltage; (ii) the BF_2 molecule is generally the most abundant beam; and (iii) the critical dose for amorphous layer production is lowered to reasonable values (1). It is a simple exercise in basic physics to show that for a BF_2 molecular beam of energy, E_0 , neglecting the molecular dissociation energy, the ^{11}B possesses $(11/49) E_0$ and the ^{19}F $(19/49) E_0$. Using secondary ion mass spectrometry (SIMS), we have observed that under certain conditions BF_2 implants can exhibit anomalous ^{11}B profiles. These conditions occur when using BF_2 molecular implants from ion implantation equipment employing preacceleration mass analysis. The following communication demonstrates the problem, proposes and verifies the mechanism, and shows that a solution can be obtained.

The samples were prepared using cleaning procedures and implantation conditions suitable for Si device fabrication. The SIMS in-depth profiles were performed on a CAMECA IMS-3f Ion Micro-analyzer employing oxygen ion bombardment and positive ion spectroscopy. To insure that profiling conditions were identical for the different implants, all samples were run with identical SIMS parameters.

In Fig. 1 we show the SIMS profile for ^{11}B resulting from a BF_2 implant into silicon. Here, the concentration and depth scales have been assigned by fitting the LSS ^{11}B distribution to the SIMS data (2). These results are obtained from unannealed material with implant conditions typical of a high throughput ion implantation process (filament ion source, maximum beam current). A pronounced shoulder on the deep

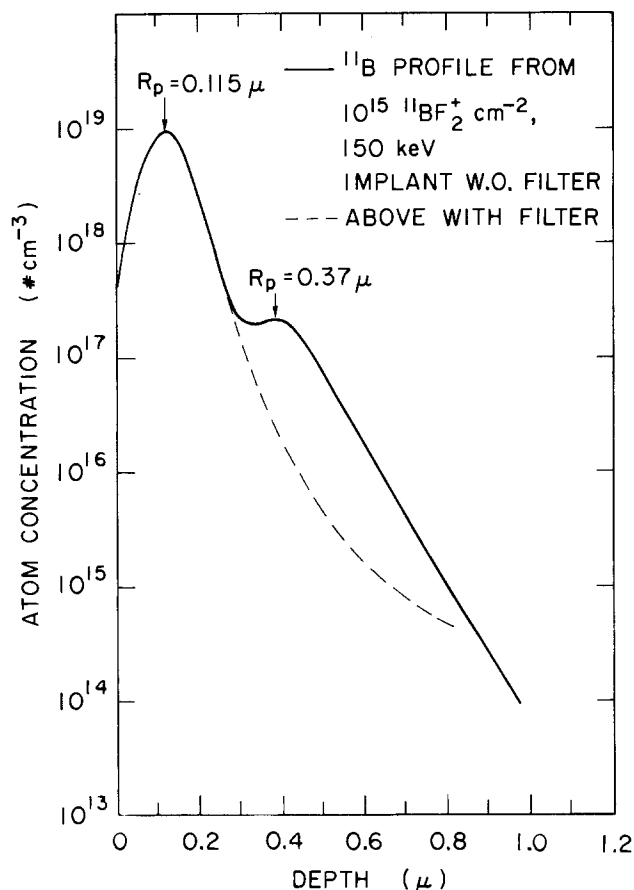


Fig. 1. ^{11}B concentration vs. depth profile resulting from a $10^{15} BF_2/cm^2$ 150 keV implant, (—) without additional filter, (- -) with additional filter.

* Electrochemical Society Active Member.

Key words: SIMS analysis, boron ion implantation.

side of the ^{11}B profile can be seen in Fig. 1 which results in a significant deviation of the measured and the expected ^{11}B -implanted profile (an ^{11}B concentration increase of over an order of magnitude at $\sim 0.4 \mu\text{m}$). The disastrous effect of this shoulder on a shallow base structure is apparent.

We propose that this shoulder results from dissociation of BF_2 molecules which have undergone mass analysis but have not yet obtained the full terminal acceleration of the ion implanter. It is possible, in the low vacuum region between the output of the mass analyzer and the collimation slits, for the BF_2 ions to undergo collisions with other ions or molecules, and fragment into both boron and fluorine ions. These boron ions then take on an energy equal to 11/49's of the preacceleration BF_2 energy plus the full postacceleration energy of the accelerator. For this work, the premass analysis energy of the molecules was 30 keV, while the final terminal acceleration voltage was 120 kV. Thus, this dissociated boron ion will have an energy of approximately 127 keV, resulting in a projected range in the Si target based on this energy, rather than on 11/49 of 150 keV as was initially desired. In Fig. 1, we show the profile of ^{11}B made using BF_2 with a velocity filter located after the normal magnetic analyzer but prior to the final acceleration stage. It can be seen that the high energy shoulder which would result from dissociated BF_2 ions does not exist, suggesting that this is in fact the cause of the anomalous profile.

A further test of this hypothesis can be made by implanting monoatomic boron ions at various energies. The BF_2 implantation with dissociation can be simulated by implanting both 34 keV and 130 keV ^{11}B . The latter implant, representing the boron atoms which have passed through the mass analyzer as a BF_2 molecule, then decompose prior to receiving the full terminal acceleration. In order to identify the mechanism clearly, we have used ^{11}B at 34 keV and ^{10}B at 130 keV, thereby allowing unequivocal identification of the two implants using SIMS. The results of this experiment are shown in Fig. 2, which depicts the SIMS profile of the ^{10}B and ^{11}B ions in Si. The individual implants, shown as the dashed lines, are then combined and result in the composite profile shown as the solid line. It can be seen that the boron profile resulting from the BF_2 implant is reproduced almost exactly by this composite profile resulting from the 34 keV and 130 keV B implants, and each individual implant profile is as expected. The difference in the tails of the profiles is believed to be due to further dissociation of the BF_2 beam during final acceleration. This is supported by the fact that the tails occur only for the BF_2 implants (opposite to what would be expected if this were an ion channeling phenomena), and that the results are reproducible, thereby eliminating SIMS parameter artifacts.

We conclude from these results that, when using molecular ion beams for a source of implant atom, care must be exercised to insure that a significant amount of molecular dissociation (in our case $\sim 0.4\%$) does not occur in the ion implanter. This dissociation can be reduced by better operating vacuum in the critical regions of the implanter (with an associated loss in beam current), and/or with the use of a second stage of mass analysis prior to the final acceleration stage of the implanter. In this work, we have shown that this effect can be minimized for a preanalysis type implanter (within the sensitivity of our SIMS instrument) by the use of a velocity filter before the final acceleration stage without a large sacrifice of beam current. Moreover, this experiment indicates that the

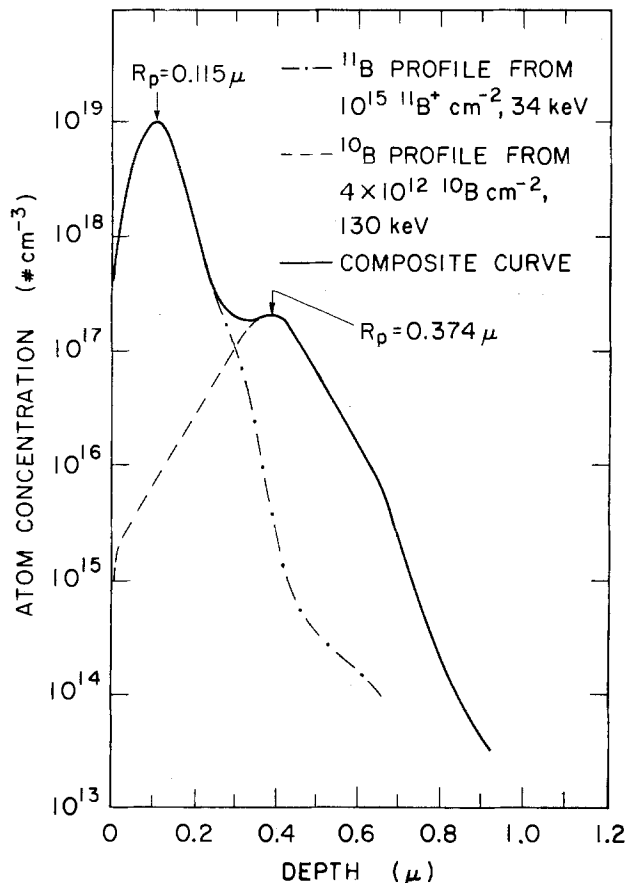


Fig. 2. ^{11}B and ^{10}B concentration vs. depth profiles resulting from a $10^{15} \text{ }^{11}\text{B}/\text{cm}^2$ 34 keV and $4 \times 10^{12} \text{ }^{10}\text{B}/\text{cm}^2$ 130 keV implant. The solid line represents the composite profile and should be compared with the solid line in Fig. 1.

majority of the dissociation occurs prior to the exit slits of the magnetic deflection mass analyzer rather than during final acceleration. Should the majority occur during final acceleration, a continuum of boron energies below 130 keV would be produced, resulting in a less well-defined back side shape for the implant profile.

Acknowledgments

The West Coast contributors to this work would like to acknowledge the support of Dr. R. Reynolds, DARPA, Contract MDA903-78-C-0290. The University of Illinois work was supported by the National Science Foundation under the MRL Grant DMR-77-23999.

Manuscript submitted June 4, 1979; revised manuscript received Aug. 13, 1979.

Any discussion of this paper will appear in a Discussion Section to be published in the December 1980 JOURNAL. All discussions for the December 1980 Discussion Section should be submitted by Aug. 1, 1980.

Publication costs of this article were assisted by Stanford University.

REFERENCES

1. H. Müller, H. Ryssel, and I. Ruge, "Ion Implantation in Semiconductors II," p. 85, Springer-Verlag, Berlin (1971).
2. J. F. Gibbons, W. S. Johnson, and S. Mylroi, "Projected Range Statistics," Dowden, Hutchinson, and Ross, Stroudsburg (1975).

Potential Profiling as a Means to Determine Conductivity Type: Application to ZnSe

G. F. Neumark, B. J. Fitzpatrick,* P. M. Harnack, S. P. Herko, K. Kosai, and R. N. Bhargava

Philips Laboratories, Briarcliff Manor, New York 10510

In characterizing semiconductors it is important to determine whether these materials are n- or p-type. The usual method of determining conductivity type is the Hall effect. However, this measurement cannot be conveniently carried out on high resistivity material. Alternative methods are thus required for this case. In the present paper, we suggest use of Schottky barrier contacts together with potential profiling as an appropriate method. Essentially, this approach gives a large potential drop at the cathode if the material is n-type, and at the anode if the material is p-type. Both the theory and the experimental setup for this profiling method are relatively simple. We are, however, not aware of its prior use to determine conductivity type of semiconductors, and have therefore checked the method with GaP and ZnSe of known conductivity type. The method was then used to characterize high resistivity ZnSe layers. These layers were grown from Bi solution. In an attempt to obtain p-type material, some of these layers were grown with Li, Na, or P as dopants, and/or annealed in Se vapor.

The present method hinges on the use of barrier contacts such that the direction of easy electron transfer across the barrier is known with respect to the voltage polarity. This direction depends on the type of carrier transport which dominates the current: activation over the barrier, or tunneling (1, 2). However, it is known (3-5) that tunneling is not important except for high doping and at low temperature. Now, the aim of our method is measurement at room temperature on high resistance material. We shall thus assume that we are dealing with carrier transport by activation. For this case, under an applied bias the energy band configuration for two symmetric Schottky¹ barriers on an n-type semiconductor (Fig. 1a) changes (1, 3) qualitatively to the situation shown in Fig. 1b, where V_A is the applied voltage. Also indicated on Fig. 1b is a resistive voltage drop (V_R) across the bulk. The corresponding voltage distribution (1, 3) is shown in Fig. 2, which shows that the main voltage drop is at the cathode. An analogous analysis for a p-type semiconductor would show the main voltage drop at the anode.

A more quantitative treatment of the barrier voltages, although not strictly required in the present application of the method, is useful to bring out some sidelights. For ideal¹ reverse-biased Schottky barriers, the voltage distribution is given by (1, 3)

$$V(x) = [4\pi e(N_D - N_A)/\kappa](wx - \frac{1}{2}x^2) \quad [1]$$

$$w^2 = [V_B\kappa/2\pi e(N_D - N_A)] \quad [2]$$

where V_B is the voltage drop across the barrier [and where it is assumed that $V_B \gg V_0$, with V_0 the zero bias barrier height (Fig. 1a)], x is the distance along the field, κ is the dielectric constant, $(N_D - N_A)$ is the net doping density, and w is the barrier width. With use of cgs units in these equations, x is in cm and $(N_D - N_A)$ is in cm^{-3} , which is convenient for

* Electrochemical Society Active Member.

Key words: semiconductors, ZnSe, conductivity type, potential distribution.

¹The terminology of what is meant by a Schottky barrier contact is not always clearly defined. In recent literature the term has sometimes been used interchangeably with "metal-semiconductor" barrier contact [see, for example, Rhoderick or Padovani, Ref. (3)]. In earlier literature [see, for example, Henisch, Ref. (1)], a Schottky barrier usually meant a barrier whose width (w) varied with voltage. Here we use the term "ideal" for barriers for which Eq. [1] and [2] are valid.

resistivity calculations (used below). For these units, $e = 4.8 \times 10^{-10}$ esu, and the voltage is in statvolts, or, for V in volts a value of $V/300$ is used. It is worth noting that $(N_D - N_A)$ can, in principle, be obtained within the barrier region. However, in practice the probing dimensions are inconveniently small except for quite high resistance material. And, of more importance, if the resistance is too high, practical dimensions result in a limitation on the method. Thus, if $(N_D - N_A)$ is very low, the barrier widens appreciably. Since sample sizes, in practice, are limited, this restricts the method. An example will clarify the extent of the limitation. Assume a sample size $\lesssim 1$ cm. It appears desirable to have a barrier width $\lesssim 1/3$ of the sample, so that adequate bulk material is also available. The barrier width can be adjusted through the applied

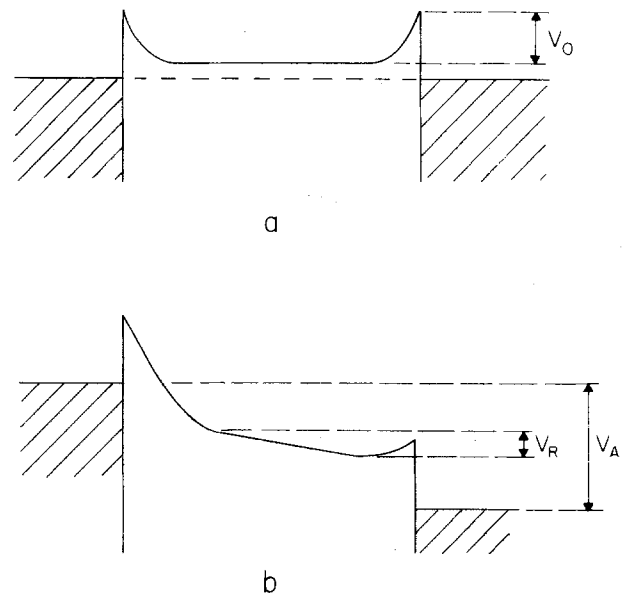


Fig. 1. (a) The zero bias case for an n-type semiconductor with two symmetric Schottky contacts (of height V_0); (b) the same system with a positive applied bias ($\equiv V_A$), with the left contact reverse biased, the right contact forward biased, and with the bulk showing some resistive drop ($\equiv V_R$).

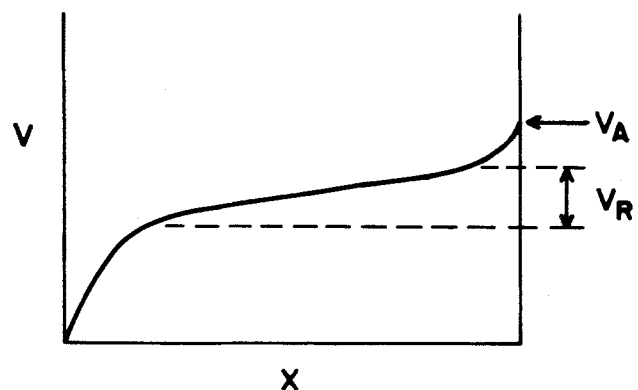


Fig. 2. Voltage vs. distance (x) corresponding to the case of Fig. 1(b).

voltage, but for measurements on high resistance materials the minimum voltage required, in practice, is $\sim 100\text{V}$ ($=1/3$ statvolts). Assuming $\kappa \approx 10$, the lowest $(N_D - N_A)$ which can be measured is $\sim 10^{10}\text{ cm}^{-3}$. To convert this value to resistivity ρ (where $\rho = 1/ne\mu$), one requires a value of mobility μ and the relation between carrier concentration n and $(N_D - N_A)$. For example, for $\mu \approx 100\text{ cm}^2/\text{Vsec}$ and $n \approx (N_D - N_A)$, the corresponding resistivity is $6 \times 10^6\ \Omega\text{-cm}$. In practice, one usually has $n < (N_D - N_A)$, so that somewhat higher resistivities should also give satisfactory results, but actual limits cannot be predicted without knowledge of the relation between n and $(N_D - N_A)$.

To carry out the present method, one requires a measurement of potential along a sample. This, in principle, is relatively simple. Using a probe which can be positioned along the sample (e.g., via a micro-manipulator), one can measure the voltage at the probe by use of the condition of zero current through the probe. Appropriate circuits are standard. Nevertheless, in practice some difficulties may arise, and it seems worth mentioning some of the problems.

The measurement, as actually carried out, had some usual difficulties due to high sample resistance. The main problem here was the high contact resistance at the probe, leading to poor sensitivity. However, we found that an adequately low contact resistance could generally be obtained by evaporating a pattern of Au dots on the sample, and then moving the probe along a row of such dots. (We used Au since it was convenient—also see below for further discussion on contact aspects.)

Another caution worth mentioning is that the measurement should be done in the dark, in order to avoid photoconductive and/or photovoltaic effects. It is, for instance, known (6) that high resistance p-material can give an n-type photo-Hall effect. This arises when the concentration of the carriers generated by the light is comparable to or higher than the dark concentration, since the conductivity is then dominated by the higher mobility of the electrons.

A further problem is that the present method requires Schottky contacts, and it is not always known which metals and which preparation conditions yield this type of contact. Fortunately, the probing method also yields information on the contact type. Firstly, if the contacts are of the Schottky type, one end of the sample will show a high voltage drop, the other end a lower one (see Fig. 2), and this condition will reverse if the voltage polarity is reversed. Secondly, if the contact resistance is dominated by an intrinsic layer, there will be a potential drop at the contact, but this drop will remain approximately constant with reversal of the polarity. Thirdly, if a contact is ohmic, there are two possible potential profiles (Fig. 3). There may be no extra voltage drop at the contacts, and the voltage distribution will be linear across the sample (dashed line on Fig. 3). The second possibility is a voltage drop at both anode and cathode, approximately equal, giving a symmetric voltage distribution (solid line on Fig. 3). The former case will occur by definition if the contact geometry is such as to give a true one-dimensional situation, e.g., if the contacts extend across the two end faces of a rectangular shaped sample. However, in practice the contacts were usually evaporated on the top surface of a sample. Thus, the current lines can spread downward into the sample (and for point contacts also laterally) leading to a lower resistance away from the contact ends. This is strictly a geometric effect. Various aspects of this problem have frequently been discussed in the literature (7).

Regarding the applications of the profiling method, we first checked it on materials of known conductivity type, namely n-ZnSe, and n- and p-GaP. The method was then applied to several ZnSe layers grown by liquid phase epitaxy from Bi solution. For probing contacts, we used evaporated Au dots for most of the

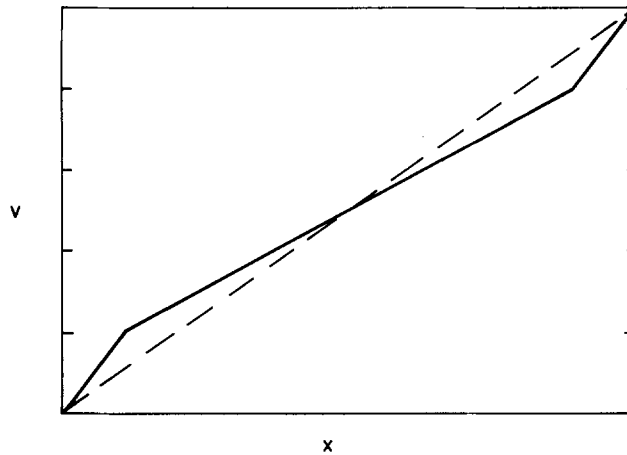


Fig. 3. Potential vs. distance for an ohmic contact. The dashed line is the ideal case of even current lines. The solid line shows the case where current lines can spread out from the contact region (see text).

measurements. As discussed earlier, these gave adequately low contact resistance. The one disadvantage of gold is that under certain conditions [e.g., sputtering or heating in H_2 (6, 8)] it may give an ohmic contact to p-ZnSe. However, using a plain evaporation procedure, we obtained sharp contact barriers on a number of high resistance ZnSe layers with p-type characteristics (anode drop—see below).

The profiling method has been carried out on various as-grown layers, both undoped and doped with Li, Na, and P. Also, some of these layers were annealed in Se vapor, since such treatment is expected (9) to result either in better p-type material, or at least in more resistive n-type material. In general, the layers were high resistance, and it was not possible to measure a Hall effect. Probing results showed that some Li and Na doped layers were p-type, and that some undoped layers could be converted to p-type by Se annealing.² Results for one typical p-type sample (Na doped) are shown in Fig. 4. The straight lines extending over the bulk part of the sample were obtained by a least squares fit over the measured points.

² A more systematic investigation of the conditions which give p-type behavior is presently in progress. However, we believe that a problem in this respect is the role of impurities in providing compensation. See R. N. Bhargava, S. P. Herko, and B. J. Fitzpatrick, *Bull. of the Am. Phys. Soc.*, 24, 402 (1979); and G. F. Neumark, *ibid.*, 24, 402 (1979); G. F. Neumark, To be published in *J. Appl. Phys.*, June, 1980.

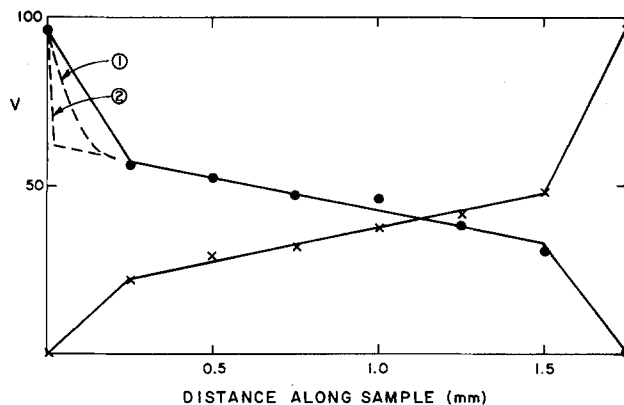


Fig. 4. Potential vs. distance along a sample of p-ZnSe (Na doped). The points correspond to a row of Au dots on the sample (0.25 mm apart). The circles denote voltage decreasing to the right, the crosses are for the opposite polarity, and the lines are drawn to connect the points (the actual barrier shape is not known since the doping is not known, see Eq. [1], [2]). The main potential drop is at the anode, denoting p-material. The dashed lines indicate the theoretical barrier shape (Eq. [1], [2]), with curves (1) and (2) for $(N_A - N_D) = 10^{12}\text{ cm}^{-3}$ and 10^{14} cm^{-3} , respectively.

Similar measurements were also carried out at higher voltages (140, 190V). A least squares fit of current *vs.* bulk voltage gave the resistance between two Au dots as $2 \times 10^9 \Omega$. For an estimated layer thickness of $\sim 10 \mu\text{m}$, and since for our Au dots the inter-dot spacing was comparable to the dot diameter, this leads to a resistivity $\sim 2 \times 10^8 \Omega\text{-cm}$; assuming $\mu \sim 5 \text{ cm}^2/\text{Vsec}$, one obtains $p \sim 7 \times 10^{11} \text{ cm}^{-3}$. We have also plotted on Fig. 4 (dashed lines) the theoretical relation (Eq. [1], [2]) for $V(x)$ for $(N_A - N_D) = 10^{12} \text{ cm}^{-3}$ and for $(N_A - N_D) = 10^{14} \text{ cm}^{-3}$. As can be seen, any value $(N_A - N_D) \gtrsim 10^{12} \text{ cm}^{-3}$ fits the observed result—the probing with the present dot distances cannot differentiate. Note that we know only that $(N_A - N_D) \geq p$, but do not know how much greater, so it may take an appreciable reduction in probing distance to evaluate $(N_A - N_D)$. Due to probing difficulties with smaller dot sizes, this aspect has therefore not been pursued. In any case, the resistivity and the barrier shape results are consistent with each other.

Overall, we have shown that for Schottky contacts the profiling method can be used to differentiate between n- and p-type material. Moreover, it has been successful on high resistance material on which Hall measurements could not be carried out.

Manuscript submitted Dec. 22, 1978; revised manuscript received Oct. 10, 1979.

Any discussion of this paper will appear in a Discussion Section to be published in the December 1980

JOURNAL. All discussions for the December 1980 Discussion Section should be submitted by Aug. 1, 1980.

Publication costs of this article were assisted by Philips Laboratories.

REFERENCES

1. See, for example, H. K. Henisch, "Rectifying Semiconductor Contacts," Oxford University Press, London (1957).
2. N. F. Mott and R. W. Gurney, "Electronic Processes in Ionic Crystals," Oxford University Press, London (1948).
3. For recent reviews, see, for example, F. A. Padovani in "Semiconductors and Semimetals," Vol. 7A, R. K. Willardson and A. C. Beer, Editors, p. 75, Academic Press, New York (1971), and E. H. Rhoderick, Institute of Physics Conference Series, Bristol and London, England, 22, 3 (1974).
4. F. A. Padovani and R. Stratton, *Solid-State Electron.*, 9, 695 (1966).
5. C. Y. Chang and S. M. Sze, *ibid.*, 13, 727 (1970).
6. G. B. Stringfellow and R. H. Bube, *Phys. Rev.*, 171, 903 (1968).
7. See, for example, L. B. Valdes, *Proc. IRE*, 42, 420 (1954); and D. S. Perloff, *Solid-State Electron.*, 20, 681 (1977).
8. Y. S. Park and C. H. Chung, *Appl. Phys. Lett.*, 18, 99 (1971).
9. See, for example, A. Sakalas, *Phys. Status Solidi A*, 27, 175 (1975); or F. A. Kroger, *J. Phys. Chem. Solids*, 26, 1707 (1965).



Influence of Surface Damage on Stabilization Against Photodecomposition of n-Type GaAs*

Marc J. Madou, Karl W. Frese, Jr.,[†] and S. Roy Morrison

SRI International, Menlo Park, California 94025

Recently noteworthy progress has been made in the development of photoelectrochemical solar cells (1,2,3). However, a major difficulty remains, that is, the photocorrosion of desirable anode materials such as n-GaAs and n-Si. Ultimately, the goal is to make solar cells using polycrystalline materials, (4) and such materials will contain different defects. Simple theory suggests that defective areas of the crystal surface will be more difficult to stabilize. From an experimental point of view, it has not been clear what effects these defects will have on the photoelectrochemical corrosion process. Therefore an important objective of our work is to investigate the effect of dislocations and grain boundaries on the corrosion rate and stabilization efficiency. Before this can be done, however, suitable stabilizing agents must be identified. We report some of our results toward these goals, both the identification of stabilizing agents for GaAs and studies of the influence of defects on the stability of the GaAs. Measurements of conversion efficiencies of radiant energy to electricity and of the influence of surface treatment on those efficiencies are planned for the near future.

A rotating-ring-disc electrode was assembled using a n-GaAs disc and a ring that was made of either amalgamated copper or pure grade gold. The collection efficiency anticipated from the geometric parameters was about 36%. In practice an efficiency of 32% was obtained. This number was independent of rotation speed in a wide range and the most commonly used speed was around 1000 rpm. The etch used for the GaAs disc was $\text{H}_2\text{SO}_4:\text{H}_2\text{O}_2:\text{H}_2\text{O}$, (3:1:1 v/v) at 80°C. Until now, only the (111)-face (As) was investigated. The GaAs disc was illuminated with chopped light (at a frequency of 1 Hz) from a 150-W xenon lamp. In the experiments reported, we used an aqueous solution containing $\text{Fe}(\text{ClO}_4)_2$ in 0.1 M EDTA.

The photoproduced holes coming to the surface of the GaAs disc can oxidize the Fe(II)-

EDTA or can corrode the GaAs. The disc potential was always kept in the flat portion of the photocurrent-voltage characteristic (+ 0.8 V versus SCE). The ring voltage was maintained on the saturation portion of the reduction wave at -1.0 versus SCE. Thus Fe(III)-EDTA formed at the disc is reduced at the ring, and its presence is monitored. The stabilization is expressed as the ratio of the hole current that oxidizes Fe(II)-EDTA, i_{ox} , to the total ac hole current i_{photo} through the GaAs disc. The value of i_{ox} is determined by measuring the periodic component of the ring current and dividing by a collection-efficiency factor.

Figure 1 shows the effect of the pH on the percentage stabilization of the etched n-type GaAs for two different concentrations of $\text{Fe}(\text{ClO}_4)_2$ in 0.1 M EDTA. The pH was adjusted with either HClO_4 or NH_4OH . One region below pH = 2.5 is inaccessible because precipitation of EDTA occurs in such a solution. The light intensity was found to influence the percentage stabilization in such a way that higher light intensities gave lower percentage stabilization. Therefore all points given in Figure 1 were taken for the same disc current of about 1 mA/cm². Another important observation is that if the percentage stabilization was low, perhaps because of the presence of an oxide film, a cathodic current temporarily passed through the disc could result in the recovery of the initial higher percentage stabilization. The experiments in Figure 1 were always started after the disc had been held cathodic for a few minutes. Both the effect of light intensity and the effect of cathodic pretreatment will be dealt with in greater detail in another publication (5).

From Figure 1 it can be seen that for both concentrations and with the prevailing light intensities the stabilization is complete in the intermediate pH region. Within the accuracy of our apparatus, we concluded the stabilization is > 99% under these conditions. For hole currents of 1 mA/cm² the stabilization at both high and low pH

decreases rapidly. We note that the highest stabilization occurs where the oxidation products in Ga are most insoluble (6). This result is completely analogous to the one found in the stabilization of n-GaP with $\text{Fe}(\text{CN})_6^{4-}$ (7). Although in this case we found that at lower light intensities in acid solution (e.g., 0.04 M Fe(II)-EDTA, pH = 3, 100% stabilization can be found.

Further investigation is required to fully explain this pH dependence of the percentage stabilization. Possible explanations are (1) a change in redox properties of the solutions with pH [in the case of Fe(II)-EDTA], (2) a shift in energy levels of the n-GaAs relative to the Fe(II)-EDTA level or (3) a change in electrode stability towards holes because of a thin oxide layer on the GaAs surface (8).

Figure 2 shows the effect of surface damage on the stabilization. In the figure we plot percentage stabilization versus concentration curve in 0.1 M EDTA at constant photocurrent and an intermediate pH. Since the disk current was lowered by the introduction of surface damage the light intensity had to be adjusted to maintain a constant photocurrent. Curve (a) was determined using well-etched samples and showed reproducible levels of stabilization as long as fresh solutions and freshly etched (e.g., 10-sec etch) electrodes were used. Curve (b) was determined on specimens etched and subsequently polished with 0.3- μm Al_2O_3 powder for 30 sec. This treatment may be assumed to introduce unspecified surface damage, primarily dislocations. We note that for conditions of constant concentration of Fe(II)-EDTA and photocurrent, the effect of surface damage is to lower the stabilization efficiency. We have also observed several times that if corrosion is allowed to proceed on such a damaged surface, the stabilization will recover with time, reaching a value characteristic of a damage-free surface in about 15 min. Curve (c) shows data taken with a more severely damaged electrode. This surface was prepared for successive polishing with Buehler 4/0 polishing paper, a 6- μm diamond paste, and 1- μm Al_2O_3 and 0.3- μm Al_2O_3 powders. Importantly, the sample was not etched before measurement. The results show that lower stabilization was obtained at all concentrations and that the highest Fe(II)-EDTA concentration was needed to reach values close to 100%. These results demonstrate that damaging single crystal surfaces leads to changes in the competition between oxidation of the redox component in solution and the crystal lattice.

These results show clearly that for well-etched single crystals, Fe(II)-EDTA is a good stabilizing agent for n-GaAs. We concluded that within the limitations of our ring-disc apparatus, the stabilization is > 99%. We observed a very distinct effect of the mechanical damage on the amount of stabilization; that is, the more damaged surfaces had lower percentage stabilization. Finally we observed a dependence of the corrosion on the light intensity and found that a cathodic current passage can produce large positive changes in the amount of stabilization of a semiconductor.

REFERENCES

1. B. A. Parkinson, A. Heller, and B. Miller, *J. Electrochem. Soc.* 126, 954 (1979).
2. P. A. Kohl and A. J. Bard, *J. Electrochem. Soc.* 126, 603 (1979).
3. S. Wrighton, M. Bolts, A. B. Bocously, M. C. Palazzotto, and E. G. Walton, *Proc. 5th Annual Conference on the Physics of Compound Semiconductor Interface*, P. Mark, Ed., New York, 1976.
4. A. Heller, B. Miller, S. S. Chu, and Y. T. Lee, *J. American Chem. Soc.* 101, 7633 (1979).
5. In preparation, to be submitted to the *Journal of Electrochemical Society*.
6. M. Pourbaix, *Atlas of Electrochemical Equilibrium*, Pergamon Press, London, 1966.
7. R. Memming in "Semiconductor Liquid-Junction Solar Cells," Adam Heller, Ed., Airline, 1977.
8. M. J. Madou, F. Cardon, and W. P. Gomes, *Ber. Bunsenges. Physik. Chem.* 81, 1186 (1977).

* Supported by Solar Energy Research Institute.

† Electrochemical Society Member.

Keywords: n-GaAs, photodecomposition, surface damage, stabilizing agent, photoelectrochemical solar cells.

Manuscript submitted Oct. 25, 1979;
revised manuscript received Jan. 25, 1980.

Publication costs of this article were assisted by SRI International.

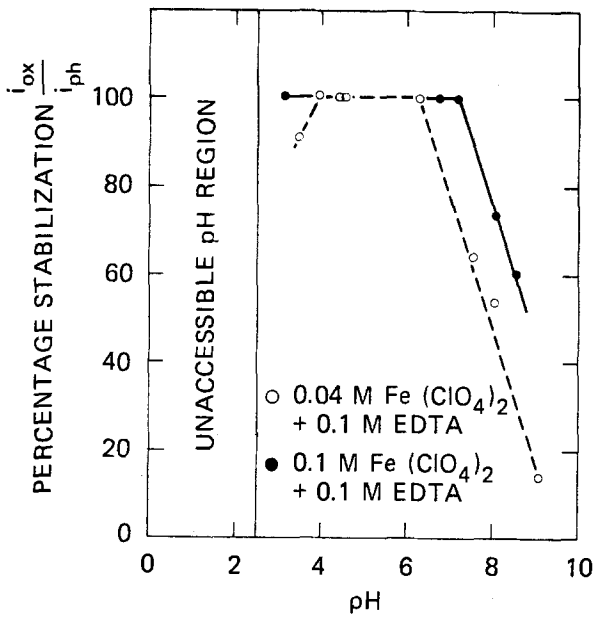


FIGURE 1 PERCENT STABILIZATION OF n-GaAs VERSUS pH
Disc Current $\approx 1 \text{ ma/cm}^2$. The pH is adjusted with NH_4OH or HClO_4 .

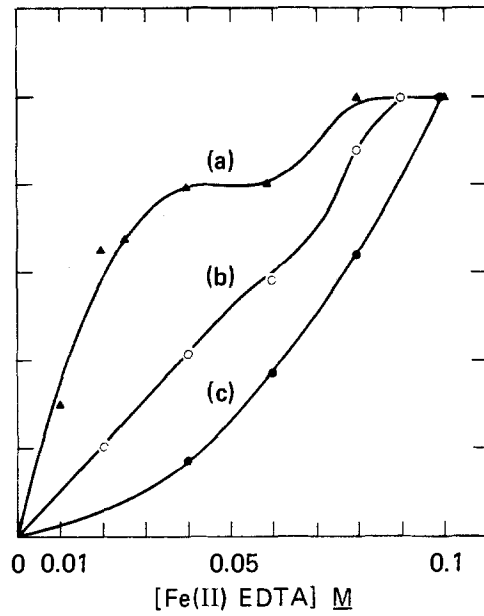


FIGURE 2 PERCENT STABILIZATION OF n-GaAs VERSUS Fe(II) EDTA CONCENTRATION IN 0.1 EDTA AQUEOUS SOLUTIONS, INTERMEDIATE pH RANGE
Curve (s), surface undamaged. Curves (b) and (c), surface damaged. See text.

Preferential Etching of Boron-Doped Polysilicon Electrodes for CCD's

H. S. Gamble, N. E. Evans, and S. H. Raza

Department of Electrical and Electronic Engineering,
The Queen's University of Belfast, Belfast BT9 5AH, Ireland

The standard techniques for fabricating charge-coupled devices employ multiple layers of phosphorus doped polycrystalline silicon for the phase electrodes. Several oxidation steps are required and these result in an increase in the grain size of the polysilicon. Fine line structures are difficult to fabricate due to these large grains and the critical etching time of the polysilicon. The faster etch rate of phosphorus doped oxide can lead to problems with undercutting of the fine polysilicon electrodes during etch out of the masking and gate oxides. This problem can be overcome by using a nitride layer as part of the gate dielectric.

To avoid growth of large polysilicon grains and the critical nature of polysilicon etching it was decided to investigate the possibility of fabricating CCD's with boron doped polysilicon. The use of boron doped polysilicon and pyrocatechol etch avoids these problems. Bohg⁽¹⁾ has shown that ethylene diamine-pyrocatechol-water mixture will only etch silicon which has a boron concentration of less $5 \times 10^{19} \text{ cm}^{-3}$ and Nicholas et al² have used this property for producing fine polysilicon lines.

For polysilicon deposited at 620°C, in a furnace tube at atmospheric pressure and boron doped at 1000°C from a boron nitride wafer source, the maximum sheet resistivity of a 5000 Å layer that was unaffected by the pyrocatechol etch was found to be $65 \Omega \square^{-1}$.

The effect of impurity type and post diffusion temperature cycles on the resultant grain size of our polysilicon layers was determined by transmission electron microscopy. The results given in Table I show that the average grain size of boron doped polysilicon is much smaller than that of phosphorus-doped polysilicon for both low and high temperature processing. All diffusions were carried out at 1000°C for 15 minutes and phosphorus oxychloride was used as the phosphorus source.

One disadvantage, however, of using boron doped polysilicon is the high diffusion

TABLE I. POLYSILICON GRAIN SIZE		
POST DIFFUSION TEMP. CYCLE	IMPURITY TYPE	AVERAGE GRAIN SIZE (Å)
55 min. 1150°C	UNDOPED	1,500
55 min. 1150°C	PHOSPHORUS	4,400
55 min. 1150°C	BORON	1,500
60 min. 1000°C	PHOSPHORUS	2,700
60 min. 1000°C	BORON	1,300

rate of boron in SiO_2 , especially in water vapour or hydrogen atmospheres.⁽³⁾ To prevent boron from the first polysilicon layer diffusing through the oxide into the substrate during subsequent oxidation steps, a layer of silicon nitride is used as part of the gate dielectric. As stated above the use of a nitride layer also removes the problems associated with undercutting of the polysilicon.

The fabrication sequence for producing four phase CCD's with two polysilicon layers is outlined in Fig 1 a-e. The process steps up to the deposition of the first polysilicon layer are the same as for standard four phase CCD's incorporating phosphorus doped polysilicon electrodes. A masking oxide is thermally grown and subsequently patterned to expose the polysilicon where the phase electrode is required (Fig 1b). The polysilicon is then boron diffused, the masking oxide removed and the wafer immersed in pyrocatechol. The polysilicon remaining is that which was boron diffused and is slightly wider than the original window in the masking oxide due to the lateral diffusion of the boron. (Fig 1c)

An isolating oxide is then thermally grown over the polysilicon electrodes and a second layer of polysilicon deposited. The second layer is patterned using the same techniques as for the first polysilicon

Keywords: Charge-transfer devices, pyrocatechol, silicon nitride, fine geometry structures

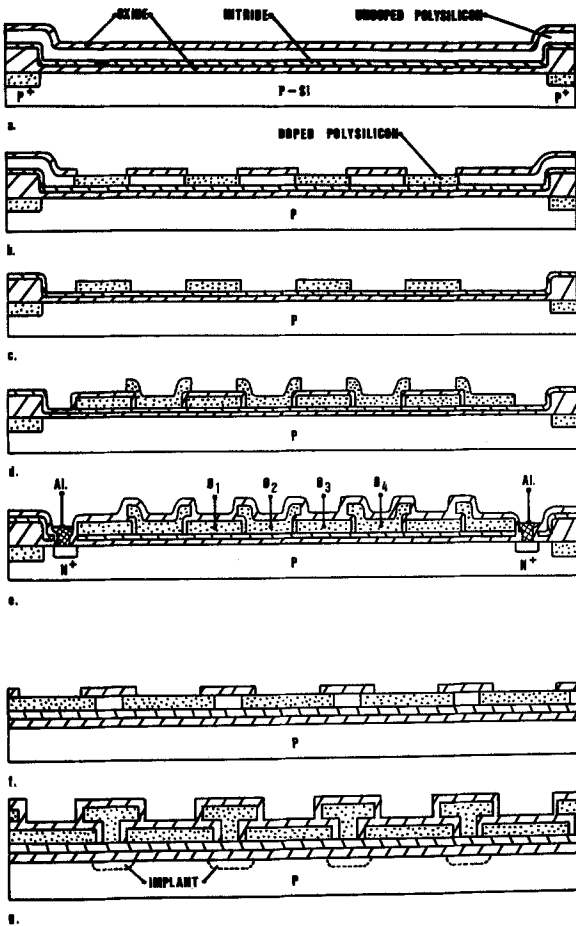


Fig 1. Processing sequence, incorporating a pyrocatechol preferential etching technique for the fabrication of two layer polysilicon CCD's.

layer. (Fig 1d) It should be noted that since the masking oxide is removed before the second polysilicon layer is etched the isolating oxide covering the first polysilicon layer electrodes is not removed. This reduces the risk of polysilicon to polysilicon shorts at the overlap edges and aids aluminium coverage over polysilicon rails in the field region. The remaining steps in the device processing are as for conventional four phase CCD's. (Fig 1e)

The lateral diffusion of boron can be used to reduce the gap between the phase 1 and phase 3 electrodes of the first polysilicon layer. If the electrode gap on the photographic mask is of minimum dimension then the inclusion of a boron drive in stage, producing significant lateral diffusion, results in a very small electrode gap. (Fig 1g) The second polysilicon layer is patterned as before, without any drive in step, to produce a device with long storage wells under the electrodes of phases 1 and 3

and short transfer regions under the electrodes of phases 2 and 4.

The lateral spread of the polysilicon electrode, after an initial diffusion at 1000°C giving a sheet resistivity of $45 \Omega_{\square}^{-1}$, was found to have a square root dependence on drive in time and an exponential dependence on drive in temperature. (Fig 2) The etching time of the 5000 \AA layer of polysilicon in pyrocatechol at 160°C was 30 seconds and no change was determined in the polysilicon electrode width after 400% over etching.

The resistivity of boron doped polysilicon is a factor of three higher than that of phosphorus doped polysilicon and the work function is increased by approximately one volt. A further increase in the resistivity of boron doped polysilicon is observed after oxidation in a water vapour ambient due to out-diffusion of boron.

Devices have been fabricated as outlined above on P-type $\langle 100 \rangle$ substrates of $25\text{--}50 \Omega\text{-cms}$. The gate dielectric consists of a 600 \AA dry thermal oxide grown at 950°C and covered with a 900 \AA layer of silicon nitride deposited at 850°C . The mask dimensions of the electrodes and gaps for the first polysilicon layer were equal at six microns. Various drive in times were then used to fabricate devices with electrode gaps on the first polysilicon layer ranging from one to five microns. The wafers were given a thirty minute hydrogen anneal at 500°C to reduce the fast state density. For a device with input gate and transfer electrodes of $2.5 \mu\text{m}$ the second harmonic content of the output, for sinewave input by the diode cut-off method, was 55 dB down. This value was obtained for signals of near maximum capacity using four phase double storage clocks of 10 volts.

A transfer region barrier could be provided, for two and pseudo single phase operation, by ion implanting boron through the small gap between the first polysilicon electrodes. (Fig 1g) The use of very short transfer regions enables almost 50% of the total CCD to be used for charge storage. This is particularly important for single phase operation where the charge handling capability is greatly reduced.

A processing sequence for the fabrication of four phase CCD's with boron doped polysilicon electrodes has been determined. It requires no critical etching steps as the fine grain polysilicon electrodes are patterned using a self-stopping etch. Neither gate dielectric nor isolating oxide is required to be etched out so problems associated with undercutting are virtually eliminated. The technique also allows very

short electrodes to be fabricated using standard photolithography for two and single phase CCD's.

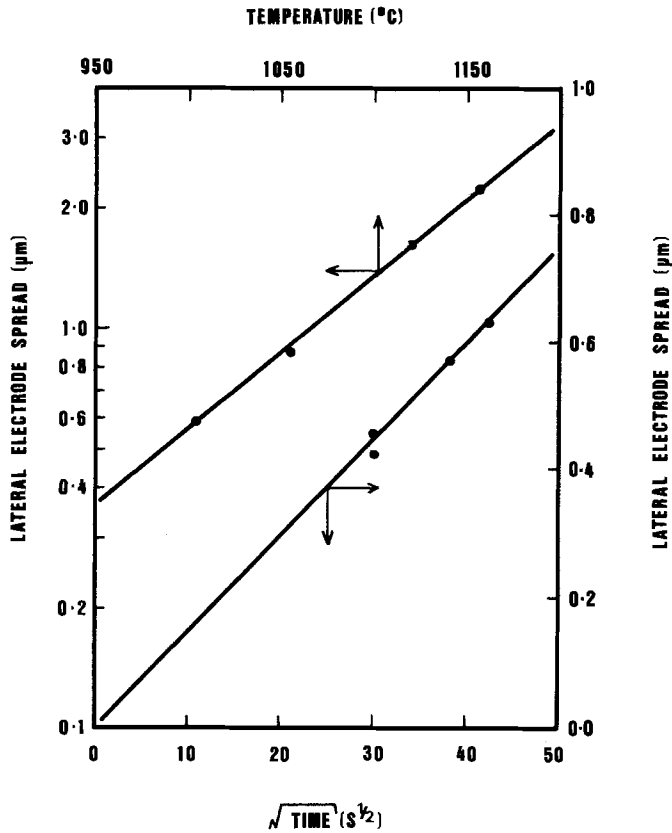


Fig 2. Lateral spread of polysilicon versus boron drive in time and temperature.

Acknowledgements The financial support of the Science Research Council is gratefully acknowledged.

References

1. A. Bohg, This Journal, 118, 401 (1971).
2. K.H. Nicholas, H.E. Brockman, and I.J. Stamp, Appl. Phys. Letts., 26 Nov 7, (1975).
3. A.S. Grove, "Physics and Technology of Semiconductor Devices", p 70, John Wiley & Sons, Inc, New-York, (1967).

Manuscript submitted June 14, 1979;
revised manuscript received Jan. 4, 1980.

Publication costs of this article were assisted by The Queen's University of Belfast.

Index of Refraction of Steam Grown Oxides on Silicon

E. A. Taft*

General Electric Company, Corporate Research and Development, Schenectady, New York 12301

In a recent paper the indices of refraction of oxides grown on silicon in dry oxygen were reported.⁽¹⁾ The index was shown to depend upon the temperature of growth of the oxide. The purpose of this note is to show further results of ellipsometric measurements on a series of oxides grown in 95°C saturated water vapor.

As in the previous work⁽¹⁾ oxide films of about 1200Å in thickness were grown on <111> and <100> lightly doped silicon wafers at several temperatures. The index of refraction of each oxide was measured on a Gaertner L119 ellipsometer. The data are shown in Fig. 1. These curves have the same general appearance as those of the oxides grown in dry oxygen. The index for both <111> and <100> decreases with increasing temperature until it reaches the minimum limiting value of 1.462, remaining constant thereafter. This value is the same as that for oxides grown in dry oxygen. This observation is consistent with the previous assumption that this index limit is associated with the properties of fused quartz. However, in the current case of wet oxidation this constant minimum index begins at the lower temperature of about 1025°C rather than the 1140°C found for the dry oxide. (These are the approximate intercept temperatures of the two straight line portions of the curves.) At these intercepts it may also be noted that there is no difference in the indices of oxides grown on either orientation of silicon used. The slopes of the rising index portions of the curves are slightly steeper for the steam-grown oxides than for the dry oxygen oxides; but at ~750°C the dry oxides still have ~0.3% higher indices. When a film grown on the low temperature slope of the curves is annealed in nitrogen at a temperature

higher than that at which it was formed, it decreases in index (though never below the value for fused silica). The higher the annealing temperature the more rapidly does the index move to lower values. This observation might be compared with the results of Douglas and Isard⁽²⁾. Their studies on the density of fused silica give indications of the time constants expected for equilibrium densities to be obtained. More importantly they find the equilibrium density of silica to increase with temperature in the opposite sense to the behavior of our grown oxide films. This fact indicates that the high densities for films grown at lower temperatures are not directly related to the properties of fused silica.

The oxide structure is clearly influenced by the silicon lattice from which it was formed. At the lower temperatures the oxide retains some of this structure. High temperature annealing allows the oxide structure to relax toward fused silica equilibrium properties. The viscosities of vitreous silica have been measured by Hetherington et al.⁽³⁾ The viscosity is not easily ascertained in silica as, for example, the glass structure changes with temperature and the previous thermal history of the sample must be considered. Metallic impurities and, especially, the water content of the silica are also important. The equilibrium viscosities reported for silicas of very low and of very high hydroxyl content may be viewed with the thought of comparison with the 1140°C and 1025°C temperatures found for our dry and our wet oxides which attain the index of refraction of silica. Hetherington et al.⁽³⁾ show that IR Vitreosil glass must be heated to 1150°C in order to exhibit

a viscosity of 13.8 poise (near the defined annealing point of glasses), whereas Spectrosil samples need be heated only to 1025°C. These vitreous silicas contain the lowest and the highest hydroxyl amounts, respectively, of all their silicas tested. The Spectrosil appears to contain nearly the saturation value of water in silica⁽⁴⁾ so that it would seem reasonable to compare it with our steam oxide. At least the temperature differences in the two cases to obtain the same viscosity is the same as the temperature difference for wet and dry oxides to attain the index of refraction of fused quartz or vitreous silica. The viscosity also seems to be an acceptable value for the growth times involved.

REFERENCES

1. E. A. Taft, *This Journal*, **125**, 968 (1978).
2. R. W. Douglas and J. O. Isard, *J. Soc. Glass Technol.*, **35**, 206 (1951).
3. G. Hetherington, K.H. Jack and J. C. Kennedy, *Phys. & Chem. of Glasses*, **5**, 130 (1964).
4. B. E. Deal and A. S. Grove, *J. Appl. Phys.*, **36**, 3770 (1965).

* Electrochemical Society Active Member
Manuscript received Jan. 8, 1980.

Publication costs of this article were assisted by General Electric Company.

Key Words: ellipsometry, silicon oxide, temperature dependence

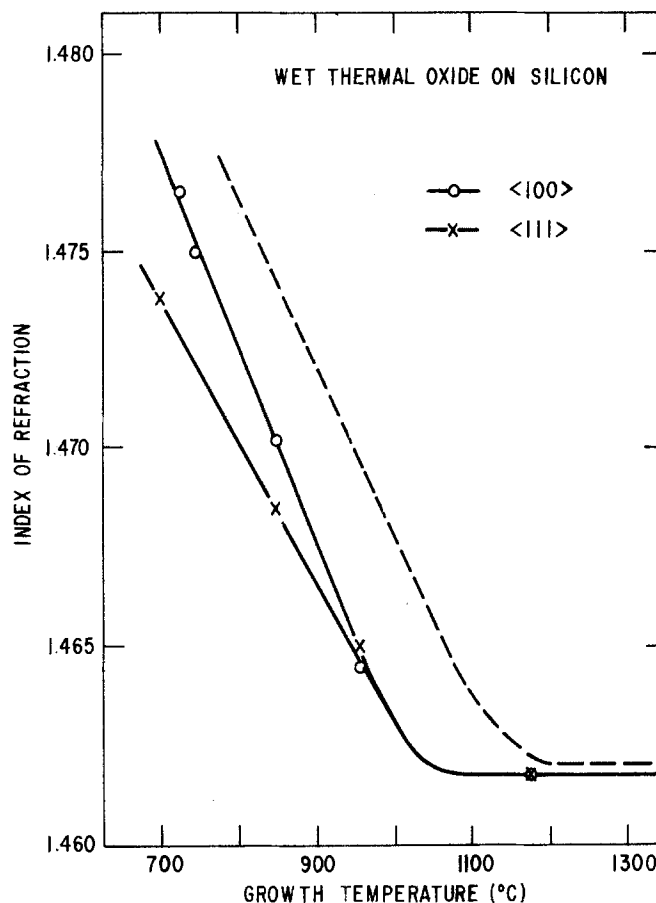


Fig. 1 Index of refraction of steam oxides grown on silicon crystal. The dashed curve is for a dry oxide on <100> silicon (Ref. 1).



Titanium Dioxide Electrode in Molten Sodium Tetrachloroaluminate; Photocurrent and Flatband Potential

I. Uchida,* H. Urushibata, H. Akahoshi, and S. Toshima

Department of Applied Chemistry, Faculty of Engineering, Tohoku University, Sendai 980, Japan

ABSTRACT

The electrochemical behavior of single crystal n-TiO₂ electrodes has been investigated in molten sodium tetrachloroaluminate (AlCl₃ + NaCl) at 175°C. The impedance and photoanodic current were measured as functions of electrode potential and of melt acidity specified by $pCl (= -\log a_{Cl^-})$. The flatband potential and the onset potential of photocurrent show pronounced pCl dependence with a variation rate of 2 (2.3 kT/e) per unit pCl , and this anomaly has been ascribed to the specific adsorption of Cl⁻ on TiO₂. Characterization of the melt-oxide interface and the photoelectrochemical oxidation of Cl⁻ via adsorbed intermediates are discussed on the basis of semiconductor energetics.

Since titanium dioxide received great attention from the viewpoint of the photoassisted electrolysis of water by utilizing solar energy (1), a number of investigations on the photoeffect at various semiconductor electrodes have been reported (2). Naturally, most studies have been concerned with aqueous systems, although some nonaqueous organic solvents have been also used (3). However, there has been little work on the use of molten salt solvents with respect to semiconductor-liquid junctions. Recently, we reported the interfacial behavior of Sb-doped tin oxide electrodes in molten LiCl-KCl eutectic (4, 5) and in AlCl₃-NaCl melts (6). There are some advantages in the use of molten salts for studying semiconductor electrodes because of the absence of neutral solvent molecules in the melt systems. The absence of this molecular solvation may lead to reversible reactions, and to a simple double layer structure without a solvent dipole layer oriented on electrode surfaces.

Among a number of molten salt systems, sodium tetrachloroaluminate melts have some salient features; (i) noncorrosive, (ii) liquidus at relatively low temperature, (iii) a relatively wide potential span, and (iv) well-established acid-base character. The characterization of the acid-base property of this melt was a recent subject and now we have detailed knowledge on its acid-base chemistry, where tetrachloroaluminate ions, AlCl₄⁻, act as chloride ion donors yielding Cl⁻ and Al₂Cl₇⁻, and the melt acidity is specified by the quantity $pCl (= -\log a_{Cl^-})$ derived from the acid-base equilibrium (7-9). In the present work our effort was mainly focused on characterizing the interfacial property between the melt and oxide. Thus we undertook to measure the photocurrent and differential capacity on single crystal n-TiO₂ electrodes in the melt of various pCl at 175°C. In connection with this study we will also present a photoelectrochemical process in the melt system.

Experimental

The sodium tetrachloroaluminate melt was prepared from the AR grade AlCl₃ and NaCl. The melt purification

* Electrochemical Society Active Member.

Key words: fused salts, semiconductor electrodes, photo-oxidation.

was carried out by employing sublimation, Al-displacement, and preelectrolysis as reported previously (6).

The reference electrode was a coiled Al wire (1 mm diam, 99.99%) immersed in the chloroaluminate melt saturated with NaCl, and the counterelectrode was W foil. Both of them were separated from the bulk of melt with fine fritted disks.

A Ψ -shaped Pyrex cell equipped with an electrode mount at the bottom is illustrated in Fig. 1. The cell assembly was set in a Pyrex container placed in a vertical electric furnace. The bottom of the cell was designed to have a flange with an optically flat surface, to which a disk of single crystal TiO₂ was attached via a Teflon O-ring. Construction details of the mount is shown in Fig. 1(B). An electrical contact to the electrode was made at the back side by alloying indium solder.

The disk of TiO₂ was reduced in a vacuum at 800°C for 1 hr to improve the bulk conductivity, then it was polished to a mirror finish with fine alumina powder ($\sim 0.3 \mu m$, Buehler Limited) on a wetted polishing cloth. Before the experiments, the electrode surfaces were chemically etched with CP4.

The assembled cell was evacuated in a container and then the purified melt was transferred into the cell under a dry nitrogen atmosphere. Experimental procedures for capacity measurements and the adjustment of pCl were described elsewhere (6).

In measurements of photocurrent the electrode surfaces were illuminated from the top with a 100W mercury lamp as illustrated in Fig. 1. A Nihon Bunko CT-25N monochromator was used for measurements of photocurrent spectra. All the experiments were carried out at $175^\circ \pm 2^\circ C$ under a dry N₂ atmosphere. Electrode potentials in this work are given with respect to the Al electrode in the melt saturated with NaCl.

Results and Discussion

Background characteristics.—Typical background cyclic traces of a TiO₂ electrode obtained in the melt of $pCl = 1.1$ in dark is shown in Fig. 2, being compared with the behavior of a SnO₂ electrode reported in the previous work (6). The anodic limit of the melt is

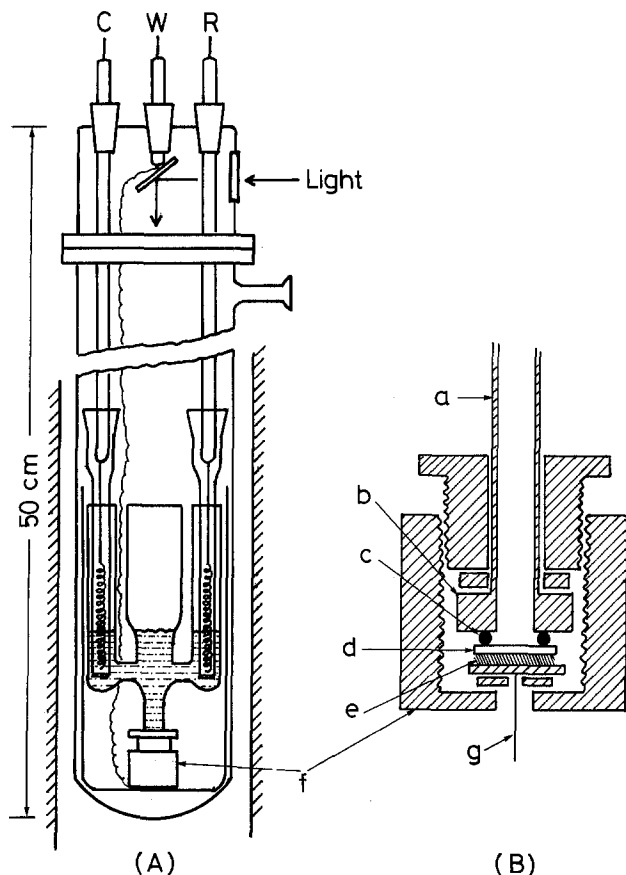


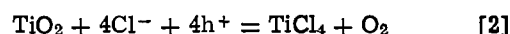
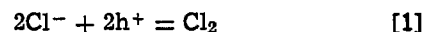
Fig. 1. Photoelectrochemical cell assembly. (A). C, counterelectrode; W, working electrode; R, reference electrode. (B). (a) Pyrex tube, (b) flange, (c) Teflon O-ring, (d) single crystal TiO_2 , (e) Indium solder, (f) electrode mount, (g) lead wire.

chlorine evolution, which occurs at potentials positive to 2.15V vs. Al at 175°C (7). The increase of anodic current at SnO_2 is due to chlorine evolution as described in our comparative study on chlorine evolution at SnO_2 and glassy carbon electrodes (10). In comparison with the SnO_2 electrode, it is noted that the chlorine evolution on the TiO_2 electrode is quite irreversible in dark, no detectable chlorine evolution taking place even at 3.0V vs. Al.

Anodic photocurrent.—When electrons at electrode surfaces of TiO_2 are depleted at potentials positive of the flatband potential, illumination of the light with higher photoenergies than the bandgap produces anodic photocurrent induced by the generation of

holes. In aqueous solutions this is the case leading to oxygen evolution which was reported by Fujishima and Honda (1). The photoeffect observed at the melt/ TiO_2 interface is shown in Fig. 3. The photocurrent begins to increase at a more negative potential than 2.15V which is the thermodynamic reversible potential of Cl^-/Cl_2 at $p\text{Cl} = 1.1$ (7). The reverse potential scan shows a current peak at 1.5V, which is presumably due to the reduction of the product accumulated at the interface during the anodic photoprocess.

Anodic processes responsible for the photocurrent in this melt containing Cl^- ions are chlorine evolution and/or the decomposition of TiO_2



Therefore, it is necessary to know whether TiO_2 electrodes in the melt are stable under illumination or not. Many investigators discussed the stability of semiconductors for photodecomposition on the basis of the energetics to semiconductor electrodes (11). According to them, competitive oxidation reactions which are located at potentials negative of the photodecomposition potential (E°_{decomp}) can effectively stabilize the semiconductor. In order to check this stabilization effect, we calculated the thermodynamic potential difference between [1] and [2] at 175°C using JANAF Table. Since E°_{decomp} of TiO_2 was shown to be positioned at 0.4V more positive potential than that of [1], the preferable photoprocess must be chlorine evolution which occurs much faster than the photodecomposition. A postulated surface band, which will be described later, can also assist the stability of TiO_2 photoanodes in the melt.

Since the sodium tetrachloroaluminate melt has an excellent optical window with 200 nm cutoff (12), the photocurrent measurement is not disturbed by the bulk adsorption. In our experimental setup, however, the light source was too remote from the electrode surface to supply sufficient light intensity. Thus, we unfortunately failed in having chemical confirmation that the product under illumination was chlorine, because of small photocurrent. However, there were several indications suggesting the chlorine evolution. In the melt saturated with chlorine gas, the reduction wave for chlorine was observed in dark at the same potential region as Fig. 3. It may be noteworthy in this context that the photodecomposition products, TiCl_4 and O_2 , are not reduced at 1.5V; the reduction potential of TiCl_4 is more negative than 1.5V (13) and oxygen seems to be electrochemically inactive. Additionally, the TiO_2 electrodes used in the melt showed no visible attack on the surfaces. Consequently, we

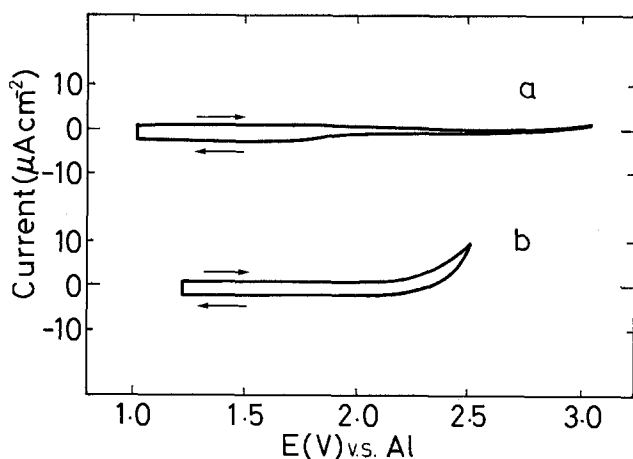


Fig. 2. Background cyclic traces for (curve a) TiO_2 , and (curve b) SnO_2 electrodes in molten sodium tetrachloroaluminate ($p\text{Cl} = 1.1$) at 175°C in dark. $V = 0.02$ V/sec.

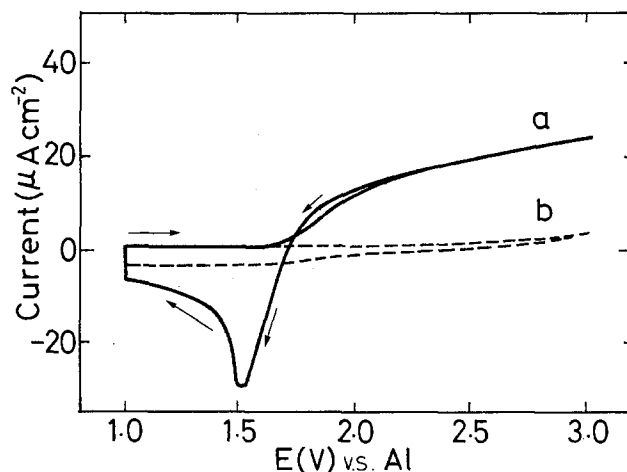
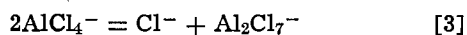


Fig. 3. Current-potential curves for TiO_2 electrode in molten sodium tetrachloroaluminate ($p\text{Cl} = 1.1$) at 175°C, curve a under illumination, and curve b in dark. $V = 0.02$ V/sec.

believe that the anodic photocurrent is due to chlorine evolution and the cathodic wave is due to the reduction of Cl_2 .

The photocurrent spectrum is shown in Fig. 4. Since the light intensity obtained through a monochromator was very weak, we had to use relatively large exit slit (2 mm) of the monochromator to obtain measurable photocurrent. Accordingly, the wavelength accuracy was questionable throughout the spectral region, where the light intensity is shown in Fig. 4c. For convenience's sake, we compared the apparent spectrum obtained in the melt with that in an aqueous 1N H_2SO_4 solution (Fig. 4b) where the photoprocess is oxygen evolution. Because both experiments were carried out with an identical condition of illumination by using the same electrochemical cell, the agreement of the spectra indicates that the photoelectrochemical process in the melt has essentially the same wavelength dependence with that in the aqueous solution, suggesting that the photoelectrolysis of the melt proceeds by consuming the photogenerated holes. It is also obvious from Fig. 4 that the process in the melt takes place with a comparable efficiency with the oxygen evolution in the aqueous solution.

The tetrachloroaluminate melts have the acid-base equilibrium expressed by the following equation



changing the melt composition therefore results in a change in the activity of Cl^- (7-9). With an analogy to the definition of pH, the activity of Cl^- is related to pCl, i.e., $\text{pCl} = -\log a_{\text{Cl}^-}$; for example, $\text{pCl} = 1.1$ in the melt saturated with NaCl (basic melt), $\text{pCl} = 2.5$ at equimolar composition (neutral melt), and $\text{pCl} > 2.5$ in acidic melt. Figure 5 shows the dependence of the photocurrent on pCl, indicating that the onset potential of photocurrent shifts towards the positive direction with increasing pCl. If the flatband potential does not depend on pCl, the onset potential would be identical regardless of pCl values. Thus the observed dependence strongly suggests that the location of flatband potential shifts towards the positive direction with increasing pCl.

Flatband potential.—It might be necessary to mention briefly the double layer structure in melt systems,

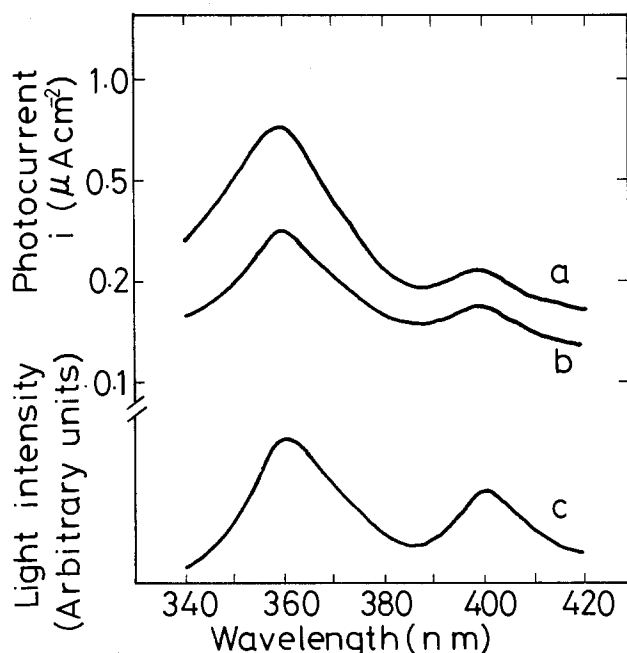


Fig. 4. Photocurrent spectra for TiO_2 electrode at constant potential. Curve a, in molten sodium tetrachloroaluminate ($\text{pCl} = 1.1$) at 175°C , $E = 3.0\text{V}$ vs. Al; curve b, in 1N H_2SO_4 at room temperature, $E = 2.0\text{V}$ vs. SCE; curve c, light intensity at the monochromator exit (2 mm slit width).

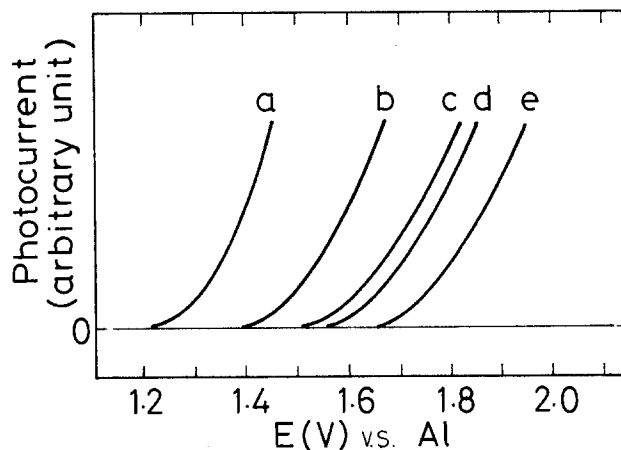


Fig. 5. Rising portion of photocurrent in molten sodium tetrachloroaluminates of various pCl at 175°C . Curve a, $\text{pCl} = 1.1$; curve b, $\text{pCl} = 2.0$; curve c, $\text{pCl} = 2.7$; curve d, $\text{pCl} = 3.5$; curve e, $\text{pCl} = 4.1$. Curves measured with chopped light from a 100W mercury lamp are corrected for dark currents.

because our knowledge is rather limited to that in aqueous systems. The potential distribution at the semiconductor/melt interface may be schematized like Fig. 6. The surface potential (ψ_s) is related to the space charge capacity of the electrode side (C_{sc}), which is given by the well-known Mott-Schottky equation (14), while ψ_H is related to the double layer capacity of the melt side (C_H). According to the multilayer model proposed to melt systems (15), the double layer of the melt side is highly compressed because of their high ionic strength. The excess charge is located several ionic layers deep, the layers being alternately negatively and positively charged. Thus ψ_H is regarded as the potential drop across the multilayer where the greater part of the potential drop is imposed on the two charged layers, i.e., the inner layer in contact with the electrode surface and the outer layer at the melt side. In the ordinary sense of the double layer concept, ψ_H is the potential drop inside the compact double layer.

Both capacities, C_{sc} and C_H , are combined in series, where C_H is much larger than C_{sc} as noted in the previous paper (6). Therefore, the measured capacity closely approximates to C_{sc} . The electrode potential (E) is the sum of the interfacial potential differences, and the flatband potential (E_{FB}) is defined as [5] because ψ_s equals zero at the flatband situation

$$E = \psi_s + \psi_H + \text{constant} \quad [4]$$

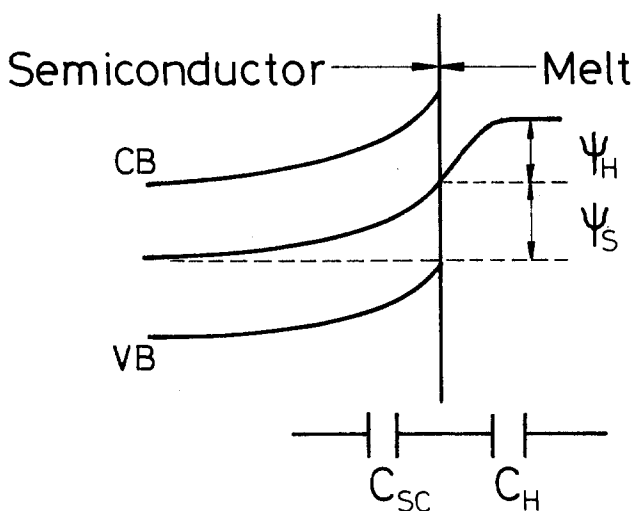


Fig. 6. Potential distribution and equivalent circuit for the semiconductor-melt interface.

$$E_{FB} = \psi_H + \text{constant} \quad [5]$$

If ψ_H is independent of E , ψ_s is replaced with $E - E_{FB}$. This assumption means that the applied potential drops inside the space charge layer. Then the reciprocal square of measured capacity becomes a linear function of electrode potentials which is known as the Mott-Schottky relationship

$$1/C^2 = (2/\epsilon\epsilon_0 e N_d) (E - E_{FB} - kT/e) \quad [6]$$

where e is the electronic charge, N_d the carrier concentration, ϵ the dielectric constant, and ϵ_0 the permittivity of vacuum.

The flatband potential obtained from this relationship has a special meaning; it is the zero charge potential with respect to the electrode. From [5] it is easily shown that a shift of E_{FB} relative to a constant-potential reference electrode is related to a change in the potential distribution of the double layer

$$\Delta E_{FB} = \Delta\psi_H \quad [7]$$

For a given electrode, $\Delta\psi_H$ may be brought about by changing the melt composition, i.e., by changing pCl values.

Mott-Schottky plots for TiO_2 electrodes in the melts with different pCl values were constructed from capacitance data measured at 1 kHz with a phase-sensitive detector. Typical plots at different pCl are shown in Fig. 7, where the capacity is the equivalent series capacity converted from the electrode admittance. In agreement with the shift of the onset potential of photocurrent, the Mott-Schottky plots were found to move towards the positive direction with increasing pCl . Although the plots were observed to deviate from linearity as they approached E_{FB} , the E_{FB} were determined by extrapolation of the linear parts and the carrier concentrations were obtained from the slope. In the calculation of N_d the dielectric constant of TiO_2 at 175°C is needed, but the exact value is not known. The data of the temperature dependence are available only for sintered polycrystalline rutile (16), indicating that the temperature coefficient is negative at temperatures below 120°C and becomes positive at higher temperatures. Taking into account this temperature dependence (16), it is considered that the ϵ value at 175°C is not considerably different from the ϵ at room temperature (= 172°C). The N_d of this specimen measured in an aqueous 1N H_2SO_4 at room temperature

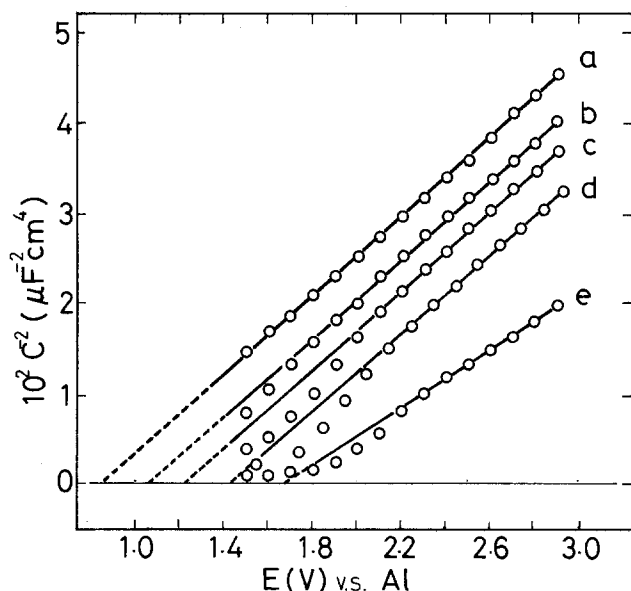


Fig. 7. C^{-2} vs. potential plots for TiO_2 electrode in molten sodium tetrachloroaluminate of various pCl at 175°C. $f = 1$ kHz. Curve a, $pCl = 1.1$; curve b, $pCl = 2.0$; curve c, $pCl = 2.7$; curve d, $pCl = 3.5$; curve e, $pCl = 4.1$.

was $3.0 \times 10^{19} \text{ cm}^{-3}$, being in good agreement with the $N_d (= 3.8 \times 10^{19} \text{ cm}^{-3})$ calculated from the slope of Fig. 7 and the above ϵ value. Thus there is no inconsistency in our analysis of capacity data based on the Mott-Schottky relationship.

The pCl dependence of E_{FB} is shown in Fig. 8 together with that of the onset potential of photocurrent. The E_{FB} shows a positive shift of 230 mV per unit pCl . Correspondingly, the onset potential of photocurrent moves to the positive direction with a variation rate of about 160 mV per unit pCl . In the case of SnO_2 electrodes in the same system, the variation rate is 170 mV as reported previously (6). Since $2.3(kT/e)$ is 89 mV at 175°C, the observed pCl dependence ($\partial E_{FB}/\partial pCl$) is close to two times of $2.3(kT/e)$. It is uncertain whether or not the somewhat large deviation from 178 mV/ pCl is real in the case of TiO_2 . The deviation appeared to increase in more acidic melts ($pCl > 2.5$) which may suggest some electrode instability at high pCl or may suggest a change in the type of ions adsorbed on the TiO_2 surface. An interesting feature of the Mott-Schottky plots is that the E_{FB} shifts to negative potentials with increasing the activity of Cl^- and its variation rate is close to $2(2.3 kT/e)$ per one decade of the activity change. The pCl dependence of the onset potential of photocurrent is regarded as a quantitative confirmation of this feature.

Specific adsorption of Cl^- .—The well-known pH dependence of E_{FB} in aqueous systems, $\partial E_{FB}/\partial pH = 2.3 kT/e = 59$ mV, is explained in terms of the change in the potential distribution across the dissociation double layer, which is caused by the acid-base equilibrium between the surface hydroxyl groups and bulk H^+ ions (17). The observed pCl dependence is, however, two times as large as the pH dependence, and cannot be explained quantitatively with the analogous acid-base concept. As suggested in the previous study on SnO_2 electrodes (6), this anomalously large variation rate can be ascribed to the discreteness-of-charge effect of specifically adsorbed Cl^- ions. According to the Esin-Markov effect (18), the point of zero charge (E_{pzc}) shifts towards increasingly negative potentials for anion specific adsorption and varies linearly with the logarithm of the anion concentration.

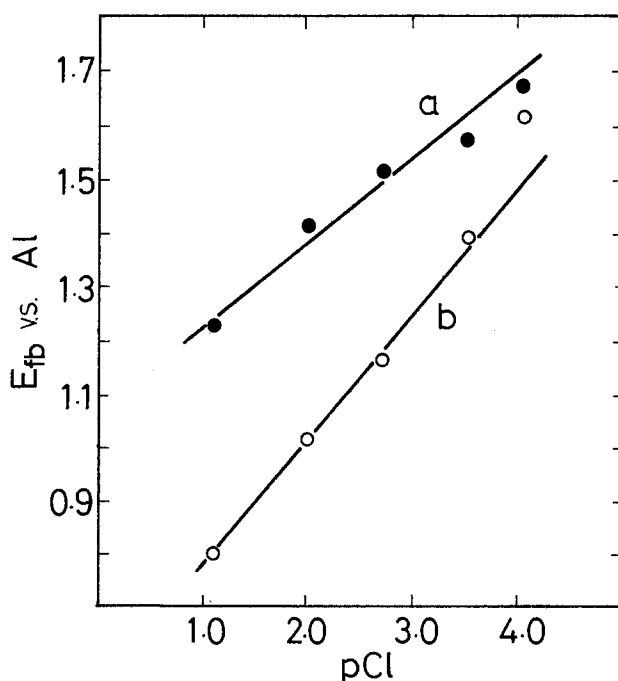
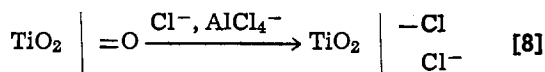


Fig. 8. pCl dependence of (curve a) the onset potential of photocurrent, and of (curve b) the flatband potential for TiO_2 electrode in molten sodium tetrachloroaluminate at 175°C.

The variation rate is reported to be about 100 mV at room temperature, i.e., $\partial E_{pzc}/\partial \log a_{x^-} \approx 2(2.3 kT/e)$ (19).

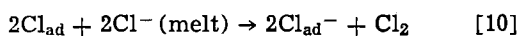
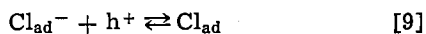
As discussed in the preceding section, the shift of E_{FB} reflects the change in the potential difference across the compact double layer present at the melt-oxide interface. When the first ionic layer in contact with the oxide surface consists of Cl^- ions, these anions populated on the surface are regarded as specifically adsorbed anions because there is no solvation layer present on the surface in this case. In addition, the original oxide surface which is covered with surface $=O$ (or $-OH$) groups must be considerably modified with the anions. Considering that $AlCl_4^-$ are oxide ion acceptor (20), the TiO_2 surface may be subjected to the following chemical change



where the surface $=O$ are replaced by chemically bonded $-Cl$ groups, and the specifically adsorbed Cl^- are present at vacant sites available for coordination. It is likely that the first ionic layer takes a hexagonal array, where some of constituents are chemically bonded $-Cl$ and the others are Cl_{ad}^- with negatively charged states. Thus the discreteness-of-charge effect is expected to influence the potential distribution between the first and the second ionic layers, and may result in the anomalous dependence of E_{FB} on pCl . With the analogy to the compact double layer theory developed in aqueous systems (21), the quantity $\partial E_{FB}/\partial pCl$ corresponds to the Esin-Markov coefficient at zero surface charge.

Hole transfer at the melt-oxide interface.—As shown in Fig. 3, the product of photo-oxidation is reduced at potentials considerably positive of E_{FB} . It was shown separately that dissolved chlorine in the melt is also reduced at TiO_2 electrodes in dark. The occurrence of reduction at potentials positive of E_{FB} strongly suggests the participation of surface states or an intermediate band in the electron transfer process as discussed by Bard *et al.* (3). Judging from the occurrence, the upper edge of the surface levels extends towards the conduction band, but its exact position is uncertain. The presence of the levels at the middle of bandgap is also suggested by the discrepancy between the onset potential of photocurrent and the flatband position, as noted in Fig. 8. When the band bending is relatively weak, these states must be more effective in the recombination of photogenerated hole-electron pairs, i.e., the back-reaction, rather than in the electron capturing from the melt side species.

Shub *et al.* studied chlorine evolution on TiO_2 photoanodes in aqueous solutions containing Cl^- ions (22), suggesting that the photo-oxidation mechanism consists of two elementary reactions involving adsorbed intermediates; the hole-capturing reaction by adsorbed Cl^- and the following recombination reaction of adsorbed Cl radicals. Taking into account the specific adsorption of Cl^- at the melt-oxide interface, similar reaction scheme can be applicable to this system



The energy levels of Cl_{ad}^- may be distributed below $E^\circ_{Cl^-/Cl_2}$, while the levels of Cl_{ad} must be positioned above $E^\circ_{Cl^-/Cl_2}$. In the case of strong adsorption the electronic energy levels of adsorbates are practically part of the electron system of the electrodes, and both energy levels will come much closer with increase of the adsorption interaction, approaching the range of the standard potential of the redox couple, as described by Gerischer (23). Thus a surface band consisting of the levels of the intermediates is placed tentatively near $E^\circ_{Cl^-/Cl_2}$ as shown in Fig. 9, which is

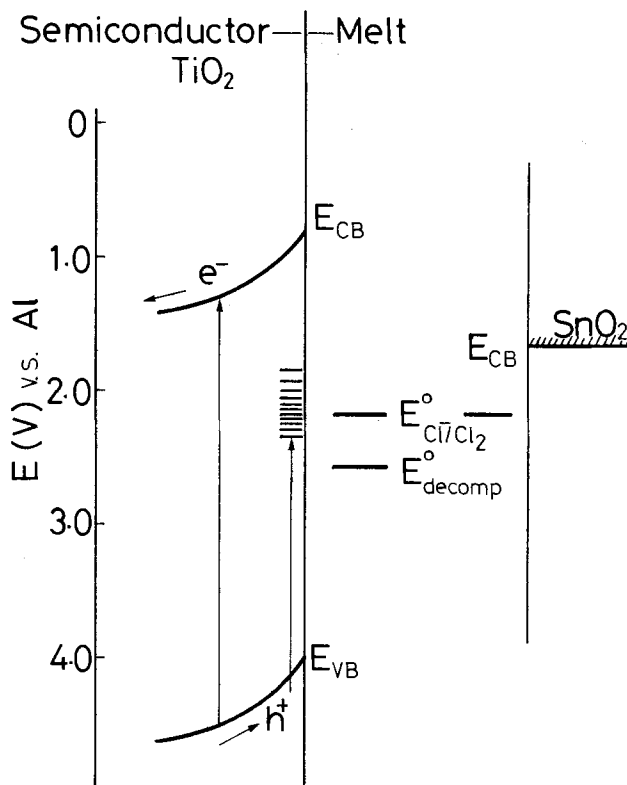


Fig. 9. Schematic energy diagrams for TiO_2 ($N_d = 3 \times 10^{19} \text{ cm}^{-3}$), and SnO_2 ($N_d = 7 \times 10^{19} \text{ cm}^{-3}$) electrodes in molten sodium tetrachloroaluminate ($pCl = 1.1$) at 175°C . The flatband position of SnO_2 is presented for comparison.

a schematic representation for the energetic relationship of the melt- TiO_2 interface obtained from the results of $pCl = 1.1$. The flatband position of $n\text{-SnO}_2$ at the same pCl taken from the previous work (6) is presented for comparison. We feel that the intermediate surface band noticed in the above section is associated with the specific adsorption of Cl^- on TiO_2 . The hole transfer under illumination can take place via the surface levels of Cl_{ad}^- , and the yielded radicals either recombine each other or accept the electrons from the melt side Cl^- to evolve chlorine.

Acknowledgments

The authors are indebted to Dr. Kingo Itaya for many helpful discussions. This research was supported partly by The Grant in Aid for Scientific Research, 1979.

Manuscript submitted Sept. 14, 1979; revised manuscript received Dec. 18, 1979.

Any discussion of this paper will appear in a Discussion Section to be published in the December 1980 JOURNAL. All discussions for the December 1980 Discussion Section should be submitted by Aug. 1, 1980.

Publication costs of this article were assisted by Tohoku University.

REFERENCES

1. A. Fujishima, K. Honda, and S. Kikuchi, *Kogyo Kagaku Zasshi*, **72**, 108 (1969).
2. c.f. "Semiconductor Liquid-Junction Solar Cells," A. Heller, Editor, The Electrochemical Society Softbound Proceedings Series, Princeton, N.J. (1977).
3. S. N. Frank and A. J. Bard, *J. Am. Chem. Soc.*, **97**, 7427 (1975); A. J. Bard and P. A. Kohl, in "Semiconductor Liquid-Junction Solar Cells," A. Heller, Editor, p. 222, The Electrochemical Society Softbound Proceedings Series, Princeton, N.J. (1977).
4. I. Uchida, H. Asano, and S. Toshima, *J. Electroanal. Chem. Interfacial Electrochem.*, **93**, 221 (1978).

5. I. Uchida, K. Niki, and H. A. Laitinen, *This Journal*, **125**, 1759 (1978).
6. I. Uchida, H. Urushibata, and S. Toshima, *J. Electroanal. Chem. Interfacial Electrochem.*, **96**, 45 (1979).
7. B. Tremillon and G. Letisse, *ibid.*, **17**, 371 (1968).
8. G. Torsi and G. Mamantov, *Inorg. Chem.*, **10**, 1900 (1971).
9. L. G. Boxall, H. L. Jones, and R. A. Osteryoung, *This Journal*, **120**, 223 (1973).
10. I. Uchida, H. Urushibata, and S. Toshima, *ibid.*, To be published.
11. H. Gerischer, in "Semiconductor Liquid-Junction Solar Cells," A. Heller, Editor, p. 1, The Electrochemical Society Softbound Proceedings Series, Princeton, N.J. (1977); A. J. Bard and M. S. Wrighton, *ibid.*, p. 195; T. Inoue, T. Watanabe, A. Fujishima, and K. Honda, *ibid.*, p. 210.
12. D. E. Bartak and R. A. Osteryoung, *This Journal*, **122**, 600 (1975).
13. J. A. Plambeck, in "Encyclopedia of Electrochemistry of Elements," Vol. X, Fused Salt Systems, A. J. Bard, Editor, p. 233, Marcel Dekker, New York (1976).
14. H. Gerischer, in "Advances in Electrochemistry and Electrochemical Engineering," Vol. 1, P. Delahay and C. W. Tobias, Editors, p. 139, Interscience, New York (1961).
15. A. D. Graves and D. Inman, *J. Electroanal. Chem. Interfacial Electrochem.*, **25**, 357 (1970).
16. "Gmelins Handbuch," Titan, **41**, p. 248, Verlag Chemie (1951).
17. M. Hoffmann-Pérez and H. Gerischer, *Z. Elektrochem.*, **65**, 771 (1961).
18. O. A. Esin and B. F. Markov, *Zh. Fiz. Khim.*, **13**, 318 (1939).
19. C. A. Barlow, in "Physical Chemistry," Vol. IXA, Electrochemistry, H. Eyring, Editor, p. 167, Academic Press, New York (1970).
20. B. Tremillon, A. Bermond and R. Molina, *J. Electroanal. Chem. Interfacial Electrochem.*, **74**, 53 (1976).
21. D. M. Mohilner, in "Electroanalytical Chemistry," Vol. 1, A. J. Bard, Editor, p. 241, Marcel Dekker, New York (1966).
22. D. M. Shub, A. A. Remnev, and V. I. Veselovskii, *Sov. Electrochem.*, **9**, 988 (1972).
23. H. Gerischer, in "Electrocatalysis on Non-Metallic Surfaces," A. D. Franklin, Editor, p. 1, NBS Special Publication 455 (1976).

Safety Studies on Li/SO₂ Cells

III. Differential Thermal Analysis of Miniature Li/SO₂ Cells

A. N. Dey*

P. R. Mallory & Company, Incorporated, Laboratory for Physical Science, Burlington, Massachusetts 01803

ABSTRACT

The differential thermal analysis (DTA) of miniature Li/SO₂ cells made with several design variables including separator material, organic solvent, and electrolyte salts were carried out with fresh, discharged, force-discharged (reversed), and charged cells. The observed thermal transitions were successfully identified by comparing these with the transitions observed in the DTA of cell constituents. The method appears to be a useful tool in studying the thermal runaway process of the Li/SO₂ cells.

Although the state-of-the art hermetically sealed high rate D cells were found to be exceedingly abuse resistant (1-5) we carried out a detailed study in order to gain increased understanding of the thermal runaway process of the Li/SO₂ cells in an effort to make the cells safe under all possible use and abuse conditions. We carried out differential thermal analysis of the cell constituents in order to identify the possible exothermic reactants which could initiate and/or propagate a thermal runaway process in a Li/SO₂ cell and reported earlier (6). In this paper we have attempted to augment the above DTA studies by doing the DTA of the actual Li/SO₂ cells themselves.

We chose to use a miniature spirally wound Li/SO₂ cell instead of the LO26 cells (D size). The design of the miniature cell was such that it reflected the behavior of the larger D size cell insofar as the heat generation characteristics are concerned. The purpose of these DTA studies is to determine the heat generation characteristics of the actual Li/SO₂ cells and compare them with the behavior predicted from the DTA studies of the cell constituents as well as to determine the effect of some of the cell design variables on the heat generation characteristics of the Li/SO₂ cells. The cell design variables studied were: separator material (porous polyethylene and glass), electrolyte salt (LiBr and LiAsF₆), and organic solvent (AN and PC + AN). The experimental details and the results are presented here.

Experimental

Miniature Li/SO₂ cell.—The cross-sectional view of the miniature Li/SO₂ cell is shown in Fig. 1. The cell was made in a nickel-plated cold rolled steel can, 0.302 in. diameter and approximately 1.5 in. high. The cell top consists of a G/M seal having a tantalum tube feed through which serves both as the positive terminal and as electrolyte fill port. The G/M seal was welded to the cell can. The cell bottom has a thermocouple well for the measurement of internal temperature. The cell was made with spirally wound electrodes: 1.2 in. × 1.3 in. × 0.012 in. cathode; 1.2 in. × 1.4 in. × 0.005 in. Li anode. The carbon cathode had an expanded aluminum current collector, but the Li anode did not have any current collector. The cells were filled with electrolyte having 70% SO₂ by weight. The fill tube was welded shut after the cell filling. The cells were made with the following variables:

Separator:	porous polypropylene, (celgard) (standard) glass filter paper
Electrolyte salt:	LiBr (standard) LiAsF ₆
Organic solvent:	AN (standard) PC + AN (1:1)

DTA fixture.—A cross-sectional view of the DTA fixture is shown in Fig. 2. It consists of an aluminum heating block having two cavities for the reference and the sample miniature cells. The differential thermocouples are inserted into the thermocouple wells (of the

* Electrochemical Society Active Member.
Key words: battery, organic, electrolyte.

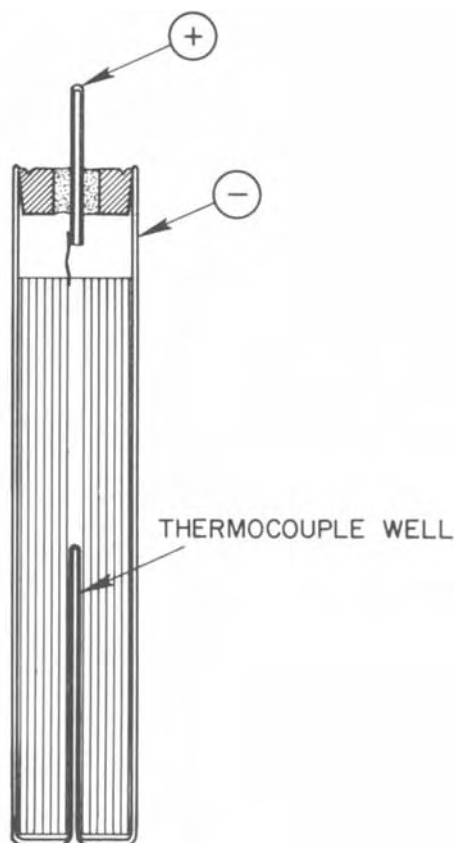


Fig. 1. Cross-sectional view of the miniature Li/SO₂ cell

cells) by means of heat-transfer compounds. The heating elements were wrapped around the aluminum block which was insulated all around by means of fiber glass. The heating block itself served as the negative terminal of the sample cell and the positive terminal was carefully insulated from the aluminum heating block. The DTA runs consisted of heating the aluminum block at a fixed rate from room temperature to a maximum of 250°C and monitoring both the block

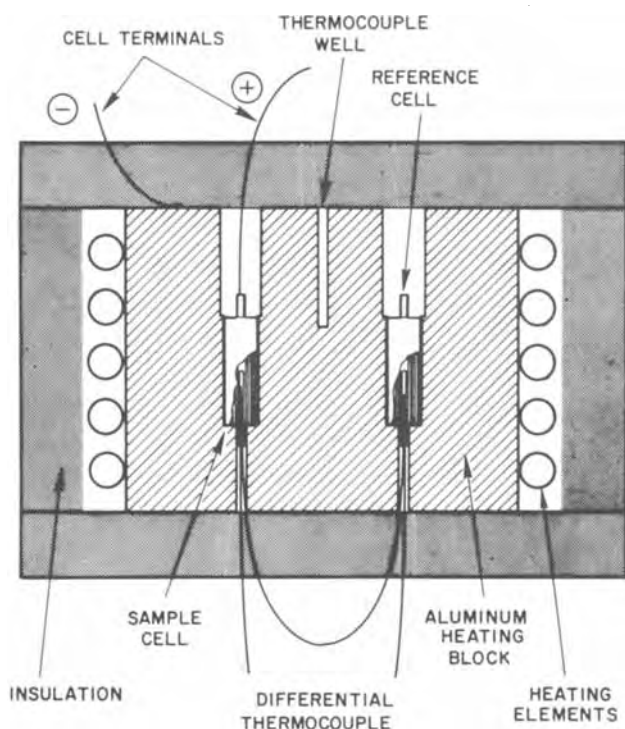


Fig. 2. Fixtures for DTA of miniature cell

temperature as well as the differential temperature on a strip chart recorder. The open-circuit voltages of the cells were also monitored during the DTA run. In some experiments the differential temperature of the cell was monitored during discharge, reversal, and charging of a cell.

Results and Discussion

The miniature cell was designed to reflect the thermal characteristics of the larger LO26S (D size) cells with the exception that the potential explosive energies involved would be substantially lower and hence less destructive of the available DTA fixtures. The electrochemical heat evolved per unit volume, as measured by the current density (i), over voltage (η) and the cell volume, turned out to be 9.1 ($i\eta$)_L W/cm³ for the LO26S cells and 11.5 ($i\eta$)_S W/cm³ for the miniature cell. Thus, if the cells are discharged at comparable current densities where they would experience comparable overvoltages, the heat evolution per unit volume would be approximately the same for the two cells and so would their thermal excursions under adiabatic conditions.

The miniature cells delivered 227 mA-hr at 1 mA and 180, 210, 180, and 180 mA-hr at 10 mA when discharged at 25°C. At -30°C, the cells delivered 90, 83, and 97 mA-hr at 90 mA to a cutoff voltage of 2.0V. A 90 mA current for the miniature cell corresponds to approximately 2A for the LO26S cells, in terms of equivalent current density.

DTA runs with two empty cell cans and with two cell cans filled with Al₂O₃ showed no transitions as expected. DTA runs with two fresh cells also showed no transitions. Cell cans filled with Al₂O₃ were chosen as a reference for all further DTA runs.

Altogether four different types of cells were tested. These will be referred to as (i) standard cells, (ii) cells with PC (propylene carbonate), (iii) cells with glass filter paper separator, and (iv) cells with LiAsF₆ electrolyte salt.

Almost all the DTA experiments were done in triplicate and the results were found to be quite reproducible.

Standard cells.—The standard cells contained 0.005 in. thick Li anode, 70% SO₂ + 7% AN (acetonitrile) + 23% LiBr electrolyte, and porous polypropylene (celgard) separator. The stoichiometric ratio of Li:SO₂ was approximately 1:1.3 based on the cell reaction



The cells were discharged at currents of 1, 10, and 90 mA at 25°C and then these were subjected to DTA runs by heating from 25° to 170°C. The differential thermocouple showed one small exothermic transition starting at temperatures of 150°C. A typical thermogram is shown in Fig. 3. There was no significant effect of the discharge current on the size of this exotherm, although the exothermic transition was somewhat smaller for a partially discharged cell. The exothermic transition is attributed to the exothermic decomposition of the discharge product Li₂S₂O₄. However the upper limit of the temperature of the DTA run was too low for most of the other exothermic reaction. The sharp lowering of the open-circuit voltage of the cell at temperatures of 140°C was probably due to the formation of shorts in the cell after melting of the polypropylene separator.

Miniature cells were force-discharged to reversal at 25° and -30°C in triplicate. One typical plot of the cell voltage, differential temperature, and the aluminum block temperature during the cell discharge is shown in Fig. 4. The differential temperature increased sharply at the point of the cell polarization. The block temperature was increased only slightly. The cell was at reversal for only 0.75 hr corresponding to a capacity of 67.5 mA-hr. There was no cell

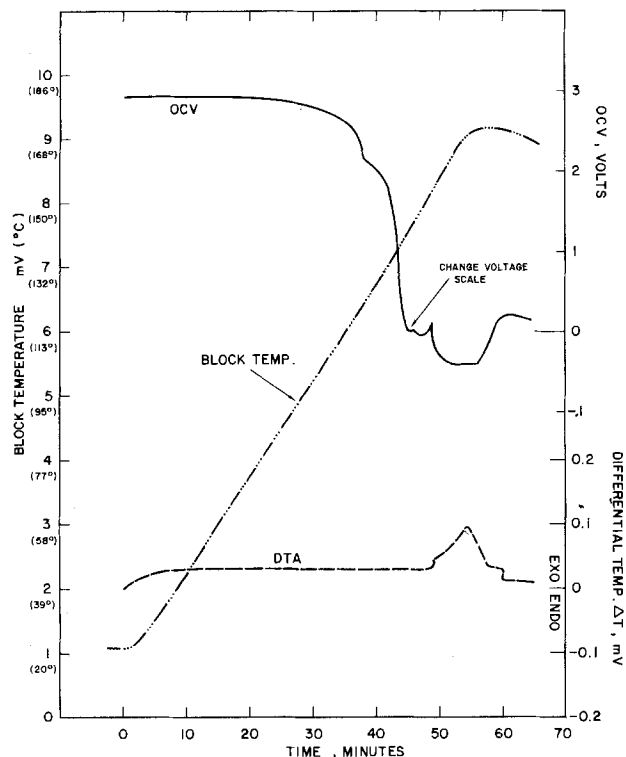


Fig. 3. Thermogram of a discharged miniature Li/SO₂ cell of standard construction. Discharge current 1 mA; discharge capacity 193 mA-hr.

venting or explosion. The cell was then subjected to a DTA run. The thermogram, as shown in Fig. 5, has two strong exothermic peaks very similar to those observed in thermograms of mixtures of powdered Li and Na₂S₂O₄ (analogous to Li₂S₂O₄). The first exotherm was attributed to the decomposition of Li₂S₂O₄ to produce S and the second one was most likely due to the Li + S reaction. Li + AN reaction may also occur simultaneously in view of the lower concentration of SO₂. The similarity of the thermograms of actual cells with that of the synthetic mixtures of

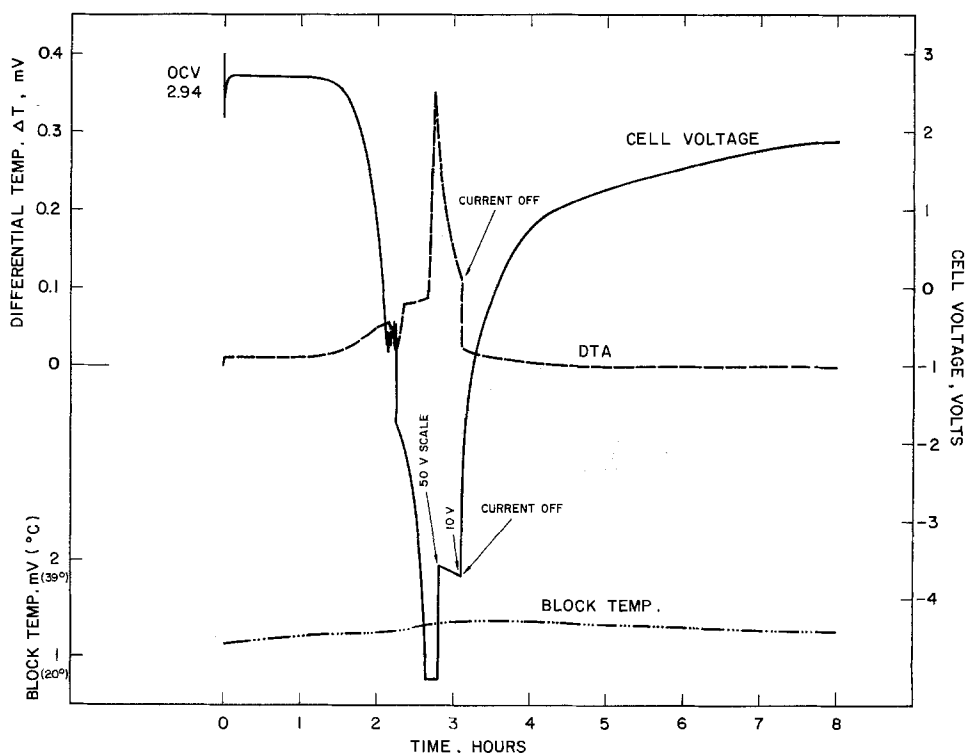
chemicals, done earlier, supports our conclusions regarding the identification of chemicals responsible for thermal runaway of Li/SO₂ cells. In the cell, Li₂S₂O₄ is formed during discharge and Li is formed during the reversal in the cathode. The presence of Li enhanced the exothermic caloric output of Li₂S₂O₄ as observed earlier (6) in DTA experiments with cathodes as well as in synthetic mixtures. A second DTA run with the same cell showed virtually no exothermic transition indicating that the active constituents (Li and Li₂S₂O₄) had reacted almost completely during the first DTA run, similar to our observations on Li/SOCl₂ cells (7).

The intensity of the exothermic transitions of the cells which were reversed appeared to be independent of the temperature at which the reversal occurred but dependent on the extent of reversal. Prolonged reversal produces more Li in the cathode than a short reversal and this leads to the increased caloric output as observed (6) in the thermograms of mixtures of Li + Na₂S₂O₄.

Miniature cells were also charged at 90 mA for 7 hr without any cell explosion. The DTA thermogram of the charged cell is shown in Fig. 6. Note that there is a small endotherm at 180°C most likely indicating the melting of Li. The strong exotherm above 200°C indicates the Li + AN reaction in the presence of excess SO₂ which protects Li from reaction with AN at a lower temperature. Since the cell was not discharged, there was no strong exotherm corresponding to the decomposition of Li₂S₂O₄, although some Li₂S₂O₄ may have formed by chemical reaction with the dendritic Li formed on the anode during charging. Again, the thermograms of the cells appeared to be interpretable based on the DTA results of the individual chemicals. A repeat DTA run of the above cell showed considerably reduced exothermic transitions indicating the consumption of the active materials during the first run.

Cells with PC.—These cells have the same size electrodes as the standard cells, only the electrolyte consists of 70% SO₂ + 23% mixture of AN and PC (3:1) + 7% LiBr. The thermogram of a discharged cell, as shown in Fig. 7, was found to be identical to that of the standard cell. Note that the upper limit of the temperature was only 170°C. The voltage and the differen-

Fig. 4. Voltage, differential temperature, and the block temperature profiles of a Li/SO₂ miniature cell of standard construction during discharge and force-discharge at 25°C at a current of 90 mA.



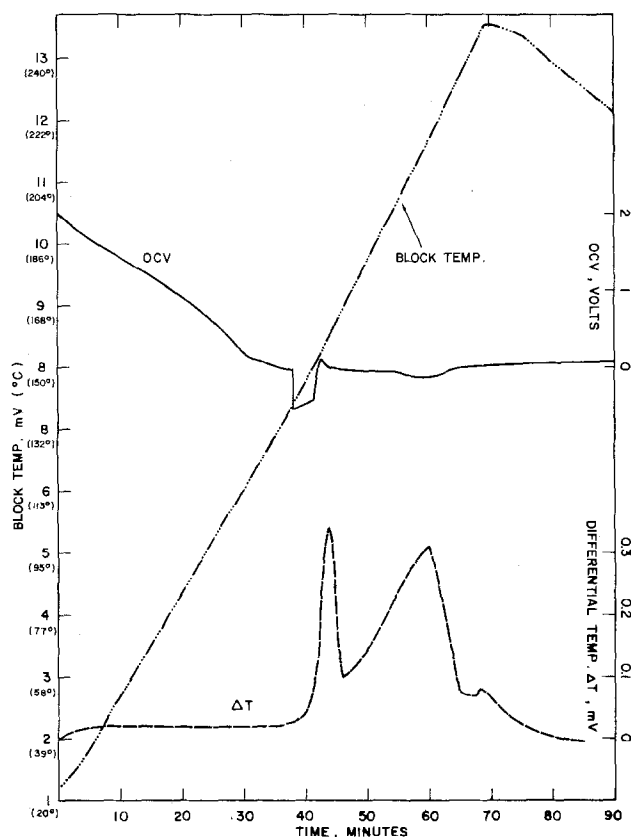


Fig. 5. Thermogram of the force-discharged Li/SO₂ miniature cell of Fig. 4.

tial temperature profile during discharge and reversal at 25°C at 90 mA for 3 hr, as shown in Fig. 8, also are very similar to those of the standard cell. However the DTA thermogram of the above reversed cell, as

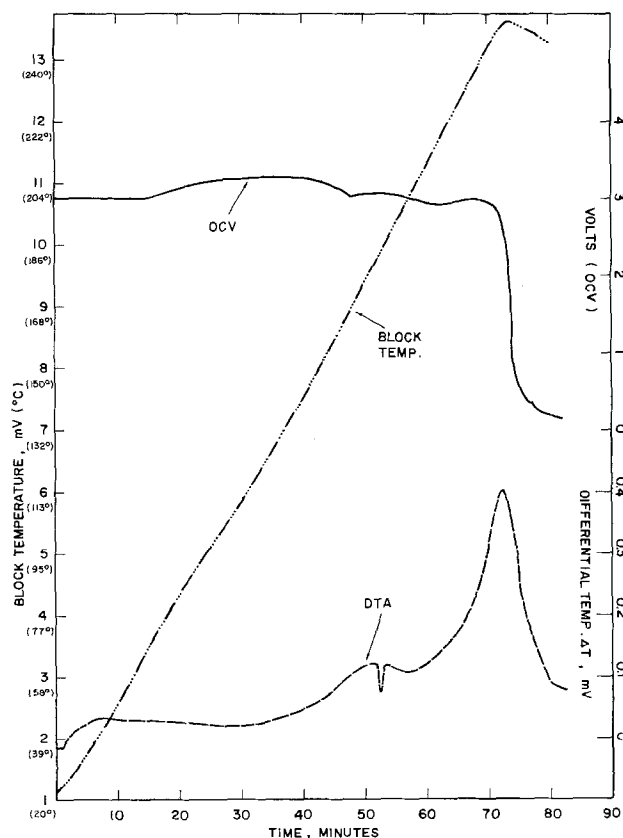


Fig. 6. Thermogram of a miniature Li/SO₂ cell of standard construction after being charged at 25°C for 7 hr at 90 mA.

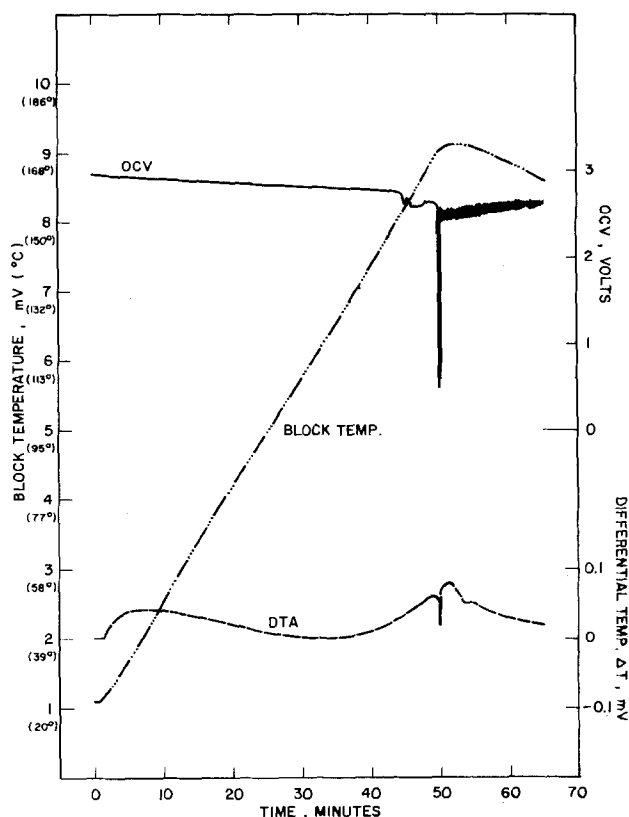


Fig. 7. Thermogram of a discharged miniature Li/SO₂ cell with PC in the electrolyte; discharge current, 10 mA; discharge temperature, 25°C.

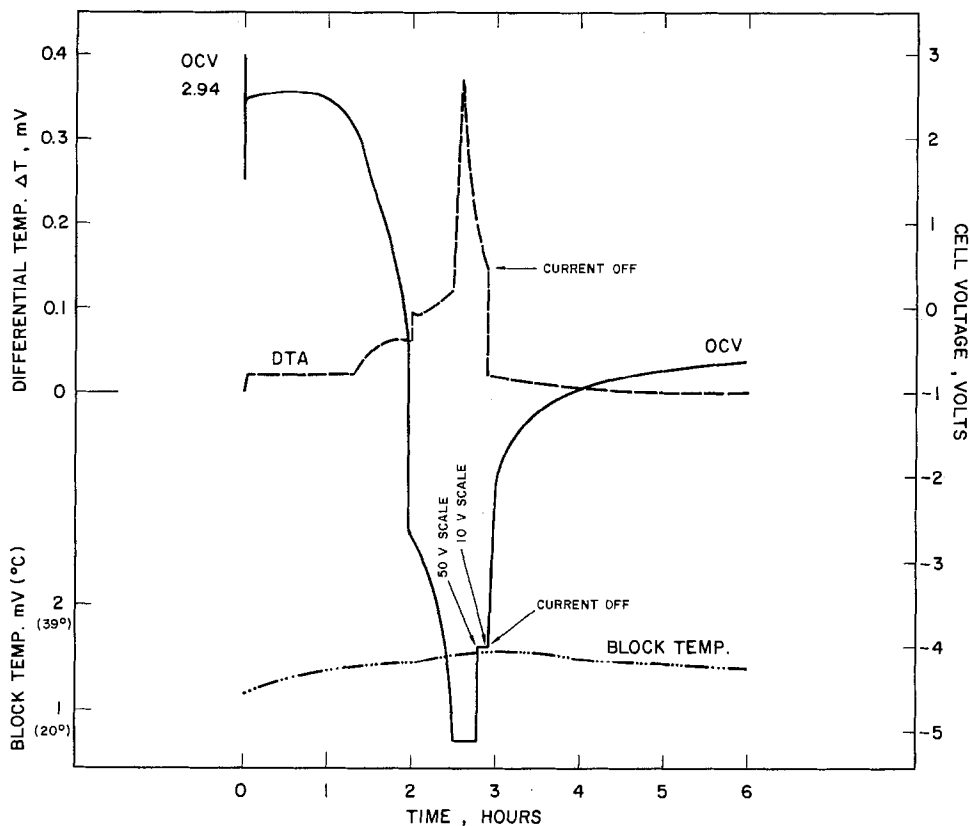
shown in Fig. 9, is interesting. Note that the upper limit of the temperature was 250°C. It shows three exothermic transitions prior to a very sharp exotherm occurring during the cooling cycle of the DTA. The repeat DTA run shows no significant exotherms. The thermogram of another cell force discharged at -30°C for 3 hr at 90 mA, is shown in Fig. 10. Note that it shows only the three exothermic peaks. But on the repeat run, the fourth strong exothermic peak appears as shown in Fig. 11. The above experiment was repeated and the DTA thermograms were found to be identical to the above. We believe that the three peaks are due to the following three reactions, viz., Li + AN, decomposition of Li₂S₂O₄ and Li + PC. The fourth sharp peak in Fig. 9 is most likely due to the Li + S reaction. We found earlier that Li + S reaction produced the sharpest exothermic transitions indicating a very fast reaction.

All the DTA experiments were carried out at least one day after the discharge and reversal of the cells; thus the exothermic transitions reflect reactions of relatively stable species and not transient species.

Cells with glass filter paper separator.—These cells are similar to the standard cells in every respect except the separator is made of glass filter paper. The thermogram of a fresh cell heated to 170°C is shown in Fig. 12. Note that the OCV remained unchanged during the run indicating the absence of shorting that occurred in cells with celgard separator which melts at approximately 140°C causing shorting. Also, there were no significant transitions as expected. The thermogram of a completely discharged cell showed a small exotherm very similar to that of the standard cells, most likely because the upper limit of the temperature was 170°C. Note also that the OCV of the cell did not drop to zero; indicating lack of cell shorting. The repeat run did not show any transition as before.

The DTA thermogram of a cell which was force-discharged at -30°C at 90 mA showed only a small

Fig. 8. Voltage, differential temperature, and the block temperature profiles of a Li/SO₂ miniature cell with PC in the electrolyte during discharge and force-discharge at 25°C at a current of 90 mA.



exotherm when the upper limit of the DTA run was kept at 170°C. However, when the upper limit of the DTA temperature was increased to 250°C of a similarly force-discharged cell, stronger exothermic trans-

sitions were observed again (Fig. 13) very similar to those of the standard cells.

The efficacy of the glass separator in preventing cells shorting at elevated temperatures is demon-

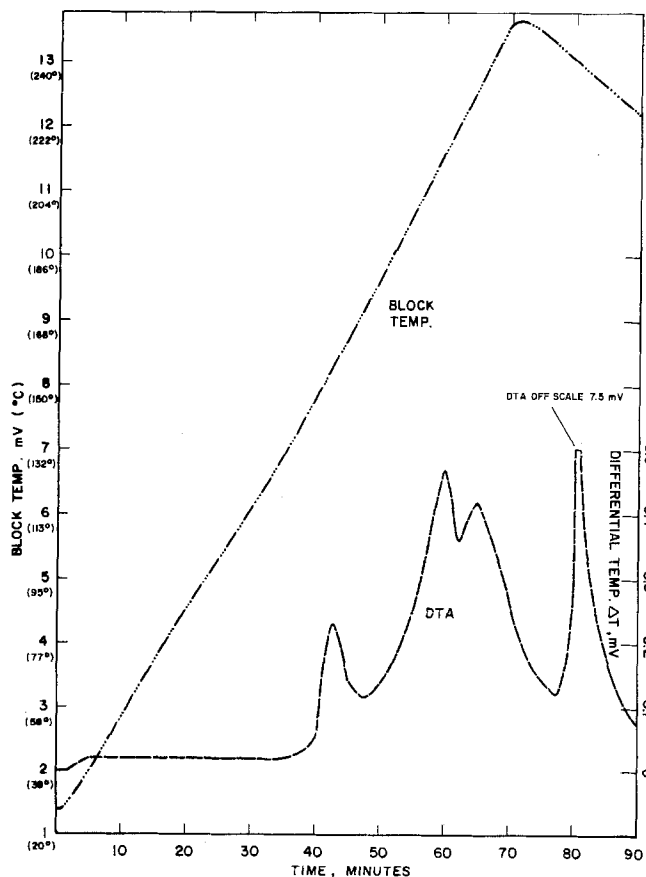


Fig. 9. Thermogram of the Li/SO₂ miniature cell with PC in the electrolyte after the force-discharge as shown in Fig. 8.

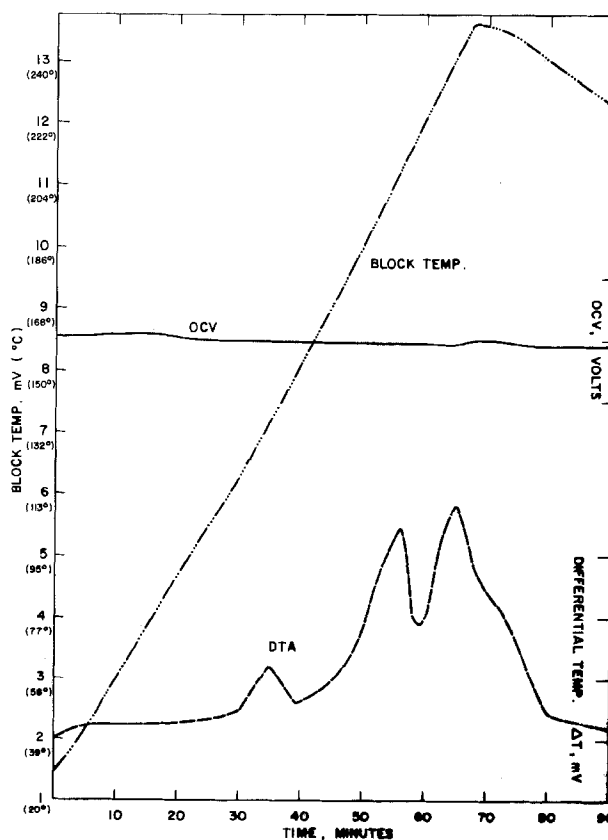


Fig. 10. Thermogram of a Li/SO₂ miniature cell with PC in the electrolyte after being force-discharged at -30°C for 3 hr at 90 mA.

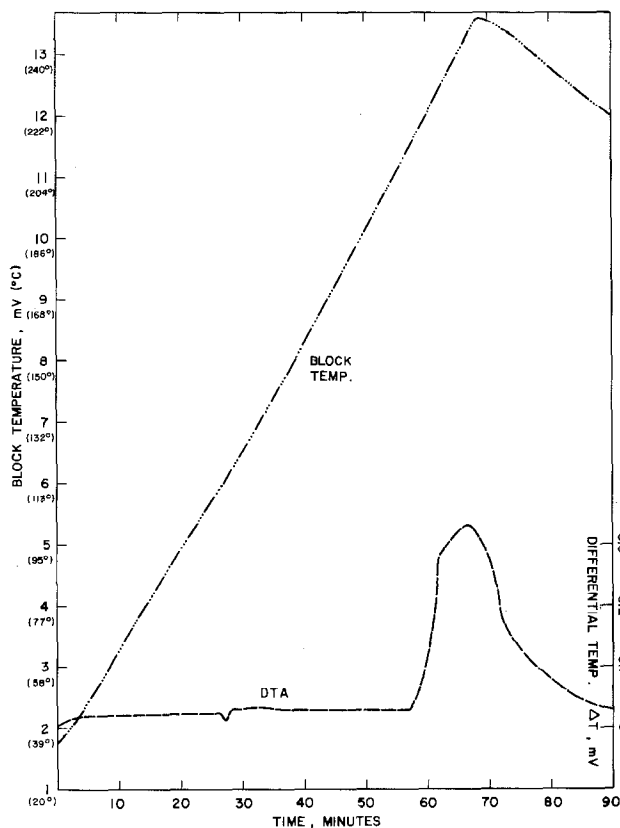


Fig. 11. Thermogram of the repeat DTA run after the one in Fig. 10.

strated from the above experiments. However, the exothermic reactions at 150°C are not thus preventable, as expected.

Cells with LiAsF_6 electrolyte salt.—These cells are identical to the standard cells except the electrolyte salt is LiAsF_6 instead of LiBr . The electrolyte con-

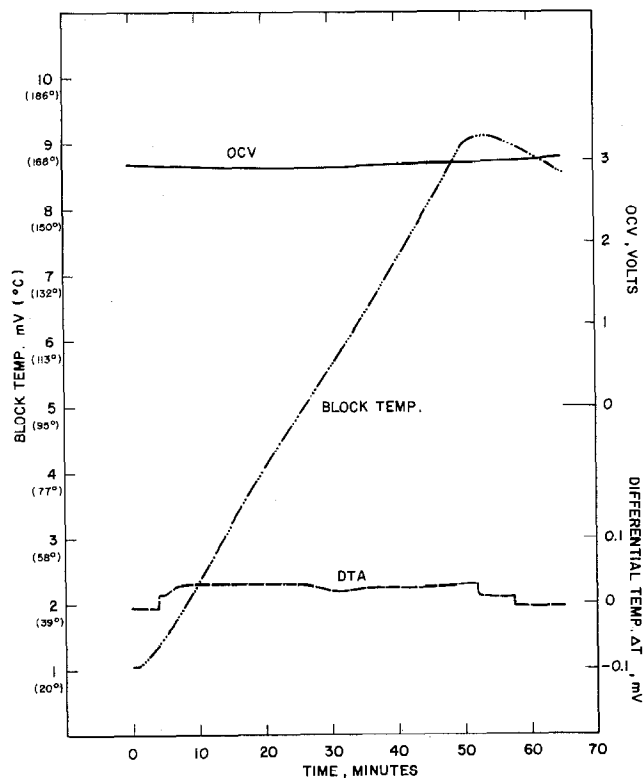


Fig. 12. Thermogram of an undischarged Li/SO_2 miniature cell with glass filter paper separator.

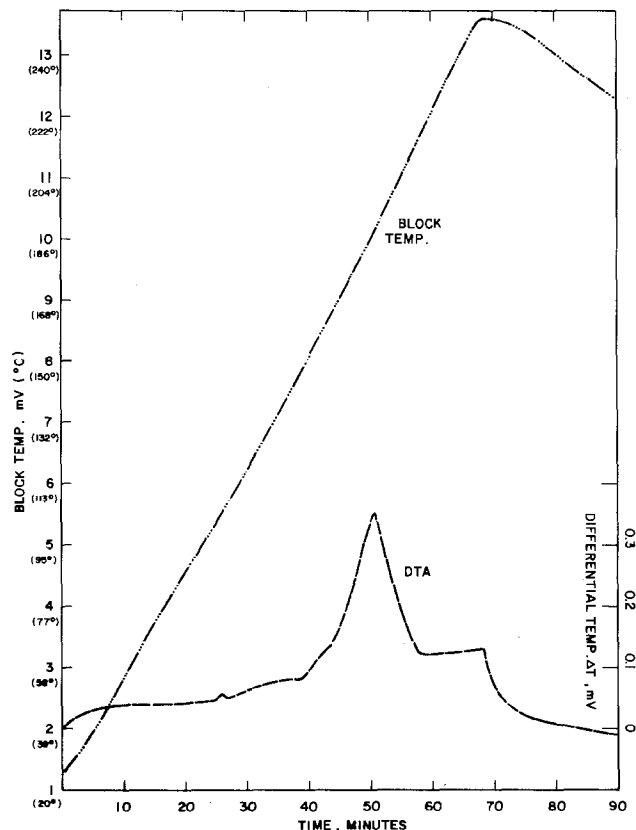


Fig. 13. Thermogram of a Li/SO_2 miniature cell with glass filter paper separator after being force-discharged at -30°C for 3 hr at 90 mA; the upper limit of the temperature was 250°C .

sisted of 70% SO_2 + 21% AN + 9% LiAsF_6 . The thermogram of a fresh cell is shown in Fig. 14. The

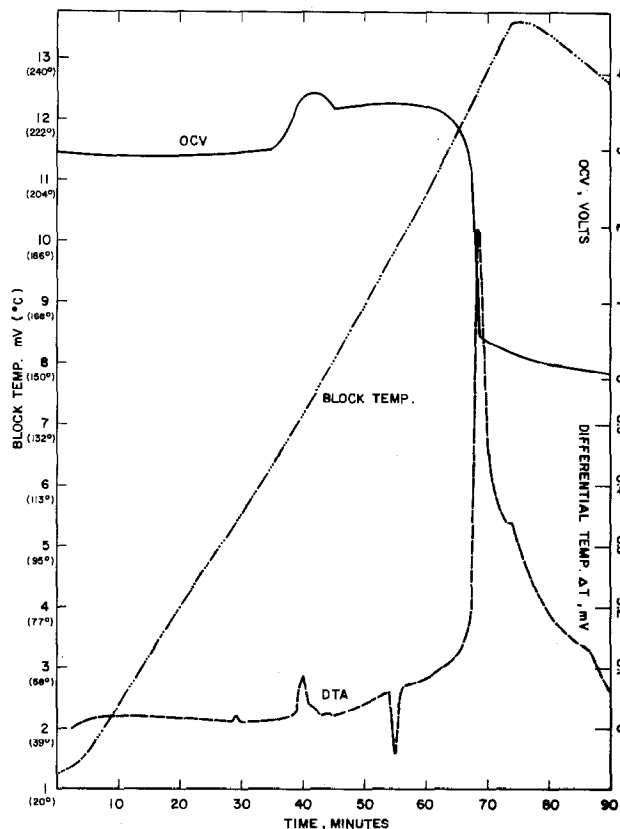


Fig. 14. Thermogram of an undischarged Li/SO_2 miniature cell with LiAsF_6 electrolyte.

open-circuit voltage of the cell curiously increased above 132°C from 2.95 to 3.66V. We found this phenomenon to be quite reproducible. There is a small exotherm in the thermogram corresponding to this increase in OCV. Our earlier DTA studies were incomplete insofar as this electrolyte salt is concerned and as such the reason for this increased OCV is not quite clear. The thermogram showed an endotherm corresponding to the melting of Li. Curiously, the cell did not short in spite of the fact that the cell temperature exceeded the melting point of the celgard separator. It is possible that the electrode assembly was not tight enough to create a short when the separator melted. The thermogram then showed a sharp exothermic transition corresponding to the shorting of the cell as indicated by the sudden drop of OCV. This cell did not explode at this point although another cell did in a subsequent run. A repeat run of the same cell showed no significant transitions, indicating complete decomposition of any electrochemically and thermally active materials including $\text{Li}_2\text{S}_2\text{O}_4$ formed during shorting. The temperature of the cell must have been high enough to complete all the thermally active processes discussed earlier.

The thermograms of discharged cells showed relatively smaller exotherms compared to those of a forced-discharged cell as observed earlier with the standard cells. The thermogram of a charged cell (Fig. 15) was similar to that of a fresh cell with the exception that the OCV was higher initially (3.44V) and it was re-

duced to 2.85V prior to shorting which resulted in a very large exotherm corresponding to both electrochemical and chemical heats. Note that the cell shorting occurred after the lithium melted as indicated by the small endotherm prior to the sharp drop of OCV. Repeat run showed no transitions as before.

The above results demonstrate the applicability of the cell DTA technique, in resolving the chemical processes occurring in cells during thermal excursions, and this method, in conjunction with the DTA of cell constituents, provides a useful tool for studying the thermal runaway processes of Li/SO_2 and other cells.

Conclusions

The differential thermal analysis (DTA) of miniature Li/SO_2 cells was found to be a useful tool in elucidating the chemical processes that occur in a cell during thermal excursions, as in thermal runaways. The DTA data of cell constituents were particularly useful for the identification of the various processes occurring in the cell by comparing the nature of the transitions of the cell with those of synthetic mixtures of cell constituents. The effect of the cell construction variables such as glass filter paper separator on the DTA thermograms of the miniature cells was found to be predictable in most cases based on the DTA data of the cell constituents. The major reactions which contribute to the thermal runaway process are the Li-organic solvent reaction and the decomposition of $\text{Li}_2\text{S}_2\text{O}_4$ as well as the $\text{Li} + \text{S}$ reaction, where S was produced from $\text{Li}_2\text{S}_2\text{O}_4$. The cell reversal results in stronger exothermic transitions due to the formation of Li in the cathode containing $\text{Li}_2\text{S}_2\text{O}_4$.

Acknowledgments

The author wishes to thank Dr. Sol Gilman and Dr. Per Bro for helpful discussions and Sarah Spencer for experimental assistance.

The work was carried out under a contract from U.S. Army, ERADCOM, Contract No. DAAB07-77-C-0472.

Manuscript received Dec. 27, 1978.

Any discussion of this paper will appear in a Discussion Section to be published in the December 1980 JOURNAL. All discussions for the December 1980 Discussion Section should be submitted by Aug. 1, 1980.

Publication costs of this paper were assisted by P. R. Mallory & Company Incorporated.

REFERENCES

1. P. Bro, R. Holmes, N. Marincic, and H. Taylor, Paper No. 45, "Proc. Intl. Power Sources Symposium," Brighton, England, 1974.
2. P. Bro, H. Y. Kang, C. Schlaikjer, and H. Taylor, "Tenth Intersociety Energy Conversion Engineering Conference," Newark, Delaware, p. 432 (1975).
3. H. Taylor and B. McDonald, "Proc. 27th Power Sources Symposium," p. 66, Atlantic City, N.J. (1976).
4. E. S. Brooks, "Proc. 26th Power Sources Symposium," p. 42, Atlantic City, N.J. (1974).
5. H. F. Hunger, and J. A. Christopolos, R&D Technical Report ECOM-4292, February 1975.
6. A. N. Dey and R. W. Holmes, *This Journal*, **127**, 775 (1980).
7. A. N. Dey, Paper 23 presented at The Electrochemical Society Meeting, Pittsburgh, Pa., Oct. 15-20, 1978.

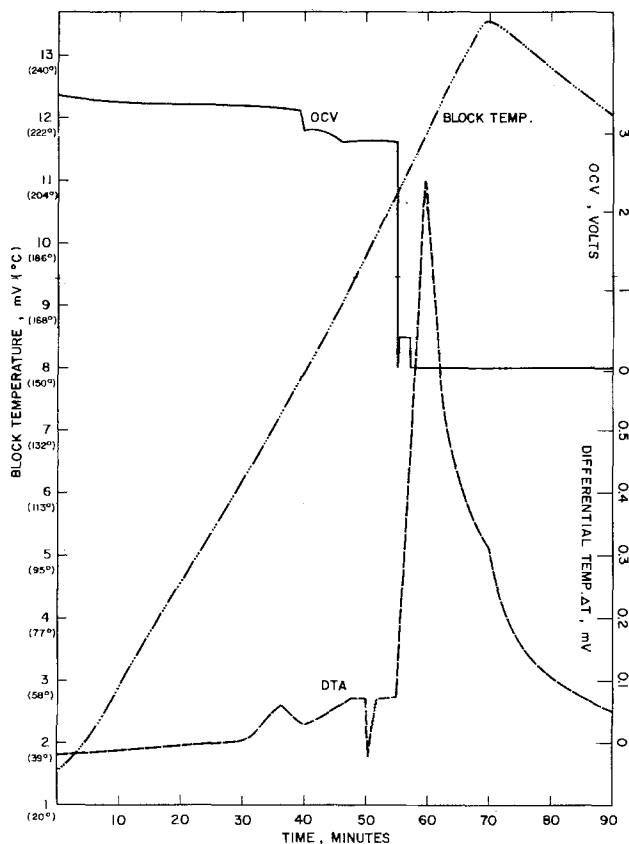


Fig. 15. Thermogram of a Li/SO_2 miniature cell with LiAsF_6 electrolyte after charging at 25°C for 7 hr with 90 mA.

The Formation of Ferrous Monosulfide Polymorphs during the Corrosion of Iron by Aqueous Hydrogen Sulfide at 21°C

David W. Shoesmith,* Peter Taylor, M. Grant Bailey, and Derrek G. Owen

Atomic Energy of Canada Limited, Research Chemistry Branch,
Whiteshell Nuclear Research Establishment, Pinawa, Manitoba, Canada R0E 1L0

ABSTRACT

The initial stages of corrosion of iron by unstirred saturated aqueous H₂S solutions at 21°C and atmospheric pressure have been examined as a function of time, pH (from 2 to 7, adjusted by addition of H₂SO₄ or NaOH), and applied current. Detailed examination of the morphology and phase identity of the corrosion products has led to a qualitative mechanistic understanding of the corrosion reactions. Mackinawite (tetragonal FeS_{1-x}) is formed by both solid-state and precipitation processes. Cubic ferrous sulfide and troilite occur as precipitates between pH = 3 and pH = 5, subsequent to metal dissolution upon cracking of a mackinawite base layer formed by a solid-state mechanism. The corrosion rate, and the relative amounts of these phases produced, are controlled by pH, applied current, and the degree of convection. The corrosion rate increases with decreasing pH; the quantity of precipitated material peaks near pH = 4, below which dissolution becomes the dominant process as the solubilities of the sulfide solids increase. Significant passivation was observed only at pH = 7, when the initial mackinawite base layer remained virtually intact. The solid-state conversion of cubic ferrous sulfide to mackinawite at 21°C was monitored by x-ray diffractometry. The resulting kinetics are consistent with the Avrami equation for a nucleation and growth process with a time exponent of 3.

The initial corrosion of iron or carbon steel by hydrogen sulfide saturated water at low temperatures is complex (1-5). There is considerable confusion regarding product identity in the earlier literature (5, 6) but it is now established that the initial corrosion involves the formation of up to three iron monosulfide phases (1-4): mackinawite (tetragonal FeS_{1-x}), cubic ferrous sulfide, and troilite (stoichiometric hexagonal FeS). Solubility measurements (7, 8) and interconversion studies (1, 2, 9) indicate the order of stability troilite > mackinawite > cubic ferrous sulfide. Troilite is a stable phase in the Fe-S system (10), but it is metastable with respect to pyrite in the solutions used in the present study (11). Mackinawite appears to be metastable under all conditions, but it occurs widely both naturally (9, 12) and as a precipitate under a wide range of laboratory conditions (8, 13) as well as in corrosion products. Little is known about cubic ferrous sulfide, other than its occurrence as a corrosion product, and its ease of conversion to mackinawite (1, 2).

Although there is a substantial body of literature describing the occurrence of these phases, no systematic examination of the chemical conditions of their formation on corroding surfaces has hitherto been reported. The purpose of the present study was to make such an examination, and to elucidate the mechanisms whereby the three solid corrosion products are formed. We have therefore examined the sequence of corrosion of iron in unstirred saturated aqueous H₂S at 21°C as a function of pH, reaction time, and applied current.

This work formed part of a study of corrosion and deposition phenomena in Canadian Girdler Sulfide heavy water production plants.

Experimental

Reactions were performed in a standard three-compartment glass cell. Deoxygenated aqueous hydrogen sulfide solutions (about 300 cm³) of desired pH were prepared *in situ* by purging appropriate NaOH or H₂SO₄ solutions with N₂, and then saturating the solu-

tions with H₂S. A slow H₂S purge was maintained during the experiments, to minimize ingress of oxygen. Experiments were performed at pH values in the range 1.7-7.0, at atmospheric pressure and usually at a temperature of 21°C. (A few experiments were performed at higher temperatures.) The solubilities of mackinawite and troilite, and the concentration of SH⁻, under these conditions are given in Table I. Most experiments were not stirred; in some experiments the solution was stirred using a magnetic stirrer bar at the bottom of the cell. Cylindrical iron electrodes (surface area = 5 cm²) were cut from bar stock (99.95% Fe), and one end of each was polished using 600 grit paper. The electrodes were mounted with the polished surface facing downward. In a few experiments, a more highly polished surface was prepared, using Metadi diamond polishing compound (1 μm). Some experiments were performed with two single crystals of iron, with polished [100] and [110] faces. These were immersed in aqueous H₂S at pH = 6 and 7, without electrical connections.

The potential of corroding specimens was monitored with a Dana Model 5330 digital voltmeter connected to a strip-chart recorder. Constant currents were applied using a Hewlett Packard Model 6186B current generator or a PAR Model 173 Galvanostat. All po-

Table I. Bisulfide ion concentrations, and solubilities of troilite and mackinawite, as a function of pH in saturated aqueous H₂S at 21°C and atmospheric pressure; concentrations in mole · dm⁻³

pH	[SH ⁻]	[Fe ²⁺] (mackinawite) ^a	[Fe ²⁺] (troilite) ^a
2	1.0 × 10 ⁻⁶	—	0.04
3	1.0 × 10 ⁻⁵	0.01	5 × 10 ⁻⁴
4	1.0 × 10 ⁻⁴	5 × 10 ⁻⁴	6 × 10 ⁻⁵
5	1.0 × 10 ⁻³	2 × 10 ⁻⁵	—
6	0.010	—	—
7	0.10	—	—

^a Estimated solubilities, expressed as pseudo-equilibrium iron concentrations, based on 25°C data from Ref. (7). No data are available for cubic ferrous sulfide, but the fact that it transforms spontaneously to mackinawite at 21°C indicates that it is more soluble than mackinawite.

* Electrochemical Society Active Member.

Key words: sulfide corrosion, iron sulfide phases, mackinawite, troilite, cubic ferrous sulfides.

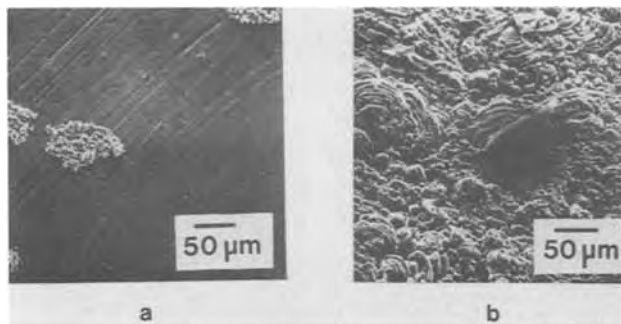


Fig. 1. Iron surfaces exposed to saturated aqueous H_2S solution, $\text{pH} = 7$, for 24 hr at 21°C . (a) Open circuit; (b) applied current, $I = 40 \mu\text{A}\cdot\text{cm}^{-2}$.

tentials quoted are on the saturated calomel electrode scale. The reference electrode was an Orion Model 90-02 double-junction silver-silver chloride electrode. The Orion KCl filling solution was of such a concentration that the electrode matched the response of a saturated KCl calomel electrode. It was necessary to use such an electrode because a single-junction electrode was found to degrade in sulfide solution, presumably due to formation of silver sulfide (14).

Corrosion products on the polished electrode surfaces were identified by direct x-ray diffractometry of the surfaces, using a Philips Model PW1050 diffractometer equipped with a diffracted-beam monochromator and using $\text{CuK}\alpha$ radiation. The morphology of corrosion products was examined using a Cambridge Mark IIA Stereoscan scanning electron microscope. Correlation of diffraction data with microscope studies permitted the visual identification of particles of the three iron sulfide phases. Rough quantitative estimates of the three phases were made from the heights of major diffraction peaks, but the accuracy of these estimates was severely limited by the very high absorption coefficient of iron for $\text{CuK}\alpha$ x-rays ($\mu \approx 10^5 \text{ m}^{-1}$ for each phase) and, in the case of mackinawite, by a significant degree of preferred orientation and a tendency to spall from the surface. A few samples of material which had spalled from electrodes were analyzed by x-ray powder photography.

Results

Reaction at $\text{pH} = 7$.—In the experiments performed at $\text{pH} = 7$ for 24 hr, with applied anodic currents, I , of 0, 1, 40, 80, and $130 \mu\text{A}\cdot\text{cm}^{-2}$, mackinawite was the only corrosion product observed, with the exception

of a trace of cubic ferrous sulfide at $I = 40 \mu\text{A}\cdot\text{cm}^{-2}$. Microscopic examination of surfaces after open-circuit reactions ($I = 0$) showed two types of corrosion product: a coherent, featureless base layer, and a loose deposit of precipitated material at a few sites (Fig. 1a). Enhancement of the $hk0$ diffraction peaks of mackinawite indicated a preferred orientation with the sheets of iron atoms in the crystal structure (15) lying perpendicular to the metal surface. The same orientation of the base layer was observed on both [100] and [110] faces of iron single crystals. We associate this preferred orientation with the coherent layer observed microscopically, and suggest that it is formed by a solid-state reaction.

Figure 2a shows the potential of the iron electrode as a function of time and applied current. The positive potential shift indicates that the base layer at least partially passivates the surface. The duration of this shift decreases with increasing anodic current, as the rate of formation of the base layer increases. Cracking of this layer causes local dissolution of iron and precipitation of the loose mackinawite deposit (Fig. 1a). Under applied currents, the enforced increase in corrosion rate results in more rapid and extensive cracking of the base layer, and consequently a much greater amount of precipitated material. The time at which cracking commences is indicated by the sudden negative shift in the potential, Fig. 2, as the electrode surface becomes more active due to the exposure of bare metal. At the higher applied currents, much of the mackinawite spalls from the electrode. This has been used at these laboratories as the basis for a synthesis of mackinawite, using much higher applied currents ($4 \text{ mA}\cdot\text{cm}^{-2}$). At $I = 40 \mu\text{A}\cdot\text{cm}^{-2}$, the mackinawite has a layered appearance (Fig. 1b), indicative of successive cracking, repair, and re-cracking of the base layer.

The initial negative potential excursions in the transients of Fig. 2a at $I = 40 \mu\text{A}\cdot\text{cm}^{-2}$, and particularly at $I = 0$, may be due to the removal of an oxide film, resulting in an increased electrode activity. The transients of Fig. 2b show that stirring retards the positive shift of the potential, indicating that a soluble species, presumably Fe^{2+} , is produced concurrently with the film formation.

Reaction at $\text{pH} = 6$.—In the relatively few experiments performed at $\text{pH} = 6$, all under open-circuit conditions, the sole product was again mackinawite, with a high degree of preferred orientation. However, the 001 diffraction peaks were enhanced, indicating orientation with the sheets of iron atoms in the struc-

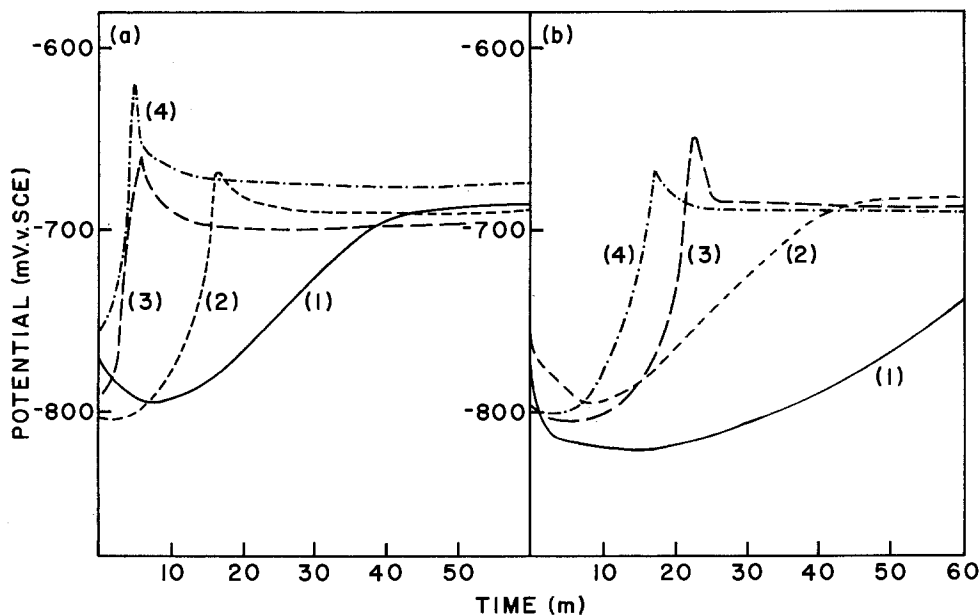


Fig. 2. Potential of iron surfaces exposed to saturated aqueous H_2S solution, $\text{pH} = 7$, at 21°C . (a) Stagnant; (b) stirred. Curve (1) $I = 0$; curve (2) $I = 40$; curve (3) $I = 80$; curve (4) $I = 130 \mu\text{A}\cdot\text{cm}^{-2}$.

ture lying parallel to the surface rather than perpendicular as at pH = 7. The intensities of the 001 mackinawite reflections after a given reaction time were enhanced for a more polished surface, which probably reflects a greater degree of perfection of orientation rather than a greater thickness of the layer. Again, the same mackinawite orientations were observed for both [100] and [110] iron crystal faces, although greater enhancement of the 001 reflections was observed for the [100] face. The association of a high degree of preferred orientation of film growth with highly polished surfaces independent of the crystallographic orientation of the substrate, and the phenomenon of changing orientation with changing growth rate, have been discussed by Finch *et al.* (16).

The oriented layer was not sufficiently coherent to passivate the surface. This is indicated by the corrosion potential, which does not show a positive shift, unlike the situation at pH = 7 (Fig. 3). The high corrosion rate resulted in a dense upper layer of very fine-grained, precipitated mackinawite, which covered the surface completely after 24 hr.

Reaction at pH = 5.—All three phases, mackinawite, cubic ferrous sulfide, and troilite, were observed at pH = 5, necessitating a more detailed examination of the reaction. A series of open-circuit experiments was performed over reaction times up to 24 hr, and a series of 24 hr experiments was carried out with applied currents, I , from -50 to $+70 \mu\text{A}\cdot\text{cm}^{-2}$.

The early stages of natural corrosion at pH = 5 resemble those at pH = 6, but the higher corrosion rate results in earlier cracking of the base layer and associated mackinawite precipitation. The upper layer material covered the surface completely after 9 hr. Both cubic ferrous sulfide and troilite were observed after 16 hr reaction. Both phases occurred as well-developed crystals, evidently grown from solution, scattered over the mackinawite base layer. Cubic ferrous sulfide typically formed large irregular blocks up to $20 \mu\text{m}$ across, while troilite occurred as pointed needles (up to $10 \times 2 \mu\text{m}$), of hexagonal cross section.

The appearance of the cubic phase at a comparatively late stage of the reaction, and its known metastability with respect to mackinawite (1, 2), show that the source of iron for its formation is the metal rather than the mackinawite. The dense upper layer of mackinawite obscured any changes in the base layer associated with the formation of cubic ferrous sulfide, but cracking or pitting of the base layer must have resulted in very high local supersaturation. This is demonstrated more clearly by the results obtained at pH = 4.

The relative amounts of cubic ferrous sulfide and troilite were more poorly reproducible at pH = 5 than at pH = 4. When large amounts of troilite were formed, it tended to occur at the expense of cubic ferrous sul-

fide, reflecting competition for the same source of iron. The greater irreproducibility is reflected in the corrosion potentials as a function of time. A spread of 30 mV was obtained for a series of nominally identical runs at pH = 5, compared with an 8 mV spread at pH = 4. The plot shown in Fig. 3 is for a single experiment which approximated the average behavior at pH = 5. Experiments performed with applied currents are discussed below.

Reaction at pH = 4.—All three phases were again produced at pH = 4. Since results tended to be more reproducible than at pH = 5, the reaction was studied most extensively at this pH. Open-circuit experiments were run from 0.25 to 96 hr, in addition to a series of 24 hr experiments with I ranging from -120 to $+120 \mu\text{A}\cdot\text{cm}^{-2}$, and a small number of 24 hr, open-circuit runs at temperatures up to 90°C . Figure 4 shows changes in surface morphology with time and Fig. 5 shows the relative amounts of the three phases as a function of time.

After 0.25 hr, a very small quantity of mackinawite was detected. Enhancement of the [001] diffraction peak indicates a significant degree of preferred orientation. The surface film was sufficiently thin that scratch marks from polishing the electrode were still visible on micrographs, and an upper layer of wispy particles was also observed. After 0.5 hr (Fig. 4a), the quantity of mackinawite was greater, the degree of orientation was somewhat lower, and the density of coverage by fine material was higher. However, scratch marks were still visible.

After 1 hr (Fig. 4b), severe blistering was observed, as the coherent base layer peeled from the surface. The blistered material was covered by a dense mass of small crystals, presumably developed by growth of the wispy particles noted after shorter reaction periods. The quantity of mackinawite detected by x-ray diffraction was higher than that after 0.5 hr, but no preferred orientation was apparent, which is consistent with the severe disruption of the base layer. The effect of stirring on the corrosion potential recorded at pH = 7 indicates that some iron dissolution was occurring. This process is more significant at pH = 4, and the fine mackinawite particles seen in these early stages are likely to have precipitated from solution.

After 2 hr, scratch lines were no longer visible and the quantity of mackinawite continued to increase. There was some indication of the redevelopment of preferred orientation with [001] parallel to the surface. This suggests the redevelopment of a coherent base layer below the debris of the original film.

After 4 hr (Fig. 4c) scratch marks were visible once again, indicating that the blistered material had fallen away; the diffraction results showed less mackinawite than at 2 hr, but with a fairly high degree of orientation. The surface was covered with a slightly pitted, dense layer of fine-grained ($< 1 \mu\text{m}$) mackinawite with larger (ca. $5 \mu\text{m}$) crystals of cubic ferrous sulfide scattered over the surface. The cubic ferrous sulfide did not display significant preferred orientation in this or any other experiment, nor was any preferred orientation of troilite ever observed. Most of the electrodes displayed a marked [110] preferred orientation of the iron metal, but this did not appear to affect the course of reaction.

In a second 4 hr experiment with a more polished specimen, mackinawite was the sole product. The initial base layer appeared not to have blistered and fallen away, although some cracking had evidently occurred, for much of the surface was covered with fine-grained precipitated mackinawite. This run thus resembled the behavior at pH = 5 with less polished specimens.

Between 4 and 12 hr, cracking and pitting of the second mackinawite base layer occurred, but its thick-

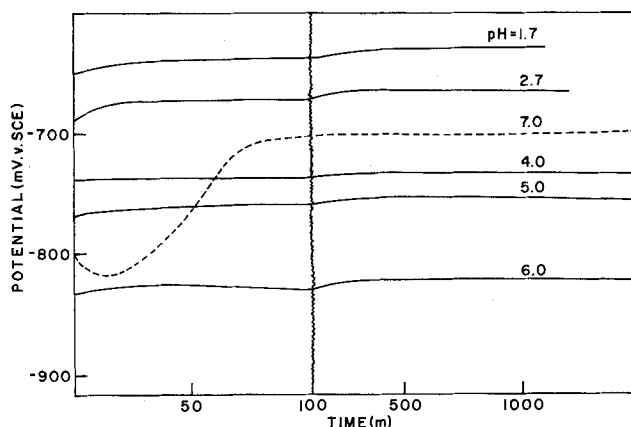


Fig. 3. Potential of iron surfaces exposed to saturated aqueous H_2S solution at 21°C as a function of time and pH.

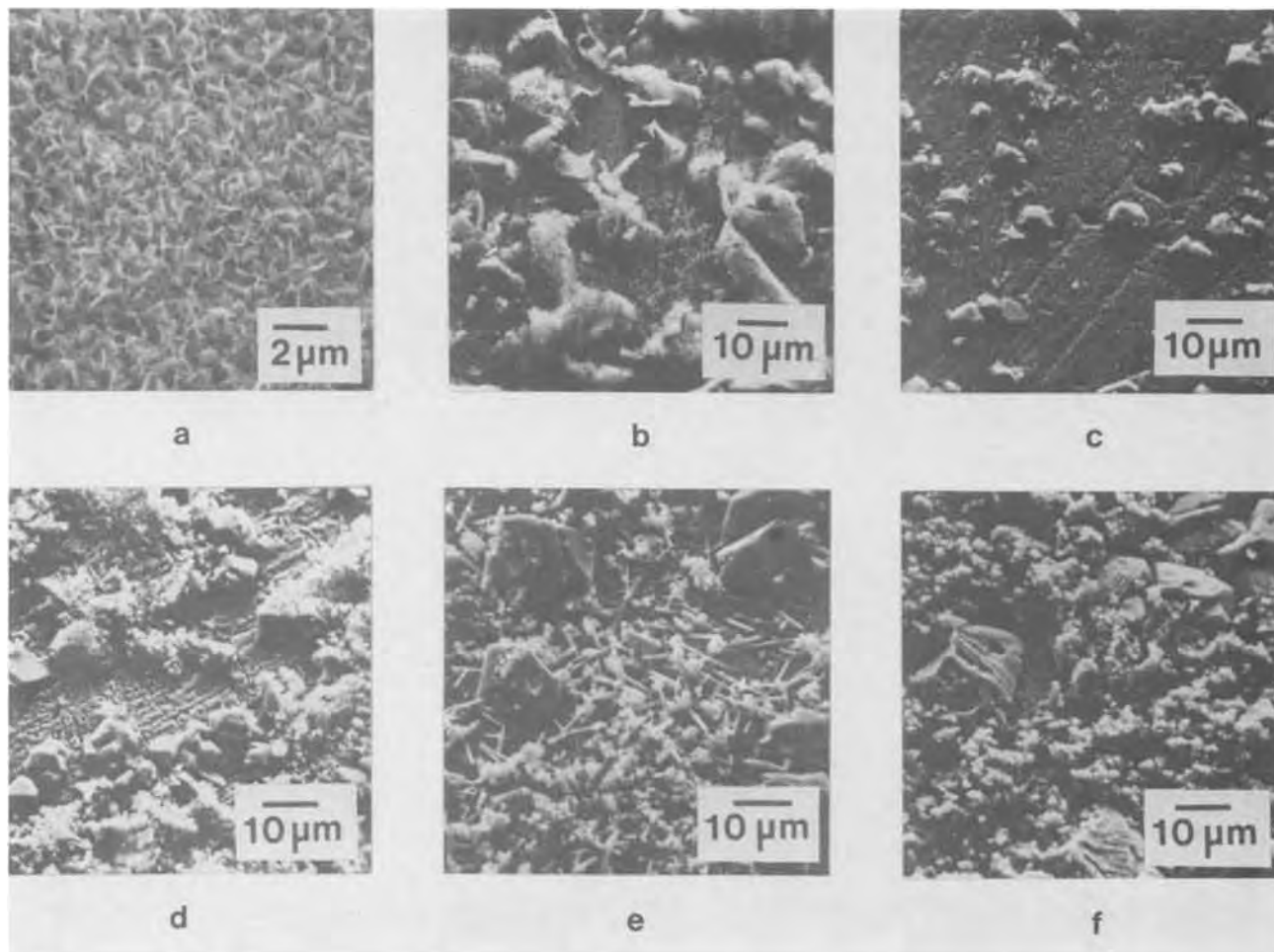


Fig. 4. Scanning electron micrographs of iron surfaces exposed to saturated aqueous H_2S solution at $21^\circ C$ and $pH = 4$ for (a) 0.5 hr, (b) 1.0 hr, (c) 4 hr, (d) 12 hr, (e) 16 hr, (f) 24 hr.

ness remained approximately constant (Fig. 4d). The amount of precipitated mackinawite increased somewhat, but much more was seen to spall from the surface. The number and size of cubic ferrous sulfide crystals increased over this period, showing that both nucleation and growth had continued. Crystals of cubic ferrous sulfide tended to be more adherent than those of mackinawite, and only trace quantities were observed in analyses of spalled material.

The only change observed between 12 and 16 hr was the appearance of a small quantity of troilite needles (Fig. 4e). The cubic ferrous sulfide crystals were now up to $15 \mu m$ across. A 16 hr experiment with a more polished iron specimen yielded a very similar surface to that obtained with a routinely prepared specimen. Evidently, although rupture of the initial

mackinawite base layer was retarded on the more polished surface, the subsequent development of the corrosion sequence was not significantly altered at the high corrosion rates obtained at $pH = 4$.

Surface coverage by cubic ferrous sulfide continued to increase, up to about 80% after 24 hr (Fig. 4f). At longer reaction times, the quantity of the cubic phase fell as it underwent solid-state conversion to mackinawite (1, 2; see below). As at $pH = 5$, the development of troilite was the least reproducible feature of the experiments. When significant quantities of troilite were formed, it again tended to occur at the expense of cubic ferrous sulfide. Even after 96 hr reaction at $pH = 4$, troilite was not the preponderant phase, although it was consistently a major component after reaction times ≥ 37 hr.

If the solution was stirred, only a thin base layer of mackinawite was formed after 24 hr, confirming that the upper layer material was precipitated from solution.

As with the open-circuit experiments, behavior under applied currents was more reproducible at $pH = 4$ than at $pH = 5$. The relative amounts of the three phases formed as a function of applied current at $pH = 4$ are shown in Fig. 6.

Even with an applied current of $-120 \mu A \cdot cm^{-2}$, a small quantity of mackinawite was formed, indicating a substantial corrosion current at $pH = 4$. The mackinawite had a preferred orientation with [001] perpendicular to the surface, similar to that observed in open-circuit experiments at $pH = 7$. At $I = 100 \mu A \cdot cm^{-2}$, the amount of mackinawite had increased, and its orientation had switched to [001] parallel to the surface, characteristic of the higher corrosion rates in open-circuit runs at $pH \leq 6$. The quantity of mackinawite did not change greatly over the range $-80 \leq$

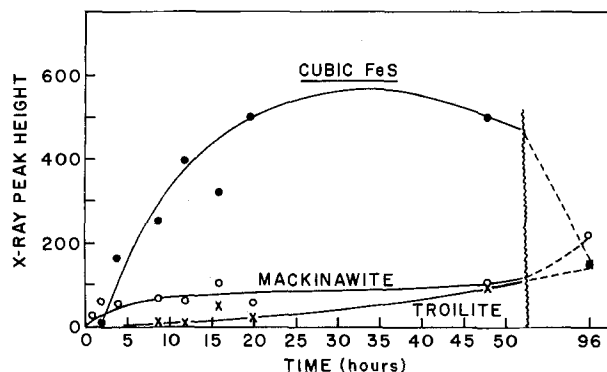


Fig. 5. Relative amounts of ferrous monosulfide phases formed on iron surfaces exposed to saturated aqueous H_2S solution at $21^\circ C$ and $pH = 4$ as a function of time.

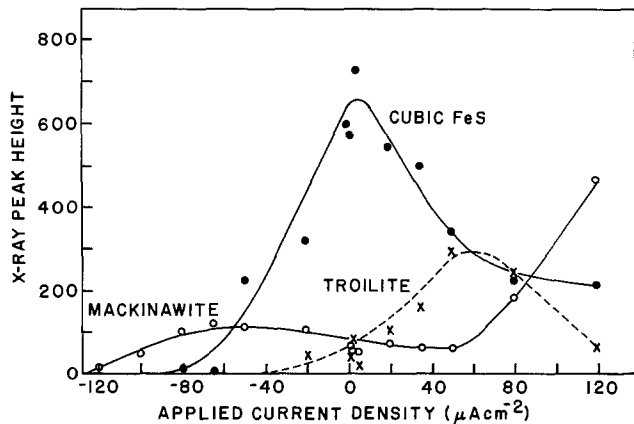


Fig. 6. Relative amounts of ferrous monosulfide phases formed on iron surfaces exposed to saturated aqueous H_2S solution at 21°C and $\text{pH} = 4$ for 24 hr as a function of applied current.

$I \leq 0 \mu\text{A}\cdot\text{cm}^{-2}$, except for a gradual increase in precipitated material. The amount of material spalling from the electrode increased as the applied current became less negative, but losses were small in this range. Mackinawite decreased somewhat as I increased to $+50 \mu\text{A}\cdot\text{cm}^{-2}$, then increased massively at still higher applied currents.

Although the amount of mackinawite changed only slightly over the range $-80 \leq I \leq +50 \mu\text{A}\cdot\text{cm}^{-2}$, major changes occurred in the quantities of both troilite and cubic ferrous sulfide. The latter appeared in minor quantities at $I = -80 \mu\text{A}\cdot\text{cm}^{-2}$, was a major product at $I = -50 \mu\text{A}\cdot\text{cm}^{-2}$, increased rapidly to a peak at $I \approx 0$, then gradually fell to about 30% of its peak value at $I = +120 \mu\text{A}\cdot\text{cm}^{-2}$. Troilite was not observed at $I < -20 \mu\text{A}\cdot\text{cm}^{-2}$, and only became a major product at $I \geq 20 \mu\text{A}\cdot\text{cm}^{-2}$. It peaked at $ca. I = 50 \mu\text{A}\cdot\text{cm}^{-2}$, then also gradually fell, concurrently with the increase in mackinawite at $I > 50 \mu\text{A}\cdot\text{cm}^{-2}$.

As noted above, results at $\text{pH} = 5$ were generally less reproducible than at $\text{pH} = 4$, but similar trends in the quantities of the three phases with changing applied current could be detected.

Figure 7 shows polarization curves obtained at $\text{pH} = 4$ and $\text{pH} = 5$, constructed from plots of the corrosion potential against time for a given applied current. The corrosion currents at the two pH values were estimated by extrapolating the anodic and cathodic linear regions of these curves to the corrosion

potential for $I = 0$. At $\text{pH} = 4$, the "initial" ($t = 2$ min) corrosion current density is $ca. 35 \mu\text{A}\cdot\text{cm}^{-2}$, falling to around $30 \mu\text{A}\cdot\text{cm}^{-2}$ at 30 min and $ca. 27 \mu\text{A}\cdot\text{cm}^{-2}$ after 24 hr. The slight fall in corrosion rate indicates that none of the corrosion products passivate the surface. At $\text{pH} = 5$, the lower corrosion rate of $ca. 10 \mu\text{A}\cdot\text{cm}^{-2}$ is consistent with the reduced amounts of material precipitated, compared with $\text{pH} = 4$. These corrosion current densities are only very approximate values. However, they are sufficiently accurate to indicate variations with time and pH .

There is little variation of size or morphology of cubic ferrous sulfide crystals as a function of applied current at $\text{pH} = 4$. At lower currents the crystals tend to possess sunken faces (Fig. 8a, $I = -50 \mu\text{A}\cdot\text{cm}^{-2}$), indicative of depletion of iron supply at the growth sites. At higher currents the crystals are better formed, and sometimes nucleate in clumps (Fig. 8b, $I = +35 \mu\text{A}\cdot\text{cm}^{-2}$), reflecting the faster iron supply rate achieved at the higher currents.

Reactions at $\text{pH} < 4$.—Only two experiments were performed at pH values below 4, the natural pH of H_2S -saturated water. The pH was lowered by addition of H_2SO_4 , and two 24 hr, open-circuit experiments were run at $\text{pH} = 1.7$ and $\text{pH} = 2.7$. At $\text{pH} = 1.7$, the solubilities of all three phases are sufficiently high that no precipitate was observed, but severe attack of the metal surface due to direct dissolution was apparent. At $\text{pH} = 2.7$, much of the metal surface was again bare and attacked, but small quantities of cubic ferrous sulfide and precipitated mackinawite were scattered on the surface.

The relative amounts of each phase formed after 24 hr of open-circuit reaction as a function of pH are summarized in Fig. 9. The mackinawite data are less reliable than those for troilite and cubic ferrous sulfide because of the preferred orientation phenomena discussed above, and because of the undetermined quantities of mackinawite which spalled from the electrode.

Reactions at elevated temperature.—A small number of 24 hr, open-circuit experiments were performed in a thermostatted cell at temperatures up to 90°C and $\text{pH} = 4$. Reproducibility of results was poor, and ripening of crystals at higher temperatures gave rise to unfamiliar morphologies. However, a few trends could be detected. At 35°C (Fig. 10a) the coverage of the surface by large ($20 \mu\text{m}$) crystals of cubic ferrous sulfide approached 100% (cf. 85% at 21°C), and rather less mackinawite was present than at 21°C . At 50°C , coverage by cubic ferrous sulfide was still close to

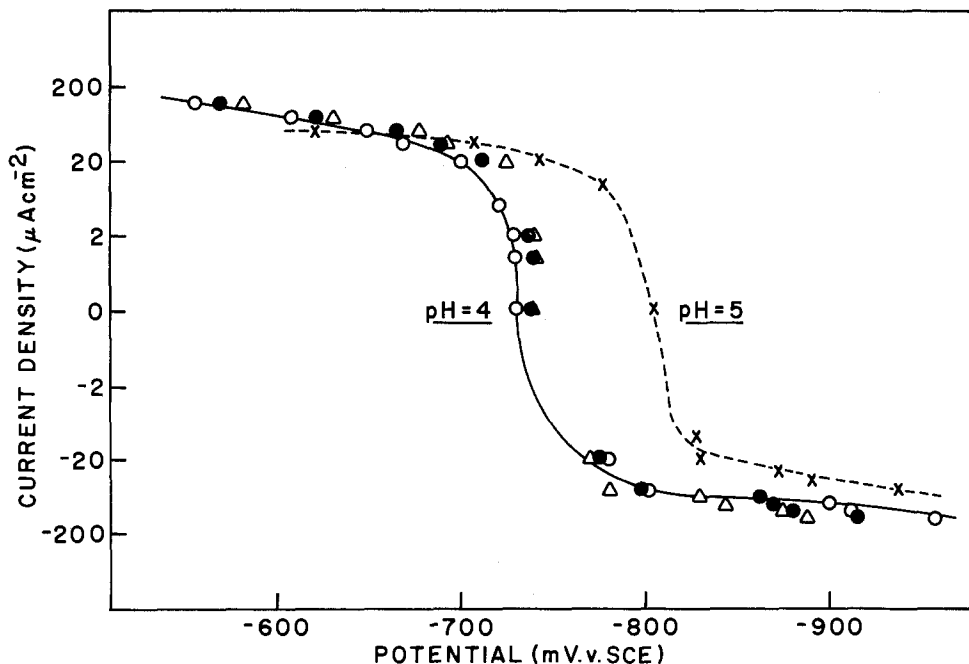


Fig. 7. Polarization curves for iron surfaces exposed to saturated aqueous H_2S solution at 21°C and $\text{pH} = 4$; Δ —2 min; \bullet —30 min; \circ —24 hr and $\text{pH} = 5$, \times —24 hr.

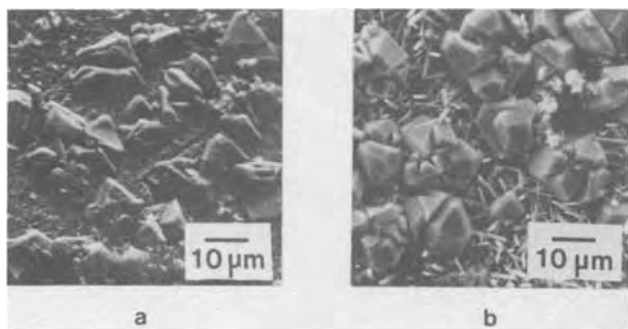


Fig. 8. Comparison of the morphology of cubic ferrous sulfide produced on iron surfaces exposed to saturated aqueous H_2S solution at $21^\circ C$ and $pH = 4$ under applied currents of (a) -50 and (b) $+35 \mu A \cdot cm^{-2}$.

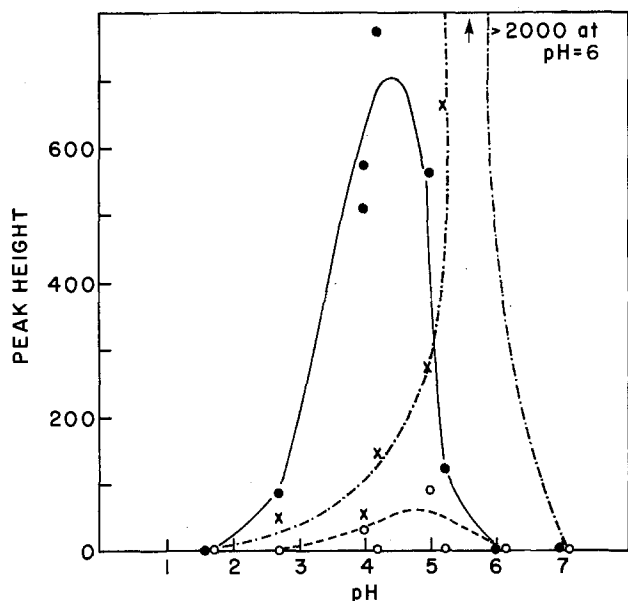


Fig. 9. Relative amounts of ferrous monosulfide phases formed on iron surfaces exposed to saturated aqueous H_2S solution at $21^\circ C$ for 24 hr as a function of pH ; —○— cubic ferrous sulfide, ---○--- troilite, -·-·-·- mackinawite (high values at $pH > 5$ due to preferred orientation in the deposit).

100%, but the crystals were only *ca.* $5 \mu m$ across (Fig. 10b), indicating a higher nucleation rate. The small amount of precipitated mackinawite was somewhat better formed than that at lower temperatures. At $75^\circ C$ (Fig. 10c), cubic ferrous sulfide was still present, but covered only about 25% of the surface, on top of a fine-grained mackinawite base layer. Some small blocks *ca.* $1 \mu m$ across were tentatively identified as precipitated mackinawite. At $90^\circ C$ (Fig. 10d), the dominant phase was troilite, but a small amount of the cubic phase still persisted. A fine-grained mackinawite base layer was still visible. In one experiment in which the temperature rose to *ca.* $75^\circ C$ for *ca.* 1 hr, then was maintained at $35^\circ C$ for 23 hr, troilite was the major product.

The conversion of cubic ferrous sulfide to mackinawite.—Cubic ferrous sulfide is known to transform spontaneously to mackinawite at room temperature, with reported rates of *ca.* 10% per hour (2) and *ca.* 2% per hour (1). The ease with which the transformation occurs is readily understood in view of the close structural relationship between the phases. The interconversion involves the migration of one-half of the iron atoms between adjacent tetrahedral sites in a cubic close packed sulfide lattice (2, 15).

We have monitored the transformation of cubic ferrous sulfide to mackinawite at $21^\circ C$ by x-ray diffractometry. Samples were prepared by open-circuit

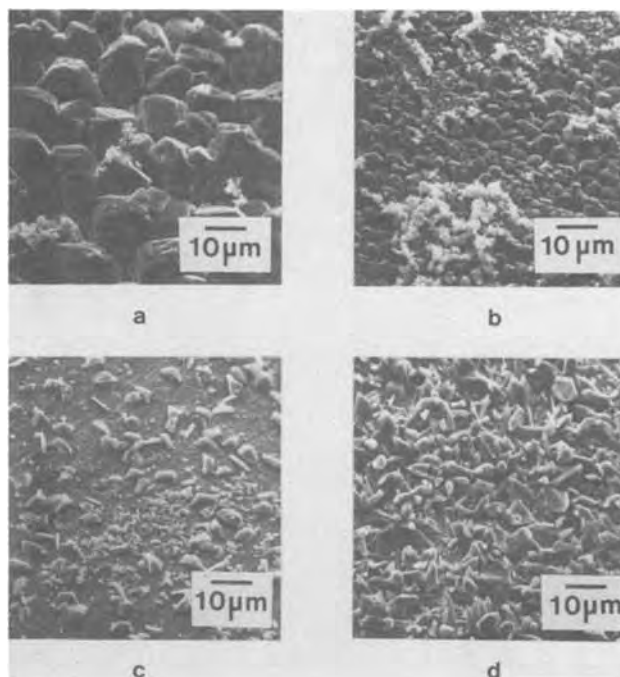


Fig. 10. Scanning electron micrographs of iron surfaces exposed to saturated aqueous H_2S solution at $pH = 4$ for 24 hr at (a) $35^\circ C$, (b) $50^\circ C$, (c) $75^\circ C$, (d) $90^\circ C$.

corrosion of iron for 24 hr at $pH = 4$, and the kinetic study was performed on the corrosion products on the metal surface. The intensities of three major diffraction lines of each phase ([001], [101], and [111] of mackinawite; [111], [220], and [311] of cubic ferrous sulfide) were monitored by direct counting. The peaks were scanned at 1° per min, with stationary counting of the background on either side of each peak. Each set of intensity data was scaled using the [110] peak of the iron substrate as a standard, to compensate for long-term fluctuations in the x-ray beam intensity. The relative decrease in the intensity of each cubic ferrous sulfide peak and the relative increase of each mackinawite peak were normalized, and found to follow very similar courses. The decline of the cubic ferrous sulfide intensity was slightly faster for the higher angle reflections; this may be a consequence of strain at the transformation interface. The progress of the summed intensities of the three peaks of each phase is depicted in Fig. 11 (after subtraction of the x-ray intensity due to mackinawite formed directly in the corrosion process). No troilite

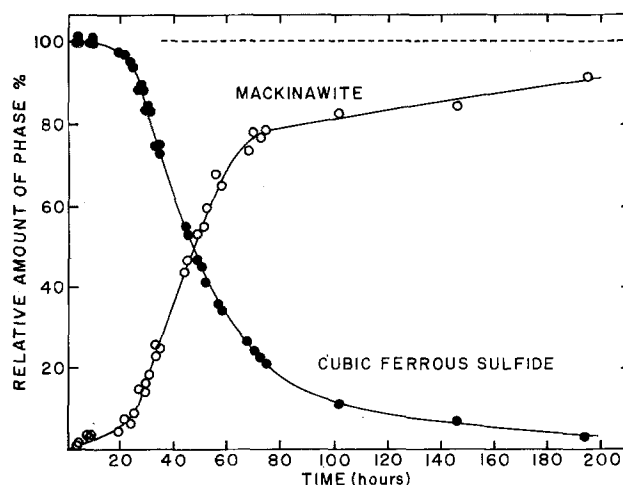


Fig. 11. Relative amounts of cubic ferrous sulfide and mackinawite in the course of their interconversion at $21^\circ C$, determined by x-ray diffractometry.

nor any other phase was detected at any stage. The clean interconversion of the two phases is clearly apparent. At longer reaction times the mackinawite intensities were slightly lower than anticipated. This is probably due to slight oxidation concurrent with the interconversion; no effort was made to exclude air from the sample during the diffraction experiment.

Figure 12 shows that the data up to about 60% conversion can be fitted to the Avrami equation [1] (17, 18), with a time exponent of 3

$$X = 1 - \exp(-1/3 \pi N_v U^3 t^3) \quad [1]$$

where X = extent of conversion, N_v = number of nucleation centers per unit volume, U = linear growth rate of nucleation centers; whence

$$\ln\left(\frac{1}{1-X}\right) = Kt^3 \quad [2]$$

The data are thus reasonably consistent with a constant rate of spherical growth of nuclei, all of which are present at the start of the transformation. The value of K depends on the choice of "zero time." If this is chosen as the point at which the corrosion reaction was terminated, $K \approx 1.1 \times 10^{-16} \text{ sec}^{-3}$. Earlier zero times result in lower values of K ; since the cubic ferrous sulfide was formed continuously over a period of about 20 hr, a true zero time does not exist.

Beyond about 60% conversion, the reaction rate becomes slower than that predicted by the Avrami equation. This may reflect a variation in nucleation center density between different crystallites, perhaps between portions precipitated at different stages of the corrosion process. We found that cubic ferrous sulfide prepared at pH = 5 underwent considerably faster conversion at 21°C than that obtained at pH = 4, and we attribute this also to variation in density of nucleation centers. This may also account for the different rates indicated by the work of de Médicis (2) and Takeno *et al.* (1).

Scanning electron microscopic examination of a corroded carbon steel surface before, during, and after the conversion (Fig. 13) showed no detectable change of morphology of the cubic ferrous sulfide, except for the appearance of cracks in a few crystals. Thus the 14% reduction in crystallographic volume appeared to be accommodated by microscopic voids between mackinawite grains within the original crystallites. Broadening of diffraction peaks of both phases in the course of the experiment indicated that the transformation was accompanied by a substantial reduction in crystallite size. This was not quantified, since it is likely that there was also a substantial lattice strain contribution to the diffraction line broadening.

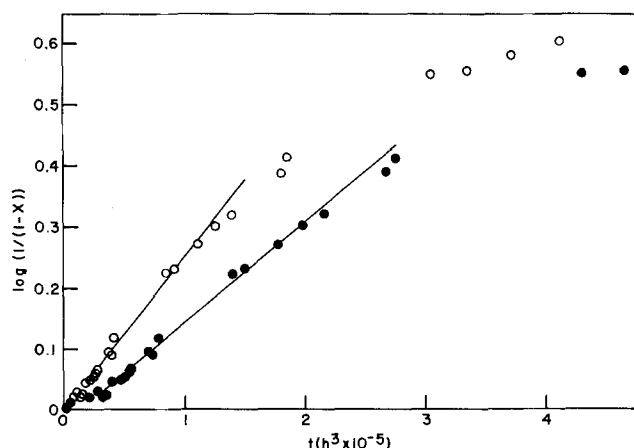


Fig. 12. Plot of $\ln(1/(1-X))$ vs. t^3 for the transformation of cubic ferrous sulfide to mackinawite at 21°C; \circ — $t = 0$ when corrosion reaction terminated; \bullet — $t = 0$ eight hours before corrosion reaction complete.

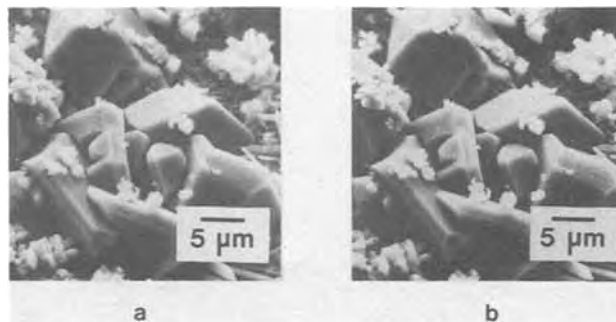
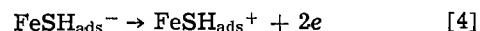


Fig. 13. Scanning electron micrographs of cubic ferrous sulfide crystals (a) before and (b) after their conversion to mackinawite at 21°C.

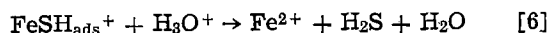
Discussion

The results of corrosion experiments at all pH values suggest that film growth and metal dissolution occur simultaneously; the relative importance of the two processes varies with pH. At pH = 7, where the least precipitation occurs, a dissolution process is suggested by the effect of stirring on the observed potential transient (Fig. 2). The presence of precipitated sulfides in the pH range 2.7-6.0, and the clean but roughened metal surface obtained at pH = 1.7 are evidence that the importance of metal dissolution increases with decreasing pH. The results of experiments with stirring at pH = 4 confirm that the upper layer of sulfides, comprising mackinawite, cubic ferrous sulfide, and troilite, is precipitated from solution. In the absence of stirring, metal dissolution leads to local supersaturation with Fe^{2+} at the electrode surface and hence sulfide precipitation. However, even in the presence of nominal stirring as used in these experiments, the local Fe^{2+} concentration can be reduced below the levels necessary for precipitation at the electrode surface.

According to Iofa *et al.* (19), SH^- ions chemisorb on iron to form an approximate monolayer. A similar process with OH^- is known to accelerate the anodic process on iron (20). We therefore propose the corrosion of iron in aqueous H_2S to occur by sequential chemisorption [3] and anodic discharge [4] (19) reactions



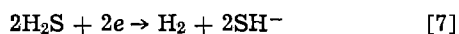
The hydroxide reaction analogous to [4] is often described as two consecutive electron transfers, the first of which is deemed to be rate determining (20). Subsequent to reaction [4], the species $\text{FeSH}_{\text{ads}}^+$ may be incorporated directly into a growing layer of mackinawite [5], or it may be hydrolyzed to yield a dissolved species [6]



If reaction [6] leads to local supersaturation at the electrode surface, then nucleation and growth of one or more of the iron sulfides, mackinawite, cubic ferrous sulfide, and troilite occurs.

The fact that the corrosion potential does not vary very much with time in the pH range 1.7-6.0 (Fig. 3), indicates that there is little change in polarization of the anodic and cathodic reactions with time. This is consistent with the presence of a cracked, porous base layer of mackinawite which does not passivate the surface and thereby polarize the electron transfer reactions occurring. This is not the case at pH = 7 where an anodic potential shift was observed, indicating that at this pH the anodic reaction (represented by steps [3]-[6]) is inhibited by the presence of the mackinawite base-layer.

Except at $pH = 2.7$ and 1.7 , a solid-state grown film of mackinawite was always observed, indicating that reaction [5] predominates over reaction [6] in the pH range 4-7. This is supported by the very large Tafel slopes (≈ 240 mV) estimated from Fig. 7 at pH values of 4 and 5, which suggest that the anodic reaction and the cathodic reaction



are both highly polarized when a current is applied, due to the presence of the mackinawite base layer.

The currents, plotted logarithmically in Fig. 7, give an almost linear anodic plot (for current values $\geq +250 \mu A$) when plotted directly against the potential. This suggests that the anodic reaction is controlled by transport through the base layer of mackinawite at the higher current values. Mass transport of Fe^{2+} and/or H_2S within the pores and cracks in this base layer is the most likely polarizing mechanism, since the anodic reaction, at least, will be occurring on the limited area of exposed metal. A similar observation was made by Hausler *et al.* (21). They also demonstrated that the polarization can be reduced by stirring. This is further evidence for rate control in macroscopic pores and cracks as opposed to transport through the actual mackinawite film.

At the lower pH values (2.7 and 1.7) metal dissolution via reaction [6] predominates and very little iron sulfide is formed. This is due to the increased solubility of the iron sulfide phases at these pH values. Although no major investigation of the effect of pH on corrosion rate was undertaken, the evidence suggests that the rate increases with a decrease in pH . This can be attributed mainly to the effect of increased proton concentration on the cathodic reaction, since the total concentration of H_2S remains constant, and the total sulfide concentration ($H_2S + SH^-$) decreases, with decreasing pH . At the pH values used here, the concentration of S^{2-} is negligible. The more specific effects of H_2S and SH^- have been investigated by others (22, 23) and will not be discussed here.

Major amounts of precipitated material form only after the base layer of mackinawite cracks and spalls, as illustrated by the electron-micrographs of Fig. 4. A higher degree of surface polishing results in a longer life of the mackinawite film prior to cracking. This suggests that the cracking of the base layer originates primarily at macroscopic irregularities on the metal surface.

Significant passivation of the iron surface occurs only at $pH = 7$, and even this is incomplete. The survival of the mackinawite base-layer at this pH is mainly due to the much lower corrosion rate than at $pH = 4$ or 5. Acceleration of the film growth rate by application of an anodic current causes more stress, and more extensive cracking (Fig. 1).

At lower pH values, this film ruptures much earlier, and at $pH = 4$, it is replaced after 2-4 hr by a second base layer which grows on the metal surface beneath the spalling initial film. This second film appeared to grow to a substantial thickness (Fig. 4). The development of stress appears to have been prevented by a network of cracks and pores, and the film adhered to the surface for the duration of the experiments. These cracks and pores are also sites for high rates of release of soluble iron from the underlying metal. Their persistence up to at least 96 hr accounts for the very slight fall in the corrosion rate observed over this time span.

The nature and amount of precipitated material is strongly dependent on pH (Fig. 9). At $pH \geq 6$, only mackinawite is precipitated. At $pH = 7$, the amount is small, but it is localized in clumps at fault sites in the base layer, where iron dissolution is enhanced. Since the solubility of mackinawite is low at $pH = 7$ [$<10^{-8}$ mole dm^{-3} (7)], its nucleation is local and

rapid, leading to the growth of a large number of small particles of ill-defined morphology. At $pH = 6$, the corrosion rate is higher, and after 24 hr precipitated material covers the surface completely.

In the pH range 2.7-5.0, all three phases were observed, and the total amount of precipitated material reached a maximum at *ca.* $pH = 4$. The quantity of precipitated material formed is determined by the rate of iron release (reaction [6]), which increases with decreasing pH , and the solubilities of the solid phases, which also increase with acidity (7). For precipitation to occur, the rate of iron release must be sufficient to cause local supersaturation with respect to the precipitating phase. Thus, as the pH decreases from 7 to 4, local supersaturation is easily maintained, and the increase in the iron release rate leads to an increase in the quantity of precipitated sulfides. As the pH decreases below 4, the solubilities of mackinawite and troilite increase above 10^{-3} and 10^{-5} mole \cdot dm^{-3} , respectively (Table I). The solubility of cubic ferrous sulfide has not been determined, but its instability with respect to mackinawite shows that it is the most soluble of the three phases. The increasing solubilities with decreasing pH cause a reduction in the amount of precipitate. Below *ca.* $pH = 2.5$, all the soluble iron diffuses into solution, and no precipitation occurs.

Application of an anodic current is expected to accelerate reaction [4], with consequent changes in the rates of reactions [5] and [6]. At $pH = 4$, as the applied current was increased from -80 to $+30 \mu A \cdot cm^{-2}$, the amounts of cubic ferrous sulfide and, less markedly, troilite increased (Fig. 6). The amount of precipitated mackinawite also increased, but most of it spalled from the electrode, and was not readily quantified. Evidently the rate of reaction [6] increases at the expense of reaction [5] with increasingly positive current over this range. However, at large applied anodic currents, $>50 \mu A \cdot cm^{-2}$, the reverse is true, and reaction [5] increases at the expense of [6]. This is demonstrated by the sudden increase in the amount of mackinawite, coincident with a decrease in the quantities of both cubic ferrous sulfide and troilite. At these high applied currents, cracks which form in the base layer are rapidly repaired by the solid-state mechanism, and the release of soluble iron and consequent precipitation are reduced.

Thus the amount of precipitated material is controlled by the rates of cracking and repair of the initial mackinawite base-layer formed by solid-state reaction, and by the rate of release of soluble iron from crack sites. These rates are controlled by both the pH and applied current. The dependence on the nature of the base layer is the chief cause of experimental irreproducibility, which was most marked at $pH = 5$.

The nature of the precipitated material is also dependent on the experimental conditions. As discussed above, both cubic ferrous sulfide and troilite were observed only at $pH < 6$, where film cracking is extensive and the rate of iron release (reaction [6]) is high. This is readily understood for cubic ferrous sulfide, which is the most soluble of the three phases and would be expected to form only under conditions of high iron release rate from the underlying metal. However, troilite is the most stable of the three phases under all the experimental conditions, and its formation might reasonably be expected to be ubiquitous.

The general difficulty of troilite formation appears to lie in the nucleation step. Thus, although cubic ferrous sulfide is the first phase formed as the applied current is increased from a minimum of $-120 \mu A \cdot cm^{-2}$ (Fig. 6), once the iron release rate is sufficiently high to cause nucleation of troilite ($I > 0$), its growth occurs at the expense of that of cubic ferrous sulfide. For $I > 50 \mu A \cdot cm^{-2}$, further enhancement of troilite yield is suppressed by the accelerated solid-state, film-repair process of mackinawite formation.

The amount of troilite also increases at the expense of cubic ferrous sulfide at temperatures above 50°C, as the troilite nucleation rate increases. In one experiment maintained at 75°C for 1 hr, then 35°C for 23 hr, a major quantity of troilite was produced. This is consistent with a high nucleation rate at the higher temperature, and a subsequent enhanced growth rate at 35°C.

Conclusion

A systematic study of the nature of the corrosion products formed on iron exposed to aqueous H₂S has led to the qualitative elucidation of the mechanisms of formation of the three ferrous monosulfide phases: mackinawite, troilite, and cubic ferrous sulfide. This mechanistic information is summarized by the reaction scheme shown in Fig. 14, which depicts the corrosion of iron (or carbon steel, which behaves very similarly) in H₂S-saturated water (pH = 4).

Initially a solid-state reaction produces a layer of mackinawite, which readily cracks and spalls from the metal surface (Fig. 4 and 5). This layer is replaced by a second solid-state grown mackinawite layer, which is cracked and pitted. High local release rates of soluble iron from these cracks and pits lead to the precipitation of cubic ferrous sulfide and, to a lesser extent, troilite. Neither the mackinawite base-layer nor the upper layer of precipitated material can passivate the surface, so nucleation and growth of cubic ferrous sulfide continue steadily. Nucleation of troilite, the most stable of the three phases, is evidently difficult, but it comprises a substantial portion of the film after 96 hr. Cubic ferrous sulfide transforms extensively to mackinawite by a solid-state mechanism between 35 and 96 hr.

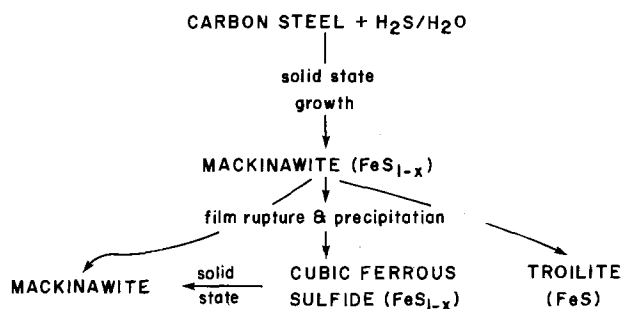


Fig. 14. Schematic reaction sequence representing processes occurring on an iron surface exposed to saturated aqueous H₂S at 21°C and pH = 4.

Manuscript submitted Jan. 15, 1979; revised manuscript received Sept. 12, 1979.

Any discussion of this paper will appear in a Discussion Section to be published in the December 1980 JOURNAL. All discussions for the December 1980 Discussion Section should be submitted by Aug. 1, 1980.

Publication costs of this article were assisted by Atomic Energy of Canada Limited.

REFERENCES

1. S. Takeno, H. Zōka, and T. Niihara, *Am. Mineral.*, **55**, 1639 (1970).
2. R. de Médicis, *Science*, **170**, 1191 (1970); *Rev. Chim. Miner.*, **7**, 723 (1970).
3. R. A. Berner, *Science*, **137**, 669 (1962).
4. A. G. Wikjord, T. E. Rummery, F. E. Doern, and D. G. Owen, Submitted to *Corros. Sci.*
5. F. H. Meyer, O. L. Riggs, R. C. McGlasson, and J. D. Sudbury, *Corrosion*, **14**, 69 (1958).
6. J. B. Sardisco and R. E. Pitts, *ibid.*, **21**, 245 and 350 (1965).
7. P. H. Tewari, G. Wallace, and A. B. Campbell, Atomic Energy of Canada Limited Report, AECL-5960 (1978).
8. R. A. Berner, *Am. J. Sci.*, **265**, 773 (1967).
9. E. H. Schot, J. Ottemann, and P. Omenetto, *Rend. Soc. Ital. Mineral. Petrol.*, **28**, 241 (1972).
10. J. C. Ward, *Rev. Pure Appl. Chem.*, **20**, 175 (1970).
11. R. J. Biernat and R. G. Robins, *Electrochim. Acta*, **17**, 1261 (1972).
12. H. T. Evans, Jr., C. Milton, E. C. T. Chao, I. Adler, C. Mead, B. Ingram, and R. A. Berner, Art. 133 in U.S. Geol. Survey Prof. Paper 475-D, pp. D64-D69 (1964).
13. D. T. Rickard, *Acta Univ. Stockho.*, **20**, 67 (1969).
14. D. W. Shoesmith, P. Taylor, M. G. Bailey, and B. Ikeda, *Electrochim. Acta*, **23**, 903 (1978).
15. L. A. Taylor and L. W. Finger, *Carnegie Inst. Washington Yearb.*, **69**, 319 (1971).
16. G. I. Finch, H. Wilman, and L. Yang, *Disc. Faraday Soc.*, **1**, 144 (1947).
17. M. Avrami, *J. Chem. Phys.*, **7**, 1103 (1939).
18. V. Raghavan and M. Cohen, in "Treatise on Solid State Chemistry," Vol. 5, N. B. Hannay, Editor, Chap. 2, Plenum, New York (1975).
19. Z. A. Iofa, V. V. Batrakov, and Cho-Ngok-Ba, *Electrochim. Acta*, **9**, 1645 (1964).
20. I. A. Ammar, *Corros. Sci.*, **17**, 583 (1977).
21. R. H. Hausler, L. A. Goeller, and R. H. Rosenwald, *Ann. Univ. Ferrara, Sez 5*, 399 (1971).
22. J. Gutzeit, *Mater. Prot.*, **17**, Dec. 1968.
23. R. Bartonicek, *Proc 3rd Int. Congr. Met. Corros. Moscow*, **1**, 119 (1969).

Kinetics of Growth of Amorphous WO₃ Anodic Films on Tungsten

F. Di Quarto, A. Di Paola, and C. Sunseri

Istituto di Ingegneria Chimica, University of Palermo, Palermo, Italy

ABSTRACT

The kinetics of growth of anodic WO₃ films have been studied in 0.01N solutions of H₃PO₄, H₂SO₄, HNO₃, and HClO₄ at room temperature. The validity of the relationship $i = A \exp BE$ was verified in the current density range 0.2-16 mA·cm⁻². Nearly constant B values were found in all investigated solutions. A lower value of dielectric constant was measured for the anodic films grown in phosphoric acid solutions. The effect of phosphate ions incorporation on the breakdown voltage is also discussed. The hypothesis of growth in presence of high space charge is carefully considered.

Although numerous experimental works (1) have been carried out on the anodic behavior of tungsten in aqueous solutions, only a few papers have been concerned with the kinetics of growth of anodic oxide films on tungsten in different acids. Apart from the works of Güntherschulze and Betz (2) and Boosz (3) on the valve-metal behavior of tungsten, the first extensive study on the kinetics was performed by Pitman and Hamby (4) in a wide current-density range (C.D.) but only in 0.1N H₂SO₄ solutions at 25°C. In this study the steady-state relationship

$$i = A \exp BE \quad [1]$$

was verified in the C.D. range 0.037-8.6 mA · cm⁻². In this range the B value was $(5.22 \pm 0.08) \times 10^{-6}$ cm V⁻¹. A film formation current efficiency of 100% was reported above 2 mA · cm⁻² and a lower efficiency was found below this C.D. value.

The relationship [1] between the C.D., i , and the electric anodizing field E was confirmed by Vas'ko *et al.* (5,6) in a wide range of temperatures (15°-175°C), again in 0.1N H₂SO₄. The B value $3.32 \cdot 10^{-6}$ V · cm⁻¹ at 25°C reported by these authors differs significantly from that found by Pitman and Hamby.

Ammar and Salim (7) have investigated extensively the growth kinetics of anodic films on tungsten in 1N solutions of five different acids in a range of C.D.'s below 1 mA · cm⁻². Also these authors confirmed the validity of Eq. [1], but they reported electric field intensities and B values which are not in agreement with either the previous ones or the theoretically estimated activation distances.

Recently, Arora and Kelly (8) claimed the valve-metal behavior of tungsten also in an acetic acid-based solution containing 1.0M additional water. Only Ord *et al.* (9,10) reported a nonlinearity in the plot of $\ln i$ vs. E in the C.D. range 20-200 μA · cm⁻² both in 0.1M H₂SO₄ and in an acetic acid-based electrolyte which was 2.0M in water. This result was obtained by the analysis of open-circuit transients by assuming that the logs of the C.D. were linearly dependent on the effective electric field (the latter was defined as the product of the applied field and the dielectric constant of the film). The nonlinearity was attributed to the dependence of the dielectric constant of the film on the applied electric field.

As for the nature of the mobile ionic species, mention should be made of the work of Davies *et al.* (11) who reported the transport number of cation was in the range 0.30-0.37, by anodizing tungsten in 0.4M KNO₃ + 0.04M HNO₃ and in the C.D. range 0.1-1 mA · cm⁻² at 25°C.

Key words: passivity, reflectance, semiconductor, electrode, dielectrics.

As for the composition and morphology of the anodic oxide films on tungsten, all authors agree that in the first instants of anodization there occurs the formation of an amorphous barrier film whose composition is mainly WO₃. To explain the optical behavior of the anodic films, Sarakinos and Spyridelis (12) suggested the formation of a duplex structure involving sulfate ion incorporation, but this claim was not confirmed by Ord *et al.* (10).

In the present work, the influence of different anions on the kinetics of growth of anodic barrier films on tungsten in acid solutions was investigated in a wide range of C.D.'s and at room temperature.

Experimental

Preliminary experiments were performed on different electrodes in order to check the reproducibility of the experimental data. Tungsten foils and rods sealed either directly to glass or to Teflon cylinders with epoxy resins were extensively studied. The best reproducibility was obtained using rods sealed to Teflon hollow cylinders with an insulating mixture of epoxy resins and 1 μm ceramic grains. In the other cases, boundary effects, due to the electrode edges or to a thermally grown oxide, shortened the linear region of the charging curves (see below). All experimental results reported below concern electrodes obtained from spectrographically pure tungsten rods 4 mm diam sealed to Teflon cylinders. The ohmic contact was ensured by a silver paste sealed to the back side of the electrode.

After each measurement at high voltages (80-140V) the electrode surface was freshly prepared by a mechanical polishing with abrasive papers and diamond pastes until 0.1 μm. Afterwards, the electrode was ultrasonically cleaned and then anodized several times in 2M HNO₃ until about 30V; this voltage was much less than the breakdown voltage. The oxide film was removed in 15% (w/v) NaOH, and the bare surface was rinsed with distilled water and dried in a nitrogen stream. At the end of this treatment, a mirror-like surface was obtained which showed even interference colors after anodization.

The galvanostatic measurements were performed using a Keithley Model 227 constant current generator. The cell voltage was monitored with a Keithley Model 610C electrometer and recorded on an Amel Model 862/A x, y, t recorder. A Simpson Model 360 digital multimeter was used in some experiments at high C.D.'s when voltage values higher than 118V were reached.

The reflectance measurements were carried out using a monochromatic light beam obtained by filtering the light from a Bausch & Lomb 150W xenon arc lamp

through a high intensity Bausch & Lomb Model 5 UV-Vis monochromator. The intensity of the reflected light was measured by an RCA Model 5819 photomultiplier tube. Both the cell voltage and the output current from the photomultiplier were recorded, respectively, on the x and y axes of the recorder.

The capacitance of the metal/oxide/electrolyte system was measured by monitoring the 90° out-of-phase component of the a.c. with a PAR Model 128 A lock-in amplifier. The lock-in was equipped with an internal oscillator which drove both an AMEL Model 567 function generator and an AMEL Model 552 potentiostat. The a.c. was obtained by superimposing a 20 mV peak-to-peak a-c voltage on the anodic triangle waveform which modulated the working electrode. The frequency of the a-c voltage was 158 Hz and the sweep of the triangle waveform was 20 mV·sec⁻¹.

All the capacitance measurements were performed in 1N H₂SO₄ solutions, the counterelectrode was a 10 cm² Pt foil and the reference electrode was Hg/Hg₂SO₄ (1N H₂SO₄). The electrode surface was 0.1256 cm² and the C.D. was calculated on the basis of the apparent area.

The anodizations were carried out in 0.01N solutions of H₃PO₄, H₂SO₄, HNO₃, HClO₄ in the C.D. range 0.2-16 mA·cm⁻². Solutions were prepared from distilled water and analytical grade reagents. All experiments were carried out at 25° ± 1°C.

Results and Discussion

Galvanostatic measurements.—As reported in other works (7, 12, 13) the shape of the voltage vs. time plots at constant current (charging curves) shows a linear rise until a voltage value is reached at which an inflection appears. This inflection point is preceded or followed, depending on the C.D. and the electrolyte composition, by the occurrence of oscillations in the cell voltage.

The inflection point and the final quasi steady-state value of the voltage can be very different if the anodization is performed at equal C.D. but in different acid solutions. This aspect is more noticeable at the higher than at the lower C.D.'s where it is always present. At a C.D. of 8 mA·cm⁻², the voltage value at the inflection point is about 135-140V in 0.01N H₃PO₄, while it decreases to about 90-95V in 0.01N HClO₄, HNO₃, and H₂SO₄ solutions. Voltage values found in HClO₄ are lower than those in H₂SO₄ and HNO₃.

It is noteworthy to mention that in 1N H₃PO₄ solutions, whose resistivity (14) is practically coincident with that of the 0.01N H₂SO₄ or HNO₃ solutions employed in our experiments, the inflection point in the charging curves also appears at a voltage value of about 120-125V. Different behavior of tungsten in H₃PO₄ was also found for long times of anodization but this aspect has been widely discussed in another work (13).

In all solutions only a slight influence of the surface finishing on the breakdown voltage was found. For a film growing at constant current, the following relation (15) can be written

$$\frac{dV}{dt} = \frac{dV}{dD} \cdot \frac{dD}{dt} = E_d \frac{i_{ion}M}{zF\rho} \quad [2]$$

where E_d is the differential field strength which corresponds to the applied C.D., i_{ion} is the ionic C.D., M the oxide molecular weight, D the thickness, ρ the density of the film, and the remaining symbols have their usual meanings.

Equation [2] shows that, by assuming a unitary film formation current efficiency, it is possible to obtain the anodizing electric field from the slope of the charging curves. According to Pitman and Hamby (4) a good agreement between the E values obtained from this method and from optical measurements (see below) is found only for $i \geq 2$ mA·cm⁻². Leakage currents and dissolution processes, which reduce

the current efficiency in an unpredictable way, are responsible for the scanty agreement of data obtained from two methods in the experiments performed at low C.D. (≤ 2 mA·cm⁻²). This source of error can significantly affect the electric field values obtained by using Eq. [2] and the B values in Eq. [1] (7).

As for the experiments performed in H₃PO₄, it is noteworthy to mention some gravimetric information obtained in 0.01 and 1N solutions. In experiments at high C.D. (8 mA·cm⁻²), so that the stay of the electrode in solution was short enough, the growth of the film was stopped in the linear region of the charging curves. The oxide covered electrode (in this case a tungsten foil) was weighed before and after the oxide dissolution in NaOH solution. The ratio between the weight of oxide removed and the weight of WO₃ estimated from the metal loss was larger than unity (1.05) for films formed in 0.01N H₃PO₄ and less than unity (0.97) for films formed in 1N solutions. The former ratio is in agreement with the hypothesis of phosphate ions incorporation (see also Capacitance Measurements) in the anodic films, the latter seems to indicate a strong dissolving action of H₃PO₄ when it is present in high concentration (13).

Interferometric measurements.—Due to the variable efficiency of film formation current, whose influence is noticeable in the lower C.D. range, an interferometric method was preferred for determining the film thickness and the anodizing electric field in the galvanostatic measurements.

Figure 1 reports typical interference patterns of the light reflected during the growth of oxide films on tungsten at low (0.2 mA·cm⁻²) and high (8 mA·cm⁻²) current density in 0.01 H₃PO₄ solutions.

The thickness of the film can be obtained from the relationship (16)

$$\Delta D = \frac{\lambda}{2(n_1^2 - \sin^2 \phi_0)^{1/2}} \quad [3]$$

where ΔD is the change in film thickness, D corresponding to two adjacent maxima or minima in the interference patterns, n_1 is the refractive index of the layer, λ is the vacuum wavelength, and ϕ_0 the angle of incidence of the light. The film thickness can be determined by this method if the value of the refractive index n_1 is known at the light wavelength employed.

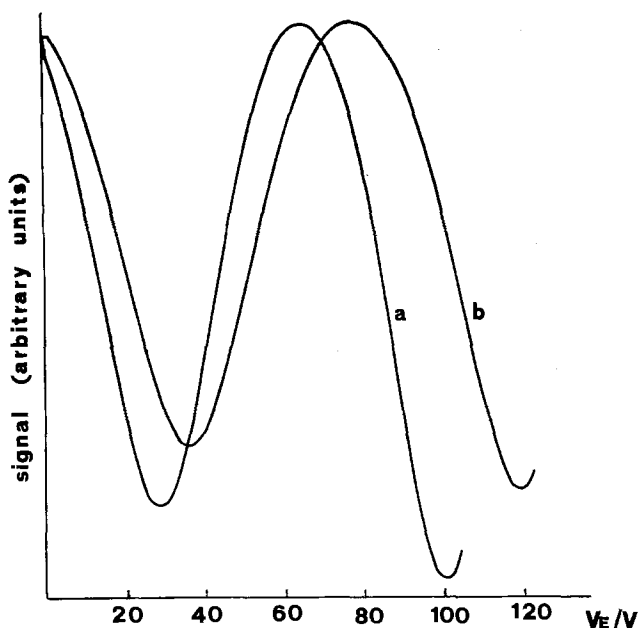


Fig. 1. Interference patterns of the light reflected during the growth of films in 0.01N H₃PO₄ solutions. Curve a: $i = 0.2$ mA·cm⁻²; curve b: $i = 8$ mA·cm⁻². ($\lambda = 6000\text{\AA}$, $\sin^2 \phi_0 = 0.155$).

The choice of the light wavelength was made so that the light absorption within the film was minimized and the number of minima and maxima in the interference pattern were maximized in the range of accessible thicknesses before the breakdown. Both conditions were reasonably fulfilled using monochromatic light at $\lambda = 6000\text{\AA}$ ($\lambda\nu < E_g \cong 3.1\text{ eV}$).

The n_1 value was calculated by means of Eq. [3], using the value reported by Ord *et al.* (9, 10) for films formed in $0.2N\text{ H}_2\text{SO}_4$ at $i = 0.2\text{ mA}\cdot\text{cm}^{-2}$ and relative to a wavelength of 6328\AA . In fact, assuming a negligible light absorption in the film, from the interference patterns obtained in two separate series of experiments at the same C.D. in $0.2N\text{ H}_2\text{SO}_4$ at 6000 and 6328\AA , respectively, it is possible to write

$$\left(\frac{\Delta D}{\Delta V}\right)_{\text{Max}}^{\text{Min}} = A = \frac{\lambda_1}{4\Delta V_1(n_1^2 - \sin^2 \phi_0)^{1/2}} = \frac{\lambda_2}{4\Delta V_2(n_2^2 - \sin^2 \phi_0)^{1/2}} \quad [3a]$$

The first member of Eq. [3a] is a quantity experimentally accessible and represents the anodizing ratio A which is not dependent on the light wavelength. ΔV_1 and ΔV_2 represent the measurable voltage drops in the interference patterns when the light intensity goes from a minimum to a maximum. The reasonable assumption was made that Eq. [2] still remains valid after the substitution of $\lambda/2$ with $\lambda/4$.

Assuming, according to Ord *et al.* (9, 10), an n_2 value equal to 2.145 at $\lambda = 6328\text{\AA}$, a value of 2.162 is obtained for n_1 at $\lambda = 6000\text{\AA}$. This last n_1 value was assumed constant in all tested solutions and C.D.'s. To neglect the possible variation of n_1 with the anodizing field (9, 10), gives an error less than 0.5% in the measured thickness.

As Fig. 1 shows, in the measurements performed in $0.01N\text{ H}_3\text{PO}_4$, in all the C.D. range investigated it was possible to detect a second minimum in the interference patterns before the breakdown phenomenon occurred. In the other solutions, it was impossible to obtain a second minimum before the film breakdown, and the electric field was obtained measuring both the change in the film thickness ΔD corresponding to the adjacent minimum and maximum, and the relative voltage drop. This assumption is supported by the experimental interference patterns in H_3PO_4 (see Fig. 1) which show a voltage drop between two minima almost exactly the double of the minimum-maximum voltage drop.

Figure 1 also shows that at the lower C.D. a decrease of the light intensity is observed in the first instants of anodization at a nearly constant cell voltage. This is in good agreement with the results reported by Ord *et al.* (9) and can be attributed to an initial islandlike growth of the film. When all the metal surface is covered by the oxide, the typical valve-metal behavior begins.

Figures 2 and 3 report the plots of the average anodizing electric field against the logarithm of the corresponding C.D., in the various solutions. A linear relationship between $\log i$ and E can be observed in the C.D. range $0.2\text{--}16\text{ mA}\cdot\text{cm}^{-2}$.

The electric field was obtained, as previously reported, by $E = \Delta V/\Delta D$. The accuracy in the measured electric field was estimated to be better than 2% . The agreement with the E values obtained from the charging curves was within this value for $i \cong 2\text{ mA}\cdot\text{cm}^{-2}$.

In all solutions, the electric field values measured at $i = 0.2\text{ mA}\cdot\text{cm}^{-2}$ do not fall on the straight line but are lower. This is indicative of a true decrease in the film formation current efficiency as previously discussed. The values of the slopes of the $\ln i$ vs. E lines are reported in Table I. A little variation in the B values is found in the different solutions.

Capacitance measurements.—Capacitance measurements of anodic films grown at different thicknesses

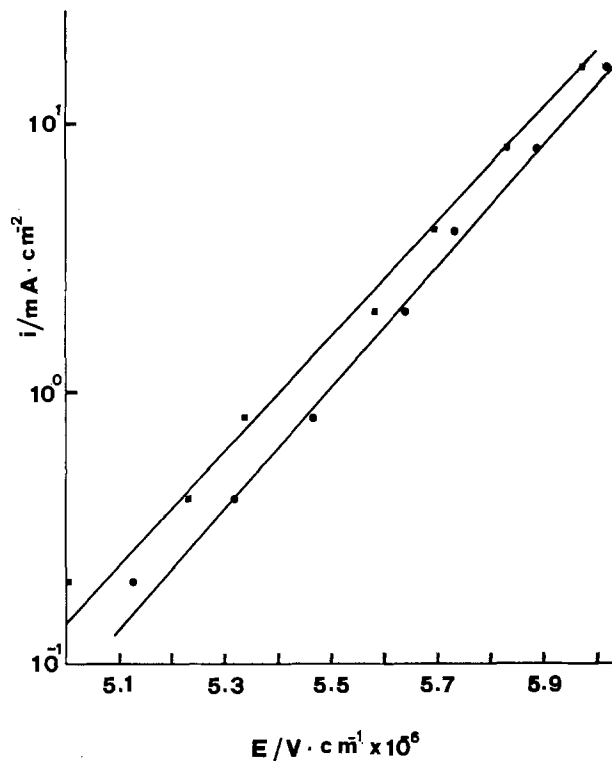


Fig. 2. Dependence of $\log i$ on electric field E . ■ $0.01N\text{ H}_2\text{SO}_4$; ● $0.01N\text{ HNO}_3$.

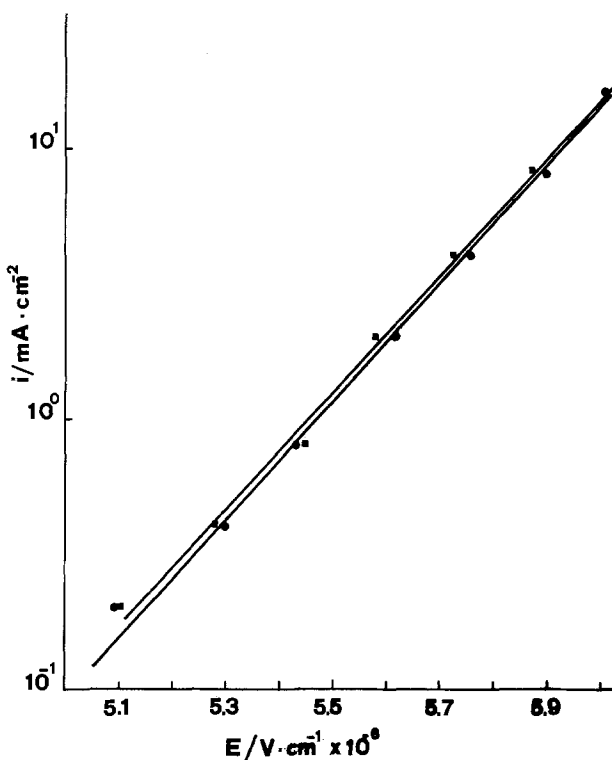


Fig. 3. Dependence of $\log i$ on electric field E . ■ $0.01N\text{ H}_3\text{PO}_4$; ● $0.01N\text{ HClO}_4$.

and C.D.'s were carried out in order both to obtain more information on the ion transport controlling process and to detect eventual anion incorporation. The capacitance measurements were performed soon after the interruption of the growth of the films which were obtained by anodization at constant current until the voltage reached a prefixed V_F value. In this way the measured reciprocal capacitance was related to the final voltage and then both to the film thickness and the anodizing electric field. In Fig. 4 the electrode capacitance C is plotted vs. the electrode

Table I. *B* values obtained from the slopes of Fig. 3 and 4

Electrolyte (0.01N)	<i>B</i> (V · cm ⁻¹)
H ₃ PO ₄	4.90 × 10 ⁻⁶
HNO ₃	5.17 × 10 ⁻⁶
HClO ₄	5.00 × 10 ⁻⁶
H ₂ SO ₄	4.90 × 10 ⁻⁶

potential for two specimens anodized until different final voltages *V_F*. In the capacitance measurements the maximum value of anodic potential *V_E* was 3 for *V_F* values up to 40V, and 5 for *V_F* values higher than 50V.

Figures 5 and 6 show the plots of the final voltage values *V_F* against the reciprocal value of the oxide film capacitance at two different C.D.'s. The capacitance values of Fig. 5 and 6 were obtained taking into account the fact that for large anodic polarization—where the space charge layer equals the thickness—the capacity of an n-type semiconductor film with a wide bandgap becomes constant, being a measure both of the thickness and of the dielectric constant (17).

The measured capacitance is given by the relation

$$\frac{1}{C} = \frac{1}{C_{ox}} + \frac{1}{C_H} \cong \frac{1}{C_{ox}} \quad [4]$$

where *C_{ox}* and *C_H* are, respectively, the oxide and the Helmholtz double layer capacitances. Since usually *C_H* >> *C_{ox}*, the measured capacitance corresponds practically to the oxide film capacitance. In Fig. 5 and 6, corrected capacitance values were used for the thinnest films by using a 20 μF·cm⁻² value for *C_H*.

The excellent linearity in the plots of *V_F* vs. 1/*C_{ox}*, found in all solutions and C.D. range seems in agreement with the hypothesis of kinetic control at one of the two metal/oxide or oxide/electrolyte interfaces (18).

A noticeable difference was found in the slopes of the lines in Fig. 5 and 6 for electrodes anodized in

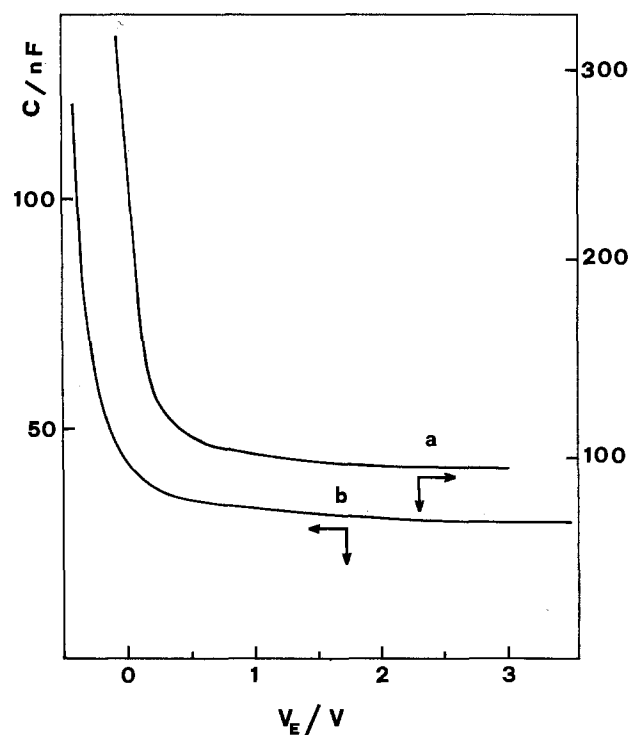


Fig. 4. Electrode capacitance *C* vs. electrode potential *V_E* for electrodes anodized at *i* = 8 mA · cm⁻² in 0.01N H₃PO₄ until different final cell voltages, *V_F*. Curve a: *V_F* = 32V; curve b: *V_F* = 101V.

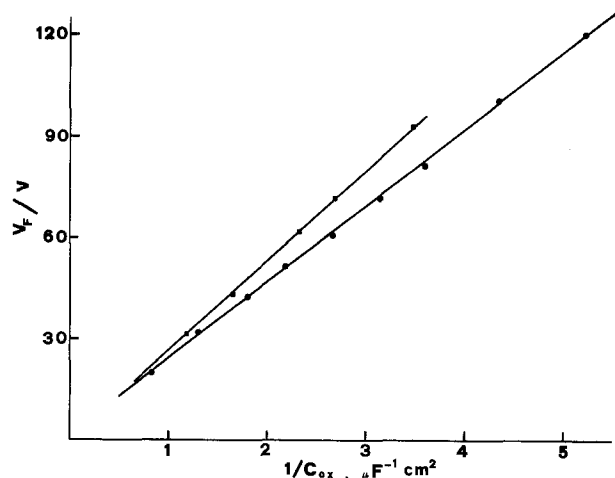


Fig. 5. Final cell voltage *V_F* vs. reciprocal value of oxide film capacitance 1/*C_{ox}* for electrodes anodized at *i* = 8 mA · cm⁻² in different solutions. ● 0.01N H₃PO₄; ■ 0.01N HNO₃.

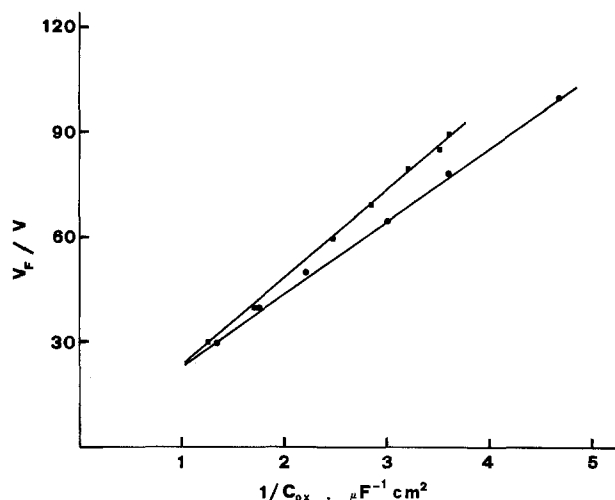


Fig. 6. Final cell voltage *V_F* vs. reciprocal value of oxide film capacitance 1/*C_{ox}* for electrodes anodized at *i* = 0.4 mA · cm⁻² in different solutions. ● 0.01N H₃PO₄; ■ 0.01N H₂SO₄.

H₃PO₄ or in the different solutions. In all C.D. ranges, a lower value of the slopes of the lines relative to the measurements in H₃PO₄ was found. Higher, nearly equal, values of the slopes were obtained for the remaining acids (see Table II).

This result can be explained recalling that

$$\left[\frac{\partial V_F}{\partial (1/C_{ox})} \right]_{i,T} = \epsilon_{ox} \epsilon_0 E \quad [5]$$

where *E* is the anodizing field at the chosen C.D., *ε_{ox}* and *ε₀* are, respectively, the oxide and vacuum dielectric constants and assuming a decrease in the di-

Table II. Dielectric constant values for WO₃ oxide films obtained in different solutions and C.D.'s. The *ε_{ox}* values were determined by using Eq. 5.

Electrolyte (0.01N)	<i>ε_{ox}</i>	<i>E</i> (V · cm ⁻¹)	<i>∂V_F</i>	
			<i>∂</i> (1/ <i>C_{ox}</i>) (μC · cm ⁻²)	<i>i</i> (mA · cm ⁻²)
H ₃ PO ₄	44.3	5.87 × 10 ⁶	23.0	8.0
	44.0	5.28 × 10 ⁶	20.5	0.4
HClO ₄	52.6	5.90 × 10 ⁶	27.5	8.0
	55.4	5.30 × 10 ⁶	26.0	0.4
H ₂ SO ₄	55.0	5.83 × 10 ⁶	28.4	8.0
	54.0	5.23 × 10 ⁶	25.0	0.4
HNO ₃	52.0	5.89 × 10 ⁶	27.0	8.0
	54.0	5.33 × 10 ⁶	25.5	0.4

electric constant of the films obtained in H_3PO_4 . In fact, as shown by Table II, the E values obtained from interferometric measurements are practically equal in all acid solutions at the same C.D. Table II also reports the dielectric constant values of oxide films grown in different solutions and at different C.D.'s. The ϵ_{ox} values were calculated by Eq. [5] using the experimental values of the electric fields and of the slopes of the V_F vs. $1/C_{ox}$ lines.

Average dielectric constant values of 43.5 and 54 were obtained for WO_3 anodic films formed respectively in H_3PO_4 or in the different acid solutions. Both these ϵ_{ox} values are in good agreement with the literature data (4, 9); they should be compared to the static and zero electric field ϵ_{ox} values.

Further interesting information was obtained from a detailed analysis of the capacitance measurements at low anodic potentials (19). They concern: (i) the noticeable influence of the thickness on the donor concentration N_D in the films. A decrease in N_D was revealed with increasing thickness. A similar result was reported by Heusler *et al.* (20, 21) for Nb_2O_5 anodic films; (ii) the existence of a region near the oxide/electrolyte interface with constant donor concentration. In this region, whose thickness is about 60% of the total film thickness, the N_D value may be related to D by the relation $N_D \propto d^{-n}$, with $n = 1.8 \pm 0.2$ (19, 20). A higher donor concentration in the neighboring metal/oxide interface (22) could cause the decreasing slopes measured in the $1/C^2$ vs. V_E curves with increasing electrode potential; (iii) the absence of any influence of the investigated electrolyte compositions on the above-mentioned properties.

Conclusions

On the basis of the experimental results, it is possible to draw some conclusions on the kinetics of growth of amorphous barrier films on tungsten in weakly acid solutions of different anions.

The most important result concerns the absence of curvature in the plots of $\ln i$ against E in the C.D. range 0.2-16 mA·cm⁻². The disagreement with the results reported by Ord *et al.* (10) could be attributed to a breakdown of Ord's anodic oxidation model in the range of investigated C.D.'s as well as to the fact that experimental information obtained by different measuring techniques cannot be interpreted by the same mathematical relationship (23).

Moreover, in the anodic oxidation of tungsten special attention must be paid to the side parasitic reactions which reduce the film formation current efficiency especially at the lowest C.D.'s.

As for the influence of the anions, they are very significant in determining both the breakdown voltage in the different solutions and the dielectric constant of the anodic oxide films. The lower values of the dielectric constant measured for films grown in H_3PO_4 , could be attributed to the incorporation of phosphate ions in the films as reported for other valve-metals (24, 25).

Different breakdown mechanisms can explain the different breakdown voltage values, which in H_2SO_4 , $HClO_4$, and HNO_3 are lower than in H_3PO_4 (13). In fact, in the former solutions a mechanical breakdown due to very high internal stresses (a very high Pilling-Bedworth ratio of 3.34 is found for WO_3 films) probably occurs during the anodization process (26). Otherwise, the incorporation of phosphate ions could decrease the internal stresses (27, 28) favoring the achievement of higher thicknesses of the barrier film and the occurrence of an electrical breakdown (29, 30).

As mentioned above, an interfacial barrier kinetic control can be invoked on the basis of the V_F vs. $1/C_{ox}$ curves. However, it is noteworthy to mention that an alternative model of growth with kinetic control within the anodic film cannot be discarded *a priori*. In fact, if it is assumed according to the Fromhold theory (31, 32) that the formation of the anodic oxide

films on tungsten occurs under very large electric fields and in the presence of high space charge, a very good linearity can be found in the V_F vs. D (i.e., $1/C_{ox}$) curves by assuming a space charge screening parameter of about 10Å. This assumption could result in a defect concentration of about 10^{19} ·cm⁻³ at the injecting interface.

Moreover, if the donors in WO_3 anodic films are identified with the injected defects which are frozen in when the film growth is stopped, two further considerations could support the Fromhold model: (i) first is the agreement between the defect concentration mentioned above and the donor concentration value found by extrapolating the $N_D \propto d^{-n}$ relationship (19) at 1V thickness; (ii) the second is the qualitative agreement found between the defect concentration profile foreseen by the model and the donor distribution mentioned above (see Capacitance Results). In this frame the kinetics of growth of anodic WO_3 amorphous films would be controlled by the transport within the anodic film of the oxygen vacancies injected at the metal/oxide interface. The nearly equal B values could support this mechanism.

It is noteworthy that a constant electric field with increasing thickness as revealed by the interferometric measurements is partially conflicting with the above-reported model (32).

Acknowledgments

Thanks are due to P. Anastasi for performing some experiments. The financial support of C.N.R. Technological Committee (Rome) is gratefully acknowledged.

Manuscript submitted Sept. 19, 1979; revised manuscript received Nov. 21, 1979.

Any discussion of this paper will appear in a Discussion Section to be published in the December 1980 JOURNAL. All discussions for the December 1980 Discussion Section should be submitted by Aug. 1, 1980.

Publication costs of this article were assisted by the Istituto Ingegneria Chimica.

REFERENCES

1. A. Di Paola, F. Di Quarto, and G. Serravalle, *J. Less-Common Met.*, **42**, 315 (1975); and references therein.
2. A. Güntherschulze and H. Betz, *Elektrolytkondensatoren*, Cram, Berlin (1952).
3. H. J. Boosz, *Metall.*, **11**, 511 (1957).
4. H. W. Pitman and D. C. Hamby, PB Rep. 146, p. 794, published by U.S. Department of Commerce, Office of Technical Services (1959).
5. A. T. Vas'ko, V. V. Tobolich, and A. V. Gorodysky, *Ukr. Khim. Zh.*, **39**, 728 (1973).
6. A. T. Vas'ko, in "Encyclopedia of Electrochemistry of the Elements," Vol. V, A. J. Bard, Editor, p. 103, M. Dekker, New York (1976).
7. I. A. Ammar and R. Salim, *Corros. Sci.*, **11**, 591 (1971).
8. M. R. Arora and R. Kelly, *This Journal*, **124**, 1493 (1977).
9. J. L. Ord, M. A. Hopper, and W. P. Wang, *ibid.*, **119**, 439 (1972).
10. J. L. Ord, J. C. Clayton, and K. Brudzewski, *ibid.*, **125**, 908 (1978).
11. J. A. Davies, B. Domeij, J. P. S. Pringle, and F. Brown, *ibid.*, **112**, 675 (1965).
12. J. Sarakinos and J. Spyridelis, *Thin Solid Films*, **27**, 239 (1975).
13. A. Di Paola, F. Di Quarto, and C. Sunseri, *Corros. Sci.*, To be published.
14. "Handbook of Chemistry and Physics," 56th ed., C. R. C. Press, Cleveland, Ohio (1975/1976).
15. L. Young, in "Anodic Oxide Films," p. 6, Academic Press, New York (1961).
16. O. S. Heavens, in "Optical Properties of Thin Films," p. 114, Dover Publications Inc., New York (1965).
17. U. Stimming and J. W. Schultze, *Ber. Bunsenges. Phys. Chem.*, **80**, 1297 (1976).
18. M. J. Dignam, in "Oxides and Oxide Films," Vol.

- I, J. W. Diggle, Editor, p. 181, Marcel Dekker, New York (1972).
19. F. Di Quarto, Unpublished results.
 20. D. Stütze and K. E. Heusler, *Z. Phys. Chem. Neue Folge*, **65**, 201 (1969).
 21. K. E. Heusler and M. Schultze, *Electrochim. Acta*, **20**, 237 (1975).
 22. W. Gissler and R. Memming, *This Journal*, **124**, 1710 (1977).
 23. J. L. Ord, J. C. Clayton, and W. P. Wang, *ibid.*, **124**, 1671 (1977).
 24. J. J. Randall, W. J. Bernard, and R. R. Wilkinson, *Electrochim. Acta*, **10**, 183 (1965).
 25. S. Ikonopisov, E. Klein, A. Stanchev, and T. S. Nikolov, *Thin Solid Films*, **26**, 99 (1975).
 26. F. Di Quarto, K. Doblhofer, and H. Gerischer, *Electrochim. Acta*, **23**, 195 (1978).
 27. L. C. Archibald and J. S. L. Leach, *ibid.*, **22**, 15 (1977).
 28. L. C. Archibald and J. S. L. Leach, *ibid.*, **22**, 21 (1977).
 29. S. Ikonopisov, *ibid.*, **22**, 1077 (1977).
 30. S. Ikonopisov, A. Girginov, and M. Machkova, *ibid.*, **24**, 451 (1979).
 31. A. T. Fromhold, Jr., in "Oxides and Oxide Films," Vol. 3, J. W. Diggle and A. K. Vijn, Editors, p. 1, Marcel Dekker, New York (1976).
 32. A. T. Fromhold, Jr., *This Journal*, **124**, 538 (1977).

A Study on Activation and Acceleration by Mixed PdCl₂/SnCl₂ Catalysts for Electroless Metal Deposition

Tetsuya Osaka* and Hideki Takematsu

Department of Applied Chemistry, Waseda University, Tokyo 160, Japan

and Kohji Nihei

OKI Electric Industry Company, Limited,

OKI Basic Materials Research and Development Department, Tokyo 160, Japan

ABSTRACT

Five different compositions of mixed acidic PdCl₂/SnCl₂ catalysts for electroless plating were investigated mainly by electrochemical and x-ray photoelectron spectroscopy measurements, and also by ultraviolet and visible photoelectron spectroscopy, transmission electron microscopy, and Auger electron spectroscopy. It is shown that the potential sweep technique using a catalyzed gold electrode in 1M HCl yields voltammograms which depend upon the catalyst activity, and that this technique is applicable for simple diagnosis of the activity of mixed PdCl₂/SnCl₂ catalyst systems. It was found by transmission electron microscopy that large colloidal particles are required for high catalytic activities. X-ray photoelectron spectroscopy showed that these colloidal particles consist of a system in which Pd and Sn atoms have an interaction such as in Pd-Sn intermediates or alloys. The ratio of Pd/Sn after acceleration is not constant but depends on the catalyst activity. The accelerator (1M NH₄BF₄ or 1:1 HCl) not only removes Sn(IV) ions from the substrate but also causes coagulation of small particles adsorbed on the substrate, and these actions result in a drastic increase in the activity of low activity catalysts.

The mixed PdCl₂/SnCl₂ solution containing hydrochloric acid is most commonly used in electroless plating to make metallic or nonmetallic substrate surfaces catalytically active to initiate the metal deposition. A two-step immersion procedure consisting of sensitization (SnCl₂ solution) and activation (PdCl₂ solution) was used for many years in the past, while a significant development has been achieved more recently by a single-step mixed PdCl₂/SnCl₂ catalyst system, which was first described by Shipley (1). He claims that the catalyst solution contains colloidal particles, and D'Ottavio (2) mentions the presence of uniform stable colloidal particles in the mixed catalyst system which gives active sites on substrates. On the contrary, other investigators in patents claim that the activity results from Pd-Sn solute complexes and not from the colloidal particles (3, 4).

Two groups of investigators have reported on the same catalyst systems as those described in the patent literature cited above. Rantell and Holtzman (5) concluded that the activity of the mixed catalysts is not

due to a colloid but to a SnPd₇Cl₁₆-type solute complex. de Minjer and Boom (6) showed that the activity results from a Pd-Sn complex containing one Pd atom per two Sn atoms. Feldstein *et al.* (7) also reported that the complex of Pd₃Sn gives the most active sites on substrate surfaces. Joisson and Devand (8) discussed the same Pd₃Sn complex formation by precipitation in acidic Pd(II)/Sn(II) complex solutions.

Contrary to the above proposals involving solute or deposited complexes, Cohen *et al.* (9a, b) concluded by ultracentrifugation, electron microscopy, and Mössbauer spectroscopy that the mixed acidic catalyst systems are colloidal and that the metal deposition is initiated by the formation of a Pd-Sn alloy core with a stabilizing layer of adsorbed Sn(II) ions. Cohen and Meek (9b) reported the ratio of Pd/Sn \approx 6 for the Pd-Sn alloy core and discussed this result in comparison with other conflicting results. Nagai *et al.* (10) also concluded that the active sites are in the colloidal state. Finally, Matijević *et al.* (11) investigated the various catalysts commercially available and also prepared in their laboratory, and concluded that the catalytic activity is exhibited only by the colloidal

* Electrochemical Society Active Member.

Key words: electroless plating, mixed PdCl₂/SnCl₂ catalyst, XPS measurement.

bottom layer obtained by separation using prolonged ultracentrifugation and not by the supernatant liquid.

In the case of selective electroless plating using ultraviolet irradiation, D'Amico *et al.* (12) found that the metal deposition does not initiate when Sn(II) species is photo-oxidized by exposure to ultraviolet light in air. Furthermore, Baylis *et al.* (13) reported that the copper plating does not initiate without ultraviolet irradiation when a Sn(IV) sensitizer-Pd(II) activator is used. Kelly and Vondeling (14) also described the nucleation of Pd on photosensitive TiO₂ by ultraviolet irradiation. Hamilton and Logel (15) concluded by using evaporated Pd that large Pd particles (4 ~ 20 atoms) are required to initiate electroless nickel deposition. Thus, for the two-step immersion procedure, it can be concluded that Pd(O) nuclei on substrate surfaces are the catalytically active sites which initiate electroless plating. In the case of a single-step procedure using mixed PdCl₂/SnCl₂ catalyst solution, the active sites consisting of Pd-Sn alloy, Pd₃Sn, or PdSn₂ on substrate surfaces have been suggested by Cohen *et al.* (9a, b), Feldstein *et al.* (7) and de Minjer *et al.* (6).

The other important process in the single-step procedure using mixed PdCl₂/SnCl₂ catalyst is the acceleration which enhances the activity of the mixed PdCl₂/SnCl₂ catalyst. Typical accelerators reported are ammonium fluoroborate, ammonium bifluoride, fluoroboric acid, hydrochloric acid, sulfuric acid, or sodium hydroxide (5c, 9c).

In this communication, we will investigate the mixed acidic catalysts and also the accelerator effects for the single-step procedure using the mixed PdCl₂/SnCl₂ catalyst mainly by means of electrochemical methods. We will also describe an electrochemical method of diagnosing the surface activity and the results of our attempt to find the form of catalytically active palladium using x-ray photoelectron spectroscopy.

Experimental

Preparation of catalysts.—Typical samples, including a commercial one, of mixed acidic PdCl₂/SnCl₂ catalysts were chosen and prepared by referring to the patents (1-4) and Matijević's experiments (11). Sample "E" (Hitachi Kasei Company, HS-101B) was used as a typical commercial sample. Preparation procedures and compositions of these catalysts are shown in Table I. All solutions were prepared with reagent grade chemicals and doubly distilled water. A freshly prepared solution of stannous chloride was always used because stannous chloride is easily oxidized by oxygen in air. Samples "A" and "B" contained, respectively, large and small concentrations of PdCl₂, sample "C" was an improved Shipley solution containing Na₃SnO₃ which was added as a stabilizing agent for colloidal particles (5b), and sample "D" was prepared by a process which was an improved

version of that described in Zebli's patent (3a). The surfactant such as C₂F_{n+1}SO₂Z (Z is a hydrophilic group), which in the Zebli's patent (3b) is claimed to improve "wetness" of substrates, was omitted in this preparation.

Functionality test for electroless plating.—The catalytic activity of mixed acidic PdCl₂/SnCl₂ catalysts was tested using an electroless nickel plating bath with the basic composition previously given in Ref. (16) (NiCl₂ · 6H₂O 29.4 g/liter, malonic acid 20 g/liter, DMAB (dimethylamine borane) 3.54 g/liter, pH 9.5 adjusted with NH₄OH, bath temperature 70°C). Glassy epoxy plastic boards (Hitachi Kasei Company, JIS-G10) and copper wires were selected as the substrate to be plated. The redox potential measurement for monitoring the initiation time of plating was performed with copper wire. The process of electroless plating consisted of these steps: (i) degrease in ethanol, (ii) rinse with water, (iii) activate in mixed acidic PdCl₂/SnCl₂ catalyst solution (3 min), (iv) rinse with water (this step was omitted when 1:1 HCl¹ was used as accelerator), (v) immerse in accelerator solution (1M NH₄BF₄ or 1:1 HCl) (3 min), (vi) rinse with water, (vii) start electroless plating.

Electrochemical measurement.—A gold wire or disk electrode was used as the test electrode, because gold does not have a catalytic activity to initiate electroless plating and also because gold shows a wide double layer region in 1M HCl. The counterelectrode was a gold wire. All potentials were measured against a saturated calomel electrode or a hydrogen electrode, and they are referred to as the saturated calomel electrode (SCE). Potential sweep was applied on the gold electrode after immersing into the activator for 1 min and then into the accelerator for 15 sec. Measurements were performed at 25°C.

Photospectroscopy (u.v. and v.l.), transmission electron microscopy, Auger electron spectroscopy, and x-ray photoelectron spectroscopy.—Ultraviolet and visible spectra of mixed catalyst solutions were measured between 200 and 700 nm with a Shimadzu double beam UV-140 spectrophotometer. Sample solutions were prepared by diluting the catalysts with 1M HCl or water. Electron microscope measurements were made using a JEOL JEM-7A instrument with 100 kV electron source. Samples for transmission electron microscopy were prepared by immersing the copper grid coated with collodion film into the catalyst and/or accelerator solutions for 3 min. Auger electron spectroscopy was performed with an Anelva EMAS II instrument, and electroless plated Ni-P sheets (plated by the Sumer method) were used as substrates instead of gold, since the characteristic peaks of gold interfere with the spectra due to surface materials.

¹ 1:1 hydrochloric acid was prepared by diluting 37% HCl with the same volume of water.

Table I. Compositions and preparation procedures of mixed PdCl₂/SnCl₂ catalyst solutions

A	B	C	D	E
37% HCl (60 ml)	37% HCl (60 ml)	37% HCl (300 ml)	37% HCl (300 ml)	37% HCl (320 ml)
← water	← water	← water (600 ml)	← water (600 ml)	← water (620 ml)
← PbCl ₂ (1g)	← PbCl ₂ (0.25g)	← PbCl ₂ (1g)	← PbCl ₂ (1g)	← HS101B* (60 ml)
← SnCl ₂ 2H ₂ O (22g)	← SnCl ₂ 2H ₂ O (12g)	← Na ₃ SnO ₃ (1.5g)	← SnCl ₂ 2H ₂ O (4g)	
		← SnCl ₂ 2H ₂ O (37.5g)	← SnCl ₂ 2H ₂ O (46g)	
← adjust volume with water to 1000 ml	← adjust volume with water to 1000 ml			
catalyst	catalyst	catalyst	catalyst	catalyst

* Commercial catalyst marketed by Hitachi Kasei Company.

X-ray photoelectron spectroscopy was carried out on a modified JASCO ESCA I spectrometer (17). Samples for XPS were made by immersing copper plates into sample solutions for ca. 3 min, dried under vacuum, and irradiated with Al K α x-ray with energy of 1486.6 eV. Solution samples for the freeze-dry method (FDM) were frozen with Dry Ice on copper plate and dried under vacuum.

Results and Discussion

Functionality test of catalysts for electroless nickel plating.—Electroless nickel plating on glassy epoxy plastic boards for the functionality test of mixed acidic PdCl₂/SnCl₂ catalysts was performed for 3 min after pretreatment processes which were described in the experimental section (1:1 HCl was used as accelerator in this case). All samples showed catalytic activities, and especially samples "D" and "E" gave completely uniform nickel films on glassy epoxy plastic boards within the 3 min plating time. Samples "A", "B", and "C" gave patched nickel films, and among the five samples the "C" catalyst gave the worst nickel film on glassy epoxy plastic board.

In order to investigate the functionality of catalysts more precisely, the mixed potential of copper wire in the plating bath was measured after activation and after acceleration (where 1M NH₄BF₄ was used as accelerator instead of 1:1 HCl in order to avoid copper dissolution). Time dependence of the mixed potential is demonstrated in Fig. 1(a) and (b). Figure 1(a) shows the time dependence of mixed potential only with activation (without acceleration). Since the mixed potential changes drastically at the time when a nickel layer covers the copper substrate surface, the initiation time of electroless plating after copper immersion can easily be determined as shown in Fig. 1(a)

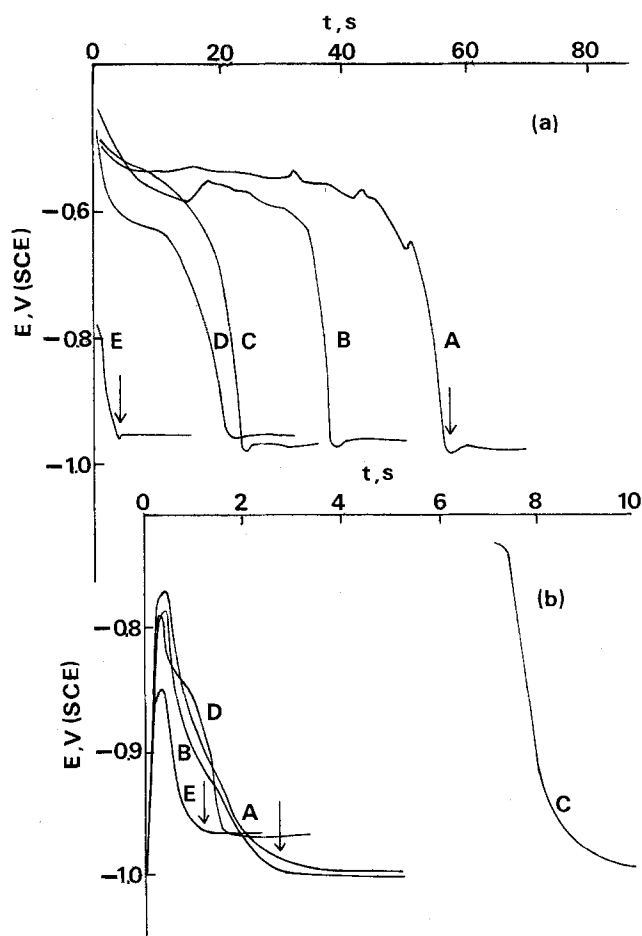


Fig. 1. Functionality test for electroless nickel plating. (a) Time dependence of mixed potentials after activation; (b) time dependence of mixed potentials after acceleration.

(cf. the arrows in the figure). This provides the basis for diagnosing the catalyst functionality. The reciprocal order of the induction time corresponds to the order of the catalyst activity; $E > D > C > B > A$. The time dependence of mixed potential after acceleration procedure shown in Fig. 1(b) demonstrates that the induction times are greatly shortened especially for samples "A" and "B". Sample "C" showed an exceptional behavior or a long induction time after acceleration. This can be explained by the facts that the solution color of sample "C" was more greenish than the other catalyst solutions (cf. next section) and that the acceleration effect of removing Sn(IV) ions from substrates was less for this sample because of the presence of sodium stannate for stabilizing Sn(II) ions. Since sample "E", commercial HS-101B, shows the shortest induction time and the most anodic potential after the initiation of plating, this sample is the most active among the five catalysts. Among the samples prepared in our laboratory, sample "D" which showed almost the same catalytic activity as sample "E" in terms of the induction time and catalyst color, was the most active. The results from the actual plating on glassy epoxy plastic board shown above correspond to the information obtained by the redox potential measurements shown in Fig. 1(b).

Spectrophotometric measurement of mixed PdCl₂/SnCl₂ in hydrochloric acid solution.—The solution of mixed PdCl₂/SnCl₂ in HCl shows green color, which gradually changes to dark brown. A precipitation occurs after keeping the dark brown catalyst solution in air.² This precipitate redissolves and finally yields a light yellow solution. Typical absorption spectra of mixed PdCl₂/SnCl₂ in 1M HCl at each stage and those of PdCl₂ and SnCl₂ in HCl solutions are shown in Fig. 2. The Pd(II) ion gives absorption peaks at 280 and 475 nm, while the Sn(II) ion does not give characteristic absorption peaks in the ultraviolet and visible regions though the extinction coefficient of SnCl₂ increases with decrease in wavelength in the ultraviolet region. A typical sample of green PdCl₂/SnCl₂ (molar ratio 1:10) mixture has three absorption peaks at 280, 330, and 420 nm. Since the characteristics of the absorption spectrum of green catalyst solution neither coincide with that of PdCl₂ nor SnCl₂, it indicates the formation of a soluble Pd-Sn complex. The absorption spectrum taken after the color change from green to dark brown contains a somewhat wavy linear portion with a high extinction coefficient. In this case the peak at 280 nm due to Pd(II) ions was still observed. However, in the actual samples shown in Fig. 3, only approximately straight lines without the peak at 280 nm were observed. This may be due to the differences in Pd(II)/Sn(II) ratio and in aging of colloidal solutions. According to Nagai *et al.* (10), the first green intermediate complex is (Pd(II)Sn(II)_m-Cl₂)ⁿ⁻ (where $m = 2$ and 6) with various ratios of Pd(II)/Sn(II), and the complex ions are decomposed gradually by the intermolecular redox reaction of Pd(II) with Sn(II) to form free Pd(O) and Sn(IV) and form the second dark brown intermediate of colloidal palladium particles. Cohen *et al.* (9a, b) concluded by their Mössbauer spectroscopy that the solid particles are protective colloids which consist of Pd-Sn alloy core with a stabilizing Sn(II) ion layer and that the precipitation occurs by the oxidation reaction of Sn(II) layer to Sn(IV). In view of the above authors' and Matijević's reports, the spectrum of somewhat wavy linear line with a high extinction coefficient is considered to be the feature of colloidal state. This interpretation was confirmed by the electron microscopy measurement described later.

The absorption spectra of the five catalyst samples are shown in Fig. 3, where the sample solutions were

² Contrary to Nagai's report (10), the induction time for the precipitate formation depended upon not only the molar ratio of Sn(II)/Pd(II) but also the Pd(II) concentration.

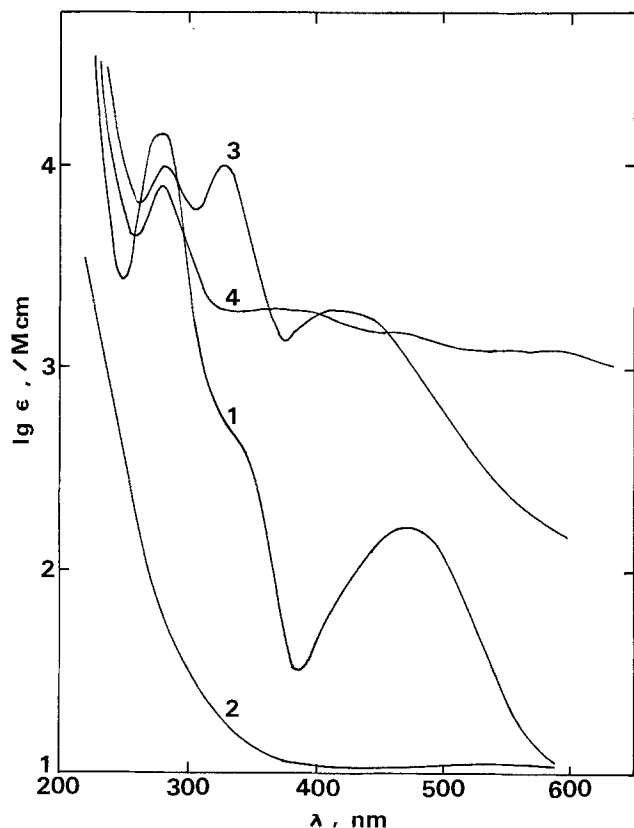


Fig. 2. Absorption spectra of PdCl_2 , SnCl_2 and mixed $\text{PdCl}_2/\text{SnCl}_2$ catalyst solutions in the ultraviolet and visible regions. Curve 1, PdCl_2 , curve 2, SnCl_2 , curve 3, mixed $\text{PdCl}_2/\text{SnCl}_2$ solution with green color ($\text{Pd}/\text{Sn} = 1/10$), curve 4, mixed $\text{PdCl}_2/\text{SnCl}_2$ solution with dark brown color ($\text{Pd}/\text{Sn} = 1/10$).

diluted with water. All spectra show almost the same tendency corresponding to the dark brown solution shown in Fig. 2; this result indicates that the catalyst solutions are in colloidal state. Samples "D" and "E", the most active catalysts, show the best linearity in the visible region.³

Since the spectrum of the redissolved solution after precipitation agreed with that of PdCl_2 solution, the redissolved solution is considered to consist of PdCl_2 containing oxidized Sn(IV) ions. The preparation of catalyst solution in nitrogen atmosphere prevented the precipitate formation, and the precipitation did not take place for a long time when the catalyst solution was stored in a nitrogen atmosphere. Therefore, oxygen produces the precipitate by oxidizing Sn(II) to Sn(IV), and this result supports the contention that Sn(II) ions stabilize the Pd-Sn colloidal particles.

Transmission electron microscopy.—The colloidal particles of catalyst solutions adsorbed on collodion film were observed by the transmission electron microscopy after activation and/or acceleration (see Fig. 4). The particles adsorbed after activation with sample "A" are unevenly distributed and measured several tens of angstroms or less. In the case of sample "D," more uniform distribution was observed as patches measuring $400 \sim 700\text{\AA}$ and consisting of small (several tens of angstroms) particles. The commercial sample "E" after activation displayed a uniform, high density distribution of large particles $300 \sim 600\text{\AA}$ in diameter. These particles give the most uniform distribution on a collodion film. Therefore, the catalyst solutions are considered to be colloidal, and the catalytic sites formed on substrates after activation consist

³The data in Fig. 3 were obtained by diluting with distilled water. In the case of dilution with HCl solution, samples "A", "B", and "C" gradually lost the linearity in the absorption spectra, and their spectra became close to that of the first green intermediate complex. A large excess of chloride ions is considered to decompose the colloidal state of the mixed catalyst solutions.

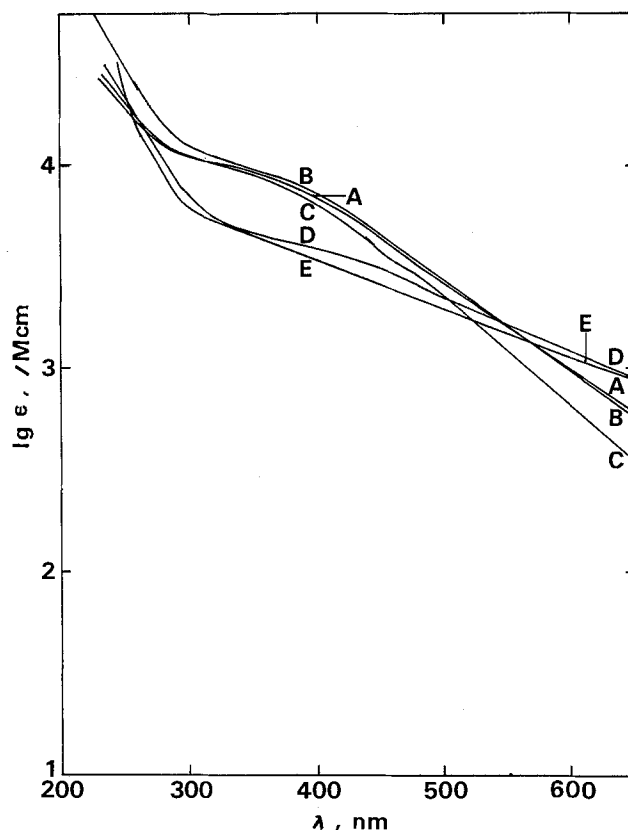


Fig. 3. Absorption spectra of five samples of mixed $\text{PdCl}_2/\text{SnCl}_2$ catalyst solutions. Each character in figure shows sample designation.

of colloidal particles. The large size of colloidal particles adsorbed on substrates is required at the activation stage to produce a high catalytic activity. The surface conditions after activation and acceleration are demonstrated in Fig. 4 (a'), (b'), and (c'). In the case of sample "A," there are two kinds of distribution, i.e., the high and low density regions consisting of several tens of angstroms particles. Sample "D" also displays the two kinds of particle distribution; the high density regions consisting of large particles, $400 \sim 700\text{\AA}$, show a relatively uniform distribution, and the low density regions consist of small (several tens of angstroms) particles. The commercial sample "E" was somewhat different from the other two samples. Although there are two types of distribution, the high density regions are almost circular in shape with $ca. 1000\text{\AA}$ in diameter, whereas particles with $100 \sim 200\text{\AA}$ in diameter are distributed uniformly in the low density regions. The accelerator is considered to not only remove the Sn(IV) ions but also coagulate the small particles to produce high density particles.⁴

Electrochemical Approaches Using Gold Substrate

Anodic sweep in 1M HCl after activation.—Figure 5 shows current-potential curves obtained on single anodic sweep at a gold electrode in 1M HCl after immersion into the five different catalyst solutions (i.e., after the activation procedure). In the case of the most active catalyst solutions, samples "D" and "E", three distinct anodic peaks were obtained at -0.10 (P1), 0.21 (P2), and 0.43V (P3). With the other three samples each anodic scan gave only two peaks at -0.10 (P1) and 0.20V (P2). This electrochemical technique can be used for rapid diagnosis of the activity of mixed catalysts. In order to identify the cause of each peak in the single anodic sweep after activation, a single anodic sweep was performed after each step in the two-step procedure. Figure 6 shows the anodic sweep in 1M HCl

⁴The action to remove the Sn(IV) ions will be discussed later.

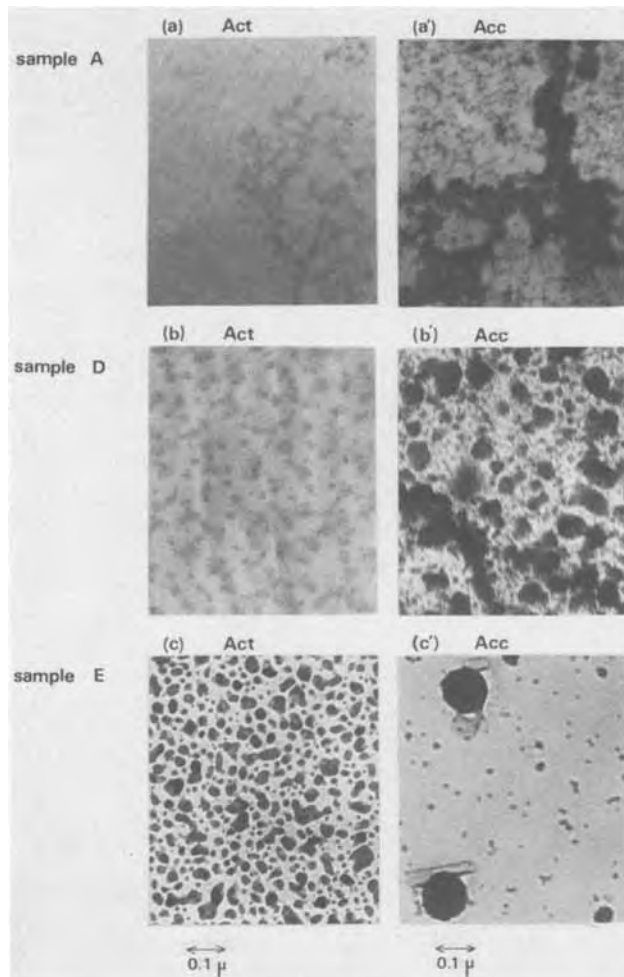


Fig. 4. Transmission electron micrographs of various samples on collodion film after activation or after acceleration. (a), (b), (c): after activation, (a'), (b'), (c'): after acceleration.

after immersion into SnCl_2 solution⁵ (sensitization), immersion into SnCl_2 and PdCl_2 solutions⁶ (activation), and immersion into PdCl_2 solution only. In the case of sensitization, only two peaks appeared corresponding to "P1" and "P2" in Fig. 5. After activation in the two-step procedure, three anodic peaks similar to those of samples "D" and "E" were observed. It is concluded by considering (a) and (b) in Fig. 6 and the more detailed experiments shown later, that the anodic peaks "P1" and "P2" correspond to the desorption of adsorbed $\text{Sn(II)}_{\text{ad}}$ or Sn(O)_{ad} ⁷ and the oxidation reaction from Sn(II) to Sn(IV) , respectively, and that the anodic peak "P3" is caused by the dissolution of Pd. The anodic sweep after immersion only into PdCl_2 solution seen in Fig. 6(c) is identical to that obtained without immersion into PdCl_2 solution. This result indicates that Pd(O) adsorbed on gold is not produced in the absence of adsorbed Sn(II) formed by the sensitization procedure.

Cyclic voltammograms on gold in 1M HCl containing Sn(II) ions or Pd(II) ions.—In order to obtain further insight into the anodic peak in Fig. 5, cyclic voltammograms were taken in 1M HCl containing SnCl_2 or PdCl_2 . The cyclic voltammograms on gold with various amounts of SnCl_2 in 1M HCl are shown in Fig. 7. Two anodic peaks are seen at -0.10 (P4) and 0.20V (P5). It was confirmed by the cyclic voltammograms with changing cathodic scanning potential range that the cathodic peak at -0.10V (P4') corresponds to that of

⁵ SnCl_2 solution was prepared by dissolving 90 g/liter $\text{SnCl}_2 \cdot 2\text{H}_2\text{O}$ in 37% HCl in nitrogen atmosphere.

⁶ PdCl_2 solution was prepared by dissolving 0.5 g/liter in 37% HCl solution.

⁷ The possibility of the peak "P1" being due to the desorption of $\text{Sn(II)}_{\text{ad}}$ or Sn(O)_{ad} will be discussed later.

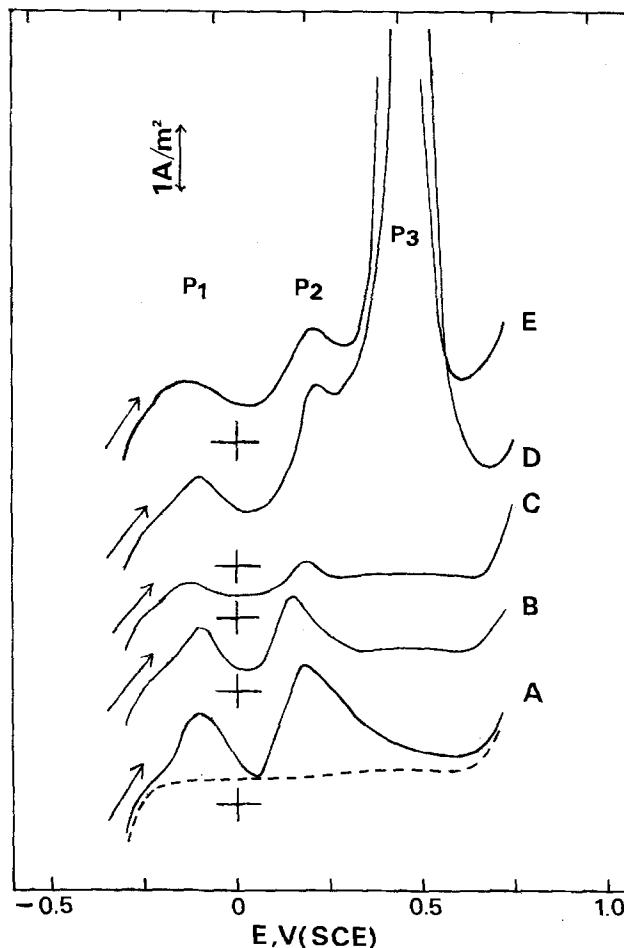


Fig. 5. Voltammograms on Au electrode in 1M HCl. Solid lines: single anodic sweep after activation, dashed line: anodic sweep without activation, sweep rate: 0.1 V/sec. Each character shows sample designation.

"P4" in the anodic sweep. The anodic and cathodic peaks "P4" and "P4'" give the saturation value of $85.2 \mu\text{C}/\text{cm}^2$, while the peak "P5" gradually increases within the concentration of SnCl_2 . Therefore, it is clear that the peak "P4" or "P4'" is due to the desorption or adsorption of Sn(O) or Sn(II) , i.e., the so-called underpotential deposition, and that the peak "P5" is caused by the oxidation reaction $\text{Sn(II)} \rightleftharpoons \text{Sn(IV)} + 2e$. The peaks "P1" and "P2" in the single anodic sweep after sensitization shown in Fig. 6(a) or activation shown in Fig. 5 or Fig. 6(b) clearly correspond to those of "P4" and "P5" in Fig. 7. Since the cyclic voltammograms on gold in 1M HCl containing Sn(IV) (as SnCl_4) ions was approximately the same as that of the blank solution, the cathodic peak "P4'" in Fig. 7 is not due to $\text{Sn(II)}_{\text{ad}}$ but to the Sn(O)_{ad} adsorption reaction $[\text{Sn(II)} + 2e \rightleftharpoons \text{Sn(O)}_{\text{ad}}]$.⁸ When the saturated adsorption value of Sn_{ad} is compared with that of O_{ad} of $395 \mu\text{C}/\text{cm}^2$,⁹ it is clear that the coverage is very small ($1/4 \sim 1/5$), and there may be a possibility of co-adsorption of $\text{Sn(II)}_{\text{ad}}$ without accompanying a charge transfer $[\text{Sn(II)} \rightleftharpoons \text{Sn(II)}_{\text{ad}}]$.

Figure 8 demonstrates cyclic voltammogram on gold in 1M HCl containing PdCl_2 . The three anodic peaks at -0.20 , -0.08 , and 0.45V correspond to

⁸ The observation of the Mössbauer effect by Bowles and Cranshaw (18) showed that the spectra of adsorbed Sn at -0.145V (SCE) (underpotential region) is in fact remarkably similar to those of metallic tin on platinum. The adsorption of Sn(O) may be caused by the starting potential being more cathodic than the rest or open-circuit potential, and at the open-circuit potential the Sn is considered to be in the state of $\text{Sn(II)}_{\text{ad}}$.

⁹ The value of the saturated O_{ad} on polycrystalline gold was determined by the reduction peak. Rand and Woods (19) reported the value of $386 \mu\text{C}/\text{cm}^2$ on (100) gold surface.

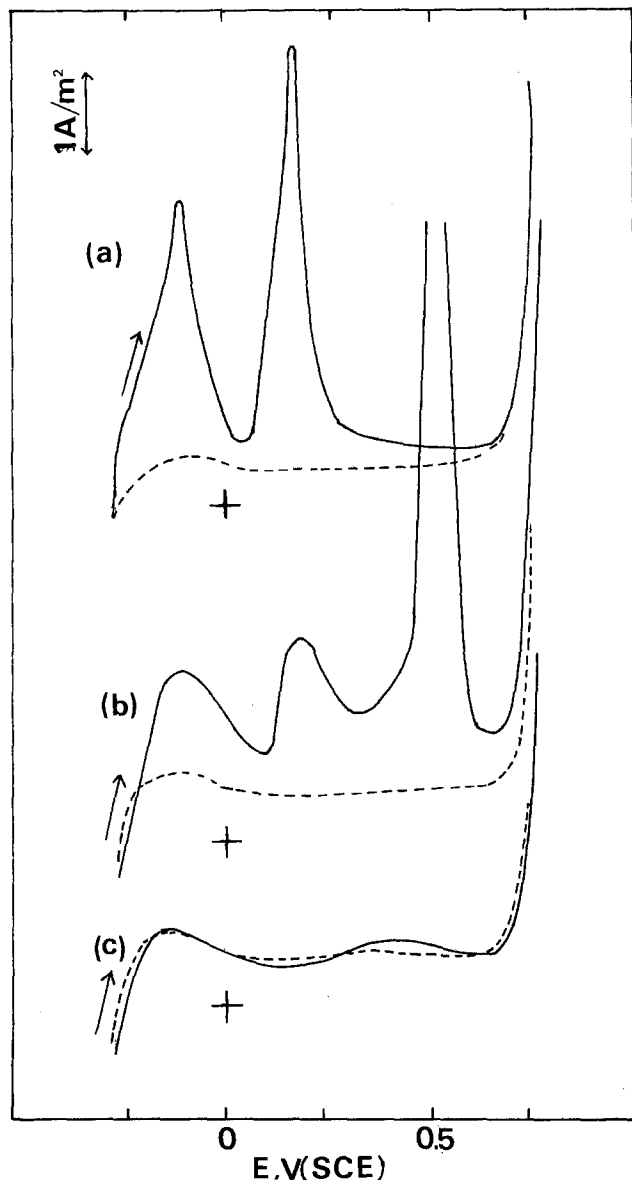


Fig. 6. Voltammograms on Au electrode in 1M HCl in the case of two-step procedure. Dashed lines: anodic sweep without immersion steps, sweep rate: 0.1 V/sec. (a) Single anodic sweep after immersion into SnCl_2 solution, (b) single anodic sweep after immersion into SnCl_2 solution and PdCl_2 solution. (c) single anodic sweep after immersion into only PdCl_2 solution.

the three cathodic peaks. From a comparison with the results on palladium deposition (20, 21), the peaks at -0.20 , and -0.08V are considered to be the desorption peaks of H_{ad} on Pd deposited on gold. The anodic peak at 0.45V was determined to be the dissolution peak of Pd(O) upon referring to the literature (20, 21). Therefore, the peak "P3" shown in Fig. 5 and Fig. 6(b) is identical with the dissolution peak of palladium in Fig. 8.

Anodic sweep in 1M HCl after acceleration.—As typical accelerators we chose 1M NH_4BF_4 and 1:1 HCl solutions. The hydrochloric acid solution was recommended by Cohen and Meek (9c), because of several advantages, i.e., material cost, simple processing due to the elimination of one-step (water rinse), easier water disposal, and a less toxic material. Figure 9 shows two voltammograms obtained after activation in sample E' and acceleration in 1M NH_4BF_4 or 1:1 HCl. When 1:1 HCl was used as accelerator, the water rinse step after activation was omitted as pointed out by Cohen and Meek (9c). It is interesting that both curves show only one anodic peak of Pd dissolution at $0.45 \sim 0.50\text{V}$ in the single anodic sweep as compared

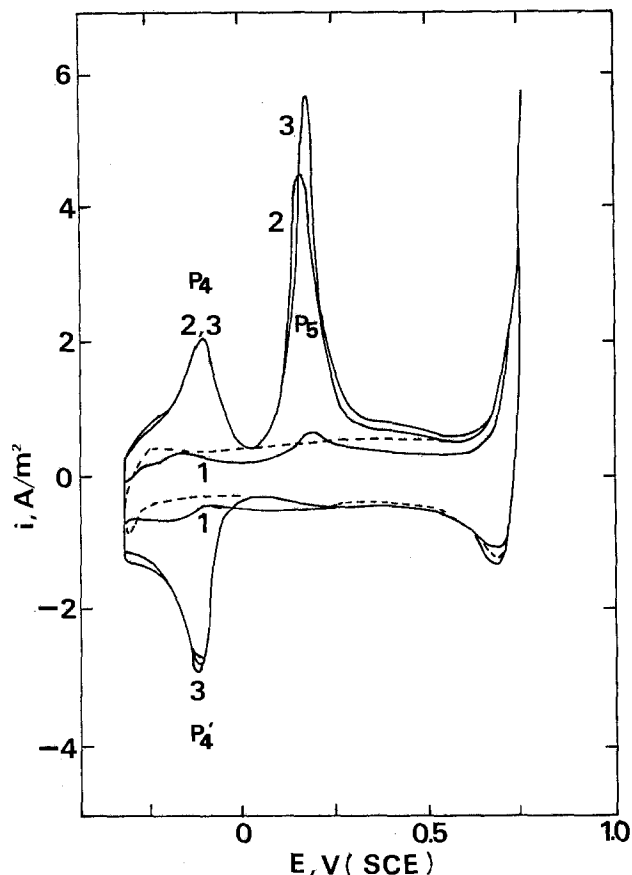


Fig. 7. Cyclic voltammograms on Au electrode in 1M HCl containing various concentrations of SnCl_2 . Sweep rate: 0.1 V/sec, curve 1, $9.0 \times 10^{-5}\text{M}$ SnCl_2 , curve 2, $1.8 \times 10^{-4}\text{M}$ SnCl_2 , curve 3, $2.2 \times 10^{-4}\text{M}$ SnCl_2 .

with the case of three anodic peaks after activation shown in Fig. 5. The acceleration procedure clearly

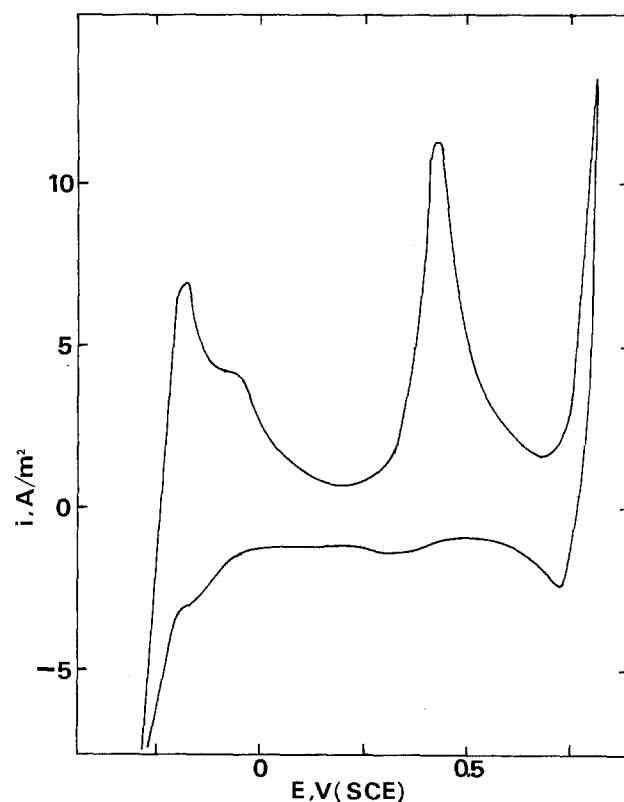


Fig. 8. Cyclic voltammogram on Au electrode in 1M HCl containing $5.10 \times 10^{-4}\text{M}$ PdCl_2 . Sweep rate: 0.1 V/sec.

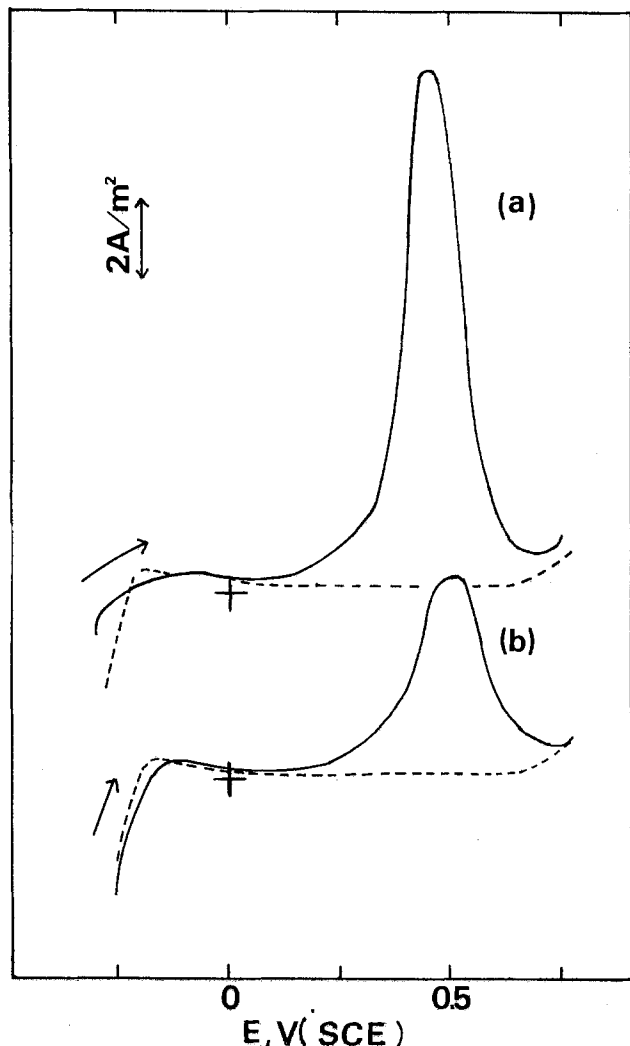


Fig. 9. Voltammograms on Au electrode in 1M HCl after activation and acceleration in the case of sample "E". Solid lines: single anodic sweep after activation and acceleration, dashed lines: anodic sweep without immersion steps, sweep rate: 0.1 V/sec, accelerator: (a) 1M NH_4BF_4 , (b) 1:1 HCl.

removes Sn adsorbed on Au, leaving Pd nuclei on gold. The most active catalysts, "D" and "E", gave clearly the dissolution peak of palladium, while the other less active samples, "A", "B", and "C", showed no distinct peak in the single anodic sweep after acceleration. It can be concluded that the active catalyst forms palladium nuclei¹⁰ on gold and that the anodic sweep on gold in HCl solution provides a reliable and simple method of diagnosing the activity of the mixed acidic catalyst. In view of the fact that the induction time before the initiation of metal deposition (cf. Fig. 1) is greatly shortened by the acceleration, it appears that the adsorbed Sn(O), Sn(II), or Sn(IV) ions on substrates formed after the activation mask the catalytic activity of palladium nuclei, and that they are removed in the acceleration step.

Kelly and Vondeling (14) reported that the nucleation reaction of palladium takes place upon u.v. irradiation of photosensitive TiO_2 films in contact with palladium ions and that the photoreaction product consisting of polycrystalline metallic palladium initiates electroless nickel deposition. Hamilton and Logel (15) investigated evaporated palladium deposits and concluded that large palladium particles (4 ~ 20 atoms) are required for nickel deposition. Clearly, metallic palladium particles also provide the catalytic activity. In the mixed $\text{PdCl}_2/\text{SnCl}_2$ catalytic system,

¹⁰ It was confirmed by the XPS measurements shown later that the final active sites on substrate are formed not by pure palladium but by the intermediate Pd-Sn system.

however, several Pd-Sn complexes such as SnPd_7Cl_6 (5), PdSn_2 (6), and Pd_3Sn (7) have been reported as catalytically active species. In the next section, an attempt will be made, based on XPS (ESCA) measurements, to determine whether the catalytic activity is due to metallic palladium or to some Pd-Sn complexes in the mixed $\text{PdCl}_2/\text{SnCl}_2$ catalyst system.

Auger electron spectroscopy (AES) and x-ray photoelectron spectroscopy (XPS) measurements for the $\text{PdCl}_2/\text{SnCl}_2$ catalysts.—For surveying the surfaces after each step, the AES measurement was done after activation and after acceleration of an electroless plated Ni-P substrate. The AES spectra after activation of Ni-P substrate indicated the peaks of Pd, Sn, O, C, and Cl and the peaks of Ni and P of the substrate were unclear after activation. The peaks of Ni and P after acceleration, however, were clearly observed in the spectra. The carbon is considered to be due to surface contamination. The XPS measurement, which was performed to confirm the chemical states of Pd and Sn on the surfaces, also indicated the presence of Pd, Sn, O, C, Cl, and Cu after activation and after acceleration (where a copper sheet was used as substrate). After acceleration there was a tendency for the Cu peaks to increase, which means that the area of the exposed substrate surface increases with acceleration. Also a tendency of decreasing Pd and Sn was observed except for sample "A" (cf. Table III), which means that the absolute amounts of Pd and Sn on the surface are decreased by the acceleration. Typical examples of XPS spectra are shown in Fig. 10, and the values of measured binding energies and

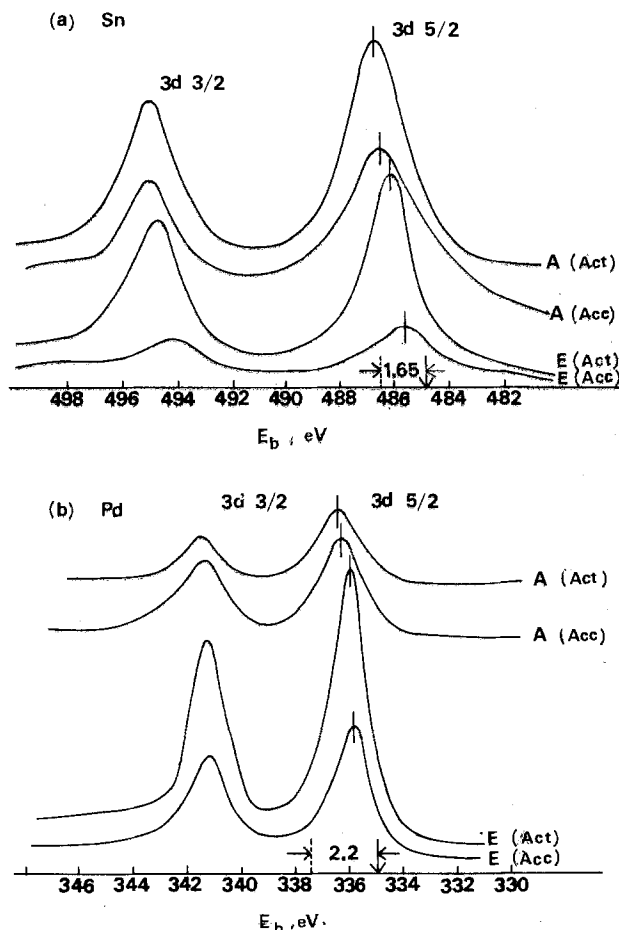


Fig. 10. XPS spectra of sample "A" and "E" for Pd $3d_{5/2}$ and Sn $3d_{5/2}$ levels. (a) Spectra for Sn $3d_{5/2}$, (b) spectra for Pd $3d_{5/2}$. Vertical arrows and dashed lines indicate E_b values for metals and charged species (24, 26), respectively. The numbers between the two markings are the corresponding chemical shifts.

Table II. Measured binding energies of the $3d_{5/2}$ levels of Pd and Sn

Samples	Binding energies (eV) and shifts (eV)				
	Pd $3d_{5/2}$	Shifts	Sn $3d_{5/2}$	Shifts	
metal	335.2	0.0	485.1	0.0	
A	{ Act ^a	336.5	1.3	486.7	1.6
	{ Acc ^b	336.3	1.1	486.6	1.5
D	{ Act	336.0	0.8	486.6	1.5
	{ Acc	336.0	0.8	485.9	0.8
E	{ Act	335.9	0.7	486.1	1.0
	{ Acc	335.8	0.6	485.7	0.6
A (F D M) ^c	336.8	1.6	487.4	2.3	
B (F D M)	336.8	1.6	487.4	2.3	
D (F D M)	336.4	1.2	487.4	2.3	
SnCl ₂ soln., PdCl ₂ soln. ^d	335.6	0.4	487.0	1.9	

^a After activation.

^b After activation and acceleration (1M NH₄BF₄).

^c Freeze-dry method.

^d After dipping into SnCl₂ solution and PdCl₂ solution (two-step procedure).

chemical shifts for the Pd $3d_{5/2}$ and Sn $3d_{5/2}$ levels are given in Table II. Three sets of data (after activation, after acceleration, and for freeze-dried catalyst solutions) are tabulated. The binding energies were measured within ± 0.2 eV. The most reasonable values in the literature are considered to be 335.2 eV for Pd metal (22) and 484.9 eV for Sn metal (23) at $3d_{5/2}$ levels. The chemical shift for Pd(II) using PdCl₂ was reported to be 2.2 eV (24). The results on the chemical shifts for the Sn $3d_{5/2}$ reported by various investigators (25) disagree with each other, and Lau and Wertheim (26) discussed the above inconsistencies and concluded that the chemical shifts of Sn $3d_{5/2}$ for SnO and SnO₂ are approximately the same. The chemical shift of Sn $3d_{5/2}$ in the direction of higher binding energies against metal was reported to be 1.65 eV for Sn(II) or Sn(IV) (as SnO or SnO₂) by Lau and Wertheim (26). It is interesting that the binding energies of Pd $3d_{5/2}$ level for various samples observed lie between palladium metal and charged palladium (as PdCl₂). It is difficult to recognize from the shape of sharp peaks that the peak of Pd $3d_{5/2}$ level for each sample consists of a mixture of Pd(O) and Pd(II).¹¹ In the step after activation, the correlation between binding energy and catalytic activity is such that the binding energy of a more highly active catalyst becomes close to the low value of palladium metal, and the acceleration procedure causes the binding energy to shift toward lower values than that observed after the activation step. As for the Sn $3d_{5/2}$ level, the tendency similar to the Pd $3d_{5/2}$ level is observed in both cases after activation and after acceleration procedures.¹² The results of the freeze-dry method indicate that the palladium and tin of the colloidal particles in solution are in more highly charged states than those on substrates, and that the more active catalysts also display the lower binding energies in solution similarly to those adsorbed on substrates. There may be also a possibility, however, that the results on the freeze-dried catalysts are caused by the coexistence of original elemental composition and colloidal particles.

It was reported by Masai *et al.* (27) that the Pd 4d state peaks in the XPS spectra for the Pd-Sn alloy system are shifted to higher binding energies with decreasing ratio of Pd/Sn. (The shift of ca. 2.2 eV for Pd 4d state was shown from Pd/Sn = ∞ to 0.54.) It may be concluded from the above results on the Pd

¹¹ The peak breadth of half-maximum intensity of each sample for Pd $3d_{5/2}$ and Sn $3d_{5/2}$ was nearly equal to that of the metal, respectively, except for "A Acc." in the case of which the peak breadth of half-maximum intensity was somewhat larger.

¹² Since it was reported that Sn(II) can be oxidized to Sn(IV) by the irradiation of u.v. light on photosensitive TiO₂ (12), it was thought probable that a similar reaction might occur upon x-ray irradiation. The above possibility, however, was shown to be non-existent by the fact that no time dependence of the observed binding energy of Sn $3d_{5/2}$ was found upon x-ray irradiation.

$3d_{5/2}$ level that the active sites in the final form consist of a Pd-Sn intermediate or alloy system, and that the active site of the more active catalyst is formed by the Pd-Sn alloy containing the larger amount of palladium. The results of the Sn $3d_{5/2}$ level that the ratio of charged states decreases upon acceleration can be explained on the assumption that the accelerator removes mainly Sn(IV) ions from the surfaces. This interpretation agrees well with the results of the electrochemical measurement.

The relative amounts and ratios of Pd and Sn on the surfaces were calculated from the peak area ratios corrected by the photoionization cross section (28) and tabulated in Table III, where the correction for the mean free path and the instrumental factor were ignored because the kinetic energies of the peaks observed are nearly equal. The line shape problems and the presence of satellites were not observed, and there were no problems in the quantification of the relative amounts of Pd and Sn. The value of Pd for sample "E Act" was used as 100 for normalization. The amounts of Pd and Sn on the surface decreased upon acceleration except for the palladium found with sample "A." It is interesting that the final ratio of Pd/Sn after acceleration is not constant but increases with increasing catalyst activity. Meek (9b) showed by the elemental analysis of commercial catalysts (Shibley 9F and MacDermid 9070) using Rutherford ion backscattering technique that the Pd/Sn ratio becomes ≤ 1 after activation and ≈ 3 after acceleration and finally ≈ 6 at the initial stage of copper plating at which the Pd-Sn alloy core remains. The smaller values of our results for Pd/Sn ratio may be partly due to the difference in catalyst activity.¹³ The values obtained by the freeze-dry method were small, which may be due to the original elemental composition. The Pd-Sn alloy particles which constitute active sites on surfaces are considered to consist of a system in which the ratio of Pd/Sn depends on the catalyst activity. Feldstein *et al.* (7) concluded the active sites to consist of Pd₃Sn alloy on the basis of the fact that the lattice parameters determined from the electron diffraction pattern closely matched those of Pd₃Sn in fcc form. Our results (29) of electron diffraction analysis of the catalyst on collodion surfaces after acceleration were also close to those of fcc Pd₃Sn. However, it was difficult to obtain accurate values because of the broad diffraction rings and of each lattice factor deviating somewhat to larger values.¹⁴ Cohen and Meek (9b) discussed the conflicting results by various investigators (5-9) on the catalytic centers

¹³ Since the information obtained by XPS technique is assumed to correspond to that of the shallower surface region than that obtained by Rutherford ion backscattering technique, our results for Pd/Sn ratios are also considered to become smaller than those of Meek because of the influence of the residual Sn ion layer on Pd-Sn active center.

¹⁴ Feldstein *et al.* (7) and Rantell *et al.* (5) also reported the slightly larger values of each lattice factor, and it was discussed by Cohen and Meek (9b).

Table III. Relative amounts* and ratios of Pd and Sn

Sample	Sn	Pd	Pd/Sn	
A	{ Act	247	25	0.10
	{ Acc	173	42	0.25
D	{ Act	313	80	0.26
	{ Acc	61	45	0.74
E	{ Act	233	100**	0.43
	{ Acc	55	47	0.84
A (F D M)	227	27	0.12	
B (F D M)	147	7	0.05	
D (F D M)	200	37	0.17	
SnCl ₂ soln., PdCl ₂ soln.	21	55	2.70	

* Relative peak areas corrected with the photoionization cross section (the electron mean free path and the instrumental factor were omitted).

** The value of Pd for sample "E Act" was used as 100 for normalization.

consisting of colloidal particles of Pd-Sn alloy, and concluded that the catalytically active centers would be designated as Pd-Sn alloy, rather than Pd₃Sn. Thus, it is concluded that the final active sites or centers consist of a disordered Pd-Sn alloy system in which the more active catalyst has the higher palladium to tin ratio, and that the actual conditions are such that compounds with various Pd/Sn ratios exist on the surface.

Acknowledgments

The authors wish to thank Professor Dr. Tadashi Yoshida, Department of Applied Chemistry, Waseda University, for advice and support of this research. They also wish to thank Professor Dr. Yoshimasa Nihei and Dr. Masahiro Kudo, Institute of Industrial Science, University of Tokyo, for their support of XPS experiments and discussions of the results.

Manuscript submitted July 9, 1979, revised manuscript received Nov. 26, 1979.

Any discussion of this paper will appear in a Discussion Section to be published in the December 1980 JOURNAL. All discussions for the December 1980 Discussion Section should be submitted by Aug. 1, 1980

Publication costs of this article were assisted by OKI Electric Industry Company, Limited.

REFERENCES

- C. R. Shipley Jr., U.S. Pat. 3,011,920 (1961).
- E. D. D'Ottavio, U.S. Pat. 3,532,518 (1970); U.S. Pat. 3,650,913 (1972).
- R. J. Zeblicky, (a) U.S. Pat. 3,672,938 (1972); (b) U.S. Pat. 3,682,671 (1972).
- E. J. Fadgen and E. B. Saubestre, U.S. Pat. 3,767,583 (1973).
- A. Rantell and A. Holtzman, (a) *Plating*, **61**, 326 (1974); (b) *Trans. Inst. Metal Finishing*, **51**, 62 (1973); (c) *ibid.*, **52**, 31 (1974).
- C. H. de Minjer and P. F. J. v. d. Boom, *This Journal*, **120**, 1644 (1973).
- N. Feldstein, M. Schlesinger, N. E. Hedgecock, and S. L. Chow, *ibid.*, **121**, 738 (1974).
- M. D. Joisson and M. M. Devand, *C. R. Acad. Sci. Paris*, **275**, 1363 (1972).
- R. L. Cohen and K. W. West, *This Journal*, **120**, 502 (1973); *Chem. Phys. Lett.*, **16**, 128 (1972); R. L. Cohen, J. F. D'Amico, and K. W. West, *This Journal*, **118**, 2042 (1971).
- R. L. Meek, *This Journal*, **122**, 1177 (1975); R. L. Cohen and R. L. Meek, *J. Colloid Interfacial Sci.*, **55**, 156 (1976).
- R. L. Cohen and R. L. Meek, *Plating*, **63**, 47 (1976).
- M. Tsukahara, T. Kishi, H. Yamamoto, and T. Nagai, *Kinzoku Hyomen Gijutsu*, **23**, 83 (1972); M. Kose, T. Kishi, H. Yamamoto, and T. Nagai, *ibid.*, **24**, 203 (1972).
- E. Matijević, A. M. Poskanzer, and P. Zuman, *Plating*, **62**, 958 (1975).
- J. F. D'Amico, M. A. de Angelo, J. F. Henrickson, J. T. Kenny, and D. J. Sharp, *This Journal*, **118**, 1695 (1972).
- B. K. W. Baylis, A. Busuttill, N. E. Hedgecock, and M. Schlesinger, *ibid.*, **123**, 348 and 1376 (1976); *ibid.*, **124**, 346 (1977).
- J. J. Kelly and J. K. Vondeling, *ibid.*, **122**, 1103 (1975).
- J. F. Hamilton and P. C. Logel, *J. Catal.*, **29**, 253 (1973).
- K. Nihei, T. Osaka, and H. Sawai, *Denki Kagaku*, **44**, 402 and 656 (1976).
- M. Kudo, Y. Nihei, and Kamada, *Rev. Sci. Instrum.*, **49**, 756 (1978).
- B. J. Bowles and T. E. Cranshaw, *Phys. Lett.*, **17**, 258 (1965).
- D. A. J. Rand and R. Woods, *J. Electroanal. Chem. Interfacial Electrochem.*, **31**, 29 (1971).
- M. F. Bell and J. A. Harrison, *ibid.*, **41**, 15 (1973); J. A. Harrison, R. P. J. Hill, and J. Thompson, *ibid.*, **47**, 431 (1973); J. A. Harrison, H. B. S. Alcazar, and J. Thompson, *ibid.*, **53**, 145 (1974).
- D. A. J. Rand and R. Woods, *ibid.*, **44**, 83 (1973); R. Woods, in "Electroanalytical Chemistry," Vol. 9, A. J. Bard, Editor, p. 1, Marcel Dekker, New York (1976).
- G. Schön, *J. Electron Spectrosc. Relat. Phenom.*, **1**, 377 (1972/1973).
- M. Cardona and L. Ley, "Topics in Applied Physics Photoemission in Solid I," General Principles (1978).
- G. Kummer, J. R. Blackburn, R. G. Albridge, W. E. Moodeman, and M. M. Jones, *Inorg. Chem.*, **11**, 296 (1972).
- P. A. Grutsch, M. V. Zeller, and T. P. Fehlner, *ibid.*, **12**, 1431 (1973); R. J. Bird, *Met. Sci.*, **7**, 109 (1973); T. Farrell, *ibid.*, **10**, 87 (1976); W. E. Morgan and J. R. Van Wazer, *J. Phys. Chem.*, **77**, 964 (1973).
- C. L. Lau and K. Wertheim, *J. Vac. Sci. Technol.*, **15**, 622 (1978).
- M. Masai, K. Honda, A. Kubota, S. Ohnaka, Y. Nishikawa, K. Nakahara, K. Kishi, and S. Ikeda, *J. Catal.*, **50**, 419 (1977).
- J. H. Scofield, *J. Electron Spectrosc. Relat. Phenom.*, **8**, 129 (1976).
- Unpublished data.

The Effect of Copper and Silver Substrates on the Structure, Internal Stress, and Electrode Potential during the Initial Stages of Gold Electrodeposition

S. T. Rao^{*,1} and R. Weil*

Department of Materials and Metallurgical Engineering,
Stevens Institute of Technology, Hoboken, New Jersey 07030

ABSTRACT

The initial stage of epitaxial electrocrystallization of gold from an additive-free, alkaline, sulfite solution on polycrystalline copper and silver substrates was found to be three-dimensional crystallite formation. The crystallites on the copper substrates were laterally considerably smaller than those on silver. This effect is attributed to the larger lattice mismatch between gold and copper. On silver, substrate coverage occurred earlier and was followed by the formation of smaller, secondary crystallites. The internal stress in the gold deposits on silver was initially very small and tensile due to the small lattice mismatch and the large crystallite size. The stress rose to a maximum during secondary crystallite formation. On copper substrates, the stress was initially compressive because of the negative lattice-mismatch component and then changed to tensile when crystallite coalescence became predominant.

Recent studies (1-7) of the early stages of epitaxial electrocrystallization of nickel on copper substrates have shown it to consist of the formation of three-dimensional crystallites all in the size range of 5-8 nm. This uniform size, which was also independent of the presence of addition agents in the plating solution, was attributed (7) to lateral-growth inhibition by basic nickel compounds produced during the deposition reactions. Substrate coverage occurred by the formation of new crystallites between existing ones and their subsequent coalescence. The crystallite nucleation was manifested by a maximum in the magnitude of the cathode potential. The attainment of a steady-state potential was indicative of substrate coverage by the electrodeposit. Crystallite coalescence resulted in the development of dislocations (3) and was the main cause of the internal stress after the initially large, extrinsic component due to the lattice mismatch between substrate and deposit decreased (5).

The purpose of this investigation was to determine whether the relationships of structure, potentials, and internal stress which were found for electrodeposited nickel on copper substrates held for other metals. The intent of this study was also to determine the effect on the internal stress of different lattice mismatches between substrate and deposit. In order that this effect should not be masked, it was necessary to use a plating solution which neither contained or produced substances having a predominant lateral-growth inhibiting effect as was found with nickel.

Gold electrodeposition on copper and silver substrates was selected for this investigation. The substrates can be readily dissolved leaving the gold deposit for transmission-electron-microscopic examination which is necessary to resolve the initial crystallite formation. An alkaline, sulfite solution without addition agents was chosen because deposition therein does not result in the production of lateral-growth-inhibiting substances. As the interatomic distances of gold are only 0.17% smaller than those of silver and 12.8% greater than those of copper, the effects of the sign and magnitude of the lattice mismatch could be de-

termined. This communication reports the result of the investigation of the structures, electrode potentials, and internal stresses during the initial stages of epitaxial electrocrystallization of gold on copper and silver substrates.

Experimental Procedure

The substrates were oxygen-free, high conductivity copper and 99.99% pure silver sheet which had been rolled and recrystallized to produce a texture such that {110} planes were parallel to the surface in most grains. The samples were 55 mm long and 5.5 mm wide. The silver substrates were 125 μm thick; the copper pieces were 25 μm thick. In order that deposition occurred on only one face of the substrate, which was necessary for the stress measurement, two layers of photoresist were applied to one side of the samples. The uninsulated side was electropolished to a mirror-bright finish. The copper substrates were prepared in the same way as those used in the previous study (5) involving nickel electrodeposition. The silver pieces were electropolished in an aqueous solution of 100 g/liter KCN and 100 g/liter $\text{K}_4\text{Fe}(\text{CN})_6$ and rinsed successively in a 20 g/liter KCN solution, essentially organic-free (5) distilled water, a 5% NaOH solution, and two more times in the distilled water.

The electrodeposition was performed in a proprietary² solution from which the usual additives had been omitted. The pH was 9.5 and the temperature 20°C. On the copper substrates the current density was 2.5 mA/cm². In order to prevent a replacement reaction from occurring, the copper substrates were either maintained at an anodic current density of 0.5 mA/cm² while the necessary adjustments for the stress measurement were made or the concentrate containing the gold ions was added just at the time when plating was desired to start. For deposition on the silver substrates, the current densities were 2.5 and 1.5 mA/cm².

The instrumentation for measuring the internal stress and the cathode potential was described in earlier papers (5, 8). Briefly, the stresses were determined from the attempted deflection of the free

* Electrochemical Society Active Member.

¹ Present address: Exxon Corporation, Optical Information Systems, Elmsford, New York 10523.

Key words: gold electrodeposition, substrate effect, internal stress.

² BDT 510 solution produced by Oxy-Metal Industries Corporation, Sei-Rex Division, Nutley, New Jersey.

end of the horizontally held substrate strip clamped at the other end, while deposition occurred on only one face. The deflection of the free end was prevented by the application of a force by a null-point electrobalance. As in previous studies (5, 9), the instantaneous stress was determined. Also as was done previously (5, 9), the deposit thicknesses were calculated from the charge densities assuming a uniform layer, 100% plating efficiency, and the same density as the bulk metal.

Samples were plated to a nominal thickness of 100 nm while the stress and cathode potentials *vs.* SCE were monitored. Samples were also plated to thicknesses less than 100 nm at which significant changes in either the stresses or potentials occurred. The very thin gold deposits on copper were backed by a Ni-P film (5) and those on silver by vapor-deposited platinum (10). The copper substrates were dissolved in a solution containing chromic and sulfuric acids (5). The silver substrates were dissolved in nitric acid. The gold deposits, including the thin ones, with their backing films were examined by transmission electron microscopy.

Results

Gold deposits on silver substrates.—Figure 1 shows the cathode potential and the instantaneous stress *vs.* deposit thickness of gold electrodeposits on silver substrates when the current density was 1.5 mA/cm². The magnitude of the cathode potential is seen to rise to a maximum at a nominal thickness of about 2 nm. Passing a charge density equivalent to a thickness of 2 nm was found not to have resulted in any gold deposit visible electron microscopically or detectable by electron diffraction. The structure at a nominal thickness of 4 nm, *i.e.*, just after the potential peak is shown in Fig. 2. The larger dark areas are three-dimensional crystallites. The fine dots are the platinum backing. A dark-field electron micrograph of a similar deposit showing the large gold crystallites is Fig. 1a in Ref. (13). A Moiré pattern in Fig. 2 probably resulted from the difference in the lattice dimensions of very thin electrodeposited gold crystallites and the

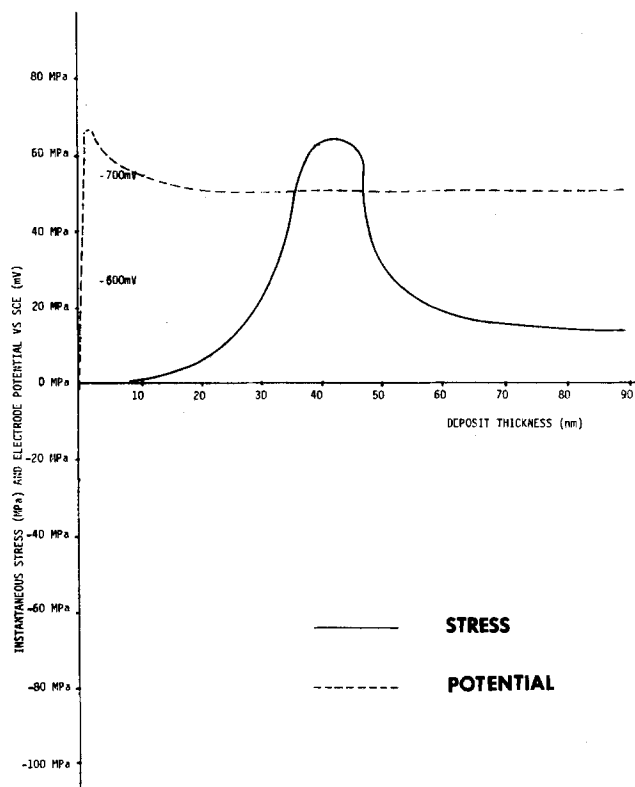


Fig. 1. Graphs of electrode potential and internal stress *vs.* nominal deposit thickness for gold on silver substrates.

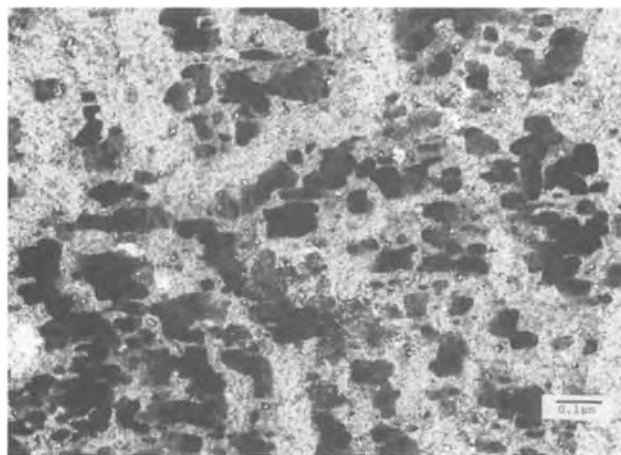


Fig. 2. Transmission electron micrograph showing three-dimensional gold crystallites which grew on silver substrate.

vapor-deposited platinum backing. It does not appear that there is a continuous gold electrodeposit underlying the large three-dimensional crystallites as the Moiré pattern is not visible over the entire sample. The large gold crystallites have an average size of about 60 nm. The electron-diffraction pattern of the gold deposit was that of a single crystal showing that all the crystallites had grown epitaxially on one substrate grain. The majority of the electron-diffraction patterns showed that {110} planes were parallel to the surface, *i.e.*, they had the same texture as the substrates.

The internal stress shown in Fig. 1 is initially small and tensile when the current density was 1.5 mA/cm². The same result was found at a current density of 2.5 mA/cm². The stress is seen to rise to a maximum value at a thickness of about 40 nm. The structure at the stress maximum is shown in Fig. 3. This sample did not have a platinum backing and was therefore a continuous film. A continuous gold deposit covered the substrate already at a thickness of 15 nm where the cathode potential attained a steady-state value. The deposit was also continuous at the same thickness when the current density was 2.5 mA/cm². In Fig. 3 a number of small hillocks which grew out of the continuous film are indicated by an arrow. These small, secondary crystallites were only observed in the thickness range of the stress maximum. Much larger pyramidal hillocks were found to have developed in thicker deposits.

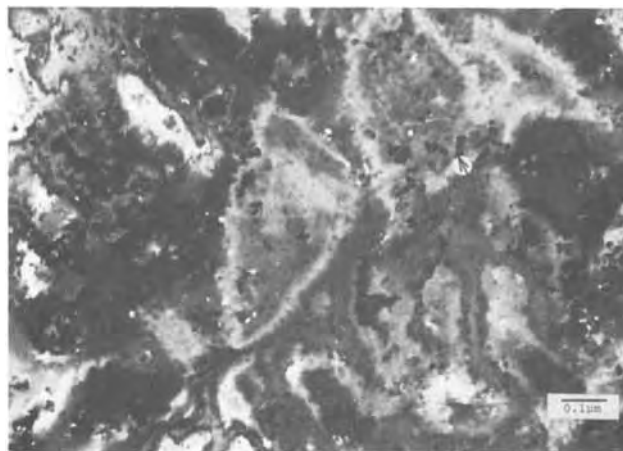


Fig. 3. Transmission electron micrograph of a continuous gold film which had been plated on a silver substrate. Arrow points to secondary crystallites.

Gold deposits on copper substrates.—Cathode potential and instantaneous stress *vs.* thickness curves for gold electrodeposits on copper substrates are shown in Fig. 4. Again the magnitude of the potential is seen to rise to a maximum. However, the nominal thickness or charge density at which the peak occurs is greater than in Fig. 1. Also the magnitude of the potential peak is greater for the deposits on copper. The structure at a nominal thickness of about 20 nm is shown in Fig. 5. Discrete crystallites with an average size of about 20 nm can be seen. The crystallites are considerably thicker than the ones which grew on silver. The effect of substrate-grain orientation is shown in Fig. 6. The deposit on the right, which is almost a complete film, had an electron-diffraction pattern indicative of a {110} plane parallel to the surface. The sparser growth on the left had a {100} plane parallel to the surface. No enhanced crystallite formation on the substrate grain boundary is visible. From an analysis of the crystallographic directions of

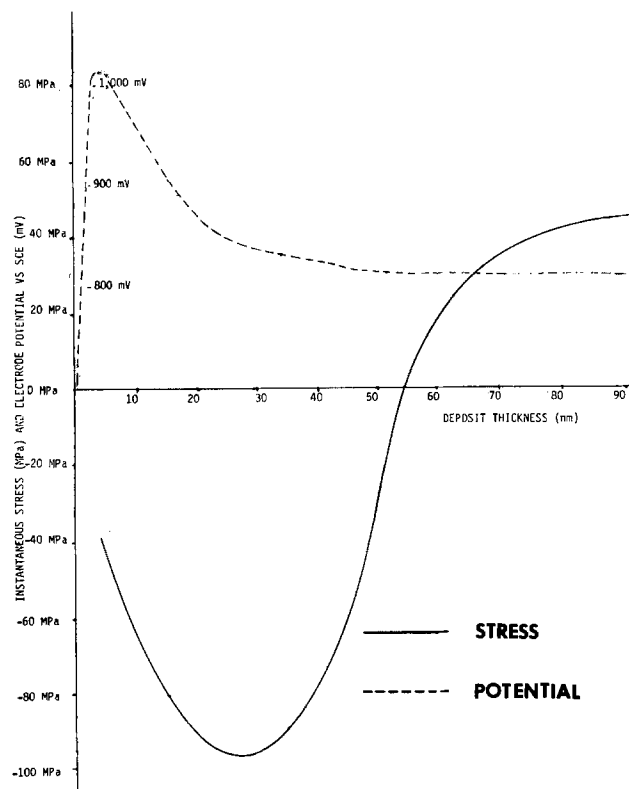


Fig. 4. Graphs of electrode potential and internal stress *vs.* nominal deposit thickness for gold on copper substrates.

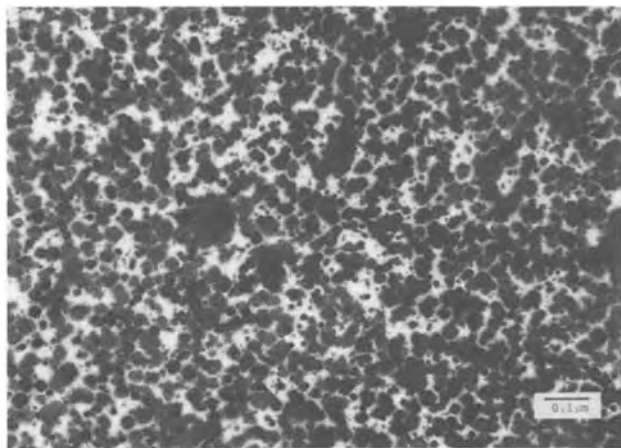


Fig. 5. Transmission electron micrograph showing three-dimensional gold crystallites which grew on copper substrates.

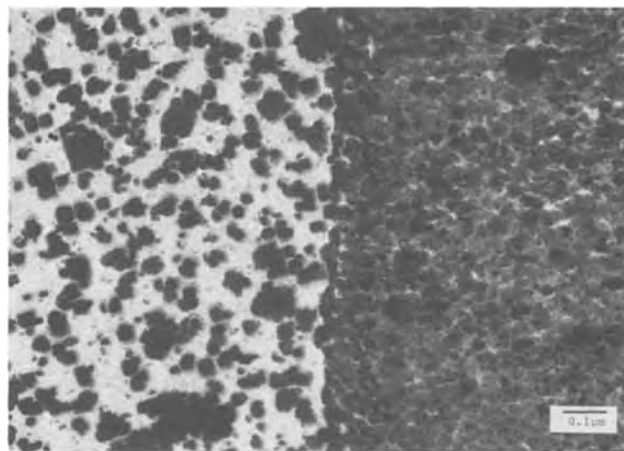


Fig. 6. Transmission electron micrograph showing an almost continuous gold deposit which grew on a {110} copper substrate grain on the right. On the left side discrete crystallites are seen which grew on {100} substrate grain.

the edges of the crystallites such as those in Fig. 5 and 6, it was determined that they were mostly bounded by {110} planes. Substrate coverage by a complete deposit film was found to have been attained at a thickness of about 40 nm, again where the cathode potential leveled off to a steady-state value.

The instantaneous stress shown in Fig. 4 is initially compressive; its magnitude reaches a maximum at a thickness of 27 nm and then increases to become tensile beyond 54 nm. The structure at the thickness where the compressive-stress maximum occurs is the one shown in Fig. 6. No significant structural features were observed in deposits having the thickness where the sign of the stress changed. No secondary crystallization such as seen in Fig. 3 in the deposits on silver was observed in the samples plated on copper substrates. The larger pyramidal hillocks were seen in thicker deposits on copper. No essential differences in the stress *vs.* thickness graphs were observed in samples in which the displacement reaction was prevented by the anodic potential or by the addition of the gold ions just prior to the start of plating. When a displacement reaction was permitted to occur, the first part of the stress graph was not recorded.

Discussion

As was previously found in epitaxial nickel deposits on copper, the initially observed electrocrystallization process of gold on the two substrates of this study was the formation of three-dimensional crystallites. It could not be definitely determined from the results of this study whether in the absence of lateral-growth inhibiting substances, a few monolayers form first and then the crystallites grow on this very thin film as discussed by Matthews, Jackson, and Chambers (11) for vapor deposits. Their analysis of the involved energies indicated that three-dimensional crystallite formation becomes more favorable than a film of uniform thickness with increasing lattice mismatch between deposit and substrate. It is, however, doubtful whether gold deposited as a continuous film even on silver substrates in view of the fact that the Moiré pattern in Fig. 2 is not continuous. Also, Stucki (12) found monolayers to be unstable in underpotential deposition of gold on both copper and silver substrates. The instability was attributed to either three-dimensional-crystallite formation or alloying with the substrate. For the explanation of the results of this study, it appears to be insignificant whether the three-dimensional growth in Fig. 2 and 5 which is clearly discontinuous, developed on a thin continuous layer or not.

The principal effect of the substrate on the initial electrocrystallization process was the size of the crystallites. On the silver substrate, which has the smaller lattice mismatch to gold, the lateral crystallite size is about three times that on copper. The determination of the crystallite size had to be done after depositing at a slightly lower current density than on copper. It was necessary to use the lower current density of 1.5 mA/cm² in order to allow sufficient time for removal from the electrolyte of a deposit on the silver substrate which was not yet continuous. It is very unlikely that the crystallite size on silver was significantly smaller when the current density was 2.5 mA/cm² as it was found that the deposits were continuous at both current densities after passing approximately the same charge density. Also the electrode potential *vs.* thickness relationships were nearly the same at 2.5 mA/cm² as that in Fig. 1. Therefore the difference between the crystallite sizes of gold plated on silver at 1.5 mA/cm² and on copper at 2.5 mA/cm² should be primarily due to the effect of the substrate.

In another study (13), the crystallite size was found to be nearly the same, *i.e.*, 8-10 nm on both silver and copper substrates, when gold was deposited from a solution containing additions of arsenic, all other conditions having been the same as in this investigation. It is therefore evident that the substrate mismatch affects the crystallite size only in the absence of lateral-growth-inhibiting substances.

As was shown (3, 5, 6) to be the case for nickel deposits, the peak in the magnitude of the cathode potential was associated with the nucleation of three-dimensional crystallites. The larger magnitude of the potential when copper was the substrate was associated with more crystallite nucleation. However, the greater current density used and the potential of copper in the gold electrolyte were also responsible for the greater peak. The presence of an oxide on the copper substrate may also have been a contributing factor. The greater charge density to reach the potential peak where the first crystallites were nucleated on copper may have been due to the need to first reduce the oxide.

The formation of a coherent deposit layer on the copper substrate occurred as it did in the case of nickel (3) by the formation of new crystallites between existing ones. The crystallites, which are still recognizable on the right side of Fig. 6, have a size which is essentially the same as that in Fig. 5. Thus it appears that there is little lateral crystallite growth once a certain size has been attained. This size was probably determined here by the lattice mismatch. Due to the fact that formation of a continuous film on silver substrates occurred after passage of a relatively small charge density and that the crystallites were no longer recognizable then, it was not possible to determine whether the same growth mechanism was operative on silver substrates as on copper.

The thinness of the crystallites on silver substrates probably resulted in relatively few defects such as voids developing during coalescence. The greater number of defects which resulted during coalescence of the crystallites on copper is the likely reason for their being still recognizable in the continuous films. The exposure of the copper substrate to the electrolyte at voids in the deposits probably accounts partly for the magnitude of the steady-state potential in Fig. 4 being greater than that in Fig. 1.

The extrinsic component of the internal stress due to the lattice mismatch between deposit and substrate can be calculated by a formula due to van der Merwe (14). For epitaxial gold on copper this value is about -120 MPa, *i.e.*, compressive, as the deposit has the larger interatomic distance. On silver substrates, the extrinsic stress in the gold deposit is 2 MPa (tensile) which is negligibly small. The intrinsic compo-

nent of the internal stress is due to the pulling together of crystallites due to surface tension before the spaces between them are completely filled (5, 15). This component is therefore always tensile and varies inversely with the lateral crystallite size. The initial stress of the deposits on silver as seen in Fig. 1 is thus small and tensile because of the large crystallite size and the negligible misfit component. The intrinsic component in the deposits on copper is estimated to be about 50 MPa, which is the value of the stress at 100 nm where the extrinsic one essentially vanishes. The extrinsic stress, which decreases with the reciprocal of the thickness according to the van der Merwe (14) formula when it is relieved by the formation of interfacial dislocations, should be negligibly small at 100 nm. The value of the stress in Fig. 4 at the compressive maximum should therefore be the algebraic sum of the extrinsic component of -120 MPa and the intrinsic one of 50 MPa, *i.e.*, -70 MPa. The agreement with the experimental value of -95 MPa is not bad considering that the reproducibility was about ± 10 MPa. This poor reproducibility was primarily due to uncertainties in the deposit thickness. The greater experimentally determined value of the compressive-stress maximum may also be due to the fact that at the thickness where it occurred there were still a number of crystallites which had not yet coalesced as seen on the left in Fig. 6 resulting in the subtraction of a smaller tensile component.

The variation of the stress with thickness in the gold deposits on copper in Fig. 4 can be explained in terms of the mismatch and crystallite-coalescence components. Initially the compressive, mismatch component predominated. Thus, the magnitude of the stress increased to a compressive maximum. When interfacial dislocations develop, the mismatch stress is relieved and the tensile, coalescence component becomes more dominant. The stress then changes sign and approaches a tensile steady state which, as already discussed, is due essentially only to the intrinsic component.

The stress in the deposits on silver starts very small and tensile as already discussed. The rise to a tensile maximum in Fig. 1 is probably due to the formation and coalescence of the secondary crystallites seen in Fig. 3. As these crystallites are much smaller than the original ones shown in Fig. 2, their coalescence results in a greater intrinsic stress. The maximum stress value of 60 MPa is about the same as the intrinsic stress in deposits on copper substrates, which have about the same crystallite size. The reason for the formation of the secondary crystallites has not been determined. They may be associated with certain crystal defects in the underlying deposit layer. The decrease in the stress beyond the maximum in Fig. 1 probably resulted because there was no observed formation and consequently no coalescence of the small secondary crystallites seen in Fig. 3 except in the one thickness range.

Conclusions

1. The initial structure of the epitaxial gold deposits on silver and copper substrates consists of three-dimensional crystallites.
2. The gold crystallites on the copper substrate are laterally smaller than those on silver, indicating that a larger mismatch results in smaller crystallites.
3. An initial peak in the magnitude of the electrode potential was associated with crystallite nucleation; a steady-state value indicated substrate coverage.
4. The stress in gold deposits on copper was initially compressive due to the predominant extrinsic, mismatch component. With increasing thickness the coalescence component became dominant resulting in a change in the sign of the stress and the development of a tensile stress.
5. The stress in gold deposits on silver were initially small and tensile because of the small lattice mis-

match and large crystallite size. A rise to a stress maximum was due to the formation and coalescence of small, secondary crystallites.

Acknowledgments

This study was partially supported by the National Science Foundation Grant SER77-06938 and is based on a thesis submitted by S. T. Rao to the faculty of Stevens Institute of Technology in partial fulfillment of the requirements for the degree of Doctor of Philosophy.

Manuscript submitted Sept. 21, 1979; revised manuscript received Nov. 29, 1979. This was Paper 149 presented at the Pittsburgh, Pennsylvania, Meeting of the Society, Oct. 15-20, 1978.

Any discussion of this paper will appear in a Discussion Section to be published in the December 1980 JOURNAL. All discussions for the December 1980 Discussion Section should be submitted by Aug. 1, 1980.

Publication costs of this article were assisted by Exxon Corporation.

REFERENCES

1. S. Nakahara and R. Weil, *This Journal*, **120**, 1462 (1973).
2. R. Weil and J. B. C. Wu, *Plating*, **60**, 622 (1973).
3. R. Weil, G. J. Stanko, and D. E. Moser, *Plating Surf. Finish.*, **63**, 34 (Sept. 1976).
4. R. Weil, H. Feigenbaum, and K. Raghunathan, *ibid.*, **64**, 52 (Oct. 1977).
5. H. Feigenbaum and R. Weil, *ibid.*, **66**, 64 (May 1979).
6. H. Feigenbaum and R. Weil, *This Journal*, **126**, 2085 (1979).
7. K. Raghunathan, Doctoral Thesis, Stevens Institute of Technology (1979).
8. E. Klockholm, *Rev. Sci. Instrum.*, **40**, 1054 (1969).
9. L. Souzis and R. Weil, *Surf. Technol.*, **4**, 41 (1976).
10. E. W. Dickson, M. H. Jacobs, and D. W. Pashley, *Philos. Mag.*, **4**, 575 (1965).
11. J. W. Matthews, D. C. Jackson, and A. Chambers, *Thin Solid Films*, **26**, 129 (1975).
12. S. Stucki, *J. Electroanal. Chem. Interfacial Electrochem.*, **78**, 31 (1977).
13. S. T. Rao and R. Weil, *Trans. Inst. Met. Finish.*, **53**, 97 (1979).
14. J. H. van der Merwe, in "Single Crystal Films," M. H. Francombe and M. Sato, Editors, p. 139, Pergamon Press (1964).
15. R. W. Hoffman, *Thin Solid Films*, **34**, 185 (1976).

Deposition of Copper in Cylindrical Pores by a Pulse Plating Technique

H. K. Ng* and A. C. C. Tseung*

Department of Chemistry, The City University, London EC1, England

and D. B. Hibbert*

Department of Chemistry, Bedford College, University of London, London NW1, England

ABSTRACT

The deposition of copper from acid copper sulfate solution in cylindrical holes was studied by potentiostatic and galvanostatic methods. Steady-state plating gave deposits of poor quality and uneven thickness ($S/H > 1$). A pulsed square wave potential resulted in good, coherent deposits. The deposition is discussed in terms of the rate of diffusion to the electrode surface and the rate of diffusion into the pore. For pores of small diameter the latter process limits the plating efficiency under steady-state conditions.

In any plating process, the supply of ions to the electrode surface is often limiting. Thus during the plating of copper under steady-state conditions effects due to the depletion of ions at the cathode (e.g., uneven deposit, hydrogen embrittlement in galvanostatic plating) are often seen (1). Methods involving agitation or air sparging (2) may alleviate these problems by reducing the thickness of the diffusion layer, but pulse techniques (3) have been shown to provide the best possibility of obtaining an even deposit with an efficient use of the current (1, 4, 5). Three methods employing periodically changing currents have been proposed; all are based on an "off" period when the depleted layer of ions at an electrode may be replenished. These use (3) reversed current, d.c. with superimposed a.c., and pulsed current. Potentiostatic methods may have an advantage over galvanostatic methods for two reasons. First, the overall current is an integral of local current densities, which, in the case of galvanostatic plating, may follow an unpredictable pattern and second, the controlled current is used for double layer charging as well as deposition.

The charging and discharging of the double layer leads to a smoothing out of the Faradaic wave.

Plating inside pores holds further problems due to the geometry of the system. At constant potential or current the thickness of the deposit inside a pore is less than that of the flat surface and in addition a buildup of copper at the mouth of the pore is observed (6).

In this paper we describe the effect of a pulsed square wave potential and a pulsed square wave current on the deposition of copper in a cylindrical pore such as may be found in printed circuit boards. A mathematical model has been developed to solve the diffusion equations in such a pore. The model gives an insight into the observed difference in plating efficiency inside and outside a pore and may be used to predict optimum plating parameters.

Mathematical Model

Various models of different complexity have been proposed to analyze diffusion in different geometries (4, 7-9). Most recently Popov *et al.* (4) have employed a numerical technique, the central difference method, with the Runge-Kuta method to solve the resulting differential equations.

* Electrochemical Society Active Member.

Key words: diffusion, mathematical model, through-hole plating.

By taking a sufficiently large mesh and small time intervals an all numeric method [the forward difference method (7)] may be used. This method has the advantages that no differential equations need be solved and it is not necessary to know precisely the nature of the perturbation on the system.

However, a considerable increase in the requirement of computer time and memory results.

The system modeled is shown in Fig. 1. The mesh (200×200 points) was taken over ABCD, where $AD = 2R$ ($R =$ radius of pore) and $AB = L$ ($L =$ length of pore). The cylindrical axis AB and axis AX allowed calculation of the concentration in all parts of the solution from the value at a point within ABCXYZ. The point A was taken as the origin of the cylindrical coordinate system; the electrode surface being $r = R, l < L/2$ (XY in Fig. 1) and $r > R, l = L/2$ (YZ in Fig. 1). For a volume element which has dimensions sufficiently small relative to the diffusion length ($2\sqrt{D\Delta t}$) the following relations hold

$$C(r + \Delta r, l, t) \simeq C(r, l, t) - \Delta r \partial C / \partial r \quad [1]$$

$$C(r, l + \Delta l, t) \simeq C(r, l, t) - \Delta l \partial C / \partial l \quad [2]$$

$$C(r, l, t + \Delta t) \simeq C(r, l, t) - \Delta t \partial C / \partial t \quad [3]$$

The change in concentration at a mesh point is the change in the number of species within the volume element divided by the volume of that element. Thus for diffusion in an infinite cylinder

$$C(r, l, t + \Delta t) - C(r, l, t) = \frac{\Delta t D}{\Delta r V(r)} \{A(r) (C(r + \Delta r, l, t) - C(r, l, t)) - A(r - \Delta r) (C(r, l, t) - C(r - \Delta r, l, t))\} \quad [4]$$

For the case of a cylindrical hole the effect of diffusion parallel to the axis of the cylinder must be added to Eq. [4]

$$\frac{\Delta t D}{\Delta l^2} \{C(r, l + \Delta l, t) - C(r, l, t) - (C(r, l, t) - C(r, l - \Delta l, t))\} \quad [5]$$

which is

$$\frac{\Delta t D}{\Delta l^2} (C(r, l + \Delta l, t) + C(r, l - \Delta l, t) - 2C(r, l, t)) \quad [6]$$

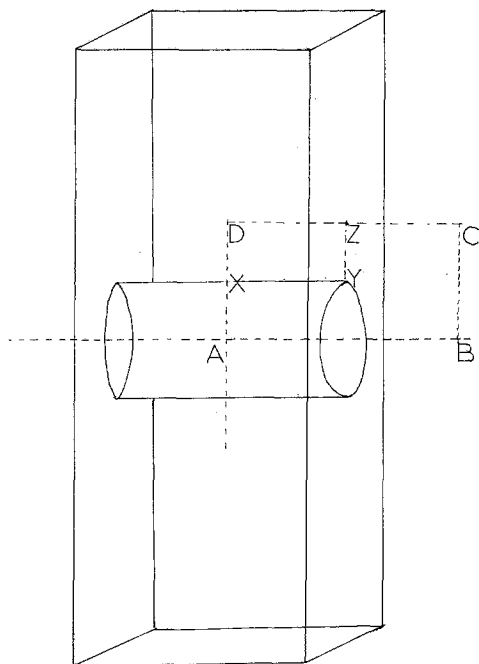


Fig. 1. Diagram of the volume matrix taken for the mathematical model ABCD. Origin is at A.

The area of a cylindrical element is $A(r) = 2\pi r$, and the volume element $V(r) = \pi l(r^2 - (r - \Delta r)^2)$. For a plane $A = \Delta l^2, V = \Delta l^3$.

There remains the boundary conditions at the electrode which are: electrode surface YZ (Fig. 1) ($\partial C / \partial l = i/nFD$ for $r > R, l = L/2$; electrode surface XY ($\partial C / \partial r = i/nFD$ for $r = R, l < L/2$; solution boundary CB for $r < 2R, l = L, C = C_0$; and solution boundary ZC for $r = 2R, l > L/2, C = C_0$.

It is assumed that the boundaries CB and ZC are sufficiently distant from the pore not to affect the solution of the diffusion equations in that region.

Therefore in Eq. [4] at $r = R, C(r + \Delta r, l, t) - C(r, l, t)$ becomes $i\Delta r/nFD$ and in Eq. [6] at $l = L/2, C(r, l, t) - C(r, l - \Delta l, t)$ becomes $i\Delta l/nFD$.

In potentiostatic plating the current from an element of electrode area A_e is

$$i = \text{const.} \times C_e \times A_e \quad [7]$$

and for galvanostatic plating

$$i = \text{const.} \quad [8]$$

A periodic pulsed potential was introduced into the model by setting $i = 0$ for the "off" period. No account was taken of double layer charging which therefore limits the viability of the model at high pulse frequencies ($>10^3$ Hz).

Diffusion of Cu^{2+} only was considered (with $D = 5.5 \times 10^{-6}$ cm²/sec), which was assumed to discharge to copper at the electrode surface. Thus no account was made of the effect of Cu^+ . The experimental results show that this is a valid assumption in this case, and work is in progress to model the system containing Cu^+ for other experimental conditions.

The model was used to investigate the depletion of ions within the pore and the buildup of copper at the mouth of the pore for potentiostatic plating (pulsed and steady-state). The ratio of the thickness of the deposit inside and outside the hole was estimated from the integrated current densities at selected areas on the electrode.

The model was implemented on the CDC7600 computer of London University.

Experimental

The deposition of copper was studied by plating on to a brass electrode drilled with holes of different diameters (0.6, 1.0, 1.3, and 1.6 mm). The brass cathode was positioned vertically between two copper anodes (Goodfellow Metals, 99.95%) in a rectangular Perspex tank. For all experiments the electrolyte was a solution of copper sulfate (0.34 mole dm⁻³) and sulfuric acid (1.76 mole dm⁻³).

In steady-state deposition a saturated calomel reference electrode was used in a Luggin capillary. A copper wire (Goodfellow Metals 99.99%) was the reference in pulse studies. Provision was made in the cell for air agitation. The potential (or current in galvanostatic experiments) was held constant against the reference electrode by a Chemical Electronics TR40-3A potentiostat. A pulsed current was achieved with a waveform generator (square wave 0.1-10⁵ Hz) in conjunction with the potentiostat. The current and voltage were displayed on an oscilloscope.

The brass boards were cleaned in the following sequence (10): (i) mechanical polishing, (ii) degreasing in trichloroethylene in an ultrasonic bath (5 min), (iii) washing in an alkaline bath (NaOH 4%, trisodium phosphate 2%) for 3 min, (iv) washing in an acid bath (H_2SO_4 5 volume percent HCl) for 5-10 sec, (v) washing in distilled water.

After plating for a time to give a deposit thickness of 0.025 mm (assuming the density of copper to be 8.96 g-cm⁻³) the brass boards were washed with distilled water and ethanol, dried, weighed, and mounted in acrylic resin for metallurgical sectioning. The sec-

tioned sample was etched in alcoholic ferric chloride (11) and examined under a microscope to measure the thickness of the deposit inside, outside, and at the mouth of the pore. From the increase in weight of the brass board and the charge passed, the current efficiency was determined.

The following plating conditions were studied:

1. Steady-state potentiostatic polarization, with and without air sparging.
2. Steady-state galvanostatic plating.
3. Pulsed galvanostatic plating with $T_{ON} = 1$ sec, $T_{OFF} = 2$ sec, and current densities in the range $34\text{--}80$ mA cm^{-2} .
4. Pulsed potentiostatic polarization. A range of frequencies ($1\text{--}7.5 \times 10^5$ Hz) was studied with $T_{ON}/T_{OFF} = \frac{1}{2}$.

Results

Steady-state potentiostatic plating.—Figure 2 shows current-voltage curves for plating with and without air sparging. It is seen that without agitation a limiting current density of 40 mA cm^{-2} is quickly reached. The ratio of the deposit thickness outside to inside the pore (S/H) (6) is plotted as a function of overpotential in Fig. 3 for the unagitated and agitated electrolyte. Although a greater current density is possible with air agitation little effect on S/H is observed. Figure 4 is a micrograph of the cross section of a typical pore under unagitated conditions, when dendritic growths were frequently seen. Agitation reduced these growth to a minimum.

Steady-state galvanostatic plating.—Deposits were essentially similar to those obtained potentiostatically.

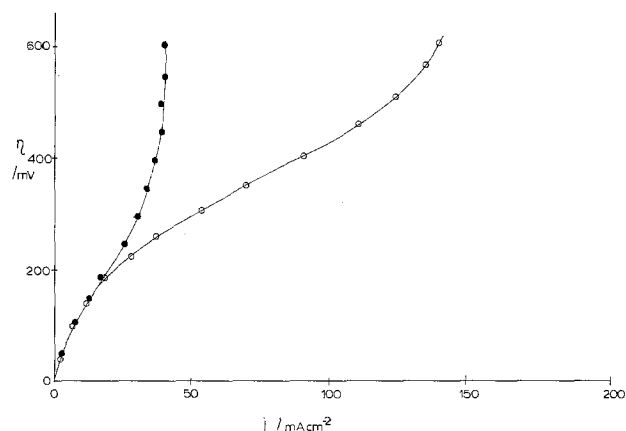


Fig. 2. Current voltage relations for steady-state potentiostatic plating. ● = Without agitation, ○ = with agitation.

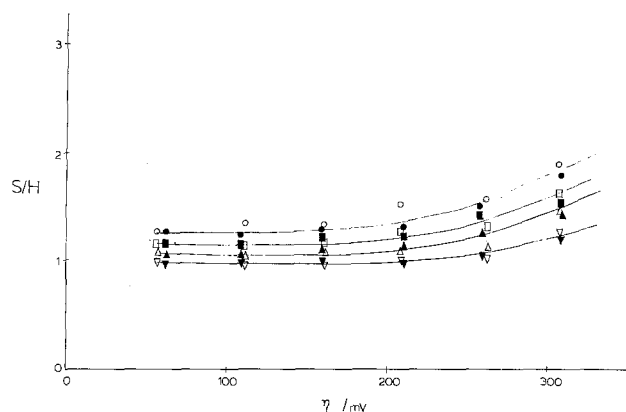


Fig. 3. Ratio of deposit thickness inside and outside the pore (S/H) at different overpotentials (open symbols) and unagitated (filled symbols) steady-state potentiostatic plating. ○, ● = Pore radius 0.6 mm; □, ■ = pore radius 1.3 mm; △, ▲ = pore radius 1.3 mm; ▽, ▼ = pore radius 1.6 mm.

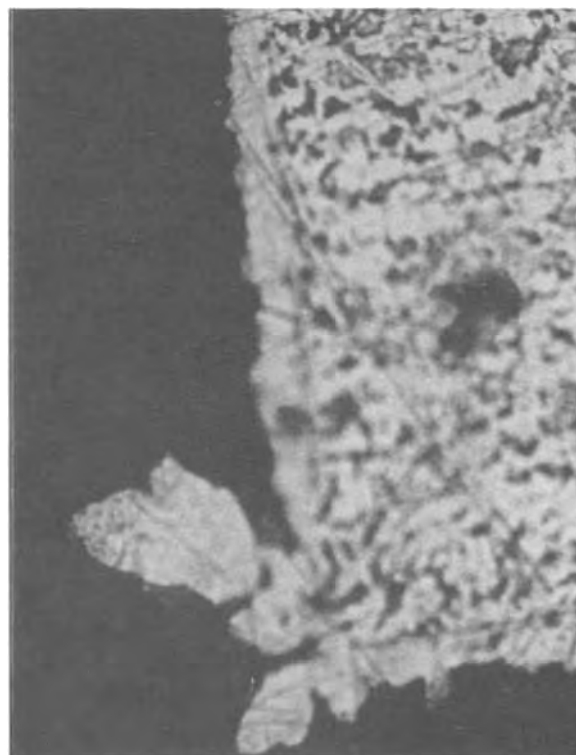


Fig. 4. Copper deposit in 1.6 mm diameter pore after steady-state potentiostatic plating, $\zeta = 357$ mV, without agitation.

However at high current densities S/H was greater for galvanostatic plating (Fig. 5). In addition a thicker deposit at the mouth of the pore was observed (Fig. 6).

Pulsed galvanostatic plating.—With a constant pulse profile $T_{ON} = 1$ sec, $T_{OFF} = 2$ sec, a plot of S/H against current density gave values of S/H near 1 for the larger holes and smaller current densities (Fig. 7). No variations in S/H were found when the period of the pulse was decreased. A smooth copper deposit was found at low current densities (<50 mA cm^{-2}) but as the current increased at a constant pulse of $T_{ON} = 1$ sec, $T_{OFF} = 2$ sec, the deposit became rough with pronounced growth at the mouth of the pore (Fig. 8a and b). Increasing the frequency of the pulse gave a smoother deposit at high current density (Fig. 8c). The current efficiency of the deposition was $100 (\pm 2)\%$ at current densities below 100 mA cm^{-2} . Above this current the efficiency fell linearly to 96% at 150 mA cm^{-2} .

Pulsed potentiostatic plating.—With a constant pulse profile, $T_{ON} = 1$ sec, $T_{OFF} = 2$ sec, S/H approached

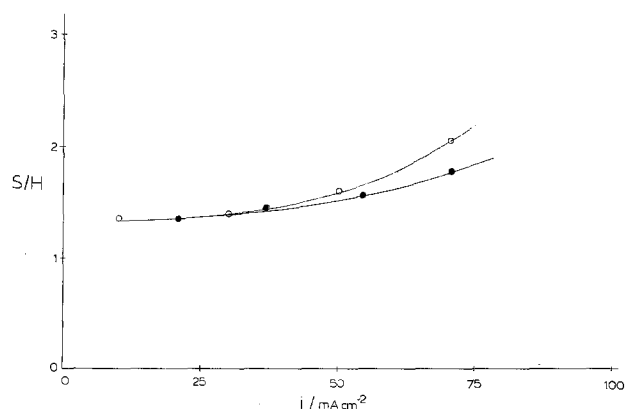


Fig. 5. S/H at different current densities for galvanostatic (○) and potentiostatic (●) steady-state plating. Pore diameter 0.6 mm.

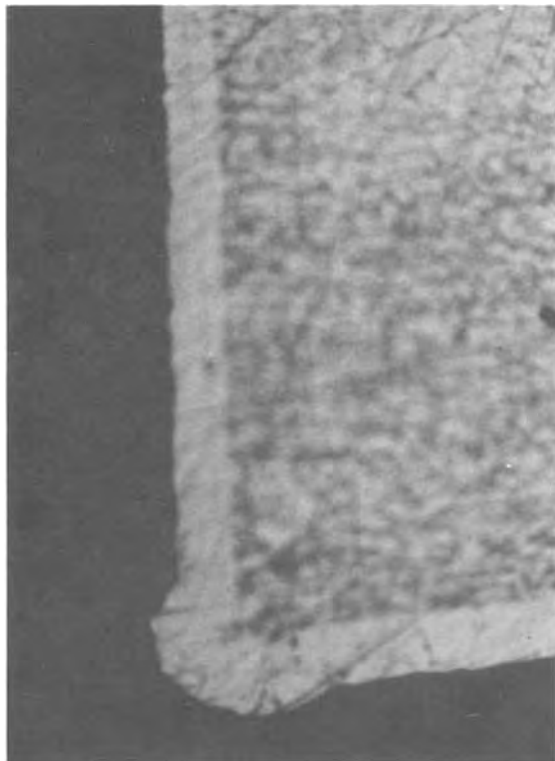


Fig. 6. Copper deposit in 0.6 mm diameter pore after steady-state galvanostatic plating, $i = 50 \text{ mA cm}^{-2}$, with agitation.

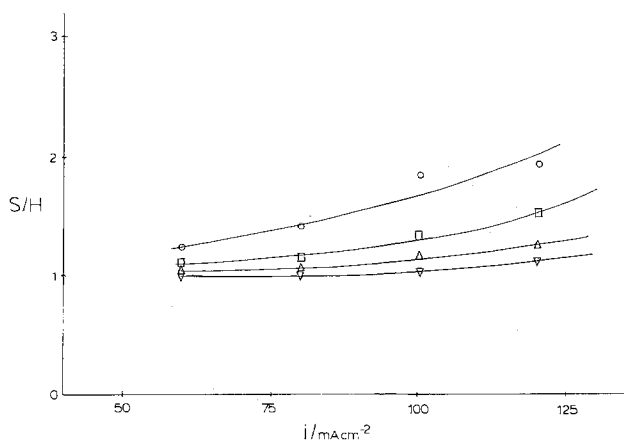


Fig. 7. S/H at different current densities for pulsed galvanostatic plating. $T_{\text{ON}} = 1 \text{ sec}$, $T_{\text{OFF}} = 2 \text{ sec}$. \circ = Pore diameter 0.6 mm, \square = pore diameter 1.0 mm, \triangle = pore diameter 1.3 mm, ∇ = pore diameter 1.6 mm.

unity for overpotentials less than 300 mV (Fig. 9). As with galvanostatic pulse plating, the frequency of the pulse had no great effect on S/H .

Surface roughness increased with increasing overpotential at constant pulse frequency and decreased with increasing frequency at constant potential (Fig. 10a and b).

The average current densities measured during pulse plating had higher values than the steady-state current densities and the variation of the average current density with pulse frequency at constant overpotential gave a maximum at $\nu = 100 \text{ Hz}$ (Fig. 11).

Mathematical model.—Figure 12a and b show a simulated contour map of the concentration of copper ions near the electrode surface at the mouth of a 1.6 mm diameter pore, after steady-state potentiostatic plating for 0.5 and 5 sec at 455 mV. The graph of current against time is given in Fig. 13. Figures 14 and 15 give corresponding contours and graphs of

the same system under a potentiostatic pulsing potential of 455 mV with $T_{\text{ON}} = 0.1 \text{ sec}$, $T_{\text{OFF}} = 0.2 \text{ sec}$. The model parameters were chosen to give a steady-state current of 40 mA cm^{-2} (see Fig. 2). It was noted that for high overpotentials (and currents) and a pulse of $T_{\text{ON}} = 0.1 \text{ sec}$, $T_{\text{OFF}} = 0.2 \text{ sec}$, while the concentration near the electrode surface during the "off" period increased, the boundary of the bulk concentration continued to move away from the electrode.

Discussion

The distribution of copper ions in a pore during plating.—It is known (5, 11), and has been confirmed here, that under steady-state conditions less copper is deposited inside a pore than on a flat electrode. This is obviously due to the deficiency of copper ions at the electrode surface in the pore, but may have two different causes. First, the rate of diffusion inside the pore to the electrode may be less than that to a flat surface by virtue of their different geometries. Second, the ions in the pore may be rapidly consumed with a slow diffusion of ions into the pore from outside. The contour maps of Fig. 12 and current-time graph of Fig. 13 show that at small time intervals after the start of plating (when copper is still present at its bulk concentration in the pore) the difference between the concentration of ions at the electrode in the pore and outside the pore is small. That the concentration is slightly less in the pore is a geometrical effect. However, the difference becomes much greater as more copper is deposited, because the rate of diffusion into the pore is much less than that required to maintain the same concentration gradient as at the flat electrode. This will occur when the boundary of the solution having the bulk concentration reaches the radius of the pore. Therefore, while air agitation and pulse techniques may allow the concentration of copper ions to be maintained in the pore to negate the second effect, the first effect, that of the geometry of the system, will remain.

At high current densities a greater S/H may be expected for galvanostatic plating than potentiostatic plating, as was observed in practice, for the following reasons. Under galvanostatic conditions the copper ion concentration within the pore will allow a lower current density than on the flat electrode. To maintain the total current, a higher current density is forced on the outer electrode, leading to a greater S/H . In potentiostatic steady-state plating, the total current falls to accommodate the smaller ion concentration in the pore, and thus there is no exacerbation of the increased S/H .

The buildup of copper at the mouth of the pore is a geometrical effect. Here the supply of ions to the edge is much greater than that to a flat electrode or cylindrical pore. It is therefore expected that this phenomenon will be seen when plating reduces the concentration below the bulk concentration. This is the case in steady-state plating, especially in galvanostatic plating (see Fig. 8) and in pulse plating when a high current or potential is held in a long pulse.

The choice of pulse parameters.—The increase in S/H at high current densities suggests that potentiostatic pulsing may be preferred to galvanostatic pulsing, and the following discussion on the optimum plating conditions is concerned with the former technique. It must be noted, however, that monitoring of the overall deposition rate may be more difficult in practical applications of potentiostatic pulse plating.

Four factors must be optimized in plating: (i) evenness of deposit ($S/H = 1$) and no increased deposition at the mouth of the pore, (ii) surface morphology, (iii) current efficiency, and (iv) total plating time.

We have shown that the current efficiency is 100% independent of potential and of frequency below 10^3 Hz , when the effect of the disproportionation of Cu^+

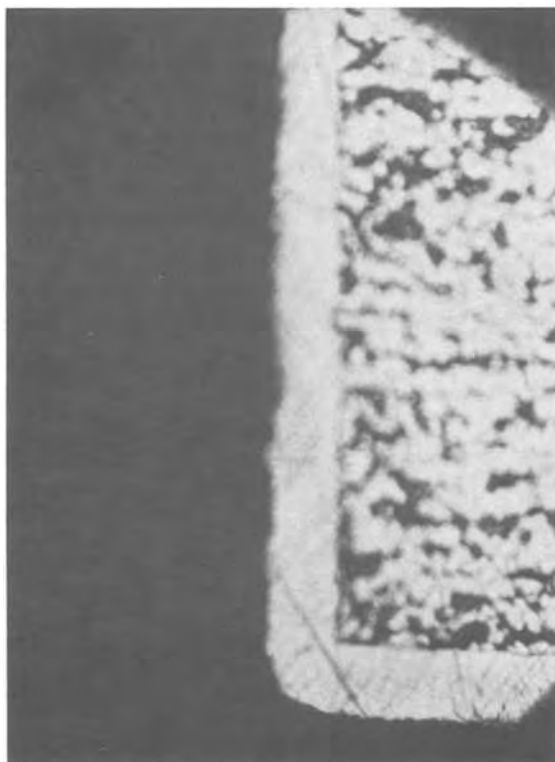
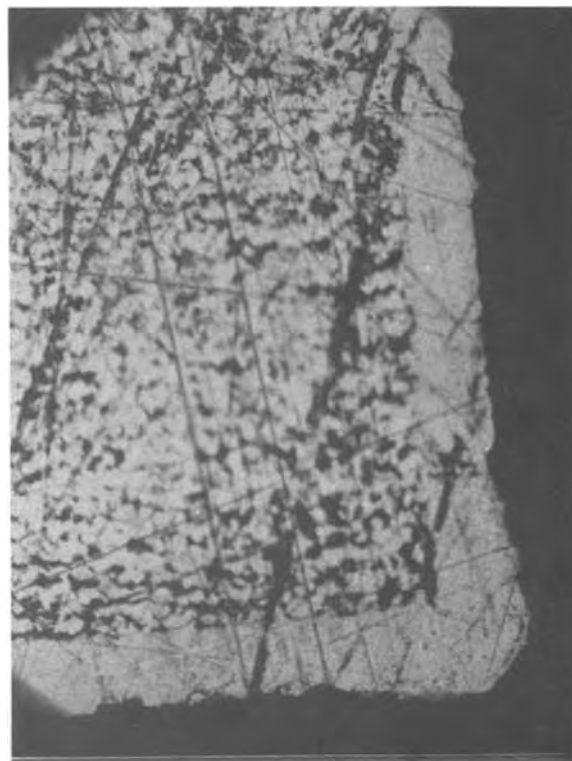
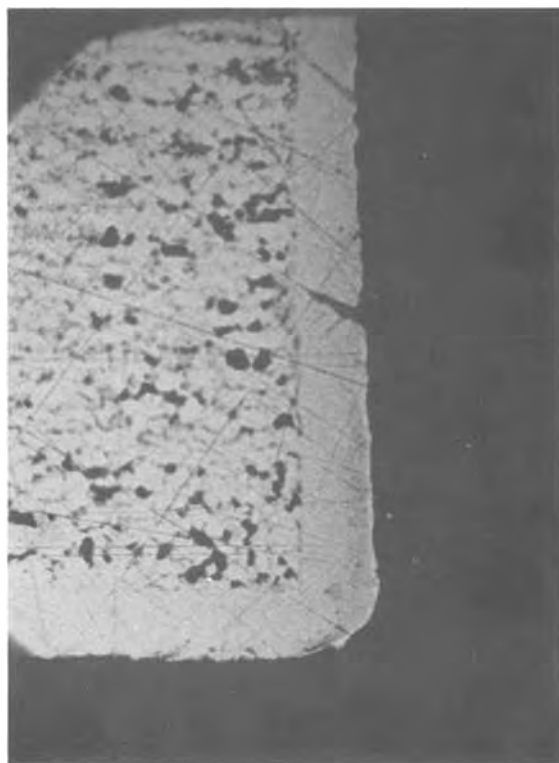


Fig. 8. Copper deposits in 0.6 mm diameter pore after pulse galvanostatic plating with agitation. a (upper left), $i = 54.5 \text{ mA cm}^{-2}$, $T_{\text{ON}} = 1 \text{ sec}$, $T_{\text{OFF}} = 2 \text{ sec}$; b (upper right), $i = 145.5 \text{ mA cm}^{-2}$, $T_{\text{ON}} = 1 \text{ sec}$, $T_{\text{OFF}} = 2 \text{ sec}$; c (lower left), $i = 145.5 \text{ mA cm}^{-2}$, $T_{\text{ON}} = 7 \times 10^{-5} \text{ sec}$, $T_{\text{OFF}} = 1.4 \times 10^{-4} \text{ sec}$.

is seen. This has been reported by Cheh and co-workers for high frequency pulse deposition of copper (14, 15). However for the most part a current efficiency near 100% found here would suggest this mechanism contributes little to the deposition process for our experimental conditions. The total plating time is reduced by increasing the potential and decreasing the "off" time, but both of these factors are limited by the morphology and evenness of the deposit.

The choice of mathematical model.—The model of pulsed deposition described by Despic and Popov (13),

assumes the concentration at the electrode surface follows the pulse, falling from C_0 to a small value and rising again to C_0 . Experimental observation of the current variation during a pulse would suggest that the initial fall in concentration does not recover immediately in the "off" period. A comparison of the diffusion layer thickness predicted by each approach may be made. The diffusion thickness for a pulse of T sec with an equal "off" time has been calculated by Despic and Popov (13). The concentration in the n th "on" period is

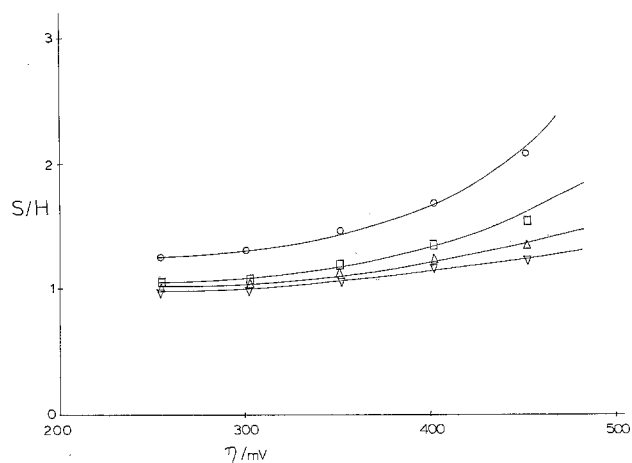


Fig. 9. S/H at different overpotentials for pulsed potentiostatic plating. $T_{ON} = 1$ sec, $T_{OFF} = 2$ sec. ○ = Pore diameter 0.6 mm, □ = pore diameter 1.0 mm, △ = pore diameter 1.3 mm, ▽ = pore diameter 1.6 mm.

$$C_{ON} = C(x, (2n + 1)T) = \frac{2C_0}{\pi^{1/2}} \left(\int_0^{x/2D^{1/2}[(2n+1)T]^{1/2}} \exp(-u^2) du + \int_{x/2D^{1/2}(2nT)^{1/2}}^{x/2D^{1/2}[(2n-1)T]^{1/2}} \exp(-u^2) du + \dots + \int_{x/2D^{1/2}(2T)^{1/2}}^{x/2D^{1/2}T^{1/2}} \exp(-u^2) du \right) \quad [9]$$

$$\delta N = \frac{C_0}{(\partial C / \partial x)_{x=0}} = \frac{D^{1/2} \pi^{1/2} T^{1/2}}{a}$$

where

$$a = [(2n + 1)^{-1/2} - (2n)^{-1/2} + (2n - 1)^{-1/2} - \dots + 1] \quad [10]$$

We have modified this equation to accommodate a pulse of period P sec and length T sec when the equations become

$$C_{ON} = \frac{2C_0}{\pi^{1/2}} \left(\int_0^{x/2D^{1/2}[(nP+T)]^{1/2}} \exp(-u^2) du + \int_{x/2D^{1/2}(nP)^{1/2}}^{x/2D^{1/2}[(n-1)P+T]^{1/2}} \exp(-u^2) du + \dots + \int_{x/2D^{1/2}P^{1/2}}^{x/2D^{1/2}T^{1/2}} \exp(-u^2) du \right) \quad [11]$$

$$\delta N = \frac{D^{1/2} \pi^{1/2}}{b}$$

where

$$b = [(nP + T)^{-1/2} - (nP)^{-1/2} + ((n + 1)P + T)^{-1/2} \dots + T^{-1/2}] \quad [12]$$

For $P = 0.3$ sec, $T = 0.1$ sec, Eq. [12] gives $\delta N = 1.68 \times 10^{-3}$ cm. From measurements made from Fig. 14b $\delta N = 3.4 \times 10^{-3}$ cm. At present it is not apparent how the two theories may be distinguished.

Acknowledgment

The authors acknowledge the use of the University of London Computer Centre's graphical package DIMFILM for the production of the contour maps and simulated graphs.

Manuscript submitted Aug. 24, 1979; revised manuscript received Nov. 19, 1979. This was Paper 173 pre-

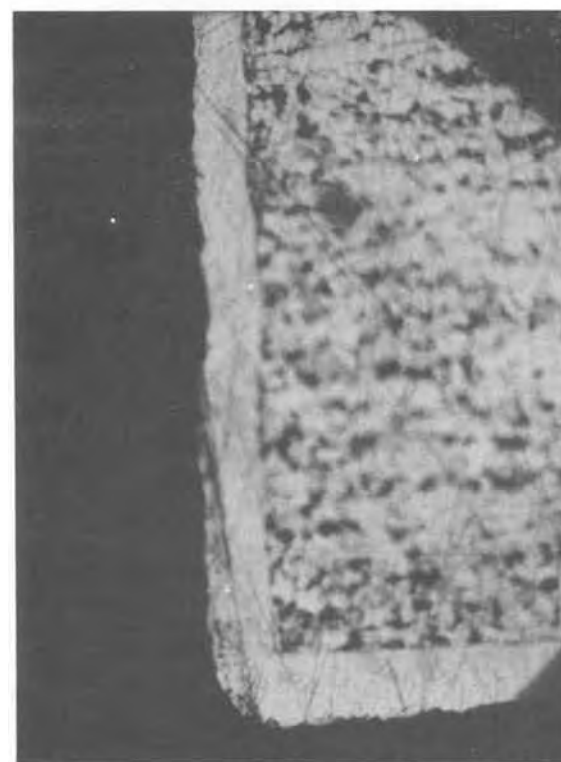
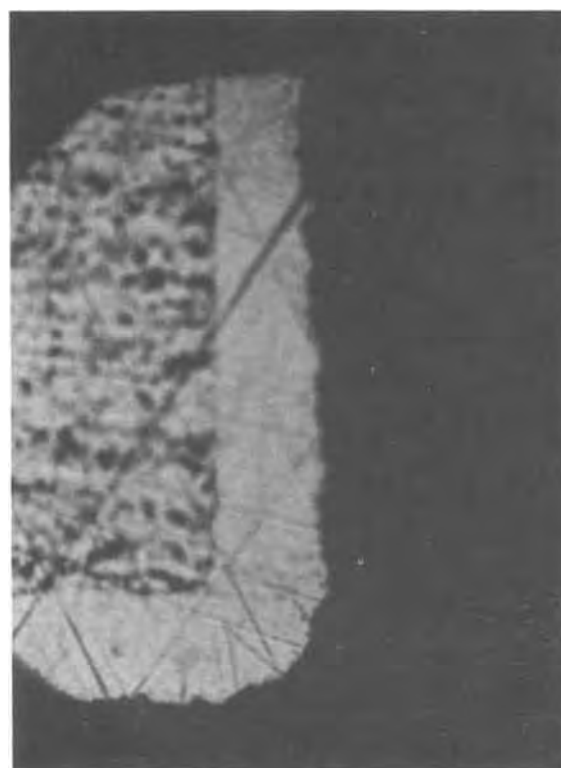


Fig. 10. Copper deposits in 0.6 mm diameter pore after pulse potentiostatic plating with agitation. a (top), $\zeta = 455$ mV, $T_{ON} = 1$ sec, $T_{OFF} = 2$ sec; b (bottom), $\zeta = 455$ mV, $T_{ON} = 7.5 \times 10^{-5}$ sec, $T_{OFF} = 1.5 \times 10^{-4}$ sec.

sented at the Boston, Massachusetts, Meeting of the Society, May 6-11, 1979.

Any discussion of this paper will appear in a Discussion Section to be published in the December 1980 JOURNAL. All discussions for the December 1980 Discussion Section should be submitted by Aug. 1, 1980.

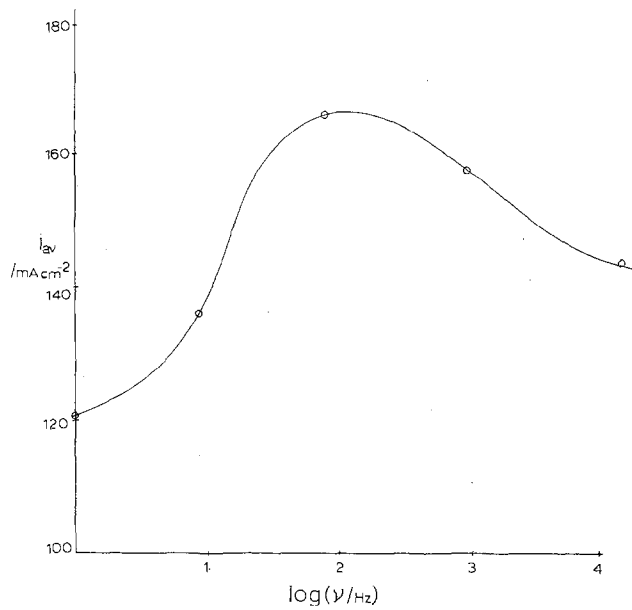


Fig. 11. Variation of average current density with frequency of pulse at constant overpotential 455 mV and constant $T_{ON}/T_{OFF} = 1/2$.

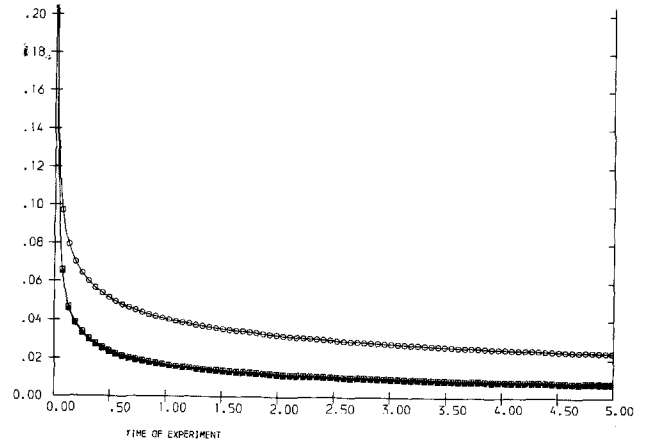


Fig. 13. Simulated current-time curve for steady-state potentiostatic plating. Current in arbitrary units. \circ = current at mouth of pore, Δ = current inside pore, \square = current on flat electrode surface.

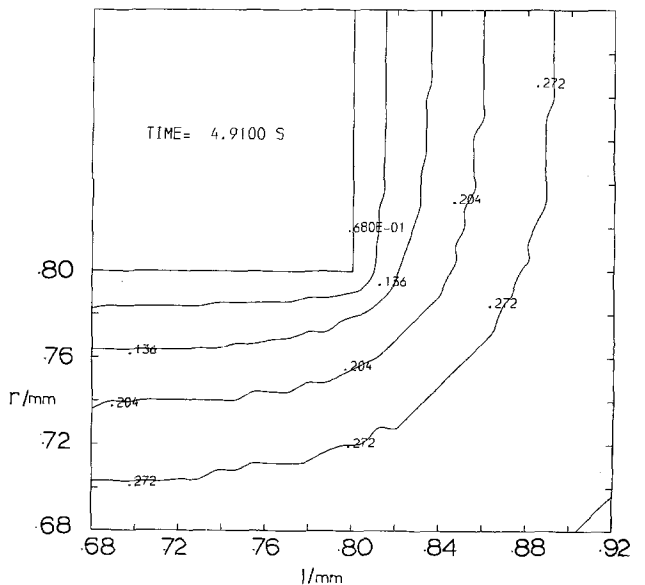
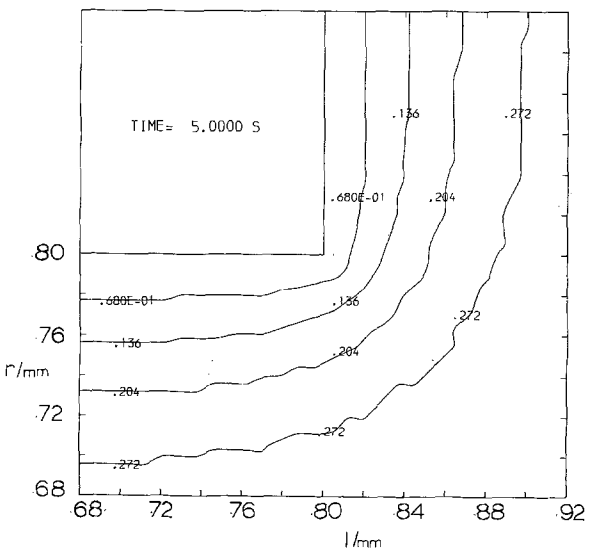
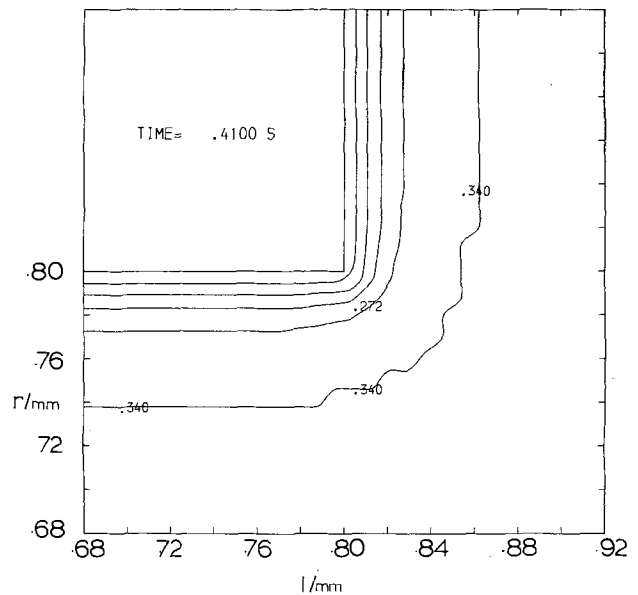
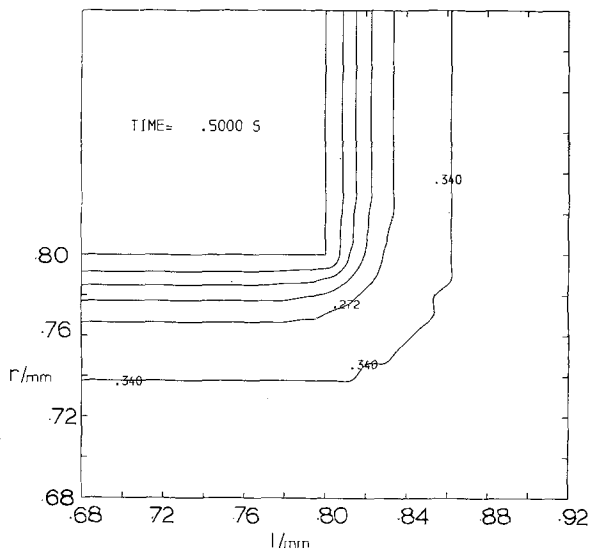


Fig. 12. Simulated contour map of the concentration of copper ions near the electrode surface during steady potentiostatic plating. Radial distances r and axial distances l are measured from point A in Fig. 1. a (top), After 0.5 sec; b (bottom), after 5 sec.

Fig. 14. Simulated contour map of the concentration of copper ions near the electrode surface during pulse potentiostatic plating. Radial distances r and axial distances l are measured from point A in Fig. 1. $T_{ON} = 0.1$ sec, $T_{OFF} = 0.2$ sec. a (top), After 0.41 sec; b (bottom), after 4.91 sec.

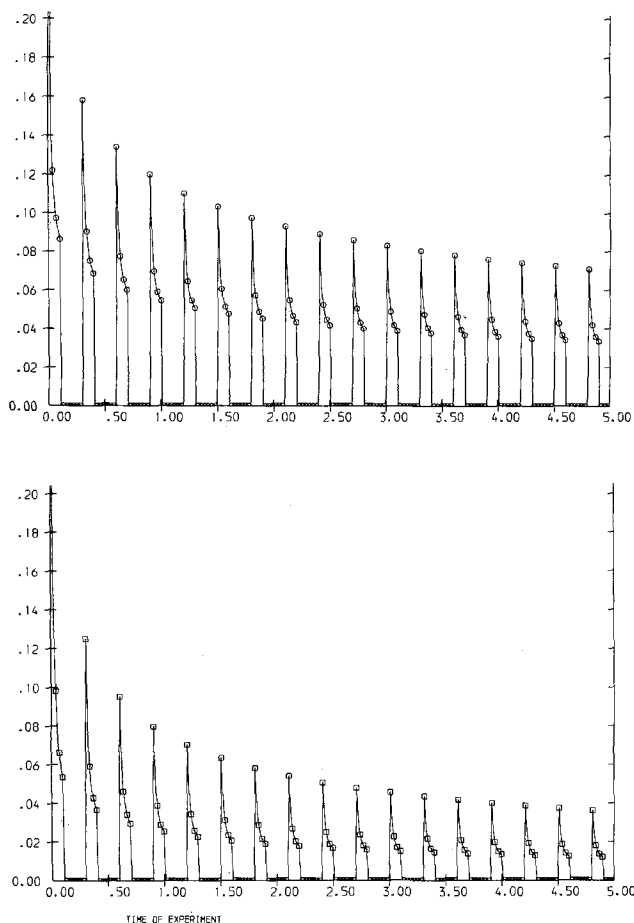


Fig. 15. Simulated current-time curve for pulse potentiostatic plating. a (top), ○ = current at mouth of pore, b (bottom), □ = current on flat electrode surface. Current in arbitrary units.

LIST OF SYMBOLS

- $A(r)$ area of a volume element at radius r
 A_e area of element on electrode surface
 $C, C(r, l, t)$ concentration of copper ions (at r, l, t)
 C_e concentration of copper ions in element at electrode surface
 D diffusion coefficient; for $\text{Cu}^{2+} = 5.5 \times 10^{-6}$

- F Faraday's constant
 H thickness of deposit in hole
 i current density
 $l, \Delta l$ length measured from center of pore, increment in l
 n number of electrons in electrochemical reaction
 $r, \Delta r$ radial length measured from center of pore, increment in r
 S thickness of deposit on flat electrode
 t time
 $V(r)$ volume of element at radius r
 ζ overpotential
 ν frequency of pulse

REFERENCES

1. N. Foran, *Plating*, **44**, 1071 (1957).
2. W. Engelmaier and T. Kessler, *This Journal*, **125**, 36 (1978).
3. A. R. Despic and K. I. Popov, in "Modern Aspects of Electrochemistry," Vol. 7, B. E. Conway and J. O'M. Bockris, Editors, p. 199, Plenum, New York (1972).
4. K. I. Popov, D. N. Keca, S. I. Vidojkovic, B. J. Lazarevic, and V. B. Milojkovic, *J. Appl. Electrochem.*, **6**, 365 (1976).
5. A. J. Avila and M. J. Brown, *Plating*, **57**, 1105 (1970).
6. R. F. Rothschild, *ibid.*, **53**, 437 (1966).
7. S. W. Feldberg, in "Electroanalytical Chemistry," Vol. 3, A. J. Bard, Editor, p. 199, Marcel Dekker, Inc., New York (1969).
8. K. I. Popov, B. J. Lazarevic, D. N. Keca, M. V. Vojnovic, and D. S. Dojcinovic, *Bull. Soc. Chem. Beograd*, **40**, 379 (1975).
9. K. I. Popov, B. J. Lazarevic, V. B. Milojkovic, D. N. Keca, M. V. Vojnovic, and D. B. Damjanovic, *ibid.*, **40**, 385 (1975).
10. A. K. Graham, "Electroplating Engineering Handbook," p. 197, Van Nostrand Reinhold Co., New York (1971).
11. W. Canning Ltd., "The Canning Handbook on Electroplating," p. 882 (1978).
12. M. W. Jawitz, *Metal Finishing*, **71**, 31 (1973).
13. A. R. Despic and K. I. Popov, *J. Appl. Electrochem.*, **1**, 275 (1971).
14. H. Y. Cheh, C. C. Wan, and H. B. Linford, Abstract 170, p. 412, The Electrochemical Society Extended Abstracts, New York, N.Y., Oct. 13-17, 1974.
15. H. Y. Cheh, H. B. Linford, and C. C. Wan, *Plating Surf. Finishing*, 66 (May 1977).

Polymer-Metal Composite Thin Films on Electrodes

Karl Doblhofer and Werner Dürr

Fritz-Haber-Institut der Max-Planck-Gesellschaft, D-1000 Berlin 33, Germany

ABSTRACT

The electrocatalytic activity of thin, metal-containing polymer films was studied. The films were prepared on glassy carbon electrodes in a glow-discharge which was established in mixtures of acrylonitrile and metal acetylacetonate vapors at 300°C. The produced films were electronically conductive and solution permeable. It is proposed that electrochemical reactions can proceed not only on the surface but also inside these films at the active sites formed by the incorporated metal. The cathodic dioxygen reduction in acidic and alkaline electrolytes was used as a test reaction for the electrocatalytic activity and stability of the electrodes.

Ultrathin polymer films can be deposited on electrodes with the method of glow-discharge-polymerization (1). Such films adhere well, are chemically stable during electrolysis in liquid electrolytes, and can render inert electrodes catalytically active. Moreover, the catalytic activity can be increased by incorporation of metals in the form of clusters or chelates (2, 3) so that the film-covered electrodes may find

Key words: polymers, films, electrolyte.

practical applications, such as in fuel cells. In this work we discuss basic aspects of such polymer-metal composite films on electrodes and propose a method to prepare such films.

The Concept of a Polymer/Metal Electrocatalyst

To be effective in electrochemical processes catalytically active centers in the polymer matrix must be accessible to the electrolyte containing the depolarizer

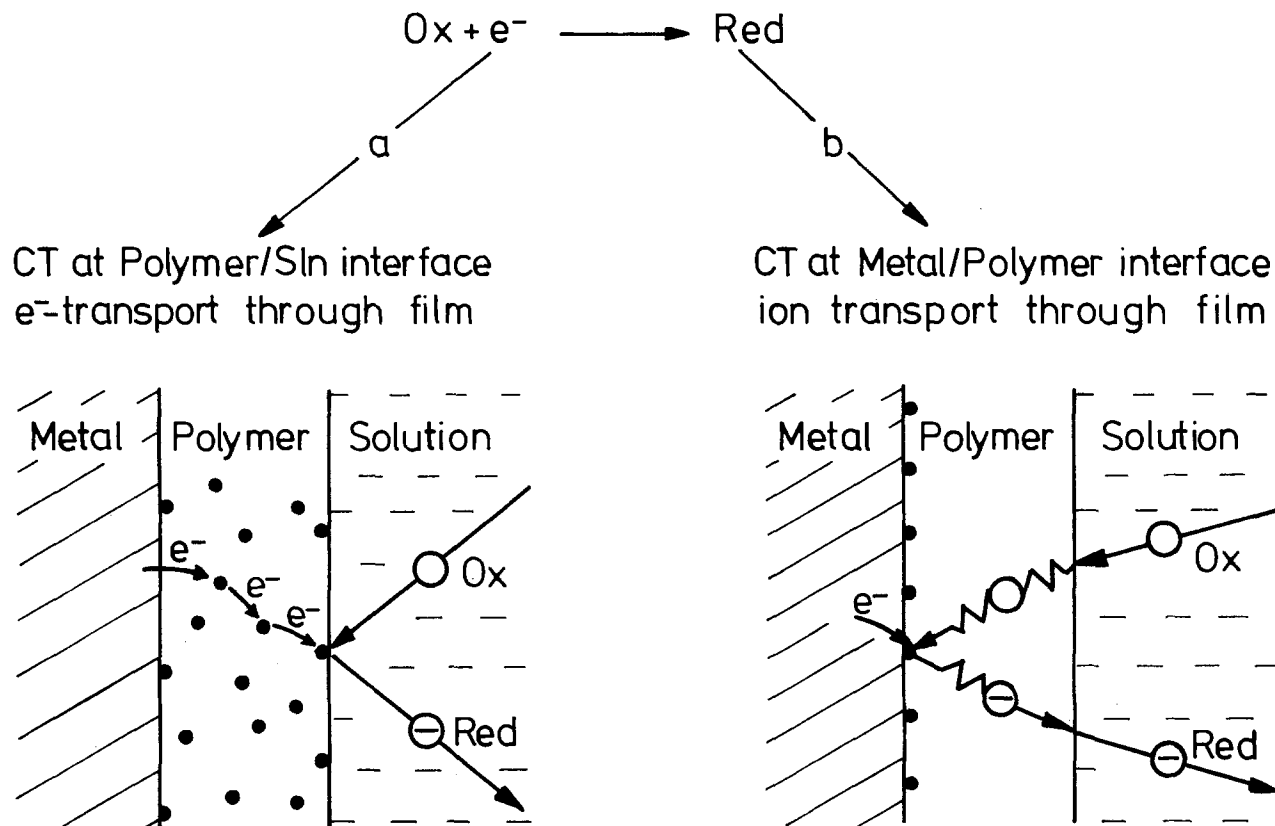


Fig. 1. Two mechanisms of electrochemical charge-transfer (CT) reactions (shown for the reduction step) proceeding on polymer-covered electrodes. The small dots in the polymer are catalytic or electron hopping sites.

species and, secondly, they must be in electrical contact with the conducting support of the polymer film. Both conditions are fulfilled for the two mechanisms (a) and (b) shown schematically in Fig. 1.

(a) The electrochemical process takes place at the interface polymer/electrolyte and the electron is transported through the film. [Note that in the discussion a metallic electrode is assumed as support for the polymer film, and, in fact, many of the experiments have been made with Pt/polymer systems. In practical applications, however, carbon, particularly glassy carbon would be preferable, as discussed in Ref. (1).]

Two steps can be distinguished in this process. Step 1: the electron transfer from (to) the electroactive species in solution to (from) the polymer surface. This process can be discussed on the basis of the accepted interfacial electron transfer theory (4-6). In particular, the predicted strong dependence of the rate of charge transfer on the concentration of the polymer electronic states demonstrated with electrochemical experiments on conducting polymer-covered electrodes (1). Step 2: the electron transport through the polymer film. This process was studied previously, also with metal/polymer/metal sandwich systems (7). From the temperature and field dependence of the film conductivity it was concluded that hopping of electrons along percolation paths was the dominant conduction mechanism.

Mechanism (a) will be favored when the film permeability for the electrolyte solution is low and its electronic conductivity is high. In this case it would be important to introduce the catalytically active (metal) centers on the polymer-surface. Inside the polymer film these centers may contribute to the film conductivity by forming electronic states which participate in the electronic percolation process.

(b) The polymer matrix acts as a membrane permitting the electroactive species and the electrolyte to reach the supporting metal/polymer interface region where the charge-transfer reaction takes place. Glow-discharge polymer films can be prepared to be

permeable to electrolyte solutions (8). The permeability is high when the polymer structure interacts with the solvent molecules and when the matrix is not cross-linked (9).

Catalytically active sites in an insulating membrane-type film are expected to be electrocatalytically effective when they are in contact with the metallic support. Such a system could be of considerable practical use to improve the stability of "modified electrodes" (3, 10). It is likely that the decomposition of certain catalytically active compounds, such as chelates or clusters attached to the electrode, is retarded when the compound is imbedded in the polymer matrix.

We propose in the following a third system which is based on a combination of the schemes (a) and (b) of Fig. 1: the polymer matrix of this proposed film is permeable to the solution and electronically conducting. When such a film contains the active sites distributed throughout the matrix an electrocatalytic reaction could proceed at the active centers in a reaction zone inside the polymer film, as schematically shown in Fig. 2. Note, that in this three-dimensional reaction zone a larger number of sites is available for the electrochemical process than on a plane "modified electrode." The electronic current to or from the active sites flows because of an electric field across the film, while the electroactive species (O_2 in Fig. 2) reaches the sites by diffusion. Active centers in the polymer which can transfer electrons reversibly to a redox species are expected to be also electronic states which are energetically accessible for the electrons in the corresponding hopping conduction process, thus increasing the film conductivity. Relatively unstable catalytically active compounds could be stabilized by the polymer matrix and thus rendered usable for electrocatalytic processes, as discussed above.

Depending on the conductivity and permeability properties of an actual, experimental film the reaction zone will deviate in its location and thickness from the idealized picture, Fig. 2. In fact, the situations (a) and (b) of Fig. 1 might be considered to be the limiting cases of the proposed scheme.

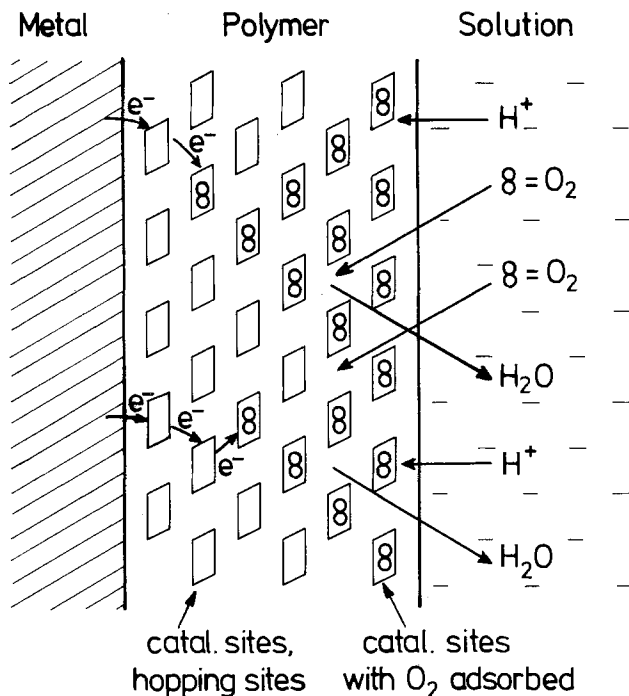


Fig. 2. Model of a solution-permeable, conducting thin polymer film with imbedded active sites, at which the electrochemical O_2 reduction proceeds. O_2 molecules are shown adsorbed on the sites; O_2 , H^+ , and H_2O as well as electrons (e^-) are mobile in the matrix.

Preparation of the Polymer-Metal Composite Films

The basis of the preparation of the polymer matrix was the cathodic glow-discharge polymerization (GDP) at elevated temperature, as described previously (1). Acrylonitrile was used as the monomer, which had been found to lead to a conducting polymer with a certain solution permeability. At $300^\circ C$ the nitrile groups of the polyacrylonitrile break up to form an unsaturated, nitrogen-containing ladder polymer. With the nonbonding N-electron pairs, coordinate bonds can be formed with metal ions in the matrix. In fact, it is likely that the ions are complexed by more than one ligand from the polymer matrix. This leads to a chelate-type structure which would protect the metallic central ions in the film from being extracted by the electrolyte solution. Such structures should have a certain catalytic activity, e.g., for the cathodic dioxygen reduction reaction (2).

To introduce the metal into the film, metal-containing volatile species, mainly metal acetylacetonates, were added to the monomer in the GDP reactor during the polymerization process. Acetylacetonates are stable at elevated temperatures and are readily available in high purity for a number of metals. Unfortunately, the necessary vapor pressure is obtained only at temperatures of the order of $150^\circ C$. Thus, it was necessary to construct the glow-discharge reactor in such a way that the temperature was nowhere lower, to avoid condensation of the acetylacetonate. A schematic picture of the apparatus is given in Fig. 3. It was built from glass and stainless steel. The temperature of the small vessel at the bottom which contained the acetylacetonate, could be controlled independently. Its temperature was raised to increase the chelate vapor pressure for the polymerization. The process could be continuously monitored with a quadrupole mass-spectrometer attached to the reactor via a narrow nozzle. Electrodes prepared from glassy carbon disks (Sigri Elektrographit GmbH, D-8901 Meitingen, Germany) of diameter 8 mm and thickness 3 mm were used as the substrate for the films. To permit only one face of these disks to be exposed to the solution in the electrochemical experiments, the disks were sealed into glass by melting the ends of

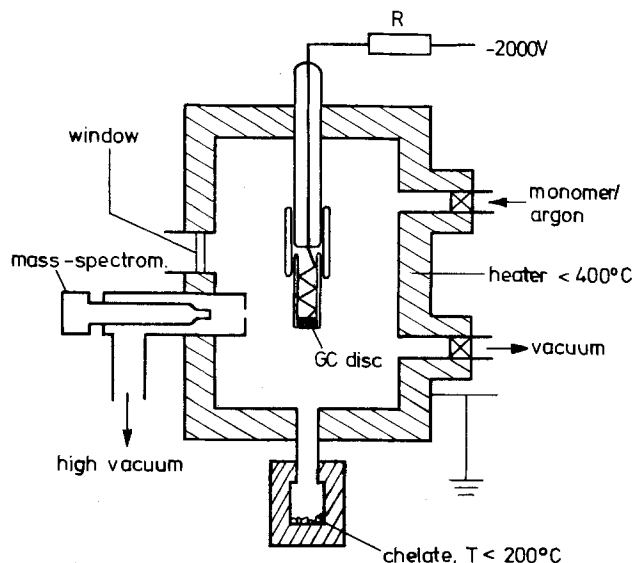


Fig. 3. Glow-discharge polymerization apparatus. The polymer-metal composite film is deposited on the exposed glassy carbon (GC) face of the electrode.

glass tubes around them, and thereafter polishing until a flat surface was obtained. Polymerization was initiated by applying the high voltage to the glow-discharge reactor when the mass-spectrometer indicated the desired vapor composition. To characterize the produced films optical reflection spectra and electrochemical measurements were routinely made. ESCA spectra were taken to estimate the amount of metal incorporated.

Results and Discussion

The properties of the produced films could be varied over a wide range by changing the acetylacetonate, by varying the ratio of the acetylacetonate-acrylonitrile vapor pressures and the polymerization temperature. In the following, a typical film is discussed. It was prepared at $300^\circ C$ from cobalt(II)-acetylacetonate and acrylonitrile (AN). Vapor composition in the GDP reactor: 0.5 mbar acrylonitrile plus approximately 0.01 mbar acetylacetonate. The latter vapor pressure value can only be estimated, whereas it could be adjusted reproducibly via the acetyl-peak ($m/e = 43$) in the mass spectrum. The cathodic oxygen reduction reaction was used as a test reaction for the electrocatalytic performance of the electrode. Oxygen diffuses well through polymeric structures (11), as do H^+ ions and the produced water; mass transport from the polymer surface to and from the metallic centers was therefore not current limiting.

Figure 4 shows the performance of this electrode (AN + Co) compared with the metal-free (AN) film-covered glassy carbon, the untreated glassy carbon (GC), and a platinum electrode, in acid solution, saturated with oxygen. The curves were obtained from cyclic voltammetry experiments with the electrodes rotated at 40 revolutions per second. The sweeps were slow (5 mV/sec), i.e., the Faradaic currents shown in the figure could be measured under quasi-stationary conditions. Clearly, the catalytic activity of the film with respect to oxygen reduction is significantly enhanced by the incorporated cobalt. ESCA spectra taken after 2 hr of O_2 reduction in acid electrolyte showed a decrease in Co content by approximately one third. After two days of electrolysis no significant amounts of Co could be detected by ESCA, i.e., in the upper 2 nm of the film. The catalytic activity, however, was practically unchanged. Thus, the reaction must have taken place at cobalt centers deep inside the film. This is a strong indication that the electrocatalytic reaction proceeds at this film-covered electrode, according to the mechanism illustrated in Fig. 2.

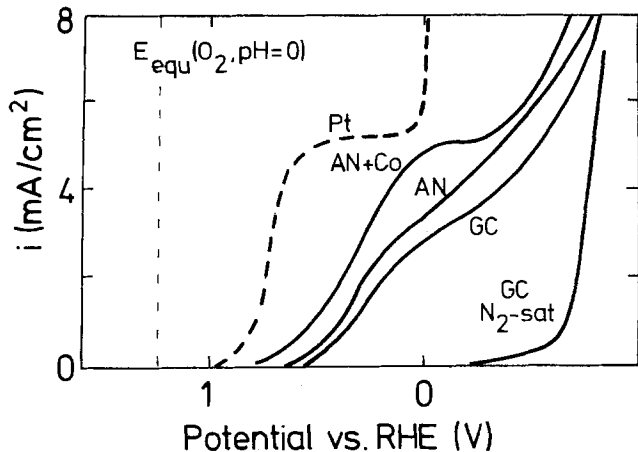


Fig. 4. O_2 reduction in 1M H_2SO_4 on the disk electrodes: glassy carbon (GC), acrylonitrile-polymer on glassy carbon (AN), Co-acetylacetonate/acrylonitrile polymer on glassy carbon (AN + Co), and platinum (Pt). The electrodes were rotated at 40 rps. RHE is the reversible hydrogen electrode in the same electrolyte.

The electrocatalytic activity of the acrylonitrile GDP film was increased by the incorporated cobalt ions also with respect to the O_2 reduction in alkaline solution, as shown in Fig. 5. The stability of the electrodes was at least as high as in acid solution.

With the apparatus shown in Fig. 3 a wide range of different polymer/metal composite films can be prepared on electrodes. The obtained systems are stable, for at least several days when used for electrochemi-

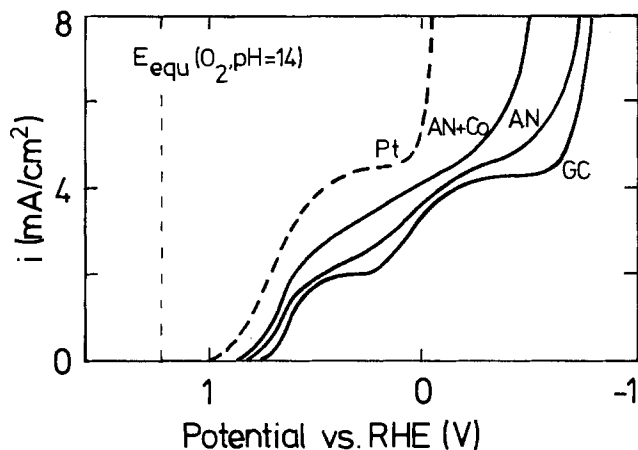


Fig. 5. O_2 reduction in 1M KOH. Electrodes are as in Fig. 4

cal processes in aqueous electrolytes. One can easily conceive of a large number of metal/polymer combinations which could on this basis, lead to electrodes with desirable electrocatalytic properties, and therefore have practical applications, e.g., in fuel cells.

Acknowledgments

The authors wish to thank Prof. H. Gerischer for valuable discussions and support of the work. The technical assistance of Mrs. I. Eiselt and Mr. R. de Boer is gratefully acknowledged.

Manuscript submitted Aug. 31, 1979; revised manuscript received Dec. 4, 1979. This was Paper 298 presented at the Boston, Massachusetts, Meeting of the Society, May 6-11, 1979.

Any discussion of this paper will appear in a Discussion Section to be published in the December 1980 JOURNAL. All discussions for the December 1980 Discussion Section should be submitted by Aug. 1, 1980.

REFERENCES

1. K. Doblhofer, D. Nölte, and J. Ulstrup, *Ber. Bunsenges. Phys. Chem.*, **82**, 403 (1978).
2. L. I. Boguslavskii and A. V. Vannikov, "Organic Semiconductors and Biopolymers," Plenum Press, New York (1970).
3. R. J. Burt, G. J. Leigh, and C. J. Pickett, *J. Chem. Soc., Chem. Commun.*, p. 940 (1976).
4. R. R. Dogonadze and Yu. A. Chizmadzev, *Dokl. Akad. Nauk SSSR*, **144**, 1077 (1962); *ibid.*, **145**, 848 (1962).
5. R. R. Dogonadze, and A. M. Kuznetsov, *Prog. Surf. Sci.*, **6**, 1 (1975).
6. H. Gerischer, in "Advances in Electrochemistry and Electrochemical Engineering," Vol. 1, P. Delahay and C. W. Tobias, Editors, p. 139, Interscience, New York (1961).
7. K. Doblhofer and J. Ulstrup, *J. Phys. Suppl.*, **38**, C5-49 (1977).
8. T. Wydeven and J. R. Hollahan, in "Techniques and Applications of Plasma Chemistry," J. R. Hollahan and A. T. Bell, Editors, Chap. 6, John Wiley & Sons, New York (1974).
9. K. Doblhofer, Prepared for publication; cf. also C. E. Rogers, J. R. Semancik, and S. Kapur, in "Structure and Properties of Polymer Films," R. W. Lenz and R. S. Stein, Editors, p. 297, Plenum Press, New York (1973).
10. J. C. Lennox and R. W. Murray, *J. Electroanal. Chem. Interfacial Electrochem.*, **78**, 395 (1977) and *J. Am. Soc.*, **100**, 3710 (1978); other references are given there and in: K. Doblhofer, Vortragszusammenfassung V/1, 16. Tutzing Symposium der DECHEMA, February 12-15, 1979.
11. D. W. Van Krevelen and P. J. Hoftzyer, "Properties of Polymers," Chap. 18, Elsevier Publishing Company, New York (1972).

Electrochemical Synthesis of N-Alkylformamides

Divna Cipris*

Allied Chemical Corporation, Corporate Research Center, Morristown, New Jersey 07960

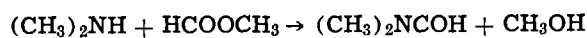
ABSTRACT

Dimethylformamide, diethylformamide, and other mono- and disubstituted N-alkylformamides are produced from carbon monoxide, methanol, and corresponding alkylamine by electrolysis. The electrolysis is conducted in a one-compartment cell under up to 100 atm of carbon monoxide at 20°-40°C. The reaction is highly electrolyte dependent. The efficiencies exceed 100% (based on 1 F/mole of amide). Electrochemical generation and continuous regeneration of catalyst appear responsible for the observed high reaction rates and high yields of formamides. The process is described and the reaction mechanism discussed.

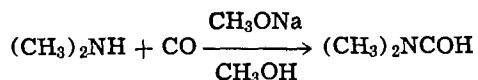
Electrochemical synthesis of N-alkylformamides is a result of our continuing interest in the electrochemical utilization of carbon monoxide in the production of commercially important chemicals. The synthesis of organic carbonates by electrolysis of carbon monoxide and the corresponding alcohol in the presence of a halide electrolyte has been previously reported (1, 2). The process as described here is an alternative to the existing chemical processes, and appears to have some advantages over the latter.

Several processes are described for chemical production of N-alkylformamides, based on various homogeneous and heterogeneous catalysts (3). The most relevant to our work are the processes for the production of N,N-dimethylformamide, described as follows (4-6):

1. By reaction of dimethylamine with methyl formate, according to



2. By reaction of dimethylamine with carbon monoxide, in the presence of dissolved alkali metal alcoholate (or CuCl_2 and potassium acetate), according to



Since methyl formate can be produced from methanol and carbon monoxide (5), these two processes can be viewed as one, differing only in number of steps.

The main problem in the one-stage commercial synthesis of N,N-dimethylformamide appears to be the plugging of equipment caused by precipitation of salts (sodium alcoholates) (6). This can be apparently avoided by the constant presence of some methyl formate added to the reaction mixture. The reaction is conducted at 90°C, at 175 atm of carbon monoxide. While the residence time of the one-stage process is not specified, methyl formate formation under comparable conditions proceeds apparently at a slow rate (8 days for 84% conversion). The electrochemical synthesis of N-alkylformamides requires ~3 hr for 60-80% conversion (based on amine), and it is conducted at milder conditions (20°-40°C and up to 100 atm of carbon monoxide). No salt precipitation occurs in the course of electrolysis. The syntheses of N,N-dimethylformamide are studied in greatest detail in this work.

Experimental

Constant current electrolysis.—Electrolyses were conducted at constant current, using cell and equipment previously described (1, 7). Graphite anode and stainless steel cathode were used throughout the work unless stated otherwise. Anodic and cathodic chambers

were not separated. Commercial chemicals were used without further purification or drying. The temperature was generally maintained in the range of 20°-40°C by cold water circulating coil. In a typical experiment, 200 ml of methanolic alkylamine [25-50 weight percent (w/o)] and 13.0g (0.04 mole) of tetrabutylammonium fluoroborate were charged into the reactor and pressurized with carbon monoxide to 100 atm. A total of 0.45F was usually passed. Product analyses were performed by GC, GC-mass spectrometry, and IR. For GC analysis of liquid samples a 5 ft \times 1/8 in. stainless steel column packed with POROPAK PS (70 \rightarrow 730°C/8°/min) was generally used. A Finnigan Model 3300 gas chromatograph/mass spectrometer operated in a chemical ionization mode with methane as the reagent gas was employed.

Potentiodynamic measurements.—The cell used for the potentiodynamic studies was of a conventional type with anolyte and catholyte separated by a fritted glass disk. A graphite rod (~1 cm² geometric area) and stainless steel or stainless steel (T316 SS, ~1 cm² geometric area) and platinum-clad tantalum were working and auxiliary electrodes, respectively. A saturated calomel electrode served as a reference electrode. Solutions were purged with argon prior to the recording. The electrical equipment used in potentiodynamic measurements consisted of a Function Generator, Model CHF-1 Elscint, a Wenking Potentiostat, and a Hewlett-Packard Autograph Model 7030AM X-Y recorder.

Results

Effect of electrolyte and electrolyte concentration.—The effect of electrolyte employed in the synthesis of various alkylformamides is shown in Table I. These data indicate that the selection of cation plays an essential role in determining the course of the reac-

Table I. Effect of electrolyte on alkylformamide formation*

Starting amine	Electrolyte, 0.2M	Products (mole/F)
Methylamine**	Et ₄ NBr	Methylformamide (~1.0)
	Et ₄ NBF ₄	Methylformamide (~1.0)
	NH ₄ Br	None
	NH ₄ Br + Et ₃ N	None
Ethylamine**	Et ₄ NBr	Ethylformamide (~1.0)
	Et ₄ NBF ₄	Ethylformamide (~1.0)
	NH ₄ Br	None
Dimethylamine***	Et ₄ NBF ₄	Dimethylformamide (~1.0)
	Bu ₄ NBr	DMF (~1.0)
	NaBF ₄	DMF (~1.0)
Diethylamine***	Et ₄ NBF ₄	Diethylformamide (~1.0)
	NaBF ₄	Diethylformamide (~1.0)

* Graphite anode, SS cathode, 100 atm CO, 20°-40°C, 0.45F.

** 25 w/o in methanol.

*** 50 w/o in methanol.

* Electrochemical Society Active Member.

Key words: carbon monoxide, catalysis, electrolyte, solvent.

tion. When tetraalkylammonium or alkali metal cations are substituted by ammonium salts, no formamides are formed. The electrolyte concentration appears to have an effect on reaction efficiencies, with higher yields obtained at lower concentrations (Table II). This, however, may be due to the experimental data scattering caused by IR effect (see Discussion).

Effect of current density and electrode material.—The efficient synthesis of formamides was generally carried out in a one-compartment cell on graphite anodes and stainless steel cathodes with current densities of 20 and 200 mA cm⁻² (geometric area), respectively. When a stainless steel cathode was substituted by graphite, identical results were obtained. Reversing the current densities (200 mA cm⁻² anode; 20 mA cm⁻² cathode) has a substantial effect on product efficiency in dimethylformamide formation. Higher yields are obtained invariably with higher cathodic current densities (Table III). Separation of the anolyte and the catholyte (Cation Exchange Membrane Ionics 61 DYG 067) increases the yields at both low and high cathodic current densities. The effect is more pronounced at higher current density (Table III).

Effect of carbon monoxide pressure and temperature.—The effect of carbon monoxide pressure on product efficiencies was studied in the cases of dimethylformamide and diethylformamide formation. Tetra-butylammonium fluoroborate (0.2M) electrolyte and a one-compartment cell were employed in all cases. The reactions were conducted at 20°–40°C. The dependence is illustrated in Fig. 1. These data suggest that in both cases there is at least a 5% yield increase for each 6.8 atm (100 psi) increment of carbon monoxide.

When the reactor is not externally cooled, the temperature rises to 65°–75°C. Some of the experiments were conducted without external cooling. Increased temperature had invariably beneficial effects on product yields. The data of some comparative runs are presented in Table II.

Current-potential data.—Current-potential curves were recorded in methanol solutions with Bu₄NBF₄ and NH₄Br electrolytes in the absence of carbon monoxide. The effect of dimethylamine and diethyl-

Table II. Efficiency of dimethylamine conversion to DMF*

Electrolyte, M	Temp., °C	DMF,** mole	Conversion, %
Bu ₄ NBF ₄ (0.2)	20°–30°	0.5 (110)	60
	30°–75°	1.0 (220)	90
Bu ₄ NBF ₄ (0.1)	20°–40°	0.8 (180)	80
Bu ₄ NBF ₄ (0.05)	20°–40°	0.8 (180)	80
NaBF ₄ (0.2)	20°–90°	0.5 (110)	50
Bu ₄ NBr (0.2)***	20°–30°	0.2 (40)	40
	30°–75°	0.8 (18)	75

* Graphite anode, SS cathode, 100 atm CO, 0.45F, residence time = 2.5 hr.

** Parentheses = apparent current efficiency, % (1 F/mole).

*** Dimethyl carbonate formed also.

Table III. One- vs. two-compartment cell in DMF formation*

Electrolyte	Cell	Cathodic current density, mA cm ⁻²	DMF, apparent current efficiency, %	
0.2M Bu ₄ NBF ₄	One-compartment	20	20	
		200	~100	
	Two-compartment (Cation exchange membrane)	20	20	~200
			200	~300
		200	20	~200
			200	~300

* Conditions: 100 atm CO, 20°–40°C, stainless steel cathode, 0.45F.

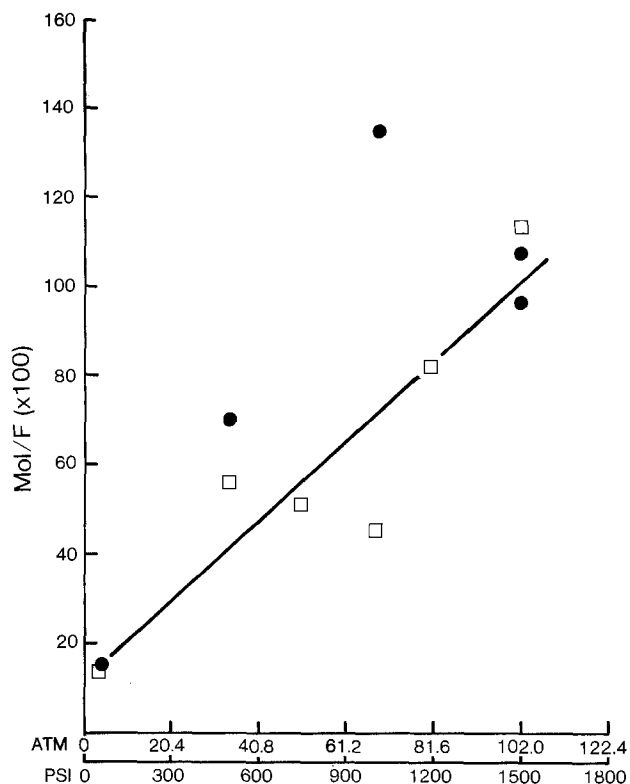


Fig. 1. Effect of CO pressure on efficiency of N,N-alkylformamide formation: □ N,N-dimethylformamide, ● N,N-diethylformamide.

amine additions (as well as corresponding formamides) on current-potential profiles of methanolic solutions was studied. The data are summarized in Table IV. As evident, current rise commences at substantially higher negative potentials upon addition of amines than in pure methanol. The reaction is accompanied by gas evolution, as in the case of pure methanol. E_{10} for methanol/NH₄Br compared to methanol/Bu₄NBF₄ solution is 300 mV less negative.¹ In all investigated cases, oxidation of amines takes place at substantially lower potentials than methanol (Bu₄NBF₄ electrolyte). With NH₄Br electrolyte simultaneous oxidation of Br⁻ and amines appears possible (bromine evolution visible). Some typical cyclic voltammograms are presented in Fig. 2.

Discussion

The synthesis of N-alkyl amides from carbon monoxide, alkyl amines, and methanol proceeds generally with apparent current efficiency of $\geq 100\%$ (based on 1 F/mole of amide). Without methanol present, no alkyl amides are formed. In the chemical synthesis of

¹ E_{10} represents the electrode potential at 10 mA cm⁻².

Table IV. Potential sweep data for methanol and methanol/amine systems*

Reactant	Electrolyte, 0.2M	E_{10} (mV/SCE)		
		Stainless steel, cathodic	Graphite****	
			Anodic	Cathodic
Methanol	Bu ₄ NBF ₄ NH ₄ Br	1500	1550	1400
		1200	—	—
Dimethylamine**	Bu ₄ NBF ₄	1800	600	1800
Diethylamine***	Bu ₄ NBF ₄ NH ₄ Br	1800	700	—
		1500	800	—

* Sweep rate: 50 mV sec⁻¹; 25°C.

** 50 v/o in methanol.

*** 30 v/o in methanol.

**** — = not determined.

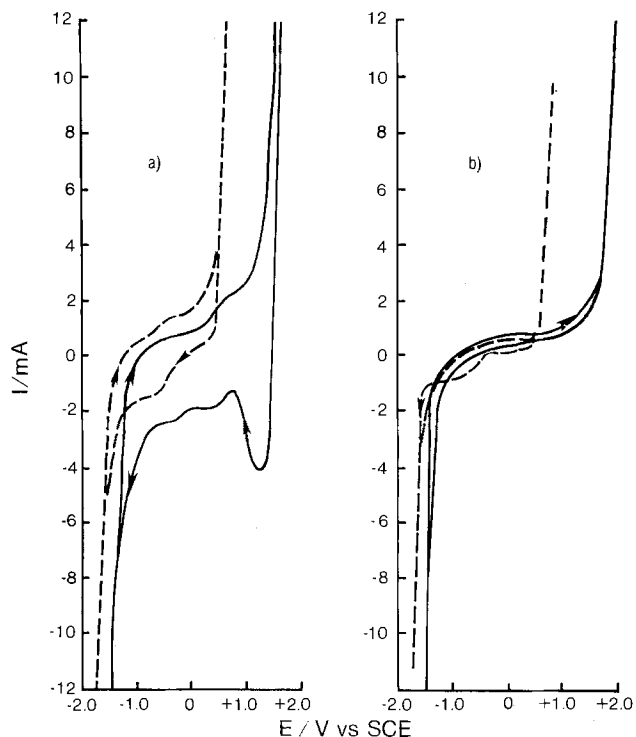


Fig. 2. *E/I* profiles of 0.2M Bu_4NBF_4 /methanol w/o dimethylamine. Sweep rate: 50 mV sec^{-1} ; 25°C . a) graphite, b) stainless steel. — Pure Bu_4NBF_4 /methanol, --- 50 w/o $(\text{CH}_3)_2\text{NH}$.

formamide the reaction takes place via methyl formate intermediate and its subsequent reaction with alkyl amines, as already seen. Methyl formate is formed from carbon monoxide and methanol in the presence of sodium alcoholates.

During our studies of electrochemical dimethyl carbonate synthesis from carbon monoxide and methanol, we discovered that methyl formate was formed preferentially when ammonium bromide electrolyte was substituted by tetrabutylammonium bromide (1). Yields of methyl formate indicated a process involving 1 F/mole of ester. Subsequently, the $\text{CO}/\text{CH}_3\text{OH}$ electrolysis was carried out employing tetrabutylammonium fluoroborate; methyl formate was a major product (Table V). The choice of anion, thus, had no essential bearing on the course of the reaction, but catalysis by R_4N^+ cation was clearly implied. When this reaction was carried out in the presence of alkyl amines, the corresponding formamides were formed, as shown in the present work (Table I). This suggests that electrochemical synthesis of formamides proceeds via methyl formate intermediate in much the same way as a chemical one.

Table V. Effect of electrolyte on product distribution in carbon monoxide/methanol electrolysis*

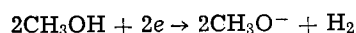
$\text{CH}_3\text{OH} + \text{CO}$	$n\text{F}$	LiBr	$(\text{CH}_3\text{O})_2\text{CO}$ (0.35)	$(\text{CH}_3\text{O})_2\text{CH}_2$ (0.05)	CH_3OOCH (0.05)
		NH_4Br	$(\text{CH}_3\text{O})_2\text{CO}$ (0.35)	None	None
		LiClO_4	None	$(\text{CH}_3\text{O})_2\text{CH}_2$ (0.35)	CH_3OOCH (0.12)
		Bu_4NBr	$(\text{CH}_3\text{O})_2\text{CO}$ (0.10)	None	CH_3OOCH (0.80)
		Bu_4NBF_4	None	$(\text{CH}_3\text{O})_2\text{CH}_2$ (0.10)	CH_3OOCH (1.00)

* Graphite anode, stainless steel cathode, one-compartment cell, 100 atm, $20^\circ\text{--}40^\circ\text{C}$, 0.45F; parentheses = mole/F.

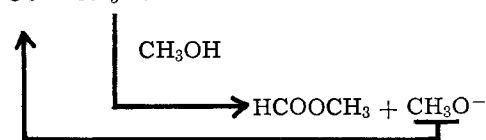
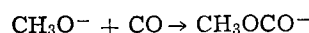
ducted at 90°C and 175 atm, but no residence time was given (6). The electrolysis of CO , methanol, and alkyl amine, in the presence of R_4N^+ or Na^+ salts as electrolytes, converts 60-80% amine to formamide in approximately 1-3 hr at 100 atm. It is believed that the role of electrochemistry is in generation of homogeneous catalyst, R_4N^+ methoxide or Na^+ methoxide. The reaction sequence leading to amides can then be depicted as follows

SCHEME 1

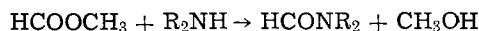
Cathode:



Chemical:



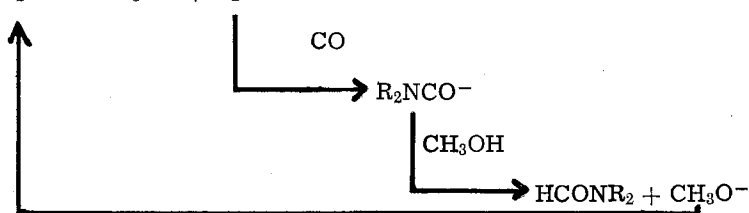
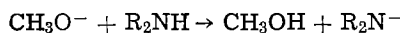
followed by



In the above scheme, for each mole of hydrogen evolved, two moles of CH_3O^- are formed cathodically. Local concentration of CH_3O^- should thus be sufficiently high to act as catalyst for formate and/or formamide formation. Concentration of R_4N^+ in the cathodic double layer is also expected to be high due to the adsorption phenomena.

An alternative scheme for the chemical reaction of electrochemically generated methoxy ions leading to formamide formation is suggested as follows

SCHEME 2



The chemical synthesis of methyl formate is catalyzed by sodium methoxide. It requires high temperatures, high pressures of carbon monoxide, and long reaction times ($100^\circ\text{--}120^\circ\text{C}$, 160 atm, 8 days for 84% conversion) (5). Chemical synthesis of formamides is, likewise, catalyzed by sodium alcoholates; it is con-

In the present work no attempt has been made to distinguish between these two possibilities of follow-up chemical reactions.

Anodic reaction in the methanol/amine system will depend on the electrolytic conditions and the concentration of the amine present. In constant current

electrolysis, at low current densities and high amine concentrations, oxidation of amine will take place in preference to methanol (Table IV). As the electrolysis progresses and amine gets depleted, oxidation of methanol will take over (batch-wise operation). It is also possible that oxidation of CH_3O^- (rather than CH_3OH) would compete with amine oxidation. High anodic current densities, even at relatively high amine concentrations, might also change the course of anodic reaction.

We have not attempted (so far) to determine the products of anodic reaction. In the case of methanol (or CH_3O^-) oxidation, formaldehyde is expected as product according to the following reaction (8)



Further oxidation of CH_3O^- to formate (and ultimately CO_2) is possible, but takes place only in the presence of OH^- or H_2O , according to (9)



This cannot happen to any substantial degree under our experimental conditions (H_2O concentration below 1%). Small amounts of CO_2 detected in the gas phase may also come from carbon monoxide oxidation. The products derived from amines oxidation are less certain. The literature data (10) suggest that secondary and tertiary aliphatic amines are dialkylated on anodic oxidations in nonaqueous solvents. The data relating directly to dimethylamine or diethylamine oxidation could not, however, be found. The solutions after $\text{CH}_3\text{OH}/\text{amine}/\text{CO}$ electrolytes contain small amounts of dark solids, whose nature remains to be determined. It is important to notice that no fouling of the electrodes was ever observed.

With Bu_4NBr electrolyte, in the presence of amine, formation of dimethyl carbonate was observed along with formamide, in agreement with previously observed reactions (Table V). Bromine evolution and subsequent COBr_2 formation is postulated in such cases (1). The fact that $(\text{CH}_3\text{O})_2\text{CO}$ forms in a much lesser degree than either methyl formate or formamide indicates different respective rates of follow-up chemical reactions. With amine present, simultaneous oxidation of amine and Br^- seems possible (Table IV), decreasing the rate of Br_2 generation. Employment of NH_4Br failed to produce any methyl formate or formamide (Tables I and V). In the presence of NH_4Br , hydrogen evolution in methanol takes place at substantially lower potentials than with Bu_4N^+ electrolytes (Table IV). It is quite obvious that, in this case, NH_4^+ serves as a primary proton source, thus diminishing high local concentration of methoxide. Also, NH_4^+ is more acidic than R_4N^+ . These two factors can adequately account for the lack of formamide (or methyl formate) formation with NH_4Br electrolyte.

Due to the relatively low conductivity of methanol/amine solutions with Bu_4NBF_4 (and especially NaBF_4) and our experimental setup, fairly high IR drop is observed, with subsequent generation of heat. Without cooling, the temperature of the reactor would rise to $65^\circ\text{--}75^\circ\text{C}$. In order to reduce the temperature, the reactor was cooled externally (by water circulating coil) to $20^\circ\text{--}40^\circ\text{C}$. It is believed, however, that external cooling could not adequately prevent internal local overheating, so that actual reaction temperature might have been higher than $20^\circ\text{--}40^\circ\text{C}$. The absence of the precise temperature control may account for some of the observed results scattering. The experiments carried out without external cooling were, in general, producing higher yields of amides than the cooled ones (Table II).

Interestingly enough, however, heating by itself (even to the temperature of 100°C) was not sufficient for the continuation of the reaction to any substantial

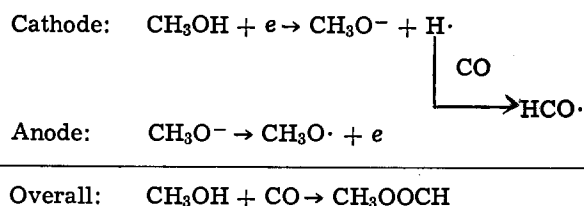
degree once the current flow was discontinued. This is remarkable if we assume that the essential role of electrolysis is indeed the generation of homogeneous catalyst, R_4N^+ or Na^+ alcoholates. Once generated, the reactions would be expected to proceed regardless of the further current flow. Discontinuation of the current should not, therefore, have such a profound effect on the product yield.

The answer for this inconsistency might be found in the possibility that, in the electrochemical synthesis, very high concentration of the catalyst may be generated locally. Concentration of the catalyst in the diffusion electrical double layer (layer adjacent to the electrode) may be many times higher than in the bulk of the solution, influencing thus the rate of the reaction. Such phenomena are known in electrochemistry (11), and it was suggested that it might be the case here (12). The slow rate of the chemical reaction may be thus attributed to the low bulk concentration of the catalyst. Solubility of NaOCH_3 in CH_3OH is fairly low. In the chemical process of methyl formate synthesis, difficulties are experienced due to the catalyst precipitation (6). The higher activity of R_4N^+ compared to Na^+ electrolyte in our process may be partially due to the higher solubilities of R_4N^+ salts.² Catalysis by metals (leached from the stainless steel container electrode) was ruled out, based on experiments employing both electrodes made of graphite.

Increase in carbon monoxide pressure (one-compartment cell) favors N-alkylformamide formation, as evidenced in Fig. 1. The reaction was not examined at pressures higher than 100 atm.

The observed higher rates (lower residence time) in the electrochemical synthesis of methyl formate (and probably formamides) are thus likely to be due to the higher local concentration of the catalyst, and/or to the continuous catalyst generation. The active catalyst state is continuously regenerated. The direct electrochemical formation of methyl formate is ruled out, even in the one-compartment cell, since it would require fast recombination of cathodic and anodic radical products, preceded (or followed) by chemical reactions, in order to account for the observed 1 F/mole efficiency. This unlikely situation can be depicted as follows

SCHEME 3



No other direct mechanism can account for the observed 1 F/mole efficiency. Preferential oxidation of amines prevents $\text{CH}_3\text{O} \cdot$ generation, while in the two-compartment cell separation of catholyte and anolyte practically eliminates the possibility of cathodic and anodic products recombination (even if they are both derived from methanol). In either of these two cases, no methyl formate, and consequently formamide, formation could be possible according to the above scheme. In both cases, however, high yields of formamide are formed, eliminating thus even remote credibility of a direct electrochemical mechanism.

Furthermore, separation of catholyte and anolyte (cation exchange membrane) produced DMF with yields highly exceeding 100% (1 mole/F) (Table III). This can be explained in terms of further increase in catalyst (R_4N^+ methoxide) concentration in the catholyte. Loss of CH_3O^- is prevented, while R_4N^+ ion con-

² It was suggested by one of the reviewers that the higher rates for R_4N^+ -containing electrolytes vs. Na^+ -containing electrolytes probably has most to do with the "nakedness" of the alkoxide ion when the counterion is R_4N^+ .

centration gradually increases due to the transfer through the cation exchange membrane. In addition, anodic decomposition of product intermediate(s) which might take place in an undivided cell is also prevented. It is obvious that chemical reaction following the electrochemical catalyst generation (and continuous regeneration) is responsible for the yields exceeding 100% current efficiency.

Acknowledgment

I am highly indebted to Mr. Arthur T. Walsh for conducting the high pressure electrolyses and GC analytical work. I also wish to thank Dr. Miroslav Novotny for useful discussions and the members of the Allied Chemical Physics Department for their contributions: Dr. Danne E. Smith (GC-mass spectrometry) and Mr. James M. Hanrahan (preparative GC and IR). Comments provided by Professor E. Gileadi are also greatly appreciated.

Manuscript submitted Sept. 17, 1979; revised manuscript received Nov. 26, 1979. This was Paper 320 presented at the Boston, Massachusetts, Meeting of the Society, May 6-11, 1979.

Any discussion of this paper will appear in a Discussion Section to be published in the December 1980

JOURNAL. All discussions for the December 1980 Discussion Section should be submitted by Aug. 1, 1980.

Publication costs of this article were assisted by Allied Chemical Corporation.

REFERENCES

1. D. Cipris and I. L. Mador, *This Journal*, **125**, 1954 (1978).
2. D. Cipris and I. L. Mador, U.S. Pat. 4,131,521 (1978).
3. D. L. Smathers, U.S. Pat. 4,101,577 (1978).
4. R. Kirk and D. F. Othmer, "Encyclopedia Chemical Technology," Vol. 10, p. 109, Wiley, New York (1964).
5. B. S. Lacy, U.S. Pat. 1,787,483 (1931).
6. VEB Leuna-Werke "Walter Ulbricht," British Pat. 925,588 (1956).
7. D. Cipris, *J. Appl. Electrochem.*, **8**, 537 (1978).
8. G. Sundholm, *J. Electroanal. Chem. Interfacial Electrochem.*, **31**, 265 (1971).
9. C. I. Wakuza, T. Hayachi, S. Kikkawa, and H. Tamura, *Electrochim. Acta*, **17**, 1085 (1972).
10. N. L. Weinberg, Editor, "Technique of Electroorganic Synthesis," Part I, p. 573, John Wiley, New York (1974).
11. M. R. Ort and M. M. Baizer, *J. Org. Chem.*, **31**, 1646 (1966).
12. E. Gileadi, Private communication.

Free-Convective Mass Transfer to a Rod-Shaped Vertical Electrode

J. R. Selman* and J. Tavakoli-Attar

Department of Chemical Engineering, Illinois Institute of Technology, Chicago, Illinois 60616

ABSTRACT

The limiting-current method is used to measure mass transfer rates by free convection to the faces of a rod-shaped electrode as commonly used in molten salts. Mass transfer rates to the horizontal (disk) face and the vertical (curved) face are measured separately and in combination. The two rates are not additive; there is significant interaction caused by leading edge effects at the vertical face and by solution streaming from the horizontal to the vertical face. At the horizontal face a new and unusual but well-characterized type of convective mass transfer, driven by buoyancy, is measured and correlated.

Electrochemical measurements of mass transfer rates and mass transfer coefficients are applied frequently because of their inherent accuracy and convenience. In the present work the limiting current technique (1) is used to investigate mass transfer by free convection at a vertical cylinder of finite length, and its horizontal end face, immersed in a liquid. This problem is of interest to electrochemists active in molten-salt technology.

In molten salts, as in aqueous electrolytic solutions, one prefers to use an electrode of well-defined area and known hydrodynamic characteristics, e.g., a rotating disk electrode. However, the ideal electrode of this type, which has its active area embedded in an insulating surface, is difficult to make and maintain crevice-free for any length of time in common molten salt media such as LiCl-KCl eutectic (mp 625°K) or equimolar Li₂CO₃-K₂CO₃ (mp 778°K). Consequently, one often employs as working electrode a metal or carbon rod partly immersed in the melt.

In a molten salt which contains a minor electroactive component, e.g., a sparingly soluble heavy-metal ion or a dissolved gas, the mass transfer rate to the rod

electrode in free convection or in rotation (2) determines the limiting current due to this component.

The mass transfer limiting current to the rod electrode, which consists of a vertical cylinder of finite length with a circular disk as the end face (Fig. 1a), is not as well defined as at a rotating disk electrode (Fig. 1b) or at a vertical electrode by free convection, e.g., at a cylindrical electrode confined between bottom and top of the cell (Fig. 1c). The objective of this work was to measure the mass transfer rate at a rod-shaped electrode in free convection and compare it with rates predicted by classical free-convection correlations for vertical and horizontal surfaces.

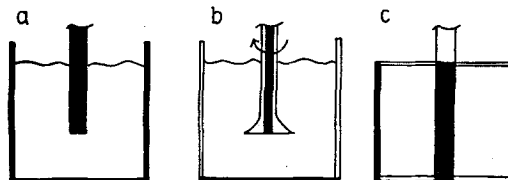


Fig. 1. Cell configurations for: a, vertical rod electrode; b, rotating disk electrode; c, cylindrical electrode confined between bottom and top of the cell. Black surfaces are electrode surfaces; white, insulator.

* Electrochemical Society Active Member.

Key words: free convection, mass transfer, limiting current, molten salt, cylinder, rod, CuSO₄.

The mass transfer rates to the vertical, curved surface and to the horizontal, disk face of the cylinder were measured in separate exposures; and, finally, in combined exposure, the mass transfer rate to the entire rod electrode. This was carried out by limiting-current measurements in aqueous solutions. The system used was copper deposition from a CuSO_4 solution containing excess H_2SO_4 as supporting electrolyte (1).

It appears justified to apply the results obtained in this aqueous system to the molten-salt solution described above: the major components of the latter, e.g., LiCl-KCl eutectic or equimolar $\text{Li}_2\text{CO}_3\text{-K}_2\text{CO}_3$, besides functioning as ionic solvent, have a high enough conductivity to cause the migration fluxes of minor components to become negligible. Thus there is a nearly complete analogy with a well-supported solution in an electrolytic solvent.

Free Convection at Vertical and Horizontal Electrodes

Free-convective heat transfer at an isothermal vertical surface is one of the classical problems of heat transfer theory (3), solved mathematically by similarity transformation. Wagner (4) first gave an approximate solution for the analogous, but more complicated case of free convection caused by copper deposition in a CuSO_4 solution containing H_2SO_4 . The limiting current density depends inversely on the 0.25 power of x , the distance from the leading (lower) edge of the electrode. It also depends on the 1.25 power of the bulk CuSO_4 concentration.

Wagner's approximate expression for the average limiting current over a distance L may be written in the dimensionless form

$$\text{Sh}_L = \frac{i_{\text{lim}}L}{2FD_{\text{Cu}^{++}}c_{\text{Cu}^{++}}} = 0.806 \left[\frac{gL^3c_{\text{Cu}^{++}}}{\nu D_{\text{Cu}^{++}}} (\alpha_{\text{CuSO}_4} - 0.66\alpha_{\text{H}_2\text{SO}_4}) \right]^{0.25} \quad [1]$$

Here α_i is the densification coefficient of species i , defined by

$$\alpha_i = \frac{1}{\rho} \left(\frac{\partial \rho}{\partial c_i} \right)_{T,c_{j \neq i}} \quad [2]$$

The negative coefficient of $\alpha_{\text{H}_2\text{SO}_4}$ in Eq. [1] means that H_2SO_4 accumulates at the cathode by migration, while CuSO_4 is depleted. The density difference driving the convection is therefore less than it would be in the case of CuSO_4 depletion only.

Accurate estimation of the density difference ($\Delta\rho$) is essential if one wants to use the limiting-current technique to establish free-convection correlations. Such correlations contain the characteristic Grashof number

$$\text{Gr}_L = \frac{gL^3}{\nu^2} \left(\frac{\Delta\rho}{\rho} \right) \quad [3]$$

which is also implicit in Eq. [1]. The density difference $\Delta\rho$ depends obviously on the extent of H^+ ion migration and thus on the ratio of supporting electrolyte (H_2SO_4) to reactant (CuSO_4) concentration in the bulk. A constant coefficient of $\alpha_{\text{H}_2\text{SO}_4}$ as in Eq. [1] is evidently an oversimplification.

Wilke, Eisenberg, and Tobias (5, 6), using an improved, semiquantitative procedure to estimate $\Delta\rho$, obtained for the mass transfer coefficient in free convection at vertical electrodes the correlation

$$\text{Sh}_L = 0.670 (\text{Gr}_L\text{Sc})^{0.25} \quad [4]$$

This is in excellent agreement with the theoretical solution for very large Schmidt numbers, characteristic of electrolytic solutions. In the experiments of Wilke *et al.* (5, 6) the vertical plate electrode was bounded on its lower edge, where the convection boundary layer originates, by the bottom of the cell.

The effect of migration on limiting currents was analyzed in more detail by Selman and Newman (7). From their results the accumulation of H_2SO_4 at the electrode may be expressed as a polynomial function of the ratio (supporting electrolyte/total electrolyte), see Table I. This table also presents a coefficient for the ratio of the limiting current in the presence of migration to that expected for pure convective diffusion only. The correlations in Table I are valid for the case of complete dissociation of H_2SO_4 , which more closely approximates the chemistry of most experimental solutions than partial dissociation to HSO_4^- (8). The correlations of Table I were used in the present work to calculate $\Delta\rho$ and k .

Free convection at a vertical cylinder differs from that at a flat vertical plate by the effect of transverse curvature; this is the more important as the cylinder (or wire) radius, r , is smaller. Ravoo *et al.* (9) investigated the effect of curvature theoretically and experimentally. They applied a correction function $f(\gamma)$ to the mass transfer correlation

$$\text{Sh}_L = 0.670 f(\gamma) (\text{Gr}_L\text{Sc})^{0.25} \quad [5]$$

where

$$\gamma = \frac{L}{r} (\text{Gr}_L\text{Sc})^{-0.25} \quad [6]$$

At high Gr_LSc combinations or small L/r ratios, γ is $\ll 1$ and $f(\gamma) \rightarrow 1$. The practical limit for absence of curvature effect is $\gamma = 0.2$; this was not exceeded in the present work.

Germane to free convection at a finite vertical cylinder is free convection at a sphere. Schütz (10) investigated this case and found that between Gr_dSc numbers of 1.22×10^7 and 1.5×10^{10} mass transfer rates were well correlated by

$$\text{Sh}_d = 2 + 0.590 (\text{Gr}_d\text{Sc})^{0.25} \quad [7]$$

where d is the sphere diameter.

Finally it should be noted that free convection at a horizontal surface is possible only if heavier fluid overlies a lighter one (unstable stratification). At a downward facing cathode in a cell as shown in Fig. 2a, deposition of copper from CuSO_4 solution will not produce free convection. Conversely, in the cell of Fig. 2b free convection will arise if Jeffreys' criterion (11) is met

$$\text{Gr}_h\text{Sc} > 1709$$

Here Gr_h is based on the cell height, h .

Usually Gr_hSc exceeds 10^7 in electrolytic solutions and a turbulent free-convection regime is established; in this case mass transfer rates are correlated by expressions such as

$$\text{Sh}_d = C (\text{Gr}_d\text{Sc})^{1/3} \quad [8]$$

If C is a constant, e.g., $C = 0.152$ (12), the mass transfer coefficient is independent of the electrode di-

Table I. Correlations for H_2SO_4 accumulation at the electrode by migration and for migration effect on limiting current based on data of Selman and Newman (7)

Function: $p = a_0 + a_1r^{1/3} + a_2r^{2/3} + a_3r$

p	$\Delta\text{CH}_2\text{SO}_4$	i_{lim}
	ΔCCuSO_4	$i_{\text{lim, diffusion}}$
a_0	-0.000215	1.91143
a_1	0.113075	-0.77174
a_2	0.85576	-0.71969
a_3	-0.50496	+0.53115
Standard error	0.0030	0.0043

$$r = \frac{\text{CH}_2\text{SO}_4}{\text{CCuSO}_4 + \text{CH}_2\text{SO}_4}$$

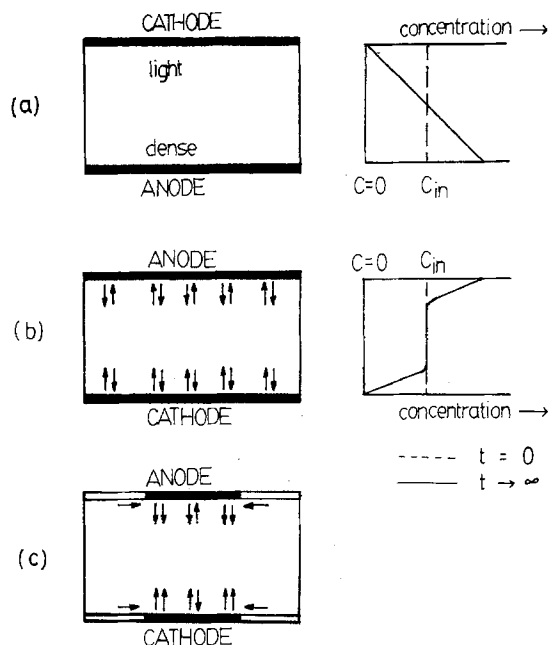


Fig. 2. Three cells with horizontal electrodes (black). System: Cu deposition and dissolution in $\text{CuSO}_4\text{-H}_2\text{SO}_4\text{-H}_2\text{O}$. (a) Stable stratification with pure diffusion. To the right: schematic concentration profile; (b) unstable stratification leading to uniform turbulent free convection. To the right: schematic concentration profile; (c) unstable stratification leading to nonuniform turbulent free convection. Horizontal arrows: advection of bulk solution.

mension, d . This is evidently the case in Fig. 2b where the current distribution cannot be otherwise than uniform.

However, if the horizontal cathode is embedded, as in Fig. 2c, the coefficient in Eq. [8] depends on the cathode dimensions: bulk electrolyte solution streams slowly toward the cathode from the inert side surfaces. Fenech (13) found for such a case that in Eq. [8] the coefficient is

$$C = 0.122 Sc^{1/24} \epsilon \quad [9]$$

where $\epsilon = 1$ if the plate is bounded by vertical surfaces. (Fig. 2b) and $\epsilon = f(d) > 1$ if it is embedded (13).

In the present study streaming caused by adjacent free convection is found to occur in a different context, as is shown below.

Experimental

The experiments were carried out in a cylindrical Lucite vessel of 16.5 cm diam and 15.9 cm height containing 2.5 liters of electrolytic solution. The working electrode was a stainless steel or OFHC copper cylinder of 0.63-5.08 cm diam; it could be screwed into the spindle of a Pine Instruments Rotator,¹ with which it had been carefully aligned, and was immersed in the center of the electrolytic solution by lowering the arm of the rotator. The counterelectrode was a $\frac{1}{8}$ in. thick sheet of OFHC copper, centered and attached to the bottom of the cell. The entire electrolytic cell was immersed in a constant temperature bath maintained at $25.0^\circ \pm 0.1^\circ\text{C}$.

A capillary adjacent to the working electrode was used to connect the bulk solution to the reference electrode compartment, which was filled with the same electrolytic solution as the main cell. A 1/16 in. diam wire of OFHC copper was used as a reference electrode.

The electrolytic solution consisted of approximately 0.05, 0.1, and 0.25M CuSO_4 solutions containing 1.5-2.0M H_2SO_4 . To some solutions glycerol was added. The concentration of CuSO_4 was determined by iodometric titration (14) and the H_2SO_4 concentration by

¹ Pine Instruments Company, Grove City, Pennsylvania 16127.

Table II. Physical property correlations of $\text{CuSO}_4\text{-H}_2\text{SO}_4\text{-H}_2\text{O}$ solutions at 25°C

$$p = a_0 + a_1c_{\text{CuSO}_4} + a_2c_{\text{H}_2\text{SO}_4} + a_{11}c_{\text{CuSO}_4}^2 + a_{22}c_{\text{H}_2\text{SO}_4}^2 + a_{12}c_{\text{CuSO}_4}c_{\text{H}_2\text{SO}_4}$$

p	ρ (g/cm ³)	μ (cp)	$\mu D \times 10^4$ (cp — cm ² /sec)
a_0	0.998706	0.904272	5.897
a_1	0.143219	0.426667	6.986
a_2	0.062387	0.132113	—
a_{11}	0.005594	0.254115	—
a_{22}	-0.000776	0.031502	—
a_{12}	-0.003197	0.108582	—
Standard error	0.0018	0.0076	0.17

potentiometric titration with NaOH (15). Glycerol was titrated with ceric ion. The solution density, viscosity, and diffusivity at 25°C were found from correlations (Table II) established in earlier work (16).

Before each run the solution was routinely deaerated by sparging nitrogen slowly for 2 hr. The electrodes were carefully polished with grade 0000 emery paper and degreased. If stainless steel electrodes were used, a 2-5 micron thick layer of copper was plated onto the cathode *in situ* while it was rotated at 100-300 rpm, at a constant current density of 3-6 mA/cm².

The limiting current measurement was started after the solution had become completely quiescent and following a visual check to ensure that no bubbles were sticking to the electrode.

The power supply used was a PAR Model 371 Potentiostat/Galvanostat.² Limiting current curves were generated by means of a VCF ramp generator (Exact Electronics³ Model 7030) and recorded on a Houston Instruments⁴ Series 2000 Omnigraphic X-Y Recorder.

After each series of experiments the electrode, if it was stainless steel, was first stripped potentiostatically at +300 to +500 mV; the electrode was then rinsed and washed with isopropanol, dried, and prepared for the next run.

In all experiments in which only part of the working electrode was to be exposed to the solution, e.g., the horizontal end face, or a certain length of the cylindrical vertical surface, the nonexposed parts were masked with a thin layer of glyptol paint.

Results and Discussion

Horizontal end face exposed.—As it was expected that no free-convective limiting current would be established in this case (see Fig. 2a), attention was focused on the unsteady-state diffusive process expected to occur at the exposed disk electrode. At a 1.27 cm diam electrode, potential scans were applied with varying scan rates (dV/dt from 2.94 to 50 mV/sec). A typical diffusion-limited process should exhibit a maximum current at approximately 22 mV (at 298°K) and the peak current should be proportional to the square root of the scan rate a [Sevcik-Randles equation (17)]

$$i_{\text{max}} = -0.6105c_b n F (aD)^{1/2} \quad [10]$$

where

$$a = \frac{nF}{RT} \frac{dV}{dt} \quad [11]$$

A typical scan result is shown in Fig. 3. Current maxima were observed at overpotentials ranging between -75 and -160 mV; this is considerably more negative than predicted by the Sevcik-Randles theory, although the copper deposition reaction has an exchange-current density of 0.1-0.5 mA/cm² and is practically diffusion controlled (18).

A similar discrepancy between predicted and observed peak potentials was observed earlier in unsteady-state limiting current measurements at a rotat-

² Princeton Applied Research, Incorporated, Princeton, New Jersey 08540.

³ Exact Electronics, Incorporated, Hillsboro, Oregon 97123.

⁴ Houston Instruments Incorporated, Austin, Texas 78753.

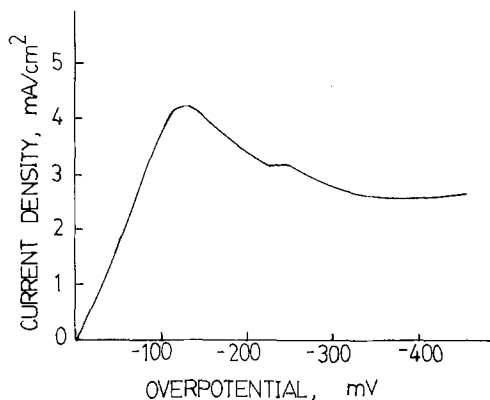


Fig. 3. Typical potential scan at the horizontal electrode surface (1.27 cm diam). Scan rate: 2.94 mV/sec. Solution: 0.05M CuSO_4 , 1.6M H_2SO_4 . Temperature: 25°C.

ing disk electrode (19). Here it was probably caused in part by uncompensated ohmic drop and in part by the presence of convection.

It was evident that, after a lapse of time, convection set in: (i) a smaller second peak was observed at -250 mV in almost all cases and (ii) the current did not decay to zero but to a small finite value which could be maintained indefinitely by holding the potential at a value between -350 and -400 mV.

Moreover, the peak current densities for the first (Randles-Sevcik) peak were only about 70% of the theoretical prediction, Eq. [10], as shown in Fig. 4. Convection clearly caused an increased supply of CuSO_4 to the electrode, thereby lowering the peak current density as well as shifting the peak potential to more negative values (i.e., lower CuSO_4 concentration at the electrode when the current peaks).

The steady-state limiting current was subsequently studied at electrodes of various diameters. The limiting current was generated simply by applying a large negative potential, but not so negative as to cause hydrogen evolution; in most cases a potential step of -400 mV was used. Figure 5 shows a typical current response to such a potential step. The limiting current is established after 3-4 min during which the initial oscillations die out. After 5-6 min the current starts increasing slowly due to buildup of surface roughness; if the applied potential was chosen too high, e.g., -500 mV, the current kept on decreasing because hydrogen

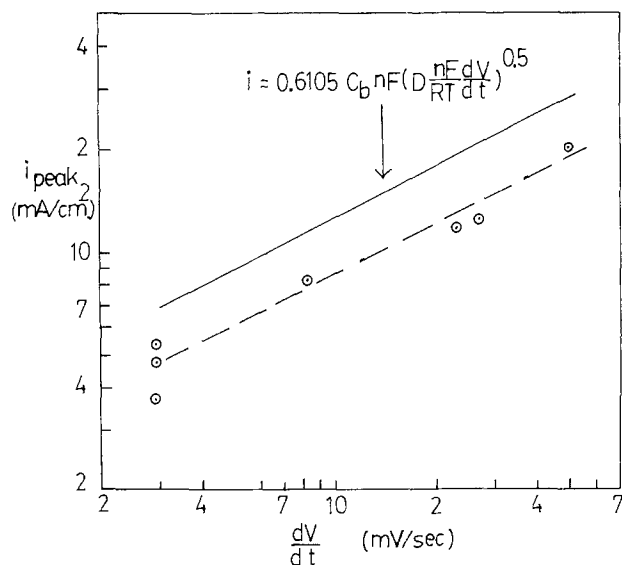


Fig. 4. Correlation of peak currents from potential scans with the scan rate (horizontal electrode surface, 1.27 cm diam). Solution 0.05M CuSO_4 , 1.6M H_2SO_4 (25°C). Solid: Eq. [10]. Dashed: least squares line through experimental results.

bubbles forming at the edge of the exposed disk surface slowed down convection.

Evidently, the convection responsible for the observed limiting current is caused by upward escape of light solution, depleted in CuSO_4 , around the edge of the exposed disk surface. The buoyant solution forms a plume around the circumference of the disk and this plume induces a very slow flow of bulk solution up toward the disk, where it is depleted in CuSO_4 . The depleted solution flows radially outward to the edge of the disk (Fig. 6).

This convection is an example of bulk flow streaming induced by buoyancy (advection) similar to that observed by Fenech (13) and Wragg and co-workers (20) adjacent to a horizontal electrode at which turbulent free convection is taking place.

The mass transfer coefficient corresponding to the present buoyancy-induced convection was found to be inversely proportional to the diameter of the disk surface (Fig. 7). Measurements with various CuSO_4 concentrations of approximately equal Sc number (2330 ± 50) yielded the correlation

$$\text{Sh}_d = 9.80 \text{Gr}_d^{0.167} \quad [12]$$

with a standard error of 8%.

Measurements with solutions containing 2.97M glycerol ($\text{Sc} = 9084$) yielded the same Gr dependence as Eq. [12] and indicated an approximate Sc dependence of 0.20. This would yield for the overall correlation

$$\text{Sh}_d = 2.075 \text{Gr}_d^{0.167} \text{Sc}^{0.2} \quad [13]$$

with an error of $\pm 6\%$ (Fig. 8)

Experimental data are given in Table III.

The dependence of Sh_d on $\text{Gr}_d^{1/6}$ is quite different from the dependence on $\text{Gr}_d^{1/4}$ in free convection at a sphere, Eq. [7], although the two geometries are extreme cases of the same general flow pattern combining free convection with stagnation flow. Whereas

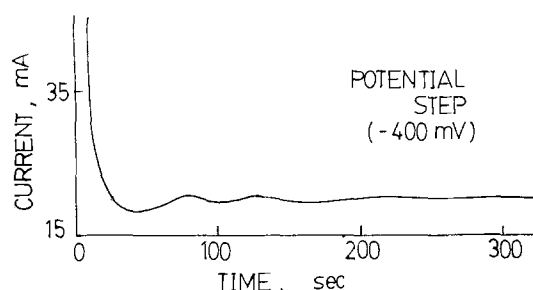


Fig. 5. Typical current response to -400 mV potential step at horizontal electrode surface.

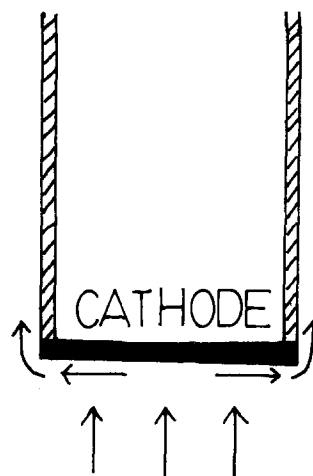


Fig. 6. Schematic flow pattern at horizontal electrode surface in copper deposition from CuSO_4 - H_2SO_4 - H_2O . Black: cathode; shaded: insulator.

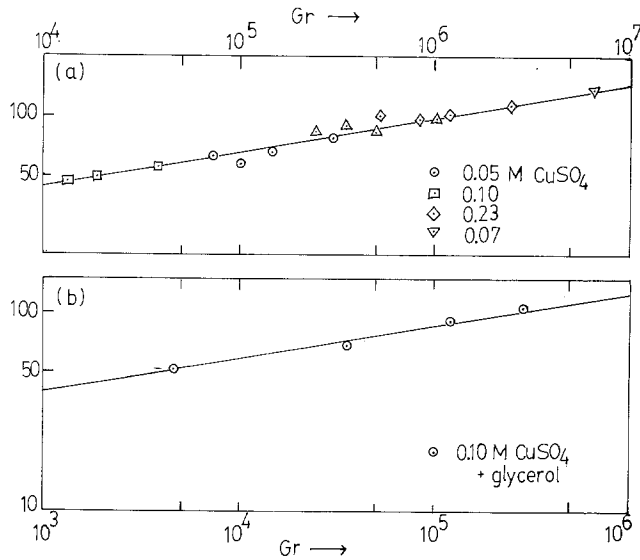


Fig. 7. Correlation of limiting currents at the horizontal electrode surface with Grashof number. (a) Solutions without glycerol. Solid line: Eq. [12]; (b) solutions with glycerol. Solid line: $Sh = 12.79Gr^{0.1687}$.

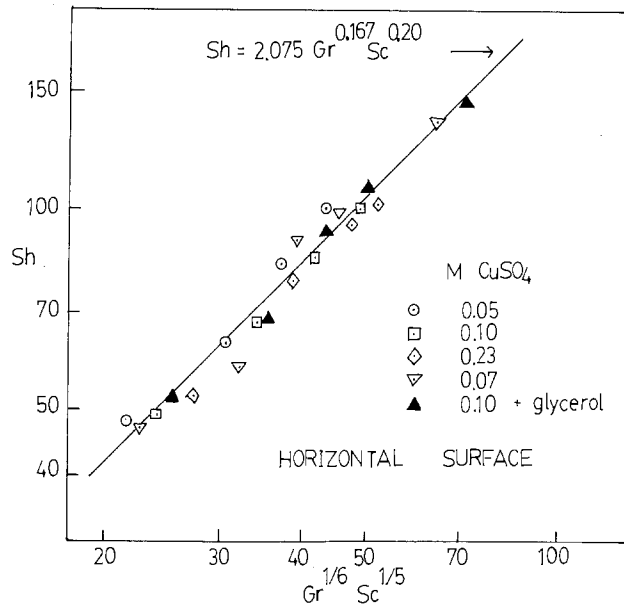


Fig. 8. Overall correlation for mass transfer at the horizontal electrode surface.

free-convection mass transfer dominates at the sphere, in the present case stagnation flow characteristics dominate if the disk is large enough.

Thus the dependence of Sh_d on $Gr_d^{1/6}$ may be explained by considering the streaming toward the disk and the radial outflow as a case of three-dimensional stagnation flow similar to that at a stationary disk perpendicular to a uniform main flow. Matsuda and Yamada (21) found a $d^{-1/2}$ dependence for the mass transfer coefficient at such a disk

$$Sh_d = 0.752Re_d^{0.5}Sc^{0.333} \quad [14]$$

where $Re_d = v_\infty d/\nu$ and v_∞ is the main stream velocity. In this case the main stream velocity v_∞ toward the disk is related to the initial velocity and thickness of the buoyant plume at the edge of the disk.

It is reasonable to assume that the velocity of this plume depends primarily on its buoyancy and on the diffusivity of the reactant species. In the simplest case one would expect from dimensional considerations

Table III. Experimental data for mass transfer to the horizontal face only

Diameter (cm)	CuSO ₄ (M)	CH ₂ SO ₄ (M)	i_{lim} (mA/cm ²)	Sh	Gr	Sc
0.635	0.050	1.598	3.59	48.27	9,545	2,402
0.635	0.099	1.550	7.53	49.22	18,252	2,340
0.635	0.232	1.560	20.99	54.93	37,735	2,316
1.270	0.0492	1.572	2.29	62.80	73,438	2,384
1.270	0.099	1.550	5.13	67.74	149,528	2,340
1.270	0.232	1.560	14.93	78.78	309,122	2,316
1.905	0.0492	1.572	2.03	83.03	245,908	2,384
1.905	0.099	1.550	4.20	82.89	500,693	2,340
1.905	0.232	1.560	12.10	95.57	1,035,092	2,316
2.540	0.050	1.598	1.855	100.45	626,703	2,402
2.540	0.099	1.550	3.85	101.24	1,196,221	2,340
2.540	0.232	1.560	10.46	110.25	2,472,973	2,316
0.635	0.0663	1.740	4.72	46.87	13,017	2,285
1.270	0.0663	1.740	2.92	58.01	104,138	2,285
1.905	0.0663	1.740	3.03	90.18	351,464	2,285
2.540	0.0663	1.740	2.49	98.74	833,101	2,285
5.080	0.0663	1.740	1.712	136.00	6,664,805	2,285
0.635	0.09566*	1.592	3.79	51.91	4,504	9,084
1.270	0.09566*	1.592	2.51	68.81	36,034	9,084
1.905	0.09566*	1.592	2.26	93.05	121,616	9,084
2.540	0.09566*	1.592	1.973	108.18	288,274	9,084
5.080	0.09566*	1.592	1.327	145.48	2,306,194	9,084

* Also 2.97M glycerol.

$$v_\infty \sim (g\alpha\Delta C D)^{1/3} \quad [15]$$

This is similar to the mass transfer velocity associated with turbulent free convection, but larger by a factor of the order of $Sc^{1/3}$.

If Eq. [15] was valid, one would expect Sh_d to depend on $Sc^{1/6}$. Such a dependence does fit the experimental data fairly well

$$Sh_d = 2.715(Gr_d Sc)^{0.167} \quad [16]$$

with a slightly larger standard error than Eq. [14]. The experimental data do not allow a meaningful decision between Eq. [14] and [16]. It is possible that the dependence on Sc is not as simple as either of these expressions.

Vertical cylindrical face exposed.—Here, too, one would expect some deviation from the classical free-convection correlation Eq. [4] and this was indeed found to be the case.

Table IV presents experimental data for various exposed lengths at three different bulk concentrations of CuSO₄. In Fig. 9 the mass transfer coefficients are compared with Eq. [4]. Almost all the measured values exceed the predictions (indicated in Fig. 9 by lines since Sc does not vary significantly). The largest deviations are systematically found for small lengths L and small concentrations c .

This indicates that the deviation is caused by a leading-edge effect and increases with the thickness

Table IV. Experimental data for mass transfer to the vertical surface only (electrode diameter 1.270 cm)

Length (cm)	CuSO ₄ (M)	CH ₂ SO ₄ (M)	i_{lim} (mA/cm ²)	Sh ($\times 0.01$)	k ($\times 10^4$)
0.635	0.0547	1.952	5.18	0.63	4.78
	0.0500	1.598	4.340	0.59	4.50
	0.1023	1.657	9.38	0.67	4.75
	0.2455	1.526	30.12	0.71	6.36
1.27	0.2440	1.680	28.02	0.69	5.95
	0.0547	1.952	3.55	0.97	3.68
	0.0500	1.598	3.40	0.93	3.53
	0.1023	1.657	7.30	0.89	3.70
1.905	0.2455	1.526	22.38	1.05	4.72
	0.0547	1.952	3.80	1.38	3.49
	0.1023	1.657	7.00	1.28	3.55
	0.2455	1.526	20.80	1.46	4.39
2.54	0.0547	1.952	3.44	1.85	3.49
	0.0500	1.598	3.11	1.71	3.22
	0.1023	1.657	6.50	1.59	3.29
	0.2455	1.526	19.38	1.82	4.09
3.175	0.1023	1.657	6.45	1.97	3.27
	0.2455	1.526	18.20	2.13	3.84
3.81	0.0547	1.952	3.01	2.26	2.85
	0.0500	1.598	2.57	2.11	2.66
	0.1023	1.657	5.94	2.17	3.00
	0.2455	1.526	17.00	2.39	3.59

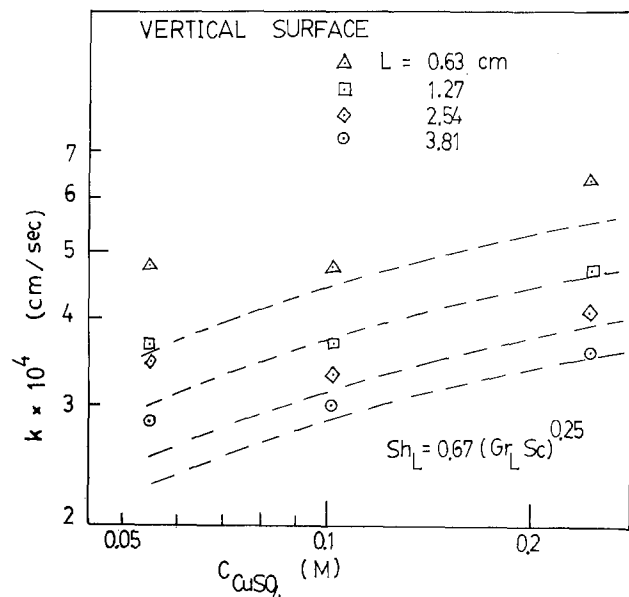


Fig. 9. Experimental and predicted mass transfer coefficients for the vertical electrode surface. Dashed lines: predicted values for (top to bottom) 0.63, 1.27, 2.54, and 3.81 cm electrode length.

of the free-convective boundary layer, which is inversely proportional with $c_b^{1/4}$.

In the classical boundary-layer model (Fig. 10a) inflow of fresh bulk solution takes place only perpendicular to the surface (y direction), not from below the leading edge (x direction). However, near the leading edge the boundary-layer equations break down and diffusion in the longitudinal (x) direction contributes significantly to the local mass transfer rate; see, e.g., Newman (22).

In many previous free-convection measurements (5, 6, 9) the geometry was that of Fig. 10b; longitudinal diffusion could not contribute to the flux, and inflow of solution necessarily was perpendicular to the electrode. Thus, the conditions for agreement with Eq. [4] were optimal. However, the present geometry (Fig. 10c) allows diffusion over a 270° angle to contribute to the leading-edge flux. From the results of Fig. 9 one can infer also that inflow from below the leading edge takes place, since the leading-edge effect is dependent on c_b and, therefore, on the thickness of the developing diffusion layer.

Combined exposure.—Table V presents the results for mass transfer to the entire surface and Fig. 11

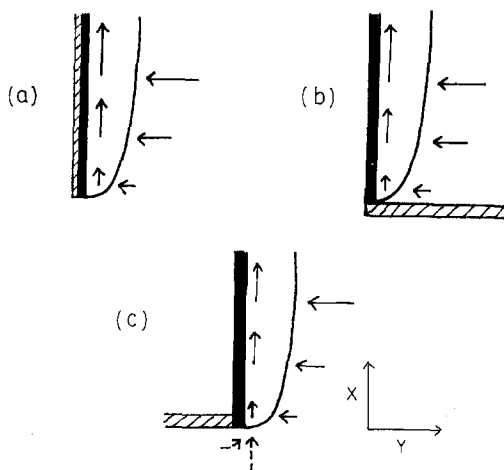


Fig. 10. Leading-edge configurations in free convection at a vertical electrode: (a) idealized boundary layer; (b) electrode extending to the bottom of the cell; (c) immersed electrode. Shaded surfaces are insulators.

Table V. Limiting currents measured at vertical surface, horizontal surface, and combined surfaces (electrode diameter 1.270 cm)

Length (cm)	C_{CuSO_4} (M)	$C_{H_2SO_4}$ (M)	I_v (mA)	I_H (mA)	$I_{comb.}$ (mA)
0.635	0.0547	1.952	13.0	2.87	14.7
	0.1023	1.657	23.5	8.25	26.0
	0.2455	1.526	75.5	24.5	82.2
	0.0547	1.952	18.0	2.87	20.4
1.270	0.1023	1.657	37.0	8.25	36.9
	0.2455	1.526	113.4	24.5	123.0
	0.0547	1.952	28.8	2.87	28.3
	0.1023	1.657	53.1	8.25	53.1
1.900	0.2455	1.526	157.6	24.5	169.9
	0.0547	1.952	34.8	2.87	36.4
	0.2455	1.526	196.4	24.5	211.9
	0.1023	1.657	81.6	8.25	87.9
2.54	0.2455	1.526	230.2	24.5	245.0
	0.0547	1.952	45.7	2.87	49.0
	0.1023	1.657	90.0	8.25	94.5
	0.2455	1.526	257.7	24.5	286.0

compares these with the summed rates for the separate surfaces. In all cases the total mass transfer rate is less than one would expect if the rates were additive. The difference is especially marked for small electrode lengths. For the larger concentrations the difference appears to approach a constant value as L increases.

From the results discussed earlier in this section it is evident that the nonadditivity is caused by the streaming of depleted solution around the edge of the horizontal end face into the leading edge of the vertical mass transfer boundary layer. The latter thus suffers an initial depletion, which decreases the overall mass transfer rate by an amount largely independent of the active electrode length.

Conclusions

Mass transfer rates and limiting currents by free convection at a truncated vertical rod electrode are significantly different from those predicted by the well-known correlation for mass transfer at a vertical electrode.

This is due to the development of an unusual but well-characterized limiting current on the horizontal, disk-shaped face of the electrode. It is caused by a buoyancy-driven stagnation flow and its mass transfer rate satisfies the correlation

$$Sh_d = 2.075 Gr_d^{0.167} Sc^{0.2} \quad [13]$$

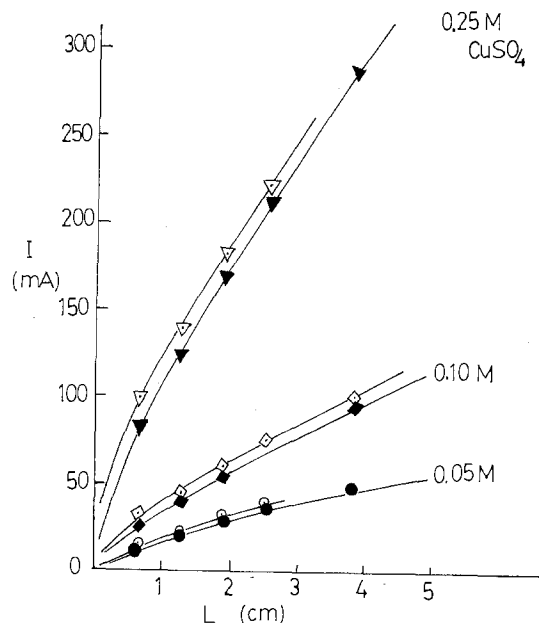


Fig. 11. Total and additive currents for immersed rod electrodes. Open symbols: sum of currents to horizontal and vertical faces; filled symbols: current to both in combined exposure. Electrode diameter = 1.27 cm.

In addition there is a significant leading-edge effect, exceeding 5% for short vertical electrode lengths (<1 cm) and for dilute solutions (<0.1M CuSO₄). Mass transfer to the vertical surface alone is increased by diffusion and by inflow of bulk solution at the leading edge. Both act to increase the limiting current.

If the entire electrode surface is accessible, this positive leading-edge effect is overwhelmed by a negative effect: the inflow of depleted solution from the horizontal surface (disk), which causes an overall decrease of the mass transfer rate. The mass transfer rates to the vertical surface and the horizontal electrode, therefore, are not additive.

Free-convection limiting currents at a rod electrode, e.g., in a molten salt, may be estimated with 10-15% accuracy by means of established correlations if positive and negative leading-edge correlations are accounted for.

Acknowledgment

This work was in part supported by Argonne National Laboratory under Contract No. 31-109-38-3975. Analyses were made in part using equipment provided under National Science Foundation Grant ENG77-17840. The authors are grateful to Mr. Dusan Bozinovich for carrying out part of the measurements and analyses.

Manuscript submitted Aug. 6, 1979; revised manuscript received Nov. 11, 1979.

Any discussion of this paper will appear in a Discussion Section to be published in the December 1980 JOURNAL. All discussions for the December 1980 Discussion Section should be submitted by Aug. 1, 1980.

Publication costs of this article were assisted by the Illinois Institute of Technology.

LIST OF SYMBOLS

<i>a</i>	dimensionless potential scan rate, Eq. [11]
<i>c</i>	concentration, g-mole/cm ³ or M
<i>C</i>	coefficient in Eq. [8] and [9]
<i>d</i>	diameter of disk or sphere, cm
<i>D</i>	diffusivity, cm ² /sec
<i>F</i>	Faraday, 96,501 C/equiv.
<i>g</i>	acceleration of gravity, cm/sec ²
<i>h</i>	height of cell, cm
<i>i</i>	current density, A/cm ²
<i>I</i>	current, A
<i>k</i>	mass transfer coefficient, cm/sec
<i>L</i>	vertical length of electrode, cm
<i>n</i>	number of electrons transferred
<i>r</i>	radius of cylindrical electrode, cm
<i>R</i>	gas constant, 8.314 CV/g-mole-°K
<i>t</i>	time, sec
<i>T</i>	temperature, °K
<i>v</i>	velocity, cm/sec
<i>V</i>	applied electrode potential vs. reference electrode, V
<i>x</i>	longitudinal (vertical) distance, cm
<i>y</i>	perpendicular (horizontal) distance, cm
<i>α</i>	densification coefficient, °K ⁻¹
<i>γ</i>	curvature parameter, Eq. [6]
<i>Δ</i>	difference bulk/electrode

<i>e</i>	correction factor for advection, Eq. [9]
<i>μ</i>	dynamic viscosity, g/cm-sec
<i>ν</i>	kinematic viscosity, cm ² /sec
<i>ρ</i>	density, g/cm ³

Subscripts

<i>b</i>	bulk electrolyte
<i>i</i>	species <i>i</i>
<i>in</i>	initial
<i>lim</i>	limiting current condition
<i>∞</i>	main stream

Dimensionless numbers

<i>Gr</i>	Grashof number, Eq. [3]
<i>Ra</i>	Rayleigh number, <i>Gr</i> × <i>Sc</i>
<i>Re</i>	Reynolds number, Eq. [14]
<i>Sc</i>	Schmidt number, <i>v/D</i>
<i>Sh</i>	Sherwood number, Eq. [1]

REFERENCES

- J. R. Selman and C. W. Tobias, *Adv. Chem. Eng.*, **10**, 211 (1978).
- J. R. Selman and J. C. McClure, To be published in *J. Electroanal. Chem. Interfacial Electrochem.*
- H. Schlichting, "Boundary-Layer Theory," 6th ed., Chap. XIV, New York (1968).
- C. Wagner, *Trans. Electrochem. Soc.*, **95**, 161 (1949).
- C. R. Wilke, M. Eisenberg, and C. W. Tobias, *This Journal*, **100**, 513 (1953).
- C. R. Wilke, C. W. Tobias, and M. Eisenberg, *Chem. Eng. Progr.*, **49**, 662 (1953).
- J. R. Selman and J. Newman, *This Journal*, **118**, 1070 (1971).
- L. Hsueh and J. Newman, *Ind. Eng. Chem. Fundam.*, **10**, 615 (1971).
- E. Ravoo, J. W. Rotte, and F. W. Sevenstern, *Chem. Eng. Sci.*, **25**, 1637 (1970).
- G. Schütz, *Int. J. Heat Mass Transfer*, **6**, 873 (1963).
- H. Jeffreys, *Proc. R. Soc. London, Ser. A*, **118**, 195 (1928).
- E. Ravoo, Dissertation Techn. Univ. Twente, Enschede, Netherlands, p. 101 (1971).
- E. J. Fenech, Ph.D. Thesis, Univ. of California, Berkeley, 1960 (UCRL-9079).
- I. M. Kolthoff, E. B. Sandell, E. J. Mehan, and S. Bruckenstein, "Quantitative Chemical Analysis," 4th ed., Toronto (1969).
- S. K. Arapkoske and J. R. Selman, UCRL-20510 (1971).
- J. R. Selman, Ph.D. Thesis, Univ. of California, Berkeley, 1971 (UCRL-20557).
- R. S. Nicholson and I. Shain, *Anal. Chem.*, **36**, 706 (1964).
- E. Mattson and J. O'M. Bockris, *Trans. Faraday Soc.*, **55**, 586 (1959); also: J. Newman, "Electrochemical Systems," p. 177, Prentice Hall, Englewood Cliffs, N.J. (1973).
- J. R. Selman and C. W. Tobias, *J. Electroanal. Chem. Interfacial Electrochem.*, **65**, 67 (1975).
- A. A. Wragg and M. A. Patrick, *Electrochim. Acta*, **19**, 929 (1974).
- H. Matsuda and J. Yamada, *J. Electroanal. Chem. Interfacial Electrochem.*, **30**, 261 (1971).
- J. Newman, in "Electroanalytical Chemistry," Vol. 6, A. J. Bard, Editor, p. 187, Marcel Dekker, Inc., New York (1973).

Semiconductor Electrodes

XXVIII. Rotating Ring-Disk Electrode Studies of Photo-oxidation of Acetate and Iodide at n-TiO₂

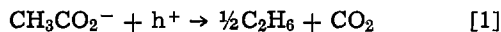
Katsuhiko Hirano and Allen J. Bard*

Department of Chemistry, The University of Texas at Austin, Austin, Texas 78712

ABSTRACT

The photo-Kolbe reaction (electro-oxidation of acetate) on TiO₂ in aqueous solution has been studied by means of a rotating ring-disk electrode (RRDE) with a TiO₂ disk and Pt ring. The oxidation of acetate competes very efficiently with water for photogenerated holes on the illuminated n-TiO₂ disk as shown by a decrease in the collection efficiency for oxygen reduction. No oxidation product of acetate was detected on the ring. Competitive oxidation of iodide with acetate and water was also investigated. Equations for determining relative rate constants for competitive reactions are derived and the applicability of the RRDE in studying such systems discussed.

Since the initial studies of the photo-oxidation of water at n-type TiO₂ (rutile) electrodes by Fujishima and Honda (1), investigations of this and many other reactions on this material have been reported. For example, the oxidation of many other substances (e.g., iodide, bromide, and cyanide ions) can be carried out at n-TiO₂ in competition with water oxidation (2, 3). Of particular recent interest has been the photo-Kolbe reaction in which a carboxylic acid is photo-oxidized (4, 5). For example, previous studies from this laboratory have established that in aqueous solutions containing acetate (Ac⁻)/acetic acid (HAc) mixtures irradiation of an n-TiO₂ electrode leads almost exclusively to the oxidation of acetate



(where h^+ represents a hole photogenerated at the TiO₂ surface). Photocatalytic decomposition of acetate (predominantly to methane and CO₂) has also been carried out by irradiation of suspensions of platinized TiO₂ (6, 7). While total product yields and current-potential (i - E) curves have yielded information about the overall course of the reaction (5) and electron spin resonance spin trapping experiments have established the intermediacy of methyl radicals in the reaction (8), studies of the relative rates of acetate vs. water oxidation have not been reported.

We describe here an investigation of acetate oxidation at a TiO₂-disk Pt-ring rotating ring-disk electrode (RRDE). In this research, products generated by photo-oxidation at the n-TiO₂ disk are swept to the Pt ring where they are detected. Relative values of the disk current (i_D) and the ring current (i_R) are then employed to obtain information on reaction rates. Previous photoelectrochemical studies employing the RRDE have proven very useful in elucidating reaction paths, relative reaction rates, and semiconductor stability (2, 9-13). In work closely related to that reported here, a TiO₂ disk RRDE was employed to study photo-oxidation of halide ions and reducing agents (2, 9).

Experimental

Chemicals.—Sodium sulfate, sodium acetate, glacial acetic acid (Fisher Scientific Company), and sodium iodide (Mallinckrodt Chemical Works) were of reagent grade. Triply distilled water was used as a solvent.

Apparatus and procedure.—A Tascussel Electronique Bipotentiostat, Model Bipad 2, was used for all experiments. A Wavetek function generator provided a

d-c potential ramp for voltammetric experiments recorded on a Mosley Model 7005A X-Y recorder.

The construction of the RRDE generally followed that described by Fujishima *et al.* (9). The TiO₂ disk electrode was a single crystal, which was prepared by cutting a 1 mm thick slice, 5.5 mm in diameter, from a large single crystal (Fuji Titanium, Japan). This piece was reduced at 750°C under hydrogen for 30 min. The TiO₂ disk and Pt ring electrodes were mounted in a Teflon rod. On the back side of the TiO₂ disk an ohmic contact was made with Ga-In alloy to which a Cu-wire was attached with conducting silver epoxy. The Cu-wire was connected to a brass shaft. The platinum ring electrode had an inner radius (r_2) of 3 mm and an outer radius (r_3) of 6.25 mm. The collection efficiency for this electrode, N_o , defined as $-i_R/i_D$ for a stable system, was calculated to be 0.648 from the geometry (14). The measured value of N_o , determined by reduction of ferricyanide at the TiO₂ in the dark and oxidation of the resulting ferrocyanide at the Pt ring, was 0.65. The electrode was rotated with a Motomatic Model E-550 motor and controller (Electrocraft Corporation, Hopkins, Minnesota). Electrical contact to the shaft was made using two sets of silver graphite brush and leaf assemblies.

A saturated calomel electrode (SCE) was used as a reference and platinum foil served as the counter-electrode. The electrochemical cell had a 4 cm diameter and was 4.5 cm high; a glass basket inside prevented vortex formation at high rotation rates (15). The TiO₂ disk was irradiated through the cell bottom by the focused beam of a 400W xenon lamp. In all experiments, the solution was purged with nitrogen gas for more than 30 min before measurements.

Results

Acetate-free solutions.—The irradiation of the TiO₂ disk electrode immersed in 0.2M Na₂SO₄ solutions produces an anodic disk current and a flux of O₂ and some H₂O₂ to the ring electrode (Fig. 1, curve A) (1, 2, 16). The products are reduced at the ring electrode (Fig. 2, curve A). The ring current, attributed to oxygen (and H₂O₂) reduction, was very dependent upon solution purity. It is well known, see, e.g., Ref. (17), that oxygen reduction at a platinum electrode depends critically on the nature of the electrode surface and the presence of adsorbed impurities. To obtain reproducible ring currents for oxygen reduction, the ring electrode was cycled repeatedly between potentials for hydrogen and oxygen evolution just before the measurement of i_R (17, 18). With this procedure the value of i_R at -0.2V vs. SCE divided by the disk photocurrent resulted in a collection efficiency of 0.63

* Electrochemical Society Active Member.

Key words: photoanode, photoelectricity, voltammetry, kinetics.

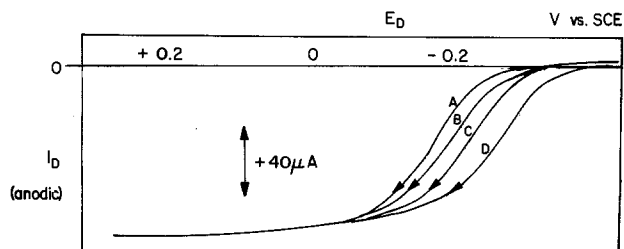


Fig. 1. Current-potential curves for an illuminated $n\text{-TiO}_2$ disk electrode in $0.2\text{M Na}_2\text{SO}_4$. (Curve A) no acetate; (curve B) 1 mM acetate; (curve C) 10 mM acetate; (curve D) 0.14M acetate; (curve E) in the dark. Rotation rate = 700 rpm ; potential scan rate, 22 mV/sec ; $[\text{NaAc}]/[\text{HAc}] = 1$.

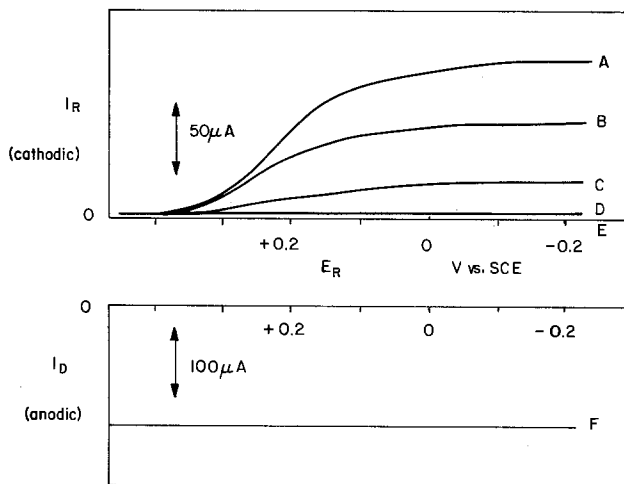


Fig. 2. Current-potential curves for Pt-ring electrode with illuminated $n\text{-TiO}_2$ disk electrode in $0.2\text{M Na}_2\text{SO}_4$. (Curve A) no acetate; (curve B) 0.03M acetate; (curve C) 0.14M acetate; (curve D) in the dark; (curve E) disk current in the dark (along X-axis); (curve F) disk current under illumination. $E_D = 1.0\text{V vs. SCE}$. Rotation rate, 700 rpm ; potential scan rate, 22 mV/sec . $[\text{NaAc}]/[\text{HAc}] = 1$.

which is quite close to the theoretical and experimental N_o -value (0.65).

Acetate-containing solutions.—The effect of addition of equimolar mixtures of sodium acetate and acetic

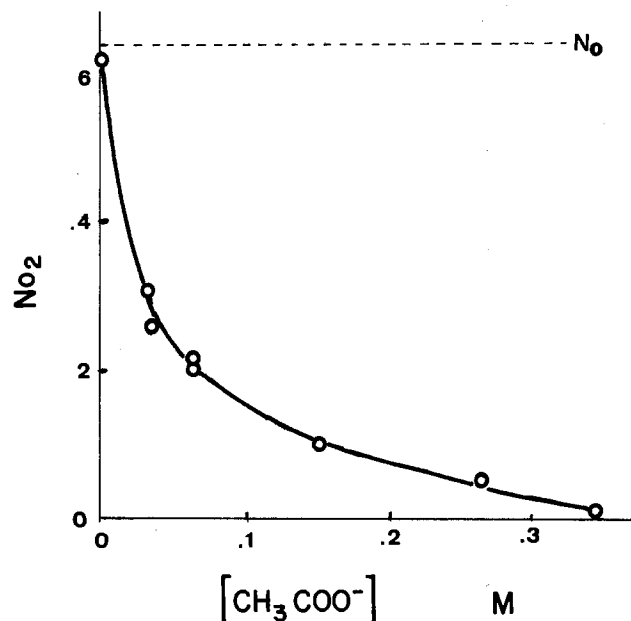


Fig. 3. Dependence of the collection efficiency for oxygen on the concentration of acetate. Rotation rate, 700 rpm ; $E_D = 1.0\text{V vs. SCE}$; $E_R = -0.2\text{V vs. SCE}$. $[\text{NaAc}]/[\text{HAc}] = 1$.

acid to the $0.2\text{M Na}_2\text{SO}_4$ solution ($\text{pH} = 4.7$) on the disk photocurrent at TiO_2 and the Pt ring current is shown in Fig. 1 and 2. The potential for the onset of the anodic photocurrent at TiO_2 shifts towards more negative values with the addition of acetate (Fig. 1, curves B-D), as found in a previous study (5). The limiting anodic disk current was unchanged by addition of acetate or rotation rate, demonstrating that this current was governed by the rate of generation of holes by light absorption and their flux to the electrode surface. The ring current was reduced by the addition of acetate (Fig. 2, curves B-C). The shape of the i_R - E_R curves was unchanged however by the addition of acetate and no new waves appeared. This demonstrates that the effect of acetate is to compete with water oxidation. Addition of acetate to an oxygen-saturated solution does not affect the limiting current for oxygen reduction at a platinum electrode, so that this decrease cannot be ascribed to this source. No product from the oxidation of acetate at the disk can be detected at the ring. This is in line with expectations, since the acetoxy radical produced by the initial oxidation step decomposes very rapidly to $\text{CH}_3\cdot$ and CO_2 . The methyl radicals rapidly react to form ethane and neither this species nor CO_2 is reducible at these potentials. Thus the ring current in acetate-containing solutions can only be ascribed to the reduction of products from the oxidation of water that competes with acetate for the photogenerated holes at the TiO_2 disk surface. We might note that the reduction of oxygen occurs on an $n\text{-TiO}_2$ electrode at potentials positive to the flatband potential (5, 18-20). In all of our studies of the collection efficiency, however, the disk potential was fixed at 1.0V vs. SCE , which is so positive that no oxygen reduction can occur.

The dependency of the oxygen collection efficiency, N_{O_2} [defined as $-i_R(E_R = -0.2\text{V})/i_D(E_D = 1.0\text{V})$ under illumination] upon total acetate concentration is shown in Fig. 3. No effect of electrode rotation rate was found with the concentrations of acetate shown in this figure. At very low concentrations of acetate (less than 1 mM) some effect of electrode angular velocity, ω , was observed however. As shown in Fig. 4, with 0.25 mM acetate the decrease in N_{O_2} was greater at larger ω , showing that at these concentra-

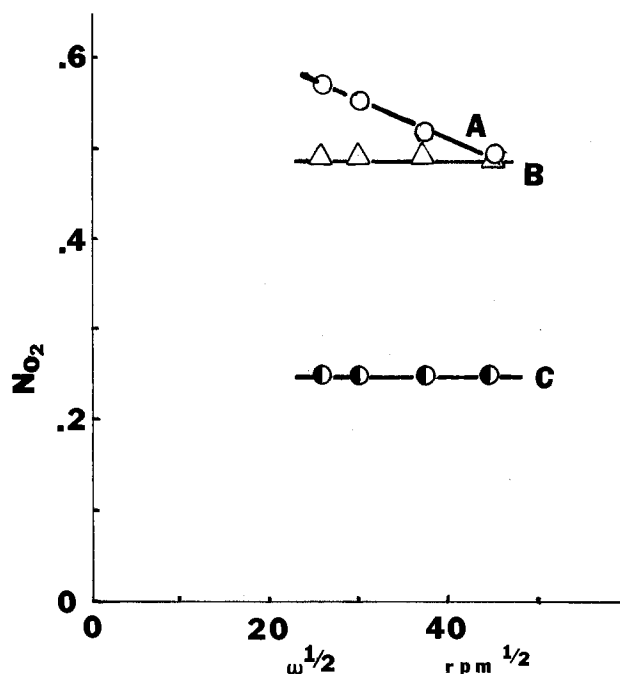


Fig. 4. Effect of rotation rate on the collection efficiency for oxygen in acetate solutions. (Curve A) 0.25 mM acetate; (curve B) 1 mM acetate; (curve C) 0.06M acetate. $E_D = 1.0\text{V vs. SCE}$; $E_R = -0.2\text{V vs. SCE}$.

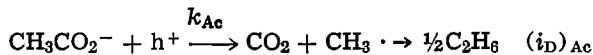
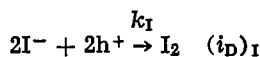
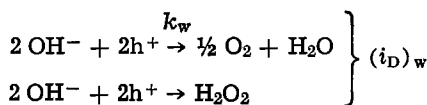
tions the rate of mass transfer of acetate to the disk governs its rate of oxidation.

Iodide solutions.—In the presence of I^- , oxidation of this species competes with water oxidation at the irradiated TiO_2 disk (2, 3). Because concentrations of I^- as low as $10^{-7}M$ suppress the oxygen reduction reaction on platinum, the addition of only small amounts of I^- decrease N_{O_2} to negligible values. To determine the competition between the water and I^- oxidation processes in this case, the ring current due to iodine reduction was determined (Fig. 5) and from this the iodine collection efficiency, N_{I_2} [defined as $-i_R'(E_R = -0.2V)/i_D(E_D = 1.0V)$ in the presence of I^-], was calculated. The variation of N_{I_2} , for solutions in the absence and presence of acetate, as a function of the concentration of sodium iodide is shown in Fig. 6. No effect of ω on N_{I_2} was observed for these concentrations of iodide ion.

Discussion

The reactions which give rise to the different disk and ring currents can be summarized as follows

Disk:



Under conditions where mass transfer rates to the disk surface are unimportant, we assume that the rate of consumption of a given species at the electrode surface is a first-order process (just as most electrochemical reactions) with relative rate constants of k_w , k_I , and k_{Ac} for water, iodide, and acetate, respectively. Under these conditions the total disk current, i_D , can be represented as

$$i_D = (i_D)_w + (i_D)_I + (i_D)_{Ac} \quad [6]$$

$$i_D = k_w[OH^-] + k_I[I^-] + k_{Ac}[Ac^-] \quad [7]$$

For solutions of acetate (in the absence of iodide) the ring current for oxygen reduction is

$$-i_R = N_o(i_D)_w = N_o k_w [OH^-] \quad [8]$$

and the collection efficiency is

$$N_{O_2} = \frac{-i_R}{i_D} = \frac{N_o k_w [OH^-]}{k_w [OH^-] + k_{Ac} [Ac^-]} \quad [9]$$

This equation can be rearranged to the form

$$(N_o/N_{O_2}) - 1 = (k_{Ac}/k_w [OH^-])[Ac^-] \quad [10]$$

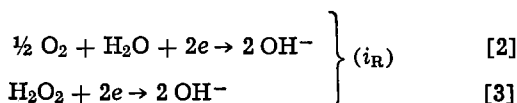
A plot of $N_o/N_{O_2} - 1$ vs. $[Ac^-]$ should be linear with zero intercept and slope $k_{Ac}/k_w [OH^-]$. Such a plot is shown in Fig. 7. From the slope of the line and the solution pH (4.7) a value of $k_{Ac}/k_w = 2.0 \times 10^{-8}$ is obtained.

A similar treatment for iodide solutions (in the absence of acetate) yields

$$N_{I_2}/N_o = k_I[I^-]/(k_w[OH^-] + k_I[I^-]) \quad [11]$$

so that the slope of a plot of $(N_o/N_{I_2}) - 1$ vs. the reciprocal of the iodide concentration should yield k_w/k_I . Such a plot at pH = 5.8 (shown in Fig. 8, curve

Ring:



A) yields $k_w/k_I = 8.8 \times 10^5$. The current efficiency for iodide oxidation at illuminated TiO_2 has previously been studied and for a 0.01M iodide solution has been estimated as 60% (3) and 70% (2). From the value of k_w/k_I found here, a current efficiency of 65% is predicted, which is in good agreement with the previous values.

For solutions containing both iodide and acetate, the following equation holds

$$\frac{N_{I_2}}{N_o} = \frac{k_I[I^-]}{k_w[OH^-] + k_I[I^-] + k_{Ac}[Ac^-]} \quad [12]$$

In this case a plot of $(N_o/N_{I_2}) - 1$ vs. $[I^-]^{-1}$ at a constant acetate concentration has a zero intercept and a slope of $(k_w/k_I)[OH^-] + (k_{Ac}/k_I)[Ac^-]$. Such a plot is shown in Fig. 8, curve B, for a 0.5M total acetate solution at pH = 4.7. The experimental slope combined with the value of k_w/k_I determined above yields $k_{Ac}/k_w = 4.5 \times 10^{-8}$ which is in reasonable agreement

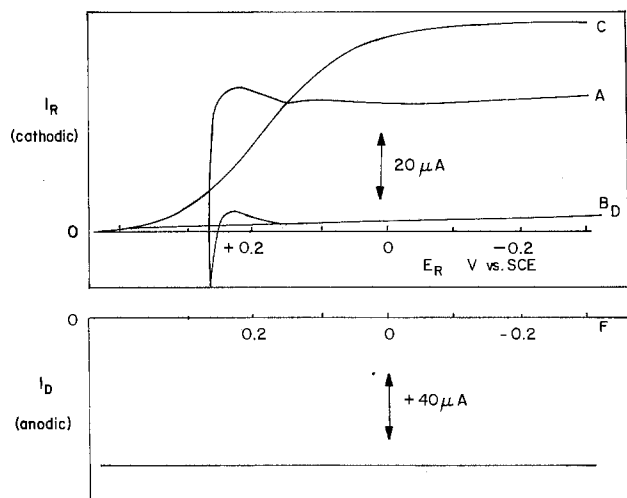


Fig. 5. Current-potential curves for Pt-ring electrode with illuminated $n-TiO_2$ disk electrode. (Curve A) 0.01M NaI under illumination; (curve B) 0.01M NaI in the dark; (curve C) no NaI under illumination; (curve D) no NaI in the dark; (curve E) 0.01M NaI disk current under illumination; (curve F) 0.01M NaI disk current in the dark. $E_D = 1.0V$ vs. SCE; rotation rate, 700 rpm; potential scan rate, 22 mV/sec.

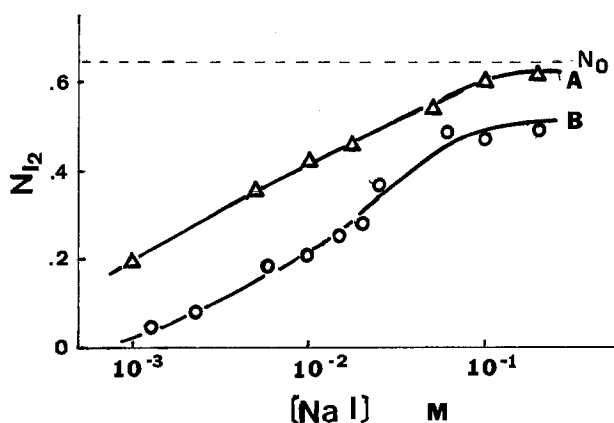


Fig. 6. Dependence of collection efficiency for iodine on the concentration of sodium iodide. (Curve A) no acetate; (curve B) 0.5M acetate; $E_D = 1.0V$ vs. SCE; $E_R = -0.2V$ vs. SCE; rotation rate, 700 rpm.

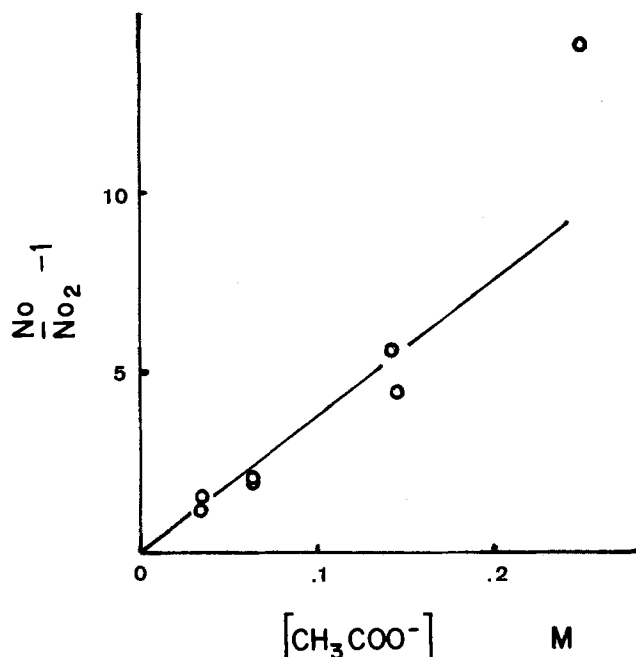


Fig. 7. Reciprocal plot on NO_2 and acetate concentration with the value found from Fig. 7. The relatively good agreement of the experimental results with the theo-

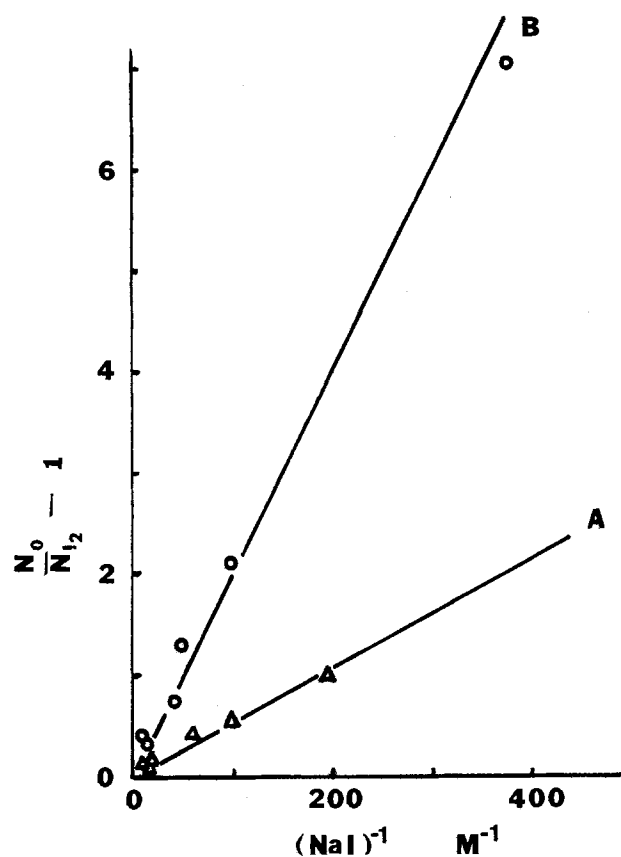


Fig. 8. Reciprocal plot of NI_2 and iodide concentration. (Curve A) no acetate; (curve B) 0.5M acetate.

retical equations suggests that there is no direct interaction of the oxidation processes, i.e., that k_w , k_{Ac} , and k_f are independent of the concentrations of acetate and iodide in the solution.

The results above demonstrate the utility of the RRDE technique in determining competitive reaction rates at an illuminated semiconductor, even when, as in the case of acetate above, the product generated is not electroactive at the ring electrode. The method is clearly easier for surveying possible reactions at semiconductors than long-term bulk electrolysis methods, and should also prove useful in the design of heterogeneous photocatalysts (6, 7).

Acknowledgment

The rotating ring-disk electrode was constructed by Dr. G. H. Brilmyer whose assistance is greatly appreciated. We are indebted to Drs. Rolf Hulnhagen, Fu-Ren F. Fan, and Ikuichiro Izumi for their helpful suggestions during the course of this research. The support of this research by the National Science Foundation is gratefully acknowledged.

Manuscript submitted Sept. 17, 1979; revised manuscript received Dec. 10, 1979.

Any discussion of this paper will appear in a Discussion Section to be published in the December 1980 JOURNAL. All discussions for the December 1980 Discussion Section should be submitted by Aug. 1, 1980.

Publication costs of this article were assisted by The University of Texas at Austin.

REFERENCES

1. A. Fujishima and K. Honda, *Nature*, **238**, 37 (1972).
2. T. Inoue, T. Watanabe, A. Fujishima, and K. Honda, *Chem. Lett.*, 1073 (1977).
3. S. N. Frank and A. J. Bard, *J. Am. Chem. Soc.*, **99**, 4667 (1977).
4. B. Kraeutler and A. J. Bard, *ibid.*, **99**, 7729 (1977).
5. B. Kraeutler and A. J. Bard, *Nouv. J. Chim.*, **3**, 31 (1979).
6. B. Kraeutler and A. J. Bard, *J. Am. Chem. Soc.*, **100**, 2239 (1978).
7. B. Kraeutler and A. J. Bard, *ibid.*, **100**, 5985 (1978).
8. B. Kraeutler, C. Jaeger, and A. J. Bard, *ibid.*, **100**, 4903 (1978).
9. A. Fujishima and K. Honda, *Seisan Kenkyu*, **22**, 478 (1970).
10. T. Inoue, T. Watanabe, A. Fujishima, K. Honda, and K. Kohayakawa, *This Journal*, **124**, 719 (1977).
11. T. Kobayashi, H. Yoneyama, and H. Tamura, *Chem. Lett.*, 457 (1979).
12. B. Miller, S. Menezes, and A. Heller, *J. Electroanal. Chem. Interfacial Electrochem.*, **94**, 85 (1978).
13. R. Memming, *Ber. Bunsenges. Phys. Chem.*, **81**, 732 (1977).
14. W. J. Albery and S. Bruckenstein, *Trans. Faraday Soc.*, **62**, 1920 (1966).
15. J. T. Maloy, K. B. Prater, and A. J. Bard, *J. Am. Chem. Soc.*, **93**, 5959 (1971).
16. M. S. Wrighton, D. S. Ginley, P. T. Wolczanski, A. B. Ellis, D. L. Morse, and A. Linz, *Proc. Natl. Acad. Sci. U.S.A.*, **72**, 1518 (1975).
17. A. Damjanovic, M. A. Genshow, and J. O'M. Bockris, *This Journal*, **114**, 466 (1967).
18. K. L. Hardee and A. J. Bard, *ibid.*, **122**, 739 (1975).
19. P. Clechet, C. Nartelet, J. R. Martin, and R. Olier, *Electrochim. Acta*, **24**, 457 (1979).
20. B. Parkinson, F. Decker, J. F. Juliao, and M. Abramovich, *ibid.*, In press.

Influence of Nickel Oxide Transformation Reaction on Oxygen Evolution Kinetics as Ascertained by Temperature Effects

C. R. Davidson^{*1} and S. Srinivasan^{*}

Brookhaven National Laboratory, Department of Energy and Environment, Upton, New York 11973

ABSTRACT

The O₂ evolution reaction and nickel oxide transformation reactions were investigated on Ni electrodes in 50 w/o KOH as a function of temperature using steady-state and cyclic voltammetric techniques, respectively. A change in the valence state of the oxide occurs in the region of oxygen evolution at temperatures above 150°C. The previously reported change in Tafel slope at elevated temperatures is explained on the basis of the role played by the transformation of surface oxides, and its effect on the kinetics of the OER.

The oxygen evolution reaction (OER) was investigated recently on nickel electrodes in 50 weight percent (w/o) KOH as a function of temperature (1). A change in the Tafel slope from 3 RT/2F at temperatures below 208°C to RT/4F at temperatures above this value was reported. The main purpose of the present work was to determine the influence of oxide transformation reactions on the change in Tafel slope and hence on the mechanism of the OER.

The existence of correlations between the activity of heterogeneous catalysts and their magnetic properties has been well documented (2-6). In addition, it has been speculated that magnetic properties influence electrocatalysis as well (7-10). The Neel temperature (antiferromagnetic to paramagnetic transition) of nickel oxide (NiO) is 247°C and the reported change in Tafel slope lends support to the concept of magnetic influences in electrocatalysis. However, as for oxygen evolution on anodized nickel, further experimental evidence now suggests an alternate explanation for the change in mechanism at elevated temperatures. For there to exist a magnetic transformation of the type mentioned on anodized Ni, the surface oxide formed would necessarily be dehydrated NiO with a cubic structure. This condition is considered to be highly unlikely (11). Cyclic voltammetric studies on Ni electrodes have been carried out by a number of workers (12, 13). Although there are some disagreements and ambiguities, it is generally believed that in alkaline solutions, nickel is first oxidized to the hydroxide, Ni(OH)₂, and subsequently to the oxyhydroxide, NiOOH; the exact stoichiometry varies around those given, and neither exhibits magnetic transformations.

In the present work, steady-state current-potential measurements were made for the oxygen evolution reaction on nickel from 50% KOH as a function of temperature. In addition, cyclic voltammograms were recorded with the aim of obtaining information on surface oxides in the oxygen evolution potential region.

Experimental

For this study, a stainless steel pressure vessel described in a previous paper (1) was utilized. A Teflon cell containing separate reference and auxiliary electrode compartments was introduced into this pressure vessel. A stainless steel clad Chromel-Alumel thermocouple, sheathed in platinum, was inserted into the electrolyte. The reference electrode was a pre-calibrated dynamic hydrogen electrode, connected to

a 1 mA/cm² power supply. A large cylindrical piece of Ni 200 (99.5% Ni, 0.15% Fe, 0.06% C, 0.05% Cu, 0.25% Mn, nominal) screen was used as the auxiliary electrode. The electrolyte was prepared from Baker analyzed KOH with doubly distilled water and pre-electrolyzed for 10-15 hr using Ni screen electrodes. The test electrode was a Ni 200 wire ($d = 0.35$ cm) of 0.2 cm² total area. The vessel and cell were heated with asbestos wrapped resistance wires; a magnetic stirrer was used to reduce thermal gradients in the cell.

Current density-potential relations were obtained using a steady-state potential step technique with a PAR 173 potentiostat. The electrodes were preanodized for a few minutes to ensure an equilibrium coverage of oxide on the surface. The measurements were made from high to low potentials while monitoring the current on a strip chart recorder during the establishment of steady-state conditions. Ohmic losses between the Luggin capillary tip and the test electrode were experimentally measured using the interrupter technique with an Adlake relay and Tektronix 7623A oscilloscope. Ohmic potentials were plotted vs. current density to confirm the expected linear relation. Cyclic voltammograms were obtained at the same temperatures as the steady-state measurements, using a PAR 175 voltage programmer in conjunction with the potentiostat. The results were recorded on an HP 7044A X-Y recorder. These experiments are described in greater detail in the following section. In addition, anodic polarization studies on the test electrode were carried out by scanning from the open-circuit potential to potentials well within the oxygen evolution region at a sweep rate of 1 mV/sec.

Results and Discussion

The temperature dependence of the potential, at which the mechanism of oxygen evolution changes, emphasizes the role of oxide films on the kinetics of this reaction. Each experiment at the various temperatures was repeated at least three times to confirm reproducibility. The cyclic voltammogram for Ni at 47°C, shown in Fig. 1, is in agreement with those of other investigators (12-14). The peak before O₂ evolution is believed to correspond to Ni²⁺/Ni³⁺ oxidation. However, there is evidence in the literature which suggests that this peak represents oxidation to the 4+ state. It is interesting to note that the overpotential for the oxygen evolution reaction at room temperature is high enough that the higher oxide formation peak remains well below the onset of evolution. Both the overpotential and oxide formation potential are temperature dependent. One would expect, however, the oxygen overpotential to have a

^{*} Electrochemical Society Active Member.

¹ Present address: General Electric Company, Direct Energy Conversion Programs, Wilmington, Massachusetts 01887.

Key words: anode, electrode, catalysis, oxygen evolution.

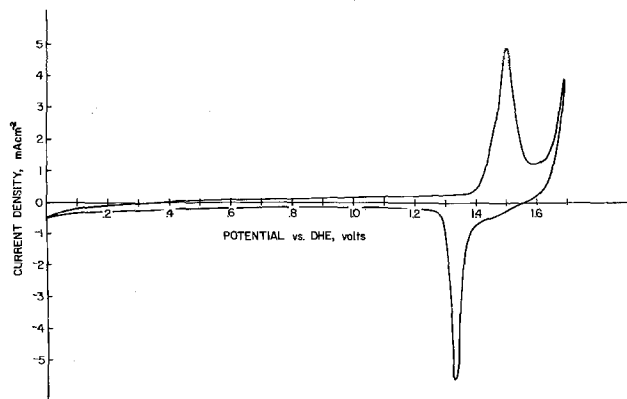


Fig. 1. Cyclic voltammogram for Ni in 50 w/o KOH at 47°C. Sweep rate 50 mV sec⁻¹.

more significant temperature dependency. This is, in fact, observed experimentally. Figure 2 shows a portion of the cyclic voltammogram obtained at 127°C. It is clear that the large oxygen evolution current obscures the higher oxide formation peak. At still higher temperatures, the higher oxide formation peak is totally masked by oxygen evolution, as exemplified in Fig. 3 for a temperature of 183°C. The corresponding reduction peak for this process is not affected by oxygen evolution and this finding can aid in determining the approximate higher oxide formation potential in this region. Cyclic voltammograms were carried out at 50 mV/sec, first sweeping in the anodic direction and then back to the initial potential. If the potential at which the sweep is reversed is not anodic enough for the higher oxide to form, there was no corresponding reduction peak on the cathodic sweep. Upon stepping up the potential of sweep reversal continuously more anodic, a cathodic reduction peak was eventually observed. Since this could only occur if the higher oxide is present, the potential at which this oxide forms can be approximately deter-

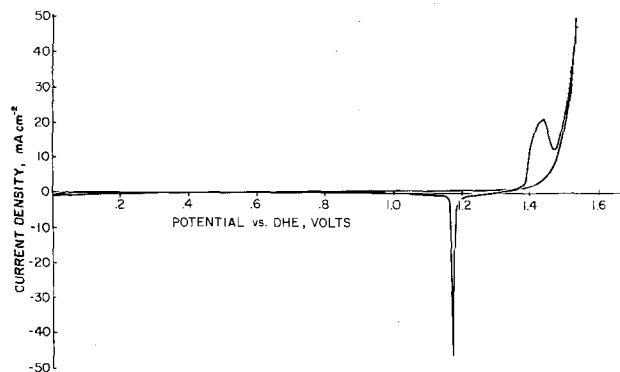


Fig. 2. Cyclic voltammogram for Ni in 50 w/o KOH at 127°C. Sweep rate 50 mV sec⁻¹.

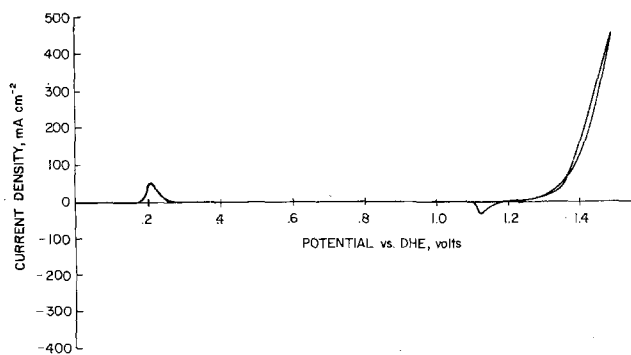


Fig. 3. Cyclic voltammogram for Ni in 50 w/o KOH at 183°C. Sweep rate 50 mV sec⁻¹.

mined, even though the oxidation peak is completely masked by the oxygen evolution current (Fig. 4). The potentials at which the higher oxide forms were determined in this manner and are shown as a function of temperature in Fig. 5.² The line in Fig. 5 represents the least squares fit of these points (coefficient of determination, $r = 0.9580$). The steady-state Tafel plots at selected temperatures are shown in Fig. 6. Below approximately 150°C, only one Tafel region is observed. The transfer coefficient at high overpotentials is again 0.67, while at low overpotentials the transfer coefficient increases with increasing temperature from approximately 1.5 at 150°C to 3.0-4.0 at 275°C. In addition, there is more scatter in the steady-state points in this low overpotential region, even to the extent that in some experiments a true Tafel region could not clearly be defined. It is extremely important to note the potentials at which the Tafel slopes change in the steady-state curves above 150°C.³ This break potential is plotted vs. temperature in Fig. 7. In the same figure, the line corresponding to the higher oxide formation potential is also shown. From this figure, one may conclude that the potential at which a break in the Tafel line occurs when making the measure-

² All potentials are with respect to the dynamic hydrogen electrode except those at room temperature, which have been corrected for the overpotential on the DHE. Above 150°C this correction is approximately constant at 30-40 mV (14).

³ This break potential is defined as being that potential at which the extrapolation of the two Tafel lines intersect.

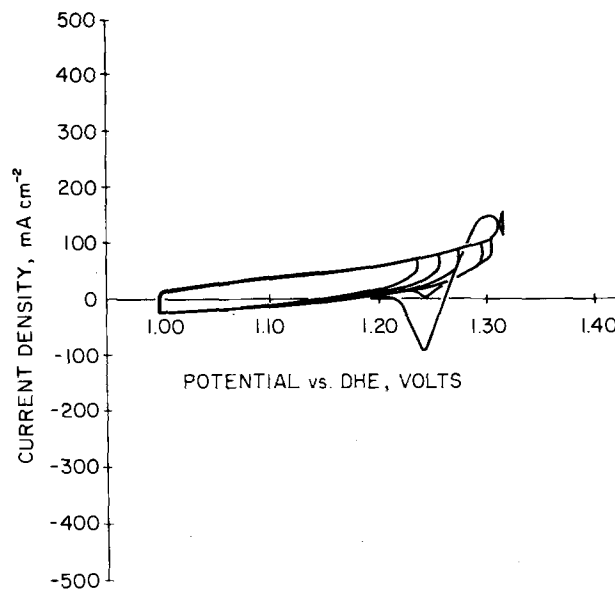


Fig. 4. Cyclic voltammogram for Ni in 50 w/o KOH at 224°C. Sweep rate 50 mV sec⁻¹.

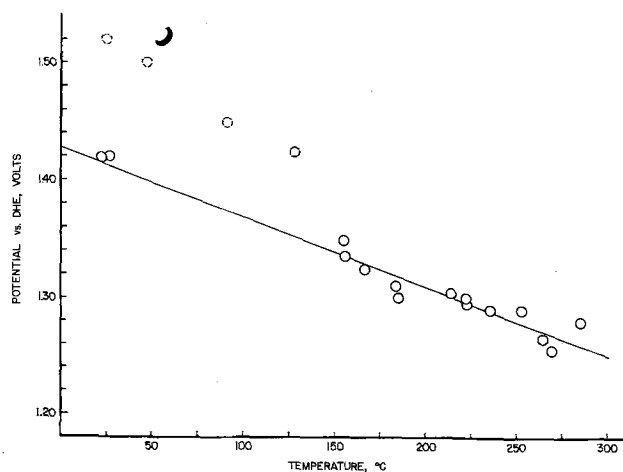


Fig. 5. Higher oxide formation potential of Ni vs. temperature

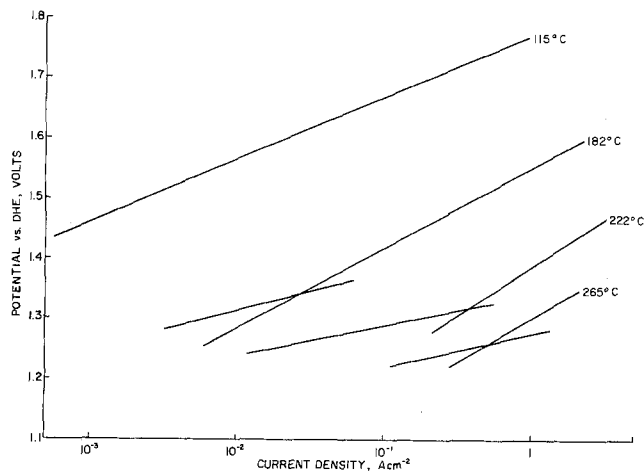


Fig. 6. Steady-state Tafel plots for oxygen evolution on Ni from 50 w/o KOH. Temperature range 115°-265°C.

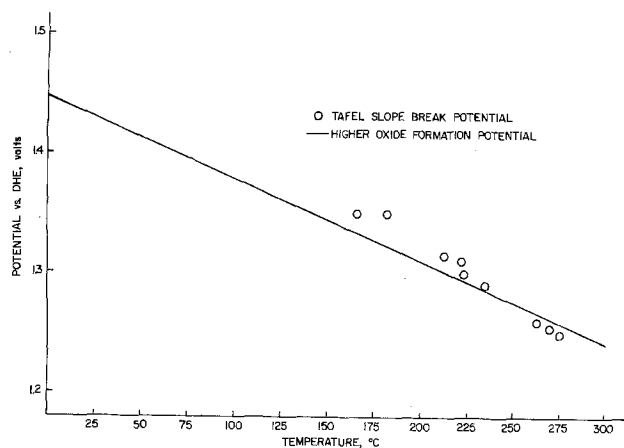


Fig. 7. Tafel slope break potential for oxygen evolution on Ni from 50 w/o KOH vs. temperature. Dependence of higher oxide formation potential on temperature.

ments from high to low current density in the steady-state measurements coincides with the potential of the higher oxide formation. To illustrate the importance of this potential, the dependence of current densities on potentials, using the slow sweep technique, were conducted at elevated temperatures to determine the potential required for "visible" oxygen evolution as seen in Fig. 8. These potentials were determined and are shown in Fig. 9. "Visible" oxygen evolution does not apparently occur until the higher oxide is present on the surface. This is direct evidence supporting the arguments made by Tseung (15) concerning the necessity of forming the appropriate oxide for good oxygen evolution electrocatalysts. Evidently the higher oxide is the catalytically active oxide for this reaction.⁴ At the lower temperature (i.e., below 150°C), the oxygen overpotential is high enough that oxygen evolution does not occur at significant rates until this higher oxide is formed. As the temperature increases, the overpotential for this reaction decreases significantly and a two-section Tafel plot is observed, corresponding to oxygen evolution on the partially reduced and higher oxides.

Because "visible" oxygen evolution takes place only on the higher oxide surface as seen from the slow potential scans (Fig. 5), one may suggest a correlation between the higher oxide formation potential and the break in the Tafel line. At high overpotentials, the higher oxide is present and the Tafel lines correspond to a transfer coefficient of 0.67 for the oxygen evolution reaction. Cathodic to the higher oxide formation

⁴ It should be stated that it is the highest oxide stable with respect to oxygen evolution (as seen from Pourbaix diagrams) which is required.

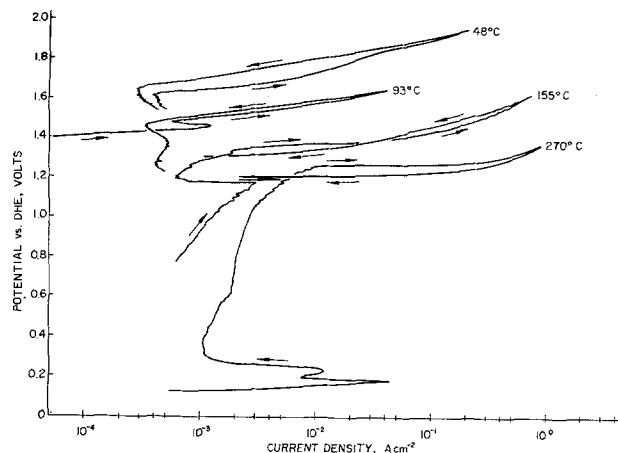


Fig. 8. Current potential relations on Ni in 50 w/o KOH using slow sweep method. Sweep rate 1 mV sec⁻¹.

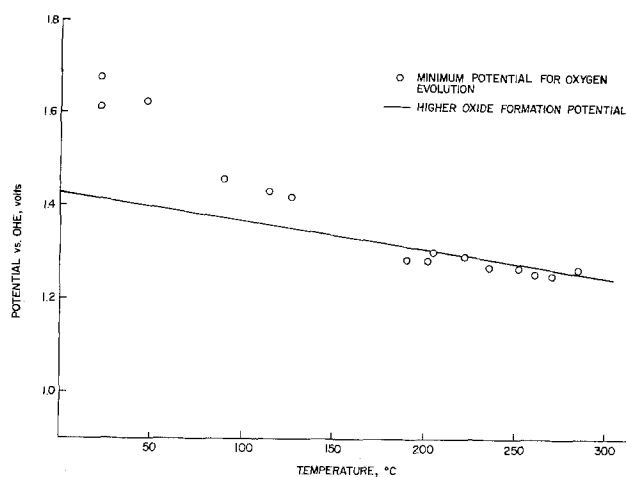


Fig. 9. Higher oxide formation potential, "visible" O₂ evolution potential, and O₂ equilibrium potential vs. temperature.

potential, there is a continuously growing ratio of lower to higher oxide on the surface.⁵ It is believed that this may interfere with the surface diffusion or desorption reactions. Transfer coefficients approaching 4.0 are calculated from the Tafel lines at higher temperatures.

Conclusions

The higher oxide formation potential for nickel has been determined as a function of temperature up to 275°C. It has been shown that at elevated temperatures (i.e., >150°C), the kinetics of the oxygen evolution reaction are fast enough that changes in reaction mechanism are observed at this potential. The consequences of reduction of the higher oxide manifests itself as a break in the Tafel slope indicating a recombination or desorption rate-determining step below this critical potential.

An interesting feature of the prerequisite of the higher oxide for the oxygen evolution reaction is a minimum in the overpotential for oxygen evolution vs. temperature curve (Fig. 10). Again, Fig. 9 shows the higher oxide formation line, the potential for "visible" oxygen evolution, and the equilibrium potential (16) for the oxygen reaction. The equilibrium potential has a larger temperature dependence than the higher oxide formation potential. Because oxygen is visibly evolved only at this higher potential, a minimum in the oxygen evolution overpotential vs.

⁵ One may argue that the higher is reduced at potentials more cathodic to the oxidation potential. The present case is not one of bulk reduction, but of a slow increase in the number of lower oxide atoms on the surface between the oxidation and reduction peaks.

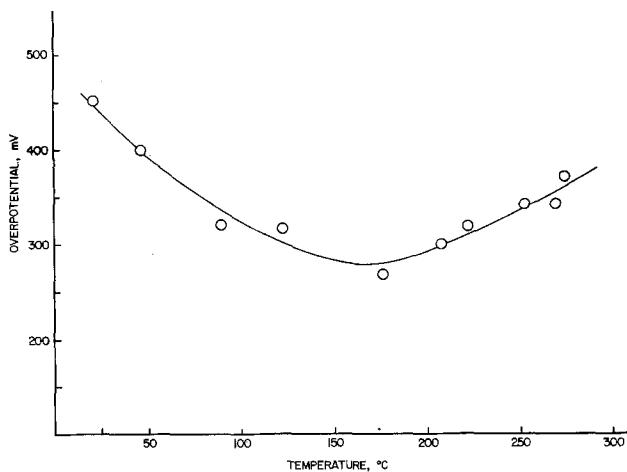


Fig. 10. "Visible" O_2 evolution overpotential on Ni vs. temperature

temperature curve results (Fig. 10). It should be realized that although there is a minimum in the overpotential vs. temperature plot for "visible" evolution, the potential for oxygen evolution continuously decreases with increasing temperature, although at a much slower rate after the temperature of the minimum than before. This information can be utilized to screen potential oxygen electrocatalyst materials. Oxygen evolution will be catalyzed on the appropriate conducting oxide stable with respect to oxygen. In addition if the temperature dependence of the oxide formation is known (either calculated from existing thermodynamic data or experimentally determined), the overpotential for oxygen evolution can be determined at any temperature. This can then be used to elucidate the activity at elevated temperatures of various electrocatalysts and associated mechanism changes with minimum high temperature experimentation.

Acknowledgments

The authors wish to acknowledge the help of G. Kissel, P. W. T. Lu, and A. C. C. Tseung. One of us (C. R. Davidson) also wishes to thank Professor Glenn

E. Stoner of the University of Virginia, Charlottesville, for his guidance during this work. This work was carried out under the auspices of the U.S. Department of Energy and in partial fulfillment of the requirements for the doctorate degree from the Materials Science Department of the University of Virginia.

Manuscript submitted July 30, 1979; revised manuscript received Dec. 20, 1979. This was Paper 538 presented at the Seattle, Washington, Meeting of the Society, May 21-26, 1978.

Any discussion of this paper will appear in a Discussion Section to be published in the December 1980 JOURNAL. All discussions for the December 1980 Discussion Section should be submitted by Aug. 1, 1980.

Publication costs of this article were assisted by Brookhaven National Laboratory.

REFERENCES

1. M. H. Miles, G. Kissel, P. W. T. Lu, and S. Srinivasan, *This Journal*, **123**, 332 (1976).
2. J. A. Hedvall, "Solid State Chemistry," Elsevier, Amsterdam.
3. P. W. Selwood, "Magnetochemistry," Interscience, New York (1956).
4. G. Parravano, *J. Am. Chem. Soc.*, **75**, 1497 (1953).
5. H. B. Clarman, R. M. Dell, and S. Teele, *Trans. Faraday Soc.*, **59**, 453 (1963).
6. E. R. S. Winter, *J. Catal.*, **6**, 35 (1966).
7. A. C. C. Tseung and H. L. Bevan, *J. Electroanal. Chem. Interfacial Electrochem.*, **45**, 429 (1975).
8. A. C. C. Tseung, B. S. Hobbs, and A. D. S. Tatrum, *Electrochim. Acta*, **15**, 473 (1970).
9. J. Brenet, 27^{eme} Reunion de la S. I. E. (1976).
10. D. B. Hibbert and A. C. C. Tseung, Paper 296 presented at The Electrochemical Society Meeting, Philadelphia, Pennsylvania, May 8-13, 1977.
11. H. Isaacs and J. McBreen, Private discussions.
12. J. D. E. McIntyre and D. M. Kolb, *Symp. Faraday Soc.*, No. 4.99a (1970).
13. J. L. Weininger and M. W. Breiter, *This Journal*, **110**, 484 (1963).
14. P. W. T. Lu, Ph.D. Dissertation, State University of New York at Stony Brook (1975).
15. A. C. C. Tseung and S. Jasem, *Electrochim. Acta*, **22**, 31 (1977).
16. H. L. Bevan, Ph.D. Dissertation, City University of London (1970).

The Zn-KOH System: Fragmentation of Dendritic Zinc Clusters on Electrode Cycling

S. Szpak* and C. J. Gabriel

Naval Ocean Systems Center, Electronic Material Sciences Division, San Diego, California 92152

and T. Katan*

Lockheed Palo Alto Research Laboratory, Materials and Structures, Palo Alto, California 94304

ABSTRACT

An *in situ* examination of dendritic clusters in Zn-KOH electrode analogs reveals that fragmentation frequently occurs during cycling. Fragments on the order of 10^{-3} cm or less are formed and are propelled through the bulk electrolyte. Initially the fragments move as though their surfaces are positively charged, but shortly after fragmentation the movement is in accord with a negatively charged surface. Fragments that are larger than ca. 10^{-3} cm are found to exhibit motion principally by displacement, generated by dissolution at one end and deposition at the other. Conditions for fragmentation during cycling are discussed and the relevance is given to zinc electrode operation.

The deleterious effects of the formation of dendrites during the operation of rechargeable systems, par-

ticularly those involving zinc electrodes, are well documented. Growing dendrites not only cause internal short circuits but they also contribute to the loss of cell capacity and to the deterioration of cell

* Electrochemical Society Active Member.
Key words: particles, electrode, transport.

performance. The formation of dendritic clusters has been studied rather extensively. Evidently, their growth is controlled by mass transport (1-4) while the initiation of growth may take place by several modes (5-10).

A somewhat different aspect of dendritic behavior, encountered in alkaline zinc batteries, is the subject of the present study, namely, the fragmentation of dendritic structures and their subsequent behavior during the course of electrode cycling. The phenomenon of fragmentation considered here is similar to that described by Vermilyea (11) in studies of the dissolution of whiskers and identical with that described by Wranglen in comments on the behavior of "living crystals," which were first observed at the beginning of this century (12).

The purpose of this communication is to describe the behavior of dendritic clusters during discharge of a zinc electrode analog. In particular, we consider fragmentation of dendritic structures and behavior of the fragments in an electric field associated with the passage of current.

Experimental

The electrolytic cell and associated electronic and optical equipment are shown in Fig. 1 in the form of a block diagram. The electrolytic cell is of the ultrathin type to minimize the development of convective flow usually initiated because of the evolution of hydrogen and localized at dendritic tips. The dimensions of the electrolytic cells, together with the details of their construction and assembly, are displayed in the insert. The working electrodes were made of 99.999% polycrystalline zinc sheet and mounted in plastic holders. Experimental cells were operated in the galvanostatic mode with an electrolyte of saturated zincate in 10M aqueous KOH solution.

The *in situ* examination of the fragmentation of dendritic structures was carried out with the aid of a Zeiss metallurgical microscope equipped with a Nomarski interference objective and a TV camera for monitoring and recording the progress. The post test details of the dendritic structures were viewed with a scanning electron microscope.

The behavior of the metallic zinc fragments that were intentionally placed in an impressed electric field was examined visually. Single crystals of zinc, about 300 μm in size, were placed in a glass capillary tube, 650 μm in diameter, containing the specified electrolyte. Morphological manifestations were examined with a Bausch and Lomb Sterozoom 7 microscope during the passage of a 2.5 mA current through the cell.

Results

An examination of the behavior of dendritic clusters revealed the occurrence of three distinctly different phenomena, aside from the straightforward anodic

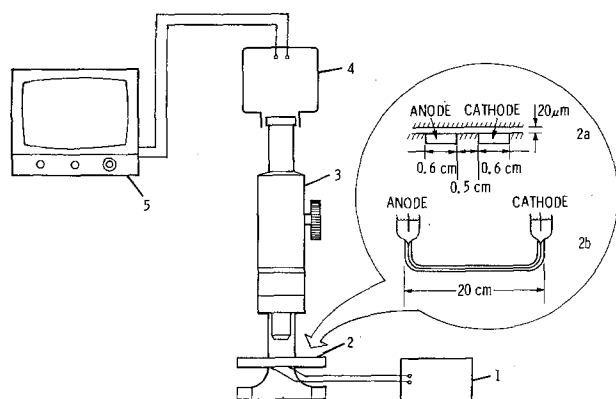


Fig. 1. Block diagram of the experimental arrangement: 1, power source; 2, electrode analog, (a) ultra thin cell, (b) capillary cell; 3, microscope; 4, recording camera; 5, display screen.

dissolution: first, a fracturing of dendritic clusters from a parent dendritic stem during the passage of anodic current, yielding fragments of various sizes; second, a motion of the smaller fragments, on the order of 10 μm or less in size, following separation from the parent stem; and, third, over a somewhat longer time, a motion of displacement through bipolar activities of larger fragments.

In particular, Fig. 2a shows the situation immediately after fracturing of a dendritic cluster from its parent stem. A typical trajectory observed for fragments of approximately 5 μm in size, as they are propelled through the electrolyte, is indicated in Fig. 2b. Such a curvilinear trajectory cannot be attributed to a convective flow because no gas evolution occurred during the passage of the anodic current, and any gas bubbles that were generated during the period of dendritic growth remained stationary and retained their shape. Trajectories of fragments were obtained by tracing their motion recorded on video tape. Typically, the velocities were on the order of 5-10 $\mu\text{m sec}^{-1}$.

The isolated zinc fragments that were placed in capillary cells and subjected to the passage of an electric current of 2.5 mA developed dendrites at their cathodic ends and underwent dissolution at their anodic ends, as indicated in Fig. 3. Initially, however, passive films with particulate residues were formed at the anodic ends. After the passage of current for approximately 20 min, the dendritic mass of clusters forming at the cathodic end of a fragment had grown to fill the transverse cross section of the cell. Subsequently, the dendritic mass appeared to be moving along the capillary tube with a velocity on the order of 0.1 $\mu\text{m sec}^{-1}$. The motion was clearly by displace-

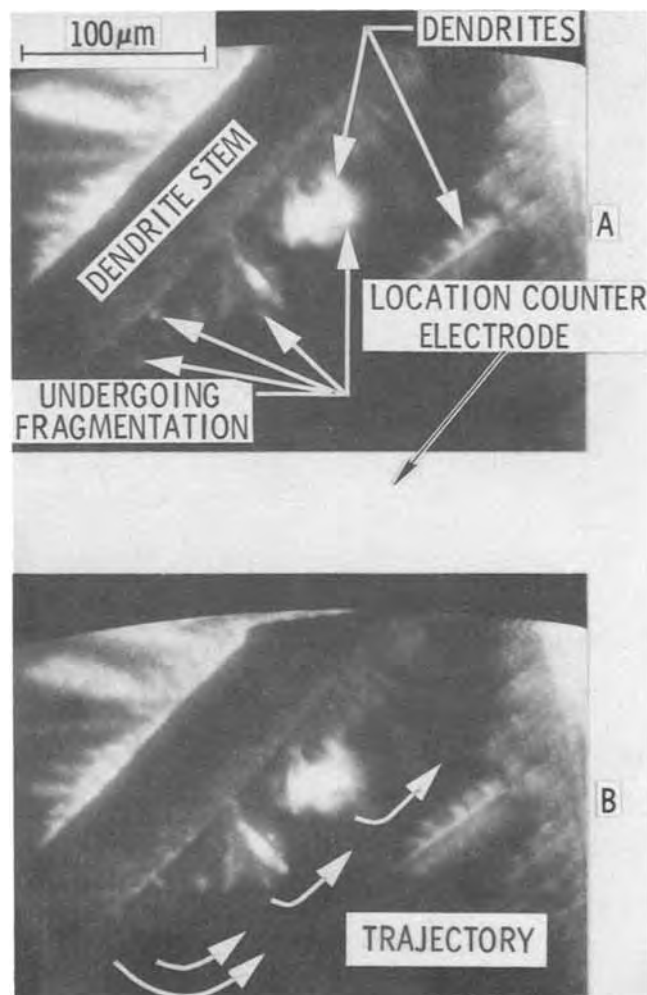


Fig. 2. Dissolution of dendritic clusters: (A) position of dendrites shortly before fracture, (B) trajectory of motion after fracture and fragmentation.

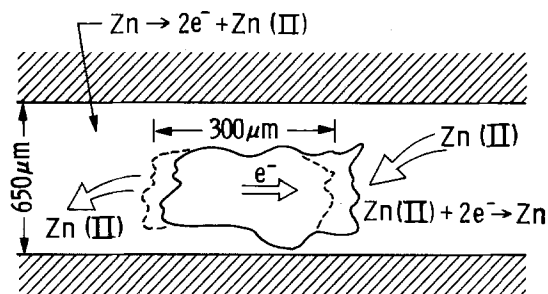


Fig. 3. Representation of motion by displacement: particle size, $300 \mu\text{m}$; initial position, dashed outline; velocity of displacement (at 2.5 mA and $650 \mu\text{m}$ diam), $0.1 \mu\text{m sec}^{-1}$.

ment due to dissolution at one end and deposition at the other.

Discussion

The physical motion of the small particles and the apparent motion by electrochemical displacement of the large ones may, in fact, represent two divergent examples of the balance of the electric and hydrodynamic forces acting on isolated zinc particles immersed in an electrolyte. Indeed, the experiments indicate that small fragments are set into motion in a curved path by dominating electrical forces while the viscous forces acting on large fragments limit their velocity thus accentuating the motion by displacement.

To account for these phenomena, we will develop the discussion as follows. First, we will consider the distribution of the current density within the electrolytic cell and within the porous structure of dendritic clusters. We will be primarily interested in clarifying the conditions that lead to anomalous transfer C.D. profiles that may account for fracturing. Following this, we will discuss the motion of small fragments and the bipolar activities of larger particles in the context of the theory of electrophoretic motion (13-15), especially as the theory applies to a corroding system (16). Finally, we will show the relevance of these phenomena to battery technology.

Fragmentation within dendritic clusters.—The *in situ* observation and the post test examination of the growth of dendritic clusters can be summarized as follows. The dendritic clusters originate at the electrode rim and extend into the bulk electrolyte in the form of three dimensional growths. This extension, shown in Fig. 4a, can be viewed as equivalent to a porous struc-

ture and as such can be represented by an equivalent electric circuit; a typical one is shown in Fig. 4b. A typical scanning electron microscope (SEM) photograph of a small fraction of the dendritic cluster is shown in Fig. 4c. Evidently, the stems of the dendritic cluster may have various geometrical forms of which two have been selected to illustrate the process of fracturing: those with nonuniform cross section, as indicated in Fig. 4c by arrow A, and those with cross sections being almost uniform, as indicated by arrow B.

The fragmentation of dendritic clusters during the anodic part of the cycle is easy to visualize. When the dendritic stem is of nonuniform cross section, the constricted regions will dissolve first even if the transfer C.D. is relatively uniform throughout. When the dendritic stem is of uniform cross section, an anomalous distribution of the transfer C.D. is required. Such distributions may arise, e.g., because of the formation of localized resistive oxides, shifting the dissolution to areas of lower reaction impedance to generate undercutting and separation. Fragmentation of dendritic structures during their growth is less straightforward, since it requires the reversal of the transfer current within a part of the growing structure.

While the equivalent circuit shown in Fig. 4b provides a convenient visualization of the reaction profile, a more phenomenological description can be obtained from the two-phase model of porous electrodes. The mathematical formulation of this model, when resistivities in both phases may be comparable and complications arising from mass transport may be excluded, is based on (a) the application of Ohm's law

$$\nabla u_n + \rho_n i_n = 0 \quad (n = s, m) \quad [1]$$

(b) the conservation of charge

$$\nabla \cdot i_s - j = 0, \quad \nabla \cdot i_m + j = 0 \quad [2]$$

together with (c), the linearized transfer C.D.-overpotential relation

$$Zj + V_{\text{rest}} = u_m - u_s \quad [3]$$

where u is a potential, i is a current density, j is the transfer C.D., ρ is a resistivity, and Z is the reaction impedance. Subscripts s and m denote the solution and metallic phases, respectively.

Within regions of constant parameters, Eq. [1]-[3] can be reduced in number by casting them in the more familiar second-order form (see Appendix)

$$\nabla^2 j - \kappa^2 j = 0 \quad [4]$$

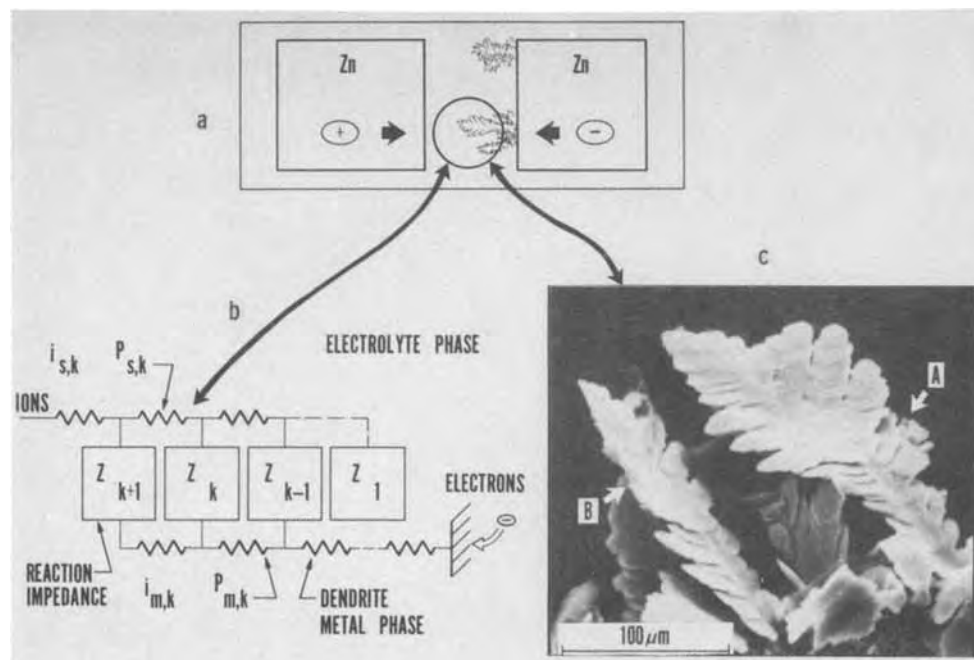


Fig. 4. Dendritic clusters in experimental analog; (a) top view of the cell showing the location of three dimensional clusters; (b) equivalent electric circuit; (c) SEM photograph of representative dendritic forms.

$$\Delta^2\phi = 0 \quad [5]$$

where $\kappa^2 = \rho_s + \rho_m/Z$ and

$$u_s = \phi - \frac{\rho_s}{\kappa^2} j \quad [6]$$

$$u_m = \phi + \frac{\rho_m}{\kappa^2} j + V_{rest} \quad [7]$$

The nonuniformity of cross section of the parent stems, the distribution of localized coverage with resistive oxides, or the variation in electrolyte concentration can be viewed as producing a number of regions characterized by the parameters $\rho_{n,k}$, Z_k , and $V_{rest,k}$, with $n = s, m$ and $k = 1, 2, 3 \dots$. For simplicity of computation and illustration, we will consider variation of parameters in only one direction.

Examples of computed, one-dimensional transfer C.D. profiles are shown in Fig. 5 and 6. These profiles were generated for dendritic clusters of unit thickness divided into five segments. The length of each segment is arbitrary but the parameters characterizing the

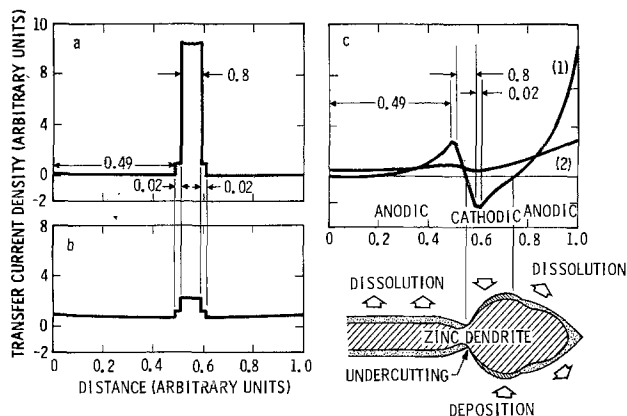


Fig. 5. Calculated anodic transfer C.D. profiles for $J = 1$: a, the effect of changing Z : $\rho_m = \rho_s = 1$, and $V_{rest} = -1$ for all segments, $Z_1 = 10$, $Z_2 = 1$, $Z_3 = 0.1$, $Z_4 = 1$, and $Z_5 = 10$; b, the effect of changing V_{rest} : $\rho_m = \rho_s = Z = 1$ for all segments, $V_{rest,1} = -0.5$, $V_{rest,2} = -1$, $V_{rest,3} = -2$, $V_{rest,4} = -1$, and $V_{rest,5} = -0.5$; c, the effect of changing resistivities; $V_{rest} = -1$ for all segments of all curves. Curve 1, $\rho_{s,1} = 10$, $\rho_{s,2} = 1$, $\rho_{s,3} = 0.1$, $\rho_{s,4} = 1$, and $\rho_{s,5} = 10$; $\rho_{m,1} = 0.1$, $\rho_{m,2} = 1$, $\rho_{m,3} = 10$, $\rho_{m,4} = 1$, and $\rho_{m,5} = 0.1$; $Z = 0.1$ for all segments. Curve 2, same parameters as curve 1, except that $Z = 1$ for all segments.

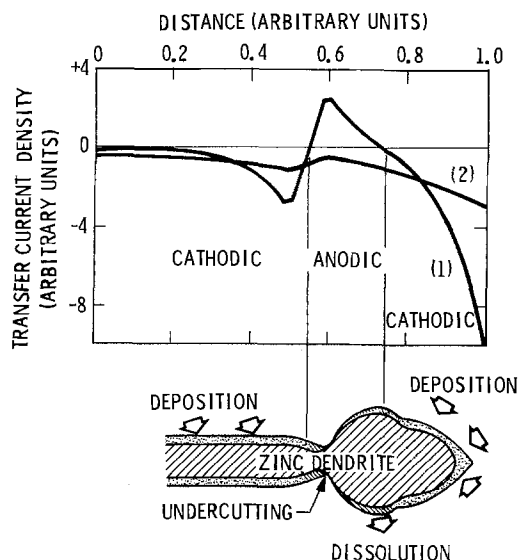


Fig. 6. Calculated cathodic transfer C.D. profiles for $J = -1$. Curve 1, parameters as in Fig. 5c. Curve 2, parameters as in Fig. 5c.

behavior within each segment were selected to indicate the changing conditions along the dendritic stem/electrolyte interphase. Numerical values that were assigned to these parameters were chosen to exaggerate the desired effect for purposes of illustration.

Transfer C.D. profiles leading to the fragmentation of clusters during the anodic part of the cycle are shown in Fig. 5a-5c. In particular, Fig. 5a illustrates the effect of blocking of the second kind (17), accomplished through changes in the reaction impedance, Z_k . Physically, such a situation should occur at high dissolution rates in zincate-saturated solutions. Figure 5b illustrates the effect of changes in concentration, which are expressed through changes in the value of V_{rest} , on the transfer C.D. profile. Finally, Fig. 5c represents the effect of precipitation in the electrolyte phase as well as the nonuniformity of cross section of the metallic phase, i.e., the combined effect of the blocking of the first kind and morphology of the dendritic growth. This example suggests that in the course of dissolution, we might find segments where the transfer current is reversed. Such reversal is attributed to local variation in resistivities in both phases and is strongly modified by the degree of polarization. Consequently, a smoothing effect of additives, e.g., surfactants, on the fragmentation is anticipated.

Conditions leading to fragmentation of dendritic clusters during their growth period are less obvious, because no insoluble species are generated in the electrolyte phase and no nonconductive material is deposited on the electrode surface during a cathodic period. In the absence of such mechanical factors as vibration or shock, the reversal of the transfer current is the only condition associated with fragmentation. As demonstrated in Fig. 6, the anomalous transfer C.D. profiles arise when a proper ratio of resistivities within the growing cluster is realized, especially when combined with low reaction impedance. These conditions are expected to be fulfilled frequently in the Zn-KOH system because of low overpotentials for the electrodeposition and a particular morphology of growing clusters, consisting of numerous branching and nonuniformity in the cross section of individual stems.

Motion of dendritic fragments.—The motion of particles in the electrolyte arises from the interaction of the interphase region with either phase. The disperse phase may be set in motion by a temperature gradient, by a concentration gradient, or by any number of factors affecting the energetics of the interphase. In electrochemical systems, there is the interaction of the diffuse part of the electric double layer with an externally impressed electric field and their relation to the ensuing hydrodynamic motion.

Upon immersion of a solid particle in an electrolyte, an interphase region of a complex structure is established. A satisfactory theory of electrophoretic motion can be developed using a simple model, that of a capacitor with electrically charged planes, capable of motion relative to each other. The essential features of this simple model are shown in Fig. 7. A charged plane, S_2 , is substituted for the diffuse part of the electric double layer. This plane is located outside of the Helmholtz outer layer, i.e., within the region of allowed hydrodynamic activity. The ensuing hydrodynamic flow arising from the interaction between the charge Q^+ and the electric field, E , in the direction parallel to plane S_1 is measured across the plane S_3 placed perpendicular to the direction of flow. The velocity and the direction of flow are proportional to the magnitude and the sign of the excess charge accumulated on the electrode surface, respectively. This simple picture of the interphase region, however, is of doubtful validity when applied to concentrated electrolytes, where the diffuse part of the electric double layer is compressed (15, 18).

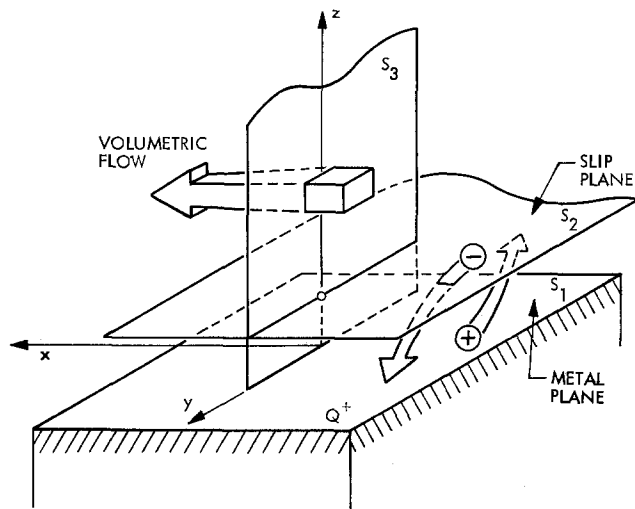


Fig. 7. Capacitor representation of electrophoretic motion: S_1 , metal surface; S_2 , slip plane parallel to S_1 ; S_3 , reference plane for flow measurements. The volume flow and charge transfer are indicated by arrows.

Prior to fragmentation, the dendritic particle is thermodynamically unstable with respect to the electrolyte phase. This instability is forced by the impressed anodic overpotential which, in turn, results in the establishment of concentration profiles of relevant ionic species in the immediate neighborhood of the dissolving dendrite. At the moment of separation, the instability due to the impressed overpotential is removed and replaced by a thermodynamic driving force leading to the attainment of a steady state.

Qualitatively, the approach to the rest potential following the separation of the fragment can be conveniently studied with the aid of a Pourbaix diagram, part of which is reproduced in Fig. 8. Starting at point A, located within the domain of stability of water, the decaying potential crosses the hydrogen reversible potential, point B, the point of zero charge potential, point C, and slowly approaches its rest potential at E. The rest potential of corroding zinc is very close to the reversible potential (19), as indicated by the dashed line.

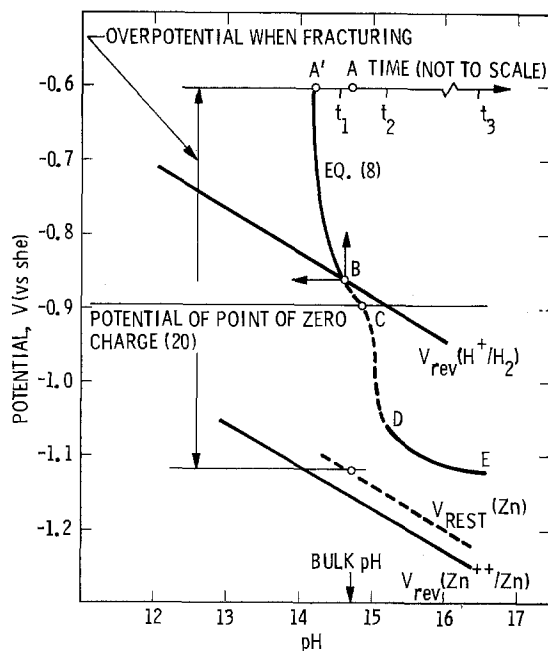


Fig. 8. Schematic representation of the approach to the corrosion potential of fragmented zinc particles.

The potential decay within the first time interval, curve AB, and the approach to the steady state, curve DE, can be treated analytically. Thus, the potential decay within the first time interval, $0 < t < t_1$, can be obtained from the expression of charge conservation

$$i_m = \sum_k j_k + d(CV)/dt \quad (k = 1, 2 \dots) \quad [8]$$

where j_k is the participating reaction current density and C and V are the capacitance and potential, respectively, of the electric double layer.

Equation [8] represents the electrode response to perturbations in current or potential. This equation must be substantially modified when it is applied to a fragmented dendrite. First, we set $i_m = 0$ to indicate a complete separation. Additional simplifications may arise from considerations involving the magnitudes of respective j_k . Thus, immediately after separation, within the time interval $0 < t < t_1$, we assume that only the Zn^{2+} ions participate in the potential-determining events and that no other processes affecting the capacitance of the electric double layer, e.g., adsorption or desorption, are involved. Choosing for C the value $100 \mu F \text{ cm}^{-2}$ and assuming the exponential form of the $j(V)$ relation with $j_0 = 0.3 \text{ A cm}^{-2}$ (8), $b = 50 \text{ mV/decade}$, and $V(0) = 0.6V$ (an arbitrarily selected value within the stability domain of water), on integration of Eq. [8], we conclude that the initial period of potential decay is completed within milliseconds, i.e., this relaxation would not affect the observation of the particulate motion.

Another time interval, $t_2 < t < t_3$, for which the $V(t)$ curve yields to analytical treatment is the final approach to its steady-state value, from D to E, Fig. 8. The dominating elementary processes within this period is the increase in surface coverage by the ZnO film that results from the reaction between the Zn^{2+} ions and OH^- ions. This final approach usually occurs over an extended period of time (20).

Of interest to the present investigation is the period $t_1 < t < t_2$, during which the decaying potential moves away from the hydrogen reversible potential, crosses the potential of point of zero charge, V_{pzc} , located at -0.8 to $-0.9V$ (vs. SHE) (19), and approaches the rest potential and during which the curvilinear path, shown in Fig. 2, was observed. As the decaying potential crosses the point of zero charge, the character of the excess charge on the surface also changes, thus accounting for the change in the direction of particle motion, as required by the theory of electrophoretic phenomenon.

The theory of electrophoretic motion is usually developed for insulating or ideally polarized particles. Here, however, a different situation arises: the zinc particle is unstable with respect to the electrolyte. The ideally polarized particle is replaced by a corroding one, i.e. a system of local cells on the particle surface, as a result of which electrical charges are being transferred across its double layer, as indicated by arrows in Fig. 7. Under these conditions, a correction term must be included in the expression for the particle velocity, which effectively slows down the motion compared to insulating particles carrying the same excess charge (16).

The velocity of the corroding zinc particle is governed by dissipation due to viscous forces and interfacial charge transfer. As the size of the particle increases, both effects contribute more, and the particle slows down to the point that no motion is observed. Instead, because of the low overpotentials for both cathodic and anodic reactions, a metallic particle placed in an electric field suffers dissolution at one end and deposition at the other, cf. Fig. 3.

This type of behavior can be demonstrated by intentionally placing a zinc particle of considerable size, e.g., $300 \mu m$, in a capillary-type cell. The small cell dimensions dampen the development of convective flow,

and the geometrical form of uniform cross section assures a uniform primary current distribution except in the immediate vicinity of the metallic particle. Using this cell design, we created conditions such that the motion by displacement could be demonstrated. The observed velocities were on the order of $0.1 \mu\text{m sec}^{-1}$, and depended on the current flow and the capillary diameter. Further discussion of this observation and its relevance to battery technology will be given in a companion paper.

Relevance to battery technology.—One approach to the rational design of battery electrodes is via electrode modeling. It is generally agreed that the concepts and mathematics of the modeling of porous electrodes are well understood and formulated with a sufficient degree of completeness. The application to real systems, however, has not kept pace with the theoretical advances. The principal weakness involving the modeling of the zinc electrode pertains to the transport coefficients associated with the various growth forms when a new phase appears as a result of an electrochemical process. At present, there is little information concerning the rate at which the various elementary processes occur, *i.e.*, on the numerical inputs that govern the computed transfer C.D. profiles. This is probably the reason why there is substantial disagreement between the predicted (21, 22) and observed (23, 24) performances of the Zn-KOH system.

Here, we have elaborated on one aspect not included in modeling, that of the motion and reactivity of metallic zinc particles in an electrolyte during the passage of current. The disengagement of zinc particles from cycled zinc electrodes has, indeed, been observed (24, 25). However, the fact that these particles may experience motion and, moreover, a change in shape has never been included in the source of modeling. The electrophoretic and displacement velocities were found to be of such magnitude that, from the size of the zinc particles, it appears that the dimensions of pores in real electrodes can be breached in just a few cycles.

Particles found in the main body of the electrolyte should affect the primary current distribution, and their effect would magnify with each cycle, causing progressively severe nonuniformities. The migration of these isolated zinc fragments with systematic cycling could contribute to the commonly observed overall change in the zinc electrode's shape. Indeed, a recent postmortem examination conducted on a 10 A-hr silver/zinc cell after 157 cycles, revealed the presence of isolated zinc fragments, *ca.* 10^{-2} cm in size, at numerous locations removed from the zinc electrode, *i.e.*, on the nylon cloth and reprocessed cellophane separator material (26). Although the effects of these fragments could not be determined, their presence lends credence to the importance of the phenomena causing fragment migration in practical battery systems.

Fragmentation of the electrode structure can reduce the cell capacity if the fragments become electrically isolated, and then capacity can be restored only after the dissolution of the fragments and subsequent deposition onto the conductive matrix. In addition, the isolated metallic particles trapped within the electrode pores are likely to affect the current flow in the electrolyte phase, thus producing additional anomalies in the transfer C.D. profile.

The examination of conditions leading to fracturing, especially during the cathodic cycle, suggests the use of additives designed to cause an increase in polarization. Such an increase in polarization would reduce the occurrence of transfer current reversal thus minimizing fragmentation of dendritic clusters.

Conclusions

1. Fragmentation may occur during either the anodic or cathodic part of the cycles. Fracturing during the

anodic part of the cycle may result from either an anomalous distribution of the transfer C.D. or from nonuniform cross section of metallic stems. Fracturing during the cathodic part requires a reversal of transfer current.

2. Small fragments, on the order of 10^{-3} cm across in our experiments, exhibit what appears to be an electrophoretic motion with an average velocity of $5\text{--}10 \mu\text{m sec}^{-1}$. Large particles, longer than *ca.* 10^{-3} cm, placed in an electric field move by displacement with a velocity on the order of $0.1 \mu\text{m sec}^{-1}$.

3. The presence and migration of particles in the bulk electrolyte may affect the distribution of the primary current, thus contributing to the electrode shape change with systematic cycling.

4. The addition of surface active agents designed to increase the polarization of the Zn/Zn⁽²⁺⁾ reaction may increase the cycle life of the zinc electrode.

Acknowledgment

This work was supported, in part, by the Naval Ship Engineering Center, Electrochemical Power Sources, and, in part, by DOE's Division of Energy Storage. The authors wish to acknowledge the continuous interest of Mr. A. Himy, NAVSEC, and Mr. R. Shivers, DOE.

Manuscript submitted Sept. 10, 1979; revised manuscript received Nov. 26, 1979.

Any discussion of this paper will appear in a Discussion Section to be published in the December 1980 JOURNAL. All discussions for the December 1980 Discussion Section should be submitted by Aug. 1, 1980.

Publication costs of this article were assisted by Lockheed Palo Alto Research Laboratory.

APPENDIX

For constant $\rho_{n,k}$ ($n = s, m; k = 1, 2, 3 \dots$) and Z_k the reduction of Eq. [1]–[3] is as follows. Taking the gradient of Eq. [3] and using Eq. [1] we have

$$Z\nabla j = -\rho_m i_m + \rho_s i_s \quad [\text{A-1}]$$

Taking the divergence of Eq. [A-1] and using Eq. [2] to eliminate i_m and i_s , we obtain Eq. [4].

The divergence of Eq. [1] yields

$$\nabla^2 u_s + \rho_s j = 0 \quad [\text{A-2}]$$

Here, Eq. [2] has been used to eliminate i_m . Taking the gradient of Eq. [A-2] followed by the divergence, we have

$$\nabla^4 u_s - \kappa^2 \nabla^2 u_s = 0 \quad [\text{A-3}]$$

where Eq. [4] and [A-2] have been used to eliminate j . Now, since Eq. [A-3] can be rewritten as either

$$\nabla^2 (\nabla^2 u_s - \kappa^2 u_s) = 0 \quad [\text{A-4}]$$

or

$$(\nabla^2 - \kappa^2) \nabla^2 u_s = 0 \quad [\text{A-5}]$$

it follows that there are solutions to Eq. [A-3] of the form

$$u_s = \phi + \psi \quad [\text{A-6}]$$

where

$$\nabla^2 \phi = 0 \quad [\text{A-7}]$$

and

$$\nabla^2 \psi - \kappa^2 \psi = 0 \quad [\text{A-8}]$$

Substituting Eq. [A-6] into Eq. [A-2] and making use of Eq. [A-7] to eliminate ϕ and Eq. [A-8] to evaluate $\nabla^2 \psi$, we obtain

$$\psi = -\frac{\rho_s}{\kappa^2} j \quad [\text{A-9}]$$

Thus, Eq. [A-6] becomes Eq. [6], which then combined with Eq. [3], yields Eq. [7].

For the one dimensional case considered here, the solutions to Eq. [4] and Eq. [5] for the k th segment, respectively, of the forms

$$j = A_k e^{\kappa x} + B_k e^{-\kappa x} \quad [\text{A-10}]$$

and

$$\phi = C_k x + D_k \quad [\text{A-11}]$$

At the current collector and at the electrode/solution interface, the current densities are known, this permits the boundary conditions on the current at the collector to be expressed as

$$\frac{dj}{dx} = -\frac{\rho_m}{Z} J \quad [\text{A-12}]$$

$$\frac{d\phi}{dx} = -\frac{\rho_s \rho_m}{\rho_s + \rho_m} J \quad [\text{A-13}]$$

and at the electrolyte interface as

$$\frac{dj}{dx} = \frac{\rho_s}{Z} J \quad [\text{A-14}]$$

$$\frac{d\phi}{dx} = -\frac{\rho_s \rho_m}{\rho_s + \rho_m} J \quad [\text{A-15}]$$

where J is total cell current density.

At each intersection of segments of constant parameters $i_s + i_m$, i_s , u_s , and $u_m - u_s$ must be continuous. This provides enough linear equations to find j as a function of J and the other parameters.

REFERENCES

1. A. R. Despic and K. I. Popov, in "Modern Aspects of Electrochemistry," Vol. 7, B. E. Conway and J. O'M. Bockris, Editors, Plenum Press, New York (1972).
2. J. W. Diggle, A. R. Despic, and J. O'M. Bockris, *This Journal*, **116**, 1503 (1969).
3. A. R. Despic, J. W. Diggle, and J. O'M. Bockris, *ibid.*, **115**, 507 (1968).
4. J. W. Diggle and A. Damianovic, *Sov. Electrochem.*, **7**, 1603 (1971).
5. R. V. Moshtev and P. Zlatilova, *J. Appl. Electrochem.*, **8**, 213 (1978).
6. F. Mansfield and S. Gilman, *This Journal*, **117**, 558 (1972); *ibid.*, **117**, 1154 (1972).
7. A. R. Despic and M. M. Purenovic, *ibid.*, **121**, 329 (1974).
8. J. O'M. Bockris, Z. Nagy, and D. Drazic, *ibid.*, **120**, 31 (1973).
9. R. D. Naybour, *ibid.*, **116**, 520 (1969).
10. N. A. Pangarov, *Electrochim. Acta*, **9**, 721 (1964).
11. D. A. Vermilyea, *J. Chem. Phys.*, **27**, 814 (1957).
12. G. Wranglen, *Electrochim. Acta*, **2**, 130 (1960).
13. J. Newman "Electrochemical Systems," chap. 9 and 10, Prentice Hall, Inc., Englewood Cliffs, N.J. (1973).
14. V. G. Levich, "Physicochemical Hydrodynamics," chap. 9, Prentice Hall, Inc., Englewood Cliffs, N.J. (1962).
15. J. O'M. Bockris and A. K. N. Reddy, "Modern Electrochemistry," Vol. 2, chap. 7, Plenum Press, New York (1970).
16. A. Frumkin and B. Levich, *Acta Physicochem., URSS*, **21**, 193 (1946).
17. S. Szpak and T. Katan, *This Journal*, **122**, 1063 (1975).
18. S. D. James, *ibid.*, **123**, 1857 (1976).
19. J. O'M. Bockris, Z. Nagy, and A. Damjanovic, *ibid.*, **119**, 285 (1972).
20. L. Z. Vorkapic, D. M. Drazic, and A. R. Despic, *ibid.*, **121**, 1385 (1974).
21. K. W. Choi, D. N. Bennion, and J. Newman, *ibid.*, **123**, 1616 (1976).
22. K. W. Choi, D. Hamby, D. N. Bennion, and J. Newman, *ibid.*, **123**, 1628 (1976).
23. D. Hamby and J. Wirkkala, *ibid.*, **125**, 1020 (1978).
24. T. Katan, J. Savory, and J. Perkins, *ibid.*, **126**, 1835 (1979).
25. J. McBreen and E. J. Cairns, in "Advances in Electrochemistry and Electrochemical Engineering" Vol. II, H. Gerischer and W. C. Tobias, Editors, John Wiley & Sons, Inc., New York (1978).
26. T. Katan, H. F. Bauman, and W. C. Spindler, Unpublished data.

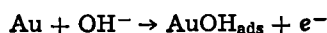
The Electrochemical Formation of Au(I) Hydroxide on Gold in Aqueous Potassium Hydroxide

D. W. Kirk,* F. R. Foulkes,* and W. F. Graydon

Department of Chemical Engineering and Applied Chemistry, University of Toronto, Toronto, Canada M5S 1A4

ABSTRACT

The behavior of gold in aqueous potassium hydroxide was studied using potentiodynamic methods. Three peaks found at potentials more negative than the gold (III) oxide formation region were identified as adsorption reactions. These reactions were shown to depend on the hydroxyl ion in solution. The following reaction was proposed



Each of the peaks was found to correspond to the formation of only a monolayer of adsorbed species, with each peak being restricted to a particular type of surface site. By means of the work function values and the ease of oxidation of the three most common crystal planes, the peaks at -1.2 to -0.7V vs. SCE , -0.7 to -0.3V vs. SCE , and -0.3 to $+0.3\text{V vs. SCE}$ were identified with monolayer hydroxide adsorption on the (110), (100), and (111) crystal faces, respectively.

The gold oxidation process has been the subject of considerable study in the literature, principally for acid media (1-21). Although there are fewer works for alkaline media (22-29), it has been shown that anodization at less than $0.1 \text{ A} \cdot \text{cm}^{-2}$ does not build up visible oxide films on gold (21, 30-33). The oxide layer has been shown to grow in thickness in the region of oxygen evolution and different oxide structures are reported to form (14, 34).

Although these works provide clear evidence of the formation of the gold (III) oxide at potentials anodic of its theoretical potential (E°), the formation of lower valent oxides or hydroxides at less anodic potentials is usually disputed. Hoare has postulated that the formation of AuO might account for the value of the rest potential of gold in acidic solutions (35, 36). The increase of the double layer capacity of gold electrodes when oxygen is introduced into the solution was used as support for this proposal (37). Ellipsometric measurements in alkaline solutions by Sirohi and Genshaw (29) indicated that adsorption of an undeter-

* Electrochemical Society Active Member.
Key words: anode, adsorption, kinetics, gold.

mined nature occurs on gold over a wide potential region (-0.8 to $+0.2V$) cathodic of the gold (III) oxide region. Difficulty with the interpretation of differential capacitance measurements by Carr and Hampson (38) also led to the suggestion of adsorption phenomena in the region -0.6 to $+0.6V$. The nature of this adsorption was not made clear.

The lack of reaction of an electrode with electrolyte is a desirable feature for the study of organic reactions, and gold is often recommended as an electrode material because of its wide potential region which is reportedly free of reactions. It is therefore important to determine whether the adsorption phenomena were artifacts of the measurement techniques or represented interactions between gold and the electrolyte. Therefore linear sweep voltammetry (a technique suitable for the detection of electrochemical reactions) was used to study the interactions between gold and aqueous alkaline hydroxide solutions at potentials cathodic of the Au(III) oxide formation.

Experimental

The electrochemical measurements were carried out in a typical electrochemical cell. The details of the cell and electronic equipment may be found in Ref. (39). For fast potential scan measurements a Tektronix storage oscilloscope (Model 5113) was used to record the data. Polycrystalline gold (>99.99% purity) wire (0.0254 cm diam) was used as the working electrode in potential scan measurements because cylindrical geometry is not subject to edge effects, and the positioning of the reference electrode to reduce IR drop is not as critical as for the case of planar electrodes. The Luggin capillary was drawn to a 0.1 mm diam (OD) capillary at the tip and was located approximately 0.2 mm from the working electrode. Calculations showed that, under the worst condition ($100 V \cdot sec^{-1}$), the maximum IR drop would be only 1.8 mV. Details of the calculation method may be found in Ref. (40-42).

The solutions, prepared from analytical grade reagent and doubly distilled water, were deoxygenated by bubbling with oxygen-free nitrogen during the experiments. The alkaline solutions were also treated with a preelectrolysis step before being used. This additional precaution was taken because of the sensitivity of the fast linear scan technique to trace impurities. The preelectrolysis was conducted for a minimum of 4 hr using two gold foil electrodes with the potential at one of the electrodes set at $-1.8V$ and a cell potential of $2.61V$. Measurements were recorded photographically from the oscilloscope screen and the data taken from the developed prints.

Gold dissolution rates were determined from weight losses and electrode surface areas. The weight loss measurements were accurate to within $\pm 20 \mu g$. The surface area of the electrode was determined from potential scan measurements, using the linear relationship between the current peak height and the square root of the voltage scan rate for the oxidation of $Fe(CN)_6^{4-}$. The relationship given by Nicholson and Shain (43) is

$$\frac{i_p}{nFA C_0 \left(D_0 \frac{nFv}{RT} \right)^{1/2}} = 0.4463$$

where C_0 is the concentration of $Fe(CN)_6^{4-}$ (mole $\cdot cm^{-3}$), D_0 is the diffusion coefficient of $Fe(CN)_6^{4-}$ ($cm^2 \cdot sec^{-1}$), i_p is the peak current (A), A is the area of the electrode (cm^2), n is the number of electrons transferred in the oxidation, v is the scan rate ($V \cdot sec^{-1}$), and F , R , and T have their usual meanings.

A standard pretreatment of the electrode was necessary to achieve reproducibility. The electrode was first heated to redness in air, then etched in hot aqua regia for 5 sec, washed in doubly distilled water,

dried, and weighed (in the dissolution measurements). It was immediately given a further treatment consisting of a 5 min reduction period in the electrolyte at $-1.2V$. This latter procedure was found to improve the reproducibility of the weight loss and potentiodynamic measurements but did not affect the measured weight of the electrode.

Results and Discussion

A typical slow scan potential sweep in 0.01M potassium hydroxide is shown in Fig. 1. Although similar profiles have appeared in the literature for acid media (44) and alkaline media (28, 45) it is useful to review some of the features for an alkaline medium. The slow scan profile has been divided into four regions which correspond to the following main processes (neglecting double layer charging)

region 1: hydrogen evolution ($H_2O + e^- \rightarrow OH^- + \frac{1}{2} H_2$)

region 2: surface oxide reduction

region 3: surface oxide formation

region 4: oxygen evolution ($2 OH^- \rightarrow H_2O + 2e^- + \frac{1}{2} O_2$) and oxide buildup

From Fig. 1 it can be seen that region 1 is characteristic of a faradaic reaction, that of hydrogen evolution without adsorption. Indeed, unlike other precious metals such as Pt, In, and Pd, gold is known not to display any tendency to adsorb hydrogen (10, 46). The anodic portion of region 2 appears to display only the double layer charging current, but it is shown later that several important reactions take place in this region which are not visible at slow potential sweep rates. The separation observed in Fig. 1 between the oxide formation (region 3) and reduction (region 2) is characteristic of an irreversible surface reaction. Recently it has been shown (44, 47-49) that the oxidation of gold in acid media involves the formation of a surface film which, although initially reversible, undergoes a rearrangement to form an irreversible surface species. In alkaline solutions the oxidation in region 3 has been shown to be complex (34) with the oxide structure dependent on the extent and duration of potential sweep. Figure 2 shows potential scans at much faster sweep rates. It can be seen that there are three peaks cathodic of the the formation of the gold (III) oxide (peak D). These peaks have been designated as peaks A, B, and C. It can be seen that the peaks are easily observed only at higher sweep rates ($>1 V \cdot sec^{-1}$) which would account for the fact that their existence has not been reported before. At slower sweep rates ($<1 V \cdot sec^{-1}$), the peaks are difficult to separate from the double layer charging current. Indeed, even at the sweep rate of $10 V \cdot sec^{-1}$, the complete separation of the peak current and the double layer charging current can only be estimated. (The method of estimation is given later.)

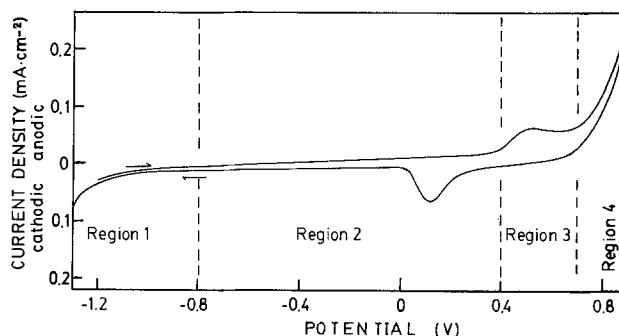


Fig. 1. Potential sweep profile in 0.01M potassium hydroxide electrolyte; sweep rate = $10 mV \cdot sec^{-1}$; temperature = $23.0^\circ C$. All potentials vs. SCE.

¹ All potentials are reported vs. a saturated calomel electrode.

The area under the potential sweep curves may be used to estimate the extent of oxidation of the surface atoms, assuming there is no significant dissolution or ion discharge at the potential in question. Oxygen evolution will not be important cathodic of region 4 (see Fig. 1); however, the anodic dissolution of gold must be considered.

The dissolution rate of gold in highly alkaline solutions has not been reported in the literature and the experimental determination was therefore necessary. The results of the dissolution measurements shown in Table I reveal that no measurable dissolution could be found at potentials less than +0.7V even though the potentials were applied for periods up to 29 hr. Therefore, current which flows in the peak regions cannot result from a dissolution process. Since the three peaks A, B, and C are found at potentials less than +0.7V, the area under the potential sweep curve could be used to calculate the charge on the surface atoms.

Determination of the charge per surface atom for most metals involves comparison of the charge passed in the anodic region and the total charge required for discharge of a monolayer of adsorbed hydrogen. However, because gold does not display any hydrogen adsorption, this method could not be used and it was necessary to measure the surface area of the electrode and estimate the number of gold atoms per unit surface area. The geometric area does not indicate the real area available for a surface reaction; hence the area determination was carried out using an electrochemical method suggested by Nicholson and Shain (43). The electrochemical method gives a better indication of the real surface area because the reaction depends to some extent on the number of active sites.

The nature of the surface structure can also affect the gold (III) oxidation behavior (50-53). For this work the electrodes were assumed to be polycrystalline. Reflection electron diffraction pictures of the electrode after cleaning did not indicate any preferred orientation. In addition, the shape and position of the gold (III) oxidation peak in Fig. 1 is similar to that found for a polycrystalline gold surface by Dickertmann, Schultze, and Vetter (15), who showed that different crystal orientations have unique potential sweep profiles. It was assumed, therefore, that the number of atoms on the surface could be calculated from an average atomic density of the three most prominent crystal faces, (111), (100), and (110), (see Table II). Similar values have been reported in the literature (4).

In order to use the area under the potential sweep profile as an estimate of the extent of reaction, the amount of current corresponding to the double layer charging also must be determined. In a study of reflectance changes on Au and Pt electrodes in acid media, Conway, Angerstein-Kozłowska, and Laliberté (54) showed that double layer charging corrections should be made from the potential of zero charge (pzc) to the potential of monolayer oxide coverage. Changes in the charging current once a complete layer

Table I. Weight loss measurements in 1.0M KOH electrolyte for potentials less than +0.7V at 23°C

Potential (V)	Time duration (hr)	Measured weight loss (g) (area of electrode = 1.8 cm ²)	Dissolution rate** (g · cm ⁻² · sec ⁻¹)
-0.5	29	N.D.*	$\leq 5 \times 10^{-11}$
-0.23	21.5	N.D.	$\leq 7 \times 10^{-11}$
+0.58	16	N.D.	$\leq 9 \times 10^{-11}$
+0.7	16	N.D.	$\leq 9 \times 10^{-11}$
+1.2	34	3×10^{-8}	8.2×10^{-9}

* N.D. = not detected.

** Dissolution rate calculated from error limits in weighing procedure ($\pm 1 \times 10^{-9}$ g).

Table II. Charge density on individual crystal planes

Crystal plane	Atomic density (atoms · cm ⁻²) (calculated)	Charge density* (C · cm ⁻²)
(100)	1.2×10^{15}	1.92×10^{-4}
(110)	0.85×10^{15}	1.36×10^{-4}
(111)	1.39×10^{15}	2.22×10^{-4}

The average charge density based on equal proportions of (100), (110), and (111) crystal planes is 1.83×10^{-4} C · cm⁻².

* Based on 1 electron per gold surface atom.

of oxide had been formed were shown to be small. The actual value of the reported pzc of polycrystalline gold in alkaline solutions may be questioned, since the work of Carr and Hampson (38) indicated that the double layer structure was complicated by oxide films or the adsorption of solution species. Their measurements indicated a value of approximately -0.50V in contrast to a value of approximate 0V reported by Gileadi (55), of -0.32V reported by Bode (56), or of -0.16V reported by Lin (57). Regardless of the value, starting the double layer correction from any of these potentials does not seem appropriate in view of the shape of the curves in Fig. 2.

Therefore, the double layer charging current was estimated graphically (see Fig. 2) by drawing a line from the $i = 0$ point to the minimum current between peaks A and B. The area under the line was used as the value of the double layer charging for peak A. From the minimum between peaks A and B, the line was extended through the minimum between peaks B and C and extended past peak C. Since the peak potentials of A, B, and C are well separated (>0.4 V), it is unlikely that there is serious overlap of the peaks A, B, and C which would elevate the double layer charging current erroneously. There is, however, overlap between peaks C and D and therefore the measurements for peak C were made up to the peak maximum and then corrected to give the value for full surface coverage by assuming the surface coverage at the peak maximum to be 0.5 of full surface coverage. This type of correction has been shown to be valid for reversible reactions (58). The reversibility of peak C will be established later.

The magnitude of the charging correction depended on the sweep rate. For the data shown in Fig. 2 ($10 \text{ V} \cdot \text{sec}^{-1}$) the corrections for the area under the curve in the peak A, B, and C regions were 9.0×10^{-6} C, 9.9×10^{-6} C, and 9.9×10^{-6} C, respectively.

It is clear that this estimation of the charging current represents the maximum value and thus may bias the value of the surface charge density. A smaller estimate of the double layer charging current would yield larger values of the surface charge density.

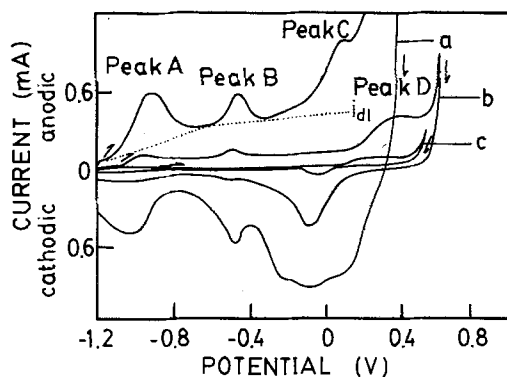


Fig. 2. Potential sweep profiles in 1.0M potassium hydroxide electrolyte at fast sweep rates: a, $v = 10 \text{ V} \cdot \text{sec}^{-1}$; b, $v = 1.0 \text{ V} \cdot \text{sec}^{-1}$; c, $v = 0.1 \text{ V} \cdot \text{sec}^{-1}$; area of electrode = 0.16 cm²; temperature = 23.4°C. All potentials vs. SCE.

Using the above graphical method to correct for the double layer charging contribution, the area under the peaks was measured using a planimeter and the data presented in Table III as the charge accumulated (mC) per surface area of the electrode. It is clear from the table that although the charge accumulated under each peak varies from run to run, the total charge accumulated for the three peaks approaches one electron per surface atom. This suggests that there is only a certain fraction of the surface which will accommodate each of the individual reactions A, B, and C. This view is supported by measurements taken from cyclic potential sweep experiments which are also shown in Table III. The reactions at peak A and peak B gradually disappear after many (>10) cycles, but the reaction at peak C does not. The charge accumulated for peak C in this case is approximately the same as if it had occurred with reactions A and B. Thus the reactions of peak A and peak B are not necessary for peak C to occur. Similarly it can be shown that peak B can be made to appear without peak A, if potential cycling is carried out in the region of peak A before the normal single sweep. It appears, therefore, that the three reactions are independent but restricted to a total accumulated charge of one electron per surface atom. Measurements in 0.1M KOH were found to have lower values for the total accumulated charge ($\sim 0.6 e^-/\text{Au}$), but this was most likely the consequence of smaller peak currents and the greater difficulty in separating the peak currents from the double layer charging at the lower hydroxide concentration.

The effect of sweep rate on peak current for each of the peaks A, B, and C was studied over several orders of magnitude of sweep rate and the results are presented on a log-log plot in Fig. 3. There is good correlation ($r > 0.99$), indicating linearity for the data when plotted as peak current *vs.* sweep rate on rectilinear axes for each of the three peaks. The data do not follow the $i_p \propto v^{1/2}$ behavior observed for diffusion controlled oxidation-reduction reactions and thus the oxidation of electrolyte contaminants may be ruled out. Linearity of the i_p *vs.* v plot is typical for activation-controlled adsorption reactions (41). The adsorption of impurities may also be ruled out because of the concentration (0.02M) of the impurity that would be required to yield the currents observed at sweep rates of $10 \text{ V} \cdot \text{sec}^{-1}$. A reaction between the gold and the electrolyte is therefore indicated.

The effect of sweep rate on the peak potential was also determined and the results are shown in Fig. 4. The potential for peak A shifts anodically at the rate of 0.053 V/decade of sweep. The constant shift of potential with sweep rate is characteristic of an irreversible reaction (58). The correlation coefficient was 0.95 and the slope was shown to be statistically significant. Peaks B and C do not shift significantly with sweep

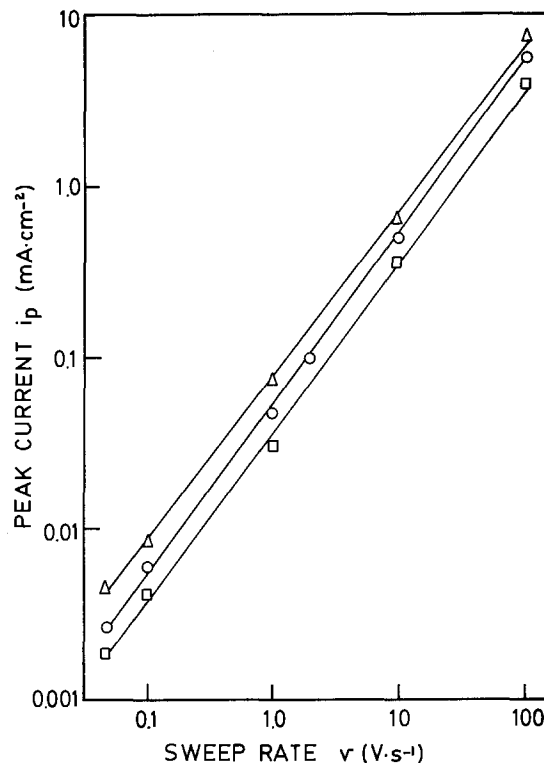


Fig. 3. Effect of sweep rate on peak currents of peaks A, B, and C; 1.0M KOH; ○, peak A; □, peak B; △, peak C; temperature = 23.3°C.

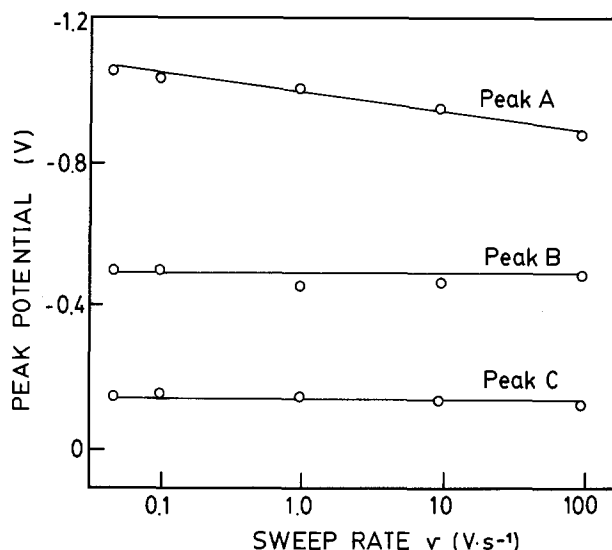


Fig. 4. Effect of sweep rate on peak potentials of peaks A, B, and C; 1.0M KOH; temperature = 23.0°C. All potentials vs. SCE.

Table III. Accumulated charge per unit surface area

Sweep rate (V · sec ⁻¹)	Surface area (mC · cm ⁻²)			Total area (mC · cm ⁻²)	<i>e</i> ⁻ /Au
	Peak A	Peak B	Peak C		
1.0M KOH					
1	0.175	0.00625	0.00475	0.186	1.01
1	0.094	0.02	0.062	0.176	0.96
1	0.0969	0.0656	0.0	0.163	0.88
10	0.0748	0.0588	0.051	0.184	1.00
10	0.0981	0.0095	0.039	0.147	0.80
10	0.0895	0.0228	0.041	0.153	0.83
Average = 0.91					
1.0M KOH using cyclic voltammetry					
1	0	0	0.0375		
1	0	0	0.0244		

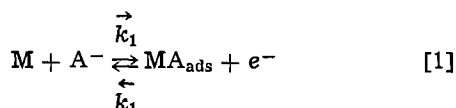
Potential range for: peak A = -1.20 to -0.68V, peak B = -0.68 to -0.39V, peak C = -0.39 to +0.08V.

rate and are therefore characteristic of a reversible type of reaction (58). It is clear in Fig. 2 that peak B shows features of a reversible reaction with the cathodic peak almost identical in shape and position with the anodic peak. The cathodic peak A representing the reduction of peak A is different in shape from the anodic peak, and the peak potential is shifted cathodically from the anodic peak position. Thus the potential difference between the anodic and cathodic peaks also indicates irreversibility, while the nonsymmetrical shape of the cathodic curve indicates interaction among the surface species involved in the reduction reaction. The effect of interaction on the shape of peaks in simulated potential sweep experiments has been studied by Angerstein-Kozlowska, Klinger, and Conway (59) and indicated for this type of behavior a positive interaction parameter, *g*, for

peak A. Using the peak width at half the peak current (0.22V) the interaction parameter can be estimated from the theoretical plot of $\Delta V^{1/2}$ vs. g presented in Ref. (59). The value of $N \approx 5$ found for peak A indicates that there is repulsion within the adsorbed layer. One can speculate that significant repulsion effects could arise in the peak A region on account of the electrode surface charge. The literature values for the potential of zero charge, referred to earlier, indicate that the gold surface may have a negative charge in the region of peak A. Such a charge would tend to repel adsorbing anions, which would have to overcome this surface repulsion effect before adsorption could take place. In addition, repulsion among adsorbed anions would be more significant when combined with the negative surface charge. In contrast, the surface bonding energy would be the dominant energy barrier to overcome in the desorption process. These factors could cause the irreversibility observed in the behavior of peak A.

Once the extent of reversibility of the reaction has been determined for peaks A, B, and C, the slope of the peak current vs. sweep rate can be used to estimate the fraction of the surface involved in each of the reactions for the run which generated the data.

Consider the adsorption reaction given below



where M = the metal and A^- = the anion in solution. If the reaction is activation controlled with no mass transfer limitation and if the species A^- does not undergo any reactions other than by step [1] the following equation may be set up assuming Langmuir-type adsorption

$$i = \vec{i} - \overset{\leftarrow}{i}$$

$$= k_1 F (1 - \theta) [A^-] \exp(\beta F \Delta \phi / RT) - k_1 F \theta \exp[-(1 - \beta) F \Delta \phi / RT] \quad [2]$$

where F = Faraday constant, i = current, \vec{i} , $\overset{\leftarrow}{i}$ = partial currents, k_1 , k_1 = electrochemical rate constants, R = gas constant, T = temperature, β = symmetry factor for anodic rate-determining step (≈ 0.5), $\Delta \phi$ = electrode potential, and θ = fractional surface coverage of MA_{ads} . For the reversible adsorption case $\vec{i} = \overset{\leftarrow}{i}$, and for the irreversible adsorption case $\vec{i} \approx \overset{\leftarrow}{i}$.

Using the procedure outlined in Ref. (58), but including the concentration term $[A^-]$ the following relationships can be found

For the reversible case

$$\frac{i_p}{v} = 0.25 \frac{QF}{RT}$$

For the irreversible case

$$\frac{i_p}{v} = 0.368 \frac{Q\beta F}{RT}$$

where i_p = peak current ($A \cdot cm^{-2}$), v = sweep rate ($V \cdot sec^{-1}$), and Q = charge associated with the formation of a monolayer of adsorbed species ($C \cdot cm^{-2}$).

Therefore, from the data in Fig. 3: for peak A, $Q = 8.26 \times 10^{-5} C \cdot cm^{-2}$; for peak B, $Q = 4.36 \times 10^{-5} C \cdot cm^{-2}$; for peak C, $Q = 8.23 \times 10^{-5} C \cdot cm^{-2}$; total = $2.09 \times 10^{-4} \pm 0.12 \times 10^{-4} C \cdot cm^{-2}$ (95% confidence limits).

The value calculated earlier for a unit charge per surface atom based on an average of the atomic surface density of three crystal planes, (111), (100), and (110), was $1.84 \times 10^{-4} C \cdot cm^{-2}$. The agreement might be better than indicated if the three crystal structures were not present in equal amounts. The surface charge density, calculated from the data in Fig. 3 and shown above, and the determination of surface charge density from the measurement of total accumulated charge (Table III) both indicate that, after peak C, there is a net charge of approximately one electron per surface atom. No gold dissolution could be measured in this potential region and it is reasonable to conclude that there is an adsorbed surface layer with the gold atoms in the +1 state.

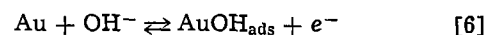
Furthermore, the potentials for the reactions at peaks A, B, and C were found to depend on pH, thus indicating a reaction involving the hydroxyl ion. Figure 5 shows the linear dependence of the potential for the reactions at peaks A, B, and C with the logarithm of the hydroxide concentration. The influence of the sweep rate on peak A was eliminated by plotting $(\Delta \phi_{pAnodic}^A + \Delta \phi_{pCathodic}^A)/2$ (60). The potentials for peaks B and C were not affected by sweep rate for the range studied. The data indicate that the peak potentials for the reactions may be written as (*indicates based on 95% confidence limits)

$$\Delta \phi_p^A = -1.013(\pm 0.019) - 0.061(\pm 0.02) \log [OH^-] \quad *r = 0.965 \quad [3]$$

$$\Delta \phi_p^B = -0.55(\pm 0.04) - 0.058(\pm 0.033) \log [OH^-] \quad *r = 0.926 \quad [4]$$

$$\Delta \phi_p^C = +0.113(\pm 0.034) - 0.082(\pm 0.034) \log [OH^-] \quad *r = 0.937 \quad [5]$$

Therefore, the following adsorption reaction is proposed to account for the three reactions of peaks A, B, and C



That three peaks might arise from the adsorption of a

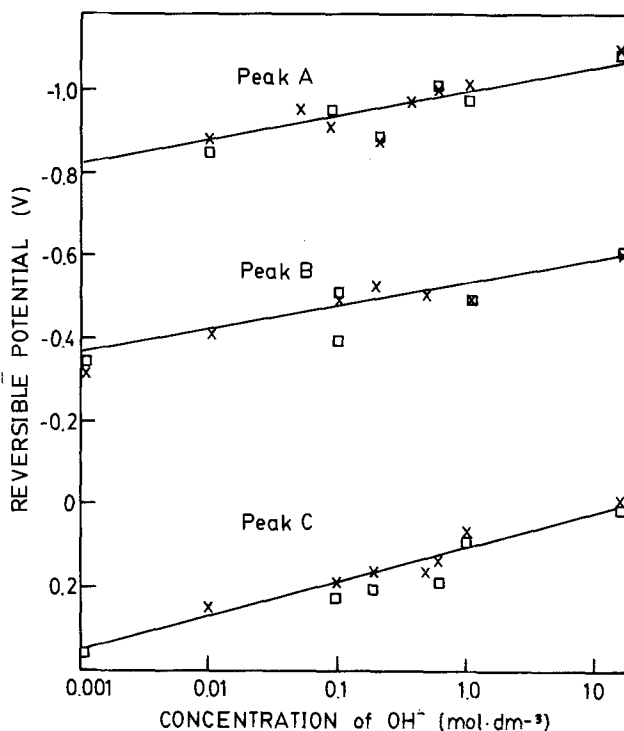


Fig. 5. Effect of hydroxide concentration on reversible potentials of peaks A, B, and C: □, 1.0 $V \cdot sec^{-1}$; ×, 10 $V \cdot sec^{-1}$; temperature = 23.0°C. All potentials vs. SCE.

single species is not unexpected in view of the known behavior of gold (III) oxide, for which the crystal structure has been shown to affect the potential of the Au_2O_3 formation (15, 50-53). On a (100) plane in acid media, Dickertmann, Schultze, and Vetter (15) found the oxidation peak to occur at +1.26V, while on the (111) plane, the oxidation peak occurred at +1.46V. Work on desorption of various adsorbed metal ions on gold single crystal substrates by Schultze and Dickertmann (61) has shown that the desorption peaks from different crystal surfaces may be separated by as much as 0.3V. The actual value for the peak separation was found to depend on the particular ion in question and was interpreted as being related to the work function difference between the gold and the solvated adsorbing ionic species. Although the work functions for the crystal planes (111), (100), and (110) of gold have been estimated to be 5.11, 5.01, and 4.80 eV, respectively, (62, 63), the contribution from the solvent and the hydroxide ion is unknown. The work on the formation of Au_2O_3 (15) indicated that the susceptibility of the crystal planes to oxidation followed the sequence (110) > (100) > (111); that is, the crystal plane with the smallest work function being oxidized first, and the crystal plane with the largest work function being oxidized last. This feature was also noted for the desorption of the metal ions of Bi and Pb from gold single crystals by Schultze and Dickertmann (61), although the ions of Sb, Cu, and Tl did not always show the same sequence. In addition, broadened desorption peaks were observed by them on the (110) crystal plane for Bi^{+3} , Pb^{+2} , and Sb^{+3} . This broadening of the peak was said to be the result of repulsion effects between the metal ions. In the present work, this effect was observed for peak A (Fig. 2), and therefore, as a result of this and the work function value, peak A can be associated with a reaction on the crystal face (110). Likewise, because of the theoretical values of the work function for the planes (100) and (111), the reactions at peak B and peak C are assumed to be related to the crystal planes (100) and (111), respectively.

The reason for the variation observed from run to run in Table III is now apparent. A change in the relative proportion of each crystal face would change the relative peak sizes, but the total charge accumulated would always approximate $1 e^-/\text{Au}$ atom.

Previously reported work (64-66) indicated that three peaks might arise in the adsorption of a single species on platinum electrodes as a result of preferred bonding sites. These preferred bonding sites were said to be unrelated to crystal structure but were a consequence of the proximity of neighboring adsorption sites. However, the peak separations resulting from this phenomenon were quite small (<0.1V) and therefore it is unlikely that the peaks A, B, and C found in the present work were caused as a result of the preferred bonding site phenomenon.

It is possible to correct the theoretical value for the unit charge per surface atom by using the relative proportions of each crystal face indicated from the data, rather than the arithmetic mean value used earlier. Thus, for the data in Fig. 3, the relative area for each peak was measured and is recorded in Table IV. The value calculated by this method is $1.91 \times 10^{-4} \text{ C} \cdot \text{cm}^{-2}$ compared with $1.84 \times 10^{-4} \text{ C} \cdot \text{cm}^{-2}$ for the mean value calculated assuming equal proportions of the (100), (110), and (111) planes for this case. Thus the correlation between the surface charge calculated from the i_p vs. v data in Fig. 3 ($2.09 \times 10^{-4} \text{ C} \cdot \text{cm}^{-2}$) and the surface charge calculated from the relative proportions of each crystal face in Table IV ($1.91 \times 10^{-4} \text{ C} \cdot \text{cm}^{-2}$) is improved. Therefore, if the crystal faces have been correctly assigned to the peaks, the correction applied to the data in Table III should yield a surface charge density which is closer to unity than the previous values. The values calculated are listed in Table V. The average charge per surface atom

Table IV. Unit surface charge density based on the identification of the peaks with distinct crystal planes

Peak	Crystal plane	% of total surface	Calculated unit charge density ($\text{C} \cdot \text{cm}^{-2}$)	Theoretical charge ($\text{C} \cdot \text{cm}^{-2}$) for $1 e^-/\text{surface atom}$
A	(110)	0.291	1.36×10^{-4}	0.40×10^{-4}
B	(100)	0.215	1.92×10^{-4}	0.41×10^{-4}
C	(111)	0.494	2.22×10^{-4}	1.10×10^{-4}
Total charge for $1 e^-/\text{surface atom} = 1.91 \times 10^{-4} \text{ C} \cdot \text{cm}^{-2}$.				

Measurements are for a sweep rate of $1 \text{ V} \cdot \text{sec}^{-1}$, in 1.0M KOH.

cathodic of peak D is $0.98e^-$ for the measurements in 1.0M KOH.

From Table V it is clear that the value of $1 e^-/\text{surface atom}$ is more closely predicted when the relative proportions of each crystal plane are considered. Thus the identification of peaks A, B, and C, with the crystal planes (110), (100), and (111) is further supported.

The data presented here have demonstrated that adsorption reactions do occur on gold electrodes in alkaline solutions at potentials cathodic of the formation of gold (III) oxide. These adsorption reactions are related to the hydroxyl ion via reaction [6] and are apparently limited to monolayer formation on each crystal plane.

Summary

The oxidation process of gold in alkaline solutions has been studied in detail. The potential regions in which the major electrochemical reactions occur for a gold electrode in alkaline solutions were identified in Fig. 1. No gold dissolution in 1.0M KOH was found cathodic of +0.7V vs. SCE [the region of the gold (III) oxidation peak].

At potentials less anodic than the oxidation peak (regions 1 and 2 in Fig. 1), the fast scan potential measurements reveal the presence of three distinct peaks. These peaks could not easily be identified at sweep rates less than $1 \text{ V} \cdot \text{sec}^{-1}$, which would account for the fact that they have not been reported in the literature. The magnitude of the peaks at sweep rates of 10 and $100 \text{ V} \cdot \text{sec}^{-1}$ precluded the possibility that the peaks were the result of impurity oxidation. Since the peak current-sweep rate data (Fig. 3) indicated activation rather than diffusion control for each peak, the parameter i_p/v was used to predict the number of coulombs required to achieve complete surface coverage by the species at peaks A, B, and C. The reaction at each peak was found to occupy only a fraction of the available number of surface sites, but the combined fractions approached the value for monolayer coverage of a univalent species. The fraction of surface occupied by each reaction varied from run to run, but the com-

Table V. Total accumulated surface charge density for the three peaks when the peaks are assigned to the distinct crystal planes

Sweep rate ($\text{V} \cdot \text{sec}^{-1}$)	Previous value ($e^-/\text{surface atom}$)	Corrected value
1.0M KOH		
1	1.01	1.00
1	0.96	1.01
1	0.88	1.03
10	1.00	1.03
10	0.80	0.91
10	0.83	0.91
Average = 0.91		Average = 0.98

Data from Table III using corrected unit theoretical charge for each crystal plane.

bined total was always $\approx 1 e^-$ /surface atom (Table III).

The potentials of the reactions at peaks A, B, and C were found to be linearly dependent on the logarithm of the hydroxide concentration and the involvement of the species OH^- was therefore indicated. Differentiation between the surface sites for the reactions at peaks A, B, and C could therefore only be the result of different bonding energies for the types of bonding sites. Two explanations for different bonding energies on a pure metal electrode had been reported. The first (64) was the result of preferred bonding sites arising from repulsion effects of the adsorbing species. The peak separations found in the potential sweep data (Fig. 2) appear to be too great to be caused by the preferred bonding site phenomenon. The second explanation results from the differences in the work function values between various crystal structures in the metal (63). The peak separations resulting from this effect were much greater. The major crystal faces of a gold electrode have been shown to have different bulk oxide (Au_2O_3) formation potentials (15). Thus the three peaks were identified as hydroxide adsorption reactions on different crystal planes. Based on the work function values for the three most common gold crystal planes, the adsorption peaks A, B, and C were identified with the planes (110), (100), and (111), respectively. Comparison with work on desorption phenomena on gold single crystals (61) revealed that the (110) plane was found to show noticeable interaction effects similar to that found for peak A in the cathodic sweep (Fig. 2), thus supporting the identification of peak A with the (110) crystal plane. Corrections to the data in Table III, based on the identification of the reactions at peaks A, B, and C with the crystal planes (110), (100), and (111), improved the correlation between the total accumulated charge density and the theoretical value of $1 e^-$ /surface atom cathodic of peak D. From these data and from the variation of peak potential with hydroxide ion concentration, reaction [6] was identified with the reactions at peaks A, B, and C.

Acknowledgment

The authors gratefully acknowledge financial assistance from the Natural Sciences and Engineering Research Council of Canada.

Manuscript submitted Aug. 3, 1979; revised manuscript received Oct. 22, 1979.

Any discussion of this paper will appear in a Discussion Section to be published in the December 1980 JOURNAL. All discussions for the December 1980 Discussion Section should be submitted by Aug. 1, 1980.

Publication costs of this article were assisted by the University of Toronto.

REFERENCES

- S. Barnartt, *This Journal*, **106**, 722 (1959).
- H. A. Laitinen and M. S. Chao, *ibid.*, **108**, 726 (1961).
- G. M. Schmid and N. Hackerman, *ibid.*, **109**, 243 (1962).
- J. W. Schultze and K. J. Vetter, *Ber. Bunsenges. Phys. Chem.*, **75**, 470 (1971).
- G. M. Schmid and N. Hackerman, *This Journal*, **110**, 440 (1963).
- R. D. Frankenthal and D. E. Thompson, *ibid.*, **123**, 799 (1976).
- T. Dickinson, A. F. Povey, and P. M. A. Sherwood, *Trans. Faraday Soc.*, **71**, 298 (1975).
- J. W. Schultze, *Electrochim. Acta*, **17**, 451 (1972).
- F. D. Will and C. A. Knorr, *Z. Elektrochem.*, **64**, 270 (1960).
- S. B. Brummer and A. C. Makrides, *ibid.*, **111**, 1122 (1964).
- S. El Wakkad and A. S. El Din, *J. Chem. Soc.*, **9**, 3098 (1954).
- K. Ogura, S. Hariyama, and K. Nagasaki, *This Journal*, **118**, 531 (1971).
- M. D. Goldshtein, T. S. I. Zalkind, and V. I. Veselovskii, *Sov. Electrochem.*, **9**, 699 (1973).
- M. M. Lohrengel and J. W. Schultze, *Electrochim. Acta*, **21**, 957 (1976).
- D. Dickertmann, J. W. Schultze, and K. J. Vetter, *Electroanal. Chem.*, **55**, 429 (1974).
- M. C. Banta and N. Hackerman, *This Journal*, **111**, 144 (1964).
- G. M. Schmid and R. W. O'Brien, *ibid.*, **111**, 832 (1964).
- A. K. N. Reddy, M. Genshaw, and J. O'M. Boçkris, *J. Electroanal. Chem. Interfacial Electrochem.*, **8**, 406 (1970).
- F. F. Faizullin and N. P. Nikandrov, *Elektrokhimiya*, **3**, 998 (1967).
- T. Takamura, K. Takamura, W. Nippe, and E. Yeager, *This Journal*, **117**, 626 (1970).
- G. Armstrong, F. R. Himsworth, and J. A. V. Butler, *Proc. R. Soc. London, Ser. A*, **43**, 89 (1934).
- J. N. Gaur and G. M. Schmid, *J. Electroanal. Chem. Interfacial Electrochem.*, **24**, 279 (1970).
- A. Hickling, *Trans. Faraday Soc.*, **42**, 518 (1946).
- S. H. Cadle and S. Bruckenstein, *Anal. Chem.*, **46**, 16 (1974).
- B. E. Conway, E. Gileadi, and M. Dzieciwch, *Electrochim. Acta*, **8**, 143 (1963).
- M. Knobel, P. Caplan, and M. Eiseman, *Trans. Electrochem. Soc.*, **43**, 55 (1923).
- A. Hickling and S. Hill, *Discuss. Faraday Soc.*, **1**, 236 (1947).
- D. E. Icenhower, H. B. Urbach, and J. H. Harrison, *This Journal*, **117**, 1500 (1970).
- R. S. Sirohi and M. A. Genshaw, *ibid.*, **116**, 910 (1969).
- J. J. MacDonald and B. E. Conway, *Proc. R. Soc. London, Ser. A*, **269**, 419 (1962).
- W. J. Müller and E. Löw, *Trans. Faraday Soc.*, **31**, 1291 (1935).
- W. I. Shutt and A. Walton, *ibid.*, **30**, 914 (1934).
- R. Thacker and J. P. Hoare, *Electrochem. Technol.*, **2**, 61 (1964).
- R. Cordova, M. E. Martins, and A. J. Arvia, *This Journal*, **126**, 1172 (1979).
- J. P. Hoare, *ibid.*, **110**, 245 (1963).
- J. P. Hoare, "The Electrochemistry of Oxygen," Interscience, New York (1968).
- J. P. Hoare, *Electrochim. Acta*, **9**, 1289 (1964).
- J. D. Carr and N. A. Hampson, *This Journal*, **119**, 325 (1972).
- D. W. Kirk, F. R. Foulkes, and W. F. Graydon, *ibid.*, **125**, 1436 (1978).
- E. Gileadi, E. Kirova-Eisner, and T. Penciner, "Interfacial Electrochemistry," p. 210, Addison-Wesley Publishing Co., Reading, Mass. (1975).
- S. Barnartt, *This Journal*, **99**, 549 (1952).
- S. Barnartt, *ibid.*, **108**, 102 (1961).
- R. S. Nicholson and I. Shain, *Anal. Chem.*, **36**, 706 (1964).
- C. M. Ferro, A. J. Calandra, and A. J. Arviá, *J. Electroanal. Chem. Interfacial Electrochem.*, **50**, 403 (1974).
- D. M. MacArthur, *This Journal*, **119**, 672 (1972).
- M. W. Breitner, *Electrochim. Acta*, **8**, 973 (1963).
- C. M. Ferro, A. J. Calandra, and A. J. Arviá, *J. Electroanal. Chem. Interfacial Electrochem.*, **65**, 936 (1975).
- C. M. Ferro, A. J. Calandra, and A. J. Arviá, *ibid.*, **55**, 321 (1974).
- N. R. DeTacconi, J. O. Zerbino, M. E. Folquer, and A. J. Arviá, *ibid.*, **85**, 213 (1977).
- M. J. Clavilier, A. Hamelin, and G. Valette, *C. R. Acad. Sci. Ser. C*, **265**, 221 (1967).
- A. Hamelin and M. Sotro, *ibid.*, **271**, 609 (1970).
- M. Sotro, *ibid.*, **274**, 1776 (1972).
- G. Ertl, *Ber. Bunsenges. Phys. Chem.*, **75**, 967 (1971).
- B. E. Conway, H. Angerstein-Kozłowska, and L. H. Laliberté, *This Journal*, **117**, 626 (1970).
- E. Gileadi, Editor, "Electrosorption," pp. 87-103, Plenum Press, New York (1967).
- D. D. Bode Jr., T. N. Andersen, and H. Eyring, *J. Phys. Chem.*, **71**, 792 (1967).
- K. F. Lin, *This Journal*, **125**, 1077 (1978).
- S. Srinivasan and E. Gileadi, *Electrochim. Acta*, **11**, 321 (1966).
- H. Angerstein-Kozłowska, J. Klinger, and B. E.

- Conway, J. *Electroanal. Chem. Interfacial Electrochem.*, **75**, 61 (1977).
60. H. Angerstein-Kozłowska, J. Klinger, and B. E. Conway, *ibid.*, **75**, 45 (1977).
61. J. W. Shultze and D. Dickertmann, *Surf. Sci.*, **54**, 489 (1976).
62. A. Hamelin and J. Lecoœur, *Collect. Czech. Chem. Commun.*, **36**, 714 (1971).
63. S. Trasatti, *Adv. Electrochem. and Electrochem. Eng.*, **10**, 274 (1977).
64. H. Angerstein-Kozłowska, B. E. Conway and W. B. A. Sharp, *J. Electroanal. Chem. Interfacial Electrochem.*, **9**, 43 (1973).
65. S. Gottesfeld and B. E. Conway, *J. Chem. Soc. Faraday Trans. I*, **69**, 1090 (1973).
66. B. V. Tilak, B. E. Conway, and H. Angerstein-Kozłowska, *J. Electroanal. Chem. Interfacial Electrochem.*, **48**, 1 (1973).

Electrochemical Properties of Iron Naphthalocyanine on Carbon Black for O₂ Reduction and Evolution in Alkaline Media and Applicability to Air Cathodes

G. Magner, M. Savy,* and G. Scarbeck

Laboratoire d'Electrochimie Interfaciale du C.N.R.S., 92190 Meudon-Bellevue, France

ABSTRACT

The synthesis, optical spectra, and x-ray pattern of iron naphthalocyanine as the pure powder are reported. The electrochemical properties for O₂ reduction and evolution of this compound loaded on carbon black supports have been determined by ultrathin and rotating ring-disk electrode techniques. While on the carbon black support O₂ reduction occurs through a two electron pathway followed by HO₂⁻ decomposition, four electron reduction is obtained on the loadings with a high efficiency. Stability tests proved their applicability as useful catalysts as the air cathode in metal-air generators.

While the capacity of monomeric phthalocyanine materials for nearly reversible charge transfer reaction (1) has been demonstrated, the main objection to their use as practical catalysts in metal-air or fuel cell generators has been their lack of stability. However, by synthesizing polymeric materials, high stability (2) during continuous operation in 3M SO₄H₂ for times up to 3000 hr has been obtained. The working potentials of the oxygen electrode remain about 400 mV below the four electron reversible potential. In these types of compounds the effect of the enlargement of the π -electron system on their activity has been emphasized by several groups (3a, b).

One might hope to be able to apply such materials to metal-air systems due to the lower current densities (C.D.) involved. On different types of polymeric iron phthalocyanines (4) spectroscopic and electrochemical investigations have been performed in alkaline media and correlations between the activity and the structural properties have been found. The role of the π -electron delocalization in the optimization of the free energy of oxygen adsorption on the iron sites (due to π -d hybridization) has been confirmed by ESCA techniques (5). In the case of compounds of larger sizes the π -electron delocalization is inhibited due to spin-spin interactions. Such effects upon chemical reactivity have already been noticed in the chemistry of conjugated ring systems (6), the activity decreasing in the order anthracene > naphthalene > benzene.

Besides this π -electron density condition, many factors can affect the electrochemical activity, for example, the junction with the support, the wettability, or the d orbital configuration of the iron which is very critical (2-4). The difficult problem is to meet all these requirements simultaneously. Several types of synthesis have been worked out. A rapid technique for the comparison of the electrochemical activity is the ultrathin electrode (7). The preparations were tested

by easy to perform spectroscopic techniques, in order to check the electronic configuration.

In this paper different syntheses of iron naphthalocyanine are briefly summarized. Investigation of the samples by optical spectroscopy and x-rays is presented. Then more complete studies of the electrode performances for the electroreduction in 1M alkaline medium are made using the ultrathin electrode technique and the rotating ring-disk electrode (RRDE) to determine the reaction path and the kinetic constants.

Previous investigations have been performed on a type of carbon black formed from CO (8a, b), which gave a life expectancy, as air electrode material, of 1000 to 1500 2 hr cycles. However the oxygen electrode carbon black catalysts have the disadvantage of a strong H₂O₂ generation which perturbs the activity of the metal electrode. By application of the rotating disk technique, investigations can be made of the amount of H₂O₂ formed and of the favored reaction path (9). A diagram of the energies of intermediates involved in the overall process was given by Morcos and Yeager (10).

Experimental

Synthesis and Characterization

The details of the synthesis and EPR investigation of samples are given elsewhere (11). Briefly two syntheses of iron naphthalocyanine have been achieved. Synthesis I corresponds to the reaction of orthodicyanonaphthalene with Fe dipivalolymethane. Synthesis II is identical to synthesis I with the addition of ammonium paramolybdate under the same experimental conditions. From EPR and ESCA data (11,12) these molybdenum ions which were added as a probe are partially dispersed in the naphthalocyanine structure with valencies 4, 5, and 6.

Instead of 7.3% w/w as theoretically expected, the amount of iron with synthesis I is 5.3%. With synthesis

* Electrochemical Society Active Member.
Key words: battery, carbon, catalysis, chelates.

II only 4.3% w/w iron has been found with approximately 1 Mo atom per iron. The molybdenum ions with valencies 4 or 5 are distributed either substitutionally for the iron in the naphthalocyanine structure or are in the oxide form (10, 11).

X-ray analysis.—Debye-Scherrer patterns on the powder resulting from synthesis I are shown in Fig. 1. The pattern is similar to that shown by the γ -form of phthalocyanines (13). This form involves small size crystallites of some 10 nm or less in diameter as shown by electron microscopy. Further investigations will be conducted in order to determine the structural properties.

Iron naphthalocyanine is difficult to vacuum sublime: at 320°C after 2 hr at 10^{-7} Torr the thickness of the deposited layers is about 160 nm as measured by a Talystep recorder. For a similar deposit of iron phthalocyanine the time required is less than 5 min.

Optical spectroscopy.—The optical transmission absorption spectrum was obtained using a Cary 17 spectrometer in a layer deposited onto a quartz slab. The spectrum in Fig. 2 is similar to that of phthalocyanine compounds (14, 15). It presents the characteristic Soret bands due to charge transfer transitions between the central ion and the ligand. In the visible, the absorption band due to π - π^* and π -d transitions can also be observed.

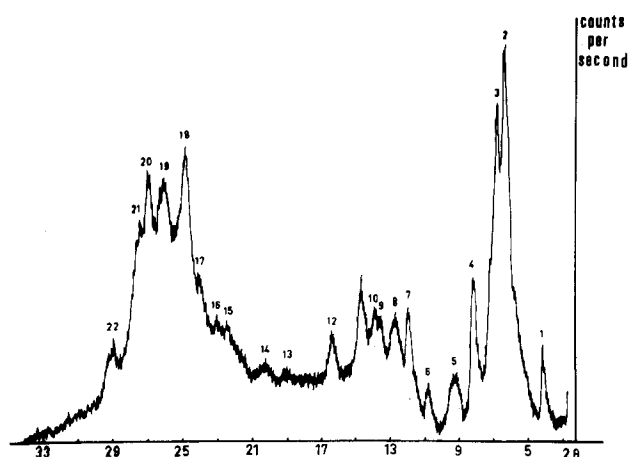


Fig. 1. X-ray diffraction spectrum

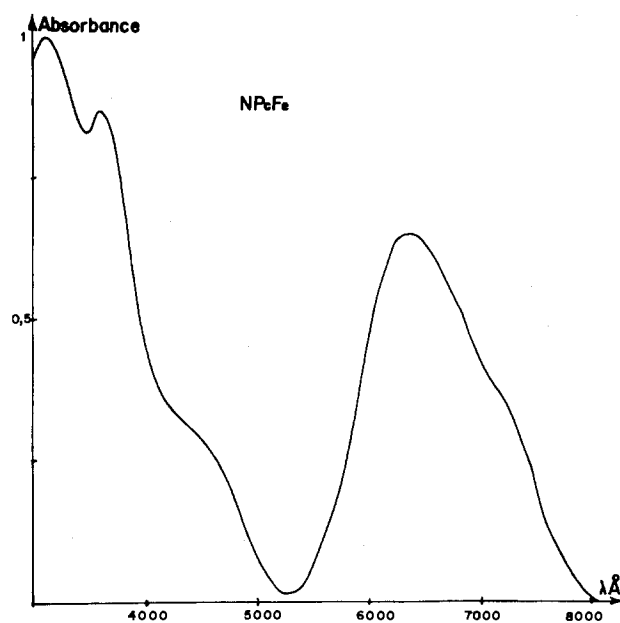


Fig. 2. Optical absorption spectrum by transmission

Electrochemical Investigations

Previous investigations (16) on a phthalocyanine dimer have stressed the role of $\text{Fe}^{\text{II}}/\text{Fe}^{\text{III}}$ couple on its electrochemical activity. Due to the action of reducing couples the stoichiometry discrepancy in iron and H_2 may therefore affect the properties of these series of compounds, especially in the range of polarization where the conductivity in the solid phase is the limiting factor. Using different iron donors in the synthesis of naphthalocyanine it is possible to modify the iron content. For example with ferrocene it drops to 2.2% w/w.

Ultrathin electrode.—Preliminary experiments have been conducted using the Lundquist-Vogel ultrathin electrode technique (6) to determine the influence of the stoichiometry on the activity of these samples. The most active samples were investigated using the rotating disk electrode.

1M alkali has been chosen as the medium for the comparison with the dimer. Structural effects of the carbon black support were also found to be an important factor in the activity of the loadings (17). Best performances were obtained with low microporosity materials. For these preliminary tests Vulcan carbon blacks have been chosen as support, with a 10% loading synthesis.

The activity may vary as a function of the charge of the catalyst on the nickel grid or with the grinding. After thorough grinding the activity as a function of the charge presents a plateau value at 0.2 mg cm^{-2} , independent of the applied potential. This value has been chosen, therefore, for all the samples investigated.

As seen in Fig. 3 for synthesis I the activity is noticeably increased with the iron content in the naphthalocyanine structure, depending upon the iron donor used in the synthesis. Between ferrocene (2.2% w/w iron) and iron dipivaloylmethane (5.3% w/w iron) the zero current potential increases from -100 mV to -72 mV SCE with the corresponding increase in current densities. The use of Mo catalysts (syntheses II) extends the Tafel zone of polarization over almost one decade of current densities.

The activity of high iron content samples can also be compared with that of the phthalocyanine dimer previously investigated (16, 17). For low polarizations the rest potential and current densities are identical. The increase in current obtained at high polarizations is a factor of about 10.

Rotating ring-disk electrode.—Equipment.—The basic experimental equipment has been previously reported (18). In this work a ring disk electrode has been substituted for the disk electrode. Its main interest lies in the wide range of the speeds available from 4 to 500 rps with a stability of 1%. The mechanical accuracy $\pm 3\mu$ in the rotation plane can be maintained independent of the rotation speed. In addition, within these characteristics several types of disks in different metals or of different diameters can be fitted and provided with rings. The electrode support can be changed without any modification of the initial accuracy of the equipment. This apparatus is represented in Fig. 4 with the modifications required for the present work. In order to avoid any possible contamination, a gold ring has been used for current collection. The disk diameter was 4 mm. Preliminary experiments have been conducted to test the validity of the equipment.

This first condition of the validity of this technique concerns the surface of the metal and of the insulator which should be situated in a plane perpendicular to the rotation axis. A slight deformation of this plane can modify the diffusion layer in such a way that the collection factor does not remain constant but decreases in a noticeable fashion as the rotation speed increases. After thorough polishing and machining of the surface, $5 \cdot 10^{-3} \text{ M K}_3\text{Fe}(\text{CN})_6$ in 1M KOH supporting electrolyte gave a constant collection factor

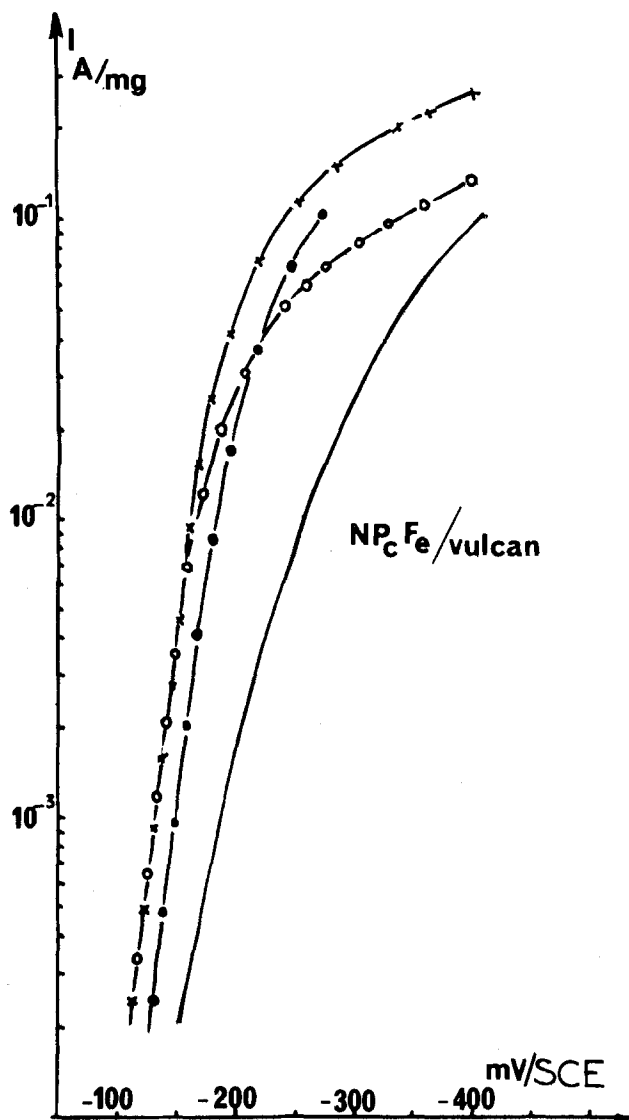


Fig. 3. *i*-*V* curves by ultrathin electrode technique. — continuous: Vulcan support. ● synthesis 2.2% iron w/w. ○ synthesis 5.6% iron w/w. × synthesis with Mo added.

of 0.26 up to 196 rps. If surface defects of the order of 0.05 mm were present a constant collection factor was not observed under the same experimental conditions. In order to work with carbon black powder under similar conditions, a hollow cavity 0.25 mm in depth was made on the disk. Tests of this electrode are described below.

Electrode preparation: binding agent.—Several tests were performed in order to choose appropriate binding agents. Initially, a spectroscopically pure paraffin wax "Uvasol" (19) was used. By mixing with the carbon powder, a plastic paste can be obtained which can be introduced into the disk cavity and which remains adherent. This paste can be smoothed mechanically with a razor blade to meet the above conditions. With this mixture, limiting currents on the disk do not present the classical linear relationship as a function of the square root of the rotation speed. As the diffusion does not appear to be the limiting factor in the overall reaction this assumption was tested by plotting the current densities as a function of the applied scanning voltage velocity v for a rotation speed initially equal to zero. Two domains can be observed for the peak current I_p

$$\text{Domain I} \quad I_p \propto \sqrt{v} \quad [1]$$

$$\text{Domain II} \quad I_p \propto v \quad [2]$$

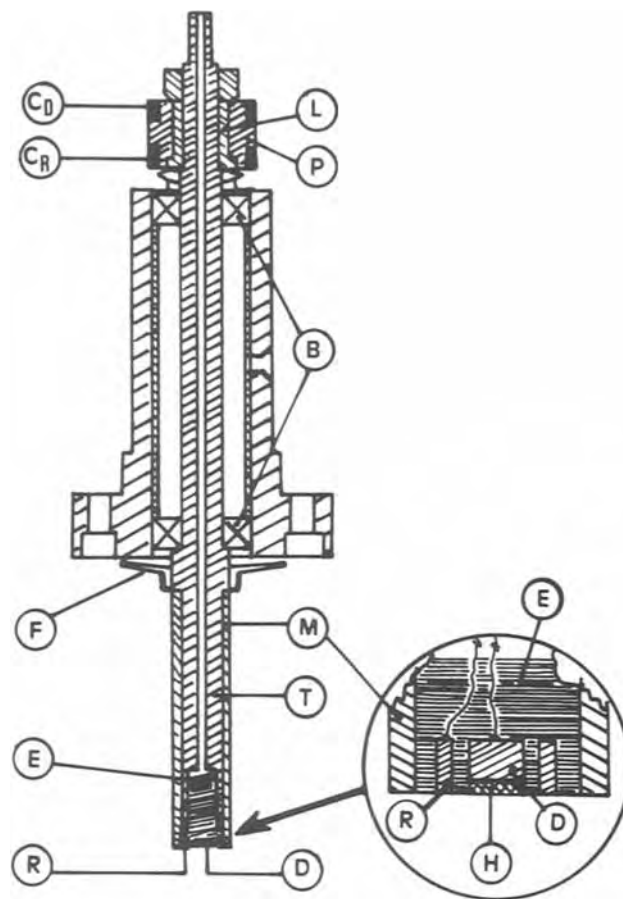


Fig. 4. Ring disk apparatus. Cross sectional of the RRDE assembly. C_D : disk rotating silver contact, C_R : ring rotating silver contact, L: brass cylinder fitted on the Plexiglas support, P: Plexiglas cylinder supporting rotating contacts, T: hollow shaft on the rotating system, M: Kelf sleeve tightly covering the immersed part of the electrode holder, E: epoxy resin, F: Kelf deflector shielding the bottom bearing, B: bearings, R: gold ring, D: gold disk, H: hollow cavity for the carbon black electrode.

Depending upon the scanning velocity the limiting step is first the diffusion then the adsorption. At 9 rps data are similar but the diffusion domain is smaller, the adsorption domain being extended. Using this type of binding agent the RRDE technique seems to be inappropriate due to slow adsorption kinetics.

In the rest of this study Soreflon¹ has been used as the binding agent. A mixture of carbon black and 40% w/w Soreflon is prepared. A typical preparation was, for example, C 50 mg, Soreflon 0.14 ml of 98 mg/ml solution.

The paste is immediately introduced into the cavity and then smoothed mechanically as above. To avoid any poisoning after the preparation, the electrode is cautiously washed with ethanol. For comparison with "Uvasol," data are presented in Fig. 5.

A pseudo plateau is visible with the Soreflon preparation which is linear as a function of the square root of the rotation speed while the *i*-*V* slope is steeper. The increase in *C.D.* at -650 mV SCE is compatible with the reduction of NiO present at high concentration (18%) w/w in the carbon black structure.

Results

Loadings.—The collection factor was determined before and after plotting the *i*-*V* curves, as described above, using the same solution deaerated with Ar. A constant factor $0.22 < N < 0.26$ was measured over a wide range of rotation speeds.

¹ Societe Francaise des Matieres Colorantes.

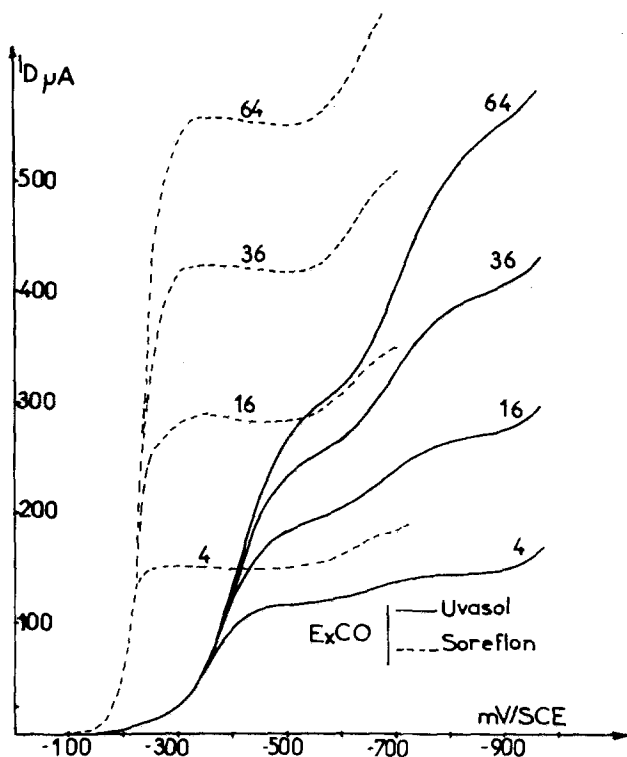


Fig. 5. Effects of the binding agent on the O_2 electroreduction. Continuous line Uvasol, dashed line Soreflon.

Vulcan support.—A preliminary study has been performed for the reasons stated above on a 10% loading on Vulcan carbon black in order to compare the properties of the phthalocyanine dimer studied previously (4) with those of the iron naphthalocyanine (synthesis I). Data are presented in Fig. 6a, b, c. In Fig. 6a are represented the ring currents obtained on the three types of samples at 64 rps. The drastic drop in H_2O_2 generation from the carbon black support on loading can be seen. In the active range of polarizations (for

potentials higher than 375 mV) the ring current remains much lower with the iron naphthalocyanine loading (0.02 μA) than with the dimer (0.45 μA). Correspondingly, in Fig. 6b, which shows the disk current in the region of diffusion limitation, the current densities with the iron naphthalocyanine loading are approximately twice those of the support whereas with the dimer they are less than twice. In the Tafel region, the current densities with the dimer and the iron naphthalocyanine are similar, as observed with the ultrathin electrode technique. In Fig. 6c, the linear relationship as a function of the square root of the rotation speed is obeyed. As in the other figures, in Fig. 6a and b the improved efficiency of the four electron reduction process with the iron naphthalocyanine loading can immediately be seen. The slight deviation from the value 2 in the slope, compared with that on the Vulcan, can be attributed to a decrease of the surface area in the case of this loading.

Ex CO carbon black (holding recycling) support.—In the rest of this work 2.5% loadings on carbon black ex CO have been used. Data on both the loading and the support at 64 rps for the disk and the ring are presented on Fig. 7a and b, respectively.

In Fig. 7a, a hump is visible on both plots at a scanning velocity of 2 mV/sec, which vanishes for the lower rate of 0.1 mV/sec. The plateau domain is better defined with the loading than with the support, an effect which can be due to the presence of nickel. In the Tafel region the slope is about 30 mV per decade with the loading as against 60 mV with the support. Potentials at constant current densities are between 120 and 150 mV more positive with the loading than with the support. In the plateau region, in the presence of the loading, the current densities are twice those of the support alone, as previously found with the Vulcan.

In Fig. 7b, the corresponding ring currents are represented. In the range of useful polarizations they remain below 1 μA on the loaded electrode. In contrast, on the support alone they rise with the disk current, being one and a half orders of magnitude higher. The corresponding efficiencies for H_2O_2 formation are about 57% on the support and 0.45% on the loaded electrode.

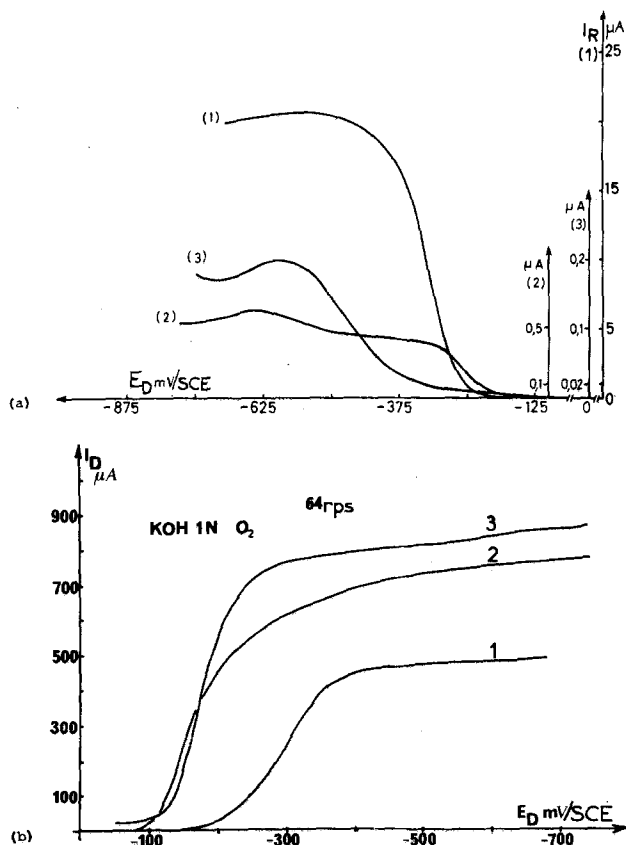


Fig. 6. Comparison Vulcan-dimer-FeNPc on the O_2 electroreduction. (a) Ring currents at 64 rps. Curve 1, Vulcan; curve 2, dimer; curve 3, NPc. (b) Corresponding disk currents. (c) Disk current vs. $(rps)^{1/2}$.

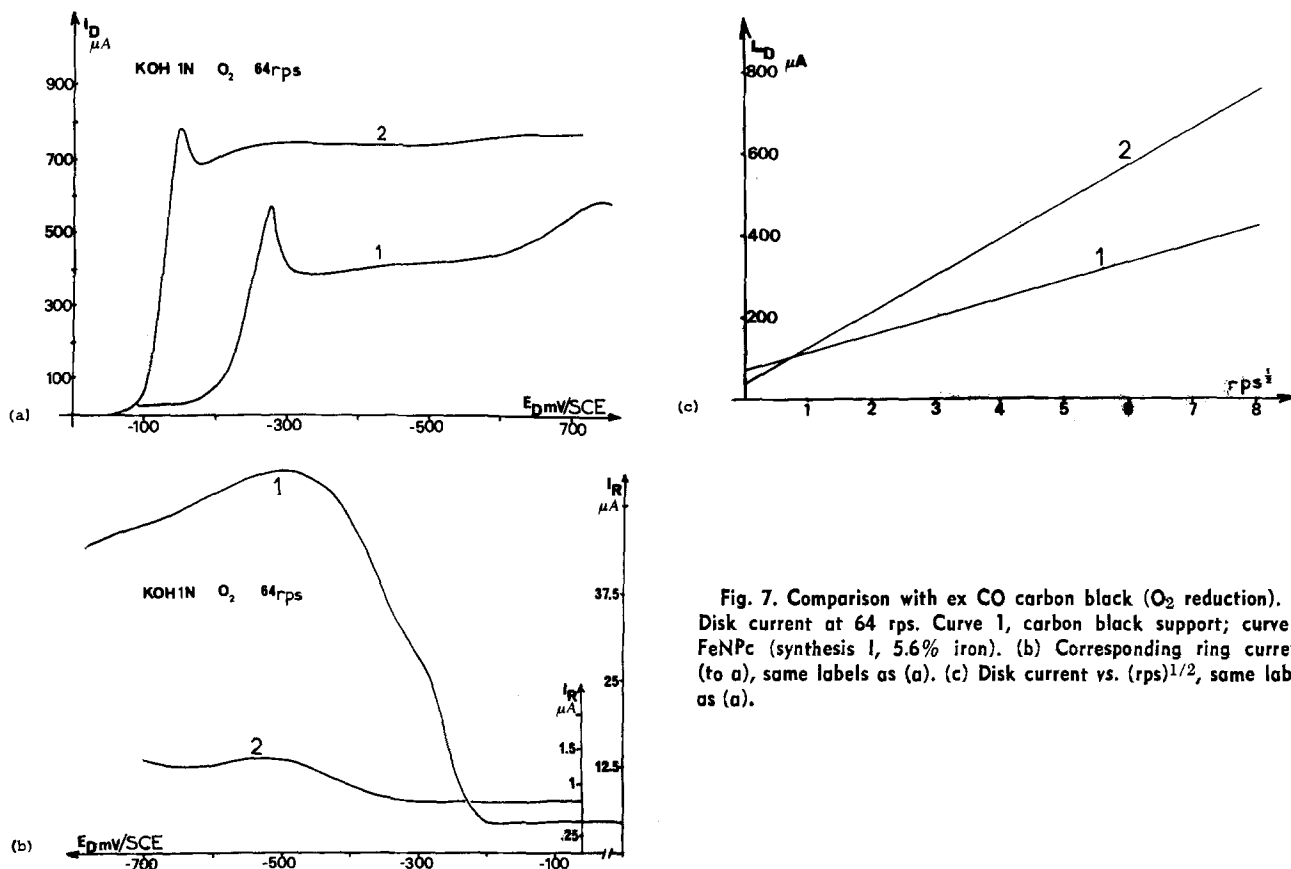


Fig. 7. Comparison with ex CO carbon black (O_2 reduction). (a) Disk current at 64 rps. Curve 1, carbon black support; curve 2, FeNpC (synthesis I, 5.6% iron). (b) Corresponding ring currents (to a), same labels as (a). (c) Disk current vs. $(\text{rps})^{1/2}$, same labels as (a).

In Fig. 7c, disk currents are represented on the loaded electrode and the support as a function of the square root of the rotation speed. Linear plots are found which do not pass through the origin. Because this does not occur in thoroughly deaerated solutions (see Fig. 8b), this discrepancy can be attributed to the presence of adsorbed oxygen. After correction for the residual current, the disk currents with the loading are found to be double that those for the support alone. This is in accord with the above data on Vulcan.

On the anodic side the activity of the loading is increased compared to that of the ex CO carbon black support. The overpotential for O_2 evolution drops initially by approximately 200 mV. Under oxygen the system is relatively stable but under nitrogen the activity tends towards that of the support.

Carbon black ex CO alone.—Disk and ring currents as a function of the square root of the rotation speed under 1 atm of O_2 are shown in Fig. 8a. As the rotation speed increases, the ring current tends towards a limit. The first explanation of this feature may be associated with the roughness of the electrode or the insulation surface. However it has to be pointed out that under thoroughly deaerated solutions, classical disk and ring currents are obtained which are linear functions of the square root of the velocity passing through the origin, similar to the data obtained on the loading. The collection factor with the loading and with deaerated solutions on the support remains constant up to 81 rps. In the presence of O_2 the ring current begins to deviate for rotation speeds higher than 16 rps. If H_2O_2 was decomposed before flowing to the ring, the reverse phenomena would be observed. Nonnegligible recycling of oxygen into the electrochemical reaction coming from the H_2O_2 decomposition would increase the disk current and not yield a factor of about 2 in the current densities between the support and the loading in the plateau region (9). An adsorption limiting step can also be ruled out by investigation of the ring current in the presence of H_2O_2 solution. A Tafel slope is observed which is compatible with charge transfer limiting kinetics without any detection of an adsorption-limiting step.

Stability under recycling conditions.²—Thin porous electrodes have been prepared from a mixture of 20% Teflon with carbon black powder with or without a loading of iron naphthalocyanine. The porous electrodes were obtained after compressing the powder at 50 kg/cm² on an expanded nickel grid. Tests were conducted in 6M KOH solutions at ambient temperatures. Potentials were monitored using an automated system between +10 and -10 mA cm⁻² during 2 hr cycles. The life expectancy for the carbon black support with 10, 5, and 2.5 w/w percent loading synthesis I and II are shown in Fig. 9. The activity increases with the dilution, the greatest activity being obtained for the 2.5% loadings. The enhancement is about 100 cycles with a factor of 2 in dilution. No differences are visible between synthesis I and II (at 2.5% w/w). With the most dilute loadings, up to 375 cycles, the activity on the cathodic side remains higher than that of the support, the drop in activity occurring at 600 cycles.

On the carbon black support, by applying cycles at 1 mV/sec, HO_2^- formation can be detected. Voltammetric scans after 300 cycles are presented in Fig. 10. Potentials are measured in this case vs. Hg/HgO reference electrode.

While the cathodic currents are comparable, on the anodic side, the gain in potential at 100 mA cm⁻² is about 100 mV for the loading. The high intensity peak due to HO_2^- visible on the support at 0 mV potential is not present on the loading on which the formation of HO_2^- remains negligible. The reduction peak at 300 mV on the support alone is slightly depleted for the loading. On the support alone as the recycling increases the HO_2^- formation is inhibited while the peak observed in reduction is enlarged.

Discussion

In this section we will discuss first the data obtained on the ex CO carbon black alone. The practical problem is to avoid the H_2O_2 generation and the techniques used may bring some insight on this problem.

² We acknowledge Dr. Feuillade and Mr. Dupeyr r  from CGE Marcoussis who obtained these data.

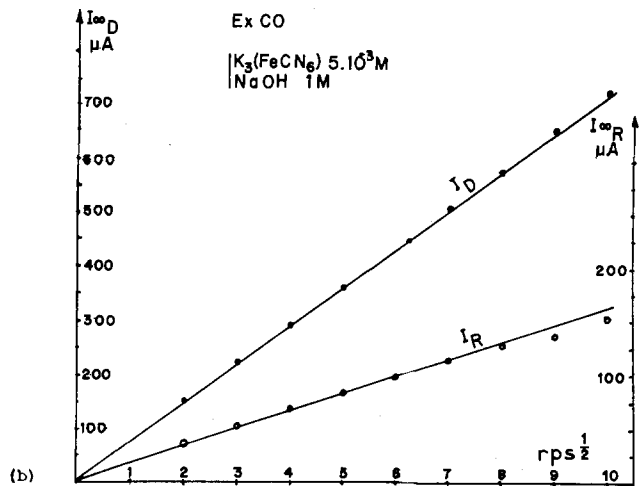
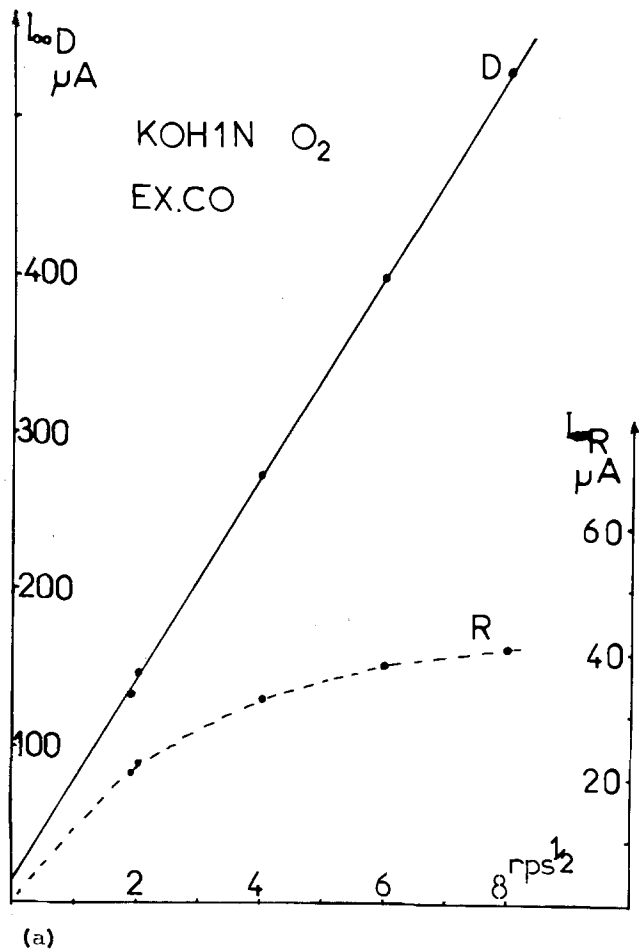


Fig. 8. Ring and disk currents on ex CO carbon black vs. $(rps)^{1/2}$. (a) In presence of O₂: D, disk; R, ring. (b) In ferrocyanide de-aerated solutions (same labels).

Ex CO alone (O₂ reduction mechanism).—Damjanovic, Genshaw, and Bockris (20) first established a criterion for the determination of the kinetic parameters of O₂ reduction in using the RRDE. They started from a simple model in which the reaction intermediate can diffuse into the solution or undergo a reducing process. Linear plots of NI_D/I_R (N : collection factor, I_D and I_R disk and ring currents, respectively) as a function of $\omega^{-1/2}$ were obtained on the basis of their assumptions.

More recently Wroblowa *et al.* (21) considered a more general scheme of reaction for O₂ electroreduction. Diagnostic criteria were derived from the shape of the NI_D/I_R plots vs. $\omega^{-1/2}$ in accord with the different reaction paths. This type of interpretation can be applied in the case investigated here. Following

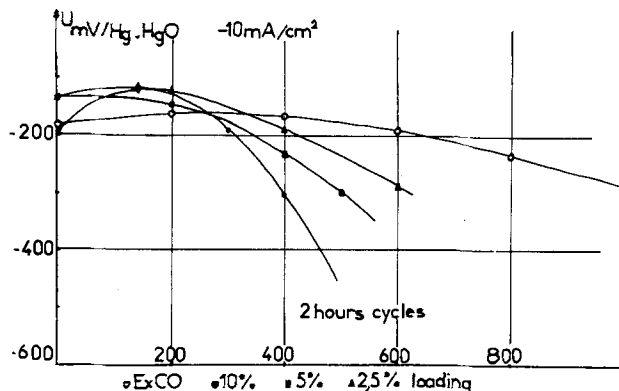


Fig. 9. Potential stability vs. recycling at 10 mA cm^{-2} . \circ carbon black; \bullet 10% loading; \blacksquare 5% loading; \blacktriangle 2.5% loading.

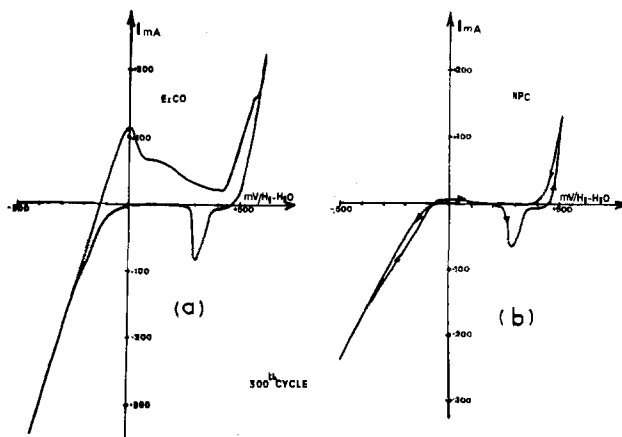


Fig. 10. Voltammetry after 300 cycles. (a) Carbon black (alone). (b) Loading (2.5%).

the latter paper with a desorption controlled ring current, the variation of the slope and intercept of these plots as a function of the applied voltage are not linear vs. $\omega^{-1/2}$.

In the present study it is also not possible to obtain such linear plots (NI_D/I_R vs. $\omega^{-1/2}$). However linear plots NI_D/I_R vs. $\omega^{+1/2}$ were obtained and are represented on Fig. 11b using the original data presented in Fig. 11a. For low applied overvoltage the plots extrapolated to $\omega = 0$ intersect the ordinate axis at $NI_D/I_R = 1$. This ordinate then increases with the overvoltage, the slope of the different plots remaining invariant.

In the case of a desorption controlled ring current the expression NI_D/I_R has been calculated in Ref. (9) as a function of the kinetic parameters taking into account the rate of recycling. The rate of loss of the peroxide from the system is given by

$$k_D[\text{HO}_2^- \text{ Sol}] = \vec{k}_5[\text{HO}_2^- \text{ ads}] - \overleftarrow{k}_5[\text{HO}_2^- \text{ Sol}] \quad [3]$$

where

$$k_D = 0.62 D^{2/3} \nu^{-1/6} \omega^{1/2} \quad [4]$$

D and ν being the diffusion coefficient for HO_2^- and the kinematic viscosity. \vec{k}_5 and \overleftarrow{k}_5 are the rate constants for adsorption and desorption respectively.

I_R is given by

$$I_R = 2FN \frac{\vec{k}_5 k_D}{k_D + \overleftarrow{k}_5} [\text{HO}_2^- \text{ ads}] \quad [5]$$

writing

$$B = 0.62 D^{2/3} \nu^{-1/6} \quad [4']$$

and the experimental relationship

$$I_D = B\omega^{1/2} \quad [6]$$

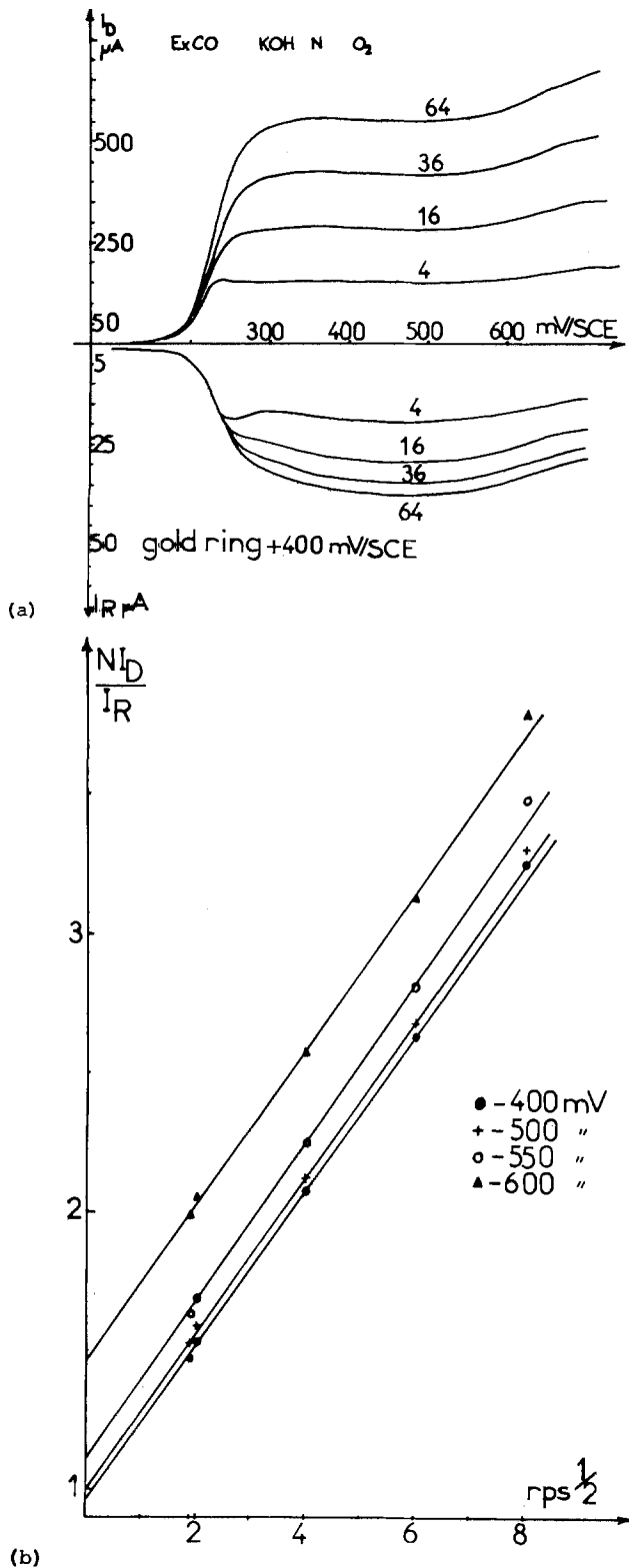


Fig. 11. $N I_D / I_R$ vs. $\omega^{1/2}$ vs. applied potentials. (a) Initial disk and ring currents under oxygen. Data presented on Fig. 8 and 9 have been obtained on another variety of carbon black ex CO than those presented on Fig. 7, 0.1 mV/sec scanning (numbers indicated are rps). (b) Calculated curves from (a) $N I_D / I_R$ plots vs. $\omega^{1/2}$.

A correction is made for the residual current

$$\frac{N I_D}{I_R} = \frac{B \omega^{1/2} + \overleftarrow{k}_5}{\overrightarrow{k}_5} \cdot \frac{1}{[\text{HO}_2^- \text{ ads}]} \quad [7]$$

As the overvoltage increases, the near constancy of the slopes implies

$$\overrightarrow{k}_5 [\text{HO}_2^- \text{ ads}] = c t^0 \quad [8]$$

$$\text{or also } k_5 \text{ and } [\text{HO}_2^- \text{ ads}] \text{ are constant.} \quad [9]$$

In the region (low overvoltages) where I_D is found to be twice as large on the loaded material as for the support alone, it follows that in Eq. [36] of Ref. (9)

$$\overrightarrow{k}_1 \neq \overrightarrow{k}_3 \neq 0 \quad [10]$$

where \overrightarrow{k}_1 = kinetic constant for the four electron process reduction, \overrightarrow{k}_2 = kinetic constant for the two electron process, \overrightarrow{k}_3 = kinetic constant for the HO_2^- reduction process, and k_4 = kinetic constant for HO_2^- decomposition.

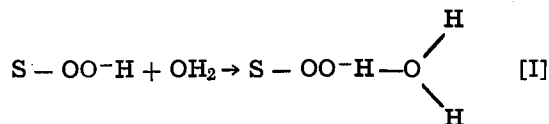
From Eq. [36] of Ref. (9) Eq. [10] means

$$\overrightarrow{k}_2 \propto k_4 \quad [10']$$

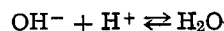
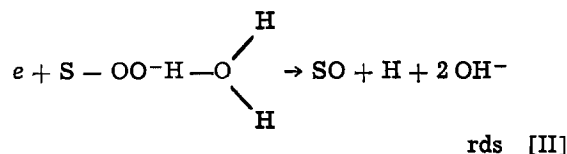
The velocity of decomposition of HO_2^- is practically equal to its velocity of formation. The reaction path is a two electron process with a totally irreversible desorption limiting step.

Remarks.—The dependence of k_4 upon cathodic polarization can be interpreted as a succession of two electrochemical reactions, cathodic and anodic, in the adsorbed phase.

The cathodic reaction should be the rate-determining step, the anodic reaction being very fast. The data are compatible with the following mechanism



(Due to the symmetry considerations (11) the wetting is faster when the water molecule is fixed by the oxygen atom on the surface than the reverse.)



The rds corresponds to the formation of hydrogenated free radical. In addition, due to the applied potential, step [III] can be fast.

Without any additional hypothesis about the HO_2^- decomposition mechanism this information can be introduced into Eq. [37] of Ref. (9) by considering two cases

$$1) \quad k_1 = k_3 = 0$$

$$\frac{N I_D}{I_R} = \tau \left[\frac{k_4 \overrightarrow{k}_5}{k_D \overrightarrow{k}_5} + \frac{k_4 + \overrightarrow{k}_5}{\overrightarrow{k}_5} \right] \quad [11]$$

τ being the rate of recycling.

Writing the condition

$$k_4 = \alpha' k_D \quad [12]$$

$$\frac{N I_D}{I_R} = \tau \left[\alpha' \frac{\overleftarrow{k}_5}{\overrightarrow{k}_5} + \frac{\alpha' k_D}{\overrightarrow{k}_5} + 1 \right] \quad [13]$$

For low overvoltages

$$\tau = 1, \text{ i.e., } k_4 < 5 k_D \quad [14]$$

and also

$$\frac{\overleftarrow{k_5}}{\overrightarrow{k_5}} \ll 1 \quad [15]$$

The increase of the ordinate at $\omega = 0$ cannot be accounted for only by an increase of τ because from Eq. [13] this would simultaneously increase the slope. Two conditions should be considered; either an increase of $\overleftarrow{k_5}$ or a second condition

$$2) \overrightarrow{k_1} = 0 \quad \overrightarrow{k_3} \neq 0$$

As the current densities on the disk with the loadings are less than twice those on the support alone the Eq. [11] becomes

$$\frac{NI_D}{I_R} = 1 + \frac{\overrightarrow{k_3} + \alpha' k_D}{\overrightarrow{k_5}} \quad [17]$$

The increase at $\omega = 0$ with the overvoltage corresponds to an increase of $\overrightarrow{k_3}$ (velocity of reduction of HO_2^-) and is detectable only at high overvoltages above the useful range of polarizations.

It may be concluded that the interpretation of the data obtained on the support alone from the models developed in Ref. (9) and (21) yields kinetics limited by a slow desorption step of HO_2^- produced. At low overvoltages one obtains a two electron reduction process followed by a decomposition of adsorbed HO_2^- . For higher overvoltages the HO_2^- reduction process takes place with a possible increase of the kinetics of desorption which means that the reduction may occur outside the initial reaction zone on the electrode.

Improvements of the carbon support may consist of adding HO_2^- decomposition catalysts which are stable under recycling conditions.

Naphthalocyanine loadings on ex CO carbon black (Improvements for O_2 electroreduction and evolution).—Our search for organic compounds presenting a useful stability and activity to serve as air cathode catalysts in alkaline media for zinc-air or fuel cell generators has led to the fabrication of iron naphthalocyanine. The materials synthesized as the pure powder have an optical absorption spectrum and x-ray pattern similar to those given in literature for the corresponding phthalocyanines.

As loadings on carbon black support, the activity of the samples prepared were investigated by the ultrathin electrode technique and were found to be higher than that of the dimer previously studied. The improvement of the performance is due to the increase of the conductivity of the naphthalocyanine. As with the phthalocyanine dimer, the differences in structure are associated with the existence of noticeable amounts of fixed oxygen which act as a well for π -electrons, a greater density of π -electrons involving (3a, b, 5) a greater activity. This result is in accord with the predictions made in Ref. (6).

As in the case of the phthalocyanine dimer (4), the reaction involves radical formation. Rest potentials and current densities at low polarizations turn out to be highly sensitive to the iron content bound to the structure. The highest iron content corresponds to the best activity. This result agrees with the models of charge transfer complexes investigated in Ref. (16). In these models as previously reported, the conductivity between superimposed molecules takes place with $\text{Fe}^{\text{II}}/\text{Fe}^{\text{III}}$ exchange [$D_h \leq 10^{-12} \text{ cm}^2 \text{ sec}^{-1}$ (22a, b)] simultaneously with electron hopping on the oxygen covalently bound to the iron sites: H_2/H^+ couples in the solid phase act as reducing agents for $\text{Fe}^{2+}/\text{Fe}^{3+}$ couples decreasing the density of sites for oxygen activation. Therefore the activity is related to the purity of the samples in Fe and the elimination of any

reducing couple which can be introduced during the synthesis or in contact with the support. A possible way to improve the performances would be by doping. Introduction of Mo^{+5} ions enhanced the activity but results in stability are similar for 2.5% loadings w/w.

While the optical spectrum and x-ray pattern are similar, there are important differences in the EPR spectra compared to those of the monomeric iron phthalocyanine. Those concern primary the amount of Fe^{III} which increases with the π -electron density (5). Due to the π -d hybridization requirement for $\text{Fe}-\text{O}_2$, the electrochemical activity seems therefore to be more dependent upon two species in resonance, one in which the Fe^{II} is covalently bound to oxygen and a second where the Fe^{III} is ionically bound to O_2^- . More excited states of the molecule do not seem to play any important role in the activity.

On the loading surface the kinetics consist mainly of a four electron reduction process with a reaction scheme similar to the one obtained with phthalocyanine dimer type (4). Rotating ring-disk techniques have shown that on the same support, the efficiency of the four electron reduction process is better with the naphthalocyanine material than with the oxygen fixing phthalocyanine dimer, confirming the correlation of activity vs. π -electron density. This low rate of HO_2^- formation can present an important advantage for zinc-air generators. Experiments have been conducted on a type of carbon black support holding for more than 1000 2 hr cycles. As above, on naphthalocyanine loadings, on this support RRDE techniques show a rate of HO_2^- formation to be less than 5% of that observed on carbon within the whole range of useful polarizations.

A main cause of the drop in the performance of the loading is generally a modification of the junction properties at the naphthalocyanine-carbon black interface. However, this type of explanation appears to be at variance with the increase of the life expectancy observed with dilution. The above data seem to be better interpreted by seeking a correlation between the overall conduction and the life expectancy; the better is the conduction the better is the life expectancy. Therefore as a working hypothesis one may assume that the development of an electric field inside the layer may involve long-range structural changes which inhibit the catalytic properties. With the aid of EPR (11) and pulse techniques (21) the formation of dipoles within the naphthalocyanine layer has been shown. They are due to the strong difference in mobility between the holes on the iron sites ($\text{Fe}^{2+}/\text{Fe}^{3+}$ couple) and the electrons associated with the oxygen molecules which can diffuse more rapidly (22b). Due to the low mobility of the positive charges Fe^{3+} or Mo^{V} ions are segregated at the surface. This view seems to be supported by ESCA investigations (12) under progress. One solution for increasing the life expectancy might consist of introducing doping agents into the naphthalocyanine lattice which would decrease the existing initial electric field.

Compared to the support, the most significant feature of Fig. 9 is the blocking of the activity after 600 cycles on loadings corresponding to coverages of naphthalocyanine lower than one monolayer. This result can be interpreted by the fact that active sites for oxygen reduction on the carbon support alone are also active sites for the fixation of the naphthalocyanine layers.

From M. O. symmetry considerations (23) the sites in the naphthalocyanine molecule presenting a high degree of symmetry should play a special role, i.e. mainly the iron sites or corresponding sites with an A_4 axial symmetry and the external carbon atoms on the naphthalene ring with A_2 axial or planar symmetry. In the first case, of sites A_4 , the adherence of the naphthalocyanine deposit would be higher than with the second case, sites A_2 , which requires a special spacing be-

tween the sites of the support in order to fit with the distances in the plane of the naphthalocyanine lattice. The relative stability of the loading under both cathodic reduction of oxygen and its evolution would suggest that the first type of fixation should be considered. If according to Yeager (10, 24) the active sites for O_2 reduction on carbon surfaces are the planes possessing π -type of orbitals, symmetry requirements for the fixation of the naphthalocyanine molecules can be encountered in this case, carbon orbitals and high symmetry sites being allowed to combine.

Conclusion

On the ex CO alone this study has shown a kinetic limitation due to a slow desorption of H_2O_2 interpreted using models developed earlier. In the present case linear plots of NI_D/I_R vs. $\omega^{+1/2}$ are obtained instead of the usual $\omega^{-1/2}$.

On the naphthalocyanine loadings tests of stability have underlined the absence of H_2O_2 generation. The limitation of the performances due to the conduction in the solid phase has been emphasized.

Using loadings on a suitable carbon black support, iron naphthalocyanine has proved to be a useful catalyst for practical applications in zinc-air generators working in alkaline media. Improvements in activity and stability may consist of a synthesis yielding an iron content as close as possible to the theoretical value and in a parallel the elimination of the reducing couples in the structure. Doping techniques may also be usefully used.

Another point of interest is the illustration of the relationship existing in such compounds between the activity and stability vs. oxygen reduction and the density of π -electrons in the conjugated rings as already reported on similar compounds. The search for larger molecules such as the six unit polymer does not take into account electronic interaction between molecules in the crystal lattice which perturbs the π -electron density. With smaller size molecules the highest π -electron densities can be obtained. A major fact seems to be the simultaneous presence of Fe^{3+} with Fe^{II} covalently bounded to oxygen which is always present on active and stable materials, cf. ESCA investigations.

Acknowledgments

We acknowledge the Direction des Recherches et Etudes Techniques for financial support, Dr. Feuillade and M. Duperray of Compagnie Generale d'Electricité (Marcoussis) for the development of the industrial electrodes and their tests of stability, and Dr. Roger Parsons for his interest to this work.

Manuscript submitted July 31, 1979; revised manuscript received Nov. 23, 1979. This was Paper 349 presented at the Boston, Massachusetts, Meeting of the Society, May 6-11, 1979.

Any discussion of this paper will appear in a Discussion Section to be published in the December 1980

JOURNAL. All discussions for the December 1980 Discussion Section should be submitted by Aug. 1, 1980.

Publication costs of this article were assisted by the Centre National de la Recherche Scientifique.

REFERENCES

1. H. Tachikawa and L. R. Faulkner, *J. Am. Chem. Soc.*, **100**, 4379 (1978).
2. H. Meier, V. Tschirwitz, E. Zimmerhackl, W. Albrecht, *J. Phys. Chem.*, **81**, 712 (1977).
3. (a) H. Meier, W. Albrecht, V. Tschirwitz, and E. Zimmerhackl, *Ber. Bunsenges. Phys. Chem.*, **77**, 843 (1973). (b) H. Jahnke, M. Schonborn, and G. Zimmermann, *Top. Curr. Chem.*, **61**, 135 (1976).
4. A. J. Appleby, J. Fleisch, and M. Savy, *J. Catal.*, **44**, 281 (1976).
5. S. Maroie, M. Savy, and J. Verbist, *Inorg. Chem.*, **18**, 2560 (1979).
6. L. Salem, "M.O. Theory of Conjugated Ring Systems," W. Benjamin, Editor, p. 287, New York (1966).
7. W. H. Vogel and J. T. Lundquist, *This Journal*, **117**, 1512 (1970).
8. (a) M. Audier, M. Renaud, and L. Bonnetain, *J. Chim. Phys.*, **3**, 296 (1977). (b) M. Audier, M. Renaud, and L. Bonnetain, *J. Chim. Phys.*, **5**, 533 (1977).
9. A. J. Appleby and M. Savy, *J. Electroanal. Chem. Interfacial Electrochem.*, **92**, 15 (1978).
10. I. Morcos and E. Yeager, *Electrochim. Acta*, **15**, 953 (1970).
11. M. Savy, J. E. Guerschais, J. Sala Pala, J. B. Nagy, and E. Derouane, Submitted to *Inorg. Chem.*
12. J. Riga, M. Savy, and J. Verbist, Submitted to *Inorg. Chem.*
13. J. W. Eastes, U.S. Pat. 2,770,629.
14. S. C. Mathur and J. Singh, *Inst. J. Quant. Chem.*, **6**, 57 (1972).
15. R. Taube, H. Dreiss, E. Fluck, P. Juhn, and K. F. Brauch, *Z. Anorg. Allg. Chem.*, **364** (1969).
16. A. J. Appleby and M. Savy, in "Electrode Materials and Processes for Energy Conversion and Storage," J. D. E. McIntyre, S. Srinivasan, and F. G. Will, Editors, p. 321, The Electrochemical Society Softbound Proceedings Series, Princeton, N.J. (1977).
17. A. J. Appleby and M. Savy, *Electrochim. Acta*, **22**, 1315 (1977).
18. M. Etman, E. Levart, and G. Scarbeck, *J. Electroanal. Chem. Interfacial. Electrochem.*, **101**, 153 (1979).
19. M. Appel, C.N.A.M. Thesis, Paris (1974).
20. A. Damjanovic, M. A. Genshaw, and J. O'M. Bockris, *J. Chem. Phys.*, **45**, 4057 (1966).
21. H. Wroblowa, Y.-C. Pan, and G. Razumney, *J. Electroanal. Chem. Interfacial Electrochem.*, **69**, 195 (1976).
22. (a) O. Contamin, E. Levart, and M. Savy, *This Journal*, **126**, 147C (1979). (b) O. Contamin, E. Levart, and M. Savy, Submitted to *J. Electroanal. Chem. Interfacial Electrochem.*
23. R. B. Woodward and R. Hoffman, *J. Am. Chem. Soc.*, **87**, 395, 2046, 2511, 4389 (1965).
24. E. Yeager, O_2 Electrochemistry Symposium, Painesville, Ohio, May 2-4, 1979.

Mass Transfer in Packed Bed Electrochemical Cells Having Both Uniform and Mixed Particle Sizes

Richard Alkire,* Brian Gracon, Thomas Grueter, James Marek, and Paul Blackburn*

Department of Chemical Engineering, University of Illinois, Urbana, Illinois 61801

ABSTRACT

An electrochemical method was used to measure the mass transfer coefficient in packed beds containing spherical particles. The electrochemical reaction was reduction of ferricyanide ions on stainless steel ball bearings in the presence of potassium nitrate supporting electrolyte. The correlation found in this study was

$$j_D = 2.944 \text{Re}^{-0.554} \left(\frac{L}{d_p} \right)^{-0.15}$$

where $1.8 < \text{Re} < 27$, $2.98 < L/d_p < 7.45$, and $\text{Sc} = 1421$. The mass transfer coefficient for randomly packed beds containing up to five different sizes of spheres (0.398-0.952 cm diam) was correlated by the above equation when the average particle diameter was determined by

$$d_{pm} = \frac{1}{\sum_i \frac{x_i}{d_{pi}}}$$

where d_{pi} is the particle diameter of size i , and x_i is the volume (or weight fraction) of particles of size i in the packed bed. It was found that when the bed packing was segregated into two parallel flow zones, each having different particle sizes, then the average mass transfer coefficient was less than the value given by the correlation above.

The design of porous electrode systems usually depends critically upon mass transfer between electrode and fluid. Although convective heat and mass transfer in packed beds has received vigorous attention in the chemical engineering literature, these studies have been primarily carried out at high flow rates and on packing materials of uniform size. Most practical porous electrode systems, however, employ electrode packing material of nonuniform size and shape. The purpose of this investigation is to obtain mass transfer correlations for flow-through porous electrodes containing mixed sizes of spherical particles.

Heat and mass transfer correlations for single phase flow in uniformly packed beds have been collected by Karabelas *et al.* (1), Froment (2), Gupta *et al.* (3), Marivoet *et al.* (4), and Sherwood *et al.* (5). Flow in nonuniform packed beds containing high and low porosity zones has also been studied recently (6), and the flow patterns within such nonuniform beds were found to be complex (7, 8), and to affect adversely the bed contact efficiency (9). The majority of the foregoing work was carried out at high flow rates characteristic of chemical engineering separation processes.

Electrochemical reactors involving porous flow-through electrodes have been studied extensively during the past decade (10). It has been found that optimum operating conditions invariably involve low flow rates, and that flow channeling therefore represents a serious practical limitation on performance. Although electrochemical methods have been used to measure mass transfer rates in packed beds at low flow rates (11-15), studies to date have addressed the more fundamental aspects for which electrodes of uniformly dimensioned packing material, usually spheres or stacks of screens, were most appropriate.

In the present study, the electrochemical limiting current method was used to measure mass transfer coefficients in porous flow-through electrodes having nonuniform properties of two different types. In the

first type, different sizes of spherical particles were thoroughly mixed and then dumped to form a porous bed which was nonuniform on a microscopic scale but uniform on a macroscopic scale (16-18). In the second type, different sizes of spherical particles were placed in different parts of a bed to create regions which were each uniformly porous on a microscopic scale but, when taken together, were not uniform on the macroscopic scale (16).

Apparatus

The porous flow-through electrode was fabricated by packing a Plexiglas tube (5.1 cm diam) with spherical metal particles. In all but one series of experiments reported below, Type-440 stainless steel ball bearings (McMaster-Carr, Chicago) were used; eight different sizes of bearings were employed ranging from 0.397 to 0.952 cm diam (5/32-3/8 in.); the machine tolerance on these bearings was 0.0025 cm.

The tube containing the packed bed was 40 cm long. The upstream region (about 23 cm) was packed with glass beads (0.6 cm diam) in order to establish plug flow (19). The packed bed electrode (cathode) was assembled upstream from the anode, and was separated from the anode by a 2.5 cm layer of glass beads. The surface area of the anode was more than twice that of the cathode. Platinum contact wires were inserted into the two electrodes through serum stoppers in the cell wall.

The electrolytic solution used with stainless bearings was 0.95M KNO_3 containing 0.002M of both potassium ferricyanide and potassium ferrocyanide. The ferricyanide ion was reduced at the cathode and was re-oxidized at the anode, which was downstream. Solution samples were withdrawn from the downstream side of the working electrode and were analyzed by iodometric titration, accurate to within one percent, to determine the exit concentration of ferricyanide (20). The ferricyanide concentration in the external flow loop was found to remain constant, permitting continuous recirculation of electrolyte to the cell.

Solution was pumped by a magnetic drive "Metl-Less" pump (March Manufacturing, Glenview, Illinois)

* Electrochemical Society Active Member.

Key words: mass transfer, porous electrode, nonuniform porosity, channeling.

and was controlled by needle valves placed downstream from each rotameter. Other than the electrolysis cell, all parts of the flow system were fabricated from glass or leached Tygon tubing. The flow system was blanketed with nitrogen except in the small number of early experiments; in these, appreciable oxygen background currents were present, as described in the discussion of Fig. 2 below.

Polarization curves were obtained with a potentiostatic power supply (Wenking 70TS1) driven by a voltage ramp generator. In the cell, a plastic pipette was used as the capillary tube for a saturated calomel reference electrode; the tip of the capillary was positioned 0.35 cm downstream from the working electrode. Determination of cell current was made with use of a precision resistor.

Procedure

Electrolytic solution was prepared from AR grade chemicals and was deaerated by water-saturated nitrogen (30 liters/hr) for 3 hr prior to initiation of experiments. To prepare for use, the stainless steel bearings were tumbled in a slurry of 80-grit grinding powder, rinsed with deionized water, mildly etched in 1M H₂SO₄ to dislodge final traces of grit, rinsed with deionized water, and dried in warm air.

The electrolysis cell was fabricated by filling the Plexiglas tube with alternate regions of glass beads and ball bearings, taking care at each step to dislodge air bubbles. In particular, the working electrode bed was carefully assembled with forceps to insure that the interface between glass beads and ball bearings was perpendicular to the cell wall. "Type 1" electrodes were prepared by random placement of particles to form an electrode. "Type 2" electrodes were prepared by establishing concentric zones each composed of single-sized particles.

The flow rate was measured both by rotameters and by collecting measured volumes of solution. The needle valve was found to provide steady flow control to within 2% of the mean value reported.

Polarization curves were obtained at various flow rates in order to determine the mass transfer limiting current. Background currents were measured separately by following the above procedure with use of solutions containing only 0.95M KNO₃; limiting current data reported below have been corrected for background current. For over 60% of the data points, background currents were less than 1% of the limiting current; at the highest flow rates, the background currents were at most 10% of the limiting amount. For the data presented in Fig. 2, the background current was neither measured nor corrected for; these data are, therefore, presented for qualitative examination only.

Results and Discussion

Measurement of ferricyanide concentration in the cathodic effluent gave material balances which agreed, after correcting for background current, to within 1% of Faraday's law with $n = 1$. Because the electrolysis rate was limited solely by mass transfer in the catholyte, the mass transfer coefficient was found by measurement of current, inlet concentration, and surface area

$$I_1 = nFC_b(aLA\epsilon)k \quad [1]$$

Table I. Physical properties of solutions studied

Property	Value
ρ , g/cm ³	1.058 ± 0.001
μ , g/cm sec	8.68 ± 0.07 × 10 ⁻³
ν , cm ² /sec	8.2 × 10 ⁻⁵
D , cm ² /sec	5.77 × 10 ⁻⁶
Sc , dimensionless	1.42 × 10 ³
n , g-equiv./g mole	1

Source: Ref. (14).

where the surface area for reaction is ($aLA\epsilon$). In this study, the mass transfer coefficient was correlated by

$$j_D = GRe^p \left(\frac{L}{d_p} \right)^q \quad [2]$$

where G , p , and q are constants to be found by analysis of experimental data. Combination and rearrangement of Eq. [1] and [2] provides the equation used for correlation of experimental data

$$\frac{I_1 \rho Sc^{2/3}}{\epsilon a n F C_b A \mu} = GRe^{p'} \left(\frac{L}{d_p} \right)^{q'} \quad [3]$$

where

$$p' = p + 1$$

$$q' = q + 1$$

Uniform particle size results.—Properties of the electrolytic solutions used in this study are compiled in Table I. Geometric properties of the stainless steel ball bearings are listed in Table II. The bed porosity, ϵ_1 , was measured by placing a known quantity of uniformly sized bearings into tubes having inside diameters of 3.8, 5.1, and 8.9 cm. A least squares fit of the data indicated that the bed porosity was a weak linear function of bearing diameter

$$\epsilon_1 = 0.3754 + 0.04744d_p \quad [4]$$

Equation [4] was used to compute the bed porosity values given in Table II. The specific surface area, a_1 , was defined as surface area per unit volume

$$a_1 = \frac{(1 - \epsilon_1) \frac{S_1}{V_1}}{\epsilon_1} = \frac{6(1 - \epsilon_1)}{d_{p1}\epsilon_1} \quad [5]$$

Table III lists the geometric properties of the eleven electrode configurations which comprised the studies on uniform bed particles. The length of the packed bed was calculated by

$$L = \frac{V_b}{A(1 - \epsilon)} \quad [6]$$

The volume of the bearings V_b , was determined by counting the number of bearings placed in the bed. The eleven configurations exhibited L/d_p ratios ranging between 2.98 and 7.45.

Table II. Properties of 440 stainless steel balls

Property	Size 1	Size 2	Size 3	Size 4	Size 5	Size 6	Size 7	Size 8
d_{p1} , cm	0.397	0.476	0.556	0.635	0.714	0.794	0.873	0.952
v_1 , cm ³	0.0327	0.0565	0.0898	0.134	0.191	0.262	0.348	0.452
s_1 , cm ²	0.495	0.712	0.970	1.27	1.60	1.98	2.40	2.85
w_1 , g	0.2455	0.4335	0.6892	1.029	1.454	2.001	2.664	3.464
a_1 , cm ⁻¹	23.3	19.1	16.1	13.8	12.1	10.7	9.61	8.66
ϵ_1	0.394	0.398	0.402	0.406	0.409	0.413	0.417	0.421

Table III. Uniform particle size summary

Run No.	d_{p1} (cm)	ϵ_i	L (cm)	Wt elec. (g)
1	0.794	0.413	2.603	236.1
2	0.476	0.398	2.538	236.1
3	0.556	0.402	2.541	234.8
4	0.635	0.406	2.542	233.3
5	0.397	0.394	2.541	237.9
6	0.714	0.409	2.546	232.5
7	0.794	0.413	3.817	346.2
8	0.794	0.413	5.074	460.2
9	0.397	0.394	1.694	158.6
10	0.873	0.417	2.602	234.4
11	0.873	0.417	6.507	586.1

The value of q was found by plotting the left side of Eq. [3] vs. (L/d_p) at constant Re . A least squares analysis of the slope gave a value of 0.83 for $Re = 6$, and 0.87 for $Re = 11$. The average value gave $q' = 0.85$, or $q = -0.15$.

The values of p and G were found by analysis of the limiting current data indicated by solid points in Fig. 1. The set of 184 data points was treated by linear regression analysis which gave $p = -0.554$ and $G = 2.944$. That is, the mass transfer correlation was found to be

$$j_D = 2.944Re^{-0.554} \left(\frac{L}{d_p} \right)^{-0.15} \quad [7]$$

$$1.8 < Re < 27$$

$$2.98 < \frac{L}{d_p} < 7.45$$

$$Sc = 1421$$

$$0.397 < d_p < 0.952 \text{ cm}$$

By linear regression analysis, the slopes on either side of $Re = 12$ in Fig. 1 were found to be statistically different

For $Re < 12$ (112 data points, 95% confidence level):

$$p = 0.567 \pm 0.005$$

$$G = 3.039 \quad [8]$$

For $Re > 12$ (72 data points, 95% confidence level):

$$p = 0.533 \pm 0.015$$

$$G = 2.797 \quad [9]$$

Because the confidence bands do not overlap, these results indicate that the linear correlation reported in Eq. [7] is a simplification. Since limiting current data were corrected by subtraction of background current, the difference in slope would not be attributed to a second electrolysis reaction. Indeed, the results of Karabelas, Wegner, and Hanratty (1) indicate that the range of Reynolds numbers used in this study does not lie in a region where a straight-line asymptotic correlation would be expected. Values of j_D calculated by Eq. [7], however, are within 3% and 1% of the values calculated with use of constants in Eq. [8] and [9], respectively.

Glass beads were used in the upstream section of the cell to establish uniform hydrodynamic conditions. The beads were of uniform size for all experiments (0.6 cm) whereas the packing particles ranged in size from 0.398 to 0.952 cm. Therefore, the data may be influenced by modest hydrodynamic rearrangement which accompanies flow into the porous electrode. Also, mass transfer entrance effects may be operative in the shallow beds used in this study, as would be indicated by the results of Fedkiw and Newman (21). Therefore, the weak L/d_p dependence found in Eq. [7] may be the result of various entrance effects which would not be experienced in deeper beds. Whereas these results indicate the need for additional investigation at the fundamental level, the point remains that most industrial porous electrodes are "shallow" (in order to accommodate potential distribution requirements), so that the correlations reported here are therefore useful for practical applications.

Nonuniform particle sizes: microscopic nonuniformity.—Results were obtained for working electrodes having two, three, four, and five different sizes of ball bearings placed randomly in the packed bed. These results are summarized in Table IV.

Eight sets of two-ball mixtures were studied as indicated in part A of Table IV. The upper portion of part A gives the weight fraction and size of each component in the electrode mixture. The average diameter for the mixture material was calculated with the rule

$$d_{pm} = \frac{1}{\sum_i \left(\frac{x_i}{d_{pi}} \right)} \quad [10]$$

This average diameter was then used to calculate values for ϵ_m , a_m , and L in a manner analogous to that

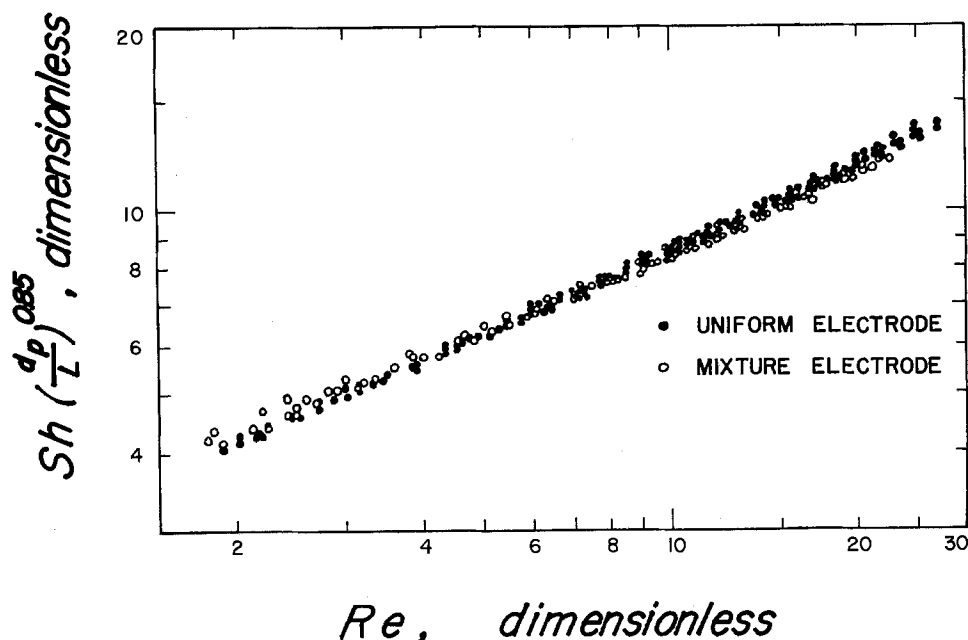


Fig. 1. Mass transfer correlation for packed bed electrochemical cells having both uniform and mixed particles sizes.

used for uniform packing as described previously. Since all bearings had the same density, the weight fraction in Eq. [10] is equivalent to the volume fraction occupied within the bed by each bearing size. The hollow circles in Fig. 1 illustrate how Eq. [7] and [10] correlate data in nonuniform beds.

The lower portion of part A contains examples of results for mixtures of two bearings. It was found that the discontinuity between the high and low flow rate regions centered about $Re = 12$ was not as distinct as had been the case with uniform packings. Therefore, the overall correlation given in Eq. [7] was used to predict the mass transfer limiting current for the entire range of flow rates studied. The second column in the lower portion of part A of Table IV lists the limiting current predicted by Eq. [7] for one particular example

flow rate ($V_{\infty} = 309$ ml/min). The third column gives the experimental data measured at that flow rate.

To gain a measure of comparison between data and correlation, it is helpful to determine what the limiting current would have been had the electrode consisted only of the large bearings used in the mixture; in the lower portion of each section of Table IV, column four (labeled "0% smaller balls") lists those values for each run as computed with use of Eq. [7] at a flow rate of 309 ml/min. In a similar manner, column five lists the limiting current which would be expected, at a flow rate of 309 ml/min, had the electrode been constructed from only the smaller bearing size. These results will be used below when comparing experimental data with calculated values.

Table IV. Mixture electrode summary

A. Two ball sizes

Mixture run No.	Smaller balls		Larger balls		Mixture properties			Wt elec. (g)
	d_{p1} (cm)	x_1	d_{p1} (cm)	x_1	d_{pm} (cm)	ϵ_m	L (cm)	
1	0.397	0.253	0.714	0.747	0.5941	0.404	2.916	268.5
2	0.397	0.499	0.714	0.501	0.5105	0.400	2.577	238.9
3	0.476	0.501	0.714	0.499	0.5712	0.402	2.581	238.5
4	0.476	0.750	0.714	0.250	0.5195	0.400	2.572	238.4
5	0.476	0.253	0.714	0.747	0.6341	0.405	2.602	239.2
6	0.476	0.499	0.952	0.501	0.6353	0.406	2.561	235.0
7	0.476	0.251	0.873	0.749	0.7221	0.410	2.614	238.3
8	0.476	0.500	0.873	0.500	0.6161	0.405	2.905	267.2

 I_{lim} , mA ($V_{\infty} = 309$ ml/min)

Mixture run No.	Calc	Data	0% smaller balls	100% smaller balls	Eq. [11] % error
1	64.44	68.6	50.17	111.24	4.96
2	71.42	73.2	45.43	100.73	1.44
8	61.18	59.7	45.36	78.63	2.99
4	69.60	67.4	45.34	78.60	4.08
5	53.41	50.5	45.47	78.82	6.76
6	52.54	50.2	30.77	77.65	4.48
7	45.02	41.1	34.91	78.57	8.47
8	61.02	60.73	38.46	86.58	2.39

B. Three ball sizes

Mixture run No.	Mixture composition		Mixture properties			Wt elec. (g)
	d_{p1} (cm)	x_1	d_{pm} (cm)	ϵ_m	L (cm)	
9	0.794	0.333	0.5814	0.403	3.900	359.6
	0.556	0.333				
	0.476	0.334				
10	0.873	0.488	0.6223	0.405	3.272	300.7
	0.635	0.256				
	0.397	0.256				
11	0.873	0.335	0.6228	0.405	3.290	302.4
	0.635	0.333				
	0.476	0.332				
12	0.873	0.261	0.5814	0.403	3.103	286.1
	0.635	0.467				
	0.397	0.272				
13	0.873	0.248	0.5771	0.403	2.912	268.6
	0.635	0.249				
	0.476	0.503				
14	0.952	0.305	0.7283	0.410	3.983	363.0
	0.714	0.496				
	0.556	0.199				
15	0.952	0.333	0.7059	0.409	3.297	301.0
	0.714	0.333				
	0.556	0.334				

 I_{lim} , mA ($V_{\infty} = 309$ ml/min)

Mixture run No.	Calc	Data	0% smaller balls	100% smaller balls	Eq. [11] % error
9	84.97	85.59	55.87	111.42	1.63
10	66.65	67.12	42.53	122.48	2.22
11	66.86	65.34	42.73	96.19	1.63
12	69.97	71.38	40.77	117.41	2.44
13	66.98	67.47	38.64	86.98	2.91
14	63.40	61.65	44.53	91.27	4.68
15	56.36	55.97	37.97	77.83	2.64

Continued on next page

Table IV. Mixture electrode summary (continued)

C. Four and five ball sizes

Mixture run No.	Mixture composition		Mixture properties			
	d_{p1} (cm)	x_i	d_{pm} (cm)	ϵ_m	L (cm)	Wt elec. (g)
16	0.873	0.249	0.6579	0.407	3.729	341.7
	0.794	0.251				
	0.635	0.250				
	0.476	0.250				
17	0.952	0.253	0.5529	0.402	3.259	301.2
	0.635	0.249				
	0.476	0.249				
	0.397	0.249				
18	0.952	0.246	0.7258	0.410	3.544	323.1
	0.794	0.253				
	0.714	0.252				
	0.556	0.249				
19	0.952	0.205	0.7030	0.409	3.883	354.5
	0.873	0.197				
	0.794	0.198				
	0.635	0.203				
		0.476	0.197			
I _{lim} , mA (V _∞ = 309 ml/min)						
Mixture run No.	Calc	Data	0% smaller balls	100% smaller balls	Eq. [11] % error	
16	68.95	68.40	47.42	106.55	1.93	
17	78.19	78.48	38.00	122.65	3.08	
18	57.67	54.33	40.33	82.65	5.92	
19	65.14	71.38	43.63	110.11	9.57	

The last column in the lower portion of part A of Table IV gives the percent error between calculated and observed limiting currents for the two ball mixtures as computed by

$$\% \text{ error} = \frac{100}{N} \sum \left| \frac{I_{lim,data} - I_{lim,calc}}{I_{lim,calc}} \right| \quad [11]$$

where there are N data points. The percentage error listed in the last column was computed by averaging all data for which the system was under mass transfer control.

In a similar manner, parts B and C of Table IV provide data and analysis for three, four, and five ball mixtures. The average of all errors for the two, three, four, and five ball mixtures were: 4.4, 2.6, 2.6, and 9.6%, respectively. These results illustrate that, over the range of parameters investigated here, Eq. [10] provides a good method for selecting the average diameter needed for predicting the mass transfer coefficient in porous electrodes fabricated from randomly mixed spherical particles.

Nonuniform particle sizes: macroscopic nonuniformities.—Nonuniform packed beds were also prepared by placing particles in two concentric zones each of which contained particles of a single size. Two different combinations of particle sizes were investigated, as listed in Table V. Different proportions of each pair of particle size were studied, ranging between all small particles and all large particles. The fraction of large and small particles is listed in Table V under headings

Table V. Properties of stainless steel composite electrodes

Electrode	x_1	x_s	ϵ_m	a_m	d_{pm}
$d_{p1} = 0.714$ cm, $d_{ps} = 0.397$ cm:					
No. 1	0.208	0.792	0.396	20.9	0.437
No. 2	0.280	0.720	0.397	20.1	0.453
No. 3	0.393	0.607	0.398	18.9	0.481
No. 4	0.455	0.545	0.399	18.2	0.497
No. 5	0.480	0.520	0.399	17.9	0.505
No. 6	0.597	0.403	0.401	16.6	0.540
$d_{p1} = 0.873$ cm, $d_{ps} = 0.397$ cm:					
No. 7	0.200	0.800	0.397	20.5	0.446
No. 8	0.256	0.744	0.397	19.7	0.461
No. 9	0.380	0.620	0.399	18.0	0.501
No. 10	0.441	0.559	0.400	17.2	0.523
No. 11	0.570	0.430	0.403	15.4	0.576

x_1 and x_s , respectively. Also given in Table V is the value of d_{pm} computed by Eq. [10], and of ϵ_m and a_m computed by Eq. [4] and [5].

When the average geometric properties listed in Table V were used to compare the limiting current by Eq. [7], deviations between calculated values and measured data were found. The nature of these deviations was characterized by the following definition of percentage error

$$E_1 = \left(\frac{I_{measured}}{I_{Eq. [7]}} - 1 \right) \times 100 \quad [11a]$$

Figure 2 illustrates how E_1 varied with the fraction of large particles in the bed (x_1) for the two systems studied. As mentioned previously, the early experimental data reported in Fig. 2 were measured under conditions where appreciable background current was present owing to dissolved oxygen. Thus it was ex-

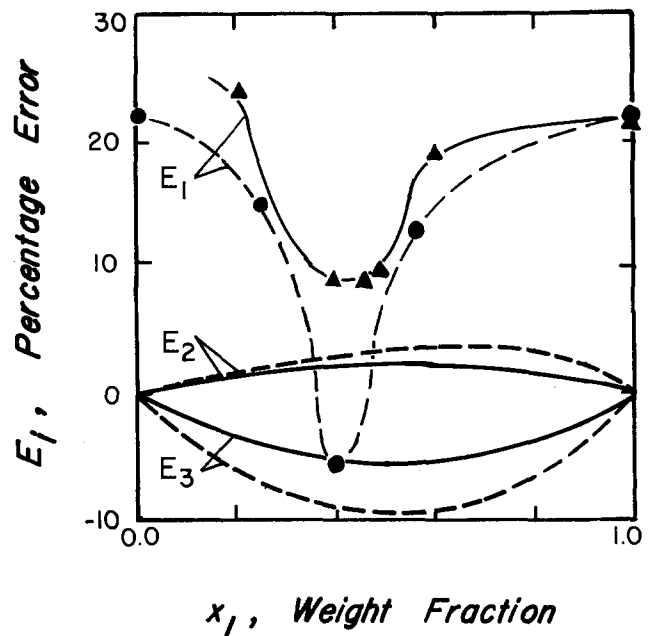


Fig. 2. Deviations from Eq. [7] for macroscopically nonuniform porous electrodes. (—: $d_{p1} = 0.714$, $d_{ps} = 0.397$; - - - -: $d_{p1} = 0.873$, $d_{ps} = 0.397$). Errors defined by Eq. [11]-[13].

pected that positive errors should be observed. It is seen that when the bed consisted of nearly all small, or nearly all large particles, then the experimental data were indeed higher than the value computed by Eq. [7] and this (positive) deviation is attributed to the presence of oxygen. For intermediate ranges of $0.2 < \alpha_1 < 0.6$, experimental data dip sharply. Since the correlation illustrated in Fig. 1 served adequately to characterize uniformly dispersed mixtures of particles, it is tentatively concluded that the strong (negative) deviations in Fig. 2 must be the result of the macroscopic nonuniformities present in the packed bed.

Two routes were used to seek improved correlations of experimental data. In the first, it was assumed that fluid passed through the mixed bed at a rate which was everywhere uniform (plug flow). Such a situation would be encountered in practice if the flow resistance external to the packed bed was large and if no rearrangement of flow pattern occurred within the packed bed. The limiting current calculated by this method, $I_{\text{plug flow}}$, was put on the same comparative basis by defining

$$E_2 = \left(\frac{I_{\text{plug flow}}}{I_{\text{Eq. [7]}}} - 1 \right) \times 100 \quad [12]$$

Results are shown in Fig. 2. It is seen that this method of prediction gives limiting currents which were slightly larger than the values computed by Eq. [7].

In the second method of calculation, it was assumed that the fluid distributed itself between the two portions of the bed such that the pressure drop across each portion was the same, and that no intermixing of fluid occurred between the two portions. By this method, the fluid flow rate was larger in the region having the larger particles since that region had the lower flow resistance. The limiting current calculated by this method, $I_{\Delta p}$, was also put on the same comparative basis by defining

$$E_3 = \left(\frac{I_{\Delta p}}{I_{\text{Eq. [7]}}} - 1 \right) \times 100 \quad [13]$$

Results are shown in Fig. 2. It is seen that this method of prediction gave limiting currents which were slightly less than the values computed by Eq. [7].

On the basis of results given in Fig. 2, several observations can be made. Since the correlation given by Eq. [7] serves adequately to characterize uniformly dispersed mixtures of particles, it is tentatively concluded that the strong variations seen between $0.2 < \alpha_1 < 0.6$ in Fig. 2 are the result of macroscopic nonuniformities present in the packed bed. Calculations based on plug flow (E_2 curves) exhibit incorrect qualitative trends: experimental data (E_1 curves) exhibit deviations which are in the opposite direction from the plug flow results (E_2 curves). On the other hand, the constant pressure drop method gave results (E_3 curves) which are more like experimental data: (i) deviations in the negative direction are predicted, (ii) the deviations for the dashed lines are greater by a factor of two than the solid line.

Conclusions

Mass transport coefficients have been correlated by Eq. [7] over a range of operating conditions. When the bed is randomly packed with a mixture of up to five different spherical particle sizes, the average particle diameter defined by Eq. [10] may be used in the mass transfer correlation. It may therefore be anticipated that an integral form of Eq. [10] would be useful in situations where the packing material is characterized by a particle size distribution.

When the bed packing is segregated into two parallel flow zones having different particle sizes, then it was found that Eq. [10] may still be used to estimate mass transfer behavior via Eq. [7] although the results may be in error if $0.2 < \alpha_1 < 0.6$. Failure of simple

correlations thus indicates that flow patterns are undoubtedly complex and are deserving of additional study at the fundamental level. The hydrodynamic studies of Stanek and Szekely (6) represent a fruitful starting position since these authors provide equations for predicting cross-flows in multiple porosity regions of the type investigated here.

The widest disparity between diameters of the largest and smallest sphere in an electrode was a factor of 2.40 in this study. A still greater disparity in size would eventually beget wholly different packing structures (like buckshot in an array of tennis balls) for which the foregoing correlations would not be expected to hold.

The present study has not addressed the role of particle shape on electrode performance. Gamson (22) was evidently the first to use empirical shape factors to correlate heat transfer data for beds containing spheres, cylinders, and various commercial packing materials. Those methods have been actively pursued in the chemical engineering literature and could be applied with relative ease to electrochemical analogues.

Acknowledgments

This research was supported by the National Science Foundation via Grant NSF ENG 76-83379. Mr. Edward Yung assisted by making the calculations reported in Table V and Fig. 2.

Manuscript submitted April 16, 1979; revised manuscript received Nov. 8, 1979.

Any discussion of this paper will appear in a Discussion Section to be published in the December 1980 JOURNAL. All discussions for the December 1980 Discussion Section should be submitted by Aug. 1, 1980.

Publication costs of this article were assisted by the University of Illinois.

LIST OF SYMBOLS

English Characters

a	specific surface area, cm^2/cm^3 pore volume
A	electrode cross-sectional area, cm^2
C_b	bulk reactant concentration, g moles/liter
d_p	characteristic packing diameter, cm
D	diffusion coefficient, cm^2/sec
F	Faraday's constant, 96,487 C/g-equiv.
I_{lim}	limiting cell current, A
j	current A/cm^2 wetted electrode surface area
j_D	$(k/V_\infty)Sc^{2/3}$, mass transfer parameter, dimensionless
k	mass transfer coefficient, cm/sec
L	electrode length, cm
n	electrons passed, g-equiv./g mole
Re	$V_\infty d_p/\nu$, Reynolds number, dimensionless
s	surface area, cm^2
Sc	ν/D , Schmidt number, dimensionless
Sh	$I_p Sc^{2/3}/\epsilon an F C_b A \mu$, Sherwood number, dimensionless
v	volume, cm^3
V_b	volume of bearings in electrode, cm^3
V_∞	electrolyte flow rate, ml/min
w	mass, g
x	weight fraction

Greek Characters

ϵ	porosity, dimensionless
κ	electrolyte conductivity, $\Omega^{-1} \text{cm}^{-1}$
μ	viscosity, g/cm sec
ν	kinematic viscosity, cm^2/sec
ρ	electrolyte density, g/cm^3

Subscripts

i	particle size number
m	average property for mixture electrode

REFERENCES

1. A. J. Karabelas, T. H. Wegner, and T. J. Hanratty, *Chem. Eng. Sci.*, **26**, 1581 (1971).
2. G. F. Froment, *Adv. Chem. Ser.*, **109**, 19 (1972).
3. S. N. Gupta, R. B. Chaube, and S. N. Upadhyay, *Chem. Eng. Sci.*, **29**, 839 (1974).

4. J. Marivoet, P. Teodoraiu, and S. Wajc, *ibid.*, **29**, 1836 (1974).
5. T. K. Sherwood, R. L. Pigford, and C. R. Wilke, "Mass Transfer," p. 244, McGraw-Hill, Inc., New York (1975).
6. V. Stanek and J. Szekely, *Can. J. Chem. Eng.*, **50**, 9 (1972); *AIChE J.*, **20**, 974 (1974).
7. J. Szekely and J. Poveroms, *ibid.*, **21**, 769 (1975).
8. E. M. Sparrow, G. S. Beavers, L. Goldstein, Jr., and P. Bahrami, *ibid.*, **22**, 194 (1976).
9. L. P. McMaster and E. R. Gilliland, *Chem. Eng. Sci.*, **27**, 2265 (1972).
10. J. S. Newman and W. Tiedemann, *Adv. Electrochem. Electrochem. Eng.*, **11**, 353 (1978).
11. K. R. Jolls and T. J. Hanratty, *AIChE J.*, **15**, 199 (1969).
12. R. E. Sioda, *J. Electroanal. Chem. Interfacial Electrochem.*, **34**, 411 (1972); *Electrochim. Acta*, **15**, 783 (1970); *ibid.*, **22**, 439 (1977); *J. Appl. Electrochem.*, **8**, 297 (1978).
13. R. Alkire and B. Gracon, *This Journal*, **122**, 1594 (1975).
14. P. W. Appel and J. Newman, *AIChE J.*, **22**, 979 (1976).
15. F. Coeuret, *Electrochim. Acta*, **21**, 185 (1977).
16. B. E. Gracon, Ph.D. Thesis, University of Illinois, Urbana-Champaign, Illinois (1976).
17. T. A. Grueter, B. S. Thesis, University of Illinois, Urbana-Champaign, Illinois (1978).
18. P. Blackburn and J. Marek, Ch.E. 390 Report, University of Illinois, Urbana-Champaign, May 9, 1978.
19. T. Baker, J. Chilton, and H. Vernon, *Trans. Am. Inst. Chem. Eng.*, **31**, 296 (1935).
20. I. M. Kolthoff, E. B. Sandell, E. J. Meehan, and S. Bruckenstein, "Quantitative Chemical Analysis," MacMillan, New York (1969).
21. P. Fedkiw and J. Newman, *AIChE J.*, **23**, 255 (1977); *Chem. Eng. Sci.*, **33**, 1043, 1563 (1978).
22. B. W. Gamson, *Chem. Eng. Prog.*, **47**, 19 (1951).

Electrochemical Studies of Triethylammonium Dichlorocuprate(I), A Room Temperature Fused Salt

James R. Silkey and John T. Yoke

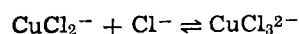
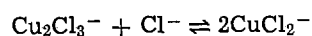
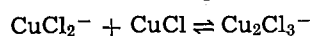
Department of Chemistry, Oregon State University, Corvallis, Oregon 97331

ABSTRACT

Density, conductivity, and viscosity data are reported in the 25°-50°C range for the neat liquid $\text{Et}_3\text{NHCuCl}_2$ and for solutions containing CuCl and CuCl_2 . The Walden product of the room temperature fused salt is not much lower than that of a molten alkali metal halide. A relation proposed by Frenkel,

$\mu\Lambda(E_{\mu}^{\oplus}/E_{\Lambda}^{\oplus}) = \text{constant}$, is followed closely by triethylammonium dichlorocuprate (I) and by solutions containing CuCl and CuCl_2 . The $\text{Cu}/\text{Et}_3\text{NHCuCl}_2$ electrode was found usable as a reference electrode. A solution of CuCl_2 in $\text{Et}_3\text{NHCuCl}_2$ has an absorption maximum at 402 nm ($\epsilon = 2.02 \times 10^3$ liters mole⁻¹ cm⁻¹). Spectrophotometric studies in an optically transparent gold minigrad electrode cell are reported. Potentiometric data from this and from a $\text{Cu}/\text{Et}_3\text{NHCuCl}_2/\text{Et}_3\text{NHCuCl}_2$, $\text{CuCl}_2(\text{M})/\text{Pt}$ cell show approximate Nernstian behavior. Overpotential-current studies permit calculation of the exchange current density at each of the above electrode interfaces. Anodic and cathodic current-voltage plots obtained with a platinum working electrode in neat $\text{Et}_3\text{NHCuCl}_2$ in the region of the $\text{Cu(I)}/\text{Cu(II)}$ redox couple have a remarkable appearance. They resemble a conventional cyclic voltammogram of a dilute solution even though the electrode reaction involves a constituent ion of the solvent itself. This is due to formation of a viscous film of the anodic product CuCl_2 on the electrode surface. Practical development of galvanic cells based on $\text{Et}_3\text{NHCuCl}_2$ electrolytes is limited by their high internal resistance.

Dichlorocuprate(I) salts with certain tertiary aliphatic ammonium and phosphonium cations are oils at room temperature and form glasses when cooled. Triethylammonium dichlorocuprate(I), $\text{Et}_3\text{NH}^+\text{CuCl}_2^-$, the prototype of these materials, is formed merely by bringing triethylammonium chloride and copper(I) chloride powders into physical contact. That such liquids truly are salts is proved by observation of the characteristic dichlorocuprate(I) ion frequencies in their infrared and Raman spectra (1). One postulate to explain why these salts are liquid is that a steric effect causes abnormally low lattice energies. A second reason is that a mixture of species is present, resulting in mutual melting point depression. The mixture arises from the operation of such complex anion equilibria as

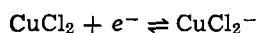
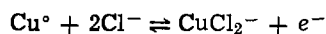


Key words: fused salts, copper complexes, viscosity.

The existence of such equilibria was demonstrated by the effect of added triethylammonium (or phosphonium) chloride, and of added copper (I) chloride, on the intensities and frequencies of the complex anion vibrations. The electrolytic nature of these neat liquids was also demonstrated (1, 2) by their conductivities, which were, however, several orders of magnitude lower than typical for high temperature molten alkali metal chlorides.

Porterfield and his students at Hampden-Sydney College showed (2) that liquid triethylammonium dichlorocuprate(I) (which has only a light yellow color) is a chloride ion-rich solvent useful for observing the visible spectra of chloro complexes of various transition metals. They also observed the cyclic voltammogram of triethylammonium dichlorocuprate (I) dissolved in acetonitrile, demonstrating oxidation and reduction of the copper(I) in the complex anion. Finally, they showed that a voltaic cell with a potential of 0.85V results from partial electrolysis of neat triethylammonium dichlorocuprate(I) between inert

electrodes. The electrode reactions were taken to be



We now report additional electrochemical and related physical studies of systems based on triethylammonium dichlorocuprate(I).

Experimental

Materials.—Reagent Grade chemicals were used. Copper(I) chloride was prepared by the method of Keller and Wycoff (3). Triethylammonium chloride was prepared from freshly distilled triethylamine and 6M hydrochloric acid. The water was evaporated. The residue was recrystallized three times from absolute ethanol, dried at 110°, and ground. It was then finally dried at 110° for 18 hr, as was anhydrous lithium chloride. Copper(II) chloride dihydrate was converted to the anhydrous salt by similar heating.

Inert atmosphere techniques.—The dried chlorides were stored in a stainless steel dry box fitted with an evacuable entry port. The box atmosphere of Pre-purified Grade nitrogen was continuously circulated through a tower containing BTS catalytic oxygen remover and through tubes of 4A, 5A, and 13X molecular sieves (4). All fused salt mixtures were prepared and transferred in this box. Mixtures were prepared by accurate weighing of the constituents with the exception of saturated solutions of lithium chloride and of triethylammonium chloride in liquid triethylammonium dichlorocuprate(I). These were prepared by equilibrating the fused salt solvent with an excess of each solid chloride and then filtering the mixture through a medium porosity glass frit. The filtrates were then analyzed for lithium and copper content, respectively. Lithium was determined by flame emission and copper by atomic absorption using an Instrumentation Laboratory 351 AA/AE spectrophotometer. All cells and vessels for physical, spectrophotometric, and electrical measurements were loaded and sealed with appropriate closures under nitrogen in the glove box. In no case was any interaction observed of the fused salt with the materials used for constructing and sealing the cells.

Densities.—These were measured using a specially constructed dilatometer, of approximately 5 ml capacity, whose bulb and graduated stem had been calibrated using a weighed quantity of freshly boiled distilled water (5). Precision was limited by measurement of volume, which was shown to be reproducible to two parts in 10,000; measurements of mass were one order of magnitude more precise. The assembly was then immersed in a bath whose temperature was controlled to $\pm 0.1^\circ$.

Viscosities.—A modified Cannon-Fenske viscosimeter was constructed, which could be closed to maintain a dry nitrogen atmosphere. A rubber bulb on the side could be squeezed to pump the liquid into the upper reservoir. The viscosimeter was calibrated using aqueous solutions of glycerol (J. T. Baker Reagent Grade). Temperatures were controlled to $\pm 0.05^\circ$ and measured with a National Bureau of Standards calibrated thermometer. Calibration reference viscosities, μ , were inferred from solution compositions, which in turn were obtained from densities, ρ , determined using a dilatometer of about 50 ml capacity and calibrated as described previously. Density-composition-viscosity interpolations were made in the extensive "Table of Absolute Viscosities of Glycerol-Water Solutions" given by Segur (6). Solutions of 79, 91, and 96% concentration were measured at 25° and 30°. From the efflux times, t , the viscosimeter constant, k , was calculated, using the equation $\mu = k\rho t$, to be 0.4727 with an accuracy of $\pm 0.2\%$ in the viscosity range 30–200 cp and $\pm 2\%$ in the range 200–440 cp.

Conductivities.—An Industrial Instruments Model RC16 B2 bridge was used. The cell consisted of two parts with a standard taper joint in the middle; the platinized platinum electrodes were sealed in the top and dipped into the test liquid in the bottom part. The cell, whose constant was 0.100 cm^{-1} , was immersed in a bath controlled to $\pm 0.1^\circ$. Conductivities were measured at a frequency of 1 kHz.

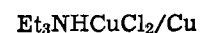
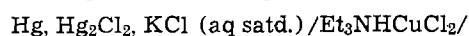
Electronic spectra.—Spectra of fused salt mixtures in stoppered 1 mm cells were recorded with a Cary 16 spectrophotometer. A Cary 118 spectrophotometer was used with the OTTLE cell, for which a special sample compartment carriage was constructed.

Electrochemical cells.—Copper and platinum wire and foil electrodes were polished with emery cloth and washed with nitric acid and distilled water. Working and auxiliary cell compartments were separated by coarse porosity glass frits. The OTTLE, an optically transparent thin layer electrode cell similar to that described by DeAngelis and Heineman (7), was also used in potentiometric, spectrophotometric, and electrolysis experiments. Microscope slides (Corning No. 2947) were cut in 6 cm lengths and, with the electrodes in place, were sandwiched together using strips of 2 mil adhesive-backed Teflon tape (Dilectrix Corporation Fluorofilm DF 1200) as spacers. The cell sides were glued and sealed with epoxy cement. The reference electrode, a strip of 0.005 in. copper foil, was mounted at the top, partly extending out of the cell. The auxiliary and slightly smaller working electrodes were made of gold minigrid mesh (Buckbee Mears Company) of 100 wires/inch with an optical transmittance of 82%. After the cell had been loaded in the dry box, its ends were sealed with Pyseal black wax (Fisher). External electrical contacts to the protruding gold minigrid leads were made with folded and clamped strips of aluminum foil. The optical path-length of the OTTLE was calculated to be 0.168 mm from measurement of the absorbance at 426 nm of a potassium chromate solution in it and in a calibrated 1 mm spectrophotometer cell.

Electrochemical instrumentation.—Polarization and electrolysis studies were carried out with a Princeton Applied Research Model 173 potentiostat/galvanostat fitted with a Model 179 digital coulometer. Current and potential data were recorded on a Heath Model SR 204 recorder or read directly from a Fairchild Model 7030 digital voltmeter. Potential-current relationships for various electrode-fused salt interfaces were investigated using a Princeton Applied Research Model 174 polarograph. Current-voltage curves for slow voltage sweep experiments were recorded with a Varian F80A X-Y recorder. EMF measurements on galvanic cells were made using a Leeds and Northrup Student's Potentiometer or with a Fairchild Model 7030 digital voltmeter.

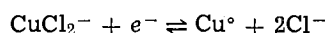
The Cu/Et₃NHCuCl₂ reference electrode.—All metal-fused salt interfacial potentials were measured with respect to this electrode. To test the polarizability of the reference electrode, galvanostatic currents were applied to a cell containing copper wire working, auxiliary, and reference electrodes immersed in neat triethylammonium dichlorocuprate(I). A length of glass tubing shielded the reference electrode from most of the bulk electrolyte but allowed electrical contact with the liquid through an open end. The area of the working electrode was about 1 cm². The potential of the working electrode was shifted by 1 mV on passage of a 1 μA current for 30 sec, and recovered the equilibrium value in 30 sec. This means that using such a Cu/Et₃NHCuCl₂ electrode as a reference with instrumentation of 1 M Ω impedance, a 1V potential could be measured to within an error of 1 mV.

Using the three compartment cell

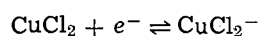


the operational potential of the copper reference electrode plus junction potential was found to be -0.241V vs. SCE at 25° .

Overpotential measurements.—A two-compartment cell was used. One compartment contained an 18 cm^2 copper foil auxiliary electrode immersed in triethylammonium dichlorocuprate(I). For study of the electrode process



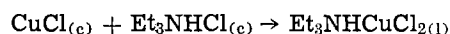
the second compartment contained a sheathed copper wire reference electrode and a 1 cm^2 copper foil working electrode mounted orthogonally to the direction of the auxiliary electrode and coated with Apiezon black wax on its back side. The electrodes were immersed in triethylammonium dichlorocuprate(I). Similar platinum wire reference and 1 cm^2 platinum foil working electrodes were used, immersed in a solution of copper(II) chloride in triethylammonium dichlorocuprate(I), for overpotential studies of the electrode process



In both cases, the electrolyte was stirred magnetically.

Results and Discussion

Densities.—Density data for triethylammonium dichlorocuprate(I) and for fused salt mixtures at several temperatures are listed in Table I and permit concentrations to be expressed both on weight and molarity bases. The molar volume of the fused salt exceeds the molar volumes of its solid constituents by 10.9%, corresponding to the expansion taking place during the markedly endothermic reaction



The greater densities of copper(I) and copper(II) chlorides than of triethylammonium dichlorocuprate(I) account for the correspondence between increasing concentrations of these salts and the densities of fused salt mixtures containing them.

Spectra.—Pure triethylammonium dichlorocuprate(I) has no absorption maximum in the visible region; its pale yellow color is due to the tail of a u.v. charge-transfer absorption. A solution of copper(II) chloride in triethylammonium dichlorocuprate(I) is green, appearing nearly black if the concentration or path length is large. Such a solution absorbs continuously across the visible region and shows no maximum vs. air, but with the neat fused salt solvent in the reference beam it has a well-resolved absorption peak at 402 nm ($\epsilon = 2.02 \times 10^3$ liters mole $^{-1}$ cm $^{-1}$). These values are typical of various chlorocuprate(II) complexes (8). No special behavior is observed of the "intervalence transfer absorption" type (9-11), common for complexes containing a transition metal in two different oxidation states. Solutions of concentration up to 0.1M copper(II) chloride in triethylammonium dichlorocuprate(I) were found to obey Beer's law.

Electrolysis products.—That the cathodic product of electrolysis of neat triethylammonium dichlorocuprate(I) is metallic copper was determined by visual inspection of the deposit on a graphite electrode. The nature of the anodic product was determined using the OTTLE. The absorption spectrum of the solution in the region of the gold anode after electrolysis was identical to the spectrum of copper(II) chloride in triethylammonium dichlorocuprate(I).

Viscosities and conductivities.—Listed in Table I are viscosity and specific conductivity data at several temperatures for triethylammonium dichlorocuprate(I) and for solutions in it containing added copper(I) and copper(II) chlorides. Addition of either compound markedly increases the viscosity and decreases the conductivity. This was true for other solutes as well. For example, at 25° the specific conductance of a saturated solution of lithium chloride (LiCl mole fraction 0.00747) was $3.68 \times 10^{-3}\ \Omega^{-1}\text{ cm}^{-1}$ and of a saturated solution of triethylammonium chloride (total Et_3NHCl mole fraction 0.5098) was $3.74 \times 10^{-3}\ \Omega^{-1}\text{ cm}^{-1}$.

The viscosity times the specific conductance (Walden) product of triethylammonium dichlorocuprate(I) in the 25° - 50°C temperature range is compared with data (12) for two molten alkali metal halides in Table II. The Walden product of molten salts over a temperature range is not constant. It is noteworthy, however, that the values of this product for triethylammonium dichlorocuprate(I) near room temperature are not all that different from the values for the much hotter molten alkali metal halides. The lower order of magnitude of the conductivity of the room temperature fused salt relative to an ordinary molten electrolyte can be attributed to the higher order of magnitude of its viscosity. This complements the vibrational spectroscopic evidence that the room temperature liquid is completely made of ions.

The equivalent conductance Λ ($\Omega^{-1}\text{ cm}^2$ equiv. $^{-1}$) of neat triethylammonium dichlorocuprate(I) was calculated from its equivalent weight, W , density, ρ , and specific conductance, κ , by the equation

$$\Lambda = \kappa W / \rho$$

For the solutions, the same form of equation was used, with the weighted average equivalent weight \bar{W} calculated from

$$\bar{W} = \sum f_i W_i$$

where f_i is the fraction of the total equivalents contributed by the i th component of concentration C_i and cation charge Z_i

$$f_i = C_i Z_i / \sum C_i Z_i$$

Arrhenius-type behavior was observed for the temperature variation both of the viscosities, μ , and equivalent conductances, Λ , of the neat fused salt as well as of solutions in it. Plots of $\log \mu$ and $\log \Lambda$ vs. $1/T$ had good linearity, in accordance with the functions

$$\mu = A \exp(-E_{\mu}^{\ddagger}/RT)$$

Table I. Densities, viscosities, and specific conductivities of fused salt mixtures at various temperatures*

Electrolyte composition (mole fraction)			Density (g/cm ³)				Viscosity (cp)				10 ³ × sp. cond. ($\Omega^{-1}\text{ cm}^{-1}$)			
CuCl	Et ₃ NHCl	CuCl ₂	25°C	30°C	40°C	50°C	25°C	30°C	40°C	50°C	25°C	30°C	40°C	50°C
0.5000	0.5000	—	1.398	1.394	1.386	1.378	123	91.7	54.4	34.8	4.30	5.55	8.36	11.8
0.4720	0.4720	0.0559	1.443	1.439	1.431	1.422	207	149	85.6	53.3	2.87	3.77	5.98	8.78
0.4455	0.4455	0.1090	1.522	1.517	1.509	1.501	421	297	158	92.8	1.87	2.48	4.25	6.80
0.5697	0.4303	—	1.519	1.515	1.506	1.497	183	133	75.4	46.8	3.60	4.55	7.40	10.8
0.6237	0.3763	—	1.627	1.622	1.613	1.603	270	189	105	62.0	2.70	3.65	6.12	9.30
0.6667	0.3333	—	1.743	1.738	1.729	1.720	388	272	143	82.7	2.53	3.43	5.86	8.95

* Estimated precision is: density, 0.5 part per thousand; viscosity, 2 parts per thousand below 200 cp and 2 parts per hundred above 200 cp; conductivity, 5 parts per hundred; temperature, $\pm 0.05^\circ$ in viscosity measurements and $\pm 0.1^\circ$ in other measurements.

Table II. Viscosity \times specific conductance product of molten salts ($\text{cp } \Omega^{-1} \text{ cm}^{-1}$)

	$^{\circ}\text{C}$	μ	κ	$\mu\kappa$
Et ₃ NHCuCl ₂	25	123	0.00430	0.529
	30	91.7	0.00555	0.509
	40	54.4	0.00836	0.455
	50	34.8	0.0118	0.411
KI*	750	1.90	1.43	2.70
	800	1.51	1.52	2.30
	850	1.22	1.61	1.96
	900	1.00	1.67	1.67
NaCl*	850	1.28	3.75	4.80
	900	1.02	3.91	3.99
	950	0.82	4.05	3.32
	1000	0.70	4.16	2.91

* Ref. (12).

and

$$\Lambda = A' \exp(-E_{\Lambda^{\pm}}/RT)$$

The energies of activation for viscous flow ($E_{\mu^{\pm}}$) and for electrolytic conductance ($E_{\Lambda^{\pm}}$) are given in Table III. The $E_{\mu^{\pm}}$ values are in the range generally found for fused salts (13), but the $E_{\Lambda^{\pm}}$ values are about three times larger than usually observed. Values of the empirical function proposed by Frenkel (14)

$$\mu\Lambda^{(E_{\mu^{\pm}}/E_{\Lambda^{\pm}})} = \text{constant}$$

are also given in Table III. It is interesting that these values do indeed show remarkable constancy in the 25°-50°C range for each given composition.

Potentiometry.—Potential measurements were made on galvanic cells of the type

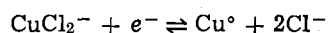


in a two-compartment cell and with varying concentrations of copper(II) chloride and corresponding variations in the copper(I) concentration [as dichlorocuprate(I) ion] in the catholyte. Similar measurements were made in the OTTLE cell



The data were combined in a plot of $\log [\text{Cu}(\text{I})]/[\text{Cu}(\text{II})]$ vs. potential, which was linear at copper(II) concentrations of 0.1M or less with a least squares slope of 55.1 mV/decade. This agrees well with the Nernstian theoretical slope of 59.2 mV/decade at 25°. There was marked deviation at higher copper(II) concentrations.

Overpotential measurements.—The effects of anodic and cathodic polarizing currents were determined for the processes



on a copper electrode surface and

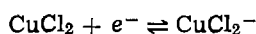


Table III. Energies of activation* and values of the Frenkel viscosity conductance function†

Electrolyte composition (mole fraction)			$\mu\Lambda^{(E_{\mu^{\pm}}/E_{\Lambda^{\pm}})}$					
CuCl	Et ₃ NHCl	CuCl ₂	$E_{\mu^{\pm}}$	$E_{\Lambda^{\pm}}$	25°C	30°C	40°C	50°C
0.5000	0.5000	0	9.6	7.8	35.5	36.3	35.9	35.4
0.4720	0.4720	0.0559	10.4	8.6	34.0	34.2	34.5	34.4
0.4455	0.4455	0.1090	11.6	10.0	40.5	39.8	39.9	40.7
0.5697	0.4303	0	10.4	8.6	38.2	37.0	38.0	37.6
0.6257	0.3763	0	11.2	9.6	38.2	38.4	39.2	38.1
0.6667	0.3333	0	11.8	9.8	43.7	44.4	44.6	43.2

* Kcal/mole.

† $\text{CP } \Omega^{-1} \text{ cm}^2 \text{ equiv.}^{-1}$.

Table IV. Current-voltage relations in the low overpotential region

Interface	$di/d\eta^*$	i_0^{**}
Cu/Et ₃ NHCuCl ₂	3.70	94
CuEt ₃ NHCuCl ₂ + CuCl†	2.92	74
Pt/Et ₃ NHCuCl ₂ + CuCl ₂ ‡	5.20	132

* $\mu\text{A cm}^{-2} \text{ mV}^{-1}$.** $\mu\text{A cm}^{-2}$.† Mole fractions Et₃NHCl 0.4545 + CuCl 0.5455.‡ Mole fractions Et₃NHCl 0.4940 + CuCl 0.4940 + CuCl₂ 0.0119.

on a platinum surface. In the low overpotential region $5 \text{ mV} \cong \eta \cong -5 \text{ mV}$, plots of current vs. overpotential showed no discontinuity at zero potential and indeed were quite linear. The values of $di/d\eta$, which are useful criteria of electrode behavior (15), are given in Table IV. The linearity of these plots is in accord with the simplified form (for a one-electron process with a change transfer rate-determining step) which the Butler-Volmer equation assumes in the limit of low overpotential

$$i = i_0 F \eta / RT$$

and permitted determination of the exchange current densities, i_0 given in Table IV.

Cyclic voltage sweep studies.—In unstirred neat triethylammonium dichlorocuprate (I), potential scans were carried out, first anodic and then cathodic, with sweep rates of 2-10 mV/sec using a conventional three-electrode potentiostat. The cell had a platinum or glassy carbon working electrode, a copper reference electrode, and a platinum auxiliary electrode. The general features of the current-voltage curves obtained in this way were reproducible, but details depended on the age and history of the electrolyte.

Such curves have a remarkable and unexpected appearance, considering that the anodic process



involves a constituent ion of the solvent itself, with a copper(I) concentration of 5.9M. [Of course, the actual electroactive species may or may not be the dichlorocuprate(I) ion; however, reversible dissociation reactions of chloro complexes of d¹⁰ copper(I) would be expected to have rapid rates.] A typical scan at 21° is shown in Fig. 1(a), and resembles a cyclic voltammogram of an electroactive species in dilute solution, where the limiting current-voltage relations involve diffusion control.

Qualitatively, current-voltage relations of the type observed here are attributed to blockage of the electrode surface by formation of a poorly conducting

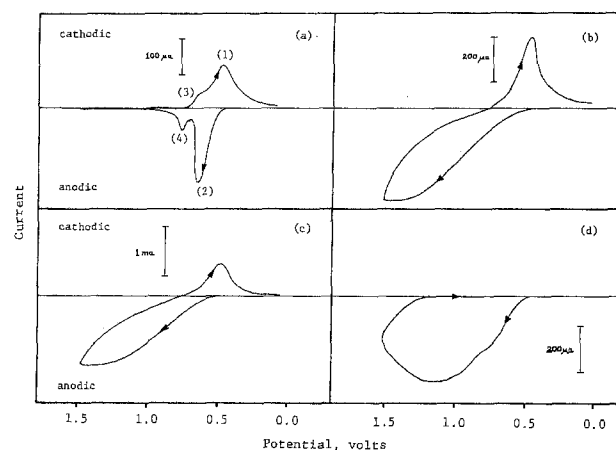


Fig. 1. Effect of temperature on voltammetry curves obtained at a platinum electrode in triethylammonium dichlorocuprate (I): (a), 21°C; (b), 34°C; (c) 51°C; (d), then cooled to 13°C.

film (16). This dark green copper(II) chloride film can be seen on the electrode surface after the anodic portion of the scan and has the same appearance as that electrogenerated in the OTTLE experiments. The previously described physical measurements demonstrated that as the concentration of copper(II) chloride in triethylammonium dichlorocuprate(I) increases, there is a marked increase in viscosity and decrease in conductivity.

Quantitatively, according to the theoretical treatment developed by Calandra and co-workers (17) and supported by their experimental observations in cases of insoluble films of anodic products blocking electrode surfaces, one expects a linear dependence on the square root of the scan rate of both the potential of the peak maximum and of the current at that point. As shown in Fig. 2, this square root dependence is observed in the present work.

The cyclic voltage sweep in Fig. 1(a) provides evidence for two anodic and two cathodic reactions. The larger anodic and cathodic peaks are a combination based on one oxidation-reduction process, and the smaller anodic and cathodic peaks correspond to another. This was proved by carrying out the scan sweep over limited parts of the range. The first anodic reaction commenced at about 0.5V with respect to the copper reference electrode. Following onset of the reaction, a green deposit was observed adhering to the working electrode. That this first anodic product is copper(II) is implied by the resemblance between this potential and appearance of the product to those observed in the OTTLE coulometric experiment. It is not known what the second anodic product is.

The peak shapes are very temperature dependent as shown in Fig. 1(b, c, d). Polarograms at 34° and 51°C, in addition to showing the expected increase in current, lack the definition observed at 21°. The polarogram obtained at 13°C, made following the 51° scan, shows the same lack of anodic peak definition observed at 51°. The cathodic process on reversing the sweep direction has vanished at 13°, indicating some change in the nature of the anodic deposit. The considerable decrease in viscosity of the anodic film on raising the temperature accounts for the changes seen in Fig. 1(b, c). The viscous gel formed by the concentrated film of anodic product on the electrode surface evidently has become completely rigid on cooling to 13°C, as indicated by the disappearance of the cathodic process on reversing the scan, seen in Fig. 1(d).

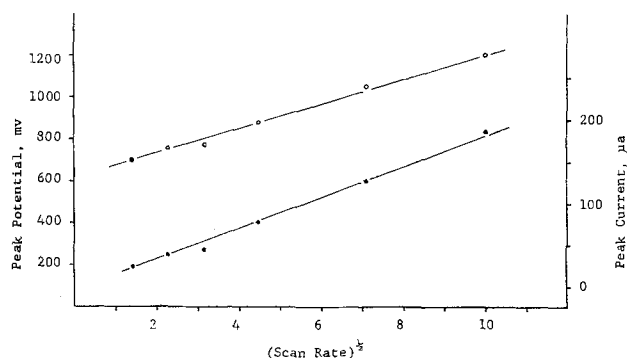


Fig. 2. Dependence of the peak potential (upper line) and peak current (lower line) on the scan rate.

Galvanic cells.—Several types of cells were prepared using copper foil and platinum or graphite (Grafoil) foil electrodes and various separator materials (18). The electrolyte was prepared either by preelectrolysis of neat triethylammonium dichlorocuprate(I) in the cell, or by using various triethylammonium dichlorocuprate(I)-triethylammonium chloride mixtures on the anode side and various triethylammonium dichlorocuprate(I)-copper(II) chloride mixtures as the catholyte. Several current-voltage-time tests of such cells were undertaken (19). Open-circuit voltages of about 0.75V were generally observed. In limited studies, performance of the cells under conditions of sustained discharge was found unsatisfactory due to their high electrolyte viscosity and high internal resistance.

Acknowledgments

We thank the Oregon State University Research Council for funds used in the construction of the OTTLE and other apparatus. Helpful discussions with Professors Harry Freund and Allen B. Scott are acknowledged with thanks.

Manuscript submitted May 28, 1979; revised manuscript received Nov. 11, 1979.

Any discussion of this paper will appear in a Discussion Section to be published in the December 1980 JOURNAL. All discussions for the December 1980 Discussion Section should be submitted by Aug. 1, 1980.

REFERENCES

- D. D. Axtell, B. W. Good, W. W. Porterfield, and J. T. Yoke, *J. Am. Chem. Soc.*, **95**, 4555 (1973).
- W. W. Porterfield and J. T. Yoke, *Adv. Chem. Ser.*, **150**, 104 (1976).
- R. N. Keller and H. D. Wycoff, *Inorg. Synth.*, **2**, 1 (1946).
- D. F. Shriver, "The Manipulation of Air-sensitive Compounds," chap. 8, McGraw-Hill Book Co., New York (1969).
- I. B. Joedicke, H. V. Studer, and J. T. Yoke, *Inorg. Chem.*, **15**, 1352 (1976).
- J. B. Segur, in "Glycerol," C. G. Miner and N. N. Dalton, Editors, pp. 278-281, Reinhold Publishing Co., New York (1953).
- T. DeAngelis and W. Heinemen, *J. Chem. Educ.*, **53**, 594 (1976).
- W. E. Hatfield and T. S. Piper, *Inorg. Chem.*, **8**, 841 (1964).
- G. C. Allen and N. S. Hush, *Prog. Inorg. Chem.*, **8**, 357 (1967).
- N. S. Hush, *ibid.*, **8**, 391 (1967).
- M. B. Robin and P. Day, *Adv. Inorg. Chem. Radiochem.*, **10**, 247 (1967).
- A. Klemm, in "Molten Salt Chemistry," M. Blander, Editor, pp. 564-578, Interscience Publishers, New York (1964).
- G. Kortum, "Treatise on Electrochemistry," 2nd ed., chap. 7, Elsevier, New York (1965).
- J. Frenkel, "Kinetic Theory of Liquids," p. 441, Oxford University Press, London (1947).
- R. H. Cousens, D. J. G. Ives, and R. W. Pittman, *J. Chem. Soc.*, 3972 (1953).
- W. J. Muller, *Trans. Faraday Soc.*, **27**, 737 (1931).
- A. J. Calandra, N. R. De Tacconi, R. Pereiro, and A. J. Arvia, *Electrochim. Acta*, **19**, 901 (1974).
- J. R. Silkey, M. S. Thesis, Oregon State University, 1979.
- N. C. Cahoon and G. W. Heise, Editors, "The Primary Battery," Vol. II, John Wiley & Sons, Inc., New York (1976).

Theoretical and Experimental Modeling of Surface Leveling in ECM under Primary Current Distribution Conditions

R. Sautebin, H. Froidevaux, and D. Landolt*

Materials Department, Swiss Federal Institute of Technology, Lausanne, Switzerland

ABSTRACT

Finite element (FE) numerical simulation was employed for studying the influence of geometrical factors on the rate of leveling of a triangular surface profile during anodic dissolution in ECM at constant interelectrode gap under conditions of primary current distribution. Theoretical results were verified experimentally with a laboratory ECM apparatus using active dissolution of copper in NaNO_3 as model reaction. The experimentally observed decrease with time of profile amplitude corresponds well to that predicted theoretically. At long dissolution times, experimental surface roughness does not reach zero, however, because microroughness develops due to crystallographic etching of the anode.

Electrochemical machining (ECM) is a high rate electrolysis process involving time dependent shape change of the anode. Shape prediction problems in ECM can be divided into two categories: prediction of tool shape necessary to produce a given workpiece, and prediction of the shape evolution of the workpiece during machining with a given tool. Deburring and surface smoothing are ECM operations falling into the second category. They are based on the observation that, upon machining with a flat tool, protruding parts of a rough surface dissolve at a higher rate than receding parts. The degree of preferential dissolution determines how much metal has to be dissolved overall to achieve a desired leveling effect. It will depend on geometrical and on electrochemical parameters.

A study involving theoretical and experimental modeling was initiated at our laboratory with the aim of learning more about the mechanism of surface leveling under ECM conditions and providing guidelines for predicting the memory effect of the anode, i.e., the extent of metal dissolution necessary to change a given anode surface profile into that of the cathode.

Theoretical modeling of surface smoothing requires calculation of the current distribution on the anode and of the resulting change in its shape with time. The problem of current distribution on a time invariant triangular two-dimensional surface profile has been treated analytically by Wagner (1). McGeough (2) has given a solution for the time dependence of the amplitude of a sinusoidal profile during anodic dissolution. For the calculation of complex shape changes the use of numerical rather than analytical procedures is indicated. Riggs (3) has developed a sophisticated computer program for predicting the influence of ECM operating variables on the accuracy of shape reproduction obtained during simple cavity sinking operations. The author used a finite difference method of calculation and was able to take into account local conductivity variations in the gap due to joule heating and to the presence of gas. In recent years the finite element method (FEM) has become increasingly popular in different branches of engineering including structural engineering and heat transfer (4-7). Compared to finite difference methods the FEM requires less elaborate programming and is more easily adaptable to time-dependent geometrical conditions. At the time the present work was initiated no application of FEM to electrochemistry was known to the authors. However, recently an excellent discussion of

the relative merits of FEM and finite difference methods for solving electrochemical problems has been published by Alkire and Bergh (8) who used FEM to predict the shape change of the cathode in an electrodeposition cell.

Experimental modeling of the ECM leveling process requires the availability of an anode of well-defined surface profile and knowledge of reaction stoichiometry, kinetics, and mass transport conditions. High rate anodic copper dissolution in KNO_3 solution has been extensively studied in the past (9-11). Copper dissolution in this electrolyte proceeds in the active mode up to a critical current density, the value of which is mass transport controlled and may be many A/cm^2 under ECM flow conditions. The copper-sodium nitrate system was therefore chosen for simulating leveling behavior under active dissolution conditions.

In the present paper, surface leveling under conditions approaching primary current distribution, where geometrical parameters rather than electrode overvoltage are controlling, is investigated. Surface leveling under secondary and tertiary current distribution conditions is being studied at this time in our laboratory and results will be reported at a later date. Original surface roughness is modeled by a two-dimensional triangular wave profile. Shape evolution with dissolution time is computed numerically using FEM based on a general computer program (7). Calculations are tested experimentally in an ECM test rig under conditions of constant interelectrode gap.

Theoretical Simulation by FEM

Fundamental equations.—The two-dimensional model of the interelectrode gap is schematically shown in Fig. 1. Throughout the present calculations, it is assumed that the average interelectrode distance l is much longer than the original surface profile amplitude ϵ_0 , $l \gg \epsilon_0$. Potential distribution in the interelectrode gap at any time is given by Laplace's equation

$$\nabla^2\phi = 0 \quad [1]$$

It is assumed that local conductivity changes due to joule heating or gas evolution are negligible. The current density i at any point in space is given by Eq. [2] where κ is the specific electrolyte conductivity

$$i = -\kappa\nabla\phi \quad [2]$$

The local anodic dissolution rate v_a (cm/sec) is given by Faraday's law

* Electrochemical Society Active Member.
Key words: dissolution, anode, FEM.

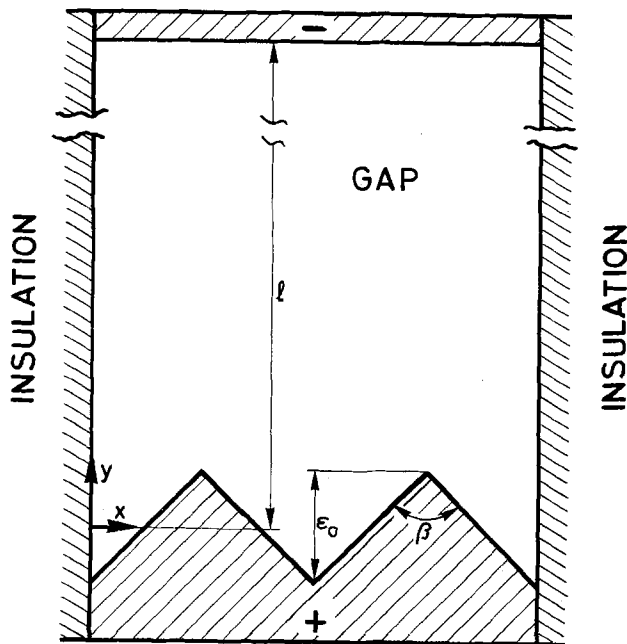


Fig. 1. Electrochemical cell geometry with triangular wave surface profile of the workpiece.

$$v_a = \frac{M\theta i}{n\rho F} \quad [3]$$

Here M is the atomic weight of the metal, θ is the current efficiency for metal dissolution, ρ is the density of the anode metal.

The boundary conditions are the following

at the anode $\phi = \phi_A \quad [4]$

at the cathode $\phi = 0 \quad [5]$

at insulating boundaries (planes of symmetry) $\frac{d\phi}{dX} = 0 \quad [6]$

Equations [1]-[6] allow one to calculate the local dissolution rate on the anode at any given time. To obtain the decrease in amplitude as a function of dissolution time, the calculation is repeated for suitably chosen time intervals using the computed roughness profile of each preceding calculation as the initial condition for the subsequent step.

Method of solution.—The system of Eq. [1]-[6] was solved numerically by FEM using a CDC Cyber 7328 computer. For the theory of FEM the reader is referred to the literature (6, 7). In brief, the method consists in finding a function ϕ which minimizes the energy density of the electric field in the interelectrode space and which satisfies the boundary conditions. For this purpose, the interelectrode space is divided into a finite number of small elements, in this case triangles (Fig. 2). Discrete linear potential functions ϕ_i are defined for each node i corresponding to the peak of a triangle. The problem of searching the unknown potential ϕ then reduces to solving a system of linear equations expressed by Eq. [7].

$$A\phi = \underline{f} \quad [7]$$

Here ϕ is a vector $\phi = (\phi_1 \phi_2)$, A is a symmetrical matrix (rigidity matrix) the value of which depends on the triangulation employed, and \underline{f} is a vector depending only on boundary conditions.

With the FEM, the potential gradient at the nodes is not well defined but it can be approximated using Eq. [8]

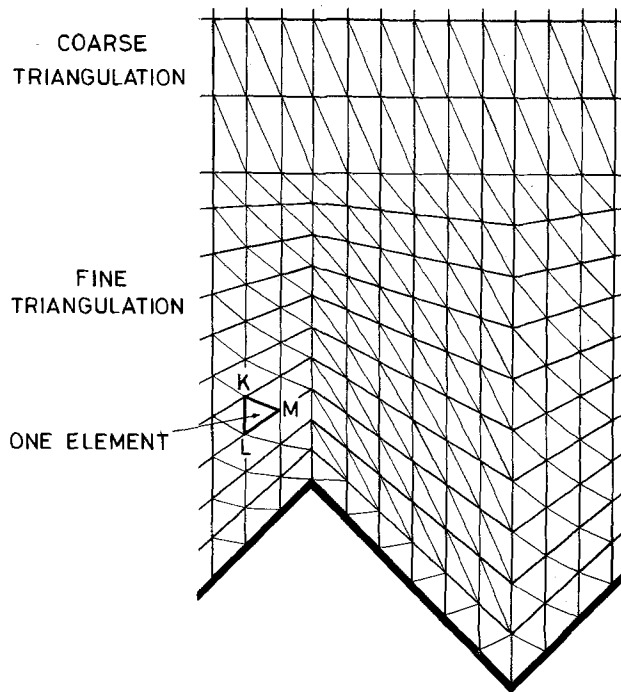


Fig. 2. Division of interelectrode space in finite triangular elements. K, L, M are the nodes of an element.

$$\bar{E}_s = \frac{\sum_{i=1}^k S_i E_i}{\sum_{i=1}^k S_i} \quad [8]$$

Here \bar{E}_s is the mean potential gradient at node s , S_i is the area, and E_i the (constant) gradient corresponding to a given triangle i . The summation is made over all k triangles having a common node s . Equation [8] is applicable to the computation of the potential gradient at sharp corners of the profile.

The accuracy of the approximation of the potential distribution depends on the node density which has to be chosen sufficiently high. The FEM allows one to have a higher node density in the region of primary interest, i.e., nearer the anode surface than in the rest of the gap (Fig. 2). For the present computations, it was ascertained that a further increase in node density did not change obtained results significantly.

The numerical calculation involves the following steps:

1. Read data, initial geometry, electrochemical parameters, and boundary conditions;
2. Label triangles in interelectrode space;
3. Compute rigidity matrix A and second member \underline{f} ;
4. Solve system of linear equations by overrelaxation;
5. Calculate potential gradients at the anode and the corresponding shape change for a given time interval;
6. Repeat procedures 1-5 until the original profile has disappeared;
7. Print out results of computations in dimensionless form.

Experimental Method and Apparatus

To test theoretical predictions experiments were carried out in a laboratory ECM rig at constant interelectrode gap. The apparatus consists of an electrochemical cell with moving anode through which the thermostated and filtered electrolyte is recirculated by means of a controlled volume two piston pump equipped with an attenuator to dampen flow pulsations. The electrochemical cell is shown in Fig. 3. It consists of two transparent plexiglass bodies (J, K) separated by a Teflon spacer (F) which fixes the dimensions of the rectangular flow channel (0.5×3 mm cross section). The flat stainless steel cathode (B) is in a fixed posi-

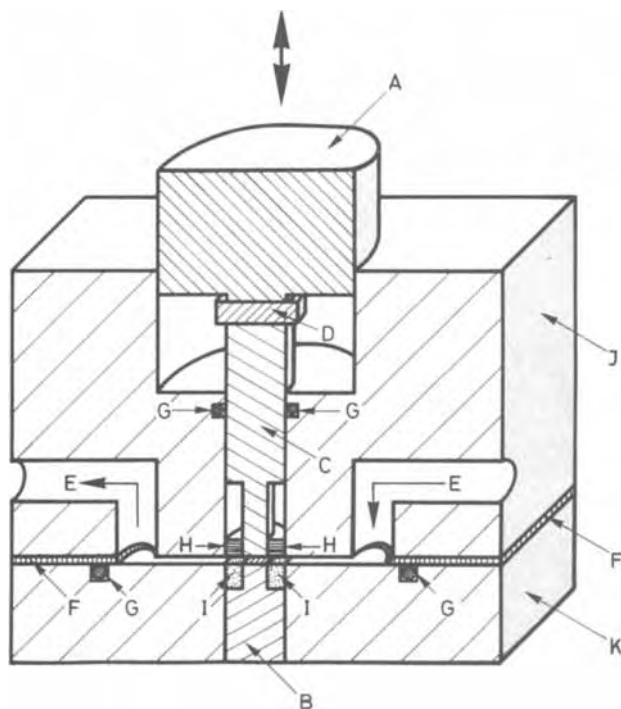


Fig. 3. Flow channel cell with moving anode (schematic): (A) anode support with controlled rate of advance; (B) fixed cathode; (C) moving anode; (D) connecting screw; (E) electrolyte flow; (F) Teflon spacer; (G) O-ring; (H) Teflon joints; (I) araldite mould; (J) fixed plexiglass cell body; (K) detachable plexiglass cell body.

tion flush with the channel wall. The anode (C) is sealed with Teflon joints (H) and O rings (G). It can be advanced continuously towards the cathode at rates varying from 1 μ /min to 6 cm/min. Anode movement is controlled by a stepping motor allowing for precise control of feed rate and position ($\pm 1\mu$). The anode is 99.9% copper, the geometrical surface area exposed to the electrolyte is the same as that of the cathode (0.5×3 mm). The anode surface is machined mechanically to a triangular profile of amplitude $\epsilon_0 = 50\mu$ and an opening angle of $\beta = 95.5^\circ$. Real anode surface at the beginning of an experiment is 0.203 cm². During the experiments the triangular profile is oriented parallel or perpendicular to the flow direction.

All experiments are performed at a constant linear flow rate of the electrolyte of 20 m/sec corresponding to a Reynolds number of 19,000. A 2M NaNO₃ solution prepared from analytical grade chemicals is employed as electrolyte. Electrolyte temperature is 25°C in all experiments. Due to the high flow velocity employed conductivity changes in the electrolyte gap due to joule heating and cathodic gas evolution are negligible.

To simulate leveling experimentally under conditions approaching primary current distribution, operating variables have to be chosen in such a way that electrode polarization and mass transport effects are negligible. In the present study, a current density of 10 A/cm² was applied at a linear flow rate of the electrolyte of 20 m/sec. Under these conditions the value of applied current density corresponded to approximately 10% of the value of the critical mass transport controlled current density for the transition from active to transpassive dissolution. Mass transport effects, therefore, should not affect obtained results. The importance of activation polarization for current distribution can be estimated by considering the Wagner number W_a

$$W_a = \left(\frac{d\eta}{di} \right) \frac{\kappa}{L} \quad [9]$$

Here $d\eta/di$ is the slope of the current voltage curve, κ

is the electrolyte conductivity, and L is a characteristic length of the system. Primary current distribution prevails if $W_a \ll 1$, secondary current distribution if $W_a \gg 1$. For active copper dissolution Tafel polarization can be assumed (10). The characteristic length L for surface leveling may be taken equal to ϵ_0 . Equation [9] then becomes

$$W_a = \frac{b\kappa}{2.3 i \epsilon_0} \quad [10]$$

Numerical values typical for the present experiments are $b = 40$ mV [Tafel slope for high rate copper dissolution in sulfuric acid (10)], $\kappa = 0.112$ Ω^{-1} cm⁻¹, $i = 10$ A/cm², $\epsilon_0 = 5 \times 10^{-3}$ cm, and the resulting value for the Wagner number is $W_a = 0.04$. The condition for primary current distribution, $W_a \ll 1$ is therefore well fulfilled.

All experiments were performed at constant current. At the beginning of an experimental run, the anode was positioned flush with the channel wall. Anode feed rate was then adjusted such that the position of the electrode surface with respect to the channel wall remained unchanged during an experiment, i.e., the feed rate was equal to the average dissolution rate. Dissolution experiments were carried out in successive steps. After each step, the surface profile was determined with a mechanical surface tester (Talysurf, Model 10), then the electrode was reintroduced into the electrolysis cell. Some surface profiles were also observed by means of a scanning electron microscope. Figure 4 illustrates the original triangular surface profile of the anode and its shape evolution with increasing dissolution time.

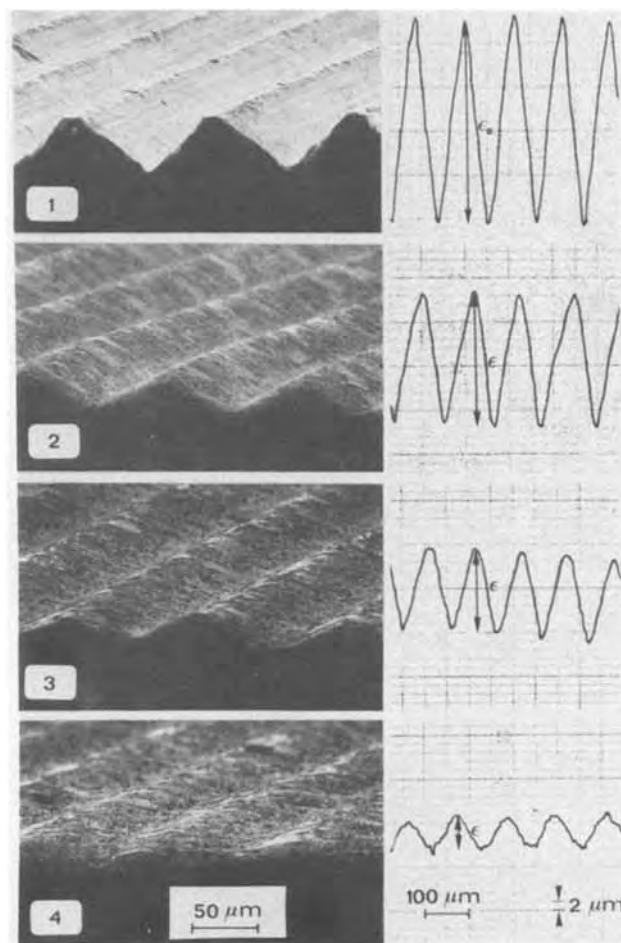


Fig. 4. SEM micrographs and surface tester traces illustrating the time evolution of a triangular profile during leveling. Pictures 1-4 correspond to points marked in Fig. 7.

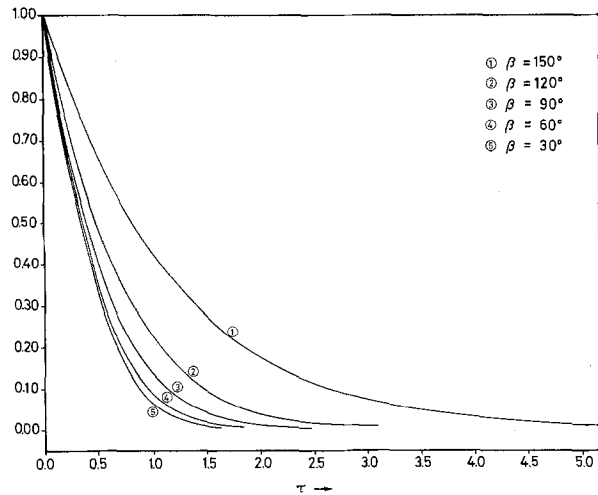


Fig. 5. Computed curves showing the influence of profile angle β , on leveling rate. $\epsilon_0/l = 0.095$.

Results and Discussion

Figures 5 and 6 give results of numerical computations. The decrease in relative amplitude ϵ/ϵ_0 is plotted as a function of the dimensionless dissolution time τ which is defined by Eq. [11]

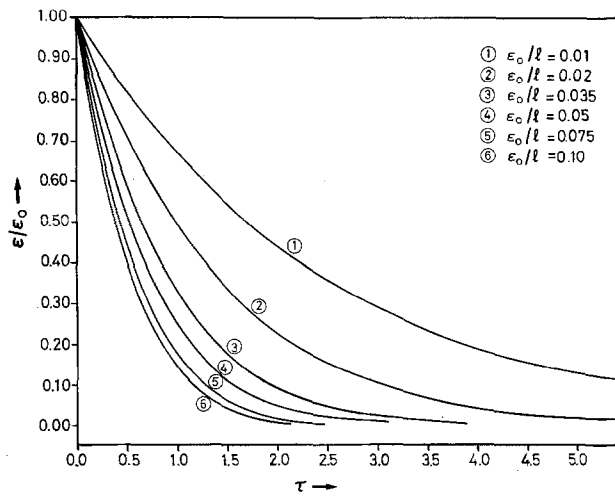


Fig. 6. Computed curves showing the influence of relative rugosity, ϵ_0/l , on the leveling rate, $\beta = 95.5^\circ$.

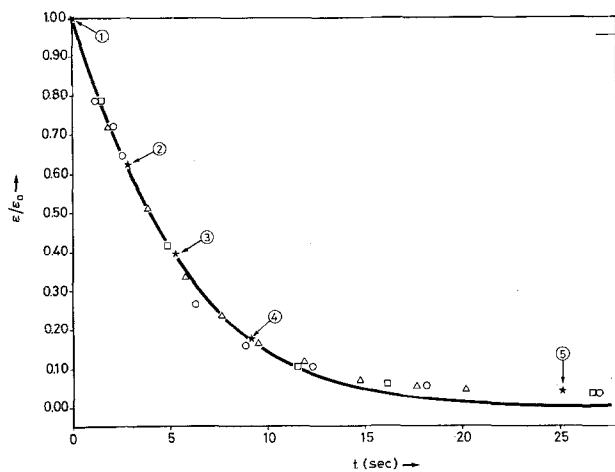


Fig. 7. Theoretical (solid line) and experimental leveling rates as a function of dissolution time, surface profile oriented perpendicular (\circ , Δ), and parallel (\square) to the flow direction. The symbol ($*$) designates experimental points shown in Fig. 4 and 8. Profile angle $\beta = 95.5^\circ$.

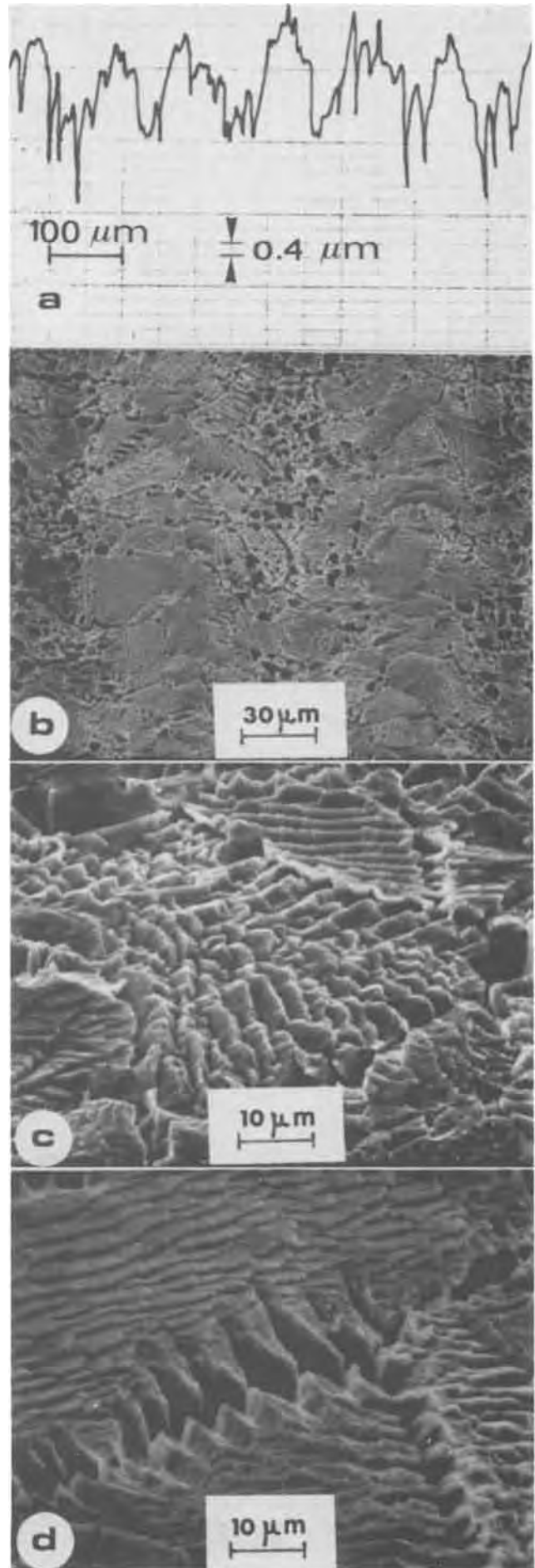


Fig. 8. SEM micrographs and profilograms illustrating micro-rugosity resulting at long dissolution times. Experimental conditions correspond to Pt. 5 in Fig. 7.

$$\tau = t \frac{M\theta I}{nF\rho\epsilon_0 A} = \frac{tv}{\epsilon_0} \quad [11]$$

Here I is the applied current, A is the geometrical area of the anode, t is the dissolution time, and v is the average rate of dissolution of the anode which for equilibrium gap conditions is equal to the cathode feed rate.

Figure 5 shows the influence of opening angle β . The larger β , the less efficient is the leveling process, i.e., the longer is the time required to achieve a desired surface smoothness. Decreasing the value of β leads to faster leveling but a limiting value is reached at small angles when dissolution proceeds almost exclusively from the peaks. The influence of the magnitude of the initial amplitude of the surface profile with respect to the electrode distance l is shown in Fig. 6. The smaller the ratio ϵ_0/l , the less efficient is the leveling process. This behavior is intuitively understandable since for small values of ϵ_0/l the potential difference relative to the applied cell voltage between the location of peaks and valleys is smaller.

The rate of mass transport controlled leveling of a sinusoidal surface profile in presence of a stagnant diffusion layer at the anode has been calculated by Wagner (12) who gave an analytical solution of Fick's law for the limiting conditions $\epsilon_0/\delta \ll 1$, and $\lambda \gg \epsilon_0$ where δ is the thickness of the stagnant diffusion layer, and λ the wavelength of the sinusoidal profile. From a mathematical point of view Wagner's solution corresponds to the solution of Laplace's equation given by McGeough (2), with the difference that the characteristic distance is the diffusion layer thickness δ in the first case, and the interelectrode distance l in the second case. It can be shown that present numerical computations applying to triangular profiles of different opening angle β at different interelectrode distance l approach Wagner's limiting solution for very large values of opening angle and of interelectrode distance, i.e., when $\beta \rightarrow 180^\circ$ and $\epsilon_0/l \rightarrow 0$.

Figure 7 shows a comparison between theoretical and experimental results for a ratio $\epsilon_0/l = 0.1$ and an opening angle of $\beta = 95.5^\circ$. The good correspondence of theoretical and experimental data for dissolution times smaller than 15 sec confirms the validity of the numerical computations and experimental procedures used. The experimentally determined rate of leveling is independent of the orientation of the triangular profile with respect to flow direction. This confirms that mass transport effects were indeed absent under the conditions of present experiments. For dissolution times longer than 15 sec or $\epsilon/\epsilon_0 < 0.05$ measured points in Fig. 7 deviate from the calculated curve. This behavior is due to the development of surface microroughness the wavelength of which is independent of the wavelength of the original triangular surface profile. This is evidenced by the SEM micrographs of Fig. 8 which clearly reveal the grain structure of the anode indicating that the development of microroughness is due to the crystallographic nature of the dissolution process. The role of crystallographic factors in high rate anodic copper dissolution in the active potential region has been discussed previously (11).

In principle, under ideal primary current distribution conditions crystallographic factors should play no role since by definition system behavior is governed entirely by geometrical factors. To explain the ap-

parent discrepancy between observed and calculated behavior at long dissolution times, one has to consider the value of the Wagner number W_a . It was shown above that at the beginning of the dissolution experiment $W_a = 0.04$, i.e., $W_a \ll 1$. However, as the surface profile amplitude decreases the value of W_a increases since one may set now $W_a = b\kappa/2.3i\epsilon$. Indeed, for $\epsilon/\epsilon_0 \approx 0.05$ corresponding to $t \geq 15$ sec one obtains $W_a \approx 1$, i.e., the condition for primary current distribution, $W_a \ll 1$, is no longer fulfilled. Electrode polarization, therefore, is no longer negligible and crystallographic factors which introduce local variation of overvoltage on a microscopic scale become significant.

Summary and Conclusions

The present study confirms that FEM is useful for simulating current distribution in electrochemical cells involving electrode shape changes. The influence of geometrical variables on the rate of anode leveling under ECM conditions at constant gap has been modeled for primary current distribution conditions and theoretical results have been verified experimentally. The use of FEM to predict leveling behavior can be extended to include other surface profiles and/or electrochemical kinetics including transpassive behavior. The approach outlined in this paper involving theoretical and experimental modeling, therefore, should eventually contribute to further our present understanding of the mechanisms which determine surface finish resulting from anodic dissolution processes such as ECM and electropolishing.

Acknowledgment

This work is part of a research program financially supported by CERS (Commission pour l'encouragement de la recherche scientifique), Bern, Switzerland.

Manuscript submitted Aug. 3, 1979; revised manuscript received Dec. 3, 1979.

Any discussion of this paper will appear in a Discussion Section to be published in the December 1980 JOURNAL. All discussions for the December 1980 Discussion Section should be submitted by Aug. 1, 1980.

Publication costs of this article were assisted by the Swiss Federal Institute of Technology.

REFERENCES

1. C. Wagner, *This Journal*, **98**, 116 (1951).
2. J. A. McGeough, in "Principles of Electrochemical Machining," p. 182ff, Chapman and Hall, London (1974).
3. J. Riggs, Ph.D. Thesis, University of California, Berkeley, Calif. (1977).
4. L. C. Wellford and R. M. Ayer, *Int. J. Num. Methods Eng.*, **11**, 933 (1977).
5. F. M. Orr and L. E. Scriven, *J. Fluid Mech.*, **84**, 145 (1978).
6. J. J. Oden, "Finite Elements of Nonlinear Continua," McGraw-Hill, New York (1972).
7. H. Froidevaux, "Mode d'emploi d'un programme de résolution aux limites." Ecole Polytech. Féd. Lausanne, Switzerland (1974).
8. R. Alkire and T. Bergh, *This Journal*, **125**, 1981 (1978).
9. D. Landolt, R. H. Muller, and C. W. Tobias, *ibid.*, **116**, 1384 (1969).
10. D. Landolt, R. H. Muller, and C. W. Tobias, *ibid.*, **118**, 40 (1971).
11. D. Landolt, R. H. Muller, and C. W. Tobias, *ibid.*, **118**, 36 (1971).
12. C. Wagner, *ibid.*, **101**, 225 (1954).



Dependence of Lithium-Silicon Electrode Potential and Lithium Utilization on Reference Electrode Location

Randall N. Seefurth* and Ram A. Sharma*

General Motors Research Laboratories, Electrochemistry Department, Warren, Michigan 48090

Lithium-silicon electrodes are undergoing development for use as negative electrodes in Li/FeS₂ compact cells (1). Lithium utilizations obtained from Li-Si electrodes having an initial composition of Li₁₅Si₄ were reported in a recent publication (2). The measurements were made at current densities between 20 and 1000 mA/cm² and at temperatures between 675° and 750°K using a cell similar to the one shown in Fig. 1A. During cycling, the voltages of the Li-Si working electrode were monitored by use of a 40 atomic percent (a/o) Li-Al reference electrode placed behind it. The working electrode was discharged to a 0.5V cutoff voltage with respect to the reference electrode and exhibited three voltage plateaus. The lithium utilizations were then calculated by dividing the plateau(s) capacity obtained during discharge by the theoretical capacity of the corresponding plateau(s).

Normally, in the measurement of overpotential of an electrode, a capillary which is connected through the electrolyte column to a reference electrode is placed in front of the electrode. The design and location of this capillary has been the topic of a number of research papers (3-6). It has been concluded in these papers that the overpotentials of an electrode measured by locating a capillary end at a distance larger than four times the external radius of the capillary from the electrodes face, and correcting for the electrolyte resistance losses, do not involve any appreciable error. It was also pointed out that significant error in overpotential measurements can occur when the capillary is placed on the insulated back side of the electrode.

In the measurement of lithium utilizations reported earlier (2), the capillary reference electrode approach was not adopted because capillary construction material which was compatible with the cell environment was not easily available. It also appeared difficult to avoid shielding of current from the electrode by the use of a capillary in this type of cell.

Due to the above reasons, lithium utilizations were measured placing the Li-Al reference electrode on the back side of the working electrode. The unconventional location of the reference electrode could cause errors in the monitored working electrode voltages, particularly at higher current densities. This was brought to our attention by one of the referees of our paper (2). He pointed out that these voltage errors in turn could lead to errors in the lithium utilizations we reported. Therefore, the present experiments were carried out to determine the variation in the measured value of the working electrode voltage with different locations of the reference electrode, the extent of error in the working electrode voltage when the reference electrode is placed behind it, and subsequently, the magnitude of any errors in the lithium utilizations reported earlier (2).

* Electrochemical Society Active Member.
Key words: fused salt, battery, current density, efficiency, energy storage.

Experimental

The materials used, electrode preparation, and experimental setup procedures were the same as reported in Ref. (2).

The working electrode was prepared by inserting a 98% porous nickel current collector into a 5 mm long and 25 mm diam stainless steel chamber with one end enclosed by spot-welding a double layer of screens (400 followed by 150 mesh). The electrode was completed by vibration-loading it with 60/100 mesh particle-size Li₂Si and enclosing the open end with screens.

In the present experiments, a liquid lithium counter-electrode was used instead of the Li₂Si-Si counterelectrode, and two 40 a/o Li-Al reference electrodes were used, one behind the working electrode and one beside it (Fig. 1B). Liquid lithium electrode preparation has been reported before (7, 8); this electrode also has been used as a reference electrode (9, 10). However, it is not normally used as a counterelectrode in Li-Si alloy electrode tests because it reacts with the LiCl-KCl electrolyte (11).

The cycling was carried out at various constant current densities at 675°K, and the discharges were terminated at a 1.0V cutoff voltage with respect to the liquid lithium counterelectrode. The working electrode-to-counterelectrode voltages were corrected for electrolyte resistance losses using the electrolyte conductivity value of 1.247 Ω⁻¹·cm⁻¹ reported by Van Artsdalen and Yaffe (12), with an electrode separation of 0.5 cm and an area of 5.0 cm² for the cell constants. These working electrode voltages with respect to lithium were then converted to those with respect to 40 a/o Li-Al using emf data published earlier (13).

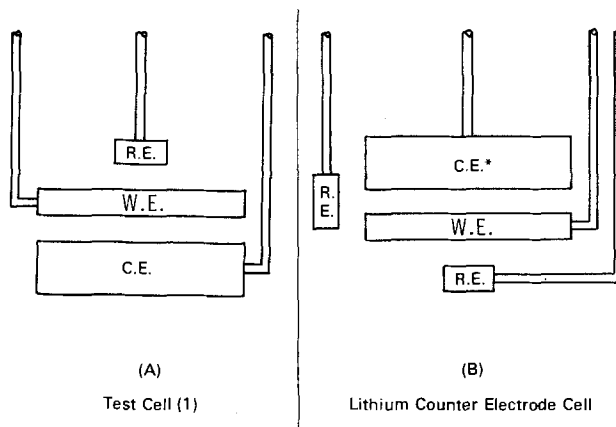


Fig. 1. Schematic representation of electrode placement in the various test cells. Where W.E. = Li-Si alloy working electrode; C.E. = Li₂Si-Si counterelectrodes; C.E.* = liquid lithium counter-electrode; and R.E. = 40 a/o Li-Al alloy reference electrode.

Results and Discussion

During the charge-discharge cycles, voltages of the $\text{Li}_{15}\text{Si}_4$ working electrode with respect to the liquid lithium counterelectrode were monitored at current densities of 50, 100, 200, 300, and 400 mA/cm^2 . In addition, the voltages were monitored with respect to the two Li-Al reference electrodes; one placed behind the working electrode and the other placed by its side (Fig. 1B). The voltages, with respect to the liquid lithium electrode, were corrected for electrolyte resistance and then converted to potentials *vs.* a 40 a/o Li-Al reference electrode. The voltages, with respect to these reference electrodes, are plotted against capacity density at current densities of 100 and 200 mA/cm^2 in Fig. 2 and 3. The plots at other current densities were similar to these plots. The voltages of the working electrode with respect to these three reference electrodes at three different locations were observed to fall within 50 mV. The calculated voltages of the working electrode with respect to the 40 a/o Li-Al reference electrode (in place of lithium) after correcting for the electrolyte resistance losses should be the most accurate. It was observed that the voltages, with respect to the reference electrode placed on the back side of the working electrode, are within 10 mV of these values at current densities up to 200 mA/cm^2 . However, the working electrode voltages, with respect to the back side reference electrode, were ~ 25 mV lower than the calculated voltages at current densities of 300 and 400 mA/cm^2 . This small difference in the two voltage values might indicate that lithium concentration gradients developed in the Li-Si electrodes during discharge at higher current densities. Apparently, under these conditions, an Li-Si compound with a lithium deficiency forms in the front of the electrode while the same Li-Si compound with a lithium excess predominates at the back of the electrode.

The voltages of the $\text{Li}_{15}\text{Si}_4$ working electrode, with respect to the liquid lithium counterelectrode after correcting for electrolyte resistance losses, are plotted

Table I. Total lithium utilizations at different current densities at 675°K

Current density (mA/cm^2)	U_T (%)	U_T^* (%)
50	79	84
100	82	83
200	78	80
300	66	—
400	55	—

where U_T = total lithium utilization from $\text{Li}_{15}\text{Si}_4$ to Si (calculated from the voltages measured with respect to a liquid lithium counterelectrode after correcting for electrolyte resistance losses),

and U_T^* = total lithium utilization from $\text{Li}_{15}\text{Si}_4$ to Si (calculated from the voltages measured with respect to a 40 a/o Li-Al reference electrode placed behind the working electrode (Ref. 2)).

against capacity density at current densities between 50 and 400 mA/cm^2 in Fig. 4. These plots are similar to those obtained with an Li_2Si -Si counterelectrode and a 40 a/o Li-Al reference electrode placed behind the working electrode as reported before (2). In fact, the total cycle lithium utilizations are within 5% of those earlier values at comparable temperatures and current densities (Table I), and the overpotential during cycling determined from current-voltage plots in the regions of the three voltage plateaus were mostly ohmic as observed before (2).

Acknowledgments

The authors are thankful to Mr. Ernest J. Verrier for assistance with the experimental work, and Drs. Elton J. Cairns and John S. Dunning of the Electrochemistry Department for useful suggestions and discussions.

Manuscript submitted March 5, 1979; revised manuscript received Nov. 30, 1979.

Any discussion of this paper will appear in a Discussion Section to be published in the December 1980

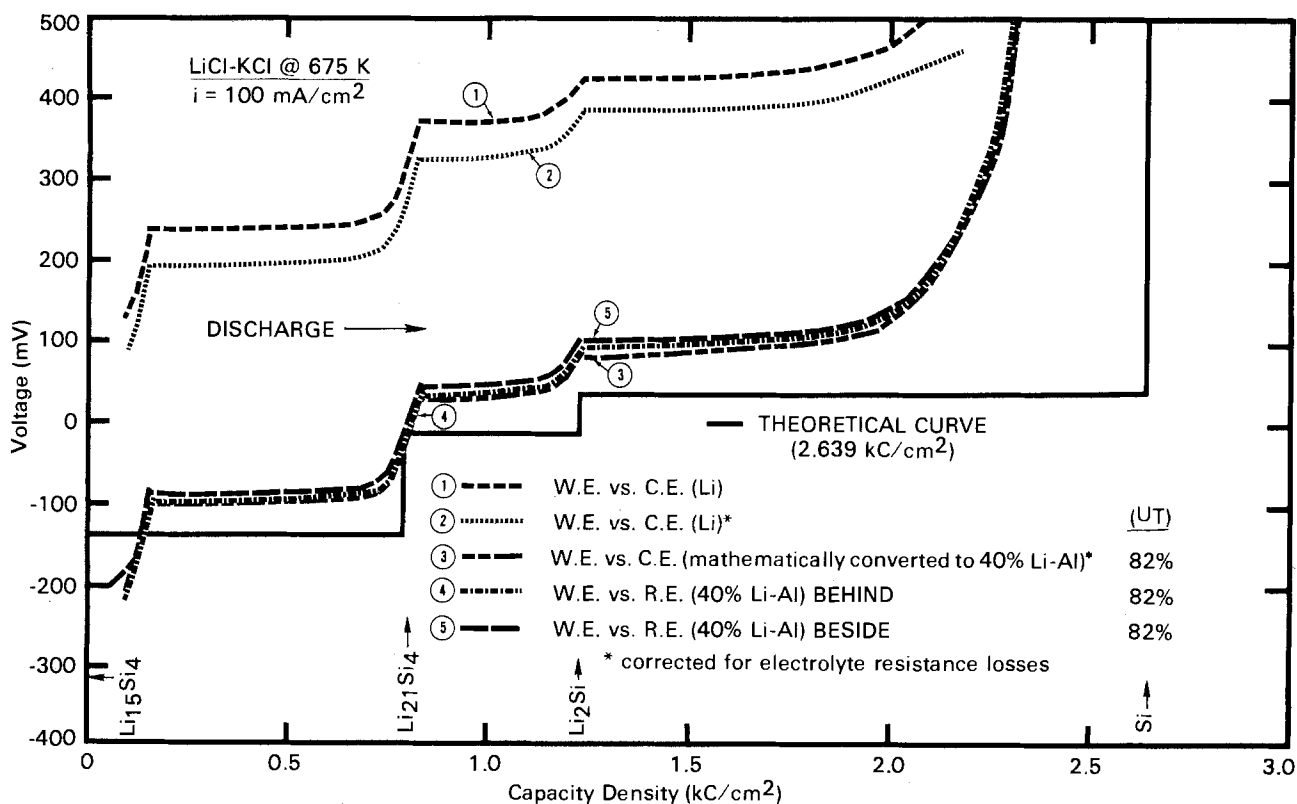


Fig. 2. Voltage-capacity density curves for a Li-Si electrode with respect to a lithium counterelectrode and two Li-Al reference electrodes at 100 mA/cm^2 .

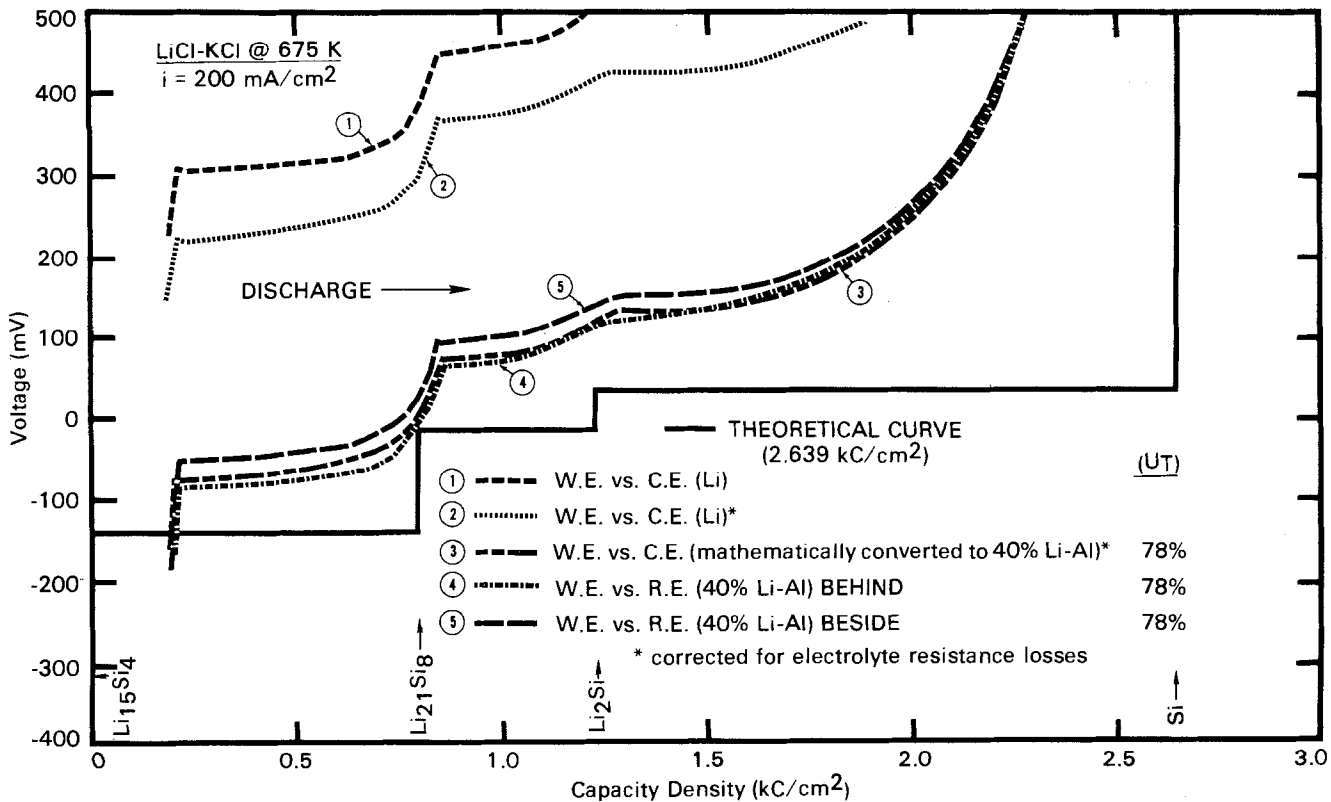


Fig. 3. Voltage-capacity density curves for a Li-Si electrode with respect to a lithium counterelectrode and two Li-Al reference electrodes at 200 mA/cm².

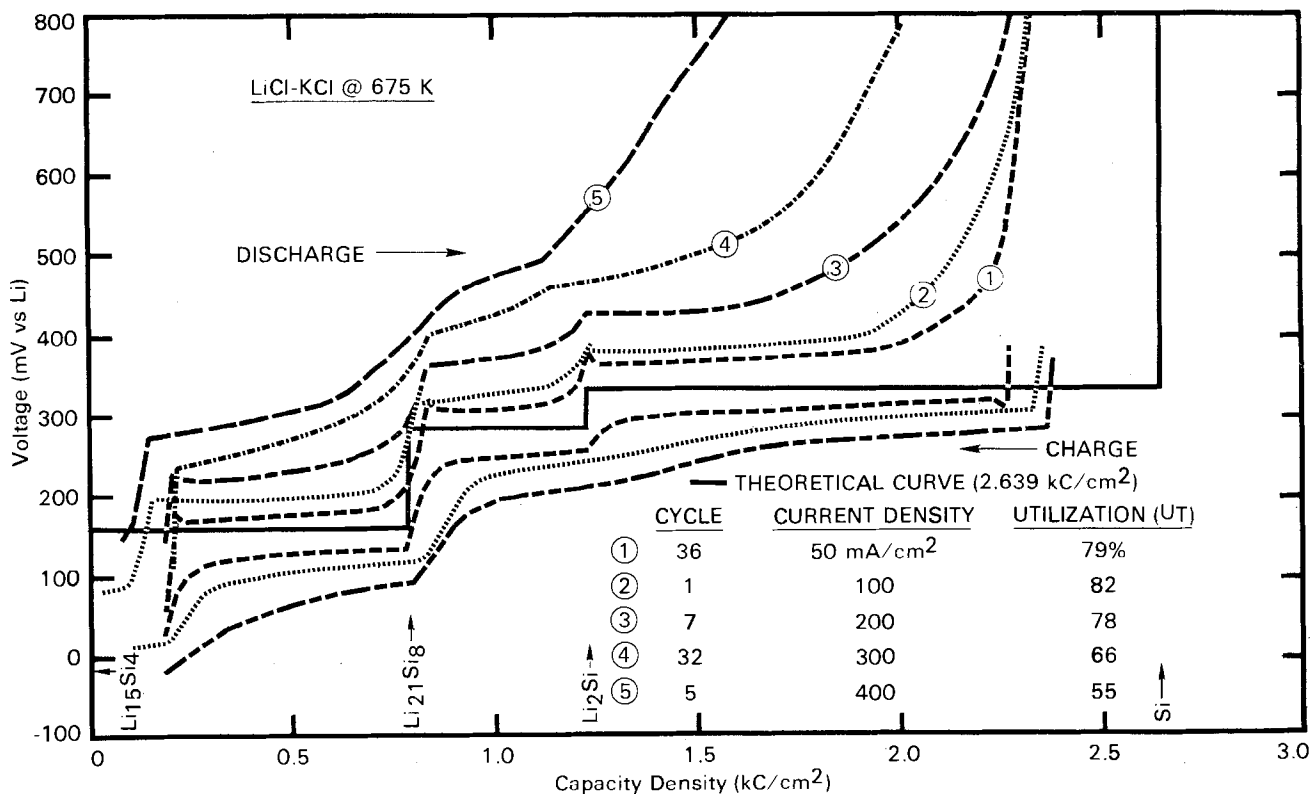


Fig. 4. Voltage-capacity density curves for a Li-Si electrode with respect to a lithium counterelectrode at different current densities

JOURNAL. All discussions for the December 1980 Discussion Section should be submitted by Aug. 1, 1980.

Publication costs of this article were assisted by General Motors Research Laboratories.

REFERENCES

1. J. S. Dunning *et al.*, *Proc. Intersoc. Energy Convers. Eng. Conf.*, **11**, 491 (1976).
2. R. N. Seefurth and R. A. Sharma, *This Journal*, **124**, 1207 (1977).
3. R. Piontelli and G. Bianchi, *ibid.*, **100**, 295 (1953).
4. R. Piontelli *et al.*, *Z. Elektrochem.*, **56**, 86 (1952).
5. S. Barnartt, *This Journal*, **99**, 549 (1952).
6. M. Eisenberg *et al.*, *ibid.*, **102**, 415 (1955).
7. R. N. Seefurth and R. A. Sharma, *ibid.*, **122**, 1049 (1975).

8. R. A. Sharma, *Am. Ceram. Soc. Bull.*, **57**, 1103 (1978).
 9. N. P. Yao *et al.*, *This Journal*, **118**, 1039 (1971).
 10. J. R. Selman *et al.*, Abstract 35, p. 75, The Electrochemical Society Extended Abstracts, Vol. 75-1, Toronto, Canada, May 11-16, 1975.
 11. R. N. Seefurth and R. A. Sharma, *This Journal*, **122**, 1049 (1975).
 12. E. R. Van Artsdalen and I. S. Yaffe, *J. Phys. Chem.*, **59**, 118 (1955).
 13. R. A. Sharma and R. N. Seefurth, *This Journal*, **123**, 1763 (1976).

Mixed Potential Analysis of Sulfation of Molten Carbonate Fuel Cells

Dan Townley and Jack Winnick

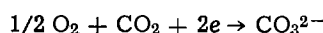
Georgia Institute of Technology, Atlanta, Georgia 30332

and H. S. Huang

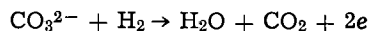
Argonne National Laboratory, Argonne, Illinois

Theory

At the anode of the molten carbonate fuel cell, reducing gas is oxidized to water and CO₂. The reaction proceeds through the intermediacy of carbonate ion as the charge carrier in the electrolyte. At the cathode, oxygen and carbon dioxide are electronated to form carbonate ion



At the anode, hydrogen reduces the carbonate ion to water and carbon dioxide

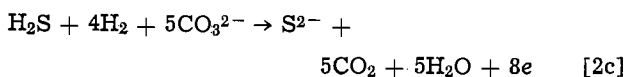
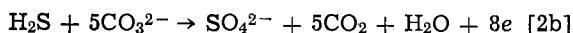
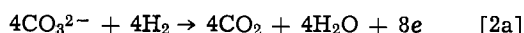


Recent experiments (1, 2) have shown that low levels of H₂S in the reducing gas at the anode have profound effects on cell performance. The potential drop due to the presence of 10 ppm of H₂S is on the order of 100 mV, indicating that the activity of H₂S may not be equal to its partial pressure. For this model, we assume a linear Henry's law relation between the activity and the partial pressure

$$a_{H_2S} = H^{-1} P_{H_2S} \quad [1]$$

where H⁻¹ is experimentally determined.

There are two reactions that may take place at the anode in which H₂S will compete with the desired reaction. In one sulfate ion is formed and in the other sulfide ion is formed. So, on the basis of eight electron transfer, there are three anode reactions to consider



If the relative extent of each of these reactions is determined by chemical equilibrium, then each will occur at the same potential as predicted by the Nernst relation

$$E = E_1^\circ - \frac{RT}{8F} \left\{ \ln \left[\frac{a_W^4 a_{CO_2}^4}{a_{CO_3^{2-}}^4 a_{H_2}^4} \right]_{an} + \ln \left[\frac{a_{CO_3^{2-}}^4}{a_{CO_2}^4 a_{O_2}^2} \right]_{ca} \right\} \quad [3a]$$

Key words: coal gasification, hydrogen sulfide, anode.

$$= E_2^\circ - \frac{RT}{8F} \left\{ \ln \left[\frac{a_{SO_4} a_{CO_2}^5 a_W}{a_{CO_3^{2-}}^5 a_{H_2S}} \right]_{an} + \ln \left[\frac{a_{CO_3^{2-}}^4}{a_{CO_2}^4 a_{O_2}^2} \right]_{ca} \right\} \quad [3b]$$

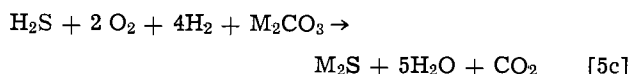
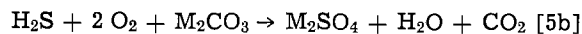
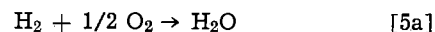
$$= E_3^\circ - \frac{RT}{8F} \left\{ \ln \left[\frac{a_S a_{CO_2}^5 a_W^5}{a_{CO_3^{2-}}^5 a_{H_2}^4 a_{H_2S}} \right]_{an} + \ln \left[\frac{a_{CO_3^{2-}}^4}{a_{CO_2}^4 a_{O_2}^2} \right]_{ca} \right\} \quad [3c]$$

We assume that the activities of all gases except H₂S are equal to the corresponding partial pressures. If we also assume that in the electrolyte melt

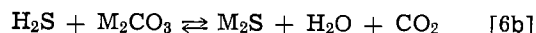
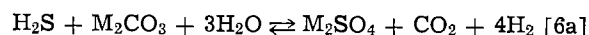
$$a_{CO_3} + a_{SO_4} + a_S = 1.0 \quad [4]$$

then we have five equations in five unknowns. In the experimental determination of H⁻¹, E is known and the five unknowns are H⁻¹, a_{H₂S}, a_{CO₃}, a_{SO₄}, and a_S.

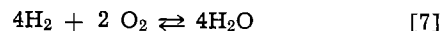
The overall cell reaction corresponding to each of the half-cell reactions in [2a-c] are



The metal in these equations corresponds to the binary eutectic composition of lithium and potassium carbonates used as the electrolyte in these cells. Equation [5a] gives a standard potential E₁⁰ = 1.027V. Data from the Institute of Gas Technology (IGT) (3) show that the free energy change for [6a] is +7.7 and for [6b] is -1.7 kcal/mole.



Combining these equations with



shows that E₂⁰ = 0.986 and E₃⁰ = 1.037V.

Calculations

We have six experimental data points relating partial pressure of H₂S in the anode feed and potential drop (Table I). The first two points, taken by United Tech-

Table I. Experimental data points (1, 2)

PT	$P_{H_2S} \times 10^6$ (atm)	Potential drop (mV)	Inlet anode gas composition	Outlet anode gas composition
UTC No. 1	8	100	0.51 H ₂ 0.105 CO ₂	0.057 H ₂ 0.443 CO ₂
UTC No. 2	31	183	0.0785 CO 0.286 H ₂ O	0.477 H ₂ O
IGT No. 1	10	44	0.572 H ₂	0.091 H ₂
IGT No. 2	50	104	0.104 CO ₂	0.412 CO ₂
IGT No. 3	100	154	0.262 H ₂ O	0.456 H ₂ O
IGT No. 4	200	169		

nologies Corporation (UTC) are at 650C and a current density of 160 A/ft². The hydrogen utilization is 96% for both data. The other four points were taken by the Institute of Gas Technology (IGT) at the same temperature and current density, in a similar apparatus, but at only 76% hydrogen utilization.

The first point, UTC No. 1, has been used to calculate H^{-1} . This H^{-1} was used to predict the other five points. Using Eq. [3a], we first calculate the Nernst potential at the inlet conditions when no sulfur is present, that is when $a_{CO_2} = 1$. Although the cathode gas composition is not important in this model, we based our calculations on a composition of 0.67 CO₂ and 0.33 O₂. The potential calculated is 1.100V. The observed potential drop of 100 mV is subtracted to give the potential produced by the cell ignoring all overvoltages. Thus, E is set equal to 1.000V in Eq. [3a-c], and these equations along with Eq. [4] are solved for a_{CO_2} , a_{SO_4} , a_S , and a_{H_2S} . Equation [1] then gives $H^{-1} = 1.5 \times 10^4$.

In this model the voltage drop caused by H₂S is presumed to be due entirely to the replacement of carbonate in the electrolyte.

Discussion

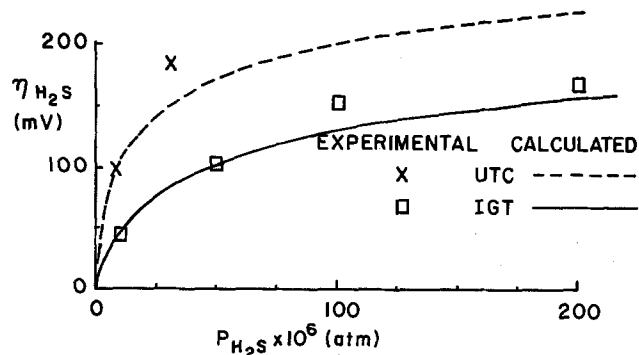
If the same H^{-1} is used to calculate the potential drop due to H₂S at the anode outlet, the value is on the order of 150 mV. This value assumes that steady state has been reached at the anode and that no sulfur is absorbed. Allowing for the increased volumetric flow rate at the outlet, P_{H_2S} is decreased by a factor of 1.5 from the inlet value. A different H^{-1} may be calculated using the outlet gas composition for UTC No. 1. Using the same method as before, $H^{-1} = 5.3 \times 10^3$ at the outlet. Using this H^{-1} , the potential drop at the inlet should be in order of 50 mV.

These calculations predict that the effect of H₂S is progressively greater from the inlet to the outlet. This is in agreement with results of the UTC study (3) which showed that the amount of sulfur in the electrolyte increased from inlet to outlet. This means, for example, that for UTC No. 1, η_{H_2S} at the inlet is less than 100 mV and η_{H_2S} at the outlet is greater than 100 mV. The overpotentials not due to H₂S are thus changed and the current density becomes redistributed across the cell. The local current density increases at the inlet and decreases at the outlet. Therefore, the true H^{-1} will be somewhere between 5.3×10^3 and 1.5×10^4 . Table II shows the results of using $H^{-1} = 5.3 \times 10^3$ to calculate the activities in the melt and the potential drops due to H₂S at the outlet.

Figure 1 illustrates the effect of increasing H₂S composition. Note that different curves are predicted

Table II. Predicted anode outlet conditions

PT	P_{H_2S} $\times 10^6$	a_{H_2S}	a_{CO_2}	a_{SO_4}	a_S	η_{H_2S} calc	η_{H_2S} meas
UTC No. 1	5.3	0.0281	0.082	0.887	0.031	(100)	100
UTC No. 2	20.7	0.110	0.022	0.931	0.091	152	183
IGT No. 1	6.7	0.0355	0.287	0.567	0.146	50	44
IGT No. 2	33.3	0.176	0.075	0.734	0.191	104	104
IGT No. 3	66.7	0.354	0.039	0.768	0.193	130	154
IGT No. 4	133.3	0.706	0.020	0.785	0.195	157	169

Fig. 1. Effect of H₂S pressure on overvoltage

for the two sets of experiments. This is due to the difference in hydrogen content of the fuel used by the two laboratories. The hydrogen content affects Eq. [3a-c].

Since the H^{-1} we calculate is not the true thermodynamic value, it is only valid for data points with the same electrochemical hydrogen utilization and current density. The effect of the H₂S is greatest at the outlet, where P_{H_2} is low, so our calculated H^{-1} will be greater for a higher utilization. The UTC points are for a utilization of 96% and the IGT points for 76%. If IGT No. 1 is used to calculate H^{-1} , a value of 4.3×10^3 is found, so that the difference is only about 20%.

The mixed potential found disregards differences in the kinetics of the three anodic reactions. The effect of incorporating the true kinetics, when they are available, would be to change the predicted anion compositions as well as the Henry's constant. The calculated η_{H_2S} - P_{H_2S} curve is very insensitive to changes in the potential. However, the compositions are very sensitive to such changes. For example, a change of $-0.150V$ in E^0 for Eq. [3b] will have the same effect on the calculated mixed potential as a change by a factor of 5/2 in the exchange current densities of the reactions. This change produces essentially no change in the predicted curve of η_{H_2S} vs. P_{H_2S} . Yet, a dramatic shift in compositions is calculated. The sulfate ion activity decreases while the sulfide ion increases. The Henry's constant increases also. Since we have no kinetic data, we must consider our predicted compositions (activities) approximate at best.

UTC (4) ran free-electrolyte experiments with varying ratios of sulfate to carbonate ion in the electrolyte. They found that the voltage produced was qualitatively related to the sulfate content of the electrolyte, in agreement with our predictions.

Although this model is not an entirely accurate representation of the effects of H₂S on fuel cell performance, it is a first attempt to describe these effects based on changes in the electrolyte. The Henry's law constant calculated may include effects other than solubility, such as the kinetics of electrode sulfidation. The kinetics of the reactions will also play a role in a working cell. Although we neglected the Henry's law constant for all gases other than H₂S, the effects of these constants are implicitly included in the overpotentials not due to H₂S. The partial pressures of these gases do not change enough between the two sets of data to have a significant effect on the observed voltages.

The true H^{-1} could be determined from cells run with zero utilization but at the same current density as before. A more exact prediction of η_{H_2S} could then be made using this H^{-1} and the polarization curve for an uncontaminated cell by numerically integrating local current densities across the cell for any utilization.

Conclusion

A simple thermodynamic model has been used to estimate the effect of H₂S on molten carbonate fuel cell performance. One datum was needed to fix the

single floating parameter. Predictions were compared with data from two independent laboratories under somewhat different conditions, with surprisingly good agreement.

The predictions of electrolyte composition are no doubt inaccurate due to the uncertainties involved in the calculation of the Henry's constant.

Manuscript submitted May 21, 1979; revised manuscript received Oct. 15, 1979.

Any discussion of this paper will appear in a Discussion Section to be published in the December 1980 JOURNAL. All discussions for the December 1980 Discussion Section should be submitted by Aug. 1, 1980.

Publication costs of this article were assisted by Jack Winnick.

LIST OF SYMBOLS

E	equilibrium Nernst potential, V
E°	standard potential, V
H^{-1}	inverse Henry's law constant, atm ⁻¹
P_{H_2S}	partial pressure of H ₂ S, atm

a_{CO_2}	activity of CO ₂ in gas phase
a_{CO_3}	activity of M ₂ CO ₃ in electrolyte
a_{H_2}	activity of H ₂ in gas phase
a_{H_2S}	activity of H ₂ S in gas phase
a_{O_2}	activity of O ₂ in gas phase
a_S	activity of M ₂ S in electrolyte
a_{SO_4}	activity of M ₂ SO ₄ in electrolyte
a_W	activity of water in gas phase
η_{H_2S}	potential drop due to presence of H ₂ S, mV

REFERENCES

1. United Technologies Corporation, "Advanced Technology Fuel Cell Program," EPRI, September 1978; Molten Carbonate Fuel Cell Workshop, Oak Ridge National Laboratories, October 1978.
2. IGT Project 8984, Final Report, Vol. 1, p. 77, September 1977; Molten Carbonate Fuel Cell Workshop, Oak Ridge National Laboratories, October 1978.
3. Institute of Gas Technology, "Development of Sulfur-Tolerant Components for Second Generation Molten Carbonate Fuel Cells," EPRI, July 1979.
4. United Technologies Corporation, "Advanced Technology Fuel Cell Program," EPRI, December 1978.

Synergism in Hydrogen Evolution on Platinized Tungsten Trioxide in Acid Medium

S. A. Abbato and A. C. C. Tseung*

Department of Chemistry, The City University, London, England

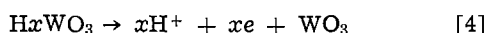
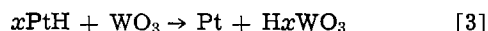
and D. B. Hibbert*

Department of Chemistry, Bedford College, University of London, London, England

Platinum when supported on tungsten trioxide shows synergism towards reactions in acid involving hydrogen atoms. Hobbs and Tseung (1-3) have demonstrated this effect for hydrogen oxidation in sulfuric acid, as have Hibbert *et al.* (4) for the hydrogenation of *p*-nitrophenol in sulfuric acid. Tungsten trioxide functions as an active support due to the reaction between hydrogen atoms and tungsten trioxide giving a conducting hydrogen tungsten bronze, H_xWO₃ (0 < *x* < 1). For hydrogen oxidation, therefore, two routes may be postulated; a normal route



and a bronze route



The rate of reaction, compared to that on pure platinum is thus enhanced if spill-over (Eq. [3]) and the subsequent reaction of tungsten bronze are fast. In this note we report the results of experiments which show synergism for hydrogen evolution in acid solution on platinized tungsten trioxide, and comment on the possible mechanism of the effect.

Experimental

A stock sample of 1 weight percent (w/o) platinum on tungsten trioxide was prepared by freeze-drying (5) chloroplatinic acid on tungsten trioxide followed by reduction in hydrogen (50°C for 30 min, 90°C for 3 hr). By this method, a great dispersion of platinum on the tungsten trioxide substrate is obtained. The specific surface area of the platinum prepared in this

manner has been shown to be 35 m²g⁻¹ (1). All other loadings (0.2-0.9 w/o) were prepared by mechanically mixing tungsten trioxide with the stock sample. It is of some importance to ensure that the morphology of the platinum particles remains constant (4), and thus it was not possible to freeze-dry each loading.

Teflon-bonded electrodes were prepared by ultrasonically mixing a 60% P.T.F.E. dispersion with the freeze-dried catalyst in the ratio 3:10 by weight. The mixture was painted onto a carbon plaque, dried, and cured at 300°C for 1 hr. Catalyst loadings were typically 10-15 mg cm⁻². A graphite rod was used as the counterelectrode.

Steady-state polarization curves were determined in 2.5M sulfuric acid at 25°C, against a dynamic hydrogen reference electrode. The measured potential was corrected for the IR drop between Luggin capillary and electrode by the interruptor technique.

Several determinations were made at temperatures up to 60°C, a fresh electrode being used on each temperature cycle. Atomic adsorption analysis of the electrolyte solution was performed for tungsten.

Results

We define the specific activity of an electrode (*J*) as the current density at a given overpotential divided by the platinum loading. For a system in which the support plays no part, *J* is constant with platinum loading.

Figure 1 shows a series of curves of *J* against platinum loading for electrodes at different overpotentials. Similar results were obtained for many electrodes, the reproducibility being 15% between different electrodes. An electrode prepared from pure tungsten trioxide gave almost no current in the overpotential range studied. The characteristic blue color of hydrogen tungsten bronze was observed on all electrodes.

* Electrochemical Society Active Member.
Key words: synergism, spill-over, hydrogen.

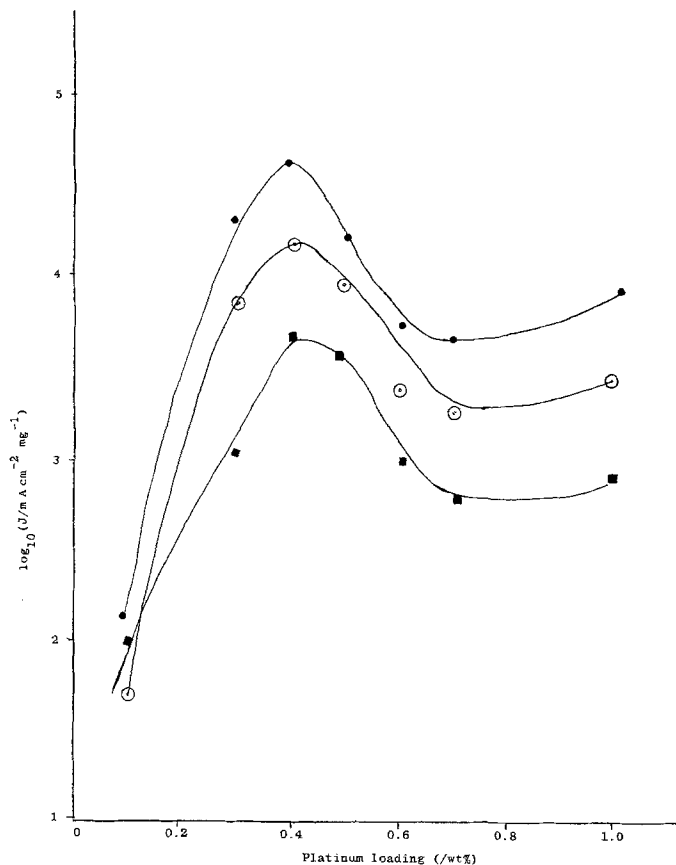


Fig. 1. Variation of specific activity (J) of a platinized tungsten trioxide electrode with platinum loading. ■: $\xi = -10$ mV; ○: $\xi = -30$ mV; ●: $\xi = -80$ mV. 2.5M H_2SO_4 , 25°C, IR corrected.

The temperature dependence of the current at $\xi = -30$ mV for an electrode of platinum loading 0.3 w/o is given in Fig. 2. The poor performance at 60°C remained when the electrode was cooled, suggesting some permanent change had occurred. No tungsten was observed in solution. This effect was observed for each platinum loading.

Discussion

The existence of a maximum in the curve of J against platinum loading at 0.4 w/o platinum indicates a synergistic effect. The fall in performance at low platinum loadings may be correlated with the number of particles of platinum and tungsten trioxide. At 0.2 w/o platinum, a simple calculation shows that the number of platinum particles just equals the number of tungsten trioxide particles. Below this loading, tungsten trioxide particles exist which are not in contact with platinum, and thus may not contribute to the activity if the migration of hydrogen atoms between tungsten trioxide particles is slow.

A simple scheme to explain synergism in this system may be postulated in which adsorbed hydrogen atoms on platinum may react immediately to give hydrogen (Eq. [6]) or migrate on to tungsten trioxide to give a tungsten bronze (Eq. [7])

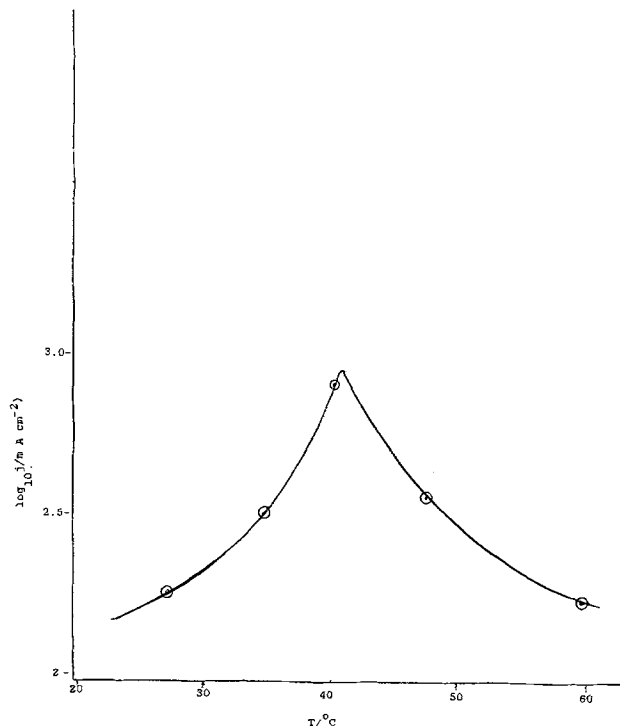
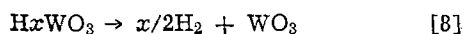
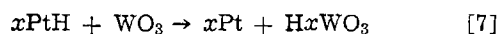
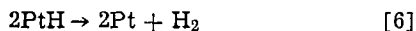
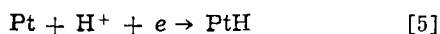


Fig. 2. Variation in the current from a platinized tungsten trioxide electrode (Pt loading 0.3 w/o) with increasing temperature. $\xi = -30$ mV. 2.5M H_2SO_4 , IR corrected.

The tungsten bronze may decompose (Eq. [8]) or act as a hydrogen evolution catalyst itself. However, the inactivity of pure tungsten trioxide at low overpotentials, even though the blue color of the bronze was seen, suggests the latter step does not contribute greatly. It has been shown (6) that the rate-determining step of hydrogen evolution on platinum is hydrogen recombination.

Thus, a fractional coverage of hydrogen atoms on platinum of near 1, would allow spill-over to occur easily and thus facilitate synergism.

The initial increase in activity with temperature yields an activation energy of 5 kcal mol⁻¹, which falls close to values in the literature (6, 7). The subsequent permanent fall in activity may be due to dissolution of platinum followed by its reprecipitation, causing a growth in platinum particle size (8).

Manuscript submitted Sept. 19, 1979.

Any discussion of this paper will appear in a Discussion Section to be published in the December 1980 JOURNAL. All discussions for the December 1980 Discussion Section should be submitted by Aug. 1, 1980.

REFERENCES

1. B. S. Hobbs and A. C. C. Tseung, *This Journal*, **119**, 580 (1972).
2. B. S. Hobbs and A. C. C. Tseung, *ibid.*, **120**, 766 (1973).
3. B. S. Hobbs and A. C. C. Tseung, *ibid.*, **122**, 1174 (1975).
4. D. B. Hibbert, N. Thomas, and A. C. C. Tseung, *J. Chem. Soc., Chem. Commun.*, 193 (1977).
5. A. C. Tseung and H. L. Bevan, *J. Mater. Sci.*, **5**, 604 (1970).
6. J. O'M. Bockris and A. K. N. Reddy, in "Modern Electrochemistry," Vol. 2, p. 1231, Plenum Press, New York (1970).
7. A. K. Vijb, *J. Phys. Chem.*, **72**, 1148 (1968).
8. A. C. C. Tseung and S. C. Dhara, *Electrochim. Acta*, **20**, 681 (1975).



Volatile Products from Interaction between Steel and H₂O/CO₂ at High Temperatures

Sin-Shong Lin

Army Materials and Mechanics Research Center, Watertown, Massachusetts 02172

ABSTRACT

A combined technique of mass spectrometry and high pressure sampling was used to analyze vapor products emanating from this interaction between steel and H₂O/CO₂. Only metal containing species of MoO₂(OH)₂, MoO₂(OH) were identified at 1400°C near the melting point of steel under water atmosphere. These vapor species might be one of the contributing factors to the initiation of high temperature steel erosion.

The ablative and erosive interactions between metal and hot flowing media have been widely investigated (1, 2). Under the extreme conditions near the melting point of steel and subjected to high pressure gases, such as repetitive gun firing, explosion, rocket exhausts, and high temperature flames, the mechanism of corrosion differs significantly from those mechanisms at low and medium temperatures. The dominant causes of material failures at low temperatures, such as mechanical stress rupture, thermal degradation, and chemical deterioration, are no longer distinguishable from each other at high temperature where an evaporation loss of material prevails. And the interaction of all failure mechanisms act simultaneously to the limited useful life of a material. The study reported here is aimed at elucidating the chemical aspect of ablative and erosive interactions under evaporative loss of materials near the melting point of steel. The experiments described in this study have simulated the hostile environment as close as possible within current available technologies. With the novel combined technique of sampling atmospheric gases and mass spectrometric detection, it might be possible to find one of major contributing factors for the initiation of high temperature erosion.

The volatile high temperature vapors originated from the interactions between metals and water have been known (3). The vapor species frequently observed from those metals used in steel are listed in Table I. The vapor pressures as well as thermodynamic properties of these species are well documented (4-15),

Key words: corrosion, erosion, steel, gas-solid interaction.

Table I. High temperature vapor species observed over iron alloys and water below 1400°C

Metal	Reaction with H ₂ O	Reaction with low pressure oxygen or over oxides	References
Fe	Fe(OH) ₂ , Fe(OH)	FeO	(4-6)
Cr	CrO ₂ (OH) ₂	CrO, CrO ₂ , CrO ₃	(7-9)
Ni	None	NiO	(10)
Mn	None	None	(11)
Mo	MoO ₂ (OH) ₂ , MoO ₂ (OH)	MoO ₂ , MoO ₃ , (MoO ₃) _n	(7, 12-14)
Si	None	SiO	(15)

but the behaviors of each individual species over a molten solution of steel are not well examined. The iron alloys react vigorously with water near the melting point to form iron and other oxides. Thus some vapor species derived from the reaction are similar to that under low pressure oxygen, and they are also listed in the table. A typical iron alloy contains less than 10 weight percent (w/o) of minor elements, and the presence of these minor elements might play a key role in the promotion of high temperature erosion. The situation might be similar to a small concentration of sulfur associated with fuel, which often is a major cause of corrosion in combustion processes.

Experimental

The experimental apparatus has been described previously (16, 17). And the schematic diagram of the sampling apparatus is shown on Fig. 1 together with the miniature furnace assembly in Fig. 2. The only modification made from previous arrangements was to locate a water reservoir adjacent to the combustion tube of the furnace. This was accomplished by directly coupling the reservoir to the fitting of the combustion tube. The core of the furnace consisted of a 1/2 in. OD closed-end alumina tube. On the tip of the tube, a 0.005 or 0.010 in. sampling orifice was drilled along the axial direction, and the depth of the orifice varied with the tubes from 0.02 to 0.06 in. The metal samples in the forms of chips, filings, and powders, were loaded in the

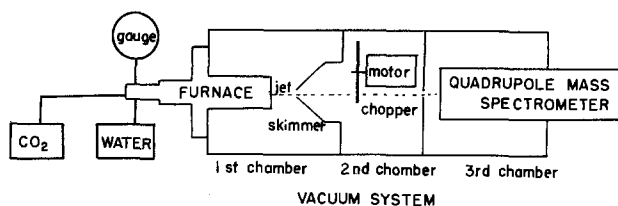


Fig. 1. Schematic diagram of sampling apparatus. The apparatus consists of three chambers differentially evacuated; the first chamber is an expansion chamber where a molecular jet beam is formed through the sampling orifice, the second chamber contains a beam modulation mechanism, and the third chamber houses the quadrupole mass spectrometer for the detection of beam. The furnace is flanged to the wall of the first chamber.

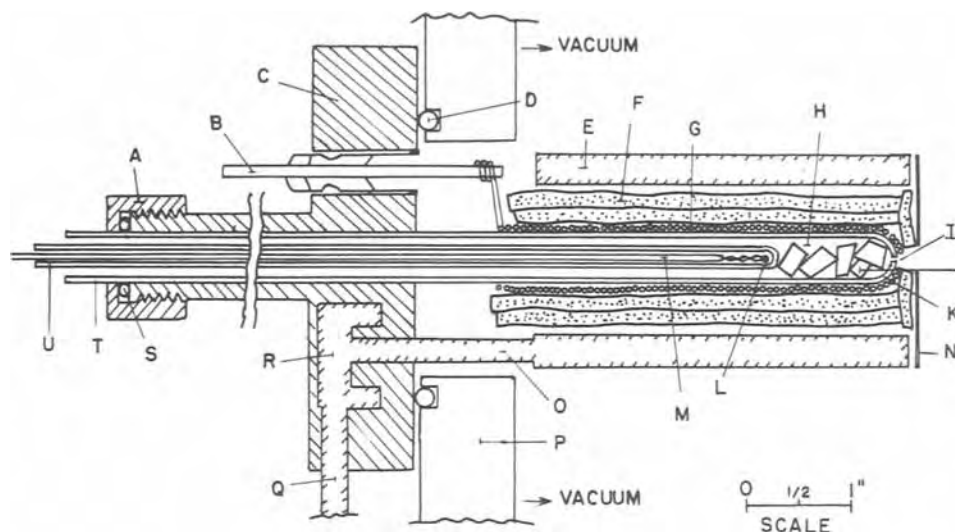


Fig. 2. High temperature miniature furnace, cross-sectional view. (A), Quick coupling; (B), electric feedthrough; (C), vacuum flange; (D), O-ring; (E), cylindrical water jacket; (F), zirconia felt; (G), molybdenum heating wire; (H), reaction chamber; (I), jet sampling orifice; (J), metal sample, e.g., steel chips; (K), tip of closed-end alumina tube; (L), thermocouple sensor; (M), thermocouple protection tube; (N), stainless steel tubing for water passage; (O), vacuum wall of first chamber; (P), inlet and outlet water tubing; (Q), O-ring seal; (S), 1/2 in. OD closed-end alumina combustion tube; (U), 1/4 in. OD closed-end alumina combustion tube.

tube within one inch from the tip. For wire samples, a several-fold concentric coil was made so that a maximum surface area could be exposed. The reactor chamber was resistance heated by a molybdenum wire winding covering the orifice area and about 4 in. from the end of the tube. The a-c power input to the heater was regulated by a proportional temperature controller, and the temperature was measured by a Pt/10%Rh-Pt thermocouple protected by a 1/4 in. OD alumina sheathing tube in the 1/2 in. combustion tube. The reacting gases including water vapor were introduced into the reactor through the annular opening of two alumina tubes, and the pressure was recorded by a digital pressure gauge connected to the steel fitting at the open end of the combustion tube. For mass spectrometric detection, the quadrupole mass filter was operated at 40 eV electron ionization energy and at an appropriate resolution throughout the experiments.

After the sample had been loaded into the reactor and good vacuum was obtained in the first chamber of the sampling apparatus, heating began. The temperature of the furnace was raised quickly to a predetermined level up to 1400°C. During this period the reactant gas (H_2O or CO_2) was introduced gradually to a selected setting of not more than 1/2 atm. Often the sampling orifice was found to clog due to a sudden introduction of the gas. To examine vapor species originating from the interaction, the mass spectrometric scans were made repeatedly during the entire heating period. Moreover many experiments had to be repeated several times so that the reproducibility of ion vapor species present in a minute amount could be confirmed. Even at the maximum temperature of 1400°C, the signals of ion vapors observed over steel and Fe samples were so weak that a positive identification was almost impossible. Alternatively a suspected source of pure metal was substituted for a better and clear identification. The identity of an ion peak was established from mass number, isotopic distribution, temperature, pressure and time dependences. A summary of experiments performed is listed in Table II.

Results

Fe.—Extensive search was made to detect metal-containing vapor from the interaction between a high purity Fe and water, CO_2 , CO_2/H_2 mixture. In the water reaction, the H_2O^+ intensity diminished considerably at the initial period of heating above 1200°C. Evidently a strong interaction took place between water and Fe. The Fe coil after the heating was a partially molten chunk of black appearance presumably consisting of iron oxides. In the CO_2 reaction, the oxidation of Fe was found to be the only reaction. The

sample after heating consisted of iron oxides. No ion vapor species was detected.

No metal-containing vapor species was detected in scan mass spectra except in some spectra obtained at 1400°C and a high H_2O pressure near 1/2 atm. Ion peaks corresponding to masses $Fe(OH)_2$, FeO , and Fe in order of increasing magnitudes were observed. Since their ion intensities were only a few times more than the background noise level which was about 10^{-5} relative to H_2O^+ , no identity could be established from their isotopic abundances. Some ions at masses 88, 64, and 44 were frequently detected. These ions were probably hydrocarbons from the preparation of the Fe sample, they were discarded because of their temperature and time dependent behaviors.

Fe_2O_3 , Fe_3O_4 .—The experiments were performed because these oxides instead of Fe might accelerate the formation of Fe containing vapor species. However only in two mass spectra obtained from the Fe_3O_4 sample, a very weak signal slightly above background noises corresponding to FeO was observed. Since the signal was so weak, no definite conclusion about the existence of FeO could be established. The powder samples after the interaction were partially molten black aggregates.

Steel.—The extensive search was made to identify exotic vapor species effusing from the steel + H_2O interaction up to temperatures of 1400°C. In order to increase surface areas of steel, not only chips but also filings were used for the investigation. After every run, the sample was found to be partially molten and oxidized. In some instances, the melts were found to diffuse into the alumina tubes and they could not be sep-

Table II. Summary of experiments
Metal + H_2O/CO_2 reaction

Sample	Source	Ion vapor species observed	
		H_2O reaction	CO_2/H_2 reaction
Fe	99.9% wire	Yes, not confirmed	None
Fe_2O_3 , Fe_3O_4	99.8% powders	None	Not performed
Steel	Gun tube ^(a)	$MoO_2(OH)_2$ & others	Not performed
Cr	99.9% powders	None	Not performed
Ni	99.9% powders	None	Not performed
Mo	99% wire	$MoO_2(OH)_2$, $MoO_2(OH)$, $Mo-O$ vapors	$MoO_2, MoO_3 (MoO_3)_n$ $n = 2,3$

^(a) Wet chemical analysis, Ni; 1.76, Cr; 1.43, Mn; 0.74, Mo; 0.30, C; 0.31, Si; 0.18, S; 0.022 w/o.

arated from the tubes. Alternatively a ZrO_2 boat was used to avoid the contamination of alumina, but the wetting of melt still existed. Moreover in these ZrO_2 boat runs, more spurious ions were observed in mass spectra. The impurities associated with ZrO_2 might be a cause of these spurious ions, and the presence of these ions in observed spectra made the interpretation of data more tedious and difficult.

No ion peak was detected in the initial period of heating. But after several hours of heating, ion signals slightly above the background level began to emerge. The only signals constantly present in mass spectra and yet reproducible, were at masses 64, 48, and 44 amu plus two broad peaks at masses 140-150 and 155-165 amu. The ions at masses 64 and 48 were found to diminish slowly with the extent of heating, and they were probably SO_3 and SO_2 . The ion at mass 44 was presumably SiO or CO_2 , and it could not be definitely identified. The two broad peaks were identified later as $MoO_2(OH)_2^+$ and $MoO_2(OH)^+$ ions with the aid of mass spectra obtained from the $Mo + H_2O$ experiments.

Cr.—The purpose of the experiment was to identify Cr-O vapor species which might be evolved from the interaction between Cr and H_2O . Although vapor species such as CrO_3 and $CrO_2(OH)_2$ are reported (7, 8), no trace of these ions was detected in the present experiments.

Ni.—A single run was made with Ni and H_2O to examine Ni-O, or Ni-OH vapor species from the interaction. No ion signal other than those derived from H_2O was detected in mass spectra even at $1400^\circ C$ and $1/2$ atm of water pressure.

Mo.—The Mo and H_2O/CO_2 experiments were performed in order that the broad peaks observed in the steel-water runs could be identified. As one might expect (7) numerous ion species were detected. The relative intensities of these Mo-O species at the highest isotopic peak together with Mo hydroxide ions are listed in Table III. The data were taken directly from scan spectra without corrections for isotopic abundance, ionization cross section, and ion transmission efficiency. The most important species in the water reaction were $MoO_2(OH)_2$ and $MoO_2(OH)$ ions. The mass positions of these ions in the spectra agreed well with those broad peaks observed in the steel-water experiments. Thus the trace amount of ion peaks observed in the steel experiment were identified as those ion peaks of $MoO_2(OH)_2$ and $MoO_2(OH)$.

In addition to these Mo hydroxide ions, a lesser abundant ion $Mo_2O_6 \cdot H_2O$ was also observed in mass

spectra taken at $1190^\circ C$ and 304 mm Hg water pressure. The neutral precursors of two abundant hydroxide ions were not determined from the present experiments. The molecule $MoO_2(OH)_2$ is reported (7, 12) to exist in high temperature vapors. Upon electron impact ionization, $MoO_2(OH)_2$ could produce fragmented ions MoO_2^+ and $MoO_2(OH)^+$ in addition to the parent ion $MoO_2(OH)_2^+$. However the observed intensity ratios of $MoO_2(OH)_2^+$ to $MoO_2(OH)^+$ varied with temperatures and pressures of the system. Therefore the existence of $MoO_2(OH)$ as a neutral molecule is highly probable.

The Mo-O vapors observed in the $Mo + CO_2$ reaction were very similar to those vapor species observed over Mo oxides. The observed Mo-O species up to Mo_3O_9 in the runs are listed in Table III. The higher polymers of Mo-O ions such as Mo_4O_{12} , Mo_5O_{15} might exist in the system but they were not recorded.

Discussion

The results from the steel-water experiments indicated that Mo hydroxide vapors were only major metal containing species emanating from the interaction. Other vapors such as CO_2 , SiO , SO_2 , and SO_3 might exist at $1400^\circ C$, but the result was not very conclusive. Thus near the melting point, the erosion of steel could be initiated by evolution of these vapors just below partially molten steel surfaces. The absence of the vapors in the initial heating period of the experiments further suggested the reacting gas H_2O , must diffuse into interiors of steel and produced the volatile Mo containing vapors.

The vapor pressures (18, 19) of metals and metal oxides commonly observed in the composition of steel are plotted on reciprocal temperatures in Fig. 3. Iron comprises 90 w/o of the steel composition. At the temperature of $1400^\circ C$, the vapor pressures of Fe or FeO are so low as indicated in the figure, that they are not a substantial fraction of evaporation loss. Chromium, the second important element of steel, tends to form a protective compact oxide layer by reaction with water,

Table III. Vapor species observed in $Mo + H_2O/CO_2$ reaction

Ion species	Relative abundances ^(a)	
	H_2O reaction $P = 304$ mm Hg, $T = 1190^\circ C$ H_2O^+ as 100	CO_2 reaction $P = 272$ mm Hg, $T = 1093^\circ C$ CO_2^+ as 100
O	—	2.5
H_2O	100	—
CO	—	10.4
CO_2	—	100
MoO	0.24	0.125
MoO_2	2.5	1.92
MoO_3	—	0.79
$MoO_2(OH)$	6.4	—
$MoO_2(OH)_2$	9.4	—
Mo_2O_4	0.33	0.25
Mo_2O_5	0.56	0.5
Mo_2O_6	0.65	0.5
$Mo_2O_6 \cdot H_2O$	0.03	—
Mo_3O_7	0.02	0.04
Mo_3O_8	0.11	0.33
Mo_3O_9	0.46	1.92
Mo_4O_{11}	0.02	*
Mo_4O_{12}	0.04	*

— Not observed.

* Not recorded.

(a) The ion intensity of the highest isotopic peak without corrections for ion transmission, ionization cross section.

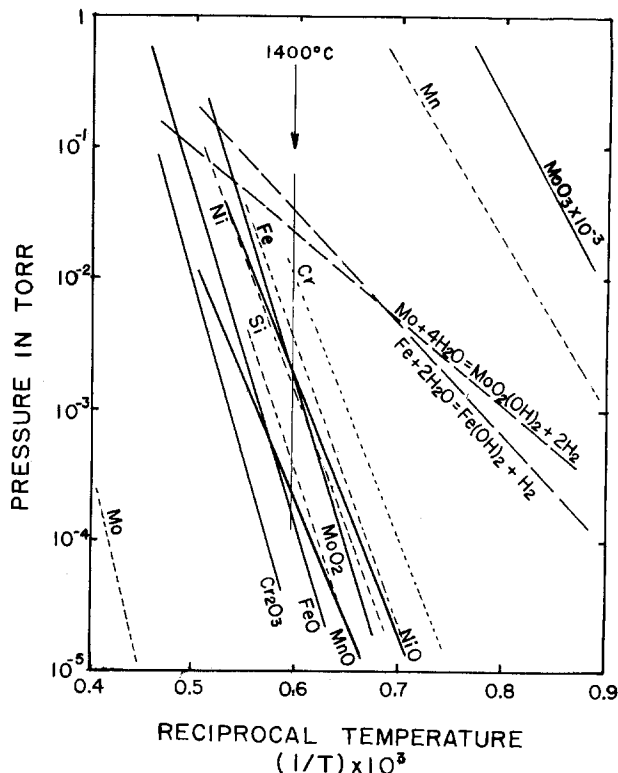
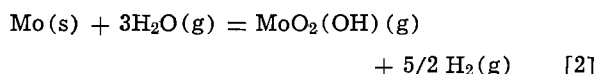
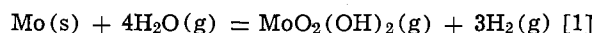


Fig. 3. Vapor pressures of metals, oxides, and hydroxides. Metal in dotted line, oxide in solid line, and hydroxide in dashed line. The pressures of hydroxides are calculated by assuming $P_{H_2O} = P_{H_2} = 1/2$ atm.

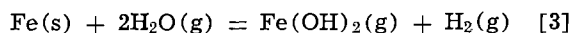
which is well known for oxidation resistance. The vapor pressure of Cr oxides is lower than that of Fe except under a very high oxygen pressure. Consequently the evaporation loss resulting from chromium could be neglected. The third abundant element of steel, nickel, consists of less than 5 w/o of the solid solution. The volatility of Ni is less than that of Fe and there is no stable nickel oxide. The minor constituents of steel such as Mn, Mo, C, Si, and S occupy less than 1 w/o of a steel composition. Manganese had a higher vapor pressure, but Mn oxide is more stable than Fe oxides. Molybdenum could form many volatile vapors MoO_2 , MoO_3 , and $(\text{MoO}_3)_n$ polymers upon oxidation. The evaporation of Mo-O vapors at temperatures far below the melting point of steel is not a major concern because the Mo content in steel is only a few fraction of one percent. Except at a high oxygen pressure near the melting point, they could cause a serious problem of ablation and erosion. Other elements such as sulfur to form SO_2 and SO_3 , silicon to form SiO , and carbon to form CO and CO_2 , are believed to cause no severe evaporation loss because these elements are present in a minute concentration and exist in the solid solution as stable carbides, sulfides, and silicides.

The formation of Mo-hydroxide vapors appears to be the most important process of steel near the melting point under H_2O atmospheres. In an equilibrium system, the magnitudes of the hydroxide vapors increase drastically with the 3rd and 4th powers of the H_2O pressure as indicated by the equilibrium constants of the reactions

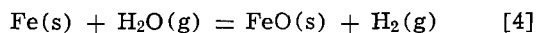


In the case of gun and rocket firings, the temperature and the pressure of exploding gases in which H_2O is a major constituent, are up to minima (20) of 2500°K and 20,000 psi, respectively. Thus the evaporation of Mo as hydroxide vapors from steel would be greatly enhanced. This evaporation would provide a recession in steel or a diffusion through fissure which may lead to fracture of the film or loss of protective metal layers. The exact role of Mo hydroxide vapors in the erosion and ablation process is not clear, but they are the first metal containing vapors to escape from molten steel surfaces.

The formation of $\text{Fe}(\text{OH})_2$ vapor from the Fe- H_2O interaction seems to be more favorable than that of Fe vapor at high temperatures as shown in the pressure vs. temperature diagram of Fig. 3. However $\text{Fe}(\text{OH})_2$ vapor from the reaction



was not positively identified. The dominant reaction observed in the Fe- H_2O reaction is the formation of iron oxide solids, such as



According to the thermodynamic calculation (4, 12) at various water pressures, the magnitudes of Fe hydroxide vapor in the system should be more than 10^{-6} relative to the H_2O^+ intensity. And at the water and hy-

drogen pressures of 1/2 atm, both Fe and Mo hydroxide vapors should have a comparable magnitude at the present experimental conditions as shown in Fig. 3. However the Mo hydroxide vapors were found to be much more abundant than $\text{Fe}(\text{OH})_2$. The $\text{MoO}_2(\text{OH})_2^+$ and $\text{MoO}_2(\text{OH})^+$ were observed in a large amount from 10^{-1} to 10^{-5} relative to H_2O^+ , but little evidence of $\text{Fe}(\text{OH})_2^+$ was obtained. The source of this discrepancy is not clear, but it is likely due to the fact that the gas-solid equilibrium in the Fe system is not established. The gas-solid equilibrium can be easily attained in the Mo system because a large concentration of Mo-O vapors is present at the temperature range of experiments. And the vapor phase reaction of Mo-O vapors and H_2O kinetically promote the completion of the equilibrium.

Manuscript submitted Oct. 1, 1979; revised manuscript received Dec. 6, 1979.

Any discussion of this paper will appear in a Discussion Section to be published in the December 1980 JOURNAL. All discussions for the December 1980 Discussion Section should be submitted by Aug. 1, 1980.

Publication costs of this article were assisted by the Army Materials and Mechanics Research Center.

REFERENCES

1. E. A. Gulbransen and S. A. Janssen, in "Heterogeneous Kinetics at Elevated Temperatures," G. R. Belton and W. L. Worrell, Editors, p. 181, Plenum Press, New York (1970).
2. M. G. Fontana, *Corrosion*, **27**, 129 (1971).
3. J. W. Hastie, "High Temperature Vapors," A. M. Alper, J. L. Margrave, and A. S. Nowick, Material Science Service Editors, p. 69, Table 2.3, Academic Press, New York (1975).
4. G. R. Belton and F. R. Richardson, *J. Phys. Chem.*, **67**, 1562 (1962).
5. D. E. Jensen and G. A. Jones, *J. Chem. Soc. Faraday Trans. I*, **69**, 1448 (1973).
6. M. Farber, P. Harris, and R. D. Srivastava, *Comb. & Flame*, **22**, 191 (1974).
7. G. C. Fryburg, R. A. Miller, F. J. Kohl, and C. A. Stearns, *This Journal*, **124**, 1738 (1977).
8. R. T. Grimley, R. P. Burns, and M. G. Inghram, *J. Chem. Phys.*, **34**, 664 (1961).
9. M. Farber and R. D. Srivastava, *Comb. & Flame*, **20**, 43 (1973).
10. R. T. Grimley, R. P. Burns, and M. G. Inghram, *J. Chem. Phys.*, **35**, 551 (1961).
11. P. J. T. Zeegers, W. P. Townsend, and J. D. Winefordner, *Spectrochim. Acta*, **B24**, 243 (1969).
12. G. R. Belton and A. S. Jordan, *J. Phys. Chem.*, **69**, 2065 (1965).
13. R. P. Burns, G. DeMaria, J. Drowart, and R. T. Grimley, *ibid.*, **32**, 1363 (1960).
14. G. DeMaria, R. P. Burns, J. Drowart, and M. G. Inghram, *ibid.*, **32**, 1373 (1960).
15. R. F. Porter, W. A. Chupka, and M. G. Inghram, *ibid.*, **23**, 216 (1955).
16. Sin-Shong Lin, *This Journal*, **125**, 1877 (1978).
17. Sin-Shong Lin, *ibid.*, **122**, 1405 (1975).
18. K. S. Pitzer and L. Brewer, "Thermodynamics," 2nd ed., McGraw-Hill Book Co., New York (1970).
19. D. R. Stull and H. Prophet, Project Director, JANAF Thermodynamic Tables, 2nd ed., NBS (June 1971).
20. Jean-Paul Picard and Iqbal Ahmad, Editors "Proceedings of the Tri-Service Gun Tube Wear and Erosion Symposium," March 1977.

Work Function and Chemical Diffusion of Nonstoichiometric Oxide Materials

Z. Adamczyk and J. Nowotny

Institute of Catalysis and Surface Chemistry, Polish Academy of Sciences, 30-239 Kraków, Poland

ABSTRACT

A particular solution of Poisson's equation and of Fick's second law leads to the determination of the chemical diffusion coefficient for the near-to-surface layer of nonstoichiometric oxide materials. The proposed method is based on the work function measurements applied to determine the surface reequilibration kinetics. Metal deficient oxide $Me_{1-y}O$ is taken as an object of quantitative considerations.

Application of the work function measurements in studies of kinetics and the mechanism of heterogeneous processes between gaseous oxygen and metal oxide surfaces was the subject of several works (1-5). It has been shown that the work function may be used to monitor the reequilibration kinetics of oxide surfaces involving chemisorption and lattice ionic diffusion. The purpose of the present work is to discuss correlations between surface potential and work function changes accompanying the reequilibration, surface charge in the boundary layer, and concentration of lattice defects in order to determine the chemical diffusion coefficient in the near-to-surface layer.

Both gravimetric and electrical conductivity methods, widely used to determine the reequilibration kinetics and the chemical diffusion coefficient (6-10), may be applied at higher temperatures (above 800°C). The methods provide information about the crystalline bulk. Recently, however, considerable experimental material has been accumulated which is not in accordance with current theories for the typical bulk-controlled mechanism of reequilibration processes. The conflicting data are referred to a "surface reaction" (11-12) which apparently occurs at the surface or in the near-to-surface layer. The diffusion data obtained from the work function measurements may be useful to characterize both transport and structural properties of the surface layer. This layer may differ essentially from the crystalline bulk especially when segregation of lattice components occurs.

Chemical Reactions and Electrical Effects Accompanying Reequilibration Processes in $MeO-O_2$ Systems

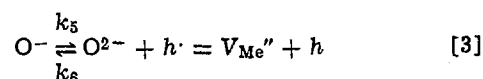
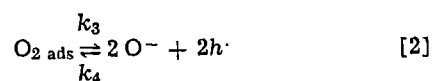
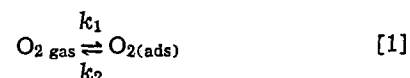
The reequilibration occurs when an initially equilibrated oxide crystal is subjected to a new value of oxygen pressure (or temperature). The reequilibration process involves the propagation of chemical potential gradients from the surface into the bulk until a new equilibrium is achieved.

As an object of our considerations we assume the nonstoichiometric oxide expressed by the general formula $Me_{1-y}O$ showing doubly ionized cation vacancies as predominant ionic lattice defects which are compensated by electron holes. This type of defect structure is represented by such widely investigated oxide materials as NiO, CoO, MnO, and FeO. We also assume that the cation vacancies are the only mobile ionic species, whereas the anion sublattice remains relatively immobile (13). At low concentrations cation vacancies may be considered as an ideal solution in the lattice and thus their concentrations may be considered as activities.

The following equilibria which seem to be most important may be considered at the oxide surface and in

Key words: semiconductor, defects, charge, potential.

the oxide crystal when oxygen pressure is isothermally changed in the ambient gas atmosphere



where $O_{2(\text{ads})}$ is a physically adsorbed molecule, O^- is the most stable ionic form of oxygen adsorbed at the surface of transition metal oxides (14), and O^{2-} is the final ionization form which is stable in the crystal field (14-16). Therefore we consider the form O^{2-} as doubly ionized cation vacancy V_{Me}'' .

Assuming isothermic conditions of experiment involving admission of a certain oxygen dose over an oxide surface initially equilibrated under low oxygen pressure (10^{-6} Torr) the following relationship may be written for oxygen pressure as a function of the amount of oxygen adsorbed

$$p_{O_2} = p_{O_2}^0 - [O_{2(\text{ads})}] S \frac{kT}{V} \quad [4]$$

where $p_{O_2}^0$ = initial oxygen pressure, V = volume of the experimental chamber, $[O_{2(\text{ads})}]$ = surface concentration of oxygen adsorbed, and S = total surface area of the investigated oxide.

As results from recent works (1-5) the work function changes for the metal oxide-oxygen system may be considered regarding experimental conditions applied.

Isobaric conditions.—The experiment occurs isobarically when the following inequality is fulfilled

$$[O_{\text{ads}}] S \frac{kT}{V} \ll p_{O_2}^0 \quad [5]$$

The work function changes accompanying oxygen chemisorption in these conditions $\Delta\phi_t$ is schematically illustrated in Fig. 1, curve 1. As seen $\Delta\phi_t$ rapidly increases achieving $\Delta\phi_{\text{eq}}$ which refers to a chemisorption equilibrium involving generation of charged oxygen species at the surface (3).

Sorption of small oxygen dose.—When a small oxygen dose equivalent to a fraction of the monolayer coverage is admitted into the reaction chamber p_{O_2} rapidly decreases as a result of the inequality

$$[O_{2(\text{ads})}^{\infty}] S \frac{kT}{V} \gg p_{O_2}^0 \quad [6]$$

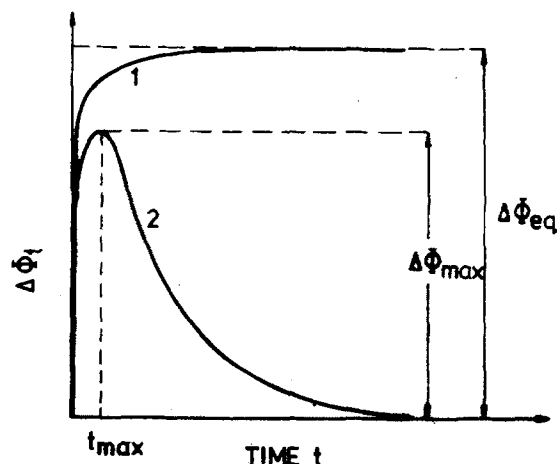


Fig. 1. Schematic plots for the work function changes vs. time accompanying isothermal sorption of oxygen for nonstoichiometric oxide surface. 1, At higher pressures when $p_{O_2} = \text{const.}$ and 2, at small oxygen doses equivalent to the fraction of the monolayer coverage.

Accompanying changes Φ_t vs. time (Fig. 1, curve 2) show a rapid initial increase due to ionization of adsorbed oxygen, reach maximum $\Delta\Phi_{\text{max}}$, and then slowly decrease as a result of diffusion of lattice ionic defects (1, 2).

The following expression may be written for O_2 adsorbed as a result of Eq. [1]

$$\frac{d[O_{2(\text{ads})}]}{dt} = k_1 \left\{ p_{O_2} - [O_{2(\text{ads})}] S \frac{kT}{V} \right\} - k_2 [O_{2(\text{ads})}] - k_3 [O_{2(\text{ads})}] + 4k_4 [O^-][h\cdot] \quad [7]$$

where $[O_{2(\text{ads})}^\infty]$ is the maximal surface concentration of oxygen adsorbed and k_1 , k_2 , k_3 , and k_4 are rate constants of corresponding processes expressed in Eq. [1] and [2]. Similarly, we can write

$$\frac{d[O^-]}{dt} = k_3 [O_{2(\text{ads})}] - 4k_4 [O^-][h\cdot] - k_5 [O^-] + k_6 [V_{\text{Me}}''] [h\cdot] \quad [8]$$

where k_5 and k_6 are appropriate rate constants in Eq. [3]. Finally for cation vacancies we obtain

$$\frac{d[V_{\text{Me}}'']}{dt} = k_5 [O^-] - k_6 [V_{\text{Me}}''] [h\cdot] - j_v \quad [9]$$

where j_v denotes the flux of vacancies from the surface into the crystalline bulk. All concentration terms in Eq. [7]-[9] correspond to the surface.

Distribution of Electrical Potential in the Boundary Layer

Shift of Eq. [1], [2], and [3] to the right leads to the formation of doubly ionized cation vacancies localized initially at the surface and to generation of surface charge q_s

$$q_s = -2e [V_{\text{Me}}''] \quad [10]$$

Consequently, the surface charge causes increase in surface potential and formation of electrical double layer (boundary layer) enriched with electron holes.

In the considerations below we assume that before admission of an oxygen dose, the initial surface potential, with respect to the bulk of the oxide crystal, is negligible comparing its changes accompanying further chemisorption of O_2 .

The electrical potential in the boundary layer is related to charge density according to Poisson's equation

$$\frac{d^2\psi}{dx^2} = -\frac{4\pi}{\epsilon} \rho(x) \quad [11]$$

where ψ = surface potential, x = distance from the crystal surface, ϵ = dielectric constant, and $\rho(x)$ = charge density. It is also assumed that ϵ is independent of both x and electric field. $\rho(x)$ may be expressed as

$$\rho(x) = e \{ [h\cdot]_b \exp(-e\psi/kT) - [e^-] \exp(e\psi/kT) - 2[V_{\text{Me}}''] + \sum_i [F_i] z_i \} \quad [12]$$

where $[F_i]$ is the concentration of impurities of effective charge z_i . The Boltzmann distribution of electronic carriers is assumed because of their large mobilities as compared with mobilities of ionic defects. The lattice electroneutrality condition for the crystalline bulk is

$$[h\cdot]_b - [e^-]_b - 2[V_{\text{Me}}'']_b + \sum_i [F_i]_b z_i = 0 \quad [13]$$

where subscript b refers to the bulk. The concentrations expressed in Eq. [12], [13], and below are considered as volume concentrations in cm^{-3} (contrary to Eq. [7], [8], and [9] where surface concentrations were used). Assuming condition [13] the relation for $\rho(x)$ may be expressed

$$\rho(x) = e \{ [h\cdot]_b \{ \exp(-e\psi/kT) - 1 \} + [e^-]_b \{ 1 - \exp(e\psi/kT) \} \} - 2e \{ [V_{\text{Me}}''] - [V_{\text{Me}}'']_b \} \quad [14]$$

Therefore, Poisson's equation may be written

$$\frac{d^2\psi}{dx^2} = -\frac{8\pi e [h\cdot]_b}{\epsilon} \frac{1}{2} \left\{ \exp(-e\psi/kT) - 1 \right\} + \frac{1}{2} \alpha \left\{ 1 - \exp(e\psi/kT) \right\} - \frac{[V_{\text{Me}}''] - [V_{\text{Me}}'']_b}{[h\cdot]_b} \quad [15]$$

where $\alpha = [e^-]_b/[h\cdot]_b$. The boundary conditions for Eq. [15] are

$$\left. \begin{aligned} \psi &= 0 \\ \frac{d\psi}{dx} &= 0 \end{aligned} \right\} x \rightarrow 0 \quad [16]$$

$$\left(\frac{d\psi}{dx} \right)_0 = \Delta q_s \frac{4\pi}{\epsilon} \quad x = 0 \quad [17]$$

where Δq_s is the surface charge generated due to formation of cation vacancies and localized at the surface.

In order to solve Eq. [15] we have to determine $[V_{\text{Me}}'']$ (which varies with both x and time t) using the diffusion equation

$$\frac{\partial [V_{\text{Me}}'']}{\partial t} = \frac{\partial}{\partial x} \left\{ D_v \frac{\partial [V_{\text{Me}}'']}{\partial x} + \frac{2eD_v}{kT} \frac{\partial \psi}{\partial x} [V_{\text{Me}}''] \right\} \quad [18]$$

where D_v is the diffusion coefficient of cation vacancies.

In further considerations we describe the outward surface diffusion of cation vacancies being formed at $t = 0$ and localized initially at the surface layer of the thickness, a , which in the first approximation is referred to the first monolayer. During the diffusion process the surface concentration of vacancies is assumed to be uniform and independent of surface topography and its energetic state. Therefore, the initial and boundary conditions for Eq. [18] are

$$\left. \begin{aligned} [V_{\text{Me}}'']_s &= [V_{\text{Me}}'']_s^0 \text{ for } -a < x < 0 \text{ and } t = 0 \\ [V_{\text{Me}}''] &= [V_{\text{Me}}'']_b \text{ for } a < x < \infty \text{ and } t = 0 \end{aligned} \right\} \quad [19]$$

$$\frac{\partial [V_{\text{Me}}'']_s}{\partial t} = D_v \left\{ \frac{\partial [V_{\text{Me}}'']_s}{\partial x} \text{ for } x = 0 \text{ and } t > 0 \right. \quad [20]$$

and

$$[V_{Me}'''] = [V_{Me}''']_s \text{ for } x = 0 \text{ and } t > 0 \quad [21]$$

The schematic diagram in Fig. 2 illustrates the distribution of cation vacancies near the surface at $t = 0$ and at $t > 0$.

Equations [15] and [18], as well as conditions [16] and [17], form a nonlinear partial boundary value problem. Its analytical solution is impossible. Only iterative, numerical methods may be applied.

Equations [7], [8], and [9] should be considered together with Eq. [15] and [18]. However, it results from the experimental data that formation of the surface charge due to ionization of the adsorbed species is much faster than the subsequent discharging of the surface caused by ionic diffusion (1, 2). Therefore, t_{\max} (Fig. 1) may here be considered as $t = 0$. We also assume that at $t = 0$ the initial concentration of cation vacancies $[V_{Me}''']_s^0$ refers to the surface layer within $a < x < 0$.

Let us now estimate the term in Eq. [18], responsible for defect migration under potential gradient, regarding the thermal diffusion term

$$b = \frac{D_v \frac{\partial [V_{Me}''']}{\partial x}}{D_v \frac{2e}{kT} \frac{\partial \psi}{\partial x} [V_{Me}''']} = \frac{\Delta [V_{Me}''']}{\frac{\Delta \psi}{L} [V_{Me}''']} \frac{kT}{2e} \quad [22]$$

where Δd is the thickness of diffusion layer increasing with time as the concentration gradient propagates inwards and L is the screening depth. According to the experimental conditions we may estimate: $\Delta [V_{Me}'''] \cong [V_{Me}''']$; $\Delta d = 10^{-7}$ cm; $\Delta \psi = 200$ mV; $L = 10^{-5}$ cm; $T = 675^\circ\text{K}$. Therefore $b = 15$, indicating the thermal diffusion is 15 times faster than migration. For longer times Δd increases but at the same time $\Delta \psi$ decreases. Hence, assuming the thermal diffusion as predominant, Eq. [18] acquires the form

$$\frac{\partial [V_{Me}''']}{\partial t} = D_v \frac{\partial^2 [V_{Me}''']}{\partial x^2} \quad [23]$$

assuming that D_v is independent of defect concentration (16). The term of thermal diffusion involves diffusion of lattice species which occurs within the thermally equilibrated crystal.

Solution of Poisson's Equation

We introduce the following nondimensional variables

$$\begin{aligned} \tilde{x} &= x/L \\ \tilde{\psi} &= e\psi/kT \\ \tilde{q} &= \Delta q_s \frac{4\pi\epsilon L}{kT} \end{aligned} \quad [24]$$

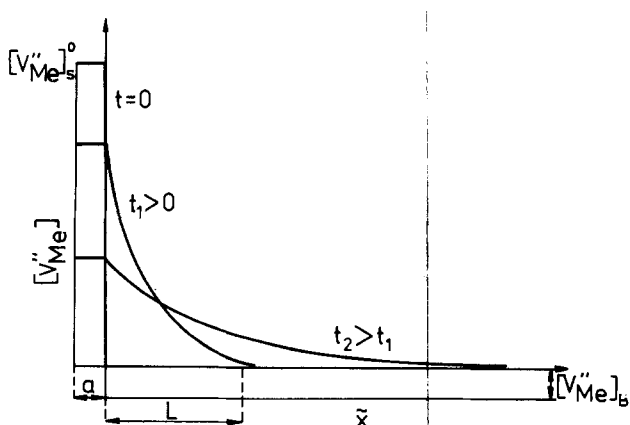


Fig. 2. Schematic distribution of cation vacancies in the boundary layer at different times.

where

$$\frac{1}{L} = \left\{ \frac{8\pi e^2 [h^+]_b}{\epsilon kT} \right\}^{1/2} \quad [25]$$

Taking into account conditions [24], Eq. [15] assumes the form

$$\frac{d^2 \tilde{\psi}}{dx^2} = -\rho_0 - \frac{1}{2} \exp(-\tilde{\psi}) + \frac{1}{2} \alpha \exp \tilde{\psi} + f \quad [26]$$

where

$$\begin{aligned} \rho_0 &= \frac{1}{2} (\alpha - 1) \\ f &= \frac{[V_{Me}'''] - [V_{Me}''']_b}{[h^+]_b} \end{aligned}$$

This is an inhomogeneous nonlinear differential equation of the second order. Its analytical solution seems impossible at any form of f . Solving Eq. [26] we consider two limiting cases.

The first case concerns $t = 0$ when generated cation vacancies are located at the surface and therefore the term f is negligible. For short times $\tilde{\psi}$ assumes maximal value and then nonlinearity of Eq. [26] is pronounced. Neglecting f Eq. [26] can be integrated

$$\frac{d\tilde{\psi}}{dx} = \{ \alpha \exp \tilde{\psi} + \exp(-\tilde{\psi}) + (\alpha - 1) \tilde{\psi} + C \}^{1/2} \quad [27]$$

where C is a constant.

Applying the boundary condition

$$\frac{d\tilde{\psi}}{dx} \rightarrow 0 \text{ and } \tilde{\psi} = 0 \text{ when } x \rightarrow \infty$$

we receive for \tilde{q}

$$\begin{aligned} \tilde{q} = - \left(\frac{d\tilde{\psi}}{dx} \right)_0 &= \{ \alpha \exp \tilde{\psi}_s + \exp(-\tilde{\psi}_s) \\ &+ (\alpha - 1) \tilde{\psi}_s - (1 + \alpha) \}^{1/2} \quad [28] \end{aligned}$$

where $\tilde{\psi}_s$ is the surface potential.

As seen the relation between $\tilde{\psi}_s$ and \tilde{q} is nonlinear. Let us determine limits of this nonlinearity. By expanding $\exp \tilde{\psi}_s$ and $\exp(-\tilde{\psi}_s)$ in a power series near zero and neglecting terms of the order greater than three we obtain after some rearrangements

$$\begin{aligned} \tilde{q} = -\tilde{\psi}_s \sqrt{\frac{1+\alpha}{2}} &\left\{ 1 + \frac{(\alpha-1)\tilde{\psi}_s}{(\alpha+1)3} + \frac{\tilde{\psi}_s^2}{6} \right. \\ &\left. + \frac{(\alpha-1)\tilde{\psi}_s^3}{(\alpha+1)30} + \dots \right\}^{1/2} \quad [29] \end{aligned}$$

For $\alpha = 0$ and $\tilde{\psi} = 1$ (for NiO refer to $\psi = 70$ mV at 400°C) the deviation from linearity assumes 7%.

The second case refers to small values of $\tilde{\psi}$ for which the expression $\exp(-\tilde{\psi})$ and $\exp \tilde{\psi}$ in Eq. [26] may be substituted by terms $(1 - \tilde{\psi})$ and $(1 + \tilde{\psi})$, respectively. Then Eq. [26] assumes the linear form

$$\frac{d^2 \tilde{\psi}}{dx^2} = \beta \tilde{\psi} + f \quad [30]$$

where $\beta = \frac{1}{2} (1 + \alpha)$.

This form of Poisson's equation is suitable for describing reconstructions of the surface charge layer for longer times when $[V_{Me}''']_s$ achieves a low value. Ap-

plying Lagrange's indefinite multilayers method we obtain the solution of Eq. [30] in the form

$$\begin{aligned} \tilde{\psi} = A \exp(-\sqrt{\beta\tilde{x}}) - \frac{1}{2\sqrt{\beta}} \exp \sqrt{\beta\tilde{x}} \\ \int_x^\infty f \exp(-\sqrt{\beta\tilde{x}}) d\tilde{x} + \frac{1}{2\sqrt{\beta}} \\ \exp(-\sqrt{\beta\tilde{x}}) \int_x^\infty f \exp(\sqrt{\beta\tilde{x}}) d\tilde{x} \end{aligned} \quad [31]$$

The constant A may be determined from the condition

$$\left(\frac{\partial \tilde{\psi}}{\partial \tilde{x}} \right)_0 = -\tilde{q} \quad [32]$$

Then we obtain

$$\begin{aligned} \left(\frac{\partial \tilde{\psi}}{\partial \tilde{x}} \right) = -\sqrt{\beta} A \exp(-\sqrt{\beta\tilde{x}}) \\ - \frac{1}{2} \exp(\sqrt{\beta\tilde{x}}) \int_x^\infty f \exp(-\sqrt{\beta\tilde{x}}) d\tilde{x} \\ - \frac{1}{2} \exp(-\sqrt{\beta\tilde{x}}) \int_x^\infty f \exp(\sqrt{\beta\tilde{x}}) d\tilde{x} \end{aligned} \quad [33]$$

For $\tilde{x} = 0$ we have

$$\left(\frac{\partial \tilde{\psi}}{\partial \tilde{x}} \right)_s = -\tilde{q} = A\sqrt{\beta} + \frac{1}{2} (\Gamma_1 + \Gamma_2) \quad [34]$$

where

$$\begin{aligned} \Gamma_1 = \int_0^\infty f \exp(-\sqrt{\beta\tilde{x}}) d\tilde{x} \\ \Gamma_2 = \int_0^\infty f \exp(\sqrt{\beta\tilde{x}}) d\tilde{x} \end{aligned} \quad [35]$$

Combining Eq. [31] and [34] we obtain for surface potential $\tilde{x} = 0$

$$\begin{aligned} \tilde{\psi}_s = \frac{\tilde{q}}{\sqrt{\beta}} - \Gamma_1 = \frac{1}{\sqrt{\beta}} \tilde{q} \\ - \int_0^\infty \frac{[V_{Me''}] - [V_{Me''}]_b}{[h']_b} \exp(-\sqrt{\beta\tilde{x}}) d\tilde{x} \end{aligned} \quad [36]$$

Solution of Fick's Second Law

In order to determine the vacancy concentration we solve Eq. [23]. Let us introduce the following terms

$$\begin{aligned} [\tilde{V}] = \frac{[V_{Me''}]}{V_{Me_0}} \\ \tau = tD_v/L^2 \\ \tilde{x} = x/L \end{aligned}$$

Accordingly Eq. [23] assumes the form

$$\frac{\partial [\tilde{V}]}{\partial \tau} = \frac{\partial^2 [\tilde{V}]}{\partial \tilde{x}^2} \quad [37]$$

Equation [37] may be solved applying Laplace's transformations. Its final solution assumes the form

$$\begin{aligned} [V_{Me''}] = \{ [V_{Me''}]_s^0 - [V_{Me''}]_b \} \exp(r\tilde{x} + r^2\tilde{x}) \\ \operatorname{erfc} \left(\frac{\tilde{x}}{2\sqrt{\tau}} + r\sqrt{\tau} \right) + [V_{Me''}]_b \end{aligned} \quad [38]$$

where $r = L/a$. In our case $r \gg 1$.

Substituting the expression for $[V_{Me''}]$ into Eq. [36] we obtain

$$\begin{aligned} \tilde{\psi}_s = \frac{\tilde{q}}{\sqrt{\beta}} - \int_0^\infty \frac{[V_{Me''}]_s^0 - [V_{Me''}]_b}{[h']_b} \exp(r\tilde{x} + r^2\tau) \\ \operatorname{erfc} \left(\frac{\tilde{x}}{2\sqrt{\tau}} + r\sqrt{\tau} \right) \exp(-\sqrt{\beta\tilde{x}}) d\tilde{x} \end{aligned} \quad [39]$$

Taking into account that

$$\begin{aligned} \tilde{q} = \frac{q_s 4\pi e L}{\epsilon k T} = - \frac{8\pi e^2 L a}{\epsilon k T} \{ [V_{Me''}]_s - [V_{Me''}]_b \} \\ = \frac{[V_{Me''}]_s - [V_{Me''}]_b}{[h']_b \tau} \end{aligned} \quad [40]$$

and considering that

$$[V_{Me''}] = \frac{[V_{Me''}]_s^0 - [V_{Me''}]_b}{r} \exp\left(-\frac{\tilde{x}^2}{4\tau}\right) \quad \text{for } r\sqrt{\tau} \gg 1 \quad [41]$$

we obtain for $\tilde{\psi}_s$

$$\begin{aligned} \tilde{\psi}_s = \frac{1}{r\sqrt{\beta}[h']_b} \left\{ \Delta [V_{Me''}]_s + \frac{\sqrt{\beta}}{\sqrt{\pi\tau}} \int_0^\infty \{ [V_{Me''}]_s^0 - [V_{Me''}]_b \} \exp\left(-\frac{\tilde{x}^2}{4\tau}\right) \exp(-\sqrt{\beta\tilde{x}}) d\tilde{x} \right\} \end{aligned} \quad [42]$$

where

$$\begin{aligned} [V_{Me''}]_s = \{ [V_{Me''}]_s - [V_{Me''}]_b \} \\ = \frac{1}{r\sqrt{\pi\tau}} \{ [V_{Me''}]_s^0 - [V_{Me''}]_b \} \end{aligned} \quad [43]$$

Finally Eq. [42] may be transformed into

$$\begin{aligned} \tilde{\psi}_s = \frac{[V_{Me''}]_s^0 - [V_{Me''}]_b}{r[h']_b} \left\{ \frac{1}{r} + \sqrt{\beta} \int_0^\infty \exp\left(-\frac{\tilde{x}^2}{4\tau}\right) \exp(-\sqrt{\beta\tilde{x}}) d\tilde{x} \right\} \end{aligned} \quad [44]$$

As seen from Eq. [44] the term related to surface charge $1/r$ has a negligible effect on $\tilde{\psi}_s$ when $\tau > r^2$. For longer times we can write

$$\sqrt{\beta} \int_0^\infty \exp\left(-\frac{\tilde{x}^2}{4\tau}\right) \exp(-\sqrt{\beta\tilde{x}}) d\tilde{x} = 1 \quad [45]$$

and consequently

$$\tilde{\psi}_s = - \frac{[V_{Me''}]_s^0 - [V_{Me''}]_b}{r\sqrt{\beta}[h']_b} \quad [46]$$

For $\tau = 0$ surface potential assumes maximum

$$\tilde{\psi}_{\max} = \frac{[V_{Me''}]_s^0 - [V_{Me''}]_b}{r[h']_b} \quad [47]$$

Then we obtain final relation between D_v , ψ_s , and ψ_{\max}

$$\frac{\psi_s}{\psi_{\max}} = \frac{1}{\sqrt{\beta\pi\tau}} = \frac{L}{\sqrt{\beta\pi D_v t}} \quad [48]$$

We assume that the surface potential in Eq. [48] refers to work function changes

$$\begin{aligned} e\psi_s = \Delta\Phi_t \\ e\psi_{\max} = \Delta\Phi_{\max} \end{aligned} \quad [49]$$

For calculations we also assume $t_{\max} = 0$.

Combining Eq. [48] and [25] we obtain

$$D_v = \frac{10^{-2} \epsilon k T}{2.4 \pi^2 e^2 [h^{\cdot}]_b \{1 + [e^-]_b / [h^{\cdot}]_b\} t g^2 \gamma} \quad [50]$$

where $t g \gamma$ is the slope of the linear part of the relation $\Delta \Phi_i / \Delta \Phi_{\max}$ vs. $1/\sqrt{t}$.

Taking into account relation between chemical diffusion coefficient and diffusion coefficient of defects

$$\tilde{D} = (1 + Z) D_v \quad [51]$$

and assuming $z = 2$ and $[h^{\cdot}]_b \gg [e^-]_b$, we finally obtain

$$\tilde{D} = \frac{10^{-2} \epsilon k T}{0.8 \pi^2 e^2 [h^{\cdot}]_b t g^2 \gamma} \quad [52]$$

The presented quantitative considerations and the proposed particular solution of Fick's second law for near surface layer enables the calculation of the chemical diffusion coefficient for this layer. Therefore, for \tilde{D} in Eq. [52] we may write

$$\tilde{D} = \tilde{D}_{SL}$$

Determination of \tilde{D}_{SL} leads to a possibility of a quantitative analysis of transport properties for near surface layer of oxide materials and also of other nonstoichiometric compounds. \tilde{D}_{SL} and \tilde{D}_{bulk} may differ essentially if segregation of lattice components occurs. Independent determination of \tilde{D}_{SL} and \tilde{D}_{bulk} is therefore especially important for appropriate characterization of compounds and their surface properties at elevated temperatures after segregation. Data of \tilde{D}_{SL} may be especially useful for understanding and correct interpretation of several technological processes as standardization of semiconducting materials, sintering of ceramic materials, reduction of ores in metallurgy, and heterogeneous catalytic reactions.

Conclusions

It has been found that the dependence between surface potential and surface charge obeys a linear relationship at higher reequilibration times when discharging of the oxide surface is produced mainly by thermal diffusion. Appropriate solution of Fick's second law leads to chemical diffusion coefficient for near-to-surface layer of oxide materials. The described method of measuring \tilde{D}_{SL} from the work function data creates a possibility of studying transport properties of the outer surface layer independently of the bulk. It should be emphasized that both structure and diffusion parameters for the bulk and the surface layer may differ essentially, especially for oxide solid solutions exhibiting the effect of segregation of lattice components.

Surface-controlled mechanism in heterogeneous reequilibration processes for oxide-oxygen systems may find an explanation in investigations of \tilde{D}_{SL} and \tilde{D}_{bulk} , independently.

Acknowledgments

This work was supported by the National Science Foundation through the M. Sklodowska-Curie Fund, Grant No. OIP-7621956, as well as by the Metallurgical Institute, Academy of Mining and Metallurgy in

Kraków, Grant No. MR-1.19-1.6.5. These supports are gratefully acknowledged.

Manuscript submitted Aug. 1, 1979; revised manuscript received Nov. 21, 1979.

Any discussion of this paper will appear in a Discussion Section to be published in the December 1980 JOURNAL. All discussions for the December 1980 Discussion Section should be submitted by Aug. 1, 1980.

LIST OF SYMBOLS

a	monolayer thickness
d	diffusion layer thickness
\tilde{D}	chemical diffusion coefficient
D_v	diffusion coefficient of cation vacancies
e	elementary charge
e^-	quasi-free electron
F_i	impurity
h^{\cdot}	quasi-free electron hole
j_v	flux of cation vacancies
k	Boltzmann constant
k_1, k_2, \dots, k_6	rate constants
L	screening depth (Debye thickness)
$O_{2(ads)}, O^-, O^{2-}$	adsorbed oxygen species
p_{O_2}	oxygen partial pressure
q	electric charge
S	surface area
t	time
T	absolute temperature
v	volume
$V_{Me''}$	double ionized cation vacancy
x	distance from the surface
z	effective charge
ϵ	dielectric constant
Φ	work function
ψ	potential
ρ	charge density
$[]$	concentrations
$[]_b$	bulk concentrations
$[]_s$	surface concentrations

REFERENCES

1. J. Deren and J. Nowotny, *Oxid. Met.*, **1**, 73 (1969).
2. J. Nowotny, *J. Mater. Sci.*, **12**, 1143 (1977).
3. J. Nowotny, *J. Chim. Phys.*, **75**, 689 (1978).
4. I. Sikora, Ph.D. Thesis, Institute of Catalysis and Surface Chemistry, Polish Academy of Sciences, Kraków, 1978.
5. J. Nowotny and I. Sikora, *This Journal*, **125**, 781 (1978).
6. J. B. Price and J. B. Wagner, Jr., *Z. Phys. Chem., N.F.*, **49**, 257 (1966).
7. P. E. Childs, L. W. Laub, and J. B. Wagner, Jr., *Proc. Br. Ceram. Soc.*, **19**, 29 (1971).
8. G. J. Koel and P. J. Gellings, *Oxid. Met.*, **5**, 185 (1972).
9. Y. Ikeda and K. Nii, *Trans. Jpn. Inst. Met.*, **17**, 419 (1976).
10. R. Fahri and G. Petot-Ervas, *J. Phys. Chem. Solids*, **39**, 1169 (1978).
11. P. E. Childs and J. B. Wagner, Jr., "Heterogeneous Kinetics at Elevated Temperature," p. 269, Plenum Press, New York (1970).
12. J. Nowotny and J. B. Wagner, Jr., *Oxid. Met.*, In print.
13. P. Kofstad, "Nonstoichiometry, Diffusion and Electrical Conductivity in Binary Metal Oxides," Wiley-Interscience, New York (1972).
14. A. Bielanski and M. Najbar, *J. Catal.*, **25**, 398 (1972).
15. K. Dyrek, *Bull. Acad. Polon. Sci., Ser. Sci. Chim.*, **21**, 675 (1973).
16. A. Bielanski and M. Najbar, *ibid.*, **24**, 665 (1976).
17. J. Deren, J. Nowotny, and A. Sadowski, *ibid.*, **21**, 503 (1973).

Near-Surface and Bulk Chemical Diffusion of Undoped NiO

Z. Adamczyk and J. Nowotny

Institute of Catalysis and Surface Chemistry, Polish Academy of Sciences, 30-239 Kraków, Poland

ABSTRACT

Work function is applied to monitor the reequilibration kinetics at the NiO surface after sorption of small oxygen doses. Using appropriate solution of Fick's second law and of Poisson's equation the chemical diffusion coefficient for the near-to-surface layer of undoped NiO was calculated in the range 300°-425°C

$$\tilde{D}_{SL} = 4 \cdot 10^{-5} \exp [(-21,000 \pm 2,100)/RT] \quad [\text{cm}^2 \text{sec}^{-1}]$$

The obtained results are discussed regarding the available diffusion data for NiO obtained at high temperatures.

Chemical diffusion coefficients for nonstoichiometric oxide materials may be calculated from the reequilibration kinetic data. The reequilibration kinetics may be followed directly by measuring changes in crystal nonstoichiometry *vs.* time. The gravimetric method is applicable when changes in crystal composition are sufficiently high (1-3). However, for compounds showing a small deviation from stoichiometry, the electrical conductivity method is more convenient (4). Both methods refer to the crystalline bulk and therefore may be applied at sufficiently high temperatures at which equilibrium in a gas-solid system may be reached relatively fast. On the other hand, the method based on the work function data leads to chemical diffusion coefficient \tilde{D}_{SL} for the near-to-surface layer of the oxide crystals (5).

The purpose of the present work is to determine the surface reequilibration kinetics and to calculate \tilde{D}_{SL} for undoped NiO. NiO is a convenient object for diffusion investigations exhibiting a very small concentration of defects which may be considered to form an ideal solution in the crystal. The available data of D for this oxide material (4, 6-12) may serve as a comparative material to discuss the results obtained from the work function measurements.

Discussion of Chemical Diffusion Data for NiO

The available data of chemical diffusion for NiO differ considerably concerning the absolute values and the reported activation energies (4, 6-12). The electrical conductivity method applied in most cases is a very accurate one (13). The differences seem to consist in crystal geometry. Also concentration of impurities may have an essential effect on the measured values of reequilibration kinetic data, especially when segregation of lattice components occurs (14). Then a surface-controlling mechanism may be observed (1, 2).

Table I illustrates available data of both the chemical diffusion coefficient \tilde{D} and the diffusion coefficient of defects D_v . Both are correlated according to the expression

$$\tilde{D} = (1 + Z)D_v \quad [1]$$

On one side, data of Wagner *et al.* (4, 9), of Koel and Gellings (8), and of Nowotny and Sadowski (12, 13) show an excellent agreement as concerns the activation energy varying between 21 and 24 kcal · mole⁻¹. Another group of data shows high values of the activation energy ranging from 31 to 37 kcal · mole⁻¹ (6, 7, 10, 11).

Key words: work function, semiconductor, defects, potential.

Several experimental details are important to determine \tilde{D} correctly. First, the oxide sample should be well equilibrated with the gas phase. It is also important to determine ranges of the equilibration kinetics for which appropriate equations (logarithmic and parabolic) are fulfilled. The calculated diffusion data are self-consistent when calculations according to both parabolic and logarithmic equations (at appropriate ranges) lead to identical values (13). Several papers do not involve any experimental details which could answer these questions (6, 7, 11). The results of Ikeda and Nii (10) show different reduction and oxidation kinetics, which are not in accordance with the bulk diffusion mechanism found for NiO (12, 13). Also impurity concentration required for critical analysis of conflicting results is lacking in several cases (6, 10).

As it results from experimental work of Sadowski (13) crystal geometry has no effect on the measured activation energy of \tilde{D} but as a strong effect on the calculated value of \tilde{D} as a consequence of concentration profiles during the reequilibration.

In the present studies the work function is used to follow the reequilibration kinetics at the surface of NiO crystal and appropriate solution of Fick's second law (5) is utilized to calculate \tilde{D}_{SL} .

Comparison of the results obtained presently and those from the electrical conductivity method may bring further arguments concerning diffusion data for NiO.

Experimental

An undoped, polycrystalline NiO sample was taken for investigation. The sample was prepared by calcination of nickel carbonate at 1000°C for 4 hr in air. The specific surface area was 0.42 m² g⁻¹. Average particle size was 0.05 mm. Results of spectral analysis for impurity concentrations are given in Table II.

The work function was measured using the dynamic capacitor method (15). The compact polycrystalline sample was located on the stainless steel plate of the dynamic condenser. The chemisorption system is able either to maintain $p_{O_2} = \text{const.}$ in the measuring system or to admit the required oxygen dose in it. The electronic device made it possible to monitor fast changes of the work function in time (15, 16). Before measurements the sample was standardized at 400°C for 1 hr under 10 Torr and then outgassed in vacuo referring to $p_{O_2} = 10^{-6}$ Torr. After the standardization the temperature was set on the experimental level and the sample was equilibrated at given conditions of T and p_{O_2} until a constant value of the work function Φ_t

Table I. Data of \tilde{D} and D_v for NiO

No.	Authors	p_{O_2} range (atm)	T range (°C)	Concentration of mono- and three-valent impurities (ppm)	\tilde{D} or D_v vs. T (cm ² sec ⁻¹)	Remarks
1	Price and Wagner (4)	$3 \cdot 10^{-6}$ -1	800-1100	200	$\tilde{D} = 7.52 \cdot 10^{-4} \exp(-21,900/RT)$	
2	Morlotti (6)	10^{-3} -1	750-1000	Not available	$D_v = 14 \exp(-31,000/RT)$	
3	Deren <i>et al.</i> (7)	$3 \cdot 10^{-6}$ -0.21	1000-1300	100	$\tilde{D} = 6.45 \cdot 10^{-2} \exp(-33,700/RT)$	
4	Koel and Gellings (8)	10^{-3}	975-1300	100	$\tilde{D} = 2.2 \cdot 10^{-3} \exp(-24,600/RT)$	
5	Nowotny and Wagner (9)	$9 \cdot 10^{-5}$ -0.1	900-1170	10	$\tilde{D} = 2.9 \cdot 10^{-3} \exp(-21,700/RT)$	
6	Ikeda and Nii (10)	10^{-4} -1	950-1100	Not available	$D_v = 0.069 \exp(-33,000/RT)$ $D_v = 0.13 \exp(-36,000/RT)$	Reduction Oxidation
7	Fahri and Petot-Ervas (11)	$1.9 \cdot 10^{-4}$ -1	1000-1400	30	$\tilde{D} = 0.244 \exp(-36,600/RT)$	
8	Nowotny and Sadowski (12)	10^{-5} -1	900-1200	200	$\tilde{D} = 1.64 \cdot 10^{-2} \exp(-22,480/RT)$ $\tilde{D} = 9.68 \cdot 10^{-3} \exp(-21,430/RT)$	Oxidation Reduction

vs. time t was reached. Then the required oxygen dose was admitted into the measuring system and at that moment both $\Delta\Phi_t$ and Δp_{O_2} were measured isothermally in time. The amount of the NiO sample taken for each experiment was always equal to 0.31g. Two different oxygen doses (indicated as A_1 and A_2) were used. Table III gives their amount and corresponding fraction of monolayer coverage at $t = 0$.

Results and Discussion

The data of $\Delta\Phi_t$ vs. t taken after admission of an O_2 dose show a nonmonotonous character involving rapid initial increase and then slower decrease (16). The increase of Φ_t is produced by chemisorption of O_2 and the subsequent decrease refers to ionic diffusion and leads to building up of new lattice elements. Accordingly the work function assumes the initial value. It has been found that p_{O_2} rapidly decreases (after admission of an O_2 dose) from the initial value listed in Table II and achieves vacuum (below 10^{-6} Torr) before $\Delta\Phi_t$ reaches maximum ($\Delta\Phi_{max}$). We assume then that Φ_t changes at time higher than t_{max} (corresponding to $\Delta\Phi_{max}$) are determined only by transfer of ionic species from the surface into the crystalline bulk. The experimental data of $\Delta\Phi_t$ corresponding to discharging the surface are plotted as a function of $\Delta\Phi_t/\Delta\Phi_{max}$ vs. $1/\sqrt{t}$ in Fig. 1. Data of $\Delta\Phi_t$ vs. t are presented elsewhere (16). The times when $\Delta\Phi_t \approx 0$ correspond to diffusion within several outer layers only, however relatively small amounts of O_2 used experimentally (16) lead to the negligible final $\Delta\Phi_t$ value after relatively short times. The chemical diffusion coefficient was calculated according to the follow-

ing equation which is a solution of Fick's second law (5)

$$D_{SL} = (1 + Z) \frac{L^2}{60\pi\beta t g^2 \gamma [h \cdot] (1 + [e^-]/[h \cdot])} \quad [2]$$

where: ϵ = dielectric constant (for NiO, $\epsilon = 10$), Z = effective charge of diffusing defects, L = the screening depth expressed by the formula, $\beta = 1/2$, and $[e^-]$ and $[h \cdot]$ are concentrations of quasifree electrons and electron holes, respectively

$$L = \sqrt{\frac{\epsilon kT}{8\pi e^2 ([h \cdot] + [e^-])}} \quad [3]$$

$Tg\gamma$ is the slope of the linear part of the dependence $\Delta\Phi_t/\Delta\Phi_{max}$ vs. $1/\sqrt{t}$ in the range of higher reequilibration times where Poisson's equation holds linearity. It has been found that $tg\gamma$ is independent of the amount of oxygen used experimentally, Fig. 2.

As results from quantitative considerations (5), Eq. [2] is valid only for longer reequilibration times when the surface potential can be sufficiently low and the migration term in the diffusion process may be neglected as compared to the thermal diffusion term. This is the reason that the linearity of $\Delta\Phi_t/\Delta\Phi_{max}$ vs. $1/\sqrt{t}$ dependence (Fig. 1 and 2) is fulfilled only at higher equilibration times. At lower times the surface potential acquires highest values, the migration term becomes comparable to the thermal diffusion term, and as a result a marked deviation from the linearity is observed. In the experimental conditions applied we may assume doubly ionized cation vacancies and electron holes to be predominant NiO lattice defects (16,

Table II. Impurity concentrations in NiO crystal

Impurity	Concentration (atom per cent)
Co	0.05
Al	0.001
Mg	0.001
Mn	0.0005
Fe	0.0005
Si	0.001
Cu	0.0005
Pb	0.001
Ca	0.0005

Table III. Experimental O_2 doses

Oxygen dose	Amount (moles)	Fraction of the monolayer coverage (%)	Initial oxygen pressure (Torr)
A_1	$4.23 \cdot 10^{-8}$	4.1	$9.2 \cdot 10^{-4}$
A_2	$1.24 \cdot 10^{-7}$	12.0	$2.7 \cdot 10^{-3}$

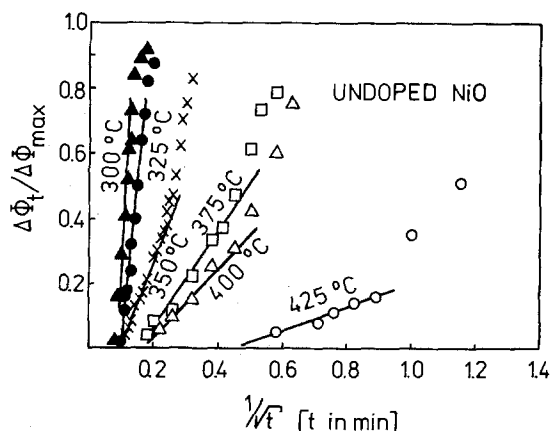


Fig. 1. Experimental work function data for NiO plotted as $\Delta\Phi_t/\Delta\Phi_{max}$ vs. $1/\sqrt{t}$ for oxygen dose A_1 .

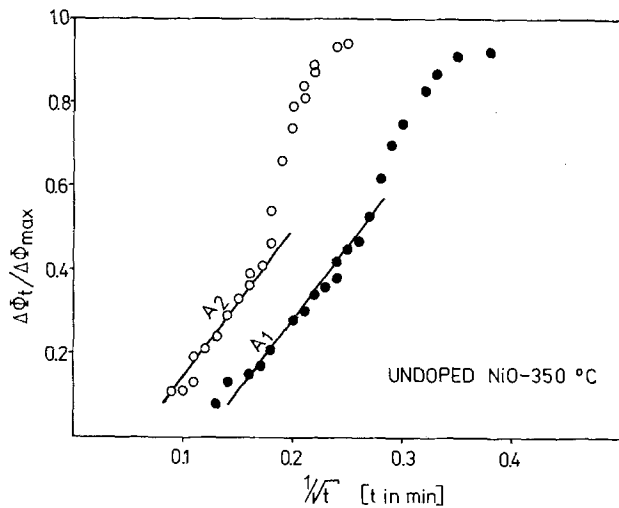


Fig. 2. Work function data for NiO plotted as $\Delta\Phi_t/\Delta\Phi_{\max}$ vs. $1/\sqrt{t}$ for oxygen doses A₁ and A₂ at 350°C.

17). Therefore, Eq. [2] and [3] may be expressed in simpler forms

$$D_{SL} = (1 + Z) \frac{\epsilon L^2}{60\pi\beta t g^2 \gamma [h \cdot]} \quad [4]$$

$$L = \sqrt{\frac{\epsilon k T}{8\pi e^2 [h \cdot]}} \quad [5]$$

The concentration of electron holes was assumed to fulfill the electroneutrality condition

$$[h \cdot] = 2[V_{Ni''}] \quad [6]$$

where $[V_{Ni''}]$ was calculated according to high temperature data of Mitoff (18)

$$[V_{Ni''}] = 11p_{O_2}^{1/6} \exp\left(-\frac{1/3 \Delta H_f}{RT}\right) \quad [7]$$

where ΔH_f is the activation enthalpy of formation of cation vacancies equal to 54 kcal · mole⁻¹ (13, 18). Assuming condition [6] we neglect the effect of impurities on $[h \cdot]$. Using the work function data (Fig. 1) and applying relations [4], [6], and [7] we obtain

$$\tilde{D}_{SL} = 4 \cdot 10^{-5} \exp\left[(-21,000 \pm 2,100)/RT\right] \quad [8]$$

Table IV shows data of both \tilde{D}_{SL} and L calculated according to Eq. [4] and [5], respectively. Figure 3 illustrates the present results as well as the high temperature data of Price and Wagner (4) and of Nowotny and Sadowski (12) extrapolated to the temperature range 300°-425°C. Taking into account the two different methods applied, two different states of the samples used (single and polycrystalline), and different temperature ranges, there is surprising agreement concerning the activation energy values. Moreover, it should be emphasized that the electrical conductivity method applicable at high temperatures refers to the

Table IV. Values of L , $tg\gamma$, and \tilde{D}_{SL} at different temperatures

Temp (°C)	L (cm)	$tg\gamma$	\tilde{D}_{SL} (cm ² /sec ⁻¹)
300	$4.56 \cdot 10^{-5}$	11.2	$5.1 \cdot 10^{-13}$
325	$3.36 \cdot 10^{-5}$	7.4	$6.6 \cdot 10^{-13}$
350	$2.55 \cdot 10^{-5}$	3.2	$2.04 \cdot 10^{-12}$
375	$1.97 \cdot 10^{-5}$	2.0	$3.0 \cdot 10^{-12}$
400	$1.55 \cdot 10^{-5}$	1.25	$4.8 \cdot 10^{-12}$
425	$1.24 \cdot 10^{-5}$	0.69	$1.02 \cdot 10^{-11}$

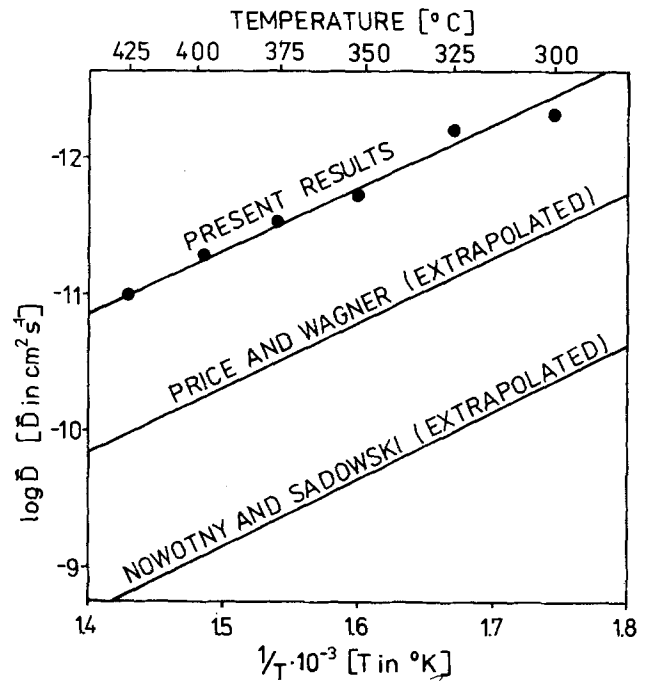


Fig. 3. Arrhenius plots of chemical diffusion coefficient calculated from the work function data (present results) and extrapolated high temperature data of Price and Wagner (4) and of Nowotny and Sadowski (12).

bulk of the crystal, whereas the work function method applied presently concerns the near-to-surface layer which is limited mainly to several outer crystal layers.

Specific surface interactions, resulting, e.g., from segregation of lattice components, may have an essential effect on the measured value of \tilde{D}_{SL} from the work function data. There is, however, some evidence indicating that the segregation effect does not occur for undoped NiO crystal (13, 14). Therefore, the observed agreement between the diffusion coefficient determined from Eq. [3] and high temperature diffusion data is understandable.

The observed differences in absolute values of \tilde{D} in Fig. 3 are apparently connected with several assumptions and approximations introduced to solve Poisson's equation (5).

Conclusions

Appropriate solution of Fick's second law and of Poisson's equation leads to the determination of the chemical diffusion coefficient from the work function data accompanying reequilibration of NiO surface. The determination of \tilde{D}_{SL} is possible at higher reequilibration times when the migration under electrical potential becomes negligible and the dependence $\Delta\Phi_t/\Delta\Phi_{\max}$ vs. $1/\sqrt{t}$ holds linearity. The data of $\tilde{D}(T)$ obtained for undoped NiO from the work function measurements show excellent agreement, concerning the activation energy term, with the high temperature data of Wagner and co-workers (4, 9) and of Sadowski (13). The agreement indicates the negligible effect of the segregation of lattice components in undoped NiO crystal.

Acknowledgments

This work was supported by the National Science Foundation through the M. Skłodowska-Curie Fund, Grant No. OIP-7621956, and by the Polish Academy of Sciences through Special Funds "Catalysis," Grant No. 03.10.2.02.02. Their support is gratefully acknowledged.

Manuscript submitted Aug. 1, 1979; revised manuscript received Nov. 21, 1979.

Any discussion of this paper will appear in a Discussion Section to be published in the December 1980 JOURNAL. All discussions for the December 1980 Discussion Section should be submitted by Aug. 1, 1980.

REFERENCES

1. J. B. Wagner, Jr., "Mass Transport in Oxides," p. 65, NBS Special Publication (1968).
2. L. W. Laub, Ph.D. Thesis, Northwestern University, Evanston, 1971.
3. P. E. Childs, L. W. Laub, and J. B. Wagner, Jr., *Proc. Br. Ceram. Soc.*, **19**, 29 (1971).
4. J. B. Price and J. B. Wagner, Jr., *Z. Phys. Chem., N.F.*, **49**, 257 (1966).
5. Z. Adamczyk and J. Nowotny, *This Journal*, **127**, 1112 (1980).
6. R. Morlotti, *Z. Naturforsch., Teil A*, **24**, 441 (1969).
7. J. Deren, Z. M. Jarzebski, S. Mrowec, and T. Walec, *Bull. Acad. Polon. Sci., Ser. Sci. Chim.*, **19**, 153 (1971).
8. G. J. Koel and P. J. Gellings, *Oxid. Met.*, **5**, 185 (1972).
9. J. Nowotny and J. B. Wagner, Jr., *J. Am. Ceram. Soc.*, **56**, 397 (1973).
10. Y. Ikeda and K. Nii, *Trans. Jpn. Inst. Met.*, **17**, 419 (1976).
11. R. Fahri and G. Petot-Ervas, *J. Phys. Chem. Solids*, **39**, 1169 (1978).
12. J. Nowotny and A. Sadowski, *J. Am. Ceram. Soc.*, **62**, 24 (1979).
13. A. Sadowski, Ph.D. Thesis, Institute of Materials Science, Academy of Mining and Metallurgy, Kraków, 1979.
14. J. Nowotny and J. B. Wagner, Jr., *Oxid. Met.*
15. R. Chrusciel, J. Deren, and J. Nowotny, *Exp. Techn. Phys.*, **14**, 127 (1966).
16. J. Nowotny, *J. Mater. Sci.*, **12**, 1143 (1977).
17. P. Kofstad, "High Temperature Oxidation of Metals," John Wiley & Sons, Inc., New York (1966).
18. S. P. Mitoff, *J. Chem. Phys.*, **35**, 882 (1961).

Preparation of Molybdenum Silicide Films by Reactive Sputtering

S. Yanagisawa and T. Fukuyama

Cooperative Laboratories, VLSI Technology Research Association, Takatsu-ku, Kawasaki, 213 Japan

ABSTRACT

A new deposition technique for molybdenum silicide films is presented whereby the films are deposited by magnetron-d-c-reactive sputtering using a Mo target in a silane argon atmosphere. The influence of sputtering conditions upon the film properties was investigated by utilizing mass spectroscopy, Auger electron spectroscopy, and x-ray diffractometry. Films with various Si/Mo atomic ratios up to 1.9 were obtained by controlling the sputtering power and the silane partial pressure. The crystal structures were found to be continuously transformed from Mo-rich silicides to Si-rich ones, including Mo_3Si , Mo_5Si_3 , and MoSi_2 , with increasing Si/Mo atomic ratio.

Studies toward the production of high density, high speed MOSLSI have explored the use of refractory metals such as Mo and W as gate and interconnection materials to replace conventional polysilicon (1-4). The refractory metals are much more conductive than polysilicon, and can withstand high temperature processing. However, these metals have poor resistance to the chemical reagents and oxidizing ambients used in MOS fabrication process, as compared with polysilicon (5, 6). This may limit the use of refractory metals. In order to overcome these disadvantages, the refractory metal silicides such as MoSi_2 and WSi_2 , have been examined because of their oxidation resistance (7-9). Several deposition techniques of the silicide films were used, including sputtering and coevaporation of the elements with a dual electron beam evaporation unit.

This paper presents a new deposition method for molybdenum silicide films whereby the films are deposited by reactive sputtering using silane as a reactive gas. This method can easily provide the silicide films, i.e., Mo_3Si , Mo_5Si_3 , and MoSi_2 , by adjusting sputtering conditions. The film properties are investigated by Auger electron analysis and x-ray analysis. The sputtering mechanism is also discussed, based upon these experimental results.

Experimental

The apparatus used is a magnetron-d-c-sputtering system (Varian S-Gun), as shown schematically in

Key words: molybdenum, magnetron sputtering, silane, crystal structure.

Fig. 1. Substrates are thermally oxidized silicon wafers of 3 in. diam and were mounted by spring clamps on a spherical rotating planetary substrate fixture. The Mo target is a 5 in. diam water-cooled circular conical

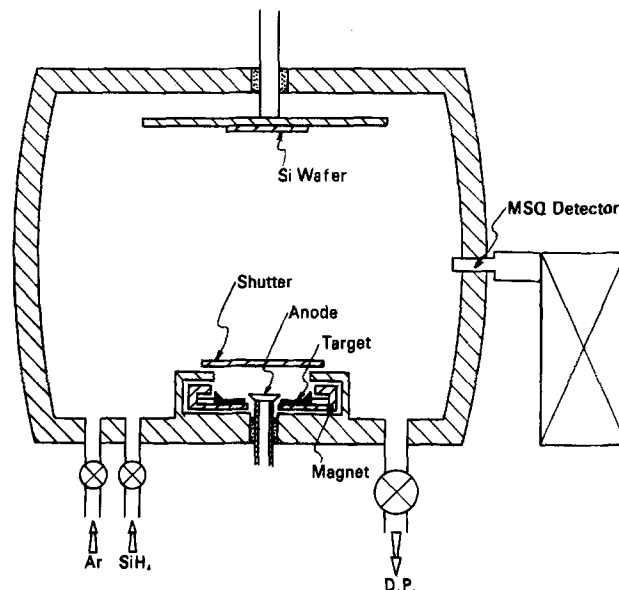


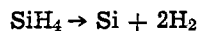
Fig. 1. Schematic diagram of the magnetron type d-c reactive sputtering apparatus.

cathode (99.99% pure). The system was pumped down to 2×10^{-6} Torr, and then backfilled to the sputtering pressure by introducing argon and silane. The substrates were preheated to about 200°C by radiation emitted from quartz lamp heaters. In this system, their heating during sputtering is negligible (10). Initially, the silane was admitted into the reaction chamber, followed by argon, until the total sputtering pressure reached 3×10^{-3} Torr. The silane partial pressure was varied up to 1.8×10^{-3} Torr. The film composition can be controlled by changing the silane partial pressure. Another method uses a mixture of argon and silane. In this case, the reproducibility of the film composition is superior to that of the first method. The sputtering pressure was measured by an ionization gauge within the high vacuum range prior to backfill. After backfill, a Schulz gauge which withstands corrosion in silane environments was used. After applying power, the sputtering pressure was found to rise higher than that before, indicating an increase of hydrogen due to the decomposition of silane in the argon plasma, as described later. During sputtering, a quartz crystal rate monitor was used to monitor the film thickness and the deposition rate. Since the change in frequency of the quartz crystal is dependent upon the density of the deposited film, the monitor was adjusted for each sputtering condition by which the film composition is determined. After deposition, the thickness was determined using Talystep. The nominal thickness of all the films deposited was 3000\AA . The deposition rate was found to be nearly constant under constant sputtering power, within the silane partial pressure range used.

The decomposed products of silane were detected by a quadrupole mass spectrometer. The detector was positioned sufficiently far from the discharge region, as shown schematically in Fig. 1, and was protected from direct impingement by the particles sputtered from the target. Therefore, the species detected are considered to include only the neutral gas species which diffuse from the discharge region. Auger electron spectroscopy was used together with Ar sputtering to investigate the relative amounts of Si incorporated within the films. The electrical resistivity of the films was determined by the usual four-point probe technique in conjunction with thickness measurements using Talystep. The crystal structure of the film was investigated by x-ray diffraction using Cu-K α radiation.

Results and Discussion

Sputtering procedure and film composition.—The sputtering power dependence of product species at an initial silane partial pressure of 6×10^{-4} Torr is shown in Fig. 2. The signals correspond to the ion currents in the mass spectrometer. The decomposition of silane is marked by a rise in the H_2 signal and a simultaneous fall in each of the Si, SiH_n ($n = 1$ to 4) signals. The initial Si and SiH_n signals could be attributed to the fragmentation of silane in the mass spectrometer ion source. The increase of molecular hydrogen H_2 as a decomposed product is consistent with the overall decomposition reaction



As seen in Fig. 2, as the sputtering power was increased, all signals varied by an order of magnitude and then became constant, indicating that most of the silane is decomposed at powers greater than 0.6 kW. Figure 3 shows in-depth profiles for Si and Mo in the deposited film of 3000\AA thickness. The profiles were measured by an Auger electron spectrometer. The sputtering power and the silane partial pressure were 2 kW and 1.2×10^{-3} Torr, respectively. Si was found to be uniformly distributed in the film. Si/Mo atomic ratios in the films, which were evaluated from the Auger electron signals, are plotted as a function of silane partial pressure for two levels of sputtering power, as shown in Fig. 4. The Si/Mo ratio was found

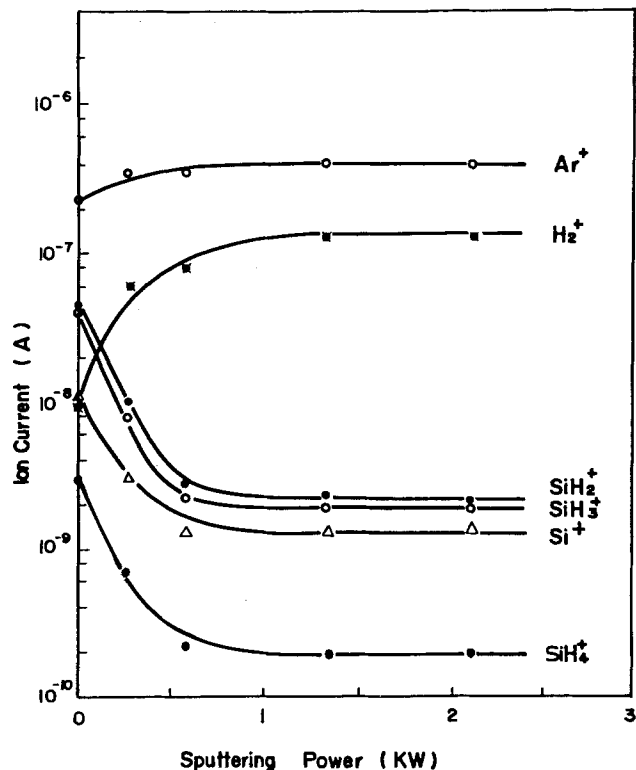


Fig. 2. Decomposed silane species as a function of sputtering power. Silane partial pressure is 6×10^{-4} Torr.

to increase superlinearly with the silane partial pressure and decrease inversely to the power.

In the magnetron sputtering system used here, most of the silane is decomposed within the intense argon plasma region which is sustained close to the target (10). The resulting Si atoms would be mostly adsorbed on a target surface (11). Because the substrate is positioned sufficiently far from the discharge region, it is improbable that Si atoms originating from the silane decomposed in the discharge region, would directly impinge on it. The main process for Si impinging on

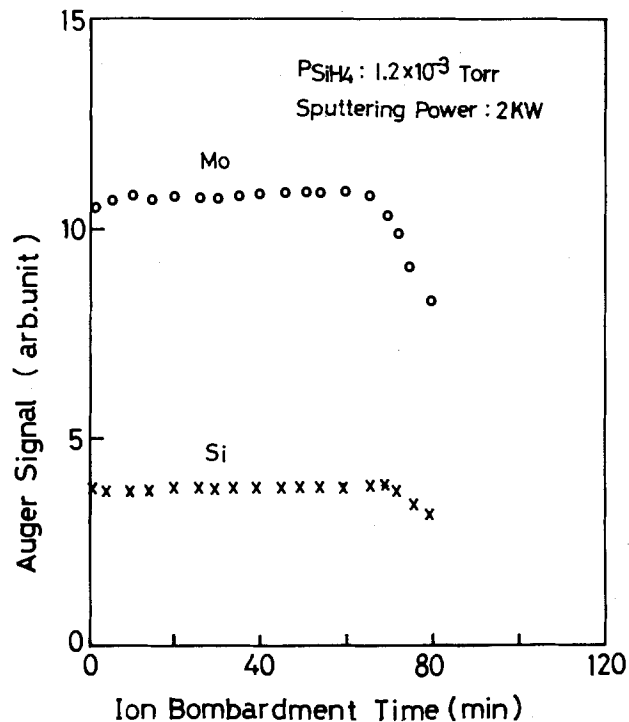


Fig. 3. In-depth profile of the deposited film measured by Auger electron analysis followed by Ar ion bombardment.

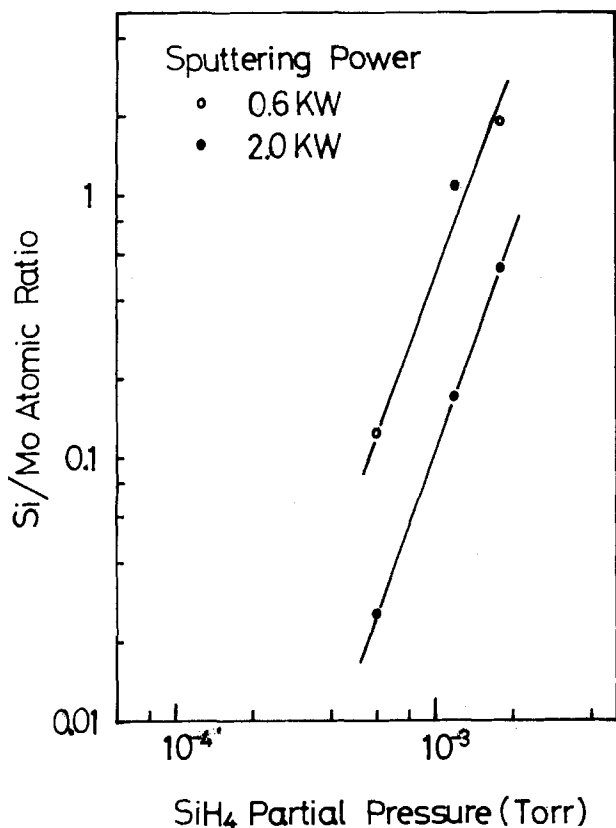


Fig. 4. Si/Mo atomic ratio of the film as a function of silane partial pressure using sputtering power as a parameter. The system pressure is 3×10^{-3} Torr.

the substrate may be the bombardment, by Ar ions, of a target surface which has adsorbed a layer of Si. From such an adsorption model, the influence of silane partial pressure on the film composition may be qualitatively understood as follows.

If the silane partial pressure is low enough that the surface coverage is much less than unity, the sputtering yield of the Mo target is little affected by the silane partial pressure. In this case, a linear dependence of the Si/Mo ratio on the silane partial pressure may be expected, because the surface coverage increases linearly with the silane partial pressure (11, 12). However, when the silane partial pressure becomes high enough that the surface coverage is comparable to unity, the sputtering yield of the Mo target is considerably reduced when the silane partial pressure is increased, and sputtering of the adsorbed layer increases. In this case, there may be a deviation from a linear dependence of the film composition on the silane partial pressure, as shown in Fig. 4. With respect to the effect of the sputtering power on the film composition, the amount of Mo deposited on a substrate increases linearly with the power, while that of Si is constant. This is because the decomposed silane species are invariant at powers greater than 0.6 kW, as shown in Fig. 2. As a result, the Si/Mo ratio is inversely proportional to the power (12).

The deposition rate has been known to decrease as the reactive gas partial pressure is increased, that is, if oxygen or nitrogen is used as the reactive gas (11, 13). This is believed to be due to the decrease of sputtering of the nitride or oxide layer synthesized on the target material. However, the deposition rate observed here was found to hold nearly constant when the silane partial pressure was varied. In order to investigate this discrepancy, the effect of reactive gas on the target current-voltage relationship was measured as shown in Fig. 5. Three different gases were used as the sputtering gases: pure argon for curve a, a silane-argon mixture for curve b, and a nitrogen-argon mixture for

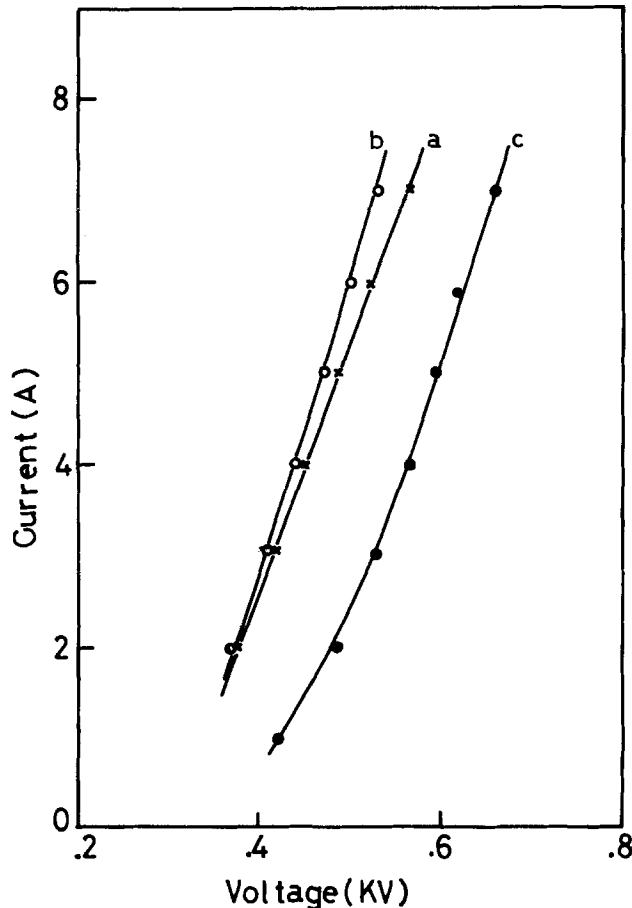


Fig. 5. Target current-voltage relationship for three different sputtering gases. Curve a, pure argon ($P_{Ar}: 1.8 \times 10^{-3}$ Torr); curve b, silane-argon mixture ($P_{SiH_4}: 1.2 \times 10^{-3}$ Torr, $P_{Ar}: 1.8 \times 10^{-3}$ Torr); curve c, nitrogen-argon mixture ($P_{N_2}: 1.2 \times 10^{-3}$ Torr, $P_{Ar}: 1.8 \times 10^{-3}$ Torr).

curve c. The current increased when silane was added to the pure argon sputtering gas, but decreased when nitrogen was added. This result suggests that electrons supplied by the decomposed silane remain within the discharge region, thereby contributing to ionizing collisions with argon gas molecules. Such a mechanism may result in an increase of the target current and thereby compensate the decrease of the sputtering of the adsorbed layer on the target surface. It appears that the decomposition of nitrogen gas does not supply electrons.

Crystal structure.—The crystal structures were investigated by x-ray diffraction. As-deposited films, except for the pure Mo film, were found to be amorphous and to change to a polycrystalline structure after heat-treatment. The continuous transformation from Mo-rich to Si-rich silicides, including Mo_3Si , Mo_5Si_3 , and $MoSi_2$, was observed as the Si/Mo ratio was increased up to 1.9. Figures 6(a)-(d) show x-ray diffractometer traces of films within the range $28^\circ \leq 2\theta \leq 51^\circ$, where each film was about 3000 Å thick. Films with various Si/Mo ratios were annealed in an N_2 atmosphere for 30 min at temperatures from 600° to 1200°C. For the film with a Si/Mo ratio of 0.17, as shown in Fig. 6(a), the Mo(110) reflection is the only detectable peak when the annealing temperatures were below 1000°C. Mo_3Si appears with the preferred reflection (210) at temperatures higher than 1000°C. The structure shows a mixture of Mo with Mo_3Si . In Fig. 6(b) for the Si/Mo ratio of 0.54, the Mo(110) reflection was not observed in any temperature range. The film was changed to single phase Mo_3Si with the preferred reflection (200) at temperatures over 800°C. Further addition of Si leads to mixtures of Mo_5Si_3 and $MoSi_2$ at temperatures over 800°C, as shown in Fig. 6(c). In Fig. 6(d)

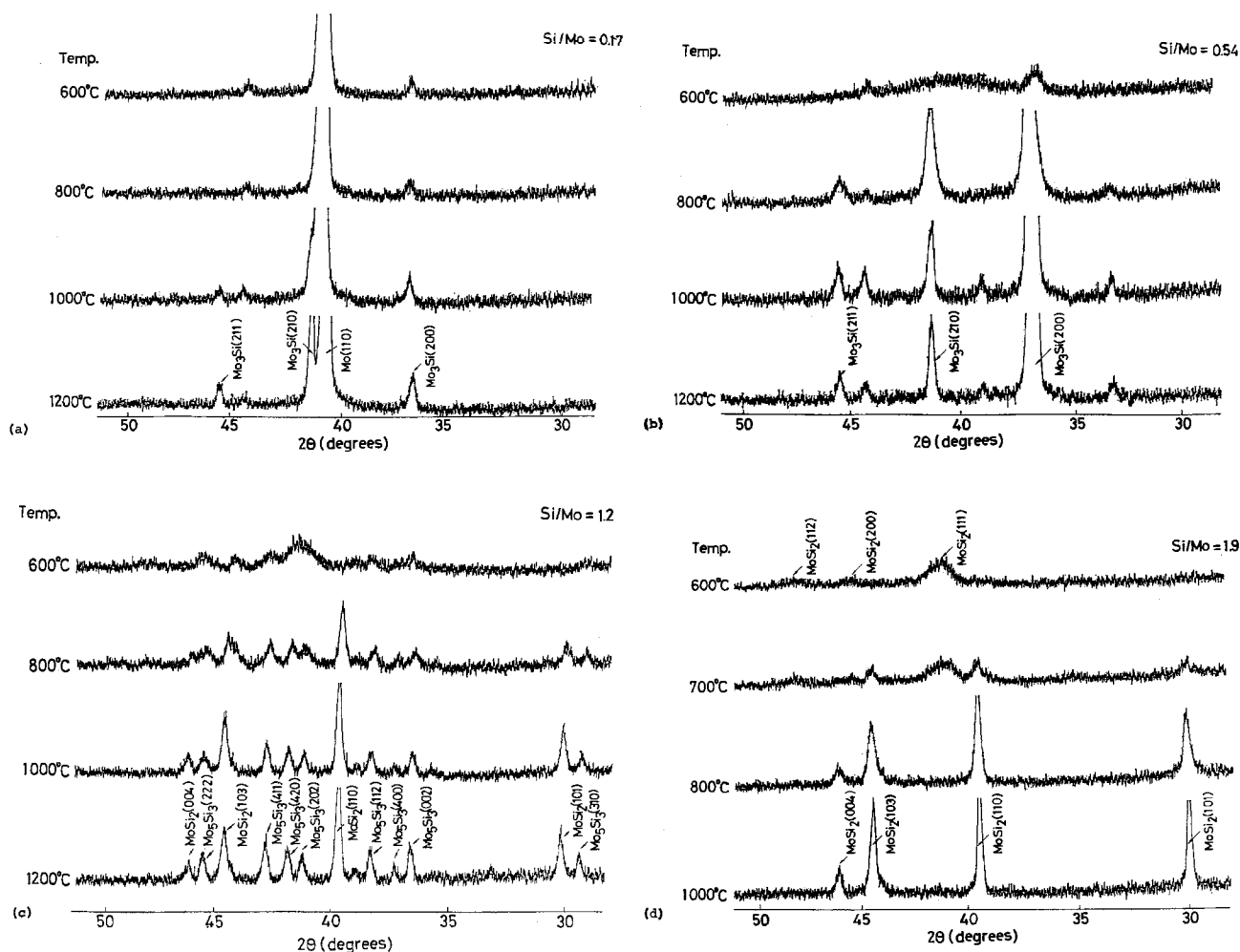


Fig. 6. X-ray diffractometer traces from the films annealed for 30 min at various temperatures. Si/Mo ratios of the films are (a) 0.17, (b) 0.54, (c) 1.2, (d) 1.9.

for the Si/Mo ratio of 1.9, the hexagonal MoSi_2 appears at 600°C, and is continuously transformed to the tetragonal MoSi_2 as the temperature is increased over 800°C.

Resistivity.—The effect of the Si/Mo atomic ratio on the film resistivity was evaluated as shown in Fig. 7. Each film thickness is about 3000 Å. The resistivity of the as-deposited films was quite high for a relatively large Si/Mo ratio. When the films were annealed for 30 min at 1000°C in N_2 atmosphere, a significant decrease in resistivity is observed for films with larger Si/Mo ratios. The amount of hydrogen incorporated within the film during sputtering results in an additional increase in as-deposited film resistivity. This hydrogen may be removed by high temperature annealing (14). This may cause a significant decrease in resistivity as a function of the annealing temperature for the larger Si/Mo ratio films. Furthermore, as shown by x-ray analysis, the recrystallization temperatures differ from each other depending upon the film composition. This also may explain the differences in temperature dependence of resistivity among the films having the various Si/Mo ratios.

Conclusion

Molybdenum silicide films were prepared by magnetron-d-c-reactive sputtering within an argon-silane atmosphere. Most of the silane is decomposed within the intense argon plasma close to the target, resulting in the silicon being adsorbed on the target surface. The silicon within the film is considered to originate from the adsorbed Si layer on the target surface. This mechanism is qualitatively consistent with the measured results concerning dependence of the Si/Mo

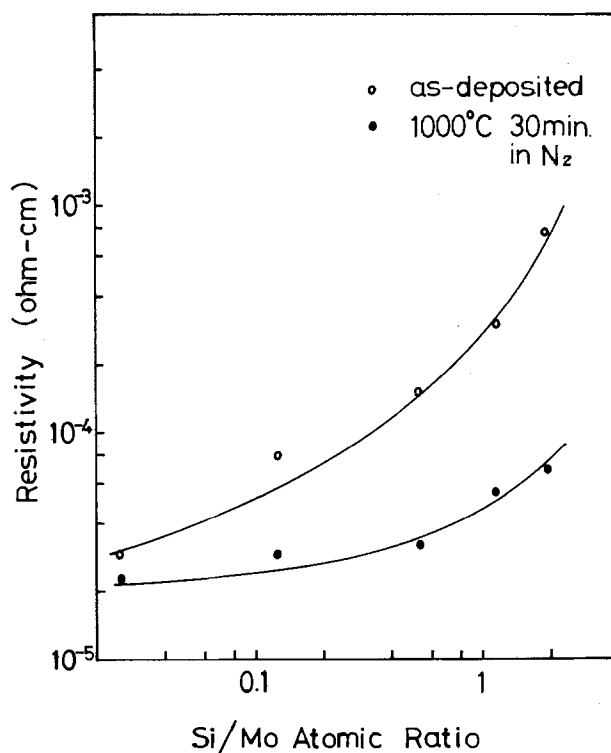


Fig. 7. Resistivity as a function of Si/Mo ratio for the as-deposited films and the films annealed for 30 min at 1000°C in N_2 atmosphere.

atomic ratio of the film upon the sputtering parameters. Corresponding to the Si/Mo ratio, the various silicide structures such as Mo_3Si , Mo_5Si_3 , and MoSi_2 were observed by using x-ray analysis. The crystal structures were found to be continuously transformed from Mo-rich to Si-rich silicides, as the Si/Mo atomic ratio was increased. This result enables us to obtain the various silicides by controlling the sputtering power and the silane partial pressure. The reactive sputtering technique reported here may be applicable for the preparation of other metal silicide films as well.

Acknowledgments

The authors wish to thank Drs. Y. Tarui and T. Oku for their encouragement.

Manuscript submitted Sept. 4, 1979; revised manuscript received Dec. 14, 1979.

Any discussion of this paper will appear in a Discussion Section to be published in the December 1980 JOURNAL. All discussions for the December 1980 Discussion Section should be submitted by Aug. 1, 1980.

Publication costs of this article were assisted by VLSI Technology Research Association.

REFERENCES

1. W. E. Engeler and D. M. Brown, *IEEE Trans. Electron Devices*, **ed-19**, 54 (1972).
2. M. Kondo, T. Mano, F. Yanagawa, H. Kikuchi, T. Amazawa, K. Kikuchi, N. Ieda, and H. Yoshimura, *IEEE J. Solid-State Circuits*, **sc-13**, 611 (1978).
3. T. Ohgishi, A. Doi, T. Akiyama, and N. Enomoto, *ibid.*, **sc-13**, 555 (1978).
4. P. L. Shah, *IEEE Trans. Electron Devices*, **ed-26**, 631 (1979).
5. L. H. Lee and V. Y. Doo, *This Journal*, **118**, 443 (1971).
6. J. A. Cunningham, C. R. Fuller, and C. T. Hayward, *IEEE Trans. Reliab.*, **r-19**, 182 (1970).
7. B. L. Cowder and S. Zirinsky, *IEEE J. Solid-State Circuits*, **sc-14**, 291 (1979).
8. T. Mochizuki, K. Shibata, T. Inoue, and K. Ohuchi, *Jpn. J. Appl. Phys. Suppl.*, **17-1**, 37 (1978).
9. T. Mochizuki and M. Kashiwagi, Abstract 201 presented at The Electrochemical Society Meeting, Pittsburgh, Pennsylvania, Oct. 15-20, 1978.
10. V. Hoffman, *Solid State Technol.*, p. 57 (Dec. 1976).
11. J. Hrbek, *Thin Solid Films*, **42**, 185 (1977).
12. T. Fukuyama and S. Yanagisawa, *Jpn. J. Appl. Phys.*, **18**, 987 (1979).
13. K. Wasa and S. Hayakawa, *Thin Solid Films*, **52**, 31 (1978).
14. T. Abe, T. Sasaki, and T. Yamashina, *Shinku*, **22**, 56 (1979) (in Japanese).

Interdiffusion Studies of Au/Ni and Au/Ni-P

A. van Wijngaarden, M. Schlesinger,* N. E. Hedgecock, and B. K. W. Baylis

Department of Physics, University of Windsor, Windsor, Ontario, Canada N9B 3P4

ABSTRACT

A comparative study is presented of the interdiffusion properties of Au/Ni and Au/Ni-P. Anomalous diffusion of gold through nickel is described. It is concluded that electrolessly deposited nickel (Ni-P) could be used to inhibit substrate contamination by gold contacts.

In a recent article (1) we described the use of proton backscattering to determine the surface concentration of palladium present on a catalyzed glass slide. Proton backscattering can also be used to determine concentrations at different depths (2) and can, therefore, be used to follow diffusion of one thin film into another. Nickel is often used as a diffusion barrier between integrated circuitry and gold contacts, for example, see Ref. (3). Therefore, diffusion of Au into Ni and Ni-P, as well as the diffusion of Ni from Ni and Ni-P into Au, was studied. Because Au, Ni, and P are very different in atomic number, the proton backscattering peaks are sufficiently separated to allow the identification of contributions to the spectrum from these three elements at various depths. Unfortunately, the interdiffusion of Ni and Cu cannot be studied by proton backscattering because Cu and Ni are too close in atomic number.

Backscatter techniques, especially involving MeV He^+ projectiles, have been used to study interdiffusion of vacuum-evaporated thin films. For examples involving Ni/Au interdiffusion, see Ref. (4-5). The films studied in this work include Ni-P deposited from an electroless plating bath. Although the attendant impurities complicate the interpretation of the diffusion results, these films should nonetheless be studied because they are used industrially and have particular characteristics that make them preferable to vacuum-deposited films for certain applications. Empirical dif-

fusion data should be helpful, even if the theory on diffusion involving highly disordered or amorphous films is not sufficiently well developed (6) to allow any detailed interpretation.

In the present study keV protons were used to determine surface and near-surface concentrations of diffused matter. Furthermore, the phosphorus concentration in the Ni-P deposited from our pH 5.3 solution (7) was determined, and good agreement was found with results obtained by other methods (8).

Apparatus and Experimental Procedure

Sample preparation.—Thin Ni-P films were deposited electrolessly on quartz substrates using the conventional sensitizing and activating catalytic process in conjunction with a pH = 5.3 nickel metallizing bath, as described by Marton and Schlesinger (7). For comparison pure Ni films were also vacuum deposited on quartz. The vacuum facility used for metal deposition and for heat-treatment was liquid- N_2 baffled, and the pressure in the system was brought to 1×10^{-6} Torr prior to either film deposition or heat-treatment. Both Ni-P and Ni samples were then coated with thin Au films, subjected to proton backscatter analysis, heated under vacuum to around 650°K, and reanalyzed.

In order to assure identical heat-treatment procedures, samples were made with both Ni and Ni-P on the same quartz slide. First, the entire surface of the slide was metallized in a Ni-P bath. A layer of Ni was evaporated on a part of the Ni-P covered surface, then the whole surface was coated with a thin layer

* Electrochemical Society Active Member.

Key words: diffusion, diffusion barrier, electroless nickel, backscatter.

of gold. Therefore, the gold layer thickness on the Ni and Ni-P films was the same. This thickness was controlled during evaporation by monitoring the decrease in electrical resistance as the gold film was built up. This, however, proved to be only partially reliable as we found that the resistance is a function of not only the instantaneous film thickness, but also of the deposition rate. If deposition is rapid, the film contains more vacancies than if it is slow. After the cessation of film deposition a further decrease in resistance is observed as vacancies diffuse from the bulk to the surface, improving film continuity. Similar effects in gold were observed by others (9). It should be noted that no such effect was observed after deposition of nickel films; i.e., once deposited their resistance remained constant.

Heat-treatment.—The samples were heated in a vacuum of 10^{-6} Torr inside a thick-walled cylindrical copper furnace. This form was chosen to assure a uniform temperature throughout the sample. It proved important to control not only the length of time the sample was at the elevated temperature, but also the lengths of time needed for raising and lowering the temperature of the sample. About an hour was needed to raise the temperature to 650°K . (Heat-treatments were performed at temperatures of from 615° to 723°K , see Table I.) The temperature inside the furnace was maintained for various lengths of time (2–24 hr) and then the samples were allowed to cool under vacuum. About an hour was required for cooling to a temperature of about 500°K . The samples were nonetheless left in vacuum until they had cooled to room temperature, a process which took several hours. This was necessary to prevent any possible reactions in air, for example, oxidation of Ni.

Proton backscattering.—The detailed setups (Fig. 1) for the proton backscattering experiments have been described previously (2). Some modifications have been introduced to improve the solid angle of observation and to eliminate errors arising from ion beam fluctuations. Briefly, the magnetically analyzed beam of protons has fixed energy to within one part in 700 of about 90 keV.

We use in our experiments a beam current density of 5×10^{-5} A/cm². Thin film targets are mounted in an evacuated system which is made entirely free of pump oil vapors. The target film is scanned by moving it across the path of the proton beam. The energy distribution spectrum of protons scattered through a laboratory angle of $\theta_L = 154^{\circ}$ is analyzed with a cylindrical electrostatic field sector of $\pi/2$ radians with radius $r = 19.05$ cm. The widths of the entrance and exit slits (S_1 and S_2 , respectively, in Fig. 1) are set

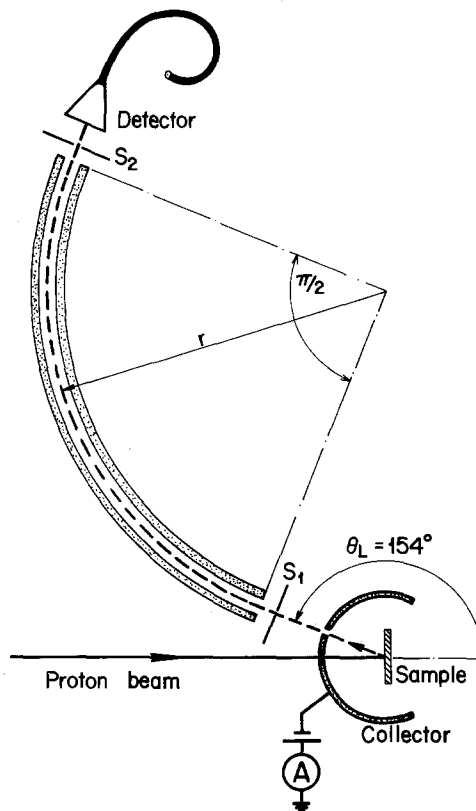


Fig. 1. A schematic diagram of the backscatter apparatus (see text).

with a view to achieving an energy resolving power R sufficient for a surface depth resolution of about 10\AA in either Au or Ni. The energy resolving power is given by

$$R = \frac{E}{\delta E} = \frac{r}{(S_1 + S_2)} = 175 \quad [1]$$

The channeltron detector is used in conjunction with standard counting equipment and the resulting counts are electronically normalized to a constant beam current. This is done (10) by monitoring the total backscatter current yield on the collector, which in turn is connected to a current to frequency (C to F) converter. The C to F converted signals serve as the time standard for the length of the counting periods. Information about the atomic composition of the surface region is obtained from the analysis of the energy distribution spectrum of the backscattered projectiles. A thorough analysis of backscattering from thin films, especially as applied to He^+ projectiles, is given in Ref. (11).

The disadvantage of depth profiling by protons, rather than by He^+ ions, is that the mass resolution is small due to the correspondingly small recoil energy of the target atom. At energies below 100 keV, however, we found that the straggling in the energy loss with He^+ is appreciably larger [see for example Ref. (11), section 2.6] than for protons. At these energies it is only with protons that the desired depth resolution of 10\AA can be achieved.

Results and Discussion

Phosphorus concentration in Ni-P films.—Thin Ni-P films plated from an acidic solution were analyzed for P content. A typical backscatter energy distribution for a film of 1100\AA thickness bombarded by a proton beam of 90.72 keV is shown in Fig. 2. The backscatter yield on the high energy end of the curve on Fig. 2 is due to Ni atoms; the step at 80 keV is due to P atoms at the surface; and the yield below 57 keV arises from scattering off the substrate.

Table I. Relative Ni surface concentration after diffusion through Au

x_0^* (\AA)	Time (hr)	T ($^{\circ}\text{K}$)				Ratios Ni-P/Ni
		615	623	675	723	
182	22.5		0.13 [†] 0.09			1.4
192	5			0.11 [†] 0.06		1.7
235	2				0.15 [†] 0.10	1.5
244	24	0.10 [†] 0.06				1.7 1.5
254	4.75			0.14 [†] 0.10		1.4
320	2				0.14 [†] 0.09	1.5
520	3				0.13 [†] 0.08	1.6 1.4

* Gold film thickness.

[†] Values with a dagger refer to the diffusion of Ni through Au from an Ni-P medium. Those without a dagger refer to the diffusion of Ni through Au from a pure Ni medium.

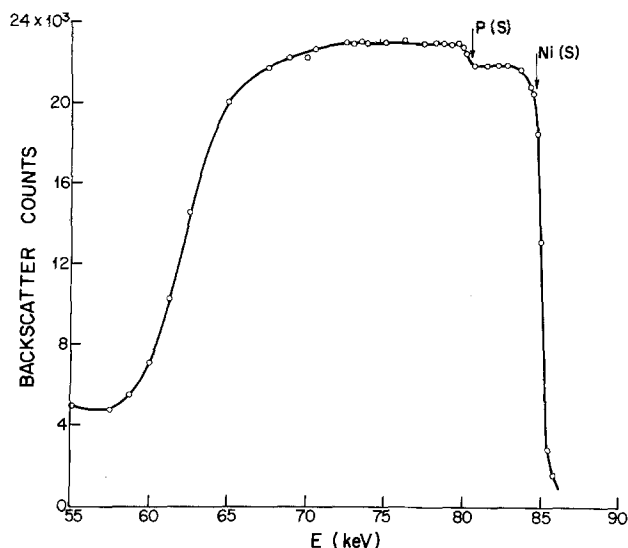


Fig. 2. The energy distribution of 90.7 keV protons backscattered off an Au/Ni film system. (a) Before heating (dotted curve); Ni film with an (S).

Since the backscatter yield, B , from a given atomic species is proportional to the square of its atomic number, Z , the atomic phosphorus concentration is

$$C_p = \frac{B_p/Z_p^2}{\frac{B_{Ni}}{Z_{Ni}^2} + \frac{B_p}{Z_p^2}} \times 100\% \quad [2]$$

The average C_p for several samples was $15.1 \pm 0.7\%$. This value is in agreement with Marton (8) who obtained, for Ni-P films grown under the same conditions, a value $C_p = 16.6 \pm 0.8\%$ from neutron activation analysis. The stopping cross section needed to calculate the film thickness from the observed energy loss data was estimated using the cross-section tabulation by Andersen (12).

Au/Ni film system.—The energy distribution spectrum of backscattered protons from a double layer Au/Ni thin film is shown by the dashed curve in Fig. 3. The sample consists of a 170Å thick Au film vacuum deposited onto a 455Å thick Ni film, itself vacuum deposited onto a quartz substrate. The solid curve represents the backscatter energy distribution spectrum after heat-treatment for 8 hr at 748°K in a vacuum of 10^{-6} Torr. Only minor changes were noted upon completion of a further 8 hr long heat-treatment: the Au concentration near the substrate increased slightly at the expense of the surface gold concentration, while

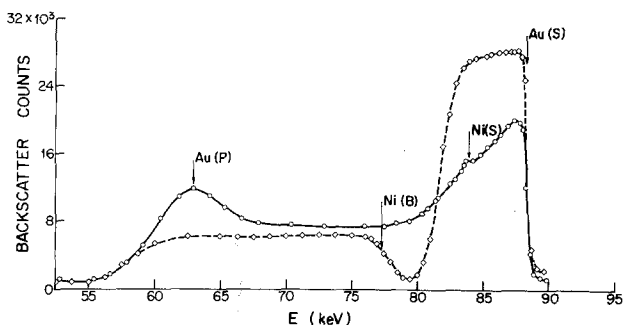


Fig. 3. The energy distribution of 90.2 keV protons backscattered off an Au/Ni film system. (a) Before heating (dotted curve); Ni film 455Å thick; Au film 170Å. (b) After heat-treatment for 8 hr at 748°K (solid curve). (S) refers to surface atoms; (B) refers to atoms immediately beneath the Au layer; and (P) refers to atoms that have penetrated through the Ni layer to the quartz.

the shoulder representing nickel at the surface developed into a small peak.

Figure 3 illustrates the tendency of Au to diffuse through the Ni layer rather than to remain dissolved in it. This behavior can readily be explained by considering the miscibility gap in the Au/Ni phase diagram (13). During cooling, the reduced solubility of Au in Ni (and vice versa) causes these elements to separate out into layers.

A sample with an 810Å thick Ni film and a slightly thinner Au film was treated in the same way. After 5 hr at 730°K the backscatter energy spectrum shown in Fig. 4 was obtained. In this case, the buildup of Au at the substrate is even more pronounced and very little Au remains at the surface. This anomalous behavior would be understood if a "sink" for Au were present at the substrate surface or a "sink" for Ni at the sample surface. [See Ref. (4, 5, 14) for examples of "sinks."] Au does not react with or dissolve in quartz: heating samples of gold on quartz did not give any broadening of the backscatter curve, indicating that the Au does not diffuse into the quartz. It is possible that the small quantity of oxygen present during heat-treatment could react with the Ni arriving at the surface, creating a Ni sink. Certainly if samples were still warm (about 470°K) when brought into contact with air, the Ni film was observed to boil up to the surface.

In some samples (see Fig. 4), the Ni plateau in the backscattering spectrum showed small irregular peaks and valleys. This was especially noticeable in a few samples which were rapidly cooled after annealing by admitting Ar gas into the vacuum chamber. This effect was not very reproducible, and it probably is due to the precipitation of gold in the nickel layer, arising from the large miscibility gap in the Au/Ni system. Similar effects have been observed in Au/Ni in an x-ray study (15) and a surface diffusion study (16). It is possible that the phenomenon is related to spinodal decomposition. [See Ref. (13) for a description of spinodal decomposition.] These features of the backscatter spectrum could be explained if there were a tendency for the islands of gold to accumulate in layers about 200Å apart in the nickel. In this work, only variations in the concentration gradients at different depths can in principle be seen. The large size of the beam (1 mm²) prevents the measurement of possible concentration gradients in the plane of the film.

Diffusion between Au and Ni-P.—The backscatter energy spectrum after heat-treatment of a composite film where Ni-P replaced Ni, did not show this anomalous

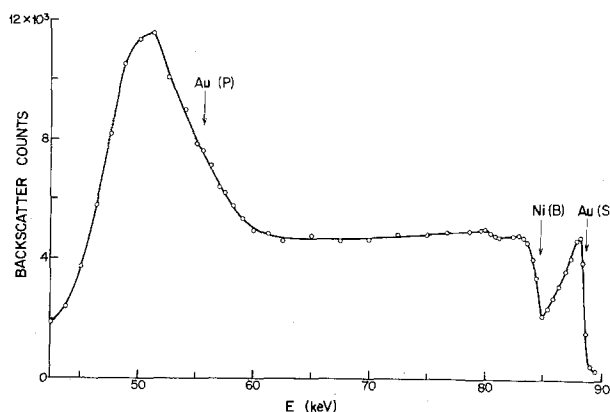


Fig. 4. The energy distribution of 90.2 keV protons backscattered off an Au/Ni film system after heat-treatment at 730°K for 5 hr. The initial Ni film thickness was 810Å; the Au film thickness was slightly less than 170Å. (S) refers to surface atoms; (B) refers to atoms immediately beneath the Au layer, and (P) refers to atoms that have penetrated through the Ni layer to the quartz.

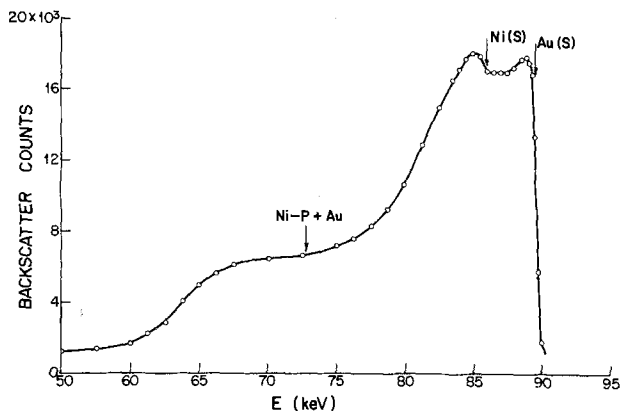


Fig. 5. A representative energy distribution curve of 91.3 keV protons backscattered off an Au/Ni-P film system after heat-treatment to 748°K for 5 hr. Initial Au film thickness was 138Å. (S) refers to surface atoms.

lous migration. The results for a 138Å thick Au film on Ni-P are shown in Fig. 5. It appears in this case that "normal" diffusion has occurred: Au into the Ni-P layer and Ni into the Au layer. Although many samples with Au on Ni-P were heat-treated none showed the anomalous behavior reported above. In fact, for samples in which the Ni was evaporated onto a Ni-P layer rather than directly onto quartz, the Au layer diffused into the Ni layer but showed no tendency to accumulate at either the Ni/Ni-P interface or the Ni-P/quartz interface. Hence, Au appears to diffuse "normally" through Ni-P, with the establishment of a concentration gradient. This suggests that the ternary Au-Ni-P system may lack a miscibility gap. Nonetheless, from a purely practical point of view, this behavior indicates that Ni-P is a better barrier with respect to penetration by Au than Ni is.

Interpretation of these observations is complicated by the fact that during the heat-treatment used to study the diffusion process, a change in the Ni-P structure also occurs. Above 590°K, the initially amorphous Ni-P transforms into a two-component system of Ni and Ni₃P, with small amounts of free P (17). Hence, any discussion of a detailed diffusion mechanism becomes highly speculative.

Ni/Au interdiffusion.—Samples were prepared consisting of quartz covered with Ni-P, then half-covered with evaporated Ni. The whole sample was then covered with Au and analyzed before and after heat-treatment. (See section on Sample preparation for details.) Figures 6 and 7 show the backscatter energy spectra for such a sample; in Fig. 6 the Au is on Ni

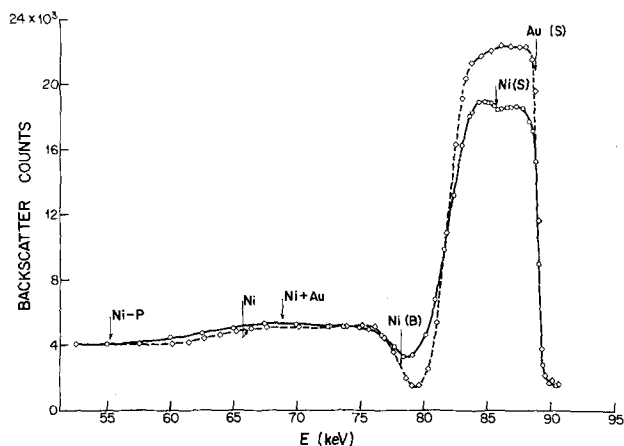


Fig. 6. The energy distribution of protons backscattered off an Au/Ni film system. (a) Before heating (dotted curve); Au film thickness was 182Å. (b) After heat-treatment for 22.5 hr at 623°K (solid curve). (S) refers to surface atoms.

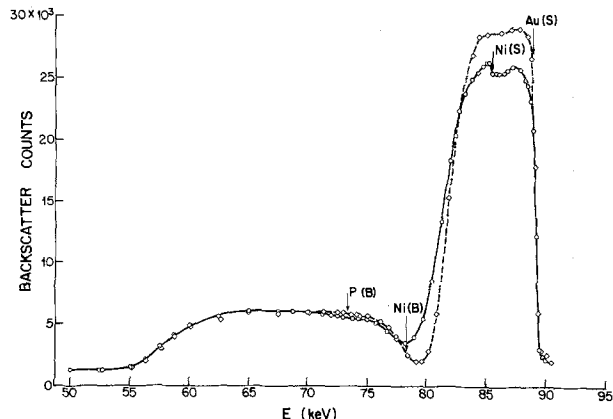


Fig. 7. The energy distribution of protons backscattered off an Au/Ni-P film system. (a) Before heating (dotted curve); Au film thickness was 182Å. (b) After heat-treatment for 22.5 hr at 623°K (solid curve). (S) refers to surface atoms; (B) refers to atoms immediately beneath the Au layer.

(which is on Ni-P); in Fig. 7 the Au is directly on Ni-P. It can be seen on Fig. 6 that the backscatter yield decreases as the projectiles pass from Ni into Ni-P. This is a result of the fact that in the Ni-P medium the concentration of the heavier Ni atoms is lower than in the pure Ni medium. The phosphorus "step" on the Ni-P plateau in Fig. 7 is not very well defined as a result of energy straggling of the protons having passed through the Au film twice.

As noted in the section on Diffusion between Au and Ni-P, the small peaks at 85 keV in Fig. 6 and 7 represent Ni that has migrated to the surface of the Au. The heights of these peaks above the Au baseline were measured for several samples. The ratios of the peak height to the plateau height of the main Ni layers are recorded in Table I. These ratios represent the surface density of diffused Ni relative to that for a pure Ni surface. The plateau heights used for the main Ni-P layers have been adjusted to account for the fact that these layers contain only 85% Ni.

It can be seen from Table I that Ni migrates into Au from Ni-P more readily than from Ni. The ratio between the amount of diffused Ni from Ni-P vs. from Ni remains 1.5 ± 0.2 , independent of temperature, heating time, and film thickness. This behavior might be attributable to the influence on grain boundary diffusion by differences in structure between Ni and Ni-P. Furthermore, the structure of the Au layer deposited on polycrystalline Ni might well differ from that of Au deposited on amorphous Ni-P. However, the equipment for properly determining structures of films of these thicknesses being unavailable to us, no determinations of grain sizes, etc., could be made.

The amount of Au diffusing into the Ni (or Ni-P) films can, in principle, be estimated by comparing the backscatter spectra before and after heating. The valley in the spectrum between the Au and Ni peaks fills in as gold travels into the Ni layer. This region of the curve cannot be unfolded unequivocally, but a rough estimate of the amount of Au in the Ni layer could be made. This amount of Au was only about one-fifth as much as the amount of Ni that had traveled into the Au layer. This is in agreement with data for the Au-Ni system obtained by Ziegler (4). It is also consistent with our previously mentioned resistivity data, which show that freshly deposited Au has more vacancies than Ni.

Summary

From the above analyses of the effect of heat-treatment on Au/Ni and Au/Ni-P interdiffusion, the following observations can be made.

1. If the conditions of heat-treatment in vacuum are the same for both samples, the amount of Ni diffusing from a Ni-P film into an Au film is 1.5 ± 0.2 times that

diffusing from a vacuum-evaporated Ni film. Various conditions were studied: temperature, from 615° to 732°K; times of heat-treatment, from 2 to 24 hr; and Au film thickness, 182-520Å.

2. Roughly five times more Ni atoms diffuse into Au than Au atoms diffuse into Ni.

3. If the sample is not allowed to cool very slowly under vacuum, the gold may leave the Ni surface and accumulate at the Ni/quartz interface. The phenomenon is only observed with Ni; never with Ni-P or with Ni on Ni-P.

4. Observation 3 suggests that Ni-P is useful in preventing contamination of a substrate by a gold contact.

Acknowledgments

It is a pleasure to acknowledge the skillful technical assistance of Mr. Tim Scholl and very useful discussions with Dr. W. E. Baylis and G. W. F. Drake of our Department, and Dr. D. F. Watt of the Engineering Materials Department. This research was supported by the Natural Sciences and Engineering Research Council of Canada.

Manuscript submitted June 27, 1979; revised manuscript received Nov. 26, 1979.

Any discussion of this paper will appear in a Discussion Section to be published in the December 1980 JOURNAL. All discussions for the December 1980 Discussion Section should be submitted by Aug. 1, 1980.

Publication costs of this article were assisted by the University of Windsor.

REFERENCES

1. B. K. W. Baylis, N. E. Hedgecock, M. Schlesinger, and A. van Wijngaarden, *This Journal*, **126**, 1671 (1979).
2. A. van Wijngaarden, B. Miremadi, and W. E. Baylis, *Can. J. Phys.*, **49**, 2440 (1971).

3. M. R. Pinnel and J. E. Bennett, *Met. Trans.*, **7A**, 629 (1976).
4. J. F. Ziegler, J. E. E. Baglin, and A. Gangulee, *Appl. Phys. Lett.*, **24**, 36 (1974).
5. A. Barcz, A. Turos, and L. Wielunski, in "Ion Beam Surface Layer Analysis," O. Meyer, G. Linker, and F. Käppeler, Editors, p. 407, Plenum Press, New York (1976).
6. J. E. E. Baglin and J. M. Poate, in "Thin Films-Interdiffusion and Reactions," J. M. Poate, K. N. Tu, and J. W. Mayer, Editors, p. 307, Wiley-Interscience, New York and Toronto (1978).
7. J. P. Marton and M. Schlesinger, *This Journal*, **115**, 16 (1968).
8. J. P. Marton, Ph.D. Thesis, University of Western Ontario, 1968.
9. J. R. Lloyd and S. Nakahara, *This Journal*, **125**, 2037 (1978).
10. A. van Wijngaarden, B. Miremadi, and E. J. Brimmer, *Can. J. Phys.*, **48**, 1026 (1970).
11. W. K. Chu, J. W. Mayer, and M. A. Nicolet, "Backscattering Spectrometry," Academic Press, New York (1978).
12. H. H. Anderson, "Experimental Range and Stopping Power Data," Vol. 2, Bibliography and Index, Pergamon Press (1977).
13. P. G. Shewmon, "Transformation in Metals," pp. 292-299, McGraw-Hill Book Co., New York (1969).
14. H. G. Tompkins and M. R. Pinnel, *J. Appl. Phys.*, **47**, 3804 (1976); C. C. Chang, S. P. Muraska, V. Mumar, and G. Quintana, *ibid.*, **46**, 4237 (1975).
15. J. L. Richards and W. H. McCann, *J. Vac. Sci. Technol.*, **6**, 644 (1969).
16. T. Nenadovic, B. Perovic, M. Adamov, and B. Meckel, *Thin Solid Films*, **25**, 515 (1975).
17. A. H. Graham, R. W. Lindsay, and H. J. Read, *This Journal*, **112**, 401 (1965); M. Schlesinger and J. P. Marton, *J. Phys. Chem. Solids*, **29**, 188 (1968).

Characterization of Thin Film Molybdenum Silicide Oxide

T. Mochizuki and M. Kashiwagi

NEC-Toshiba Information Systems Incorporated, 72, Horikawa-cho, Saiwai-ku, Kawasaki, Japan 210

ABSTRACT

Dielectric properties and growth kinetics of oxide film of molybdenum silicide (MoSi_2) on SiO_2 have been investigated. The oxide of MoSi_2 is composed of SiO_2 , and the oxidation rate of MoSi_2 is described by the same general relationship as of the crystalline silicon. The molybdenum in MoSi_2 is partly vaporized through the oxide and is partly piled up at the oxide- MoSi_2 interface during oxidation. The ratio of MoSi_2 thickness to corresponding thickness of oxide produced from MoSi_2 decreases from 0.48 to 0.3 with increasing oxide thickness due to increasing piled-up molybdenum. The dielectric constant and the dielectric breakdown strength of MoSi_2 -oxide are very close to those of n^+ -poly-Si oxide. The MoSi_2 oxide shows the self-healing breakdown, more frequently than the n^+ -poly-Si oxide, which is due to the interface roughness induced by the pile-up of molybdenum. The dielectric breakdown strength is improved at higher oxidation temperatures.

In very large scale integrated circuits (VLSI) the electrical conductivity of poly-crystalline silicon (poly-Si) for interconnection and gate electrode ($\sim 10^{-3} \Omega\text{-cm}$) is one of the major limitations on circuit performance. Studies of refractory metals having low resistivity of $\sim 10^{-5} \Omega\text{-cm}$, such as tungsten (W) and molybdenum (Mo), have been made to replace poly-Si (1-3). However, they frequently show poor abilities to withstand chemical reagents and oxidizing

Key words: molybdenum silicide, gate electrode, oxidation, oxide.

ambients especially at high temperatures. An alternative approach is to utilize refractory metal silicides such as MoSi_2 and WSi_2 , which also show relatively low resistivity ($\sim 10^{-4} \Omega\text{-cm}$) and good abilities to withstand chemical reagents (4, 5). For the application to VLSI's, it is generally required to cover the electrode with its own oxide layer for better stability and controllability as in the case of silicon gate technology. MoSi_2 and WSi_2 exactly meet this requirement. Therefore, the studies of oxidation mechanism of the silicides and dielectric properties of the oxide are of

practical importance to establish the silicide process as one of the VLSI technologies.

Since the earlier works of molybdenum silicide oxidation, it has been recognized that the high oxidation resistance of MoSi_2 is due to the protective silicon dioxide layer formation (6). The oxidation products of molybdenum silicides have been comprehensively investigated by Berkowitz-Mattuck *et al.* (7). The kinetics of MoSi_2 has been discussed by Chang where the oxidation follows the parabolic law (8). However, the interest of previous works stayed in the refractory behavior relating to heater coating material for resistance furnace. Therefore, the detailed oxidation mechanism and the grown oxide properties of the refractory metal silicide have not been carried out yet.

More recently, studies on the oxidation of WSi_2 and MoSi_2 as gate electrodes of MOS devices have been reported. (9, 10). The authors have briefly reported the oxidation kinetics of MoSi_2 film and the dielectric properties of the oxide grown on MoSi_2 previously (10). In this paper, the thermal oxidation kinetics of MoSi_2 film and microscopic oxide- MoSi_2 interface morphology are described in detail, and the oxide formed on MoSi_2 is proved to have good dielectric properties.

Experimental Procedures

Molybdenum silicide films were deposited on oxidized Si wafers by means of planar magnetron type d-c sputtering at the power of 700W. The MoSi_2 film thickness was approximately 3000Å. The oxidation was carried out in dry oxygen (dry O_2) ambients at 900°, 1000°, and 1100°C. The oxide thickness on MoSi_2 was measured by Talystep after the oxide was selectively removed by buffered or diluted HF. Silicon nitride films were employed as oxidation masks for selective molybdenum silicide oxidation. The composition of molybdenum silicide or the oxide formed on the surface, and microscopic oxide-silicide interface or oxide surface morphologies were investigated with Auger electron spectroscopy (AES), scanning electron microscopy (SEM), and transmission electron microscopy (TEM).

Diodes with the structure of $\text{Al}/\text{SiO}_2/\text{MoSi}_2$ were fabricated in order to evaluate the leakage current and dielectric breakdown strength of the oxide formed by the oxidation of MoSi_2 which will be called as MoSi_2 -oxide in the remainder of this paper. The upper aluminum electrodes were successively deposited on MoSi_2 -oxide by electron beam evaporator. The oxide and aluminum were measured approximately a thickness of 1100 and 2000Å, respectively. The aluminum electrodes of 640 $\mu\text{m}\phi$, were patterned by the usual photolithography. The diodes were annealed for 30 min in forming gas at 450°C.

The phosphorus-doped polycrystalline silicon (n^+ -poly-Si), as a reference, was employed in order to compare with the oxidation behavior and dielectric properties of the MoSi_2 -oxide.

Experimental Results

The oxidation of MoSi_2 .—Oxidation rate.—The thermal oxidation of MoSi_2 , as is described above, results in the silicon dioxide (SiO_2) formation on the MoSi_2 surface. Figure 1 shows the thickness of MoSi_2 -oxide vs. oxidation time in dry oxygen at 900°, 1000°, and 1100°C. As references, results from (100) crystalline silicon and phosphorus-doped poly-Si are illustrated by broken lines. The oxidation rates of MoSi_2 -oxide are similar to the rate of single crystalline silicon. Therefore, the general relationship for silicon oxidation, given by

$$\text{Xo}^2 + \text{AXo} = \text{B}(t + \tau) \quad [1-A]$$

or

$$\text{Xo}/\text{A}/2 = \sqrt{1 + \frac{t + \tau}{\text{A}^2/4\text{B}}} - 1 \quad [1-B]$$

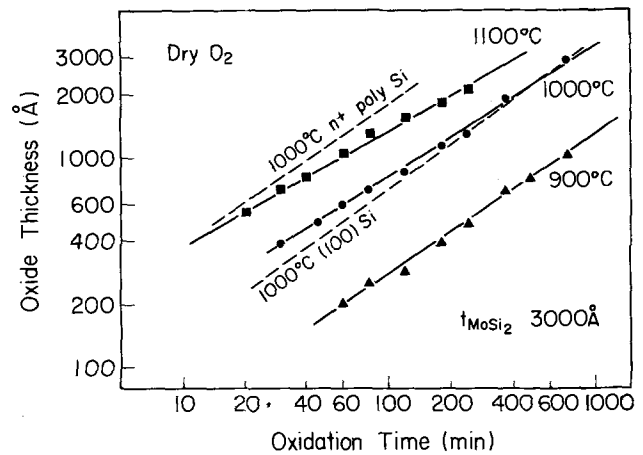


Fig. 1. Growth rates of MoSi_2 -oxide in dry oxygen at 900°, 1000°, and 1100°C.

is applicable to the oxidation of MoSi_2 (11). Figure 2 shows the fitting of the experimental results shown in Fig. 1 with the curve derived from the general relationship for silicon oxidation. As is clearly indicated in Fig. 2, the experimental results show excellent agreement with the crystalline silicon oxidation model. As oxidation proceeds, the oxidation kinetics continuously changes from the so-called reaction-controlled region ($\text{Xo} = \text{B}/\text{A}(t + \tau)$) to the diffusion-controlled region (limited by $\text{Xo}^2 = \text{B}(t + \tau)$). Figure 3 shows the Arrhenius plots of the parabolic rate constant B and linear rate constant B/A which are derived from Fig. 1. The activation energies of B and B/A are estimated to be E_a , (parabolic) = 1.6 eV and E_a , (linear) = 1.9 eV, respectively. The former is two times larger than the value reported by Chang, which was derived from the consumed oxygen during oxidation by monitoring the amount of oxygen at the inlet and the outlet of the furnace (8). Taking account of the deviation of the published results for silicon oxidation where E_a , (parabolic) and (linear) are 1.2 to 2.2 and 1.5 to 2.2 eV, respectively, these activation energies of MoSi_2 oxidation are very close to the respective activation energies of silicon oxidation (12). Thus, the experimental results indicate that the oxidation of MoSi_2 eventually follows the same oxidation mechanism as crystalline silicon as far as the oxide growth rate is concerned.

Etching rate.—The MoSi_2 -oxide grown at 900°, 1000°, and 1100°C in dry oxygen shows the same etch rate of 3Å/sec as the thermal silicon dioxide grown under the same conditions in the thickness range of 500-2000Å with 5% HF.

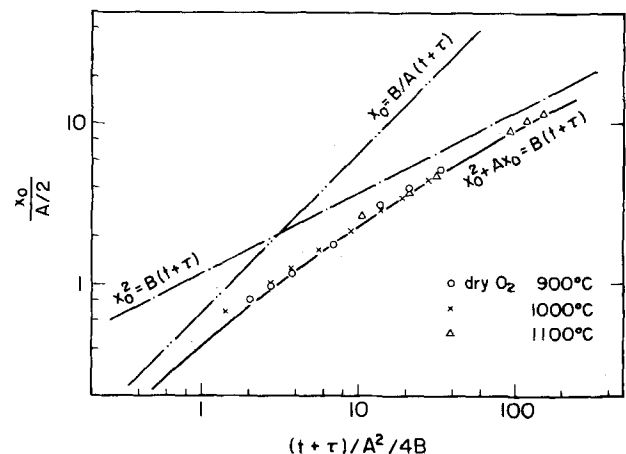


Fig. 2. Relationship for the oxide growth rate of MoSi_2 film showing the linear and parabolic region.

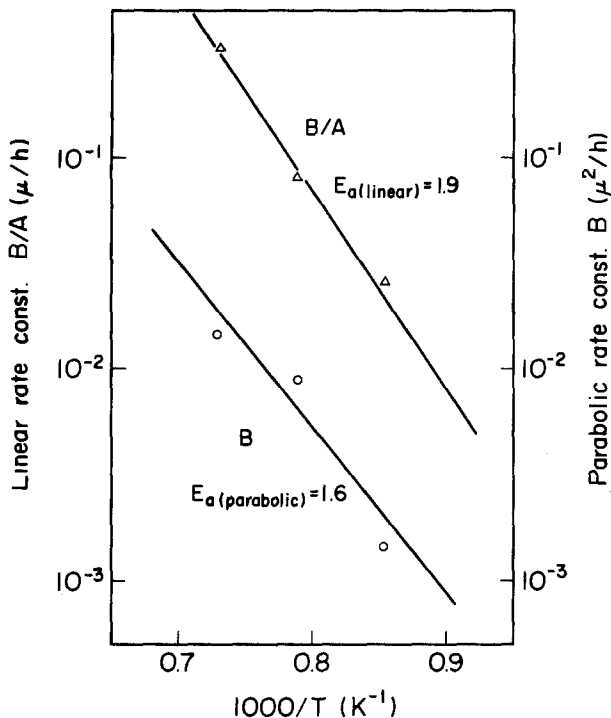


Fig. 3. The Arrhenius plots of the parabolic rate constant B and linear rate constant B/A .

Thickness ratio.—The ratio of MoSi_2 thickness (t_m) to the corresponding thickness of MoSi_2 -oxide produced from the MoSi_2 (t_s), $R_o = t_m/t_s$, was measured as a function of grown oxide thickness, which is shown in Fig. 4. t_m was estimated from the difference in height between the initial and the oxide removed surface as shown in Fig. 4. The error bars are mostly attributed to the asperities of the oxidized MoSi_2 -oxide/ MoSi_2 interface as described later. The ratio, R_o for silicon oxidation is well known as 0.44. On the other hand, that of MoSi_2 oxidation decreases with increasing oxide thickness. At the earlier oxidation stages, the thin oxide layer is less protective for oxidation, so that both silicon and molybdenum in MoSi_2 are oxidized, and the most of molybdenum oxide should be vaporized completely through the thin silicon dioxide layer because of its low sublimation temperature.

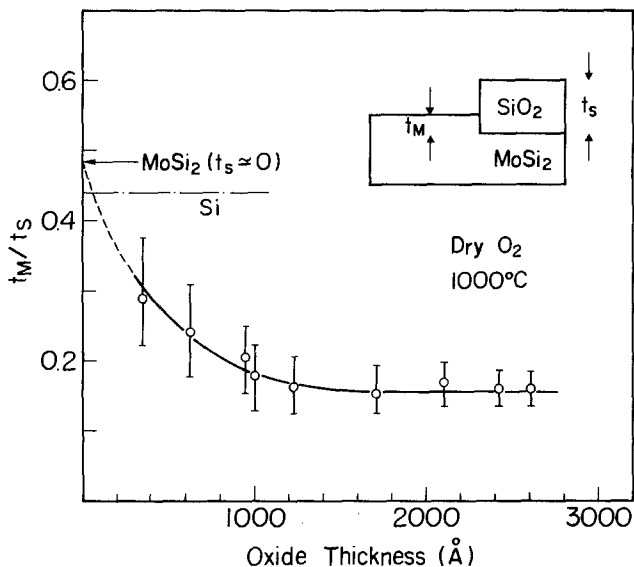


Fig. 4. Change in thickness ratios of the consumed MoSi_2 film to the grown SiO_2 layer during oxidation in dry O_2 at 1000°C . The ratio decreases with increasing thickness of MoSi_2 -oxide.

This means the MoSi_2 -oxide will not contain molybdenum, thus the ratio should be described as

$$R_o = t_m/t_s = \frac{\rho_s}{\rho_m} \frac{W_{\text{Si/SiO}_2}}{W_{\text{Si/MoSi}_2}} \quad [2]$$

where $W_{\text{Si/SiO}_2}$ and $W_{\text{Si/MoSi}_2}$ are the atomic weight ratios of silicon in SiO_2 and MoSi_2 , ρ_s and ρ_m are the densities of silicon and molybdenum, respectively. By simple calculation, Eq. [2] leads to the constant 0.48.

Dielectric properties of MoSi_2 -oxide.—**Dielectric constant.**—The dielectric constant of MoSi_2 -oxide, ϵ , was estimated to be 3.1 by measurements of oxide capacitance and thickness of MoSi_2 -oxide with aluminum/ MoSi_2 -oxide/ MoSi_2 structure diode. This is smaller than that of thermal silicon dioxide, 3.9, but is close to that of n^+ -poly-Si oxide, 3.4.

Dark current and breakdown.—Figure 5 shows the dark current of aluminum (Al)/ MoSi_2 -oxide/ MoSi_2 diode and along with those of Al/ n^+ -poly-Si oxide/ n^+ -poly-Si diode. The both signs denote the Al electrode polarities and the arrows show the so-called shorting breakdown (final breakdown). The MoSi_2 -oxide shows the so-called self-healing breakdown, especially, in the case of positively biased Al electrode. In spite of this, the MoSi_2 -oxide shows low dark current compared with that of n^+ -poly-Si oxide.

Figure 6 shows breakdown probabilities of both MoSi_2 and n^+ -poly-Si oxides as a function of the electric field (Al⁺). The initial breakdown is defined by the voltage when the leakage current exceeds 5×10^{-7} A/cm², or the voltage when the initial self-healing breakdown takes place. Both types of breakdown were successively measured with the same ramp voltage sweep. The most of the initial breakdown of MoSi_2 and

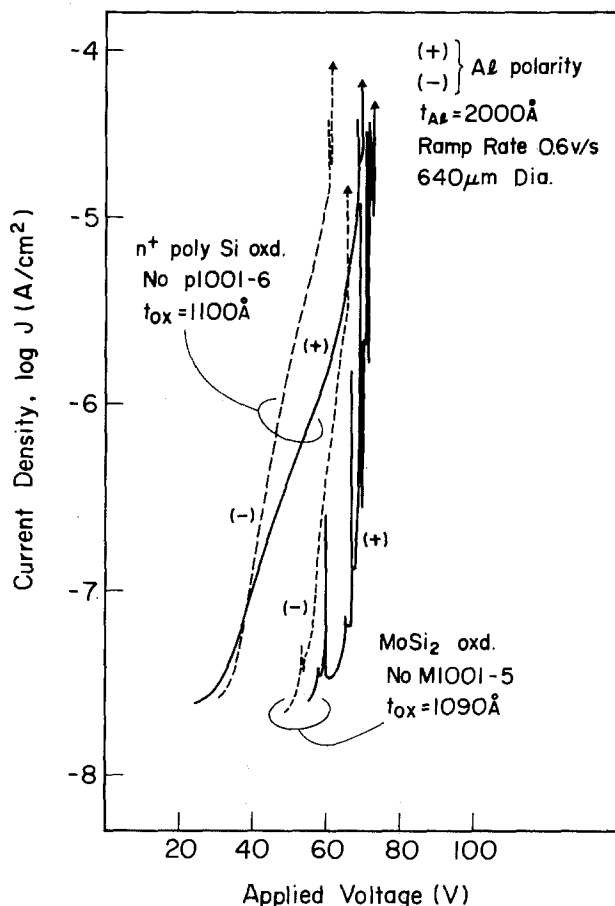


Fig. 5. The dark current densities of Al/ MoSi_2 -oxide/ MoSi_2 diode, as references, those on n^+ -poly-Si oxide are plotted. The arrows show the so-called shorting breakdown. The signs, (+) and (—), denote Al polarities.

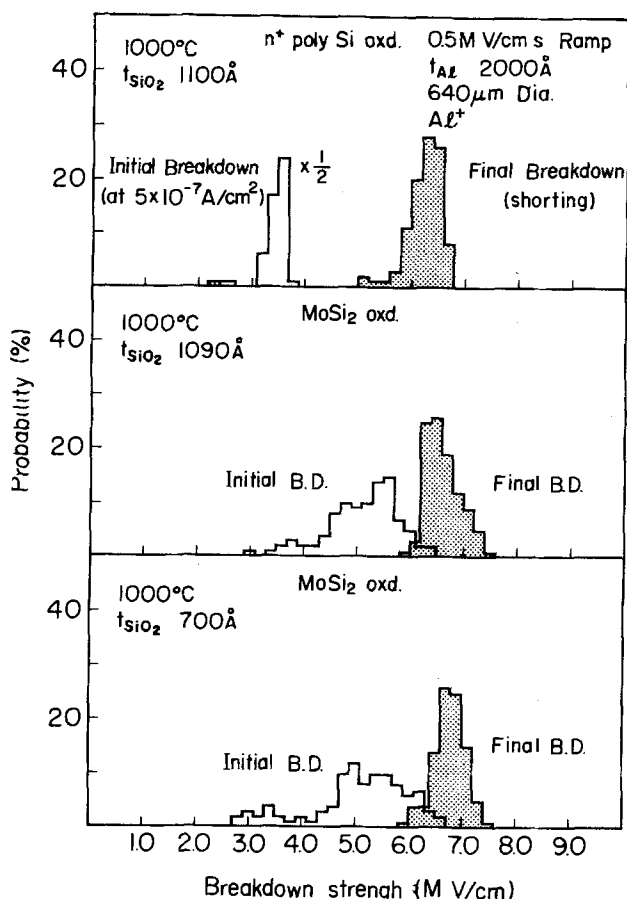


Fig. 6. The breakdown probabilities of the n^+ -poly-Si oxide, 1100 Å in thickness (upper); the MoSi_2 -oxide, 1090 Å in thickness (middle); and the MoSi_2 -oxide, 700 Å in thickness (bottom). The initial breakdown is defined as the voltage when the current density exceeds to $5 \times 10^{-7} \text{ A/cm}^2$.

n^+ -poly-Si oxide are determined by the self-healing breakdown and the dark current, respectively. There are no MoSi_2 -oxide thickness dependence for breakdown fields of both initial and final breakdown.

Figure 7 shows the breakdown probabilities of the MoSi_2 -oxides made at various oxidation temperatures. As is clearly indicated from the figure, the higher temperature oxidation gives rise to the higher initial breakdown strength and less fluctuation in the final breakdown strength.

Discussion

Molybdenum pile-up and vaporization.—The oxidation (oxide growth rate) of MoSi_2 , as is described, follows nearly the same oxidation mechanism as that of crystalline silicon. In other words, the molybdenum within MoSi_2 takes no part in the silicon dioxide formation rate. However, the oxidation shows the different behavior such as $R_o (= t_m/t_s)$. It is important to consider the behavior of molybdenum during oxidation. Figure 8 (a), (b) and (c) show Auger in-depth profiles of MoSi_2 -oxides made at various oxidation temperatures. As is clearly seen in the figures, the silicon dioxide is formed on the MoSi_2 surface during the oxidation. This is also confirmed by backscattering analysis with He^+ . The molybdenum in the oxide is less than the Auger electron detection limits which is a few percent in concentration. Figure 8 also shows a peak in molybdenum concentration at the MoSi_2 -oxide/ MoSi_2 interface. The molybdenum pile-up region increased in concentration and in depth with increasing oxidation (10), which indicates the preferential oxidation of silicon in MoSi_2 because of the difference in the oxide formation energies between silicon and molybdenum in MoSi_2 .

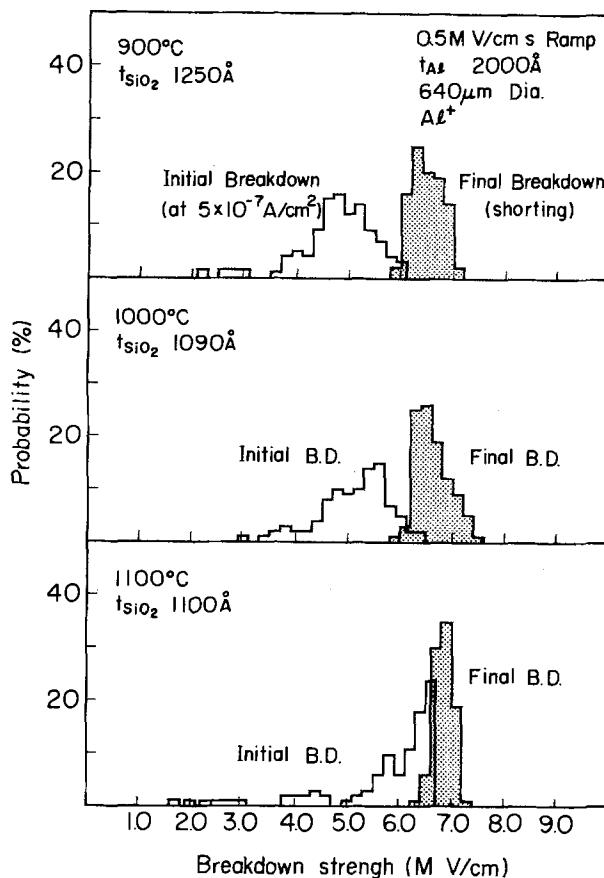


Fig. 7. The breakdown probabilities of MoSi_2 -oxide oxidized at 900°C (upper), 1000°C (middle), and 1100°C (bottom).

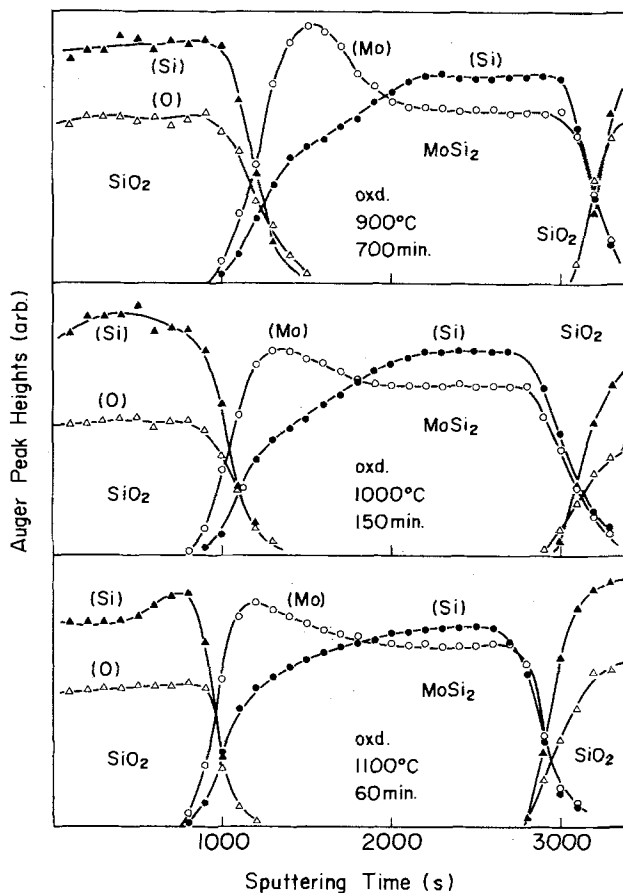


Fig. 8. The Auger in-depth profiles of the MoSi_2 film oxidized at 900°C for 700 min (upper), 1000°C for 150 min (middle), and 1100°C for 60 min (bottom).

In order to investigate the structure and composition of the high molybdenum concentration layer, the oxidized MoSi_2 film was examined with transmission electron diffraction and the diffraction pattern was obtained as shown in Fig. 9 where the MoSi_2 film was 1500Å and was oxidized in dry oxygen for 5 hr at 1000°C. The diffraction lines are assigned to be those of the higher molybdenum silicide Mo_3Si and the elemental molybdenum with ASTM cards No. 4-0811. In addition, the intensity of the diffraction lines suggests that the elemental molybdenum is dominant in this film. This is in agreement with the previous work which identified the molybdenum rich layer as α -molybdenum solution (7).

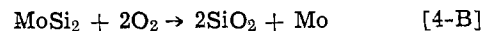
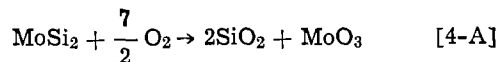
During the MoSi_2 oxidation the white particles were deposited in the cold gas trap. The ESCA spectra of the deposit revealed that the deposit was mostly composed of molybdenum trioxide (MoO_3). It is reasonable to assume the vaporization of MoO_3 can occur because of its low sublimation temperature, 790°C.

According to the above results, the oxidation of MoSi_2 is accompanied by the silicon dioxide formation with nearly the same growth rate as that of silicon and the piled-up molybdenum. The negative oxide formation energies of silicon and molybdenum, ΔH_{Si} and ΔH_{M} , were reported to be -77.2 and -35.5 kcal/g-atom at 1000°C, respectively (13). This means that the silicon oxide is stable compared with molybdenum oxide. The oxidation reaction subsequent to thick oxide growth will be controlled by the diffusion of oxidant through the oxide, and the oxidant concentration will be reduced to the lower levels at the interface at which the oxidation reaction takes place. The ratio of reaction products of silicon-oxidant system to molybdenum-oxidant system, γ , will be given by

$$\gamma = \exp \left(\frac{-\Delta H_{\text{Si}} + \Delta H_{\text{M}}}{KT} \right) \quad [3]$$

The value γ is 4×10^4 at 1000°C, which means the oxidation of silicon is dominantly carried out in MoSi_2 . Thus, unoxidized molybdenum will be piled up at the MoSi_2 -oxide/ MoSi_2 interface. However, a part of piled-up molybdenum is actually oxidized and therefore vaporizes as molybdenum oxide even in the diffusion-controlled region because of the decrease of silicon atom to form the silicon dioxide. On the other hand, analysis for the reaction-controlled region is difficult due to lack of knowledge of the reaction rate process. However, when we consider that vaporization of molybdenum oxide through a thin MoSi_2 -oxide layer will take place at the earlier oxidation stage, the

molybdenum silicide oxidation system will be described by



At the initial oxidation stage and at a further oxidation stage after thick oxide formation, MoSi_2 oxidation will follow the reaction and diffusion-controlled oxidation rules, which correspond to Eq. [4-A] and [4-B], respectively. However, at the intermediate stage the oxidation of MoSi_2 will be described by a hybridization of [4-A] and [4-B].

The experimental results in Fig. 2 suggest that the higher temperature oxidation rapidly reaches to the diffusion-controlled region. Therefore, piled-up molybdenum will be expected at higher temperature oxidation. However, this is not the case as shown in Fig. 8, where the pile-up of molybdenum is remarkable at lower oxidation temperature. It should be due to the fact that the reaction ratio γ increases with decreasing temperature. Thus, the MoSi_2 -oxide growth rate will be close to that of crystalline silicon oxidation as long as the silicon reacting with oxidant in the molybdenum rich region is high enough in concentration to form the silicon dioxide.

Thickness ratio.—The thickness ratio, R , will be rewritten and given by

$$R = (t_m - t_{\text{mo}})/t_s = R_0 - t_{\text{mo}}/t_s \quad [5\text{-A}]$$

where

$$t_{\text{mo}} = \alpha \frac{\rho_s}{\rho_{\text{mo}}} W_{\text{Mo/MoSi}_2} \cdot t_m \quad [5\text{-B}]$$

Here $W_{\text{Mo/MoSi}_2}$ and t_{mo} are the atomic weight ratio of molybdenum in MoSi_2 and the thickness of the piled-up molybdenum layer, respectively. The notation α is defined as the ratio of piled-up molybdenum to the total amount of molybdenum at the interface. From Eq. [2], [5-A] and [5-B], the ratio is given by

$$R = 0.48 - 0.18 \alpha \quad [5\text{-C}]$$

The ratio R , for instance, is estimated to be $R = 0.3$ when molybdenum in the consumed MoSi_2 completely piles up (i.e., $\alpha = 1$). This value is larger than the experimental results as shown in Fig. 2. The experimental results may involve certain errors due to the surface asperities. However, the ratio obtained from Fig. 10 (c) is $R = 0.25$, which is rather close to the calculated value. Thus, the value of R decreases with increasing oxide thickness due to the existence of piled-up molybdenum.

Morphologies.—The morphologies of the MoSi_2 -oxide and the MoSi_2 -oxide/ MoSi_2 interface after the oxidation were investigated with SEM observation. Figures 10 (a), (b), and (c) show the SEM photographs of the MoSi_2 surface annealed in nitrogen at 1000°C for 30 min, the MoSi_2 -oxide surface and MoSi_2 -oxide/ MoSi_2 interface oxidized in oxygen at 1000°C for 3 hr, and the cross-sectional view of the selectively oxidized MoSi_2 covered with MoSi_2 on the oxide and silicon nitride as an oxidation mask. The MoSi_2 -oxide shows the flat surface and roughened interface. The white and small grains at the concave of the MoSi_2 surface, shown in Fig. 11 (b), are assumed to be elemental molybdenum. The average grain sizes are 500 and 2000Å in diameter for annealed and oxidized MoSi_2 , respectively, while the as-deposited MoSi_2 film has an amorphous state. The localization of the elemental molybdenum in the MoSi_2 -oxide/ MoSi_2 interface suggests the nonuniform oxidation of MoSi_2 . In other words, the preferential silicon oxidation simultaneously induces nonuniform pile-up of molybdenum at the interface as shown in Fig. 10 (b). The additional oxidation should cause the oxidation of the piled-up molybdenum and at the same

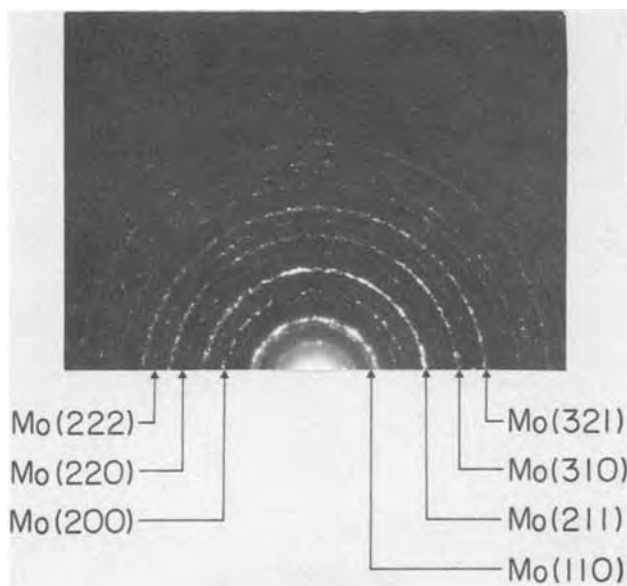


Fig. 9. Diffraction pattern of MoSi_2 oxidized in dry O_2 at 1000°C for 5 hr.

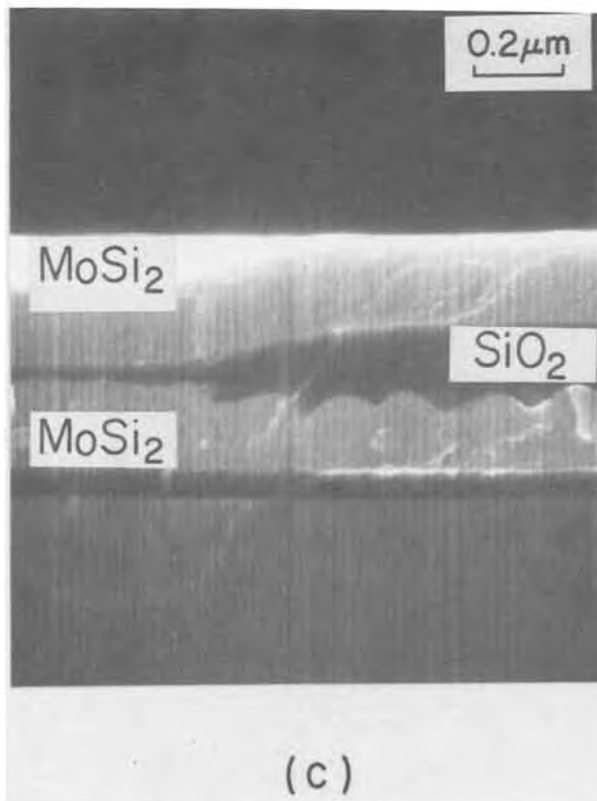
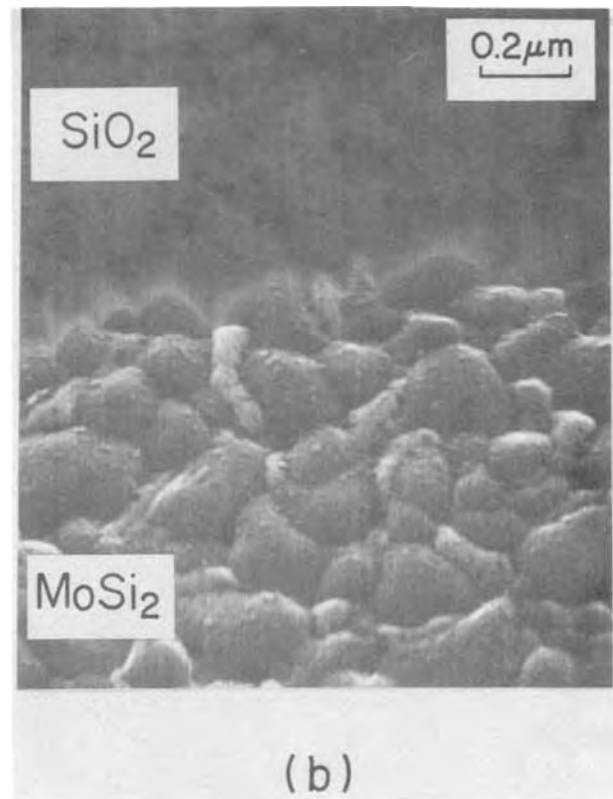
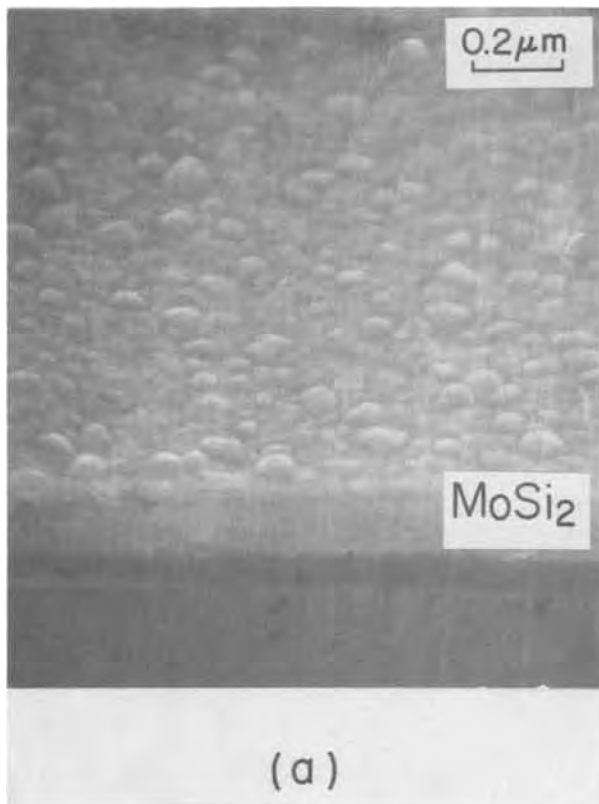


Fig. 10. The MoSi₂ surface annealed in N₂ at 1000°C for 30 min (a). MoSi₂ surface oxidized in dry O₂ at 1000°C for 2.5 hr (b). Cross-sectional view of the MoSi₂/MoSi₂-oxide/MoSi₂ structure (c). The MoSi₂ layer (upper) was deposited on Si₃N₄ and SiO₂ layer after the MoSi₂ oxidation at 1000°C for 7 hr.

time another pile-up of molybdenum around the MoSi₂ grain could occur.

Dielectric properties.—There is no notable difference between both types of oxides as far as the shorting breakdown is concerned. However, the dark current and the initial breakdown show a remarkably different behavior. The low initial breakdown of poly-Si oxide comes from the high dark current due to the high trap densities in the oxide (14). The MoSi₂-oxide shows the low dark current, so that the initial breakdown of MoSi₂-oxide is limited by the self-healing breakdown which is generally attributed to the defects in the

oxide, such as molybdenum in the MoSi₂-oxide smaller than Auger detectability. At higher oxidation temperature, more molybdenum vaporizes as oxide leaving less molybdenum in the MoSi₂-oxide which will lead to improvement on the self-healing breakdown. Furthermore, it is likely to consider that the MoSi₂-oxide has high pin hole densities because of the vaporization of molybdenum oxide through the MoSi₂-oxide. Actually, the pin holes are sometimes observed in the MoSi₂-oxide formed in wet oxygen. The rapid oxidation such as in wet oxygen may cause the explosive vaporization through the MoSi₂-oxide. Therefore, such a kind of pin

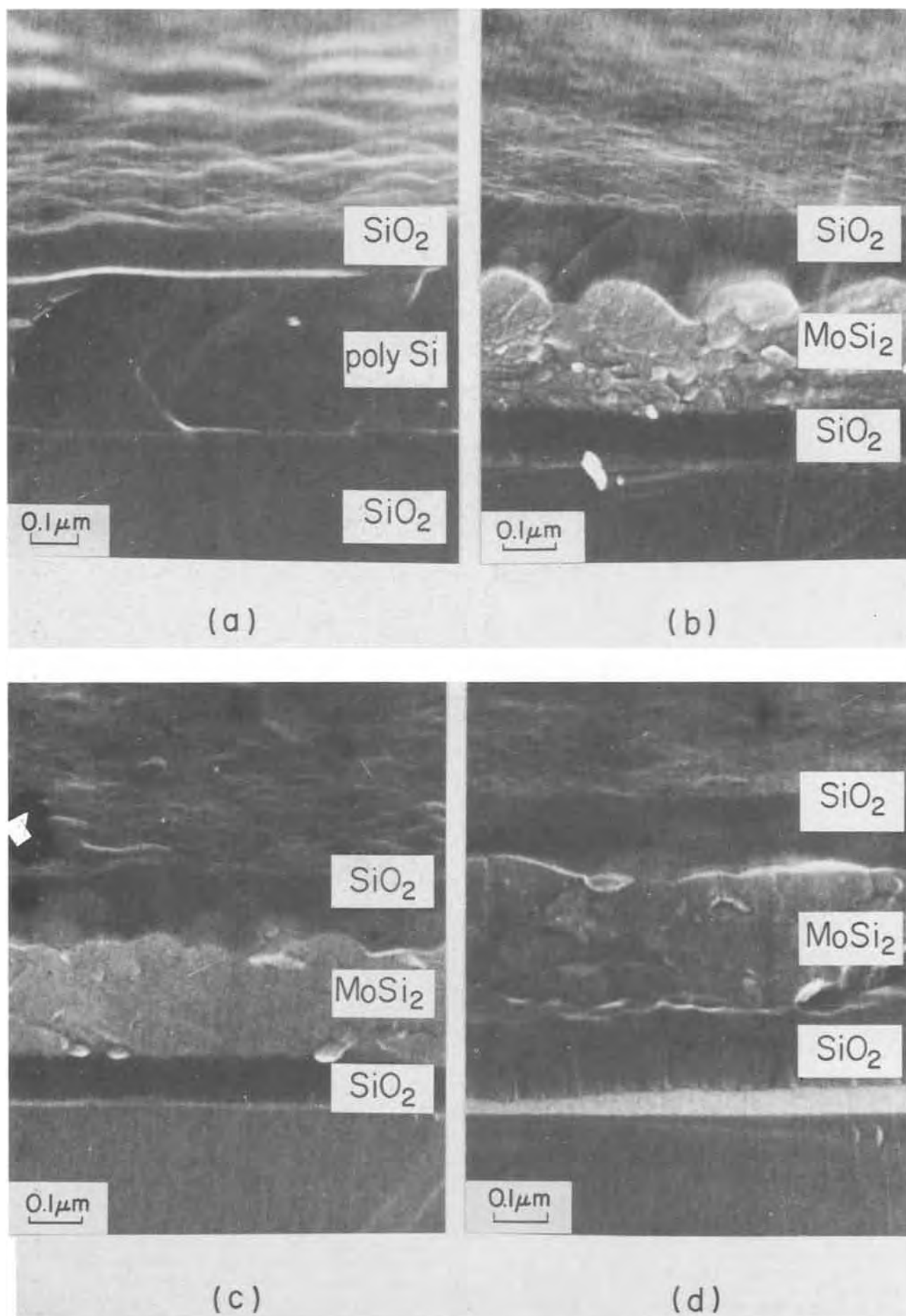


Fig. 11. Cross sectional view of n^+ -poly-Si oxidized at 1000°C (a) and those of MoSi₂ oxidized at 900°C (b), 1000°C (c), and 1100°C (d). Their oxide layers were 1100, 1250, 1090, and 1100\AA thick, respectively.

hole could be formed even in the MoSi_2 -oxide formed in dry oxygen as far as the oxidation temperature is high enough. The experimental results derived in Fig. 8 indicate that higher temperature oxidation induces low molybdenum pile-up, resulting from high molybdenum vaporization compared with that of low temperature oxidation. Therefore, the pin-hole density in high temperature oxidized MoSi_2 -oxide would be large. However, Fig. 7 shows that the higher temperature oxidation improves the self-healing breakdown strength. Therefore, the vaporization of molybdenum through the MoSi_2 -oxide will have no notable influence on the oxide breakdown.

Figures 11 (a) to (c) show the SEM photographs of the cross-sectional view of n^+ -poly-Si oxide and the MoSi_2 -oxide formed at 900° , 1000° , and 1100°C , respectively. As is clearly indicated in the figures, the MoSi_2 -oxides have the roughened interfaces compared with that of n^+ -poly-Si. This is more remarkable at lower temperatures which is qualitatively in agreement with the experimental findings on the breakdown strength, i.e., with increasing interface asperities, the probability of the self-healing breakdown at low supply field increases. The remarkable self-healing breakdown when the Al electrode is positively biased, as shown in Fig. 5, will be caused by the electron emission from the convex MoSi_2 (or molybdenum) into the MoSi_2 -oxide, and the electrons emitted into the oxide will increase the electric field in the MoSi_2 -oxide near the Al/oxide interface up to the oxide breakdown strength. Thus, the self-healing breakdown frequently occurs in the MoSi_2 -oxide formed at low temperature even at the low supply field, while, the high temperature oxidation improves the breakdown strength because of less pile-up of molybdenum.

Conclusions

The growth rate and the composition of the oxide formed by oxidation of molybdenum silicide are investigated in comparison with those of single crystal silicon. The oxidation rate of MoSi_2 can be well described by the same general relationship as of single crystal silicon. The activation energies of the parabolic and linear rate constant of MoSi_2 oxidation are estimated to be 1.6 and 1.9 eV, respectively, which are also close to those of crystalline silicon. A part of molybdenum in the consumed MoSi_2 is vaporized through the oxide in a form of MoO_3 during the oxidation. The MoSi_2 oxidation is governed by preferential silicon dioxide formation, in particular, in the diffusion-controlled oxidation region. The pile-up of molybdenum at the MoSi_2 -oxide/ MoSi_2 interface occurs as a result of oxidation of silicon in MoSi_2 , which depends on the oxidation temperature. The ratio of MoSi_2 thickness to the corresponding thickness of oxide produced from MoSi_2 decreases with increasing

oxide thickness due to the pile-up of molybdenum at the interface. The interface asperities of MoSi_2 -oxide are attributed to the local oxidation of MoSi_2 induced by molybdenum pile-up.

The dielectric constant of MoSi_2 -oxide is estimated to be 3.1. The final breakdown strength of MoSi_2 -oxide is close to that of n^+ -poly-Si oxide. The MoSi_2 -oxide frequently showed the self-healing breakdown due to the interface asperities. The higher temperature oxidation decreases the interface asperities of the MoSi_2 -oxide due to less pile-up of molybdenum, and hence, it results in higher breakdown field.

Acknowledgment

The authors would like to thank Drs. S. Kohyama and Y. Nishi for their critical reading of the manuscript.

Manuscript submitted Aug. 8, 1979; revised manuscript received Dec. 14, 1979.

Any discussion of this paper will appear in a Discussion Section to be published in the December 1980 JOURNAL. All discussions for the December 1980 Discussion Section should be submitted by Aug. 1, 1980.

Publication costs of this article were assisted by NEC-Toshiba Information Systems Incorporated.

REFERENCES

1. W. E. Engeler and D. M. Brown, *IEEE Trans. Electron Devices*, ed-19, 54 (1972).
2. R. C. Henderson, R. F. Pease, A. M. Voshenkov, R. P. Helm, and R. Wadsak, *IEEE J. Solid-State Circuits*, sc-10, 92 (1975).
3. F. Yanagawa, T. Amazawa, and H. Oikawa, *Jpn. J. Appl. Phys.*, 18, suppl. 18-1, 237 (1979).
4. T. Mochizuki, K. Shibata, T. Inoue, and K. Ohuchi, *ibid.*, 17, suppl. 17-1, 37 (1977).
5. B. Crowder and S. Zirinsky, *IEEE J. Solid-State Circuits*, sc-14, 291 (1979).
6. R. Kieffer and E. Cerwenda, *Z. Metallk.*, 43, 101 (1952).
7. J. B. Berkowitz-Mattuck and R. R. Dils, *This Journal*, 112, 583 (1965).
8. Y. A. Chang, *J. Mater. Sci.*, 4, 641 (1959).
9. S. Zirinsky, W. Hammer, F. d'Heurle, and J. Baglin, *Appl. Phys. Lett.*, 33, 76 (1978).
10. T. Mochizuki and M. Kashiwagi, Abstract 201, p. 537, The Electrochemical Society Extended Abstracts, Vol. 78-2, Pittsburgh, Pa., Oct. 15-20, 1978.
11. B. E. Deal and A. S. Grove, *J. Appl. Phys.*, 36, 3770 (1965).
12. E. A. Irene, *This Journal*, 125, 1146 (1978).
13. I. E. Campbell and E. M. Sherwood, "High-Temperature Material and Technology," p. 160, John Wiley, New York (1967).
14. O. L. Curtis, Jr. and J. R. Srowr, *J. Appl. Phys.*, 48, 3819 (1977).

Process-Induced Effects on Carrier Lifetime and Defects in Float Zone Silicon

A. Rohatgi and P. Rai-Choudhury*

Westinghouse Research and Development Center, Pittsburgh, Pennsylvania 15235

ABSTRACT

The effects of cooling rate, oxidation temperature, back surface damage gettering, and HCl oxidation on the generation lifetime and defects in float zone silicon have been investigated. Silicon used in this study does not show stacking faults after the oxidation; instead, dominant oxidation-induced defects are saucers. The combination of back surface damage gettering and HCl oxidation reduces the oxidation-induced saucer density by three orders of magnitude. Lifetime of a fast-cooled sample is always low and bears no relationship with the saucer density, while the lifetime of slow-cooled samples shows an inverse relationship with the saucer density. High temperature HCl oxidation, with back surface damage and slow cool, is a very effective process which gives lifetimes of the order of 2 msec. Oxidation-induced saucer density is not the only reason for low lifetime, e.g., impurities and/or decorated saucers may play an important role.

The oxidation-induced defects and their deleterious effects on the electrical performance of the devices have been an area of major concern. It is important to understand what defects degrade the device performance and how to minimize them by selecting the right process. Several investigators (1-4) have discussed the conditions for the initiation of oxidation-induced stacking faults and the methods (5-7) of suppressing them by various gettering techniques, e.g., preoxidation gettering (3), HCl gettering (7,19), and high temperature anneal in inert ambient (8). It has been shown (5, 17) that reduction of stacking fault density improves the carrier lifetime. Some investigators (9, 10) believe that oxidation-induced saucers are indicative of metallic contaminants and may also degrade the device performance. Generation lifetime is a good and sensitive indicator of the device performance and has been utilized in this work to study the process-induced effects on device performance and defects in silicon. This paper discusses the effects of process variables, such as cooling rate after the oxidation, oxidation temperature, back surface damage (BSD) gettering, and HCl oxidation on float zone silicon.

Experimental Procedure

Studies were conducted on 4-8 Ω -cm, n-type, (100) float zone silicon. MOS capacitors were fabricated to evaluate the process-induced effects on lifetime and defects. Cleaning involved organic solvents to degrease, a hot sulfuric-nitric acid mix, a detergent to remove lapping residues, and a preoxidation peroxide treatment. In order to keep the oxidation-induced stacking faults to a minimum, no HF treatment was given to the wafers prior to the oxidation (12). Oxidation time was selected to obtain approximately 1500Å thick oxide. These samples were annealed for 20 min in N_2 at the oxidation temperature after the oxidation and prior to cooling. The oxidation was carried out in a quartz furnace and 50 mil diameter aluminum electrodes were evaporated on the oxide.

Generation lifetime in the bulk silicon was determined by the pulse MOS-C technique, which is well documented in the literature (10, 18). In this technique the capacitor is pulsed into deep depletion and the capacitance is recorded as a function of time as it recovers from the deep depletion to its equilibrium state of inversion. Modified Zerbst analysis was used to calculate the lifetime. A simple approximation can be used to obtain the generation lifetime (τ_g) if the

surface-state effects are small and the capacitor is pulsed from inversion into the deep depletion. This approximation has been discussed in detail by Schroder (13) and is given by

$$\tau_g = \frac{n_i}{8N_D} \frac{C_F}{C_o} t_F \left(1 + \frac{C_i}{C_F} \right)^2 \quad [1]$$

where N_D is the doping density, C_o is the oxide capacitance, C_i is the initial capacitance in deep depletion, C_F is the inversion capacitance, and t_F is the time it takes to recover from deep depletion to the inversion. In order to keep the surface generation small, the capacitors were sintered at 425°C for 1 hr in H_2 . An average of 10 or more data points, near the central region of the wafer, was used to obtain the lifetime.

In selected instances, oxidation-induced defects in silicon were delineated by first removing the metal and the oxide and then preferentially etching $\sim 3 \mu\text{m}$ silicon with Secco etch (20). The $3 \mu\text{m}$ region lies within the active area of the device during the lifetime measurement since the deep depletion width was $\sim 5 \mu\text{m}$. The oxidation-induced defects on the etched surface were observed with the help of an optical microscope. An average of 10 or more data points was taken to obtain the defect density on a wafer.

The effect of cooling rate after oxidation was studied by either quenching or slow cooling the samples. Quenching was done by rapidly removing the sample to room temperature after the 20 min N_2 anneal. Slow cooling was performed at a rate of 1°C/min in N_2 until a temperature of 600°C was reached and then the sample was removed to room temperature. The effect of oxidation temperature was investigated by varying the temperature in the range of 900°-1200°C. The influence of back surface damage gettering was evaluated by lapping the back side of the wafer with 60 μm Al_2O_3 powder prior to the oxidation. The effect of HCl oxidation was studied by oxidizing the wafers in ambients containing mixtures of HCl and O_2 gases. HCl concentration was varied in the range of 1-6% of the total gas flow during the oxidation. The first 100Å of oxide was grown in dry oxygen and the remaining oxide was grown in the HCl/ O_2 mixture.

Results

Float zone silicon used in this study did not show stacking faults after the oxidation (Fig. 1). In a few instances stacking fault density was at most 25 cm^{-2} . The dislocation density was also quite small, less than 100 cm^{-2} . The dominant defects were saucers. Saucers

* Electrochemical Society Active Member.

Key words: oxidation, saucers, impurities, gettering.

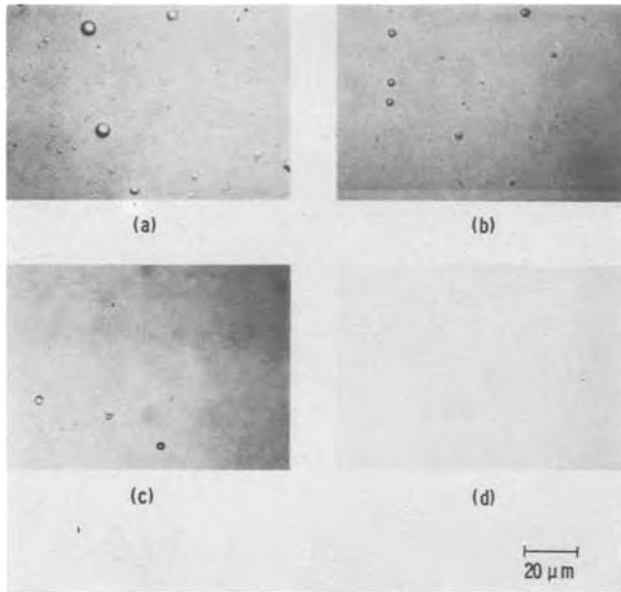


Fig. 1. Effect of back surface damage gettering and HCl oxidation on saucer defects (a) 0% HCl oxidation without back surface damage, $\sim 1 \times 10^6$ saucers/cm², (b) 1% HCl oxidation without back surface damage, $\sim 1 \times 10^5$ saucers/cm², (c) 0% HCl oxidation with back surface damage, 1×10^4 saucers/cm², (d) 1% HCl oxidation with back surface damage, $\sim 1 \times 10^3$ saucers/cm².

are small, circular, shallow and flat-bottomed pits (Fig. 1).

Table I shows the effects of cooling rate, damage gettering, and HCl oxidation on the lifetime and defects for 1100°C oxidation. The data show that when a sample is quenched after the oxidation, the lifetime is very small, ~ 20 μ sec, regardless of damage gettering and/or HCl oxidation. Figure 1 and Table I show that the damage gettering reduces the oxidation-induced saucer density by two orders of magnitude, $10^6 \rightarrow 10^4$ cm⁻², that HCl oxidation reduces the saucer density by an order of magnitude, $10^6 \rightarrow 10^5$ cm⁻², and that a combination of the two brings down the saucer density to $\sim 10^3$ cm⁻². The saucer density on the starting wafer was in the range of 500-1000 cm⁻². Slow cooling, without damage and HCl gettering, gives somewhat higher lifetime (~ 100 μ sec) but the saucer density remains in the range $1-5 \times 10^6$ cm⁻². Introducing back surface damage gives a substantial increase in the lifetime, ~ 500 μ sec, if the sample is slow cooled. One percent HCl oxidation with damage and slow cool gives lifetime of the order of 2 msec. Increasing the HCl concentration from 1 to 6% has very little effect on the lifetime and saucer density.

Figure 2 shows the effect of oxidation temperature on the lifetime. When a sample is quenched after oxidation, the lifetime is very low and relatively insensitive to the oxidation temperature. Slow cool without

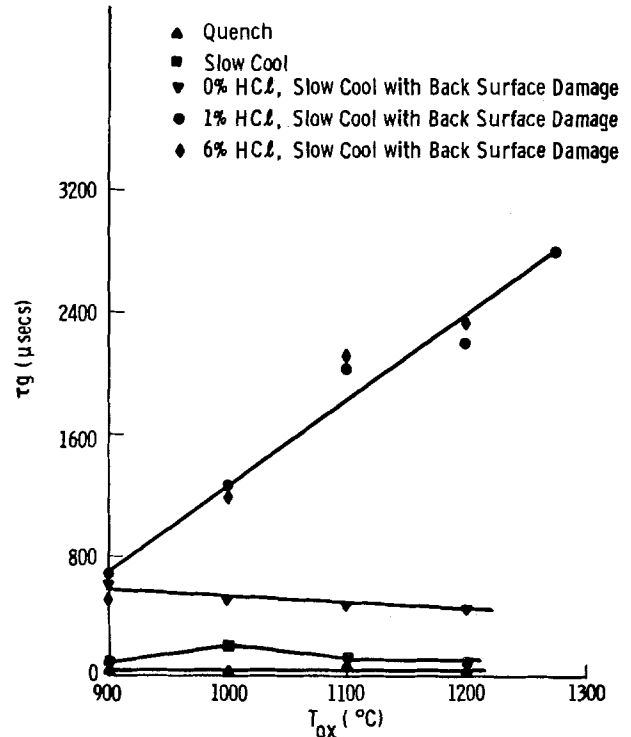


Fig. 2. Minority carrier lifetime as a function of oxidation temperature for different oxidation conditions.

back surface damage gives somewhat higher lifetime which does not depend strongly on the oxidation temperature. Slow cool with damage gettering gives a substantial increase in the lifetime which is also not a strong function of the oxidation temperature. HCl oxidation with back surface damage and slow cool gives high lifetime which increases monotonically with the increase in oxidation temperature. Increasing the HCl concentration from 1 to 6% has no appreciable effect on lifetime. This is in agreement with Wang *et al.* (16). Table II shows that the saucer density remains unchanged, despite the systematic increase in lifetime, with increasing HCl oxidation temperature.

Discussion

The data showed that quenching after oxidation is very detrimental to device lifetime, regardless of back damage and HCl gettering. It has been shown by Wang (16) that quenching gives rise to recombination centers, at $E_c - 0.26$ eV and $E_c - 0.49$ eV, which may result from the dissolved impurities quenched in the interstitial sites. Thus, in quenched samples, lifetime is probably controlled by these centers and has no relationship with the saucer density (Table I). On the other hand, in the slow-cooled samples, the lifetime is inversely related to the saucer density. During slow cooling, the dissolved impurities get enough time to migrate, precipitate, and become electrically inactive, therefore, they do not seem to limit the lifetime as in the case of quenched samples. Moreover, according to

Table I. Effect of cooling rate, back surface damage gettering, and HCl oxidation on lifetime and defects in FZ silicon

Process	Life-time (μ sec)	Saucer density (cm ⁻²)
No BSD 0% HCl quench	20	$10^6 - 5 \times 10^6$
BSD 0% HCl quench	20	$10^4 - 5 \times 10^4$
BSD 1% HCl quench	20	$10^3 - 5 \times 10^3$
No BSD 0% HCl slow cool	100	$10^6 - 5 \times 10^6$
No BSD 1% HCl slow cool	200	$10^5 - 5 \times 10^5$
BSD 0% HCl slow cool	500	$10^4 - 5 \times 10^4$
BSD 1% HCl slow cool	2000	$10^3 - 5 \times 10^3$
BSD 6% HCl slow cool	2100	$10^3 - 5 \times 10^3$

Oxidation temperature 1100°C.

Table II. Effect of HCl oxidation temperature on lifetime and defects in FZ silicon

Oxidation temperature (°C)	Lifetime (μ sec)	Saucer density (cm ⁻²)
900	660	$10^3 - 5 \times 10^3$
1000	1275	$10^3 - 5 \times 10^3$
1100	2000	$10^3 - 5 \times 10^3$
1200	2200	$10^3 - 5 \times 10^3$

1% HCl oxidation with back surface damage and slow cool.

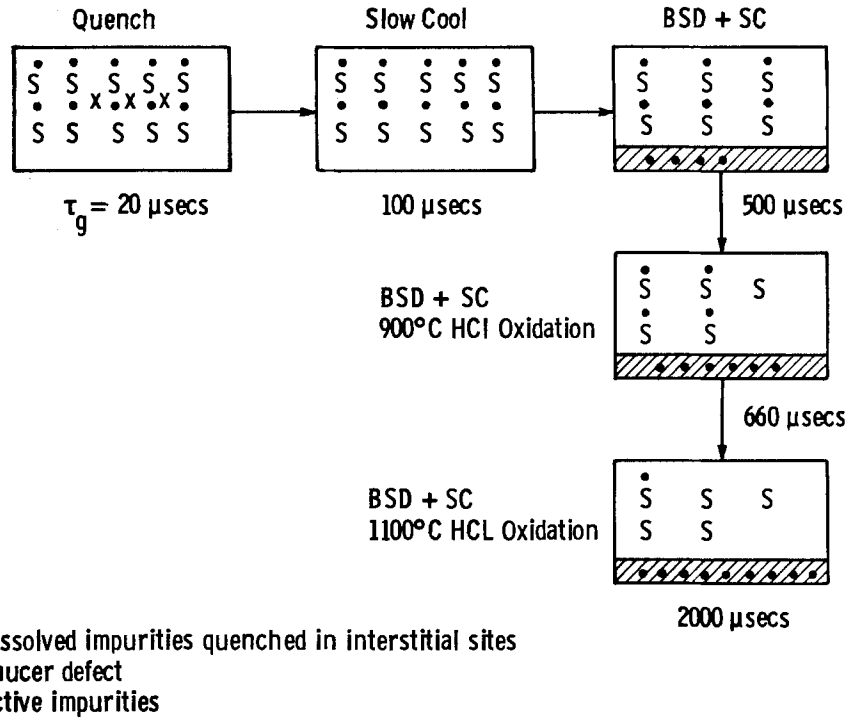


Fig. 3. Schematic representation of process-induced effects on lifetime and defects.

Pearce *et al.* (9), the oxidation-induced saucers can be generated from heavy metals incorporated during handling, cleaning, and processing of the wafer. They found that saucers are the result of a dislocation loop formed by heavy metal precipitates, although no satisfactory model has yet been proposed to account for their behavior. These saucers, being indicative of metallic contaminant, can reduce lifetime. Therefore, in the absence of other lifetime limiting sources, the lifetime is expected to vary inversely with the saucer density (Table I).

Table II showed that the HCl oxidation with the damage and slow cool is a very effective process for achieving high lifetime. The lifetime increases monotonically with the increase in the HCl oxidation temperature, however, the saucer density remains unchanged indicating that this systematic increase in lifetime cannot be attributed to the saucer density alone. Several investigators (8, 17) have pointed out that the defects should be decorated with impurities in order to be detrimental to the device performance. It appears from the data that higher HCl oxidation temperature cleans the bulk silicon more effectively either by extracting the impurities and/or by preventing them from getting into the bulk during the oxidation. Therefore, the concentration of the decorated saucers diminishes with higher HCl oxidation temperature, which may account for the monotonic increase in the lifetime, in spite of a constant saucer density.

The model in Fig. 3 illustrates these process-induced effects on lifetime and defects. It shows that when a sample is quenched, after the oxidation, the lifetime is very low primarily due to the dissolved impurities in the silicon lattice. When a sample is slow cooled, some of the dissolved impurities are able to precipitate and become electrically inactive, resulting in an increase in the lifetime. Slow cooling by itself has no effect on the saucer density. However, slow cooling with back surface damage reduces the saucer density by two orders of magnitude because the damage provides a sink for the point defects and fast diffusing impurities. This results in a substantial increase in the lifetime. HCl oxidation reduces the saucer density by an order of magnitude resulting in some additional increase in the lifetime. Increasing the HCl oxidation temperature has no appreciable effect on the net saucer density but it decreases the concentration of the decorated saucers to improve the lifetime further. Thus, by se-

lecting the right process the lifetime can be increased from 20 μsec to 2 msec.

Conclusions

Quenching of devices after the oxidation results in very low lifetime ($\sim 20 \mu\text{sec}$), regardless of damage or HCl gettering. The lifetime of quenched samples bears no relationship to the saucer density. Slow cooling has no effect on the saucer density but it gives somewhat higher lifetime ($\sim 100 \mu\text{sec}$). Slow cooling with back surface damage gives a substantial improvement in the lifetime ($\sim 500 \mu\text{sec}$). HCl oxidation with damage and slow cool is a very effective process which can give lifetimes of the order of 2 msec. Higher HCl oxidation temperature is more important than the HCl concentration for achieving better lifetimes. Back surface damage reduces the oxidation-induced saucer density by two orders of magnitude and the HCl oxidation reduces the density by an order of magnitude. The saucer density is not always the only reason for low lifetime, *e.g.*, dissolved impurities and/or decorated saucer density play an important role.

Acknowledgments

The authors wish to thank S. G. Hitchins and R. R. Adams for their help in the experimental work.

Manuscript submitted July 13, 1979; revised manuscript received Dec. 12, 1979.

Any discussion of this paper will appear in a Discussion Section to be published in the December 1980 JOURNAL. All discussions for the December 1980 Discussion Section should be submitted by Aug. 1, 1980.

Publication costs of this article were assisted by the Westinghouse Research and Development Center.

REFERENCES

- G. A. Rozgonyi, S. Mahajan, M. H. Read, and D. Brasen, *Appl. Phys. Lett.*, **29**, 531 (1976).
- M. Conti, G. Corda, R. Matteucci, and C. Ghezzi, *J. Mater. Sci.*, **10**, 705 (1975).
- G. A. Rozgonyi, P. M. Petroff, and M. H. Read, *This Journal*, **122**, 1725 (1975).
- Y. M. Chang and L. J. Bemer, in "Semiconductor Characterization Techniques," P. A. Barnes and G. A. Rozgonyi, Editors, p. 324, The Electrochemical Society Softbound Proceedings Series, Princeton, N.J. (1978).
- S. Prussin, S. P. Li, and R. H. Cockrum, in "Semi-

- conductor Characterization Techniques, P. A. Barnes and G. A. Rozgonyi, Editors, p. 357, The Electrochemical Society Softbound Proceedings Series, Princeton, N.J. (1978).
6. H. Shiraki, *Jpn. J. Appl. Phys.*, **14**, 747 (1975).
 7. H. Shiraki, *ibid.*, **15**, 1 (1976).
 8. C. L. Claeys, G. J. Declerck, and R. J. Van Overstraeten, in "Semiconductor Characterization Techniques," P. A. Barnes and G. A. Rozgonyi, Editors, p. 366, The Electrochemical Society Softbound Proceedings Series, Princeton, N.J. (1978).
 9. C. W. Pearce and R. McMahon, *J. Vac. Sci. Technol.*, **14** (40), 1977.
 10. G. A. Rozgonyi and C. W. Pearce, *Appl. Phys. Lett.*, **32** (11), 747 (1978).
 11. T. Hattori and T. Suzuki, *ibid.*, **33** (4), 347 (1978).
 12. C. M. Drum and W. Van Gelder, *J. Appl. Phys.*, **43**, 4465 (1972).
 13. D. K. Schroder and J. Guldberg, *Solid-State Electron.*, **14**, 1285 (1971).
 14. K. L. Wang, *This Journal*, **125**, 1664 (1978).
 15. F. Secco D'Aragona, *ibid.*, **119**, 948 (1972).
 16. K. L. Wang and R. J. Connery, in "Semiconductor Characterization Techniques," P. A. Barnes and G. A. Rozgonyi, Editors, p. 386, The Electrochemical Society Softbound Proceedings Series, Princeton, N.J. (1978).
 17. H. Strack, K. R. Mayer, and B. O. Kolbesen, *J. Solid-State Electron.*, **22**, 135 (1979).
 18. M. Zerbst, *Z. Angew. Phys.*, **22**, 30 (1966).
 19. E. J. Janssens and G. J. Declerck, in "Semiconductor Characterization Techniques," P. A. Barnes and G. A. Rozgonyi, Editors, p. 376, The Electrochemical Society Softbound Proceedings Series, Princeton, N.J. (1978).
 20. F. Secco D'Aragona, *This Journal*, **119**, 948 (1972).

Inhomogeneities in Silicon Crystals Grown from the Melt

Gene F. Wakefield*¹

Texas Instruments Incorporated, Dallas, Texas 75265

ABSTRACT

A brief review is given of some of the methods used to describe incorporation of impurities into silicon crystals grown from the melt. It is concluded that the concept that allows the equilibrium segregation coefficient to vary to an "effective" segregation coefficient is misleading and disguises the actual solid/liquid dynamics. Impurity concentration is controlled in crystals by their actual (changing) concentration at the interface and their equilibrium (essentially constant) segregation coefficient. This paper presents calculations on the effect of growth rate on impurity incorporation. Growth rate fluctuations lead to solute nonuniformities on a microscale with dopant, carbon, and metals concentrated into areas of a silicon slice separate from oxygen-rich "swirl" bands. The measured fluctuation in dopant concentration across a slice can be used to estimate other impurity concentration variations. Discrepancies between experimentally determined and the calculated values are considered to result primarily from lack of an appropriate value of boundary layer thickness.

The subject of chemical inhomogeneities in semiconductor crystals has received considerable attention, with the major focus on dopant and oxygen nonuniformities. Several crystal growth models (1-6, 8, 9) have been proposed which have aided understanding of the cause of the microscale variations prevalent in crystals. A critical analysis of the models reveals that though each covers certain aspects, the silicon crystal from large commercial Czochralski pullers is not as well described as desired.

Silicon crystals are now grown as long, cylindrical ingots which are sliced into thin wafers for semiconductor device manufacture. During growth of a silicon crystal, constant thermal and chemical changes occur within the crystal puller which cause each individual wafer to differ in content and distribution of impurities from every other wafer. A macroscale longitudinal variation is inherent in batch growth due to concentration of impurities into a decreasing melt volume. Also, thermal convection causes microscopic growth rate fluctuations to occur in the interface dynamics, and introduces inhomogeneities on a microscale. Since the interface shape is usually a curved surface, nonuniform bands reflecting the instantaneous melt-solid interface shape are frozen into the crystal. These nonuniformities have been shown to be bands which have different

solute concentration from the interband silicon. As each planar wafer may intersect several of the curved interface shapes, each wafer then also varies across its surface on a microscale basis as illustrated in Fig. 1. Compounding these nonuniformities within a crystal, each crystal is somewhat unique in quality because of the nature of any batch process, the variations in pullers, and the variations in starting polysilicon quality.

Microscale fluctuations are now recognized to result primarily from thermal convection currents within the melt (1-5). These currents periodically disturb the microscopic growth rate of the crystal. The magnitude and nature of the convection currents also varies as the melt aspect (melt height to diameter) ratio is decreased as a crystal is grown. The major source of the convection currents is clearly the temperature gradient (4) which exists due to a high heat input through the crucible walls which must then be lost from the top and bottom of the melt.

The microscale conditions of the solid-liquid interface of a growing crystal include solute rejection (for a solute with a segregation coefficient, $K < 1$) just ahead of the advancing solid, increasing the solute concentration at this interface. Between the solid and the well mixed (bulk) liquid is a 100-500 μm "boundary layer" of liquid, consisting of a momentum and solute concentration gradient. The excess solute moves from the interface against a silicon solution flowing normal to the interface, and with the radial flowing solution. A precise definition of solute boundary layer

* Electrochemical Society Active Member.
Present address: ARCO Solar Incorporated, Chatsworth, California 91311.
Key words: interface, integrated circuits, crystallization, diffusion.

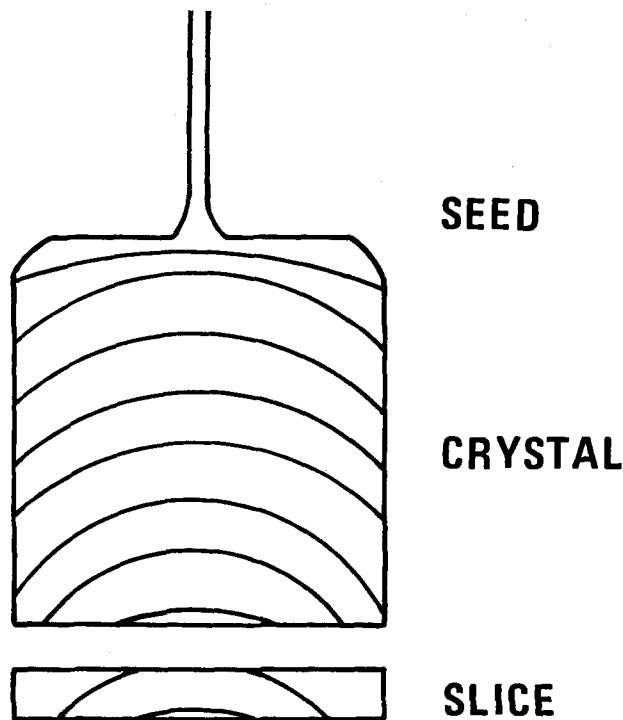


Fig. 1. Schematic illustration of a silicon crystal cross section containing curved melt interface surfaces which result in inhomogeneities on a slice surface.

thickness would be the distance from the solid into the melt at which concentration level becomes constant and equal to the bulk melt composition.

It is preferred to assume that the segregation coefficient is unchanged within the small range of the relevant silicon-impurity phase diagram, since it is a thermodynamic parameter relating the activity of the impurity in the solid and liquid. A crystal growth description which treats K as a variable parameter, such as K_{eff} , masks a true understanding of the interface dynamics since microscale concentration variations are caused by concentration changes occurring at the interface, not by a variation in K .

The purpose of this paper is to present calculations on relationships of solute nonuniformities in a silicon crystal and to suggest a method to use measured dopant variations to predict variations in other impurities. This analysis is based on the two assumptions: (i) the segregation coefficient is a constant; and (ii) the boundary layer thickness is defined by physical parameters (both are unchanged by growth rate).

Background

The Burton, Prim, Slichter (BPS) description of crystal growth relates variations in impurity incorporation into the solid by varying the equilibrium segregation coefficient K to an effective $K(K_{\text{eff}})$ value (6). The main equation of the BPS model is

$$K_{\text{eff}} = \frac{K_0}{K_0 + (1 - K_0)e^{-f\delta/D}} \quad [1]$$

using the Cochran (7) definition of boundary layer thickness

$$\delta = 1.6 D^{1/3} \nu^{1/6} \omega^{-1/2} \quad [2]$$

where f is the growth rate solid, δ is the boundary layer thickness, D is the diffusion coefficient of the solute in the melt, ν is the kinematic viscosity of the liquid, and ω is the angular velocity of crystal rotation. The K_{eff} equation is applicable to a (at least instantaneous) steady-state condition and can be used to relate the concentration in the solid to the bulk liquid concentration. Variation in K is used to account for solute concentration changes occurring at the solid-

liquid interface. The application of this model is usually done by fitting solute concentration profiles in crystals grown at various macroscopic growth rates using δ/D as a parameter, and subsequent calculation of K_{eff} . This technique has been used to derive a consistent description of a macroscopic situation and also has been the major technique used to obtain values for diffusivities (7).

A description of solute buildup in zone refining was given by Tiller, Jackson, Rutter, and Chalmers (8). The main equation describing buildup is

$$C_T = \frac{C_s}{K} = C_0 \left\{ \left[\frac{1-K}{K} \right] \left[1 - \exp\left(-K \frac{R}{D} x\right) \right] + 1 \right\} \quad [3]$$

where C_T is the solute concentration at the growing interface, C_s the solid, C_0 the initial concentration in the melt, R rate of advance of the interface, and x the distance the interface has traveled. This description applies to a constant and limited melt volume, melt replenishment of C_0 concentration, and no melt stirring, i.e., only diffusion of the excess solute away from the interface. The approach has the attraction of focusing on impurity buildup and gives a valid macroscopic view of zone refining. Nonmonotonic solute incorporation into the solid, "banding" is briefly ascribed to changes in heat input to the liquid. The description has limited application to a Czochralski configuration with a large and varying, stirred, melt volume.

A modification of the BPS description was used by Hall (9) to correlate the effect of varying growth rate on incorporation of multiple impurity dopants in germanium crystals. The equation was

$$K_{\text{eff}} = K \exp(V/V_d) \quad [4]$$

where V is the growth velocity and V_d a characteristic growth parameter which depended upon the degree of stirring and diffusion in the melt. The technique was used to develop a process for the growth of crystals having a series of p-n junctions, using gallium and antimony dopants, by varying the growth rate. The important interplay between segregation, growth rate, and melt stirring are included in this model, but emphasis is placed on a K_{eff} , rather than interface concentration.

The development of a technique (10) to determine the microscopic growth rate in a Czochralski puller enabled analysis of actual interface dynamics. The measured dopant variations were found to follow the general shape of the microscopic growth rate curve. Analysis of the data was done using the form of the BPS model

$$C_s = K_{\text{eff}} C_L = \frac{K C_L}{K + (1 - K) \exp(-V\delta/D)} \quad [5]$$

where C_L is the solute concentration in the bulk liquid and V is the microscopic growth rate obtained from the constant time marks. Crystal dopant levels and microscopic growth rate data were used to obtain the value of δ/D as a parametric fit to Eq. [5] and then the best fit δ/D used to calculate the expected dopant concentration. A value of δ/D of 133.3 sec/cm was obtained which led to a boundary layer thickness of 266 μm taking $D = 2 \times 10^{-4} \text{ cm}^2/\text{sec}$. The value of D was originally obtained (11) by a similar treatment using the BPS model. An independent evaluation of D would be preferred.

The technique of determining microscopic growth rate aided significantly to understanding actual Czochralski crystal growth. Several works (4, 11, 12) support the concept that microscopic growth rate changes are caused by thermal convection currents within the melt.

Analysis and Discussion

Thermal fluctuations which disturb the rate of crystal growth change the rate of solute rejection. The limitation of diffusion of the solute through the boundary layer causes the interface solute concentration to continually change. This is illustrated in Fig. 2 (a and b) where (a) depicts the solute concentration as the microscopic growth rate increases and (b) depicts the solute concentration as the microscopic growth rate decreases. Periodic thermal convection currents cause fluctuations in growth rate, especially during crystal growth from melts having a height-to-diameter (h/d) aspect ratio $> 1/2$. As the volume of remaining melt is decreased, h/d decreases and the microscopic growth rate may at times be negative, i.e., remelting of the crystal may occur.

Crystal growth without remelt.—During periods of increasing microscopic growth rate, solutes with $K < 1$ will be enriched at the solid-liquid interface, and solute diffusivity is insufficient to avoid increasing concentration at the interface. For solutes with $K > 1$ such as oxygen, the concentration at the solid-liquid interface will be depleted and a decreasing amount of these solutes will be incorporated into the crystal.

During periods of decreasing microscopic growth rate, solutes with $K < 1$ will have greater time for diffusion away from the solid-liquid interface and the interface concentration will be decreasing. Solute with $K > 1$ will have more time for concentration replenishment to the melt-liquid interface and thus will show increasing concentration in the solid.

When microscopic growth is at a minimum positive value, interface solute concentrations closer to the bulk melt concentration result. As the microscopic growth rate then begins to increase, the maximum concentration of oxygen ($K C_L$) can be incorporated into the crystal. This is consistent with the observations that oxygen is at a maximum on the melt side of growth striation (12). Correspondingly, the initial acceleration period after a pause will incorporate the minimum of components with $K < 1$ and this minimum approaches $K C_L$. Table I summarizes the solute changes as the microscopic growth rate varies and the limits in impurity concentrations that can conclude from this approach.

When the microscopic growth rate reaches a maximum, the minimum of solutes with $K > 1$ are incorporated into the crystal at some value of $< K C_L$. The maximum in microscopic growth rate corresponds to the maximum in solute incorporation for $K < 1$, and the maximum may be $>> K C_L$ for these solutes.

Crystal growth with extensive remelt.—Crystal growth at conditions where extensive remelt is occurring, such as at low melt aspect ratios, is less well characterized since the microscopic growth rate determination technique is not applicable. The previous discussion showed that as microscopic growth rate decreases, diffusion through the boundary layer decreases the concentration of solutes with $K < 1$ at the solid-liquid interface. If a portion of the crystal is remelted,

Table I. Summary of solute concentration dynamics during crystal growth

Microscopic growth rate	$K < 1$			$K > 1$		
	C_i	C_s	C_b	C_i	C_s	C_b
Increasing	$>> C_L$, inc.	$> K C_L$, inc.	$> C_L$	$< C_L$, dec.	$< K C_L$, dec.	$< C_L$
Decreasing	$> C_L$, dec.	$> K C_L$, dec.	$> C_L$	$< C_L$, inc.	$< K C_L$, ins.	$< C_L$
Pause	$\rightarrow C_L$	$\rightarrow K C_L$	$\rightarrow C_L$	$\rightarrow C_L$	$\rightarrow K C_L$	$\rightarrow C_L$
Negative (remelting)	dec.	—	dec.	inc.	—	inc.

Note: Maximum C_s for any $K > 1 = K C_L$
 Minimum C_s for any $K < 1 = K C_L$

\rightarrow = approaches
 inc. = increasing
 dec. = decreasing

a further decrease in solute concentration at the interface occurs, since concentration in the melting crystal was less than the interface concentration. Depending upon the amount and speed of remelting, as the crystal begins to refreeze, a reduced concentration of $K < 1$ solutes may result. For solutes with $K > 1$, remelting of the crystal causes the interface concentration to increase. As the crystal begins to refreeze, the concentration of these solutes in the solid is likely similar to the remelted crystal. Lacking detailed information on the dynamics occurring during such remelting periods, limits on the solute concentration in the solid cannot be established.

Float zone crystal growth.—The growth mechanism perspective which focuses on solute buildup at the interface is consistent with the occurrence of solute concentrations in float zone crystals. It was shown (13) that carbon concentration bands occur on the seed side of melt striae (as they most likely also do in Czochralski crystals). Correspondingly then, associated with the carbon banding will be higher concentrations of metallic impurities and dopant since the striae are also caused by thermal convection current disturbance of the microscopic growth rate.

Investigation of the impurity striation in float zone crystals having various carbon levels showed that at an average carbon level of 8×10^{16} atoms/cm³, significant banding of carbon occurred (14). Associated with the maxima and minima of carbon across a wafer surface, correspondingly were maxima and minima of the phosphorous dopant. Subsequent diffusion of gold into the high carbon, striated wafers resulted in gold preferentially distributed into carbon and phosphorous-rich areas and performance of power devices made on this material was substantially degraded.

Impurity distribution calculation.—The impurity concentration of the solid is related to the interface concentration $C_s = K C_i$. The fractional change in C_i with varying (microscopic) growth rates can be calculated from

$$\Delta C_i = \frac{C_i - C_L}{C_L} = \frac{(1 - K)(1 - e^{-\Delta})}{K + (1 - K)e^{-\Delta}}$$

where $\Delta = f\delta/D$.

This equation for ΔC_i was used to calculate the expected changes in concentration for several common impurities. The Cochran (15) derivation of boundary layer thickness was used since it was judged that a more consistent alternative was not available. A kinematic viscosity of 0.0106, as calculated by Kodera (7), was also chosen. The magnitude, but not the trends, in ΔC_i would be slightly sensitive to other selected values. Growth rates of 25, 50, and 75 $\mu\text{m}/\text{sec}$ and rotation rates of 10, 15, and 20 rpm were selected to represent typical values for silicon crystal production.

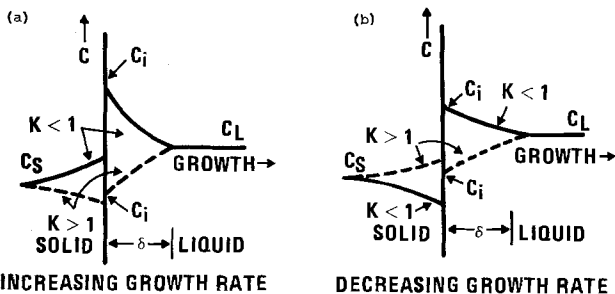


Fig. 2. Schematic of solute profile at solid-liquid interface during growth. (a) Increasing microscopic growth rate. (b) Decreasing microscopic growth rate.

Table II. Calculated interface concentration change in silicon

Impurity	K	D (10 ⁴ cm ² /sec)	ω (sec ⁻¹)	δ (μ m)	ΔC_i			
					f (μ m/sec)	f (μ m/sec)	f (μ m/sec)	f (μ m/sec)
Boron	0.8	2.4 (Ref. 5e)	1.05	455	8	25	51	76
			1.57	372		0.08	0.14	0.18
			2.10	322		0.07	0.12	0.16
Phosphorus	0.35	5 (Ref. 5e)	1.05	540	0.33	25	0.48	0.72
			1.57	441		0.19	0.39	0.58
			2.10	381		0.16	0.33	0.50
Antimony	0.023	1.5 (Ref. 5e)	0.52	551	0.33	1.45	2.53	5.32
			1.05	389		0.89	1.81	3.60
			1.57	318		0.68	1.45	2.78
Oxygen	1.25	1*	0.52	481	-0.07	-0.15	-0.17	-0.19
			1.05	340		-0.13	-0.16	-0.18
			1.57	278		-0.11	-0.16	-0.18
Carbon	0.07	0.485 (Ref. 10)	1.05	267	0.42	2.34	6.89	10.90
			1.57	218		1.73	5.07	8.97
			2.10	189		1.45	4.04	7.49
Iron	8 \times 10 ⁻⁶	1*	0.52	481	0.42	1.91	3.25	6.16
			1.05	340		1.16	2.37	4.50
			1.57	278		0.89	1.90	3.56
Aluminum	0.002	7 (Ref. 5e)	0.52	608	0.27	1.16	1.98	4.14
			1.05	430		0.73	1.44	2.81
			1.57	350		0.56	1.16	2.18
Copper	4 \times 10 ⁻⁴	2*	0.52	304	0.27	0.47	0.60	1.03
			1.05	460		0.21	0.47	0.78
			1.57	430		0.18	0.40	0.65
			1.05	430		0.72	1.96	4.10
			1.57	350		0.56	1.45	2.77
			2.10	304		0.47	1.16	2.17

* Assumed values.

The calculated values for ΔC_i are given in Table II along with the values used for K and D. Two calculations were made for carbon using an assumed value for D of 1×10^{-4} cm²/sec [this value was used in Fig. 3(b)], and also a measured value of 0.485×10^{-4} cm²/sec (16). The latter value was determined by an independent method and differs significantly from many of the other D values. The ΔC_i values are plotted in Fig. 3.

The large calculated increases in interface concentration for carbon and antimony are consistent with the tendency for single crystal growth breakdown even at C_L concentrations substantially less than equilibrium liquid solubility values. The expectation of improved uniformity of boron over phosphorous-doped crystals is also consistent with observations.

This approach can be used to predict impurity concentration variations by measurement of dopant variations. Data (1) on antimony variations at minimum (8 μ m/sec) and maximum (26 μ m/sec) microscopic growth rates indicated a ΔC_i of 0.11 and 0.40, respec-

tively, for a fitted parameter boundary layer thickness of 266 μ m. This compares to calculations based on the assumptions of this paper which predict a ΔC_i for antimony of 0.33 and 1.45 for the two growth rates and also ΔC_s of -0.08 and -0.15 for oxygen, 0.42 and 1.91 for carbon, 0.27 and 1.16 for iron for the respective growth rates. Selection of a thinner boundary layer value would reduce these predicted values. However, the areas of higher antimony concentration (fast growth rate) will have relatively lower oxygen, higher carbon and iron.

Deficiencies in calculations.—The discrepancies between the experimental data and the calculated values are likely influenced most from inaccuracy in the appropriate boundary layer thickness and to a lesser extent in the accuracy of the impurity diffusion coefficients and the viscosity of liquid silicon.

The Cochran (7) calculation for the momentum boundary layer was derived for liquid flow normal to the interface. Within the boundary layer adjacent to the crystal, radial velocity significantly exceeds normal

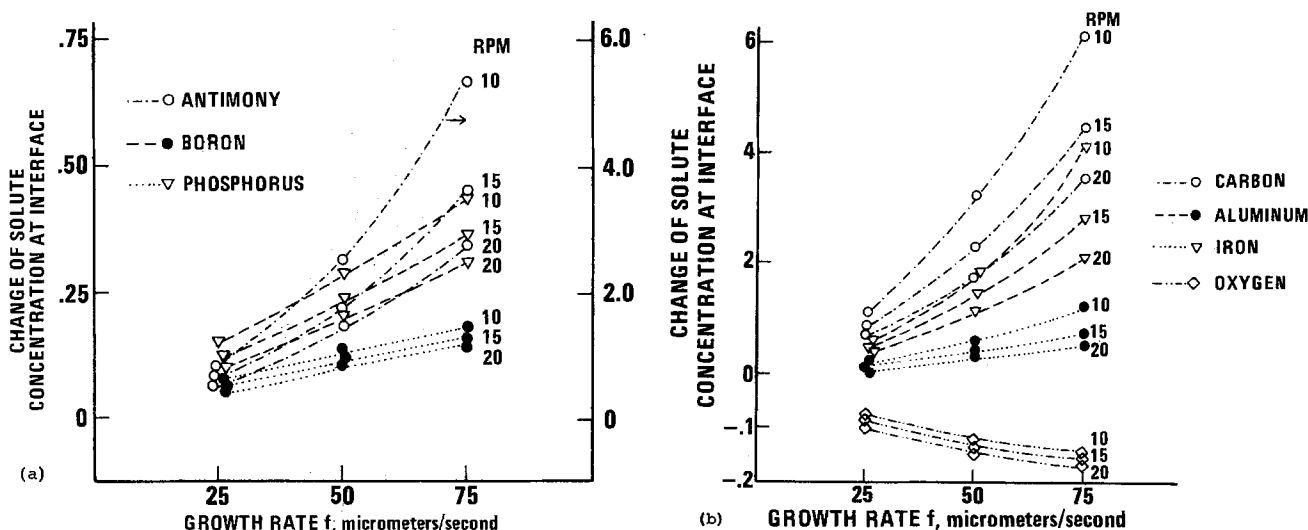


Fig. 3. Calculated change in impurity concentration at solid-liquid interface. (a) Common dopants, (b) impurities

velocity. Accurate calculations require a boundary layer thickness which relates the concentration, rather than momentum, boundary layer thickness established due to diffusion and physical mixing. Estimates of diffusion coefficients have usually been derived from solid concentration values at varying growth rate using a boundary layer value calculated by the Cochran analysis. Later use of such diffusion numbers and adjusting the boundary layer thickness to fit experimental data is a rather questionable, circular procedure. Independent measurement of diffusion coefficients is required.

The one independent check on carbon diffusion (16) in a nonstirred melt (assumed equivalent to silicon self-diffusion) was self-consistent with experimental results and less than one-half most commonly used diffusion values. It would seem consistent to speculate that diffusion coefficients for all impurities should approach the value for silicon self-diffusion. To assume that a weak impurity/silicon bonding (short-range ordering) could occur within the liquid state to allow deviation from silicon self-diffusion values would likely require consideration of impurity/impurity bonding also.

An error in the values for kinematic viscosity of silicon 0.0106 (calculated) (7) and 2.9×10^{-3} (experimental) (17) could lead to a small error in model calculations. However, viscosity enters only into the boundary layer thickness equation to the one-sixth power, so this is of less concern than accuracy of diffusivity or boundary layer thickness values.

Conclusions

Several conclusions can be obtained from this approach. (i) Treating K as a constant and focusing on solute concentration at the interface allows additional information to be gained regarding microscale distribution of oxygen, carbon, and other impurities. Both Czochralski and float zone distributions are consistently explained. (ii) Microscale dynamics of the growth interface have critical impacts on inhomogeneities in the crystal and some limits on concentrations can be elucidated, at least in the portion of crystal grown without extensive remelt. (iii) Silicon crystals with reduced microscale and macroscale inhomogeneities could be obtained from crystal pullers designed with minimum temperature gradients in the melt. A steady-state growth condition from a constant melt volume would aid in stabilizing the microscopic growth rate.

To capitalize on this approach a new mathematical model needs to be developed which defines both the

dynamics of the chemical environment at the interface and the transient thermal effects. Additional experimental efforts are needed to quantify the microscale nonuniformities, and relate their impact on device fabrication and performance.

Manuscript submitted Sept. 11, 1978; revised manuscript received March 21, 1979.

Any discussion of this paper will appear in a Discussion Section to be published in the December 1980 JOURNAL. All discussions for the December 1980 Discussion Section should be submitted by Aug. 1, 1980.

Publication costs of this article were assisted by ARCO Solar, Incorporated.

REFERENCES

1. A. Murgai, H. C. Gatos, and A. F. Witt, *This Journal*, **123**, 224 (1976).
2. A. Murgai, A. F. Witt, and H. C. Gatos, *ibid.*, **122**, 1276 (1975).
3. A. F. Witt, M. Lichtensteiger, and H. C. Gatos, *ibid.*, **120**, 1119 (1973).
4. J. R. Carruthers, A. F. Witt, and R. E. Reusser, in "Semiconductor Silicon 1977," H. R. Huff and E. Sirtl, Editors, p. 61, The Electrochemical Society Softbound Proceedings Series, Princeton, N.J. (1977).
5. K. M. Kim, A. F. Witt, and H. C. Gatos, *This Journal*, **119**, 1218 (1972).
6. J. A. Burton, R. C. Prim, and W. P. Slichter, *J. Chem. Phys.*, **21**, 1987 (1953).
7. H. Kodera, *Jpn. J. Appl. Phys.*, **2**, 212 (1963).
8. W. A. Tiller, K. A. Jackson, J. W. Rutter, and B. Chalmers, *Acta Metall.*, **1**, 428 (1953).
9. R. N. Hall, *Phys. Rev.*, **88**, 1987 (1953).
10. M. Lichtensteiger, A. F. Witt, and H. C. Gatos, *This Journal*, **118**, 1013 (1971).
11. A. Murgai, H. C. Gatos, and A. F. Witt, in "Semiconductor Silicon 1977," H. R. Huff and E. Sirtl, Editors, p. 61, The Electrochem. Society Softbound Proceedings Series, Princeton, N.J. (1977).
12. A. Murgai and W. A. Westdorp, *ibid.*, p. 83.
13. T. Abe, K. Kikuchi, and S. Shirai, *ibid.*, p. 95.
14. M. J. Hill and P. M. Van Iseghem, *ibid.*, p. 715.
15. W. C. Cochran, *Proc. Cambridge Philos. Soc.*, **30**, 365 (1934).
16. G. Gnesin and A. J. Raichenko, *Povoshkovaya Metallurgia*, No. 5, **125**, 35 (1973).
17. B. A. Baum, R. V. Gel'd, and P. V. Kocherov, "The Viscosity of Liquid Silicon, Chromium and Chromium Silicides," Translated from *Russ. Metall.*, **1**, 27, 28 (1967).

Thermal Manipulation of Deactivation Processes in Luminescent Photoelectrochemical Cells Employing Tellurium-Doped Cadmium Sulfide Photoelectrodes

Bradley R. Karas,* David J. Morano,* Daniel K. Bilich, and Arthur B. Ellis**

Department of Chemistry, University of Wisconsin-Madison, Madison, Wisconsin 53706

ABSTRACT

Temperature significantly modifies the efficiencies of luminescence and photocurrent in an n-type, single crystal, CdS:Te-based photoelectrochemical cell (PEC) employing aqueous polyselenide electrolyte. Between 20° and 100°C photocurrent (quantum yield Φ_x) from ultrabandgap 501.7 nm excitation increases modestly by \lesssim 20%, whereas photocurrent from bandgap edge 514.5 nm excitation increases by about an order of magnitude, reaching 50-100% of the 20°C 501.7 nm photocurrent. Undoped CdS exhibits a similar photocurrent-temperature profile. Higher temperatures thus extend the wavelength response of CdS- and CdS:Te-based PEC's. In contrast to the increase in photocurrent, emissive efficiency (quantum yield Φ_r) of CdS:Te drops by a factor of \sim 10-20 over the same temperature range; this decline is relatively insensitive to potential and excitation wavelength (501.7 or 514.5 nm). Little change in the spectral distribution of emission ($\lambda_{\max} \sim$ 600 nm) is observed with temperature. A dependence of emission intensity on potential is observed for the first time with 514.5 nm excitation in the high temperature regime. These results are interpreted in terms of band bending, optical penetration depth, the known red-shift of the CdS bandgap edge with temperature, and the competitive nature of emission and photocurrent. Relationships among Φ_x , Φ_r , and Φ_{r0}/Φ_r (out-of-circuit to in-circuit emission intensity) are discussed.

We recently reported that n-type, tellurium-doped CdS (CdS:Te) serves as a luminescent photoelectrode in photoelectrochemical cells (PEC's) used to convert optical energy to electricity (1). In this manner CdS:Te permits determination of the effect of PEC parameters such as incident excitation wavelength, electrolyte, and potential upon the various deactivation routes of the semiconductor electrode excited state. In particular, luminescence is a probe of electron-hole recombination processes which compete with electron-hole separation leading to photocurrent.

In the course of our studies, we noted that the emission intensity and, in some instances, the photocurrent of CdS:Te-based PEC's were temperature dependent. We demonstrate herein that temperature may be used to significantly modify the relative efficiencies of excited state deactivation pathways in a manner which underscores the competitive nature of luminescence and photocurrent. In addition, higher temperatures extend the wavelength response of both CdS- and CdS:Te-based PEC's.

Theory

The bandgap of undoped CdS, E_{BG} , is \sim 2.4 eV at 298°K (2). Although CdS:Te has a low energy tail in its absorption spectrum which masks the bandgap, the highest absorptivities ($>10^4$ cm $^{-1}$) occur at $\lambda \lesssim$ 500 nm in both undoped CdS and CdS:Te (2-6). Ultrabandgap wavelengths are therefore taken as those with $\lambda \lesssim$ 500 nm; absorption occurs within \sim 0.1-1 μ of the surface, a distance typically corresponding to the depletion region. This zone is characterized by maximum band bending and is conducive to ready separation of photogenerated electron-hole ($e^- - h^+$) pairs leading to maximum photocurrent (7).

Longer excitation wavelengths penetrate farther into the crystal, and the diminished band bending favors $e^- - h^+$ recombination at the expense of separation. Luminescent CdS:Te-based PEC's exhibit more emis-

sion and less photocurrent with bandgap edge 514.5 nm than with ultrabandgap 501.7 nm excitation, for example (1).

Figure 1(a) illustrates the interrelationship of penetration depth and band bending at these wavelengths. The dashed line represents the discrete states involved in the emissive process which are introduced by the Te dopant; holes trapped at Te sites (Te presumably substitutes for S in the lattice) may coulombically bind an electron in or near the conduction band to form an exciton whose subsequent radiative collapse leads to luminescence (3-6).

Our chief guide for predicting thermal effects in the PEC was the known optical bandgap temperature coefficient, dE_{BG}/dT , for undoped CdS. This coefficient has a value of -5.2×10^{-4} eV/°K between 90° and 400°K (8). To the extent that CdS:Te resembles CdS, this relationship predicts that the bandgap edge red shifts with increasing temperature; at a sufficiently high temperature 514.5 nm will become an ultrabandgap wavelength like 501.7 nm, for example. Figures 1(b) and (c) illustrate the anticipated effect of increased temperature on the band diagram and absorption spectrum. The decline of E_{BG} with increasing temperature has been interpreted as arising from two effects: lattice dilation and energy level broadening at the edges of the bandgap due to collisions between electrons and phonons (9).

Implicit in the comparison of Fig. 1(a) and (b) is the relative insensitivity of the depletion region width, W , to temperature. The expression for W is given by Eq. [1] where

$$W = (2\epsilon_0 V_B / qN)^{1/2} \quad [1]$$

N is the charge carrier density in the semiconductor, q is the electronic charge, ϵ_0 is the permittivity of free space, ϵ is the semiconductor dielectric constant, and V_B is the amount of band bending in the depletion region (10). For a given electrolyte we do not expect W to change drastically over the 20°-100°C temperature range investigated. That is, we are assuming variations in ϵ , N , and V_B to be small. We note that ϵ changes by less than 15% between -196° and 25° C for undoped

* Electrochemical Society Student Member.

** Electrochemical Society Active Member.

Key words: photoelectrochemistry, luminescence, semiconductors.

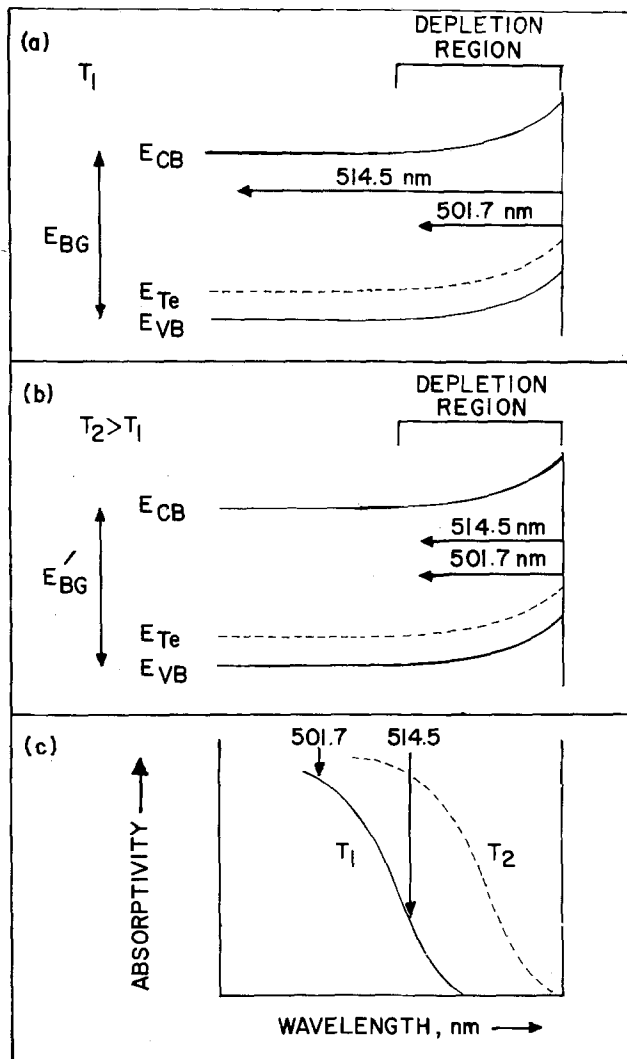


Fig. 1. (a) Comparison of penetration depths for bandgap edge (514.5 nm) and ultrabandgap (501.7 nm) excitation relative to the width of the depletion region at temperature T_1 for CdS:Te (not to scale). E_{CB} and E_{VB} refer to the conduction and valence band energies. Doping CdS with Te is believed to introduce discrete states at energy E_{Te} . E_{BG} is the bandgap energy at T_1 ; (b) at temperature $T_2 > T_1$ the bandgap is expected to shrink, $E_{BG}' < E_{BG}$; as a consequence, the penetration depth of 514.5 nm light would be reduced; (c) the expected effect on the CdS:Te absorption spectrum caused by an increase in temperature. Solid and dashed lines represent the spectra at T_1 and T_2 , respectively (curves are crude approximations and not drawn to scale).

CdS (11) and that donors in 50 ppm CdS:Te are $\geq 90\%$ ionized at room temperature (Hall measurements) (5). The maximum value of V_B is controlled by the relative energies of the semiconductor Fermi level and the electrolyte redox potential, E_{redox} (7, 10). While the explicit temperature dependence of V_B is not known for the electrolyte employed, our results are consistent with small changes in V_B and W . We emphasize that these are assumptions, however, and that a rigorous analysis requires knowledge of the depletion width. With this in mind, we treat Fig. 1 as an approximation whose validity can be qualitatively probed by the PEC of Fig. 2.

The PEC consisted of an n-type, single crystal, 100 ppm CdS:Te working electrode, a 2.0×0.8 cm Pt foil counterelectrode, an Ag pseudoreference electrode (PRE), and an aqueous polyselenide electrolyte of approximate composition 5M OH⁻/0.1M Se²⁻/0.001M Se₂²⁻. Temperature control was achieved with resistive heating, as sketched in Fig. 2. Emission and photocurrent could be monitored simultaneously by placing the

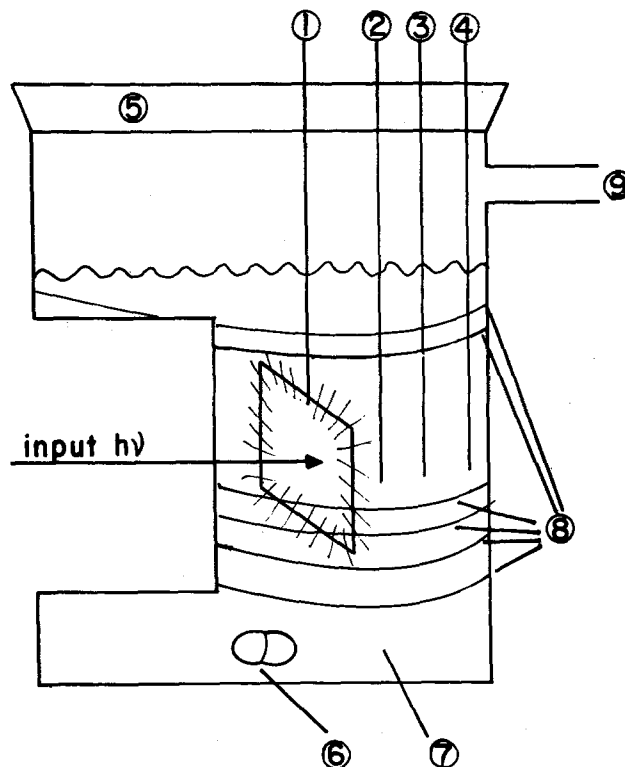
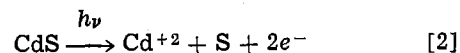


Fig. 2. Components of the CdS:Te-based variable temperature PEC: (1) n-type CdS:Te photoelectrode, site of polyselenide oxidation; (2) thermometer; (3) Pt foil counterelectrode, site of polyselenide reduction; (4) Ag pseudoreference electrode (PRE); (5) rubber stopper, positioned loosely enough to serve as a vent, through which (1)-(4) are inserted; (6) magnetic stir bar; (7) aqueous polyselenide electrolyte; (8) Nichrome wire wound outside the cell for resistive heating; (9) N₂ inlet, the N₂ passing first through an aqueous reservoir. Components (1), (3), and (4) are connected to a potentiostat.

PEC inside an emission spectrometer and inclining the electrode at $\sim 45^\circ$ with respect to both the Ar ion laser excitation beam and the emission detection optics; the laser beam was expanded and masked to fill the electrode surface. The electrochemistry occurring corresponds to oxidation of polyselenide electrolyte at the photoanode and the reduction of polyselenide at the counterelectrode (12). No net change occurs in the electrolyte under these conditions, thus permitting sustained conversion of optical energy to electricity, while inhibiting the competitive photoanodic dissolution process, Eq. [2] (12)



Polyselenide electrolyte is also an advantageous choice because of its relative transparency to the excitation wavelengths employed (12).

Results and Discussion

Emissive properties.—While $E_{BG} = |E_{CB} - E_{VB}|$ is expected to vary inversely with temperature, the temperature dependence of the CdS:Te emission spectrum will hinge on the relative positions of E_{Te} , E_{CB} , and E_{VB} . We and others have found that at 77°K the emission maximum blue shifts slightly from its 298°K ~ 600 nm value; the spectrum also sharpens and increases in intensity dramatically (1, 3-6). As the photoelectrode in a PEC, CdS:Te shows little change in the emitted spectral distribution (bandwidth ~ 5 nm; 540-800 nm) over the $\sim 20^\circ$ - 100° C temperature range investigated in polyselenide electrolyte. A few samples displayed a modest red shift of λ_{max} (~ 10 nm) and/or more of a low energy tail at the high temperature extreme. Typical spectra obtained at open circuit are shown in Fig. 3. In

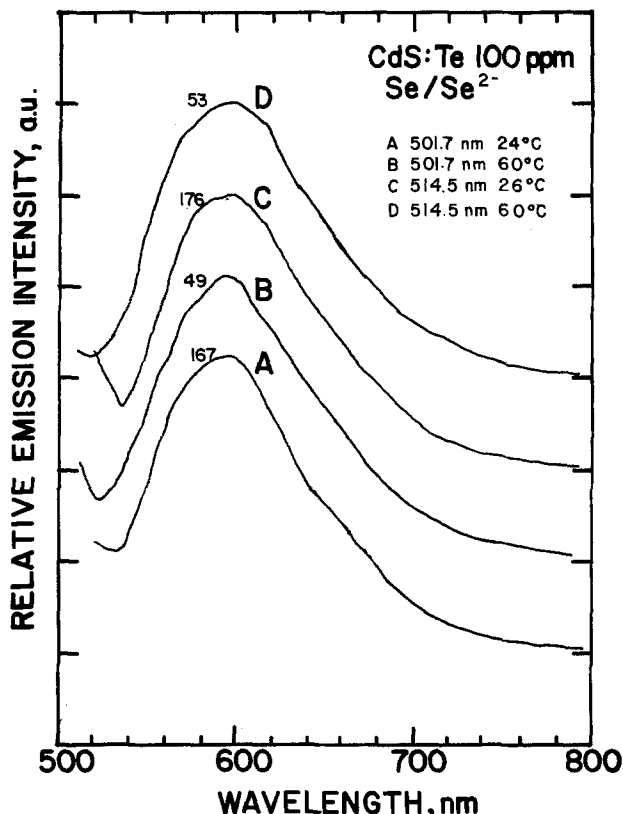


Fig. 3. Uncorrected emission spectra at open circuit of a CdS:Te electrode in $5M OH^-/0.09M Se^{2-}/0.001M Se_2^{2-}$ electrolyte. Temperature and excitation wavelength employed for each curve are identified in the figure. Although the curves have all been normalized to the same intensity at $\lambda_{max} \sim 600$ nm, the number above each curve gives the actual intensity before normalization. A filter solution was used to eliminate the exciting light (see Experimental) and is responsible for the deviations from baseline at the short wavelength extreme.

agreement with our earlier studies, the spectral distribution is independent of whether 501.7 or 514.5 nm excitation is used and independent of electrode potential between $+0.7V$ vs. Ag (PRE) and the onset of cathodic current. Changes in potential alter the degree of band bending in an n-type semiconductor: negative bias diminishes and positive bias augments band bending (7). If the Te state energies were not affected by potential in the same manner as the conduction and valence bands, we would expect to see potential dependent spectral distributions. This not being the case, we show E_{Te} bent in parallel with E_{CB} and E_{VB} in Fig. 1(a) and (b).

Another noteworthy feature of Fig. 3 is the considerable decline in CdS:Te emission intensity with increasing temperature. The effect is reversible; luminescence reappears with reproducible intensity upon cooling. A more quantitative measure of this effect is provided by Fig. 4(a) which displays the open-circuit emission intensity monitored at λ_{max} (~ 600 nm) vs. temperature for both excitation wavelengths in polyselenide electrolyte. Earlier studies of CdS:Te in the absence of electrolyte show analogous thermal quenching; plots of $\ln(I_o/I_T - 1)$ vs. T^{-1} (I_o is the maximum emission intensity observed at low temperature; I_T is the emission intensity at temperature T) yielded straight lines over the range of $150^\circ \lesssim T \lesssim 300^\circ K$ and activation energies, corresponding to the exciton binding energy, of ~ 0.2 eV (3-5, 13). The radiative efficiency is expected to decline from its maximum value, I_o , with increasing temperature, as progressively more thermal energy becomes available to ionize Te-bound holes. We find the rates of decline in emission to be comparable for 514.5 and 501.7 nm excitation. Because emission from the latter is gen-

erally weaker (1b, d), the data in Fig. 4(a) were obtained with 501.7 nm excitation of ~ 6 times the 514.5 nm intensity in order to match incipient luminescence intensity at room temperature. Note that both curves fall by a factor of ~ 10 -20 over the $75^\circ C$ interval. This factor is comparable to literature data obtained in the absence of electrolyte and with excitation sources consisting of ultrabandgap light (3b, 5), electron beams (4), and α particles (13).

We also wished to determine whether the decline in emission intensity with temperature was potential dependent. Figures 4(b) and (c) present emission-temperature curves for equivalent numbers of 514.5 and 501.7 nm photons, respectively, at three potentials: open-circuit, 0.0V, and 0.7V vs. Ag (PRE). The irradiated CdS:Te electrode emits more intensely with the longer excitation wavelength so that "100" on Fig. 4(b) represents ~ 5 times the intensity of "100" on Fig. 4(c). To a first approximation the rate of decline in both figures is independent of potential. This is seen more clearly with 514.5 nm excitation where there is very little dependence of emission intensity on potential until high temperatures are reached (*vide infra*). However, even with the more potential dependent emission intensity from 501.7 nm excitation, the rates of decline are similar as evidenced by the parallel shapes of the three curves. As a unit, Fig. 4 indicates that the decline of CdS:Te emission intensity with temperature is relatively insensitive to both penetration depth (501.7 and 514.5 nm) and potential ($+0.7V$ vs. Ag to the onset of cathodic current).

iLV curves.—Simultaneous measurement of current, luminescence, and voltage (*iLV* curves) as a function of temperature is facilitated by the cell of Fig. 2. The emission intensity is conveniently monitored by sitting at a single wavelength, generally λ_{max} . Our previous observations regarding *iLV* curves for CdS:Te-based PEC's at $298^\circ K$ in aqueous (poly)chalcogenide electrolytes may be summarized as follows: for ultrabandgap wavelengths (e.g., 501.7 nm), we observe high quantum efficiencies for electron flow, Φ_x , and potential dependent emissive quantum efficiencies, Φ_r ; in general Φ_r and Φ_x vary inversely as a function of potential. For bandgap edge (e.g., 514.5 nm) excitation we observe lower values of Φ_x and higher values of Φ_r ; however, Φ_r is largely independent of potential (1).

The ratio of open-circuit to in-circuit emission intensity, Φ_{r0}/Φ_r , is a useful expression of the potential dependence with the in-circuit value taken at a potential where saturation of photocurrent is evident. For bandgap edge excitation Φ_{r0}/Φ_r is roughly unity, whereas with ultrabandgap light we have observed ratios from ~ 1.2 to as high as 15. To some extent Φ_{r0}/Φ_r correlates with Φ_x which is invariably low (< 0.1) for bandgap edge excitation. Ultrabandgap light often gives $0.5 < \Phi_x < 1.0$. By pulsing the electrode between potentials corresponding to open circuit and maximum photocurrent, the discrepancy of Φ_{r0}/Φ_r from unity is visibly apparent. The same effect may be observed at different potential sweep rates including point-by-point. We have so frequently observed this phenomenon that we have come to regard it as jointly diagnostic of ultrabandgap excitation and a high value of Φ_x .

The prediction afforded by Fig. 1 is that increasing the temperature will increase Φ_x for 514.5 nm excitation. Should this occur we would also predict that Φ_{r0}/Φ_r will exceed unity. In Fig. 5(a) we present plots of photocurrent vs. temperature for 501.7 and 514.5 nm excitation (equal photons/sec) of CdS:Te in aqueous polyselenide electrolyte. The photocurrent at the former wavelength increases by less than 20% over the thermal excursion, but rises by a factor of ~ 10 with 514.5 nm excitation. In most cases this increase is sufficient to either match the 501.7 nm photocurrent or produce a large fraction ($\geq 50\%$) of it. Since 501.7 nm photocurrent is relatively insensitive to tempera-

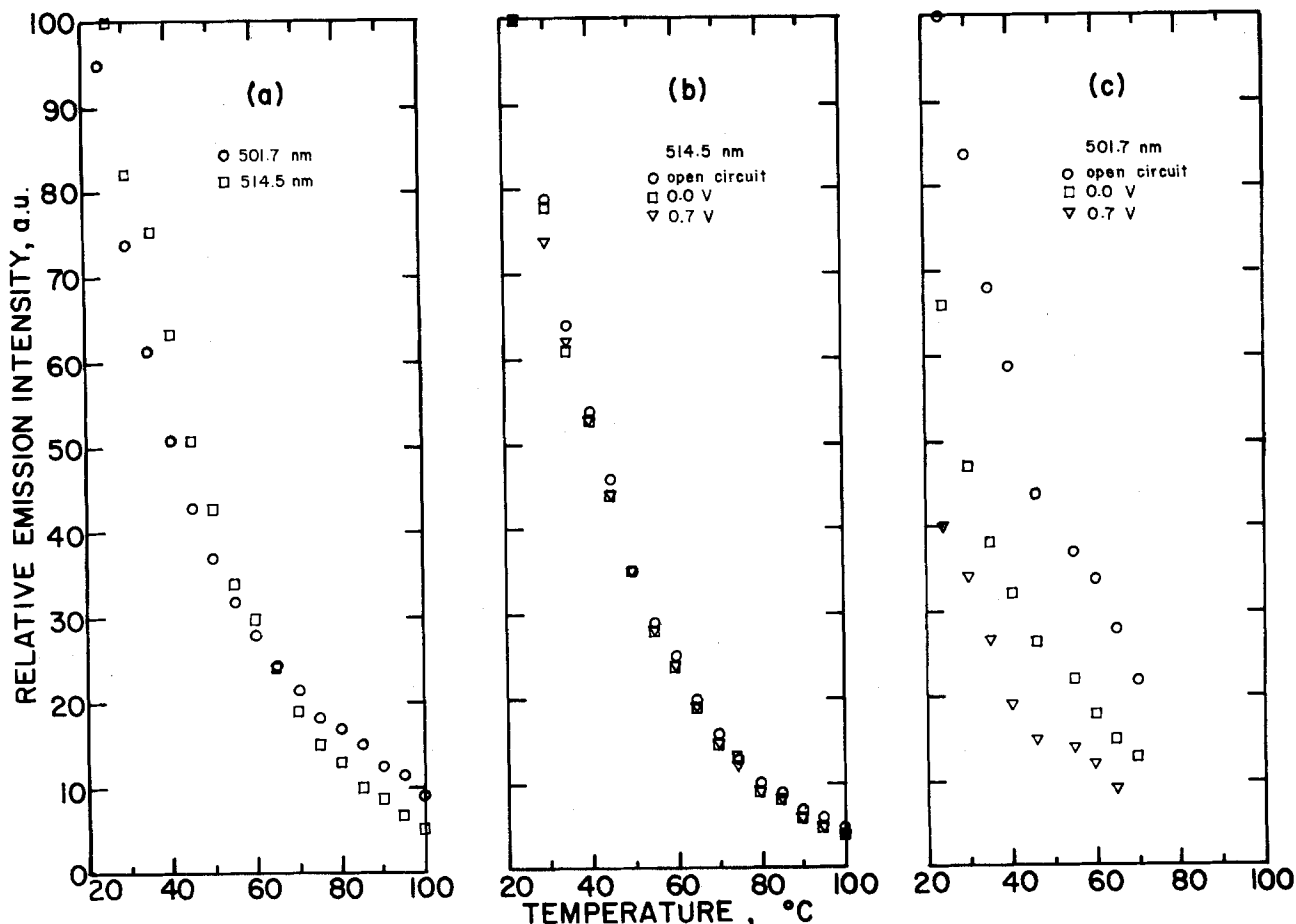


Fig. 4. (a) Relative emission intensity monitored at 600 nm vs. temperature in polyselenide electrolyte ($5M OH^-/0.09M Se_2^{2-}/0.001M Se_2^{2-}$) of CdS:Te excited at open circuit with 501.7 nm (circles) and 514.5 nm (squares) light. The excitation intensity at 501.7 nm is $6\times$ that at 514.5 nm in order to approximately match emission intensity at room temperature; (b) relative emission intensity vs. temperature for 514.5 nm excitation of a CdS:Te electrode [different sample than in (a)] in polyselenide electrolyte ($5M OH^-/0.02M Se_2^{2-}/0.001M Se_2^{2-}$) at three potentials. Circles, squares, and triangles correspond to open circuit, 0.0V, and 0.7V vs. Ag(PRE), respectively; (c) relative emission intensity vs. temperature for the same electrode and geometric configuration as in (b), but now excited with an equivalent number of 501.7 nm photons as in (b). The point "100" on the emission scale is \sim one-fifth the corresponding point in (b). The symbols in (c) have the same significance in terms of potential as in (b). Typical photocurrent behavior at 0.7V accompanying the emission changes shown in (b) and (c) is given in Fig. 5(a).

ture in this range and is not substantially exceeded with shorter wavelength excitation (e.g., 457.9 nm), we regard it as a saturation photocurrent.

Perhaps not surprisingly, undoped CdS yields a similar photocurrent-temperature plot, Fig. 5(b). Because both undoped CdS and 100 ppm CdS:Te have about the same absorptivity for 514.5 nm light (6), it is difficult to determine what role, if any, the low energy absorption tail of CdS:Te plays in the photocurrent-temperature profile. Longer excitation wavelengths should be helpful in resolving this question. We can say that the rate at which 514.5 nm photocurrent approaches 501.7 nm photocurrent in Fig. 5 is in qualitative agreement with the bandgap temperature dependence (*vide supra*). This calculation is made by noting that the two wavelengths differ by ~ 0.061 eV, predicting a temperature range of $\sim 120^\circ C$ for matching penetration depths from the model and assumptions described above.

Full iLV curves for a CdS:Te-based PEC employing polyselenide electrolyte are presented in Fig. 6. Equivalent intensities (photons/sec) of 501.7 and 514.5 nm excitation were used at both room temperature and elevated temperature ($49^\circ C$ for 501.7 nm; $86^\circ C$ for 514.5 nm). These plots succinctly summarize many of the properties described previously: photocurrent at $23^\circ C$ is ~ 18 times greater for 501.7 nm excitation (curve A vs. curve B) and emission intensity at open circuit is ~ 5 times smaller (curve A' vs. curve B'). The value of Φ_r/Φ_r is unity for 514.5 nm (curve B') and 3.5

for 501.7 nm light (curve A'). At $49^\circ C$ photocurrent with 501.7 nm excitation only increased by $\sim 15\%$ (curve C) but has dramatically increased at $86^\circ C$ with 514.5 nm light by a factor of almost 8 (curve D). Emission intensity has dropped by more than a factor of 2 with 501.7 nm light while retaining a similar value of Φ_r/Φ_r of 3.4 (curve C'); for the first time and despite its lower absolute intensity, emission from 514.5 nm excitation has resulted in a nonunity value of $\Phi_r/\Phi_r = 1.27$ (curve D', note tenfold scale expansion). We visually confirmed the discrepancy from unity by pulsing the electrode between the extreme voltages shown on curve D'. As mentioned above, this phenomenon is characteristic of larger values of Φ_x . All of the aforementioned changes were reversible simply by returning to the lower temperature. Similar photocurrent and emissive trends were also observed in OH^-/S^{2-} electrolyte.

Energy conversion efficiency.—Another feature of Fig. 6 worth noting is the enhancement of optical to electrical energy conversion efficiency at higher temperature with 514.5 nm excitation. The efficiency, η , is given by Eq. 3 for bandgap energy excitation

$$\eta = \frac{\Phi_x E_V}{E_{BG}} \quad [3]$$

E_V is the output voltage; extraction of this value from $i-V$ curves has been described (12).

In Table I we present a summary of the energy conversion parameters for both undoped CdS- and CdS:

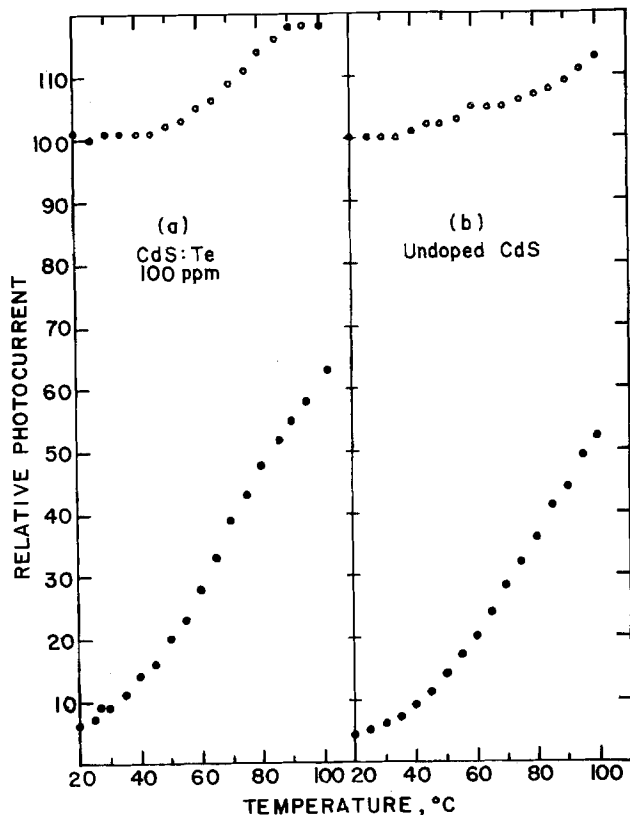


Fig. 5. (a) Relative photocurrent vs. temperature for a CdS:Te electrode in aqueous polyselenide electrolyte ($5M OH^-/0.02M Se_2^{2-}/0.001M Se_2^{2-}$) excited with equivalent photons of 514.5 nm (filled circles) or 501.7 nm (open circles) light at 0.7V vs. Ag(PRE). The scale is such that the photocurrent at 25°C from 501.7 nm excitation has been arbitrarily set at 100 and corresponds to a current density of ~ 0.36 mA/cm² and a quantum yield for electron flow, Φ_x , of ~ 0.50 ; (b) relative photocurrent vs. temperature for an undoped CdS electrode in the same electrolyte as in (a), excited with an equivalent photon flux of 514.5 nm (filled circles) and 501.7 nm (open circles) light. Again, "100" has been arbitrarily set as the 25°C photocurrent from 501.7 nm excitation and represents a current density of ~ 0.44 mA/cm² and a Φ_x of ~ 0.60 .

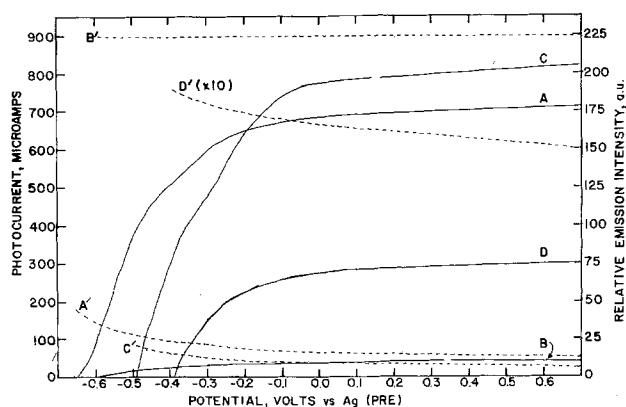


Fig. 6. Current-luminescence-voltage (*iLV*) curves for a CdS:Te electrode in polyselenide electrolyte. Unprimed, solid line curves are photocurrent (left-hand scale). Primed, dotted line curves are luminescence intensity (right-hand scale) monitored at λ_{max} , ~ 600 nm. Curves A and A' were obtained from excitation at 501.7 nm, 23°C; curves B and B' from 514.5 nm, 23°C; curves C and C' from 501.7 nm, 49°C; curves D and D' from 514.5 nm and 86°C. Note that the ordinate of curve D' has been expanded by a factor of 10. Equivalent numbers of 501.7 and 514.5 nm photons were used in identical PEC geometric configurations. The exposed electrode area is ~ 0.41 cm² and the estimated value of Φ_x for 501.7 nm excitation at 23°C and 0.7V vs. Ag(PRE) is ~ 0.50 , uncorrected for reflection losses and solution absorbance.

Table I. Optical to electrical energy conversion parameters^a

Electrode	T, °C	λ_{exc}	η_{max} , % ^b	E_V , V ^c	Φ_x at η_{max} ^d	Φ_x max ^e
CdS:Te	23°	501.7	5.6	0.32	0.44	0.75
		514.5	0.23	0.28	0.02	0.04
	73°	501.7	3.8	0.21	0.44	0.74
CdS	24°	514.5	1.0	0.18	0.14	0.26
		501.7	5.0	0.27	0.46	0.68
	73°	514.5	0.21	0.27	0.02	0.03
		501.7	2.5	0.19	0.32	0.68
		514.5	0.90	0.24	0.09	0.20

^a The indicated crystal served as the photoanode in a PEC similar to that shown in Fig. 2, but with only two electrodes (Pt counterelectrode and photoanode). Electrolyte composition is $5M OH^-/0.3M Se_2^{2-}/0.001M Se_2^{2-}$. Table entries represent typical values.

^b (Maximum electrical power out divided by input optical power) $\times 100$.

^c Output voltage at η_{max} .

^d Quantum efficiency for e^- flow at η_{max} ($\pm 15\%$), uncorrected for reflection losses and electrolyte absorption.

^e Maximum quantum efficiency ($\pm 15\%$) for e^- flow, measured at $\sim 0.7V$ vs. Ag(PRE), uncorrected for reflection losses and electrolyte absorption.

Te-based PEC's employing polyselenide electrolyte and a two electrode configuration (photoanode and Pt counterelectrode). The great improvement in η with temperature for 514.5 nm excitation is readily traced to an increase in Φ_x . At higher temperatures η from 514.5 nm excitation begins to rival that obtainable with 501.7 nm light for both electrodes. We do see a decline in output voltage at the higher temperatures; in general the i - V curves shift ~ 50 - 200 mV anodic between 20° and 100°C. This may indicate, as noted earlier, some difference in the relative energetic positions of the semiconductor Fermi level and E_{redox} with temperature.

While the enhanced red response is certainly desirable from the standpoint of solar energy conversion, we also wished to determine the extent to which it could be sustained. We found that photocurrent from 514.5 nm excitation of CdS:Te at $78^\circ \pm 5^\circ C$ declined at a respectably slow rate of 3%/hr over 9 hr at a current density of 0.56 mA/cm² at 0.08V vs. Ag(PRE). The emission spectrum was unaffected but for its 25% decline in intensity over this period. Neither the optical density of the electrolyte nor its redox potential changed noticeably during the experiment.

Implications regarding excited state decay routes.—

The striking inverse dependence of photocurrent and emission intensity on temperature depicted in Fig. 4-6 highlights their roles as competitive deactivation processes for the CdS:Te electrode excited state. While photocurrent is a unique probe of $e^- - h^+$ pair separation, emission is the minor product of $e^- - h^+$ pair recombination. Nonradiative recombination, (quantum yield Φ_{nr}) leading to heat is the dominant recombination process; room temperature emissive efficiencies for 100 ppm CdS:Te are at best only $\sim 1\%$ (1, 3-6).

Our intent has been to probe the manner in which input optical energy is partitioned among the three deactivation paths as a function of PEC parameters. In steady-state experiments such as these, the redistribution of energy is determined using measures of quantum efficiency, Φ_i . Our analysis is necessarily limited because we have only been able to obtain absolute numbers for Φ_x and relative values for Φ_r . We lack measures of Φ_{nr} entirely except insofar as they can be determined by difference, although photothermal spectroscopy has recently been used to provide quantitative information on nonradiative recombination (14). Despite these limitations, several important features do emerge from the thermal perturbation studies.

First, the ratio of Φ_x to Φ_r can be tuned over many orders of magnitude by a combination of excitation wavelength, electrode potential, and temperature. Previous work established the relative insensitivity to potential of Φ_r during excursions where Φ_x was varied

from zero (open circuit) to ~ 0.1 with 514.5 nm excitation (1). Figures 4-6 demonstrate for 501.7 nm excitation that changes in temperature leave Φ_x relatively constant while Φ_r varies by a factor of up to 20.

Recasting these observations, a given value of Φ_x does not affix unique values to Φ_r and Φ_{nr} . Besides the example just cited, consider Fig. 6 in more detail. At room temperature equivalent Φ_x can be achieved with 514.5 nm excitation at $+0.7V$ or with 501.7 nm excitation at $\sim -0.62V$ vs. Ag(PRE). Yet the emission intensity, Φ_r , corresponding to these two conditions is quite different. In a similar vein, a value of Φ_x attained at $-0.52V$ vs. Ag(PRE) with 501.7 nm excitation at room temperature can be matched at $0.7V$ with 514.5 nm excitation at $86^\circ C$, each condition accompanied by a different Φ_r . These differences can be ascribed to variations in optical penetration depth, band bending, and efficiencies of excited state deactivation processes.

Second, there is now additional evidence linking Φ_x with Φ_{r0}/Φ_r : (i) ratios exceeding unity for 514.5 nm excitation appear only at elevated temperatures where Φ_x has increased dramatically [Fig. 4(b) and 6]; (ii) neither Φ_x nor Φ_{r0}/Φ_r changed appreciably for 501.7 nm excitation as a function of temperature even though Φ_{r0} and Φ_r both changed drastically [Fig. 4(c) and 6]. A simplistic model correlating Φ_x with Φ_{r0}/Φ_r can be constructed with the assumption that the ratio of Φ_r to Φ_{nr} is independent of potential (band bending). The ratio Φ_r/Φ_{nr} is, of course, dependent on temperature and optical penetration depth. For the purposes of the model, any recombining $e^- - h^+$ pairs are subject to the Φ_r/Φ_{nr} ratio appropriate for the experimental conditions. Photocurrent serves to divert $e^- - h^+$ pairs from recombining by separating them; at open circuit it plays no role in the excited state description. In passing from a given potential to open circuit, changes in photocurrent are changes in Φ_x and determine how many more $e^- - h^+$ pairs are returned to recombination. The significant quantity is the magnitude of this change relative to how many pairs were recombining before the change, $\Phi_x/(1 - \Phi_x)$. This represents the fractional increase expected in Φ_r , Eq. [4]

$$\frac{\Phi_{r0}}{\Phi_r} - 1 = \frac{\Phi_x}{1 - \Phi_x} \quad [4]$$

Table II lists typical values of Φ_{r0}/Φ_r and Φ_x derived from [4]. The same logic predicts that Φ_x and Φ_r at any two potentials will be related by [5] for a constant, monochromatic excitation wavelength and temperature

$$\frac{1 - \Phi_{x2}}{1 - \Phi_{x1}} = \frac{\Phi_{r2}}{\Phi_{r1}} \quad [5]$$

While Eq. [4] and [5] have been approximately satisfied by several combinations of luminescent electrodes, electrolytes, excitation wavelengths, and tem-

Table II. Relationship between Φ_x and Φ_{r0}/Φ_r^a

Φ_x	Φ_{r0}/Φ_r
0.001	1.00
0.01	1.01
0.05	1.05
0.10	1.11
0.20	1.25
0.30	1.43
0.40	1.67
0.50	2.00
0.60	2.50
0.70	3.33
0.80	5.00
0.90	10.00
1.00	∞

^a Calculated from Eq. [4]. Φ_x is the quantum yield for e^- flow in the external circuit (photocurrent), and Φ_{r0}/Φ_r is the ratio of the emission quantum yield between open circuit ($\Phi_x = 0$) and the potential where Φ_x was measured.

peratures (1, 15, 16), they are still oversimplifications. Under certain conditions a nearly mirror image relationship between photocurrent and emission intensity in an iLV curve has been observed with ZnO photoelectrodes and a derivation presented to account for it (16). A rigorous model, however, will need to incorporate the following features: (i) nonexponential emission lifetimes (1, 3-6); (ii) nonlinear intensity effects on Φ_x and Φ_r (1, 6); (iii) local traps, surface imperfections, surface states, grain boundaries, impurity states, etc., all of which can alter Φ_i ; (iv) electroabsorption (dependence of absorptivity on potential) which mixes optical penetration and band bending effects (17); (v) conditions leading to humps or plateaus in the luminescence portion of iLV curves: in these regions Φ_r and Φ_x are decidedly not inversely related (1d). Studies designed to construct a more realistic model are currently in progress.

Experimental

All experiments were performed with $\sim 5 \times 5 \times 1$ mm plates of single crystal, 100 ppm CdS:Te or undoped CdS obtained from Cleveland Crystals, Cleveland, Ohio. The $\sim 5 \times 5$ mm face is oriented perpendicular to the c-axis and sample resistivities are $\sim 2 \Omega\text{-cm}$. Crystals were etched with Br_2/MeOH (1:10 v/v) before use. Electrode and polyselenide electrolyte preparation has been described previously (1d).

The basic PEC configuration, illustrated in Fig. 2, was assembled inside an Aminco-Bowman SPF-2 Spectrophotofluorometer when emission data were desired; the photoelectrode was inclined at $\sim 45^\circ$ to both the incident Coherent Radiation CR-12 Ar ion laser beam (501.7 or 514.5 nm) and the emission detection optics. The ~ 3 mm diam beam was $10\times$ expanded and masked to fill the electrode surface. A $0.03M$ $\text{Na}_2\text{Cr}_2\text{O}_7$ solution was placed in front of the detection optics to filter the exciting light. In experiments where only current-voltage data were obtained, the PEC was simply set on a stir plate and the electrode irradiated "head-on." The electrochemical instrumentation has been described previously (1d).

Temperatures in the PEC were maintained by resistive heating employing a Nichrome wire and a Sepco variable transformer. A thermometer accurate to $\pm 1^\circ C$ was calibrated by measuring melting points of several solids; adjustment of its immersion depth into the electrolyte indicated that significant thermal gradients were absent.

Changes in electrolyte absorption over the thermal excursion were probed by single beam experiments using the 501.7 and 514.5 nm laser lines and found to be small ($<5\%$ change in $\%T$ in a 1 mm pathlength). Light intensity in this and other experiments was measured with a Tektronix J16 radiometer equipped with a J6502 probe head.

The suitability of the 25×0.5 mm diam Ag wire as a PRE was checked by measuring its potential vs. that of a 2.0×0.8 cm Pt foil electrode with a high impedance Data Precision 1450 multimeter. Between 20° and $100^\circ C$ potential only varied from 100 to 123 mV and was stable for minutes at a time at temperatures in this range. Moreover, $i-V$ curves run at several temperatures with an Ag(PRE) or an SCE were practically superimposable. Energy conversion efficiencies at all temperatures were derived using a two electrode PEC (semiconductor and Pt counterelectrode; reference and counterelectrode leads from the potentiostat were shorted) whose $i-V$ curves also matched those obtained with an Ag(PRE) or SCE three-electrode PEC. The Pt electrode exhibited good reversibility for the polyselenide redox couple over the entire temperature range.

Curves of photocurrent and emission intensity (monitored at ~ 600 nm) vs. temperature were obtained by heating from 20° - $100^\circ C$ over a span of 80 min with readings taken \sim every 5° . Reproducibility of the data upon cooling was generally better than $\pm 10\%$. The

procedure and equipment involved in the sustained PEC experiment have been described (1d).

Acknowledgment

We thank the Office of Naval Research for their generous support of this work. BRK is grateful to The Electrochemical Society for summer support through a Joseph W. Richards Fellowship. Professors John Wiley and Dennis Evans are acknowledged for several helpful discussions.

Manuscript submitted Oct. 15, 1979; revised manuscript received ca. Jan. 4, 1980.

Any discussion of this paper will appear in a Discussion Section to be published in the December 1980 JOURNAL. All discussions for the December 1980 Discussion Section should be submitted by Aug. 1, 1980.

REFERENCES

- (a) A. B. Ellis and B. R. Karas, *J. Am. Chem. Soc.*, **101**, 236 (1979); (b) A. B. Ellis and B. R. Karas, *Adv. Chem. Ser.*, **184**, 185 (1980); (c) A. B. Ellis and B. R. Karas, Abstract No. 65, 176th ACS Meeting, Miami Beach, Sept. 1978; (d) B. R. Karas and A. B. Ellis, *J. Am. Chem. Soc.*, **102**, 968 (1980).
- D. Dutton, *Phys. Rev.*, **112**, 785 (1958).
- (a) A. C. Aten and J. H. Haanstra, *Phys. Lett.*, **11**, 97 (1964); (b) A. C. Aten, J. H. Haanstra, and H. deVries, *Philips Res. Rep.*, **20**, 395 (1965).
- J. D. Cuthbert and D. G. Thomas, *J. Appl. Phys.*, **39**, 1573 (1968).

- D. M. Roessler, *ibid.*, **41**, 4589 (1970).
- P. F. Moulton, Ph.D. Dissertation, Massachusetts Institute of Technology (1975).
- H. Gerischer, *J. Electroanal. Chem. Interfacial Electrochem.*, **58**, 263 (1975).
- R. H. Bube, *Phys. Rev.*, **98**, 431 (1954).
- A. R. Hutson in "Semiconductors," N. B. Hannay, Editor, pp. 578-580, ACS Monograph Ser. No. 140, Reinhold Publishing Corp., New York (1959).
- A. J. Nozik, *Ann. Rev. Phys. Chem.*, **29**, 189 (1978).
- D. Berlincourt, H. Jaffe, and L. R. Shiozawa, *Phys. Rev.*, **129**, 1009 (1963).
- A. B. Ellis, S. W. Kaiser, J. M. Bolts, and M. S. Wrighton, *J. Am. Chem. Soc.*, **99**, 2839 (1977).
- J. E. Bateman, F. E. Ozsan, J. Woods, and J. R. Cutter, *J. Phys. D. Appl. Phys.*, **7**, 1316 (1974).
- (a) A. Fujishima, G. H. Brilmyer, and A. J. Bard, in "Semiconductor Liquid-Junction Solar Cells," A. Heller, Editor, p. 172, The Electrochemical Society Softbound Proceedings Series, Princeton, N.J. (1977); (b) A. Fujishima, Y. Maeda, K. Honda, G. H. Brilmyer, and A. J. Bard, *This Journal*, **127**, 840 (1980); (c) G. H. Brilmyer, A. Fujishima, K. S. V. Santhanam, and A. J. Bard, *Anal. Chem.*, **49**, 2057 (1977).
- K. H. Beckmann and R. Memming, *This Journal*, **116**, 368 (1969).
- G. Petermann, H. Tributsch, and R. Bogomolni, *J. Chem. Phys.*, **57**, 1026 (1972).
- D. F. Blossey and P. Handler in "Semiconductors and Semimetals," Vol. 9, R. K. Willardson and A. C. Beer, Editors, pp. 302-304, Academic Press, New York (1972).

Reaction of Mo Thin Films on Si (100) Surfaces

S. Yanagisawa and T. Fukuyama

Cooperative Laboratories, VLSI Technology Research Association,

4-1-1 Miyazaki, Takatsu-ku, Kawasaki, 213 Japan

ABSTRACT

The reaction between Mo thin films and single crystal Si (100) substrates has been studied as a function of various heat-treatments. In the temperature range between 520° and 550°C, MoSi₂ has been observed to grow linearly with time and with an activation energy of about 4.1 eV. X-ray diffraction indicates that the hexagonal phase of MoSi₂ changes continuously to the tetragonal phase as the temperature increases from 600° to 800°C. In contrast, the presence of native oxide prohibits formation of any silicide phases in the above temperature range and leads to the formation of a Mo₃Si phase at temperatures near 1000°C. The formation of MoSi₂ results in large compressive strains in the MoSi₂ layer and in strains of the opposite sign in the underlying Si. In limited reaction areas the corresponding stresses were found to be sufficient to cause the nucleation and propagation of dislocations in the Si substrates. The dislocations are propagated for considerable distances away from the reaction areas. An anomalous growth of silicide occurs at the edges of the reaction areas. These phenomena are shown to result from cumulative stress effects. Stresses enhance the formation of MoSi₂ layers, and thereby modify the kinetic laws of growth.

Mo has been considered as a suitable material for gates and interconnections in MOS-LSI technology because of its ability to withstand high temperature processing (1-6). The physical properties of Mo films, such as electrical resistivity, stress, and MOS characteristics have been extensively studied (7-9). Because it controls the electrical and metallurgical characteristics of the contacts, the reaction between Si and Mo films is quite significant. The reaction is known to occur at temperatures considerably below the eutectic temperature; this may impose restrictions of time and temperature on fabrication processes subsequent to metallization. Several papers on the formation of the disilicide of Mo have been published. Oertel et al. (10), using x-ray diffraction, have observed the growth of

the tetragonal form of MoSi₂ with a square root of time dependence. Bower et al. (11) used the backscattering of He ions to determine the thickness of the silicide layers; they found that at relatively high temperatures (1200°C) MoSi₂ grows linearly with time. Aleksandrov et al. (12) reported that MoSi₂ grows according to a square root of time law in the temperature range of 525° ~ 600°C. They determined the thickness of the silicide layers from the quantity of electricity consumed in anodic dissolution. Guivarc'h et al. (13) found that the hexagonal phase of MoSi₂ grows linearly as a function of the square of the time with an activation energy of 2.4 eV. They used 800Å thick Mo films and investigated the temperature range from 475° to 550°C. The measurement methods and the experimental conditions were different in each case, which might explain the diversity of these results. However, infor-

Key words: molybdenum, molybdenum silicide, stress, strain, dislocation.

mation sufficient to explain the different growth kinetics is still missing. It is necessary to understand the factors affecting the laws of silicide formation, so that through the control of these factors stable contacts might be obtained. It is well known that the reaction being studied is quite sensitive to cleaning of the Si surface. Guivarc'h *et al.* (13) observed that the growth kinetics varied as a function of Mo film thickness. They suggested that stresses might play a dominant role but offered no supporting experimental evidence. Stresses could be important not only with respect to the growth kinetics but also to the metallurgical stability of the contacts. In this paper we present the results of our investigation of the reaction between Mo and single crystal (100) Si in the temperature range between 520° and 800°C, with emphasis on understanding the effect of stresses on the kinetics of silicide formation.

Experimental Procedures

The substrates were 3 in. diam wafers of p-type Si of (100) orientation, doped with boron to 1 Ω -cm resistivity. The Si wafer was etched in dilute HF solution, rinsed in H₂O, and then dried in an N₂ atmosphere just before mounting in a vacuum system. A magnetron d-c sputtering system (Varian S-Gun) was used to deposit Mo films onto Si substrates. The Mo target was a 5 in. diam water-cooled circular conical cathode (99.99% pure). The system was pumped down to 2×10^{-6} Torr, and then backfilled to a sputtering pressure of 3×10^{-3} Torr by introducing argon gas. The substrates were preheated to about 200°C by radiation emitted from quartz lamp heaters. In all runs, the Mo films were deposited at a rate of 180 Å/min to a thickness of 3000Å. In some cases, to confirm the effect of native oxide on silicide formation, the Mo films were deposited on n⁺ (100) Si substrates by using the rf sputtering system. Then, the samples were annealed in a flowing nitrogen tube furnace at various temperatures and times. The thicknesses of Mo and silicides were measured by using Talystep after step-etching. Dilute nitric acid was used to etch the Mo films, and HNO₃:NH₄F:H₂O = 10:1:30 etchant was used for silicides. With the second etchant, the Si substrate and the silicide layer near the silicon-silicide interface were etched simultaneously. However, the etching end point was determined easily by utilizing the fact that silicon repels water and silicide does not.

The measurement error was estimated to be on the order of 200Å. This value is probably larger than that obtainable with other methods such as He⁺ ion backscattering and x-ray analysis. However, the accuracy of thickness measurements actually depends on the surface roughness of the silicide layer, which becomes more pronounced as the reaction progresses. This decreases the effective depth resolution of these methods by which average thicknesses can usually be detected within a range of several square millimeters or square centimeters on Si substrates. Thus, when measuring silicide thicknesses above several thousand angstroms, the etching method used here may be more reliable than the other methods because the space resolution is only limited by the probe diameter of 10 μ m.

In order to evaluate the stress in the silicide layer, the deflection profile of Si substrate over which the silicide was grown was measured by using a laser-scanning flatness tester (Canon LSF-500) where the operating principle was reported earlier (14). The bowing of the Si substrate was then obtained from the deflection profile. The difference h in a bowing between a bare silicon wafer and one from which the residual Mo has been removed after annealing is directly proportional to the product of silicide stress σ and thickness d by

$$\sigma d = \frac{4E_s}{3(1-\nu_s)} \cdot \frac{d_s^2 h}{D^2}$$

where E_s is Young's modulus for the Si substrate, ν_s

is its Poisson's ratio, and d_s and D are the thickness and diameter of the Si substrate, respectively. The sense of h is a direct indication of the kind of stress in the silicide. An upward-curved h indicates compressive stress, and a downward curve indicates tensile stress. In order to determine the stress accurately, substrates with deflection profiles that were symmetrical with respect to the center were chosen. The measurements were made at room temperature.

The silicide phases were investigated by x-ray diffraction analysis where CuK α radiation was used. A scanning electron microscope was used to observe the silicide textures.

Results

Homogeneous reaction.—Figure 1 shows the silicide thickness as a function of annealing time at a temperature of 540°C. The difference in the Mo film thickness before and after the heat-treatment, which denotes the Mo transformed to the silicide, are also plotted. The thickness of the silicide was found to be about 2.7 times that of consumed Mo. As shown in the figure, the silicide formation follows a linear-growth time dependence. This indicates that the reaction being studied is not diffusion-limited. Figure 2 shows the thicknesses of the silicide and the Mo transformed to the silicide as a function of annealing temperature. The samples were annealed for 30 min. The measured points fall on straight lines with the same slope, indicating an activation energy of about 4.1 eV. This value is significantly larger than those previously reported.

The phases of the formed silicides were identified by x-ray analysis. To confirm the phase transformation, the samples were annealed in a higher temperature range as follows. After being annealed for 30 min at 550°C, the residual Mo films were removed by chemical etching. The silicide thickness was estimated to be about 5000Å. Then, the samples were annealed further for 30 min at various temperatures over 600°C. The above two-step annealing was necessary to avoid film failure arising from excessive silicide formation. Figure

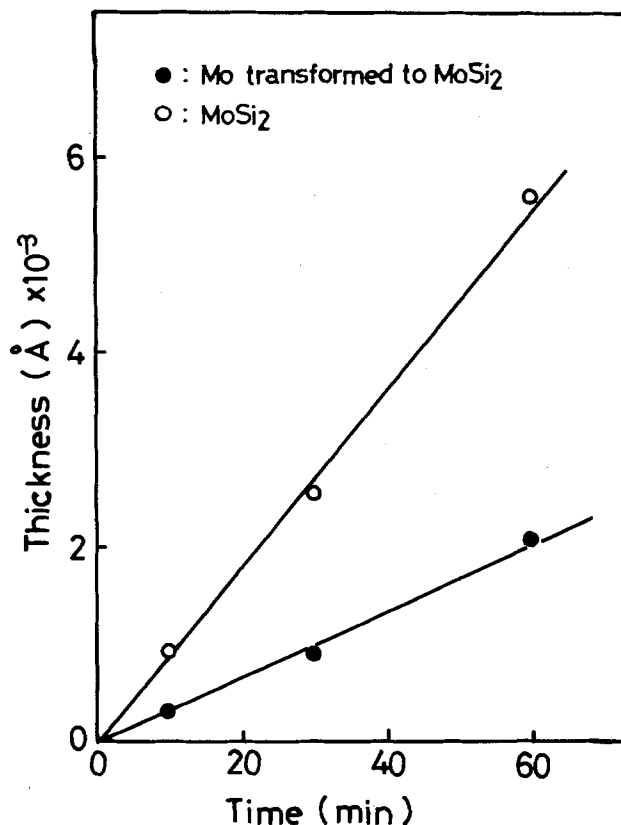


Fig. 1. The thicknesses of MoSi₂ (○) and Mo transformed to MoSi₂ (●) as a function of annealing time. Annealing temperature was 540°C.

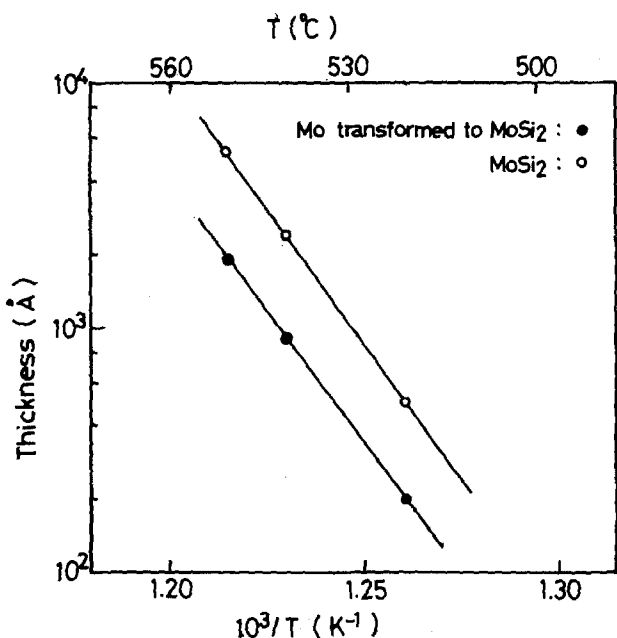


Fig. 2. The thicknesses of MoSi₂ (○) and Mo transformed to MoSi₂ (●) as a function of reciprocal annealing temperature. Annealing time was held at 30 min.

3 shows x-ray diffractometer traces for samples annealed at three different temperatures. These results clearly indicate that the hexagonal phase of MoSi₂ changes continuously to the tetragonal phase as the temperature increases from 600° to 800°C. At an intermediate temperature of 750°C, these phases coexist. The x-ray diffractometer traces showed no direct evidence of the presence of other silicide phases even before the removal of Mo film. It is possible that other phases did exist, but in quantity too small to be detected by x-ray analysis (13).

Silicide formation on the heavily doped Si substrates was found to be quite different from that presented above. When n⁺ (100) Si substrates doped with phosphorous to 1 × 10²⁰ cm⁻³ were used, silicides did not form at temperatures below about 800°C; no amount of silicide was detected by the x-ray analysis. However, annealing at higher temperatures was found to lead to formation of Mo₃Si. Figure 4 shows a typical x-ray diffractometer trace for an n⁺ sample annealed at 1000°C for 30 min. The occurrence of Mo₃Si and the presence of residual Mo were shown in the figure, although the amount of Mo₃Si was found to differ even between samples annealed under the same conditions. In some samples, Mo₃Si and MoSi₂ were found to have formed simultaneously. The native oxide existing be-

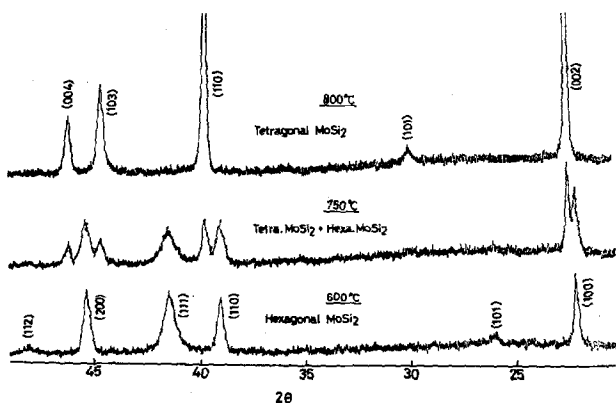


Fig. 3. X-ray diffractometer traces of silicide layers. After the silicides were formed to a thickness of about 5000Å, further heat-treatments were performed at 600°, 750°, and 800°C for 30 min.

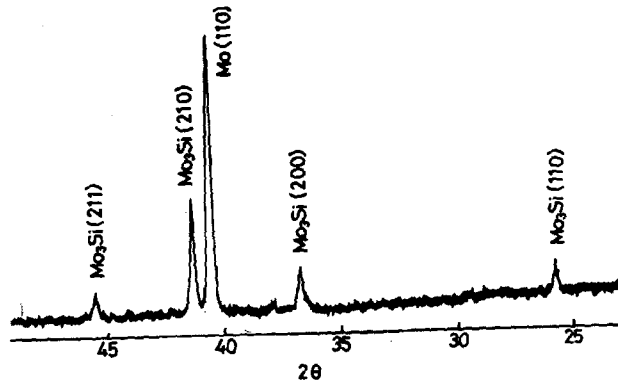


Fig. 4. X-ray diffractometer trace of silicide formed on n⁺ Si substrate. The sample was annealed for 30 min at 1000°C.

tween the Mo and the Si substrate may play an important role in these results. The chemical cleaning used here is usually ineffective in removing the native oxide because the Si surface is exposed to air just before Mo deposition (15). In addition, the heavily doped Si generally shows a greater growth rate of native oxide than that which is lightly doped (16). This may result in a pronounced effect of native oxide on the formation of silicide on the heavily doped Si. The effects of surface cleaning on silicide formation were examined by using n⁺ silicon prepared by sputter etching on which the native oxide was considered to be completely removed. The results were found to be similar to those shown in Fig. 1 and Fig. 2, only the MoSi₂ phase was observed. This suggests that the effect of native oxide is negligible for the lightly doped Si, even after chemical cleaning.

Figure 5 shows the product of silicide stress σ and thickness d as a function of silicide thickness d. Silicides of various thicknesses were obtained from the samples annealed for 30 min in the range of 525° ~

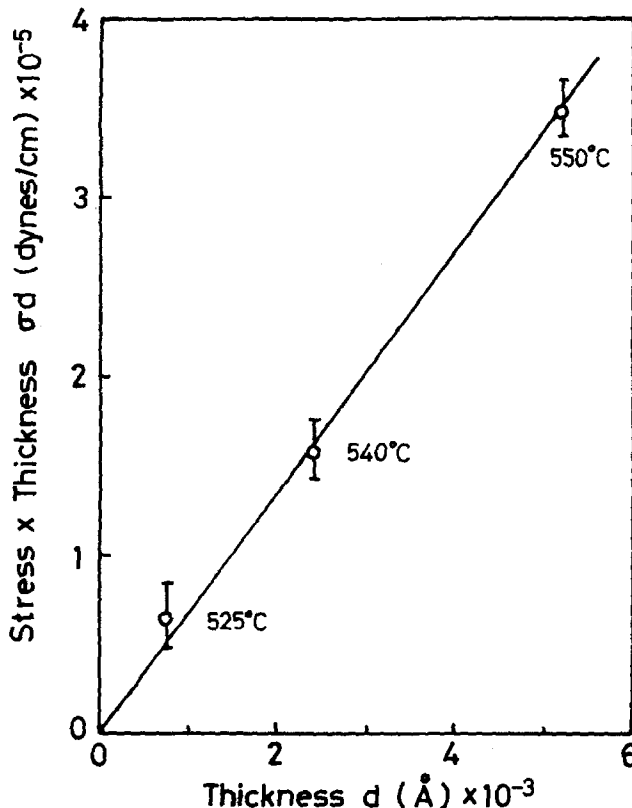


Fig. 5. The product of silicide stress σ and thickness d as a function of silicide thickness d. The annealing temperatures which correspond to the different thicknesses are indicated on the figure.

550°C. The temperatures which correspond to the different thicknesses are shown in the figure. σd is linearly dependent on d through the zero point, indicating that the stress has almost no temperature dependence in the range of 525° ~ 550°C. The stress was found to be compressive and was evaluated to be about 7×10^9 dyn/cm². The measured stress σ consists of two components, an intrinsic component σ_i at reaction temperature, and a thermal component σ_{th} caused by the difference between the thermal expansion coefficients of MoSi₂ and Si on cooling from the reaction temperature (T_R) to room temperature (T_0): $\sigma = \sigma_{th} + \sigma_i$. σ_{th} is approximately estimated by

$$\sigma_{th} = \frac{E'}{1 - \nu'} (\alpha' - \alpha) \cdot (T_R - T_0)$$

where E' is the Young's modulus for the MoSi₂, ν' is its Poisson's ratio, and α' and α are the thermal expansion coefficients of MoSi₂ and Si, respectively. Here, E' and ν' are 3.8×10^{12} dyn/cm² and 0.165, α' and α are $8.1 \times 10^{-6}/^\circ\text{C}$ and $2.5 \times 10^{-6}/^\circ\text{C}$ at room temperature, respectively (17). Using these values, the thermal stress σ_{th} was found to be tensile and was calculated to be about 6×10^9 dyn/cm² in the above temperature range. This leads to the compressive stress of about 1.3×10^{10} dyn/cm² for the intrinsic stress σ_i in the range of 525° ~ 550°C. On the other hand, it can be concluded from lattice parameters on the hexagonal MoSi₂ (3 molecules in a unit cell volume of 120.699 Å³) (18) that this formation involves about a 27% decrease in volume with respect to the components Mo and Si. This result suggests that the intrinsic stress would be tensile. However, it should be noted that Si is the dominant diffusing species (18); the reaction progresses by its insertion into the molybdenum lattice. Therefore, MoSi₂ formation is accompanied by a volume expansion of the deposited Mo film, resulting in the compressive stress in the MoSi₂ and, simultaneously, a void accumulation at the MoSi₂-Si interface.

As previously mentioned, the silicide surface becomes rougher as the reaction progresses. In the course of our experiments, the silicide layers were often observed to fail when they grew to more than about 6000Å. Figure 6 shows the surface texture of the sample annealed for 10 min at 600°C. This annealing condition may lead to a silicide thickness of about 6000Å, as estimated from extrapolations of the data shown in Fig. 1 and 2, that is, if the reaction continues uniformly over the entire substrate. As clearly observable in the figure, excessive silicide formation results both in blistering and cracking of the formed silicide. This is probably attributable to the two different stresses; the blistering may be due to the compressive stress during MoSi₂ formation, and the cracking may be due to the tensile stress on cooling from the reaction temperature to room temperature. Furthermore, the void accumulation which can occur at the MoSi₂-Si interface, might also lead to poor silicide adhesion and rough surface texture. In contrast, when the reaction area was limited to within a range of several tenth μm^2 on the Si substrate, no film failure was observed in any annealing condition. This is described more fully in the next section.

Localized reaction.—Mo film was deposited to a thickness of 3000Å on an Si substrate covered with SiO₂ film which was selectively etched to expose regions of bare silicon. Heat-treatment then permits MoSi₂ to form in a limited silicon region. Such MoSi₂ formation was found to generate dislocations outside the reaction region, suggesting that the strain field which the MoSi₂ formation exerts on the surrounding silicon lattice is relieved through the formation of dislocations. This probably prevents silicide failure in the contact region. The nucleation and propagation of dislocations and their relationship to MoSi₂ formation were investigated in some detail, as follows. The samples annealed were etched for 20 sec in Sirtl etch after the residual Mo

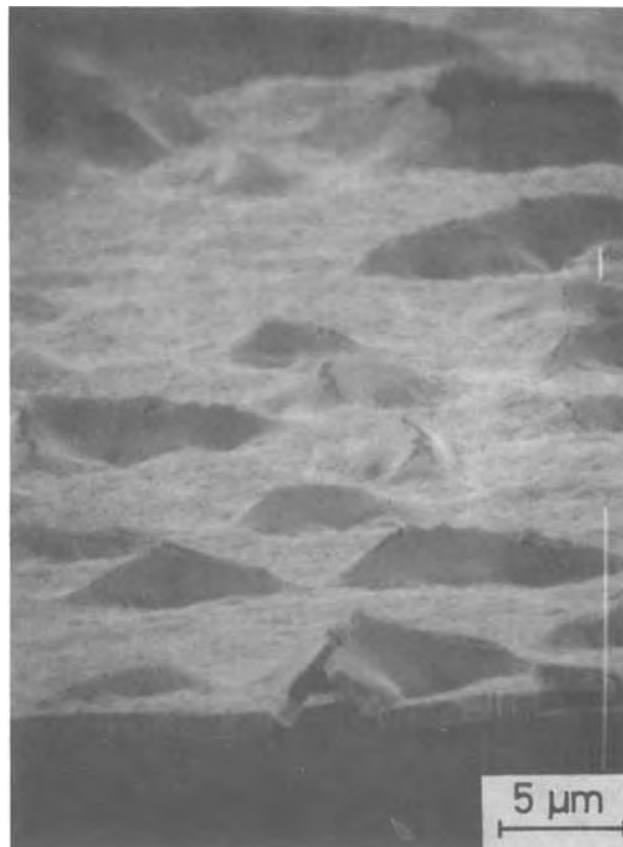


Fig. 6. Surface texture of MoSi₂ on Si substrate. The sample was annealed for 10 min at 600°C.

and SiO₂ films were removed. This etching produces etch pits at the sites of dislocations. Figure 7 shows the dislocation patterns on those samples annealed for 10 min at 560° and 600°C, respectively. The dislocation patterns near the reaction regions of various areas are shown in Fig. 8 where the sample's annealing temperature and time were 600°C and 10 min, respectively. In both figures, the contact edges are along $\langle 110 \rangle$ direction. The dislocations extend more laterally outside of the reaction region into the silicon, by increasing the layer thickness and the reaction area. Figure 9 shows the distribution of dislocations on sample whose contact edges are inclined by 45° to $\langle 110 \rangle$ direction. The annealing temperature and time were 600°C and 10 min, respectively. A comparison of the dislocation patterns shown in Fig. 7-9 indicates that the disloca-

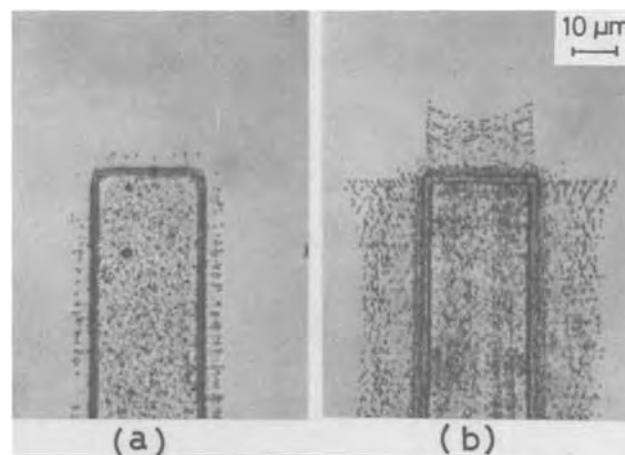


Fig. 7. Dislocation patterns around reaction regions on the wafers annealed for 10 min at 560°C for (a) and at 600°C for (b), respectively. The contact edges are along $\langle 110 \rangle$ direction.

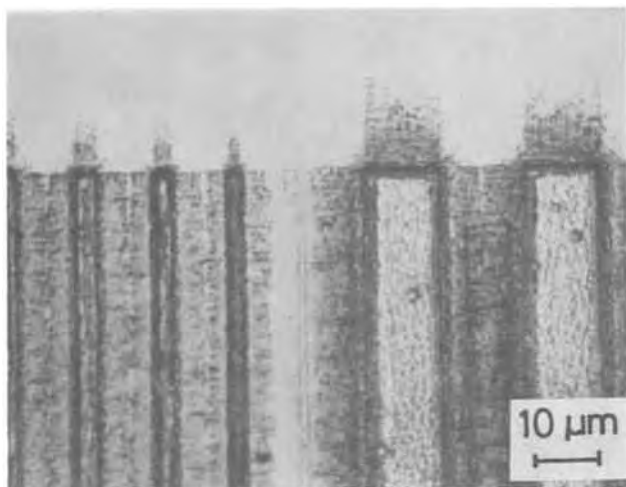


Fig. 8. Dislocation patterns around reaction regions of various areas on the wafer annealed for 10 min at 600°C. The contact edges are along $\langle 110 \rangle$ direction.

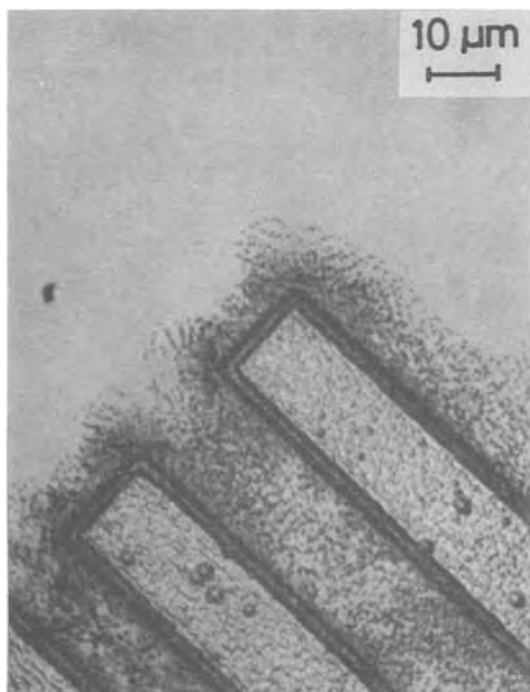


Fig. 9. Dislocation distributions around reaction regions on the wafer annealed for 10 min at 600°C. The contact edges are inclined by 45° to $\langle 110 \rangle$ direction.

tions propagate along $\langle 110 \rangle$ direction. In addition, as observed in Fig. 10, the dislocations were found to extend for considerable distances perpendicularly down into the silicon substrate. In this sample, the vertical cross section was etched through silicide layers of various widths for 5 sec in Sirtl etch. The dislocations glide on the inclined (111) plane. The dislocation density seems to be greatest at the contact edge, indicating cumulative strain. Corresponding to the above observations, an anomalous growth of the MoSi₂ layer was observed near the edge of the reaction region. Figure 11 shows SEM photographs of the vertical cross sections through the edges of MoSi₂ layers where the samples were annealed at 550°C for 10 min and 60 min, respectively. The reaction tends to become nonuniform near the edge, as the thickness of MoSi₂ layer increases. Figure 12(a) shows a similar observation for MoSi₂ layers of various widths. The sample was annealed for 10 min at 600°C. This observation suggests that strain exerted on Si substrates by MoSi₂ layers of the nar-

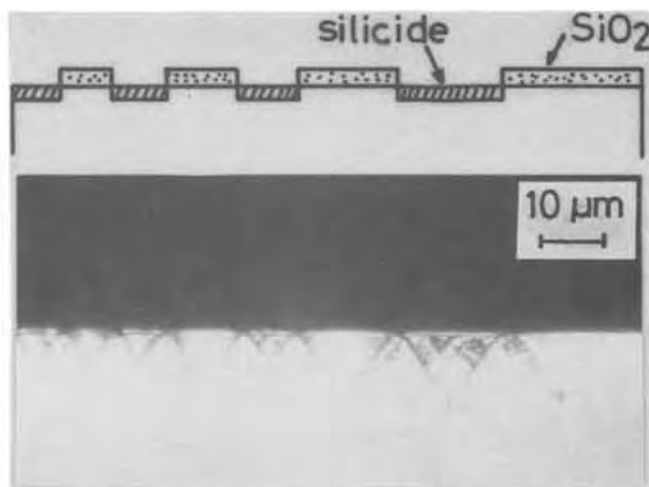


Fig. 10. Dislocation distributions around vertical cross section through the reaction regions on the wafer annealed for 10 min at 600°C.

rower widths is less uniform and results in less uniform growth. The sample for which the width of MoSi₂ layer is comparable to its thickness clearly confirms this. Figure 12(b) is an enlarged photograph of a MoSi₂ layer with a width of 2 μm. The fiber structured MoSi₂ layer is seen to be split at the center of reaction region. Figure 13(a) shows the vertical cross section of the MoSi₂ layer edge and Fig. 13(b) shows an inclined view. The surface of MoSi₂ layer lies below the level of the original silicon surface, indicating that the reaction is enhanced near the edge. It is interesting to note, as shown by Fig. 11 and 13, that the behavior of MoSi₂ near the edge is different even among samples for which the MoSi₂ layer is of the same thickness; the anomalous growth of the MoSi₂ layer is more enhanced for the sample annealed at the higher temperature. This suggests that the effect of stress on the growth of MoSi₂ becomes more pronounced at higher temperatures.

Discussion

Marker experiments show that Si is the dominant diffusing species in MoSi₂ formation (18, 19). Thus, one may expect that the diffusion of Si through the growing MoSi₂ layer is the rate-limiting factor and that the reaction therefore obeys the parabolic growth-time law. But, the results obtained here, such as those indicating linear-growth time dependence, abnormally high activation energy, and anomalous formation of MoSi₂ at the contact edge, would rule out such a simple diffusion model. Bower *et al.* (11) have observed two types of behavior in the formation of silicide contacts; one where the reaction is self-limited to the exposed contact area, and the other where the reaction continues beyond the contact region. Further, they pointed out that these two types of behavior correlate with reaction kinetics; the thickness of the silicide increases with parabolic-time dependence in the first case, and linearly with time in the second case. The MoSi₂ formation studied here corresponds to the second case. Although it is difficult at this time to establish a firm model to explain such phenomena, a discussion of the possible contributory mechanism follows.

Silicide formation is significantly delayed due to the native oxide, which acts as a barrier against the diffusion of Si. In addition, the native oxide clearly leads to the formation of Mo-rich silicide, *i.e.*, Mo₃Si. This indicates that the growth mechanism is different for the cases with and without the native oxide. The formation of Mo₃Si may be due to an insufficient supply of Si to the Mo-silicide interface. However, as previously mentioned, extremely thin oxide was found not to affect the growth kinetics of MoSi₂.

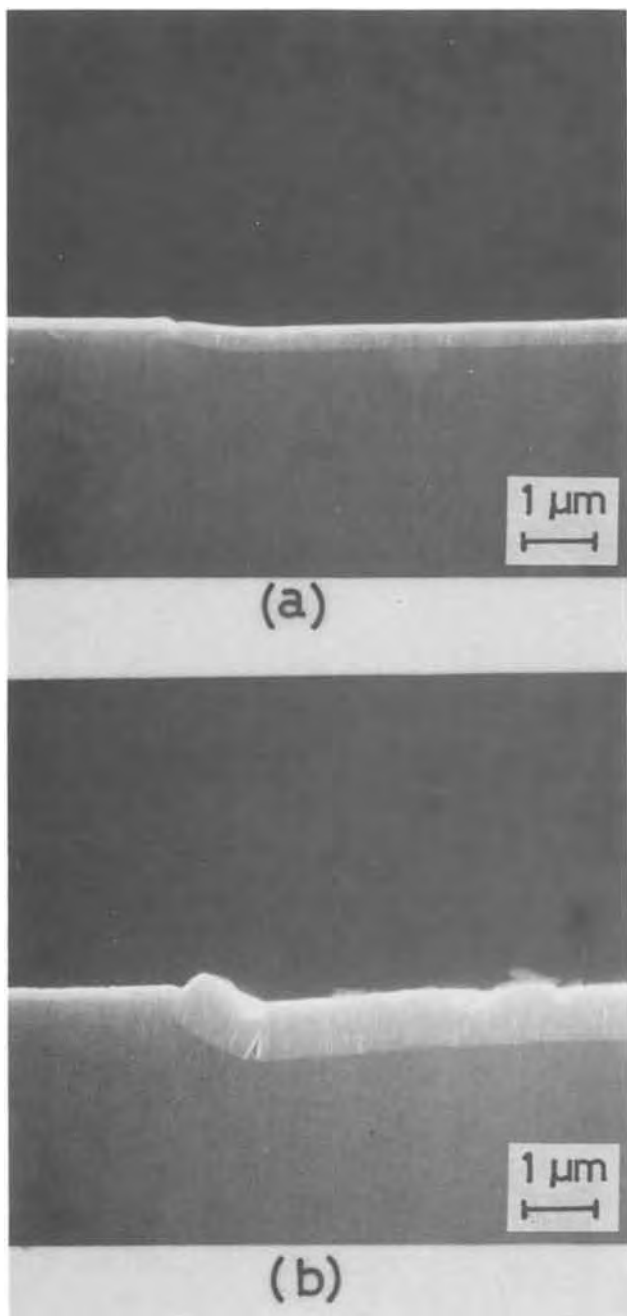


Fig. 11. SEM photographs of the vertical cross sections through the MoSi₂ layer edges on the wafer annealed at 550°C for 10 min for (a) and for 60 min for (b), respectively.

Stress seems to be a more important influence on the growth kinetics of MoSi₂. The generation of dislocations and the corresponding anomalous growth of MoSi₂ appear to correlate closely with the stress in the growing MoSi₂ layer. It may be reasonable to consider that such stress weakens the covalent bonds in the substrate and dissolves silicon atoms from their lattice more easily. This may increase the supply of Si to the Mo-MoSi₂ interface, enhancing MoSi₂ formation. This assumption may be confirmed by the anomalous growth of MoSi₂ which corresponds to the cumulative strain at the contact edge. In this case, it is apparent that the reaction is not confined to the exposed silicon region because the strain field extends outward from the reaction region. The variety of data for MoSi₂ formation can be qualitatively accounted for by the stress-enhanced reaction mechanism proposed here. The strain increases with the thickness of MoSi₂ layer and results in more pronounced growth-time dependence, that is, from a parabolic law to a linear one. The overall stress originates from the bilayer which consists of the formed

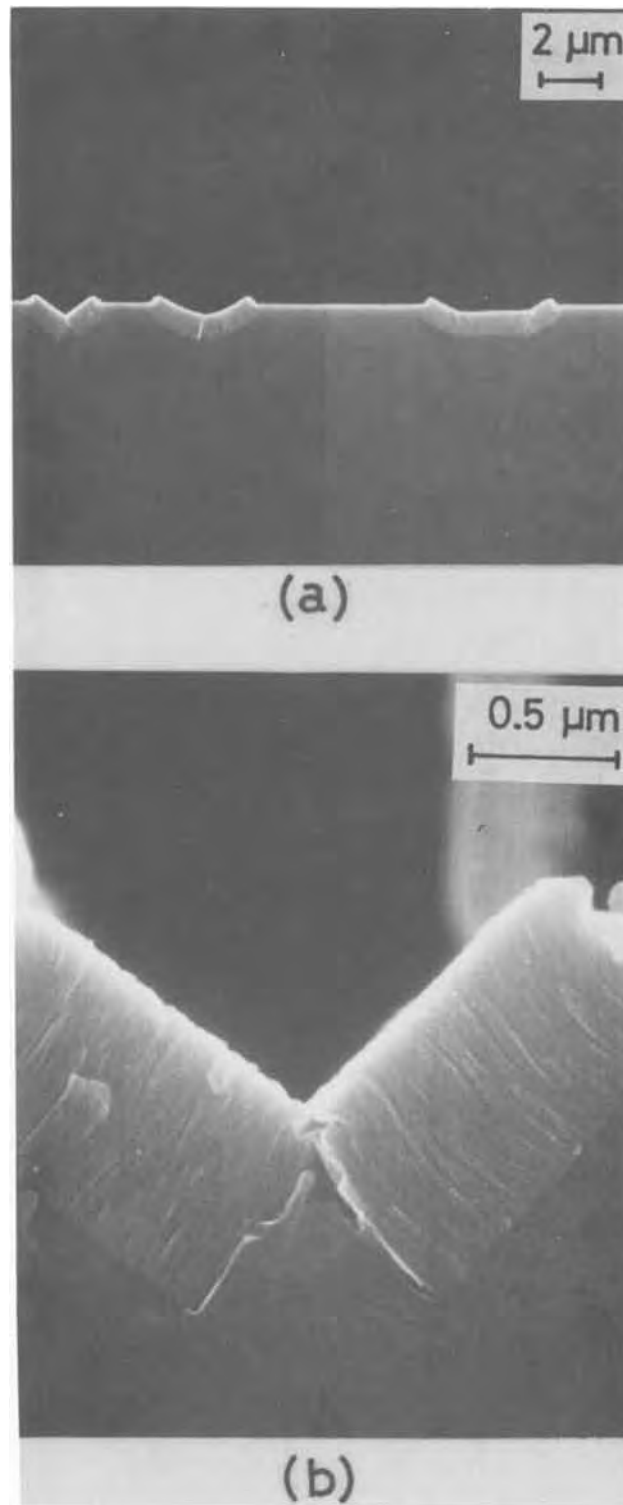


Fig. 12. (a) SEM photograph of the vertical cross sections through MoSi₂ layers of various widths. (b) An enlarged photograph of (a). The annealing temperature and time were 600°C and 10 min, respectively.

MoSi₂ and the residual Mo. Therefore, the stress in the Mo, which has been shown to be significantly dependent on the deposition condition (20), might also affect the growth kinetics. Considering that the stress in the Mo is on the same order of magnitude and of the opposite sign to that in the silicide under normal deposition condition (21), the overall stress is smaller for samples with the thicker Mo films and may thereby suppress the growth rate. This appears to agree with the results reported by Guivarc'h *et al.* (13) where they observed a linear-growth time dependence for 1500Å Mo film, and a square-growth time for 800Å Mo

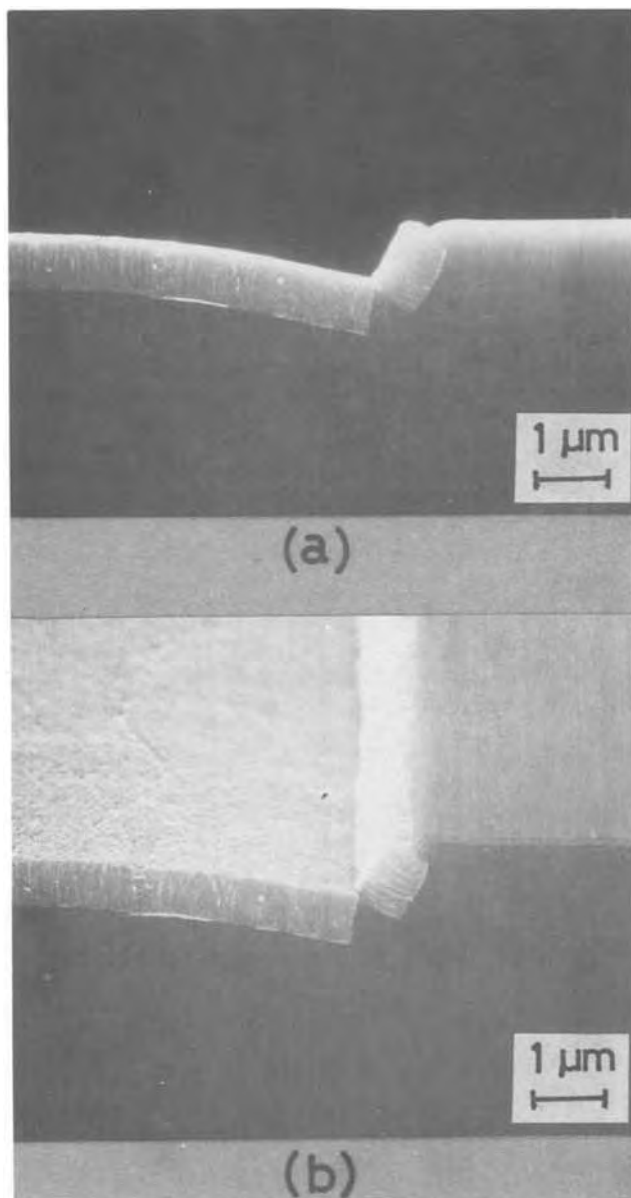


Fig. 13. (a) SEM photograph of the vertical cross section of the MoSi_2 layer edge on the wafer annealed for 30 min at 650°C . (b) An inclined view of (a).

film. Furthermore they showed that when 800\AA Mo film was coated with an Si layer of about 4000\AA thick before annealing, the silicide formation was delayed and followed a linear-growth time dependence. It is worth considering if a coating film might change the overall stress and thus modify the growth time dependence. As previously described, as the growth temperature of MoSi_2 becomes higher, the strain field may increase. This also may enhance the reaction, resulting in the high activation energy observed. Thus, it is possible that the growth kinetics of MoSi_2 are modified due mainly to the differences in the stress existing under various experimental conditions.

From a practical point of view, it is anticipated from the results presented here that the stress associated with the Mo-Si reaction will result in potentially detrimental effects on the mechanical and electrical characteristics of the devices. To avoid these disadvantages, it is necessary to suppress the dissolution of Si into the Mo film. This consideration may lead to the

possibility of using the Mo-Si compound film (22). Further investigation is required to clarify these problems.

Conclusion

It was found that the stress generated in MoSi_2 layers enhanced MoSi_2 formation. The stress is affected by various factors such as the properties of the deposited Mo film and the annealing temperature range. This suggests that the stress-enhanced reaction mechanism may play an important role in accounting for the differences in data on growth kinetics presented by us and other investigators.

The presence of native oxide also modifies the growth kinetics, but in a different way, as suggested by the formation of Mo_3Si but not of MoSi_2 .

Acknowledgments

The authors wish to thank Drs. Y. Tarui and T. Oku for their encouragement.

Manuscript submitted July 6, 1979; revised manuscript received Dec. 6, 1979.

Any discussion of this paper will appear in a Discussion Section to be published in the December 1980 JOURNAL. All discussions for the December 1980 Discussion Section should be submitted by Aug. 1, 1980.

Publication costs of this article were assisted by the VLSI Technology Research Association.

REFERENCES

1. D. M. Brown, W. E. Engeler, M. Garfinkel, and P. V. Gray, *This Journal*, **115**, 874 (1968).
2. W. E. Engeler and D. M. Brown, *IEEE Trans. Electron Devices*, **ed-19**, 54 (1972).
3. D. M. Brown and R. J. Connery, *ibid.*, **ed-25**, 1302 (1978).
4. P. L. Shah, *ibid.*, **ed-26**, 631 (1979).
5. M. Kondo, T. Mano, F. Yanagawa, H. Kikuchi, T. Amazawa, K. Kiuchi, N. Ieda, and H. Yoshimura, *IEEE J. Solid-State Circuits*, **sc-13**, 611 (1978).
6. T. Ohgishi, A. Doi, T. Akiyama, and N. Enomoto, *ibid.*, **sc-13**, 555 (1978).
7. H. Oikawa, *J. Vac. Sci. Technol.*, **15**, 1117 (1978).
8. H. Oikawa and Y. Nakajima, *ibid.*, **14**, 1153 (1977).
9. R. S. Nowicki, W. D. Buckley, W. D. Mackintosh, and I. V. Mitchell, *ibid.*, **11**, 675 (1974).
10. B. Oertel and R. Sperling, *Thin Solid Films*, **37**, 185 (1976).
11. R. W. Bower and J. W. Mayer, *Appl. Phys. Lett.*, **20**, 359 (1972).
12. L. N. Aleksandrov, A. E. Gernshinskii, R. N. Lovyagin, P. A. Simonov, B. I. Fomin, and E. I. Cherepov, *Thin Solid Films*, **45**, 87 (1977).
13. A. Guivarc'h, P. Auvray, L. Berthou, M. Le Cun, J. P. Boulet, P. Henoc, G. Pelous, and A. Martinez, *J. Appl. Phys.*, **49**, 233 (1978).
14. A. K. Sinha, H. J. Levinstein, and T. E. Smith, *ibid.*, **49**, 2423 (1978).
15. V. Kumar, *This Journal*, **123**, 262 (1976).
16. L. D. Locker and C. D. Capio, *J. Appl. Phys.*, **44**, 4366 (1973).
17. "Engineering Properties of Selected Ceramic Materials," American Ceramic Society, Columbus, Ohio (1966). P. T. B. Shaffer *et al.*, "Plenum Press Handbook of High Temperature Materials," No. 1, Plenum Press, New York (1964).
18. J. Baglin, J. Dempsey, W. Hammer, F. d'Heurle, S. Petersson, and C. Serrano, *J. Electron. Mater.*, **8**, 641 (1979).
19. J. Baglin, F. d'Heurle, and S. Petersson, *Appl. Phys. Lett.*, **33**, 289 (1978).
20. J. A. Thornton, *J. Vac. Sci. Technol.*, **14**, 164 (1977).
21. E. Klokholm and B. S. Berry, *This Journal*, **115**, 823 (1968).
22. S. Yanagisawa and T. Fukuyama, *ibid.*, To be published.

Thermodynamic Study of Ga-Ge-Zn Ternary Alloys by EMF Measurements

C. Girard, R. Baret, and J. Riou

Laboratoire de chimie générale, Faculté de Pharmacie, 13385 Marseille, Cedex 4, France

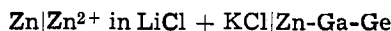
and J. P. Bros

Laboratoire de "Thermodynamique des systèmes métalliques à composants multiples,"

Université de Provence, 13331 Marseille, Cedex 3, France

ABSTRACT

An electrode potential study of the liquid Ga-Ge-Zn system has been conducted with the cell



in the temperature range 623°-1123°K. Zinc partial mixing functions were determined for 22 alloys. These measurements allow us to give the surface corresponding to zinc partial free energy at 1233°K and a large part of the liquidus surface of this system.

In the course of the thermodynamic study carried out by our laboratory at the Université de Provence concerning ternary systems formed by adding to gallium-germanium alloys another metal of group II or III Al (1), In (2), Sn (2), we have measured, by potentiometry, the zinc activity in a number of gallium-germanium-zinc liquid alloys over a large temperature range. The thermodynamic functions and the phase diagram of this ternary system have not been previously studied.

The three limiting binary systems: Ga-Ge, Ga-Zn, and Ge-Zn, the phase diagrams of which are shown in Fig. 1, have the same characteristics: each eutectic composition is very near the most fusible element and terminal solid solutions are small.

Gallium-germanium system.—The eutectic point practically coincides with the melting point of pure gallium ($x_{\text{Ge}} = 5 \cdot 10^{-7}$) (3, 4). Greiner (5) suggested a retrograde solidus curve exhibiting a maximum solubility of gallium in germanium ($x_{\text{Ga}} = 0.026$) at 1053°K. Trumbore (6) confirmed the shape of this solidus limit and found a maximal solubility at 923°K ($x_{\text{Ga}} = 0.011$). Thermodynamic functions for Ga-Ge liquid alloys were determined by Predel (7) at 1273°, by Bergman (8) at 1270°, by Eslami (1) at 1241°, and by Batalin at 1240°K (9).

Gallium-zinc system.—The eutectic point coordinates (T_e, x_e) have been proposed by several authors (10-13) ($298.15 \leq T_e \leq 298.55$ and $0.037 \leq x_{\text{Ga}} \leq 0.050$). The maximal molar fraction of gallium in solid zinc would be 0.0195 (14) or 0.009 (13). The solid solubility of zinc in gallium corresponds to $x_{\text{Zn}} = 0.085$ (13). Mixing enthalpy was measured calorimetrically at 723°K by Kleppa (15) and Gambino (16); at 978°K Predel (17) obtained activities using a comparative vapor pressure method. The galvanic cell measurements of Genta, 723°-818°K (18); Kleppa 850°K (19), Svirbely 693°-793°K (20); Gerasimenko, 723°-823°K (21); Ryabov, 933°-1033°K (22); and Moser 714°-877°K (23) have yielded partial molar functions of zinc in Ga-Zn system. The last author, Moser, thinks emf measurements are unsatisfactory with such a binary alloy since the components are close together in the electropotential series; he recommends a vapor pressure method. These two kinds of measures will be compared in the Results section.

Germanium-zinc system.—The liquidus curve has been reported by Gebhart (24) and Thurmond (4).

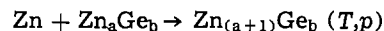
Key words: free energy, Ga-Zn, Ge-Zn, Ga-Ge-Zn, liquidus.

The eutectic point coordinates are: $T_e = 671.15^\circ\text{K}$ for $x_{\text{Ge}} = 0.055$ (24), or $x_{\text{Ge}} = 0.044$ (4). The maximal solubility of zinc in solid germanium corresponds to $x_{\text{Zn}} = 7.2 \cdot 10^{-5}$ at 1032°K (6). Emf measurements performed by Kleppa, 850°K (19); Batalin, 950°-1230°K (25); and Predel, 1000°K (26) have yielded the thermodynamic functions of this binary system. At 687°, 708°, and 739°K Voronin (27) determined zinc activities using an effusion method.

In this paper we report experimental values of zinc activity in some Ga-Zn and Ge-Zn alloys, and partial mixing entropy and free energy of zinc in 22 Ga-Ge-Zn alloys.

Theory

The formation of a binary (or ternary) alloy by a reaction of the type



may be investigated by a concentration cell represented schematically by: $\text{Zn}|\text{Zn}^{2+} \text{ in molten } \text{LiCl-KCl}|\text{Zn}$ in Ga-, or in Ge-, or in Ga-Ge- (T, p). Electric conduction

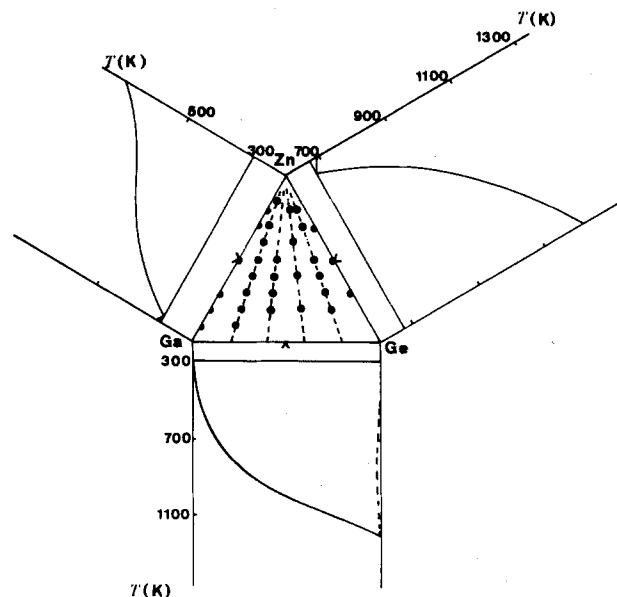


Fig. 1. Phase diagrams of the three limiting binary systems and studied ternary alloys compositions. The temperature scale is larger for the Ge-Zn system than for the two other binary systems.

is due to ions Zn^{2+} because this metal is more electro-positive than gallium and germanium. In effect, standard electrode potentials (ϵ°) for zinc and gallium in molten LiCl-KCl eutectic mixture at 723°K: $Zn(II) - Zn(0)$; $\epsilon^\circ_{Zn} = -1.566V$; $Ga(III) - Ga(0)$; $\epsilon^\circ_{Ga} = -0.84V$ have been investigated by Laitinen and Liu (28). These authors have not measured standard potential for germanium; however, from the values of free energy of formation of gallium, germanium, and zinc chlorides (29) listed in Table I, we can deduce that germanium is the least electro-positive of these three metals. The differences between the standard free energies of formation of gallium, germanium, zinc, lithium, and potassium chlorides are large enough to avoid exchange reactions at experimental temperatures.

From the knowledge of the emf value (E) at temperature T , partial free energy and activity of zinc in an alloy may be calculated using the following equation

$$-zFE = \Delta_{mix}G_{Zn} = RT \ln a_{Zn}$$

since we have

$$\Delta_{mix}G_{Zn} = \Delta_{mix}H_{Zn} - T\Delta_{mix}S_{Zn}$$

the determination of $\Delta_{mix}S_{Zn}$ and $\Delta_{mix}H_{Zn}$ requires the measurement of the change in E with temperature

$$\Delta_{mix}S_{Zn} = zF \left(\frac{\partial E}{\partial T} \right)_P$$

$$\Delta_{mix}H_{Zn} = -zF \left(E - T \frac{\partial E}{\partial T} \right)$$

If the emf of the cell is a linear function of T ($E = A + BT$), then molar partial enthalpy and molar partial entropy of zinc do not vary perceptibly with temperature: they are proportional to the coefficients A and B .

Experimental

Apparatus.—We have developed the apparatus previously described by Massart (30) and shown in Fig. 2. The large external crucible (I), the lead wire sheath (D), and the thermocouple sheath (E) are of alumina. The pure zinc and alloys are also contained in pure alumina crucibles (A). The electrode crucibles are wedged in place on the bottom of the crucible (I) by several alumina tubes (C). Each cell contains ten electrodes: two with pure zinc and the others with alloys. The tantalum lead wires (D) for the electrodes and Pt-Pt 10% Rh thermocouple (E) are aligned by two covers (G and H). In the cover (G) suitable fittings permit a flowing argon.

The cell is heated by a cylindrical vertical furnace with two kanthal resistors; one of which is connected to a-c supply and the other to an electronic regulator. A more uniform temperature distribution along the electrodes is obtained by enclosing the cell inside the furnace in a concentric refractory steel cylinder (K) which also acts as an electric shield.

Emf values are measured with a digital millivoltmeter (Tacussel Aries 20,000) with a large input impedance ($10^{12}\Omega$).

Materials.—99.9999 gallium was donated by Alusuisse France S.A., and 99.999 germanium and 99.9998 zinc

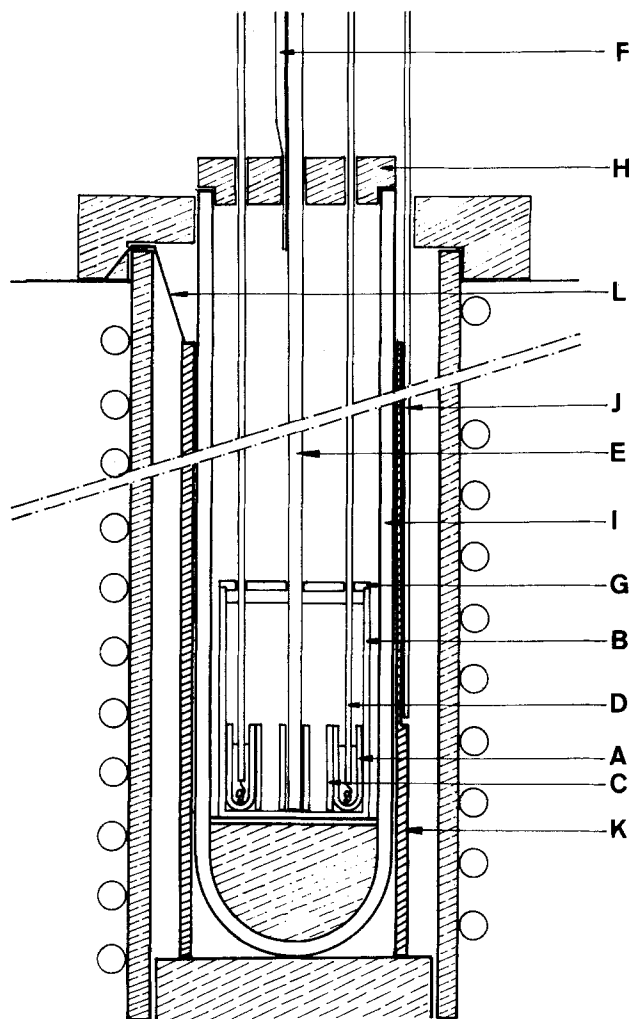


Fig. 2. Schematic diagram of the apparatus. (A) Alumina crucible, (B) alumina crucible containing molten electrolyte, (C) alumina wedge, (D) lead wire sheath, (E) thermocouple sheath, (F) argon delivery pipe, (G) alumina cover, (H) alumina cover, (I) external alumina crucible, (J) thermocouple connected to the regulator, (K) refractory steel cylinder, (L) earth-wire.

were supplied by Koch-Light Company. Lithium, potassium, and zinc chlorides were analytical grade salts (Prolabo and Merck). The cell was supplied with pure argon (grade U-Air liquide Company).

Cell preparation.—The molten electrolyte has to be carefully prepared to avoid considerable problems in experiments. Eutectic mixture of lithium and potassium chlorides (55.8 weight percent (w/o) LiCl; $T_{fus} = 623^\circ K$) was dried at $523^\circ K$ for 24 hr under dynamic vacuum and molten under flowing argon. After addition of 5 w/o zinc chloride, kept under vacuum at $383^\circ K$, the decanted mixture of salts is transferred to the cell after putting metals in the crucibles. The cell is heated until about $1100^\circ K$ and held for 2 hr at this temperature to stabilize. Potentials are then measured at intervals of about $30^\circ K$ after stabilization of the cell.

Accuracy.—It is difficult to make a correct evaluation of emf measurement errors. Careful attention has been paid to the experiments preparation but the major problem is knowing if values correspond well to one reversible reaction. During experiments we took the following precautions: (i) attainment of equilibrium by alloys after each change in temperature was verified by observing the course of emf over a period of time; (ii) the emf between two reference electrodes was always lower than 0.0002V at moderate temperatures and lower than 0.0003V at upper temperatures; (iii) since zinc vapor pressure becomes important

Table I. Standard free energies of formation at two temperatures of five chlorides (29).

Reaction	$\Delta_r G^\circ$ (kcal _{th} mole ⁻¹)	
	$T = 500^\circ K$	$T = 1050^\circ K$
$1/3 Ga + 1/2 Cl_2 = GaCl_3$	-34	-32
$1/4 Ge + 1/2 Cl_2 = 1/4 GeCl_4$	-13	-11
$1/2 Zn + 1/2 Cl_2 = 1/2 ZnCl_2$	-40	-34
$K + 1/2 Cl_2 = KCl$	-93	-81
$Li + 1/2 Cl_2 = LiCl$	-88	-79

above 900°K ($p = 10132$ Pa at 991°K), all measurements were repeated on the next day to check that measured voltages were constant during this period; (iv) for each composition, three independent experiments were carried out; (v) Ga-Zn and Ge-Zn binary alloys were studied in the same cells as ternary alloys. Results were compared with published data to verify the smooth working of the cells; (vi) at fusion of reference metal (M) the slope change of $E = f(T)$ diagrams is proportional to metal fusion enthalpy

$$\Delta_{\text{fus}}H_m(M) = zT_{\text{fus}}F \left[\left(\frac{\partial E}{\partial T} \right) (M,s) - \left(\frac{\partial E}{\partial T} \right) (M,l) \right]$$

In our case, however, it was difficult to determine accurately the slope $(\partial E/\partial T)$ (M,s) because melting points of zinc and the salt mixture are close. We have seen that there is no correlation between the difference calculated value, generally accepted value (1750 cal_{th} mole⁻¹), and zinc concentration.

Experimental Results

Limiting binary systems.—Ga-Zn system.—Six alloys ($x_{\text{Zn}} = 0.1; 0.2; 0.3; 0.5; 0.7; 0.8$) were studied. In Table II are reported equations $E = f(T)$ calculated from emf experimental measurements of Genta (18), Kleppa (19), Svirbely (20), Gerasimenko (21), Moser (23), and Ryabov (22)

Using these equations we calculated zinc activity at 850° and 978°K; resulting values are compared in Table III.

Results proposed by Kleppa, Svirbely, and Moser are in good agreement; the maximal discrepancy is about 4% at 978°K for $x_{\text{Zn}} = 0.6$. Comparing our values with the mean of those found by these three authors, we find a maximal deviation of 4.7% for the

alloy $x_{\text{Zn}} = 0.1$ at 978°K; at 850°K this deviation was lower than 3%. We have also reported in this table results from a comparative vapor pressure method used at 978°K by Predel (17). The difference between his values and the same mean values is about 1.5%, except for the alloy $x_{\text{Zn}} = 0.5$ for which it is about 5%, which is very satisfactory for two such different methods. Consequently, although Genta, Gerasimenko, and Ryabov give somewhat different values, the potentiometric method seems well reproducible and as reliable as the vapor pressure method.

Ge-Zn system.—In Table IV are reported experimental results found by Kleppa (19), Batalin (25), and Predel (26) with the potentiometric method, and Voronin's (27) obtained by an effusion method.

Table V, giving zinc activity values calculated at 739° and 1000°K from the data of Table IV, shows that the deviation between values of Kleppa and Batalin increases with germanium molar fraction from 1% ($x_{\text{Ga}} = 0.1$) to 11% ($x_{\text{Ge}} = 0.7$). The maximal difference between these values and Predel's is 4%. Our results are very near to those of Kleppa (maximal difference 1%). At 739°K, values calculated from Kleppa's and Batalin's data are coherent but not in good agreement with Voronin's results. This discrepancy probably reflects the method used by Voronin.

Emf values vs. temperature for different Ge-Zn alloys, which are plotted in Fig. 3, vary linearly across the one-phase field as expected from equilibrium considerations. $E = f(T)$ curves exhibit sharp discontinuities at the phase boundaries. Liquidus temperatures so obtained agree well with those found by Kleppa and with the phase diagram published by Hansen (14).

Ga-Ge-Zn system.—In Fig. 4-7 are reported $E = f(T)$ curves for 22 alloys disposed along four sections,

Table II. Analytical expressions of $E = A + BT$ curves for Ga-Zn alloys $E(V)$; A ($V \cdot 10^3$); B ($V \cdot 10^3 \text{ K}^{-1}$)

Genta (18) 761.4°K			Svirbely (20) 693°-793°K			Ryabov (22) 933°-1033°K		
x_{Zn}	A	B	x_{Zn}	A	B	x_{Zn}	A	B
0.042	-26.614	0.1574	0.1	-24.233	0.11532	0.099	-27.12	0.1164
0.150	-23.236	0.1001	0.2	-19.587	0.08188	0.201	-20.85	0.0830
0.260	-18.131	0.0720	0.3	-17.292	0.06400	0.299	-16.81	0.0635
0.370	-16.179	0.0565	0.37	-15.338	0.05425	0.399	-13.28	0.0488
0.480	-18.060	0.0500	0.40	-13.558	0.04888	0.497	-10.72	0.0377
0.590	-13.029	0.0363	0.50	-11.066	0.03838	0.600	-8.16	0.0281
0.697	-9.771	0.0264	0.60	-7.314	0.02722	0.700	-5.34	0.0193
0.775	-5.035	0.0167	0.70	-4.976	0.01916	0.799	-3.55	0.0120
0.841	-1.103	0.0082	0.80	-2.799	0.01195	0.901	-2.00	0.0062
0.910	-1.071	0.0054	0.90	-0.862	0.00505	0.950	-1.53	0.0035
0.957	-1.063	0.0033						
Kleppa (19) 850°K			Gerasimenko (21) 723°-823°K			Moser (23) 714°-877°K		
x_{Zn}	A	B	x_{Zn}	A	B	x_{Zn}	A	B
0.606	-7.685	0.0273	0.10	-27.941	0.117	0.01	-15.913	0.19892
0.669	-5.67	0.0214	0.20	-20.440	0.080	0.03	-17.710	0.15555
0.751	-3.44	0.0146	0.30	-16.307	0.059	0.05	-19.572	0.13696
0.826	-1.41	0.0088	0.40	-12.712	0.044	0.07	-17.433	0.12031
0.863	-2.075	0.0081	0.50	-9.036	0.032	0.10	-20.744	0.1113
0.908	-0.92	0.0048	0.60	-5.806	0.022	0.20	-19.412	0.0819
			0.70	-2.922	0.014	0.30	-11.704	0.05693
			0.80	-1.657	0.009	0.40	-8.916	0.043038
			0.90	-1.065	0.005	0.50	-6.264	0.032141
						0.60	-2.612	0.020808
						0.70	-2.674	0.016117
						0.80	-1.794	0.0105
						0.90	-0.504	0.00517
Our values 623°-1123°K								
x_{Zn}	A	B						
0.10	-17.118	0.10607						
0.20	-12.019	0.07229						
0.30	-10.635	0.05502						
0.50	-8.918	0.03562						
0.70	-4.046	0.01762						
0.80	-0.930	0.00937						

Table III. Ga-Zn system: zinc activity values calculated at 850° and 978°K from analytical expressions of *E*. Predel's results at 978°K are experimental ones.

azn at 850°K							
<i>x</i> _{Zn}	Genta (18)	Kleppa (19)	Svirbely (20)	Gerasimenko (21)	Ryabov (22)	Moser (23)	Our values
0.10	0.160		0.133	0.142	0.182	0.133	0.137
0.20	0.285		0.255	0.273	0.307	0.254	0.259
0.30	0.405		0.363	0.397	0.414	0.368	0.373
0.40	0.500		0.465	0.509	0.512	0.469	
0.50	0.587		0.556	0.608	0.605	0.563	0.557
0.60	0.672	0.650	0.649	0.703	0.688	0.662	
0.70	0.752	0.737	0.734	0.782	0.769	0.740	0.742
0.80	0.830	0.822	0.819	0.849	0.854	0.824	0.824
0.90	0.912	0.905	0.911	0.916	0.925	0.899	

azn at 978°K								
<i>x</i> _{Zn}	Genta (18)	Kleppa (19)	Svirbely (20)	Gerasimenko (21)	Ryabov (22)	Moser (23)	Our values	Predel (17)
0.10	0.200		0.122	0.128	0.128	0.123	0.128	
0.20	0.335		0.238	0.254	0.259	0.237	0.248	
0.30	0.450		0.341	0.374	0.341	0.352	0.359	
0.40	0.540		0.444	0.487	0.441	0.455		
0.50	0.625		0.533	0.590	0.540	0.550	0.541	0.570
0.60	0.702	0.630	0.632	0.689	0.632	0.656		0.650
0.70	0.772	0.725	0.721	0.774	0.725	0.733	0.731	0.737
0.80	0.845	0.818	0.810	0.844	0.823	0.818	0.823	0.827
0.90	0.920	0.905	0.908	0.913	0.908	0.898		0.907

$x_{Ga}/x_{Ge} = \text{constant}$, of the Ga-Ge-Zn phase diagram. The compositions of the investigated ternary alloys are

$$\frac{x_{Ga}}{x_{Ge}} = 4; x_{Zn} = 0.1; 0.2; 0.3; 0.4; 0.5; 0.6; 0.7; 0.85$$

$$\frac{x_{Ga}}{x_{Ge}} = \frac{3}{2}; x_{Zn} = 0.2; 0.3; 0.4; 0.5$$

$$\frac{x_{Ga}}{x_{Ge}} = \frac{2}{3}; x_{Zn} = 0.2; 0.4; 0.6; 0.8$$

$$\frac{x_{Ga}}{x_{Ge}} = \frac{1}{4}; x_{Zn} = 0.2; 0.3; 0.4; 0.5; 0.7; 0.8$$

For an alloy containing a large amount of germanium, the plot of *E* vs. *T* is a straight line at upper temperatures and a curved line at moderate temperatures; this part is interrupted by a break point at 693°K, the melting temperature of zinc. For an alloy containing a large amount of gallium or zinc, the curved part is very short or absent. These results may be easily explained: the straight line corresponds to one liquid phase equilibrium; therefore, the partial mixing en-

thalpy and entropy of zinc, deduced from the zero abscissa ordinate and the slope, vary very little or not at all with temperature changes. Analytical equations of these straight lines and partial functions of zinc are listed in Table VI.

For all the studied alloys, from the partial mixing enthalpy and entropy of zinc, we have calculated $\Delta_{mix}G_{Zn}$ at 1233°K, the temperature at which the Ga-Ge-Zn system is always composed of one liquid phase: corresponding values are reported in Table VII, and Fig 8 gives the general shape of the $\Delta_{mix}G_{Zn}$ function over all the concentration range.

The curved line of each *E* = *f*(*T*) diagram corresponds to a two-phase equilibrium (liquid-solid) with a sharp discontinuity when the liquidus surface is reached. Liquidus temperatures so determined are listed in Table VIII and plotted in Fig. 9. We can compare these results with those recently obtained by Fornaris (31) using a high temperature Calvet type microcalorimeter: we notice small deviations which are not significant.

For the ternary alloy: $x_{Ga}/x_{Ge} = 1/4$, $x_{Zn} = 0.8$, the *E* = *f*(*T*) curve shows a third break point at 738°K, the temperature at which the emf value is near to zero.

Table IV. Experimental data for Ge-Zn alloys: analytical expressions of *E* = *A* + *BT*, or zinc fugacity, or activity values *E* (V); *A* (V · 10³); *B* (V · 10³ K⁻¹) () value extrapolated for liquid state.

<i>x</i> _{Zn}	Kleppa (19) emf 850°K		<i>x</i> _{Zn}	Batalin (25) emf 950°-1230°K		<i>x</i> _{Zn}	Voronin (27) effusion <i>f</i> _{Zn}		
	<i>A</i>	<i>B</i>		<i>A</i>	<i>B</i>		739°K	708°K	687°K
0.965	-0.960	0.00260	0.9079	-1.661	0.00649	0.985	0.718	0.820	0.906
	(-0.669)	(0.00360)	0.8588	-2.129	0.00962	0.975	0.668	0.783	0.875
0.936	(-0.485)	0.00330	0.7400	-3.417	0.01715	0.950	0.650	0.751	0.836
	(-0.955)	(0.00530)	0.6248	-3.528	0.02516	0.925	0.650	0.738	0.811
0.906	(-1.005)	0.00530	0.5061	-4.763	0.03610	0.900	0.650	0.731	0.834
0.879	-1.515	0.00730	0.4253	-11.411	0.05038	0.875	0.650	0.752	0.860
0.842	-2.490	0.01020	0.3794	-15.480	0.04900	0.850	0.669	0.774	0.885
0.822	-2.595	0.01150	0.3221	-21.922	0.07230				
0.796	-3.925	0.01470	0.2240	-45.373	0.11112				
0.756	-3.485	0.01650							
0.697	(-4.305)	(0.02150)							
0.680	(-3.510)	(0.02200)							
0.648	(-4.885)	(0.02630)							
0.597	(-3.370)	(0.02900)							
0.552	(-4.440)	(0.03360)							
0.551	(-4.340)	(0.03400)							
0.503	(-4.480)	(0.03880)							
0.500	(-7.085)	(0.04230)							
0.453	(-4.735)	(0.04430)							
0.449	(-6.440)	(0.04780)							
0.400	(-5.323)	(0.05171)							

Predel (26) emf 1000°K		Our values emf 623°-1123°K		
<i>x</i> _{Zn}	<i>a</i> _{Zn}	<i>x</i> _{Zn}	<i>B</i>	
0.9	0.916	0.8	-3.811	0.01440
0.8	0.799	0.7	-5.684	0.02280
0.7	0.468	0.6	-6.457	0.03120
0.6	0.391	0.5	-8.812	0.04400
0.55	0.370	0.4	-10.955	0.05720
		0.3	-17.278	0.07733

Table V. Ge-Zn alloys: zinc activity values calculated at 739° and 1000°K from analytical expressions of E compared with corresponding experimental results of Voronin (27) and Predel (26). () value extrapolated for liquid state.

x_{Zn}	at 739°K			at 1000°K			
	Kleppe (19)	Batalin (25)	Voronin (27)	Kleppe (19)	Batalin (25)	Our values	Predel (26)
	0.975	0.980	0.975	0.651			
0.950	0.955	0.947	0.617				
0.925	0.930	0.922	0.601				
0.900	0.905	0.895	0.585	0.895	0.880		0.916
0.875	0.880	0.870	0.569				
0.800				0.785	0.777	0.782	0.799
0.700				0.667	0.680	0.672	
0.600				0.547	0.570	0.563	
0.500				(0.440)	(0.470)	(0.442)	
0.400				(0.335)	(0.372)	(0.342)	
0.300				(0.250)	(0.280)	(0.246)	

Table VI. Analytical expressions of $E = A + BT$ curves and partial thermodynamic functions of zinc in Ga-Ge-Zn alloys

x_{Ga}/x_{Ge}	x_{Zn}	A (V 10 ³)	B (V 10 ³ K ⁻¹)	$\Delta_{mix}H_{Zn}$ (cal _{th} mole ⁻¹)	$\Delta_{mix}S_{Zn}$ (cal _{th} mole ⁻¹)	$\Delta_{mix}S_{Zn}^E$ (cal _{th} mole ⁻¹ K ⁻¹)
4/1	0.1	-16.66	0.1072	768	4.94	0.37
	0.2	-15.27	0.0777	704	3.58	0.38
	0.3	-11.63	0.0580	536	2.68	0.29
	0.4	-10.01	0.0440	462	2.03	0.36
	0.5	-7.50	0.0328	346	1.51	0.14
	0.6	-5.35	0.0240	247	1.11	0.09
3/2	0.7	-3.49	0.0163	161	0.75	0.04
	0.85	-1.10	0.0068	51	0.32	-0.006
	0.2	-6.59	0.0693	304	3.20	-0.0002
	0.3	-6.30	0.0480	291	2.21	-0.150
	0.4	-4.97	0.0377	229	1.73	-0.084
	0.5	-4.94	0.0320	228	1.48	0.098
2/3	0.2	-12.43	0.0771	573	3.56	0.36
	0.4	-8.38	0.0470	387	2.17	0.35
	0.6	-5.85	0.0264	270	1.22	0.20
	0.8	-4.23	0.0128	195	0.59	0.15
1/4	0.2	-14.68	0.0843	677	3.89	0.69
	0.3	-5.18	0.0600	239	2.77	0.37
	0.4	-4.67	0.0465	215	2.14	0.32
	0.5	-6.15	0.0369	284	1.70	0.33
	0.7	-2.79	0.0170	129	0.78	0.07
	0.8	-2.47	0.0117	114	0.54	0.09

Thus, solid zinc appears and this temperature is probably the upper limit of the three-phase zone [liquid + Ge(s) + Zn(s)].

For the alloy $x_{Ga}/x_{Ge} = 4/1$, $x_{Zn} = 0.85$, when $E = 0$ solid zinc is in equilibrium with liquid solution; the equilibrium temperature may be calculated from the following simplified equation (32)

$$T = \frac{\Delta_{mix}H_{Zn(l)} - \Delta_{fus}H_m(Zn)}{\Delta_{mix}S_{Zn(l)} - \Delta_{fus}H_m(Zn)/T_{fus}(Zn)}$$

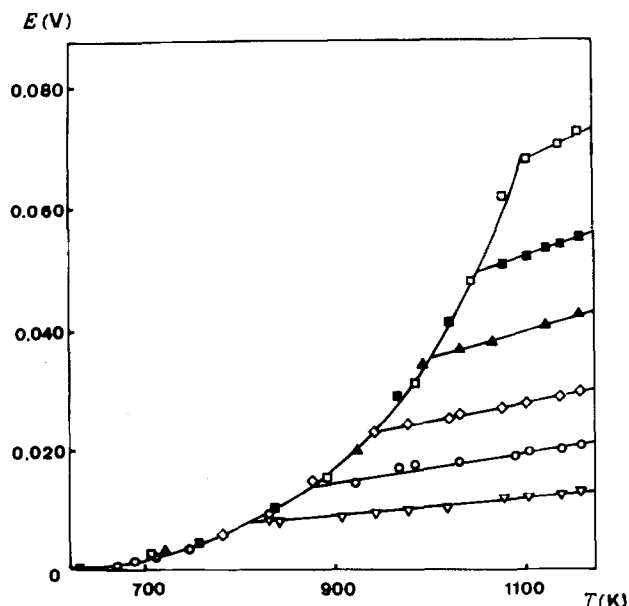


Fig. 3. Experimental values of emf plotted against temperature for 6 alloys of the Ge-Zn system: $x_{Zn} = 0.3$ (□); 0.4 (■); 0.5 (▲); 0.6 (◇); 0.7 (○); 0.8 (▽).

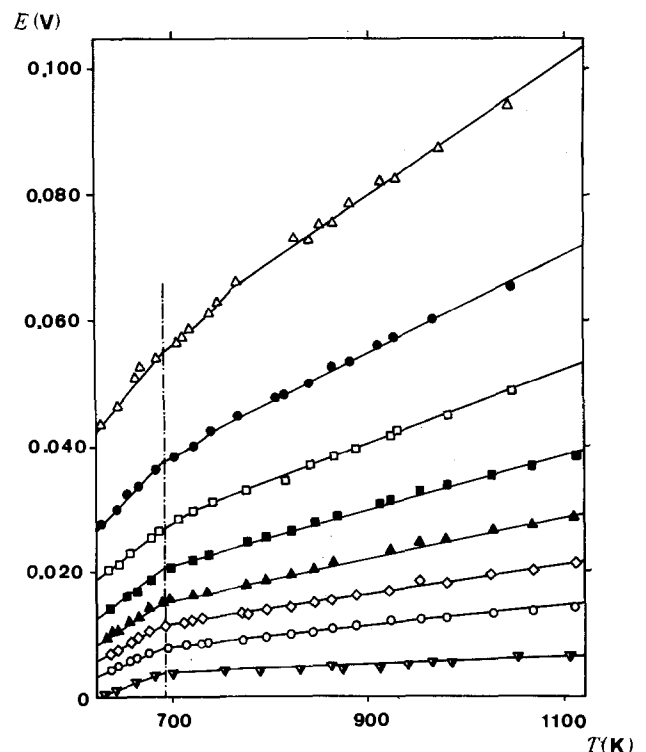


Fig. 4. Experimental values of emf plotted against temperature for 8 alloys of the Ga-Ge-Zn system: $x_{Ga}/x_{Ge} = 4/1$; $x_{Zn} = 0.1$ (△); 0.2 (●); 0.3 (□); 0.4 (■); 0.5 (▲); 0.6 (◇); 0.7 (○); 0.85 (▽).

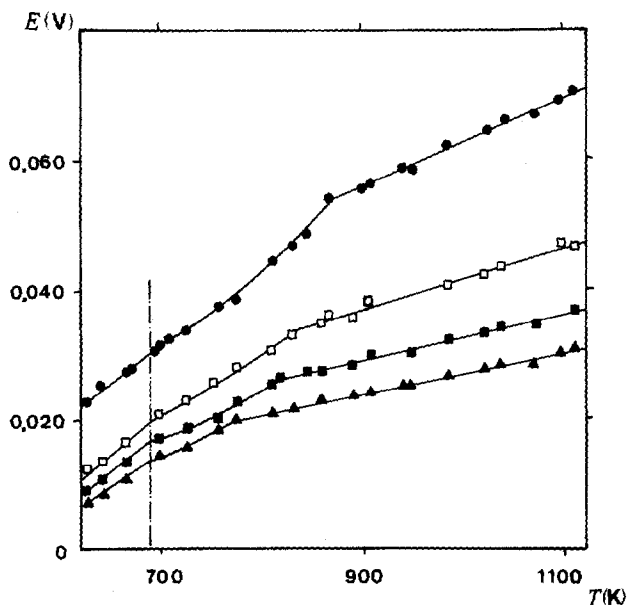


Fig. 5. Experimental values of emf plotted against temperature for 4 alloys of the Ga-Ge-Zn system: $x_{Ga}/x_{Ge} = 3/2$; $x_{Zn} = 0.2$ (●); 0.3 (□); 0.4 (■); 0.5 (▲).

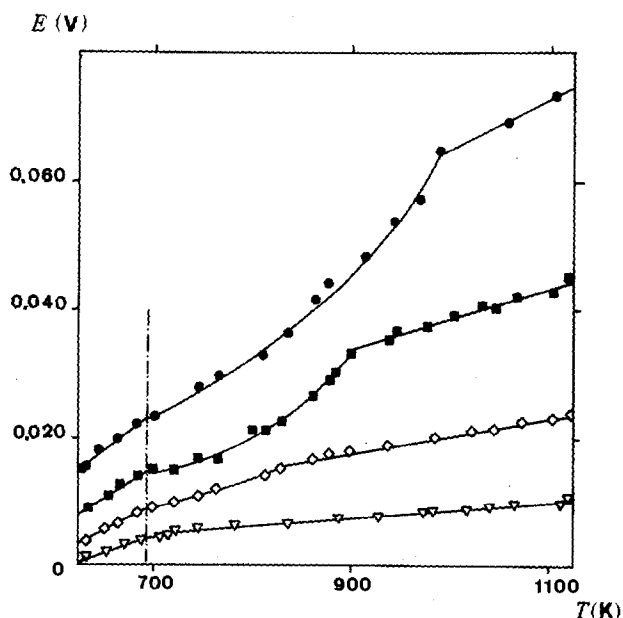


Fig. 6. Experimental values of emf plotted against temperature for 4 alloys of the Ga-Ge-Zn system: $x_{Ga}/x_{Ge} = 2/3$; $x_{Zn} = 0.2$ (●); 0.4 (■); 0.6 (◇); 0.8 (▽).

The value obtained, 633°K, is in good agreement with the experimental value of 629°K.

Table VII. Partial free energy of zinc $\Delta_{mix}G_{Zn}$ (cal_{th}mole⁻¹) at 1233°K in Ga-Zn, Ge-Zn and Ga-Ge-Zn systems. () interpolated value

x_{Zn}	Ga-Ge-Zn x_{Ga}/x_{Ge}					Ge-Zn
	Ga-Zn	4/1	3/2	2/3	1/4	
0.1	-5420	-5323				-6238
0.2	-3758	-3719	-3642	-3816	-4119	-4414
0.3	-2892	-2768	-2434	(-2920)	-3176	-3312
0.4	-2144	-2041	-1904	-2289	-2424	-2513
0.5	-1637	-1516	-1597	(-1720)	-1812	-1893
0.6	-1210	-1122		-1234	(-1280)	-1388
0.7	-852	-764		(-940)	-833	-961
0.8	-529	(-440)		-532	-552	-627
0.9	-245	-343				-322

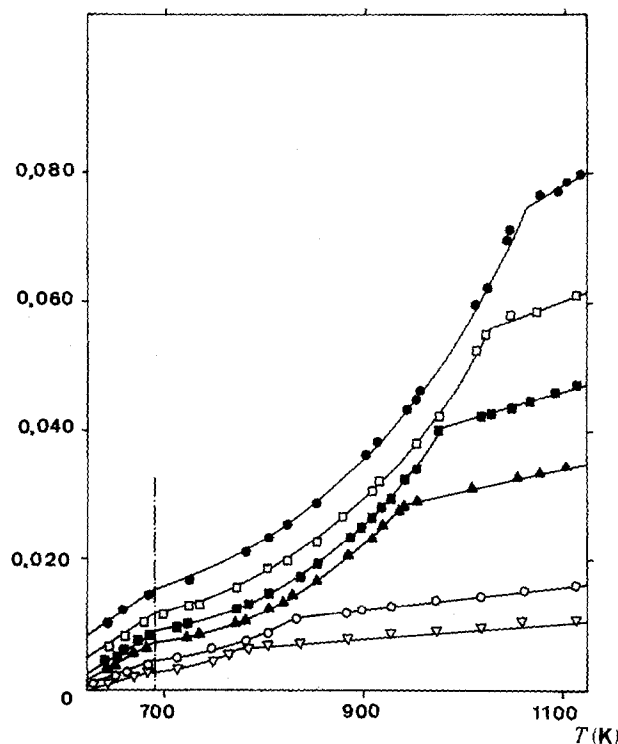


Fig. 7. Experimental values of emf plotted against temperature for 6 alloys of the Ga-Ge-Zn system: $x_{Ga}/x_{Ge} = 1/4$; $x_{Zn} = 0.2$ (●); 0.3 (□); 0.4 (■); 0.5 (▲); 0.7 (○); 0.8 (▽).

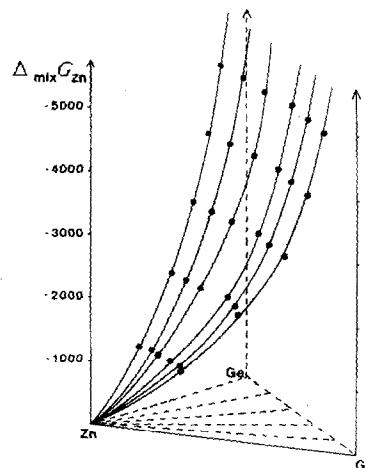


Fig. 8. Partial free energy of zinc $\Delta_{mix}G_{Zn}$ (cal_{th} mole⁻¹) at 1233°K in Ga-Zn, Ge-Zn, and Ga-Ge-Zn systems.

Conclusion

The activities of zinc measured in 22 Ga-Ge-Zn alloys between 623° and 1123°K allowed us to propose partial molar mixing entropy and free energy of zinc. From the shape of the $E = f(T)$ plot we have deduced a large part of the liquidus surface of the ternary system.

Manuscript submitted June 27, 1978; revised manuscript received Nov. 9, 1979.

Any discussion of this paper will appear in a Discussion Section to be published in the December 1980 JOURNAL. All discussions for the December 1980 Discussion Section should be submitted by Aug. 1, 1980.

Publication costs of this article were assisted by the Université d'Aix-Marseille II.

LIST OF SYMBOLS

For all our results, the standard is zinc in liquid state.

Table VIII. Temperatures corresponding to break points of $E = f(T)$ curves

x_{Ga}/x_{Ge}	x_{Zn}	T (°K)	x_{Ga}/x_{Ge}	x_{Zn}	T (°K)
4/1	0.1	765	2/3	0.2	983
	0.2	743		0.4	903
	0.3	731		0.6	835
	0.4	703		0.8	723
	0.85	629*			
3/2	0.2	878	1/4	0.2	1063
		833		0.3	1023
	0.3	833	0.4	979	
	0.4	808	0.5	943	
	0.4	808	0.7	831	
	0.5	763	0.8	733-638*	

* At this temperature $E = 0V$ thus zinc crystallizes.

In this paper, we are using the nomenclature of the publication project by the Commission on Thermodynamics and Thermochemistry of the IUPAC (September 1976): "States and transformations notations and definitions of the word "Standard" in chemical thermodynamics." This text will be an appendix of the "Manual of Symbols and Terminology for Physicochemical Quantities and Units," Butterworths, London (1975). So we recall that

x_A	molar fraction of metal A in an alloy
a_A	activity of metal A
T	temperature (in kelvins)
$T_{fus}(A)$	melting temperature of metal A
$\Delta_{fus}H_m(A)$	molar enthalpy of fusion of metal A

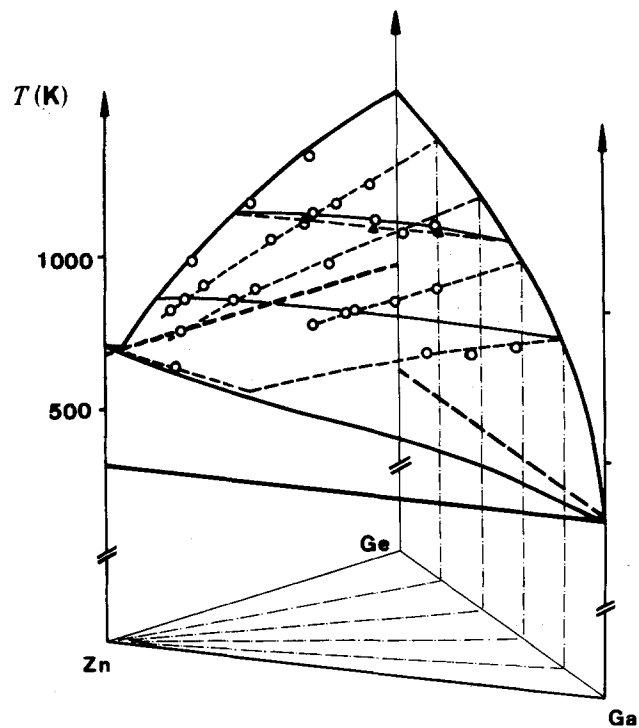


Fig. 9. Liquidus surface of the Ga-Ge-Zn ternary system. (○) Point of the liquidus obtained by potentiometry; (▲) point of the liquidus obtained by calorimetry (31). To clarify this figure, the temperature scale is not respected in the lower part.

$\Delta_{mix}H_{A(l)}$, $\Delta_{mix}S_{A(l)}$, $\Delta_{mix}G_{A(l)}$ = mixing partial molar enthalpy (or entropy or free energy) of liquid metal A

$\Delta_f G^\circ$	formation standard free energy
E	electromotive force (in volts)
z	charge number of the cell reaction
F	Faraday constant = 96487 coulombs
R	gas constant = 8.31433 JK ⁻¹ mole ⁻¹
1 cal _{th}	4.184J

REFERENCES

- H. Eslami, Thèse Doct. Spéc., Université de Provence, Marseille (1977).
- M. Fornaris, Thèse Doct. Spéc., Université de Provence, Marseille (in press).
- M. Hansen and K. Anderko, in "Constitution of Binary Alloys," McGraw Hill, New York (1958).
- C. D. Thurmond and M. Kowalchik, *Bell Syst. Tech. J.*, **39**, 169 (1960).
- E. S. Greiner, *J. Metals*, **4**, 1044 (1948).
- F. A. Trumbore, *Bell Syst. Tech. J.*, **39**, 205 (1960).
- B. Predel and D. W. Stein, *Z. Metallkd.*, **62**, 499 (1971).
- C. Bergman, J. P. Bros, and M. Laffitte, *Thermochim. Acta*, **2**, 259 (1971).
- G. I. Batalin, E. A. Beloborodova, V. A. Stukalo, and S. S. Trofimova, *Ukr. Khim. Zh.*, **38**, 1231 (1972).
- N. A. Puschin, S. Stepanovic, and V. Stajic, *Z. Anorg. Chem.*, **209**, 329 (1932).
- B. Siede, *Metall.*, **17**, 1031 (1963).
- S. Delcroix, A. Defrain, and I. Epelboin, *J. Phys.*, **24**, 17 (1963).
- T. Heumann and B. Predel, *Z. Metallkd.*, **49**, 90 (1958).
- D. A. Davies and E. A. Owen, *Br. J. Appl. Phys.*, **15**, 1309 (1964).
- O. J. Kleppa, *Acta Metall.*, **6**, 225 (1958).
- M. Gambino, Thèse Doct. Etat Sci. Phys., Université de Provence, Marseille (1976).
- B. Predel, R. Mohs, and D. Rothacker, *J. Less-Common Met.*, **12**, 483 (1967).
- V. Genta, M. Fiorani, and V. Valenti, *Gazz. Chim. Ital.*, **85**, 103 (1955).
- O. J. Kleppa and C. E. Thalmayer, *J. Phys. Chem.*, **63**, 1953 (1959).
- W. J. Svirbely and S. M. Read, *J. Phys. Chem.*, **66**, 658 (1962).
- L. N. Gerasimenko, V. A. Zaitsev, L. N. Lozhkin, and A. C. Morachevskii, *Izvest V. U. Z., Isvetn. Med.*, **1**, 46 (1966).
- V. G. Ryabov and I. T. Sryvalin, *Isv. Akad. Nauk SSSR, Met.*, **2**, 78 (1971).
- Z. Moser, *Metall. Trans.*, **4**, 2399 (1973).
- E. Gebhardt, *Z. Metallkd.*, **34**, 255 (1942).
- V. I. Batalin, E. A. Beloborodova, and V. A. Stukalo, *Izv. Akad. Nauk SSSR, Met.*, **2**, 82 (1970).
- B. Predel and U. Schallner, *Z. Metallkd.*, **63**, 119 (1972).
- G. F. Voronin and A. M. Evseev, *Zh. Fiz. Khim.*, **33**, 2024 (1959).
- H. A. Laitinen and H. Liu, *J. Am. Chem. Soc.*, **80**, 1015 (1958).
- T. B. Reed, in "Free Energy of Formation of Binary Compounds," M.I.T. Press, Cambridge, Mass. (1971).
- G. Massart, F. Durand, and E. Bonnier, *Bull. Soc. Chim.* **87** (1965).
- M. Fornaris, Private communication.
- O. J. Kubaschewski and E. L. L. Evans, in "La Thermochemie en Métallurgie," Gauthier-Villars, Paris (1964).

The Effects of Titanium Impurities in N⁺/P Silicon Solar Cells

A. M. Salama* and L. J. Cheng*

California Institute of Technology, Jet Propulsion Laboratory, Pasadena, California 91103

ABSTRACT

To understand the degradation mechanisms associated with the presence of titanium impurities of concentration level 3.6×10^{14} atoms/cm³ in silicon solar cells, microscopic and electrical measurements were performed on these cells. The measurements included x-ray topography, transmission electron microscopy, and deep level transient spectroscopy, before and after processing. The results indicated the presence of TiO₂ precipitates, the density of which increased after phosphorus diffusion. A majority carrier trapping level located at $E_v + 0.27$ eV was observed in the wafers before processing. Two additional majority carrier trapping levels located at $E_v + 0.20$ eV and $E_v + 0.40$ eV and a minority carrier level at $E_c - 0.24$ eV were observed at the junction after phosphorus diffusion. It was concluded that about 10% of the Ti in the N⁺/P silicon solar cells formed electrically active centers which caused degradation of the cell junction. About 14% of the remaining Ti precipitated out as TiO₂, forming electrically active defects, which also caused junction degradation. The details of the degradation mechanisms are given.

Titanium is one of the impurities of concern in metallurgical grade silicon. Therefore, this work was performed to determine its effect on solar cell performance, in order to establish a definition of low cost solar grade silicon.

From previously reported investigations (1, 2), it was found that deliberate titanium doping in N⁺/P silicon solar cells caused degradation in the cell conversion efficiency to about 61% of that of the undoped baseline silicon solar cells.

During deep level transient spectroscopy studies (DLTS) (3), a majority (hole) carrier trap at $E_v + 0.29$ eV was observed in the as-grown titanium-doped silicon wafers. A minority (electron) carrier trap, at energy level $E_c - 0.24$ eV, was also seen for titanium in p-type silicon diodes. The electrically active concentration of the minority trap was estimated to be 1.5×10^{13} /cm³, and the hole trap concentration was 1.35×10^{13} /cm³.

By means of electron spin resonance measurements, titanium was found (4) to have occupied interstitial sites in silicon. It was also reported (5) that diffused titanium in silicon acted as a donor at the level $E_c - 0.24$ eV.

In addition, titanium is known to have a high affinity to react with oxygen and form a wide range of titanium oxides (6). Therefore, one expects a great tendency for the titanium to react with the oxygen in the Czochralski-grown ingots or wafers, during growth or annealing, thus forming titanium-oxygen complexes.

To understand the mechanism of the titanium-doped solar cell degradation, a series of microscopic and electrical measurements were performed on these cells, before and after phosphorus diffusion and solar cell fabrication. By comparing the results of these measurements, it was possible to track the critical step for defect generation and determine the defects that caused the junction degradation.

Description of the Silicon Wafers and Cells under Investigation

The 0.025 cm thick, 3.12 cm diam silicon wafers were cut from ingots with <111> growth axes, prepared by Czochralski techniques (3). The titanium was added to the ingots during the melting process at $\sim 1412^\circ\text{C}$. The seed silicon material was boron-doped to a concentration of $\sim 10^{16}$ atoms/cm³. The titanium doping

level was 3.6×10^{14} atoms/cm³, as determined by neutron activation analysis (3). The ingot was pulled out of the furnace at a rate of 7.5 cm/hr, then rapidly cooled. Some of these wafers were characterized before and after processing, and the results are included in this paper.

The diffusion process was performed at 825°C using standard solar cell fabrication techniques with POCl₃ as the phosphorus source. Thin films of Ti/Pd/Ag metallization were evaporated on the diffused wafers to form the contacts of the solar cells.

Devices for capacitance studies were prepared as follows: (i) titanium Schottky barrier diodes on silicon wafers, (ii) mesa structure diodes etched from solar cells, and (iii) diodes made by the usual integrated circuit techniques.

Experiments and Results

Microscopic Evaluation of the Silicon Wafers

Transmission x-ray topography on the as-grown wafers.—Wafers of <111> crystal orientation were examined using the Lang transmission method. A Rigaku-Denki camera and MoK_α radiation from a Jarrell-Ash microfocussing x-ray generator were used. All exposures were recorded on Ilford K-5, 50 μm nuclear plates. Three Ti-doped silicon wafers of each ingot were examined, and topographs of both the (111) and (220) crystal reflections from those wafers were taken.

Figure 1 shows a typical (220) topograph of a titanium-doped silicon wafer before processing. The dislocation density of this wafer was 700 d/cm², and the precipitates, shown as bright spots, had a density of 1.9×10^2 p/cm².

Transmission x-ray topography on wafers after phosphorus diffusion.—After the x-ray topography examination, the same wafers were processed for p-n junction formation by phosphorus diffusion. The back sides of those wafers were etched off as done for standard solar cell fabrication. Then they were examined again by the nondestructive transmission x-ray topography technique.

Figure 2 shows a typical (220) topograph of the same wafer as in Fig. 1, after the phosphorus diffusion. The topograph indicated that there were new precipitates at the central part of the wafer at A. The dislocation density had changed slightly to 800 d/cm², whereas the precipitate density had increased significantly to 4×10^2 p/cm².

* Electrochemical Society Active Member.

Key words: silicon, titanium, impurity, defects, solar cells.

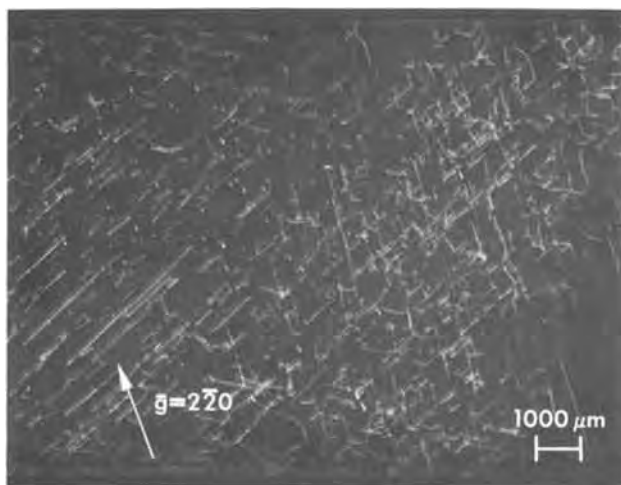


Fig. 1. A (220) x-ray topograph of a Ti-doped silicon wafer before processing.

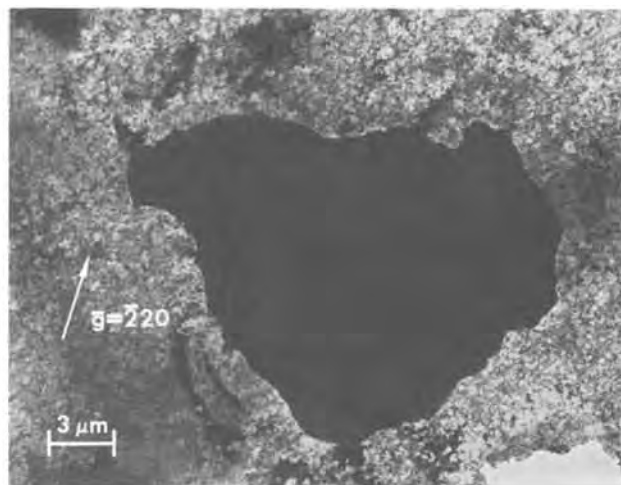


Fig. 3. A TEM micrograph showing a large precipitate particle in the bright field.

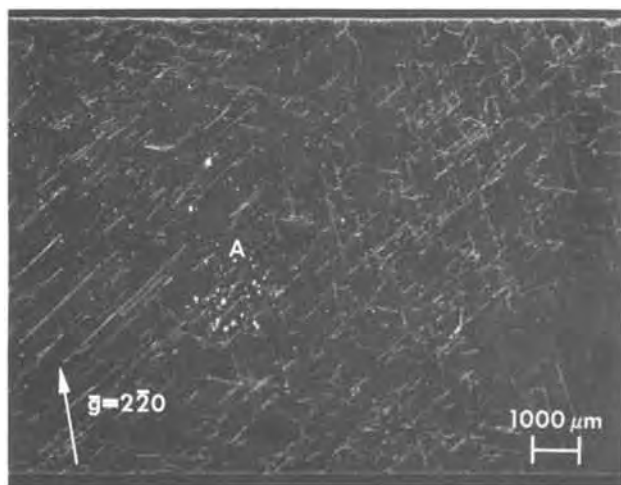


Fig. 2. A (220) x-ray topograph of the same wafer as in Fig. 1, after processing.

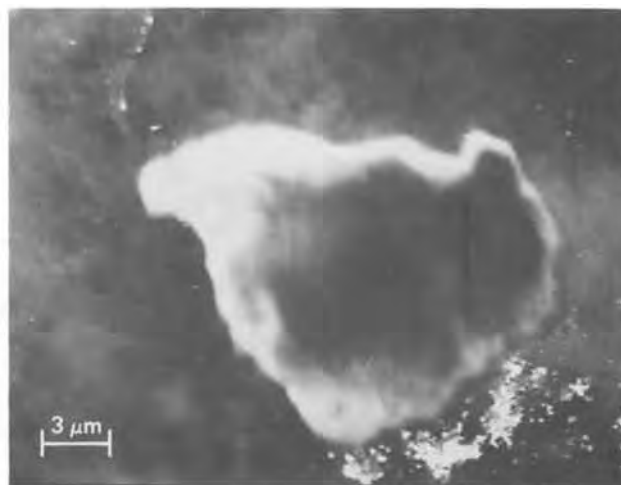


Fig. 4. A TEM micrograph of the same large particle as in Fig. 3, in the dark field.

From the two figures, it was found that the precipitate concentration increased from 2.6×10^{13} atoms/cm³ to 4.9×10^{13} atoms/cm³ after the diffusion process. Some of these precipitates were associated with dislocations.

Transmission electron microscopy (TEM).—Titanium-doped silicon specimens were cut from the previously examined wafers, around the areas that showed precipitates in the x-ray topographs (area A in Fig. 2). Thin foils were prepared chemically using HF, HNO₃, CH₃COOH, and iodine, in an ice bath, then examined by Siemens' Elmiskope TEM at 100 keV. The foils were examined in the (111) plane. Other results (not included here) were obtained for foils tilted in the (110) and (100) planes. Selected area diffraction (SAD) patterns were taken, both for the silicon material and the precipitate particles in the silicon.

Figures 3 and 4 show a large precipitate particle in bright and dark fields, respectively, and Fig. 5 shows the selected area diffraction pattern for the precipitate particle. The average size of the precipitate particles was 1.2×10^{-12} cm³. The diffraction spots correspond to the precipitate interplanar spacings of 1.8907, 1.343, and 1.044 Å for the (200), (220), and (321) reflections, respectively. By comparing the obtained lattice spacings with those of the ASTM index cards, it was determined that the precipitate is the tetragonal titanium dioxide, TiO₂ (anatase).

Physical and Electrical Evaluation of the Solar Cells

Physical evaluation.—Scanning electron microscopy (SEM) using the electron beam induced current

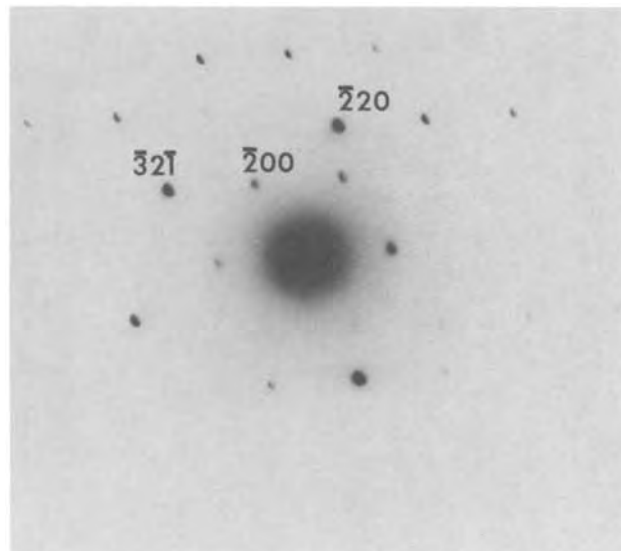


Fig. 5. Selected area diffraction pattern for the precipitate particle in Fig. 3 and 4.

(EBIC) mode was employed on solar cells incorporating the titanium impurities of interest. A Cambridge S-410 scanning electron microscope was used. At ~ 10 keV, the electron beam penetration depth is $\sim 0.5 \mu\text{m}$, which gives an image of the p-n junction depletion region. The junction depth, as determined by the incremental sheet resistance technique (3), is $0.3\text{--}0.4 \mu\text{m}$. Figure 6 shows an EBIC micrograph at 10 keV. A precipitate clump is shown in the center of a hole-like region. It is believed that these defects are the TiO_2 precipitates found in the TEM experiments.

Electrical evaluation.—Deep level transient spectroscopy (DLTS) method used to measure the carrier trapping centers is similar to the deep level transient spectroscopy method reported by Lang (7, 8). The measured activation energies for carrier emission are accurate to about ± 0.02 eV.

The samples used were in the form of Schottky diodes or diffused diodes. They were prepared from wafers of Czochralski ingots grown from the melt as described previously. The Schottky barrier was prepared by titanium evaporation on freshly etched wafers.

Figure 7 shows typical DLTS spectra of the Ti-doped samples, in which the upper spectrum is that obtained from the Schottky diodes made of as-grown materials, and the other two spectra are measured from the two diffused diodes. These two diodes were prepared from the same Ti-doped material fabricated as previously described. It should be mentioned that one kind of the diffused diodes (cell-s) was prepared by mesa etching of solar cells, while the other (cell-W) was made by etching and photolithographic techniques. Four DLTS peaks were observed, corresponding to three majority carrier trapping levels and one minority carrier trapping level.

The temperature dependence of carrier emission rate of each level was measured as shown in Fig. 8. The activation energies for the emission process of the levels estimated from those data revealed their locations in the forbidden gap. They were $E_V + 0.18$ eV, $E_V + 0.27$ eV, and $E_V + 0.38$ eV for the majority carrier trapping levels and $E_C - 0.24$ eV for the minority carrier trapping level.

The $E_V + 0.27$ eV level was the only majority carrier trapping level in the as-grown samples. The measured concentration was about $5\text{--}6 \times 10^{13}/\text{cm}^3$, which is much lower than the total concentration of titanium determined by neutron activation analysis. The $E_V + 0.27$ eV level was also observed in the diffused samples but with lower concentrations, $\sim 1 \times 10^{13}/\text{cm}^3$, indicating the existence of some diffusion-induced effect.

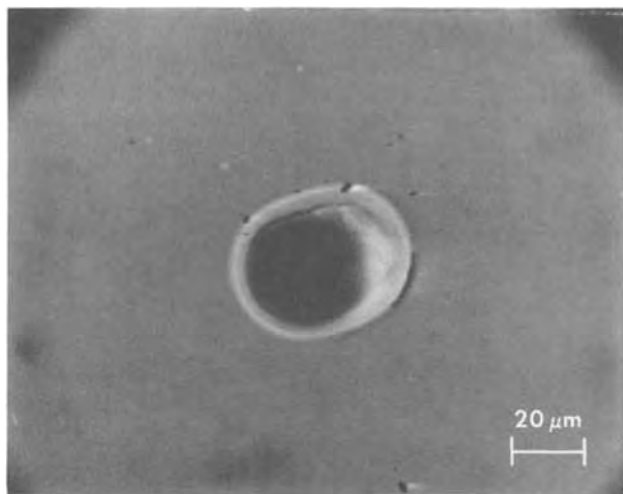


Fig. 6. An SEM/EBIC micrograph of a defect in the Ti-doped silicon solar cell junction depletion region.

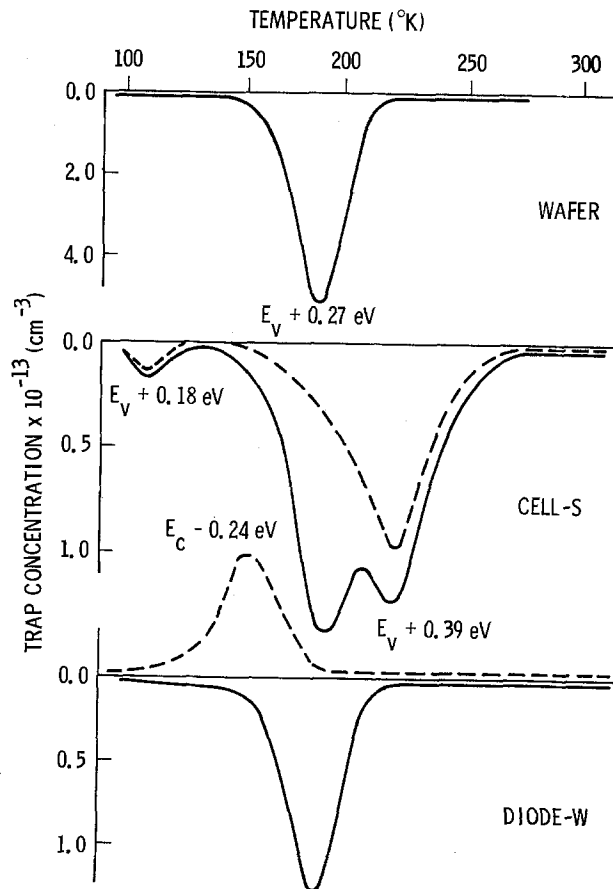


Fig. 7. Typical DLTS spectra of Ti-doped samples. The upper one corresponds to that of as-grown materials, and the other two are for the two types of diffused diodes. The solid curves were taken without carrier injection and the dashed curves with carrier injection.

In order to explore the effect further, the diffused layer of the wafer was removed by etching off $10\text{--}30 \mu\text{m}$. Then, several Schottky diodes were made. The DLTS measurements on these Schottky diodes revealed that the concentration of the $E_V + 0.27$ eV level in the etched wafer is about $5 \times 10^{13}/\text{cm}^3$, being the same as that in the as-grown material.

Discussion

The effect of titanium in silicon.—Titanium was found to have diffused interstitially in silicon (4). In the presence of a high concentration of oxygen of $\sim 7.8 \times 10^{17}$ atoms/ cm^3 in the Czochralski crystals (3), it reacts very rapidly with oxygen, forming Ti-O complexes and consequently precipitates out as TiO_2 (anatase). If the precipitates' molar volume is greater

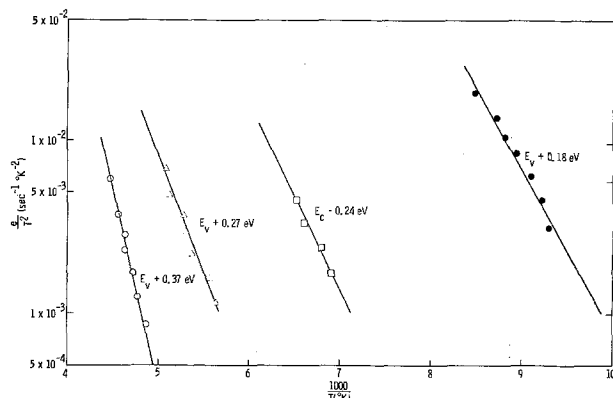


Fig. 8. Arrhenius plot of the carrier emission rate of the levels observed by DLTS.

than the molar volume of the matrix as in the case of TiO_2 , interstitials or dislocations are introduced to relax the stress field which will develop. The x-ray topographs in the present work indicated the presence of a high density of dislocations due to this effect. It is known that impurities segregate to the dislocations. If the titanium interstitial impurities act as donors, this means that a p-n junction forms around each dislocation, degrading the solar-cell quality.

Gettering of titanium during the solar cell processing.—X-ray topography showed that more precipitates are formed during the diffusion process, which was supported by the deep level transient spectroscopy measurement results. It was found that about 10% of the titanium in the N^+/P silicon solar cells is electrically active centers. About 14% of the remaining titanium precipitated out. It is therefore believed that the remaining titanium was either gettered out during the solar cell fabrication process or cannot be detected by these techniques.

The DLTS results also indicated a reduction in the concentration of the $E_v + 0.27$ eV level, in the depletion region of the diffused diodes. This reduction can be attributed to the diffusion of titanium in the n^+ region (gettering effect) or the transformation of titanium into other complexes such as titanium oxide TiO_2 or the occurrence of both effects simultaneously.

Also, the observation of additional DLTS peaks corresponding to $E_v + 0.18$ eV, $E_v + 0.38$ eV, and $E_c - 0.24$ eV levels and the TEM results which indicated the presence of TiO_2 precipitates could serve as an indication of formation of titanium oxide complexes in the depletion region during the diffusion process. The $E_c - 0.24$ eV level may correspond to the $E_c - 0.24$ eV level found earlier (5) for a titanium donor level in a diffused titanium sample.

Moreover, the titanium oxide precipitates, which were not associated with dislocations, were electrically active defects as was revealed by the SEM/EBIC results. Therefore, the presence of these defects in the solar-cell depletion region causes further degradation of the solar-cell conversion efficiency.

Conclusion

For titanium-doped silicon solar cells of concentration level 3.6×10^{14} atoms/cm³, the mechanism of the significant degradation is attributed to the presence of electrically active titanium or titanium oxide complexes in the junction depletion region. In spite of the fact that the active trapping center concentration was reduced during the phosphorus diffusion process, due either to the increase in the TiO_2 precipitate density or to the gettering of titanium to the n^+ region, the TiO_2

(anatase) precipitate particles were also active in the depletion region when not associated with dislocations. However, dislocations act as recombination centers in the depletion region. The precipitates or impurity atoms segregate to the dislocations and probably degrade the junction. This is consistent with the findings of other investigators that diffused titanium forms a donor level at $E_c - 0.24$ eV. The DLTS and x-ray topography measurements strongly suggest that titanium diffuses during the processing steps. However, the rate of titanium diffusion in silicon is slow compared to that of other metals such as copper.

Acknowledgments

The authors wish to thank JPL and Materials Research Incorporated staff for the use of the facilities and the services performed during the course of this evaluation. Special thanks are extended to Danny Leung for the DLTS measurements and to Mary McGough of the Photolab for her excellent efforts in reproducing the photographs.

The research described in this paper was carried out for the Low-Cost Silicon Solar Array Project by the Jet Propulsion Laboratory, California Institute of Technology, and was sponsored by the U.S. Department of Energy through an agreement with NASA.

Manuscript submitted July 20, 1979; revised manuscript received Nov. 20, 1979.

Any discussion of this paper will appear in a Discussion Section to be published in the December 1980 JOURNAL. All discussions for the December 1980 Discussion Section should be submitted by Aug. 1, 1980.

Publication costs of this article were assisted by the California Institute of Technology.

REFERENCES

1. A. M. Salama, in "Proceedings of the Thirteenth IEEE Photovoltaic Specialists Conference," p. 496 (1978).
2. J. Scott-Monck and F. M. Uno, Spectrolab Second Quarterly Report, under JPL/DOE Contract No. 954694 (1977).
3. R. H. Hopkins, J. R. Davis, P. Rai-Choudhury, and P. D. Blais, Westinghouse Research and Development Laboratories, Quarterly Reports under JPL/DOE Contract No. 954331 (1976-1978).
4. F. T. Tsay, Private communication, To be published.
5. J. Y. Chen, A. G. Milnes, and A. Rohatgi, *Solid-State Electron.*, To be published.
6. Metals Handbook Vol. I on "Titanium and Titanium Alloys," 8th ed., pp. 1147-1153, American Society for Metals (1961).
7. D. V. Lang, *J. Appl. Phys.*, **45**, 3014 (1974).
8. D. V. Lang, *ibid.*, **45**, 3023 (1974).

Liquid Phase Epitaxial Silicon Diodes: N-Epitaxial Layers on Boron-Doped Substrates

B. Jayant Baliga*

General Electric Company, Corporate Research and Development Center, Schenectady, New York 12301

ABSTRACT

It is demonstrated that both abrupt and graded junction diodes can be fabricated by the growth of n-type epitaxial layers on heavily boron-doped substrates by using silicon liquid phase epitaxy with tin as the solvent. It is found that the breakdown voltage is enhanced by the presence of the graded p-type region at the epi-substrate interface when the layers are grown with meltback prior to growth. In spite of a high measured tin concentration in the epitaxial layers, the diodes exhibit characteristics which are in good agreement with theoretically calculated values based upon bulk silicon properties. In addition a high minority carrier lifetime has been measured in the epitaxial layers, indicating that the incorporation of tin does not introduce a large density of recombination centers in silicon.

The growth of epitaxial layers of silicon by liquid phase epitaxy offers an interesting alternative to the presently used vapor phase epitaxial deposition techniques. Early reports on silicon liquid phase epitaxy have been directed towards reducing epitaxial layer defects (1) and for the formation of ohmic pedestal contacts to planar-diffused diodes (2). More recently, Girault *et al.* (3) and Sumner and Foley (4) have reported on the growth and electrical properties of silicon epitaxial layers grown from gallium and aluminum melts. Since both gallium and aluminum exhibit shallow acceptor levels in silicon and are readily incorporated into the epitaxial layer, these layers were found to be p-type with carrier concentrations above 10^{18} cm^{-3} and to have a short minority carrier lifetime. The growth of high resistivity epitaxial layers with high lifetime, therefore, requires that the solvent used for the silicon must not introduce active centers in the silicon lattice. Since tin lies in the same column as silicon in the periodic table, its incorporation in the silicon lattice is not expected to introduce either shallow dopant levels or deep lying recombination levels in the silicon energy gap. It has been previously shown that specular films can be grown at reasonable growth rates by silicon liquid phase epitaxy with tin as a solvent (5-7). More recently, measurements of the doping profiles in these epitaxial layers has also been reported (8). These measurements have demonstrated that in spite of a tin concentration in excess of 10^{19} per cm^3 in the epitaxial layers, carrier concentrations in the range of 1×10^{15} cm^{-3} to 1×10^{16} cm^{-3} could be achieved. In addition, it was shown that meltback prior to epitaxial growth had a strong influence on the doping profile of these n-type epitaxial layers when grown on heavily boron-doped substrates. Although an abrupt doping interface was observed between the epitaxial layer and the substrate in the absence of meltback, a graded p-type layer was produced at the substrate interface in the presence of meltback.

The quality of junctions fabricated using silicon liquid phase epitaxy with tin as the solvent is of importance in evaluating its potential for device applications. The incorporation of a high concentration of tin in these layers has been found by electron microprobe analysis. The presence of this high tin concentration may be expected to have an influence on the junction characteristics, particularly, since some studies have implied that the tin introduces deep recombination levels in silicon (9). In addition, meltback prior to epitaxial growth is expected to improve the crystalline quality of the epitaxial growth because it

provides an *in situ* substrate surface cleaning prior to growth. However, it has been found that meltback cannot be used for the growth of n-type layers on heavily boron-doped substrates if an abrupt interface is required (8). The objective of this paper is to examine the quality of junctions fabricated by silicon liquid phase epitaxy on heavily boron-doped substrates both with and without meltback. It is shown here that in spite of the high tin concentration in the epitaxial layers, the junction characteristics are in agreement with theoretical calculations based upon bulk silicon parameters.

Experimental Procedure

The technique used for the growth of the epitaxial layers in this study has been reported in detail in a previous paper (5). Briefly, the layers were grown by using the dipping technique with tin as a solvent for the silicon. The tin melt was maintained at the growth temperature in a quartz crucible within a hydrogen ambient. In order to grow the epitaxial layers, the melt was first saturated with silicon at 950°C . The saturation was done with phosphorus-doped, float zone wafers having resistivities in excess of $100 \Omega\text{-cm}$. The carrier concentration in the epitaxial layers was found to be independent of the phosphorus concentration in the saturation wafers, thus indicating the presence of an n-type contaminant in the high purity tin (five nines purity) used as the melt. After saturation, (111) oriented, boron-doped substrate wafers with a resistivity of $0.01 \Omega\text{-cm}$ were introduced into the melt and the temperature of the melt was reduced at known cooling rates to initiate the epitaxial growth.

After epitaxial growth, the wafers were etched in aqua regia to remove any tin that may have adhered to the wafer surface. A piece of each wafer was then used for spreading resistance measurements using an ASR100 spreading resistance probe to obtain the doping profile. An abrupt doping profile was observed between the epitaxial layer and the substrate in the absence of meltback. However, in the presence of meltback prior to growth,¹ a graded p-type layer was observed at the interface between the epitaxial layer and the substrate. The origin of this graded profile has been discussed in detail in an earlier paper, and it has been shown that the doping concentration decreases exponentially with distance away from the epi-substrate interface (8). To examine the effect of this graded profile upon the junction characteristics, diodes were fabricated from these wafers. The diode fabrication procedure consisted of first performing a phos-

* Electrochemical Society Active Member.

Key words: silicon, liquid phase epitaxy, junctions, diodes.

¹ The meltback was caused by raising the temperature of the melt by 1° to 5°C after saturation as described in Ref. (8).

phorus diffusion into the epitaxial layer to obtain a good ohmic contact. This diffusion was performed well below the growth temperature for a short duration to avoid any impurity redistribution in the epitaxial layers. Aluminum was then evaporated on both sides of the wafers, and sintered at 400°C for 30 min. The wafers were then scribed apart into 60 × 60 mil chips and mounted on TO-5 headers. After bonding a gold lead to the top surface, the edges of the chips were etched in a freon plasma just prior to passivation. A polyimide passivant similar to that described in Ref. (13) was used here. This method of mounting and passivation has been found to be successful in reducing the surface electric field to an extent that allows observation of bulk diode characteristics.

For this study, the diodes were fabricated from epitaxial layers grown at various cooling rates ranging from 0.2°C/min to 7°C/min. In addition, some of these layers were grown with meltback prior to epitaxial growth to allow examination of the influence of the graded p-type region upon diode characteristics. The avalanche breakdown voltage of many diodes was measured both at room temperature and at 77°K for each of the wafers. Table I lists some of the diode breakdown data together with the growth conditions and the diode doping profile in the order of increasing exponent factor. This exponent factor (α) is a measure of the gradient of the junction and is described analytically in the next section. It should be noted that the diode breakdown voltage at 77°K is lower than the value at room temperature. This is an indication that bulk avalanche breakdown is being observed during these measurements. In addition it can be seen that the breakdown voltage decreases with increasing exponent factor, α , and is not sensitive to the cooling rate used during epitaxial growth.

In addition to the breakdown characteristics, the capacitance of these diodes was also measured as a function of the reverse applied voltage. The C-V characteristics of four typical diodes are shown in Fig. 1. The broken lines in this figure have been drawn to indicate the shape of the curves for an abrupt junction diode (C proportional to $V^{-1/2}$) and a linearly graded junction diode (C proportional to $V^{-1/3}$). It can be seen that the curves for diodes with large exponent factors (α) approach the abrupt junction case while those for diodes with smaller exponent factors (α) approach the linearly graded case.

Analysis

Electron microprobe measurements of the epitaxial layers grown in this study indicate that the layers contain tin concentrations in excess of 10^{19} per cm^3 . This incorporation of tin in the layers may be expected to degrade the quality of the junctions being discussed in this paper. To assess the influence of tin on the junction characteristics, it is, therefore, necessary to obtain a comparison with theoretically calculated values of the breakdown voltage based upon bulk silicon properties. As shown in a previous paper, the doping profile in the epitaxial layers can be described as (8)

$$N_A = N_D \exp(-\alpha x) \quad [1]$$

Table I. Diode breakdown voltage data

Experimental data					
Sample number	Cooling rate (°C/min)	Exponent factor (α) (cm^{-1})	N_D (cm^{-3})	77°K (volts)	RT (volts)
GBG-21	0.2	1×10^3	6×10^{15}	120	150
GBG-26	2	1.5×10^3	3×10^{15}	100	120
GBG-14	0.5	2.3×10^3	7×10^{15}	130	160
GBG-11	7	2.4×10^3	6×10^{15}	70	80
GBG-5	7	1.5×10^4	8×10^{15}	60	70
GBG-7	0.75	1×10^5	5×10^{15}	40	50
GBG-23	0.2	1×10^5	1×10^{16}	30	50

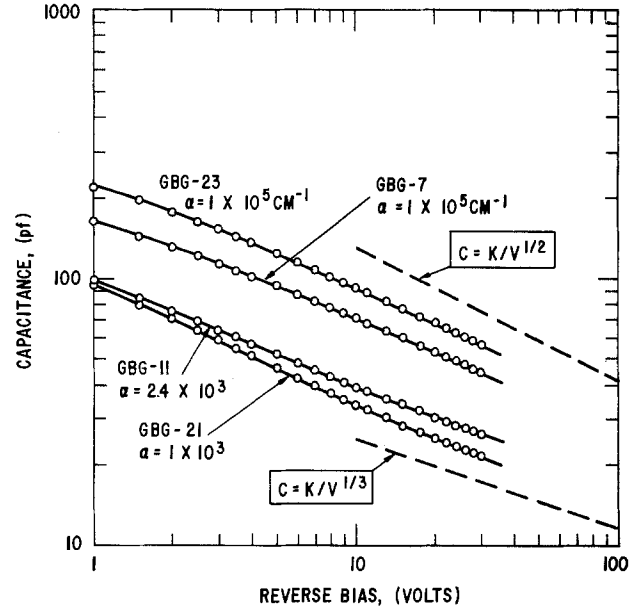


Fig. 1. Capacitance-voltage characteristics of diodes fabricated with abrupt and exponentially graded junctions using silicon liquid phase epitaxy.

where N_A is the acceptor concentration (boron), and N_D is the background donor concentration in the epitaxial layer in the absence of meltback. This doping profile and the electric field distribution are indicated in the inset of Fig. 2. The electric field distribution is described by Poisson's equation

$$\frac{d^2V}{dx^2} = -\frac{dE}{dx} = -\frac{\rho(x)}{\epsilon} = -\frac{qN_D}{\epsilon} [1 - \exp(-\alpha x)] \quad [2]$$

where $\rho(x)$ is the charge distribution in the junction depletion layer. Integration of this equation provides the electric field distribution

$$E(x) = \frac{qN_D}{\epsilon} \left[\frac{\exp(-\alpha x)}{\alpha} - W_N - \frac{\exp(-\alpha W_N)}{\alpha} + x \right] \quad [3]$$

where W_N is the depletion layer width on the n-type side of the junction. This depletion width is related to the applied junction voltage

$$V_A = \frac{qN_D}{\epsilon} (W_P + W_N) \left[\left(\frac{W_P + W_N}{2} \right) - \frac{1}{\alpha} + \frac{\exp(-\alpha W_N)}{\alpha} \right] \quad [4]$$

with

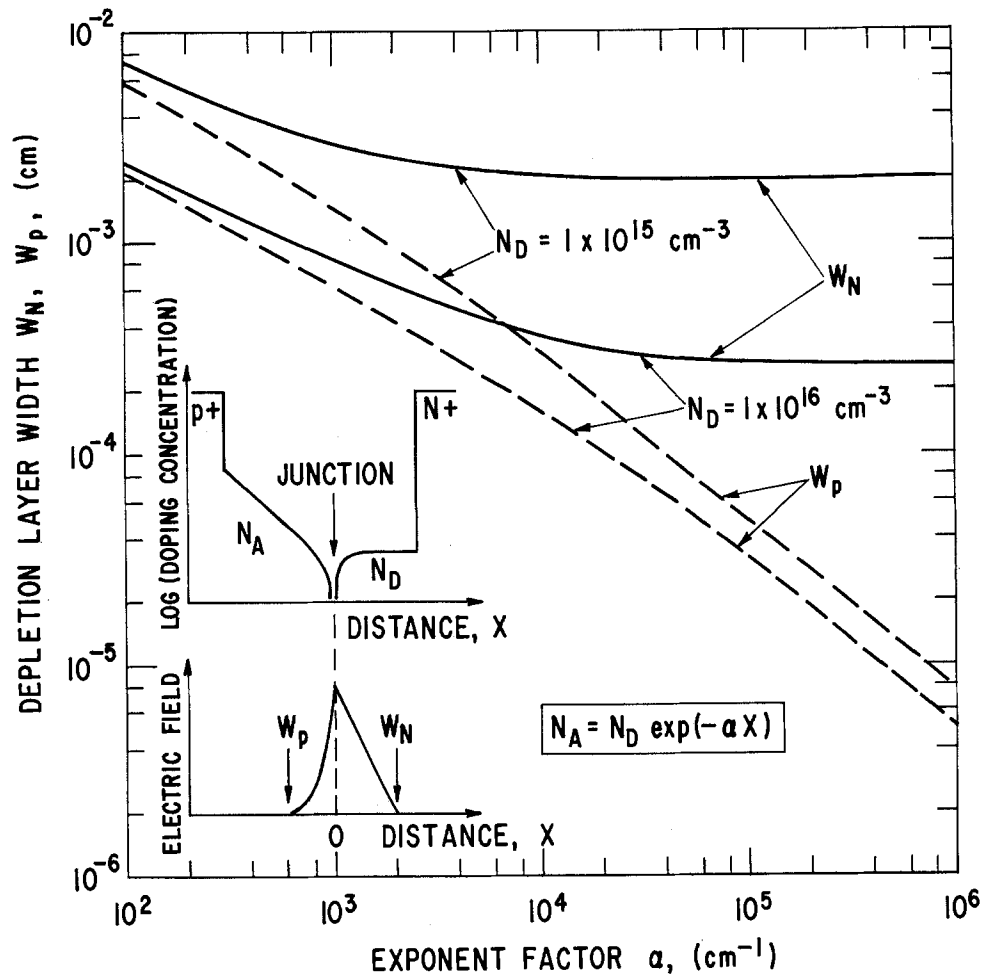
$$W_N + \frac{\exp(-\alpha W_N)}{\alpha} = \frac{\exp(\alpha W_P)}{\alpha} - W_P \quad [5]$$

where W_P is the depletion layer width on the p-type side of the junction. In addition, if avalanche breakdown is assumed to occur when the peak electric field in the junction reaches a critical value (E_C), then at breakdown

$$W_N + \frac{\exp(-\alpha W_N)}{\alpha} = \frac{1}{\alpha} + \frac{\epsilon E_C}{qN_D} \quad [6]$$

From the last equation, the depletion layer widths at breakdown, as well as the breakdown voltage, can be calculated as a function of the background doping (N_D) and the exponent factor (α). Using the critical electric field values given by Sze and Gibbons (10), the depletion layer widths on both sides of the junc-

Fig. 2. Variation of depletion layer widths on the p-side (W_P) and n-side (W_N) of the junctions with exponent factor. (The inset shows the doping profile and the electric field distribution.)



tion and the breakdown voltage have been calculated over a selected range of background doping and exponent factor values and are plotted in Fig. 2 and Fig. 3. It can be seen that when the exponent factor (α) exceeds 10^5 cm^{-1} , the breakdown voltage and the depletion layer width on the n-type side of the junction become independent of α , and the depletion layer width on the p-type side of the junction becomes far smaller than that on the n-side. Consequently, at these large exponent factor values, the diodes will essentially have an abrupt junction characteristic. Similarly, at small values of the exponent factor ($\alpha < 10^2 \text{ cm}^{-1}$), the depletion layer widths on both sides of the junction become nearly equal, indicating that the junction is now approaching the linearly graded case.

A comparison of these theoretically calculated values can now be made with the measured values listed in Table I. For the wafers with large values for the exponent factor (GBG-7 and GBG-23), the breakdown voltage is within 10% of the calculated values. This indicates that in spite of the junction being located at the epi-substrate interface and in spite of the high tin concentration in the layers, good diode breakdown characteristics can be achieved with this liquid phase epitaxial growth process for making abrupt junctions. This is of particular significance to the fabrication of devices which require an abrupt transition in doping between the epitaxial layer and the substrate. The achievement of good diode breakdown characteristics in the absence of meltback prior to epitaxial growth is also of significance to the fabrication of buried grid regions (11). However, the quality of the diodes grown in the presence of meltback is also of interest because the junction is now located within the epitaxial layer and away from the epi-substrate interface. In addition, Fig. 3 shows that the grading of the doping concentration on the p-type side of the junction enhances the breakdown voltage. The measured break-

down voltage of the diodes with exponent factors of $2 \times 10^3 \text{ cm}^{-1}$ (GBG-14) are indeed about three times larger than those with exponent factors of 10^5 cm^{-1} (GBG-7), in reasonable agreement with the calculated values. It is also worth pointing out that the breakdown voltages of the diodes listed in Table I are essentially controlled by the magnitude of the exponent factor (α) and are insensitive to the cooling rate (and hence the growth rate) at which the epitaxial layers were grown. Thus, although a high cooling rate has been found to cause a deterioration in the surface quality of the films (6), it does not cause any significant degradation in the breakdown characteristics.

In addition to obtaining a comparison between the experimental breakdown data and the theoretical values determined using bulk silicon parameters, it is also interesting to examine the capacitance voltage characteristics of these diodes. The theoretical ca-

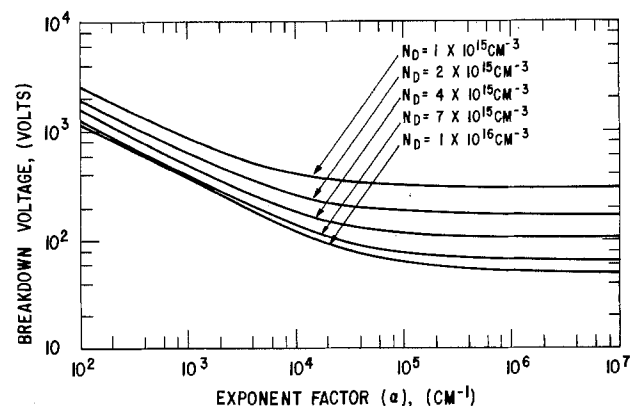


Fig. 3. Theoretical plots of junction breakdown voltage as a function of the exponent factor and the background doping level.

capacitance per unit area can be determined from the calculated depletion layer widths at each applied bias by using the relationship

$$\frac{C}{A} = \frac{\epsilon}{(W_P + W_N)} \quad [7]$$

where A is the area of the diode. Using this relationship with Eq. [4] and [5], the capacitance per unit area has been calculated for diodes with background carrier concentration of $2 \times 10^{15} \text{ cm}^{-3}$ on the n-type side of the junction. These calculated curves are shown as a function of reverse bias in Fig. 4 using the exponent factor as a parameter. From this figure, it can be concluded that when the exponent factor exceeds 10^6 cm^{-1} , the capacitance varies inversely as the square root of the reverse bias. Even at lower exponent factors in the range of 10^5 cm^{-1} , the curves asymptotically approach the curve for $\alpha = 10^6 \text{ cm}^{-1}$ at the larger reverse bias voltages. This theoretically predicted behavior can be observed to occur in the C-V curves of diodes made from wafers GBG-23 and GBG-7 as shown in Fig. 1. In contrast, the curves in Fig. 4 for small values of the exponent factor (less than 10^3) approach the linearly graded case where the capacitance varies inversely as the cube root of the reverse bias voltage. This can be observed in the experimental data obtained for the diodes fabricated from wafers GBG-11 and GBG-21 at the larger reverse bias voltages (see Fig. 1). In addition to this, the theoretical calculations predict an increase in capacitance with increasing values of the exponent factor (α). In spite of some expected variation in the diode area due to the sample preparation technique used in this study, it can be seen from Fig. 1 that a roughly threefold increase in capacitance occurs when the exponent factor increases from 1×10^3 to $1 \times 10^5 \text{ cm}^{-1}$ in agreement with the theoretical calculations.

Discussion and Conclusions

The analysis presented in the previous section demonstrates that diodes, which are fabricated by the growth of n-type layers using silicon liquid phase epitaxy on heavily boron-doped substrates, have the breakdown and C-V characteristics that is expected of bulk silicon diodes. However, it is possible that the presence of tin in the epitaxial layers may cause the introduction of deep levels in the silicon energy gap in spite of tin being in the same column as silicon in

the periodic table. Schulz (9) has reported that when tin is introduced in silicon by ion implantation several deep levels are observed even after annealing. If these levels were due to the tin incorporation and were not associated with any residual defects after the implantation and annealing procedures, then the lifetime in the epitaxial layers grown in this study should be very low because the tin concentration in the layers exceeds 10^{19} per cm^3 . To evaluate the lifetime, reverse recovery measurements (12) were made using the diodes fabricated in this study. It was found that the minority carrier lifetime was in the neighborhood of 2-10 μsec at room temperature. The observation of these reasonably high lifetime values is another indication that the tin is inactive in the silicon lattice, and that the lifetime is controlled by some other impurity or defect center. An idea of the location of this deep level which is controlling the lifetime may be obtained by measuring the lifetime as a function of ambient temperature. Typical results of such measurements are shown for three diodes in Fig. 5. These data show an increase in lifetime with increasing temperature. This indicates that the dominant recombination center lies below midgap. At present, the nature of the defect center responsible for this recombination level is not known.

In conclusion, it has been determined that both abrupt and exponentially graded junction diodes can be fabricated by the growth of n-type layers on heavily boron-doped substrates by using silicon liquid phase epitaxy with tin as the solvent. In spite of a high tin concentration in the layers, the diode break-

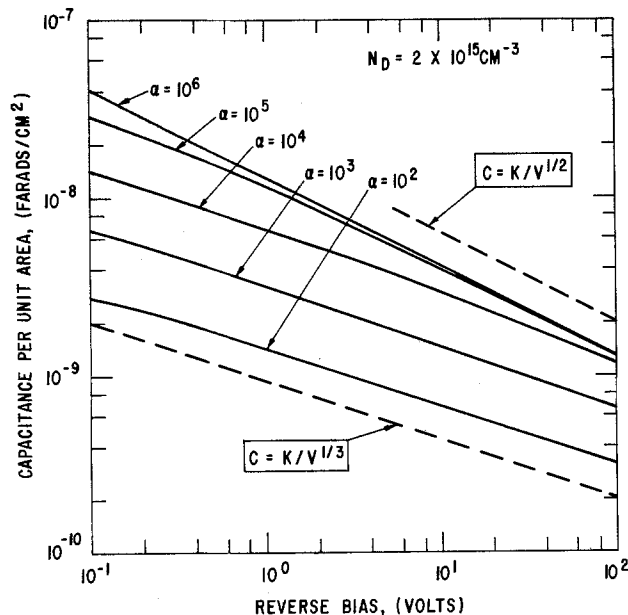


Fig. 4. Theoretical capacitance-voltage characteristics of diodes with various exponent factors.

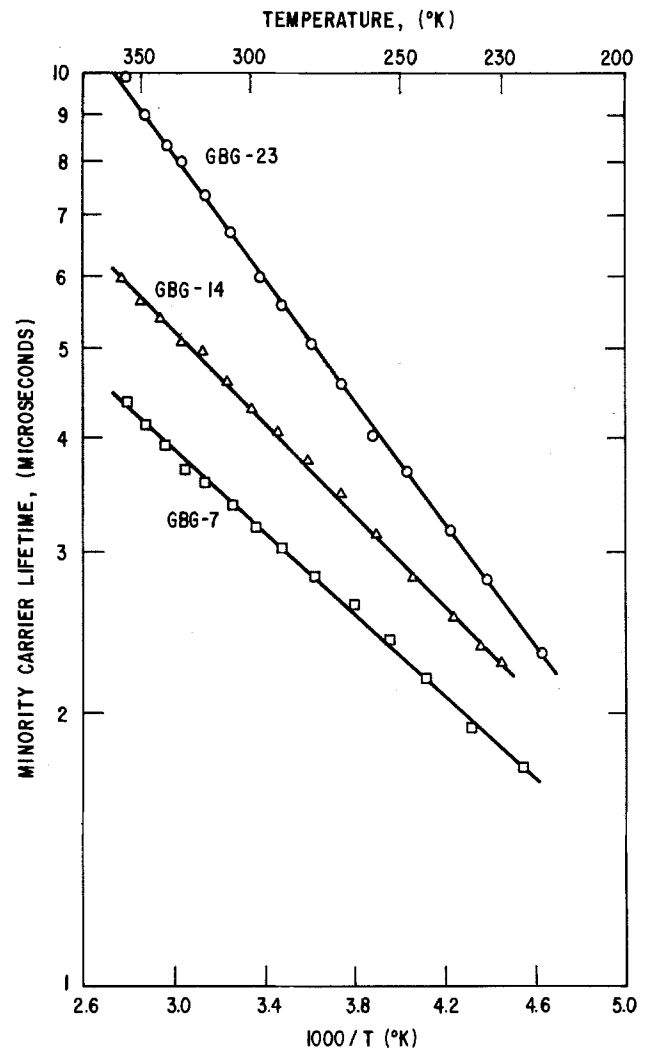


Fig. 5. Variation of the minority carrier lifetime with ambient temperature.

down and capacitance-voltage characteristics are in agreement with the theoretically calculated values using bulk silicon properties. Although good breakdown characteristics are observed, even for diodes made with an abrupt junction (without meltback), the breakdown voltage can be increased by creating the graded junction (using meltback prior to growth). In addition, these diodes have been used to measure the lifetime in the epitaxial layers. The reasonably high lifetime values observed in this study are an indication that the tin in the layers does not introduce a high concentration of recombination levels in the silicon energy gap. The results, thus, indicate that the fabrication of junctions by silicon liquid phase epitaxy using tin as a solvent is a promising technique for device applications.

Manuscript submitted May 4, 1979; revised manuscript received Nov. 15, 1979.

Any discussion of this paper will appear in a Discussion Section to be published in the December 1980 JOURNAL. All discussions for the December 1980 Discussion Section should be submitted by Aug. 1, 1980.

Publication costs of this article were assisted by General Electric Company.

REFERENCES

1. L. A. D'Asaro, R. W. Landorf, and R. A. Furnanage, in "Semiconductor Silicon," R. R. Haberecht and E. L. Kern, Editors, p. 233, The Electrochemical Society Softbound Proceedings Series, Princeton, N.J. (1969).
2. H. J. Kim, *This Journal*, **119**, 1394 (1972).
3. B. Girault, F. Chevrier, A. Joullie, and G. Bougnot, *J. Cryst. Growth*, **37**, 169 (1977).
4. B. E. Sumner and R. T. Foley, *This Journal*, **125**, 1817 (1978).
5. B. J. Baliga, *ibid.*, **124**, 1627 (1977).
6. B. J. Baliga, *J. Cryst. Growth*, **41**, 199 (1977).
7. B. J. Baliga, *This Journal*, **125**, 598 (1978).
8. B. J. Baliga, *ibid.*, **126**, 138 (1979).
9. M. Schulz, *Appl. Phys.*, **4**, 225 (1974).
10. S. M. Sze and G. Gibbons, *Appl. Phys. Lett.*, **8**, 111 (1966).
11. B. J. Baliga, *ibid.*, **34**, 789, (1979).
12. D. C. Lewis, *Solid State Electron.*, **18**, 87 (1975).
13. R. R. Verderber, G. A. Gruber, J. W. Ostroski, J. E. Johnson, K. S. Tarneja, D. M. Gillott, and B. J. Coverston, *IEEE Trans. Electron Devices*, **ed-17**, 797 (1970).

Distinction Between Clean and Decorated Oxidation-Induced Stacking Faults by Chemical Etching

Motonobu Futagami

Sony Corporation Research Center, Hodogaya-ku, Yokohama 240, Japan

ABSTRACT

Decorated stacking faults in (100) silicon were distinguished from clean faults by Sirtl etch at any etching stage. The decorated faults were delineated as hillocks, while the clean faults were delineated as flat and geometric pit-features by Sirtl etch. These observations were confirmed by transmission electron microscopy. The formation of the different etch features of the faults can be explained in terms of the solution etch rate and the activity of the etch agent on the decorating precipitates.

There is considerable interest in oxidation-induced stacking faults (OSF's) (1-7) in semiconductor manufacturing. These faults which form during a high temperature thermal oxidation of silicon wafers are extrinsic in nature and are bounded by Frank partial dislocations (2). The presence of such faults is well known to have a deleterious effect on device performance (8-11). A number of techniques have been applied to eliminate the formation of OSF's (12-17). None of the methods, however, has been found to be effective in completely eliminating the formation of OSF's in actual devices. The electrically active OSF's are decorated with impurity precipitates and the electrical activity differs with varying degrees of impurity decoration on OSF's (9, 10). This fact suggests that the clean OSF's which are free of precipitates will be electrically nearly inactive. The development of a simple and reliable method to distinguish them is therefore highly desirable.

Rozgonyi and Kushner (18) have reported that there are differences in etch pit features by Secco etching (19) between OSF's due to varying amounts of decoration and electrical activity. The Secco etch, however, is not satisfactory to precisely distinguish the faults with small amounts of decoration from the faults without decoration. A suitable or an improved preferential etch is now expected to be developed for this purpose.

In this paper it is demonstrated that decorated faults frequently induced during oxidation of silicon wafers were clearly distinguished by the Sirtl etch (20) from clean faults obtained by the subsequent gettering treatment using boron diffusion on the back-side of the wafer. Etch features of clean and decorated faults are compared using the Secco and the Wright (21) etches as well as the Sirtl etch. It was found that the Sirtl etch is superior in distinguishing them. These observations were confirmed by transmission electron microscopy (TEM).

Experimental

Silicon wafers used in this work were prepared from boron-doped p-type dislocation-free Czochralski-grown crystals with a (100) surface plane. They were 5 cm diam, 300 μm thick wafers with resistivities ranging from 40 to 60 Ωcm and mirror polished on one side. The front side (polished side) of the wafers was used to study OSF's. The wafers were cleaned using a standard cleaning procedure prior to oxidation. The oxidation was carried out in steam at 1100°C for 2 hr (giving $-0.85 \mu\text{m}$ of oxide) to enable OSF's to grow to a microscopically visible size. Some of the oxidized wafers were boron-diffusion gettered at their back surfaces to extract impurity precipitates from the OSF's. In these cases a control was built into each sample. This was accomplished by the

Key words: preferential etch, precipitation, gettering.

following method. Conventional photolithographic procedures were used on these oxidized wafers to strip the oxide from the half of the back-side while the oxide layers were retained on the front. Boron was then diffused into the exposed half of the wafer at 1000°C for 15 min from a BBr_3 source. A 0.85 μm thick SiO_2 layer was sufficient to mask the silicon underneath against the diffusing boron atoms.

Regardless of any test sample processing prior to defect examination all samples were stripped of oxide in concentrated hydrofluoric acid solution. The etchants used to delineate the OSF's were those due to Sirtl, Secco, and Wright. The samples were etched with manual agitation for a desired length of time in each etch solution. The etched samples were rinsed, dried, and examined with the optical microscope, if necessary, using differential interference contrast.

After stripping of oxide the sample was waxed onto a flat stainless steel plate and thinned by chemical etching from the back surface to a thickness of about 1 μm using a $HF:HNO_3:CH_3COOH$ mixture. Specimens thinned in this manner were examined using a JEOL JEM 200A TEM operated at an accelerating voltage of 200 kV.

Results

Decorated Fault Delineation

Surface stacking faults which were in the uniform size of about 20 μm in length were formed during thermal oxidation on mirror polished wafers. They were uniformly distributed in the entire area of the wafer with a typical density of $5 \times 10^8 \text{ cm}^{-2}$. The transmission electron micrograph of a typical OSF is shown in Fig. 1. The partial dislocations bounding a fault were decorated with impurity precipitates while the faulted regions were free of precipitates. The presence of impurity precipitates around the partial dislocations will be demonstrated in detail in the following section.

A comparison of stacking fault delineation after preferential etching is shown in Fig. 2. Portions of an oxidized wafer were etched using the following etch solutions: (a) Sirtl etch, (b) Secco etch, and (c) Wright etch. The etching time for each etch was 5 min, which was long enough to reveal entire features of OSF's. The most well-defined stacking fault etch pits were produced by the Wright etch. It was found that the Sirtl etch produced OSF etch hillocks while the Secco etch produced deep OSF etch pits. These observations were confirmed by the following examinations of OSF's on the cleavage face.

Figures 3(a) and (b) show the Sirtl-etched (100) surface and the subsequently cleaved (110) surface, respectively. It can be seen that both ends of the fault located at the edge of the (100) surface present hillocks

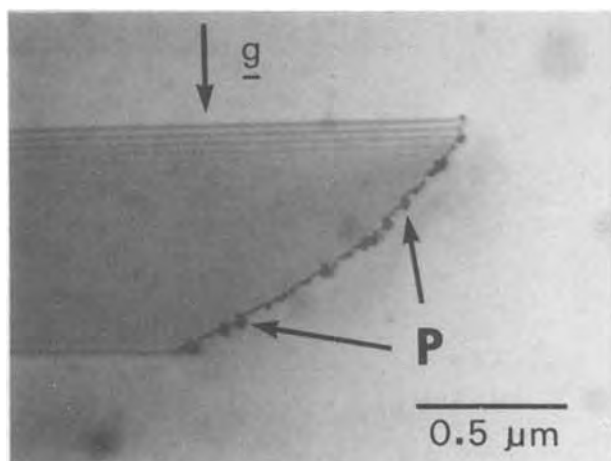


Fig. 1. Bright field transmission electron micrograph of a typical oxidation-induced stacking fault. Note the impurity precipitates (P) around the partial dislocations.

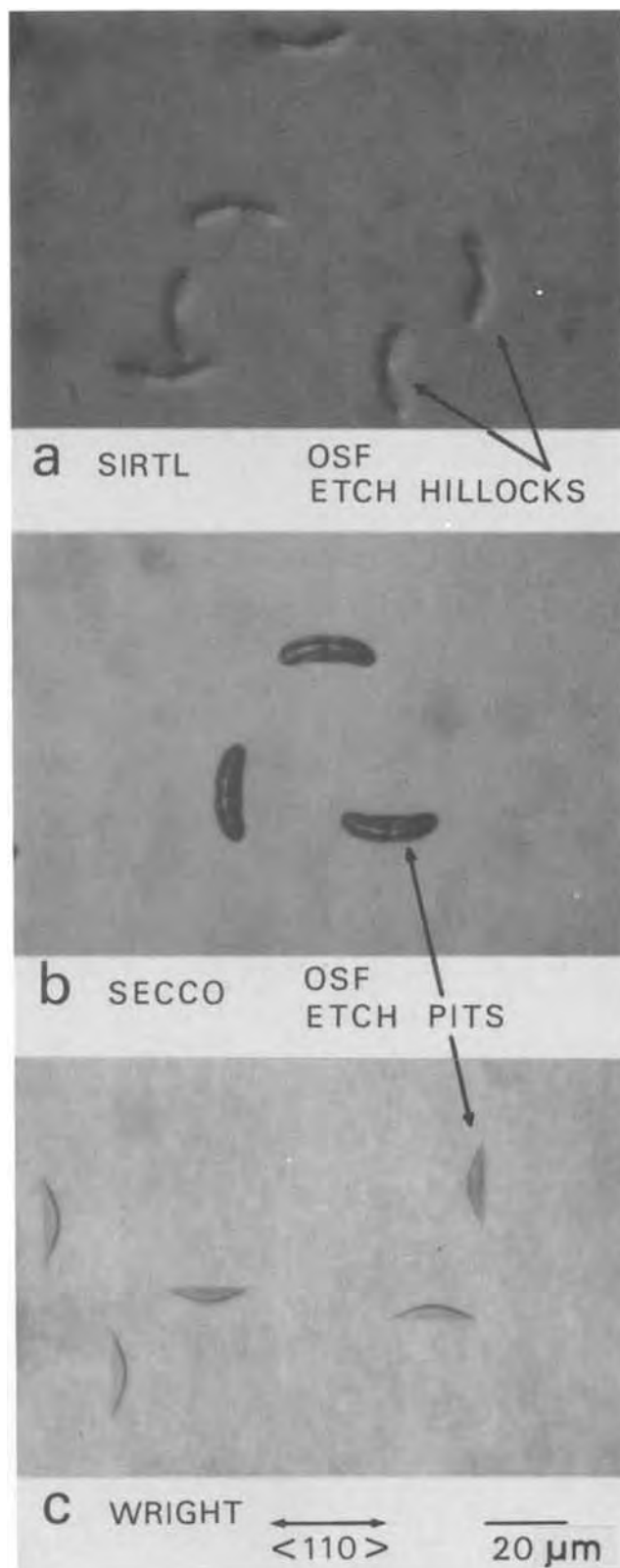
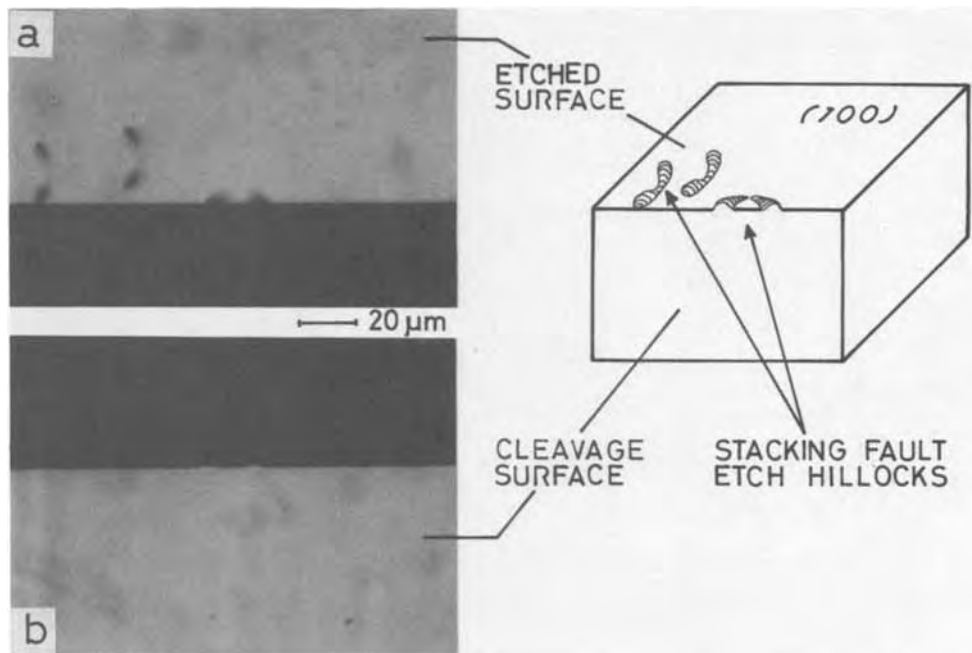


Fig. 2. A comparison of stacking fault delineation of a (100) oriented wafer after oxidation and preferential etching. (a) Sirtl etch, 5 min; interference contrast; (b) Secco etch, 5 min; (c) Wright etch, 5 min.

as shown in Fig. 3. Figure 4 shows the similar examination by the Secco etch at the intersection of the cleavage edge and the stacking fault. In this case, the stacking fault was delineated as the deep pit. By microstructural examination of the pit in Fig. 4 the bounding dislocation had a deeper profile in depth than the faulted region.

Fig. 3. Optical micrographs of (a) Sirtl-etched (100) and (b) subsequently cleaved adjacent (110) surface of the oxidized wafer showing protrusion of the OSF etch hillock. Etching period 3 min.



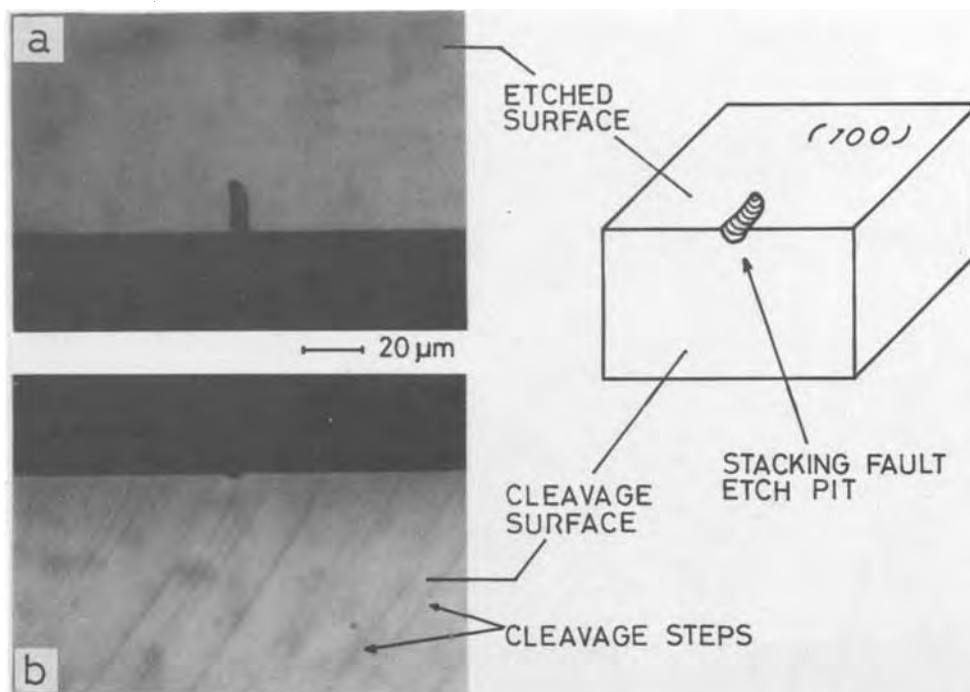
Comparison of Clean and Decorated Faults

Detailed TEM studies of impurity precipitates.—Diffraction-contrast experimental results proving the presence or absence of impurity precipitates on stacking faults are demonstrated in Fig. 5. Figures 5(a) and (c) are bright field micrographs of stacking faults in the ungettered (controlled) and gettered regions, respectively. These micrographs were obtained under two-beam dynamical conditions (diffracting vector $g = [220]$, Bragg deviation parameter $Sg > 0$). In Fig. 5(a), it is observed that the partial dislocation is decorated with impurity precipitates. In Fig. 5(c), precipitates are not observed both at the partial dislocation and in the faulted region. To confirm the presence or absence of precipitates, further diffraction-contrast experiments were performed. As a result it was confirmed that the precipitates were present on the faults which were in the ungettered region and the precipitates were absent on the faults which were in the gettered region. These

results are demonstrated in Fig. 5(b) and (d). Figures 5(b) and (d) were obtained under quasikinematical conditions. Figure 5(b) is the bright field micrograph of the same stacking fault as shown in Fig. 5(a), and Fig. 5(d) is that of the same stacking fault as shown in Fig. 5(c). In Fig. 5(b), the array of grain-contrast images is observed around the defective area defined by the partial dislocation. Based on the dynamical theory of electron diffraction [e.g., Ref. (22) and (23)], this shows the presence of impurity precipitates around the partial dislocation. In Fig. 5(d), no grain-contrast image is observed in the defective area defined by the fault and bounding partial dislocation. This shows that the fault and bounding partial dislocation are free of precipitates.

A selective area diffraction pattern analysis was performed to characterize the precipitates. However, the extra spots due to the precipitates could not be observed because of too small amounts of precipitates.

Fig. 4. Optical micrographs of (a) Secco-etched (100) and (b) subsequently cleaved adjacent (110) surface of the oxidized wafer showing extension of the OSF etch pit. Etching period 5 min.



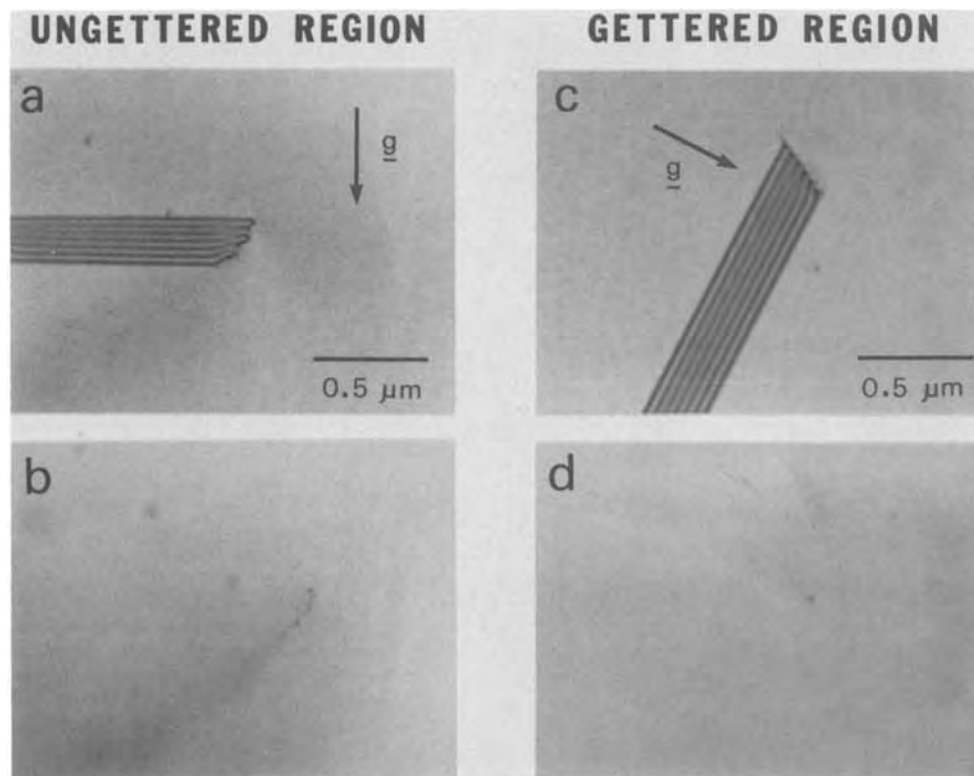


Fig. 5. Bright field TEM micrographs of stacking faults in (a and b) ungettered and (c and d) gettered regions. (a) and (b) show the presence of impurity precipitates around the bounding partial dislocations. (c) and (d) show the absence of precipitates on the fault and the bounding partial dislocations. (a) and (c): two-beam dynamical conditions, $g = [220]$, and $Sg > 0$. (b) and (d): quasikinematical conditions, no Bragg reflection strongly excited.

Sirtl etch results.—The difference in Sirtl etch features between clean and decorated OSF's is shown in the optical micrographs using differential interference contrast in Fig. 6. In the early stages of etching, the decorated OSF's, top left in Fig. 6, were delineated as pairs of etch hillocks at both ends of each fault, where the bounding dislocations intersect the silicon surface. The clean OSF's, top right in Fig. 6, however, were delineated as the very shallow etch grooves which show intersections between fault planes and the (100) silicon surface. On further etching, pairs of etch hillocks of the decorated faults became more pronounced. The morphology of the faults became an oxbow-like hillock as shown in the bottom left in Fig. 6. The appearance of these oxbows, similar to those shown in Fig. 2(a), can be interpreted as the etching-out of the decorated partial dislocations bounding the faults. On the other hand, the shallow grooves of clean faults broaden but not deepen on extended etching. The morphology of the faults, which is shown in the bottom right in Fig. 6, was geometrically similar to the images of stacking faults obtained with the TEM and also similar to the Wright etch figures of OSF's [see Fig. 2(c)].

The above results show that decorated OSF's are distinguished from clean OSF's at any etching stage by using the Sirtl etch. The Sirtl etch, however, produced a rough surface, which is the well-known drawback for (100) silicon. Care should be taken in optical microscopic observation, since the clean stacking fault etch grooves or pits produced by Sirtl etching are so shallow that they cannot be observed clearly without using interference contrast. No interference contrast may lead to a wrong conclusion; one may conclude that no stacking faults are present in this area.

Secco and Wright etch results.—The Secco and Wright etch results are shown in Fig. 7 and Fig. 8. No remarkable difference in etch features between clean and decorated OSF's was observed except that the decorated OSF etch pit appeared prior to the clean OSF etch pit appearance, when Secco or Wright etched lightly. Both the Secco and Wright etches produced clear OSF etch grooves in the early stages of the etching at both the gettered and ungettered regions. With extended etching, familiar OSF etch pits which are peculiar to the respective etching were produced in

the both regions. The etch features observed in the bottom left and right in Fig. 7 and those in Fig. 8 were

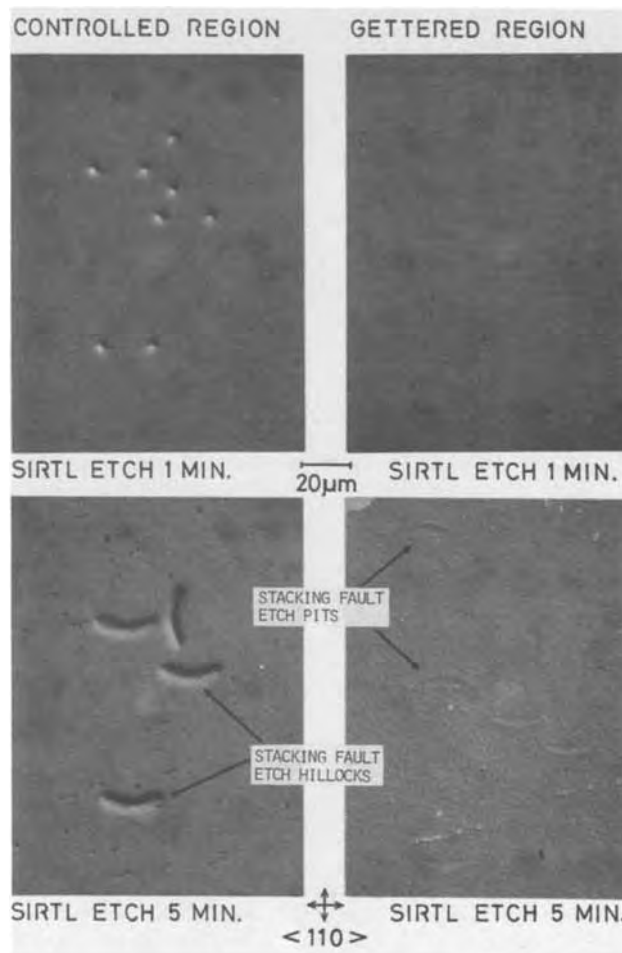


Fig. 6. Comparison of Sirtl etch features of stacking faults which are (top and bottom left) decorated, and those which are (top and bottom right) clean. Interference contrast optical micrographs.

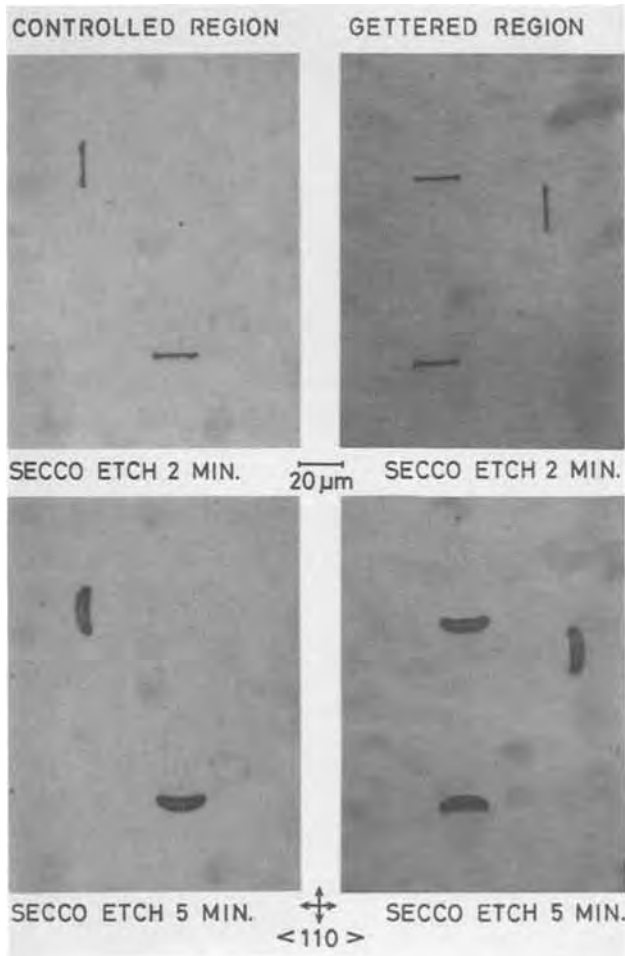


Fig. 7. Comparison of Secco etch pits of stacking faults which are (top and bottom left) decorated, and those which are (top and bottom right) clean.

the same as the etch features in Fig. 2(b) and (c), respectively.

Discussion

The Sirtl etch features of OSF's which have been presented by many workers are similar to those observed in the oxidized wafers in the present work. This suggests that the OSF's generated during the usual oxidation are generally decorated with impurities around the partial dislocations, in some degree. When the degree of decoration on OSF's is large, precipitates exist not only around the partial dislocations but on the faulted regions (9). Rozgonyi and Kushner have showed in an actual device that there are differences in Secco etch pit features between decorated faults from a heavily swirled wafer and clean faults from a "POGO" treated wafer (18). No remarkable difference in etch features by the Secco etch, however, was observed in the present study. This is believed to be related to the degree of decoration and the difference in precipitated materials on the faults between Rozgonyi and Kushner's samples and the present samples, though they did not show the details about precipitates.

The defect delineation can be described as follows (24). The chemical etching of silicon results from an oxidation of the silicon followed by removal of the oxide by HF. In order to delineate a crystal defect as an etch pit, the defect area must be oxidized and removed at a faster rate than the surrounding area. If HF, which removes the oxide immediately, is in excess in the etching solution, the delineation of the defect will be determined by the oxidation rate differential, i.e., etch rate differential, between the defect and surrounding areas. This etch rate differential is accentuated by the slowing down of the solution etch rate.

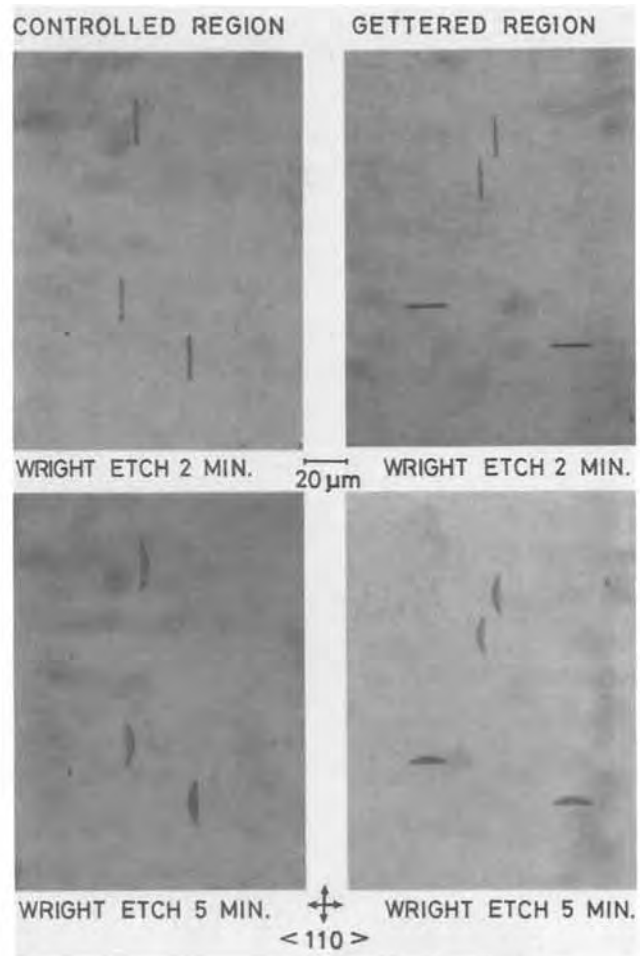


Fig. 8. Comparison of Wright etch pits of stacking faults which are (top and bottom left) decorated, and those which are (top and bottom right) clean.

The reason for the occurrence of the remarkable difference in Sirtl etch features between clean and decorated faults can be explained as follows.

The Sirtl etchant has much oxidizing agent and a higher solution etch rate compared with the Secco and Wright etchants. The etch rates of the Sirtl, Secco, and Wright etches are about 3, 1.5, and 1 $\mu\text{m}/\text{min}$, respectively (19-21, 24). If the etch rate of the defect area is denoted by R_D and that of the surrounding area by R_S , the relationship as $R_D \approx R_S$ will be given in the Sirtl etch because of the higher solution etch rate. This corresponds to the experimental result that the Sirtl etch pits of the clean faults are very shallow and cannot be observed clearly without using interference contrast.

If precipitates on the defect resist the etching, the situation $R_D < R_S$ will be realized easily in the Sirtl etching. The decorated partial dislocations are etched at a slower rate than the surrounding area and consequently, remain as the hillocks. Lawrence has reported that copper precipitates in silicon resist the Sirtl etching (25). The present precipitates are thought to be fast diffusing metallic impurities, such as Cu, Fe, and Au, because the precipitates could be gettered at a lower temperature (1000°C) and for a short period (15 min). Therefore, it is reasonable to assume that the precipitates around the partial dislocations resist the Sirtl etching and affect to slow down the etch rate at the partial dislocations. If the partial dislocation of the fault is free of precipitates, the faulted plane and the partial dislocation will be etched at approximately the same rate, producing a flat figure. On the other hand, both the Secco and Wright etches have a relatively slow solution etch rate, thus $R_D \gg R_S$. In addition, it is believed that the precipitates are dissolved

and removed readily with $K_2Cr_2O_7$, a strong oxidizing agent, in the Secco etch formulation. Similarly, HNO_3 in the Wright etchant is considered to act also as a solvent for the precipitates. These are reasons why clear and relatively deep etch pits of both the clean and decorated faults were formed by the Secco and the Wright etches.

The observations that the decorated OSF etch pit appeared prior to the clean OSF etch pit appearance when Secco or Wright etched lightly, can be interpreted that the decorated partial dislocations are etched at a rather higher rate than the clean dislocations.

Schimmel has showed that the Sirtl etch reveals fewer dislocation etch pits and saucer pits, and produces some mounds in virgin and/or oxidized (100) wafers compared to the Secco etch (24). These facts can be explained by the relationship between defect appearance and effects of Sirtl etch on the impurity decoration of the defects in (100) silicon discussed above.

The Sirtl etch produces a rough surface and gives rise to loss of details for the very small stacking faults. An improved or modified Sirtl etch formulation with minimum surface roughness and with good (deep) definition of the clean faults is expected to be developed for the present purpose.

Conclusions

Decorated faults could be distinguished from clean faults by the Sirtl etching at any etching period. The decorated faults were delineated as hillocks, while the clean faults were delineated as flat and geometric pit-features by the Sirtl etch. It was found that the Sirtl etch was more effective in delineating decorated stacking faults than the Secco and the Wright etches.

Acknowledgment

The author would like to thank T. Yanada and T. Ishibashi for providing the TEM analysis, and T. Hoshina and T. Hattori for comments on the manuscript.

Manuscript submitted July 3, 1979; revised manuscript received Dec. 5, 1979.

Any discussion of this paper will appear in a Discussion Section to be published in the December 1980 JOURNAL. All discussions for the December 1980 Discussion Section should be submitted by Aug. 1, 1980.

Publication costs of this article were assisted by SONY Corporation Research Center.

REFERENCES

1. D. J. D. Thomas, *Phys. Status Solidi*, **3**, 2261 (1963).
2. G. R. Booker and W. J. Tunstall, *Philos. Mag.*, **13**, 71 (1966).
3. W. A. Fischer and J. A. Amick, *This Journal*, **113**, 1054 (1966).
4. K. V. Ravi and C. J. Varker, *J. Appl. Phys.*, **45**, 263 (1974).
5. C. M. Drum and W. van Gelder, *ibid.*, **43**, 4465 (1972).
6. T. Y. Tan, L. L. Wu, and W. K. Tice, *Appl. Phys. Lett.*, **29**, 765 (1976).
7. M. Futagami and M. Hamazaki, *Jpn. J. Appl. Phys.*, **17**, 1343 (1978).
8. H. Shiraki, J. Matsui, T. Kawamura, M. Hanaoka, and T. Sasaki, *ibid.*, **10**, 213 (1971).
9. K. V. Ravi, C. J. Varker, and C. E. Volk, *This Journal*, **120**, 533 (1973).
10. C. J. Varker and K. V. Ravi, *J. Appl. Phys.*, **45**, 272 (1974).
11. R. Ogden and J. M. Wilkinson, *ibid.*, **48**, 412 (1977).
12. H. Shiraki, *Jpn. J. Appl. Phys.*, **13**, 1514 (1974).
13. H. Shiraki, *ibid.*, **14**, 747 (1975).
14. G. A. Rozgonyi, P. M. Petroff, and M. H. Read, *This Journal*, **122**, 1725 (1975).
15. P. M. Petroff, G. A. Rozgonyi, and T. T. Sheng, *ibid.*, **123**, 565 (1976).
16. T. Hattori, *Appl. Phys. Lett.*, **30**, 312 (1977).
17. S. P. Murarka, H. J. Levinstein, R. B. Marcus, and R. S. Wagner, *ibid.*, **48**, 4001 (1977).
18. G. A. Rozgonyi and R. A. Kushner, *This Journal*, **123**, 570 (1976).
19. F. Secco d'Aragona, *ibid.*, **119**, 948 (1972).
20. E. Sirtl and A. Adler, *Z. Metallkd.*, **52**, 529 (1961).
21. M. Wright, *This Journal*, **124**, 757 (1977).
22. P. B. Hirsch, A. Howie, R. B. Nicholson, D. W. Pashley, and M. J. Whelan, "Electron Microscopy of Thin Crystals," Butterworths, London (1969).
23. R. Gevers, "Electron Microscopy in Materials Science," p. 302, Academic Press, New York (1971); L. M. Brown, *ibid.*, p. 360.
24. D. G. Schimmel, *This Journal*, **123**, 734 (1976).
25. J. E. Lawrence, *Trans. AIME*, **242**, 484 (1968).

The Dissolution Kinetics of GaAs in Undersaturated Isothermal Solutions in the Ga-Al-As System

M. B. Small, R. Ghez,* R. M. Potemski, and W. Reuter

IBM Thomas J. Watson Research Center, Yorktown Heights, New York 10598

ABSTRACT

Experiments are described which demonstrate that during the isothermal dissolution of GaAs wafers into undersaturated Ga-Al-As solutions a graded layer of the alloy (GaAl)As is present on the surface. Such a layer can only be formed by solid diffusion. A kinetic analysis of the situation using a value of $5 \times 10^{-12} \text{ cm}^2 \text{ sec}^{-1}$ for the diffusion coefficient of Al in the solid gives a good agreement with the experimental results. The fact that a layer is formed during dissolution is counter to a number of recent publications on the subject, while the measured diffusion coefficient is very different from that measured in bulk MBE material. The significance of obtaining an understanding of this situation is relevant to the formation of all heterojunctions by near-equilibrium processes.

When a GaAs wafer is exposed to an isothermal, undersaturated solution in the Ga-Al-As system, the surface dissolves and a layer of (GaAl)As forms on

the surface. This situation has been encountered when determining the phase diagram of the system (1) and in the fabrication of solar cells (2). In both these cases the kinetics have been assumed to involve dissolution, in order to saturate the solution, followed

* Electrochemical Society Active Member.
Key words: kinetics, dissolution, GaAs.

by regrowth to form the layer. A recent analysis of experimental results by Kordos *et al.* (3) has been based on the same assumption. On the other hand, our kinetic analysis (4) suggests that dissolution should be continuous and that Al enters the dissolving solid by diffusion.

This paper describes experiments designed to test which of two models of the process is correct. In order to do this, the solid and liquid phases have been allowed to interact for a range of times about the diffusion relaxation time, t_R (see below), for the liquid. In this time the liquid would become essentially uniformly saturated and if there were any change in the behavior of the interface (such as a reversal of its direction of motion), then it may occur at about that time. Measurements were made of the amounts dissolved from these samples and of the profiles of Al concentration into the solid. Particular attention has been paid to the measurement of the Al concentration at the surface of the solid. If a dissolution-regrowth model was correct, then one would expect some change in the surface concentration between these two states, while our analysis predicts that the surface concentration should be essentially constant. Also, if dissolution is shown to be continuous with time, while at the same time the thickness of a surface layer containing Al becomes greater, then this must disprove the dissolution-regrowth model. Our model suggests that the Al enters the dissolving solid by diffusion, and the measurements enable the coefficient of diffusion under these conditions to be calculated.

The import of obtaining a correct understanding of the process is neither limited to this crystal system nor to the process for fabricating solar cells. The liquid phase epitaxy (LPE) process is used to make a number of heterostructure devices in a variety of crystal systems. It is vital, therefore, to have a satisfactory understanding of the chemical physics of heterostructure formation and a reliable model of the kinetic processes which occur.

Experimental

GaAs wafers were prepared for LPE using a normal combination of chemical-mechanical polishing and chemical etching. The LPE process was performed using an apparatus which has been described elsewhere (5), but the essence of which is a graphite crucible in which a number of solutions may be presented to a wafer in sequence. Two solutions were used for each of the experiments described here. The purpose of the first was to grow a layer of approximately 20 μm of GaAs onto the wafer to present a clean surface to the second solution. The first solution was originally saturated and the layer was produced by cooling the system by 23° to 835°C. The cooling program was then stopped for a period of 15 min after which time the system had reached a stable temperature for the isothermal part of the experiment.

The second solution was made up to contain 1.41g of Ga and 20.5 mg of Al. The geometry of the well containing the solution defined the depth, L , to be 1.5 mm. Using the measured value for the diffusion coefficient, D_{As} , of As in a Ga solution at this temperature, $5 \times 10^{-5} \text{ cm}^2 \text{ sec}^{-1}$ (6, 7), one can calculate the diffusion relaxation time, $t_R = L^2/D_{\text{As}}$, of the solution to be 450 sec and then define dimensionless time $\tau = t/t_R$. The experiment was repeated with the exposure times of the wafers to the solutions being fixed at $t = 45, 180, 720, \text{ and } 2790 \text{ sec}$, or $\tau = 0.1, 0.4, 1.6, \text{ and } 6.2$. By exposing only part of the area of the wafer to this second solution, the remainder served as a reference plane from which the amount dissolved could be measured. If, following the processing of a wafer, any drops of solution were left on parts of the surface, these areas were cleaved away.

It can be seen, both from the simulation and the experimental results, that for $\tau \leq 1$ the process was

dominated by large changes in the compositions of the solutions as they become saturated. For longer times the driving force is for the bulk solid to tend towards equilibrium; this is a very much slower process limited by solid diffusion. Thus the dissolution rate becomes very small for $\tau > 1$, Fig. 2; and, consequently, during this phase of the process the experiment becomes very sensitive to both temporal and spatial thermal variations. We calculate, for example, that a layer as thick as that formed on the sample exposed for $\tau = 1.6$ would be either dissolved or as much grown if the temperature fluctuated by 0.5°C in the time interval between this and $\tau = 6.2$. For this reason we have only used the latter experiment to demonstrate that dissolution was taking place when the first three samples were removed from their solutions.

The amount dissolved from each surface was determined using the calibrated focusing mechanism of a microscope to measure the displacement of the surface exposed to the second solution compared to the reference surface. Since this involved traversing the sample from one region to another, checks were made that the traversing plane was normal to the measurement direction by rotating the sample. There was considerable roughness on the dissolved surfaces, which both precluded some alternate methods of measurement and produced a larger error than is inherent in this method. One form of surface roughness was on the scale of the sides of the solution well and was thought to be due to solutal convection during rapid dissolution. Figure 1 shows two finer scaled morphologies. One of these has a spacing of the order of 20 μm and may be similar to those observed by Nishinaga *et al.* (8) on dissolved surfaces of InP. The closed loops shown in the figure were unusual, but the same spacing was normally present in a linear array. Also shown in the figure is a finer structure, which does not appear to have been remarked upon before. Although one of these patterns might be explicable in terms of the constitutional variations which occur on a perturbed interface, and the resulting two-dimensional transport effects in the two phases (9), it is difficult to associate both with such a mechanism. The uncertainties in the measurements shown in Fig. 2 are a result of a combination of these morphologies. Of these, the contribution due to the larger features shown in Fig. 1 could be as great as 1 μm . In sputter etching these surfaces, it has been assumed that the rate of removal was uniform over the surface.

Secondary ion mass spectroscopy (SIMS) was used to determine the profiles of Al into the dissolved surfaces. The secondary ion mass spectrometer is



Fig. 1. A Nomarski interference contrast micrograph of a dissolved surface illustrating the two finer scale morphologies which occur. The longer side of the figure represents 680 μm .

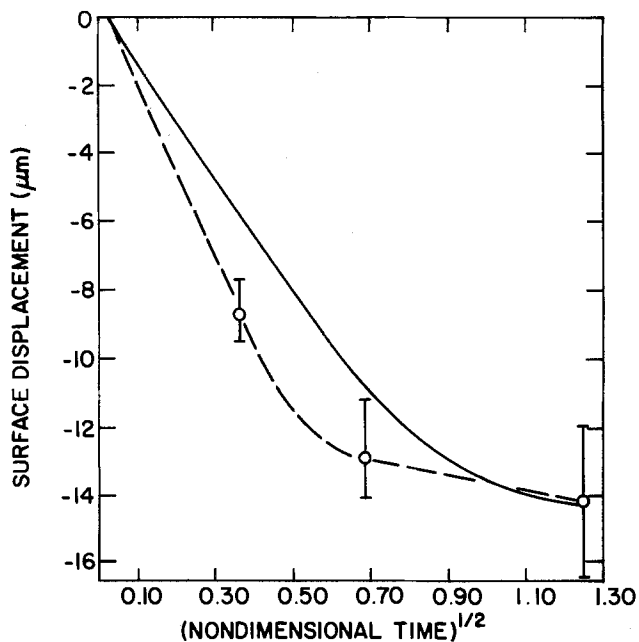


Fig. 2. This illustrates the amounts dissolved from the surfaces as a function of $\tau^{1/2} = (D_{As}t)^{1/2}/L$. The data points may be compared with the results (solid line) of the computer simulation.

an integral part of a surface analysis system including Auger and photoemission spectroscopy. A detailed description of this system will appear shortly elsewhere. Primary ion beams of reactive or inert gases are produced in an ion gun built by Atomike Technische Physik, GmbH, Munich, which is discussed by Wittmaack (10). In this study we used a 12 and 6 keV O_2^+ beam mass analyzed by a Wien filter and focused to about 20 μm onto the target with an Einzel lens. The beam was raster scanned to cover an area of $750 \times 950 \mu\text{m}$, but the scaler was gated to count only during the central 5% of the scanned area. Secondary ions emitted from the target are first energy analyzed by an energy filter (11) before mass separation by a quadrupole mass spectrometer. This filter was set to transmit positive ions of approximately 10 eV and the energy distribution was scanned by variation of the bias potential of the target. For the data presented here we used a fixed bias potential corresponding to the peak in the energy distribution of the secondary ions $^{27}\text{Al}^+$ and $^{69}\text{Ga}^+$.

This analytical technique is generally utilized to measure the relative concentrations of components which are present in the host lattice at low concentrations, such that one would not expect the secondary ion yield to vary as material was removed. In this instance the components of interest constitute a substantial proportion of the lattice. A separate experiment was carried out to investigate this. The $^{27}\text{Al}^+$ concentration was measured through a heterostructure laser grown by LPE in which the compositional ratio between the active region and the clad layers was known, from the phase diagram (12) and growth conditions, to be 3.5. The measured ratio was 3.2. Because the active layer was thin ($\sim 0.2 \mu\text{m}$), the measured concentration in this layer was likely to be high tending to reduce the measured ratio. Thus, the change in secondary ion yield is less than 10% in this range. This calibration is sufficiently accurate for our present purpose, which is to demonstrate constant surface composition during dissolution and obtain an estimate for the diffusion coefficient of Al in the solid.

Results and Analyses

The three data points in Fig. 2 are the displacements of the interface of the three samples processed for the shortest times. They are plotted against $\tau^{1/2}$.

The additional data point mentioned earlier was $-16.8 \mu\text{m}$ at $\tau = 6.2$ and this is cited to demonstrate continuous dissolution for the first three samples.

The data points in Fig. 3 illustrate the Al concentrations as functions of depth into the solid as measured using SIMS. For each sample the data set is representative of a number of repeated measurements which showed no significant differences. Absolute measures of concentration are not possible using this technique so these are expressed in terms of the numbers of counts. Some samples were profiled using different sputtering current densities and these have been normalized to the same value. Manual adjustments were made to maintain a constant sputtering current. The corresponding changes in the numbers of counts can be seen as noise on the data set for the sample with the smallest change in Al concentration. At the end of the sputtering process the depths of a number of craters between 1 and 2 μm deep in relatively smooth regions of the surface were measured using a Talysurf to transform a time scale into a depth scale.

The data in Fig. 2 and 3 show quite clearly that there is an Al-containing layer of finite thickness on the surfaces of the samples which were dissolving when withdrawn from their solutions. Also, it can be seen that the sharpest profile occurs at the fastest dissolution rate, as one would expect for a diffusive process.

An important test of our kinetic analysis is that it predicts an essentially constant surface concentration for all components in all phases (4). We have access to that concentration frozen into the solid. The dissolution-regrowth model (3), on the other hand, does not attempt to provide a consistent model for the whole of the process, but assumes dissolution to a point where the solution is supersaturated, as a whole, and hence regrowth must follow from this assumption. Because there has been no attempt to describe the dissolution process, our only argument against this model must be based upon our interpretation of it. We assume that if the direction of motion of the interfaces changes, then this must be reflected in a change in the surface concentrations; otherwise there would be no driving force for such a change since the phases "sense" one another at the interface. We have used two methods for determining the surface concentration. First, the data points in Fig. 3 have been fitted to polynomial forms (see below) to allow us to extrapolate to the values at the surface. These are the points shown, as open symbols, on the

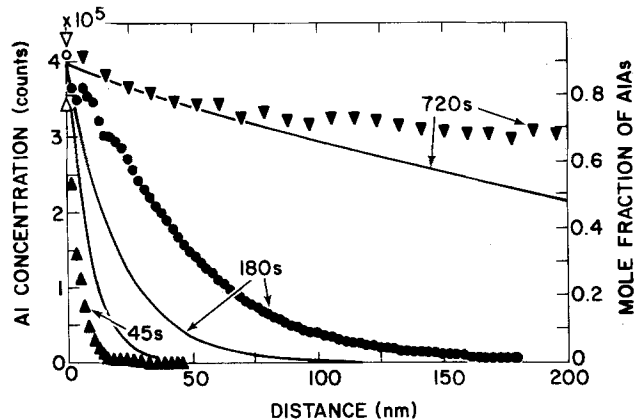


Fig. 3. This illustrates the $^{27}\text{Al}^+$ concentrations as functions of depth from the solid surface. The data points were measured under the conditions described in the text while the open symbols show the extrapolated values at the surface for the three profiles shown. The full lines are profiles produced by the computer simulation and refer to the scale on the right. The two scales were matched at the surface of the crystal.

origin of the spatial axis. It can be seen that they are the same within the reproducibility of SIMS measurements, $\pm 10\%$.

The above procedure may be subject to doubt, particularly for the sample $\tau = 0.1$ which was only in contact with the melt for 45 sec and hence exhibits a very steep decline in the $^{27}\text{Al}^+$ signal near the surface. For this reason we have repeated the SIMS experiment using only 50 msec counting time, increasing the scanned area to $800 \times 800 \mu\text{m}$, and reducing the primary ion current to 50 nA operating at 12 keV. For these conditions we estimate a removal rate of $0.06 \text{ \AA sec}^{-1}$ from Talysurf measurements made at 500 nA but otherwise identical conditions. The results are shown in Fig. 4. The upper six curves show the \log_{10} intensity of $^{27}\text{Al}^+$ and $^{69}\text{Ga}^+$ for each of the three samples sputtered for 1000 sec corresponding to the removal of about 60 \AA of material. In the early phase of the sputtering process both signals increase, probably due to the removal of a hydrocarbon contamination layer (see below) from the surface. Note that the rate of increase during this early phase is much higher for Al than for Ga. This can be attributed to the preferred sputtering of the lower atomic weight component as discussed by Kelly (13) and studied in detail also by Liao *et al.* (14) and Ho *et al.* (15). More difficult to understand is the appearance of a maximum in the $^{69}\text{Ga}^+$ emission near the surface, which recovers in intensity after about 300 sec of sputtering time. This effect is reminiscent of a similar observation by Anderson (16) when bombarding Al with O^{2+} ions. Anderson attributed the initial peak to the presence of a thin Al_2O_3 layer on Al and the final recovery of the Al intensity later in the sputtering process due to the conversion of the Al to an Al_2O_3 film under O_2 bombardment at a depth corresponding to the range of the primary projectile. Implantation of oxygen, which is more electronegative than arsenic, may indeed explain the initial intensity variation in the $^{69}\text{Ga}^+$ signal. Note that the transient features in the sputtering process can be discussed without invoking, but not necessarily excluding, the possibility of compositional variations near the surface. After about 300 sec a steady state is reached, when the value for the intensity ratio of $^{27}\text{Al}^+$ to $^{69}\text{Ga}^+$ is constant within 5% for the samples $\tau = 0.4$ and $\tau = 1.6$. This indicates an identical composition of both samples after the removal of about 20 \AA . For the sample $\tau = 0.1$, which is of primary interest in this study, we find the concentration of Al already decreasing when steady-state conditions are attained. In the lower part of Fig. 4 we have plotted the $^{27}\text{Al}^+$ signal on a linear scale as a

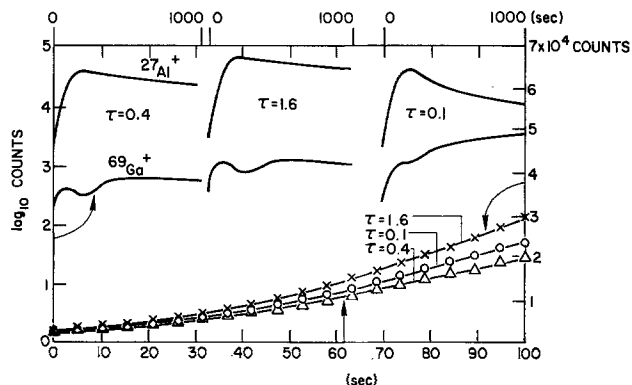


Fig. 4. The intensity of $^{27}\text{Al}^+$ and $^{69}\text{Ga}^+$ as a function of time raster scanning a 12 keV O_2^+ beam of 50 nA over an area of $800 \times 800 \mu\text{m}$ gating 5% of the central portion of the scanned area and counting each isotope for 50 msec. The upper six curves show the \log_{10} intensity of $^{69}\text{Ga}^+$ and $^{27}\text{Al}^+$, sputtering each sample for 1000 sec ($\sim 60 \text{ \AA}$), whereas the three lower curves show the counts for $^{27}\text{Al}^+$ on a linear scale in the first 100 sec of each run.

function of time for the first 100 sec of the sputtering process, thus removing only a few monolayers of the targets. Extrapolation of the $^{27}\text{Al}^+$ signal to the start of the experiment clearly demonstrates that within the experimental error of $\pm 10\%$ the composition is identical for all samples at the surface.

We now fit these data to our model (4). Specifically, we seek an estimate of the diffusion coefficient D_s of Al in the solid, and a reasonable description of the Al concentration profiles. For short times we expect our analytic solution to hold. With minor changes in notation, Eq. [3.6] and [3.7c] of Ref. (4) for the amount dissolved, h , and the local mole fraction x of Al in the solid are

$$h = 2\beta(D_s t)^{1/2} \quad [1]$$

$$\frac{x - x_\infty}{x_0 - x_\infty} = \frac{\text{erfc}(|z|/2(D_s t)^{1/2} - \beta)}{\text{erfc}(-\beta)} \quad [2]$$

Here, $|z|$ is the distance measured from the actual interface into the solid, x_∞ is the initial composition of the substrate ($x_\infty = 0$ for these experiments), x_0 is the surface composition (approximately equal to the equilibrium value, 0.85), and β is a constant that describes the growth rate. For long times one expects β to be a slowly varying function of time, as is clear from Fig. 2. Now, for small values of $|z|/2\sqrt{D_s t}$ one can expand the function [2] to get

$$\frac{x - x_\infty}{x_0 - x_\infty} = 1 - \frac{|z|}{(D_s t)^{1/2}} \frac{1}{\text{experfc}(-\beta)} - \frac{|z|^2}{2D_s t} \frac{\beta}{\text{experfc}(-\beta)} + \dots \quad [3]$$

where

$\text{experfc}(\cdot)$ stands for the abbreviation

$$\text{experfc}(-\beta) = \pi^{1/2} \exp(\beta^2) \text{erfc}(-\beta) \quad [4]$$

and is asymptotically equal to $(-\beta)^{-1}$ for large negative values of β , as will be the case. The polynomial approximation [3] is compared to a polynomial representation of the 45 sec data of Fig. 3, namely

$$C = C_0(1 + a_1|z| + a_2|z|^2) \quad [5]$$

where C is the number of counts. Least squares fitting yields the values

$$\left. \begin{aligned} C_0 &= 3.46 \times 10^5 \\ C_0 a_1 &= -9.22 \times 10^{11} (\text{cm}^{-1}) \\ C_0 a_2 &= 8.99 \times 10^{17} (\text{cm}^{-2}) \end{aligned} \right\} \quad [6]$$

With these values, the first data point of Fig. 2, namely $h = -8.7 \mu\text{m}$ at $t = 45$ sec, and the above formulas, we find $\beta = -34.05$, hence, $D_s = 3.6 \times 10^{-12} \text{ cm}^2 \text{ sec}^{-1}$.

A value for D_s of $5 \times 10^{-12} \text{ cm}^2 \text{ sec}^{-1}$ was then used for our simulation. The diffusion coefficient D_{Al} of Al in the liquid was assumed equal to D_{As} (a tenfold change in $D_{\text{Al}}/D_{\text{As}}$ produced no significant changes in the kinetics). The methods are described in Ref. (4). Briefly, we generate an analytic solution for $\tau = 0.04$, and march this forward in time by finite-difference methods. The results are displayed in Fig. 2, 3, 5, and 6. Figures 5 and 6 show the profiles of As and Al in the solution, assumed stagnant, at $\tau = 0.04$ (the analytic solution) and at those times at which samples were removed from the solutions. It can be seen that there are very steep gradients at short times and that the solution is essentially uniform at $\tau = 1.6$. Also calculated was the dissolution, h , as a function of time; this is compared with the data points in Fig. 2. It can be seen that there is excellent agreement at $\tau = 1.6$. This is to be expected because the solution is then saturated and the amount of dissolution necessary to achieve this is simply determined by the phase diagram. The fact that at short times the dissolution was more than predicted is further

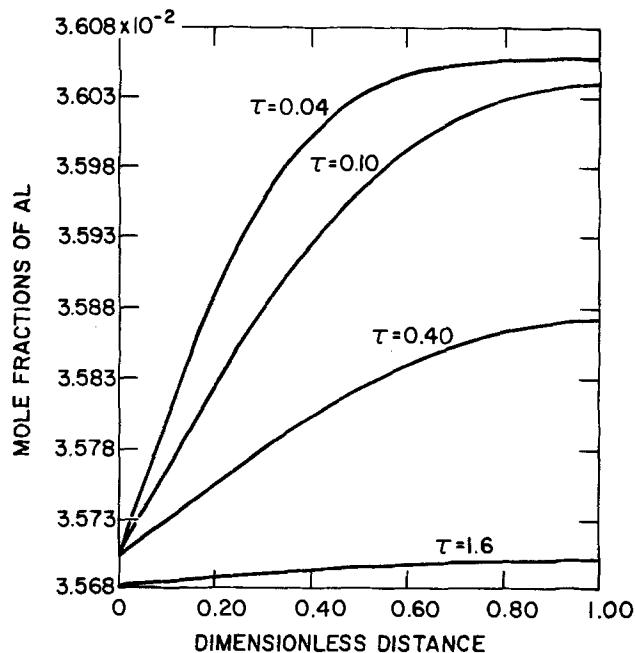


Fig. 5. Showing the concentration profiles of Al in the solutions, as calculated by computer simulation, at a series of times including those when the substrates were withdrawn.

evidence for the fact that the large solutal gradients produced convection in the solutions. The simulation also calculates the Al profiles in the solid and these are compared with the data points in Fig. 3. The measured concentrations were not absolute and so have been scaled to have the same surface concentration as the calculated profiles. The correspondence between theory and experiment is good except for the profile at the intermediate time. In this case, because of the assumed convection, the actual dissolution rate was substantially less than the predictions and this would tend to produce a deeper diffusion profile as the results show.

Two points should be made here concerning the diffusion of Al into the solid. First, the full profile at $\tau = 1.6$, of which only a part is shown, has an inflection point deeper in the material than is shown

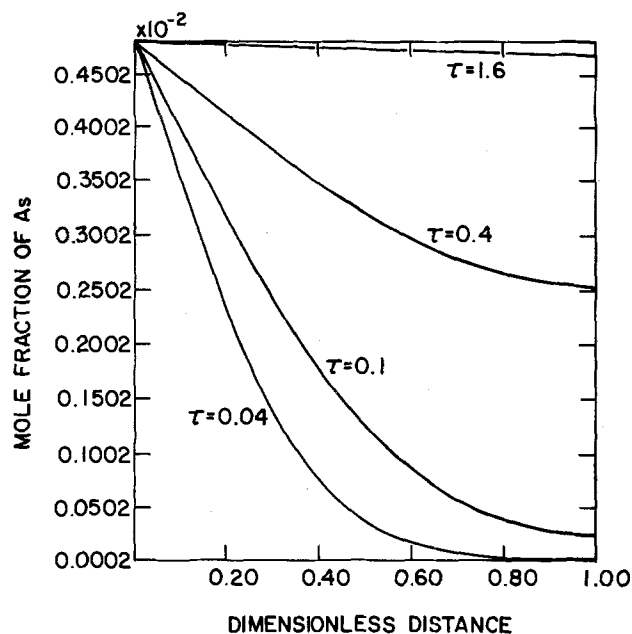


Fig. 6. Showing the As profiles in solution corresponding to those for Al in Fig. 5. Both figures show the initially very large gradient and that the solutions are essentially uniform at $\tau = 1.6$.

in the figure. This implies that the diffusion coefficient is not a constant. Secondly, earlier measurements (17, 18) of the diffusion coefficient of Al in (GaAl)As super-lattice structures grown by MBE gives a value of $\sim 10^{-18} \text{ cm}^2 \text{ sec}^{-1}$ for the diffusion coefficient at this temperature. Although one may argue that LPE material has a higher concentration of arsenic vacancies (19) and that the diffusion process could involve such vacancies acting in a ring mechanism, the fact that LPE may be used to grow heterostructures in this system with very thin layers (20) indicates that it is not simply a difference between these two materials that accounts for this large effect. It would appear, therefore, that the diffusion coefficient is larger in dissolving than in growing material.

Summary and Conclusions

These experiments have demonstrated the following:

1. That GaAs wafers withdrawn from isothermal Ga-Al-As solutions while they were dissolving had layers of finite thicknesses of (GaAl)As on their surfaces.

2. That the surface compositions of these layers are constant, within the accuracy of our measurement technique. This also discounts suggestions that the process occurs in two stages.

3. That data fitting between theory and experiment for a time when the liquid was essentially semi-infinite gave a value of $\approx 5 \times 10^{-12} \text{ cm}^2 \text{ sec}^{-1}$ for the diffusion coefficient of Al in the solid close to the surface. (It has also been noted that the diffusion coefficient is a function of either concentration or distance from the surface.)

4. A reasonably good fit has been obtained, when using the above value, for D_s , between a computer simulation and the measured concentration profiles and amounts dissolved.

Thus, it has been demonstrated that our kinetic model of the process is certainly correct inasmuch as these layers are not produced by regrowth. The diffusion coefficient for Al in the solid necessary to explain these results is larger than one would expect. It is obviously of interest to pursue this matter further.

Manuscript submitted Aug. 15, 1979; revised manuscript received Jan. 18, 1980. This was Paper 177 presented at the Boston, Massachusetts, Meeting of the Society, May 6-11, 1979.

Any discussion of this paper will appear in a Discussion Section to be published in the December 1980 JOURNAL. All discussions for the December 1980 Discussion Section should be submitted by Aug. 1, 1980.

Publication costs of this article were assisted by IBM Corporation.

REFERENCES

1. M. Ilegems and G. L. Pearson, in "Proc. 1968 Symposium on GaAs," p. 3, Institute of Physics, London (1969).
2. J. M. Woodall and H. Hovel, *Appl. Phys. Lett.*, **30**, 493 (1977).
3. P. Kordos, R. A. Powell, W. E. Spicer, G. L. Pearson, and M. B. Panish, *ibid.*, **34**, 366 (1979).
4. M. B. Small and R. Ghez, *J. Appl. Phys.*, **50**, 5322 (1979).
5. M. B. Small, J. C. Blackwell, and R. M. Potemski, *J. Cryst. Growth*, **46**, 253 (1979).
6. I. Crossley and M. B. Small, *ibid.*, **11**, 157 (1971).
7. D. L. Rode, *ibid.*, **20**, 13 (1973).
8. T. Nishinaga, K. Pak, and S. Uchiyama, *ibid.*, **42**, 315 (1977).
9. R. F. Sekerka, in "Crystal Growth," W. Bardsley, D. T. J. Hurle, and J. B. Mullin, Editors, pp. 403-441, North-Holland (1973).
10. K. Wittmaack, *Nucl. Instrum. Meth.*, **143**, 1 (1977).
11. K. Wittmaack, in "Proc. 7th Int. Vac. Congress," Vol. 3, A. Dobrozemsky, et al., Editors, p. 2573, F. Berger and Shone, Austria (1977).
12. M. B. Panish and M. Ilegems, *Prog. Solid State Chem.*, **7**, 39 (1972).

13. R. Kelly, *Nucl. Instrum. Meth.*, **149**, 533 (1978).
14. Z. L. Liao, W. L. Brown, R. Homer, and J. M. Poate, *Appl. Phys. Lett.*, **30**, 626 (1977).
15. P. S. Ho, J. E. Lewis, H. S. Wildman, and J. K. Howard, *Surf. Sci.*, **57**, 393 (1976).
16. C. A. Anderson, *J. Mass. Spectrosc. Ion Phys.*, **2**, 61 (1969).
17. L. L. Chang and A. Koma, *Appl. Phys. Lett.*, **29**, 138 (1976).
18. P. M. Petroff, *J. Vac. Sci. Technol.*, **14**, 973 (1977).
19. J. A. VanVechten, "A Simple Man's Guide to Defect Thermochemistry" in *Semiconductor Handbook*, Vol. 3, S. Keller, Editor, North Holland (In press).
20. H. Kressel and M. Ettenberg, *J. Appl. Phys.*, **47**, 3533 (1976).

Microdistribution of Oxygen in Silicon

A. Murgai,^{*1} J. Y. Chi, and H. C. Gatos*

Department of Materials Science and Engineering,
Massachusetts Institute of Technology, Cambridge, Massachusetts 02139

ABSTRACT

The microdistribution of oxygen in Czochralski-grown, p-type silicon crystals (75 mm in diameter and with a resistivity of 10 Ω -cm) was determined by using the SEM in the EBIC mode in conjunction with spreading resistance measurements. The crystals were heat-treated at 450°C to activate oxygen donors. When the conductivity remained p-type, (the oxygen donor concentration did not exceed the dopant concentration), bands of contrast were observed in the EBIC image which were found to correspond to maxima in resistivity, *i.e.*, to dopant compensation maxima and hence, to maxima in oxygen concentration. When at the oxygen concentration maxima the oxygen donor concentration exceeded (locally) the p-type dopant concentration, an inversion of the conductivity occurred. It resulted in the formation of p-n junctions in a striated configuration and the local inversion of the EBIC image contrast. A chemical etching procedure was developed, in conjunction with phase contrast microscopy, to delineate the n-type oxygen striations. By heat-treating silicon at 1000°C prior to the activation of oxygen donors, some silicon-oxygen micro-precipitates were observed in the EBIC image within the striated oxygen concentration maxima.

Variations in oxygen thermal donor concentration, activated by 450°C heat-treatment have been observed in Si (1-3) and determined by spreading resistance measurements (4, 5). The thermal donor concentration is proportional to the oxygen concentration and provides direct information on the microdistribution of oxygen. Such measurements, however, do not provide direct knowledge of the overall state of oxygen, *e.g.*, on the morphology of oxygen concentration variations, on oxygen clusters (6), and on precipitates (7-9). X-ray topography (10) has also been employed for the observation of oxygen concentration variations. This technique is at best qualitative in nature, as no quantitative relationship between topographic contrast and oxygen concentration is as yet available. In addition, the resolution of inhomogeneities by this technique is rather limited.

The electron beam induced current (EBIC) mode of scanning electron microscopy offers several advantages over the above characterization techniques. Dopant striations (11, 12), impurity precipitates (13), and other electrically active defects (14) can be simultaneously observed in the EBIC image with a relatively high resolution. Recently, the EBIC technique has been applied to the quantitative determination of dopant concentration variations (15), and employed in the study of impurity segregation (16). In addition, basic electronic parameters, such as minority carrier diffusion length, lifetime, and their variations (15, 16) can be readily determined with the EBIC technique.

In the present investigation, the EBIC technique has been applied to the study of microscale variations in oxygen concentration and their effects on p-type silicon crystals.

Experimental Procedure

Dislocation-free silicon crystals 75 mm in diameter and boron-doped to a level of about $5 \times 10^{14}/\text{cm}^3$ were pulled in the (100) direction from the melt. They were grown with a seed rotation of 5 rpm and a pulling rate of 75 mm/hr. The average oxygen concentration in the crystals, as determined from IR measurements (17), was found to be $1.8 \times 10^{18}/\text{cm}^3$.

All measurements were made on (100) longitudinal slices, 0.5 mm thick. The slices were heat-treated at 450°C for 50 hr, lapped, and polished with Syton HT. After cleaning with an organic solvent and etching in $\text{HF} + \text{HNO}_3 + \text{CH}_3\text{COOH}$, a 0.5 μm Al layer (2×2 cm) was deposited on these slices to obtain a semiconductor-metal Schottky barrier (collecting field).

Impact traces of spreading resistance probes were introduced (at 5 or 25 μm intervals) on the Schottky diode to serve as location markers (see also below). EBIC measurements were subsequently conducted in the region of the impact traces with an electron beam accelerating voltage of 35 kV. At the above accelerating voltage the electron range, R , lies outside the depletion width of the Schottky barrier for 10 Ω -cm Si (18). The experimental arrangement for the EBIC measurements and imaging is indicated schematically in Fig. 1.

Following EBIC measurements, the metal layer was stripped from the slice with concentrated HCl. Longitudinal variations in the thermally activated donor concentration (introduced by the 450°C heat-treatment) were determined from spreading resistance measurements (at 5 μm intervals) carried out near and parallel to the impact traces introduced earlier, the traces were still present after the metal layer was stripped. The spreading resistance measurements were made employing both polarities of the d-c bias between the two probes. From such measurements, the presence of any

* Electrochemical Society Active Member.

¹ Present address: IBM Corporation, East Fishkill, New York 12533.

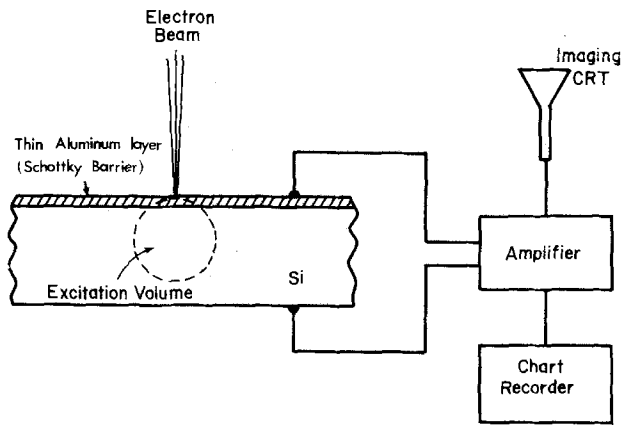


Fig. 1. Schematic diagram of experimental arrangement for EBIC measurements.

p-n junctions formed during the 450°C heat-treatment was readily determined.

The slices were subsequently heat-treated at 700°C for 1 hr to eliminate the oxygen thermal donors (1-3); following this heat-treatment EBIC and spreading resistance measurements were repeated in the identical regions using the impact traces of the spreading resistance probe as reference.

In certain instances, the slices were heat-treated at 1000°C for 12 hr in ultrahigh purity argon prior to the 450°C heat-treatment. The 1000°C heat-treatment induces some form of silicon-oxygen precipitation in the slices as confirmed by IR measurements.

Results and Discussion

Oxygen striations—compensation.—Following the 450°C heat-treatment, the presence of oxygen striations is seen in Fig. 2 for a longitudinal slice cut 0.5 mm from the periphery of a typical 75 mm diam. The oxygen striations are seen in the EBIC image [Fig. 2(a)] as bright bands and the corresponding variations in the normalized EBIC and resistivity (as determined from spreading resistance measurements at 5 μm intervals) are shown in Fig. 2(a) and (b), respectively.

As can be seen from Fig. 2(a) and (b), there is direct spatial correspondence of the variations in the normalized EBIC and resistivity; the large variations (exceeding a factor of 10) in resistivity following the 450°C heat-treatment reflect corresponding variations in the oxygen thermal donor concentration (and, hence, in the oxygen concentration), since variations in the boron acceptor concentration are less than 12% (see below); the oxygen striations in the EBIC image, Fig. 2(a), manifested as bright bands, correspond to the maxima in resistivity [Fig. 2(b)] which in turn correspond to oxygen concentration maxima. Maxima in resistivity are expected to coincide with maxima in oxygen thermal donors, since the higher the concentration of the thermal donors, the higher the compensation of the p-type dopant and hence the higher the resistivity (provided the concentration of thermal donors does not exceed the concentration of the acceptors).

In the regions of maximum resistivity, the space charge region (depletion width) of the Schottky diode is significantly increased. For resistivities of about 200 $\Omega\text{-cm}$ the depletion width is several microns but well within the excitation volume of a 35 keV electron beam. Accordingly, the collection efficiency of the excess carriers is enhanced in these regions of the oxygen concentration maxima and consequently appear as bright bands in the EBIC image.

As seen in Fig. 2(a) and 2(b), the width of the EBIC maxima (e.g., the width at half the maximum value) is larger than that of the resistivity maxima. This result is apparently due to interference effects of the electric fields resulting from the resistivity variations.

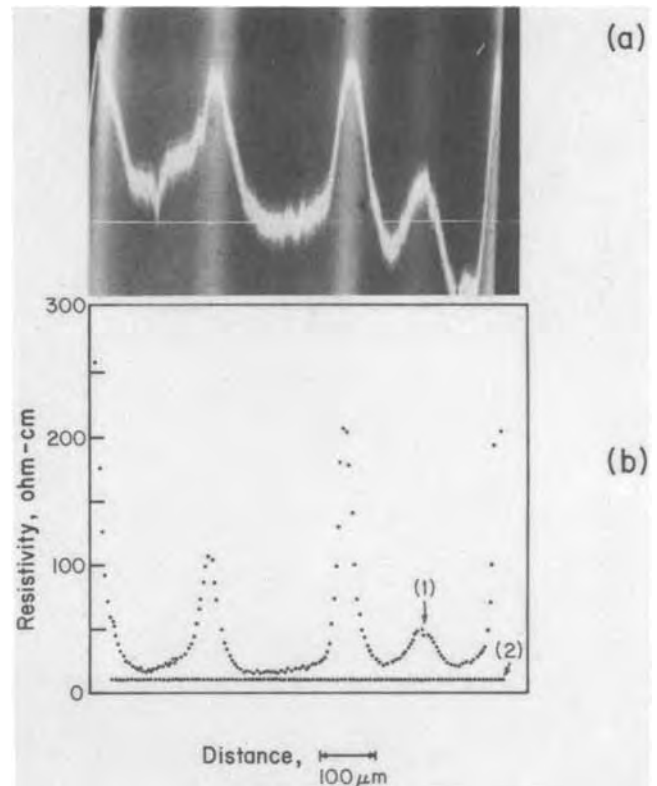


Fig. 2. (a) EBIC image and superimposed EBIC tracing taken along indicated line on a sample cut near crystal periphery (see text). (b) Resistivity profile as determined by spreading resistance measurements at 5 μm intervals along the line indicated in EBIC image after 450°C heat-treatment, curve 1; profile taken prior to 450°C heat-treatment, curve 2; small variations of boron concentration are not visible on this scale.

Since the spacing of the spreading resistance impact traces in the EBIC image is 5 μm , it is seen from a comparison of the resistivity and the normalized EBIC that the linear resolution attained by the EBIC technique in the present case is about 10 μm .

It has been found that heat-treatment of Si at 700°C eliminates oxygen thermal donors (1-3). Consistent with this finding, after heat-treatment of the slices studied above at 700°C for 1 hr, their EBIC images exhibited no bands. The normalized EBIC and resistivity measurements carried out in the same regions as discussed above exhibited small variations.

These variations are due to B-dopant fluctuations which in 10 $\Omega\text{-cm}$ Si are about 12% [Fig. 2(b)]. These B-dopant fluctuations are not resolved in the EBIC image.

Oxygen striations and overcompensation.—Longitudinal slices cut 1 cm from the crystal periphery were also investigated. They were also treated at 450°C for 50 hr and prepared for EBIC and spreading resistance measurements as discussed above.

The EBIC image of one of these slices is shown in Fig. 3(a). Spreading resistance measurements were carried out at 5 μm intervals, 20 μm below the horizontal impact trace markers which are spaced 25 μm apart and are clearly shown in the EBIC image. Dark bands are seen in the EBIC image which correspond to resistance minima in Fig. 3(b). These dark bands (regions of low collection efficiency of excess carriers) correspond to oxygen striations in which the donor concentration exceeds the concentration of the p-type dopant forming striated n-type regions (see below). Since the donor concentration is a direct function of the oxygen concentration (2), the presence of n-type regions only in the slices cut 1 cm away from the periphery shows that the mean oxygen concentration is higher

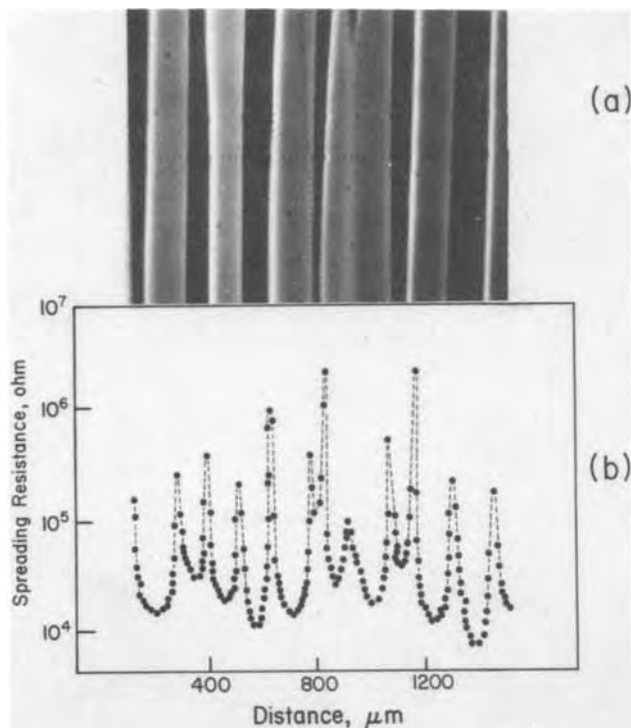


Fig. 3. (a) EBIC image on sample cut away from crystal periphery. Reference impact traces are clearly visible. (b) Spreading resistance profile taken at 5 μm intervals, 20 μm below horizontal line of reference tracers.

away from the periphery than near the periphery of the crystals. The bright bands (adjacent to the dark bands) in Fig. 3(a) correspond to regions of maxima in compensation as in the case of Fig. 2(a) but not to maxima in oxygen concentration.

The conductivity type within the dark bands was determined as follows: employing a two-probe spreading resistance measurement arrangement, measurements were carried out at 5 μm intervals with one of the probes positioned at all times on a dark band as shown in Fig. 4(a). As shown in Fig. 4(b) with the probe on the dark band having a negative polarity the measured resistance was about $8 \times 10^5 \Omega$. When the bias was reversed the resistance increased by about three orders of magnitude. Thus, there is a p-n junction at the boundary of each dark band and the adjacent bright band; the dark band is n-type and corresponds to a region overcompensated by thermal oxygen donors. After a 700°C heat-treatment (which eliminates the thermal oxygen donors) no dark bands in the EBIC image nor pronounced variations in resistance were present; this result confirms that the n-type regions (dark bands) are the result of oxygen donors.

Chemical etching.—It was found that oxygen striations can be conveniently revealed by chemical etching when they form n-type regions in p-type silicon. The etchant found suitable for this purpose is 20 parts $\text{CH}_3\text{COOH} + 3\text{HNO}_3 + 1\text{HF}$. An interference contrast photomicrograph of the slice etched for 20 min (after the metal layer was removed) is shown in Fig. 5. The area depicted in this figure is identical to that in the EBIC image of Fig. 3(a). It is seen that the striations in Fig. 5 correspond exactly to the dark band in Fig. 3(a). The bright bands (region of compensation maxima) could not be revealed by etching. Thus, a bright band in location D of Fig. 3(a) does not appear in Fig. 5; similarly, no oxygen striations could be revealed by etching on slices cut near the crystal periphery which correspond to oxygen concentration maxima but lead to maxima in compensation as in the case shown in Fig. 2(a).

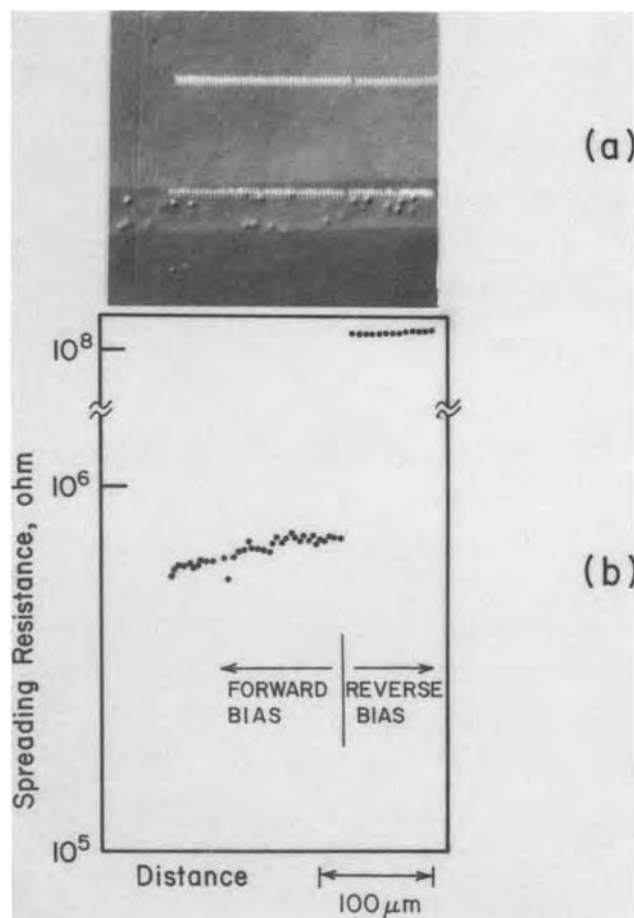


Fig. 4. (a) Optical photomicrograph of chemically etched surface (see text) showing impact traces of two-probe spreading resistance measurements. Traces of one probe are within dark band measurements of EBIC image (Fig. 2) while traces of other probe are outside dark band (for convenience the dark band is shown in the horizontal position). (b) Spreading resistance measured with both polarities of the d-c bias. Polarity was reversed at the discontinuity of the impact traces.

SiO_2 precipitation.—Silicon slices heat-treated at 1000°C for 12 hr prior to heat-treatment at 450°C (for activating thermal donors) exhibited silicon-oxygen precipitation (19). An EBIC image of a slice cut from near the periphery of the crystal is shown in Fig. 6(a). It is seen that within the bright bands [corresponding to maxima in resistivity, Fig. 6(b); compare also with Fig. 2] there are dark spots with low excess carrier

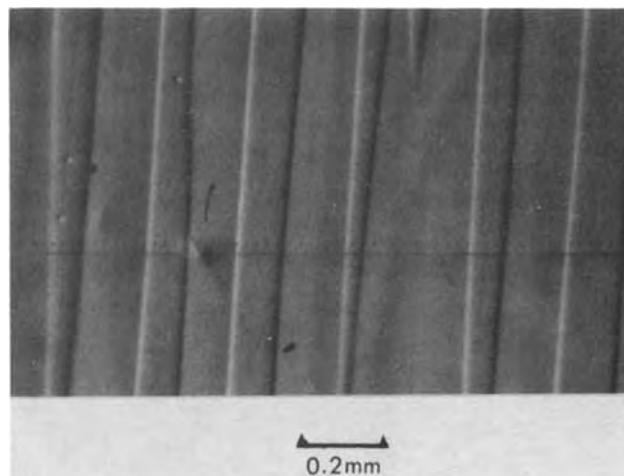


Fig. 5. Optical photomicrograph of chemically etched sample showing the identical region as EBIC image of Fig. 3(a).

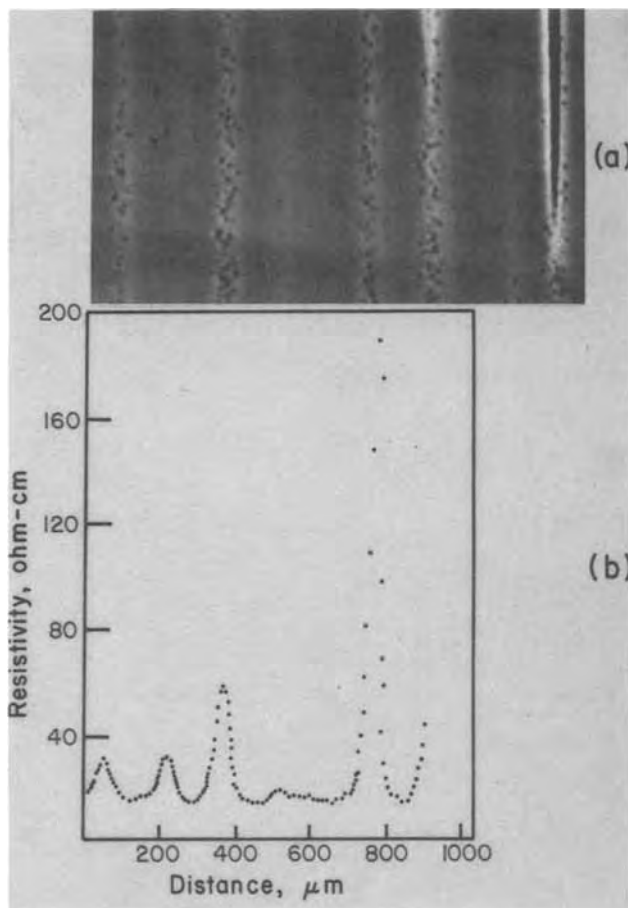


Fig. 6. (a) EBIC image of sample heat-treated at 1000°C prior to a 450°C heat-treatment. (b) Resistivity as determined from spreading resistance measurements.

collection efficiency which are associated with micro-precipitates (and related loops and stacking faults). On the right-hand side of the EBIC image there are two dark bands, corresponding to overcompensated, n-type regions, which also contain microprecipitates. Apparently, the 12 hr 1000°C heat-treatment causes only partial precipitation of oxygen, since a subsequent 450°C heat-treatment leads to the formation of thermal oxygen donor striations (bright and dark bands in the EBIC image). The fact that the microprecipitates are associated with oxygen was confirmed by IR transmission measurements which showed that after the 1000°C, and prior to the 450°C, heat-treatment the interstitial oxygen content in Si was reduced.

As in the cases discussed earlier, heat-treatment at 700°C eliminates the oxygen donor striations, however, the microprecipitates can still be seen (Fig. 7).

Although the detailed nature of the micro-defects generated by these precipitates will not be discussed in the present communication, it should be pointed out that the morphology of the etch pits, revealed by the Sirtl etchant, was found to correspond to that associated with stacking faults as discussed in the literature.

Summary and Conclusions

The distribution of oxygen in Czochralski-grown p-type silicon was studied by scanning electron microscopy in the EBIC mode in conjunction with spreading resistance measurements. A linear resolution of about 10 μm was achieved in the determination of oxygen distribution. Through generation of thermal oxygen donors (by heat-treating at 450°C) it was found that oxygen is distributed in a striated pattern. At the oxygen concentration maxima, maxima in dopant compensation occur, provided the thermal donor concentration does not exceed the p-type dopant concentra-

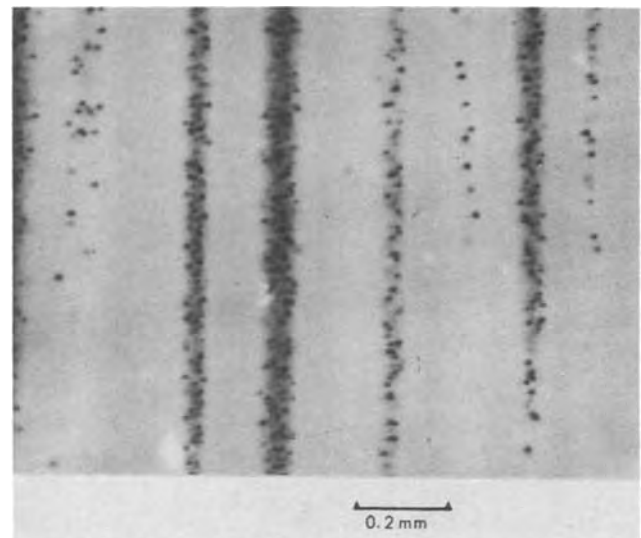


Fig. 7. EBIC image of sample heat-treated at 700°C after heat-treatments at 1000°C and 450°C.

tion. These compensation maxima appear as bright bands in the EBIC images (high collection efficiency regions of excess carriers) and exhibit high resistivity as determined by spreading resistance measurements. If at the oxygen concentration maxima the thermal donor concentration exceeds that of the p-type dopant, then dopant overcompensation takes place. These regions become n-type and appear as dark bands (low collection efficiency regions of excess carriers) adjacent to bright bands (highly compensated regions). The boundaries of these regions constitute p-n junctions which could be individually characterized with a two-probe spreading resistance arrangement.

Oxygen precipitates resulting from a heat-treatment at 1000°C were found to be distributed in a striated pattern and within the regions of oxygen concentration maxima. Unlike the thermal oxygen donors the precipitates were not eliminated by prolonged heat-treatment at 700°C.

Etching with a mixture of 20 parts CH_3COOH + 3HNO₃ + 1HF was found to delineate conveniently and accurately the oxygen striations in the cases where the oxygen donors overcompensate the p-type dopant (dark bands in the EBIC image); this etchant also revealed oxygen precipitates. However, the oxygen striations could not be revealed by etching in the cases where the oxygen donors do not overcompensate the p-type dopant.

The EBIC technique employed in the present study, in conjunction with spreading resistance measurements, is well suited for quantitative study of the microsegregation of oxygen in silicon and its quantitative interactions with electronic phenomena and defect structure. It should be finally noted that controlled formation of p-n patterns through controlled incorporation of oxygen in silicon could be advantageously employed for photovoltaic cell and other device applications.

Acknowledgment

The authors are grateful to the International Business Machines Corporation and the National Aeronautics and Space Administration for financial support and to Dr. W. A. Westdorp for stimulating discussions.

Manuscript submitted April 24, 1979; revised manuscript received Oct. 29, 1979.

Any discussion of this paper will appear in a Discussion Section to be published in the December 1980 JOURNAL. All discussions for the December 1980 Discussion Section should be submitted by Aug. 1, 1980.

Publication costs of this article were assisted by the Massachusetts Institute of Technology.

REFERENCES

1. C. S. Fuller, J. A. Ditzenberger, N. B. Hannay, and E. Buehler, *Phys. Rev.*, **96**, 833 (1954); *Acta Metall.*, **3**, 97 (1955).
2. W. Kaiser, H. L. Frisch, and H. Reiss, *Phys. Rev.*, **112**, 1546 (1958).
3. V. N. Mordkovich, *Sov. Phys. Solid State*, **6**, 654 (1964).
4. T. Abe, K. Kikuchi, and S. Shirai, in "Semiconductor Silicon 1977," H. R. Huff and E. Sirtl, Editors, p. 95, The Electrochemical Society Soft-bound Proceedings Series, Princeton, N.J. (1977).
5. A. Murgai, H. C. Gatos, and W. A. Westdorp, *This Journal*, **126**, 2240 (1979).
6. J. R. Patel and B. W. Batterman, *J. Appl. Phys.*, **34**, 2716 (1963).
7. W. Kaiser, *Phys. Rev.*, **105**, 1751 (1957).
8. D. M. Maher, A. Staudinger, and J. R. Patel, *J. Appl. Phys.*, **47**, 3813 (1976).
9. T. Y. Tan and W. K. Tice, *Philos. Mag.*, **34**, 615 (1976).
10. G. H. Schwuttke, *J. Appl. Phys.*, **33**, 2760 (1962).
11. A. J. R. de Kock, S. D. Ferris, L. C. Kimerling, and H. J. Leamy, *J. Appl. Phys.*, **48**, 301 (1977).
12. C. N. Varker and K. V. Ravi, in "Semiconductor Silicon 1973," H. R. Huff and R. R. Burgess, Editors, p. 670, The Electrochemical Society Soft-bound Proceedings Series, Princeton, N.J. (1973).
13. L. C. Kimerling, H. J. Leamy, and J. R. Patel, *Appl. Phys. Lett.*, **30**, 217 (1977).
14. H. J. Leamy, L. C. Kimerling, and S. D. Ferris, in "Scanning Electron Microscopy 1976," Part IV, p. 526, ITT Research Institute, Chicago (1976).
15. J. Y. Chi and H. C. Gatos, *J. Appl. Phys.*, **50**, 3433 (1979).
16. J. Y. Chi, A. Murgai, and H. C. Gatos, Unpublished.
17. 1977 Annual Book of ASTM Standards, Part 43, ASTM, Philadelphia (1971).
18. T. E. Everhart and P. H. Hoff, *J. Appl. Phys.*, **42**, 5837 (1971).
19. K. H. Yang, P. Anderson, and H. Kappert, *Appl. Phys. Lett.*, **33**, 225 (1978).

The Influence of Preparation on Semiconducting Rutile (TiO₂)

L. A. Harris and R. Schumacher

General Electric Corporate Research and Development, Schenectady, New York 12301

ABSTRACT

Three processes for doping rutile crystals, vacuum reduction, hydrogen reduction, and electrochemical hydrogen loading are considered. The mechanisms by which n-type conductivity is produced, the relative disorder in the crystal, and the effects on photoelectrochemical behavior are compared for these different processes.

Rutile has received a great deal of attention as an electrode in photoelectrochemical studies. It is usually made conducting by some form of reduction such as heating in vacuum, in hydrogen, or by introducing an appropriate impurity such as fluorine. More recently it has been shown that conductivity can be induced by electrochemically charging the TiO₂ with hydrogen at room temperature (1, 2). It is the purpose of this note to suggest that the materials produced by these doping processes have different chemical and physical structures that influence their electronic behavior as photoelectrochemical electrodes.

Vacuum Reduction

To produce conductivity in a TiO₂ crystal by vacuum treatment, temperatures exceeding about 700°C are required (3). It has been established that the crystal loses weight during this treatment due to the loss of water and oxygen (4, 5). The oxygen vacancies so formed leave some of the Ti atoms in the 3+ state and these can readily act as donors, providing electrons to the conduction band. Relatively high temperatures are required because bonds between an O atom and the remainder of the lattice must be broken so that O can diffuse out of the crystal.

Some disorder is introduced by this reduction process, and interstitial Ti atoms have been detected by channeling experiments (6). As oxygen content is decreased the crystal rearranges itself to accommodate the various Magneli phases by introducing shear planes or grain boundaries where extra titanium atoms are located (7-9).

The disorder in the crystal manifests itself in the photoelectrochemical characteristics. The poor response

to longer wavelengths of light which are absorbed deep in the crystal and the low quantum efficiency are indicative of short hole diffusion lengths due to a high density of bulk recombination sites (3).

Vacuum reduction appears to be the only process by which hydrogen, evidenced by OH absorption peaks in the infrared spectrum, can be removed from these crystals (10, 11).

Hydrogen Reduction

If rutile is heated in hydrogen, conductivity can be induced at temperatures roughly 200°C lower than those required to induce comparable conductivities by heating in vacuum (3). The presence of hydrogen in the crystal is shown by the appearance of OH absorption peaks, indicating that the hydrogen is bound to O atoms of the lattice. There are usually two peaks, one at 3276 cm⁻¹ and a smaller one at 3323 cm⁻¹ (10, 11). One might speculate that the peak at 3276 cm⁻¹ is due to H bonded between two lattice O atoms (10) and that the peak at 3323 cm⁻¹ is due to H bonded to a single lattice O atom. These peaks are not to be confused with those due to surface-adsorbed OH which occur at 3620 and 3680 cm⁻¹ (12). This interpretation is consistent with the appearance of a third peak at 3345 cm⁻¹ in samples etched in molten NaOH (Fig. 1). This third peak, attributable to interstitial OH groups is removed by heating in H₂ but not by heating in O₂.

Recent observations of the diffusion of tritium in TiO₂ agree with computed values under the assumption that the tritium is bonded to lattice O atoms (13, 14). In contrast to the vacuum reduced case no O atoms need be lost from the crystal and the crystal order is not so seriously disturbed. We may think of the conductivity as being produced by the change of divalent O ions to monovalent OH ions, thus leaving Ti³⁺ ions

Key words: semiconductor electrodes, photoelectrochemistry, hydrogen, doping.

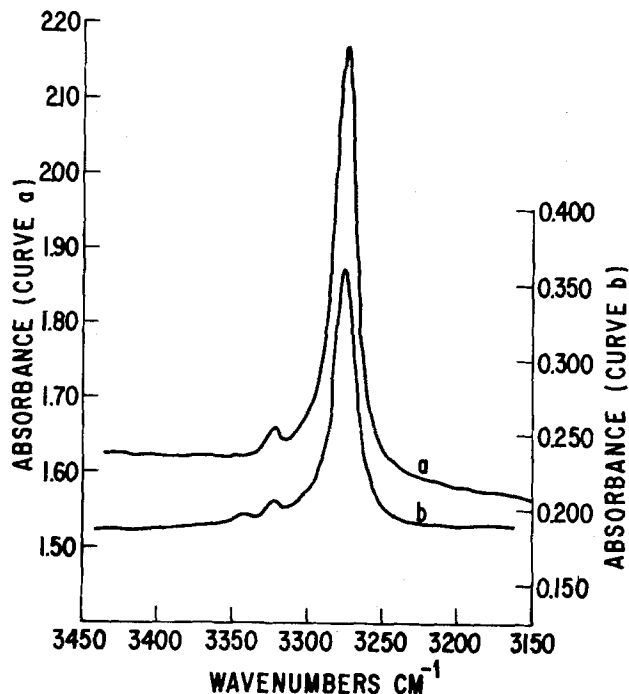


Fig. 1. Infrared absorption peaks due to OH groups in rutile: (a) crystal reduced in H₂; (b) unreduced crystal, etched in molten NaOH, and oxidized. Note the difference in scales.

to act as donors, without leaving their central positions in the surrounding octahedra of O atoms. This process is analogous to doping with fluorine, in which divalent O is replaced by monovalent F, leaving an extra electron on the Ti atom (15).

To produce an OH group, one of the oxygen bonds must be switched from a Ti to an H atom. The activation energy for this process must be less than that to simply break O-Ti bonds, without reestablishing them, so that O vacancies can be produced, hence the lower temperatures required for reduction in hydrogen than in vacuum. Hydrogen reduction at higher temperatures can result in the production of both OH groups and oxygen vacancies with the attendant crystal disorder.

The photoelectrochemical behavior of electrodes reduced in hydrogen at the relatively low temperatures of 550°-650°C are consistent with a high degree of order, hence longer hole lifetimes and fewer bulk recombination centers. The observed quantum efficiencies are higher than for vacuum reduced samples, particularly in the long wavelength region approaching the edge of the absorption band (3).

Electrochemical Loading

It has been demonstrated that the density of donors in a lightly doped rutile electrode can be enormously, but temporarily, increased by operating the electrode cathodically so as to generate hydrogen at its surface. The original doping of the crystal, necessary to operate it as an electrode, can be done either in hydrogen or in vacuum. The extra conductivity induced by the generation of hydrogen is attributed to the diffusion of H atoms into the crystal where they donate their electrons to the conduction band, leaving interstitial protons (2).

There are several indications that the protons are not bound to the crystal lattice. This form of doping is much more temporary than the higher temperature processes. The increased donor density induced by electrochemical loading disappears in the course of a few hours if the crystal is just left standing, either in electrolyte or in air. The capacitance of the depletion layer, which reflects the donor density, decreases more rapidly as the field strength in the depletion layer is increased, suggesting the presence of mobile positive charges (2). Recent measurements indicate that the

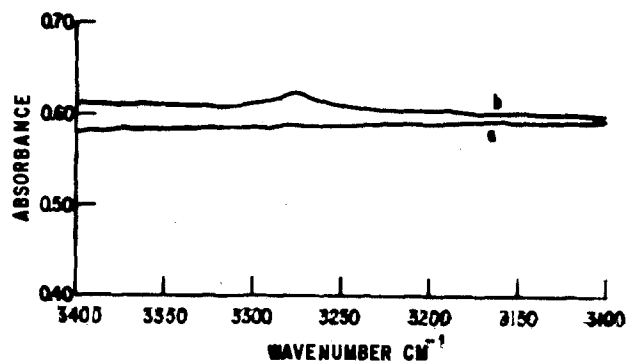


Fig. 2. Infrared absorption of a vacuum reduced crystal: (a) after vacuum reduction; (b) same crystal after hydrogen loading.

hydrogen, which usually leaves the crystal as it entered as neutral H atoms, leaves as protons if the surface field exceeds the critical value of about 10⁶ V/cm (16).

Vacuum reduced TiO₂ crystals can be heavily loaded electrochemically with hydrogen, enough to give the crystal a temporarily bluish cast, yet the infrared absorption spectrum taken promptly after loading does not show an appreciable density of OH groups (Fig. 2). Thus the hydrogen introduced electrochemically cannot be bound to the lattice, except possibly where some O atoms had dangling bonds due to the original vacuum reduction.

As might be expected, the photoelectrochemical properties of rutile electrodes charged with hydrogen at room temperature are similar to those of well-ordered hydrogen-reduced crystals previously annealed in oxygen. The quantum efficiencies are relatively high and the short wavelength response is improved by the loading (2). There is some decrease in long wavelength response near the absorption edge. This decrease at heavy loadings can be shown to result from the decrease in depletion layer width. In this case most long wavelength photons are absorbed well beyond the depletion layer and in a field-free region where the collection efficiency of holes is somewhat reduced. These electrode properties are of only academic interest in this case, because in normal operation the hydrogen soon leaves the crystal.

This brief review of some of the properties of semiconducting rutile is far from complete, neglecting as it does, possible changes in band structure, the results of ESR studies, and other components of the extensive literature on TiO₂. Nevertheless, the viewpoint offered here, it is hoped, may be helpful to others in clarifying some of the controversies regarding the nature of donor species produced by different preparatory treatments.

Acknowledgment

The authors are grateful to D. V. Temple for the infrared absorption measurements and to R. H. Wilson for useful discussions.

Manuscript received Aug. 31, 1979.

Any discussion of this paper will appear in a Discussion Section to be published in the December 1980 JOURNAL. All discussions for the December 1980 Discussion Section should be submitted by Aug. 1, 1980.

Publication costs of this article were assisted by General Electric Company.

REFERENCES

1. P. F. Chester and D. H. Bradhurst, *Nature*, **199**, 1056 (1963).
2. L. A. Harris, M. E. Gerstner, and R. H. Wilson, *This Journal*, **126**, 850 (1979).
3. R. H. Wilson, L. A. Harris, and M. E. Gerstner, *ibid.*, **126**, 844 (1979).
4. A. W. Czanderna and J. M. Honig, *J. Phys. Chem.*, **63**, 620 (1959).
5. G. J. Hill, *J. Phys. D.*, **1**, 1151 (1968).

6. E. Yagi, A. Koyama, H. Sakairi, and R. R. Hasiguti, in "Inst. Phys. Conf. Ser. No. 31," N. B. Urli and J. W. Corbett, Editors, p. 485, The Institute of Physics, Bristol and London (1977).
7. T. Hurlen, *Acta Chem. Scand.*, **13**, 365 (1959).
8. L. A. Bursill, B. G. Hyde, O. Terasaki, and D. Watanabe, *Philos. Mag.*, **20**, 347 (1969).
9. J. S. Anderson, *Rev. Pure Appl. Chem.*, **21**, 67 (1971).
10. A. von Hippel, J. Kalnajs, and W. B. Westphal, *J. Phys. Chem. Solids*, **23**, 779 (1962).
11. B. H. Soffer, *J. Chem. Phys.*, **35**, 940 (1961).
12. G. Munuera, V. Rives-Arnau, and A. Saucedo, *J. Chem. Soc. Faraday Trans. 1*, **75**, 736 (1979).
13. J. B. Bates, J. C. Wang, and R. A. Perkins, *Phys. Rev. B*, **19**, 4130 (1979).
14. J. V. Cathcart, R. A. Perkins, J. B. Bates, and L. C. Manley, *J. Appl. Phys.*, **50**, 4110 (1979).
15. N. Subbarao, Y. H. Yun, R. Kershaw, K. Dwight, and A. Wold, *Inorg. Chem.*, **18**, 488 (1979).
16. R. Schumacher, *Ber. Bunsenges. Phys. Chem.*, **84**, No. 2 (1980).

Arsenic Doping of Chemical Vapor Deposited Polycrystalline Silicon Using SiH₄-H₂-AsH₃ Gas System

Junichi Murota and Eisuke Arai

Nippon Telegraph and Telephone Public Corporation,

Musashino Electrical Communication Laboratory, Musashino, Tokyo, 180 Japan

and Kiyoshi Kudo

Nippon Telegraph and Telephone Public Corporation,

Ibaraki Electrical Communication Laboratory, Tokai, Ibaraki, 319-11 Japan

ABSTRACT

The arsenic concentration (C_{As}) in polycrystalline silicon (poly-Si) deposited under various deposition conditions in the deposition temperature range 670°-760°C using SiH₄-H₂-AsH₃ gas system has been determined by neutron activation analysis. From the experimental results, it was found that C_{As} increases with decreasing deposition temperature and with increasing partial pressure of AsH₃ in the gas introduced into the reactor ($P_{AsH_3}^{(1)}$), and that for lower $P_{AsH_3}^{(1)}$ region, C_{As} decreases with decreasing gas velocity and with increasing deposition rate, and for higher $P_{AsH_3}^{(1)}$ region, C_{As} is independent of gas velocity and deposition rate. From the analyses of the experimental data, it was suggested that (i) for lower $P_{AsH_3}^{(1)}$ region, C_{As} is limited by the diffusion of As-containing species, such as As molecule, As₂ molecule, and As₄ molecule, in the stagnant layer formed by gas stream, and for higher $P_{AsH_3}^{(1)}$ region, C_{As} is controlled by the surface reaction; (ii) monatomic As existing at wafer surface is incorporated in poly-Si in accordance with Henry's law; (iii) the transfer coefficient of As atoms in gas phase increases slightly with increasing deposition temperature and gas velocity; (iv) the segregation coefficient of monatomic As between gas phase and poly-Si (m) is approximated by $m = 1.5 \times 10^8 \exp(-71.5 \text{ kcal/mole}/RT)$; (v) the energy of As-Si bond is 44.5 kcal/mole.

Arsenic-doped polycrystalline silicon (As-doped poly-Si) is an important material as a diffusion source for the emitters of microwave transistors (1, 2) and as a gate electrode of MOSLSI's (3). In the fabrication process of fine pattern silicon devices, the deposition temperature of As-doped poly-Si has been selected in the range between 650° and 800°C, taking account of grain size (4-6). The deposition rate, structure, and resistivity of As-doped poly-Si have been investigated by many workers (5-7), however, little has been known about As doping mechanism of chemical vapor deposited poly-Si at deposition temperature between 650° and 800°C, which is a basic knowledge for using As-doped poly-Si.

In the present work, the As concentration (C_{As}) in poly-Si deposited under various deposition conditions in the deposition temperature range 670°-760°C using the SiH₄-H₂-AsH₃ gas system was obtained by neutron activation analysis. From the experimental results, it was suggested that, for lower $P_{AsH_3}^{(1)}$ region, C_{As} is limited by the diffusion of As-containing species in the stagnant layer (8) formed by gas stream, and for higher $P_{AsH_3}^{(1)}$ region, C_{As} is controlled by the surface reaction, and that monatomic As existed at wafer sur-

face is incorporated in poly-Si in accordance with Henry's law. The temperature dependences of the transfer coefficient of As atoms in H₂ and the segregation coefficient of monatomic As between gas phase and poly-Si were also obtained, and the energy of As-Si bond was determined using Weiser's model (9).

Experimental

The As-doped poly-Si was deposited in an rf heated reactor using the SiH₄-H₂-AsH₃ gas system. Figure 1 shows the schematic view of the reactor used for the deposition of poly-Si. Total gas flow rate, which is nearly equal to H₂ gas flow rate, was 15-50 l/min. Deposition temperature range was 670°-760°C. Deposited thickness was about 4500Å. Deposition temperature on wafer surface was measured with an optical pyrometer, corrected for the emissivity of Si and the absorption of quartz. Substrates used were p-type Si wafers of 1-2 Ω-cm with mirror polished (100) surface. The oxide film was grown on the substrates in the atmosphere of dry O₂ gas before poly-Si deposition.

The deposition rate was obtained by measuring both deposition time and deposited thickness. The deposited thickness was measured with a Taylor Hobson Talystep

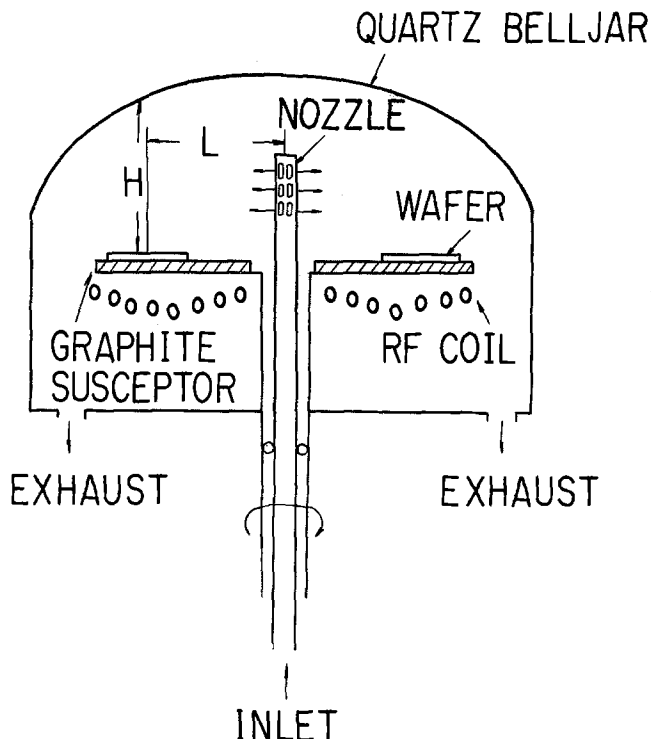


Fig. 1. Schematic view of the reactor used for the deposition of poly-Si.

after the poly-Si on SiO₂ had been locally removed. The As concentration in poly-Si was determined by neutron activation analysis. The samples, together with As₂O₃ as a comparative standard, were irradiated in the nuclear reactor JRR-4 in Japan Atomic Energy Research Institute at a thermal neutron flux of 8×10^{13} n/cm² sec for 60 min. Radioactivity of As in poly-Si removed by chemical etching method was measured by a Ge(Li) detector coupled with a 4096 channel pulse height analyzer.

Results and Discussion

Relationships between C_{As} and deposition conditions.—Figures 2 and 3 show the dependence of deposition rate of poly-Si and C_{As} upon the total gas flow rate of the gas introduced into the reactor (F) at the

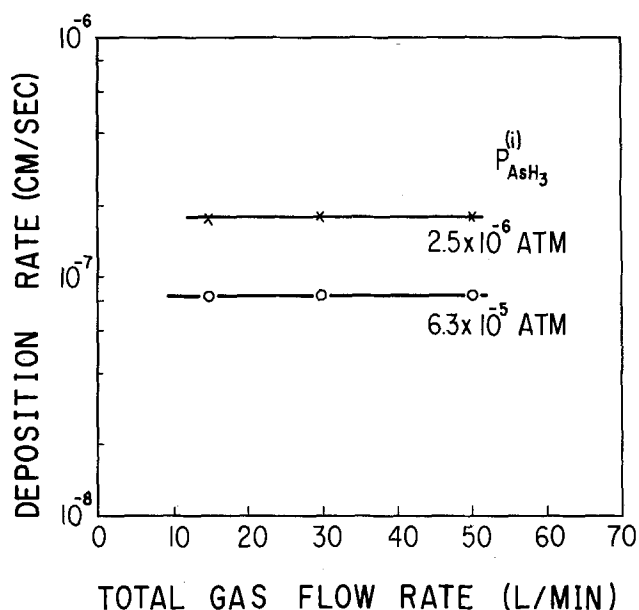


Fig. 2. Dependence of deposition rate of poly-Si upon the total gas flow rate at deposition temperature of 730°C and P_{SiH₄}⁽ⁱ⁾ = 5.0 × 10⁻³ atm.

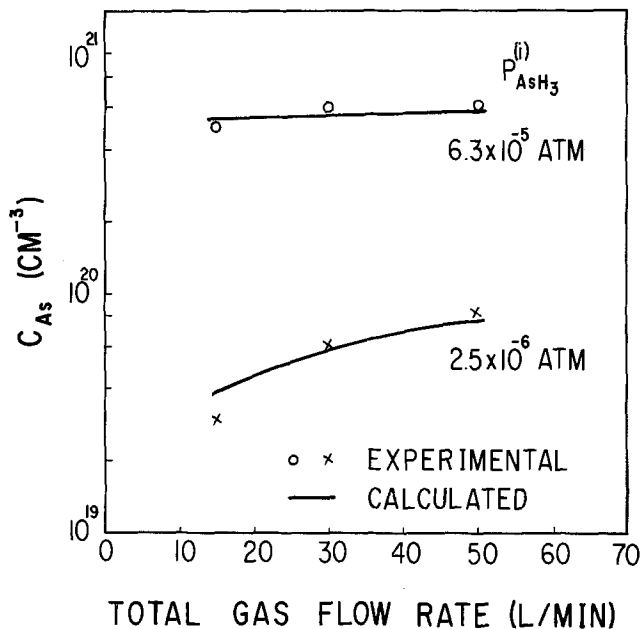


Fig. 3. Dependence of C_{As} upon total gas flow rate at deposition temperature of 730°C and P_{SiH₄}⁽ⁱ⁾ = 5.0 × 10⁻³ atm. Solid curves were calculated from Eq. [10] and [11] with the data of Fig. 2 and m = 3.8 × 10⁻⁸ atm.

deposition temperature of 730°C when the partial pressure of AsH₃ in the gas introduced into the reactor (P_{AsH₃}⁽ⁱ⁾) and the partial pressure of SiH₄ in the gas introduced into the reactor (P_{SiH₄}⁽ⁱ⁾) are constant. From Fig. 2, it is seen that the deposition rate is not influenced by F, i.e., gas velocity although the deposition rate decreases with increasing P_{AsH₃}⁽ⁱ⁾ as reported by many investigators (5-7). From Fig. 3, it is seen that, for lower P_{AsH₃}⁽ⁱ⁾ region, C_{As} tends to increase with increasing F, i.e., gas velocity, and for higher P_{AsH₃}⁽ⁱ⁾ region, C_{As} becomes to be independent of F, i.e., gas velocity. These results suggest that the deposition rate of poly-Si and C_{As} for higher P_{AsH₃}⁽ⁱ⁾ region is controlled by the surface reactions, while C_{As} is limited by the mass transport of As atoms in gas phase for lower P_{AsH₃}⁽ⁱ⁾ region. Figure 4 shows the dependence of C_{As} upon P_{AsH₃}⁽ⁱ⁾ for several deposition temperatures at F = 30 l/min and P_{SiH₄}⁽ⁱ⁾ = 5.0 × 10⁻³ atm. The slope of log C_{As} vs. log P_{AsH₃}⁽ⁱ⁾ curve decreases with increasing P_{AsH₃}⁽ⁱ⁾, and C_{As} increases with decreasing deposition temperature. The deposition rate dependence of C_{As} for several P_{AsH₃}⁽ⁱ⁾'s at the deposition temperature of 730°C and F = 30 l/min is shown in Fig. 5. The deposition rate was controlled by changing P_{SiH₄}⁽ⁱ⁾. From Fig. 5, it is seen that, for lower P_{AsH₃}⁽ⁱ⁾ region, C_{As} decreases with increasing deposi-

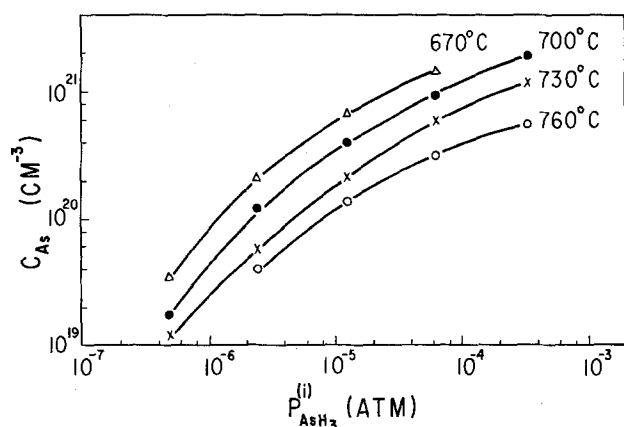


Fig. 4. Dependence of C_{As} upon P_{AsH₃}⁽ⁱ⁾ for several deposition temperatures at F = 30 l/min and P_{SiH₄}⁽ⁱ⁾ = 5.0 × 10⁻³ atm.

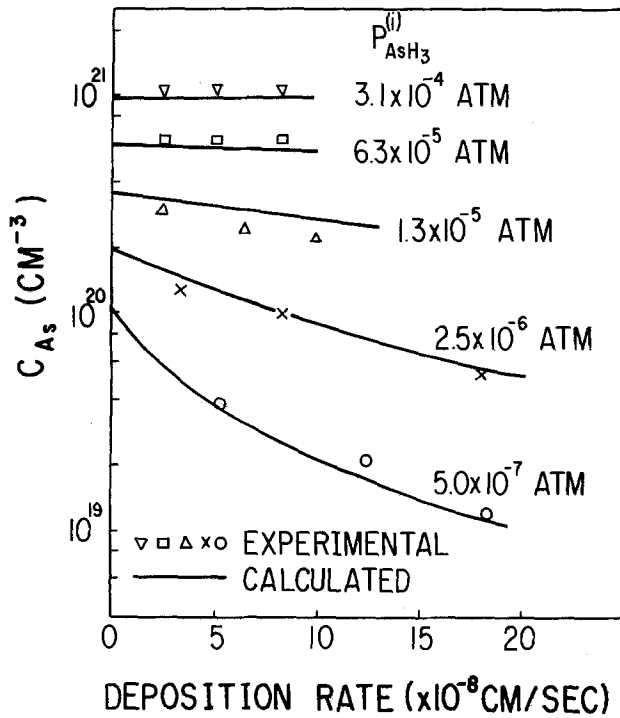


Fig. 5. Dependence of C_{As} upon deposition rate for several $P_{AsH_3}^{(i)}$'s at deposition temperature of 730°C and $F = 30$ l/min. Solid curves were calculated from Eq. [10] with $m = 3.8 \times 10^{-8}$ atm and $\pi = 5.6 \times 10^{-1}$ cm/sec.

tion rate, and for higher $P_{AsH_3}^{(i)}$ region, C_{As} is independent of deposition rate.

These results are summarized as follows: (i) C_{As} increases with decreasing deposition temperature and with increasing $P_{AsH_3}^{(i)}$, (ii) for lower $P_{AsH_3}^{(i)}$ region, C_{As} decreases with decreasing gas velocity and with increasing deposition rate, and for higher $P_{AsH_3}^{(i)}$ region, C_{As} is independent of deposition rate and gas velocity.

Relationships between C_{As} and partial pressure of As-containing species.—In the present section, the decomposition of AsH_3 , the mass transport of As atoms in gas phase and the relationships between C_{As} and the partial pressure of As-containing species at wafer surfaces are discussed using the above results, and finally the empirical equation to determine C_{As} is proposed.

The reliable thermodynamic data of AsH_3 have not been reported. In the present work, the equilibrium relationship among AsH_3 molecules, As_4 molecules, and H_2 molecules, reported by Kirwan (10), is assumed, which is proved to be appropriate in the below discussions.

Under the $P_{AsH_3}^{(i)}$ and deposition temperature ranges in the present experiment, AsH_3 molecules are decomposed completely into As molecules, As_2 molecules, and As_4 molecules. Then, the equilibrium relation near the wafer surface in the gas phase is as follows

$$K_1 = P_{As}^{(s)} / (P_{As_2}^{(s)})^{1/2} \quad [1]$$

$$K_2 = P_{As_4}^{(s)} / (P_{As_2}^{(s)})^2 \quad [2]$$

where $P_{As}^{(s)}$, $P_{As_2}^{(s)}$, and $P_{As_4}^{(s)}$ are the partial pressure of As molecule, As_2 molecule, and As_4 molecule near the wafer surface in the gas phase, respectively, formed by the decomposition of AsH_3 gas; K_1 and K_2 , equilibrium constants (11).

Next, the mass transport of As atoms in gas phase is considered, assuming a model analogous to that for the deposition of Si epitaxial layer (12, 13). Then, the number of As atoms (n_T) transported towards the wafer surface per square centimeter per second is

$$n_T = \pi(n_1 - n_2) \quad [3]$$

$$n_1 = P_{AsH_3}^{(i)} / kT \quad [4]$$

$$n_2 = [P_{As}^{(s)} + 2P_{As_2}^{(s)} + 4P_{As_4}^{(s)}] / kT \quad [5]$$

where it is also assumed that all the transfer coefficients of As-containing species have the same value and that As molecules, As_2 molecules, and As_4 molecules are the most abundant As-containing species at the wafer surface, but the other As-containing species such as AsH_3 molecules are not. π is the transfer coefficient for As atoms in H_2 ; n_1 and n_2 , the number of As atoms introduced into the reactor and that existed at the wafer surface, respectively. Equation [3] is similar to Eq. [3] in Ref. (14) shown by Craig.

The number of As atoms (n_p) incorporated in poly-Si per square centimeter per second is

$$n_p = vC_{As} \quad [6]$$

where v is the deposition rate of poly-Si.

In the steady-state condition ($n_T = n_p$), combining Eq. [3] and [6]

$$\pi(n_1 - n_2) = vC_{As} \quad [7]$$

This equation means that, at $v = 0$, n_1 is equal to n_2 , i.e.

$$P_{AsH_3}^{(i)} = P_{As}^{(s)} + 2P_{As_2}^{(s)} + 4P_{As_4}^{(s)} \quad [8]$$

Therefore, from the calculation of Eq. [1], [2], and [8], and the experimental data of C_{As} at $v = 0$ for various $P_{AsH_3}^{(i)}$'s, the dependences of C_{As} upon $P_{As}^{(s)}$, $P_{As_2}^{(s)}$, and $P_{As_4}^{(s)}$ under the equilibrium condition, respectively, are estimated, which are shown in Fig. 6. Here, C_{As} at $v = 0$ was approximated by linearly extrapolating the deposition rate to zero in Fig. 5. From Fig. 6, it is found that C_{As} at $v = 0$ is nearly proportional to $P_{As}^{(s)}$, $(P_{As_2}^{(s)})^{1/2}$, and $(P_{As_4}^{(s)})^{1/4}$. This means that monatomic As is incorporated in poly-Si in accordance with Henry's law. Then, the relationship between $P_{As}^{(s)}$ and C_{As} under the equilibrium condition is given by

$$P_{As}^{(s)} = mC_{As} / C_{Si} \quad [9]$$

where m is the segregation coefficient of monatomic As between gas phase and poly-Si, and C_{Si} is the concentration of Si lattice sites, 5.5×10^{22} cm $^{-3}$. Here, it should be noted that the above assumption in regard to the decomposition of AsH_3 is effective because C_{As} at $v = 0$ in Fig. 5 is nearly proportional to $(P_{AsH_3}^{(i)})^{1/2}$ for lower $P_{AsH_3}^{(i)}$ region and $(P_{AsH_3}^{(i)})^{1/4}$ for higher $P_{AsH_3}^{(i)}$ region. In other words, if AsH_3 molecules or AsH_3 molecules are the most abundant As-containing species at the wafer surface under the present conditions (15, 18), C_{As} at $v = 0$ should be proportional to $P_{AsH_3}^{(i)}$ and as a result, Eq. [9] could not be obtained.

Combining Eq. [1], [2], [4], [5], and [9], Eq. [7] is rewritten as

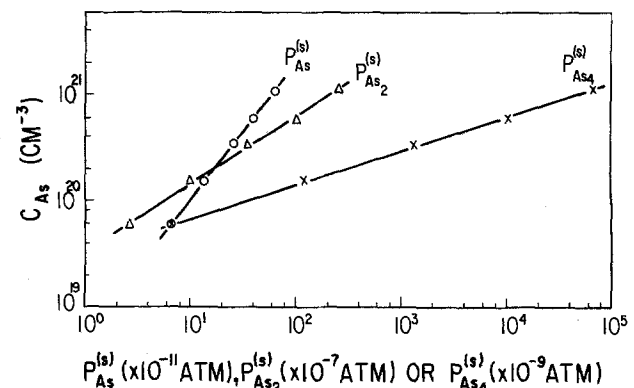


Fig. 6. Dependence of C_{As} upon $P_{As}^{(s)}$, $P_{As_2}^{(s)}$, and $P_{As_4}^{(s)}$ under the equilibrium condition, obtained from the calculation of Eq. [1], [2], and [8], and the experimental data of C_{As} at $v = 0$ for various $P_{AsH_3}^{(i)}$'s. Here, C_{As} at $v = 0$ was approximated by linearly extrapolating the deposition rate to zero in Fig. 5.

$$vC_{As} = \frac{\pi}{kT} [P_{AsH_3}^{(i)} - mC_{As}/C_{Si} - 2m^2C_{As}^2/C_{Si}^2K_1^2 - 4m^4K_2C_{As}^4/C_{Si}^4K_1^4] \quad [10]$$

The C_{As} vs. deposition rate curves calculated from Eq. [10] with $m = 3.8 \times 10^{-8}$ atm, $\pi = 5.6 \times 10^{-1}$ cm/sec, and $T = 730^\circ\text{C}$ is also shown in Fig. 5, where m and π are determined from two point data in Fig. 5. These curves give best fits to all the experimental data. Looking at Eq. [7] and [10] with $m = 3.8 \times 10^{-8}$ atm, $\pi = 5.6 \times 10^{-1}$ cm/sec, and $T = 730^\circ\text{C}$, it is found that for higher $P_{AsH_3}^{(i)}$ region, vC_{As} is negligibly small compared with πn_2 , i.e., n_2 becomes to be nearly equal to n_2 , but not for lower $P_{AsH_3}^{(i)}$ region. Therefore, for lower $P_{AsH_3}^{(i)}$ region, C_{As} is limited by the mass transport of As atoms in gas phase and decreases with increasing the deposition rate, and for higher $P_{AsH_3}^{(i)}$ region, C_{As} is not limited by the mass transport of As atoms in gas phase and as a result, becomes to be independent of deposition rate. In the same way, the total gas flow rate dependence of C_{As} can be explained using the results that π is dependent upon total gas flow rate as shown in the next section and that the deposition rate is independent of total gas flow rate. Further, using Eq. [10], the deposition temperature dependence of C_{As} is discussed. For lower $P_{AsH_3}^{(i)}$ region, C_{As} depends strongly upon deposition rate and π/kT , and for higher $P_{AsH_3}^{(i)}$ region, C_{As} depends strongly upon $P_{As}^{(s)}$ and m . From the data shown in Table I, the deposition temperature dependences of deposition rate are obtained. Substituting the experimental data shown in Table I and the value of K_1 and K_2 in Ref. (11) in Eq. [10], the deposition temperature dependences of π/kT , $P_{As}^{(s)}$, and m are obtained under the conditions that $P_{AsH_3}^{(i)}$, $P_{SiH_4}^{(i)}$, and total gas flow rate are constant. It is found that π/kT (see Fig. 7) decrease slightly, but the deposition rate, $P_{As}^{(s)}$ and m (see Eq. [12]) decrease rapidly with decreasing deposition temperature. Therefore, considering that the deposition rate decreases and $P_{As}^{(s)}/m$ increases with decreasing deposition temperature, the experimental facts shown in Fig. 4 that C_{As} increases with decreasing deposition temperature in lower and higher $P_{AsH_3}^{(i)}$ region can be explained. From these results, it is confirmed that Eq. [10] is a basic approximate equation to explain the As doping process in lower and higher $P_{AsH_3}^{(i)}$ regions.

Transfer coefficient.—Table I shows the data of deposition rate and C_{As} for various deposition conditions. Using the data in Table I and the values of K_1 and K_2 in Ref. (11), π was calculated from Eq. [10]. The deposition temperature dependence of π is shown in Fig. 7. π increases slightly with increasing deposition temperature. As described in the above section, for lower $P_{AsH_3}^{(i)}$ region, it is suggested that C_{As} is limited by the mass transport of As atoms in the gas phase. If the mass transport of As atoms in the gas phase is limited by the diffusion of As-containing species in the stagnant layer formed by gas stream, a model similar to that for the P doping in Si epitaxial layer (19, 14) based upon the stagnant layer model

Table I. Deposition rate and C_{As} for various deposition conditions

Deposition temperature (°C)	$P_{AsH_3}^{(i)}$ (atm)	Deposition rate (cm/sec)	C_{As} (cm ⁻³)
670	2.5×10^{-6}	3.4×10^{-8}	2.3×10^{20}
670	6.3×10^{-3}	2.2×10^{-8}	1.5×10^{21}
700	2.5×10^{-6}	6.5×10^{-8}	1.3×10^{20}
700	6.3×10^{-3}	4.2×10^{-8}	9.5×10^{20}
730	2.5×10^{-6}	1.8×10^{-7}	5.4×10^{19}
730	6.3×10^{-3}	8.3×10^{-8}	6.0×10^{20}
760	2.5×10^{-6}	2.5×10^{-7}	4.0×10^{19}
760	6.3×10^{-3}	1.4×10^{-7}	3.1×10^{20}

$F = 30$ l/min, $P_{SiH_4}^{(i)} = 5.0 \times 10^{-3}$ atm.

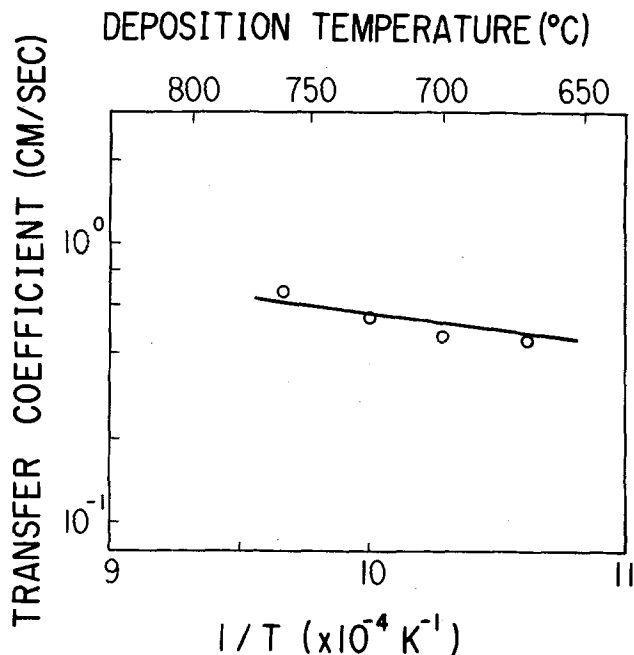


Fig. 7. Deposition temperature dependence of transfer coefficient at $F = 30$ l/min. Open circles were calculated from Eq. [10] and Table I. Solid curve was calculated from Eq. [11].

proposed by Eversteyn *et al.* (8) can be assumed. Then, π is given by

$$\pi = D/d \quad [11]$$

with $D = D_0(T/T_0)^2$, $d = a/\sqrt{V_T} - b$ in Ref. (8), $V_T/T = V_r/T_r$, and $V_r = F/2\pi L(H - d)$, where it is assumed that the temperature of gas is equal to wafer surface temperature; D , the diffusion coefficient of As-containing species in H_2 at deposition temperature (T); D_0 is D at $T_0 = 273^\circ\text{K}$, about $0.2 \text{ cm}^2 \text{ sec}^{-1}$ in Ref. (12) because As-containing species are mainly composed of As_2 molecules and As_4 molecules; d , the thickness of the stagnant layer; a and b , $7 \text{ cm}^{3/2} \text{ sec}^{-1/2}$ and 0.2 cm in Ref. (8), respectively; V_r , gas velocity at $T_r = 300^\circ\text{K}$, which is determined by the structure of reactor; L , distance from the nozzle of gas to the wafer surface, about 13 cm ; H , distance from the bell-jar surface to the wafer surface, about 15 cm .

The π calculated from Eq. [11] is also shown in Fig. 7, and is in good agreement with that from Eq. [10]. The C_{As} vs. F curves calculated from Eq. [10] and [11] with the data of Fig. 2 and $m = 3.8 \times 10^{-8}$ atm are also shown in Fig. 3. The calculated values are in good agreement with the experimental data in Fig. 3. For the determination of stagnant layer thickness in Eq. [11], the empirical equation obtained in a horizontal reactor reported by Eversteyn *et al.* (8) is used. The above results may mean that the gas flow dynamics of the present reactor are the same as those of horizontal reactor.

From these results, it is confirmed that the mass transport of As atoms in gas phase for lower $P_{AsH_3}^{(i)}$ region is limited by the diffusion of As-containing species in the stagnant layer formed by gas stream.

Segregation coefficient.—The deposition temperature dependence of m is shown in Fig. 8. Data (i) were calculated from Eq. [10] using the data in Table I. Data (ii) were calculated from Eq. [10] using the data of Swanson *et al.* (16). Data (iii) were obtained by Shepherd (13) using $SiCl_4$ - H_2 - $AsCl_3$ gas system. Data (iv) were calculated from the vapor pressure data of Sandhu *et al.* (17). From Fig. 8, it is seen that m increases with increasing deposition temperature and the temperature dependence of m , except for one point in the data (iv), is expressed approximately by

$$m = 1.5 \times 10^8 \exp(-71.5 \text{ kcal/mole}/RT) \quad [12]$$

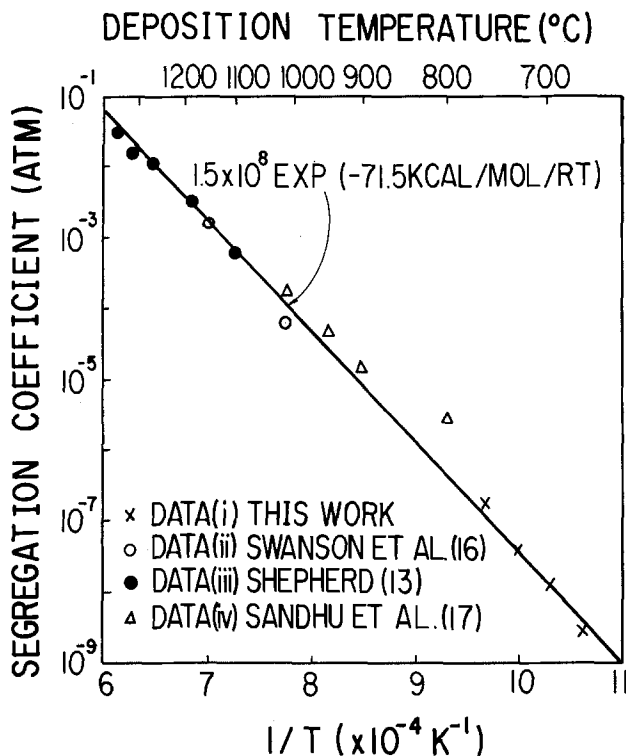


Fig. 8. Deposition temperature dependence of the segregation coefficient of monatomic As.

According to the theoretical relation for m proposed by Weiser (9), the temperature dependence of m is given by

$$\frac{d \ln m}{d(1/RT)} = \Delta H_{\text{Si}}^{\text{subl}} - 4E_{\text{As-Si}} + E_{\text{As-Si}}^{\text{strain}} \quad [13]$$

where the energy of Si-Si bond is assumed to be equal to one-half the heat of sublimation of Si (20); $E_{\text{As-Si}}$, the energy of As-Si bond; $E_{\text{As-Si}}^{\text{strain}}$, the strain energy caused by the difference of normal tetrahedral radius between As and Si, about 0.1 kcal/mole (9); $\Delta H_{\text{Si}}^{\text{subl}}$, the heat of sublimation of Si, 106.5 kcal/mole (21). Using Eq. [12], the right-hand side of Eq. [13] becomes -71.5 kcal/mole. Therefore, $E_{\text{As-Si}}$ becomes 44.5 kcal/mole. On the basis of a rule suggested by Allen (22), $E_{\text{As-Si}}$ is estimated by

$$1/E_{\text{As-Si}} = (1/E_{\text{As-As}} + 1/E_{\text{Si-Si}})/2 \quad [14]$$

where $E_{\text{As-As}}$ is the energy of As-As bond, 40.3 kcal/mole, which is calculated from Ref. (18); $E_{\text{Si-Si}}$, the energy of Si-Si bond, 53.25 kcal/mole with the assumption of $E_{\text{Si-Si}} = \Delta H_{\text{Si}}^{\text{subl}}/2$. The $E_{\text{As-Si}}$ calculated from Eq. [14] is 45.9 kcal/mole and is in good agreement with that obtained by the present work. Consequently, the value of $E_{\text{As-Si}}$ obtained by the present work, 44.5 kcal/mole is correct.

Conclusions

The incorporation of As in poly-Si is dependent upon deposition temperature, $P_{\text{AsH}_3}^{(1)}$, deposition rate, and gas velocity. From the experimental results, it was suggested that, for lower $P_{\text{AsH}_3}^{(1)}$ region, C_{As} is limited by the diffusion of As-containing species in the stagnant layer formed by gas stream, and for higher $P_{\text{AsH}_3}^{(1)}$ region, C_{As} is controlled by the surface reaction, and that monatomic As existing at wafer surface is incorporated in poly-Si in accordance with

Henry's law. The relationships between C_{As} and deposition conditions are given by

$$vC_{\text{As}} = \frac{\pi}{kT} [P_{\text{AsH}_3}^{(1)} - mC_{\text{As}}/C_{\text{Si}} - 2m^2C_{\text{As}}^2/C_{\text{Si}}^2K_1^2 - 4m^4K_2C_{\text{As}}^4/C_{\text{Si}}^4K_1^4]$$

where π is estimated by D/d using the stagnant layer model. By the above empirical equation, the As doping process in lower and higher $P_{\text{AsH}_3}^{(1)}$ region can be explained. The segregation coefficient (m) is approximated by $m = 1.5 \times 10^8 \exp(-71.5 \text{ kcal/mole}/RT)$. From the temperature dependence of m , the energy of the As-Si bond is determined to be 44.5 kcal/mole.

Acknowledgments

The authors wish to express their gratitude for encouragement of Mr. M. Kondo and Mr. F. Yanagawa in executing the study. They also would like to thank Mr. M. Tabe and Mr. H. Nakamura for their useful discussions and valuable advice, and Mr. K. Kobayashi for carrying out the experiments of neutron activation analysis.

Manuscript submitted Dec. 14, 1978; revised manuscript received Nov. 27, 1979.

Any discussion of this paper will appear in a Discussion Section to be published in the December 1980 JOURNAL. All discussions for the December 1980 Discussion Section should be submitted by Aug. 1, 1980.

Publication costs of this article were assisted by Nippon Telegraph and Telephone Public Corporation.

REFERENCES

1. M. Takagi, K. Nakayama, C. Terada, and H. Kamio, in "Proc. 4th Conf. on Solid State Devices," Tokyo, 1972, *Oyo Buturi (J. Jpn. Soc. Appl. Phys.)* 42, Suppl. p. 101 (1973).
2. T. Sakai, Y. Sunohara, Y. Sakakibara, and J. Murota, in "Proc. 8th Conf. on Solid State Devices," Tokyo, 1976, *Jpn. J. Appl. Phys.*, 16, Suppl. 16-1, p. 43 (1977).
3. E. Arai and N. Ieda, *IEEE J. Solid-State Circuits*, sc-13, 333 (1978).
4. N. Nagasima and N. Kubota, *Jpn. J. Appl. Phys.*, 14, 1105 (1975).
5. F. C. Eversteyn and B. H. Put, *This Journal*, 120, 106 (1973).
6. P. Rai-Choudhury and F. L. Hower, *ibid.*, 120, 1761 (1973).
7. R. F. C. Farrow *ibid.*, 121, 899 (1974).
8. F. C. Eversteyn, P. J. W. Severin, C. H. J. v. d. Brekel, and H. I. Peek, *ibid.*, 117, 925 (1970).
9. K. Weiser, *J. Phys. Chem. Solids*, 7, 118 (1958).
10. D. J. Kirwan, *This Journal*, 117, 1572 (1970).
11. Stull and Sinke, "Thermodynamic Properties of Elements," *Advances in Chemistry Series No. 8* (1956).
12. W. H. Shepherd, *This Journal*, 112, 988 (1965).
13. W. H. Shepherd, *ibid.*, 115, 541 (1968).
14. S. E. Craig, Jr., *ibid.*, 122, 840 (1975).
15. P. Duchemin, *Rev. Tech., Thomson-CSF*, 9, 411 (1977).
16. T. B. Swanson and R. N. Tucker, *This Journal*, 116, 1271 (1969).
17. J. S. Sandhu and J. L. Reuter, *IBM. J. Res. Dev.*, 15, 464 (1971).
18. D. T. J. Hurle, R. M. Logan, and R. F. C. Farrow, *J. Crystal Growth*, 12, 73 (1972).
19. J. Bloem, *J. Cryst. Growth*, 13/14, 302 (1972).
20. L. Pauling, "Nature of the Chemical Bond," 2nd ed., Cornell University Press (1948).
21. JANAF Thermochemical Tables, 2nd ed., NSRDS-NBS 37 (1971).
22. T. L. Allen, *J. Chem. Phys.*, 27, 810 (1957).

Recrystallization of Polycrystalline CVD Grown Silicon

W. J. H. Schins, J. Bezemer, H. Holtrop, and S. Radelaar

Technical Physics Department, State University Utrecht, 3508 TA Utrecht, The Netherlands

ABSTRACT

The recrystallization of fine-grained polycrystalline silicon (0.1-10 μm) obtained by chemical vapor deposition (CVD) was investigated. Recrystallization of sharply $\langle 110 \rangle$ textured material heated at 1350°-1400°C yields an inhomogeneous assembly consisting of 0.02-2 mm long grains of 0.02-0.1 mm diam. New grains are elongated in the direction of growth of the starting material. Grains do not grow further when impinging on each other. Textured material yields a sharply textured primary matrix. No influence of large temperature gradients (up to 500°C/mm) on recrystallization phenomena was observed. The degree of recrystallization as a function of time for fine-grained material can be described with a constant nucleation rate. From the dependence of the degree of recrystallization upon time and temperature an activation energy of 4.2 eV can be deduced for growth in fine-grained regions.

In recent years interest in polycrystalline silicon especially for photovoltaic solar-cell application has increased considerably. Polycrystalline silicon can be fabricated easily in large area sheets by chemical vapor deposition (CVD). However, the efficiency of a cell made of polycrystalline silicon is strongly affected by numerous randomly oriented grain boundaries acting as recombination centers for charge carriers. A grain size of at least 100 μm and grain boundaries lying perpendicular to the p-n junction are necessary for an acceptable overall cell efficiency (1). As reported earlier (2, 3) CVD grown polycrystalline silicon can be recrystallized to larger grains. We made a more thorough investigation of the influence on recrystallization phenomena of parameters like crystal orientation, specimen thickness, and heating temperature. A recrystallized sheet of silicon can either be doped and consequently be used as a photovoltaic layer or it might serve as a substrate on which a more perfect layer of silicon is grown epitaxially.

Experimental Techniques

Material specification.—The starting material used for our experiments is grown by the CVD method. We used both commercially available, high purity (99.999%) polycrystalline bars (Wacker Chemitronic) with a diameter of about 55 mm and layers grown on a flat substrate by CVD using SiHCl_3 as a source. As usual the bars were grown on a long polycrystalline silicon core from which silicon grains grow out radially. Optical examination shows that for different bars there is a difference in structural details as a result of growth conditions. Typical examples are shown in Fig. 1 and 2 which are optical micrographs of samples cut parallel to the growth direction, henceforth called material A and B, respectively. Material A consists of clusters of crystals elongated in the radial growth direction. The various crystals (0.1-10 μm in diameter) in a cluster are separated by straight grain boundaries. Optical examination of material B (crystals 0.1-10 μm in diameter) gives the impression that the growth process was interrupted a number of times. Upon further growth new nuclei are formed on discrete spots and growth continues in tree-like structures which often recrystallize during or shortly after deposition.

For x-ray measurements (4) samples of $8 \times 8 \text{ mm}^2$ were sawn from various sections of the bars in order to minimize the influence of the direction of growth. The samples cannot have larger dimensions because of the radial symmetry of the bars. The samples were ground and polished and then CP4-etched. Reflections from $\{111\}$ and $\{220\}$ crystal planes were recorded using a Siemens 3 kVA texture-goniometer with $\text{CuK}\alpha$ radiation.

Key words: CVD, nucleation, texture, grain growth.

The resulting pole figures show that material A has a sharp $\langle 110 \rangle$ fiber texture coinciding with the radial growth direction. An illustration is given in Fig. 3a which shows a part of a $\{111\}$ pole figure of a sample cut perpendicular to the growth direction. The thickness of the lines indicates the intensities relative to the intensities of a random sample. The thickest lines correspond to an eight times larger intensity. The observed spread in reflection angle is mainly due to the radial symmetry of the bars from which the samples are sawn. This is in agreement with earlier results for this kind of material (5). The same kind of analysis on only one of the striated clusters (area 10 mm^2) show it to be very strongly $\langle 110 \rangle$ fiber textured. The grains of material B do not show a preferred orientation as shown in Fig. 3b: all x-ray intensities are between 0.5 and 2 times the intensity of a random sample.

Thin polycrystalline silicon layers of thickness varying from 20 to 150 μm were grown in the laboratory by CVD at various temperatures in the range 1000°-1250°C at an average deposition rate of 2 μm per minute. The substrate consisted of thermally oxidized or nitridized silicon single crystals of various orientations. The crystallographic structure of these layers (henceforth to be called material C) is similar to the structure of material A.



Fig. 1. Sample of silicon material A cut from a CVD grown bar. Growth direction is from left to right.



Fig. 2. Sample of silicon material B cut from a CVD grown bar. Growth direction is from left to right.

Pole figures reveal a sharp $\langle 110 \rangle$ fiber texture coinciding with the growth direction. This is in agreement with earlier results on CVD grown polycrystalline silicon layers reported in the literature (6, 7).

For experiments with material A and B, samples were sawn from the rods with known angles ϕ as indicated in Fig. 4. The growth direction makes angles from 0 to $\frac{1}{2}\phi$ with the normal to the sample surface.

Grinding of the samples was followed by polishing with 6 and $\frac{1}{4}$ μm diamond paste. Samples were etched with CP4 for chemical polishing and with Sirtl etch (CrO_3 , HF) for preferential grain boundary etching.

Heating.—The samples were heated either in resistance-heated furnaces with gas-tight alumina tubes or in rf-heated furnaces in a silica tube. For the recrystallization experiments with relatively short heating times an rf-heated furnace was used which was modified in such a way that highly stable temperatures and temperature gradients under reproducible conditions could be obtained ($\pm 10^\circ\text{C}$).

Recrystallization experiments were carried out by heating samples of different orientations and thicknesses varying from 20 μm to a few millimeters at temperatures in the range of $1100^\circ\text{--}1400^\circ\text{C}$ and heating times of a few seconds up to 48 hr. Samples were either CP4 or Sirtl-etched or unetched before recrystallization. As oxygen in air causes the samples to oxidize considerably at high temperatures heating was performed in a variety of protective atmospheres like ultrahigh purity argon, Ar with a few percent H_2 , Ar with 30 volume percent HCl, N_2 with 8% H_2 , pure N_2 , and pure H_2 .

To remove oxygen and water from these ambients a palladium de-oxo-catalyst and a 5A molecular sieve were used, respectively.

A number of experiments were carried out in vacuum of various pressures.

Results

Recrystallization structure.—Recrystallization at 1380°C during 3 hr of samples of material A parallel to the $\langle 110 \rangle$ growth direction with a 200 μm thickness yields oblong grains with an inhomogeneous grain size (Fig. 5).

Grain size in these samples varies from 0.02 to 2 mm in length and from 0.02 to 0.1 mm in diameter and increases only slightly with heating temperature in the range $1350^\circ\text{--}1400^\circ\text{C}$. The structure of the recrystallized material obviously depends on the structure of the starting material. The new grains are elongated in the original $\langle 110 \rangle$ growth direction and consequently most of the high angle grain boundaries lie in this direction. The resulting grain size is not influenced by the heating rate ($0.1^\circ\text{--}100^\circ\text{C}/\text{sec}^{-1}$), a strong temperature gradient ($500^\circ\text{C}/\text{mm}$ at 1300°C), or grinding and polishing of the samples before heating.

Examination of samples with various values of the angle ϕ leads to the conclusion that nucleation occurs at discrete sites and nuclei grow out to a primary matrix. The moment these growing primary grains impinge on each other no further grain growth occurs even after prolonged heating. This will be discussed in the section "Kinetics."

Texture-goniometer measurements of recrystallized samples with various values of ϕ revealed a sharp $\langle 111 \rangle$ fiber texture with free rotation around this axis. This $\langle 111 \rangle$ fiber axis is always parallel with the original $\langle 110 \rangle$ growth direction in the samples, independent of the value of ϕ . This means that when recrystallizing samples sawn from the bar in such a way

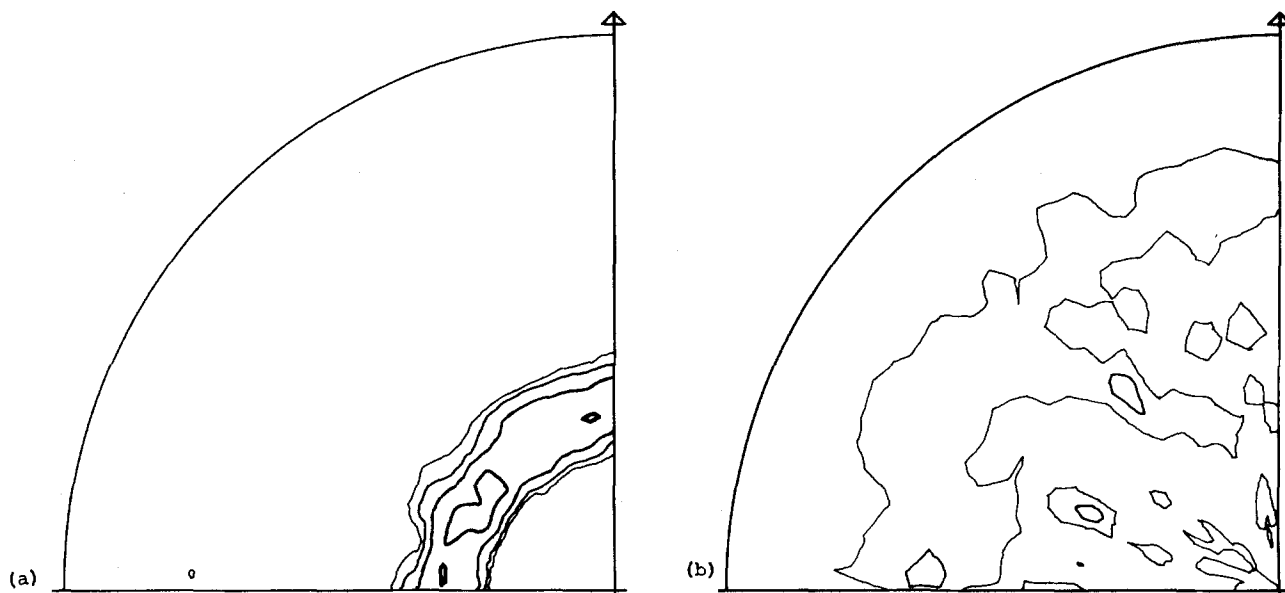


Fig. 3. Part of pole figures for $\{111\}$ reflections of CVD grown silicon grains of material A and B (a and b, respectively)

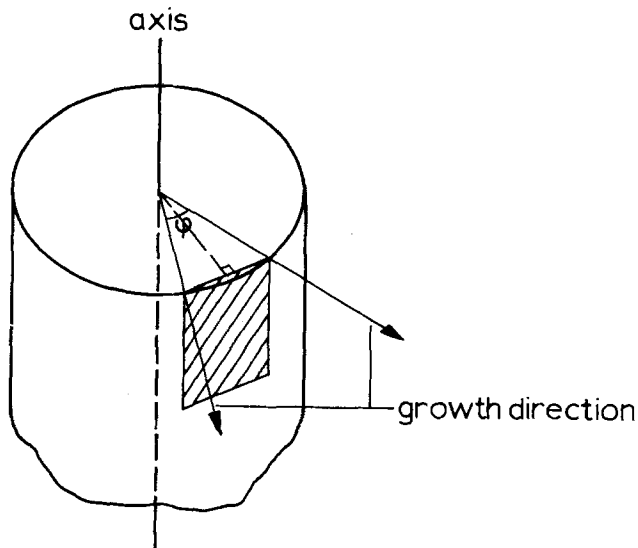


Fig. 4. Sample from a bar of polycrystalline silicon. The angle ϕ is a measure for the spread of the growth direction over the sample surface.

that the $\langle 110 \rangle$ growth direction is normal to the sample's surface we find that the newly formed grain boundaries lie also mainly normal to this surface but now the grains are $\langle 111 \rangle$ oriented.

The behavior of material B upon recrystallization is different compared to material A for the same experimental conditions. Nucleation occurs very readily in fine-grained regions whereas the tree-like coarse-grained regions keep their geometrical shape although they become coarser to some extent. This yields a fairly homogeneous matrix of grains of about $30 \mu\text{m}$ in diameter containing the coarser grained structures as mentioned (see Fig. 6). The same features are observed when using samples sawn in different orientations from the bar. As in the case of material A the grain size and structure cannot be influenced by a variation in heating temperature or very long heating. Texture-goniometer measurements show that recrystallized samples of material B are still randomly oriented.

The behavior upon recrystallization of material C is comparable to the case of material A. This is not

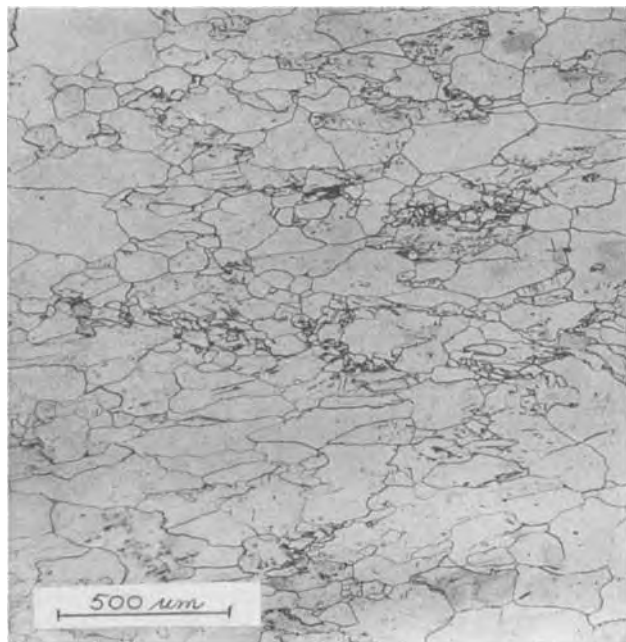


Fig. 5. Grains of material A after recrystallization at 1380°C during 3 hr. The sample is sawn parallel to the original $\langle 110 \rangle$ growth direction which is from left to right on the micrograph.



Fig. 6. Grains of material B after recrystallization at 1380°C during 3 hr. The sample is sawn parallel to the original growth direction which is from left to right on the micrograph.

surprising since structure and texture are very similar. Due to the texture the newly formed high-angle grain boundaries of material C lie mainly perpendicular to the surface of the substrate. Grain size of the samples varies from 50 to $100 \mu\text{m}$. When one does not remove the substrate and the SiO_2 interface layer before heating one finds a large number of stacking faults in the silicon crystals. This is probably caused by diffusion of oxygen out of the SiO_2 interface layer into the polysilicon layer.

Texture-goniometer measurements on a sample grown at 1100°C and subsequently recrystallized at 1380°C showed a sharp $\langle 322 \rangle$ fiber texture. To be sure that this is not only a surface texture, measurements were done again after removing $60 \mu\text{m}$ from the surface. The same amount of $\langle 322 \rangle$ fiber texture was found.

However, when we tried to recrystallize CVD-grown layers which were coarse-grained already (diameter $> 20 \mu\text{m}$) we found that these grains did not recrystallize so the original structure is unchanged.

Kinetics.—The degree of recrystallization $X(t)$ as a function of heating time at a constant temperature was measured for material A at various temperatures on samples of the kind depicted in Fig. 4, sawn very close to the edge of the bar. Series of samples were partly recrystallized in discrete steps and micrographs taken after every heating step were compared. Values of $X(t)$ were measured using the point-counting method. The results of these measurements for two different bars are shown in Fig. 7. $X(t)$ depends strongly on the grain structure of the different bars, as will be explained later.

The same series of micrographs were used to determine values for nucleation and growth rates. As an example three stages of the recrystallization process at 1313°C are shown in Fig. 8 after 45, 60, and 90 min of heating, respectively. New nuclei develop and existing grains grow out further upon prolonged heating. As one can see in Fig. 8(a) the grain size of the original material is very inhomogeneous. The higher the density of grain boundaries, the more readily nucleation will occur. For a more detailed description of the nucleation process in the samples we will split up the material into separate regions, namely fine-

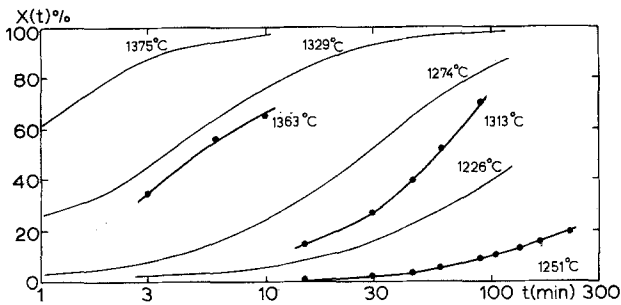


Fig. 7. Degree of transformation of CVD grown silicon material A as a function of time for various temperatures for two different bars of the kind of material A.

grained regions ($0.1-1 \mu\text{m}$) and coarse-grained regions consisting of clusters of larger crystals ($1-10 \mu\text{m}$) with rather straight grain boundaries. Because of the continuously changing grain size pattern this is somewhat arbitrary, but one can consider roughly $25 \pm 5\%$ of the total volume to be fine-grained and $75 \pm 5\%$ to be coarse-grained.

The nucleation rate in the samples was determined by counting the number of visible grains after the various steps of the isothermal process and correcting these data for the actually recrystallized part of a sample surface by multiplying them by $1/(1 - X(t))$. Results are shown in Fig. 9 where the number of nuclei is plotted as a function of heating time. The number of nuclei present at a given time is difficult to measure accurately because of the impossibility of recognizing nuclei before they have grown out. From the nucleation

rates at two temperatures (1251° and 1313°C , respectively) an activation energy can be calculated using the Arrhenius relation

$$N = N_0 \exp(-\epsilon/kT) \quad [1]$$

Results are summarized in Table I.

In the determination of growth rates the same distinction has to be made between fine-grained and coarse-grained regions. Moreover, growth in the coarse-grained regions differs in directions parallel to the straight grain boundaries (growth rate V_p , averaged over all grains) and normal to these boundaries (growth rate V_n , averaged over all grains) indicated in Fig. 8(a). All growth rates were determined at about 30 positions on a sample surface.

Growth rates were determined by measuring the displacement of newly formed high-angle boundaries into the unrecrystallized assembly after the various isothermal heating steps. Growth rates in the fine-grained regions were determined only during unimpeded growth of the new crystals. In Fig. 10 the growth rate V_f in the fine-grained regions averaged over all grains considered is plotted as a function of time elapsed after nucleation of each grain. Activation energies for primary recrystallization were determined from the time averages of V_f , V_n , and V_p (denoted by \overline{V}_f , \overline{V}_n , and \overline{V}_p , respectively). Values of \overline{V}_f , \overline{V}_n , and \overline{V}_p and the activation energies derived are listed in Table I. The estimated inaccuracy in the values for the activation energies amounts to $\pm 0.5 \text{ eV}$.

Discussion

Material A merely consists of strongly $\langle 110 \rangle$ textured clusters of closely spaced crystals parallel to the

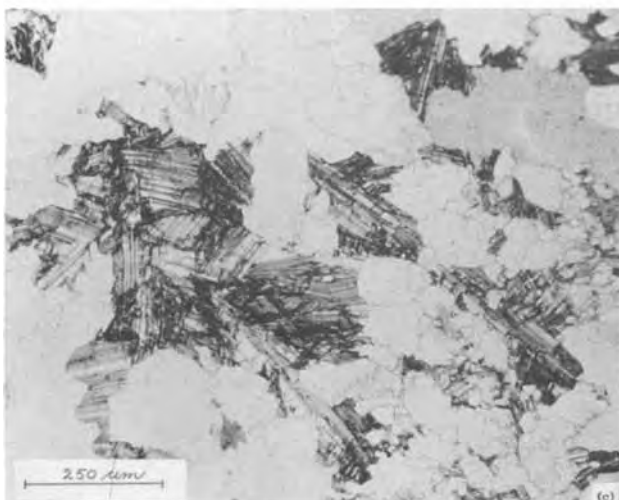
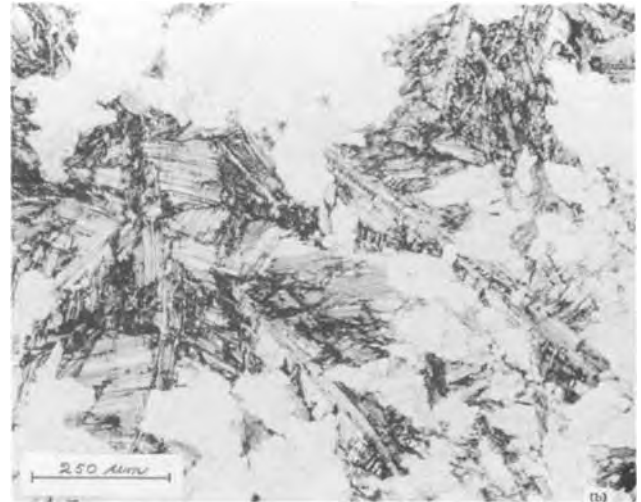
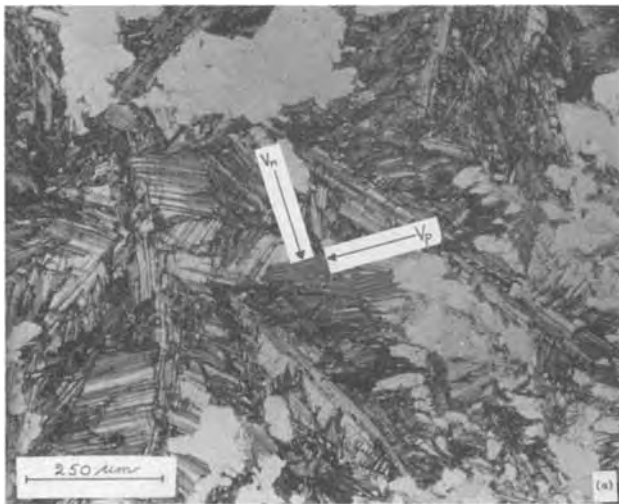


Fig. 8. Three stages of the recrystallization process of material A at 1313°C . Micrographs are taken after 45, 60, and 90 min of heating.

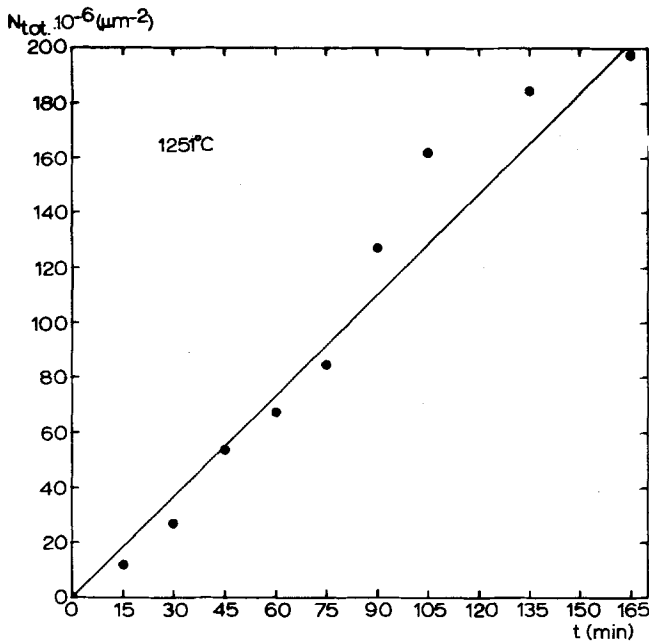


Fig. 9. Number of visible nuclei as a function of heating time at 1251°C.

growth direction. If the straight lines are closely spaced twin boundaries we would, however, expect a double texture. To explain the single <110> texture one must assume that if the lines are twin boundaries a crystal should return to its parent state immediately following the generation of a twin, so the percentage twin orientation is very small. Another possibility, suggested by Ravi (9) as an explanation for striation on EtG silicon ribbons, is to assume that the straight lines are stacking faults as a limiting case of twinning, with two extra planes of atoms between twinned regions in the case of extrinsic faults.

The recrystallization process of material A is rather complex. The main features can be summarized as follows.

1. The recrystallization process proceeds by development and subsequent growth of newly formed high-angle grain boundaries.

2. Nucleation occurs only in very fine-grained regions having a high density of grain boundaries. The higher the grain boundary density, the more readily nucleation occurs. Nucleation in coarse-grained regions does not occur.

3. Nuclei develop with a nucleation rate that is nearly constant for an isothermal process as indicated in Fig. 9 for 1251°C.

4. Nuclei grow out in the fine-grained regions until they impinge on each other or on coarse-grained material. The latter is consumed only to a small extent during the transformation of the fine-grained regions.

5. For most nuclei the rate at which they grow out in the course of the transformation process (after nucleation at $t = \tau$) is initially high but decreases

Table I

	1251°C	1313°C	Act. energy (eV)
Nucleation rate in fine-grained area ($\mu\text{m}^{-2} \text{min}^{-1}$)	1.2×10^{-6}	19.5×10^{-6}	9.4
\bar{V}_τ (fine-grained) ($\mu\text{m min}^{-1}$)	0.7	2.3	4.2
\bar{V}_n ($\mu\text{m min}^{-1}$)	0.07	0.45	6.5
\bar{V}_p ($\mu\text{m min}^{-1}$)	0.20	0.62	3.8

The activation energy for silicon volume self-diffusion is 5.0 eV (8).

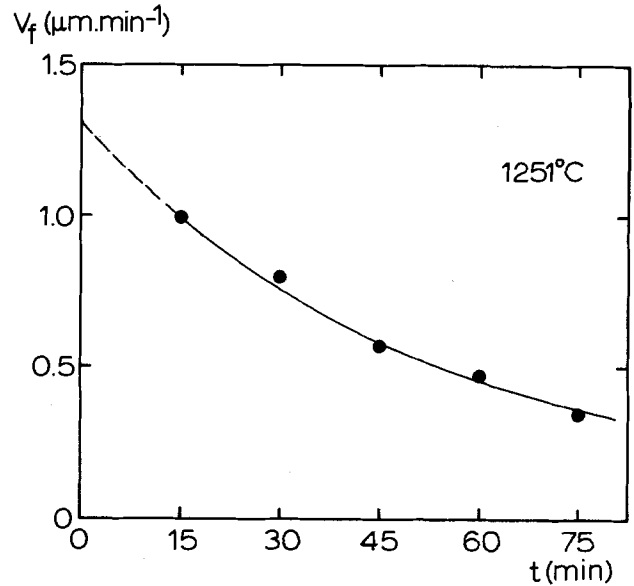


Fig. 10. Growth rate V_f of newly formed silicon grains as a function of time, averaged over all grains at 1251°C in fine-grained regions.

gradually with continuing growth of the new grain. Also the average value of the growth rate for all grains (V_f) is a decreasing function of the time after nucleation $t - \tau$ as illustrated in Fig. 10.

6. In the coarse-grained regions no nucleation takes place but they are consumed by the growing grains originating from the fine-grained regions. As mentioned before there are two distinguishable growth rates V_n and V_p in the coarse-grained material.

7. The primary assembly so obtained does not alter its structure even after prolonged heating. Apparently grain growth and/or secondary recrystallization does not occur.

Because of the different recrystallization behavior of the fine- and coarse-grained regions the overall degree of transformation as a function of time cannot be described by a simple Avrami-relation (10). For the fine-grained regions in which nucleation and growth of nuclei are defined accurately we can set up a model as derived from general kinetics of transformation processes (10). The average growth rate as a function of time at 1251°C as shown in Fig. 10 can be described empirically by

$$V_f = V_0 \exp(-(t - \tau)/t_0) \quad [2]$$

In this equation V_0 is the average value of the initial growth rate of nuclei ($V_0 = 0.02 \mu\text{m sec}^{-1}$) and t_0 is a relaxation time determined by the dragging forces for growth ($t_0 = 3 \cdot 10^3 \text{ sec}$).

All sample surfaces are normal to the <110> growth direction. As growth in this particular direction is much faster than normal to it (shown in Fig. 5) we can consider the degree of recrystallization of the bulk $X_f(t)$ to be equal to the fraction of the surface area recrystallized at time t .

The radius of the growing grains (r) obeys

$$r = V_f(t - \tau) \text{ for } t \geq \tau \text{ and} \quad [3]$$

$$X_f(t) = \int_0^t N \pi r^2 d\tau \quad [4]$$

in which N is the (constant) nucleation rate. Calculating $X_f(t)$ (Eq. [4]) and taking the impingement of grains on each other into account the degree of recrystallization of the fine-grained regions is found

$$X_f(t) = 1 - \exp[-\pi V_0^2 t_0^2 N \{t - 3t_0/2 + 2t_0 \exp(-t/t_0) - t_0/2 \exp(-2t/t_0)\}] \quad [5]$$

which in fact represents a modified Avrami-Johnson-Mehl equation (10).

To compute the contribution of $X_f(t)$ to the overall degree of recrystallization $X(t)$ the former must be multiplied by the fraction fine-grained material in the sample in which nucleation can occur. As mentioned before an approximate amount of $25 \pm 5\%$ of total volume is very fine-grained. At the time the coarse-grained material starts to be transformed, nucleation in fine-grained regions has occurred in $20 \pm 5\%$ of total volume. In Fig. 11 the calculated $X_f(t)$ is shown in graphical form for three different values for the fraction fine-grained regions bounding the range of calculated $X_f(t)$ values.

The reasonable agreement between experimental and calculated values for $X_f(t)$ confirms the proposed growth model for the fine-grained area.

The observed decrease in growth rate of the unimpeded-growth grains cannot be explained by a decrease in driving force as a consequence of the occurrence of recovery processes in the as yet untransformed matrix. Initially all grains grow out relatively fast when they develop in the course of the transformation process, but when the size of these new grains increases, growth rate decreases. The measured values of the growth rate at 1251°C decrease from 1 to $0.35 [\mu\text{m min}^{-1}]$ as shown in Fig. 10. This latter value approximates the average value of the growth rate \bar{V}_p ($0.2 [\mu\text{m min}^{-1}]$, see Table I) of the coarse-grained regions. Nucleation occurs in very fine-grained regions and new grains grow out in the surrounding matrix which has a larger grain size. This probably means that the growth rate is a function of the density of grain boundaries in the matrix, ranging from very fine- to very coarse-grained regions.

Another reason why grain growth decreases with time may be the segregation of impurities on newly formed grain boundaries which tends to decrease boundary mobility.

As nucleation and/or growth processes connected with the transformation of the coarse-grained regions are not accurately defined, the involved kinetics are difficult to describe quantitatively.

The observed $\langle 111 \rangle$ recrystallization fiber texture of material A is not a consequence of surface free-energy driving forces which in thin layers tend to bring lowest energy planes, in our case $\{111\}$ (11), at the sample's surface. In that case we would expect a $\langle 111 \rangle$ fiber axis normal to a sample's surface, whatever the orientation of the sample with respect to the original $\langle 110 \rangle$ growth direction. However, as mentioned earlier, in all cases the $\langle 111 \rangle$ direction is parallel to the $\langle 110 \rangle$ direction of the original grains even if the original $\langle 110 \rangle$ growth direction lies in the plane of specimen. Moreover, the $\langle 111 \rangle$ recrystallization texture also develops in the case of thick

samples (1.2 mm) and thin samples ($<100 \mu\text{m}$) even when applying very long heating times. Samples normal to the $\langle 110 \rangle$ growth direction consequently have mainly (111) planes exposed at the sample surface. This prohibits the occurrence of tertiary recrystallization where the driving force is caused by differences in surface free-energy of the crystallographic planes exposed at the sample-free surface.

Figure 7 shows that complete recrystallization of samples at temperatures above 1350°C occurs within 100 min time. The growing grains impinge on each other and growth ceases. There are several reasons why this primary assembly does not alter its structure any more during prolonged heating. In samples with grain size of the order of the sheet thickness boundary movement might have been impeded by preceding etching of the samples before heating by pinning boundaries at the sample free surface. This was not the case because both etched and unetched samples yield the same structure. Pinning of grain boundaries also may result by the occurrence of thermal etch grooves (12) which develop at high temperatures in all ambients used. However, this cannot be the main reason for growth inhibition as also grain boundaries in the bulk of the recrystallized silicon do not migrate. The third possibility is that growth ceases because of the sample thickness (specimen thickness effect) which implies that grains can grow in two directions only when the size is of the order of the sheet thickness. This does not apply to our case as thick samples (1.2 mm) yield the same structure. A fourth possibility lies in the pinning of moving boundaries by segregated particles on grain boundaries after the stage of primary recrystallization (13). Although infrared absorption measurements show that the oxygen content in the starting materials is very low (less than 2 ppm) and does not change upon recrystallization, there might be an increase in content of other impurities due to contamination during the heat-treatment.

Conclusions

1. CVD grown polycrystalline silicon grains (1-10 μm) can be recrystallized (final grain size 20-200 μm) by heating at temperatures above 1200°C .
2. Nucleation readily starts in regions with a high grain boundary concentration (grain size 0.1-1 μm). These nuclei grow out until they impinge on each other and further growth is inhibited. A randomly oriented starting material yields a randomly oriented recrystallized matrix as, e.g., our material B. In the case of $\langle 110 \rangle$ fiber textured material however, as our materials A and C we find a sharp $\langle 111 \rangle$ resp. $\langle 322 \rangle$ fiber texture after recrystallization.
3. The recrystallization behavior can be described approximately by an Avrami-Johnson-Mehl type relation using a constant nucleation rate. The resulting grain size for material A is 20-100 μm for samples normal to the $\langle 111 \rangle$ recrystallization fiber texture axis. This final grain size is not influenced by prolonged heating, heating rate ($0.1^\circ\text{C}/\text{sec}$), a temperature gradient, or by different ambients.
4. The recrystallized grains are elongated in the original $\langle 110 \rangle$ growth direction since the mobility of the interface between recrystallized and unrecrystallized material is highest in this direction.
5. In originally $\langle 110 \rangle$ textured material no tertiary recrystallization induced by differences in surface free-energy of exposed planes occurs due to the strong recrystallization texture.

Acknowledgments

The authors are very indebted to Eindhoven University of Technology (Lab. for Physical Chemistry, particularly Dr. J. Maas and co-workers), Delft University of Technology (Lab. for Metallurgy), and Twente University of Technology (Metallurgy Department, Mr. H. Heller and co-workers) for co-

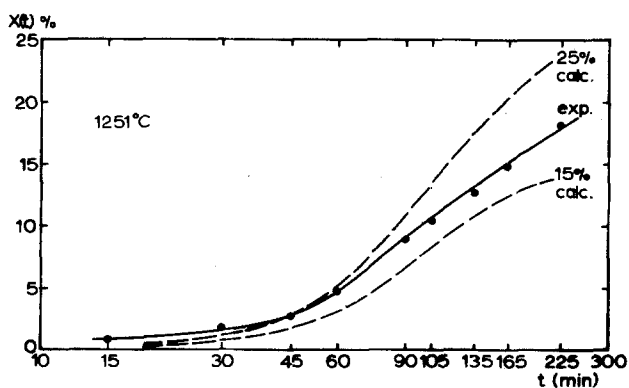


Fig. 11. Calculated values for $X(t)$ for two values of the percentage fine-grained area in comparison with the experimentally determined $X(t)$ curve for 1251°C .

operation in x-ray measurements. Dr. J. W. Drijver of State University of Utrecht (Technical Physics Department) is thanked for valuable discussions. Mr. E. Smit of Delft University of Technology (Dept. for Electrical Engineering) is thanked for supplying some CVD specimens.

This work was financially supported by the Directorate-General for Research, Science and Education of the European Communities under Contract No. 444-78-4 ESN.

Manuscript submitted March 26, 1979; revised manuscript received Sept. 11, 1979.

Any discussion of this paper will appear in a Discussion Section to be published in the December 1980 JOURNAL. All discussions for the December 1980 Discussion Section should be submitted by Aug. 1, 1980.

Publication costs of this article were assisted by State University Utrecht.

REFERENCE

1. H. Fischer, in "Proc. Int. Photovoltaic Conf.," p. 52, Luxemburg, (1977).

2. C. Daey Ouwens and H. Heijligers, *Appl. Phys. Lett.*, **26**, 569 (1975).
3. W. J. H. Schins, J. Bezemer, C. Daey Ouwens, and S. Radelaar, in "Proc. Int. Photovoltaic Conf.," p. 52, Luxemburg (1977).
4. B. D. Cullity, "Elements of X-ray Diffraction," Add. Wesley Series in Metall. and Mat. (1959).
5. B. Pratt, S. Kulkarni, D. P. Pope, and C. D. Graham, Jr., *This Journal*, **123**, 1760 (1976).
6. P. Rai-Choudhury and P. L. Hower, *ibid.*, **120**, 1761 (1973).
7. T. I. Kamins and T. R. Cass, *Thin Solid Films*, **16**, 147 (1973).
8. B. J. Masters and J. M. Fairfield, *Appl. Phys. Lett.*, **8**, 280 (1966).
9. K. V. Ravi, *J. Cryst. Growth*, **39**, 1 (1977).
10. J. W. Christian, "The Theory of Transformations in Metals and Alloys," Part I, Pergamon Press (1975).
11. R. J. Jaccodine, *This Journal*, **110**, 524 (1963).
12. W. W. Mullins, *Acta Metall.*, **6**, 414 (1958).
13. F. Haessner, "Recrystallization of Metallic Materials," Papers presented at a seminar of the Institut für Metallkunde of the University of Stuttgart and the Max Planck Institut für Metallforschung (1970).

Characterization of Cobalt-Hardened Gold Electrodeposits by Mössbauer Spectroscopy

II. Production of Co Metal Precipitates

R. L. Cohen, F. B. Koch,* L. N. Schoenberg,* and K. W. West

Bell Laboratories, Murray Hill, New Jersey 07974

ABSTRACT

Annealing of cobalt-hardened gold electrodeposits at 400°C and above leads to the formation of microprecipitates of cobalt metal clearly identified from their hyperfine structure. This finding removes the conflict between a previous study, which has claimed to observe precipitated cobalt, and our previous work, which shows that in unannealed deposits, most of the cobalt is a substitutional solute in the gold. The solubility of cobalt in gold has been redetermined, confirming the earlier results. A number of interesting properties of extremely fine cobalt precipitates in gold are observed and analyzed.

A previous paper (1) (henceforth referred to as "I") reported on the atomic-level structure of cobalt-hardened gold electrodeposits as observed by Mössbauer spectroscopy with particular attention to the coordination of the cobalt atoms. Most of the cobalt (~70%) was found to be dissolved substitutionally in the gold host with the remainder complexed as a hexacyanocobaltate. This result was in reasonable agreement with another recently published analysis (2). However, there are three reports in the literature claiming that cobalt microprecipitates are found, either in the as-deposited material (3), or after heat-treatment (4, 5). Since this issue is important in defining the relation between the microstructure and possible hardening mechanisms, we have carried out further experiments to study this point.

The Mössbauer spectroscopy technique is very useful for this type of measurement, because (i) it is very effective for examining the early stages of clustering and precipitation and (ii) the spectrum of magnetically ordered cobalt metal is distinctive allowing immediate identification of that phase. An additional advantage of the Mössbauer spectroscopy approach in this case is that the phenomenon of superparamagnetism allows

us to distinguish between small and large cobalt precipitates. When a particle of cobalt is so small that its magnetic anisotropy energy is comparable to thermal excitation energies, the magnetization direction of the particle fluctuates rapidly and tends to average out the magnetic splitting so that only a single line is observed for very small (<~60Å) precipitates. This effect is clearly seen in the data, and allows us to observe and distinguish early-stage precipitates of cobalt.

Experimental Techniques

Samples of cobalt-hardened gold doped with radioactive Co⁵⁷ were electrodeposited as described in I. The deposited layer was approximately 2.5 μm (100 μin.) thick, plated from a CI¹ solution adjusted to give a cobalt concentration of 0.67 atomic percent (a/o) in the deposit. The substrate was removed by dissolving it in nitric acid, leaving the thin gold foil as a self-supporting layer. This foil was held between graphite disks and annealed in a hydrogen atmosphere to provide the heat-treatments discussed below. Between anneals, the samples were measured either at room temperature or 78°K by the Mössbauer spectrometer described in I.

* Electrochemical Society Active Member.

Key words: superparamagnetism, microprecipitates, Au-Co alloys.

¹CI is a proprietary hard gold solution supplied by Sel-Rex Corporation, a division of Oxymetal Industries.

Table I. Anneal schedule for samples studied in this experiment, and fraction of dissolved cobalt and absolute cobalt solubility determined by least squares fits to the Mössbauer spectra

Anneal No.	Temp. (°C)	Time hot (hr)	Cool down	Fraction of cobalt dissolved	Solubility of Co in Au (a/o)
1	740 625	1.5 38	11.5°C/min to 625°C 0.145°C/min to 270°C 3°C/min to RT	0.72	0.48
2	460	23	45°C/min to 160°C 5°C/min to RT	0.57	0.38
3	511	24	5°C/min to RT	0.87	0.58
4	460	72	5°C/min to RT	0.63	0.42
5	400	22.5	5°C/min to RT	0.46	0.31
6	400	68	5°C/min to RT	0.44	0.30
7	360	71	5°C/min to RT	0.43	0.29
8	360	140	5°C/min to RT	0.30	0.20*

* Upper limit value—equilibrium not demonstrated.

Table I shows the anneal schedule used. Spectra taken at various points in the anneal cycle are shown in Fig. 1 with least-squares fits to the data (see I for a fuller description of the techniques involved).

Results

For the materials scientist concerned with the properties and microstructure of cobalt-hardened gold, the significant results can be directly seen in the sequence of spectra in Fig. 1. Figure 1A shows that there are no cobalt precipitates in the as-deposited layer, Fig. 1B shows that all the cobalt has been put into solid solution in a CI deposit which has been heated to 800°C and rapidly cooled (12°/min), and Fig. 1C shows that after heating and slow cooling through 400°C, cobalt metal precipitates out of the gold-cobalt alloy. After the 800° anneal, the deposit is essentially equivalent to an alloy made by standard metallurgical processes. The complex spectra obtained after annealing at <600°C show a number of interesting physical and metallurgical phenomena, and we have carried out a complete analysis of the data to understand all of these effects, although they have no direct bearing on the properties of CI gold in the as-deposited state. Some of these effects may be significant if the deposit is subjected to high temperatures either in manufacture or service.

The spectra shown in Fig. 1 can be shown to come from cobalt in three environments: Co⁵⁷ substitutional in the gold matrix, small (<60Å) superparamagnetic precipitates of fcc cobalt metal, and larger precipitates of fcc Co metal, which produce the split 6 line spectrum. The detailed identification of these species is given below. Although there is considerable overlap between some of the spectral components, the use of constrained least squares fitting routines (6, 7) allows accurate evaluation of the relative intensities under the spectra of the three phases. We do not believe that Co₂C or Co₃C are present in these samples. Although the spectra of these carbides have not been measured, we would expect the hyperfine (HF) fields to be similar to those observed for iron in the analogous Fe₂C and Fe₃C, 160-200 kG. No components of the spectrum with splittings corresponding to HF field values in this range were observed.

At 78°K, the iron recoil-free-fraction, f , is about 0.90 for the cobalt host (8) and 0.84 for the gold host (9). Since the recoil-free fractions are essentially the same, the Mössbauer spectrum area from each phase is proportional to the presence of that phase in the sample. Thus, the relative area corresponding to each spectrum can be used to determine directly the fractions of dissolved and coarse and fine precipitated cobalt. Since the total cobalt concentration is known (1) to be 0.67 a/o, the solubility of cobalt in gold can be determined by dividing the 0.67% among the dissolved and precipitated phases. The new results from these studies are shown in Table I and Fig. 2 superimposed on the previously published phase dia-

gram (10, 11). Considering the difficulties of determining equilibrium solubilities in dilute alloys at low temperatures, the agreement between our result and the earlier results is very good.

As stated in I, the isomer shift of the line arising from the dissolved cobalt, -0.68 mm/sec (*vs.* iron metal at 78°K), is consistent with that obtained for metallurgically prepared material. The isomer shift for the split spectrum of cobalt precipitates is ~ -0.06 mm/sec, essentially the same as that observed by Krop and Williams (12, 13) for fcc cobalt precipitated from cobalt-copper alloy, for precipitates larger than 10^{-17} cm³. The unsplit (superparamagnetic) line appears in our spectra at ~ -0.14 mm/sec, close to the value -0.10 mm/sec observed by Krop and Williams (13) for small precipitates of cobalt in copper. The difference between the values for small and large precipitates has been attributed (13) to the coherency of the small precipitates with the host, which places them under dilational stress. This stress increases the lattice constant, and alters the isomer shift slightly.

Linewidths, ~ 0.33 mm/sec full width at half maximum (FWHM) for the dissolved-phase cobalt and ~ 0.4 - 0.5 mm/sec for the superparamagnetic small cobalt precipitates, are consistent with what would be expected for these phases. The observed HF field, 308 kG at 78°K, is significantly smaller than that of either iron in hcp cobalt, 323 kG (7), or iron in fcc cobalt, 334 kG (14) at the same temperature. Thus, the value of the HF field does not tell us which cobalt phase has precipitated. We believe that the precipitate phase is fcc for all annealing temperatures including 360°C. There is some question about this one temperature since the fcc to hcp transformation takes place at about 400°C for pure Co. However, the transformation temperature is depressed by about 50°C for each a/o of gold in solid solution (11). As will be discussed subsequently, it is likely that there is more than enough Au in the Co precipitates to lower the transition temperature 40°C. Another study (16) on the precipitation of cobalt from gold at 202°C also concluded that the precipitates were fcc, on the basis that no x-ray diffraction lines from hcp cobalt were observed.

For the cobalt precipitates after anneal No. 8, the temperature dependence of the HF field is $H(300)/H(78) = 0.96$. For bulk cobalt, $H(300)/H(78) = 0.98$ (7). Thus, both the absolute size and the temperature dependence of the HF field are different from bulk values. These differences arise from two causes, and give us further information on the properties of these fine precipitates.

Mørup and Topsøe (17) have recently shown that there is a temperature dependent reduction in the effective HF field for fine particles, $H = H(\text{bulk}) (1 - kT/2\kappa V)$, for $kT \ll \kappa V$, where κ is related to the magnetic anisotropy constant for the magnetic microcrystals and V is the particle volume. We observe that the HF field decrease with temperature

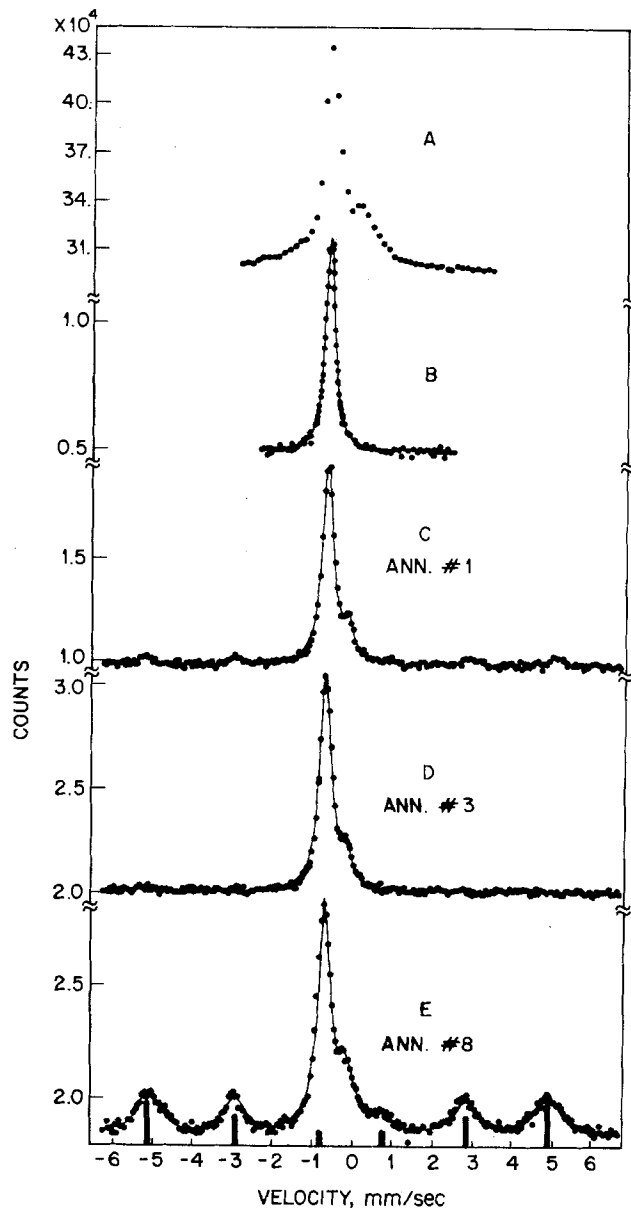


Fig. 1. Mössbauer spectra of cobalt-hardened gold deposit at 78°K after various heat-treatments. A, as deposited; B, after high-temperature treatment in hydrogen and rapid cooling; C-E, as shown in Table I. The line at -0.68 mm/sec comes from cobalt substitutional in gold, the line at -0.14 mm/sec from very fine ($<60\text{\AA}$) superparamagnetic precipitates of fcc cobalt, and the 6 line split spectrum from fcc cobalt precipitates $>60\text{\AA}$, which show the magnetic hyperfine (HF) splitting. The solid lines are constrained least squares fits of Lorentzian lines to the data points. Line positions and relative intensities for the magnetically split spectrum are shown at the bottom. The shoulder near zero velocity in the as-plated sample is at 0.14 mm/sec [see Ref. (1)], distinctly displaced from the line at -0.14 mm/sec from the superparamagnetic precipitates. This shoulder is believed to arise from $\text{Co}(\text{CN})_6^{3-}$ inclusions in the deposit [see Ref. (1)] and these inclusions decompose in the high temperature anneal.

is 2% larger for the cobalt precipitates than for bulk cobalt over the range from 78° to 300°K. If we consider that decrease to arise from the term $kT/2\kappa V$, we can calculate the mean effective size of the precipitates producing the split spectrum. If we approximate κ by $|K_1|$, and use $K_1 = -1.1 \times 10^6$ erg cm^{-3} (18), we find an effective particle volume of 0.63×10^{-18} cm^3 , or cubic particles about 90\AA on a side. This is similar to the particle size studied by Krop and Williams (12).

The overall loss in HF field, from the 334 kG expected at 78°K for fcc cobalt to the 308 kG we observe,

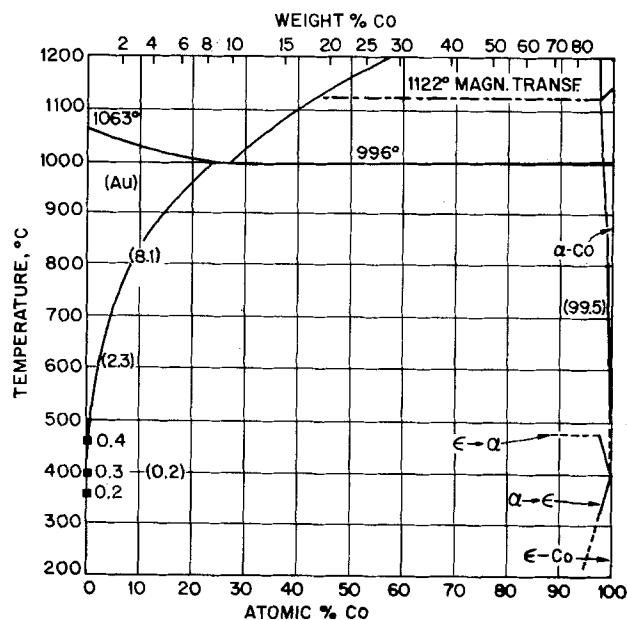


Fig. 2. Phase diagram of the gold-cobalt system, from Ref. (10), with new solubility values determined for cobalt in gold from this work. Previous solubility values are in parentheses. Agreement with the older values is good, especially in view of the difficulties of determining equilibrium solubilities at low temperatures.

however, obviously comes from another cause since at 78°K the term discussed above is negligible. We believe this decrease is due to the fact that the cobalt microcrystals contain a significant amount (e.g., a few percent) of dissolved gold. The presence of this nonmagnetic alloying constituent would decrease the HF field observed at both 78° and 300°K. In the work of Krop and Williams (12), a similar decrease (to 320 kG at 300°K) was observed, but not commented on. The presence of a few percent of gold in the fcc cobalt crystals would also explain the large line widths (FWHM 0.6-0.7 mm/sec) and deviations from Lorentzian line shapes observable in Fig. 1E. The variation of line shapes and effective widths among the different split lines is also characteristic of spectra of dilute alloys. The random alloy statistics provide a range of environments, and the relationship of isomer shift, quadrupole coupling and HF field affects the individual lines differently, producing a different variation of line position for each line in the spectrum. This variation leads to complex line shapes, typically different for each line.

The phase diagram both supports and contests our inference that the cobalt crystallites contain a significant amount of gold. According to Köster and Horn (11), only ~ 0.5 a/o of gold is soluble in cobalt below $\sim 500^\circ\text{C}$. This amount of gold would be too small to produce the effects we observe. However, they show that the fcc \rightarrow hcp transition is depressed by the alloying of the Co with up to 8 a/o of Au. Moreover, this supersaturated solid solution approaches equilibrium very slowly [Ref. (11) cites a heat-treatment of 24 hr at 700°C as being insufficient to fully achieve the equilibrium concentration of Au]. This metastable equilibrium would allow our conclusion that the reduced HF field and large line widths arise from a few percent of gold included in the cobalt microcrystals.

Discussion

The Mössbauer spectra in Fig. 1 show clearly that no cobalt metal precipitates are present in as-deposited or annealed and quenched samples of CI cobalt-hardened gold electrodeposited layers. Thus, hardening by cobalt precipitates is not an operative mechanism in providing the observed hardness. This

contradicts the claim of Ref. (3). The Mössbauer spectra also show, however, that after heating and slow cooling through $\sim 400^\circ\text{C}$, magnetic cobalt precipitates do form. This explains the conclusions of Ref. (5), which reported magnetic properties in slowly cooled CI samples. [The cooling rate used in anneal 1 was chosen to approximate the conditions of Ref. (5) so the spectrum Fig. 1C should correspond to their sample.] The effects of long anneals at 300°C and below without an earlier high-temperature anneal, are different from the results presented here, and will be presented in a later paper. After the 800°C heat-treatment, the light impurities (H, O, C, N) should no longer be present, and the sample should be equivalent to a metallurgically prepared alloy of 0.67 a/o Co in gold. Effects observed in the subsequent anneals are thus characteristic of annealing and precipitation phenomena in metallurgical gold-cobalt alloys.

The results observed here parallel those obtained by Krop and Williams for the precipitation of cobalt crystals from dilute copper (12, 13). The precipitation of small superparamagnetic crystals and larger magnetically ordered crystals, and the retention of dissolved-phase cobalt in gold are evident from the data. In fact, our data are much more successful in resolving the line from the dissolved cobalt from that of the superparamagnetic precipitates than the data of Ref. (13). The improvement in resolution occurs because of the sharper linewidths obtained here, and the isomer shift difference between cobalt in gold and cobalt in copper. In the copper-cobalt system, the dissolved-phase line cannot be distinguished from that of the superparamagnetic precipitates, whereas it is clearly resolved in our spectra.

In addition to the effects already reported by Krop and Williams for these fine precipitates of cobalt, we have observed the superparamagnetic reduction of the HF field (17) and also determined that there is significant dissolved gold in the cobalt precipitates. We believe this to be the first report of the superparamagnetic reduction of HF field in a metallic system.

Acknowledgments

We thank S. Voris for enthusiastic help with the radiochemical procedures, and R. Sard for encouragement and advice during the research.

Manuscript submitted June 11, 1979; revised manuscript received Sept. 24, 1979.

Any discussion of this paper will appear in a Discussion Section to be published in the December 1980 JOURNAL. All discussions for the December 1980 Discussion Section should be submitted by Aug. 1, 1980.

Publication costs of this article were assisted by Bell Laboratories.

REFERENCES

1. R. L. Cohen, F. B. Koch, L. N. Schoenberg, and K. W. West, *This Journal*, **126**, 1608 (1979).
2. H. Leidheiser, Jr., A. Vértés, M. L. Varsányi, and Czako-Nagy, *ibid.*, **126**, 391 (1979).
3. E. C. Darby and S. J. Harris, *Bull. Inst. Metal Finishing*, **53** (1975).
4. A. F. Mohrnhelm, *This Journal*, **117**, 833 (1970).
5. Ch. J. Raub, H. R. Khan, and J. Lendvay, *Gold Bull.*, **9**, 123 (1976).
6. Lorentzian line shapes were used with the 6 lines of the magnetically split spectrum constrained to have the same widths, intensity ratios close to 3:2:1:1:2:3, and relative positions determined from the magnetic moment ratio (Ref. 7) $\mu_e/\mu_g = 1.7135$.
7. G. J. Perlow, C. E. Johnson, and W. Marshall, *Phys. Rev.* **140A**, 875 (1965).
8. Estimated from the value measured at room temperature in nickel, D. G. Howard and J. G. Dash, *J. Appl. Phys.*, **38**, 991 (1967).
9. W. A. Steyert and R. D. Taylor, *Phys. Rev.*, **134A**, 716 (1964).
10. M. Hansen, "Constitution of Binary Alloys," 2nd ed., p. 196, McGraw-Hill, New York (1958).
11. W. Köster and E. Horn, *Z. Metallkund.*, **43**, 333 (1952).
12. K. Krop and J. M. Williams, *J. Phys. F*, **1**, 938 (1971).
13. K. Krop and J. M. Williams, *ibid.*, **3**, 1261 (1973).
14. Results of C. E. Johnson, M. S. Ridout, and T. E. Cranshaw, *Proc. Phys. Soc.*, **81**, 1079 (1963), extrapolated to 100% cobalt and 78°K .
15. J. Crangle, *Phil. Mag. Ser. 7*, **46**, 499 (1955).
16. R. M. Asimow, *Trans. Met. Soc. AIME*, **233**, 401 (1965).
17. S. Mørup and H. Topsøe, *Appl. Phys.*, **11**, 63 (1976).
18. C. P. Bean and J. D. Livingston, *J. Appl. Phys. (Suppl)*, **30**, 120 (1959).

Technical Notes



Rectifying and Ohmic Contacts to GaInAsP

D. V. Morgan,¹ J. Frey, and W. J. Devlin

School of Electrical Engineering, Cornell University, Ithaca, New York 14853

The high value predicted for the electron mobility in the quaternary alloy GaInAsP lattice-matched to InP (1) may make this material valuable for the fabrication of high frequency transistors and integrated optical switching circuits. Two important technological ingredients required for such fabrication are the ability

to fabricate good quality ohmic and rectifying contacts to the material. In this letter we report on some preliminary results on both these problems, and suggest a possible technology for these contacts which overcomes problems associated with the low intrinsic Schottky barrier height inherent in the material.

The material used for the present study was LPE n-type GaInAsP layers ($N_D \approx 10^{16}/\text{cm}^3$) grown lattice-matched to a semi-insulating InP substrate. The band-

¹ On leave from the Department of Electrical and Electronic Engineering, the University of Leeds, England.

Key words: contacts, resistivity, diodes.

gap of the layers ranged from 0.99 to 1.1 eV. Metal contacts were deposited by evaporation in a vacuum of $\sim 2 \times 10^{-6}$ Torr using either resistance heating or electron beam heating.

Ohmic Contacts

For the ohmic contacts a eutectic alloy of gold/germanium (88:12) was chosen, partly because of its previous success on III-V compounds (2) and partly to allow direct comparison of the present results with these earlier results. Specific contact resistances were determined by the transmission line method (3). The pattern of contact pads was defined by photolithography and consisted of a series of $100 \times 300 \mu\text{m}$ pads where the spacing between successive pads increased from 8 to $90 \mu\text{m}$. For this system, a plot of resistance vs. gap length produces a straight line whose extrapolation to zero resistance may be analyzed to yield a value of ρ_c , the specific contact resistance. Samples were annealed at temperatures ranging from 380° to 550°C for 20 sec in flowing hydrogen gas. Prior to annealing, the contact's electrical characteristic corresponded to that of a leaky Schottky diode with a reverse leakage of approximately $50\text{-}80 \mu\text{A}$. After annealing the specific contact resistance fell, decreasing to a broad minimum for alloying temperatures in the range $425^\circ\text{-}510^\circ\text{C}$ (Fig. 1). The minimum measured value of ρ_c is about $3.5 \times 10^{-7} \Omega\text{-cm}^2$, considerably lower than the corresponding value of $10^{-6} \Omega$ generally observed in GaAs. This low resistance is partially a reflection of the lower intrinsic barrier heights observed in the quaternary compound (0.4 compared to 0.85 eV in GaAs).

Rectifying Contacts

Gold was chosen as a rectifying contact material to allow comparison with previous studies on other III-V compounds. Samples were degreased and etched lightly in a mixture of 1% bromine in methanol. Ohmic contacts were made as described above to one-half of the samples, using Au/Ge and alloying at 450°C for 20 sec. An array of gold Schottky pads ($\approx 160 \mu\text{m}$ diam) was evaporated onto the remaining half of the slice.

Figure 2 shows semilogarithmic I-V plots for these diodes indicating the typical results and spread in characteristics obtained. From the value of current density, J_s , obtained from this data, a value of effective barrier height may be estimated using the relationship

$$\phi_{bn} = (kT/q) \ln[A^*T^2/J_s] \quad [1]$$

where A^* is the effective Richardson constant and T the absolute temperature.

This estimate yields $\phi_{bn} = 0.39 \pm 0.015$ eV, the uncertainty being related to the spread in J_s values. These characteristics show good rectification with ideality factors, n , near unity. The barrier height obtained from the C-V characteristic yields a value of 0.4 eV which is consistent with the above value. The reverse charac-

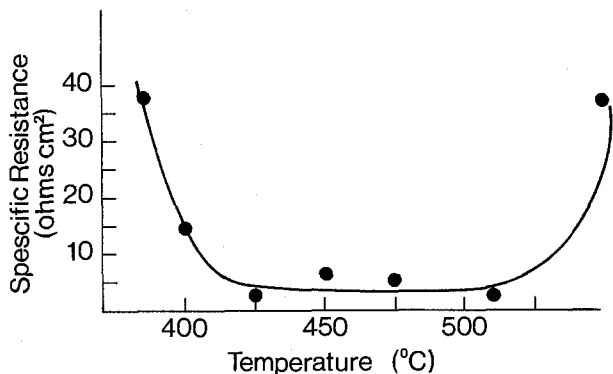


Fig. 1. Specific contact resistance ρ_c of Au/Ge alloyed contacts to GaInAsP as a function of alloying temperature. The broad minimum is at a value of $\rho_c = 3.5 \times 10^{-7} \Omega\text{-cm}^2$.

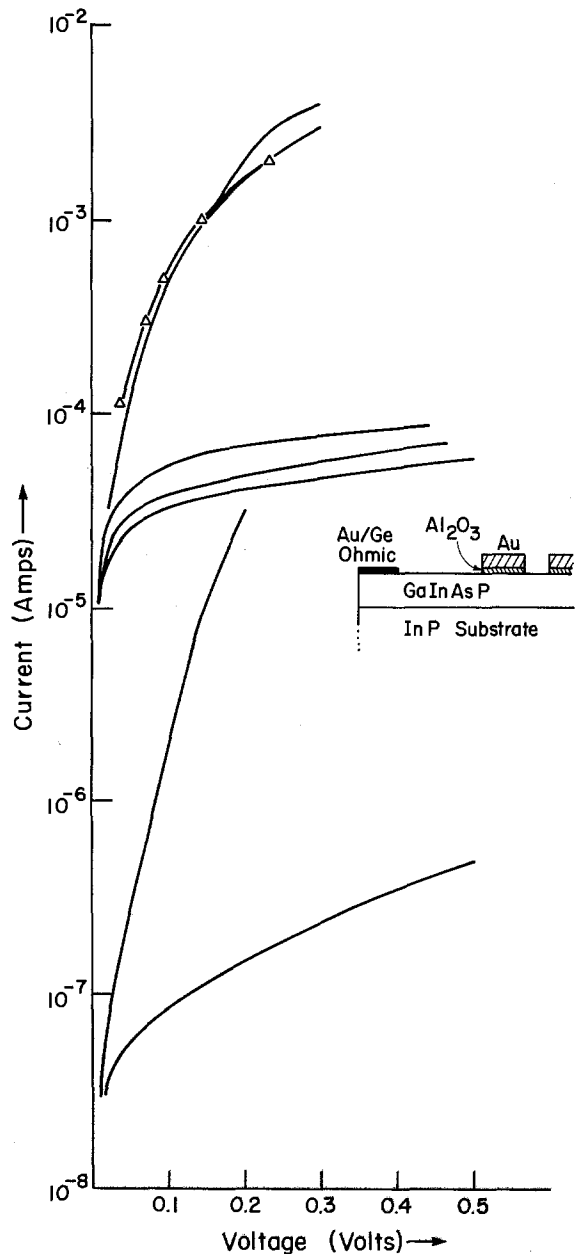


Fig. 2 (a). Forward and reverse current-voltage characteristics for Au-GaInAsP diodes. The top curves correspond to a direct Au contact and the lower set of curves corresponds to the situation where an aluminum oxide layer 7 nm thick is positioned between the metal and semiconductor.

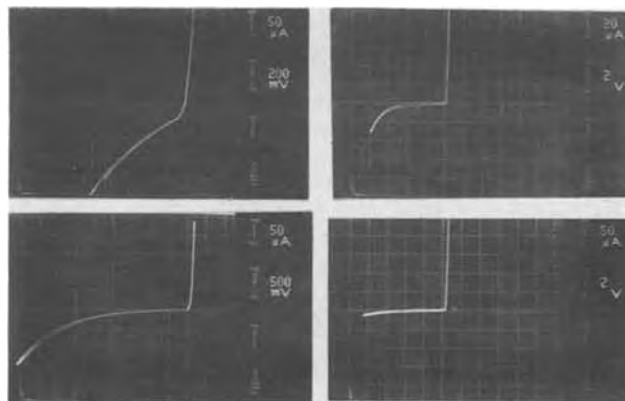


Fig. 2 (b)-(e). A series of I-V curves for (b) a direct gold contact; (c) a direct gold contact after heating in air for 24 hr at 160°C ; (d) an Au/aluminum oxide/semiconductor contact; (e) an Au/SiO₂/semiconductor contact.

teristics are quite soft (see inset in Fig. 2) with breakdown values which range from 2 to 4V. Absence of guard rings and mesa etching of these test devices certainly contribute to the soft characteristics.

In the results described above, all the samples were cleaned and etched immediately prior to loading into the vacuum system for the deposition of the gold contacts. Considerable, but unpredictable, reduction in the reverse leakage could be achieved by subjecting the diodes to heating in air at 160°C for up to 24 hr. This procedure reduces the reverse leakage in some cases from $\approx 40 \mu\text{A}$ to typically (1-10) μA at 0.1V (i.e., $\phi_{\text{bn}} \approx 0.46 \text{ eV}$), and the reverse breakdown voltage increases. This improvement may be a result of the migration of oxygen through the gold film to stabilize the interfacial oxide film. Because electrons are required to tunnel through this interfacial film, transport across the junction is made more difficult (4). One could exploit this phenomenon by fabricating a metal-insulator-semiconductor structure in which a controlled thin insulating film is placed at the interface (5). If the oxide thickness is $< 10 \text{ nm}$, the metal will be in equilibrium with the semiconductor surface, and the contact should exhibit the characteristics of a Schottky barrier with an increased effective barrier height, giving a reduced reverse saturation leakage as defined in Eq. [1]. Although this procedure has been shown to work for a range of semiconductors including InP and the ternary compound GaInAs (5), it is difficult to fabricate a thin insulating film with the required electrical and structural properties. Once again, therefore, the lack of a serviceable natural oxide on the III-V compounds seems a severe handicap in the technology of these materials.

In this paper, we shall consider procedures for fabricating the insulating dielectric which is compatible with FET technology. These are: (i) the oxidation of a thin Al film to produce aluminum oxide; (ii) the oxidation of a thin magnesium film to produce magnesium oxide; and (iii) low temperature ($\sim 80^\circ\text{C}$) plasma deposition of a thin silicon dioxide layer. Aluminum oxide is formed by depositing a thin aluminum layer at the interface and subsequently oxidizing it by heating in air at temperatures up to 250°C for up to 24 hr. In an attempt to achieve a uniform layer 5-10 nm thick and free of pinhole defects, the Al was deposited by electron beam evaporation. A deposition rate of 12 nm/min resulted in a controllable process with reasonable uniformity. Again, a gold contact was deposited over the Al_2O_3 layer. In Fig. 2, we show the current voltage curve corresponding to a typical diode with an oxide thickness $70 \pm 20 \text{ nm}$. The improvement in leakage is dramatic with the reverse saturation current, I_s , falling by three orders of magnitude to $\approx 4 \times 10^{-8} \text{ A}$, and yielding an effective barrier height, $\phi_{\text{bn}} \approx 0.57 \text{ eV}$. The existence of the thin oxide does not alter the n value appreciably ($n \approx 1.04$), and the overall reverse characteristics of the diodes are seen to have improved appreciably. The reverse characteristic is much improved, with breakdown voltages of the order of 8V being typical.

A typical capacitance voltage curve for an aluminum oxide device is shown in Fig. 3. Due to the capacitance associated with the oxide, a plot of $(1/C^2)$ vs. V cannot be used to obtain meaningful values of barrier height (5). The sequence of curves shown in Fig. 3 indicates that these devices exhibit a capacitive hysteresis effect as the devices are voltage-ramped into reverse bias, probably because of deep levels in the oxide. This hysteresis would be very undesirable if these contacts were used in FET applications; or if such oxide layers were used to increase the barrier height for DLTS or TSC studies, as the peaks from the oxide traps would interfere with the signals from the semiconductor traps.

An alternative explanation for these hysteresis effects is that they are a result of the defects known to exist at the interface between the InP semi-insulating

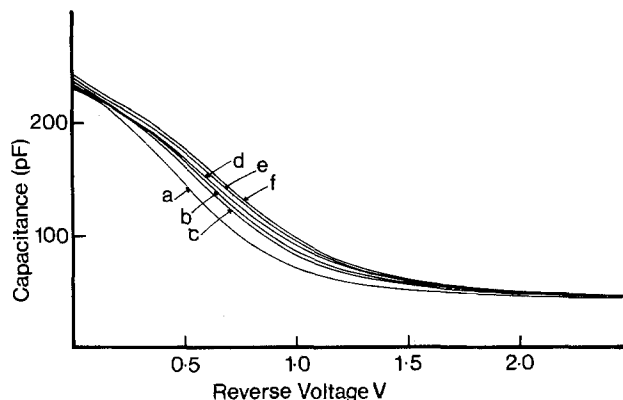


Fig. 3. Reverse bias capacitance-voltage curves measured at 1 MHz for an Au/aluminum oxide/GaInAsP contact. The curves a-f correspond to consecutive voltage scans. Delay between scans $\sim 5 \text{ sec}$.

substrate and the GaInAsP epitaxial layer. However, this can be ruled out since these effects were not observed in the basic Au/GaInAsP diodes which were fabricated on the same slice.

Similar results have been obtained for the magnesium oxide system. The basic procedure is the same as that described above for aluminum, except that for the oxidation of magnesium temperatures up to 300°C were used. Magnesium oxide was investigated because it was thought that it might be possible to obtain thicker oxides than with aluminum at these low temperatures. Oxide layers produced in this way were, however, structurally inferior to the aluminum oxide layer. Furthermore, although the same general trends as those observed for aluminum were obtained, the detailed results were considerably inferior. The reverse leakage with a 10 nm oxide was $\sim 1 \mu\text{A}$ and the reverse characteristic was soft and very unstable. It is possible that these results could be improved if the correct conditions for oxidation of the magnesium layer could be found. These studies are currently being pursued on InP (6).

The third insulating layer studied was SiO_2 , deposited by a low temperature plasma process. These devices yielded results comparable to those with aluminum oxide. The diodes exhibited an abrupt turn-on voltage and ideality values of $n \sim 1.1$ in forward bias. A typical current-voltage characteristic is shown in Fig. 2(e) for an approximate oxide thickness of 15 nm. We note also from this figure that these diodes exhibit very good reverse characteristics with breakdown voltages $\leq 8 \text{ V}$. One unfortunate feature of these diodes is their sensitivity near breakdown; the characteristics become unstable and the diodes easily destroyed (i.e., exhibited low resistance).

Discussion

On the basis of the interfacial oxide tunneling theory applied to these structures, the reduction in reverse leakage as a function of oxide thickness, d , yields an effective barrier height (4, 5)

$$\phi_{\text{bn}}' = \phi_{\text{bn}} + Dd$$

where ϕ_{bn} is the clean surface value (no oxide) and D is the coefficient of increase in barrier height with oxide thickness. D may be estimated from simple tunneling theory. Figure 4 shows the result of the present work and compares these with previous studies of Si, GaAs, InP, and GaInAs. The consistency of all these results is apparent from these curves. In the majority of cases, the experimental values of D are consistently less than the theoretical values. The theoretical calculations are always subject to a great deal of uncertainty due to the lack of realistic information on the shape of the tunneling barrier. On the experimental side, the major uncertainty is the thickness of the oxide film.

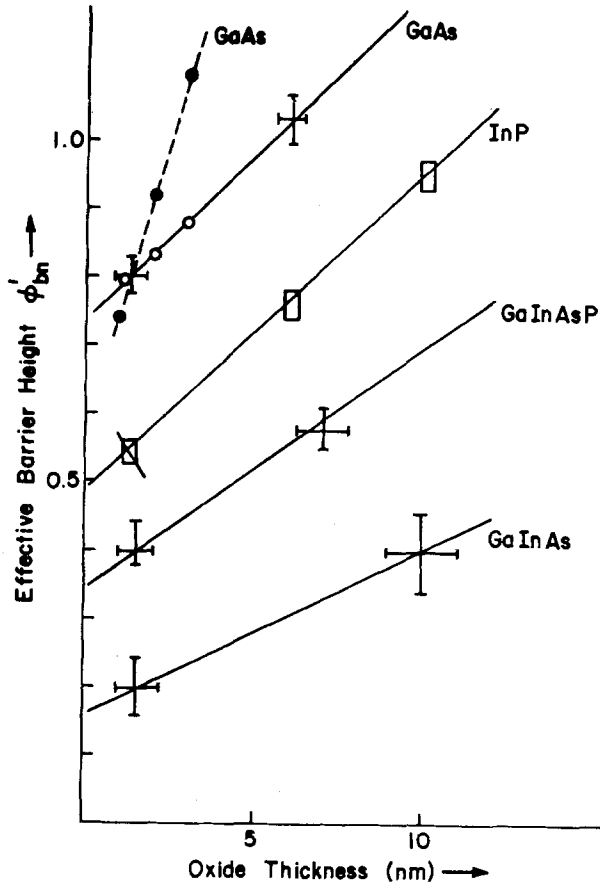


Fig. 4. Effective barrier height ϕ'_{bn} plotted as a function of oxide thickness, d , for a range of different semiconductors. The results of the present study are compared with previous work. The two curves shown for GaAs (solid line and broken line) indicate the two extreme results cited in Ref. (5). The solid line indicates the more typical results.

Conclusions

The current studies, aimed at improving the technology of ohmic and rectifying contacts to the quaternary alloy GaInAsP, yield the following conclusions.

(i) Specific contact resistances of $\approx 3.5 \times 10^{-7} \Omega\text{-cm}^2$ have been obtained with Au/Ge eutectic alloyed

at 450°C for 20 sec. The contact resistance is insensitive to alloying temperature over a wide temperature range from $\approx 425^\circ$ to 500°C.

(ii) Rectifying characteristics of evaporated Au contacts are characterized by a barrier height of 0.4 eV, with the current-voltage and capacitance-voltage techniques yielding consistent values.

(iii) Large increases in effective barrier have been demonstrated using interfacial layers of Al_2O_3 , MgO, and SiO_2 . These layers are all produced by low temperature processes and are compatible with current FET technology. Although these layers produce desirable effects on the current-voltage characteristics, they do induce some undesirable hysteresis in the capacitance-voltage curves which probably could be reduced by improving the structure of the interfacial oxide.

Acknowledgment

We are grateful to Dr. P. D. Greene (STL Limited) and Dr. R. W. Brander (Post Office Research Centre, England), for supplying the material used in this study, and to Drs. J. Comas and W. A. Schmidt (NRL Washington) for depositing the SiO_2 layers. We are also grateful to Dr. C. J. Palmström (University of Leeds) and J. Berry (Cornell) for technical assistance, and to Drs. E. C. Wood, L. F. Eastman, and K. Board for constructive criticism.

This work was supported by the National Aeronautics and Space Administration.

Manuscript submitted Oct. 2, 1979; revised manuscript received Dec. 20, 1979.

Any discussion of this paper will appear in a Discussion Section to be published in the December 1980 JOURNAL. All discussions for the December 1980 Discussion Section should be submitted by Aug. 1, 1980.

REFERENCES

1. M. A. Littlejohn, J. R. Hauser, and T. H. Glisson, *Appl. Phys. Lett.*, **30**, 242 (1977).
2. V. L. Rideout, *Solid-State Electron.*, **18**, 541 (1975).
3. H. H. Berger, *This Journal*, **119**, 507 (1972).
4. H. C. Card and E. H. Rhoderick, *J. Phys. D*, **4**, 1589 (1971).
5. D. V. Morgan and J. Frey, *Phys. Status Solidi. A*, **51**, K29 (1979).
6. B. Van Rees and L. F. Eastman, Private communication.

A Quantitative AES Study of the Compositional Profile of Thin Oxide Films

Katsuhiko Ishiguro and Teiichi Homma

Institute of Industrial Science, University of Tokyo, Tokyo, Japan

It is desirable to obtain quantitative information about the composition and structure of thin film corrosion products in order to understand the growth of such thin films and how they develop into thick scales.

Although Auger electron spectroscopy (AES) coupled with inert ion sputter etching can be a powerful technique for studying in-depth compositional profiles of oxidized surfaces, it is difficult to obtain quantitative results on multicomponent metal alloys. Thus, quantitative interpretations of Auger peak intensities have rarely been attempted for oxide/alloy systems. An exception is the work of Hammer *et al.* (1) who pro-

posed an internal calibration technique for evaluating pseudobinary systems and applied it to the quantitative analysis of a variety of systems including oxide solid solutions, pseudobinary intermetallic compounds, etc.

In this paper, their method is further extended by using relative sensitivity factors to explain Auger peak intensity changes obtained by sputter etching oxide films formed on an Fe-Cr alloy. A procedure for estimating the variation of the composition with depth from the AES data is described.

Experimental

Electropolished specimens of an Fe-18 weight percent (w/o) Cr alloy ($0.15 \times 20 \times 10 \text{ mm}^3$ in size)

were oxidized in a UHV microbalance system at 620°C and 1×10^{-3} Pa O_2 for 120 min; the total weight gain was $14 \mu\text{g}/\text{cm}^2$. The oxide crystal structure was subsequently studied using the reflection high energy electron diffraction technique.

Auger analysis was performed using a commercial scanning micro-probe analyzer (ANELVA, EMAS II). Using a primary electron beam energy of 5 kV and a current $1 \mu\text{A}$ yielded a beam $\sim 1 \mu\text{m}$ diam. The modulation amplitude was 2V peak-to-peak. A 1 mm diam sputter ion beam was used at 2 kV, and 20 mA, and an argon pressure of 3×10^{-3} Pa. Since the average grain size of the specimen was $100 \sim 200 \mu\text{m}$, the AES result provided information about the oxide formed on individual grains. Thus, measurements on several grains gave similar, quite reproducible results. The Auger signals used were oxygen (510 eV), chromium (529 eV), and iron (651 eV).

Results and Discussion

A typical change in Auger peak intensities during ion sputtering the oxidized alloy surface is shown in Fig. 1. Note that iron is enriched in the outermost layer while chromium is concentrated in the remainder of the oxide film. Surface contaminants (*e.g.*, C) picked up during specimen exposure to room air were neglected.

In order to explain the results of Fig. 1 by means of the internal calibration technique (1), the data were replotted in Fig. 2 and 3. In the I_{Cr} vs. I_{Fe} plot of Fig. 2, the directions of the arrows indicate the changing Auger intensities with increasing sputtering. Note that I_{Cr}^{**} and I_{Fe}^* correspond to the Auger intensities of pure chromium oxide and pure iron oxide, respectively. Also, I_{Cr}° and I_{Fe}° represent the AES strengths of the pure metals, under the same experimental conditions. The change in the peak intensities along the $I_{\text{Cr}}^{**}-I_{\text{Fe}}^*$ line (1-9) can be attributed to a concentration variation in the oxide film with depth. The results in Fig. 2 indicate the outermost surface is comprised of pure iron oxide. This was then identified to be Fe_3O_4 by RHEED. The composition of the mixed oxide layer approaches that of Cr_2O_3 at point 9. Note that deeper into the material (pt. 10-18), the data do not fall on the $I_{\text{Cr}}^{**}-I_{\text{Fe}}^*$ line but tend instead to fall on the $I_{\text{Cr}}^\circ-I_{\text{Fe}}^\circ$ line. To a first approximation, this can be interpreted to mean that the film at this depth is comprised of a metallic iron- Cr_2O_3 mixture. Since the points 10-18 fall slightly above this line, this suggests as an added refinement that a small amount of metallic chromium

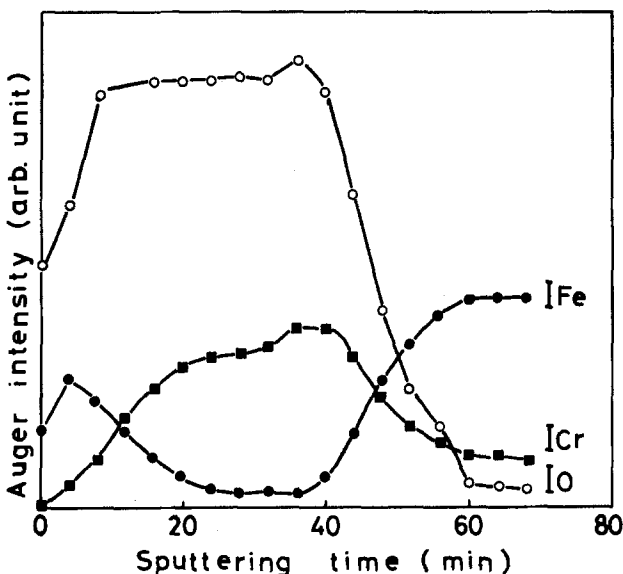


Fig. 1. Sputtering in-depth profile of Fe-18Cr alloy oxidized for 120 min at 620°C and at an oxygen pressure of 1×10^{-3} Pa.

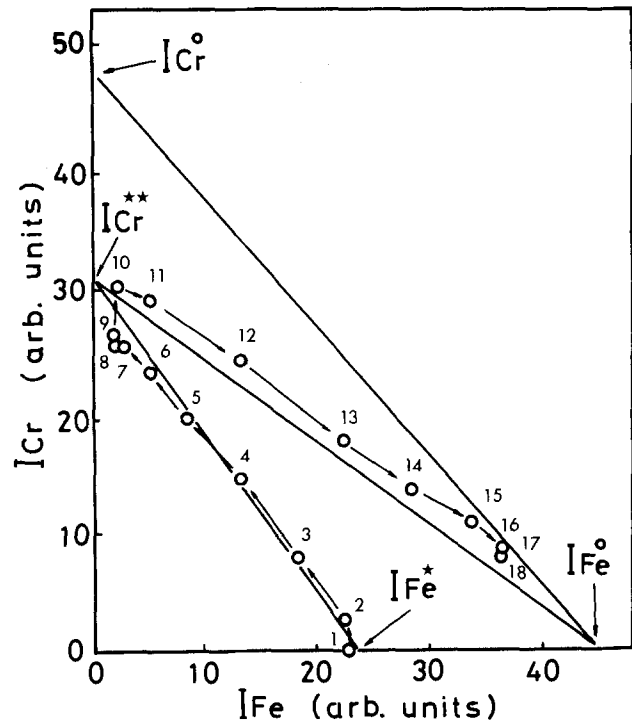


Fig. 2. Chromium peak intensity vs. iron peak intensity during sputtering. Auger peak intensities, I_{Cr}^{**} and I_{Fe}^* , for Cr_2O_3 and Fe_3O_4 , respectively. I_{Cr}° and I_{Fe}° for pure metals.

is also present. The $I_{\text{O}}/I_{\text{Fe}}$ vs. $I_{\text{Cr}}/I_{\text{Fe}}$ plot of Fig. 3 provides additional information. The straight line (L) indicates a concentration change in the pseudobinary system, $(\text{FeO}_n)_{1-x}(\text{CrO}_m)_x$. In other words, a variation of the points 1-9 along the line corresponds to

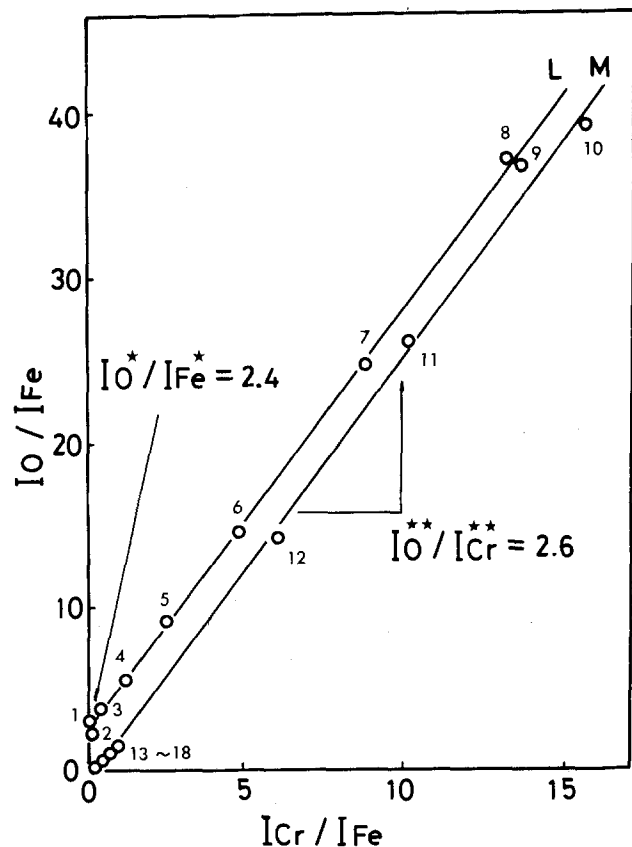


Fig. 3. Plot of peak intensity ratio $I_{\text{O}}/I_{\text{Fe}}$ vs. $I_{\text{Cr}}/I_{\text{Fe}}$. Intersection and slope in L line give $I_{\text{O}}^*/I_{\text{Fe}}^*$ for Fe_3O_4 and $I_{\text{O}}^{**}/I_{\text{Cr}}^{**}$ for Cr_2O_3 .

that on the $I_{Cr^{**}}-I_{Fe^*}$ line of Fig. 2. The intersection with the ordinate axis and the slope give the values of the I_{O^*}/I_{Fe^*} and $I_{O^{**}}/I_{Cr^{**}}$ ratios for pure iron oxide and pure chromium oxide, respectively. Further in, the points 10-18 fall on a second straight line (M), having the same slope as L, but passing through the origin, i.e., where $I_{O^*}/I_{Fe^*} = 0$. Thus, Fe exists in the metallic state along this line. The change on M line corresponds to that on the $I_{Cr^{**}}-I_{Fe^*}$ line in Fig. 2. Accordingly, the present results show that the composition varies along L towards the chromium-rich direction (pt. 1-9), and then changes to the M line where it varies towards an iron-rich direction. This means that the oxide/alloy interface begins to appear at point 10. The slight deviation of pt. 10-18 from the M line suggests that some chromium is present in the metallic state.

The concentrations of these elements in different states were evaluated so as further to quantify the compositional in-depth profiles. For determining concentrations, the following empirical formula with the relative sensitivity factor (2) was employed.

$$X_i = \alpha_i I_i / \sum \alpha_j I_j \quad [1]$$

where the sum of the iron and chromium concentrations has been normalized to 100%. In this case,

$$X_i = \alpha_i I_i [\alpha_{Cr} (I_{Cr^{Ox}} + I_{Cr^{Me}}) + \alpha_{Fe} (I_{Fe^{Ox}} + I_{Fe^{Me}})]^{-1} \quad [2]$$

$$I_{Cr} = I_{Cr^{Ox}} + I_{Cr^{Me}} \quad [3]$$

$$I_{Fe} = I_{Fe^{Ox}} + I_{Fe^{Me}} \quad [4]$$

$$I_O = K_1 I_{Cr^{Ox}} + K_2 I_{Fe^{Ox}} \quad [5]$$

$$K_1 = I_{O^{**}}/I_{Cr^{**}}, \quad K_2 = I_{O^*}/I_{Fe^*} \quad [6]$$

where I_i^{Ox} represents the Auger intensity for the oxide, I_i^{Me} for the metal and α_i is an inverse relative sensitivity factor. A value of 1.22 for α_{Fe}/α_{Cr} was used here. $K_1 (=2.6)$ and $K_2 (=2.4)$ were determined by the slope and the intersection of L at the point of a vertical line in Fig. 3. The following approximations have been introduced to determine $X_{Cr^{Ox}}$, $X_{Cr^{Me}}$, $X_{Fe^{Ox}}$, and $X_{Fe^{Me}}$ from Eq. [2]-[6]

$$(i) \quad I_{Cr^{Me}} = I_{Fe^{Me}} = 0 \quad \text{on L line in Fig. 3 (pt. 1-9)}$$

$$(ii) \quad I_{Fe^{Ox}} = 0 \quad \text{on M line in Fig. 3 (pt. 10-18)}$$

The validity of these approximations has been confirmed by measurements of the low energy Auger peaks of iron and chromium in order better to evaluate their chemical valence states (3).

The compositional profile obtained from these procedures has been shown in Fig. 4, where the chemical state of each element was denoted in parentheses. Thus, Cr^{+3} ions were established to be the dominant cation state in the chromium oxide layer. In addition, the $I_{O^{**}}/I_{Cr^{**}}$ value (=2.6) in Fig. 3 is quite close to that for bulk Cr_2O_3 (=2.6), and the I_{O^*}/I_{Fe^*} (=2.4) in Fig. 3 is also quite close to that for bulk

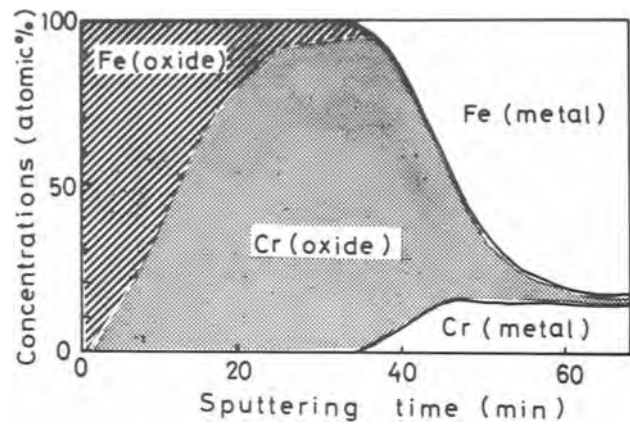


Fig. 4. Concentration profiles for chromium and iron

Fe_3O_4 (=2.6). Most likely, the bulk of the oxide between the Fe_3O_4 and Cr_2O_3 regions is a spinel, $Fe_{3-x}Cr_xO_4$ ($0 < x \leq 2$). In this discussion, we do not consider effects due to preferential sputtering and decomposition of the oxides by bombardment, because it has been confirmed that these effects are negligible for the Cr_2O_3 and Fe_3O_4 mixture system (5).

The present results are similar to those obtained for thick scales formed at 600°C and higher O_2 pressures, as determined (1 atm) by using the Electron Probe Micro Analyzer (4). The formation of α - Fe_2O_3 was expected for the present oxidation conditions from thermodynamical consideration. However, this phase did not appear. At lower oxygen pressures (below 10^{-3} Pa) α - Fe_2O_3 formation has not been reported for pure iron oxidation (6). An average oxide film thickness was evaluated from the total weight gain of $14 \mu g/cm^2$. This thickness is $\sim 900 \text{ \AA}$, assuming an average density for the Cr_2O_3 and Fe_3O_4 mixture of 5.2 g/cm^3 .

Manuscript submitted May 16, 1979; revised manuscript received Nov. 26, 1979.

Any discussion of this paper will appear in a Discussion Section to be published in the December 1980 JOURNAL. All discussions for the December 1980 Discussion Section should be submitted by Aug. 1, 1980.

Publication costs of this article were assisted by the University of Tokyo.

REFERENCES

1. R. Hammer, N. J. Chou, and J. M. Eldridge, *J. Electron. Mater.*, **5**, 557 (1976).
2. C. C. Chang, *Surf. Sci.*, **48**, 9 (1975).
3. K. Ishiguro, To be published.
4. B. Chattopadhyay and G. C. Wood, *Oxid. Met.*, **2**, 373 (1970).
5. N. S. McIntyre and D. G. Zetaruk, *J. Vac. Sci. Technol.*, **14**, 181 (1977).
6. R. J. Hussey and M. Cohen, *Corros. Sci.*, **11**, 699 (1971).

Anomalous Etch Structures Using Ethylenediamine-Pyrocatechol-Water Based Etchants and Their Elimination

A. Reisman, M. Berkenblit, C. J. Merz, A. K. Ray, and D. C. Green

IBM Thomas J. Watson Research Center, Yorktown Heights, New York 10598

Recently, several of the authors published the results of studies on pyrazine catalyzed ethylenediamine-pyrocatechol-water etchant solutions (1). Two quaternary etchant compositions were defined for use in slow and fast etching applications S and F etch, respectively. S etch was found useful in the temperature range from 50°C up to the solution boiling point at approximately 118°C. In using S etch at 50°C, a new phenomenon was observed, which was found not to be an attribute of S etch composition, but was in fact observed with uncatalyzed solutions as well. This phenomenon, manifests itself on single crystal material by the appearance of a dense etch structure pattern reminiscent of dislocation mound etch structures, as shown in Fig. 1. The effect is odd, in that with repeated 50°C etchings conducted in a bath contained in the apparatus shown in Fig. 1 of Ref. (1), some baths never exhibited the effect, some exhibited it immediately, while others did so only after several wafers had been etched.

This indicates that whatever causes the effect does not necessarily do so by itself, but first participates in a slow reaction in the etching bath forming something else which causes the effect. Based on the above, it would appear that because some baths show the effect immediately while others do so only after a period of time, that the time of first observation of the etch

structure depends on the level of contamination of the unknown contaminant in the as constituted bath.

The problem was traced to the use of different lots of ethylenediamine. The effect was found using ethylenediamine which was contaminated with pyrazine as well as with ethylenediamine which was pyrazine free. Our best efforts have thus far been unsuccessful in identifying the causative agent. Photon absorption techniques show no difference between lots of ethylenediamine which cause the effect and those which do not. Similarly, high pressure liquid phase chromatographic isolation techniques have not provided any clues.

We have been unable to create the effect by contaminating ethylenediamine with NH_3 , CO_2 , HCl , or a colloidal silica suspension, but have developed a simple procedure which eliminates it. If after constituting an etchant bath, it is heated for 1 hr at 115°C under an inert gas ambient atmosphere, as for example might be done with the apparatus described in Ref. (1), the effect is absent even with baths that would yield the etch structure immediately. Preheating of the ethylenediamine by itself under the same conditions works equally well. If the time of 115°C treatment is less than 1 hr, the freedom from the effect cannot be guaranteed. For example, following 20 min 115°C pretreatments, some known bad baths used at 50°C did not show the effect again until several wafers had been etched, and several hours had elapsed. Others did not exhibit the effect again at all. All baths, however, showed an alleviation from the effect for at least several hours. When treated at 115°C for 1 hr instead of 20 min, however, no previously bad bath has been found to revert to its bad status. This indicates that whatever it is that causes the effect is either decomposed or volatilized by the extended 115°C treatment. Incidentally, it is not uncommon to use pyrocatechol based baths in an open beaker at from 105°C to its boiling point. We constituted such a bath using ethylenediamine which was known to yield the etch structure, but which was pyrazine free, and used it to etch (100) wafers at the solution boiling point with a 5 min pretreatment at the boiling point. The etch structure was observed and of course, as is the case with such uncatalyzed baths exposed to air, the bath exhibited significant darkening due to oxidation. Consequently, even if such pyrazine free solutions are to be used in air at temperatures above 100°C, it would be necessary first to pretreat them or the ethylenediamine at 115°C for 1 hr in an inert gas ambient atmosphere prior to their use in air.

REFERENCE

1. A. Reisman, M. Berkenblit, S. A. Chan, F. Kaufman, and D. C. Green, *This Journal*, **126**, 1406 (1979).

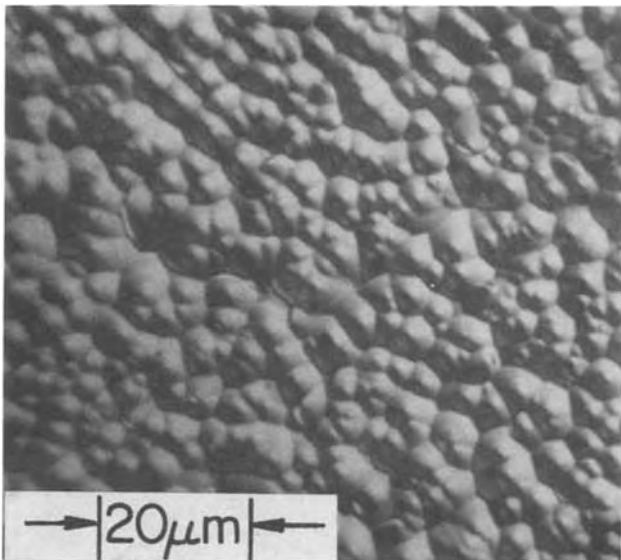


Fig. 1. Photomicrograph of an Si surface etched at 50°C

Photoelectrochemistry of Hydrogenated Amorphous Silicon (a-Si:H)

Yitzhak Avigal, David Cahen, Gary Hodes, Joost Manassen, and Baruch Vainas*

The Weizmann Institute of Science, Rehovot, Israel

and R. A. G. Gibson

Carnegie Laboratory of Physics, Dundee, Scotland

Photoelectrochemical cells (PEC's; semiconductor-liquid junction solar cells) have attracted much attention as candidate systems for practical conversion of solar energy into electricity since the pioneering work by Fujishima and Honda (1), Gerischer (2), and others (3). Several studies have been reported, using crystalline silicon (c-Si) as the semiconducting photoelectrode in a PEC containing an aqueous electrolyte (4, 5). The results show that c-Si is grossly unstable in such a PEC, probably because of the very rapid formation of an electrically blocking surface oxide layer. The same material has been used in organic solvents, both as a photoanode (6, 7) and a photocathode (7). Relatively low photocurrents were reported and no information on conversion efficiency and stability under solar conditions was presented.

Lately, since the discovery that glow-discharge deposited amorphous silicon (a-Si:H) can be successfully doped (8) there has been much interest in the potential use of this material in solid-state photovoltaic cells (9) [see, for example, the recent reviews by Gibson *et al.* (10) and Wilson *et al.* (11)]. a-Si:H has the advantage over c-Si of ease of preparation and, because direct optical transitions dominate its absorption/reflection spectrum, it can be used in thin layers ($\sim 1\mu$ compared to $\sim 100\mu$ for c-Si). The photoanode properties of vapor-deposited a-Si in aqueous solution have been mentioned briefly, and its output instability noted (4). Here we present preliminary results on the properties of an a-Si:H based PEC which uses the nonaqueous electrolyte system of Legg *et al.* (6), *i.e.*, ferrocenium/ferrocene in ethanol, and compare them to those for a similar c-Si based system.

Experimental

Stainless steel or titanium were used as the substrates for the glow-discharge deposition of a-Si:H layers as n-type material ($N_D \sim 10^{17} \text{ cm}^{-3}$) (8). Except for the photoactive area the electrode was encapsulated in epoxy resin. Photoelectrodes of c-Si were prepared from wafers of n-type Si, cut along the (111) plane with 1-10 $\Omega\text{-cm}$ resistivity (kindly provided by Dr. J. Mandelkorn of the Weizmann Institute of Science). Ohmic contacts were made using In-Ga alloy and silver epoxy. The electrolyte was an absolute ethanolic solution of ferrocene (70 mM, Aldrich) and 0.5 mM ferrocenium, prepared by electrochemical oxidation of ferrocene in a separate H-cell. The supporting electrolyte was tetrabutyl-ammonium perchlorate (TBAP) (0.1M, G. Frederick Smith Chemical Company). Potentiostatic experiments were carried out with a Wenking LT73 potentiostat, using a Pt gauze counterelectrode and standard calomel electrode (SCE) as the reference electrode, connected to the working solution via a salt bridge of TBAP in ethanol. All experiments were done under an argon atmosphere in deaerated solutions. Stability tests were carried out under constant temperature conditions.

Both types of electrodes were etched by 40% aqueous HF: a-Si:H three times for 5 sec and rinsed with absolute ethanol after each etch. c-Si was etched three

times for 20 sec and rinsed with absolute ethanol after each etch.

Results and Discussion

Figure 1 shows dark and light potentiostatic *I-V* curves of a-Si:H and c-Si. The onset of photocurrent for these two photoelectrodes occurs at quite similar electrode potentials, (100 mV difference under the conditions of Fig. 1), which reflects their similar flat-band potentials. The saturation open-circuit voltage at high illumination intensities suggests a value of 740 mV (-440 mV vs. SCE) for the a-Si:H flatband potential, which should be compared with 700 mV (-400 mV vs. SCE) for c-Si (6). On the basis of this information and the measured values of the optical energy gap of 1.1 eV for c-Si and 1.7 eV for a-Si:H, the energy diagram of Fig. 2 can be constructed. The band-edge energies shown are minimum ones only, and it is quite possible that they may be more negative, because of differences between E_F and E_C , both in a-Si:H and c-Si. Such a shift, however, does not affect the conclusions of this work. Figure 1 also shows that the cathodic overpotential for dark, forward currents for a-Si:H is considerably larger than that for c-Si. This may be caused by the much lower concentration of surface states on a-Si:H than on c-Si, something which may influence the photocurrents as well (12).

Variable load (nonpotentiostatic) *I-V* curves of a-Si:H based PEC's show, at an illumination intensity of 100 mW/cm^2 ($\sim \text{AM1}$ solar irradiation), a photocurrent of 1.2 mA/cm^2 , and a photopotential of $\sim 500 \text{ mV}$, with a fill factor of ~ 0.4 ($\sim 0.24\%$ efficiency). At 1500 mW/cm^2 , under these conditions, a photopotential of $\sim 700 \text{ mV}$ is obtained (quite close to saturation), a photocurrent of $\sim 4.5 \text{ mA/cm}^2$, and a fill factor of

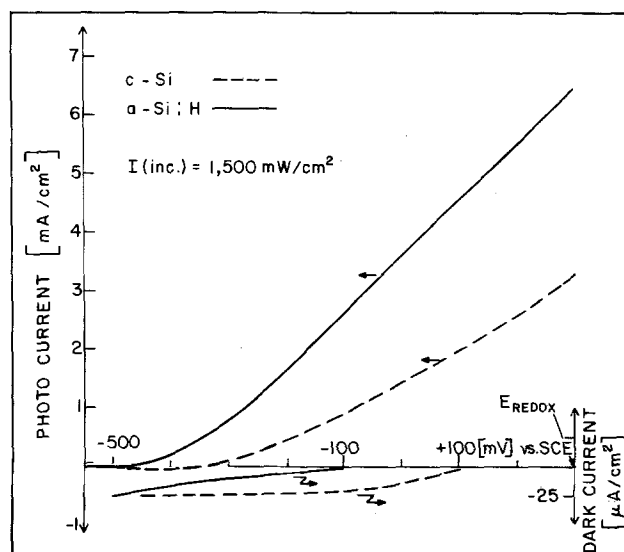


Fig. 1. Light and dark potentiostatic *I-V* curves for a-Si:H (solid lines) and c-Si (dashed lines). E_{REDOX} : Redox potential of the 70 mM ferrocene, 0.5 mM ferrocenium ethanolic solution. Note the different current scales for dark and light currents. $I(\text{inc})$ = Incident light intensity.

* Electrochemical Society Active Member.
Key words: amorphous Si, photoelectrochemistry, solar energy conversion, nonaqueous electrolytes.

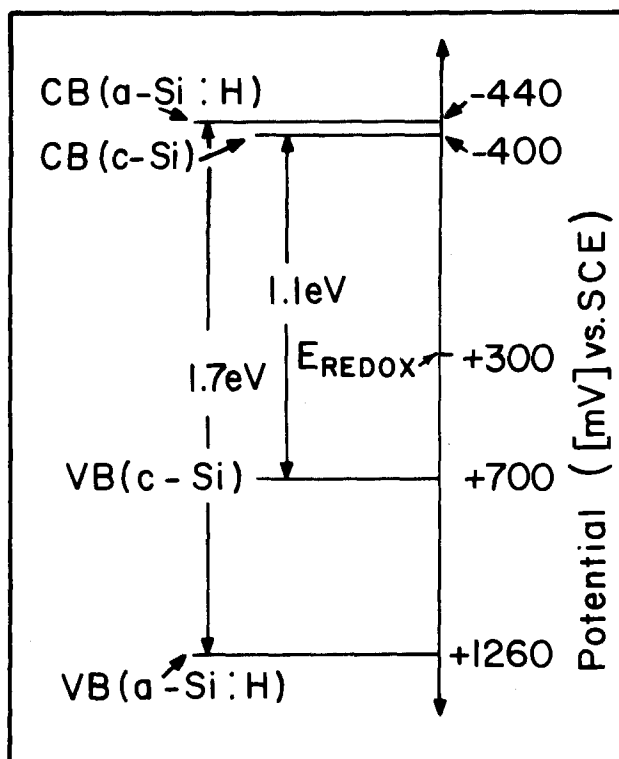


Fig. 2. Scheme of relevant energy levels for a-Si:H and c-Si/ferrocene-ferrocenium semiconductor-electrolyte junctions. E_{REDOX} as in Fig. 1.

~ 0.2 . The relatively small photocurrent (as compared to Fig. 1) is due to the fact that the electrode was at ~ 0 mV vs. SCE under short-circuit conditions, and not at the electrolyte redox potential of +300 mV vs. SCE, as it ideally should have been. This is probably because of the larger resistance drop between the electrodes in the rather dilute organic electrolyte.

Spectral response measurements show the onset of photocurrent for a-Si:H to be around 700 nm, with a maximum response around 530 nm. This spectral response agrees quite well with a superposition of the solution absorption spectrum and the a-Si:H reflectance spectrum, and that of a-Si:H based Schottky cells (when electrolyte absorption losses are taken into account).

In Fig. 3 the photocurrent of an a-Si:H-based PEC is shown as a function of charge passed, reflecting the cell output stability. The photocurrent decreases to about half its initial value during the first ten hours (~ 30 C passed), after which the deactivation process virtually stops. It is quite probable that this deactivation is due to a buildup of an insulating silicon oxide layer on the electrode surface. Also, after deactivation, the photoelectrode dark potential shifted by ~ 100 mV to a more negative value. Deactivated photoelectrodes were easily reactivated by etching with 40% aqueous HF. (The electrode performance was found to be very sensitive to the exact surface etching process.) a-Si:H photoelectrodes of small surface area (down to 5 mm²) were found to give better and more reproducible performance than larger ones, possibly pointing to the existence of pinholes.

The stability of a-Si:H based PEC's is similar to that of c-Si ones under our (near short-circuit) conditions (those of Fig. 3), and under those conditions it seems to be a function of the initial photocurrent density, mainly. However, because of the consistently higher photocurrents of a-Si:H PEC's as compared to c-Si ones under identical illumination conditions, photocurrent decay of a-Si:H cells may start at lower illumination levels than is the case for c-Si ones. The stability referred to in Ref. 6 (with monochromatic excitation at 632.8 nm of ~ 10 mW/cm², and short-circuit photocur-

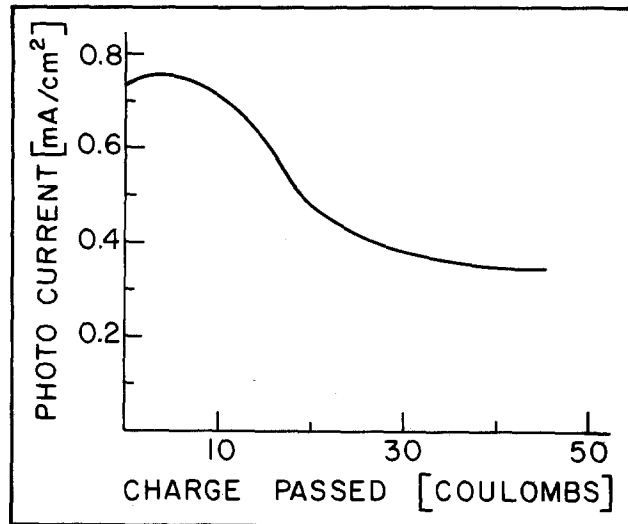


Fig. 3. Photocurrent of a-Si:H as function of charge passed. AM1 simulated illumination. $R = 100\Omega$ (near short-circuit for this, organic electrolyte-containing, PEC). Temp.: 30°C.

rent densities between 0.3 and 1.2 mA/cm²) is not found by us under the conditions used in this study.

The similarities and differences between these two forms of silicon can be understood further by investigating the transient photocurrents obtained from them, and this study, presently in progress, will be reported elsewhere. Figure 2 does show, however, that the electron affinities of a-Si:H and c-Si are quite similar and thus it seems that this physical quantity is dictated mainly by the similar immediate environment of the Si-atoms in the two materials, possibly by the similar Si-Si bonds, and much less so by long-range forces. Additional evidence for this explanation comes from: (i) the reported decrease in optical bandgap with decreasing hydrogen content of a-Si:H (13), and (ii) photoelectron spectroscopic data, that show that increasing the hydrogen content in a-Si:H shifts the valence band edge down with respect to the conduction band edge, which remains fixed (14). This suggests that Si-H interaction plays a role in determining the valence band position but that the conduction band position is not (or very much less so) affected by it.

Also, from Fig. 2 we see that the energy gained by a hole in the semiconductor which reaches the surface and interacts with the ferrocene in solution is nearly 600 mV more in the case of a-Si:H than in that of c-Si. If it is necessary to overcome an activation energy (overpotential) for this reaction to take place, then this difference in energy gain may explain the larger photocurrents observed for a-Si:H than for c-Si, under similar illumination conditions.

In summary, the above results show that the photoelectrochemical behavior of a-Si:H is in most respects superior to that of c-Si in the redox electrolyte used here. However, this electrolyte system is still far from ideal, from both stability and efficiency considerations, for a-Si, as well as for c-Si, photoelectrodes.

Acknowledgment

We thank Y. Merovsky for the spectral response data, the Ministry of Research and Technology of the FRG (through Kernforschungsanlage Jülich) for support (to WIS group), and Lucas Industries for the award of a Fellowship to R.A.G.G.

Manuscript submitted Aug. 30, 1979, revised manuscript received Nov. 11, 1979.

Any discussion of this paper will appear in a Discussion Section to be published in the December 1980 JOURNAL. All discussions for the December 1980 Discussion Section should be submitted by Aug. 1, 1980.

Publication costs of this article were assisted by The Weizmann Institute of Science.

REFERENCES

1. A. Fujishima and K. Honda, *Nature*, **238**, 37 (1972).
2. H. Gerischer, *J. Electroanal. Chem.*, **58**, 263 (1975).
3. "Semiconductor-Liquid Junction Solar Cells," A. Heller, Editor, The Electrochemical Society Soft-bound Proceedings Series, Princeton, N.J. (1977).
4. T. S. Jayadevaiah, *Appl. Phys. Lett.*, **25**, 399 (1974).
5. R. M. Candea, M. Kastner, R. Goodman, and N. Hickok, *J. Appl. Phys.*, **47**, 2724 (1976).
6. K. D. Legg, A. B. Ellis, J. M. Bolts, and M. S. Wrighton, *Proc. Natl. Acad. Sci. USA*, **74**, 4116 (1977).
7. D. Laser and A. J. Bard, *J. Phys. Chem.*, **80**, 459 (1976).
8. W. E. Spear and P. G. Le Comber, *Solid State Commun.*, **17**, 1193 (1975); W. E. Spear and P. G. Le Comber, *Philos. Mag.*, **33**, 935 (1976).
9. D. E. Carlson and C. R. Wronski, *Appl. Phys. Lett.*, **28**, 671 (1976); D. E. Carlson, *IEEE Trans. Electron Devices*, **ED-24**, 449 (1977).
10. R. A. Gibson, P. G. Le Comber, and W. E. Spear, *Solid State and Electron Devices*, **2**, S3-S6 (1978).
11. J. I. B. Wilson, J. McGill, and D. Weaire, *Adv. Phys.*, **27**, 365 (1978).
12. S. R. Ovshinsky and D. A. Adler, *Contemp. Phys.*, **19**, 109 (1978).
13. C. C. Tsai, H. Fritzsche, M. H. Tanielian, P. J. Gaczi, P. D. Persans, and M. A. Vesaghi, in "Proceedings of the Seventh International Conference on Amorphous and Liquid Semiconductors," W. E. Spear, Editor, p. 339, CICL, Edinburgh University, Edinburgh (1977).
14. B. V. Roedern, L. Ley, and M. Cardona, *Solid State Commun.*, **19**, 415 (1979).

Erratum

In the paper "Formation Mechanism of Porous Silicon Layer by Anodization in HF Solution," by Takashi Uragami which appeared on pp. 476-483 in the Feb-

ruary 1980 JOURNAL, Vol. 127, No. 2, the word "fluoride" which appeared on pp. 477 and 478 should read: "fluorine ion".



On the Design of Silver-Hydrogen Electrochemical Cells

P. O'D. Offenhardt and G. L. Holleck*

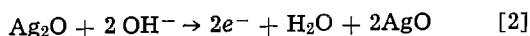
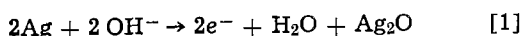
EIC Corporation, Newton, Massachusetts 02158

ABSTRACT

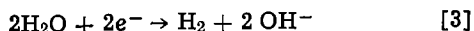
With a projected energy density of 70-110 W-hr/kg and an estimated lifetime in excess of 1000 cycles, silver-hydrogen cells represent a promising electrochemical energy storage device for specialized applications. A cell design using a rolled stack configuration is especially attractive. A comprehensive computer simulation has been used to optimize the energy density of such a cell. The parameters considered include: cell geometry, electrode and lead dimensions, water generation and consumption, electrolyte movement, heat generation and dissipation, and active material utilization. The results show that balancing of electrolyte transport processes is essential for stable long term operation. Energy density is a strong function of rate, with incomplete silver electrode utilization the main factor. At higher rates no more than three or four layers can be used if the maximum temperature increase on discharge is to be kept below 5°-10°C to avoid electrolyte loss via evaporation/condensation processes. Conversely, use of only one or two layers leads to an unacceptably high penalty in the energy density.

A metal-gas battery based on the Ag-H₂ couple is an attractive power source, particularly in terms of the weight energy density. By replacing the Zn electrode in the Ag-Zn system with the H₂ electrode, the main drawback of Ag/Zn batteries, short cycle life, can be overcome. However, the relatively high solubility of silver oxide in alkaline electrolytes still requires use of argentistatic membranes similar to those employed in Ag-Zn cells.

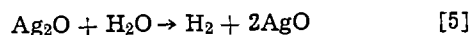
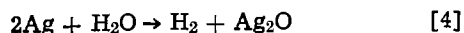
Oxidation of the silver electrode during charging nominally takes place in two steps



In alkaline media the relevant reaction at the H₂ electrode is



so that the overall cell reactions are



At 25°C the relevant thermodynamic data (1) for the first reaction are $\Delta G^\circ = 54.104$ kcal/mole, $\Delta H^\circ = 61.011$ kcal/mole, and $\Delta S^\circ = 23.17$ ($\epsilon^\circ = 1.173\text{V}$); for the second reaction, $\Delta G^\circ = 66.202$ kcal/mole, $\Delta H^\circ = 70.085$ kcal/mole, and $\Delta S^\circ = 13.02$ ($\epsilon^\circ = 1.435\text{V}$). In practice, during charging the cell voltage increases sharply to the second plateau after roughly 30% of the ultimate net capacity has been reached; during discharge, the cell voltage drops after about 35% of capacity. A typical voltage-time trace for an Ag-H₂ cell is shown in Fig. 1. Charge utilization of the Ag electrode is generally in the range 40-70%, and, as shown in Fig. 2, is a strong function of the current density.

* Electrochemical Society Active Member.
 Key words: cell, energy density, electrolyte.

Several aspects of Ag-H₂ cell design have been considered in the literature (2-5). Electrolyte management is the main problem area (6). In this paper we briefly summarize the design implications of the earlier work, which has focused on cells with stacked electrodes (4, 5), and then proceed to a discussion of a computer simulation model for rolled Ag-H₂ cells. The model takes into account both the mechanical and electrochemical aspects of design, and can optimize such features as pressure vessel radius and length for maximum energy density subject to constraints on volumetric density, thermal gradients, and discharge rate.

Electrolyte Management

Unless the two electrodes are separated by an argentistatic membrane, dissolved silver oxide will migrate

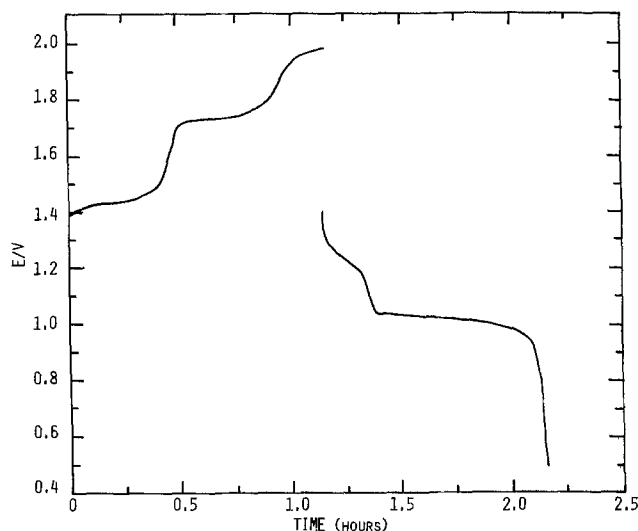


Fig. 1. Typical voltage-time trace during a charge-discharge cycle of an Ag/H₂ cell.

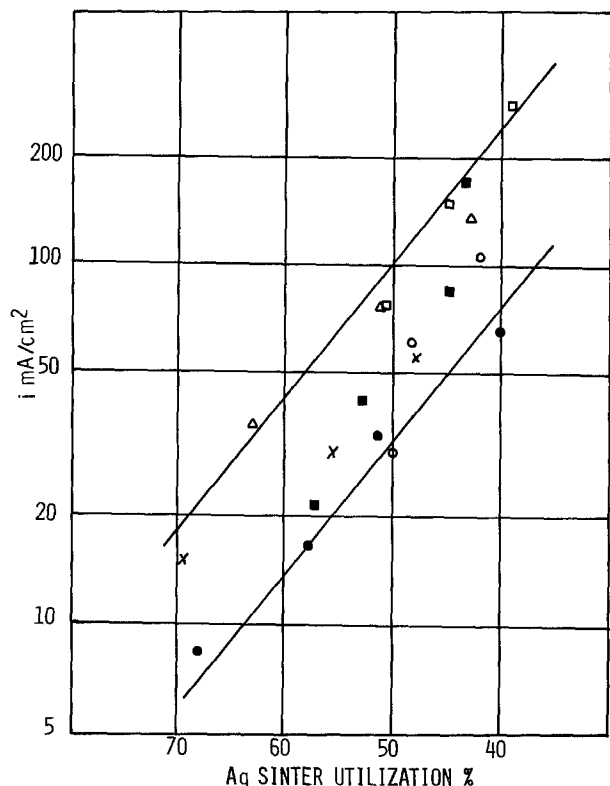


Fig. 2. Effect of current density on silver electrode utilization. \times = thin (0.028 cm) Conf. I (one-sided use); \circ , \bullet = thin Conf. II (two-sided use); \triangle = thick (0.063 cm) Conf. I; \square , \blacksquare = thick Conf. II.

to the H_2 electrode. This not only causes reduced cell capacity but also leads to internal shorting when the dissolved oxide is reduced to silver. Indeed, migration is such a serious problem that the barrier membrane must be extended well beyond the edges of the electrodes to eliminate rapid Ag bridging and shorting. However, in a pressure vessel with stacked electrodes, extension of the membranes would seriously reduce heat transfer between the electrodes and the vessel walls, leading to high thermal gradients and possible evaporation of water from the electrolyte and condensation on the vessel walls. This problem can be solved by using a rolled electrode configuration, in which the barrier membrane extensions do not increase the gap between the vessel wall and the electrode. As we demonstrate in the next section, this approach is limited by the thermal conductivity of the electrode roll in the direction perpendicular to its axis, which is much lower than the thermal conductivity in the parallel direction. A rolled configuration is hence limited to a few layers.

A second problem in electrolyte management is consumption of water during charging, which, as can be seen from Eq. [4] and [5], is inherent in the cell chemistry. To prevent the electrodes from drying out it is essential to use electrolyte reservoirs. Casual examination of Eq. [1]-[3] indicates that the H_2 electrode is likely to dry out during the charging step. In practice, drying out of the Ag electrode during charge is the real problem (6). This is because electromigration of KOH tends to increase the KOH concentration in the H_2 electrode reservoir. The diffusion constant for water is larger than for KOH, but both are sufficiently large that the concentration gradient on the two sides of the barrier membrane is small. Thus, electromigration of KOH into the H_2 electrode reservoir leads to large-scale diffusion of water out of the Ag electrode reservoir, thus drying it. Careful analysis indicates that this problem cannot be solved merely by increasing the volume of the Ag electrode reservoir; the excess of charge over discharge current (i.e., overcharge) will lead to drying in a few cycles. It is hence necessary to select

and adjust the various transport parameters through the argentostatic membranes such that a suitable balance of the mass flow can be maintained. Of the four membranes investigated—Visking, Permion 2291, Permion 2193, and the NASA IO separator—only the latter could meet these requirements. A significantly higher rate of electrolyte backwicking is the main distinguishing parameter. This topic will be treated more fully in a subsequent paper (7).

Experimental and theoretical considerations along the lines above have led to a preferred cell design consisting of a 25 mil thick porous Ag electrode, an inorganic-organic NASA separator (similar to the earlier "Astropower" separator) with the membrane side away from the Ag electrode, and a 20 mil asbestos absorber layer between the separator and the H_2 electrode. Such test cells have survived over 500 charge/discharge cycles to 70% depth of discharge at the C/1.4 rate with capacity loss under 10%. (On this basis we project a lifetime in excess of 1000 cycles.) The simulation program used the gravimetric and thermal properties of this electrode arrangement in optimizing the overall cell design.

Computer Model for Ag- H_2 Cells

The generalized mechanical design for Ag- H_2 cells is shown in Fig. 3-7. The labels for the various dimensions, which are the FORTRAN variable names, are explained in Table I. Although the program makes it possible in principle to vary any of these dimensions, only the pressure vessel radius, length, and thickness were routinely and systematically altered, along with the number of Ag- H_2 electrode pairs in the "roll."

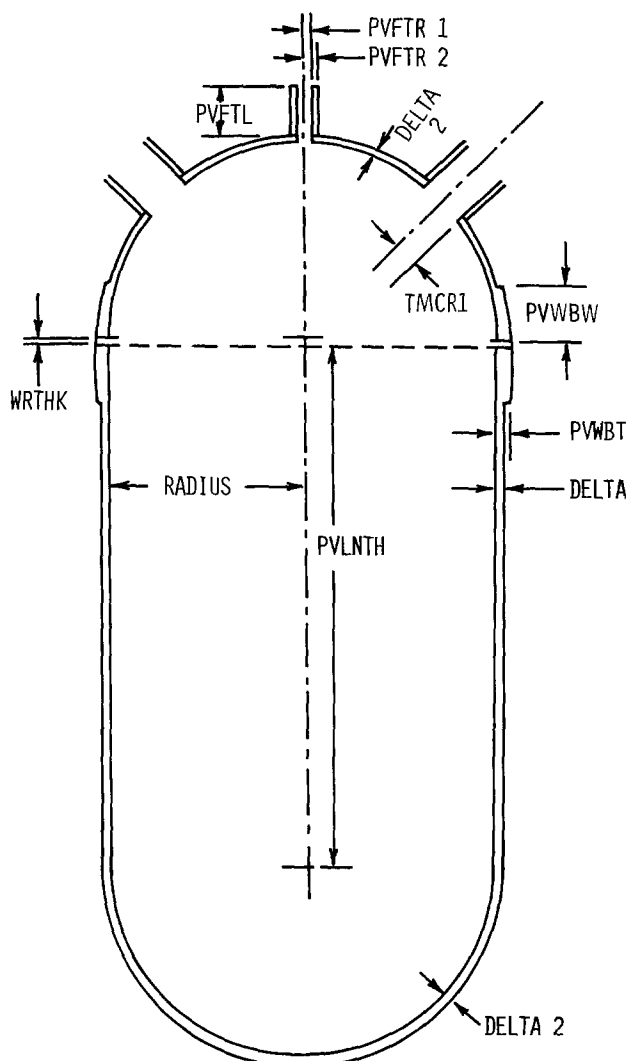


Fig. 3. Basic dimensions of the generalized pressure cell design

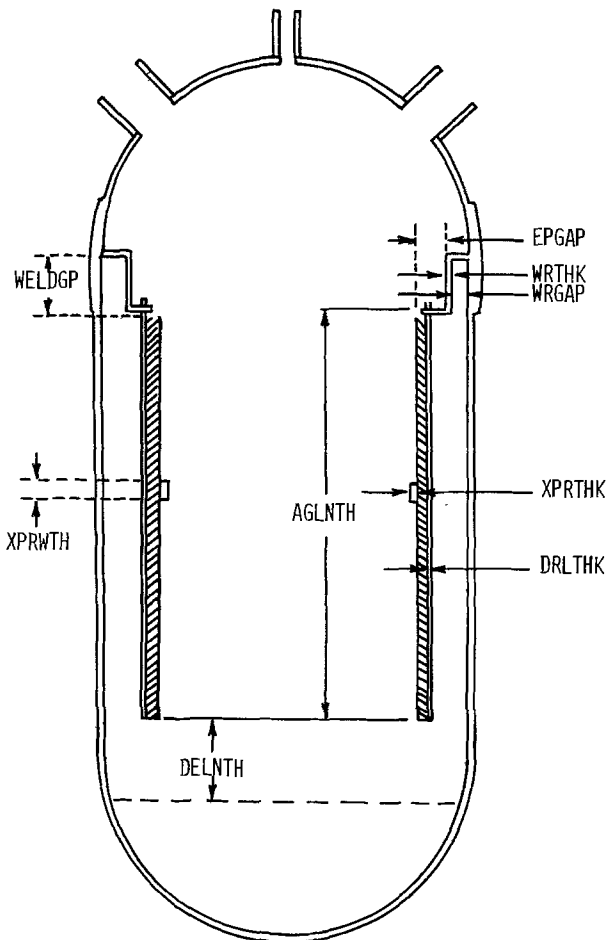


Fig. 4. Interior details of the generalized pressure cell design

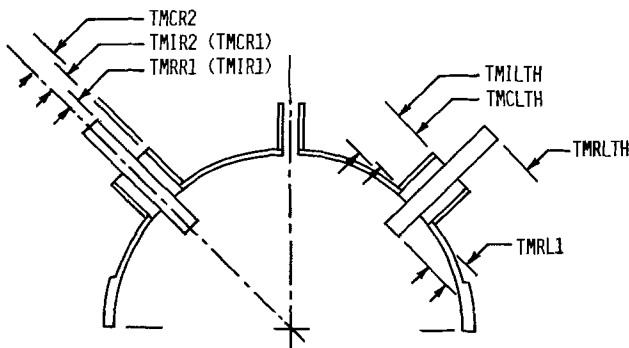


Fig. 5. Details of the electrode terminals

Given the cell capacity, the thickness of the Ag electrode, and the number of electrode pairs, knowledge of the silver utilization allows calculation of the electrode area. The experimental relationship between utilization U and discharge current density i_d is approximately represented by the equation

$$U = 0.208 - 0.286 \log (i_d) \quad [6]$$

Since the current density depends on plate area, an iterative technique is used to obtain both the Ag utilization and the plate area. The current density is inversely proportional to the discharge time, so required plate area is also a function of discharge time.

Since the plate area is known, the radius and length of the pressure vessel are no longer independent variables. The program provides values for both variables in the following fashion. First, an arbitrary radius is chosen, and the length of the pressure vessel is calculated using the known plate area. The entire weight and volume calculations follow. A new (and larger) radius is chosen, and the calculations are repeated.

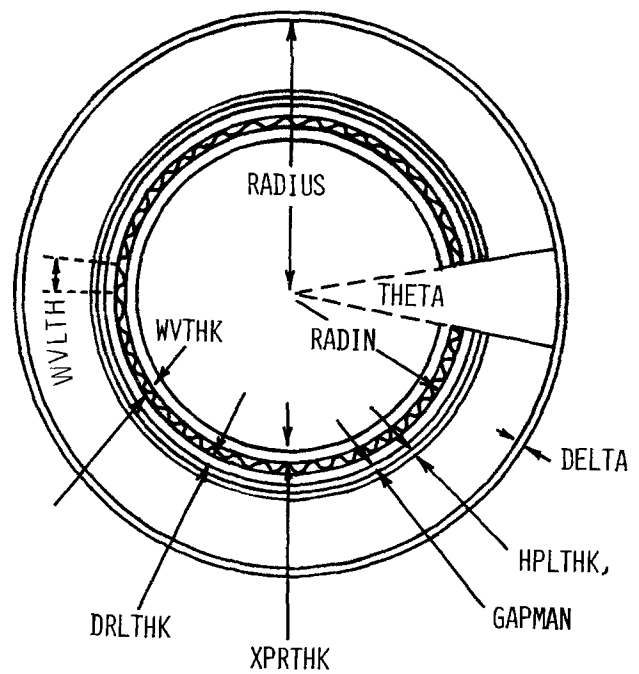


Fig. 6. Details of the support structure for the electrode roll

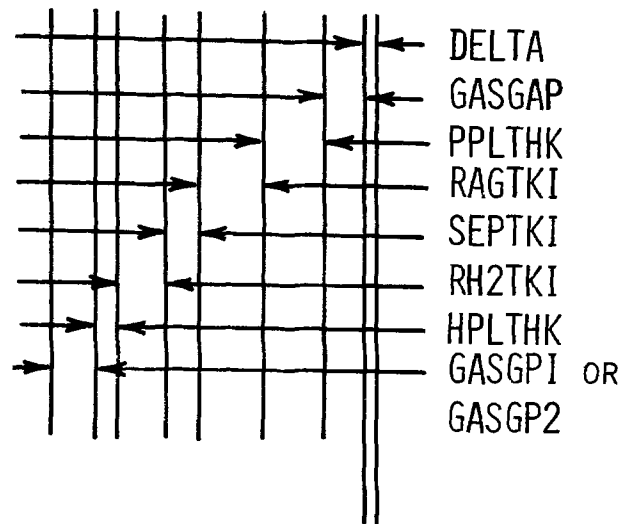


Fig. 7. Electrode roll structure. Gas gap between H_2 and Ag electrodes is GASGP2; between adjacent H_2 electrodes, GASGP1.

This process is continued until the selected volumetric energy density is bracketed; the program then interpolates the correct radius and repeats the calculations once more. In this way the program provides a cell design with a preselected volumetric energy density.

The quantity of H_2 in the cell is of course determined by the cell capacity, and the volume is fixed by the pressure vessel radius and length. (Excluded volumes, e.g., mandrel, electrode roll, leads, and terminals, are taken into account). The maximum cell pressure is hence determined by the assumed maximum temperature ($20^\circ C$). This in turn fixed the thickness of the pressure vessel walls (Inconel 718, with a safety factor of 2).

With three main exceptions, the remaining components in the cell are of fixed design, and are assumed to have fixed weights and volumes. The exceptions are the H_2 electrodes (Ni Exmet™ screen supporting the Teflon bonded platinum black) and the H_2 and Ag electrode leads. These elements make a substantial contribution to the overall weight, and also affect the net cell energy due to resistive heat losses. Thus, the thickness of each of these three elements is optimized so

Table I. Definitions of the cell dimensions (FORTRAN variable names) in the generalized mechanical design shown in Fig. 3-7

FORTRAN Variable names	Definition
AGLNTH	Length of Ag electrode.
DELNTH	Gap between end of electrode roll and beginning of hemispherical end cap.
DELTA	Thickness of pressure vessel wall, cylindrical section.
DELTA2	Thickness of pressure vessel wall, hemispherical section.
DRLTHK	Mandrel thickness.
EPGAP	Length of support ring section.
GAPMAN	Gap thickness between mandrel and innermost electrode.
GASGAP	Gap thickness between pressure vessel and outermost electrode.
GASGP1	Gap thickness between adjacent H ₂ electrodes.
GASGP2	Gap thickness between H ₂ and Ag electrodes.
HPLTHK	Thickness of H ₂ electrode.
PPLTHK	Thickness of Ag electrode.
PVFTL	Length of pressure vessel fill tube.
PVFTL1	Inner radius of pressure vessel fill tube.
PVFTL2	Outer radius of pressure vessel fill tube.
PVLNTH	Length of cylindrical section of pressure vessel.
PVWBT	Thickness of pressure vessel weld band.
PVWBW	Width of pressure vessel weld band.
RADIN	Inner radius of electrode roll.
RADIUS	Inner radius of pressure vessel.
RAGTKI	Thickness of Ag electrode reservoir.
RH2TKI	Thickness of H ₂ electrode reservoir.
SEPTKI	Thickness of separator.
THETA	Angular gap in electrode roll.
TMCLTH	Length of the terminal case.
TMCR1	Inner radius of terminal case.
TMCR2	Outer radius of terminal case.
TMILTH	Overall length of terminal case.
TMRL1	Length of the inner terminal section.
TMRLTH	Overall length of the terminal.
TMRR1	Radius of the terminal.
WELDGP	Length of support ring section.
WRGAP	Gap between support ring and pressure vessel wall.
WRTHK	Thickness of weld ring (support ring).
WVLTH	"Wavelength" of corrugation.
WVTHK	Overall thickness of corrugation.
XPRTHK	Thickness of expansion ring.
XPRWTH	Width of expansion ring.

as to maximize the gravimetric energy density. The technique for optimizing the plate thickness is a bit more difficult than that required for the leads, so we confine the present discussion to the leads. A discussion of plate thickness optimization is available elsewhere (8).

We consider a set of n electrode leads, each of length l and resistance R . The material properties of the leads are the resistivity ω (in $\Omega\text{-cm}$), the density ρ , and the thermal conductivity K (in $\text{W}\cdot\text{cm}^{-1}\cdot\text{deg}^{-1}$). The current through each lead will be designated by i . Then, for each lead, we may write the weight, W , cross-sectional area A , and energy dissipation E as

$$A = \frac{\omega l}{R} \quad [7]$$

$$W = Al\rho \quad [8]$$

$$E = i^2R/C \quad [9]$$

where $1/C$ is the discharge time in hours.

We also designate the energy stored in the battery by SV , where S is the capacity in ampere-hours and V the voltage. The net energy N that can be obtained from the battery is

$$N = SV - ni^2R/C \quad [10]$$

The current i depends on the rate of discharge. At the 1 hr rate, $ni = S$; at an arbitrary rate C (hours^{-1}), $ni = SC$. Thus, the net energy may be written as

$$N = SV - S^2C/R/n \quad [11]$$

In order to optimize the energy density, we also require an expression for the total weight of the battery, T . Approximately, T is proportional to the cell capacity, to which we add the weight of the leads. Thus

$$T = aS + nW \quad [12]$$

where a is a proportionality factor. We can now solve the lead resistance R such that

$$\frac{d(N/T)}{dR} = 0 \quad [13]$$

A little manipulation yields the quadratic equation

$$R^2 + \frac{2n\omega l^2\rho}{aS}R - \frac{n^2V\omega l^2\rho}{aS^2C} = 0 \quad [14]$$

In the cases we have considered, the linear term is negligible, so that

$$R \approx \frac{nl}{S} \sqrt{\frac{V\omega\rho}{aC}} \quad [15]$$

It is then easily shown that the heat dissipation is

$$E = Sl \sqrt{\frac{V\omega\rho C}{a}} \quad [16]$$

and the total weight of the leads is

$$nW = Sl \sqrt{\frac{a\omega\rho C}{V}} \quad [17]$$

Both E and nW are independent of the total number of leads.

It is useful to consider a specific example. For a 20 A-hr cell designed to discharge at the $2C$ rate at 1.1V, the net energy is

$$N = 22 - 800R/n$$

Let us assume that the leads are 5 cm long, and are made of Ag ($\omega = 1.6 \times 10^{-6} \Omega\text{-cm}$; $\rho = 10.5$) or Ni ($\omega = 9.5 \times 10^{-6} \Omega\text{-cm}$; $\rho = 8.9$). We also assume that the battery weight (exclusive of leads) is 220g, i.e., $a = 11 \text{ g/A-hr}$. Then

$$\frac{R}{n} = 5.14 \times 10^{-4} \Omega \text{ (Ni)}$$

$$= 2.29 \times 10^{-4} \Omega \text{ (Ag)}$$

$$EC = 0.82W \text{ (Ni)}$$

$$= 0.37W \text{ (Ag)}$$

$$nW = 4.11g \text{ (Ni)}$$

$$= 1.83g \text{ (Ag)}$$

The energy density is reduced from $22/220 = 0.100$ to $21.41/225.94 = 0.0948$, a reduction of about 5%.

It is of interest to consider the reduction in energy density due to off-design conditions. Suppose the resistance of the Ni leads is deliberately decreased by a factor of two to reduce the heat dissipation. Then it is easily shown that the lead weight doubles and the i^2/R loss is halved. The energy density is now $21.61/230.05 = 0.0939$, a further reduction of about 1%. Thus, because the lead resistance was initially optimized to satisfy Eq. [14], relatively large changes in R away from the optimum value do not strongly effect the energy density.

We have also calculated the temperature rise along the leads, assuming that all heat dissipation takes place at one end. We find that at optimum thickness the temperature rise in the Ni lead can be of the order of 40°C . Doubling the Ni lead thickness reduces the temperature rise by a factor of four. For this reason we routinely specify that the lead thickness should be double the optimum; as we have seen, this penalizes the energy density by about 1%. For similar reasons, the thickness of the Ni ExmetTM screen was set at 150% of optimum.

Thermal Simulation

Given the mechanical details of the cell design, it is possible to simulate the thermal performance of the cell if the thermal properties of the components are

known, and if the sources and sinks of heat can be assumed. For this purpose we use a constant case temperature, and assume that all heat generation occurs at the Ag electrode. The program permits the electrode roll to be segmented into volume elements in all three directions, but generally we only considered radial "peels," thus reducing the thermal problem to one dimension. Three charge steps (including overcharge) and three discharge steps are considered. Conduction of heat through the gas is ignored except in the gaps between electrodes, and in the gap between the outer electrode and the pressure vessel.

During charge or discharge, heat generation due to electrochemical reactions will be largely uniform throughout the surface of the Ag electrode. However, heating caused by reaction of H_2 and O_2 during overcharge will occur primarily at the ends of the H_2 electrodes. Similarly, heating due to the leads and due to voltage drops will occur at the ends. This is accounted for when the volume elements are axially segmented.

Since overcharge can be limited by appropriate controls, it is not generally the most important step from the point of view of cell design. Aside from overdischarge, maximum heat generation occurs during the second discharge step. Here the cell voltage has dropped to the second plateau, but the electrochemical process is still described by Eq. [4]. For this process, the electroneutral voltage—the potential derived from the relation $\Delta H^\circ = -n\tau e$ —is 1.5V, while the cell voltage is around 1.15V. The rate of heat generation is proportional to the difference between the cell voltage and the electroneutral voltage, ca. 0.35V. This voltage difference is roughly 20% of the overcharge voltage.

The rate of heat generation is of course a direct function of the rate of discharge. For a given temperature rise, more layers can be provided in a cell discharged at low rate. For this reason, a low-rate cell can be designed in a relatively compact shape, with a relatively low ratio of length to radius, and with a thicker electrode roll. Together with improved Ag utilization, this is a factor in the increased energy density of low-rate cells.

Simulation Results for 50 A-hr Cells

The calculated variation of weight energy density with the number of electrode pairs in the roll is shown in Fig. 8 for a cell with 25 mil Ag electrodes discharged at the 1 hr (C) rate. Use of only a single pair of electrodes reduces the energy density by about a third. For two pair, the reduction is about 15%; for three pair, less than 10%. The improvement beyond 3 or 4 pairs is quite small. Figure 9 illustrates the calculated profile of maximum and minimum cell temperatures during C/2 charge and C-rate discharge for a cell with three pairs of electrodes; the maximum temperature on discharge is only 4°C above the case temperature, and even on overcharge the temperature rise is less than 11°C. The variation of maximum discharge temperature with number of electrode pairs is shown in Fig. 10; for C-rate discharge, cells are probably limited by thermal effects to 3 or 4 layers. Fortunately, as seen in Fig. 8, this does not greatly limit the energy density.

In most of the calculations reported here, the volume energy density was fixed at 0.07 W-hr/cm³. As shown in Fig. 11, this is not optimal for the weight energy density, which peaks at roughly twice this volumetric energy density. However, optimal cells with high volumetric energy density tend to be extremely long and thin, and the weight penalty for a more conventionally shaped vessel (with ratio of length to radius in the range 2-4) is not large.

The projected variation of energy density and temperature rise with discharge rate is shown in Fig. 12; as mentioned earlier, low rate cells show quite small temperature increases and high energy densities. However, the improvement of energy density with number of electrode pairs is a relatively small effect even at

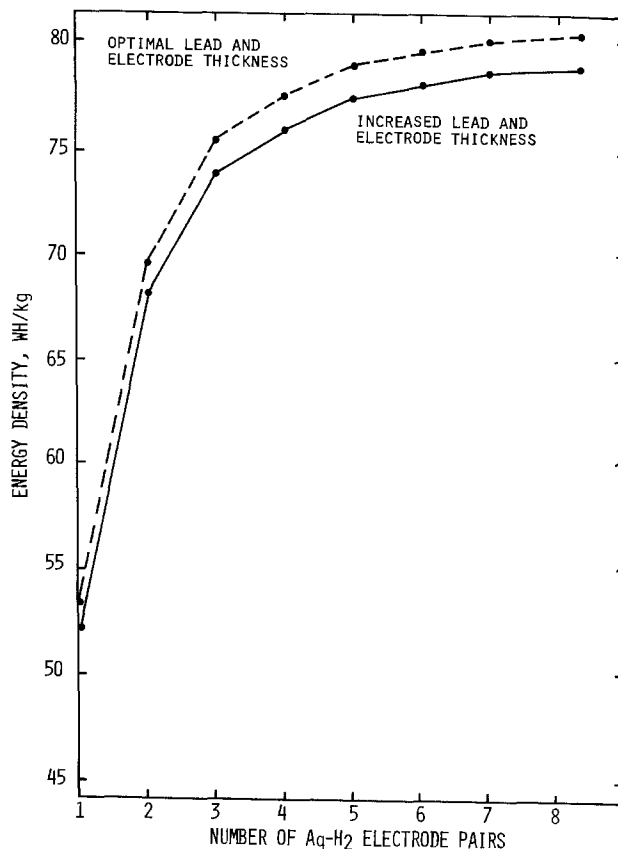


Fig. 8. Effect on energy density of increasing the number of electrode pairs.

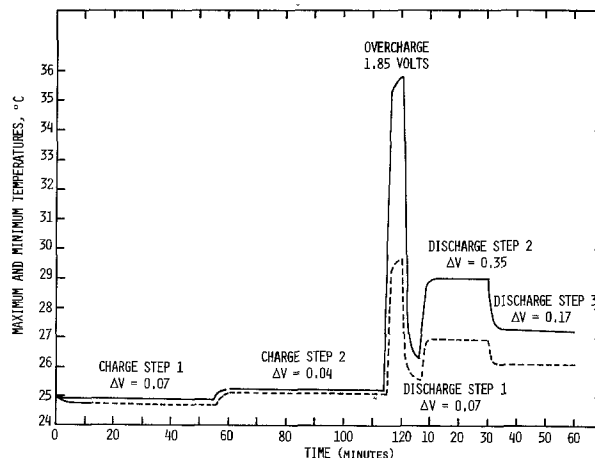


Fig. 9. Temperature changes in a battery with 3 pairs of Ag/H₂ electrodes. ΔV is the difference between the cell potential and the thermoneutral potential.

low rates, and there seems to be little gain in increasing the number of electrode pairs beyond 3 or 4.

One final comparison is shown in Fig. 13; here the number of Ag electrodes has been varied simultaneously with their thickness. It appears that the 25 mil thickness we have selected is close to optimal, particularly for low-rate cells. Thinner electrodes are probably not practical, since their use would require a larger number of layers or a pressure vessel with a greater ratio of length to radius.

Conclusions

We have demonstrated the feasibility of Ag-H₂ cells with energy densities in the range 70-110 W-hr/kg, depending on the rate of discharge. Such cells are capable of extended cycle life, in excess of 1000 deep discharge cycles, despite the solubility of silver oxide. We have

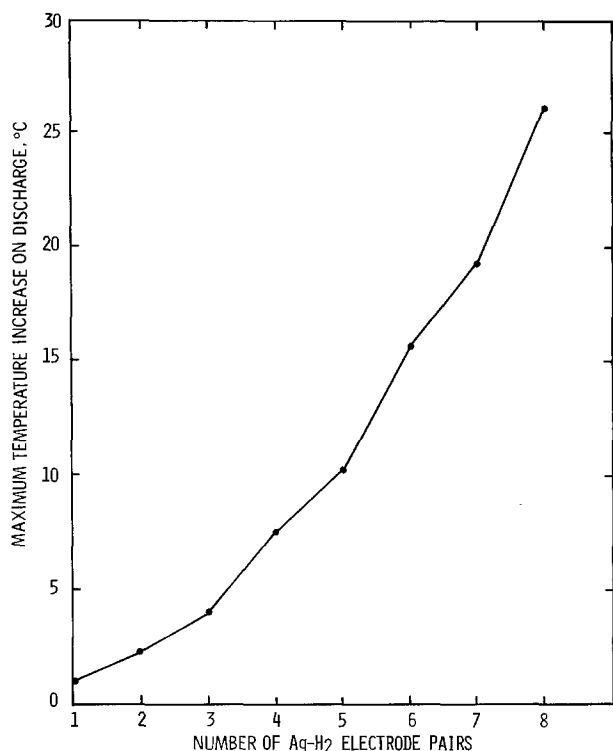


Fig. 10. Effect on maximum discharge temperature of increasing the number of electrode pairs; C-rate discharge.

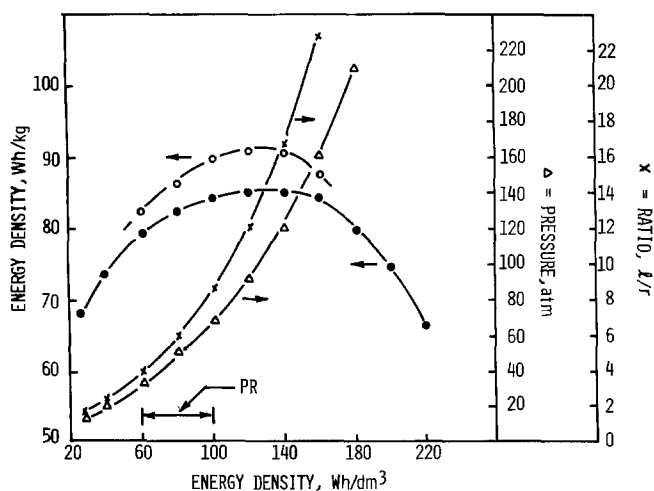


Fig. 11. Change in weight energy density as a function of volume energy density of a rolled 50 A-hr Ag/H₂ cell with corresponding changes in cell pressure and ratio between cell length and radius. Discharge rate C/1.5. ● = 3 electrode layers, ○ = 4 electrode layers, PR = practical range.

systematically investigated the dependence of the energy density on a number of factors, including pressure vessel length, radius, thickness, volumetric energy density, electrode thickness, and number of layers in the electrode roll. We showed that Ag-H₂ cells of rolled design with reasonably conventional shapes are practical and have attractive performance characteristics.

Acknowledgments

This investigation was supported by the U.S. Air Force Aero Propulsion Laboratory, Wright Patterson AFB, Ohio, under Contract No. F33615-76-C-2093.

Manuscript submitted Aug. 6, 1979; revised manuscript received Dec. 13, 1979.

Any discussion of this paper will appear in a Discussion Section to be published in the December 1980

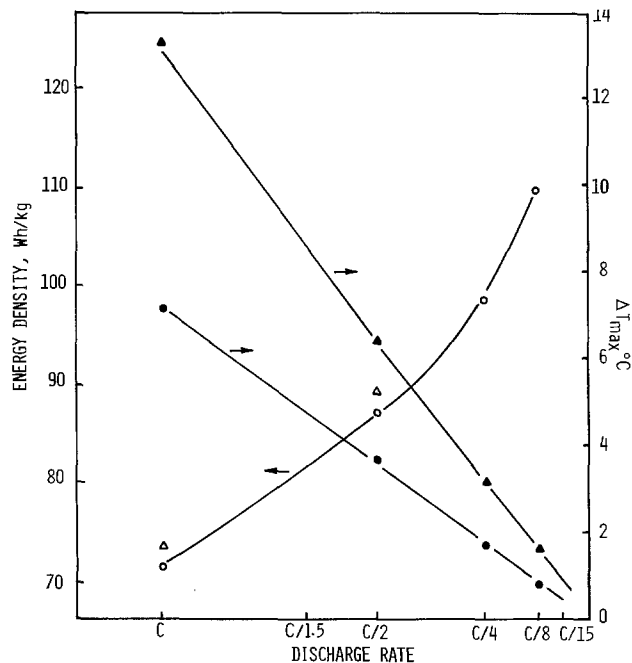


Fig. 12. Energy density and maximum temperature difference of a rolled 50 A-hr Ag/H₂ cell as a function of cell configuration and discharge rate. ●, ○ = 3 electrode layers; △, ▲ = 4 electrode layers.

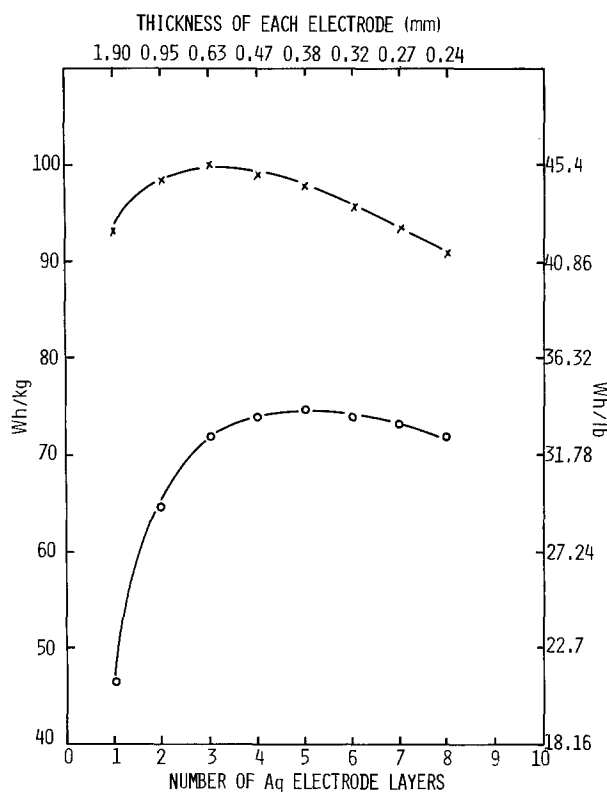


Fig. 13. Energy density of a rolled 50 A-hr Ag/H₂ cell with a constant amount of Ag as a function of the number of Ag electrodes. × = C/4 rate, ○ = C rate.

JOURNAL. All discussions for the December 1980 Discussion Section should be submitted by Aug. 1, 1980.

REFERENCES

- H. H. Bode *et al.*, in "Zinc-Silver Oxide Batteries," A. Fleischer and J. J. Lander, Editors, John Wiley & Sons, Inc., New York (1971).
- R. J. Haas and D. C. Briggs, in "Proc. 8th IECEC," p. 116, Philadelphia, Pa. August 1973.
- G. L. Holleck, M. J. Turchan, F. S. Shuker, D. J. DeBiccari, and P. O'D. Offenhardt, in "Power

- Sources 7," J. Thompson, Editor, p. 271, Academic Press, New York (1979).
4. M. Klein, "Power Sources 5," p. 375, Academic Press, New York (1975).
 5. A. Charkey and M. Klein, in "Proc. 28th Power Sources Symposium," p. 145, Atlantic City, N.J. (1978).
 6. G. L. Holleck, M. J. Turner, and P. O'D. Offenhardt, *This Journal*, **124**, 275C (1977).
 7. P. O'D. Offenhardt and G. L. Holleck, In preparation.
 8. G. L. Holleck, M. J. Turchan, F. S. Shuker, D. DeBiccari, M. J. Turner, and P. O'D. Offenhardt, Final Report AFAPL-TR-78-65 for Air Force Aero Propulsion Lab., Wright-Patterson AFB, Ohio.

Surface Area Loss of Platinum Supported on Carbon in Phosphoric Acid Electrolyte

G. A. Gruver,* R. F. Pascoe,¹ and H. R. Kunz*

United Technologies Corporation, Power Systems Division, South Windsor, Connecticut 06074

ABSTRACT

An experimental study was conducted to determine the surface area loss of platinum supported on carbon in a 191°C phosphoric acid fuel cell environment and to define the mechanism for this process. The surface area was found to decline rapidly initially, but remains above 20 m²/g for 20,000 hr, the longest time period investigated. A study of the effect of operating potential, transmission electron microscope studies of electrodes, and Pt deposited on a carbon film, and the results of other previous studies indicate that crystallite migration and coalescence are the major mode by which Pt surface area is lost in this situation.

A significant mode of decay of the performance of fuel cells which use phosphoric acid (H₃PO₄) as the electrolyte and platinum (Pt) catalyst on the cathode is the loss of surface area of that catalyst with time. Platinum black fuel cell electrodes have been reported to experience a rapid decrease in the surface area of the Pt during operation (1-5) which results in a decrease in electrode performance. A densification of the Pt black agglomerates accompanies this loss of area (4). This sintering process occurs by surface diffusion of Pt atoms to sites of lower surface energy (3-5).

Supported Pt has also been found to experience an area loss in the fuel cell environment. Connolly *et al.* (6) found that a rapid growth of supported platinum crystallites occurred when in contact with a conducting electrolyte. The associated Pt area losses ranged from 5 to 90% of the initial area depending on initial crystallite size, temperature, type of support, and electrolyte. No detectable area losses were found due to heating in air or argon at temperatures 100°C higher than those at which large area losses occurred in electrolytes. The loss of surface area was therefore thought to be caused (possibly) by the migration of complex platinum ions through solution.

Tseung and Dhara (5) similarly found that the area of Pt supported on graphite did not change when heated in air whereas the Pt area did decrease when the Pt was used in a fuel cell electrode. As a result they also concluded that supported Pt sintered by a dissolution/redeposition mechanism, i.e., small particles dissolve in solution by virtue of their greater surface energy and the dissolved Pt diffuses along a concentration gradient to the larger particles. However, others (7-9) found that Pt supported on graphite did lose surface area when heated in a gaseous environment, thus suggesting a different sintering mechanism or that a reinterpretation of the supported Pt sintering mechanism was required.

In addition to the dissolution/redeposition mechanism, surface area loss by supported catalysts is thought

to occur (10, 11) either by crystallite migration over the surface of the support material accompanied by liquid-like coalescence of the crystallites (12, 13) or by interparticle migration of single atoms (14, 15). Bett *et al.* (16) found rapid crystal growth of Pt supported on graphitized carbon black below 200°C when exposed to H₃PO₄ and other liquid environments. The nature of the liquid environment did not appear to have an influence on the rate of Pt surface area loss although exposure to hydrogen gas at temperatures below 600°C did not result in significant area loss. Since the crystallite growth did not depend on potential or the Pt content of the catalyst, they concluded that the migration of Pt atoms on the surface of the carbon was the likely mechanism of area loss. They had previously concluded that crystallite migration was the mechanism of area loss of this supported catalyst in a gaseous environment (17). Blurton *et al.* (18) also found little effect of operating potential on the rate of Pt surface area loss in H₃PO₄ electrolyte. They concluded, however, that crystallite migration is the most likely mode in this environment.

Wong *et al.* (19) studied the surface area loss of Pt supported on graphite single crystals. They found that both atom and crystallite migration occurred at 100°C depending on the nature of the gaseous environment.

Because of the importance of Pt surface area on the performance of H₃PO₄ electrolyte fuel cells, further studies were performed to evaluate the extent of the area loss and to define the mechanism of this loss.

Experimental Procedures

Fuel cell electrodes.—Teflon-bonded fuel cell electrodes, such as those described by Kunz and Gruver (20), were used to determine the effect of time and operating potential on Pt area loss. The catalyst used was 10 weight percent (w/o) Pt dispersed on carbon (Vulcan XC-72, Cabot Corporation). Catalyst loadings were in the range of 0.25-0.60 mg Pt/cm² of electrode area. The initial Pt areas for these catalysts were in the range of 80-120 m²/g. These electrodes were used in operating 5.08 by 5.08 cm fuel cells to determine the

* Electrochemical Society Active Member.

¹ Present address: Union Camp Corporation, Princeton, New Jersey 08540.

Key words: fuel cells, sintering, catalyst, crystallite, platinum.

effect of operating time on area loss; the test electrode was the cathode. These cells were operated continuously at a constant temperature of 191°C and at a current density of 215 mA/cm² with ambient pressure air as the cathode reactant. This resulted in a cathode potential of about 0.7V with respect to the hydrogen potential in the same electrolyte. H₃PO₄ concentrations were maintained at 100-101% by appropriate anode fuel saturation with water.

Experiments to determine the effect of operating potential on Pt area loss were done in a 2000 ml Teflon-lined reaction kettle. Provisions were made so that up to ten samples could be tested simultaneously. A de-ganged potentiostat system provided individual potential control for each test sample, using a common static hydrogen reference electrode and a common Pt counterelectrode in the same electrolyte. The test electrodes were pre-flooded with electrolyte and potentiostated at the desired potential for 100 hr at 191°C. Adequately humidified N₂ was passed over the surface of the electrolyte to maintain the H₃PO₄ concentration at 101%.

Surface areas of the Pt catalysts were determined using both the transmission electron microscope (TEM) and an electrochemical technique. The TEM approach consisted of photographing catalyst fragments supported on a nickel grid at a direct magnification of 113,000× in a Phillips EM-300 TEM. Positive transparencies of these micrographs were prepared at an additional 3× magnification. The diameters of a large sampling of Pt crystallites were measured from the transparencies using a Zeiss Particle Analyzer. Since most of the crystallites observed in the photomicrographs appeared to be roughly circular in shape, it was assumed the crystallites were spheres of diameter d_i . By considering the surface area, volume, and density of such spheres, the final calculated surface area was expressed by

$$\text{Pt Surface Area (m}^2\text{/g)} = a \frac{\sum d_i^2}{\sum d_i^3} \quad [1]$$

where a is a proportionality constant involving the density of Pt as well as the magnification factor when d_i is measured directly in millimeters off the micrograph. Pt surface areas derived in this manner were in good agreement with those measured electrochemically.

Electrochemical areas were measured on electrode samples by pre-flooding them with electrolyte and measuring the charge associated with hydrogen adsorption capacity (9) in 50% H₃PO₄, recorded during potentiodynamic sweeps. The electrochemical measurements were made in a conventional three-chambered cell at room temperature with nitrogen degassing of the electrolyte for 20 min prior to the measurement. Reagent grade 85% H₃PO₄ (Mallinckrodt) was used without additional purification and was diluted to 50 w/o with distilled water.

Platinum deposited on carbon films.—Conventional TEM carbon support films were prepared on surfactant-coated microscope slides and floated off onto gold grids. These were then placed in a vacuum system and fine table salt was applied directly onto the films prior to evacuation. The salt was used to shield areas on the film and prevent uniform Pt deposition. After establishing a vacuum of 1×10^{-5} Torr, a 1 mm length of platinum-carbon pellet (30% Pt) was evaporated onto the support film at a distance of 5 cm. Upon removal from the vacuum system, the specimen was inverted and lightly tapped to remove the salt crystals. A second gold "finder grid" was aligned with the support grid and spot-welded into place. An annealed 0.02 cm diam gold wire (2.5 cm length) was also spot-welded to the grid edge to facilitate specimen handling.

Several observations of the sample in the microscope at various direct magnifications up to 113,000× were required to identify and locate for future reference regions where an interface existed between areas of Pt on carbon and the salt-shielded zones of the carbon

film. Bright-field observations and darkfield Pt (111) reflections were used to establish the presence of Pt on one side of the interface and the absence of Pt on the other side. The "finder grid" enabled one to locate these same areas for viewing after the sintering tests.

Once several suitable areas were identified, the sample (gold grid/platinum on carbon substrate/gold grid) was submerged in 102 w/o H₃PO₄ at 191°C and potentiostated at 0.7V (*vs.* NHE in the same electrolyte). The volume of acid in the test cell was approximately 0.6 liters; appropriately humidified nitrogen was continuously passed over the surface of the acid to exclude oxygen and to maintain a constant acid concentration. The counterelectrode used was a porous graphite ring. The sample was withdrawn after 24 hr at these conditions, washed in distilled water, vacuum dried, and then observed in the TEM. Photomicrographs were made and the sample was returned to the electrochemical environment for an additional 76 hr of testing. The sample was again processed as above and observed in the TEM.

Results

The experimental data of Pt surface area from fuel cell electrodes as a function of operating time are shown in Fig. 1. Results obtained using both the TEM and electrochemical area determinations are presented. The surface area of the Pt can be seen to decline rapidly at first and then tends to level off with an area of about 20 m²/g being reached after 20,000 hr. Figure 2 shows that a good linear relationship exists between ln surface area and ln t , as would be predicted using various theoretical models (12).

TEM photographs of the catalysts from four of the electrodes used in this study are shown in Fig. 3. These photographs show more dramatically the changing rate of surface area loss with time.

The effect of operating potential on the loss of surface area is shown in Fig. 4. The fraction of the initial surface area remaining after 100 hr can be seen to be

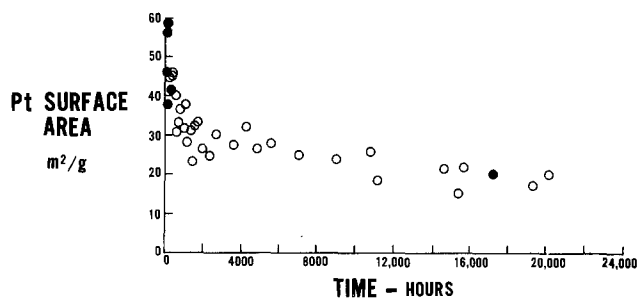


Fig. 1. Surface area loss with time at 191°C in H₃PO₄ for Pt supported on Vulcan XC-72. ○ Determined electrochemically; ● determined using transmission electron microscope.

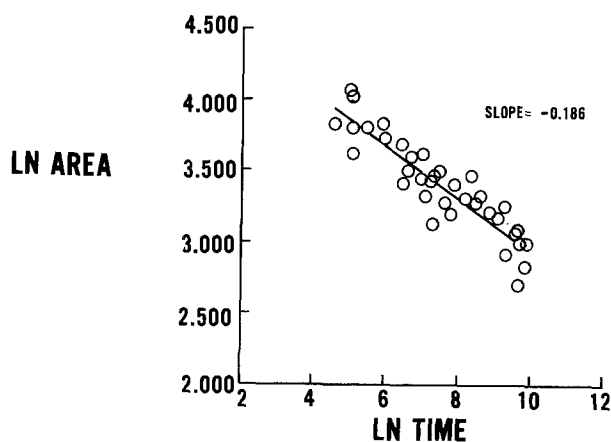


Fig. 2. Plot of ln area as a function of ln t for Pt supported on Vulcan XC-72 at 191°C in H₃PO₄.

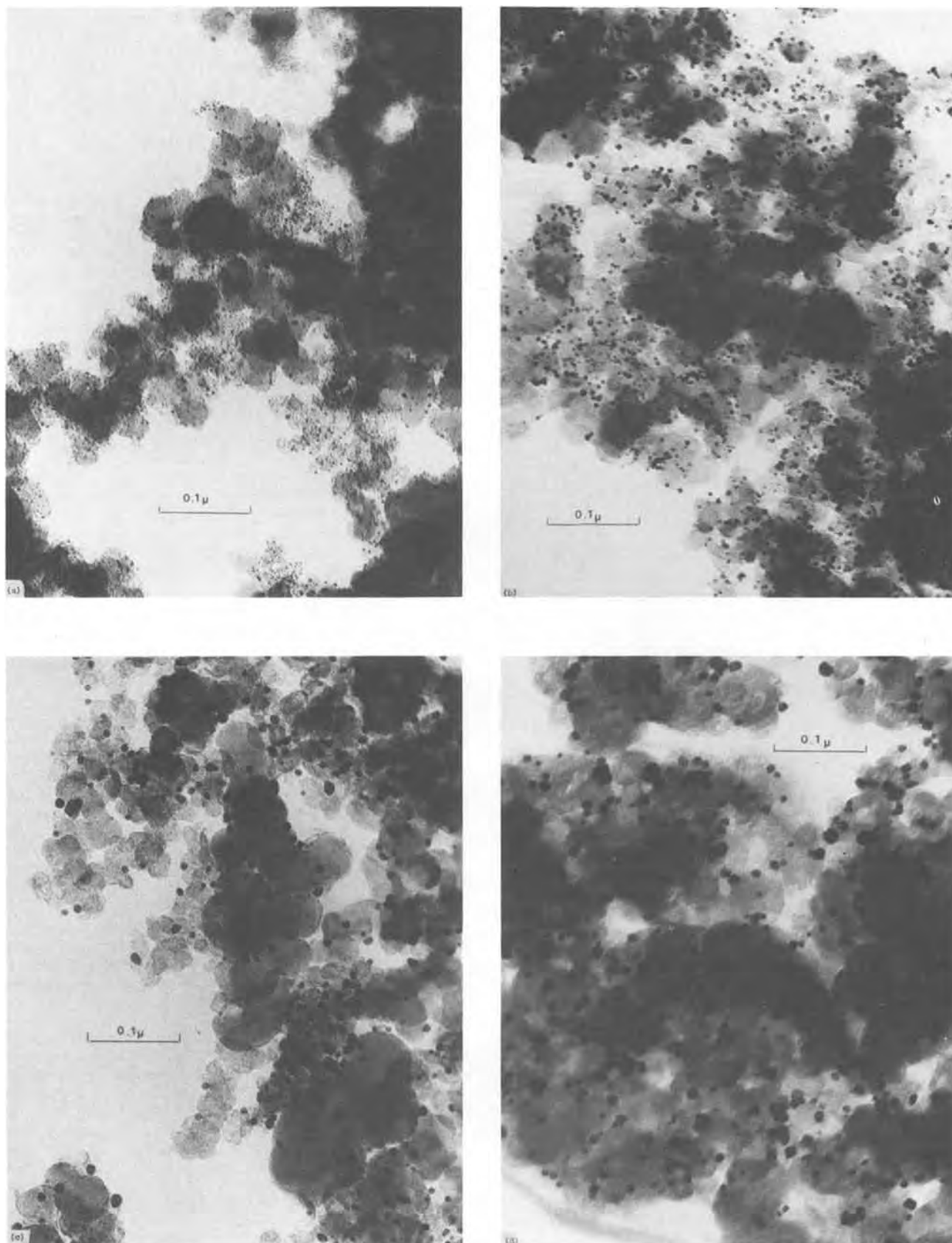


Fig. 3. Electron micrographs of Pt supported on Vulcan XC-72 after various times of operation at 191°C in H_3PO_4 . (a) 0 hr; (b) 100 hr; (c) 1,050 hr; (d) 20,201 hr.

relatively insensitive to operating potential, although the final area is somewhat lower at 0.7V (fuel cell cathode potential) than 0.0V (fuel cell anode potential).

The results of the carbon film experiments are shown in Fig. 5 and 6. Figure 5(a) shows a transmission electron micrograph of the sample before any exposure to H_3PO_4 . An extremely fine (1.0-1.5 nm particle size) and

uniform distribution of the Pt is evident. After 24 hr of exposure to the H_3PO_4 , agglomerates of significantly enlarged Pt particles of fairly uniform size can be seen [Fig. 5(b)]. After further exposure to 100 hr accumulated time, further agglomeration of the Pt particles can be seen [Fig. 5(c)]. The size of the prime particles appears to have changed little between 24 and 100 hr.

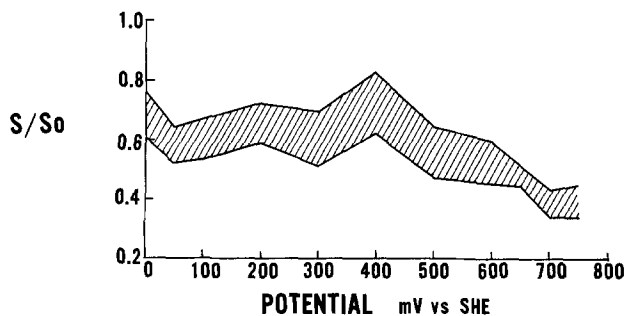


Fig. 4. Platinum area (S) relative to initial area (S_0) as a function of electrode potential after 100 hr at 191°C in H_3PO_4 .

Figure 6 is a micrograph taken after 24 hr exposure showing a region where an interface between the Pt on carbon and the salt-shielded carbon zone exists.

Discussion

The surface area of Pt supported on carbon decreases considerably in H_3PO_4 at 191°C at fuel cell cathode potentials, from between 50 and 60 m^2/g at 100 hr to about 20 m^2/g after 20,000 hr. The surface area, however, is maintained much above that which would result for unsupported Pt black. The initial surface area for Pt black is 20–30 m^2/g and rapid surface area loss results; a surface area equal to about 10 m^2/g is reached after 200 hr at 150°C in 96% H_3PO_4 (4).

The significance of this area loss on fuel cell performance depends on the change in activity of the catalyst as the surface area of the catalyst changes. For a constant Tafel slope of 90 mV/decade (9) and constant catalyst activity per unit Pt area, a change in surface area by a factor of 2 results in a loss in performance of 27 mV and a factor of 3 in 42 mV. However, Bregoli (21) has shown that the catalytic properties of Pt are crystallite size dependent, with the current per unit of Pt surface area and the Tafel slope for oxygen reduction increasing as the surface area of the Pt decreases. The changing activity of the Pt results in a reduced performance loss due to loss of Pt surface area.

The experimental data obtained in this study can be used to help ascertain the mechanism by which Pt surface area loss occurs. As shown in Fig. 2, a good linear relationship exists between \ln area and $\ln t$. This would be predicted if the general sintering model of Ruckenstein and Pulvermacher (12), which considers crystallite migration, collision, and coalescence, applies to the present experimental situation and if the initial surface areas of the catalysts tested were the same. A least squares correlation of the data is highly significant (considering the catalysts tested had slightly different initial metal areas) and would indicate that the sintering mechanism is rate controlled by particle migration rather than particle coalescence [calculated n value is 6.4; see Ref. (12)] and that the mechanism does not change as the catalyst ages. Routine TEM analysis of sintered catalysts (see Fig. 3) always show the Pt crystallites to be roughly spherical and not elongated or "necked" as one might expect to see if coalescence of particles was rate limiting. One must be cautioned, however, against attaching too much significance to conclusions based on agreement between results using the model of Ruckenstein and Pulvermacher and experimental data obtained here since there are experimental data previously reported which cannot be explained by this model (22), and other parameters not included in the model are thought to be important. Therefore, other experimental data must also be used to determine the mechanism by which Pt surface area is lost.

The study of the effect of operating potential and the TEM studies can be used to provide additional information. Figure 4 shows that the electrode operating potential has only a small effect on the rate of surface area loss. If the dissolution of an electroactive species

such as a platinum ion were the mechanism by which Pt surface area is lost, a much stronger potential dependency would be expected. A small potential dependency was also found for Pt black (4) and Pt supported on graphitized carbon black (16, 18). The nature of the liquid environment (organic liquids, water, 96% H_3PO_4) also was found to have a smaller effect on the rate of Pt area loss than would be expected if Pt dissolution were important (16). Post-test quantitative analyses for Pt on the electrodes which provided the area loss data shown in Fig. 1 and 2 showed no significant change in Pt loadings over the duration of the tests. If dissolution occurred to a high degree, decreased Pt loadings would be expected on the cathodes and corresponding loading increases would result at either the anodes or matrices where dissolved Pt would be reduced out of solution. Based on the results of these tests at various potentials, a dissolution-redeposition mechanism can be eliminated as the primary mechanism by which Pt area is lost over the potential range investigated.

The TEM photographs of fuel cell catalyst in Fig. 3 show that the Pt crystallites are initially distributed uniformly over the carbon support material but are located at the interstices of the carbon prime particles after a period of operation. Little clustering of the Pt crystallites is evident. Pt migration might occur through the migration of adsorbed atoms or atom clusters or by the migration of entire crystallites along the carbon surface. If the entire crystallite migrates, sintering of clusters of crystallites must be occurring rapidly in the time scale of this experiment.

The distribution of particle sizes of sintered supported catalysts is believed to allow discrimination between crystallite and atom migration processes (23, 24). Pt particle size distributions for the present sintered catalysts were typically like those previously reported for Pt supported on graphitized carbon black (18), with no tail on the small particle diameter side of the peak in the distribution curves such as would be expected if an Ostwald ripening/atom migration process were occurring (23). The absence of small particles in the sintered catalysts shown in Fig. 3b, c, and d adds visual support to this argument. However, there is disagreement on the interpretation of crystallite size distribution analyses for distinguishing between these two mechanisms (25, 24). The TEM photomicrographs of Pt deposited on carbon film shown in Fig. 5 provided additional information on this question.

Figure 5a shows the initial, uniform dispersion of 1.0–1.5 nm Pt particles on the surface of the carbon film substrate. Figure 5b shows the Pt crystallites after being potentiostated at 0.7V for 24 hr in 102 w/o H_3PO_4 at 191°C. The crystallites have increased in size to about 8 nm and considerable clustering is observed. An approximate mass balance calculated by analyses of TEM micrographs of this sintered Pt indicates that the Pt cannot all be present as spherical crystallites, but that some of it must be present as flat rafts or islands. The variation in darkness of some of the crystallites indicates that some regions are thickening into more spherical particles. This first stage of area loss could have occurred either by atom or crystallite migration. If atom migration occurred, some Pt particles less than 1.0 nm would be expected to be present. However, these are difficult to observe. If particle migration occurred, some coalescence of particles must have taken place since the Pt particles have grown from the 1.0–1.5 nm range to about 8 nm. A considerable degree of necking can be seen between these larger particles, indicating that smaller particles might have completely coalesced. After 100 hr of exposure (Fig. 5c), the size of the prime particles does not appear to have changed significantly, but much more clustering and sintering of clusters is evident. This change can occur only if the Pt crystallites move; atom migration would be expected to result in growth of the 8 nm crystallites.

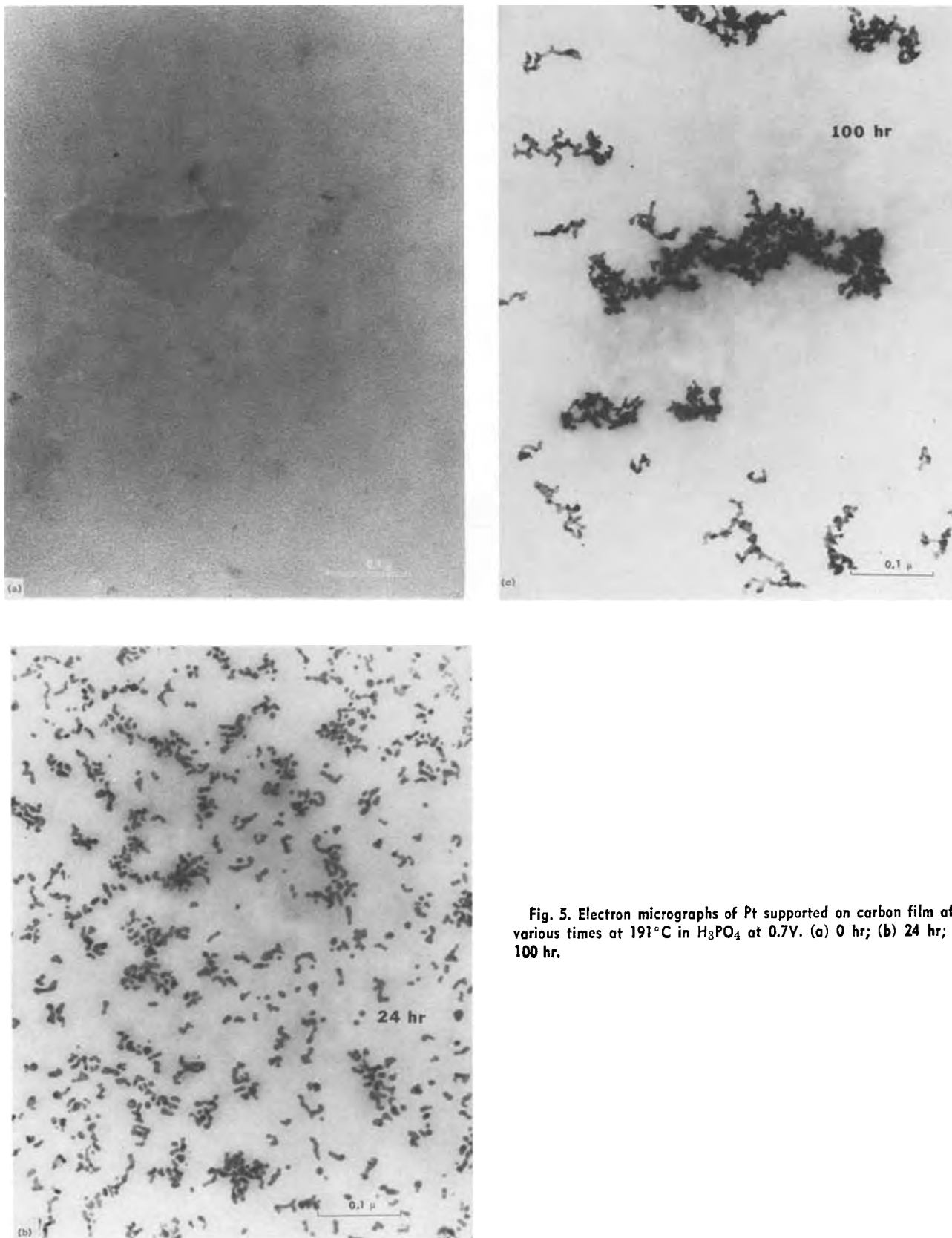


Fig. 5. Electron micrographs of Pt supported on carbon film after various times at 191°C in H_3PO_4 at 0.7V. (a) 0 hr; (b) 24 hr; (c) 100 hr.

This clustering implies that the rate-determining step for sintering during this time period on the carbon film is coalescence and not migration or the activation of a crystallite to migrate. This clustering is not evident for the fuel cell catalysts supported on high surface area carbon (Fig. 3). It may be that this type of surface requires more activation for the crystallites to become mobile and migrate, such that coalescence is not rate determining. The fact that the Pt has sintered so much more rapidly on the carbon film lends support to this hypothesis.

Several observations can be made from areas which were partially shielded during the Pt vapor deposition and show an interfacial region between the Pt on carbon and the bare carbon areas. Figure 6 shows such a region after 24 hr exposure to the acid environment. In this region the Pt chain length is less and the clean void space around clusters indicate that some of the Pt was transported over distances in excess of 100 nm. This observation also provides evidence against a process involving significant dissolution/redeposition of the Pt. Dissolution would be most likely to occur with the

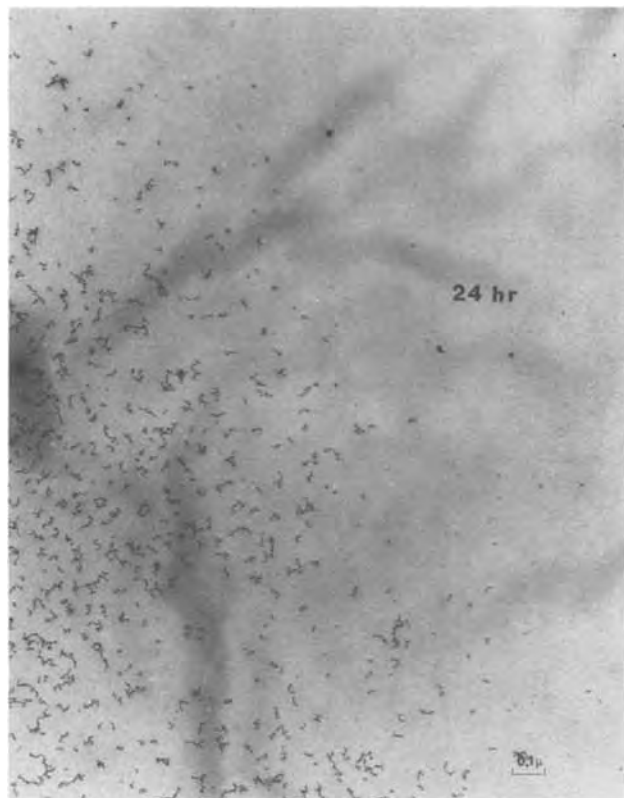


Fig. 6. Electron micrograph showing the interfacial region of the Pt-carbon and salt-shielded carbon areas after exposure to H_3PO_4 at 191°C for 24 hr.

Pt in its original highly dispersed state. In addition, the Pt is supported on essentially a planar carbon surface and is exposed to a relatively large volume of electrolyte. Under these circumstances, it is very unlikely that any Pt which might dissolve could plate out of solution somewhere else on the carbon surface. Thus, the presence of clusters formed by Pt which has been transported over large distances argues against significant dissolution of the Pt, and implies that the forces between the carbon surface and the Pt are sufficient to restrict the Pt crystallites to the carbon surface.

All things considered, this study using Pt supported on a carbon film indicates that crystallite migration is the major mode of surface area loss. And, in fact, the surface treatment of graphitic supports to retard crystallite migration was found to affect the rate of Pt area loss in 102% H_3PO_4 at 191°C (18). Previously, Bett *et al.* presented data demonstrating that the rate of area loss for Pt supported on graphitized carbon black is dependent on the concentration of the dispersed Pt in a gas phase environment (17), but is independent of Pt concentration over a range of 5-20 w/o in a H_3PO_4 environment (16). They reasoned that, if in the mechanism of crystallite migration the rate-determining step is the migration of the crystallite across the surface of the support, the rate of Pt area loss should depend on the Pt concentration. Thus they concluded that in the gas phase environment the migration of Pt crystallites on the carbon surface is the process by which Pt is transferred from one crystallite to another, but that atom migration was the mechanism in H_3PO_4 . However, since the present studies indicate that crystallite migration is the major mode of area loss, the rate-determining step is apparently not the migration but some other process, perhaps the activation of a crystallite to become mobile.

Conclusions

The experimental results lead to the following conclusions:

1. Supporting Pt on carbon results in an H_3PO_4 fuel cell catalyst that maintains a surface area above $20\text{ m}^2/\text{g}$ for 20,000 hr at 191°C . Longer time data are not yet available.

2. The mechanism by which Pt surface area is lost for Pt supported on carbon in an H_3PO_4 acid environment is not a dissolution-redeposition mechanism in the potential range from 0 to about 0.75V. Although atom migration on the support may be a secondary factor, crystallite migration is the major mode of area loss.

Acknowledgment

The authors gratefully acknowledge the technical contributions of D. G. Pilney of United Technologies Research Center in preparing the Pt-carbon film specimens and for all TEM work reported in this study.

Manuscript submitted May 1, 1979; revised manuscript received Oct. 11, 1979. This was Paper 311 presented at the Pittsburgh, Pennsylvania, Meeting of the Society, Oct. 15-20, 1978.

Any discussion of this paper will appear in a Discussion Section to be published in the December 1980 JOURNAL. All discussions for the December 1980 Discussion Section should be submitted by Aug. 1, 1980.

Publication costs of this article were assisted by United Technologies Corporation.

REFERENCES

1. R. Thacker, *Nature*, **212**, 182 (1966).
2. J. Giner, J. M. Parry, S. Smith, and M. Turchan, *This Journal*, **116**, 1692 (1969).
3. P. Stonehart and P. A. Zucks, *Electrochim. Acta*, **17**, 2333 (1972).
4. K. Kinoshita, K. Routsis, J. A. S. Bett, and C. S. Brooks, *ibid.*, **18**, 953 (1973).
5. A. C. Tseung and S. C. Dhara, *ibid.*, **20**, 681 (1975).
6. J. F. Connolly, R. J. Flannery, and B. L. Meyers, *This Journal*, **114**, 241 (1967).
7. K. F. Blurton, *Carbon*, **10**, 305 (1972).
8. L. J. Hillenbrand and J. W. Lacksonen, *This Journal*, **112**, 245 (1965).
9. J. Bett, K. Kinoshita, K. Routsis, and P. Stonehart, *J. Catal.*, **29**, 160 (1973).
10. S. C. Wanke and P. C. Flynn, *Catal. Rev. Sci. Eng.*, **12**, 93 (1975).
11. P. Wynblatt and N. A. Gjostein, *Prog. Solid State Chem.*, **9**, 22 (1975).
12. E. Ruckenstein and B. Pulvermacker, *AIChE J.*, **19**, 356 (1973).
13. E. Ruckenstein and R. Pulvermacker, *J. Catal.*, **29**, 224 (1973).
14. P. C. Flynn and S. E. Wanke, *ibid.*, **34**, 390 (1974).
15. P. C. Flynn and S. E. Wanke, *ibid.*, **34**, 400 (1974).
16. J. A. S. Bett, K. Kinoshita, and P. Stonehart, *ibid.*, **41**, 124 (1976).
17. J. A. S. Bett, K. Kinoshita, and P. Stonehart, *ibid.*, **35**, 307 (1974).
18. K. F. Blurton, H. R. Kunz, and D. R. Rutt, *Electrochim. Acta*, **23**, 183 (1978).
19. S. Wong, M. Flytzani-Stephanopoulos, M. Chen, T. E. Hutchinson, and L. D. Schmidt, *J. Vac. Sci. Technol.*, **14**, 452 (1977).
20. H. R. Kunz and G. A. Gruver, *This Journal*, **122**, 1279 (1975).
21. L. Bregoli, *Electrochim. Acta*, **23**, 489 (1978).
22. S. E. Wanke and P. C. Flynn, *Catal. Rev. Sci. Eng.*, **12**, 93 (1975).
23. C. G. Granqvist and R. A. Buhrman, *J. Catal.*, **42**, 477 (1976).
24. C. G. Granqvist and R. A. Buhrman, *ibid.*, **46**, 238 (1977).
25. S. E. Wanke, *ibid.*, **46**, 234 (1977).

Electrical Data of Sodium/Sulfur Cells Operating with Dissolved Catholyte

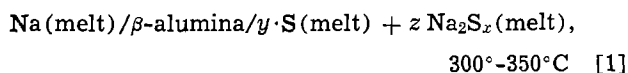
G. Weddigen

Brown, Boveri & Cie AG., Central Research Laboratory, D-6900 Heidelberg, Germany

ABSTRACT

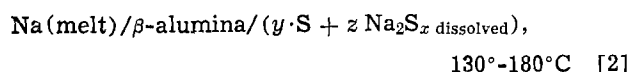
Usual sodium/sulfur cells have an operating temperature of 300°C or higher. Thus the precipitation of solid polysulfides can be avoided during discharge until a stoichiometry of Na₂S₃ has been obtained in the sulfur compartment. Using organic solvents it becomes possible to discharge sodium/sulfur cells even up to the catholyte composition of Na₂S. Besides this the operating temperature can be lowered to 150°C (1). It is shown how rechargeability and internal resistance depend on temperature, solvent, and additives.

Many groups throughout the world are developing Na/S cells of the type

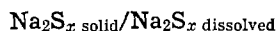


Even at this relatively high operating temperature of 300°-350°C the cells can only be discharged up to an average sodium polysulfide composition of Na₂S₃ as the more sodium-rich compounds exhibit melting temperatures above 350°C. Thus only one-third of the theoretical cell capacity and only three-fifths of the theoretical energy density can be realized.

Experiments with cells of the type (1-3)



show that the following cell properties are changed in comparison to cell type [1]: (i) the internal resistance is increased, (ii) capacity and sulfur utilization are increased, (iii) the current density is decreased, (iv) the corrosion rate is decreased, (v) the operation temperature is lower, (vi) plastic materials with lower specific weight can be used as cell components and (vii) in the sulfur electrode a new phase boundary occurs



The organic solvent has to fulfill the following requirements: (i) stability with respect to sulfur and sodium polysulfide at 130°-180°C, (ii) solubility for polysulfides and sulfur, and (iii) high dissolution speed of liquid sulfur layers and solid Na₂S layers in organic Na₂S_x solutions.

In the case of cell type [1] the open-circuit voltage of a charged cell amounts to 2.08V. In case of cell type [2] a higher open-circuit voltage (2.14-2.17V) is obtained. It can be explained by the temperature dependence on the emf and by the solvation energy arising from the reactions

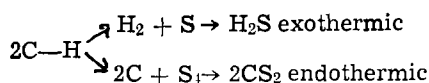


and



Results

Stability tests.—The organic solvents considered are hydrocarbon compounds. In contact with sulfur the C—H bond can be decomposed and the following reactions are imaginable



Key words: organic electrolyte, Na/S cells, solubility, energy density.

One can conclude that the C—H bond must be stabilized by the fact that the reaction conditions do not promote a fast reaction rate.

In order to study the thermal stability of solvents in the presence of sulfur and Na₂S_x, the solvents were boiled under reflux over several weeks. 50g of solvent and 5g of sulfur were used in these experiments which were carried out in a nitrogen atmosphere.

The H₂S gas generated by the attack of sulfur on C—H groups and N—H groups was determined daily over a period of several weeks.

Figure 1 shows some examples of the stabilities of different solvents as reacted with sulfur. It is obvious that the structure and nature of functional groups in the different solvents must lead to different results in stability. Theoretical considerations show that sulfur, being a nucleophilic chemical substance, exhibits a great reactivity towards CH acidic C—H groups. The result of such an attack consists of the evolution of H₂S gas and in the formation of a C=C double bond. Certain neighboring functional groups such as —SO₂— or —O— can increase the acidic character of the C—H bond. On the other hand, basic groups such as —N(CH₃)₂— can decrease the acidic character of a C—H bond in a solvent molecule. The solvents diethylene glycoldimethylether (curve 1) and tetrahydrothiophene —S—S dioxide (curve 2) have CH groups and neighboring functional groups which increase the CH acidic character. These solvents were decomposed in contact with sulfur.

In the case of tetramethylurea and of NN'diacetyl NN'dimethylethanediamine no H₂S evolution could be observed (curves 3 and 4).

Solubility and conductivity tests.—Some examples of solubilities of sodium polysulfides in organic solvents are given in Table I. One can conclude from this table that the solubilities of Na₂S₄ and Na₂S are

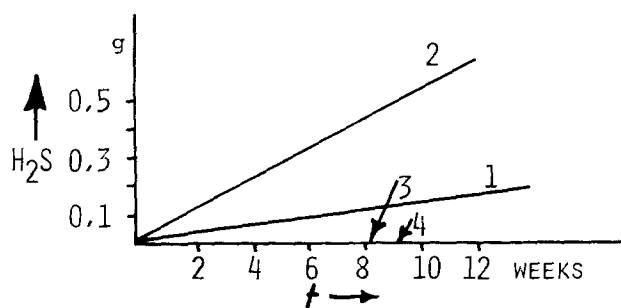


Fig. 1. H₂S evolution of solvents as a function of time. Curve 1, diethylene glycoldimethylether; curve 2, tetrahydrothiophene-S-S dioxide; curve 3, tetramethylurea; and curve 4, NN'diacetyl NN'dimethylethanediamine.

Table I. Solubilities of Na_2S_x in organic solvents

Substance	Solvent	Temperature (°C)	Solubility (g/l)
Na_2S_4	Glycol	166	583.9
Na_2S	Glycol	170	175.0
Na_2S_4	Ethanol	55	108.0
Na_2S_4	Phenol	140	27.0

Table II. Resistivities of saturated Na_2S_4 and Na_2S -solutions

Solvent	Dis-solved sub-stance	ρ (Ωcm)				
		90°C	110°C	130°C	150°C	170°C
Ethyleneglycol	Na_2S_4	58.8	35.5	22.9	14.8	10.9
Diethylenetri-amine	Na_2S_4	67.6	36.3	21.7	14.0	77.6
Furfuryl alcohol	Na_2S_4	216.0	166.0	137.0	105.0	X
Dimethylform-amide	Na_2S_4	65.3	46.0	36.8	28.8	X
Ethyleneglycol	Na_2S	26.9	19.9	14.0	10.6	8.6

high enough in the above mentioned solvents. Unfortunately glycol is not sufficiently stable during long time tests due to the weak acidic character of the OH groups.

The resistivities of saturated Na_2S_4 and Na_2S solutions have been determined. The results (Table II) show that the resistivities are of the same order of magnitude as the resistivity of β -alumina at 150°C.

Half-cell tests.—The results of cathodic half-cell measurements are summarized in Table III.

One can conclude from Table III that mixtures of solvents enable in most cases higher cathodic current densities to be obtained than with pure solvents. This can be explained by the fact that the additives have increased the solubility of Na_2S_4 and the dissolution speed of cathodically deposited Na_2S .

Cell tests.—Cell tests were carried out in reusable glass and metal cells (4). β -alumina containing 2 weight percent (w/o) of magnesia was used as a sodium ion conductor. This solid electrolyte has a specific resistance of approximately 30 Ωcm at 150°C.

A complete cycle (stoichiometry variations between S and Na_2S) could be measured with O-toluenitrile as solvent. This solvent exhibits a relatively weak polarity. Therefore, only a current density of 0.1 mA/cm^2 could be obtained. In another cell 90 cycles with a practical capacity of 70% (100% corresponds to stoichiometry changes between sulfur and Na_2S) were obtained using N methylpyrrolidon as solvent. This is shown in Fig. 2. In this case the current density increased up to 2 mA/cm^2 during discharge and to 4 mA/cm^2 during charge. The addition of tetracyanoethylene enabled one to charge the cell with a higher current density. This experiment was interrupted by the destruction of the β -alumina tube.

Table III. Results of half-cell measurements in different Na_2S_4 solutions, scan rate = 2 mV/sec

Solution No.	Na_2S_4 (g)	Solvent (ml)	Additive (g)	u^* (V)	t (min)	Cath (mA/cm ²)
I	0.5	10 Tetramethylurea	—	-1	4	67.2
II	0.5	9 Tetramethylurea	1 Tetramethylsulfonamide	-1	4	78.4
III	0.5	8 Tetramethylurea	2 Tetramethylsulfonamide	-1	4	58.8
IV	0.5	10 N-methylpyrrolidon	—	-1	4	46.2
V	0.5	9 N-methylpyrrolidon	1 Tetramethylsulfonamide	-1	4	92.4
VI	0.5	8 N-methylpyrrolidon	2 Tetramethylsulfonamide	-1	4	77
VII	0.5	9 N-methylpyrrolidon	1 ml O-tolonenitrile	-1	4	54.6
VIII	0.5	8 N-methylpyrrolidon	2 ml Tolonenitrile	-1	4	61.6

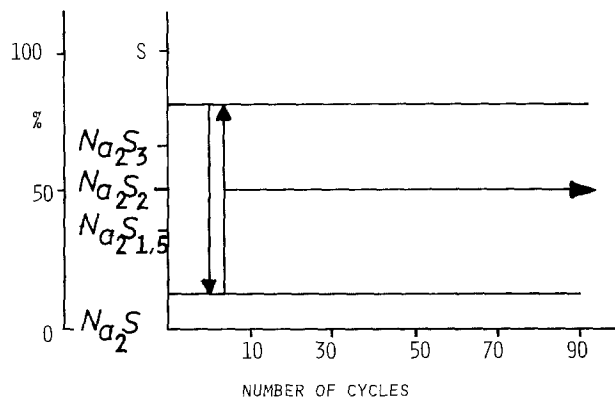
* u = voltage between the working electrode and the reference electrode.

Fig. 2. Stoichiometry changes during cycle tests. Solvent: N methylpyrrolidon.

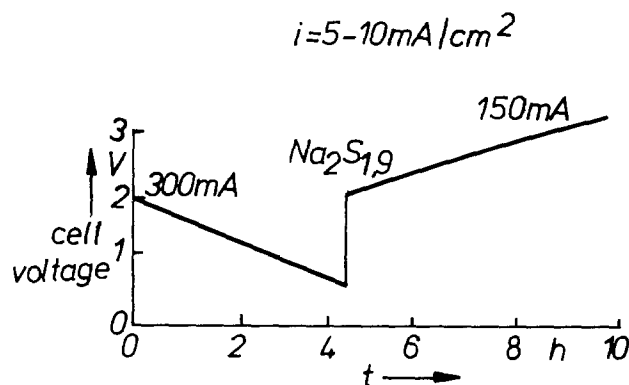


Fig. 3. First cycle of i.t. Na/S cell solvent: N methylpyrrolidon

Another cell with an electrolyte area of 40 cm^2 could be discharged with a current density of 8 mA/cm^2 . The sulfur electrode contained C_6N_4 and tetramethylsulfonamide as additive and N methylpyrrolidon as solvent. In the first discharge cycle 52% of the theoretical capacity could be realized (Fig. 3).

The results of some other cell measurements are represented in Table IV. If the ratio between the mass of sulfur and solvent is higher than 0.1 and the current density higher than 5 mA/cm^2 only small capacity values $C/C_0 < 50\%$ can be obtained. In this case the existence of a solid Na_2S_x phase in the sulfur electrode causes a high diffusion resistivity as the mass transfer between this phase and the liquid phase is very slow. This resistivity contribution could be prevented during the charge cycle of experiment 7. Here the resistivity of surface unity amounted to only 13 Ωcm^2 . This value is to be expected with respect to the specific resistivity of β Al_2O_3 at 150°C and the results of the half-cell measurements.

Table IV. Results of cell tests

Exper. No.	m_s/m_{solvent}	Solvent + additive	T (°C)	i (mA/cm ²)	C/C (%)	Surf. (Ωcm^2)
1	0.11	13 ml NN'dimethylacetamide	130	3.5	53	142
2	0.03	12 ml N-methylpyrrolidone	130	5 → 10	75	50
3	0.10	12 ml tetramethylurea	150	15	23	33
4	0.10	18 ml N-methylpyrrolidone + 18 ml NN'dimethylacetamide	130	10	42	50
5	0.06	10 ml N-methylpyrrolidone + 2g catalyst + 10 ml N-methylpyrrolidone	150	6	85	83
6	0.36	10 ml N-methylpyrrolidone	150	10	15	50
7	0.07	5 ml glycol + 5 ml diethelene-triamine	150	10-20	80	50 13*

* Charge.

Conclusions

It has been shown that solvents exist which are stable against sulfur and sodium polysulfides at 150°C. By using these solvents or mixtures, the sulfur utilization can be doubled in comparison to the capacity of cell type (1). Low temperature sodium sulfur cells can be operated at 150°C with charging and discharging current densities between 3 and 20 mA/cm². The cell properties of the 300°C cell and the 150°C cell are compared in the Tables V and VI. The energy densities of the two cell types become equal when the power of the 150°C cell is 1/10 of the 300°C cell.

Acknowledgments

Thanks are due to Professor Dr. G. Ege and to Dr. W. Fischer for many interesting discussions. The author is grateful to the Brown, Boveri & Cie AG for permission to publish this paper. This work was supported by the German Federal Ministry for Research and Technology (Reference: NT 4471).

Table V. Comparison of cell mass

Mass (g)	300°C molten catholyte	150°C dissolved catholyte
Sulfur	150	60
Solvent	—	200*
Sodium	100	130
β Al ₂ O ₃	50	50
Remaining cell components	280	160
Total	580	600

* $m_s/m_{\text{solvent}} = 0.3$.

Table VI. Comparison of electrical data

Cell type	300°C molten catholyte	150°C dissolved catholyte
A-hr theoretical, C ₀	83	99
A-hr practical, C	66	55
C/C ₀ (%)	80	54
W-hr practical	95	79
W-hr/kg	164	146
Surface unity resistivity (Ωcm^2)	2-3	15-215 ↓ 0-200 (diffusion)
Power density (mW/cm ²)	120 → 220	7 → 30

Manuscript submitted March 27, 1979; revised manuscript received Dec. 29, 1979. This was Paper 37 presented at the Pittsburgh, Pennsylvania, Meeting of the Society, Oct. 15-20, 1978.

Any discussion of this paper will appear in a Discussion Section to be published in the December 1980 JOURNAL. All discussions for the December 1980 Discussion Section should be submitted by Aug. 1, 1980.

Publication costs of this article were assisted by Brown, Boveri & Cie AG.

REFERENCES

- G. Weddigen, U.S. Pat. 1,495,371.
- K. M. Abraham, R. D. Rauh, and S. B. Brummer, *Electrochim. Acta*, **23**, 501 (1978).
- G. Weddigen and W. Fischer, *Chem.-Ing.-Tech.*, **4**, 345 (1977).
- H. Kleinschmager, W. Haar, W. Fischer, and G. Weddigen, in "Proc. of the 10th International Power Sources Symposium," Paper 45, Brighton, England, Sept. 1976.

The Corrosion of Steel by Aqueous Solutions of Hydrogen Sulfide

D. R. Morris,* L. P. Sampaleanu,¹ and D. N. Veysey²

Department of Chemical Engineering, University of New Brunswick, Fredericton, New Brunswick, Canada

ABSTRACT

Steel corrosion has been investigated through polarization studies in aqueous H₂S systems of acid pH using a rotating disk electrode cell. H₂S does not change the Tafel slopes of the anodic and cathodic processes. The anodic curves are shifted toward more negative potentials mainly due to the decrease of the reversible potential of iron, while the exchange current density appears to remain unchanged. The cathodic process maintains the reversible potential and the exchange current density of the H₂S free system, but the H⁺ diffusion control gradually disappears. A corrosion current density dependence on the H₂S concentration is found which matches that obtained from published weight-loss experiments. The product of corrosion, mackinawite is essentially nonadherent and in certain circumstances enhances the corrosion rate. A new method for the compensation of ohmic overpotential in polarization measurements is described.

The corrosion of steel by aqueous H₂S is a significant technical problem in two major industrial areas. In oil refineries and natural gas treatment facilities, the process conditions vary widely due to natural causes (1-4). Replication of the conditions for laboratory work is difficult. The Girdler-Sulphide (GS) process for the production of heavy water involves the use of H₂S as the deuterium exchange agent. The process prescribes the basic pressure/temperature conditions, hence laboratory replication is simpler.

This paper presents the results of studies of the corrosion of carbon steel by deaerated aqueous solutions of H₂S at 25°-30°C using the potentiostatic polarization method and under long term (up to 1000 hr) dynamic exposure conditions.

Theory

According to the electrochemical theory of corrosion, the corrosion process takes place at a mixed potential, E_{corr} between the reversible potentials, E_{revFe} for the anodic process and E_{revH} for the cathodic process, in the absence of oxygen.

The reversible potential, E_{revFe} for the Fe²⁺/Fe electrode is given generally by (5)

$$E_{\text{revFe}} = -0.44 + 0.030 \log [\text{Fe}^{2+}] \quad [1]$$

For the particular case involving aqueous H₂S solutions, the concentration of ferrous ions, [Fe²⁺] is related to the first and second ionization constants of H₂S, K_1 and K_2 , the solubility product of FeS, K_s , and the Henry law constant, k , for the H₂S solution. Inserting numerical values of K_1 , K_2 , and K_s equal to 9.1×10^{-8} , 1.1×10^{-12} , and 3.7×10^{-19} at 18°C, respectively (6), and k equal to 8.3 atm (mole liter⁻¹)⁻¹ (7) at 18°C gives

$$E_{\text{revFe}} = -0.39 - 0.06 \text{pH} - 0.03 \log p_{\text{H}_2\text{S}} \quad [2]$$

where $p_{\text{H}_2\text{S}}$ is the partial pressure of H₂S.

According to Hilbert *et al.* (8), iron with a high density of crystal imperfections dissolves by a catalyzed mechanism (CM) whereas iron with low surface activity dissolves by a noncatalyzed mechanism (NCM). The dissolution reaction is activation controlled with a Tafel slope $b^a = 0.04$ V/decade for the NCM (8-10) and $b^a = 0.03$ V/decade for the CM (11).

The influence of the ferrous ion concentration on the reaction rate is disputed; Bockris and Reddy (12) claim an electrochemical reaction order, $p_{\text{Fe}^{2+}}$

$$p_{\text{Fe}^{2+}}^a \equiv \left(\frac{\partial \log i}{\partial \log [\text{Fe}^{2+}]} \right)_{E, \text{pH}} = 1 \quad [3]$$

where i is the current density. Hilbert *et al.* (8) state that all authors agree that the reaction rate shows no dependence on [Fe²⁺].

The electrochemical reaction order related to pH, $p_{\text{pH}}^a \equiv (\partial \log i / \partial \text{pH})_{E, \text{Fe}^{2+}}$ is agreed to be (8, 12), $p_{\text{pH}}^a = 1 \pm 0.1$ (NCM) and $p_{\text{pH}}^a = 2 \pm 0.3$ (CM).

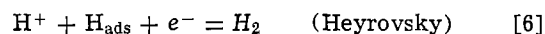
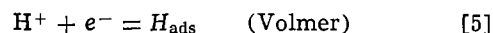
The exchange current densities, i_0 A-cm⁻² for the Fe/Fe²⁺ electrode at pH = 0 and [Fe²⁺] = 1 are reported as (8), $\log i_0 = -8.11$ to -8.51 (NCM) and $\log i_0 = -10.28$ to -12.7 (CM).

The influence of anions on the process of iron dissolution is not well understood. Florianovich *et al.* (13) conclude that anions in addition to OH⁻ ions play a direct part in the anodic reaction; an effect consistent with a model in which specific adsorption of the anion changes the surface area for the Fe/Fe²⁺ exchange has also been advanced (9, 10).

The reversible potential, E_{revH} for the H⁺/H electrode is given by (5)

$$E_{\text{revH}} = -0.06 \text{pH} - 0.03 \log p_{\text{H}_2} \quad [4]$$

The reaction proceeds in two stages, according to the generally accepted Volmer-Heyrovsky mechanism (14)



The cathodic reaction of hydrogen exhibits a Tafel slope $b^c = 0.118$ V/decade (12) which may vary slightly depending on the degree of H₂ coverage of the electrode. The bulk of reported Tafel slopes is between 0.110 and 0.120 V/decade. According to Bockris *et al.* (9), the exchange current density i_0 is pH dependent, $\partial \log i_0 / \partial \text{pH} = -0.5$; at pH = 3, $i_0 = 1.6 \times 10^{-6}$ A-cm⁻².

The total amount of hydrogen produced by the cathodic reaction is equivalent to the metal weight loss and may be used as a measure of the overall corrosion rate. However, in certain circumstances, dangerous corrosion effects may occur with little weight loss due to hydrogen embrittlement of the metal. This situation arises when the Heyrovsky mechanism is hindered, leading to the diffusion of H atoms into the metal and the phenomenon of hydrogen embrittlement. H₂S is known to promote this phenomenon but a mechanism for its action has not been generally accepted. Technically, a solution to the problem has been found

* Electrochemical Society Active Member.

¹ Present address: Ontario Hydro, Toronto, Ontario, Canada.

² Present address: Boise Cascade Limited, Newcastle, New Brunswick, Canada.

Key words: corrosion film, H₂S-H₂O system, mackinawite scale.

through the specification of the maximum applied stress and/or hardness of the steel used.

Experimental

Polarization cells.—Polarization measurements about the corrosion potential were conducted with two designs of cell, the ASTM standard cell (15) and a rotating disk electrode cell (RDE). The design of the working electrodes used in the two cells is shown in Fig. 1. The auxiliary electrode for the ASTM cell was located on a chord plane in front of the working electrode to improve the spatial symmetry of the electrical field. This arrangement gave good reproducibility of the experimental results.

The detailed design of the RDE cell is described elsewhere (16). It was fabricated such that the only materials in contact with the electrolyte, aside from the electrodes, were glass and Teflon. Electrical contact to the rotating shaft was made via copper and mercury.

The steel specimens used as the working electrodes were machined from rod stock of 1020 carbon steel and sleeved as shown in Fig. 1. The surfaces were prepared according to standard procedures (15). Auxiliary electrodes were platinized platinum (17). As the electrolyte was sodium chloride based, no treatment was applied to remove occluded chloride.

A KCl saturated calomel reference electrode was used for all measurements; $E_{ref} = +241.5$ mV SHE. The reference electrode was bridged to the Luggin capillary with cell electrolyte via a beaker containing 1M NaCl solution.

The electrolyte solutions were prepared from reagent grade chemicals and twice distilled water. The solutions were NaCl based, blended with HCl for pH control with a total chloride concentration of 0.2M. The buffering agent used was acetic acid-sodium acetate. Before use the solutions were deoxygenated with bubbling nitrogen for at least 30 min, followed by H₂S

bubbling for another 30 min when required. The cells were purged with nitrogen before the electrolyte was siphoned in and once wet, the electrode did not contact oxygen. The composition of the H₂S/N₂ gas mixture was controlled by the use of calibrated rotameters.

Auxiliary equipment comprised a Wenking potentiostat, a Keithley electrometer, and Honeywell digital multimeter and a thermostated water bath in which the polarization cells were immersed. Additionally for the RDE cell a speed control unit and a stroboscope were used.

The current-voltage curves were obtained using a hand-switched potentiostatic potential step every five to ten minutes, to give at least five experimental points per current decade. The current densities observed were essentially stable. The bulk of the experiments were conducted with the RDE cell at 200 rpm.

Results from initial experiments were obscured by significant ohmic overpotentials. Compensation for the ohmic overpotential is usually effected with the aid of a positive feedback circuit (18) (FBC) in conjunction with a cell substitute circuit representing the equivalent of the cell circuit, including a polarization voltage and two resistors to satisfy the relation

$$R_t/R_g = R_c/R_\Omega \quad [7]$$

where R_c and R_Ω are the resistors in the substitute circuit; R_t and R_g are compensating resistors in the FBC. The essential difficulty is the determination of the ratio R_c/R_Ω . An elaborate method using a rapid response voltmeter, an oscilloscope, and a fast switching device to create transients shorter than 1 msec is recommended (18). To overcome these difficulties an alternative method was devised (see Appendix). This method is fast, accurate, and provided that the position of the Luggin capillary may be controlled by a screw movement, does not require any extra equipment. In the present work, the cell did not have this provision and the capillary was adjusted manually through the cell top passage. The exact position was followed with a crossline reticle finder with micrometer control.

Flow loop.—A flow diagram of the corrosion test loop is shown in Fig. 2. It consisted essentially of standard 1 in. (2.54 cm) diam glass pipeline in the form

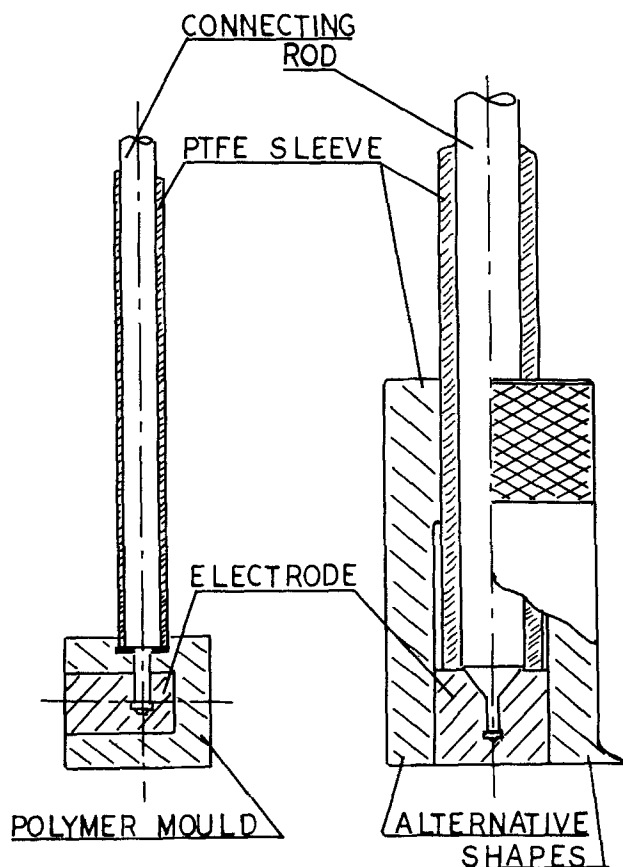


Fig. 1. Sectional view of working electrodes. Left: ASTM cell, right: RDE cell.

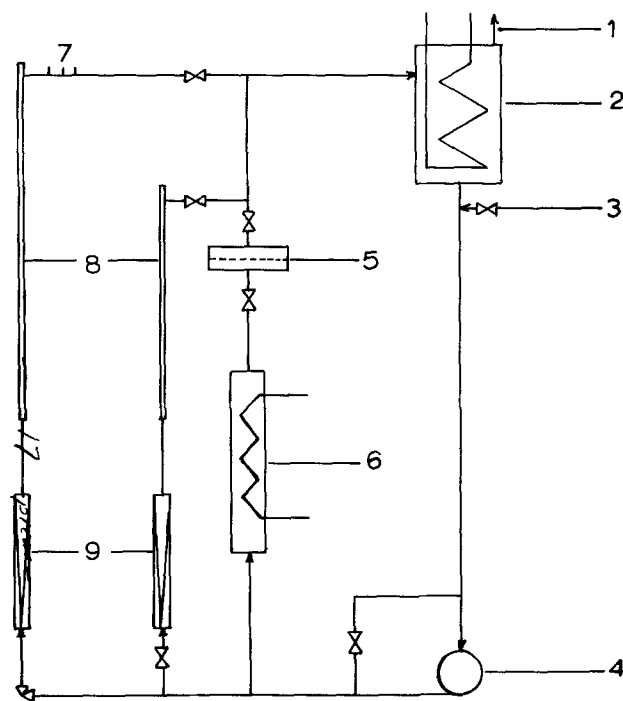


Fig. 2. Diagram of flow loop. Legend: 1. Gas outlet, 2. Header tank, 3. Gas inlet, 4. Pump, 5. Filter, 6. Heat exchanger, 7. Location of electrodes, 8. Test sections, 9. Rotameters.

of a closed circuit with two parallel test sections, a stainless steel header tank fitted with the (stainless steel) cooling coil of a refrigerator unit (Blue M Electric Company Model PCC 24SSA3), and a pump (Crane Dynapump Model 880E) incorporating a bypass. A third parallel line incorporated a Q.V.F. heat exchanger and a sieve plate filter to trap particles of corrosion product. Calibrated rotameters were installed upstream of each test section; the solution flow rate to each test section was controlled manually. Gas connections were fitted as shown in order that the distilled water could be deoxygenated initially with nitrogen and subsequently saturated with H_2S gas. The gas outlet line included a trapping arrangement to prevent ingress of air. Deoxygenation of the distilled water was achieved in the loop by purging with nitrogen over a 2 hr period; this reduced the oxygen concentration to 0.3 ppm or less. H_2S gas at 1 atm was then introduced and the solution circulated for at least 4 hr prior to insertion of the test specimens. A continuous flow of H_2S gas was maintained during the experimental work. The test loop was mounted on plywood and situated in a polyethylene enclosed cage in front of a walk-in fume hood. Ancillary equipment, installed to monitor the solution properties and the corrosion potential of the test specimens, comprised a glass pH electrode (Fisher Scientific Model E-12), a sulfide ion electrode (Orion Research, Model 94-16), and a double junction reference electrode DJE (Orion Research, Model 90-02). Output signals were recorded via a digital pH meter (Orion Research, Model 701) using a strip chart recorder (Yokagawa Company, Model LER 12A).

The pH electrode in conjunction with the DJE was calibrated periodically using standard buffer solutions of pH 4.0, 7.0, and 11.0 at 25°C. The sulfide ion electrode in conjunction with the DJE was calibrated at 25°C using standard solutions of NaOH saturated with H_2S at 1 atm. The slope $\partial E_s / \partial \log [S^{2-}]$, where E_s is the potential of the sulfide ion electrode and $[S^{2-}]$ is the sulfide ion concentration, was measured as -26.7 mV/decade in satisfactory agreement with the calculated value -29.6 mV/decade.

The corrosion potential was measured in conjunction with the DJE by adapting the assembly holder such that electrical contact with a corrosion specimen was achieved. The potential of the DJE was determined to be $+125$ mV SHE at 25°C.

Carbon steel test specimens were machined from AISI 1020 rod stock to a diameter of 0.5 in. (1.27 cm) and an exposed length of 1.5 in. (3.81 cm), Fig. 3. Test specimens were prepared according to ASTM specification (17), weighed, and mounted in a test assembly within 30 min of preparation. A test assembly comprised multiple specimens and was mounted in an annular geometry in the test section, Fig. 3.

Each test specimen was electrically insulated from others in the assembly using fiberglass impregnated Teflon spacers machined to the same dimensions as the test specimens. The two test assemblies were centered in the test sections using spiders. The upper and lower assembly holders were machined from Perspex; the lower was sufficiently long (6.7 in. 20 cm) to act as a calming section for the inflowing solution. The upper holder was of an adjustable length to accommodate changes in the overall length of the test assembly arising from variations in the number of specimens installed. The above arrangement of test specimens permitted the rapid removal and replacement of specimens comprising the assembly at any time within the overall duration of an experiment. Hence the average corrosion rate could be determined over different time intervals at the solution flow rates prevailing in the two test sections.

Upon removal from the loop each specimen was washed in acetone, gently air dried, and weighed. The corrosion product was mechanically removed by rubbing with acetone-soaked paper towels while rotating

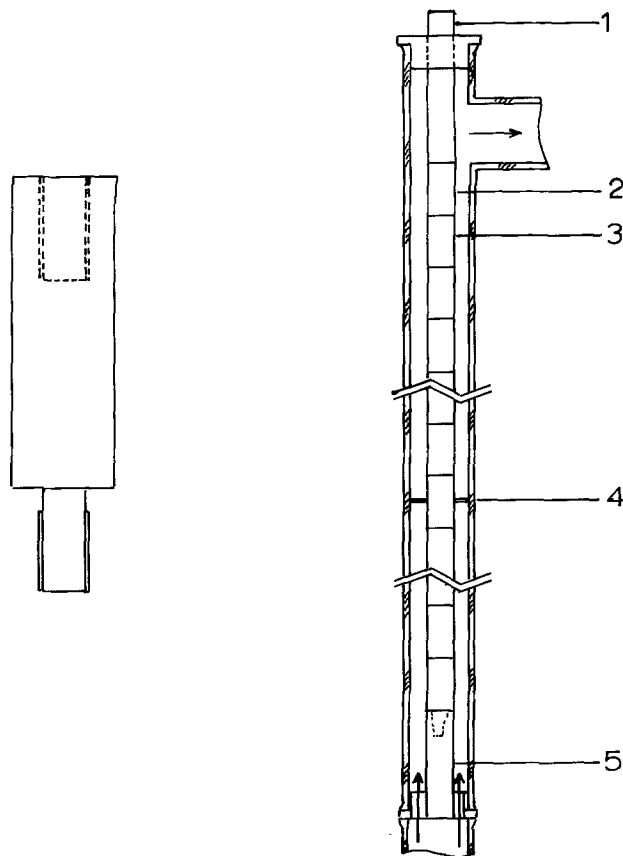


Fig. 3. Corrosion specimen and test assembly for flow loop. Legend: 1. Top holder, 2. Test specimen, 3. Teflon spacer, 4. Centering spider, 5. Bottom holder.

a drill press at low speed. This was sufficient to remove lightly adherent corrosion product. The specimen was again washed in acetone, air dried, and weighed. In later experiments the specimen was then cleaned in a special solution (25 g/liter stannous chloride, 10 g/liter antimony trioxide in 50% hydrochloric acid). It was found that this solution did not appreciably attack bare metal during exposures up to 2 min. The specimen was immersed for 10-20 sec in the cleaning solution at room temperature, washed with water, and rubbed with a soft pencil eraser. This was repeated until no more scale was visible. The specimen was then washed in acetone, air dried, and weighed.

Samples of the corrosion product were kept under nitrogen and subsequently analyzed by x-ray diffraction using Co radiation.

Experiments were conducted in the manner described at $25^\circ \pm 0.5^\circ C$ using water saturated with H_2S at 1 atm with solution velocities in the range 0.1-13.3 ft/sec (0.03 - 4.05 msec $^{-1}$) and for specimen exposure times in the range 5-1400 hr.

Results and Discussion

The corrosion potential.—Over the pH range investigated, the corrosion potential of steel, E_{corr} , in systems with and without H_2S exhibited a linear relationship

$$E_{corr} = E^{\circ}_{corr} - 0.059 \text{ pH} \quad [8]$$

where E°_{corr} is a constant. At $\text{pH} > 4$ slight curvature was observed in agreement with other data (9, 13, 19).

For H_2S -free electrolytes, E°_{corr} had a spread of up to 80 mV depending on the degree of agitation. With the RDE cell, the corrosion potential at $\text{pH} = 2$ was shifted from -318 mV SHE at 300 rpm to -394 mV at rest; the largest variation took place between rest and 100 rpm.

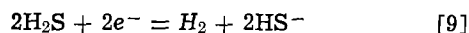
In H_2S systems, the corrosion potential becomes more negative, due to the change in the reversible potential

of iron with H_2S concentration according to Eq. [2]. The hydrogen reversible potential is unaffected by the H_2S concentration. Further, the presence of H_2S at low concentrations reduced the corrosion potential variation with rotational frequency; for $p_{H_2S} > 0.5$ atm the corrosion potential was independent of frequency. The largest variation of the corrosion potential was 60 mV with the RDE at 2000 rpm observed as the partial pressure of H_2S was raised from 0 to 1 atm; the major part of this change occurred over the dilute range of H_2S partial pressure.

The changes of corrosion potential of specimens in the flow loop with exposure time and flow rate were small over the ranges studied. The initial corrosion potential of a new test specimen was approximately -460 mV SHE changing to -450 mV after 5 hr exposure to the corroding solution at $pH = 4$. Thereafter it remained essentially constant for exposure times up to 6 days. An increase of the linear velocity of the corroding solution from 0 to 10 ft/sec (0 to 3 msec⁻¹) after 2 hr exposure was accompanied by a change in the corrosion potential of 1.4% in the noble direction. After six days exposure, a change of solution velocity had no influence on the corrosion potential.

These results indicate that the presence of H_2S progressively eliminates the strong concentration polarization of the H_2S -free system.

Polarization studies.—As a preliminary to the polarization measurements, the performance of the RDE cell was examined by measurements of the limiting current density i_L as a function of the rotational frequency, w . Plots of i_L vs. $w^{1/2}$ were linear in accord with theory (20). At $pH = 2.1$ $p_{H_2S} = 0.19$ atm, i_L increased by a factor of approximately 1.3 relative to the value for the H_2S -free system, again indicating the progressive elimination of concentration polarization. This is attributed to additional hydrogen discharge from H_2S by the overall reaction



Over the same H_2S concentration variation but at higher pH , Bolmer (21) obtained about one order of magnitude increase of i_L . However, Bolmer's work was conducted in a static system under which circumstances, stirring by the evolved gas would have a decisive effect. These effects would be minimized in the RDE cell.

The anodic polarization curves are shown in Fig. 4 and 5. Data for Fig. 4 were obtained at $pH = 3.9$ -4.0; the parameter is p_{H_2S} equal to 0, 0.19, 0.50, and 1.0 atm. With the exception of data at $p_{H_2S} = 0.5$ atm, all data were taken in acetate buffered solutions. On Fig. 5 the parameter is the solution pH at p_{H_2S} equal to 0 and 0.19 atm. From these data, Tafel slopes are in the range $38 < b^a < 45$ mV/decade in good agreement with values reported by Bockris *et al.* (9).

The spacing of the curves of Fig. 4 is essentially the same as the spacing calculated for the reversible potential of iron at $pH = 4$ from Eq. [2]. This is illustrated

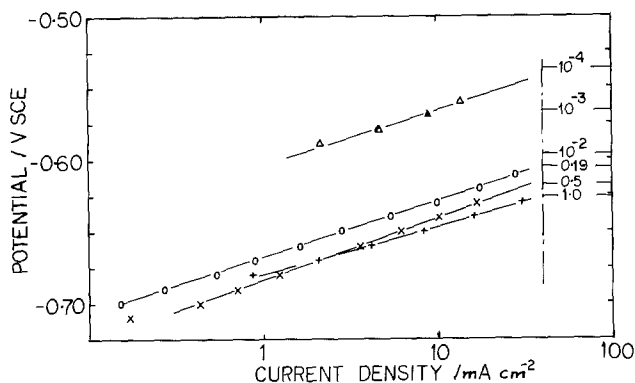


Fig. 4. Influence of H_2S concentration on anodic polarization. Solution pH : 3.9 to 4.0; Parameter is p_{H_2S} (atm).

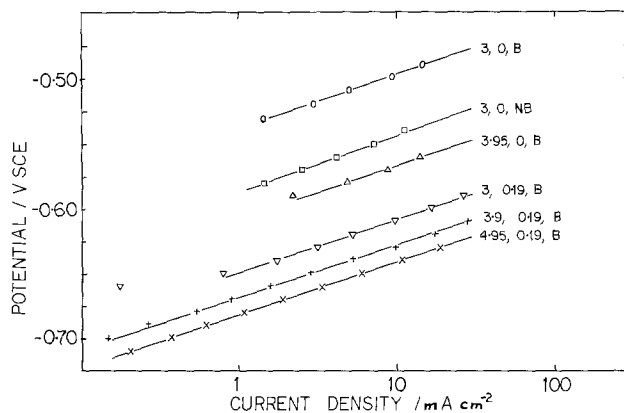


Fig. 5. Influence of buffering and pH on anodic polarization. Parameter is solution pH at $p_{H_2S} = 0$ and 0.19 atm. B = buffered, NB = no buffer.

on Fig. 4 arbitrarily taking as reference the curve at $p_{H_2S} = 1$ atm. Thus, variations of H_2S concentration are only causing changes in the reversible potential of iron; the exchange current density remains the same. The latter is thus calculated to be $i_0 = 8.9 \times 10^{-6}$ A-cm⁻², in good agreement with reported values for the Fe/Fe²⁺ electrode (8, 9).

From Fig. 5, based on just two pH values, the buffered, H_2S -free solutions show an electrochemical reaction order, $p_{pH^a} = +1.8$ consistent with the reaction proceeding by the catalyzed mechanism (8). At $p_{H_2S} = 0.19$ atm, $p_{pH^a} \sim +0.4$ suggesting a change of mechanism relative to the H_2S -free system.

The results of some cathodic polarization experiments using buffered solutions of $pH = 3$ are presented in Fig. 6. For the H_2S -free solution, a limiting current density, $i_L = 1.06$ mA cm⁻² was observed at an overpotential of 170 mV in agreement with the measurements of Bockris *et al.* (9). This diffusion control is eliminated by the presence of H_2S as noted earlier. Tafel slopes, $b^c = 110$ and 116 mV/decade are observed at $p_{H_2S} = 0.5$ and 1.0 atm in agreement with the theory for the discharge of the H^+ ion (9). The Tafel line is insensitive to $[H_2S]$ changes in agreement with previous observations (21, 22); the slight shift observed at $p_{H_2S} = 0.5$ and 1.0 atm is within the fluctuations due to hydrogen preconditioning of the electrode.

Polarization diagram and corrosion current density.—The results of this work and those of Bockris *et al.* (9) are presented in the polarization diagram, Fig. 7. It was shown experimentally that the shift of the anodic curves by a change of H_2S concentration is due to the shift of the reversible potential of iron. Hence the corrosion reaction order $n \equiv (\partial \log i_{corr} / \partial \log [H_2S])_{pH} = 0.20$ from geometrical considerations with $b^c = 0.110$ V/decade and $b^a = 0.041$ V/decade. At $pH = 3$ the

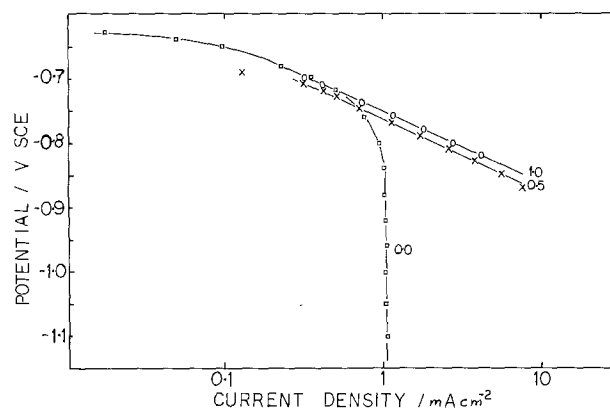


Fig. 6. Influence of H_2S concentration on cathodic polarization, at $pH = 3$. Parameter is p_{H_2S} (atm).

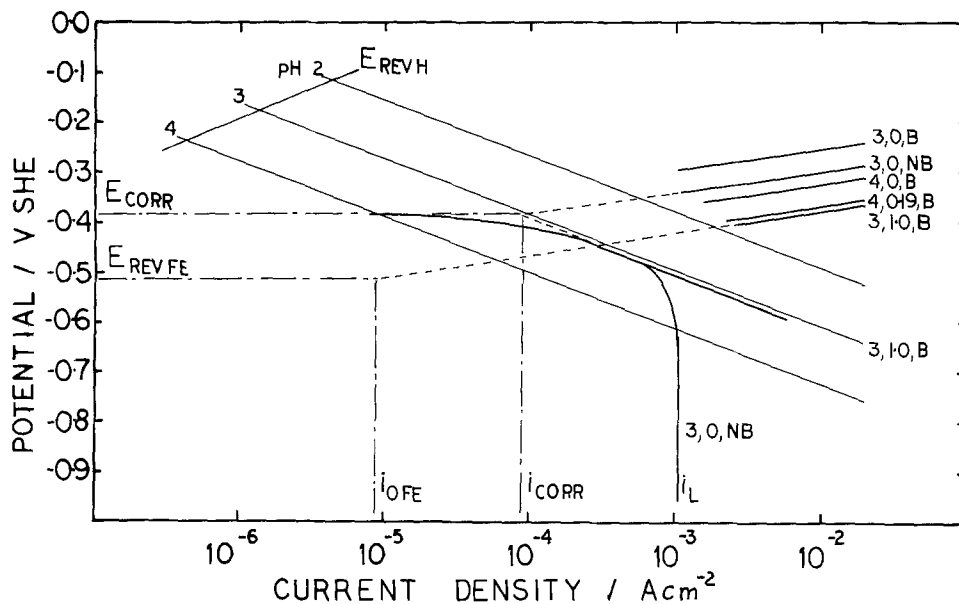


Fig. 7. Polarization diagram, system Fe + H₂S + H₂O. Light lines, from Bockris et al. (9). Numerals indicate solution pH. Heavy lines, this work. Numerals indicate solution pH and p_{H₂S} (atm), respectively. B = buffered, N.B. = no buffer.

corrosion current density, i_{CORR} is given by

$$i_{\text{CORR}} = 3.1 \times 10^{-4} p_{\text{H}_2\text{S}}^{0.20} \text{ A-cm}^{-2} \quad [10]$$

This is the form of dependence reported by Bartonicek (23), based on weight-loss experiments. Since the data obtained in this work reflect initial corrosion rates, whereas those of Bartonicek are averaged over the 6 hr duration of his experiments, direct comparison is not possible. For this reason his corrosion rates are approximately 85 and 38% smaller at $p_{\text{H}_2\text{S}} = 1$ atm and 10^{-4} atm, respectively, than values calculated from Eq. [10].

Based on a limited number of experiments, the experimental finding that $\Delta E = \Delta E_{\text{REVFe}}$ might be true only over a narrow pH range. A more general expression may be obtained considering that H₂S causes not only a change of E_{REVFe} but also of the exchange current density $i_{0\text{Fe}}$. In this case, again from geometrical considerations

$$n = \frac{1}{b^c + b^a} \left(0.03 + b^a \frac{\partial \log i_{0\text{Fe}}}{\partial \log [\text{H}_2\text{S}]} \right) \quad [11]$$

Besides including the previous case, this expression produces smaller or larger n depending on the sign of the derivative.

Rate of corrosion.—A summary of the corrosion rate data obtained from the flow loop as a function of the solution velocity and exposure time are presented in Table I and illustrated in Fig. 8. The time average corrosion rate \bar{r} is defined by the expression

$$\bar{r} = m/s\theta \quad [12]$$

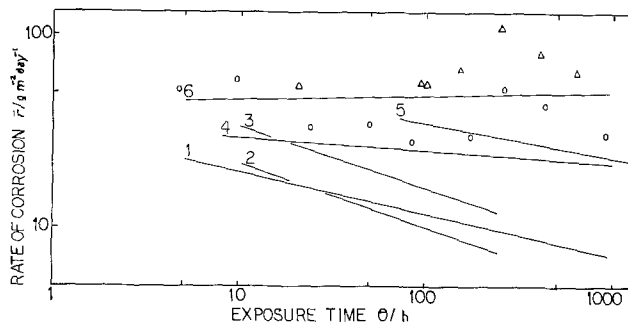


Fig. 8. Time-average corrosion rate of AISI 1020 steel. $p_{\text{H}_2\text{S}} = 1$ atm, temperature = 25°C. Legend: see Table I. \circ Solution velocity = 3.0 msec⁻¹, Δ solution velocity = 3.1 msec⁻¹.

where m is the mass of metal ionized in the exposure time θ and s is the surface area of the specimen exposed to the corroding solution. A power law relation between \bar{r} and θ of the form

$$\bar{r} = \alpha\theta^\gamma \quad [13]$$

is assumed where α and γ are constants. Values of α and γ are given in Table I together with the correlation coefficients as a measure of the fit of the data to the assumed equation. Owing to the large scatter of data, only those pertaining to line 6 are shown in Fig. 8.

Time-average corrosion rates were generally in the order range 10–100 gm⁻² day⁻¹, (equivalent to 0.5–5 mm penetration per year), the lower order values

Table I. Summary of experimental results. Corrosion of AISI 1020 steel by the H₂S + H₂O system at 25°C

Solution	0.60	0.98	1.91	2.32	3.05	4.05
Velocity/msec ⁻¹	0.60	0.98	1.91	2.32	3.05	4.05
Reynolds number	3530	13,800	27,000	32,800	43,700	57,400
Experimental data						
No. of data points	24	16	6	14	16	11
Line No., Fig. 8	1	2	3	4	6	5
Time average corrosion rate, parameters of Eq. [13]						
α /gm ⁻² day ⁻¹	32.3	45.8	69.9	34.8	44.0	79.7
γ	-0.22	-0.33	-0.32	-0.07	+0.02	-0.18
Correlation coefficient	-0.63	-0.61	-0.96	-0.24	+0.09	-0.47
Instantaneous corrosion rate, Eq. [14]						
r_{av} /gm ⁻² day ⁻¹	13.5	14.4	15.3	23.4	54.2	34.2
Standard deviation, σ	9.0	12.1	11.7	69.8	35.6	103
Corrosion product removal parameter P, Eq. [16]						
$P \pm \sigma$, all data	0.83 ± 0.15	0.90 ± 0.07	0.89 ± 0.03	0.84 ± 0.13	0.97 ± 0.03	0.98 ± 0.02
$P \pm \sigma$, time span 0 to 100 hr	0.78 ± 0.20	0.87 ± 0.07	0.89 ± 0.03	0.73 ± 0.13	0.95 ± 0.04	—

corresponding to long term exposure ($\theta > 10^2$ hr) at solution velocities less than about 2 msec^{-1} . At solution velocities in excess of about 2 msec^{-1} , corrosion rates generally retained initially high values and in certain instances exceeded these values. This observation will be discussed later. The "initial" corrosion rate observed at $\theta = 1$ hr (values of α listed in Table I) averaged $50 \pm 19 \text{ gm}^{-2} \text{ day}^{-1}$, in satisfactory agreement with the value $75 \text{ gm}^{-2} \text{ day}^{-1}$ calculated from Eq. [10]

The corrosion rate r defined as

$$r = \frac{1}{s} \left(\frac{m_2 - m_1}{\theta_2 - \theta_1} \right) \quad [14]$$

where m_1 and m_2 are the masses of metal ionized during the exposure times θ_1 and θ_2 were also calculated. Neglecting changes in the surface area of the specimen, the value r approximates the instantaneous corrosion rate at the mean exposure time $\bar{\theta} = (\theta_1 + \theta_2)/2$. Due to the large scatter of data, the values r show wide variations; the results are included in Table I as the average value, r_{avg} together with the standard deviation. These data emphasize the increasing corrosion rate with increasing solution velocity though the trend is somewhat obscured at high flow rates by the large standard deviation.

The corrosion product release rate, \bar{r} is a measure of the rate of removal of metal from the specimen. It is defined by the expression

$$\bar{r} = (m - 0.64f)/s\theta \quad [15]$$

where f is the mass of the corrosion product, taken to be FeS, adhering to the specimen after the exposure time θ . From the definitions of \bar{r} and r , the ratio P may be defined

$$P = \bar{r}/r = 1 - (0.64f/m) \quad [16]$$

with the limiting values, $P = 0$ in which case all the corrosion product remains on the specimen, and $P = 1$ in which case all the corrosion product is removed. Values of P with the standard deviation σ are included in Table I both for all the data at a given solution velocity and for data obtained in the time span 0-100 hr exposure. It is evident that in all experiments, the corrosion product is largely removed by the flowing solution ($P \rightarrow 1$). At low solution velocity ($< \sim 2 \text{ msec}^{-1}$) there is a suggestion of greater retention of corrosion product particularly in the first 100 hr exposure. Thus the lower corrosion rates observed may be due to a protective action of the corrosion product film.

X-ray diffraction measurements of samples of the corrosion product revealed the presence of mackinawite (Fe_{1+x}S). Pyrite (FeS_2) was not present. No significant differences in the nature of the products were observed for either static or dynamic exposure conditions.

Metallographic examination of cross sections of specimens showed an increasing extent of surface roughness with increasing exposure time to the corroding solution. The surface roughness is defined as the standard deviation of the surface from the mean surface line observed with a microscope. The results obtained at the solution velocity of 3.1 msec^{-1} are presented in Table II. Similar measurements were made of the scale rough-

ness and thickness which also increased with increasing time of exposure. However the scale was observed to be discontinuous on the surface due, presumably, to occasional and random removal by the solution. The metal then exposed would exhibit a larger apparent corrosion rate than a fresh specimen due to the increased surface area with increasing roughness. Evidently, at high solution velocities ($> \sim 2 \text{ msec}^{-1}$) the scale is more readily sloughed off leading to enhanced apparent corrosion rates in some instances.

These results complement those of Tewari and Campbell (24, 25) who studied the corrosion of carbon steel using the rotating disk technique. In the laminar flow regime at 22°C , $p_{\text{H}_2\text{S}} = 1$ atm, these authors reported corrosion rates in the order of $10 \text{ gm}^{-2} \text{ day}^{-1}$, and concluded that the corrosion rate was controlled by the rate of the chemical reaction between mackinawite and hydrogen ion and by the transport of FeSH^+ ions to the bulk solution. At 120°C , $p_{\text{H}_2\text{S}} = 15.8$ atm in the transition and turbulent flow regimes, corrosion rates in the order range $20\text{-}200 \text{ gm}^{-2} \text{ day}$ were observed. The authors also noted that the mass of iron sulfide scale remaining on the steel specimen ($\sim 200 \text{ gm}^{-2}$) was approximately independent of the rotational frequency and exposure time indicating that the corrosion product was continuously removed from the specimen. In the work reported here, in the fully turbulent regime ($\text{Re} > 8500$) the corrosion product is largely removed ($P \rightarrow 1$) as noted earlier. The mass of product remaining on the specimens varied in the order range $6\text{-}60 \text{ gm}^{-2}$ for exposure times of 10-1000 hr.

The nature of the various iron sulfides and their influence on the corrosion of steel have been reviewed by Smith and Miller (26) in which they point out that the formation of iron sulfides will in certain conditions not give protection to the metal, but will contribute a new corrosion mechanism to such systems. Thus they quote the work of King (27) who showed that the presence of mackinawite depressed the potential required for cathodic protection of steel below that normally considered adequate. Earlier, Greco and his co-workers (28) found that with increasing concentration of H_2S , increasing amounts of mackinawite [identical to Kansite (29)] relative to other sulfides were formed and that the formation of mackinawite was accompanied by an increasing corrosion rate. Meyer *et al* (30) found the initial corrosion product to be mackinawite tarnish, which provided some protection to the underlying metal. After some 200 hr exposure to the corroding solution the mackinawite tarnish grew into a thicker mackinawite scale and was accompanied by an increasing corrosion rate. Subsequent behavior depended on the presence or absence of sodium chloride in the solution; in the absence of NaCl, the outer layers of mackinawite transformed to pyrrhotite and pyrite, which provided protection to the metal. They proposed that the mackinawite tarnish, consisting of discrete crystallites consolidated into a disjointed permeable scale leading to increased electronic conductivity consequent upon an increased defect density. Similar results regarding the influence of NaCl were found by Ewing (31). This proposal is supported by the work of Mara and Williams (32) who found in particular that mackinawite was an excellent anodic and cathodic depolarizing agent.

Further evidence regarding the influence of the morphology of the scale is provided by the work of Macdonald *et al.* (33), who studied the corrosion of steel in the presence of wet elemental sulfur under aerobic and anaerobic conditions. Corrosion rates were found to increase rapidly after an induction period which was found to be a function of the initial pH of the system, the particle size of sulfur, and the presence of oxygen. In particular they noted that the onset of catastrophic corrosion was accompanied by the formation of H_2S and mackinawite and a shift in the corrosion potential to more positive values. They postulated

Table II. Surface examination of steel specimens exposed to $\text{H}_2\text{S} + \text{H}_2\text{O}$ solutions. Solution flow rate: 3.1 msec^{-1}

Duration of exposure/hr	Surface roughness/ μm	Scale roughness/ μm	Scale thickness/ μm
0	1.9		
260	6.2	8.9	26
980	33	28	55

a mechanism in which the mackinawite acted as a catalyst of the corrosion process.

It is evident from the above discussion that iron sulfide is unreliable as a protective scale; on the contrary the formation of mackinawite may promote the corrosion process. Some evidence in support of the concept of an induction period noted by Meyer *et al.* (30) and by Macdonald *et al.* (33) was obtained in this work. This is shown in Fig. 8 in which the time-average corrosion rates at the solution velocities of 3.0 and 3.1 msec⁻¹ are included. These two sets of data are combined in the line 6 of Fig. 8. A significant increase in the time average corrosion rate is observed after an exposure time of the order 200 hr. Data obtained at other solution velocities showed the same phenomenon. However, the scatter of data is such as to preclude quantitative evaluation.

Conclusions

1. In the presence of H₂S, the corrosion potential of steel becomes more negative. This change is due to the change in the reversible potential of iron with change of H₂S concentration according to Eq. [2].

2. The presence of H₂S does not change the Tafel slopes of the anodic and cathodic processes within the investigated pH domain.

3. The exchange current density of the anodic process is unaffected by H₂S.

4. The cathodic process maintains the reversible potential and the exchange current density of the H₂S free system, but the H⁺ diffusion control gradually disappears with increasing H₂S concentration.

5. The necessity for ohmic overpotential correction has been emphasized and a new method for compensation is described.

6. A corrosion current dependence on H₂S concentration has been found which agrees with that found from published weight-loss experiments.

7. The product of corrosion, mackinawite, is essentially nonadherent, particularly at solution velocities in excess of about 2 msec⁻¹, equivalent to a Reynolds number of about 28,000.

8. The presence of mackinawite scale in certain circumstances may enhance the corrosion rate above the initial value obtained from polarization measurements. This is in accord with earlier observations.

Acknowledgment

Thanks are due to Atomic Energy of Canada Limited for financial support of this work.

Manuscript submitted Oct. 24, 1979; revised manuscript received Dec. 31, 1979.

Any discussion of this paper will appear in a Discussion Section to be published in the December 1980 JOURNAL. All discussions for the December 1980 Discussion Section should be submitted by Aug. 1, 1980.

APPENDIX

Compensation of Ohmic Voltage Drops in the Polarization Experiments

As noted earlier, the results of initial polarization experiments were obscured by significant ohmic overpotentials; a compensation method necessitating substantial additional equipment is described by the potentiostat manufacturers (8). Britz has recently reviewed the general problem (34). In what follows, a simple method of compensation is described suitable under conditions of stable current density; this method requires little extra equipment. The method is enumerated as follows in conjunction with Fig. 9 and Ref. (18).

1. Select the polarizing voltage of the feedback circuit (FBC) as usual with no current through the loop cell-FBC. The potentiometer for R_g is turned to $R_g = 0$.

2. Place the tip of the Luggin capillary at the normally required distance S from the electrode.

3. Select the control voltage E_1 on the potentiostat control. When the current density is stable, at i_1 , the following relation holds

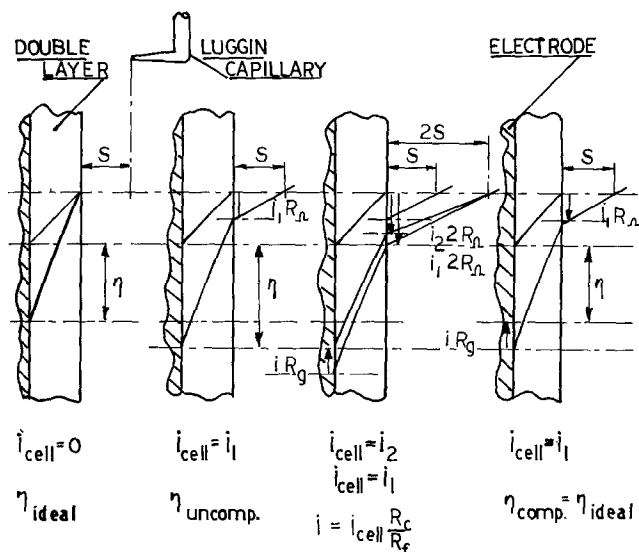


Fig. 9. Principle of new method for compensation of ohmic overpotential.

$$\eta_1 + i_1 R_\Omega = E_1 \quad [\text{A-17}]$$

where η is the process overpotential under study and $iR_\Omega = E_\Omega$ is the ohmic overpotential to be compensated.

4. Change the Luggin tip location from S to $2S$. To this corresponds an electrolyte resistance $2R_\Omega$. The current density and the overpotential change to new values

$$\eta_2 + i_2 2R_\Omega = E_1 \quad [\text{A-18}]$$

5. Compensate the FBC to a value R_{g1} which returns the current to i_1 . Then one has

$$\eta_1 + i_1 2R_\Omega = E_1 + i R_{g1} \quad [\text{A-19}]$$

The last term is a compensating voltage produced by the current i of the FBC over the resistor R_{g1} . Subtracting Eq. [17] and [19], one obtains

$$i_1 R_\Omega = i R_{g1} \quad [\text{A-20}]$$

The total resistance of the FBC is selected to be much larger than that of the cell so the current i is small relative to i_{cell}

$$i = (R_c/R_f) i_{\text{cell}} \quad [\text{A-21}]$$

In view of Eq. [7], Eq. [20] and [21] are identical; hence R_{g1} is the value which will compensate the ohmic overpotential due to R_Ω corresponding to the distance S .

6. Return the Luggin capillary from $2S$ to S . The adjustment is now complete and the control voltage matches the process overvoltage, η since

$$\eta_3 + i_3 R_\Omega = E_1 + i_3 \frac{R_c}{R_f} R_{g1} = E_1 + i_3 R_\Omega \quad [\text{A-22}]$$

or, for any other change of E , $\eta = E$.

The above method was found to be fast and accurate in the polarization experiments described.

REFERENCES

1. R. V. Comeaux, *Corrosion (Houston)*, **11**, 189t (1959).
2. C. B. Hutchinson and W. B. Hughes, *ibid.*, **17**, 514t (1961).
3. J. Gutzeit, *Mater. Prot.*, **7**, 20 (1968).
4. R. H. Hausler and N. D. Coble, *API Proc., Division of Refining*, **52**, 586 (1972), *Met. Abstr.*, **6**, 35-0282 (1973).
5. M. Pourbaix, "Atlas of Electrochemical Equilibria in Aqueous Solutions," Pergamon, New York (1966).
6. R. C. Weast, Editor, "Handbook of Chemistry and Physics," 58th ed., CRC Press, Inc. (1977).
7. J. H. Perry, Editor, *Chemical Engineers Handbook*, 3rd Ed., McGraw Hill Book Co., Inc., New York (1950).
8. F. Hilbert, Y. Miyoshi, G. Eichkorn, and W. J. Lorenz, *This Journal*, **118**, 1919 (1971).

9. J. O'M. Bockris, D. Drazic, and A. R. Despic, *Electrochim. Acta*, **4**, 325 (1961).
10. J. J. Podesta and A. J. Arvia, *ibid.*, **10**, 171 (1965).
11. K. E. Heusler, *Z. Elektrochem.*, **62**, 582 (1958).
12. J. O'M. Bockris and A. K. N. Reddy, "Modern Electrochemistry," Plenum Press, New York (1970).
13. G. M. Florianovitch, L. A. Sokolova, and Y. M. Kolotyркиn, *Electrochim. Acta*, **12**, 879 (1967).
14. K. J. Vetter, "Electrochemical Kinetics," Academic Press, New York (1967).
15. ASTM Standards, Standard No. GS-72.
16. L. Sampaleanu, M.Sc. Thesis, University of New Brunswick, (1978).
17. ASTM Standards, Standard No. G3-68.
18. Operating Manual, Wenking potentiostat Model No. 68.
19. F. K. Nauman and W. Carius, *Arch. Eisenhuettenwes.*, **30**, 283 (1959).
20. A. C. Riddiford, *Adv. Electrochem. Electrochem. Eng.*, **4**, 47 (1965).
21. P. W. Bolmer, *Corrosion (Houston)*, **21**, 69 (1965).
22. B. Leboucher, *Rev. Inst. Fr. Pet.*, **18** (1963).
23. R. Bartonicek, *Proc. 3rd Int. Congr. Met. Corros., Moscow*, **1**, 119 (1969).
24. P. H. Tewari and A. B. Campbell, *Can. J. Chem.*, **57**, 188 (1979).
25. P. H. Tewari, M. G. Bailey, and A. B. Campbell, *Corros. Sci.*, **19**, 573 (1979).
26. J. S. Smith and J. D. A. Miller, *Br. Corros. J.*, **10**, 136 (1975).
27. R. A. King, Ph.D. Thesis, University of Manchester (1971) [quoted by Smith and Miller, Ref. (26)].
28. E. C. Greco and J. B. Sardisco, *Proc. 3rd Int. Congr. Met. Corros., Moscow* 130 (1969).
29. C. Milton, *Corrosion (Houston)*, **22**, 191 (1966).
30. F. H. Meyer, O. L. Riggs, R. L. McGlasson, and J. D. Sudbury, *ibid.*, **14**, 109t (1958).
31. S. P. Ewing, *ibid.*, **11**, 497t (1955).
32. D. D. Mara and D. J. A. Williams, *Br. Corros. J.*, **7**, 94 (1972).
33. D. D. Macdonald, B. Roberts, and J. B. Hyne, *Corros. Sci.*, **18**, 411 (1978).
34. D. Britz, *J. Electroanal. Chem. Interfacial Electrochem.*, **88**, 309 (1978).

Mechanism of Passivity Breakdown of High Purity Cadmium

M. G. Alvarez and J. R. Galve*

Comisión Nacional de Energía Atómica, Departamento de Materiales, 1429 Buenos Aires, Argentina

ABSTRACT

The passivity breakdown of high purity cadmium in NaCl, Na₂SO₄, and KI aqueous solutions was studied. The pitting potential was measured by potentiostatic polarization techniques, surface scratching techniques, and galvanostatic techniques. The effect of pH and aggressive anion concentration on the pitting potential was investigated. The passivity breakdown potential of cadmium in 1.0M NaCl solution (pH 11 and 12.5) and in 0.5M Na₂SO₄ solution (pH 9-12.5) was found to be due to localized acidification on the metal-solution interface. No pitting potential was found for cadmium either in 1.0M KI solution (pH 11) or in 1.0M NaCl solution (pH 9). Thermodynamic considerations showed that no stable oxide film is formed in those solutions.

The present work is part of a research program in which the passivity breakdown mechanism of several high purity metals and binary alloys was studied in the presence of different electrolytes. The results obtained in the case of high purity aluminum (1-5), high purity zinc (6), high purity iron (7, 8), and binary Al-Cu (2, 9), Al-Mg (10), and Al-Zn (10) alloys have been published. These results suggested that in all the systems so far studied the pitting potential was the potential above which localized acidification could be maintained on the metal-solution interface (11-13). The purpose of the present work is to prove that such a mechanism can be applied to the passivity breakdown of high purity cadmium.

The literature about pitting of cadmium is not abundant. According to Kadyrov *et al.* (14) cadmium exhibits pitting in NaCl solutions and in NaCl plus NaOH solutions at $-0.50V_{(NHE)}$. Augustynski (15) measured the pitting potential of zinc, cadmium, and manganese in borate buffered solutions with different aggressive anions. This author found that in all cases the pitting potential was close to the normal equilibrium potential of the metal with its ions.

In the present work the anodic behavior and passivity breakdown of cadmium were studied in alkaline solutions of the following salts: NaCl, Na₂SO₄, and KI. The effect of the pH and the aggressive anion con-

centration on the pitting potential was also investigated. The results obtained indicated the pitting potential changes with the composition of the solution in the way predicted by the theory (11-13). This came to confirm that with this metal, too, localized corrosion appeared above the pitting potential as a result of localized acidification on the metal-solution interface.

Experimental

Specimens 1 mm thick were prepared by hot-rolling 8 mm diam 99.999% cadmium rods from "Colnbrook-Buck," England. Intermediate etchings with HNO₃ 10% (v/v) were made in the preparation sequence of the samples to minimize metal contamination. The hot-rolled material was cut into rectangular 20 mm long × 10 mm wide coupons which were annealed for 2 hr at 270°C in argon and furnace cooled. A copper wire lead was soldered to one of the faces of the samples. The soldered face and the edges of the samples were covered with an epoxy resin cured at 70°C, leaving a free surface of about 1 cm² exposed. Before the measurements the samples were chemically polished for 1 min in a solution of 5 cm³ HNO₃ conc plus 5 cm³ H₂O₂ (100 vol.) plus 30 cm³ ethanol, at room temperature.

The anodic behavior of high purity cadmium was studied in the following solutions: (i) 1.0M NaCl (pH 12.5, 11.0, 9.0, and 3.0); (ii) 2.5, 0.25, 0.1, 0.025,

* Electrochemical Society Active Member.

Key words: metals, anode, corrosion, passivity.

and 0.01M NaCl (pH 11.0); (iii) 0.5M Na₂SO₄ (pH 12.5, 11.0, 10.0, 9.0, and 3.0); and (iv) 1.0M KI (pH 11.0).

The solutions were prepared with analytical grade reagents and doubly distilled water and were deaerated with purified nitrogen (16). Nitrogen was bubbled through the solutions during the tests. The pH of the solutions was adjusted by addition of the corresponding acid or base.

All measurements were made at 25° ± 0.5°C in a Pyrex glass cell with a platinum counterelectrode. Potentials were measured through a Luggin capillary with a mercurous sulfate reference electrode for the experiments with Na₂SO₄ solutions and with a saturated calomel electrode for the other solutions. An intermediate salt bridge with the working solution and a porous plate were used to avoid electrolyte contamination during the measurements in KI solutions. All potentials are reported in the normal hydrogen electrode scale (NHE).

Potentials were kept constant with a Tacussel PRT 40-1X potentiostat, while they were measured with a Tacussel S6Z-R2 electronic millivoltmeter. The currents were recorded with a Sefram BS recorder. A LYP Electronic Potentiostat and a Toshin Electron TO2N1 recorder were used for galvanostatic experiments.

Quasi-stationary potentiostatic curves were obtained by changing the potential in steps of 10 or 20 mV, starting from the corrosion potential. The current was measured after 10 min at constant potential. The breakdown potential was also measured by the scratching technique developed by Pessall and Liu (17), with the modifications described in a previous publication (6). Before the experiments, the samples were subjected to a cathodic reduction in the test solution by means of a 20 min polarization at -0.86V. Afterward, the samples were left at open circuit to reach a stationary potential. This occurred after about 15 min.

The galvanostatic technique was also used to measure the pitting potential in some of the solutions. In those cases a constant anodic current density of 2·10⁻⁵ A/cm² was applied to the specimens, allowing the potential to reach a stationary value. In these galvanostatic experiments the specimens were pre-treated for 15 min with a cathodic current density of 10⁻⁶ A/cm².

Results

Anodic behavior of cadmium in NaCl solutions.—Anodic polarization curves were obtained for high purity cadmium in the following solutions: 1.0, 0.1, and 0.01M NaCl solutions, pH 11.0. All the curves showed a passive zone, where the current density was lower than 10⁻⁶ A/cm², and a breakdown potential above which high current increases and passivity breakdown were observed. The breakdown potentials obtained through this method had a considerable dispersion, particularly in solutions with low chloride ion contents. Figure 1 shows the dispersion found in 0.1M NaCl solution (pH 11.0). A similar dispersion was observed in 0.01M NaCl solution (pH 11.0), Table I. Wide dispersion in the pitting potentials measured by potentiostatic methods was also reported for zinc (6).

Due to this difficulty the breakdown potential had to be determined through the scratching technique. Figure 2 shows the repassivation time values obtained for high purity cadmium in 0.1M NaCl solution (pH 11.0). The values obtained in three independent experiments are plotted and show a good reproducibility of the method. Above the pitting potential, -0.48V, the repassivation time was one order of magnitude above that found at lower potentials. Similarly, when plotting the changes in current, after scratching, the current was found to increase sharply below the pitting potential, Fig. 3, but after a few seconds it returned

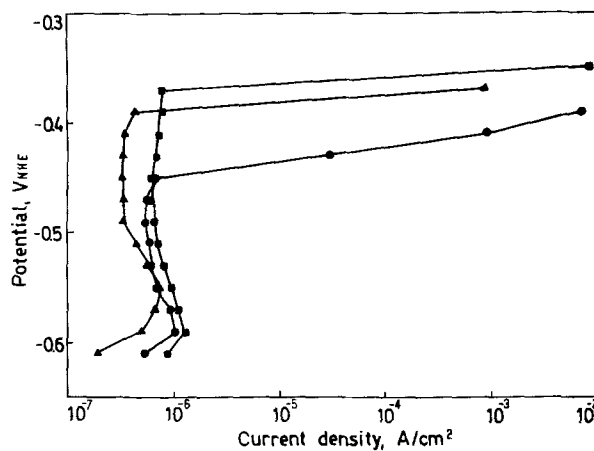


Fig. 1. Anodic potentiostatic polarization curves of high purity cadmium in deaerated 0.1M NaCl solution, pH 11.0, 25°C. High dispersion is found in the pitting potentials measured by this technique.

to values typical of the passive zone. However, when the surface scratching was performed at a potential just 10 mV higher than the pitting potential, the initial current rise was more abrupt and decreased slowly with frequent oscillations. It took above 4000 sec to reach a current value of the order of the initial one. The progressive accumulation of corrosion products on the scratch itself clearly indicated that this current decrease was not the result of a true repassivation process but that of a mechanical obstruction due to the corrosion products plugging up the scratched zone. Finally, when a potential of -0.46V was applied, the current did not decay after scratching, but reached values two orders of magnitude above those of the passive zone. The small dispersion found in the repassivation time, at potentials below the pitting potential, is attributed to differences in the scratch length and depth. Similar observations were made for 2.5, 1.0, 0.25, 0.025, and 0.01M NaCl solutions, pH 11.0. Table I summarizes the measured breakdown potentials. As reported by many authors (13) for the passivity breakdown of other metals, the pitting potential of high purity cadmium changes with the change in the aggressive anion concentration. The higher the aggressive anion concentration, the lower the pitting potential. A semilogarithmic representation of the data in Table I shows that there is a linear relation between the pitting potential and the logarithm of the NaCl concentration.

For the lowest NaCl concentration solutions (0.025 and 0.01M) there is a slight deviation from this law, leading to higher pitting potentials. Disregarding these two values, a logarithmic curve fitting gives the

Table I. Passivity breakdown potentials for high purity cadmium

	Measuring techniques		
	Anodic polarization curves (V)	Surface scratching (V)	Galvanostatic E vs. time (V)
NaCl (0.01M, pH 11)	-0.36 to -0.30	-0.38	—
NaCl (0.025M, pH 11)	—	-0.41	—
NaCl (0.1M, pH 11)	-0.45 to -0.37	-0.48	—
NaCl (0.25M, pH 11)	—	-0.49	—
NaCl (1.0M, pH 9)	-0.56	*	—
NaCl (1.0M, pH 11)	-0.45	-0.53	—
NaCl (1.0M, pH 12.5)	-0.41	-0.50	—
NaCl (2.5M, pH 11)	—	-0.55	—
Na ₂ SO ₄ (0.5M, pH 9)	—	—	-0.47
Na ₂ SO ₄ (0.5M, pH 10)	—	—	-0.47
Na ₂ SO ₄ (0.5M, pH 11)	-0.47 to -0.40	-0.45	-0.45
Na ₂ SO ₄ (0.5M, pH 12.5)	—	—	-0.41 to -0.44†
KI (1.0M, pH 11)	-0.64	*	—

* No repassivation was observed after scratching, at any potential.

† Oscillations. No stable potential was found.

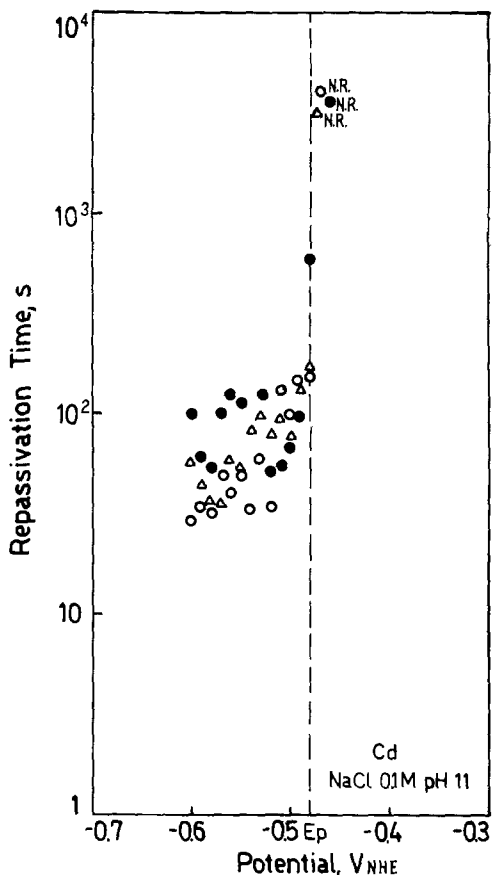


Fig. 2. Repassivation time, after scratching, at constant potential, for high purity cadmium in deaerated, 0.1M NaCl solution, pH 11.0, 25°C. N.R.: no repassivation. Broken line: breakdown potential. Good reproducibility is found in the breakdown potentials measured by this technique.

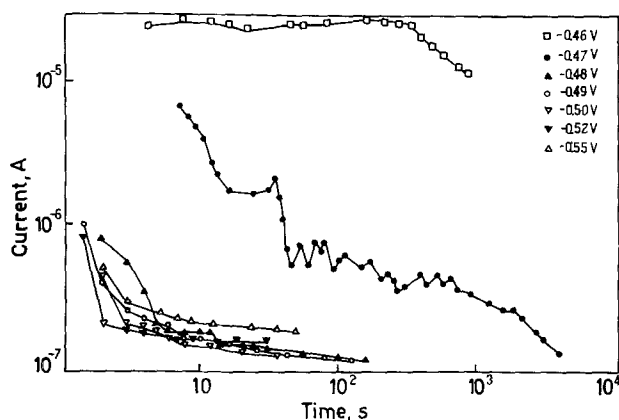


Fig. 3. Potentiostatic current-time curves, after scratching the metal surface. High purity cadmium in deaerated 0.1M NaCl solution, pH 11.0.

following relation between the pitting potentials and the NaCl concentration

$$E_p = -0.528 - 0.053 \log C_{NaCl} \quad [1]$$

where E_p is the pitting potential, in volts, and C_{NaCl} the molar NaCl concentration. The deviation observed for the two lowest concentrations is assumed to be due to uncompensated ohmic drop in the solution, in front of the pits.

The effect of pH on the pitting potential of cadmium in NaCl solutions was investigated in 1.0M NaCl solutions at pH 12.5, 11.0, 9.0, and 3.0. The results are reported in Table I. An increase in the pH from 11.0 to 12.5 was found to produce an increase in the pitting potential of about 30 mV. No passivity was found in

the 1.0M NaCl solution, pH 3.0. The stationary corrosion potential in this solution after a 4 hr exposure was $-0.61V$. The samples showed corrosion at all the potentials above the corrosion potential. A linear relation was found between the potential and the logarithm of the current density in the range between 10^{-5} and $10^{-3} A/cm^2$. The slope of the curve was approximately 27 mV, Fig. 4.

The behavior of cadmium in 1.0M NaCl solution, pH 9.0, was intermediate between those observed in acid solutions and in strongly alkaline solutions. The polarization curve in this medium, Fig. 5, showed a sort of passive zone followed by a breakdown potential. Nevertheless, repassivation time measurements, Fig. 6, showed that the pseudo-passive zone observed in Fig. 5 was not a stable condition. No repassivation was detected at any potential, in the pH 9.0, 1.0M NaCl solution.

Anodic behavior of cadmium in Na₂SO₄ solutions.—The anodic polarization curves of high purity cadmium in deaerated 0.5M Na₂SO₄ solutions, pH 11.0 were found to be similar to those obtained in NaCl solutions. A passive zone was found, followed by a passivity breakdown potential. A remarkable dispersion was observed in the values of the breakdown potentials thus obtained. As in NaCl solutions, the surface scratching technique gave more reproducible results of pitting potentials than the potentiostatic polarization technique. At potentials below $-0.45V$ slight current fluctuations were observed even before scratching. But it was only when higher potentials were applied that a sensible change in current behavior took place after scratching. Duplicate experiments suggested that $-0.45V$ was the most probable value for the breakdown potential.

The galvanostatic method was used to confirm the pitting potential value of cadmium in the Na₂SO₄ solution, pH 11.0. Figure 7 shows an example of the

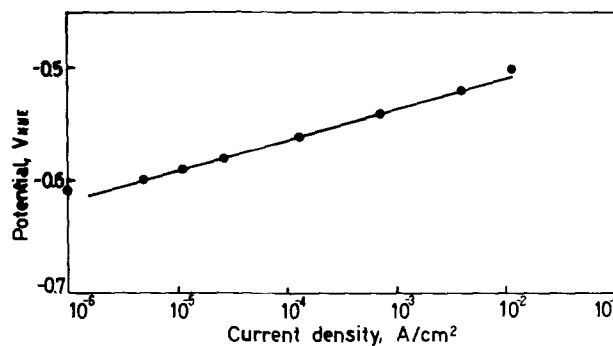


Fig. 4. Potentiostatic anodic polarization curve of high purity cadmium in deaerated 1.0M NaCl solution, pH 3.0, 25°C.

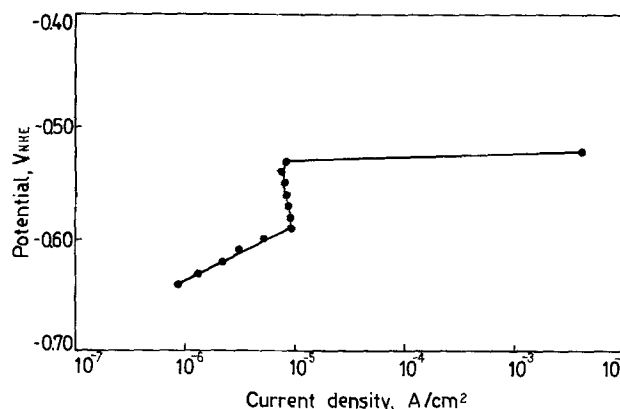


Fig. 5. Pseudo-potentiostatic anodic polarization curve of high purity cadmium in deaerated 1.0M NaCl solution, pH 9.0, 25°C. The passive zone is unstable when tested with other techniques.

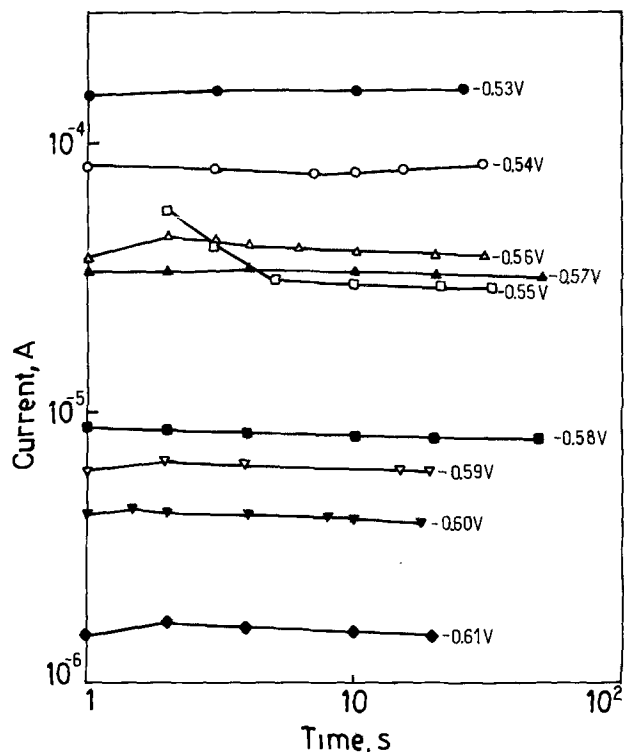


Fig. 6. Potentiostatic current-time curves, after scratching the metal surface. High purity cadmium in deaerated 1.0M NaCl solution, pH 9.0, 25°C. No passivity is found at any of the potentials tested.

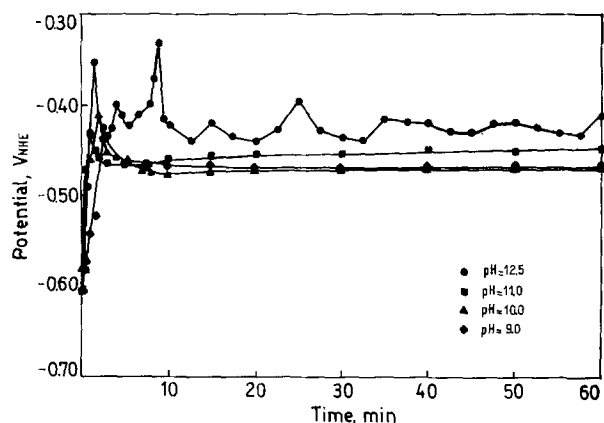


Fig. 7. Galvanostatic potential-time curves for high purity cadmium in deaerated 0.5M Na₂SO₄ solution, at 25°C and various pH values. Current density: 2×10^{-5} A/cm². The stationary potential is taken as the pitting potential of the metal.

potential-time curves obtained. At the beginning of the anodic polarization the potential rise denoted that a passivating film was being formed. Once the attack had started, the potential began to decrease and, after about 40 min, a stationary potential, taken as the pitting potential, was obtained. The value obtained was equal to that found by the surface scratching technique. Corroded areas were observed on the metallic surface as soon as the potential began to decrease.

The galvanostatic method was used to study the effect of pH on the pitting potential of cadmium in Na₂SO₄ solutions (Fig. 7). Measurements were performed in deaerated 0.5M Na₂SO₄ solutions, pH 12.5, 11.0, 10.0, and 9.0. The results are reported in Table I. Up to pH 10.0 the pH had no effect on the pitting potential. At higher pH values, the higher the pH the higher the pitting potential. Stationary potentials were observed in all the solutions, with the only exception the pH 12.5 solution. In this solution the

potential was observed to oscillate between -0.44 and -0.41V, the pitting potential was assumed to be somewhere in between. In the region of pH values where the pitting potential changed with the pH, a linear relation between pitting potential and pH was observed. By linear regression the following equation was found

$$E_p = -0.647 + 0.018 \text{ pH} \quad [2]$$

Electrochemical measurements were also performed in pH 3.0, 0.5M Na₂SO₄ solution. Cadmium did not show passivity in this solution. Anodic polarization experiments, Fig. 8, showed that there was a linear relation between the potential and the logarithm of the current density. A Tafel slope found was of approximately 18 mV/decade. The corrosion potential of cadmium, after a 4 hr exposure in this solution, was found between -0.53 and -0.56V.

Anodic behavior of cadmium on KI solutions.—Potentiostatic anodic polarization curves of cadmium in deaerated 1.0M KI solutions, pH 11.0, showed an apparent passive zone, followed by a breakdown potential. An important difference was found though: the passive range was very narrow, between -0.70 and -0.64V, and the breakdown potential was about 200 mV lower than that in the other solutions when applying the same technique (Table I). The passive current density, above 10^{-6} A/cm², was higher than the corresponding values in chloride and sulfate solutions.

Repassivation-time measurements proved that there was no actual passivity breakdown process in this medium, similarly to what was observed in pH 9.0, 1.0M NaCl solution. The after-scratching current-time curves showed that no potential could be found where a discontinuity occurred. Moreover, there was a clear increase in the current when the potential was increased, indicating the absence of any repassivation process.

Pitting morphology.—The attack observed on high purity cadmium, above the pitting potential, had the same characteristics for all the electrolytes tested. After passivity breakdown, the pits spread quickly, covering great areas of the metallic surface, Fig. 9. Dissolution developed along certain preferential crystallographic planes and looked like crystallographic etching. As dissolution proceeded, heavy accumulation of corrosion products was detected on the metal surface. This morphology, lacking the characteristic pit localization, was also observed on high purity zinc in the presence of the same aggressive solutions (6).

As shown for high purity zinc (6), the type of attack is a function of the properties of the surface oxide film. When the film is easily soluble in the acidified solution in the pit, the attack spreads easily along the surface. When the dissolution rate of the

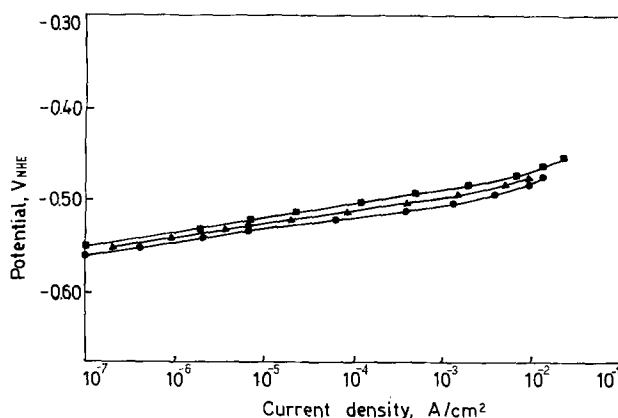


Fig. 8. Potentiostatic anodic polarization curve of high purity cadmium in deaerated 0.5M Na₂SO₄ solution, pH 3.0, 25°C.

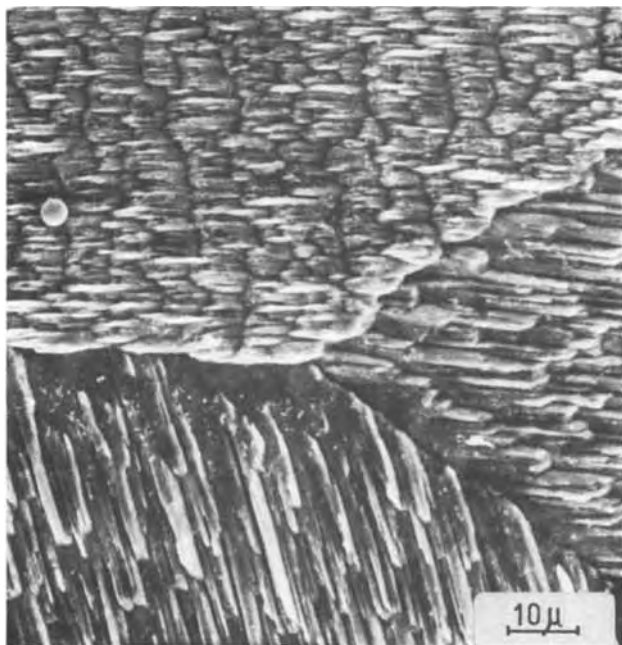


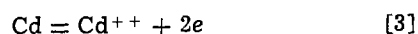
Fig. 9. Scanning electron micrograph of high purity cadmium exposed to deaerated 1.0M NaCl solution, pH 11.0, 25°C, above the breakdown potential.

oxide film, in the acid solution, is sluggish, the surface propagation of the attack is hindered by the film, and typical pits are found. In the case of cadmium, the surface oxide film offers little opposition to the spreading of the attack.

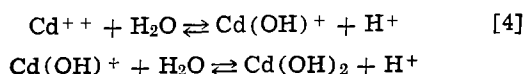
Discussion and Conclusions

Anodic polarization curves and surface scratching experiments performed in alkaline NaCl solutions and Na₂SO₄ solutions indicated that cadmium undergoes passivity breakdown in the presence of these electrolytes. For the attack to begin on the passive metallic surface, the potential must exceed a certain critical value: the breakdown potential. Even when the passivating film is mechanically disrupted, no pitting develops if the potential is below the pitting potential. The exposure of the bare metal to the corrosive environment leads to repassivation at potentials lower than the pitting potential. This suggests that the oxide film is acting as an inert barrier in the pitting process, but does not interfere with the anodic reaction that occurs at the breakdown potential. Similar conclusions were drawn when the surface scratching technique was used to study the pitting of zinc in several electrolytes (6). The same conclusion was reached through straining metal experiments with aluminum in NaCl and NaNO₃ solutions (4, 5), with zirconium in NaCl solutions (18), and with stainless steels in NaCl solutions (19).

According to a pitting mechanism recently proposed by Galvele and co-workers (4, 6, 7, 10-12) the necessary condition for pitting initiation and propagation is the maintenance of local acidification on the metal-solution interphase. Then the pitting potential is the minimum potential at which such local acidification can be maintained. The source of protons in the acidified zone is the metal ions produced by anodic dissolution



followed by metal ions hydrolysis equilibrium

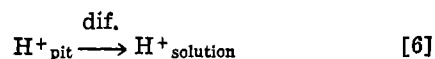


As first pointed out by Hoar (20), the aggressive anions for pitting are strong acid anions. This is because they will not interfere with the reaction [4].

If reducible anions are absent, there are only two processes responsible for proton consumption in the acidified zone. One will be hydrogen evolution, which is the only cathodic reaction possible in the locally acidified zone



and the other will be proton diffusion from the acidified zone to the bulk of the solution



The open-circuit potential of the metal in the acidified solution, E_c^* , will be that at which the rate of reaction [3] equals the rate of reaction [5]. If the metal in the neutral or weakly alkaline unbuffered solution of a strong acid salt is exposed to a potential equal to E_c^* , the acidification will not survive. Since the rate of reactions [3] plus [4] is equal to the rate of reaction [5] no net production of protons will occur. Meanwhile, process [6] will dissipate any previously existing acidity.

At a potential below E_c^* reaction [5] will be greater than reaction [3]. Protons will be consumed, and eventually an alkalization will take place on the metal solution interface. The metal ions will precipitate as oxides, or hydroxides, and will plug any defects on the passive film. Consequently, for values of the potential below E_c^* , the metal will form protective films and any disruption of the film will lead to its reformation. The dissolution process due to the existence of localized acidity in the solution close to the metal surface will only be possible when the potential surpasses E_c^* . According to this, the breakdown potential should be equal to, or higher than, the corrosion potential of the metal in the pit-like solution

$$E_p \geq E_c^* \quad [7]$$

As shown in previous publications (11, 12) to compensate for process [6], and keep the pits active, a net anodic current density should circulate through the pits, i.e., a certain polarization, η , should be applied. Then, the minimum potential for pitting would be

$$E_p \simeq E_c^* + \eta \quad [8]$$

The value of η could be estimated from either Fig. 4 or 8 if the current density inside the pits at the pitting potential is known. No direct measurements of the current density inside the pits of cadmium are available. Nevertheless, during the anodic polarization curves, it was found that the current density, when the corrosion was extended to all the surface, was of the order of 10^{-2} A/cm². These values were measured above the pitting potential, and it can be expected that at the pitting potential the current density should be lower. From Fig. 4 and 8 it is found that to have a current density of the order of 10^{-3} A/cm² a potential of -0.53 V would be necessary in the chloride containing pit-like solution (Fig. 4) and a potential of -0.50 V in the sulfate containing pit-like solution. These values compare very well with the pitting potentials reported in Table I. The pitting potential measured in 1.0M NaCl solution, pH 11, was -0.53 V, while the value measured in 0.5M Na₂SO₄ solution, pH 9.0 and 10.0, was -0.47 V.

Equation [8] gives the minimum pitting potential, according to the localized acidification mechanism. Transport considerations (11) showed that the pitting potential is increased by the presence of inhibitors in the solution. If the metal has a logarithmic type of polarization curve, then, in the presence of inhibiting anions, the pitting potential follows an equation of the type

$$E_p = A + B \log C_{inh} \quad [9]$$

A and B are constants, and C_{inh} is the concentration of the inhibiting species. According to the localized acidification mechanism for pitting, the inhibitors could be either anions of weak acid salts (buffers) or OH^- ions. From the ionic concentration diagrams (11) it was also concluded that the value of B in Eq. [9] should be close to the Tafel slope for the metal in the acidic pit-like solution. Equation [2], which is of the type of Eq. [9], was found for cadmium in alkaline Na_2SO_4 solutions. As predicted by the theory, the value of the constant B , 0.018V, was found to be equal to the value of the Tafel slope for cadmium in acid Na_2SO_4 solution, Fig. 8. In NaCl solutions, on the other hand, an increase of one unit in the pH of the solution was found to lead to an increase of 20 mV in the pitting potential. Here again there is good agreement with the theory, since the Tafel slope found for cadmium in acid NaCl solutions was 27 mV.

When the concentration of the aggressive anion is modified over a big range of concentrations, the change of the potential gradient, ϕ , inside the pits must be accounted for (11). According to the pitting theory, when the change of the value of ϕ is the only cause for the changes observed in the value of E_p , an equation of the type

$$E_p = A - 0.059 \log C_x \quad [10]$$

should be found, where A is a constant, and C_x is the concentration of the aggressive anion. Equation [1] is in good agreement with Eq. [10], showing that the change in ϕ is the only cause for the observed changes of E_p .

From transport considerations of the pitting process (11) an equation of the type

$$E_p = E_c^* + \eta + \phi + E_{inh} \quad [11]$$

should hold true for the passivity breakdown of metals. Good correlations were reported for pitting of aluminum and binary aluminum alloys (10), of molybdenum containing ferritic stainless steels (21), and of high purity zinc (6), iron (8), and nickel (8). The present results show that the same equation could be applied for high purity cadmium.

As pointed out by Augustynski (15), the passivity breakdown for cadmium is close to the normal equilibrium potential of the metal with its ions. This is shown in Fig. 10, where the pitting potential values are plotted on the Pourbaix diagram for cadmium (22). As shown in Fig. 10, the corrosion potential of cadmium in the acid solution, E_c^* , is very close to the equilibrium electrode potential of the metal for a very dilute solution of metal ions. This is because of the high overpotential for hydrogen evolution on cadmium (23). The current densities involved in the pitting process of cadmium are low, and since the Tafel slope is low too, the contribution of η to the pitting potential will be small. The same happens with ϕ . In conclusion, the value of E_p will be still in the range of the equilibrium electrode potentials of the metal.

The results in 1.0M NaCl solution, pH 9.0 (Fig. 6) and those in 1.0M KI solution, pH 11.0 are difficult to explain in view of the equilibrium Pourbaix diagram of Fig. 10. According to this diagram a $\text{Cd}(\text{OH})_2$ oxide film should be stable in both solutions. Hence, a passivity breakdown process should be expected. Nevertheless, the diagram in Fig. 10 does not account for the soluble complexes formed by cadmium in chloride and in iodide solutions. If new diagrams are drawn (24), accounting for all these complexes, Fig. 11 and 12, no stable solid film is found in those solutions. The hydroxide stability range in KI solution is very small, and the metal remains active at almost any pH value. In the 1.0M NaCl solution, on

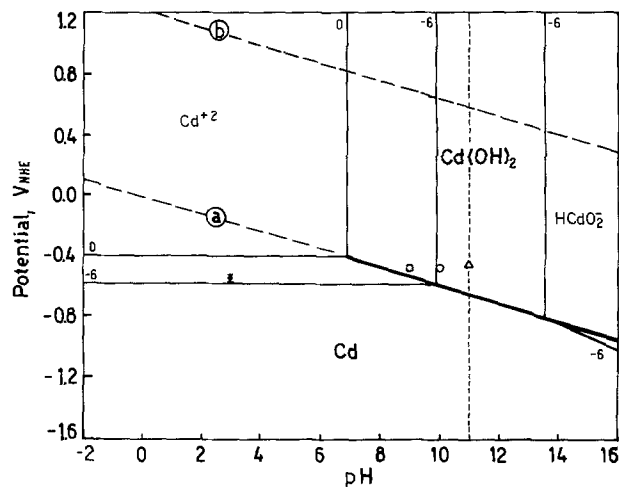


Fig. 10. Potential/pH diagram for the Cd-H₂O system at 25°C. Line a corresponds to the hydrogen reaction equilibrium and line b corresponds to the oxygen reaction equilibrium. Light lines represent equilibrium conditions between a solid phase and an ion at activities 1 and 10⁻⁶M. Heavy line represents equilibrium conditions between two solid phases. Broken line represents equilibrium condition between two ions for a ratio of these ions equal to unity [after Zoubov and Pourbaix (22)]. □, ○, △: pitting potentials for Cd in 0.5M Na_2SO_4 solutions. ✕: corrosion potential for Cd in pH 3, 0.5M Na_2SO_4 solution.

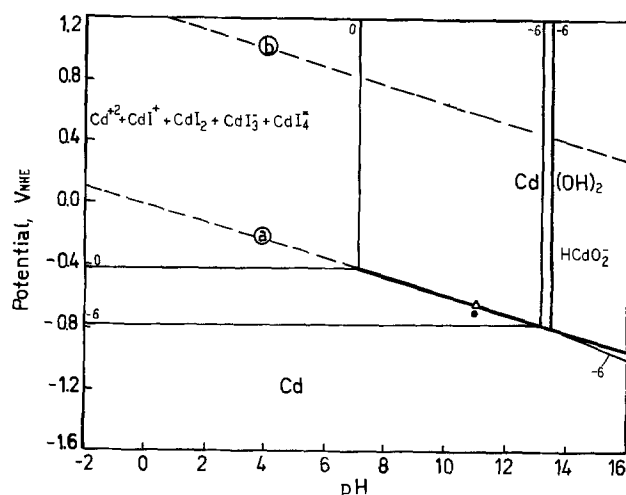


Fig. 11. Potential/pH diagram for the Cd-I-H₂O system, for 1.0M KI solution at 25°C. Line a corresponds to the hydrogen reaction equilibrium and line b corresponds to the oxygen reaction equilibrium. Light lines represent equilibrium conditions between a solid phase and a solution containing a total concentration of dissolved Cd of 1.0 and 10⁻⁶M. Heavy line represents equilibrium conditions between two solid phases [after Alvarez (23)]. ●: Corrosion potential, and △: pseudopitting potential for Cd in 1.0M KI , pH 11.0.

the other hand, passivity could be found at pH values between 11.0 and 13.5.

Acknowledgments

This work was sponsored by the Comisión de Investigaciones Científicas, Pcia. Buenos Aires, by the Programa Multinacional de Metalurgia (PMM-OEA), and by the Servicio Naval de Investigación y Desarrollo, Programa ECOMAR.

Manuscript submitted July 13, 1979; revised manuscript received Nov. 2, 1979.

Any discussion of this paper will appear in a Discussion Section to be published in the December 1980

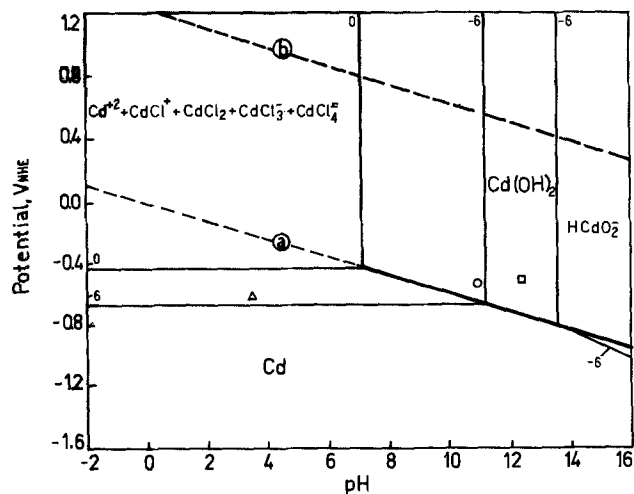


Fig. 12. Potential/pH diagram for the Cd-Cl⁻-H₂O system, for 1.0M NaCl solution at 25°C. Line a corresponds to the hydrogen reaction equilibrium and line b corresponds to the oxygen reaction equilibrium. Light lines represent equilibrium conditions between solid phase and a solution containing a total concentration of dissolved Cd of 1.0 and 10⁻⁹M. Heavy line represents equilibrium conditions between two solid phases [after Alvarez (23)]. Δ: corrosion potential in pH 3, 1.0M NaCl solution. ○ and □: breakdown potentials in 1.0M NaCl solution.

JOURNAL. All discussions for the December 1980 Discussion Section should be submitted by Aug. 1, 1980.

Publication costs of this article were assisted by the Comisión de Investigaciones Científicas, Pcia. Buenos Aires.

REFERENCES

- J. R. Galvele and S. M. de De Micheli, *Corros. Sci.*, **10**, 795 (1970).
- S. M. de De Micheli and J. R. Galvele, *Metalurgia (ABM)*, **27**, 588 (1971).
- J. R. Galvele, S. M. de De Micheli, I. L. Muller, S. B. de Wexler, and I. L. Alanis, in "Localized Corrosion," R. W. Staehle, B. F. Brown, J. Kruger, and A. Agrawal, Editors, p. 580, NACE, Houston (1974).
- S. B. de Wexler and J. R. Galvele, *This Journal*, **121**, 1271 (1974).
- I. A. Maier and J. R. Galvele, *ibid.*, **125**, 1594 (1978).
- M. G. Alvarez and J. R. Galvele, *Corrosion (Houston)*, **32**, 285 (1976).
- C. J. Semino and J. R. Galvele, *Corros. Sci.*, **16**, 297 (1976).
- M. G. Alvarez and J. R. Galvele, IV Reunión Argentina de Electroquímica, La Plata, 5 to 7 November, 1975.
- I. L. Muller and J. R. Galvele, *Corros. Sci.*, **17**, 179 (1977).
- I. L. Muller and J. R. Galvele, *ibid.*, **17**, 995 (1977).
- J. R. Galvele, *This Journal*, **123**, 464 (1976).
- J. R. Galvele, in "Passivity and Its Breakdown on Iron and Iron Base Alloys," R. W. Staehle and H. Okada, Editors, p. 118, NACE, Houston (1976).
- J. R. Galvele, in Fourth International Symposium on Passivity, Airlie House, October 1977.
- M. Kh. Kadyrov and A. L. Golubev, *Zashch. Met.*, **6**, 569 (1970).
- J. Augustynski, *Corros. Sci.*, **13**, 955 (1973).
- D. Gilroy and J. E. O. Mayne, *J. Appl. Chem.*, **12**, 382 (1962).
- N. Pessall and C. Liu, *Electrochim. Acta*, **16**, 1987 (1971).
- G. Cragnolino and J. R. Galvele, in Fourth International Symposium on Passivity, Airlie House, October 1977.
- M. de Castro and J. R. Galvele, 1ra. Reunión Latinoamericana de Electroquímica, La Plata, August 1972.
- T. P. Hoar, in "Electrode Processes," Discussions of the Faraday Society, No. 1, 1947, p. 299, Butterworths, London (1961).
- J. R. Galvele, J. B. Lumsden, and R. W. Staehle, *This Journal*, **125**, 1204 (1978).
- N. de Zoubov and M. Pourbaix, in "Atlas of Electrochemical Equilibria in Aqueous Solutions," M. Pourbaix, Editor, Pergamon Press, Oxford (1966).
- R. Piontelli, *Bull. Nat. Inst. Sci. Indian*, **29**, 80 (1965); see also, R. Piontelli, "Scientific Papers 1935-1971," p. 2820, Milan (1974).
- M. G. Alvarez, Thesis, Universidad de Buenos Aires, 1977.

The Electrosorption of Methane and Its Potentiodynamic Electrooxidation on Platinized Platinum

M. G. Sustersic, R. Córdova O.,¹ W. E. Triaca, and A. J. Arvía*

*Instituto de Investigaciones Físicoquímicas Teóricas y Aplicadas,
División Electroquímica, Sucursal 4—Casilla de Correo 16, 1900 La Plata, Argentina*

ABSTRACT

The electrosorption of methane on platinized platinum and the potentiodynamic oxidation of the electrosorbed species in 1N H₂SO₄ solution is studied at 60°C. Two electrosorbed species are distinguished through the *I/E* characteristics recorded under different perturbation conditions. These species are assigned to COH-type and CO-type adsorbed species. The latter can be transformed into the former by electrochemical reduction in the potential range of the hydrogen adatoms. The number of the electrocatalyst sites per adsorbed species is estimated. The reported results contribute to the understanding of the kinetics of the methane electrooxidation under both stationary and non-stationary electrolysis conditions.

The electrooxidation of methane on a platinum electrocatalyst occurs at an appreciable rate in aqueous phosphoric, sulfuric, or perchloric acids in the 60°–150°C range (1–5). The electrochemical adsorption characteristics of this reaction on platinum-Teflon diffusion electrodes has also been investigated (6, 7). When methane is brought into contact with a platinized-platinum electrode, a shift of the potential in the cathodic direction is observed (2, 3). The rest potential in acid solutions in the presence of methane is determined by the hydrogen adatom electrooxidation reaction (2, 3). This has been taken as evidence of a dehydrogenation reaction on the platinum surface involving the organic molecule (2, 3, 8).

The studies of the methane adsorption by different electrochemical pulse techniques indicate that the electrode contains an adlayer of the so-called C₁ species, which were considered as partially oxygenated species (4, 6, 7). In the anodic polarization of the electrode under stationary conditions, the overall methane electrooxidation reaction occurring at potentials preceding that of the oxygen evolution reaction yields CO₂ and H⁺ ions with practically 100% efficiency. The corresponding Tafel line involves a slope equal to the *RT/F* ratio (5). When the equilibration potential of the Pt/H₂SO₄(aq) (methane) interface is larger than 0.35V, there is practically no chemisorbed product accumulated and the electrochemical reaction actually takes place on a platinum surface free of chemisorption products (6).

Despite these results, the structural and energetic characteristics of the surface species involved in the reaction, as well as the kinetics and mechanism of the reaction under both stationary and nonstationary conditions, are not yet clearly established. Thus, from the differences observed between the results obtained on smooth platinum and on platinized platinum for various electrocatalytic reactions involving reactants such as carbon monoxide and formaldehyde, it follows that they are due not so much to an actual difference in the adsorption process itself but rather to the possible occurrence of processes involving the interconversion of electrosorbed species (9). By using adequate perturbation techniques it would be possible to ascertain the nature and quantity of the electrosorbed species on the electrocatalyst surface and to establish the character-

istics of the predominant electrosorbed species when the electrooxidation process takes place under stationary conditions. Following these lines of thought, the present paper attempts to elucidate the electrosorption characteristics of methane on platinized platinum in sulfuric acid solution and its relation to the hydrocarbon electrooxidation process through the application of different combined potentiodynamic sweep techniques.

Experimental

A conventional three-compartment Pyrex glass electrolysis cell and platinized-platinum electrodes prepared as previously described in the literature (10, 11) were used. The working electrode real area was determined through the charge of the hydrogen electro-sorption current peaks. A hydrogen reference electrode (RHE) in the free-methane electrolyte (1N H₂SO₄) was employed. The potentials of the working electrode are referenced to the RHE.

The 1N H₂SO₄ solution was prepared from the AR chemical (Merck) and triply distilled water. The standard purity criterion for the electrolyte solution consisted in reproducing the conventional potentiodynamic current/potential (*I/E*) profile of the Pt/H₂SO₄(aq) interface (12) after holding the potential at a value close to that of the potential of zero charge of the system for at least a 2 hr period.

Experiments were run either in the nitrogen-saturated electrolyte (blanks) or in the presence of methane (ultrahigh purity, Matheson) under 1 atm saturation at 60°C. Most of the runs were made under a continuous gas bubbling at 30 cm³/min.

Preceding the hydrocarbon adsorption, the working electrode was subjected to the pretreatment already described (11, 13). After the electrode pretreatment the potential was held at a preset value, *E*_{ad}, to adsorb methane during a certain time, *t*_{ad}. Immediately afterward a triangular potential sweep was applied either toward the positive, program (a), or the negative-going potential direction, program (b), at a constant potential sweep rate, *v* (Fig. 1). From the potentiodynamic *I/E* displays the charge required to electrooxidize the adsorbed hydrocarbon layer, *Q*_{ox}, was determined after the proper corrections for both the double layer effect and the electrode surface oxidation (10).

Experiments at constant *E*_{ad} and *t*_{ad} and different *v*'s were performed in order to select the suitable potential sweep rate range for the methane electrooxidation under hydrocarbon readsorption-free conditions. From the charge/potential sweep rate plot (10) it was found that

* Electrochemical Society Active Member.

¹ Present address: Departamento de Química, Universidad Católica de Valparaíso, Valparaíso, Chile.

Key words: methane electrooxidation, hydrocarbon electro-sorption, platinized platinum electrocatalyst.

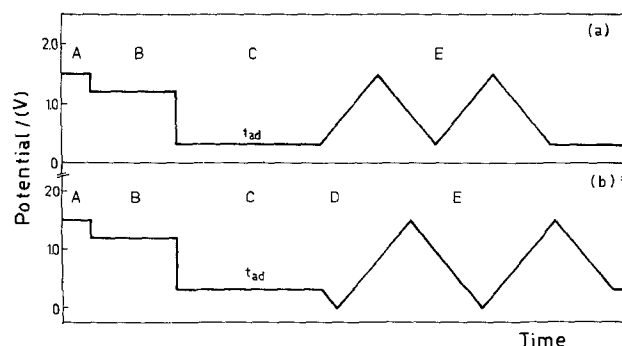


Fig. 1. Potential perturbation programs. Time axis arbitrary scale. Step width: A = 15 sec; B = 120 sec (gas bubbling); C = t_{ad} ; D = initial negative going potential sweep; E = triangular potential sweep.

at $v \geq 0.05$ V/sec the methane readsorption-free condition for the electrochemical reaction was fulfilled.

Results and Interpretation

The adsorption characteristics of methane on platinum.—The adsorption of methane on platinized-platinum electrodes was studied over a wide range of E_{ad} (0.1–0.4V) at a constant t_{ad} and over a wide range of t_{ad} (5–250 min) by keeping E_{ad} constant. The amount of adsorbed species was evaluated through the charge integrated from the potentiodynamic anodic I/E curves. The electrooxidation of the adsorbed species takes place within the 0.5–0.8V range and it exhibits a double anodic current peak under the experimental conditions shown in Fig. 2. At $E_{ad} = 0.3V$ and short t_{ad} , the I/E displays exhibit a predominant contribution of the anodic current peak located at more positive potentials. Contrarily, as t_{ad} increases the overall anodic charge also increases but the relative contribution of the anodic current peak located at more negative potentials becomes more noticeable (Fig. 2). Simultaneously, the residual hydrogen adatoms electrooxidation charge located between 0.30 and 0.40V decreases as t_{ad} increases. At a constant E_{ad} , the adsorbed hydrocarbon electrooxidation charge reaches a maximum value at the time required in order to attain a hydrocarbon stationary coverage, $t_{ad,ss}$. Reasonable straight lines are obtained in the Q_{ox} vs. $\log t_{ad}$ plot (Fig. 3), whose slope depends on E_{ad} . The I/E displays obtained after the hydrocarbon adsorption at $t_{ad,ss}$ and at a constant E_{ad} in the 0.2–0.4V range (Fig. 4) exhibit a maximum electrooxidation charge, $Q_{ox,M}$, equal to 0.113 mC/real cm^2 at 0.26V (Fig. 5). The maximum anodic charge associated with the methane electrooxidation is lower than that corresponding to one monolayer of hydrogen adatoms. The anodic current peak exhibits again the partial overlapping of the two anodic current peaks whose contributions change accordingly with E_{ad} (Fig. 4). At $E_{ad} = 0.2V$ and $E_{ad} = 0.4V$ the anodic current peak located at more positive potentials contributes predominantly

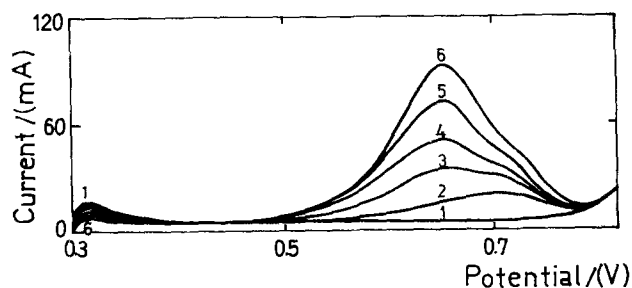


Fig. 2. Potentiodynamic I/E profiles at 0.1 V/sec run from $E_{ad} = 0.3V$ at different t_{ad} . Real electrode area = 1366 cm^2 . Curve 1, blank; curve 2, $t_{ad} = 5$ min; curve 3, $t_{ad} = 15$ min; curve 4, $t_{ad} = 30$ min; curve 5, $t_{ad} = 60$ min; curve 6, $t_{ad} = 120$ min.

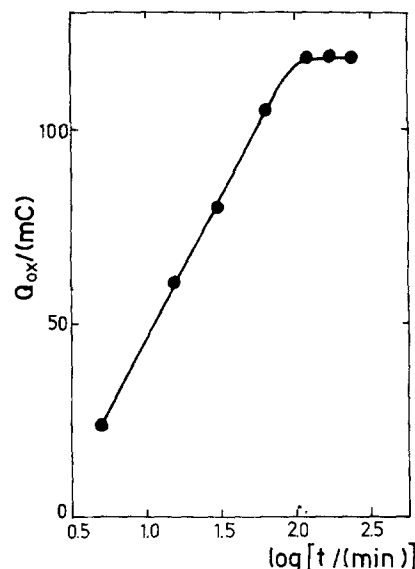


Fig. 3. Dependence of Q_{ox} on t_{ad} at $E_{ad} = 0.3V$. Real electrode area = 1366 cm^2 .

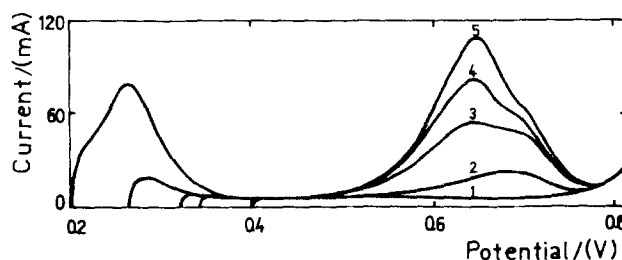


Fig. 4. Potentiodynamic I/E profiles at 0.1 V/sec after the hydrocarbon adsorption at $t_{ad,ss}$ and at different E_{ad} . Real electrode area = 1366 cm^2 . Curve 1, blank at $E_{ad} = 0.4V$; curve 2, $E_{ad} = 0.2$ and $0.4V$; curve 3, $E_{ad} = 0.34V$; curve 4, $E_{ad} = 0.32V$; curve 5, $E_{ad} = 0.26V$.

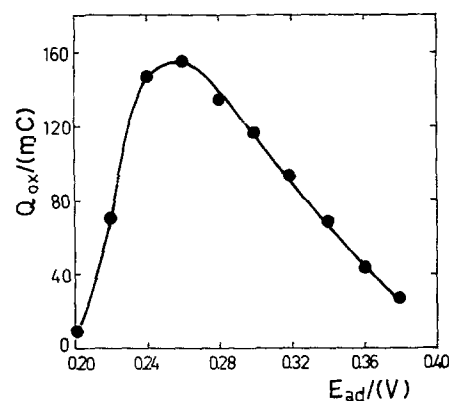


Fig. 5. Dependence of Q_{ox} at $t_{ad,ss}$ on E_{ad} . Real electrode area = 1366 cm^2 .

to the total anodic current while the reverse is observed when E_{ad} is close to the potential where the maximum hydrocarbon adsorption takes place.

The methane electrosorption process.—The occurrence of an electrosorption process was made evident by applying to the interface a potentiostatic step at E_{ad} just after step B of the electrode pretreatment (Fig. 1) and simultaneously recording the anodic current transient up to its stationary value. The major contribution in the overall transient current is attributed to the electrooxidation of hydrogen adatoms produced during the electrosorption process and presents an initial abrupt increase followed by a smooth decay (Fig. 6). The current related to the electrooxidation

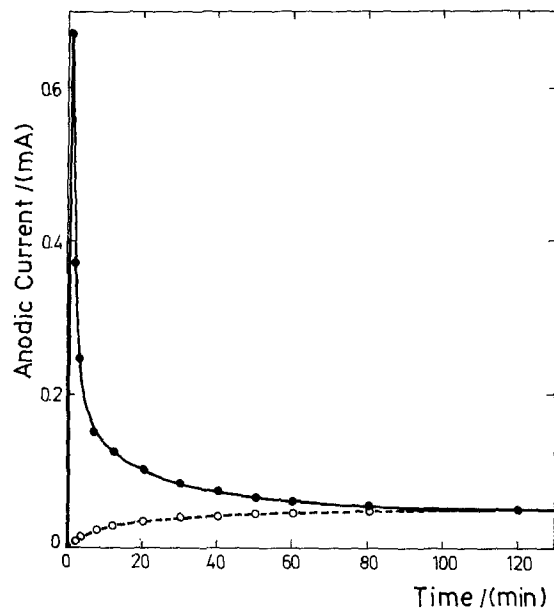


Fig. 6. Potentiostatic I/t plot at $E_{ad} = 0.28V$. Real electrode area = 1366 cm^2 . ●, Overall transient anodic current after correction for the blank; ○, estimated current related to the electrooxidation of the residual electrosorbed species.

of the residual electrosorbed organic species is subtracted from the overall transient anodic current after assuming that the former depends linearly on the hydrocarbon surface coverage degree (14) and that the surface coverage by the adsorbed hydrocarbon species increases linearly with $\log t$. The anodic charge, Q_D , after correction both for the blank and for the electrooxidation reaction is ascribed to the methane dehydrogenation. The charge corresponding to the electrooxidation of the residual organic species, Q_{ox} , is determined through the potentiodynamic scan immediately after the stationary current is attained. For $t_{ad} = t_{ad,ss}$, the Q_D/Q_{ox} experimental ratio approaches two limiting values. Thus, when $0.24V \leq E_{ad} \leq 0.36V$, $(Q_D/Q_{ox})_{exp} \rightarrow 2$ while when either $E_{ad} = 0.2V$ or $E_{ad} = 0.4V$, $(Q_D/Q_{ox})_{exp} \rightarrow 3$ (Table I). Similarly, when $t_{ad} = 0.3V$ for $t_{ad} \leq 5 \text{ min}$, $(Q_D/Q_{ox})_{exp} \rightarrow 3$ while for $t_{ad} > 5 \text{ min}$, $(Q_D/Q_{ox})_{exp} \rightarrow 2$ (Table II).

Kinetic relationships from the potentiodynamic runs.—Within the range of either E_{ad} or t_{ad} where only the anodic current peak located at more positive potentials is observed the anodic current peak height, I_p , after the correction for the blank fits a linear dependence with v and the current peak potential, E_p , fits an E_p vs. $\log v$ relationship whose slope is equal to the $2.3(2RT/F)$ ratio (Fig. 7 and 8). An E vs. $\log I$ linear plot is derived from the initial ascending portion of the

Table I. Q_D/Q_{ox} ratio at $t_{ad,ss}$ and different E_{ad}

E_{ad} (V)	$(Q_D/Q_{ox})_{exp}$	$(Q_D/Q_{ox})_I$	$(Q_D/Q_{ox})_{II}$
0.20	2.5	2.8	1.9
0.24	2.0	2.1	2.6
0.26	2.2	2.2	2.7
0.28	2.0	2.2	2.8
0.30	2.2	2.0	2.7
0.32	1.9	2.1	2.6
0.34	2.1	2.0	2.7
0.36	2.2	2.2	2.5
0.40	3.2	2.9	1.8

Table II. Q_D/Q_{ox} ratio at $E_{ad} = 0.3V$ and different t_{ad}

t_{ad} (min)	$(Q_D/Q_{ox})_{exp}$	$(Q_D/Q_{ox})_I$	$(Q_D/Q_{ox})_{II}$
5	3.0	2.6	2.2
30	2.3	2.0	2.7
120	2.2	2.0	2.7

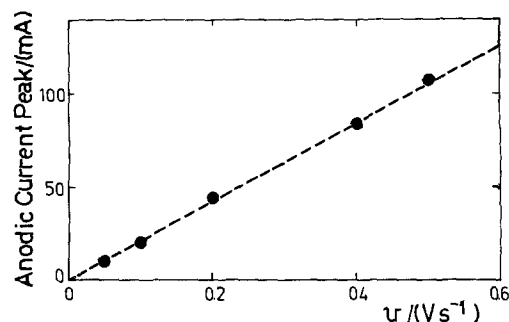


Fig. 7. Dependence of the anodic current peak related to the electrooxidation of the adsorbed hydrocarbon species on v . $E_{ad} = 0.4V$; $t_{ad} = t_{ad,ss}$. Real electrode area = 1366 cm^2 .

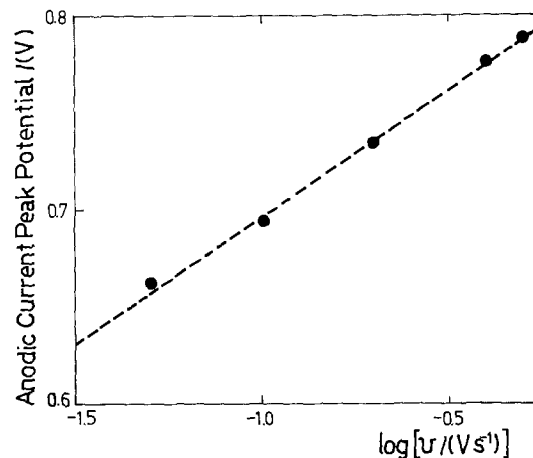


Fig. 8. Dependence of the anodic current peak potential related to the electrooxidation of the adsorbed hydrocarbon species on v . $E_{ad} = 0.4V$; $t_{ad} = t_{ad,ss}$. Real electrode area = 1366 cm^2 . The dashed line corresponds to the slope $2.3(2RT/F)$.

I/E display at any v in the $0.01\text{--}0.1 \text{ V/sec}$ range (Fig. 9). The slope of the best straight line is also equal to the $2.3(2RT/F)$ ratio.

The potentiodynamic I/E displays under controlled electroadsorption.—The shape of the I/E display in the $0.3\text{--}1.5V$ range is modified when after adsorption at E_{ad} during t_{ad} , a negative-going potential excursion is run from 0.3 to $-0.025V$ covering the hydrogen adatom potential region, e.g., after applying program (b) (Fig. 10). Thus, during the first potential sweep the charge pertaining to the hydrogen adatoms is lower than that

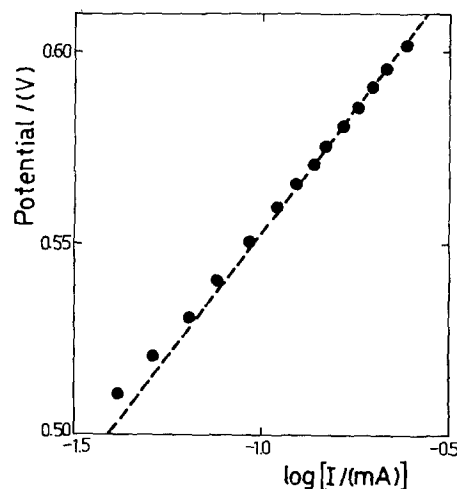


Fig. 9. $E/\log I$ plot derived from a potentiodynamic run at 0.05 V/sec . $E_{ad} = 0.4V$; $t_{ad} = t_{ad,ss}$. Real electrode area = 144 cm^2 . The dashed line corresponds to the slope $2.3(2RT/F)$.

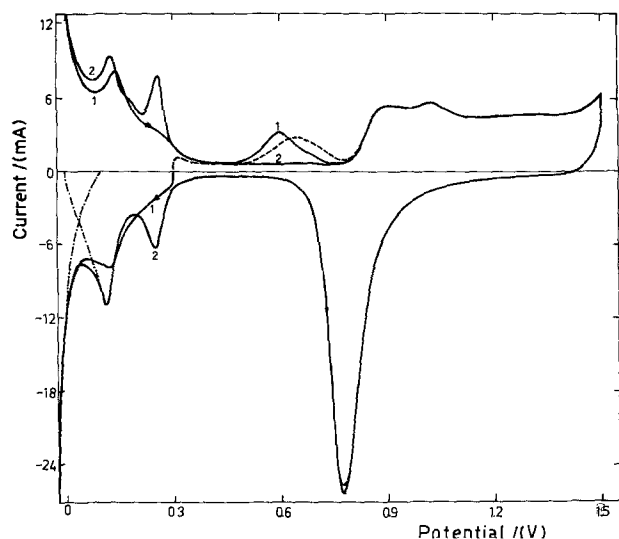


Fig. 10. Potentiodynamic I/E profiles at 0.05 V/sec. $E_{ad} = 0.3V$; $t_{ad} = 15$ min. Real electrode area = 144 cm². ---, First I/E profile run with program (a); —, first (curve 1) and second (curve 2) I/E profiles run with program (b); - - - - , estimated hydrogen electroreduction and hydrogen evolution I/E profiles.

recorded during the following triangular potential scan due to the blocking of the electrode surface by the residual organic species. During the second successive potential sweep, as the electroadsorbed organic species are electrooxidized and no hydrocarbon readsorption becomes possible, the hydrogen adatom current peaks whether anodic or cathodic appreciably increase in height. Nevertheless, the surface blockage affects mainly the hydrogen adatom current peaks located at more positive potentials. During the second positive going potential excursion the anodic charge associated with the electrooxidation of the organic species in the 0.5–0.8V range is practically no longer observed.

To evaluate the charge related to the hydrogen adatom monolayer the following procedure was followed. The hydrogen evolution I/E line, depicted in Fig. 10 which fits an $E/\log I$ plot was extrapolated down to $I = 0$. The extrapolated line yields the cathodic charge related to the hydrogen evolution reaction and permits a reasonable estimation of the I/E profile corresponding to the adsorption of hydrogen adatoms. The decreasing portion of the latter exhibits an inflection point near 0.05V and reaches the $I = 0$ condition corresponding to full hydrogen adatom coverage at $-0.01V$ as given by pseudocapacity data (15).

The blocking charge Q_b is defined as the difference between the hydrogen adatom charge required to form a monolayer in the absence of methane and the charge related to the hydrogen adatoms formed in the methane-saturated solution. The Q_b/Q_{ox} ratio in the 0.24–0.34V range is close to one (Table III).

The comparison of the I/E displays run with the perturbation programs (a) and (b) shows a remarkable difference in the potential range associated with the electrooxidation of the methane electroadsorbed species. Thus, the first I/E profile (Fig. 10) obtained after applying program (a) starts with a surface which is appreciably covered by the electroadsorbed species which is electrooxidized at more positive potentials. This is obtained by the proper adjustment of both E_{ad} and t_{ad} . If the electrooxidation of the electroadsorbed species is preceded by a negative-going potential scan covering

the whole potential range related to the hydrogen adatoms species, e.g., after applying program (b), the immediately following positive potential-going I/E profile shows that the complex anodic current peak after hydrogenation shifts toward more negative potentials and simultaneously the charge involved in the electrooxidation process is practically equal to that observed in the first positive-going potential I/E profile run with program (a).

To confirm the different hydrogenation capabilities of the electroadsorbed species, experiments were also made having the electrocatalyst surface mainly covered by the electroadsorbed species which is electrooxidized at the more negative potential. In this case after the potentiodynamic hydrogenation the immediately following positive-going potential scan shows that the I/E profile corresponding to the electrooxidation of the adsorbed species remains practically unaltered.

Further evidence of the different hydrogenation capability of the two types of electroadsorbed organic species is obtained by running the same kind of experiment as described above but including a potential holding at 0.05C for different periods of time, t_c (Fig. 11). As the cathodization time increases the electrooxidation profiles of the electroadsorbed species progressively moves toward more negative potentials yielding a reasonably stable I/E profile only when the cathodization time exceeds 5 min. The potentiodynamic I/E profile in the hydrogen adatom region changes as already described regardless of the type of perturbation applied to the interface.

All these experiments indicate that the electroadsorption of methane on platinum implies the formation of at least two adsorbed species, one of which can be transformed into the other through a potential-controlled hydrogenation.

Stationary I/E measurements.—The stationary I/E measurements were made by applying to the electrochemical interface different potentiostatic steps at preset potentials in the 0.20–0.55V range just after step B of the electrode pretreatment (Fig. 1). The steady current value at the preset potentials are attained after periods of time comprised between 10 and 190 min depending on the preset potential value (Fig. 12). The experimental $E/\log I$ plot corresponds to a curve (Fig. 13). The lower potential region of the $E/\log I$ plot approaches a limiting straight line whose slope is equal to the 2.3 (RT/F) ratio while the upper potential region approaches a limiting current.

Discussion

The electrocombustion of methane on platinum is expressed by the following overall anodic reaction

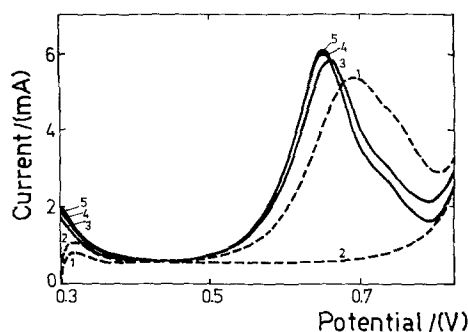
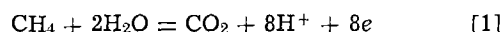


Fig. 11. Potentiodynamic I/E profiles at 0.2 V/sec. $E_{ad} = 0.3V$; $t_{ad} = 30$ min. Real electrode area = 42 cm². ---, First (curve 1) and second (curve 2) I/E profiles run with program (a); —, I/E profiles run with program (b) but including a potential holding at 0.05V just after step D for different t_c : curve 3, $t_c = 10$ sec; curve 4, $t_c = 1$ min; curve 5, $t_c = 5$ min.

Table III. Q_b/Q_{ox} ratio at $t_{ad} = 15$ min and different E_{ad}

E_{ad} (V)	Q_b/Q_{ox}
0.24	1.0
0.30	0.9
0.34	0.8

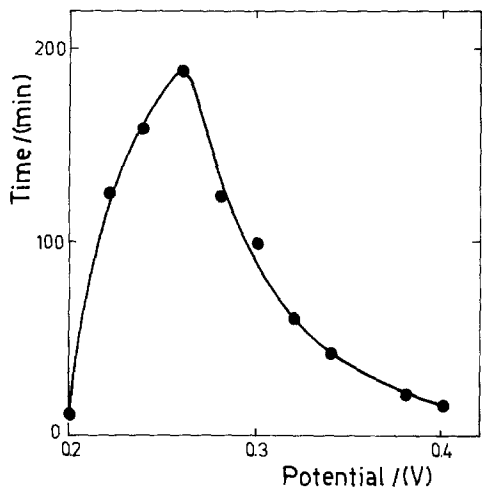


Fig. 12. Plot of the time required to attain the stationary current at different potentials.

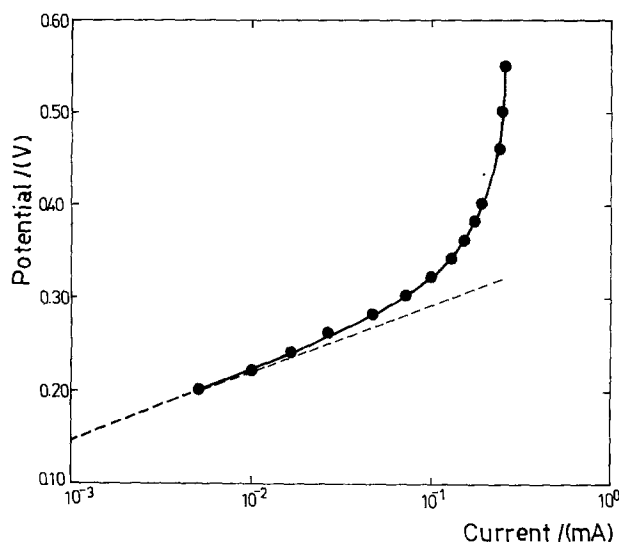
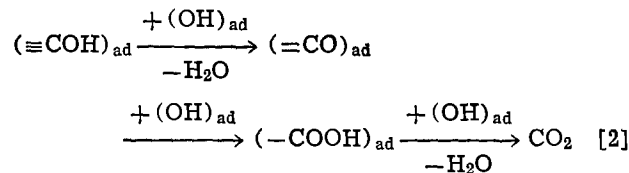


Fig. 13. $E/\log I$ plot derived from stationary measurements under a continuous methane bubbling. Real electrode area = 1366 cm². The dashed line corresponds to the slope $2.3(RT/F)$.

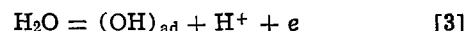
This reaction is free of hydrocarbon readsorption contribution when it proceeds potentiodynamically at potential sweep rates larger than 0.05 V/sec. Under potentiostatic conditions reaction [1] involves an electro-sorption process preceding the proper electrooxidation reaction. Methane electro-sorbs slowly on platinum through a dissociative mode. Under most of the experimental conditions chosen to study the adsorption process, the reaction is partially diffusion controlled (14). This is not unexpected since the solubility of methane in water at 25°C and 1 atm pressure is 24.4g CH₄/10⁶g H₂O (16). In the adsorption of methane, hydrogen- and oxygen-containing chemisorbed species were shown to appear on the Pt electrocatalyst after a prolonged contact of the latter with the methane-saturated electrolyte at open circuit (3).

The present results indicate that in the electro-sorption process at least two well-distinguished hydrocarbon residual surface species are involved. It has been suggested that the surface species resulting from methane adsorption on platinum in acid electrolytes may be -CHO, ≡COH, or a similar species (4, 7). The former involves a single bond with platinum and three electrons per platinum site while the latter implies bonds with three platinum sites, requiring one electron per site. The CO-type species are produced on platinum during the adsorption of different compounds such as CO and formaldehyde (17, 18), although COH-

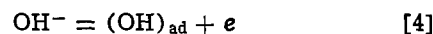
type species are also formed from both substances as revealed by radiochemical techniques (19, 20). Furthermore, it has been demonstrated that the adsorbed surface species can interact with each other or with hydrogen adatoms or adsorbed OH radicals so as to form new adsorbed species or to desorb as stable organic molecules (9). Thus, it has been proposed that the electrooxidation of methanol on platinum occurs via the interaction of adsorbed ≡COH particles with adsorbed OH radicals (21, 22)



The adsorbed OH radicals are produced in the preceding fast electrochemical step in acid solutions

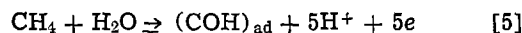


and in alkaline solutions

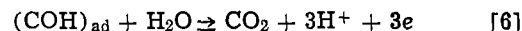


which at 0.3-0.9V (RHE) can be regarded as being in equilibrium (23, 24). Hence, all these results suggest the possibility of a gradual hydrogenation of the CO-type species into the COH-type species, as is experimentally demonstrated in the present paper. Then, the $Q_{\text{D}}/Q_{\text{ox}}$ experimental ratio furnishes an indication as to the most probable type of adsorbed species which predominates during the electro-sorption process under constant potential conditions.

The existence of the first electro-sorbed species can be explained through the electro-sorption of methane according to the following reaction

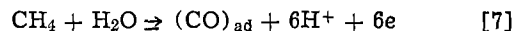


Therefore, the major contribution in the anodic transient current recorded during the potentiostatic electro-sorption at a potential which is in the neighborhood of the maximum adsorption potential, corresponds to the deprotonation of methane yielding the adsorbed COH species. Reaction [5] is probably a complex process involving 5 F/mole of electro-sorbed species. Now, under potentiodynamic conditions, the electro-sorbed species is electrooxidized according to

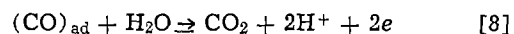


where 3 F/mole of electro-sorbed species play a part in the reaction. Therefore, from reactions [5] and [6] the $Q_{\text{D}}/Q_{\text{ox}}$ ratio equals 1.7, a figure which is near to the lowest limit for the $Q_{\text{D}}/Q_{\text{ox}}$ experimental ratio.

On the other hand, the existence of the second adsorbed species from the methane electro-sorption process results from the reaction



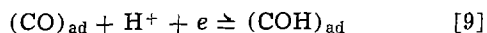
yielding a CO adsorbed species and six protons per adsorbed methane molecule. Reaction [7] corresponds to another limiting situation for the electro-sorption of methane on platinum which predominates at short t_{ad} or at constant E_{ad} or when either $E_{\text{ad}} = 0.2\text{V}$ or $E_{\text{ad}} = 0.4\text{V}$ at $t_{\text{ad,ss}}$. When reaction [7] occurs the potentiodynamic electrooxidation corresponds to the following process



This second possibility for the electro-sorption and electrooxidation of methane on platinum involves a $Q_{\text{D}}/Q_{\text{ox}}$ ratio equal to 3. Therefore, the relative contribution of the two electro-sorption processes depends on E_{ad} and t_{ad} , so that the experimental values which lie between 1.9 and 3.2 indicate the composite nature of the electro-

sorption process preceding the proper electrooxidation reaction.

The existence of two different adsorbed species opens the possibility that the CO species can be electrochemically reduced to the COH species according to



Reaction [9] is obviously potential dependent. Furthermore, if two residual organic species are formed during the electrodeposition process whose relative contributions depend on E_{ad} and t_{ad} , the fact that Q_{b} is essentially equal to Q_{ox} (Table III) implies that each COH species blocks three adsorption sites of the electrocatalyst while each CO species involves only two adsorption sites. According to reaction [9] the electrooxidation current peak located at more negative potentials is that related to the COH species and that located at more positive potentials corresponds to the contribution of the CO species. As a matter of fact, the potential range of the current peak assigned to the electrooxidation of the CO-type adsorbed species coincides with the potential range where the CO-electrosorption current peaks are observed (25-27), although the corresponding I/E profile is apparently more complex than thought earlier (28).

On the assumption that the electrooxidation of COH-type species occurs at more negative potentials while that of the CO-type species takes place at more positive potentials, the electrooxidation charge of each species can be related to the dehydrogenation charge involved in the electrosorption process. Thus, the total dehydrogenation charge, Q_{D} can be related to the corresponding electrooxidation charges according to

$$Q_{\text{D}} = 1.7(Q_{\text{ox}})_{\text{COH}} + 3(Q_{\text{ox}})_{\text{CO}} \quad [10]$$

The $(Q_{\text{D}}/Q_{\text{ox}})_{\text{I}}$ and $(Q_{\text{D}}/Q_{\text{ox}})_{\text{II}}$ ratios shown in Tables I and II involve the experimental Q_{ox} and the Q_{D} estimated according to Eq. [10] from the decomposition of the overall anodic potentiodynamic I/E profiles into two partial current contributions represented by two Gaussian functions (Fig. 14). The former ratio denoted by the subscript I implies that the peak location at more negative potentials corresponds to the COH species while that located at more positive potential values is related to the CO species. The charge ratio indicated with the subscript II corresponds to the reverse assignment of the two current peaks. Nevertheless, it should be pointed out that evaluation of Q_{D} from the potentiostatic transients may involve a small contribution due to the probable electroreduction of traces of CO_2 present at the electrochemical interface generated during the electrosorption process particularly when the latter occurs at $E_{\text{ad}} < 0.24\text{V}$. This means that the experimental Q_{D} values used up in Tables I and II are the minimum Q_{D} values and, consequently, the reported $(Q_{\text{D}}/Q_{\text{ox}})_{\text{exp}}$ figures should be taken as the lower limiting values of the $(Q_{\text{D}}/Q_{\text{ox}})_{\text{exp}}$ ratios. Therefore, from the data assembled in Table I one deduces that in the 0.24-0.36V range, under hydrocarbon stationary coverage conditions, the main electrosorbed species is the one identified as the COH-type species.

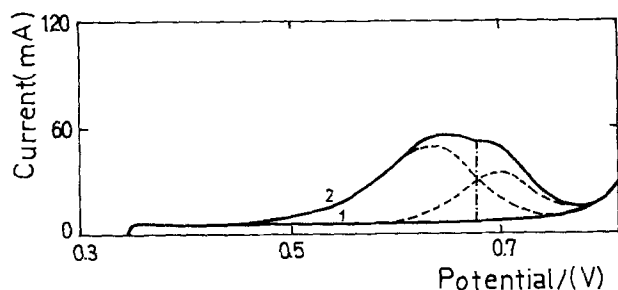
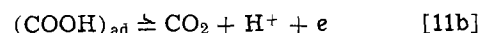


Fig. 14. Potentiodynamic I/E profile at 0.1 V/sec, $E_{\text{ad}} = 0.34\text{V}$ and $t_{\text{ad,ss}}$ (curve 2). Real electrode area = 1366 cm^2 . The estimated separate current contributions are represented by the dashed curves. Blank (curve 1).

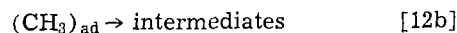
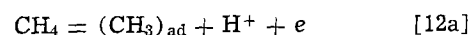
Contrarily, when the hydrocarbon adsorption takes place at either 0.2 or 0.4V during $t_{\text{ad,ss}}$ the CO species is apparently the predominant species on the electrocatalyst surface. Furthermore, for those experiments run at a constant E_{ad} and different t_{ad} (Table II), during the initial electrosorption the CO species apparently predominates on the surface while on increasing t_{ad} the COH species becomes the main species on the electrocatalyst surface. These conclusions are relevant to understanding the kinetics and mechanisms of the overall reaction under different experimental conditions.

The dependence of both I_{p} and E_{p} on v and the Tafel slope equal to the $2.3(2RT/F)$ ratio, which are worked out from the potentiodynamic data at $E_{\text{ad}} = 0.4\text{V}$, should be directly related to the electrooxidation of the CO-type species. Accordingly, this reaction which finally yields CO_2 and H^+ ions should comprise an initial single electron transfer step as rate determining. The possible sequence of consecutive reactions can be written in the following way



where step [11a] is rate determining, under a Langmuirian type of adsorption isotherm for the CO-type species. This means that any interaction effect should be, in principle, negligible, a situation which is not far from reality as the prevalence of the CO-type species on the electrode surface is only accomplished under a low degree of surface coverage, that is, when the adsorption occurs either at low adsorption times or at potentials located at both sides far enough from the maximum electrosorption potential.

Finally, a comment on the Tafel plot related to the methane overall electrooxidation process is relevant at this stage. The fact that the average composition of the adsorbed species depends both on E_{ad} and t_{ad} , and that different times are required to reach the hydrocarbon stationary surface coverage at each E_{ad} , indicates that any Tafel-type plot derived from stationary measurements should be handled with extreme care in order to draw mechanistic conclusions on the electrochemical reaction. Under these circumstances it is not surprising that the Tafel plot corresponds in face to a curve which approaches a limiting current at potentials higher than 0.3V (Fig. 13). However, the initial portion of this curve can be to a certain extent arbitrarily approximated to a straight line which approaches the slope RT/F on a $\log I$ region less than one decade. This slope has been recently reported for the stationary electrooxidation of methane at potentials lower than 0.2V (5) and was used, together with the pH and the hydrocarbon partial pressure dependences of the electrochemical reaction, for the mechanistic interpretation of the reaction in terms of the following successive stages



where stage [12b] was assumed to be rate determining. Nevertheless on the basis of the previous discussion this slope cannot be taken as a definitive criterion to derive the mechanism of the electrochemical process. Furthermore, under stationary conditions, the actual situation may be even more complex since, apart from a possible diffusional contribution at the higher overpotentials, the reaction may involve in addition to the COH- and the CO-type species, a relative number of other adsorbed intermediates such as COOH-type, CH, CH_2 , and CH_3 species, as already pointed out for the electrooxidation of more complex organic molecules on platinum (26, 29).

Acknowledgment

INIFTA is sponsored by the Consejo Nacional de Investigaciones Científicas y Técnicas, the Universidad

Nacional de La Plata, and the Comisión de Investigaciones Científicas (Provincia de Buenos Aires). This work was partially supported by the Regional Program for the Scientific and Technological Development of the Organization of American States. R.C.O. thanks the Universidad Católica de Valparaíso (Chile) for the leave of absence.

Manuscript submitted July 20, 1979; revised manuscript received Jan. 3, 1980.

Any discussion of this paper will appear in a Discussion Section to be published in the December 1980 JOURNAL. All discussions for the December 1980 Discussion Section should be submitted by Aug. 1, 1980.

Publication costs of this article were assisted by the Instituto de Investigaciones Fisicoquímicas Teóricas y Aplicadas.

REFERENCES

- W. T. Grubb and C. J. Michalske, *Nature*, **201**, 287 (1964).
- L. W. Niedrach, *This Journal*, **111**, 1309 (1964).
- R. V. Marvet and O. A. Petrii, *Elektrokhimiya*, **3**, 153 (1967).
- A. H. Taylor and S. B. Brummer, *J. Phys. Chem.*, **72**, 2856 (1968).
- S. Y. Hsieh and K. M. Chen, *This Journal*, **124**, 1171 (1977).
- L. W. Niedrach, *ibid.*, **113**, 645 (1966).
- L. W. Niedrach and M. Tochner, *ibid.*, **114**, 17 (1967).
- O. A. Petrii, R. V. Marvet, and Zh. N. Malysheva, *Elektrokhimiya*, **3**, 1141 (1967).
- Yu. B. Vasiliev, V. S. Bagotskii, and O. A. Khazova, *ibid.*, **11**, 1406 (1975).
- W. E. Triaca, T. Rabockai, and A. J. Arvia, *This Journal*, **126**, 218 (1979).
- W. E. Triaca, A. M. Castro Luna, and A. J. Arvia, *ibid.*, **127**, 826 (1980).
- B. E. Conway, H. Angerstein-Kozłowska, W. B. A. Sharp, and E. E. Criddle, *Anal. Chem.*, **45**, 1331 (1973).
- S. Gilman, *Trans. Faraday Soc.*, **62**, 466 (1966).
- E. J. Cairns, in "Advances in Electrochemistry and Electrochemical Engineering" Vol. 8, C. W. Tobias and P. Delahay, Editors, Wiley-Interscience, New York (1971).
- R. Woods, *J. Electroanal. Chem. Interfacial Electrochem.*, **49**, 217 (1976).
- C. McAuliffe, *Nature (London)*, **200**, 1092 (1963).
- S. Gilman, *J. Phys. Chem.*, **67**, 78 (1963).
- T. Loucka and J. Weber, *J. Electroanal. Chem. Interfacial Electrochem.*, **21**, 329 (1969).
- V. E. Kazarinov, V. N. Andreev and G. Ya. Tsyachnaya, *Elektrokhimiya*, **8**, 927 (1972).
- G. Ya. Tsyachnaya and V. E. Kazarinov, *ibid.*, **7**, 1879 (1971).
- O. A. Khasova, Yu. B. Vasiliev, and V. S. Bagotskii, *ibid.*, **2**, 267 (1966).
- V. S. Bagotskii and Yu. B. Vasiliev, *Electrochim. Acta*, **12**, 1323 (1967).
- A. N. Frumkin, O. A. Petrii, and A. M. Kossaya, *Elektrokhimiya*, **4**, 475 (1968).
- O. A. Petrii, A. N. Frumkin, and V. V. Topolev, *ibid.*, **4**, 1104 (1968).
- M. W. Breiter, "Electrochemical Processes in Fuel Cells," Springer-Verlag, New York (1969).
- B. Damaskin, O. A. Petrii, and V. V. Batrakov, "Adsorption of Organic Compounds on Electrodes," Plenum Press, New York (1971).
- A. B. Fasman and G. L. Padyukova, *Elektrokhimiya*, **10**, 39 (1974).
- S. A. Bilmes, N. R. de Tacconi, and A. J. Arvia, *This Journal*, In press.
- A. A. Michri, A. G. Pshenichnikov, and R. Kh. Burshtein, *Elektrokhimiya*, **8**, 276 (1972).

Galvanostatic Oxidation of Nickel in Borate Buffer Solution

B. MacDougall,* D. F. Mitchell, and M. J. Graham

National Research Council of Canada, Division of Chemistry, Ottawa, Ontario K1A 0R9, Canada

ABSTRACT

Anodic oxide films formed on nickel in pH 7.65 borate buffer solution in both the passive potential and oxygen evolution regions have been analyzed by RHEED, Auger spectroscopy (in conjunction with argon ion sputtering), and O K α x-ray emission spectroscopy. In the passive potential region, a highly epitaxial, single crystal NiO film is formed with a limiting thickness of $\sim 12\text{\AA}$. In this potential range, even very long times of anodizing do not alter the oxide epitaxy or increase its thickness. In contrast, polarization in the potential range where oxygen is evolved results in the development of considerable oxide misorientation and a significant increase in oxide thickness. While long times of polarization (>20 hr) in this potential region produce oxide films hundreds of angstroms thick, the current efficiency for oxide growth is $<1\%$. These thick anodic oxide films are quite different from thermally prepared, compact films of NiO and appear to have an open-cellular, sponge-like structure with an oxygen:nickel ratio approaching 1.3. This oxide probably forms by a direct oxidation rather than a dissolution/precipitation reaction.

The passive oxide film produced by potentiostatic oxidation of nickel in neutral and acid sulfate solutions is NiO (1-4). The stability of this film towards open-circuit breakdown and cathodic reduction depends strongly on both the time and potential of anodic treatment, in contrast to the overall film thickness which is almost constant at 9-12 \AA (0.13-0.17 μg oxygen cm^{-2}) (5-8). It has been reported

by other workers (9-11) that oxide films several thousand angstroms thick can be produced galvanostatically on nickel in neutral borate solution but not in sulfate solutions. The reason for the difference appears to be the much higher solubility of the oxide film in sulfate solution in comparison with the borate electrolyte. While it is agreed that thicker oxide films can be formed on nickel in neutral borate solutions, little is known about their nature and their relationship to the passive films formed in the potential

* Electrochemical Society Active Member.

Key words: films, electrode, current efficiency, sputtering.

region between nickel dissolution and oxygen evolution.

The present paper presents the results of an investigation of the anodic oxidation of nickel in pH 7.65 borate buffer solution under galvanostatic conditions. The electrochemical data are complemented by solution analysis for Ni^{2+} to determine the current efficiency for oxide growth. Also, electron diffraction, Auger electron spectroscopy, and x-ray emission analysis have been used to determine the structure, thickness, and composition of the oxide films.

Experimental

Polycrystalline specimens, $1 \times 2.5 \times 0.02$ cm thick, were prepared from Materials Research Corporation zone-refined nickel sheet of 99.996% purity (1). They were degreased with benzene, chemically polished, electropolished for 2 min at 23°C in a 57 volume percent (v/o) sulfuric acid solution at 0.5 mA cm^{-2} , and then annealed at 800°C in a vacuum of 10^{-8} Torr. The specimens were again electropolished immediately before use in an experiment. Potentials quoted in this paper are referred to the saturated calomel electrode which is 0.245V with respect to the standard reversible hydrogen electrode. Electropolished nickel electrodes were galvanostatically anodized either with or without cathodic reduction of the prior oxide film, as discussed in detail elsewhere (12). Solutions were deaerated pH 7.65 borate buffer, and were analyzed for Ni^{2+} by carbon rod atomic absorption spectroscopy, the lower limit of detection by this method being $0.2 \mu\text{g cm}^{-2}$ (sample area = 5 cm^2 ; cell volume = 50 ml). X-ray emission (13, 14) and Auger electron spectroscopy (Physical Electronics Incorporated Model 590) were used to determine oxide film thickness. The structure of the oxide film on a Ni(111) single crystal electrode was investigated by reflection high energy electron diffraction (RHEED).

Results and Discussion

Anodic galvanostatic charging data.—Electropolished nickel has a 6Å ($0.087 \mu\text{g oxygen cm}^{-2}$) "air-formed" film of NiO (1, 2, 4, 7) which can be cathodically reduced in neutral borate solution (9, 15). In this work, anodic charging curves were obtained for both the oxide-covered and oxide-free electropolished nickel electrodes (Fig. 1), the latter being obtained after cathodic reduction at $80 \mu\text{A cm}^{-2}$ for 5 min. For the oxide-free surface (Fig. 1, curve a), an initial potential arrest is followed by a region of almost linear increase of anodic potential, V_a , with anodic charge,

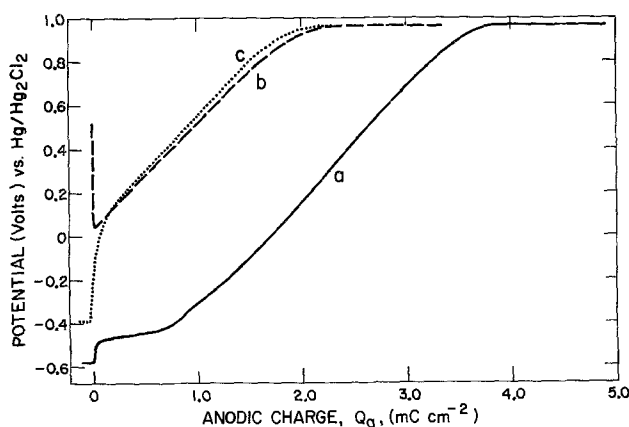


Fig. 1. Anodic galvanostatic charging profiles for electropolished polycrystalline nickel electrodes in pH 7.65 borate buffer at $80 \mu\text{A cm}^{-2}$ following different pretreatments: curve a, cathodic reduction at $80 \mu\text{A cm}^{-2}$ and open-circuit exposure (—); curve b, immersion in solution at $80 \mu\text{A cm}^{-2}$ (---); curve c, immersion in solution on open circuit for 10 min (····).

Q_a ; eventually a steady-state potential plateau is reached. The initial region is usually considered to be due to active nickel dissolution ($\text{Ni} \rightarrow \text{Ni}^{2+} + 2e$) whereas the linear transition region is thought to be mainly due to growth of an oxide film, e.g., $\text{Ni} + \text{H}_2\text{O} \rightarrow \text{NiO} + 2\text{H}^+ + 2e$, and corresponds to the passive potential region in constant potential experiments. The potential plateau at 0.95V could be associated with transpassive nickel dissolution and/or oxygen evolution and/or a thickening of the oxide film.

If an electropolished nickel electrode is immersed in the solution under anodic galvanostatic polarization, i.e., without cathodic reduction of the air-formed oxide (Fig. 1, curve b), the active metal dissolution region is avoided. At $80 \mu\text{A cm}^{-2}$, the immersion potential is 0.05V and V_a increases almost linearly with Q_a to the plateau region at 0.95V. The slope between 0.05 and 0.95V is similar for curves a and b, suggesting that the state of an electropolished nickel surface is similar to that of an initially oxide-free nickel surface which has been anodically polarized to 0.05V at $80 \mu\text{A cm}^{-2}$ [cf. Ref. (12)]. The anodic charging profile for electropolished nickel is not influenced by a prior 10 min open-circuit exposure to the pH 7.65 borate solution (Fig. 1, curve c), which means that the open-circuit treatment has little influence on the nature of the air-formed film. The transient charge associated with curve b, $\sim 2.0 \text{ mC cm}^{-2}$, is independent of charging rates between 5 and $80 \mu\text{A cm}^{-2}$, a result compatible with a surface charging process.

In order to detect changes in the nature of the oxide film during galvanostatic charging, an anodically polarized Ni(111) single crystal was removed at various stages during anodic charging at $10 \mu\text{A cm}^{-2}$ (Fig. 2), and examined by RHEED. [One specimen was reimmersed in the solution after examination by diffraction and the subsequent charging profile almost immediately approached that for an electrode maintained in solution. It thus appears that removal of the electrode from solution, washing, and vacuum pumping in the diffraction apparatus have little influence on the state of the surface oxide as anticipated from previous work (5).] The electron diffraction patterns included in Fig. 2 indicate that the epitaxy of the NiO film is maintained throughout the transient region but is lost in the plateau region. As the potential increases to more anodic values in the transient region, the metal reflections become less pronounced, an indication that there is additional oxygen uptake. At the same time, the measured NiO lattice parameter changes gradually from 2% expanded on electropolished nickel to 1% expanded (Fig. 2, point B) to $<0.2\%$ expanded at the end of the transient region (Fig. 2, point C), i.e., the oxide lattice parameter gradually approaches that expected for stoichiometric NiO. In the plateau region, the oxide changes from a highly epitaxed, single crystal overgrowth to an NiO with a fiber axis normal to the surface (Fig. 2, point D). The absence of metal reflections after charging in the plateau region for 24 hr (Fig. 2, point E) indicates that the oxide thickness increases in this region. This last observation agrees with the results of Ord *et al.* (9, 10) who found that the oxide thickness increases considerably with time of anodic treatment in the plateau region.

To determine the current efficiency for oxide growth in the transient region, the solution was analyzed for Ni^{2+} after charging electropolished nickel to 0.9V (Fig. 1). The amount of nickel in solution is $0.3 \mu\text{g Ni}^{2+} \text{ cm}^{-2}$ of electrode, corresponding to 1.0 mC cm^{-2} of charge. Since the total anodic charge is 2.0 mC cm^{-2} , the current efficiency for oxide growth is 50%. Thus, the total oxide thickness after charging is 12Å ($0.17 \mu\text{g oxygen cm}^{-2}$) because the oxide on electropolished nickel is 6Å thick ($0.087 \mu\text{g oxygen cm}^{-2}$). It is unlikely that the 1.0 mC cm^{-2} of charge asso-

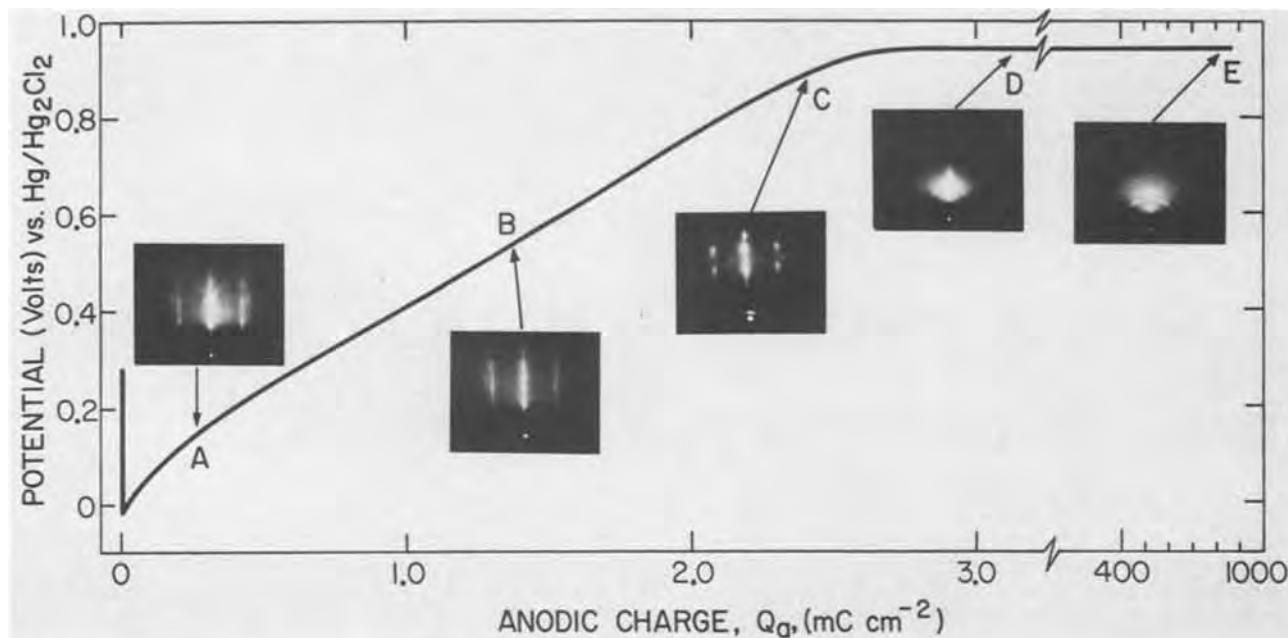


Fig. 2. Anodic galvanostatic charging profile for an electropolished Ni(111) electrode at $10 \mu\text{A cm}^{-2}$. The electrode was removed at points A, B, C, D, and E for reflection high energy electron diffraction (RHEED) examination; the diffraction patterns are from the [112] direction using 75 kV electrons.

ciated with nickel dissolution is simply due to chemical dissolution of the oxide since the oxide is resistant to dissolution in pH 7.65 borate buffer solution (Fig. 1, curve c). Also, as mentioned earlier, the transient charge is independent of charging rate between 5 and $80 \mu\text{A cm}^{-2}$ and if chemical dissolution were playing a major role, the decrease in transition time by a factor of ca. 16 should greatly diminish the extent of chemical dissolution and thus the transient charge. It thus appears that the anodic potential causes nickel to dissolve and thereby lowers the efficiency of oxide growth.

To determine the current efficiency for the oxide formation in the plateau region, the solution was analyzed for Ni^{2+} and the thickness of the oxide determined by Auger analysis as a function of time of anodic charging of electropolished nickel. A charging rate of $80 \mu\text{A cm}^{-2}$ was chosen in order to develop a thick oxide film and to compare with previous work in the borate solution (9, 10). The amount of Ni^{2+} in solution did not increase above the 1 mC cm^{-2} equivalent dissolved in the transition region even for extended time periods in the plateau region [cf. Ref. (15)]. This may not, however, mean that the current efficiency for oxide growth is 100% in the plateau region since oxygen evolution may be consuming a significant portion of the anodic charge.

Quantitative Auger analysis.—Auger analysis of the oxide film on polycrystalline nickel (see Appendix) after anodic charging to 0.9V indicates the presence of 12Å of NiO ($0.17 \mu\text{g oxygen cm}^{-2}$), a value in excellent agreement with that obtained for anodic films on nickel formed in neutral or acid sulfate solutions (1-8). After 5 min in the plateau region at $80 \mu\text{A cm}^{-2}$, the oxide thickness was determined by Auger analysis to be 16Å ($0.23 \mu\text{g oxygen cm}^{-2}$) indicating a current efficiency for oxide formation of $\sim 10\%$. The oxide stoichiometry was estimated to be close to NiO from the ratio of nickel to oxygen signal intensities. Such an increase in oxide film thickness above the 12Å ($0.17 \mu\text{g oxygen cm}^{-2}$) detected in the passive region can only be achieved by polarization in the potential plateau region. Indeed, potentiostatic anodic polarization of electropolished nickel, either with or without a prior cathodic reduction, for very long periods of time ($\geq 24 \text{ hr}$) in the passive

potential region (e.g., at 0.7V) will not increase the film thickness above $\sim 12\text{Å}$.

Thicker oxide films prepared by anodizing electropolished nickel at $80 \mu\text{A cm}^{-2}$ for times $> 10 \text{ min}$ were analyzed by the Auger technique in conjunction with Argon ion sputtering. Figure 3 shows the ratio of the oxygen to nickel peak to peak intensities (denoted by P/P) of a number of films, anodized for various periods of time, as a function of sputtering time. Because the analysis comes from an area encompassing about ten grains of the polycrystalline sheet, the signal intensities are average values. The same general result is obtained from analysis of only one grain, but there is a grain-to-grain variation in the P/P ratio of as much as a factor of three. There is an almost uniform decrease in the P/P ratio with sputtering time for the anodically formed films (Fig.

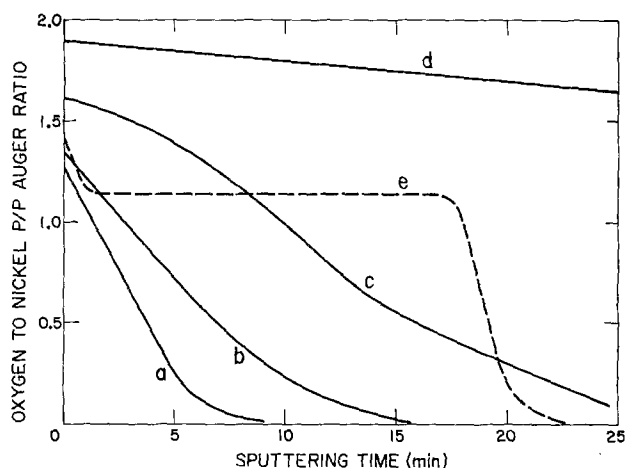


Fig. 3. Variation of the oxygen 510 eV (peak to peak) to nickel 848 eV (peak to peak) Auger signal intensity ratio (P/P) with time of argon ion bombardment for electropolished nickel electrodes anodized at $80 \mu\text{A cm}^{-2}$ in pH 7.65 borate buffer for the following times: curve a, 5 min; curve b, 30 min; curve c, 24 hr; curve d, 200 hr. Also shown is the sputter profile (---) for a thermally grown NiO film (curve e). Argon ion beam condition is 1 kV, 53° from normal incidence; sputter rate is $0.07 \mu\text{g oxygen cm}^{-2} \text{ min}^{-1}$ for the thermal NiO film.

3, curves a-d), a result which is different from that normally obtained with a thick ($>25\text{\AA}$), thermally formed NiO film (Fig. 3, curve e). With the latter, there is an initial decrease in P/P representing disproportionation due to sputtering, followed by a period of constant P/P ratio representing 90-95% of the time required to sputter through the film. Finally a rapid decrease is observed on sputtering through the metal-oxide interface. The most likely interpretation of the "long" interface observed for the anodic oxide films is that they are present as an open-cellular sponge with a large variation in point to point mass on a lateral scale in the 10\AA range.¹

An alternate but less likely interpretation is that some form of severe disproportionation is occurring during sputtering. The initial P/P ratio for specimens anodized for long times (curves c and d) is higher than that for the thermal NiO film (curve e), and indicates an oxygen to nickel ratio approaching 1.3. High oxygen-content material is probably also present in the films formed at shorter times of anodic treatment but its analysis is masked by the "thinness" of the oxide in some areas which allows a signal contribution from the underlying metal.

As indicated in the Appendix, the oxide thickness can be estimated from the time required for the P/P ratio to decrease to $\sim 2/3$ of its initial value. This is approximately the time required to remove one-half of the oxide layer. Using this time and assuming that the anodic film sputters at the same rate as the thermal film, i.e., $0.07 \mu\text{g oxygen cm}^{-2} \text{ min}^{-1}$, oxide thicknesses calculated for the various anodic treatments are given in Table I.² To verify that the oxide thicknesses determined by this method are accurate, the samples anodized for 30 min, 24 hr, and 200 hr were also analyzed by O $K\alpha$ x-ray emission spectroscopy to determine the average oxygen uptake. The values, as seen in Table I, are in agreement with those determined by Auger analysis.

The anodic film formed on electropolished polycrystalline nickel after 24 hr at $80 \mu\text{A cm}^{-2}$ was examined in some detail by the Auger technique. The analysis from a number of grains indicates that the average thickness of the oxide sponge is $\sim 1.3 \mu\text{g oxygen cm}^{-2}$. To determine the oxide thickness variation from one metal grain to another, a large sample area was sputtered for set periods of time, after which oxygen Auger signal maps of the surface were obtained. In this way, assuming a uniform sputtering rate from grain to grain, variations in oxide thickness over the surface could be obtained. The minimum

¹ Replica electron micrographs of the oxide surfaces show a uniform roughening, with height variations of $\sim 50\text{\AA}$.

² Oxide thicknesses are quoted as $\mu\text{g oxygen cm}^{-2}$. While it is reasonable to convert to angstroms the thickness of thin oxides produced in the transient region (assuming a roughness factor of 1 and an NiO density of 6.75, i.e., $1 \mu\text{g oxygen cm}^{-2} = 69.2\text{\AA NiO}$), it is not so for the oxides produced at long anodization times in the plateau region which are open-cellular sponges of unknown density.

Table I. Average oxide film thicknesses as a function of time of anodizing of electropolished Ni electrodes at $80 \mu\text{A cm}^{-2}$ in pH 7.65 borate buffer solution determined by (a), Auger electron spectroscopy in conjunction with Argon ion sputtering, and (b), O $K\alpha$ x-ray emission analysis of some of the samples

Time of anodic treatment	Oxide film thickness ($\mu\text{g oxygen cm}^{-2}$)	
	(a) Auger analysis	(b) X-ray emission analysis
5 min	$0.23 \pm 0.02^*$	
30 min	0.5 ± 0.1	0.58 ± 0.02
24 hr	1.3 ± 0.2	1.23 ± 0.06
200 hr	6.5 ± 1.0	>5

* Thickness obtained by quantitative thin film Auger analysis (see Appendix) where sputtering is not required.

oxide thickness was found to be $\sim 0.6 \mu\text{g oxygen cm}^{-2}$ whereas the maximum was $\sim 1.7 \mu\text{g oxygen cm}^{-2}$. The fact that the oxide thickness depends on the metal substrate orientation is an indication that the oxide does not form by a dissolution/precipitation mechanism; also, the electron diffraction pattern for this oxide (Fig. 2, point E) is not as compatible with a precipitated oxide as it is with one formed via a surface oxidation process. It thus appears that growth of this oxide probably occurs at the metal interface with electrolyte penetrating through the existing oxide to reach the bare nickel metal. Each new layer of oxide forms beneath the existing oxide and pushes the latter further into the solution. The penetration of electrolyte through the oxide should not be too difficult when the oxide is in the form of a sponge.

Using the average thickness value of $1.3 \mu\text{g oxygen cm}^{-2}$ for the oxide sponge, the current efficiency for oxide growth at long times of anodic charging is extremely small ($<1\%$). The majority of the charge must be consumed by the oxygen evolution reaction, and the occurrence of this reaction may be contributing to the breakdown of oxide epitaxy in going from the transient to plateau regions. It is interesting to note that the thickness of the oxide formed in the transient region is limited to $\sim 12\text{\AA}$ ($0.17 \mu\text{g oxygen cm}^{-2}$) no matter how long the time of anodizing. This limiting thickness may correlate with the fact that the oxide epitaxy is maintained throughout the transient region and is only lost in the plateau region (Fig. 2). Upon loss of the oxide epitaxy, the film thickness increases above the 12\AA limiting value, but with a very low current efficiency for oxide growth.

Summary

The present work shows that the thickness and structure of anodic oxide films formed galvanostatically on nickel in pH 7.65 borate solution change dramatically at potentials more anodic than 0.9V. At lower anodic potentials, the NiO film thickness is limited to $\sim 12\text{\AA}$ ($0.17 \mu\text{g oxygen cm}^{-2}$) whereas at the higher potentials the thickness can increase to more than $1.5 \mu\text{g oxygen cm}^{-2}$. This increase in oxide thickness is correlated with a degeneration of the single crystal oxide epitaxy and a conversion of the oxide from a compact film to a porous, sponge-type oxide. The thickness of this oxide film depends on the conditions of polarization and the metal substrate orientation. At long times of polarization in the plateau region at $80 \mu\text{A cm}^{-2}$, e.g., 24 hr, the oxide thickness variation from grain to grain is between ~ 0.6 and $\sim 1.7 \mu\text{g oxygen cm}^{-2}$. This anisotropy of film thickness indicates that the oxide grows by a direct surface oxidation reaction rather than a dissolution/precipitation mechanism.

Acknowledgment

The authors thank Mr. G. I. Sproule for helpful assistance with the Auger analysis.

Manuscript submitted Sept. 25, 1979; revised manuscript received Dec. 20, 1979.

Any discussion of this paper will appear in a Discussion Section to be published in the December 1980 JOURNAL. All discussions for the December 1980 Discussion Section should be submitted by Aug. 1, 1980.

Publication costs of this article were assisted by the National Research Council of Canada.

APPENDIX

Auger Analysis

The quantitative thin film Auger analysis used was based on the concepts of Gallon (16) and Pons *et al.* (17). In the latter treatment for a sample containing various elements, the contribution from each atomic layer (i) of a given element I towards the overall

Auger peak to peak signal (P/P) for element I is given by $h_I^{(i)} = \alpha_I k_I^i N_I^{(i)}$. In this equation, α_I is the sensitivity coefficient for element I, k_I^i is the contribution coefficient (also known as the absorption coefficient) of layer (i) to the total signal, and $N_I^{(i)}$ is the number of atoms of element I in layer (i). H_I is the sum of all the individual layer contributions for element I, which for a total of x layers is

$$H_I = \sum_{i=0}^{i=x} h_I^{(i)} = \sum_{i=0}^{i=x} \alpha_I k_I^i N_I^{(i)} \quad [\text{A-1}]$$

It should be noted that the contribution coefficient (of value <1) is raised to the power i ; i.e., for the first atomic layer of the surface (which is not covered by any layer), $i = 0$ and $k_I^0 = 1$.

Using Eq. [A-1], Auger analysis of bulk NiO of uniform composition gives a P/P ratio ($\equiv H_O/H_{Ni}$)

equal to the ratio $\frac{\alpha_O}{\alpha_N} \frac{(1 - k_{Ni})}{(1 - k_O)}$. For thin films of

NiO on Ni, the increase in P/P with increasing layer by layer NiO coverage can be calculated using this ratio (1.43) and Eq. [A-1], in conjunction with the approximation of Pons *et al.* (17) for calculating the contribution coefficients. The results of these calculations are represented graphically in Fig. 4 for a total of 15 layers, or 30Å of NiO assuming 1 layer of NiO is equivalent to 2Å. Nickel samples were prepared with 6 and 12Å of NiO [thicknesses were determined independently by x-ray emission spectroscopy (13, 14)] and the oxygen to nickel P/P Auger ratios were found to be in good agreement with those given by Fig. 4. Oxide film thickness up to ~16Å can thus be accurately obtained from the measured oxygen to nickel P/P ratio. For thicker NiO films, this P/P ratio falls off significantly with increasing oxide thickness as seen in Fig. 4. Sputtering is required in order to determine the oxide thickness which is estimated from the time required for the P/P ratio to decrease to ~2/3 of its initial value. This is approximately the time required to remove 1/2 of the oxide layer.

REFERENCES

1. B. MacDougall and M. Cohen, *This Journal*, **121**, 1152 (1974).
2. B. MacDougall and M. Cohen, *ibid.*, **123**, 191 (1976).
3. B. MacDougall and M. Cohen, *ibid.*, **123**, 1783 (1976).
4. B. MacDougall and M. Cohen, in "Passivity of Metals," R. P. Frankenthal and J. Kruger, Editors, p. 827, The Electrochemical Society, Princeton, N.J. (1978).

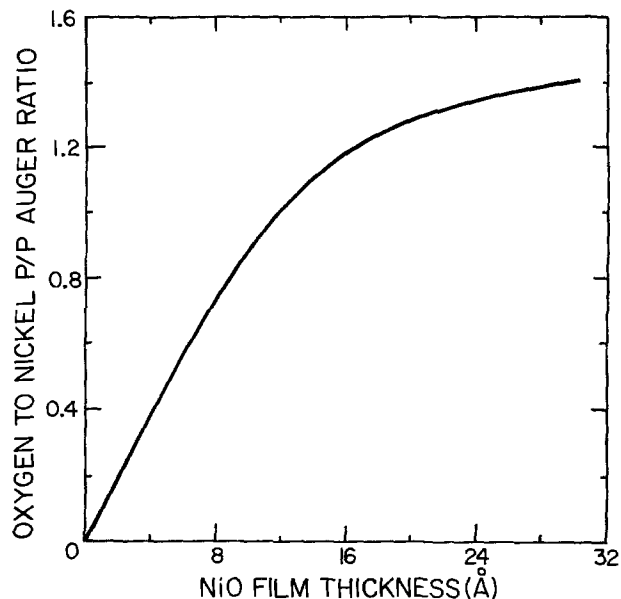


Fig. 4. Variation of the calculated oxygen 510 eV (peak to peak) to nickel 848 eV (peak to peak) Auger signal intensity ratio (P/P) with NiO film thickness.

5. B. MacDougall and M. Cohen, *This Journal*, **124**, 1185 (1977).
6. B. MacDougall and M. Cohen, *Electrochim. Acta*, **23**, 145 (1978).
7. B. MacDougall, *This Journal*, **125**, 1183 (1978).
8. B. MacDougall, D. F. Mitchell, and M. J. Graham, *Isr. J. Chem.*, **18**, 125 (1979).
9. J. L. Ord, J. C. Clayton, and D. J. De Smet, *This Journal*, **124**, 1714 (1977).
10. M. A. Hopper and J. L. Ord, *ibid.*, **120**, 183 (1973).
11. J. L. Ord, in "Passivity of Metals," R. P. Frankenthal and J. Kruger, Editors, p. 273, The Electrochemical Society, Princeton, N.J. (1978).
12. B. MacDougall, *This Journal*, **127**, 789 (1980).
13. D. F. Mitchell and P. B. Sewell, *Thin Solid Films*, **23**, 109 (1974).
14. P. B. Sewell, D. F. Mitchell, and M. Cohen, in "Development in Applied Spectroscopy," Vol. 7A, pp. 61-79, Plenum Press, New York (1969).
15. N. Sato and K. Kudo, *Electrochim. Acta*, **19**, 461 (1974).
16. T. E. Gallon, *Surf. Sci.*, **17**, 486 (1969).
17. F. Pons, J. Le Hérycy, and J. P. Langeron, *ibid.*, **69**, 565 (1977).

Anodic Polarization Behavior of Mild Steel in Hot Alkaline Sulfide Solutions

Desmond Tromans*

Department of Metallurgical Engineering, University of British Columbia,
Vancouver, British Columbia, V6T 1W5 Canada

ABSTRACT

Anodic polarization studies have been conducted in an aqueous solution of 2.5M NaOH + 0.423M Na₂S, at 92°C, and compared with studies in 3.35M NaOH. Anodic films were examined by electron diffraction and x-ray energy analysis and all results compared with published data on S-H₂O and Fe-S-H₂O equilibria. In particular, it was concluded that the delay of passivity in the sulfide solution, relative to NaOH, was due to the incorporation of S²⁻ ions into the Fe₃O₄ lattice to render it nonprotective. Passivity did not occur until the lattice S²⁻ content was decreased at more noble potentials, this process being influenced by anodic oxidation of aqueous S²⁻ ions. The polarization behavior is relevant to corrosion and stress corrosion cracking in the pulp and paper industry.

Mild steel is frequently exposed to hot aqueous alkaline sulfide solutions in the Kraft process (1) for converting (digesting) wood chips into pulp. The industrial solutions, known as white liquors, usually contain 2.1-2.8M NaOH and 0.21-0.64M Na₂S, together with several impurities and a room temperature pH near 14 (2). They encounter mild steel at ~90°C in white liquor clarifiers and storage vessels, and at 150°-170°C in digesters. However, in spite of the importance and long-term use (>50 years) of the Kraft process in the pulp and paper industry, few electrochemical polarization studies have been conducted on mild steel in hot alkaline sulfide solutions, and no studies have been reported on the anodic films.

The major reported polarization studies on mild steel in simulated alkaline sulfide pulping solutions were conducted by Mueller (2) at 30°-97°C, and Kesler and Bakken (3) at 35°C. Electrochemical interpretation of their data was limited and important details at low current densities were not revealed by their data plots of linear current density vs. linear potential. However, they demonstrated an active-passive transition and their work has been used as the basis for understanding corrosion in white liquors (4), and the use of polysulfide oxidants (4, 5) and impressed anodic currents (6) for corrosion protection.

The present study was designed to provide a more thorough understanding of the anodic polarization behavior of mild steel in a hot NaOH + Na₂S solution representative of white liquor. Polarization curves were obtained containing more detail than those previously reported (2-4), and were compared with those obtained in NaOH only. Anodic corrosion films were identified, and the results were interpreted using the data of Biernat and Robins on S-H₂O (7) and Fe-S-H₂O (8) equilibria.

Experimental

Test-piece.—Studies were conducted on mild steel having a weight percentage composition of 0.22 C, 0.55 Mn, 0.28 Si, 0.11 Ni, 0.10 Cr, 0.01 P, 0.032 S, and remainder Fe. It was in the form of cold drawn 9.5 mm diam rod, with a Rockwell hardness of R_B78. Cylindrical test pieces were sectioned, each having a total surface area of 500 mm². The surfaces were mechanically polished with 240 grit paper, degreased in clorethane, cleaned in 10 volume percent (v/o) HCl, and rinsed in water, alcohol, and dried. This procedure gave reproducible corrosion potentials and polarization behavior.

* Electrochemical Society Active Member.

Key words: anodic films, passivity, stress corrosion, white liquor.

Solutions.—The alkaline sulfide solution was similar to that used by Kesler and Bakken (3). Its molar composition was 2.5 NaOH + 0.423 Na₂S (total Na⁺ of 3.35M). Comparative tests were conducted in 3.35M NaOH. All solutions were freshly prepared from distilled water purged with nitrogen, reagent grade NaOH, and hydrated Na₂S flake containing 59.4% Na₂S by weight.

Polarization.—Polarization tests were conducted in 800 ml of solution at 92°C, using a Princeton Applied Research (PAR) single compartment corrosion cell (Model 9700) with two graphite counterelectrodes and Model 178 electrometer probe. The cell was heated with a Corning heating mantle connected to a variable transformer, allowing manual control of temperature to within ±1°C. The solution was continuously stirred and purged with nitrogen.

Test-pieces were introduced into the cell at 92°C and allowed to remain under free corrosion conditions for 900 sec before conducting a single anodic scan on each specimen. The potential was potentiodynamically increased at 1 mV/sec with a PAR potentiostat (Model 173) coupled to a universal programmer (Model 175) and logarithmic current converter (Model 376). The potentials were measured with respect to a saturated calomel electrode (SCE) placed outside the test cell at 25°C. A Luggin capillary, placed 1 mm from the test piece, was connected to the reference electrode via a KCl salt bridge. No attempt was made to correct for the small potential differences arising from concentration effects and thermal gradients in the salt bridge. Potential and logarithmic current were plotted automatically on a Houston Omnigraph 2000 recorder. All data are reported as logarithmic current density (*i*) vs. potential (*E*) with respect to the standard hydrogen electrode scale (*V*_{SHE}), where *E*_{SCE} = +0.2416 *V*_{SHE}.

Film analysis.—Following polarization, anodic films were investigated by *in situ* electron diffraction analysis at 100 keV in the high resolution diffraction chamber of an Hitachi HU 11A electron microscope. The test-pieces were washed in water, rinsed in alcohol, dried, and placed in the chamber. Diffraction patterns were obtained by transmission through protuberances on the specimen surface. Films beneath loose corrosion products were studied after wiping away the loose products with soft tissue in alcohol. In addition, films were studied via x-ray energy analysis at 20 keV in an ETEC Autoscan scanning electron microscope using an Ortec Si/Li detector (7000 series) and multichannel analyzer (Model 6200).

Results

Polarization behavior.—Representative anodic polarization curves for the NaOH and alkaline sulfide solutions are shown in Fig. 1. In both cases, mild steel exhibited a corrosion potential (E_{corr}) near -0.89 V_{SHE} in the active state and underwent an active-passive transition. However, current densities were higher in the alkaline sulfide, the peak current density exceeding that in NaOH by a factor of ~ 35 and the minimum passivation current density being in excess by a factor of ~ 25 .

The onset of passivity occurred above -0.77 V_{SHE} in NaOH, whereas in the alkaline sulfide it commenced above the major current peak at -0.66 V_{SHE}. A minor current peak occurred in the sulfide solution at -0.77 V_{SHE}.

Anodic potentials near the major current peak in the alkaline sulfide solution were associated with a visible brownish discoloration of the solution around the specimen and formation of a loosely adherent brown-black corrosion film. This film ceased to thicken above -0.63 V_{SHE} and the increased anodic currents above -0.5 V_{SHE} were not associated with any additional discoloration of the solution. The onset of passivation in the NaOH solution above -0.8 V_{SHE} was accompanied by formation of an adherent black film.

Anodic films.—Electron diffraction studies of specimens removed from the alkaline sulfide solution at -0.6 V_{SHE} failed to disclose any diffraction spots or rings from the loosely adherent brown-black film, indicating an amorphous structure. Figure 2 is a scanning electron micrograph of the *in situ* film showing its porous and fine powdery nature. Samples of the film were isolated from the specimen by carefully scraping with a wooden spatula. X-ray energy spectra were obtained from samples mounted on a carbon substrate. These were compared with spectra obtained from FeS₂ (pyrite) and FeS (pyrrhotite) under identical instrument conditions. Ratios of the integrated intensities S/Fe for the K_α peaks, after allowing for background subtraction, were FeS₂ = 2.01, FeS = 1.06, film = 1.03. Hence, the brown-black film was identified as amorphous FeS. This conclusion was consistent with the fact that freshly precipitated FeS has been shown by Berner (9) to be both noncrystalline and black in color.

In situ electron diffraction studies of anodic films formed in the passive region beneath amorphous FeS were obtained after wiping away the loose FeS, as described in the "Film analysis" section. Studies were also conducted on the unwiped adherent film formed in the passive region in NaOH. In all cases, ring patterns were obtained characteristic of a cubic spinel structure. The details are shown in Table I. The lattice parameters for iron oxide spinels are reported to be $a_0 = 8.32$ – 8.34×10^{-10} m for γ -Fe₂O₃, and 8.39×10^{-10} m for Fe₃O₄ (10). The lattice parameter for the thio-spinel, Fe₃S₄, is reported to be $a_0 = 9.876 \times 10^{-10}$ m

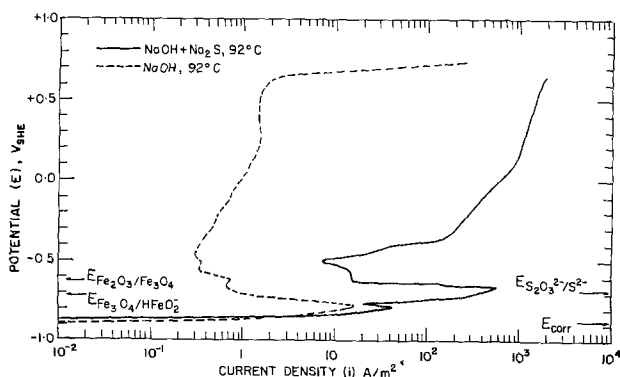


Fig. 1. Anodic polarization behavior of mild steel in NaOH and NaOH + Na₂S solutions.

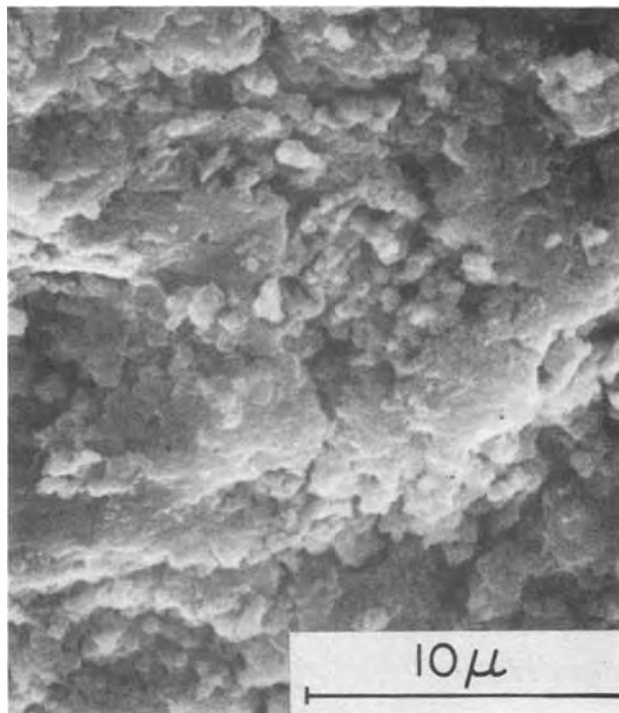
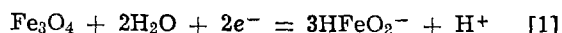


Fig. 2. Scanning electron micrograph of loosely adherent, amorphous FeS film.

(11). Thus, at -0.6 V_{SHE} in the alkaline sulfide, the film is believed to be basically an Fe₃O₄ spinel containing substitutional S²⁻ ions, e.g., Fe₃O_{4-x}S_x, where $x \approx 0.19$ based on a weighted average of lattice parameters.

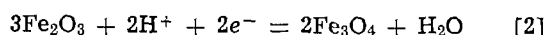
Discussion

Aqueous equilibria.—Biernat and Robins (8) have calculated Fe-S-H₂O equilibria at 100°C which are relevant to the present study. The data show that at the commencement of the polarization test (E_{corr}), the stable dissolved S species is S²⁻ and Fe dissolves in the active condition as HFeO₂⁻. Equations which are particularly useful are shown below

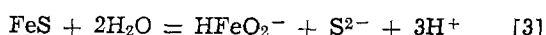


$$E_{\text{Fe}_3\text{O}_4/\text{HFeO}_2^-} = -1.74 + 0.037 \text{ pH} -$$

$$0.037 \log [\text{HFeO}_2^-]^3, \text{ V}_{\text{SHE}} \quad [1a]$$



$$E_{\text{Fe}_2\text{O}_3/\text{Fe}_3\text{O}_4} = +0.261 - 0.074 \text{ pH}, \text{ V}_{\text{SHE}} \quad [2a]$$



$$3 \text{ pH} = 40.09 + \log ([\text{HFeO}_2^-] [\text{S}^{2-}]) \quad [3a]$$

With reference to Eq. [1a] and [2a], the pH values of the test solutions were estimated from the dissociation constant for water at 100°C [1.62×10^{-12} (12)], the activity of [OH⁻] and the activity of [H₂O]. The value of [OH⁻] was estimated by approximating molar concentrations to molalities (*M*) and extrapolating the activity coefficient data of Harned and Owen (13) to 100°C. The activity of water was assumed to be ~ 0.95 (14). The estimated pH values are shown in Table II.

Table I. Experimental lattice parameters of spinel passive films

Solution	E (V _{SHE})	a_0 (10^{-10} m)	Probable film
NaOH	-0.5	8.36 ± 0.02	γ -Fe ₂ O ₃ + Fe ₃ O ₄
NaOH + Na ₂ S	-0.6	8.46 ± 0.02	Fe ₃ O ₄ containing S ²⁻ ions (Fe ₃ O _{4-x} S _x)
NaOH + Na ₂ S	-0.5	8.39 ± 0.02	Fe ₃ O ₄

Table II. Calculated E values

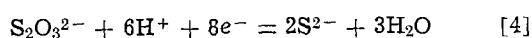
Solution	pH	[HFeO ₂ ⁻] (M)	$E_{\text{Fe}_3\text{O}_4/\text{HFeO}_2^-}$ (V _{SHE})	$E_{\text{Fe}_2\text{O}_3/\text{Fe}_3\text{O}_4}$ (V _{SHE})
NaOH	~12.1	6.83×10^{-6}	-0.719	-0.634
NaOH + Na ₂ S	~12.0	6.6×10^{-6}	-0.721	-0.627

The activities of [HFeO₂⁻], required for Eq. [1a], were calculated after traversing the large current peak in NaOH and the minor current peak in alkaline sulfide (see Fig. 1). The total coulombs passed was determined and the concentration of HFeO₂⁻ estimated by assuming all current involved dissolution of Fe to form HFeO₂⁻. The concentrations were assumed to be the same as the activities, and are shown in Table II.

The potentials corresponding to Eq. [1a] and [2a] at 100°C are shown in Table II. Within the accuracy of the thermodynamic data and activity estimates, the E values may be compared with the tests at 92°C and are placed on Fig. 1.

Equation [3a] represents deposition of FeS from solution. The pH at which this occurs may be estimated from [S²⁻] and [HFeO₂⁻] activities. In the alkaline sulfide test solution, [S²⁻] was approximated to the molar concentration of S²⁻ (i.e., 0.423) and the maximum value of [HFeO₂⁻] was estimated by determining the number of coulombs required to reach the major current peak at -0.66 V_{SHE} and assuming this represented dissolution of Fe as HFeO₂⁻. In this manner [HFeO₂⁻] was found to be $\sim 1.04 \times 10^{-4}$ M, which upon inserting in Eq. [3a] yielded a pH of ~12. This pH value was in agreement with the pH of the solution (see Table II) and shows that formation of the amorphous FeS film occurred via Eq. [3] and [3a]. In practice, concentration gradient effects in the diffusion layer at the metal surface (kinetic factors) could locally raise the value of [HFeO₂⁻] and produce formation of FeS before the major current peak was reached, as was frequently observed.

One additional reaction which must be considered is the anodic oxidation of S²⁻ during polarization. Generally, in oxidation of white liquors, oxidation to S₂O₃²⁻ is the first and most rapid stage (15, 16). Therefore, this reaction will be considered using the data of Biernat and Robins (7) at 100°C, as shown below



$$E_{\text{S}_2\text{O}_3^{2-}/\text{S}^{2-}} = 0.034 - 0.056 \text{ pH}$$

$$+ 0.0093 \log ([\text{S}_2\text{O}_3^{2-}]/[\text{S}^{2-}]^2) \quad [4a]$$

Consequently, approximating [S²⁻] to the molar concentration of S²⁻, and using a value of [S₂O₃²⁻] equivalent to 10⁻⁶ M, which is a reasonable activity to form during polarization without invalidating the previous calculations, it is seen that $E_{\text{S}_2\text{O}_3^{2-}/\text{S}^{2-}}$ is equal to -0.68 V_{SHE}. This value is placed on Fig. 1. Thus, the marked increase in current above -0.5 V_{SHE} is believed to be due to oxidation of S²⁻ via Eq. [4].

Overall events.—The present results and calculations suggest that the onset of passivation (reduction of current) in NaOH is associated with formation of Fe₃O₄ films, with maximum passivation being associated with formation of γ-Fe₂O₃ at $E_{\text{Fe}_2\text{O}_3/\text{Fe}_3\text{O}_4}$. This is consistent with Vetter's (17) view of the Flade potential.

In alkaline sulfide solution, it appears that Fe₃O₄ starts to form, causing a minor current peak (near -0.77 V_{SHE}), and then becomes nonprotective due to the incorporation of S²⁻ ions into the lattice to form Fe₃O_{4-x}S_x. Thus, dissolution of Fe continues with increasing E and is accompanied by deposition of amorphous FeS when the solubility product is exceeded (near the major current peak at -0.66 V_{SHE}). The onset of passivation occurs when the S²⁻ content of the Fe₃O_{4-x}S_x film is decreased to $x \approx 0.19$, maximum passivation occurring when $x \approx 0$ and Fe₃O₄ is formed.

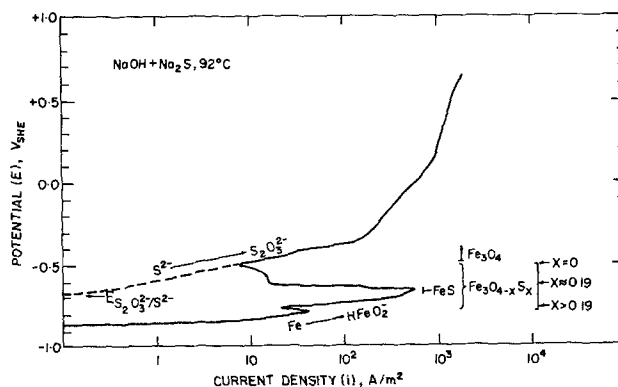


Fig. 3. Schematic diagram of anodic polarization behavior of mild steel in NaOH + Na₂S showing sequence of events.

Stabilization of the film by reduction of the lattice S²⁻ content appears to be related to oxidation of aqueous S²⁻ to S₂O₃²⁻. The sequence of events is shown schematically in Fig. 3.

It should be noted that the onset of passivity in the sulfide solution also appears coincident with $E_{\text{Fe}_2\text{O}_3/\text{Fe}_3\text{O}_4}$ (see Fig. 1). However, this is believed to be fortuitous because the electron diffraction data do not reveal the presence of γ-Fe₂O₃ (Table I). Furthermore, the higher minimum current densities observed at maximum passivation in the sulfide solution, relative to NaOH, indicate different passive films in the two solutions. This is consistent with the views of Foley *et al.* (18) on the higher electrical conductivity of Fe₃O₄ relative to γ-Fe₂O₃.

Stress corrosion cracking.—The occurrence of stress corrosion cracking of mild steel in highly alkaline solutions has been associated with a small range of potentials near the nose of the active-passive current peak (19, 20). Thus, the displacement of the nose of the active-passive current peak to higher E values in the alkaline sulfide solution, relative to NaOH (see Fig. 1), indicates that stress corrosion cracking will occur at more noble potentials in the sulfide solution. This prediction is being investigated further.

Conclusions

Anodic polarization studies on mild steel exposed to aqueous NaOH, and NaOH + Na₂S solutions at 92°C were consistent with the following conclusions:

1. An active-passive transition was observed in both environments. Larger current densities and displacement of the active-passive transition to higher potentials were observed in the sulfide solution.
2. Passivation commenced in NaOH with formation of Fe₃O₄, maximum passivation occurring with formation of γ-Fe₂O₃ at $E_{\text{Fe}_2\text{O}_3/\text{Fe}_3\text{O}_4}$.
3. Passivation was delayed in NaOH + Na₂S, due to incorporation of S²⁻ into the Fe₃O₄ lattice to form a nonprotective film, possibly Fe₃O_{4-x}S_x. Further active dissolution of iron occurred, exceeding the solubility product of FeS to deposit a nonprotective amorphous layer.
4. Passivation commenced in NaOH + Na₂S at higher potentials when the lattice S²⁻ content of Fe₃O_{4-x}S_x was decreased to a critical value (probably at $x \approx 0.19$), maximum passivation occurring when Fe₃O₄ was formed. The decrease in lattice S²⁻ content was influenced by anodic oxidation of aqueous S²⁻ to S₂O₃²⁻.

Acknowledgments

The author wishes to thank the National Research Council of Canada for providing financial support.

Manuscript received March 27, 1979.

Any discussion of this paper will appear in a Discussion Section to be published in the December 1980 JOURNAL. All discussions for the December 1980 Discussion Section should be submitted by Aug. 1, 1980.

Publication costs of this article were assisted by the University of British Columbia.

REFERENCES

1. S. A. Rydholm, "Pulping Processes," Interscience Pub., New York (1965).
2. W. A. Mueller, *Tappi*, **40**, 129 (1957).
3. R. B. Kesler and J. F. Bakken, *ibid.*, **41**, 97 (1958).
4. W. A. Mueller, "Pulp and Paper Industry Corrosion Problems," Vol. 1, pp. 109-116, NACE, Houston (1974).
5. W. A. Mueller, *Corrosion (Houston)*, **17**, 73 (1961).
6. T. R. B. Watson, *Pulp Paper Mag. Can.*, **63**, T-247 (1962).
7. R. J. Biernat and R. G. Robins, *Electrochim. Acta*, **14**, 809 (1969).
8. R. J. Biernat and R. G. Robins, *ibid.*, **17**, 1261 (1972).
9. R. A. Berner, *Am. J. Sci.*, **265**, 773 (1967).
10. P. B. Sewell, C. D. Stockbridge, and M. Cohen, *This Journal*, **108**, 933 (1961).
11. B. J. Skinner, R. C. Erd, and F. S. Grimaldi, *Am. Mineral.*, **49**, 543 (1964).
12. J. W. Cobble, *J. Am. Chem. Soc.*, **86**, 5394 (1964).
13. H. S. Harned and B. B. Owen, "The Physical Chemistry of Electrolytic Solutions," p. 560, Reinhold Publishing Corp., New York (1943).
14. H. E. Barner and R. V. Scheuerman, "Handbook of Thermochemical Data for Compounds and Aqueous Species," p. 10, John Wiley & Sons, New York (1978).
15. W. A. Mueller, "Reduction and Oxidation Reactions in Kraft Liquor Recovery: Sources, Effects and Preventions," PPR/53, Pulp and Paper Res. Inst., Canada (1971).
16. E. Uusitalo, *Suom. Kemistil. B*, **30**, 157 (1957); **31**, 367 (1958).
17. K. J. Vetter, "Electrochemical Kinetics," p. 780, Academic Press, New York (1967).
18. C. L. Foley, J. Kruger, and C. J. Bechtoldt, *This Journal*, **114**, 994 (1967).
19. H. Grafen, *Corros. Sci.*, **7**, 177 (1967).
20. M. Humphries and R. N. Parkins, *ibid.*, **7**, 747 (1967).

Trapped Oxygen in Aluminum Oxide Films and Its Effect on Dielectric Stability

Walter J. Bernard* and Philip G. Russell

Sprague Electric Company, North Adams, Massachusetts 01247

ABSTRACT

Anodic oxide films formed on aluminum in aqueous borate solutions contain substantial amounts of trapped oxygen, presumably in an adsorbed state within film cavities. Under some conditions the film has relatively stable electrical properties, but the release of the uncombined oxygen by reaction of the film with hot water brings about a sudden and nearly complete loss of barrier properties. The Faradaic charge required to restore high dielectric strength to the film is related to the quantity of oxygen evolved.

The anodic oxidation of aluminum foil, on which a surface layer of hydrous oxide has been previously formed, results in the growth of a duplex oxide film whose barrier portion suffers from an unusual instability. Alwitt and Dyer (1) refer to this phenomenon as "relaxation" and cite a number of ways in which it may be induced. In some instances it appears to occur spontaneously in the anodizing electrolyte, after a variable and ill-defined induction period.

This instability, if uncorrected at the time of processing, can result in a serious reduction of the ability of the dielectric film to sustain a high electric field, and the passage of a substantial charge in a suitable electrolyte is needed to restore the barrier oxide to its original state. A practical method for correcting this instability (widely practiced commercially) is through a brief treatment of the freshly anodized foil in hot distilled water, followed by the recharging to the original anodization voltage (1-3). The reaction of the water with the oxide greatly accelerates the complete relaxation of the dielectric and reanodization results in a stable oxide.

The effect may be better understood by reference to Fig. 1, in which it is graphically demonstrated. Aluminum foil is coated with a hydrous oxide layer by immersion for a short period (typically, 5-10 min) in boiling water and is then anodized to several hundred volts in an aqueous borate solution. If the anode foil is held at constant potential (V_A) for several minutes, the current (I_D) decays to a small fraction of the

anodization current (I_A), showing the normal behavior of a stable anodic oxide. But if the foil is then removed from the electrolyte, treated in boiling water for, say, 2 min, and returned to the anodization cell with the application of the same current (I_D) that was measured at the termination of the oxide formation step, it will display an initial barrier voltage close to zero. A substantial passage of charge, of the order of a few percent of the anodization charge, will then be required in

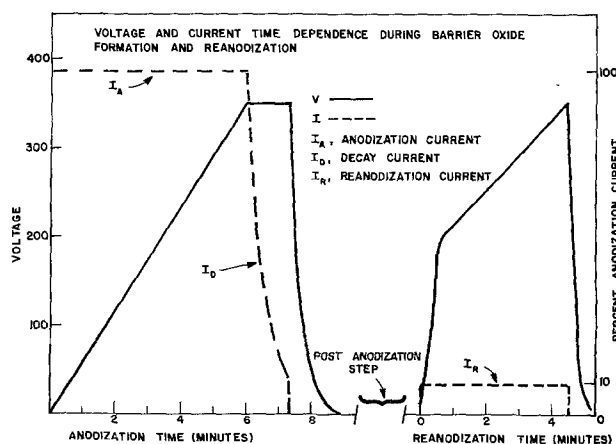


Fig. 1. Voltage and current-time curves for barrier oxide formation on aluminum foil. The reanodization voltage-time curve was obtained after a 5 min barrier postboil. These curves are typical of the results obtained with both polished and etched foils.

* Electrochemical Society Active Member.

Key words: anodic oxidation, hydrous aluminum oxide, dielectric relaxation.

order for the anode to sustain the original anodization voltage. An important conclusion drawn from these observations is that the dielectric damage incurred during relaxation is not uniform over the entire surface of the anode, since the apparently complete loss of barrier properties can be restored by a relatively small degree of reanodization.

An analysis of the process is complicated by the fact that the barrier oxide itself can undergo hydration in contact with boiling water (4) and the repair of dielectric damage from this reaction would also contribute to the charge passed after relaxation. The hydration reaction alone, however, cannot account for the observations since it has been established that hydration of anodic oxide occurs with relative uniformity across the oxide surface (5) and not at isolated areas as is indicated by the evidence in this case. A quantitative measurement of the relaxation effect must therefore separate these two contributions to the reanodization charge.

It has been suggested by Alwitt and Dyer (1) that the cause of the unstable dielectric is the presence of voids which are sealed off in the growing oxide during the anodization process and subsequently exposed during a boiling water treatment. Through transmission electron microscopy, Kudo and Alwitt (6) have detected the presence of fine vertical cracks in the barrier film, which may possibly represent the voids that have been postulated. Such oxide-free cavities or channels are consistent with our observations. However, it is our belief that these cavities are not empty but are filled with oxygen acting as a trapped dielectric that the postanodization water reaction releases as a gas. This belief is based on the observation of an apparent evolution of a gas from the oxide surface within seconds of the immersion of the foil in boiling water, and which has been identified by us as oxygen. The presence of gaseous oxygen in the unrelaxed film has also been detected by Alwitt and Dyer (1) and by Crevecoeur and deWitt (7). In the latter paper the authors attribute the generation of oxygen during anodization to the presence of crystalline γ - Al_2O_3 in the film. They have shown that at 90°C the development of γ - Al_2O_3 can begin at voltages as low as 30V and that beyond 150V the predominant oxide in the barrier layer is the crystalline form.

In this paper we present quantitative measurements on the amount of oxygen trapped in the oxide film and relate these measurements to the relaxation phenomenon.

Experimental

Barrier film formation.—Barrier films were formed on both high purity (99.99%) electropolished foil and commercially etched high voltage anode foil (99.97%). The plain foil was electropolished by a standard procedure using an acetic anhydride-perchloric acid mixture. All samples had an apparent surface area of 77.4 cm². Deionized water further purified through distillation was used in all aqueous solutions, water rinses, and for boiling water treatment of the foil both before and after the formation of barrier oxide, referred to as "preboil" and "postboil," respectively.

The anodization electrolyte (30 g/liter H_3BO_3 + 2.1 g/liter borax) had a pH of \sim 6.3 and a resistivity at 90°C of 500 Ω -cm. Anodizations were carried out at 90°C in a jacketed cell containing two platinum cathodes mounted on a Teflon support. Pyrex rods extending from this support into the electrolyte kept the anode foil well centered between the cathodes during anodization. A stream of nitrogen gas directed at the electrolyte surface minimized spattering.

The following procedure was established for producing barrier films on foil samples: first, a hydrous oxide layer (pseudoboehmite) was grown during a 10 min preboil step. Anodization was then carried out at constant current, I_A , to 350V (Fig. 1) and held at this voltage until the decay current, I_D , was one-tenth the

value of I_A . The cell was then disconnected from the power supply and the field was allowed to decay to zero. The slow field decay shown in Fig. 1 was observed with barrier oxide formations on polished foil. The field decayed much faster with etched foil samples. After a water rinse, one of several postanodization steps was carried out: (i) barrier hydration (postboil); (ii) high temperature treatment (500°–600°C); (iii) storage in air at room temperature; and (iv) storage at 85°C in a glycol-borate electrolyte. This was then followed by reanodization to the original barrier voltage (350V) which was carried out at constant current, I_R , (final value of I_D). When the sample was used for O_2 analysis the reanodization step was omitted in most cases. The anodization current was 1A and 100 mA for etched foil and polished foil, respectively. In the case of etched foils where I_R was 100 mA the voltage drop across the electrolyte was less than 2.0V, and therefore the subsequent measurement of potential at 100 mA provides an accurate estimate of the thickness of the barrier oxide. The charge passed during the constant voltage period was measured graphically on a recorder trace.

The 10 min preboil step insures that the barrier film on polished foil does not suffer from short-term instability; that is, the relaxation of the dielectric can be delayed until it is deliberately induced by a procedure such as postboiling. In most samples examined here it was observed that if the barrier film was given a water rinse little or no charge was required to reach the barrier voltage during the reanodization step.¹ On the other hand, barrier films on etched foil show some instability. After a water rinse usually 1–2% of the anodization charge, q_A , (see Fig. 1) is required to reach the barrier voltage during reanodization. Further details on the stability of barrier films is given later.

Measurement of capacitance.—The capacitance of a given sample was measured at 120 Hz after three different steps in the formation process: (i) anodization, (ii) postanodizing treatment, and (iii) reanodization. The sample cell contained two platinized platinum electrodes suspended from a Teflon support, approximately 1.25 in. apart, and a measuring electrolyte (50 g/liter H_3BO_3 + 1.9 g/liter NH_3 ; pH \sim 7.0) kept at 25°C. The sample was placed midway between the electrodes and the capacitance recorded after a 2 min stabilizing period.

Gas chromatographic analysis for O_2 .—Quantitative measurement of the total uncombined oxygen (i.e., available in the gaseous form) in the oxide film was made by gas chromatographic (GC) analysis of the gas evolved during chemical stripping of the oxide from the aluminum substrate. The amount of O_2 lost from the film during a relaxation process was then determined by difference.

The oxygen gas was stored in a sample storage tube. This storage tube consisted of a test tube made from heavy wall Pyrex tubing (\sim 5 in. in length with an OD of $\frac{3}{4}$ in.) and an O-ring seal (Cajon Ultra-Torr Fitting) connected to a needle valve outlet (Hoke 3700 series with O-ring stem packing) which formed a gas-tight container with the test tube. During analysis a storage tube was connected to the sample loop of the chromatograph (F&M Model 720). After evacuation of the loop the stored gas sample was divided between the loop and the storage tube. In this way the sample loop contained the same molar fraction of oxygen that was contained in each sample storage tube before a given analysis. Separation of O_2 and N_2 was carried out with helium as the carrier gas on a column containing Linde molecular sieve 5A, 60–80 mesh, at 60°C. Detection was made by a thermal conductivity bridge.

A typical recorder trace made during O_2 analysis is shown in Fig. 2 for both polished and etched foil sam-

¹ The preboil time was varied from 0 to 10 min in a series of formation experiments on polished foil. A preboil of at least 5 min was found to be necessary for the formation of a stable barrier film.

RECORDER TRACE OF OXYGEN AND NITROGEN
SIGNALS FROM GC DETECTOR

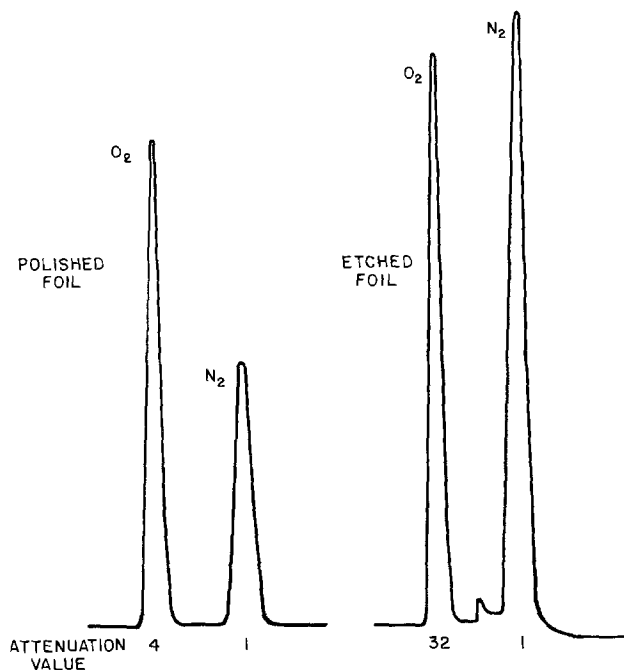


Fig. 2. Recorder trace from polished and etched foil samples prepared with freshly boiled and cooled stripping solution. The signal attenuation is given under each peak. The variation in the strength of the N_2 signal from sample to sample as shown here is due to small differences in the air content of the stripping solution just prior to the degassing step. Small variations in time of boiling, rate of boiling, and cooling time most likely account for changes in the air content of the stripping solution.

ples. The area under each curve is given by the product of the peak height above the base line times the half-width. A correction to the observed O_2 signal is made by subtracting from this signal the O_2 signal equivalent to the observed N_2 signal. This correction is especially important for polished foil samples where the observed N_2 signal may be as large as $\sim 25\%$ of the observed O_2 signal. The N_2 signal is the result of dissolved air being released from the stripping solution in the sample storage tube during the stripping process which was carried out at $85^\circ C$ for a period of several hours.

The following procedure for sample preparation was found to minimize the amount of N_2 present; each sample is cut into 12 strips and placed in a sample tube along with 10 ml of stripping solution (2% CrO_3 + 4.25% H_3PO_4) which has been boiled for 1 min and cooled immediately before using. The storage tube is evacuated and then backfilled with purified helium (99.995%). This degassing procedure is repeated a second time. The storage tube containing a degassed sample is then placed in a water bath at $85^\circ C$ where stripping of the barrier film occurs for a specified period of time prior to GC analysis for O_2 and N_2 . In some of the earlier experiments where the stripping solution was not boiled just before degassing, larger amounts of N_2 were found to be present during O_2 analysis.

Correction factors for use in subtracting the unwanted O_2 component from dissolved air were determined from reference experiments. In these experiments polished foils without either a preboil layer or barrier film and with both freshly boiled and nonboiled stripping solutions were used during sample preparation. The results in Table I show that a 1 min boil of the stripping solution just prior to degassing removes $\sim 73\%$ of the dissolved air. In each case the O_2 to N_2

Table I. Determination of correction factor, O_2/N_2

No. of samples	Sample and preparation*	O_2 signal area (cm^2)	O_2/N_2
6	Polished foil, stripping solution not boiled	11.30 ± 1.62	0.533 ± 0.012
5	Polished foil, stripping solution freshly boiled†	3.07 ± 1.49	0.524 ± 0.013
7	Polished foil given 10 min preboil. Stripping solution not boiled	2.82 ± 0.58	0.470 ± 0.032
4	Etched foil given 10 min preboil. Stripping solution freshly boiled†	1.25 ± 0.30	0.454 ± 0.021

* In these experiments 10 ml of stripping solution is added to the sample tube containing foil cut into 12 strips. The stripping process is carried out for 5 hr prior to GC analysis for O_2 and N_2 .

† The stripping solution was boiled for 1 min and cooled just before addition to the sample tube.

correction ratio does not vary much from the mean value and is in close agreement with the value expected for air dissolved in water.² It should be noted that when the solution degassing process is carried out with foil having a hydrous oxide layer, the O_2 signal and the O_2/N_2 ratio are decreased. This has been attributed to the observation that there is a significant retention of the H_2 within the hydrous oxide produced by the reaction with boiling water; this loosely trapped gas escapes under reduced pressure and helps to remove dissolved air, enhancing the solution degassing process. This enhancement does not occur with samples having a barrier film formed on a foil with a hydrous oxide layer. In this case there is much less gas (dissolved air) escaping under reduced pressure.

A calibration curve (Fig. 3) for converting the O_2 signal area to moles of O_2 was constructed using eight air-helium gas mixtures from Matheson (Certified Standards). A wide range of gas mixtures was required since the maximum quantity of O_2 obtained from the etched foil samples was 9.6 times larger than the amount from polished foil samples. (This number, which is a measure of the increase in surface area of etched foil over polished foil, is in good agreement with the value of 8.9 obtained by capacitance measurements). An expansion of the lower portion of this curve (4 points) was used in order to obtain a more accurate calibration factor for determining the moles of O_2 from polished foil samples. The moles of O_2 present in a calibration sample were calculated from

² The O_2 to N_2 signal ratio observed for air ($\sim 21.0\% O_2$, $\sim 78.1\% N_2$) is 0.284. In water $\sim 33.8\%$ of the dissolved air is O_2 . Assuming that N_2 is the only other dissolved component the ratio expected for an air sample obtained from water is 0.539.

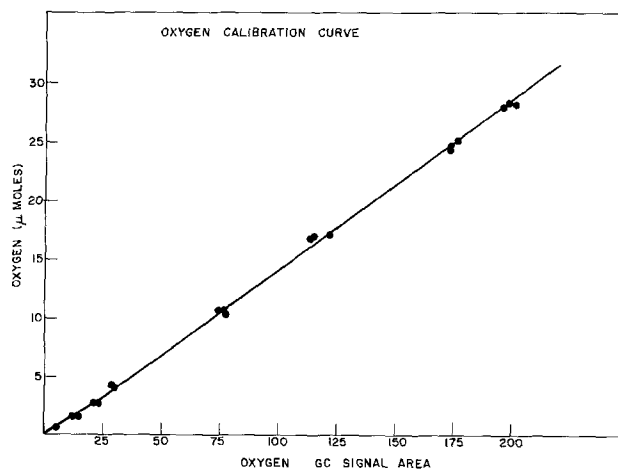


Fig. 3. Calibration curve for conversion of the O_2 GC signal area to micromoles of O_2 .

the ideal gas law. A mercury manometer was used to measure pressure during backfilling of the storage tube with one of the air-helium gas mixtures. The volume of the gas space in the storage tube was determined after O_2 analysis.

The amount of O_2 released from the barrier increases rapidly with stripping time (Fig. 4 and 5). About three-quarters of the total O_2 from etched foil is released during the first 15 min while the corresponding amount from polished foil is only one-third. Furthermore, since the results in Table I show that chemical stripping of the hydrous oxide alone does not result in any detectable generation of O_2 , all the O_2 that is measured must be contained within the barrier portion of the final film structure. After 3 hr there is little if any increase in the O_2 signal; however, in all the experiments reported here, the samples were stripped for 5 hr prior to O_2 analysis to ensure complete removal of O_2 from the oxide. Even with such prolonged treatment it was found that a small amount of residual oxide was not dissolved. Investigation by reflection electron diffraction showed that the aluminum substrate was still covered in places by crystalline $\gamma-Al_2O_3$.

Results and Discussion

In Fig. 1 a 5 min postboil on a 350V barrier oxide on polished foil is shown to reduce the barrier to about 10V. That this reduction occurs over only a small fraction of the surface is indicated by the fact that the voltage rises to 200V on the passage of only 0.39C, or

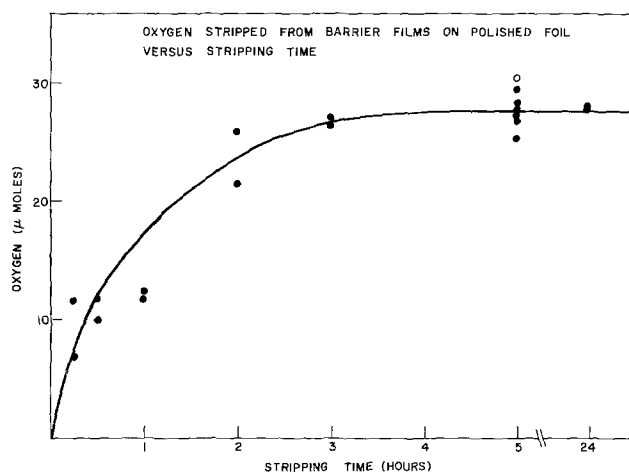


Fig. 4. O_2 content of barrier films on polished foil. The mean value of the O_2 content is $0.0357 \mu\text{mole}/\text{cm}^2$. This value was obtained with the results for 5 hr (except 0) and 24 hr stripping.

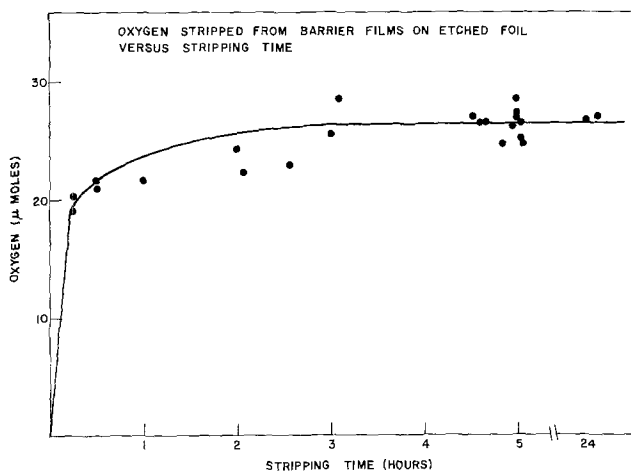


Fig. 5. O_2 content of barrier films on etched foil. The mean value of the O_2 content is $0.343 \mu\text{mole}/\text{cm}^2$. This value was obtained from the results of samples stripped for more than 4 hr.

1.0% of the original anodization charge. An additional 2.37C is then required to restore the film to its original barrier thickness at the decay current of 10 mA. Similar results were obtained with etched foil samples. In one case after a 4 min barrier postboil only 11.4C or 2.7% of the original anodization charge was required for the voltage to reach 200V.

The presence of cavities in the film containing uncombined oxygen can be postulated to explain the reanodization curve. The first steps in the curve, i.e., the region up to 200V, can be ascribed to the filling with fresh oxide of deep-lying film cavities exposed during the boiling water treatment. The slower final stage is probably only partially due to the filling of cavities since at least some portion must be associated with the repair of barrier oxide that had been converted to hydrous oxide during the postboil (5). It would be difficult to determine how much hydrous oxide is generated since it is obviously not a uniform process but only occurs at those locations where barrier oxide has been exposed on the opening of the cavities. The bulk of the barrier oxide is protected by a thick layer of hydrous oxide and would not undergo any significant attack during the short postboil, but the interior of the barrier layer would be susceptible to hydration.

It is also apparent from the rate of reanodization that the process is not uniform over the entire oxide surface. The original rate of anodization is 0.96 V/sec, while the rate of reanodization (normalized to I_A) is 6.76 V/sec.

The relaxation of the dielectric oxide is accompanied by the release of oxygen gas. In Fig. 6 and 7 the rate at which oxygen is evolved for polished and etched

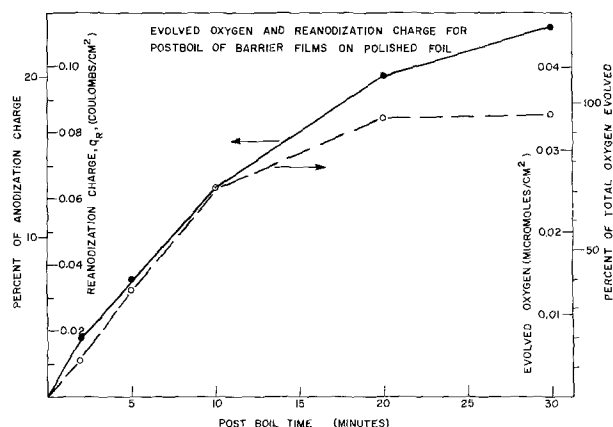


Fig. 6. The percent of total O_2 evolved and the percent of anodization charge required during reanodization for various post-boil times of barrier films on polished foils.

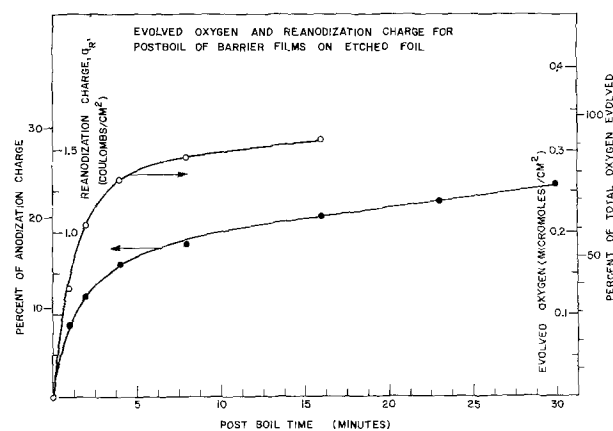


Fig. 7. The percent of total O_2 evolved and the percent of anodization charge required during reanodization for various post-boil times of barrier films on etched foils.

foils is compared to the charge required to reanodize to the original film thickness. The percent of the total oxygen available that was evolved during the postboil period was determined by measuring the residual oxygen and comparing it to the total amount known to be present after anodization (Fig. 4 and 5). The fact that the amount of reanodization parallels the quantity of oxygen evolved suggests that the presence of oxygen is intrinsic to the phenomenon. Capacitance measurements (Fig. 8 and 9) also show that the reaction is not a uniform one but must involve penetration through the dielectric nearly to the substrate. Values of capacitance after postboiling are many times larger than can be accounted for simply on the basis of uniform hydration of the dielectric.

These observations are consistent with the following picture of the overall process: in the anodization of aluminum, part of the dielectric is grown through the conversion of low density hydrous oxide to barrier oxide (8), and the resulting reduction in volume results in shrinkage cavities which are filled with electrochemically generated oxygen. Crevecoeur and deWitt have reported that crystalline γ - Al_2O_3 is formed when the anodization is carried out in hot solutions, as we have done here, and they attribute the evolution of oxygen to the presence of this oxide (7). The oxygen trapped within the cavity also functions as a dielectric and thus permits the continued growth of the oxide film. Although the final film displays an apparent stability, the presence of the oxygen-filled cavities leaves it susceptible to mechanical damage and chemical attack that may bring about a sudden and catastrophic loss in dielectric strength. Boiling water, through its

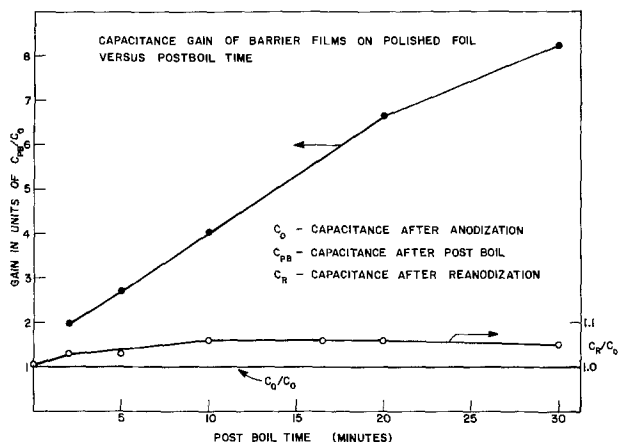


Fig. 8. Effect of postboil time on capacitance gain for barrier films on polished foil. The mean value of C_0 on polished foil is $0.0239 \mu\text{F}/\text{cm}^2$.

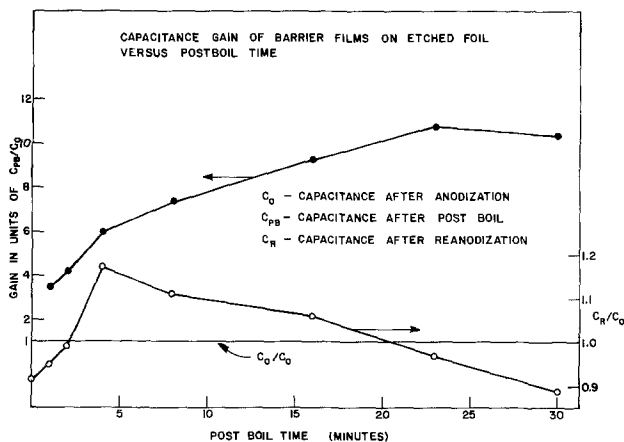


Fig. 9. Effect of postboil time on capacitance gain for barrier films on etched foil. The mean value of C_0 on etched foil is $0.213 \mu\text{F}/\text{cm}^2$.

ability to hydrate anodic oxide, apparently attacks singularities in the oxide associated with the oxygen-filled cavities. This action effectively ruptures the "sealed" cavity and allows the oxygen to escape. We have shown that hydration (or some other form of chemical attack) is a necessary step since the use of boiling aqueous phosphate solutions, which are known to prevent hydrous oxide formation (5), does not bring about dielectric relaxation or the evolution of oxygen. For example, it was found that treatment in boiling $0.1\text{M NH}_4\text{H}_2\text{PO}_4$ for periods up to 10 min has a constant, and small, effect on the reanodization charge. Little more than 1% of the original charge required to form the oxide was needed, or about the same that was measured after a single cold water rinse. The concentration of uncombined oxygen in the film was undisturbed by this treatment.

The manner in which oxygen is retained within the oxide cavities is a matter of some speculation. That it cannot be contained as a gas at ordinary pressures is easily demonstrated by consideration of the volumes involved. In Fig. 4 the total amount of O_2 from complete film stripping was found to be $0.036 \mu\text{moles}/\text{cm}^2$, equivalent to $8.06 \times 10^{-4} \text{ ml}/\text{cm}^2$ at STP. Since this greatly exceeds the calculated volume of the oxide dielectric itself ($4 \times 10^{-5} \text{ ml}/\text{cm}^2$) it is apparent that the O_2 before release must be under extremely high pressure or in a condensed state. It seems likely that it is strongly adsorbed on the surface of the oxide walls and is released upon reaction of the oxide with water. O_2 adsorption on alumina has been reported by a number of investigators (9, 10) and has been shown to be stable at relatively high temperatures. We have found this to be the case with oxygen in these films as well, as shown in Table II. Storage in air or in a glycol-borate electrolyte at 85°C results in an extremely slow loss of O_2 and barrier properties, while vacuum treatment alone had no measurable effect. However, heating to 600°C for 1 hr allowed about 55% of the entrapped oxygen to escape.

It was also observed that the reanodization charge after high temperature treatment was much less than that required after a postboil since there is no barrier damage from hydration. It should be possible to obtain a relaxation charge due to the release of entrapped O_2 during the dielectric relaxation from this charge but only qualitative measurements are possible at this point because heat-treatment introduces other complicating factors (hydrous oxide dehydration and possible thermal oxidation of the aluminum substrate) that can affect the results.

Table II. Barrier stability on etched foil

No. of samples	Time (days)	Percent of anodization charge required to reanodize	Percent of total barrier O_2 remaining	Percent of initial capacitance*
A. Storage in air at 25°C				
4	212	1.52	92	94
4	212	—	87	—
B. Storage in glycol-borate electrolyte at 85°C				
4	37	0.92	—	97†
2	102	1.54	—	—
1	102	—	84	—
C. Effect of temperature				
	Time (min) at 600°C in air			
1	15	4.15	—	199
2	15	—	58	—
1	30	3.81	—	204
2	30	—	54	—
1	60	4.78	—	309
2	60	—	44	—

* Capacitance measured before reformation; use mean value for initial capacitance. (See legend of Fig. 9.)

† Average value of 2 samples.

Acknowledgment

The authors wish to express their appreciation to Mr. John E. Barry for his assistance in the gas chromatographic measurements.

Manuscript submitted Oct. 18, 1979; revised manuscript received Jan. 16, 1980.

Any discussion of this paper will appear in a Discussion Section to be published in the December 1980 JOURNAL. All discussions for the December 1980 Discussion Section should be submitted by Aug. 1, 1980.

Publication costs of this article were assisted by Sprague Electric Company.

REFERENCES

1. R. S. Alwitt and C. K. Dyer, *Electrochim. Acta*, **23**, 355 (1978).
2. J. J. Randall, Jr. and W. J. Bernard, U.S. Pat.

- 4,113,579 (1978).
3. N. F. Jackson, in Proceedings of Symposium of British Aluminum Foil Rollers Association, University Aston in Birmingham, Sept. 24, 1979, p. 50.
4. W. J. Bernard and J. J. Randall, Jr., *This Journal*, **108**, 822 (1961).
5. W. J. Bernard, *Ibid.*, **109**, 1082 (1962).
6. T. Kudo and R. S. Alwitt, *Electrochim. Acta*, **23**, 341 (1978).
7. C. Crevecoeur and H. J. deWitt, Abstract 174, p. 413, The Electrochemical Society Extended Abstracts, Seattle, Washington, May 21-26, 1978.
8. R. S. Alwitt, *This Journal*, **114**, 843 (1967).
9. I. N. Frantsevich, V. A. Lavrenko, A. A. Chekhovskii, V. A. Kravets, and K. V. Nazarenko, *Dokl. Phys. Chem.*, **211**, 563 (1973).
10. V. A. Kotel'nikov and T. K. Skaletskaya, *High Energy Chem., USSR*, **10**, 239 (1976).

The Polarographic and Potentiostatic Reduction of Dichloromalononitrile: A Carbene Intermediate

Robert C. Duty and Barry V. Pepich

Chemistry Department, Illinois State University, Normal, Illinois 61761

ABSTRACT

The polarographic reduction of dichloromalononitrile in acetonitrile produced one polarographic wave ($E_{1/2} = 0.47V$ at $0^\circ C$ vs. Ag/AgBr reference electrode). A plot of E_{dme} vs. $i/i_d - i$ produced a 1-electron reduction for the rate-controlling step. A postulated mechanism suggested a dicyanocarbene, and a large-scale potentiostatic reduction with tetramethylethylene as the trapping agent produced the adduct of dicyanocarbene, 1,1-dicyano-2,2,3,3-tetramethylcyclopropane. The yield of the cyclopropane adduct was less than 1%, and was identified by chromatographing the reduction mixture on two different SCOT columns, OV-101 and OV-17. Dicyanocarbene has been prepared previously by debromination of dibromomalonitrile and dehydrobromination of bromomalononitrile, but this is the first reported generation of dicyanocarbene via electrochemical processes.

The existence of dicyanocarbene was proposed as early as 1957 by Cairns *et al.* (1), who debrominated dibromomalononitrile with copper powder in boiling benzene. Cairns was unable to establish direct proof for the carbene's existence because he was unable to isolate their predicted product, 7,7-dicyanobicyclo[4.1.0]heptane. In the absence of a carbene acceptor, tetracyanoethylene was isolated as the main product which led Cairns to postulate the existence of dicyanocarbene. Since 1957, dicyanocarbene has been examined more closely.

In 1965, Swenson *et al.* (2) presented more evidence for the carbene's existence by preparing 1,1-dicyano-tetramethylcyclopropane from tetramethylethylene (TME) and bromomalononitrile. The proposed carbene was postulated to form by the extraction of hydrogen bromide from bromomalononitrile using triethylamine. However, Boldt *et al.* (3) published a paper in 1966 demonstrating that Swenson's cyclopropane derivative could be obtained under the same conditions without the formation of a dicyanocarbene intermediate. Also, during 1965, Ciganek (4) published a comprehensive manuscript on the reactions of dicyanocarbene. He generated the carbene using dicyanodiazomethane in two different ways. It was found that simple heating at $70^\circ C$ or irradiation with ultraviolet light were both efficient ways to generate the desired intermediate, dicyanocarbene. At the present, these various methods are the only documented ways to generate the proposed dicyanocarbene.

According to available literature, no electrochemical studies have been conducted on the generation of dicyanocarbene. Dichlorocarbene has been generated electrolytically from carbon tetrachloride by Wawzonek *et al.* (5) who also reported the generation of phenylcarbene from the electrochemical reduction of benzal chloride (6). The phenylcarbene was trapped as the 1-phenyl-2,2,3,3-tetramethylcyclopropane adduct with tetramethylethylene albeit in very low yields. A carbene precursor, 9,9-dichlorofluorene, was reduced polarographically and potentiostatically and yielded a dimerized product of fluorenylidene, a diradical, or triplet carbene (7). These two methods, polarograph and potentiostat, were used to reduce dichloromalononitrile in the presence of tetramethylethylene to establish proof for the existence of the dicyanocarbene intermediate.

Experimental

Apparatus.—A Heath Model EUW-401 polarograph with Heath Model EUW-19-2 operational amplifier was used to record the polarograms on a Heath Model EU-20B recorder. The polarographic cell was a three electrode cell with a platinum anode and an Ag/AgBr reference electrode.

The potentiostat used in this experiment was a Princeton Applied Research Model 173 Potentiostat/Galvanostat with a Princeton Applied Research Model 178 Electrometer Probe. The reduction mixture was analyzed using a Hewlett Packard Model 5830A Gas Chromatograph with a Hewlett Packard Model 18850A G.C. Terminal. To obtain good separation two 50 ft

Key words: polarography, chromatography, reduction.

Perkin Elmer Scot Columns were used; substrates OV-17 and OV-101.

Reagents.—Aldrich dichloromalononitrile (97%) and Aldrich tetramethylethylene (99+%) were used in the reduction without further purification. Eastman Reagent Grade tetra-*n*-butylammonium bromide (0.175M) was used as the supporting electrolyte after it had been recrystallized from anhydrous ethyl acetate to insure a polarographically pure product. Three recrystallizations were required.

In the preparation of 1,1-dicyano-2,2,3,3-tetramethylcyclopropane, Eastman practical grade malononitrile, Baker reagent grade bromine (99.7%), and Mallinckrodt reagent grade triethylamine were used. Acetonitrile (Mallinckrodt-Nanograde) was refluxed with 0.5g sodium hydride per liter and distilled through a glass helice column (70 × 2 cm OD) under a dry nitrogen atmosphere. The distilled acetonitrile was stored under dry nitrogen in brown bottles.

Polarographic procedure.—A polarogram was recorded in an acetonitrile solution of 1×10^{-3} M in dichloromalononitrile and 0.175M in supporting electrolyte (tetra-*n*-butylammonium bromide in acetonitrile). The capillary had a drop time of 3.10 sec in distilled water at a mercury height of 60 cm. The $m^{2/3}t^{1/6}$ value for the capillary was 4.56. The value obtained for αn at 0°C equaled 0.42 and was in the range (0.4-0.6) for the gain of one electron (8, 9).

Potentiostatic reduction procedure.—An H-cell (7) was used in which the cathode and anode were separated by a medium fine sintered glass frit. The volume of the cathode was 60 ml and the anode volume was 50 ml. The mercury pool cathode was vigorously stirred throughout the reduction by a small magnetic stirrer. A coiled 12-gauge platinum wire was used as the anode with an Ag/AgBr nonaqueous reference electrode which contained the supporting electrolyte. The cell resistance was approximately 30Ω as measured from the anode potential (1.2V) and the initial cell current (40 mA). The reduction was carried out in a thermostat bath in the temperature range of 0° to +5°C under a purified nitrogen atmosphere.

Five grams of dichloromalononitrile (0.0371M) was added to the cathode compartment which contained 10 ml TME and 25 ml of the 0.175M supporting electrolyte in acetonitrile. The anode contained 40 ml of the acetonitrile solution. The current ranged between 100 and 160 mA. The potentiostat was turned off after 4.5 hr with the current reading 20 mA.

The catholyte at the beginning of the reduction immediately changed color from clear to yellow and finally to an opaque reddish-brown color. The catholyte was rotary evaporated, and the distillate and pot residue were collected. An ether extraction of the pot residue ensured that no product was left behind. The yellow ether extract and the distillate were combined and concentrated on a steam bath for G.C. analysis.

Preparation of 1,1-dicyano-2,2,3,3-tetramethylcyclopropane (I).—Bromomalononitrile was starting material for the preparation of I, and 1.6g (2% yield) was prepared with a melting point of 62.0°-62.5°C. (Lit. mp 64°-65°C) (10). Compound I was prepared by a scaled-down procedure of Swenson (11). Long needle-like clear crystals from hexane (0.1g) were obtained with a melting point of 49°-51°C (Lit. mp 51.5°-52°C) (11).

Gas chromatographic analyses.—The initial G.C. column, which was used to establish retention times, was a Perkin-Elmer Scot OV-17 column. The instrumental conditions used appear in Table I. A 0.1 μl sample of 1,1-dicyano-2,2,3,3-tetramethylcyclopropane in hexane was injected and found to have a retention time of 27.7 min. The reduction mixture was chromatographed, and only a single peak occurred within ±10 min of the standard peak at 27.7 min. To establish whether or not both peaks corresponded to the compound in question

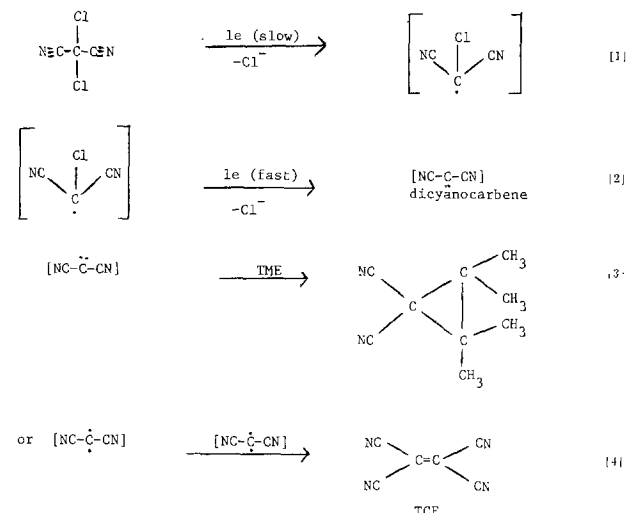
Table I. Instrumental conditions used for gas chromatography

Column	OV-17	OV-101
Initial temp.	50°C	50°C
Time at T ₁	10 min	5.0 min
Rate	4°C/min	4°C/min
Final temp.	200°C	140°C
Time at T ₂	4 min	2.0 min
Carrier gas	7 ml/min (He)	6 ml/min (He)

(1,1-dicyano-2,2,3,3-tetramethylcyclopropane), the reduction mixture was spiked with a small amount of the standard solution and injected again. The only peak found in the 20 min window had a retention time of 27.7 min. Thus, the cyclopropane structure had been formed as one of the reduction products and its yield as measured by spiking the sample was less than 1%. To further confirm the validity of this conclusion, the same procedure was utilized with a Perkin-Elmer OV-101 column under different instrumental conditions (see Table I). Again, the standard solution, the reduction solution, and the spiked reduction solution were run, and a retention time of 17.8 min was recorded. The closest peak in the reduction mixture was located at 27.06 min. This peak exhibited no notable change in retention time (0.06 min) or peak area (701 area counts) as compared to the peak in question (8992-34,218 area counts). Consequently, with two different substrates producing different retention times for 1,1-dicyano-2,2,3,3-tetramethylcyclopropane which agreed with unknown peaks in the reduction mixture, the generation of dicyanocarbene at the electrode surface was confirmed. This technique of identifying compounds with retention times from different chromatographic columns has been documented by a study of isomers of aromatic mono, di, and trichlorinated toluenes (12).

Results and Discussion

A Heath Polarograph Model EUW-401 (see Apparatus section) was used to ascertain the reduction pathway for dichloromalononitrile. In Fig. 1, the polarogram is shown with the half-wave potential at 0.47V at 0°C. Only one polarographic wave was observed for which a reduction scheme is proposed



This mechanism is supported by ascertaining the number of electrons involved in the rate-controlling step according to the procedure of Meites (13). In this method for irreversible polarographic waves, a plot of E_{dme} vs. $i/i_d - i$ was constructed for dichlorodicyanomethane. The values of E_{dme} and i (the current at each equal increment of 20 mV) were taken from the rising portion of the polarogram. The slope of this plot is equal to $-0.0542/\alpha n$ where α is the transfer coefficient and n is the number of electrons in the rate-controlling step. The value of αn has been shown to fall in the range of 0.4-0.6 for a one-electron reduction in a rate-

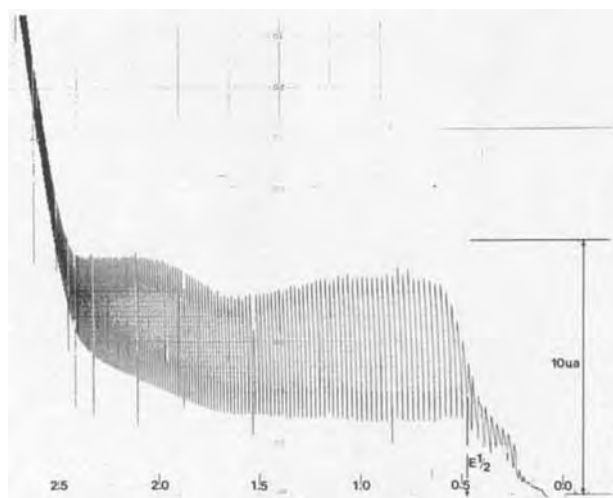


Fig. 1. Polarogram of dichlorodicyanomethane

controlling step (8,9). Consequently, since αn was 0.42 for dichlorodicyanomethane, this is consistent, but not absolute proof, for the mechanism shown above. In fact, since a very low yield of trapped product was obtained (less than 1%), more than one mechanism is undoubtedly occurring. A most plausible mechanism for reduction of organic halides is through a one-electron reduction to the free radical which, subsequently, is reduced to the carbanion.

Simonet (14) has published evidence of this for his α -bromo acetylene compounds, and Erickson has demonstrated an equivalent mechanism with his excellent study of gem-dihalocyclopropane structures (9). In addition, Casanova has shown this to be true for the reduction of α -bromoketones (15).

The diffusion current constant ($I_d = i_d/cm^2/3t^{1/6}$) as calculated from Fig. 1 was 1.38. This value has limited significance because it is readily apparent from observing the solution prior to a polarographic run that a reaction is occurring, undoubtedly, with the mercury. These observations have been noticed previously with reactive halides by Wawzonek (16). This was confirmed in our polarogram by running the same solution at 15 min intervals. In the second run the diffusion current had decreased by approximately 25%.

Additional evidence for a reaction with mercury was obtained by running the reaction at 25°C. At this higher temperature a very rapid increase in current (greater than 20 μ amp) appeared at 0.1V. This initial wave had the same appearance as the prewaves which were shown for benzyl mercuric iodide (16) which was polarographed under similar conditions as the dichloromalonitrile. The prewave had a maximum current which dropped back to the level of the residual current after a few tenths of a volt. This maximum could be caused by the adsorption onto the surface of the mercury drop of the reduction product, an organomercurial free radical, as explained by Wawzonek for benzyl mercuric chloride (16).

The reduction of dichlorodicyanomethane was diffusion-controlled and did not exhibit a kinetic or an absorption current at the electrode surface. The diffusion-controlled reduction current was directly proportional to the square root of the mercury height. Thus, one would expect a rapid gain of the second electron in Step 2 leading to the formation of a carbene intermediate. A similar electrochemical mechanism has been proven for 9,9-dichlorofluorene (7). A carbene formed in this manner can add to a double bond yielding a cyclopropane derivative, or dimerize to form TCE. An explanation of these two products is more easily explained if one examines the dicyanocarbene spin states.

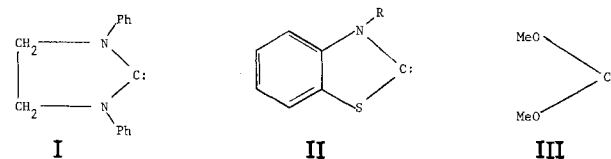
It seems reasonable that the cyclopropane derivative was formed mostly from the singlet state of the car-

bene. Singlet states have been shown to be much more reactive toward substrate molecules and to react stereospecifically by Ciganek (4). Unfortunately, there was no way to examine the stereospecificity of the reaction since TME was employed as the substrate.

It is felt that the TCE product is formed via the triplet or diradical spin state. Due to the nature of the experimental procedure it seems plausible that some TCE would be formed. The reducing surface employed was a small pool of mercury. Thus, due to migration of dichloromalonitrile towards the cathode surface the concentration of TME would be reduced. If two carbenes were formed and had time to relax to the triplet state, one could observe TCE as a product. At the present only Cairns *et al.* (1) have observed TCE as a product of a proposed carbene intermediate.

Cairns explains that the formation of TCE was due to the absence of a suitable substrate since benzene was employed as a solvent. If one accepts that Cairns had actually formed a carbene intermediate, then it seems very likely that the TCE produced was also formed via triplet dicyanocarbene since the benzene molecules would have aided in the singlet-triplet transition.

It has been shown that the ground state for dicyanocarbene is a linear triplet (17, 18). This triplet is resonance stabilized by the two cyano groups which account for its extended lifetime and ability to dimerize. Some work has been done with stabilized carbenes where the carbene carbon is attached to two atoms each bearing an unshared pair of electrons. It has been reported that I (19), II (20), and III (21) have long enough half-lives to exist in equilibrium with their dimers, although this conclusion has been proved incorrect in the case of I via crossover experiments (22)



If this is in fact the case, then one might expect a very small equilibrium between dicyanocarbene and its dimer, TCE, although it would not be expected to exhibit as much stability as the above species. Further work might be attempted on trapping this diradical with a different substrate. If the diradical does exist in any residual amount at all, it should be possible to shift this equilibrium using mild conditions. A consideration might also be made on attempting to generate dicyanocarbene from TCE.

Manuscript submitted May 8, 1979; revised manuscript received Jan. 14, 1980.

Any discussion of this paper will appear in a Discussion Section to be published in the December 1980 JOURNAL. All discussions for the December 1980 Discussion Section should be submitted by Aug. 1, 1980.

REFERENCES

1. T. L. Cairns, R. H. Carboni, D. D. Coffman, V. A. Engelhardt, R. E. Heckert, E. L. Little, E. G. McGreer, B. C. McKusick, W. J. Middleton, R. M. Scribner, C. W. Theobald, and H. E. Winberg, *J. Am. Chem. Soc.*, **87**, 2775 (1958).
2. J. S. Swenson and D. J. Renaud, *ibid.*, **87**, 1394 (1965).
3. P. Boldt and L. Schultz, *Tetrahedron Lett.*, **13**, 1415 (1966).
4. E. Ciganek, *J. Am. Chem. Soc.*, **88**, 1979 (1966).
5. S. Wawzonek and R. C. Duty, *This Journal*, **108**, 1135 (1965).
6. S. Wawzonek and J. M. Shradel, *ibid.*, **126**, 401 (1979).
7. R. C. Duty, G. Biolchini, and W. Matthews, *Anal. Chem.*, **46**, 167 (1974).
8. R. Annino, R. E. Erickson, J. Michalovic, and B. McKay, *J. Am. Chem. Soc.*, **88**, 4424 (1966).
9. R. E. Erickson, R. Annino, M. D. Scanlon, and G. Zon, *ibid.*, **91**, 1767 (1969).
10. P. Boldt, L. Schultz, and J. Etzemuller, *Chem.*

- Ber.*, **100**, 1285 (1967).
11. J. S. Swenson and D. J. Renaud, *J. Am. Chem. Soc.*, **87**, 1394 (1965).
 12. R. C. Duty, *Anal. Chem.*, **49**, 743 (1977).
 13. L. Meites and Y. Israel, *J. Am. Chem. Soc.*, **83**, 4903 (1968).
 14. J. Simonet, H. Doupeux, and D. Bretelle, *C. R. Acad. Sci.*, **270**, 59 (1970).
 15. J. Casanova, J. Dirlam, and L. Ebersson, *J. Am. Chem. Soc.*, **94**, 240 (1972).
 16. S. Wawzonek, R. C. Duty, and J. H. Wagenknecht, *This Journal*, **111**, 74 (1964).
 17. R. Hoffman, G. Zeiss, and G. VanDine, *J. Am. Chem. Soc.*, **90**, 1485 (1968).
 18. J. Olsen and L. Bunnelle, *Tetrahedron*, **25**, 5452 (1969).
 19. H. W. Wanzlick and E. Schikora, *Agnew. Chem.*, **72**, 494 (1960); *Chem. Ber.*, **94**, 2389 (1961); H. W. Wanzlick and H. Ahrens, *Chem. Ber.*, **97**, 2447 (1964).
 20. H. W. Wanzlick and H. J. Kleiner, *Agnew. Chem. Int. Ed. Engl.*, **3**, 65 (1964).
 21. R. W. Hoffman and H. Haeuser, *Tetrahedron Lett.*, **11**, 1365 (1964).
 22. D. M. Lemal, R. A. Lovald, and K. I. Kawano, *J. Am. Chem. Soc.*, **86**, 2518 (1964). See also H. W. Wanzlick, B. Lachmann, and E. Schikora, *Chem. Ber.*, **98**, 3170 (1965).

Oxidation State Changes and Structure of Electrochromic Iridium Oxide Films

J. D. E. McIntyre,* W. F. Peck, Jr., and S. Nakahara*

Bell Laboratories, Murray Hill, New Jersey 07974

ABSTRACT

Oxidation state changes, completeness of oxidation, and densities of anodically formed, electrochromic iridium oxide films have been determined by combined gravimetric, coulometric, and reflection spectroscopy analyses. The results show that the oxidation state of Ir ions in the oxide is changed from III to IV during the anodic coloration process [0.25 to 1.25V(RHE)], rather than II to IV as previously postulated, and that virtually all Ir ions in the film are accessible for electrochemical oxidation and reduction. The mean density of the oxide film is 2.0g cm⁻³, as compared to 11.68 for bulk crystalline IrO₂. The structure of the film was shown by electron microscopy to consist of oxide grains 0.05-0.1 μm in diameter, surrounded by voids. In addition, the presence of a high density of microvoids ~25Å in diameter was detected. The highly porous structure of the film permits ready access of the electrolyte to the oxide grains throughout the entire film and facilitates the rapid coloration and bleaching (~40 msec) observed in aqueous electrolytes. The apparent accessibility of all Ir ions in the film also implies rapid transport, within the oxide grains, of the mobile charge-compensating ions which must be injected and ejected to preserve electroneutrality. Mechanisms of ion and electron transport are discussed.

In recent communications from this laboratory (1, 2), the results of studies of the anodic formation and electrochemical and spectroscopic properties of hydrous anodic iridium oxide films have been presented. Owing to the rapid and reversible coloration and bleaching which these films exhibit during redox cycles (transparent ⇌ blue-black), this electrochromic system has potential application in electro-optic display devices (1, 3). In contrast to other electrochromic oxides such as WO₃ (4), coloration in these films is produced by anodic oxidation rather than cathodic reduction.

The structure and composition of these hydrous oxide films and their influence on the kinetics and mechanism of the electrochromic effect are of considerable current interest. In addition, highly conducting iridium and ruthenium oxide films are excellent electrocatalysts for O₂ evolution (5-11) and serve as stable anode materials for Cl₂ evolution (12-16). From analyses of the anodic oxygen layer on iridium by x-ray emission, electron diffraction, and electron microscopy, Michell *et al.* (17, 18) concluded that in the oxidation process Ir(OH)₂ is converted to IrO₂ on the iridium metal electrode surface by a reaction involving transfer of $n = 2$ electrons to the metal substrate and simultaneous ejection of an equal number of protons into the electrolyte. For a film with a charge capacity of 24 mC cm⁻², measured with a linear potential sweep extending from 0.06V to 1.5V(RHE), the thickness was estimated to

be 22 nm. In their soft x-ray emission measurements, determination of the n -value necessitated an estimation of the parameters, R_{∞} , the ratio of the peak height of the oxygen emission line to background for an oxide of infinite thickness, and μ , the absorption coefficient, from a calibration for tantalum oxide (19). This method was stated to permit the weight of the oxide film to be determined within 10% (17, 18). Film thicknesses were calculated by assuming the anodic oxide film density to be the same as that for bulk IrO₂ (11.68g cm⁻³).¹

Although iridium forms a variety of chemical species in which the metal ion oxidation state ranges from 0 to VI, only the I, III, and IV compounds are commonly found (20-23). The report of the electrochemical formation of a stable divalent oxide which could repeatedly be cycled to a higher oxidation state was therefore surprising. Secondly, the film thicknesses calculated by Michell *et al.* (17) are smaller by a factor of ~10 than those calculated on the basis of recent optical measurements (11, 24, 25). In order to resolve these apparent discrepancies we have determined the oxidation state changes, completeness of oxidation, and densities of anodic iridium oxide films by alternative techniques, using combined weight-loss, coulometry, and reflection spectroscopy measurements. In addition, the structures of these films were investigated by scanning and transmission electron microscopies.

* Electrochemical Society Active Member.

Key words: ion transport, electrochromism, microscopy, anodic film.

¹ At the time of the work of Michell *et al.*, optical constant data for anodic iridium oxide films (11) were not yet available for determination of film thicknesses by ellipsometry or reflectometry.

Experimental

Iridium metal is highly resistant to corrosion under static potential conditions, but a hydrous anodic oxide film can be grown on its surface by square-wave or triangular-wave potential cycling (2). Subsequently, this film can be completely removed from the electrode surface by cycling in 5M H₂SO₄ (18, 26), or by soaking in hot 5M H₂SO₄ (2) or hot chromic acid (27). In addition, the oxide film can be removed by holding the electrode at an anodic potential >1.63V (RHE) in 1M H₂SO₄ or by repetitively cycling to ~1.7V (28). This fact suggested that the weight of the film could be determined directly by accurately weighing the electrode with a microbalance before and after film stripping. Although the exact composition of the hydrous electrochromic oxide is not yet known with certainty, the atomic weight of Ir (192.22) is so high relative to those of O and H that the total Ir content in the oxide film should be approximated quite closely by the weight loss. Further, the amounts of Ir lost from the metal electrode due to dissolution in the electrolyte during film growth can be estimated by also weighing the bare metal electrode before film growth and after film stripping.

In the present studies, anodic iridium oxide films were grown on precleaned-and-weighed Ir metal electrodes in 0.5M H₂SO₄ at 25°C by cycling the potential with 0.5 Hz square waves between 0.0 and 1.5V (RHE), as previously described (2), until films with the desired charge capacity (20-25 mC cm⁻²) were obtained. The number of coulombs required to oxidize a film in color-bleach cycles with cathodic and anodic limits of 0.25 and 1.25V (RHE), respectively, was measured with an analog coulometer during triangular potential sweeps at 150 mV sec⁻¹. As shown previously (2), these potential limits prevent changes in film thickness and also the evolution of O₂ and H₂ gases. After completion of the coulometric measurements, the sample electrode was removed from the electrolyte in the bleached state while under potential control at 0.25V (RHE). The electrode was then rinsed in distilled water, air-dried at room temperature, and further dried in an oven at 110°C for 1 hr to remove excess water. The electrode was then reweighed to determine the net weight change produced by growth of the oxide film and dissolution of Ir metal ions in solution.

The film was next stripped from the electrode to determine the residual weight of the Ir substrate. Oven-dried oxide films were found not to be soluble in hot 5M H₂SO₄ or chromic acid, even on long exposure. It was found, however, that the dried film could be stripped from the electrode by cycling in 0.5M H₂SO₄ with 150 mV sec⁻¹ linear potential sweeps between 0.25 and 1.75V (RHE) for ~5 min. This procedure "undetermined" the dehydrated oxide film and allowed it easily to be wiped off the surface. Final stripping of any residual oxide was accomplished by soaking in hot 5M H₂SO₄ at ~80°C for 1 hr. After rinsing and drying at 110°C, the electrode was weighed again to determine the weight of the bare Ir substrate and hence the weight of the oxide film removed. Blank runs with nonoxidized Ir metal electrodes showed that there was negligible weight loss of metal (≤1 μg) produced by this stripping procedure.

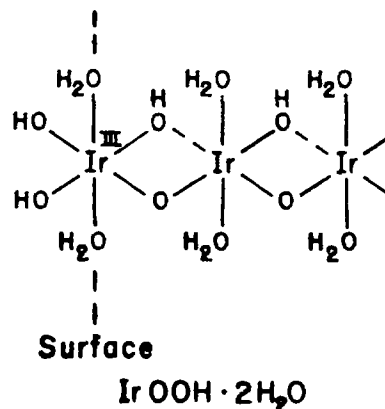
All weights were determined with a Perkin-Elmer Autobalance Microbalance, Model AD2Z, employing a substitution weighing method which permitted use of a 20 mg full-scale range with a resolution of 1 μg. The average precision of the weighings was ±1 μg.

Scanning electron micrographs of an anodic iridium oxide film grown on an Ir metal substrate were taken in the secondary electron emission mode with an ETEC Corporation Autoscan Scanning Electron Microscope operated with an accelerating voltage of 20 kV. For transmission electron microscopy, an anodic oxide film was grown in 0.5M H₂SO₄ by cycling the potential of a thin (400 nm) Ir metal film, which had been elec-

tron-beam evaporated onto a pyrolytic graphite substrate, until the metal was completely converted to oxide. The oxide film was then lifted from the graphite surface with transparent adhesive tape. Subsequently this tape was dissolved in CCl₄ to free the film. TEM micrographs of the isolated film were taken with a Japan Electron Optics Laboratory JEM-200 electron microscope operated at 200 kV.

Results and Discussion

The results of the weight-loss and charge measurements on three different samples are summarized in Table I. The number of coulombs of positive charge injected during film coloration [0.25 to 1.25V (RHE)] was corrected for the component due to double-layer charging. This correction is small, amounting to only ~3% of the total charge passed. Its magnitude (~0.7 mC cm⁻²), however, indicates that the real surface area of the oxide layer is very high. The oxidation state change per Ir atom was calculated assuming the composition of the bleached state to be Ir(OH)₃ (≡ IrOOH · H₂O). This composition is in best agreement with the results of nuclear reaction and Rutherford backscattering analyses of the H and O contents of the film, measured by bombarding the film with 0.9 MeV ³He⁺ ions in a Van de Graaff ion accelerator (30). These analyses showed that there are significant amounts of strongly bound H contained in both bleached and colored states of the film, which are not removed by extended pumping under high vacuum conditions (<10⁻⁶ Torr). If the bleached film were assumed to consist of IrOOH · 2H₂O units bound in a network configuration, viz.



the molecular weight would be increased from 243.3 to 261.3 and the calculated oxidation state changes would be increased correspondingly from 0.99 to 1.06. Similarly, if foreign anions such as SO₄²⁻ are incorporated in the oxide film during growth, as shown to be the case by infrared spectroscopy measurements (31), then the calculated oxidation state changes should also be slightly higher than the values shown in Table I. Since the anodic tail of the main oxidation peak centered at 0.98V (RHE) appears to overlap part of an anodic peak at higher potentials (Fig. 1), the end point of 1.25V chosen for the coloration step must also be regarded as uncertain to about this extent.

Table I. Oxidation state changes of anodic iridium oxide films [0.25-1.25V (RHE)]

Specimen	Square-wave growth cycles (0.0-1.5V)	Q _a * (mC cm ⁻²)	Weight of surface oxide (μg cm ⁻²)	Oxidation state change
A	250	23.0 (24.4)	59.0	0.98
B	250	23.1 (23.7)	59.2	0.98
C	250	23.2 (23.9)	58.0	1.01

* (), before correction.

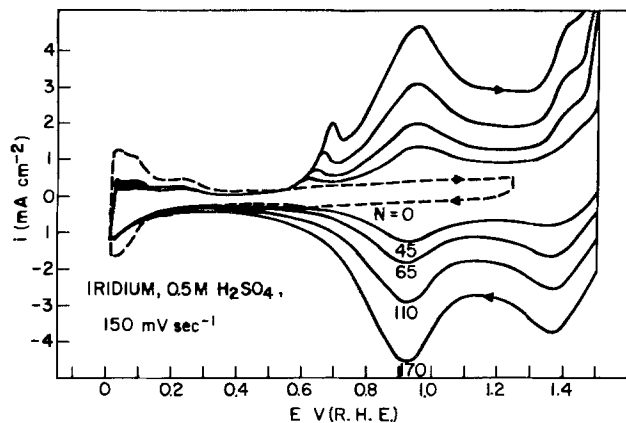
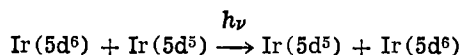


Fig. 1. Cyclic voltammograms of an Ir electrode in aqueous 0.5M H_2SO_4 electrolyte at 25°C . ---, oxide-free surface; —, oxide-covered electrode after N growth cycles. Potential sweep rate = 150 mV sec^{-1} .

Oxidation state changes were also calculated from the weight differences of the bare Ir electrodes before and after film growth and stripping. With this method, no assumption need be made concerning the actual film composition, since the measured weight loss is entirely due to Ir. If, however, some of the Ir metal dissolves into the electrolyte during oxide film growth, as shown (18, 26), then the net weight loss will correspond to the sum of these processes and the calculated oxidation state changes will be too low. In the present experiments, the average n -value calculated by this method was 0.87 ± 0.015 , indicating that an amount of Ir metal corresponding to 10–20% of that incorporated in the oxide is lost to the electrolyte by dissolution during film growth.

The above results are in very good agreement with an oxidation state change of 1 during color-bleach cycles, rather than 2 as postulated by Michell *et al.* (17, 18). The transformation of the color of the film from transparent to blue-black during oxidation strongly indicates that this process corresponds to a change of oxidation state from III to IV. The final blue color of the anodic film is very similar to that of thin IrO_2 films formed by thermal oxidation. The coloration of this mixed valence system may be attributable to intervalence transitions of the type



made possible by the introduction of holes into the $5d(t_{2g})$ subband of the oxide. The conclusion that the final valence state is IV is further supported by Raman (32) and XPS (33) studies of the geometric structure and electronic properties of the anodic films in both colored and bleached states.

The anomalously high values of the oxidation state changes reported by Michell *et al.* appear to have arisen from their choice of the potential limits 0.06 and 1.5V (RHE) for coulometry in 1M H_2SO_4 . As noted previously (1, 2), such limits are suitable for film growth, but not for color-bleach cycles. It is evident from the forms of the cyclic voltammograms of an Ir electrode in acid solution (cf. Fig. 1) that both a second redox process and O_2 evolution can occur if the anodic limit is extended to 1.5V (RHE). In the present studies, the measured values of anodic charge passed during linear potential sweeps at 150 mV sec^{-1} from 0.25 to 1.50V (RHE) were $\sim 50\%$ greater than those recorded with a limit of 1.25V. Still greater values might result from increased evolution of O_2 during the slower (40 mV sec^{-1}) sweeps employed in Ref. (17) and (18).

From combined optical and coulometric measurements (24, 25), it is possible to determine the film thickness very accurately. For a film such as specimen

A (Table I), which had a charge capacity of 23.0 mC cm^{-2} (corrected), the thickness was calculated to be 295 nm. The density of the hydrous oxide film is, therefore, $\sim 2.0 \text{ g cm}^{-3}$. This value is much lower than that of anhydrous bulk IrO_2 (11.68 g cm^{-3}) and reflects the very porous nature of the anodic oxide layer (see below). This high porosity is also evidenced by the low apparent refractive index of the anodic film (1.41–1.44), determined by *in situ* ellipsometry (11). The latter value is actually a composite of the refractive index of the oxide grains and that of the electrolyte contained within the film pores.

If it is assumed that the coulometric values of Michell *et al.* (17) are higher by a factor of ~ 2 than those measured in the present studies for oxide films containing equal amounts of Ir, then it can be seen that the film weight determinations by the two independent techniques are in quite good agreement. Studies of contrast ratio enhancements produced by optical interference effects in these electrochromic surface films (24, 25) have confirmed that the films used in the present work were *ca.* one-half the wavelength of visible light in thickness. The film thickness estimates of Michell *et al.* (17) are apparently low by a factor of 7–10, owing to their use of the density of bulk IrO_2 in their calculations.

The porous nature of the film deduced from these results was confirmed directly by scanning and transmission electron microscopy studies. Figure 2 is an SEM micrograph of an anodic oxide film grown on an Ir metal substrate, which reveals a high density of pores $0.05\text{--}0.07 \mu\text{m}$ in diameter. Figure 3 is a TEM micrograph of an anodic iridium oxide film grown on a pyrolytic graphite substrate and stripped. It is evident that the film structure consists of oxide grains $0.05\text{--}0.1 \mu\text{m}$ in diameter surrounded by voids. The oxide grain size determined in the present studies is in close agreement with the TEM measurements made by Michell *et al.* (5) using a replication technique. In addition to macrovoids, the presence of microvoids $\sim 25 \text{ \AA}$ in diameter was detected in the present study. Such structures are very similar to those of chromate films grown by elec-

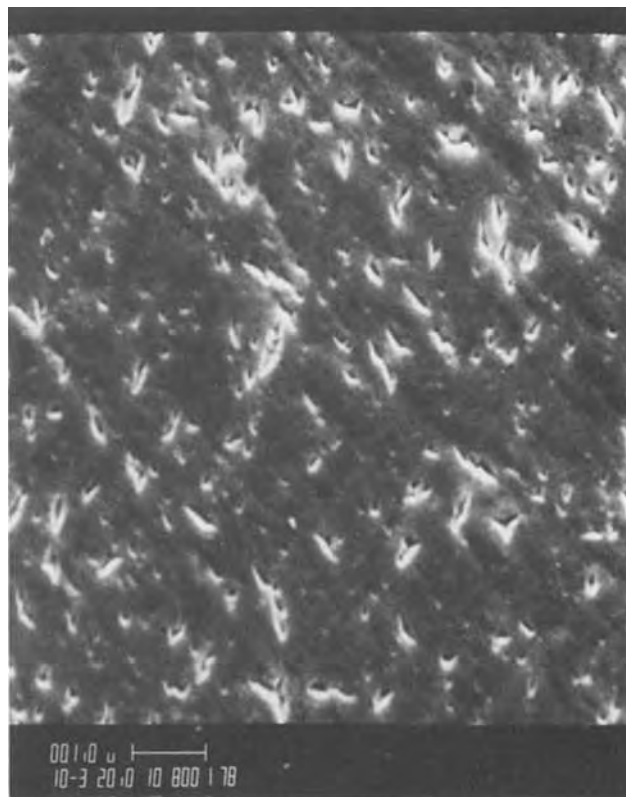


Fig. 2. SEM micrograph of an anodic iridium oxide film showing the high density of pores. Original magnification: $10,000\times$.

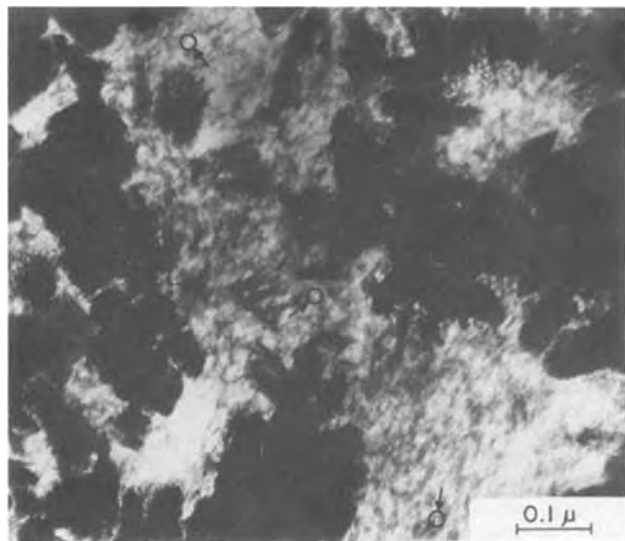


Fig. 3. TEM micrograph of an anodic iridium oxide film showing the large density of macrovoids and microvoids (arrows). Original magnification: 200,000 \times .

trochemical precipitation (34). This suggests that anodic iridium oxide layers may be formed by a dissolution-precipitation process induced by potential cycling. Results of a more detailed electron microscopy study of film structure will be presented separately. The highly porous structure observed in the present study permits ready access of the electrolyte to the oxide grains throughout the entire film and is presumed to be responsible in large part for the rapid coloration and bleaching times (~ 40 msec) observed for electrochromic iridium oxide films in aqueous electrolytes.

The above results have significant implications for establishing the mechanism of charge neutralization within the oxide during coloration and bleaching. During anodic coloration, electrons are transferred from the oxide to the Ir metal substrate. Simultaneously, an equivalent amount of ionic charge is transferred across the oxide-electrolyte interface to maintain electro-neutrality inside the oxide (2). In principle, this charge compensation can be accomplished either by ejection of cations or by injection of anions. From the close agreement of the measured oxidation state change with that expected on chemical grounds, we conclude that virtually all of the Ir ions in the oxide film are accessible for oxidation and reduction. It would be highly improbable that such close agreement could be obtained if the oxidation state change were 2. This would require that exactly half of the Ir ions in the film be oxidized and reduced in each color-bleach cycle, the other half remaining inaccessible or inert.

Reflectivity transients observed during bleaching in aqueous, unbuffered Na_2SO_4 (pH 3.5) electrolyte show that part of the film is bleached in an initial rapid step (2). At low cathodic overpotentials, the remainder is bleached in a much slower process, controlled by diffusion of ionic species in solution. The relative magnitudes of these two components are dependent on the amplitude of the applied cathodic potential, indicating that the compensator ions required to maintain local charge neutrality inside the bulk oxide can be supplied by three sources in this dilute acid solution: (i) bound H_2O and OH groups on the oxide surface; (ii) free H_2O in the electrolyte contained within the film pores; and (iii) hydrated H^+ species in the bulk electrolyte. The rapid bleaching component is attributed to sources (i) and (ii), which do not require mass transport. Now the charge-compensating ions must be externally supplied to the bulk oxide phase, either from the oxide surface or from the bulk electrolyte. The oxide grain-size determinations in the present study indicate that

the majority of the Ir ions are situated within the bulk of the oxide rather than at its surface. Also, it may be assumed that no more than one or two OH or H_2O groups bound to the surface Ir ions are exposed to the electrolyte at the interface (see above). These facts imply that the majority of the compensator ions must be supplied from the bulk electrolyte, i.e., sources (ii) and (iii). There are insufficient bound species initially present on the surface [source (i)] to satisfy the charge neutralization requirements.

Both cation (1, 2, 35) and anion (36, 37) transport mechanisms have been postulated to occur in electrochromic iridium oxide films. In the first, protons are proposed to migrate along a hydrated IrO_2 chain network (see above), by a Grotthuss-type mechanism analogous to that occurring in water and ice (35). This process may be assisted by quantum mechanical proton tunneling. Desolvated protons could also migrate through open tunnels in the oxide lattice similar to those which occur in anhydrous crystalline IrO_2 (38). The structure of the anodic iridium oxide film, however, is amorphous (32, 33) and it is not yet known whether similar tunnels exist in the grains of this material. Tunnels of the type occurring in the rutile-like structure of IrO_2 are much too narrow ($r \approx 0.65\text{\AA}$) to permit insertion of anions such as F^- ($r = 1.36\text{\AA}$), OH^- ($r = 1.53\text{\AA}$), or CN^- ($r \approx 1.9\text{\AA}$). It is therefore not evident how compensator ions such as these could be injected into the bulk oxide, as proposed in the anion mechanism (36, 37), so that all Ir ions are oxidized and reduced in the solid-state electrochromic redox reaction. A high concentration of point defects in the amorphous oxide film, e.g., $\text{O}^=$ vacancies, might make such insertion possible, but normally this process should be very slow at 25°C . Nor is it clear why, in a hydrous oxide/ aqueous electrolyte system, the mobility of an OH^- ion in the solid oxide should be greater than that of a free proton, which has the same absolute charge but much lower mass and no geometric barriers to prevent its migration. A lower proton mobility would imply that this species is more tightly bound in the solid, e.g., to $\text{O}^=$ ions, than are mobile OH^- ions to the Ir cations. The rapid isotopic exchange of D and H observed in these hydrous oxide films (30) indicates that the protons are highly labile.

Finally, we note that on the basis of measurements of the small amplitude a-c response of anodic iridium oxide films, it has been suggested (39) that the kinetics of the redox reaction are controlled by the mobility of reduced lattice sites in the oxide. The structural studies in the present investigation suggest an alternative but related phenomenon should also be considered as a possible rate-limiting factor, viz., electron transport across oxide grain boundaries.

Manuscript submitted Nov. 16, 1979; revised manuscript received Jan. 22, 1980.

Any discussion of this paper will appear in a Discussion Section to be published in the December 1980 JOURNAL. All discussions for the December 1980 Discussion Section should be submitted by Aug. 1, 1980.

Publication costs of this article were assisted by Bell Laboratories.

REFERENCES

1. S. Gottesfeld, J. D. E. McIntyre, G. Beni, and J. L. Shay, *Appl. Phys. Lett.*, **33**, 208 (1978).
2. S. Gottesfeld and J. D. E. McIntyre, *This Journal*, **126**, 742 (1979).
3. G. Beni, S. Gottesfeld, J. D. E. McIntyre, and J. L. Shay, U.S. Pat. 4,191,453 (1980).
4. B. W. Faughnan, R. S. Crandall, and P. M. Heyman, *RCA Rev.*, **36**, 177 (1975).
5. J. P. Hoare, "The Electrochemistry of Oxygen," Wiley-Interscience, New York (1968).
6. S. Trasatti and G. Buzzanca, *J. Electroanal. Chem. Interfacial Electrochem.*, **29**, App. 1 (1971).
7. D. Galizzioli, F. Tantardini, and S. Trasatti, *J. Appl. Electrochem.*, **4**, 57 (1974); **5**, 203 (1975).

8. W. O'Grady, C. Iwakura, J. Huang, and E. Yeager, in "Electrocatalysis," M. W. Breiter, Editor, p. 286, The Electrochemical Society Softbound Proceedings Series, Princeton, N.J. (1974).
9. D. N. Buckley and L. D. Burke, *J. Chem. Soc. Faraday Trans. I*, **72**, 2431 (1976).
10. C. Iwakura, H. Tada, and H. Tamura, *Denki Kagaku*, **45**, 202 (1977).
11. S. Gottesfeld and S. Srinivasan, *J. Electroanal. Chem., Interfacial Electrochem.*, **86**, 89 (1978).
12. O. De Nora, *Chem. Eng. Technol.*, **42**, 222 (1970).
13. G. Faita and G. Fiori, *J. Appl. Electrochem.*, **2**, 31 (1972).
14. P. C. S. Hayfield and M. A. Warne, "Industrial Electrochemical Processes," Chap. 14, Elsevier, Amsterdam (1971).
15. A. T. Kuhn and C. J. Mortimer, *J. Appl. Electrochem.*, **2**, 283 (1972).
16. A. T. Kuhn and P. M. Wright, *J. Electroanal. Chem. Interfacial Electrochem.*, **41**, 329 (1973).
17. D. Michell, D. A. J. Rand, and R. Woods, *ibid.*, **84**, 117 (1977).
18. D. A. J. Rand, R. Woods, and D. Michell, in "Electrode Materials and Processes for Energy Conversion and Storage," J. D. E. McIntyre, S. Srinivasan, and F. G. Will, Editors, p. 217, The Electrochemical Society Softbound Proceedings Series, Princeton, N.J. (1977).
19. D. F. Mitchell and P. B. Sewell, *Thin Solid Films*, **23**, 109 (1974).
20. N. V. Sidgwick, "The Chemical Elements and Their Compounds," Vol. II, p. 1530 et seq., Oxford, London (1950).
21. W. P. Griffith, "The Chemistry of the Rarer Platinum Metals," Chap. 5, p. 227, Wiley-Interscience, New York (1977).
22. S. E. Livingstone, in "Comprehensive Inorganic Chemistry," Vol. 3, J. C. Bailar, Jr., H. J. Emeléus, R. Nyholm, and A. F. Trotman-Dickenson, Editors, Chap. 43, p. 1371, Pergamon, New York (1973).
23. J. F. Llopis and F. Colom, in "Encyclopedia of Electrochemistry of the Elements," Vol. VI, A. J. Bard, Editor, Chap. 5, p. 222, Dekker, New York (1976).
24. J. D. E. McIntyre, To be published.
25. J. D. E. McIntyre and W. F. Peck, Jr., Paper 302 presented at The Electrochemical Society Meeting, Los Angeles, California, Oct. 14-19, 1979.
26. D. A. J. Rand and R. Woods, *J. Electroanal. Chem. Interfacial Electrochem.*, **55**, 375 (1974).
27. A. Capon and R. Parsons, *ibid.*, **39**, 275 (1972).
28. D. N. Buckley and L. D. Burke, *J. Chem. Soc. Faraday Trans. I*, **71**, 1447, 1896 (1975).
30. W. L. Brown, J. D. E. McIntyre, and W. F. Peck, Jr., Paper 43 presented at The Electrochemical Society Meeting, St. Louis, Missouri, May 11-16, 1980.
31. J. D. E. McIntyre, G. A. Pasteur, and W. F. Peck, Jr., To be published.
32. J. D. E. McIntyre and G. P. Schwartz, To be published.
33. J. D. E. McIntyre and G. K. Wertheim, To be published.
34. S. Nakahara, *Thin Solid Films*, **45**, 421 (1977).
35. J. D. E. McIntyre, Paper 301 presented at The Electrochemical Society Meeting, Los Angeles, California, October 14-19, 1979.
36. C. E. Rice, *Appl. Phys. Lett.*, **35**, 563 (1979).
37. C. E. Rice, G. Beni, and J. L. Shay, 717 RNP, *This Journal*, **126**, 458C (1979).
38. G. M. Clark, "The Structure of Non-Molecular Solids," Chap. 5, p. 227, Wiley-Interscience, New York (1967).
39. S. H. Glarum and J. H. Marshall, Submitted to *This Journal*.

Metal Filmed-Semiconductor Photoelectrochemical Cells

S. Menezes,* A. Heller,* and B. Miller*

Bell Laboratories, Murray Hill, New Jersey 07974

ABSTRACT

Voltammetric and light to electrical energy conversion characteristics of metallized semiconductor Schottky junctions with redox solution contacts are reported. Electrodeposited noble metal films on n-GaAs establish contacts to reversible aqueous redox couple solutions that can sustain solar photocurrent levels with low loss, requiring only a thin metal layer adequate to photovoltaic barrier formation. Possible advantages in lateral conductivity, relative to solid-state Schottky devices, and in surface stability and redox electrolyte independence, relative to semiconductor-liquid junction solar cells, are weighed against both the absorptive losses in the metal layer and the practicalities of obtaining sufficient integrity in the film to serve the semiconductor corrosion protection function. Gold, platinum, and rhodium plated n-GaAs with carbon counter-electrodes and ferro-ferricyanide solutions give 2-6% conversion efficiency under solar irradiance.

Stability of the semiconductor-liquid electrolyte interface is essential for practical solar-to-electrical conversion or electrosynthesis with cells based on the photovoltaic properties of these junctions. Among the expedients proposed to circumvent the chemical or photoanodic reaction of the semiconductor with the electrolyte is the limiting case of total removal of the active junction from electrolyte contact by interposition of a thin, unreactive metal film between the two phases (1-5). This requires that, in the hybrid cell, the metal and semiconductor form a Schottky barrier for the photoactive junction. In this scheme, the electrolytic redox couple solution with necessary counterelectrode becomes a simple front contact (4).

* Electrochemical Society Active Member.

Key words: energy conversion, photovoltaic, solar, voltammetry.

Prior workers have reported cyclic current-voltage curves of metallized GaP at stationary electrodes (1-4). That the photopotentials of such cells are a function of the metal-semiconductor pairing and relatively independent of the redox couple was demonstrated therein for gold-coated GaP and Si electrodes (1). Analyses of voltammetric behavior and issues in light to electrical power conversion were not described.

Recent suggestions in this area (6-8) utilize illuminated p-n junctions, metallized to form ohmic contacts at both the p and the n regions which, in contact with an electrolyte, drive a net electrolytic reaction. In this concept, based on silicon particles, the current flow is local rather than to an external load, but the considerations of metal-semiconductor interface stability determining the long-term performance in corrosive elec-

trolytes are related, whether this junction is ohmic (6-8) or blocking (1-5).

Schematic possibilities for these cells are given in Fig. 1. The hybrid cell is B, containing elements of a Schottky barrier solid-state cell A, and a semiconductor-liquid junction cell C. Cell A in practice has additional metallization and contact fingers on the metal layer to supply a low resistance front contact whereas cell C necessarily has a counterelectrode (CE) to complete the equivalent function. In all cases, the semiconductors themselves would have an ohmic back contact, not indicated in Fig. 1.

Cell B has a semiconductor-metal barrier with two electrolytic contacts in series (anode and cathode). This implies that lateral conductivity in the metal plane is less of a constraint on overall device series resistance than in cell A, since the electrolytic solution provides a parallel path. The electrolytic part of the hybrid depends in its dynamic contact resistance (I - V slope) on both anode and cathode voltammetry, but the Fermi level (Nernst potential) of the solution itself ought not to influence open-circuit voltage. If the solution presents a low enough resistance, the M layer in cell B may be made as thin (for improved light transmission) as needed for its functioning in a Schottky junction and for isolation of the semiconductor from the electrolyte. The electrolyte interface in cell C is profoundly different. It is involved in defining the barrier height, band bending, cell voltage, and power output.

The arrows in Fig. 1 indicate the light path through the respective cells to the photoactive junction. The light must traverse the metal layer and/or the solution plus cell window in the respective cases. Contact fingers in cell A structure cause further light loss. The dashed lines over the counterelectrode of Fig. 1 indicate that the losses will vary to the extent that the counterelectrode affects light transmission. This loss is a function both of geometry and electrode material. All the present experiments employ configurations in which the counterelectrode does not block the light path.

When the hybrid cell contains a kinetically reversible redox couple, the exchange currents at both the Schottky barrier metal and counterelectrode can be higher than the photogenerated currents. If, in addition, the electrolyte is highly conductive, the hybrid cell will have an ohmic contact characteristic and low impedance. With suitably transparent redox couples, not now restricted by the severe requirements of competing against semiconductor corrosion, and with appropriate counterelectrode design, this "contact" might absorb very little light. Then, if the metallization of the semiconductor did not produce too severe light absorption and reflection, or if transparent conductive electrodes such as SnO_2/Sb or $\text{In}_2\text{O}_3/\text{Sn}$ were used, a hybrid cell like B might have interesting properties as an energy converter relative to both the conventional solid-state (A) and liquid junction (C) counterparts. This work is an examination of some characteristics of the metallized semiconductor-electrolyte structure, with such possibilities in mind.

Our previous consideration (5) of type B cells was restricted to their use for modeling light and mass transfer flux limitations in liquid junction cells, C, in a case where the interface was not subjected to parallel

photocorrosion. In this paper, we are drawing the first quantitative comparison between the hybrid cell B and the metal Schottky cell A with respect to their impedance and kinetic characteristics. We have continued in the present effort to prepare all metal films by electrodeposition (5, 9) as the method of choice for large areas, rather than by evaporation (1-4).

Experimental

n-Gallium arsenide of $2.4 \times 10^{15} \text{ cm}^{-3}$ carrier concentration, not deliberately doped, was cut in either (111) or (100) directions. Back ohmic contacts were applied prior to shaping specimens into disks and attaching them to steel shafts with silver epoxy. Electrodes were potted in insulating epoxy and the n-GaAs surface was repolished to a Linde A (0.3 micron) finish, followed by 1:1 H_2SO_4 - H_2O_2 etch to a semimatte (gray) condition.

The plating solutions and conditions employed for Au, Pt, and Rh films were, respectively, 20 g/liter $\text{KAu}(\text{CN})_2$ -50 g/liter diammonium citrate at 70°C and 10 mA/cm^2 , "Platinex III" (OxyMetal Industries) at 80°C and 20 mA/cm^2 , and "Rhodex" (OxyMetal Industries) at 50°C and 10 mA/cm^2 . The latter two are proprietary baths. Plate thicknesses were calculated from the faradaic efficiency, nearly 100% for deaerated gold baths, and the supplied manufacturer's plating rate estimates for Pt and Rh. They were not otherwise measured.

A front contact for Au-plated GaAs type A electrodes was made by pressing on a ring of indium with an inner opening just less in diameter than that of the gold film. For the size of the active electrode disks in these and also type B cells, 0.5 cm or less, imperfect circularity and the nonuniformity of the incident laser beam lead to perhaps $\pm 10\%$ relative uncertainty in power efficiency determination.

Electrochemical experiments were performed in two- or three-electrode configurations, with potential control, in a cell with an optical window at its bottom, under nitrogen atmosphere. In three electrode runs either the saturated calomel electrode (SCE) or the poised electrolyte redox potential from carbon or platinum electrodes was used as reference.

Radiant sources were either a 10 mW He-Ne laser or a 100W tungsten-halogen lamp. Light intensity was varied by a Glan prism polarizer based optical attenuator (Karl Lambrecht Corporation) with a rotatable element driven by a 1 rpm motor. A pellicle beam splitter (Oriol Corporation) inserted in the light beam directed 8% of the light to a silicon detector (Metrologic Corporation) whose analog output was linearly or logarithmically recorded. The 100W lamp, a 160 Hz chopper (Bulova Corporation) and an Oriol Corporation 7240 grating monochromator comprised the spectral source. Photocurrent response was synchronously detected (PAR 128) and corrected for light source and grating output within the $\pm 10\%$ flat region of the power detector, between 400 and 1000 nm. For transmission spectra Au or Pt films evaporated on glass slides were inserted between the spectral source and the detector.

Electrolytes were prepared with reagent grade chemicals and triply distilled water.

Solar power conversion efficiency data were obtained as previously described (10). Rotating disk electrode methodology was also identical to established practice (11).

Results and Discussion

The current-voltage curve of a type A cell of electrodeposited Au on a n-GaAs single crystal disk, with circumferential indium contact to the Au at the disk edge, is shown in Fig. 2, curve a. The open-circuit voltage of a different specimen, similarly prepared, is displayed as a function of laser beam power, P , in curve b.

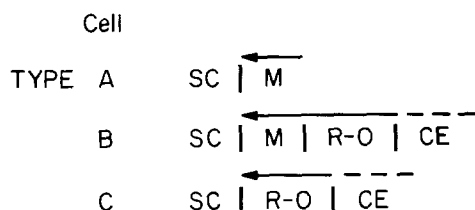


Fig. 1. Schematic of photocell structures. Arrows indicate light path. SC = semiconductor, M = metal, CE = counterelectrode, and R-O = redox electrolyte.

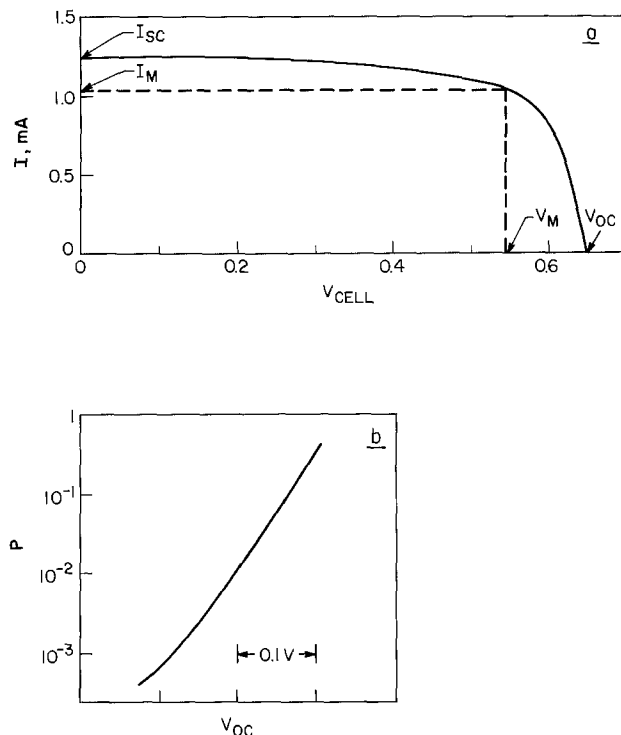


Fig. 2. Behavior of electroplated Au on n-GaAs diode with indium front contact under 632.8 nm laser illumination; (a) photocurrent-voltage characteristic with open-circuit voltage (V_{oc}), short-circuit current (I_{sc}), and maximum power product ($I_m V_m$) defined on figure and (b) V_{oc} as a function of illumination intensity, P , normalized to approximate intensity of (a).

The current-voltage curve has a fill factor, $I_m V_m / V_{oc} I_{sc}$, of 0.7 and a power conversion efficiency of about 6%. The open-circuit voltage increases by 67 mV for each tenfold increase in irradiance over the linear region of the plot, corresponding to a quality factor (ratio to $2.3 kT/q$) of 1.1 for the Schottky barrier. The absolute value of the voltage (not shown) varies with film thickness, average irradiance, and light spot size.

These data indicate that the electroplated structure operates as anticipated for an Au-n-GaAs Schottky device. When employed as a rotating disk electrode (RDE), it shows the behavior of Fig. 3. curve a, with a 2 mm $\text{Fe}(\text{CN})_6^{4-}$ -pH 5 buffer solution under controlled potential scan and laser illumination. The level of illumination is so maintained that the limiting current is due to mass transfer of $\text{Fe}(\text{CN})_6^{4-}$, not light flux (5). The dark current of the electrode is essentially nil through the potential region of Fig. 3. The curve for a conventional gold disk, under the same experimental conditions, save illumination, is shown

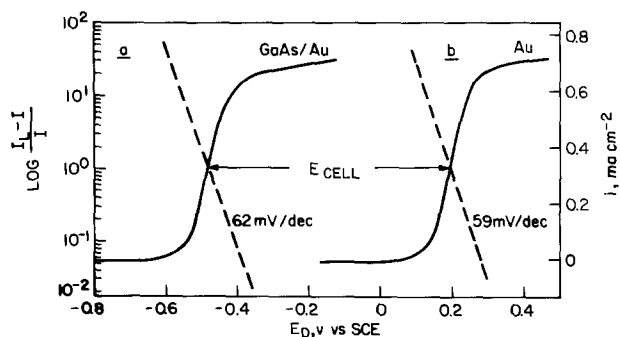


Fig. 3. Current-voltage curves at 1600 rpm rotating disk electrodes of (a) electroplated Au on n-GaAs (laser illuminated) and (b) Au (unilluminated), both in 2 mm $\text{Fe}(\text{CN})_6^{4-}$ + pH 5 0.5M acetate buffer. $\log [(I_L - I)/I]$ vs. disk potential, E_D , plots are superimposed on the respective curves, with I_L = convective diffusion limited current.

as curve b of Fig. 3. The curves are displaced in potential by the Schottky barrier voltages expected for the junction in Fig. 1, cell type B.

Logarithmic analysis of the two waves, also included in Fig. 3, confirms their similar shape, $\log [(I_L - I)/I]$ vs. E_D plots giving 59 and 62 mV/decade values for the Au and illuminated Schottky junction electrodes, respectively. These logarithmic slopes are those of one-electron reversible redox couples, as normally found for $\text{Fe}(\text{CN})_6^{4-}$ on gold.

Open-circuit voltage, V_{oc} , and short-circuit current, I_{sc} , for a typical Au-n-GaAs type electrode in a $\text{Fe}(\text{CN})_6^{4-}/\text{Fe}(\text{CN})_6^{3-}$ solution, recorded separately as a function of input power, are shown in Fig. 4. The 0.25M concentration of $\text{Fe}(\text{CN})_6^{4-}$ is more than sufficient to produce a light-limited short-circuit current condition at laser source or solar irradiance levels. I_{sc} is linear (unity slope in the log-log coordinates) with beam intensity over the more than three decades displayed, showing constant quantum efficiency. The slope of the V_{oc} plot in the linear region at higher intensities is 65 mV/decade, in good agreement with the equivalent data of Fig. 2 for the solid-state cells.

Electrodeposited Schottky barriers have been made on the n-GaAs single crystal substrate with nominally 200Å thick Pt and Rh, as well as Au. Examples of each of the three are shown in the V - I plots collected in Fig. 5 for the 0.25M $\text{Fe}(\text{CN})_6^{4-}$ electrolyte, with the appropriate maximum power conversion efficiency for 632.8 nm light indicated on the respective curves. Open-circuit voltages in the 0.6-0.7V range are obtainable for all three metals, which are sufficiently noble (have high enough work function) to act as stable anodes in the oxidation of $\text{Fe}(\text{CN})_6^{4-}$ in an acetate buffer, as needed in hybrid (type B) cells.

For Au and Pt electroplates, the photocurrent spectra for both type A (classical Schottky) and B (hybrid) cells and the transmission spectra of the respective metal films, evaporated on glass, are compiled in Fig. 6 and 7. Since the thickness of metal layers for each of the traces for the same element differs, the results within the figures cannot be rigorously compared. The

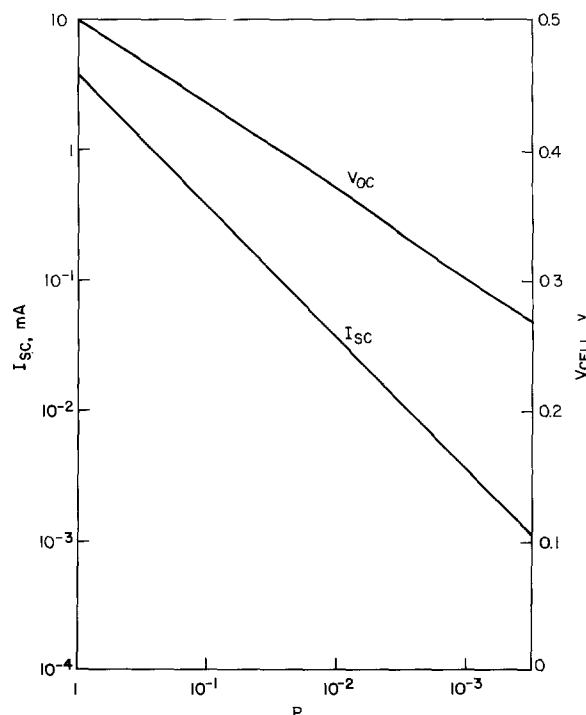


Fig. 4. I_{sc} and V_{oc} each as a function of the intensity, P , of the 632.8 nm laser beam with a gold-plated n-GaAs electrode and carbon counterelectrode. I_{sc} and P scaled logarithmically with P normalized to maximum intensity. Solution is 0.25M $\text{Fe}(\text{CN})_6^{4-}$. 0.01M $\text{Fe}(\text{CN})_6^{3-}$ in pH 5 acetate buffer.

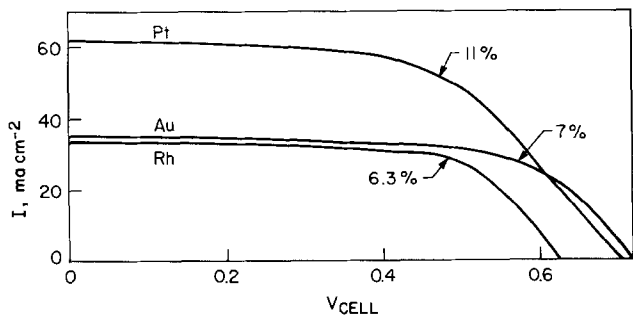


Fig. 5. Current-voltage characteristics of n-GaAs plated with Au, Pt, or Rh as run in the cell of Fig. 4 and with the laser irradiance. Maximum power conversion efficiency of each cell indicated on the curves.

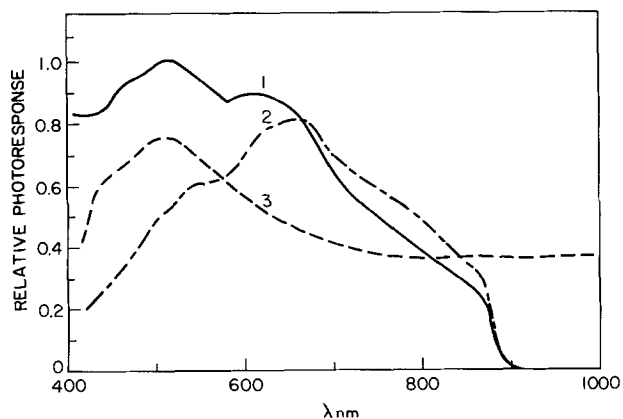


Fig. 6. Short-circuit photocurrent spectrum of curve 1, Au on n-GaAs electrode, and curve 2, same in 5 mm $\text{Fe}(\text{CN})_6^{-4}$; and curve 3, transmission spectrum, Au evaporated on glass. The curves are normalized to either maximum photocurrent or transmission, as applies.

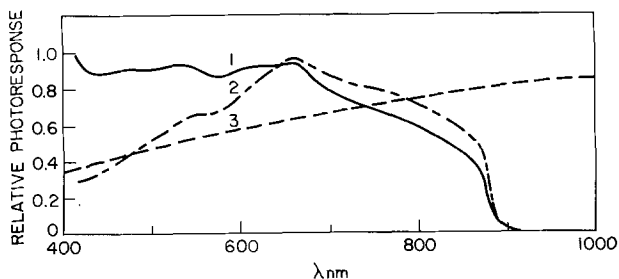


Fig. 7. Curves identical to those of Fig. 6 with Pt substituted for Au.

spectra indicate, however, the loss in type B cells due to electrolyte absorption at short wavelengths and, for the gold case, the increase in transmission for the metal around 500 nm. The choice of the colored $\text{Fe}(\text{CN})_6^{-3/4}$ solution reflects our inability to find completely transparent redox solutions in which the metal film semiconductors would be stable under prolonged photoanodic use. Attack by some colorless redox media is attributed to residual porosity and undercutting, leading to eventual adhesive failure of the metal film (4), when the exposed GaAs does not form sufficiently protective anodic products (passivating oxides). This process is often evidenced in a current peak prior to attainment of the limiting current in rotating disk potential scans.

Current-voltage curves under solar irradiance for a set of Au, Pt, and Rh electroplates are shown in Fig. 8. The conversion efficiencies are indicated on the curves. Values in the range 2-6% are typical. These values are difficult to reproduce closely because of deficiencies in control of the plating step.

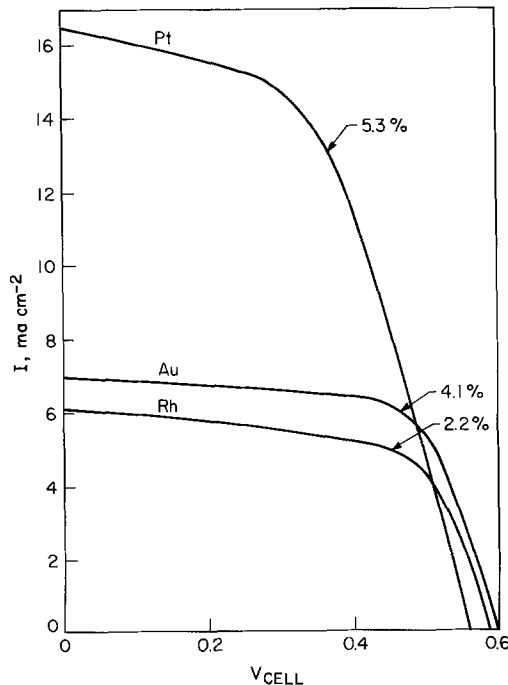


Fig. 8. Experiments as in Fig. 5 but with solar irradiances of 69, 93, and 90 mW/cm^2 ; respectively, for Au, Pt, and Rh plated n-GaAs electrodes.

Of the three solutions used to plate the electrodes of Fig. 8, the gold plating bath is the least corrosive to the GaAs substrate and yields the most reproducible electrodes. The other, proprietary, baths are acidic and sensitive to contamination by the corrosion reaction products, Ga(III) and As(III). Such effects add to the porosity and thus to substrate attack in the hybrid solar cells.

The behavior of the gold bath is reproducible enough to investigate the behavior of the hybrid (B) cell as a function of metal thickness. The data obtained are shown in Fig. 9. The abscissa is calculated from the coulombic increments of constant current electroplating. For each point the short-circuit current was measured after an added layer of gold was plated. As expected, the short-circuit current drops with thickness. However, a straight line for Beer-Lambert law conformity with the data of Fig. 9 requires constant reflectivity and absorptivity of the gold film and constant current efficiency and film uniformity in the deposition. Extrapolation of the experimental plot to zero thickness yields an intercept corresponding to a $60\% \pm 10\%$

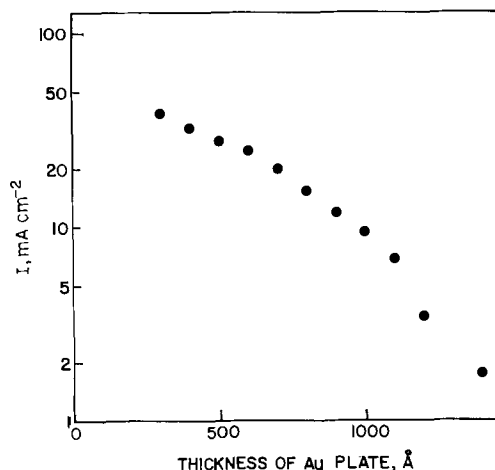


Fig. 9. Short-circuit current, I_{sc} , plotted logarithmically as a function of the thickness of Au electroplate on the n-GaAs substrate for the conditions of Fig. 4.

quantum efficiency for the incident laser beam. (The irradiance was measured by replacing the cell by a detector. The quantum yield or current efficiency for the metal thickness corresponding to that of the electrode used in obtaining the solar efficiency in Fig. 8 is about 32%).

It has been suggested above that the Au-n-GaAs electrode operates stably in the pH 5 $\text{Fe}(\text{CN})_6^{-4}$ solution. The observed change in photocurrent under tungsten-halogen illumination is shown in Fig. 10. I_{sc} is stable under these conditions only for about an hour before significant decline is apparent. However, replacement of the solution from a reservoir, without doing anything further to the electrode, at intervals marked by the arrows on Figure 10, restores the initial activity. Thus, the decline is due to photodegradation of the electrolyte rather than the electrode.

Other solutions that were used, e.g., colorless Fe(II)-Fe(III) phosphate media at pH 2, proved corrosive and the output decline with time was indeed associated with metal layer disruption and GaAs attack. Activity could not be restored without etching and replating.

Passage of current in the cathodic direction for type B cells and the equivalent forward conduction curve for the type A structure are shown in Fig. 11. The essentially straight (log current)-voltage regions have virtually the same decade slopes (65 mV for B, 67 mV for A) over several orders of magnitude. The type B cell begins to deviate from linearity at the highest currents when mass transfer of $\text{Fe}(\text{CN})_6^{-3}$ exerts influence and the cathodic current approaches a limit. Subject to this transport effect, the electrolytic contact operates without introducing extraneous behavior and the exponential factors are in agreement with those earlier observed for the open-circuit voltage shift with light intensity, as is expected for such Schottky junctions.

Conclusions

Hybrid cells with metallized semiconductors and electrolytic contacts (type B) have interesting characteristics as photovoltaic power sources. The power conversion efficiencies of the examples cited are, however, below those of semiconductor-liquid junction cells of type C. The major loss is in short-circuit current, which is roughly half that of the presently leading 12% n-GaAs selenide-polyselenide cell (12). However, the behavior of the series junctions (photoactive semiconductor-metal, metal-redox plus redox-counterelectrode) yields relatively high fill factors even under intense illumination. The operating characteristics prove the expected low resistance of the metal/redox couple contact.

The cell output is independent of redox potential and dependent on the electron transfer kinetics at both metal and counterelectrode electrolyte interfaces. This behavior is shown by logarithmic analysis of the I - V trace in the rotating disk electrode regime to be re-

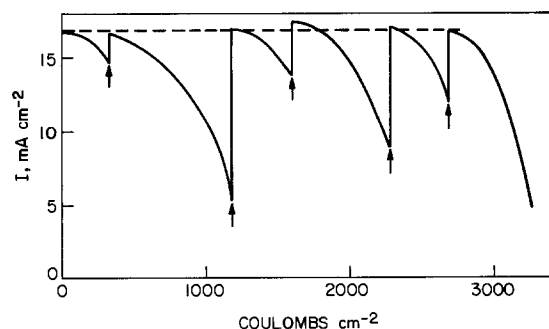


Fig. 10. Stability curve (I_{sc} vs. total coulombs/cm² passed) for a gold-plated n-GaAs electrode in the electrolyte of Fig. 4 under fixed tungsten-halogen illumination approximating at least solar levels. Arrows indicate times at which solution in cell was renewed; dotted line is the maximum current attained in fresh solution.

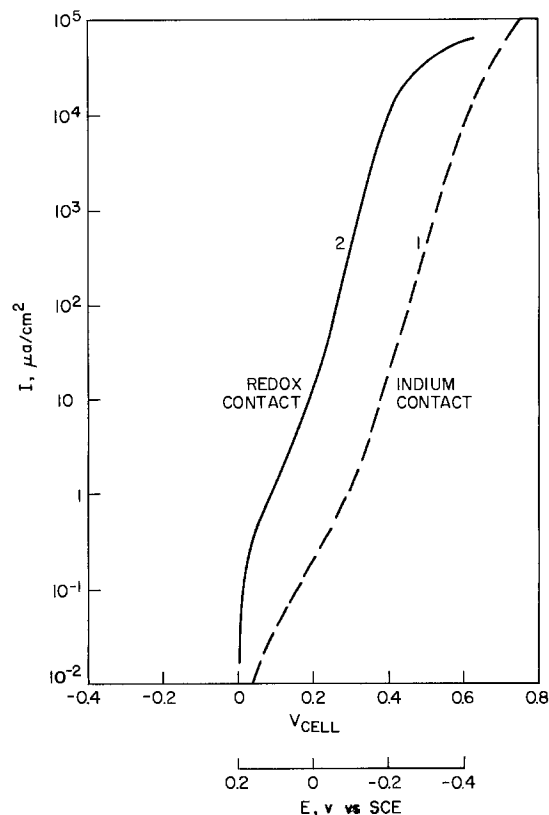


Fig. 11. Forward (cathodic) conduction current vs. voltage for the electroplated Au on n-GaAs structure with curve 1 (dashed) indium contact as in Fig. 1 and curve 2, 0.20M $\text{Fe}(\text{CN})_6^{-3}$ -0.01M $\text{Fe}(\text{CN})_6^{-4}$ -pH 5 acetate solution with carbon counterelectrode. Electrode in curve 2 rotated at 1600 rpm and potential is given with respect to saturated calomel electrode. Data taken without electrode illumination.

versible for the $\text{Fe}(\text{CN})_6^{-4/-3}$ couple at the gold-plated n-GaAs surface and therefore to contribute negligibly to cell loss with decimolar redox couple concentrations (plus supporting electrolyte for increased conductivity). Cell characteristics are basically determined by the quality of the as-plated metal-semiconductor interface. Open-circuit voltage-light intensity and forward conduction V - I plots both give ~ 1.1 ($2.3 kT/q$) decade slopes, very close to ideal for Schottky barriers, and independent of whether the electrolyte contact is present or not. This further confirms the low loss at the electrolyte interfaces, until mass transfer limitations are reached.

Plating thickness studies show that, on the single crystal substrate, quantum efficiencies of 50% ought to be obtainable with very thin (tens of angstroms) films for the type B cell. Platinum films, though more difficult to reproduce than gold with available electrodeposition methods, show better quantum efficiencies at sufficient metal thickness for electrode stability in pH 5 acetate buffered solutions.

Porosity in the deposited layers and photoanodic attack at the base of the pores appear to be the mechanism of the thin film failure in the electrolyte solutions. This is reflected voltammetrically by peaks in the RDE current response on initial voltage scan under illumination and from the n-GaAs substrate behavior in the different electrolytes. Only data from the pH 5 acetate- $\text{Fe}(\text{CN})_6^{-4/-3}$ system is shown here, although the initial curves in other electrolytes, aside from porosity effects, are comparable to the extent that the redox couples in question are kinetically reversible. Photodegradation in the acetate buffer is due to reactions of the $\text{Fe}(\text{CN})_6^{-4/-3}$ couple rather than failure of the gold-plated n-GaAs electrode.

Improvements in the integrity of the metal film, either by modification of the electrodeposition step or by the use of other preparative procedures, are necessary to find a combination of electrode and electrolyte that has useful photostability. Applying a matte etch (12) to reduce the semiconductor reflectance and thus to increase the short-circuit current (as done in the n-GaAs-selenide cells) is not feasible in the present work as the surface becomes too rough for the electrodeposited products to cover the semiconductor protectively at the desired metal thickness.

Manuscript received Dec. 17, 1979.

Any discussion of this paper will appear in a Discussion Section to be published in the December 1980 JOURNAL. All discussions for the December 1980 Discussion Section should be submitted by Aug. 1, 1980.

Publication costs of this article were assisted by Bell Laboratories.

P-Type GaP as a Semiconducting Photoelectrode

M. A. Butler* and D. S. Ginley*

Sandia Laboratories, Albuquerque, New Mexico 87185

ABSTRACT

The nature of p-type GaP photocathodes as employed in photoelectrochemical cells has been explored in some detail. These cathodes are found to be unstable in both acid and base. The flatband potential has been measured, using capacitance techniques, as well as the pH for zero surface charge, the point of zero zeta potential (PZZP). These data provide a measure of the electron affinity which is in excellent agreement with that calculated using our electronegativity model. The onset of photocurrent occurs at $\sim 0.7V$ negative of the flatband potential. It is demonstrated that this is due to a localized state acting as a recombination center. Experimental evidence for this state comes from the infrared photoresponse of these photoelectrodes. It is suggested that this is the same bulk state which controls the efficiency of GaP electroluminescence diodes.

While a number of groups have examined p-GaP with respect to its fundamental properties (1) and as a photocathode for use in photoelectrolysis (2-5), there exists in the literature considerable conflicting information. This is especially true with regard to its stability as a photoelectrode. Therefore we have undertaken a detailed study of the properties of p-GaP photocathodes. In addition to the stability question we wished to study the discrepancy which exists between the flatband potential as measured by capacitance data and the potential for photocurrent onset. For p-GaP, this difference is $\sim 0.7V$. While such effects have not been observed for the metal-oxide semiconductors in aqueous media, they appear to be more prevalent in the nonoxide semiconductors, particularly p-type materials, and will obviously play an important role in determining the usefulness of these materials. This study of p-GaP electrodes also provided the first check of our electronegativity model (6) for predicting flatband potentials in a nonoxide p-type semiconductor.

The samples were single crystals of GaP cut perpendicular to the [111] axis, and Zn doped to a density of $\sim 5 \times 10^{17} \text{ cm}^{-3}$ as determined by Hall mobility and conductivity measurements. The contacts were made by alloying in In:2 weight percent Zn. All electrochemical measurements were made using a conventional three-electrode electrochemical cell with a PAR

- ### REFERENCES
1. Y. Nakoto, T. Ohnishi, and H. Tsubomura, *Chem. Lett.*, 883 (1975).
 2. Y. Nakato, K. Abe, and H. Tsubomura, *Ber. Bunsenges. Phys. Chem.*, **80**, 1002 (1976).
 3. R. H. Wilson, L. A. Harris, and M. E. Gerstner, *This Journal*, **124**, 1233 (1977).
 4. L. A. Harris, M. E. Gerstner, and R. H. Wilson, *ibid.*, **124**, 1511 (1977).
 5. B. Miller, S. Menezes, and A. Heller, *ibid.*, **126**, 1483 (1979).
 6. J. S. Kilby, J. W. Lathrop, and W. A. Porter, U.S. Pat. 4,021,323 (1977).
 7. J. S. Kilby, J. W. Lathrop, and W. A. Porter, U.S. Pat. 4,100,051 (1978).
 8. J. S. Kilby, J. W. Lathrop, and W. A. Porter, U.S. Pat. 4,136,436 (1979).
 9. Y. Nakato, S. Tonomura, and H. Tsubomura, *Ber. Bunsenges. Phys. Chem.*, **80**, 1289 (1976).
 10. A. Heller, K. C. Chang, and B. Miller, *This Journal*, **124**, 697 (1977).
 11. B. Miller, *ibid.*, **116**, 1677 (1969).
 12. B. A. Parkinson, A. Heller, and B. Miller, *Appl. Phys. Lett.*, **33**, 521 (1978).

173 potentiostat and 174 programmer. Illumination was by a 150W Schoeffel xenon lamp with Schoeffel grating monochromator. The list of electrolytes used in these experiments is shown in Table I. All were prepared from spectral quality reagents and solvents.

Stability

Since stability is of crucial importance in determining the eventual utility of any photoelectrode for photoelectrolysis, we took particular care in ascertaining the electrode's stability in both acidic and basic solutions. The normal techniques for evaluating stability were employed: photocurrent stability, observation of the electrode surface, mass loss, and analysis of the electrolyte. Table I summarizes some of the stability experiments. In general with no stabilizing redox couples present it is found that the p-GaP photocathode is unstable. Approximately one to three electrons

Table I. Stability of p-GaP

Electrolyte	Fraction of current contributing to decomposition and end products.
0.1M NaOH	10^{-3} current produces Ga^{3+} in solution
0.1M H_2SO_4	3×10^{-4} current produces Ga^{3+} in solution and grayish surface layer
0.1M HClO_4	Similar to H_2SO_4 but more active surface etching
0.1M H_3PO_4	Deposition of Ga metal on surface

* Electrochemical Society Active Member.

Key words: interfaces, infrared, energy conversion.

per thousand in the photocurrent take part in a decomposition reaction in all of the electrolytes.

Interestingly the photocurrent degradation rate depends strongly on the nature of the electrolyte as is illustrated in Fig. 1. Here we plot photocurrent *vs.* total charge through the external circuit. Note the expanded scale at the top of the figure which refers to the H₂SO₄ results. In general the HClO₄ results (not shown) closely parallel those in H₂SO₄, though detailed differences do show up in voltammetric measurements. All of the experiments were run under identical conditions. In a 0.1M NaOH electrolyte the photocurrent was observed to decay very rapidly with time. Analytical atomic absorption results indicate that Ga was going into solution probably as the hydroxide. The rapid decay of the current implies that as surface Ga is leached a passivating phosphate layer is formed which is insulating. Etching of these electrodes in aqua regia restores their performance.

In 0.1M H₃PO₄ we again observe a rapid decay of the photocurrent. However, in this case, no Ga is observed in solution. Instead a dark gray surface layer forms on the electrode. We feel that this layer is Ga metal caused by the reductive decomposition reaction. This is substantiated by linear sweep voltammetry as shown in Fig. 2. Here trace one represents the initial photocurrent and trace two the photocurrent after aging. If at this point we scan from the cathodic regime (trace 2) to the anodic regime, a peak is observed centered between +0.25 and +0.5V *vs.* SCE. The larger peak

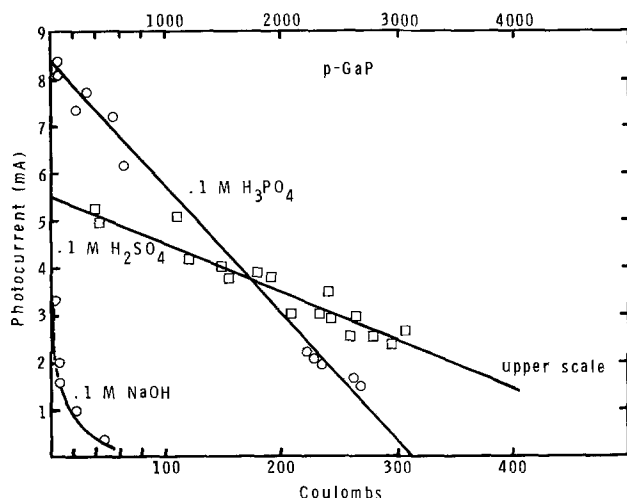


Fig. 1. Photocurrent for p-GaP illuminated with white light as a function of total charge passed through the interface. Note the different scales for different electrolytes.

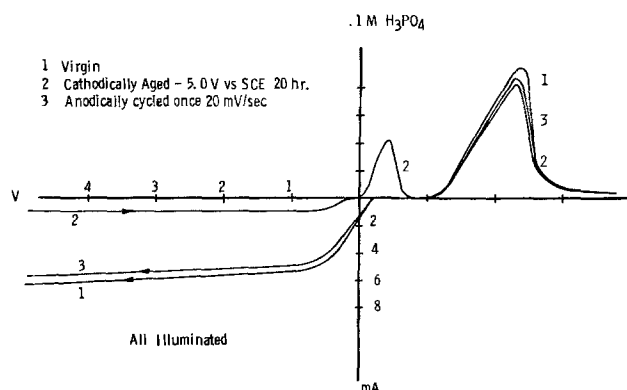


Fig. 2. The current-voltage characteristics for Zn-doped GaP in 0.1M H₃PO₄ illuminated with white light. The data were taken in the order shown. The potential is measured *vs.* SCE. The peak at +0.4V observed only for the first scan after cathodic aging corresponds to stripping of Ga metal from the surface. The peak observed in all scans around +2V is not light sensitive.

at a more positive potential is discussed below. After one scan through this oxidative peak the electrode surface returns to its original orange color and the initial photocurrent is restored as shown in trace 3. The peak cannot be reproduced until the electrode has been aged again. This peak corresponds well with the potential for Ga oxidation and we feel that the metallic gallium on the surface is being oxidized into a soluble form.

The decrease in the photocurrent in Fig. 1 most probably comes from adsorption of the light by the Ga metal surface film. The observed linear decrease in photocurrent with total charge is only an approximation. Assuming a film thickness \bar{X} proportional to total charge and a frequency independent optical absorption coefficient α for the Ga film, we would expect an exponential decay of the form

$$i_{\text{photo}} = i_0 \exp(-\alpha\bar{X}) \quad [1]$$

However, the initial form of the decay will appear linear within the accuracy of the data.

In the more oxidizing acids, HClO₄ and H₂SO₄, a slightly different behavior is observed. Again Ga is observed in solution but the photocurrent decreases more slowly. The reason for this is that the Ga produced is reoxidized into the electrolyte at the interface by the acids and leaves an essentially fresh electrode surface. The fact that the surface remains essentially virgin and that the photocurrent does not decline rapidly explains the previous observations in the literature indicating that this electrode is stable in H₂SO₄. For HClO₄ linear sweep voltammetric measurements show oxidative current peaks after aging in the potential range for which they were observed for H₃PO₄. This may be gallium metal or other gallium compounds on the surface. The apparent darkening of the electrode surface in these electrolytes may be due to formation of such gallium compounds and/or surface roughening.

It is clear from this data that p-GaP is unstable in acidic or basic media and that the observed relative stability of the photocurrent is a function of the electrolytes' ability to remove the gallium products from the electrode surface. Since the actual rate of decomposition, approximately one part in a thousand, is basically independent of the electrolyte, it might be possible to modify the electrode surface to stabilize the electrode as has been recently shown for ZnO (7) and Si and Ge (8, 9).

The above results are all for cathodically biased p-GaP, as it would be operated in a photoelectrochemical cell. For anodic bias another effect of interest is observed. Figure 2 shows that for scans to anodic potentials in 0.1M H₃PO₄ a peak in the *I-V* characteristics is observed around +2V (SCE). We believe that this is evidence of passivation of the GaP surface by growth of an insulating film. This behavior is also observed in 0.1M HClO₄ but not in 0.1M H₂SO₄ or 0.1M NaOH for our particular experimental conditions. When scanning in the reverse direction, the peak is smaller and the electrode can be cycled back and forth many times with reproducible results.

Flatband Potential

The flatband potential V_{FB} has been measured using the Mott-Schottky technique (9). As illustrated in Fig. 3 the data are well behaved and show little frequency dependence. The doping density extracted from the slope agrees well with the value from solid-state measurements. Our measured V_{FB} agrees well with previous data (10) as shown in Fig. 4.

An important question is whether our electronegativity model (6) that has been previously applied to n-type semiconductors would work as well for this p-type main group semiconductor. The relationship which exists between V_{FB} and the semiconductor electron affinity EA is given by

$$eV_{\text{FB}} = EA + E_g - E_o - e\Delta_{\text{FC}} - e\Delta_{\text{pX}} \quad [2]$$

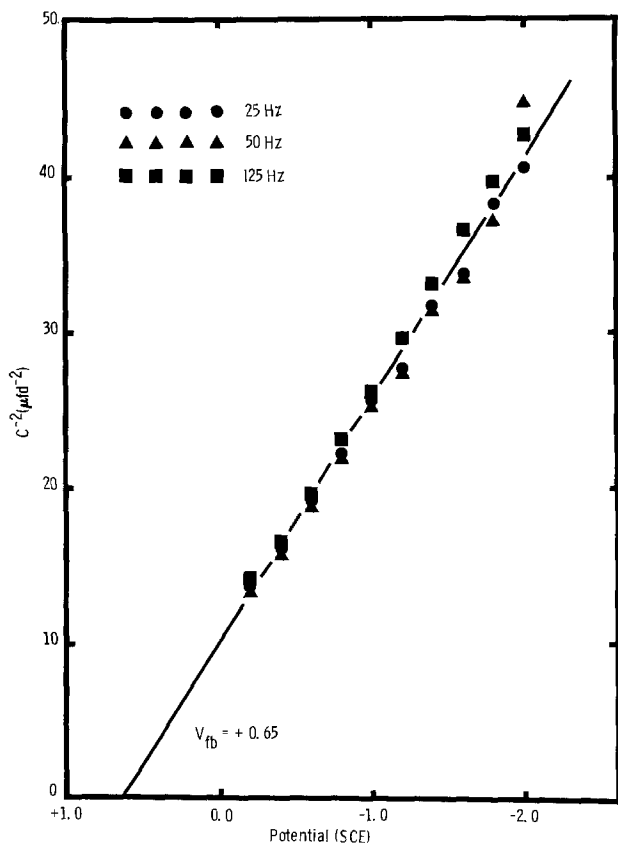


Fig. 3. Mott-Schottky plot for Zn-doped GaP in 0.1M H_3PO_4 . The data were taken by modulating the potential with a sawtooth and detecting the square-wave component of the current. The slope corresponds to a doping density of $\sim 7 \times 10^{17}/cm^3$ for the electrode area of $1 cm^2$.

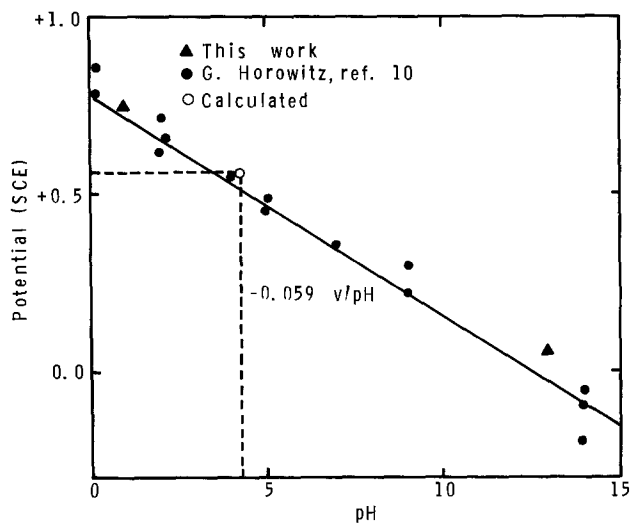


Fig. 4. Variation of the flatband potential with pH. The solid line has a slope of 59 mV per pH unit. The open circle is the calculated V_{FB} at the measured PZZP.

where E_g is the semiconductor bandgap, E_o is the position of the reference electrode (SCE) with respect to the vacuum level (4.75 eV), Δ_{FC} is the difference between the doped Fermi level and the top of the valence band, and Δ_{pX} the potential drop in the Helmholtz layer due to adsorbed ions. Note that for p-type materials the additional term E_g occurs in this relationship to account for the position of the Fermi level in the p-type semiconductor. For Zn-doped GaP the term Δ_{FC} is $< 0.1V$ and may be neglected.

The various potential-determining ions in the electrolyte will contribute charge to the Helmholtz layer

as a function of the relative equilibrium constants for chemisorption on the electrode surface. For aqueous electrolytes and semiconductors where the hydroxyl and the proton are potential determining there will exist a unique pH, which is a function of the intrinsic pK_a of the electrode, where equal numbers of H^+ and OH^- are adsorbed. At this point, the zero zeta potential (PZZP), the net charge of the ions adsorbed on the electrode surface is zero and therefore the potential drop across the Helmholtz layer, Δ_{pX} , is also zero. This point may be evaluated by a number of techniques, the simplest of which is the pH drift technique. Here, the pH of the solution is monitored while adding powdered semiconductor material. The pH will drift to the PZZP from either side, and at the PZZP the addition of more powdered semiconductor results in no net change in pH. The data for a series of drift experiments on GaP are illustrated in Fig. 5. As can be seen the PZZP is observed to be at a pH of approximately 4.3. Thus, at this pH the correction term Δ_{pX} will be equal to zero. It is interesting that a well-defined PZZP is observed for this electrode in contrast to many nonoxides which do not show a clearcut pH dependence of V_{FB} . This is most probably due to the fact that the phosphide ions on the GaP surface are oxidized to phosphates which interact strongly with the aqueous media.

The electron affinity (EA) of the semiconductor is given by (6)

$$EA = [\chi(Ga)\chi(P)]^{1/2} - \frac{1}{2} E_g \quad [3]$$

where χ is Mulliken's atomic electronegativity. Using a bandgap of 2.2 eV (12) we obtain a value for EA of 3.1 eV. Thus the flatband potential at the PZZP (pH = 4.3) is predicted to be +0.55V (SCE). As we can see in Fig. 4, this calculated value is in excellent agreement with the measured flatband potential. This result further confirms the general applicability of the electronegativity model to semiconductor-electrolyte interfaces.

Photoresponse

GaP is a semiconductor with an indirect gap at ~ 2.2 eV and a direct gap at ~ 2.8 eV (12). These characteristics are clearly evident in its spectral response shown in Fig. 6. The small quantum efficiency is related to the small depletion layer thickness (less than $0.1 \mu m$ for this sample) and short diffusion length (typically $1 \mu m$ or less for these poor quality samples). The optical absorption depth for photon energies below the direct gap is several microns. Therefore improvements in the quantum efficiency should be possible by decreasing the doping level to increase the depletion layer thickness to near the optical absorption depth.

A more interesting question is the dependence of the photoresponse on applied potential. Generally one

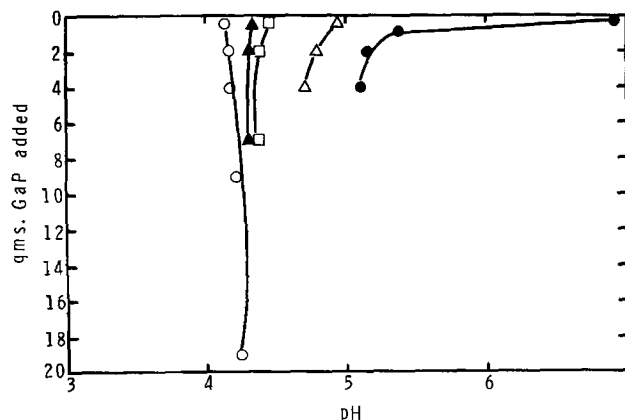
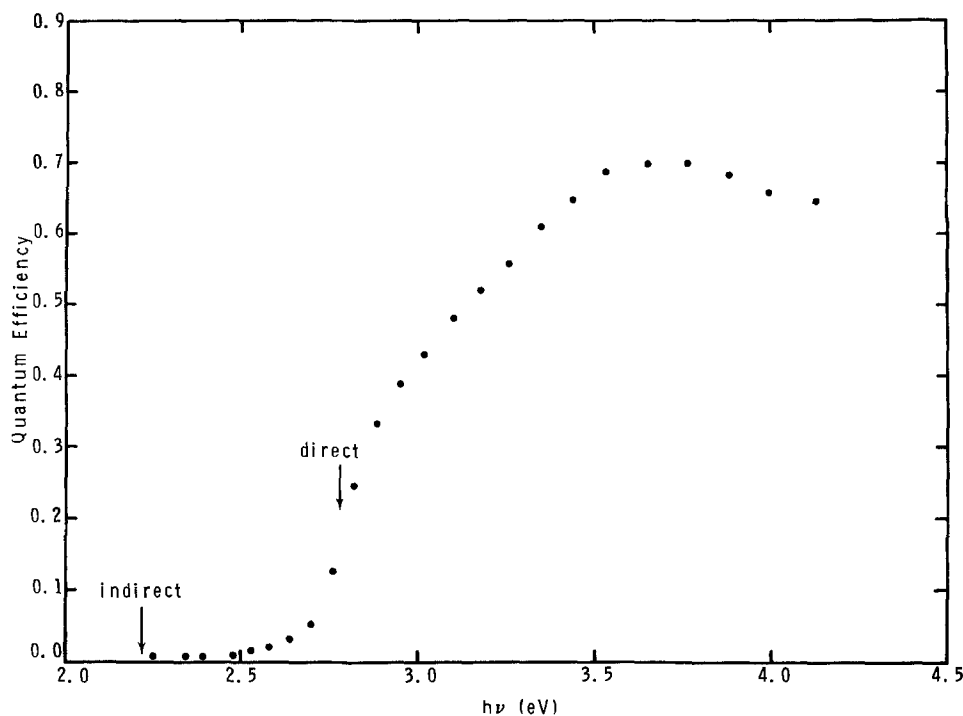


Fig. 5. A series of experiments where the pH of the solution as a function of the amount of powdered GaP added has been demonstrated. The data shows that zero net surface charge occurs at about pH = 4.3.

Fig. 6. The spectral response of GaP:Zn in 0.1M H_3PO_4 biased at $-1.0V$ (SCE). The data is uncorrected for reflection and adsorption losses.



would expect that the photocurrent onset should occur at the flatband potential. This is true for the metal oxide semiconductors, such as WO_3 in aqueous electrolytes (13). However we see in Fig. 7 that the photocurrent onset occurs $\sim 0.7V$ negative of the flatband potential for p-GaP. This behavior has been previously noted (14). The obvious explanation for this behavior is the existence of a recombination center at or near the semiconductor surface which short circuits the

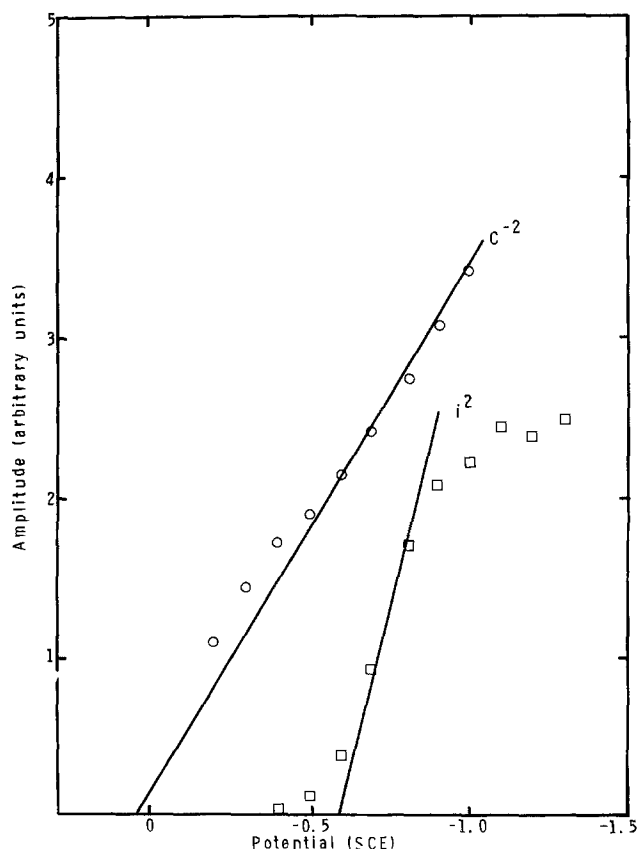


Fig. 7. Comparison of the flatband potential as determined by capacitance measurements (C^{-2}) and the photocurrent (i^2) onset for Zn-doped GaP in 0.1M NaOH. The discrepancy between the two is about 0.7V.

photoelectrolysis process (15). This mechanism is illustrated more clearly in Fig. 8. In Fig. 8a the empty localized state allows the photoexcited electron in the conduction band to take path 1 as well as path 2. Path 1 short circuits the photocurrent. In Fig. 8b the localized state is filled and path 1 is not available to the photoelectron in the conduction band. Thus we would expect the photocurrent through the interface to drastically decrease or stop when the Fermi level falls below the energy of the localized state in the gap. The discrepancy between the flatband potential and photocurrent onset in p-GaP could be explained by such a localized state ~ 0.7 eV above the top of the valence band.

Confirming evidence for this picture can be obtained by considering Fig. 8b. Since the localized state is filled with electrons, it should be possible to photoexcite them into the conduction band, where they can contribute to the photocurrent. The experiment has been done and the results are shown in Fig. 9. The peak occurring at 1.4 eV is very near where it would be expected. Since the localized state is ~ 0.7 eV above the valence band and the bandgap is ~ 2.2 eV, the IR peak should occur at about 1.5 eV. The measurements were extended down to 0.4 eV and no other IR photoresponse was observed. The IR photocurrent has the same turn on potential as the photocurrent induced by bandgap radiation. This is

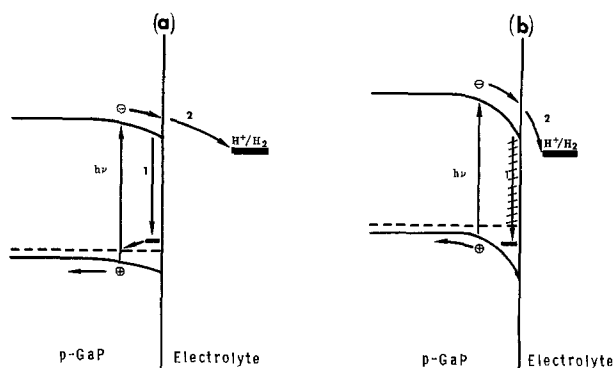


Fig. 8. The p-GaP electrolyte interface for two different bias conditions. (a) Here the Fermi level is below the localized state and thus it is empty. It can act as an electron recombination center. (b) Here the Fermi level is above the localized state and here the localized state cannot act as an electron recombination center.

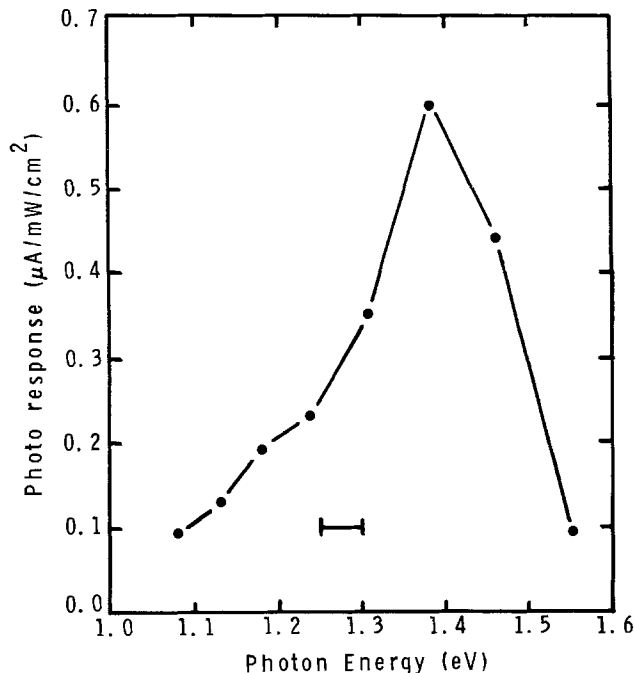


Fig. 9. Infrared photoresponse of p-GaP in 0.1M HClO_4 at -1.5V (SCE). The resolution of the monochromator is indicated.

exactly what would be expected if the same state were responsible for both effects.

An important question to ask is the nature of this localized state. To act as an efficient recombination center it must occur near the GaP surface. The strength of the IR photoresponse (up to $0.6 \mu\text{A}/\text{mW cm}^2$) shown in Fig. 9 would be very difficult to explain for states confined to the interface (true surface states). A state related to the bulk properties of the material is thus implied. However we noticed that the IR response is enhanced if the sample is previously aged cathodically in HClO_4 with incident white light, again suggesting that the phenomenon is somehow tied to the surface.

There was a possibility that the localized state is related to the oxygen content of the p-GaP. Experiments were performed on epitaxial single crystal p-GaP samples in which oxygen was intentionally excluded. The flatband potential and photocurrent onset potential were not significantly shifted from those where oxygen was present.

The most likely explanation of the recombination center is the following. A bulk state is known to exist 0.75 eV above the valence band (16). This state is not related to any known impurity but by acting as a nonradiative recombination center it plays an important role in determining the efficiency of GaP electroluminescence diodes. The number of these recombination centers has been found to be directly related to the concentration of gallium vacancies (17). This does not necessarily imply that the center is a gallium vacancy, but rather that the possible complexes (18) forming the defect center may involve gallium vacancies. Further evidence for this state comes from photoemission and electron energy loss spectroscopy which show a "surface state" 0.8 eV above the valence band in phosphorus-rich GaP (19). We believe that this bulk state is the one responsible for the discrepancy between the flatband potential and photocurrent onset potential in p-GaP photocathodes. The increased IR response and thus concentration of recombination centers with aging probably comes from the gallium leaching during the photocorrosion of the p-GaP as was discussed in the stability section.

Summary

In this paper we have attempted to explore the properties of p-GaP as a photocathode in a photoelectrolysis

cell. Our results indicate that this material is unstable in both acid and base with essentially the same decomposition pathway in both but that the photocurrent stability depends strongly on the nature of the electrolyte. Passivation of the electrode was observed for aging in the anodic regime. The pH at which the net surface charge is zero (PZZP) was found to be 4.3. These results, together with the capacitively measured flatband potential, allowed the first test of our electronegativity model for p-type semiconductors. The good agreement found further supports the contention that the electronegativity model is applicable to all semiconductor-electrolyte interfaces. The discrepancy between the flatband potential and the photocurrent onset potential was shown to be due to a bulk recombination center located 0.7 eV above the valence band. This localized state was observed directly by optical excitation of electrons from this state into the conduction band. We suggest that this state is the same recombination center which controls the efficiency of solid-state electroluminescence in LED's made from GaP.

These results offer some encouragement for the practical application of p-GaP photocathodes. The sensitivity of the photocurrent stability to the electrolyte composition suggests that modification of the decomposition kinetics may be possible. Identification of the recombination center as the bulk state which determines the efficiency of electroluminescence diodes means that the same techniques may be used to improve the performance of both devices.

Acknowledgments

The authors are indebted to L. R. Dawson of these laboratories for providing most of the GaP used in these experiments and for contacting the samples and to E. G. Bylander of Texas Instruments for providing the low oxygen content p-GaP samples. The authors are also indebted to Ron P. Hellmer for excellent technical assistance. This work was supported by the Materials Science Program, Division of Basic Energy Sciences, U.S. Department of Energy under Contract DE-ACO4-76-DP00789.

Manuscript submitted Nov. 2, 1979; revised manuscript received Dec. 20, 1979. This was Paper 239 presented at the Boston, Massachusetts, Meeting of the Society, May 6-11, 1979.

Any discussion of this paper will appear in a Discussion Section to be published in the December 1980 JOURNAL. All discussions for the December 1980 Discussion Section should be submitted by Aug. 1, 1980.

Publication costs of this article were assisted by Sandia Laboratories.

REFERENCES

1. R. Memming and G. Schwandt, *Electrochim. Acta*, **13**, 1299 (1968).
2. H. Yoneyama, H. Sakamoto, and H. Tamoura, *ibid.*, **20**, 341 (1975).
3. A. J. Nozik, *Appl. Phys. Lett.*, **29**, 150 (1976).
4. M. Tomkiewicz and J. M. Woodall, *Science*, **196**, 4293 (1977).
5. K. Ohashi, J. McCann, and J. O'M. Bockris, *Int. J. Energy Res.*, **1**, 259 (1977).
6. M. A. Butler and D. S. Ginley, *This Journal*, **125**, 228 (1978).
7. K. G. McGregor, J. W. Otvos, and M. Calvin, 2nd International Conference on the Photochemical Conversion and Storage of Solar Energy, Aug. 10-12, 1978, Cambridge, England.
8. M. S. Wrighton, J. M. Bolts, A. B. Bocarsly, M. C. Palazzotto, and E. G. Walton, *J. Vac. Sci. Technol.*, **15**, 1429 (1978); J. M. Bolts and M. S. Wrighton, *Trans. Am. Chem. Soc.*, **100**, 5257 (1978).
9. H. Gerischer, in "Physical Chemistry: An Advanced Treatise," Vol. 9A, H. Eyring, D. Henderson, and W. Jost, Editors, Academic Press, New York (1970).
10. G. Horowitz, *J. Appl. Phys.*, **49**, 3571 (1978).

11. D. S. Ginley and M. A. Butler, *This Journal*, **125**, 1968 (1978).
12. W. H. Strehlow and E. L. Cook, *J. Phys. Chem. Ref. Data*, **2**, 163 (1973).
13. M. A. Butler, *J. Appl. Phys.*, **48**, 1914 (1977).
14. Y. Nakato, S. Tonomura, and H. Tsubomura, *Ber. Bunsenges. Phys. Chem.*, **80**, 1289 (1976).
15. A. J. Bard and P. A. Kohl, in "Semiconductor Liquid-Junction Solar Cells," by A. Heller, Editor, p. 222, The Electrochemical Society Soft-bound Proceedings Series, Princeton, N.J. (1978).
16. A. R. Peaker, B. Hamilton, D. R. Wight, I. D. Blenkinsop, W. Harding, and R. Gibb, *Inst. Phys. Conf. Ser.*, **33a**, 326 (1977).
17. A. S. Jordan, A. R. Von Neida, R. Caruso, and C. K. Kim, *This Journal*, **121**, 153 (1974).
18. J. A. Van Vechten, *ibid.*, **122**, 419 (1975).
19. K. Jacobi, *Surf. Sci.*, **51**, 29 (1975).

Transient Studies of Glucose, Oxygen, and Hydroquinone at a Membrane-Covered Rotated Disk Electrode

David A. Gough and John K. Leypoldt

Department of Applied Mechanics and Engineering Sciences, Bioengineering Group, University of California at San Diego, La Jolla, California 92093

ABSTRACT

The membrane-covered rotated disk electrode was used to evaluate transport and reaction of three representative solutes after a step change in electrode potential. An analysis is proposed that allows complete characterization of solute transport properties in the membrane from a single measurement for diffusion-limited processes. For partially reaction-limited processes, certain kinetic constants can be estimated provided that transport properties are known from independent experiments. Using a well-characterized membrane, reactions of oxygen and hydroquinone were studied as examples of diffusion-limited processes. Glucose oxidation, a process in which there is a complex dependency on reaction kinetics, was also studied and certain rate constants estimated. These results provide a foundation for characterization of transport in novel membranes.

In previous papers (1-3), we described a membrane-covered, rotated disk electrode that may be useful in the development of membranes for use with new chemical-specific sensors. In this device both a disk electrode and a reference electrode are mounted on a rotating shaft over which a hydrophilic membrane is placed. With such a configuration the current distribution between the working electrode and the nonrotated counterelectrode can be made symmetrical by using a high conductivity background electrolyte. This allows the disk electrode to be uniformly accessible to both reactant and electrolyte, thus ensuring a uniform potential distribution across the disk surface. Under these conditions, a well-defined mass transport regime is established in which the diffusion boundary layer thickness in solution is precisely determined by electrode rotation rate and the limiting current reflects combined membrane and solution mass transfer resistances. At low rotation rates the diffusion boundary layer is relatively large, making transport through solution the major contribution to total diffusional resistance. Under such conditions, the current is analogous to the conventional Levich current (4) and proportional to the square root of rotation rate. At high rotation rates, however, where the solution diffusion boundary layer is small, the resistance of the solution becomes negligible. Here, the diffusion current is independent of rotation rate and limited by permeability of the membrane.

The steady-state diffusion current i_d is given by the following equation (1)

$$i_d = i_L \left[\frac{1}{1 + \frac{P_s}{P_m}} \right] \quad [1]$$

Key words: membrane characterization, rotating disk electrode, chemical analysis.

where i_L is the Levich current without membrane (4)

$$i_L = 0.62nF\pi R^2 D^{2/3} \nu^{-1/6} \omega^{1/2} C_B \quad [2]$$

in which n is the number of electrons transferred, F is the Faraday constant, R is the electrode radius, D is the molecular diffusion coefficient in solution, ν is the kinematic viscosity, ω is the angular rotation rate, and C_B is the bulk solute concentration. P_s is the solution permeability or mass transfer coefficient given by

$$P_s = \frac{D}{\delta_d} \quad [3]$$

where δ_d is the diffusion boundary layer thickness (4) in solution

$$\delta_d = 1.61 D^{1/3} \nu^{1/6} \omega^{-1/2} \quad [4]$$

and P_m is the membrane permeability

$$P_m = \frac{\alpha D_m}{\delta_m} \quad [5]$$

in which α is the partition coefficient or equilibrium ratio of solute concentration in the membrane to solute concentration in solution, D_m is the solute diffusivity in the membrane, and δ_m is the membrane thickness.

We used the relationship in Eq. [1] to estimate the permeability of Cuprophane PT-150, a commercial hydrophilic membrane, to $\text{Fe}(\text{CN})_6^{-3}$ (1) and to O_2 and hydroquinone (2). Steady-state diffusion currents were measured over a range of rotation rates and the membrane permeability for each solute was calculated from plots of $1/i_d$ vs. $1/\omega^{1/2}$ by extrapolation to infinite rotation rate. The values of permeability thus determined were in agreement with results for solutes of comparable molecular weight obtained by conventional meth-

ods. It was not possible to further resolve the permeability into its components of the partition coefficient and diffusivity without additional independent measurements.

In another paper (3), we developed a method for estimation of solute diffusivity in the membrane based on analysis of the transient current after a step change of bulk solute concentration. This method is analogous to standard time lag methods commonly used for gas-membrane systems except that the concentration boundary layer in solution was taken into account. Thus, with values for diffusivity obtained by this method and of membrane permeability from steady-state measurements, the partition coefficient and diffusivity in the membrane can be calculated, allowing a complete characterization of transport properties of the membrane from a single experiment.

In the present paper we analyze the transient produced after abruptly imposing the measurement potential. Experimental results are reported for oxygen and hydroquinone as examples of processes that are strictly diffusion limited, and for glucose, where there exists a complex dependence on electrode kinetics. The analysis of this transient is proposed as an alternative method of characterizing solute transport in the membrane for diffusion-limited processes or, in the case of kinetic-limited processes, for estimation of certain kinetic constants.

Previous Work

It has been shown by Levich (4) that the conventional rotated disk electrode has some unique advantages for the investigation of kinetic-limited processes. The concentration boundary layer is of constant thickness across the disk making the electrode surface uniformly accessible to the diffusant. Since conditions for mass transfer are therefore identical at any point on the disk surface, the concentration of reacting species and the reaction rate are also uniform over the entire surface. For a given concentration boundary layer thickness, there exists a single-valued relationship between the concentrations at the surface and in the bulk. Thus, the thickness of the concentration boundary layer is not a function of reaction kinetics. Although these features are not generally characteristic of other mass transfer regimes, they are obtained when the electrode is covered by a hydrophilic membrane and greatly simplify the analysis of kinetic-limited processes.

Some fixed-potential studies have been previously conducted with the solutes employed in this investigation. In our previous studies on steady-state oxygen reduction at a platinized-platinum electrode both with and without a membrane (2), it was found that electrode prepolarization is helpful for obtaining highly stable and reproducible oxygen diffusion currents. In the absence of oxygen a small but significant anodic background current was observed at the working potential of -200 mV *vs.* a saturated silver, silver chloride electrode (SSCE). This current was independent of rotation rate and quantitatively the same with or without the membrane. Taking the background current into account, a Levich current corresponding to a four-electron process was obtained and membrane permeability was determined as before.

Some relevant previous work has also been reported on electrochemical glucose oxidation. Lerner *et al.* (5) employed a platinized-platinum rotated disk electrode without a membrane to study glucose oxidation over the potential range of -200 to 200 mV *vs.* SSCE. An electrode prepolarization treatment was used for surface activation in which the electrode was polarized first at 900 mV for 2 min, then at -300 mV for 3 min before recording each current-time curve at the specified measurement potential. These investigators found that the current-time curves were strongly dependent on electrode potential and that excellent reproducibility could be obtained with this measurement protocol.

Nevertheless, they found that the current constantly decayed and did not attain a steady-state value even after several hours, suggesting the existence of a slow electrode deactivation process occurring in parallel with glucose oxidation. Over a limited potential range of -200 to -50 mV the current decay exhibited a logarithmic dependence on time. In this potential region the current i was described by the following relationship

$$i = k_e C (1 - \theta) \quad [6]$$

where k_e is a constant at a particular electrode potential, C is the glucose concentration at the electrode surface, and θ is the fraction of the electrode surface covered by deactivating species as a function of time, given by

$$\theta = k_2 \ln(t/k_3) \quad \text{for } 1 \leq t/k_3 < e^{1/k_2} \quad [7]$$

where t is time and k_2 and k_3 are constants having, respectively, no units and dimensions of time. Variable electrode rotation rate had little effect on the glucose current showing that the process was predominately kinetic controlled. The overall charge transfer number for glucose oxidation was dependent on potential and time, and under the conditions studied ranged from 4 to 20. Gebhardt *et al.* (6) obtained similar results.

The oxidation of hydroquinone at a rotated disk electrode has also been studied previously both with (2) and without (4) a membrane. This process involves uncomplicated reaction at the electrode surface and the diffusion coefficient has been reported (4). We found, as did previous investigators (7), that without the membrane the electrode surface roughness had no effect on diffusion-limited processes, suggesting that electrodes with high roughness factors can be employed without precluding application of the Levich analysis.

Theoretical Analysis

We consider a disk electrode rotating at constant angular frequency ω , covered by a homogeneous gel membrane of thickness δ_m . As before (1), we let $z = 0$ at the membrane-solution boundary with z positive in the direction normal to the plane of the membrane away from the membrane surface. Initially, the electrode potential is such that there is no reaction of the chemical of interest at the electrode surface. Thus, there is no flux of that solute across the membrane-electrode interface and the solute is distributed at equilibrium between the membrane and solution. At time $t = 0$ the electrode potential is abruptly adjusted to a new value at which the chemical of interest can now react at the electrode surface. For a thin membrane, neglecting mass transfer at the edge, the governing equation within the membrane is

$$\frac{\partial C_m}{\partial t} = D_m \frac{\partial^2 C_m}{\partial z^2} \quad -\delta_m \leq z \leq 0 \quad [8]$$

where C_m is the chemical concentration in the membrane and D_m is the molecular diffusion coefficient within the membrane. If the initial bulk solute concentration is C_B , then

$$C_m(z, 0) = \alpha C_B \quad [9]$$

where α is the partition coefficient of the solute in the membrane. For $t > 0$ we assume that the reaction follows a first-order kinetic law with a first-order reaction constant k . The boundary condition at the electrode-membrane interface is therefore

$$D_m \frac{\partial C_m}{\partial z} (-\delta_m, t) = k \frac{C_m}{\alpha} (-\delta_m, t) \quad [10]$$

where the rate constant depends on the roughness factor and takes into account any differences between the membrane geometric area and the effective electrode

area. In certain cases, the rate constant may also depend on electrode potential. The partition coefficient is included in this expression to account for the equilibrium concentration difference between the membrane phase and the thin, aqueous layer adjacent to the electrode surface. The boundary condition at the membrane-solution interface is more difficult to model exactly and we therefore assume a linear concentration profile in solution with a boundary layer thickness equal to the Levich diffusional boundary layer thickness given previously in Eq. [4]. Thus, at the membrane-solution interface we have the following boundary condition

$$D_m \frac{\partial C_m(0, t)}{\partial z} = \frac{D}{\alpha \delta_d} [\alpha C_B - C_m(0, t)] \quad [11]$$

The above equations can be expressed in nondimensionalized form by introducing the following variables and parameters

$$\tau = \frac{D_m t}{\delta_m^2} \quad [12]$$

$$\bar{C}_m = \frac{\alpha C_B - C_m}{\alpha C_B} \quad [13]$$

$$y = 1 + z/\delta_m \quad [14]$$

$$h = \frac{k \delta_m}{\alpha D_m} \quad [15]$$

$$Bi = \frac{D \delta_m}{\alpha D_m \delta_d} \quad [16]$$

Equations [8], [9], [10], and [11] then become

$$\frac{\partial \bar{C}_m}{\partial \tau} = \frac{\partial^2 \bar{C}_m}{\partial y^2} \quad 0 \leq y \leq 1 \quad [17]$$

$$\bar{C}_m(y, 0) = 0 \quad [18]$$

$$\frac{\partial \bar{C}_m}{\partial y}(0, \tau) - h \bar{C}_m(0, \tau) = -h \quad [19]$$

$$\frac{\partial \bar{C}_m}{\partial y}(1, \tau) + Bi \bar{C}_m(1, \tau) = 0 \quad [20]$$

A method for solving equations of this form has been given elsewhere (8). The solution is

$$\bar{C}_m(y, \tau) = \frac{-1}{1 + Bi^{-1} + h^{-1}} [y - (1 + Bi^{-1})] - 2 \sum_{k_n} \frac{h(k_n^2 + Bi^2)(k_n \cos k_n y + h \sin k_n y)}{k_n \{(k_n^2 + h^2)(k_n^2 + Bi^2 + Bi) + h(k_n^2 + Bi^2)\}} e^{-k_n^2 \tau} \quad [21]$$

where the summation is over the roots of the following equation

$$\tan k_n = \frac{k_n(h + Bi)}{k_n^2 - hBi} \quad [22]$$

The measurable quantity of interest is the flux $j(\tau)$ at the electrode surface, which in nondimensionalized form is

$$\frac{j(\tau)}{P_m C_B} = \frac{-\partial \bar{C}_m}{\partial y}(0, \tau) = \frac{1}{1 + Bi^{-1} + h^{-1}} + 2 \sum_{k_n} \frac{h^2(k_n^2 + Bi^2)}{\{(k_n^2 + h^2)(k_n^2 + Bi^2 + Bi) + h(k_n^2 + Bi^2)\}} e^{-k_n^2 \tau} \quad [23]$$

From this equation it can be seen that after a sufficiently long time the flux approaches a steady-state value given by

$$\frac{j_{ss}}{P_m C_B} = \frac{1}{1 + Bi^{-1} + h^{-1}} \quad [24]$$

The steady-state current is therefore

$$i_{ss} = nF\pi R^2 j_{ss} = i_L \left[\frac{1}{1 + Bi + \frac{Bi}{h}} \right] \quad [25]$$

where i_L is the limiting Levich current given in Eq. [2]. From Eq. [25] it can be seen that the steady-state current is reduced by the presence of membrane and finite electrode kinetics. The parameter Bi is the Biot number (9) and represents the ratio of membrane to solution mass transfer resistance. The parameter Bi/h in Eq. [25] represents the ratio of finite kinetic to solution resistances.

The anticipated results of a partially kinetic-limited process can be obtained from conversion of the flux described by Eq. [23] into current density. Figure 1 is a plot of time-dependent, normalized current density for various values of h at constant Biot number. Experimentally, these conditions could be realized for different values of the rate constant obtained by operating at different electrode potentials or by varying the electrode roughness factor. The figure shows that the time to reach steady state increases with decreasing values of h and that the steady-state current decreases with h . The effect of different Biot numbers at constant h is plotted in Fig. 2. Such results might be obtained in practice by varying rotation rate or by using membranes of different molecular permeability. With increasing values of Bi , where transport through solution becomes relatively rapid, the time to reach steady state decreases and the ultimate current density increases.

An important special case of the above equations is when kinetics of the electrode are very rapid compared to diffusion within the membrane. This corresponds to the parameter h becoming very large and therefore in the limit as $h \rightarrow \infty$ the time-dependent current becomes

$$\frac{i'(\tau)}{nF\pi R^2 P_m C_B} = \frac{j'(\tau)}{P_m C_B} = \frac{1}{1 + Bi^{-1}} + 2 \sum_{k'} \frac{k'^2 + Bi^2}{k'^2 + Bi^2 + Bi} e^{-k'^2 \tau} \quad [26]$$

where values for k' are the roots of the following equation

$$k' \cot k' = -Bi \quad [27]$$

This provides a means of determining the solute diffusivity in the membrane. For τ of order 1, Eq. [26] can be approximated by the following monoexponential expression

$$\frac{i(t)}{nF\pi R^2 P_m C_B} = \frac{1}{1 + Bi^{-1}} + 2 \frac{k_1'^2 + Bi^2}{k_1'^2 + Bi^2 + Bi} e^{-k_1'^2 t} \quad [28]$$

where k_1' is the smallest root of Eq. [27]. At steady-state Eq. [26] becomes

$$\frac{i_{ss}}{nF\pi R^2 P_m C_B} = \frac{1}{1 + Bi} \quad [29]$$

which is equivalent to Eq. [1].

In Fig. 3 the normalized current density for a solute that reacts under strict diffusion control as described by Eq. [26] is plotted as a function of dimensionless time.

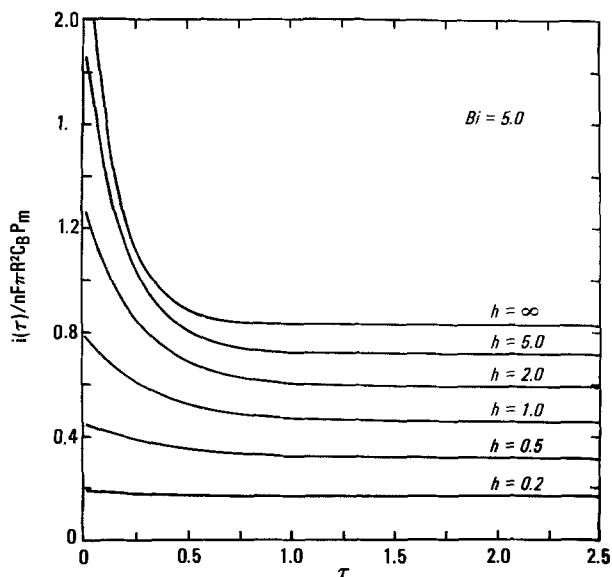


Fig. 1. The effect of variable h at constant Bi on the normalized, time-dependent current density.

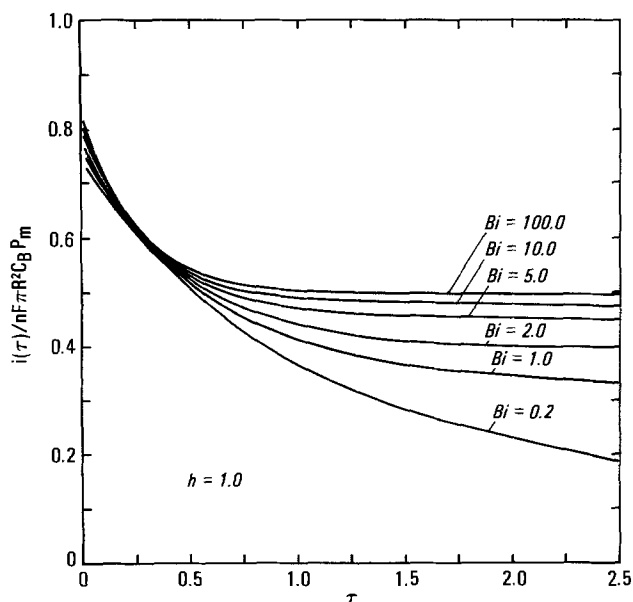


Fig. 2. The effect of variable Bi at constant h on the normalized, time-dependent current density.

The curves are given for different values of Bi that, in practice, could be obtained with the same membrane at different rotation rates or with membranes of various permeabilities. The values of Bi chosen represent a linear increase in $\omega^{1/2}$, and it can be seen that the steady-state current densities yield the characteristic nonlinear dependency on rotation rate described previously (1). The figure demonstrates that the time to reach steady state increases with decreasing values of Bi , as would be anticipated from the contribution of the concentration boundary layer.

We now consider a special case in which the effective electrode area is a slowly varying function of time, as is observed in glucose oxidation (5).

The expressions for the effective electrode area, the rate constant, and the partially kinetic-limited current are modified to include a time dependency. The effective electrode area as a function of time $A_{eff}(t)$ is described by Eq. [6] and [7], which state that

$$A_{eff}(t) = A_0(1 - k_2 \ln t/k_3) \quad [30]$$

where A_0 is the original effective surface area at time $t = k_3$. The kinetic parameter is written as

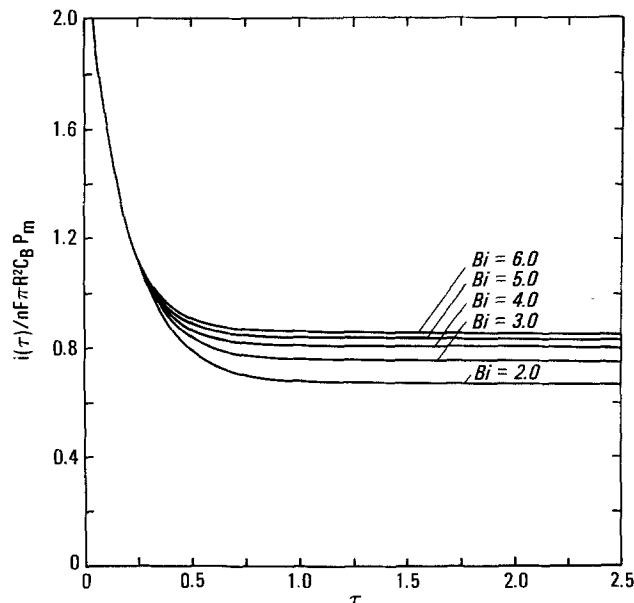


Fig. 3. The effect of variable Bi under strict diffusion control on the normalized, time-dependent current density.

$$h^* = \frac{k_1 A_0 (1 - \theta) \delta_m}{\alpha D_m A_g} \quad [31]$$

where A_g is the electrode geometric area, k_1 is a rate constant for glucose oxidation, and θ is given by Eq. [7]. The partially kinetic-limited current given by Eq. [25] then becomes

$$i(t) = \frac{nFA_0 k_1 C_B}{A_g} (1 - k_2 \ln t + k_2 \ln k_3) \left[\frac{1}{1 + h^* + \frac{h^*}{Bi}} \right] \quad [32]$$

Consequently, although the current decays approximately with the logarithm of time, the slope of the decay would be affected by a relatively impermeable membrane. Assuming that the kinetic constants k_1 , k_2 , and k_3 are not altered by the presence of the membrane, the anticipated ratio Φ of the current slope without membrane to the current slope with membrane is given by the equation

$$\Phi = 1 + h^* + \frac{h^*}{Bi} \quad [33]$$

Equations [32] and [33] provide a means for estimation of either certain kinetic constants or mass transfer properties, provided that values for the complementary process are known from independent experiments.

Experimental

Apparatus and electrode construction.—A disk electrode 0.80 cm in diameter was machined from 0.5 mm thick platinum plate and spot welded at the center to a length of platinum wire. The disk and wire were cemented into an electrode body fashioned from 1.9 cm diam Lucite rod and the disk surface polished to a mirror finish. A cavity in the electrode body with a small opening at the inactive portion of the disk surface near the edge of the platinum electrode was the receptacle of the reference electrode. This cavity was filled with saturated KCl and a chlorided silver wire inserted. The liquid junction at the edge of the disk electrode was partially occluded with a linen fiber to minimize convective outflow of electrolyte. A conventional Luggin capillary reference electrode was employed in studies without a membrane. In either case, electrode potentials are reported with reference to the saturated silver, silver chloride electrode, which is

+600 mV vs. the reversible hydrogen electrode under these conditions. The counterelectrode was a high surface area platinum wire that had been sealed in an adjustable glass tube and mounted to the vessel lid.

The rotating shaft was mounted on a Teflon bearing and attached to the vessel lid. Electrical contact was made between the rotating electrodes and the potentiostat through concentric, mercury-filled channels. Further details of electrode construction have been given elsewhere (1).

The electrochemical cell was a single compartment, water-jacketed vessel in which all three electrodes were placed. The lid was mounted to the vessel with a gas-tight seal and provision was made for passage of the purge gas through the cell.

The rotating shaft was directly coupled to a stepper motor (Model M-062, Minarik Corporation) and rotation rate controlled by a complementary regulator (Model TBM of the same manufacturer). The apparatus was adjusted so that each complete revolution of the shaft was made in 200 equal steps, each step being initiated only after a train of 4 pulses from a voltage-controlled oscillator (Model 180, Wavetek Corporation). The voltage input for determination of oscillation frequency was supplied by a voltage programmer (Model 176, Princeton Applied Research Corporation). Thus, the electrode rotation rate could be precisely maintained over a range of 0-3000 rps.

The electrochemical measurements were made with a potentiostat (Model 173, Princeton Applied Research Corporation), equipped with a digital coulometer (Model 178). Measurements were recorded on an X-Y recorder (Model 7037, Hewlett-Packard Corporation). Thermostatic conditions were maintained by a constant temperature water circulator (Model FE, Haake Corporation).

All solutions were prepared from analytical grade reagents and distilled, deionized water. Studies involving glucose and oxygen were conducted at 37°C with a supporting electrolyte of 0.1N KCl in $10^{-2}M$ sodium phosphate buffer, pH 7.3. In experiments with oxygen, the supporting electrolyte was equilibrated with the atmosphere and concentration calculated using standard solubility tables. In all other experiments the solution was purged with prepurified nitrogen. Glucose solutions were made from anomerically equilibrated stock solutions. Studies with hydroquinone were conducted with $20 \times 10^{-3}M$ solute in 0.1N KCl containing $5 \times 10^{-4}M$ H_2SO_4 at 37°C.

Properties of the membrane, Cuprophane PT-150 were characterized elsewhere (10) by conventional methods. The membrane ionic resistivity measured previously (1) was negligible compared to the membrane resistance to reactants. Thickness of the hydrated membrane was estimated to within ± 0.0005 cm with a precision micrometer.

Procedures.—A platinized-platinum electrode was used in all but specifically mentioned experiments with the intent of operating under diffusion control. The following method was employed for platinization (7). After polishing and cathodic cleaning in 1N HCl, the electrode was platinized in a solution containing 5% (w/v) chloroplatinic and 0.03% (w/v) lead acetate. Six alternate anodic and cathodic galvanostatic pulses of 100 mA/cm² current density, each 1 min in duration, were applied to the electrode while rotating. This treatment was followed by a thorough rinse with distilled water. This platinization method typically produced an initial electrode roughness factor of approximately 2000. However, the surface area dropped dramatically during the first several days of use to a stable value of approximately 650. We found, as did previous investigators (7), that the surface area remained remarkably stable over a period of months after the initial aging phase, provided that care was taken during the membrane mounting procedure to avoid disturbing the deposit. Surface area was determined with-

out a membrane in place by galvanostatic hydrogen stripping in 1N H_2SO_4 . A value at $210 \times 10^{-6}C$ was used for the equivalent charge of 1 cm² adsorbed hydrogen.

A suitable working potential for each solute was first determined without the membrane using a Luggin capillary reference electrode. This was done by recording current-time curves at fixed potentials in increments of 50 mV over the potential range of interest. For oxygen and glucose, each measurement was immediately preceded by a sequence of electrode pre-polarizations for surface activation consisting of anodization for 2 min at +900 mV followed by cathodization for 3 min at -300 mV. The background current in the absence of reactant was similarly recorded. With hydroquinone, prepolarization was not necessary and experiments were conducted by stepping the potential from approximately +300 mV where the current was insignificant to the working potential. Some acceptable working potentials were: oxygen, -200 mV; glucose, -100 mV; and hydroquinone, +700 mV. For oxygen and hydroquinone, steady-state measurements at various rotation rates and concentrations were also made. Calculations of diffusion coefficients in solution were based on the limiting Levich currents or, in the case of glucose, estimated from other studies (11). It was not necessary to activate the electrode before individual measurements of solutes that attained steady state. Moreover, a reproducible Levich current was obtainable for several hours after a single activation treatment. In certain measurements, slight compensation for iR drop was necessary.

These experiments were then repeated with the membrane in place using the internal reference electrode. Steady-state membrane permeability for oxygen and hydroquinone was calculated from plots of i_d^{-1} vs. $\omega^{-1/2}$ by extrapolating to the intercept at $\omega^{-1/2} = 0$, taking the background current into account. No significant IR drop was observed using the internal reference electrode with the membrane in place.

Results and Discussion

Hydroquinone.—Transient results for hydroquinone are shown in Fig. 4. The dashed lines are recordings without a membrane of current density normalized by concentration for several values of $\omega^{1/2}$. The steady-state current densities were linearly proportional to $\omega^{1/2}$ and used in determination of the diffusion coefficient of hydroquinone in solution. The time required for the current to reach steady state decreased slightly with increasing values of $\omega^{1/2}$, as predicted by previous models of the current transient at rotated disk electrodes without membranes (12, 13). The normalized current density with the membrane for two values of $\omega^{1/2}$ is recorded in the solid lines. With a membrane, the current density at comparable values of $\omega^{1/2}$ was reduced, and longer time was required to reach steady state. Nevertheless, the shape of the curves with or without the membrane was similar, with the exception of the initial slope at less than 1 sec. Initially, the background current density with membrane decayed rapidly, then slowly approached steady state. The background current density was independent of rotation rate and the presence of the membrane.

Oxygen.—As shown in Fig. 5, the results were qualitatively different with oxygen. The anodic movement of the electrode potential from the prepolarization potential of -300 mV to the working potential of -200 mV caused the transients to come from the anodic direction and cross through zero before finally arriving at cathodic steady-state values. In addition to the direction of the transients, the time to reach steady state for the background currents was substantially greater than for the oxygen currents. Moreover, the transient component of the background current was strongly dependent on the rotation rate and working potential and was affected by the presence of the mem-

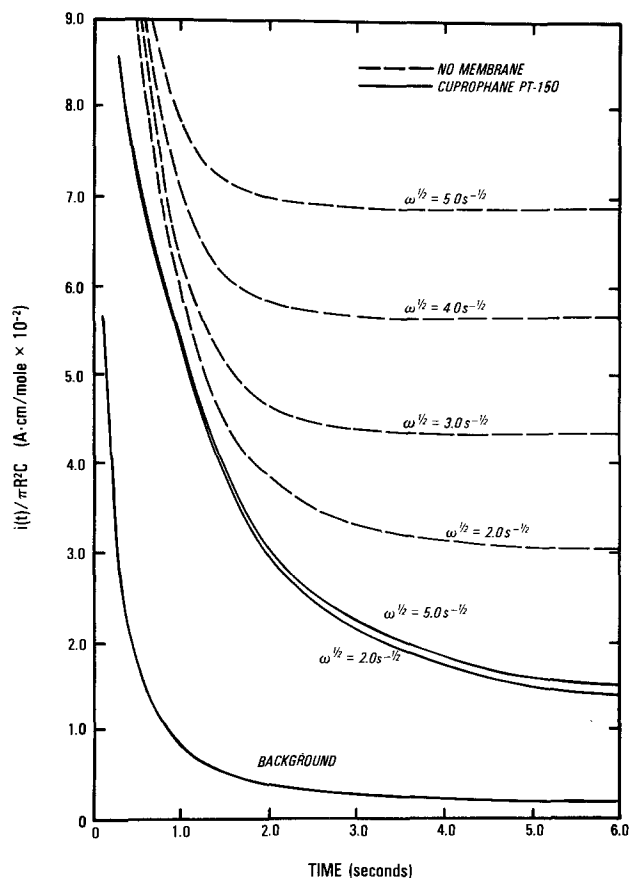


Fig. 4. The transient response with hydroquinone

brane. Nevertheless, the transient background currents, both with and without the membrane, eventually reached a common steady-state value that was independent of rotation rate.

The use of these data for determination of the diffusion coefficients of oxygen and hydroquinone in the membrane is shown in Fig. 6. Here, the logarithm of individual values of normalized current density minus the normalized steady-state current density was plotted as a function of time. Data points were calculated

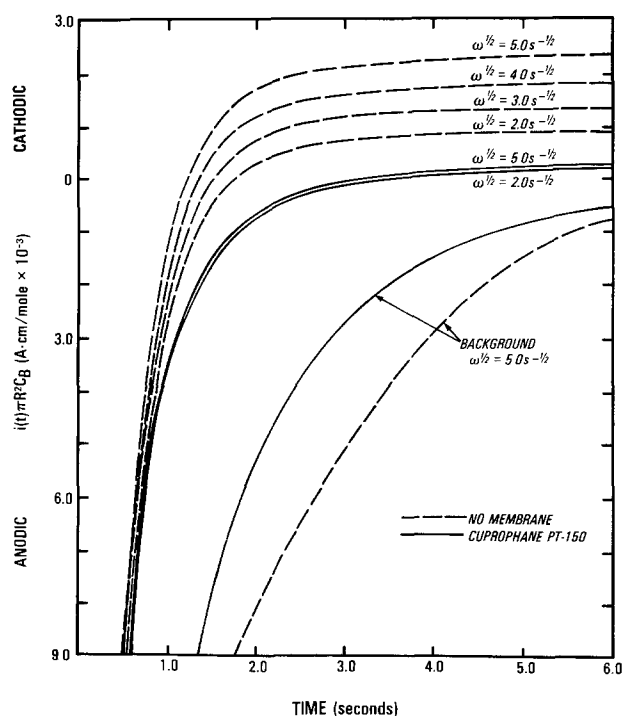


Fig. 5. The transient response with oxygen

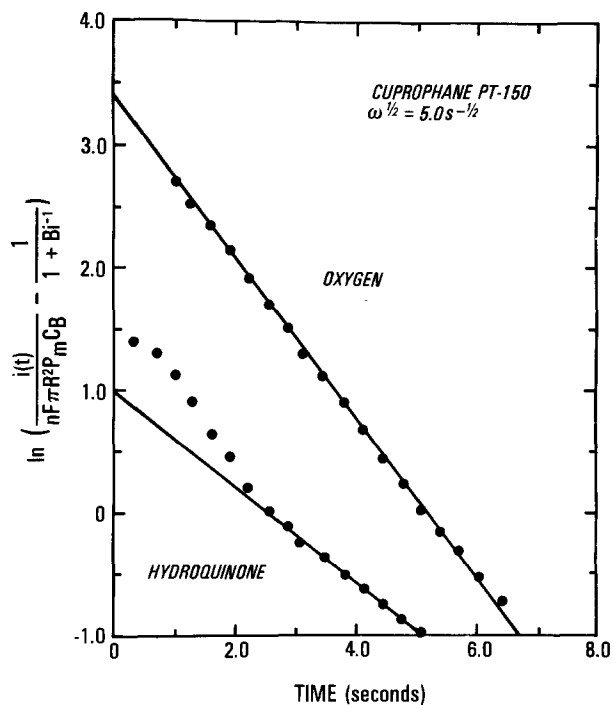


Fig. 6. The determination of the diffusion coefficient in the membrane for oxygen and hydroquinone.

from Fig. 4 and 5 for the same rotation rate. The diffusion coefficients were estimated from the slopes according to Eq. [28].

Although the oxygen data points closely approximated a straight line, the hydroquinone data points deviated significantly from linearity during the first 2 sec. Some degree of nonlinearity was representative of most trials. Departure from linearity suggests the possibility that various electrochemical process with distinguishable relaxation constants may have been involved in the transient response. While the physical nature of such processes and their significance to the eventual operation of chemical-specific sensors are not presently clear, these results may provide a point of departure for future studies. Thus, although the method proposed here is useful for the determination of diffusion coefficients in membranes, the analysis is based on a monoexponential transient and must be acknowledged as an approximation in certain cases.

The experimentally determined transport properties for oxygen and hydroquinone are summarized in Table I and compared to previous results for ferrocyanide (1). Values of the membrane molecular resistivity R_m , of membrane permeability, and of the diffusivity in solution were obtained from steady-state measurements. The effective diffusivity in the membrane D_{eff} is the product of the partition coefficient and the solute diffusivity in the membrane and was calculated from the steady-state permeability. In our previous study (1), D_{eff} was resolved into the components of α and D_m by an independent measurement of α , but in the present study D_m and D_{eff} were measured directly and α calculated.

Since transport of these solutes in cellulosic membranes has not been characterized previously there is no standard for direct comparison of these results. Nevertheless, indirect comparison based on other solutes (10, 11) can be made by reference to the ratio D_{eff}/D and the solute molecular weight. The present results are consistent with predictions based on such comparisons. In addition, the values reported here are comparable within experimental error to our other results (3) obtained with a time lag method.

Glucose.—The transient glucose current with the membrane in place is shown in Fig. 7. The current

Table I. Mass transfer properties in cuprophane

Solute and conditions	R_m (min/cm)	P_m (cm/ sec $\times 10^4$)	D (cm ² / sec $\times 10^6$)	D_{eff} (cm/ sec $\times 10^7$)	D_{eff}/D	D_m (cm ² / sec $\times 10^7$)	α
Oxygen; 0.1N KCl, 0.01M phosphate buffer, pH 7.3, 37°C	12.0	13.9	23.2 27.6 (3)	34.7	0.15	41.0	0.85
Hydroquinone; 0.1N KCl, 10 ⁻⁴ M H ₂ SO ₄ , 30°C	26.2	6.37	11.6 8.5* (4)	15.8	0.14	24.1	0.66
Ferrocyanide (1); 1N KCl, 0.01M phosphate buffer, pH 7.3, 30°C	99.7	1.67	6.3	4.2	0.07	5.6	0.74

* 15°C.

initially dropped rapidly, then began a logarithmic decay analogous to that described previously without the membrane (5). The current density at any given time was nonlinear with concentration, indicating that the process was still partially reaction limited. The background current shown by the dashed line decayed exponentially rather than logarithmically and was comparable to or larger than the glucose current at low concentrations. This is probably a result of the complex glucose oxidation process and invalidates the simple subtraction of the background current. Kinetic control of this process was evident from the nonlinearity of the current with concentration, the dependence of the current on the electrode roughness factor, and the relatively small effect of rotation rate.

The logarithmic nature of the glucose current decay is shown in Fig. 8. Values of glucose current density taken from Fig. 7 without subtraction of the background current density were plotted against the logarithm of time. While most values at greater than 75 sec closely fit a straight line, the current density at shorter times was frequently higher than expected. The deviation was probably due to initial glucose oxidation by an alternate mechanism involving a greater charge transfer number. Such an explanation would be consistent with the observations of Lerner *et al.*

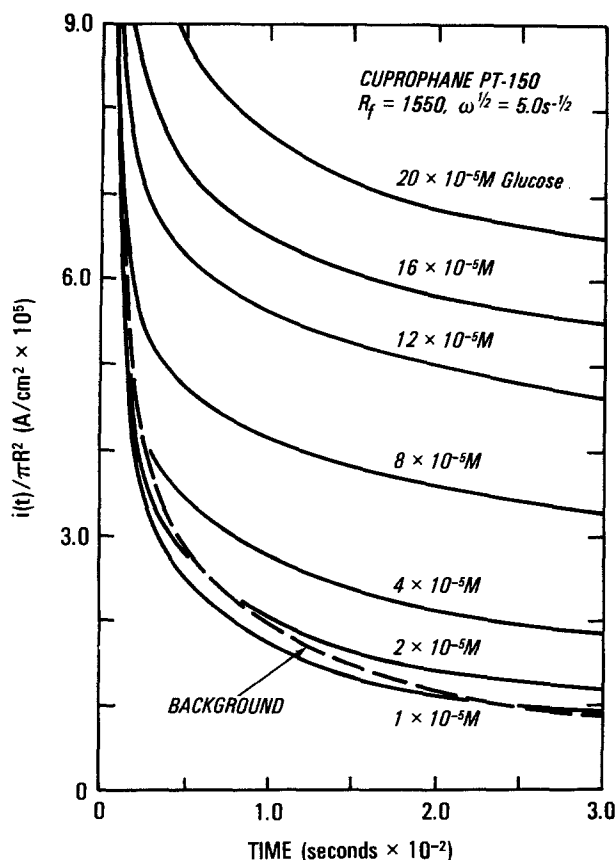


Fig. 7. The transient response to glucose with a membrane present.

(5) of a decreasing charge transfer number during the initial phase of fixed potential glucose oxidation without a membrane. The time during which this initial oxidation phase was significant is represented by the constant k_3 in Eq. [32] and was estimated from Fig. 8 to be approximately 75 sec. Thus, for times greater than k_3 , characterization of the glucose current decay as linear with the logarithm of time seems reasonable.

In Fig. 9 a comparison is made of the glucose current density with and without a membrane for two electrode roughness factors. Both with and without the membrane, the current density was substantially greater at the higher roughness factor, reflecting reaction control. However, with the membrane, the current density at a given time was reduced by proportional amounts for both roughness factors. Although the process was clearly under reaction control, the membrane had a slight effect on the slope of the current density decay, thus permitting the use of Eq. [33]. Since the reaction and transport properties could not be determined independently in these experiments, we chose to estimate the transport properties by linear interpolation from Table I on a basis of molecular weight and to use Eq. [31] and [33] to calculate values of the kinetic constants. These values could then be used in future studies with other membranes for determination of relative transport properties. The values used were: D , 9.0×10^{-6} cm²/sec; D_{eff}/D , 0.1; and α , 0.75. For the conditions of our experiment, this led to values of 3.60×10^{-4} and 2.91×10^{-4} cm/sec for P_m and P_s , respectively, and 8.08 for Bi . Results of the calculations are summarized in Table II. Values of ϕ were determined from averages of several measurements. At either roughness factor the magnitude of h^* was substantially smaller than that of Bi , as expected for a process under reaction control. There was no measurable dependence of ϕ on time, suggesting that θ in Eq. [31] may be negligible, thereby permitting determination of values for the product k_1A_0 . Further resolution of k_1 and A_0 on the basis of roughness factor was not warranted because the roughness factor as determined by hydrogen stripping was not expected to be equivalent to the surface area after prepolarization in the presence of the reactant. Values of k_2 were determined from the slopes of the current decay without membrane in Fig. 9 at greater than 75 sec using Eq. [32]. For this calculation, the charge transfer number was assumed to be 4, as suggested by previous studies (5). The values of k_2 shown in Table II were small compared to unity, justifying the treatment above in which θ was neglected. Rate constants have not been reported in the literature so that quantitative comparisons with previous studies could not be made. However, the glucose current density without the mem-

Table II. Reaction constants for glucose oxidation

R_f	Bi	ϕ	h^*	k_1A_0 (cm ³ / sec $\times 10^4$)	k_2 ($\times 10^3$)	k_3 (sec)
1550	8.08	3.17	2.48	4.46	16.52	75 (approx)
640	8.08	2.91	1.70	3.06	2.34	75 (approx)

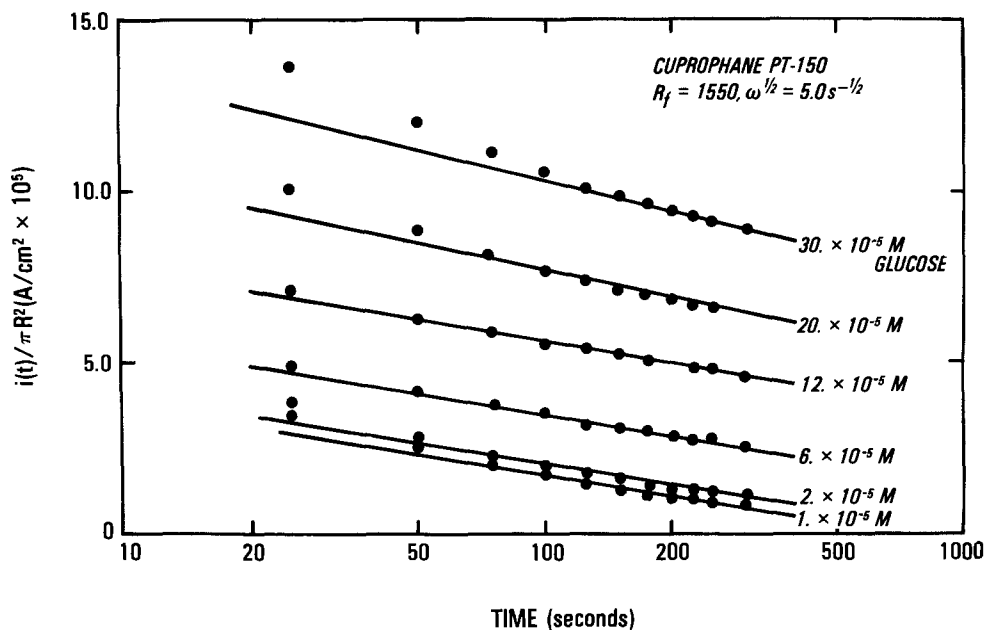


Fig. 8. The transient response to glucose with a membrane present plotted as a function of the logarithm of time.

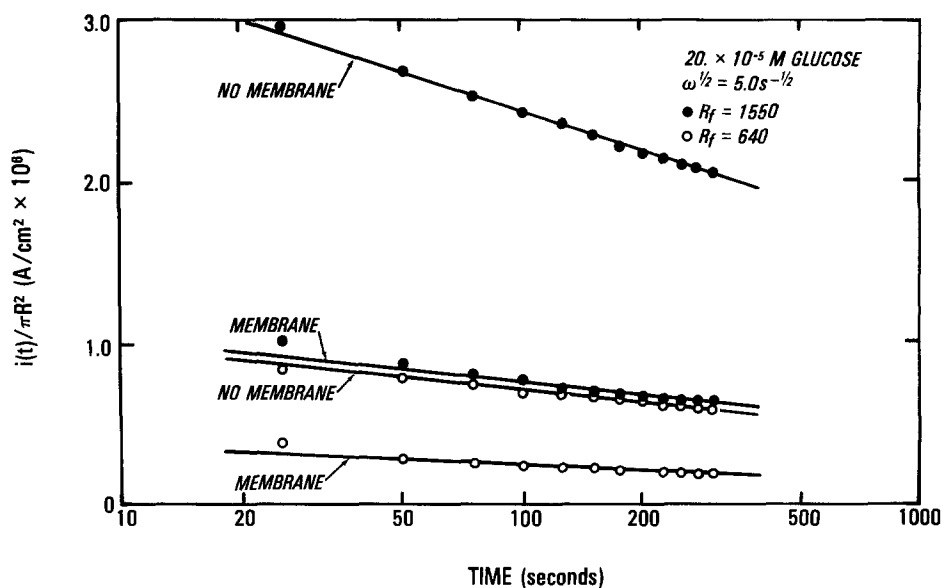


Fig. 9. The effect of roughness factor on glucose oxidation, with and without a membrane.

brane observed throughout our study was about 50% that reported by Lerner *et al.* (5) when adjusted for roughness factor, rotation rate, and concentration. This discrepancy may be due to the differences in iR drop compensation and may have an effect on the value of k_2 . Nevertheless, the rate of current decay as calculated from the values of k_2 and k_3 obtained in our study was comparable to previous experimental findings (5).

The nature of the glucose current can depend on the electrochemical technique employed. In another study (3), we analyzed the fixed potential glucose current at a membrane-covered rotated disk electrode after incremental increases in glucose concentration. A treatment for surface activation was not employed. The current decayed linearly with time after each addition of glucose and although the current density with the membrane for a given concentration was much higher, the process was still nonlinear with concentration and limited by reaction. Thus, the kinetic constants and logarithmic decay described in the present study are not necessarily observed for other modes of electrode operation.

One general feature of the analysis is the assumption that transients in solution are sufficiently rapid to produce a linear concentration profile in the concentra-

tion boundary layer. It has been shown elsewhere (13, 14) that transients within the concentration boundary layer at a rotating disk electrode decay with a time scale

$$t_s \sim \frac{\delta_d^2}{3.10D} \quad [34]$$

whereas transients in the membrane die out with a time scale

$$t_m \sim \frac{\delta_m^2}{k'_1{}^2 D_m} \quad [35]$$

For the assumption of a linear profile within the concentration boundary layer it is necessary that

$$\frac{t_m}{t_s} \gg 1 \quad [36]$$

The plausible values for transport parameters obtained for oxygen and hydroquinone suggest that this assumption is reasonable. However, the attainment of this condition may be in question where the analysis is applied to more highly permeable membranes.

An essential condition in the analysis was the assumption of an equilibrium distribution of the reactant

in the membrane at the time of imposing the measurement potential. In the case of oxygen and glucose significant reaction was likely during the prepolarization treatment, with the result that this condition may not have been completely satisfied. Nevertheless error due to the initial reactant distribution was expected to be minor for membranes of high permeability.

These studies prepare the way for characterization of new membranes that may eventually be incorporated in novel, biochemical-specific sensors.

Conclusions

1. An analysis of current transients after adjusting the electrode potential at the membrane-covered rotated disk electrode is given. Cases are described in which the process is strictly diffusion limited, partially reaction limited, and partially reaction limited with the effective surface area decreasing with the logarithm of time.

2. The membrane-covered rotated disk electrode and the transient analysis can be employed to evaluate the permeability, the partition coefficient, and the diffusion coefficient in membranes from a single experiment for solutes that are readily consumed at the electrode. The system may also be useful to analyze transport and reaction of solutes that are partially reaction limited.

3. This study confirms previous reports of the effectiveness of certain electrode prepolarization procedures for obtaining highly reproducible glucose oxidation currents. At a potential of -100 mV vs. Ag/AgCl without a membrane, the glucose oxidation current decays with the logarithm of time, as previously reported. Moreover, we find that these properties are also obtained with a membrane covering the electrode, although the membrane decreases the current density and the slope of current decay.

4. The analysis developed here is useful to describe the process of glucose oxidation at the membrane-covered electrode and to estimate certain reaction rate constants.

Acknowledgments

We gratefully acknowledge support from the U.C.S.D. Academic Senate Committee on Research. J. K. L. was supported by NIH grant HL-10881 to B. W. Zweifach.

Manuscript submitted Aug. 17, 1979; revised manuscript received Dec. 17, 1979.

Any discussion of this paper will appear in a Discussion Section to be published in the December 1980 JOURNAL. All discussions for the December 1980 Discussion Section should be submitted by Aug. 1, 1980.

LIST OF SYMBOLS

A_{eff}	effective electrode surface area (cm^2)
A_0	original effective electrode surface area (cm^2)
Bi	Biot number, a dimensionless transport parameter
C_B	solute concentration in the bulk (mole/cm^3)
C_m	solute concentration in the membrane (mole/cm^3)
\bar{C}_m	dimensionless solute concentration in the membrane
D	solute diffusion coefficient in the bulk (cm^2/sec)

D_m	solute diffusion coefficient in the membrane (cm^2/sec)
h	dimensionless reaction parameter defined in Eq. [15]
h^*	dimensionless reaction parameter for glucose
i_d	diffusion current (A)
i_L	Levich current (A)
i	time-dependent glucose current (A)
i'	time-dependent current with no reaction limitation (A)
i_{ss}	steady-state current (A)
i'_{ss}	steady-state current with no reaction limitation (A)
j_{ss}	steady-state flux ($\text{mole}/\text{cm}^2 \text{ sec}$)
j'_{ss}	steady-state flux with no reaction limitation ($\text{mole}/\text{cm}^2 \text{ sec}$)
$k, k_1, k_2, k_3, k_e, k_n, k', k'_1$	constants, variously defined
P_s	solution permeability or mass transfer coefficient (cm/sec)
P_m	membrane permeability (cm/sec)
R	electrode radius (cm)
t	time (sec)
t_s	time constant of transient in solution (sec)
t_m	time constant of transient in membrane (sec)
v_z	solution velocity (cm/sec)
y	dimensionless distance from the electrode surface
α	partition coefficient (cm^3/cm^3)
δ_d	concentration boundary layer thickness (cm)
δ_m	membrane thickness (cm)
θ	fraction of electrode surface covered by adsorbate
Φ	ratio of the glucose current slope without and with a membrane
τ	dimensionless variable defined in Eq. [12]
ν	kinematic viscosity (cm^2/sec)
ω	angular rotation rate (sec^{-1})

REFERENCES

- D. A. Gough and J. K. Leyboldt, *Anal. Chem.*, **51**, 439 (1979).
- D. A. Gough and J. K. Leyboldt, *ibid.*, In press.
- D. A. Gough and J. K. Leyboldt, *AIChE J.*, In press.
- V. G. Levich, "Physicochemical Hydrodynamics," Prentice-Hall, Englewood Cliffs, N.J. (1962).
- H. Lerner, J. Giner, J. S. Soeldner, and C. K. Colton, *This Journal*, **126**, 237 (1979).
- U. Gebhardt, G. Luft, G. J. Richter, and F. von Sturm, *Bioelectrochem. Bioenergetics*, **5**, 607 (1978).
- L. Marincic, J. S. Soeldner, C. K. Colton, J. Giner, and S. Morris, *This Journal*, **126**, 43 (1979).
- M. N. Ozisik, "Boundary Value Problems in Heat Conduction," International Textbook Co., Scranton, Pa. (1968).
- E. R. G. Eckert and R. M. Drake, Jr., "Analysis of Heat and Mass Transfer," McGraw-Hill Book Co., New York (1972).
- K. A. Smith, C. K. Colton, E. W. Merrill, and L. B. Evans, *Chem. Eng. Prog.*, **64**, 45 (1968).
- C. K. Colton, K. A. Smith, E. W. Merrill, and P. C. Farrell, *J. Biomed. Mater. Res.*, **5**, 453 (1971).
- S. Bruckenstein and S. Prager, *Anal. Chem.*, **39**, 1161 (1967).
- Y. V. Pleskov and V. Y. Filinovskii, "The Rotating Disc Electrode," Consultants Bureau, New York (1976).
- V. Y. Flinovskii and V. A. Kiryanov, *Dokl. Phys. Chem.*, **156**, 650 (1964).

Influence of Electrolyte Composition on Electrode Kinetics in the Molten Carbonate Fuel Cell

P. G. P. Ang* and A. F. Sammells*

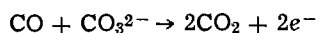
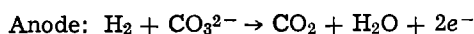
Institute of Gas Technology, Chicago, Illinois 60616

ABSTRACT

Electrode kinetics of fuel oxidation on nickel and cobalt electrodes is discussed for three selected molten carbonate mixtures. The measurements were made using a potential step technique. The highest exchange current values were found on nickel anodes in all melts, and the highest of these values were found in the melt comprised of 43.5 mole percent Li_2CO_3 -31.5 mole percent Na_2CO_3 -25 mole percent K_2CO_3 . In this ternary melt the exchange current density on nickel varied from 78 mA/cm² for intermediate-BTU fuel to 22 mA/cm² for low-BTU fuel at 650°C. The exchange current density was found to have an electrochemical reaction order parameter at constant overpotential of around 0.25 for hydrogen, carbon dioxide, and water. Electrochemical performance of the two anode materials in the three melts is discussed, and a tentative reaction mechanism is suggested for the oxidation reaction.

The molten carbonate fuel cell (MCFC) operates at 650°C and consists of a porous nickel anode together with a porous nickel cathode, both of which are pressed against what is called the electrolyte tile. This tile contains both an inert matrix into which can be supported a variety of alkali carbonate mixtures which, at the fuel cell operating temperature, are molten.

The empirical electrode reactions taking place in this cell are



The CO present at the fuel cell anode may react electrochemically as indicated above, but at the cell operating temperature of 650°C the water-gas shift equilibrium $\text{CO} + \text{H}_2\text{O} \rightleftharpoons \text{CO}_2 + \text{H}_2$ will be attained more rapidly. Hence the major contribution of CO to the fuel cell anode performance may be in hydrogen produced via the water-gas shift reaction.

Several factors must be considered in the selection of a molten carbonate mixture supported on the lithium-aluminate (LiAlO_2) matrix of the tile. These factors are (i) ionic conductivity, (ii) solubility of reactants and reaction products, (iii) the diffusion coefficients of reactants and products, (iv) the rate of the anodic and cathodic reactions, (v) electrolyte vapor pressure, and (vi) stability of the lithium-aluminate matrix. Electrolyte vaporization losses appear to be related to the hydroxide content in the molten carbonate mixture, with the highest concentrations occurring in lithium carbonate (1). Projected electrolyte tile lifetimes have already been reported (2). Reactant-gas solubility has generally been found to decrease with increasing lithium carbonate content. Maximum solubilities have been found in ternary mixtures rich in K_2CO_3 and lean in Li_2CO_3 (3).

Polarization data for hydrogen oxidation has shown little dependency on the nature of the metal (4). Experimental evidence has indicated that polarization at such electrodes for the hydrogen-oxidation reaction in molten carbonates may be controlled more by the local buildup of reaction products (H_2O , CO_2) than by the diffusion of hydrogen in the melt (5). Some work has already been reported for hydrogen oxidation on fully

immersed (6,7) and partially submerged anodes in molten carbonate melts (8,9). This latter work has shown that diffusion of reactants through the thin film electrolyte meniscus can play a significant role in the overall rate of the anodic reaction. Determination of the electrode kinetics for fuel oxidation requires the use of techniques that will enable effective separation of activation overpotential from any diffusion overpotential that may exist at the anode under the experimental conditions.

Experimental

Anode materials (nickel and cobalt rod) were purchased from commercial sources (Materials Research Corporation, Orangeburg, New York). The nickel and cobalt were Marz grade with purities of 99.995% and 99.99+, respectively. All measurements were performed in an electrochemical half-cell. Fuel gas mixtures were purchased premixed from Matheson Gas Company. The initial and after humidification gas compositions were determined by gas chromatographic analysis and were in agreement with predicted values. Humidification of the inlet gas was performed by passing it through a column of water in a large test tube. A gold wire in equilibrium with 33.3% O_2 -66.7% CO_2 inside an alumina tube served as a reference electrode (10, 11). The wire communicated with the melt through a small hole (0.015 in. diam) at the bottom of the tube. The potential of the working electrode was controlled by a Wenking ST72 potentiostat. The potentiostat had a risetime of about 1 μsec when a step voltage was applied. A piece of round gold foil was used as the counterelectrode. Electrolyte mixtures were prepared from a mixture of Li_2CO_3 , Na_2CO_3 , and K_2CO_3 (Mallinckrodt, Analytical Reagent). Compositions used in the study were Li_2CO_3 -38 mole percent (m/o) K_2CO_3 (Li/K), which has a high ionic conductivity and a reasonably high reactant-gas solubility; 52 m/o Li_2CO_3 -48 m/o Na_2CO_3 (Li/Na), which combines good electrolyte conductivity and a high sodium content for low vapor pressure to minimize electrolyte vaporization losses; and the ternary 43.5 m/o Li_2CO_3 -31.5 m/o Na_2CO_3 -25 m/o K_2CO_3 (Li/Na/K) to evaluate electrochemical performance at temperatures below 650°C.

A Tacussel Type GSTP2B pulse-sweep generator was used to control the potentiostat. The output voltage of the Tacussel generator was monitored with a digital voltmeter (Fluke, Type 8020A). Steady-state, linear voltage sweep, and transient pulse techniques were

* Electrochemical Society Active Member.

Key words: electrode kinetics, molten carbonate fuel cell.

used to study the current/voltage relationships of the electrode. The signals were recorded on a Hewlett-Packard 7046 X-Y recorder. Signals from the transient techniques were displayed and photographed on a Tektronix Type 547 oscilloscope. To eliminate errors caused by mass-transfer effects, the transient potentiostatic technique was used so that more precise kinetic information could be obtained. Electrode measurements made with this transient potentiostatic technique were performed using appropriate IR compensation within the potentiostat. Without such compensation, a large transient capacitive current was usually seen. Such an effect can cause some error in the current extrapolated to time zero. In order to achieve IR compensation, part of the voltage at the current recorder terminal of the potentiostat was picked up from an external potentiometric voltage divider (250Ω) and fed back into one of the potentiostat control inputs. The feedback voltage was then adjusted until the system almost started to oscillate. The positive feedback resulted in an increase of the control voltage proportional to the cell current. A Lindberg Hevi-Duty SB furnace with 3-zone temperature control was used to heat the cell. The temperature of the melt was read by an alumina-sheathed thermocouple and was displayed on a digital readout (Newport Laboratories, Incorporated, Model 267A-KCl-07). Fuels used in the course of this work are listed in Table I.

Results and Discussions

Before kinetic data could be obtained for the hydrogen-oxidation reaction, it was essential to determine whether the rate of the anodic reaction was controlled by diffusion- or mixed-control. Linear voltage sweep measurements at various sweep rates are shown in Fig. 1 for a completely immersed nickel wire anode in the ternary Li/Na/K melt at 650°C under conditions of fuel (intermediate-BTU) bubbling (50 ml/min). Figure 2 shows the voltage sweep measurements taken with the fuel bubbling turned off immediately prior to the linear voltage sweep. In both cases, we can see a dependency of the current density measured on the voltage sweep rate; the higher the sweep rate, the higher the observed current density. If we compare the measured current at a fixed voltage sweep rate, higher values are obtained for the melt subjected to continuous bubbling. Linear sweep measurements were also performed on a nickel wire partially submerged in the melt (approximately 50%) so that the half of the nickel wire above the electrolyte bulk would be covered with a thin film of the melt and would, therefore, approximate those electrochemical conditions present within the fuel cell porous electrode. With continuous fuel bubbling, linear voltage sweep measurements were performed with sweep rates between 0.15 and 150 mV/sec, and a dependency of the current density on the voltage sweep rate was again observed, indicating the continued presence of diffusion- or mixed-control effects at a partially submerged nickel wire. The limiting current density obtained with a sweep rate of 0.15 mV/sec at an overpotential of approximately 150

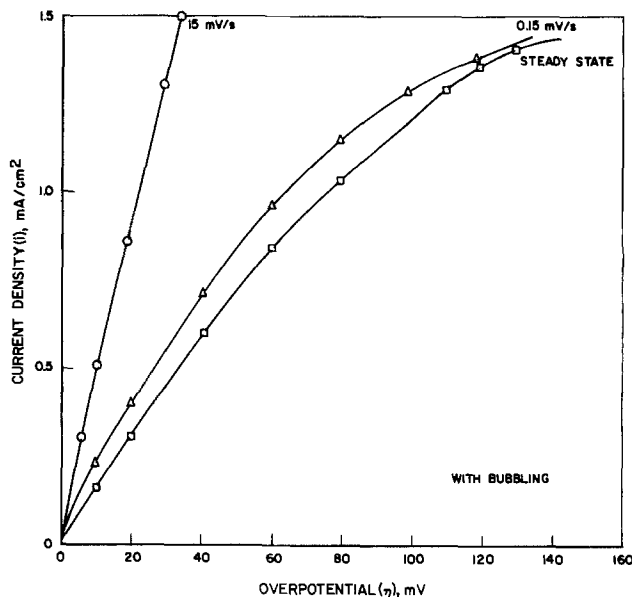


Fig. 1. Dependency of polarization curve on linear voltage sweep rate for a fully immersed nickel wire (fuel continuously bubbled into melt).

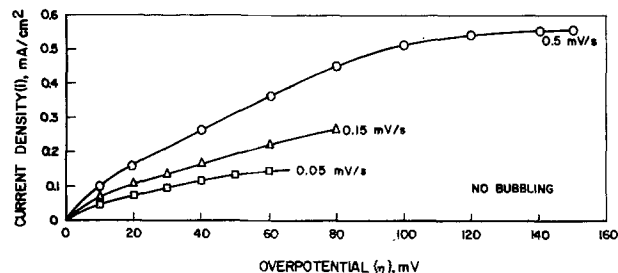


Fig. 2. Dependency of polarization curve on linear voltage sweep rate for a fully immersed nickel wire (no fuel bubbling into melt at time of measurement).

mV is around 3 mA/cm². In a porous electrode where the ratio of real to apparent area can be expected to be about 400, this current density would correspond to an apparent value of 1.2 A/cm².

Steady-state polarization measurements for completely immersed nickel and cobalt are shown in Fig. 3 and 4, respectively.

These steady-state polarization curves differ from those obtained initially on new electrodes by exhibiting rapidly increasing currents at high anodic overpotentials (~ 150 mV for nickel and ~ 100 mV for cobalt).

Upon removal of the high anodic potentials, approximately 30 min was required to reach the initial open-circuit potential. However, if upon removal of the anodic overpotential the working electrode was potentiostated back to its initial open-circuit potential, large (several mA/cm²) cathodic currents were observed. It can be speculated that the sudden increase in currents at high anodic overpotentials is a consequence of electrode surface oxidation. The oxidation potentials of nickel and cobalt are expected to be within the potential range of these steady-state experiments.

In order to gain some mechanistic understanding of the electrochemical process occurring it was of interest to make electrode kinetic measurements.

The measurement of the electrode kinetic parameters under the mixed-control conditions have been performed using transient potentiostatic techniques (12) on both nickel and cobalt electrodes under conditions of total and partial immersion in the candidate molten carbonate electrolytes. This technique involves applying a potential step to the nickel or cobalt working electrode, and recording the current as a function of time. Under such conditions of mixed control, the as-

Table I. Fuel gas composition calculated from the water-gas shift equilibrium reaction at 650°C

	%					
	H ₂	CO ₂	H ₂ O	CO	CH ₄	N ₂
High-BTU (53°C)*	60.0	7.42	22.47	10.11	—	—
Intermediate-BTU (71°C)*	40.5	16.4	32.8	10.3	—	—
Low-BTU (36°C)*	21.16	9.16	5.54	17.76	1.13	45.25
Very low-BTU (36°C)*	11.71	5.71	4.40	7.75	0.57	69.86
High-BTU (71°C)*	53.68	8.08	31.11	7.12	—	—

* Number in parentheses corresponds to the humidifier temperature.

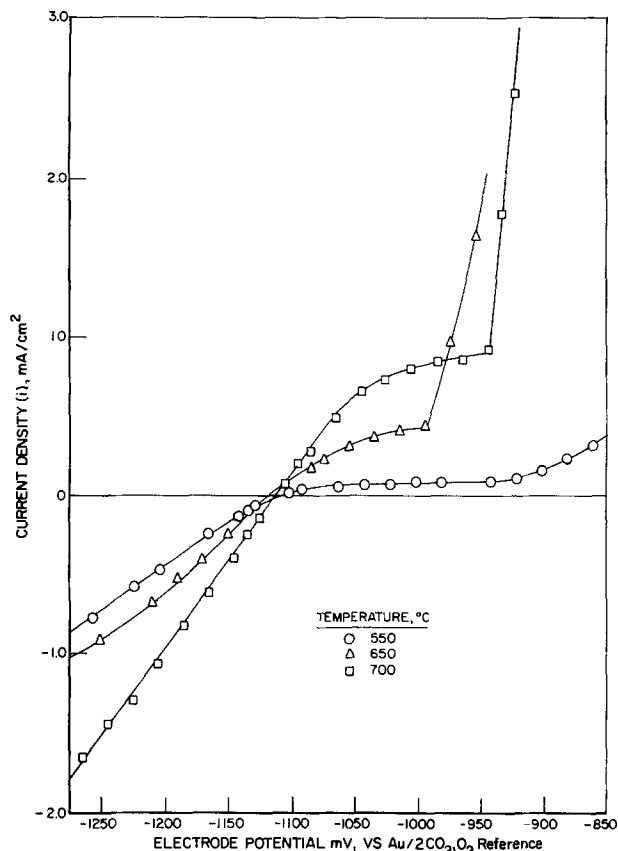


Fig. 3. Steady-state polarization curves for nickel in Li/Na/K carbonate melt.

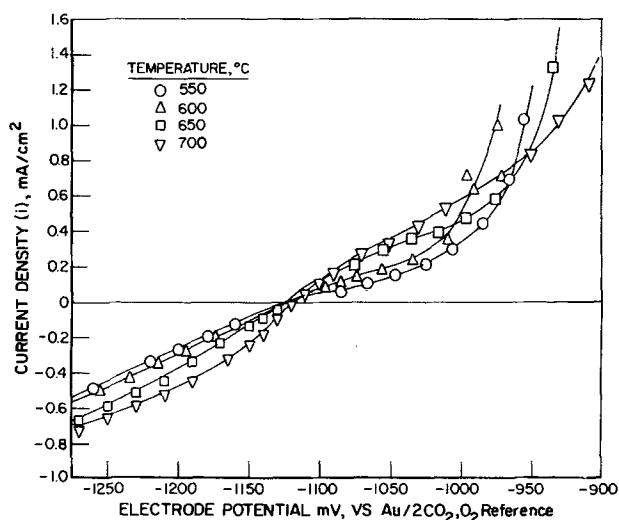


Fig. 4. Steady-state polarization curves for cobalt in Li/Na/K carbonate melt.

sumption is made that at time zero only activation control will be present; that is, sufficient supply of electroactive species will be present, together with minimum reaction products, so that any mass-transfer effects will be minimized. A typical oscillograph obtained using this transient potentiostatic technique is shown in Fig. 5. A 20 mV anodic voltage step (from the resting potential) is shown for a nickel electrode (top traces). The bottom traces show the current variations on three different time scales between 0.05 and 2.0 msec/div. Highest reproducibility of the kinetic current, $i(0)$, was obtained by extrapolating currents between 0.3 and 0.5 msec to time zero. Here, the kinetic current is found to be 39 mA/cm² for the Li/Na/K melt at 650°C in the intermediate-BTU fuel. Care was taken so that the extrapolated current values were free of interference

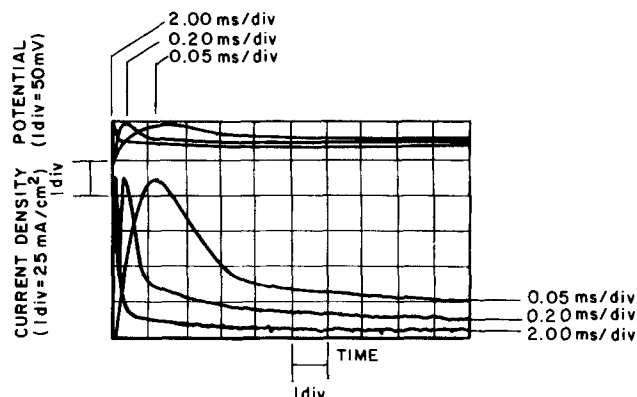


Fig. 5. IR-compensated potentiostatic measurement on nickel wire in Li/Na/K at 650°C with intermediate-BTU fuel [three time scales were used for potential (top traces) and current (bottom traces)].

from capacitive currents. With appropriate IR compensation the capacitive current can be clearly distinguished. Following the transient capacitive spike, the current can be seen to decrease because of diffusional processes.

This potential step technique has been applied to both nickel and cobalt electrodes in the three candidate molten carbonate mixtures discussed earlier. Various fuel compositions and different temperatures were used so that comparative kinetic data could be obtained from the three candidate melts. Extrapolated current densities at time zero $i(0)$ were plotted vs. the applied potential steps η . Figure 6 shows a representative activation polarization plot for nickel in the Li/Na/K ternary melt using intermediate-BTU fuel. For an activation-controlled process the current-voltage is given by the relationship

$$i(0) = i_0 [e^{\alpha_A \eta F/RT} - e^{-\alpha_C \eta F/RT}] \quad [1]$$

In the low overpotential region, this equation can be approximated by

$$i(0) \approx i_0 (\alpha_A + \alpha_C) \eta F/RT$$

or

$$i_0 \approx \frac{RT}{(\alpha_A + \alpha_C) F} \frac{di(0)}{d\eta} \quad [2]$$

Thus, the exchange current density, i_0 , can be calculated from the slope of the current density, $i(0)$, vs. overpotential, η , curve. We assume a value of 2 for the sum of the apparent transfer coefficient α_A and α_C based on a total of two electron transfer processes and a stoichiometric number 1. For the specific case above i_0 was

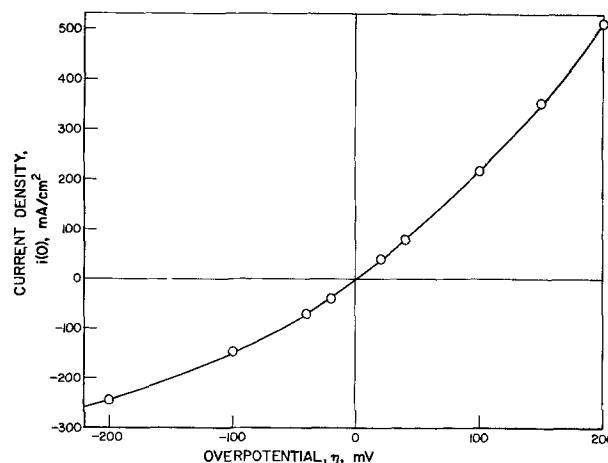


Fig. 6. Polarization curve at a nickel electrode from $i(0)$ values extrapolated via potential step technique (fuel: 40% H₂, 17% CO₂, 10% CO, and 33% H₂O at 650°C).

calculated using Eq. [2] to be 78 mA/cm² for a nickel electrode. This potential step technique was applied to electrodes that were both fully and partially immersed in molten carbonate mixtures. Under each experimental condition, the extrapolated kinetic current densities agreed within 20%, the major source of inaccuracy being caused by instrumentation noise effects in the fuel bubbled, partially raised, electrode case. This gave good support to the validity of this technique for separating activation kinetic data under the mixed-control conditions present.

Exchange current density values were also obtained from Allen-Hickling plots of the potential step data. For the Allen-Hickling plot, Eq. [1] can be rewritten as

$$\log \frac{i}{e^{(\alpha_A + \alpha_C)\eta F/RT} - 1} = \log i_0 - \frac{\alpha_C \eta F}{2.303RT} \quad [3]$$

If we assume $\alpha_A + \alpha_C = 2$, then a plot of

$$\log \frac{i}{e^{(\alpha_A + \alpha_C)\eta F/RT} - 1} \text{ vs. } \eta \quad [4]$$

can give the value of α_C from the slope and a value of i_0 from the intercept.

Typical Allen-Hickling plots at 650°C for nickel and cobalt are compared in Fig. 7 using intermediate-BTU fuel. From the intercept at zero overpotential, exchange current densities were generally found to be higher for nickel (85 mA/cm²) compared with those for cobalt (28 mA/cm²).

Agreement between 10 and 20% was generally found between exchange current density values obtained from low overpotential data and Allen-Hickling plots. The curves for the anodic and cathodic side of the Allen-Hickling plots shown in Fig. 7 differ for both cobalt and nickel, probably indicating a change in the reaction mechanism between the anodic and cathodic direction. The cathodic reaction mechanism has yet to be clarified.

From the anodic slope shown in Fig. 7 for nickel, we obtain $\alpha_A = 0.7$ and $\alpha_C = 1.3$, and for cobalt $\alpha_A = 0.74$ and $\alpha_C = 1.26$. From the cathodic slope, for nickel we obtain $\alpha_C = 0.48$ and $\alpha_A = 1.52$, and for cobalt $\alpha_C = 0.59$ and $\alpha_A = 1.41$.

The above charge-transfer coefficients given for the ternary melt are representative of values obtained for all three melts with the temperatures and fuel compositions used in this work.

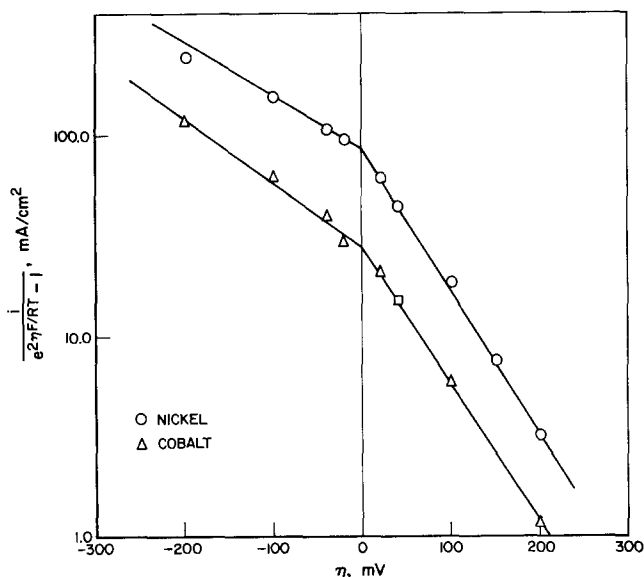


Fig. 7. Allen-Hickling polarization curve from potential step data (nickel and cobalt electrodes, Li/Na/K melt, intermediate-BTU fuel, 650°C)

In the high anodic overpotential region, oxidation of the electrode surface may become significant, giving currents higher than that caused by fuel oxidation only (see Fig. 3 and 4). This would result in higher α_A values in the anodic region. As a consequence, only data obtained from the low overpotential region was used for mechanistic interpretations. To gain more insight into the validity of the α_A and α_C values corresponding to fuel oxidation at nickel and cobalt electrodes, activation data were generated on a gold electrode in the Li/K melt at 650°C using intermediate-BTU fuel, as shown in Fig. 8. The corresponding Allen-Hickling plot from this activation data is shown in Fig. 9. Here we obtain $i_0 = 16$ mA/cm², $\alpha_C = 1.56$, and $\alpha_A = 0.44$. These values of α_A and α_C on a gold electrode where gold dissolution is absent are in close agreement to values obtained using nickel and cobalt electrodes. We can, therefore, tentatively conclude that nickel and cobalt anodic dissolution at low applied overpotentials is minimal and consequently the oxidation of fuel proceeds with $\alpha_C = 1.5$ and $\alpha_A = 0.5$ in the absence of electrode oxidation effects.

The dependency of the i_0 on hydrogen content is shown for both nickel and cobalt for the Li/K, Li/Na/K, and Li/Na melts at 650°C in Fig. 10, 11, and 12, respectively. In these figures, a straight line was drawn through the data points; however, those points falling off these lines should not be interpreted as experimental error, but rather as reflecting the interdependency between H₂, CO₂, H₂O, and CO by way of the water-gas shift reaction.

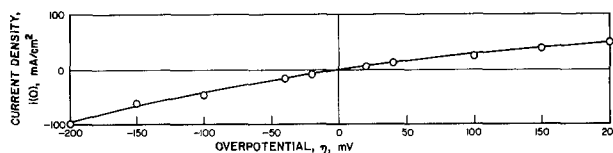


Fig. 8. Current-voltage characteristics from transient potentiostatic experiments on gold in 650°C Li/K melt with intermediate-BTU fuel.

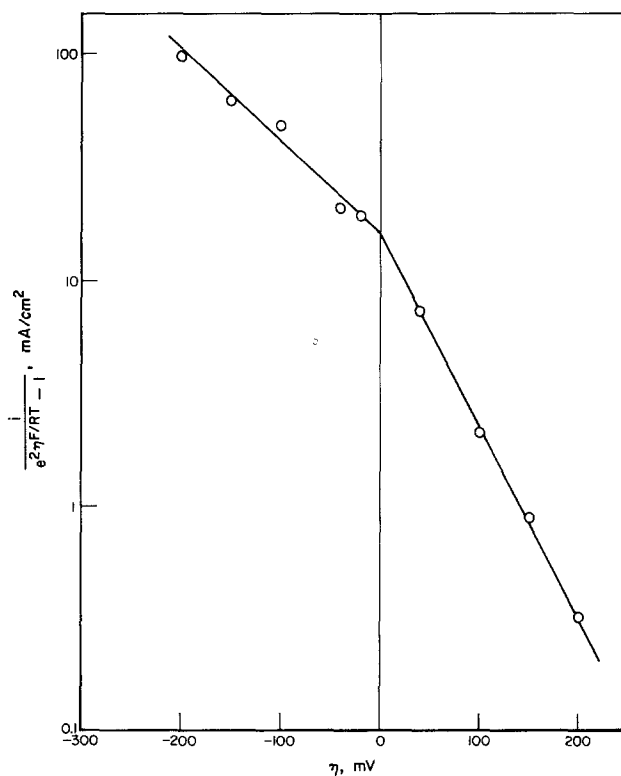


Fig. 9. Allen-Hickling polarization curve from potential step data (gold electrode, Li/K melt, intermediate-BTU fuel, 650°C).

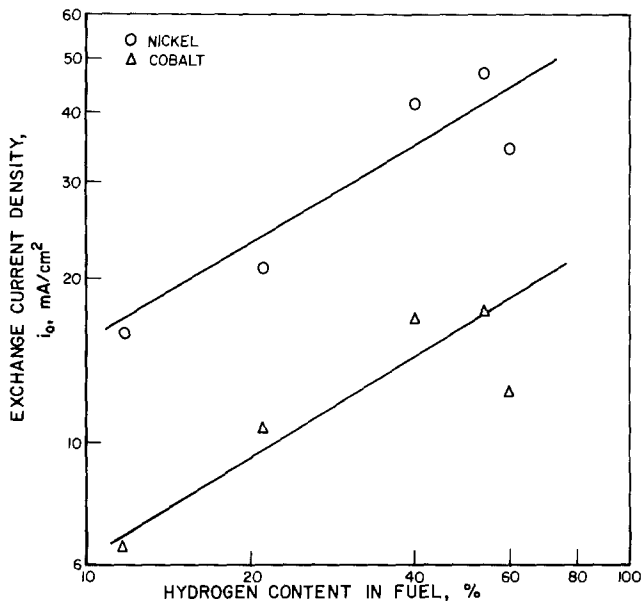


Fig. 10. Dependency of exchange current densities of nickel and cobalt on hydrogen content using various fuels (Li/K melt at 650°C).

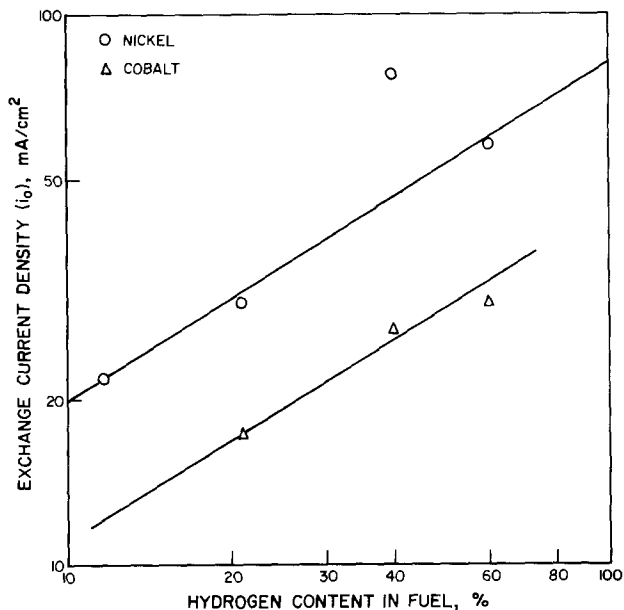
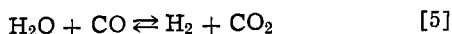


Fig. 11. Dependency of exchange current densities of nickel and cobalt on hydrogen content using various fuels (Li/Na/K melt at 650°C).



The slope of these lines would suggest an electrochemical reaction order parameter at constant overpotential of approximately 0.5 for hydrogen. However, this value could not be considered reliable since it is not possible to independently vary the hydrogen content without changing the overall gas composition (see Table I). The open-circuit potential of the working electrode upon changing the gas composition was observed to vary by around 60 mV, in agreement with calculated values.

An estimation of these electrochemical reaction order parameters at constant overpotential (13, 14) for hydrogen, carbon dioxide, and water in the fuel were calculated from the following equation

$$i_0 = k^* (\text{H}_2)^a (\text{CO}_2)^b (\text{H}_2\text{O})^c \quad [6]$$

where k^* is a proportionality constant; a , b , and c are, to a first approximation, the electrochemical reac-

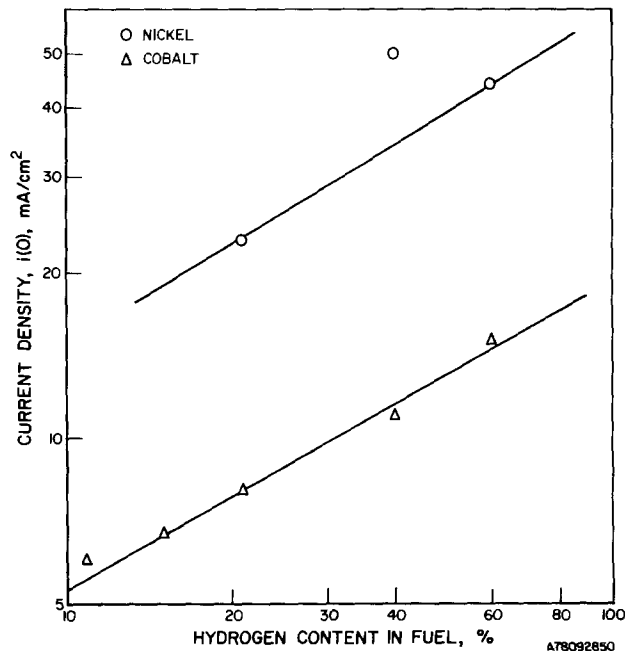


Fig. 12. Dependency of exchange current densities of nickel and cobalt on hydrogen content using various fuels (Li/Na melt) at 650°C.

tion order at constant overpotential for H₂, CO₂, and H₂O, respectively.

Knowing the respective concentrations of H₂, CO₂, and H₂O, then, by the water-gas shift reaction (Eq. [5]) the CO content is automatically fixed. If i_0 is measured in four different fuels, then the four unknowns k^* , a , b , and c can be determined. The above equation can be written in the logarithmic form

$$\log i_0 = k + a \log (\text{H}_2) + b \log (\text{CO}_2) + c \log (\text{H}_2\text{O}) \quad [7]$$

where $k = \log k^*$. Using i_0 values obtained with fuel gas compositions corresponding to high-, medium-, low-, and very-low-BTU fuel (Table I), Eq. [8] can be written in a matrix form, e.g., for nickel in Li/K

$$\begin{bmatrix} 1.54 \\ 1.62 \\ 1.34 \\ 1.20 \end{bmatrix} = \begin{bmatrix} 1 & -0.22 & -1.13 & -0.65 \\ 1 & -0.39 & -0.79 & -0.48 \\ 1 & -0.67 & -1.04 & -1.26 \\ 1 & -0.93 & -1.24 & -1.36 \end{bmatrix} \begin{bmatrix} k \\ a \\ b \\ c \end{bmatrix} \quad [8]$$

These linear simultaneous equations were solved on a programmable calculator to find the solution

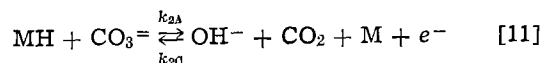
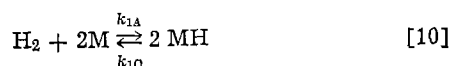
$$\begin{bmatrix} k \\ a \\ b \\ c \end{bmatrix} = \begin{bmatrix} 2.02 \\ 0.258 \\ 0.275 \\ 0.178 \end{bmatrix}$$

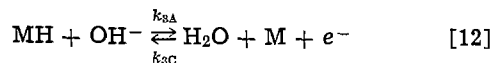
Thus, Eq. [7] can be written as

$$i_0 = 104.7 (\text{H}_2)^{0.258} (\text{CO}_2)^{0.275} (\text{H}_2\text{O})^{0.178} \quad [9]$$

A variety of approaches can be pursued for the development of the reaction mechanism (13-15). We have followed the general procedure described by Newman (13).

We considered several reaction mechanisms for fuel oxidation that might give the i_0 dependency shown in Eq. [9]. These mechanisms have been discussed by us at length in our earlier report (16). We have found the following reaction mechanism to satisfy this criterion





This mechanism assumes that (i) Eq. [11] is the rate-determining step; (ii) Langmuir adsorption isotherm; and (iii) there is low coverage, θ , of MH.

At equilibrium, one can write for Eq. [10]

$$\frac{\theta}{1 - \theta} = \left(\frac{k_{1A}}{k_{1C}} C_{\text{H}_2} \right)^{1/2} = K_1^{1/2} C_{\text{H}_2}^{1/2} \quad [13]$$

The net current from Eq. [12] is

$$i_3 = F[k_{3A}\theta C_{\text{OH}^-} - e^{\beta_3 FV/RT} - k_{3C} C_{\text{H}_2\text{O}}(1 - \theta) e^{-(1-\beta_3)FV/RT}] \quad [14]$$

V is the potential difference between the electrode and the electrolyte. At equilibrium, when $i_3 = 0$

$$C_{\text{OH}^-} = \frac{k_{3C}}{k_{3A}} C_{\text{H}_2\text{O}} \frac{1}{(K_1 C_{\text{H}_2})^{1/2}} e^{-FV/RT} \quad [15]$$

For Eq. [11] the net current is

$$i_2 = F[k_{2A}\theta C_{\text{CO}_3} = e^{\beta_2 FV/RT} - k_{2C} C_{\text{OH}^-} C_{\text{CO}_2} (1 - \theta) e^{-(1-\beta_2)FV/RT}] \quad [16]$$

Upon substitution for C_{OH^-} from Eq. [15] into the equilibrium expression for Eq. [16] for the equilibrium potential V_0 , we can write

$$e^{FV_0/RT} = \left[\frac{k_{2C}}{k_{2A}} \frac{k_{3C}}{k_{3A}} \frac{1}{K_1 C_{\text{H}_2}} \frac{C_{\text{H}_2\text{O}} C_{\text{CO}_2}}{C_{\text{CO}_3}} \right]^{1/2} \quad [17]$$

Replacing V for $V_0 + \eta$ in Eq. [16], where η is the overpotential, we obtain

$$i_2 = F \left\{ k_{2A}\theta C_{\text{CO}_3} = e^{\beta_2 F\eta/RT} \left[\frac{k_{2C}}{k_{2A}} \frac{k_{3C}}{k_{3A}} \frac{1}{K_1 C_{\text{H}_2}} \frac{C_{\text{H}_2\text{O}} C_{\text{CO}_2}}{C_{\text{CO}_3}} \right]^{\beta_2/2} - k_{2C} \frac{k_{3C}}{k_{3A}} \frac{C_{\text{H}_2\text{O}}}{(K_1 C_{\text{H}_2})^{1/2}} C_{\text{CO}_2} (1 - \theta) e^{(-2+\beta_2)F\eta/RT} \left[\frac{k_{2C}}{k_{2A}} \frac{k_{3C}}{k_{3A}} \frac{1}{K_1 C_{\text{H}_2}} \frac{C_{\text{H}_2\text{O}} C_{\text{CO}_2}}{C_{\text{CO}_3}} \right]^2 \right\} \quad [18]$$

From Eq. [13] for low coverage we have $\theta = K_1^{1/2} C_{\text{H}_2}^{1/2}$ and $1 - \theta \approx 1$. Thus, Eq. [18] becomes

$$i_2 = F \left\{ k_{2A} K_1^{1/2} C_{\text{H}_2}^{1/2} C_{\text{CO}_3} = \left[\frac{k_{2C}}{k_{2A}} \frac{k_{3C}}{k_{3A}} \frac{1}{K_1 C_{\text{H}_2}} \frac{C_{\text{H}_2\text{O}} C_{\text{CO}_2}}{C_{\text{CO}_3}} \right]^{\beta_2/2} e^{\beta_2 F\eta/RT} - k_{2C} \frac{k_{3C}}{k_{3A}} \frac{C_{\text{H}_2\text{O}}}{(K_1 C_{\text{H}_2})^{1/2}} C_{\text{CO}_2} e^{(-2+\beta_2)F\eta/RT} \left[\frac{k_{2C}}{k_{2A}} \frac{k_{3C}}{k_{3A}} \frac{1}{K_1 C_{\text{H}_2}} \frac{C_{\text{H}_2\text{O}} C_{\text{CO}_2}}{C_{\text{CO}_3}} \right]^2 \right\} \quad [19]$$

Comparing this with the general relationship for activation polarization

$$i = i_0 (e^{\alpha_A F\eta/RT} - e^{-\alpha_C F\eta/RT}) \quad [20]$$

we obtain

$$\alpha_A = \beta_2 \quad \text{assuming } \beta_2 = 0.5 \quad \text{we obtain } \alpha_A = 0.5$$

$$\alpha_C = 2 - \beta_2 \approx 1.5$$

The dependency of i_0 on the gases (for $\beta_2 = 0.5$) is

$$i_0 \sim [C_{\text{H}_2}]^{0.25} [C_{\text{CO}_2}]^{0.25} [C_{\text{H}_2\text{O}}]^{0.25} \quad [21]$$

The theoretical value of $\alpha_A = 0.5$ compares reasonably well with our experimentally determined α_A of 0.7 for nickel and cobalt and 0.5 for gold. Table II compares experimentally determined i_0 values at 650°C with those calculated, assuming electrochemical reaction order parameters at constant overpotential of 0.25 for H_2 , CO_2 , and H_2O on nickel anode in three different melts and with four gases. Similar data for cobalt is shown in Table III.

The highest exchange current densities were measured on nickel and cobalt in the Li/Na/K ternary melt with all fuel compositions used. In these tables, we can see that good agreement exists between experimental and calculated i_0 values.

We have seen in Fig. 1 and 2 that currents were dependent upon the rate of fuel bubbling through the melt. The current increased further when the nickel wire was partially raised from the electrolyte. This suggests that in this system the current is limited by the rate of fuel gas delivery through the melt into the electrode. In the porous electrode of an actual fuel cell, the situation is rather different, however. Fuel gas is delivered directly at the electrode from the rear side while the front side is facing the electrolyte tile. Thus, the gas can reach electroactive sites directly, or through a layer of melt, or by diffusion through the metal. Diffusion of hydrogen through nickel may be quite significant (17). Thus, there may be a very high local concentration of hydrogen in the porous electrode. The solubility of hydrogen in nickel at 650°C has been shown to be around 2.5×10^{-5} g mole/cm³ atm (18), and its diffusivity to be 3×10^{-5} cm²/sec (19).

We have seen from Eq. [9] that the exchange current density does not depend only on hydrogen concentra-

Table II. Exchange current densities, i_0 , for nickel in different melts and using various gases at 650°C

	Measured	Calculated
	mA/cm ²	
Li/K		
		$k^* = 110$
High-BTU	35.0	34.70
Medium-BTU	42.0	42.17
Low-BTU	21.0	19.84
Very low-BTU	16.0	14.37
Li/Na/K		
		$k^* = 299.09$
High-BTU	57.0	55.34
Medium-BTU	78.0	66.80
Low-BTU	30.0	31.44
Very low-BTU	22.0	22.78
Li/Na		
		$k^* = 135$
High-BTU	44.0	41.70
Medium-BTU	54.0	50.70
Low-BTU	23.0	23.85
Very low-BTU	—	17.30

Table III. Exchange current densities, i_0 , for cobalt in different melts and using various gases at 650°C

	Measured	Calculated
	mA/cm ²	
Li/K		
		$k^* = 45$
High-BTU	12.5	14.10
Medium-BTU	17.0	17.18
Low-BTU	10.7	8.08
Very low-BTU	6.5	5.90
Li/Na/K		
		$k^* = 71.59$
High-BTU	30.0	22.60
Medium-BTU	26.0	27.50
Low-BTU	17.4	13.00
Very low-BTU	10.5	9.40
Li/Na		
		$k^* = 55.2$
High-BTU	15.0	17.46
Medium-BTU	11.0	21.00
Low-BTU	8.0	9.90
Very low-BTU	6.7	7.20

tion but also on the other fuel components. In particular, the significance of water present in the melt appears to play an important role in the overall reaction rate.

Some preliminary work was performed on the temperature dependency of the exchange current density on nickel and cobalt electrodes in the Li/Na/K melt over the temperature range of 550°-700°C. No correction was made for changes in hydrogen concentrations caused by the temperature dependency of Eq. [5]. However, the calculated changes over this temperature range were below 10%. Figure 13 shows plots of $\log i_0$ vs. $1/T$ for nickel and cobalt using low-BTU fuel.

The activation energy (ΔE) was calculated from the relationship

$$\Delta E = \frac{R}{0.434} \frac{d(\log i_0)}{d(1/T)} \quad [22]$$

Here we get activation energies of 6.65 kcal/mole and 7.31 kcal/mole for nickel and cobalt, respectively.

Of the three molten carbonate compositions evaluated, the highest kinetic rates for fuel oxidation were found in the ternary melt of 43.5 m/o Li_2CO_3 -31.5 m/o Na_2CO_3 , and 25 m/o K_2CO_3 with both nickel and cobalt anodes. The higher α_A and i_0 values found for nickel and cobalt compared with those found for gold may indicate that stable surface oxide species may be responsible for the enhanced kinetics in the former two anode materials.

Comparison of the ionic conductivities at 600°C for all three melts gives values of $1.20 \Omega^{-1} \text{cm}^{-1}$, $1.15 \Omega^{-1} \text{cm}^{-1}$, and $1.79 \Omega^{-1} \text{cm}^{-1}$ for, respectively, the Li/Na/K, Li/K, and Li/Na melts. If ionic conductivity were the only consideration, then clearly the Li/Na melt would be favored. This melt, however, does not have such favorable kinetics as the ternary melt.

From a consideration of gas solubility of the three candidate melts, the highest values for both fuel and oxidant appear to occur in the ternary melt (20, 21), thereby possibly giving higher limiting current density values than the other two candidates. Some work has been reported (22) on the expected lifetimes of each of these melts, based upon projected carbonate vaporization losses and the corresponding extrapolated cell lifetimes. For the Li/Na/K, Li/K, and Li/Na carbonate melts at 600°C, projected cell lifetimes were, respectively, 6.4×10^5 , 6.3×10^5 , and 10.3×10^5 hr. Clearly, the Li/Na melt has a 40% greater projected lifetime compared with the other two melts.

The Li/Na/K melt is worthy of further consideration because of a higher fuel and oxidant solubility, faster electrode reactions for fuel oxidation, and, particularly, because its lower melting point, compared with the other two candidates, offers the possibility of operating the molten carbonate fuel cell at temperatures somewhat below the normal operating temperature of 650°C. This lower operating temperature may not only

extend the electrolyte tile life, but also that of the other fuel cell components. The relatively low activation energy values (≈ 7 kcal/mole) from the ternary melt, using both nickel and cobalt electrodes, also acts as further encouragement for low operating temperatures without sacrificing too much kinetic performance for the fuel oxidation reaction. However, at lower operating temperatures, diffusional factors may become predominant under the probable mixed-control conditions present.

Manuscript submitted Feb. 6, 1979; revised manuscript received ca. Dec. 15, 1979.

Any discussion of this paper will appear in a Discussion Section to be published in the December 1980 JOURNAL. All discussions for the December 1980 Discussion Section should be submitted by Aug. 1, 1980.

Publication costs of this article were assisted by the Institute of Gas Technology.

LIST OF SYMBOLS

i	current density
$i(0)$	kinetic current at time zero
i_0	exchange current density
η	overpotential
F	Faraday's constant
R	gas constant
T	absolute temperature
k^*	proportionality constant
k	$\log k^*$
a	reaction order parameter for H_2
b	reaction order parameter for CO_2
c	reaction order parameter for H_2O
θ	degree of electrode coverage
V	potential difference between electrode and electrolyte
V_0	equilibrium electrode potential
α_A	anodic transfer coefficient
α_C	cathodic transfer coefficient
β	symmetry coefficient

REFERENCES

- B. K. Andersen, Ph.D. Thesis, Technical University of Denmark, Lyngby (1975).
- J. R. Selman, H. C. Maru, V. Sampath, and L. G. Marianowski, in "Electrode Materials and Processes for Energy Conversion and Storage," J. D. E. McIntyre, S. Srinivasan, and F. G. Will, Editors, p. 656, The Electrochemical Society Softbound Proceedings Series, Princeton, N.J. (1977).
- H. C. Maru, A. Pigeaud, E. Ong, J. R. Selman, V. Sampath, L. G. Marianowski, and K. F. Blurton, Project 8984 Quarterly Status Report, July-October, 1976, Institute of Gas Technology, Chicago.
- L. P. Klevtsov, G. G. Arkhipov, and G. K. Stepanov, *Elektrokhimiya*, **3**, 785 (1967).
- G. H. J. Broers and M. Schenke in "Hydrocarbon Fuel Cell Technology," B. S. Baker, Editor, pp. 225-250, Academic Press, New York (1965).
- P. Degobert and O. Bloch, *Bull. Soc. Chim., Fr.*, 1887 (1962).
- M. L. Kronenberg, *This Journal*, **109**, 753 (1963).
- F. Will, *ibid.*, **110**, 152 (1963).
- M. B. Knaster and M. I. Temkin, *Dokl. Akad. Nauk SSSR*, **152**, 658 (1963).
- A. Borucka, *Electrochim. Acta*, **13**, 295 (1968).
- A. Borucka, *This Journal*, **124**, 972 (1977).
- H. Gerischer, *Z. Elektrochem.*, **59**, 604 (1955).
- J. Newman, "Electrochemical Systems," p. 175, Prentice-Hall, Englewood Cliffs, N.J. (1973).
- E. Gileadi, E. Kirowa-Eisner, and J. Penciner, "Interfacial Electrochemistry," p. 329, Addison-Wesley Publishing Company Inc., Reading, Mass. (1975).
- J. O'M. Bockris and A. K. N. Reddy, "Modern Electrochemistry," Plenum/Rosseta, New York (1973).
- IGT Final Technical Report; project 9105 Fuel Cell Research on Second-Generation Molten Carbonate Systems, p. 2-97, April 1979.
- A. D. S. Tantram, A. C. C. Tseung, and B. S. Harris, "Hydrocarbon Fuel Cell Technology," B. S.

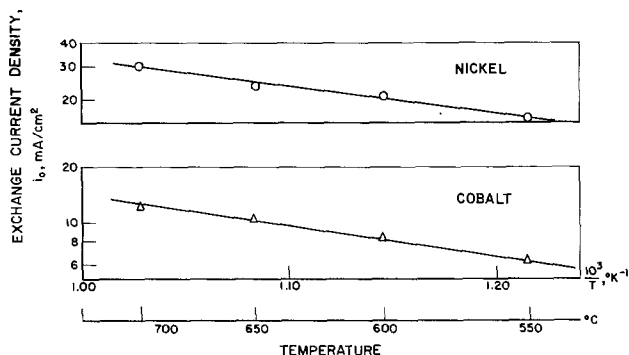


Fig. 13. Dependency on temperature of i_0 values obtained using transient potentiostatic measurements (nickel and cobalt electrodes in low-BTU fuel).

Baker, Editor, pp. 187-212, Academic Press, New York (1965).

18. R. Speiser, in "Metal Hydrides," W. M. Mueller *et al.* Editors, p. 87 (1968).
19. J. Volkl and G. Alefeld, in "Diffusion in Solids," A. S. Nowick and J. J. Burton, Editors, p. 231 (1975).
20. G. H. J. Broers, International Rept. No. 69-0667/1272-7211, Apeldoorn, Netherlands, Central Technisch Instituut T.N.O. (1969).
21. M. A. Volgin, A. L. L'vov, and V. A. Loskutkin, *Sov. Electrochem.*, **9**, 353 (1973).
22. H. C. Maru, J. Dullea, E. Ong, A. Pigeaud, V. Sampath, and J. R. Selman, Project 8984 Quarterly Status Report, October-December 1976, Institute of Gas Technology, Chicago.

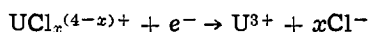
Electrochemistry of Uranium (IV) in Acidic AlCl₃-NaCl Melts at 175°C

F. Meuris, L. Heerman, and W. D'Olieslager

Laboratorium voor Radiochemie, Katholieke Universiteit te Leuven, Celestijnenlaan 200 F, 3030 Heverlee, Belgium

ABSTRACT

Solutions of uranium (IV) in acidic AlCl₃-NaCl melts (52-70 mole percent AlCl₃) at 175°C were prepared by dissolving uranium (IV) oxide or chloride. The electrochemistry of uranium (IV) in these melts, investigated by pulse polarography and cyclic voltammetry, corresponds to two reversible one-electron reactions. For the U(IV)/U(III) redox couple, the reaction is given by



where $3 \geq x \geq 1$, the lower values of x being found for the most acidic melts. Thus, uranium (IV) exists in solution as UCl₃⁺, UCl₂²⁺, and UCl³⁺. For the U(V)/U(IV) redox couple, the reaction is written as



where $(y-x) = 3$ over almost the entire $p\text{Cl}$ range covered in this work. Therefore, the uranium (V) species in solution are formulated as UCl₆⁻, UCl₅, and UCl₄⁺. However, since some oxide impurities are probably always present in molten chloroaluminates, the existence of a UOCl_y^{(3-y)+} species cannot be totally excluded.

The electrochemical behavior of uranium (IV) oxide (UO₂) and uranium (VI) oxide (UO₃) in the NaCl-saturated AlCl₃-NaCl melt at 175°C was reported previously (1). This paper reports some results on the electrochemistry of uranium (IV) in acidic melts [52-70 mole percent (m/o) AlCl₃] at the same temperature. Morrey (2) investigated the absorption spectrum of UCl₄ in AlCl₃-KCl melts and concluded that his data are consistent with the postulate that the species is U(AlCl₄)_x^{(4-x)+} (such as U(AlCl₄)₆²⁻; the coordination number of the uranium species is six or less) is present in solutions containing an excess of AlCl₃. The same author also determined the solubility of UCl₄ in AlCl₃-KCl melts as a function of the temperature (250°-400°C). A rough extrapolation of the data given in his paper indicates a solubility of approximately $2 \times 10^{-2}\text{M}$ (after conversion from mole fraction to molar concentrations) for a melt with a 55 m/o AlCl₃-45 m/o KCl composition at 175°C. In this work, solutions of uranium (IV) were prepared by dissolving either uranium (IV) oxide (UO₂) or uranium (IV) chloride (UCl₄) and it was found possible to use concentrations as high as $4 \times 10^{-2}\text{M}$, at least in more acidic solutions.

Experimental

All experiments were carried out in Pyrex glass cells (with a tight fitting Teflon top) (3) under a purified nitrogen atmosphere (VAC dry box equipped with a Model HE-493 Dri-Train for constant recirculation of the inert gas through a column of activated copper and molecular sieves). A homemade proportional temperature controller with a Chromel-Alumel

Key words: uranium, fused salts, AlCl₃-NaCl melt, pulse polarography, cyclic voltammetry.

Pyrex-sheathed thermocouple was used to maintain the temperature of the melts at $175^\circ \pm 1^\circ\text{C}$.

The NaCl-saturated AlCl₃-NaCl melt was prepared and purified by the procedure described by Boxall *et al.* (3). The melts were acidified by adding solid AlCl₃ (Fluka AG; puriss.) which was purified by sublimation in sealed glass ampuls (samples which remained colored after sublimation were rejected). The $p\text{Cl}$ of the melts was calculated from the potential of an aluminum wire electrode (Alfa Inorganics; m5N) using the equilibrium constants given by Boxall *et al.* (4).

The working electrodes used for cyclic voltammetry and pulse polarography were made by sealing a 3 mm diam tungsten rod (Alfa Inorganics; m3N8) or a glassy carbon rod (Le Carbone-Lorraine) in a Pyrex glass tube. A tungsten foil electrode (3 × 3 cm; Alfa Inorganics; m3N8) was used for the coulometry experiments. The reference electrode was a 1 mm diam aluminum wire spiral placed in a separate compartment with a leak-free ceramic filter tip. The reference electrode compartment was filled with a NaCl-saturated AlCl₃-NaCl melt. The potential of this reference electrode against an aluminum electrode in a 1:1 melt (50 m/o AlCl₃) was calculated as -0.176V and corresponds well with the value quoted by Bartak and Osteryoung (5), $-0.175 \pm 0.001\text{V}$ [for the calculation, the composition of the NaCl-saturated melt was taken as 49.75 m/o AlCl₃ (6)]. The aluminum counterelectrode was also placed in separate compartment.

Uranium (VI) oxide (UO₃), uranium (IV) oxide (UO₂), and uranium (IV) chloride (UCl₄) (all obtained from Alfa Inorganics) were used as received. The uranium content of the melts was determined by standard analytical procedures and converted to

molar concentrations using the density data of Fannin *et al.* (7).

A PAR Model 173/176 potentiostat, a PAR Model 175 function generator, and a Houston Model 2000 X-Y recorder were used for cyclic voltammetry. A PAR Model 379 digital coulometer was used for controlled-potential coulometry. A Tacussel unit UAP-4 was used for pulse polarography. Potentials were measured with a Beckman Model 4500 digital pH meter.

Results and Discussion

Experiments with solutions of uranium (IV) oxide (UO_2).—The cyclic voltammograms of uranium (IV) oxide solutions for different melt acidities, shown in Fig. 1, exhibit two well-defined reduction-oxidation waves (peaks A/A' and B/B'). Controlled-potential coulometry at 1.1V indicates a one-electron reduction ($n = 1.01 \pm 0.04$) and, therefore, peaks A/A' are attributed to the U(IV)/U(III) redox couple.

The separation between the cyclic voltammetric peaks, approximately 0.090V, is very close to its theoretical value (0.086V) and is independent of the scan rate, as is expected for a reversible electrode reaction (results obtained with either tungsten or glassy carbon electrodes are identical). The peak potentials shift toward more positive values as the acidity of the melt is increased, but quantitative data on this point are given in a separate section. The peak heights ($i_p^A/i_p^{A'} \cong 1$) increase linearly with $v^{1/2}$ ($v =$ scan rate; 0.020–0.400 V/sec) and with the concentration (0.93 – $4.25 \times 10^{-2}M$). Furthermore, the peak heights are independent of the acidity of the melt.

The second reduction-oxidation wave, peaks B/B', is observed at rather positive potentials, very close to the potential limit of the solvent. For this reason, only the height of the anodic peak B' can be measured accurately (and then only if the acidity of the melt is not too high). This peak has almost the same height as peaks A/A' and, therefore, peaks B/B' are attributed to the U(V)/U(IV) redox couple.

The peak separation is again independent of the scan rate and close to its theoretical value for a

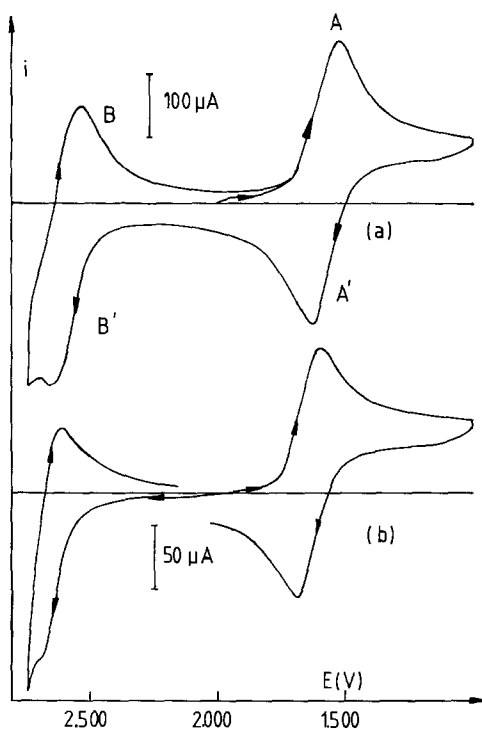


Fig. 1. Cyclic voltammogram of uranium (IV) oxide solution. Area of tungsten indicator electrode = 7.07 mm^2 . Scan rate = 0.1 V/sec . (a) Mole percent $\text{AlCl}_3 = 59.0$; uranium concentration = $3.13 \times 10^{-2} \text{ mole/liter}$, (b) $m/o \text{ AlCl}_3 = 65.0$; uranium concentration = $1.63 \times 10^{-2} \text{ mole/liter}$.

reversible one-electron process. Solutions of uranium (V) can be prepared by the controlled-potential oxidation of uranium (IV) solutions but some evolution of chlorine is difficult to avoid at the positive potentials necessary for the reaction to be complete.

A normal pulse polarogram and a differential pulse polarogram of a uranium (III) solution (prepared by the controlled-potential reduction of uranium (IV)) are shown in Fig. 2. The plots of $\log(i/i_d - i)$ vs. E , shown in Fig. 3, have slopes of 0.088V for the U(IV)/U(III) couple and 0.085V for the U(V)/U(IV) couple,

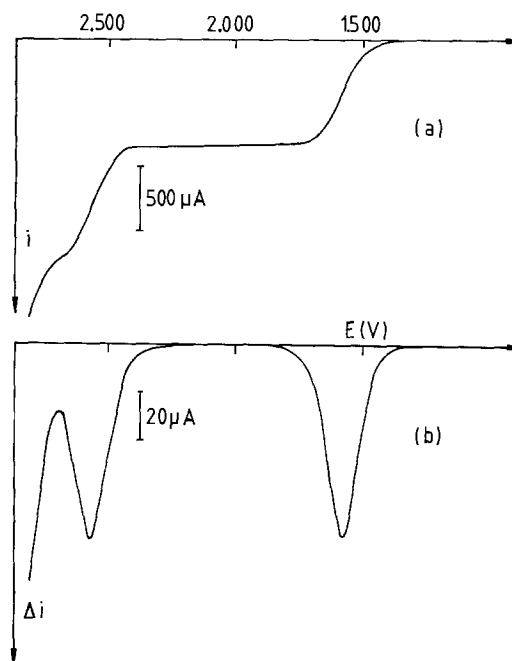


Fig. 2. Normal pulse polarogram (a) and differential pulse polarogram (b) of uranium (III) solution. Area of tungsten indicator electrode = 7.07 mm^2 . Scan rate = 2 mV/sec . Mole percent $\text{AlCl}_3 = 59.2$. Uranium concentration = $2.88 \times 10^{-2} \text{ mole/liter}$. Normal pulse polarogram: pulse width = 50 msec ; pulse delay = 200 msec ; current sampling = 80 – 85% . Differential pulse polarogram: pulse width = 50 msec ; pulse delay = 300 msec ; current sampling = 40 – 60% ; pulse amplitude = 10 mV .

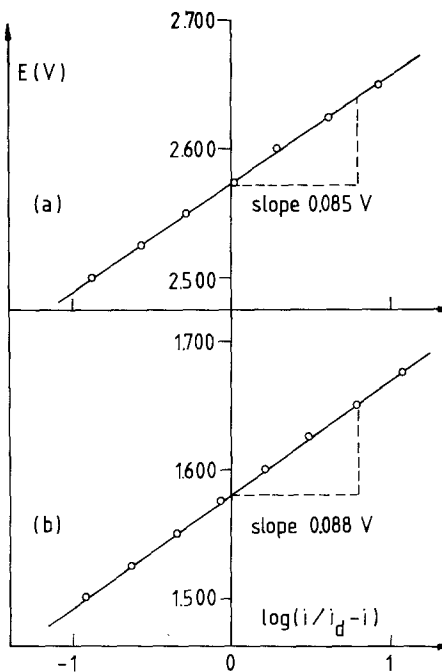


Fig. 3. Logarithmic analysis of the normal pulse polarogram of Fig. 2. (a) U(V)/U(IV) wave, (b) U(IV)/U(III) wave.

indicating the reversibility of the electrode reactions (the Nernst slope for a one-electron process is 0.089V at 175°C). The peak heights determined from differential pulse polarography increase linearly with the concentration and with the pulse amplitude as is shown in Fig. 4. From the data of this figure, the diffusion coefficient of the uranium (IV) species was calculated as $D = 2.98 \pm 0.24 \times 10^{-6}$ cm²/sec (cyclic voltammetry gives $D = 2.85 \pm 0.30 \times 10^{-6}$ cm²/sec; since $i_p^A/i_p^{A'} \cong 1$, the diffusion coefficient of the uranium (III) species has approximately the same value).

Experiments with solutions of uranium (IV) chloride (UCl₄).—A series of experiments was performed with solutions of uranium (IV) chloride. The cyclic voltam-

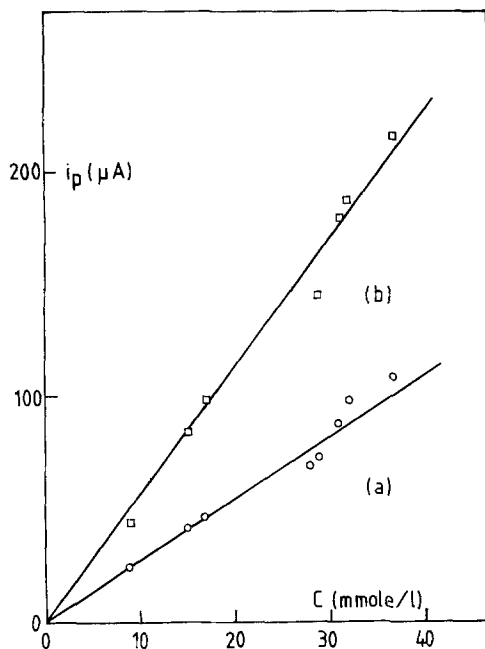


Fig. 4a. Peak height of differential pulse polarograms vs. uranium (IV) oxide concentration for the U(V)/U(IV) wave. Pulse amplitude = 10 mV (a) 20 mV (b). Other conditions as for Fig. 2.

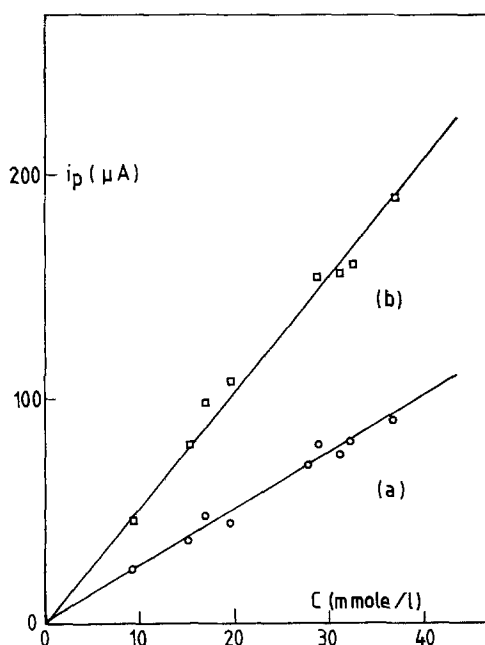


Fig. 4b. Peak height of differential pulse polarograms vs. uranium (IV) oxide concentration for the U(IV)/U(III) wave. Pulse amplitude = 10 mV (a) 20 mV (b). Other conditions as for Fig. 2.

mogram of such a solution, shown in Fig. 5, exhibits the same reduction-oxidation waves as described in the preceding section. It turns out indeed that the results obtained with solutions of uranium (IV) chloride and uranium (IV) oxide are identical. This indicates that the same uranium species (for the different oxidation states participating in the electrode reactions) are present in solution, irrespective of whether the solutions are prepared by dissolving either the oxide or the chloride.

Experiments with uranium (VI) oxide (UO₃).—Uranium (VI) oxide (UO₃) reacts with the melt to give solutions of uranium (V) as can be expected from the results presented in the preceding sections. Normal and differential pulse polarograms of the resulting solution are shown in Fig. 6 (these polarograms were recorded approximately 90 min after adding uranium (VI) oxide to the melt). The waves for the reduction of uranium (V) to uranium (IV) and uranium (III) are already described in the preceding section. However, an additional wave is observed at about 1.87V (for the polarograms of Fig. 6). This wave is much higher when a polarogram is recorded

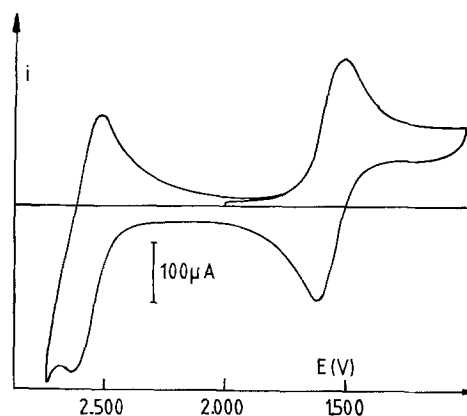


Fig. 5. Cyclic voltammogram of uranium (IV) chloride solution. Area of tungsten indicator electrode = 7.07 mm². Scan rate = 0.1 V/sec. Mole percent AlCl₃ = 58.5. Uranium concentration = 3.00×10^{-2} mole/liter.

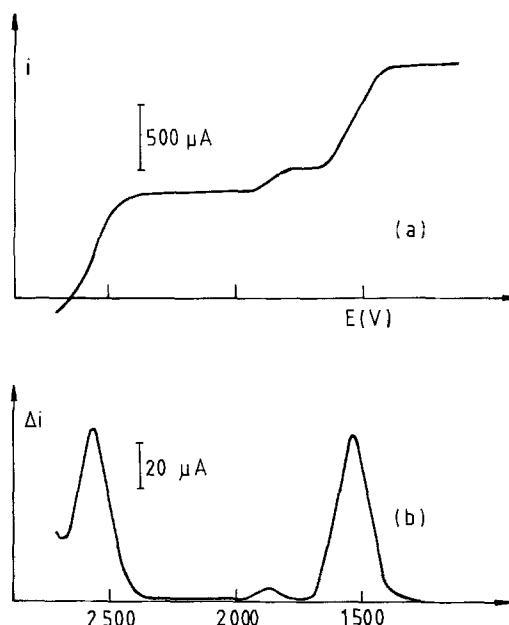
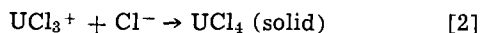
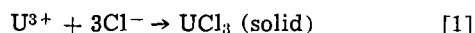


Fig. 6. Normal pulse polarogram (a) and differential pulse polarogram (b) recorded approximately 90 min after the addition of uranium (VI) oxide to the melt. Mole percent AlCl₃ = 56.8. Uranium concentration = 2.79×10^{-2} mole/liter. Other conditions as for Fig. 2.

immediately after adding uranium (VI) oxide to the melt but decreases rapidly with time and finally disappears completely. Therefore, it is believed that this wave is due to the reduction of a product formed in the reaction between UO_3 and the melt. However, because of its transient nature, this species has not been identified.

Effect of melt composition on half-wave potentials.—Nernst plots constructed from potential measurements during the controlled-potential reduction or oxidation of uranium (IV) solutions are shown in Fig. 7. The standard potentials determined from these measurements and the half-wave potentials obtained from differential pulse polarography and cyclic voltammetry are plotted vs. $p\text{Cl}$ (molar fraction scale) in Fig. 8 and 9 for the U(IV)/U(III) and U(V)/U(IV) redox couples, respectively. The values obtained with either uranium (IV) oxide or uranium (IV) chloride solutions fit nicely on the same lines for both redox couples. Numerical data are given in Table I.

Poturaj-Gutniak (8) concluded from spectral data that uranium (III) exists in acidic $\text{AlCl}_3\text{-NaCl}$ melts either as U^{3+} or as a chlorocomplex (he formulated the species quite generally as $\text{U}(\text{Al}_2\text{Cl}_7)_n\text{Cl}_{3-n}$; for the sake of brevity, solvation by Al_2Cl_7^- ions is omitted further in this paper). Gilbert *et al.* (9) studied the precipitation of uranium (III) and uranium (IV) from acidic $\text{AlCl}_3\text{-NaCl}$ melts at 175°C by cyclic voltammetry and pulse polarography and concluded that the reactions are given by



According to these authors (9), the differences observed by Morrey (2) between the spectrum of uranium (IV) in basic and acidic chloroaluminate melts can be accounted for by the transition from UCl_6^{2-} to UCl_3^+ species.

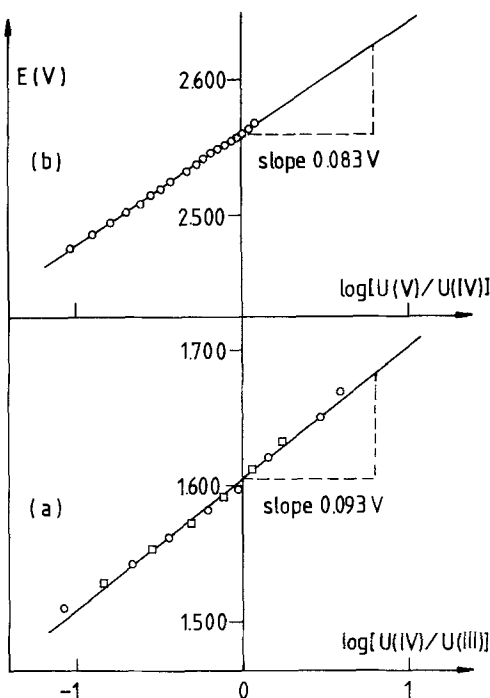


Fig. 7. Nernst plot obtained from potential measurements during the coulometric titration of uranium (IV) oxide solutions. (a) Reduction of uranium (IV) solutions (circles) and reoxidation of the reduced solution (squares); $m/o \text{ AlCl}_3 = 61.4$; uranium concentration = 2.29×10^{-2} mole/liter. (b) Oxidation of uranium (IV) solution (the potential was kept constant during the oxidation at a value slightly more positive than the half-wave potential of the U(V)/U(IV) wave; $m/o \text{ AlCl}_3 = 58.2$; uranium concentration = 1.57×10^{-2} mole/liter.

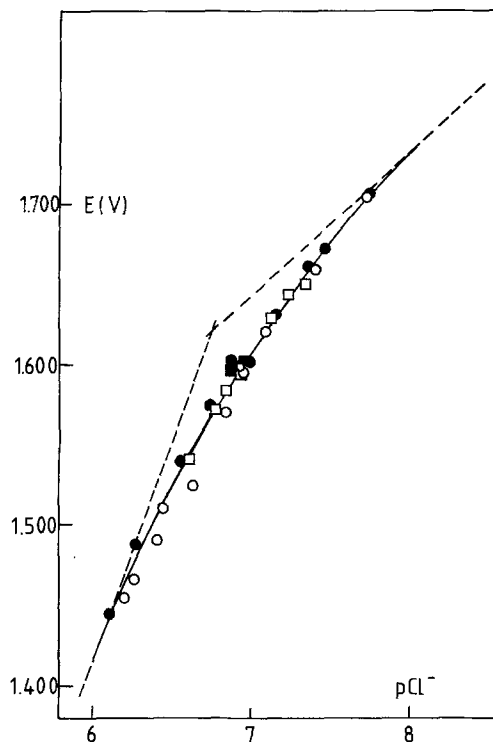


Fig. 8. Effect of the melt composition on the half-wave potentials of the U(IV)/U(III) wave. Values of $p\text{Cl}$ are given in the molar fraction scale. The broken lines are drawn with slopes of 0.267 and 0.089V, respectively. \circ , Differential pulse polarography of UCl_4 solutions, other experiments with UO_2 solutions; \bullet , pulse polarography; \square , cyclic voltammetry; \blacksquare , emf measurements.

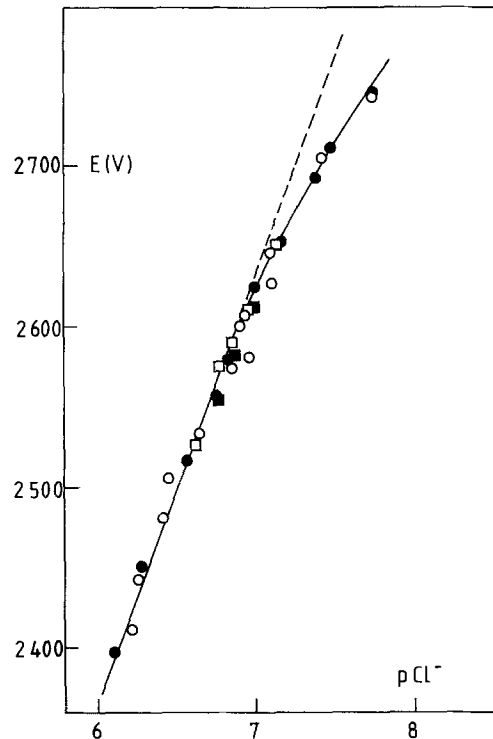


Fig. 9. Effect of the melt composition on the half-wave potentials of the U(V)/U(IV) wave. Values of $p\text{Cl}$ are given in the molar fraction scale. The broken line is drawn with a slope of 0.267V. \circ , Differential pulse polarography of UCl_4 solutions, other experiments with UO_2 solutions; \bullet , pulse polarography; \square , cyclic voltammetry; \blacksquare , emf measurements.

If one accepts that uranium (III) exists in solution as the U^{3+} ion, then the electrode reaction for the U(IV)/U(III) couple can be written as

Table I. Half-wave potentials of the U(V)/U(IV) and U(IV)/U(III) redox couples in acidic AlCl_3 -NaCl melts at 175°C (a)

Mole % AlCl_3	pCl	$E_{1/2}$ (V/IV)	$E_{1/2}$ (IV/III)	Remark
70.75	7.76	2.745	1.705	(b)
67.65	7.48	2.711	1.672	(b)
66.65	7.38	2.692	1.661	(b)
64.25	7.17	2.653	1.631	(b)
61.75	6.99	2.625	1.603	(b)
60.35	6.91	2.599	1.604	(b)
59.30	6.83	2.580	1.582	(b)
58.30	6.76	2.565	1.575	(b)
56.05	6.57	2.516	1.540	(b)
53.70	6.28	2.451	1.488	(b)
52.65	6.10	2.396	1.445	(b)
66.25	7.35	—	1.650	(c) (d)
65.05	7.24	—	1.643	(c) (d)
63.80	7.14	2.652	1.628	(c)
60.95	6.94	2.610	1.595	(c)
59.45	6.85	2.590	1.582	(c)
58.40	6.77	2.577	1.572	(c)
61.40	6.97	—	1.601	(e)
60.80	6.88	—	1.595	(e)
61.90	7.00	2.612	—	(f)
59.60	6.86	2.583	—	(f)
58.20	6.75	2.559	—	(f)
70.70	7.74	2.743	1.705	(g)
67.10	7.42	2.705	1.660	(g)
63.40	7.10	2.628	1.620	(g)
63.25	7.07	2.645	1.620	(g)
61.45	6.97	2.580	1.595	(g)
60.85	6.94	2.607	1.600	(g)
59.50	6.85	2.575	1.570	(g)
56.80	6.64	2.533	1.525	(g)
54.95	6.45	2.505	1.510	(g)
54.60	6.41	2.480	1.490	(g)
53.50	6.26	2.442	1.465	(g)
53.25	6.21	2.410	1.455	(g)

(a) Potentials are given in volts against the Al(III)/Al(O) electrode in the NaCl-saturated AlCl_3 -NaCl melt; pCl values are expressed in the molar fraction scale.

(b) From differential pulse polarography of uranium (III) solutions prepared by controlled potential reduction of uranium (IV) oxide solutions; concentration $9.30 \times 10^{-3}\text{M}$; precipitation of UCl_4 (and UCl_3) is observed for pCl < 6.1.

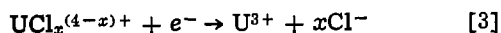
(c) From cyclic voltammetry of uranium (IV) oxide solutions; concentration $1.82 \times 10^{-2}\text{M}$.

(d) Peaks for U(V)/U(IV) couple are distorted by chlorine evolution.

(e) From emf measurements; coulometric reduction of uranium (IV) oxide solutions.

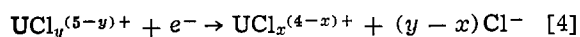
(f) From emf measurements; coulometric oxidation of uranium (IV) oxide solutions.

(g) From differential pulse polarography of uranium (IV) chloride solutions.

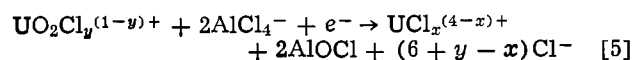


The slope in Fig. 8 diminishes from approximately 0.267V ($x = 3$) to 0.089V ($x = 1$) as the acidity of the melt increases in the range $6.1 \leq \text{pCl} \leq 7.8$. The slope of 0.267V, which is obtained as a limiting value for the lowest pCl values used in this work, is in agreement with the work of Gilbert *et al.* (9). Thus, the results reported here confirm the existence of UCl_3^+ in the less acidic solutions used in this work (just before the precipitation of UCl_4). In the more acidic region, however, the species in solution must be formulated as UCl_2^{2+} and UCl^{3+} . It is perhaps worthwhile to note that a vapor complex between uranium tetrachloride and aluminum chloride, $\text{UCl}_2(\text{AlCl}_3)_2$, has been described by Gruen and McBeth (10, 11).

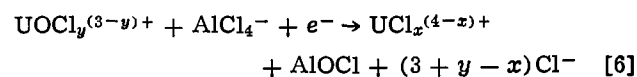
The electrode reaction for the U(V)/U(IV) redox couple can be written similarly as



The slope in Fig. 9 is 0.267V ($y - x = 3$) in the range $6.1 \leq \text{pCl} \leq 7$ and diminishes somewhat as the acidity of the melt is increased. The uranium (V) species in solution can then be formulated as UCl_6^- , UCl_5 , UCl_4^+ , and UCl_3^{2+} (with increasing acidity of the melt). However, since some oxide impurities are probably always present in molten chloroaluminates (12), reactions such as



and



cannot be excluded *a priori* [AlOCl is the aluminum oxochloro complex most likely present in acidic melts (13)]. The variation of the half-wave potentials expected for reaction [5] ($dE_{1/2}/d\text{pCl} = 6 + y - x$) is much greater than was actually found in the experiments. On the same basis, however, reaction [6] and thus the existence of $\text{UOCl}_y^{(3-y)+}$ species cannot be totally excluded. Nevertheless, the existence of uranium (V) chloro complexes is not altogether unexpected. A vapor complex between uranium pentachloride and aluminum chloride, formulated as $\text{UCl}_5 \cdot \text{AlCl}_3$, has been described by Gruen and McBeth (11). Furthermore, UCl_6^- is a well-known species in a number of nonaqueous solvents. For example, solutions of UCl_6^- in thionyl chloride are readily obtained by dissolving uranium trioxide in the refluxing solvent (14, 15); these solutions are quite stable toward hydrolysis and/or disproportionation (16) and a number of hexachloro-uranates (V), MUCl_6 , can be obtained from these solutions (15, 17). Since the spectrum of UCl_6^- is well-known (18), spectroscopic measurements would be helpful to confirm the existence of the uranium (V) species postulated in this paper.

Acknowledgment

The authors wish to express their thanks to the I.K.W., Belgium, for the financial support of this research and for granting a fellowship to one of them (F. M.). Part of the work described in this paper was presented at the Journées d'Etudes des Sels Fondus, Liège, Belgium, June 6-8, 1979.

Manuscript submitted July 27, 1979; revised manuscript received Jan. 3, 1980.

Any discussion of this paper will appear in a Discussion Section to be published in the December 1980 JOURNAL. All discussions for the December 1980 Discussion Section should be submitted by Aug. 1, 1980.

Publication costs of this article were assisted by Katholieke Universiteit te Leuven.

REFERENCES

1. F. Meuris, L. Heerman, and W. D'Olieslager, Paper presented at the 7th EuChem Conference on Molten Salts, Lysekil, Sweden, June 19-23, 1978, ZAED Library, B12-4882 (1978).
2. J. R. Morrey, *Inorg. Chem.*, **2**, 163 (1963).
3. L. G. Boxall, H. L. Jones, and R. A. Osteryoung, *This Journal*, **121**, 212 (1974).
4. L. G. Boxall, H. L. Jones, and R. A. Osteryoung, *ibid.*, **120**, 223 (1973).
5. D. E. Bartak and R. A. Osteryoung, *J. Electroanal. Chem.*, **74**, 69 (1976).
6. G. Torsi and G. Mamantov, *Inorg. Chem.*, **10**, 1900 (1971).
7. A. A. Fannin, F. C. Kibler, L. A. King, and D. W. Seegmiller, *J. Chem. Eng. Data*, **19**, 266 (1974).
8. S. Poturaj-Gutniak, *Nukleonika*, **14**, 269 (1969).
9. B. Gilbert, J. P. Schoebrechts, and G. Duykaerts, Paper presented at the Journées d'Etude des Sels Fondus, Liège, Belgium, June 6-8, 1979.
10. D. M. Gruen and R. L. McBeth, *Inorg. Nucl. Chem. Lett.*, **4**, 299 (1968).
11. D. M. Gruen and R. L. McBeth, *Inorg. Chem.*, **8**, 2625 (1969).
12. N. J. Bjerrum, R. Fehrman, and J. H. von Barner, Paper presented at the 30th ISE Meeting, Trondheim, Norway, Aug. 26-31, 1979; Extended Abstracts, p. 254.
13. B. Gilbert and R. A. Osteryoung, *J. Am. Chem. Soc.*, **100**, 2725 (1978).
14. D. C. Bradley, B. B. Chakravarti, and A. K. Chatterjee, *J. Inorg. Nucl. Chem.*, **3**, 367 (1957).
15. K. W. Bagnall, D. Brown, and J. G. H. du Preez,

J. Chem. Soc., 1965, 5217.
16. D. Brown, "Halides of the Lanthanides and Actinides," p. 129, Wiley-Interscience, New York (1968).

17. E. Stump and G. Piltz, *Z. Anorg. Allg. Chem.*, **409**, 53 (1974).

18. J. Selbin, J. D. Ortego, and G. Gritzner, *Inorg. Chem.*, **7**, 976 (1968).

Fluoride Electrodes with Reversible Solid-State Contacts

T. A. Fjeldly* and K. Nagy

Electronics Research Laboratory and Division of Applied Chemistry, SINTEF, The University of Trondheim, The Norwegian Institute of Technology, N-7034 Trondheim—NTH, Norway

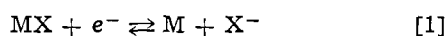
ABSTRACT

Fluoride-selective LaF_3 membranes with reversible solid-state contacts have been prepared as layered structures of LaF_3 , AgF , and Ag . In this report the preparation and properties of such contacts are discussed. All-solid-state fluoride electrodes with the present membrane structures have been tested, and the results compare favorably with those of conventional electrodes with internal filling solution.

With the advance of microelectronic techniques in the manufacture of ion-selective electrodes, a growing need for suitable solid-state inner membrane contacts has emerged. Solid contacts are more compatible with microelectronic manufacturing techniques than the conventional solution contacts, but also offer advantages in terms of miniaturization and electrode ruggedness, and permit the construction of electrodes that can withstand high temperature and pressure (i.e., autoclaving).

In order to achieve the desired electrode quality in terms of sensitivity, response time, and stability, it is essential to use reversible membrane contacts. Reversibility is assured when a unique electrode reaction occurs when the electrode operates as an anode, and the inverse of the same reaction takes place when it operates as a cathode. Furthermore, at zero current, the contacted materials should be in thermodynamic equilibrium (1). Thus, nonreversibility does not assure thermodynamic equilibrium, and long-term potential drift can generally be expected (2). These effects depend on the rate of relaxation processes, for instance at the blocked interface between an electronic and an ionic conductor (3). In the basic ISFET (ion sensitive field effect transistor), like in conventional glass membranes, deviation from thermodynamic equilibrium within the membranes is responsible for increased response time (4). With a regular MOSFET (metal oxide field effect transistor) connected properly to an ion-selective membrane (4-6), the potential gradient across the oxide layer also represents a lack of thermodynamic equilibrium, but here the relaxation processes proceed extremely slowly and will normally not interfere with the measurements.

For the case of a solid junction between an electronic and an ionic conductor, reversibility is normally achieved when the parent metal M is in contact with a solid electrolyte MX . The reversible reaction taking place at the interface is then



Other metal contacts are also possible provided their salt formation free energies are positive relative to the parent metal (7). Thus, the construction of proper contacts is straightforward in the case of the silver salt membranes (5, 7), where silver metal is conveniently used.

Similarly, the natural choice in the case of LaF_3 appears to be lanthanum metal. However, this material is difficult to handle since it oxidizes rapidly in air.

Accordingly, the fabrication of such contacts will have to involve either a multilayer vacuum-deposited thin film structure, where the lanthanum is sealed from contact with air, or possibly the use of a lanthanum amalgam.

Another approach, which is the one used here, is to consider the LaF_3 as an ordinary electrolyte and construct a proper compound electrode of the second kind with which to contact it. The most obvious choice seems to be the structure (6)



which has the overall reversible reaction



In this case F^- ions are exchanged reversibly at the AgF-LaF_3 interface and electrons are exchanged reversibly at the Ag-AgF interface, as indicated in Fig. 1. The particular advantage of the Ag-AgF contact is that AgF itself is an Ag^+ ionic conductor (8), assuring a reasonably low overall ohmic resistance in the system. In this paper special attention has been given to the preparation and properties of this particular contact. But, other systems of the basic design, i.e.



are also possible. Thus, contacts were also constructed based on a layered structure with Cu and $\text{CuF}_2 \cdot 2\text{H}_2\text{O}$. Recently a Czech patent appeared, reporting the use of a Bi-BiF_2 contact (9).

Preparation of the Contacts

In a first attempt at constructing an Ag-AgF contact on LaF_3 , a near-saturated solution of AgF was applied

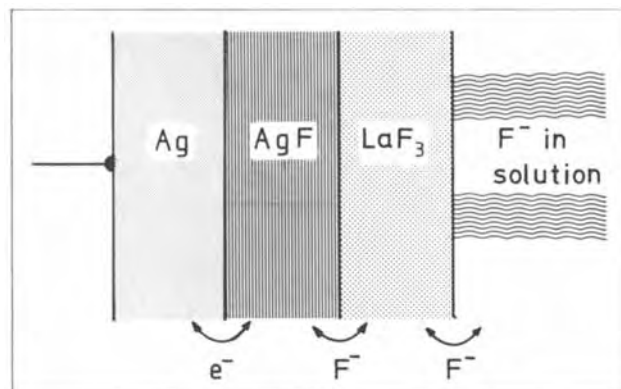


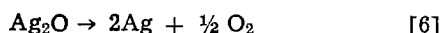
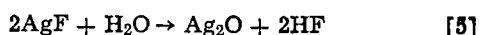
Fig. 1. Structure of the reversible solid-state contact on LaF_3

* Electrochemical Society Active Member.
Key words: ion-selective electrodes, contacts.

dropwise to the membrane surface. The water was evaporated by gently heating the membrane. Finally, a silver conducting epoxy contact was applied. All solid-state ion-selective electrodes based on such membrane structures at first performed quite satisfactorily, but after a few days the contact deteriorated, presumably due to residual water left in the hygroscopic AgF.

By a similar procedure, Cu-CuF \cdot 2H $_2$ O contacts were also prepared, i.e., by heating drops of CuF \cdot 2H $_2$ O solution to dryness on the surface of LaF $_3$. In this case the outer contact consisted of silver conducting epoxy admixed with copper metal powder. Solid-state ion-selective electrodes prepared from these structures performed satisfactorily for months, but eventually also deteriorated, for reasons unknown.

Satisfactory contacts were prepared by again turning to AgF. This time AgF, admixed with small amounts of LaF $_3$ (both Lab. grade chemicals from Merck), were melted on the surface of LaF $_3$ membranes at a temperature of about 450°C. This procedure served a dual purpose: a high quality fused contact was established and, at the same time, water was effectively expelled from the AgF. This process required great care, and the melting had to be performed in an inert, dry atmosphere in order to avoid excessive decomposition of AgF through the reaction path (10)



Apparently, some reduction of silver still took place, and in a separate analysis on the contacts, about 80% water soluble fluoride was found to be retained through the melting. Metallic silver is therefore probably dispersed throughout the AgF.

Immediately upon cooling, the AgF was sealed by the application of a silver-conducting paint or epoxy, which also served to complete the contact.

The properties of the melted junctions were tested electrically and evaluated after incorporation into solid-state ion-selective electrodes. For the electrical measurements LaF $_3$ specimens with symmetrical, double-sided contacts were prepared. For comparison, similar structures with blocked silver contacts and with conventional solution contacts were also tested. The contact areas were in all cases about 10 mm 2 .

Electrical Measurements

Electrical properties such as the frequency-dependent admittance and the low frequency current-voltage characteristics were measured with the symmetrically connected LaF $_3$ specimens.

Complex impedance and admittance plots have been shown to be useful for determining the equivalent circuit for electrochemical systems (11-14). In the present case, similar measurements are useful to determine the electrical properties of the contacts. The complex admittance $Y(\omega)$ (ω is the angular frequency) of a system is the inverse of the impedance $Z(\omega)$, and may be written as

$$Y(\omega) = G(\omega) + jB(\omega) \quad [7]$$

The real part, $G(\omega)$, is the conductance and the imaginary part, $B(\omega)$, is the susceptance.

Figure 2 shows an admittance plot for the Ag-AgF-LaF $_3$ -AgF-Ag structure, measured in the frequency range 50 Hz to 4 MHz. The measurements were mostly performed with automatic LCR meters of the type: Hewlett-Packard Models 4275A and 4261A. The data points below about 100 kHz can be fitted with the arc of a circle centered slightly below the conductance axis.

Since the effects of the contacts and of the membrane substrate can be regarded as sequential physical processes, the consistent choice of an equivalent circuit requires that appropriate network elements be coupled in series (11). To a good approximation each such element can be represented by a resistance and a capaci-

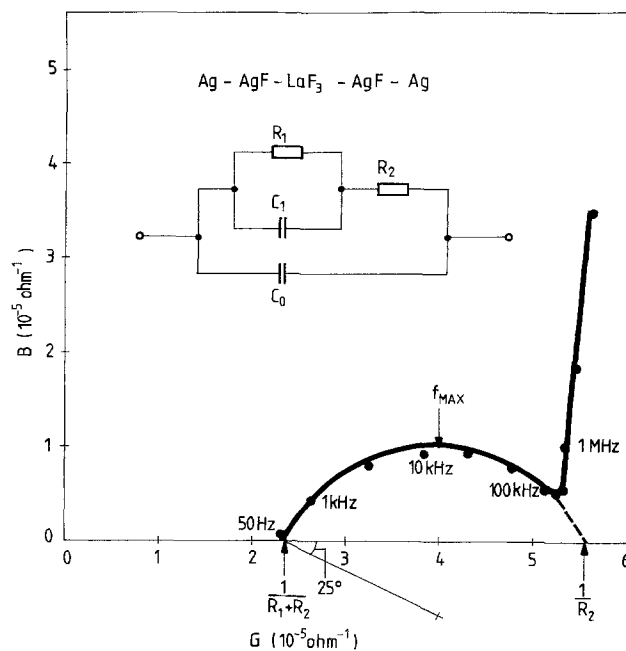


Fig. 2. Admittance plot for an LaF $_3$ membrane with symmetric Ag-AgF contacts. Dots indicate measured admittance at the frequency 50 Hz (curve tracer) and between 1 kHz and 4 MHz (LCR meters).

tance in parallel. At high frequencies the whole sequence will be shorted by the geometric capacitance. Based on such a model the admittance plot of the present sample suggests an equivalent circuit as shown in Fig. 2. The upper circuit branch, which contains a resistance in series with a parallel R-C network, gives rise to a semicircle centered somewhere along the positive conductance axis. The sharp increase in the susceptance at high frequencies results from C $_0$, a lumped combination of geometric and stray capacitance, represented by the lower branch of the equivalent circuit. In terms of the present structure it seems reasonable to associate the parallel R-C network in the upper branch with the two identical contacts (here lumped together for simplicity), while the series resistance is that of the LaF $_3$ substrate. There is no measurable parallel capacitance within the substrate. Such capacitance is often associated with grain boundaries in polycrystalline samples (11), and is not to be expected in the present LaF $_3$ single crystals.

As noted, the admittance arc of Fig. 2 was depressed somewhat below the ideal semicircle of the suggested equivalent circuit, indicating that the present model for the contacts may be too simple. A more complete model should incorporate the fact that each contact possesses two interfaces, one at either side of the AgF-layer. Furthermore, the material boundaries are not well defined, both as a result of partial reduction of AgF to metallic silver, and because of the fused junction between AgF and LaF $_3$. Thus, at the next level of refinement the equivalent circuit model for the contacts should contain three R-C parallel circuits in series which, along with possible nonsymmetry in the system, would account for the observed distortion in the admittance plot. But numerical values for the electrical parameters can only be obtained for the simplest circuit model, for which a resultant ohmic resistance of $R_1/2 \approx 12$ k Ω , and an effective parallel capacitance of $2C_1 \approx 2.5$ nF are found for each contact. The series resistance of the 2 mm thick LaF $_3$ substrate is determined to be $R_2 \approx 18$ k Ω .

The main source of the ohmic contact resistance is probably the overall electrode reaction of Eq. [3]. The ohmic resistance in the thin (~ 0.05 mm) AgF layer is expected to be quite negligible (8). The parallel capacitance probably originates at the smeared out material interfaces of the contacts.

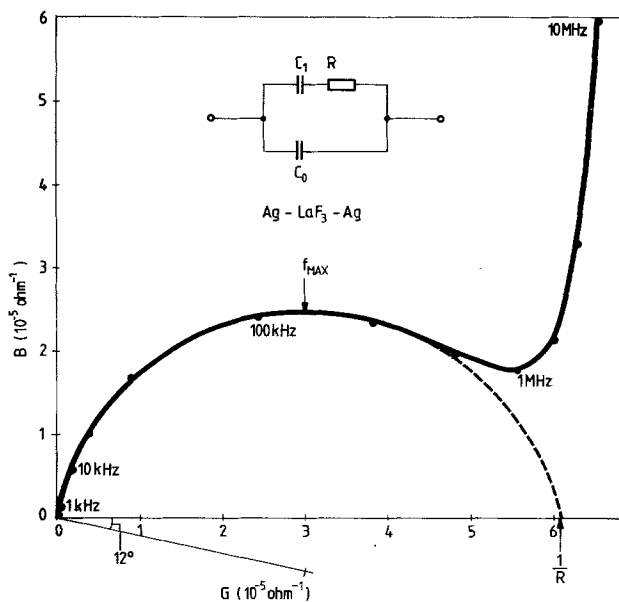


Fig. 3. Admittance plot for an LaF_3 membrane with symmetric silver contacts. Dots indicate measured admittance at frequencies between 120 Hz and 10 MHz (LCR meters).

Figure 3 shows the admittance plot for an LaF_3 substrate with blocked silver contacts. Qualitatively, this plot looks very much like the foregoing, except for the notable difference that the low frequency portion of the arc now passes through the origin. This suggests a similar equivalent circuit as before, but this time with negligible conductance in the contacts. The relative simplicity of the resulting circuit yields a particularly straightforward expression for the admittance behavior

$$B = \frac{C_0}{C_1} \left(\frac{G/R}{1 - GR} \right)^{1/2} + \left[\frac{G}{R} (1 - GR) \right]^{1/2} \quad [8]$$

The first term represents the steep increase at high frequencies as G approaches $1/R$, and the second term is the semicircle passing through the origin and with diameter $1/R$. The analysis of the experimental admittance plot yields an ohmic resistance of 16 k Ω for the substrate, in good agreement with the previous result. The relatively high frequency associated with the maximum point of the semicircle yields an effective parallel capacitance per contact of $2C_1 \approx 0.14$ nF ($C_1 = (2\pi R f_{\text{max}})^{-1}$). The reason for this small value is not immediately obvious, but it may be associated with the use of silver-conducting epoxy for the contacts.

The admittance behavior was also measured for a commercial fluoride electrode with a conventional internal filling solution. The outer surface of the LaF_3 membrane was contacted with a solution of 0.5M NaCl and 0.5M NaF, in which a silver wire electrode was introduced. The resulting admittance plot for this structure is shown in Fig. 4. Presumably, the abrupt increase in the imaginary part of the admittance is again caused by the geometric capacitance. The intercept with the conductance axis suggests a total series resistance of 102 k Ω for the system. Using previous results for the LaF_3 bulk contribution, the effective single contact resistance is found to be about 40 k Ω for this case. At the frequencies considered, the effective parallel capacitance of the contacts appears to be quite small ($C_1 \ll [R_1 \omega (10 \text{ kHz})]^{-1} \approx 0.1$ nF). There has been some speculation on the possible formation of a gel layer on the surface of LaF_3 exposed to aqueous solutions (15). If so, this will have a significant bearing on the extent of the effective width of the interfacial space charge, and tend to reduce the double layer capacitance. On the other hand, a large interfacial capacitance will represent a short at the fre-

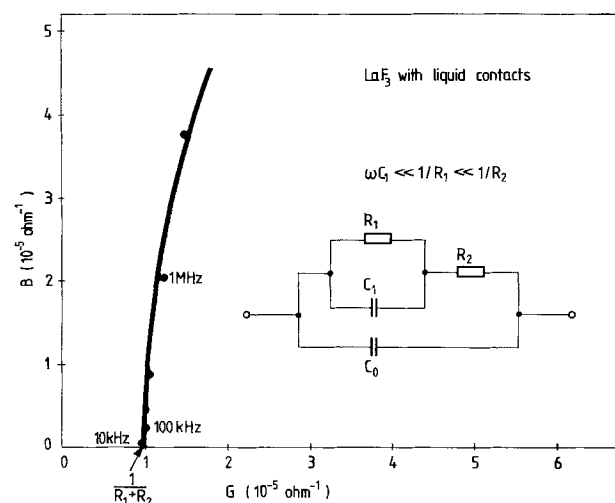


Fig. 4. Admittance plot for an LaF_3 membrane with liquid contacts (see text). Dots indicate measured admittance at frequencies between 10 kHz and 2 MHz (LCR meters).

quencies considered, and may instead combine with Warburg behavior to produce structure at low frequencies (16).

In applications, the low frequency behavior of the membrane structure is of particular interest, since it governs the electrode response times typically of interest in practical analysis. As an illustration of this behavior, Fig. 5 shows a 50 Hz curve tracer (Tektronix, Type 576) current-voltage characteristic for each of the three membrane structures discussed above. In general, the shape of the loop reflects the relative size of the real and the imaginary parts of the admittance. Thus, the loop degenerates into a straight line when the admittance is purely real and nonrectifying, *i.e.*, when the contacts are truly ohmic. It is interesting to note that the membranes with Ag-AgF and liquid contacts both give rise to similar, near degenerate loops while the blocked silver contacts produce a pronounced, elliptical shape.

Solid-State Fluoride Electrodes

Solid-state fluoride electrodes were prepared in two versions, one with a microelectronic impedance transference network contained within the sensor body, and one with a direct electrical connection to an external high impedance voltmeter. The electrodes manufactured according to the microelectronic approach have a single chip preamplification circuit positioned in close proximity to the membrane, in order to reduce noise pick-up. Details of the electrode construction have previously been discussed (5, 6).

The electrodes were evaluated by determining their response in fluoride standards (*i.e.*, potential response *vs.* fluoride concentration), as well as their response time and stability. Lifetime is of vital importance, and is currently being investigated by continuous exposure of electrodes to fluoride solutions. So far, this test has lasted for five months without signs of electrode failure.

In Fig. 6 are shown typical response curves obtained with the present fluoride electrodes. The response was measured by pipetting known additions of NaF standard into stirred buffer solutions of either TISAB or 1M HCl. The curves are in close agreement with theory, with sensitivities of about 59 mV/decade (1M HCl) and 58 mV/decade (TISAB) at 24°C. The logarithmic Nernstian response extends down to about 2×10^{-6} M NaF when using the 1M HCl buffer, and to about 8×10^{-6} M NaF in the TISAB buffer. Both values are in reasonable agreement with the reported solubility of LaF_3 (17), and are in the same range as commercial electrodes with internal filling solution. The higher detection limit in TISAB is presumably the

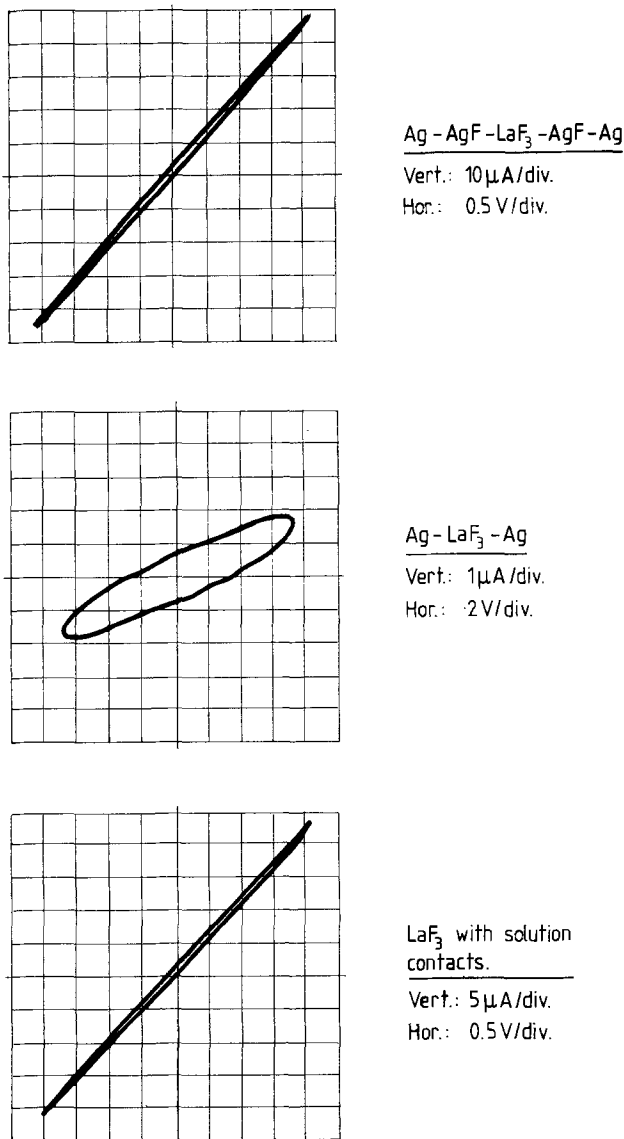


Fig. 5. 50 Hz curve-tracer current-voltage characteristics for LaF₃ membranes with different contacts.

result of complexing of lanthanum, which is compensated for by increased dissolution of membrane material (18).

The response times of the electrodes were measured both with an injection technique and in a regular analytical setup. With the injection technique the fluoride electrode and a reference electrode were pointed against each other (6). A small drop of an initial solution provided contact between the electrodes, and a new solution with a different fluoride content was rapidly injected into the gap to displace the initial solution. With a suitable trigger arrangement the time response of the system could be monitored on a storage oscilloscope (Tektronix, Type 549). With this technique time constants in the range 20-100 msec, depending on the experimental circumstances, were measured for the present fluoride electrodes as well as for a commercial electrode (Orion, Model 94-09). Further details on these experiments will be published elsewhere (19).

In the regular analytical setup a stirred sample solution (50 ml 1M HCl buffer) was monitored under successive additions of known quantities of NaF. The time response was recorded on an x-t recorder (Watanabe Servo Recorder, Type 652) with a highest recording speed of 0.4 cm/sec. Typical results for a fluoride electrode with the Ag-AgF contact are shown in Fig. 7. For the highest concentrations (accumulated NaF concentration shown to the right) potential stability was

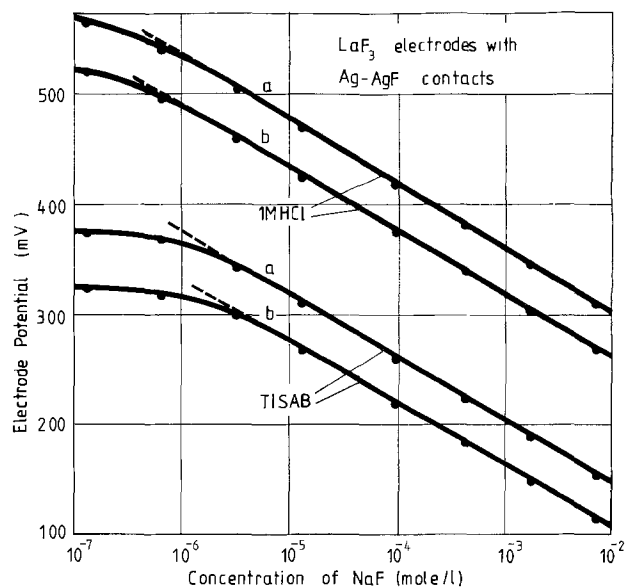


Fig. 6. Calibration curves obtained with LaF₃ electrodes with Ag-AgF contacts. Curves (a) are for electrode with integral impedance transforming network and curves (b) are for electrode with direct electrical connection to an external high impedance voltmeter. Reference electrode: Orion 96-01.

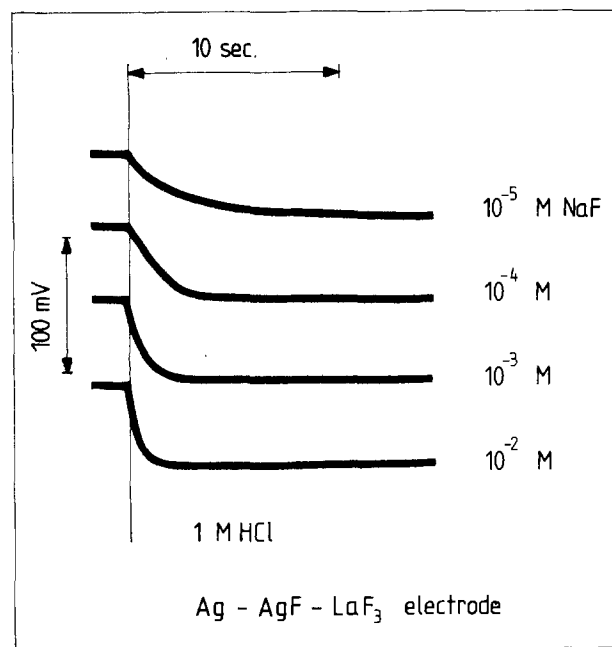


Fig. 7. Total response time of LaF₃ electrode with Ag-AgF contacts and integral impedance transforming network measured in a regular analytical setup (see text).

achieved within one or two seconds, probably limited by the mixing and reaction times (*i.e.*, $F^- + H^+ \rightleftharpoons HF$ and $HF + F^- \rightleftharpoons HF_2^-$) in the liquid. Below about 10^{-4} M NaF, however, a steady increase in the response time became evident. It appears that under identical circumstances the present electrodes and the electrode with internal filling solution responded about equally fast (19). In contrast to these results Fig. 8 shows the response of an LaF₃ electrode with a blocked silver contact (3). In this case the response time was typically several minutes and, in addition, a long-term potential drift on the order of millivolts per minute was observed. It is reasonable to assume that this effect is associated with the lack of reversibility at the inner contact. In a comparable time scale (*i.e.*, up to 10 min)

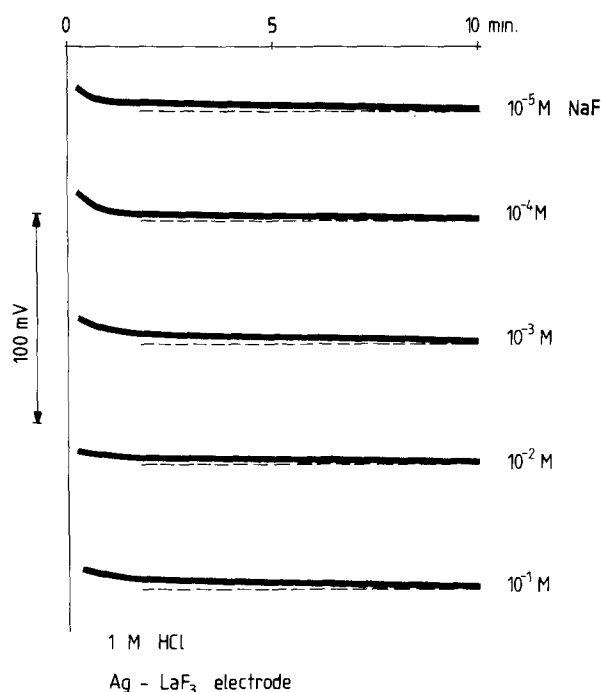


Fig. 8. Total response time of LaF_3 electrode with silver contacts

the potential drift in the Ag-AgF- LaF_3 electrode was an order of magnitude less.

Summary

Reversible solid-state contacts on LaF_3 , based on the use of AgF and Ag, have been prepared and tested. The electrical properties of the contacts were investigated by means of the frequency-dependent complex admittance. This yielded values for the effective ohmic resistance ($\sim 1.2 \text{ k}\Omega/\text{cm}^2$) and the parallel capacitance ($\sim 25 \text{ nF}/\text{cm}^2$) of the contacts. For comparison, similar analyses were also performed on samples with conventional solution contacts and with blocked silver contacts. A low frequency (50 Hz) curve tracer plot indicates that the current-voltage characteristics for both the Ag-AgF contacts and for the solution contacts are almost purely ohmic, i.e., degenerate and nonrectifying.

Fluoride electrodes using the present Ag-AgF solid-state contacts behave very satisfactorily. In tests on sensitivity, response time, stability, and lifetime they

compare favorably with commercial solution contact electrodes, while electrodes with blocked silver contacts suffer from increased response time, and lack of long-term stability.

Manuscript received Nov. 26, 1979. This was Paper 669 presented at the Los Angeles, California, Meeting of the Society, Oct. 14-19, 1979.

Any discussion of this paper will appear in a Discussion Section to be published in the December 1980 JOURNAL. All discussions for the December 1980 Discussion Section should be submitted by Aug. 1, 1980.

Publication costs of this article were assisted by The University of Trondheim and The Royal Norwegian Council for Scientific and Industrial Research.

REFERENCES

1. G. B. Benedek and F. M. H. Villars, "Physics with Illustrative Examples from Medicine and Biology," Vol. 3, Addison-Wesley, Reading, Mass. (1979).
2. R. G. Kelly, *Electrochim. Acta*, **22**, 1 (1977).
3. K. Nagy, T. A. Fjeldly, and J. S. Johannessen, in "Ion-Selective Electrodes," E. Pungor, Editor, p. 491, Akadémia Kiado, Budapest (1978).
4. R. P. Buck, in "Ion-Selective Electrodes in Analytical Chemistry," Vol. 1, H. Freiser, Editor, Plenum Press, New York (1978).
5. T. A. Fjeldly, K. Nagy, and J. S. Johannessen, *This Journal*, **126**, 793 (1979).
6. T. A. Fjeldly and K. Nagy, SINTEF report STF21 79009 (1979).
7. R. P. Buck and V. R. Shepard, Jr., *Anal. Chem.*, **46**, 2097 (1974).
8. A. M. Raaen, I. Svare, and T. A. Fjeldly, *Phys. Rev. B*, In press.
9. L. Miroslav, J. Vesely, and J. Jindra, Czech, Pat. 172.449, 15. May 1978.
10. "Gmelins Handbuch der Anorganischen Chemie," 8th ed., 61B1 Verlag Chemie, Weinheim (1971).
11. J. E. Bauerle, *J. Phys. Chem. Solids*, **30**, 2657 (1969).
12. R. P. Buck, *J. Electroanal. Chem. Interfacial Electrochem.*, **18**, 381 (1968).
13. R. P. Buck and I. Krull, *ibid.*, **18**, 387 (1968).
14. J. Ross McDonald, *J. Chem. Phys.*, **61**, 3977 (1974).
15. J. Vesely, *Electroanal. Chem. Interfacial Electrochem.*, **41**, 134 (1973).
16. J. Mertens, P. Van der Winkel, and J. Vereecken, Paper 666 presented at The Electrochemical Society Meeting, Los Angeles, California, Oct. 14-19, 1979.
17. J. Butler, in "Ion-Selective Electrodes," R. A. Durst, Editor, NBS Special Publication 314, Washington, D.C., (1969).
18. M. S. Frant and J. W. Ross, *Anal. Chem.*, **40**(7), 1169 (1968).
19. K. Nagy and T. A. Fjeldly, Abstract 665, p. 1669, The Electrochemical Society Extended Abstracts, Los Angeles, California, Oct. 14-19, 1979.

Primary Current Distribution on a Sinusoidal Profile

Peter Fedkiw*

Department of Chemical Engineering, North Carolina State University, Raleigh, North Carolina 27650

ABSTRACT

The primary current distribution at a sinusoidal profile has been solved as a perturbation problem in the amplitude-to-wavelength parameter. The results are also applicable to diffusion-limited reactions on sinusoidal surfaces. The solution for the potential has been developed to the fourth order term. Wagner's solution to this problem can be recovered by including only the first two terms in the perturbation expansion. The expansion technique enables an estimate of the error caused by the neglected terms. The leveling efficiency of a mass-transfer controlled dissolution reaction is predicted to be always less than that given by Wagner's equation. Applications of the perturbation technique to other relevant problems are discussed.

The surface of any real metal on the microscopic scale is not smooth and will contain low and high spots. The greater accessibility to the counterelectrode of the high areas in comparison to the low areas causes these protrusions to preferentially receive more current during an electrochemical reaction. For a metal deposition reaction in the absence of leveling agents these peaks may grow with a consequent increase in surface roughness. It has been proposed that leveling agents induce a smooth metal deposit by preferentially adsorbing and reacting at the high points of the surface and thereby increasing the polarization required for the metal deposition (1-3). In the anodic direction (electropolishing), the high points of the surface preferentially dissolve in comparison to the low points. Wagner (4) examined the initial dissolution of a sinusoidal surface whose dissolution rate was controlled by the diffusion of an acceptor species for the metal ions from the bulk of the solution to the surface. Wagner's solution of the diffusion equation was limited to a sinusoid with an amplitude which was much less than the wavelength. His solution satisfied the boundary condition of zero acceptor concentration at the metal surface only in an approximate manner. In this paper a parameter perturbation in the amplitude-to-wavelength is applied to the primary current distribution at a sinusoidal surface. This is the electrical analog of the diffusion-limited dissolution of the profile. The current distribution is found for a uniform potential at the surface and the counterelectrode at infinity. The perturbation solution developed here identically satisfies all boundary conditions and furthermore, the error of the neglected terms can be assessed. It is demonstrated that Wagner's solution can be recovered from the first two terms in the expansion. The parameter perturbation solution technique may be used in other relevant problems. A short discussion is given on the application of this technique to computing the potential variation in the electrolyte adjacent to a sinusoidal surface at which a uniform current density is applied. This is physically relevant to the action of potential dependent adsorption of leveling agents on metal surfaces. A discussion on applying the solution technique to pulsating potential deposition is also presented. Work at this laboratory is currently in progress in these two areas.

Problem Statement

Figure 1 is a plot of the sinusoidal profile under consideration. The profile consists of a single frequency with a period length l' and an amplitude A' . (The prime signifies a dimensional length.) The origin of the coordinate system is placed such that the valley corresponds to $x' = 0$. The profile shape is described by the equation

$$y_w' = -A' \cos(2\pi x'/l) \quad [1]$$

The potential at the sinusoidal surface is uniform and the counterelectrode at which a uniform current density is applied is at infinity. The potential in the solution will satisfy Laplace's equation subject to appropriate boundary conditions

$$\frac{\partial^2 \phi}{\partial x'^2} + \frac{\partial^2 \phi}{\partial y'^2} = 0 \quad [2]$$

$$\phi(y' = y_w', x') = 0 \quad [3i]$$

$$-\kappa \frac{\partial \phi}{\partial y'} \Big|_{x', y' \rightarrow \infty} = i_A \quad [3ii]$$

$$\frac{\partial \phi}{\partial x'} \Big|_{y', x' = 0, l/2, l} = 0 \quad [3iii]$$

Condition [3iii] results from the symmetry of Laplace's equation and its boundary conditions. We therefore will only need to consider the region

$$y' \geq y_w', \quad 0 \leq x' \leq l/2$$

The concentration of a species which is controlled by diffusion to (or from) the electrode surface will also be governed by Eq. [2] and [3]. One need only replace the potential by the properly defined concentration, the conductivity by the diffusivity, and the applied current density by an expression for the diffusion flux which is usually written

$$j = -D\Delta C/\delta \quad [4]$$

where δ is the diffusion layer thickness and ΔC is the driving force of bulk concentration minus the surface concentration of the reacting species. In order to formulate the concentration field problem in terms of the diffusion layer thickness however, it must be assumed that $\delta \gg A'$. This follows if the concentration analog of Eq. [3ii] is to apply. Consequently, we prefer to consider the potential field problem in our discussion and to translate the results to the concentration field problem at the end of the analysis. Krichmar (5) has

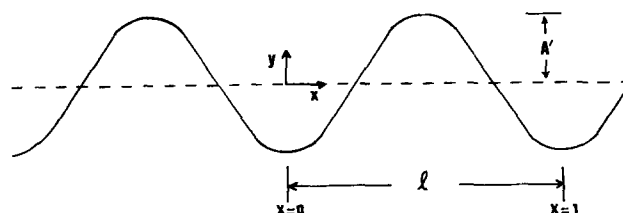


Fig. 1. Profile of a sinusoidal surface

* Electrochemical Society Active Member.
Key words: diffusion, current distribution, potential.

analyzed in an approximate manner the situation where δ is a function of position along the sinusoidal surface.

Mathematical Development

Define the following dimensionless quantities

$$X = x'/l, \quad Y = (y' - y_w')/l, \quad \Phi = (\kappa\phi)/(li_A) \quad [5]$$

Laplace's equation and its boundary conditions then transform to

$$\frac{\partial^2 \Phi}{\partial X^2} + \frac{\partial^2 \Phi}{\partial Y^2} + AL_1(\Phi) + A^2L_2(\Phi) = 0 \quad [6]$$

$$\Phi(Y=0, X) = 0 \quad [7i]$$

$$\left. \frac{\partial \Phi}{\partial Y} \right|_{X, Y \rightarrow \infty} = -1 \quad [7ii]$$

$$\left. \frac{\partial \Phi}{\partial X} \right|_{X, Y=0, 1/2} = 0 \quad [7iii]$$

The operators $L_1(\Phi)$ and $L_2(\Phi)$ are given by

$$L_1(\Phi) = -4\pi \sin 2\pi X \frac{\partial^2 \Phi}{\partial X \partial Y} - 4\pi^2 \cos 2\pi X \frac{\partial \Phi}{\partial Y} \quad [8]$$

$$L_2(\Phi) = 4\pi^2 \sin^2 2\pi X \frac{\partial^2 \Phi}{\partial Y^2} \quad [9]$$

The solution for Φ may be written as a perturbation in the dimensionless amplitude-to-period length ratio A

$$\Phi = \Phi_0 + A\Phi_1 + A^2\Phi_2 + \dots \quad [10]$$

[Perturbation methods are discussed in the text by Nayfeh (6).] Equation [10] is substituted into Eq. [6]. Equations governing each of the expansion functions are found by equating equivalent terms in the A expansion

$$\frac{\partial^2 \Phi_0}{\partial X^2} + \frac{\partial^2 \Phi_0}{\partial Y^2} = 0 \quad [11]$$

$$\frac{\partial^2 \Phi_1}{\partial X^2} + \frac{\partial^2 \Phi_1}{\partial Y^2} = -L_1(\Phi_0) \quad [12]$$

$$\frac{\partial^2 \Phi_n}{\partial X^2} + \frac{\partial^2 \Phi_n}{\partial Y^2} = -L_1(\Phi_{n-1}) - L_2(\Phi_{n-2}) \quad n \geq 2 \quad [13]$$

The boundary conditions on the zero-order solution may be written

$$\Phi_0(Y=0, X) = 0 \quad [14i]$$

$$\left. \frac{\partial \Phi_0}{\partial Y} \right|_{X, Y \rightarrow \infty} = -1 \quad [14ii]$$

$$\left. \frac{\partial \Phi_0}{\partial X} \right|_{Y, X=0, 1/2} = 0 \quad [14iii]$$

Consequently the higher order solutions satisfy homogeneous conditions

$$\Phi_n(Y=0, X) = 0 \quad [15i]$$

$$\left. \frac{\partial \Phi_n}{\partial Y} \right|_{X, Y \rightarrow \infty} = 0 \quad [15ii]$$

$$\left. \frac{\partial \Phi_n}{\partial X} \right|_{Y, X=0, 1/2} = 0 \quad [15iii]$$

Equations [11]-[15] have been solved through the fourth order term. The calculations are tedious but straightforward

$$\begin{aligned} \Phi(X, Y) = & -Y + A [1 - e^{-2\pi Y} \cos 2\pi X] \\ & + \pi A^2 [(1 - e^{-2\pi Y}) + (e^{-4\pi Y} - e^{-2\pi Y}) \cos 4\pi X] \\ & + \pi^2 A^3 \left[2(e^{-4\pi Y} - e^{-2\pi Y}) \cos 2\pi X \right. \\ & \left. + \left(2e^{-4\pi Y} - \frac{1}{2}e^{-2\pi Y} - \frac{3}{2}e^{-6\pi Y} \right) \cos 6\pi X \right] \\ & + \pi^3 A^4 \left[(1 - 5e^{-2\pi Y} + 4e^{-4\pi Y}) \right. \\ & \left. + \left(\frac{1}{6}e^{-2\pi Y} - 4\pi Y e^{-4\pi Y} + \frac{13}{3}e^{-4\pi Y} \right. \right. \\ & \left. \left. - \frac{9}{2}e^{-6\pi Y} \right) \cos 4\pi X + \left(-\frac{1}{6}e^{-2\pi Y} + 2e^{-4\pi Y} \right. \right. \\ & \left. \left. - \frac{9}{2}e^{-6\pi Y} + \frac{8}{3}e^{-8\pi Y} \right) \cos 8\pi X \right] + 0(A^5) \quad [16] \end{aligned}$$

The current along the wall can be evaluated by taking the normal derivative of Eq. [16]

$$\frac{i_n}{i_A} = -\frac{\partial \Phi}{\partial n} \quad [17]$$

The normal derivative is evaluated according to the procedure presented in the Appendix. We find

$$\begin{aligned} \frac{i_n}{i_A} = & \sqrt{1 + 4\pi^2 A^2 \sin^2 2\pi X} [1 - 2\pi A \cos 2\pi X] \\ & + 2(\pi A)^2 \cos 4\pi X - 1 - 2(\pi A)^3 (\cos 6\pi X - 2\cos 2\pi X) \\ & + (\pi A)^4 \left(6 - \frac{16}{3} \cos 4\pi X + 2\cos 8\pi X \right) + 0(A^5) \quad [18] \end{aligned}$$

In order to track the change in the surface roughness during a reaction, we are particularly interested in the current at $X = 0$ (valley) and $X = 1/2$ (peak). These are given by

$$\frac{i_p}{i_A} = 1 + 2\pi A - 2(\pi A)^3 + \frac{8}{3}(\pi A)^4 + 0(A)^5 \quad [19]$$

$$\frac{i_v}{i_A} = 1 - 2\pi A + 2(\pi A)^3 + \frac{8}{3}(\pi A)^4 + 0(A)^5 \quad [20]$$

The shape of the profile will change in the course of the deposition (or dissolution) reaction. An initial sinusoidal profile will become distorted to higher harmonics. Riggs (7) has developed a numerical routine which has included this shape change phenomenon. As a first approximation, however, let us assume that the profile retains its sinusoidal shape. The rate of change of the amplitude will be proportional to the difference between the peak and valley current. The amplitude of the profile can be tracked during the deposition (or dissolution) reaction by solving the following mass balance equation

$$\frac{dA'}{dt} = \frac{1}{2} \frac{V_i s_i}{n_R F} (i_p - i_v) \quad [21]$$

where s_i is the stoichiometric coefficient of the reactant from the general reaction under consideration



and V_i is the solid phase molar volume of reactant i . (The current is negative for a cathodic reaction and $s_i < 0$, therefore $dA'/dt > 0$, whereas for the anodic case, $dA'/dt < 0$.)

Equation [21] may be solved for $A(t)$ by use of Eq. [19] and [20]

$$\frac{A}{A_0} = \left[\frac{e^{4\pi v_s t/l}}{1 - \pi^2 A_0^2 (1 - e^{4\pi v_s t/l})} \right]^{1/2} \quad [23]$$

where A_0 is the initial dimensionless amplitude and v_s is the equivalent velocity of the solid phase if the current density i_A is applied at a flat surface

$$v_s = V_i \frac{s_i}{n_R F} i_A \quad [24]$$

Results and Discussion

Equations [16], [18], and [23] are the main results of this analysis. The perturbation solution in the parameter A has enabled us to estimate the accuracy of the solution. Table I demonstrates the convergence of this solution for $A = 0.10$. It shows the normal current evaluated at the valley and the peak. The current is given using various orders of the solution. The normal current at the valley has converged to within at least 6% with use of the highest order term. Wagner's solution for the same profile is given by the A^1 term in the expansion (see following discussion). The potential field (which is not illustrated) shows a greater convergence rate than its derivative, the current.

It can be demonstrated that Wagner's solution can be recovered by including only the first-order term in the perturbation solution, i.e.

$$\phi = \phi_0 + A\phi_1 + O(A^2) \quad [25]$$

Due to the nature of the ϕ function at $X = 0$ and $1/2$, the second order contribution to the current at these two points is zero. Thus even though Wagner's solution for the potential is accurate to $O(A^2)$, the peak and valley current which is calculated from his solution is accurate to $O(A^3)$. The nature and approximation of Wagner's solution to this problem have been developed and expanded upon. In Wagner's development the denominator of Eq. [23] is equal to 1.

Figures 2 and 3 are plots of the potential variation in the solution and the current distribution at the surface, respectively. These plots are for a dimensionless amplitude of 0.1. The abscissa length scale for both figures is measured in terms of the number of amplitude lengths above the average wall position.

Figure 2 shows that the potential in the solution quickly becomes independent of X . The three lines become indistinguishable on the scale of this graph for y/A values much larger than indicated. Equation [16] evaluated at $y/A = 6$ demonstrates that the maximum variation in the dimensionless solution potential (valley-peak) is $-0.56347 - (-0.56797) = 0.00450$. This corresponds to a deviation of $\pm 0.40\%$ about the average potential at this elevation. The counterelectrode may be placed anywhere above $y/A = 6$ and have very little effect on the profile's current distribution. We can utilize this result to interpret a diffusion-limited reaction at a sinusoidal surface. Thus if the concentration boundary layer for a mass-transfer controlled reaction

Table I. Convergence of perturbation solution for the normal current distribution on a sinusoidal surface with $A = 0.10$

Order of solution	i_n/i_A	
	$X = 0$	$1/2$
A^0	1.0000	1.0000
A^1	0.3717 (-62.8)	1.6283 (62.8)
A^2	0.3717 (0)	1.6283 (0)
A^3	0.4337 (16.7)	1.5663 (-3.81)
A^4	0.4597 (5.99)	1.5923 (1.66)

() = $\frac{\text{term}(A^{n+1}) - \text{term}(A^n)}{\text{term}(A^n)} \times 100$.

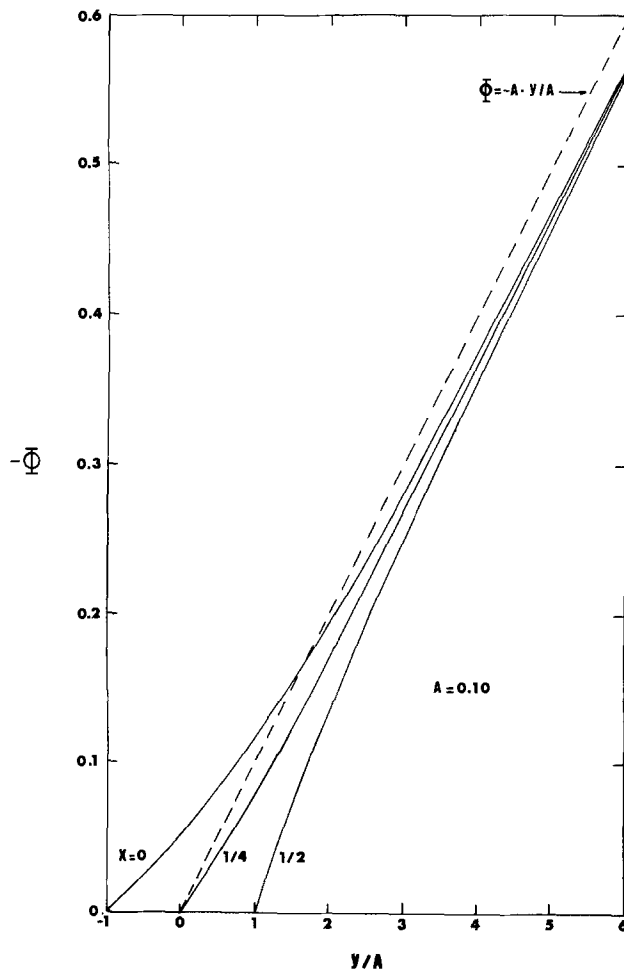


Fig. 2. Potential distribution above a sinusoidal surface with a primary current distribution.

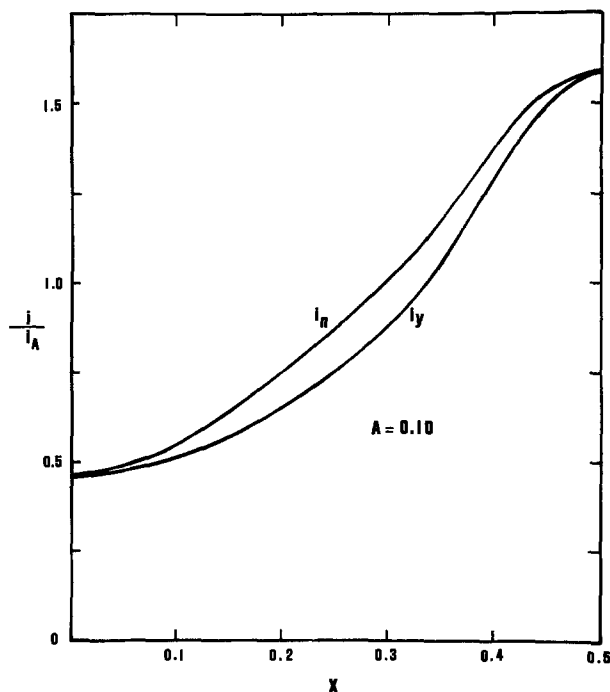


Fig. 3. The normal and y component of the current for the primary current distribution at a sinusoidal surface.

extends much above $y/A = 6$, the thickness of the boundary layer will have little effect on the current distribution at the surface. Of course the greater the boundary layer thickness for a given system, the lower

will be the resulting current. The analysis of this work enables us to quantify the statement $\delta \gg A'$. The dashed line on Fig. 2 indicates the dimensionless solution potential if the current was applied at a flat surface. Less energy will be required to distribute the current to the peak areas in comparison to a flat surface. Furthermore, more current is distributed to the high points of the profile ($X > 1/4$) than to the low points of the profile ($X < 1/4$). Therefore for the same applied current, the dimensionless solution potential drop is greater (in absolute value) for the flat surface than the sinusoidal surface. Equation [16] shows that this difference is given by $\pi A^2 + \pi^3 A^4 + O(A^6)$.

Figure 3 shows that at the average wall position ($X = 1/4$) neither the normal current nor the y component of the current equals the average applied current density. This would follow from Eq. [18] only if the first-order term is retained which is $O(A)$ after the square root term is expanded.

As an application of the analysis in this paper, the leveling efficiency of an anodically dissolved surface is discussed. Consider the sinusoidal profile of Fig. 1 to be anodically reacting under the mass-transfer controlled condition of an acceptor species diffusing from the bulk to the surface. This is the case discussed by Wagner. Following Wagner's nomenclature, let u represent the displacement of the surface from the initial position if the entire surface were flat. If t_R represents the reaction time, it follows that

$$u = v_s t_R$$

Equation [23] may be plotted to illustrate the leveling efficiency. The ordinate of Fig. 4 is the quantity $\ln(A/A_0)/(2\pi u/l)$ and the abscissa is the initial amplitude A_0 . Inclusion of the higher order correction terms illustrate that the leveling efficiency is dependent upon the initial amplitude and the parameter u/l which is a measure of the number of wavelengths of the surface reacted. The leveling is always less than that predicted by Wagner's solution.

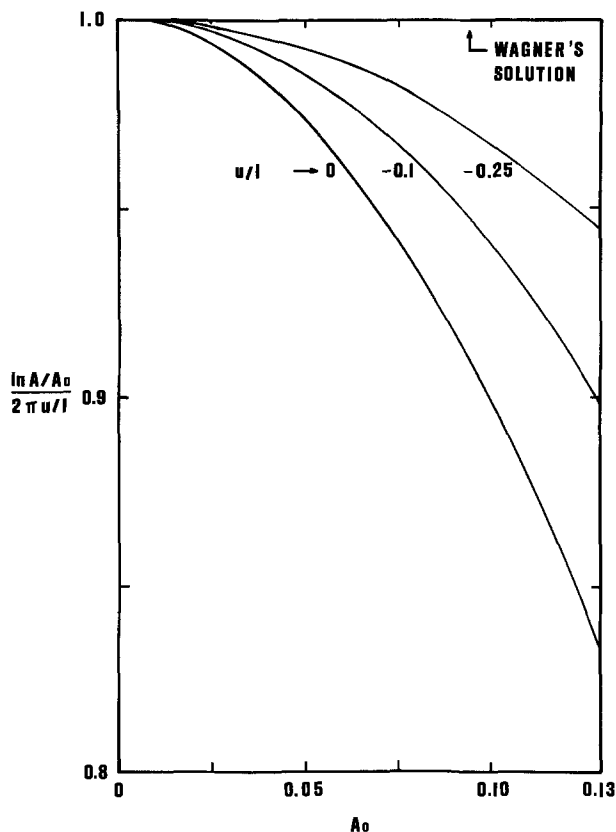


Fig. 4. Leveling of a sinusoidal surface as a function of the initial amplitude and the equivalent displacement of a flat profile.

As the surface is dissolved away u/l increases. Initially the deviation between the leveling predicted by Wagner's solution and the perturbation solution can be significant for nonzero A_0 . However, as more and more of the surface is dissolved away, regardless of the initial amplitude, Wagner's solution is again a good approximation. As $u/l \rightarrow \infty$, all of the curves on Fig. 3 approach the value one for their abscissa.

The perturbation analysis given in this work may be applied in other physically important situations. If the normal current is uniform along the sinusoidal surface, a solution of the form assumed in Eq. [10] may still be applied to the potential. Laplace's equation will apply; however, the boundary conditions must be changed. The zero of potential may be defined to be at some reference plane located at $y = y_R$. This can be translated to the Y coordinate system by further assuming that $y_R' \gg A'$. The wall boundary condition on the current will involve the parameter A as can be seen from the Appendix. Since the perturbation parameter appears in both the governing equation and its boundary conditions, this problem is mathematically more complicated than that developed here, but it is solvable. The solution of this problem will quantify the potential variation in the solution adjacent to the surface. This variation has relevance for the potential dependent adsorption of leveling agents.

The perturbation solution technique outlined here may also be applied to the transient problem of a pulsating potential applied to a sinusoidal profile. The various orders of the solution will thus be time-dependent in addition to their spatial dependence. Various boundary conditions at the surface can be applied. The surface concentration might respond in a Nernstian manner to the applied potential. Linear kinetics will be another limiting case of interest.

Manuscript submitted May 29, 1979; revised manuscript received Dec. 18, 1979.

Any discussion of this paper will appear in a Discussion Section to be published in the December 1980 JOURNAL. All discussions for the December 1980 Discussion Section should be submitted by Aug. 1, 1980.

Publication costs of this article were assisted by North Carolina State University.

APPENDIX

A. Normal derivative

Let (n', t') be a local normal and tangent coordinate system along the surface

$$\frac{\partial \phi}{\partial n'} \Big|_{t'} = \frac{\partial \phi}{\partial x'} \Big|_y \frac{\partial x'}{\partial n'} \Big|_{t'} + \frac{\partial \phi}{\partial y'} \Big|_x \frac{\partial y'}{\partial n'} \Big|_{t'}$$

$$\text{but: } \frac{\partial x'}{\partial n'} \Big|_{t'} = -\sin \theta \quad \frac{\partial y'}{\partial n'} \Big|_{t'} = \cos \theta$$

where θ is the angle between the tangent and x axis. Therefore

$$\frac{\partial \phi}{\partial n'} = \cos \theta \left[\frac{\partial \phi}{\partial y'} - \left(\frac{dy_w'}{dx'} \right) \frac{\partial \phi}{\partial x'} \right] \quad [\text{A-1}]$$

Since $\tan \theta = dy_w'/dx'$

$$\text{it follows that } \cos \theta = \frac{1}{\sqrt{1 + \left(\frac{dy_w'}{dx'} \right)^2}}$$

B. Normal derivative in (X,Y) coordinate system

The derivatives transform as

$$\begin{aligned} \frac{\partial \phi}{\partial x} \Big|_y &= \frac{\partial \phi}{\partial X} \Big|_Y \frac{\partial X}{\partial x} \Big|_y + \frac{\partial \phi}{\partial Y} \Big|_X \frac{\partial Y}{\partial x} \Big|_y \\ &= \frac{\partial \phi}{\partial X} - \left(\frac{dy_w'}{dx'} \right) \frac{\partial \phi}{\partial Y} \end{aligned}$$

Also

$$\frac{\partial \phi}{\partial y} \Big|_x = \frac{\partial \phi}{\partial Y} \Big|_x$$

Substitution of these two terms into the nondimensional Eq. [A-1] gives

$$\frac{\partial \phi}{\partial n} = \cos \theta \left[\left(1 + \left(\frac{dy_w'}{dx'} \right)^2 \right) \frac{\partial \phi}{\partial Y} \Big|_x - \left(\frac{dy_w'}{dx'} \right) \frac{\partial \phi}{\partial X} \Big|_y \right]$$

If this is evaluated along the surface for the primary distribution

$$\frac{\partial \phi}{\partial n} \Big|_t = \sqrt{1 + \left(\frac{dy_w'}{dx'} \right)^2} \left(\frac{\partial \phi}{\partial Y} \right)_x$$

LIST OF SYMBOLS

A	dimensionless amplitude, A'/l
F	Faraday's constant, C/equiv.
i	current density, mA/cm ²
i_A	current density applied at counterelectrode, A/cm ²
l	period length, cm
n_R	number of electrons transferred in reaction
n	dimensionless normal coordinate, n'/l
s_i	stoichiometric coefficient of reactant i
t	time, sec
u	equivalent displacement of flat profile, cm
V_i	solid phase molar volume of reactant i , cm ³ /mole
v_s	plane solid phase velocity, $V_i s_i i_A / (nF)$, cm/sec
x	dimensionless coordinate, x'/l

X	dimensionless coordinate, x'/l
y	dimensionless coordinate, y'/l
Y	dimensionless coordinate, $(y' - y_w')/l$

Greek

δ	diffusion layer thickness, cm
ϕ	potential, V
Φ	dimensionless potential, $\phi\kappa/(i_A l)$
κ	conductivity, $\Omega^{-1} \text{cm}^{-1}$

Superscript

' denotes a dimensional length

Subscript

n	normal
p	peak
v	valley
w	wall
y	y coordinate

REFERENCES

- O. Kardos, *Plating*, February, 129 (1974); March, 229 (1974); April, 316 (1974).
- O. Kardos and D. G. Foulke, in "Advances in Electrochemistry and Electrochemical Engineering," Vol. 2, P. Delahay and C. Tobias, Editors, Interscience Publishers, New York (1962).
- S. S. Kruglikov, *et al.*, *Electrochim. Acta*, **10**, 253 (1965).
- C. Wagner, *This Journal*, **101**, 225 (1954).
- S. I. Krichmar, *Russ. J. Phys. Chem. Engl. Transl.*, **37**, 1298 (1963).
- A. Nayfeh, "Perturbation Methods," John Wiley and Sons, Inc., New York (1973).
- J. B. Riggs, Dissertation, University of California, Berkeley (1977).

Technical Notes



Glassy Electrolyte Galvanic Cells

Tsutomu Minami, Tadashi Katsuda, and Masami Tanaka

Department of Applied Chemistry, University of Osaka Prefecture, Sakai-Shi, Osaka-Fu 591, Japan

Solid-state batteries have been studied extensively because of their advantages such as long shelf life, no cell leakage, wide temperature range of operation, miniaturization, and so on, compared with aqueous systems. These batteries are based on polycrystalline superionic conductors. Solid-state batteries using glassy superionic conductors have been reported in only a few papers (1-3), in spite of the fact that glasses have higher potentialities than polycrystals in the use as electrolytes in solid-state batteries; for

Key words: solid-state battery, superionic conductor, glassy electrolyte, solid-state ionics.

example, higher conductivities than crystals (4, 5), isotropic properties, ease of forming no-grain boundary disks, formation of thin films, and especially miniaturization.

In previous papers (4, 5), we have reported glass-forming regions and conductivities of the glasses in the systems AgI-Ag₂O-MoO₃ and AgI-Ag₂O-P₂O₅; some of these have conductivities as high as 10⁻² Ω⁻¹ cm⁻¹ at room temperature. The purpose of this paper is to present electrolytic properties of these glasses used in galvanic cells. Three compositions were chosen, as shown in Table I; two of these have very high

Table I. Properties of glassy electrolytes at 25°C

Glass No.	Composition (mole percent)	Total conductivity ^a (Ω ⁻¹ cm ⁻¹)	Electronic conductivity (Ω ⁻¹ cm ⁻¹)	Silver ion transport number ^b		Decomposition voltage (V)
				Emf method	Tubandt's method	
1	75AgI · 25Ag ₂ MoO ₄	1.1 × 10 ⁻²	8.7 × 10 ⁻⁹	0.999 ₆	0.992 ± 0.001	0.72
2	60AgI · 40Ag ₂ MoO ₄	6.0 × 10 ⁻⁴	—	0.999 ₆	0.972 ± 0.021	—
3	80AgI · 20Ag ₃ PO ₄	1.2 × 10 ⁻²	4.7 × 10 ⁻⁹	0.597 ₂	—	0.74

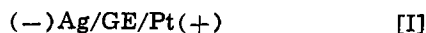
^a Ref. (4-6).

^b Ref. (4).

conductivities and are the most promising, and the other one a lower conductivity, for comparison with the above two. In the table several properties are summarized, some of which were cited from previous papers (4-6), and some will be shown below.

Pulverized samples were used in this experiment, as a first step toward miniaturized thin film batteries, on account of easy assembling of reproducible cells. The impedance of intergranules was reported to be small in these glassy superionic conductors (5-7).

As already reported (4, 5), the transport number of the glasses studied was determined to be practically unity by the emf and the Tubandt method. In the present investigation the small values of electronic transport number were measured by the Wagner d-c polarization technique (8). The cell used was the type



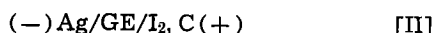
where GE denotes the glassy electrolyte. According to Wagner's analysis, the total electronic current, I , is given by

$$I = I_e + I_h = \frac{RTA}{FL} \left\{ \sigma_e \left[1 - \exp\left(-\frac{EF}{RT}\right) \right] + \sigma_h \left[\exp\left(\frac{EF}{RT}\right) - 1 \right] \right\} \quad [1]$$

where I_e and I_h are the current due to electrons and holes, respectively, R the gas constant, T the absolute temperature, A the electrode area, L the sample thickness, F the Faraday constant, E the applied voltage, and σ_e and σ_h the conductivity due to electrons and holes, respectively. If $\sigma_e \gg \sigma_h$, the second term in the braces is negligible and I becomes independent of E . If $\sigma_e \ll \sigma_h$, the first term is negligible and I varies exponentially with E . The experimental results shown in Fig. 1 indicate that $\sigma_e \gg \sigma_h$ holds for the present glassy electrolytes; $\sigma_e = 8.7 \times 10^{-9} \Omega^{-1} \text{cm}^{-1}$ for curve 1 (Glass No. 1) and $\sigma_e = 4.7 \times 10^{-9} \Omega^{-1} \text{cm}^{-1}$ for curve 2 (Glass No. 3) were obtained (Table I).

When the voltage is further increased, the decomposition voltage is determined. Figure 2 shows the current-voltage curve of cell [I] at 25°C for Glass No. 1; the decomposition voltage of 0.72V is obtained. The voltage for Glass No. 3 was 0.74V (Table I).

Open-circuit voltages (OCV) were measured for the cell



The anode (silver powder) and the electrolyte layer

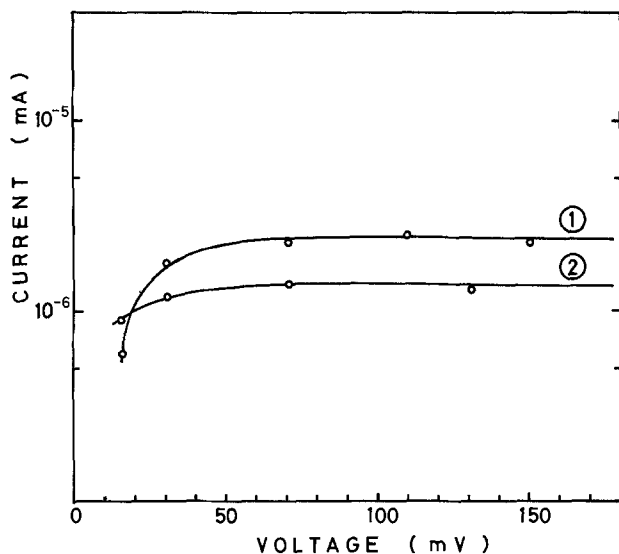


Fig. 1. D-C polarization behavior of glassy electrolytes in cell [I] at 25°C. 1: Glass No. 1, 2: Glass No. 3.

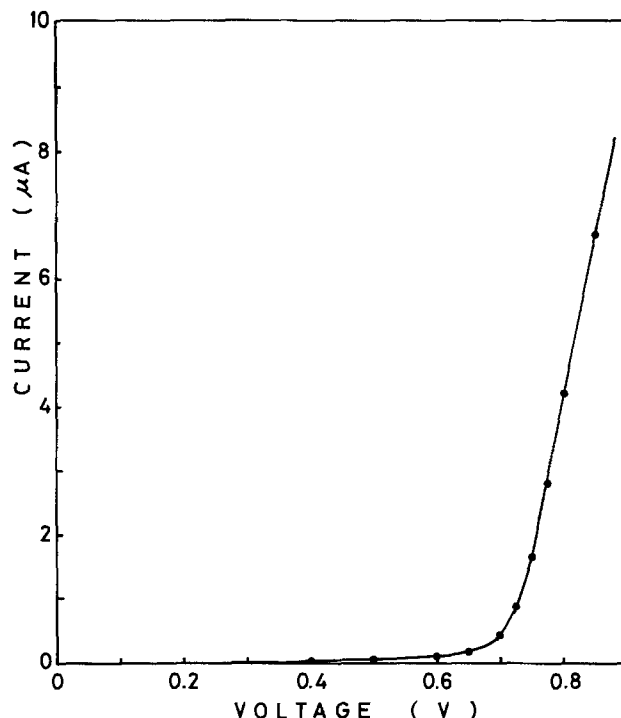
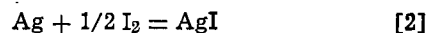


Fig. 2. Decomposition potential of Glass No. 1 at 25°C

were pressed under 2 t/cm² to form a pellet of 13 mm in diameter. The cathode mixture of iodine and carbon black (4:1 in weight ratio) was pressed to form a pellet. The cell was sealed with epoxy resin after the above two pellets were tightly contacted with screw bolts. The time dependence of OCV is shown in Fig. 3; the curves 1, 2, 3 are respectively for Glass No. 1, 2, 3. The initial values are 687.0, 687.0, and 685.4 mV for curves 1, 2, and 3, respectively, which were measured by the combination of a high impedance (>10¹⁴Ω) electrometer with a digital voltmeter. These values are very close to the theoretical value, 687.3 mV (9), for the standard emf of the formation of AgI by the reaction



The OCV are stable and decrease by 1-2 mV in 30 days.

Figure 4 shows the voltage-current characteristics of the cell



The anode was a mixture of silver powder and the sample electrolyte (1:1 in weight ratio) and the cathode was a mixture of I₂, carbon black, and the electrolyte (5:1:5 in weight ratio). The cell was con-

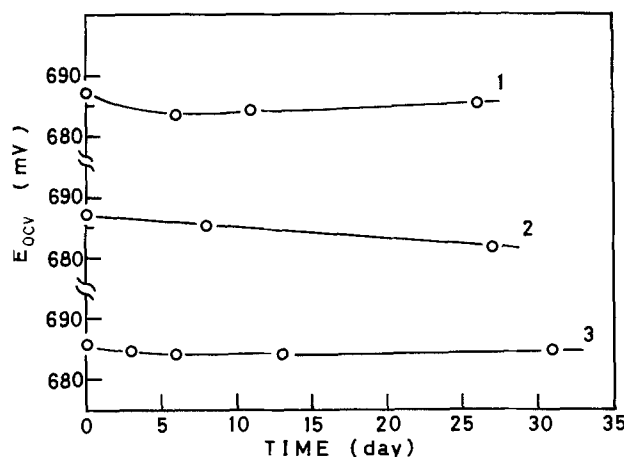


Fig. 3. Variation of open-circuit voltage of cell [II] with time. 1: Glass No. 1, 2: Glass No. 2, 3: Glass No. 3.

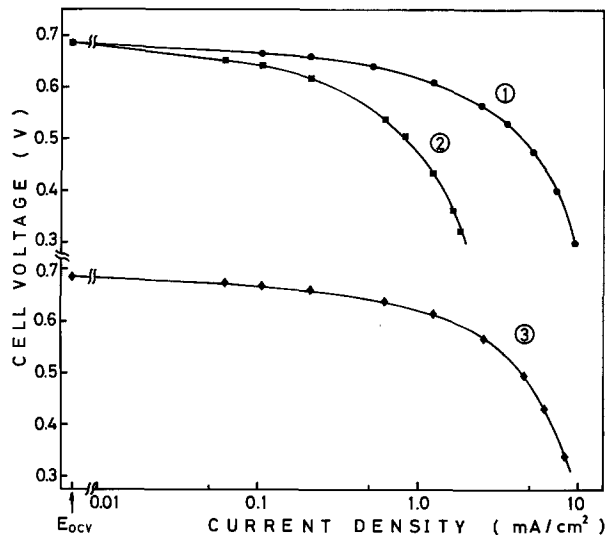


Fig. 4. Current-voltage curves of cell [III] at 25°C. 1: Glass No. 1, 2: Glass No. 2, 3: Glass No. 3.

structed by the same way as cell [II]. The voltage shown in the figure is plotted after 30 sec discharge at each current density. The curves 1, 2, and 3 are respectively for Glass No. 1, 2, and 3. The cells for Glass No. 1 and 3 give the current density of 1 mA/cm² without serious polarization. The reason for the voltage decrease at higher current densities is probably attributed to cathodic and anodic polarization (3); the improvement of the cathode and anode assembly will serve the higher current density.

Discharge curves of cell [III] under different loads are shown in Fig. 5. The cell of Glass No. 1 (curve 1), for example, showed the initial current density of 73, 137, and 600 μ A/cm² for the load of 10, 5, and 1.1 k Ω , respectively.

Figure 6 shows the steady current discharge curves of cell [III] for Glass No. 1; under 0.5 mA, for example, the cell had the capacity of 7.0 mA-hr and the energy density of about 1.7 W-hr/kg. The discharge parameters are summarized in Table II. These parameters are comparable to the cell using crystalline electrolytes (10). In view of the fact that the present results were obtained from handmade laboratory type cells, results from production type cells using the good qualities inherent in glasses would be expected to be even better.

Acknowledgment

This research was financially supported by a Grant-in-Aid for Developmental Scientific Research from the Ministry of Education of Japan and by the Asahi

Table II. Characteristics and performances of cell [III] (Glass No. 1) at 25°C

	Drain	
	0.2 mA	0.5 mA
Cell weight (g)	2.12	2.12
Electrolyte		
Thickness (cm)	0.11	0.11
Diameter (cm)	1.3	1.3
Operating time from OCV to 0.3V (min)	2300	840
Discharge capacity (mA-hr)	7.7	7.0
	(~10% theoretical of anode capacity)	
Energy density (W-hr/kg)	~2.1	~1.7

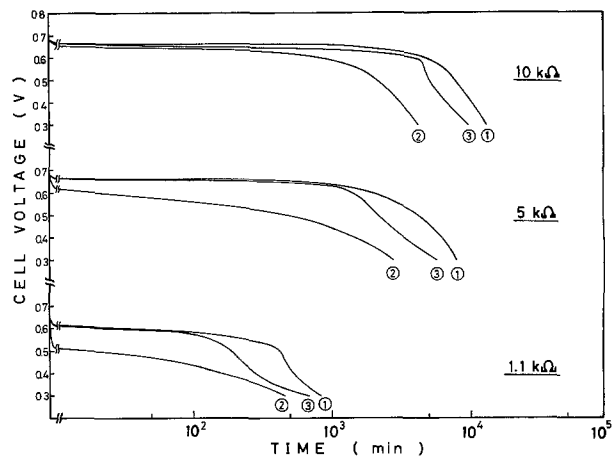


Fig. 5. Discharge curves of cell [III] under different loads at 25°C. 1: Glass No. 1, 2: Glass No. 2, 3: Glass No. 3.

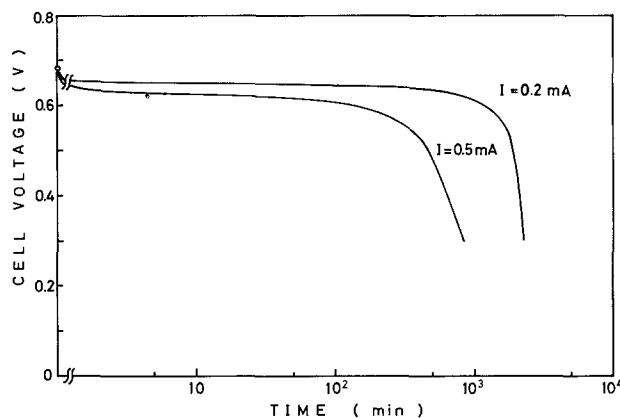


Fig. 6. Time dependence of voltage of cell [III] for Glass No. 1 at 25°C.

Glass Foundation for the Contribution of Industrial Technology.

Manuscript submitted Oct. 5, 1979; revised manuscript received Dec. 4, 1979.

Any discussion of this paper will appear in a Discussion Section to be published in the December 1980 JOURNAL. All discussions for the December 1980 Discussion Section should be submitted by Aug. 1, 1980.

Publication costs of this article were assisted by the University of Osaka Prefecture.

REFERENCES

1. B. Scrosati, F. Papaleo, and G. Pistoria, *This Journal*, **122**, 339 (1975).
2. A. Schiraldi, G. Chiodelli, and A. Magistris, *J. Appl. Electrochem.*, **6**, 251 (1976).
3. G. Chiodelli, A. Magistris, and A. Schiraldi, *Electrochim. Acta*, **23**, 585 (1978).
4. T. Minami, H. Nambu, and M. Tanaka, *J. Am. Ceram. Soc.*, **60**, 283 and 467 (1977).
5. T. Minami, Y. Takuma, and M. Tanaka, *This Journal*, **124**, 1659 (1977).
6. T. Minami and M. Tanaka, *J. Solid State Chem.*, **32**(2) (1980), In press.
7. A. Magistris, G. Chiodelli, and A. Schiraldi, *Electrochim. Acta*, **24**, 203 (1979).
8. C. Wagner, *Proc. C.I.T.C.E. VII*, 361 (1955).
9. T. Takahashi and O. Yamamoto, *Electrochim. Acta*, **11**, 779 (1966).
10. B. Scrosati, *J. Appl. Chem. Biotechnol.*, **21**, 223 (1971).

Some Aspects on the Self-Discharge of LiAl/FeS Experimental Cells with Molten Salt Electrolyte

Reinhard Knödler* and Gotthold Böhme

Battelle-Institut e.V., Frankfurt am Main, Germany

and Waldemar Borger

VARTA Batterie AG, Kelkheim, Germany

The LiAl/FeS battery with molten KCl-LiCl electrolyte operates at a temperature of about 450°C and is a promising candidate for load-leveling and traction applications (1-4).

As part of the general R&D program of VARTA Batterie AG, Kelkheim, Battelle-Institut e.V., Frankfurt am Main was commissioned to conduct investigations into the self-discharge behavior of LiAl/FeS cells. Although it is well known from the measurement of coulomb efficiencies that the self-discharge rate is relatively low, quantitative data on this important property are not available. The objectives of the work described were therefore (i) to determine quantitatively the rate of self-discharge, (ii) to discover the reasons for self-discharge, and (iii) to examine the effect of cell leakages on the rate of self-discharge. In order to isolate the principal effects, the investigations were carried out in cell types in which self-discharge reactions caused by contacts between the electrodes could be excluded from the start. Thus, it was possible to determine the smallest possible self-discharge rate of this battery system. Since this work is in a preliminary stage, an explanation of possible mechanisms of self-discharge is not given. Work in this direction is now in progress.

Experiment

The cells had a utilized capacity of 6 A-hr, limited by the positive electrode. They were assembled in an argon atmosphere in a glove box and operated in open air.

Figure 1 shows the cell configuration. The electrodes were about 6 mm thick. The positive electrode was in contact with the stainless steel casing. It was prepared in the uncharged state by hot-pressing a mixture of Li₂S, Fe, and electrolyte powders. In order to prevent mass losses, the electrode was wrapped in a 300-mesh stainless steel screen. The preparation of the negative electrode is described in detail elsewhere (5). This electrode consists of a porous aluminum disk, also wrapped in a stainless steel screen. The distance between the electrodes was about 10-15 mm (investigations involving smaller spacings are now in progress). The capacity of the negative electrode was made about 30% higher than that of the positive electrode. Thus, the β -field of the Li-Al phase diagram has not been reached. The observed increase in voltage (see Fig. 2) therefore may be due to the formation of small amounts of FeS₂.

After having been assembled in the glove box the cells were soldered with a special solder. Conventional current feed throughs with ceramic bodies or spark plugs were used, which were carefully sealed with a ceramic cement. As the feed throughs were not in contact with the melt (see Fig. 1), it was possible to use 99.9% Al₂O₃ for the insulating ceramic. No

attack was observed at these materials after the experiments. After heating to the operating temperature of 430°C, the cells were charged to 1.6V with constant current (in most cases at a 20 hr rate).

The actual rate of self-discharge was determined by operating the cell for some time at OCV (i.e., without current) and subsequently recharging it to 1.6V with a constant current density of 20 mA/cm². The capacity loss, expressed in percent per day, has been calculated from the amount of charge needed for this procedure. This is called the self-discharge rate of the cell.

Results

Figure 2 shows an example of the behavior of the OCV as a function of the operating time. The decrease of the OCV to its final value of 1.33V was relatively rapid at the beginning of the experiment and slowed down as the operating time progressed. The self-discharge rate, as calculated from the various amounts of charge indicated in Fig. 2, is shown in Fig. 3a. This is a typical behavior which was observed in a series of cells. It shows that (i) at the beginning of the experiment the self-discharge rate is relatively high; it may reach values of up to 10% per day, (ii) the self-discharge rate decreases in the course of the experiment to values below 1% per day. This low value can be maintained even if the cell is cycled between

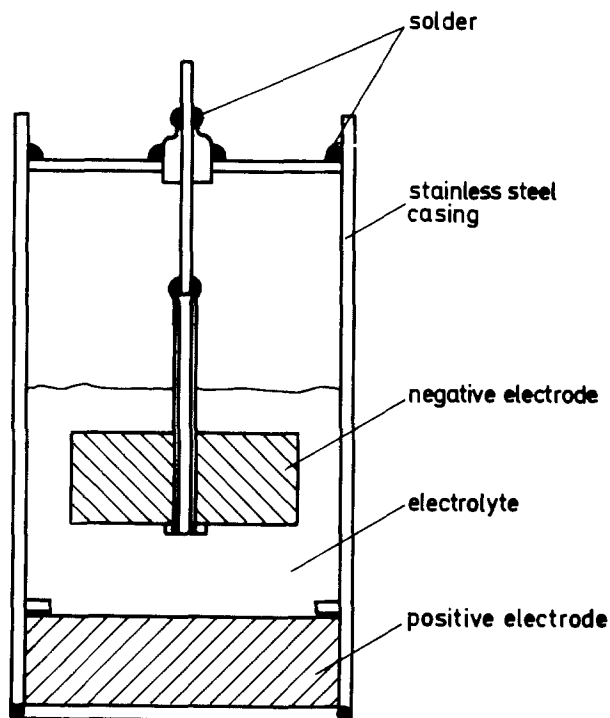


Fig. 1. Cell configuration

* Electrochemical Society Active Member.

Key words: lithium metal sulfide battery, self-discharge, molten salt electrolyte.

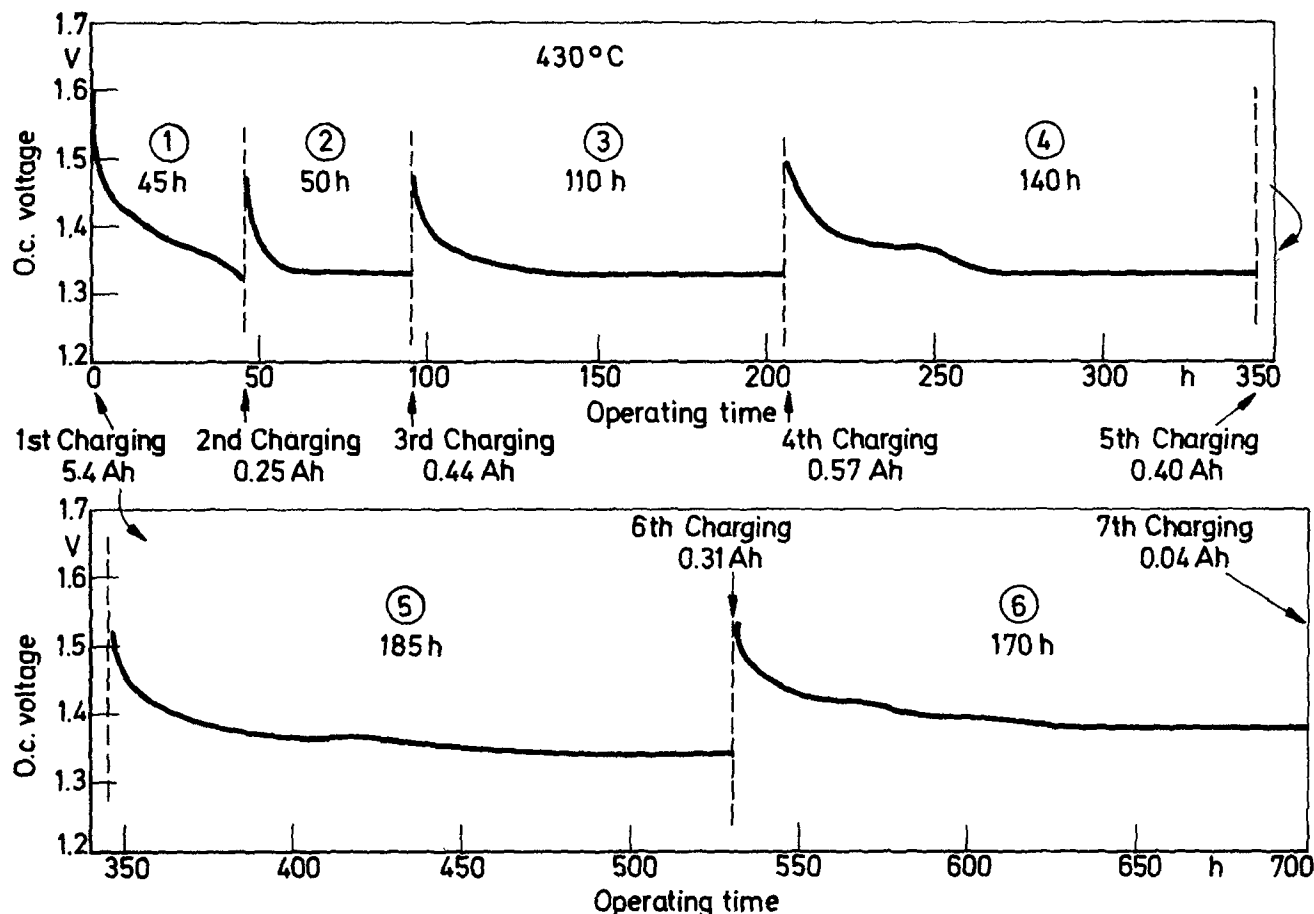


Fig. 2. Open-circuit voltage after repeated charging to 1.6V with 10 mA/cm²

0.8 and 1.6V with current densities of up to 50 mA/cm². The decrease of the self-discharge rate can also be seen from the upward trend both in the starting voltage and the final voltage.

Experiments were carried out in order to determine the influence of a gas leakage into a cell on the self-discharge rate. For this purpose the cell atmosphere, normally consisting of argon, was replaced successively by nitrogen, oxygen, and air. Figure 3b shows the effect of these operations on the self-discharge rate. Within the accuracy of measurement, nitrogen did not influence the rate, whereas oxygen and air had a substantial effect. Air is obviously more dele-

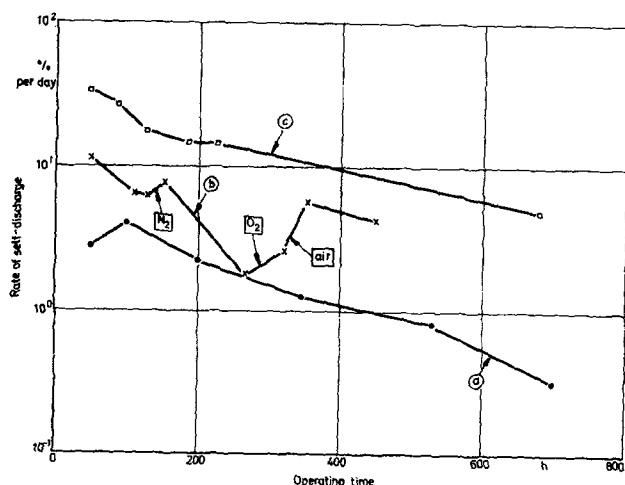


Fig. 3. Rate of self-discharge of different cells: curve a, argon atmosphere (pure electrolyte); curve b, nitrogen, oxygen, and air atmosphere (pure electrolyte); curve c, argon atmosphere and addition of 2 weight percent Li₂O to the electrolyte.

terious than oxygen. This may be attributed to the moisture in the air. These observations were confirmed by examining the cell by x-ray spectroscopy after the experiment. Li₃N or related nitrides have not been detected within the limits of error, but considerable amounts of Li₂O₂ were present. The effect of H₂O is currently under study.

A further confirmation of the finding indicating that the occurrence of Li₂O₂ is responsible for the enhanced self-discharge rate was obtained by an experiment in which 2% by weight of Li₂O was added to the electrolyte before the experiment. Figure 3c shows that in this case the self-discharge rate is considerably higher than in the absence of Li₂O. It decreases as the operating time progresses, but the final value is still as high as about 5% per day. After the experiment, examination of the cell revealed that Li₂O was no longer present in the electrolyte but Li₂O₂ was formed instead. Thus, in the case of a cell leakage, an increase in the self-discharge rate to about 5% per day has to be expected, probably as a result of the formation of Li₂O₂. This statement is, of course, only valid if—as in the experimental cells used in this case—the electrodes are covered with electrolyte.

In order to confirm these findings, the electronic conductivities of pure LiCl-KCl melts and of melts with Li₂O and Li₂O₂ additions were measured in conductivity cells with blocking electrodes (made of molybdenum). These measurements were carried out by determining the frequency dependence of the cell impedance. In order to remain in the linear region of the current voltage curve according to the Hebb-Wagner theory (6), the sinusoidal voltage was always kept below RT/F . This is the reason why we were not able to distinguish between electron and hole conductivity.

Figure 4 shows measurements in pure LiCl-KCl melts and in melts with additions of Li₂O and Li₂O₂. At

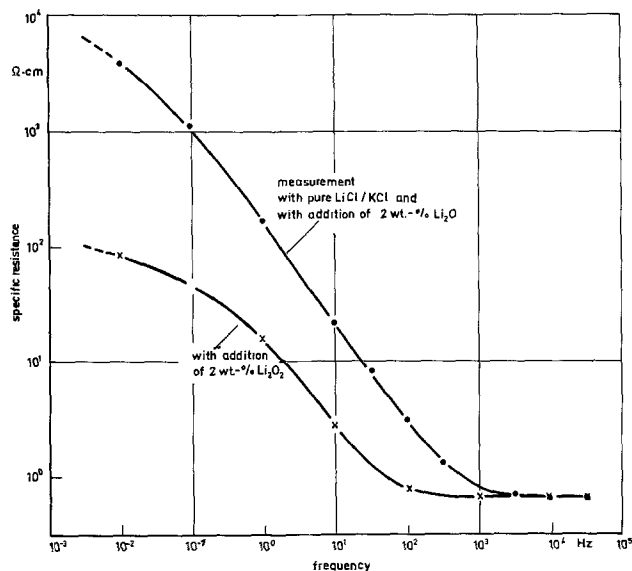


Fig. 4. Frequency dependence of the specific resistance of a cell with blocking molybdenum electrodes.

high frequencies the value for the pure ionic conductivity of the melt was obtained independent of the substances added. In the case of the pure melt and the melt with Li_2O the curve can be extrapolated to low frequencies to obtain a value of the order of magnitude of about $10^4 \Omega\text{-cm}$. This corresponds well with data already available on the electronic conductivity of the melt (7). If, however, Li_2O_2 is added instead of Li_2O , the specific resistance is about two orders of magnitude lower. According to these findings, the reason for the higher self-discharge in the presence of air may be the electronic conductivity of the melt caused by the formation of Li_2O_2 . However, other possible mechanisms may be considered, e.g., shuttle mechanisms as observed in the Ni-Cd battery. In this case an "intermediate" product, e.g., Li_2O , would migrate between the two electrodes, becoming alternately oxidized and reduced thus causing self-discharge effects. Investigations in this direction are being continued.

Conclusions

The findings described above allow the following conclusions:

1. The self-discharge rate of LiAl/FeS cells is less than 1% per day. The rate decreases during operation

of the cell and can be kept low even if the cell is being cycled.

2. The electronic conductivity of the molten electrolyte is drastically increased by the addition of Li_2O_2 . In contrast, this effect does not occur with Li_2O . In a complete cell, Li_2O will be oxidized to Li_2O_2 , thus causing self-discharge due to electronic conductivity.

3. The presence of air or oxygen in the cell atmosphere causes an increase in the self-discharge rate. Nitrogen has no effect. The consequence of the presence of air (or oxygen) is the formation of Li_2O_2 in the electrolyte. Thus, increased conductivity of the melt may be one of the reasons for the enhanced self-discharge.

Acknowledgment

This work was supported by the Bundesministerium für Forschung und Technologie within the Energy Research program directed by Kernforschungsanlage Jülich (project No. ET 5138 A) and by VARTA Batterie AG. We wish to thank Prof. Dr. Winsel, Dr. Voss, and Dr. Binder for many valuable discussions in the course of this work.

Manuscript submitted Sept. 10, 1979; revised manuscript received Dec. 5, 1979.

Any discussion of this paper will appear in a Discussion Section to be published in the December 1980 JOURNAL. All discussions for the December 1980 Discussion Section should be submitted by Aug. 1, 1980.

Publication costs of this article were assisted by Battelle-Institut e.V.

REFERENCES

1. P. A. Nelson *et al.*, Argonne National Laboratory Report, ANL 79-1 (March 1979).
2. R. J. Rubischko, L. W. Eaton, Y. M. F. Marikar, E. J. Chaney, and R. E. Thompson, Abstract 92, p. 245, The Electrochemical Society Extended Abstracts, Pittsburgh, Pennsylvania, Oct. 15-20, 1978.
3. R. Hudson and K. Gentry, Abstract 91, p. 242, The Electrochemical Society Extended Abstracts, Pittsburgh, Pennsylvania, Oct. 15-20, 1978.
4. L. R. McCoy and S. Sudar, Abstract 90, p. 240, The Electrochemical Society Extended Abstracts, Pittsburgh, Pennsylvania, Oct. 15-20, 1978.
5. R. Knödler, W. Baukal, and G. Böhme, *This Journal*, 126, 1853 (1979).
6. H. Rickert, "Einführung in die Elektrochemie fester Stoffe," Springer Verlag, Berlin, Heidelberg, New York (1973).
7. R. J. Heus and J. J. Egan, *J. Phys. Chem.*, 77, 1989 (1973).

Electrochemical Deionization Via Ion Adsorption Electrodes

Arnold Factor

General Electric Corporate Research and Development Center, Schenectady, New York 12301

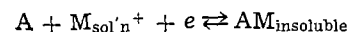
and Thomas O. Rouse

General Electric Large Transformer Technical Resources Operation, Pittsfield, Massachusetts 01201

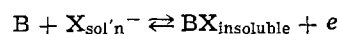
This report describes the first successful example of electrochemical deionization using ion adsorption electrodes based on organic redox polymers. In this system cations are reversibly bound to electrochemically generated anionic groups and anions to electrochemically generated cationic groups. The requirements for this type of electrochemical ion adsorption are illustrated in Eq. [1] and [2]. In these reactions,

Key words: redox polymers, desalination, water deionization.

A and B must be insoluble and, when fabricated into an electrode, be able to undergo electrochemical reaction leading to the reversible formation of an insoluble



Cation adsorption (cathode) [1]

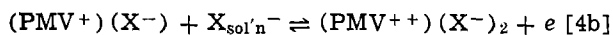
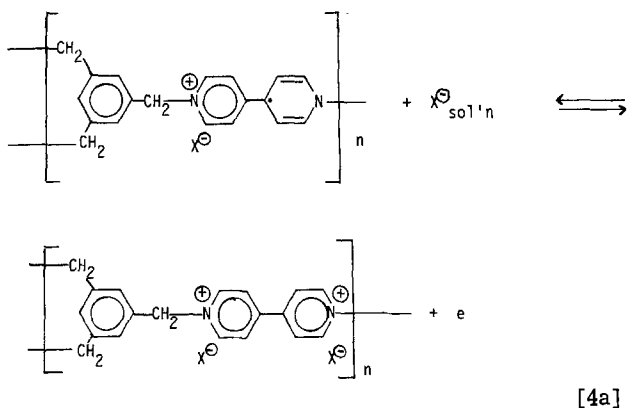
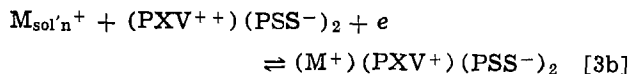
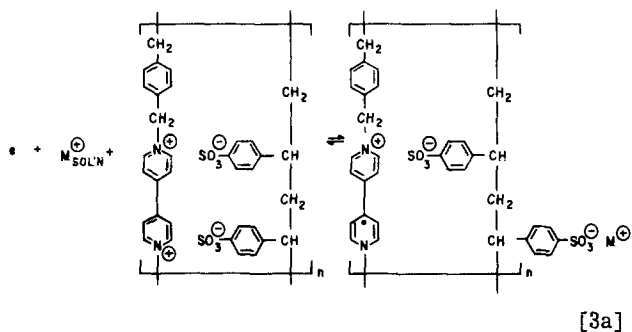


Anion adsorption (anode) [2]

product within the electrode. Cations M^+ and anions X^- must be removed from the water electrolyte in the formation of these insoluble products. Cation and anion-adsorbing electrodes together form an electrochemical cell which under an applied voltage is capable of demineralizing water for practical use. As illustrated in Fig. 1, the electrochemical reactions should proceed in either direction so that the cell can be rejuvenated by reversing the cell voltage and the adsorbed cations and anions rejected into a waste stream. On repetitively reversing the voltage, ions can be repeatedly removed from one stream and rejected into another.

Previously, this type of ion adsorption cell was examined by Arnold and Murphy (1) using activated carbons as the insoluble reactants. However, these cells showed limited adsorption capacities and poor cycle life.

It has been found that a deionization cell could be successfully produced based on the previously reported redox polymers, polyviologens (2). In this cell, the cation-absorbing cathode involved the reduction of the neutral, water-insoluble polyelectrolyte complex of polyxylylviologen and poly(styrene sulfonate) ($PXV(PSS)_2$) (2) to its anionic form, Eq. [3]. The anion-absorbing anode involved the oxidation of the cross-linked radical cation on polvmesitylviologen ($PMV-V_2$) (2) to its dicationic form, Eq. [4]



Experimental

Electrode preparation.—Electrodes were prepared by intimately mixing weighed amounts of Pettinos 6427 graphite powder (surface area-10 m^2/g) and ground (to pass 400 mesh) redox polymer. The usual proportions were two parts graphite to one part electroactive material. An anhydrous solution of polyvinylidene fluoride (PVF) (Pennsalt Corporation) in dimethylacetamide (DMA) was added to the mixture as a binder. The resulting paste was painted on the lower section of one side of a 10 mil thick rectangular graphite foil (Union Carbide Company), and immersed

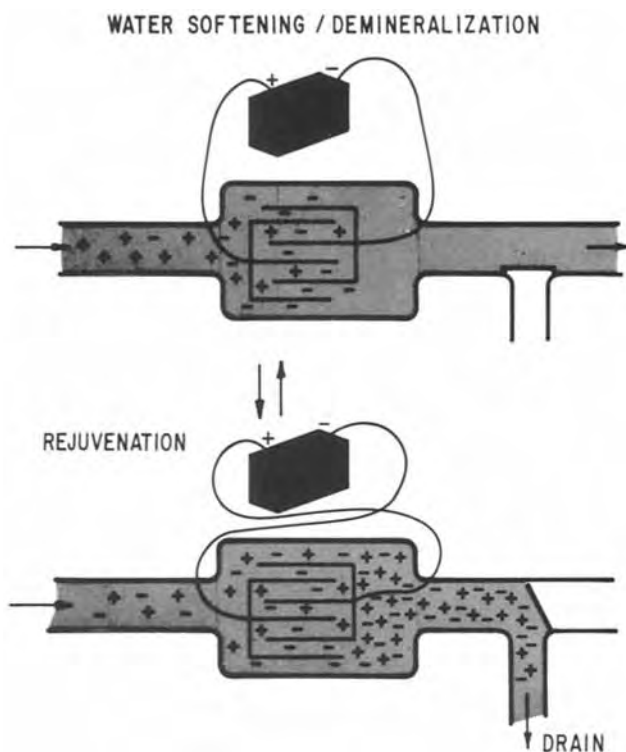


Fig. 1. Reversible ion absorption

in distilled water to leach out the DMA and set the binder. Leaching was continued in several fresh portions of water for a minimum of 12 hr. The binder content of the final porous body was normally 5%. The electrode normally consisted of 25 mg of porous material per cm^2 of foil. A contact was riveted to the foil prior to electrode fabrication.

The electrode capacity was found to greatly depend on the degree of dispersion of graphite in the polymer. The highest electrochemical capacities were achieved by forming the redox polymer in the presence of graphite followed by the addition of more graphite in the grinding step. In the case of the $PXV(PSS)_2$ electrode, the most efficient electrodes were prepared by precipitation of the complex onto an equal weight of graphite by flash vacuum evaporation of acetone from a $NaBr/acetone/H_2O$ (30/55/15 by weight) ternary solution (2, 4) of the complex. In this manner, electrodes were obtained with capacities up to 0.5 meq/g in 0.1M $NaCl$ or 80% of the theoretical capacity. In the case of the electrodes formed from the cross-linked $PMV(Br)_2$, the most efficient electrodes were formed by polymerizing the redox polymer in the presence of graphite. Capacities up to 0.5 meq/g were obtained for electrodes containing 50% graphite, half of which was added during the grinding step.

Electrolysis—electrode optimization.—In this work, the final cell was constructed with a cathode and anode which had been separately optimized using constant current electrolysis (3). The electrochemical cells used in this study consisted of two compartments separated by a medium fritted glass disk and an agar-KCl plug. Generally, the electrolyte in the test electrode compartment was 0.5M $NaCl$. A reference electrode dipped into this same compartment. The electrolyte solutions were deaerated with nitrogen and covered with flowing nitrogen during electrolysis. The solutions were not stirred.

Electrolysis was performed at constant current against a silver sheet preanodized in chloride solution. Potentials were measured against a Beckman silver-silver chloride reference electrode. No evidence of silver migration into the test compartment was observed on prolonged cycling. Electrolysis currents

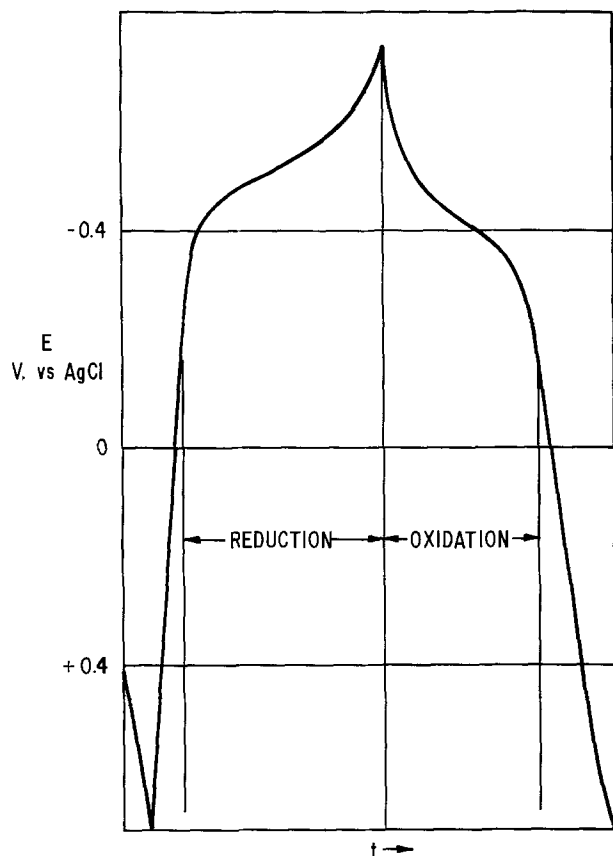


Fig. 2. Potential-time curve for poly-p-xylylviologen polystyrene sulfonate [PXV(PSS)₂], electrolysis time ~5 hr per half-cycle.

were in the range of 0.3-2 mA/cm², usually the former. Provision for automatically reversing the current at preset values of working electrode potential was made through a circuit activated by an optical meter and controller (Assembly Products, Incorporated) as illustrated in Fig. 2. Electrodes prepared without redox polymers gave only rapid and linear potential changes in the potential range of interest on current application and reversal. The coulombs consumed in these charging processes were subtracted in the data below.

Sodium and calcium analyses were done by atomic adsorption.

Demonstration of reversible deionization.—The cell used was assembled with a silver electrode between the cation and anion electrodes. The silver electrode was a fine screen, heat-sealed into a double wrap of nylon screen. The cell was filled with 0.0125M NaBr and the solution was deaerated by bubbling with nitrogen gas presaturated with water. The electrolysis current was held constant at 5.65 mA. The potential-time curves for the electrode of interest were recorded against a silver-silver chloride reference electrode. In addition, the cell potential was recorded when the ion adsorption electrodes were electrolyzed against each other. Duplicate analytical

Table I. Electrolysis of (PXV⁺⁺)(PSS⁻)₂^a

Electrolyte — 0.025M NaCl ^b								
Cycle No.	%C _c	C _c	C _c ^{N_a} /C _c	%C _a	C _a	C _a ^{N_a} /C _a		
1	46	0.32	0.84	37	0.26	0.85		
2	37	0.25	0.80	30	0.20	1.00		
3	35	0.24	0.87	30	0.20	1.00		
30	19	0.13	0.77	16	0.11	0.91		
31	19	0.13	0.77	16	0.11	0.91		
Electrolyte — 0.0125M CaCl ₂ ^b								
Cycle No.	%C _c	C _c	C _c ^{Ca} /C _c	%C _a	C _a	C _a ^{Ca} /C _a		
1	34	0.33	0.85	25	0.25	0.80		
2	27	0.27	0.81	23	0.23	0.87		
3	26	0.26	0.77	21	0.21	0.90		
Electrolyte — 0.0125M NaCl + 0.0125M CaCl ₂ ^c								
Cycle No.	%C _c	C _c	C _c ^{N_a} /C _c	C _c ^{Ca} /C _c	%C _a	C _a	C _a ^{N_a} /C _a	C _a ^{Ca} /C _a
1	24	0.21	0.05	0.90	17	0.15	0.06	0.87
2	18	0.17	0.00	0.82	16	0.14	0.00	0.93
3	18	0.17	0.06	0.82	16	0.14	0.00	0.93
51	11	0.12	0.00	0.92	11	0.10	0.02	1.10

^a Electrode material — 50% PXV(PSS)₂, 50% graphite in precipitate, no added graphite, 5% PVF; area — 6.0 in.²; solution volume — 30.0 ml; potential limits +0.2 and -0.7V vs. AgCl.

^b Electrode weight — 200 mg/cm², current 0.3 mA/cm².

^c Electrode weight — 100 meq/cm², current 0.15 mA/cm².

samples of electrolyte were removed at each step of the electrolysis and stored in polyethylene bottles.

Results and Discussion

In reporting the results of this work, the following abbreviations were used: %C = percent of theoretical coulombic capacity; C_{c,a} = coulombic capacity in milliequivalents calculated from the coulombs passed during the cathodic, c, or anodic, a, half-cycle; C_{c,a}^A = adsorption capacity in milliequivalents calculated for ion A from the change in solution concentration; and C_{c,a}^A/C_{c,a} = coulombic efficiency for removal (or replacement) of ion A from solution.

As indicated above, the electrode capacity was found to greatly depend on the degree of dispersion of graphite in the polymer. The highest percent capacities (%C) were achieved by forming the redox polymer in the presence of graphite followed by the addition of more graphite in the grinding step. While experimental electrodes were not subjected to exhaustive cycle life tests, the electrochemical capacity was observed to remain constant over a large number of cycles. For example, the capacity of a PXV(PSS)₂ electrode cycled in a solution of 0.0125M NaCl and in NaBr was 0.39 meq/g in the first cycle, and 0.33 meq/g in the second through 160th cycle. Generally, similar behavior was found for both PXV(PSS)₂ and PMV(X)₂ electrodes in even more concentrated NaCl or CaCl₂ for as many as 300 cycles.

In the case of the PXV(PSS)₂ electrode, cations were shown to be electrochemically removed and replaced in solution with a coulombic efficiency of greater than 80%. The results of three electrolyses

Table II. Electrode characteristics^a

Electrode	Material	ω _a	ω _b	ω _c	ω _d	DMA, ml	A _{cm} ²	C ₀ , meq	%C ₁	%C ₂
Cation-adsorbing	Meta-PXV(PSS) ₂	0.488	0.488	0.588	0.078	1.75	55	0.68	26	21
Anion-adsorbing	PMV(Br) ₂	0.129	0.101	0.125	0.018	0.41	18	0.307	70	72

^a ω_a = weight of polymer in grams; ω_b = weight of graphite powder in precipitated sample; ω_c = weight of graphite powder added during fabrication; ω_d = weight of polyvinylidene fluoride; DMA = total volume dimethylacetamide; C₀ = calculated electrode capacity, meq; %C₁ = percent actually available coulombic capacity found for similar small test electrodes; %C₂ = percent actually available coulombic capacity found for this experiment.

Table III. NaBr solution demineralization by ion-absorbing electrodes

Step	Operation ^e	Electrolyte volume, ml	C _{Br} , meq/ ml × 10 ²	Br, ^f meq × 10	C _{Na} , meq/ ml × 10 ²	Na, meq × 10	ΔBr ^g observed, meq × 10	ΔNa observed, meq × 10	ΔBr ^h cal- culated, meq × 10	Na cal- culated, meq × 10	Current efficiency ⁱ	
											Br	Na
1	Introduced electro- lyte and deaerated	Beginning—25.0	1.29 ± 0.015	3.22	1.23 ± 0.005	3.08	+0.20 ± 0.04	+0.14 ± 0.02	0.00	0.00	—	—
		End—25.0	1.37 ± 0.005	3.43	1.29 ± 0.005	3.22						
2	a) Removed 1.2 ml b) 02 cathode vs. Ag [†] , 70.3 min	23.8	1.37 ± 0.005	3.26	1.29 ± 0.005	3.08	-0.09 ± 0.03	+0.16 ± 0.04	[0.00]	0.00	0.94	—
		23.8	1.33 ± 0.01	2.17	1.36 ± 0.015	3.24						
3	a) Removed 1.2 ml b) 02 anode vs. Ag, 62.5 min	22.6	1.33 ± 0.01	3.01	1.36 ± 0.015	3.08	+0.18 ± 0.02	+0.05 ± 0.03	[0.00]	0.00	0.91	—
		22.6	1.41 ± 0.01	3.10	1.58 ± 0.000	3.58						
4	a) Removed 1.2 ml b) 02 cathode vs. Ag, 61.3 min	21.4	1.41 ± 0.01	3.02	1.58 ± 0.000	3.38	+0.06 ± 0.11	+0.11 ± 0.02	[0.00]	0.00	1.03	—
		21.4	1.44 ± 0.05	3.08	1.63 ± 0.010	3.49						
5	a) Removed 1.2 ml b) Added 5.0 ml 0.0129 (M) NaBr	20.2	1.44 ± 0.05	2.91	1.63 ± 0.010	3.29	+0.57 ± 0.12	+0.36 ± 0.05	+0.64	+0.64	—	—
		25.2	1.38 ± 0.02	3.48	1.48 ± 0.015	3.65						
6	a) Removed 1.2 ml b) 02 anode vs. 01, 49.5 min	24.0	1.38 ± 0.02	3.31	1.45 ± 0.015	3.48	-1.05 ± 0.05	-1.01 ± 0.04	-1.71	-1.71	0.62	0.59
		24.0	0.94 ± 0.00	2.26	1.03 ± 0.000	2.47						
7	a) Removed 1.2 ml b) 02 cathode vs. 01, 26.2 min	22.8	0.94 ± 0.00	2.14	1.03 ± 0.000	2.35	+0.23 ± 0.07	+0.36 ± 0.04	+0.91	+0.90	0.21	0.40
		22.8	1.04 ± 0.03	2.37	1.19 ± 0.020	2.71						

¹Br = $X \times C_{Br}$. Bromine was determined by silver ion titration.

² ±σ = $\sqrt{\sigma_{beginning}^2 + \sigma_{end}^2}$.

³ ΔBr_{calc} = $\frac{t/F}{V + Br_{best}(initial) + 5.0 \times 1.29 \times 10^{-2}}$.

ΔBr_{calc} = $\frac{V + 5.0}{V + 5.0}$

⁴ Current efficiency = ΔBr_{obs.}/ΔBr_{calc.}.

⁵ Calculated ΔBr if the anion electrode reaction failed.

⁶ 01 is cation-absorbing electrode, 02 is anion absorbing electrode.

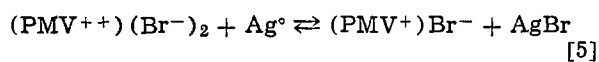
[†] Stands for 02-anion absorbing electrode operated as cathode against Ag anodes.

are given in Table I. The last electrolysis, which contained both sodium and calcium ions, demonstrated that calcium ions were selectively removed and replaced with 90% coulombic efficiency even in the presence of a fourfold excess of sodium ions.

Additional chemical effects were apparent in this experiment. During equilibration of the electrode in the mixed electrolyte prior to the start of electrolysis, the sodium ion in solution increased by 0.14 meq while the calcium ion decreased by a like amount. This is due to the replacement of residual sodium ions in the electrode by calcium ions. During the 50 cycles, the calcium ion in solution had decreased by an additional 0.27 meq. The electrode was calculated to contain 0.86 meq of PXV(PSS)₂. Thus after 50 cycles the system lost 48% of its initial capacity to reversibly absorb ions.

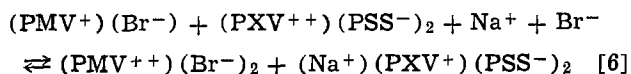
The reversible adsorption of anions by a PMV(Br)₂ electrode and the demonstration of reversible demineralization by a cell made of a PMV(Br)₂ anode and a PXV(PSS)₂ cathode was demonstrated in the same experiment. The characteristics of the electrodes used are given in Table II.

In the first part of this experiment, anion adsorption by the PMV(Br)₂ electrode was demonstrated in a cell where a silver screen was used as the counter-electrode (Steps 2 through 4 in Table III). The theoretical cell reaction, shown in Eq. [5], predicts no net change in bromide ion concentration



The occurrence of other reactions of the anion-adsorbing material would cause changes in bromide ion concentration. The analytical results for bromide ions show that the postulated reaction did take place and bromide ions were removed from and returned to the solution nearly quantitatively.

Demineralization, Eq. [6], was demonstrated in the second segment of the experiment consisting of electrolysis of the anion-adsorbing electrode against the cation-adsorbing electrode (Steps 6 and 7 in Table III)



In Step 6, the reaction proceeded as written, both sodium and bromide ions were removed, and demineralization was demonstrated. In Step 7, the reaction was reversed and both cations and anions were returned to the electrolyte. The results for Step 6 reinforce the earlier conclusion that the reaction of the anion adsorbing material proceeded as anticipated.

Conclusions

These preliminary experiments demonstrate that an ion adsorption cell based on polyviologen redox polymers is feasible. In addition, the high selectivity shown for calcium ions over sodium ions for the PXV(PSS)₂ electrode would be particularly useful in applications requiring the selective removal of multivalent ions in the presence of monovalent ions, e.g., water softening. Further work will be required to fully define the requirements needed to use the above cell in a practical application.

Acknowledgments

The authors would like to gratefully acknowledge J. R. Wilfore for his able assistance and the United States Department of Interior, Office of Saline Water for financial support for part of this work under Contract No. 14-01-0001-612.

Manuscript submitted Nov. 7, 1979; revised manuscript received Jan. 8, 1980.

Any discussion of this paper will appear in a Discussion Section to be published in the December 1980 JOURNAL. All discussions for the December 1980 Discussion Section should be submitted by Aug. 1, 1980.

Publication costs of this article were assisted by General Electric Company.

REFERENCES

1. B. B. Arnold and G. W. Murphy, *J. Phys. Chem.*, **65**, 135 (1961).
2. A. Factor and G. E. Heinsohn, *Polym. Lett.*, **9**, 289 (1971).
3. T. O. Rouse and A. Factor, Office of Saline Water, Research and Development Progress Report No. 524 (April 1970).
4. A. S. Michaels, *Ind. Eng. Chem.*, **57**, 32 (1965).

The Morphology of Viologen Films on Transparent Oxide Electrodes

Gabriel G. Barna*

Texas Instruments Incorporated, Dallas, Texas 75265

Viologens, the dialkyl derivatives of 4,4'-dipyridinium salts, have been widely investigated for possible use in electrochromic displays. Although electrochemical studies have been performed on the various alkyl derivatives (1), the 1,1'-diheptyl-4,4'-dipyridinium salts have been typically employed in display development. The kinetics of the cathodic deposition of this species, and the subsequent reoxidation of the purple film, have been studied (2, 3). Other work has been performed on the effect of the anions on the film formation and its adherence to the electrode (4). These papers have also addressed the question of the nucleation of the film (2) and have shown indirect evidence for the recrystallization of the deposited film (5).

* Electrochemical Society Active Member.

Key words: electrochromics, viologen films, reorientation.

During our development of a display package, a procedure was generated which resulted in the uniform deposition of this heptylviologen onto transparent oxide electrodes (6). By following the rigorous cleaning and surface activation procedures, sealed patterned cells could be constructed such that the deposited viologen film would be typically uniform in appearance. However, these cells generally degraded by a mechanism that prevented the complete erasure of the deposited film.

This paper describes the experimental technique that was employed to show that there is an open-circuit reorientation of the deposited heptylviologen film. The demonstrated change in the birefringence of the film proves that the material gradually assumes a greater degree of optical anisotropy. The nature of this ordered phase can only be surmised. Considering

that the molecular geometry of this species is very similar to the class of biphenyl liquid crystals, it is possible that the film gradually reorients itself into a liquid crystal-like phase, with some degree of intermolecular orientation between adjacent molecules. Or, the film can assume a truly crystalline form. The data generated cannot distinguish between these two cases. Therefore, in this paper, the less constraining term of "reorientation" will be employed. The "recrystallization" terminology sometimes used in the existing literature to describe this phenomenon is deemed to have more rigorous implications than can be supported by the available data. It is postulated that an accumulation of this reoriented material is responsible for the incomplete erasure of the film.

Experimental

The data were collected in sealed, patterned cells. The front plate was a piece of Nesatron 20 (PPG Industries) indium-tin oxide glass etched to form the usual seven segment "1888" pattern, with an insulating layer of SiO_2 then deposited over the leads. The backplate was a piece of regular soda-lime glass, with Pd thermally evaporated around its perimeter. Pd-black was subsequently electroplated onto this film, this perimeter electrode serving as the counterelectrode in the sealed cell. Prior to assembly, the backplate was extracted with deionized water and the front plate was cleaned and treated as previously described (6). The cell was assembled with an epoxy perimeter seal and filled, under nitrogen, with a 0.1M n-heptyl-viologen phosphate/1M dihydrogenphosphate solution. The fill hole was then epoxy filled.

Leads were attached to the counterelectrode and several individual segments on the front plate. One segment was turned on by applying -1 VDC between it and the counterelectrode. This viologen-deposited segment (poised by the equilibrium potential between the solid and dissolved radical cation) was then employed as the reference electrode in all the subsequent electrochemical experiments.

The cells were driven with a Wenking Model ST72 potentiostat and a Wenking VSG Voltage Scan Generator. The timing was obtained from an HP 3311A Function Generator and the charge measured with a PAR Model 379 digital coulometer. The electrooptical measurements were all performed in the three-electrode potentiostatic drive mode. For the cycling experiments, the viologen film was deposited during a 5 sec cathodic pulse at variable potentials, and reoxidized at $+400$ mV for 5 sec.

With the described perimeter counterelectrode, optical measurements could be made, in transmission, with a Leitz Wetzlar polarizing microscope. Using the 25X objective, the field of view was contained entirely within the driven segment. The transmitted light was fed directly, via the vertical optics of the trioptic head, into a Gamma Scientific photomultiplier tube equipped with a photopic filter. The signal was analyzed by a Gamma Scientific DR-2 Digital Radiometer. Illumination was provided by a tungsten lamp powered by a Leitz power supply. When the cell was first examined optically, it was noticed that the deposit was visible between crossed polarizers while the field of view was dark in the absence of the film. This proves that the film is birefringent, and hence that there exists an optical anisotropy in the individually visible $1\text{-}5\ \mu\text{m}$ "crystallites." Since the purpose of this study was to monitor the change in the morphology of the film, all measurements were performed with the cell between crossed polarizers. The beam focuser was not used so as to keep the cell temperature at 30°C . The electrical and optical responses were monitored simultaneously on a two-channel strip-chart recorder. The mechanical offset between the two pens has been left unretouched in Fig. 1, i.e., there is no

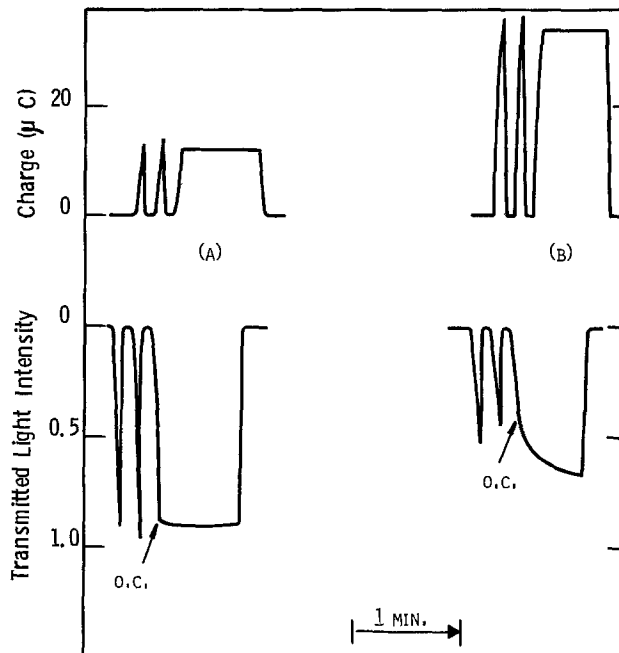


Fig. 1. Electro-optical response of a single segment under cycling and open circuit (O.C.) conditions: (A) -25 mV/ $+400$ mV pulsing at 0.1 Hz (B) -30 mV/ $+400$ mV pulsing at 0.1 Hz.

delay time between the charge accumulation and the optical response.

Results and Discussions

Cyclic voltamograms inside the sealed cells exhibited the typical reversible one-electron reduction and oxidation peaks. With respect to the internal reference electrode, the reduction and oxidation peaks are at -38 and $+28$ mV, respectively, at a 5 mV/sec scan rate.

The typical response of a single segment to the cathodic/anodic cycling is shown in Fig. 1. The top tracing is the charge response (ΔQ), the one on the bottom is the optical response. The experiment consisted of cycling the segment a few times, at a given cathodic potential limit, and then pulling the working electrode lead. This places the system on open circuit, at around 4 sec into the 5 sec cathodic pulse.

The optical response demonstrates the following sequence in the morphology of the growing film. When the film is first formed, part of it is immediately birefringent. However, the significant aspect of the data is the optical response of the deposit, after the segment has been placed on open circuit. For films deposited at the lowest overpotential (-25 mV vs. the internal reference segment), the optical response is constant on open circuit [Fig. 1(A)]. Films deposited at the higher overpotentials (-30 , -50 , and -75 mV vs. the same reference) exhibit a continually increasing optical leakage through the crossed polarizers [Fig. 1(B)]. This leakage cannot be due to the continual deposition of the viologen film, since at the open-circuit potential there is no driving force to plate more material. In addition, the amount of the optical transmission through the film at the time when the segment is placed on open circuit, as a function of the increasing cathodic potentials, is tabulated in Table I. During the approximately same time periods, more

Table I. Electro-optical characteristics of a deposited viologen film placed on open circuit, under crossed polarizers

Cathodic potential (mV)	ΔQ ($\times 10^{-4}$ C)	Δ Intensity	Optical leakage
-25	0.12	0.88	None
-30	0.34	0.40	Continuing
-50	0.47	0.18	Continuing
-75	0.53	0.12	Continuing

charge is deposited at the more negative cathodic potentials. This results in a denser film, which is characterized by a proportional relationship between the charge passed and the calculated absorbance of the film between parallel polarizers. However, the light transmitted through the crossed polarizers, when the segment is placed on open circuit, is inversely related to ΔQ . This implies that during the faster deposition of the film, there is less of a tendency for it to deposit in an oriented fashion. Left on open circuit, the film reorients itself to a phase with a higher degree of ordering and hence a greater optical anisotropy. The final morphology of films deposited at various overpotentials is not the same. The higher the overpotential, the less the optical transmission at steady state, implying a less ordered film.

These data firmly support the previous hypothesis (5) that the "aging" of the heptylviolegen radical cation film involves a reorientation process. However, it is now clear that in addition to other influencing factors, this phenomenon is very dependent on the overvoltage at which the film is deposited. The data also confirm previous arguments (2, 6) that the number of active sites available for film nucleation is potential-dependent. Visual examination of the deposited films shows that the -25 mV film contains larger "crystallites" ($3-5 \mu\text{m}$) arranged in a discontinuous fashion, while the -50 mV film contains smaller "crystallites" ($<1 \mu\text{m}$) spaced more densely together. Hence films formed at more negative potentials nucleate at a larger number of sites, providing a greater number of less oriented deposits.

From a device point of view, these data can be used to postulate a cause for the commonly observed

erasure problem. The typical timekeeping mode requires that the segments be switched as fast as possible, and that they be then placed on open circuit for 1 min. Hence the film is formed at high overpotential, which provides a dense deposit of small aggregates. During the open-circuit time period, the deposit reorients into an ordered phase. It can be postulated that this reoriented film is more difficult to erase, leaving after a large number of cycles, a visible residue on the segments.

Acknowledgment

The author wishes to thank Ms. B. Moussa for her meticulous work in all aspects of the cell preparation.

Manuscript submitted July 31, 1979; revised manuscript received Jan. 2, 1980.

Any discussion of this paper will appear in a Discussion Section to be published in the December 1980 JOURNAL. All discussions for the December 1980 Discussion Section should be submitted by Aug. 1, 1980.

Publication costs of this article were assisted by Texas Instruments Incorporated.

REFERENCES

1. H. T. van Dam and J. J. Ponjeé, *This Journal*, **121**, 1555 (1974).
2. J. Bruinink and C. G. A. Kregting, *ibid.*, **125**, 1397 (1978).
3. J. Bruinink and P. van Zanten, *ibid.*, **124**, 1232 (1977).
4. R. J. Jasinski, *ibid.*, **124**, 637 (1977).
5. J. Bruinink, C. G. A. Kregting, and J. J. Ponjeé, *ibid.*, **124**, 1854 (1977).
6. R. J. Jasinski, *ibid.*, **125**, 1619 (1978).

DISCUSSION SECTION



This Discussion Section includes discussion of papers appearing in the *Journal of The Electrochemical Society*, Vol. 126, No. 4, 5, 9, 10, and 12, April, May, September, October, and December 1979.

Electrochemical Potential Spectroscopy

J. Thompson (pp. 608-616, Vol. 126, No. 4)

Brian E. Conway:¹ In a recent paper by Thompson, interesting effects associated with sorption of lithium ions into layer lattices leading to intercalation compounds, for example with TiS_2 and MoS_2 , have been reported.

Special attention was directed to a "spectrum" of capacitance maxima which arise as the host lattice becomes progressively occupied by the guest ion, Li^+ , on account of the electrode potential being sequentially changed in small steps. The response of the system was referred to as Electrochemical Potential Spectroscopy.

We would like to mention that very similar phenomena have been known for some years²⁻⁴ with the occupation in two dimensions of two-dimensional lattices⁴ on the surface of various noble metals, leading to multiple states of adsorption. The study of this kind of two-dimensional, multi-state surface com-

pound formation has usually been followed by linear-sweep potentiodynamic methods² which lead directly to the observation of the corresponding capacitance measured as the current \div sweep-rate.

The characteristic of most two-dimensional lattice occupation processes is that multiple capacitance peaks arise, corresponding to a series of distinguishable states of adsorption below a monolayer.²⁻⁴ Thus, the concept of electrochemical potential spectroscopy has existed with regard to the response of two-dimensional systems to a linear potential sweep for some time, really commencing with the experimental work of Will and Knorr in 1960.²

Various explanations of the multiple state adsorption which arises in a number of systems in monolayer formation on noble metals such as platinum, gold, rhodium, or palladium, have been offered.⁵⁻⁷ The obvious possibility of polycrystallinity arises but multiple state adsorption is nearly always still observed on well-prepared single crystal surfaces.^{8,9} Hence some kind of indirect heterogeneity at the atomic level must arise,^{5,6} even on single crystal

¹ Chemistry Department, University of Ottawa, Ottawa, Ontario, Canada.

² F. G. Will and C. A. Knorr, *Z. Elektrochem.*, **64**, 258 (1960).

³ T. Takamura, F. Watanabe, and K. Takamura, *Electrochim. Acta*, **18**, 933 (1974).

⁴ H. Angerstein-Kozłowska and B. E. Conway, *J. Electroanal. Chem. Interfacial Electrochem.*, **43**, 9 (1973).

⁵ B. E. Conway, H. Angerstein-Kozłowska, and W. B. A. Sharp, "Electrocatalysis," M. W. Breiter, Editor, p. 94, The Electrochemical Society Softbound Proceedings Series, Princeton, N. J. (1974).

⁶ T. Toyoshima and G. Somorjai, *Catal. Rev.*, **19**, 105 (1979).

⁷ B. E. Conway, H. Angerstein-Kozłowska, and F. C. Ho, *J. Vac. Sci. Technol.*, **14**, 351 (1977).

⁸ A. T. Hubbard, R. Ishikawa, and J. Katekaru, *J. Electroanal. Chem. Interfacial Electrochem.*, **86**, 271 (1978).

⁹ A. Bewick and B. Thomas, *ibid.*, **84**, 127 (1977); **65**, 911 (1975).

planes, so that an adsorbate exists in distinguishable states and experiences a range of energies of adsorption as the monolayer is filled up. These can correspond to different overlay lattice structures with different geometrical arrangements^{4,5} of the adsorbate on the host lattice, utilizing different groupings of hybrid-orbital bonds emerging from the surface, as the surface sites are occupied. In the case of lead deposition in a monolayer on gold,¹⁰ there appears to be a sharp transition which could correspond (cf. 11) to a rearrangement of the surface lattice structure at about 55% of full final coverage, as is indicated by the reversibility of the sharp peak observed at this coverage. Reordering amongst various overlay structures is believed¹¹ to be involved, i.e., similar to the effects in three dimensions.

We thought it would be worth directing attention to the relation between the three-dimensional lattice observations of Thompson and those found in two-dimensions for a number of elements as reported in recent and earlier papers, using cyclic voltammetry.

A. H. Thompson:¹² In his discussion, B. E. Conway compares measurements on Li_xTiS_2 to previous studies on surface adsorption and suggests that similar effects have been known for a number of years. In particular he states "... the concept of electrochemical potential spectroscopy has existed with regard to the response of two dimensional systems to a linear potential sweep for some time ...". This statement shows that there is some confusion about what I have called Electrochemical Potential Spectroscopy (ECPS) that I would like to clarify.

I agree with Professor Conway that differential capacity curves have been used for a number of years to analyze surface studies of the type that he describes. They have also been used to study electrochemical cells such as Zn/MnO_2 ,¹³ to study the double layer capacitance¹⁴ and to study liquid metal alloys.¹⁵ The differential capacity is clearly not a new feature of ECPS.

As I have defined ECPS, it is a method involving a sequential stepping of the electrochemical potential. The constant voltage steps are terminated when the current decays to a small value. The series of voltage steps produces not only the voltage-charge relation but also a discrete, precise measure of the derivative of V vs. Q . The derivative used is called the incremental capacity to distinguish it from the differential capacity obtained by continuous techniques such as linear sweep voltammetry. The following are comparisons of the method and further definition.

With ECPS the effective rate discharge may be very low so as to obtain quasi thermodynamic results. The data were taken at a rate equivalent to a linear sweep in voltage at a rate of 10^{-2} $\mu\text{V}/\text{sec}$. It would require three years for linear sweep voltammetry to give equivalent data at the same effective rate.

The ECPS measurement is not simply another coulometric titration since no attempt is made to obtain ideal equilibrium conditions. Rather, by stepping the voltage at a fixed current level, data are obtained under quasi thermodynamic conditions with the deviation from equilibrium being well defined. On a typical voltage step in my paper, it would require more than 36 hr to obtain a voltage that is constant within the voltage resolution employed of 100 μV . "True open-

circuit data" would then require a minimum of one year to collect.

The ECPS measurement gives both quasi thermodynamic and kinetic data on each step.

The small voltage steps and low cutoff currents apply mild perturbations to the cell. These conditions are required in organic electrolyte based systems where large voltage excursions and high current levels may easily cause irreversible damage to the system.

With regard to the structural effects on surfaces as compared to those in intercalate systems, it would be quite interesting to compare two-dimensional deposition on a surface to the two-dimensional intercalation problem since the intercalate does not permit multiple layers to form. In fact, ECPS may provide useful data for the surface problem since measurements can be made at low rates which would be particularly attractive for low temperature measurements where equilibration times may be large and surface structures well formed.

Quantity of the Metal Deposited in Pulsed Plating vs. Direct Current Plating

Richard Haynes (pp. 881-882, Vol. 126, No. 5)

P. Radhakrishnamurty:¹⁶ The author tried to show that the condition $\eta_P > \eta_{dc}$ must be satisfied to get a higher weight of the metal in pulse plating compared to d-c plating. That there exist several possibilities to achieve this result, besides $\eta_P > \eta_{dc}$ can be shown by means of a trivial exercise from basic principles.

It should be mentioned first of all that neither the mechanism of the deposition reaction nor the mode of control of the reaction is needed for the calculation of the weight of the deposit, as has been done in the paper under discussion. Thus the whole discussion regarding the presence of simultaneous HER/some other parallel reaction at the electrode surface, is of first order or second order etc., whether the metal deposition is under pure diffusion control, pure activation control, etc., are all irrelevant.

Secondly substitution of $(i_P)_1/(i_{dc})_1 = 3.76$ in Eq. [1] of Haynes paper is incorrect because $(i_P)_1$, $(i_{dc})_1$ refer to the current densities at a particular instant of time during the deposition whereas i_P , i_{dc} refer to the constant or average values of current density in pulse plating and d-c plating.

From basic principles, we have: weight of metal deposited = rate of metal deposition \times time of deposition

$$\begin{aligned} W &= I_M \times E \times t \\ &= I_T \times \eta \times E \times t \\ &= i_T \times A \times \eta \times E \times t \end{aligned}$$

In the case of pulse plating

$$W_P = i_T \times \frac{\theta_1}{\theta} \times t \times A \times E \times \eta_P$$

Thus the necessary and sufficient condition for $W_P > W_{dc}$ is

$$i_T \times \frac{\theta_1}{\theta} \times t \times A \times E \times \eta_P > i_T \times t \times A \times E \times \eta_{dc}$$

Since $\theta_1/\theta < 1$, $W_P < W_{dc}$ if all other parameters are same in both d-c and pulse plating. However, by choosing the parameters conveniently W_P can be made greater than W_{dc} . Of a number of combinations of parameters available for example

$$\left[\frac{i_P}{i_{dc}} > \frac{\theta}{\theta_1} \right]_{\eta, A, t}, \left[\frac{\eta_P}{\eta_{dc}} > \frac{\theta}{\theta_1} \right]_{i, A, t}, \left[\frac{A_P}{A_{dc}} > \frac{\theta}{\theta_1} \right]_{i, \eta, t}$$

are some to achieve $W_P > W_{dc}$.

¹⁶ Central Electrochemical Research Institute, Karaikudi 623006, India.

¹⁰ J. Horkans, B. D. Cahan, and E. Yeager, *This Journal*, **122**, 122 (1975).

¹¹ A. Bewick and B. Thomas, *J. Electroanal. Chem. Interfacial Electrochem.*, **85**, 329 (1979).

¹² Exxon Research and Engineering, Corporate Research Scientific Laboratories Company, Linden, New Jersey 07036.

¹³ Y. Balewski and J. P. Brenet, *This Journal*, **5**, 527 (1967).

¹⁴ E. Gileadi, E. Kirrowa-Eisner, and J. Penciner, "Interfacial Electrochemistry," Addison-Wesley Publishing Co., Reading, Mass. (1975).

¹⁵ J. C. Thompson, K. Ichikawa, and S. M. Granstaff, Jr., *Phys. Chem. Liq.*, **5**, 157 (1976).

In conclusion, it may be said that to get a higher weight of metal deposited in pulse plating than in d-c plating there exist several possibilities to compensate for the drawback $\theta_1/\theta < 1$ present in pulse plating and one need not know about the mechanism of deposition for the above purpose.

LIST OF SYMBOLS

W	weight of the metal deposited (g)
I_M	partial current utilized for metal deposition reaction of interest, ampere
I_T	total current passing through the cell, ampere
E	electrochemical equivalent of the metal, g/A·sec
t	time of deposition, sec
θ	period of the pulse, sec
θ_1	time for which pulse is on, sec
η	current efficiency of the metal deposition reaction of interest
A	the surface area of the electrode, cm ²

Subscripts P and dc denote pulse plating and direct current conditions.

Richard Haynes:¹⁷ What I have shown is a condition where pulsed current plating can yield a greater quantity of deposited metal than direct current plating when both are compared at the maximum possible rates. I have used the quantity of the deposit only as a simple indicator of the maximum possible deposition rates. The limit for the maximum possible reaction rate in my model is considered to be mass transport of the depositing metal for both pulsed and direct current plating. A parallel reaction scheme is always imposed when the current efficiency is less than 100% efficiency. The example given is easily shown to become the same as my equations when the weights are compared at the maximum possible rates of the deposition reaction

$$i_{T1P} \frac{\theta_1}{\theta} AE\eta_P > i_{T1dc} AE\eta_{dc}$$

For comparison at the maximum possible rates: A and E drop out and

$$i_{T1P} \text{ becomes } i_{T1P)_{\max}}$$

and

$$i_{T1dc} \text{ becomes } i_{T1dc)_{\max}}$$

For my model the rate limiting step is mass transport controlled so

$$i_{T1P)_{\max}} \equiv i_{T1P)L}$$

and

$$i_{T1dc)_{\max}} \equiv i_{T1dc)L}$$

which then becomes the same as my equation once substituted above. A definition of $(i_p)_1$ is given by K. Viswanathan *et al.*¹⁸

In summary, I have shown that there can, in theory, exist electrochemical conditions such that pulse plating can yield a greater quantity of metal when compared at the maximum plating rates which in my model is mass transport limited. I thank P. Radhakrishnamurty for asking for clarification on these points.

H. Y. Cheh (Divisional Editor):¹⁹ The assumption that the upper limit of i_p/i_{dc} is equivalent to $(i_p)_1/(i_{dc})_1$, which has been made by Haynes is of doubtful validity. On the other hand, Radhakrishnamurty's analysis is not conclusive either. This is because E_p and E_{dc} are generally both functions of applied current density. Without kinetic information, there is no knowledge on the magnitude of E_p and E_{dc} . The three conditions presented are therefore meaningless. We have completed a more rigorous analysis on the current efficiency for simultaneous reactions by pulsed electrolysis. This

¹⁷ Western Electric, Princeton, New Jersey 08540.

¹⁸ K. Viswanathan, M. A. Farrell Epstein, and H. Y. Cheh, Paper 156 presented at The Electrochemical Society Meeting, Pittsburgh, Pa., Oct. 15-20, 1978.

¹⁹ Department of Chemical Engineering and Applied Chemistry, Columbia University, New York, N. Y. 10027.

work has been submitted to **This Journal** for publication.

The Potential Distribution at the TiO₂ Aqueous Electrolyte Interface

Micha Tomkiewicz (pp. 1505-1510, Vol. 126, No. 9)

David L. Ullman:²⁰ In this article, the author attributes nonlinearity in the Mott-Schottky plot of an unetched sample of TiO₂ to surface states that change their charge state in the course of varying the electrode potential. He then proceeds to present an analysis that ostensibly shows these to be fluctuating levels energetically located approximately in the center of the bandgap.

However, it appears from the author's Fig. 3 that these supposed states exchange charge most rapidly when there are practically no electrons at the surface. From data the author supplies, $n_s = n_1$ at the peak of this curve, and these may be calculated as follows

$$\begin{aligned} n_1 = n_s &= 3.8 \times 10^{19} \exp((-0.48-0.8)/0.0256) \\ &= 7 \times 10^{-3} \text{ cm}^{-3} \quad [1] \end{aligned}$$

The intrinsic carrier concentration may be estimated²¹ to be not much more than $2 \times 10^{-5} \text{ cm}^{-3}$, so it is clear that holes could not play much of a part in this process, either.

From the usually accepted model of trap kinetics,²² it is clear that if transport through the space charge region is sufficiently rapid that n_s stays constant after the electrode potential has been changed, that as the traps exchange electrons to come into equilibrium with the surface potential, the equilibration will be a first-order process. A simple analysis shows that the relaxation time for this process is

$$\tau = \frac{1}{\sigma_n v_{th} (n_s + n_1)} \quad [2]$$

To evaluate this expression, we shall take for σ_n the value that Morrison²³ suggests as an upper limit for capture cross section, 10^{-12} cm^2 . Assuming unit effective mass, we shall take the electron thermal velocity to be 10^7 cm/sec . We thus find

$$\tau = 7 \times 10^6 \text{ sec} = 2000 \text{ hr} \quad [3]$$

This argument applies whether we speak of filling or emptying the traps. Obviously, this is too long a time for the measurements to be made in any reasonable length of time. The slow rate of filling may be seen intuitively as due to the excessively low concentration of electrons at the surface at this potential; the slow rate of emptying, as due to the great energy difference between the states and the conduction band (on the order of 1.3 eV) and the resulting improbability of the transition.

In answer to these arguments, one might claim that the fluctuating nature of the energy levels causes them to exchange charge at a much faster rate than my analysis above shows. However, I will show that this is impossible.

In the case of filling empty traps, a "downward" fluctuation of trap energy would not change the situation, since both n_1 and n_s would remain infinitesimal. An "upward" fluctuation of energy might raise n_1 to some reasonable value, but only thereby making the probability of filling nil for thermodynamic reasons, since the trap energy would now be far above the surface Fermi level.

²⁰ Littleton, Colorado 80120.

²¹ W. Huybrechts and J. Devreese, *Solid State Commun.*, **17**, 401 (1975). The rather tentative value of effective mass ratio given here was used to calculate an estimate of the intrinsic carrier concentration.

²² A. S. Grove, "Physics and Technology of Semiconductors," Chap. 5, John Wiley, New York (1967).

²³ S. R. Morrison, "The Chemical Physics of Surfaces," p. 44, Plenum Press, New York (1977).

For the case of emptying, one might argue that when a filled trap fluctuates upward, it is both thermodynamically and kinetically capable of emptying (from my Eq. [2]), and what is actually implied by my arguments is that the traps can empty going from cathodic to anodic potentials, but going from anodic to cathodic, will fill only as flatband is approached (that is, when n_s becomes substantial). Thus what would be implied by my arguments is a hysteresis in the capacitance vs. potential curves.

Unfortunately, this leads to a thermodynamic inconsistency. We see that these arguments lead to a mechanism of rapid emptying when n_s is low, but no comparably rapid method of refilling. Since the traps must be half-filled, and the rate of emptying equal to the rate of filling when $n_s = n_1$, this situation is impossible.

Yet another argument might be that the traps do indeed rapidly empty as they rise in energy, but refill by extracting electrons from (injecting holes into) the valence band upon downward fluctuation. However, it is a principle of catalysis (actually thermodynamics) that a route of forward reaction must also be a route of backward reaction. Thus the electrons and holes must be able to recombine through these states. But we have shown that trapping rates at vanishing carrier concentration is excessively slow, and reasonable carrier concentrations for this process to occur must imply an "equilibrium" n - p product far greater than n_1^2 , and this is again thermodynamically impossible.

Tunneling is another relatively rapid process that might be contemplated, but while my knowledge of quantum mechanics is rather nil, it does seem to me that tunneling to and from a state near the intrinsic level is rather improbable. Rapid tunneling to and from an "upward" fluctuated state is impossible for the thermodynamic reasons discussed earlier.

Another defense that might be relied upon could be that there was error in the potential determination. Shifting the peak of the curve 180 mV cathodically would decrease the relaxation time by a factor of 1000, although 2 hr still seems unacceptably slow. However, it is difficult to see how such an error could be justified, particularly with modern measuring equipment. Flatband potentials are quoted to within 20 or 30 mV, and the curve appears well behaved on the cathodic side.

Finally, the crux of the matter appears to be this: at this range of potential there are practically no carriers at the surface, and whatever the mechanism, it is difficult to envision any physical entity responding so sharply to such vanishing concentrations, as required by the interpretation of Tomkiewicz.

As an alternative interpretation of the author's Fig. 2, I suggest that it is interesting, and perhaps not irrelevant, to note that the "nonlinear" portion of the upper curve is almost a straight line with a slope equal to that of the lower curve. However, I cannot say whether or not the roughness factor changed during the etching. If we hypothesize that the upper curve is the result of a lightly doped layer on top of the more heavily doped substrate, depletion region theory²⁴ allows us to estimate this thickness, noting that the break occurs at about 1V positive of flatband, and using other data we find in the article. This yields a top layer thickness of about 0.22 μm . Just how much the etch might have removed is impossible to say without knowledge of the etching time and kinetics.

The scatter in the "nonlinear" portion could be due to unavoidable error in the extraction of the capacitance element by relaxation analysis.²⁵ We note that the points showing greatest deviation represent the smallest values of capacitance, in series with an assumed constant resistance.

²⁴ A. S. Grove, "Physics and Technology of Semiconductors," Chap. 6, John Wiley, New York (1967).

²⁵ M. Tomkiewicz, *This Journal*, 126, 2220 (1979).

However, we must confess that we do not know why there should be a thin layer of lightly doped material on top of a more heavily doped substrate, with an abrupt junction between the two.

Another criticism I have concerns the author's apparent assumption that flatband potential is invariant with doping level. This is inconsistent with the fact that two differently doped samples of a semiconductor must display an electronic potential difference when brought into intimate contact; they cannot then have the same potential relative to a third potential. The conclusion is that it is the bandedges that will remain constant when the Helmholtz potential is constant; flatband potential must vary Nernstianly with the bulk electron concentration.

The author also assumes that the various samples will have the same Helmholtz potentials in the same electrolyte. Considering that different samples may respond differently to the etching procedure due to different dopant concentrations, etc., this assumption seems to us to be rather dangerous.

M. Tomkiewicz:²⁶ While not fully agreeing with the authors detailed discussion on the possible mechanism of charge exchange between the bulk of the semiconductor and the surface or bulk states which reside near the middle of a gap of wide band semiconductors, his comments illustrate well our deficiency in understanding these processes. The existence of surface states on TiO_2 at this energy range was implied before,²⁷ with even more pressing need for efficient charge exchange between the surface and the bulk. This does not preclude the possibility of different interpretation but, just points to the fact that additional work is needed to clarify this problem. My data did not address the kinetic problem but it did demonstrate that under certain conditions the potential of the Helmholtz layer does not remain constant during a potential scan. The change in potential indicates charging and discharging in the layer. Because of the dimensions of this layer in concentrated aqueous solutions every state that lies in the layer in the potential range within the gap is attributed to surface states. The fluctuating level model explained the experimental energy distribution of the state but as I have shown in a later publication²⁸ this model is not unique in explaining the energy distribution. As to the authors comments on the dependence of the flatband potential on doping, it should be emphasized that the intercept to "zero doping" is at relatively high doping level and puts the flatband potential approximately 0.15V below the conduction bandedge.

Aside from this, there is some basic difference of interpretation of the flatband potential between the author and myself. It is true that the difference in energy between the Fermi level and the bottom of the conduction band will change with the doping level but the result will be shift in the conduction bandedge relative to the electrolyte. The flatband potential is the only measurable quantity which establishes the energy relationship of the semiconductor electrolyte system provided that the only potential drop in the system is across the space charge layer.

Occurrence of the Salt Film during Initiation and Growth of Corrosion Pits

T. R. Beck and R. C. Alkire (pp. 1662-1666, Vol. 126, No. 10)

J. Toušek:²⁹ In the last years considerable attention has been paid to the mechanism of localized corrosion of metals. Among others persuasive arguments have appeared about the presence of a thin salt layer along

²⁶ Department of Physics, Brooklyn College of the City University of New York, Brooklyn, New York 11210.

²⁷ S. N. Frank and A. J. Bard, *J. Am. Chem. Soc.*, 97, 7427 (1975).

²⁸ M. Tomkiewicz, *Surf. Sci.*, To be published.

²⁹ Institute of Physical Metallurgy, Czechoslovak Academy of Science, 616 62 Brno, Czechoslovakia.

the pit surface.³⁰⁻³⁴ The paper discussed deals with the kinetics of pitting corrosion based on the salt film theory. Because the results of this work may be important for a further development of the localized corrosion mechanism, a discussion concerning this problem may be useful.

According to the authors, the purpose of their paper was to employ simple transport laws to gain a perspective of events which occur during early stages of pit initiation and growth. Under the presumption that the corrosion current in pits is controlled by the mass transport of corrosion products out of the pit, they have derived for the pit radius the equation

$$r = \left[r_1^2 + \frac{2DC_sM}{\rho} t \right]^{1/2} \quad [1]$$

and for the current density in the pits the equation

$$j_L = \frac{nFDC_s}{\left[r_1^2 + \frac{2DC_sM}{\rho} t \right]^{1/2}} \quad [2]$$

The pit growth at relatively long exposition times has been measured in our laboratory and the calculation of pit radii and of actual rates of metal dissolution in the pits has been made. Corresponding kinetic equations have been derived from the relation for the pit growth and from the experimentally ascertained time dependencies of the total current density j and of the pit number z . The pit growth is expressed by the general equation

$$(2/3)\pi abc = (V_M/zF) \int_0^{t-t_1} Idt \quad [3]$$

in which a , b , c are dimensions of the pit, V_M is the molar volume of metal, F is the Faraday constant, I is the current from one pit, t_1 is the time at which the pit was initiated, and $t - t_1$ is the age of the pit. When measuring the localized corrosion of iron in the $\text{Na}_2\text{SO}_4 + \text{KCl}$ solution, the following equations were found to be valid for the time dependence of the pit number and of the total current density³⁵

$$z = Kt \quad [4]$$

and

$$j = At^2 \quad [5]$$

In these equations, K and A are constants. The pits have a hemispherical shape. From Eq. [3], [4], and [5], it is possible to calculate the pit radius as has been shown, e.g., in^{36,37}

$$r = \sqrt[3]{(3V_M/4\pi F)} \sqrt[3]{(At^2/K)} \quad [6]$$

The correlation between the pit growth given by Eq. [6] and [1] and the experimentally found pit radii is illustrated in Fig. 1. The comparison was made for macro-size and also for micrometer-size pits whose radii were taken from the paper published by Vetter and Strehblow. From Fig. 1, a good agreement follows between experimental values and those calculated from Eq. [6], which, as it is evident, expresses well the pit growth both for long and short exposition times. On the other hand, the values of pit radii gained from Eq. [1] do not agree well with those found experimentally.

According to Eq. [6], the pit growth is characterized by the slope $d \log r / d \log t = 2/3$. This value fits well the experimental time dependence obtained for both large and micrometer-size pits. Equation [1] requires

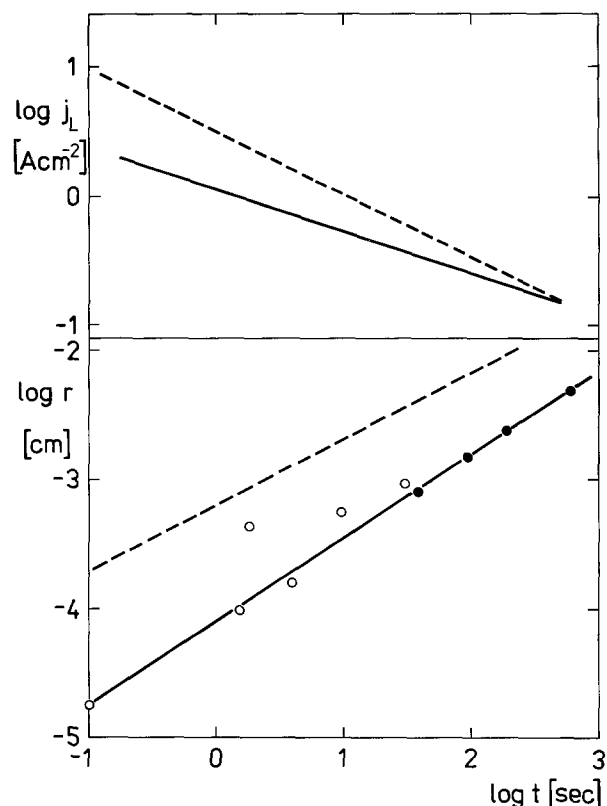


Fig. 1. Pit growth on iron in the $\text{KCl} + \text{Na}_2\text{SO}_4$ solution. ----- pit radius r and current density in the pits j_L predicted by Eq. [1] and [2]. ——— pit radius r and current density in the pits j_L predicted by Eq. [6] and [7]. Experimental values: ○ Vetter and Strehblow, ● Toušek.

for the slope [for sufficiently high exposition time, when $r_1^2 \ll (2DC_sMt/\rho)$] the value 1/2, which is at variance with the experimental results.

If we know the current from one pit and its area, the corrosion current in the pit can be evaluated³⁸

$$j_L = \sqrt[3]{(16F^2/9\pi V_M^2)} \sqrt[3]{(A/Kt)} \quad [7]$$

The drop of the current density j_L with time is given by the slope $d \log j_L / d \log t = -1/3$, whereas the slope calculated from Eq. [2] yields the value $-1/2$.

In the connection with Eq. [1] and [2] it is necessary to emphasize the experimental results, according to which the time dependence of pit radius and of current density in the pits varies with the corrosion environments composition and concentration.^{36,38,39} In some cases, the corrosion current remains constant and the pit radius rises linearly with time. These facts are not involved in Eq. [1] and [2] according to which the time dependence of localized corrosion should be always the same.

It is possible to conclude that although the paper of Beck and Alkire brings many remarkable facts about the localized corrosion mechanism, some results presented here must be taken with care. Very probably, the salt film along the pit surface does not influence the metal dissolution kinetics in that way as it is assumed by the authors. According to our opinion, the salt film theory is not clear enough to explain the localized corrosion phenomena (kinetics and mechanism in general) as it has been supposed.

T. R. Beck⁴⁰ and R. C. Alkire⁴¹ Our publication expressed a salt-film hypothesis which led, by application

³⁰ K. J. Vetter and H.-H. Strehblow, *Ber. Bunsenges. Phys. Chem.*, **74**, 1024 (1970).

³¹ H.-H. Strehblow and K. J. Vetter, *ibid.*, **75**, 822 (1971).

³² H.-H. Strehblow and J. Weners, *Z. Phys. Chem. N.F.*, **98**, 199 (1975).

³³ H.-H. Strehblow, *Werkst. Korros.*, **27**, 792 (1976).

³⁴ I. L. Rosenfeld, I. S. Danilov, and R. N. Oranskaya, *This Journal*, **125**, 1729 (1978).

³⁵ J. Toušek, *Corros. Sci.*, **12**, 15 (1972).

³⁶ J. Toušek, *ibid.*, **12**, 1 (1972).

³⁷ J. Toušek, *ibid.*, **18**, 53 (1978).

³⁸ J. Toušek, *Werkst. Korros.*, **25**, 406 (1974).

³⁹ G. Herbsleb and H.-J. Engell, *Z. Phys. Chem.*, **215**, 167 (1960).

⁴⁰ Electrochemical Technology Corporation, Seattle, Washington 98107.

⁴¹ Department of Chemical Engineering, University of Illinois, Urbana, Illinois 61801.

of first-principles, to Eq. [4] and [5] therein. This result, which introduced no adjustable parameters, gave agreement to within an order of magnitude of literature data obtained in several pit systems. It was therefore concluded that the hypothesis was reasonable, although several differences between data and hypothesis were yet to be resolved. In this work, the mathematical model represented the scientific hypothesis, and gave thereby a quantitative framework for incorporation of additional refinements in concept.

By contrast, the foregoing discussion by Tousek illustrates that an empirical fit to pit growth data can be achieved with adjustment of two parameters, K and A , along with experimental observations which support the exponents on t indicated in both Eq. [4] and [5] in the above discussion. Evaluation of the foregoing discussion indicates that;

1. In Eq. [3] in the above discussion, the quantity z should not appear but should be replaced by n , g equiv/gmole. Within the integral, the current to a single pit, I , is also given by j/z .

2. For such conditions that empirical Eq. [4] and [5] are observed, then Eq. [6] follows provided that $t_1 = 0$. This procedure, however, yields no understanding of the processes occurring in the pit.

3. Evaluation of the ten data points provided in Fig. 1 of the discussion indicates that the slope of the line which best fits the data by a least-squares analysis is 0.60, a value which lies between that put forth by Toušek (0.67) and by ourselves (0.50). If the single data point at 10^{-1} sec is disregarded, then the slope through the remaining nine points is 0.55.

While additional empirical manipulations could perhaps yield an improved fit of the data, we would encourage also the method by which hypotheses of mechanism are expressed in a fashion which permits a more rigorous comparison with first-principles and which gives, thereby, a clearer insight into the physical events which actually occur during pit initiation and growth.

The Electrochemical Behavior of Alkali and Alkaline Earth Metals in Nonaqueous Battery Systems—The Solid Electrolyte Interphase Model

E. Peled (pp. 2047-2051, Vol. 126, No. 12)

I. Warshawsky⁴² In connection with Peled's thesis concerning the presence of a solid electrolyte interphase, SEI, between the metal anode and electrolyte, a complicating factor in interpreting the kinetic data may be the presence of water as an impurity in many nonaqueous solvents. This ubiquitous impurity can be present in trace amounts even when the most stringent purification procedures and precautions have been used, including using vacuum line manipulations. Hence, in many battery systems utilizing alkali metals, a reaction can occur between the alkali metal and the aqueous impurity in the solvent, leading to hydroxide film formation at the metal-liquid interface.

In addition, the aqueous impurity can react with the SEI affecting both its thickness and texture, further complicating the problem of interpreting kinetic data obtained electrochemically during discharge.

The author's idea that a thicker more polarizable SEI occurs during discharge when the anion transference number, t_- , is greater than zero compared to the situation in which it is zero, with the electron transference number, t_e , being zero, can also be challenged. Consider, for example, the discharge process at the anode. According to the author's reasonable model for $t_- > 0$ and $t_e = 0$, film formation occurs continuously at two interfaces—at the alkali metal-solid electrolyte interface and at the solid electrolyte-liquid interface. Con-

sequently, during discharge a process of bond-making and bond-breaking takes place continuously at the alkali metal-solid electrolyte interface, affecting the interaction between these two contiguous phases. Hence, we have a possible mechanism for a loosening and a flaking off of the solid electrolyte film from the alkali metal surface, exposing new metallic surface to the liquid. This then leads to a less polarizable electrode than would be the case if the film adhered to the metal surface continuously during discharge.

As Peled points out, the polarization process is complex. The above conclusion may need modification for systems where other factors, such as stresses and strains, are significantly involved in the formation of the SEI, affecting its structure and stability. That is, ordinary thermodynamic considerations may not prevail for the temperature and peculiar circumstances under which the SEI is forming while the battery is functioning. For instance, it is possible that the cation, anion, and vacancy concentrations at the metal-solid electrolyte interphase can be characteristic of a high temperature while further away from the interphase in the SEI, they may be characteristic of a low temperature, and their respective mobilities throughout the film also characteristic of a low temperature.

In any event, it is not as obvious as the author seems to imply that during discharge in which $t_- > 0$ and $t_e = 0$ that a thicker and more polarizable film forms compared to the situation in which $t_- = 0$ and $t_e = 0$.

A Finite Difference Numerical Analysis of Galvanic Corrosion for Semi-Infinite Linear Coplanar Electrodes

P. Doig and P. E. J. Flewitt (pp. 2057-2063, Vol. 126, No. 12)

D. J. Astley⁴³ I would like to indicate an inaccuracy in the paper by P. Doig and P. E. J. Flewitt. On page 2063 the authors refer to the parameter $(i_0/wC)^{1/2}$,⁴⁴ and state that as the magnitude of this parameter increases so the "approximation of unidirectional current flow becomes more accurate." In fact although the approximation improves with decreasing w , the unidirectional current flow model becomes more appropriate as (i_0/C) decreases. This follows from first principles in that as the solution becomes less resistive and/or the electrochemical reaction becomes more polarizable, so the potential gradient normal to the electrode surface decreases.

I have demonstrated that the unidirectional current flow model approximation improves with decreasing (i_0/C) by comparing the predictions of this model with those obtained from Waber's series solution of Laplace's equation for both semi-infinite linear coplanar electrodes,⁴⁵ and for tubular coplanar electrodes with junctions perpendicular to the axis,⁴⁶ assuming linear polarization kinetics in all cases. Comparisons clearly indicate that, for a fixed anode/cathode size, corrosion potential difference (ΔE) and solution depth/tube radius, the approximation involved in using the unidirectional current flow model improves as i_0 decreases and C increases. Thus for $i_0 = 0.01 \text{ Am}^{-2}$ and $C = 4 \Omega^{-1} \text{ m}^{-1}$ (values typical for copper-base alloys, titanium, and seawater), the unidirectional model predicted interfacial potentials typically within 1 mV of those calculated from the series solution of Laplace's equation for electrode length = solution depth = 30 cm ($\Delta E = 150 \text{ mV}$). For $i_0 = 0.07 \text{ Am}^{-2}$ and $C = 0.6 \Omega^{-1} \text{ m}^{-1}$, the approximation involved in using the simpler model worsened, although still tolerable, so that the greatest difference between interfacial potential predictions was about 5 mV.

⁴² IMI Limited, Birmingham, England.

⁴³ i_0 = the free corrosion current density, w = the depth of solution above the corrosion couple surface, and C = specific conductance of the solution.

⁴⁴ J. T. Waber and B. Fagan, *This Journal*, 103, 64 (1956).

⁴⁵ J. T. Waber and J. M. Ruth, Los Alamos Scientific Laboratory Microfilm LA-1993 (Physics) July 1956.



Bare Surface Reaction Rates and Their Relation to Environment Controlled Cracking of Aluminum Alloys

I. Bare Surface Reaction Rates on Aluminum-7 Weight Percent Magnesium in Aqueous Solutions

F. P. Ford,¹ G. T. Burstein,* and T. P. Hoar

Department of Metallurgy and Materials Science, University of Cambridge, Cambridge CB2 3QZ, England

ABSTRACT

Data have been obtained for electrode reaction rates on bare aluminum-7 weight percent magnesium immersed in aqueous solutions. The reactions investigated were metal dissolution, proton reduction, and oxide growth in sulfate and chloride containing solutions in the pH range 1.0-6.5. The bare metal surface was produced by rapidly and lightly scratching a potentiostatically controlled rotating disk electrode. The resulting current transients were measured under various conditions of electrode potential, electrolyte composition, temperature, and electrode rotation rate. Current densities of up to 8 A cm^{-2} on the scratch were measured in this way. The rates of metal dissolution and proton reduction are increased by many orders of magnitude by removing the high impedance surface oxide. Dissolution of the bare surface occurs with the following rate-determining step: $\text{Al} + \text{H}_2\text{O} \rightarrow \text{AlOH}_{\text{ads}} + \text{H}^+ + \text{e}^-$, the rate being independent of pH and sulfate (0.5M) or chloride (1-4M) content. Proton reduction occurs with the discharge step being rate controlling. The rate of nucleation and growth of the oxide film follows the empirical law $i_{\text{at}} = i_{\text{am}} \exp(-at^n)$. Initially $n = 1$, but at longer times changes to 0.5, the changeover occurring earlier with increase in anodic polarization and by the presence of Cl^- .

The generalized theory of stress-corrosion cracking, originally suggested by Mears, Brown, and Dix (1) and expanded upon by others (2-4) has long been accepted for aluminum alloys since it is capable of explaining qualitatively the variation of cracking rate with second-phase morphology and, possibly, with elementary changes in electrochemical conditions at the crack edge. In essence this theory proposes that crack propagation progresses from a nucleating notch (usually formed by intergranular attack associated with discrete second-phase particles) when sufficient stress concentration exists to cause ductile tearing at the notch edge. Accelerated dissolution then occurs preferentially at the resultant film-free regions and continues until the dissolution rate is decreased by oxide formation or the intergranular penetration is halted at a grain boundary of unfavorable orientation. Thereupon the cycle of slow intergranular corrosion followed by rapid growth of the oxide film starts again.

Recently, however, there is increasing evidence (5, 6) that an alternative mechanism involving hydrogen embrittlement may be valid in humid and aqueous environments. This evidence is based primarily on the similarity between the potential dependence of stress-corrosion susceptibility and of hydrogen permeation (7, 8), the fact that the tensile ductility may be reversibly

reduced by cathodic charging (8), the observation of hydrogen gas bubbles nucleated at grain boundary precipitates (9, 10), and by the fact that slow cracking may occur at humidity levels where a bulk aqueous phase cannot theoretically exist in the crack (6, 11).

It is the prime object of this investigation to provide data that relates quantitatively the accelerated electrode reaction rate accompanying film rupture to the crack propagation rate of aluminum-7 weight percent (w/o) magnesium in aqueous solutions. Specifically, the rates of dissolution, proton reduction, and oxide growth on an initially bare metal surface are determined and these data enable theoretical propagation rates for both slip dissolution and hydrogen embrittlement models to be calculated for various conditions of electrode potential, anion content, and temperature. These theoretical rates are then compared with literature values of the crack propagation rate under static and cyclic stress conditions.

In Part I the data on the bare surface reaction rates are reported, and in Part II a comparison is made between the calculated and observed environmentally controlled crack propagation rates.

Experimental

The alloy investigated was a high purity binary of nominal analysis Al-7 w/o Mg (supplied by Alcan International Research Laboratories, Banbury, England); spectrographic analysis gave: 7.03% Mg, 0.001% Si, 0.001% Fe, 0.001% Cu, 0.004% Zn, 0.002% Ti, 0.001%

* Electrochemical Society Active Member.

¹ Present address: General Electric Company, Research and Development Center, Schenectady, New York 12301.

Key words: metal dissolution, proton reduction, oxide growth.

Mn, and the balance Al. The original hot-rolled sheet was heat-treated at 370°C for 4 hr and water quenched to retain a single phase magnesium supersaturated condition; this ensured that the measured current on the potentiostatically controlled specimen emanated from a homogeneous structure of known area. Results showed that there was no difference between mechanically polished and electropolished (in HClO₄, CH₃OH, glycerol) surfaces; for convenience experiments were conducted on surfaces polished to 6 μm diamond finish. These were degreased with alcohol.

Solutions were made up from AR grade NaCl or Na₂SO₄ to strengths 0.5-4M in doubly distilled water (conductivity $1 \times 10^{-6} \Omega^{-1} \text{cm}^{-1}$). The pH was adjusted to the required value in the range 1.0-6.5 by addition of HCl or H₂SO₄; after an experiment the pH was within 0.1 pH units of the initial value and the solutions were thus not further buffered. Prior to introduction to the experimental cell the solutions were either aerated (8 ppm oxygen) or deaerated to <0.01 ppm oxygen by flushing with nitrogen which had been previously purged of oxygen by the technique of Gilroy and Mayne (12). The electrolyte temperature was normally 21° ± 3°C but in experiments where the temperature was purposely altered, control was achieved either by a Teflon-coated immersion heater or by the addition of liquid nitrogen to the cell.

The specimen, in the form of a disk of area 0.50 cm², was force-fitted into the end of a cylindrical Lucite holder and the interface sealed with lacquer (Fig. 1). Electrical contact between the specimen and the stainless steel shaft (externally coated with Teflon) was made with a compression spring and that between the revolving shaft and an external terminal made with a mercury seal, which minimized spurious effects due to contact noise. The use of mercury as an electrical contact did not introduce any effects vis à vis possible reaction with the working electrode (which was separated from the contact by the glassware) as indicated by similar current density/time results obtained using a conventional carbon-brush contact. The solution flow was visibly turbulent for $\omega > 100$ Hz, although departure from laminar flow probably occurred at lower speeds. The Pt counterelectrode (area ~10 cm²) was mounted on a Teflon base and placed symmetrically below the specimen surface in order to give a uniform

potential field. The Luggin probe emerged from the center of the counterelectrode and was aimed at a point midway between the center and the periphery of the specimen. Preliminary results based on the dependence of current response on the probe position and size, and on interrupter-galvanostat experiments, indicated that negligible shielding and impedance effects were obtained using a 0.7 mm OD probe tip placed 1.0 mm from the specimen surface.

The electrode potential was potentiostatically controlled, the potential being monitored with respect to a saturated calomel electrode. A colorimetric check was made that no chloride was diffusing into the cell over time periods far in excess of those normally used.

In order to achieve a bare metal surface the surface oxide was mechanically removed by scratching the exposed circular surface of the rotating disk electrode with a diamond stylus. The diamond assembly, shown in Fig. 1, consisted of a gramophone stylus of tip radius 13 μm cemented to a Lucite holder which was mounted rigidly on a double bearing assembly. By the use of a calibrated screw the diamond could be made to traverse the specimen surface to create up to 10 separate concentric scratches during an experimental session. The diamond was normally held away from the specimen surface by a solenoid attracting a steel bolt let into the Teflon rod connected to the Lucite diamond holder. When appropriate the diamond was raised a height of ~2 mm onto the specimen by opening the solenoid circuit; the tracking weight was 2g. The diamond was allowed to bounce on the surface to produce individual scratches approximately 13 μm wide, 2 μm deep, and a length that was calculated from the linear velocity of the scratch v_s and the contact time. The contact time was controlled by the inertia of the diamond assembly and was independent of ω for $\omega > 10$ Hz; the contact time used in these experiments was 1 msec.

This method of production of a known area of bare surface is a modification of the technique developed by Lees (13), who relied on the production of a continuous scratch on a rotating disk to give a regenerated bare annulus. This latter method is powerful in that it provides an indication when a bare surface is maintained over the whole of the scratched area by monitoring the cell current with rotation speed, i.e., the cell current becomes independent of rotation speed when the rotation periodicity is less than the nucleation time for oxide growth. Although this technique has been successful for such systems as stainless steel/chloride and brass/ammonia it is unsuitable for systems having nucleation times for oxide growth less than the 5 msec, since it is experimentally difficult to achieve the required rotational frequency (>200 Hz) and maintain mechanical stability. Hence the modification in these experiments is a discontinuous scratching mode with a contact time ~1 msec.

In experiments which were to be conducted in deaerated solutions the cell was flushed with nitrogen and the previously deaerated solution then pumped into the cell until the rotating specimen was ~2.5 cm below the liquid surface. The corrosion potential was monitored for 3 hr by which time an approximately steady-state potential was achieved. The specimen was then potentiostatically controlled and the current recorded until a steady value was obtained on the filmed surface. The diamond was then dropped onto the surface and the current surge due to oxide removal was photographically recorded on the oscilloscope. A typical oscillogram is shown in Fig. 2. In this example the current surge deviates from the initial linear time relationship (shown dotted in Fig. 2). At less noble potentials this deviation does not occur; the reason for this is discussed below. The transient was quantified in terms of the initial current density on the filmed surface, the maximum anodic or cathodic current densities on the scratch (i_{am} and i_{cm} , respectively) during the first bounce and the subsequent rate of decay in

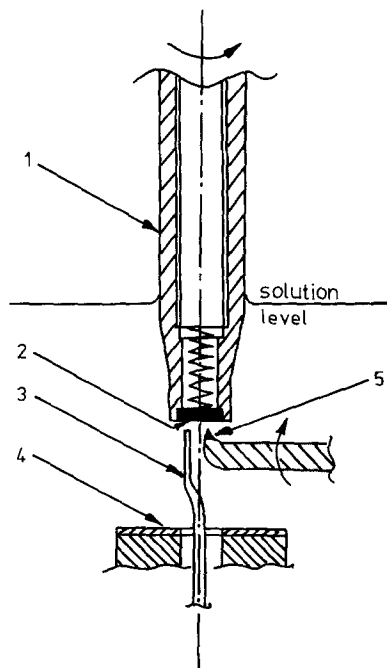


Fig. 1. Rotating disk electrode equipped for scratching. 1, Specimen holder; 2, specimen; 3, Luggin capillary; 4, counterelectrode; 5, diamond stylus.

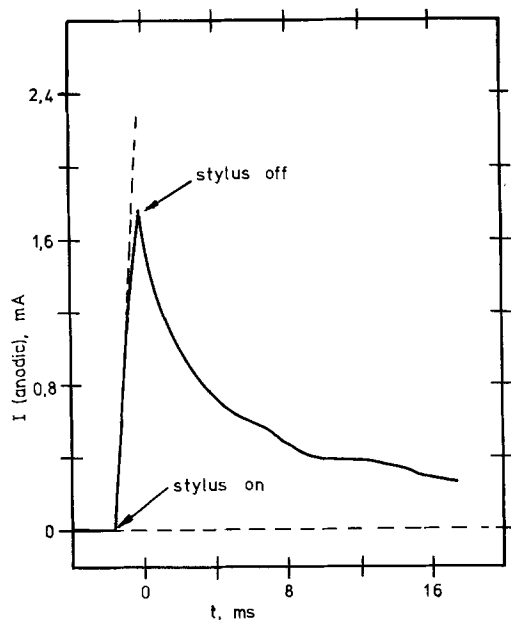


Fig. 2. Current transient caused by scratching electrode at constant $E = -825$ mV (SCE). $v_s = 384$ cm sec $^{-1}$. 1.0M HCl, pH = 1.0. $I_p = 0.0165$ mA.

current density. The current density on the scratch was calculated as $(I_s - I_p)/A$, where I_s is the current recorded during the transient, I_p the current recorded before scratching, and A the measured area of the scratch. There is a degree of uncertainty in this calculation due to an unknown surface-roughness factor on the scratch; this uncertainty is believed to be small, however, since the surface profile appears smooth when observed at magnifications of X10K.

Results

Polarization characteristics on filmed surfaces (steady state before scratching).—Figures 3a and 3b illustrate the polarization characteristics in deaerated 0.5M Na₂SO₄ and 1M NaCl, respectively, at pH 1.0 and 6.5. The curves were produced potentiodynamically at a sweep rate of 0.225 mV sec $^{-1}$. Reduction of H⁺ with a linear $E/\log_{10} i_c$ predominates in the cathodic region; at more noble potentials anodic oxidation of Al occurs. The high degree of polarization of the latter ceases at -800 mV (SCE) in halide solutions when pitting is observed on the specimen. Reduction of O₂ was observed in aerated solutions; all results presented here were from deaerated solutions.

The addition of halide ions to the electrolyte increased i_a at constant E ; in acid solutions this increase is approximately threefold and is constant over the range 1-4M NaCl. At more noble potentials pitting occurs in the halide solutions; the pitting potential varies between -805 mV (SCE) in 1M NaCl and -880 mV (SCE) in 4M NaCl.

The reduction reaction rate at constant E decreases with bulk pH and, in strongly acidic solution, is almost independent of halide content. At higher pH, however, the reduction rate is slightly higher in chloride solutions. The temperature dependence of i_c in the potential range -1200 to -1700 mV (SCE) gives an activation energy between 31 and 42 kJ mole $^{-1}$. Tafel plots are linear over some orders of magnitude of i_c , but changes in slope are observed at higher current densities. Values of $b_c = \partial E/\partial \log_{10} i_c$ in the linear region vary from -200 mV at pH = 1 to -120 mV at pH = 6.5.

Maximum dissolution and proton reduction rates on an oxide-free surface.—Figure 4 illustrates the variation of the maximum anodic current density i_{am} , on the scratched surface at -900 mV (SCE) with the linear velocity of the scratch v_s , for $1 < \omega < 200$ Hz. (Com-

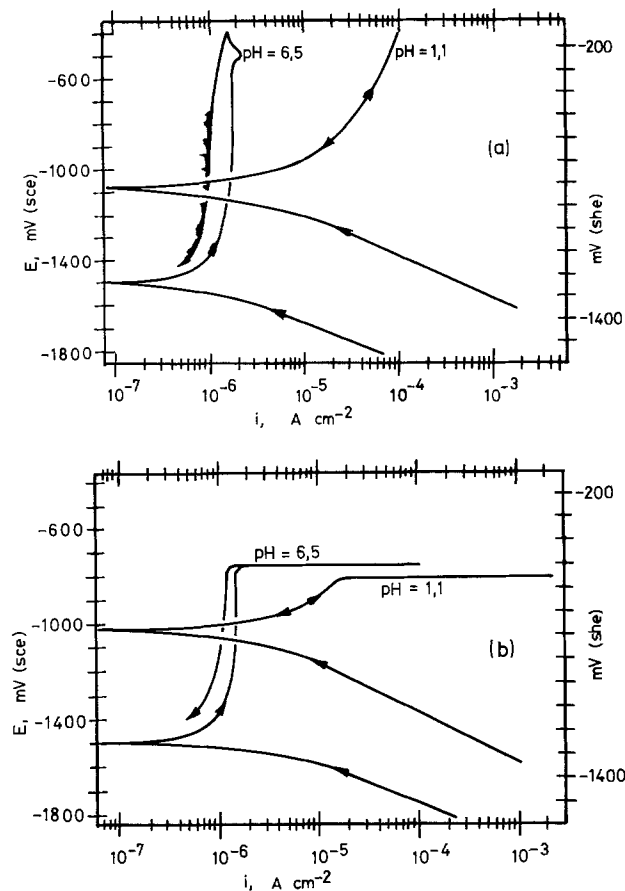


Fig. 3. Steady-state polarization of Al-7 w/o Mg. $dE/dt = 0.225$ mV sec $^{-1}$; $\omega = 10$ Hz. (a) 0.5M Na₂SO₄; (b) 1.0M NaCl.

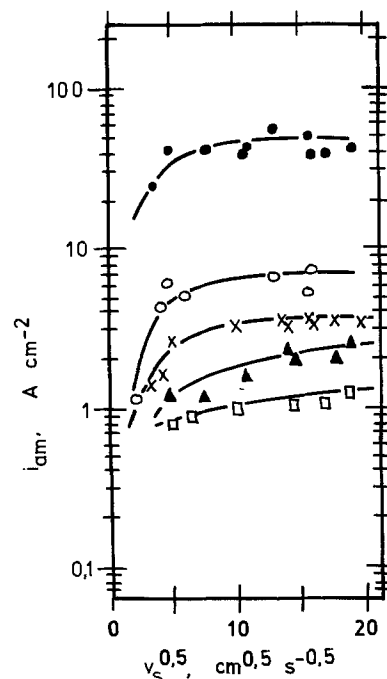


Fig. 4. Dependence of i_{am} on v_s at $E = -900$ mV (SCE) for electrolytes of different pH and anion content. ●, 4M NaCl, pH = 1.0; ○, 1M NaCl, pH = 1.0; ×, 0.5M Na₂SO₄, pH = 1.0; ▲, 1M NaCl, pH = 4.0; □, 1M NaCl, pH = 6.0.

pare the magnitudes of i_{am} with i_a in Fig. 3.) v_s is defined at $2\pi r\omega$, where r is the distance between the center of rotation of the disk and the scratch. Although the reaction rate varies with anion content and electrolyte pH (Fig. 4), it is constant for $v_s > 100$ cm sec $^{-1}$. At lower v_s there is a small dependence of i_{am} on

v_s . Similar relationships were observed at -1000 mV (SCE) and -1300 mV (SCE). All subsequent experiments were conducted at $v_s > 200$ cm sec $^{-1}$.

The dependence of i_{am} on E is summarized in Fig. 5 for 1M NaCl solutions at various pH values and in Fig. 6 for acid solutions of various anion contents. Also shown in these figures are the data of Hagyard and Earl (14), who rapidly scratched pure Al in 1M KCl at pH = 3.2. The graphs illustrate two major points. First, i_{am} at constant E is the same in all solutions over some potential range, the extent of which is specific to the solution pH and anion content; this common characteristic is denoted by the dotted line. (Note that this line is extrapolated beyond the experimental data at approximately 6 A cm $^{-2}$.) Second, at potentials just noble to this common range i_{am} may decrease or remain constant, before increasing upon further anodic polarization; this is most pronounced for the more acidic electrolytes.

The fact that the dotted line corresponds to the condition where a bare surface is maintained throughout the 1 msec scratch period is discussed in more detail below. Deviation from the dotted line at more noble potentials is due to the formation of a surface film of appreciable coverage within the 1 msec scratch time. It cannot be due to an ohmic potential drop since this was measured (using an interrupter-galvanostat) and found to have a maximum value of 10 mV. Neither can it be due to diffusion control at the high velocities used ($v_s > 200$ cm sec $^{-1}$, see Fig. 4). In addition the activa-

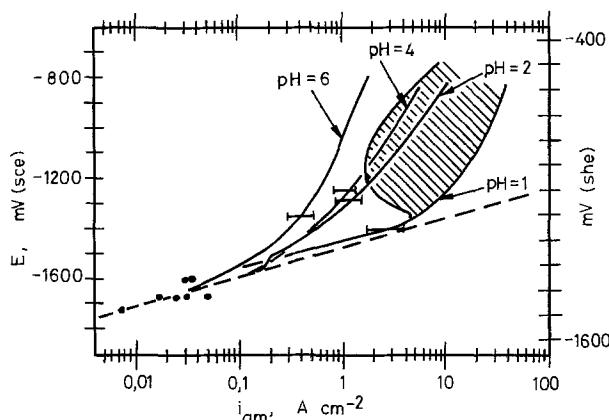


Fig. 5. Anodic polarization curve for bare metal dissolution in 1M NaCl as a function of pH. $v_s = 200$ - 400 cm sec $^{-1}$. Numbers give the electrolyte pH. Hatched area represents scatter of results which occurred at pH = 1 only. Error bars give the maximum deviation. Data points (●) are for pure aluminum in 1M KCl at pH 3.2 (14).

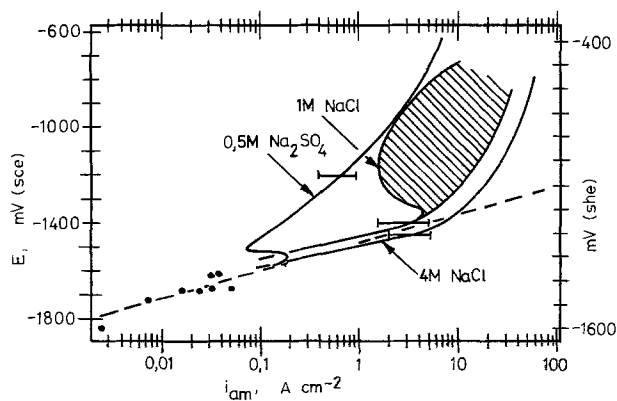


Fig. 6. Anodic polarization curve for bare metal dissolution in electrolytes of pH = 1 for different anion contents. $v_s = 200$ - 400 cm sec $^{-1}$. Hatched area represents scatter of results which occurred in 1M NaCl only. Error bars give maximum deviation. Data points (●) are for pure aluminum in 1M KCl at pH 3.2 (14).

tion enthalpy for dissolution on the scratched surface in the potential region -1500 to -1000 mV (SCE) is low (15) in the range 12-17 kJ mole $^{-1}$, in contrast to 84-92 kJ mole $^{-1}$ observed on dissolving surfaces with an initially air-formed film at pH 6.5.

At potentials more negative than -1500 to -1600 mV (SCE) the net current density on the scratch is dominated by the cathodic reaction. The maximum cathodic current density i_{cm} is shown as a function of pH and anion content in Fig. 7a and 7b. At high i_{cm} and less acidic pH, the reaction rate tends to become potential independent; under these conditions the rate is limited by diffusion of H $^+$ since the limiting value of i_{cm} is inversely proportional to pH (Fig. 7) and depends on $\omega^{1/2}$ (15). However, linear regions in $E/\log_{10} i_{cm}$ are apparent which are independent of ω and have a slope $b_c = -290$ to -320 mV in both sulfate and chloride electrolytes. Note that a similar b_c value was observed by Hagyard and Earl (14) for the proton reduction reaction on oxide-free pure aluminum in 1M KCl at pH 3.2.

Decay of reaction rate of scratched surfaces.—The change in reaction rate due to oxide growth on the scratch was examined in terms of the time dependence of the ratio i_{at}/i_{am} , where i_{at} is the anodic current density at time t after the diamond has bounced off the surface. The choice of this was based on the assumption that the decay would follow a law of the type $i_{at} = i_{am}f(t)$.

Figure 8 illustrates the effect of potential on the electrode reaction rate for various anion contents at pH = 1.0. In 0.5M Na $_2$ SO $_4$ the decay rate due to oxide growth on the scratch increases as E becomes more noble (i.e., as the overpotential for oxide formation increases). The same dependence is noted in the solutions containing Cl $^-$ except that anomalous behavior is observed as the potential approaches the pitting potential. This is shown in Fig. 8 by the dotted lines and is characterized by a significantly slower decay rate than that observed in sulfate solutions. The effect becomes more marked as

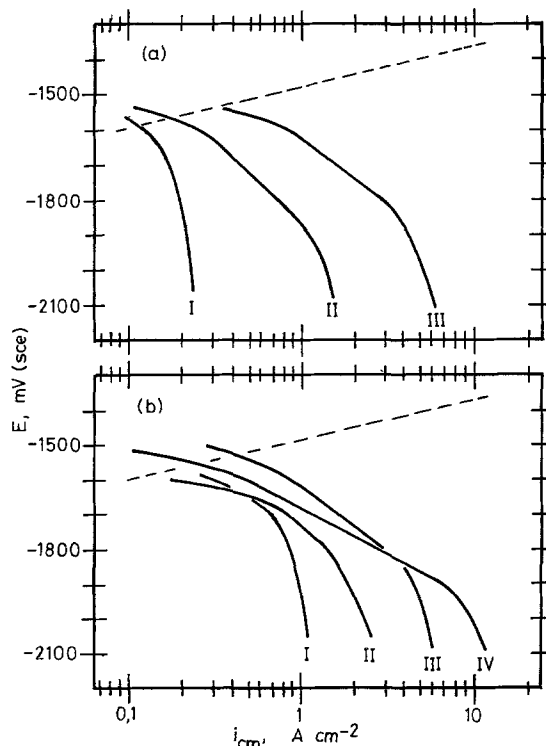


Fig. 7. Cathodic polarization curves for reduction of H $^+$ on bare metal surface. (a) 1M NaCl: I, pH = 2.0; II, pH = 1.5; III, pH = 1.0. (b) pH = 1.0: I, 4M NaCl; II, 2M NaCl; III, 1M NaCl; IV, 0.5M Na $_2$ SO $_4$. Bare surface anodic dissolution is shown as the broken line.

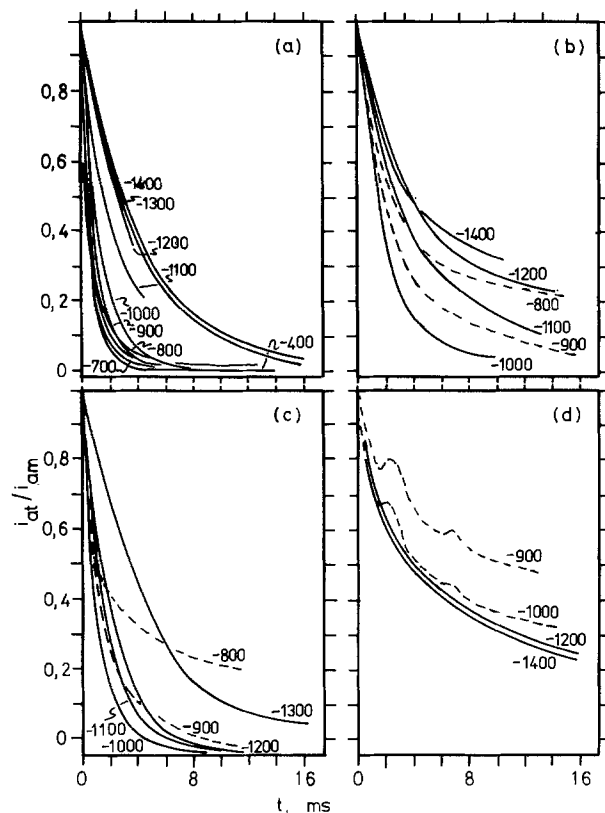


Fig. 8. Decay of i_{at}/i_{am} with t as a function of E (mV (SCE)) at $\text{pH} = 1.0$. (a) $0.5\text{M Na}_2\text{SO}_4$; (b) 1M NaCl ; (c) 2M NaCl ; (d) 4M NaCl .

the Cl^- concentration increases, and in 4M NaCl "breakaway" current surges are observed during decay. It is expected that the decay rate should increase as the pH increases (i.e., as the oxide becomes more thermodynamically stable at a given potential). In general this was observed, but the effect was not reproducible, possibly owing to the buildup of localized acidity associated with oxide formation.

Figure 9 shows the decay in cathodic reaction rate after scratching in various solutions at potentials approaching the reversible potential for solid-state oxide formation (~ -1800 mV (SCE) at $\text{pH} = 1.0$). As E becomes more cathodic and the oxide becomes less stable, so the effect of Cl^- in slowing down the decay rate becomes more appreciable, in a manner similar to that noted as the pitting potential is approached.

Discussion

Metal dissolution on a bare surface.—The linear regions in Fig. 5 and 6 (shown dotted) are summarized in Fig. 10, together with the data of Hagyard and Earl (14) (who used a $5 \mu\text{sec}$ contact time). That the data shown in Fig. 10 do in fact correspond to the condition where a bare surface is maintained throughout the 1 msec scratch period is indicated as follows. First, the $E/\ln i_a$ relationship is independent of sulfate (0.5M) and chloride ($1\text{--}4\text{M}$) content and solution pH and is linear. This is expected for a simple charge-transfer rate-controlled anodic dissolution reaction. Second, the data form a direct extrapolation of the work of Hagyard and Earl, whose scratch period was far shorter and thus even more likely to maintain a bare surface. Finally, the extent of the potential range over which the bare surface is maintained (Fig. 5 and 6) depends inversely on the expected stability of the oxide, i.e., the potential range increases as the pH decreases, and as the concentration of Cl^- increases.

Figure 10 shows that the dissolution kinetics obey Tafel's law and gives a slope $b_a = 118 \pm 25$ mV. Lin-

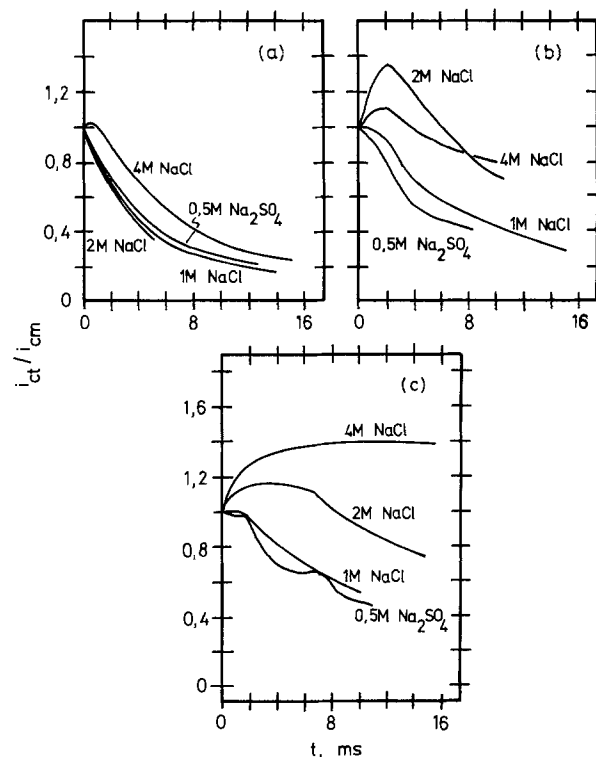


Fig. 9. Decay of i_{ct}/i_{cm} with t as a function of anion content at $\text{pH} = 1.0$. (a) $E = -1600$ mV (SCE); (b) $E = -1800$ mV (SCE); (c) $E = -2000$ mV (SCE).

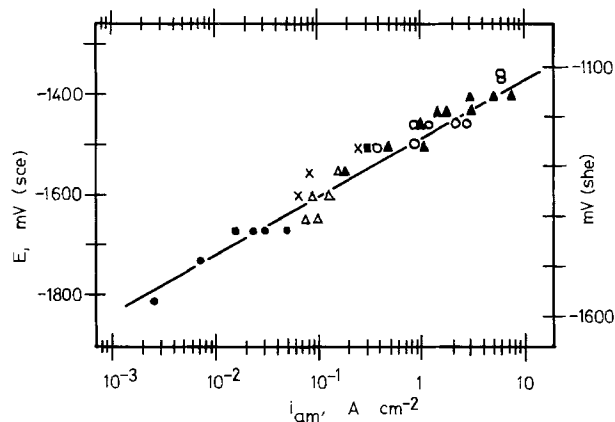
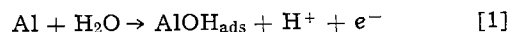


Fig. 10. Anodic Tafel line for dissolution of bare metal showing independence of reaction on electrolyte composition. $b_a = 118 \pm 25$ mV. \blacktriangle , 4M NaCl , $\text{pH} = 1.0$; \circ , 1M NaCl , $\text{pH} = 1.0$; \triangle , 1M NaCl , $\text{pH} = 4.0$; \times , 1M NaCl , $\text{pH} = 6.0$; \blacksquare , $0.5\text{M Na}_2\text{SO}_4$, $\text{pH} = 1.0$; \bullet , 1M KCl , $\text{pH} 3.2$ (14).

earity is achieved over almost 4 decades of current density.

Since the bare surface dissolution rate is independent of sulfate or chloride content (within the concentration ranges investigated) the reaction does not involve complexes of these anions, at least in the rate-determining step. It is also independent of pH . We thus conclude that the initial single electron transfer is rate determining



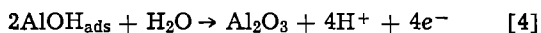
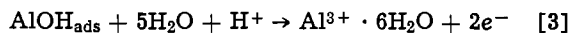
Reaction [1] proceeds with a rate given by

$$i_a = 3Fk_1 \exp(\beta_a FE/RT) \quad [2]$$

which gives $b_a = 118$ mV and $\partial \log_{10} i_a / \partial \log_{10} \text{H}^+ = 0$, in good agreement with experiment, for $\beta_a = 0.5$.

Reaction [1] is probably the initial step in both the dissolution and passivation processes (which occur in parallel until the surface is completely covered with

oxide). The net remaining reactions may be, respectively



The mechanisms of reactions [3] and [4] are unknown, but they are probably electrode reactions since observations of Straumanis and Poush (16) and Spooner (17) have shown that, from the stoichiometry of the overall reaction, there are 3 electrons detected per atom of aluminum oxidized. Reaction [4] is probably a solid-state reaction with no intermediate dissolved phase at least in the early stage of oxide growth ($t < 2$ msec); the lack of dependence of i_{am} on V_s for $V_s > 100$ cm sec⁻¹ (Fig. 4) indicates that, at these high solution flow rates, passivation does not occur by a dissolution-precipitation process, despite the very high current densities.

Repassivation.—The rate of decay of i_a was interpreted in terms of the rate of oxide growth after scratching, and obeys the following law

$$i_{\text{at}} = i_{\text{am}} \exp(-\alpha t^n) \quad [5]$$

α and n have values determined by plotting $\log_{10}(\ln(i_{\text{am}}/i_{\text{at}}))$ against $\log_{10} t$, shown in Fig. 11. i_{at} is the anodic current density at time t after the diamond stylus has left the surface. Two values of n are revealed in Fig. 11: an initial region where $n = 1$ and at longer times a region in which $n = 0.5$. The fact that some coverage of the bare scratch surface has in some cases (at more positive E) already occurred when the stylus leaves the surface is unimportant since, although it affects the surface area of bare metal, analysis of the data via Eq. [5] involves only ratios of current density. Figure 12 shows plots of Eq. [5] as a function of electrolyte composition and potential. As E becomes more noble the transition between the two laws for the sulfate electrolyte system occurs at shorter times. Increasing the Cl⁻ concentration also decreases the transition time, especially as the pitting potential is approached. A possible explanation for the change in n value is that the $n = 1$ decay law represents growth of a continuous oxide film, probably of monolayer coverage, that is relatively defect-free, whereas the $n = 0.5$ law represents thickening of the film, which also becomes increasingly defective, perhaps because of inclusion of alternative anions (Cl⁻ or SO₄²⁻) in the solid lattice (18). It must be emphasized however, that when the oxide is ruptured in solutions containing Cl⁻ even as concentrated as 4M, rapid film growth always ensues; the effect of the Cl⁻ is merely to accelerate the onset of growth of the subsequent defective film. As indicated in Fig. 8 by the periodic current surges, partial break-

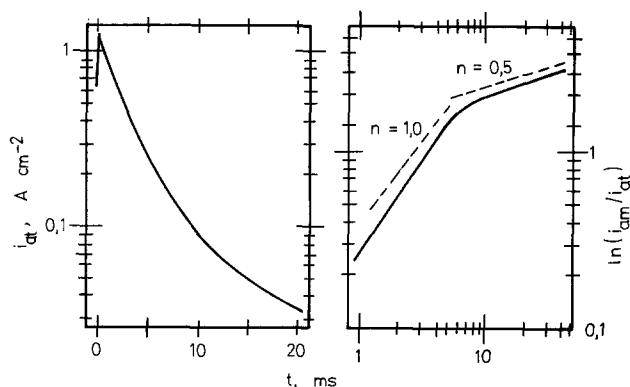


Fig. 11. Decay of anodic reaction rate in 0.5M Na₂SO₄ at pH = 1.0, $E = -1100$ mV (SCE), $v_s = 338$ cm sec⁻¹. (a) Logarithmic plot and (b) double logarithmic plot of Eq. [5]. Broken lines show slopes, n , of 1.0 and 0.5.

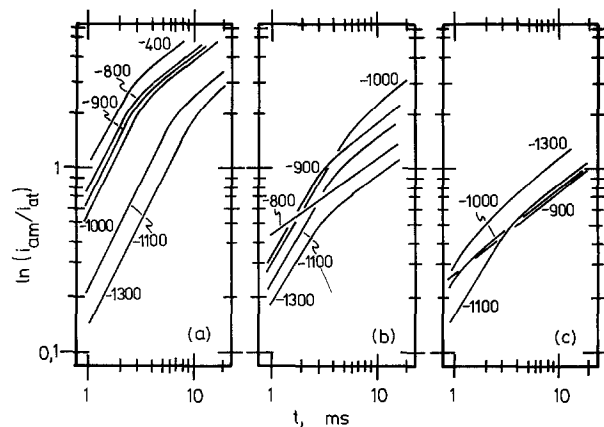
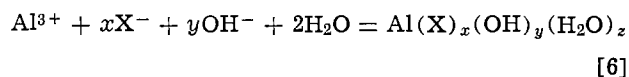


Fig. 12. Plots of Eq. [5] for decay of anodic reaction rate in solutions of pH = 1.0 as a function of E (mV (SCE)). (a) 0.5M Na₂SO₄; (b) 1M NaCl; (c) 4M NaCl.

down of the film may occur at high concentrations of Cl⁻.

The experimental results presented are in qualitative agreement with those of Adams and Foley (19) and of Foley and Trzaskama (20) who investigated the change in uncontrolled open-circuit potential of various aluminum alloys upon continuously scratching the specimen in solutions containing different concentrations of anions. For instance, their observed open-circuit values on the scratched surface are in approximate agreement with those computed from the individual anodic and cathodic current densities in Fig. 5, 6, and 7, and their resultant change in open-circuit potential with time and its dependence on, for instance, sulfate and chloride anions, is in agreement with the expected effect from Fig. 8 and 9. However a direct quantitative comparison is not possible since the use by these authors of a continuous scratching technique with a rotation periodicity > 5 msec will not maintain a bare surface over the whole of the scratched area, as discussed in the Experimental section above; thus there is some question as to the surface condition initially being examined in these other investigations.

Although the experimental results of these authors (19, 20) and the present work are in qualitative agreement, there is a divergence in interpretation. Adams and Foley (19) and Foley and Trzaskama (20) suggest that the effect of anions on the passivation rate is due solely to the following reaction occurring in the liquid



were X⁻ is any anion. The interpretation from the present work is that, although the above reaction may well occur at longer times or in more stagnant solutions, the oxide forms first by an overall reaction given by Eq. [4], followed by incorporation of the anions into the film after a finite time period, which is dependent on the potential and the anion. The precise reaction sequence must await further experimentation.

Conclusions

1. The rates of dissolution of Al-7 w/o Mg and of proton reduction are increased by several orders of magnitude when the high-impedance surface oxide is mechanically removed.

2. The anodic dissolution kinetics of the bare alloy surface follow Tafel's law, the rate being independent of pH and sulfate (0.5M) and chloride (1-4M) content. The rate-determining step is



3. By comparison with previous results on pure Al the anodic and cathodic reaction kinetics for the pure metal and for Al-7 w/o Mg are similar.

4. Growth of an oxide film on the initially bare alloy surface occurs readily in acid sulfate and chloride solutions and follows the empirical law $i_{at} = i_{am} \exp(-at^n)$, where $n = 1$ initially but changes to 0.5 after some time. The changeover time is a function of both E and Cl^- concentration.

Acknowledgment

Acknowledgment is given to the Procurement Executive of the Ministry of Defence, U. K., for financial support to one of us (F.P.F.) during the tenure of which this work was conducted.

Manuscript submitted Nov. 9, 1977; revised manuscript received Dec. 27, 1979.

Any discussion of this paper will appear in a Discussion Section to be published in the December 1980 JOURNAL. All discussions for the December 1980 Discussion Section should be submitted by Aug. 1, 1980.

Publication costs of this article were assisted by General Electric Company.

REFERENCES

- R. B. Mears, R. M. Brown, and E. H. Dix, Stress-Corrosion Cracking Symposium, ASTM/AIME, p. 329 (1944).
- E. C. Perryman and S. E. J. Hadden, *J. Inst. Metals*, **77**, 207 (1950).
- P. Brenner and W. J. Roth, *ibid.*, **94**, 159 (1948).
- P. T. Gilbert and S. E. J. Hadden, *ibid.*, **77**, 237 (1950).
- A. W. Thompson and I. M. Bernstein, Rockwell International Science Center Report No. SC-PP-75-63, To be published in *Adv. Corros. Sci. Technol.*
- M. O. Speidel, Proceedings of Conference on Hydrogen in Metals, p. 249, Seven Springs, ASM Metals Park (1974).
- J. Berggren, Ph.D. Thesis, University of Erlangen, Nurnberg (1973).
- R. J. Gest and A. R. Troiano, *Corrosion*, **30**, 274 (1974).
- P. R. Swann, Private communication.
- C. E. Eells and W. Evans, *Trans. AIME.*, **227**, 438 (1963).
- M. O. Speidel, "The Theory of Stress-Corrosion Cracking in Alloys," p. 289, NATO Conference (1971).
- D. Gilroy and J. E. O. Mayne, *J. Appl. Chem.*, **12**, 382 (1962).
- D. J. Lees, Paper presented at Stress-Corrosion Test Methods Working Group European Federation of Corrosion, Firminy, September 1978.
- T. Hagyard and W. B. Earl, *This Journal*, **114**, 694 (1967); **115**, 623 (1968).
- F. P. Ford, Ph.D. Thesis, Cambridge University (1973).
- M. E. Straumanis and K. Poush, *This Journal*, **112**, 1185 (1965).
- R. C. Spooner, *ibid.*, **102**, 156 (1955).
- M. A. Heine, D. A. Keir, and M. J. Pryor, *ibid.*, **112**, 24 (1962).
- A. A. Adams, and R. T. Foley, *Corrosion*, **31**, 84 (1975).
- R. T. Foley and P. P. Trzaskoma, *ibid.*, **33**, 435 (1977).

Effect of CO on the Low Temperature Diffusion of Cr and Si Through Thin Gold Films

Chin-An Chang*

IBM Thomas J. Watson Research Center, Yorktown Heights, New York 10598

ABSTRACT

Low temperature diffusion of Cr and Si through thin gold films is studied in N_2 and in $(N_2 + CO)$ ambients. The out-diffusion of both Cr and Si to the gold surface is suppressed in the presence of CO. The results are discussed in terms of a model which considers the roles of both the gold film and the ambients used.

Recently there have been studies of ambient effects on low temperature diffusion in thin gold films. The diffusing species include both metals and Si (1-4). The out-diffusion rates can be either enhanced or suppressed depending on the ambient used. An enhanced diffusion is often observed in an oxidizing ambient, whereas a reduced one is observed in the presence of H_2 . An understanding of such ambient effects is useful not only for the determination of the diffusion mechanism involved, but also for the control of metal-metal contacts, metal-Si contacts, Schottky barriers, and in such applications as the growth of large grain polycrystalline Si films (5).

In this paper we study the effect of CO on the out-diffusion of Cr and Si in thin gold films. As will be discussed later, CO is chosen because changes it produces in the work function of gold are different from those produced by oxidizing ambients, e.g., steam and air. We are interested in studying whether this

difference plays any role on the diffusion of Cr and Si through gold. We have found that the outdiffusion of both Cr and Si through thin gold films is suppressed in the presence of CO. This result is discussed in connection with other ambient effects on the various species diffusing through gold. A surface potential model is proposed for the observed ambient effects by considering the roles of both the gold film and the ambients used.

Experimental and Results

For the study of outdiffusion of Cr through gold, Cr and Au films, 2000-3000Å each, were successively evaporated on sapphire substrates. For that of Si through gold, thin films of gold, ~2000Å, were evaporated on (111)Si. The samples were annealed at 250°C for 1 hr in a flowing N_2 ambient and in an $N_2 + CO(5:1)$ mixture. The N_2 flow rate was kept the same in both ambients. The samples were analyzed using both He^+ -ion backscattering spectrometry and Auger spectroscopy.

* Electrochemical Society Active Member.

Key words: diffusion, gold, ambient effects, model.

Figure 1 shows the backscattering spectra for the Au/Cr samples. It shows significant out-diffusion of Cr to the gold surface, and also diffusion of Au into Cr. Less accumulation of Cr on the gold surface is observed in the presence of CO. Figure 2 shows the Auger depth profiling using Ar⁺-ion sputtering for the sample annealed in N₂. It shows both Cr and oxygen near the surface, indicating oxidation of the accumulated Cr on the gold surface. The sputtering time needed for the disappearance of the Cr signal is 50 min for this sample. In contrast, the Cr signal for the sample annealed in N₂ + CO mixture disappeared after 7 min of sputtering.

Figure 3 shows the backscattering spectra for the out-diffusion of Si through gold. Accumulation of Si on the gold surface is observed for the film heated in N₂, but not for that in the N₂ + CO mixture. This is also confirmed by Auger analysis. The small amount of Si accumulation observed on the gold surface is expected in a nonoxidizing ambient (2). The broad peak located near channel 310 in Fig. 3 corresponds to the residual Ar from plasma etching cleaning of the Si substrates prior to gold evaporation.

We have also evaporated gold films on GaAs and studied the out-diffusion of Ga and As through gold. Using N₂ and N₂ + CO ambients, the diffusion rates for both Ga and As are reduced in the presence of CO. Details of this study will be reported elsewhere.

Discussion

We have shown that the out-diffusion of both Cr and Si through thin gold films is suppressed in the presence of CO. This result is now compared with the known ambient effects on the out-diffusion of various metals and Si through gold. Table I lists both the known ambient effects from literature and results of this study. Our results on Ga and As are also included for comparison.

As Table I shows, in an oxidizing ambient such as steam, air, and oxygen, an enhanced out-diffusion rate is observed over that in vacuum or nonoxidizing ambients. The presence of CO or H₂, however, reduces the out-diffusion rates. In oxidizing ambients, the out-diffused species on the gold surface were often found to be in the oxide form. This is thought to act as a sink for the out-diffused species and is responsible for the enhanced diffusion observed. Such a sinking effect is consistent with the observed higher diffusion rate of Si through gold in steam than in air, and that for Cu in the presence of chlorine (4). This effect alone, however, considers only the role of the ambients on the oxidation of the out-diffused species. It does not take into account the ambient effect on the prop-

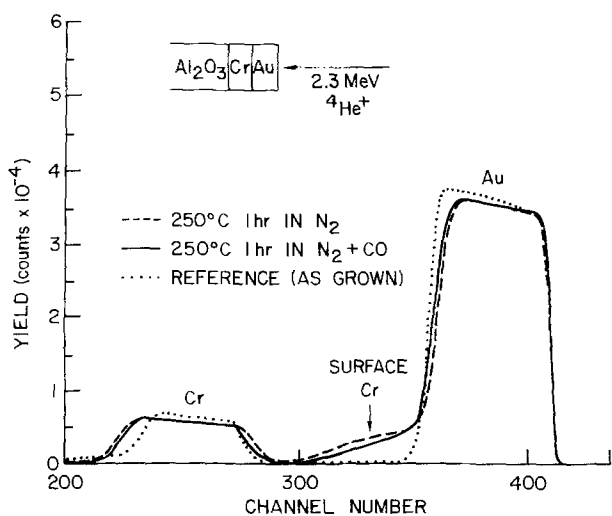


Fig. 1. Backscattering spectra of Au/Cr/sapphire samples heated in different ambients. 5 keV/channel.

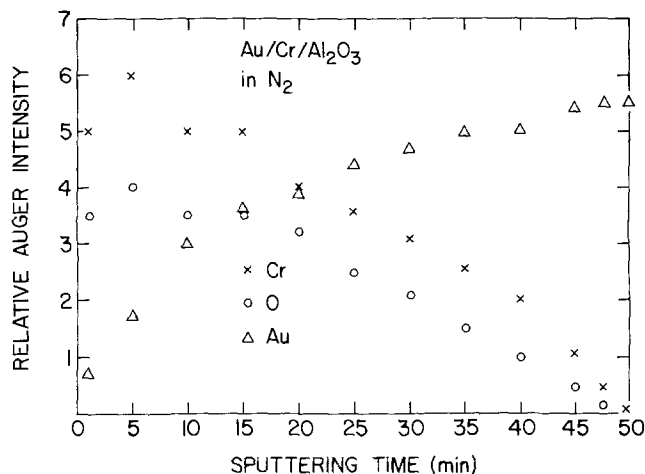


Fig. 2. Auger depth profiling of the Au/Cr/sapphire sample annealed in N₂.

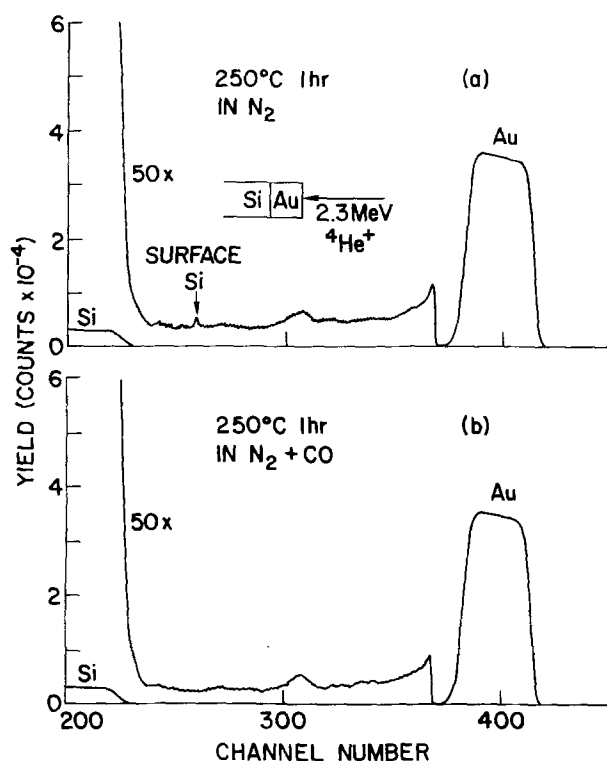


Fig. 3. Backscattering spectra of Au/Si samples: (a) 1 hr annealing at 250°C in N₂; (b) 1 hr annealing at 250°C in N₂ + CO(5:1). 5 keV/channel.

erties of the metal film, nor the role played by the metal film itself. We will show that the latter considerations provide an alternative explanation to the observed ambient effects. They also allow a generalization of the known ambient effects using similar metal films, such as gold and silver. For example, no Si accumulation on a silver surface is observed when the Ag/Si system is heated in an oxidizing ambient (2). However, using sequential Ag/Au or Au/Ag films on Si, accumulation of Si is observed on the silver surface for the Ag/Au/Si system, but not on the gold surface for the Au/Ag/Si one. A similar result has been observed for Cr (6).

Here we propose a model to consider the roles of both the ambients and the metal films. We show that this model correlates very well the observed ambient effects on the various diffusing species in both gold and silver films. It is also consistent with the higher out-diffusion rate of Si in steam than in air. For the role of the metal films, we consider the electronega-

Table I. Observed ambient dependence of the out-diffusion rates in thin gold films

Diffusing species	Difference in diffusion rates in different ambients	Remarks
Cr	in O ₂ > in vacuum	Ref. (1)
Si	in N ₂ > in N ₂ + CO in steam > in air > in oxygen; negligible in forming gas (N ₂ + H ₂)	This work Ref. (2)
Co	in N ₂ > in N ₂ + CO	This work
Cu	in N ₂ > in N ₂ + H ₂	Ref. (3)
Ga,As	in air > in vacuum	Ref. (4)
	in N ₂ > in N ₂ + CO	This work

tivity difference between the metal film and the diffusing species; for that of the ambients we consider the ambient-induced surface potential changes of the metal film. Since the metal films studied are polycrystalline, it has been suggested that grain boundary diffusion is the dominant mechanism in these films (1-4). The grain boundary diffusion scheme plays a central role in our model.

All the diffusing species listed in Table I have smaller electronegativities than gold. The electronegativities of Cr and Si, for example, are 1.6 and 1.8, respectively, that of gold is 2.4 (7). The ionicity of Cr and Si in gold can be approximately estimated using Pauling's ionicity relation (7). It gives one-seventh and one-tenth of a positive unit charge for Cr and Si in gold, respectively. Such positively charged species in gold would be attracted to the gold surface if the ambient-induced surface potential changes are favorable. Indeed, upon exposure to air and steam, a decrease in work function of 0.5 and 1.2 eV, respectively, is observed for gold (8, 9). Such a decrease in work function is equivalent to an increase in the negative surface potential of the same magnitude (10). No work function data are available for gold in dry oxygen, but the resistivity measurement of gold in dry oxygen also shows an induced negative surface potential (11). These changes result from the corresponding increases in electron charge density on the gold surface due to adsorption of the ambient species. The extra charge will penetrate into gold and establish an electric field under the surface for some layers (12). For a polycrystalline gold film, this effect can be much more pronounced due to the small grains present. The ambient species are often known to diffuse into the metal film along the grain boundaries (13). This would create an electric field under the surface of each grain, similar to that described above for the film surface. The dissolved Cr and Si in gold, for example, would be attracted to the grain surface due to the attractive force in an ambient of steam, air, or oxygen. Once they reached the grain surface, rapid diffusion through the grain boundaries to the film surface would follow (14). The larger surface potential change of gold in steam than in air is also consistent with the higher diffusion rate of Si observed in the former ambient. Hydrogen and CO ambients, on the other hand, increase the work function of gold by 0.18 and 0.9 eV, respectively (15). The ambient-induced surface potential changes of gold in hydrogen and CO are, therefore, unfavorable to the out-diffusion of Cr, Si, etc., and this out-diffusion should be suppressed. Thus, we have shown a good correlation between the different out-diffusion rates observed and the ambient-induced surface potential changes of gold in these ambients.

This model is also consistent with the work using Ag and sequential Au-Ag films. The electronegativity of silver is 1.9, and the ionicity of Si in silver, for example, is less than one-tenth of that in gold. Much less ambient-enhanced out-diffusion of Si in silver is expected even in an oxidizing ambient. For the Au-Ag sequential films, since Si mixed with the metal only near the Si-metal interface at temperatures below

the Si-metal eutectic point (2), our model shows that it is the metal film which is in direct contact with Si that determines whether the dissolved Si could be pulled to the grain surface or not. Thus, one expects an accumulation of Si on the silver surface for the Ag/Au/Si case, but not on the gold surface for the Au/Ag/Si one.

It is encouraging that our model, described in a simplistic way, correlates well the observed ambient effects on a variety of diffusing species in gold and silver films. The diffusion mechanism in these systems can, of course, be much more complicated. Other factors could also play important roles in determining the observed diffusion rates. The sinking effect mentioned earlier, for example, is clearly an additional favorable factor to enhancing the out-diffusion rates using oxidizing ambients. The effect of film thickness on the out-diffusion rate could also be incorporated into our model by considering a concentration gradient of the in-diffused ambient species along the grain boundaries. With increasing gold film thickness, fewer ambient species would be distributed along the grain surface near the interface which would weaken the described ambient effect. In addition, the in-diffused ambient species could also affect the initial interface mixing process which is very important to any subsequent out-diffusion through the metal films. Further studies are in progress to understand this last process.

Summary

We have shown that the presence of CO in an N₂ ambient suppresses the out-diffusion of Cr, Si, Ga, and As through thin gold films. A surface potential model is proposed by considering the roles of both the ambients and the metal films used. This model is shown to correlate both our results and the known ambient effects on a variety of diffusing species in both gold and silver films. Extension of this study to different ambients and to different metal films can be both interesting and useful to the semiconductor technology.

Acknowledgment

The author would like to thank L. L. Chang for discussions, W. K. Chu and W. N. Hammer for the backscattering measurement, N. Chou for the Auger spectroscopic measurement, W. W. Molzen for annealing work, and D. S. Yu for thin film evaporation.

Manuscript submitted Aug. 17, 1979; revised manuscript received Jan. 3, 1980.

Any discussion of this paper will appear in a Discussion Section to be published in the December 1980 JOURNAL. All discussions for the December 1980 Discussion Section should be submitted by Aug. 1, 1980.

Publication costs of this article were assisted by IBM Corporation.

REFERENCES

- G. C. Nelson and P. H. Holloway, "Metallurgical Applications of Surface Analysis Techniques," ASTM STP596, p. 68, Philadelphia, Pa. (1976).
- A. Hiraki, E. Lugujo, and J. W. Mayer, *J. Appl. Phys.*, **43**, 3643 (1972); A. Hiraki, E. Lugujo, M.-A. Nicolet, and J. W. Mayer, *Phys. Status Solidi A*, **7**, 401 (1971).
- S. Ohkawa, O. Akanuwa, and H. Ishikawa, *Jpn. J. Appl. Phys.*, **14**, 1589 (1975).
- H. G. Thompson and M. R. Pinnel, *J. Appl. Phys.*, **47**, 3804 (1976).
- C. A. Chang and W. J. Siekhaus, *Appl. Phys. Lett.*, **29**, 208 (1976); C. A. Chang, W. J. Siekhaus, T. Kaminska, and D. T. Huo, *ibid.*, **26**, 178 (1975).
- K. D. Kang, R. R. Burgess, M. G. Coleman, and J. G. Keil, *IEEE Trans. Electron Devices*, **ed-16**, 356 (1969).
- L. Pauling, "The Nature of the Chemical Bond," 3rd ed., Cornell University Press, New York (1960).
- N. A. Surplice and W. Brearly, *Surf. Sci.*, **52**, 62 (1975).

9. R. L. Wells and T. Fort, Jr., *ibid.*, **32**, 554 (1972).
10. F. C. Thompson, in "The Solid-Gas Interface," E. Alison Flood, Editor, Chap. 25, Marcel Dekker, Inc., New York (1967).
11. K. L. Chopra, "Thin Film Phenomena," p. 380, McGraw-Hill Co., New York (1969).
12. R. Furth and E. Morris, *Proc. R. Phys. Soc. London*, **73**, 869 (1959).
13. J. C. M. Hwang, P. S. Ho, and R. W. Balluffi, *Appl. Phys. Lett.*, **33**, 458 (1978).
14. J. E. E. Baglin and J. M. Poate, in "Thin Films—Interdiffusion and Reactions," J. M. Poate, K. N. Tu, and J. W. Mayer, Editors, p. 305, John Wiley & Sons, New York (1978).
15. G. A. Somorjai, "Principles of Surface Chemistry," p. 249, Prentice-Hall Inc., Englewood Cliffs, New Jersey (1972).

Autodoping Effects in Silicon Epitaxy

G. R. Srinivasan

IBM Data Systems Division, East Fishkill Facility, Hopewell Junction, New York 12533

ABSTRACT

This paper reviews some of the recent autodoping developments which have contributed to a quantitative understanding of this phenomenon. Special emphasis is placed on buried layer studies that are pertinent to the fabrication of integrated circuits. The paper also presents new data concerning the origin of autodoping, flow effects, autodoping differences between silane and SiCl_4 depositions, and the effect of HCl vapor etch on autodoping. An attempt is made to provide a theoretical framework within which these and other effects can be interpreted.

Autodoping in epitaxial silicon was first discovered in 1961 (1, 2), and numerous studies have appeared since then in literature (3-28) describing various aspects of this phenomenon. The term autodoping refers to the transfer of dopants from the substrates to the epitaxial layers during growth. The studies in the past have identified various mechanisms that are involved in this dopant transfer. For example, Thomas *et al.* (3) and Grossman (5) considered the transfer of dopants in the gas phase, whereas Rice (6) and Grove *et al.* (7) focused on the solid-state diffusion of the dopants from the substrate into the epitaxial layers. However, the clear separation of the solid-state and gas phase effects was not made until recently (13, 20, 24, 25, 28) when studies using high resistivity substrates with localized buried layers were begun. The use of such substrates has allowed quantification of autodoping in terms of various process and substrate parameters. In this paper, we limit our discussion to the buried layer studies, which are also more pertinent to the fabrication of integrated circuits in which buried layer structures are used as device elements. Further, this will also simplify the discussion, since complications arising out of back surface autodoping can be neglected for this case.

The vertical cross section of a buried layer structure is shown in Fig. 1a. Figure 1b shows typical vertical profiles of dopant concentration from this structure. These profiles correspond to sections on and off the buried layer. There are some characteristic similarities between the two profiles. Both show a peak near the substrate-epitaxy interface, although the peak in the "on" profile is a few orders of magnitude higher than that for the "off" profile. We can also observe that in the top layers of the epitaxy the two profiles tend to merge, which shows that the distribution mechanisms must be common for the two cases in these layers. In fact, this common region in the "on" profile corresponds to the so-called autodoping tail, which is a result of vertical autodoping. It is customary to refer to the "off" profile as the lateral autodoping peak. The region close to the substrate-epitaxy interface in the "on" profile is dominated by solid-state out-diffusion of the dopant, whereas the distribution in the autodoping tail is caused by dopant transport in the vapor

phase. Figure 2 shows the resolution of the "on" profile into various components. We consider first the out-diffusion models, followed by a discussion of gas phase autodoping, which includes both the lateral and vertical autodoping.

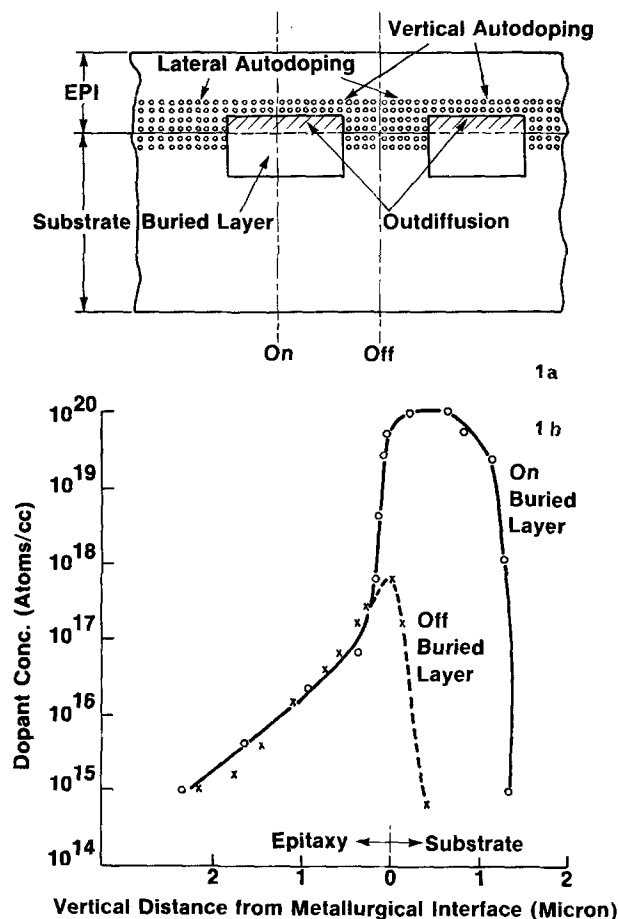


Fig. 1. (a) Vertical cross section of a buried layer structure (schematic). (b) Typical spreading resistance profiles from an arsenic buried layer structure. (Deposition temperature 950°C , growth rate $0.08 \mu\text{m}/\text{min}$, intrinsic deposition.)

* Electrochemical Society Active Member.

Key words: arsenic, buried layer, out-diffusion, prebake, incorporation, CVD.

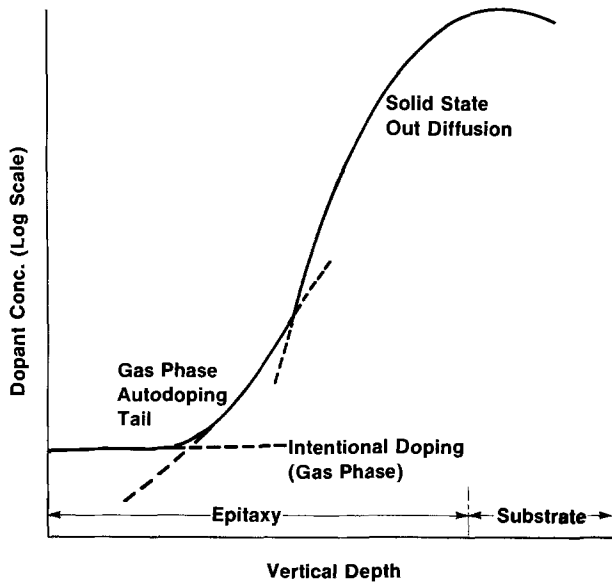


Fig. 2. Resolution of an on-buried layer profile into different components (schematic).

Out-Diffusion Models

Rice (6) and Grove *et al.* (7) have solved the one-dimensional linear diffusion equation, which describes the out-diffusion of dopants into the epitaxy from uniformly doped substrates. Their solution simplifies to a complementary error function (erfc) distribution for cases for which $Vt > 2\sqrt{Dt}$, where V is the epitaxial growth rate, D is the solid diffusivity of the dopant in the epitaxy, and t is the growth time. This distribution has been verified for several cases of uniformly doped silicon substrates which have dopant concentrations up to 10^{19} cm^{-3} (8).

In order to extend the diffusion model to the case of buried layers, one must consider the redistribution of an existing nonuniform profile. One such attempt was made by Hu (11), who considered the redistribution of an initial erfc distribution. He was able to show that satisfactory analytical solutions can be obtained for cases where the initial erfc distribution is approximated by a Gaussian. However, his model requires the assumption of zero surface concentration at the growing surface, which evidently needs to be modified in view of the autodoping component. Also, in view of the high dopant concentrations that are typical of the buried layers, concentration dependence of the diffusion coefficient needs to be taken into account. In addition to these complexities, one must also consider the redistribution that would occur in the buried layer during the heat cycle prior to deposition. Quite evidently, the above-mentioned complications render it impossible to obtain an analytical solution to the diffusion equation. Therefore, it is necessary to solve numerically the nonlinear continuity equation

$$\frac{\partial c}{\partial t} = \frac{\partial}{\partial x} \left[D(c) \frac{\partial c}{\partial x} - VC \right] \quad [1]$$

with appropriate moving boundary conditions. Computer programs such as SUPREM (29) have been written to solve the above one-dimensional equation, and it is found that close agreement between theory and experiment is possible for at least the out-diffusion portion of the dopant profile.

Lateral Autodoping

Previous studies (13, 21, 24, 25, 28) have clearly established that lateral autodoping is brought about by the gas phase transport of the dopant vapor in the reactor. In what follows, we examine the lateral autodoping process in terms of the dopant evaporation during pre-epitaxial thermal cycle, and its redistribu-

tion in the reactor flow system and, finally, its reincorporation into the substrate and epitaxy.

Origin of autodoping.—Before we attempt to understand the detailed mechanism of autodoping, it is necessary to establish the time sequence in the epitaxial process at which most of the dopant transfer occurs. Clearly, since the maximum in the lateral autodoping profile occurs near the substrate-epitaxy interface, a major portion of the dopant redistribution must occur in the initial stages of epitaxial growth. In order to further define this stage of maximum autodoping, the following experiments were conducted. A P^- silicon wafer which had a localized (2.5 mm^2) arsenic diffusion at the center, was cut into parts, A and B, such that part A had the diffusion region and part B did not. The two parts were then placed on the susceptor of a horizontal epitaxial reactor. The cut between parts A and B was made close to the edge of the diffused area such that part B can be placed very close to, but not in contact with, the diffused region in part A. The spacing between parts A and B could be varied in order to obtain information on the dependence of the lateral autodoping with lateral distance from the edge of the diffused area.

The experiment consisted of prebaking parts A and B together in the epitaxial reactor using typical epitaxial H_2 flow conditions. The prebake was at 1150°C for 10 min without deposition. After cooling to room temperature, part A was taken out and was replaced by another P^- silicon wafer (C) which did not have any localized arsenic diffusion in it. The reactor was heated again to 1150°C with wafers B and C, and a standard $2 \mu\text{m}$ thick silicon epitaxy was deposited.¹ In a separate experiment, another P^- silicon wafer (D), which had an arsenic-diffused region as in A, was given a normal epitaxial deposition using the same growth and flow conditions as in the previous experiment but without any interruption between the prebake and deposition cycles. The wafers B, C, and D were subsequently profiled for several lateral distances from the diffused area by the spreading resistance technique. It was found that the profile from wafer C did not show any p-n junction (*i.e.*, the epitaxy was p-type), thus indicating that there was no autodoping on this wafer. On the other hand, wafer B showed substantial autodoping. In addition, wafer D showed arsenic autodoping, as expected. It was also found that the autodoping peak maximum concentration decreased with increased lateral distance from the diffused region for wafer D and also with the increase in lateral distance from the cutoff edge in wafer B.

In order to facilitate a comparison of these autodoping results, profiles are shown in Fig. 3 for wafers B and D, measured 2 mm laterally from the diffused region. We can see from this figure that the peak maximum concentration is about the same for both wafers B and C within the experimental uncertainty, although the integrated dose for wafer D is $\sim 20\%$ larger than that for wafer B.

On the basis of these observations, we draw the following conclusions: (i) since wafer C did not show any autodoping while wafer B did, although both were together during the deposition cycle, the autodoping in B is the result of its prebake with the diffused wafer A; (ii) the near equality of autodoping in wafers B and D show that the bulk of autodoping has already occurred at the prebake stage. We recall that wafer D had the diffusion area through the entire epitaxial cycle, whereas wafer B had the diffused silicon source only during the prebake part of the epitaxial cycle.

The fact that the major portion of autodoping occurs in the prebake cycle has also been noted by Joyce *et al.* (8) and by Deines and Spiro (34). Recently, Tabe and Nakamura (40) have also reported similar results. It is clear, then, that any satisfactory model for

¹ Unless otherwise noted, all epitaxial depositions in the autodoping experiments described in this paper are intrinsic depositions without the addition of an external dopant.

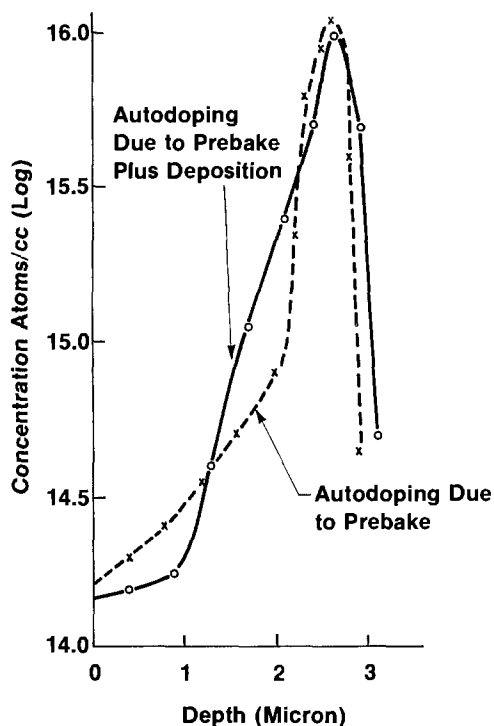


Fig. 3. Spreading resistance profiles from wafers B and D. (Wafer B, autodoping contribution due to prebake; wafer D, total autodoping.)

autodoping has to take into account the dopant transport that occurs during prebake. In the next section, we describe such a model developed by the present author (25).

Another interesting observation drawn from the above experiments is that autodoping occurred even when the source wafer A and the autodoped wafer B were not in physical contact. This fact rules out surface diffusion as the mechanism of dopant transport involved in lateral autodoping. Similar conclusions were reached by Pogge *et al.* (13), who found that autodoping from a diffused wafer occurred even when the diffused region was surrounded by an oxide ring.

Evaporation kinetics during hydrogen prebake.—This aspect of autodoping has been considered in some detail by the present author (25) who found that the maximum in a lateral autodoping profile is a decreasing function of both prebake time and temperature. This analysis showed that the autodoping peak maximum concentration can be related to these prebake parameters on the basis that the maximum in a lateral autodoping profile is directly proportional to the surface concentration over the diffused layer that existed just prior to epitaxial deposition. This expression for the autodoping peak concentration due to an initial rectangular dopant distribution in the diffused layer is given by (25)

$$C(T,t) = A \exp(\beta^2 t) \cdot \operatorname{erfc}(\beta t^{1/2}) \quad [2]$$

where A is a constant of proportionality independent of temperature, T and t are prebake temperatures and time, respectively. $\beta = K/\sqrt{D}$, where K and D are, respectively, the evaporation velocity and solid diffusivity of the dopant in silicon. Both K and D were assumed to be Arrhenius functions of temperature. The above expression gave a good fit to the data yielding values for the arsenic evaporation velocity as a function of temperature. We also note that since the evaporation rate, r , is given by $r = KC_0(t)$, where $C_0(t)$ is the surface concentration, which can also be described by an expression similar to Eq. [2], the above equation describes the variation of evaporation

rate with prebake time and temperature. The results of this study thus support the view that the dopant redistribution during a pre-epitaxial bake cycle is controlled by the evaporation of the dopant from the buried layer.

Effect of HCl vapor etch during prebake.—In the previous section, we considered the release of dopants during prebake in H_2 . The dopant redistribution could conceivably change if there were other etchants in the system during prebake. HCl vapor etching is a common practice for silane epitaxial deposition, and hence it is instructive to study its effect on autodoping. Maeda and Takayama (17) studied this effect in the silane epitaxy grown on antimony-diffused silicon substrates. They found that the etched samples had less out-diffusion than the controls. They argued that the amount of silicon etching was not enough to account for this difference and interpreted this decreased out-diffusion as evidence for decreased arsenic diffusivity in silicon near the surface.

The effect of HCl etching on substrates with an arsenic buried layer has not been reported in the literature. To study this effect, the following experiments were conducted: P^- (100) silicon wafers of 10-20 Ωcm resistivity were diffused with arsenic ($C_0 \sim 1.5 \times 10^{21}/\text{cm}^3$, $x_j \sim 1 \mu\text{m}$) to cover 62% of the wafer surface area in a dense pattern which had buried layers varying in size from 50×100 to $200 \times 400 \mu\text{m}$. A standard 1150°C epitaxial deposition of 2 μm thickness was made on one of these substrates in an rf heated horizontal reactor. The pre-epitaxial bake cycle used was 10 min at 1150°C in flowing H_2 . In subsequent runs, HCl vapor etching (0.04% by volume) was included in the middle of the prebake cycle while keeping all other conditions unchanged. The HCl etching times used were 10 sec, 20 sec, and 1 min. The samples were profiled, both on and off the buried layers, using the spreading resistance technique. Profiles were made at the same distance and direction with respect to flow in all cases.

The autodoping results are shown in Fig. 4. We observe that while there is no significant change in autodoping due to the 10 sec etching, further increase in etching time caused a decrease in the autodoping peak maximum concentration. Since etching is also expected to produce changes in the buried layer characteristics, we show these data in Table I. We note from these data that (i) the decrease in off-profile maximum is accompanied by an increase in the buried layer sheet resistance, and (ii) the junction depth of the buried layer decreases with an increase in etching time. These two facts show clearly that the top layer of the buried layers are being etched away during the HCl etch, which, in turn, implies a change in the surface concentration, C_0 , over the buried layers. Thus, it would appear that changes in autodoping due to HCl etching can be related to changes in C_0 . In further experiments, we varied the etch cycle such that HCl was injected for 10 sec at different times in the prebake cycle and found no significant change in autodoping.

We conclude from the above results that the effect of HCl etching in the prebake cycle can be understood in

Table I. Autodoping effects of pre-epitaxial HCl vapor etch (0.04% HCl by volume, 1150°C deposition temperature, 0.25 $\mu\text{m}/\text{min}$ growth rate)

Etch time (sec)	Buried layer characteristics Sheet resistance (Ω/\square)	Junction depth (μm)	Lateral autodoping characteristics	
			Peak max (atoms/ cm^3)	EPI sheet resistance (Ω/\square)
0	9.01	4.24	2.2×10^{17}	1340
10	9.96	4.03	2.2×10^{17}	1370
20	15.70	4.01	1.37×10^{17}	1730
60	94.30	3.35	7.6×10^{16}	2780

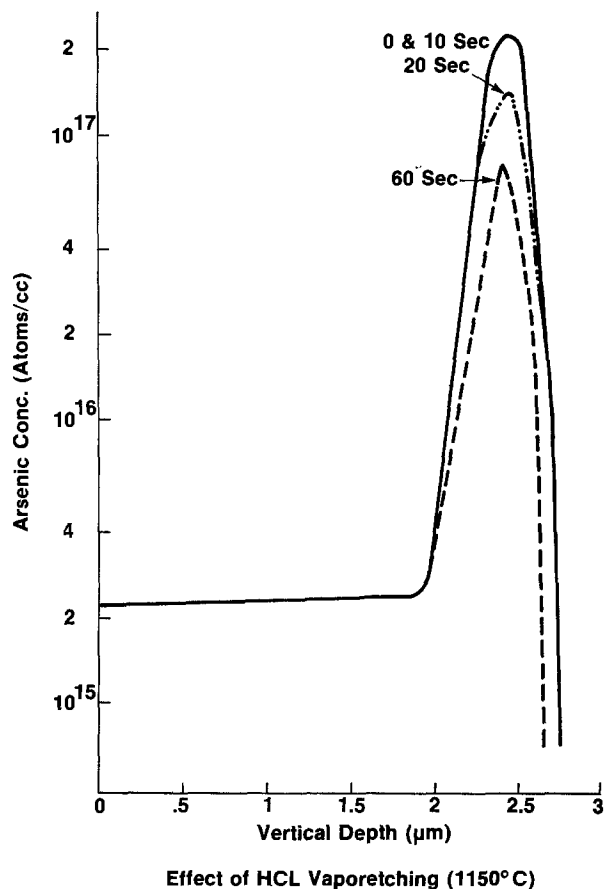


Fig. 4. Off-buried layer spreading resistance profiles for various periods of pre-epitaxial HCl vapor etch (etch temperature 1150°C).

terms of a change in C_0 , which is consistent with the model developed in the previous section. We point out here, however, that HCl (or any other etchant) present during the deposition cycle could alter the autodoping characteristics through a different mechanism that involves changes in dopant incorporation. We shall consider this aspect later, when we discuss the autodoping differences between silane and SiCl_4 depositions.

Vapor distribution and gas flow effects.—The dopant vapor that is produced during the prebake is carried away by the reactor flow system which redistributes this vapor onto different areas of the substrate as well as to different substrates in the reactor. The fact that lateral transport of dopant occurs over large distances has been well documented (13, 20, 24). It is also known that transport in the direction of flow (i.e., downstream autodoping) is larger than that against the main gas flow (upstream autodoping). A detailed understanding of this redistribution requires a knowledge of the flow pattern that exists in any particular reactor. Eversteyn *et al.* (30) have proposed a boundary layer concept according to which there is a relatively stagnant layer of gas above the susceptor. The boundary layer is estimated to be a few millimeters thick in a typical epitaxial run, and dopant impurities could become trapped in this layer. This model has been used to explain the qualitative features of autodoping in silicon epitaxy (13); however, this concept has not been quantitatively developed for autodoping.

Attempts have recently been made to characterize the flow system in terms of temperature and concentration profiles that exist in the gas of an epitaxial reactor. Sedgwick *et al.* (31) have measured the temperature profiles using Raman light scattering in an rf heated horizontal epitaxial reactor. They found that a thermal boundary layer exists in the flow system above the heated susceptor and that the vertical temperature

distributions in the gas vary along the gas flow. Their results indicated a linear velocity distribution in the layer at the leading edge, and this distribution became more complex further downstream. Ban (32) has essentially confirmed these findings. At present, however, there is no good mathematical model that describes the flow distribution in an epitaxial reactor.

The effect of the variations in the main gas flow rate on lateral autodoping has been observed before. Bozler (21) reported a decrease in vertical autodoping of arsenic in silicon epitaxy as the flow rate was increased. However, Pogge *et al.* (13) reported that arsenic lateral autodoping in epitaxial silicon was relatively insensitive to changes in the main gas flow. In order to clarify this point and to provide a quantitative understanding of the flow effects, a systematic study was undertaken by the present author. The details of this study will be reported elsewhere (33a, b, and c).

Briefly, the experiments consisted of silicon epitaxial depositions made at 1150°C on P^- (100) silicon substrates which had a diametrical stripe of arsenic diffusion. The H_2 flow rates used in these experiments varied from 7 to 30 liters/min while other deposition conditions were kept constant. The growth rate was maintained constant at 0.13 $\mu\text{m}/\text{min}$ for all different hydrogen flow rates by suitably adjusting the SiCl_4/H_2 ratio. Epitaxial vertical profiles for arsenic were measured at several distances from the stripe, both along the flow direction (downstream) and against it (upstream).

Figure 5 shows the variation of the autodoping peak concentration with lateral distance for a 15 liters/min flow rate. It can be seen that autodoping decreases with increase in the lateral distance, both for upstream and for downstream flow. This decrease is much faster in the upstream direction than for the downstream case. The present author has shown (33b) that the following equations describe the variation of autodoping peak maximum concentration with distance x from the stripe for both upstream and downstream cases

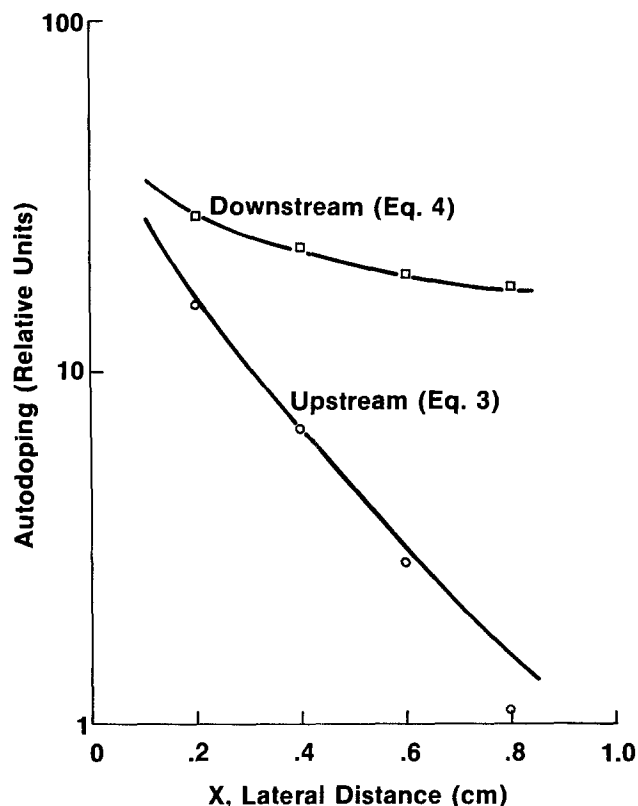


Fig. 5. Variation of autodoping peak maximum with lateral distance. (Deposition temperature 1150°C, growth rate 0.13 $\mu\text{m}/\text{min}$, H_2 flow rate 15 liters/min.)

$$C(\text{upstream}) = (A/u) (r/\sqrt{\pi}) \{ \operatorname{erf} \sqrt{u(x+h)/D} - \operatorname{erf} \sqrt{u(x-h)/D} \} \quad [3]$$

$$C(\text{downstream}) = (A/\sqrt{u}) (r/\sqrt{\pi D}) \{ \sqrt{x+h} - \sqrt{x-h} \} \quad [4]$$

where C and D are the concentration and diffusivity of arsenic vapor in H_2 , u is the linear velocity of H_2 flow, r is the evaporation rate per unit length of the stripe, x is the lateral distance from the edge of the diffused region, and $2h$ is the width of the stripe. A is a constant of proportionality that is constant for identical epitaxial deposition conditions. We can see from Eq. [3] and [4] that the gas concentration decreases roughly as $1/u$ for the upstream case and as $1/\sqrt{u}$ for the downstream case. The solid lines in Fig. 5 represent the plot of Eq. [3] and [4], respectively, for the upstream and downstream cases. This analysis yields a value of D (As/H_2) = 2.5 cm^2/sec , which is in reasonable agreement with the kinetic theory estimation of D . Figure 6 shows the variations of autodoping with gas velocity for both the upstream and downstream flows as measured at 4 mm distance from the stripe source. The solid lines represent Eq. [3] and [4] for $D = 2.5$ cm^2/sec . Once again, the agreement between the theory and experiment is quite good.

Autodoping under low pressure.—It is clear from the preceding discussion that changes in the flow patterns could significantly alter the dopant redistribution. One of the effective means to change the flow dynamics in an epitaxial reactor is to change the pressure. There have been several studies in literature (24, 27, 34-36) which show that lateral autodoping can be significantly reduced by lowering the reactor pressure to ~ 5 kPa (~ 40 Torr). It is found (27) that the reduced pressure also results in sharper profiles over buried layers.

Ogirima *et al.* (24) have studied recently the effect of pressure variation on autodoping and on growth kinetics for the case of silicon epitaxy using silane. They found that, for substrates with arsenic buried layers, autodoping decreases with increasing lateral distance from the buried layer region for all pressures studied. However, this variation is more isotropic with respect to the flow direction for pressures below 20 kPa (~ 150 Torr). Above 40 kPa (~ 300 Torr) pressure, the

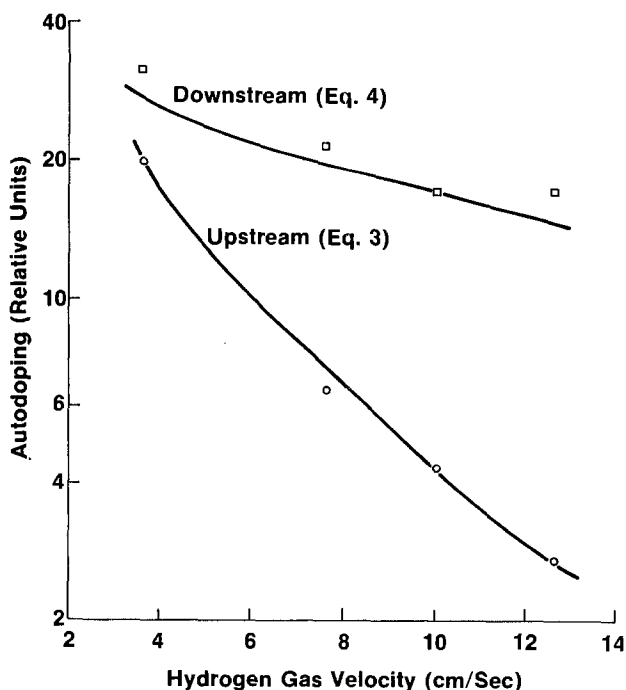


Fig. 6. Variation of autodoping peak maximum with carrier gas velocity. (Deposition temperature 1150°C, diffused stripe 4 mm.)

autodoping was found to be anisotropic, similar to the case for atmospheric pressure as discussed in the preceding section. They found, in addition, that lateral autodoping decreased linearly with the decrease in pressure. That is, a factor of 10 decrease in autodoping occurred when pressure was reduced to about 10 kPa (~ 80 Torr). Since autodoping is linearly proportional to reactor pressure, it is also proportional to the dopant partial pressure, providing that the dopant evaporation rate is itself not a function of pressure. This proportionality is to be expected when Henry's law is obeyed (25) which, in turn, implies that autodoping at reduced pressures may be controlled by the equilibration of arsenic at the vapor-solid interface.

The observation that there is considerably less flow-induced anisotropy in lateral autodoping at reduced pressures indicates that vapor diffusional transport is the dominant mechanism involved. The transport equation under such conditions yields an exponential decrease in vapor concentration with increasing distance from the vapor source, as indeed was the case in Ogirima's experiments.

Dopant incorporation and growth parametric effects.—In the preceding sections, we considered the production of dopant vapor during prebake and its redistribution in the reactor flow system. We now examine the effects of growth parameters on the incorporation of the dopant vapor into the crystal.

Effect of deposition temperature.—Although the effect of epitaxial deposition temperature on the out-diffusion profiles is well documented in the literature, there was, until recently, very little information available on the temperature dependence of lateral autodoping. In a recent report (25), the present author has described the details of this effect for arsenic in silicon epitaxy using $SiCl_4$ depositions. Silicon substrates with localized arsenic diffused layers were used in this investigation, which allowed a separation of out-diffusion and lateral autodoping effects. It was found that lateral autodoping increased with decreasing deposition temperature, and that the slope in the autodoping vs. temperature curve was a function of deposition rate. These results indicated that lateral autodoping is not determined by the thermodynamic equilibrium between arsenic in the vapor and the arsenic incorporated into the epitaxy. The analysis suggested a kinetic limitation for the incorporation process.

Ogirima *et al.* (28) have recently repeated these measurements. They also found that the logarithm of the maximum concentration in the autodoping peak varies inversely as the deposition temperature. To account for this variation, they propose that the dopant incorporated into the epitaxy is directly proportional to that adsorbed on the substrate as given by the equation

$$C = (A/RT) \exp(E/RT)$$

where A is a constant, R is the gas constant, and E is the adsorption energy. However, the situation could be more complex than that suggested by the above equation, for the temperature variation of autodoping has to include both the prebake as well as the growth effects. It is also quite likely that these two components may be controlled by entirely different mechanisms (25), and hence it is necessary to separate out these two effects. Experimentally, it can be done by keeping one of these constant, while changing the other. As indicated in the section on Evaporation kinetics during hydrogen prebake, the autodoping variation due to changes in prebake suggests an evaporation mechanism. The autodoping changes due to changes in deposition temperature, on the other hand, may be due to the temperature variation of dopant trapping in the epitaxial layer. This aspect is considered next.

Effect of growth rate.—It has been known for some time that a reduction in the epitaxial growth rate has

a beneficial effect in reducing the vertical autodoping (21) as well as lateral autodoping (37). In a recent study (25) the present author had made quantitative measurements of the effect of growth rate on lateral autodoping using substrates with arsenic diffusions covering 20% of the wafer surface. These measurements showed that arsenic lateral autodoping in silicon epitaxy decreases almost exponentially with a decrease in growth rate down to a growth rate value of $0.2 \mu\text{m}/\text{min}$. Below this value, the autodoping had remained insensitive to growth rate changes. We repeated these experiments using substrates which had 62% of the surface area covered by arsenic diffusion in a dense pattern as described previously. Autodoping results are shown in Fig. 7 in which the autodoping peak maximum concentration is plotted as a function of growth rate. The figure also shows a plot of the integrated dose in the lateral autodoping curve as a function of growth rate. We note from this figure that both the peak maximum as well as the total amount vary similarly, and that the growth variation extends to much lower growth rates for these high density buried layer wafers than for the case reported earlier.

The results were analyzed as before (25) on the basis of an impurity trapping model. The variation of the autodoping peak concentration is described by the following equation

$$C = C_b + (C_s - C_b) \exp(-V_i/V) \quad [5]$$

where C_b and C_s are the equilibrium dopant concentration in the bulk and surface, respectively, and V_i is a characteristic velocity for which the diffusional relaxation time at the surface is equal to the time for the growth of one monolayer of epitaxy. The model predicts an excess dopant concentration ($C - C_b$) over the equilibrium value due to trapping, and this excess increases with the increase in growth rate, as described by Eq. [5]. A least squares fit to the peak concentration data, as shown by the solid line in Fig. 7, yields: $C_b = 2.3 \times 10^{16} \text{ cm}^{-3}$, $C_s = 9.7 \times 10^{17} \text{ cm}^{-3}$, and $V_i = 0.14 \mu\text{m}/\text{min}$. These values for densely patterned substrates are different from those obtained earlier for substrates with only 20% of the surface covered by the buried layers. For the present case, the results indicate

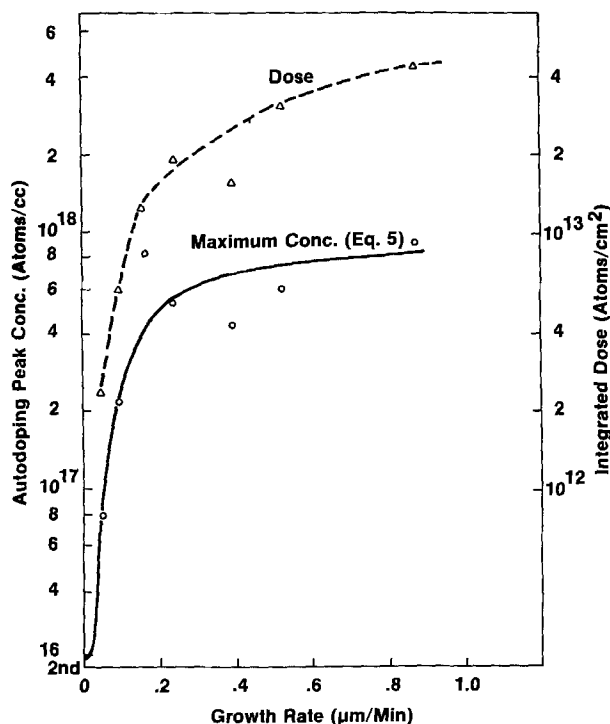


Fig. 7. Variation of autodoping peak concentration and integrated dose (area under the autodoping peak) with growth rate. (Deposition temperature 1100°C .)

a saturation effect, at moderately low growth rates, which was not observed for wafers with low density buried layers.

Effect of silicon source species.—Epitaxial depositions of silicon use either silane or chlorosilanes as the source species. The two most common species are SiH_4 and SiCl_4 . In the literature there is some indication that there is a difference in autodoping between the two. Many of the experiments, however, had used different growth conditions for the two cases, so that a one-to-one comparison was not possible. However, Suzuki and Endo (14) have compared the autodoping differences between silane and SiCl_4 using identical growth conditions. Their results showed that, for a growth temperature of 1100°C , a growth rate of $0.7 \mu\text{m}/\text{min}$, and an H_2 flow rate of 3 liters/min, the silane produces a sharper profile than SiCl_4 on arsenic-doped substrates. They attributed this result to the absence of chlorine in the silane system which was presumed to be the dopant carrier. We have made detailed comparison of autodoping between SiH_4 and SiCl_4 depositions using localized buried layer substrates. Since our results are at variance with those of Suzuki and Endo, we will describe them here.

In our buried layer experiments, we used 10-20 Ωcm P^- (100) silicon substrates, which had arsenic diffusions ($C_0 \sim 1.5 \times 10^{21} \text{ cm}^{-3}$, $x_1 \sim 1.0 \mu\text{m}$) to cover 20% of the surface area in a 5-square pattern. Two-micron thick intrinsic epitaxial depositions were made at $0.08 \mu\text{m}/\text{min}$ and at $0.25 \mu\text{m}/\text{min}$ growth rates using an rf heated horizontal reactor. The main gas flow rate used was 20 liters/min. Results of these experiments are shown in Fig. 8-10. Figure 8 shows the autodoping peak maximum concentration as a function of deposition temperature for both silane and SiCl_4 depositions and for the two growth rates. Figure 9 shows the variation of the integrated area under the autodoping peaks with deposition temperature for the cases shown in Fig. 8. It is clear from these figures that autodoping for silane is worse than that for SiCl_4 for all the temperatures and growth rates tested. In Fig. 10 we show a typical comparison of on-profiles for silane and SiCl_4 depositions made at 1050°C and $0.08 \mu\text{m}/\text{min}$ growth rate.

The fact that SiCl_4 epitaxy produced a lower autodoping than silane epitaxy can be understood in terms of strain-enhanced etching of the depositing film that might occur at the impurity lattice sites by HCl (or Cl_2) released by the H_2 reduction of SiCl_4 . Such an

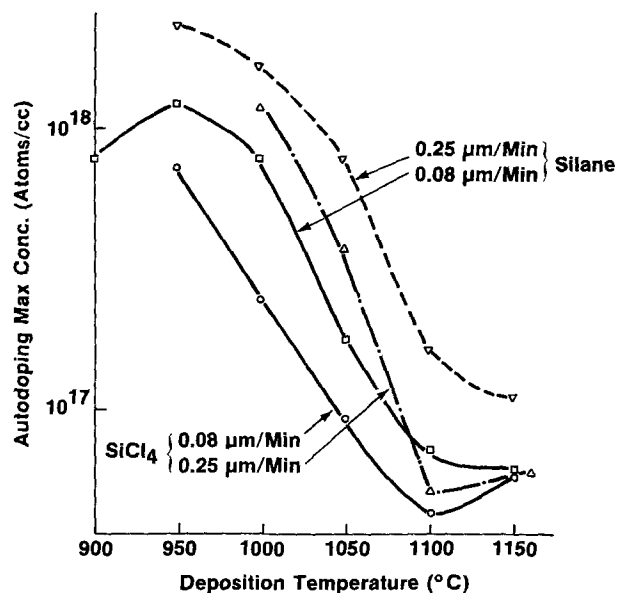


Fig. 8. Variation of autodoping peak maximum concentration with deposition temperature for silane and SiCl_4 depositions, using dose (area under the autodoping peak) with growth rate. (Depo-

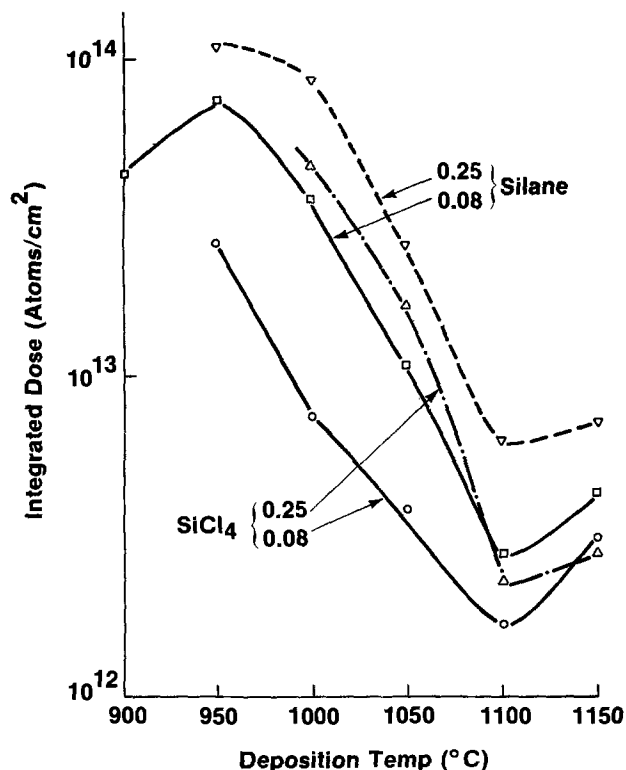


Fig. 9. Variation of autodoping dose (area under the autodoping peak) with deposition temperature for silane and SiCl_4 depositions using growth rates of 0.08 and 0.25 $\mu\text{m}/\text{min}$.

in situ etching could reduce the dopant incorporation in the film and, hence, autodoping. In silane deposition, such a mechanism for *in situ* etching does not exist. It would be interesting to see if reduction in autodoping would occur when HCl is included with silane during the entire deposition cycle. In fact, such an experiment was conducted by Langer and Goldstein (38) who observed a reduction in boron autodoping due to the addition of HCl during silane epitaxial growth. This result is consistent with the above model.

Dependence of autodoping on substrate parameters.—Among the primary factors that influence epitaxial

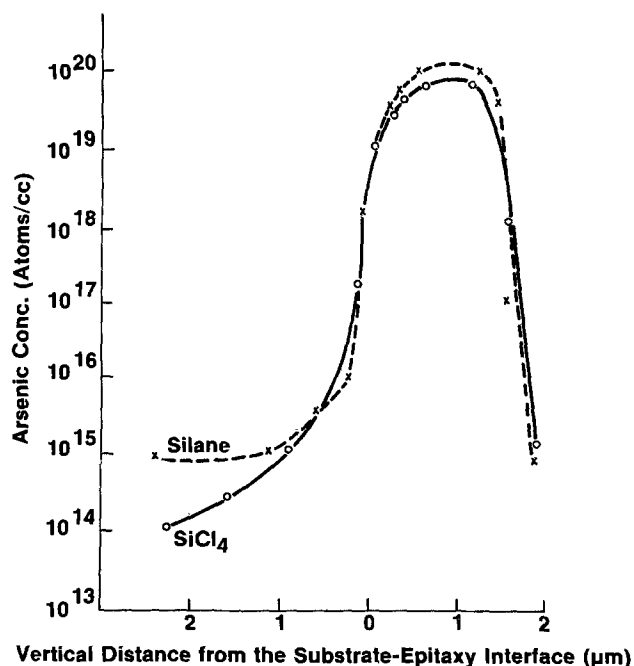


Fig. 10. Spreading resistance profiles over the arsenic buried layers for silane and SiCl_4 depositions. (Deposition temperature 1050°C, growth rate 0.08 $\mu\text{m}/\text{min}$.)

autodoping are the characteristics of the substrate, which include the area of the buried layers on the wafer surface, the initial dopant distribution in the buried layers, the presence of other compensating impurities in the substrate and, finally, the number of substrates used in any given deposition run. Qualitatively, these factors are simple to account for in terms of the total amount of the dopant vapor produced during the prebake stages. For example, Fig. 11 shows the lateral autodoping peak obtained for two wafers, one with 20% of the wafer surface covered by arsenic diffusion, and the other with 62% covered. The epitaxial deposition conditions on these wafers were identical (deposition temperature, 1050°C; growth rate, 0.08 $\mu\text{m}/\text{min}$, species, SiCl_4), and profiles were made at 100 μm from the edge of the diffused region. It is clear from this figure that autodoping increases with an increase in the surface area of the buried layer. A theoretical model has been recently developed by the present author (33a, c) to account for this effect, which shows that autodoping increases as the square root of the buried layer density in the substrate.

Further we found, by etching a diffused arsenic layer to different depths and then growing epitaxy, that the logarithm of the maximum concentration in the autodoping peak was directly proportional to the logarithm of the surface concentration over the buried layer.

The effect of the variation on autodoping with the number of substrates in the run is well known. The larger the number of substrates, the larger is the autodoping (21). However, we found a saturation effect. That is, autodoping initially increases with the number of wafers in the load up to a point beyond which it does not change with any addition to the load. At this level of saturation, we assume that the gas layer region is saturated with the dopant vapor.

Autodoping profile modeling.—We have seen several process and wafer variables that factor into the autodoping effect. The next step is to use this information to arrive at a comprehensive model that allows an accurate dopant profile prediction in the epitaxy for a given set of process and substrate conditions.

The problem is quite complex, not so much for the number of factors that have to be included into any given model, but for the way in which these factors

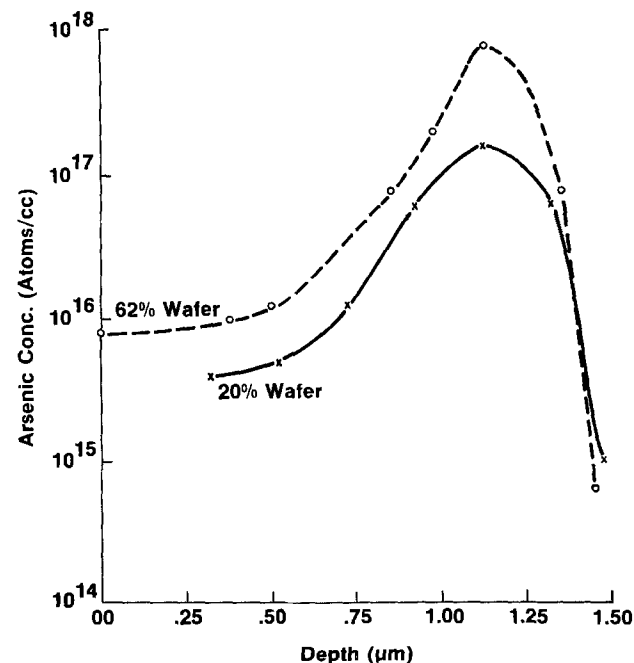


Fig. 11. Variation of autodoping with the percent area of the buried layer on the wafer surface. (Deposition temperature 1050°C, growth rate 0.08 $\mu\text{m}/\text{min}$.)

interact. For example, as discussed in the section on Dopant incorporation and growth parametric effects, the growth rate effect due to trapping is also a function of deposition temperature. It is therefore necessary to decouple these effects as much as possible before formulating a general autodoping model.

There have been several previous attempts to model the autodoping profile. A study by Thomas *et al.* (3) represents the first attempt at such a modeling, and they were able to obtain an exponential decrease in dopant concentration with epitaxial thickness on the assumption that silicon and the dopant atoms are deposited in the ratio that is present in the gas phase. Grossman (5) obtained a similar expression by assuming that the dopant vapor reincorporates into the epitaxy with a rate proportional both to the growth rate and to the concentration at the surface. His expression for gas phase autodoping is given by

$$C = C_0 \exp(-aKZ)$$

where a is a constant, K is the distribution coefficient between the solid and the adsorbed phase, and Z is the epitaxial thickness. However, it is known (39) that K itself is a function of growth rate and, indeed, it is this effect that gives rise to the dopant trapping discussed earlier.

Variations of this approach have also been used recently to model the autodoping profile. Bozler (21) considered the variations in vapor concentration due to flow and treated the dopant escape into the flow as a first-order kinetic equation. The vapor concentration in the flow stream thus falls off exponentially in time which, in turn, through a direct proportionality to the dopant concentration incorporated at the growing surface, yields an exponential decay of the dopant concentration with the film thickness. Bozler's model is attractive for its simplicity, but it does not consider the molecular diffusion of vapor in the gas flow. In addition, as before, the model does not include a growth rate effect on the partition coefficient.

Recently, Tabe and Nakamura (40) have proposed an adsorption model to account for the dopant profile in silicon epitaxial growth. Their model assumes, in contrast to the impurity trapping model discussed earlier, a thermodynamic equilibrium between the impurity in the adsorbed layer and that in the bulk epitaxy. However, their model yields a decrease, rather than an increase, in autodoping with increased growth rate, which is contrary to observations in the buried layer studies.

Yet another model for dopant profile is due to Langer and Goldstein (18). In this numerical approach, they consider dopant fluxes arising out of the substrate through evaporation and solve the one-dimensional linear diffusion equation. When they applied this to the case of boron autodoping (38), they found that, while a good agreement between the experimental and calculated profiles was found for areas at the center of a uniformly doped wafer, the model could not account satisfactorily for the lateral variation of autodoping in the wafer.

One way of dealing with the complex problem of autodoping modeling is to isolate various kinetic steps such as described in the preceding sections. The evaporation, redistribution, and incorporation should be factored into the total equation. The wafer effects could then be included into the equation as a scaling factor. We are at present proceeding in this direction and hope to communicate our results in the near future.

Autodoping Control Techniques

Previous discussion on the parameters that influence autodoping leads us to devise ways to reduce autodoping in epitaxial processes. These are: (i) low pressure epitaxial deposition, (ii) prolonged baking prior to epitaxy, (iii) use of high deposition and baking temperatures, (iv) use of low growth rate, (v) use of high

flow rates, (vi) use of low vapor pressure species such as antimony over arsenic, (vii) reduced batch size, (viii) use of low surface concentration and surface density of the buried layers, and finally (ix) use of compensating doping. Obviously a whole range of these options is not available in any given situation. For example, use of deposition temperature may be dictated by the amount of out-diffusion allowed in the epitaxy and by the abruptness of the profile. Also, selection of the kind of dopant species may be restricted by other considerations such as solubility limit, lattice strain, and the resultant epitaxial quality. Reduced batch size is a throughput consideration. Use of low growth rate is limited by the amount of out-diffusion and throughput considerations. As far as the flow rates are concerned, the commercial reactors use flow rates which have been optimized in terms of thickness and dopant uniformity in the epitaxial films, and, as such, any significant change in the flow rate will have adverse impact on these parameters. The buried layer characteristics such as surface concentration and the surface density are mainly dictated by the device design constraints. The use of a purge in the deposition cycle is only slightly effective in reducing autodoping.

One of the promising ways to deal with autodoping problems is the low pressure technique. This technique, as discussed earlier, reduces autodoping in direct proportion to the reduction in pressure. Even here, there remain serious concerns regarding epitaxial quality and thermally induced slip. Another technique that combines the advantages of both low pressure and low temperature is molecular beam epitaxy. It has been demonstrated that atomically abrupt layer compositions can be obtained using this technique. However, the molecular beam technique as applied to silicon technology is still in its infancy, and further progress in terms of epitaxial quality and dopant uniformity is needed before it becomes an effective tool for fabricating integrated circuits.

Concluding Remarks

In the discussion presented here, we have attempted a quantification of the effects of various process parameters on autodoping in silicon epitaxial growth. We have examined several plausible models that are capable of quantitative explanation of these effects. While at present no comprehensive autodoping model exists, a reasonable amount of understanding has begun to develop, which should result in one in the near future.

Acknowledgments

I thank Messrs. J. A. Miller and W. Patterson for assistance in many of the experiments reported here.

Manuscript submitted Oct. 15, 1979; revised manuscript received Dec. 4, 1979. This was Paper 403 presented at the Los Angeles, California, Meeting of the Society, Oct. 14-19, 1979.

Any discussion of this paper will appear in a Discussion Section to be published in the December 1980 JOURNAL. All discussions for the December 1980 Discussion Section should be submitted by Aug. 1, 1980.

Publication costs of this article were assisted by IBM Corporation.

REFERENCES

1. H. Basseches, R. C. Manz, C. O. Thomas, and S. K. Tung, AIME Semiconductor Metallurgy Conference, Los Angeles, Vol. 15, J. R. Schroeder, Editor, p. 69, Interscience Publishers, New York (1961).
2. D. Kahng, R. C. Manz, M. M. Atalla, and C. O. Thomas, Paper 135 presented at The Electrochemical Society Meeting, Detroit, Mich., Oct. 1-5, 1961.
3. C. O. Thomas, D. Kahng, and R. C. Manz, *This Journal*, **109**, 1055 (1962).
4. R. S. Bholra and A. Mayer, *RCA Rev.*, **24**, 511 (1963).
5. J. J. Grossman, *This Journal*, **110**, 1065 (1963).
6. W. Rice, *Proc. IEEE*, **52**, 284 (1964).

7. A. S. Grove, A. Roder, and C. T. Sah, *J. Appl. Phys.*, **36**, 802 (1965).
8. B. A. Joyce, J. C. Weaver, and D. J. Maule, *This Journal*, **112**, 1100 (1965).
9. T. Abe, Y. Nisha, K. Sato, and N. Oi, *Denki Kagaku*, **35**, 142 (1967).
10. W. H. Shepherd, *This Journal*, **115**, 652 (1968).
11. S. M. Hu, *J. Appl. Phys.*, **39**, 3844 (1968).
12. D. C. Gupta and R. Yee, *This Journal*, **116**, 1561 (1969).
13. H. B. Pogge, D. W. Boss, and E. Ebert, in "Chemical Vapor Deposition, Second International Conference," J. M. Blocher and J. C. Withers, Editors, p. 767, The Electrochemical Society Softbound Proceedings Series, Princeton, N.J. (1970).
14. K. Suzuki and M. Endo, Abstract 96, p. 256, The Electrochemical Society Extended Abstracts, Los Angeles, Calif., May 10-15, 1970.
15. L. D. Dyer and F. Padovani, in "Semiconductor Silicon 1973," H. R. Huff and R. R. Burgess, Editors, p. 201, The Electrochemical Society Softbound Proceedings Series, Princeton, N.J. (1973).
16. G. Skelly and H. C. Adams, *This Journal*, **120**, 116 (1973).
17. L. Maeda and T. Takayama, *Jpn. J. Appl. Phys.*, **13**, 1903 (1974).
18. P. H. Langer and J. I. Goldstein, *This Journal*, **121**, 563 (1974).
19. V. I. Shachnev, *Inorg. Mater.*, **10**, 176 (1974).
20. G. Mitsuhashi, *NEC Res. Dev.*, **36**, 68 (1975).
21. C. O. Bozler, *This Journal*, **122**, 1705 (1975).
22. H. Nihira, T. Shirasu, T. Terasaki, and J. Nishizawa, *ibid.*, **122**, 781 (1975).
23. T. Ishii, K. Takahashi, A. Kondo, and K. Shirahata, *ibid.*, **122**, 1523 (1975).
24. M. Ogirima, H. Saida, M. Suzuki, and M. Maki, *ibid.*, **124**, 903 (1977).
25. G. R. Srinivasan, *ibid.*, **125**, 146 (1978). Also in "Semiconductor Silicon 1977," H. R. Huff and E. Sirtl, Editors, p. 218, The Electrochemical Society Softbound Proceedings Series, Princeton, N.J. (1977).
26. R. W. Dutton *et al.*, Tech. Rep. No. 5021-1, Integrated Circuits Laboratory, Stanford University, Stanford, California, 1977.
27. P. H. Lee, M. T. Wauk, and W. C. Genzing, *IEDM*, 482 (1977).
28. M. Ogirima, H. Saida, and M. Maki, Abstract 218, p. 583, The Electrochemical Society Extended Abstracts, Pittsburgh, Pa., Oct. 15-20, 1978.
29. D. A. Antoniadis, S. E. Hansen, R. W. Dutton, and G. A. Gonzalez, Tech. Rep. No. 5019-1, Stanford Electronics Laboratories, Stanford University, May 1977. Also, SUPREM-2, Tech. Rep. No. 5019-2.
30. F. C. Eversteyn, P. J. W. Severin, C. H. J. van den Brekel, and H. J. Peek, *This Journal*, **117**, 925 (1970).
31. T. O. Sedgwick, J. E. Smith, Jr., R. Ghez, and M. E. Cowher, *J. Cryst. Growth*, **31**, 264 (1975).
32. V. S. Ban, *This Journal*, **125**, 317 (1978).
33. (a) G. R. Srinivasan, Second Joint Special VLSI Issue of *IEEE Trans. Electron Devices* and *IEEE J. Solid State Circuits*, Aug. 1980; (b) G. R. Srinivasan, To appear in *J. Appl. Phys.*; (c) G. R. Srinivasan, To appear in *This Journal*.
34. J. L. Deines and A. Spiro, Abstract 62, p. 161, The Electrochemical Society Extended Abstracts, San Francisco, Calif., May 12-17, 1974.
35. M. Ogirima, H. Saida, M. Suzuki, and M. Maki, *This Journal*, **125**, 1879 (1978).
36. M. J. Duchemin, M. M. Bonnet, and M. F. Koelsch, *ibid.*, **125**, 637 (1978).
37. A. V. Badami *et al.*, U.S. Pat. 3,669,769 (1972).
38. P. H. Langer and J. I. Goldstein, *This Journal*, **124**, 591 (1977).
39. R. N. Hall, *Phys. Rev.*, **88**, 139 (1952).
40. M. Tabe and H. Nakamura, *This Journal*, **126**, 822 (1979).

Electrochromism of Anodic Iridium Oxide Films

III. Anion Mechanism

G. Beni,* C. E. Rice, and J. L. Shay*

Bell Laboratories, Holmdel, New Jersey 07733

ABSTRACT

We examine the electrochromic effect of anodic iridium oxide films (AIROF's) in aqueous and nonaqueous electrolytes. All experimental data in aqueous electrolytes are consistent with the hypothesis that electrochromism in AIROF's can occur via hydroxide ions, without insertion-extraction of protons from the electrolyte. We also report new experiments in which electrochromism of AIROF's takes place by insertion-extraction of anions (OH^- , F^- , CN^-) from nonaqueous electrolytes.

Several recent papers (1-7) have described the electrochromic properties of anodic iridium oxide films (AIROF's). Electrochromics are promising materials for passive display devices (8). They have a wide viewing angle and an open-circuit memory. They are suitable for large character displays and for all-solid-state devices. Earlier electrochromic research focused primarily on WO_3 in which coloration (9-12) takes place by simultaneous insertion of electrons and cations, e.g., H^+ , Li^+ , Na^+ , etc. The fastest response times (≈ 0.1 sec) are obtained with protons in a humid environment. However WO_3 -based devices degrade (13) in the presence of water. Thus, current research in WO_3 -based displays is centered around Li^+ [Ref. (14)] and Na^+ [Ref. (15)] insertion devices employing nonaqueous electrolytes. Although these devices are more stable than those based on protons in humid environments, they have considerably longer coloring and bleaching times (≈ 1.0 sec).

AIROF's do not degrade in contact with water. They have been operated in aqueous solutions for $\approx 10^6$ cycles with no detectable degradation and no electrolyte decomposition. AIROF's also have fast coloring-bleaching times (≈ 20 msec) and good contrast throughout the visible. All-solid-state (diffuse reflection) display cells have been demonstrated recently (7).

Initial descriptions of the mechanism of electrochromism in AIROF's were based on simultaneous electron and proton insertion, similar to electrochromism in WO_3 , albeit with opposite polarity (1, 5). However, since we observed (2) that the speed of coloration and bleaching in AIROF's is independent of pH, this interpretation seemed questionable. Although the lack of dependence of color/bleach speed on pH was confirmed by the detailed studies of Gottesfeld and McIntyre (5) (hereinafter referred to as II), they nevertheless retained a proton injection description since they found all alternative mechanisms unacceptable.

The purpose of this paper is twofold: (i) to demonstrate that all available experimental data concerning

* Electrochemical Society Active Member.

Key words: electrochromism, electrolyte, ions.

AIROF electrochromism in aqueous systems is satisfactorily explained by a hydroxide injection mechanism; and (ii) to report new experiments using non-aqueous electrolytes which demonstrate that AIROF coloring/bleaching in fact takes place by anion insertion/extraction in these systems.

In the next section we study the electrochromism of AIROF's in aqueous electrolytes. We reanalyze previous experiments and discuss the point of zero zeta potential. By a thermodynamic analysis of the isotherms, we show that electrochromism in AIROF's is well explained by the hydroxide ion mechanism. In the section "Water-Free Electrochromism" we present results of experiments performed in water-free electrolytes. We show that the anions OH^- , F^- , or CN^- are sufficient for electrochromism to occur in the nonaqueous systems studied. In "Discussion and Conclusions" we discuss the nature of the anion mechanism for electrochromism and its relationship to anodic film growth and electrocatalysis.

Electrochromism in Aqueous Solutions

During coloration (bleaching) an anodic (cathodic) potential typically removes (1) (injects) $\approx 10^{17}$ electrons/cm² from (into) a $\approx 3000\text{\AA}$ thick AIROF in $\lesssim 40$ msec. Preservation of electroneutrality requires a simultaneous injection (ejection) of negative charge or ejection (injection) of positive charge at the AIROF/electrolyte interface. Assuming fast interfacial processes and fast diffusion within the AIROF, coloring-bleaching times are determined by the diffusion of the charged species from the electrolyte to the AIROF surface. For ions with bulk electrolyte diffusion coefficient D , the (unbuffered) ion concentration C necessary to inject N ions per unit surface in a time t is (16)

$$C = \frac{N}{\sqrt{(4Dt)}} \quad [1]$$

For protons in aqueous solutions $D = 10^{-4}$ cm²/sec [Ref. (17)] so that, with $N = 1.6 \cdot 10^{-7}$ mole/cm² and $t = 40$ msec, we have $C = 4 \cdot 10^{-5}$ mole/cm³ or $\text{pH} = 1.4$. Thus, at $\text{pH} \gtrsim 1.4$ there are not enough protons available in the bulk electrolyte to bleach the AIROF in $\lesssim 40$ msec. But, as shown in Ref. (2), bleaching times of ≈ 20 msec are regularly obtained at pH as high as 14.

Following similar arguments, it was concluded in II that AIROF electrochromism in basic and mildly acidic aqueous solutions can be due to proton injection, only if the source of protons is free H_2O molecules and/or bound H_2O or OH groups on the oxide surface. In the latter case, the bleaching process is effectively a proton desorption from the surface into the AIROF. Since none of the electrochemical measurements discussed in II can distinguish between the desorption of a proton and the adsorption of a hydroxide ion (16), the question remains open as to whether protons or hydroxide ions give rise to the electrochromic effect in AIROF's.

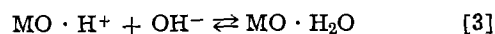
To proceed further we begin by considering the nature of the water bound to the AIROF surface. In II it has been speculated that "owing to polarization by the coordinated metal ion," the bound H_2O has a higher concentration of H^+ than the free water. We shall see, however, that the opposite is true, and in fact, there is in most cases a preponderance of OH^- on the surface of an AIROF in an aqueous solution.

Point of zero zeta potential.—The point of zero zeta potential (pzpp) is the pH at which the net surface charge is zero. There is a sizable literature on the pzpp (18-24). For metal oxides the pzpp usually refers to specific adsorption of protons or hydroxide ions. Thus the pzpp is the pH at which the concentrations of adsorbed H^+ and OH^- are equal. At $\text{pH} \neq \text{pH}(\text{pzpp})$ a net charge is present on the oxide surface.

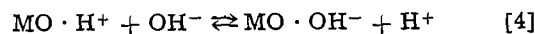
Most investigators (25-29) of the properties of the oxide/aqueous-solution interface suggest that the

mechanism by which the surface charge is established may be viewed qualitatively as a two step process: surface hydration followed by dissociation of the surface hydroxide. The hydration step is an attempt by the exposed surface atoms to complete their coordination shells of nearest neighbors. Exposed cations accomplish this by pulling OH^- ions from the aqueous phase; oxygen ions accomplish this by pulling H^+ from the aqueous phase.

The equilibria at the surface of a metal oxide MO can schematically be represented (18) by



where \cdot means "bound at the surface." Adding Eq. [2] and Eq. [3] we obtain



From which, at equilibrium

$$\Delta F + kT \log \frac{[\text{H}^+]_s}{[\text{OH}^-]_s} + kT \log \frac{[\text{OH}^-]}{[\text{H}^+]} = 0 \quad [5]$$

where ΔF is the standard free energy of the reaction; $[\text{H}^+]_s$ and $[\text{OH}^-]_s$ are the concentrations of protons and hydroxide ions at the surface; k is the Boltzmann constant; and T is the absolute temperature. By definition, at the pzpp, $[\text{H}^+]_s = [\text{OH}^-]_s$ so that at room temperature

$$\text{pH}(\text{pzpp}) = 7 - \frac{\Delta F(\text{eV})}{0.12} \quad [6]$$

Although ΔF is not known, it has been found (30) empirically that Eq. [6] is well satisfied by all studied metal oxides if one sets $\Delta F(\text{eV}) = \Delta M(\text{eV}) - 5.9$ where ΔM is the Mulliken electronegativity of the oxide. The Mulliken electronegativity of an element is the arithmetic mean of the atomic electron affinity A and the first ionization energy I , i.e.

$$\Delta M = (A + I)/2 \quad [7]$$

The Mulliken electronegativity of a compound is the geometric mean of the electronegativity of the constituent atoms.

For IrO_2 , $\Delta M = 6.7$ eV [Ref. (31)] and thus from Eq. [6], $\text{pH}(\text{pzpp}) = 0.33$. Similarly for Ir_2O_3 , $\Delta M = 6.54$ eV [Ref. (31)] and $\text{pH}(\text{pzpp}) = 1.66$. Therefore, assuming that AIROF's have compositions close to IrO_2 or Ir_2O_3 , the AIROF surface has a high concentration of hydroxide ions and a very low concentration of protons at all pH except for $\text{pH} \lesssim 1$. Moreover, it is obvious that by applying an anodic potential to the AIROF the equilibrium on the surface is further shifted toward enriching the hydroxide ion concentration.

It is clear therefore that the AIROF surface is usually covered predominantly with OH^- , and thus there is not a reservoir of H^+ as stated in II in support of the proton injection model. The extremely low value of the pzpp for the AIROF's also explains the insensitivity (2) to pH of the hydroxide ion insertion-extraction electrochromic process.

Further thermodynamic data supporting the hydroxide mechanism of electrochromism are presented in the next section.

Isotherms.—From measurements of the internal emf of AIROF's in aqueous solutions over the pH range 0-14 and temperature range 0° - 75°C , it is apparent that (i) AIROF's develop an internal emf E during coloration and have the external properties of thin film batteries; and (ii) that their internal emf is a function only of the charge per unit volume Q . As a consequence of (i) and since the charging process is sufficiently fast, cyclic voltammograms for AIROF's yield directly dQ/dE vs. E , and thus provide the most convenient way to obtain the isotherm, $E(Q)$.

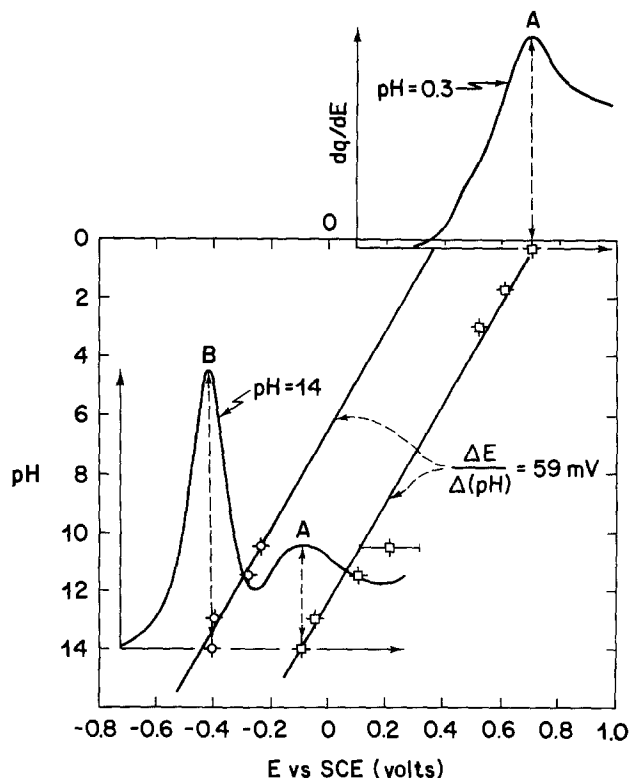


Fig. 1. pH dependence of maxima in cyclic voltammograms for AIROF's at room temperature measured at a sweep rate of 100 mV/sec. The two solid curves are anodic scans and measure dq/dE (in arbitrary units) as a function of the internal emf E (in volts vs. a saturated calomel electrode) at pH = 0.3 and pH = 14. The square (round) points trace the pH dependence of the A(B) peaks. Both peaks shift at the rate of 59 mV/pH (solid lines).

Figure 1 shows the pH dependences of the maxima in the cyclic voltammograms over the pH range 0-14 at room temperature. The two curves superimposed are anodic scans for pH = 0.3 and 14, respectively (the processes are highly reversible and the cathodic scans are almost mirror images about the abscissa). The square points trace the pH dependence of the A peak which dominates the voltammogram in acidic solutions. It can be seen that this peak shifts at a rate of 59 mV/pH, which, from the Nernst equation, is in agreement (16) with insertion-extraction of hydroxide ions during electrochromism. At high pH a new peak B appears in the voltammogram. Its dependence upon pH is shown by the round points which also shift at a rate of 59 mV/pH. Simultaneous reflectivity measurements show that for pH = 14 the electrochromic reaction takes place primarily around B.

The existence of two distinct electrochromic processes can be understood straightforwardly in terms of the hydroxide mechanism. At low pH, the hydroxide ions are supplied by the highly basic water bound at the surface. At higher pH, however, the OH^- are supplied primarily by the bulk electrolyte. We show below that these two ways of supplying hydroxide ions correspond to two thermodynamically distinct processes.

When hydroxide ions are supplied directly from the electrolyte (B process), the AIROF internal emf is given by (neglecting interactions)

$$E = E_B + kT \log[(q/(1-q))^n] \quad [8]$$

where E_B is the insertion energy per hydroxide ion and the second term is T times the configuration entropy per normalized charge $q = Q/Q_{\text{max}}$ per unit volume. The configurational exponent n is 1 or 2 according to whether or not the inserted hydroxide ion and the extracted electron are spatially correlated.

We find that Eq. [8] is experimentally verified with $n = 2$ to high accuracy for $0.02 \leq q \leq 0.98$. It follows from Eq. [8] that the shape of the current peak around the equilibrium value E_B is related to the internal emf E by

$$i \propto \frac{dq}{dE} = (4nkT)^{-1} \cosh^{-2}[(E - E_B)/2nkT] \quad [9]$$

where i is the current measured by cyclic voltammetry under reversible and fast-diffusion conditions, and absence of other reactions (we set the electronic charge $e = 1$). We find that the B peak has the form of Eq. [9] with $n = 2$. Values of dq/dE calculated from Eq. [9] using a configurational exponent $n = 2$ are compared with experiment in Fig. 2. Although there are no adjustable parameters (except for the trivial E_B) and no base line corrections, the agreement between theory and experiment is excellent over the entire range $0.02 \leq q \leq 0.98$.

The exponent $n = 2$ is also found (32, 33) for the configurational entropy of protons and electrons in WO_3 . In WO_3 however, the dominant part of the internal emf is not the configurational entropy but an interaction term linear in q . In general this interaction term dominates the internal emf of cation insertion electrochromics (34). AIROF's are instead almost ideal entropy cells (4).

When the hydroxide ions are supplied by water bound at the surface, i.e., in acidic solutions, the insertion process involves an additional statistically inde-

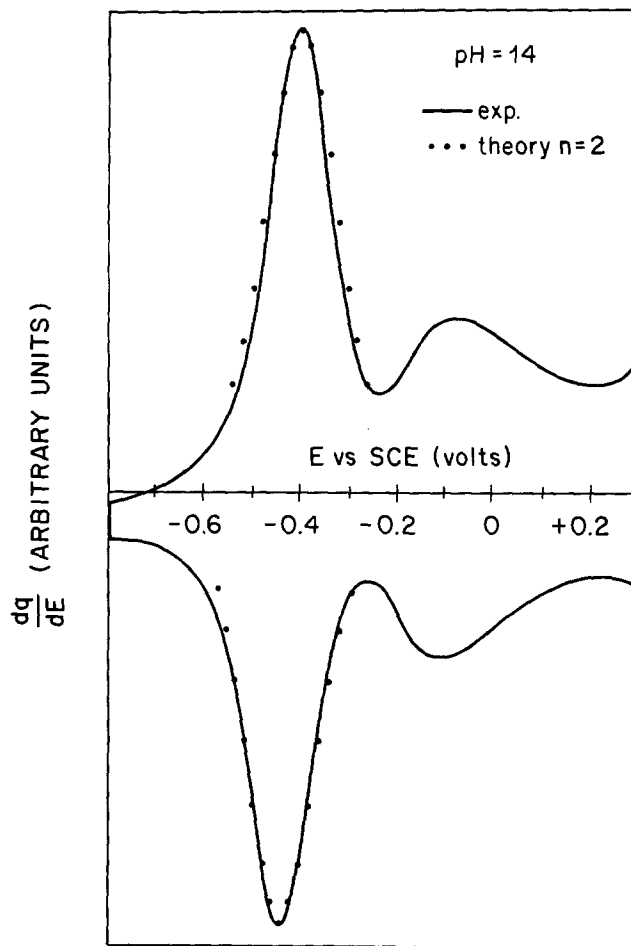


Fig. 2. The derivative of the electrochromism isotherm of process B (cf. Fig. 1) at pH = 14. The solid curve was obtained experimentally by cyclic voltammetry under reversible conditions and fast diffusion. The points are theoretical values from Eq. [9] using a configurational exponent $n = 2$. No other parameter enters the theory and no base line adjustments were made. For clarity in this figure we show only a few points rather than a continuous line.

pendent event: the removal of an OH⁻ from the surface. Thus, the configurational entropy term must have an exponent $n = 3$ or 4, according to whether or not the OH⁻ removed from the surface is spatially correlated with the OH⁻ adsorbed on the surface from the bulk electrolyte. Moreover, since at the end of the process the surface has a modified configuration, the insertion energy E_A will be, in general, larger than E_B . This is clearly shown in Fig. 1, where $E_A - E_B = 0.3V$. In addition, Fig. 3 shows that indeed the configurational exponent for the A process is $n = 3$. This figure shows experimental data (solid line) and two theoretical

curves using Eq. [9] with $E_B \leftrightarrow E_A$. The dotted line corresponds to $n = 3$ and the dashed line to $n = 4$. There are no adjustable parameters and no base line corrections. Taking the latter into account and subtracting out both the spurious component at high voltages and the small shoulder (origin unknown) at $\approx 0.45V$ (SCE), the best fit is obtained with $n = 3$. This result was independently checked by measuring the temperature dependence of the isotherms which is in good agreement with $n = 3$ (Fig. 4). As expected there is no linear term in q also for this process. An upper limit on the coefficient of the linear term is 0.01 eV for both A and B.

From Eq. [1] we estimate that the bulk electrolyte can supply enough free hydroxide ions for coloration at $pH \gtrsim 8$. Consequently we expect the B peak to appear around this value of pH and to increase with pH relative to the A peak. This effect is clearly seen in Fig. 5 which shows the significant portions of cyclic voltammograms recorded in buffered solutions at various pH. To illustrate the emergence of the B peak we

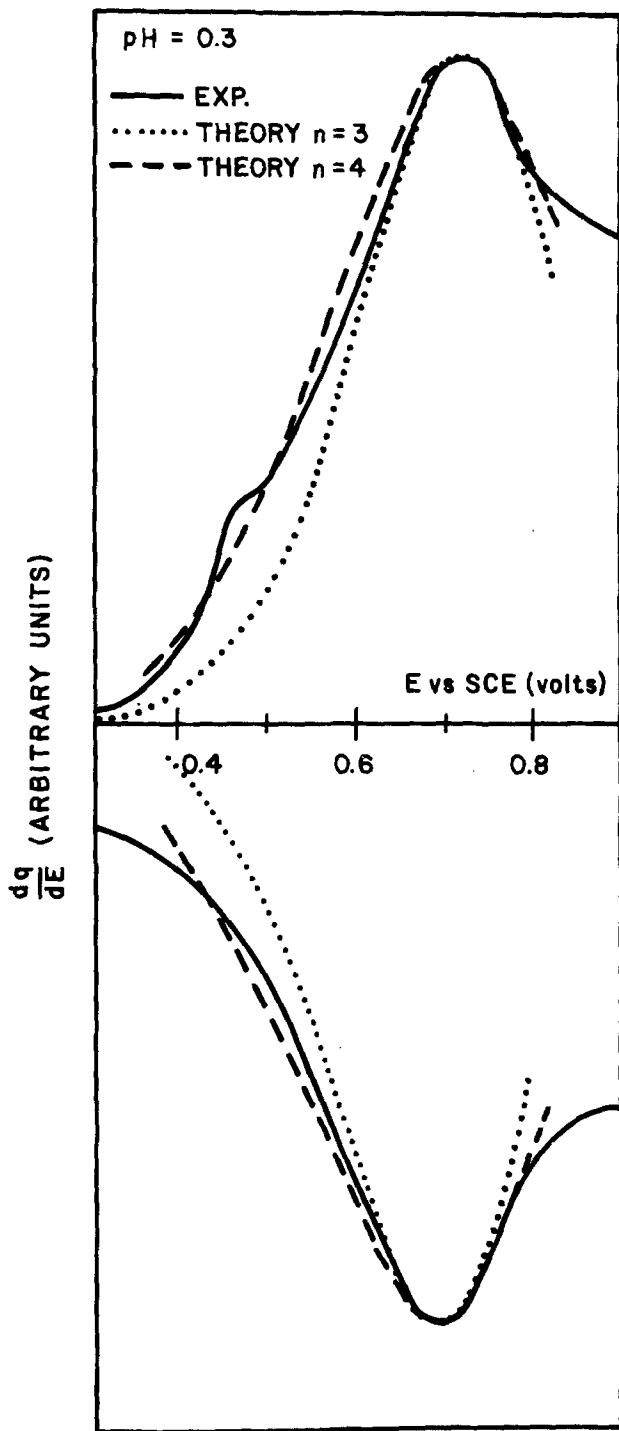


Fig. 3. The derivative of the electrochromism isotherm of process A (cf. Fig. 1) at $pH = 0.3$. The solid curve was obtained experimentally by cyclic voltammetry under reversible conditions and fast diffusion. The dotted (dashed) lines are theoretical values from Eq. [9] using a configurational exponent $n = 3$ (4). No other parameter enters the theory and no base line adjustments were made.

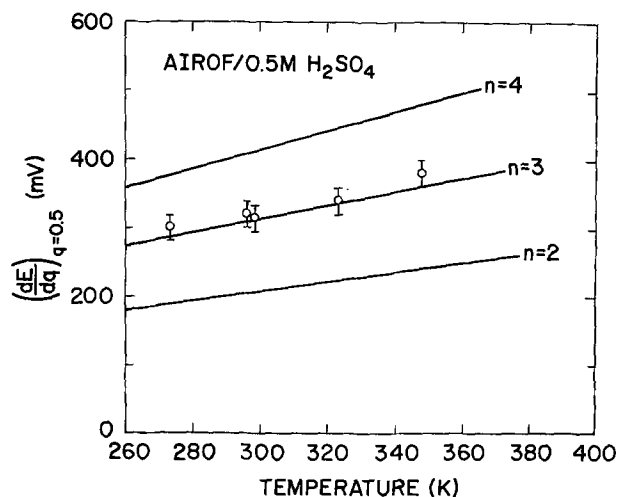


Fig. 4. Temperature dependence of the slope of the A-electrochromism isotherm at $q = 0.5$. The solid lines are theoretical values from Eq. [9] for configurational exponents $n = 4, 3,$ and $2,$ respectively.

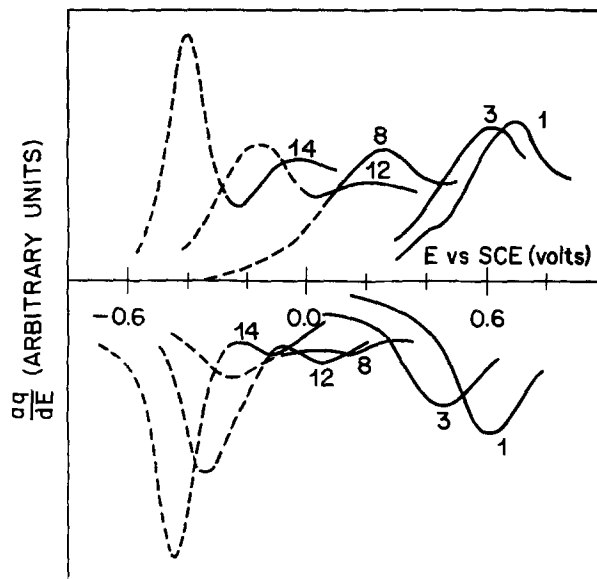


Fig. 5. pH dependence of the cyclic voltammograms for AIROF's at a sweep rate of 100 mV/sec in buffered solutions. Solid and dashed point indicate A and B peak, respectively. The emergence of the B peak is clearly visible in the cathodic scan at $pH \gtrsim 8$.

have plotted the B peak part of the voltammogram as a dashed line. Especially in the cathodic scan, it is clearly visible that around pH = 8 the A peak is disappearing while the B peak is emerging.

In conclusion, all the experimental data in aqueous electrolytes are consistent with the hypothesis that electrochromism in AIROF's takes place via hydroxide ions.

Water-Free Electrochromism

In order to establish the relative role of protons and hydroxide ions independently of water we have studied the electrochromic performance of AIROF's in various water-free solutions. In these experiments the AIROF's were grown on iridium electrodes in aqueous 0.5M H₂SO₄ as described in Ref. (1). In this solution the normal-incidence reflectivity ($\lambda = 633$ nm) of the electrode in the colored state was 50% of that in the bleached state. After growth the electrodes were placed in a desiccator over Drierite at atmospheric pressure for at least one day to remove gross surface water. However, no attempt was made to rigorously remove all traces of water from the AIROF's.

Attempts to operate these dried AIROF electrodes in nonaqueous solutions of strong proton acids, HClO₄ or H₂SO₄ in dimethylsulfide (DMSO) or acetonitrile (AN), produced no evidence of electrochromic activity. For these experiments, the potential of the electrochromic electrode vs. an Ag/Ag⁺ reference electrode (potential = 0.253V vs. aqueous SCE) was swept cyclically while gradually increasing the potential limits until a significant steady-state current flow signaled the onset of electrolyte breakdown. [A detailed description of a representative experiment has appeared in a previous communication (35)]. Figure 6(a) shows a cyclic voltammogram obtained with an AIROF working electrode in 0.01M HClO₄/DMSO. Over the entire 2.2V potential window scanned, no appreciable current was observed other than that due to electrolyte breakdown near the limits of the scan. The application of a 2.2V square wave potential with a pulse width of hundreds of seconds [Fig. 7(a)] produced no change in electrode reflectance. The same results were observed in all other nonaqueous acid solutions investigated. All solutions contained substantial concentrations of free protons as confirmed by titration with base, and by the fact that WO₃ electrodes could be electrochemically colored and bleached in these solutions [Fig. 6(c), 7(c)]. Thus in the absence of water, a supply of free protons is not sufficient for AIROF electrochromism.

A material which exhibits electrochromism by proton insertion-extraction may be expected to exhibit electrochromism also by other small cations. Indeed WO₃ can be colored not only by proton insertion but also by insertion of Li⁺ [Ref. (14)] or Na⁺ [Ref. (15)]. In

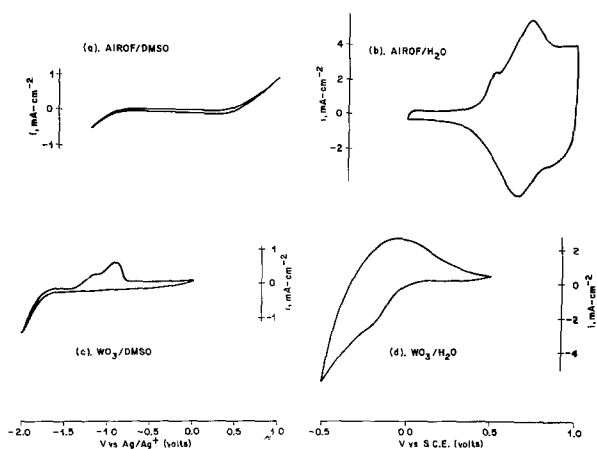


Fig. 6. Cyclic voltammograms of typical AIROF's and WO₃ films in aqueous and nonaqueous acid solutions. Scan speeds: (a) 20 mV/sec; (b) 100 mV/sec; (c) 20 mV/sec; (d) 50 mV/sec.

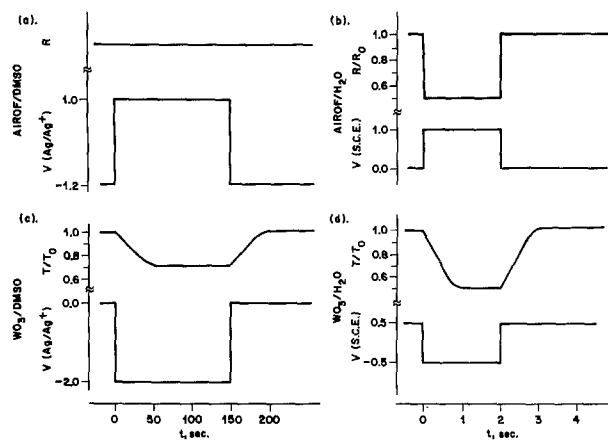


Fig. 7. Spectral response ($\lambda = 633$ nm) to abrupt potential change of AIROF's and WO₃ films in aqueous and nonaqueous acid solutions. Normalized reflectance $R/R_0 = R/R_{\text{bleached}}$; normalized transmission $T/T_0 = T/T_{\text{bleached}}$.

contrast, "lithiation" by cathodic reduction in a nonaqueous electrolyte (0.5M LiAsF₆ in acetonitrile) does not produce any electrochromic effect in AIROF's (II).

It is tempting to generalize these results and suggest that proton injection is equally unimportant for AIROF electrochromism in aqueous solutions. However, given the negative nature of these findings, several objections can be raised about this suggestion. For example, it is possible that electrochromism was not observed because the AIROF's color/bleach potential lies outside the available potential window in DMSO and AN. This explanation is improbable given the wide potential limits which were scanned. As further evidence against this possibility, the addition of trace amounts of water to these solutions causes electrochromism to be observed, with a color/bleach potential roughly equivalent to the coloration potential in totally aqueous acid solutions.

Another more serious objection is that the nonaqueous solvents may "deactivate" the AIROF by removing necessary water of hydration from within the oxide film. Indeed it is known that proton conductivity is inhibited or destroyed in solid-state proton conductors when all water is removed (36). In order to remove the objection that perhaps the AIROF cannot operate in any water-free solution, and to establish the role of hydroxide ions in the electrochromic process independently of water, we have studied AIROF electrode performance in nonaqueous solutions containing hydroxide ions.

The nonaqueous base experiments were performed in exactly the same way as the water-free acid studies described previously; in this case the solutions used were KOH or (CH₃)₄NOH in ethanol or AN. Hydroxide ion concentrations ranged from 0.1 to 1M. (Full experimental details and results for these studies will appear in a separate paper.) In contrast to the results in nonaqueous acid, electrochromism could always be observed when AIROF electrodes were operated in these water-free hydroxide solutions. Figure 8(a) shows the cyclic voltammogram obtained with an AIROF in 0.1M (CH₃)₄NOH in AN; clear evidence of coloration and bleaching peaks can be seen. This result contrasts sharply with the completely flat voltammograms obtained with solutions of acids in this solvent. Figure 8(b) shows the response of the electrode reflectance to the application of a square wave potential. The magnitude of the reflectivity change is similar to that obtained in aqueous solutions. The response time is slower due to the higher resistivity of the electrolyte. These results prove that the AIROF electrochromic reaction can indeed occur in nonaqueous electrolytes as long as the proper ion (hydroxide) is present.

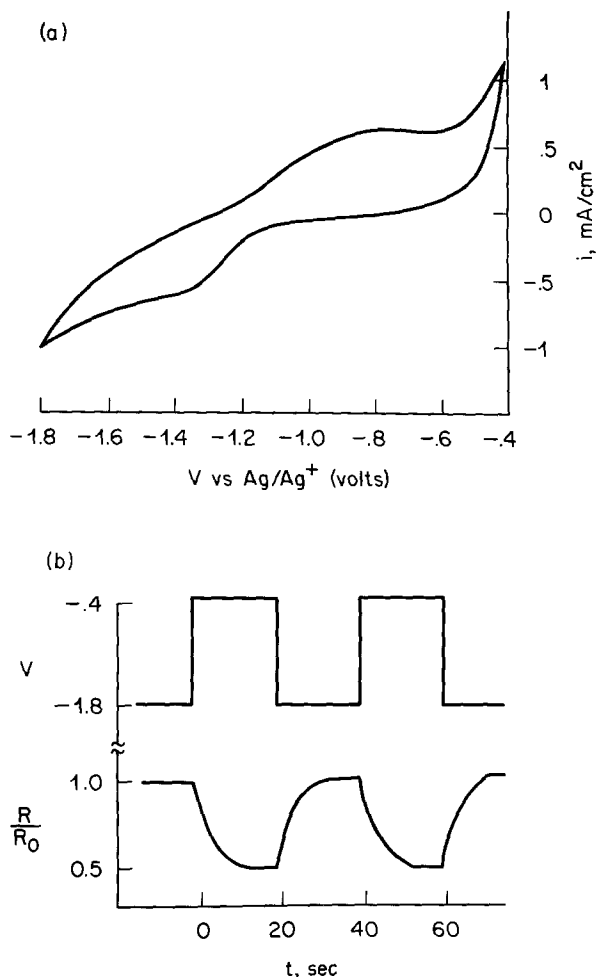
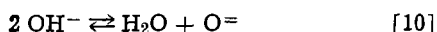


Fig. 8. (a) Cyclic voltammogram of AIROF electrode in 0.1M $(\text{CH}_3)_4\text{NOH} + 0.1\text{M} (\text{CH}_3\text{CH}_2)_4\text{NClO}_4/\text{acetonitrile}$. Scan speed 10 mV/sec. (b) Changes in AIROF electrode reflectance with abrupt potential change. The electrolyte is the same as in (a).

One might anticipate that a material which exhibits electrochromism by hydroxide ions should also exhibit electrochromism by other anions of similar size and charge. Indeed we have found that coloration-bleaching of AIROF's occurs in water-free solutions containing F^- or CN^- . Thus although no electrode reflectance changes occur when a dry $\text{NH}_4\text{Br}/\text{ethanol}$ solution is used (presumably Br^- is too large to insert readily into the AIROF), electrochromism does occur in $\text{NH}_4\text{F}/\text{ethanol}$. $\text{KCN}/\text{ethanol}$ is also an effective electrolyte for AIROF electrochromism. Details of these experiments will be published elsewhere.

Discussion and Conclusions

The hydroxide ion mechanism of electrochromism is also consistent with the close connection between AIROF growth and electrochromism. The growth of an hydrous oxide film in aqueous solution requires, in general (16), the half-reaction

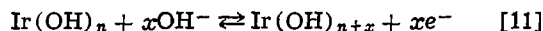


which implies diffusion of hydroxide ions and/or metal cations through the forming oxide. From Ref. (3) there is evidence that Ir ions do not diffuse easily through the AIROF's. Thus hydroxide ions must diffuse through the AIROF during its growth.

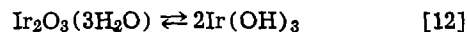
AIROF's are grown typically (1) in aqueous solutions of 0.5M H_2SO_4 by continuously sweeping the potential of the Ir electrode between -0.25 and $+1.25\text{V}$ (SCE). During the anodic (cathodic) sweep, the growth reaction Eq. [10] is shifted to the right (left), corresponding to OH^- insertion (extraction). Since coloration (bleaching) is observed during the anodic (cathodic)

growth sweep, the electrochromic process is associated with the insertion-extraction of OH^- .

The hydroxide mechanism for AIROF electrochromism can be represented by a half-reaction of the form (37)



The exact electrochromic reaction, however, must remain speculative until the exact AIROF composition is known. The AIROF composition is probably a form of hydrated iridium oxide. Iridium forms various kinds of oxides (38), the most common being Ir_2O_3 and IrO_2 . In hydrated form they correspond to



and



which describe the equilibria between the hydrated oxide form and hydroxide form of Ir_2O_3 and IrO_2 , respectively. Although AIROF's are hydrous, the amount of molecular water is not easily ascertained. In fact we can now take as generally accepted (39) that metal hydroxides are "polymers" in which the metal ions are linked by bridges of hydroxyl pairs. The closeness of the hydroxyls in these diol bridges causes the latter to be unstable as they are converted to oxobridges with liberation of water (40). The question may be raised as to whether or not the amount of hydration is related to electrochromism.

Hydration (dehydration) is indeed a part of the OH^- insertion (extraction) process as shown by Eq. [10]. It seems unlikely, however, that the hydration-dehydration step of Eq. [10] is the fundamental part of the electrochromic process. In fact this would be inconsistent with the experiments in which coloration is obtained by insertion of F^- or CN^- . On the other hand, since dehydration of a mixed valence compound generally gives rise to coloration (41), it is possible that coloration of the AIROF might be obtained by dehydration.

The fundamental part of the electrochromic process is likely to be associated not with hydration-dehydration, but with the injection-extraction of the oxygen anions. The insertion of oxygen ions could cause coloration: (i) by changing the valence or iridium from 3 to 4, Ir^{IV} coordination compounds being typically more strongly colored than their Ir^{III} counterparts; (ii) by creating a mixed valence oxide, the coloration being due to intervalence transitions; or (iii) by creating defects. None of these mechanisms can be excluded at this stage and more detailed investigations are necessary to clarify the detailed nature of the electrochromic mechanism in AIROF's.

In summary, all available data in aqueous and non-aqueous solutions show that electrochromism in AIROF's takes place via anions. This contrasts with the cation mechanism of electrochromism which has been well established for WO_3 and other cathodically colored oxides. On the other hand, it has recently been shown (42) that in lutetium diphthalocyanine "coloration" from green to red occurs by injection of Cl^- ions from the electrolyte into the electrochromic film.

Anion electrochromism is of particular significance for solid-state display devices. Solid-state fluorine fast-ion conductors are known (36) and can conceivably be used in conjunction with AIROF's. Preliminary results to be reported elsewhere have shown that this is possible.

Finally, in addition to display device applications, hydroxide ion electrochromism is of fundamental importance for its relation to oxygen electrocatalysis. In most materials, high catalytic activity for oxygen evolution from the splitting of water has been found (43) to be associated with high affinity for hydroxide ions. As we have seen, AIROF's have high affinity for hydroxide ions and indeed they have superior catalytic activity for oxygen evolution (44). The detailed rela-

tionship between electrochromism and electrocatalysis remains a problem for future investigations.

Acknowledgments

We thank W. C. Dautremont-Smith for many stimulating discussions, L. M. Schiavone for his expert technical assistance, and F. J. DiSalvo, A. M. Glass, and J. H. Wernick for useful comments on the manuscript.

Manuscript received Nov. 14, 1979.

Any discussion of this paper will appear in a Discussion Section to be published in the December 1980 JOURNAL. All discussions for the December 1980 Discussion Section should be submitted by Aug. 1, 1980.

Publication costs of this article were assisted by Bell Laboratories.

REFERENCES

- S. Gottesfeld, J. D. E. McIntyre, G. Beni, and J. L. Shay, *Appl. Phys. Lett.*, **33**, 208 (1978).
- G. Beni and J. L. Shay, *ibid.*, **33**, 567 (1978).
- J. L. Shay, G. Beni, and L. M. Schiavone, *ibid.*, **33**, 942 (1978).
- G. Beni and J. L. Shay, *Phys. Rev. B*, **21**, 364 (1980).
- S. Gottesfeld and J. D. E. McIntyre, *This Journal*, **126**, 742 (1979).
- L. M. Schiavone, W. C. Dautremont-Smith, G. Beni, and J. L. Shay, *Appl. Phys. Lett.*, **35**, 823 (1979).
- W. C. Dautremont-Smith, G. Beni, L. M. Schiavone, and J. L. Shay, *ibid.*, **35**, 565 (1979).
- "Conference Record of 1978 Biennial Display Research Conference," IEEE, New York (1978).
- B. W. Faughnan, R. S. Crandall, and P. M. Heyman, *RCA Rev.*, **36**, 177 (1975).
- M. Green, W. C. Smith, and J. A. Weiner, *Thin Solid Films*, **38**, 89 (1976).
- R. S. Crandall and B. W. Faughnan, *Appl. Phys. Lett.*, **28**, 95 (1976).
- H. N. Hersh, W. E. Kramer, and J. H. McGee, *ibid.*, **27**, 646 (1975).
- J. P. Randin, *J. Electron. Mater.*, **7**, 47 (1978).
- S. K. Mohapatra, *This Journal*, **135**, 284 (1978); and K. Matsuhiro and Y. Masuda, To be published.
- M. Green and K. S. Kang, *Thin Solid Films*, **40**, L19 (1977); M. Green, W. C. Dautremont-Smith, and K. S. Kang, Paper presented at Second Int. Sym. on Solid Electrolytes, St. Andrews, Sept. 1978; and to be published.
- See, e.g., K. J. Vetter, "Electrochemical Kinetics," Academic, New York (1967).
- "American Institute of Physics Handbook," 3rd ed., McGraw Hill, New York (1972).
- G. A. Parks and P. L. DeBruyn, *J. Phys. Chem.*, **66**, 967 (1962).
- L. Blok and P. L. DeBruyn, *J. Colloid. Interface Sci.*, **32**, 518 (1970).
- K. C. Ray and S. Khan, *Indian J. Chem.*, **13**, 577 (1975).
- Y. G. Berube and P. L. DeBruyn, *J. Colloid. Interface Sci.*, **27**, 305 (1968).
- S. Mukai, Y. Yokoyama, T. Wakamatsu, and N. Narazaki, *Suiyokai-Shi*, **17**, 49 (1970).
- J. Bjerrum, G. Schwarzenbach, and L. G. Sillen, "Stability Constants-Part II, Inorganic Ligands," The Chemical Society, London (1958).
- R. J. Atkinson, A. M. Posner, and J. P. Quirk, *J. Phys. Chem.*, **71**, 550 (1967).
- R. Zsigmondy and E. B. Spear, "Chemistry of Colloids," J. Wiley and Sons, Inc., New York (1917).
- D. J. O'Connor and A. S. Buchanan, *Aust. J. Chem.*, **6**, 278 (1953).
- D. J. O'Connor, P. G. Johansen, and A. S. Buchanan, *Trans. Faraday Soc.*, **52**, 229 (1956).
- R. K. Iler, "The Colloid Chemistry of Silica and Silicates," Cornell Univ. Press, Ithaca, New York (1955).
- A. M. Gaudin and D. W. Fuerstenau, *Trans. A.I.M.E.*, **202**, 66 (1955).
- M. A. Butler and D. S. Ginley, *This Journal*, **125**, 228 (1978).
- From Ref. (17) and from H. Hotop and W. C. Lineberger, *J. Phys. Chem. Ref. Data*, **4**, 539 (1975).
- R. S. Crandall, P. J. Wojtowicz, and B. W. Faughnan, *Solid State Commun.*, **18**, 1409 (1976).
- R. S. Crandall and B. W. Faughnan, *Phys. Rev. B*, **16**, 1750 (1977).
- T. A. Ramanarayanan and W. L. Worrell, *This Journal*, **121**, 1530 (1974).
- C. E. Rice, *Appl. Phys. Lett.*, **35**, 563 (1979).
- See, e.g., "Solid Electrolytes," P. Hagenmuller and W. Van Gool, Editors, Academic Press, New York (1978).
- C. E. Rice, Proc. of Int. Conf. on Fast Ion Transport in Solids, Lake Geneva, Wisc. (May 1979).
- W. P. Griffith, "Chemistry of the Rarer Platinum Metals," Interscience, New York (1967).
- See, e.g., N. H. Ray, "Inorganic Polymers," Academic Press, New York (1978).
- Yu. M. Polezhaev, Yu. D. Afonin, V. A. Zhilyaev, M. V. Mikshevich, and V. N. Shalaginov, *Izv. Akad. Nauk SSSR, Neorg. Mater.*, **13**, 476 (1977).
- M. B. Robin and P. Day, *Adv. Inorg. Chem. Rad.*, **10**, 247 (1967).
- M. M. Nicholson, Paper presented at the 21st Electronic Materials Conference, Boulder, Colo., June 27-29, 1979.
- See, e.g., J. P. Hoare, "The Electrochemistry of Oxygen," Interscience, New York (1968).
- G. Beni, L. M. Schiavone, J. L. Shay, W. C. Dautremont-Smith, and B. S. Schneider, *Nature*, **282**, 281 (1979).

X-Ray Diffraction Studies of Electrodeposited and Sputtered Hard Gold

E. T. Eisenmann

Bell Laboratories, Columbus, Ohio 43213

ABSTRACT

Studies of the oxidative softening of additive-free and cobalt-hardened gold lead to the conclusion that lattice strain is a major contributor to the hardness of these electrodeposits. Since strain hardening is not observed in gold from the melt, its occurrence in hard gold is claimed to derive from the polytypic structures, which seem to be characteristic of all high purity hard golds, plated as well as sputtered. Structural similarities of the gold polytypes and cobalt dicyanoaurate may be the reason for their electrolytic codeposition, which generates a distorted gold lattice. Oxidation or reduction of the light elements promotes the relaxation of lattice strains and leads, consequently, to the softening of electroplated hard gold.

Electroplated hard gold has been the subject of sustained fundamental studies ever since its use became preeminent in the electronics industry. This is not to say that the mechanical and physicochemical behavior of hard gold is thoroughly understood. Rather, new aspects of this material crop up occasionally when an industrial application fails to produce or to maintain the desirable properties. One case in point is the recent observation that cobalt-hardened gold loses its hardness within a few seconds when heated to 350°C in air.

The hardness of electroplated hard gold has been attributed to its small grain size (1). Grain growth was observed in cobalt-hardened gold at temperatures as low as 100°C, but significant softening of the deposit was found only after prolonged heating (1 hr) at temperatures in excess of 300°C (2). Nickel-hardened gold required 600°C to produce some grain enlargement and 700°C to slightly decrease the hardness (3). Isochronal annealing experiments in both investigations (2, 3) preclude, however, any judgment about the rate of the softening process. Koch (2) indicates that there is no mechanism by which hard gold could change metallurgically at 85°C to affect its performance as contact material. Structural changes of hard gold were also measured by Mohrheim (4) in dependence of time and temperature, but no hardness data were taken.

The object of this investigation was to provide an adequate data base on the kinetics of the reactive softening of various electroplated hard golds. Hardness tests, in combination with electron microscopic inspections and x-ray diffractometer scans, were chosen as analytical tools, temporarily disregarding the chemical nature of the process.

Heat-Treatment of Plated Hard Gold

A series of experiments was designed to estimate the rate at which structural changes occur in cobalt-hardened gold in response to various heat-treatments. Samples were prepared by plating 15-20 μm of gold on 0.5 \times 15 cm strips of nickel sheet, using a Selrex Autronex CI bath (Oxymetal Industries, Nutley, New Jersey), under standard conditions. Each strip was cut into 15 pieces, and each piece was used for a different heat-treatment. In the as-plated condition x-ray diffraction analysis yielded the lattice parameter $a_0 = 4.059 \pm 0.001\text{\AA}$, as calculated from the (422) peak. After heating in air at 340°C for 10 min, the lattice parameter was $a = 4.076$. Heating at the same temperature for 1 hr yielded the same result. Numerous samples were consequently heated at different temperatures for various times t , such that the resulting parameters a_t were evenly spaced over the range from

Key words: polytypism, strain hardening.

a_0 to a . Plotting $(a - a_0)/(a - a_t)$ on a logarithmic scale vs. t yields curves as shown in Fig. 1. These curves provide a convenient way of interpolating the time required for any degree of completion of the change in the lattice parameters. Alternatively, the relaxation time t_R may be defined as the inverse slope of the linear part of the curves in Fig. 1. These relaxation times are plotted in Fig. 2 to summarize the results of various heat-treatments in air and forming gas (N_2 -10% H_2).

The data are best fitted to two straight lines, suggesting that two distinct processes are operative, i.e., oxidation and reduction. The lack of curvature indicates that no change of mechanism occurs within the range of temperatures studied.

The data presented in Fig. 2 reflect primarily a surface effect, because of the limited penetration depth of x-rays in heavy metals. For copper $K\alpha$ radiation the half-value layer in gold is about 1.7 μm . This thickness value corresponds, approximately, to twice the reaction zone characterized by t_R . For structural changes occurring at depths greater than $\sim 0.5 \mu\text{m}$, x-ray diffraction is no longer a suitable tool for analysis. Scratch hardness tests (5) on cross sections of partially reacted hard gold were used, therefore, to monitor the continued progress of softening with time. This approach was also expected to elucidate the relationship between softening and the structural effects described above.

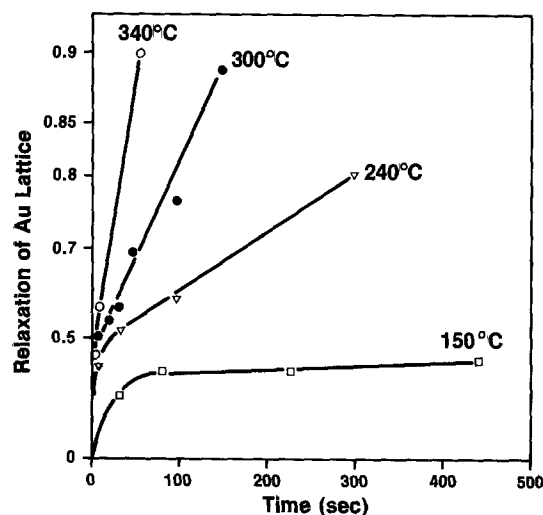


Fig. 1. Relaxation of the gold lattice in dependence of time and temperature.

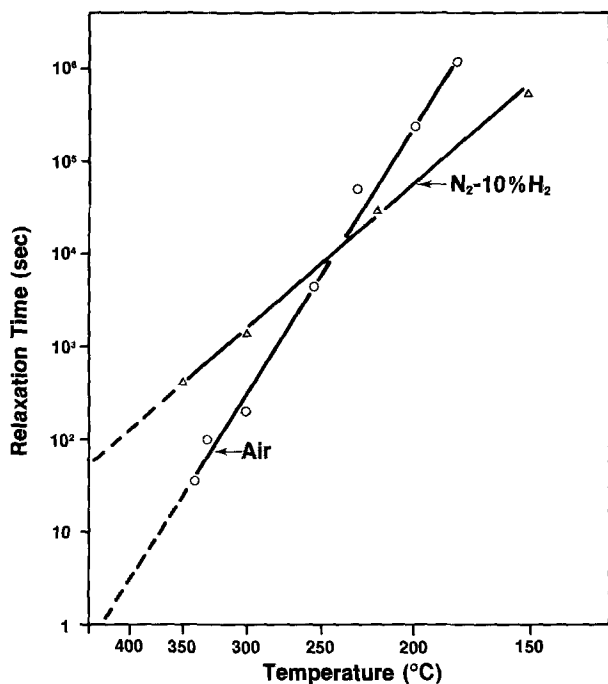


Fig. 2. Arrhenius plot of the relaxation time of structural changes in cobalt-hardened gold due to heating in air and forming gas.

The scratch hardness test is capable of detecting a hardness gradient with a spatial resolution of 1-2 μm . Within this limit numerous repetitions of the experiment indicated that a hardness step exists, rather than a continuum, between the reacted and unreacted regimes of the gold layer, Fig. 3a. Treatment of the cross section with a KCN-H₂O₂ solution led to preferred etching on the reacted part of the gold, giving rise to the formation of a spongy structure, Fig. 3b. Figure 4a shows the sharp boundary between the reacted and unreacted zones of the gold layer after prolonged etching, which in first approximation agrees with the location of the hardness step. The spongy gold shows no signs of crystallographic etching, apparently because recrystallization has not progressed very far, Fig. 4b. These observations suggest that the softening of hard gold is caused by the removal of nonmetallic material from the gold and by the formation of a spongy structure, rather than by grain growth alone.

The progress of the reaction boundary at 300°C was measured microscopically by means of the hardness step and thereafter by means of the etch pattern. According to Fig. 5 a systematic difference exists between the two measurements which is probably caused by erroneous readings of the hardness step. There is no evidence for a decrease in the velocity of the moving boundary with time as should be expected for a diffusion-controlled process. Hence it is concluded that reaction control prevails. Using the slope of the line in

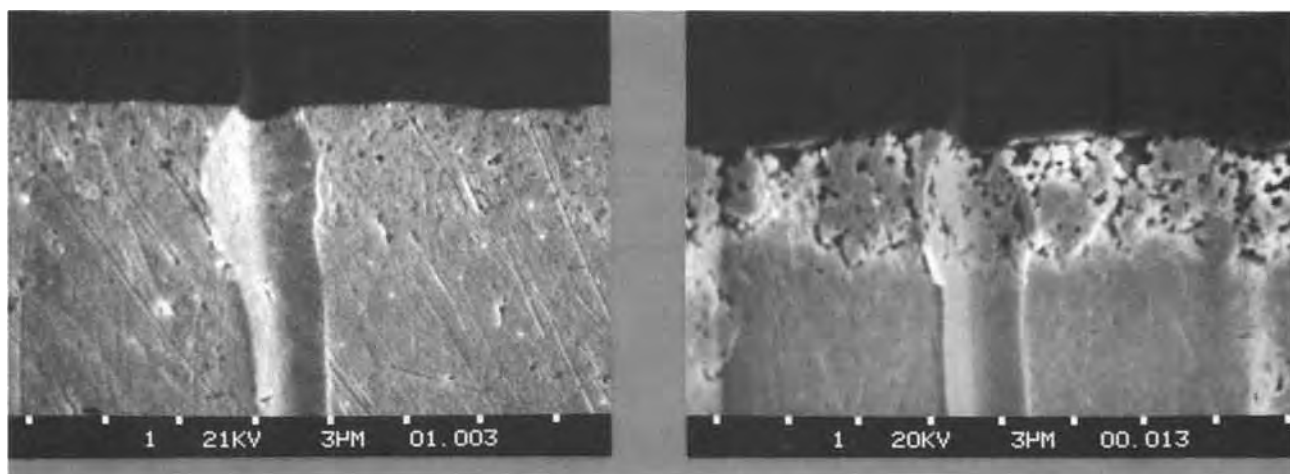


Fig. 3. Scratch hardness test on the cross section of partially softened hard gold: (a, left) polished surface, (b, right) etched surface

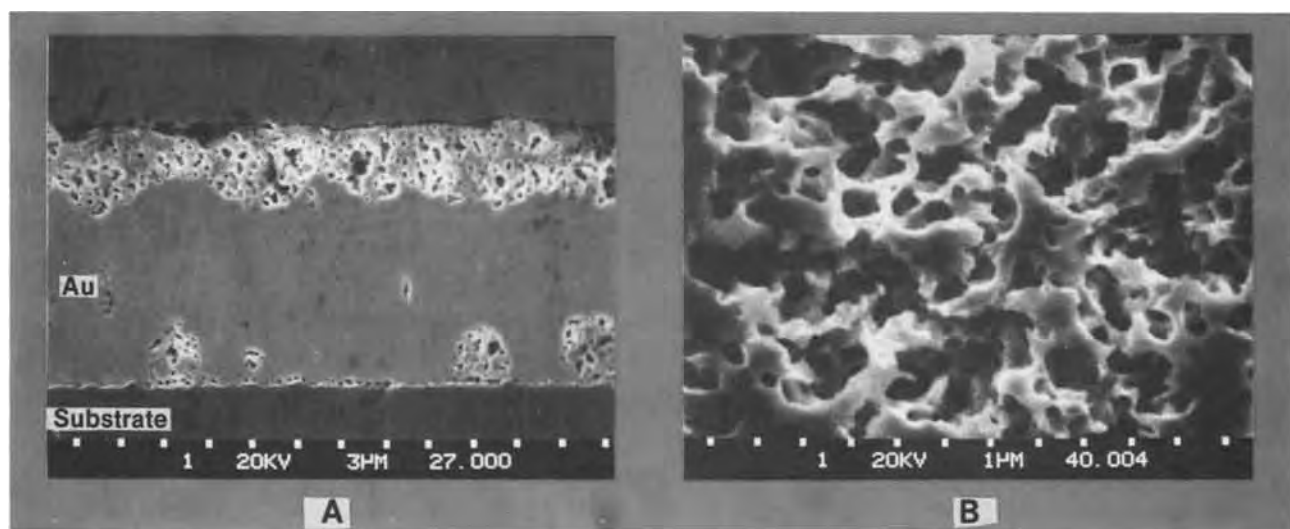


Fig. 4. (a) Boundary in partially oxidized hard gold, exposed by prolonged etching. (b) Gold sponge generated by etching oxidized hard gold.

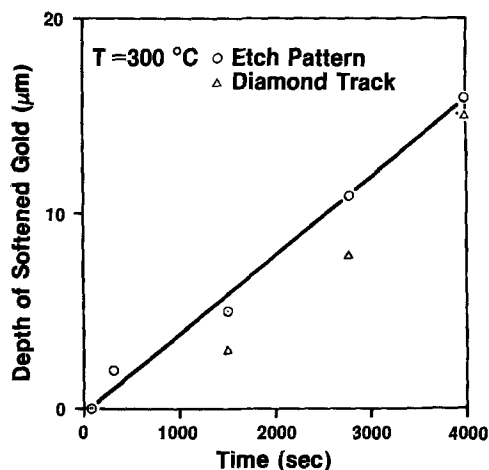


Fig. 5. Progress of the moving reaction boundary with oxidation time as measured by the etch pattern and by the scratch hardness test on cross-sectioned gold samples.

Fig. 5 one estimates a velocity of $0.004 \mu\text{m}/\text{sec}$. This result is in good agreement with the relaxation time $t_R = 200 \text{ sec}$, which follows from Fig. 2 for 300°C . Referring this time to one-half of the x-ray penetration depth of $1.7 \mu\text{m}$ yields $0.0043 \mu\text{m}/\text{sec}$.

Further studies of the annealing characteristics of plated gold were carried out with deposits from an "additive-free" cyanaurate solution at high over-voltage. This bath, which contained no hardening agent, was composed of 0.5 mole/liter monopotassium citrate and 0.5 mole/liter potassium cyanaurate. When operated at 30°C and $100 \text{ mA}/\text{cm}^2$ under vigorous agitation, deposits resulted whose hardness approached that of cobalt-hardened gold, but had a lower content of impurities. Heating in air at 350°C followed by etching produced, accordingly, no spongy structure. However, a decrease in hardness was observed, as shown in Fig. 6. These data were obtained on the plated surface using a Knoop indenter at various loads. Both the as-plated and the annealed gold exhibit increasing hardness with increasing load. This behavior is opposite to that of cobalt-hardened gold (5) and could indicate a lesser hardness of the surface. However, scratch hardness tests¹ on cross sections yielded uniform hardness throughout all test samples, regardless of their heat-treatments. Figure 7 presents the variation of the Knoop hardness with time at 350°C as percent deviation from the as-plated values at 1 and 25g load. Also shown is the increase in lattice param-

¹In scratch hardness tests, a Vickers indenter is loaded onto the surface and remains stationary, while the specimen is slowly pulled in the direction parallel to the diagonal of the square, pyramidal indentation. Variations in the rate of relative motion were suspected to influence the results due to "hydroplaning," but were never found to actually do so in a systematic evaluation.

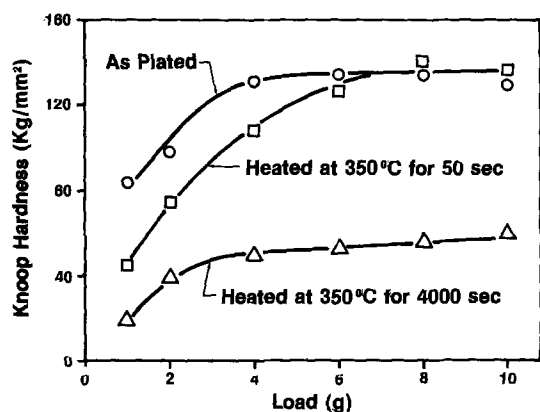


Fig. 6. Hardness of additive-free gold in dependence of the load at various stages of heat-treatments at 350°C .

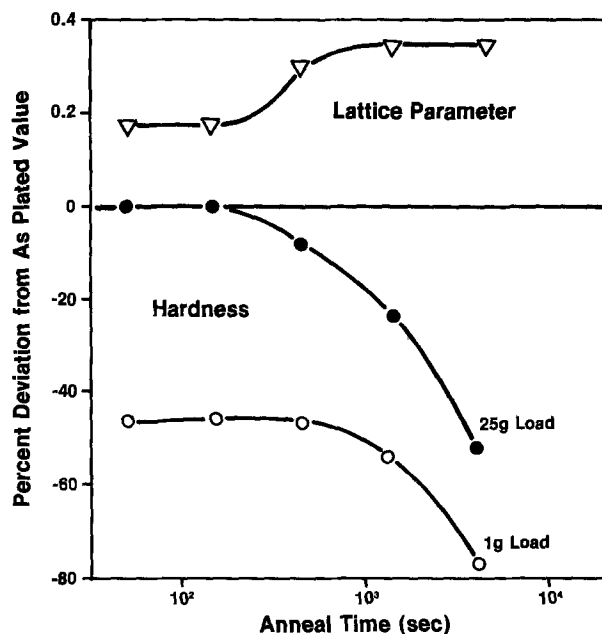


Fig. 7. The variation of hardness with anneal time at 350°C and the corresponding lattice relaxation.

eter, which accompanies the decrease in hardness. It is noted that 50 sec of heating causes a significant change in the lattice parameter, but affects only the hardness at 1g, not at 25g load. Continued heating produces a decrease of the higher load hardness as well and is associated with an additional expansion of the gold lattice.

A single principle emerges in two ways from these experiments with additive-free hard gold: (i) Electrodeposited gold can be strain hardened, contrary to gold from the melt. This follows from the load dependence of the hardness in Fig. 6, where increasing the strain imposed by the Knoop indenter produces an increase in hardness. (ii) Hard gold electrodeposits have a compressively strained lattice. Relaxation of the stress, due to heating, leads to a decrease in hardness, as demonstrated in Fig. 7.

It is concluded that hardness and lattice strains are correlated, even though strain hardening is not observed in gold from the melt. The capability of strain hardening of ("pure") plated gold appears to depend on the particular structure described in the following paragraph.

Detection of polytypism in hard gold.—Transforming cobalt-hardened gold into a gold sponge has been reported previously (6). Combined with the new observations, sponginess seems to indicate that inclusions of carbonaceous materials in as-plated gold are located in voids. From there they may be removed by reaction with oxygen (to form CO_2 , N_2) or with hydrogen (to form CH_4 , NH_3), thus exposing the already existing spongy structure. From the density of cobalt-hardened gold ($17.8 \text{ g}/\text{cm}^3$) one estimates that the impurities occupy 8% of the deposit volume. If the pores contain a crystallized material, its characteristic reflections may be detectable in the x-ray diffraction pattern. Accordingly, the previously proposed hypothesis may be tested that cobalt-gold cyanide coordination complexes are incorporated into hard gold during electrodeposition (7).

Selrex Autronex CI gold was plated under standard conditions on a $6 \text{ cm}^2 \times 4 \text{ mm}$ polished nickel substrate, to yield a thickness of approximately $20 \mu\text{m}$. This specimen was scanned on the x-ray diffractometer from $2\theta = 2^\circ$ upward. The reason for selecting this small diffraction angle was the fact that the hypothesized inclusions are characterized by large unit cells.

Confirmation of the hypothesis appeared to be at hand when reasonably strong, but diffuse and asymmetric reflections were observed at the 2θ angles 8.5° , 17° , and 26° (Cu K_α radiation). These diffraction lines coincide with the strongest reflections of $\text{Co}[\text{Au}(\text{CN})_2]_2 \cdot 10 \text{H}_2\text{O}$, which is known to decompose into gold and cobalt cyanide at 350°C in inert atmosphere (7). This information may be combined with the observation that cobalt-hardened gold changes its structural and mechanical properties under oxidizing conditions at 350°C . The extra diffraction lines were, therefore, expected to disappear in the course of such a heat-treatment. Instead, the relative intensities changed, the peak breadths and the asymmetry decreased, and additional reflections became evident.² Further sequential heat-treatments at higher temperatures produced eventually a decrease of the peak intensities, primarily because nickel diffused to the surface to form a dense layer of nickel oxide, which could not be removed with hydrochloric acid. The presence of nickel as surface oxide was concluded from electron probe measurements of the partially abraded surface. A strong nickel signal was obtained on the unabraded surface, but the abraded surface yielded no nickel signal at all.

These observations are inconsistent with the view that the extra diffraction lines are caused by a codeposited cobalt-gold cyanide coordination complex. In fact, Cohen and others (9) claim outright, on the basis of Mössbauer studies, that cobalt-gold cyanide coordination compounds are not present in cobalt-hardened gold. Yet, these authors analyzed only the bonding state of gold, rather than that of cobalt, in just two of at least four compounds worthy of consideration (10). With the precise nature of the contaminants in cobalt-hardened gold unresolved, alternatives for the origin of the extra diffraction lines were considered. Especially attractive appeared the possibility that a new modification of gold was formed due to the irreversibility of the electrocrystallization. Sputtered gold should then also crystallize with this structure because extreme irreversibility characterizes this deposition process. Numerous diffraction lines at low Bragg angles were indeed recorded for sputtered gold, as shown in Fig. 8. A sample of sputtered gold was removed from its substrate and annealed at 700°C for 56 hr. The diffraction pattern yielded then the d spacings listed in Table I, which allow indexing in the cubic system with the cell constant $a_0 = 36.72\text{\AA}$. This value is, with good accuracy, nine times larger than the cell constant of the fcc gold lattice. Because of this relationship, the extra lines in the diffraction pattern of sputtered gold are believed to indicate polytypism. As illustrated by silicon carbide (11), polytypes are formed by stacking identical layers in different arrangements.

The breadth and the asymmetry of the reflections at low Bragg angles precluded meaningful intensity measurements. None of these lines exceeded 3% of the intensity of the strongest line in the pattern, the (111) reflection of the basic fcc gold lattice. Continued annealing at up to 1000°C for 15 min was found to have little effect on the intensities.

To clarify whether or not the hardness of gold deposits is in any way tied to the polytypic structure, two additional series of tests were carried out with the following results.

1. All sputtered samples with hardness values ranging from 60 to 200 kg/mm (measured at 10g load) (1) showed numerous polytype reflections of varying intensities. However, no relationship to the as-deposited hardness data was evident. The effect of annealing on hardness was not evaluated.

² Oxidation decomposition of cobalt-hardened gold has been reported to lead to a cobalt oxide film at the surface of the gold and to a depletion of cobalt in the grain boundaries of the deposit (8). Accordingly, the intense purple discoloration observed on the present test sample was assumed to be cobalt oxide. It was removed with hydrochloric acid before the x-ray analysis.

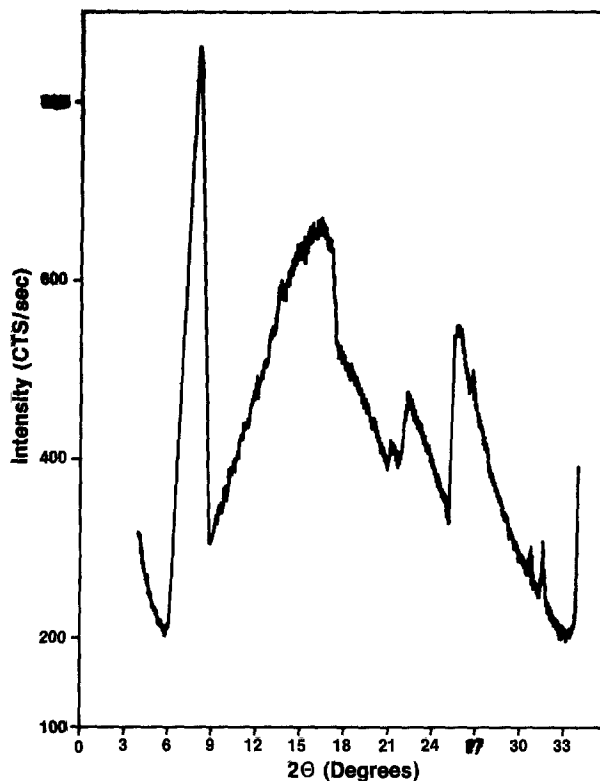


Fig. 8. Low Bragg angle reflections in as-sputtered gold

2. Various types of electroplated gold were tested for low angle reflections. High purity soft gold proved to be without additional reflections. All hard golds showed extra lines, though no correlation between the hardness and the intensity of these reflections was evident. Tested were cobalt- and nickel-hardened as well as "additive-free" hard golds plated from standard and from high speed baths. Typical patterns are listed in Table II and may be compared with that of sputtered gold in Table I.

It is surmised that polytypism in gold is a prerequisite but not a proportional factor in the development of hardness in high purity gold due to strain hardening.

An attempt was made to index the extra reflections of plated golds. Although the d spacings agree largely with those of sputtered gold, there is a conspicuous absence of the spacing $d = 36.7\text{\AA}$. Also, there is clear evidence of the interplanar spacing $d = 9.6\text{\AA}$, which is

Table I. X-ray diffraction pattern of sputtered gold after annealing at 700°C for 56 hr

Bragg angle $2\theta^\circ$		d (Å)	h	k	l
Experimental	Calculated				
2.3	2.41	38.41	1	0	0
8.3	8.34	10.652	2	2	0
13.6	13.66	6.511	4	4	0
14.2	14.26	6.237	5	3	1
17.2	17.41	5.155	7	1	1
22.4	22.45	3.969	9	2	0
25.6	25.44	3.480	10	3	2
31.2	31.58	2.840	10	8	2
38.2	38.20	2.3559	9	9	9
41.2	41.21	2.1910	16	5	0
48.55	48.58	1.8751	16	8	8
77.65	77.60	1.2296	27	9	9
81.72	81.76	1.1784	18	18	18

* For copper K_α radiation. The calculated Bragg angles correspond to a cubic unit cell with $a_0 = 36.721\text{\AA}$.

Table II. Diffraction patterns of electroplated hard golds after annealing at 350°C in air

Co-hardened gold [d (Å)]	Ni-hardened gold [d (Å)]	Additive-free hard gold [d (Å)]
10.28	10.65	
9.51	9.61	9.61
7.20		
5.16	5.13	5.01
	4.13	
4.04	3.99	
3.47	3.45	3.44
3.39		
3.30	3.31	
	3.15	
		3.00
2.91	2.92	2.96
	2.88	2.86
2.83	2.84	2.84
	2.79	2.80
		2.67
		2.53
2.45	2.46	2.45
2.35	2.36	2.36
2.20	2.19	
	2.13	
1.88	1.87	1.87
	1.74	
1.73	1.73	
	1.60	

inconsistent with a cubic cell constant of 36.72Å. Further studies are necessary to clarify these differences.

Updating the model of hard gold electrodeposition.—A causative relationship has been claimed to exist between the chemistry of cobalt (and nickel) cyanaurate complexes and the deposition characteristic of hard gold (7). These compounds were assumed to be incorporated in the gold deposit at grain boundaries or, more specifically, in the pores of a gold sponge. X-ray diffraction measurements did not confirm this particular composite structure but led instead to the discovery of polytypism in gold. Therefore, the model of hard gold electrodeposition should be revised to account for this feature.

Previous studies showed that the electrode relaxation after cathodic prepolarization at constant current density is significantly slower for (cobalt) hard gold than for soft gold deposition (12). This effect indicates the enhancement of an adsorption process, possibly the change from AuCN to Co[Au(CN)₂]₂ in the adsorption layer. Concurrently, the activation energy for soft gold deposition was found to decrease with time, while it remained constant for hard gold deposition. It was suggested that the increased activation energy generates hardness via an increased nucleation rate which results in grain refinement (1). In view of the results of the present study it stands to reason that high energy levels during gold deposition are responsible for the polytypism, which by itself is insufficient to increase the hardness. Accordingly, some of the sputtered golds showed strong low angle x-ray reflections but were actually soft. Polytypisms in gold seems, however, to permit strain hardening. The strains in plated hard gold originate from the incorporation of impurities and cause extreme broadening as well as an angular shift of the x-ray diffraction peaks. Most likely, adsorption mixed crystals are formed by reason of structural equalities of the gold polytypes and the impurities. Support for this concept is derived for the case of cobalt-hardened gold from the observation that Co[Au(CN)₂]₂, the hypothesized impurity, grows epitaxially on sputtered gold.

The x-ray diffraction pattern of the epitaxial layer is significantly different from that of the crystalline powder which precipitates from homogeneous solution. This is shown in Table III. Therefore, it is concluded that sufficient analogies exist between the polytypic gold and cobalt dicyanoaurate to permit solid solution. Mismatched dimensions, on the other hand, would account for the lattice strain in hard gold.

The updated model of the electrodeposition of cobalt hardened gold presents itself as follows.

Table III. Diffraction patterns of Co[Au(CN)₂]

Precipitated Co[Au(CN) ₂] ₂ · 10 H ₂ O			Grown on polytypic gold	
d (Å)	I/I ₁	hkl*	d (Å)	I/I ₁
10.4	100	100	10.4	22
			7.83	100
6.417	3	001		
5.170	60	200	5.185	11
			4.732	2
			3.909	39
3.433	14	300	3.450	2
3.207	47	002	3.132	1
3.058	37	102		
2.983	95	220	2.964	2
2.880	52	310		
2.726	21	202	2.770	3
2.585	48	400	2.609	Au(111) CuKβ
2.347	16	302	2.356	Au(111)
2.257	18	410		
2.010	13	402		
1.953	20	420	1.951	5

* Indexed in hexagonal system with a₀ = 11.930Å and c₀ = 6.416Å.

High overvoltage initiates the deposition and produces polytypism. Chemical adsorption of Co[Au(CN)₂]₂ interferes with the crystallization of the fcc structure. In order to permit either the overgrowth or the electrochemical breakdown of the adsorbed species, the electrode potential has to remain high compared to the conditions in soft gold plating. As a result, nucleation and continued growth of the polytypic structure take place.

Summary and Conclusion

Heat-treatments of electroplated cobalt-hardened gold in air and in forming gas produced structural changes which were evaluated by x-ray diffraction, hardness tests, and metallographic cross sectioning. The experimental results suggest that the light element impurities, which are commonly present in this type of hard gold, are removed by oxidation or by reduction, causing a thorough relaxation of the gold lattice and a loss of hardness. Above 250°C, the oxidation reaction proceeds at a higher rate than the reduction reaction, though the latter is less temperature dependent. Scratch hardness tests on cross sections of gold samples, which were heated in air at 300°C, revealed a hardness step. Etching of the cross sections confirmed that the oxidation reaction advances through the gold layer with a sharp boundary, indicating reaction control of the process rather than diffusion limitation.

The annealing of additive-free hard gold resulted in a similar relaxation of the gold lattice and caused a reduction in hardness. No hardness gradient was observed, however. Strain hardening was considered to account for the observed load dependence of the hardness data.

Testing a previously proposed hypothesis about the nature of the impurities in hard golds led to the observation that all plated hard golds show signs of polytypism while plated soft gold does not. Sputtered gold exhibits polytypism, regardless of its hardness. Evidence is discussed that hardness in electrodeposited gold is due, in part, to the lattice strain introduced by the inclusion of contaminants in polytypic gold.

It is concluded that all hard gold plates from cyanaurate electrolytes are subject to principally the same deposition kinetics and, therefore, to the same hardening mechanism. Loss of hardness due to the reactive removal of the codeposited species will be similar in all of these hard golds, although the rate of softening may vary in dependence of the impurity levels. However, not even additive-free hard gold with its low impurity level is immune from the loss of hardness caused by short term heating at 350°C.

Acknowledgments

Thanks are due to J. A. Augis who provided the sputtered gold samples and contributed to this study through valuable discussions.

Manuscript submitted Aug. 29, 1979; revised manuscript received Nov. 20, 1979.

Any discussion of this paper will appear in a Discussion Section to be published in the December 1980 JOURNAL. All discussions for the December 1980 Discussion Section should be submitted by Aug. 1, 1980.

Publication costs of this article were assisted by Bell Laboratories.

REFERENCES

1. J. A. Augis, C. C. Lo, and M. R. Pinnel, *J. Appl. Phys.*, **50**, 6887 (1979).
2. F. B. Koch, Private communication.

3. P. S. Willcox and J. R. Cady, *Plating*, **61**, 1117 (1974).
4. A. F. Mohnheim, *This Journal*, **117**, 833 (1970).
5. C. C. Lo, *Plating*, **60**, 247 (1973).
6. C. J. Raub, *Plating Surf. Finishing*, **63**, 35 (1976).
7. E. T. Eisenmann, *This Journal*, **124**, 1957 (1977); see also; W. S. Rapson, *Gold Bull.*, **11**, 132 (1978).
8. J. H. Thomas III and S. P. Sharma, *This Journal*, **126**, 445 (1979).
9. R. L. Cohen, F. B. Koch, L. N. Schoenberg, and K. W. West, *ibid.*, **126**, 1608 (1979).
10. R. L. Cohen, Private communication.
11. P. T. B. Shaffer, *Acta. Crystallogr., Sect. B*, **25**, 477 (1969).
12. E. T. Eisenmann, *This Journal*, **125**, 717 (1978).

Radial Wafer-to-Wafer Uniformity of Plasma-Deposited Si-N Films

Frank D. Egitto*,¹

Texas Instruments Incorporated, Dallas, Texas 75265

ABSTRACT

A multidimensional model relating the effects of reactor pressure and rf power to wafer-to-wafer radial uniformity for plasma deposited SiN_x films has been developed for a radial flow plasma reactor. The effects of pressure from 0.4 to 1.6 Torr (53.3 to 213.3 Pa) and power from 30 to 90W on percent nonuniformity are analyzed for constant gas flows. Inward radial depletion of silane can affect uniformity of deposition rate and index of refraction. The experimental technique used to obtain a "uniformity surface" and the theoretical considerations employed in analyzing the results are described.

In using a radial flow plasma reactor (1) (see schematic, Fig. 1) for depositing silicon-containing films, radial uniformity of deposition rate can be attributed mainly to three controlling factors. These are the radial gradients of electron density n_e , residence times τ of the reactant gases, and residual concentrations C_i (number of molecules of gas i per unit volume) of the reactant gases (2). Since the gases are continually depleted as they flow inward, $C_i(r_1)$ refers to that portion of gas i which is not consumed at radii greater than r_1 . These gradients are illustrated in Fig. 2. The electron density is determined

by rf power input while the residence times are controlled by reactor pressure which, for constant inlet

* Electrochemical Society Active Member.
¹ Present address: Applied Materials, Incorporated, Plasma Dry Processing Systems Division, Santa Clara, California 95051.
 Key words: radial flow plasma reactor, silicon nitride deposition, silane depletion, reactor balancing.

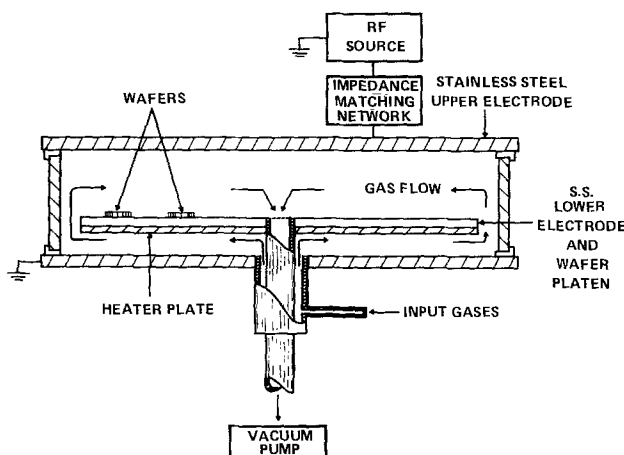


Fig. 1. Schematic of radial flow reactor used for SiN_x film depositions.

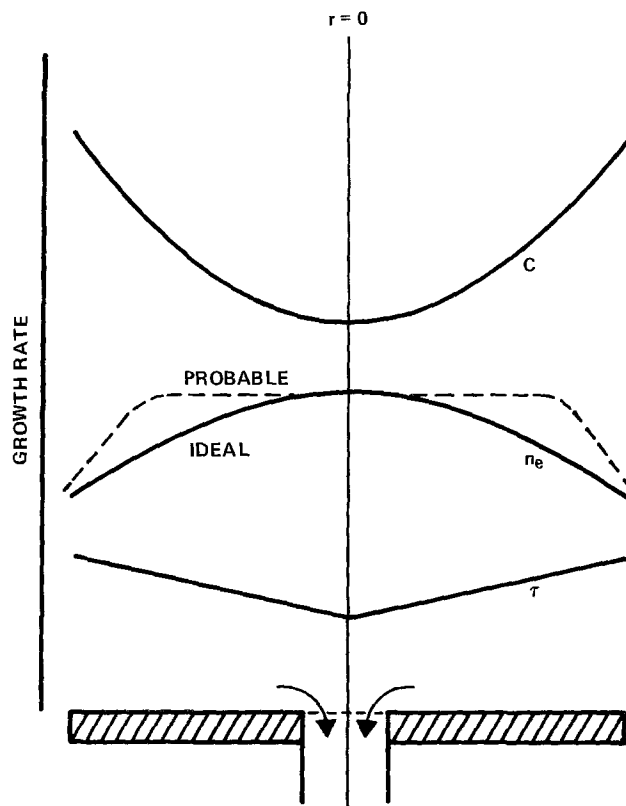


Fig. 2. Factors which affect radial uniformity: residual gas concentration (C), electron density (n_e), and residence time (τ). After Reinberg (2).

gas flows, is a function solely of pumping speed. Residual gas concentration, although influenced by gas flows, is also a function of both rf power and reactor pressure. Thus, at a given radius and constant inlet gas flows

$$\begin{aligned} n_e &= f(\text{rf power}) \\ \tau &= g(\text{reactor pressure}) \\ C &= h(\text{rf power, reactor pressure}) \end{aligned} \quad [1]$$

Near the outer wall, the electron density falls off approximately as a zeroth order Bessel function (3), promoting higher deposition rates near the center of the reactor. However, τ decreases linearly with decreasing radius (2). Ideally, a balance between the effects of power and pressure is sought in order to obtain radial uniformity.

The object of this paper is to analyze the effects of power and pressure on SiN_x film deposition at constant gas flows and to develop a three-dimensional uniformity surface which can be used as a basis for a routine to obtain the optimum combination of these parameters. Each point on the uniformity surface will identify the radial wafer-to-wafer uniformity of deposition rate (vertical axis) corresponding to a given combination of power and pressure settings (horizontal axes).

Experimental

Depositions were performed in the radial flow reactor (1) shown schematically in Fig. 1. The outer diameter of the plates which were separated by 2.5 cm was 40.6 cm. Two silicon pilot wafers were centered at radii of 10.2 and 16.5 cm, respectively, and along a common radial line. The positions were held constant to 0.2 cm between runs. The substrate plate was heated to 300°C by resistance heaters adjacent to its underside. The platen temperature was monitored and controlled via a thermocouple positioned at its underside.

A SiH_4 flow of 12 SCCM, 14 SCCM of NH_3 , 315 SCCM of N_2 , and 362 SCCM of argon were admitted

to the reactor chamber from below the substrate plate. These flows provided a reasonable film index of refraction throughout the power range of 30-90W and the pressure range of 0.4-1.6 Torr (53.3-213.3 Pa). The rf power was varied in 10W increments and at each of these power settings the pressure was varied in 0.2 Torr (26.7 Pa) increments by adjusting the pumping speed via a throttle valve. Pressure was monitored by a Validyne diaphragm vacuum gauge.²

An ellipsometer operating at 6328Å was used to measure film thickness and index of refraction of all films. Deposition times were adjusted for various powers and pressures in order to produce film thicknesses more easily measured by this technique. Measurements were taken at the centers of all test wafers.

Percent nonuniformity, *PNU*, was determined as follows

$$PNU = [(\bar{R} - R_1)/\bar{R}] \times 100 \quad [2]$$

where R_1 is the deposition rate on the inside wafer and \bar{R} is the average of the inside and outside deposition rates. Thus, a positive value for *PNU* implies a greater rate on the outside wafer, a negative *PNU* indicates a greater rate on the inside wafer, and a *PNU* of zero defines a perfect radially uniform deposition rate.

PNU is plotted as a function of pressure for various rf powers in Fig. 3. The same data is illustrated as *PNU vs. power* for various pressures in Fig. 4. The three-dimensional uniformity surface is illustrated in Fig. 5. All points at which the uniformity surface intersects the power-pressure plane represent zero *PNU*, i.e., possess radially uniform deposition rates. These power-pressure pairs constitute the balance sought in making uniform depositions. However, as explained below, not all of these uniformly thick films are suitable for semiconductor device manufacture and it is necessary to filter out those which are not.

²The AP10 Validyne Absolute Pressure Transducer is a variable reluctance transducer. Pressure displayed on the Model DM56A digital manometer is not a function of gas species.

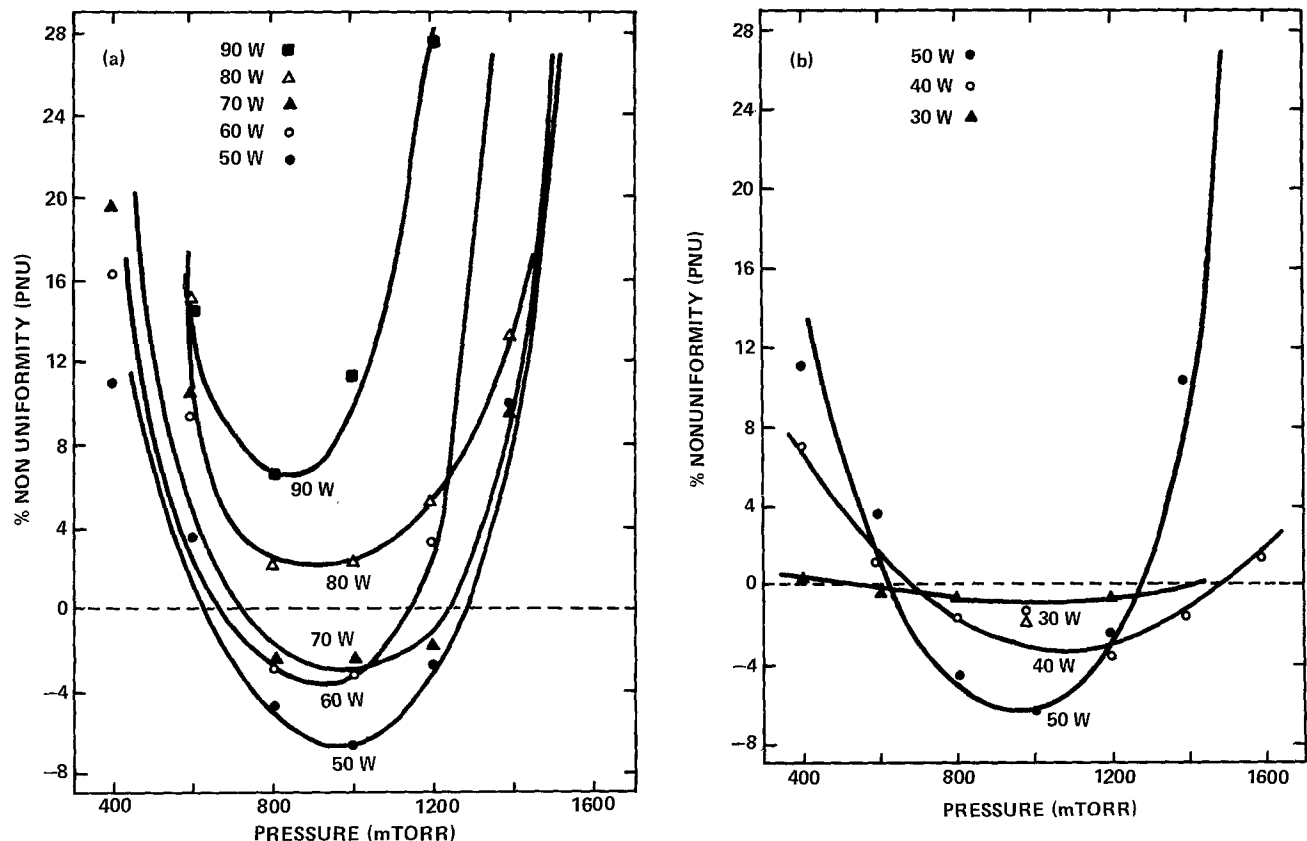


Fig. 3. *PNU vs. reactor pressure, rf power fixed: (a, left) 50-90W; (b, right) 30-50W*

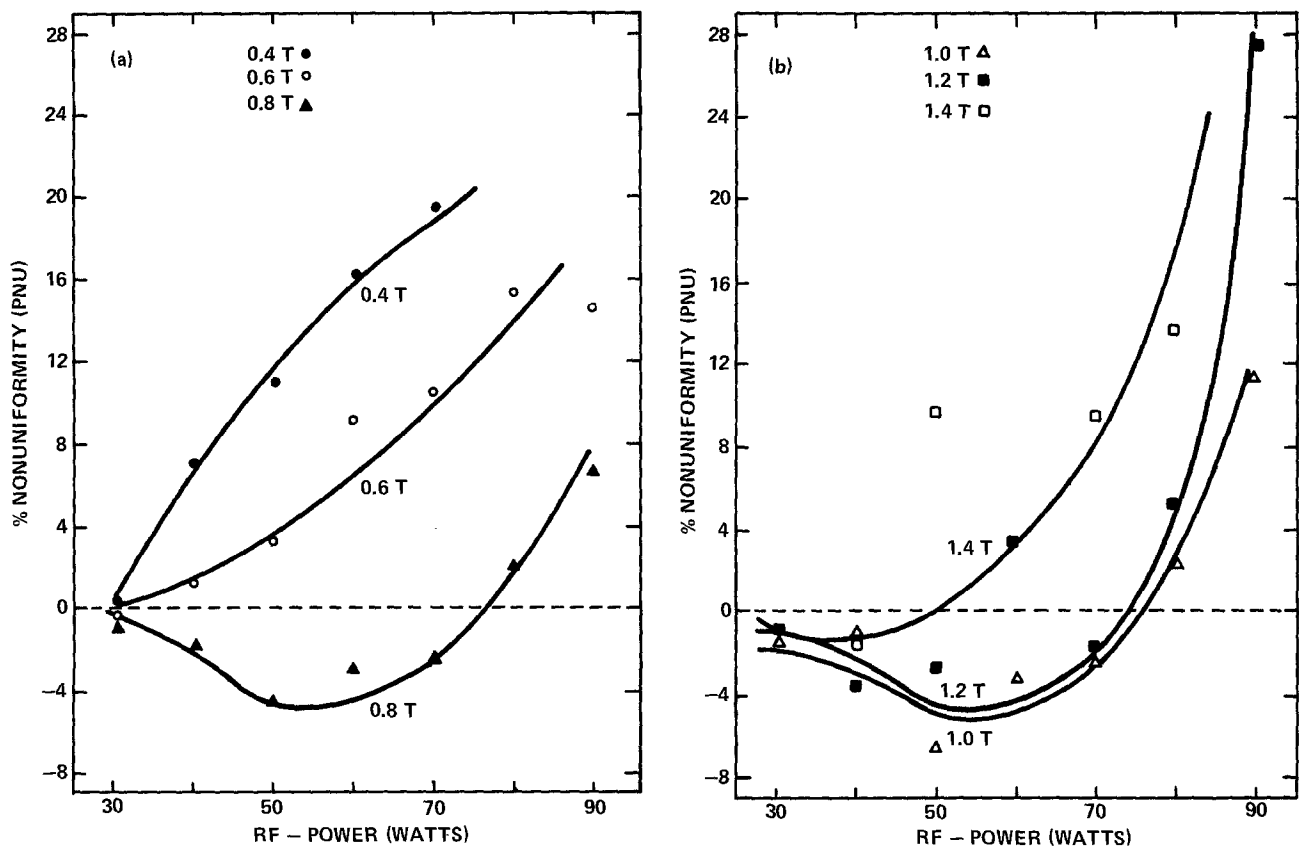


Fig. 4. PNU vs. rf power, pressure fixed: (a, left) 0.4-0.8 Torr; (b, right) 1.0-1.4 Torr

Discussion

The degree to which deposition rates vary radially due to radial variations in electron density n_e or gas residence times τ depends on the reactor chamber pressure. At high pressures, gas velocities are lowest and residence times are longest. As a result, n_e is the controlling mechanism, encouraging relatively higher deposition rates at small radii than at large radii. At low pressures, residence times are shorter and the effect of n_e is diminished. τ becomes the controlling factor, encouraging relatively higher deposition rates at large radii than at small radii. Hence, as pressures

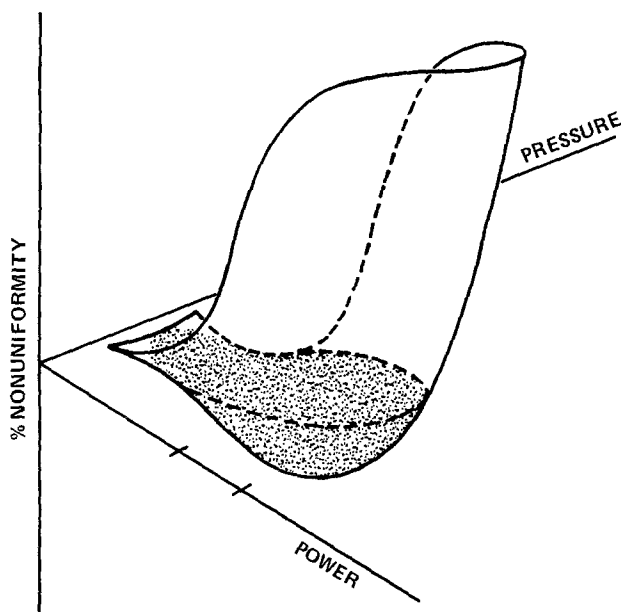


Fig. 5. Uniformity surface

are increased at a given power, a decrease in PNU is expected.

However, this behavior is observed only over a limited pressure range. As the pressure is increased to values above this range, the outside rate is enhanced, relative to the inside rate, producing a quadratic dependence of PNU on pressure (Fig. 3). At the highest pressures shown, the relative deposition rate is increasingly greater on the outside wafer. For lower powers, uniformity is obtainable at two pressures while at higher powers uniformity may not be obtained at any pressure. The reason for this becomes apparent when one observes the behavior of the refractive index of the two test wafers as illustrated in Table I and Fig. 6. In Fig. 6, percent nonuniformity of index was determined as for deposition rates. It is observed that, when a uniform deposition rate is obtained at higher pressures, a large nonuniformity in index of refraction can occur. At these points, the index of the outer film is consistently and significantly larger than the inside index. This effect is produced by a rapid inwardly radial depletion of silane at pressures which are too high. At these pressures, the reactant gases move too slowly over the outer portion of the substrate plate and are deposited at an abnormally high rate. The depletion of the rate-controlling silane leads to the behavior of PNU illustrated in Fig. 3.

It has been demonstrated (2) that for rf powers from 10 to 80W, the percentage of silane depleted in the reactor is greater than the percentage of ammonia depleted (as measured downstream from the reactor chamber). In addition, silane is more easily dissociated than nitrogen. Since the silane concentration controls the silicon content of the film, silicon deficient films are deposited on inner wafers when the pressure is too high. As a result, inner wafers exhibit the lower index characteristic of a lower silicon to nitrogen ratio in the film. As pressure is increased even further, the effect of depletion can be observed

Table I. Deposition rates and refractive indexes of SiN_x films for inner and outer reactor radii at various rf powers and reactor pressures

RF POWER (W)	PRESSURE (T)	30		40		50		60		70		80		90	
		RATE (Å/MIN)	INDEX	RATE (Å/MIN)	INDEX	RATE (Å/MIN)	INDEX	RATE (Å/MIN)	INDEX	RATE (Å/MIN)	INDEX	RATE (Å/MIN)	INDEX	RATE (Å/MIN)	INDEX
0.4	INSIDE	28	1.98	31	1.97	34	2.03	44	2.02	53	1.94				
	OUTSIDE	28	1.97	36	1.95	42	2.03	61	2.05	79	1.97				
0.6	INSIDE	37	2.03	43	2.01	50	2.09	67	2.09	77	1.98	95	1.96	136	1.91
	OUTSIDE	37	2.01	44	1.99	54	2.10	81	2.09	95	2.01	130	2.00	183	1.97
0.8	INSIDE	40	2.06	62	2.02	83	2.12	122	2.14	179	2.01	218	1.94	234	1.87
	OUTSIDE	39	2.02	60	2.01	75	2.10	115	2.15	170	2.05	228	2.02	269	1.99
1.0	INSIDE	36	2.07	67	2.07	110	2.16	168	2.13	226	1.96	250	1.91	245	1.86
	OUTSIDE	34	2.02	65	2.04	96	2.15	168	2.18	216	2.04	262	2.02	306	1.96
1.2	INSIDE	34	2.06	65	2.08	100	2.18	164	2.09	236	1.92	255	1.87	186	1.83
	OUTSIDE	33	2.02	60	2.05	95	2.16	175	2.17	228	2.05	283	2.01	329	1.96
1.4	INSIDE			58	2.13	80	2.18	68	2.11	203	1.91	225	1.85		
	OUTSIDE			56	2.09	98	2.18	191	2.14	246	2.01	296	1.99		
1.6	INSIDE			55	2.13	12	2.01	0	-	75	1.83				
	OUTSIDE			57	2.11	104	2.19	185	2.13	267	1.97				

on outer wafers. In this pressure region much silane is consumed below the substrate plate.

As rf power is increased, the effects of silane depletion are observed at lower and lower pressures (Fig. 6). The gas flow shield reported by Sinha *et al.* (4) promotes uniform deposition at powers much greater than otherwise possible. This results from confinement of the discharge to the region above the substrate plate and, hence, reduced consumption of silane below the plate.

As rf power is increased, the increase of n_e at the outer edge of the reactor exceeds the increase at the center, although n_e remains maximum at $r = 0$. Thus, higher powers promote greater relative outside deposition rates. This is in agreement with the curves of Fig. 4 except at the lowest powers. At powers less than 50W, decreasing power tends to increase PNU toward zero. At these powers, a radially uniform deposition rate is obtained at all pressures. It is possible that this effect is due to the fact that at very low powers, ionization occurs primarily near the electrodes where the gas velocities are near zero, independent of radius. This follows from the expression for gas velocity given by (5)

$$v(r, z) = \frac{-3Q}{8\pi br} \left[1 - \left(\frac{z}{b} \right)^2 \right] \quad [3]$$

where Q is the volume rate of flow, $2b$ is the electrode separation, z is the distance from the midplane between electrodes, and r is the radius. The negative sign indicates that flow is radially inward. A slow, steady, laminar, incompressible Newtonian flow is assumed. Hence, at low power, pressure variations have little effect on uniformity.

Figure 5 can be used as a basis for a computer program to aid in obtaining depositions which are radially uniform in rate and index of refraction. Two techniques have been considered: one involving a linear approximation with the use of appropriate filters and the second employing a quadratic approximation.

It is obvious that the uniformity surface is not planar and a linear approximation may, at first, seem unsuitable. However, by using filters such as refractive index nonuniformities and variations in PNU as a function of variations in rf power or reactor pressure, one can arrive at a region of the uniformity surface where a linear approximation can be applied. A sample calculator flow diagram illustrating this routine is shown in Fig. 7 and such a program has been written for the Texas Instruments SR-60 programmable prompting calculator.

As shown in Fig. 3, the dependence of PNU on pressure (power constant) is quadratic in nature. Using three data points, *i.e.*, three PNU-pressure pairs, the zeros of the parabola at a given power can easily be obtained. These zeros are the pressures at which radially uniform deposition rates are obtained. Imaginary zeros imply a power which is too large to obtain uniformity at any pressure. In addition, when real zeros exist, their proximity is an indication of the amount by which the power may be raised without exceeding the maximum power at which uniformity is obtainable. Figure 3 shows that as rf power is increased, the zeros of the parabola become closer. The index of refraction will almost always be more uniform at the lower of the two pressures at which a uniform deposition rate is achieved.

Conclusions

Silane depletion, as well as reactor pressure and rf power, acts in determining radial uniformity of plasma-deposited silicon nitride films. For a given power and constant gas flows, uniformity of deposition rate is possible at two pressures (assuming the

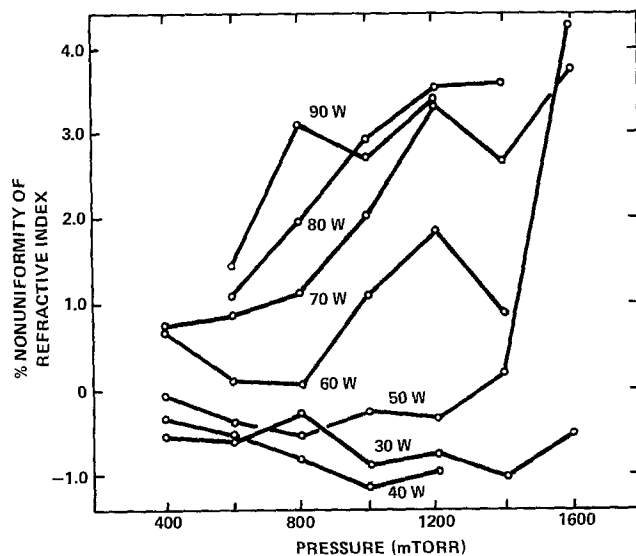
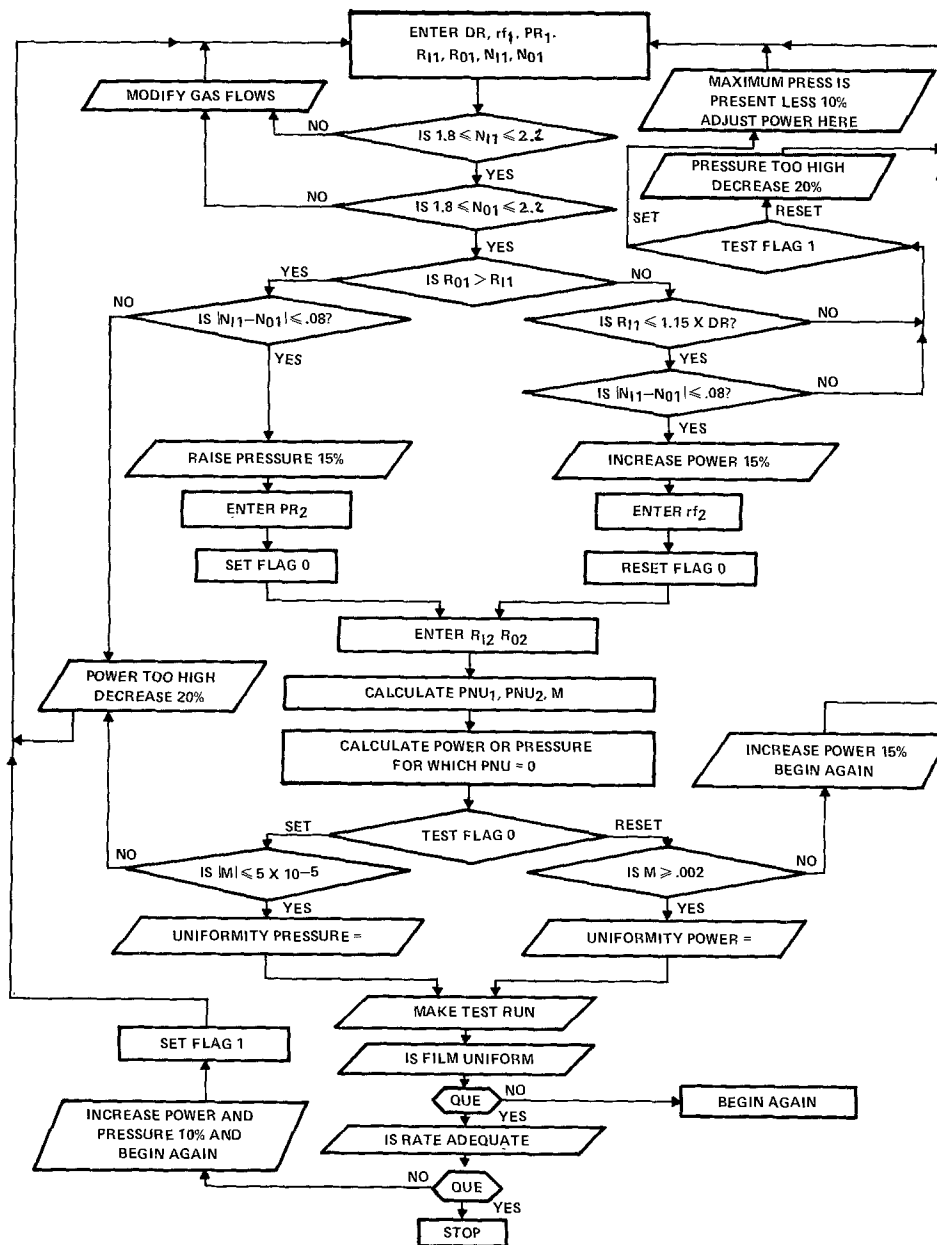


Fig. 6. Percent nonuniformity of SiN_x film refractive index as a function of pressure at various rf powers.

Fig. 7. Sample flow diagram employing linear approximations with appropriate process filters. Symbols are: *DR*, desired rate; *rf*, power; *PR*, pressure; *R*, rate; *N*, refractive index. Subscripts indicate inner (I) and outer (O) radii and test run number (1 or 2). *M* is the slope of the line containing *PNU*₁ and *PNU*₂.



power is not too great), the higher pressure usually accompanied by a large radial nonuniformity of refractive index. At very high powers, uniformity of rate is not achievable.

The three-dimensional uniformity surface can be used as a basis to develop a routine to optimize the SiN_x deposition process. Since the routine employs data taken as the process is set up, it will be reactor independent, although the shape and position of the surface may vary slightly for various radial flow reactors and reactor configurations.

Compensating for silane depletion by adjustment of inlet gas flow rates is possible, yet not straightforward. It appears obvious that the flow rate of SiH_4 should be increased. However, a corresponding increase in NH_3 flow rate would be required to avoid undesirably high refractive indexes. Assuming that pumping speed and residence times do not vary appreciably with the resulting pressure increase (throttle valve conductance remaining fixed), deposition rates at inner radii may increase relative to those at outer radii as the effects of depletion are diminished. An additional correction in reactor pressure or *rf* power may then be required.

Acknowledgment

The author is grateful to Dr. A. R. Reinberg for many useful discussions.

Manuscript submitted June 29, 1979; revised manuscript received Dec. 23, 1979.

Any discussion of this paper will appear in a Discussion Section to be published in the December 1980 JOURNAL. All discussions for the December 1980 Discussion Section should be submitted by Aug. 1, 1980.

Publication costs of this article were assisted by Texas Instruments Incorporated.

LIST OF SYMBOLS

n_e	electron density in the plasma
τ	residence times of reactant gases
C	residual gas concentration
PNU	percent nonuniformity of deposition rate (radial)
R_I	deposition rate at inner radius
\bar{R}	average of R_I and outer deposition rate
v	radial gas velocity
Q	volume rate of gas flow
$2b$	reactor electrode separation

REFERENCES

1. A. R. Reinberg, Abstract 6, p. 19, The Electrochemical Society Extended Abstracts, Spring Meeting, San Francisco, Calif., May 12-17, 1974; U.S. Pat. 3,757,733.

2. A. R. Reinberg, Private communication.
3. "Techniques and Applications of Plasma Chemistry," John R. Hollahan and Alexis T. Bell, Editors, p. 22, Wiley-Interscience, New York (1974).
4. A. K. Sinha, H. J. Levinstein, T. E. Smith, G. Quin-tana, and S. E. Haszko, *This Journal*, **125**, 601 (1978).
5. R. B. Bird, W. E. Stewart, and E. N. Lightfoot, "Transport Phenomena," p. 114, John Wiley & Sons, inc., New York (1960).

Spectroscopic Analysis of the Interface Between Si and Its Thermally Grown Oxide

D. E. Aspnes*

Bell Laboratories, Murray Hill, New Jersey 07974

and J. B. Theeten

Laboratoire d'Electronique et de Physique, Limeil-Brevannes 94450, France

ABSTRACT

Spectroscopic ellipsometric data from 1.5-5.8 eV has been analyzed to determine the *in situ* optical response of the interface between Si and its thermally grown oxide. Results for $\langle 100 \rangle$, $\langle 110 \rangle$, and $\langle 111 \rangle$ sample orientations show an interface of width $d_{ox} = 7 \pm 2 \text{ \AA}$ consisting of atomically mixed Si and O of average stoichiometry $\text{SiO}_{0.4 \pm 0.2}$. The optical data are not consistent with either microroughness at the interface or an abrupt transition between crystalline Si and SiO_2 or a significant accumulation of amorphous Si at the interface, but rather support a gradual transition region. The thickness and the average $\lambda 5461$ refractive index $n = 3.2 \pm 0.5$ of this region are in agreement with the fixed-wavelength results, $d \sim 6 \text{ \AA}$ and $n \sim 2.8$, of Taft and Cordes. The oxide on the $\langle 110 \rangle$ surface is shown to have a density about 1.2% less than that of corresponding oxides on $\langle 100 \rangle$ and $\langle 111 \rangle$ surfaces.

There has been much recent interest in studying the properties of the interface between Si and its thermally grown oxide, not only because of its technological importance but also because it is the chemically simplest, most easily managed semiconductor-oxide system and hence the one most likely to be understood in fundamental terms (1). Recent experimental results have been summarized by Wager and Wilmsen (2). In short, the interface is too narrow to be analyzed by conventional ion-milling techniques, which not only have inadequate depth resolution but also destroy the interface during the measurement process. The most reliable information has come from recent experiments using nondestructive techniques. Krivanek and co-workers (3) used transmission electron microscopy with 3Å resolution to show that the crystalline Si (c-Si) substrate terminates abruptly (within one monolayer) with a 4-8Å modulation of a period of 200-500Å. Rutherford backscattering (RBS) was used by Feldman and co-workers (4) to show the existence of about two monolayers equivalent of excess Si, which could occur for example as two layers of nonregistered Si under stoichiometric SiO_2 , or as a single nonregistered layer of Si together with $\sim 5 \text{ \AA}$ of SiO under stoichiometric SiO_2 . Fixed-wavelength $\lambda 5461$ null ellipsometry (NE) by Taft and Cordes (5) indicated an interface about 6Å wide of effective index about 2.8. XPS measurements on ultrathin or chemically profiled oxides show a gradual transition region $\sim 5 \text{ \AA}$ (6) or 7-10Å (7) with evidence that the SiO_2 bonding is affected up to 40Å from the interface (6).

In this paper, we present results of a spectroscopic ellipsometric investigation of the Si-SiO₂ interface from 1.5 to 5.8 eV. Our objective was to take advantage of the sensitivity of ellipsometry to thin films and of the widely different dielectric properties of c-Si, amorphous Si (a-Si), SiO₂, and their mixtures in the visible-

near u.v. spectral region to perform *in situ* spectroscopy on the protected interface and to determine information about its microstructure and chemical bonding from its visible-near u.v. optical response. TEM, RBS, and NE can provide general information about microstructure, but not about chemical bonding which requires some form of spectroscopy. XPS in principle can provide the latter information, but its interpretation is dependent on electron escape depths. Because spectroscopic ellipsometry does not depend on transport assumptions, requires only a transparent ambient (as, for example, SiO₂), and is sensitive to monolayers, it is a natural technique to apply to this problem. The results demonstrate also that spectroscopic ellipsometry can be used to study layers as thin as a few angstroms even though buried under hundreds or even thousands of angstroms of transparent overburden.

Analysis of the ellipsometric data shows that the interface is best represented as a $7 \pm 2 \text{ \AA}$ region of Si and O of average stoichiometry $\text{SiO}_{0.4 \pm 0.2}$. These data show clearly that the mixing is on an atomic scale rather than occurring as regions identifiable explicitly as a-Si and SiO_2 as might be expected from microroughness or incomplete oxidation of particulate material. Also rejected is an abrupt junction between Si and SiO_2 or an accumulation of a-Si at the interface. No difference in the interface region is observed for the three different interface orientations investigated here, although the SiO_2 overlayer on the $\langle 110 \rangle$ interface is about 1.2% less dense than that on the $\langle 100 \rangle$ or $\langle 111 \rangle$ interfaces. The microstructure that emerges is a laterally uniform, graded transition region of atomically mixed Si and O of thickness and composition as mentioned above. The results are consistent with the RBS alternative of a monolayer of a-Si followed by 5Å of SiO. The graded nature is in agreement with XPS measurements (6, 7). Finally, because the $\lambda 5461$ refractive index of $\text{SiO}_{0.4 \pm 0.2}$ is 3.2 ± 0.5 , the present results are also in agreement with the fixed-

* Electrochemical Society Active Member.
Key words: silicon, SiO₂, interface, ellipsometry.

wavelength λ 5461 null ellipsometric measurements of Taft and Cordes (5). Thus a completely consistent picture is obtained.

Experimental

Spectroscopic ellipsometer.—The spectroscopic rotating-analyzer ellipsometer (RAE) used to obtain these data has been discussed in detail elsewhere (8). In brief, the essential features include a Xe 75W short-arc source for high luminosity and efficient collection at relatively low power dissipation, a Cary 14 spectrometer for excellent scattered light rejection, quartz Rochon prisms for extended spectral range and source/detector depolarization, and computerized Fourier processing of the digitized detector output for high precision. The detector circuit includes a feedback loop to achieve system linearity to at least one part in 10^3 over the entire operating range. A shutter periodically interrupts the lamp output to allow component drift and stray light contributions to be evaluated and eliminated at each wavelength. The data are corrected (9) for the optical activity of the quartz Rochon prisms.

While precision of a few parts in 10^5 is achieved routinely accuracy limits are more difficult to assess. Nevertheless, the following observations are suggestive. In straight-through operation, the calculated polarization plane is constant to within $\pm 0.02^\circ$ from 1.5 to 5.8 eV. Over the same range, the apparent a-c/d-c ratio is constant to within ± 0.001 . At a fixed wavelength, the analyzer and polarizer azimuths track to within $\pm 0.01^\circ$ over the ranges used, showing that the polarizer divided circle drive and the detector system is linear, and that source/detector residual polarization effects are negligible. Finally, calibration for a variety of samples routinely yields plane-of-incidence azimuths which are invariant to within $\pm 0.05^\circ$, showing accurate reproducibility for sample alignment and also accurate compensation for the optical activity of the quartz Rochon prisms. Thus in direct angular measurements, the present photometric system is comparable to that of a good null ellipsometer, but somewhat less accurate than the $\pm 0.01^\circ$ fixed-wavelength instrument used by Taft and Cordes (5). The a-c/d-c ratio uncertainty has no direct analog in null ellipsometry, but corresponds roughly to an uncertainty of $\pm 0.1^\circ$ in ψ under worst-case conditions where the light leaving the sample is linearly polarized. These uncertainties are not large enough to affect the conclusions reached here on the basis of the data.

Sample preparation.—Three n-type single crystal Si wafers of 24–29 Ω cm resistivity and $\langle 100 \rangle$, $\langle 110 \rangle$, and $\langle 111 \rangle$ surface orientations were Syton polished to provide high quality specular surfaces. The wafers were precleaned by standard gate-oxide procedures, then cleaning oxides were grown in dry O_2 at $1000^\circ C$ to a $\langle 111 \rangle$ thickness of 1000 Å. These oxides were stripped, and final oxides were regrown under the same conditions to a $\langle 111 \rangle$ thickness of about 2000 Å. All three wafers were processed simultaneously to eliminate any possible differences due to slight variations in processing and growth conditions. All processing was done on equipment used routinely for the production of high quality gate oxides.

The resulting oxides on the $\langle 100 \rangle$ and $\langle 111 \rangle$ wafers were about 2100 and 2300 Å thick, respectively, and appeared absolutely uniform on visual inspection, although ellipsometric measurements showed a slight (5 Å) nonuniformity in thickness over the wafers. The substantially thicker 2800 Å $\langle 110 \rangle$ oxide showed an obvious thickness gradient over part of the surface, but about half the wafer was found to be sufficiently uniform for interface determinations to be performed.

To provide self-consistency checks, and particularly to establish conditions (10) for determining accurately individual model parameters such as the density of the SiO_2 overlayer, the samples were etched after the initial measurements to obtain further data at several dif-

ferent oxide thicknesses. We used a 5% HF-95% H_2O solution (5), which was observed to etch the $\langle 100 \rangle$, $\langle 110 \rangle$, and $\langle 111 \rangle$ sample oxides at 190, 120, and 200 Å/min, respectively. The $\langle 110 \rangle$ oxide also exhibited a different density than the $\langle 100 \rangle$ and $\langle 111 \rangle$ oxides, as is discussed below.

Data Processing

Determination of sample parameters.—Our general data reduction procedure has been discussed elsewhere (11). Briefly, we measure the complex reflectance ratio (optical impedance) of a composite sample from 1.5–5.8 eV and then compare these data objectively to model spectra calculated for a given hypothetical configuration by using standard equations (12) and linear regression analysis (13). The specific configuration studied here consists of a c-Si substrate, a possible interface, an oxide overlayer, and the air ambient. These constituents can be described by means of dielectric functions, thicknesses, possible void fractions and birefringence in the oxide, etc.

Because a single-wavelength ellipsometric measurement provides only two constraints, the parameters of the composite system are hopelessly underdetermined unless further conditions can be established. We generate the necessary constraints by making spectroscopic measurements and by including spectrally dependent and independently measurable data, such as the dielectric response of c-Si and SiO_2 , as known quantities. This leaves only a few spectrally independent parameters such as oxide thickness to be determined by comparing model spectra to measured spectra. Thus a given model becomes highly overdetermined, and its validity can be judged readily by how well it fits the entire spectrum, not just at a single wavelength. Linear regression analysis (13) provides an objective and systematic way of minimizing the differences between the data and spectra computed for specific models and expressing the result in terms of best-fit model parameters and the

unbiased estimator, $\hat{\sigma}$, of the mean square deviation, δ . We have shown previously (11) that linear regression analysis can be applied in this context not only as a systematic means of providing best-fit parameters, but also as a means of establishing correlations and confidence levels to show which parameters are well determined by the data and consequently should be emphasized and which parameters cannot be well determined by the data and consequently should be ignored.

Dielectric function data of constituents.—*c-Si substrate.*—No previously published c-Si dielectric function data exist that are sufficiently accurate and/or cover a sufficiently wide energy range to determine interface parameters. The best available low energy data are those of Hulthén (14), determined below 3 eV by transmission measurements. The best wide-range data are those of Philipp (15), determined by Kramers-Kronig analysis of complex reflectance measurements, from 0–27 eV, with subsequent correction for the effect of oxide overlayers. The Hulthén data are probably sufficiently accurate but do not cover an adequate spectral range. The Philipp data are probably accurate with respect to general amplitude values but are not available over a sufficiently fine grid and consequently show substantial shifts of threshold energies for interband transitions.

Accordingly, a c-Si spectrum was generated by accurately measuring the pseudodielectric function of a piece of the oxidized $\langle 110 \rangle$ sample that had been stripped in HF. Although the traditional approach is to correct these data by mathematically removing an overlayer of SiO_2 , consistent interface results could be achieved only by mathematically removing the self-consistent 6 Å overlayer of chemically mixed $\sim Si_{0.75}(SiO_2)_{0.25}$ that was determined by the interface analysis itself. This is in qualitative agreement with the results of Philipp (15), who noted previously that

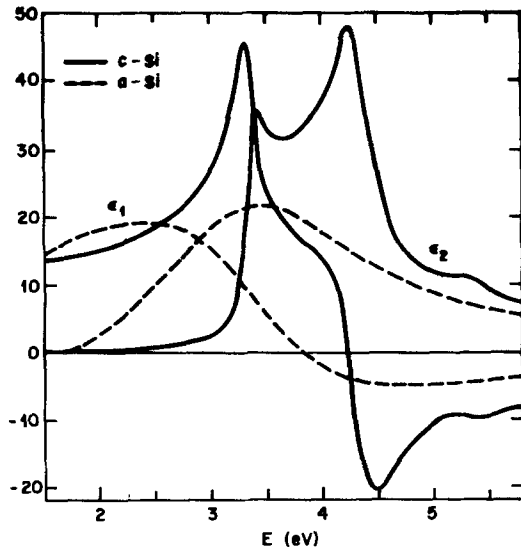


Fig. 1. Dielectric functions of c-Si and a-Si

the presence of an SiO_2 overlayer on stripped c-Si would lead to reflectance structure near 10 eV that is not observed.

Our resulting spectra are shown in Fig. 1. The ϵ_1 spectrum below the direct gap agrees with that of Hulthén (14) to within 1½% and with that of Philipp (15) to within ½%. The maximum value of ϵ_2 , 47.87, is slightly less than Philipp's value, 48.25, in agreement with discrepancies observed for Ge (16). Finally, the ϵ_2 values below the direct gap, which are exceptionally difficult to determine with an RAE, agreed with Hulthén values to within 3%. However, because the transmission data are more accurate, our ϵ_2 data were replaced with Hulthén's data below 2.5 eV. We thus believe these data to be the most accurate ever determined for c-Si over the visible-near u.v. quartz-optics range.

SiO_2 oxide.—The data base is the dispersion equation determined by Malitson (17) for fused silica. Taft (18) has shown that thermally grown oxides on c-Si differ at $\lambda 5461$ from the Malitson data in at least two significant respects. First, thermally grown oxides show birefringence. Second, the index values depend on the growth temperatures and slightly on crystal orientation (only $\langle 100 \rangle$ and $\langle 111 \rangle$ data were given). The birefringence was shown (18) to arise entirely from the compressive stress in the thermally grown oxide, which in turn derives almost entirely from the mismatch in thermal expansion coefficients (19). Less clear is the origin of the index differences, which below 1200°C growth temperatures suggest the presence of different SiO_2 polytypes (18) and thus may not be related entirely to density differences.

For simplicity, we suppose that refractive index differences between our oxides and Malitson's data arise from density differences, which can be described accurately in the Bruggeman effective medium approximation (20). But this implies an assumption about the nature of the SiO_2 dispersion which presently cannot be tested. However, such effects do not appear to be important as is discussed more fully later.

Birefringence in the SiO_2 overlayer is incorporated by supposing different threshold shifts, $+\Delta E$ and $-0.5\Delta E$, for p- and s-wave polarizations, respectively, in the two higher energy Sellmeyer oscillators in the Malitson expression. The value $\Delta E = +0.017$ eV was chosen to give $n_e - n_o = 0.0007$ at $\lambda 5461$ in agreement with the accurate measurements of Taft and Cordes (5). The effect on the complex reflectance ratio in model calculations was included by standard equations (12, 21).

Si-SiO₂ interface.—To determine the interface composition we require dielectric function spectra for the

complete range $\text{Si}_x(\text{SiO}_2)_{1-x} = \text{SiO}_{2-2x}$, $0 \lesssim x \lesssim 1$. Experimental spectra are not available, but suitable interpolations can be obtained as follows.

First, we recognize two possible types of mixtures: physical, where optically identifiable regions of a-Si and SiO_2 coexist as, e.g., microroughness or inclusions and host, on a scale small compared with the wavelength of light, and chemical, where the Si and O are mixed on an atomic scale. The former case is described by heterogeneous dielectric theory. We use the Bruggeman model together with data for a-Si that we obtained previously (22) and which are also shown in Fig. 1. The Malitson dispersion equation is used for SiO_2 .

Specifically, the Bruggeman approximation (20) gives the effective dielectric function, $\langle \epsilon \rangle$, of a heterogeneous material as

$$0 = f_a \frac{\epsilon_a - \langle \epsilon \rangle}{\epsilon_a + 2\langle \epsilon \rangle} + f_b \frac{\epsilon_b - \langle \epsilon \rangle}{\epsilon_b + 2\langle \epsilon \rangle} + f_v \frac{1 - \langle \epsilon \rangle}{1 + 2\langle \epsilon \rangle} \quad [1]$$

where f_x , ϵ_x , $x = a, b, v$ are the volume fractions and dielectric functions of the separate phases a, b, and v = void, respectively; $f_a + f_b + f_v = 1$. For the interface, we take $f_v = 0$. Because the volume associated with an SiO_2 molecule is 1.55 times larger than that associated with an Si atom in a-Si, the relation between atomic fraction x and the parameters of Eq. [1] are

$$\epsilon_a = \epsilon_{a\text{-Si}}; \quad f_a = x/[x + 1.55(1 - x)] \quad [2a]$$

$$\epsilon_b = \epsilon_{\text{SiO}_2}; \quad f_b = 1.55(1 - x)/[x + 1.55(1 - x)] \quad [2b]$$

Spectra calculated for x in increments of 0.125 are shown in Fig. 2.

Spectra for chemically mixed Si and O are calculated in a model that we developed previously for another application and which is completely described elsewhere (23). Results for x values in increments of 0.125 are also shown in Fig. 2. The physical and chemical models differ in that the peak value of ϵ_2 remains at 3.5 eV until a relatively large SiO_2 fraction is present in the former case, but immediately starts shifting to higher energies with increasing O content in the latter case. This is a result of the electronegativity difference between Si and O which moves the average oscillator strength to higher energies in the blended material. Also, boundary screening inhibits the dilution effect of O in physical mixtures, requiring more O to achieve a given reduction in the long-wavelength refractive index than for atomically mixed material. The qualitative difference can be seen immediately by comparing the spectra for the $x = 0.75$ physically mixed and $x = 0.875$

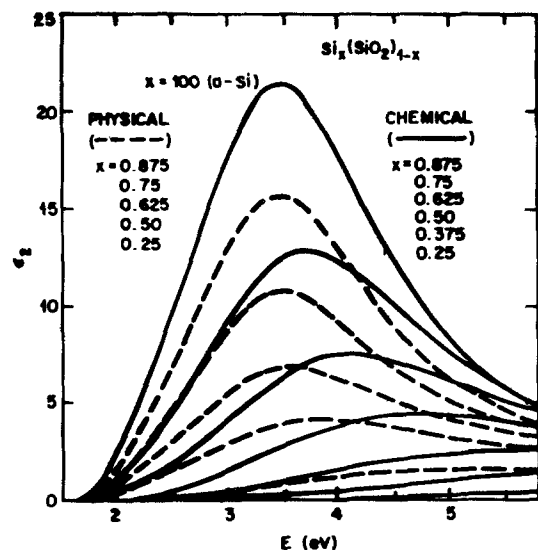


Fig. 2. Comparison of ϵ_2 spectra for physical and chemical mixtures of a-Si and SiO_2 for atomic fractions of a-Si in SiO_2 as indicated.

chemically mixed materials, which are essentially identical up to 3 eV and differ appreciably only in the u.v. Both cases have been observed: the former behavior describes spectra (24) of the composite material SIPOS, while the latter describes the atomically mixed material evaporated silicon monoxide (25).

We reemphasize that physical and chemical mixtures cannot be distinguished optically without determining the dielectric response in the near u.v. Thus the $n = 2.8$ value for the interface at $\lambda 5461$ obtained by Taft and Cordes (5) corresponds to either a physical mixture of $x = 0.65$ or a chemical mixture of $x = 0.73$. No further information can be obtained at a single wavelength.

Results

1-, 2-, and 3-parameter models.—Typical $\tan \psi$, $\cos \Delta$ data for an oxidized Si wafer of $\langle 100 \rangle$ orientation and oxide thickness 1360 Å are shown in Fig. 3. These data exhibit the characteristic interference pattern with increasing energy as the optical standing waves in the oxide pass through increasing periods. Interface sensitivity is maximized for the p- and s-wave components near minima and maxima, respectively, in $\tan \psi$ as minimum reflectance implies maximum energy density at the interface as previously discussed (11, 26).

The results of least squares fitting 1-, 2-, and 3-parameter models to these data are shown in Fig. 4. The fitting was done at 83 points equally spaced over the 1.5–5.8 eV interval to the real and imaginary parts of ρ calculated from $\tan \psi$ and $\cos \Delta$. Rather than compare spectra directly in terms of $\tan \psi$ and $\cos \Delta$, we show the differences because in every case these are small and would not be seen on the scale of Fig. 3.

Figure 4 shows that a one-parameter model consisting of an ideal c-Si substrate, no interface, and an ideal SiO₂ overlayer does not reproduce accurately the peak in $\tan \psi$. For this model the least squares procedure

yields $d_{ox} = 1368.6 \pm 0.4 \text{ \AA}$ and $\hat{\sigma} = 0.0567$. The uncertainty shown here, and those which follow, refer to 90% confidence limits based on the mismatch between model spectra and data and do not include possible systematic errors. By allowing the void volume density to vary, most of the $\tan \psi$ discrepancy near 2 eV disappears although the phase spectrum, $\cos \Delta$, and the higher $\tan \psi$ mismatch are not improved. The parameters obtained in this two-parameter model are $d_{ox} = 1363.6 \pm 0.3 \text{ \AA}$, void fraction $f_v = -0.0062 \pm 0.0004$, and $\hat{\sigma} = 0.0166$. Thus the fit as measured by $\hat{\sigma}$ is improved

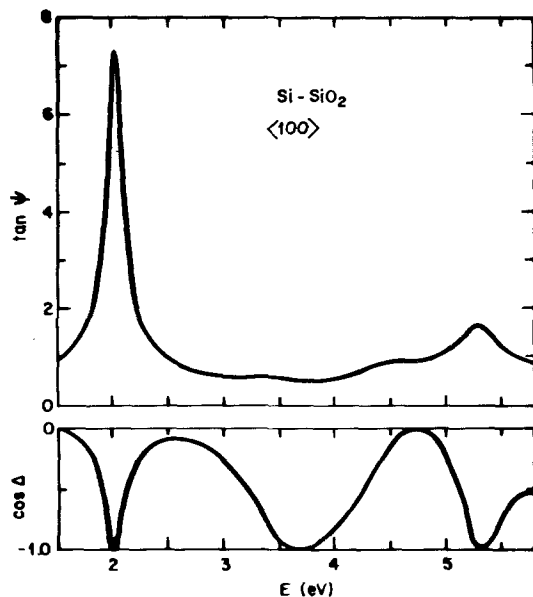


Fig. 3. Typical $\tan \psi$, $\cos \Delta$ data for an oxidized Si wafer. The orientation is $\langle 100 \rangle$ and the oxide thickness is 1360 Å.

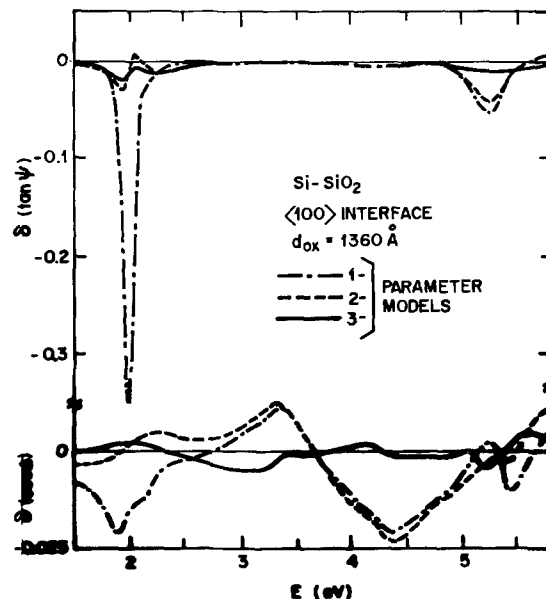


Fig. 4. Differences between theoretical and experimental $\tan \psi$ and $\cos \Delta$ spectra for 1-, 2-, and 3-parameter models of the $\langle 100 \rangle$ SiO₂ interface for an SiO₂ overlayer of approximately 1360 Å.

significantly, by more than a factor of 3. The negative void fraction simply means that the thermally grown oxide is effectively more dense than the fused-quartz reference, a result that has been well characterized for oxides on $\langle 100 \rangle$ and $\langle 111 \rangle$ wafers (18).

In terms of an equivalent refractive index at $\lambda 5461$, where $n_0 = 1.4602$ for fused quartz, the above void fraction corresponds to $n = 1.4631 \pm 0.0002$. This is less than the Taft value of 1.4678 obtained for $\langle 100 \rangle$ samples oxidized in dry O₂. Lower values obtain if traces of H₂O are present in the oxidizing atmosphere (18), whence the result is physically reasonable. Note that the thickness has decreased as n has increased to maintain the optical thickness, nd , essentially unchanged. The two-parameter model as used here includes birefringence, although its effect is relatively minor.

By incorporating an interface of chemically mixed Si_{0.75}(SiO₂)_{0.25}, the periodic discrepancy between data and model computations for $\cos \Delta$ and the remaining 5 eV discrepancy for $\tan \psi$ are both largely eliminated. Specifically, we find $d_{ox} = 1359.9 \pm 0.5 \text{ \AA}$, the interface thickness $d_{int} = 6.6 \pm 0.9 \text{ \AA}$, $f_v = -0.0065 \pm 0.0002$, and $\hat{\sigma} = 0.0098$ in this three-parameter model. Thus the presence of an interface improves the overall fit by nearly another factor of 2. The void fraction is essentially unchanged but d_{ox} has decreased by nearly 4 Å, showing that the oxide is trying to simulate the effect of the interface in the two-parameter model. The above improvement constitutes the existence proof for the interface.

Interface composition and thickness.—Having dielectric function spectra for the possible interface compositions, one can now use linear regression analysis in a 4-phase model with three free parameters (d_{int} , f_v , d_{ox}) to determine the "best" interface. Figure 5 shows the

variation of $\hat{\sigma}$ for three oxide thicknesses on the $\langle 100 \rangle$ sample for the full range of interface composition Si _{x} (SiO₂)_{1- x} from no interface ($x = 0$) to pure a-Si ($x = 1$) for both chemical and physical mixture models. Generally speaking, a consistent set of values of d_{ox} , d_{int} , and f_v was obtained near the residual minimum for each oxide thickness, although values away from the minimum showed wide variations as the least squares approach attempted to compensate the interface compositional error imposed by the model through various combinations of the three free parameters.

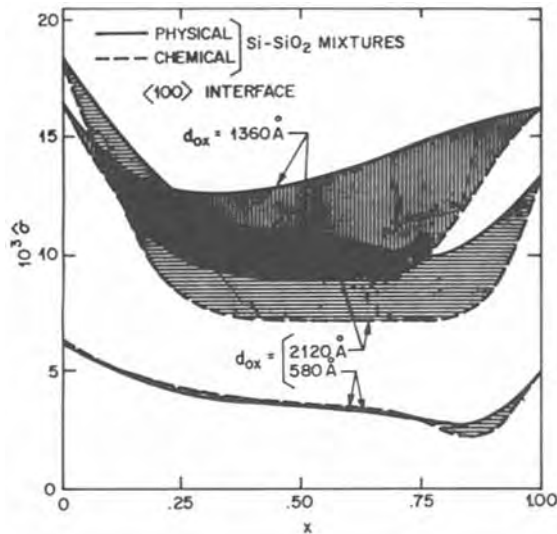


Fig. 5. Variation of 3-parameter 4-phase model residuals with interface composition for <100> Si-SiO₂ interface for SiO₂ overlayers of approximately 580, 1360, and 2120 Å. Limits corresponding to physical and chemical mixtures are shown.

Conclusions immediately obvious from Fig. 5 are as follows. First, an interface is present, in agreement with previous work (1-7). $\hat{\sigma}$ always decreased for a finite interface, regardless of oxide thickness or assumed interface composition. Second, a chemically mixed Si-O interface gives better results than a physical mixture of Si and SiO₂. For the orientation shown, the difference is greatest for the thicker oxides although this is not generally true. Third, the statistically favored interface composition range is approximately $0.3 < x < 0.8$ based on Fig. 5.

The relatively broad compositional range allowed by Fig. 5 can be narrowed significantly by requiring consistency of the free parameters determined by the individual least squares fits on samples that differ only by etching the oxide to new thicknesses. In this context d_{ox} is clearly a meaningless parameter. However, f_v is the key to the analysis because its value is determined at $d_{ox} \sim 1400 \text{ \AA}$ with an order-of-magnitude less sensitivity to interface properties than at other thicknesses, owing to a particular favorable combination of parameters and measurement conditions (10). This occurs because of exceptionally good impedance-matching characteristics for s-wave polarization near 2 eV for the given combination of materials and measurement conditions, which for the small interface thicknesses used here depends almost entirely on the refractive index of the oxide overlayer. The independence on interface composition can be understood immediately by noting that at 2 eV all mixtures are transparent, as shown in Fig. 2.

If one requires that the values of f_v determined for overlayer thicknesses near 1400 Å must also apply at other thicknesses, the results shown in Table I are obtained. Here, df_v/dx is calculated from least fit spectra for $x = 0.625, 0.75,$ and 0.875 , and the interpolated values of x obtained by requiring all f_v values to be equal to that at $d_{ox} \sim 1400 \text{ \AA}$, for which $df_v/dx \cong 0$, are also shown. Uncertainties in x are calculated from equivalent uncertainties in f_v . The values of d_{int} are then obtained by interpolation from solutions for $x = 0.625, 0.75,$ and 0.875 .

The results of the analysis are shown in Table I and plotted in Fig. 6 and 7. We repeat that the error bars shown derive from 90% confidence levels based on the fits of specific models to the data, and do not include systematic errors. Nevertheless, all data are consistent with an interface $7 \pm 2 \text{ \AA}$ wide composed of a chemical (atomic) mixture of Si and O of average stoichiometry

Table I. Interface compositions determined by requiring consistency in f_v among all data for a given sample. Due to insensitivity to interface parameters, the value of f_v for $d_{ox} \approx 1400 \text{ \AA}$ is chosen as reference unless otherwise noted by parentheses (see text).

Sample	d_{ox} (Å)	df_v/dx	f_v	x	d_{int} (Å)		
<100>	2120	-0.028	-0.0065 ± 0.0002	0.78 ± 0.06	8.3 ± 1.0		
	1360	-0.003				(0.75)	6.6 ± 0.9
	584	-0.016				0.81 ± 0.03	5.4 ± 0.9
<111>	2282	-0.028	-0.0059 ± 0.0008	0.83 ± 0.08	7.7 ± 1.4		
	1445	-0.002				(0.75)	6.0 ± 3.7
	659	-0.023				0.83 ± 0.06	6.0 ± 1.1
<110>	2805	-0.034	$+0.0065 \pm 0.0005$	0.74 ± 0.06	8.3 ± 1.5		
	2318	-0.037				(0.75)	9.6 ± 1.5
	2142	-0.031				0.82 ± 0.05	8.8 ± 1.1
	1407	0.000				(0.75)	4.7 ± 2.1
	604	-0.014				0.91 ± 0.09	6.3 ± 3.4

$\text{Si}_{0.8 \pm 0.1}(\text{SiO}_2)_{0.2 \pm 0.1} \cong \text{SiO}_{0.4 \pm 0.2}$. The three points corresponding to $d_{ox} \sim 1400 \text{ \AA}$ are shown without error bars in Fig. 7 because they cannot be determined from f_v and the residual minimum (see Fig. 4) is too broad to yield a definitive result. All three actually have a weak residual minimum near $x = 0.6$, but this value is not consistent with the well-defined values obtained at other oxide thicknesses. In deference to this tendency we have shaded the average x value slightly to lower values for these points. A second <110> point also failed to provide an f_v value consistent with the re-

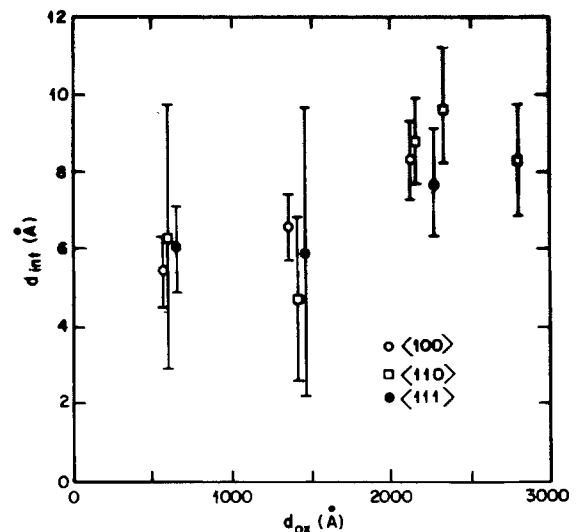


Fig. 6. Calculated interface thicknesses for <100>, <110>, and <111> samples after initial growth and at various stages of etching, from Table I.

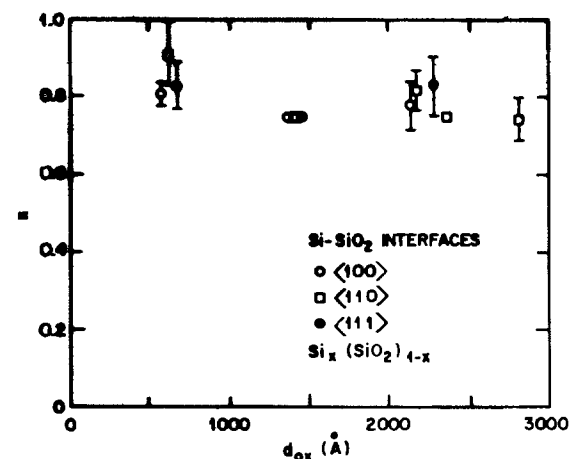


Fig. 7. Calculated interface composition x in chemically mixed $\text{Si}_x(\text{SiO}_2)_{1-x}$ after initial growth and at various stages of etching, from Table I.

maining data. Its contribution was defined similarly and its datum also shown in Fig. 7 without error limits.

The values of interface width determined here agree with that given in our initial report (11), which discussed data obtained on a single sample at a single value of oxide thickness. The uncertainty in the previously determined stoichiometry, SiO, could not be established from the single-thickness data and should be considered as superceded by the present results. All work, however, supports the conclusion that the interface Si and O are atomically mixed.

Discussion

Systematic errors.—If the data and analysis were exact and totally self-consistent, the interface parameters would be invariant with respect to oxide thickness and the residuals would reach negligibly small values. It is clear that this ideal has been approached but not completely reached; while the compositional data of Fig. 7 are reasonably constant, the results given in Fig. 6 show a trend of decreasing interface thickness as the oxide overlayer is gradually removed by etching. Because the interface is protected and cannot be affected by etching, this suggests that a small systematic error may be present.

The most probable sources of systematic errors are instrumental accuracy, nonuniformity (either in thickness or composition) of the oxide overlayer both in the as-grown and etched conditions, the ϵ spectrum for c-Si, or the ϵ spectrum for SiO₂. In self-consistent tests we have shown that the instrument accuracy approaches null ellipsometer accuracy as discussed in the Experimental section. Taft and Cordes have discussed the oxide uniformity problem at length and have concluded that the overlayer is uniform to the extent needed to analyze the interface problem (5). Moreover, their data show clearly that the etching procedure used there (and followed here) yields consistent results for 200Å increments from 7000Å to zero.

We next consider the ϵ data bases. With respect to that of c-Si, the effect of removing mathematically compositions and thicknesses from the stripped <110> sample data other than the self-consistent 6Å of chemically mixed \sim Si_{0.75}(SiO₂)_{0.25} has been examined. No difference results if physically mixed spectra are used in place of chemically mixed spectra. Decreasing the removed thickness causes a general shift of all interface widths to lower values but does not affect either the trend or the conclusion that a chemically mixed interface is preferable to a physically mixed interface. Thus in principle the width data are subject to a general systematic uncertainty of no more than 2Å depending on possible future improvements of the ϵ data for c-Si. But we do not feel the possibility likely because of the agreement of the ϵ data with the Hulthén and Philipp work as discussed in the section on Data Processing, and the fact that our interface results agree at λ 5461 with those of Taft and Cordes.

We are left with the SiO₂ ϵ data. Taft has shown that the n values at λ 5461 cannot be described below 1200°C as a simple compression of fused quartz and has suggested that other polymorphs of SiO₂ may be present in the oxide (17). Because these polymorphs should have different absorption thresholds and/or oscillator strengths, this implies that the Malitson dispersion equation will have only approximate validity: the dispersion in ϵ_1 at higher energies for thermally grown oxides may well deviate from the Malitson values. In principle, if sufficiently thick oxides can be grown this hypothesis can be checked directly with spectroscopic ellipsometry by reducing the data for the oxide ϵ_1 values assuming the presence of a known substrate and interface. If the oxide thickness approaches 1 micron, one could expect that the spectra are dominated by the oxide and that substrate and interface discrepancies would be minor.

A better SiO₂ representation was attempted by reducing the 2120Å <100> oxide data within the three-phase model and fitting the resultant spectrum to a three-term Sellmeyer oscillator with energies at the Malitson values and using the amplitudes as free parameters. The smoothly varying Sellmeyer terms average over the interference oscillations arising from the interface and extract the background, which is the intrinsic response of SiO₂. The results showed amplitudes of 12.73 ± 0.35 , 4.36 ± 0.18 , and 0.17 ± 0.10 eV for the oscillators at 18.2, 10.67, and 0.125 eV, respectively, compared to the Malitson values 12.617, 4.351, and 0.112 eV. The differences are not statistically significant, although the trend indicates a shift of the oxide absorption edges to lower energy. But the revised values changed interface thickness values by less than a few percent and did not affect the systematics of the results. Therefore, oxide effects alone appear to be ruled out.

Thus systematic errors cannot be traced to individual sources but rather may be an accumulation of effects from several sources. A further assignment of their origin would require more accuracy than presently attainable.

Microscopic structure of the interface.—The unusual effective average composition SiO_{0.4±0.2} suggests that the layer whose effective thickness is 7 ± 2 Å is actually graded in composition (6, 7), though laterally uniform. The connection between effective average and actual position-dependent dielectric functions, where the spatial variation is restricted to one dimension, has been considered in many contexts and most recently by Plieth and Naegele (27). In short, the spatial dependence can be replaced by a spatial average if the region is sufficiently thin, as is the case here. Specifically, for a thin layer on a uniform substrate (three-phase model) the change in the complex reflectance ratio is given by

$$\rho = \rho_0 \left\{ 1 + \frac{4\pi i n_a d \cos \phi}{\lambda} \frac{\epsilon_s(\epsilon_s - \epsilon_0)(\epsilon_0 - \epsilon_a) \sin^2 \phi}{\epsilon_0(\epsilon_s - \epsilon_a)[\epsilon_s \cos^2 \phi - \epsilon_a \sin^2 \phi]} \right. \\ \left. \times \left[1 - \frac{\epsilon_a \epsilon_0 \epsilon_s}{(\epsilon_s - \epsilon_0)(\epsilon_0 - \epsilon_a)} \delta \epsilon \right] \right\} \quad [3]$$

where ϵ_s and $\epsilon_a = n_a^2$ are the dielectric functions of the uniform substrate and ambient, respectively, and

$$\epsilon_0 = \frac{1}{d} \int_{-d}^0 dz \epsilon(z) \quad [4a]$$

$$\delta \epsilon_0 = \frac{1}{d} \int_{-d}^0 dz [\epsilon^{-1}(z) - \epsilon_0^{-1}] \quad [4b]$$

It is supposed that the nonuniform response extends only over $-d < z < 0$.

The term involving $\delta \epsilon_0$ is a correction that does not appear in the classical three-phase model, that is, if the dielectric response of the interface is spatially invariant. If the interface is graded, it arises because the functional dependence on $\epsilon(x)$ of the wave equation for p-polarization is different from that for the s-polarization, leading to a different weighting in the spatial average (27). We express it as in Eq. [3] to estimate more easily its relative effect. Using the data of Fig. 1 and 2, it is straightforward to show that its magnitude is of the order of 0.2 for an assumed linear variation in dielectric response. Since we are concerned only with estimating possible limits to the variation, this is small enough to be neglected and the effective dielectric response obtained in the previous section can be taken to be the simple spatial average of the actual variation.

We consider next the probable location of the interface as determined by optical measurements. The interface is operationally defined as that region whose optical response is measurably different from that of the c-Si substrate and the SiO₂ overlayer. Considering the c-Si side first, the atoms in the outermost c-Si plane

have neither lattice nor lateral symmetry because they are bonded on one side to the adjacent disordered region. Moreover, at least some of those atoms will be involved in oxygen bonding to the disordered region even though the total oxygen concentration there may be small. Their dielectric response should therefore be more like a-Si than c-Si. Thus optical measurements would view the interface as containing the outermost c-Si plane. On the SiO₂ side, the optical interface would terminate before full stoichiometry is reached because, by Fig. 2, it is not possible to distinguish between SiO_{1.5} and SiO₂ in the 1.5–6.0 eV region with presently attainable accuracy. We should not expect to distinguish from SiO₂ a possible slightly perturbed ~40Å SiO₂ region as suggested by XPS measurements (6). As mentioned earlier, the preference for chemical, rather than physical, mixing rules out microroughness and the possibility of small Si inclusions near the interface resulting from nonuniform oxidation.

From the spatial average argument, Fig. 2, and the results of the preceding section, it is apparent that no more than one-third (~2Å) of the interface could appear as a-Si if the remainder were at least as oxygen-rich as SiO. We can reject the case of a-Si followed by stoichiometric SiO₂ because the optical data would have shown a narrower interface, and in any event a-Si is not the favored stoichiometry. Thus the accumulation of a-Si at the interface does not occur. Because the outermost ~c-Si plane is fulfilling optically the function of an a-Si layer, we are left with a region that is effectively about 5Å of SiO, in agreement with one of the RBS alternatives. Although the interface is undoubtedly graded, the width is small enough for the spatial-average limit to be valid whence the optical data can provide no further information on its distribution.

We note finally that the average refractive index of the $7 \pm 2\text{Å}$ region of SiO_{0.4±0.2} at $\lambda 5461$ is 3.2 ± 0.5 , as compared to the Taft-Cordes $\lambda 5461$ value of ~2.8 determined for their ~6Å interface. Thus the fixed-wavelength null ellipsometric and spectroscopic ellipsometric results are in agreement at the wavelength at which they overlap.

Acknowledgments

We thank E. Povilonis for kindly growing the oxide films used here. One of us (D.E.A.) wishes to thank H. R. Philipp for supplying a numerical listing of the c-Si ϵ data reported in Ref. (15).

Manuscript submitted Sept. 10, 1979; revised manuscript received Dec. 21, 1979.

Any discussion of this paper will appear in a Discussion Section to be published in the December 1980 JOURNAL. All discussions for the December 1980 Discussion Section should be submitted by Aug. 1, 1980.

Publication costs of this article were assisted by Bell Laboratories.

REFERENCES

1. See, for instance, "Physics of SiO₂ and Its Interfaces," S. T. Pantelides, Editor, Pergamon Press,

2. J. F. Wager and C. W. Wilmsen, *J. Appl. Phys.*, **50**, 874 (1979).
3. O. L. Krivanek, D. C. Tsui, T. T. Sheng, and A. Kamgar, in "Physics of SiO₂ and Its Interfaces," S. T. Pantelides, Editor, p. 356, Pergamon Press, New York (1978).
4. L. C. Feldman, P. J. Silverman, J. S. Williams, T. E. Jackman, and I. Stensgaard, *Phys. Rev. Lett.*, **41**, 1396 (1978); L. C. Feldman, I. Stensgaard, P. J. Silverman, and T. E. Jackman, in "Physics of SiO₂ and Its Interfaces," S. T. Pantelides, Editor, p. 344, Pergamon Press, New York (1978).
5. E. Taft and L. Cordes, *This Journal*, **126**, 131 (1979).
6. F. J. Grunthaler and J. Maserjian, in "Physics of SiO₂ and Its Interfaces," S. T. Pantelides, Editor, p. 389, Pergamon Press, New York (1978).
7. S. I. Raider and R. Flitsch, in *ibid.*, p. 384.
8. D. E. Aspnes and A. A. Studna, *Appl. Opt.*, **14**, 220 (1975); in "Optical Polarimetry-Instrumentation and Applications," Vol. 112, R. M. A. Azzam and D. L. Coffeen, Editors, p. 62, SPIE, Bellingham, Wash. (1977); *Rev. Sci. Instrum.*, **49**, 291 (1978).
9. D. E. Aspnes, *J. Opt. Soc. Am.*, **64**, 812 (1974).
10. J. B. Theeten and D. E. Aspnes, *Thin Solid Films*, **60**, 183 (1979).
11. D. E. Aspnes, J. B. Theeten, and R. P. H. Chang, *J. Vac. Sci. Technol.*, **16**, 1374 (1979).
12. R. M. A. Azzam and N. M. Bashara, "Ellipsometry and Polarized Light," chap. 4, North Holland, Amsterdam (1977); D. E. Aspnes, in "Optical Properties of Solids: New Developments," B. O. Seraphin, Editor, p. 799, North-Holland, Amsterdam (1976).
13. E. S. Keeping, "Introduction to Statistical Inference," chap. 12, Van Nostrand, Princeton, N.J. (1962).
14. R. Hulthén, *Phys. Scr.*, **12**, 342 (1975).
15. H. R. Philipp, *J. Appl. Phys.*, **43**, 2835 (1972).
16. D. E. Aspnes and A. A. Studna, in 1979 Ellipsometry Conference Proceedings, *Surf. Sci.*, In press.
17. I. H. Malitson, *J. Opt. Soc. Am.*, **55**, 1205 (1965). The dispersion equation actually used in these computations is that given in "American Institute of Physics Handbook," third edition, D. E. Gray, Editor, pp. 6-29, McGraw-Hill Book Co., New York (1973).
18. E. A. Taft, *This Journal*, **125**, 968 (1978).
19. R. J. Jaccodine and W. A. Schlegel, *J. Appl. Phys.*, **37**, 2429 (1966).
20. D. A. G. Bruggeman, *Ann. Physik (Leipzig)*, **24**, 636 (1935).
21. D. den Engelsen, *J. Opt. Soc. Am.*, **61**, 1460 (1971).
22. D. E. Aspnes, J. B. Theeten, and F. Hottier, *Phys. Rev.*, **820**, 3292 (1979).
23. D. E. Aspnes and J. B. Theeten, *J. Appl. Phys.*, **50**, 4928 (1979).
24. D. E. Aspnes, W. R. Knolle, and H. R. Maxwell, Jr., Unpublished.
25. H. R. Philipp, *J. Phys. Chem. Solids*, **32**, 1935 (1971).
26. J. B. Theeten, D. E. Aspnes, and R. P. H. Chang, *J. Appl. Phys.*, **49**, 6097 (1978).
27. W. J. Plieth and K. Naegle, *Surf. Sci.*, **64**, 484 (1977).

GaAs Oxidation and the Ga-As-O Equilibrium Phase Diagram

C. D. Thurmond,* G. P. Schwartz,* G. W. Kammlott, and B. Schwartz*

Bell Laboratories, Murray Hill, New Jersey 07974

ABSTRACT

The phases formed from the oxidation of GaAs have been considered in the light of an estimated equilibrium Ga-As-O condensed phase diagram. Thermal oxidation leads to phases consistent with the phase diagram. Plasma oxidation and anodic oxidation lead to phases inconsistent with the phase diagram. Thermal annealing of the plasma and anodic oxide layers leads to reactions producing phases consistent with the phase diagram. It is concluded that plasma and anodic oxides are produced far from equilibrium and that the estimated phase diagram is a satisfactory approximation to the equilibrium ternary phase diagram.

The gallium-arsenic-oxygen equilibrium phase diagram is not known. We have been able to estimate an important portion of it from a combination of experiments and thermodynamics. Condensed phase equilibria below the melting point of As_2O_3 (278°C) have been considered. The stable phases occurring in this temperature region are assumed to be Ga(l, s), GaAs(s), As(s), As_2O_3 (s), As_2O_5 (s), GaAsO_4 (s), and Ga_2O_3 (s) based on an evaluation of available literature information (1).¹

Two different approaches have been taken to obtain an estimate of the low temperature condensed phase ternary diagram. Both rest on the key assumption that all equilibria are between nearly pure phases. This implies that the solubility ranges of each of the eight phases are sufficiently narrow to assure they are pure phases insofar as their thermodynamic properties are concerned. In particular, it follows that the Gibbs energy of formation of each phase is that of the pure phase to an acceptable degree of approximation. An additional consequence of this assumption is that all ternary equilibria are pseudobinary.

The first approach is based on the fact that there are 13 possible phase diagrams under the pure phase assumption. Only a few experiments are needed to obtain a reasonable approximation to the equilibrium phase diagram.

The second approach makes use of the Gibbs energy of formation of each compound phase to calculate the equilibrium phase diagram. The Gibbs energy of formation of GaAsO_4 and As_2O_5 , however, are not known. Nevertheless an important section of the phase diagram obtained from the first approach can be tested without this information.

Experimental and Results

At a chosen temperature below the melting point of As_2O_3 , seven phases will make up the Ga-As-O condensed phase diagram. Various crystalline modifications of both Ga_2O_3 and As_2O_3 are known as well as a vitreous phase for As_2O_3 . Cubic As_2O_3 (arsenolite) and β - Ga_2O_3 were selected because thermodynamic data for the other structural modifications were either not available or the differences in their Gibbs energies of formation were sufficiently small (a few kilocalories per mole) to enable only one phase to be considered. The assumption is made that at equilibrium these

condensed phases are essentially pure in all reactions with other phases. This means that the ternary diagram will be made up of straight lines connecting one phase to another. The lines are called pseudobinary lines and the proposed ternary diagram will consist entirely of such lines.

We will take advantage of the fact that there are only 13 possible ternary phase diagrams that can occur from seven phases each of which is nearly pure. One of the 13 ternary phase diagrams will be the equilibrium phase diagram, and an estimate can be made of which it is from the results of several experiments. The 13 possible ternary diagrams are shown in Fig. 1 and have been found by inspection.

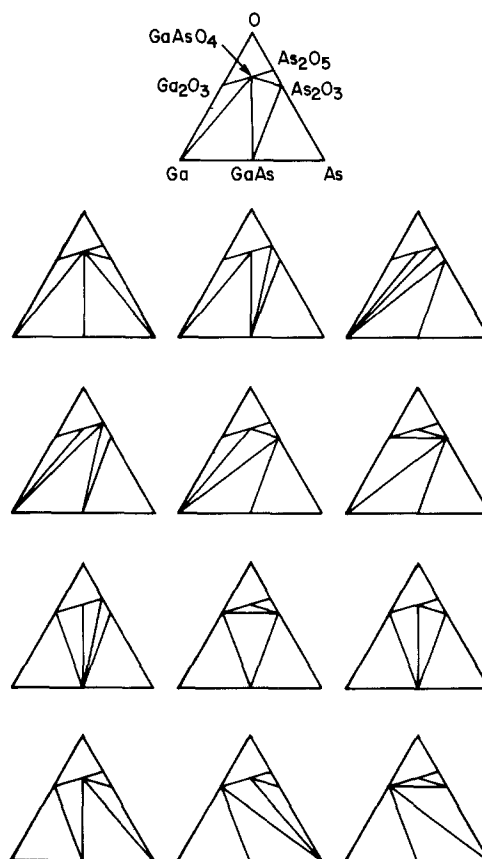


Fig. 1. The 13 ternary phase diagrams possible for the seven phases (Ga(s, l), GaAs(s), As(s), As_2O_3 (s), As_2O_5 (s), GaAsO_4 (s), and Ga_2O_3 (s)). All phases are assumed to be pure.

* Electrochemical Society Active Member.

Key words: thermal oxidation, plasma oxidation, ternary phase diagram.

¹ Although Ga_2O is a well-documented gas phase species, there is as yet no conclusive structure data to substantiate the assignments of Brukl and Ortnner and Klemm and Von Vogel (1) that the brown-black powder which results from the reaction between Ga_2O_3 and Ga actually constitutes single phase stoichiometric Ga_2O .

Experiments with binary mixtures.—The first experiment was to anneal a mixture of powdered GaAs and As_2O_3 in an evacuated (5×10^{-7} Torr) quartz tube for 48 hr at 630°C . The molar ratio of GaAs to As_2O_3 was 3 to 1. X-ray diffraction identified the resulting products as crystalline As (hexagonal, A7 structure), $\beta\text{-Ga}_2\text{O}_3$ and unreacted GaAs which was initially present in excess. The absence of As_2O_3 in the recovered products was taken to indicate that the reaction had proceeded to completion. The experiment was repeated with the same results.

The kinetics of the reaction were sufficiently slow that incomplete reaction occurred in 48 hr for temperatures of $\sim 500^\circ\text{C}$. Although 630°C is above the melting point of As_2O_3 , it is still below the temperature at which GaAs ceases to evaporate congruently, i.e., direct thermal decomposition of GaAs is not involved in generating arsenic. In addition, no evidence for metallic Ga is obtained after reaction. The only significant modification expected in the ternary phase diagram for some temperature range above the melting point of As_2O_3 (278°C) is the dissolution of other solid phases in the As_2O_3 -rich liquid. We assume that the amount of dissolution of the other phases in liquid As_2O_3 is small and consequently the higher temperature anneals we have used give the phases that are stable at the lower temperatures. The fact that the reactions involved are for condensed phases implies that the heat capacities for the reactions will be small and therefore the Gibbs energies of the reactions will not depend much on temperature. We conclude from the results of the first experiment that As and Ga_2O_3 are the phases in equilibrium with GaAs. There are only two of the 13 possible diagrams that have this feature, the last two diagrams of Fig. 1.

A second experiment was carried out to distinguish between the two remaining phase diagrams. Thermal reaction of a 1:1 molar mixture of GaAs- As_2O_3 should produce GaAsO_4 according to one diagram; the other predicts Ga_2O_3 and As. Table I shows that As (hexagonal), $\beta\text{-Ga}_2\text{O}_3$, and vitreous As_2O_3 were detected. For the molar ratio utilized (1:1), the latter product represents excess unreacted As_2O_3 . Raman scattering was used to identify this vitreous phase. GaAsO_4 was not observed by either x-ray diffraction or Raman scattering. In addition, the absence of GaAs indicated that the reaction had gone to completion. Figure 2 thus emerges as the phase diagram suggested by these experiments.

An additional experiment was used to check the conditions predicted by the derived phase diagram to give GaAsO_4 . A mixture of As_2O_5 and GaAs in the mole ratio 2 to 1 was heated to 600°C for 48 hr. Raman scattering showed that the products were GaAsO_4 and vitreous As_2O_3 . These are just the products anticipated from the phase diagram according to the reaction $2\text{As}_2\text{O}_5 + \text{GaAs} \rightarrow \text{GaAsO}_4 + 2\text{As}_2\text{O}_3$.

Thermodynamic calculations.—A check on the phase diagram of Fig. 2 can be made if the Gibbs energies of formation of the compound phases, GaAs, As_2O_3 ,

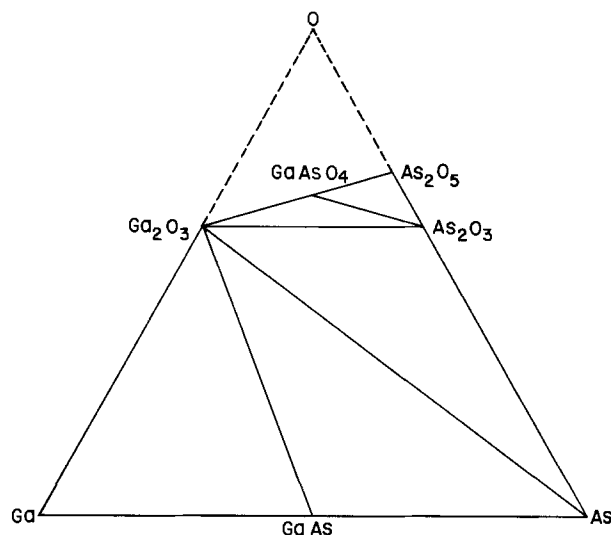


Fig. 2. An estimate of the Ga-As-O ternary condensed phase diagram for temperatures below the melting point of As_2O_3 (278°C, arsenolite). A portion of this phase diagram, the oxygen-rich region above the line $\text{Ga}_2\text{O}_3\text{-GaAsO}_4\text{-As}_2\text{O}_5$ and bounded at the sides by the dashed lines, has not been studied and is an excluded part of the Ga-As-O ternary diagram.

As_2O_5 , GaAsO_4 , and Ga_2O_3 , were known. In fact, the Gibbs energy of formation is not known for GaAsO_4 and is not very certain for As_2O_5 . The derived phase diagram Fig. 2 shows, however, that the portion of the diagram below the $\text{Ga}_2\text{O}_3\text{-As}_2\text{O}_3$ pseudobinary line does not involve the GaAsO_4 and As_2O_5 phases. Therefore, it is possible to calculate that portion of the phase diagram from the thermodynamic information available for GaAs, As_2O_3 , and Ga_2O_3 .

The total number of pseudobinary lines possible for the lower portion of the phase diagram of Fig. 2 is five and they are shown in Fig. 3. The equilibrium pseudobinaries can be found in a simple way from the three points where pseudobinaries cross. Such crosspoints have been used for many years to guide experiments in the determination of phase diagrams (2). They can also be used to obtain the stable pseudobinary of the crossing pair from the Gibbs energies of formation of GaAs, As_2O_3 , and Ga_2O_3 .

The composition of a crosspoint can be expressed in terms of the components of either of the pseudobinaries. This is equivalent to writing a stoichiometric equation giving the transformation of one set of compounds into the other. The conservation of atoms corresponds to the crosspoint composition. The three equations representing the three crosspoints of Fig. 3 are given in Table II. The stable pseudobinary may now be obtained by calculating the standard Gibbs energy for each of these equations from the Gibbs energies of formation of the compound phases. For the first crosspoint equation of Table II, the standard Gibbs energy is given by

Table I. Pseudobinary reactions

Pseudobinary	Composition (mole ratio)	Temperature ($^\circ\text{C}$)	Time (days)	Products	Detection method*	Comments
1. $\text{As}_2\text{O}_3\text{-GaAs}$	1:3	652	2	Arsenic Ga_2O_3 GaAs	XRD XRD, XRF XRD	As_2O_3 not detected
2. $\text{As}_2\text{O}_3\text{-GaAs}$	1:1	630-650	2	Arsenic Ga_2O_3 As_2O_3	XRD XRD Raman	GaAsO_4 not detected GaAsO_4 not detected
3. $\text{As}_2\text{O}_3\text{-GaAs}$	2:1	630-650	2	Arsenic Ga_2O_3 As_2O_3	XRD XRD Raman	GaAsO_4 not detected GaAsO_4 not detected
4. $\text{As}_2\text{O}_3\text{-GaAs}$	2:1	630-650	2	GaAsO_4 As_2O_3	Raman Raman	Ga_2O_3 not detected

* XRD = x-ray diffraction, XRF = x-ray fluorescence.

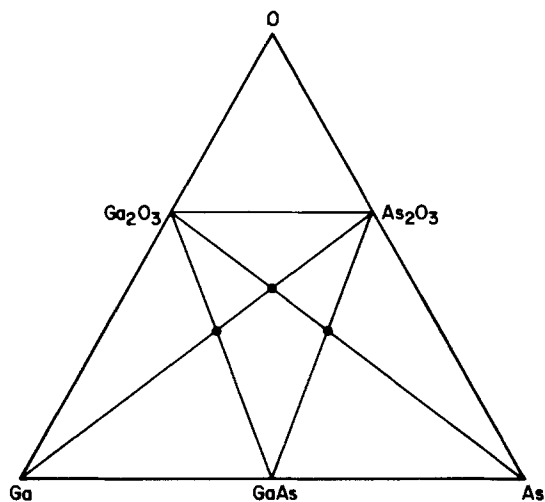


Fig. 3. The three crosspoints below the $\text{Ga}_2\text{O}_3\text{-As}_2\text{O}_3$ pseudobinary generated by the four pseudobinaries $\text{Ga-As}_2\text{O}_3$, $\text{GaAs-Ga}_2\text{O}_3$, $\text{GaAs-As}_2\text{O}_3$, and $\text{As-Ga}_2\text{O}_3$.

$$\Delta G^\circ = 2\Delta G^f(\text{GaAs}) + \Delta G^f(\text{Ga}_2\text{O}_3) - \Delta G^f(\text{As}_2\text{O}_3)$$

If ΔG° is greater than zero the reaction will not proceed and the $\text{Ga-As}_2\text{O}_3$ pseudobinary would be more stable than the $\text{GaAs-Ga}_2\text{O}_3$ pseudobinary. In fact, as shown in Table II, ΔG° is less than zero and consequently $\text{GaAs-Ga}_2\text{O}_3$ is the stable pair. A similar procedure was used for the other two crosspoint equations. The standard Gibbs energies have been calculated for the two temperatures 300° and 500°K. The Gibbs energies of formation used are given in Table III with the reference states indicated. The conclusion is reached that the stable pseudobinaries are $\text{Ga}_2\text{O}_3\text{-GaAs}$ and $\text{Ga}_2\text{O}_3\text{-As}$. These are the two shown in Fig. 2 previously deduced from experiment.

Finally it is important to note that the two independent estimates of the diagram employing binary mixture experiments run at $T \approx 630^\circ\text{-}650^\circ\text{C}$ and thermodynamic calculations applicable to the condensed phase ($T < 278^\circ\text{C}$) diagram were observed to yield equivalent results in all phase fields which

Table II. Standard Gibbs energies for crosspoint reactions

Crosspoint reactions	$\Delta G^\circ/\text{kcal}$	
	300°K	500°K
1. $4\text{Ga} + \text{As}_2\text{O}_3 = 2\text{GaAs} + \text{Ga}_2\text{O}_3$	-142	-134
2. $2\text{Ga} + \text{As}_2\text{O}_3 = 2\text{As} + \text{Ga}_2\text{O}_3$	-102	-98
3. $2\text{GaAs} + \text{As}_2\text{O}_3 = 4\text{As} + \text{Ga}_2\text{O}_3$	-62	-62

Table III. Gibbs energies of formation

Formation reaction	T/°K	$\Delta G^f/\text{kcal}$
$\text{Ga}(s,l) + \text{As}(s) = \text{GaAs}(s)$	300	-20 ^(a,b,e)
	500	-18 ^(a,b,e)
$2\text{Ga}(s,l) + 3/2 \text{O}_2(g) = \text{Ga}_2\text{O}_3(s,\beta)$	300	-240 ^(d,e)
	500	-223 ^(d,e)
$2\text{As}(s) + 3/2 \text{O}_2(g) = \text{As}_2\text{O}_3(\text{arsenolite})$	300	-133 ^(f)
	500	-125 ^(f)

^a B. D. Lichten and P. Sommelet, *Trans. Met. Soc. AIME*, **245**, 1021 (1969), and for a correction, *Met. Trans.*, **1**, 1087 (1970). GaAs free energy function.

^b R. Hultgren et al., "Selected Values of the Thermodynamic Properties of the Elements," American Society for Metals (1973). Ga and As free energy functions.

^c J. R. Arthur, *J. Phys. Chem. Solids*, **28**, 2257 (1967). Table I for ΔH_{298}° (GaAs).

^d J. P. Coughlin, *Bull. No. 542*, Bureau of Mines, p. 21 (1954).

^e A. Mah, *Rep. Invest.*, 5965, U.S. Dept. of Interior, Bureau of Mines (1962).

^f Ref. ^a, p. 9.

were examined. In the following section, we assume that the thermal oxidation products of GaAs generated at elevated temperatures are consistent with the derived condensed phase diagram.

Applications of the Diagram

Despite the fact that a ternary phase diagram composed solely of pseudobinary tie lines constitutes a somewhat limited thermodynamic description of any real system, it is still possible to extract useful information from such a diagram. In this section we wish to consider the application of the phase diagram to predicting the oxide phases which result from the oxidation of GaAs.

Phases and their compositions.—The Ga-As-O diagram of Fig. 2 can be used to give the equilibrium phases expected under certain conditions used to oxidize GaAs. The composition of the phases can be determined by constructing a line which connects the oxidant to GaAs and examining the intersection of this line and the phase field boundaries it crosses.

The predicted phase compositions appropriate to oxidation using either $\text{O}_2(g)$ or $\text{As}_2\text{O}_3(s)$ are given in Fig. 4. As an example, consider $\text{O}_2(g)$ oxidation. The chemical potential of O_2 will be lowest at the GaAs interface and increase monotonically to its gas phase value across the thickness of the growing oxide film. Consequently in describing the phases formed during oxidation, movement along the line from GaAs toward the O apex of the diagram will describe the formation of interface, bulk, and surface layers in that order. The process terminates at a point on the GaAs-O line which is fixed by the oxidation potential of the gas phase, i.e., by the temperature and partial pressure of O_2 . The three oxidizing conditions (weak, intermediate, and strong) given in Fig 4 correspond to terminations within the $\text{GaAs-Ga}_2\text{O}_3\text{-As}$, $\text{Ga}_2\text{O}_3\text{-As}_2\text{O}_3\text{-As}$, or $\text{Ga}_2\text{O}_3\text{-GaAsO}_4\text{-As}_2\text{O}_3$ phase fields, respectively. The molar ratios of the pseudobinary pairs (As, Ga_2O_3 ; 2:1) and (As_2O_3 , Ga_2O_3 ; 1:1) are fixed at their intersection point values with the GaAs-O line.

O_2 oxidation can yield one, two, or three distinct composition regions depending on the oxidizing conditions (Fig. 4). For the case of $\text{As}_2\text{O}_3(s)$ oxidation, only a single composition is predicted under all oxidizing conditions. Finally it should be remarked that the phase diagram cannot predict the relative thickness of the oxide film layers; Fig. 4 portrays a schematic representation of the oxidation of GaAs with emphasis on phase compositions not relative thicknesses of oxide layers.

Experimental oxidation results.—Six conditions are frequently employed in the oxidation of GaAs. Data pertinent to the various conditions have been divided into two tables comprised of thermal oxidation under O_2 , As_2O_3 , air, or $\text{O}_2/\text{As}_2\text{O}_3$ (Table IV) and anodiza-

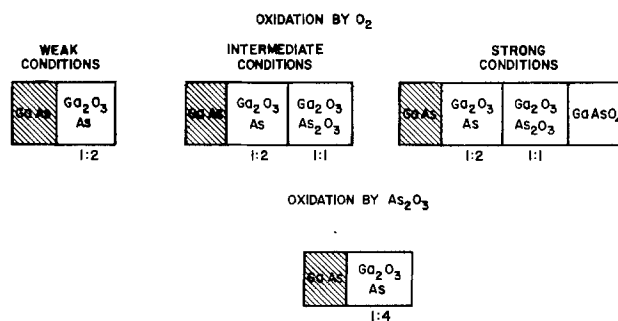


Fig. 4. Schematic diagrams of the phases formed in the oxidation of GaAs by oxygen and As_2O_3 under various oxidizing conditions according to the Ga-As-O phase diagram of Fig. 2. The predicted molar ratio of the upper to lower phase constituents is given beneath the oxide phase.

Table IV. Experimental results on thermally oxidized GaAs

Conditions	Interface	Bulk	Surface	Analysis technique*	Reference	Comments
I. O₂/air						
O ₂ /600°-900°C	β-Ga ₂ O ₃	β-Ga ₂ O ₃	β-Ga ₂ O ₃	ED, XRD	(4)	Crystalline, no arsenic-containing phases detected
O ₂ /740°-1040°C	β-Ga ₂ O ₃ (90%) GaAsO ₄ (10%)	β-Ga ₂ O ₃ (90%) GaAsO ₄ (10%)	β-Ga ₂ O ₃ (90%) GaAsO ₄ (10%)	XRD XRD	(5) (5)	
O ₂ /840°C	β-Ga ₂ O ₃ (85%) GaAsO ₄ (15%)	β-Ga ₂ O ₃ (85%) GaAsO ₄ (15%)	β-Ga ₂ O ₃ (85%) GaAsO ₄ (15%)	XRD XRD	(6) (6)	
O ₂ /450°-750°C	β-Ga ₂ O ₃	β-Ga ₂ O ₃	β-Ga ₂ O ₃	TEM	(7)	Amorphous films at 450°C, no evidence for crystalline arsenic-containing phases
O ₂ /610°C	β-Ga ₂ O ₃	β-Ga ₂ O ₃	β-Ga ₂ O ₃	ED, XPS	(8)	Arsenic present as a minor constituent (form not identified)
Air/530°C	Ga ₂ O ₃ (major) As (minor)	Ga ₂ O ₃ (major) As (minor) As ₂ O ₃ (trace)	Ga ₂ O ₃ (major) As ₂ O ₃ (minor) GaAsO ₄ (?)	XPS	(9)	Linewidth evidence for both As ³⁺ and As ⁵⁺ at the surface
Air/530°C	Ga ₂ O ₃ , As	Ga ₂ O ₃ (major) As (minor)	Ga ₂ O ₃ (major) As ₂ O ₃ (minor)	XPS	(10)	Broad As 3d linewidth on surface, indication of As ³⁺ /As ⁵⁺
Air/900°C		Ga ₂ O ₃ GaAsO ₄ (?)	Ga ₂ O ₃ GaAsO ₄	XPS XPS	(10) (10)	Argon beam reduction of GaAsO ₄ obscures bulk content of that product
O ₂ /450°C	Crystalline As	—	—	Raman	(11)	Chemical etching shows arsenic is at the interface
O ₂ /450°C	—	Crystalline As	—	Raman	(12)	Identification of crystalline As, spatial location of deposits not analyzed
II. As₂O₃/O₂; As₂O₃						
As ₂ O ₃ /O ₂ 500°C	Ga ₂ O ₃ (major) As ₂ O ₃ , As (minor)	Ga ₂ O ₃ , As ₂ O ₃ (major) As (minor)	GaAsO ₄ As ₂ O ₃	RHEED, XPS RHEED, XPS	(9) (9)	Amorphous film by RHEED
As ₂ O ₃ /O ₂ 750°C	Ga ₂ O ₃ (major)	Ga ₂ O ₃ , As ₂ O ₃ (major) As (minor)	GaAsO ₄	RHEED, XPS RHEED, XPS	(9) (9)	Interface phase not completely profiled
As ₂ O ₃ /O ₂	Ga ₂ O ₃ As ₂ O ₃ , As	Ga ₂ O ₃ , As ₂ O ₃	GaAsO ₄ Ga ₂ O ₃ , As ₂ O ₃	XPS XPS	(10) (10)	Retention of As ₂ O ₃ in bulk oxide
As ₂ O ₃ /500°C		β-Ga ₂ O ₃ (major) Arsenic species (minor) (form not identified)		ED ED	(13) (13)	Auger detects arsenic species in bulk film whose concentration increases at the interface
As ₂ O ₃ 350°-500°C		Crystalline As		Raman	(14)	Arsenic detected at all temperatures, spatial location not analyzed

* ED, electron diffraction; TEM, transmission electron microscopy; RHEED, reflection high energy ED; IXE, ion-induced x-ray emission; ELLIP, ellipsometry; XRD, x-ray diffraction; XPS, x-ray photoelectron spectroscopy; RBS, Rutherford backscattering; MS mass spectroscopy.

tion via electrochemical and plasma methods (Table V). Two points should be mentioned prior to comparing the experimental data with the phase diagram predictions. Such a comparison involves the implicit assumption that oxide growth is sufficiently slow for phase formation to occur under "near equilibrium" conditions. Finally, care must be taken to account for volatilization phenomena which can alter the concentration of certain film components such as As₂O₃ and As.

Thermal oxidation.—Table IV presents a compilation of experimental results for the thermal oxidation of GaAs utilizing O₂, air, As₂O₃, or As₂O₃/O₂ mixtures as oxidants. The scope of the table has been limited somewhat to emphasize those analytical techniques which provide either direct bulk crystalline phase identification or spatial profiling information with concomitant valence state identification of the chemical components. An extensive processing review and bibliography containing III-V oxidation data up to 1977 can be found in Ref. (3).

For oxidation with O₂ or air, Table IV indicates that GaAsO₄, Ga₂O₃, As, and As₂O₃ have all been detected as phases resulting from the oxidation process. The diffraction techniques have identified β-Ga₂O₃ as the major film constituent (4-7) for all temperatures sufficiently high to produce crystalline products (7) ($T \geq 500^\circ\text{C}$). Similar observations are available from x-ray photoelectron spectra (XPS) profiles (8-10).

In the case of GaAsO₄, relatively strong oxidizing conditions (high temperatures) are required before this product is observed by the diffraction techniques. The reasons for this are essentially twofold: XPS (9) results indicate that for low temperature growth an amorphous modification may exist which would not

be identified by diffraction techniques; second, the measurement volume involved in x-ray diffraction requires that a significant quantity of that phase be generated before detection is possible. XPS (9, 10), on the other hand, provides evidence that GaAsO₄ may be formed at lower temperatures, primarily as a surface product. The spatial extent to which GaAsO₄ extends into the bulk oxide is difficult to ascertain due to artifacts associated with ion milling, but a conservative estimate would be less than 150Å for growth below 600°C.

As₂O₃ is generally not observed in the bulk films except in trace amounts [a few mole percent (m/o)] although XPS does detect small quantities of this product (~10 m/o) right at the gas/oxide surface where it is normally accompanied by an additional pentavalent arsenic species. Since As₂O₃ is readily identified via XPS even when present in vitreous form, its absence throughout the bulk of thermally oxidized films is primarily associated with its high vapor pressure and subsequent loss through volatility.

Finally, Raman scattering (11, 12) has unambiguously identified the presence of crystalline arsenic in thermally oxidized films, and chemical etching experiments have shown that its concentration increases in the interfacial region. Similar concentration gradients of elemental arsenic have been observed by XPS (8-10) in conjunction with ion milling. The failure of the diffraction techniques to observe this crystalline phase is believed to be due to the low total concentrations actually present following extensive volatility losses.

Oxidation with As₂O₃/O₂ mixtures in closed tube (10) and "leaky box" (9) configurations both resulted in the incorporation of As₂O₃ in the outer sections

Table V. Experimental results on anodic oxides

Electrolyte	Interface	Bulk	Surface	Technique	Reference	Comments
I. Electrochemical						
Tartaric acid-glycol	β -Ga ₂ O ₃ on the GaAs surface	—	—	ED	(15)	Bulk oxides amorphous
Tartaric acid-glycol	Insufficient structural order to identify phases			ED	(16)	Structural differences in oxides grown at high and low current densities
As ₂ O ₃ saturated and buffered	Ga ₂ O ₃ /As ₂ O ₃ ~1:1 mole ratio throughout the oxide	Ga ₂ O ₃ /As ₂ O ₃	Ga ₂ O ₃ /As ₂ O ₃	XPS	(9)	
Tartaric acid-glycol	Ga ₂ O ₃ /As ₂ O ₃ ~1:1 mole ratio throughout the oxide	Ga ₂ O ₃ /As ₂ O ₃	Ga ₂ O ₃ /As ₂ O ₃	XPS	(10)	
Dilute phosphoric acid solution	As (?) trace levels	—	—	XPS	(17)	Chemically stripped films
Neutral borate	Film formed from Ga ⁺³ and As ⁺³			Coulometry	(18)	Electron number of 6.0 measured per gram mole of GaAs consumed
Not given	Ga:As ratio constant (~1:1) throughout the oxide except for surface (~200Å) arsenic depletion			RBS, IXE	(19)	Arsenic component decreases rapidly with thermal annealing
Tartaric acid-glycol	Ga:As ratio constant (1:1) throughout the oxide including the surface			RBS, MS	(20)	H ₂ O, As ₂ O ₃ , and As evolved on heating
H ₃ PO ₄ -glycol	Arsenic below detection limits of Raman; ellipsometric analysis indicates ~25Å interface with roughly 6Å of arsenic			RAMAN ELLIP	(21, 22) (23)	Thermal annealing in vacuo generates interfacial arsenic
II. Plasma						
Low pressure rf discharge ~2 × 10 ⁻³ Torr oxygen	Amorphous bulk films			TEM	(24)	Crystalline arsenic observed at interface after thermal annealing
Low pressure rf discharge	O:Ga:As 3:1.07:1 for oxides greater than 1000Å thick			RBS, IXE	(25)	Incomplete oxidation in thinner films
Low pressure rf discharge	Bulk oxides contain 1-2 v/o elemental arsenic, 84% Å wide interface contains ~25Å arsenic			ELLIP	(26)	Quantity of interfacial arsenic depends on growth rate
Low pressure rf discharge	Thick interfacial deposits of arsenic detected in thermally annealed samples			ELLIP	(27)	
D-C discharge (0.1-0.3 Torr)	Raman detects arsenic in bulk films, thermal generation of thick arsenic deposits verified			XPS, RAMAN	(28)	Evidence for mixed As ⁺³ /As ⁺⁵ surface signal

of the film. In the latter configuration the As₂O₃:Ga₂O₃ ratio was nearly 1:1 and the outermost surface (~150Å) of a film grown at 750°C was identified by reflection high energy electron diffraction (RHEED) as a single phase layer of GaAsO₄ (9). Complete profiling of the thinner films of Ref. (10) indicate that elemental arsenic was present throughout most of the bulk film and exhibits a concentration gradient which increases toward the substrate. Evidence for the retention of some As₂O₃ in the interfacial region is also present (10).

Limited data are available concerning the oxidation of GaAs under pure As₂O₃. Electron diffraction has identified beta phase Ga₂O₃, and Auger sputter profiling indicates that the major film constituents are gallium and oxygen with evidence for a weak arsenic signal which increases substantially in the interfacial region (13). The chemical form of the arsenic (elemental or As₂O₃) was not identified. Raman scattering explicitly demonstrates that elemental crystalline arsenic is present in these films (14).

The fundamental patterns observed in the experimental data on thermally oxidized GaAs are seen to be generally consistent with the phase predictions of the proposed phase diagram. In particular, GaAsO₄ surface layers can be formed under strong oxidizing conditions followed by a region composed primarily of Ga₂O₃ and As₂O₃ when conditions are such that volatilization of As₂O₃ is suppressed. The interfacial region is dominated by the presence of Ga₂O₃ and As, although the latter product always exhibits a strong concentration gradient resulting from its high diffusivity and volatility. For As₂O₃ as an oxidant, both Ga₂O₃ and As have been shown to be present, again with a strong concentration variation in the latter product which increases toward the substrate.

Anodic and plasma oxidation.—The situation for electrochemically (9-10, 15-23) and plasma (24-28) oxi-

dized GaAs (Table V) stands in distinct contrast to what was observed for the case of thermal oxidation. Room temperature electrochemical anodization leaves amorphous oxide films (15, 16) whose major phase constituents are Ga₂O₃ and As₂O₃ (9, 10, 24). Water and As₂O₃ have been observed to volatilize from films anodized in aqueous base electrolytes during heating (20). Coulometry supports the trivalent assignments of the bulk film constituents with a measured electron number in the passive film formation regime of 6.0/g mole of GaAs consumed (18). Electrochemically anodized films appear to contain elemental arsenic only at the trace level (9-10, 17, 21-22); recent ellipsometric evidence suggests an unobservable concentration in carefully prepared bulk films and perhaps 6Å of absorbing material (assumed to be arsenic) in a 25Å wide interface (23).

Plasma oxides are likewise amorphous (24) and can be prepared as approximately 1:1 molar mixtures of Ga₂O₃ and As₂O₃ (25). Films prepared at high current densities contain ~1-2 volume percent (v/o) arsenic in the bulk films with an estimated interfacial arsenic concentration of 25Å in an approximately 84Å wide interface (26). Low current density (slow) growth has been observed ellipsometrically to yield significantly thicker arsenic deposits in the interfacial region (26). Thermally annealed plasma oxides have been examined by TEM (24), ellipsometry (27), and Raman scattering (28) and were observed to contain thick, crystalline arsenic deposits in the interfacial region in all cases. The implications of thermal annealing are considered in detail later.

The experimental data found in Table V thus indicate that the room temperature electrochemical or plasma oxidation of GaAs results in a reasonably uniform mixture of Ga₂O₃ and As₂O₃ which extends from the surface to the interface. Elemental arsenic has been detected as a component of very low con-

centration in plasma oxidized films (1-2 v/o); its presence in electrochemically anodized samples is below that level. The low arsenic concentration is in direct contradiction to the expectations of the phase diagram under any set of oxidizing conditions using O₂. For room temperature growth, loss by diffusion and volatilization would not be expected to account for the absence of this component. Finally, an interfacial mixture of GaAs, Ga₂O₃, and As₂O₃ is not consistent with the equilibrium phases predicted by the proposed phase diagram. Although the phase diagram is not appropriate for predicting phases grown from oxidants containing hydrogen (H₂O, OH⁻, H₃O⁺), the virtual equivalence of the observed products for electrochemical (aqueous electrolyte) and plasma (O₂ gas) anodization suggests that this is not the source of the noted discrepancies. One is led to conclude that either the proposed phase diagram is in error or that the oxidation products evolved in electrochemical and plasma anodizations form under conditions far from thermodynamic equilibrium.

The phase diagram indicates that As₂O₃ in contact with GaAs should react according to the equation



yielding at the interface Ga₂O₃ and As as the stable phases which can coexist at equilibrium with GaAs. The annealing experiments on anodic and plasma grown oxides previously mentioned support the above reaction. Chemical etching experiments in conjunction with Raman scattering (21, 22) have revealed that metallic arsenic deposits are being generated next to the GaAs substrate as they must if Eq. [1] is assumed to hold. TEM (24) measurements on thermally annealed plasma oxides likewise reveal the existence of crystalline arsenic domains next to the substrate. Anodic and plasma oxide films thus seem to grow under strongly nonequilibrium conditions; thermal annealing is observed to drive the system toward the favored equilibrium phases.

Summary

An estimate of the Ga-As-O phase diagram has been made from a combination of experiments and free energy calculations. The experiments were carried out at temperatures above the melting point, 278°C, of As₂O₃ (arsenolite) whereas the thermodynamic estimates were made for temperatures below the melting point of As₂O₃. A number of regions of the estimated phase diagram were explored by the higher temperature anneals. The phases found on cooling were in accord with the low temperature phase diagram. Thermal oxidation of GaAs by O₂ or As₂O₃ produces phases in the grown layer agreeing with the estimated phase diagram. Low temperature electrochemical and plasma oxidation of GaAs lead to phases which are not in agreement with the estimated phase diagram. Thermal anneals of these layers do produce phases consistent with the phase diagram, suggesting that the phases produced by electrochemical and plasma oxidation are due to nonequilibrium reactions. Experimental analysis of oxide layers by a number of complementary techniques are reported including relevant work reported in the literature.

Manuscript received Sept. 24, 1979.

Any discussion of this paper will appear in a Discussion Section to be published in the December 1980 JOURNAL. All discussions for the December 1980 Discussion Section should be submitted by Aug. 1, 1980.

Publication costs of this article were assisted by Bell Laboratories.

REFERENCES

1. A. Brukl and G. Ortner, *Z. Anorg. Allg. Chem.*, **203**, 23 (1931); W. Klemm and H. U. Von Vogel, *ibid.*, **219**, 45 (1934).
2. G. Masing, "Ternary Systems," Reinhold, New York (1944), see p. 57. Masing in translation uses the term quasibinary for pseudobinary.
3. C. W. Wilmsen and S. Szpak, *Thin Solid Films*, **46**, 17 (1977).
4. H. T. Minden, *This Journal*, **109**, 733 (1962).
5. M. Rubenstein, *ibid.*, **113**, 540 (1966).
6. A. V. Emelyanov, A. V. Nikitin, V. N. Timofeev, and A. N. Shoken, *Sov. Phys. Crystallog.*, **20**, 373 (1975).
7. C. J. Bull and B. J. Sealy, *Philos. Mag. A*, **37**, 489 (1978).
8. J. Sealy and P. L. F. Hemment, *Thin Solid Films*, **22**, S38 (1974).
9. G. P. Schwartz, G. J. Gualtieri, G. W. Kammlott, and B. Schwartz, *This Journal*, In press.
10. Y. Mizokawa, H. Iwasaki, R. Nishitani, S. Nakamura, *Jpn. J. Appl. Phys.*, **17**, 327 (1978).
11. J. A. Cape, W. E. Tennant, and L. G. Hale, *J. Vac. Sci. Technol.*, **14**, 921 (1977).
12. R. L. Farrow, R. K. Chang, S. Mroczkowski, and F. H. Pollack, *Appl. Phys. Lett.*, **31**, 768 (1977).
13. H. Takagi, G. Kano, and I. Teramoto, *This Journal*, **125**, 579 (1978).
14. G. P. Schwartz, J. E. Griffiths, D. Distefano, G. J. Gualtieri, and B. Schwartz, *Appl. Phys. Lett.*, **34**, 742 (1979).
15. B. L. Weiss, "Final Technical Report," University of Newcastle upon Tyne, Grant No. Da-ERO-75-G-038 (1976).
16. S. Szpak, J. L. Thomlinson, and G. Hari Narayanan, *This Journal*, **124**, 466 (1977).
17. C. C. Chang, P. H. Citrin, and B. Schwartz, *J. Vac. Sci. Technol.*, **14**, 943 (1977).
18. W. W. Harvey and J. Kruger, *Electrochim. Acta*, **16**, 2017 (1971).
19. L. C. Feldman, J. M. Poate, F. Ermanis, and B. Schwartz, *Thin Solid Films*, **19**, 81 (1973).
20. T. Ishii and B. Jeppson, *This Journal*, **124**, 1784 (1977).
21. G. P. Schwartz, B. Schwartz, D. DiStefano, G. J. Gualtieri, and J. E. Griffiths, *Appl. Phys. Lett.*, **34**, 205 (1979).
22. G. P. Schwartz, J. E. Griffiths, and B. Schwartz, Presented at 6th Conference on Physics of Compound Semiconductor Interfaces, Asilomar, 1979, and *J. Vac. Sci. Technol.*, In press.
23. D. E. Aspnes, G. P. Schwartz, G. J. Gualtieri, and B. Schwartz, Presented at the Annual Materials Research Society Meeting, Cambridge, 1979.
24. R. P. H. Chang, T. T. Sheng, C. C. Chang, and J. J. Coleman, *Appl. Phys. Lett.*, **33**, 341 (1978).
25. R. L. Kauffman, L. C. Feldman, J. M. Poate, and R. P. H. Chang, *Appl. Phys. Lett.*, **30**, 319 (1977).
26. D. E. Aspnes, J. B. Theeten, and R. P. H. Chang, Presented at the 6th Conference on Physics of Compound Semiconductor Interfaces, Asilomar, 1979, and *J. Vac. Sci. Technol.*, In press.
27. J. B. Theeten, D. E. Aspnes, and R. P. H. Chang, *J. Appl. Phys.*, **49**, 6097 (1978).
28. G. P. Schwartz, J. E. Griffiths, B. Schwartz, and T. Sugano, Unpublished data on d-c and rf plasma oxidized films.

Contact Reliability Studies on Lead-Salt Diode Lasers

Wayne Lo and Fay E. Gifford

General Motors Research Laboratories, Physics Department, Warren, Michigan 48090

ABSTRACT

Deleterious changes in the electrical and optical properties of lead-salt semiconductor diode lasers have been traced to the diffusion of In into the surface layer of the lead-salt crystals. New contacting methods have been developed to eliminate this mode of degradation for $Pb_{1-x}Sn_xTe$ and $PbS_{1-x}Se_x$ diode lasers.

For lead-salt diode lasers made in our laboratories, we have observed two major modes of contact degradation. They are catastrophic failure (operation ceases abruptly) and a slow change in electrical and optical properties during room temperature storage. The first mode of degradation can be eliminated by using a properly designed mounting package (1). The second mode of degradation is manifested by a slow increase in contact resistance. In order to understand this latter mode of degradation, an investigation of contacting procedures was undertaken. The lasers used in this study were fabricated from single crystals of $PbS_{1-x}Se_x$ (2) and $Pb_{1-x}Sn_xTe$ (3) grown from the vapor phase.

Contact Degradation

For cw operation at temperatures approaching 40°K, we find that a contact resistance of $10^{-4} \Omega\text{-cm}^2$ or less is necessary. This is attributed to the low thermal conductivity of lead-salt materials (typically 0.07 W/cm-K vs. 3.0 W/cm-K for GaAs at 77°K) (4). Since lead-salt crystals have very high electron affinities, low resistance, ohmic contact to the n-type side of diodes can be obtained easily by using either Au, In, or In-Au combinations. It is the p-type contact that normally causes problems.

For the p-type side In-Au (5), In-Pt (6), and In-Pt-Au (7) structures have been reported as producing low resistance, ohmic contacts. More recently only In-Au combinations have been used (8, 9). We are not aware of any systematic studies on the long-term reliability of In-Au contacts. However, we found that they are not stable in our devices. During storage at room temperature over periods that range from days to months, the resistance of In-Au contacts can increase. Such increases are typically accompanied by increases in cw threshold current densities and laser emission frequencies, while at the same time laser output powers tend to decrease (10).

Figure 1 shows the I-V characteristics of a laser that has been subjected to life testing. It is evident that once a laser is mounted and tested, slow degradation occurs during room temperature storage, rather than during cw operation (including thermal cycling).

$PbS_{1-x}Se_x$ Lasers

We found that the increase in contact resistance is caused by the diffusion of In into the surface layer of the p-type side. Figure 2 shows an electron microprobe analysis of In and Pb concentration profiles near the metal-semiconductor interface before and after degradation. The samples were prepared with In-Au as the p-type contact. The degradation was accelerated by heating the sample to 100°C for 1 hr. This test condition is equivalent to room temperature storage of approximately one week (11). Both the degraded and the control samples were angle-lapped at a 3° inclination to provide a twentyfold improvement in spatial resolution normal to the interfaces.

Key words: contacts, IV-VI, lasers, reliability, interdiffusion.

The typical electron beam penetration depth is about 1-2 μm . The x-rays generated by the E-beam (the signal strength shown in Fig. 2) are absorbed partially by the contact metals before being detected. Au and Pt are good absorbers for the x-rays. We calculated that 70% of the x-rays generated in the crystal are absorbed by Au in a distance of 0.2 μm . This explains the sharp change in the Pb x-ray signal near the interface (and hence the good accuracy in identifying the interface). From Fig. 2 it is also noted that for a degraded sample, traces of In were found in the first few microns of the crystal below the contact. Since In is a donor in lead-salt materials, a reduction in hole carrier concentration near the surface is expected. We think that this is the reason for the increase in contact resistance (12).

Further study revealed that Au or Pt alone cannot form a barrier against In penetration, but a combination of Pt-Au does (1). It was also noticed that the reliability of the lasers depends on the thickness of the Pt and Au layers. We found that both layers have to be at least 0.2 μm thick in order to form a barrier against In diffusion. After depositing the Au and Pt layers on the p-type side of the diode a 10 μm layer of In is added. The n-type contact consists of a 0.2 μm layer of Au plus 5 μm of In. The entire contact structure is shown in Fig. 3. The p-type side of the crystal surface was purposely oxidized by exposure to air before evaporating the first layer of Au.

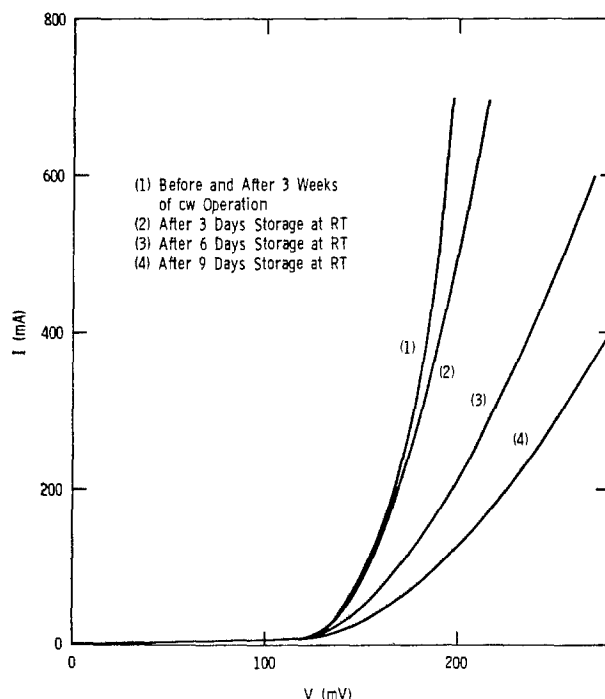


Fig. 1. I-V characteristics of a $Pb_{0.92}Sn_{0.08}Te$ laser during operation and after storage at room temperature.

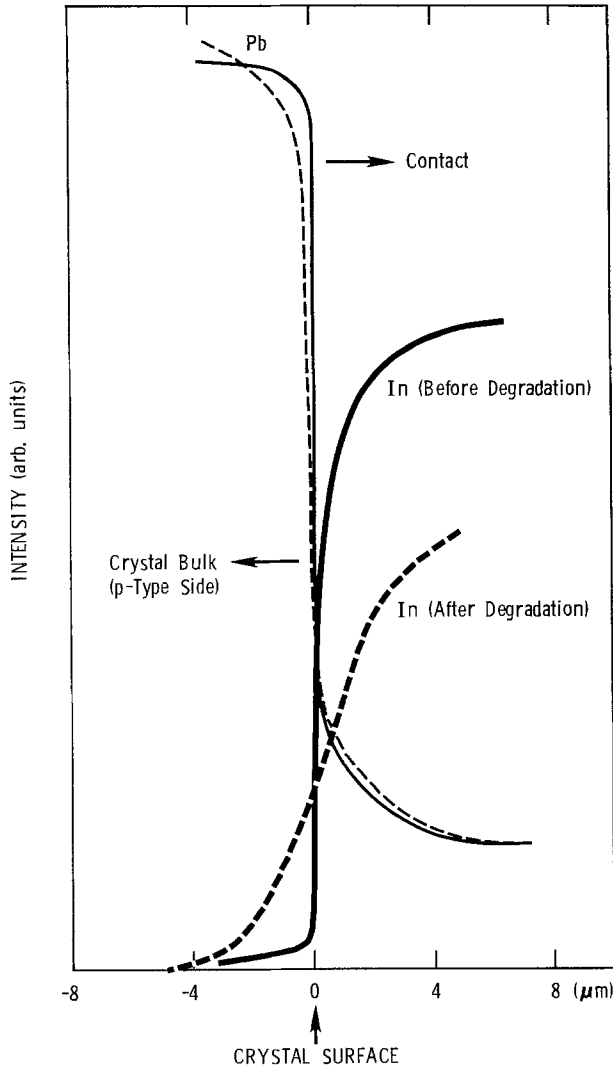


Fig. 2. Electron microprobe analysis of a crystal-contact interface for $Pb_{0.82}Se_{0.18}$.

This increases the hole carrier concentration near the surface and tends to stabilize the contact resistance (13).

$Pb_{1-x}Sn_xTe$ Lasers

The same three-layer structure of In-Pt-Au did not produce consistent results for $Pb_{1-x}Sn_xTe$ lasers. Different results were obtained for $Pb_{1-x}Sn_xTe$ with different x values. It is apparent that the Au- $Pb_{1-x}Sn_xTe$ interface properties vary as x changes. We have studied this interface and found methods

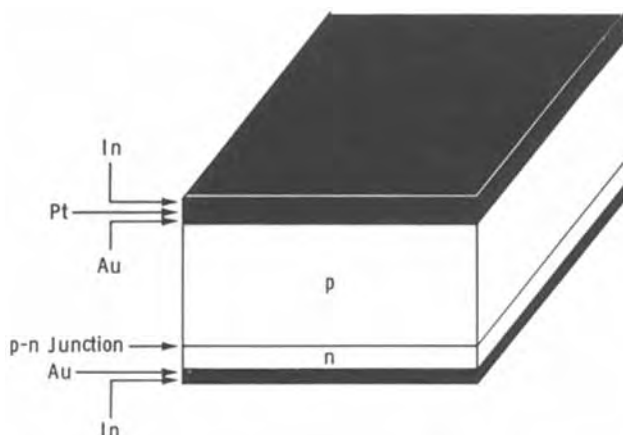


Fig. 3. Contacts for $Pb_{1-x}Se_x$ lasers

for making low resistance, reliable contacts for all compositions of $Pb_{1-x}Sn_xTe$.

As shown in Fig. 4(a), the work function of a metal ($q\phi_M$) is defined as the energy difference between the vacuum level and the Fermi level (E_F). In semiconductors, the equivalent energy unit is called the electron affinity ($q\chi$). It is defined as the energy difference between the vacuum level and the conduction band minimum. A semiconductor is also characterized by its bandgap (E_g) and its quasi-Fermi level [E_{FP} for p-type material—Fig. 4(a)]. When a metal makes intimate contact with a semiconductor, the Fermi levels in the two materials must coincide at thermal equilibrium. Whether the contact is ohmic or a barrier depends on the energy difference between the metal work function and the total of the semiconductor electron affinity and bandgap.

In a p-type semiconductor, the barrier height (ϕ_{BP}) is defined as (14)

$$q\phi_{BP} = (E_g + q\chi) - q\phi_M \quad [1]$$

where the effect of surface states has been ignored (15). This is consistent with the high dielectric constant. If ϕ_{BP} is positive, as shown in Fig. 4(b), charge carriers (holes) are depleted in the surface and the contact is a barrier. However, if ϕ_{BP} is negative, as shown in Fig. 4(c), an accumulation layer is formed in the surface and the contact is ohmic.

It has been reported that Au makes barrier contacts on p-type PbTe (15). It is speculated that, since the work function of Au and the electron affinity of PbTe are both 4.6 eV, the contact is not ohmic. Al-

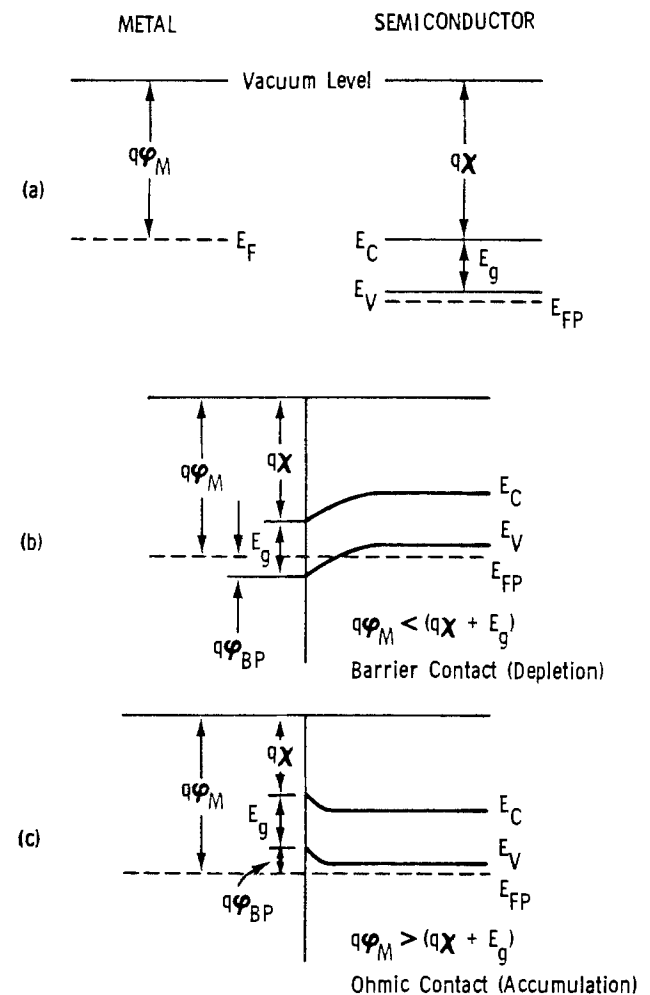


Fig. 4. Energy levels of a metal-semiconductor interface

though the exact value of the work function for Au is not certain (16), the approximate equality of work function and electron affinity could explain the barrier contacts. From Eq. [1], it is seen that the barrier height would be positive and equal to the energy bandgap E_g . It is interesting to note that as SnTe is added to PbTe to form $Pb_{1-x}Sn_xTe$, the bandgap of the semiconductor decreases. This tends to lower the barrier height and improves the contact resistance. However, in order to change the contact from barrier to ohmic (ϕ_{BP} goes from positive to negative) the electron affinity of the $Pb_{1-x}Sn_xTe$ system would have to decrease. The crossover between barrier contact and ohmic contact should then occur at a certain SnTe concentration. This has been observed in our experiments as will be discussed later.

From the previous analysis it is clear that the best contact metal for p-type $Pb_{1-x}Sn_xTe$ is not Au, but a metal with a higher work function. Among the metals, Pt is the one with the highest work function (5.4 eV). Therefore it was selected for experimentation.

Platinum can be applied to $Pb_{1-x}Sn_xTe$ by either vacuum deposition or electroplating techniques. Although the former is done in a cleaner environment, there are several practical problems. Films deposited at room temperature have very poor adhesion. Attempts to heat samples during evaporation lead to further degradation in contact resistance. For these reasons, only the electroplating method was used in our work.

Three Pt-plating solutions have been tried. Characteristics of these solutions and the results are summarized in Table I. The alkaline solution is not desirable because it attacks the sample surface and produces high contact resistance. The strong acid solution is also undesirable, because the results are not consistent (contact resistance varies widely). Best results have been obtained with the moderate acid solution.

Although properly plated Pt routinely produces low resistance ($\sim 10^{-5} \Omega\text{-cm}^2$) contacts on p-type $Pb_{1-x}Sn_xTe$ (17), the simple addition of a little In to facilitate mounting lasers on heat sinks did not provide reliable contacts. The Pt-In contacts degraded (resistance increased) after storage at room temperature for a few days. As found previously, the resistance increase was due to diffusion of the In through the Pt and into the $Pb_{1-x}Sn_xTe$. Therefore a more complex structure was tried.

The p-type material was originally plated with 0.15 μm of Au, followed by 0.2 μm of Pt and 10 μm of In. The contact resistance was $1-2 \times 10^{-5} \Omega\text{-cm}^2$ for $Pb_{1-x}Sn_xTe$ with $x > 12\%$, but was much higher ($8-15 \times 10^{-5} \Omega\text{-cm}^2$) for $x < 8\%$. This is consistent with the physics of metal-semiconductor interfaces as applied to Au and $Pb_{1-x}Sn_xTe$. However, the contacts were very stable. No significant degradation was observed over extended life tests.

The results for the lower Sn concentration suggested that Pt should be applied first. We found that the best method starts with 0.2 μm of Pt followed by 0.15 μm of Au and 10 μm of In. The n-type side of the diode is contacted with Au and In. Typical contact resistance for diodes fabricated this way is in the $8-15 \times 10^{-6} \Omega\text{-cm}^2$ range for $Pb_{1-x}Sn_xTe$ with all values of x .

Laser Tests

Over a period of ten months, groups of $PbS_{1-x}Se_x$ and $Pb_{1-x}Sn_xTe$ lasers (made with three-layer contacts on the p-type side) have been tested for thermal cycling, room temperature storage, and cw operation. For up to sixty thermal cycles and five hundred hours of cw operation, no significant changes in contact resistance, threshold current density, or optical properties were observed. The test results are summarized in Table II. This is a significant improvement over lasers that have been fabricated in the past, whose performance could degrade in a matter of a few days at room temperature.

However, we found that contact degradation can be induced by heating lasers to temperatures above 160°C, even for only a few seconds. Degradation can also be induced by operating lasers at cw current densities above 3 kA/cm². We believe that both of these processes enhance the diffusion of In through the Pt-Au barrier and change the surface properties of the p-type side of the laser. With proper handling and avoidance of high temperature, high current operation, these lasers should be reliable devices.

It is also noted that interdiffusion between In and Au, which has received much attention recently (18), cannot account for the change in contact resistance discussed in this paper (Fig. 1). The problem we are dealing with is In diffusion into the semiconductor surface. We found that the use of multilayered structures of Pt-Au or Au-Pt has significantly retarded this process. Further improvements over this con-

Table I. Pt plating parameters and results

	pH values	Temperature (°C)	Current density (mA/cm ²)	Agitation	Time to plate 200 nm (min)	Contact resistance (m Ω)
Strong acid (Technic Pt TP) *	1.2	45	10	None	30	20-50
Moderate acid (Engelhard E-401) **	4.0	45	1	Moderate	10	8-15
Alkaline (Engelhard E-209) **	8.0	45	5	Moderate	20	80-100

* Technic Incorporated, Providence, Rhode Island.

** Engelhard, Newark, New Jersey.

Table II. Laser test results (ten-month test period)

		R_c ($\Omega\text{-cm}^2$) $\times 10^6$ Contact resistance		J_{th} (A/cm ²) Threshold current density		P (mW) Total output power at $I = 1A, T = 20^\circ K$		Remarks
		Initial	Final	Initial	Final	Initial	Final	
$PbS_{0.82}Se_{0.18}$	No. 1	1.10	1.18	260	280	0.85	0.80	<ul style="list-style-type: none"> • 500 hr cw operation • Thermal cycling 26 times • Thermal cycling 45 times
	No. 2	0.87	0.91	365	380	3.2	2.6	
$Pb_{0.86}Sn_{0.14}Te$	No. 1	0.74	0.80	95	105	0.65	0.58	<ul style="list-style-type: none"> • 300 hr cw operation • Thermal cycling 25 times • 420 hr cw operation • Thermal cycling 33 times
	No. 2	0.65	0.73	125	135	0.90	0.86	

tacting method have since been developed and will be published elsewhere (11).

Conclusions

Slow degradation for lead-salt diode lasers has been attributed to a slow increase in contact resistance. This mode of degradation has been traced to migration of In into the surface layer of the p-type side of the lasers. By using combinations of Au-Pt or Pt-Au as barriers to prevent In migration, we have substantially increased the lifetime of these lasers.

Acknowledgments

The authors thank Don E. Swets for providing the single crystals.

Manuscript submitted May 23, 1979; revised manuscript received Nov. 9, 1979.

Any discussion of this paper will appear in a Discussion Section to be published in the December 1980 JOURNAL. All discussions for the December 1980 Discussion Section should be submitted by Aug. 1, 1980.

Publication costs of this article were assisted by General Motors Research Laboratories.

REFERENCES

1. W. Lo, *Jpn. J. Appl. Phys.*, **18**, suppl. 18-1, 367 (1979).
2. W. Lo and D. E. Swets, *Appl. Phys. Lett.*, **33**, 938 (1978).
3. W. Lo, G. P. Montgomery, Jr., and D. E. Swets, *J. Appl. Phys.*, **47**, 267 (1976).
4. "American Institute of Physics Handbook," pp. 4-156, McGraw Hill, New York (1975).
5. R. W. Ralston, I. Melngailis, A. R. Calawa, and W. T. Lindi, *IEEE J. Quantum Electron.*, **qe-9**, 350 (1973).
6. G. A. Antcliffe and S. G. Parker, *J. Appl. Phys.*, **44**, 4145 (1973).
7. R. W. Ralston, J. N. Walpole, A. R. Calawa, T. C. Harman, and J. P. McVittie, *ibid.*, **45**, 1323 (1974).
8. J. N. Walpole, A. R. Calawa, T. C. Harman, and S. H. Groves, *Appl. Phys. Lett.*, **28**, 552 (1976).
9. K. J. Linden, K. W. Nill, and J. F. Butler, *IEEE J. Quantum Electron.*, **qe-13**, 720 (1977).
10. E. D. Hinkley, Private communication; Frank Alario, Private communication; Herb Flicker, Private communication.
11. W. Lo, To be submitted for publication.
12. W. Lo, *J. Electron. Mater.*, **6**, 39 (1977).
13. G. F. McLane and J. N. Zemel, *Thin Solid Films*, **7**, 229 (1971).
14. S. M. Sze, "Physics of Semiconductor Devices," John Wiley & Sons, Inc., New York (1969).
15. K. W. Nill, A. R. Calawa, and T. C. Harman, *Appl. Phys. Lett.*, **16**, 375 (1970).
16. A. G. Milnes and D. L. Feucht, "Heterojunction and Metal-Semiconductor Junctions," p. 158, Academic Press, New York (1972).
17. W. Lo, *IEEE J. Quant. Electron.*, **qe-13**, 591 (1977).
18. V. Simic and Z. Marinkovic, *Thin Solid Films*, **41**, 57 (1977).

The Growth of, and the Formation of Grain Boundaries in, Cu_2S Films Grown on Faceted Single Crystal CdS Substrates

C. H. Cheng and K. A. Jones*

Electrical Engineering Department, Colorado State University, Fort Collins, Colorado 80523

ABSTRACT

It is shown that large angle grain boundaries are formed in the Cu_2S film at the intersection of adjacent prismatic CdS planes and that small angle grain boundaries are formed at the intersection of adjacent prismatic and nonprismatic CdS planes and at the intersection of a nonprismatic plane with the basal plane. The large angle grains are formed because the orthorhombic Cu_2S c-axis is at most a 2-fold axis whereas the CdS axis is a 6-fold axis. It is shown that the open-circuit voltage is reduced in the vicinity of these grain boundaries. The small angle grain boundaries form because the effective c/a axis of Cu_2S is different than the c/a axis of CdS so that the Cu_2S is distorted when it is made to conform with the CdS substrate. The open-circuit voltage in the vicinity of these grain boundaries did not noticeably decrease. It is also shown that the growth rate and morphology of the Cu_2S films depend on the orientation and morphology of the CdS substrate.

The Cu_2S -CdS solar cell is usually made by growing a Cu_2S film on a textured polycrystalline CdS substrate film. Because the CdS film is so highly textured, it is frequently assumed that the Cu_2S -CdS interface is parallel to the basal plane of each. However, the interface plane is usually parallel to a number of different planes because the CdS grains are highly faceted (1, 2). In addition they can contain hexagonal flat tops and pyramids (3, 4) and hexagonal etch pits (5, 6), and even originally smooth CdS surfaces can be roughened by the preferential grain boundary attack by the Cu_2S (1, 7). Sometimes the CdS film is also purposely roughened using an HCl etch in order to reduce the reflection losses (8).

It has been shown that increasing the surface roughness increases the amount of lattice mismatch at the

interface (9, 10) and therefore the density of interface recombination centers (11, 12). These recombination centers have the undesirable effects of decreasing the short-circuit current via interface recombination and of decreasing the open-circuit voltage by increasing the reverse saturation current by increasing the generation-recombination and the tunneling currents (13).

In this paper we show that grain boundaries form in the Cu_2S when it grows on a faceted CdS surface, even though the CdS is a single crystal, and that these grain boundaries can reduce the cell efficiency (14). Grain boundaries are formed because the Cu_2S (orthorhombic) and CdS (hexagonal) crystals belong to different crystal systems. That the Cu_2S grows at different rates (1, 15-17) with different morphologies is also confirmed. This has important implications for the manufacture of Cu_2S -CdS cells using a rough CdS substrate because a Cu_2S film of uniform thickness

* Electrochemical Society Active Member.

Key words: growth rate, morphology, orientation, open-circuit voltage.

cannot be grown on it and the reflectivity of the different exposed Cu_2S surfaces can be different.

This study was done by growing the Cu_2S on a number of faceted single crystal surfaces. Growth on the prismatic surfaces, which occurs during grain boundary penetration, was studied by growing the Cu_2S on CdS platelets containing ridges (18) and hexagonally shaped c-oriented needle single crystals of CdS. Growth on the rough substrate surface was modeled by growing the Cu_2S on the tapered tip of the c-oriented needles and on an etched (0001) single crystal surface.

Theoretical Background

It has been shown that the (100), (010), and (001) Cu_2S planes grow respectively parallel to the (2110), (0110), and (001) CdS planes (1, 15). Using the equivalent lengths of the Cu_2S unit cell, $a/3$, $b/4$, and $c/2$, and the three index notation for the CdS, it can be shown that the planar orientation relationship is given by $\bar{h}_o = \bar{A}\bar{h}_h$ where \bar{h}_h is the CdS plane normal, \bar{h}_o is the equivalent Cu_2S plane normal, and \bar{A} is (9)

$$\bar{A} = \begin{pmatrix} 3 & 0 & 0 \\ 4 & 8 & 0 \\ 0 & 0 & 2 \end{pmatrix} \quad [1]$$

The d spacings for the equivalent planes are slightly different because the equivalent lattice parameters are slightly different, and most of the equivalent planes are not quite parallel because the mismatch, $\Delta a/a$, $\Delta b/b$, and $\Delta c/c$, in the directions parallel to the Cu_2S lattice parameters is slightly different. This lack of parallelism is what causes the small angle grain boundaries discussed below to form.

As is shown in Fig. 1, a small angle grain boundary can form at the intersection of adjacent prismatic planes. The (080) Cu_2S plane is parallel to the (0110) CdS plane but the (340) Cu_2S plane is not quite parallel to the equivalent (1010) CdS plane since $\Delta a/a$ is a bit smaller than $\Delta b/b$. The Cu_2S must, however, conform

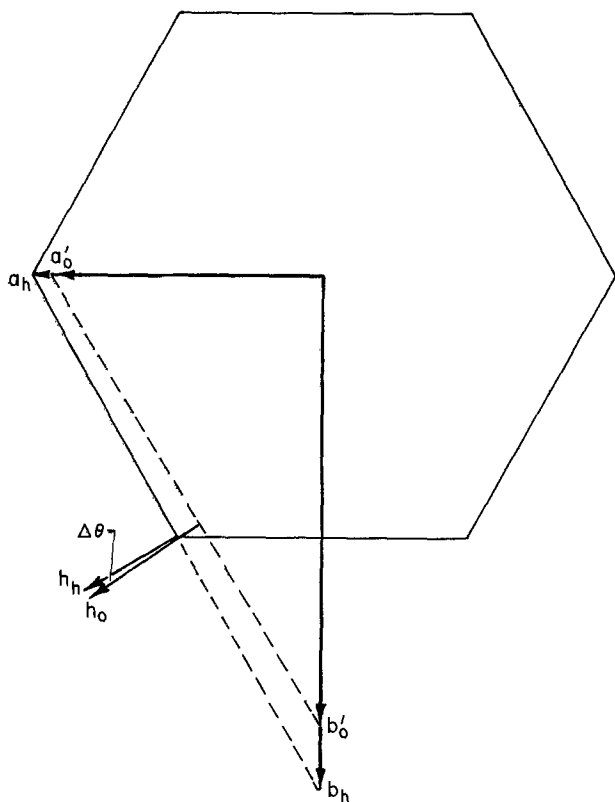


Fig. 1. The angular misorientation in the Cu_2S film at the intersection of adjacent prismatic CdS surfaces due to the difference in the mismatch in the a and b directions.

to the CdS substrate so that the (340) Cu_2S plane must be rotated $\Delta\theta$ in a clockwise rotation about the basal plane normal. This rotation can be accomplished by a tilt boundary which has a linear dislocation density, ρ

$$\rho \approx \frac{\Delta\theta}{b} \quad [2]$$

where b is the Burger's vector. For the prismatic planes $\Delta\theta = 0.0075^\circ$. If one assumes that $b = 4\text{\AA}$, which is about equal to the a-lattice vector of CdS, then $\rho \approx 3.2 \times 10^8$ dislocations/cm. This, in turn, yields a dangling bond density of 8×10^{10} dangling bonds/cm² when it is assumed that the repeat distance along the dislocation line is 4\AA and there is one atom with one dangling bond in the repeat distance (19).

Small angle grain boundaries are formed at the intersections of a nonprismatic plane with the basal plane and with a prismatic plane primarily because the effective $c/a = c/2/a/3$ ratio (1.69) is different than it is for CdS (1.63). The lack of parallelism of all the prismatic planes also has an effect, but the effect of the different c/a (γ) ratios is enough larger so that this effect can essentially be ignored. As is shown in Fig. 2, the nonprismatic Cu_2S film can be made to conform by a rotation, $\Delta\theta_r$, about the line formed by the intersection of the nonprismatic and basal planes. The amount of rotation is found from the difference in the angle, θ , that \bar{h}_h and \bar{h}_o make with the c-axis where θ is found from the equation (9)

$$\cos \theta_i = \frac{\sqrt{3l}}{2\gamma_i(h^2 + hk + k^2 + 3l^2/4\gamma_i^2)^{1/2}} \quad [3]$$

where h , k , and l are the Miller indexes referred to the CdS lattice and the γ 's are those of Cu_2S and CdS.

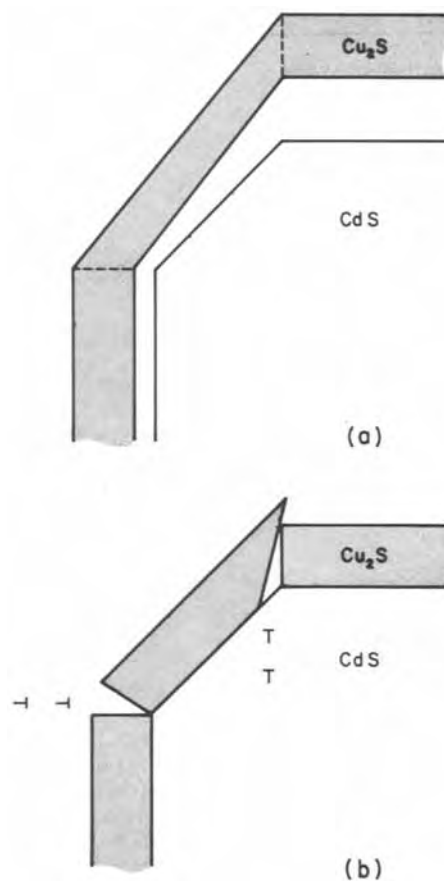


Fig. 2 (a) Schematic diagram illustrating that the effective γ for Cu_2S is larger than γ for CdS and (b) the tilt boundaries formed at the intersections of a nonprismatic CdS plane with a prismatic plane when the Cu_2S is compressed to conform to the CdS.

The value of $\Delta\theta_r$ depends on which nonprismatic CdS plane is parallel to the interface. This is shown in Fig. 3 where $\Delta\theta_r$ is plotted as a function of θ for the (hOl) type planes. There it is seen that the maximum tilt occurs for $\theta \sim 45^\circ$ where it is 1.15° . Values for specific planes are shown in Table I. For a tilt of 1° the tilt boundary will contain $\sim 4.4 \times 10^5$ dislocations/cm which, in turn, corresponds to a dangling bond density of 1.1×10^{13} per cm^2 .

Small angle grain boundaries will also form at the intersections of adjacent nonprismatic planes. They form because the Cu_2S hexagonal flat top is "split down the seams" when it is compressed in order to conform to the hexagonal flat top. This is shown in Fig. 4. It has been shown elsewhere (20) that the tilt due to this splitting, $\Delta\theta_s$, is found from the equation

$$\sin \frac{\Delta\theta}{2} = \frac{\sqrt{3}}{2} \sin \phi_2 (\cot \phi_1 - \cot \phi_2) \quad [4]$$

where ϕ is the angle formed by the line that is parallel to the intersection of adjacent nonprismatic planes and the line that is parallel to the intersection of the nonprismatic and basal planes. It is found from the equation (20)

$$\cot \phi_1 = \frac{2l[h_1^2 + h_1k_1 + k_1^2 - h_1h_2 - \frac{1}{2}h_1k_2 - \frac{1}{2}h_2k_1 - k_1k_2]}{(h_2k_1 - h_1k_2)[3l^2 + 4\gamma_1^2(h_1^2 + h_1k_1 + k_1^2)]^{1/2}} \quad [5]$$

where the subscripts designate the nonprismatic planes \bar{h}_1 and \bar{h}_2 described in Fig. 4a. $\Delta\theta_s$ is also plotted as a function of θ in Fig. 3. There it is seen that it is less than $\Delta\theta_r$ and it peaks near $\theta = 60^\circ$ where it has a value ~ 0.85 . The values for specific CdS planes are shown in Table I. Also, the dislocation and dangling bond densities are determined in exactly the same way as they were in the previous discussion.

Large angle grain boundaries can also be formed at the intersection of adjacent prismatic planes and ad-

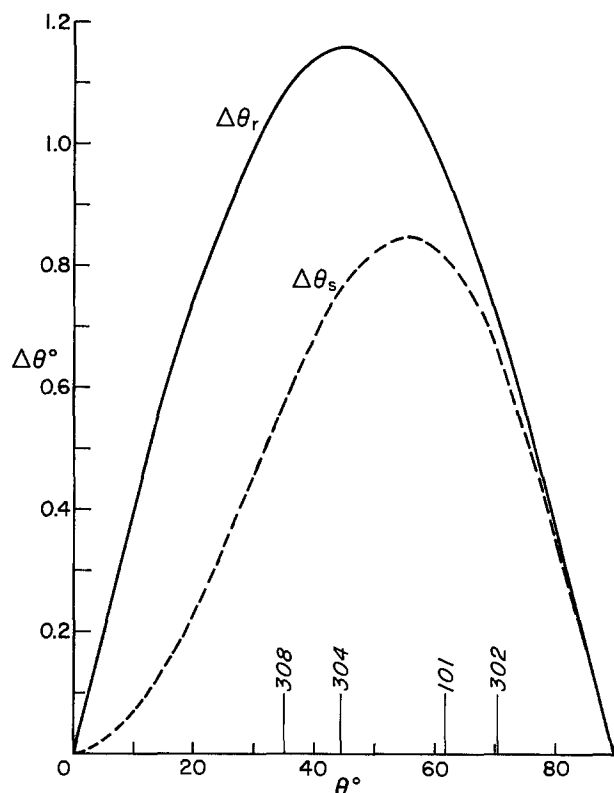


Fig. 3. The angular misorientation in the Cu_2S film at the intersections of a nonprismatic CdS plane with a prismatic plane and with the basal plane, $\Delta\theta_r$, and the angular misorientation at the intersection of adjacent nonprismatic planes that is due to splitting, $\Delta\theta_s$, that is plotted as a function of the angle between the nonprismatic (hOl) type planes and the basal plane.

Table I. The amount of tilt due to rotation about the axis parallel to the intersection of a prismatic CdS plane and the basal plane, $\Delta\theta_r$, and that due to splitting along the intersection of adjacent nonprismatic planes, $\Delta\theta_s$, for selected CdS planes

hkil	$\Delta\theta_r^\circ$	$\Delta\theta_s^\circ$
(3032)	0.720	0.669
(1011)	0.952	0.816
(3034)	1.087	0.848
(1012)	1.158	0.739
(3038)	1.098	0.580
(1121)	0.641	0.606
(1122)	1.026	0.842
(1123)	1.153	0.798

acent nonprismatic planes because the basal plane normal for the CdS is a 6-fold axis whereas the equivalent Cu_2S direction is only a 2-fold axis. As is shown in Fig. 5, the (021) Cu_2S plane grows on the (01 $\bar{1}$ 2) CdS plane and the (344) Cu_2S plane grows on the (10 $\bar{1}$ 2) CdS plane if the orientation relationship is obeyed. However, the (01 $\bar{1}$ 2) and (10 $\bar{1}$ 2) CdS planes

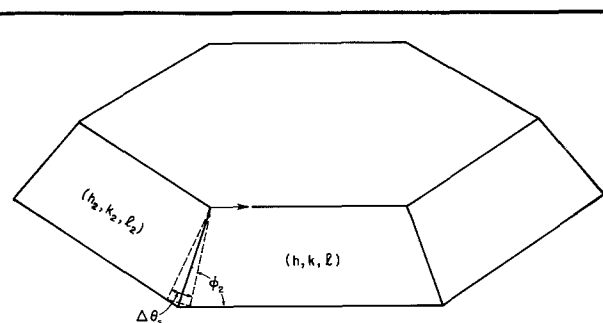


Fig. 4a. Schematic illustration of the splitting of the Cu_2S hexagonal flat top at the intersection of adjacent nonprismatic CdS planes, \bar{h}_1 and \bar{h}_2 , when it is compressed to conform with the CdS hexagonal flat top.

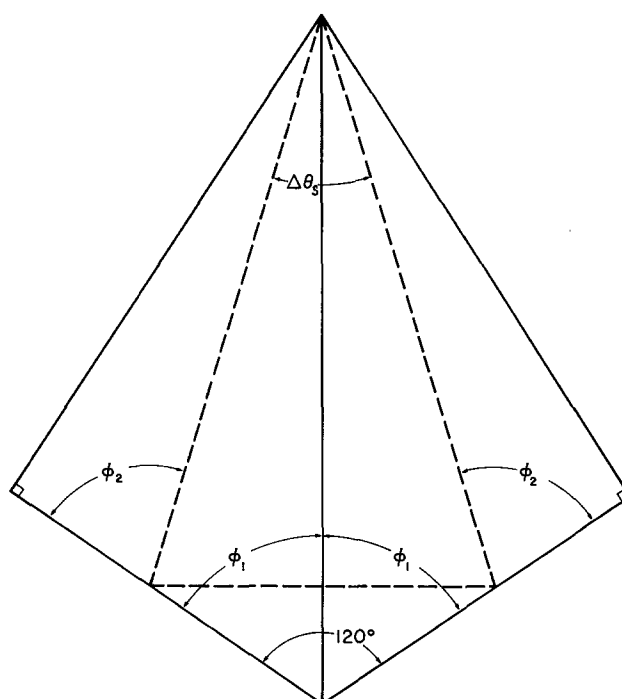


Fig. 4b. An enlargement of the split section

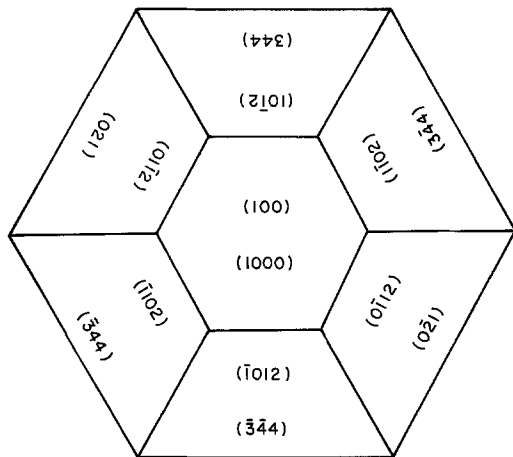


Fig. 5. The basal and $\{10\bar{1}2\}$ type CdS planes and their equivalent Cu_2S planes.

are crystallographically equivalent, but the (021) and (344) Cu_2S planes are not. If, as is more likely, crystallographically equivalent Cu_2S planes grew on these CdS planes, a 60° grain boundary would form at the intersection of these two planes.

Experimental Procedure and Results

The CdS needle single crystals were grown using five 9's pure CdS powder by placing the powder in a 25 cm evacuated quartz tube and then putting the tube in a temperature gradient of $\sim 2^\circ\text{C}/\text{cm}$ with the hot end being at 1200°C . The platelets were grown using a modified Frerich's technique with the five 9's pure CdS being evaporated at $\sim 1100^\circ\text{C}$ transported by an argon carrier gas flowing at ~ 1 cm/sec and then being deposited at $\sim 900^\circ\text{C}$ (18). The bulk CdS crystals were donated to us by the 3M Company.

The bulk crystals were cut with an (0001) orientation, the positive (0001) face was identified after the crystal had been etched in HCl, and then it was mechanically polished with the last polish being made with 0.3 micron alumina. The surface was partially covered with a protective layer of black wax and the unprotected area was then etched for ~ 5 min in concentrated HCl. The prismatic surfaces of the CdS needles were left as is, and the nonprismatic surfaces were formed by polishing the tip so that the nonprismatic plane made an angle of 45° with both the $(10\bar{1}0)$ and the (0001) planes. The nonprismatic plane was then almost parallel to the low energy $(10\bar{1}2)$ plane (3).

Some of the crystals were examined in an optical microscope and a SEM, and then the Cu_2S was grown using the dipping technique described by Lindquist and Bube (17). Usually some of the crystal surfaces were protected with black wax, and they were dipped for times ranging from 5 min to 2 hr.

Photographs of the z-oriented CdS and Cu_2S are shown in Fig. 6. As is seen in Fig. 6a, the etched z CdS surface is composed of small hexagonal flat tops. Figure 6b shows how the surface morphology changes when a Cu_2S film covers the CdS substrate. There it is seen that the Cu_2S appears to nucleate on the different exposed CdS surfaces, and that grains appear to form when the film on the different surfaces grows together. In Fig. 6c and 6d it is seen that the morphology of the Cu_2S grown on the etched face (Fig. 6c) is very different from that grown on the smooth face (Fig. 6d).

Photographs of the Cu_2S film growing on adjacent prismatic surfaces of a CdS needle are shown in Fig. 7. The intersection of the Cu_2S film growing on adjacent prismatic CdS planes is shown in Fig. 7a and the same intersection after it had been treated with a KCN etch is shown in Fig. 7b. In the former it appears as if the Cu_2S film does not grow together perfectly, and in the

latter it is seen that the intersection is preferentially attacked by the etch much as it would if there was a grain boundary there.

The effects of growing Cu_2S on a rough platelet surface is shown in Fig. 8 where there are photographs of a Cu_2S -coated CdS platelet cleaved parallel to the (0001) plane. There it is seen that the Cu_2S films growing on the different CdS planes appear to have different orientations, and there are boundaries at the intersections of the CdS planes. These boundaries could

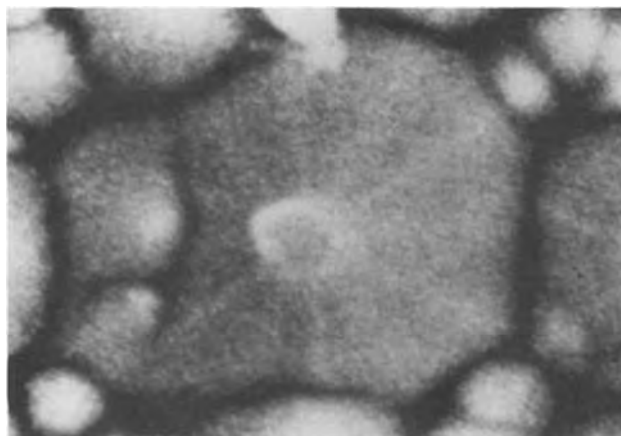


Fig. 6a. A photomicrograph of a typical protuberance on an etched (0001) CdS surface ($5000\times$).

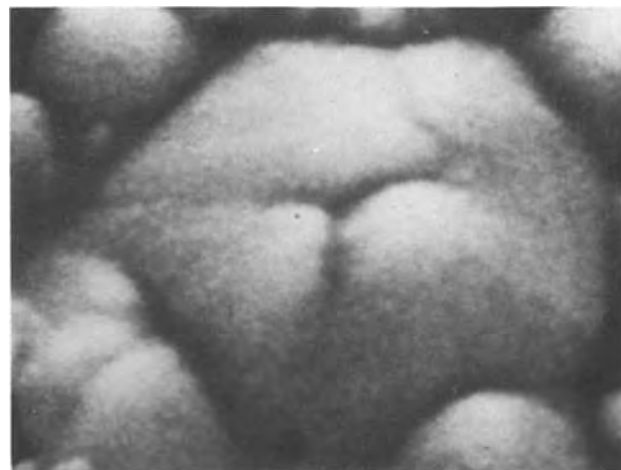


Fig. 6b. The growth of the Cu_2S over the protuberance ($5000\times$).



Fig. 6c. A Cu_2S film grown on an etched (0001) CdS surface ($2000\times$).

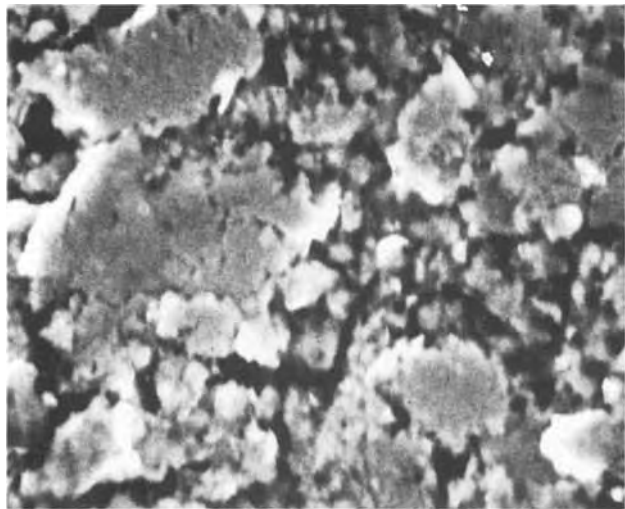


Fig. 6d. A Cu_2S film grown on a polished (0001) CdS surface ($2000\times$).

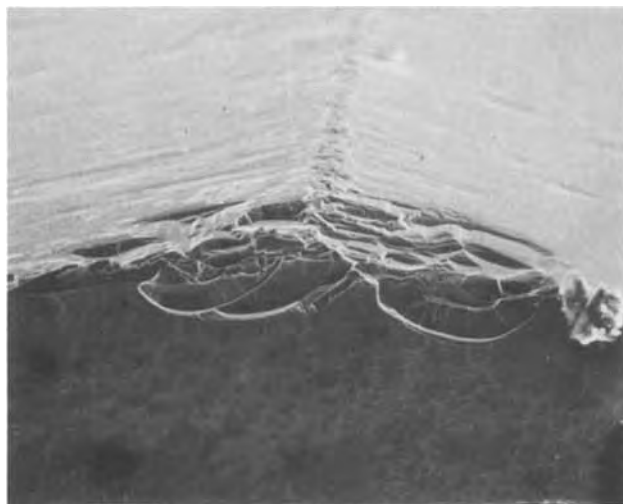


Fig. 7a. A photomicrograph of the Cu_2S film growing together at the intersection of adjacent CdS prismatic planes ($200\times$).



Fig. 7b. A photomicrograph of the Cu_2S film at the same intersection after being treated by a KCN etch ($500\times$).

only be cracks formed by stress concentrations at the notches, but they could also be caused by Cu_2S films with different orientations growing together.

A photograph of the Cu_2S growing near the intersection of the $(10\bar{1}0)$ and $(10\bar{1}2)$ CdS planes is shown in Fig. 9a. There it is seen that the morphology on the two surfaces is different and that the film on the $(10\bar{1}2)$ plane is thinner. That it is thinner is shown by the ridge formed at the intersection, the Cu_2S film on the $(10\bar{1}2)$ is thin enough to still replicate the scratches on the CdS substrate, and the film on the $(10\bar{1}2)$ surface is thin enough so that growth cracks have not yet formed. That the Cu_2S has substantially different growth rates on the different CdS surfaces is also shown in Fig. 9b where it is seen that the Cu_2S growing on the basal plane (horizontal) is thicker than it is growing on a prismatic plane (vertical).

The rocking curves for the $(10\bar{1}0)$ and (0002) CdS planes and the corresponding (080) and (004) Cu_2S planes made using a Cu_2S fine focus tube and a Lang camera are shown in Fig. 10. The dotted lines are parallel to the x-ray line source, and the tall, narrow double peaks are the α_1 and α_2 CdS peaks and the short, broad peaks are the Cu_2S peaks. An important point to be elaborated on in the next section is that the α_1 and α_2 CdS peaks for the $(10\bar{1}0)$ reflection in Fig. 10a and 10b are all located in the same position, but the (080) Cu_2S peaks shift or do not exist. Also, in Fig. 10c the (0002) CdS peaks are fixed but the (004) Cu_2S peaks are not and there is more than one peak.

A back wall cell was fabricated from a needle crystal that had one prismatic surface polished flat, but the back surface contained two sets of intersecting prismatic planes. These intersections are represented by dotted lines in Fig. 11a and 11b. Indium contacts were evaporated on to the front surface and ohmic contacts were made by annealing in nitrogen at 200°C for 5 min. The front surface was then covered by black wax and the crystal was dipped into a CuCl solution for ~ 2 hr. The black wax was removed and then a contact to the rear wall was made using silver paint. The results of a scanning light spot scan using a He-Ne laser is shown in Fig. 11c. There it is seen that the open-circuit voltage is less in the front wall contact area and, more significantly, in the vicinity of the intersecting prismatic planes. This is what one would expect if a grain boundary was formed parallel to the lines of intersection.

Another back wall cell was constructed in a similar manner. The only difference is that the rear side of the CdS crystal contained a 45° beveled edge. This is represented by a dotted line in Fig. 12a. The solid curved line in the lower right-hand corner shows that the sides of the crystal were not everywhere normal to the front surface. The scanning light spot scan shown in Fig. 12b differs from that in Fig. 11c in that there is not a line of lower output that corresponds to the intersection of the two CdS planes on the back wall.

Discussion and Conclusions

The photographs in Figs. 6-9 support the idea that a grain boundary forms in the Cu_2S film at the intersection of adjacent planes in the CdS substrate. In Fig. 6a and 6b it appears that grain boundaries separate sections of the Cu_2S film that nucleate on different nonprismatic planes of the CdS hexagonal flat top. In Fig. 7 the Cu_2S film growing on adjacent prismatic planes of a CdS needle appears to grow together imperfectly at the intersection (Fig. 7a). That this is the case is supported by the observation that the Cu_2S at the intersection is preferentially attacked by an etch (Fig. 7b). In Fig. 8 there also appears to be an angular mismatch in the Cu_2S film at the intersection of prismatic CdS planes, and the Cu_2S growing on the different CdS surfaces has a different orientation.

One can also see from these photographs that the morphology of the Cu_2S depends on the surface preparation and orientation of the CdS substrate and that the Cu_2S growth rate has an orientation dependence.

In Fig. 6c and 6d one sees that the Cu_2S film is much rougher when it is grown on an etched z-face (Fig. 6c) than it is when the face is not etched (Fig. 6d). In Fig. 9a it is seen that the morphology of the Cu_2S growing on a prismatic CdS surface is different than it is growing on a nonprismatic surface. For reasons given in the previous section the film on the nonprismatic surface is also thinner. That the Cu_2S growth rate has an orientation dependence is also shown in Fig. 9b where it is seen that the film growing on the basal CdS surface is thicker than the one growing on the prismatic surface. An additional observation we made is that the rate of growth of the Cu_2S decreases with time more rapidly when growth occurs on polished z-face than it does on an etched z-face. This could be due to the fact that the growth of Cu_2S is diffusion limited, and the diffusion rate is greater for films grown on an etched surface because these films contain more grain boundaries due to the fact that growth occurs on a rough substrate surface.



Fig. 8a. A photomicrograph of a (0001) cross section of a CdS platelet with a Cu_2S film growing on it (100 \times).



The x-ray rocking curve data in Fig. 10 can be explained by the formation of small angle grain boundaries at the intersections of a nonprismatic plane with a prismatic plane and with the basal plane, and the formation of large angle grain boundaries at the intersection of adjacent nonbasal planes. That small angle grain boundaries form can be seen in Fig. 10a. The angular separation ($\sim 0.3^\circ$) of the (01 $\bar{1}$ 0) CdS and (080) Cu_2S rocking curves for growth on the prismatic (01 $\bar{1}$ 0) surface (lower curves) is such that the two planes must be parallel. The (080) curve has a larger θ value since its d spacing is less. However, when the same reflections are recorded in the tapered region the (080) curve is shifted about a degree. It is shifted because the Cu_2S on the nonprismatic plane is related to the Cu_2S on the prismatic plane by a rotation of 1° about the horizontal axis. This is about what was predicted in the section on Theoretical Background.

It should also be pointed out that there is only one (080) reflection from the Cu_2S on the nonprismatic planes so that there is no splitting between adjacent nonprismatic planes. Rather, the sections of the Cu_2S film on the adjacent nonprismatic and prismatic planes make an angle of 60° with each other. This is due to the fact that a (010) Cu_2S plane grows parallel to all six of the crystallographically equivalent {01 $\bar{1}$ 0} type CdS planes and this is shown in Fig. 10b. There is no (080) reflection from the Cu_2S growing on the top CdS plane because the (010) plane has been rotated 60° away from the (010) plane on the middle CdS plane in order to conform with the CdS crystal. When the crystal is rotated 60° about the c-axis, the reflections from the section that was originally the top section and is now the middle section are identical to those of the original middle section.

It should also be pointed out that there is only one (080) reflection from the middle section. Thus the Cu_2S growing on the nonprismatic CdS plane is not misaligned from the Cu_2S growing on the prismatic CdS plane by a rotation about the c-axis; it is only misaligned about an axis normal to the c-axis as was shown in Fig. 10a.

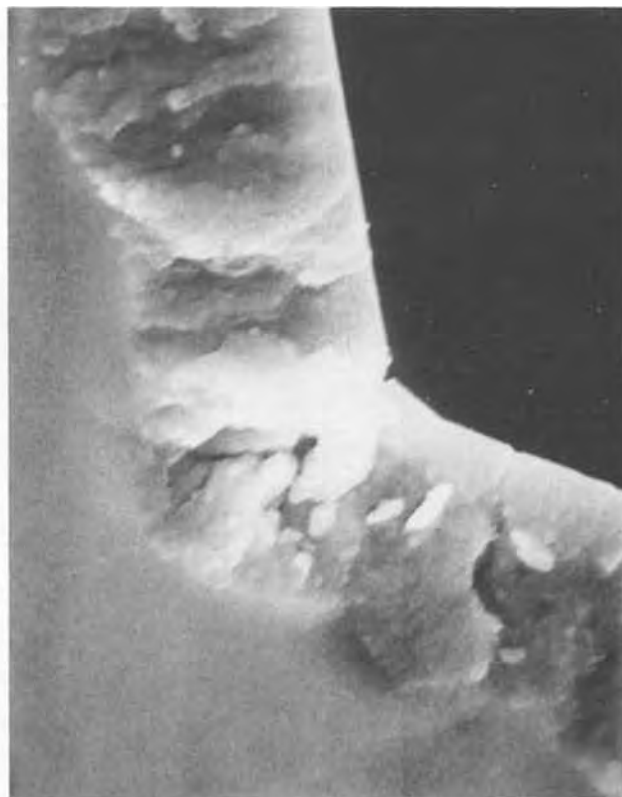


Fig. 8b and c. Enlargements of two regions at the intersection of two CdS planes (5000 \times)

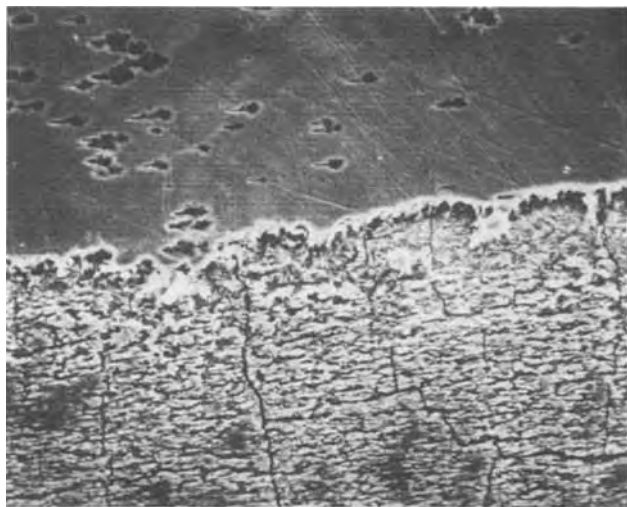


Fig. 9a. A photomicrograph of the Cu_2S growing near the intersection of a prismatic (lower) plane and a nonprismatic (upper) plane ($500\times$).



Fig. 9b. A photomicrograph of the Cu_2S film growing on the (0001) CdS plane (horizontal) and on a prismatic plane (vertical) ($500\times$).

The large angle rotations about the c-axis do not change the orientation of the basal plane, only rotations about axes in the basal plane do, and this is shown in Fig. 10c where the (0002) CdS and (004) Cu_2S rocking curves are recorded. There it is seen that the Cu_2S (001) plane in the sections of the Cu_2S film growing on the nonprismatic surfaces is related to the (001) Cu_2S growing on the basal surface by a rotation of 1° about the intersection of the nonprismatic and basal planes. The (004) reflection for the lower set of rocking curves is for a film with its (001) plane growing parallel to the (0001) CdS plane. The second (040) peak must be due to reflections from the Cu_2S growing on the nonprismatic planes.

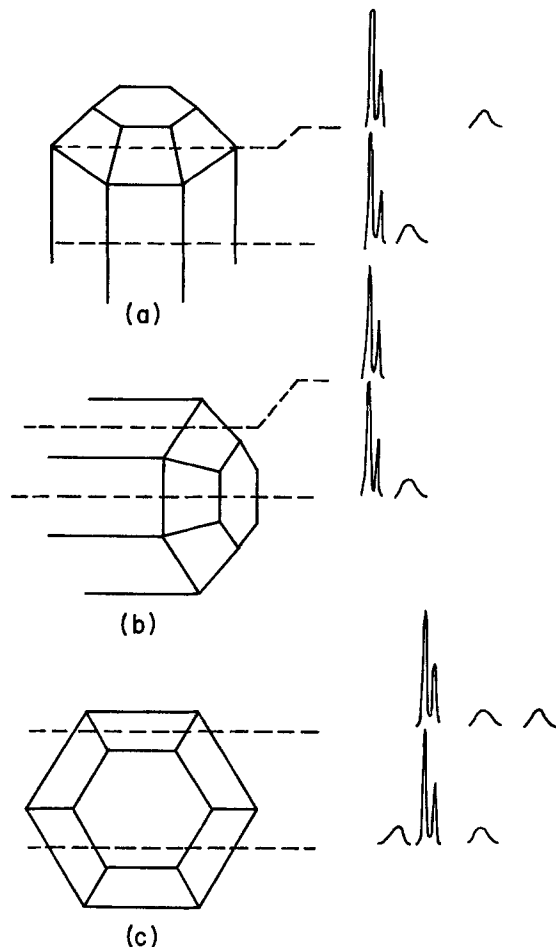


Fig. 10. (a) $(0\bar{1}\bar{1}0)$ CdS and (080) Cu_2S rocking curves with the x-ray beam normal to the c-axis for growth on the prismatic (lower) and nonprismatic (upper) CdS planes. (b) $(0\bar{1}\bar{1}0)$ CdS and (080) Cu_2S rocking curves with the x-ray beam parallel to the c-axis for growth of Cu_2S on a prismatic surface parallel to the plane of the paper (lower) and for growth on an adjacent prismatic plane. (c) (0002) CdS and (004) Cu_2S rocking curves for Cu_2S growth on the CdS basal plane and two nonprismatic planes (lower) and on three nonprismatic planes (upper).

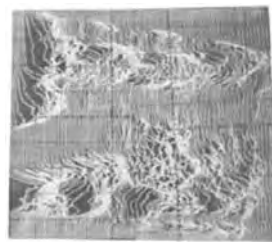
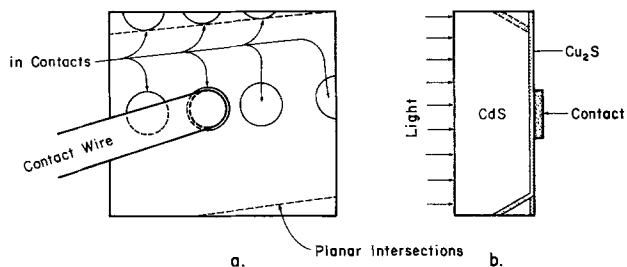


Fig. 11. The top (a) and side (b) view of the back wall cell with the Cu_2S film growing on adjacent prismatic CdS planes. (c) A scanning light spot scan of this cell.

There is a shift since there is a component of the rotation axis that is parallel to the x-ray line.

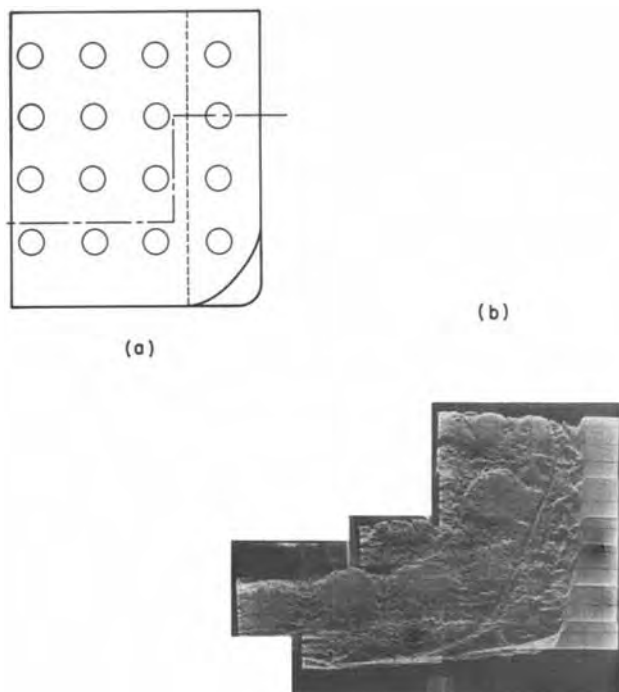


Fig. 12. (a) The top view of the back wall cell with the Cu_2S growing on adjacent prismatic and nonprismatic CdS planes. (b) A scanning light spot scan of the portion of this cell dotted in (a).

There are two (040) peaks, both of them shifted away from parallelism, in the upper set of curves. The closer peak is from the two sections of the film that have a component of the rotation axis parallel to the x-ray beam, and the more distant peak is from the section of the film for which the rotation axis is parallel to the x-ray beam.

That the large angle grain boundary formed at the intersection of adjacent prismatic planes has a detrimental effect on the cell characteristics is shown in the scanning light spot scan in Fig. 11c. There it is seen that the open-circuit voltage in the vicinity of the grain boundaries is reduced. It is likely that the reduction is due to an increased leakage current due to the shunts formed at the intersection of the grain boundary and the junction.

There is no equivalent detrimental effect in the open-circuit voltage at the intersection of the prismatic and nonprismatic planes in Fig. 12b. This could be due to the fact that the small angle grain boundary at the intersection does not have as detrimental effect as the large angle grain boundary formed at the intersection of adjacent prismatic planes. It could also be due to the

fact that the intersection was formed by polishing so that the intersection was a bit rounded. Therefore the change in orientation could occur over a larger distance.

Acknowledgments

We would like to acknowledge the support of the NSF Grant DMR-75-09329 and the Research Corporation Grant 7785. We also would like to thank V. A. Surprenant and N. Inoue for their technical assistance, C. W. Wilmsen for the use of some of his equipment, and M. H. Christmann and the 3M Company for supplying the bulk CdS crystals.

Manuscript submitted Aug. 16, 1979; revised manuscript received Jan. 2, 1980.

Any discussion of this paper will appear in a Discussion Section to be published in the December 1980 JOURNAL. All discussions for the December 1980 Discussion Section should be submitted by Aug. 1, 1980.

Publication costs of this article were assisted by the Colorado State University.

REFERENCES

1. L. R. Shiozawa, F. Augustine, G. A. Sullivan, J. M. Smith III, and W. R. Cook, Jr., Clevit Corp. Rept., Contract AF33 (615)-5224 (1969).
2. J. I. B. Woods and J. Phys. Chem. Solids, **34**, 171 (1973).
3. W. H. Strehlow, *J. Appl. Phys.*, **41**, 1810 (1970).
4. M. H. Christmann, K. A. Jones, and K. H. Olsen, *ibid.*, **45**, 4295 (1974).
5. D. C. Reynolds and S. J. Czyzak, *ibid.*, **31**, 94 (1960).
6. G. A. Wolff, J. J. Frawley, and J. R. Hietanen, *This Journal*, **111**, 22 (1964).
7. S. Martinuzzi, F. Cabane-Brouty, and J. F. Bretzner, in 9th IEEE Photovoltaics Specialist Conference, 1972, p. 111.
8. K. W. Boer *et al.*, NSF/RANN/AER 72-03478 A03/FR/75, p. 36.
9. K. A. Jones, *J. Cryst. Growth*, **43**, 165 (1978).
10. K. A. Jones, C. H. Cheng, and B. F. Shirreffs, Proceedings of 13th IEEE Photovoltaics Specialists Conference, 1978, p. 513.
11. W. G. Oldham and A. G. Milnes, *Solid State Electron.*, **7**, 153 (1964).
12. H. Kressel, *J. Electron. Mater.*, **4**, 1081 (1975).
13. A. Rothwarf, NSF/RANN/AER 72-03478 A03/TR75/4.
14. A. Rothwarf, Proceedings of 12th IEEE Photovoltaics Conference, 1976, p. 488.
15. J. Singer and P. A. Faeth, *Appl. Phys. Lett.*, **11**, 130 (1967).
16. R. W. Buckley and J. Woods, *J. Phys. C (Appl. Phys.)*, **7**, 663 (1974).
17. P. F. Linquist and R. H. Bube, *This Journal*, **119**, 936 (1972).
18. K. A. Jones, *J. Cryst. Growth*, **19**, 33 (1973).
19. K. A. Jones, To be published in *J. Cryst. Growth*.
20. K. A. Jones, To be published.

Generation Mechanism of Dislocations in Local Oxidation of Silicon

Kenji Shibata and Kenji Taniguchi

NEC-Toshiba Information Systems Incorporated, Kawasaki, Kanagawa, 210, Japan

ABSTRACT

Local oxidation conditions and film thickness combinations of Si_3N_4 and SiO_2 are studied to investigate the generation mechanism of dislocations using (001) oriented silicon wafers. The nature of dislocations in Si is examined by Secco etching and transmission electron microscopy is used for the determination of Burgers vectors. Dislocations have been generated in the film combinations with more than 2000Å Si_3N_4 or with less than 78Å SiO_2 at 1000°C oxidation in wet O_2 . Edge and screw dislocations are found underneath and close to Si_3N_4 film, respectively. These dislocations are generated in the initial stage of oxidation.

Application of silicon local oxidation technology for the fabrication of integrated circuits has various significant advantages, such as packing density increase, reliability improvement in metal interconnection, and a capacitance reduction of the active regions. This technology has been increasingly advanced and adapted to LSI fabrications. At present, however, there are still a few problems to be solved. Local oxidation of silicon is performed by masking a part of the silicon surface with a chemical vapor deposited Si_3N_4 film. As is well known, high density dislocations are induced in the silicon substrate during local oxidation processing, if the intrinsic stress of the Si_3N_4 film exceeds the yield stress for silicon. A few works have been carried out on the crystallographic analysis of the dislocations (1) and on the processing method to reduce the defects (2-4). The induced defects were reported to be 60° type dislocations (1).

In this paper, the nature and distribution of dislocations induced by local oxidation are studied in detail, for various combinations of local oxidation conditions and film thicknesses of Si_3N_4 and pad SiO_2 . It has been analyzed by transmission electron microscopy that two types of dislocations are induced, that is, edge dislocations located underneath Si_3N_4 film and screw dislocations near the Si_3N_4 film edges. On these results, the generation mechanism of dislocations is discussed.

Experimental

Substrates used were boron-doped, P-type, (001) silicon wafers of 6 ~ 8 Ω-cm. The sample preparation and experimental procedure employed in this study are shown in Fig. 1. Silicon substrate surfaces were covered with thermal SiO_2 films (pad SiO_2) ranging from 0 to 330Å thick, grown at 1000°C in dry O_2 . Subsequently, Si_3N_4 films ranging between 500 and 3000Å in thickness were deposited chemically onto the pad SiO_2 films by $\text{SiH}_4\text{-NH}_3$ reaction at 800°C. After patterning these films as shown in Fig. 1, the exposed regions of silicon substrate were oxidized locally from 1.0 to 1.5 μm at temperatures of 900°, 1000°, and 1100°C in wet O_2 . The film edges of Si_3N_4 were aligned parallel to <110> Si directions on the (001) surface.

After removing all the films, crystalline defects induced in the silicon substrate were examined by etch pits revealed by Secco etching (5). Furthermore, transmission electron microscopy (TEM) at 100 keV was used for the analysis of Burgers vectors and dislocation characterization. The samples for TEM observations were prepared by thinning the silicon substrates by chemical etching from the back side.

Results

Effects of pad SiO_2 and Si_3N_4 film thicknesses.—High intrinsic tensile stress (6) of Si_3N_4 film generates

Key words: local oxidation, integrated circuit, silicon nitride, silicon dioxide, dislocation.

crystalline defects in silicon substrates, if it exceeds the yield stress for silicon during thermal oxidation. In this work, in order to study this stress effect, the relationship between the pad SiO_2 and Si_3N_4 film thicknesses on crystal defects was examined. Figure 2 shows the Secco-etched Si surface for a combination of no pad SiO_2 and 2000Å Si_3N_4 film as an example. In Table I, the degree of crystalline damage induced in the silicon substrates is summarized for various thickness combinations. These results were obtained from the etch pit observations by Secco etching. "Yes" and

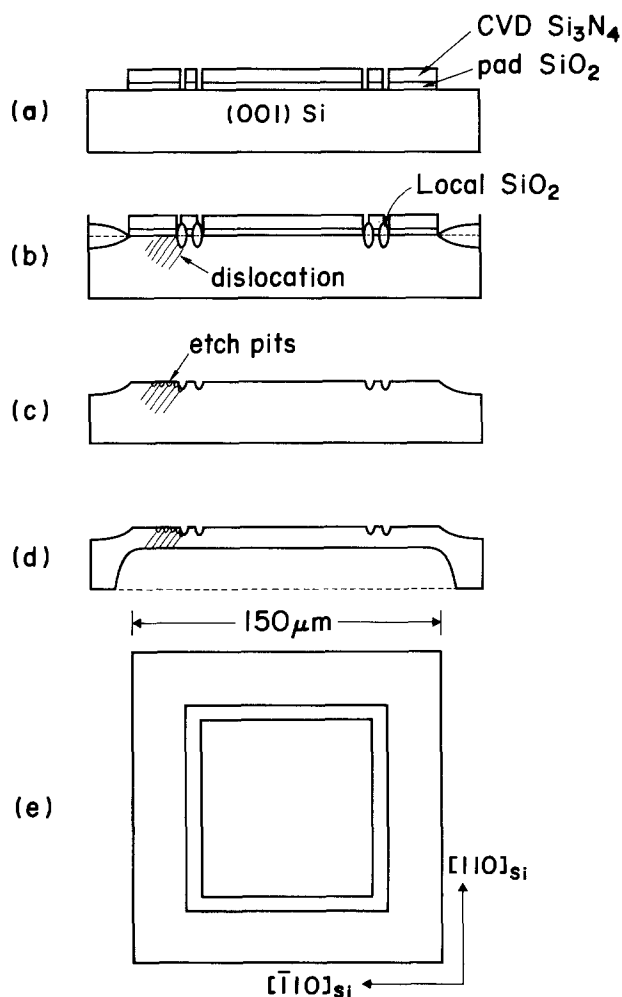


Fig. 1. Sample preparation and experimental procedure: (a) after patterning Si_3N_4 and SiO_2 films, (b) local oxidation, (c) sample for optical microscope inspections, (d) sample for transmission electron microscope inspections, (e) dimensions of top view observed.

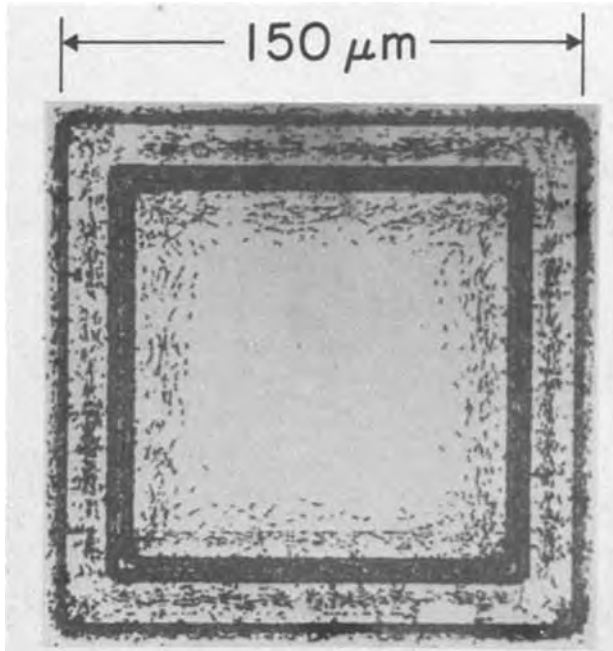


Fig. 2. Secco-etched Si surface for a combination of no pad SiO₂ and 2000Å Si₃N₄ film.

"Yes*" in this table indicate the amounts of etch pits in increasing order. The following results are obtained from Table I: (i) no dislocation is generated under Si₃N₄ thickness less than 2000Å except for no pad SiO₂, (ii) in the case of 3000Å Si₃N₄ film thickness, dislocations are generated regardless of pad SiO₂ thickness, and (iii) in the case of no pad SiO₂, a high density of dislocations is generated along Si₃N₄ film edges regardless of the Si₃N₄ film thickness, as seen in Fig. 2. These results mentioned above were studied in detail by transmission electron microscopy. The detailed examinations of these dislocations will be discussed later.

Effects of oxidation temperature and time.—No pad SiO₂ case was examined because the influence of oxidation conditions on the crystalline damages remarkably appear. The oxidation was carried out at 900°, 1000°, and 1100°C in wet O₂. Figures 3 and 4 show optical micrographs of Secco-etched silicon surfaces oxidized under the conditions of 1000 and 3000Å thick Si₃N₄ films, respectively. In the case of 1000Å Si₃N₄ film, a marked dependence on the oxidation temperature can be observed (Fig. 3). For a 900°C local oxidation, etch pits due to dislocations are randomly distributed in the vicinity of Si₃N₄ film edges. The amount of etch pits and the randomly distributed ones are decreased with increasing oxidation temperature, as seen in Fig. 3(b). It should be noted that no dislocations are formed in regions apart from the Si₃N₄ film edges at a higher oxidation temperature. On the other hand, in the case of 3000Å thick Si₃N₄ films, there is no significant

Table I. Crystalline damage degree induced in the silicon substrates for various thickness combinations of pad SiO₂ and Si₃N₄ films. "No" indicates no dislocations are generated. "Yes" and "Yes*" indicate the amount of etch pits in the increasing order.

Pad SiO ₂	Si ₃ N ₄			
	500Å	1000	2000	3000
0Å	—	Yes*	—	Yes*
78	No	No	No	Yes
143	No	No	No	Yes
240	No	No	No	Yes
330	No	No	—	Yes

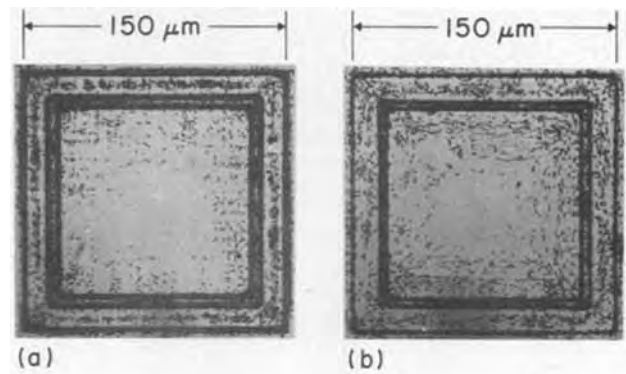


Fig. 3. Oxidation temperature dependence for 1000Å Si₃N₄ film with no pad SiO₂.

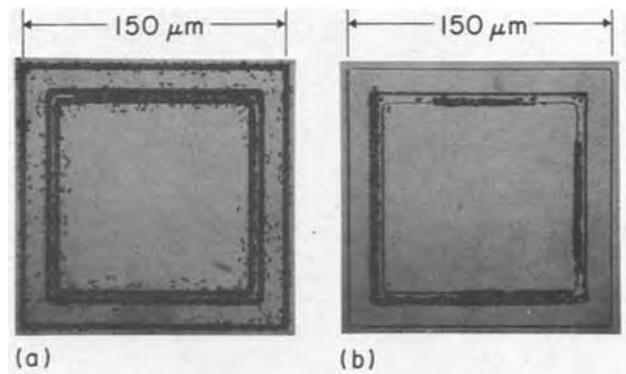


Fig. 4. Oxidation temperature dependence for 3000Å Si₃N₄ film with no pad SiO₂.

difference due to the oxidation temperature, as shown in Fig. 4. Furthermore, it can be seen that many dislocations are arrayed along the Si₃N₄ film edges and generated even in the region away from the Si₃N₄ film edges. These results are summarized in Table II. The localization degree of the generated dislocations increases in the order "E", "L", "VL", and "VVL." Table II shows the dislocations are localized with increasing oxidation temperature and with decreasing Si₃N₄ film thickness.

In the following, the oxidation time dependence is examined. It was found that density of dislocations does not depend upon the oxidation time (i.e., local oxide thickness) in the range more than 20 min, for any oxidation temperatures and any combinations of pad SiO₂ and Si₃N₄ film thickness. This result suggests that the density of dislocations saturates within 20 min, and that the silicon substrate which has not been damaged at early stages of oxidation remains dislocation-free. The generation mechanism of dislocations can be explained by these results. It will be discussed later.

Observations of crystalline defects by transmission electron microscopy.—In Fig. 3 and 4, we divided the generated dislocations into two types, that is, one is

Table II. Localization degree of the generated dislocations for various oxidation temperatures and Si₃N₄ film thicknesses. "E", "L", "VL", and "VVL" indicate the localization degree increases in the order.

Oxidation Temperature	Si ₃ N ₄		
	1000Å	2000	3000
900°C	E	E	E
1000	VL	L	E
1100	VVL	L	E

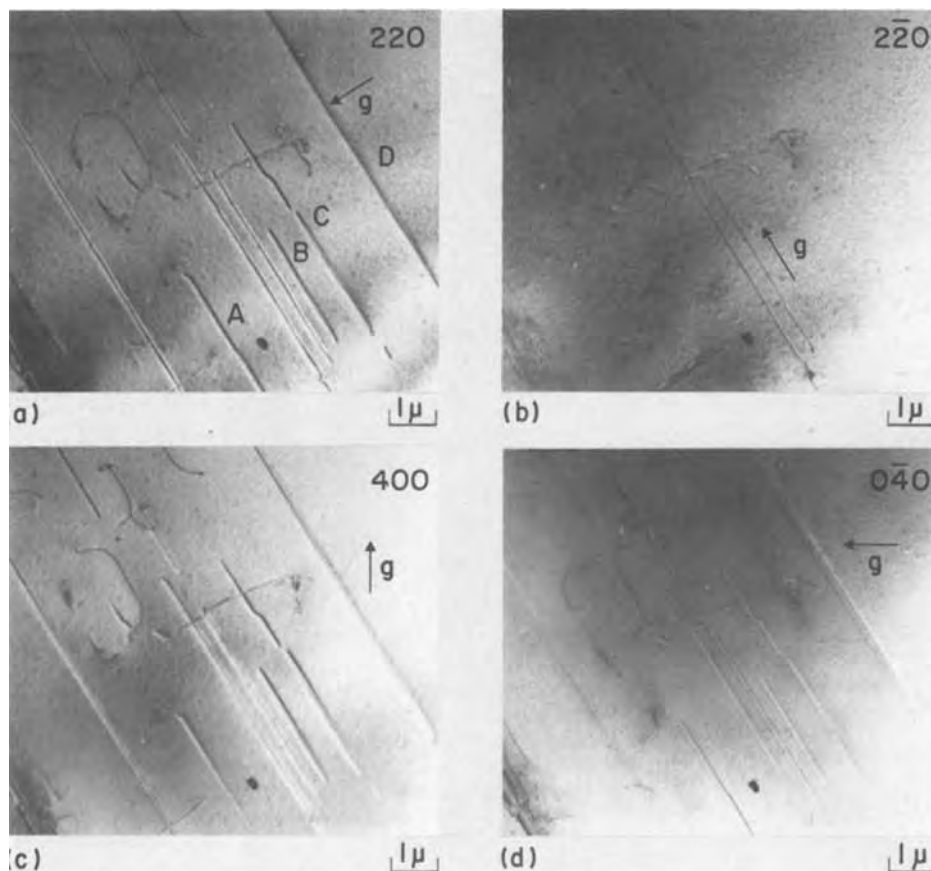


Fig. 5. Transmission electron micrographs of edge dislocations (A-type) underneath the Si_3N_4 film: in (a), (c), and (d), dislocations named A, B, C, and D are visible taken in $[220]$, $[400]$, $[040]$ reflection vectors, respectively; in (b) they are invisible taken in $[220]$ reflection vector.

arrayed close to the Si_3N_4 film edges and the other is arrayed underneath the Si_3N_4 films which is apart from the film edges. Transmission electron microscopy was used for the detailed inspection of the dislocations and the analysis of their Burgers vectors. Four different reflections of $[220]$, $[\bar{2}\bar{2}0]$, $[400]$, and $[040]$ were used to determine the crystallographic nature of the dislocations. Figure 5 is composed of four bright field images on the four different reflections in the same silicon region underneath the Si_3N_4 film which is apart from the film edges. In these micrographs, there are several

straight dislocations paralleled to the Si_3N_4 film edges along a $\langle 110 \rangle$ direction of silicon. In Fig. 5(a), (c), and (d), all of the dislocations are visible, but in Fig. 5(b), the dislocations named A, B, C, and D in Fig. 5(a) have vanished. This observation proved that these dislocations consist of pure edge component having the $a/2 [110]$ Burgers vector, and are named A-type dislocation hereafter.

Figure 6 shows bright field image transmission electron micrographs on the reflections of $[220]$ and $[\bar{2}\bar{2}0]$ in the region near the Si_3N_4 film edges. These micro-

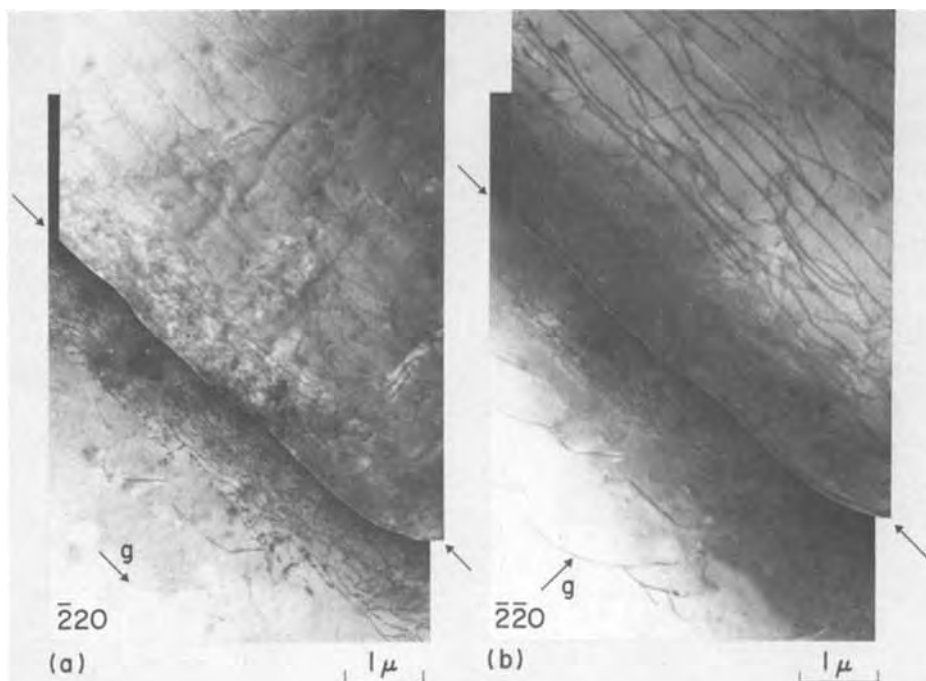


Fig. 6. Transmission electron micrographs of screw dislocations (B-type) close to Si_3N_4 film edge (indicated by arrows): in (a) dislocations are visible clearly in $[220]$ reflection vector; in (b) they are almost out of image in $[220]$ reflection vector.

graphs show both oxidized and unoxidized regions close to the film edge. High density dislocations tangling with one another have been observed along the Si_3N_4 film edges. This fact suggests that very high shear stress acts on silicon substrate, and leads to high density dislocations, which differ from A-type dislocations, and are identified as follows. As seen in Fig. 6, the dislocations close to the film edges have a clear contrast on the $[\bar{2}20]$ reflection and are almost out of image on the $[\bar{2}20]$ reflection, perpendicular to the dislocation lines. Therefore, these dislocations have the screw components, having the $a/2$ $[\bar{1}10]$ Burgers vector, and are named B-type dislocations hereafter. In conclusion, low density edge component dislocations (A-type) are generated in the regions underneath the Si_3N_4 films which are distant from the film edges. On the other hand, high density screw component dislocations (B-type) are generated in the region close to the film edges.

Discussion

In the case of no pad SiO_2 .—High density dislocations are introduced in silicon substrates during high temperature local oxidation using a Si_3N_4 film, especially for the condition of no pad SiO_2 film. This generation mechanism of dislocations is explained by high intrinsic stress of the Si_3N_4 film. It is suggested that the stress acting on the silicon substrate during the high temperature oxidation exceeds the yield stress for silicon. It has been found in this work that the dislocations introduced by the Si_3N_4 film stress can be divided into two types, A-type and B-type. From this finding, it is considered that the stress state in the region close to the Si_3N_4 film edges is different from that far away from the film edges. Serebrinsky (7) reported the stress concentration near Si_3N_4 film edges by an elastic two-dimensional model. Therefore the stress acting on the silicon substrate underneath the Si_3N_4 film is considered to be low compared to that near Si_3N_4 film edges, and to be of the same order as the yield stress for silicon, which leads to the generation of low density edge (A-type) dislocations. In this region the movement and multiplication of dislocations and their interactions could not take place easily, because the stress is not high and, in addition, the silicon substrate surface is fixed by the Si_3N_4 film. On the other hand, in the region close to Si_3N_4 film edges, the stress acting on the silicon substrate exceeds the yield stress for silicon by far, and generates high density dislocations which are confirmed to be screw ones. These results are obtained by TEM observation of the samples which are prepared by thinning the silicon wafers from the back side. This means that dislocations located near the surface of silicon substrate after the local oxidation are screw ones.

It is probable that another type of dislocation distribute in the deeper region of the silicon substrate. In view of the aim to examine the depth profile of dislocations, the cross section of the silicon substrate is observed with etch pits. It can be seen from this result that numerous dislocations are generated at the Si_3N_4 film edges and the plastic deformation occurred by the drastic motion of dislocations. The dislocation mobility should be considered to study the dislocation motion in detail.

The mobility of edge dislocations is larger than that of screw ones, and 60° dislocations move faster than screw ones in germanium as representative of crystals with a high Peierls energy especially at higher stress and temperature (8). The same results would be expected in silicon, since the crystal structure of silicon is the diamond lattice and the same as that of germanium. Therefore the distance of dislocation motion from the dislocation sources which located in the silicon surface tends to increase with edge, 60° , and screw dislocations in that order, and it is reasonable that screw dislocations are observed in the surface region of the silicon substrate after the local oxidation.

It has been found in this work that the generated dislocation density in silicon does not depend upon the time for more than 20 min. Therefore, silicon substrate remains dislocation-free, if it has not been damaged at the beginning of oxidation. It is considered that the dislocations are not introduced during the cooling down process at the end stage of oxidation, because the dislocation density is not influenced by the local oxide thickness.

These discussions lead to the following conclusions on the generation mechanism of dislocations: (i) A-type dislocations are formed in the silicon region underneath Si_3N_4 films due to intrinsic Si_3N_4 film stress in the initial stages of oxidation if the film stress is over the yield stress for silicon at a high temperature, (ii) the screw (B-type) dislocations are multiplied from the Si_3N_4 film edges since the stress of Si_3N_4 film is extremely high compared to yield stress for silicon. This multiplication stops within 20 min during local oxidation.

In the case of pad SiO_2 existence.—EerNisse (9) and Patel (10) showed that the viscous flow of thermally grown SiO_2 occurred above 960°C . Therefore, the stress acting on silicon substrates by the Si_3N_4 film can be relieved above 1000°C during local oxidation if there exists a sufficiently thick pad SiO_2 . At a lower temperature of 900°C , the stress is not relieved because the viscous flow of pad SiO_2 cannot occur, so that the crystalline damage is induced in the silicon substrate. The following results are obtained from this work: in the case of Si_3N_4 film thickness less than 2000\AA , pad SiO_2 film at least 78\AA thick is necessary in order to make the silicon substrate free of dislocations. However, in the case of Si_3N_4 film thickness more than 3000\AA , the dislocation-free silicon substrates are not obtained even if a 330\AA SiO_2 film are used. This result indicates that the stress acting on silicon substrates overcomes the yield stress for silicon in spite of the viscous flow of the pad SiO_2 for more than 1000°C oxidation.

Conclusion

The generation mechanism of the crystalline defects in silicon associated with the local oxidation technology has been investigated. Defect observations were carried out by Secco etching and transmission electron microscopy techniques.

It has been found by transmission electron microscopy observations that two types of dislocations are generated in silicon substrate by high intrinsic stress of Si_3N_4 films. A-type dislocations which have the edge component are parallel to Si_3N_4 film edges and to the $\langle 110 \rangle$ directions. These dislocations locate in the region covered by the Si_3N_4 film. On the other hand, B-type dislocations are of a high density and locate near the Si_3N_4 film edges, and have mainly the screw component. These dislocations are generated in silicon substrates at the beginning of high temperature local oxidation.

The stress in silicon due to Si_3N_4 films can be reduced by viscous flow of pad SiO_2 lying under the Si_3N_4 films at local oxidation temperatures above 960°C . The amount of induced dislocations decreases with pad SiO_2 film thickness and increase with Si_3N_4 film thickness. The dislocation-free conditions have been found in combinations of less than 2000\AA Si_3N_4 and more than 78\AA SiO_2 films.

Acknowledgments

The authors wish to thank Prof. H. Fujita, his co-workers, Dr. N. Sumida at Osaka University, Prof. R. Horiuchi, Assist. Prof. T. Kishi, and his co-workers at the University of Tokyo for their kind permission to use transmission electron microscopes. They also thank Kashiwagui and Dr. Y. Yasuda for valuable discussions and critical readings of this manuscript. Takeuchi and Chiba are also appreciated for the sample preparation.

Manuscript submitted May 3, 1979; revised manuscript received Nov. 15, 1979.

Any discussion of this paper will appear in a Discussion Section to be published in the December 1980 JOURNAL. All discussions for the December 1980 Discussion Section should be submitted by Aug. 1, 1980.

Publication costs of this article were assisted by NEC-Toshiba Information Incorporated.

REFERENCES

1. I. Magdo and A. Bohg, *This Journal*, **125**, 932 (1978).
2. A. Bogn and A. K. Gaid, *Appl. Phys. Lett.*, **33**, 895 (1978).
3. E. Bassous, H. N. Yu, and V. Maniscalco, *This Journal*, **123**, 1729 (1976).
4. P. C. Parekh, *ibid.*, **125**, 1703 (1978).
5. F. Secco d' Aragona, *ibid.*, **119**, 948 (1972).
6. E. A. Irene, *J. Electron. Mater.*, **5**, 287 (1976).
7. J. H. Serebrinsky, *Solid State Electron.*, **13**, 1435 (1970).
8. V. Celli, M. Kabler, T. Ninomiya, and R. Thomson, *Phys. Rev.*, **131**, 58 (1963); M. N. Kobler, *ibid.*, **131**, 54 (1963).
9. E. P. EerNisse, *Appl. Phys. Lett.*, **30**, 296 (1977); E. P. EerNisse and G. F. Derbenwick, *IEEE Trans. Nucl. Sci.*, **ns-23**, 1534 (1976).
10. J. R. Patel and N. Kato, *J. Appl. Phys.*, **44**, 971 (1973).

Effect of Lubricant Environments on Saw Damage in Si Wafers

T. S. Kuan, K. K. Shih,* and J. A. Van Vechten*

IBM Thomas J. Watson Research Center, Yorktown Heights, New York 10598

and W. A. Westdorp

IBM Data Systems Division, East Fishkill Facility, Hopewell Junction, New York 12533

ABSTRACT

The effect of lubricant environments on the structure of the surface damage induced in Si during the wafer sawing process was tested for four different lubricants: water, methyl silane solution, Kleenzol B, and dielectric oil. The nature of the saw damage was characterized by transmission electron microscopy and the depth profile of the damage determined by a taper-sectioning method. The results showed that the number and depth of surface damage is sensitive to the chemical nature of the saw lubricant. Lubricants that are good catalysts for breaking Si bonds can induce more fracture cleavage and produce less surface damage. Lubricants that can dampen more effectively the out-of-plane blade vibration can also reduce the surface damage. The chemomechanical effect of the lubricant environment was also tested by applying different potentials on Si crystal during the sawing. Correlation between the applied potential and the depth of damage in the dielectric oil environment was observed and possible mechanisms involved were discussed.

The sawing of boules into wafers is the most violent process to which semiconductor materials are subjected in the course of device fabrication. The damage introduced by this process into single crystal Si is so extensive that typically 90 μm must be etched off each side of the wafer in order to obtain practical yields for integrated circuit products. Careful and expensive procedures must be employed after sawing to achieve an adequate degree of wafer flatness. As the most advanced Si solar cell designs require starting wafers only 50 μm thick, this waste of a rather expensive commodity is a significant economic factor in the alternant energy field.

The nature and depth of surface damage induced in Si wafers as they are sawed from the single crystal is known to be sensitive to several operational variables, such as blade size, feed rate, blade tension, direction of sawing, etc. (1-5). When the wafers are subjected to subsequent lapping and polishing treatments, the depth of the induced damage depends mainly on the abrasive particle size (6, 7). Previously these sawing, lapping, and polishing (the so-called wafer shaping processes) were treated as physical processes in which the mechanical condition of the operating system is the controlling factor. Little attention was paid to the relation between the physico-

chemical conditions of the system and the surface damage structures. The purpose of this study is to show that the chemistry and electrochemical potential of the saw lubricant are important operational variables, and the depth of surface damage can be reduced by improving the lubricant environment.

The nature of the surface damage due to mechanical abrading has been shown to consist of a layer of chipped and cracked material at the surface and a layer containing varying density of dislocations underneath the surface (7, 8). The processes which introduce the dislocations into the damaged layers during the abrading process have not yet been determined in the literature. However, several mechanisms including the effects of local heating (8), hydrostatic pressure (6, 9), and formation of dislocation cracks (10) have been suggested. Although saw damage structures identified as microcracks have been reported (4, 5), the detailed structure of damage at different depths due to the sawing process has not been studied at high magnification.

The sawing process involves rupturing of chemical bonds to create new surface. For brittle materials, such as Si, this is believed to be largely a cleavage process although plastic flow is also possible at the surface (11). Any environment that can either reduce the surface free energy or increase the mobility of near-surface dislocations and the speed of the crack propagation should reduce the energy expended in

* Electrochemical Society Active Member.

Key words: silicon wafers, saw damage profiles, lubricant effects, transmission electron microscopy (TEM).

the sawing operation (12). On the other hand, the depth of damage, which depends on the detailed pattern of crack propagation and the dislocation motion in the plastically deformed region, can also be changed in different environments.

In this study four different lubricant environments were tested: (i) that of the standard production process—water, which is a strong catalyst for the making and breaking of Si covalent bonds (13); (ii) dielectric oil, which is chemically inert; (iii) a commercial cutting oil (Kleenzol-B); and (iv) a solution of methyl silane in 80 parts water, which is an even more active catalyst (13) for making and breaking Si and other covalent bonds than pure water. The methyl silane solution has been used in the oil drilling and ballmilling industries to minimize the energy of comminution.

Since the depth of saw damage is determined by the extent to which cracks, single dislocations, or dislocation networks can propagate into the bulk material from the surface (7, 8), any change in the mobility of dislocations in the Si crystal could affect the number and configuration of dislocations introduced during the sawing process. It has been suggested that for covalent crystals in a liquid lubricant, the electrical influence of the zeta potential can be felt at several microns below the surface, and the induced redistribution of the carriers could change the charge state of dislocations and point defects in these near-surface regions (14). It has also been predicted that the velocity of dislocations in Si or Ge crystal with the diamond structure is related to the dislocation charge (15). If these assumptions are valid, then we would expect the damage structure to be dependent on the surface potential. To test this effect, we applied, in the dielectric oil environment, a positive or negative potential on the Si crystal during the sawing and looked for the changes in the depth of damage.

In the previous studies of mechanically induced surface damage in Si, the depth of damage has been measured using a variety of techniques, e.g., the x-ray rocking-curve method (6), the etching rate method (8), the photomagnetolectric method (6), the photoconductivity decay method (6), step-etching with x-ray topography (1, 2, 16), transmission electron microscopy (5, 7), metallographic taper-sectioning method (17), etc. Only the last three methods can show the actual damage distribution. In this study the improved taper-sectioning method (18) was chosen because a rather accurate damage density profile from a large sample area can be obtained quite easily by this technique. Transmission electron microscopy was also used to study the nature of the saw damage.

Experimental Procedures

Test wafers were sawn from one vertically mounted Czochralski {100} oriented, p-type, 100 Ω -cm, Si single crystal on a commercial HAMCO ID-diamond saw with feed speed 2.54 cm/min and rotation speed 2100 rpm. The operational parameters of the six experiments are listed in Table I. The saw blade was brand new at the beginning of Experiment 1. The experiments were performed in the order listed and a total of 30 wafers were sawn in each experiment. The dielectric oil was used when the saw blade was most

worn. The wear of the diamond saw blade was considered not important since typically 3000-4000 wafers can be sawn on a new saw blade before blade replacement is required.

Since the surface damage in the wafers from different experiments will be compared directly to each other, all the operation variables, except the lubricant environments, were carefully controlled to be constant. All six experiments were performed on the same Si crystal and on the same saw. Thickness and warpage measurements were then carried out by an ADE 6043 microsense capacitance gauge, and the surface features were observed by optical microscopy.

With the modified taper-sectioning method, the six samples from different experiments were mounted at a time on a 5° beveling fixture using quartz sticky wax (see Fig. 1). Before the rough lap the samples were covered with another Si wafer and thin layer of epoxy mixed with 0.3 μ m alumina powder to protect the sharp edges from chipping off. Then, by use of 12 μ m alumina particles suspended in water, the specimens were hand-polished until a flat taper surface was attained. This was then followed by a finer polish using 5 μ m alumina powder to obtain a shiny surface. This mechanical polishing is known to generate surface damage. This damaged layer newly introduced from polishing was removed so as not to obscure the pre-existing saw damage. This was done by chem-mech polishing which does not generate additional surface damage. The polish solution used was 1 part Syton¹ HT-40 and 2 parts deionized (D.I.) H₂O. After polishing, samples were demounted and cleaned using trichlorethylene followed by acetone and ethyl alcohol. To reveal the saw damage, samples were etched for 25 sec in dilute Sirtl etch solution. The etch solution consists of one part HF and one part dilute Sirtl etch mix, which was prepared by mixing one gram CrO₃ with 4 ml D.I. H₂O. Immediately after the etch, the samples were rinsed for 5 min in D.I. H₂O. The distribution of saw damage was read directly from optical micrographs of the etched surfaces. The number of damage pits and their distances from the wafer surface were recorded and damage distribution profiles were plotted for each sample. The nature of saw damage structures were observed by transmission electron microscopy. Here the as-sawn wafers were etched from the back side to \sim 1 μ m thickness by HF/HNO₃ solution so that the damage in the very top surface layer can be observed by TEM. In order to obtain a cross-sectional view of the saw damage, TEM samples were also prepared

¹ Monsanto trade name.

Table I. The order and the different lubricant environments used in the six experiments

Experiment	Environments	Flow meter reading (mm)
1	Water	150
2	Solution of methyl silane in 80 parts water	120
3	Kleenzol B (commercial cutting oil)	150
4	Dielectric oil with no potential	150
5	Dielectric oil with +6V on crystal	150
6	Dielectric oil with -6V on crystal	150

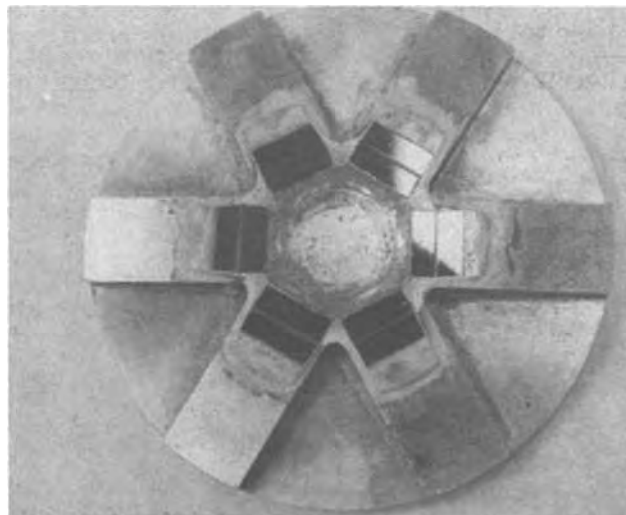


Fig. 1. 5° beveling fixture with wafer sections from six experiments mounted and polished.

by slicing the wafers along the plane perpendicular to the as-sawn surface and thinned down from both sides by an Ar-ion milling machine (19). A JEOL 200B electron microscope was used in this study.

Experimental Results

The results of thickness and warpage measurements on as-sawn wafers are listed in Table II. The thickness measurements indicated that sawing in dielectric oil can result in wafers with more uniform thickness in each wafer than sawing in water. However, the applied potential on the crystal during sawing would increase the taper to a value larger than that with water. The taper values for Kleenzol B and methyl silane solution are about the same as that for water. The measured absolute thickness values of wafers from different experiments showed that sawing in water leaves about 6-10 μm more material on the wafer than with any other process. In general, the distribution of wafer thickness is narrower in water than in any other lubricant except methyl silane, which gives a thickness distribution curve about a factor of two narrower than that for water. It is interesting to note that sawing in dielectric oil would on the average, leave about 8 μm less material on the wafer if a positive potential is applied to the crystal and about 4 μm more material for a negative potential, as compared to sawing without potential applied. The applied potential, positive or negative, also increases the warpage value as indicated in Table II (b). Here it is shown that Kleenzol B gives the largest warpage value.

The surface morphologies of wafers sawn in different environments are shown in Fig. 2. These optical micrographs indicate two kinds of surface structure: the brighter regions with scratches lying in the direction of blade motion are relatively flat, and the darker regions are places where larger pieces of silicon had chipped off. These chipped off regions are not in focus on the micrographs, but the through focus pictures showed that they are about 1 μm deep. When the saw blade cuts through the crystal, cracks are generated at the blade edge and as they propagate and meet in the crystal, small pieces of Si are knocked off and removed by the rotating blade. The diamonds plated on the edge and sides of the blade also abrade the newly cleaved surface. The cleavage and abrasive processes could give rise to two kinds of surface structure observed above. The surface morphologies of wafers sawn in Kleenzol B and in dielectric oil with +6V are very similar to that for methyl silane and dielectric oil with no potential, respectively, and,

Table II (a). Thickness measurements (μm) on wafers sawn in six different lubricant environments

Exp. No.	Number of wafers measured	Thickness variations in each wafer (Taper)		Absolute thickness (center)	
		Average	Range	Average	Range
1	11	3.3	1.6-10.2	602.4	594.3-610.4
2	11	5.5	1.5-10.5	593.0	590.6-594.8
3	12	4.7	2.5-7.7	595.8	587.3-619.3
4	12	2.6	1.5-4.1	592.5	582.9-601.6
5	12	7.2	3.0-13.2	584.5	562.0-596.0
6	12	8.8	1.6-26.9	596.7	576.4-659.8

Table II (b). Warpage measurements (μm) on wafers sawn in six different lubricant environments

Exp. No.	Number of wafers measured	Centerline warpage		Top surface warpage		Bottom surface warpage	
		Average	Range	Average	Range	Average	Range
1	11	16.6	7.9-24.1	17.5	8.4-25.5	11.2	7.4-22.5
2	11	19.1	19.5-21.3	19.1	17.3-22.8	19.3	16.7-22.6
3	12	30.0	26.4-34.3	31.0	26.1-39.5	29.1	25.5-33.0
4	12	11.2	8.2-13.7	11.8	8.0-14.6	10.7	8.0-13.5
5	12	15.6	7.7-36.7	16.4	7.9-33.4	16.0	7.1-38.9
6	12	20.0	8.9-39.5	21.5	8.8-43.6	19.7	8.5-40.1

Table III. The periodicity distance of the saw mark on wafers sawn in six different lubricant environments and the corresponding saw blade vibration frequencies

Exp. No.	Periodic distance (μm)	In unit of λ^*	Corresponding frequency (rpm)
1	21.6	1.79	1173
2	20.4	1.69	1242
3	22.5	1.86	1129
4	19.8	1.64	1280
5	23.8	1.97	1065
6	23.1	1.91	1099

$$*\lambda = \frac{\text{feed speed}}{\text{rotational speed}} = 12.1 \mu\text{m.}$$

therefore, they are not shown in Fig. 2. The continuous diamond scratches in the abrasive region have a long-range ordering with periodicity of about twice the feed distance per rotation as can easily be seen in a low magnification micrograph [Fig. 2(b)].

The periodicity distance was found to be the same on the two wafer surfaces that are on opposite sides of the saw blade, but different for different lubricant environments. The periodicity distances for the six lubricants are listed in Table III. These ordered scratches might be due to the out-of-plane blade vibration and/or the noncircularity of the center hole in the blade (4). The latter should give rise to ordered structure in unit of λ , feed distance per rotation. This is not observed. Therefore the periodic structure on sawn surface must be predominantly from the out-of-plane blade membrane vibration. This is believed to be the major damage mechanism during ID sawing of silicon wafers (4). Different environments can result in different vibration frequencies as indicated in Table III. The size and distribution of the abrasive areas (brighter areas) in Fig. 2 is sensitive to the original depth of the chipped off region and the amplitude of the blade vibration. By comparing the micrographs in Fig. 2, it is noted that dielectric oil lubricant (with zero potential) increases, while the Kleenzol B and methyl silane decrease, the abrasive area. It is noted that an applied negative potential markedly decreases this area as well.

All the observations mentioned above were made on the "A" surface, which is the wafer surface still attached to the bulk crystal during sawing. The wafer surface on the opposite side of the blade is designated "B." The rupture features on both A and B surfaces are very similar to each other for the water, Kleenzol B, and methyl silane solution cases. But the B surface in dielectric oil with no potential shows much less abraded area than the A surface. This might be due to the greater vibration amplitude of the blade and wafer in this particular lubricant during the sawing process.

Figure 3(a) shows a cross section TEM micrograph of the saw damage in the wafer sawn in water. To the left side of the micrograph is the surface line of the as-sawn wafer. This surface is protected by an epoxy layer and another Si wafer during the sample thinning process. This micrograph and many others taken indicate that the surface damage induced by the sawing is mainly an array of cracks extending

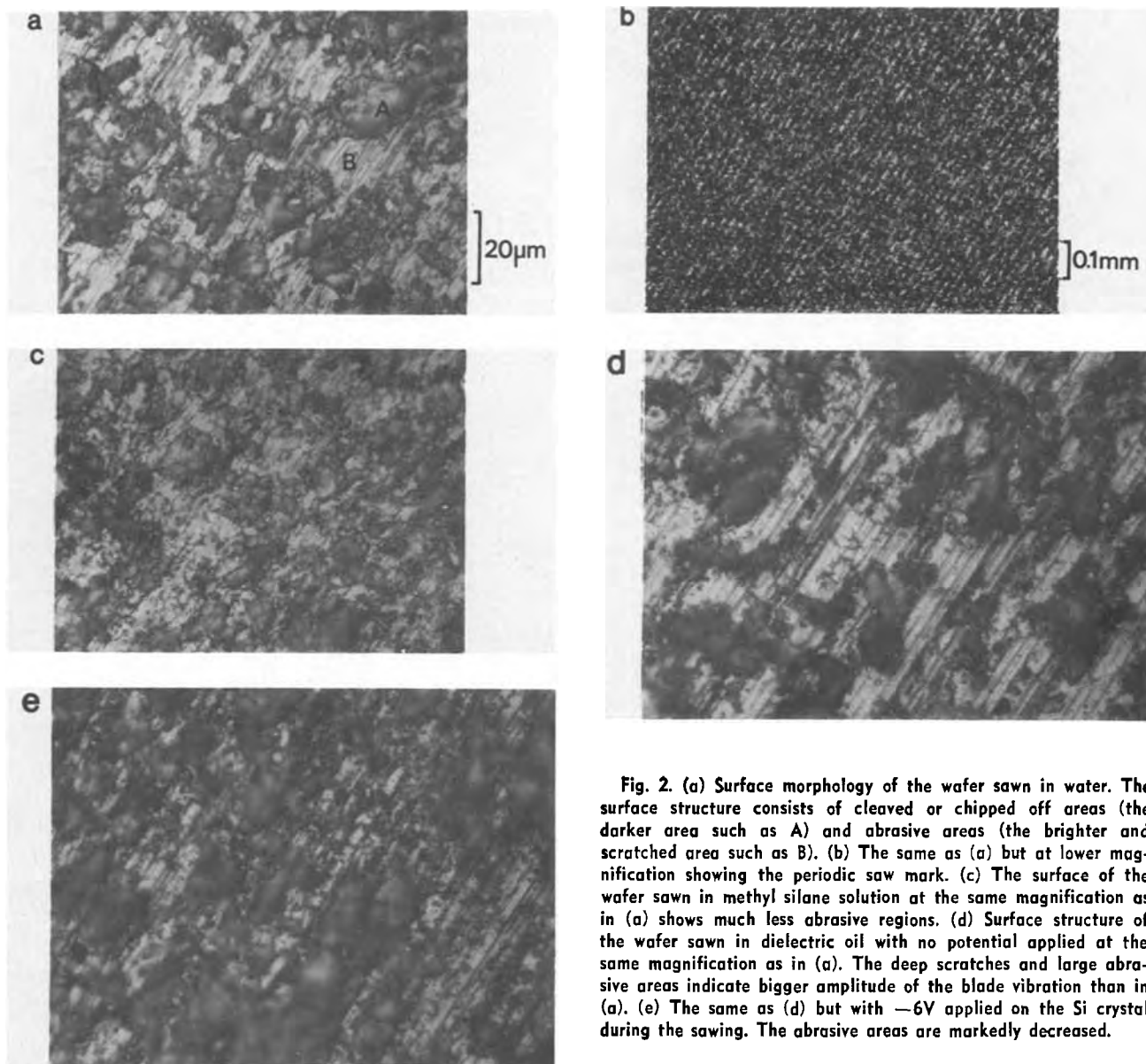


Fig. 2. (a) Surface morphology of the wafer sawn in water. The surface structure consists of cleaved or chipped off areas (the darker area such as A) and abrasive areas (the brighter and scratched area such as B). (b) The same as (a) but at lower magnification showing the periodic saw mark. (c) The surface of the wafer sawn in methyl silane solution at the same magnification as in (a) shows much less abrasive regions. (d) Surface structure of the wafer sawn in dielectric oil with no potential applied at the same magnification as in (a). The deep scratches and large abrasive areas indicate bigger amplitude of the blade vibration than in (a). (e) The same as (d) but with $-6V$ applied on the Si crystal during the sawing. The abrasive areas are markedly decreased.

from the surface to the bulk. Dislocations were found only at the very top $\sim 1 \mu\text{m}$ layer. The cracks propagate mainly along the $\{110\}$ plane [e.g., cracks A, B, and C in Fig. 3(a)] and the $\{111\}$ plane [e.g., cracks D and E in Fig. 3(a)]. In Fig. 3(a), the lengths of those cracks observed are less than $5 \mu\text{m}$, however, this length cannot be considered as the typical depth of the damaged zone, since the TEM observation is limited to a very tiny sample area [$0.5 \times 10 \mu\text{m}$ in Fig. 3(a)]. Cracks were also found by TEM technique in the sample where the top $\sim 30 \mu\text{m}$ layer has been removed by Syton polishing. The more accurate statistics of the distribution of the crack depth should be obtained by other methods which cover bigger sample area, e.g., the taper-sectioning method used in this study.

Since the dislocations are found at the "hill top" area in the top $1 \mu\text{m}$ layer [e.g., dislocation loops at F and G in Fig. 3(a)], it is believed that the occurrence of dislocation is related to the abrasive motion of the blade. This point becomes clearer if these dislocations are observed along the direction normal to the $\{100\}$ wafer surface. For this purpose the samples were prepared by etching away from the back side of the wafer the whole wafer except the top $\sim 1 \mu\text{m}$ thick layer on the front side. Figure 3(b) shows a group of dislocation half loops distributed along a straight diamond scratch at the wafer surface. These loops all lie on the $\{111\}$ plane with

their Burgers vectors also on this glide plane which demonstrates that they are punched into the surface by the diamond on the blade.

The depth profiles of the number of defects obtained by the taper-sectioning method for different saw lubricant environments are shown in Fig. 4(a) and (b). The defect numbers for each case were observed directly from 10 optical micrographs which represent the total defect underneath one line with length of 8.95 mm on the sawn wafer. Three micrographs, one for the water case and the others for the dielectric and methyl silane solution are shown in Fig. 5(a)-(c) as examples. The depth d was calculated from

$$d = b \sin 5^\circ \quad [1]$$

where b is the distance measured from the surface edge to the defect on the micrograph. The number of defects shown in Fig. 4 can be converted to crack or dislocation density D by

$$D (\text{cm}^{-2}) = 5.2 \times 10^3 \times N \text{ cm}^{-2} \quad [2]$$

where N is the number of defects shown in Fig. 3.

As shown in Fig. 5, the density of defects close to the surface is very high, thus the accuracy of the observation is limited by the size of the etch pits. Those defects that are too close to each other cannot be resolved in the micrograph, and, as shown by the TEM results, at the very edge (closest to the surface)

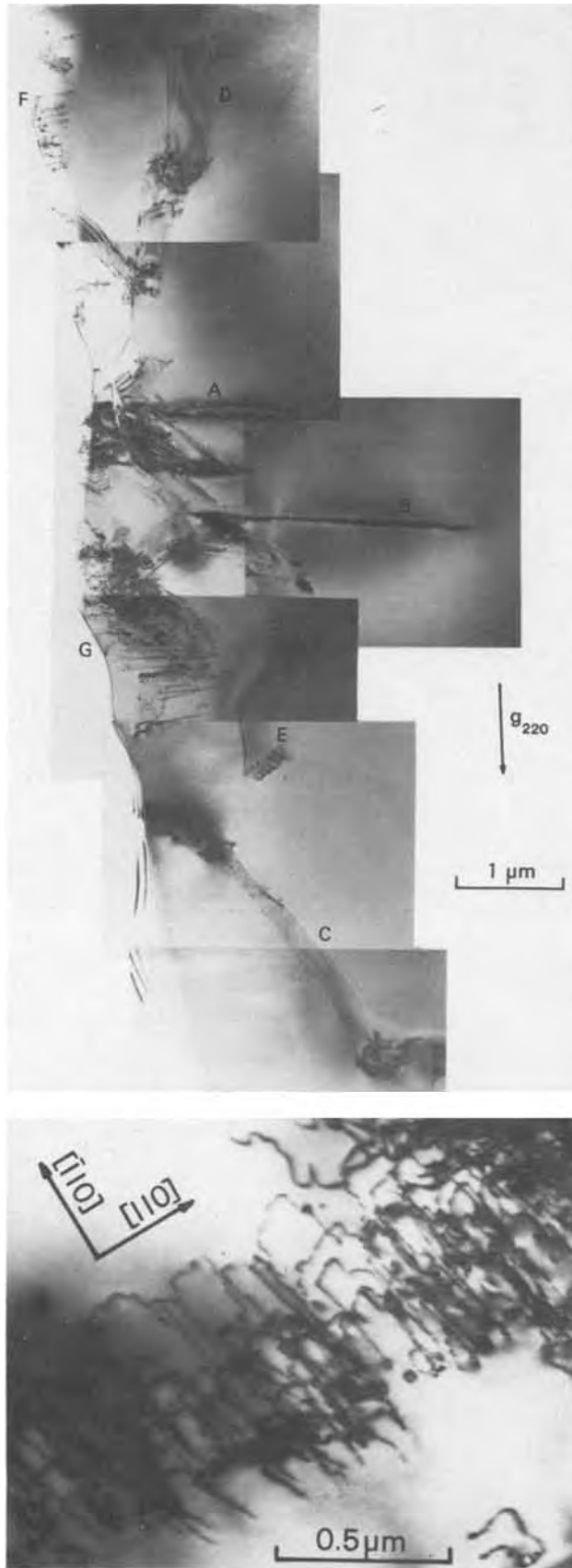


Fig. 3. (a, top) Cross-sectional TEM micrograph of the saw damage in the wafer sawn in water. (b, bottom) Dislocations in the top 1 μm surface layer of the wafer sawn in methyl silane solution.

the density of damages and the etch rate are so high that many defects are etched away from the wafer. It is therefore expected that the numbers plotted in

Fig. 4 in the top $\sim 4 \mu\text{m}$ layer are smaller than the actual values.

The damage profiles in Fig. 4 indicated that the number of defects drops markedly in the first 20 μm in the water case, and maintains a constant low value to about 50 μm . In the case of Kleenzol B and methyl silane solution, the number of cracks decreases by $\sim 20\%$ and $\sim 50\%$, respectively, as compared to the water case in the top 10 μm . In Fig. 4(b) the dielectric oil increases the number of cracks by a factor of ~ 3 as compared to water in the first 10 μm but has the rest of the profile similar to that of water. The applied positive potential very obviously increases the number of defects in the 15-30 μm range by a factor of ~ 2 and also maintains a higher value from 30 μm to the depth of 90 μm . On the other hand, the applied negative potential decreases the number by a factor of ~ 2 in the first 15 μm as compared to the zero potential case.

It is noted that in all six experiments, etch pits were observed in the area deeper than 50 μm , where the defect concentration maintained at a value approximately equal to $5 \times 10^3 \text{ cm}^{-2}$. These defects can be the very deep cracks induced during the sawing process or they can be the dislocations (e.g., swirl defects) originally present in the Si crystal. By comparing Fig. 4(a) and (b), we find that the defect density in the 50-100 μm range is slightly higher in the dielectric oil case than in the three cases plotted in Fig. 4(a), which seems to suggest that at least part of the etch pits observed in this depth range must come from the saw damage, otherwise they should maintain at the same concentration since all the experiments were performed on the same Si crystal.

Discussion

Most of the previous investigations on saw damage in Si were concentrated on measuring the depth of damage so that the damaged layer can be removed before further processing. Due to the differences in crystals, operational parameters, measurement methods, and the definitions of damage used in these investigations, the depth of damage reported varies from 7 μm to more than 50 μm (20). In this study the optical microscopy observation on etched taper-sectioned surfaces showed that the saw damage distribution can extend to 90 μm or more under the surface. Schwuttke has reported previously that some of the saw damage structures are so deep in the crystal that they can affect the reliability of the finished MOS device even after 90 μm of material has been etched off both sides of the wafer (5).

The nature of saw damage is not understood in detail prior to this work because little work on mechanically induced surface damage had been done at high magnification. Stickler and Booker (7) have reported that the damage due to different abrasive particle size consists of individual dislocations for fine abrasive and strained dislocation networks and cracking for coarser abrasives. The dislocations observed in their work indicated that plastic deformation occurs in the abrasion process. Since plastic flow cannot usually occur in Si below 600°C, the presence of dislocations were explained as due to local heating (8), hydrostatic stress from sharp corners of the particles (6, 9), or developed from healed cracks (10). The sawing of Si crystal into wafers at $\sim 2.5 \text{ cm/min}$ feed speed and 2100 rpm rotation speed is certainly a more violent process than the abrading process. Meek and Huffstutler (4) argued from their etching and fracture stress measurements that the saw damage zones are predominantly microcracks rather than dislocations. Schwuttke (5), using TEM observation, characterized the very deep saw damage as microcracks. In this work, we observed the saw damage from both the top and the cross-sectional view angles at 30,000X magnification by TEM and characterized the damage structure as mainly cracks

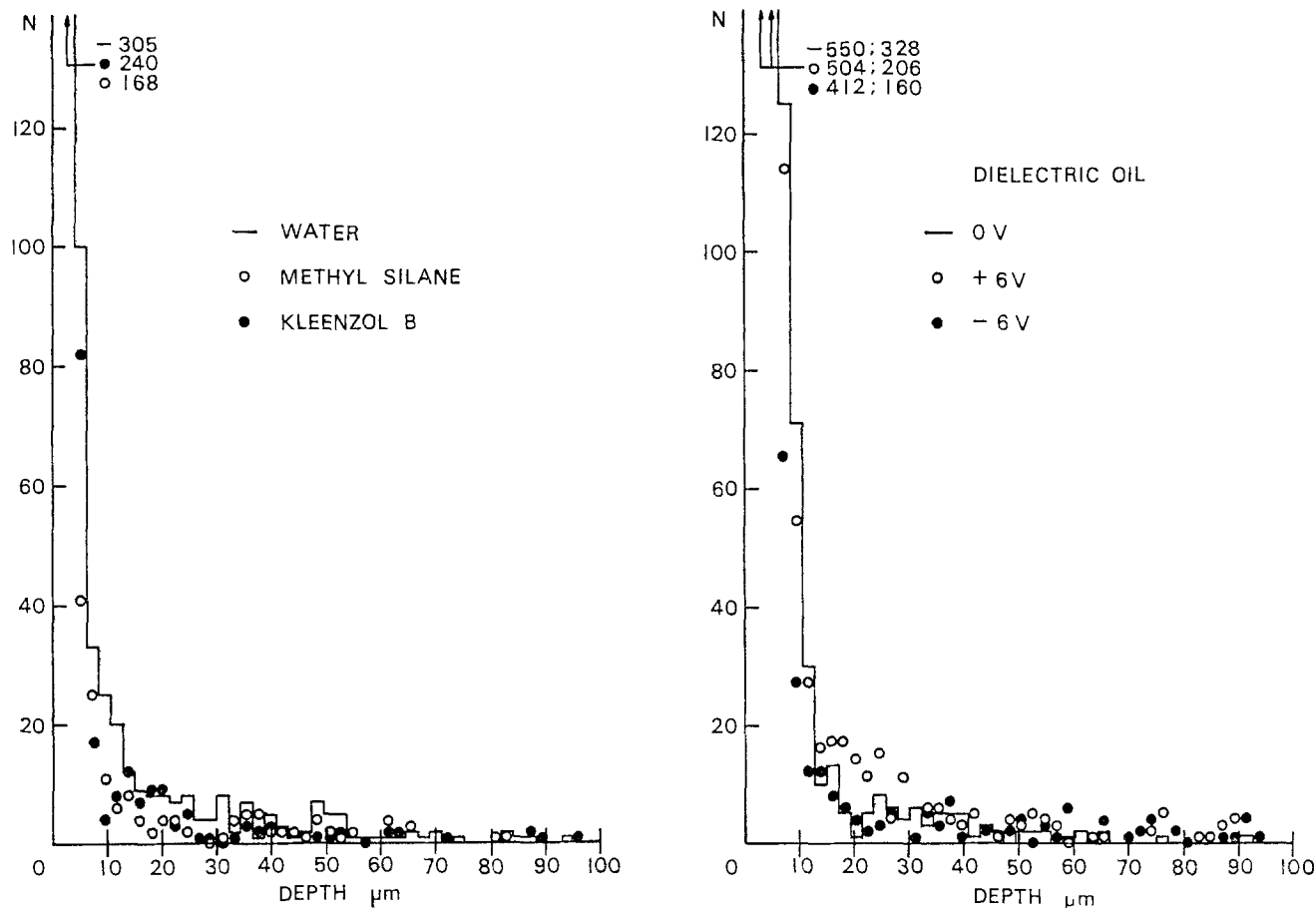


Fig. 4. (a, left) The depth profiles of the number of defects obtained by the taper-sectioning method for three different saw lubricants: water, methyl silane solution, and Kleenzol B. (b, right) The depth profiles of the number of defects induced by the sawing in dielectric oil with different potentials applied on the Si crystal.

extended roughly along both $\{110\}$ and $\{111\}$ planes. Dislocations were found only at the top $\sim 1 \mu\text{m}$ layer and their occurrence was attributed to the abrasive motion of the saw blade.

One question that is being speculated about sawing is whether plastic flow occurs at the surface when we saw Si at room temperature. The presence of dislocations strongly suggests that it does. With a constant flow of lubricant it is very unlikely that the surface temperature ever reaches 600°C , the temperature at which Si starts to deform plastically. However, detailed TEM observation on Si after microhardness indentation at room temperature by Nikitenko and Eremenko (11) and by Hill and Rowcliffe (21) and the observation of saw damage in this work indicate clearly that dislocations are produced by a slip process in the vicinity of indentation as a result of high local shear stress. Gridneva *et al.* (22) concluded from their resistivity measurement that the surface layer of Si can transform into metallic phase if the hydrostatic pressure under the indenter has reached the critical phase transition pressure, which is about 140 kb ($1.4 \times 10^{10} \text{ N/m}^2$) at room temperature [critical pressure goes as low as $9 \times 10^9 \text{ N/m}^2$ at about 600°C (23)], and that Si deforms plastically when it is in the metallic state. However, as pointed out by Hill and Rowcliffe (21), dislocations were observed to extend to several microns which is much deeper than the expected thickness of the metallic layer. Furthermore, shock wave compression experiments on Ge by Graham *et al.* (24) indicated that plastic flow can occur at stress levels less than half that required for the phase transformation. Hill and Rowcliffe (21) estimated the shear stress for plastic flow in Si to be $\sim 22.5 \text{ kb}$.

Although the observed dislocation loops indicate that the local shear stress that the diamond particles on the ID blade can introduce on the Si surface during the high speed cutting has reached the value for plastic flow to occur, the major event that creates the kerf and governs the depth of damaged zone is the initiation and propagation of cracks. If we use the water case as a standard, we can make a detailed comparison between the effects of different saw lubricants and speculate on the possible mechanisms involved. The Kleenzol B and methyl silane solution are very good catalysts for breaking Si bonds and therefore could enhance crack nucleation and propagation (13). This is evident from the presence of more chipped off regions in Fig. 2(c). The scratches in Fig. 2(c) are shallower than those in (a) and (d) which might indicate that methyl silane solution and Kleenzol B impart less drag to the saw blade so that there is less out-of-plane blade vibration than when water or dielectric oil are used. These two effects would contribute to less damage produced during the sawing. [Fig. 4(a)].

On the other hand, the noncatalytic nature of the dielectric oil would be expected to make crack nucleation and propagation more difficult and, thereby, impart more drag on the saw blade than does water and increase the amplitude of vibration. This argument is in good agreement with the observation that the scratches in dielectric oil [Fig. 2(d)] are deeper than in water and also the number and depth of cracks are substantially increased [Fig. 4(b)].

No correlation was found between the blade vibration frequency (Table III) and depth of damage (Fig. 4). It is the amplitude of the vibration that can affect the depth of crack propagation the most. The sig-

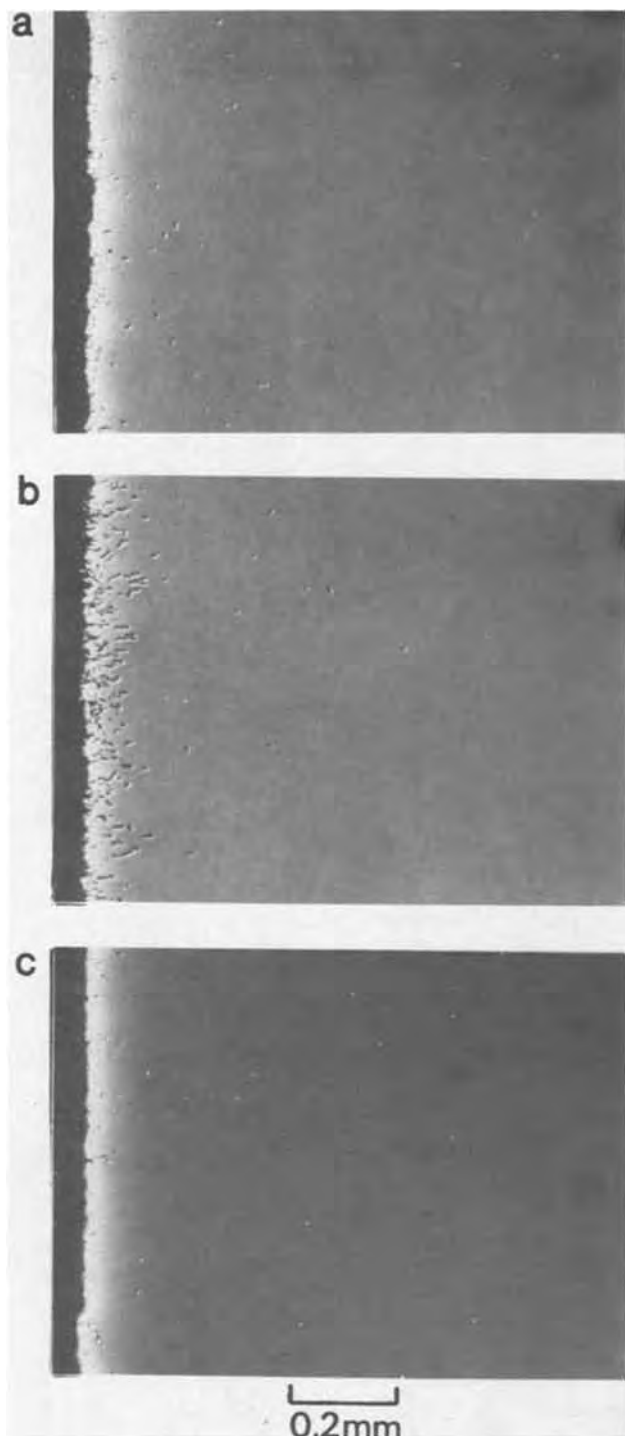


Fig. 5. (a) The beveled and etched sample section from the wafer sawn in water. The etch pits indicate the number and distribution of defects. (b) The sawing in dielectric oil introduces more surface defects than in (a). (c) The sawing in methyl silane solution introduces less surface defects than in (a).

nificance of the depth profile of crack distribution shown in Fig. 4 is that some of the cracks can extend to more than $90\ \mu\text{m}$ deep. This seems to be in agreement with the finding of Schwuttke (5). As mentioned above, the blade vibration in the dielectric oil environment with no potential is such that there is more abrasion on the A surface than the B surface. Applying a positive potential does not significantly change the surface morphology or the depth of scratch on both A and B surfaces. But applying a negative potential does markedly decrease the abrasion on the A surface and slightly increase the depth of scratch

on the B surface. It seems to suggest that the -6V potential applied on the crystal can reduce the amplitude of the blade out-of-plane vibration and the $+6\text{V}$ potential does the reverse. This can explain the increase of crack numbers in the depth ranges $10\text{-}50\ \mu\text{m}$ for the $+6\text{V}$ case and the reduction of crack numbers in the depth range under $15\ \mu\text{m}$ for the -6V case.

How the surface potential affects the blade out-of-plane vibration is not clear at present, but a possible explanation can be offered if we follow the Westwood theory (14) which states that dislocation mobility is least on a surface when the zeta potential is zero. The dielectric oil molecule may decompose during the sawing and become an electrolyte. The adsorption induced zeta potential may also be changed by the potential applied on the crystal and this change in turn affects the fracture processes. But the detailed mechanism, such as how the new charge environment affects the propagation of fast moving cracks, still needs to be worked out.

Conclusion

Six different lubricant environments were tested for the sawing of Si wafers: (i) water, which is used in the standard production process; (ii) a solution of methyl silane in 80 parts water; (iii) a commercial cutting oil (Kleenzol B); (iv) dielectric oil with no potentials; (v) dielectric oil with $+6\text{V}$ applied on Si crystal; (vi) dielectric oil with -6V applied on Si crystal. The results showed that the saw lubricant is an important operational variable, and the depth of damage can be reduced by improving the lubricant environment.

TEM observations indicated that cracks are the main surface damage induced by the sawing process. Dislocations were found only at the very top layer (several microns) and were related to the abrasive motion of the saw blade.

Results of the optical microscopy on angle-lapped specimens of the cut surfaces indicated that the number and depth of the saw damage are less for Kleenzol B and methyl silane, but are much more for dielectric oil than for water. By combining the damage depth profile and the surface structure observations, it was determined that the lubricants that are good catalysts for breaking Si bonds can dampen more effectively the out-of-plane blade vibration and produce less surface damage.

The application of a potential on the crystal should change the barrier for dislocation or for crack propagation in Si. We have observed, in the case of dielectric oil, that the applied positive potential increases the depth of damage and the negative potential decreases the depth of damage, as compared to the sawing process without applied potential.

Acknowledgments

We want to thank W. White for setting up the slicing experiments. One of us (T.S.K.) has also benefited from discussions with Z. Kovac and H. Föll.

Manuscript submitted Sept. 11, 1979; revised manuscript received Nov. 26, 1979.

Any discussion of this paper will appear in a Discussion Section to be published in the December 1980 JOURNAL. All discussions for the December 1980 Discussion Section should be submitted by Aug. 1, 1980.

Publication costs of this article were assisted by IBM Corporation.

REFERENCES

1. J. K. Howard, J. Regh, and G. H. Schwuttke, IBM TR 22.714 (1968).
2. M. L. Joshi and J. K. Howard, in "Silicon Device Processing," C. P. Marsden, Editor, pp. 313-364, NBS Spec. Publ. No. 337, Gaithersburg, Maryland (1970).
3. W. R. Runyan, "Silicon Semiconductor Technology,"

- p. 231, Mc-Graw Hill, New York (1965).
4. R. L. Meek and M. C. Huffstutler, Jr., *This Journal*, **116**, 893 (1969).
 5. G. H. Schwuttke, IBM TR 22.1588 (1973), TR 22.1692 (1973).
 6. T. M. Buck, in "The Surface Chemistry of Metals and Semiconductors," H. L. Gates, Editor, p. 107, John Wiley and Sons, Inc., New York (1960).
 7. R. Stickler and G. R. Booker, *Philos. Mag.*, **8**, 859 (1963).
 8. J. W. Faust, Jr., *Electrochem. Technol.*, **2**, 339 (1964).
 9. King and Tabor, *Proc. R. Soc. London, Ser. A*, **223**, 225 (1954).
 10. J. W. Allen, *Philos. Mag.*, **4**, 1046 (1959).
 11. V. I. Nikitenko, M. M. Myshlyaev, and V. G. Eremenko, *Sov. Phys. Solid State*, **9**, 2047 (1968).
 12. P. Somasundaran and I. J. Lin, *Ind. Eng. Chem. Process Res. Dev.*, **11**, 321 (1972).
 13. E. P. Plueddemann, *J. Adhes.*, **2**, 184 (1970).
 14. A. R. C. Westwood, *J. Mater. Sci.*, **9**, 1871 (1974).
 15. P. Haasen, *Phys. Status Solidi A*, **28**, 145 (1975).
 16. E. J. Saccocio and W. McKeown, *J. Appl. Phys.*, **37**, 2702 (1967).
 17. E. N. Pugh and J. E. Samuels, *This Journal*, **108**, 1043 (1964).
 18. T. H. Irish, IBM TR 22.1933 (1975).
 19. T. T. Sheng and C. C. Chang, *IEEE Trans. Electron Devices*, **ed-23**, 531 (1976).
 20. T. M. Buck and R. L. Meek, in "Silicon Device Processing," C. P. Marsden, Editor, pp. 419-430, NBS Spec. Publ. No. 337, Gaithersburg, Maryland (1970).
 21. M. J. Hill and D. J. Rowcliffe, *J. Mater. Sci.*, **9**, 1569 (1974).
 22. I. V. Gridneva, Yu. V. Milman, and V. I. Trefilov, *Phys. Status Solidi A*, **14**, 177 (1972).
 23. J. A. Van Vechten, *Phys. Rev. B*, **7**, 1479 (1973).
 24. R. A. Graham, O. E. Jones, and J. R. Holland, *J. Appl. Phys.*, **36**, 3955 (1965).

Kinetics of Chemical Vapor Deposition

J. Subrahmanyam,¹ A. K. Lahiri, and K. P. Abraham

Department of Metallurgy, Indian Institute of Science, Bangalore—560 012, India

ABSTRACT

A generalized mass transport model is developed for predicting the rate of deposition in chemical vapor deposition (CVD) systems. This combines the generalized method of obtaining equilibrium composition, with elemental flux balance expressions. This procedure avoids the usual problems encountered in calculating the rates in multicomponent systems, like writing overall reaction schemes. The dependence of multicomponent diffusivities on the fluxes is accounted in this model using an iterative procedure. The model developed is applied to the deposition of titanium carbide on cemented carbide tool bits from a gas mixture of titanium tetrachloride, toluene, and hydrogen. Experimental deposition rates were obtained using a thermogravimetric assembly. Mass transport controlled rates give an order of magnitude estimates of the observed rates.

Chemical vapor deposition (CVD) is a complex process with many variables to be controlled for obtaining a solid product with desired properties. Effective process control needs an understanding of the following: (i) nucleation (ii) thermodynamics, and (iii) kinetics. The theories developed for nucleation of the deposit in physical vapor deposition (1) cannot be successfully employed for chemical vapor deposition (2). However Campbell (3) showed that the supersaturation ratio can be used to predict the growth morphology in CVD systems. A thermodynamic analysis helps in eliminating some of the undesirable systems and also in identifying the systems having potential for depositing a required solid. However the thermodynamic possibilities may have to be accepted with reservation on account of the kinetic limitations.

In CVD the deposition rate is either controlled by the chemical reaction rate at the substrate surface or by the mass transport through the gas film. If the chemical reaction rate is assumed to be high, mass transport controls the process. To predict the mass-transport controlled rates, equilibrium composition is to be assumed at the substrate surface. In CVD a number of reactants and products are present and it is difficult to write an overall reaction scheme. In addition, for each reaction scheme written, a new flux value can result. Recently Nolang and Richardson (4) developed a mass transport model for the rate of

chemical transport in closed systems assuming equilibrium composition at the surface. These authors used free-energy minimization technique for computing the equilibrium composition. Average diffusivity values were used in their treatment. Their model cannot be directly applied to chemical vapor deposition process.

Chemical vapor deposition of titanium carbide on cemented tungsten carbide tool bits is an established industrial process. Lee and Richman (5) studied the effect of substrate material on the growth morphology of titanium carbide from titanium tetrachloride, toluene, and hydrogen gas mixture. They had collected some kinetic data and showed that mass transport controls the process at temperatures exceeding 1100°C and chemical reaction at lower temperatures.

In the present paper a mass transport model is developed for determining the deposition rate, applicable for all possible CVD systems. This combines the elemental flux balance expressions with generalized equilibrium computation. Moreover, more realistic multicomponent diffusivities are used in the present model in obtaining the rates. Experimental work was carried out to obtain the rates of chemical vapor deposition of titanium carbide from titanium tetrachloride, toluene, and hydrogen gas mixture on cemented tungsten carbide tool bits, using a thermogravimetric assembly. The experimental results are compared with the calculated mass transport controlled rates.

Mass Transport Model

The following assumptions are made in developing the mass-transport model:

¹ Present address: Bharat Heavy Electricals Limited, Materials Science Laboratory, Corporate Research & Development Division, Vikasnagar, Hyderabad — 500593, India.

Key words: mass transport, generalized equilibrium computation, flux balance, titanium carbide.

1. The deposition occurs from a flowing multicomponent gas mixture on a heated substrate.

2. The heterogeneous reaction rate is fast so that reaction attains equilibrium on the substrate surface.

3. No homogeneous reaction occurs within the gas film.

4. Thermal diffusivity is negligible compared to chemical diffusion.

The general expression for the flux of a species i in an n component gaseous mixture is given by (6)

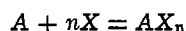
$$N_i = -K_i(X_i^b - X_i^{eq}) + X_i^{av} \sum_{i=1}^n N_i \quad [1]$$

For each species Eq. [1] can be written, but only $(n - 1)$ of them are independent since the flux of n th species can be obtained from the fluxes of other species and the equation

$$\sum X_i = 1 \quad [2]$$

Equations [1] and [2] cannot be solved to obtain N_i values since X_i^{eq} values are also unknown. X_i^b can be obtained from the input composition.

For the formation of a compound AX_n from elements A and X , we can write



equilibrium constant

$$K = \frac{a_{AX_n}}{a_A \cdot a_X^n}$$

or

$$a_{AX_n} = e^{-\Delta F/RT} \cdot a_A \cdot a_X^n$$

Generalizing this expression for gaseous species and taking

$$a_{AX_n} = X_i^{eq}$$

$$X_i^{eq} = \exp\left(-C_i + \sum_e Y_e a_{ie}^e\right) \quad [3]$$

where $\exp(Y_e)$ is the activity of the e th element in the system and $C_i = \Delta F/RT$

Similarly for solids

$$\exp\left(-C_j + \sum_e Y_e a_{je}^e\right) = 1$$

or

$$-C_j + \sum_e Y_e a_{je}^e = 0 \quad [4]$$

By assuming a film model at the deposition site and making an elemental flux balance within the film we can write

$$\sum_{i=1}^n a_{ie}^e N_i + \sum_{j=1}^m a_{je}^e r_j = 0 \quad [5]$$

for $e = 1, 2, \dots, NE$

Now substituting Eq. [1] and [3] in [5] we get

$$\begin{aligned} & \sum_{i=1}^{n-1} a_{ie}^e \left[K_i \exp\left(-C_i + \sum_e Y_e a_{ie}^e\right) \right. \\ & \left. + X_i^{av} \sum N_i \right] + a_{ne}^e N_n + \sum_{j=1}^m a_{je}^e r_j \\ & = \sum_{i=1}^n a_{ie}^e K_i X_i^b \quad [6] \end{aligned}$$

for $e = 1, 2, \dots, NE$

where N_n is the flux of n th species, whose flux is obtained from the fluxes of rest of the species and Eq. [2].

Now Eq. [1], [2], [4], and [6] can be solved together ($n + m + NE$ number of equations) for the unknowns N_i , r_j , and Y_e .

In most of the CVD processes, hydrogen is the predominant species and the bulk flow term

$$\left[X_i^{av} \sum N_i \right]$$

is insignificant for all other species. By neglecting bulk flow term for all other species except hydrogen, Eq. [6] reduces to

$$\begin{aligned} & \sum_{i=1}^{n-1} a_{ie}^e \left[K_i \exp\left(-C_i + \sum_e Y_e a_{ie}^e\right) + X_{H_2}^{av} \sum_i N_i \right] \\ & + a_{ne}^e N_n + \sum_{j=1}^m a_{je}^e r_j = \sum_{i=1}^n a_{ie}^e \cdot K_i \cdot X_i^b \quad [7] \end{aligned}$$

where hydrogen is the only predominant species, Eq. [6] can also be simplified as

$$\begin{aligned} & \sum_{i=1}^{n-1} a_{ie}^e \left[K_i \exp\left(-C_i + \sum_e Y_e a_{ie}^e\right) \right] + a_{H_2e}^e N_{H_2} \\ & + \sum_{j=1}^m a_{je}^e r_j = \sum_{i=1}^n a_{ie}^e K_i X_i^b \quad [8] \end{aligned}$$

Eq. [1], [2], [4], and [7] form a set of $(n + m + NE)$ equations with unknowns Y_e , r_j , and N_i . The unknowns Y_e , r_j , and the flux of the n th species N_n can be obtained from a solution of Eq. [2], [4], and [8] forming $(1 + m + NE)$ number of equations. In the latter case, the fluxes of species other than n th species can be obtained from the following equation

$$N_i = -K_i \left[X_i^b - \exp\left(-C_i + \sum_e Y_e a_{ie}^e\right) \right] \quad [9]$$

In this case the number of simultaneous equations to be solved is reduced by $(n - 1)$. The solution to the set of nonlinear equations was arrived at by using the Newton-Raphson method.

The multicomponent diffusivity D_{im} of a species i in the gas mixture depends on the fluxes of all the species (5), as can be seen from Eq. [10]

$$D_{im} = \frac{N_i - X_i \sum_i N_i}{\frac{1}{D_{ij}} (X_j N_i - X_i N_j)} \quad [10]$$

Since hydrogen is the only predominant species in CVD systems, the binary diffusivity of i th species with hydrogen (D_{iH_2}) gives a good approximation for the multicomponent diffusivity. Hence these diffusivity values were used to get a solution for the set of simultaneous equations [2], [4], and [8]. The fluxes obtained from this solution were used in Eq. [10] to improve the multicomponent diffusivities. The solution procedure is exemplified for TiC deposition in the following sections.

Experimental

Materials.—The hydrogen gas (99.98% purity) was supplied by Indian Oxygen Limited, Bangalore. Titanium tetrachloride (99.99% purity) was supplied by Nuclear Fuel Complex, Hyderabad. The cemented carbide tool bits were supplied by Widia (India) Limited, Bangalore. These inserts were triangular in shape (composition): WC 70%, TiC-7%, Ta(Nb)C-13%, and cobalt 10%.

Apparatus.—A conventional thermogravimetric setup with a quartz spring assembly was used to note the

weight changes during the deposition. The cemented carbide tool bits were suspended using a molybdenum wire from the calibrated quartz spring (sensitivity: 3.48 cm/g maximum load: 5g). The weight changes in the sample were noted at regular intervals of time

by means of a cathetometer (accuracy: ± 0.01 mm). A calibrated optical pyrometer was used to measure the temperature. The vapors of titanium tetrachloride and toluene were transported to the reaction site by passing hydrogen over the respective liquids kept im-

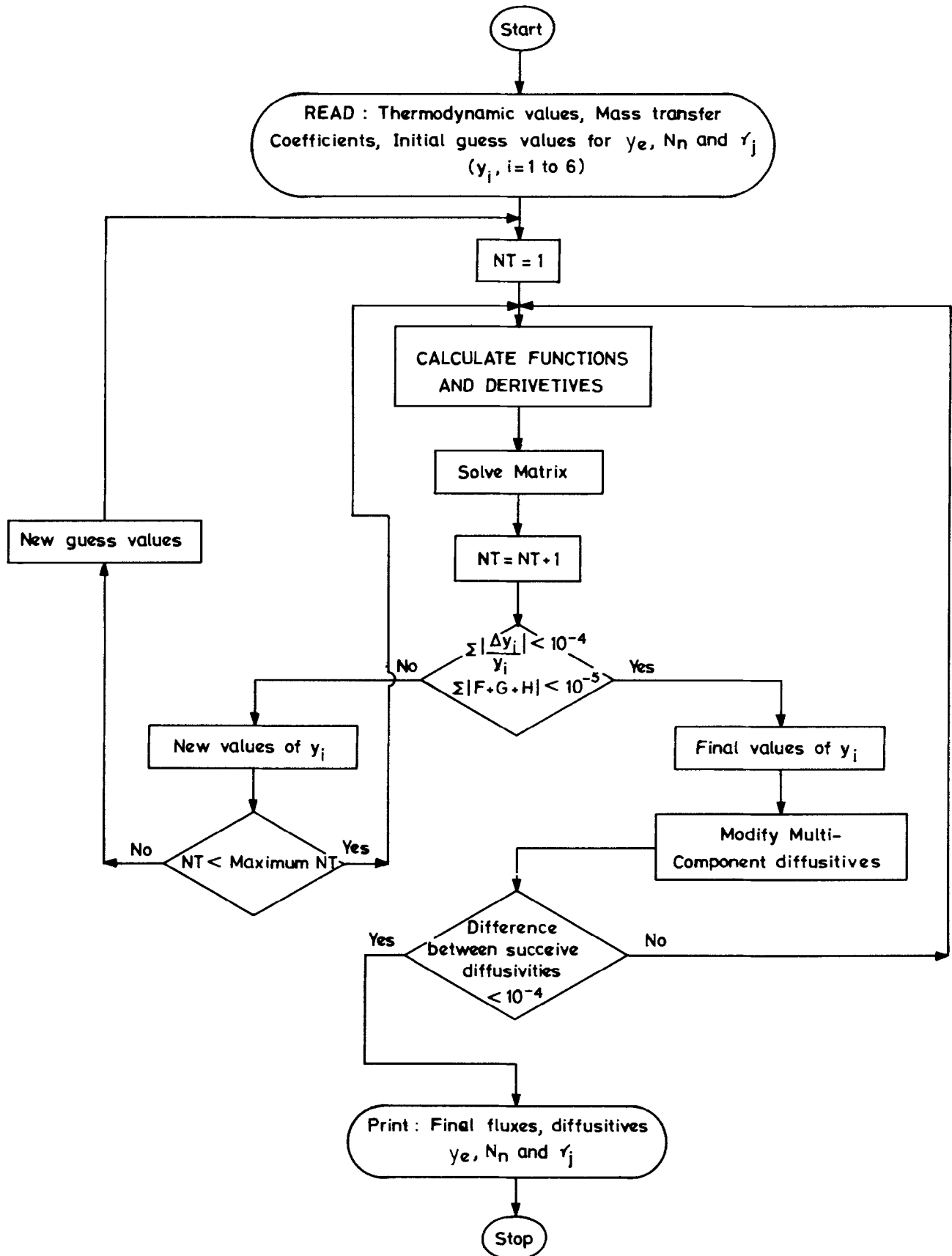


Fig. 1. Flow diagram

mersed in constant temperature baths (controlled to $\pm 1^\circ\text{C}$). The flow rate of hydrogen was measured using a calibrated flowmeter. The experiments were conducted at atmospheric pressure.

Theoretical Deposition Rates

A thermodynamic analysis of the $\text{TiCl}_4\text{-C}_7\text{H}_8\text{-H}_2$ system (7) revealed that only the following gaseous species are present in significant amount at equilibrium: TiCl_4 , TiCl_3 , TiCl_2 , C_3H_4 , H_2 , and HCl . In addition, toluene was also considered as one of the species in the calculation since toluene was an input gas. The system consists of seven gaseous species and four elements (Ti, C, H, Cl). TiC is the only solid that can be formed in the temperature range considered. For TiC deposition Eq. [8] can be expressed as

$$\sum_{i=1}^6 a_{ie}^g \left[K_i \exp \left(-C_i + \sum_e Y_e a_{ie}^g \right) \right] + a_{\text{H}_2e}^g \cdot N_{\text{H}_2} + a_{\text{TiC}e}^g \cdot r_{\text{TiC}} = \sum_{i=1}^7 a_{ie}^g \cdot K_i \cdot X_i^b \quad [11]$$

for $e = 1, 2, 3, 4$

where r_{TiC} is the rate of deposition of titanium carbide. Equation [11] together with Eq. [2] and [4] forms a set of $4 + 1 + 1 = 6$ equations. The quantities required to solve these equations are the thermodynamic functions, and the mass transfer coefficients. The thermodynamic functions were taken from Barin and Knacke (8). Mass transfer coefficient is given by $K_m = D_{\text{im}}/\delta$, where δ is the boundary layer thickness. It was difficult to evaluate the boundary layer thickness for the complex shape of the specimens used, from the available correlations. Hence independent experiments were carried out using naphthalene specimens to evaluate film thickness. These details are presented in the Appendix.

To start the iteration, the multicomponent diffusivity (D_{im}) values were approximated to D_{H_2} as mentioned earlier and the solution to the set of equations [11], [2], and [4] was obtained. The solution to these equations gives Y values for the four elements, flux of hydrogen, and rate of deposition of titanium carbide, r_{TiC} . The fluxes of all other species were obtained from the Y values using Eq. [9]. These flux values were substituted in Eq. [10] together with the binary diffusivities, to get the improved values of the multicomponent diffusivities. These improved values were used to evaluate the mass transfer coefficient in the next iteration. The binary diffusivities were calculated using Sutherland's formula (6) for all gas pairs except for pairs with TiCl_3 and TiCl_2 . Lennard-Jone's parameters required to use in Sutherland's formula were not available for TiCl_3 and TiCl_2 . Therefore, Gilliland's formula was used to arrive at the binary diffusivities with these species. The scheme of solution is presented in the form of a flow diagram in Fig. 1.

Results and Discussion

Experimental results are shown in Fig. 2-5 as weight increase with time. An error analysis of the experimental data points showed that the standard deviation in the deposition rate is 0.1 mg/min. This deviation in deposition rate corresponds to an error of 15°K in temperature, which can be either due to fluctuation in the temperature of the substrate or due to an error in temperature measurement.

As shown in Fig. 2-5 the deposition rate is independent of time because the area of depositing surface nearly remains constant throughout the experiment. In heterogeneous systems like CVD an incubation period is possible due to difficulties associated with nucleation of deposit. However in the present work no incubation period was observed.

Figures 6 and 7 show Arrhenius plots of the logarithm of the observed deposition rates as a function of re-

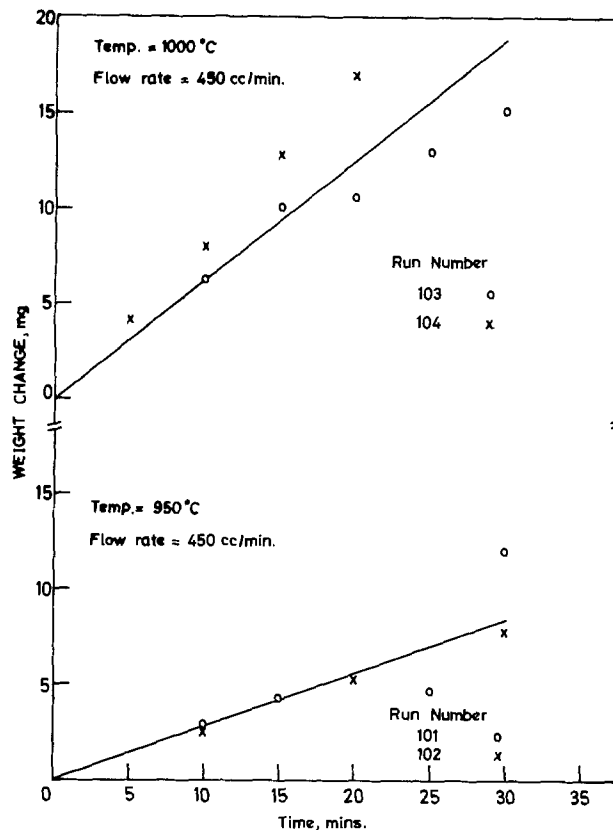


Fig. 2. Weight increase with time at 950° and 1000°C and at the flow rate of $450\text{ cm}^3/\text{min}$.

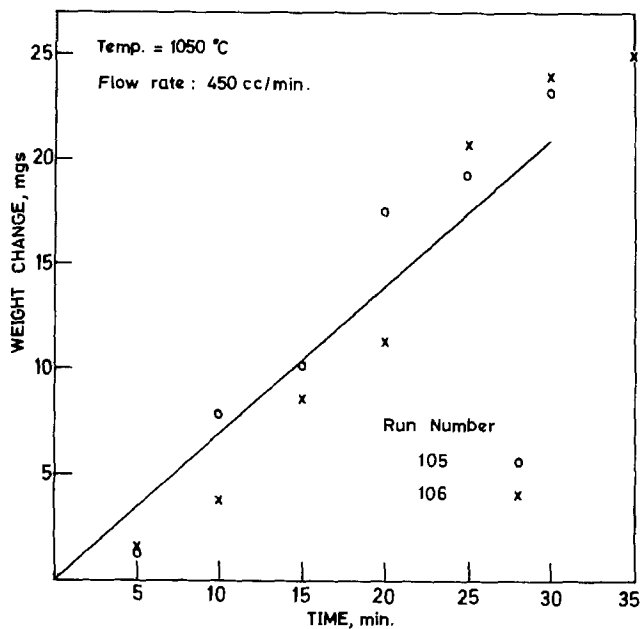


Fig. 3. Weight increase with time at 1050°C and $450\text{ cm}^3/\text{min}$

ciprocal temperature at flow rates of 450 and $950\text{ cm}^3/\text{min}$, respectively. Diffusion-controlled rates calculated using the mass transport model developed are also presented in Fig. 6 and 7. Assuming a first-order heterogeneous chemical reaction to occur on the substrate surface simultaneously with mass transfer through the film, the overall reaction rate r may be written as (9)

$$\frac{1}{r} = \frac{1}{r_1} + \frac{1}{r_2} \quad [12]$$

where r_1 = mass transport controlled rate and r_2 = chemical reaction rate. Chemical reaction rates (r_2) can be obtained from the experimental values and the cal-

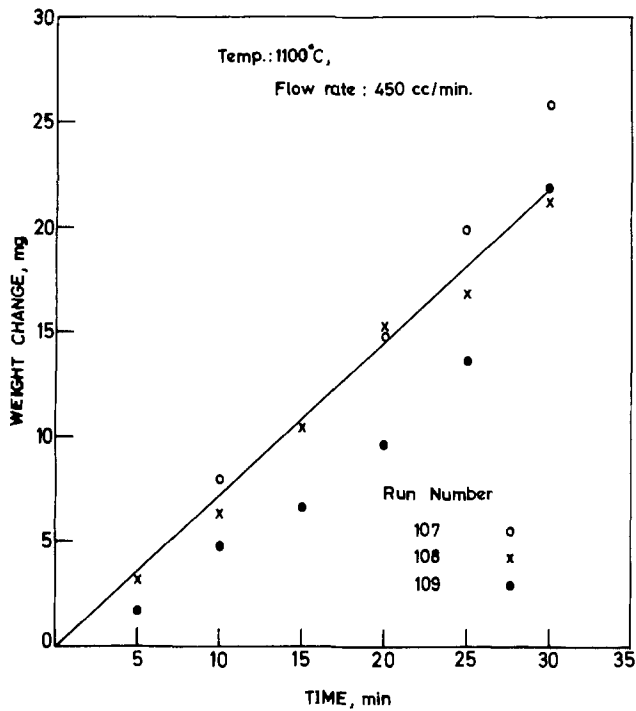


Fig. 4. Weight increase with time at 1100°C and at 450 cm³/min

culated mass transport controlled rates using Eq. [12].

From Fig. 6 it is seen that at high temperatures and at a flow rate of 450 cm³/min, the deposition rate is controlled by diffusion. It would appear that at lower temperatures both diffusion and chemical reaction are important in controlling the process. At higher flow

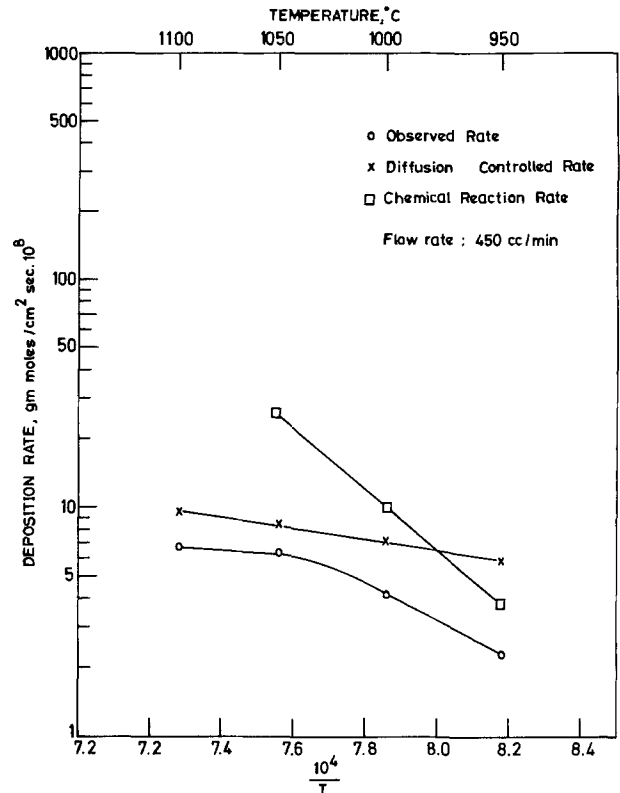


Fig. 6. Comparison of experimental and theoretical results at the flow rate of 450 cm³/min.

rate, 950 cm³/min, as can be seen from Fig. 7, the calculated mass transport controlled rates give an order of magnitude estimates of the observed rates.

It will be noted from Fig. 6 and 7 that the chemical reaction rates are different at the two flow rates 450

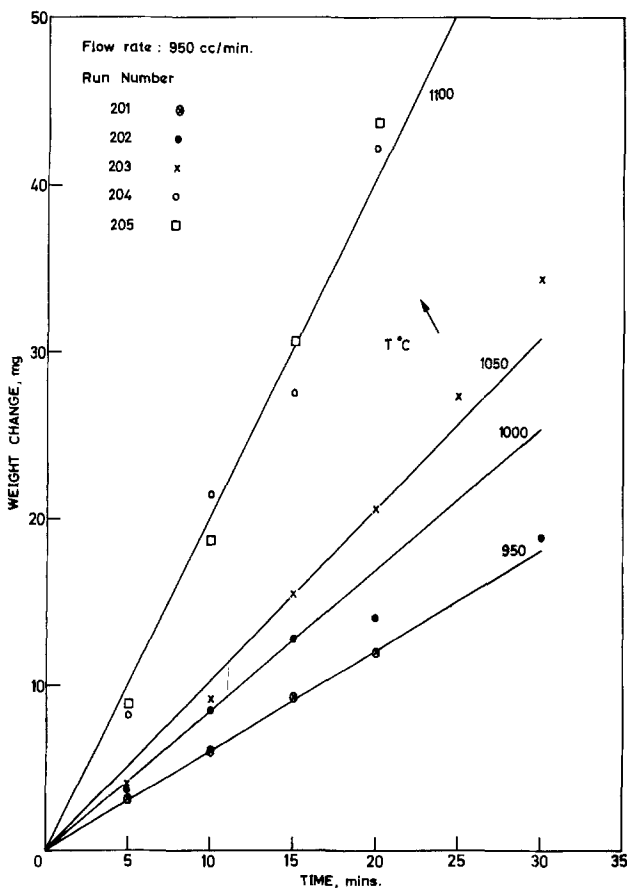


Fig. 5. Weight increase with time at the flow rate of 950 cm³/min.

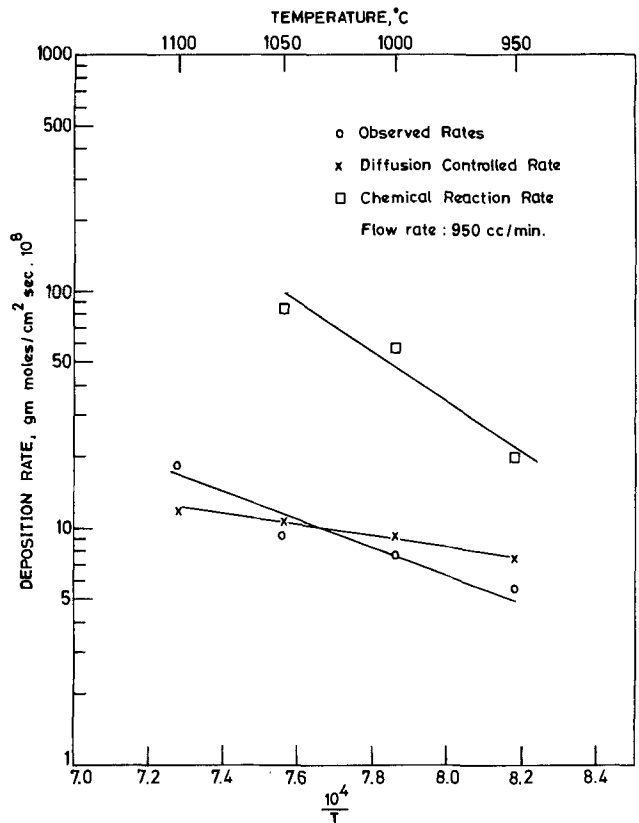


Fig. 7. Comparison of experimental and theoretical results at the flow rate of 950 cm³/min.

and 950 cm³/min. This can be attributed to the fact that in arriving at Eq. [12] it is assumed that a first-order chemical reaction occurs simultaneously with mass transfer at the reaction site. If the reaction is not first order such an equation cannot be written. In such a case chemical reaction rate r_2 calculated from Eq. [12] depends on flow rate (7).

Conclusion

A generalized mass transport model has been developed for CVD systems, combining the generalized equilibrium computation with the elemental flux balance expressions. This avoids a number of complications in calculating mass transport controlled rates in multicomponent and multiphase systems encountered in chemical vapor deposition. Kinetic experiments were conducted on the deposition of titanium carbide on cemented tungsten carbide tool bits in the temperature range 950°-1100°C and at two flow rates of hydrogen: 450 and 950 cm³/min. Theoretical deposition rates, obtained using the mass transport model, compare well with the observed rates.

Manuscript submitted Dec. 1, 1978; revised manuscript received Nov. 15, 1979.

Any discussion of this paper will appear in a Discussion Section to be published in the December 1980 JOURNAL. All discussions for the December 1980 Discussion Section should be submitted by Aug. 1, 1980.

APPENDIX

The specimens used for the kinetic experiments were triangular in shape. As it was difficult to obtain mass transfer correlations for such a shape, independent experiments were conducted to evaluate the mass transfer coefficients.

Naphthalene was used as the sample material in these experiments since it has been established (10) that mass transfer is rate controlling in its evaporation. Naphthalene specimens of nearly the same size and shape as that of cemented carbide tool bit were prepared from the commercially available naphthalene balls. The specimen was weighed and placed in the reaction chamber in the same fashion as the original samples. The hydrogen gas was passed at a constant flow rate for a specific time period. Then the flow was stopped and the sample was quickly removed and weighed again. From the weight loss, the flux N_A was calculated. The driving force ($C_A - 0$) was obtained from the vapor pressure of naphthalene at the temperature of experiments. From the flux and driving

force, the mass transfer coefficient and hence δ , the film thickness can be calculated.

LIST OF SYMBOLS

a_A	activity of element A.
a_{ie}^g	stoichiometric coefficient of the eth element in the ith gaseous species
a_{je}^s	stoichiometric coefficient of the eth element in the jth condensed species
C_i	$\Delta F^\circ/RT$ where ΔF° is Gibbs free energy change for the reaction, (cal/mole)
D_{ij}	binary diffusion coefficient, cm ² /sec
D_{im}	effective binary diffusivity of species i in a multicomponent gas mixture cm ² /sec
K_i	k_m^p/RT effective mass transfer coefficient, g·moles/cm ² ·sec
K_m	D_{im}/δ mass transfer coefficient, cm/sec
m	number of condensed phases
n	number of gaseous species
NE	number of elements
N_i	molar flux of species i with respect to stationary coordinates, g·moles/cm ² ·sec
N_n	flux of nth species, g·moles/cm ² sec
P	total pressure, atm
r_j	rate of production of solid j , g·moles/cm ² ·sec
R	gas constant, cal/mole·°K
T	temperature, °K
X_i^b	mole fraction of ith species in the bulk stream
X_i^{eq}	equilibrium mole fraction of ith species
X_i^{av}	$(x_i^b + X_i^{eq})/2$

REFERENCES

1. J. P. Hirth and G. M. Pound, "Condensation and Evaporation, Nucleation and Growth Processes," Pergamon Press, Oxford (1963).
2. J. M. Blocher, Jr., in "Proc. Conf. on CVD of Refractory Metals Alloys and Compounds," A. C. Schaffhauser, Editor, p. 3, American Nuclear Soc., Illinois (1967).
3. W. B. Campbell, *Chem. Eng. Prog.*, **62**, 68 (1966).
4. B. I. Nolang and M. W. Richardson, *J. Cryst. Growth*, **34**, 198 (1976).
5. M. Lee and M. H. Richman, *This Journal*, **120**, 993 (1973).
6. B. Bird, W. E. Stewart, and E. N. Lightfoot, "Transport Phenomena," John Wiley and Sons, New York (1960).
7. J. Subrahmanyam, Ph.D. Thesis, Indian Institute of Science, Bangalore, India (1977).
8. I. Barin and O. Knacke, "Thermophysical Properties of Inorganic Substances," Springer, Berlin (1973).
9. T. M. Besmann and K. E. Spear, *This Journal*, **124**, 786 (1977).
10. T. K. Sherwood and O. Trass, *J. Heat Transfer*, **No. 4**, 313 (1960).

Intensity Dependence of Photochemical Reaction Rates for Photoresists

John Albers and Donald B. Novotny

National Bureau of Standards, Electron Devices Division, Washington, D.C. 20234

ABSTRACT

The intensity dependence of photochemical reaction rates, and thus the exposure reciprocity, is investigated in terms of a kinetic model. This model assumes a two-step photochemical reaction and reactions that are first order in the concentrations of each of the various species. The model is applicable to both positive and negative photoresists and is specifically applied to the photoactive species of a typical negative photoresist with the efficiency of the polymer cross-linking assumed constant. The model predicts that there is a saturation effect at high intensities which serves as a rate-limiting step, thus limiting the applicability of exposure reciprocity. Calculations using this model indicate that exposure reciprocity should be obeyed for exposure times of 10 μ sec or greater.

Photoresist films are exposed to ultraviolet light to produce images for microelectronic device fabrication. These exposures are generally about 10 sec in duration. While this duration is not particularly long, the possibility of rapid, high intensity exposures to reduce this time to a fraction of a second is appealing from the aspect of increased throughput on a mask aligner or other exposure unit.

A kinetic model is presented in which the photochemical reactions take place through an intermediate, photoexcited state. This model is investigated to assess the effects of the intensity dependence of the reaction kinetics of photochemical reactions. To this end, a system of first-order kinetic equations is postulated to take into account the photon intensity as well as the presence of the intermediate excited state. This system of equations is solved exactly using Laplace transform and matrix techniques and is carried out for a two-step photochemical reaction. Approximate solutions are obtained from the exact solutions using well-defined mathematical approximations. The approximate solutions show a separation of time scales: one associated with the rapid equilibration of the ground and excited states of the photoactive species and the other associated with the formation of the product. An effective rate constant governing the formation of the final reaction product is defined and its dependence upon the photon intensity is investigated. At high photon intensity, there is a photon-induced saturation of the equilibrium between the ground and excited states of the photoactive species. This saturation serves to limit the production of the photolysis product on a pseudo time scale defined by the intensity-time product and thus limit the validity of resist exposure reciprocity.

Kinetic Model

Consider a system of photochemically active molecules whose species is denoted by M. The system is exposed to monochromatic radiation of intensity I which causes a transition from the ground state of M to an excited state denoted by M^* . Once in the excited state, the molecule may either return to the ground state or undergo a chemical reaction to form the final reaction product which is denoted by P. The kinetic model which describes the effect of the radiation upon the photochemically active species and the production of the final photolysis product may be represented by



Key words: exposure, kinetics, photochemistry, photoresist.

where k_1 is the rate constant associated with the excitation of M to M^* due to photon absorption, k_2 is the rate constant associated with the decay of the excited state species back to the ground state, and k_3 is the rate constant associated with the chemical reaction in which the final reaction product, P, is formed. In general, the rate constants k_1 and k_2 may be written as

$$k_1 = k_f I \quad [2]$$

$$k_2 = k_f I + k_s + k_q \quad [3]$$

where k_f is the Einstein coefficient associated with the induced photon absorption (emission), k_s is the rate constant associated with the spontaneous photon emission (1), k_q is the rate constant referring to all other linear decay modes of the excited state, and I is the photon intensity.

The concentrations of the three molecular species are denoted by $M(t)$, $M^*(t)$, and $P(t)$. If the photon energy is large compared to thermal energy ($h\nu/k_B T > 1$), then the initial conditions are

$$M(0) = M_0 \quad M^*(0) = P(0) = 0 \quad [4]$$

It is convenient to define a set of dimensionless concentrations as

$$m(t) = \frac{M(t)}{M_0} \quad m^*(t) = \frac{M^*(t)}{M_0} \quad p(t) = \frac{P(t)}{M_0} \quad [5]$$

If the processes involved in the model are first order, then the equations governing the temporal evolution of the dimensionless concentrations may be written as

$$\frac{dm(t)}{dt} = -k_1 m(t) + k_2 m^*(t) \quad [6a]$$

$$\frac{dm^*(t)}{dt} = k_1 m(t) - (k_2 + k_3) m^*(t) \quad [6b]$$

$$\frac{dp(t)}{dt} = k_3 m^*(t) \quad [6c]$$

While systems of coupled linear differential equations of the above form can be solved by using assumed particular solutions and solving the associated secular equations (2), the use of Laplace transforms offers a simpler and more straightforward technique for obtaining the solution. For this reason, salient details of the solution are presented here. Introducing the Laplace transform

$$\hat{f}(s) \equiv \mathcal{L}f(t) \equiv \int_0^\infty e^{-st}f(t)dt \quad [7]$$

Eq. [6] becomes

$$s\hat{m}(s) - 1 = -k_1\hat{m}(s) + k_2\hat{m}^*(s) \quad [8a]$$

$$s\hat{m}^*(s) = k_1\hat{m}(s) - (k_2 + k_3)\hat{m}^*(s) \quad [8b]$$

$$s\hat{p}(s) = k_3\hat{m}^*(s) \quad [8c]$$

This set of simultaneous equations may be solved to obtain

$$\hat{m}(s) = \frac{s + k_2 + k_3}{(s + K^+)(s + K^-)} \quad [9a]$$

$$\hat{m}^*(s) = \frac{k_1}{(s + K^+)(s + K^-)} \quad [9b]$$

$$p(s) = \frac{k_1k_3}{s(s + K^+)(s + K^-)} \quad [9c]$$

where

$$K^\pm = \frac{L \pm (L^2 - 4M)^{1/2}}{2} \quad [10]$$

$$L = k_1 + k_2 + k_3 \quad [11]$$

and

$$M = k_1k_3 \quad [12]$$

Making use of Laplace transform inversion formula

$$f(t) = \sum_{\text{residues}} e^{st}\hat{f}(s) \quad [13]$$

where the residues are evaluated at the singularities of $\hat{f}(s)$ leads to the result that

$$m(t) = \frac{Y+1}{2} \exp\left\{-\frac{L+G}{2}t\right\} - \frac{Y-1}{2} \exp\left\{-\frac{L-G}{2}t\right\} \quad [14a]$$

$$m^*(t) = W \left\{ \exp\left\{-\frac{L-G}{2}t\right\} - \exp\left\{-\frac{L+G}{2}t\right\} \right\} \quad [14b]$$

$$p(t) = 1 + \frac{Z-1}{2} \exp\left\{-\frac{L+G}{2}t\right\} - \frac{Z+1}{2} \exp\left\{-\frac{L-G}{2}t\right\} \quad [14c]$$

where

$$G = (L^2 - 4M)^{1/2} \quad [15]$$

$$Y = N/G \quad [16]$$

$$Z = L/G \quad [17]$$

$$W = k_1/G \quad \text{and} \quad [18]$$

$$N = k_1 - k_2 - k_3 \quad [19]$$

In order to investigate the dependence of the formation of the final photolysis product upon the light intensity, it is convenient to develop approximate solutions from the above exact solutions. This may be achieved by considering the exponential functions in Eq. [14]. It may be shown for all cases of physical interest that $L^2 > 4M$. Then

$$G = (L^2 - 4M)^{1/2} = L \left\{ 1 - \frac{4M}{L^2} \right\}^{1/2} \\ = L \left\{ 1 - \frac{1}{2} \frac{4M}{L^2} - \frac{1}{4} \frac{(4M/L^2)^2}{2!} + \dots \right\} \\ \simeq L - \frac{2M}{L} \quad [20]$$

where terms of second order and higher have been neglected. Therefore

$$\frac{L+G}{2} \simeq L \quad [21]$$

and

$$\frac{L-G}{2} \simeq \frac{M}{L} = \frac{k_1k_3}{k_1 + k_2 + k_3} \quad [22]$$

In a similar manner, the coefficients may be approximated by

$$\frac{Y+1}{2} \simeq \frac{k_1}{L} \quad [23]$$

$$\frac{Y-1}{2} \simeq -\frac{k_2 + k_3}{L} \quad [24]$$

$$W \simeq \frac{k_1}{L} \quad [25]$$

$$\frac{Z-1}{2} = 0 \quad [26]$$

$$\frac{Z+1}{2} \simeq 1 \quad [27]$$

Using the above approximations and assuming that there is no quenching of the photoexcited species¹ ($k_q = 0$), the explicit form of k_1 and k_2 given in Eq. [2] and [3], respectively, yields

$$m(t) = \frac{k_f I}{L} \exp(-Lt) + \frac{k_f I + k_s + k_3}{L} \exp(-\gamma t) \quad [28]$$

$$m^*(t) = \frac{k_f I}{L} \{ \exp(-\gamma t) - \exp(-Lt) \} \quad [29]$$

$$p(t) = 1 - \exp(-\gamma t) \quad [30]$$

where

$$\gamma = \frac{k_f k_3}{(2k_f I + k_s + k_3)} \quad [31]$$

There are two time scales associated with the solution. These are: the "fast" time scale which is determined by the time constant $1/L$ which is typically in the regime of 10^{-8} sec for strongly absorbing species such as the photoactive components of photoresists; and the "slow" scale which is determined by the time constant $1/\gamma I$. Physically, the "fast" time scale is associated with the equilibration of the M-M* system in the presence of the radiation field. The "slow" time scale is associated with the decay of the M-M* system into the final reaction product. Once $t > 1/L$, the "fast" time scale exponentials go to zero and then

$$m(t) + m^*(t) = \exp(-\gamma t) \quad [32]$$

and

$$\frac{m^*(t)}{m(t)} = \frac{k_f I}{(k_f I + k_s + k_3)} \quad [33]$$

Equation [33] states, on the "slow" time scale, that the ratio $m^*(t)/m(t)$ is time independent and hence

¹ It should be noted that for real processes at room temperature appreciable quenching often occurs, i.e., $k_q \neq 0$. The assumption that $k_q = 0$ is made for the purpose of calculating the minimum intensity at which reciprocity failure can occur and is discussed later in this paper.

has equilibrated. If M^* produces P by means of the chemical reaction, then M undergoes a transition to M^* to make up the difference and hence maintain the equilibrium. Hence, the M - M^* subsystem, in a restricted sense, may be viewed as decaying in a coherent manner to the reaction product on the "slow" time scale.

Reciprocity

Simply stated, the principle of reciprocity maintains that $p(t)$ is a universal function of the exposure $I \cdot t$. That is to say, if $I_1 \cdot t_1 = I_2 \cdot t_2 = \dots = I_n \cdot t_n$ then

$$p(I_1 \cdot t_1) = p(I_2 \cdot t_2) = \dots = p(I_n \cdot t_n) \quad [34]$$

and the time dependence of the final reaction product is dictated by the product $I \cdot t$. As $I \cdot t$ is a measure of the total number of photons incident upon the sample during the time, t , the concentration of the photolysis product would, if reciprocity holds, depend only upon this number. This would indicate, as far as the concentration of the final photolysis product is concerned, that long exposures at low intensity are equivalent to short exposures at high intensity.

The important thing to remember is that Eq. [33] shows that for the "slow" time scale reaction, the effect of the intensity dependence of the m^*/m equilibrium ratio becomes noticeable in the exposure process when $k_f/(k_s + k_3) \cong 10^{-2}$. At intensities smaller than this, $\gamma \cong k_f k_3 / (k_s + k_3)$, $p(t) = p(I \cdot t)$, and reciprocity holds.

The underlying physical reason for reciprocity failure may be found by considering Eq. [33]

$$\frac{m^*(t)}{m(t)} = \frac{k_f I}{(k_f I + k_s + k_3)} \quad [33]$$

and Eq. [6c]

$$\frac{dp(t)}{dt} = k_3 m^*(t) \quad [6c]$$

Equation [6c] states that the rate of production of p may be increased by increasing $m^*(t)$. Equation [33] states that this may be achieved by increasing I at low I . However, if I is made sufficiently large, then $m^*(t)/m(t) = 1$. Increasing I further does not increase the concentration of M^* and hence does not increase the rate of production of the final reaction product in a manner dictated by reciprocity. In effect, the M - M^* equilibrium saturates at high I . This saturation effect is then the rate-limiting step at high I thus leading to reciprocity failure.

Application to Photoresist

The photokinetic data published by Blais (3) for a negative photoresist are used to estimate the values of the kinetic constants used in this model. An assumption made is that all photons absorbed in the absorption band of the photoactive species of the photoresist are responsible for populating the same electronically excited state from which photolysis to the final product occurs. This assumption should assure a conservative estimate of the high intensity reciprocity limit predicted by this model.

The constant k_s of Eq. [2] corresponds to the Einstein coefficient for spontaneous emission from an excited state and may be calculated by integrating the area under the absorption curve for this state. The value of k_s with the radiation wave number and the resist extinction coefficient in reciprocal length units of μm^{-1} takes the form (4)

$$k_s = 2880 \bar{\nu}_0^2 n^2 \int \epsilon d\bar{\nu} \quad [35]$$

where $\bar{\nu}_0$ is the wave number at the maximum of the absorption band, ϵ is the extinction coefficient, and n is the refractive index of the photoresist. A value of 1.5 is used which is representative of the refractive indexes of many photoresists (5, 6). Using the value

of $\bar{\nu}_0 = 2.82 \mu\text{m}^{-1}$ which corresponds to the maximum of the extinction coefficient, a value of $k_s = 2.2 \times 10^9 \text{ sec}^{-1}$ was obtained from graphical integration of the data of Blais (3).

The rate constant k_f is calculated from the Einstein coefficient B for stimulated radiation. The probability per second for stimulated transitions over this absorption band is given by $\int \psi_\nu B d\nu = k_f I$ where the integration extends over the entire absorption band. The isotropic energy density ψ_ν at frequency ν is related to the intensity (7) by $\psi_\nu = 4\pi I_\nu / c$ where I_ν is the spectral power distribution at the exposure plane per unit area per frequency interval at ν . Assuming the intensity to be constant across the adsorption band, which approximates the spectrum of a xenon flash lamp, and using $B = (\lambda_o^3 / 8\pi n^2 h) k_s$ (8), the following relation is obtained

$$k_f = \lambda_o^3 k_s / [2c^2 (1/\lambda_s - 1/\lambda_i) n^2 h] = 4.4 \times 10^3 \text{ cm}^2 \text{ J}^{-1} \quad [36]$$

where:

- λ_o = band center wavelength, $3.65 \times 10^{-5} \text{ cm}$,
- λ_s = short wavelength edge of the adsorption band, $3.05 \times 10^{-5} \text{ cm}$, and
- λ_i = long wavelength edge of the adsorption band, $4.25 \times 10^{-5} \text{ cm}$.

The value of $k_3 = 3.6 \times 10^7 \text{ sec}^{-1}$ is calculated from Eq. [31] and the data of Blais (3) of $\gamma = 70 \text{ cm}^2 \text{ J}^{-1}$.

The high intensity limit for the onset of reciprocity failure is now calculated from the criterion $k_f I / (k_s + k_3) \cong 10^{-2}$. From this, it is found that reciprocity will fail for intensities of $I_f \cong 5 \times 10^3 \text{ W/cm}^2$. Assuming an exposure of 50 mJ/cm^2 to be typical for complete exposure of photoresist films, I_f corresponds to exposure times of $10 \mu\text{sec}$ or less for reciprocity failure to occur by this mechanism.

The assumption that no quenching occurs (i.e., $k_q = 0$ in Eq. [3]) made in applying this model to photoresist exposure and photolysis may not be obeyed. Quenching would cause the onset of reciprocity failure to occur at even higher intensities than those calculated. This is because k_q would now appear in the denominator of Eq. [33] reducing the value of $m^*(t)/m(t)$ and requiring larger intensities to satisfy the above criterion for reciprocity failure. Thus, from the values calculated using this model, it appears that this mechanism will not account for any reciprocity failures that may occur in the photolithographic fabrication of microelectronic circuits where the light intensities are generally less than 5 mW/cm^2 and exposure times are of the order of seconds.

Conclusions

Using a kinetic model, the intensity dependence of photochemical reaction rates has been investigated. At intermediate to high intensities, the equilibration of the ground and excited state concentrations of the photoreactive molecule saturates, thus limiting the production of the photolysis product on the pseudo time scale defined by the $I \cdot t$ product. Exposure reciprocity failures due to this mechanism do not occur in current photolithographic fabrication processes of microelectronic circuits. However, this model does provide a possible explanation of reciprocity failure if observed for very large I and small t .

Acknowledgment

This research was conducted as part of the NBS Semiconductor Technology Program with principal funding from the Defense Advanced Research Projects Agency (Order 2397).

Manuscript submitted June 11, 1979; revised manuscript received Nov. 26, 1979.

Any discussion of this paper will appear in a Discussion Section to be published in the December 1980

JOURNAL. All discussions for the December 1980 Discussion Section should be submitted by Aug. 1, 1980.

Publication costs of this article were assisted by the United States Department of Commerce.

REFERENCES

1. G. M. Barrow, "Introduction to Molecular Spectroscopy," pp. 61-72 and 309-311, McGraw-Hill, New York (1962).
2. A. A. Frost and R. G. Pearson, "Kinetics and Mechanism," pp. 173-177, John Wiley & Sons, Inc., New York (1961).
3. P. D. Blais, in "Proc. Microelectronics Seminar INTERFACE '75," pp. 6-15, Kodak Publication No. G-45, available from Eastman Kodak Co., Rochester, New York.
4. C. A. Parker, "Photoluminescence of Solutions," Chapt. 1 and 2, Elsevier Publishing Co., New York (1968).
5. K. G. Clark, *Solid State Technol.*, **14**, 52 (June 1971).
6. K. G. Clark, *ibid.*, **14**, 48 (September 1971).
7. A. C. G. Mitchell and M. W. Zemansky, "Resonance Radiation and Excited Atoms," p. 94, Macmillan, New York (1934).
8. C. A. Parker, *op. cit.*, p. 27.

Technical Notes



Spreading Resistance Calibration for Gallium- or Aluminum-Doped Silicon

J. R. Ehrstein*

National Bureau of Standards, Electron Devices Division, Washington, D.C. 20234

Quantitative resistivity or doping density profile analysis by spreading resistance requires several considerations. The use of a sampling volume correction is required to account for the effects of layer nonuniformity on the measurements (1, 2). The use of calibration data accounts for the effects of the metal semiconductor contact interface on the relation between specimen resistivity and measured spreading resistance (3). Calibration response for any set of probes is known to depend on specimen conductivity type, crystallographic orientation, and specimen surface preparation (4). Although it is advisable to choose and prepare calibration specimens in as equivalent a manner as possible to the specimens being profiled, it is common practice to ignore possible effects due to dopant species and to use boron and phosphorus-doped silicon for all calibration work.

This note reports the results of an experimental test of the acceptability of using boron-doped silicon to calibrate spreading resistance measurements of aluminum- or gallium-doped silicon. Specimens of boron-, aluminum-, and gallium-doped Czochralski-grown silicon were obtained with resistivity values appropriate to the use of gallium and aluminum for diffusions in thyristors and other high power devices. The four-probe resistivity values of slices cut from the crystals are given in Table I. Resistivity variations along one diameter of each slice were measured by spreading resistance. In the region measured by the four-point probe, the spreading resistance data indicated that the maximum nonuniformity ranged from 3 to 13% depending upon the specimen.

Subsequent to sawing, all specimens were etched in a DI water solution of KOH (15% by weight) at 100°C for 10 min which removed about 15 μm of silicon from each side of the slices. All slices were mounted for simultaneous polishing to minimize extraneous effects due to differences in surface preparation. Polishing was done with colloidal silica, 3-4 μm nominal particle size, 12% by weight in water, which was brought to pH 10.4-10.6 with ethylene diamine. Polishing was

done at a nominal load of 4 psi of specimen surface for 90 min. The polishing removed 25-35 μm of silicon from each of the slices. Following dismounting from the polishing fixture, the slices were degreased using a standard $\text{NH}_4\text{OH}/\text{H}_2\text{O}_2/\text{H}_2\text{O}$ process (5) and then baked at 150°C for 15 min in room ambient prior to measurement, as recommended for stabilizing p-type silicon surfaces following aqueous polishing (6).

A set of 25 spreading resistance measurements was taken over a 2.5 mm scan length near the center of each specimen and the average spreading resistance values calculated. Repeat measurement sets were then made for all specimens at locations adjacent to the original scan but at sufficient distance so as to sample a different portion of the specimen resistivity structure sensed by the four-probe technique. After all specimens had been aged for two weeks and then been freshly baked, a third set of measurements was taken on each specimen. All specimens were then repolished and baked, and a single set of spreading resistance measurements was taken. Two additional sets of measurements were taken on the gallium- and aluminum-doped specimens, one after repolishing and baking, the second within 24 hr of the first. In this manner a range of measurements over specimen non-uniformity, polishing replication, and time between polishing and measurement was obtained.

The spreading resistance data, summarized as the ratios of average spreading resistance to four-probe resistivity values, are shown in Fig. 1 for each measure-

Table I. Four-probe resistivity values of silicon specimens used in test

Dopant		
Boron ($\Omega \cdot \text{cm}$)	Aluminum ($\Omega \cdot \text{cm}$)	Gallium ($\Omega \cdot \text{cm}$)
0.121	0.692	1.54
1.072	1.14	2.31
4.98	4.62	
10.5	9.30	
17.6		

* Electrochemical Society Active Member.

Key words: semiconductor, contacts, conductance, resistivity.

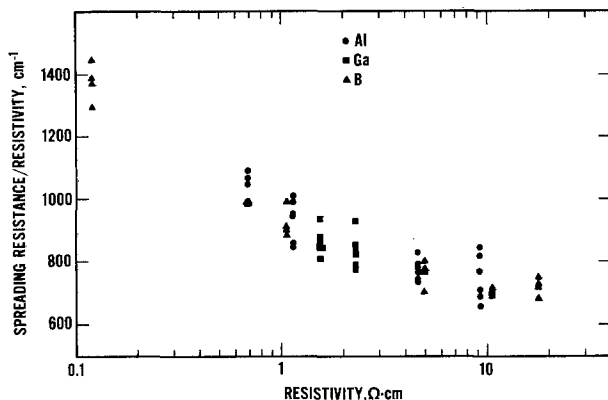


Fig. 1. Spreading resistance normalized to resistivity vs. resistivity for boron-, aluminum-, and gallium-doped (111) silicon.

ment set. This manner of representation gives a good visual magnification of variations due to resistivity or dopant species. Each point at a given resistivity represents the average of a set of spreading resistance measured over the 2.5 mm scan length. The standard deviations of the individual measurement sets ranged from less than 1% to nearly 3.5% of the measurement average. Consequently, the error bars for the sets are generally comparable to, or smaller than, the plot symbol and are not shown in the figure. The overall resistivity dependence of the plotted values is in good agreement with the response typically obtained in this laboratory on an all-boron composite specimen calibration block (4). The scatter between measurement sets for any specimen generally correlates with the magnitude of resistivity variation seen in the radial profiles for that specimen. The scatter is also caused in part by small, but measurable, changes in the response of the probes which occurred during the time span of the experiment. However, it is noted that the highest values measured for all aluminum- and gal-

lium-doped specimens and for all but two boron-doped specimens occurred when the specimens were aged for two weeks and then rebaked before measuring.

Within the limits imposed by the measurement scatter, no difference can be detected between the spreading resistance response of boron-, aluminum-, or gallium-doped specimens. The use of spreading resistance calibration data obtained on boron-doped silicon specimens for interpretation of measurements on aluminum- or gallium-doped silicon appears to be an acceptable procedure.

Acknowledgment

This work was supported by the Division of Electric Energy Systems of the Department of Energy under DOE Task Order A021-EES.

Manuscript submitted July 5, 1979; revised manuscript received Dec. 7, 1979.

Any discussion of this paper will appear in a Discussion Section to be published in the December 1980 JOURNAL. All discussions for the December 1980 Discussion Section should be submitted by Aug. 1, 1980.

Publication costs of this article were assisted by the United States Department of Commerce.

REFERENCES

1. P. A. Schumann and E. E. Gardner, *This Journal*, **116**, 87 (1969).
2. D. H. Dickey and J. R. Ehrstein, *Nat. Bur. Stand. Spec. Publ.*, 400-48 (April 1979).
3. P. Kramer and L. J. van Ruyven, *Solid State Electron.*, **15**, 757 (1972).
4. J. R. Ehrstein, in "Semiconductor Silicon 1977," H. R. Huff and E. Sirtl, Editors, p. 377, The Electrochemical Society Softbound Proceedings Series, Princeton, N.J. (1977).
5. W. Kern and D. Puotinen, *RCA Rev.*, **31**, 187 (1970).
6. J. R. Ehrstein, in *Nat. Bur. Stand. Spec. Publ.*, 400-10, p. 249 (1974).

Characterization of Dicing Process by X-Ray Section Topography

S. Yasuami

Toshiba Corporation, Toshiba Research and Development, Center, Saiwai-ku, Kawasaki 210, Japan

The dicing process usually consists of grooving a wafer with a diamond saw and then separating it by a roller into chips. The first process causes damage on the surface and this damage induces elastic strains in the wafer. Even after separating the wafer into chips, the chips are not free from these lattice distortions. It is often required that these distortions are checked in a fabrication process with nondestructive methods. X-ray diffraction topography (1) is the most suitable technique, because it is highly sensitive to the strain of crystal lattice. Schumaker and Rozgonyi (2), for example, studied the damage due to dicing by Berg-Barrett topography (3) and investigated the effects on quantum efficiency in GaP electroluminescent diode. In this paper, the effects of dicing with different kinds of diamond saw blades were studied by means of x-ray section topography (4) and the connection with the breakdown voltage of the p-n junctions was investigated.

Let us assume the (001) surface of the silicon wafer; the diameter and the thickness were about 76 mm and

Key words: defects, diodes, stress-strain.

395 μm , respectively. For the comparison of the effects of different blades, several lines were drawn on a single wafer using different diamond saw blades. The grooves were drawn along the [110] direction. A fine focused x-ray generator with an Ag target was used at 0.7 kW; the effective focus size was 40 μm square. The technique of taking section topographs was standard except that a fine slit of 10 μm width was used for limiting the width of the incident beam. Topographs were obtained using the 440 Bragg reflection. It took about 3 hr using the ILFORD L4 nuclear emulsion plate.

In Fig. 1, the grooves of (a) and (b) were made by 20 μm thick blades with different sizes of diamond abrasive particles [2-6 μm ϕ for (a), and 4-8 μm ϕ for (b)]. The grooves of (c) were drawn by the 40 μm thick blade with the same abrasive particles as that used for (b). Other conditions are listed in the figure caption. In the vicinity of the grooves, black and white intensity contrasts were observed. The resultant surface damage and its associated lattice strain are the causes of these contrasts (5). By observing the dis-

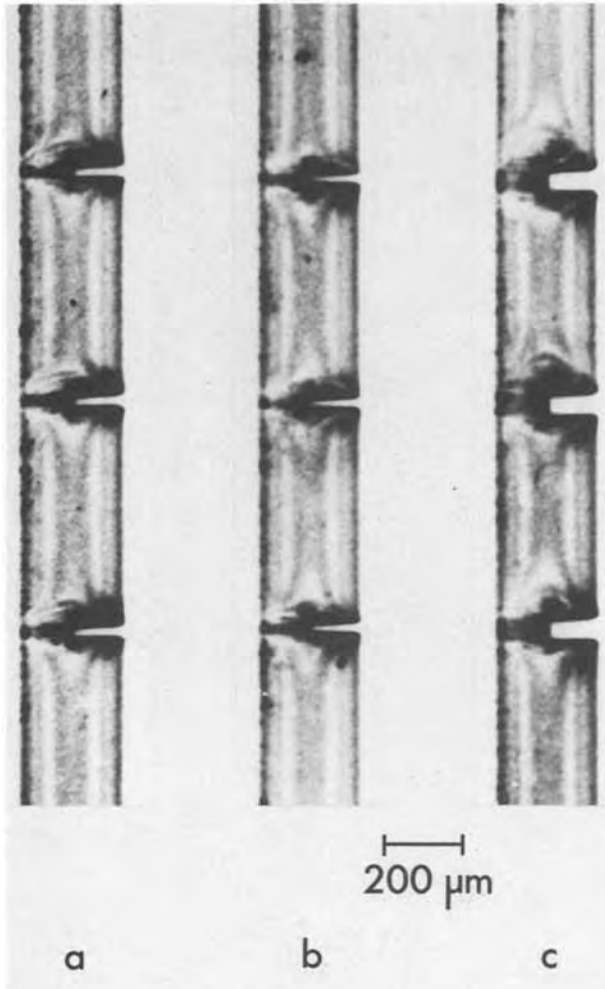


Fig. 1. Section topographs of a (001) silicon wafer grooved by different kinds of diamond saw blades. The thickness of the blades are 20, 20, and 40 μm for (a), (b), and (c), respectively. The abrasive particle sizes are 2-6, 4-8, and 4-8 μm ϕ for (a), (b), and (c), respectively. The common data are as follows: revolution rate of blades: 30,300 rpm, table leading rate: 76 mm/sec, flow rate of water for cooling: 0.5 liter/min, and groove depth: 150 μm . Reflection 440, $\text{AgK}\alpha$ radiation.

torted Pendellösung fringes, one can see that the [110] component of strain gradient is extended more than four times of the groove width. Clearly, the strain field is weaker for the thinner blade and/or for the finer abrasive particles. Here, the grooves appear narrower for the coarse abrasive particles, probably because of photographic effects.

Following the grooving process, the wafer was further pressed by a roller and separated into chips. The top of Fig. 2(a) shows the damage after the separation in the case of a groove of Fig. 1 (c). The strain still remained to the same extent as before the separation. The surface damage could be removed within 1 min in the etchant ($\text{HF}:\text{CH}_3\text{COOH}:\text{HNO}_3 = 1:2:3$) at 0°C . Figure 2(b) is the section topograph of the same specimen as that shown in Fig. 2(a) after etching. It is interesting that the net amount of etching is about 1 μm whereas the contrasts over 100 μm disappear. This fact is good indication that the lattice distortion induced by dicing in the bulk is purely elastic. The dark contrasts indicated by the arrows are caused by bending due to gravitation.

Often, some electric properties of solid-state devices are changed by the surface damage. A p-n junction was formed by diffusing boron dopants all over the face of an n-type wafer. The thickness of the p-region was about 50 μm . Grooves of about 40 μm in width, and about 160 μm in depth were drawn, and filled with

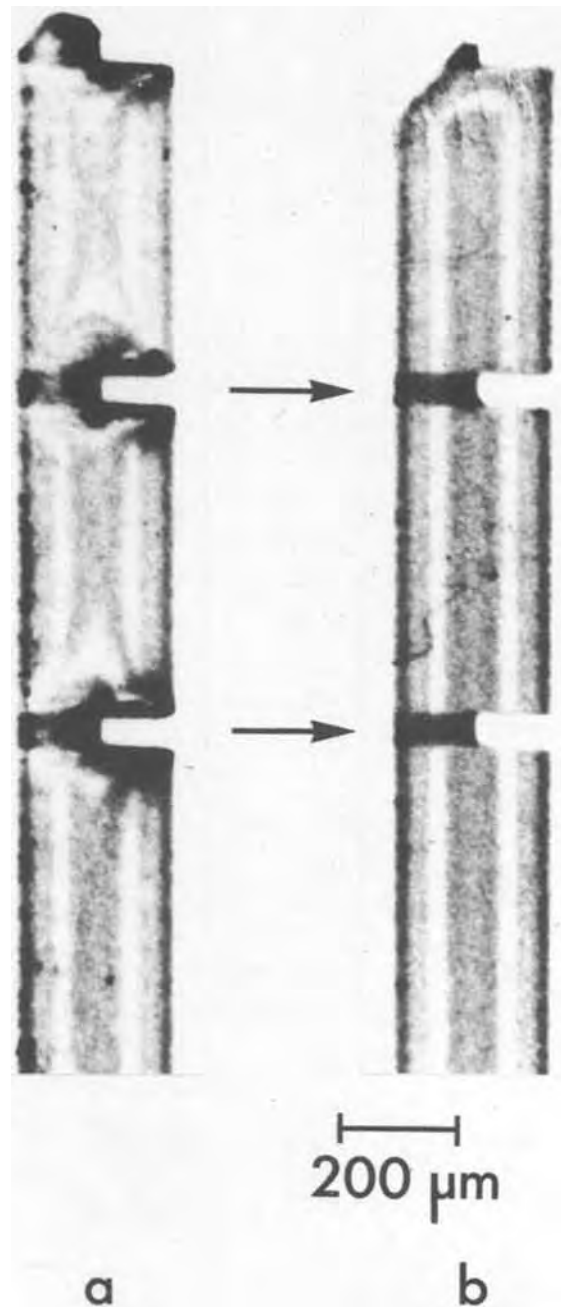


Fig. 2. (a) Section topograph of the wafer after the separation at a groove of Fig. 1(c). See the top part and compare with the grooves. (b) Section topograph after etching. Surface damage due to dicing is removed by slight etching. Reflection 440, $\text{AgK}\alpha$ radiation.

glass materials for passivation. At this stage, the breakdown voltage of the p-n junction was extremely low. If, however, the grooves were etched for about 10-60 sec, the breakdown voltage was increased by as much as 1000V. At this stage, section topographs showed that the surface damage was completely removed, although the residual strain as indicated by the arrows in Fig. 2(b) remained in the bulk crystal.

The experiments of this type are useful for the characterization of the crystals after the dicing process and the device designing.

Acknowledgments

The author would like to thank Professor N. Kato for valuable discussions. He also thanks Dr. M. Watanabe for critical comments, and M. Abe and T. Atsumi for the specimen preparation and the electric measurement.

Manuscript submitted Oct. 29, 1979; revised manuscript received Jan. 7, 1980.

Any discussion of this paper will appear in a Discussion Section to be published in the December 1980 JOURNAL. All discussions for the December 1980 Discussion Section should be submitted by Aug. 1, 1980.

Publication costs of this article were assisted by Toshiba Corporation.

REFERENCES

1. For example, see, B. K. Tanner, "X-ray Diffraction Topography," Pergamon Press, Oxford (1976).
2. N. E. Schumaker and G. A. Rozgonyi, *This Journal*, **119**, 1233 (1972).
3. W. F. Berg, *Naturwissenschaften*, **19**, 391 (1931); C. S. Barrett, *Trans. AIME*, **161**, 15 (1945).
4. A. R. Lang, *J. Appl. Phys.*, **29**, 597 (1958).
5. Y. Ando and N. Kato, *J. Appl. Crystallogr.*, **3**, 74 (1970).

Diffusion of Indium in $\text{Hg}_{1-x}\text{Cd}_x\text{Te}$

S. Margalit and Y. Nemirovsky

Department of Electrical Engineering, Technion-Israel Institute of Technology, Haifa, Israel

The semiconductor alloy system $\text{Hg}_{1-x}\text{Cd}_x\text{Te}$ has become the most useful and important material for infrared photon detectors. This alloy is very versatile: it can cover a wide wavelength range in the infrared by altering the mole fraction x of CdTe and is suitable for both photovoltaic and photoconductive detectors. An additional attractive feature of the system is the fact that the processing and technology do not vary appreciably for a wide range of composition x .

It is interesting to note that devices of $\text{Hg}_{1-x}\text{Cd}_x\text{Te}$ have been widely used as practical detectors long before their basic properties have been fully understood. Among the topics that should be further studied are the defect structure and the properties of dopants in $\text{Hg}_{1-x}\text{Cd}_x\text{Te}$.

Indium is commonly used in n-type $\text{Hg}_{1-x}\text{Cd}_x\text{Te}$ devices to form evaporated ohmic contacts. It can also be introduced into the $\text{Hg}_{1-x}\text{Cd}_x\text{Te}$ lattice during growth to control the conductivity of the "as grown" crystals, as has been done in CdTe (2, 3). Johnson and Schmit (4) have found that indium is a metal sublattice substituted donor and a very fast diffuser. During the low temperature annealing cycle of device processing and technology the indium which is present in the contacts diffuses into the lattice. Concentration gradients and consequently built-in electric fields (5) of the order of $10\text{--}20\text{ V}\cdot\text{cm}^{-1}$ are formed. The distribution and the surface recombination velocity of photoexcited minority carriers are modified by these fields. Precise knowledge of the indium diffusion is therefore needed for the analysis of the photoresponse of the devices.

In view of the practical and theoretical interest in diffusion of indium in $\text{Hg}_{1-x}\text{Cd}_x\text{Te}$, this subject has been investigated and is reported in this note. The study describes the diffusion of indium from evaporated layers of indium into unoriented crystals of $\text{Hg}_{1-x}\text{Cd}_x\text{Te}$ with $x = 0.215$ and $x = 0.29$, in the temperature range of $70\text{--}160^\circ\text{C}$. The temperature range under study is relevant for the technology of the devices and, in addition, it can be assumed that stoichiometry changes do not take place. Diffusion profiles are given as well as diffusion constants, the diffusion energy of activation, and the surface concentrations.

Experiments were performed on $\text{Hg}_{0.785}\text{Cd}_{0.215}\text{Te}$ and $\text{Hg}_{0.71}\text{Cd}_{0.29}\text{Te}$ with approximately 0.1 and 0.25 eV bandgap at 77°K , respectively. P-type wafers of low carrier concentration (approximately $1\cdot 10^{15}\text{ cm}^{-3}$) and of random orientation were used. The samples were epoxied to a flat sapphire substrate which served as a reference surface and also masked the bottom face of the $\text{Hg}_{1-x}\text{Cd}_x\text{Te}$. The wafers were mechanically polished with $0.3\text{ }\mu\text{m}$ Al_2O_3 until a mirror-like flat surface was achieved. The front surface was then etched for 1-2 sec in 20% bromine in methanol to remove the polishing damage and thoroughly rinsed in methanol

to get rid of the bromides. The thickness of the semiconductor was determined within $\pm 1\text{ }\mu\text{m}$.

The diffusion process was carried out in two steps: first, a layer of 5000 \AA of indium was vacuum evaporated on the freshly etched surface of $\text{Hg}_{1-x}\text{Cd}_x\text{Te}$. In the second step the sample was diffused in vacuum.

In order to get reproducible results the samples were brought to room temperature in a manner that was repeatable from run to run. Abrupt quenching was avoided in order to preserve excess minority carrier lifetimes. Finally, the indium was removed in concentrated HCl and after that the properties of the diffused layer were evaluated.

The diffusion profiles were plotted by carrying out van der Pauw measurements (6) at 77°K on the surface, then lapping off a thin layer of typically $1\text{--}2\text{ }\mu\text{m}$, and repeating the process. Petritz's (7) two layer formulation was used to determine the majority carrier concentration and the effective mobility of each lamina. Since the indium is believed to be electrically active substituted on metal lattice sites (4), the profile of electron concentration gives the profile of diffusion.

Typical diffusion profiles which were measured using the method outlined above are shown in Fig. 1. The calculated solid lines are the fit to the measured points, assuming the simplest possible model of a constant diffusion coefficient and an "infinite" source of deposited indium. These assumptions lead to a profile of the form of a complementary error function (5), $C(x) = C_s \text{erfc}[x/2(Dt)^{1/2}]$, where C_s is the surface concentration and D is the diffusion coefficient and their values are determined from the best fit. It is shown in Fig. 1 that as the diffusion time progresses the surface concentration remains constant within the experimental error. It was also observed that the sheet conductance increases with the square of the diffusion time. It is therefore reasonable to assume that in the temperature range under study the simple model may be used. The surface concentration of indium which is obtained is $(3\text{--}6) \times 10^{15}\text{ cm}^{-3}$.

The measured sheet conductance as a function of the reciprocal of the diffusion temperature is shown in Fig. 2. The diffused sheet conductance is given by $\sigma = (2q\mu C_s)(D_0t/\pi)^{1/2} \cdot e^{-E_A/2kT}$ where μ is the average mobility of the diffused layer, E_A is the diffusion energy of activation, and D_0 is the preexponential term of the diffusion coefficient. The data points for $x = 0.215$ are best fitted with the relation $\Delta G_{\square} = 25.7 \cdot e^{-0.37/2kT}$ leading to a diffusion energy of activation of 0.37 eV .

The energy of activation is practically the same for $x = 0.29$. However, the preexponential term of the sheet conductance differs by a factor of 2.7. It is known that the electron mobility at 77°K of bulk $\text{Hg}_{1-x}\text{Cd}_x\text{Te}$ decreases with increasing x (1). For $x = 0.215$ and $x =$

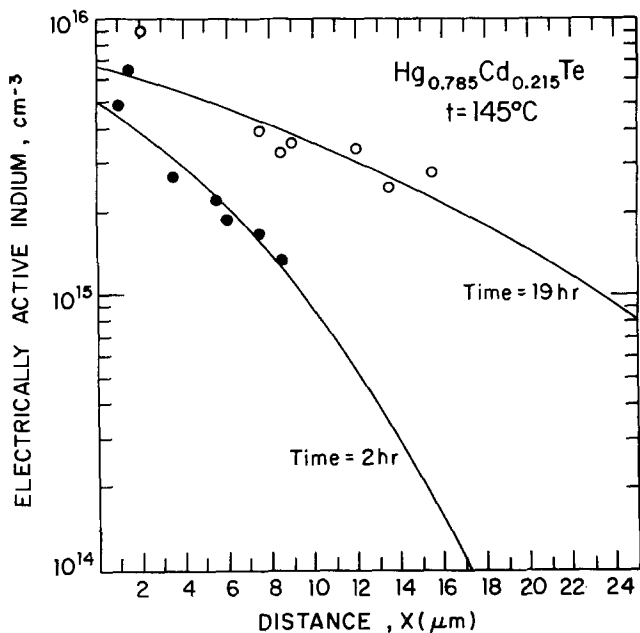


Fig. 1. Concentration profile of the electrically active indium in $\text{Hg}_{0.785}\text{Cd}_{0.215}\text{Te}$ vs. depth. The circles are measured points. The solid lines are calculated distributions assuming a complementary error function. The diffusions were carried out at 145°C for 19 hr and 2 hr for the upper and lower curves, respectively.

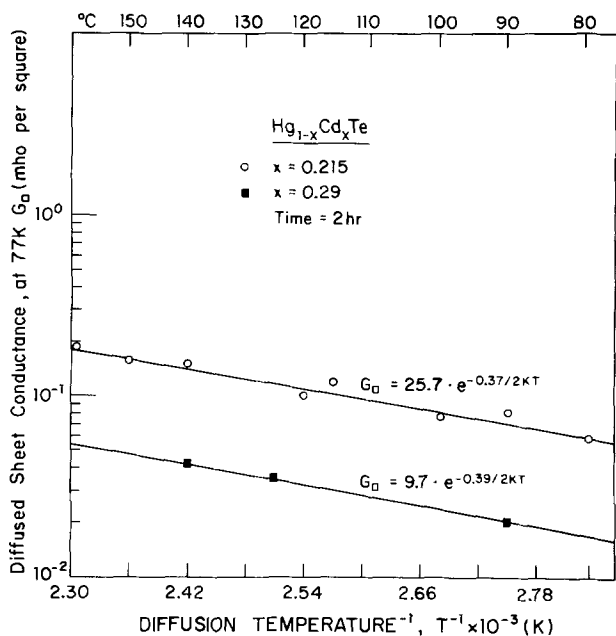


Fig. 2. The diffused sheet conductance measured at 77°K as a function of the reciprocal of the diffusion temperature. The diffusions were carried out for 2 hr. The points are for $\text{Hg}_{1-x}\text{Cd}_x\text{Te}$ with $x = 0.215$. The squares are for $x = 0.29$.

0.29 the mobility ratio is approximately 2.5. The reduced preexponential term for $x = 0.29$ is therefore due to a lower average mobility and probably to a slightly lower surface concentration.

From the slope of the lines of Fig. 2 and taking $\mu = 1.5 \cdot 10^5 \text{ cm}^2 \cdot \text{V}^{-1} \cdot \text{sec}^{-1}$ and $C_s = 6 \cdot 10^{15} \text{ cm}^{-3}$ the preexponential term of the diffusion coefficient D_0 is obtained: $D_0 (\mu\text{m}^2 \cdot \text{sec}^{-1}) = 5.1 \cdot 10^2$.

The measured temperature dependence of the diffusion coefficient is given in Fig. 3. The calculated best fit is $D (\mu\text{m})^2/\text{sec} = (5.25 \cdot 10^2) e^{-0.38/kT}$. The diffusion energy of activation and the preexponential term of the diffusion coefficient correspond to that of Fig. 2. It should be noted that the data points of Fig. 2 are based

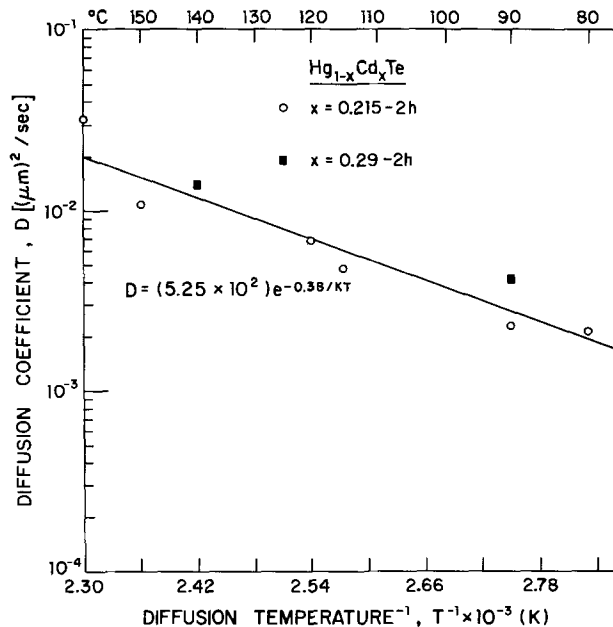


Fig. 3. The diffusion coefficients of indium in $\text{Hg}_{1-x}\text{Cd}_x\text{Te}$ for $x = 0.215$ as a function of the reciprocal of the absolute diffusion temperature. The lines are best fitted to the form $D = D_0 \cdot e^{-E_a/kT}$. The diffusions were carried out for 2 hr.

on simple and straightforward measurements and are therefore the least susceptible to experimental errors.

It is interesting to note that the activation energy of the diffusion is the same for $x = 0.215$ and $x = 0.29$ and does not depend on the bandgap. $\text{Hg}_{1-x}\text{Cd}_x\text{Te}$ with $x = 0.215$ has a bandgap which varies between 0.215 eV at 100°C and 0.229 eV at 140°C (9). The bandgap of $\text{Hg}_{0.71}\text{Cd}_{0.29}\text{Te}$ varies in the same temperature range between 0.329-0.340 eV. The activation energies of a purely substitutional mechanism of diffusion are three to four times the energy gap of the semiconductors. Such a mechanism would have shown a dependence on the composition x corresponding to the bandgap variation with x . The fact that such a dependence is not observed and the fact that indium is a fast diffuser indicate that indium diffuses through the interstices in the metal sublattice. The mechanism of the diffusion and its dependence on the defect concentration for that particular crystal have not been established.

Indium undergoes a chemical reaction with $\text{Hg}_{1-x}\text{Cd}_x\text{Te}$. The mirror-like surface acquires a gray-matte appearance after the removal of the indium, even without annealing the samples at higher temperatures. The phase diagrams of In and the constituents of $\text{Hg}_{1-x}\text{Cd}_x\text{Te}$ indicate alloying either at room temperature, or in the temperature range under study (8). Since $\text{Hg}_{1-x}\text{Cd}_x\text{Te}$ is easily oxidized, this feature of the diffusion system is very favorable and ensures reproducible results.

The process of diffusion of indium into $\text{Hg}_{1-x}\text{Cd}_x\text{Te}$ forms a distribution of ionized donors near the surface. The ionized donor sites create an electric field which is given by $dv/dx = kT/q \cdot 1/n(dn/dx)$ where n is the local concentration of ions and k is the Boltzmann's constant. For shallow diffusions the resulting surface fields are $(10-20) \text{ V} \cdot \text{cm}^{-1}$ at 77°K . Excess photoexcited minority carriers (holes in an n-type semiconductor) are pushed away from the surface and electrons are attracted there. The surface recombination velocity of excess carriers in n-type samples which were subjected to a shallow indium diffusion is therefore reduced. The measured effective lifetime of holes in n-type samples was shown to increase by approximately a factor of two as a result of such a shallow diffusion.

In summary, the diffusion of indium from evaporated layers of indium into randomly oriented crystals of

$\text{Hg}_{1-x}\text{Cd}_x\text{Te}$ with the composition $x = 0.215$ and $x = 0.29$, in the temperature range of $70^\circ\text{--}160^\circ\text{C}$, has been investigated. For $x = 0.215$ the diffusion sheet conductance at 77°K of the resulting n-type layer in mho per square is $\Delta G_{\square} = 0.3 \cdot t^{1/2} \cdot e^{-0.37/2kT}$ where $t(\text{sec})$ is the diffusion time and $T(^{\circ}\text{K})$ is the diffusion temperature. The energies of activation and the diffusion coefficients are the same within the experimental error for $x = 0.215$ and 0.29 and are shown to follow $D[(\mu\text{m})^2/\text{sec}] = (5.25 \cdot 10^2)e^{-0.38/kT}$ giving the value of 0.37 ± 0.01 eV for the diffusion energy of activation. The surface concentration of indium is of the order of $(3\text{--}6) \cdot 10^{15} \text{ cm}^{-3}$. The diffused indium forms built-in fields of the order of $10\text{--}20 \text{ V} \cdot \text{cm}^{-1}$ which reduce the surface recombination velocity of photoexcited excess carriers.

Finally, it should be noted that the experimental conditions under which the results were obtained were intentionally chosen so as to be suitable for device processing and applications.

DISCUSSION SECTION



This Discussion Section includes discussion of papers appearing in the *Journal of The Electrochemical Society*, Vol. 126, No. 7, 11, and 12, July, November, and December 1979.

The Strain Distribution of the Interface between Substrate and Epitaxial Layer of Silicon by X-Ray Double Crystal Method

N. Miyamoto and E. Kuroda (pp. 1228-1234, Vol. 126, No. 7)

J. Nishizawa, M. Fukase, and H. Tadano:¹ It seems to us that the paper under discussion was intended to describe the experimental results of strain distributions in the epitaxial crystal silicon layer as the substrate by measuring the lattice constant in the $\langle 111 \rangle$ direction using an x-ray double crystal method.^{2,3} However, we cannot be convinced of the results for the following two main reasons.⁴

(i) Lattice strain varies depending not only on the depth direction but also on the lattice plane parallel to the substrate surface as a function of the position within the sample investigated. But the authors of the paper have not described the irradiating point of the input x-ray beam on the surface of the sample. The radius of the crystal bending, and phenomena, lattice spacing, and the angle of bonding are known to vary with the direction and position of the sample.

(ii) There is no logical explanation of their conclusion that the subpeaks appearing in the rocking curve of the highly doped crystal layer epitaxially grown on the high resistivity silicon substrate is phenomenologically the same as Pendellösung fringes. Such fringes can be observed in the x-ray diffraction curve of a thin crystal film as a substrate from which the epitaxial layer is removed. We will examine in some detail the content of the paper under discussion.

Shape of the sample.—Since the elastic constant shows a variation with crystal orientation, the lattice strain exhibits very complicated changes. Therefore,

Manuscript received Sept. 10, 1979.

Any discussion of this paper will appear in a Discussion Section to be published in the December 1980 JOURNAL. All discussions for the December 1980 Discussion Section should be submitted by Aug. 1, 1980.

REFERENCES

1. D. Long, "Topics in Applied Physics," R. J. Keyes, Editor, Vol. 19, Springer-Verlag, New York (1977).
2. K. Zanio, "Semiconductors and Semimetals," Vol. 13, Academic Press, New York (1978).
3. F. A. Kroger, "The Chemistry of Imperfect Crystals," North-Holland, Inc., New York (1973).
4. E. S. Johnson and J. L. Schmit, *J. Electron. Mater.*, **6**, 25 (1977).
5. B. Tuck, "Introduction to Diffusion in Semiconductors," Peter Peregrinus Ltd., England (1974).
6. L. J. van der Pauw, *Philips Res. Rep.*, **13**, 1 (1958).
7. R. L. Petritz, *Phys. Rev.*, **110**, 1254 (1958).
8. M. Hansen, "Constitution of Binary Alloys," McGraw-Hill Book Company, Inc., New York (1958).
9. J. L. Schmit, *J. Appl. Phys.*, **41**, 2876 (1970).

the measurement of lattice strain should be carried with a highly symmetrical sample with respect to crystal orientation. The crystal surface of the sample used in the paper is parallel to the (111) plane. The crystal has three kinds of symmetry with respect to the axis of the $\langle 111 \rangle$ direction as shown in our Fig. 1. However, the shape of the sample in the paper is rectangular. In this case, the sides of the sample differ from each other. Sides A and B are $\{112\}$ planes, and C and D are $\{110\}$ planes. Therefore there is poor symmetry in the rectangular shape. When the surface of the sample is the (111) plane, it is easiest for the analysis to make the shape of the sample triangular. When the surface is parallel to the (100) plane, it is possible to make the side of the sample equivalent to the (100) plane by making the shape rectangular. Hence, it is easy to measure the lattice strain because the distribution of lattice strain is highly symmetric and the lattice strain does not show any radical change with the direction in the symmetric center. It would be interesting to measure such a sample.⁵ We have urged the authors of the paper to carry out measurements at the axis.

Measured point by x-rays.—Lattice strain depends on the position within the sample even if the shape of

⁵ J. Nishizawa *et al.*, To be published.

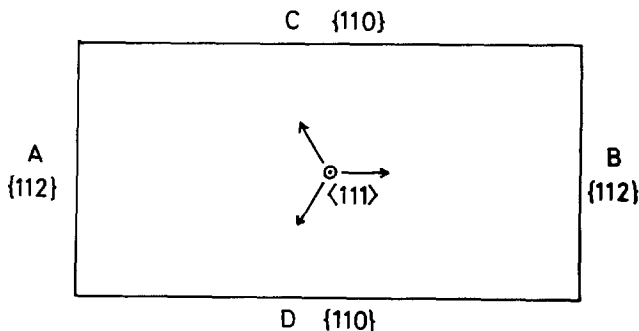


Fig. 1. Shapes of the sample and the symmetric axis of the sample. Arrow indicates the equivalent direction with the $\langle 111 \rangle$ direction.

¹ Research Institute of Electrical Communication, Tohoku University, Sendai 980, Japan.

² E. Kuroda, N. Miyamoto, and J. Nishizawa, Technical Group on Semiconductor Transistor, IECE of Japan, No. SSD 72-23 (1972).

³ N. Miyamoto, E. Kuroda, and J. Nishizawa, Technical Group on Semiconductor Transistor, IECE of Japan, No. SSD 73-29 (1973).

⁴ Private communication.

the sample is a triangle. The paper merely introduces the idea which was suggested by one of us concerning the change of lattice spacing in depth direction. But there is no description about the point of x-ray irradiation, though the sample is not symmetric to the axis owing to the nontriangular shape and the complicated distribution of lattice strain. It seems that the authors have not considered the lattice strain in the direction parallel to the interface.

Since the change of the lattice strain in the crystal is interconnected three-dimensionally, it is necessary to measure the strain in the x, y, and z directions in order to determine the lattice strain, especially, when the shape of the sample is not symmetric in terms of crystal orientation. It is possible that the lattice strain in the center direction differs from that in the perpendicular direction including the center of the crystal. For this reason it is necessary to measure the strain in at least two directions.

The atoms in the diamond structure are in tetrahedral coordination. If the length and angle of each bonding are not clear, we cannot state the true lattice strain which is measured. For this reason, it becomes necessary to measure plural lattice planes and to analyze the data multi-dimensionally.

Figure 2 shows a simulation⁶ of the change of the lattice spacings by using a two-dimensional simple cubic lattice. The change of the lattice spacing in the epitaxial layer in both directions is small near the symmetric center and becomes larger with the distance from the symmetric center. The degree of the change at the edge is more than ten times that at the symmetric center. Along with this change, the differential strain (the gap between the lower atomic plane and lattice spacing) also becomes larger with the distance from the symmetric center. Therefore the lattice constant in the vertical direction that is obtained from Young's constant or Poisson's ratio also changes widely depending on positions, though

⁶ J. Nishizawa *et al.*, To be published.

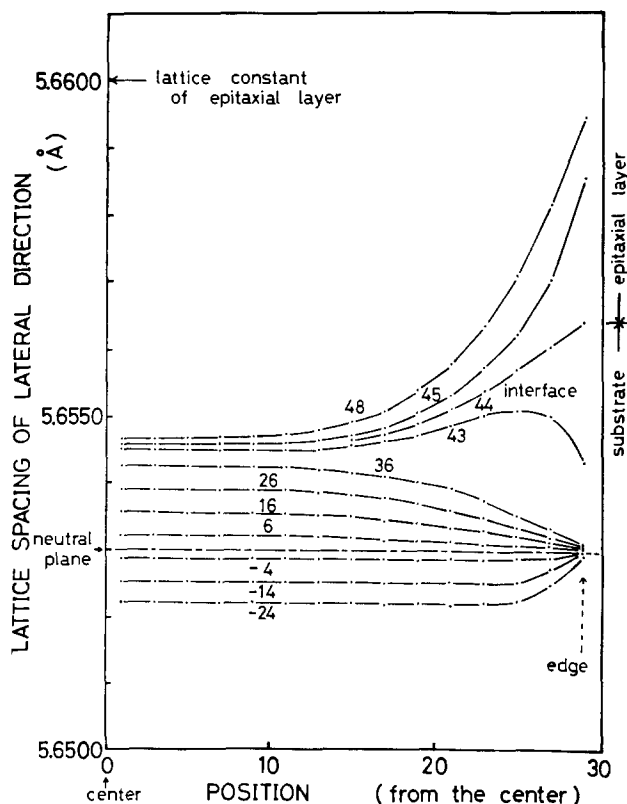


Fig. 2. Lattice spacing distribution in the lateral direction for the growing epitaxial layer made up of the atoms whose atomic radius is somewhat large.

the value is assumed to be constant in our approximate calculation. Figure 2 seems to be well suited to the actual case in spite of the simplicity of the analysis performed.

As described above, it appears that the change in lattice strain cannot be described only in terms of the findings in the depth direction, but the three-dimensional strain distribution should also be taken into consideration.

In a private communication with one of us the authors of the paper stated that the results presented are attained by measuring a crystal in which dislocations are not induced. However, the distribution of strain and stress should depend on position within the crystal. If the dislocation is induced within the sample, strain and stress around the dislocation are decreased (*i.e.*, the distribution of stress and strain around changes). But the distribution of strain and stress within the sample shows a similar distribution between dislocations or dislocation and free edge to the case between free edges where dislocations are not induced.

Curvature radius of the bending.—There is no description about the position of points x_1 and x_2 where Bragg angles θ_1 and θ_2 are measured to represent the bonding. Therefore it is not clear where and which direction is indicated by the value calculated from Eq. [2]. Lattice strain has a three-dimensional distribution as already described.

Moreover, the sample used in the paper has poor symmetry as discussed previously. Therefore the curvature radius of the bending must differ with the direction and point on the crystal surface, and their specific description should be made. For example, a sample grown on a thick substrate produces a large lattice strain especially in the epitaxial layer owing to the difference in lattice constant. Therefore the change in lattice strain with position is large and there should also be a difference in the curvature radius between the epitaxial layer and the substrate.

Even if a sample of the so-called "nonbending crystal" is macroscopically nonbending, it has considerable deformation as viewed from the crystal plane, and it naturally causes the strain which changes as a function of position. A strain in the vertical direction should result. The radius of the bending of the crystallographic plane is not infinite and the radius should also change vertically. Qualitatively there is no difference between the "nonbending" and bending of the crystallographic plane.

Strain distribution in depth direction.—Figure 9 is the sole result of the strain distribution in the paper. It is shown that the lattice strain is not constant near the interface in the range whose order is the same as the thickness of the epitaxial layer. There is a marked difference in curvature radius between the epitaxial layer and the substrate, which means that the lattice strain greatly changes with increasing layer thickness. So, the result shown in Fig. 9 seems to be reasonable. But the authors have given the following explanation by using the idea proposed by one of us: "For high concentration phosphorus-doped epitaxial layers, the lattice constant shrinks, because the covalent radius of phosphorus is smaller than that of silicon. The grown layer at the interface is pulled by the silicon substrate. Therefore, the grown layer expands in the direction parallel to the silicon surface and shrinks in the direction of the thickness. Consequently, the lattice constant distribution at the interface becomes more abrupt compared with isotropically strained samples. The actual distribution of the grown layer is considered to be more abrupt than shown in Fig. 9." But the results of Fig. 8 which constitute the basis of Fig. 9 are measured in the crystal after epitaxial growth and it shows a result of the measurements of the sample whose lattice has already been in the state of strain distribution. Therefore the lattice

strain determined from Fig. 8 is the value after the lattice has been already distorted (*i.e.*, Fig. 9 indicates the strain distribution of the lattice which involves strain to a certain extent). Therefore the authors' explanation about Fig. 9 is inconsistent with the assumption used in solving Fig. 9.

Interpretation of subpeaks.—The authors have shown the correlation between the thickness of the crystal and the period of "Pendellösung fringes" appearing on the diffraction curve of the reflected x-rays by Eq. [5], and stated that a series of the subpeaks observed between the two main peaks is due to the occurrence of Pendellösung fringes among x-rays reflected within the epitaxial layer. This conclusion is based on the fact that the correlation between the interval of neighboring subpeaks and the thickness of the epitaxial layer is analogous to that calculated from the equation. "Pendellösung fringes" appearing on the reflected x-rays are essentially some weak reflections of x-rays which appear across the strong reflection peak at the Bragg angle when the absorption of x-rays can be neglected during the impingement of x-rays on the crystal surface through the bottom. This raises two questions. In the first place, if "Pendellösung fringes" are observed on the rocking curve of x-rays reflected from the epitaxial layer, x-rays reflected at the lattice planes of the internal substrate should be included in the former reflected x-rays, because the substrate made of the same material exists under the epitaxial crystal layer. As one of us has advised the authors, it is very improper to neglect the x-rays reflected from the substrate, even if the lattice constant in the vertical direction changes abruptly at the interface. In effect, the peak of the x-ray rocking curve reflected from the substrate has been observed with the appearance of subpeaks in the immediate vicinity of the peak. The authors have only taken into account the thickness of the epitaxial layer and neglected the effect of the x-rays reflected from the substrate crystal, when the equation of "Pendellösung fringes" is applied. They have considered only the reflections from the epitaxial layer. We cannot understand such an approximation which is not fitted to the real situation. Even if the spacing of the lattice plane that causes reflections changes rapidly at the interface, it is unreasonable to take into account only the x-rays reflected from the epitaxial layer and to neglect the x-rays reflected from the substrate. When a large amount of x-rays are absorbed in the substrate and x-rays do not reach the bottom of the substrate, only a strong main peak appears and "Pendellösung fringes" should not emerge.

In the second place, if Pendellösung fringes appear in the rocking curve of x-rays reflected from the lattice plane of the epitaxial layer, subpeaks must appear at both sides of the main peak. But, judging from the authors' experiment, the subpeaks appear at only one side of the main peak in the rocking curve.

The interference of the x-ray reflected from the substrate and the x-rays reflected from the surface epitaxial layer is most likely to induce the subpeaks. Another possibility is that the deflection angle is distributed and causes a mutual interference due to a gradual change of the atomic surface distance as a function of position.

In conclusion, we would like to point out again here that the content of the paper under discussion is incomplete in the following respects. The distribution of lattice strain is considered solely in terms of the depth direction of the epitaxially grown crystal, though lattice strain has a three-dimensional distribution. We cannot agree with the view that the subpeaks appearing in the rocking curve of the epitaxially grown crystal is phenomenologically the same as Pendellösung fringes observed in the x-ray diffraction curve of a thin crystal film. We hope that

the authors of the subject paper will reexamine our comments.

Techniques of Lapping and Staining Ion-Implanted Layers

C. P. Wu, E. C. Douglas, C. W. Mueller, and R. Williams
(pp. 1982-1988, Vol. 126, No. 11)

R. S. Turner and C. L. Aley:⁷ The portion of the paper by Wu *et al* describing his research and theory of the staining mechanism using HF H₂O Cu stain seems well executed, and we agree with his conclusions within the framework of his study. However, his examination of junction depths in the article was limited to a few wafers of a very specific type. In addition to the variables that the authors define, there are other considerations that affect staining and subsequent junction depth determination. We have found in the course of measuring several thousand junctions with commercially available staining solutions somewhat similar to the Wu type stain, that some other variables include dopant concentration and type, semiconductor material type, crystal orientation, junction depth range, number of junctions, and their relative positions. We feel that because of the huge number of variables that are present, the Wu process is a good start, yet his conclusions have not necessarily been proven to be applicable to the wide range of staining applications in the industry.

In his paper, Wu goes into great detail explaining the need for, and the advantages of the geometric multiplying effect created by beveling. Although his statements and rationale are correct, he has overlooked a measuring method in wide use in industry and research that employs the same principle to a greater advantage. Happ⁸ and McDonald⁹ described a method wherein a radial section is machined into the wafer, penetrating the junction (see Fig. 1). After staining, the width of the groove at the surface and at the junction, W_1 and W_2 , respectively, in Fig. 2, is measured through a microscope.

Junction depth, X_j , is then calculated per the following equation

⁷ Philtec Instrument Company, Philadelphia, Pennsylvania 19119.
⁸ W. W. Happ and W. Shockley, *Bull. Am. Phys. Soc., Ser. II*, 1, 382 (1956).
⁹ B. McDonald and A. Goetzberger, *This Journal*, 109, 141 (1962).

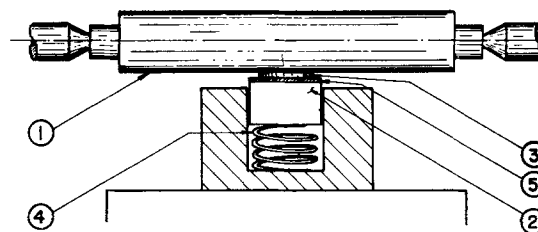


Fig. 1. Grooving apparatus: 1. grooving cylinder; 2. mounting block; 3. silicon slice; 4. spring; 5. glass cover plate.

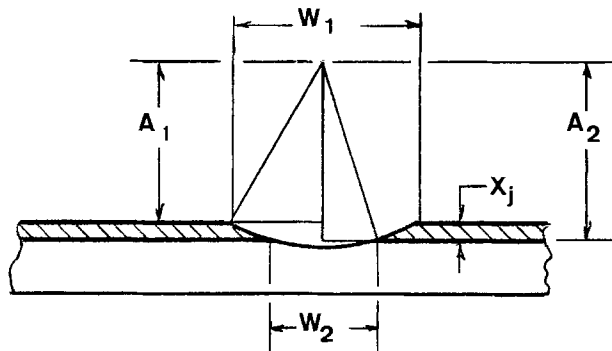


Fig. 2. Groove cross section

$$X_j = A_2 - A_1$$

$$X_j = \sqrt{R^2 - \left(\frac{W_1}{2}\right)^2} - \sqrt{R^2 - \left(\frac{W_2}{2}\right)^2}$$

The multiplying factor increases as the depth decreases, e.g., for the 540Å layer described in the Wu paper, the 50:1 geometric multiplying advantage of the 1° angle lap is credited along with a 1009× microscope as being an important factor in achieving his 200Å repeatability. With a standard sectioning machine employing a groove radius of 19 mm, the multiplying effect is greater than 2000:1 for a junction of that depth, resulting in an equivalent angle of 0.05°. This geometric multiplying factor, when used in conjunction with only a 200× microscope, provides magnification of more than 400,000×. This results in an operator-to-operator repeatability of ±10Å.

Although the grooving method is essentially limited to use on undiced wafer material, and therefore the bevel lap techniques is more suited for individual chip failure analysis, the grooving method offers some distinct advantages other than the greater multiplying effect, such as: (i) as Wu correctly emphasized, when using the angle lap technique, laser angle verification is absolutely necessary. This is not required when determining junction depth by measuring penetration of a known radius. (ii) Because the groove is exposing the same layer twice (once on each side), the resultant X_j is an average of two separate bevel readings. (iii) When considering accuracy of the measuring method, it is generally best to discuss percentage of repeatability: 540 ± 200Å for the angle lap method results in a ±37% potential error; this can be compared to results of studies done using the grooving method on ion-implanted, laser annealed layers of 360 ± 10Å, or operator-to-operator repeatability of ±3%.

C. P. Wu:¹⁰ If the manufacturers of the grooving apparatus for junction depth determination want an opportunity to describe the advantages and accuracies of their method, they should do so by submitting a paper for proper review by referees. Turner and Aley would need much more experimental data and theoretical arguments to substantiate their claim concerning their capability to determine junction depths to ±10Å, roughly two atomic layers.

High Field Intrinsic Ionic Conduction in Solids

Michael J. Dignam (pp. 2188-2195, Vol. 126, No. 12)

Lawrence Young:¹¹ In considering the alleged possibility of a quite large dependence on film thickness of the field at constant ionic current density under steady-state conditions, Dr. Dignam reproduced some of my data on the anodization of tantalum.¹² I wish to suggest that anyone interested in this point should also look at the extensive data for a range of current densities and temperatures which I gave in the second paper¹³ of the series, in which a very precise optical method was used for the thickness. Dr. Dignam (page 2193) refers to the "assumption" that the field was constant. In fact, it was just that the results came out that way. As explained,¹³ I had expected a transition from a thin film case (Mott-Cabrera), in which, with a limited space charge density, the film thickness is supposed to be too small to allow a significant total charge to be present, to the bulk or thick film case in which the condition of electroneutrality would determine the carrier concentration.

On page 2188 Dr. Dignam refers to the quadratic field term in the ionic transport equation "which was first demonstrated experimentally" by Young. He quotes

the paper on steady-state data.¹³ However, on a defect model the field dependence of both the defect concentration and the drift velocity affect the current under steady-state conditions. In a later paper¹⁴ I used a stepped field method, which, as Vermilyea had pointed out, should give direct information on ionic velocity at constant defect concentration. In this connection there is also a question of the significance of the quadratic field terms. I invented this term for the steady-state case as the most natural way of describing my experimental results. What I found experimentally was that $\log J$ was not quite linear in E for steady-state conditions in dilute sulfuric acid. Also, $\partial \log J / \partial E$ was almost independent of temperature if calculated for a constant current but showed the expected temperature dependence if calculated for constant field. The curvature of $\log J$ vs. E plots was much more pronounced for film made in more concentrated sulfuric acid. I considered a range of explanations in this paper.¹³ In the stepped field experiments¹⁴ I found (Fig. 5) that $\partial \log J / \partial E$ was to a first approximation linear in the initial (steady-state) field and had the expected temperature dependence if calculated for a fixed initial field. Although I did not find or establish (Fig. 4) the required curvature of plots of $\log J$ vs. E for stepped fields, the nonlinear dependence on field of the activation energy for ionic transport was proposed as "the simplest suggestion" to explain the results. This dependence of activation energy on field is the basis of Dr. Dignam's and others' models. Quite different possibilities exist and Dr. Dell'Oca and I¹⁵ proposed an explanation of the steady-state curvature of $\log J$ vs. E plots in terms of the two layer model of these films which is indicated by tracer and ellipsometry experiments. Mr. D. J. Smith is presently reinvestigating the kinetics of ionic conduction in these films.

On page 2189, Dr. Dignam refers to "equations proposed by Young" in which conducting species are generated "at a rate proportional to JnE ". The interested reader will not find such equations in the two references which Dr. Dignam quotes^{14,16} but should instead consult two much more recent papers.^{17,18}

M. J. Dignam:¹⁹ In response to the comments by Dr. Young on the above paper, I am grateful for these for partly redressing any negligence on my part for not fully documenting the many important contributions Dr. Young has made to the entire field of anodic films. I particularly regret the omission of his references 17 and 18.

Otherwise, I can find only one matter of disagreement arising between us in relation to this article, and that relates to whether or not there exist data of sufficient precision to rule out a dependence of field strength on film thickness (for thin films at constant current density and temperature) which for Ta₂O₅ would be of the order of a 7% decrease in field per factor of 10 increase in film thickness. Dr. Young apparently believes his data do rule out such a dependence while I am not convinced. The purpose of the paper, however, was not to contest this matter, but rather to examine certain consequences of the high field conduction model proposed by Bean, Fisher, and Vermilyea,²⁰ that had not been previously examined. Whether or not the behavior of anodically formed Ta₂O₅ is or is not in accord with a particular equation arising from this analysis is a matter of some interest, but is not the central issue in the paper. To make intelligent choices between alternative mechanisms, the full consequences of these mechanisms must be known. This paper makes a contribution in this direction.

¹⁴ L. Young, *ibid.*, 263, 395 (1961).

¹⁵ C. J. Dell'Oca and L. Young, *This Journal* 117, 1548 (1970).

¹⁶ L. Young, *Can. J. Chem.*, 50, 574 (1972).

¹⁷ L. Young and D. J. Smith, *This Journal*, 126, 765 (1979).

¹⁸ L. Young and D. J. Smith, *ibid.*, 126, 1972 (1979).

¹⁹ Department of Chemistry, University of Toronto, Toronto, Ontario, Canada M5S 1A1.

²⁰ C. P. Bean, J. C. Fisher, and D. A. Vermilyea, *Phys. Rev.*, 101, 55 (1956).

¹⁰ RCA Laboratories, Princeton, New Jersey 08540.

¹¹ Electrical Engineering Department, University of British Columbia, Vancouver, B.C., Canada V6T 1W5.

¹² L. Young, *Proc. R. Soc., London, Ser. A*, 244, 41 (1958).

¹³ L. Young, *ibid.*, 258, 496 (1960).



Effects of Chloride Ion Impurities on the High Voltage Barrier Anodization of Aluminum

D. J. Sharp and J. K. G. Panitz

Sandia Laboratories, Albuquerque, New Mexico 87185

INTRODUCTION

Anodic oxide films grown on aluminum are divided into two categories: 1) thick, porous films generally applicable for dye adsorption, and 2) high dielectric-strength barrier films for capacitor device application. It has long been recognized that the specific dielectric strength of anodic barrier oxides depends critically on the purity of the aluminum and the anodization bath. Halides (especially chlorides) at concentrations in the range of parts per million have been reported to greatly increase the defects in anodic oxide films (1).

This work reports the use of constant current anodization curves using 99.99% purity aluminum specimens for evaluating bath purity and the effects of chloride ion contaminants as low as 50 parts per billion.

EXPERIMENTAL

The anodization bath used in this study consisted of 0.23 gms. of ammonium tartrate, 47 ml. of deionized water and 2000 ml. of spectroscopic grade ethyl alcohol. The solution was made by first dissolving the ammonium tartrate in water and then adding ethyl alcohol. Unannealed high purity aluminum wire (99.99%) of 0.5 mm diameter was cleaned in 2.0 normal NaOH and rinsed in deionized water immediately prior to use. The anodization cell consisted of a

350 ml. bath using a 99.99% pure gold cathode. Anodization was performed at room temperature (23°C) using an anodic current density of 1.0 mA/cm². The constant current curves illustrated in Figure 1 show the effect of increasing amounts of chloride ion (from HCl) on the rate of rise of anodic potential.

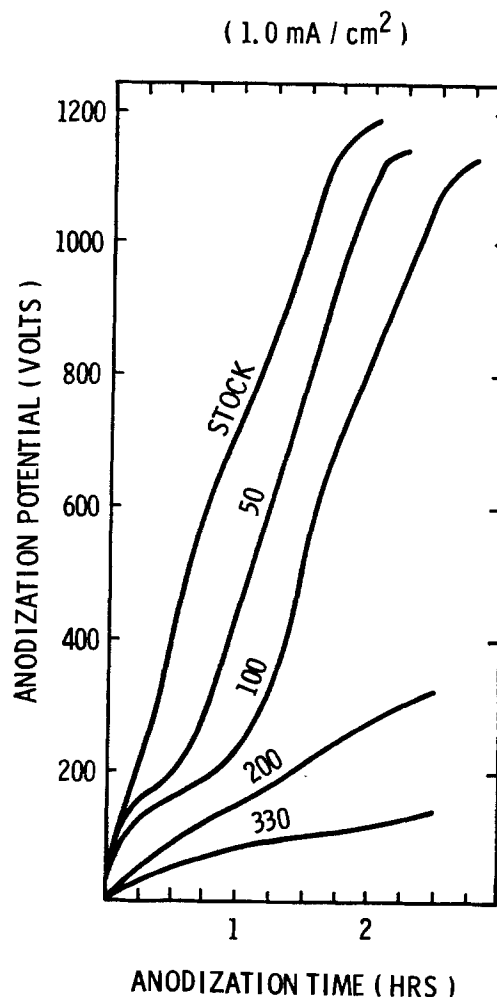


Fig. 1. Constant current anodization curves illustrate the effect of trace amounts of chloride contamination in parts per billion.

Chloride ion was introduced by aliquot dilutions of the original stock solution and added to the working bath so as to produce concentrations of 50, 100, 200, and 330 parts per billion respectively.

DISCUSSION

The first measured effect of chloride additions was noted at a concentration of 50 parts per billion, as an inflection in the rate of voltage rise. Scintillation of the aluminum wire sample was also observed at this point. At chloride ion concentrations above 100 parts per billion the potential did not rise above 400 volts, during the period of anodization (2-1/2 hrs.).

Normally during the anodization process, hydroxyl ions dissociate at the anode to produce oxygen and hydrogen ions. Chloride ions may compete with oxygen to form soluble aluminum compounds, such as AlCl_3 , forming heavily defected dielectrics rather than the insoluble Al_2O_3 barrier films.

Low power microscopic examination of the samples (Figure 2) clearly revealed increasing degradation in the form of flaking and formation of poorly adherent oxide film.

SUMMARY

The use of high purity aluminum wire samples to evaluate the effect of impurity concentrations of chloride ion, as low as 50 parts per billion, was used to provide a useful technique for trouble shooting or certifying an anodization bath. Contaminants at these low levels are easily introduced by careless handling and inadequate specification of materials used in conjunction with barrier layer anodization for capacitor applications.

ACKNOWLEDGMENT

This work is supported by the Division of Basic Energy Sciences, U.S. Department of Energy (DOE), under Contract DE-AC04-76-DP00789.

Manuscript received Oct. 4, 1979.

Publication costs of this article were assisted by Sandia Laboratories.

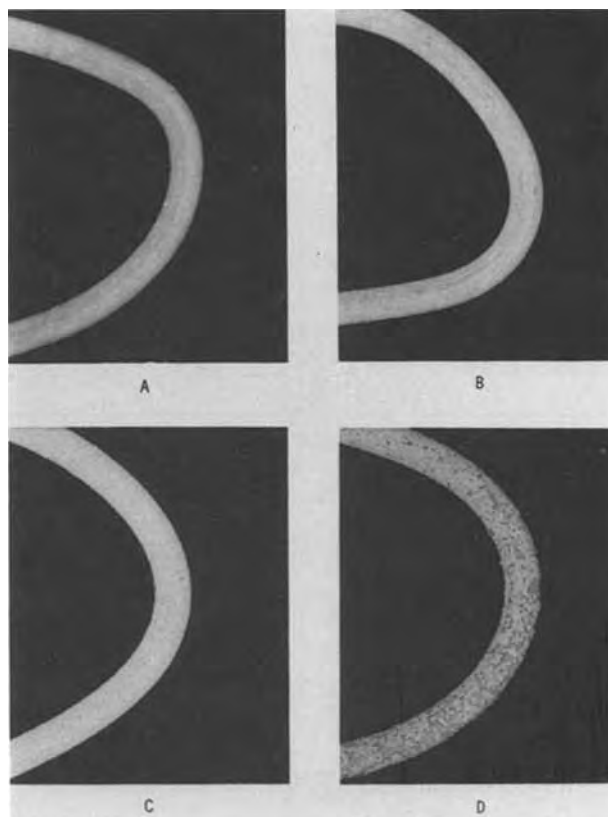


Fig. 2. Magnified view of aluminum wire samples showing degradation of oxide quality as a function of increasing chloride ion concentration. (A = 50 ppb, B = 100 ppb, C = 200 ppb, D = 330 ppb).

REFERENCES

1. H. J. Church, "The Dielectric Properties of Anodic Aluminum Oxide Films," proceedings of the International Conference on Components and Materials used in Electronic Engineering; pp. 399, June 1961.

Phosphosilicate Glass Bridge Structures*

A. Naumaan** and J. T. Boyd

*Solid State Electronics Laboratory, Department of Electrical and Computer Engineering,
University of Cincinnati, Cincinnati, Ohio 45221*

We report herein the formation of phosphosilicate glass (PSG) bridge structures which span across V-grooves formed in silicon by anisotropic etching. These bridge structures consist of a PSG layer which has been deposited by chemical vapor deposition and then shaped by surface tension during heat treatment (1). Open space is clearly apparent beneath these bridge structures. The bridge structure has been observed to span V-grooves notches over lengths of 25 mm. Formation of the bridge structures has occurred on a number of samples for several different preparation conditions.

Experimental.--The standard techniques of photolithographic definition and anisotropic etching (2,3) were used to form V-grooves (having surface dimensions of $247.45\mu\text{m} \times 25.4\text{mm}$) in {100} oriented silicon wafers. The resulting grooves were then about $175\mu\text{m}$ deep. Following groove formation a $.75\mu\text{m}$ thick layer of SiO_2 was thermally-grown on the wafer surface. PSG layers of $12\mu\text{m}$ or $22\mu\text{m}$ were then deposited by chemical vapor deposition at 400°C . Conditions for deposition were selected by considering published data (4-6). The deposited layers contained 10m% P_2O_5 . Finally, the wafers were annealed for periods of either 60 or 120 mins. at 1100°C . Ambients during anneal consisted of either dry O_2 , or O_2 or N_2 bubbled through 95°C deionized water. After annealing samples were cleaved perpendicular to the groove axis and the cleaved cross sections were observed in a scanning electron microscope (SEM). Photomicrographs of the samples were taken and used to obtain measurements of the

structures under examination.

Results and Discussion.--We have observed that for some samples surface tension during PSG flow resulted in the formation of bridges which span across the V-groove about $15\mu\text{m}$ away from the apex of the groove from one sidewall to the other sidewall leaving empty space below. One such bridge structure is apparent in the SEM picture in Fig. 1. Since all samples exhibited considerable flow of the PSG layers, we conclude that bridge formation results for a restricted set of flow conditions. The fact that bridge formation did not occur for all samples is believed to be due to local variations in phosphorous concentration. Wafers were loaded vertically in the annealing furnace with groove axes parallel to the horizontal plane. The profile of the bridges is a function of the viscosity of the flowing PSG, surface tension and gravitational drag. In structures such as that shown in Fig. 1, surface tension has dominated gravitational drag whereas the converse is true in the case of the structure shown in Fig. 2. Fig. 3 illustrates the open space between a PSG bridge and the V-groove from a different angle. The lack of any supporting material between the bridge and the V-groove is clearly evident in this SEM photograph.

Thickness of the bridges at their thinnest point ranged from $3.4\mu\text{m}$ to $7.5\mu\text{m}$. The length, considered to be the shortest distance between end points of the bridge side facing the groove apex, was in the range $10.1\mu\text{m}$ to $42.6\mu\text{m}$. Length to thickness ratios varied from 1.7 to 7.8. Grooves containing the bridge structure were about 25mm long. They exhibited a smooth, continuous PSG layer surface under the microscope. Upon cleavage into samples 5mm or longer, the bridge structure was observed at both ends. This leads us to believe that the bridge extends along the full length of the groove. Radii of curvature of the bridge surfaces ranged from $10.4\mu\text{m}$ to $37.2\mu\text{m}$.

Summary.--PSG layers were deposited

*Research sponsored by the Air Force Office of Scientific Research, Air Force Systems Command, USAF, under Grant No. AFOSR-76-3032 and the University of Cincinnati Research Council. The United States Government is authorized to reproduce and distribute reprints for Governmental purposes notwithstanding any copyright notation hereon.

which flowed in response to high temperature annealing in such a way as to form bridge structures which span V-grooves etched in silicon. Formation by flow is supported by SEM observations of bridge profiles. Based on observations of a number of samples, we speculate that the bridge profile is a function of PSG viscosity, surface tension, and gravitational forces. However, further work remains to be done before the bridge forming process is completely characterized.

REFERENCES

1. A. Naumaan and J.T. Boyd, J. Vac. Sci. and Tech., Jan/Feb Issue, 1980, accepted for publication.
2. M.J. Declerq, L. Gerzberg and J.D. Meindl, J. Electrochem. Soc., 122, 541 (1975).
3. K.E. Bean, IEEE J. Elect. Dev., ED-25, 1185 (1978).
4. W. Kern and R.S. Rosler, J. Vac. Sci. Tech., 14, 1082 (1977).
5. M. Shibata and K. Sugawara, J. Electrochem Soc. 122, 155 (1975).
6. M. Shibata, T. Yoshimi and K. Sugawara, J. Electrochem. Soc., 122, 157 (1975).

** Electrochemical Society Active Member.

Manuscript received Nov. 26, 1979.

Publication costs of this article were assisted by the University of Cincinnati.

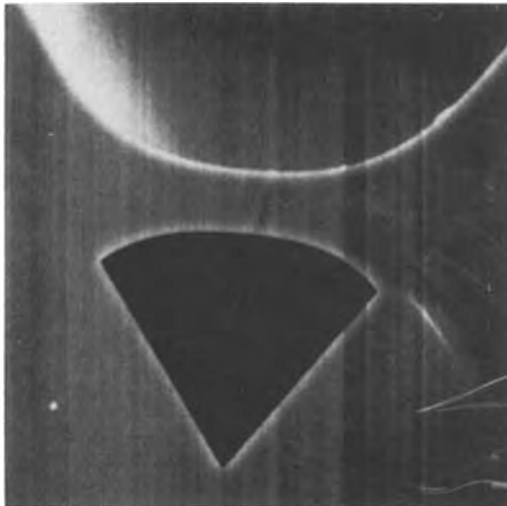


Fig. 1. SEM micrograph showing a PSG bridge structure spanning a V-groove. Bridge thickness is about 6 μm at the central region. The dark area is a clear passage under the bridge.

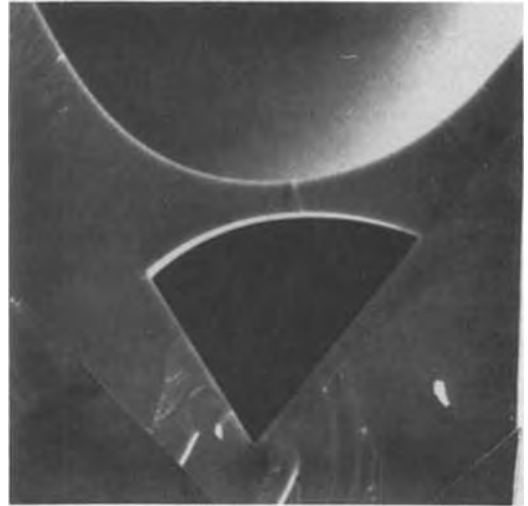


Fig. 2. SEM micrograph showing asymmetric bridge profile due to gravitational force dominating during flow of phosphosilicate glass.

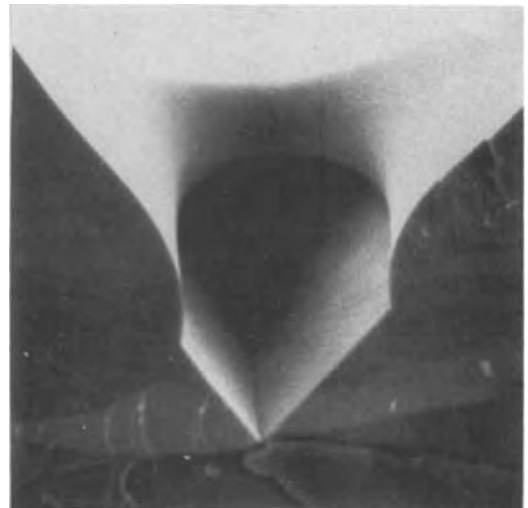


Fig. 3. Micrograph of a bridge structure taken at a different angle. The apex of the V-groove and open space under the bridge are clearly evident.

In Situ Identification of Surface Phases on Lead Electrodes by Laser Raman Spectroscopy

R. Varma,* C. A. Melendres,* and N. P. Yao*

Argonne National Laboratory, Chemical Engineering Division, Argonne, Illinois 60439

INTRODUCTION

There is need for "in-situ" characterization of electrode surfaces to determine the details of processes occurring at electrodes and facilitate the interpretation of current-potential measurements. Laser Raman Scattering appears promising in this application (1). In the work described here, we have used the technique to examine the solid phases formed on lead electrodes during anodic oxidation in sulfuric acid solution. Monitoring of surface phases on lead electrodes during cycling may provide valuable information regarding the factors affecting their cycle life and failure mechanism in lead-acid batteries (2).

Lead foils (0.5 cm x 6 cm x 0.05 cm, 99.999% purity) were anodized in 0.1N H₂SO₄ at constant potentials in a 3-compartment spectroelectrochemical cell using a PAR Model 173D Potentiostat. A Hg/Hg₂SO₄ reference and a platinum counter electrode were used. The laser beam was incident at the working electrode surface at an angle of 60°; the scattered light collected using a 90° illumination-collection optics and analyzed using a Spex Model 1401 double monochromator with photomultiplier tube detection. Coherent Radiation Model 52G Argon and Krypton Lasers were used for optical excitation. Following recording of spectra of the anodic films "in-situ", the electrode was taken out of the cell washed with distilled water, acetone, then dried, and spectra taken again. Samples of various oxides of lead were run as standards for comparison. Film composition was also determined by X-ray diffraction and the morphology examined by scanning electron microscopy (SEM).

*Electrochemical Society Active Member.
Key words: Lead Electrode, In-Situ Raman Spectroscopy

Figure 1a shows the Raman bands observed from scattering off the surface of a lead foil anodized in 0.1 N H₂SO₄ solution at -0.451 V vs. Hg/Hg₂SO₄ for 12 to 72 hrs. Under this condition the electrode is expected to be coated with a layer of PbSO₄ (3,4). Raman spectrum of a compressed pellet of reagent grade PbSO₄ is shown in Fig. 1b. Excellent correspondence is evident for the bands at 436, 450 and 980 cm⁻¹ of the 2 samples. The weaker bands at 1060, 1159, 607 and 641 are understandably not visible for the "in-situ" sample in Fig. 1a due to intensity loss by absorption and diffuse scattering. These bands were, however, also observed when the electrode was examined "ex-situ". X-ray diffraction analysis of the surface coating shows conclusively that the material is PbSO₄ with a rhombic crystal habit.

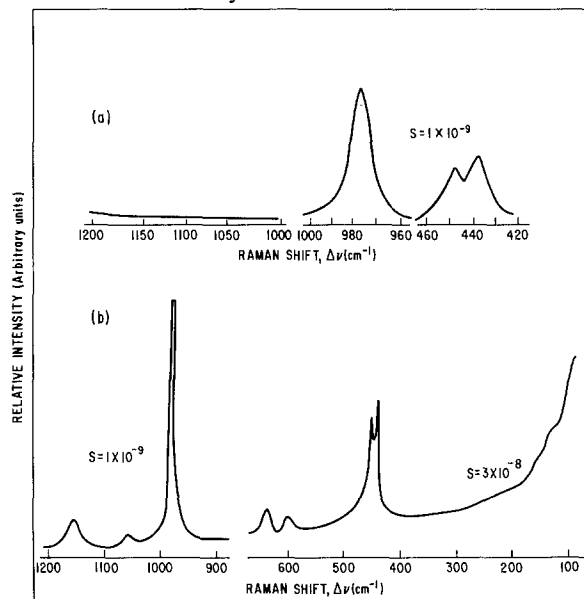


Figure 1. Raman Scattering with Ar⁺ Ion Laser, $\lambda = 4879.86 \text{ \AA}$ (a) In-Situ Spectrum Observed on Lead Electrode Anodized in 0.1N H₂SO₄ at -0.451V vs. Hg/Hg₂SO₄ (b) Spectrum Observed on Compressed Pellet (Commercial Sample) of PbSO₄. Laser beam power = 280 mW (s = detector sensitivity setting).

On anodizing a Pb foil at + 1.335 V vs. Hg/Hg₂SO₄ (following initial formation of the PbSO₄ film at -0.451 V) the white PbSO₄ coating transforms to a greyish black material. Raman scattering from the surface "in-situ" yields the spectrum shown in Fig. 2. with bands at 103, 113, 122, 138 and 286 cm⁻¹ occasionally appearing. There also appeared to be an induction period of several minutes following laser irradiation before we would observe a spectrum. From the Pourbaix diagram of Pb in H₂SO₄ (4), one anticipated obtaining a surface coating of β-PbO₂ on the electrode under the present condition of electrolysis. X-ray diffraction analysis of the coating obtained and SEM study showed it to be β-PbO₂. It, however, appeared necessary to see if the lines observed can indeed be assigned to β-PbO₂ in view of previous reports that no infrared (5) and Raman (6) bands have been observed for β-PbO₂. Moreover, application of the selection rules for lattice and molecular vibrations, indicate that only 4 vibrational modes should be Raman active. Standard samples of β-PbO₂ were obtained from the ESB Battery Company and examined "ex-situ". Initial scans of the samples at laser power of less than 175 mW yielded only a very weak band at 150 cm⁻¹. On increasing the laser power to 350 mW, relatively strong bands at 84, 144, 288, 385, 424 and 550 cm⁻¹ are observed (Fig. 3).

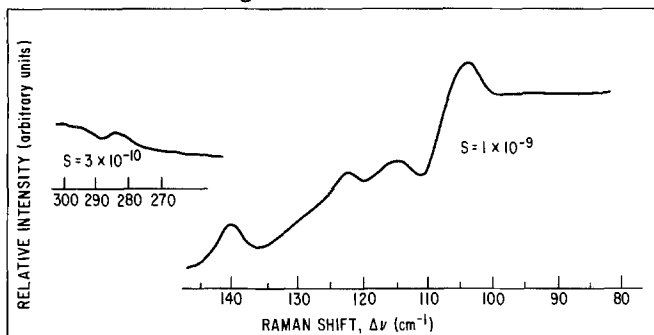


Figure 2. Raman Scattering, Ar⁺ Ion Laser, $\lambda = 4879.86 \text{ \AA}$, In-Situ Spectrum Observed on Lead Electrode Anodized for 72 hours at +1.335 V vs. Hg/Hg₂SO₄

Rotation of the sample causes these peaks to either disappear (with reappearance of the 150 cm⁻¹ band) or to shift by 2 to 8 cm⁻¹ towards lower frequency. At times, on prolonged laser irradiation of the stationary sample, we find the disappearance of the band at 84 cm⁻¹ and the appearance of medium weak bands at 80, 92 and 104 cm⁻¹. The band at 134 cm⁻¹ also shifts

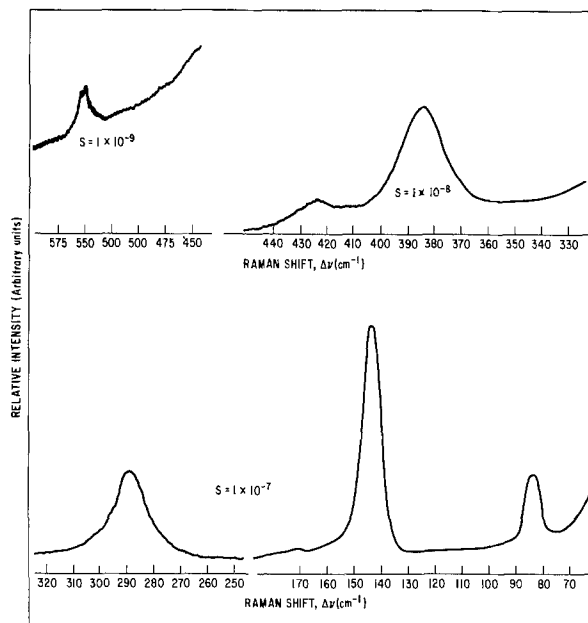


Figure 3. Raman Scattering from β-PbO₂ in KBr Pellet (60 : 40 By Weight), Ar⁺ Ion Laser, $\lambda = 5145 \text{ \AA}$, Power = 300 mW.

to 140 cm⁻¹ with significant loss in intensity. On removal of the sample from the spectrometer, we find peach-colored spots where the laser beam had impinged on the sample. It is evident that Laser irradiation has perturbed the sample significantly causing presumably some phase transformation of the β-PbO₂ to other lead-oxides which give rise to the bands observed. The bands at 92, 144 and 288 cm⁻¹ are, within experimental error, the same as found by Reid (7) and Heidersbach et al (6) for PbO. We are at this point, however, unable to assign the other bands. It is evident that the bands found "in-situ" cannot be unequivocally assigned to β-PbO₂. This lends credence to other workers (6) findings that no Raman active bands for this molecule have been observed.

Finally, we have applied the technique for in-situ monitoring of phase transformations on an actual lead-positive battery plate during discharge. A fully charged PbO₂ plate was cathodically potentiostated at -0.451V vs. Hg/Hg₂SO₄. Bands at 980, 436 and 450 cm⁻¹ were observed to grow in intensity as the β-PbO₂ layer was being converted into PbSO₄.

In summary, we have found the technique of Raman Spectroscopy to be useful for "in-situ" identification of anodic films on

lead electrodes. Caution must, however, be exercised in the assignment of observed Raman bands to a particular surface composition since laser irradiation of the sample may induce chemical and phase transformation in it. The need for supplementing "in-situ" measurements with "ex-situ" studies is evident.

ACKNOWLEDGMENT

Support of the Division of Energy Storage of the Department of Energy is hereby acknowledged.

One of the authors (CAM) thanks F. A. Cafasso and the Division of Basic Energy Sciences of the Department of Energy for their support.

We are grateful to P. R. Fields, J. Unik and J. Ferraro of the Chemistry Division of Argonne for allowing the use of their Raman Spectrometer. We thank ESB Co. for providing standard samples of β -PbO₂.

REFERENCES

1. M. Fleischmann, P. J. Hendra and A. J. McQuillan, *J. Chem. Soc., Chem. Communications* 1973, p. 80.
2. A. C. Simon, S. M. Caulder and J. T. Stemmler, *J. Electrochem. Soc.*, 122, 461 (1975).
3. J. Burbank, *J. Electrochem. Soc.*, 106, 369 (1959)
4. J. Burbank, A. C. Simon and E. Willihnganz, "The Lead-Acid Cell" in Advances in Electrochemistry and Electrochem. Eng. Vol 8, (1971) p. 157 edited by C. W. Tobias and P. Delahay.
5. N. T. McDevitt and W. L. Baun, *Spectrochim. Acta*, 20, 799 (1964).
6. R. Heidersbach, C. Brown, R. Thibeau and A. Goldfarb, Technical Report No. 4, Contract No. N00014-76-C-0889, submitted to the Department of the Navy, Office of Naval Research, Metallurgy Program-Code 471, Aug. 1978.
7. E. S. Reid, R. P. Cooney, et al, *J. Electroanal Chem.* 80, 405 (1977).

Manuscript received Nov. 2, 1979.

Publication costs of this article were assisted by Argonne National Laboratory.



Primary Li/SOCl₂ Cells

XI. SOCl₂ Reduction Mechanism in a Supporting Electrolyte

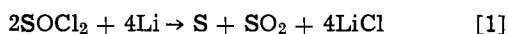
W. L. Bowden* and A. N. Dey*

P. R. Mallory & Company, Incorporated, Laboratory for Physical Science, Burlington, Massachusetts 01803

ABSTRACT

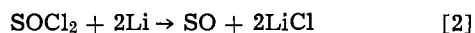
The electrochemical reduction of SOCl₂ has been investigated in organic solvents with supporting electrolytes, using cyclic voltammetry, coulometry, and UV-VIS spectroscopy. An overall 2.0F reduction was observed. Comparison of voltammograms of SO₂, S, and S₂Cl₂ with those of reduced SOCl₂ solutions demonstrated that intermediate species are formed in the reduction of SOCl₂. These intermediates decompose slowly to form S and SO₂. Reaction mechanisms consistent with these findings are discussed.

The Li/SOCl₂ inorganic electrolyte cell is the highest energy density system known to date (1-4). It consists of a lithium anode, a carbon cathode, and thionyl chloride, which functions both as solvent and cathode active material. While this system has been subject to intense development, there exist questions with regard to cell chemistry and cell safety. The cell stoichiometry [1] suggested originally by Dey and Schlaikjer (4) is the most generally accepted one. The reaction involves the formation of sulfur and sulfur dioxide in equimolar amounts, and the quantitative precipitation of LiCl (13) based on 2 F/mole of SOCl₂



Other formulations which include S₂Cl₂, SCl₂, Li₂S₂O₄, and Li₂SO₃ have also been proposed. These (1, 2, 5, 6) proposed reduction processes are accompanied by stoichiometries ranging from 2 F/mole to 2.67 F/mole SOCl₂.

Calorimetric (7) and DTA studies (8, 9) of Li/SOCl₂ D cells showed that chemical reactions occur, which liberate heat after the discharge of the cell. Since these reactions do not occur in an undischarged cell, it is reasonable to assume that the reduction of SOCl₂ is responsible, at least in part, for these spontaneous exothermic reactions. The reported spontaneous explosions of partially discharged Li/SOCl₂ cells on casual storage may also be initiated by reactions involving SOCl₂ reduction intermediates. Thus, knowledge regarding the nature of the unstable intermediates of SOCl₂ reduction may be useful as a guide for the improvement of the safety of the Li/SOCl₂ cells. We postulated (10, 11) the initial overall cell reaction to be



where SO may dimerize and then decompose to S and SO₂ or form polymers. Although there is substantial evidence (12, 13) in favor of cell stoichiometry [1] and the quantitative formation of LiCl and qualitative formation of S and SO₂, little is known regarding the intermediates formed during the discharge of SOCl₂.

Attempts to use cyclic voltammetry (6, 14, 15) in neat SOCl₂-LiAlCl₄ solutions to study the discharge reaction were complicated by electrode passivation due to the precipitation of LiCl which is insoluble in SOCl₂. We have circumvented this electrode passivation problem by using a supporting electrolyte consisting of tetrabutylammonium hexafluorophosphate (N(C₄H₉)₄PF₆) (TBAPF₆) in organic solvents such as dimethyl formamide (DMF), methylene chloride, dimethylsulfoxide (DMSO), and acetonitrile (AN) for studying the SOCl₂ reduction. The electrode passivation was absent in the above solutions since both tetrabutylammonium chloride and S are soluble in the above solvents. We carried out cyclic voltammetry, coulometry, and UV-VIS spectroscopy in the above electrolytes. The results are reported here.

Experimental

Electrochemical experiments were performed using a PAR 173 potentiostat and PAR 175 function generator with associated ancillary equipment. Data were collected using conventional X-Y and strip chart recorders. Platinum working electrodes were pretreated by chromic acid followed by a wash with distilled water and air drying. Experimental solutions were routinely degassed with argon before the substrates were added. A silver chloride coated silver wire was used as a reference electrode. This electrode has a potential of 3.30V vs. Li in PF₆⁻-DMF solutions.

Experiments were performed in cells of conventional design. Coulometric experiments were carried out in a two compartment H-cell using a glass frit to prevent passage of material from the working and auxiliary electrode compartments.

Organic solvents were either Burdick and Jackson "Distilled in Glass" DMF, CH₂Cl₂, and DMSO or Eastman Spectro Grade acetonitrile. Supporting electrolyte was prepared by metathesis of tetrabutylammonium chloride and lithium hexafluorophosphate in acetone/water and purified by multiple recrystallizations from hot ethanol.

Results

The electrochemical characteristics of some of the impurities and proposed reduction products of SOCl₂

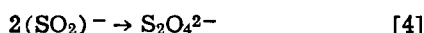
* Electrochemical Society Active Member.

Key words: cathode, voltammetry, spectroscopy.

were examined by cyclic voltammetry in the organic supporting electrolyte solutions. In particular, sulfur, sulfur monochloride, and sulfur dioxide are materials of interest, while chloride ion is known (13) to be a reduction product.

Chloride.—A cyclic voltammogram on a Pt electrode in TBAPF₆/AN is shown in Fig. 1 which demonstrates the clean background. A suitable chloride source was found in tetramethylammonium chloride (N(CH₃)₄Cl; TMACl) which is both soluble and ionized in acetonitrile solution. A cyclic voltammogram obtained with a platinum wire electrode of a solution of TMACl and TBAPF₆ in AN is shown in Fig. 2. The oxidation of free chloride to chlorine and the associated reduction to chloride are clearly located about 1.1V positive of the reference potential.

Sulfur dioxide.—The electrochemical reduction of sulfur dioxide is itself of practical importance and reasonably stable solutions of sulfur dioxide in organic solvents are easily obtained. The reduction of SO₂ in DMF, acetonitrile, and methylene chloride has been examined. In acetonitrile, SO₂ is reduced in a diffusion controlled process at $E_{1/2} = -1.15V$ vs. the silver reference as shown in Fig. 3. The oxidation wave with E_p near +0.35V is much diminished at lower sweep rates and represents the oxidation of a product of the SO₂ reduction, viz. S₂O₄²⁻ according to the reactions



Even at the relatively high sweep rate of 1 V/sec there is little evidence for any other oxidation peaks corresponding to the oxidation of species such as SO₂⁻. A similar voltammogram of SO₂ in dimethylformamide solution is shown in Fig. 4. Once more $E_{1/2}$ is near -1.15V and there is a kinetic oxidation wave due to SO₂ reduction products, but there is also a small wave near -0.13V which is due to a new product species. Finally, SO₂ was also examined in methylene chloride solution, where two oxidation peaks corresponding to the oxidation of SO₂⁻ and S₂O₄²⁻ are more apparent, as shown in Fig. 5. In general the initial reduction behavior of SO₂ in organic solvents was

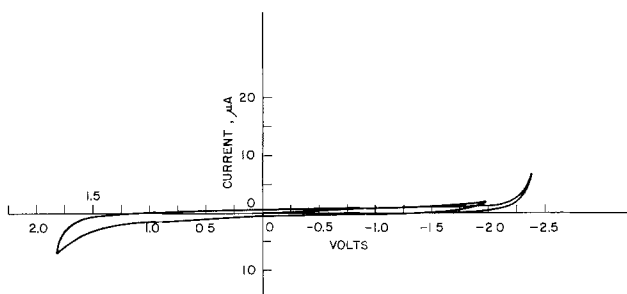


Fig. 1. Cyclic voltammograms of TBAPF₆ solution in acetonitrile on Pt electrode, background, scan rate 200 mV/sec.

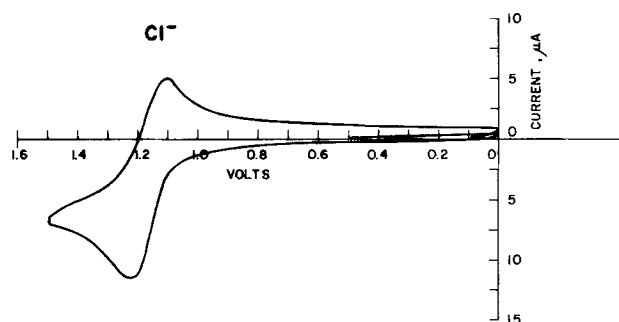


Fig. 2. Cyclic voltammogram of TMACl in acetonitrile/TBAPF₆, scan rate 200 mV/sec.

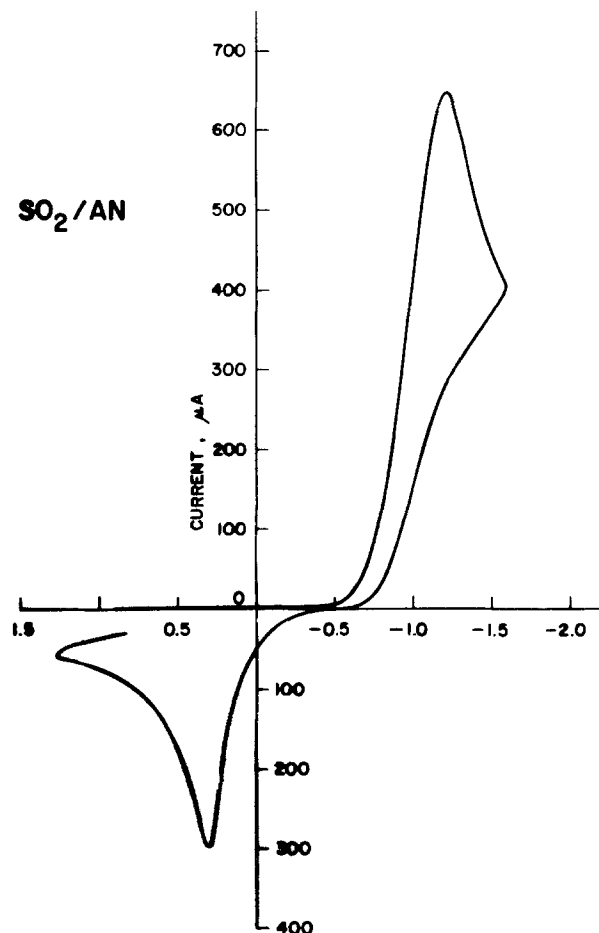


Fig. 3. Cyclic voltammogram of SO₂ in acetonitrile/TBAPF₆, scan rate 1 v/sec.

consistent with the established mechanisms (16) but the oxidation of the reduction products was substantially affected by the solvent, probably due to varying degrees of solvation of the two reduced species, SO₂⁻ and S₂O₄²⁻.

Sulfur.—The cyclic voltammetry of sulfur was examined in dimethylformamide and methylene chloride because of the difficulty of dissolving sulfur in acetonitrile. In both methylene chloride and DMF, the reduction of sulfur is a rather complex phenomenon. The reduction of sulfur in CH₂Cl₂ as shown in Fig. 6 consists of two successive reduction waves whose relative heights are sweep rate dependent (as V increases the second wave becomes less prominent) at ca. -1.1 and -1.5V with an oxidation near 0.2V which

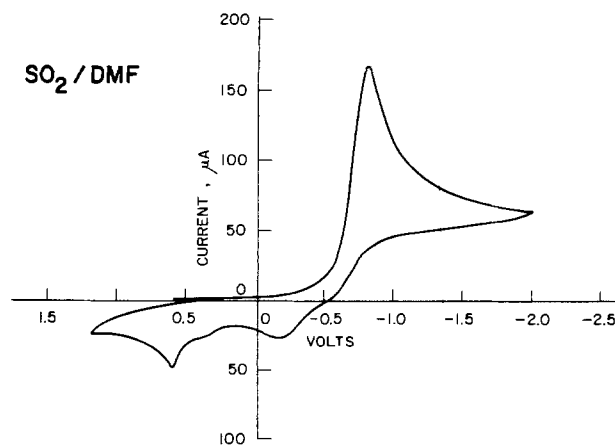


Fig. 4. Cyclic voltammogram of SO₂ in DMF/TBAPF₆, scan rate 200 mV/sec.

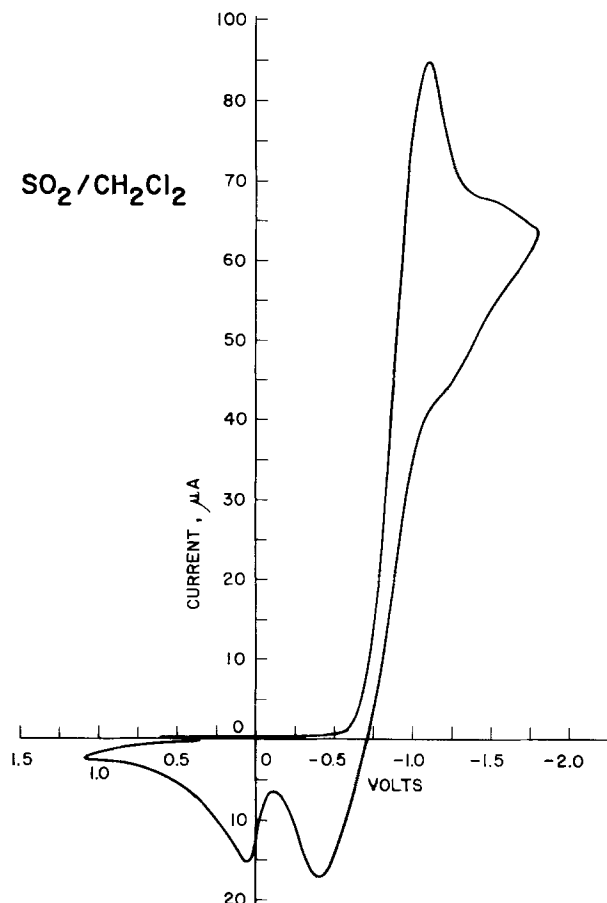


Fig. 5. Cyclic voltammogram of SO₂ in methylene chloride/TBAPF₆, scan rate 100 mV/sec.

is also sweep rate dependent and becomes more prominent as the sweep rate increases. Both of these reduction processes appear to be quite irreversible. The reduction of sulfur in DMF, as shown in Fig. 7 again consists of two irreversible, but more widely spaced waves near -0.6 and -1.15 V. The shape of this second reduction wave is dependent on sweep rate. Finally there is an oxidation wave, also irreversible, at $+0.25$ V. The species responsible for this oxidation has been shown by other voltammograms to be the product of the first reduction wave. The height of this oxidation wave is also a function of the sweep rate and becomes much more obvious at high sweep rates. In acetonitrile the cyclic voltammogram for sulfur is somewhat similar to that for DMF, although the second wave is much less well defined and the oxidation wave is near 0V.

Mixture of sulfur and sulfur dioxide.—Since both S and SO₂ are known to form in the cell, the cyclic voltammogram of a mixture of S with trace amounts of SO₂ in TBAPF₆-DMF electrolyte was obtained, and, as shown in Fig. 8, it contained only the two peaks corresponding to the reduction of S. Cyclic voltammograms of the same solution with slightly higher concentrations of SO₂, as shown in Fig. 8 curve (b), contain three reduction peaks, the middle one represents the SO₂ reduction. There was no noticeable interaction between S and SO₂ that could be detected by the cyclic voltammetry.

Sulfur monochloride.—In contrast to the other products examined, S₂Cl₂ showed a complicated electrochemical behavior in organic solvents. As shown in Fig. 9, the voltammogram of S₂Cl₂ in acetonitrile is dominated by an adsorption wave near -1.15 V. This wave is followed by an apparently reversible reduction near -1.75 V. On the return sweep there is peculiar behavior suggesting adsorption of S₂Cl₂ or

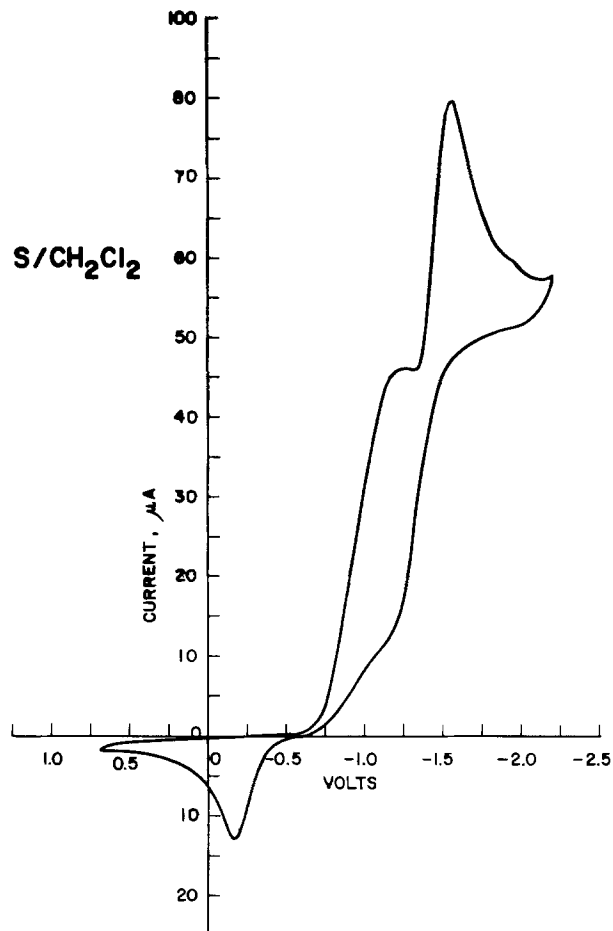


Fig. 6. Cyclic voltammogram of S in methylene chloride/TBAPF₆, scan rate 200 mV/sec.

its products on the electrode surface. At $+1.1$ V we see the oxidation of the chloride generated during the reduction of S₂Cl₂.

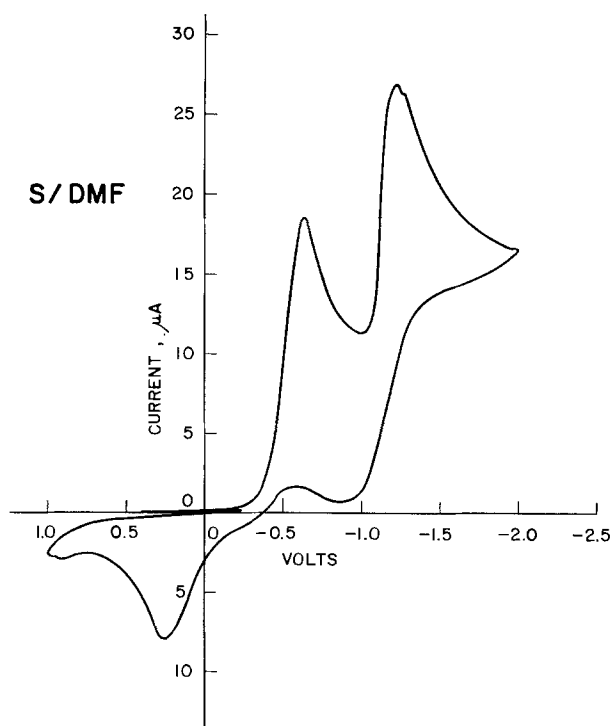


Fig. 7. Cyclic voltammogram of S in DMF/TBAPF₆, scan rate 500 mV/sec.

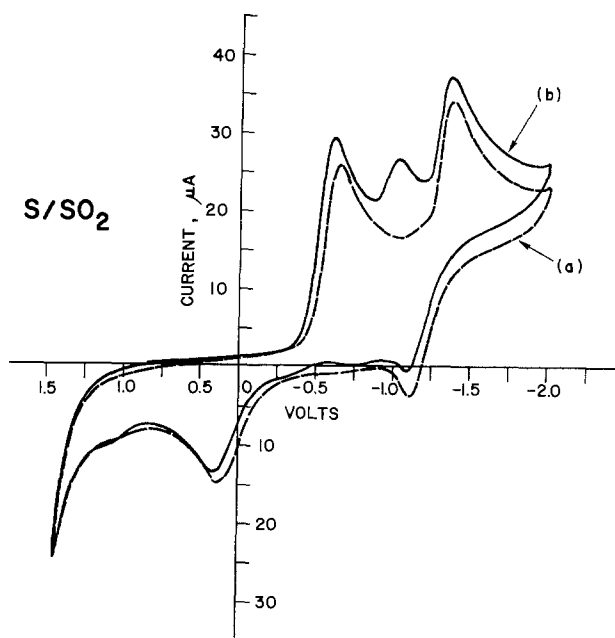


Fig. 8. Cyclic voltammograms of curve (a) S + trace SO_2 in DMF/TBAPF_6 , curve (b) S + more SO_2 , scan rate 200 mV/sec.

Thionyl chloride.—A series of voltammograms for ~ 10 mM SOCl_2 in $\text{CH}_3\text{CN}/0.1\text{N TBAPF}_6$ are shown in Fig. 10. In these voltammograms, on a constant current scale of $25 \mu\text{A/cm}$, the sweep rate, V, was varied from 0.20 to 2.0 V/sec. As the sweep rate increases, the peak current increases, but an oxidation process near 0.0V appears at 500 mV/sec and becomes more prominent at 1.0 and 2.0 V/sec. The chemical entity which is being oxidized at this potential is not present in the solution originally since there is no anodic current at this potential until some of the thionyl chloride has been reduced. The sweep rate dependence of this oxidation wave shows that the species responsible for the oxidation is reacting fairly rapidly in solution. The oxidation and coupled reduction near +1.0V is due to oxidation of chloride ion to chlorine. The chloride itself is generated by reduction of thionyl chloride.

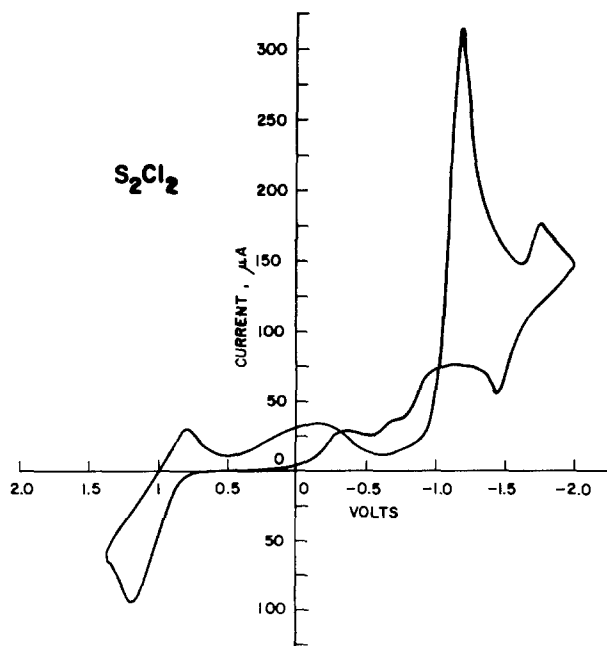


Fig. 9. Cyclic voltammogram of S_2Cl_2 in acetonitrile/ TBAPF_6 , scan rate 500 mV/sec.

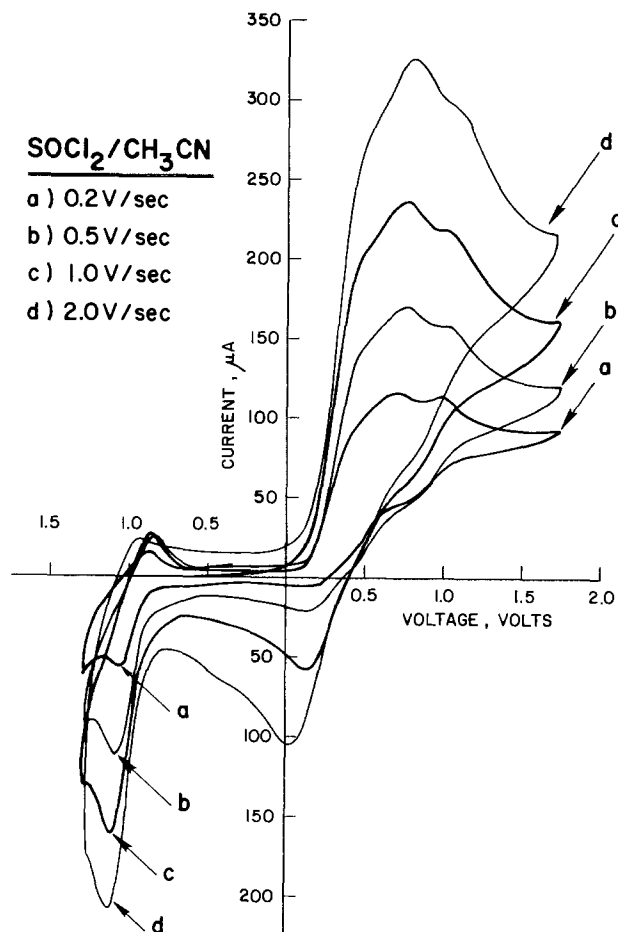


Fig. 10. Cyclic voltammogram of SOCl_2 in acetonitrile/ TBAPF_6 at a Pt wire electrode showing the effect of sweep rate: curve a) 0.20 V/sec, curve b) 0.50 V/sec, curve c) 1.0 V/sec, curve d) 2.0 V/sec.

The effect of concentration on the SOCl_2 reduction has been examined. Cyclic voltammograms of SOCl_2 at various concentrations at a Pt electrode are shown in Fig. 11. For a given sweep rate of 500 mV/sec the oxidation near 0.0V becomes less prominent as concentration increases. From the sweep rate dependence of this oxidation, we can conclude that the species responsible for this oxidation wave is reacting either with thionyl chloride or with itself. Change in the reduction behavior was also noted as the wave near -0.65V became less prominent and the one near -1.0V more prominent as the concentration increased in CH_3CN solution.

For further comparison we ran cyclic voltammograms in dimethylsulfoxide (DMSO), a solvent which is regarded as very good for reduced species because of its ability to stabilize reactive materials by complexation. DMSO is also known to have a rather low activity of residual water because of the sulfoxide's coordinating ability. A cyclic voltammogram for SOCl_2 in DMSO/TBAPF_6 is shown in Fig. 12. The pattern of two successive reduction waves and an oxidation near 0.0V are very similar to that observed in DMF. The oxidation near 0.0V is quite prominent even at the 0.05 V/sec sweep rate, indicating that the reaction species involved is greatly stabilized by the DMSO solvent. The definition of the two reduction waves is very clear and there is little evidence for the appearance of the third wave near -1.0V which we noted in other solvents.

We have continued our work on the thionyl chloride reduction in DMF where the reduction appears to take place by the same mechanism. The better separation of the two reduction waves in DMF makes it a more attractive solvent for use in strictly electro-

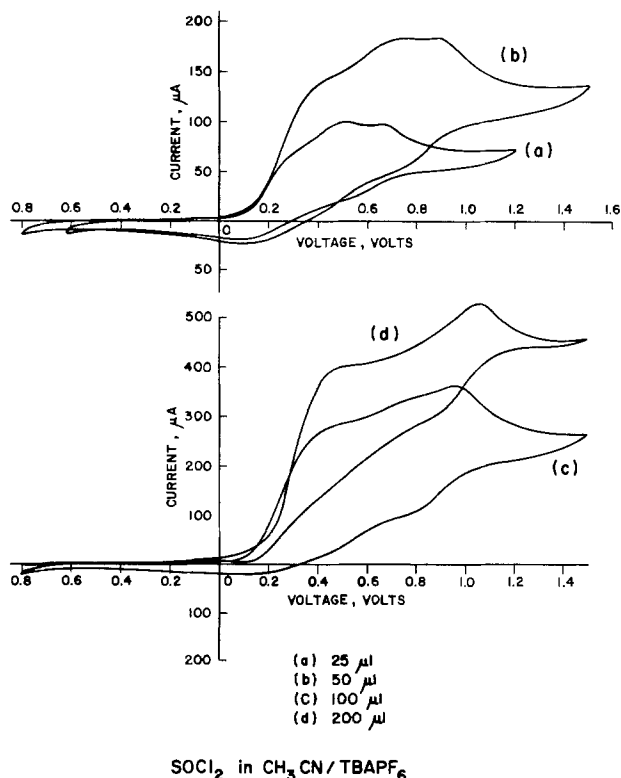


Fig. 11. Cyclic voltammograms of SOCl₂ in acetonitrile/TBAPF₆ at various concentrations. Curve a) 25 μ l SOCl₂/75 ml CH₃CN (0.5 V/sec), curve b) 50 μ l SOCl₂/75 ml (0.5 V/sec), curve c) 100 μ l SOCl₂/75 ml (0.20 V/sec), curve d) 200 μ l/75 ml (0.20 V/sec).

chemical studies on this system. Experiments in which sweep rate and concentration were systematically varied in DMF/TBAPF₆ gave similar results for the reduction of SOCl₂ to those found in acetonitrile. The second reduction wave remained more prominent in DMF, suggesting that coordination with DMF was stabilizing the species responsible for the reduction process.

To examine the formation of the intermediate species more closely we also examined the reduction at higher sweep rates than usual, recording the current/voltage trace on a storage oscilloscope. At sweep rates as high as 100 V/sec no qualitative change in the voltammogram could be observed. Except for uncompensated IR losses, the voltammogram was similar to those generated at lower sweep rates. We were also able to use the storage oscilloscope with multiple sweeps of the same voltage range to examine the relationships of the two reduction waves and the oxidation near 0V. Using this method we were able to generate a "steady-state" voltammogram of reduced thionyl chloride species. This voltammogram was unique in that the first thionyl chloride reduction wave was absent while the second reduction wave and the oxidation near 0V were still present. This indicates that the oxidation near 0.0V does not regenerate thionyl chloride since the first reduction wave, corresponding to the reduction of SOCl₂, is absent and as such the reduction of thionyl chloride is irreversible.

A cyclic voltammogram for 50 μ l SOCl₂ in approximately 75 ml DMF (~14 mM) with 0.1M N(C₄H₉)₄ PF₆ at a platinum wire electrode is presented in Fig. 13 curve (a). The reduction of thionyl chloride shows two successive reduction waves with $E_{1/2}$ at -0.20V for the first wave (17), with a peak potential which is sweep rate dependent, but near -0.37V, while the peak potential for the second reduction is near -0.65V. In addition to these reduction processes, there is an irreversible and broad oxidation on the return sweep near 0.0V. The small reduction wave near -1.25V is

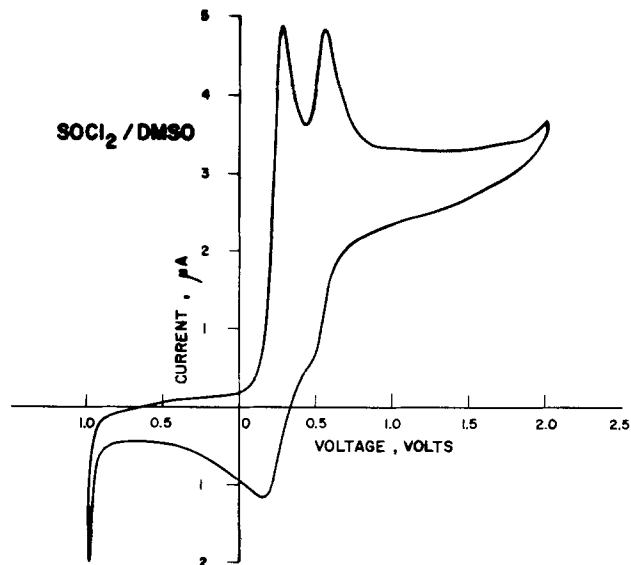


Fig. 12. Cyclic voltammogram of SOCl₂ in DMSO/TBAPF₆ at a Pt wire electrode (0.05 V/sec).

present in the background and presumably due to a trace impurity in the DMF. Both of the reduction peaks due to thionyl chloride are due to diffusion controlled processes as shown by the linear relationship of the peak cathodic current i_{pc} and \sqrt{V} , where V is the sweep rate. Under similar circumstances an adsorption controlled process would show i_{pc} linear with V and a kinetic controlled process that is not a simple function of V (17).

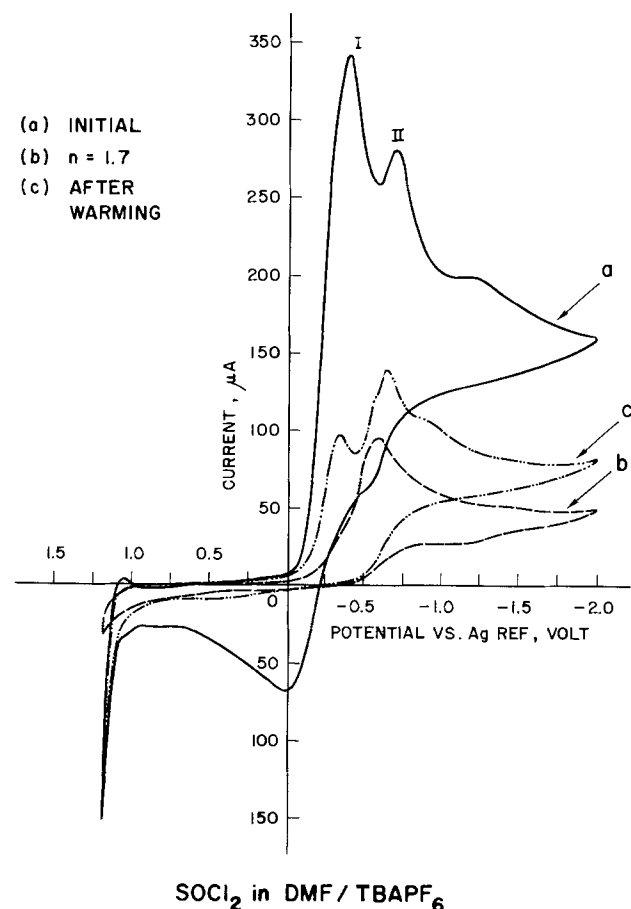


Fig. 13. Cyclic voltammograms of SOCl₂ in DMF/TBAPF₆, curve a) before electrolysis, curve b) immediately after exhaustive electrolysis at -0.25V, curve c) after warming solution, scan rate 0.2 V/sec.

This solution of DMF and thionyl chloride is sufficiently stable that an exhaustive electrolysis of the thionyl chloride can be performed at a platinum foil electrode. It is difficult to get completely reproducible n values from coulometry because of the closely spaced second reduction wave, but reduction at -0.25V gives an apparent n of 1.7-1.9 equivalents per SOCl_2 . A cyclic voltammogram of this reduced SOCl_2 solution is shown in Fig. 13 curve (b). This reduced product is characterized by a reduction wave near -0.63V with little clear evidence for any oxidation processes. If this reduced solution is either allowed to stand or is slightly warmed with a water bath, some thionyl chloride is regenerated, as shown in Fig. 13 curve (c). If this material is then further reduced at -0.25V , n is 2.04 or very nearly 2.0, while a shoulder appears near -0.9V .

We have examined the coulometric reduction of SOCl_2 in DMF, acetonitrile, and methylene chloride. In all three solvents we have observed the regeneration of thionyl chloride by destruction of an intermediate species and have confirmed the Faradaic current of 2 equivalents of charge for each mole of SOCl_2 reduced. In particular, the reduction in acetonitrile is of interest since the UV-VIS solvent cutoff of 190 nm gives a much better spectral window than DMSO (268 nm), DMF (270 nm), or methylene chloride (230 nm). We were able to monitor the course of a coulometric reduction by using both cyclic voltammetry and UV-VIS spectroscopy to monitor changes in the solution. For comparative purposes, spectra of SO_2 and S in acetonitrile are reproduced in Fig. 14 and 15, respectively. The wavelengths of maximum absorbance, 279 nm for SO_2 and 277 for S are very similar to that of SOCl_2 , 277 nm as shown in

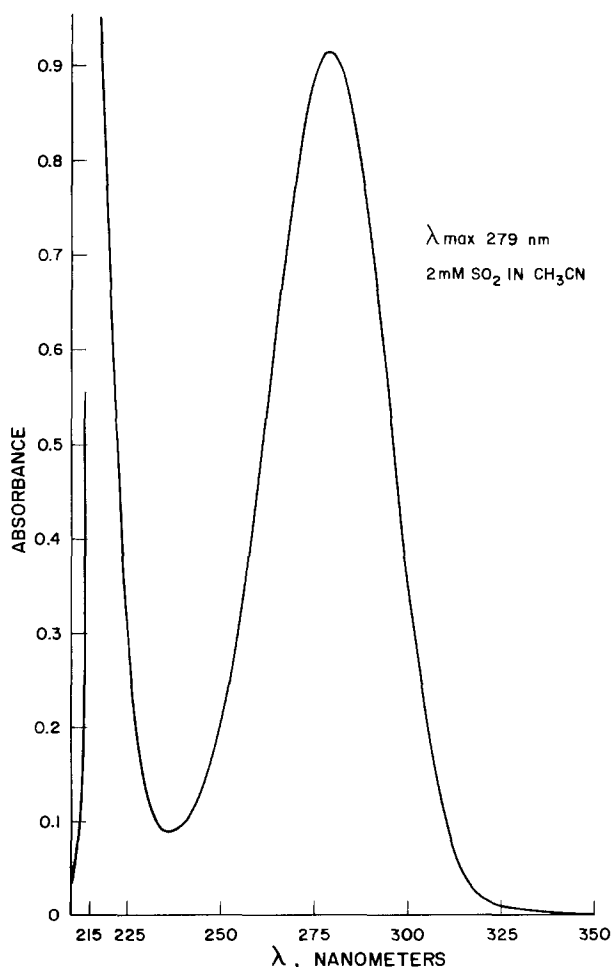


Fig. 14. UV-VIS spectrum of 2 mM SO_2 in acetonitrile, path length 1 cm.

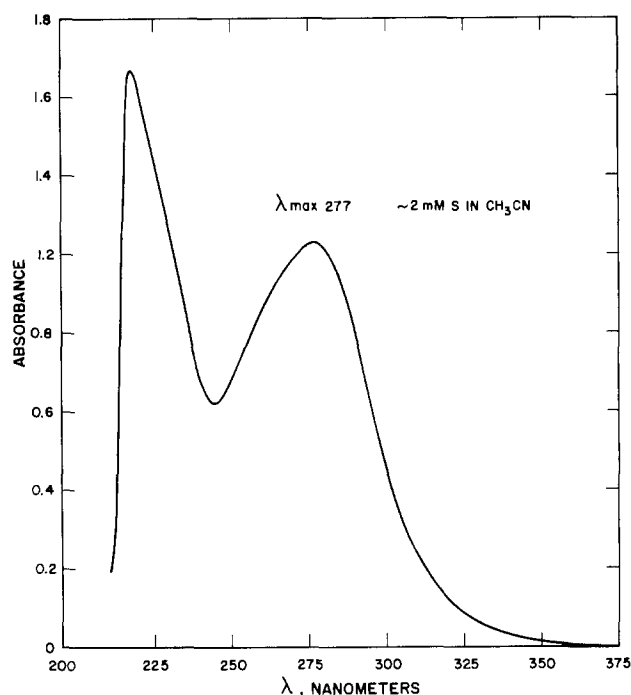


Fig. 15. UV-VIS spectrum of 2 mM S in acetonitrile, path length 1 cm.

Fig. 16, however, there is a second band in the spectrum near 234 nm which is not present in the spectra of SO_2 and S. In this particular experiment 10 μl of SOCl_2 was used in 75 ml of CH_3CN to give a concentration of 1.83 mM SOCl_2 in CH_3CN . We experimentally determined that this concentration of ~ 2 mM was suitable for UV-VIS spectroscopy, cyclic voltammetry, and coulometry. Changes in the ultraviolet spectrum as a function of charge passed in the exhaustive electrolysis are shown in Fig. 17. From λ_{MAX}

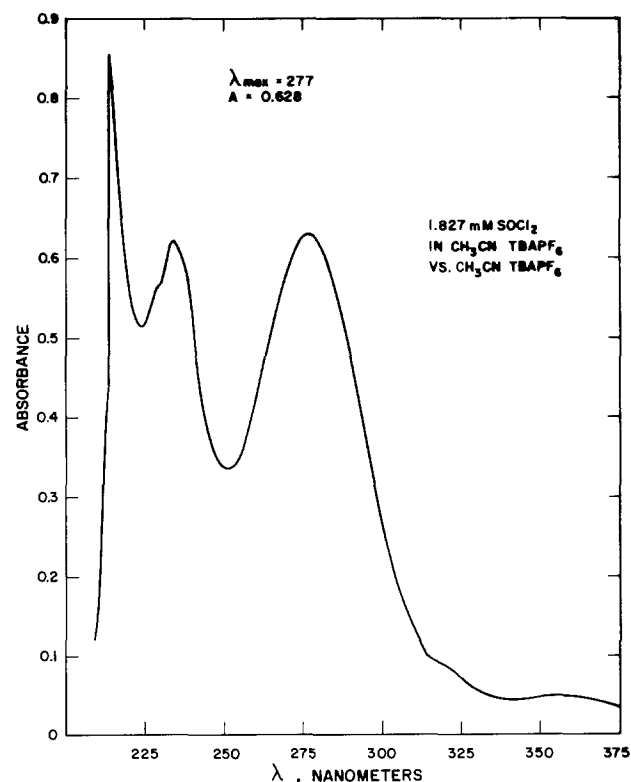


Fig. 16. UV-VIS spectrum of 1.8 mM SOCl_2 in acetonitrile/TBAPF₆, path length 1 cm.

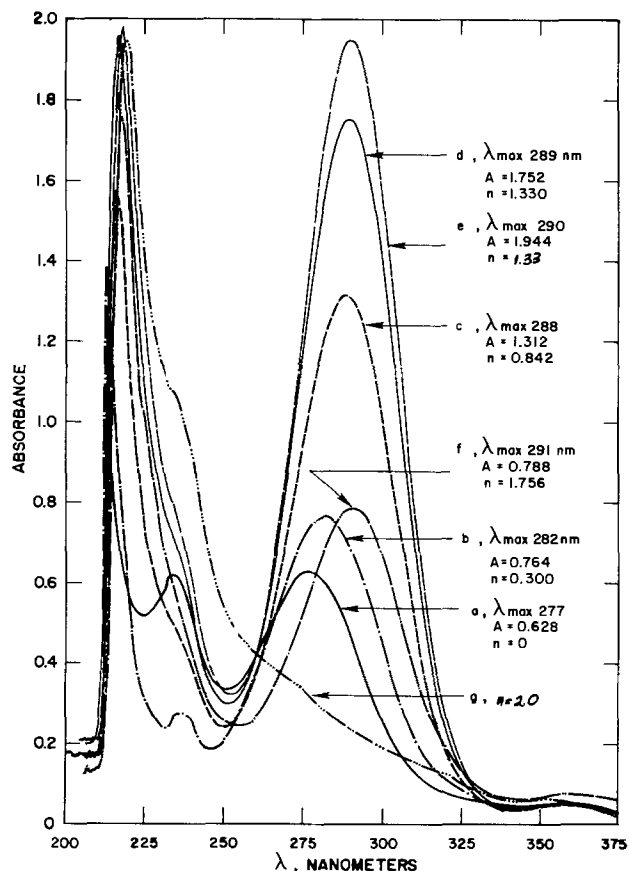


Fig. 17. Absorbance spectrum of 1.8 mM solution of SOCl₂ in acetonitrile/TBAPF₆, curve a) $n = 0.00$, curve b) $n = 0.30$, curve c) $n = 0.84$, curve d) $n = 1.33$, curve e) $n = 1.33$ after 16 hr, curve f) $n = 1.76$, curve g) $n = 2.0$ after 1 week stand.

272, $A = 0.628$ at $n = 0$ the λ_{MAX} gradually changes to 282, 288, 289, 290, 291 nm as A first increases then decreases to 0.764, 1.312, 1.752, 1.944, 0.764 corresponding to n of 0.30, 0.84, 1.33, 1.33, and 1.76, respectively. At $n = 2.0$ this absorption band is completely absent after storage for 1 week at room temperatures. During this reduction the small band near 234 nm in SOCl₂ also disappeared. The gradual change of A from 1.75 to 1.94 for $n = 1.33$ on overnight standing indicates that the intermediate species, corresponding to the absorption band, must be forming as a result of a slow secondary reaction of the intermediates of the SOCl₂ reduction. Accordingly, we cannot expect to see a simple relationship between absorbance and progress of the reduction.

Changes in cyclic voltammograms throughout the reduction are shown in Fig. 18. In Fig. 18(a) the solution was scanned before reduction ($n = 0.0$) in 18(b) at $n = 0.30$, in 18(c) at $n = 0.84$ and 18(d) at $n = 1.33$. In these voltammograms there is a consistent decrease in the first wave and relative enhancement of the second reduction wave. The wave due to electro-generated chloride also increases. In the final voltammograms for $n = 1.76$ and $n = 2.0$, the initial wave is completely absent, while a third wave appears at more negative potentials.

To examine whether the reduction processes in bulk thionyl chloride electrolytes are comparable to those observed in dilute solution, we removed an aliquot of electrolyte from a partially discharged Li/SOCl₂ cell and examined the voltammetry of this sample in DMF solution. The resulting voltammogram was identical to one observed in the reduction of SOCl₂ in DMF.

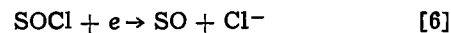
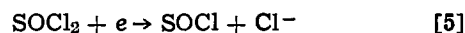
Discussion

The coulometric data demonstrate an overall n value of 2.0 for the reduction of thionyl chloride. Reduc-

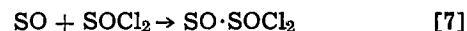
tions for extended times have given green, air-sensitive solutions possibly including polysulfides, but there is no evidence to suggest that this reflects any process occurring in SOCl₂ reduction since the cyclic voltammograms show that no further unreduced SOCl₂ is present.

The spectroscopic evidence shows that S and SO₂ are not formed during the reduction process itself. Instead a different species is formed with an absorption band near 291 nm. This is confirmed by the cyclic voltammograms which show only a slow formation of species reducing at potentials near those for S and SO₂. This intermediate species is reasonably stable and decomposes only slowly to generate more SOCl₂.

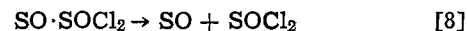
We propose the following reduction mechanism for SOCl₂ to explain the above cyclic voltammetric and UV-VIS spectroscopic observations. SOCl₂ undergoes two successive, one-electron transfers to generate SO



It is likely that the E_0 of the second step [6] may be positive of E_0 of the first step [5] and as such both the electron transfers may occur at the first reduction wave (I) shown in Fig. 13 curve (a). The highly unstable nature of SO (18) and the presence of excess SOCl₂ at the early stages of the discharge, may lead to the complexation of SO with SOCl₂



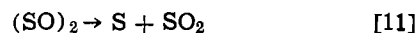
This species is sufficiently stable and is reduced in the second reduction wave (II) shown in Fig. 13 curve (a) and the unstable reduced product is oxidized at 0V corresponding to the oxidation wave shown in Fig. 13 curve (a). The complex dissociates to form SO and SOCl₂ on standing or warming of the solution



This explains the regeneration of the first reduction wave [Fig. 13 curve (c)] on overnight standing. During the latter part of the discharge, when the concentration of SOCl₂ has decreased considerably, dimerization and polymerization of SO may occur



These dimers and polymers may decompose on standing or heating to form S and SO₂ (18)



Observations regarding delayed pressure rise (20) and thermal activity in discharged cells (7) as well as lower cell capacity at lower temperature (19) are consistent with the above reaction scheme.

Although the above experiments were carried out on smooth Pt electrode, we believe that the results are applicable to the carbon substrates as well, particularly in the absence of any catalyst (homogeneous or heterogeneous). Addition of catalyst may alter the stability of the intermediate and as such may have significant effect on the performance and safety of the cells. We are in the process of investigating this aspect of the problem and the results will be reported later on.

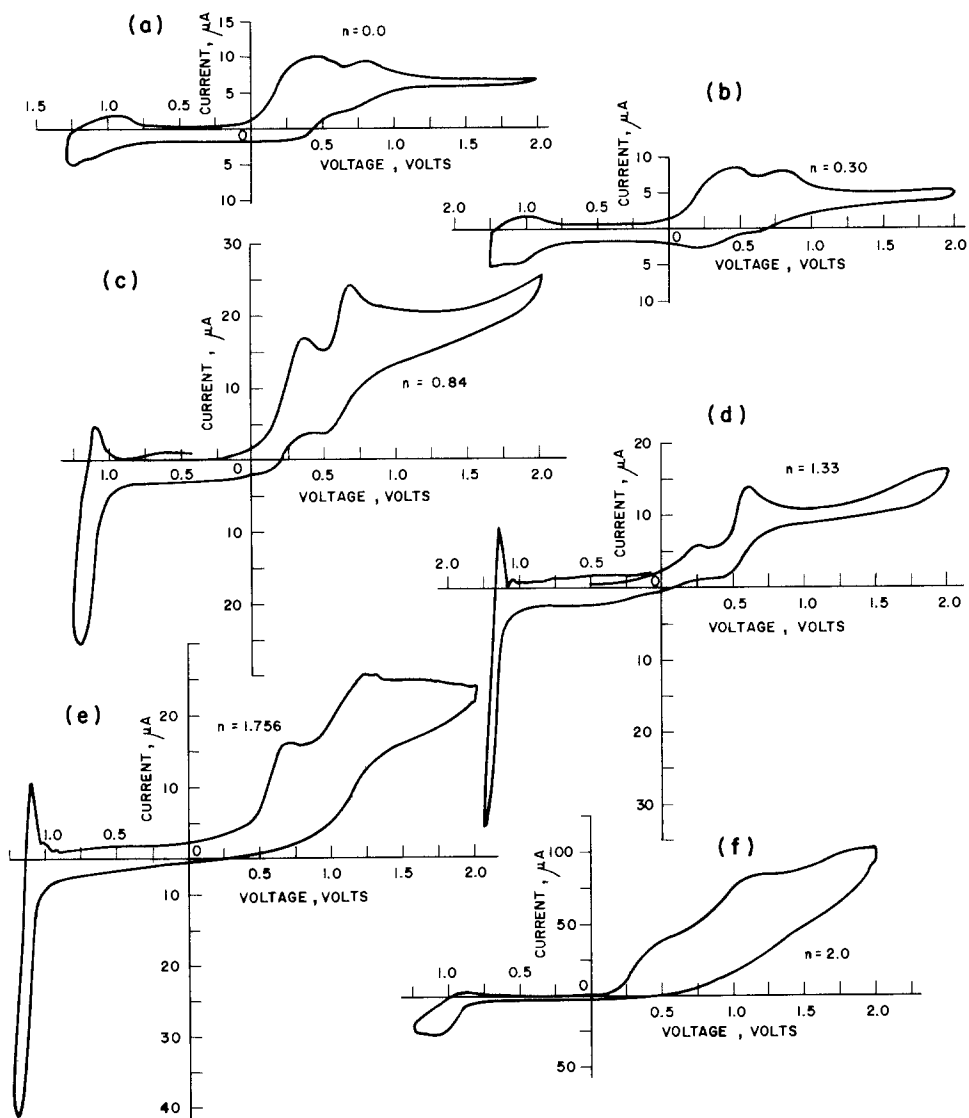
Acknowledgments

The work was carried out under a contract from ERADCOM, DAAB07-78-C-0563.

Manuscript submitted Oct. 24, 1979; revised manuscript received Jan. 30, 1980.

Any discussion of this paper will appear in a Discussion Section to be published in the June 1981 JOURNAL. All discussions for the June 1981 Discussion Section should be submitted by Feb. 1, 1981.

Fig. 18. Cyclic voltammograms of 1.8 mM SOCl_2 in acetonitrile/TBAPF₆ (a) $n = 0.00$, (b) $n = 0.30$, (c) $n = 0.84$, (d) $n = 1.33$, (e) $n = 1.76$, (f) $n = 2.03$ after 1 week stand.



SOCl_2 in CH_3CN / TBAPF₆

Publication costs of this article were assisted by P. R. Mallory and Company, Incorporated.

REFERENCES

- W. H. Behl, J. A. Christopoulos, M. Ramirez, and S. Gilman, *This Journal*, **120**, 1619 (1973).
- J. J. Auborn, K. W. French, S. I. Lieberman, V. K. Shah, and A. Heller, *ibid.*, **120**, 1613 (1973).
- D. L. Maricle, *et al.*, U.S. Pat. 3,567,515 (1971); G. E. Blomgren and M. L. Kronenberg, German Pat. 2,262,256 (1973).
- A. N. Dey and C. R. Schlaikjer, U.S. Pat. 4,020,240 (1977), "Proc. 26th Power Sources Symposium," Atlantic City, N.J., June 1974.
- D. I. Chua, J. O. Crabb, and S. L. Deshpande, "Proc. 28th Power Source Symp.," p. 247 (1978).
- G. E. Blomgren, V. Z. Leger, M. L. Kronenberg, T. Kalnoki-Kis, and R. J. Brodd, in "Proceedings 11th Internat. Power Sources Symposium," Brighton, England, 1978.
- P. Bro, *This Journal*, **125**, 674 (1978).
- A. N. Dey, Final Report, DELET-TR-74-109-F, P. R. Mallory & Co. Inc., July 1978.
- A. N. Dey, "Proc. 28th Power Sources Symp.," Atlantic City, N.J., June 1978.
- A. N. Dey, *This Journal*, **123**, 1262 (1976).
- A. N. Dey, *Thin Solid Films*, **43**, 131 (1977).
- C. R. Schlaikjer, "Proc. 27th Power Sources Symp.," Atlantic City, N.J., June 1976.
- D. R. Cogley and M. J. Turchan, Second Quarterly Report; ECOM-74-0030; AD779477, EIC Inc., May 1974, Fifth Quarterly, Sixth Quarterly.
- W. K. Behl, "Proceedings 27th Power Sources Symposium," Atlantic City, N.J., June 1976.
- W. K. Behl, *J. Electroanal. Chem. Interfacial Electrochem.*, **101**, 367 (1979).
- R. P. Martin, Thesis, Univ. of California, Riverside (1973).
- R. N. Adams, "Electrochemistry at Solid Electrodes," p. 143, Marcel Dekker, Inc., New York (1969).
- P. W. Schenk and R. Steudel, *Angew. Chem. Int. Ed. Eng.*, **4**, 402 (1965).
- W. Bowden and A. N. Dey, *This Journal*, **126**, 2035 (1979).
- C. R. Schlaikjer, F. Goebel, and N. Marincic, *ibid.*, **126**, 513 (1979).

The Reduction of Sulfuryl Chloride at Teflon-Bonded Carbon Cathodes

S. Gilman and W. Wade, Jr.

U.S. Army Electronics Technology and Devices Laboratory (ERADCOM),
Power Sources Division, Fort Monmouth, New Jersey 07703

ABSTRACT

Polarization and discharge curves were measured for sulfuryl chloride reduction at Teflon-bonded carbon cathodes fabricated using a number of different carbon powders. Lithium chloroaluminate was utilized as electrolyte solute. At moderate current densities cathode polarization tends to normalize with respect to Brunauer, Emmett, Teller (BET) surface area of the carbon. Cathode life increases with increased porosity of the electrode. The porosity is required for good accommodation of product LiCl. A formulation incorporating both high BET area and porosity was developed and found to provide good electrochemical performance against lithium counterelectrodes. When sulfuryl chloride is reduced at the optimized cathode (against a lithium anode), the main products of reaction are LiCl (which is quantitatively deposited within the electrode's pores) and SO₂. This suggests the overall cell reaction: $2\text{Li} + \text{SO}_2\text{Cl}_2 \rightarrow 2\text{LiCl} + \text{SO}_2$. The addition of Cl₂ or SO₂ to the electrolyte causes decrease or increase of cathode polarization, respectively. This may be taken as evidence that the reduction, at moderate current densities, occurs through a Cl₂ intermediate resulting from heterogeneous decomposition of SO₂Cl₂. Reduction of undissociated SO₂Cl₂ may occur at high current densities or after the active area of the electrode is significantly reduced through deposition of product LiCl.

The potential usefulness of sulfuryl chloride for lithium inorganic electrolyte cells was recognized a number of years ago (1-3). However, development of a practical lithium-sulfuryl chloride cell has generally been assigned lower priority, by both governmental and industrial organizations, than the corresponding lithium-thionyl chloride system. One reason for the relative inattention to sulfuryl chloride cell technology has been the observed dissipation of the apparent high voltage and capacity advantage (observed at low current densities) when experimental cells utilizing Teflon-bonded carbon (Shawinigan black) cathodes are discharged at high rates (4). It was the purpose of this work to improve the performance-limiting Teflon-bonded carbon cathode and to gain mechanistic insights which will suggest further refinements in technology. The present work was performed using neutral lithium chloroaluminate solution (1.5 molar) in which lithium anodes are fairly stable and which is therefore suitable for primary cell use. As is the situation for the analogous thionyl chloride system, acidic (e.g., AlCl₃-rich) solutions allow higher voltages and cathode service life under load, but are suitable only for reserve cell use.

Experimental

Preparation of electrolyte.—Sulfuryl chloride was refluxed over Li ribbon for several hours and then distilled under a positive pressure of argon, retaining the middle fraction. Lithium aluminum chloride was prepared by fusion of the salts as described previously (5). The 1.5M solutions were prepared in an argon atmosphere, in a glove box, and were stored in a tightly stoppered bottle. Electrolyte was used within a day of preparation or argon-degassed just before use.

Preparation of cathodes.—"Uncompressed" cathodes were prepared as described previously (5) by wet-blending of du Pont TFE-30 emulsion, carbon powder, and a sufficient amount of water to yield a stiff paste. The latter was then applied to a 2.5 × 2 cm Exmet

(Exmet Corporation) support. The latter support was prepared by welding two thicknesses of (Type 5 Ni7-2/0) screen together, with the mesh out of registration so as to provide maximum tortuosity for good anchoring of the Teflon-carbon mixture and to provide high electronic conduction. While still moist, the electrode was pressed to whatever thickness (depending on the particular carbon powder used) required for a final thickness of 0.89 ± 0.05 mm after vacuum drying for approximately 24 hr at 99°C. All cathodes were trimmed to the 2.5 × 2 cm dimensions of the Exmet support.

"Compressed" (the fabrication procedure finally developed for United Carbon) cathodes were prepared as described above, but compressed to an intermediate thickness of 1.56 mm while still moist. After vacuum drying the electrode was pressed in a 0.635 mm frame and after re-expansion (due to electrode resiliency) had a final thickness of 0.89 mm. The "uncompressed" electrodes made with Shawinigan black or Darco G-60 were of good, uniform appearance and possessed good adherence after the vacuum drying step. The uncompressed electrodes made of Columbia or United Carbon were badly cracked and fragile after the drying stage. The compressed United Carbon electrodes presented a good appearance and were sturdy.

Preparation of cells.—Cells were assembled in an all-Teflon jig with the planes of the electrodes parallel to the bottom of the jig. The cathode was placed between two Li anodes. An Li foil electrode placed in the same plane as the cathode served as reference. A 0.30 mm thick glass "filter-paper" provided mechanical separation between the cathode and the Li counterelectrodes facing it on each side. The lithium anodes were fabricated by pressing nickel Exmet into a 1.3 mm thick lithium foil and trimming to the same (2.5 × 2 cm) length and width as the cathodes. After assembling the cell and adding electrolyte, a Teflon weight was applied to the cell to help maintain good contact between the cell components. Unless otherwise specified, the electrolyte volume was 5 cm³. Electrical connections were made to Pt wires sealed in the cap of a glass outer container having a standard taper ground glass joint, and the cell assembly was then

Key words: polarization curves, discharge curves, cathode polarization.

enclosed in the outer container. All assembly steps were accomplished in the glove box.

Electrochemical measurements.—Discharge and polarization curves were recorded on a Moseley Strip Chart Recorder at $22^\circ \pm 2^\circ\text{C}$. The discharge curves were obtained while applying constant current from a power supply. The polarization curves were measured by applying predetermined constant currents (starting from 0.02 mA/cm²) for a period of 3 min before recording each cathode potential.

Cathode porosity determination.—The percent porosity is defined as the percent of wet cathode volume available for absorption of SO₂Cl₂. The volume of SO₂Cl₂ absorbed was determined by weighing a cathode before and after immersion in SO₂Cl₂ and "blotting" on a glass surface. The wet volume of the cathode was determined by measuring its lineal dimensions with calipers. The porosity measurements were conducted in the glove box.

Chemical analysis.—The solubility of lithium chloride at 25°C in SO₂Cl₂ was determined by preparing a saturated solution at 30°C, allowing equilibration/precipitation to proceed for several days at 25°C, and then weighing the LiCl residue after taking 10 cm³ of solution to dryness.

Determination of sulfuryl chloride-insoluble chloride in discharged cathodes was accomplished as follows. The cathode was extracted with five 20 cm³ volumes of SO₂Cl₂ (with vigorous magnetic stirring) during a 24 hr period. The cathode was then vacuum-dried, first at room temperature and then at 100°C. The cathode was then extracted with a total volume of 100 cm³ of water and aliquots of the extract titrated potentiometrically with standardized silver nitrate solution.

Aluminum was determined quantitatively to correct for occluded lithium aluminum chloride in the sulfuryl chloride-insoluble (lithium) chloride cathode product residue. The aurintricarboxylate colorimetric method (6) was employed, and aluminum concentrations were read off from a Beer's law plot at the absorption maximum of 525 mμ.

Volumetric determination of (SO₂) gas release during cell discharge.—The cell was prepared for discharge as described above. Before use, a volume of electrolyte was presaturated with SO₂ for 45 min by bubbling the gas through the solution. To minimize gas-supersaturation effects, only 2 cm³ of the presaturated electrolyte were inserted in the cell. After assembling the cell and closing the gas-tight glass outer envelope, the latter was flushed with SO₂ through its two stopcocks. The glass envelope was then connected to a manifold and gas burette assembly by means of standard taper joints. Before opening the stopcock separating the cell from the manifold-burette assembly, the latter was evacuated and backfilled with SO₂. Measurements were made more or less frequently depending on observed rate of change of volume, and a rate of gas release was derived from each pair of adjacent volume determinations.

Determination of solubilities of SO₂ and Cl₂ in SO₂Cl₂.—In an alkaline aqueous solution, SO₂ or Cl₂

when individually dissolved can be titrated through iodimetry or iodometry, respectively (7). If both gases are introduced into an alkaline solution, they will react, resulting in quantitative oxidation of the SO₂, by Cl₂, to SO₄²⁻ and Cl⁻ plus the balance of the component present in higher normality. Therefore, only the excess of equivalents may be determined iodometrically/iodimetrically for such a mixture. Pure sulfuryl chloride can be expected to behave like a stoichiometric mixture of SO₂ and Cl₂ when dissolved in alkaline solution as was confirmed.

Solutions of either gas in SO₂Cl₂ were prepared by bubbling the gas through the liquid for ½ hr. A 1 cm³ aliquot of either of the solutions was then placed in an ampul which was supported above 40 cm³ of 1-5M aqueous KOH solution in a flask with a gas-tight stopper. The ampul was dropped into the KOH solution and the latter shaken vigorously. A sample of argon-saturated SO₂Cl₂ gave a negligible iodimetric or iodometric blank determination. Iodimetric/iodometric determinations were conducted on the saturated solutions of the pure gases.

Results and Discussion

Dependence of cathode polarization and discharge capacity on cathode physical properties.—A Teflon content of 16% was chosen for preliminary comparative evaluation purposes, because it was found to provide adequate coherence of the Teflon-carbon mixtures and adherence to the screens even though this is not the optimum Teflon loading for each individual carbon powder.

Table I identifies the carbon powders used in formulating cathodes, along with their BET surface areas. Shawinigan black possesses the lowest area of the entries listed, but has been a frequent choice of lithium battery technologists because of its good mechanical working properties and porosity. The latter quality is due in part to its extensive chain-like microstructure. Darco G-60 is a relatively high-area activated charcoal. The United and Columbia carbon blacks listed possess particularly high surface areas and were originally produced for use in experimental aqueous primary cells (8, 9).

The cathodes were compared at the same thickness (0.89 mm) (rather than at the same weight) since that allows the best comparison with respect to overall performance of a practical cell. The carbon loadings obtained reflect the different packing tendencies of the Teflon-carbon mixtures when accommodating to the same volume. Previous studies revealed that the BET surface area of such electrodes is approximately the same as that of the original carbon utilized (10). On that basis, Table I presents the BET areas for the electrodes computed from the powder areas and the carbon loadings (of representative electrodes). Because the variations in carbon loadings of the electrodes tend to compensate for the variations in surface areas of the powders, the only large variation in electrode BET area is that for Shawinigan black when compared with the other three carbons.

The electrode porosity or, more precisely, the ability to absorb SO₂Cl₂ depends on the original microstructure of the powder and its interaction with the Teflon

Table I. Teflon-bonded carbon cathodes (16% TFE)

Type of carbon	Derivation	Carbon loading* (g/cm ²)	BET surface area of carbon: meter ²		
			Per gram of carbon powder	Per cm ² of electrode geometric area*	% electrode porosity
Shawinigan—50% compressed	Decomposition of acetylene	0.0194	66	1.28	87
Darco-G60	Steam-activation of charcoal	0.0048	301	14.4	64
United XC-6310-4	Decomposition of oil	0.0146	1000	14.6	81
Columbia HR 1670	Decomposition of oil	0.0104	1200	12.5	75

* Based on (length × width) area of electrode, one side.

binder. As already mentioned above, the latter properties are particularly favorable for Shawinigan black and probably account for the higher than average cathode porosity listed in the table and the fact that the electrodes have a sturdy and uniform appearance. The Darco cathodes have the lowest porosity and fair mechanical integrity. The Columbia and United carbon cathodes prepared by this method are cracked and fragile, but possess medium porosity. When swollen with electrolyte, the latter electrodes acquired a more uniform appearance.

Figure 1 shows the polarization curves obtained for the four different carbon samples, with the recorded current density based on the geometric cathode area (length \times width, one side). From the practical point of view, it can be concluded that the United carbon would provide the best and Shawinigan black the poorest initial voltage in a practical cell.

The results of Fig. 1 are replotted in Fig. 2 but with the current densities computed from the total currents and the BET carbon areas of the electrodes. It is now apparent that polarization for three of the carbons (covering more than an order of magnitude's spread in BET area) is very similar in the range of currents where "activated" processes predominate. The Darco cathode shows significantly more polarization than the other three in that range. This may possibly be attributed to the fact that Darco G-60 is an "activated charcoal" with part of the BET area intragranular in nature and consequently not readily accessible to solid/liquid reactions. The steep decline of cathode potential at high current densities may be attributed [as applies also to the similar thionyl chloride cath-

ode (10, 11)] to transport limitations in pores partially blocked by a solid product of cell discharge.

Cathodes made from the four different carbon samples were discharged at a constant current density of 5 mA/cm² in cells containing the "standard" 1 mm of electrolyte/cm² of cathode geometric area. The "full discharge capacities" were determined from the discharge curves by drawing the appropriate tangents near the "knee" of the curves. In Fig. 3, the capacities are plotted against the percent porosity values taken from Table I. The relationship is approximately linear for the particular current density employed. The slope can be conceptualized as incorporating a pore "choking coefficient" as proposed by Marincic (11) for the thionyl chloride cathode. The similarity exists because the same major product of cathode reaction (LiCl) is involved in both cases as discussed below. It may also be anticipated, as observed for the thionyl chloride cell (12), that the distribution of LiCl in the cathode, and its effect on the discharge curve, will vary with the current density.

From Fig. 1 and 3 it can be concluded that Shawinigan black affords the best cathode capacity, but the poorest cathode voltage. United Carbon black, which affords the highest cathode voltage performance, provides second-best capacity. The latter carbon black was selected for further experimentation.

Improvement of the United Carbon cathode.—Figure 4 presents discharge curves for experimental modifi-

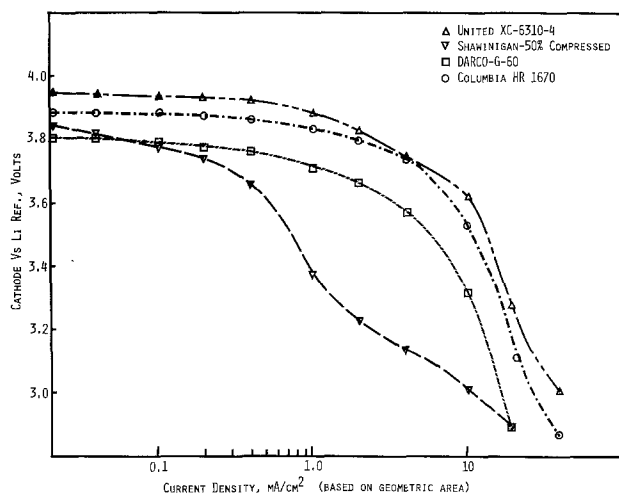


Fig. 1. Polarization curves for Teflon-bonded carbon cathodes (16% TFE, uncompressed).

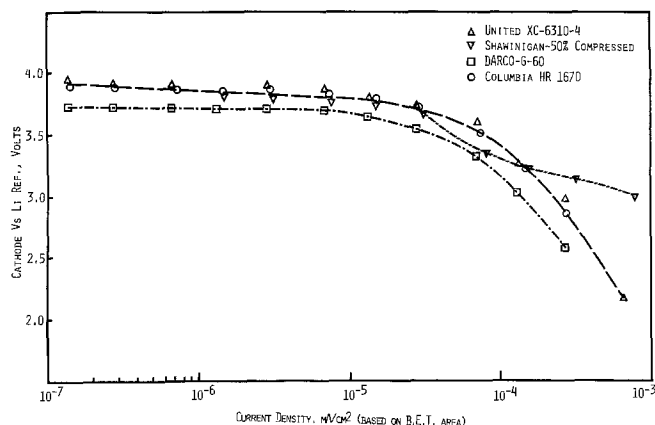


Fig. 2. Polarization curves for Teflon-bonded carbon cathodes (16% TFE uncompressed) normalized with respect to BET area.

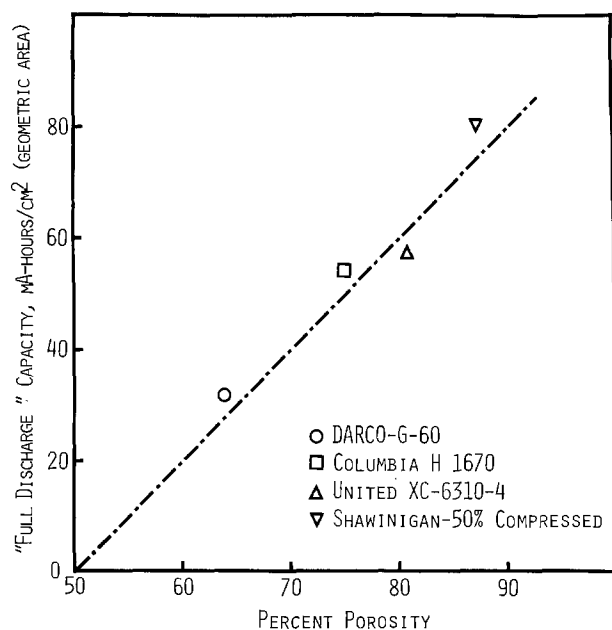


Fig. 3. Capacity-porosity relationship for Teflon-bonded carbon cathodes (16% TFE, uncompressed).

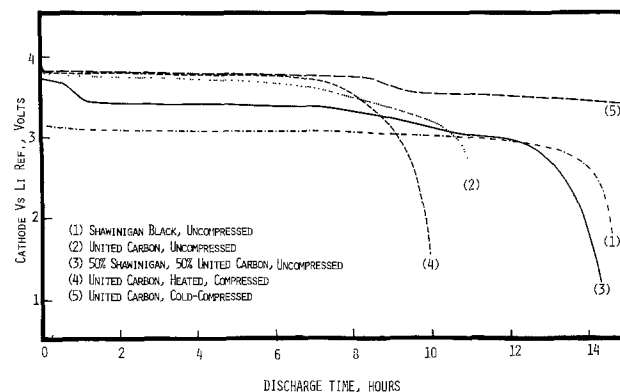


Fig. 4. Discharge curves ($I = 5 \text{ mA/cm}^2$) for differently formulated cathodes.

cations of the cathode fabrication process (16% TFE) for comparison with those obtained by the original ("uncompressed") process (curves 1 and 2). All cathodes were constructed to the same final thickness (0.89 mm), but incorporated different amounts of carbon. Admixture of the two carbons (curve 3) results in the high capacity associated with Shawinigan black, but only part of the increased voltage associated with United Carbon black. Also, the physical integrity of the electrode is not good. Heat-compression of the United Carbon cathode at 300°C (curve 4) greatly improves its sturdiness and slightly improves the voltage, but causes decreased capacity. The "cold-compression" process (curve 5) results in a cathode of highest discharge voltage and longest life. This cold-compressed United Carbon formulation was therefore selected for further optimization.

Figure 5 shows the discharge curves obtained, at a current density of 5 mA/cm², for different concentrations of TFE in the dried United Carbon-Teflon mixtures. A maximum in cathode life ("full discharge capacity") is obtained for a TFE concentration of 10.7%. Duplicate runs for 9.7% and 10.7% are presented to show typical variation of results attributable to fabrication technique variability.

The 10.7% formulation was selected for the further investigations reported below. A typical electrode had a carbon loading of 0.024 g/cm² and a porosity of 87%. The electrode swelled 11% when immersed in electrolyte.

Solubilities of LiCl, SO₂, and Cl₂ in sulfuryl chloride.

—The solubility of LiCl in sulfuryl chloride at 25°C was determined to be less than 0.009M. This corresponds to a solubility product of less than 8×10^{-5} and leads to the conclusion that LiCl is, practically speaking, insoluble in the 1.5M lithium chloroaluminate concentration of our electrolyte.

The solubilities of Cl₂ and SO₂ at 24° were determined to be 0.62 and 1.09 molal, respectively, when individually dissolved in pure SO₂Cl₂. The analysis for SO₂ correlates well with published results (13) for other temperatures.

Analysis of cell discharge products.—A discharged cathode, after rinsing in sulfuryl chloride and drying, was crushed and analyzed with an x-ray spectrometer. Diffraction lines were obtained for LiCl only. Two cathodes, A and B (formulated with 6.7% and 10.7% TFE, respectively), were discharged to a cut-off potential of 2V, treated as described in the Experimental section above, and analyzed for both Cl⁻ and Al⁺³. Table II presents the results of the analyses, assuming that all chloride in the cathode is either LiCl or

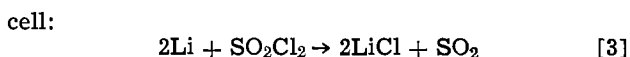
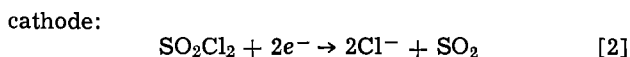
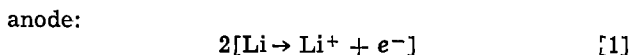
Table II. Chloride determination for discharged cathodes

	Cathode A	Cathode B
Total equivalents of Cl ⁻ determined argentimetrically	0.0146	0.02035
4 × equivalents of Al ⁺³ determined colorimetrically	0.00093	0.00103
Equivalents of Cl ⁻ as LiCl	0.0137	0.0193
Equivalents of electricity consumed in cathode discharge	0.0141	0.0189

LiAlCl₄. It can be seen that agreement between the equivalents of charge passed and LiCl formed is within 2%, which is taken as evidence that LiCl is the only ionic product of cathode discharge for the predominant discharge reaction. Quantitative precipitation of the LiCl in the cathode is a result of its insolubility as already noted above. In this respect the situation is identical to that for thionyl chloride cells (14).

One of the possible non-ionic products of cell discharge is elemental sulfur, as proposed previously (2). A cathode was fully discharged (20 hr) at a current density of 5 mA/cm². Extraction of the vacuum-dried cell components with CS₂ yielded only 15 mg of a yellow waxy substance with no distinct melting point. The substance dissolved in benzene and, therefore, was apparently not sulfur.

The simplest cell discharge reaction involving LiCl as the ionic product would produce SO₂ as the neutral product. Cells were always observed to develop positive pressure during discharge. The resulting gas phase contained SO₂ and Cl₂ which are, in any case, present above an SO₂Cl₂ volume (15). To avoid the difficulty of analyzing for SO₂ released in the presence of Cl₂, volumetric determination of gas release during discharge was made after saturating the solution with SO₂. This procedure has the benefit of suppressing Cl₂ release while forcing electrochemically produced SO₂ into the gas phase. The results of a determination appear in Fig. 6. The figure compares the observed rate of gas production with that anticipated based on the reactions



$$E^\circ = 3.909\text{V (30}^\circ\text{C)}$$

A "background" production of gas of approximately 0.06 cm³/min was measured at open circuit. That "background" may, for instance, correspond to initial reaction (corrosion) of the fresh lithium electrode

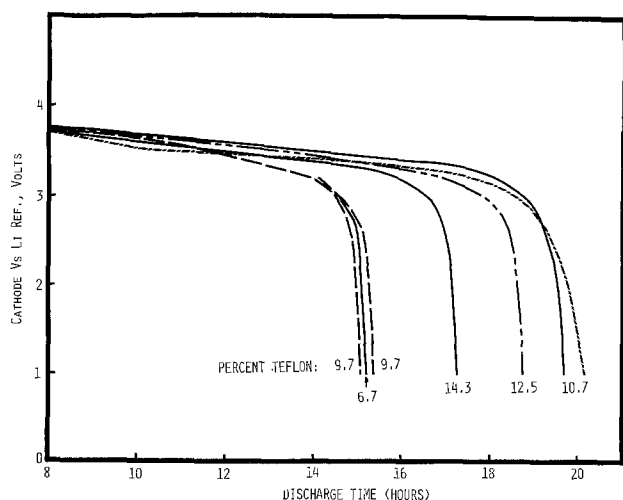


Fig. 5. Discharge curves ($i = 5 \text{ mA/cm}^2$) for cathodes formulated with varying amounts of TFE (uncompressed).

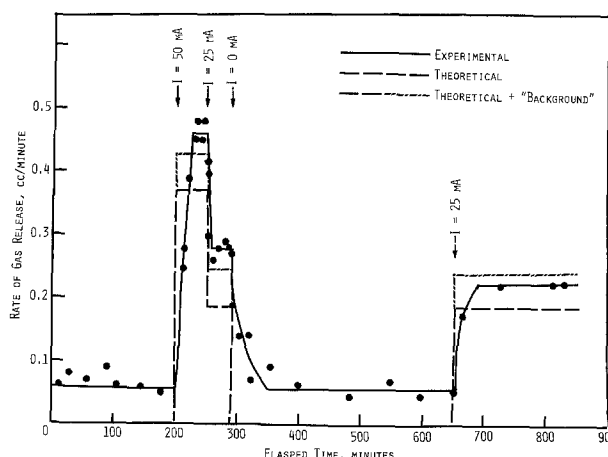
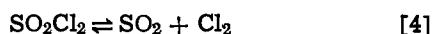


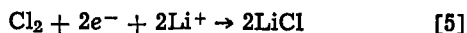
Fig. 6. Gas release during cathodic reduction of SO₂Cl₂

surface with the solvent. When the "background" and theoretical rates are added, they compare fairly well with the experimental rates eventually established when the current is increased or decreased. The results imply that the cell reactions proceed, at least largely, according to Eq. [1] and [2].

Effect of dissolved gases on cathode discharge.—Sulfuryl chloride dissociates readily into SO_2 and Cl_2 (15), and that reaction may be suspected of playing a role in the cell electrochemistry. The equilibrium constant at 30°C is 0.0288 for the reaction



The chlorine produced by reaction [4] could then be consumed as follows cathode:



The standard potential, E° , for reaction [5] vs. an Li reference electrode is 3.979V (30°C). However, the activity of Cl_2 in solution will always be equal to or less than dictated by the equilibrium constant of Eq. [4] and, therefore, always lower than unity. Correspondingly, the cell potential can never exceed that of Eq. [3] unless molecular Cl_2 is introduced from an external source.

Reaction [4] could proceed either homogeneously or heterogeneously. However, for pure SO_2Cl_2 , the homogeneous reaction is slow, while the heterogeneous decomposition is relatively rapid at a carbon surface (15).

Figure 7 compares the polarization curves obtained when the electrolyte is saturated with either argon, SO_2 , or Cl_2 . Results for solutions prepared in the glove box and stored for a few days resemble the "argon-saturated" example. Clearly, Cl_2 and SO_2 serve to enhance or diminish the current, respectively, at any particular cathode potential. The effect of Cl_2 saturation demonstrates that molecular Cl_2 is kinetically more active than SO_2Cl_2 in this electrolyte, although reduction occurs well below the appropriate thermodynamic cell potential (3.979V). Since SO_2 is itself not reduced at these high potentials, and since it could not produce any significant decrease in Cl_2 bulk concentration over that in the argon-saturated solution, it is proposed that it exerts its effect on the polarization curve by decreasing the surface concentration of the chlorine which (at moderate currents and high potentials) normally serves as an intermediate in the reduction of SO_2Cl_2 . In practical situations, (small volume of electrolyte, extended periods of discharge) the electrolyte will become SO_2 rich and the tendency for the results for the argon and SO_2 -saturated electrolytes to converge (at higher currents) is also apparent from the figure.

Discharge curves (constant current of 5 mA/cm^2) appear in Fig. 8. The results for the SO_2 -saturated, argon-saturated, and "aged" electrolytes are almost

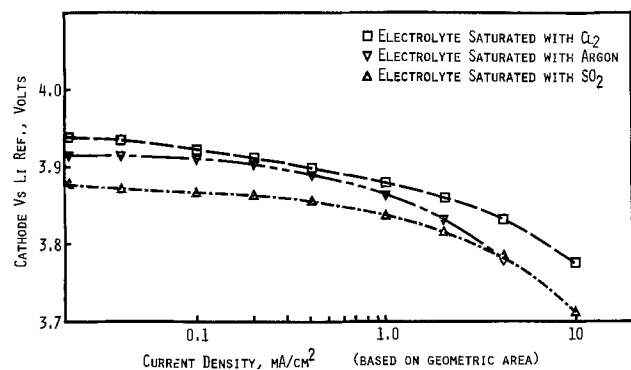


Fig. 7. Cathode polarization curves for optimized cathode electrolyte presaturated with different gases.

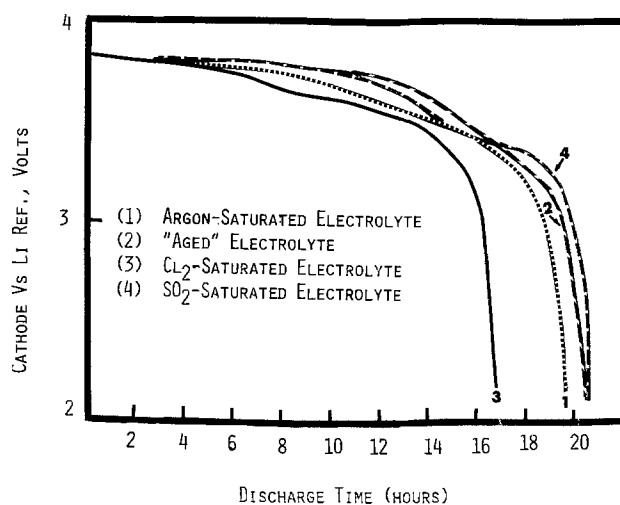


Fig. 8. Cathodic discharge curves ($I = 5 \text{ mA/cm}^2$). Electrolyte saturated with different gases.

indistinguishable in the first few hours (as might be expected due to buildup of product SO_2) in the first two cases. The variations during the later period of discharge are within the normal span for any particular (e.g., argon-saturated) starting condition. The significantly shorter discharge for Cl_2 saturation was found reproducible. A possible explanation is that the direct reduction of chlorine from the bulk of the solution occurs near the outer surface of the electrode and has a greater tendency to clog pores than the heterogeneously produced Cl_2 intermediate which would be produced and consumed throughout the electrode volume.

The discharge curves for cells with either argon/ SO_2 -saturated or "aged" electrolyte exhibit an intermediate voltage decline suggesting a two-step reduction. This is probably analogous to the two-wave reduction observed by Behl (16) during voltage-sweep studies of carbon microelectrodes. Behl attributed the first and second waves to reduction of Cl_2 and undissociated SO_2Cl_2 , respectively. A similar interpretation for the second transition in the discharge curve is tentatively adopted here. The transition to reduction of molecular SO_2Cl_2 might come about as the available surface area available to catalyze SO_2Cl_2 dissociation is diminished through coating with product LiCl .

Dependence of discharge curves (optimized United Carbon cathodes) on electrolyte volume and current density.—Figure 9 presents discharge curves for several current densities at the "standard" ratio of electrolyte volume to cathode geometric area of 1 ml/cm^2 .

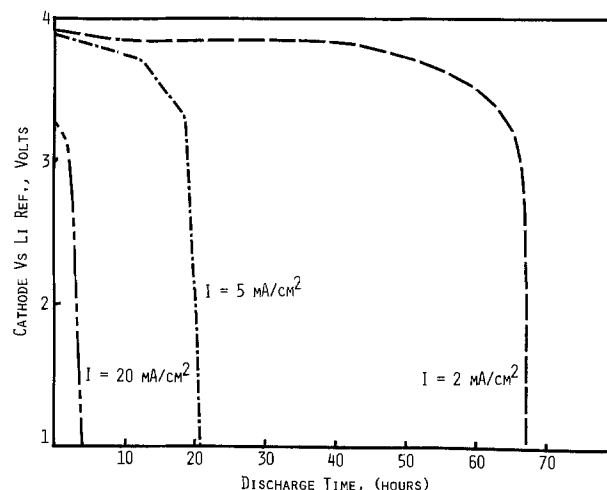


Fig. 9. Discharge curves for optimized cathode

As for thionyl chloride cells, the efficiency of cathode utilization tends to drop off with increased current density. The relatively efficient discharge current density of 2 mA/cm² was selected for exploring the effect of varying the electrolyte volume. Curves for several different volume/area ratios appear in Fig. 10. From such curves, a charge Q was estimated for "full discharge" and for discharge to a first "high voltage" transition point and the results plotted in Fig. 11. Based on Eq. [3], the values of charge, and the volume of solution in the cell, a "percent solvent utilized" was derived and plotted in Fig. 11. For volume/area rates of 0.14 or less, cell components are visibly incompletely wetted at the beginning of the experiment. No attempt has yet been made to analyze the rather sharp dependence on electrolyte volume/area ratio. Maximum solvent utilizations at "high voltage" and for "full discharge" were not observed to exceed 20% and 30%, respectively.

Let us consider how the 20% "high voltage" efficiency compares with the percentage of equivalents of Cl₂ available from the dissolved phase only. Corresponding to the Cl₂ (0.62 molal, as reported above) in a saturated solution at 24°C, 7.8% of the reducible equivalents are available from predissolved Cl₂. For degassed sulfuryl chloride, allowed to dissociate to equilibrium with the gas phase, the partial pressure of Cl₂ is approximately 0.05 atm [based on the vapor pressure of SO₂Cl₂ and dissociation constant of SO₂Cl₂ at 30°C (15)]. The corresponding percentage of equiv-

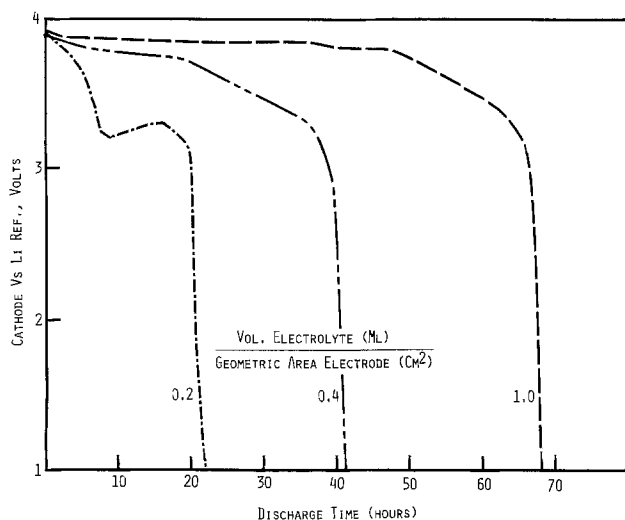


Fig. 10. Discharge curves for optimized cathode using various volumes of electrolyte.

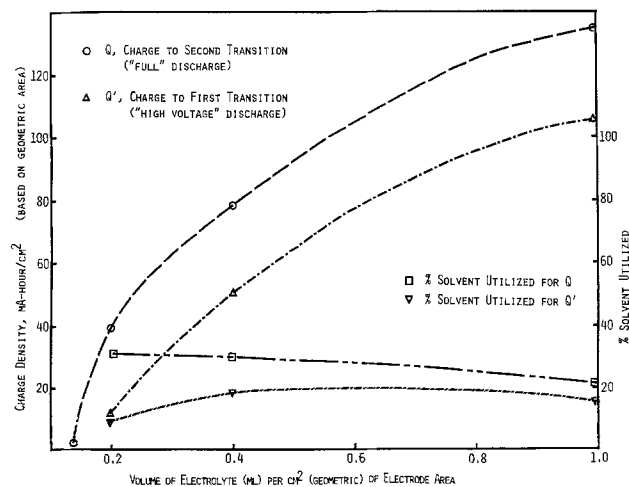


Fig. 11. Dependence of cathodic charge and solvent utilization on electrolyte volume.

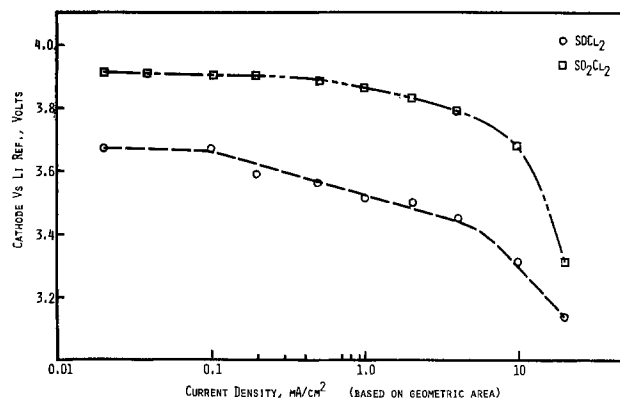


Fig. 12. Comparison of cathodic polarization curves for SO₂Cl₂ and SOCl₂.

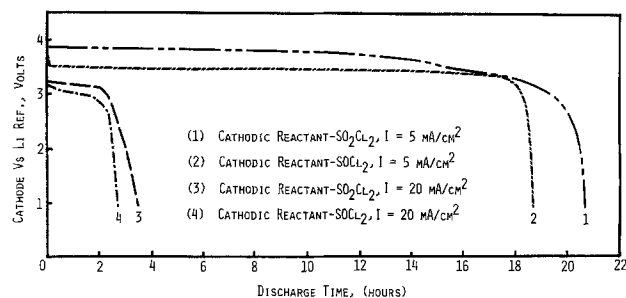


Fig. 13. Comparison of cathodic discharge curves for SO₂Cl₂ and SOCl₂.

alents available from Cl₂ can be as low as 0.4% (if Henry's law is obeyed). Hence the "high voltage" solvent utilization reported above cannot be attributed to a "reservoir" of Cl₂ resulting from dissociation of the solvent before cathodic discharge is begun, but must be supplied during the cathodic process.

Comparison of SO₂Cl₂ with SOCl₂ cathodes.—The polarization and discharge curves are compared in Fig. 12 and 13, respectively, for cathodes utilizing SOCl₂ and SO₂Cl₂ and an electrolyte volume/cathode geometric area of 1 ml/cm². Shawinigan black cathodes were used as representing the "state-of-the-art" for SOCl₂ and the optimized United Carbon cathodes were utilized for SO₂Cl₂. It can be seen from the figures that SO₂Cl₂ appears to offer an advantage in terminal voltage over SOCl₂ at high current densities, if the optimized cathodes are utilized. The comparison may be expected to vary, of course, for different proportions and concentrations of electrolyte, different temperatures, etc.

Manuscript submitted Oct. 19, 1979; revised manuscript received Feb. 8, 1980. This was Paper 33 presented at the Los Angeles, California, Meeting of the Society, Oct. 14-19, 1979.

Any discussion of this paper will appear in a Discussion Section to be published in the June 1981 JOURNAL. All discussions for the June 1981 Discussion Section should be submitted by Feb. 1, 1981.

Publication costs of this article were assisted by the U.S. Army Electronics Technology and Devices Laboratory (ERADCOM).

REFERENCES

- G. E. Blomgren and M. L. Kronenberg, German Pat. 2,262,756 (1973).
- J. J. Auburn, R. D. Bezman, K. W. French, A. Heller, and S. F. Lieberman, in Proceedings of 26th Power Sources Symposium, p. 45 (1974).
- S. Gilman, in *ibid.*, p. 29.
- J. J. Auburn and N. Marincic, in "Power Sources 5," D. H. Collins, Editor, p. 683, Academic Press, London (1975).
- W. K. Behl, J. Christopoulos, and S. Gilman, *This Journal*, 120, 1619 (1973).

6. E. B. Sandell, "Colorimetric Determination of Traces of Metals," p. 146, Interscience Publishers Inc., New York (1950).
7. I. M. Kolthoff and E. B. Sandell, "Textbook of Quantitative Inorganic Analysis," p. 614, The Macmillan Co., New York (1948).
8. Final Report by Columbian Carbon Co. Contract No. DA-36-039-AMC-03239(E) (1964).
9. J. B. Doe and D. B. Wood, in Proceedings of 22nd Annual Power Sources Conference, p. 97 (1968).
10. J. A. Christopoulos and S. Gilman, in Proceedings of Tenth Intersociety Energy Conversion Conference, p. 437 (1975).
11. N. Marincic, *J. Appl. Electrochem.*, 5, 313 (1975).
12. A. N. Dey and P. Bro, *This Journal*, 125, 1574 (1978).
13. M. Aubry, B. Gilot, and C. Jayles, "Annales Genie Chimique," Vol. 3, p. 33 (1967).
14. J. R. Driscoll, G. L. Holleck, and D. E. Toland, in Proceedings of 27th Power Sources Symposium, p. 28 (1976).
15. "Encyclopedia of Chemical Technology," Vol. 14, K. Othmen, Editor, p. 398 (1969).
16. W. K. Behl, Paper 31 presented at The Electrochemical Society Meeting, Los Angeles, Calif., Oct. 14-19, 1979.

Voltage Losses in Fuel Cell Cathodes

Raymond P. Iczkowski¹

United Technologies Corporation, Power Systems Division, South Windsor, Connecticut 06074

and Michael B. Cutlip

Department of Chemical Engineering, University of Connecticut, Storrs, Connecticut 06268

ABSTRACT

A model of the air diffusion electrode used in fuel cells was developed which accounts for the diffusion of oxygen in the gas-filled pores as well as diffusion into the liquid-filled pores, electrochemical reaction, and electrical conduction. The model was applied to a PTFE-bonded, platinum-on-carbon cathode in acid electrolyte to evaluate the relative contribution of these effects. Gas diffusion contributed 38% and ohmic loss in the electrolyte contributed 48% to the voltage loss other than activation. Knudsen diffusion was found to be as important as molecular diffusion. Diffusion of dissolved oxygen and ohmic conduction produced small voltage losses. Diffusion contributes to the utilization loss, especially at high oxygen utilizations, but ohmic effects do not.

The purpose of this study was to evaluate the importance of all of the sources of polarization in a polytetrafluoroethylene-bonded fuel cell cathode. In order to accomplish this purpose, a complete mathematical model of the electrode was required.

The type of electrode under consideration is shown in Fig. 1. The porous backing of the electrode consists of an inert, electronically conducting material which holds the catalyst layer. The catalyst layer consists of platinum supported on carbon powder which is sintered with du Pont Teflon. Air flows past the porous backing material and concentrated phosphoric acid electrolyte is present in the catalyst layer of the electrode. A microscopic view of a small region of the catalyst layer (also shown in Fig. 1) shows some pores filled with gas and other regions filled with electrolyte. The latter regions are referred to as agglomerates and consist of platinum crystallites (shown as dots), carbon (shown as grains) with electrolyte between the grains of carbon. The agglomerates can also be covered by a film of electrolyte.

The basic processes occurring in the electrode are shown in Fig. 2. In the first step, oxygen diffuses through the porous backing. Next, it diffuses into the catalyst layer, where it is transported through the gas filled pores. The oxygen then dissolves in the outer layer of the film of electrolyte which covers the agglomerates. The dissolved oxygen diffuses across the film and then diffuses into the pores of the agglomerates. By electrical conduction, electrons move through the carbon and hydrogen ions migrate through the phosphoric acid which is in the pores of the agglomerates. Finally, the oxygen reacts with the hydrogen ion and the electron. The resulting water evaporates into the gas pores and diffuses through the catalyst layer and the porous backing into the gas stream.

¹ Deceased.

Key words: fuel cells, mathematical models, polarization.

Mathematical Model

For each of these transport processes, there is a physical law and a mathematical equation which describes that process quantitatively.

Diffusion in the porous backing.—Fick's law was not used for diffusion in the porous backing because it applies only to the interdiffusion of two gases. In the present case, there are three gases: oxygen, water and, since the oxygen comes from air, nitrogen is also present. Therefore, the Stefan-Maxwell equations (1) for multicomponent diffusion were used

$$\frac{dP}{dz} = \frac{RT}{P} A_s P \quad [1]$$

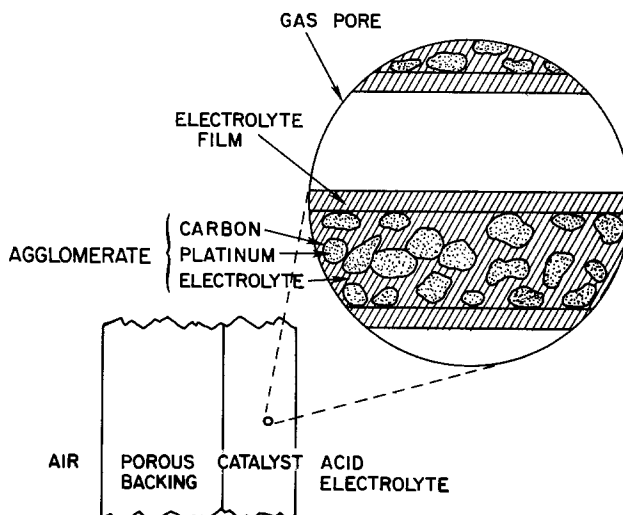


Fig. 1. Fuel cell cathode and its microstructure

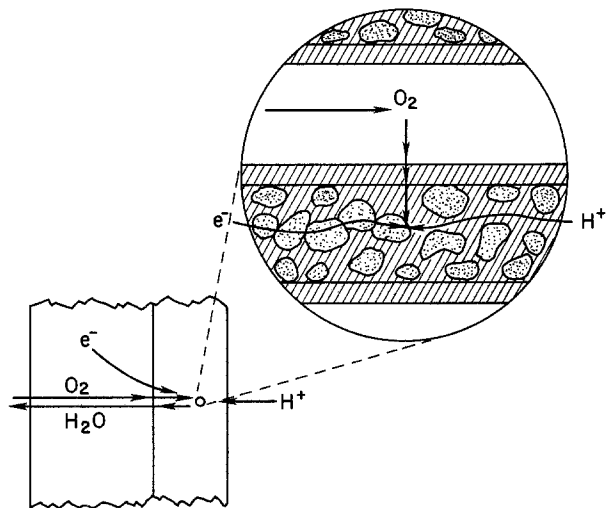


Fig. 2. Basic processes occurring in the cathode

where P represents the total pressure, \mathbf{P} is the n -tuple (P_1, P_2, P_3) whose components represent the partial pressures of oxygen, P_1 , water vapor, P_2 , and nitrogen, P_3 . The distance inside the porous backing is given by z , where the origin is at the gas stream-porous backing interface. The matrix A_s is given by

$$A_s = \begin{pmatrix} \frac{N_{20}}{D_{12p}} + \frac{N_{30}}{D_{13p}} & -\frac{N_{10}}{D_{12p}} & -\frac{N_{10}}{D_{13p}} \\ -\frac{N_{20}}{D_{12p}} & \frac{N_{10}}{D_{12p}} + \frac{N_{30}}{D_{23p}} & -\frac{N_{20}}{D_{23p}} \\ -\frac{N_{30}}{D_{13p}} & -\frac{N_{30}}{D_{23p}} & \frac{N_{10}}{D_{13p}} + \frac{N_{20}}{D_{23p}} \end{pmatrix} \quad [2]$$

The effective binary diffusion coefficients at pressure, P , are given by D_{12p} for oxygen and water, D_{13p} for oxygen and nitrogen, and D_{23p} for water and nitrogen.

The rate of diffusion of oxygen through the porous backing, N_{10} , can be found from the current density of the electrode, I_m , and is equal to $I_m/(4F)$. Water generated by the electrochemical reaction in the catalyst layer diffuses in a direction opposite to that of the oxygen at a rate N_{20} . Since nitrogen is neither produced nor consumed, the flux of nitrogen is zero: $N_{30} = 0$.

The effective diffusion coefficients in the porous backing, D_{ijp} , are equal to the gas-phase diffusion coefficients times a porosity-tortuosity factor, E_p , which is characteristic of the particular porous backing used. Furthermore, the gas-phase diffusion coefficients are, to a good approximation, inversely proportional (1) to the total pressure, P . Therefore

$$D_{ijp} = D_{ij^0} E_p / P \quad [3]$$

where D_{ij^0} is the gas phase diffusion coefficient at ordinary pressures extrapolated to unit pressure. With these substitutions, the multicomponent equations simplify to

$$\frac{d\mathbf{P}}{dz} = \frac{RTN_{10}}{E_p} \mathbf{A} \mathbf{P} \quad [4]$$

where \mathbf{A} is the matrix

$$\mathbf{A} = \begin{pmatrix} m/D_{12^0} - 1/D_{12^0} - 1/D_{13^0} \\ -m/D_{12^0} & 1/D_{12^0} - m/D_{23^0} \\ 0 & 0 & 1/D_{13^0} + m/D_{23^0} \end{pmatrix} \quad [5]$$

and where $m = N_{20}/N_{10} = -2$.

The solution of this equation is

$$\mathbf{P}(z) = e^{ARTN_{10}z/E_p} \mathbf{P}_m \quad [6]$$

where \mathbf{P}_m is the n -tuple (P_{1m}, P_{2m}, P_{3m}) whose components are the partial pressures of oxygen, water, and nitrogen, respectively, at the interface between the flowing gas stream and the porous backing. The fundamental matrix can be computed from the formula

$$e^{ARTN_{10}z/E_p} = \sum_{i=1}^3 e^{\lambda_i RTN_{10}z/E_p} \prod_{j(\neq i)=1}^3 \frac{A - \lambda_j I_u}{\lambda_j - \lambda_i} \quad [7]$$

where I_u is the unit matrix and the λ_i are the eigenvalues of \mathbf{A} , which are 0, $(m+1)/D_{12^0}$, and $1/D_{13^0} + 1/D_{23^0}$.

The purpose of solving these multicomponent diffusion equations is to obtain \mathbf{P}_c , whose components (P_{1c}, P_{2c}, P_{3c}) are the partial pressures of oxygen, water, and nitrogen at the interface between the porous backing and the catalyst layer. This value of \mathbf{P}_c is obtained by setting z equal to z_p in Eq. [6], where z_p is the thickness of the porous backing. This value of \mathbf{P}_c then serves as the boundary condition for the next step, which is diffusion in the catalyst layer.

Gas diffusion in the catalyst layer.—The diffusion in the porous backing material was entirely molecular diffusion, in which the retardation of the flow of oxy-

gen was due to collisions with other molecules. The diffusion in the catalyst layer is also partly molecular diffusion, but the pores in the catalyst layer are very narrow. The walls of the gas pores are so close together that their distance apart is nearly equal to the mean free path of the molecules. Therefore, oxygen molecules are slowed up by collisions with the walls of the pores as well as by collisions with other gas molecules. This added component of diffusion is called Knudsen diffusion. Therefore, for the catalyst layer, the Stefan-Maxwell equations must be modified (2) by adding a term for Knudsen diffusion

$$\frac{dP_1}{dz} = RTN_1 \left[\frac{1}{P_T} \left(\frac{m}{D_{12p}} P_1 - \frac{1}{D_{12p}} P_2 - \frac{1}{D_{13p}} P_3 \right) - \frac{1}{D_{k1e}} \right] \quad [8]$$

$$\frac{dP_2}{dz} = RTN_1 \left[\frac{1}{P_T} \left(-\frac{m}{D_{12p}} P_1 + \frac{1}{D_{12p}} P_2 - \frac{m}{D_{23p}} P_3 \right) - \frac{m}{D_{k2e}} \right] \quad [9]$$

$$\frac{dP_3}{dz} = RTN_1 \frac{1}{P_T} \left(\frac{1}{D_{13p}} + \frac{m}{D_{23p}} \right) P_3 \quad [10]$$

where P_T is the total pressure, $P_1 + P_2 + P_3$, inside the catalyst layer and N_1 is the flux of oxygen. The porous-backing, catalyst-layer interface is chosen for $z = 0$ and the catalyst-layer, electrolyte interface is at $z = z_l$. For a given flux ratio, m , the total pressure will not remain constant inside the catalyst layer, as was the case for entirely molecular diffusion in the

porous backing, but will vary from point to point in accordance with the above equations.

These equations can be simplified in a manner similar to that used for the porous backing. The molecular diffusion coefficients are approximately inversely proportional to the total pressure and are equal to the gas phase values times a porosity-tortuosity factor, E_T , which is characteristic of the catalyst layer

$$D_{ijp} = D_{ij^0} E_T / P_T \quad [11]$$

The Knudsen diffusion coefficient for the i th component, D_{kie} is similarly approximated by the Knudsen diffusion coefficient for a straight cylindrical tube, D_{kis} , corrected with the porosity-tortuosity factor

$$D_{kie} = E_T D_{kis} \quad [12]$$

and D_{kis} , in turn, as given in Ref. (1), is related to the radius of the tube, R_t , by

$$D_{kis} = 0.97 R_t (T/\mu_i)^{1/2} \quad [13]$$

where μ_i is the molecular weight of the diffusing molecule. With these substitutions, the equations become

$$\frac{d\mathbf{P}}{dz} = \frac{RTN_1}{E_T} (\mathbf{C} + \mathbf{A}\mathbf{P}) \quad [14]$$

where \mathbf{A} is the same matrix as was given previously for diffusion in the porous backing and \mathbf{C} is equal to $(-1/D_{k1s}, -m/D_{k2s}, 0)$.

The partial pressures of oxygen, P_1 , and water vapor, P_2 , can be expressed in terms of the partial pressure of nitrogen, P_3 , by dividing the equations for dP_1/dz and dP_2/dz by the equation for dP_3/dz . The resulting equations are independent of N_1

$$\lambda_3 P_3 \frac{d\mathbf{p}}{dz} = \mathbf{B}\mathbf{p} + P_3 \mathbf{b} + \mathbf{c} \quad [15]$$

where \mathbf{p} and \mathbf{c} are the vectors formed from the first two components of \mathbf{P} and \mathbf{C} . \mathbf{B} is the matrix formed from the first two rows and columns of \mathbf{A} and \mathbf{b} is the vector formed from the first two components of the third column of \mathbf{A} . The solution is

$$\mathbf{p} = \mathbf{Y}(P_3) [\mathbf{Y}^{-1}(P_3) \mathbf{p}_c + \mathbf{G}(P_3) - \mathbf{G}(P_{3c}) + \mathbf{H}(P_3) - \mathbf{H}(P_{3c})] \quad [16]$$

where

$$\mathbf{Y}(P_3) = I_u + (P_3^\gamma - 1) \mathbf{B} / \lambda_2 \quad [17]$$

$$\mathbf{Y}^{-1}(P_3) = I_u + (P_3^{-\gamma} - 1) \mathbf{B} / \lambda_2 \quad [18]$$

$$\mathbf{G}(P_3) = \{I_u + [P_3^{-\gamma} / (1 - \gamma) - 1] \mathbf{B} / \lambda_2\} P_3 \mathbf{b} / \lambda_3 \quad [19]$$

$$\mathbf{H}(P_3) = \{(\ln P_3) I_u - [P_3^{-\gamma} / \gamma + \ln P_3] \mathbf{B} / \lambda_2\} \mathbf{c} / \lambda_3 \quad [20]$$

$$\mathbf{p}_c = (P_{1c}, P_{2c}) \quad [21]$$

$$\gamma = \lambda_2 / \lambda_3 \quad [22]$$

Only one of the three original differential equations for gas diffusion remains to be solved.

$$\frac{dP_3}{dz} = \frac{RTN_1 \lambda_3}{E_T} P_3 \quad [23]$$

Diffusion of dissolved oxygen and electrochemical reaction.—As oxygen diffuses through the electrode, some of the oxygen reacts along the way. The flux of oxygen diffusion past any point in the electrode diminishes in proportion to the rate of reaction per unit volume of electrode, N_R , at that point

$$\frac{dN_1(z)}{dz} = -N_R \quad [24]$$

Before the oxygen can react, it must first dissolve in the outer surface of the film covering the agglomerates, diffuse across the film, and diffuse through the agglomerates. The oxygen dissolved in the outermost

layer of the film may be taken to be in equilibrium with the oxygen in the gas pores at that point and therefore has a concentration, $P_1(z)C_1^0$, where C_1^0 is the concentration of dissolved oxygen in equilibrium with oxygen at a partial pressure of one atmosphere. If the film is thin in comparison with the radius of the cylindrical agglomerates, the equation describing this diffusion can be approximated by Fick's law for a flat film

$$N_R = aD \frac{P_1(z)C_1^0 - C_1(r_a, z)}{\delta} \quad [25]$$

where $C_1(r_a, z)$ is the concentration of oxygen at the film-agglomerate interface, a is the area of the film per unit volume of electrode, δ is the thickness of the film, D is the diffusion coefficient of oxygen in the electrolyte, and r_a is the radius of the agglomerate.

After the oxygen has diffused across the film, it diffuses radially into the pores of the agglomerates. Some of the oxygen reacts along the way. The current density has been found to be first order in the oxygen concentration from experiments at constant potential. The rate of reaction in the agglomerate can be obtained (3) by multiplying the rate constant, K_e , for the reaction by the concentration of dissolved oxygen, $C_1(r_a, z)$, at the surface of the agglomerate and by an effectiveness factor, ϵ_c , which depends on the relative rates of diffusion and reaction

$$N_R = \epsilon_c K_e C_1(r_a, z) \quad [26]$$

The formula for the effectiveness factor (3) is

$$\epsilon_c = I_1(2M_c) / [M_c I_0(2M_c)] \quad [27]$$

where I_0 and I_1 are modified Bessel functions of the first kind and

$$M_c = \frac{r_a}{2} \left(\frac{K_e}{E_n E_a D} \right)^{1/2} \quad [28]$$

where E_a is the porosity-tortuosity factor for the agglomerates and E_n is the volume fraction of the agglomerates in the electrode. The effectiveness factor can be approximated (3) by the formula

$$\epsilon_c \approx \frac{3M_c \coth(3M_c) - 1}{3M_c^2} \quad [29]$$

from which it is more easily computed.

The variable $C_1(r_a, z)$ can be eliminated between the two different equations [25] and [26] for N_R above. Since diffusion in the film and diffusion and reaction in the agglomerates occur in series, the resulting expression is the reciprocal of the sum of reciprocals of terms relating to diffusion in the film and diffusion and reaction in the agglomerates alone. The result is substituted into the differential Eq. [24] for N_1 to yield the final differential equation for the effect of diffusion of dissolved oxygen and electrochemical reaction

$$\frac{dN_1}{dz} = - \frac{P_1(z)}{\frac{\delta}{aDC_1^0} + \frac{1}{\epsilon_c K_e C_1^0}} \quad [30]$$

The rate constant, K_e , can be expressed in terms of $I_T(E)$, the current density which the electrode would have if activation were the only source of voltage loss

$$K_e = \frac{I_T(E)}{4Fz_1 \mu_{1m} C_1^0} \quad [31]$$

For current densities greater than 10 A/m², I_T can be represented by

$$I_T(E) = I_T(E_r) \exp_{10} [(E_r - E)/T_s] \quad [32]$$

where E_r is some reference potential, usually 0.9V, and $I_T(E_r)$ is the current density at that potential. T_s is

the Tafel slope which is approximately 90 mV/decade at 190°C (4).

Electrical conduction.—Ohm's law governs the current of electrons through the catalyst layer

$$\frac{dE_e}{dz} = -\frac{I_e(z)}{\sigma_c} \quad [33]$$

and the current of hydrogen ions in the electrolyte

$$\frac{dE_i}{dz} = -\frac{I_i(z)}{\sigma_1} \quad [34]$$

where I_e and I_i are the electronic and ionic current densities and σ_c is the electronic conductivity of the catalyst layer material. The effective conductivity of the electrolyte in the pores, σ_1 , is equal to the porosity-tortuosity factor for the agglomerates, E_a , times E_n , the volume fraction of agglomerates, times the conductivity of the electrolyte. E_e and E_i are the potentials in the catalyst layer and the electrolyte. The flux of oxygen flowing through the plane at z is consumed in producing the electronic current density at z , flowing in the opposite direction

$$I_e(z) = -4FN_1(z) \quad [35]$$

The ionic current density $I_i(z)$ is equal to the difference between the total electronic current density through the plane at $z = 0$ and the electronic current density at z

$$I_i = I_e(0) - I_e(z) \quad [36]$$

The rate of electrochemical reaction, N_R , depends only on E , which is the difference between the potentials in the electrode and in the electrolyte

$$E(z) = E_e(z) - E_i(z) \quad [37]$$

Therefore, the two differential equations for E_e and E_i can be combined into a single differential equation for E

$$\frac{dE}{dz} = \frac{I_e(0)}{\sigma_1} + 4F \left(\frac{1}{\sigma_c} + \frac{1}{\sigma_1} \right) N_1 \quad [38]$$

The above equations constitute a model which accounts for gas diffusion, diffusion of dissolved oxygen, and ohmic effects. Previous models considered only diffusion of dissolved oxygen and ohmic loss in electrolyte (5, 6), or only gas diffusion and diffusion of dissolved oxygen but not ohmic resistance (7).

Solution of the equations.—The electrode behavior can be characterized by solving the three simultaneous equations [23], [30], and [38]. For a given value of $E(0)$, the value of $N_1(0)$ must be varied by trial and error to give a solution of the equations for which the flow of oxygen through the catalyst layer-electrolyte interface, $N_1(z_1)$, is equal to zero. [Alternatively, $N_1(0)$ could be fixed and $E(0)$ varied.] The result is N_1 , E , and P_3 . From P_3 , the values of P_1 and P_2 can be obtained using Eq. [16]. I_e and I_i can be obtained from N_1 using Eq. [35] and [36]. E_e and E_i can be obtained by quadrature from either Eq. [33] or Eq. [34] together with Eq. [37]. Since E_e and E_i are not independently observable, the boundary condition for E_i is arbitrary and $E_i(0)$ is conveniently chosen as zero. The experimentally measurable potential corresponds to the difference between the potential in the catalyst layer at the point of current collection, $z = 0$, and the potential of the reference electrode in the solution at the catalyst layer-electrolyte interface, $z = z_1$ or $E_e(0) - E_i(z_1)$. The experimentally observed performance curve corresponds to a plot of $E_e(0) - E_i(z_1)$ vs. $I_e(0)$. In the present case, the above equations were substituted into the IBM CSMP program to obtain the solution.

Approximate equations.—The partial pressure of water in the gas phase varies with the position between the two surfaces of the catalyst layer. The con-

centration of the electrolyte at various points in the catalyst layer will be determined by equilibrium with the water vapor present at that point. Therefore, the concentration of electrolyte will vary inside the catalyst layer. The conductivity of the electrolyte, σ_1 , the solubility of oxygen, C_1^0 , and the diffusion coefficient of oxygen in the electrolyte, D , are functions of the concentration of electrolyte and therefore, they will also vary with position. The diffusivity and solubility do not occur independently, but only as the product, DC_1^0 , in the above equations. This product varies less rapidly with concentration than either the diffusivity or the solubility alone. The variation of diffusivity-solubility and conductivity were taken into account in calculations made with this model.

If the dependence of the conductivity σ_1 on position is ignored, the number of simultaneous differential equations can be reduced from three to two. This can be done eliminating N_1 between Eq. [23] and [38] for P_3 and to yield

$$\frac{dE}{dz} = \frac{I_e(0)}{\sigma_1} + 4F \left(\frac{1}{\sigma_c} + \frac{1}{\sigma_1} \right) \frac{E_T}{RT\lambda_3} \frac{d \ln P_3}{dz} \quad [39]$$

By integrating this equation, P_3 can be expressed in terms of E

$$P_3 = P_{3c} \exp \left\{ \frac{RT\lambda_3}{4FE_T \left(\frac{1}{\sigma_c} + \frac{1}{\sigma_1} \right)} \left[E - E(0) - \frac{I_e(0)}{\sigma_1} z \right] \right\} \quad [40]$$

In this case, only two simultaneous differential equations, [30] and [38], remain to be solved.

Application to a Particular Electrode

In order to apply this model to a particular electrode, parameters which are characteristic of that electrode must be substituted into the model equations. The rate constant for the electrode can be determined from its behavior at low current densities, where only activation losses are important and diffusion and ohmic losses are negligible. The observed Tafel slope, T_s , and the current density $I_T(E_r)$ at a reference potential, E_r , of 0.9V can be substituted into Eq. [32] to give the electrode behavior, I_T , with only activation losses. I_T can then be substituted into Eq. [31] to yield the rate constant. The Knudsen diffusion coefficient, D_{kis} , can be estimated from Eq. [13] and the average pore radius, R_t , can be estimated to be 70 nm, using electron micrographs of the catalyst layer. In a similar way, most of the parameters used in the model such as the conductivity of the carbon, the effective diffusivity in the porous backing, etc., can be evaluated experimentally.

Four parameters exist which cannot be determined directly: (i) the radius of the agglomerates, r_a (ii) the thickness of the electrolyte film covering the agglomerates, δ , (iii) the porosity-tortuosity factor for gas diffusion in the catalyst layer, E_T , and (iv) the product of the porosity-tortuosity factor for diffusion and electrical conduction in the pores of the agglomerates times the fraction of the electrode consisting of agglomerates, $E_n E_a$. These four parameters were determined by adjusting their values until the solution of the model equations agreed with four experimental performance curves over the range of current densities from one to 3700 A/m². These performance curves were obtained using four different humidified gas mixtures: (i) air, (ii) pure oxygen, (iii) 4% oxygen in nitrogen, and (iv) 4% oxygen in helium. By changing from air to pure oxygen, the diffusion losses are practically eliminated and only ohmic and activation losses remain. Therefore, this change of gases is effective in separating the ohmic losses from the diffusion

losses. Changing from pure oxygen to 4% oxygen in nitrogen reverses the situation. Diffusion losses predominate to such an extent that they cause a limiting current. This limiting current can be caused by the porous backing or by the electrolyte film covering the agglomerates. Therefore, changing to 4% oxygen in nitrogen is helpful in obtaining the effect of the backing and the film. The effect of the backing alone is obtained from the measured effective diffusivity of the backing material. Changing from 4% oxygen in nitrogen to 4% oxygen in helium changes only the molecular diffusion coefficient for gas diffusion in the porous backing and in the gas pores of the catalyst layer. Other factors remain the same. In particular, the Knudsen diffusion coefficient remains the same, since it is independent of the other gases in the mixture. Therefore, changing from 4% oxygen in nitrogen to 4% oxygen in helium is effective in separating the effect of ordinary molecular diffusion from that of Knudsen diffusion.

Calculation of Voltage Losses

This model is useful to evaluate how much voltage loss is caused by each of the basic transport processes, such as gas diffusion, diffusion of dissolved oxygen, ohmic losses, etc. Identification of the most important sources of voltage loss allows research and development efforts to be directed toward the minimization of these voltage losses.

A given loss was evaluated mathematically by calculating the performance curve with one parameter changed in such a way as to make its contribution to the total voltage loss equal to zero. For example, an ohmic loss would be made equal to zero by setting the electrical resistance equal to zero in the calculation. Figure 3 gives an example of a performance curve calculated with the diffusion loss in the agglomerate made equal to zero by making the diffusion coefficient for diffusion into the liquid filled pores of the agglomerates very large in Eq. [28]. The voltage loss corresponding to the parameter which was changed (in this case, diffusion in the agglomerate) is equal to the difference between the voltage calculated in this way and the base line curve in which all parameters have their normal values. Voltage losses for all of the transport processes were calculated in this way for an air cathode at a current density of 2000 A/m².

The total ohmic and diffusion losses are represented by the distance from the base line to the activation only Tafel line. The activation loss is represented by the distance from the Tafel line to the theoretical equilibrium potential.

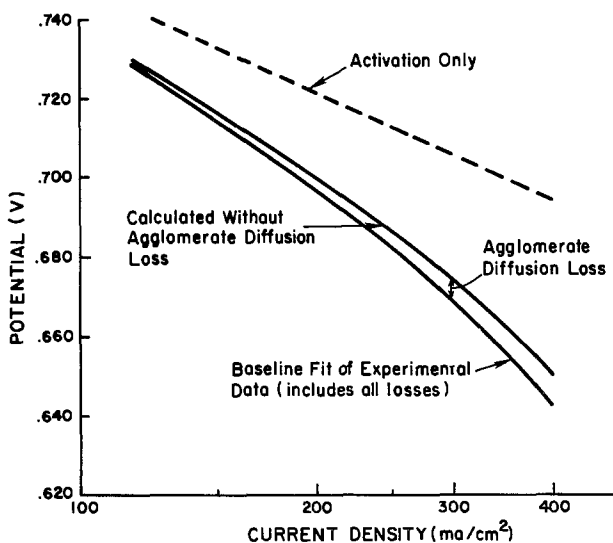


Fig. 3. Method of calculating the voltage loss due to diffusion in the agglomerates.

The relative contributions of diffusion and ohmic losses to the total voltage loss for transport processes are summarized in Fig. 4 for a typical electrode made in 1974 at the Power Systems Division of United Technologies Corporation (4). Activation loss is not shown, being much larger than the losses for the transport processes. The conclusions are that, for the electrode studied, 54% of the voltage loss due to transport processes was due to ohmic resistance in the catalyst layer. Most of this ohmic loss occurred in the acid electrolyte and only a small part was due to the resistance of the catalyst material. Next most important was diffusion in the gas phase which accounted for 38% of the voltage loss for all the transport processes. Both the porous backing and the catalyst layer are important for gas diffusion. For the catalyst layer alone, Knudsen diffusion is slightly more important than molecular diffusion. Least important were the losses due to the diffusion of dissolved oxygen which accounted for only 8% of the total voltage loss due to transport processes. The very small voltage loss calculated for the electrolyte film indicates that such films are very thin or nonexistent at the cathode.

The voltage loss caused by Knudsen diffusion can be reduced by operating the cell at higher total pressure. However, the loss caused by molecular diffusion is practically unchanged because the benefits of the increase in oxygen concentration outside the electrode are compensated for by the decrease in the molecular diffusion coefficient with pressure shown in Eq. [3] and [11].

Optimum Electrode Thickness

The catalyst is composed of platinum particles dispersed among particles of noncatalytic conducting filler. For a fixed amount of platinum, increasing the amount of filler increases the thickness of the catalyst layer. As shown in Fig. 5, the gas diffusion and electrical conduction paths are longer for a thicker electrode than for a thinner electrode, resulting in larger gas diffusion and ohmic losses. On the other hand, reducing the amount of filler reduces the thickness of the catalyst layer and decreases the total surface area of the agglomerates. Since, from Fick's law, the gradient of oxygen concentration is inversely proportional to the area across which the diffusion is occurring, a reduction of the surface area of the agglomerates reduces the concentration of oxygen in the interior of the agglomerates (at constant overall current) and therefore increases the voltage loss due to the diffusion of dissolved oxygen. The fact that the voltage losses become large if the electrode is very thick or very thin indicates that there is an optimum amount of filler

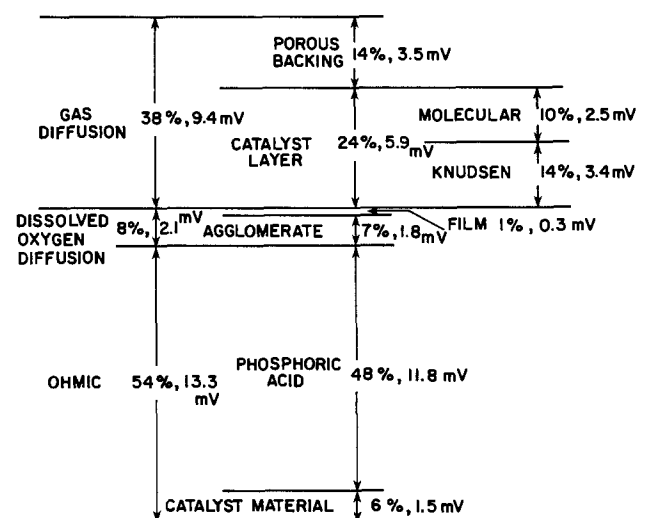


Fig. 4. Relative voltage losses for transport processes at 200 mA/cm².

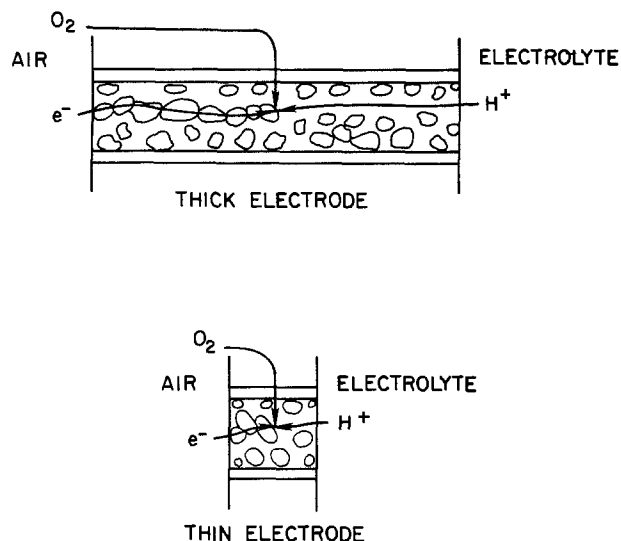


Fig. 5. Comparison of path lengths for gas diffusion and electrical conduction, and agglomerate surface areas for thick and thin catalyst layers.

and an optimum thickness for which the total voltage loss is a minimum.

Utilization

The losses given above are the only ones that apply in the laboratory situation, in which much more oxygen is made to flow past the electrode than is used to produce current. In a practical fuel cell, a substantial part of the oxygen in the air flow past the porous backing is consumed along the electrode. The parts of the electrode which are downstream operate on air which has less oxygen than the parts which are upstream. This depleted air increases the activation and diffusion losses in the electrode. Also, the downstream parts of the electrode carry a lesser than average current, while the parts nearer the inlet carry a greater than average current. The cell voltage, which is kept constant across the face of the cell by highly conductive current collectors, is less than it would be if all parts have access to the concentration of oxygen at the inlet and all parts were operating at the average current density.

The fraction of the input flow of oxygen, which is consumed to produce current, is called the air utilization. The distribution of partial pressures of oxygen in contact with the electrode at a given value, U , of the utilization can be obtained by first relating the partial pressure of oxygen to the utilization and then relating the utilization to position between the inlet and outlet. The partial pressure of oxygen, P_1 , at any point across the face of the electrode is related to the molar flow of oxygen M_1 by

$$P_1 = PM_1/M_t \quad [41]$$

where P is the total pressure and M_t is the total molar flow of all components, oxygen, water, and nitrogen. Since the molar flow of oxygen decreases in direct proportion to the utilization, it is given by

$$M_1 = P_{10}(1 - U)M_{t0}/P \quad [42]$$

where P_{10} and M_{t0} are the partial pressure of oxygen and the total molar flow, respectively, at the inlet. For every mole of oxygen consumed, two moles of water are formed, which enter the gas stream to produce a net increase in the molar flow

$$M_t = [1 - (1 + m)P_{10}U/P]M_{t0} \quad [43]$$

where $m = -2$ for the case where all of the product water is removed by evaporation into the oxidant gas stream. By eliminating M_1 and M_t , the utilization can

be expressed in terms of the partial pressure of oxygen

$$U = \frac{1 - P_1/P_{10}}{1 - (1 + m)P_1/P} \quad [44]$$

The utilization can be related to the position, x , along the electrode between the inlet at $x = 0$ and the outlet at $x = l$. The overall utilization, $U(l)$, is the value of U at the outlet. The utilization at any point is related to the distribution of current densities across the electrode, I , by

$$U(x) = \frac{h \int_0^x I dx}{4FM_{10}} \quad [45]$$

where h is the height of the electrode. Introducing the overall utilization, $U(l)$, yields

$$U(x) = \frac{U(l) \int_0^x I dx}{I_m} \quad [46]$$

where I_m is the average current density produced by the electrode. Eliminating U between the above equations yields

$$\frac{1 - (1 + m)(1/P)}{[1 - (1 + m)(P_1/P)]^2 I} dP_1 = -\frac{U(l)}{I_m} d\left(\frac{x}{l}\right) \quad [47]$$

For the range of current densities in which the electrochemical effects are much larger than ohmic effects, the current density, I , is related to the oxygen partial pressure by

$$I \approx I(P_{10})P_1/P_{10} \quad [48]$$

where $I(P_{10})$ is the current density at the inlet, or at zero utilization. The distribution of partial pressures of oxygen is obtained by substituting for I in Eq. [47] and integrating. The resulting expression with x set equal to the width of the electrode, l , is used to eliminate the quantity $U(l)I(P_{10})/I_m$ in favor of P_{11} , the partial pressure of oxygen at the outlet of the cell to yield

$$\frac{P_1}{P_{10}} = \left\{ s_p + \exp \left[\frac{x}{l} \ln \left(\frac{1}{r_p} - s_p \right) + \left(1 - \frac{x}{l} \right) \ln (1 - s_p) - \frac{1 - x/l}{1 - s_p} + \frac{1}{1 - s_p P_1/P_{10}} - \frac{x/l}{1 - s_p r_p} \right] \right\}^{-1} \quad [49]$$

where $s_p = (1 + m)P_1/P$, $r_p = P_{11}/P_{10}$, and P_{11} is calculated from Eq. [44] using the known value of the utilization, $U(l)$. This equation can be solved numerically to obtain the oxygen partial pressure, P_1 , as a function of position, x , in the cell. The oxygen partial pressure, in turn can be integrated numerically to obtain the average partial pressure of oxygen flowing past the electrode, P_{1m} . If the increase in the volume of reacting air caused by the formation of water had been neglected in the above derivation, the expression for the average partial pressure of oxygen would have reduced to

$$\frac{P_{1m}}{P_{10}} = \frac{(P_{11}/P_{10}) - 1}{\ln (P_{11}/P_{10})} \quad [50]$$

The partial pressure of water vapor, P_2 , is related to the partial pressure of oxygen by using the fact that two moles of water are produced for every mole of oxygen consumed

$$P_2 = \frac{P_{20}[P - (1 + m)P_1] - m(P_{10} - P_1)}{P - (1 + m)P_{10}} \quad [51]$$

where P_{20} is the partial pressure of water at the inlet.

When P_{1m} is substituted for P_1 in this formula, then the average water partial pressure, P_{2m} , is obtained. The average partial pressure of nitrogen, P_{3m} , is the difference between the oxygen and water partial pressures and the total pressure, P

$$P_{3m} = P - P_{1m} - P_{2m} \quad [52]$$

The average partial pressures of oxygen, water vapor, and nitrogen found in this way serve as the boundary conditions for diffusion into the porous backing for the model of electrode behavior described above in Eq. [6], from which the performance curve can be calculated.

Calculations made in this way involve the approximation to the current density distribution in Eq. [48]. This approximation can be removed by dividing the cell into rectangular regions. From an initial assumed current density distribution, the flows of gases into and out of each of the nodes and the partial pressure distributions were calculated. Diffusion of water across the matrix was also considered. These partial pressures serve as the boundary conditions for diffusion into the porous backing for the above model of cathode behavior. The cathode potential was calculated at each node. A similar model was used to find the anode potential at each node. The voltage drop across each rectangular region was found from the anode and cathode potentials and the potential drop across the matrix. The difference in voltage from the average voltage is a measure of how much the current density at each node should be changed in order to improve the current density distribution. Successively more accurate distributions were calculated and the process was repeated until the potential difference was the same across each rectangular region. The cell voltage obtained in this way using 144 nodes differs by less than 2 mV from the approximate treatment of utilization given above when the current density was 2610 A/m² and the air utilization was 70%.

The utilization loss can be broken down into contributions from separate effects. The air activation component is the amount by which the activation Tafel line is shifted to lower potentials due to the decrease in oxygen partial pressure caused by utilization. Air activation is the largest component of the utilization loss. It depends only on the Tafel slope and the partial pressure of oxygen and is equal to $-T_s \log(P_1/P_{10})$. Its value averaged over all the nodes of the cell is 20 mV at 60% utilization and 31 mV at 80% utilization.

The diffusion loss in the porous backing and catalyst layer increases as the partial pressure of oxygen in the air decreases as a result of utilization. Unlike the activation component, the diffusion component of the utilization loss is different for different electrodes. This diffusion component is small at low utilizations but increases steeply at high utilizations amounting to about 14 mV at 90% utilization.

As the oxygen partial pressure decreases due to utilization, the partial pressures of water and nitrogen increase because the total pressure remains essentially constant. In addition, water from the fuel stream migrates and diffuses from the anode across the matrix to the cathode and water is produced at the cathode by electrochemical reaction. When dry air is used, a drying effect occurs which is confined to a small neighborhood around the inlet for all but very low utilizations. The ohmic component of the utilization loss increases by 6 mV when the utilization of dry air is reduced from 10% to nearly zero. This effect is eliminated by using humidified air at low utilization. As the utilization is varied under practical operating conditions the concentration changes in the electrolyte are small, and since the electrical resistance of the acid does not change much with concentration, the ohmic loss in the cathode and matrix does not change significantly. Except for dry air at very low utilization, the ohmic component is not an important factor in the utilization loss.

Manuscript submitted Nov. 5, 1979; revised manuscript received Jan. 18, 1980. This was Paper 32 presented at the Las Vegas, Nevada, Meeting of the Society, Oct. 17-22, 1976.

Any discussion of this paper will appear in a Discussion Section to be published in the June 1981 JOURNAL. All discussions for the June 1981 Discussion Section should be submitted by Feb. 1, 1981.

Publication costs of this article were assisted by United Technologies Corporation.

LIST OF SYMBOLS

A	matrix defined by Eq. [5] (sec/m ² Pa)
A_s	matrix defined by Eq. [2] (kmole/m ²)
a	area of electrolyte film per m ³ of electrode (m ⁻¹)
B	matrix composed of the first two rows and columns of A (sec/m ² Pa)
b	vector composed of the first two components of the third row of A (sec/m ² Pa)
C	vector representing the effect of Knudsen diffusion in Eq. [14] (sec/m ²)
C_1	concentration of oxygen dissolved in the electrolyte (kmole/m ³)
C_1^0	solubility of oxygen in the electrolyte (kmole/m ³ Pa)
c	vector composed of the first two components of C (sec/m ²)
D	diffusion coefficient of oxygen dissolved in the electrolyte (m ² /sec)
D_{ij}^0	gas diffusion coefficient for components i and j at one atm total pressure extrapolated to one Pa (Pa m ² /sec)
D_{ijp}	effective gas diffusion coefficient for components i and j in the porous backing or catalyst layer at the given pressure (m ² /sec)
D_{kis}	Knudsen diffusion coefficient in the catalyst layer (m ² /sec)
D_{kis}	Knudsen diffusion coefficient for a straight cylindrical tube (m ² /sec)
E	electrode potential (V)
E_a	porosity-tortuosity factor for diffusion and electrical conduction in the agglomerates (dimensionless)
E_c	potential in the catalyst layer (V)
E_e	potential in the electrolyte (V)
E_m	fraction of the electrode consisting of agglomerates (dimensionless)
E_p	porosity-tortuosity factor for gas diffusion in the porous backing (dimensionless)
E_r	reference potential (V)
E_t	porosity-tortuosity factor for gas diffusion in the catalyst layer (dimensionless)
F	Faraday (C/equiv.)
G	function defined by Eq. [19]
H	function defined by Eq. [20]
h	height of the electrode (m)
I	current density along the electrode between the gas inlet and the gas outlet (A/m ²)
I_c	current density in the catalyst layer (A/m ²)
I_e	current density in the electrolyte (A/m ²)
I_m	average current density for the cathode (A/m ²)
I_T	current density assuming the only source of voltage loss is activation (A/m ²)
I_u	unit matrix (dimensionless)
J_0	Bessel function of the first kind (dimensionless)
J_1	Bessel function of the first kind (dimensionless)
K_e	rate constant for the electrochemical reaction of oxygen (sec ⁻¹)
l	width of the electrode (m)
M_c	modulus for diffusion and reaction in the agglomerates defined by Eq. [28] (dimensionless)
M_i	molar flow of component i (kmole/sec)
M_{io}	molar flow of component i which was input to the cell (kmole/sec)
M_t	total molar flow of all components (kmole/sec)
m	ratio of water flux to oxygen flux (dimensionless)

N_i	flux of gaseous component i diffusing past any point in the catalyst layer (kmole/m ² sec)	x	position along the electrode between the gas inlet and the gas outlet of the cell (m)
N_{i0}	flux of gaseous component i diffusing in the porous backing (kmole/m ² sec)	Y	fundamental matrix of the homogeneous part of Eq. [15]
N_R	rate of reaction of oxygen per m ³ of electrode at a given point (kmole/m ³ sec)	z	position in the porous backing or catalyst layer (m)
P	total pressure in the gas stream and porous backing (Pa)	z_1	thickness of the catalyst layer (m)
\mathbf{P}	vector whose components are the partial pressures of oxygen, water vapor, and nitrogen (Pa)	z_p	thickness of the porous backing (m)
P_c	the value of \mathbf{P} at the interface between the porous backing and the catalyst layer (Pa)	Greek letters	
P_i	partial pressure of component i (Pa)	γ	λ_2/λ_3 (dimensionless)
P_{i0}	partial pressure of component i at the inlet (Pa)	δ	thickness of the electrolyte film (m)
P_{i1}	partial pressure of component i at the outlet (Pa)	ϵ_c	effectiveness factor for diffusion and reaction of oxygen in the agglomerates (dimensionless)
P_{im}	average partial pressure of component i in the gas stream (Pa)	λ_1	eigenvalues of A (sec/m ²)
\mathbf{P}_m	average value of \mathbf{P} in the gas stream (Pa)	μ_i	molecular weight of component i (kg/kmole)
P_t	total pressure in the catalyst layer (Pa)	σ_c	conductivity of the catalyst layer ($\Omega^{-1}\text{m}^{-1}$)
\mathbf{p}	vector whose components are the partial pressures of oxygen and water (Pa)	σ_1	conductivity of the electrolyte ($\Omega^{-1}\text{m}^{-1}$)
P_c	the value of \mathbf{p} at the interface between the porous backing and the catalyst layer (Pa)	Subscripts	
R	gas constant (J/deg kmole)	$i = 1,2,3$	oxygen, water vapor, and nitrogen, respectively
R_t	average radius of the gas filled pores in the catalyst layer (m)	p	at pressure other than unit pressure, or for a porous solid
r_a	radius of the agglomerates (m)		
r_p	P_{i1}/P_{i0}		
s_p	$(1+m)P_i/P$		
T	temperature ($^{\circ}\text{K}$)		
T_s	slope of the semilog plot of the performance curve at low currents (V/decade)		
U	fraction of the amount of oxygen which was input into the cell which is consumed in producing current (dimensionless)		

REFERENCES

1. C. J. Geankoplis, "Mass Transport Phenomena," pp. 33, 64, 152, Holt, Rinehart and Winston, Inc., New York (1972).
2. L. B. Rothfeld, *AIChE J.*, **9**, 24 (1963).
3. R. Aris, "Elementary Chemical Reactor Analysis," Prentice Hall, Inc., Englewood Cliffs, N.J. (1969).
4. H. R. Kunz and G. A. Gruver, *This Journal*, **122**, 1279 (1975).
5. J. Giner and C. Hunter, *ibid.*, **117**, 1124 (1969).
6. J. Kosinski, *ibid.*, **116**, 282C (1969).
7. M. B. Cutlip, *Electrochim. Acta*, **20**, 767 (1975).

The Effect of Ammonia on Hydrogen-Air Phosphoric Acid Fuel Cell Performance

S. T. Szymanski, G. A. Gruver, M. Katz,* and H. R. Kunz*

United Technologies Corporation, Power Systems Division, South Windsor, Connecticut 06074

ABSTRACT

Laboratory experiments and tests conducted on phosphoric acid fuel cells have indicated that ammonia, when present as an impurity in either the fuel or oxidant streams, will react with the electrolyte to form $(\text{NH}_4)\text{H}_2\text{PO}_4$. Ammoniation of the acid to greater than 0.2 mole percent resulted in a loss in performance due primarily to a lowering in the rate of O_2 reduction on the the cathode catalyst. Complete recovery of the performance loss was achieved after the removal of the contaminant source. The degree of electrolyte conversion and, hence, steady-state performance loss were found to be dependent on the rate of ammonia addition to the cell relative to the rate of ammonium ion oxidation at the cathode. This oxidation process was found to be potential dependent, with an increase in cathode potential resulting in the ability of the cell to tolerate higher NH_3 concentrations in the reactant gas streams.

Small amounts of ammonia may be present as a contaminant in the processed fuel or oxidant streams of hydrocarbon-air fuel cell systems. The ammonia might be formed in a reformer used to convert a hydrocarbon fuel into a hydrogen-rich gas if nitrogen is present. Ammonia might also be introduced into the fuel because of its use as a tracer gas in natural gas distribution systems. It is also present at low concentrations in the air. Although the ammonia concentration will be on the order of a part per million, the presence of the ammonia is of concern to long-term operation of

acid electrolyte fuel cell systems, since the ammonia will react with the electrolyte. This potential problem is an analog of carbon dioxide in the fuel and oxidant reacting with the electrolyte in alkaline fuel cell systems. An experimental and theoretical study was undertaken to define the severity of the performance loss associated with ammonia and the tolerance level of acid cells to ammonia.

Ammonia reacts with phosphoric acid electrolyte to form ammonium dihydrogen phosphate. Electrochemical experiments were performed with stationary and rotating electrodes to determine the effect of ammonium dihydrogen phosphate concentration on the per-

* Electrochemical Society Active Member.

Key words: cathode catalyst, electrolyte conversion, oxidation.

formance of fuel cell cathodes in phosphoric acid electrolyte. Post-test chemical analyses were performed on subscale fuel cells, which had operated for various periods of time, to determine the rate at which the electrolyte was converted in tests in which no ammonia was intentionally added to the reactants. Other subscale cell tests were performed with controlled ammonia injection in the fuel gas. The transient performance data of these subscale cell tests were compared with the results of a mathematical model that was derived to describe the cell behavior. This approach provided the definition of the effect of ammonia on the subscale fuel cell performance.

Experiments

Half-cell tests.—In order to determine the effect of $(\text{NH}_4)\text{H}_2\text{PO}_4$ concentration in the H_3PO_4 electrolyte on the performance of fuel cell cathodes, floating electrode experiments were performed using the experimental apparatus and electrodes described in Ref. (1). Electrode performance for the reduction of oxygen was measured as a function of current density under both oxygen and air. The electrodes contained about 0.5 mg Pt/cm² supported on Vulcan XC-72 with a concentration of 10 weight percent (w/o) Pt on the carbon support. The electrolyte in the working electrode chamber was maintained at 191°C and the water vapor pressure above the electrolyte maintained constant at a level in equilibrium with pure 99 w/o H_3PO_4 . Data were obtained when various quantities of $(\text{NH}_4)\text{H}_2\text{PO}_4$ were added to the electrolyte in the working electrode chamber.

Additional half-cell experiments were conducted to determine the rate of oxidation of $(\text{NH}_4)\text{H}_2\text{PO}_4$ from H_3PO_4 electrolyte containing 1, 3, and 10 w/o $(\text{NH}_4)\text{H}_2\text{PO}_4$. The temperature and water vapor pressure of the electrolyte were maintained the same as in the previous half-cell tests. Oxidation currents were measured under N_2 over the potential range of 0.650–0.900V with respect to the hydrogen reference electrode in uncontaminated H_3PO_4 electrolyte. This potential range was selected since it is the operating potential range of fuel cell cathodes. The electrode used in this experiment consisted of a platinum-black-Teflon-bonded electrode supported on a gold-plated tantalum screen. The surface area of the Pt was determined electrochemically by hydrogen adsorption at room temperature in 50% H_3PO_4 . Experiments were performed both with the electrode stationary in the electrolyte and rotating at 2100 rpm.

Subscale cell tests.—Tests were performed on 2×2 in. active area fuel cells to determine the effect of the presence of ammonia in the fuel gas on the cell performance and decay. Some tests were performed with no ammonia introduced into the fuel and oxidant streams. Post-test chemical analyses were performed on the cells to determine the amount of $(\text{NH}_4)\text{H}_2\text{PO}_4$ present in the cell after various periods of operation. Reactant gas analyses and chemical analyses of untested cell components were also performed to determine the source of any $(\text{NH}_4)\text{H}_2\text{PO}_4$ found after the cell tests.

Other cell tests were performed with about 1 mole percent (m/o) $(\text{NH}_4)\text{H}_2\text{PO}_4$ added to the electrolyte prior to the commencement of the test. Tests were performed at two different cell voltages, 0.616 and 0.750V, to determine the effect on cell operating voltage on the cell performance history. Two cells were tested at each cell voltage. One of each pair was tested for about 150 hr and the other for about 350 hr to determine the effect of operating time on the final $(\text{NH}_4)\text{H}_2\text{PO}_4$ content in the cell. A control cell in which no $(\text{NH}_4)\text{H}_2\text{PO}_4$ was initially added was also tested for about 350 hr at 0.616V and analyzed for post-test $(\text{NH}_4)\text{H}_2\text{PO}_4$ content.

In addition, cell tests were performed on the subscale cells with controlled quantities of NH_3 intro-

duced into the fuel stream. The ammonia was introduced using permeation tubes which were placed in a dead-ended and thermally controlled branch to the inlet fuel line. The ammonia contents were set at 1, 2, and 6 ppm in the dry fuel gas in three separate cells by controlling the temperature of the permeation tubes. A control cell in which no NH_3 was introduced was also tested.

All subscale cell tests were performed at 191°C, atmospheric pressure, and 215 mA/cm². The fuel contained 80% H_2 , 18.3% CO_2 , and 1.7% CO and was provided at a flow rate such that 80% of the H_2 was consumed by the electrochemical reaction at the anode. The air flow was set at 40% O_2 utilization. Water was added to the cells using a saturator on the cathode gas stream.

Finally, three additional cell tests were performed. One test was conducted using a mixture of 20% H_2 and 80% N_2 as the fuel to determine whether NH_3 could possibly be formed within the cell. The other two tests were performed with 167 ppm NH_3 added to the fuel gas and NH_4OH injected into the fuel stream to obtain additional data on the effect of high levels of electrolyte ammoniation on cell performance.

All cells were constructed of the same materials. Both anode and cathode were Teflon-bonded electrodes of Pt supported on Vulcan XC-72. The electrode Pt loadings were nominally 0.25 and 0.50 mg/cm², respectively. The electrode spacing was approximately 125 microns.

Theory

Since some of the experimental data indicated that $(\text{NH}_4)\text{H}_2\text{PO}_4$ was oxidized at fuel cell cathode potentials, the mathematical model conceived was based on the conservation equation for $(\text{NH}_4)\text{H}_2\text{PO}_4$. This species was considered to be introduced by NH_3 present in the reactant gases and consumed by the oxidation of $(\text{NH}_4)\text{H}_2\text{PO}_4$ in the cell. All NH_3 entering the cell was assumed to react. In equation form

$$\text{input} - \text{output} + \text{generation} = \text{accumulation}$$

or

$$\Sigma C^*_{\text{NH}_3} \cdot F - 0 - kA_{\text{Pt}}C_{\text{NH}_4^+} = \frac{V(dC_{\text{NH}_4^+})}{dt} \quad [1]$$

where $\Sigma C^*_{\text{NH}_3} \cdot F$ is the sum of the products of ammonia concentrations and reactant flow rates for the two reactant streams (g moles NH_3/hr), k is the oxidation rate constant ($\text{cm}^3 \text{ acid}/\text{hr cm}^2 \text{ Pt}$), A_{Pt} is the real Pt area of cathode ($\text{cm}^2 \text{ Pt}$), $C_{\text{NH}_4^+}$ is the concentration of NH_4^+ in the cell at any time, (g moles/cm³ acid), V is the volume of acid in the cell at 191°C (cm^3), and t is the time (hr). In Eq. [1] the rate of consumption of NH_4^+ within the cell was assumed to be controlled by the rate of its electrochemical oxidation at the cathode and to be proportional to the Pt surface area.

The solution to this equation is

$$C_{\text{NH}_4^+} = \frac{\Sigma C^*_{\text{NH}_3} \cdot F}{kA_{\text{Pt}}} \left[1.0 - \exp\left(\frac{-kA_{\text{Pt}}t}{V}\right) \right] + C^0_{\text{NH}_4^+} \exp\left[\frac{-kA_{\text{Pt}}t}{V}\right] \quad [2]$$

where $C^0_{\text{NH}_4^+}$ is the initial value of $C_{\text{NH}_4^+}$.

The oxidation rate constant was calculated from subscale cell data on preammoniated electrolyte. The resulting expressions were

$$k = \exp\left[\frac{E_c - 1.034}{0.0273}\right] \text{ for } E_c \leq 0.673 \quad [3]$$

and

$$k = \exp\left[\frac{E_c - 2.625}{0.1474}\right] \text{ for } E_c \geq 0.673 \quad [4]$$

where E_c is the cathode potential.

Results

The performance loss due to electrolyte ammoniation was found to be a function of the amount of ammonium ion found in the electrolyte. The data obtained in both the half-cells and full cells are shown in Fig. 1. All of the experimental data indicate that 10 m/o conversion of H_3PO_4 to $(NH_4)H_2PO_4$ results in a performance loss of about 70 mV at 215 mA/cm². Only about 0.2 m/o conversion can be tolerated without a significant performance loss. The performance loss was found to be due to loss of cathode performance as can be seen by the good agreement between cathode half-cell data and full cell results. An inspection of the cathode Tafel plots from the half-cell tests indicated that the primary mode of performance loss is a reduction in the rate of the O_2 reduction on the cathode catalyst. Figure 2 shows the relative cathode catalyst activity for ammoniated electrolyte compared to the pure electrolyte. A loss of 84% in activity results with only 1% conversion of the H_3PO_4 .

The data from the cell which was tested with an H_2/N_2 mixture as the fuel is also shown in Fig. 1. This test resulted in no performance loss due to ammoniation and only a small degree of ammoniation which was typical of a cell in which no ammonia was introduced. Therefore, N_2 does not react with H_2 in a cell to form $(NH_4)H_2PO_4$.

The results of the electrolyte analyses for cells which were endurance tested without NH_3 deliberately added to the fuel or NH_4^+ added to the electrolyte are shown in Fig. 3. The $(NH_4)H_2PO_4$ content in the cell did not increase linearly with time as might be expected if NH_3 were in the reactants, completely reacted within the cell, and not rejected. The $(NH_4)H_2PO_4$ content reached a constant value after about 1000 hr, indicating that the cell has a capacity to reject the $(NH_4)H_2PO_4$. Analyses of the reactant gases for NH_3 and of the pretest cell components indicated that much more $(NH_4)H_2PO_4$ was introduced in the cell than was found by post-test analyses, again indicating rejection capability.

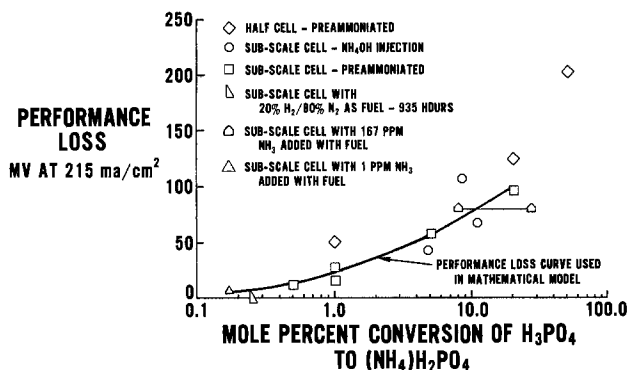


Fig. 1. Performance loss due to ammoniation of H_3PO_4

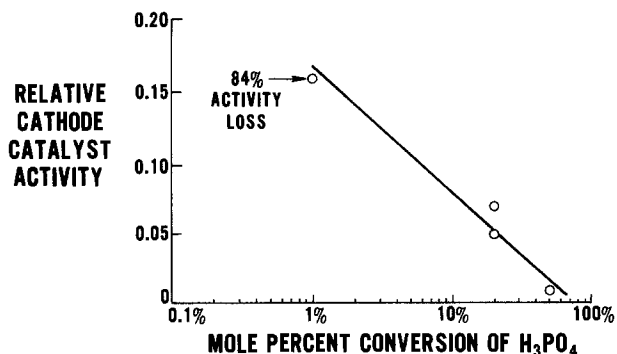


Fig. 2. Relative cathode catalyst activity as a function of percent H_3PO_4 conversion to $(NH_4)H_2PO_4$.

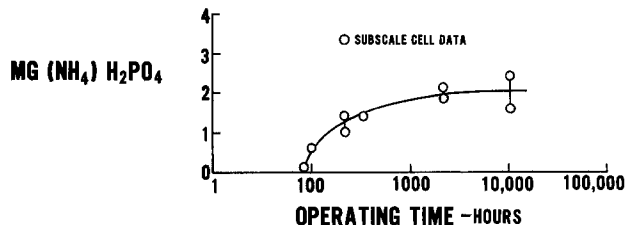


Fig. 3. Post-test analysis of subscale cell for $(NH_4)H_2PO_4$

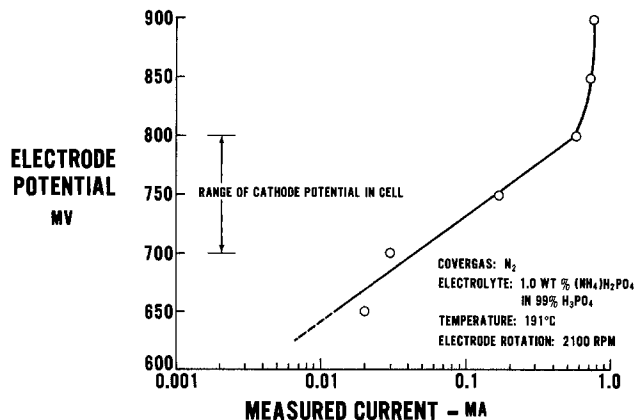
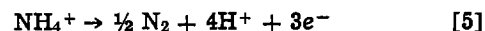


Fig. 4. Effect of electrode potential on ammonium phosphate oxidation current.

The results of the experiments to investigate the electrochemical oxidation of $(NH_4)H_2PO_4$ are shown in Fig. 4 for 1 w/o $(NH_4)H_2PO_4$ at a rotation rate of 2100 rpm. Significant oxidation currents were found for the probable reaction



The reaction rate for this reaction was found to be strongly potential dependent, increasing by a factor of about 60 in the potential range from 0.65 to 0.85V. Results at other electrolyte concentrations at 0.75V are shown in Table I. These results show that the rate of oxidation increases with the concentration of ammonium ion in solution and the rate of rotation.

Because of this strong effect of cathode potential on the oxidation rate of $(NH_4)H_2PO_4$, the rate of electrolyte purification for the cells containing pre-ammoniated electrolyte would be expected to be dependent on the cathode operating potential in the cells. These results are shown in Fig. 5. In all cases, the initial concentration of $(NH_4)H_2PO_4$ in the electrolyte was about 1 m/o. For the two cells which were tested at 0.616V, the $(NH_4)H_2PO_4$ content decreased to 0.342 m/o in 141 hr for cell D and to 0.068 m/o in 334 hr for cell E. For the two cells tested at 0.750V, the $(NH_4)H_2PO_4$ content decreased more rapidly to 0.034

Table I. Summary of half-cell data

Measured current (mA) at mV RHE

Concentration w/o ammoniation	1st Experiment		2nd Experiment	
	With rotation	Without rotation	With rotation	Without rotation
0	0.0	-0.10	+0.27	0.0
1	-0.37	-0.30	-0.25	-0.38
3	—	—	-0.68	-0.66
10	-1.20	-0.75	-1.08	-0.80

Notes:

1. Electrode (Pt black, screen electrode) surface area = 11,407 cm².
2. Minus sign indicates anodic current (oxidation), plus sign indicates cathodic current (reduction).
3. Data taken after 20 min.

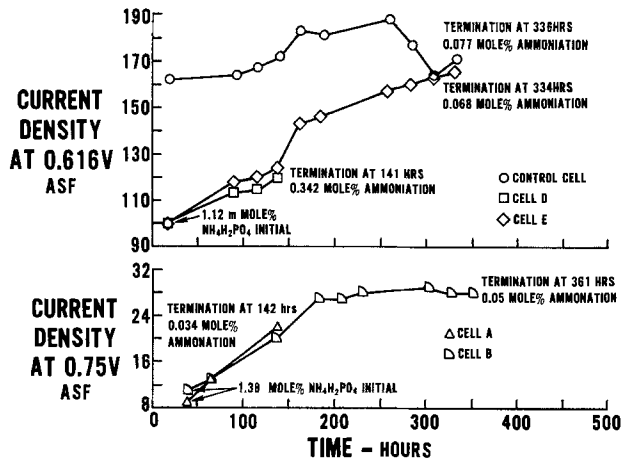


Fig. 5. Subscale cell current density at constant voltage vs. operating time.

m/o in 142 hr for cell A and 0.050 m/o in 361 hr for cell B. For cells E and B, the concentration after about 334 and 361 hr, respectively, was about the same as that of the control cell (0.077 m/o) after 336 hr. The amount of ammonium ion in the preammoniated cells had therefore been reduced to the low level of $(\text{NH}_4)_2\text{H}_2\text{PO}_4$ content of the control cell. Figure 5 shows also that the currents of the cells had also reached that of the control cell at the same potential. It is assumed that the performance had been improved by electrolyte purification provided by the cell cathodes. The data from these tests are summarized in Table II. This table shows that the percent ammonium ion oxidized is a function of operating time, initial concentration, and the potential of the cell.

Experimental data for the subscale cells in which NH_3 was injected into the fuel stream is shown in Fig. 6. Introduction of 2 ppm NH_3 into cell G at about 150 hr resulted in a decay in performance. After about 560 hr, the ammonia injection was stopped and a gradual restoration of performance resulted until it reached that of the control cell at about 1500 hr. At this time, 1 ppm NH_3 was added to the fuel gas and a smaller decay again began. Analysis of the NH_3 content in the fuel gas of the control cell indicated 0.08 ppm. For cell H, introduction of 6 ppm was started at about 150 hr and removed after performance decay to about 560 hr. Again, restoration in performance to that of the control cell resulted. These results clearly show the ability of cells in which NH_3 is introduced to self-restore performance.

Figure 7 shows the loss in performance at 215 mA/cm² of cells G and H due to the introduction of NH_3 as a function of the NH_3 content. Two lines are shown since the initial performances of the three cells were slightly different. Less than 10 mV performance loss at 215 mA/cm² results if 1 ppm NH_3 is present in the fuel gas.

The results obtained using the mathematical model are compared with the results of cells G, H, and their control in Fig. 8 and 9. In applying the mathematical model, the relationship between $(\text{NH}_4)_2\text{H}_2\text{PO}_4$ content

in the electrolyte and cell performance shown in Fig. 1 was used. In all three cases, agreement between the predicted and measured performance changes was found to be satisfactory.

The experimental data and mathematical analysis show that H_3PO_4 fuel cells can become contaminated due to NH_3 present in the reactants and be seriously

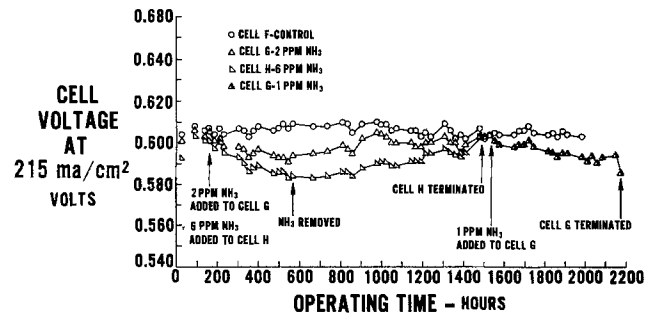


Fig. 6. Effect of ammonia on cell performance

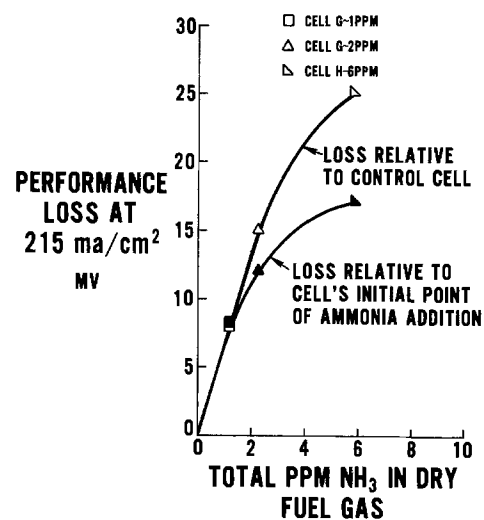


Fig. 7. Experimental cell performance loss as a function of ppm NH_3 in dry fuel gas.

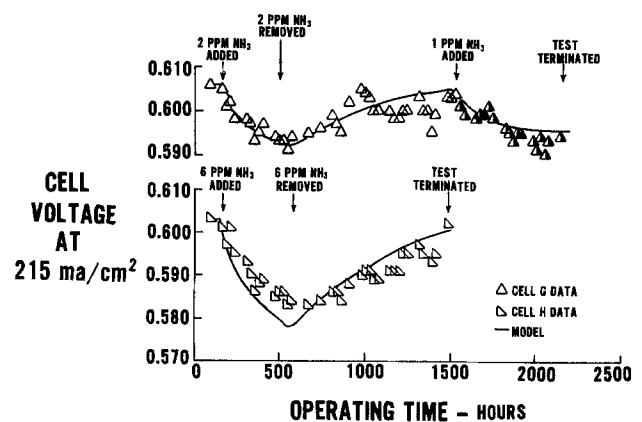


Fig. 8. Comparison of model with experimental data

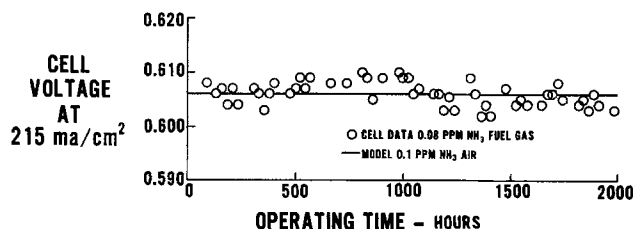


Fig. 9. Comparison of model with experimental data

Table II. Test results from preammoniated electrolyte cells

Cell	Voltage	Operating time (hr)	m/o Ammoniation		Final estimate of performance loss (mV)	% NH_3 oxidized
			Initial	Final		
A	0.750	142	1.380	0.034	0	98
B	0.750	361	1.380	0.051	0	95
Control	0.616	336	0.127	0.077	0	71
			(Background)			
D	0.616	141	1.120	0.342	5	71
E	0.616	334	1.120	0.068	0	94

affected in performance. However, they have the ability of self-purification because of the oxidative capability of the cathodes. Therefore, the performance loss depends on the relative rates at which NH_3 enters the cell and is removed by oxidation. This means that the performance loss would be strongly dependent on the operating load profile of the fuel cell.

Conclusions

This study indicates that NH_3 present in the fuel or oxidant gases supplied to an H_3PO_4 fuel cell will react with the electrolyte to form $(\text{NH}_4)\text{H}_2\text{PO}_4$ and could have a severe detrimental effect on the cell performance. The conversion of the electrolyte must be limited to less than about 0.2 m/o to avoid a significant performance loss. This performance loss is due primarily to a reduction of the rate of O_2 reduction on the cathode catalyst. The cell has the capacity to reject $(\text{NH}_4)\text{H}_2\text{PO}_4$ by oxidation at the cathode. Therefore, a cell can tolerate sustained low levels of NH_3 in the reactants with little performance loss. Also the per-

formance lost due to ammoniation can be restored if the NH_3 supply to the cell is stopped. The self-cleaning feature is dependent on the operating potential of the cathode. Therefore, the tolerance of H_3PO_4 cells to NH_3 in the reactants is dependent on the load profile that the cell is following. A mathematical model was developed to predict the loss in performance for any load profile.

Manuscript received Aug. 3, 1979. This was Paper 316 presented at the Pittsburgh, Pennsylvania, Meeting of the Society, Oct. 15-20, 1978.

Any discussion of this paper will appear in a Discussion Section to be published in the June 1981 JOURNAL. All discussions for the June 1981 Discussion Section should be submitted by Feb. 1, 1981.

Publication costs of this article were assisted by United Technologies Corporation.

REFERENCE

1. H. R. Kunz and G. A. Gruver, *This Journal*, **122**, 1279 (1975).

Voltammetric Studies at Glassy Carbon Electrodes in Sulfuryl Chloride Solutions

Wishvender K. Behl*

U.S. Army Electronics Technology and Devices Laboratory (ERADCOM),

Power Sources Division, Fort Monmouth, New Jersey 07703

ABSTRACT

The electrochemical reduction and oxidation of sulfuryl chloride in 1M $\text{LiAlCl}_4\text{-SO}_2\text{Cl}_2$ solutions were studied at glassy carbon electrodes using the technique of cyclic voltammetry. It was found that the reduction of chlorine, which is formed by the decomposition of sulfuryl chloride, precedes and obscures the reduction of sulfuryl chloride. Thus, in chlorine-rich solutions, sulfuryl chloride reduction peak in the cyclic voltammograms is completely masked by the chlorine reduction peak. However, in solutions saturated with sulfur dioxide, the chlorine reduction peak is relatively smaller than the sulfuryl chloride reduction peak. The reduction of both chlorine and sulfuryl chloride leads to the deposition of insoluble lithium chloride at the electrode surface and results in its passivation. The electrochemical oxidation of $\text{LiAlCl}_4\text{-SO}_2\text{Cl}_2$ solutions leads to the formation of chlorine, first by the oxidation of AlCl_4^- ions followed by the oxidation of sulfuryl chloride.

During the past few years, a number of studies have been reported on the ambient temperature lithium-inorganic electrolyte battery systems. However, only a few of these studies have been devoted to the lithium-sulfuryl chloride system. The scarce literature includes studies of the discharge characteristics (1-4) and discharge reaction stoichiometry (4) of lithium-sulfuryl chloride cells, conductivities (5), and voltammetric reduction of sulfuryl chloride (6) in $\text{LiAlCl}_4\text{-SO}_2\text{Cl}_2$ solutions. The electrochemical reduction and oxidation of sulfuryl chloride in 1M $\text{LiAlCl}_4\text{-SO}_2\text{Cl}_2$ solutions and in solutions containing excess of chlorine or sulfur dioxide were also investigated in this laboratory employing the technique of cyclic voltammetry. This paper summarizes our results.

Experimental

The preparation and purification of lithium tetrachloroaluminate have been described elsewhere (7). Sulfuryl chloride (Matheson, Coleman and Bell Company) was refluxed over lithium metal and distilled as colorless liquid. However, on storage, the color

slowly changed to light yellow. Solutions of lithium tetrachloroaluminate in sulfuryl chloride were light yellow in color.

A three electrode system was used for all measurements. The reference (1×5 cm) and counter (3.5×6 cm) electrodes were both made by pressing lithium ribbon (0.38 mm thick; Foote Mineral Company) onto a nickel screen. The reference electrode was contained in a Pyrex tube (10 mm diam) with a coarse porosity fritted glass bottom. Both the reference and the counterelectrodes were thoroughly washed with carbon tetrachloride before use. The working electrode consisted of a 3.18 mm diam glassy carbon rod (Beckwith Carbon Company) heat-sealed in a shrinkable Teflon tubing and the end ground flush with the seal so as to expose the cross section of the rod. The glassy carbon electrode was then polished to a mirror finish using a 0.3 μm size powdered alumina and had an area of 0.079 cm^2 .

All experiments were performed inside a Dry-train, Dry-lab (Vacuum Atmosphere Corporation) in a pure dried argon atmosphere. Other experimental details (8-10) were similar to those used for the voltammetric studies in phosphorous oxychloride and thionyl chloride solutions.

* Electrochemical Society Active Member.

Key words: electrolyte, battery, voltammetry.

In order to obtain reproducible voltammograms, the passivating lithium chloride film on the working electrode was dissolved, after each scan, in acidic $\text{AlCl}_3\text{-SO}_2\text{Cl}_2$ solution followed by washing with sulfuryl chloride and carbon tetrachloride. The electrode was then wiped clean and mechanically polished. The electrode could also be cleaned, *in situ*, by holding the electrode potential¹ at $\sim 4.5\text{V}$ for 1-2 min. However, this procedure was not employed since it led to the contamination of the solution by the oxidation products, namely, chlorine, aluminum chloride, etc. (see Discussion).

Results

Typical cyclic voltammograms obtained in $1\text{M LiAlCl}_4\text{-SO}_2\text{Cl}_2$ solution, through which pure dried argon was bubbled for 16 hr, at a scan rate of 0.1 V/sec , are presented in Fig. 1. Voltammogram A was obtained by scanning the electrode from 4.0 to 0.25V and voltammogram B by scanning the electrode from 4.0 to 5.0V . Cyclic voltammogram A shows a large increase in cathodic current beginning at $\sim 3.6\text{V}$ with a shoulder (peak I) at $\sim 3.05\text{V}$ and peak (peak II) at $\sim 2.85\text{V}$. A minor peak (peak III) is observed at $\sim 2\text{V}$ before a rapid increase in reduction current is observed at $\sim 0.75\text{V}$. On reversing the direction of polarization at 0.25V , only one small anodic peak (peak IV) is observed at $\sim 1.0\text{V}$. The anodic peak IV is not observed if the direction of polarization is reversed at potentials positive to 0.75V . Similar cyclic voltammograms were observed at scan rates of 0.01 to $\sim 0.2\text{ V/sec}$. At higher scan rates peaks I and II merged together and peak III was slightly more discernible. The peak currents increased with increasing scan rate and peak potentials shifted to less positive potentials.

Cyclic voltammogram B shows a small anodic peak (peak V) at $\sim 4.6\text{V}$ before a sharp increase in anodic current is observed at $\sim 4.75\text{V}$. Cyclic voltammograms did not show any reduction peak during the reverse scan. Similar cyclic voltammograms were obtained at scan rates of $0.01\text{-}2\text{ V/sec}$.

In $\text{LiAlCl}_4\text{-SO}_2\text{Cl}_2$ solutions containing excess of chlorine or sulfur dioxide, cyclic voltammograms for the anodic processes were similar to the voltammogram B presented in Fig. 1. However, voltammograms for the cathodic processes were distinctly different from voltammogram A.

Thus, in saturated solutions of chlorine in $1\text{M LiAlCl}_4\text{-SO}_2\text{Cl}_2$, cyclic voltammograms (Fig. 2) showed only one major reduction peak at scan rates of $0.01\text{-}2\text{ V/sec}$. The peak potential for this reduction peak was closer to the peak potential for peak I in the cyclic voltammograms shown in Fig. 1. While peak II was not

¹All potentials are reported with respect to lithium reference electrode.

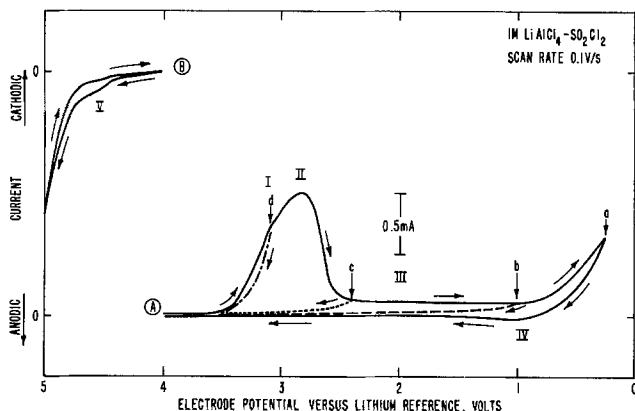


Fig. 1. Typical cyclic voltammograms at glassy carbon electrodes in argon purged $1\text{M LiAlCl}_4\text{-SO}_2\text{Cl}_2$ solutions at a scan rate of 0.1 V/sec . Roman numerals refer to the different peaks and letters a-d indicate the potential of scan reversal of different sweeps.

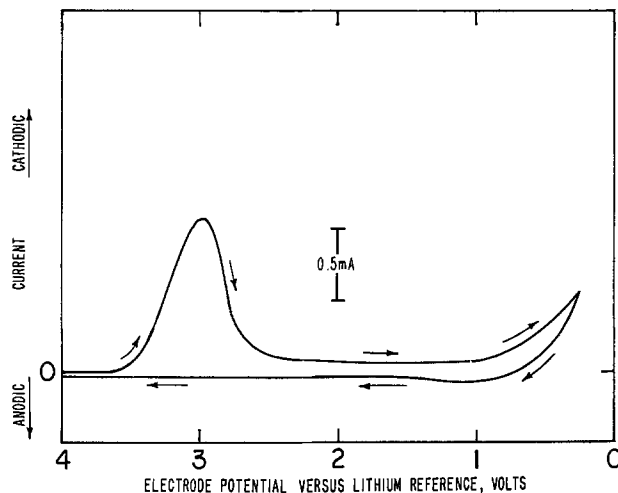


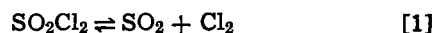
Fig. 2. Typical cyclic voltammograms at glassy carbon electrodes in saturated solutions of chlorine in $1\text{M LiAlCl}_4\text{-SO}_2\text{Cl}_2$ at a scan rate of 0.1 V/sec .

observed at all scan rates, the minor peak III became discernible only at scan rates greater than 1 V/sec .

Typical cyclic voltammograms obtained in $1\text{M LiAlCl}_4\text{-SO}_2\text{Cl}_2$ solutions, through which sulfur dioxide was bubbled for 16 hr, at a scan rate of 0.1 V/sec are shown in Fig. 3. In these solutions, peak I appears as a small step at $\sim 3.3\text{V}$ and peak II is the major peak at $\sim 2.75\text{V}$. Peak III appears as a wide peak beginning at $\sim 2\text{V}$. Again no anodic peak corresponding to reduction peaks I, II, and III is observed on the reverse scan. Similar cyclic voltammograms were observed at scan rates of $0.01\text{-}2\text{ V/sec}$. Again the peak heights for peaks I, II, and III increased with increasing scan rate and peak potentials shifted to less positive potentials. Addition of chlorine to sulfur dioxide saturated $\text{LiAlCl}_4\text{-SO}_2\text{Cl}_2$ solution caused an increase in peak height for peak I (Fig. 4) and a corresponding decrease in peak height for peak II.

Discussion

Sulfuryl chloride is known (11) to decompose to sulfur dioxide and chlorine according to the equation



Both sulfur dioxide and chlorine are soluble (11) in sulfuryl chloride and remain in solution. While solu-

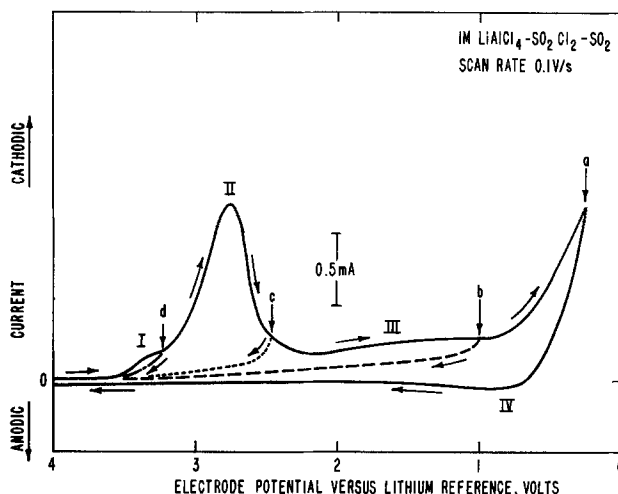


Fig. 3. Typical cyclic voltammograms at glassy carbon electrodes in saturated solutions of sulfur dioxide in $1\text{M LiAlCl}_4\text{-SO}_2\text{Cl}_2$ at a scan rate of 0.1 V/sec . Roman numerals refer to the different peaks and letters a-d indicate the potential of scan reversal of the different sweeps.

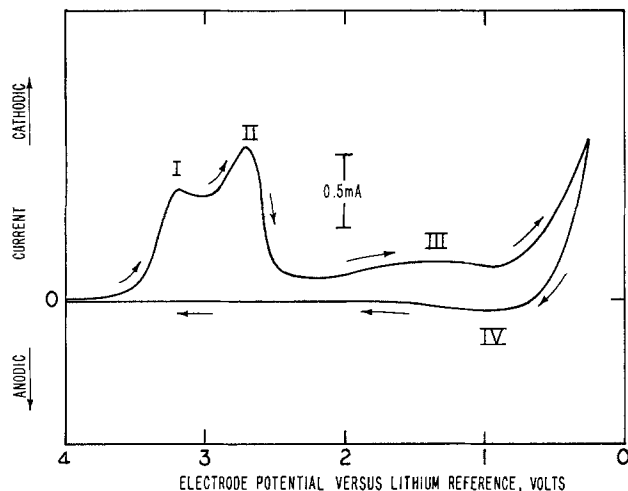
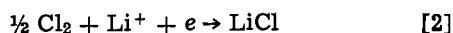


Fig. 4. Typical cyclic voltammograms at glassy carbon electrodes at a scan rate of 0.1 V/sec in 1M $\text{LiAlCl}_4\text{-SO}_2\text{Cl}_2\text{-SO}_2$ solutions to which a small amount of chlorine is added.

tions of sulfur dioxide in freshly distilled sulfuryl chloride are colorless, solutions of chlorine are light yellow in color. Solutions of lithium tetrachloroaluminate in freshly distilled sulfuryl chloride were always found to be light yellow in color. Both sulfuryl chloride and its solutions containing lithium tetrachloroaluminate became dark yellow in color on long storage. The yellow color in these solutions is attributed to chlorine which is formed by the decomposition of sulfuryl chloride according to Eq. [1]. It was not possible to completely remove the dissolved chlorine and the yellow color by purging the $\text{LiAlCl}_4\text{-SO}_2\text{Cl}_2$ solutions with argon, especially in the presence of lithium electrodes. It was, however, possible to shift the equilibrium in Eq. [1] to the left by bubbling sulfur dioxide and remove the dissolved chlorine. Thus, the $\text{LiAlCl}_4\text{-SO}_2\text{Cl}_2\text{-SO}_2$ solutions were almost colorless.

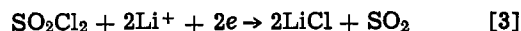
Electrochemical reduction of sulfuryl chloride.—Cyclic voltammograms (Fig. 1, voltammogram A) obtained in $\text{LiAlCl}_4\text{-SO}_2\text{Cl}_2$ solutions show three reduction peaks before a rapid increase in cathodic current is observed at $\sim 0.75\text{V}$ due to the deposition of lithium metal at the electrode surface. On the reverse scan only one anodic peak (peak IV) is observed at $\sim 1.0\text{V}$. Since peak IV is not observed if the direction of polarization is reversed prior to lithium deposition, it may be regarded due to the dissolution of the deposited lithium metal. Similarly, the rapid increase in the cathodic current at $\sim 0.75\text{V}$ and the anodic peak IV at $\sim 1.0\text{V}$ in $\text{LiAlCl}_4\text{-SO}_2\text{Cl}_2\text{-Cl}_2$ (Fig. 2) and $\text{LiAlCl}_4\text{-SO}_2\text{Cl}_2\text{-SO}_2$ (Fig. 3) solutions may also be regarded due to the deposition and dissolution of lithium metal, respectively.

In order to identify the other reduction peaks, let us first consider the cyclic voltammograms in $\text{LiAlCl}_4\text{-SO}_2\text{Cl}_2\text{-SO}_2$ solutions (Fig. 3). Peak height for peak I in these voltammograms is strongly dependent on the concentration of dissolved chlorine as demonstrated by the addition of chlorine to $\text{LiAlCl}_4\text{-SO}_2\text{Cl}_2\text{-SO}_2$ solutions (Fig. 4). Further, if these solutions are allowed to stand for a few hours or if argon is bubbled through the solutions to remove sulfur dioxide, the equilibrium in Eq. [1] is shifted to the right resulting in an increase in the chlorine concentration and a corresponding increase in peak height for peak I. Thus, peak I may be regarded as due to the reduction of chlorine



The main reduction peak (peak II) in $\text{LiAlCl}_4\text{-SO}_2\text{Cl}_2\text{-SO}_2$ solutions may be regarded as due to the reduction of sulfuryl chloride. From a study of the dis-

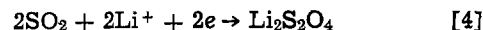
charge products in lithium-sulfuryl chloride cells, Gilman and Wade (4) have identified lithium chloride as the only solid reaction product. The reduction of sulfuryl chloride may, therefore, be represented as



The reduction of both chlorine (Eq. [2]) and sulfuryl chloride (Eq. [3]) leads to the deposition of insoluble lithium chloride at the electrode surface and causes its passivation. Since it would require a fixed amount of lithium chloride, at a fixed scan rate, to cover the electrode surface, the combined peak height for peaks I and II remains constant and independent of the chlorine concentration in the solution. Thus, the peak heights for peaks I and II are interdependent and an increase in chlorine reduction peak (peak I) due to increased chlorine concentration results in a corresponding decrease in sulfuryl chloride reduction peak (peak II).

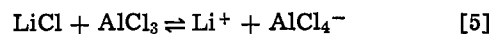
Similarly, peaks I and II in $\text{LiAlCl}_4\text{-SO}_2\text{Cl}_2$ solutions (Fig. 1) may be attributed to the reduction of chlorine and sulfuryl chloride, respectively. Since the chlorine reduction peak appears as the major reduction peak even in $\text{LiAlCl}_4\text{-SO}_2\text{Cl}_2$ solutions purged with argon for 16 hr, it seems likely that chlorine is supplied to the glassy carbon electrode not only by the migration of bulk chlorine but also by the decomposition of sulfuryl chloride at the electrode surface. Thus, at more catalytic surfaces such as platinum (12), the decomposition of sulfuryl chloride at the electrode surface is facilitated and the electrochemical reduction of sulfuryl chloride proceeds mainly through chlorine even in sulfur dioxide saturated $\text{LiAlCl}_4\text{-SO}_2\text{Cl}_2$ solutions.

The minor reduction peak III (Fig. 1 through 4) in the cyclic voltammograms may be assigned to the reduction of sulfur dioxide



While peak III is hardly discernible in $\text{LiAlCl}_4\text{-SO}_2\text{Cl}_2$ and $\text{LiAlCl}_4\text{-SO}_2\text{Cl}_2\text{-Cl}_2$ solutions, it is easily distinguishable in $\text{LiAlCl}_4\text{-SO}_2\text{Cl}_2\text{-SO}_2$ solutions. Since the electrode is already passivated due to the deposition of lithium chloride, the reduction of sulfur dioxide does not occur significantly in these solutions and results in only a very small peak in the cyclic voltammograms.

In order to further differentiate between peaks I, II, and III in the cyclic voltammograms, a small amount of aluminum chloride was added to the $\text{LiAlCl}_4\text{-SO}_2\text{Cl}_2$ solutions previously purged with argon. Since the excess of aluminum chloride increases the corrosion of lithium counterelectrode by dissolving the protective lithium chloride film and eventually results in its complete disintegration, the cyclic voltammograms were recorded immediately after the addition of aluminum chloride and are shown in Fig. 5. The excess of aluminum chloride in $\text{LiAlCl}_4\text{-SO}_2\text{Cl}_2$ solutions also partially dissolves the lithium chloride film on the glassy carbon electrode surface due to complex formation



Thus, the electrode surface continues to be partially regenerated during the life of the voltage scan and results in distinct reduction peaks for the reduction of chlorine (peak I), sulfuryl chloride (peak II), and sulfur dioxide (peak III). The peak heights are also slightly higher than those obtained in neutral $\text{LiAlCl}_4\text{-SO}_2\text{Cl}_2$ solutions. Further, due to the partial regeneration of the electrode surface, a small cathodic current is observed during the reverse scan of the cyclic voltammograms (Fig. 5) in contrast to almost no current in neutral $\text{LiAlCl}_4\text{-SO}_2\text{Cl}_2$ solutions (Fig. 1).

In $\text{LiAlCl}_4\text{-SO}_2\text{Cl}_2\text{-Cl}_2$ solutions (Fig. 2), the reduction of chlorine completely obscures the reduction of sulfuryl chloride so that only one major reduction

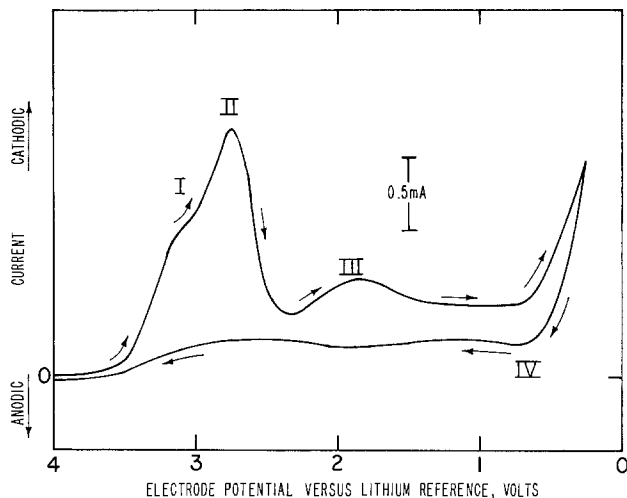


Fig. 5. Typical cyclic voltammograms at glassy carbon electrodes at a scan rate of 0.1 V/sec in 1M LiAlCl₄-SO₂Cl₂ solutions containing slight excess of aluminum chloride.

peak is observed in the cyclic voltammograms. Thus, in these solutions, the electrode surface is completely covered by lithium chloride produced as a result of chlorine reduction (Eq. [2]) and is not available for the reduction of suluryl chloride and sulfur dioxide. Cyclic voltammograms similar to those presented in Fig. 2 are also obtained in aged LiAlCl₄-SO₂Cl₂ solutions. The chlorine concentration in the aged solutions is rather large due to the decomposition of suluryl chloride and thus the chlorine reduction peak completely masks the suluryl chloride reduction peak. If the excess of chlorine in aged LiAlCl₄-SO₂Cl₂ or LiAlCl₄-SO₂Cl₂-Cl₂ solutions is removed by bubbling argon, cyclic voltammograms similar to those presented in Fig. 1 (voltammogram A) are obtained.

The total charge passed under peaks I and II of the cyclic voltammograms in LiAlCl₄-SO₂Cl₂, LiAlCl₄-SO₂Cl₂-Cl₂, and LiAlCl₄-SO₂Cl₂-SO₂ solutions was measured as a function of scan rate by integrating the area under the peaks. From the total charge passed, the thickness of the lithium chloride film on the glassy carbon electrode was then calculated taking the density of lithium chloride to be 2.068 g/cm³ at 25°C. These results are plotted in Fig. 6. The total charge passed and hence the thickness of the lithium chloride film in all three solutions was found to decrease with increasing scan rate. However, at all scan

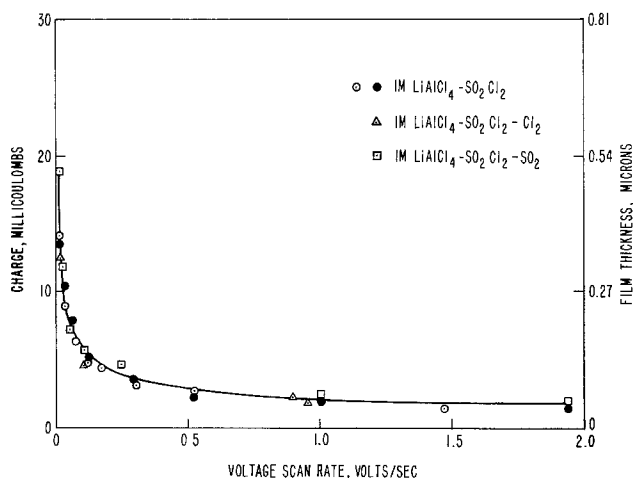
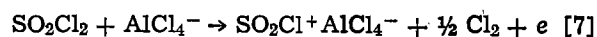
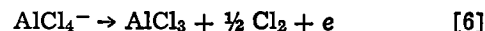


Fig. 6. Total charge passed under peaks I and II of the cyclic voltammograms and the thickness of lithium chloride film as a function of scan rate.

rates, the film thickness in LiAlCl₄-SO₂Cl₂-SO₂ solutions was found to be slightly higher than that obtained in LiAlCl₄-SO₂Cl₂ or LiAlCl₄-SO₂Cl₂-Cl₂ solutions.

Electrochemical oxidation of suluryl chloride.—Cyclic voltammograms (voltammogram B, Fig. 1) for the oxidation of LiAlCl₄-SO₂Cl₂ solutions at glassy carbon electrodes were similar to those obtained in LiAlCl₄-SOCl₂ solutions (9, 13). Thus, analogous to LiAlCl₄-SOCl₂ solutions, anodic peak V at ~4.6V and the sharp increase in anodic current at ~4.75V in these voltammograms (Fig. 1) may be regarded as due to the oxidation of AlCl₄⁻ ions and SO₂Cl₂, respectively



Thus, if the potential of the glassy carbon electrode is held at ~5V for few minutes before scanning it in the cathodic direction, the formation of chlorine at more positive potentials (Eq. [6] and [7]) causes an increase in peak height for the chlorine reduction peak (peak I) in the cyclic voltammograms. At the same time, aluminum chloride formed in Eq. [6] partially dissolves the lithium chloride film on the electrode surface and causes an overall increase in combined peak heights for peaks I and II.

Manuscript submitted Oct. 15, 1979; revised manuscript received Feb. 14, 1980. This was Paper 31 presented at the Los Angeles, California, Meeting of the Society, Oct. 14-19, 1979.

Any discussion of this paper will appear in a Discussion Section to be published in the June 1981 JOURNAL. All discussions for the June 1981 Discussion Section should be submitted by Feb. 1, 1981.

Publication costs of this article were assisted by the U.S. Army Electronics Technology and Devices Laboratory (ERADCOM).

REFERENCES

- J. J. Auburn, R. D. Bezman, K. W. French, A. Heller, and S. I. Lieberman, in "Proc. 26th Power Sources Symposium," p. 45, Atlantic City, N.J., April 29-30, May 1-2, 1974.
- J. J. Auburn and N. Marincic, in "Power Sources 5," D. H. Collins, Editor, p. 683, Academic Press, London (1975).
- S. Gilman, in "Proc. 26th Power Sources Symposium," p. 28, Atlantic City, N.J., April 29-30, May 1-2, 1974.
- S. Gilman and W. Wade Jr., *This Journal*, **127**, 1427 (1980).
- L. Nanis, V. K. Kapur, and M. A. Gencer, Final Report, ECOM-75-1676-F, Contract No. DAAB07-75-C-1676 (ECOM), University of Pennsylvania, Philadelphia, Pa., April 1977.
- C. E. Blomgren, V. Z. Leger, M. L. Kronenberg, T. Kalnoki-Kis, and R. J. Brodd, Preprint, Paper presented at the 11th International Power Sources Symposium, Brighton, England (1978).
- W. K. Behl, J. A. Christopoulos, M. Ramirez, and S. Gilman, *This Journal*, **120**, 1619 (1973).
- W. K. Behl, *J. Electroanal. Chem. Interfacial Electrochem.*, **70**, 213 (1976).
- W. K. Behl, in "Proc. 27th Power Sources Symposium," p. 30, June 24-26, 1976, Atlantic City, N.J.
- W. K. Behl, *J. Electroanal. Chem. Interfacial Electrochem.*, **101**, 367 (1979).
- J. W. Mellor, "A Comprehensive Treatise of Inorganic and Theoretical Chemistry," Vol. 10, Longmans, Green and Co., London (1930).
- W. K. Behl, Unpublished results.
- K. M. Abraham, R. M. Mank, and G. L. Holleck, Second Quarterly Report, DELET-TR-78-0564-2, Contract No. DAAB07-78-C-0564 (ERADCOM), EIC Corporation, Newton, Mass., July 1979.

Properties of Alternate Electrolytes for Secondary Zinc Batteries

Roy F. Thornton*

General Electric Corporate Research and Development, Schenectady, New York 12301

and Eric J. Carlson*

General Electric Company, Lamp Business Division, Cleveland, Ohio 44112

ABSTRACT

Several mixed aqueous electrolytes have been characterized for zinc oxide solubility, ionic conductivity, density, and nickel hydroxide utilization. These electrolytes were made by reducing the usual potassium hydroxide concentration and by adding the salts such as potassium fluoride or potassium phosphate to partially compensate for the lower ionic conductivity. These mixed electrolytes may be useful in prolonging the cycle life of the zinc electrode in secondary batteries.

Secondary batteries with zinc anodes and alkaline electrolytes offer the promise of high energy density and high rate capability. Zinc-nickel oxide batteries under development for electric vehicles have higher energy density than lead-lead dioxide and nickel-cadmium batteries. If the cycle life of zinc-nickel oxide batteries can be substantially improved, they could be cost effective in electric vehicles. However, present state-of-the-art zinc-nickel oxide batteries do not meet the cost-life-energy density goals.

The zinc electrode is responsible for the limited cycle life of zinc-nickel oxide batteries. During cycling, zinc tends to concentrate in the center of the electrodes (shape change), thicken and lose porosity (densification), and grow tree-like structures (dendrites) on charge which cause internal shorting. General discussion of the secondary zinc electrode can be found in Ref. (1) and (2). References (3), (4), and (5) specifically address zinc electrode shape change. Zinc electrode thermodynamics and electrolyte properties are found in Ref. (6), (7), and (8).

Shape change, densification, and dendrite growth on secondary zinc electrodes are all results of the high solubility of zinc hydroxide in strong KOH and NaOH electrolytes. Uneven current distribution, electroosmotic pumping in separator membranes, diffusion, and natural convection can combine to cause migration of dissolved zinc hydroxide. Supersaturation of dissolved zinc hydroxide during discharge also aggravates these problems with zinc electrodes. One approach to improving the life of rechargeable zinc electrodes would be to utilize an electrolyte in which zinc hydroxide would be substantially less soluble. Such an electrolyte must satisfy several requirements. Ionic conductivity must be high enough to give a reasonable cell resistance. Both the zinc and nickel hydroxide active materials must have good utilization at practical discharge rates. The self-discharge rates of both electrodes must be low. Preferably the cost of the electrolyte should be not much more than that of the normally used KOH and should not contain any toxic material.

Considerable research has been done on the solubility of zinc oxide and hydroxide in aqueous potassium hydroxide and sodium hydroxide solutions and on the nature of the dissolved species. Good summaries of this work are found in (1), (2), and (6). The species present in alkaline solutions is the zincate ion, $\text{Zn}(\text{OH})_4^{2-}$ (7).

The concentration of zincate in alkaline solutions depends on the solid species in contact with the solu-

tion, the method used to introduce the dissolved zinc, and the history of the solution. Data from P. R. Malory Company reported in (8) include for 31% KOH

Solid Species	Solubility mg(Zn)/ml
ZnO	54
$\text{ZnO} \cdot \frac{1}{2} \text{H}_2\text{O}$	92
$\text{Zn}(\text{OH})_2$	114

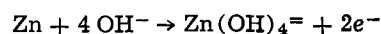
Solutions prepared by electrochemically discharging zinc into solution can be substantially supersaturated, and the decay of these solutions to saturation can be very slow (9). Solutions saturated with $\text{Zn}(\text{OH})_2$ also age, and eventually the dissolved zinc content reaches that of ZnO saturation. The $\text{Zn}(\text{OH})_2$ decomposes to ZnO releasing water (8, 9). Aging of solutions can be accelerated by introducing finely divided ZnO and agitating the solution (9).

Experimental

Solutions were made using reagent grade chemicals and distilled water. Components were weighed to within 1/2%. Care was taken to minimize the amount of carbonate buildup from absorption of CO_2 from the air. The actual amounts of carbonate in the solutions were not measured.

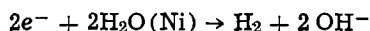
Specific conductivities of solutions were measured using a Beckman Model RC16B2 conductivity meter at 1000 Hz and a conductivity cell with platinized electrodes. The cell constant was $0.90 \pm 0.01 \text{ cm}^{-1}$. Densities were measured by weighing the amount in a 25 or 50 ml volumetric flask. Accuracy is probably $\pm 0.1\%$. A Fisher pH meter was used to measure the pH of some of the solutions, but these values are approximate because of the high alkalinity.

Dissolved zincate was produced in two ways: (i) by dissolution of ZnO powder, New Jersey Zinc USP12; and (ii) by electrochemical discharge of zinc metal into solution. The former solutions were agitated constantly with magnetic stirring bars while heat from the stirring plates warmed the solutions. After stirring was discontinued, the solutions sat at room temperature for at least one day. The latter method was accomplished by mixing 1g of nickel powder (made by the carbonyl process) and an amount of zinc metal powder, New Jersey Zinc 1223, sufficient to more than saturate the solution with zincate. The powder mix was added to 50 ml of solution and allowed to stand with occasional mixing until a white precipitate appeared. Zinc was discharged according to



* Electrochemical Society Active Member.
Key words: conductance, solubility, electrolyte.

while water decomposed on the nickel surface and hydrogen was evolved



The appearance of the precipitate indicated that saturation had been reached or exceeded and that solution aging had begun. To accelerate aging of these solutions, ZnO (NJZ USP12) was added and the solutions agitated continuously. Aliquots of clear supernatant were taken at various times for zinc analysis.

Separation of solutions from solids was accomplished by settling, centrifuging, or filtering through 0.6 micron pore polyvinyl chloride filter media. The last method is the most rapid and least troublesome.

Determination of the dissolved zinc content was done by an EDTA-Cu back titration method (10). Zinc solutions, diluted and buffered with NH_4Cl-NH_4OH buffer, were complexed with an excess of EDTA and then back titrated with copper sulfate using PAN indicator. The method was reproducible to within $\pm 1/2\%$ and accurate to the larger of $\pm 3\%$ or ± 0.03 mg/ml. The concentrations of KOH, KF, etc., reported are the starting values, uncorrected for zinc oxide dissolution or zinc discharge.

The effects of the electrolytes on the capacities of nickel hydroxide electrodes were tested in small flooded cells. A test electrode 15 cm^2 in area was placed in a 30 ml cell with a counterelectrode on each side. Test electrodes were cut from standard sintered nickel hydroxide electrodes, and the capacity was about 0.5 A-hr at 0.6A discharge. The test cells were automatically cycled using a 150 mA (5 mA/cm^2 on each side) charge for 4.2 hr followed by a discharge at 600 mA (20 mA/cm^2 on each side) to a cutoff of 0.22V vs. an Hg/HgO reference. After a test electrode had been cycled in 31% KOH several times, the cell was cleaned and refilled with a test electrolyte, and cycling was continued.

The open-circuit potentials of Zn/ZnO electrodes and of Zn/NiOOH cells were measured in the various electrolytes. A pasted zinc oxide electrode was charged in a test electrolyte and then partially discharged. A nickel electrode was fully charged in the same electrolyte. The electrodes were then transferred to another cell containing fresh electrolyte saturated by dissolution of zinc oxide. Mercury/mercuric oxide reference electrodes were prepared and vacuum filled, some with the test electrolytes and some with 31% KOH. Two reference electrodes were used for a test, one filled with the test electrolyte in the cell with the nickel and zinc electrodes, and one filled with 31% KOH in a side

compartment isolated from the cell with a salt bridge. Nitrogen was bubbled through the cell to deaerate the electrolyte. Open-circuit voltage measurements were made after a 16-20 hr stand in an incubator set to 26.5°C .

Results

Electrolyte compositions, densities, conductivities, and nickel hydroxide electrode utilization are shown in Table I. The data are for zincate-free solutions. Electrolyte specific conductivities fall in the range of $0.1\text{-}0.64\ (\Omega\text{-cm})^{-1}$ with 31% KOH the highest. Adding KF or K_3PO_4 to 5% KOH significantly increases the ionic conductivity.

The nickel hydroxide utilizations are reported as a percentage of the discharge capacity of the same electrode in 31% KOH. Physical degradation of the nickel electrode did not seem to be a problem except with electrolyte O. The electrode in this test blistered and shed active material. The cause for the increase in utilization in electrolytes C, I, and K is unknown.

The effect of most of the electrolytes on the charge and discharge voltages of the nickel electrodes was small, less than 20 mV. In the 26.8% KF + 4.8% KOH, F, and in the 30% KF + 21% KOH, G, electrolytes, the spread between the mid-charge and mid-discharge voltages increased by about 30 mV relative to the spread in 31% KOH, A, electrolyte. In the 32.7% K_3PO_4 + 4.3% KOH, L, electrolyte, the mid-charge voltage increased 50-70 mV. In the 30% K_3PO_4 , M, in the 20% K_3PO_4 , N, in the 16.1% K_2HPO_4 + 19.6% K_3PO_4 , O, and in the 30% KF adjusted to pH 13.5, H, electrolytes, the depression of the discharge voltages and the elevation of the charge voltages were unacceptably large.

Zinc solubility data are shown in Table II. Many of these values are not equilibrium values because of the slow dissolution rate of ZnO or the slow aging of solutions saturated with respect to $Zn(OH)_2$. The actual ZnO solubility is bracketed by the highest value obtained by ZnO dissolution and the lowest value obtained by zinc discharge and solution aging. Because the purpose of the study was screening and comparison of electrolytes for secondary zinc cells, tests were not continued until equilibrium had been definitively attained. The test results for electrolyte A, 31% KOH, fall within the range of the data (8) shown in the first section. The 104 mg/ml found in the freshest solution saturated by discharge is close to the reported value for equilibrium with $Zn(OH)_2$, and the aged solution, 88 mg/ml compares with the reported value of 92 mg/ml for equilibrium with $ZnO \cdot 1/2 H_2O$. The 46

Table I. Electrolyte properties

Electrolyte No.	Composition (weight percent)	Density (g/ml)	Conductivity ($\Omega\text{-cm})^{-1}$	Ni electrode utilization (%)
A	31% KOH	1.301 at 15°C	0.64 at 26.4°C 0.38 at 2°C	100
B	5% KOH	1.044 at 25°C	0.20 at 25°C	100
C	20.1% KOH + 10% KF	1.286 at $26 \pm 1^\circ\text{C}$	0.53 at 27°C	110
D	22% KF + 10% KOH	1.307 at 23.2°C	0.46 at 24.0°C	99
E	24.3% KF + 7.5% KOH	1.303 at 23.6°C	0.36 at $24^\circ\text{-}26^\circ\text{C}$ 0.22 at 2°C	nd
F	26.8% KF + 4.8% KOH	1.301 at $24 \pm 1^\circ\text{C}$	0.35 at $24^\circ\text{-}26^\circ\text{C}$ 0.21 at 2°C	95
G	30% KF + 2% KOH	1.300 at 23.3°C	0.37 at 24.0°C	75
H	30% KF (+KOH to pH 13.5)	1.286 at $24 \pm 0.5^\circ\text{C}$	0.36 at $24^\circ\text{-}25^\circ\text{C}$	28
I	23.9% K_2BO_3	1.270 at $26 \pm 1^\circ\text{C}$	0.41 at 26.3°C	110
J	32% K_2HBO_3	1.343 at $24 \pm 0.5^\circ\text{C}$	0.36 at $24^\circ\text{-}25^\circ\text{C}$	96
K	21.1% KOH + 11.8% K_3PO_4	1.268 at $26 \pm 1^\circ\text{C}$	0.49 at 27°C	104
L	32.7% K_3PO_4 + 4.3% KOH	1.416 at $24 \pm 0.5^\circ\text{C}$	0.28 at $24^\circ\text{-}25^\circ\text{C}$ 0.13 at 2°C	81
M	30% K_3PO_4	1.331 at 23.2°C	0.24 at 24.0°C	60
N	20% K_3PO_4	1.268 at 23.2°C	0.21 at 24.1°C	59
O	16.1% K_2HPO_4 + 19.6% K_3PO_4	1.382 at 23.3°C	0.22 at 24.2°C	49
P	12% KF + 16% K_2PO_4 + 7.5% KOH	1.293 at 23.6°C	0.33 at 23.6°C 0.21 at 2°C	nd
Q	10% Na_2SiO_3 + 1% NaOH	1.114 at $24^\circ\text{-}26^\circ\text{C}$	0.14 at 25.2°C	nd
R	30% Na_2SiO_3 + 1% NaOH*	1.36 at $24^\circ\text{-}26^\circ\text{C}$	0.10 at 25.2°C	nd
S	10% Na_2SiO_3 + 5% NaOH	1.161 at 22.2°C	0.22 at 25.3°C	nd
T	25.5% Na_2SiO_3 + 5.3% NaOH*	nd	nd	nd

* Small crystalline residue after dissolution.

Table II. Summary of solubility results

Electrolyte	Solution saturated by discharge			Solution saturated by ZnO dissolution	
	MgZn/ml	Days since ppt	Days stirred with ZnO	MgZn/ml	Days stirred
A	104	18	0	46.0	10
	88	55	0		
B	2.00	8	0	1.17	10
	1.61	19	11		
C	43.2	4	0	20.9	10
	40	17	0		
	35.3	15	11		
D	11.1	1	0	5.52	8
	11.1	6	5*	5.59	25
	8.7	32	4**		
E	4.8	32	0	3.3	19
	4.7	32	12		
F	2.6	30	0	1.4	>4
	2.41	185	0		
G	1.15	0	0	0.25	8
	0.53	5	5*	0.33	25
	0.33	31	4**		
I	30.5	3	0	13.9	10
	27	14	0		
	23.5	14	11		
J	22.5	15	0	11.4	5
	16.8	170	0		
K	48	8	0	22.9	10
	48	17	0		
	40.5	19	11		
L	10.4	7	0	2.7	5
	7.1	10	0		
	3.6	41	29		
M	1.35	7	0	0.51	8
	2.17	8-9	1-2*	0.51	25
	1.38	38	7-8**		
N	0.50	7	0	0.17	8
	0.52	12	5*	0.19	25
	0.42	38	4**		
O	0.11	7	0	0.09	8
	0.31	12	5*	0.11	25
	0.26	38	4**		
P	10.1	32	0	4.8	19
	10.0	32	12		
Q	—	—	—	3.9	20
R	—	—	—	39 ± 2	20
S	—	—	—	15 ± 1	20
T	—	—	—	—	—

* Solution stirred, no ZnO added, solution contained Ni powder and precipitate.

** ZnO added after * and stirring continued.

mg/ml produced by ZnO dissolution compares with the reported value of 54 mg/ml equilibrium with ZnO.

Precipitates from some of the solutions saturated by discharge and partially aged were gently dried and analyzed for major phases by x-ray diffraction. Table III lists the results.

Open-circuit potentials of zinc electrodes and Zn/NiOOH cell voltages in the various electrolytes are presented in Table IV. Stable voltage readings were obtained from all the zinc electrodes but one. In electrolyte O, the zinc electrode corroded and disintegrated overnight. The potential readings in this electrolyte were taken within a few minutes of immersion of the electrodes. Zn/NiOOH cell voltages all fall in the range 1.72-1.80. Most of the variation is in the nickel positive electrode whose potential is a function of state of charge.

The pH's of the test electrolytes were calculated using the potential differences between Hg/HgO reference electrodes in 31% KOH and in the test electrolytes. From Pourbaix (11) $E_0 = 0.926 - 0.0591 \text{ pH}$ for the Hg/HgO electrode in alkaline electrolyte. The pH of the 31% KOH at 25°C was calculated to be 15.26 using the mean molal activity coefficient, 1.93, the dis-

Table III. X-ray diffraction results

Electrolyte	Species found in dried precipitate
C	ZnO
G	ZnO
I	ZnO
K	ZnO
M	ZnO and KZnPO ₄
O	KZnPO ₄

sociation constant for water, 1.008×10^{-14} , and the activity of water in 31% KOH, 0.575. In the calculations of pH of test electrolytes, junction potentials were ignored, and the assumption was made that the presence of anions in addition to hydroxyl ions did not interfere with the Hg/HgO reaction mechanism. The potential differences and calculated pH values are shown in Table IV. The zinc electrode potentials measured at 26.5°C would be within 1 mV of those at 25°C because $(\partial E/\partial T)_p$ for the Zn/HgO cell is +0.033 mV/°C. The overall uncertainty in the calculated pH values is about ± 0.2 . For the electrolytes in which pH could be measured, the agreement with calculated values is within the uncertainty.

The measured zinc electrode potentials were adjusted by 0.025V (the potential of Hg/HgO at pH 15.26 vs. the NHE) to their values vs. the NHE. The adjusted values are listed in Table IV and are plotted against the calculated pH in the Pourbaix diagram (11) in Fig. 1. The points fall within or close to the band of potentials calculated by Pourbaix for various forms of ZnO and Zn(OH)₂. Because solid discharge product was present in all of the test electrodes, only the potential-pH curves for zinc-solid zinc oxide reactions were plotted.

Discussion

The goal of this study was to screen a number of electrolyte mixtures and select a few that appeared promising for use in nickel-zinc batteries.

The ideal additive to an electrolyte would be one which combines with the dissolved zincate ion to form insoluble species in analogy to the silver chloride precipitation. Ceneck *et al.* (12) used this approach by adding up to 10 weight percent potassium fluoride to the electrolyte or by using zinc oxalate or zinc fluoride in the anode. Their assertion that zinc fluoride is insoluble in the electrolyte is not consistent with the analysis in this study showing that ZnO is the solid species in equilibrium with 30% KF + 2% KOH. The reduction in solubility of ZnO in these electrolytes is apparently a function of the available hydroxyl ions. Note that the ZnO solubility in 5% KOH is close to that in 26.8 KF + 4.8% KOH and in 32.7% K₃PO₄ + 4.3% KOH. In phosphate-containing solutions with

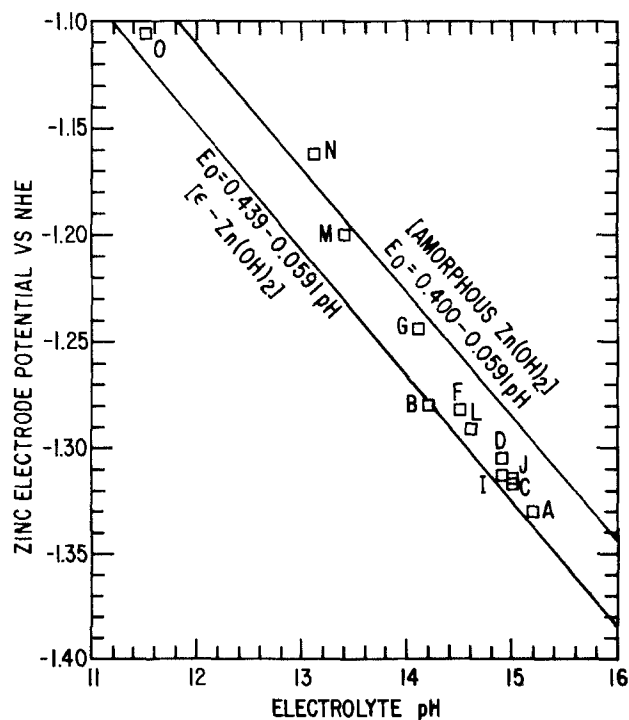


Fig. 1. Variation of zinc electrode potential with the calculated pH of the electrolyte.

Table IV. Zinc electrode potentials and electrolyte pH

Electrolyte	$V_1(\text{Zn/ZnO})$ vs. (Hg/HgO in 31% KOH)	$V_2(\text{Zn/ZnO})$ vs. NHE	$V_3(\text{Ni/Zn})$	$V_4(\text{Hg/HgO})$ vs. (Hg/HgO in 31% KOH)	pH calc. from V_4	pH meter
A	-1.355	-1.330	1.742	0.002	15.2	
B	-1.305	-1.280	1.796	0.061	14.2	
C	-1.342	-1.317	1.765	0.015	15.0	
D	-1.330	-1.305	1.762	0.022	14.9	
F	-1.307	-1.282	1.758	0.042	14.5	
G	-1.269	-1.244	1.756	0.070	14.1	
I	-1.338	-1.313	1.776	0.023	14.9	
J	-1.339	-1.314	1.777	0.018	15.0	
L	-1.316	-1.291	1.722	0.038	14.6	
M	-1.225	-1.200	1.770	0.107	13.4	13.3 ↓
N	-1.187	-1.162	1.743	0.125	13.1	13.0
O	-1.131*	-1.106	—	0.225	11.5	11.8 ↓

* Immediate reading, see text.

↓ Drifting reading.

low enough KOH concentrations, KZnPO_4 appears, but in these electrolytes, nickel hydroxide electrolyte utilization is undesirably reduced.

Borate-based electrolytes were studied by Schneider and Domiczak (13) for a bipolar Ni/Zn battery. The conductivity and zinc solubility results of this work are roughly consistent with theirs. The analysis of the precipitate from the K_3BO_3 solution again showed that ZnO is the stable species and that compounds like KZnBO_3 are not preferentially precipitated. There is an apparent anomaly in the test results for the two borate-based electrolytes, I and J. Although the compositions are substantially different, the zinc electrode potentials and calculated pH values are essentially equal, and zincate solubilities are close. This may be a manifestation of a buffering action in the borate-based electrolytes.

No anions were found which form insoluble zinc compounds at pH values compatible with nickel hydroxide electrodes. Therefore the most promising electrolytes are those in which the KOH concentration is minimized, and a highly soluble salt added to raise the conductivity. The three salts found most suitable are potassium borate, phosphate, and fluoride. Other salts such as potassium aluminate, sulfate, and chloride do not have sufficient solubility to be interesting. The mixed sodium hydroxide-silicate solutions combined low conductivity with low zincate solubility and therefore did not appear as desirable. Silicate is also reported to stabilize supersaturated zincate solutions (14.)

Because of the slow approach to equilibrium in these systems, experiments could not be continued until equilibrium was established with certainty. However, the equilibrium value for the solubility of zinc oxide is bounded below by the maximum value found by ZnO dissolution and is bounded above by the minimum value found after saturation by zinc discharge into solution. These data can serve as guidelines for selection of electrolytes for secondary cells.

There is good agreement, illustrated in Fig. 1, between the potential-pH values for zinc electrodes in the test electrolytes and the theoretical relationship for zinc electrodes in alkaline media. This agreement indicates that the presence of fluoride, borate, or phosphate anions do not alter the reaction mechanism. The x-ray diffraction data which found ZnO in most discharge products confirm this for all points except N and O.

Plots of the log of ZnO solubility (mg Zn/ml) against calculated pH are shown in Fig. 2. The values plotted were the highest obtained by direct dissolution of ZnO. For comparison, the dotted line shows the solubility-pH relationship presented by Pourbaix for $\epsilon\text{-Zn}(\text{OH})_2$. The experimental data tend to parallel this line except for the electrolytes M, N, and O which contain phosphate with little or no KOH. The data suggest that above a pH of 14, hydroxyl ion activity controls the

zinc solubility. The phosphate electrolytes below a pH of 13.5 show evidence of zinc complexing.

When the nickel hydroxide electrode utilization is plotted against the calculated pH some trends appear. Fluoride and phosphate both reduce the electrode utilization below a pH of 14.5, but at lower pH phosphate has an apparent buffering action.

Figures 2 and 3 provide a means for preliminary selection of which electrolytes might be tested in zinc-nickel oxide cells. Electrolytes with a pH greater than

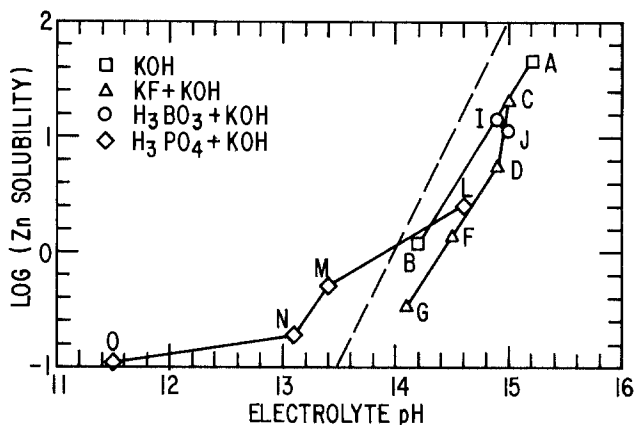


Fig. 2. Solubility of ZnO in various electrolytes

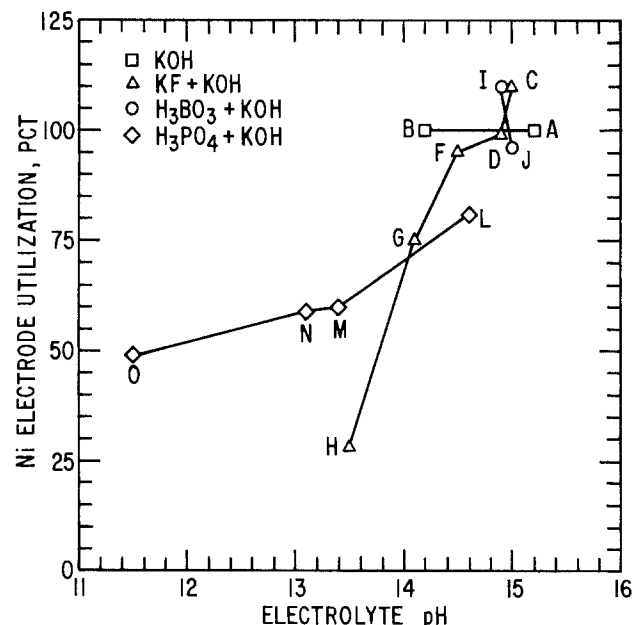


Fig. 3. Utilization of the nickel oxide electrode in various electrolytes.

14 are required for acceptable functioning of the nickel electrode. If one chooses only those electrolytes with more than a factor of 3 reduction in zinc oxide solubility, the electrolytes would be in the composition ranges represented by

- D 10% KOH + 22% KF
 E 7.5% KOH + 24.3% KF
 G 2% KOH + 30% KF
 I 24% K_3BO_3
 J 32% K_2HBO_3
 L 4.3% KOH + 32.7% K_3PO_4
 P 7.5% KOH + 16% K_3PO_4 + 12% KF

One might also consider somewhat more acidic borate-based electrolytes than I and J.

Cycling tests of zinc-nickel oxide cells using some of these electrolytes will be described in a later report.

Conclusions

Several mixed electrolytes have been selected as promising for use in secondary cells with zinc electrodes. Alkaline electrolytes containing major amounts of potassium fluoride, phosphate, or borate show low solubility for zinc oxide and conductivity reduced in most cases by less than a factor of two. These electrolytes should suppress shape change, slumping, and dendrite growth during cycling of cells with zinc electrodes. Cells using these electrolytes may show higher cell resistance and lower electrode utilization. This compromise between energy or power density and cycle life could be adjustable by varying the ratio of KOH to other salts in the electrolyte.

Manuscript submitted Oct. 29, 1979; revised manuscript received Jan. 28, 1980.

Any discussion of this paper will appear in a Discussion Section to be published in the June 1981 JOURNAL. All discussions for the June 1981 Discussion Section should be submitted by Feb. 1, 1981.

Publication costs of this article were assisted by the General Electric Company.

REFERENCES

1. A. Fleischer and J. J. Lander, "Zinc-Silver Oxide Batteries," John Wiley & Sons, New York (1971).
2. R. V. Bobker, "Zinc in Alkali Batteries," reprinted and issued by the Society for Electrochemistry, University of Southampton, England (1973).
3. J. McBreen, *This Journal*, **119**, 1620 (1972).
4. K. W. Choi, D. N. Bennion, and J. Newman, *ibid.*, **123**, 166 (1976).
5. K. W. Choi, D. Hamby, and D. N. Bennion, *ibid.*, **123**, 1628 (1976).
6. G. W. Heise and N. C. Cahoon, Editors, "The Primary Battery," Vol. I, John Wiley & Sons, New York (1971).
7. T. P. Dirkse, *This Journal*, **101**, 328 (1954).
8. S. U. Falk and A. J. Salkind, "Alkaline Storage Batteries," John Wiley & Sons, New York (1969).
9. O. V. Karpova, I. F. Reznik, and E. A. Mendzheritskii, *J. Appl. Chem. USSR*, **45**, 1751 (1972).
10. F. Welcher, "Analytical Uses of Ethylenediaminetetraacetic Acid," D. Van Nostrand Co., Inc., New York (1958).
11. M. Pourbaix, "Atlas of Electrochemical Equilibria in Aqueous Solutions," Pergamon Press, New York (1966) English Ed.
12. M. Cenek, O. Kouril, J. Sandera, A. Touskova, and M. Calabek, "Proc. 10th International Power Sources Symposium (Power Sources 6)," Academic Press, New York (1977).
13. F. A. Schneider and Z. Dominiczak, "Proc. 8th International Power Sources Symposium," p. 103 (Power Sources 4) Academic Press, New York (1973).
14. V. N. Flerov, *J. Appl. Chem. USSR*, **29**, 1913 (1956).

The Behavior of the Zinc Electrode in Alkaline Solutions

IV. The Effect of Ionic Strength in the Tafel Region

T. P. Dirkse*

Calvin College, Grand Rapids, Michigan 49506

ABSTRACT

Potentiostatic pulses have been used to obtain information about the behavior of the zinc electrode in the Tafel region. The form of the current transients obtained has been analyzed and an interpretation of it is given. Changes in the current density of zinc at a given potential have been noted as the ionic strength of the electrolyte is altered. This has been done for solutions containing high and low concentrations of OH^- ion. The current density values are only slightly affected by changes in ionic strength except that as the ionic strength increases, the results tend to become more erratic.

For some time work in this laboratory has dealt with the kinetics and the mechanism of the zinc electrode in alkaline solutions. The exchange current density for this process has been measured by different methods (1-3). However, the experimental information was all obtained within 10 mV of the equilibrium potential. Attempts to get overpotential-current information beyond this equilibrium potential region were unsuccessful because of the unusual shapes of the transients obtained. Consequently, no information was obtained in the Tafel region.

Our earlier work has also shown that the exchange current density is influenced by the ionic strength of the solution (4-6). This observation appeared to resolve the unexpected result that the exchange current density does not increase monotonically with increasing KOH concentration, but reaches a maximum in about 3-8M KOH and then decreases.

While much work has been reported on the kinetics of the zinc electrode processes, most of this has been concerned with the cathodic rather than the anodic part of the process. As a result, the cathodic or electro-deposition process is fairly well understood. This is not so true of the anodic process. There still is a difference of opinion, e.g., as to whether the cathodic and anodic

* Electrochemical Society Active Member.

Key words: electrolyte, electrode, potentiostatic pulses, Tafel slope.

paths are the reverse of each other. There is also the problem of whether the process is the same in the Tafel region as in the vicinity of the equilibrium potential. A good review of the present understanding of the zinc electrode reactions has appeared recently (7).

There were several reasons for undertaking the present work. First of all, an attempt was made to shed some light on the anodic part of the process. In doing so, an attempt was made to gather information in the Tafel region. It was suggested earlier (1) that the "peculiar" shapes of the transients might be due to metallurgical effects, i.e., lack of sufficient active sites on the zinc metal. It was also shown that a cathodic prepulse overcomes these difficulties. With this in mind, attempts were made to provide sufficient such sites. This was accomplished in part by a cathodic pretreatment and in part by the use of repetitive pulses. With this experimental approach we were able to get information in the Tafel region for solid polycrystalline zinc electrodes. No work was done with amalgam electrodes.

The second purpose of this work was to attempt to explore more systematically the effect of ionic strength on the anodic process in the Tafel region and to compare this with information obtained in the equilibrium potential region. A later article will deal with the determination of reaction orders in the Tafel region.

Much of the work dealing with the behavior of the zinc electrode in the Tafel region has been obtained galvanostatically. Very little has been reported on the use of potentiostatic pulses in studying the behavior of the zinc electrode. Potentiostatic pulses were used in this work. The intent was to add the results of this approach to the literature already available on the study of the zinc electrode.

Experimental

Stock solutions of KOH, KOH + Zn(II), and KF were prepared by using analytical reagent grade solids and doubly distilled deionized water. The Zn(II) was introduced by dissolving ZnO in a KOH solution. These stock solutions were then used to prepare the working solutions. This was done by taking prescribed volumes of the stock solutions and quantitatively diluting them. The ionic strength of the solutions was controlled by the addition of KF. Three solution variables were considered: KOH concentration, Zn(II) concentration, and total ionic strength. Two series of solutions were prepared. In each series the OH⁻ ion and Zn(II) concentrations were held constant while the ionic strength was varied. These two series represented OH⁻ ion concentrations on either side of the maximum in the i_0 vs. OH⁻ ion concentration plots.

The Tafel region information was obtained by subjecting the electrode to repetitive potentiostatic pulses from a Tacussel GATP Function Generator. These pulses were fed into the electrode by way of a Wenking Potentiostat. The pulse sequence consisted of a cathodic prepulse, an equilibrium pulse, followed by the working pulse. This series of pulses is shown on Fig. 1. All work was done at room temperature, 21° ± 1°C.

Results

The effect of repetitive pulses is shown on Fig. 2. Trace "a" was obtained from one of the first pulses. It is similar to the transients obtained with single potentiostatic pulses (3). It does not show the characteristic spike for such pulses. Trace "b" was obtained after pulsing repetitively for a few seconds. During this time a form of spike developed on the trace. Longer pulsing did not alter the shape of trace "b." Consequently, all the data were taken as soon as the trace stabilized. These were then extrapolated to zero time in the usual way. Changing the amplitude of the cathodic prepulse did not change the transient obtained during the working pulse. The change in

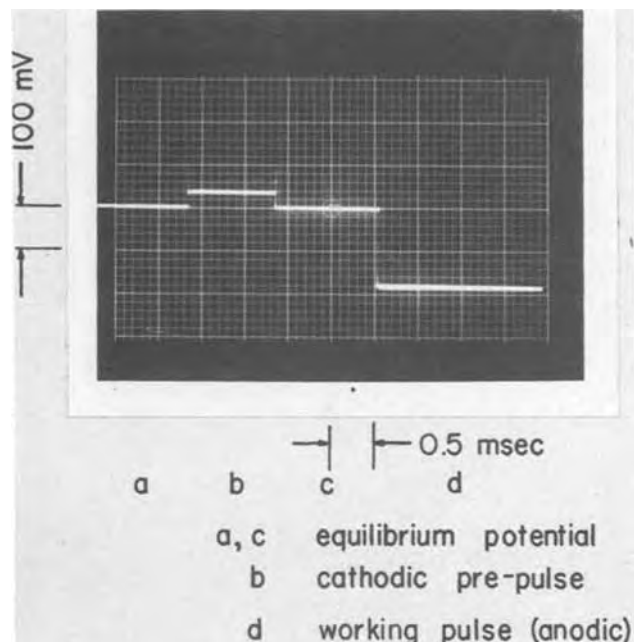


Fig. 1. Typical potentiostatic pulse sequence

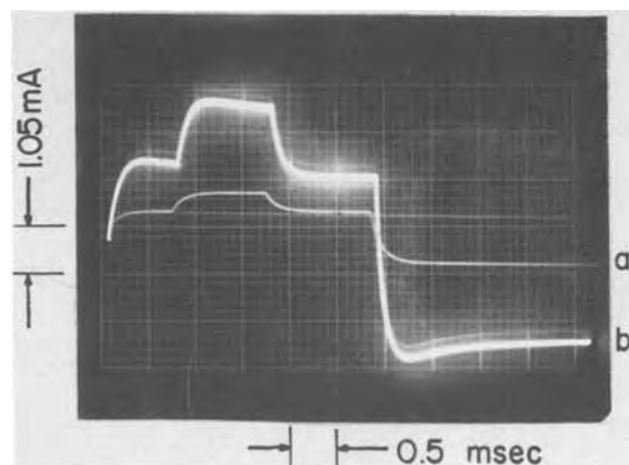


Fig. 2. Current-time transients from potentiostatic pulses in 2.04M KOH.

shape of the transients suggests that the electrode needs to be worked (or cycled) before the so-called normal effects appear. A single cathodic prepulse alone is not sufficient to bring this about—see trace "a" on Fig. 2.

Repetitive pulsing has at least two effects: (i) the amplitude of the current is increased; and (ii) the leading edge of the current transient undergoes a change in shape. In addition to this there is another fact that should be noted. When the pulsing is terminated after the shape of the transient has stabilized (trace "b", Fig. 2), then during open circuit the electrode undergoes some sort of change so that when pulsing is resumed the sequence of transients obtained is again the same as that shown on Fig. 2.

On Fig. 3 are shown two of the Tafel plots obtained in a series of solutions whose ionic strengths ranged from 2.05 to 6.55M. The plots are all very similar. Apparently, the change in ionic strength has little, if any, real effect on the Tafel plots. All of these plots showed a tendency to level off at overpotentials greater than 140 mV. This has also been observed by others (7) and it was suggested that this is due to the attaining of full surface coverage by the anodic univalent intermediate which was considered to be strongly adsorbed.

Figure 4 shows a Tafel plot for a solution in which the OH⁻ ion concentration was 6.27M, i.e., the solu-

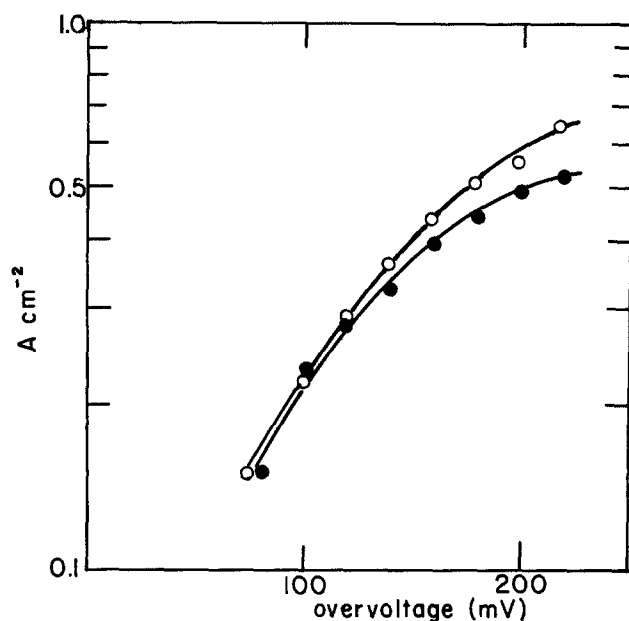


Fig. 3. Tafel plots for solutions containing 2.0M OH^- and 0.01M Zn(II) . Ionic strength is 2.05M for the open circles and 6.55M for the closed circles.

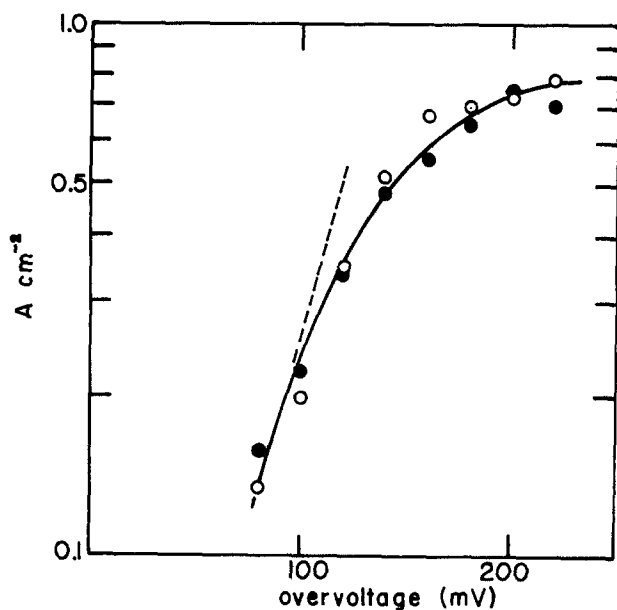


Fig. 4. Tafel plot for a solution containing 6.27M OH^- and 0.023M Zn(II) . Total ionic strength is 8.65M. The open and closed circles refer to results obtained from two different cells.

tion was on the high side of the maximum in the i_0 vs. KOH concentration plot, while the OH^- ion concentration in the solutions of Fig. 3 was on the low side of this maximum. Again, a change in the ionic strength from 6.38 to 8.65M has very little effect on the shape of the Tafel plot on Fig. 4. As on Fig. 3, the plots have a tendency to level off at the higher overpotentials.

The effect of changing ionic strength on the zinc electrode process is shown on Fig. 5. The potential in each case is chosen as 100 mV anodic to the equilibrium potential. Earlier work (8) has shown that the equilibrium potential of the zinc electrode is fairly insensitive to changing ionic strength. Consequently, selecting current densities at a given overpotential is equivalent to the selection of current densities at a given electrode potential, provided the concentrations of the OH^- and Zn(II) ions remain constant.

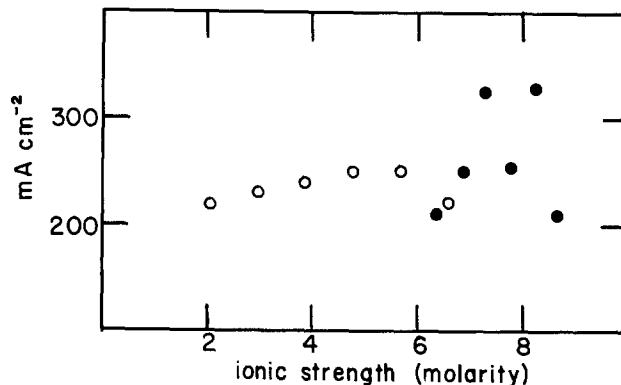


Fig. 5. Effect of ionic strength on current density in the Tafel region. Open circles, 2.0M OH^- , 0.01M Zn(II) ; closed circles, 6.27M OH^- and 0.023M Zn(II) . The potential is 100 mV anodic to the equilibrium potential.

Discussion

Shape of transients.—The stabilized transients (trace "b" on Fig. 2) do not have the classical shape of a current transient resulting from a potentiostatic pulse. Although they do have a maximum at the leading edge of the transient, they do not have the sharp spike characteristic of double layer charging. Therefore it is necessary to analyze the transients further to determine what sort of information they do contain.

The first transient (trace "a," Fig. 2) appears to be the result of increasing surface area. The current increases with time which suggests that the initial potentiostatic pulses are altering the surface condition of the electrode. There are several possible explanations for this. First, it is possible that the surface area is increasing due to the formation of etch pits (9). However, the i vs. t relationship for trace "a" does not agree with that developed for each pit formation (9). Another objection to this explanation is that it would not readily account for the fact that on open circuit the electrode surface loses its increased area, i.e., the etch pits disappear or fill in. Ordinarily, when etch pits are formed they tend to grow and thus increase the surface area (and the current) further.

A second explanation is related to the observation that the zinc electrode equilibrium potential is a mixed potential (10). As a consequence, the surface of a zinc electrode at its equilibrium potential may have hydrogen atoms adsorbed on it. The cathodic prepulse would then serve to reduce any oxide present as well as cause the adsorbed hydrogen to be evolved from the surface. This explanation would account for the fact that when the active surface is allowed to rest at the equilibrium potential the surface again becomes inactive, i.e., it would again be covered with adsorbed hydrogen. However, as noted earlier, changing the amplitude of the cathodic prepulse had no effect on the shape of the stabilized pulse. If this explanation were correct then it would seem that increasing the amplitude of the cathodic prepulse would cover the surface with still more hydrogen and reduce the activity of the surface during the anodic working pulse, unless all the hydrogen so produced would be evolved.

A third explanation assumes that the anodic pulse produces active sites or centers on the zinc surface. These would disappear during the cathodic prepulse but during a series of repetitive cycles more anodic than cathodic charge is given to the electrode and so the net result is an increase in the number of active sites with time, causing an increase in current until a stabilized or equilibrium (or steady-state) condition is reached. On open circuit these active sites would be the first ones destroyed and hence the electrode would again revert to its relatively inactive form. This explanation appears to be the most likely

one of those presented here, especially since polycrystalline (rather than amalgam) zinc electrodes were used.

The discussion above had to do primarily with the shape of the first transient ("a" on Fig. 2) and the fact that during repetitive pulsing the current increases. However, this still does not account for the changes in the shape of the leading edge of the transient during cycling. An explanation for this is that both traces on Fig. 2 are composites of at least two processes occurring simultaneously. One of these processes is that discussed above, *i.e.*, the increase of reactive area on the electrode during repetitive cycling. This is the dominant process in trace "a" on Fig. 2. The other process(es) is the one associated with a classical potential step experiment, *i.e.*, the double layer charging spike followed by the charge transfer process and then tapering off as concentration polarization sets in. A combination of such a classical transient with one such as "a" will give a transient having the shape of "b" on Fig. 2.

This means that extrapolation of the current transients in the usual way to time zero is not really straightforward and may include a bit more information than that of charge transfer. However, as will be indicated below the information obtained by using the usual method is consistent with that obtained by other techniques.

Effect of ionic strength.—For the more dilute solutions with respect to the OH⁻ ion, Fig. 5, the ionic strength has no effect on the electrode process. For solutions more concentrated in OH⁻ ion the results are not so clear-cut. There is a good deal of scatter in the results and no particular trend is apparent. This is likely due to the excessive ionic crowding in these solutions. The increase in ionic strength of these solutions was done by adding KF, and this increases the viscosity of the solutions markedly (11).

The results of Fig. 5 may be compared with those reported earlier for the zinc electrode processes in the vicinity of the equilibrium potential (5). There the increasing ionic strength had no effect on the processes at the lower OH⁻ ion concentrations but caused a decrease in i_0 at the higher OH⁻ ion concentrations. This latter effect is not observed here, Fig. 5 (closed circles). The difference in behavior is likely due to the fact that here an overpotential is applied which offsets the effect of increasing ionic strengths. This is borne out by considering data from these same Tafel plots but at a higher overpotential, Fig. 6. On Fig. 6 the current density is definitely higher for the solutions more concentrated in OH⁻ ion (closed circles) while at the lower overpotential, Fig. 5, there

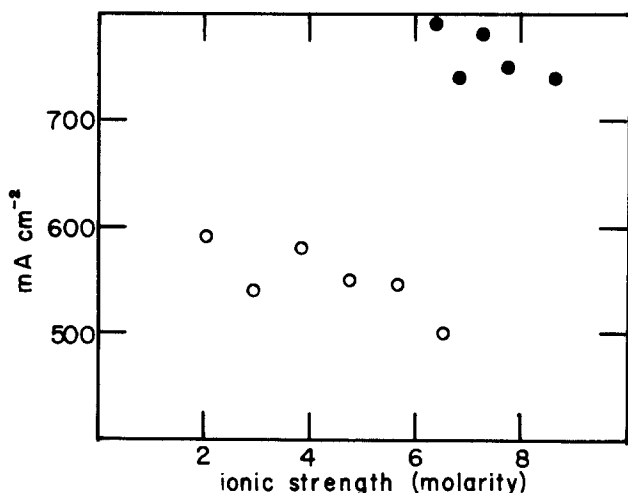


Fig. 6. Effect of ionic strength on current density in the Tafel region. Symbols the same as for Fig. 5. The potential is 200 mV anodic to the equilibrium potential.

is no marked difference in current density between the different OH⁻ ion concentrations.

Tafel slopes.—Although there probably is no really linear portion to these Tafel plots, slopes were measured as shown on Fig. 4 and extrapolated to zero overpotential to determine i_0 . The results are given in Table I. The slopes for the solutions that were more dilute in OH⁻ ion concentration are fairly constant, and are larger than the others. The exchange current densities also are substantially constant for the solutions that are more dilute in OH⁻ ion and are in fairly good agreement with the results obtained by other methods (5, 6).

The Tafel slopes in Table I are almost double those obtained by Despic, *et al.* (7). Those authors obtained their Tafel information from galvanostatic pulses. It has been noted before that the values obtained for the parameters of the zinc electrode processes are dependent on the method used for obtaining the information (3). The exchange current densities obtained by Despic and co-workers by extrapolation of Tafel slopes are at least an order of magnitude smaller than the values measured in the region of the equilibrium potential (3).

For the solutions that have a higher OH⁻ ion concentration, (B) in Table I, the Tafel slopes show some variation but this is likely due more to difficulties in determining the slopes than to any real effect. The exchange current densities, likewise, show more scatter and are much lower than those obtained by other methods.

No significant kinetic information will be deduced from these Tafel slopes for two reasons: (i) the difficulty in determining the slopes; and (ii) the intention here is merely to note the effect of ionic strength on the process and to ascertain whether it is as important to control this variable in the Tafel region as it is in the region of the equilibrium potential. In a subsequent article the effect of changing OH⁻ and zincate ion concentration on the Tafel slopes will be used to extract kinetic and mechanistic information.

Conclusions

Changes of ionic strength have little effect on the zinc electrode processes in alkaline solutions in the Tafel region. However, at concentrations of OH⁻ ion above the maximum in the i_0 vs. KOH concentration plot, *i.e.*, above about 3-6M, increasing the total ionic strength of the solutions causes the results to be rather erratic. A likely reason for this is that at these higher ionic strengths normal hydration numbers of the ions cannot be satisfied and the physical nature of the solution is changing. There may be significant ion pair formation as well as other accommodations to the increasing dearth of solvent molecules.

Acknowledgment

I wish to thank Peter Allen and Dr. N. A. Hampson for considerable help in the preparation of this paper

Table I. Effect of ionic strength on Tafel region values

(A) [OH ⁻] = 2.0M		[Zn(II)] = 0.01M
Ionic strength, as molarity	Tafel slope, mV/decade	i_0 , mA/cm ²
2.05	165	54
2.95	170	55
3.85	190	50
4.75	180	73
5.65	170	65
6.55	170	55
(B) [OH ⁻] = 6.27M		[Zn(II)] = 0.023M
6.38	105	23
6.83	110	30
7.29	135	64
7.74	100	30
8.20	74	16
8.65	69	10

and for suggestions with respect to experimental work, and to the General Electric Company for a research grant which provided the financial support for this work.

Manuscript received Sept. 17, 1979.

Any discussion of this paper will appear in a Discussion Section to be published in the June 1981 JOURNAL. All discussions for the June 1981 Discussion Section should be submitted by Feb. 1, 1981.

Publication costs of this article were assisted by the Johnson Wax Fund.

REFERENCES

1. T. P. Dirkse and N. A. Hampson, *Electrochim. Acta*, **17**, 135 (1972).

2. T. P. Dirkse and N. A. Hampson, *ibid.*, **17**, 383 (1972).
3. T. P. Dirkse and N. A. Hampson, *ibid.*, **17**, 1113 (1972).
4. T. P. Dirkse and N. A. Hampson, *J. Electroanal. Chem. Interfacial Electrochem.*, **35**, 7 (1972).
5. T. P. Dirkse, *This Journal*, **125**, 1591 (1978).
6. T. P. Dirkse, *ibid.*, **126**, 541 (1979).
7. A. R. Despic, D. J. Jovanovic, and T. Rakic, *Electrochim. Acta*, **21**, 63 (1976).
8. T. P. Dirkse, *This Journal*, **126**, 1456 (1979).
9. G. J. Bignold and M. Fleischmann, *Electrochim. Acta*, **19**, 363 (1974).
10. J. O'M. Bockris, Z. Nagy, and A. Damjanovic, *This Journal*, **119**, 285 (1972).
11. A. Marshall, N. A. Hampson, and M. P. Saunders, *J. Electroanal. Chem. Interfacial Electrochem.*, **78**, 307 (1977).

The Effect of Alloying with Bismuth on the Electrochemical Behavior of Lead

Noel A. Hampson and Sheila Kelly

Chemistry Department, Loughborough University, Leicestershire, LE11 3TU, England

and Kenneth Peters*

Chloride Technical Limited, Swinton, Manchester, M27 2HB, England

ABSTRACT

The effect of alloying bismuth on the electrochemical behavior of lead has been investigated at three levels of bismuth. Linear sweep voltammetry and potential step experiments have been carried out in sulfuric acid solution of battery strength. The results show that bismuth additions accelerate the rate of corrosion of the lead and confirm that the relationship between the extent of the anodic attack and bismuth content is not linear but goes through a minimum value. From the potential step behavior it appears that bismuth differs in effect from that of antimony, the most obvious difference being the absence of a second current peak in the step response for the development of PbO₂ with the bismuth-containing electrodes.

Despite recent concentrated efforts toward the development of small, light-weight secondary electrochemical power sources, the lead-acid battery, first introduced in 1859, remains unsurpassed at the forefront of major battery systems today. Numerous attempts have been made, however, to replace antimony as the grid alloying ingredient for reasons we outlined in a previous publication (1), not least of these being the deleterious effect of the alloy on the hydrogen overvoltage of the cell. Materials suggested as a substitute include alloys of Ca, Sn, Mg, Al, and Ti, and several workers have considered the effect of alloying lead with various amounts of bismuth (2-7). Recent work carried out in this laboratory by Casson (8) in which a whole range of alloys were subjected to extensive cycling conditions has suggested that alloying with bismuth produces favorable recharge characteristics which are worth further investigation.

Small quantities of Bi (<0.3%) do not seem to have any significant effect on the metallurgical properties of lead; as the quantity of Bi is increased the lead is found to harden, its bending strength being considerably reduced. The effect of Bi on the hydrogen evolution reaction has been studied by Kilimnek *et al.* (9) who found that the kinetic constants a and b in the equation $\eta = a + b \log_{10} i$ depend on the magnitude of the charge on the electrode surface. The values

given in Table I for Bi in 1M H₂SO₄ (9) indicate the slow rate of hydrogen gas formation.

It has been reported that the stability of bismuth-containing alloys to corrosive attack passes through a minimum at approximately 3.5 weight percent (w/o) Bi (10). These curves were based on studies of the weight loss of a corroding anode, the amount of sludge formed, and the cathode weight gain over a period of 70 days. The authors offer no explanation for the effect of bismuth in promoting the corrosion of the lead lattice. A detailed study of the effect of bismuth on battery performance (11) has shown that the presence of bismuth results in an increase in the amount of positive shedding (*i.e.*, loss of active material as sludge in the cell case) and promoted grid growth. These increases, however, do not appear to be linear with increasing bismuth content.

There seems to be some discrepancy in the literature concerning the tolerable level of Bi, with one set of workers reporting that as little as 0.01% Bi in Pb increases its corrodability (12). For this reason it was decided to carry out our own investigation using vari-

Table I. Surface charge

	Positive (V)	Negative (V)
a	0.93	1.15
b	0.12	0.115

* Electrochemical Society Active Member.

Key words: corrosion, nucleation, electrocrystallization, oxidation, passivation.

ous levels of Bi in the form of binary weight alloys with pure lead.

This paper records the LSV and potential step measurements and compares the data obtained with that from our previous work on the Pb/H₂SO₄ and Pb-Sb/H₂SO₄ systems.

Experimental

The electrolytic cell, electrode pretreatment, and electrical circuitry have all been adequately described in a previous publication (1). Linear sweeping and potentiostatic pulse experiments were made with bismuth/lead binary alloys in 5M H₂SO₄ using a Kemtron PS-40 potentiostat and function generator, the output being monitored on an (X-Y-T) recorder (Bryans, Series 26000). The rods used in the preparation of the disk electrodes were precast and aged for a month in an attempt to simulate the industrial situation as far as possible. "Stabilized" electrodes were obtained by cycling to a constant response between the limits¹ 400 and 1520 mV for approximately 1½ hr. As before (1), it was found necessary to "initiate" the reaction by sweeping to a positive limit of 2000 mV¹ in the first cycle; this provides the considerable initial overpotential first emphasized by Fleischmann *et al.* (13), otherwise negligible product lead dioxide was formed with a positive limit set at 1520 mV. The three binary alloys used in the experiments contained, respectively, 0.063%, 0.127%, and 0.267% Bi.

Results and Discussion

Linear sweep experiments.—Rate of attainment of constant response.—Noticeable features of the early cycle pattern were the two anodic current peaks obtained during the negative-going sweep with the positive potential limit set at 2000 mV. This was to be expected from our previous work on lead and antimonial lead alloys (1), and we have attributed this to lead sulfate formation at a surface previously passivated by oxygen. The quantity of charge contained in the integrated anodic area of these peaks was independent of bismuth concentration in the range studied, confirming our findings that the response is due to the base metal (Pb) itself and is also connected with oxygen and other related species because of the upper limit required.

The extent of formation of product lead dioxide showed a large variation with bismuth content such that as the Bi level was increased the corresponding alloy required a large number of cycles to give a constant response (negligible change in peak current values).

Constant response curves.—Stabilized potential curves for each alloy under test are shown in Fig. 1. The intermediate Bi concentration (0.127 w/o) appears to produce the stablest alloy with peak current values (i_p in PbO₂ formation peak) appreciably less than those for electrodes containing higher (0.267 w/o) and lower (0.063 w/o) levels of bismuth. The position of this current maximum also changes with varying Bi content, the intermediate alloy having an i_p value at the more negative potential. This suggests that the kinetic barrier to the oxidation of PbSO₄ varies with the quantity of Bi in the test electrode. The form of the maximum current (corrodibility) and peak potential variation with bismuth concentration is interesting; a maximum stability to anodic attack occurs within the range studied here. Figure 2 depicts this trend as a plot of i_p vs. Bi content for stabilized electrodes. A possible explanation for this can be given in terms of grain refinement caused by the incorporation of Bi into the lead lattice. As the amount of Bi is increased, the quantity of lead available for surface reaction is depleted, hence the stability of the alloy initially rises with increasing Bi levels. Zener (14)

¹ All potentials were measured against the Hg₂SO₄/Hg electrode in the same solution.

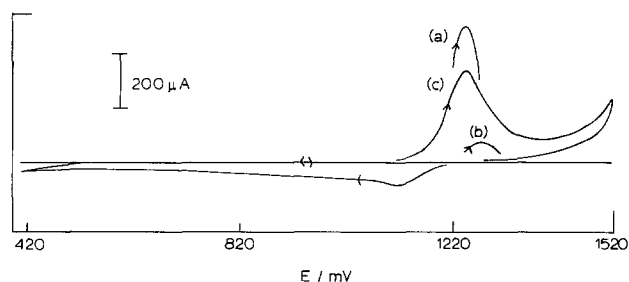


Fig. 1. Stabilized potential curves for (a) 0.063% Bi, (b) 0.127% Bi, (c) 0.267% Bi. (400-1520 mV; 50 mV/sec⁻¹, A = 0.0707 cm².)

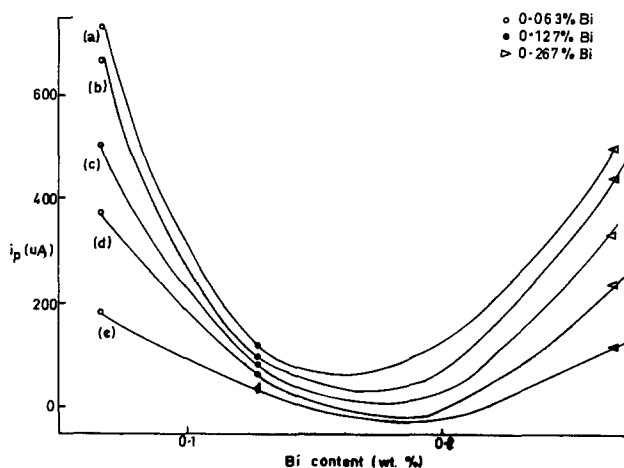


Fig. 2. Plot of i_p vs. Bi content for electrodes cycled to constant response: (a) 100 mV sec⁻¹, (b) 80 mV sec⁻¹, (c) 50 mV sec⁻¹, (d) 30 mV sec⁻¹, (e) 10 mV sec⁻¹.

has shown that grain growth should cease when the average grain size Dm is given by Eq. [1]

$$Dm = \frac{d}{F} \quad [1]$$

where d signifies the average diameter of an inclusion and F the fraction of the volume in the alloy. It is possible that this condition applies when the concentration of Bi in the alloy lies between 0.14 and 0.19 w/o and so accounts for the minimum in Fig. 2. These results contrast with those of Bryntseva (10) and Gonzales (15); Bryntseva has reported an increase in the electrochemical corrosion of lead anodes containing concentrations of Bi up to 2% and Gonzales has claimed that the corrosion rate can be doubled by increasing the Bi content from 0.01% to 0.1%. The latter author emphasized that the precise increase depended on the conditions of the test which greatly differ from those used here and probably account for the difference between their results and ours.

The relationship between peak potential (E_p) and sweep rate (v) is shown in Fig. 3 as a plot of E_p vs. $\log_{10} v$ for each alloy under test. This data is in agreement with that obtained by Canagaratna *et al.* (16) and us (17) (for both pure and antimonial lead) for the growth of a single layer on an electrode surface. Figure 4 shows the relationship between the peak current (i_p) and sweep rate (v) in the form of a plot of i_p vs. \sqrt{v} . In each case (three bismuth concentrations) the peak current values are much larger than corresponding data on Pb and Pb-Sb (5%) electrodes (1) indicating that concentrations as low as 0.06% Bi in lead result in the formation of an alloy which is much more susceptible to anodic attack than one containing a relatively high proportion of antimony.

A summary of the integrated anodic charge for stabilized electrodes is given in Table II. An interesting feature here is the similarity between Pb-Sb and

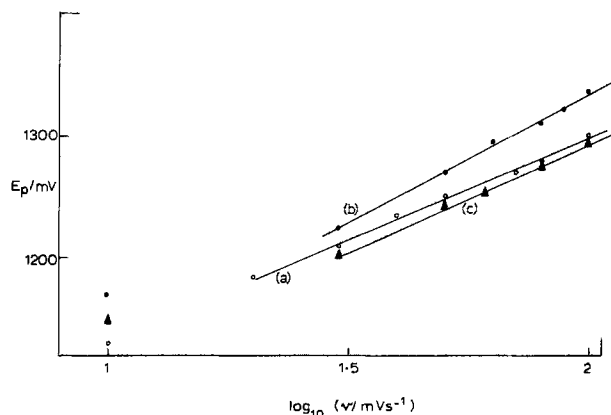


Fig. 3. Plot of peak potential vs. \log_{10} sweep rate for (a) 0.063% Bi, (b) 0.127% Bi, (c) 0.267% Bi. (Electrodes cycled to constant response.)

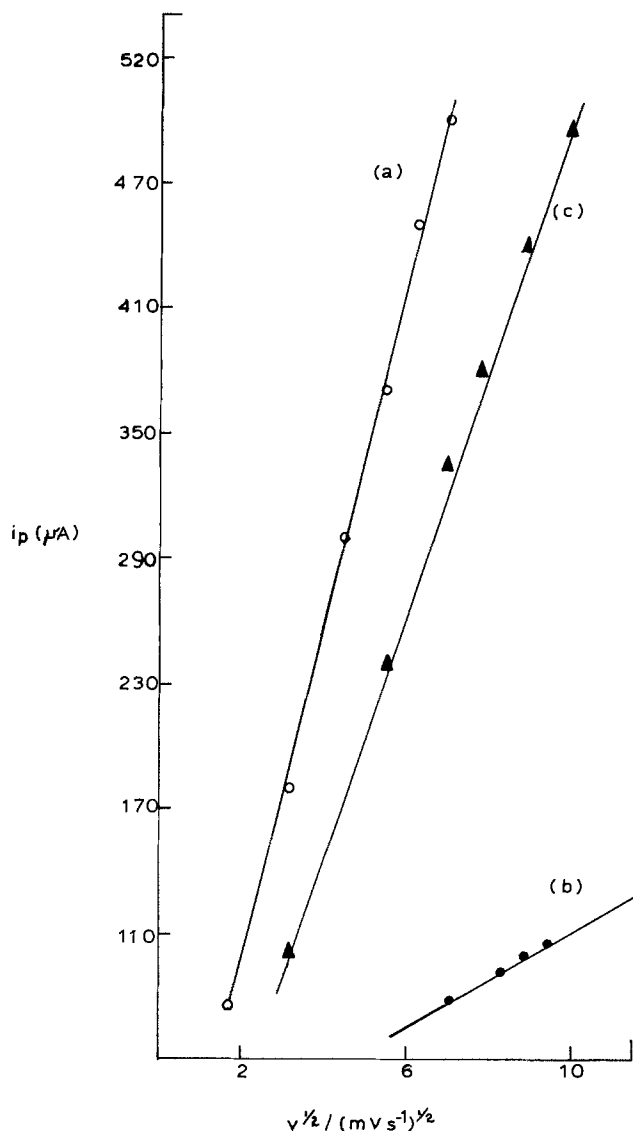


Fig. 4. Plot of peak current vs. $(\text{sweep rate})^{1/2}$ for stabilized electrodes containing (a) 0.063% Bi, (b) 0.127% Bi, (c) 0.267% Bi.

Pb-Bi electrodes, both exhibiting a much larger sweep-rate dependency of charge than pure lead. As before (1) this can be attributed to the constant thickness of the oxidized layer on pure lead which discharges to approximately the same extent throughout. The Pb-Sb and Pb-Bi alloys, on the other hand, form a layer which is more porous than that on pure lead, and so the reaction is driven deeper into the spongy mass at

Table II. Calculated anodic charge during positive-going sweep (400-1520 mV) for stabilized electrodes

Sweep rate (mV sec ⁻¹)	Anodic charge (mC cm ⁻²)		
	0.063% Bi	0.127% Bi	0.267% Bi
10	35.4	6.2	32.2
30	23.0	4.9	20.5
50	18.0	3.9	16.0
60	16.7	3.2	14.5
80	15.3	2.9	12.7
100	14.1	2.9	11.7

lower rates of sweeping. The lack of any rotation speed dependence during the electrochemical cycling indicates that the diffusion of species through the electrode occurs via a solid-state process similar to that for Pb and Pb-Sb electrodes.

Potential sweep experiments.—These were performed after formation of PbSO₄ by cyclic potential sweeping and a stabilizing period at 400 mV when the current became negligible ($\leq 1 \mu\text{A}$). We have already shown (17) that the length of time the electrodes are held in the sulfate region has a significant effect on the oxidative behavior of the lead sulfate deposit and have suggested this is due to the removal of nucleation sites formed during the stabilizing sweep. For this reason the reductive period prior to potential stepping was kept constant at approximately 20 min.

Figure 5 shows a typical current response curve when a lead sulfate deposit (formed by continuous cycling on a Pb-Bi base) is stepped into the lead dioxide region. The form of the transient is similar to that for pure lead (17) where the initial double layer charging spike is followed by an increase in current due to the formation and growth of nucleation centers. The presence of a single oxidation peak is indicative of a completely passivated film (PbO₂) with most of the residual current flow due to the oxygen evolution reaction because of the high overpotential used. These observations contrast with our previous work on antimonial lead when a thickening of the oxidized deposit does occur and a second rise in transient is obtained as a further layer of product PbO₂ is formed.

Although at the start of the transient response (Pb/Bi) the current did not rise from zero (indicating the presence of some growth centers) we were able to identify a two-dimensional growth process by the residual linear i - t correlation represented by Eq. [2]

$$i = (ZF\pi M/\rho) N_0 k^2 t \exp(-\pi M^2 N_0 k^2 t^2/\rho^2) \quad [2]$$

We have concluded (17) that the cycled electrode contains sufficient nuclei for electrocrystallization to proceed at a speed sufficient to change the process from

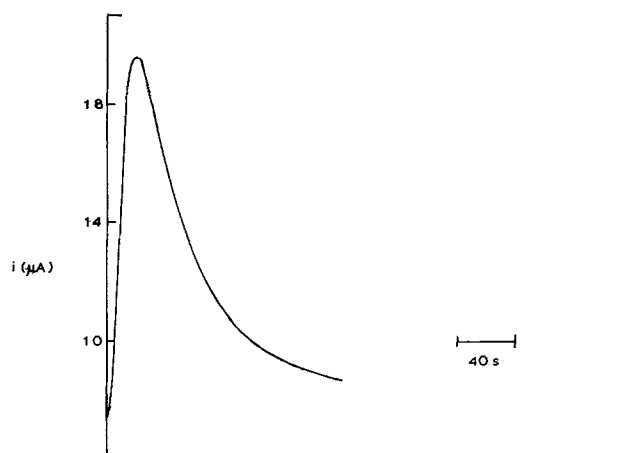


Fig. 5. Potential step experiment (400-1100 mV) on stabilized Pb-Bi (0.127%) electrode ($A = 0.0707 \text{ cm}^2$).

the relatively slow three-dimensional one reported by Fleischmann and Thirsk (13) and later by Casson (8) to the faster two-dimensional process.

Figure 6 shows a typical series of current-time curves for the rise in transient as a cyclically formed PbSO_4 deposit is stepped to various overpotentials in the PbO_2 region. The slopes of these lines are seen to increase with increasing overpotential which is to be expected from Eq. [2] ($di/dt \propto k^2 N_0$ at short times). The potential dependency of $k^2 N_0$ is shown in Fig. 7 as a plot of overpotential vs. $\log_{10} (di/dt)$. It is interesting to note that as the electrodes are stepped to a series of increasing overpotentials the peak current values rise to a limiting value then start to fall. It can be shown (18) that for instantaneous nucleation

$$i_m = (2\pi N_0)^{1/2} n F k h e^{-\theta} \quad [3]$$

which, when compared with the data in Fig. 7, shows that for a simple two-dimensional process the value of i_m should not decrease. This fall-off in peak current values is accompanied by a corresponding fall in the charge contained in the oxidation peak (calculated by a simple integration process). A possible explanation for this can be given in terms of a reduction in effective surface area of the electrode due to partial coverage of the surface by gaseous oxygen (again because of the high overpotentials used): surface area before potential step = A , surface area after potential step = $A(1 - \theta)$, where θ represents the area of the electrode covered with oxygen. (As the overpo-

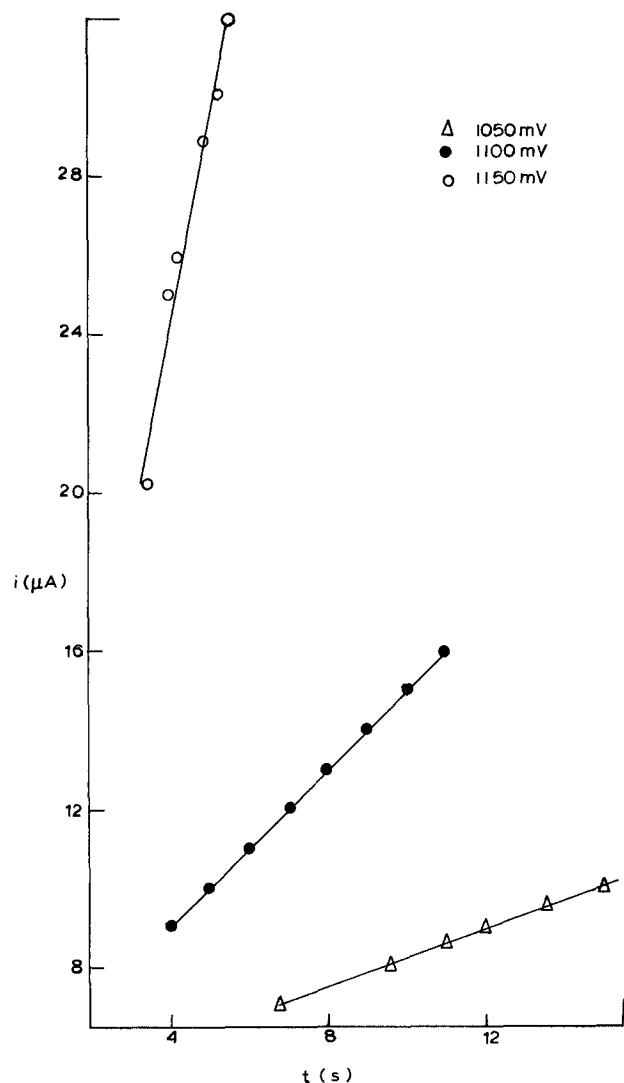


Fig. 6. Current-time plots (rise in transient) for potential step experiments on Pb-Bi (0.127%) stabilized electrodes.

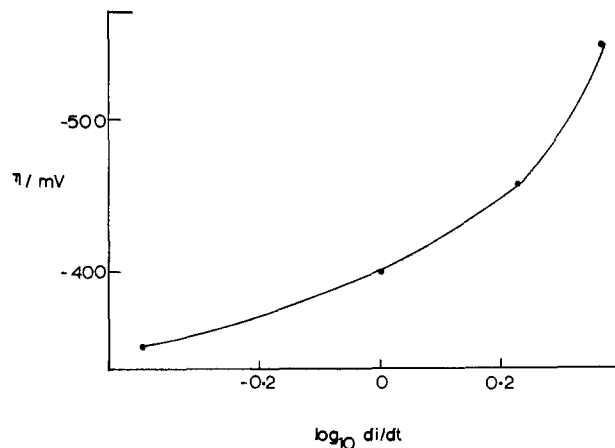


Fig. 7. Plot of overpotential vs. $\log_{10} (di/dt)$ for 0.127% Bi

tential is increased the value of θ will also increase and i_m subsequently falls). Figure 8 confirms the presence of oxygen on the electrode surface with a reduced plot of i/i_m vs. t/t_m . The current values at the tail end of the curve ($t/t_m > 1.5$) are larger than expected due to the contribution of the oxygen evolution current. A further proof that the reaction studied here follows a simple two-dimensional growth mechanism is provided in Fig. 9 with a typical plot of $\ln(i - i_r)/t$ vs. t^2 with a correction for the oxygen evolution current being made. The straight lines obtained are in good agreement with Eq. [2].

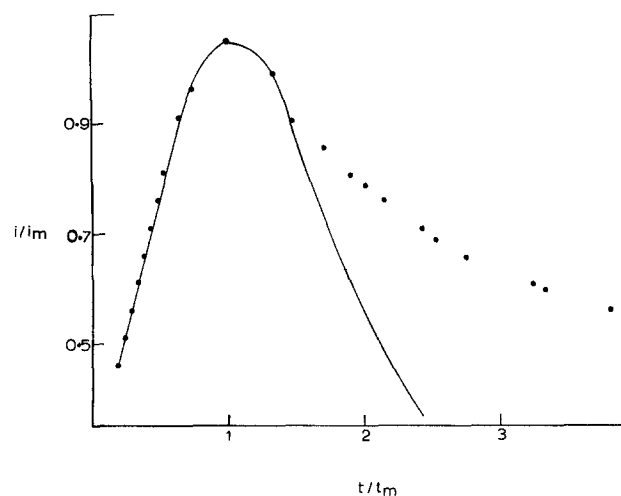


Fig. 8. i/i_m vs. t/t_m for potential step transient (0.127% Bi, 400-1100 mV).

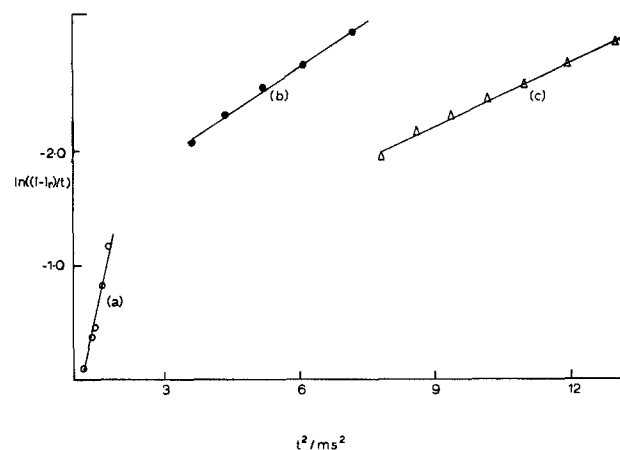


Fig. 9. $\ln(i - i_r)/t$ vs. t^2 for (a) 0.063% Bi, (b) 0.127% Bi, (c) 0.267% Bi at long times ($t/t_m > 1$).

These results are of great importance to industry and battery manufacturers in particular since they give the optimum level of bismuth for use as a grid alloying ingredient in the lead-acid battery system. They do not, however, provide any information concerning the recharge characteristics of such an alloy. Dewitt and Myers (19) found Bi to have a less harmful effect than Sb on self-discharge and gassing rates. These beneficial properties of bismuth if combined with the optimum level of the alloy (minimum anodic corrosion) in the positive battery grid could go a long way in promoting Bi as a replacement for Sb in the lead-acid system today.

Conclusions

1. The incorporation of bismuth into lead does not produce an alloy with the same electrometric behavior as antimonial lead (*viz.*, the second current peak in the step response for the development of PbO_2 is absent).

2. The oxidation of $PbSO_4$ to PbO_2 on a lead-bismuth electrode results in the formation of a completely passivating layer.

3. Concentrations as low as 0.06% Bi in lead render the alloy much more susceptible to anodic corrosion than a pure lead or antimonial (5%) lead electrode.

4. The relationship between bismuth content and depth of corrosive attack is not linear but parabolic.

5. A maximum stability concentration of bismuth in lead was found in the range studied.

Acknowledgment

We thank the Directors of Chloride Technical Limited for permission to publish this paper and for financial support (to S.K.).

Manuscript submitted July 20, 1979; revised manuscript received Feb. 11, 1980.

Any discussion of this paper will appear in a Discussion Section to be published in the June 1981 JOURNAL. All discussions for the June 1981 Discussion Section should be submitted by Feb. 1, 1981.

Publication costs of this article were assisted by Chloride Technical Ltd.

LIST OF SYMBOLS

E potential
 η overpotential
 i current

i_p current at maximum in anodic peak during cyclic sweep
 E_p potential at which i_p occurs
 v sweep rate
 Z number of electrons transferred in the rate-determining step
 F Faraday's constant
 M molar mass
 ρ density of phase
 N_0 density of nucleation sites
 k kinetic constant of Eq. [2] and [3]
 t time
 i_m maximum current in potential step experiment
 t_m time of i_m
 i_r residual oxygen evolution current
 A electrode area

REFERENCES

- N. A. Hampson, S. Kelly, and K. Peters, *J. Appl. Electrochem.*, **10**, 91 (1980).
- W. Hofmann, "Lead and Lead Alloys," Ind. ed., p. 196, Springer-Verlag, New York (1970).
- P. Casson, N. A. Hampson, and K. Peters, Unpublished work.
- J. Greenwood, *Metall. Rev.*, **23**, 279 (1961).
- M. Dasoyan, *Dokl. Akad. Nauk.*, **107**, 863 (1956).
- N. L. Parr, A. Muscott, and A. J. Crocker, *J. Inst. Met.*, **87**, 321 (1957).
- G. Kostorz and S. Mihailovich, Inst. Conf. Strength of Metal Alloys Conf. Proc., **1**, 304 (1970).
- P. Casson, N. A. Hampson, and K. Peters, *This Journal*, **124**, 1655 (1977).
- A. B. Kilimnik and A. L. Rotinyan, *Eletstrokhimiya*, **5**, 1234 (1969).
- V. I. Bryntseva, V. G. Bundzhe, Yu. D. Dunaev, G. Z. Kiryakov, and L. A. Tskhe, *Zasch. Metall.*, **3**, 504 (1967).
- E. Hoehne, *Metallwirtschaft*, **23**, 60 (1944).
- G. Bacskay, Intem. Symp. Anti. Corros. Protect, Bratislava, **1** (21), 13 pp (1962).
- M. Fleishmann and H. R. Thirsk, *Trans. Faraday Soc.*, **51**, 71 (1955).
- C. Zener, *Acta Metall.*, **6**, 147 (1948).
- J. A. Gonzales, M. Rvejula, and S. Felui, *Rev. Met. (Madrid)*, **7**, 105 (1971).
- S. G. Canagaratna, P. Casson, N. A. Hampson, and K. Peters, *J. Electroanal. Chem.*, **79**, 273 (1977).
- N. A. Hampson, S. Kelly, and K. Peters, *J. Appl. Electrochem.*, **10**, 261 (1980).
- D. D. McDonald, "Transient Techniques in Electrochemistry," p. 281, Plenum Press, New York (1977).
- J. L. Devitt and M. Myers, *This Journal*, **123**, 1769 (1976).

Structure-Reactivity Relationships of Methylated Tetrahydrofurans with Lithium

J. L. Goldman,* R. M. Mank, J. H. Young, and V. R. Koch*

EIC Corporation, Newton, Massachusetts 02158

ABSTRACT

Tetrahydrofurans methylated in the α -position manifest remarkable chemical and electrochemical stability toward Li. While tetrahydrofuran (THF) distilled off benzophenone ketyl and stored with Li at 71°C reacts in two days, 2-methyltetrahydrofuran (2-Me-THF) treated similarly was stable for over 10 months. Electrolytes comprising either 2-Me-THF or 2,5-dimethyltetrahydrofuran (2,5-di-Me-THF) were subjected to cycling studies in half-cell configurations. Average Li on Li cycling efficiencies exceeded 96% for $Q = 1$ C/cm². Unlike the α -methylated ethers, 3-methyltetrahydrofuran (3-Me-THF) was as reactive towards Li as THF. Thus, the position of the methyl substituent with respect to the cyclic ether's oxygen atom is critically important, and several mechanisms are considered.

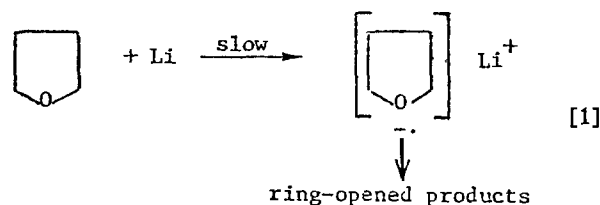
Ambient temperature Li secondary battery technology has been actively pursued for more than 20 years (1-4). Potential applications of such batteries run the gamut from vehicular propulsion to power sources for digital watches. Transition metal chalcogenides such as TiS₂ (5-7) and V_{1-x}M_xS₂ (M = Fe or Cr) (8, 9) have proved to be suitable cathode materials for ambient temperature cells. More recently, transition metal oxides with perovskite-related structures such as V₆O₁₃ show promise as rechargeable cathode materials (10). Yet, as is generally agreed, the key technical problem preventing the realization of such batteries is the cycling behavior of the Li electrode.

While Li may be plated onto a conducting substrate from a variety of aprotic organic electrolytes with 100% efficiency (2, 11), subsequent anodic dissolution is invariably less (11-14). The difference reflects Li metal electrically isolated from the substrate by passivating, albeit Li⁺ conducting films (3, 14-18). These films arise from the reduction of impurities at high rate, and electrolyte itself at a lower rate by freshly deposited Li. The underlying metal is thereby protected from further attack. The presence of such filmed or "encapsulated" Li particles results in an irregular surface which seriously distorts the morphology of subsequent plates. On the second plate, for example, Li nucleation and growth proceed irregularly forming dendrites; the surface area of the plate correspondingly increases, the rate of reaction with electrolyte increases, and more Li is isolated. Thus, the effect of a small morphological perturbation on the first cycle becomes compounded over several cycles, leading to ultimate electrode failure.

Our approach to electrolyte development has been to choose solvents expected to manifest low reactivity toward Li, and then refine electrolytes based on these solvents via stringent purification procedures. In selecting a solvent, one may be guided by Selim and Bro who have pointed out that polar solvents are necessarily reactive with Li due to the presence of a molecular dipole (11a). The dipole results from an unequal distribution of electron density about a carbon-heteroatom bond which facilitates electron transfer from Li into the bond. More recently, a thermodynamic analysis of the possible direct interaction between Li and a variety of aprotic organic solvents demonstrated that all may be reduced by Li (19). We suspected, therefore, that cyclic ethers afforded the

best chance of retarding Li/solvent reactivity, since the C—O bond is far less polar than C=O (methyl acetate, methyl formate, and propylene carbonate), or S=O (dimethylsulfite and dimethylsulfoxide), other solvents in which the Li electrode has been cycled. Lower Li/solvent reaction rates should permit more uniform Li plate morphology on charge, and smooth, nondendritic plates are a prerequisite for discharge with high efficiency. Accordingly, tetrahydrofuran (THF)/Li reactivity was investigated in depth (14, 20). We found that while LiAsF₆/THF electrolytes outperformed LiAsF₆/propylene carbonate (PC) (12, 13) and methyl acetate (21) in terms of Li electrode cycling efficiency, THF media were nonetheless too reactive for use in a practical secondary battery.

On the basis of isolated reaction products and earlier mechanistic work, we postulated a reduction mechanism involving an initial transfer of an electron from Li to the lowest unfilled molecular orbital (LUMO) centered on the oxygen atom of THF (20) (Eq. [1])



If Eq. [1] accurately describes the rate-determining step in the reduction of THF by Li, one can envisage modifying reaction kinetics by raising the activation energy of the slow step. This may be accomplished by perturbing the energy of the LUMO upward. Thus, locating an electron donating group, e.g., alkyl, in the 2-position adjacent to the oxygen atom raises the activation energy required to form the anion-radical by localizing additional electron density on the oxygen atom. In a recent patent (22) and paper (23), we showed that 2-Me-THF and 2,5-di-Me-THF were less reactive toward Li than THF itself. In this paper, we elaborate upon these findings and present data indicating that 3-Me-THF is as reactive as THF toward Li.

Experimental

General.—All purification procedures subsequent to distillation and the electrochemical experiments were conducted at ambient temperature under an Ar atmosphere in a Vacuum-Atmospheres Corporation dry box equipped with a Model HE-493 Dri-Train.

* Electrochemical Society Active Member.

Key words: organic, electrolyte, lithium, electrode.

Materials.—Tetrahydrofuran (THF) (Burdick and Jackson, distilled-in-glass), lithium hexafluoroarsenate (LiAsF_6) (U.S. Steel Agri-Chemicals, electrochemical grade), and lithium perchlorate (LiClO_4) (Anderson Physics, highest purity) were used as-received. Lithium foil (15 mil) was obtained from Foote Mineral Company sealed under Ar. 2-Methyltetrahydrofuran (2-Me-THF), 3-methyltetrahydrofuran (3-Me-THF), 2,5-dimethyltetrahydrofuran (2,5-di-Me-THF) *cis/trans* mixture, tetrahydropyran (THP), 2-methyltetrahydropyran (2-Me-THP), 2,5-dimethoxy-tetrahydrofuran (2,5-di-OMe-THF), and 1,3-dioxolane (Aldrich) were distilled off CaH_2 under Ar from a Perkin-Elmer Model 251 Auto Annular Still. The reflux ratio was 5:1; only the middle 60% fraction was collected. For some experiments, solvents were distilled off sodium benzophenone ketyl, and details regarding this procedure may be found elsewhere (20).

Activated neutral alumina (Woelm 200 neutral, activity grade Super 1) was used as received, and exposed only to the dry box atmosphere. Approximately 1g desiccant per 5 ml solvent was used in a given purification procedure. The first 10% of solvent eluting through the column was discarded.

Details regarding electrolyte preparation and purification and subsequent storage at elevated temperatures with Li may be found elsewhere (14, 20).

Cells and electrodes.—Glass rectangular cells ($10 \times 40 \times 60$ mm, Vitro Dynamics) were used for the galvanostatic cycling of Li in a half-cell configuration. The working electrode was a 5.5 cm \times 3.8 cm \times 5 mil strip cut from Ni 200 sheet (Roblinger). The counter-electrode was fabricated from 15 mil Li ribbon. Details regarding cell assembly, Li cycling experiments, and the galvanostatic preelectrolysis technique may be found elsewhere (14).

Linear sweep experiments employed a 5 mm diam vitreous carbon disk working electrode (Tokai) sealed in Pyrex. Li counter and reference electrodes dipped into the electrolyte under investigation, and these experiments were accomplished in an undivided cell.

Chronopotentiometric plating and stripping of Li were conducted with a constant current power supply and an automatic cyler (both constructed in-house). The latter allowed plating for a given period of time, then stripped to a preset potential (1.0V anodic of the stripping potential). Upon reaching this potential, stripping was terminated and the cell reverted to open circuit until plating again commenced.

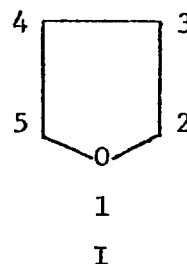
Linear sweep experiments were accomplished with a Pine Potentiostat Model RDE2 equipped with a triangle wave generator and a Houston Model 2000 Omnidigraphic X-Y recorder.

Conductivity measurements were performed with a YSI Model 31 bridge in a medium range Jones-type conductance cell equipped with Pt electrodes. The cell constant was determined with standard 0.1M KCl solution.

NMR measurements.— ^{13}C NMR spectra of the cyclic ethers with and without LiAsF_6 were run neat with an external reference tube comprising 75% D_6 acetone and 25% ^{13}C enriched TMS on a JEOL FX-60 spectrometer (Northeastern University). Spectra were recorded at ambient temperature ($\sim 30^\circ\text{C}$) in pulse/Fourier transform quadrature mode and were proton decoupled. Spectral resolution was greater than ± 0.3 Hz (± 0.02 ppm). Chemical shifts are reported as ppm downfield from TMS.

Results and Discussion

Methylated tetrahydrofurans.—The numbering scheme of the oxolane ring is shown in I. On the basis of the LUMO argument, 2-Me and 2,5-di-Me-THF are predicted to be more stable to Li than THF. 3-Me-THF, on the other hand, should



be about as stable as THF, since the inductive effect of the methyl group is rapidly attenuated through saturated C-C bonds (24). To test this hypothesis, a series of methylated-THF's were obtained and exposed to Li under static and dynamic conditions. Static tests involved the incubation of Li foil with electrolyte at 71°C . The onset of Li-electrolyte reaction visually manifests itself in terms of corrosion on the Li foil and concurrent yellowing of the electrolyte. Dynamic conditions were achieved by galvanostatically cycling Li to and from Li and Ni substrates at 25°C . A fresh Li surface, therefore, came into contact with electrolyte on every cycle. Li-electrolyte reactivity was noted in terms of a loss of cycling efficiency (Li stripped/Li plated) with increasing cycle number.

Li storage experiments.—Tables I and II summarize the results of the static tests. It is readily apparent that those solvents and electrolytes comprising 2-Me-THF or 2,5-di-Me-THF are markedly superior to THF or 3-Me-THF on exposure to Li at elevated temperature. We see that purified 2-Me-THF itself, as well as electrolyte prepared from it, require months before any sign of reaction with Li is noticeable. In fact, the ampul containing Li and 2-Me-THF off benzophenone ketyl was deliberately opened after 10 months of storage prior to the onset of reaction. The u.v. spectrum of this solvent was essentially superimposable with freshly distilled 2-Me-THF. The Li corrosion observed for unpurified 2-Me-THF and 2,5-di-Me-THF was due to the reaction between Li and BHT (butylated hydroxytoluene) added to the commercial product as a stabilizer. On the other hand, THF is quite reactive towards Li, regardless of purification procedure. Solvent distilled off benzophenone ketyl is effectively free

Table I. The onset of Li reaction with cyclic ethers at 71°C

Purification procedure	Time, days			
	THF	2-Me-THF	3-Me-THF	2,5-di-Me-THF
None	1 (3) ^a	1 (2)	1 (1)	1 (1)
A ^b	4 (7)	300	1 (1)	1 (2) ^c
Benzophenone ketyl	3 (2)	>300	—	—

^a Observable Li corrosion after 1 day; observable solvent coloration after 3 days.

^b Solvent passed through activated alumina.

^c Culture tube leaked.

Table II. The onset of Li reaction with cyclic ether based electrolytes at 71°C

Purification procedure	Time, days				
	1M LiAsF_6 /THF	1M LiAsF_6 /2-Me-THF	1M LiClO_4 /2-Me-THF	1M LiAsF_6 /3-Me-THF	1M LiAsF_6 /2,5-di-Me-THF
None	2 (16) ^a	—	—	—	—
A ^b	25 (28)	390	—	—	—
DAPA ^c	4 (7)	300	180	10 (4)	360

^a Observable Li corrosion after 2 days; observable electrolyte coloration after 16 days.

^b Solvent passed through activated alumina.

^c Solvent distilled; passed through alumina; salt added in the cold followed by preelectrolysis; electrolyte passed through alumina.

of H_2O and O_2 —substances that can form protective films on Li (14). Yet even this extremely pure THF reacts with Li. Electrolyte prepared from THF is more stable, reacting after 25 days of storage. Presumably, impurities introduced in the electrolyte form protective films, or the salt itself can to some extent scavenge reactive intermediates. The major reduction product in the reaction of THF with Li was found to be *n*-butanol from lithium *n*-butoxide after hydrolysis (20).

Electrolyte conductivities.—The specific conductivities of the methylated cyclic ethers were determined at varying concentrations of $LiAsF_6$. These data are plotted in Fig. 1 and compared with literature values for the $LiAsF_6/THF$ system (25). We see that the introduction of methyl groups on the oxolane ring lowers electrolyte conductivity. With 3-Me-THF, loss of molecular symmetry may inhibit the ability of these molecules to solvate Li^+ relative to that of THF resulting in a higher ratio of contact ion pairs to solvent separated ion pairs. With 2-Me and 2,5-di-Me-THF, the conductivity is more seriously attenuated. An attractive rationalization involves steric crowding of the oxygen atom by the α -methyl group(s), and this model has been advanced by us (23) and others (26). However, recent carbon-13 NMR measurements by us (vide infra) discount this explanation. In fact, from α -carbon chemical shift data we infer that Li^+ interacts more strongly with the oxygen atoms of 2-Me and 2,5-di-Me-THF than THF, as would be predicted on the basis of alkyl group inductive effects. It is therefore likely that α -methyl substituents simply perturb the efficient packing of solvent molecules about Li^+ leading to an increased number of contact ion pairs, as has been observed earlier (27).

Because $LiAsF_6/2,5$ -di-Me-THF electrolytes have much lower conductivity than $LiAsF_6/2$ -Me-THF, most of our electrolyte development effort was focused on the latter system.

Li cycling experiments.—A more stringent test of electrolyte inertness involves the dynamic cycling of Li to and from a conducting substrate. As indicated earlier, good cycling efficiency can only be achieved if the reactivity of electrolyte with Li is minimal. This requires the absence of reactive impurities as well as the chemical compatibility of salt and solvent with Li. In Fig. 2, the cycling efficiencies of THF and 2-Me-

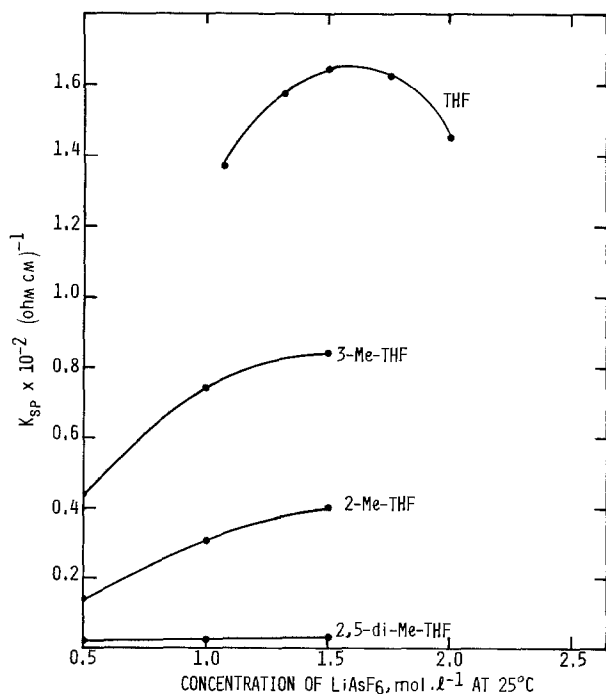


Fig. 1. Specific conductance of several tetrahydrofurans at various $LiAsF_6$ concentrations.

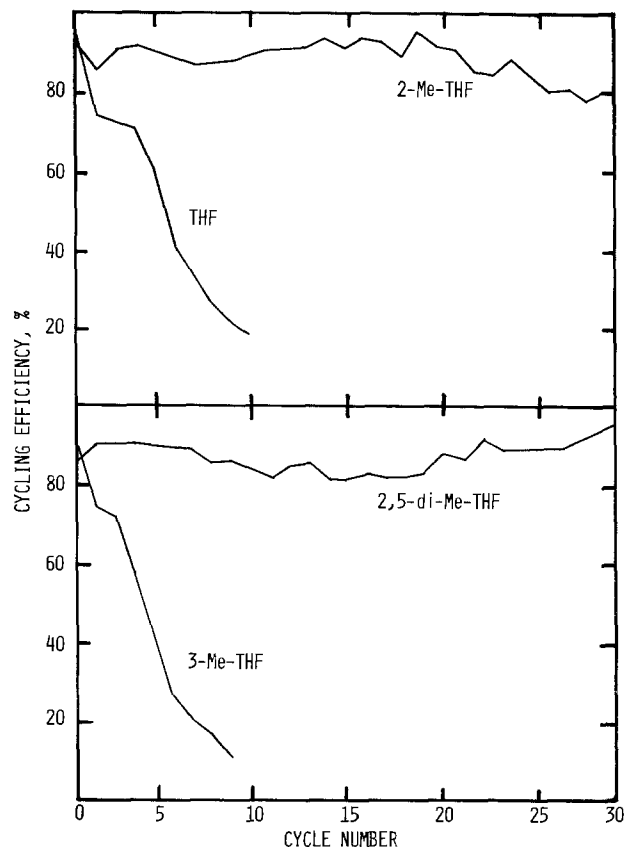


Fig. 2. Efficiencies of cycling Li on an Ni substrate. 1M $LiAsF_6$ /cyclic ethers; $Q_p = 1.1 C/cm^2$; $i_p = i_s = 1 mA/cm^2$ (2,5-di-Me-THF), and 5 mA/cm^2 (other ethers).

THF electrolytes (1M $LiAsF_6$) are presented as a function of cycle number for 1.1 C/cm^2 Li on Ni plates. On the 10th cycle run in THF-based electrolyte, 80% of the Li plated is encapsulated by films and lost to anodic dissolution. By comparison, only 7% of Li plated from 2-Me-THF based electrolyte is electrically isolated. This electrolyte nevertheless does degrade with cycle number, as evidenced by the slow decay in cycling efficiency. Either reactive impurities and/or a very slow reaction of 2-Me-THF with Li yield products which perturb the morphology of subsequent plates.

Figure 2 also compares the cycling efficiency of 2,5-di-Me-THF and 3-Me-THF, 1M in $LiAsF_6$. There is a striking similarity between these curves which is in qualitative agreement with the static storage tests, i.e., that methyl groups α to the oxygen atom improve the electrolyte's stability.

Our experimental work with cyclic ether electrolytes attempts to mimic the charge and discharge characteristics of the secondary Li electrode in a practical battery. A key experiment employed by us to evaluate electrolyte stability involved cycling Li to and from a Li rather than Ni substrate in a half-cell configuration. This was accomplished by plating a known amount of Li onto a Ni electrode, and then sequentially stripping and plating a lesser charge of Li. The amount of excess Li determines, in part, the number of "100%" cycles to be achieved. For example, a typical Li on Li cycling experiment consists of plating 4.5 C/cm^2 Li onto a Ni electrode; 1.1 C/cm^2 are then stripped leaving 3.4 C/cm^2 of the excess Li. Subsequent plating and stripping cycles employ 1.1 C/cm^2 . Were each cycle 100% efficient, the cell would cycle indefinitely with a 3.4 C/cm^2 reserve of Li (efficiency = Q stripped/ Q plated). Of course, each stripping cycle is <100% efficient which means that each strip cuts into the Li reserve yielding an apparent "100%" cycle until the Ni substrate is reached. At this point the excess Li is exhausted and one may calculate the

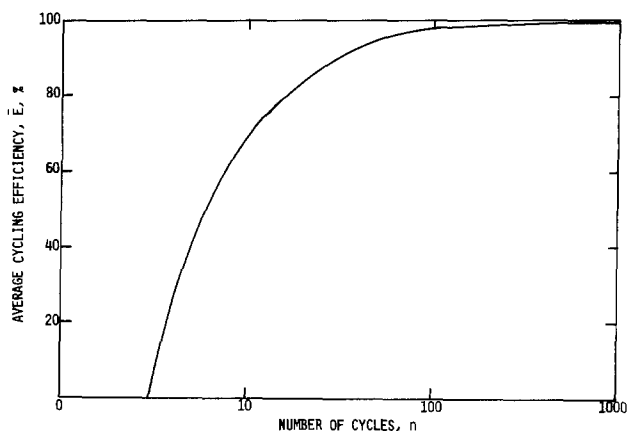


Fig. 3. Functional dependence of \bar{E} on n , where $Q_s = 1.1 \text{ C/cm}^2$ and $Q_{ex} = 3.4 \text{ C/cm}^2$.

average efficiency per cycle, \bar{E} (Eq. [2])

$$\bar{E} = \frac{Q_s - \frac{Q_{ex}}{n}}{Q_s} \quad [2]$$

where Q_s is the charge of Li stripped, Q_{ex} is the amount of excess Li, and n is the number of "100%" cycles. Beyond 100 "100%" cycles, large increases in n provide only a fractional increase in \bar{E} as seen in Fig. 3.

Li on Li cycling efficiencies for LiAsF₆/THF and 2-Me-THF were determined at three salt concentrations. The cycling results and conductivity measurements are summarized in Table III. Electrolytes containing 2-Me-THF significantly outperformed those prepared with THF, even though the conductivities of the former were much less than the latter. In addition, Li plates from 2-Me-THF electrolyte were much less dendritic than those from THF electrolyte. Thus, good conductivity and throwing power alone do not necessarily insure regular Li plate morphology.

The average cycling efficiency of 1.5M LiAsF₆/2-Me-THF electrolyte was also assessed as a function of current density. As seen in Table IV, \bar{E} increases to 97.4% as i is lowered to 0.9 mA/cm² presumably due to better Li plate morphology at lower current densities.

In an earlier paper (20), we noted the formation of a brown film on the surface of the Li electrode when it was cycled in LiAsF₆/THF media. Elemental and ESCA analyses suggested that the film was composed of LiF and a $(-\text{As}-\text{O}-\text{As}-)_n$ polymer formed from

the reaction of THF and AsF₆⁻ reduction products (20). This film was also observed to form on the Li electrode after cycling in LiAsF₆/2-Me-THF electrolyte. However, the rate of formation in 2-Me-THF is substantially lower than that in THF again indicating that 2-Me-THF is less reactive toward Li than THF.

Table III. Comparison of conductivity and cycling efficiencies for LiAsF₆/THF and 2-Me-THF electrolytes at 25°C^a

	[LiAsF ₆] (mole/l)	$K_{sp} \times 10^{-2}$ ($\Omega \text{ cm}$) ⁻²	Number of "100%" cycles	\bar{E} (%)
THF	1.0	1.37 ^b	18	83.3
	1.5	1.65 ^b	25	88.0
	2.0	1.45 ^b	17	82.4
2-Me-THF	0.5	0.14	30	90.0
	1.0	0.30	45	93.3
	1.5	0.40	84	96.4

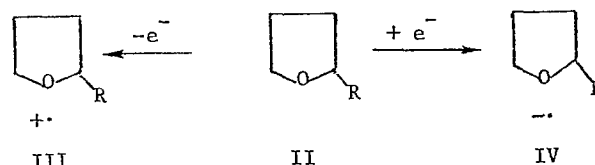
^a $Q_{ex} = 3.4 \text{ C/cm}^2$; $Q_s = 1.1 \text{ C/cm}^2$; $i_b = i_a = 5 \text{ mA/cm}^2$.
^b Ref. (25).

Table IV. Variation of average cycling efficiency with current density for 1.5M LiAsF₆/2-Me-THF^a

i , mA/cm ²	Number of "100%" cycles	\bar{E} (%)
5.0	80	96.3
2.5	95	96.8
0.9	116	97.4

^a $Q_{ex} = 3.4 \text{ C/cm}^2$; $Q_s = 1.1 \text{ C/cm}^2$; $i_b = i_a = i_s$.

Anodic limits of cyclic ethers.—We believe Li-ether reactivity to be determined by the ease with which a solvent molecule accepts an electron from Li (Eq. [1]). Data presented in earlier sections of this paper show that cyclic ethers incorporating methyl group(s) α to the oxygen atom resist reduction in consonance with the LUMO argument. If the electrophore (that part of a molecule accepting or giving up an electron) is involved in both one-electron oxidation and reduction, one would predict that those ethers more difficult than THF to reduce should be correspondingly easier to oxidize. In Scheme I, for example



R = H, Me

Scheme I

the oxidation potential of II \rightarrow III (R = Me) should be less than II \rightarrow III (R = H). Accordingly, the reduction potential of II \rightarrow IV (R = Me) should be greater than II \rightarrow IV (R = H).

Now oxidation of the ether electrophore ensues at the highest occupied molecular orbital (HOMO). And, for aliphatic ethers, the HOMO comprises an orbital including the nonbonding electrons on oxygen as has been determined earlier (28).

In order to verify the anodic side of Scheme I, a variety of cyclic ether/LiAsF₆ electrolytes were subjected to linear sweep voltammetry. Starting from the rest potential (typically +2V vs. Li), the working electrode was anodically polarized. Potentials at which the anodic current density reached an arbitrary value of 100 $\mu\text{A/cm}^2$ were recorded and are tabulated in ascending order (Table V). Although only 300 mV separate the extremities of this scale, it is clear that those compounds with electron-donating α -methyl groups oxidize more readily than unsubstituted THF or THP. Conversely, ring systems with electron-withdrawing substituents (-OMe) or with an electronegative oxygen atom in place of a methylene group (1,3-dioxolane) are more difficult to oxidize.

These data support the LUMO concept of cyclic ether reduction whereby transfer of an electron from

Table V. Anodic limits of selected cyclic ethers

Ether ^a	E_{100} , V ^b
2,5-dimethyl-THF	4.04
2-methyl-THP	4.14
2-methyl-THF	4.15
THP	4.20
THF	4.25
3-methyl-THF	4.29
1,3-dioxolane	4.31
2,5-dimethoxy-THF	4.35

^a 1M in LiAsF₆.

^b Potential vs. Li at which the current density reached 100 $\mu\text{A/cm}^2$ on a vitreous carbon working electrode; $A = 0.196 \text{ cm}^2$, $v = 100 \text{ mV/sec}$.

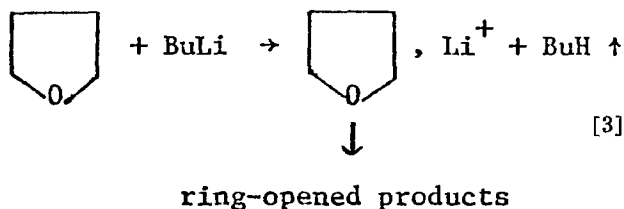
Li to an orbital approximated by a linear combination of sp^3 C and $2p$ O places excess electron density in the C—O bond (20). The excess electron density, formally a radical-anion, predisposes the C—O bond to cleavage, or ring-opening as in the case of cyclic ethers.

Knowledge of a solvent's anodic limit is critically important to Li battery technology, as has been noted previously by Dey and Rudd (29). They found that at $+4.0V$ vs. Li THF rapidly underwent anodic oxidation with subsequent polymerization. Thus, the potential at which an electrolyte oxidizes determines the maximum charging potential as well as influencing the choice of the positive electrode for secondary Li batteries.

When 1M $LiAsF_6/2\text{-Me-THF}$ was potentiostated at $4.15V$ vs. Li for several hours, no polymeric material was observed to form on the Ni working electrode surface. This is consistent with earlier work which demonstrated that 2-Me-THF and 2,5-di-Me-THF do not polymerize under conditions which readily polymerize THF (30). Nevertheless, α -methylated THF's oxidize irreversibly at potentials lower than THF, and this must be taken into account in setting battery charging limits.

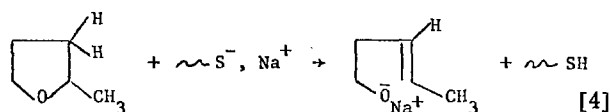
Alternative mechanisms for cyclic ether reduction.—While the LUMO argument is consistent with the chemical and electrochemical results, other possible reaction mechanisms require consideration.

Bates and co-workers found that *n*-butyllithium (BuLi), a strong base, abstracted the α -proton from THF (Eq. [3]) (31). Accordingly, a methyl



group in the 2-position might effectively shield one side of oxolane ring from attack. At best, this halves the number of abstractable protons which in turn retards the observed reaction rate. This effect is typically accounted for by multiplying the rate expression by the statistical factor (0.5 for 2-Me-THF) (32). However, on the basis of the storage and cycling data presented earlier, it appears that the reaction rate of 2-Me-THF with Li is much more than halved compared to that of THF.

Szwarc and co-workers have suggested that a proton in the 3-position of 2-Me-THF may be sufficiently acidic so as to be abstracted by a strong base (Eq. [4]) (33)



where $\sim\text{S}^{\ominus} \equiv$ polystyryl carbanion. Under the same conditions, however, Szwarc found that THF is inert to polystyryl carbanions (33). This indicates that a proton abstraction mechanism is not in force when these solvents are reacted with Li.

Another possibility is that the observed reaction rate differences are due to variations in the physicochemical properties of films on the Li surface. In the case of the cyclic ethers, such films are expected to be composed of Li alkoxide salts from solvent reduction by Li, e.g., lithium *n*-butoxide from THF (20). Propylene carbonate (PC) is "stable" toward Li due to a coherent, insoluble Li_2CO_3 film which protects the underlying Li from PC (34). Unlike Li_2CO_3 , however, lithium *n*-butoxide is soluble in hydrocarbon solvents at ambient temperatures—0.66M in *n*-hexane (25°C) (35). Now, Li-solvent reduction products from alkyl-

ated oxolane rings are expected to yield either longer or branched-chain alkoxide salts. These compounds have been shown to have even higher solubilities in alkane and cyclic ether solvents than lithium *n*-butoxide (35). Therefore, the chemical stability of the α -methylated THF's cannot be due to the intervention of protective alkoxide films. It is also difficult to invoke other, as yet unisolated reduction products or intermediates from 2-Me-THF which passivate Li, since structurally similar 3-Me-THF affords reaction products which clearly do not passivate Li.

It is known that corrosion rates generally accelerate with increasing electrolyte conductivity (36). And we have shown earlier that $LiAsF_6/THF$ media are significantly more conductive than $LiAsF_6/\alpha$ -methyl THF's. In order to demonstrate that solvent reactivity with Li (corrosion of Li) is not simply an artifact of electrolyte conductivity, we have cycled the Li electrode in electrolytes composed of $LiAsF_6/THF$ and $LiAsF_6/2\text{-Me-THF}$ with identical conductivities, i.e., $1.4 \times 10^{-3} \Omega^{-1} \text{cm}^{-1}$. With a 3.4 C/cm^2 excess, only seven "100%" 1.1 C/cm^2 plating and stripping cycles ($i = 5 \text{ mA/cm}^2$) were obtained with the THF electrolyte ($\bar{E} = 57.1\%$); while 31 "100%" cycles were obtained with the 2-Me-THF electrolyte ($\bar{E} = 90.3\%$). These sizable variations in cycling efficiencies reflect changes in the reactivity of the oxolane rings on going from THF to 2-Me-THF, and not in a conductivity effect.

A recent paper (37) and patent (38) suggest that the addition of a macroheterocycle (such as a crown ether) to an organic electrolyte retards the rate of solvent-Li reaction. According to the authors, this phenomenon involves the selective complexation of Li^+ by the macroheterocycle rather than by the solvent's electronegative heteroatom (oxygen, in the case of THF). On the basis of this interpretation and in the absence of a macroheterocycle, one would predict that Li^+ should be more strongly associated with THF than with either of the α -methylated THF's since THF electrolytes are more reactive towards Li than 2-Me and 2,5-di-Me-THF electrolytes.

Now the affinity of Li^+ for a heteroatom is largely related to the basicity of that heteroatom in a homologous series of compounds, as calculated by Hinton and co-workers (39). Thus, the computed interaction between Li^+ and an ether's oxygen atom increases with alkyl substitution. However, experimentally determined basicity orders of cyclic ethers vary with the experiment. Sisler and Perkins, for example, deduced that the oxygen atom of 2-Me-THF and 2,5-di-Me-THF was much more basic than the oxygen atom of THF on the basis of the reaction of these ethers with N_2O_4 (40). Alternatively, Arnett and Wu found THF to be a slightly more basic molecule than either of the α -methylated THF's when these ethers were reacted with H_3^+O (41). Nicholls and Szwarc measured the change in α -proton chemical shifts ($\Delta\delta$) of THF and 2-Me-THF on going from 0 to 10 mole percent Li^+ (42). They obtained $\Delta\delta$ values of 5.0 Hz for 2-Me-THF and 3.7 Hz for THF indicating a stronger interaction of the former ether with Li^+ . We have measured the chemical shift of α -carbon atoms in THF, 2-Me, 3-Me, and 2,5-di-Me-THF on going from 0 to 1M Li^+ . The chemical shift data, presented in Table VI, clearly indicate that Li^+ more strongly perturbs the electronic environment of the α -methylated THF's.

On the basis of Hinton's ab initio calculations (39) and the NMR work, we conclude that Li^+ interacts more strongly with α -methylated THF's than with THF. In addition, the nature of this interaction has been established as being ionic rather than covalent (39, 43). These results cast doubt on the proposed mechanistic role played by macroheterocycles in staving off electrolyte reduction by Li. More importantly, the NMR work coupled with ab initio calculations of Li^+ -solvent interactions illustrate the importance of funda-

Table VI. Downfield shift of cyclic ether α -carbon atoms on going from 0 to 1M LiAsF₆ at 30°C

Cyclic ethers	$\Delta\delta \pm 3$ Hz ^a
THF	29
3-Me-THF	34
2-Me-THF	41
2,5-di-Me-THF	41

$$^a \Delta\delta = \delta_{c_g} (1M Li^+) - \delta_{c_g} (0M Li^+).$$

mental studies in helping to elucidate the complex chemistry of Li-electrolyte reactivity.

Summary and Conclusions

In this paper, we have shown that α -methylated oxolane rings are more resistant to reduction by Li compared to THF itself. With regard to the secondary Li electrode, cycling efficiencies in excess of 96% can be routinely achieved in LiAsF₆/2-Me-THF electrolytes for thin (1 C/cm²) plates. On the basis of storage results at elevated temperatures, cycling data, linear sweep voltammetry, and a consideration of alternative reaction mechanisms, we believe that our results may be rationalized as follows: cyclic ether reduction is initiated by a rate-determining one-electron transfer from Li to the LUMO of the solvent molecule. Raising the activation energy of that initial step retards the rate of reduction of solvent by Li. Methyl groups bonded to α -carbon atoms inductively donate additional electron density into the LUMO making electron transfer from Li to the solvent molecule more difficult.

The use of methylated THF's as solvents in practical ambient temperature Li secondary batteries requires that high cycling efficiencies be maintained for thick (>50 C/cm²) plates. While these anode efficiencies have not been reported in the open literature, it is nevertheless encouraging to note that LiAsF₆/2-Me-THF has found use as an electrolyte in a variety of Li/TiS₂ cells. Thus, Holleck and co-workers have indicated that 500 mA-hr Li/TiS₂ batteries may be designed for 100-200 deep cycles (44). Malachuk reported obtaining 25 deep cycles in a 90 mA-hr Li/TiS₂ button cell (45). Finally, Jet Propulsion Laboratory has tested 4.5 A-hr Li/TiS₂ D cells supplied by EIC Corporation (46). The major problem limiting cycle life was found to be short circuits, presumably caused by Li dendrite growth through the separator.

Although more work is needed to better understand Li-solvent-salt interactions, we believe that a practical secondary Li electrode is at hand. Problems associated with the design and manufacture of ambient-temperature rechargeable Li batteries appear to be ones of optimization and engineering, rather than a problem with the electrochemistry itself.

Acknowledgments

We wish to thank Ms. Gail Schnaper and Prof. David Forsyth (Northeastern University) for obtaining the ¹³C NMR spectra. This work was supported by the Office of Naval Research.

Manuscript submitted Dec. 9, 1979; revised manuscript received Jan. 24, 1980. This was Paper 20 presented at the Los Angeles, California, Meeting of the Society, Oct. 14-19, 1979.

Any discussion of this paper will appear in a Discussion Section to be published in the June 1981 JOURNAL. All discussions for the June 1981 Discussion Section should be submitted by Feb. 1, 1981.

REFERENCES

- W. S. Harris, Ph.D. Thesis, University of California, Berkeley (1958).
- J. E. Chilton, Jr., W. J. Conner, G. M. Cook, and A. W. Hosinger, Lockheed Missiles and Space Co., Final Report on AG-33 (615)-1195, Feb. 1965, AFAPL-TR 64 147.
- R. J. Jasinski, "High Energy Batteries," Plenum Press, New York (1967).
- (a) G. Eichinger and J. O. Besenhard, *J. Electroanal. Chem. Interfacial Electrochem.*, **68**, 1 (1976); (b) *ibid.*, **72**, 1 (1976), and references cited therein.
- M. S. Whittingham, *Science*, **192**, 1176 (1976).
- G. L. Holleck and J. R. Driscoll, *Electrochim. Acta*, **22**, 647 (1977).
- Preliminary Application Guide 0578-1, Exxon Enterprises, Somerville, N.J.
- D. W. Murphy, J. N. Carides, F. J. DeSalvo, C. Cros, and J. V. Waszczak, *Mater. Res. Bull.*, **12**, 825 (1977); U.S. Pat. 4,125,687 (1978).
- J. R. Driscoll, Unpublished work.
- D. W. Murphy and P. A. Christian, *Science*, **205**, 657 (1979).
- (a) R. Selim and P. Bro, *This Journal*, **121**, 1467 (1974); (b) J. Jorné and C. W. Tobias, *J. Appl. Electrochem.*, **5**, 279 (1975).
- R. D. Rauh and S. B. Brummer, *Electrochim. Acta*, **22**, 75 (1977).
- V. R. Koch and S. B. Brummer, *ibid.*, **23**, 55 (1978).
- V. R. Koch and J. H. Young, *This Journal*, **125**, 1371 (1978).
- J. Butler, D. Cogley, and J. Synnott, *J. Phys. Chem.*, **73**, 4026 (1969).
- A. N. Dey, *Thin Solid Films*, **43**, 131 (1977).
- E. Peled, Abstract No. 4, p. 19, The Electrochemical Society Extended Abstracts, Atlanta, Ga., Oct. 9-14, 1977.
- J. E. Dubois, G. Tourillon, and P. C. Lacaze, *This Journal*, **125**, 1257, 1262 (1978).
- I. A. Kedrinskii, S. V. Morosov, G. I. Sukhova, and L. A. Sukhova, *Sov. Electrochem.*, **12**, 1094 (1977).
- V. R. Koch, *This Journal*, **126**, 181 (1979).
- F. W. Dampier and S. B. Brummer, *Electrochim. Acta*, **22**, 1339 (1977).
- V. R. Koch, U.S. Pat. 4,118,550 (1978).
- V. R. Koch and J. H. Young, *Science*, **204**, 499 (1979).
- E. S. Gould, "Mechanism and Structure in Organic Chemistry," p. 203, Holt, Rinehart and Winston, New York (1959).
- J. B. Doe, F. W. Dampier, K. Jeffries, P. E. Krouse, N. Margalit, E. J. Merrick, and L. C. Thompson, USAF Technical Report AFAPL-TR-63, AD-A004543, December 1974.
- D. H. O'Brien, C. R. Russell, and A. J. Hart, *J. Am. Chem. Soc.*, **101**, 633 (1979).
- (a) C. Carvajal, J. J. Tölle, J. Smid, and M. Szwarc, *ibid.*, **87**, 5548 (1965); (b) D. Nicholls, C. Sutphen, and M. Szwarc, *J. Phys. Chem.*, **72**, 1021 (1968).
- V. R. Koch and L. L. Miller, *J. Am. Chem. Soc.*, **95**, 8631 (1973).
- A. N. Dey and E. J. Rudd, *This Journal*, **121**, 1294 (1974).
- C. L. Hamermesh and V. E. Haury, *J. Org. Chem.*, **26**, 4748 (1961).
- R. B. Bates, L. M. Kropowski, and D. E. Potter, *ibid.*, **37**, 560 (1972).
- K. J. Laidler, "Chemical Kinetics," 2nd ed., pp. 84-85, McGraw-Hill, New York (1965).
- M. Van Beylen, M. Fisher, J. Smid, and M. Szwarc, *Macromolecules*, **2**, 575 (1969).
- F. P. Dousek, J. Jansta, and J. Riha, *J. Electroanal. Chem. Interfacial Electrochem.*, **46**, 281 (1973).
- C. W. Kamienski and D. H. Lewis, *J. Org. Chem.*, **30**, 3498 (1965).
- J. E. Truman, in "Corrosion," L. L. Shreir, Editor, Vol. 1, 2nd ed., 2.1, Newnes-Butterworths, London (1978).
- A. Soffer and E. Yeager, Abstract 547, p. 1367, The Electrochemical Society Extended Abstracts, Seattle, Wash., May 21-26, 1978.
- A. Soffer, U.S. Pat. 4,132,837 (1979).
- J. F. Hinton, A. Beeler, D. Harpool, R. W. Briggs, and A. Pullman, *Chem. Phys. Lett.*, **47**, 411 (1977), and references therein.
- H. H. Sisler and P. E. Perkins, *J. Am. Chem. Soc.*, **78**, 1135 (1956).
- E. M. Arnett and C. Y. Wu, *ibid.*, **81**, 1684 (1967).
- D. Nicholls and M. Szwarc, *J. Phys. Chem.*, **71**,

- 2727 (1967).
43. P. P. Schmidt and B. S. Pons, *J. Chem. Soc. Faraday Trans. 2*, Submitted for publication.
44. G. L. Holleck, K. M. Abraham, and S. B. Brummer, Abstract 29, p. 82, The Electrochemical Society Extended Abstracts, Los Angeles, Calif., Oct. 14-19, 1979; and "Power Sources for Biomedical Implantable Applications and Ambient Temperature Lithium Batteries," B. B. Owens and N. Margalit, Editors, p. 384, The Electrochemical Society Softbound Proceedings Series, Princeton, N.J. (1980).
45. P. A. Malachuk, Presented at the NASA-Goddard Battery Workshop, Goddard Spaceflight Center, Greenbelt, Md., Nov. 13-15, 1979, Proceedings in press.
46. R. B. Somoano, Presented at the NASA-Goddard Battery Workshop, Goddard Spaceflight Center, Greenbelt, Md., Nov. 13-15, 1979, Proceedings in press.

The A-C Response of Iridium Oxide Films

S. H. Glarum* and J. H. Marshall

Bell Laboratories, Murray Hill, New Jersey 07974

ABSTRACT

The dependence of the a-c response of iridium oxide films upon thickness, potential, and pH was explored in sulfuric and perchloric acid solutions. For concentrations greater than 0.1M, the response function closely resembled that for an injection process diffusively spreading from one interface throughout the film. The response time shifted by a factor of 10^5 with the potential drop across the film. A porous film model is suggested in which response is determined by the mobility of reduced lattice sites, the diffusion coefficient being controlled by a hydrogen ion exchange current within the pores.

Metal oxide films which shift color with applied potential are attractive possibilities for electrochromic display applications. Tungsten oxide has received much attention (1-4), and the discovery of analogous behavior in iridium oxide films has prompted several recent studies of their properties (5-8). At present the electrochemical kinetic response of these films is poorly understood. Most kinetic experiments have dealt with responses to large potential excursions, a property readily measured and important from a device-oriented viewpoint, but one difficult to interpret mechanistically. Analysis requires the assumption of an explicit model, such as the space-charge limited bleaching process described by Faughnan, Crandall, and Lampert for WO_3 (9).

In contrast to large potential transient studies, small amplitude modulation experiments, such as a-c impedance measurements, may be analyzed in considerable detail through complex-plane representations without recourse to any assumed model. With sufficient relaxation data it is possible to determine the requisites of a suitable model. The only a-c measurements on electrochromic films of which we are aware is a recent brief examination of WO_3 (10). We would emphasize that there need be no unique correspondence between large and small signal measurements. The former may introduce nonlinear effects absent in the latter. As one example, large perturbations could introduce nonuniform film states, whereas with small perturbations one always deals with states infinitesimally displaced from uniform, equilibrium configurations.

Figure 1 shows a cyclic voltammogram of an iridium oxide film grown in H_2SO_4 . On passing from 0.1V_{SCE} to 1.1V_{SCE} the electrode's appearance shifts from metallic to dark blue. In this study we shall examine changes in the electrode's response function across this potential region, its dependence upon film thickness and solution pH, and "aging" or slow changes which take place when a film is moved between different solutions. Our computerized instrumentation facilitates the rapid acquisition and analysis of large amounts of a-c data, allowing a more systematic study than is feasible with manual procedures.

* Electrochemical Society Active Member.

Key words: impedance, anodic films, electrochromism.

This paper encompasses a vast amount of experimental data, and it may be helpful to the reader to outline its course and content. Our philosophy for the interpretation of a-c measurements is somewhat unconventional. Rather than starting with a proposed kinetic scheme, deriving an equivalent circuit, and evaluating its parameters from the data, we prefer first to deduce an equivalent circuit description from the data and then proceed to possible interpretations. Our section on results is therefore largely a phenomenological presentation, while the discussion examines physical interpretations.

The most expedient path to find an equivalent circuit is through examination of the shape of complex-plane plots. Thus Fig. 2 indicates a series R-C circuit at low frequencies and a $\sqrt{i\omega}$ response at high frequencies. Empirical parameters can then be defined, and their dependence upon film thickness and potential determined (Fig. 3 and 4). A finite R-C transmission line is shown to have a response function close to that of the film (Fig. 5), and this simple two parameter function satisfies a test in which the characteristic relaxation time varies by a factor of 10^5 (Fig. 6). With the response function established, it is then feasible to

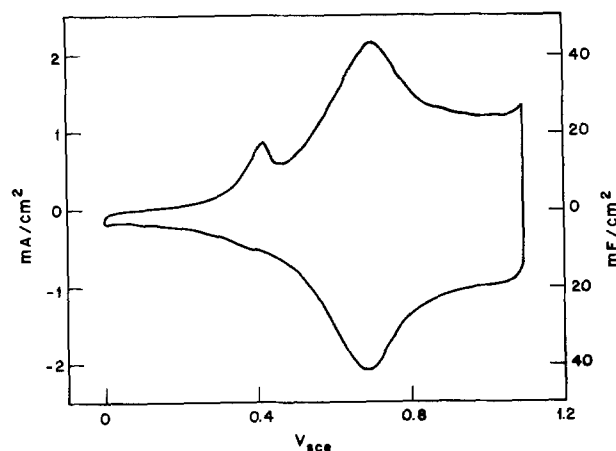


Fig. 1. Cyclic voltammogram of an iridium oxide film taken at 50 mV/sec in 0.5M H_2SO_4 .

make continuous studies *vs.* potential to illustrate solvent and aging effects (Fig. 7, 9, and 10). In dilute acid solutions the response function changes (Fig. 8). The dominant dispersion is characterized by a Warburg element which varies with concentration as expected if the supply of solute H^+ ions is rate determining.

Our discussion focuses upon the interpretation of the response function. A simple model in which a neutral species is in electrochemical equilibrium at one film interface, but spreads diffusively through the film until blocked by the other interface, leads to the equivalent circuit previously deduced. In a more complex calculation we consider the influence on the relaxation process of finite diffusion constants for both species in a double injection process. In the space-charge-free limit, justified by injection densities and measured capacitances, a more complicated relaxation function is found, which reduces to observed behavior when one species is much more mobile. Whether electron or ion motion in the film is rate determining cannot be deduced wholly from the data. Because the limiting diffusion coefficient shifts with potential by a factor greater than 10^5 , we favor a "slow" electron interpretation, and speculate upon a mechanism in which electron motion is blocked by hydroxyl groups whose lifetime is controlled by an electrochemical exchange process with electrolyte in film pores.

Experimental

Materials.—Sulfuric and perchloric acids were obtained from J. T. Baker (Ultrex). The end of a 20 mil iridium wire (0.002 cm^2) embedded in epoxy resin formed the working electrode. Use of a very small electrode was mandated by the large surface capacitance of an oxide film (0.05 F/cm^2). With larger surfaces the response is dominated by the combination of this capacitance with electrolyte resistance.

Even with such a small surface the latter resistance leads to a nonuniform current distribution which is manifest in complex plane plots at kilohertz frequencies. For each experiment the previous film was removed by abrasion with SiC paper. The electrode was then briefly polished with 15, 5, and 1 micron alumina. Extensive polishing tended to raise the metal above the resin surface. The response then appeared intermediate between that of a disk and a hemisphere. This ambiguity was eliminated by the above procedure. Films were grown on the electrode by pulsing as described by Gottesfeld and McIntyre (8).

Cell.—Details of the cell have been previously described (11). The cell was thermostated at 25°C , and all solutions were sparged with argon. All data were taken and are referenced with respect to a saturated calomel electrode.

Measurements.—Apparatus for this work has also been described previously (11). For sweep-frequency admittance measurements taken at a fixed potential, $Y_\eta^*(\omega)$, combinations of three decade sweeps covered the range between 150 kHz and 0.1 Hz. Below 1 kHz a calibrated capacitor shunted by a 1M resistor was used as a reference admittance. This led to greater accuracy over a wider frequency range, for the reference then better matched the unknown admittance.

Modifications of the phase-detector and the sweep circuitry expedited acquisition of data below 100 Hz. To avoid prolonged time constants, pulses at 0° , 90° , 180° , and 270° triggered four sample-and-hold circuits fed by the unfiltered phase detector outputs. Analog combination of these signals gave the required voltages for admittance computation. These pulses were also used to control the sweep rate, so that most time was spent at the low frequency end of the sweep. A single sweep from 100 to 0.1 Hz took 35 sec, and four such sweeps provided sufficient signal averaging for each run.

Prior to each series of experiments electrolyte resistance was determined from high frequency measurements, preferably at a high anodic potential. Following each measurement, the 500+ data points were corrected for the current distribution pattern of a disk electrode, electrolyte resistance was subtracted, and results plotted as a complex capacitance, $C^* = Y^*/i\omega$. Fifty points were listed for later identification and numerical analysis. Typically measurement, corrections, and output required 8-10 min per run.

In alternative experiments, admittance was measured *vs.* potential at a fixed frequency, $Y_\omega^*(\eta)$. Data were taken on the anodic traces of 50 mV/sec cyclic sweeps. At this sweep rate the lowest usable frequency was 5 Hz. After current distribution corrections and electrolyte resistance subtraction, data were plotted and listed in terms of an equivalent series capacitance and conductance. Each such run required a total period of about 10 min.

All reported data have been normalized with respect to the geometric electrode area.

Results

The relaxation function.—Figure 2a shows a composite complex-plane plot of measurements between 100 kHz and 0.2 Hz on an iridium oxide film charging 0.02 C/cm^2 between 0.0 and $1.2V_{SCE}$. Data were taken at $0.70V_{SCE}$ in $0.5M \text{ H}_2\text{SO}_4$, *i.e.*, at the reversible capacitance maximum (Fig. 1). An enlargement of the high frequency branch appears in Fig. 2b. Empirically this linear behavior is described by

$$C^* = C_\infty + W(i\omega)^{-\alpha} \quad [1]$$

where W is a constant and C_∞ , the intercept, equals

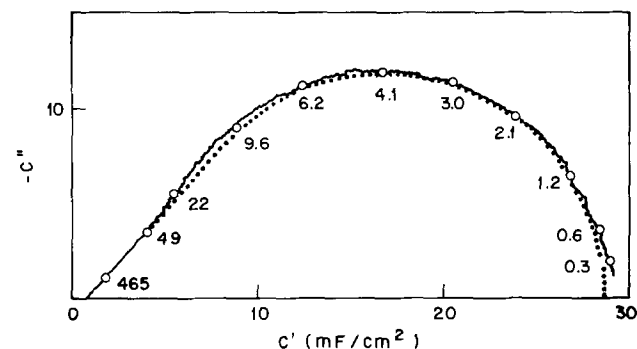


Fig. 2a. Composite complex-plane plot of C^* taken at $0.7V_{SCE}$ in $0.5M \text{ H}_2\text{SO}_4$. Frequencies are in hertz. The dotted curve is a theoretical function.

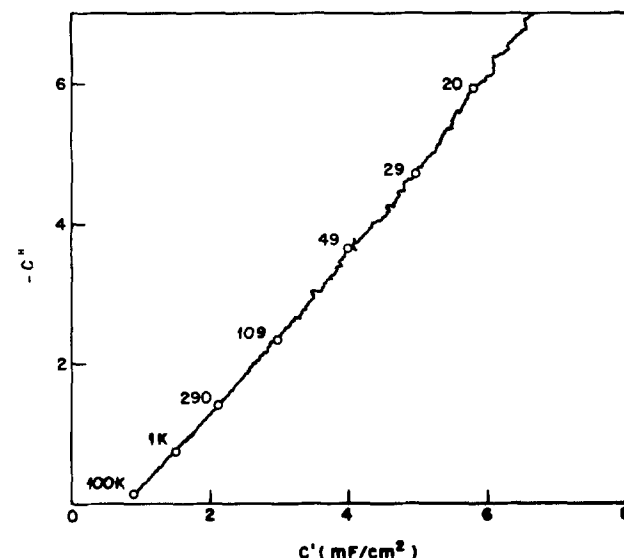


Fig. 2b. High frequency branch of the plot in Fig. 2a

750 $\mu\text{F}/\text{cm}^2$. From the angle of 47.5° , $\alpha = 0.53$. Below 20 Hz the plot shifts towards a semicircle, and one may formally define a relaxation time, $\tau = \frac{1}{2} \pi f_{\text{max}}$, a capacitance $2C_{\text{max}}''$, and a conductance $2C_{\text{max}}'/\tau$. At low frequencies the plot approaches an intercept on the real axis which roughly equals the capacitance inferred from cyclic voltammetry.

Measurements on this film at 0.1 V_{SCE} yielded much smaller capacitance values. Between 100 kHz and 100 Hz we find a broad C^* plot, indicative of a wide distribution of relaxation times, with measured values for C' ranging between 90 and 225 $\mu\text{F}/\text{cm}^2$, and an extrapolated value for C_o of 60-70 $\mu\text{F}/\text{cm}^2$.

The variation of τ with thickness was followed by subjecting the electrode to a number of 1 Hz pulses between -0.25 and $1.25V_{\text{SCE}}$, cycling 10 min between 0.0 and $1.1V_{\text{SCE}}$ to minimize a slight drift in the response function following film growth, measurement, further pulsing, etc. Cyclic voltammograms had similar shapes as the film thickened, and the height of the reversible peak was proportional to the number of pulses. The position of the irreversible anodic peak shifted anodically with increasing thickness, while that of the reversible peak remained unchanged. Figure 3 plots τ and $2C_{\text{max}}''$ vs. the peak capacitance of the cyclic voltammogram. Assuming the latter to be proportional to film thickness, the dispersion amplitude is seen to be proportional to the first power, while the relaxation time increases as the second power of thickness.

In a separate series of experiments data were taken at 50 mV intervals. Between 0.4 and $1.0V_{\text{SCE}}$ the shape of C^* plots resembled that seen in Fig. 2. The amplitude of the dispersion paralleled the cyclic voltammogram, but the relaxation times varied substantially. Below $0.4V_{\text{SCE}}$, f_{max} was less than 0.2 Hz, while above $1.0V_{\text{SCE}}$ the equivalent resistance was more than an order of magnitude less than the electrolyte resistance, and could not be accurately determined. Results for τ and $G = 4\pi f_{\text{max}} C_{\text{max}}''$ are plotted in Fig. 4. Both anodic and cathodic portions of the plot show exponential variations with potential, ~ 120 mV/decade, with an inflection near $0.7V_{\text{SCE}}$.

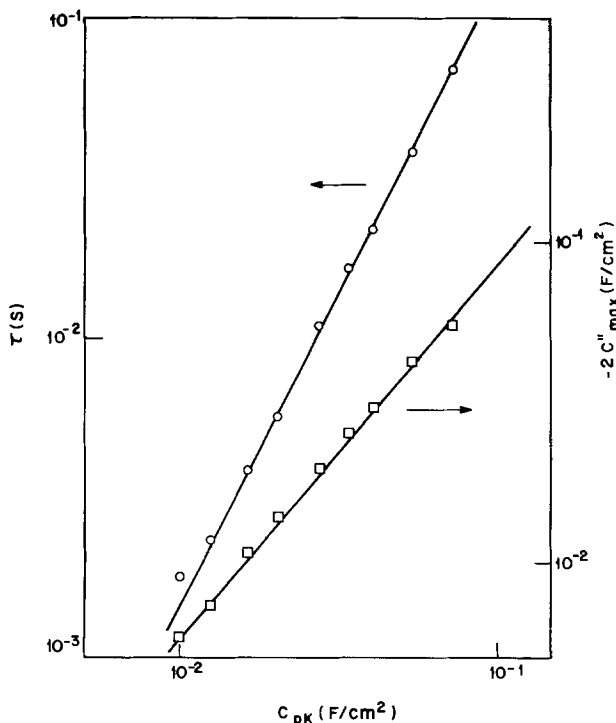


Fig. 3. Log-log plot of τ and $2C_{\text{max}}''$ vs. the peak capacitance found from a cyclic voltammogram. The respective slopes are 1.95 and 1.16. Data were taken at $0.7V_{\text{SCE}}$ in $0.5M \text{H}_2\text{SO}_4$.

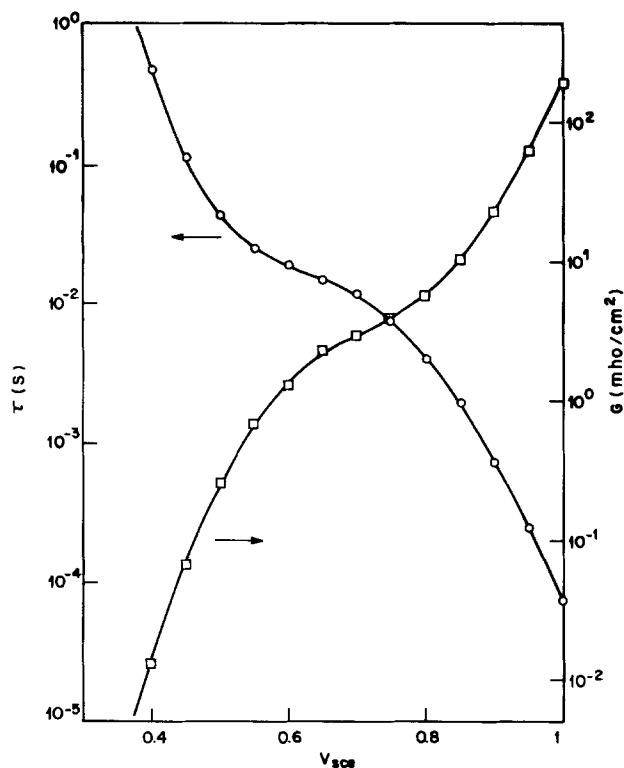


Fig. 4. Potential dependence of τ and G calculated from maxima in C^* plots. Data were taken in $0.5M \text{H}_2\text{SO}_4$.

The shape of the dispersion in the complex plane (Fig. 2) is reminiscent of the response function for a finite R - C transmission line of length l

$$C^*/C_o = \tanh \sqrt{i\omega\tau} / \sqrt{i\omega\tau}$$

$$C_o = l \cdot \partial C / \partial x$$

$$\tau = l^2 (\partial R / \partial x) (\partial C / \partial x) \quad [2]$$

This function is plotted in Fig. 5. At the maximum $\omega\tau = 2.54$, $2C_{\text{max}}''/C_o = 0.834$, and $C_{\text{max}}'/C_o = 0.582$. Although this shape is a good approximation to the experimental function, it is not exact as shown by the dotted plot in Fig. 2a. This difference may reflect a nonuniformity in the film, for the film was grown in a matter of minutes and its thickness is believed to be several thousand angstroms. Immediately after formation the angle of the high frequency branch exceeded 50° , and it gradually decreased to the cited value after an hour of cycling.

The tanh function may be tested by a comparison of W , derived from high frequency data using Eq. [1], with $\omega_{\text{max}}^{1/2} C_{\text{max}}''$. This comparison in Fig. 6 shows good agreement over several orders of magnitude and supports the hypothesis that the distinctive high and low frequency regimes reflect a common relaxation func-

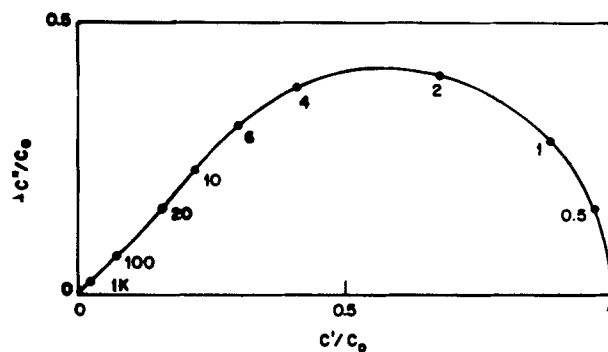


Fig. 5. Complex-plane plot of the function $\tanh \sqrt{ix} / \sqrt{ix}$. Values for x are given.

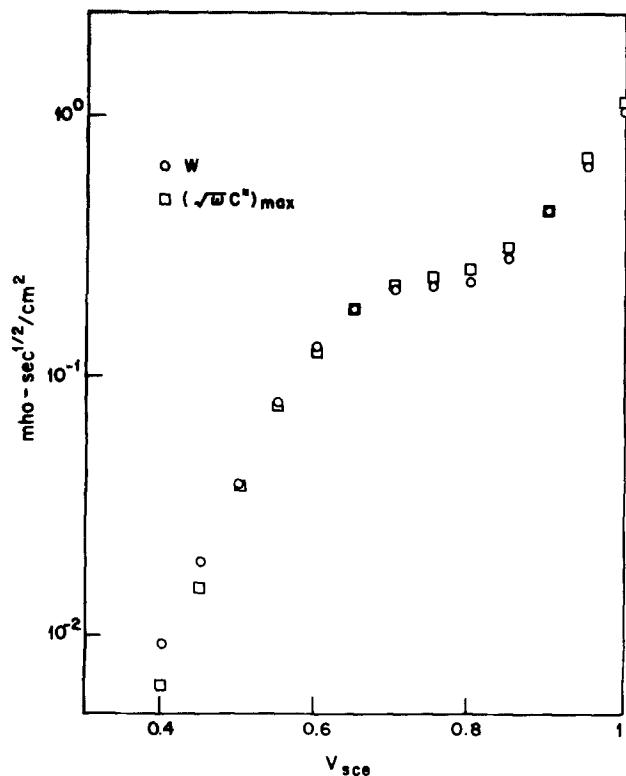


Fig. 6. Comparison of W and $\sqrt{\omega C_{\max}^*}$ vs. potential. Data were taken in 0.5M H_2SO_4 . Ordinate units are $\text{mho}\cdot\text{sec}^{1/2}/\text{cm}^2$.

tion and are not the fortuitous superposition of independent semicircular and circular-arc dispersions. Theoretically, $W/\omega_{\max}^{1/2}C_{\max}^*$ should equal 1.50. The actual ratio appears closer to 1.0 over most of the potential range. In view of the much larger variations seen in these parameters, however, it appears that the tanh function furnishes a meaningful representation for film response.

Figures 7a and 7b show the results of experiments in which data were taken at a fixed frequency during the anodic portion of a cyclic, linear potential sweep. The admittance was resolved into series G and C components, and results are plotted vs. potential. At low frequencies the capacitance plot follows the cyclic voltammogram curve, but the irreversible peak is noticeably absent. With increasing frequency the amplitude of the plot decreases, first at cathodic potentials and then spreading across the plot. The equivalent series conductance shows an exponential variation with po-

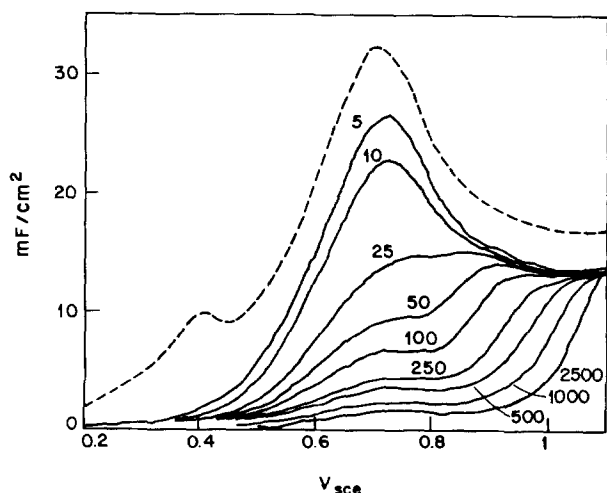


Fig. 7a. Equivalent series capacitance for a film in 0.5M H_2SO_4 . Data were taken at a fixed frequency, indicated in hertz. The dashed curve was derived from the cyclic voltammogram.

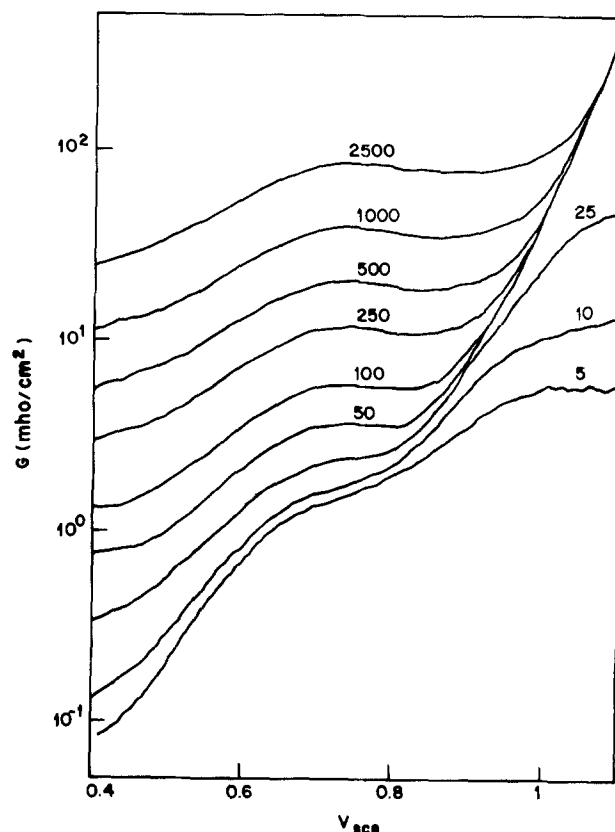


Fig. 7b. Equivalent series conductance for data in Fig. 7a

tential similar to that found in Fig. 4, but with a dispersion in values over most of the potential range.

Some caution is required in interpreting such plots, for the dispersion appears only because plots such as Fig. 2a are not semicircles. The frequency at which the capacitance is half its equilibrium value does not reflect the relaxation time, but rather a frequency at which deviations from a series R - C circuit are significant. For this data at 0.7V_{SCE}, a complex capacitance plot would have a maximum near 7 Hz, whereas Fig. 7a shows a 50% drop at 25 Hz.

At more anodic potentials the frequencies are comparable or less than the relaxation frequency, and one is in the low frequency regime where C^* plots are semicircular. Correspondingly, the dispersions in Fig. 7a and 7b decrease. In principle, at low frequencies Fig. 7a should reveal the reversible portion of the film capacitance and Fig. 7b should correspond to the conductance plot in Fig. 4. At cathodic voltages, however, relaxation frequencies are less than 5 Hz, the minimum frequency which could be used in these experiments, and G values exceed those found by a proper complex-plane analysis. At the anodic extreme, the relaxation frequency exceeds 1 kHz, and the deviation of 5 Hz values from asymptotic behavior seen at higher frequencies is related to the minor deviations from a normal low frequency intercept in Fig. 2a.

Solute effects.—In unbuffered dilute acid solutions C^* plots alter their form. To study this change, a film was grown in 0.1M HClO_4 and examined in various mixtures of 1M HClO_4 and 1M NaClO_4 . Cyclic voltammogram waveforms indicated no major changes in the desorption isotherm other than a 60 mV/pH shift for 10^{-3} to 1M $[\text{H}^+]$ solutions. At the lower concentrations slow sweeps (10 mV/sec) and stirring were necessary to determine the potential of the capacitance maximum where these measurements were carried out. Figure 8 shows our results for a 5 mM solution. The plot has clearly shifted from a semicircular function at low frequencies to a 45° circular-arc function indicative of a Warburg admittance ($\sqrt{i\omega}W$). This

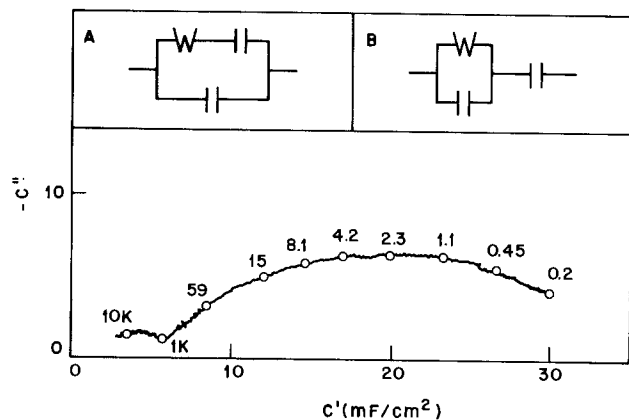


Fig. 8. Complex capacitance for a film in 1M NaClO₄/5 mM HClO₄. Frequencies are given in hertz. Insets A and B are two electrically indistinguishable equivalent circuits fitting the major dispersion.

may, in turn, be related to a bulk diffusion coefficient

$$W = (eF/kT)\sqrt{D} [c] \quad [3]$$

Two distinct equivalent circuits reproduce the observed dispersion and they are identified in the inserts in Fig. 8. Using either circuit for analysis, one finds a linear relationship between W and $[H^+]$ for 1-50 mM solutions. Circuit A gives $D = (3.8 \pm 0.4) \times 10^{-5}$ cm²/sec, while B yields $(6.5 \pm 0.4) \times 10^{-5}$. The error indicates the spread in results obtained for 1, 2, 5, 10, 20, and 50 mM solutions. A separate measurement of H⁺ diffusion in a 1M NaClO₄/1.5 mM HClO₄ solution with a platinum rotating disk electrode gave $D = 6.5 \times 10^{-5}$ cm²/sec. Circuit B is therefore favored, and it seems clear that in these dilute acid solutions the response is primarily determined by the diffusion of H⁺ ions in the electrolyte phase. For concentrations greater than 50 mM, C^* plots reverted to a semicircular low-frequency shape. From the frequency of the maximum we find $\tau = 1.1$ msec for 0.1M, and 0.6 msec for 0.2, 0.5, and 1.0M H⁺ concentrations.

Parallel studies in H₂SO₄/Na₂SO₄ solutions also showed a diffusion controlled response in dilute acids, although the rate-determining ion appears to be HSO₄⁻. In more concentrated acid sulfate solutions response is significantly slower and much more dependent upon $[H^+]$ than in corresponding perchloric acid solutions. Figure 9 shows data for a film grown and measured in 0.5M HClO₄. Direct comparison with Fig. 7a suggests a response time 20 times greater for the H₂SO₄ film.

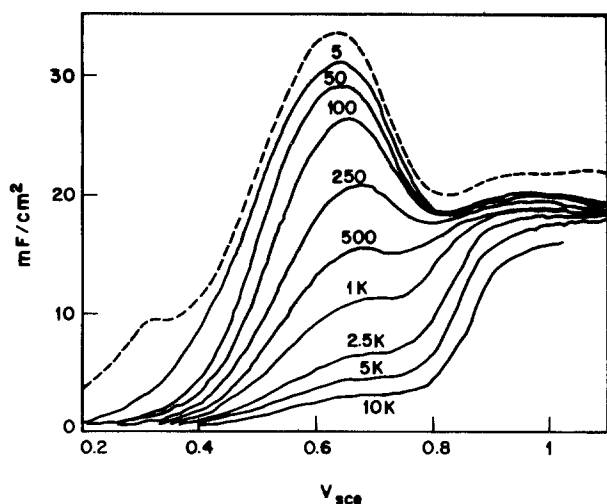


Fig. 9. Equivalent series capacitance for a film in 0.5M HClO₄. Frequencies are given in hertz. The dashed curve was derived from the cyclic voltammogram.

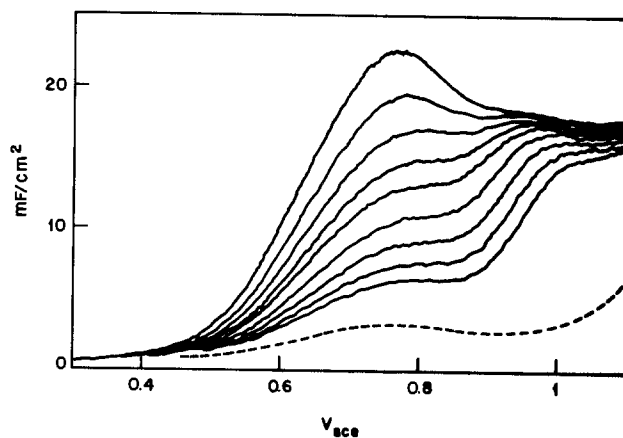


Fig. 10. Aging curves of equivalent series capacitance taken at 100 Hz after transferring a film from 0.1M H₂SO₄ to 2M H₂SO₄. The solid curves span a 2 hr period. The dashed curve was taken after 18 hr.

While in Fig. 7a the peak response is halved at 25 Hz, in 0.1 and 2.0M H₂SO₄ the corresponding frequencies are 250 Hz and <5 Hz. Figure 10 shows series capacitance results at 100 Hz for a film transferred to 2M H₂SO₄ after being grown in 0.1M H₂SO₄. A steady deterioration in response at all potentials is evident, and after 18 hr the electrode appears quite inactive. The level of response is quite similar to that of a film directly grown in 2M H₂SO₄. Nevertheless, upon replacement in 0.1M acid the original response curve was resurrected, although its amplitude had uniformly decreased 50%. The solubility of these films in concentrated H₂SO₄ has been noted by Gottesfeld and McIntyre (8).

Discussion

Cyclic voltammograms (Fig. 1) exhibit three distinct features: an irreversible prepeak at 0.4V_{SCE}, a reversible maximum at 0.7V_{SCE}, and a reversible plateau between 0.8 and 1.1V_{SCE}. A-C measurements (Fig. 7a and 9) show no indications of the prepeak. One cannot decide from Fig. 1 whether the reversible features represent the superposition of two uncoupled processes or a common process with a free energy dependent upon the level of oxidation. Admittance data favor the latter interpretation. Complex-plane plots show no signs that the capacitance can be resolved into two components with differing response functions. Throughout the potential range where overlap would be anticipated, 0.7-0.9V_{SCE}, these plots maintained the functional form seen in Fig. 2. Correspondingly, $C_\omega(\eta)$ plots (Fig. 7a and 9) do not exhibit the clustering of traces at a non-zero capacitance value expected for a superposition of different processes. The a-c results in fact suggest that the response is controlled by a single, potential-dependent parameter. Even the aging curves in Fig. 10 follow the behavior seen in Fig. 7a for an "active" electrode, implying that aging is the time-dependent variation of this parameter.

Although low frequency capacitance measurements are closely correlated with cyclic voltammograms (Fig. 7a and 9), differences beyond the bounds of systematic errors are discernible above 0.7V_{SCE}, a region where the response is sufficiently rapid to preclude the dominant relaxation process from being too slow. Quantitative comparison of cyclic voltammograms shows a slight asymmetry between anodic and cathodic currents, and together these facts may indicate a degree of irreversibility in the redox process. The discrepancy between a-c and voltammetric capacitances is reduced in more dilute solutions, and is less in perchlorate solutions than in sulfate solutions of the same concentration.

An explanation for the response function is naturally the prime object of a kinetic analysis. The thickness de-

pendence of τ (Fig. 3) rules out charge-transfer processes as rate determining. Should such a process be limiting at either the metal/oxide or oxide/electrolyte interface, the resulting resistance would be independent of thickness, and τ would then be directly proportional to film thickness. If, alternatively, limiting were due to charge-transfer occurring uniformly throughout the film, τ would be independent of thickness.

We have noted that the response function closely resembles that for a finite R - C transmission line, and a direct interpretation would be that the dispersion resistance arises from either the conductance of ions or electrons within the film. The possibility that it might reflect electrolyte conductivity within a porous film may be discounted, for increasing $[H^+]$ in sulfate solutions increases both electrolyte conductivity and the dispersion resistance, and it is rather difficult to rationalize a porous resistance change with potential by five orders of magnitude (Fig. 4).

Optical studies of films with comparable charging currents indicate thicknesses of order 10^{-5} cm (6). The maximum value of G measured then corresponds to a bulk conductivity of order 10^{-2} mho/cm. The conductivity of 0.5M H_2SO_4 is 0.3 mho/cm, while crystalline IrO_2 displays a metallic conductivity of 10^4 mho/cm (12, 13). Whether metallic behavior is expected for electrochemically formed iridium oxide films is questionable, for the structure of these films may be quite different from that of crystalline IrO_2 (14, 15).

Electronic conductivities of amorphous hydrogen tungsten oxide films, H_xWO_3 , removed from electrolyte, show ambient conductivities of 10^{-3} to 10^1 mho/cm, with a transition to metallic behavior near $x = 0.3$ (16). Although this injection level approximately equals the fraction of the iridium oxide film oxidized at 0.7V_{SCE}, our results cannot be directly interpreted in terms of such a transition because of the continued increase in conductivity with increasing film oxidation. Recent experiments by Zeller and Beyeler utilizing an amorphous WO_3 film with separated metallic and H_2SO_4 contacts suggest that the electronic conductivity of this film is small in comparison with its ionic conductance and that electron mobility is strongly dependent upon the degree of film reduction (3). Should this situation also prevail in iridium oxide films, it could account for the changes in relaxation time found with potential.

An alternative, but closely related interpretation for the function represented by Eq. [2] is a model involving diffusion through a layer of finite thickness. Let us assume the current to be a function of the concentration of a reduced species, c , formed at the interface $x = 0$ and the overpotential, η , at this interface

$$I^* = (\partial I / \partial \eta) \eta^* + (\partial I / \partial c) c^*(0) = -FD(\partial c^* / \partial x)_{x=0} \quad [4]$$

Solving the basic diffusion equation

$$i\omega c^* = D d^2 c^* / dx^2 \quad [5]$$

with a reflecting boundary at $x = l$, one obtains as a solution for the film impedance

$$\begin{aligned} Z^* &= G^{-1} + [i\omega C \tanh \sqrt{i\omega\tau} / \sqrt{i\omega\tau}]^{-1} \\ G &= \partial I / \partial \eta \\ C &= -Fl (\partial c / \partial \eta)_I \\ \tau &= l^2 / D \end{aligned} \quad [6]$$

The second term is identical with the R - C transmission line response function. The quadratic dependence of τ upon l fits our findings, and assuming $l \sim 10^{-5}$ cm, values for D vary with potential from 10^{-10} to 10^{-6} cm²/sec.

Applied to iridium oxide films, this model does not tell us where the interface is or to what species c refers. In acid solutions we believe electrons enter across one

interface and hydrogen ions across the other. Our simple calculation does not take into consideration the complications of a double-injection process involving charged species, save possibly as a limiting case.

For a more realistic analysis of our films let us therefore consider a film containing positive and negative carriers with unit charge, p and n . In addition we shall assume a certain density, c , of immobile, neutral traps formed by the 1:1 combination of p and n . We further assume that species p may pass across the interface $x = l$ without hindrance, but encounters a reflecting boundary at $x = 0$. Converse boundary conditions apply to species n . Local equilibrium between $c(x)$, $p(x)$, and $n(x)$ is also assumed, so that the model contains no kinetic constants and is wholly diffusive. The linearized kinetic equations we shall employ are

$$\begin{aligned} \frac{dp}{dt} &= D_p \frac{\partial}{\partial x} \left[\frac{\partial p}{\partial x} - \left(\frac{\partial p}{\partial \phi} \right)_e \frac{\partial \phi}{\partial x} \right] - \frac{dc}{dt} \\ \frac{dn}{dt} &= D_n \frac{\partial}{\partial x} \left[\frac{\partial n}{\partial x} - \left(\frac{\partial n}{\partial \phi} \right)_e \frac{\partial \phi}{\partial x} \right] - \frac{dc}{dt} \quad [7] \\ c(x) &= K(c)p(x)n(x) \end{aligned}$$

The subscript e denotes a derivative following local equilibrium configurations and $\phi(x)$ is the potential within the film. $\phi(x)$ satisfies Poisson's equation

$$\frac{\partial^2 \phi}{\partial x^2} = (4\pi e / \epsilon) [n(x) - p(x)] \quad [8]$$

Before attempting a calculation of the small signal a-c response for these equations, we must first examine the nature of the equilibrium configurations to be perturbed. Their solution leads to an antisymmetric function for $\phi(x)$, with equal polarizations at each interface localized within a Debye length, λ (17). When $\lambda \ll l$ the interior of the film becomes an equipotential, space-charge free region ($\bar{p} = \bar{n}$) and $\phi = \eta/2$, η being the total metal-electrolyte potential difference.

High frequency capacitance measurements indicate that this approximation is valid for iridium oxide films. At a potential of 0.1V_{SCE}, a nominally bare iridium surface exhibited a capacitance of 40 $\mu F/cm^2$. Repeating this experiment after a film had been grown on the surface gave 60 $\mu F/cm^2$. Both values indicate a potential drop localized within a short distance of a planar interface and require a large concentration of mobile charges.

We shall therefore consider the solution of Eq. [7] and [8] for a small a-c perturbation, taking the limit as $\lambda \rightarrow 0$. The narrow regions of polarization at $x = 0$, l are excluded, and we shall redefine $x = 0$, l to be the boundaries of the space-charge free region. The relevant modulation equations become

$$\begin{aligned} \frac{d^2 p^*}{dx^2} &= \left[\frac{i\omega}{D_p} \left(1 + \frac{\kappa_2}{2} \right) + \frac{1}{\lambda^2} \right] p^* \\ &\quad - \left(\frac{1}{\lambda^2} - \frac{i\omega\kappa_2}{2D_p} \right) n^* \\ \frac{d^2 n^*}{dx^2} &= \left[\frac{i\omega}{D_n} \left(1 + \frac{\kappa_2}{2} \right) + \frac{1}{\lambda^2} \right] n^* \\ &\quad - \left(\frac{1}{\lambda^2} - \frac{i\omega\kappa_2}{2D_n} \right) p^* \quad [9] \\ \frac{d^2 \phi^*}{dx^2} &= (1/\lambda^2 \kappa_1) (n^* - p^*) \end{aligned}$$

where

$$\begin{aligned} \kappa_1 &= (\partial n / \partial \phi)_e = -(\partial p / \partial \phi)_e \\ \kappa_2 &= (\partial c / \partial p)_e = (\partial c / \partial n)_e \\ 1/\lambda^2 &= (4\pi e / \epsilon) \kappa_1 \end{aligned} \quad [10]$$

At $x = 0$ three boundary conditions are given by

$$\frac{\partial p^*}{\partial x} + \kappa_1 \frac{\partial \phi^*}{\partial x} = 0 \quad x = 0 \quad [11]$$

$$p^*(0) = n^*(0) = -\kappa_1[\eta^* - \phi^*(0)]$$

while the remaining three are set at $x = l$

$$\frac{\partial n^*}{\partial x} - \kappa_1 \frac{\partial \phi^*}{\partial x} = 0 \quad x = l \quad [12]$$

$$p^*(l) = n^*(l) = -\kappa_1 \phi^*(l)$$

The total current across the metal/oxide interface is the sum of that injected and that charging surface polarization at this interface

$$\begin{aligned} I_{mo}^* &= eD_n \left(\frac{\partial n^*}{\partial x} - \kappa_1 \frac{\partial \phi^*}{\partial x} \right)_{x=0} + i\omega \sigma^*(0) \\ &= eD_n \left(\frac{\partial n^*}{\partial x} \right)_{x=0} - \left(eD_n \kappa_1 + i\omega \frac{e\lambda^2}{\kappa_1} \right) \left(\frac{\partial \phi}{\partial x} \right)_{x=0} \end{aligned} \quad [13]$$

Similarly, at the oxide/electrolyte interface

$$\begin{aligned} I_{os}^* &= -eD_p \left(\frac{\partial p^*}{\partial x} \right)_{x=l} \\ &\quad - \left(eD_p \kappa_1 + i\omega \frac{e\lambda^2}{\kappa_1} \right) \left(\frac{\partial \phi}{\partial x} \right)_{x=l} \end{aligned} \quad [14]$$

The preceding differential equations automatically lead to the equivalence of these currents.

A formal solution for Eq. [9] yields

$$\begin{aligned} p^* &= A \sinh \mu_1 x + B \sinh \mu_1 (l - x) \\ &\quad - \gamma_2 C \sinh \mu_2 x - \gamma_2 D \sinh \mu_2 (l - x) \\ n^* &= \gamma_1 A \sinh \mu_1 x + \gamma_1 B \sinh \mu_1 (l - x) \\ &\quad + C \sinh \mu_2 (x) + D \sinh \mu_2 (l - x) \end{aligned} \quad [15]$$

$$\phi^* = \alpha x + \beta (l - x) - (1 - \gamma_1)$$

$$\begin{aligned} &\frac{\lambda^2}{\mu_1^2} [A \sinh \mu_1 x + B \sinh \mu_1 (l - x)] + (1 + \gamma_2) \\ &\quad \frac{\lambda^2}{\mu_2^2} [C \sinh \mu_2 x + D \sinh \mu_2 (l - x)] \end{aligned}$$

A , B , C , D , α , and β are the integration constants.

In the limit $\lambda \rightarrow 0$

$$\begin{aligned} \mu_1^2 &= (2/\lambda^2) + (i\omega/2)(1/D_p + 1/D_n) \\ \mu_2^2 &= (i\omega/2)(1 + \kappa_2)(1/D_p + 1/D_n) \\ \gamma_1 &= -1 + (i\omega\lambda^2/2)(1/D_p - 1/D_n) \\ \gamma_2 &= -1 + (i\omega\lambda^2/2)(1 + \kappa_2)(1/D_p - 1/D_n) \end{aligned} \quad [16]$$

After a stretch of thoroughly tedious algebra fitting boundary conditions to the integration constants, one finds

$$\begin{aligned} Y^* &= I^*/\eta^* = e\kappa_1(D_n + D_p)\mu_2 \left| \left(\mu_2 l \right. \right. \\ &\quad \left. \left. + \frac{D_n^2 + D_p^2}{D_n D_p} \coth \mu_2 l + 2 \operatorname{csch} \mu_2 l \right) \right| \quad [17] \end{aligned}$$

At low frequencies

$$Y^* = i\omega e l (\partial(n + c)/\partial \eta)_e \quad [18]$$

which is the required differential isotherm capacitance. If one diffusion coefficient is much greater, i.e., $D_p \gg D_n$

$$Y^* = eD_n (\partial n / \partial \phi)_e \mu_2 \tanh \mu_2 l \quad [19]$$

This expression is essentially identical with our previous result, less rigorously derived. The effect of traps, aside from increasing the low frequency capacitance, is to reduce the effective diffusion coefficient by a factor $(1 + \kappa_2)$.

When $D_n = D_p$ the normalized admittance is given by

$$Y^*(i\omega)/Y^*(0) = (\mu l/2)^{-1} (\mu l/2 + \coth \mu l/2)^{-1} \quad [20]$$

A complex-plane plot of this function lies very close to the full semicircle. Not finding such behavior at any potential in our experiments, we conclude that over the potential range studied either $D_p \gg D_n$ or $D_p \ll D_n$, with no transition between these limits taking place. Equation [17] predicts deviation from a 45° slope towards a normal intercept at high frequencies in C^* plots when

$$\omega/\omega_{\max} \simeq (D_1/D_2)^2 \quad [21]$$

Figures 2a and 2b show no break below 10 kHz, and as f_{\max} is 4 Hz, the diffusion coefficient ratio must exceed 10^2 .

This model leads to two physically distinct pictures of film oxidation and reduction. If hydrogen ions are the more mobile species, then following a potential change, a density change of electrons, free and trapped, first occurs at the metal/oxide interface and spreads diffusively through the film. An ample supply of hydrogen ions is available to neutralize any incipient space charge. Conversely, if the film is a good electron conductor, changes will first appear at the oxide/electrolyte interface. The Zeller-Beyeler experiments with WO_3 films show the former situation prevails there (3). Repetition of that experiment with an iridium oxide film could resolve this choice.

A serious problem with the double-injection model just analyzed is the potential dependence of the diffusion coefficient or the relaxation time (Fig. 4) which shows slopes at high and low potentials temptingly close to a value of 120 mV/decade. This is perplexing since, according to this model one is dealing with the diffusion of charges in a field-free region, and the only influence of potential is indirectly through the density of charges in the film. One might simplistically assume that $n \propto \exp(-e\phi/kT) = \exp(-e\eta/2kT)$ and that $c \propto n^2$. When $c \gg n$, the trapping coefficient, κ_2 , conveniently leads to the correct potential dependence for the effective diffusion coefficient, but the requisite exponential decrease of c with η is in no way compatible with the cyclic voltammogram. An additional difficulty with this model is the reversible change found when a film is transferred between dilute and concentrated acid solutions. It does not explain why, at corresponding points on the desorption isotherm, corresponding presumably to equivalent injection levels, the diffusion coefficient of the slow species is so greatly affected.

Both difficulties may be circumvented if one postulates a model of a highly porous film with essentially all oxide sites accessible to an electrolyte phase. At equilibrium this phase, containing both anions and cations, is electrically neutral and adopts the potential of the external electrolyte. The electrochemical potential of oxide sites is determined at the metal/oxide interface. In contrast to the preceding model, the total applied potential is felt by all sites within the film. Consider the process idealized in Fig. 11 as the path by which redox changes propagate. With a stationary transition state approximation

$$\begin{aligned} db/dt &= k_a(a + c) - 2k_c b = 0 \\ da/dt &= k_c b - k_a a = k_a(c - a)/2 \end{aligned} \quad [22]$$

where k_a and k_c are anodic and cathodic electrochemical rate constants for the interfacial release and uptake of hydrogen ions. Let Δ represent the distance the reduced site moves in this transition, so that its effective diffusion coefficient is $k_a \Delta^2/2$. If only nearest neighbor transitions are allowed, Δ will be of the

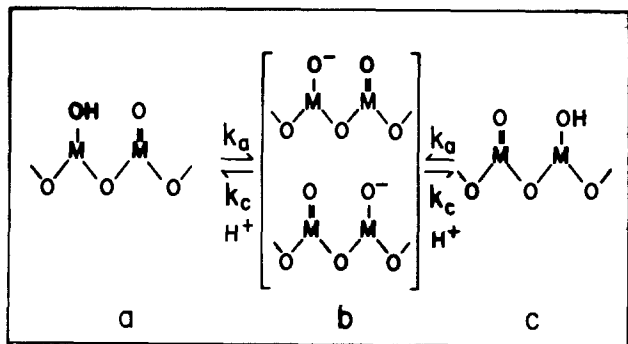
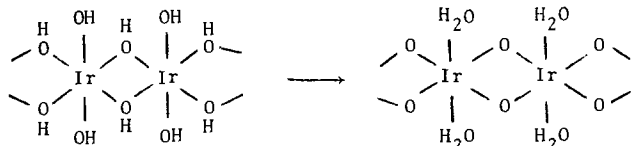


Fig. 11. Hypothetical electrochemical mechanism to describe the motion of a reduced lattice site.

order of a metal-metal distance in the oxide. The potential dependence of diffusion will be dominated by k_a , and is in accord with the observed 120 mV/decade slope.

The slow, but reversible, aging effects observed suggest that structural changes are taking place within the film which alter reduced site mobilities. To rationalize these changes we must speculate on the nature of the film. Indications are that they differ from crystalline IrO_2 in being amorphous and having a high water content (6, 14, 15). The IrO_2 rutile-like lattice can be described in terms of linear chains of edge-sharing octahedra, with adjacent, parallel chains coupled at triply coordinated oxygen vertices (13, 18). Direct hydrolysis of these interchain connections would lead to a structure $\text{Ir}(\text{OH})_4$ which might rearrange to $\text{IrO}_2 \cdot 2\text{H}_2\text{O}$



Structures of this form have been proposed for polynuclear iridium complexes (19). We may further speculate that, during the process of film growth, octahedra are created at the metal/oxide interface and combine to form chains, not necessarily linearly connected. Random crosslinking between chains with a local bonding structure of triply coordinated oxygen atoms similar to that found between chains in the IrO_2 lattice will probably occur.

The aging seen in strong acids may reflect the further hydrolysis of this structure by the introduction of additional H_2O or H_2SO_4 . This would reduce the connectivity of the network and thereby decrease the mobility of reduced sites restricted to motions along the chains. The reversibility of the aging process shows that a dynamic equilibrium exists, and the interconnections must be continually forming and breaking, even in a stable film. Under such circumstances one should be wary of direct comparisons between measurements made on desiccated films in high vacuum experiments and measurements made on "live" films. Both structure and physical properties may be significantly altered by dehydration.

One aspect of our measurements which remains unexplained are the values for C_s . For the data in Fig. 2 this value, $750 \mu\text{F}/\text{cm}^2$, is substantially larger than the double-layer capacitance, although but a fraction of the total film capacitance. For 1-10 mM solutions, c.f. Fig. 8, a capacitance of $5200\text{--}5800 \mu\text{F}/\text{cm}^2$ is seen to characterize a high frequency relaxation process. With the dimensional expression, $C = Ne^2/kT$, the equivalent number of charges is $6 \times 10^{14}/\text{cm}^2$. The

equivalent circuit (Fig. 8) requires that these charges correspond to an H^+ reservoir within the film. Qualitative observations of an unbuffered NaClO_4 solution show a rapid partial response despite the absence of a significant number of hydrogen ions. The cyclic voltammogram is comparatively featureless, as expected for a sluggish reaction, but upon stopping or reversing the sweep in the redox potential region one sees the superposition of a very rapid and a very slow relaxation. The optical response of an unbuffered dilute acid solution also indicates this composite behavior (8). We must conclude that, although in acid solutions, $\text{pH} \sim 3$, the dominant relaxation is governed by the supply of hydrogen ions, an additional mechanism arises in neutral solutions. Rapid kinetics in alkaline solutions have been found (20), but in a nominally neutral solution both hydrogen and hydroxide ion concentrations are too low to support rapid and reversible kinetics. We have postulated two structures which might result from the hydrolysis of an IrO_2 lattice, and it is conceivable that the balance between these configurations is pH dependent. Further studies are needed to reconcile the properties of films in neutral and alkaline solutions with the effort herein reported for acidic media.

Acknowledgments

We gratefully thank Shimshon Gottesfeld for attracting our attention to this interesting system, and for many discussions of our findings.

Manuscript submitted Nov. 19, 1979; revised manuscript received Feb. 4, 1980.

Any discussion of this paper will appear in a Discussion Section to be published in the June 1981 JOURNAL. All discussions for the June 1981 Discussion Section should be submitted by Feb. 1, 1981.

Publication costs of this article were assisted by Bell Laboratories.

REFERENCES

1. S. K. Deb, *Philos. Mag.*, **27**, 801 (1973).
2. B. W. Faughnan, R. S. Crandall, and P. M. Heyman, *RCA Rev.*, **36**, 177 (1975).
3. H. R. Zeller and H. U. Beyeler, *Appl. Phys.*, **13**, 231 (1977).
4. W. C. Dautremont-Smith, M. Green, and K. S. Kang, *Electrochim. Acta*, **22**, 751 (1977).
5. D. A. J. Rand and R. Woods, *J. Electroanal. Chem. Interfacial Electrochem.*, **55**, 375 (1974).
6. S. Gottesfeld and S. Srinivasan, *ibid.*, **86**, 89 (1978).
7. S. Gottesfeld, J. D. E. McIntyre, G. Beni, and J. L. Shay, *Appl. Phys. Lett.*, **32**, 208 (1978).
8. S. Gottesfeld and J. D. E. McIntyre, *This Journal*, **126**, 742 (1979).
9. B. W. Faughnan, R. S. Crandall, and M. A. Lampert, *Appl. Phys. Lett.*, **27**, 275 (1975).
10. B. Reichman and A. J. Bard, *This Journal*, **126**, 583 (1979).
11. S. H. Glarum and J. H. Marshall, *ibid.*, **126**, 424 (1979).
12. W. D. Ryden, A. W. Lawson, and C. C. Sartain, *Phys. Lett. A*, **26**, 209 (1968).
13. D. B. Rodgers, R. D. Shannon, A. W. Sleight, and J. L. Gillson, *Inorg. Chem.*, **8**, 841 (1969).
14. C. C. Schubert, C. L. Page, and B. Ralph, *Electrochim. Acta*, **18**, 33 (1973).
15. D. Michell, D. A. J. Rand, and R. Woods, *J. Electroanal. Chem. Interfacial Electrochem.*, **84**, 117 (1977).
16. R. S. Crandall and B. W. Faughnan, *Phys. Rev. Lett.*, **39**, 232 (1977).
17. J. N. Butler, *J. Chem. Phys.*, **35**, 639 (1961).
18. A. F. Wells, "Structural Inorganic Chemistry," 4th ed., p. 200, Oxford (1975).
19. N. K. Pshenitsyn, S. I. Ginsburg, and L. G. Sal'skaya, *Zh. Neorg. Khim.*, **5**, 832 (1960).
20. G. Beni and J. L. Shay, *Appl. Phys. Lett.*, **33**, 567 (1978).

Porphyrin Modified Tin Oxide Semiconductor as Photocathode

H. Ti Tien and John Higgins

Department of Biophysics, Michigan State University, East Lansing, Michigan 48824

ABSTRACT

A new sensitized semiconductor photoelectrochemical cell is described. The semiconductor is n-type SnO_2 , a wide-band material inherently less susceptible to anodic dissolution. When sensitized by a thin layer of tetraphenylporphyrin (TPP), the SnO_2 electrode acts as a photocathode. The TPP layer is considered as a p-type organic semiconductor whereas the interface between the TPP layer and redox solution is likened to that of a Schottky barrier with the aqueous solution playing the role of a metal. Under illumination, the TPP- SnO_2 electrode vs. Pt (or SnO_2) displays a potential of 400 mV and a current density of $20 \mu\text{A}/\text{cm}^2$.

One of the major problems for photoelectrochemical (PEC) cells using narrow bandgap n-type semiconductors such as CdS is anodic decomposition. The wide bandgap semiconductors such as TiO_2 and SrTiO_3 are stable against photoanodic decomposition (1-4), but unfortunately are poor absorbers of the solar spectrum (5). These semiconductors may be sensitized to enhance their absorption characteristics either by incorporating impurities into the semiconductors (6) or by absorbing dyes onto the semiconductor surface (7, 8). The latter approach has the advantages of simplicity of construction and modification and the availability of a wide range of dye absorption bands, but a PEC so sensitized has a low energy conversion efficiency because only the molecular layers near the semiconductor can inject charge into the semiconductor, the more distant molecules losing most of their energy of excitation in other ways (9, 10). Thus dye or pigment in a thick layer generally has a high electrical resistance and low quantum yield.

We report here a new sensitized semiconductor PEC cell which shows promise of overcoming the above problems. The semiconductor is n-type SnO_2 , a wide-band material ($E_g = 3.5 - 3.8 \text{ eV}$) inherently less susceptible to anodic dissolution, and previously studied as a photoanode for possible application to solar cells (11-13). We have found that, when sensitized by a layer of the pigment *meso*-tetraphenylporphyrine (herein abbreviated TPP), the SnO_2 electrode acts as a photocathode, thereby obviating the anodic dissolution problem of the sensitized photoelectrode. By depositing only the small amount of pigment that can be electroactive, the electrode remains essentially an optically transparent electrode. This permits stacking of cells (or diodes) to form a battery capable of high absorption of visible light, and thereby overcomes the weakness of low absorption of the individual cells.

In addition to its potential for conversion of solar energy, our coated electrode may be of interest in the study of the electrochemical properties of porphyrins (and other pigments) owing to the direct chemisorption of the photoactive compound itself to the electrode without the need for linking molecules or modification of the pigment.

Experimental

A piece of window glass coated on one side with heavily doped SnO_2 (Nesa glass, PPG Company, Pittsburgh, Pennsylvania) with a resistance of $60 \Omega/\text{square}$. This is cleaned in acid, rinsed successively in water and chloroform, and heated to $80^\circ\text{--}90^\circ\text{C}$ before being dipped into the coating solution of *meso*-tetraphenylporphyrine (TPP, from Strem Chemicals, Danvers,

Massachusetts) in CHCl_3 . The normal concentration is 0.65% (w/v), but we have experimented with concentrations ranging from 0.2% to 3.25%, reported here. After 10 sec (not critical) of immersion, the electrode is quickly and smoothly withdrawn. The TPP solution dries to a smooth, hard film that does not noticeably dissolve into the aqueous electrolyte (at $\text{pH} < 7$) if the coat is given sufficient time to dry, usually 2-5 min at room temperature in air. The preheating of the glass appears only to decrease the required drying time, as Nesa glass dipped at room temperature works about as well if given longer time to dry. The electrolyte is 10^{-4}M $\text{Fe}_2(\text{SO}_4)_3$, 10^{-2}M FeSO_4 , and 10^{-2}M H_2SO_4 ($\text{pH} 2.0$). For counterelectrodes we have tried platinum, glassy carbon, and SnO_2 (Nesa glass). SnO_2 was used for the data reported here. The electrical power of the cells with Pt or glassy carbon was about the same as for SnO_2 . Electrical connection was made by tinned alligator clips, which also held the electrodes in a glass container of electrolyte. The electrodes were 2.5 by 5.0 cm, with the immersed, illuminated area being 3.2 cm^2 . Illumination was from a 500W tungsten projector lamp, with spectral measurements made by a Bausch and Lomb High Intensity Monochromator (Model 33-86-02, grating 1350 grooves/mm, 350-800 nm). Both white-light and monochromatic irradiation were measured by the photocurrent from a silicon solar cell through a 1.0Ω load, whose response was calibrated by a radiometer (Yellow Springs Instruments, Incorporated).

Results

From the current-voltage (I/V) curves of two cells (Fig. 1), it can be seen that under irradiation of 200 mW cm^{-2} from tungsten lamp the cell is equivalent to a potential of 0.35-0.40V in series with a resistance of $7\text{--}15 \text{ k}\Omega\text{-cm}^2$ with a short-circuit current density of $1.6\text{--}2.0 \times 10^{-5} \text{ A-cm}^2$. The fill factor is 0.2-0.3, and typical power is $1.0\text{--}2.0 \times 10^{-6} \text{ W cm}^{-2}$. Total power conversion efficiency (maximal power delivered divided by irradiation) is a maximum of 10^{-5} in tungsten white light and 4×10^{-3} at 420 nm. Due to differences between energy spectra, conversion efficiency is expected to be somewhat higher in sunlight than that in tungsten light. The photovoltage risetime is related to the exchange current density and the physical limits on the power such a cell can deliver. The time course of the photopotential exhibits three exponential time constants: 11 sec risetime and two decay constants of 38 and 100 sec. These were measured at 420 nm, but the values of all three are independent of wavelength within our error of measurement (1 sec). All the above data are for SnO_2 counterelectrode, 0.65% TPP: CHCl_3 coating solution, and no external potential. In the dark the same cell has zero potential and current (on the

Key words: photoelectrochemical cell, solar cell, photosensitization.

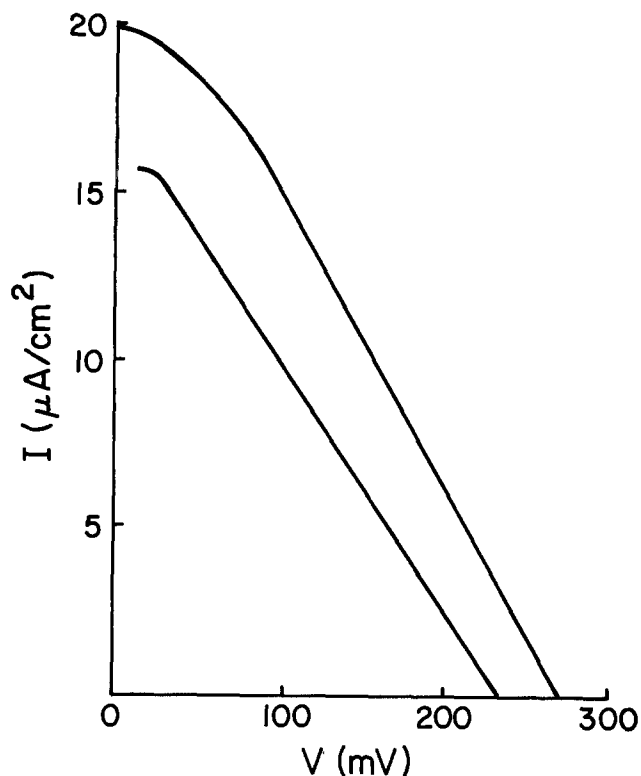


Fig. 1. Current-voltage characteristic of cell at 200 mW cm^{-2} irradiation of tungsten white light. The abscissa shows voltage difference between the electrodes when the cell is loaded by a resistor.

scale of Fig. 1) with resistance of 2-5 times that in the light. Both the photovoltaic and photoconductive effects arise solely from the sensitized electrode. Thus, the currents of Fig. 1 are a combination of a photovoltaic effect (which is the source of overpotential driving the current) and a photoconductive effect, whose presence was shown by measurement of the dark TPP-SnO₂ electrode, which passed about 50% less current at the same overpotentials (provided by an external potential source). In both cases, overpotential was measured against a saturated calomel electrode. If excited TPP is considered the dominant electroactive species, electrochemical theory shows that a photopotential generally leads to increased exchange current density, equivalent to photoconductivity.

The open-circuit photovoltage and the short-circuit photocurrent spectra are shown in Fig. 2. They exhibit the strong violet absorption (Soret band) typical of all porphyrins. The spectra are uncorrected for the spectral distribution of irradiation so that the structure below 450 nm can be seen easily. The combined tungsten lamp-monochromator spectrum rises in three nearly linear segments, from 0.05 to 1.29 mW cm^{-2} over 375 to 550 nm, peaking to 1.78 mW cm^{-2} at 750 nm, and falling to 1.71 mW cm^{-2} at 800 nm. Therefore the light source does not introduce any structure. The quantum efficiency (electron flux divided by absorbed photon flux) and absorption spectra are shown in Fig. 3. The peak positions of the action spectrum are those of the corrected voltage and current spectra. The absorbance peaks of the absorption spectrum of a dilute TPP: CHCl₃ solution differs from the peaks of relative absorption of the porphyrin film on an SnO₂ electrode. The electrode was coated exactly as that for which the action spectra were measured. The absorption of the TPP film was measured by subtracting from the incident radiant energy flux the amounts transmitted and reflected by the coated electrode as well as the amount absorbed by the SnO₂-glass substrate (measured separately).

With respect to electron transfer, Fig. 4 shows the importance of a thin layer of pigment in maximizing

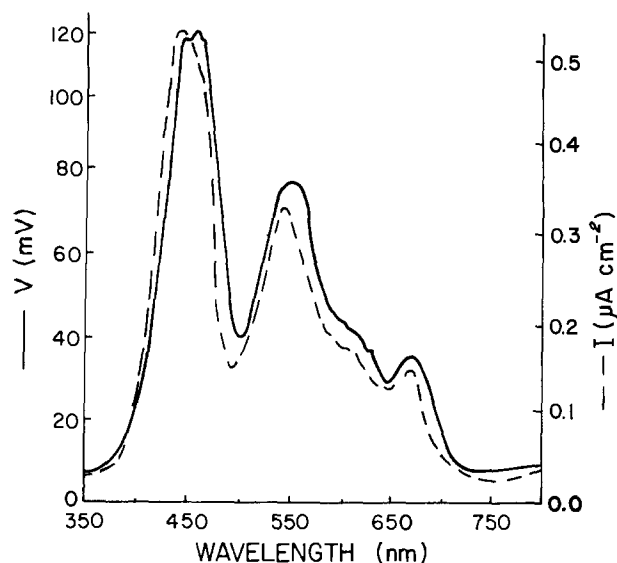


Fig. 2. Spectral photoresponse of TPP-SnO₂ electrode. Irradiation varies as described in the text. Photopotential (solid line) of electrode was measured by the voltage across the open-circuit cell after the absence of a photopotential from the clean SnO₂ counter-electrode or from the electrolyte was determined. Photocurrent (dashed line) through 100Ω , essentially a short circuit.

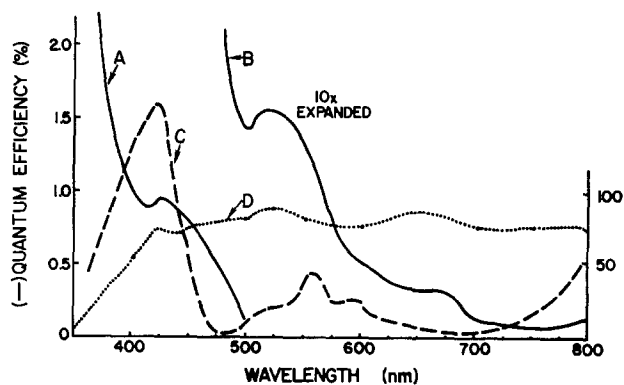


Fig. 3. Quantum efficiency (QE) spectrum (A and B) of cell and absorption spectra of TPP: CHCl₃ solution (C) and dry TPP film on SnO₂ (D, in % on right-hand scale). Note that beyond 500 nm the QE curve (B) has been expanded tenfold with respect to the illustrated scale. The scale for the solution absorption is relative.

the photovoltage and photocurrent, both of which increased as the concentration of the TPP in the coating solution decreased, and they had not reached apparent maxima even at 0.2% (w/v), at which concentration the cell was not stable for more than a few hours. We have not examined closely the relationship between the concentration of the coating solution and the mass of TPP deposited onto the electrode, although at all concentrations studied it was less than 10^{-4} g/cm^2 and there was a visible increase of pigment density with concentration.

We observed that the electrical output of batteries of 2-6 cells added approximately in series or parallel for corresponding electrical connection. That is, for a battery of cells connected in series, the observed battery voltage was close to the theoretical value predicted by the potentials and internal resistances of the individual cells. Similarly, the total current from a battery of cells connected in parallel was the sum of currents measured in isolated cells and the battery voltage was close to the average of cell voltages. These observations were made on batteries whose cells were physically arranged behind one another along the optical axis, so that a single beam of light passed through each cell in sequence, thus increasing the amount of electrical power extracted per beam area. This battery arrangement was permitted by the optical transparency

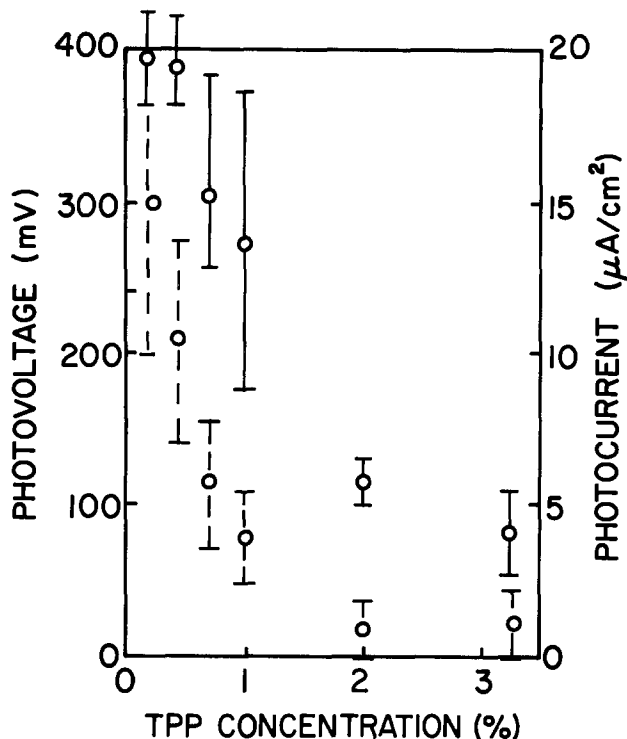


Fig. 4. Cell photopotential (filled circles) and photocurrent (open circles) vs. concentration of TPP coating solution. Bars indicate standard deviations (4-10 samples).

of the SnO_2 and the incomplete absorption of light by the films of TPP.

Discussion

We have described a new photosensitive electrode, SnO_2 coated with an insoluble film of tetraphenylporphine, that can function as a photocathode under its photopotential, in contrast to the more common anodic behavior of sensitized semiconducting electrodes. It has a quantum efficiency of 1% at 425 nm, 0.31 mW cm^{-2} irradiation. Explanation of the positive potential of the TPP- SnO_2 electrode with respect to three apparently inert electrodes, clean SnO_2 , platinum, and glassy carbon, in the iron sulfate electrolyte solution requires more information on the relative energy levels. It is presumably due to the injection of a hole by excited TPP into the semiconductor's valence band, while the excited electron is blocked by the bandgap. The actual mechanism probably involves the bandgap because the photoresponses reported here are very much greater than those of various metals coated with TPP (16).

Regarding spectral characteristics of the electrode, the solution absorption (curve C of Fig. 3) changes and broadens upon depositing the TPP as a coat of pigment on SnO_2 (curve D of Fig. 3). Band broadening is expected in the condensed state. Quantum yield decreases with wavelength faster than does absorption of radiant energy by the film. This may be due to the higher probability for electron transfer from the valence band of SnO_2 to the lowest vacant levels of the energy band of a given ground-state valence orbital of TPP, the availability of more excited-state TPP orbitals to the electrons of higher excitation energy, and the ability of the higher energy charge carriers generated in TPP by the shorter wavelengths to migrate or diffuse through molecular layers of TPP. The dependence of QE on wavelength was reported for monolayers of chlorophyll on SnO_2 (13).

As the spectral intensities used to measure quantum efficiency (QE) of Fig. 2 approach the intensities present in 200 mW cm^{-2} of tungsten light used to measure I/V curves (Fig. 1), we estimate upper limits of 40% to 50% decrease in QE as follows. The theoretical current density is proportional to both QE and irradiation

distributions, although both are unknown at the higher intensities, the fact that the irradiation distribution of the monochromatic source has the shape of a typical tungsten spectrum (at most 17% deviation) suggests that the intensity scaling factor (S) is approximately independent of wavelength. Also, our monochromator's bandwidth (BW) is independent of wavelength for fixed geometrical arrangement. Consequently S can be evaluated by numerically integrating the irradiation spectrum, to give

$$S = (0.40 \pm 0.04) BW(\text{nm}) \quad [1]$$

Because BW cancels in the final equation for current, it need not be known, but Eq. [1] provides a check on our approach if we use a value 5 nm for BW , estimated by the change in wavelength reading to make the same hue appear successively at the two edges of the electrode (2.0 cm across). We find $S = 2.0 \pm 0.2$, in agreement with the monochromator's specified efficiency of 55% at the blaze wavelength (i.e., of maximal efficiency) of 550 nm (an exact check depends upon the unknown efficiency spectrum, but efficiency is specified as high throughout the visible spectrum). The intensity scaling factor is then multiplied by the value of numerical integration over wavelength of the product of irradiation (described in text) times absorption (curve D of Fig. 3) times quantum efficiency (Fig. 3) divided by the energy quantum. The result is multiplied by the electronic charge to give a theoretical current density of $34 \pm 8 \times 10^{-6} \text{ A-cm}^{-2}$, compared with measured values of 16 and $20 \times 10^{-6} \text{ A-cm}^{-2}$ from Fig. 1. Assuming all the difference is due to a decrease in QE upon doubling irradiation permits calculation of the QE decrease. Although we expect most of the decrease in current to be accounted for by QE , the absorption percentage should also decrease a little, so the calculated QE decrease is only an upper limit.

We compare the quantum efficiency results with those of a structurally analogous electrode: chlorophyll-*lecithin* monolayers on SnO_2 (13). For a given photon flux at the relevant sensitive wavelengths (420 and 673 nm) of each electrode, the TPP- SnO_2 electrode has factors of 406 more photons absorbed, 7.4 more electrons per incident photon, and 0.018 as many electrons per absorbed photon. The greater number of photons absorbed simply reflects the greater thickness of our film. The low ratio of electrons to photons absorbed is due to the inability of excited pigment molecules too far from the semiconductor to inject a charge (9, 10). From Fig. 3 and knowledge of the radiant energy absorbed by the substrate (approximately 4% at 425 nm), it is seen that 77% of the incident photon flux reached the molecular layers near the semiconductor. If only the adjacent pigments can inject charge, the efficiency of TPP must be ten times that of chlorophyll. Lower charge injection efficiency implies that charge carriers migrate or diffuse from regions of pigment near, but not adjacent to, the semiconductor.

Previously we have used Mg-*meso*-tetraphenylporphyrin and metal-free tetraphenylporphyrin (TPP) to coat vitreous (glassy) carbon electrodes for use in a photogalvanovoltaic cell (15, 16). The photoactive TPP-electrode behaves as a photocathode. Owing to its opacity, cells made of glassy carbon electrodes cannot be stacked for better light utilization. Therefore, for the construction of a battery, electrode materials must be as transparent as possible in the visible region of the solar spectrum and have good conductivity.

On the basis of obtained data, the following mechanism may be given to account for the observed photocathodic current of the TPP-coated SnO_2 electrode. The doped SnO_2 serves as a conducting substrate with the appropriate bandgap for the TPP layer which is considered as a p-type organic semiconductor. The interface between the TPP layer and redox electrolyte is likened to that of a Schottky barrier with the aqueous solution playing the role of a metal. Upon excita-

tion by light, charge carriers are generated in the TPP layer. The excited TPP most likely decays first to the lowest singlet state and then crosses to the triplet state, at which the triplet state exciton transfers an electron to an acceptor in the bathing solution. The vacant hole left in the TPP layer is filled by an electron from the doped SnO₂ substrate, thereby giving rise to the observed direction of photocathodic current.

The present study has been restricted to inert counterelectrodes, but the behavior of this TPP-coated SnO₂ as a photocathode rather than a photoanode makes possible the use of a photoanode as the counterelectrode to increase power output. It should also be possible to sensitize this optically transparent cell to other visible bands by adding electroactive dye to the electrolyte solution. This is the photogalvanovoltic concept and has been observed from porphyrin-coated glassy-carbon electrodes with thionine in solution (15-17). Thionine did not work well in the TPP-SnO₂ cell. We are currently searching for other dyes and pigments that (i) also bond tightly to SnO₂ to produce a photocathode of different spectral sensitivity or a photoanode and/or (ii) make use of dye solution to construct a photogalvanovoltic cell. We will look at more quantitative methods of coating the SnO₂ electrode with porphyrin using Langmuir-Blodgett molecular layers, or by evaporating a known amount of TPP onto the SnO₂, a technique successful with surface active porphyrin (8).

In summary, we feel that our tetraphenylporphyrin oxide electrode is a good candidate for further investigation as the photocathode for a solar cell. Chemical attack on the sensitized electrode appears to be negligible. One problem common to sensitized semiconductors, low absorption of the incident radiation, can be alleviated by the battery design discussed above, which is made possible by the transparent substrate. No component of our cell presents an obvious cost or production limitation. Pyrolytic deposition of polycrystalline tin oxide onto glass does not require the stringent control of purity required by single crystals or some other types of polycrystalline materials; and metal-free porphyrin can be readily synthesized (14).

Manuscript submitted July 17, 1979; revised manuscript received Dec. 20, 1979.

Any discussion of this paper will appear in a Discussion Section to be published in the June 1981 JOURNAL. All discussions for the June 1981 Discussion Section should be submitted by Feb. 1, 1981.

Publication costs of this article were assisted by Michigan State University.

REFERENCES

1. G. Porter and M. D. Archer, *Interdisc. Sci. Rev.*, **1**, 119 (1976).
2. K. Rajeshwar, P. Singh, and J. DuBow, *Electrochim. Acta*, **23**, 1117 (1978).
3. R. Reisfeld, *Naturwissenschaften*, **1**, 1 (1979).
4. H. Gerischer, *J. Appl. Phys.*, **31**, 115 (1979).
5. M. W. Wrighton, D. L. Morse, A. B. Ellis, D. S. Ginley, and H. B. Abrahamson, *J. Am. Chem. Soc.*, **98**, 44 (1976).
6. A. K. Ghosh and H. P. Maruska, *This Journal*, **124**, 1516 (1977).
7. H. Tsubomura, M. Matsumura, Y. Nomura, and T. Amamiya, *Nature*, **261**, 402 (1976).
8. Y. Umezawa and T. Yamamura, *This Journal*, **126**, 705 (1979).
9. H. Gerischer, *Photochem. Photobiol.*, **16**, 243 (1972).
10. R. Memming, *ibid.*, **16**, 325 (1972).
11. K. Kim and H. A. Laitinen, *This Journal*, **122**, 53 (1975).
12. T. Osa and M. Fujihira, *Nature*, **264**, 349 (1976).
13. T. Miyaska, T. Watanabe, A. Fujishima, and K. Honda, *ibid.*, **277**, 638 (1979) (amended reprint).
14. D. Dolphin, Z. Muljani, K. Rousseau, D. C. Borg, and J. Fajer, *Ann. N.Y. Acad. Sci.*, **206**, 177 (1973).
15. J. M. Mountz and H. T. Tien, *Solar Energy*, **21**, 291 (1978).
16. H. T. Tien, J. Higgins, and J. Mountz, in "Solar Energy: Chemical Conversion and Storage," R. R. Hautala, R. B. King, and C. Kutal, Editors, pp. 203-235, Humana Press (1979).
17. Z.-H. Liu, Z.-C. Bi, D.-S. Cheng, Y.-N. Zhu, and Y.-S. Li, *Kexue Tongbao (Chinese)*, **24**, 1027 (1979).

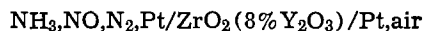
Ammonia High Temperature Solid Electrolyte Fuel Cell

Roger D. Farr and Costas G. Vayenas*

Department of Chemical Engineering, Massachusetts Institute of Technology, Cambridge, Massachusetts 02139

ABSTRACT

A study was made of the overpotential and product selectivity characteristics of the high temperature solid electrolyte fuel cell



It was found that NO is the primary oxidation product, although significant amounts of by-product N₂ are also formed due to the catalytic reaction between NH₃ and NO on Pt. The influence of this side reaction can be minimized under optimal operating conditions and yields of NO exceeding 60% can be achieved. Two dimensionless numbers have been identified which govern product selectivity and power output. The cell is a promising candidate for the cogeneration of electric energy and nitric acid.

The oxidation of ammonia to nitric oxide over a Pt-Rh alloy is the basic step for the manufacture of nitric acid (1). It is a highly exothermic reaction with

$\Delta G = -64.5$ kcal/mole NH₃ at 1000°K. More than 7·10⁶ tons of HNO₃ are produced annually in the U.S. alone. Due to the high exothermicity of the reaction large amounts of thermal energy are generated. It has been a long sought goal to obtain this

* Electrochemical Society Active Member.

Key words: solid electrolyte, fuel cell, ammonia, nitric oxide.

energy as electric rather than thermal energy by oxidizing ammonia to NO in a fuel cell (2).

Low and intermediate temperature ammonia-air cells have been investigated using strong KOH solutions (3, 4) or fused KOH in an MgO matrix (5) as the electrolyte. However N_2 was found to be the only oxidation product.

High temperature solid electrolyte fuel cells operating on H_2 , CO, or CH_4 as the fuel have been tested for years (6, 7). With Pt electrodes and H_2 as the fuel, pure resistance polarization has been observed, but with CO some activation overpotential also appears (7).

Stabilized zirconia cells have been used to monitor the activity of oxygen on metal oxidation catalysts (8) and to dissociate oxygen-containing compounds, including NO (9, 10).

Although the catalytic NH_3 oxidation is highly efficient and, under industrial conditions, mass transfer controlled (1), there have been several interesting recent studies of the intrinsic NH_3 oxidation kinetics on Pt (11, 12).

In this research NH_3 was used as the fuel in a high temperature stabilized zirconia fuel cell with Pt electrodes in order to examine the product distribution of the cell and explore the possibility of NO and electric energy cogeneration.

Experimental Apparatus

A schematic diagram of the experimental apparatus is shown in Fig. 1. It consists of a gas feed system, the fuel cell, and the analytical system. The fuel cell design is shown in Fig. 2. It consists of an 8 mole percent (m/o) yttria stabilized zirconia tube with an ID of 16 mm and 1.8 mm wall thickness. Platinum electrodes were deposited inside and outside to the dimensions given in Fig. 2 using Englehard Pt ink A3788 followed by air drying and calcining at 1300°K for 4 hr. This procedure was repeated twice with Englehard Pt ink A3788 and once with Englehard Pt 6926. Scanning electron micrographs showed electrodes prepared in this manner to be evenly applied and porous. Each electrode had a resistance of 0.24Ω and BET area of $300\text{ cm}^2/\text{cm}^2$ of superficial catalyst area. Thickness was estimated to be $3\ \mu\text{m}$. The anode was extended to one end of the tube in order to ensure good contact with the Pt wire lead. All power

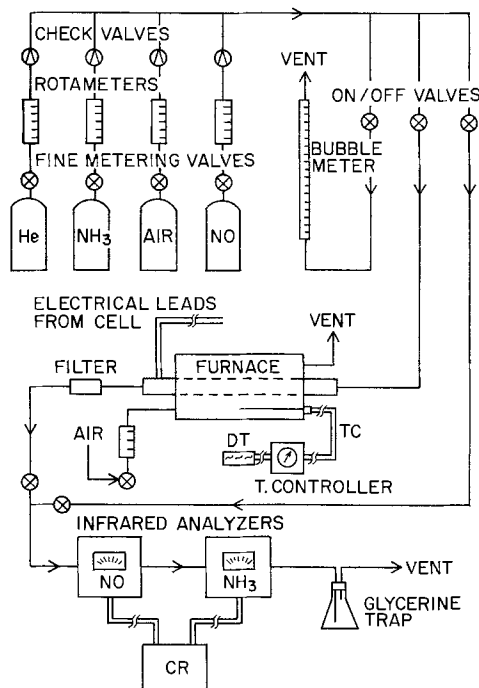


Fig. 1. Experimental apparatus

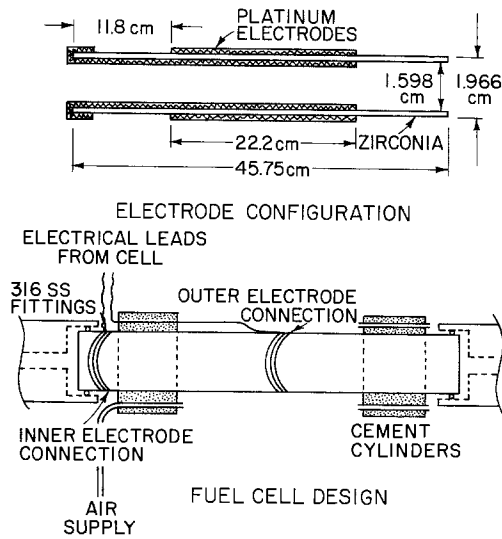


Fig. 2. Fuel cell design and electrode configuration

values reported here are based on the cathode length of 22.2 cm.

To complete the cell assembly and support the weak zirconia tube, Dylon C-3 cement cylinders were cast around the zirconia tube where it entered and exited the furnace. Thermocouple and cathode leads as well as air supply and removal tubes were set into the cylinders as shown in Fig. 2. The fuel cell temperature was held constant within 2°K by means of an on-off type controller. Stainless steel fittings with Viton O-rings were adapted to fit the ends of the zirconia tube. The assembly passed a helium leak test to 4.46×10^5 Pa. All tubing and fittings were 316 stainless steel. The product gas from the cell was immediately cooled by the exit fitting to 298°K for analysis.

Reactants and products were analyzed using Beckman 864 and 865 infrared analyzers for NH_3 and NO, respectively. The feed and exit streams were sampled as shown in Fig. 1. Cell voltage and current were measured by two digital multimeters (Fluke 8600A). A decade resistance box was used to vary cell load. In addition to this load a residual resistance of 0.873Ω was present at all times in the circuit due to connecting wires and multimeters. Additional details of the apparatus appear elsewhere (13).

Reactants used were Matheson certified standards of 4.59% ammonia in helium and 8550 ppm NO in helium. They could be further diluted with Matheson zero gas standard helium. The fuel cell was operated at atmospheric pressure.

Constant potentials could be applied to the cell, when necessary, using an AMEL 549 Potentiostat.

Results

Close agreement was observed ($\pm 0.5\%$) between measured and theoretical emf values when O_2 , N_2 , or He mixtures of known P_{O_2} were fed through the zirconia tube. This verified the pure ionic conductivity of the solid electrolyte.

Cell resistance.—With both Pt electrodes exposed to air, the potentiostat was used to apply to the cell voltages between -2 and 2V . In agreement with previous work (7) it was found that current is linear in voltage and therefore only resistance polarization appears. The cell resistance was thus determined from the slope of the voltage-current lines which have been shown to coincide with the a-c resistance of the cell (7). Results obtained in this manner are shown in Fig. 3. The dashed line between 1000° and 1200°K corresponds to single point d-c resistance measurements. Over the temperature range investigated (700° - 1200°K) the cell resistance R can be approximated by the expression

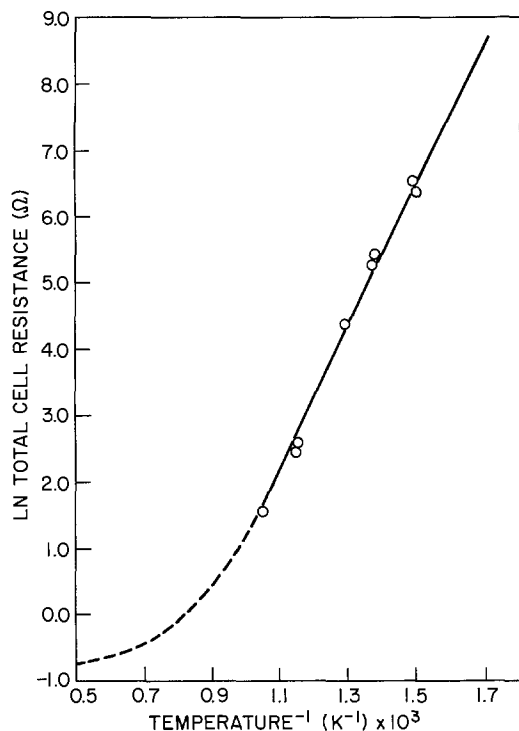


Fig. 3. Fuel cell resistance

$$R = 0.48 + 7.7 \cdot 10^{-5} \exp(10,600/T) \Omega$$

The first term roughly corresponds to the resistance of the electrodes, and the second is due to the solid electrolyte.

Fuel cell performance.—Typical current-potential plots at constant feed composition (4.59% NH_3 in He) are given in Fig. 4a and b. The current I_L corresponding to 100% ammonia conversion to N_2 is also shown for comparison. It is defined by $I_L = 3FG_{\text{NH}_3, \text{F}}$, where F is the Faraday constant and $G_{\text{NH}_3, \text{F}}$ is the feed molar ammonia flow rate. Clearly the current I_M corresponding to 100% ammonia conversion to NO equals $1.67 I_L$.

The current-potential plots indicate strongly that above 1000°K ohmic overpotential is the dominant source of polarization. Taking into account the residual resistance of connecting wires ($\sim 0.87 \Omega$) one finds that the straight line portions of these curves correspond within 30% to the cell resistance. The initial nonlinear decrease in the cell potential can be accounted for by the "Nernst loss" due to increasing conversion to products with increasing current. This gradually increasing "Nernst loss" with increasing current causes the slopes of the quasi-linear portions of the curves to be systematically higher (10%-30%) than the cell resistance.

The potential values observed (Fig. 4), including the open-circuit emf value, would indicate that NO is the primary anodic product according to the reaction



Assuming [1] to be the dominant anodic reaction and using the cell resistance values one can approximate fairly well the potential-current behavior. If O^{2-} or oxygen adsorbed on Pt were involved in N_2 formation, then the absolute emf value would be at least 250 mV higher than what is observed. This is further discussed below.

Using ammonia feed molar flow rates $G_{\text{NH}_3, \text{F}}$ in excess of $7 \cdot 10^{-7}$ mole NH_3/S , i.e., roughly 20 cm^3 STP/min of 4.59% NH_3 in He, resulted in power outputs on the order of 10^{-3} W/ cm^2 of electrolyte and almost zero selectivity to NO, nitrogen being the only oxidation product. However, a decrease in $G_{\text{NH}_3, \text{F}}$

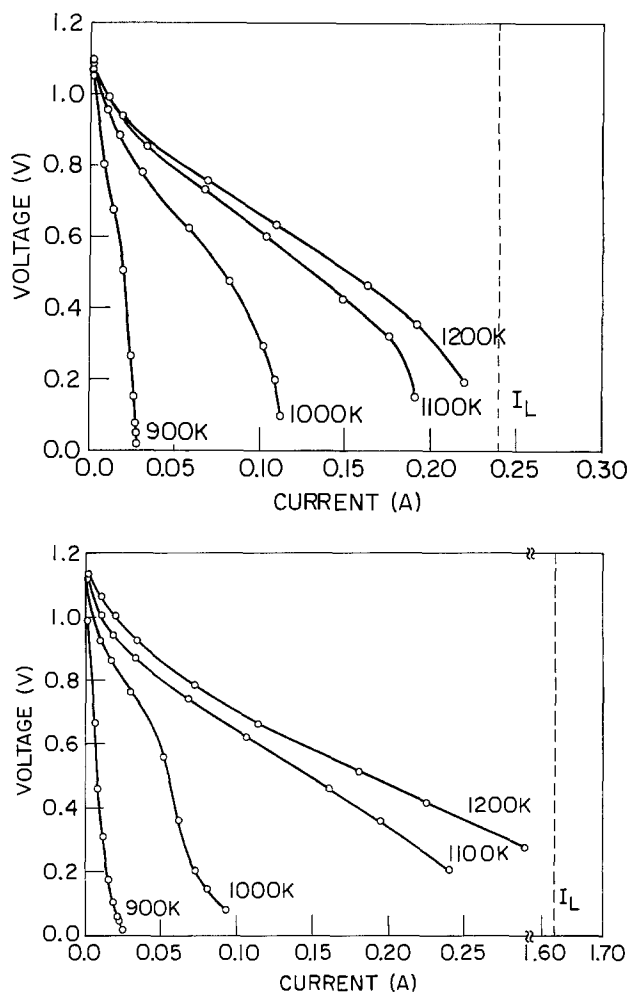


Fig. 4. Current-voltage behavior of the cell with $y_{\text{NH}_3, \text{F}} = 0.0459$. a (top). Flow rate 26 cm^3 STP/min. b (bottom). Flow rate 176 cm^3 STP/min.

below that value, by either increasing dilution or decreasing total flow rate, resulted in a dramatic increase in selectivity (moles NO formed/mole NH_3 reacted).

Accordingly, the fuel cell selectivity and power output were studied extensively at temperatures between 900° and 1200°K, NH_3 feed mole fractions $y_{\text{NH}_3, \text{F}}$ between 0.01 and 0.0459, and total flow rates between 5 and 25 cm^3 STP/min. At 1100°K, $y_{\text{NH}_3, \text{F}} = 0.02$ and with a total flow rate of 5 cm^3 STP/min the maximum selectivity was obtained (97%), although the power output had dropped to $7 \cdot 10^{-6}$ W/ cm^2 due to the very long residence time employed. Under these low flow rates the fuel cell, although tubular in shape, behaves almost exactly as a continuous flow stirred tank reactor (CSTR). This was predicted on the basis of the axial and radial Peclet numbers, but was also verified experimentally (Fig. 5).

Although the dependence of selectivity on temperature, $y_{\text{NH}_3, \text{F}}$, and flow rate initially appears complicated, it was found that selectivity is almost uniquely defined at any T , $y_{\text{NH}_3, \text{F}}$, and flow rate by a dimensionless parameter M defined as

$$M = \frac{G_{\text{O}_2}}{G_{\text{NH}_3, \text{F}}} = \frac{I}{4FG_{\text{NH}_3, \text{F}}}$$

where G_{O_2} is the molar oxygen flux, in the form of O^{2-} , through the electrolyte (Fig. 6). For M values below 0.75 the selectivity is very low but with $M = 1.0$, up to 97% selectivity can be obtained.

In light of this no distinct trend exists on plotting selectivity vs. conversion (13), i.e., selectivity does

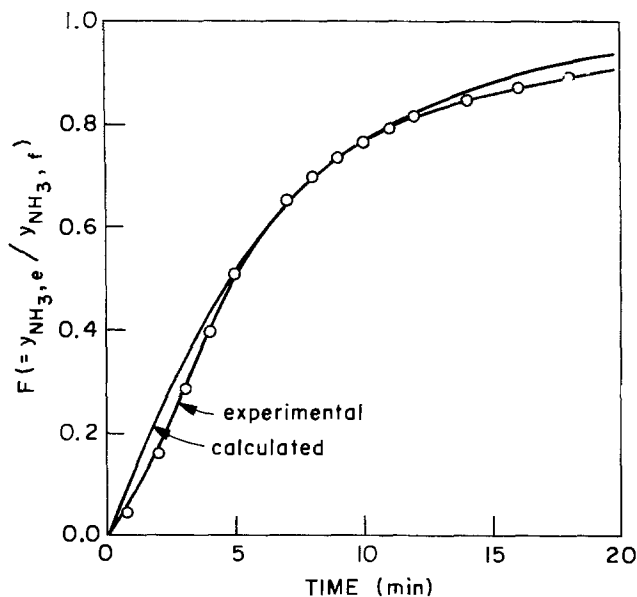


Fig. 5. Response to a step-function change in the feed concentration of ammonia and comparison with ideal CSTR response. Flow rate 18.6 cm³ STP/min, volume of reactor and associated tubing 126 cm³.

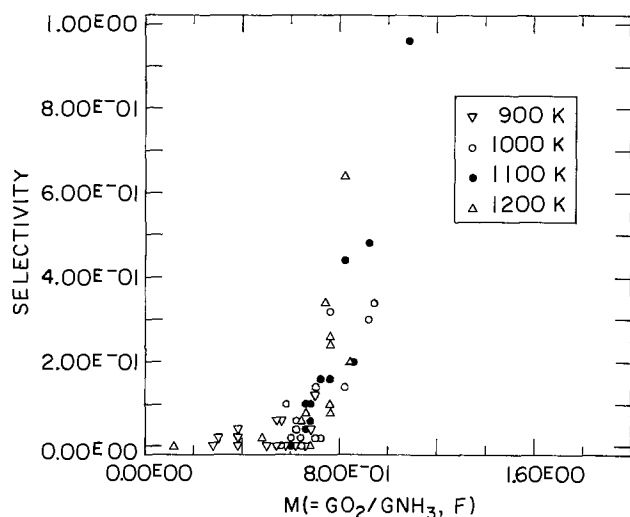


Fig. 6. Selectivity vs. dimensionless group M

not decrease with increasing conversion, and this is an attractive feature of the cell.

In order to examine if the dramatic dependence of selectivity on M is characteristic of NH₃ fuel cell only or if it is a general characteristic of the NH₃ oxidation on Pt, the following experiment was made. Small concentrations of oxygen were admixed with NH₃ fed in the cell. It was observed that when the ratio

$$M' = G_{O_2,F} / G_{NH_3,F}$$

is below 0.75 again the selectivity is practically zero, but increases sharply when $M' > 0.75$ (Fig. 7). It was thus verified that the origin of O₂ (through the zirconia or from the gas phase) plays no role on the selectivity of the cell.

With long residence times (several minutes) and with M values near 0.7 it was observed that the fuel cell voltage, current, and product concentrations exhibit self-sustained oscillations. This is shown in Fig. 8 for $M = 0.7$, $T = 1100^\circ\text{K}$, and 8 min residence time. An extended study of this phenomenon will be presented in a later communication. Only steady-state data have been presented here.

The platinum electrodes performed well over long periods of time (~ 500 hr). Scanning electron micro-

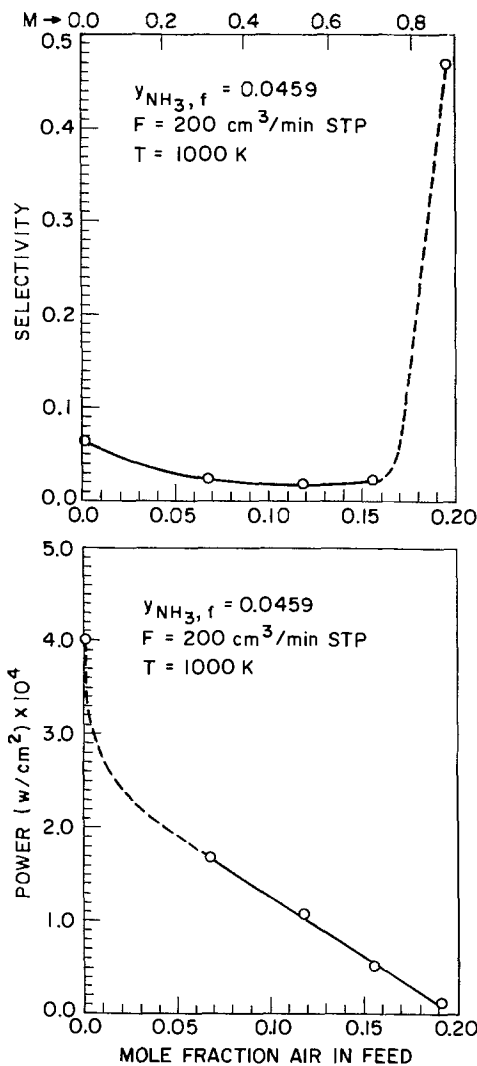


Fig. 7. Effect of oxygen addition to ammonia feed. Selectivity and power output vs. M .

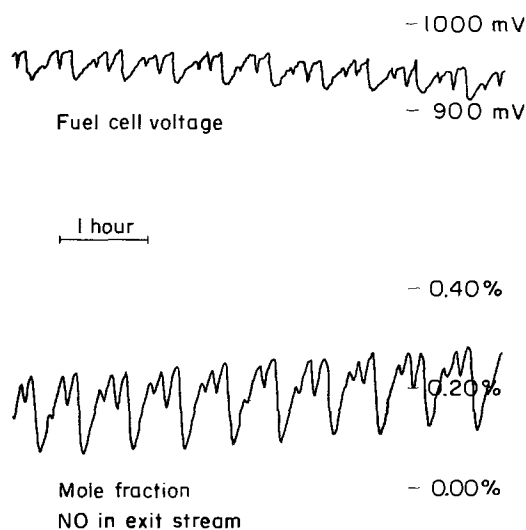


Fig. 8. Cell voltage and product oscillations. Flow rate 12.7 cm³ STP/min, $T = 1100^\circ\text{K}$, $M \approx 0.69$, $N \approx 8.6$, $Y_{NH_3,F} = 0.0459$.

graphs of the anode and cathode after 100 hr of continuous operation are shown in Fig. 9. Extensive sintering and faceting has occurred at the anode similar to that observed during the normal catalytic oxidation of NH₃ on platinum (12).

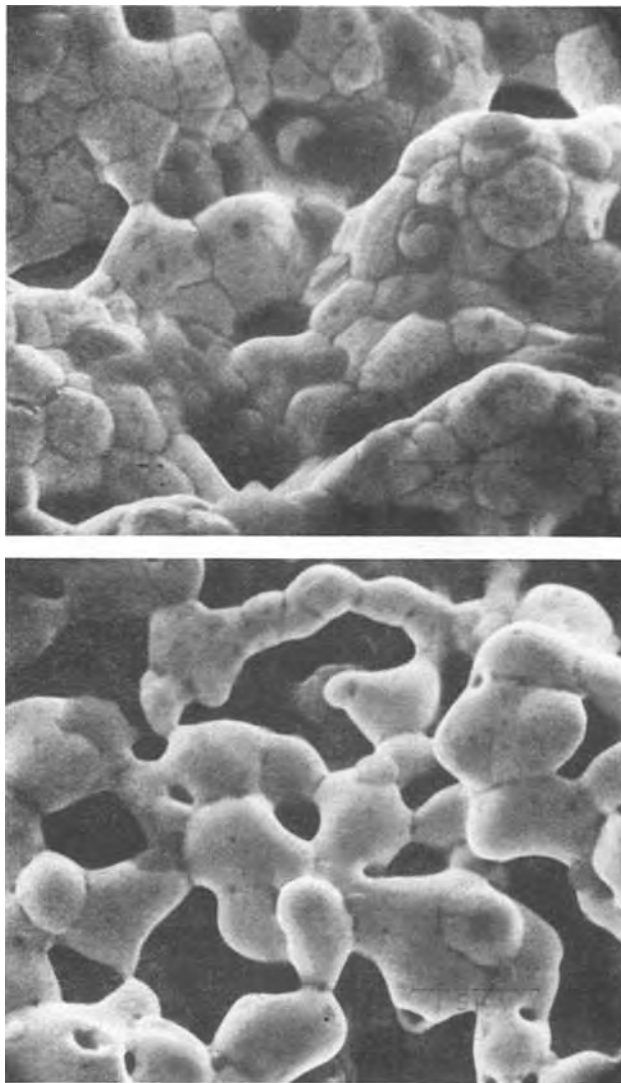
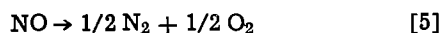
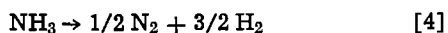
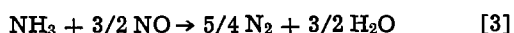


Fig. 9. Scanning electron micrographs of cathode (a, top) and anode (b, bottom).

Discussion

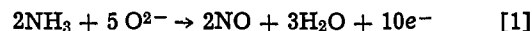
Pignet and Schmidt (11) have studied the kinetics of NH_3 oxidation on Pt wires and found the main reactions occurring to be



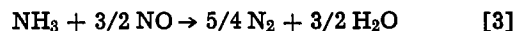
The relative importance of reactions [4] and [5] in the fuel cell was examined by passing separately NO and NH_3 through the cell under open-circuit conditions. Decomposition of NO, as reported by Chilton (1), was found to be negligible at the temperatures and residence times employed in this study. In agreement with previous work by Mason and Huggins (9, 10) we found that the rate of NO decomposition can be enhanced dramatically by application of an external voltage. Decomposition of NH_3 was found to be significant only above 1100°K, therefore, the major source of by-product N_2 is reaction [3]. This is further supported by the magnitude of the observed emf which would be considerably higher if O^{2-} or adsorbed oxygen were directly or indirectly involved in N_2 formation. That NO rather than N_2 is the primary anodic oxidation product is not surprising in view of the fact that Pt catalysts convert almost

quantitatively NH_3 to NO at temperatures between 700° and 1200°K (1).

On the basis of these observations it is safe to conclude that the dominant anodic reaction is



while N_2 is mostly formed by the catalytic side reaction



Because of the predominantly ohmic nature of the overpotential, the rate of reaction [1] is controlled by the rate of O^{2-} diffusion through the zirconia electrolyte.

The observed selectivity behavior can be explained in terms of these two reactions in a quantitative manner: mass balances of the three components NH_3 , NO, and N_2 in the CSTR yield

$$Gy_{\text{NH}_3,f} = (4/5)(i/4F) + kSy_{\text{NH}_3,e}y_{\text{NO},e} + Gy_{\text{NH}_3,e} \quad [6]$$

$$0 = (-4/5)(i/4F) + (3/2)kSy_{\text{NH}_3,e}y_{\text{NO},e} + Gy_{\text{NO},e} \quad [7]$$

$$0 = (-5/4)kSy_{\text{NH}_3,e}y_{\text{NO},e} + Gy_{\text{N}_2,e} \quad [8]$$

where k is the specific constant of reaction [3], assumed first order in both NH_3 and NO, S is the Pt anode surface area, G is the total molar flow rate, and the y 's represent mole fractions in the feed (f) and exit (e) streams. Writing these in terms of dimensionless variables and solving for the exit concentration gives

$$0 = x_D^2 + (1/N - 2M + 3/2)x_D - (4/5)(M/N) \quad [9]$$

$$x_A = \frac{(4/5)M - x_D}{(3/2)Nx_D} \quad [10]$$

$$x_F = (5/4)Nx_Ax_D \quad [11]$$

where $x_A = y_{\text{NH}_3,e}/y_{\text{NH}_3,f}$, $x_D = y_{\text{NO},e}/y_{\text{NH}_3,f}$, $x_F = y_{\text{N}_2,e}/y_{\text{NH}_3,f}$, $M = G_{\text{O}_2}/G_{\text{NH}_3,f}$, $G_{\text{O}_2} = i/4F$, and $N = k \cdot S \cdot y_{\text{NH}_3,f}/G$.

In terms of these dimensionless parameters, the selectivity is defined as

$$S' = x_D/(1 - x_A) \quad [12]$$

For very large values of N the selectivity is equal to x_D , and Eq. [9] and [10] yield

$$S' = 0 \quad \text{for } M < 0.75$$

$$S' = 2M - 3/2 \quad \text{for } 0.75 < M < 1.25$$

$$S' = 1 \quad \text{for } 1.25 < M$$

The solution of Eq. [9], [10], and [11] for various finite values of N are shown in Fig. 10 where the predicted selectivity is compared with the experimental results. At constant M , Eq. [9], [10], and [11] predict a decrease in selectivity with increasing N . This is shown in Fig. 11 where the model prediction is compared with the observed selectivity at constant $M = 0.75$.

The excellent agreement between experimental results and model prediction shows that the cell performance can be adequately described in terms of the two dimensionless groups M and N . The group M has a much more pronounced effect on selectivity than N . Due to the large thickness of the solid electrolyte employed in the present fuel cell design, maintaining values of M above 0.75 was difficult and required low values of G_{NH_3} since G_{O_2} was limited to a low value because of the high electrolyte resistance. Power production from this cell was also greatly limited due to the high electrolyte resistance.

Thinner electrolyte walls must be employed to maintain high selectivity at higher NH_3 molar flow rates. This would also increase the power output proportionally to the reduction in the electrolyte wall

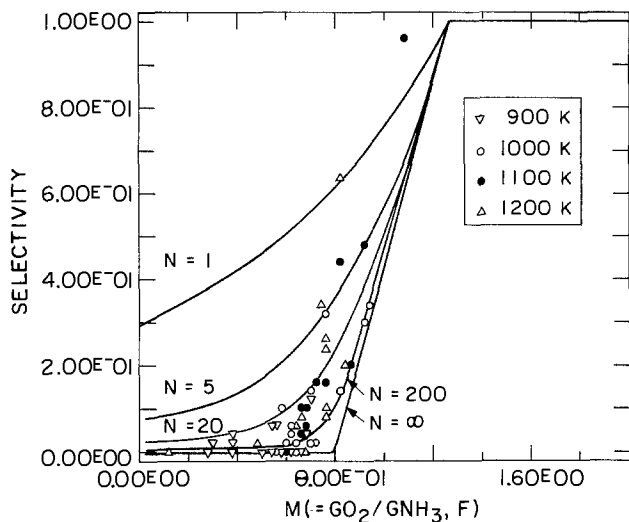


Fig. 10. Selectivity vs. M solid lines correspond to kinetic model prediction.

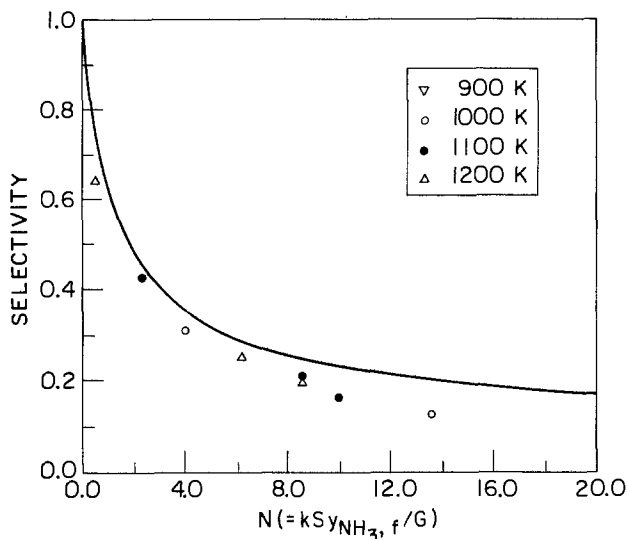


Fig. 11. Selectivity vs. N at constant $M = 0.75$ line corresponds to model prediction.

thickness. Work is currently being conducted in this direction.

Conclusions

Nitric oxide is the primary electro-oxidation product of the ammonia high temperature stabilized zirconia platinum electrode fuel cell. However the yield

of NO can be severely decreased due to the undesirable catalytic side reaction between NH_3 and NO on the Pt anode. The product selectivity is completely determined by the values of two dimensionless groups that can be used as a guide for design and operation of this fuel cell. Improving the existing technology of thin stabilized zirconia film deposition on mechanically strong cathodes has a high probability of making the high temperature NH_3 fuel cell a commercially attractive means for nitric acid and electric energy cogeneration.

Acknowledgments

This research was supported under NSF Grant ENG 77-27500. We thank C. W. Cheng, D. Ortman, and A. Ubel for their valuable assistance in the early experiments. Support from the M.I.T. Energy Lab through a Research Assistantship for R. D. F. is also gratefully acknowledged.

Manuscript submitted Oct. 15, 1979; revised manuscript received ca. Feb. 8, 1980.

Any discussion of this paper will appear in a Discussion Section to be published in the December 1980 JOURNAL. All discussions for the December 1980 Discussion Section should be submitted by Aug. 1, 1980.

Publication costs of this article were assisted by Massachusetts Institute of Technology.

REFERENCES

1. T. H. Chilton, "The Manufacture of Nitric Acid by the Oxidation of Ammonia," Chemical Engineering Press Monograph Series No. 3, Vol. 56 (1960).
2. K. Denbigh, "The Principles of Chemical Equilibrium," 2nd ed., p. 76, Cambridge University Press, New York (1968).
3. J. O'M. Bockris and S. Srinivasan, "Fuel Cells: Their Electrochemistry," pp. 587-591, McGraw-Hill Book Co., New York (1969).
4. R. O. Wynveen, in "Fuel Cells," Vol. 2, G. T. Young, Editor, chap. 12, Reinhold Publishing Corp., New York (1963).
5. M. Eisenberg, *Proc. Ann. Power Sources Conf.*, **18**, 20 (1964).
6. T. Weissbart and R. Ruka, *This Journal*, **109**, 723 (1962).
7. T. H. Etsell and S. N. Flengas, *ibid.*, **118**, 1890 (1971).
8. C. G. Vayenas and H. M. Saltsburg, *J. Catal.*, **57**, 296 (1979).
9. S. Pancharatnam, R. A. Huggins, and D. M. Mason, *This Journal*, **122**, 869 (1975).
10. T. M. Gur and R. A. Huggins, *ibid.*, **126**, 1067 (1979).
11. T. Pignet and L. D. Schmidt, *J. Catal.*, **40**, 212 (1975).
12. M. Flytzani-Stephanopoulos, S. Wong, and L. D. Schmidt, *ibid.*, **49**, 51 (1977).
13. R. D. Farr, M. S. Thesis, Massachusetts Institute of Technology (1979).

The Reaction of Electrogenerated Superoxide Ion with Nitroaromatic Amines

C. L. Hussey,* T. M. Laher, and J. M. Achord

Department of Chemistry, University of Mississippi, University, Mississippi 38677

ABSTRACT

The reaction of electrogenerated superoxide ion with 2-, 3-, and 4-nitroaniline and *N,N*-dimethyl-4-nitroaniline was studied as a function of temperature in *N,N*-dimethylformamide containing tetra-*n*-butylammonium perchlorate as the supporting electrolyte. Techniques used for the investigation were cyclic voltammetry, chronoamperometry, and absorption spectroscopy. The results obtained indicate that superoxide ion behaves as a strong base, effecting proton transfer from the amino group of 2- and 4-nitroaniline. No reaction of superoxide ion was observed with 3-nitroaniline or *N,N*-dimethyl-4-nitroaniline on the time scale of voltammetry. Pseudo-first-order rate constants for the chemical step in the ECE mechanism involving deprotonation of 2- and 4-nitroaniline by superoxide ion were estimated from chronoamperometric data to be 0.14 and 0.13 sec⁻¹, respectively, at 25.0°C and 0.46 and 0.30 sec⁻¹, respectively, at 40.0°C.

Electrochemical studies (1-7) have established that molecular oxygen undergoes a one-electron quasireversible reduction in aprotic solvents to the stable superoxide ion, O₂⁻. Electrogeneration of this species by reduction of molecular oxygen in aprotic solvents provides a convenient method for producing it in high concentrations without accompanying reactive species. In addition, various electrochemical techniques can be used advantageously to study the kinetics of the reaction of O₂⁻ generated in this fashion with substrates of interest.

The chemical reactivity of this unusual oxygen species, including its effective nucleophilicity, reducing power, and propensity to act as a strong base effecting proton transfer from organic substrates, recently was summarized (8). The latter property was postulated as the initial step in the "oxidation" of organic substrates by O₂⁻ (8).

Reactions of O₂⁻ with various organic substrates have been reviewed (9). Relatively few investigations have been concerned with reactions between O₂⁻ and aromatic hydrocarbons substituted with basic nitrogen functional groups. Chern and San Filippo (10) used chemically introduced O₂⁻ to oxidize hydrazines, hydrazones, and related compounds to azo compounds, *N*-nitrosoamines, and azines. In a recent study Crank and Makin (11) examined the reaction of O₂⁻ with aromatic amines substituted with electron donating functional groups. These workers found that the 2- and 4- isomers of phenylenediamine and aminophenol were converted by O₂⁻ to their diaminoazobenzenes and dihydroxyazobenzenes, respectively. The reaction process was postulated to involve hydrogen abstraction from the amino group of these compounds by O₂⁻.

In order to obtain additional information about the reaction of O₂⁻ with aromatic amines, particularly those substituted with electron withdrawing functional groups, reactions of electrogenerated O₂⁻ with 2-, 3-, and 4-nitroaniline and *N,N*-dimethyl-4-nitroaniline were studied. The results of this investigation are reported in this paper.

Experimental

Chemicals.—2-Nitroaniline (Eastman), 3-nitroaniline (Eastman) 4-nitroaniline (Eastman), and *N,N*-dimethyl-4-nitroaniline (Pfaltz and Bauer) were recrystallized twice from 95% ethanol and dried in a vacuum for several days. Spectrophotometric grade *N,N*-dimethylformamide, DMF (Burdick and Jack-

son), with a specified water content of less than 0.004% was used without further treatment. Tetra-*n*-butylammonium perchlorate, TBAP, was prepared and purified using established procedures. Potassium superoxide, KO₂ (Pfaltz and Bauer), potassium hydroxide, KOH (Fisher, certified A.C.S.), and 18-crown-6 ether (Aldrich) were used as received. Dry grade oxygen gas (Linde) was passed through a laboratory gas drying unit (Ace Glass) containing Drierite before it was introduced into DMF-TBAP solutions. Solvent, supporting electrolyte, and solutions for study were stored in a dry box in a dry nitrogen atmosphere prior to use.

Instrumentation.—Cyclic voltammetry, chronoamperometry, and controlled potential electrolysis were performed using an AMEL Model 551-MWR ultrafast potentiostat equipped with a positive feedback IR compensation circuit. The potentiostat was programmed by means of an AMEL Model 566 function generator during cyclic voltammetric and chronoamperometric experiments. Cyclic voltammograms and potentiostatic current-time transients were recorded using a Houston Model 100 X-Y recorder or photographed from the display of a Tektronix Model 7844 dual beam oscilloscope. Resistance compensation was employed during all electrochemical experiments according to the procedure described by Whitson *et al.* (12).

Ultraviolet-visible absorption spectra were recorded on a CARY-17 UV-VIS spectrophotometer (Varian Associates). Gas chromatographic analysis was performed using a Beckman GC-45 gas chromatograph equipped with 6 ft × 1/4 in. columns packed with 12% OV-101 on Gas Chrom-Q, operated over a temperature range of 150°-250°C, using helium carrier gas.

Electrodes and cells.—A glassy carbon working electrode was constructed by forcing a small length of 0.5 cm Tokai GC-30 grade glassy carbon rod (Continental Ore) into an undersized, heated Teflon sleeve. A male 14/20 standard taper joint was machined into the opposite end of the Teflon sleeve. Electrical contact with the glassy carbon was accomplished by inserting a small spring into the sleeve and forcing an oversized brass rod into the sleeve until contact was established. The end of the Teflon rod containing the glassy carbon was cut flush and polished to a final mirror finish with 0.1 μm metallographic polishing alumina. The geometrical area of the electrode was 0.22 cm².

The counterelectrode was a platinum wire spiral held in a 14/20 standard taper Ace Glass mini-electrode

* Electrochemical Society Active Member.
Key words: free radicals, organic, kinetics.

adapter. Potentials were measured against a saturated calomel electrode, SCE, isolated from the bulk solution by means of a Vycor-tipped bridge tube equipped with a 14/20 standard taper joint.

Cyclic voltammetric and chronoamperometric experiments were conducted in a sealed Metrohm titration vessel. In addition to the working electrode, counterelectrode, and reference electrode bridge tube, gas dispersion and outlet tubes were provided. The cell and reference electrode bridge tube were filled inside the dry box, removed, and thermostated in a constant temperature bath to within $\pm 0.2^\circ\text{C}$ of the desired temperature before electrochemical measurements were made.

Results and Discussion

Voltammetry.—A representative cyclic voltammogram, illustrating the reduction of oxygen to O_2^- at a glassy carbon electrode in DMF containing 0.1M TBAP, saturated with oxygen gas at 25.0°C , is shown in Fig. 1. Oxygen reduction at glassy carbon exhibits a degree of reversibility comparable to that of oxygen reduction at mercury or mercury-coated platinum. Use of glassy carbon to study oxygen reduction in aprotic solvents, for the most part, appears to have been ignored.

Cyclic voltammograms corresponding to the reduction of oxygen in DMF containing 2-, 3-, and 4-nitroaniline and N,N-dimethyl-4-nitroaniline are shown in Fig. 1, 2, 3, and 4, respectively. As can be seen in these figures, cyclic voltammograms representing the O_2/O_2^- couple appear notably different in the presence

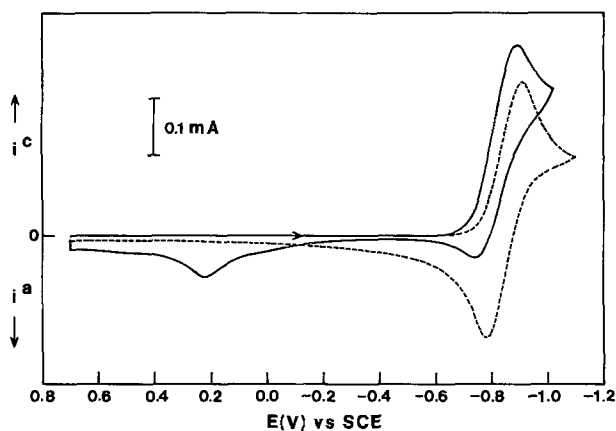


Fig. 1. Cyclic voltammograms at a glassy carbon electrode in DMF + 0.1M TBAP at 25.0°C ; (dashed line) saturated with O_2 at 1 atm, (solid line) saturated with O_2 at 1 atm and 0.05M in 2-nitroaniline. Sweep rates were 0.02 Vsec^{-1} .

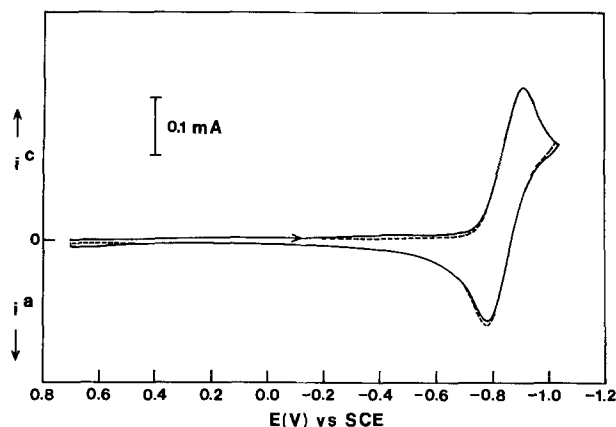


Fig. 2. Cyclic voltammograms at a glassy carbon electrode in DMF + 0.1M TBAP at 25.0°C ; (dashed line) saturated with O_2 at 1 atm, (solid line) saturated with O_2 at 1 atm and 0.05M in 3-nitroaniline. Sweep rates were 0.02 Vsec^{-1} .

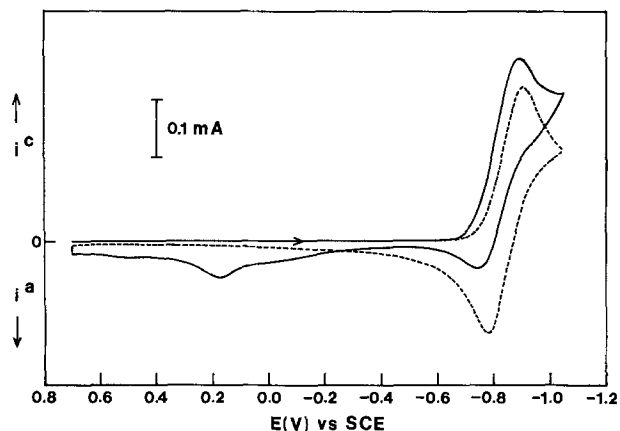


Fig. 3. Cyclic voltammograms at a glassy carbon electrode in DMF + 0.1M TBAP at 25.0°C ; (dashed line) saturated with O_2 at 1 atm, (solid line) saturated with O_2 at 1 atm and 0.05M in 4-nitroaniline. Sweep rates were 0.02 Vsec^{-1} .

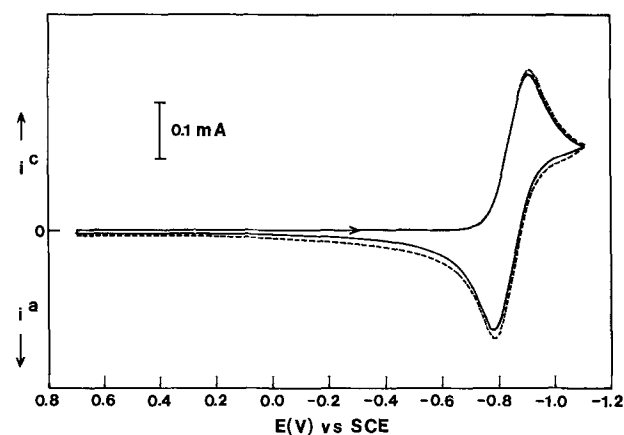


Fig. 4. Cyclic voltammograms at a glassy carbon electrode in DMF + 0.1M TBAP at 25.0°C ; (dashed line) saturated with O_2 at 1 atm, (solid line) saturated with O_2 at 1 atm and 0.1M in N,N-dimethyl-4-nitroaniline. Sweep rates were 0.02 Vsec^{-1} .

of 2- and 4-nitroaniline (Fig. 1 and 3), but virtually unchanged in the presence of 3-nitroaniline and N,N-dimethyl-4-nitroaniline (Fig. 2 and 4). At slow scan rates the peak potential for O_2 reduction is shifted positively in DMF-TBAP containing 2- or 4-nitroaniline (Fig. 1 and 3). The cathodic current due to O_2 reduction is significantly increased compared to the current observed for the O_2 reduction process in DMF-TBAP which does not contain these nitroanilines. The positive shift of the O_2 reduction half-peak potential in the presence of 2- or 4-nitroaniline averaged about $29 \pm 2 \text{ mV}$ at a scan rate of 0.020 V/sec at 25.0°C . The potential shift decreased in value as the scan rate was increased. Although relatively small in magnitude, this potential shift was always observed at slow scan rates when 2- or 4-nitroaniline was present, but was not observed in the presence of 3-nitroaniline or N,N-dimethyl-4-nitroaniline. In Fig. 1 and 3 the current corresponding to O_2^- oxidation is greatly diminished and a small peak representing the oxidation of a product formed during the initial O_2 reduction process can be seen at potentials positive of the peak representing O_2^- oxidation. The product peaks did not exhibit corresponding reduction peaks as ascertained from repetitive cyclic voltammetric scans. When the scan rate was increased above ca. $5\text{--}10 \text{ Vsec}^{-1}$, voltammograms for the O_2 reduction process in the presence of 2- or 4-nitroaniline were identical to those observed for O_2 reduction with no nitroaniline present and no product peaks were observed.

The effect of changing the scan rate on the value of n_{app} for O_2 reduction, where n_{app} is calculated from the ratio of the voltammetric peak current for O_2 reduction with added nitroaniline to the respective voltammetric peak current without added nitroaniline at the same scan rate, for solutions containing 2- or 4-nitroaniline is shown in Fig. 5. At slow scan rates n_{app} increases toward a value of 2.0 for O_2 saturated DMF-TBAP solutions containing 2- and 4-nitroaniline. This is especially evident for data obtained at 40.0°C where the rate of reaction between $O_2^{\cdot-}$ and added nitroaniline is enhanced and indicates that the O_2 reduction process in the presence of 2- or 4-nitroaniline may involve two electrons.

The cyclic voltammetric behavior observed for the O_2 reduction process in the presence of 2- or 4-nitroaniline suggests that the process may proceed via an ECE mechanism (13). In this particular type of ECE process the charge transfer arising from the product of the coupled chemical step involves one electron and occurs at a potential positive of the original charge transfer step (13).

Addition of KO_2 and 18-crown-6 ether.—The failure of *N,N*-dimethyl-4-nitroaniline to react with $O_2^{\cdot-}$, unlike 4-nitroaniline, suggests that the hydrogens attached to the amine nitrogen of 2- or 4-nitroaniline may be important in the reaction of $O_2^{\cdot-}$ with these compounds. To deduce the nature of the products formed as a result of the reaction of $O_2^{\cdot-}$ with 2- or 4-nitroaniline, large quantities of $O_2^{\cdot-}$ were introduced into DMF solutions ca. 0.1M in these nitroanilines. Superoxide ion was most conveniently added using KO_2 and 18-crown-6 ether. Solutions containing 2-nitroaniline, initially yellow, turned red when $O_2^{\cdot-}$ was added. Greenish-yellow solutions of 4-nitroaniline became orange when treated with $O_2^{\cdot-}$. Colors identical to these also could be observed to form in the electrode diffusion layer in DMF-TBAP solutions saturated with O_2 containing 2- or 4-nitroaniline upon application of a potential step of sufficient magnitude to form $O_2^{\cdot-}$. Examination of both solutions using thin layer and gas-liquid chromatography revealed no detectable product species, only the starting material. However, the quantity of starting material was greatly diminished in $O_2^{\cdot-}$ treated solutions. It could be restored simply by the addition of a small amount of proton donor (water or acetic acid).

Absorption spectra were recorded for dilute solutions of 2- and 4-nitroaniline in DMF both before and after the addition of KO_2 and 18-crown-6 ether. Figures 6 and 7 show the spectra that were obtained. The absorption peaks which appear at 516 nm (Fig. 6) and

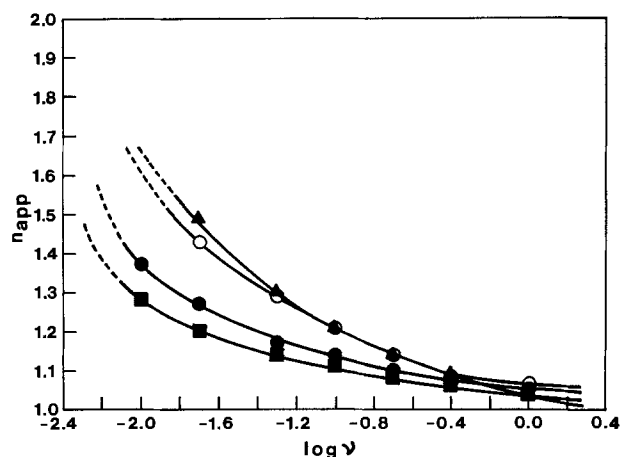


Fig. 5. Variation of n_{app} as a function of sweep rate for the voltammetric reduction of O_2 at a glassy electrode in DMF + 0.1M TBAP, saturated with oxygen at 1 atm; 0.05M in 2-nitroaniline, 25.0°C ●; 0.1M in 2-nitroaniline, 40.0°C ○; 0.05M in 4-nitroaniline, 25°C ■; and 0.1M in 4-nitroaniline, 40.0°C ▲.

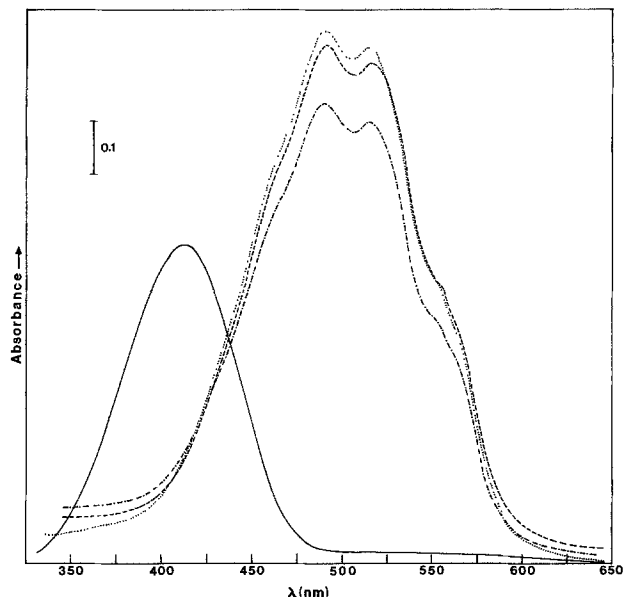


Fig. 6. Absorption spectra for 2-nitroaniline in DMF, (solid line) no base, (dashed line) addition of excess KO_2 + 18-crown-6 ether, (dotted line) addition of excess CH_3ONa , and (dashed-dotted line) addition of excess KOH + 18-crown-6 ether. The initial concentration of 2-nitroaniline in each solution was $1.0 \times 10^{-4}M$.

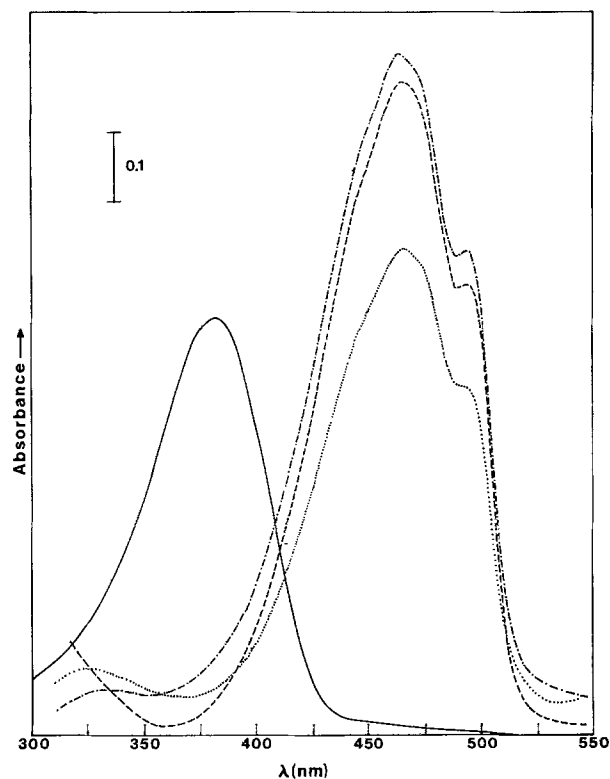


Fig. 7. Absorption spectra for 4-nitroaniline in DMF; (solid line) no base, (dashed line) addition of excess KO_2 + 18-crown-6 ether, (dotted line) addition of excess CH_3ONa , and (dashed-dotted line) addition of excess KOH + 18-crown-6 ether. The initial concentration of 4-nitroaniline in each solution was $2.8 \times 10^{-5}M$.

464 nm (Fig. 7) after the addition of $O_2^{\cdot-}$ are in excellent agreement with literature values (14) of λ_{max} for the anions of 2- and 4-nitroaniline, respectively, as shown in Table I. Unfortunately, published spectra for the 2- and 4-nitroanilide ions do not appear to be available. Values of ϵ_{max} were calculated from the spectra shown in Fig. 6 and 7 for both the neutral and ionized nitroanilines. It was assumed that the addition of excess $O_2^{\cdot-}$ to dilute solutions of 2- or 4-nitroaniline

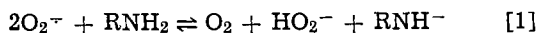
Table I. Summary of spectroscopic data

Compound	Neutral molecule		Anion		Base added	Ref.
	λ_{\max} (nm)	ϵ_{\max} ($M^{-1} cm^{-1}$)	λ_{\max} (nm)	ϵ_{\max} ($M^{-1} cm^{-1}$)		
2-Nitroaniline	413	5400	516	8700	O_2^-	This work (14)
	410	4500	515	8400	OH^-	
4-Nitroaniline	382	19,000	464	32,800	O_2^-	This work (14)
	378	16,900	467	32,300	OH^-	

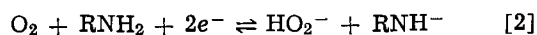
resulted in complete ionization of the nitroaniline. The values of ϵ_{\max} calculated, summarized in Table I, also are in good agreement with values of ϵ_{\max} reported in the literature (14) for the neutral and ionized nitroanilines.

Additional support for the O_2^- induced generation of the anions of 2- and 4-nitroaniline was obtained from experiments in which CH_3ONa or alternately $KOH + 18$ -crown-6 ether were added to dilute solutions of 2- or 4-nitroaniline. Both CH_3O^- and OH^- have been used extensively to generate the anions of weakly acidic organic compounds (14-16) in aprotic solvents. Absorption spectra for these solutions (Fig. 6 and 7) are identical to those obtained after the addition of O_2^- . Thus, the products of the reaction of the three bases, O_2^- , CH_3O^- , and OH^- with 2- or 4-nitroaniline appear to be equivalent for each aniline.

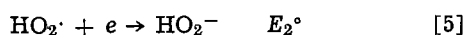
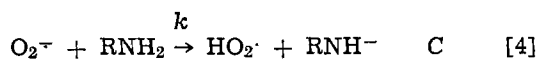
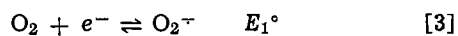
Mechanism of the reaction of O_2^- with 2- and 4-nitroaniline.—The results obtained from experiments employing the addition of O_2^- and other bases to solutions of 2- or 4-nitroaniline in DMF suggest that 2- and 4-nitroaniline undergo proton transfer to O_2^- in DMF to form their respective stable nitroanilide ions. An overall reaction sequence for the reaction of O_2^- with these nitroanilines can be written on the basis of the reaction of O_2^- with other proton donors (8) and is represented by Eq. [1]



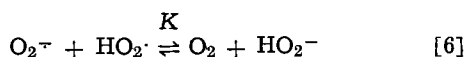
The overall process for oxygen reduction in the presence of these nitroanilines can be obtained by combining the O_2 reduction half-reaction with Eq. [1] to give



The ECE process observed for O_2 reduction in the presence of 2- or 4-nitroaniline must therefore correspond to a stepwise series of reactions whose overall sequence involves two electrons and is represented by Eq. [2]. A series of reactions that would produce an ECE response and yet meet other criteria imposed by Eq. [2] are represented by Eq. [3]-[5]. An ECE process, similar to that represented by Eq. [3]-[5], has been postulated to account for the electrochemical behavior observed during the reduction of oxygen in nonaqueous solvents in the presence of organic and inorganic acids (4, 7, 17).



An additional equilibrium involving homogeneous electron transfer also must be considered for an ECE mechanism of this type (18) since E_2° is positive of E_1°



The homogeneous electron transfer reaction represented by Eq. [6] is rapid with a k_2 value of $9 \times 10^7 M^{-1} sec^{-1}$ (8). Estimation of the rate constant, k , for the chemical step represented by Eq. [4] and the

equilibrium constant K , for the process represented by Eq. [6] is reported below.

The product peaks observed at 0.23 and 0.19V in Fig. 1 and 3, respectively, most likely correspond to the oxidation of the respective nitroanilide ions. Oxidation peaks were observed at the same potentials in degassed DMF-TBAP containing 2- or 4-nitroaniline to which KO_2 was added. Oxidation of nitroanilide ion should occur more readily than oxidation of the parent nitroaniline. Oxidation of peroxide ion, HO_2^- , was not considered in the reaction represented by Eq. [5] since no voltammetric peak attributable to HO_2^- oxidation was observed. This finding is in good agreement with a previous study (19) in which oxidation of HO_2^- was not observed in 1M NaOH at gold, glassy carbon, or pyrolytic graphite electrodes. It also was found to rapidly decompose in aprotic solvents (19).

Proton transfer rate measurements.—In order to estimate rate constants for the chemical step represented by Eq. [4] and equilibrium constants for the process described by Eq. [6], chronoamperometric measurements were employed. The resulting data were analyzed according to the procedure described by Hawley and Feldberg (18). Chronoamperometric experiments were run under pseudo-first-order conditions, i.e., with a large excess of nitroaniline present. The amount of nitroaniline necessary to impose pseudo-first-order conditions was determined by observing the increase in voltammetric peak current for O_2 reduction at a fixed scan rate of $0.010 Vsec^{-1}$ with increasing concentrations of nitroaniline. Concentrations of nitroaniline greater than 0.05M produced no measurable increase in the peak height at 25.0°C while concentrations greater than 0.10M produced similar results at 40.0°C. No change in potentiostatic current-time transients could be detected either, as the nitroaniline concentrations were increased above these values. The 2- and 4-nitroaniline were reduced to their respective radical anions at peak potentials of -1.30 and $-1.45V$. It was possible, however, to observe the foot of these reduction waves at potentials slightly negative of -1.05 and $-1.10V$, respectively, especially when the nitroanilines were present in high concentrations. To avoid any possibility of the simultaneous reduction of the nitroaniline to its radical anion during these rate measurements, potential steps of 1.00 to $-1.05V$ were employed for 2-nitroaniline and 1.00 to $-1.10V$ for 4-nitroaniline. Studies of O_2 reduction without added nitroaniline using potential steps of 1.00 to $-1.05V$ showed the O_2 reduction process to be diffusion controlled at elapsed times greater than 0.1 sec, whereas significant effects due to convection were noticeable at times exceeding 8 sec. For this reason, chronoamperometric experiments were restricted to a time window of 0.1-8 sec.

Plots of n_{app} vs. $\log t$ for the reduction of O_2 in solutions containing 2- and 4-nitroaniline are shown in Fig. 8 and 9, respectively. Chronoamperometric values of n_{app} were calculated according to Hawley and Feldberg (18). These plots were matched to n_{app} vs. $\log kt$ working curves calculated using various values of K and the best fit was determined on the basis of similarity of shape. The best fit was generally obtained for curves generated with values of K less than 0.1. This is most vividly demonstrated for data acquired at 40.0°C (Fig. 8 and 9). Unfortunately, the method used to estimate K in the present investigation is too imprecise to allow determination of a more exact value for K or to study the effect of temperature on K . However, the available evidence tends to support a value of K for Eq. [6] which is close to 0 for the present systems. Values of $\log kt$ corresponding to experimental values of $\log t$ from Fig. 8 and 9 were obtained and used to calculate the pseudo-first-order rate constant, k , for the proton transfer reaction represented by Eq. [4]. Values of k estimated in this fashion are given in Table II. Using the estimates of k given in Table II, plots of n_{app} vs. $\log t$ were generated for values of

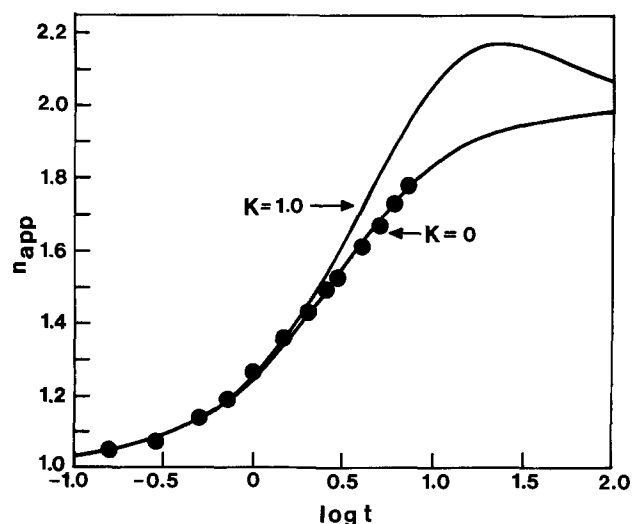
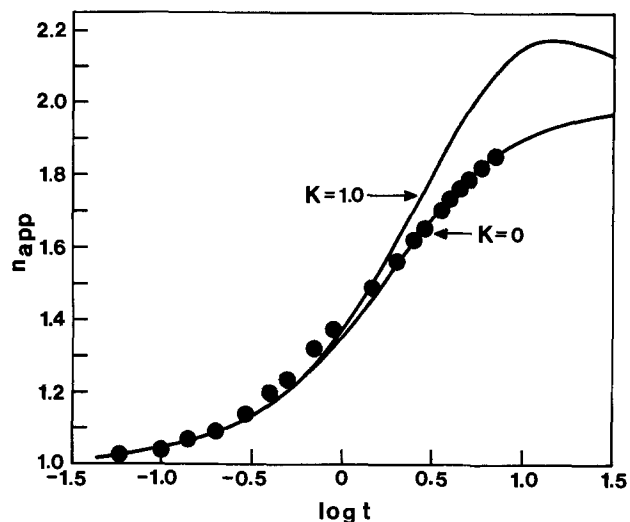
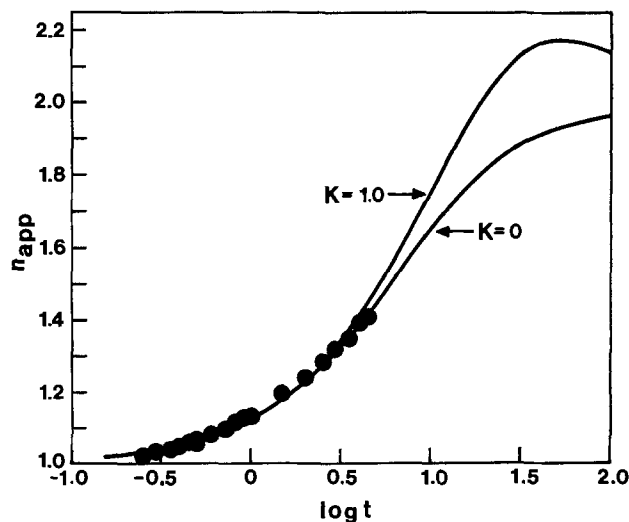
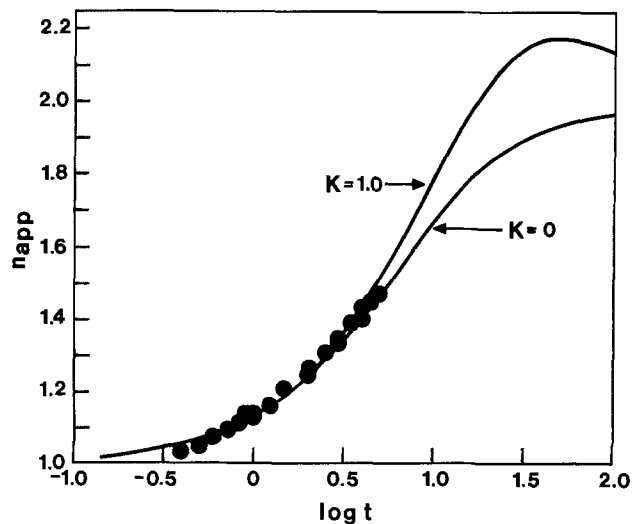


Fig. 8. Dependence of n_{app} on $\log t$ for O_2 reduction at a glassy carbon electrode in DMF + 0.1M TBAP, saturated with O_2 at 1 atm for a potential step of 1.00 to $-1.05V$ vs. SCE. Upper figure: 0.05M in 2-nitroaniline, 25.0°C. Lower figure: 0.1M in 2-nitroaniline, 40.0°C.

Fig. 9. Dependence of n_{app} on $\log t$ for O_2 reduction at a glassy carbon electrode in DMF + 0.1M TBAP, saturated with O_2 at 1 atm for a potential step of 1.00 to $-1.10V$ vs. SCE. Upper figure: 0.05M in 4-nitroaniline, 25.0°C. Lower figure: 0.1M in 4-nitroaniline, 40.0°C.

$K = 1.0$ and are shown in Fig. 8 and 9 for comparative purposes.

Examination of the data given in Table II reveals that the rate of deprotonation of the respective nitroaniline correlates well with the pK_a of the compound in the two cases studied. The failure of 3-nitroaniline to react with O_2^- is not surprising since it should be much more basic than the 2- and 4-isomers. The results of the present investigation also are in good agreement with the calculations of Sawyer *et al.* (8), who predict that superoxide ion solutions can promote proton transfer from substrates with pK_a values as large as 23.

Acknowledgment

The authors acknowledge financial support of this work by Lawrence Livermore Laboratories through Subcontract No. 4288309 and through a University of

Mississippi Faculty Research Grant. Helpful suggestions concerning this work were provided by Dr. N. E. Heimer.

Manuscript submitted Sept. 10, 1979; revised manuscript received Jan. 23, 1980.

Any discussion of this paper will appear in a Discussion Section to be published in the June 1981 JOURNAL. All discussions for the June 1981 Discussion Section should be submitted by Feb. 1, 1981.

Publication costs of this article were assisted by the University of Mississippi.

Table II. Proton transfer rate constants

Substrate	pK_a	t (°C)	k (sec $^{-1}$)
2-Nitroaniline	17.9 ^a	25.0 ± 0.1	0.14 ± 0.01
		40.0 ± 0.2	0.46 ± 0.02
4-Nitroaniline	18.4 ^a	25.0 ± 0.1	0.13 ± 0.01
		40.0 ± 0.2	0.30 ± 0.03

^a Values taken from Ref. (14).

LIST OF SYMBOLS

E°	standard electrode potential (V)
i^a	anodic current (A)
i^c	cathodic current (A)
k	first-order rate constant (sec $^{-1}$)
k_2	second-order rate constant (M $^{-1}$ sec $^{-1}$)
K	homogeneous electron transfer equilibrium constant
K_a	acid dissociation constant
n_{app}	apparent number of electrons in the overall charge transfer process
t	time (sec)
ϵ_{max}	molar extinction coefficient at λ_{max} (M $^{-1}$ cm $^{-1}$)
λ_{max}	wavelength of maximum absorption (nm)
ν	scan rate (Vsec $^{-1}$)

REFERENCES

1. M. E. Peover and B. S. White, *Chem. Commun.*, 10, 183 (1965).

2. D. L. Maricle and W. G. Hodgson, *Anal. Chem.*, **37**, 1562 (1965).
3. D. T. Sawyer and J. L. Roberts, Jr., *J. Electroanal. Chem. Interfacial Electrochem.*, **12**, 90 (1966).
4. M. E. Peover and B. S. White, *Electrochim. Acta*, **11**, 1061 (1966).
5. E. L. Johnson, K. H. Pool, and R. E. Hamm, *Anal. Chem.*, **38**, 183 (1966).
6. J. B. Headridge, D. Pletcher, and M. Callingham, *J. Chem. Soc. (A)*, 684 (1967).
7. J. E. A. Toni, *This Journal*, **116**, 212 (1969).
8. D. T. Sawyer, M. J. Gibian, M. M. Morrison, and E. T. Seo, *J. Am. Chem. Soc.*, **100**, 627 (1978).
9. E. Lee-Ruff, *Chem. Soc. Rev.*, **6**, 195 (1977).
10. C. Chern and J. San Filippo, Jr., *J. Org. Chem.*, **42**, 178 (1977).
11. G. Crank and M. I. H. Makin, *Tetrahedron Lett.*, 2169 (1979).
12. P. E. Whitson, H. W. VandenBorn, and D. H. Evans, *Anal. Chem.*, **45**, 1298 (1973).
13. R. S. Nicholson and I. Shain, *ibid.*, **37**, 178 (1965).
14. R. Stewart and J. P. O'Donnell, *Can. J. Chem.*, **42**, 1681 (1964).
15. R. Stewart, J. P. O'Donnell, D. J. Cram, and B. Rickborn, *Tetrahedron*, **18**, 917 (1962).
16. K. Bowden, *Chem. Rev.*, **66**, 119 (1966).
17. H. J. James and R. F. Broman, *J. Phys. Chem.*, **75**, 4019 (1971).
18. M. D. Hawley and S. W. Feldberg, *ibid.*, **70**, 3459 (1966).
19. M. M. Morrison, J. L. Roberts, Jr., and D. T. Sawyer, *Inorg. Chem.*, **18**, 1971 (1979).

The Electrochemical Oxidation of Substituted Catechols

Michael D. Ryan,* Alice Yueh, and Wen-Yu Chen

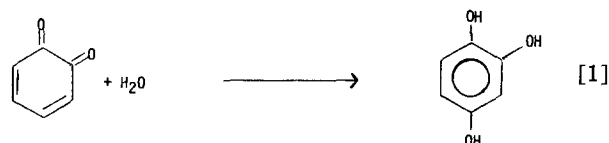
Department of Chemistry, Marquette University, Milwaukee, Wisconsin 53233

ABSTRACT

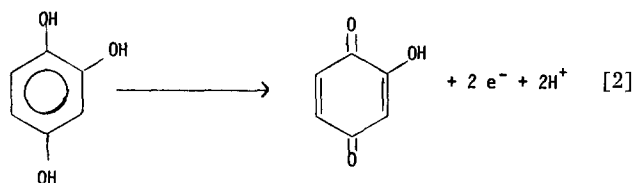
The oxidation of substituted catechols was studied by cyclic voltammetry, chronoamperometry, rotating ring-disk electrode, and coulometry. The results showed that the quinones that were formed from the oxidation of substituted catechols reacted with the basic forms of the starting material to yield the dimeric product. These products were generally unstable and rapidly polymerized or underwent some other irreversible reaction to form an electroinactive product. For 3,4-dihydroxyacetophenone and propiophenone, the intermediate was stable long enough to be observed in cyclic voltammetry. The rate of the coupling reaction was found to correlate well with the Hammett ρ - σ parameters and indicated that there was substantial negative charge in the transition state. Finally, an analysis of the coulometric n -values along with the $i_a t^{1/2}/C$ values indicated that the initial coupling product was a diphenyl ether. Analysis of the coulometry products showed extensive polymerization.

Many workers have shown that *o*- and *p*-diphenols can be oxidized electrochemically to *o*- and *p*-quinones, respectively. The quinone that is formed is quite reactive and can be attacked by a variety of nucleophiles. Adams and co-workers (1-3) have shown that 4-methyl-*o*-benzoquinone can react with nucleophiles such as ammonia, chloride, and sulfhydryl compounds to form the addition products. In addition, Adams (4, 5) has shown that *p*-benzoquinones with electron-withdrawing substituents can be nucleophilically attacked by water to yield a trihydroxy compound, which can be further oxidized to the hydroxyquinone. Several other workers (6-9) have investigated the reactions of *o*-quinones from Dopa, catechol, and 4-methyl catechol in aqueous solutions, but the emphasis has been mostly on acidic solutions and at low concentrations, which significantly suppress the coupling reaction. Outside of the work by Stum and Suslov (10), there has been little electrochemical work done on the coupling reactions of quinones.

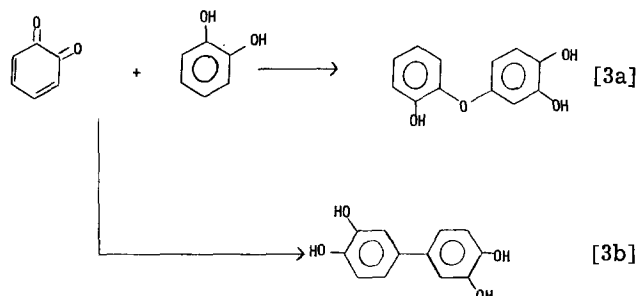
By contrast, there have been extensive chemical studies on the oxidative coupling reactions of phenols, and this area has been reviewed in a book by Musso (11). The ultimate products of catechol oxidations is a melanin-type product (12-14), but it is very difficult to characterize the material or to understand its coupling mechanism. There are several possible reactions which the *o*-quinone can undergo. The first possibility is the reaction of the *o*-quinone with water (reaction [1])



Because a *p*-quinone is formed when 1,2,4-trihydroxybenzene is oxidized, trihydroxybenzene is easier to oxidize than catechol. Thus, reaction [2] will occur when the trihydroxybenzene is formed



This species may then undergo a polymerization reaction (15). Alternatively, the *o*-quinone can react with the starting material, as shown in reaction [3]



* Electrochemical Society Active Member.

Key words: cyclic voltammetry, chronoamperometry, rotating ring-disk electrode, coulometry.

Both of these products can be further oxidized to form o-quinones. In the above reaction, the reactive phenol may also be one of the anionic forms of catechol, which is formed by the acid dissociation reaction. Finally, the coupling reaction may occur by way of a semiquinone intermediate.

Electrochemical methods are uniquely suitable to provide information on the kinetics of the coupling reaction. The rate of disappearance of the o-quinone can be monitored by the use of double-step chronoamperometry or the rotating ring-disk method. The identity of new electroactive species can be monitored by cyclic voltammetry. By this approach, it is possible to understand the initial steps that are involved in the coupling reaction.

Experimental

Equipment.—Most of the electrochemical experiments were performed on a homemade three-electrode potentiostat of conventional design. Some of the cyclic voltammetric experiments were done on a Princeton Applied Research Corporation (PAR) Model 174A polarographic analyzer. The reference electrode was a saturated calomel electrode (SCE) and the working electrode was a carbon paste electrode. A platinum wire was used as an auxiliary electrode. The chronoamperometric and cyclic voltammetric data were recorded on a Hewlett-Packard 7045A X-Y recorder or a Tektronix Model D15 storage oscilloscope. The u.v.-visible spectra were recorded on a Cary 14 spectrometer. The coulometry was performed on a PAR Model 173 potentiostat with a Model 179 integrator. The ring-disk electrode rotator was a Pine Instrument Company Model ASR, the ring and disk were platinum, and a homemade bipotentiostat was used as described in Ref. (16).

Catechol (CAT), 3,4-dihydroxyacetophenone (DHAP), 3-methyl catechol (3MC), 4-methyl catechol (4MC), 3,4-dihydroxybenzoic acid (DHBA), and 3,4-dihydroxyphenylacetic acid (DHPA) were purchased from Aldrich Chemical Company. 3,4-Dihydroxypropionophenone (DHPP) was obtained from ICN Pharmaceutical Incorporated. 3,4-Dihydroxybenzoic acid, ethyl ester (DHBE) was obtained from Pfaltz and Bauer, Incorporated. Catechol and 3-methyl catechol were purified by sublimation. DHBE was recrystallized from hot water, and pale yellow crystals were obtained with a melting point of 198°–200°C. 3,3',4,4'-Tetramethoxy biphenyl (TMBP) was synthesized by the Ullmann reaction, as described in Ref. (17), and the TMBP was reacted with boron tribromide (18) to yield the 3,3',4,4'-tetrahydroxybiphenyl (THBP).

All solutions were prepared from deionized water. The pH 1 solutions were made with sulfuric acid. The solutions that were buffered around pH 5 were made from acetic acid/acetate mixtures, while phosphate buffers were used for solutions above pH 6.

Results

Cyclic voltammetry.—Only one oxidation peak was observed for all the catechols studied except for THBP, DHAP, and DHPP. With the same exceptions, only one reduction peak was seen, except in basic solutions where the quinone was unstable. In that case, the reduction peak disappeared. The quasi-reversibility of the electron transfer reaction makes it difficult to obtain quantitative kinetic data from the cyclic voltammograms but one can see qualitatively that the quinone becomes progressively less stable as the pH is raised. The effect of pH on the cyclic voltammetry of catechol is shown in Fig. 1. In addition, the second-order nature of the reaction process can be seen by the decrease in the peak current ratio, i_{pc}/i_{pa} , as the concentration is increased at a given pH and scan rate. A quantitative measurement of this effect is described later in this work.

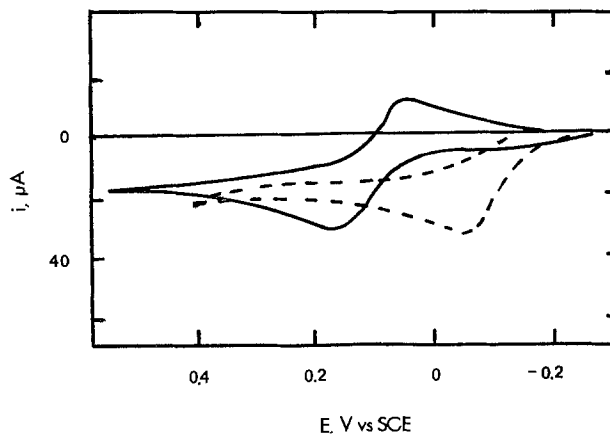


Fig. 1. Cyclic voltammetry of 0.3 mM catechol. Solid line pH 2. Dashed line pH 8. Scan rate 10 mV/sec.

The oxidation of DHAP and DHPP gives additional features that are instructive in understanding the reaction process. In solutions with a pH less than 5, the cyclic voltammetry of these two compounds is similar to the other catechols. But, for pH values between 5 and 7, a new redox couple is seen in the voltammograms, as shown in Fig. 2. For DHPP, the new oxidation wave is not seen until the second scan because its peak potential is less than the peak potential for catechol, while the new oxidation peak for DHAP is more positive than the catechol peak and hence is seen in the first scan. In Fig. 2, curve C, one can see that this new peak is reduced relative to the first peak as the scan rate is increased. At first glance, this behavior looks similar to the behavior seen for 2,5-dihydroxyacetophenone (4), where water adds to

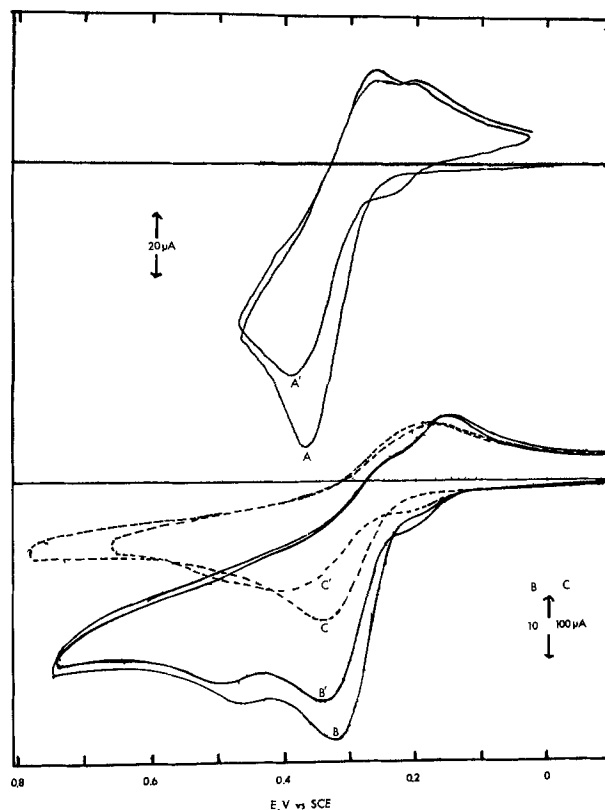


Fig. 2. A (first scan) and A' (second scan): cyclic voltammetry of 1.0 mM dihydroxypropionophenone, pH = 5.8; scan rate 30 mV/sec. B (first scan) and B' (second scan): cyclic voltammetry of 1.0 mM dihydroxyacetophenone (DHAP), pH = 6.0; scan rate 10 mV/sec. C (first scan) and C' (second scan): cyclic voltammetry of 1.0 mM DHAP; pH = 6.0; scan rate 100 mV/sec. Solid lines are the zero current for each voltammogram.

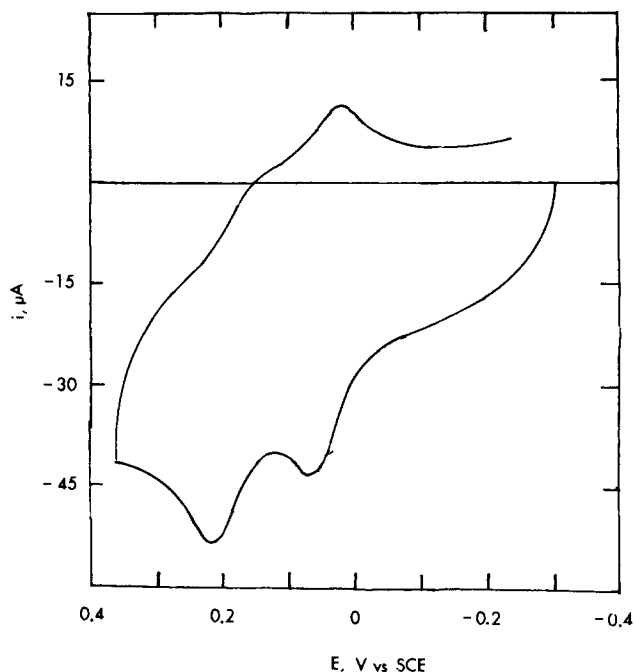
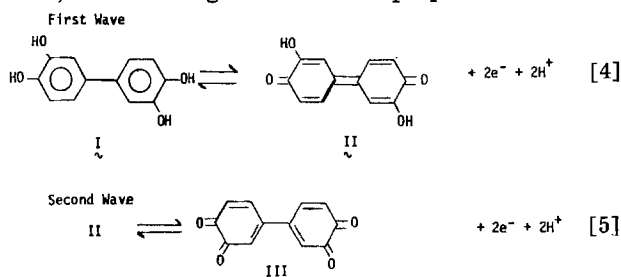


Fig. 3. Cyclic voltammery of 0.1 mM 3,3', 4,4'-tetrahydroxybiphenyl; pH 7.0; scan rate 100 mV/sec.

the quinone. But, on quantitative examination, the peak current function, $i_{pa}/v^{1/2}C$, does not increase but remains constant at the value for two electrons. This will be examined in more detail later by chronoamperometry. In more basic solutions, both reduction waves and the new oxidation wave disappear.

The oxidation of THBP is shown in Fig. 3. Two oxidation waves occur, and on the basis of previous work, the following scheme can be proposed



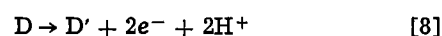
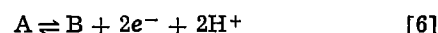
The peak potential of the second wave is approximately at the same potential as the peak potential of catechol at the same pH. It should be noted that, except for catechol and 3-methyl catechol, none of the other biphenyls formed from their respective catechols can form structure II because of the repulsion of the 4-substituents on the rings. As a result, it is impossible for the biphenyl to form the planar configuration needed for the extended *p*-quinone structure.

Chronoamperometry.—In order to calculate the rate of reaction of the electrochemically generated quinone, double-potential step chronoamperometry (DPS) was used to eliminate the effect of the electron transfer rate. The chronoamperometric behavior of catechol was typical of all the substituted catechols where no new peaks were observed in the cyclic voltammograms. The current decay of the oxidation current for catechol obeyed the Cottrell equation for all the pH values studied ($1 < \text{pH} < 12$). The value of the current constant, $i_a t^{1/2}/C$, was equal to the value expected for a two-electron oxidation, even for times when there was substantial reaction of the quinone. The current ratio i_c/i_a , was dependent on the step time, τ , the concentration of catechol, and the pH. The first two

Table I. The chronoamperometric data for catechol at pH 8

Conc (mM)	Time (sec)	i (μA)	$i_a t^{1/2}/C$	i_c/i_a	R_1
0.30	0.50	97.5	230	0.275	0.951
	1.0	67.8	209	0.262	0.904
	2.0	46.9	221	0.264	0.912
	5.0	29.4	219	0.260	0.875
	10.0	20.8	219	0.223	0.769
1.00	1.0	209	207	0.274	0.943
	2.0	148	209	0.256	0.882
	5.0	93.6	207	0.199	0.688
	10	66.6	210	0.135	0.466
	15	54.1	209	0.123	0.425
3.00	20	47.2	211	0.083	0.288
	0.5	1087	256	0.268	0.926
	1.0	679	226	0.228	0.786
	2.0	454	214	0.221	0.762
	5.0	278	222	0.131	0.450
10	210	221	0.073	0.250	
15	171	220	0.048	0.165	
20	148	221	0.037	0.127	

effects can be seen in Table I for three different concentrations of catechol at pH 8. In all cases, the current ratios are divided by 0.2928 to normalize the values. This new parameter is called R_1 . These data demonstrate the second-order nature of the reaction process. The current ratio data from Table I can be correlated with the theoretical working curve for the following coupling mechanism



It is assumed that reaction [8] is irreversible because no new wave is seen for the D/D' couple. Since reaction [8] is favorable, reaction [9] must also be occurring and may very well be the most probable means of forming D'. The current ratio data from Table I is shown in Fig. 4, along with the theoretical lines. It should be pointed out that an alternate coupling scheme could be



The chronoamperometric working curve for R_1 as a function of τ is somewhat different for this case, but the difference is not large. As will be seen later, though, the pH variation of the rate constant is more consistent with reaction [7a].

The variation of the coupling rate constant, k_{obs} , with pH is shown in Table II, along with the $i_a t^{1/2}/C$ values. This variation was consistent with the following coupling mechanism

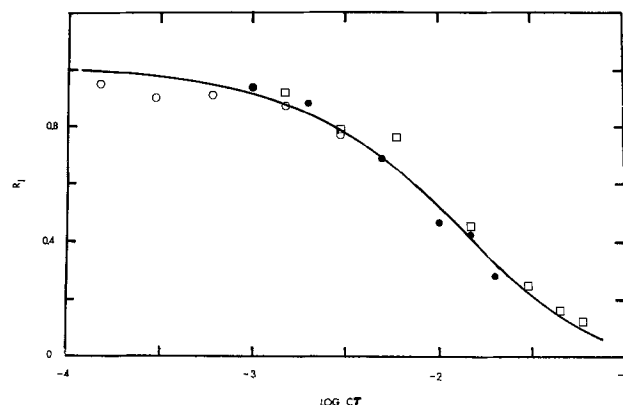


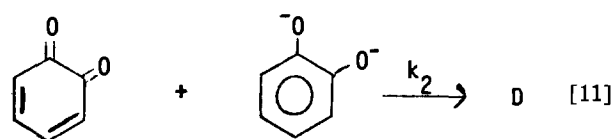
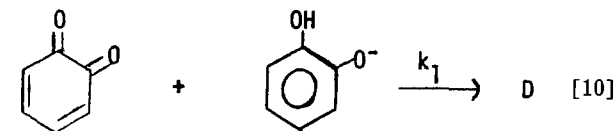
Fig. 4. Chronoamperometry of catechol at pH 8. Concentration of catechol: (○) 0.30 mM, (●) 1.00 mM, and (□) 3.00 mM. Line is theoretical line for a second-order coupling mechanism with a rate constant of $30 \text{ M}^{-1} \text{ sec}^{-1}$.

Table II. Variation of the rate of the coupling reaction as a function of pH

pH	k_{obs} (M^{-1} sec $^{-1}$)	α_1^*	k_1 (M^{-1} sec $^{-1}$)	α_2^*	k_2 (M^{-1} sec $^{-1}$)	k_{calc}^\dagger (M^{-1} sec $^{-1}$)
8.0	30	0.059	507	1.18×10^{-5}	—	29
9.0	158	0.387	410	7.71×10^{-4}	—	188
10.0	456	0.848	537	1.69×10^{-2}	—	411
11.0	1398	0.823	802	0.164	4500	754
12.0	1610	0.333	(485)‡	0.666	2175	1605

* $pK_1 = 9.2$, $pK_2 = 11.70$, Ref. (20).† Calculated value of k_{obs} from the best fit of the data.

‡ Calculated from the pH 8-11 data.

The value of k_{obs} is then

$$k_{obs} = \alpha_1 k_1 + \alpha_2 k_2 \quad [12]$$

where α_1 and α_2 are the fraction of the catechol in the first and second ionized forms, respectively, as defined in Eq. [13] and [14]

$$\alpha_1 = K_1[H^+] / ([H^+]^2 + K_1[H^+] + K_1K_2) \quad [13]$$

$$\alpha_2 = K_1K_2 / ([H^+]^2 + K_1[H^+] + K_1K_2) \quad [14]$$

where K_1 and K_2 are the first and second acid dissociation constants, respectively. If k_2 is not much larger than k_1 , then, when the $pH < pK_2$, $\alpha_2 k_2$ is negligible compared to $\alpha_1 k_1$, as a result, k_1 is then

$$k_1 \approx k_{obs} / \alpha_1$$

The calculated values of k_1 are shown in Table II, along with the k_2 values calculated from the best values of k_1 and Eq. [12]. In Table II, the best values for k_1 and k_2 are used with Eq. [12] to calculate the value of k_{obs} at each pH, and this will be called k_{calc} . The values of k_{obs} as a function of pH are shown in Fig. 5 along with the theoretical line based on the known α values and the measured rate constants.

This same procedure can be used to calculate the values of k_1 and k_2 for other catechols, except for DHPP and DHAP. The values of k_{obs} are small enough so that k_1 and k_2 can be calculated for 3MC, 4MC, and DHPA. The coupling reaction is too fast to measure the values of k_{obs} in very basic solutions which are necessary to calculate k_2 for DHBA, DHAP, DHPP, and DHBE. The variation of k_{obs} as a function of pH for these compounds are shown in Fig. 5 and 6. The values of k_1 and k_2 are given in Table III for all the

Table III. Values of k_1 and k_2 for substituted catechols

Compound	k_1 (M^{-1} sec $^{-1}$)	k_2 (M^{-1} sec $^{-1}$)	pK_1	pK_2
CAT	485	2170	9.2	11.7
3MC	82	580	9.3	11.8
4MC	440	660	9.5	11.9
DHPA	140	1500	10.0	11.6
DHBA	4,900	—	10.2	—
DHAP	60,000	—	8.20	—
DHBE	1,800	—	8.08	11.65
DHPP	66,000	—	8.20	—

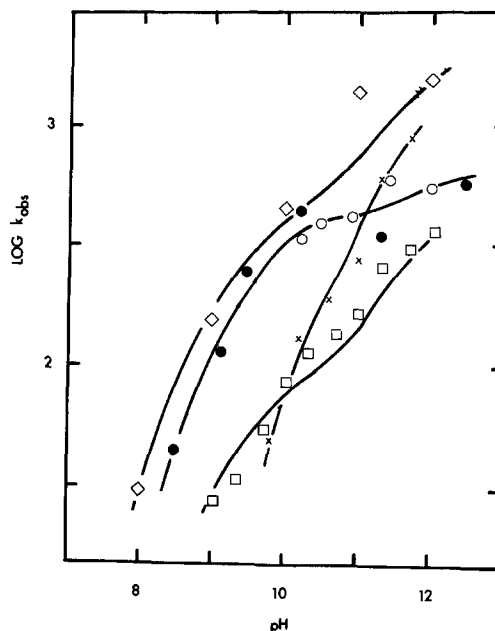


Fig. 5. Variation of the observed rate constant, k_{obs} , as function of pH. (\diamond) catechol, (\square) 3-methyl catechol, (\bullet) 4-methyl catechol using chronoamperometry, (\circ) 4-methyl catechol using rotating ring-disk method, (\times) dihydroxyphenylacetic acid. Solid lines are the theoretical curves using Eq. [12].

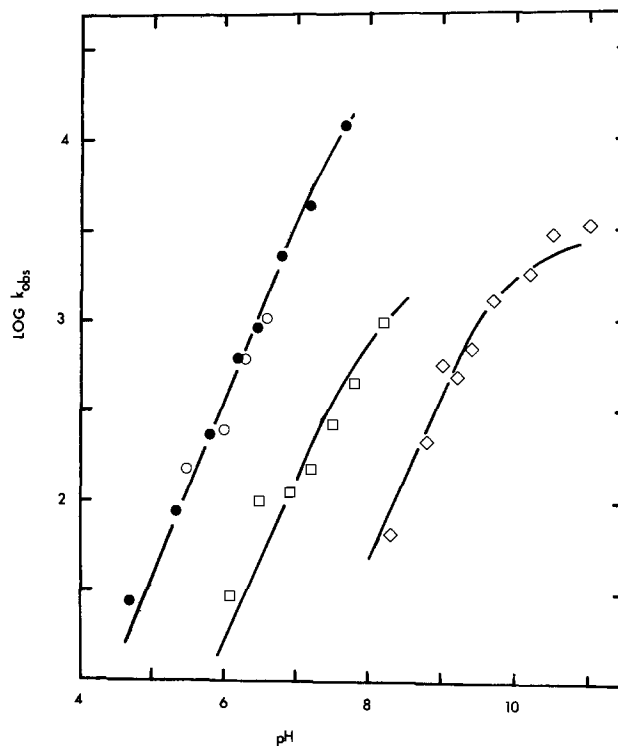
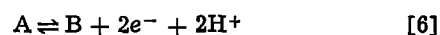
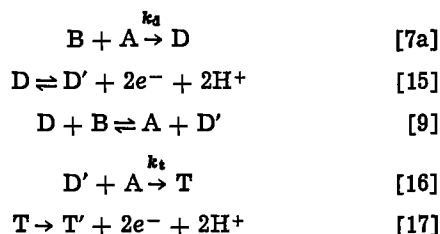


Fig. 6. Variation of the observed rate constant k_{obs} , as a function of pH. (\bullet) dihydroxypropiophenone, (\circ) dihydroxyacetophenone, (\square) dihydroxybenzoic acid, ethyl ester; (\diamond) dihydroxybenzoic acid. Solid lines are the theoretical curves using Eq. [12].

catechols studied, along with the literature values for pK_1 and pK_2 .

The measurement of k_{obs} for DHAP and DHPP must take into account the electroactivity of the reaction product. The working curve for an electroactive D/D' couple was derived by the use of the finite-difference approach (19). The following reaction mechanism was numerically solved





where T and T' are the reduced and oxidized forms of the trimer, respectively, and k_t is the rate of the trimer reaction. Qualitatively we can see from cyclic voltammetry that the stability of the dimer peak depends on the concentration of the catechol. The working curve for this mechanism for different ratios of k_d/k_t is shown in Fig. 7.

The analysis of the DHPP data is illustrated in Fig. 8 for the chronoamperometric data at pH 6.8 for three different concentrations. For $R_1 > 0.5$, the value of k_{obs} depends mostly on the dimerization rate while the value of k_t can be calculated most accurately for R_1 values less than 0.5. From this information, it was found that k_d was $1.0 \times 10^3 M^{-1} sec^{-1}$ and k_t was $1.0 \times 10^2 M^{-1} sec^{-1}$. One must remember that both k_d and k_t depend on pH and are observed rates that depend on α_1 and α_2 . Data for different pH values are shown in Fig. 9, and the variation of k_d with pH is shown in Fig. 6. From this, k_1 was found to be $6.6 \times 10^4 M^{-1} sec^{-1}$ and $k_{1,t}$ or k_1 for the trimer reaction was $1.3 \times 10^4 M^{-1} sec^{-1}$. Similar data were obtained for

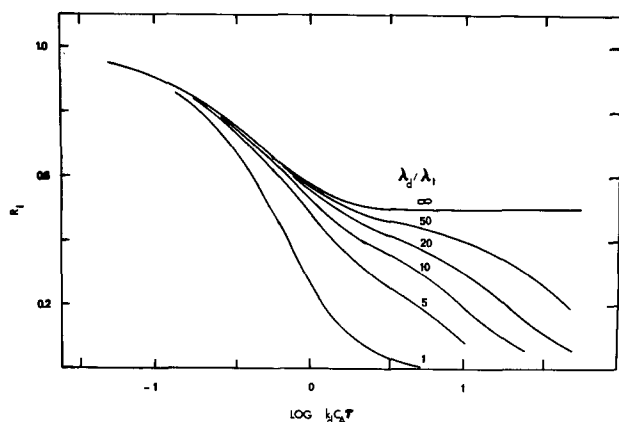


Fig. 7. Theoretical working curve for a dimer-trimer coupling reaction. $\lambda = k_d C \tau$, where k_d is the rate of dimerization reaction. $\lambda_t = k_t C \tau$, where k_t is the rate of the trimerization reaction.

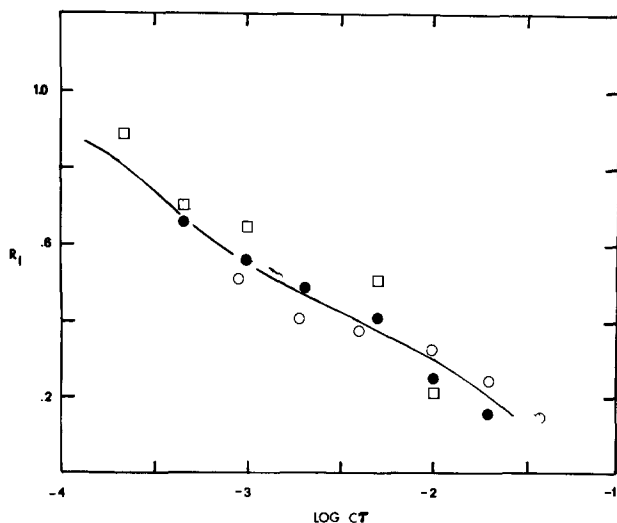


Fig. 8. Double potential step chronoamperometry of dihydroxypropionophenone at pH 6.8. Concentration of DHPP: (\square) 0.5 mM, (\bullet) 1.0 mM, (\circ) 2.0 mM.

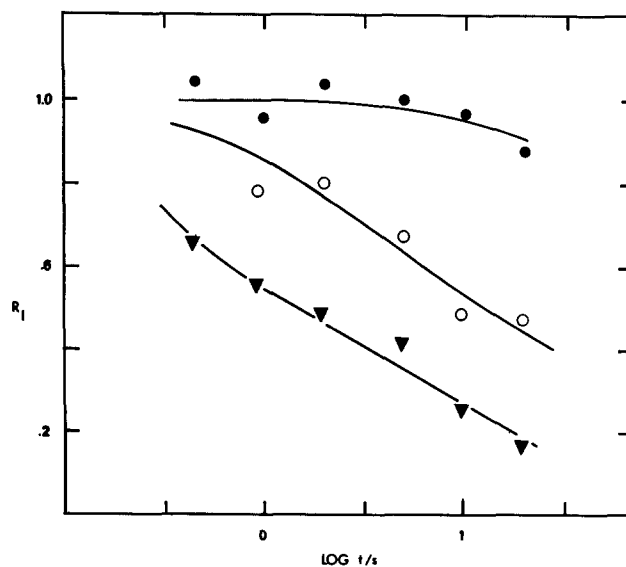


Fig. 9. Double potential step chronoamperometry of 1.0 mM dihydroxypropionophenone. (\bullet) pH = 5.8, (\circ) pH = 6.2, (\blacktriangledown) pH = 6.8.

DHAP. The potential for the anodic step was always chosen positive of the second peak. It is interesting to note that the value of $i_a t^{1/2}/C$ remained at the value indicative of two electrons even when there was substantial reaction for the quinone.

Rotating ring-disk experiments (RRDE).—4MC was studied by RRDE in order to verify that surface film-forming or other such effects were not occurring. The appearance of steady-state currents (especially for the ring) and the obtaining of kinetic data consistent with the chronoamperometry were a further verification that the homogeneous reactions were being monitored.

Only one oxidation wave was observed on the disk as the disk potential was scanned (Fig. 10). If the ring potential was held at a potential where the quinone is reduced, a reduction wave was seen as the disk potential was scanned through the oxidation wave (Fig. 10). In addition, if the disk potential was held in the limit-

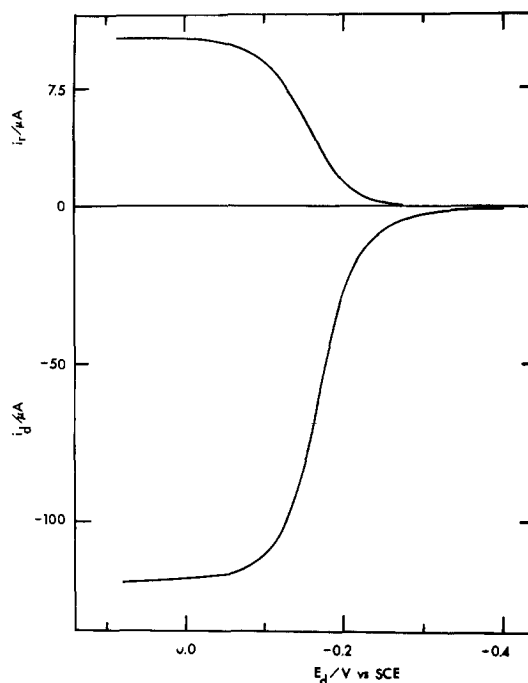


Fig. 10. Rotating ring-disk voltammogram of 0.93 mM 4-methyl catechol. i_r = ring current. i_d = disk current. pH = 12. ω = $10.5 sec^{-1}$.

ing current region and the ring potential was scanned, only one wave corresponding to the quinone reduction was observed. For all pH values studied, the disk limiting current, i_D , was proportional to the square root of the rotation rate, $\omega^{1/2}$. For $n = 2$, the diffusion coefficient, D , for 4MC was calculated to be 4.64×10^{-6} cm²/sec.

In acidic solutions, the collection efficiency, N_k , was independent of the rotation rate, ω , and was equal to 0.17, which was the maximum collection efficiency. In neutral and basic solutions, the collection efficiency decreased and was dependent on rotation rate. A typical set of data is shown in Fig. 11, along with the theoretical curve for the coupling mechanism. The second-order rate constant was calculated for different pH values and the results are shown in Fig. 5. These results were quite consistent with chronoamperometry.

Coulometry.—The coulometric oxidation of 4-methyl catechol was studied most extensively with less work being done on catechol, DHBA, and DHPP. All of these compounds gave similar results. The oxidation of these compounds leads to extensive polymerization as has been seen by previous workers (11). In particular, in this work the products of the oxidation of DHBA and DHPP were isolated and were found by mass spectrometry to be highly polymerized. Fragments were seen in the mass spectra for monomers, dimers, and trimers and the high melting point ($>200^\circ\text{C}$) indicated even larger polymers. This is consistent with the chronoamperometric work which showed the poor stability of the dimer.

The current decay curve for the oxidation of 4MC depended somewhat on pH. In very basic solutions such as pH 11.2, the coulometric n -value was 2.12 which is consistent with the voltammetric and chronoamperometric data. An analysis of the log i - t curve at this pH also gave a slope with an n -value of 2.07. In less basic solutions, the log i - t curve tended to flatten out at long times and the overall coulometric n -value rose to 3.03 at pH 9.42. Still, for the first 10-15 min of the electrolysis, the slope of the log i - t curve yielded a value of 2.05. This indicated that in less basic conditions and at longer times an electroactive product was slowly being formed. This is at much too long a time scale to be observed in chronoamperometry or voltammetry and is probably related to the polymerization reaction. During the time scale for the chrono-

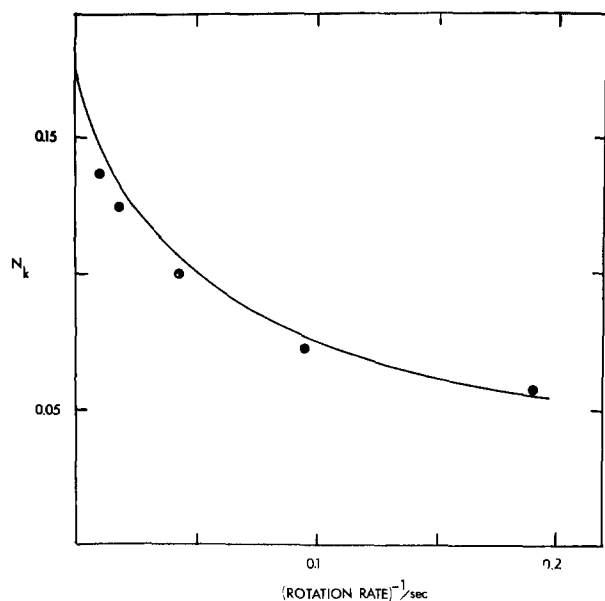
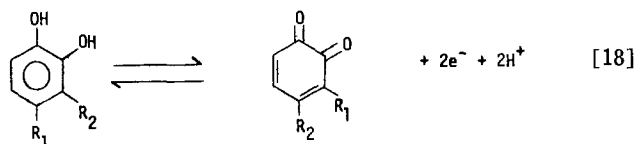


Fig. 11. Variation of the collection efficiency, N_k , as a function of the reciprocal of rotation rate for 0.93 mM 4-methyl catechol, pH = 12. Points are experimental points and solid line is the theoretical curve for $k_f = 620 \text{ M}^{-1} \text{ sec}^{-1}$.

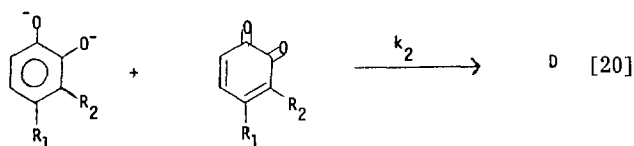
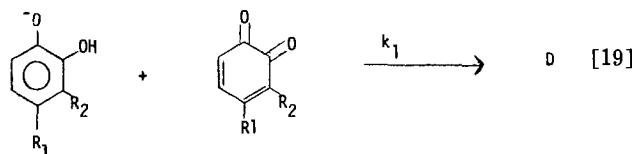
amperometric work, though, an overall $n = 2$ process occurred. Similar results were observed for DHBA where an n -value for the log i - t curve was initially 2.13 while the overall n -value was 2.91 at pH 10.62. Once again, the increased n -value was due to some slowly formed electroactive product which occurred during further polymerization.

Discussion

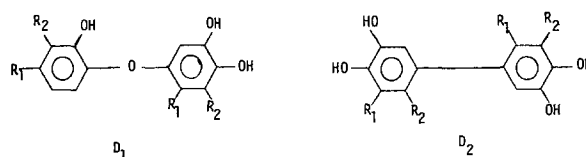
The oxidation of all the catechols studied involved initially the oxidation of the catechol to the o-quinone



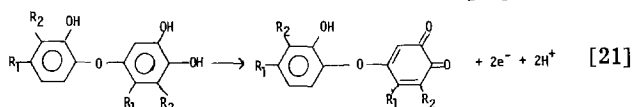
The next step was the coupling between the starting material, catechol, and the quinone



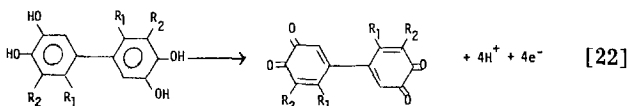
The identity of D can only be inferred because of its poor stability and the great tendency of the quinones to polymerize. Two general types of D, which are formed by C-O or C-C coupling, can be visualized



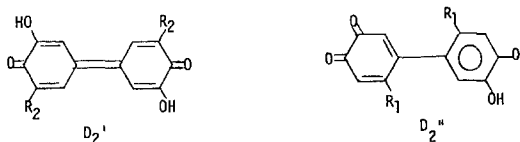
There are also several other isomers that can be formed by coupling at other positions. Dimer D₁ can be further oxidized as shown in reaction [21]



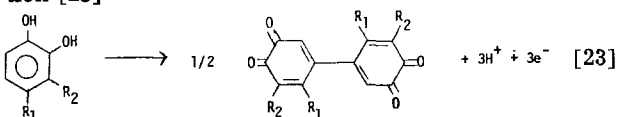
and D₂ can be oxidized as follows



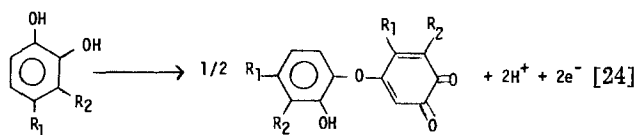
There is an intermediate two-electron oxidation state for these catechols such as D₂' for catechol ($R_2 = \text{H}$) or 3-methyl catechol ($R_2 = \text{CH}_3$) or D₂'' for the other catechols



Since D₂ can be oxidized by four electrons at the potential that the oxidation occurred the overall oxidation of catechol by the C-C coupling is given in reaction [23]



Conversely, the overall oxidation of catechol to D_1' is



Thus, if reaction [23] were occurring, the $i_a t^{1/2}/C$ values should increase by 50% when the coupling reaction occurs to a significant extent. But if reaction [24] were occurring, the $i_a t^{1/2}/C$ values should remain constant, as was observed. In addition, the coulometric n -values were consistent with an $n = 2$ oxidation process. It is only when the coupling process is slow (low pH) and when the catechol concentration is depleted (long electrolysis time) that the coulometric n -value increases. In those cases, extensive polymerization is occurring and the decreases in the catechol may cause changes in the polymerization mechanism. In general, though, the formation of dimer D_1 is the most probable step in initiating the polymerization process for catechol. The electroactivity of the product is probably due to the rapid polymerization or some yet uncharacterized irreversible reaction. Dimer D_2 has been shown in this work to be electroactive and, in all probability, dimer D_1 should also be electroactive. It is only for DHAP and DHPP that the reaction of the dimer is slow enough to be observed in voltammetry.

The coupling reaction is quite sensitive to substituent effects as was seen in Table III. The rate of the coupling reaction, k_1 , can be related with the Hammett ρ - σ parameters, where the Hammett equation is

$$\log k_1 = \log k_0 + \rho\sigma$$

where k_1 is the rate constant for the substituted catechol, k_0 is the rate constant for catechol, σ is a constant characteristic of a given substituent group, and ρ is the slope of the $\log k_1$ - σ graph. The Hammett plot is shown in Fig. 12. The ρ value was 6.2. This positive ρ value means that the transition state has a substantial negative charge because the reaction rate is increased significantly for electron-attracting substituents. This result is consistent with the attack of the catechol anion on the quinone. The only exception is the coupling of DHBE, which deviates significantly from the $\log k_1$ - σ line. This deviation may be due to steric effects.

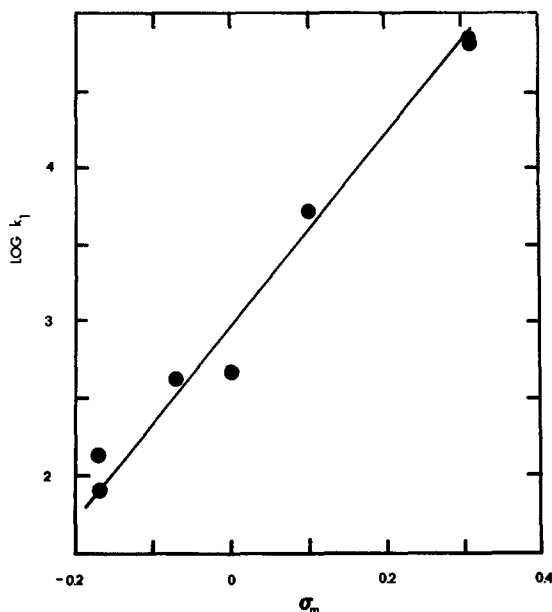


Fig. 12. Hammett σ - ρ plot for the catechols studied

The best fit was obtained for σ_m values, although σ_p gave similar results but with somewhat more scatter. This may be a reflection of the point of attack by the anion, although it is difficult to make any firm conclusions on this basis alone.

Conclusions

The results of this work show that substituted catechols are oxidized to their respective quinones. The quinone is then attacked by the various anionic forms of the catechol to form a diphenyl ether. The overall oxidation is a two-electron process, but the coulometric n -value increases at long electrolysis times due to some slowly formed polymeric products and also changes in the reaction mechanism due to the depletion of catechol. Finally, the Hammett ρ - σ plot is consistent with a substantial negative charge in the transition state.

Acknowledgment

The authors would like to acknowledge the Research Corporation and the Marquette University Committee on Research for partial support of this research. In addition, the authors would like to thank the Computer Services Division of Marquette University for computer time, Dennis H. Evans for his generous help in allowing the use of some of his equipment, and Benjamin A. Feinberg for obtaining the mass spectra.

Manuscript submitted Sept. 28, 1979; revised manuscript received Feb. 14, 1980. This was Paper 321 presented at the Boston, Massachusetts, Meeting of the Society, May 6-11, 1979.

Any discussion of this paper will appear in a Discussion Section to be published in the June 1981 JOURNAL. All discussions for the June 1981 Discussion Section should be submitted by Feb. 1, 1981.

REFERENCES

- R. N. Adams, M. D. Hawley, and S. W. Feldberg, *J. Chem. Phys.*, **71**, 851 (1967).
- M. D. Hawley, S. V. Tatawawadi, S. Piekarski, and R. N. Adams, *J. Am. Chem. Soc.*, **89**, 447 (1967).
- A. W. Sternson, R. McCreery, B. Feinberg, and R. N. Adams, *J. Electroanal. Chem. Interfacial Electrochem.*, **46**, 313 (1973).
- L. Papouchado, G. Petrie, and R. N. Adams, *ibid.*, **38**, 389 (1972).
- L. Papouchado, G. Petrie, J. H. Sharp, and R. N. Adams, *J. Am. Chem. Soc.*, **90**, 5620 (1968).
- T. E. Young, J. R. Griswold, and M. H. Hulbert, *J. Org. Chem.*, **39**, 1980 (1974).
- A. Brun and R. Rosset, *J. Electroanal. Chem. Interfacial Electrochem.*, **49**, 287 (1974).
- J. Doskocil, *Coll. Czech. Chem. Commun.*, **15**, 780 (1950).
- G. Sivaramiah and V. R. Krishnan, *Indian J. Chem.*, **4**, 541 (1966).
- D. I. Stom and S. N. Suslov, *Biofizika*, **21**, 40 (1976).
- H. Musso, in "Oxidative Coupling of Phenols," W. I. Taylor and A. R. Battersley, Editors, pp. 1-94, Marcel Dekker, Inc., New York (1967).
- W. G. C. Forsyth and V. C. Quesnel, *Biochim. Biophys. Acta.*, **25**, 155 (1957).
- A. C. Waiss, Jr., J. A. Kuhnle, J. J. Windle, and A. K. Wiersema, *Tetrahedron Lett.*, 6251 (1966).
- D. E. Hathway, *J. Chem. Soc.*, 519 (1957).
- C. R. Dawson and W. B. Tarpley, *N.Y. Acad. Sci. Ann.*, **100**, 937 (1963).
- P. J. Kinlen, D. H. Evans, and S. F. Nelsen, *J. Electroanal. Chem. Interfacial Electrochem.*, **97**, 265 (1979).
- E. Ritchie, *J. Proc. R. Soc. N.S. Wales*, **78**, 134 (1945).
- J. F. W. McOmie, M. L. Watts, and D. E. West, *Tetrahedron*, **24**, 2289 (1968).
- S. W. Feldberg, in "Electroanalytical Chemistry," Vol. 3, A. J. Bard, Editor, pp. 199-296, Marcel Dekker, Inc., New York (1969).
- P. J. Antikainen and U. Witikainen, *Acta Chem. Scand.*, **27**, 2075 (1973).

The Electrochromic Properties of 4-Benzoylpyridinium Derivatives

Nobuyuki Yoshiike, Shigeo Kondo, and Masakazu Fukai

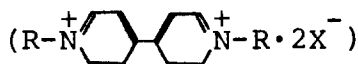
Central Research Laboratories, Matsushita Electric Industrial Company, Limited, Moriguchi, Osaka, 570 Japan

ABSTRACT

The electrochemistry and electrochromism of a number of 4-benzoylpyridinium derivatives (BpX) have been studied in aqueous electrolyte. Cyclic voltammograms demonstrate that the first reduction wave is reversible and controlled by diffusion. The radical compound (Bp) formed at the first reduction is fairly stable in the absence of oxygen. The second reduction peak potential is irreversible and it has a pH dependence. A linear relation between the first reduction potential of substituted 4-benzoylpyridines and the number of carbon atoms in normal alkyl substituents is found. The first reduction wave is shifted to positive region by using longer alkyl substituents increasing the separation from the second wave. The possibility of an electrochromic display based on BpX is also discussed.

Several electrochromic displays (ECD) have been studied in the last ten years. In general they differ from other display devices in that they are based on an electrochemical reaction which brings about a reversible color change. They have been demonstrated having a memory effect, good contrast, low switching voltage, low mean power consumption, and no viewing angular dependence.

They can be classified into two main groups; one using organic materials (1-5) such as viologen



and the other using inorganic materials (6-13) such as WO_3 .

For the studies of application to ECD, it is very important to make clear the electrochemical properties of these electrochromic materials. Polarography and/or cyclic voltammetry are useful methods for this purpose. For example, the polarographic behavior of methyl viologen (MVX_2) was examined (1) in an aqueous solution. The first reduction wave of MV^{++} has been reported to be reversible and pH independent while the second wave is irreversible. In another example, the cyclic voltammetry of WO_3 has been reported (9) to be used for the investigation of electrochemical properties.

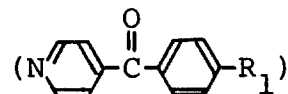
In this paper, the cyclic voltammetry of 4-benzoylpyridinium derivatives (BpX) was studied and BpX were found to give a purplish blue colored stable radical deposit by reduction reaction. The electrochemical and electrooptical behaviors of BpX for a new electrochromic material are described.

Experimental

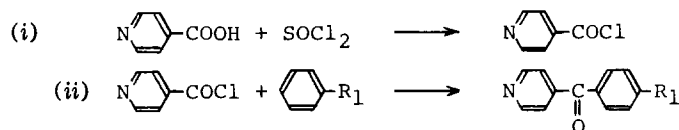
Apparatus.—The electrochemical cell is shown in Fig. 1(a). The working electrode was a platinum plate (1.0 cm^2), the counterelectrode was a platinized platinum plate (15 cm^2) and a saturated calomel electrode (SCE) was used as the reference electrode. The cell (made of Teflon) used for electrooptical studies is shown in Fig. 1(b). The working electrode was a transparent In_2O_3 electrode coated with a thin Pt layer (*ca.* $20 \Omega/\text{cm}^2$, 0.79 cm^2). The electrochemical and/or electrooptical measurements were made with the assembly shown in Fig. 2. The optical measurements fitted for luminosity factor were made with a filter (Hoya Glass Works, LB-200), a gelatin filter (Kodak No. 106), and others as in Fig. 2. Test electrolytes were

degassed with nitrogen to remove oxygen before each measurement.

Reagent.—4-(p-alkylbenzoyl) pyridine derivatives



were prepared by the following general procedure (14).



The data of elementary analyses, melting points,

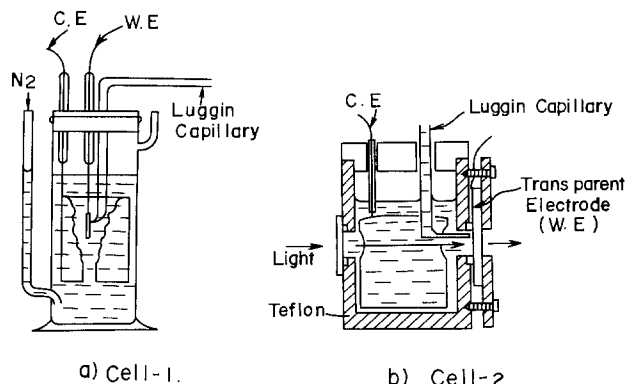


Fig. 1. Schematic diagrams of electrolysis cell

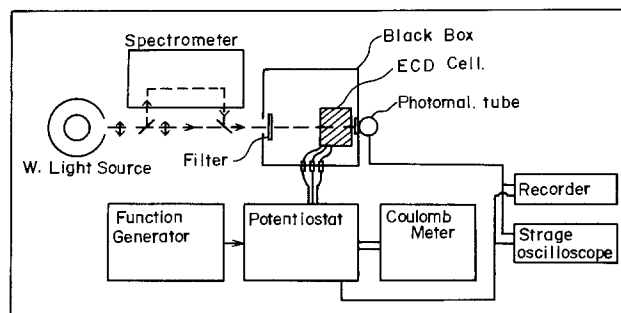
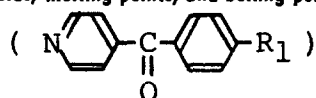


Fig. 2. Instrumental setup employed in electrochemical and electrooptical measurements.

Key words: electrochromic, electrochromic, electrochemical reduction, benzopyridine, displays.

Table I. The data of elementary analyses, yields, melting points, and boiling points of prepared 4-benzoylpyridine derivatives



	Deriva- tives	Analyses (%)						yield (%)	m.p (°c)	b.p (°c) /(m mHg)
		Calcd.			Found					
		R	C	H	N	C	H			
1	CH ₃	79.78	5.63	7.14	79.19	5.58	7.11	93	81-82	145-151 _{/2}
2	C ₂ H ₅	79.77	6.24	6.48	79.62	6.16	6.64	75	49-56	175-181 _{/5}
3	C ₃ H ₇	80.00	6.76	6.14	80.00	6.67	6.22	74	44-48	156-158 _{/3}

yields, and boiling points of prepared materials are shown in Table I. 4-Benzoylpyridine was supplied by Tokyo Kasei Kogyo Company, Limited. The 4-(p-alkylbenzoyl) pyridines were distilled under vacuum, and then refluxed with n-alkyl halide (R₂X) in alcohol. The solid obtained by filtration was washed thoroughly with acetone until washings were colorless and ex-

tracted with water. The aqueous solution was evaporated to dryness in a rotary evaporator. The solid

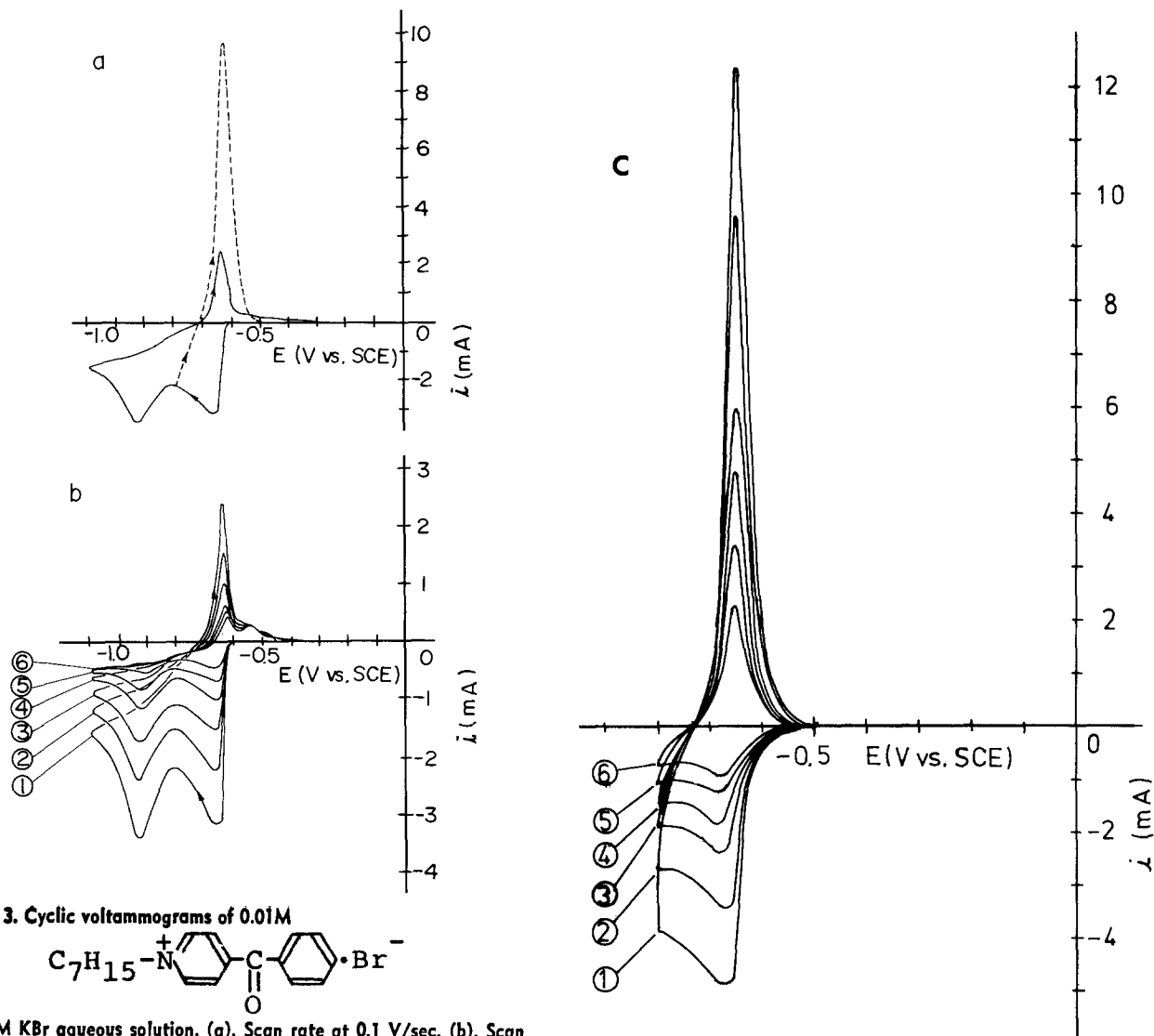
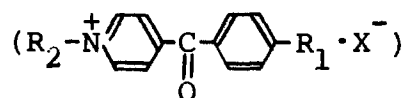
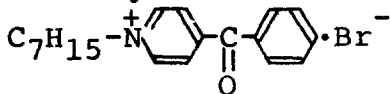


Fig. 3. Cyclic voltammograms of 0.01M



in 0.3M KBr aqueous solution. (a). Scan rate at 0.1 V/sec. (b). Scan rate (V/sec); 1, 0.10; 2, 0.05; 3, 0.025; 4, 0.01; 5, 0.005; 6, 0.002. (c). Scan rate (V/sec); 1, 0.2; 2, 0.10; 3, 0.05; 4, 0.033; 5, 0.0167; 6, 0.0083.

obtained from aqueous solution was recrystallized twice from ethanol, confirmed by elementary analyses and used in the experiments.

The data of analyses are shown in Table II. Potassium bromide (guaranteed reagent) was used as the supporting electrolyte.

Results and Discussion

Electrochemical properties.—A typical cyclic voltammogram for N-heptyl-4-benzoylpyridinium bromide is shown in Fig. 3. It has two well-defined reduction waves. A purplish blue deposit was formed on the working electrode at the first reduction wave. It was fairly stable in the absence of oxygen and reverted to the initial state by an electrochemical oxidation; however, the deposit formed at the second reduction wave was not returned to the initial state and remained on the working electrode. The anodic current peak corresponding to the first reduction wave was sharp as shown by the dotted line in Fig. 3(a), on the other hand, the anodic peak corresponding to the second

wave was not observed. In order to determine the reversibility of each reduction wave, current-potential characteristics were examined by cyclic voltammetry.

Cyclic voltammograms of N-heptyl-4-benzoylpyridinium bromide were measured at various scan rates and are shown in Fig. 3(b) and (c). The scan rate (v) dependence of the first peak potential (E_p^1), the second peak potential (E_p^2) and the first peak current (i_p^1) are obtained from the results as shown in Fig. 4 and give the following

$$\Delta E_p^1 / \Delta \log(v) = 0, \quad \Delta E_p^2 / \Delta \log(v) \neq 0 \quad [1]$$

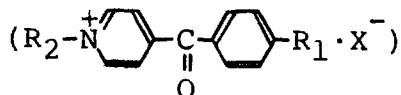
$$i_p^1 / v^{1/2} = 9.9 \times 10^{-3} \quad [2]$$

In the case that the reduction process is reversible and the activity of the deposit is equal to unity, the peak potential (E_p) is given by Delahay (15) as

$$E_p = E_0 + \frac{RT}{nF} \ln f_0 C - (0.942)^2 \frac{RT}{nF} \quad [3]$$

where E_0 is the standard potential, R is gas const., T is

Table II. The data of elementary analyses and melting points of prepared 4-benzoylpyridinium derivatives



	Derivatives			Analyses (%)								m. p (°c)
				Calcd.				Found				
	R	R	X	C	H	N	X	C	H	N	X	
1	C ₇ H ₇	H	Br	63.63	4.50	4.05	23.94	64.41	4.52	3.95	22.60	185-187
2	C ₈ H ₁₇	CH ₃	Br	63.89	7.23	3.69	20.51	64.62	7.18	3.59	20.51	194-196
3	C ₄ H ₉	H	Br	59.75	5.48	4.54	24.94	60.00	5.63	4.38	25.00	143-146
4	C ₅ H ₁₁	C ₂ H ₅	Br	63.07	6.63	3.95	21.33	62.98	6.63	3.87	22.11	175-177
5	C ₇ H ₇	CH ₃	Br	65.09	4.83	3.75	21.57	65.22	4.89	3.80	21.74	188-189
6	C ₆ H ₁₁	H	Cl	73.98	5.85	4.09	10.55	74.67	5.93	4.15	10.22	189-192
7	C ₂ H ₅	CH ₃	I	51.30	4.45	4.04	35.25	50.99	4.53	3.97	35.98	191-194
8	C ₃ H ₇	CH ₃	Br	60.39	5.58	4.35	23.91	60.00	5.63	4.38	25.00	151-152
9	C ₅ H ₁₁	CH ₃	Br	60.76	6.15	4.14	23.11	62.07	6.32	4.02	22.99	130-133
10	C ₇ H ₁₅	CH ₃	Br	61.83	6.53	3.58	22.52	63.83	6.91	3.72	21.28	158-165
11	C ₂ H ₅	C ₂ H ₅	I	53.24	4.87	3.83	32.77	52.32	4.90	3.81	34.60	125-130
12	C ₂ H ₅	C ₃ H ₇	I	53.39	5.24	3.78	33.01	53.52	5.25	3.67	33.33	110-112
13	C ₅ H ₁₁	C ₃ H ₇	Br	62.14	7.09	3.77	21.12	63.83	6.91	3.72	21.28	124-128
14	C ₇ H ₁₅	C ₃ H ₇	Br	63.97	7.36	3.60	18.10	65.35	7.43	3.47	19.80	108-110
15	C ₇ H ₁₅	H	Br	62.85	6.76	3.85	21.73	62.98	6.63	3.87	22.10	166-168
16	C ₇ H ₁₅	CH ₃	Br	61.64	6.82	3.81	20.19	61.22	6.63	3.57	20.41	190-192

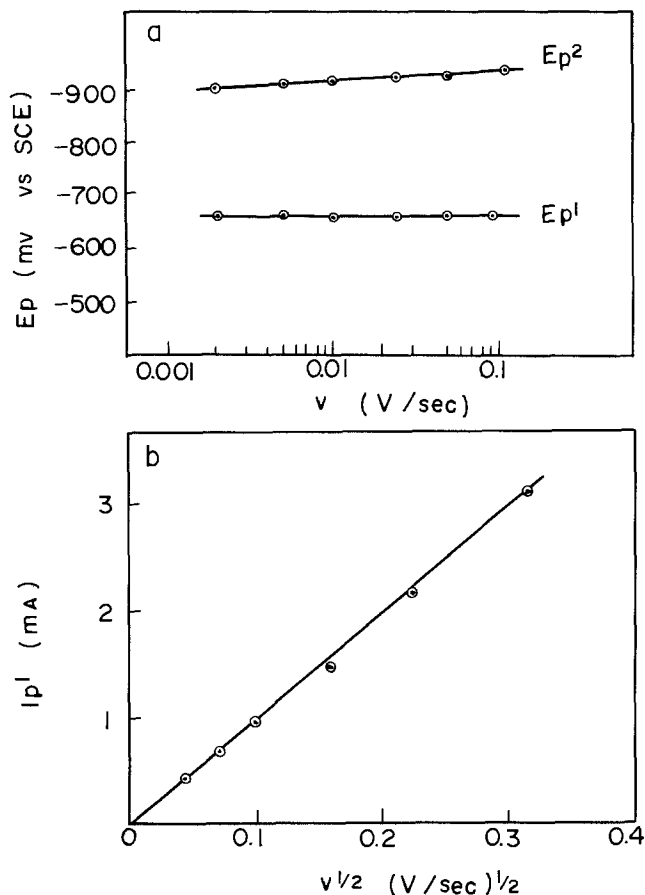
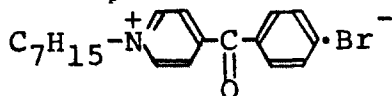


Fig. 4. Scan rate (v) dependence of the peak potential (E_p) and the first peak current (i_{p^1}) for



Data as in Fig. 3, E_{p^1} , the first peak potential, E_{p^2} , the second peak potential.

absolute temperature ($^{\circ}\text{K}$), n is the number of electrons involved, F is Faraday's constant, f_0 is the activity coefficient of the reactant, and C is the bulk concentration. The peak current (i_p) is given by

$$i_p = 3.67 \times 10^5 n^{3/2} S C D^{1/2} v^{1/2} \quad [4]$$

where S is the area of working electrode, D is the diffusion coefficient and v is the scan rate (V/sec).

Empirical relations, [1] and [2] relating to the first reduction wave agree well with the theoretical equations, [3] and [4], respectively, so that the first reduction wave is reversible and controlled by diffusion. The reversibility of the first reduction is supported by other experimental data that show that the anodic-cathodic peak potential difference for the redox couple involved is independent of scan rates of cyclic voltammetric behavior [Fig. 3(c)] and that it is small (about 35 mV). The sharp anodic peak may indicate film stripping during the anodic process. The same results were obtained with other 4-benzoylpyridinium derivatives. The tabulation of these results, E_{p^1} , E_{p^2} , $E_{p^1}/\log(v)$ and $i_{p^1}/v^{1/2}C$ ($\text{A}\cdot\text{sec}^{1/2}\cdot\text{cm}^3/\text{V}^{1/2}\cdot\text{mole}$) is made in Table III.

The number of electrons involved at the first reduction wave may be calculated from theoretical Eq. [4] and an empirical relation between E_{p^1} and $\log C$. For instance, Fig. 5 shows the $E_{p^1} - \log C$ plot of N-heptyl-4-benzoylpyridinium bromide and Eq. [5] the following

$$E_{p^1} = 0.055 \log C + K \quad [5]$$

where K is constant, and $n = 1.06 \approx 1$ is calculated from Eq. [3] and [5]. Therefore the first reduction

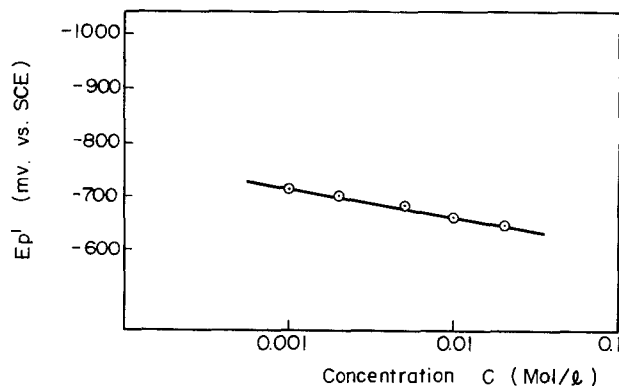
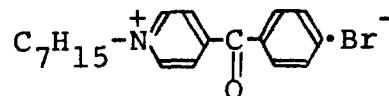


Fig. 5. Plots of the peak potential (E_p) vs. $\log(C)$ for



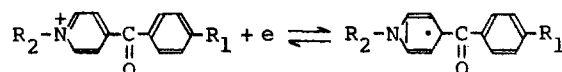
in 0.3M KBr solution at 20°C .

waves of these derivatives proceed with one-electron reduction process. The same relations were obtained on others.

The second reduction process is irreversible, because the second reduction wave had the scan rate dependence of the peak potential (E_{p^2}) and the anodic current peak corresponding to the second reduction wave was not observed clearly as shown in Fig. 3.

The pH dependences of reduction waves were measured in various $\text{H}_3\text{BO}_3\text{-KCl-Na}_2\text{CO}_3$ buffer solutions and $\text{Na}_2\text{HPO}_4\text{-NaOH}$ buffer solutions. The representative result of N-heptyl-4-benzoylpyridinium bromide is shown in Fig. 6.

The peak potential of the first reduction is independent of pH over a pH range of 8-12, and the second reduction wave varies 43 mV per pH unit. Therefore the first reduction,



is not affected by protons in the electrolyte system. The structure of the first reduction product is actually a resonance structure with the radical delocalized over both the aromatic rings and the carbonyl group; such resonance contributes to the radical stability. The extraction of proton from the electrolyte follows presumably the second reduction and the process is irreversible.

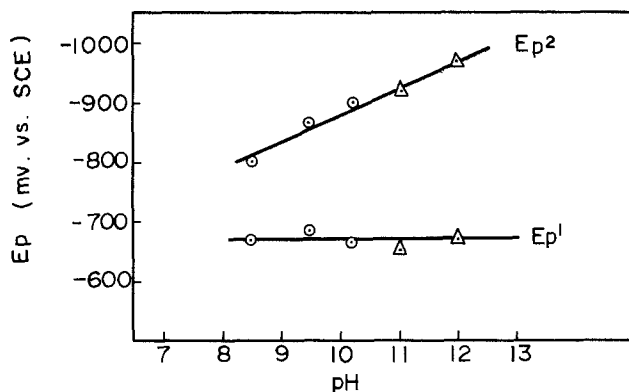
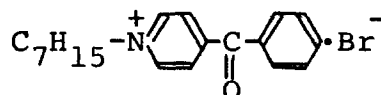
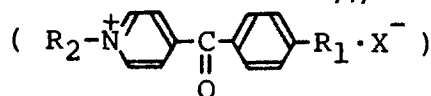


Fig. 6. Plots of the peak potential (E_p) vs. pH for 0.01M

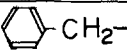


in buffer solution $\text{H}_3\text{BO}_3\text{-KCl-Na}_2\text{CO}_3$, $\text{Na}_2\text{HPO}_4\text{-NaOH}$.

Table III. Cyclic voltammetric results for 4-benzoylpyridinium derivatives

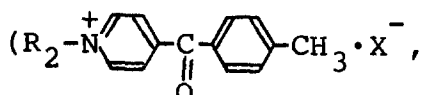


E_p at scan rate $v = 0.1$ V/sec; supporting electrolyte, 0.3M KBr

No.	R ₁	R ₂	X	C (M/l)	E_p^1 mv (vs. SCE)	E_p^2 mv (vs. SCE)	$\frac{\Delta E_p^1}{\Delta \log v}$	$\frac{ip}{v^{1/2} C}$
1	CH ₃	C ₂ H ₅	I	5×10^{-3}	-820	-922	0	1.0×10^3
2		C ₃ H ₇	Br	5×10^{-3}	-790	-940	0	1.2×10^3
3		C ₅ H ₁₁	Br	5×10^{-3}	-730	-1010	0	8.8×10^2
4		C ₇ H ₁₅	Br	5×10^{-3}	-680	-945	0	8.0×10^2
5		C ₈ H ₁₇	Br	2.5×10^{-3}	-670	-930	0	1.2×10^3
6		 -CH ₂ -	Br	1.5×10^{-2}	-700	-840	0	1.2×10^3
7	C ₂ H ₅	C ₂ H ₅	I	1.0×10^{-2}	-760	-1035	0	1.0×10^3
8	C ₃ H ₇	C ₂ H ₅	I	5×10^{-3}	-760	-960	0	1.2×10^3
9		C ₅ H ₁₁	Br	2.5×10^{-3}	-710	-880	0	9.2×10^2
10		C ₇ H ₁₅	Br	2.5×10^{-3}	-590	-890	0	8.0×10^2
11	H	C ₄ H ₉	Br	5×10^{-3}	-765	-875	0	
12		C ₇ H ₁₅	Br	1.0×10^{-2}	-690	-895	0	9.9×10^2
13	CH ₃ O	C ₇ H ₁₅	Br	2.5×10^{-3}	-660	-710	0	1.2×10^3

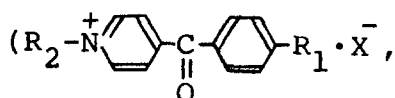
Consequently, to use BpX as an ECD material, it is necessary to use only the first reduction reaction during writing time for the purpose of reversible color change. Therefore, it is desirable to separate the first reduction potential from the second irreversible reduction potential as much as possible.

The apparent standard potential (E_0) for the couple $Bp^+ - Bp$ was obtained from the experimental data, where each activity coefficient is equivalent under the experimental conditions. For example, for the 4-(p-methylbenzoyl) pyridinium derivatives



$R_2 = n$ -alkyl group), the linear relation between m , the number of carbon atoms in the N -alkyl substituents, and the standard potential, E_0^1 , is given by $E_0^1 = 28m + b$ (mV), where b is a constant, and is shown in Fig. 7.

The effect of p -alkyl substituents



$R_1 = n$ -alkyl group) on the apparent standard potential is the same as the effect of N -alkyl substituents. For N -pentyl-4-(p -alkylbenzoyl) pyridinium derivatives, the relation between m' , the number of carbon atoms in p -alkyl substituents, and E_0^1 is almost linear and given by $E_0^1 = 15m' + b'$ (mV) where b' is constant and shown in Fig. 8.

These results demonstrate that the standard potential E_0 of the first reduction shifts to more positive

potentials with increasing carbon atoms in the alkyl substituents and that it is more efficient to use long alkyl groups, i.e., n -hexyl, n -heptyl, for N -substituents than using these groups for p -substituents. They are supported by the fact that the reduction potential shifts to a more positive region with decreasing nucleophilic effect of the substituents (16-18). The substituent effect on the second reduction potential is not clear (see Table III).

The first reduction potential may be shifted to positive potential regions and separated from the second reduction potential by using large alkyl substituents, for example, the potential difference between E_p^1 and E_p^2 is more than 200 mV for N -heptyl substituents, so

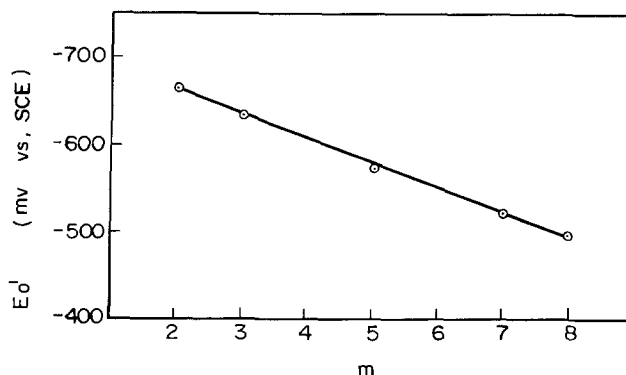


Fig. 7. The relationship between the standard potential and m for

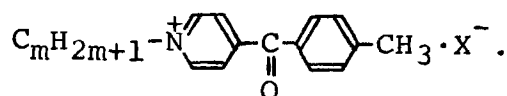
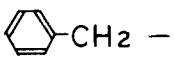
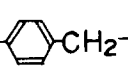


Table IV. Quasi-extinction coefficients which were obtained from the luminous transmittance (TI) and the following equation,
 $K = -(FS/q) \log (TI)$

	1	2	3	4
R ₁	H	C ₂ H ₅	CH ₃	H
R ₂	C ₇ H ₁₅ -	C ₅ H ₁₁ -		C ₂ H ₅ - 
K	5800	6230	5240	7420

it is easier to use the first reduction reaction during writing time, and possible to use BpX as an ECD material by using long alkyl groups for substituents.

The optical properties of BpX.—The electrooptical properties were measured by a potentiostatic pulsed mode with cell 2 of Fig. 1 and the assembly of Fig. 2. The reduction potential for the writing state was controlled within the first reduction peak potential (E_p^1).

The writing state of ECD is achieved by the deposition of reduced electrochromic materials on the working electrode. Absorption spectra of the deposit were obtained from the transmittance (Tr) at each wavelength (λ) and the following equation. $A = -\log Tr = kq/FS$ where A is the absorbance at each wave-

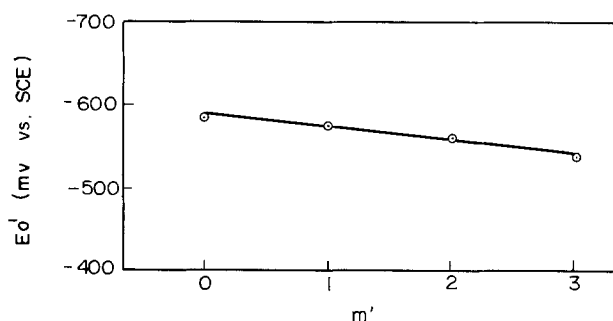


Fig. 8. The relationship between the standard potential and m' for

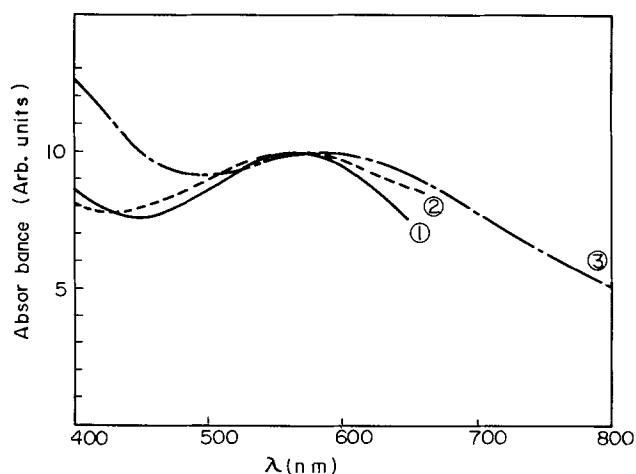
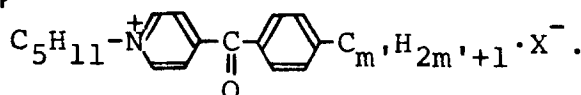
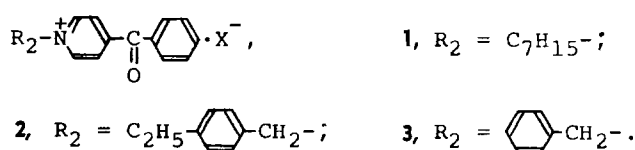
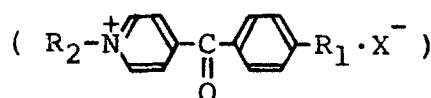


Fig. 9. Absorption spectra of radical states of

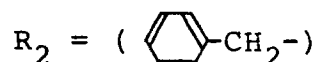


length, k is the extinction coefficient, q is the amount of charge consumed for writing, and S is the area of the working electrode. The absorption spectra of Bp show broad bands around 5800A as shown in Fig. 9.

Light absorption of Bp is based on π -electron resonance of benzoylpyridine ring, so that a small amount of adsorption spectrum shift may be achieved by changing the substituents R_1 and R_2 in



A 0.11 eV shift was observed between $R_2 = C_7H_{15}$ and



The contrast at writing state is directly determined by absorbance fitted for a luminosity factor. For convenience, constants (K) which correspond to a quasi-extinction coefficient fitted for luminosity factor were obtained from the luminous transmittance (TI) and the following equation, $K = -(FS/q) \log (TI)$ and shown in Table IV for a comparison of the absorbance fitted for luminosity factor.

Absorption spectra of the radical state of BpX are mainly fitted for luminosity spectrum having peak at 5550A, hence great contrast changes at write-erase cycles can be expected, so that absorption spectra of writing states of BpX are suitable for a display device.

From the above-mentioned results, BpX has a possibility as a new electrochromic material for ECD.

Manuscript submitted Nov. 27, 1978; revised manuscript received Jan. 23, 1980.

Any discussion of this paper will appear in a Discussion Section to be published in the June 1981 JOURNAL. All discussions for the June 1981 Discussion Section should be submitted by Feb. 1, 1981.

Publication costs of this article were assisted by the Matsushita Electric Industrial Company, Limited.

REFERENCES

1. R. M. Elefson and R. L. Edsberg, *Can. J. Chem.*, **35**, 646 (1957).
2. C. T. Shoot, J. J. Ponjee, H. T. van Dam, R. A. van Doorn, and P. T. Bolwijn, *Appl. Phys. Lett.*, **23**, 64 (1973).
3. R. J. Jasinski, *This Journal*, **124**, 637 (1977).
4. M. Yamamoto and M. Yamana, *Oyo Butsuri* **145**, 789 (1976).
5. J. Bruinink, C. G. A. Kregting, and J. J. Ponjee, *This Journal*, **124**, 1854 (1977).
6. B. W. Faughnan, R. S. Crandall, and P. M. Heyman, *RCA Rev.*, **36**, 177 (1975).
7. I. F. Chang and W. E. Howard, IBM Research, Nov. 14, 1974.
8. A. Di Paola, F. Di Quarto, and C. Sunseri, *This Journal*, **125**, 1344 (1978).
9. I. F. Chang, B. L. Gilbert, and T. L. Sun, *ibid.*, **122**, 955 (1975).

10. S. K. Deb, *Appl. Optics Suppl.*, **3**, 192 (1969).
11. S. K. Deb, *Philos. Mag.*, **27**, 801 (1973).
12. T. C. Arnoldussen, *Proc. Int. Electron Devices Meet.*, 1975, p. 389 (1975).
13. B. W. Faughnan and R. S. Crandall, *Appl. Phys. Lett.*, **31**, 834 (1977).
14. E. Klingsberg, "Pyridine and Its Derivatives," Part I ~ III, Interscience Publishers, Inc., New York (1961).
15. P. Delahay, "New Instrumental Methods in Electrochemistry," Interscience, New York (1974).
16. M. Yamamoto, T. Kawata, and M. Yamana, *Gazogijitsu* **6**, 25 (1975).
17. T. Kubota, K. Nishikida, H. Miyazaki, K. Iwatani, and Y. Oishi, *J. Am. Chem. Soc.*, **90**, 5080 (1968).
18. H. H. Jaffe, *Chem. Rev.*, **53**, 191 (1953).

Photoanodic Dissolution Reaction of an n-Type Gallium Phosphide Electrode and Its Effect on Energies of the Electronic Bands at the Surface

Yoshihiro Nakato, Akira Tsumura, and Hiroshi Tsubomura*

Department of Chemistry, Faculty of Engineering Science, Osaka University, Toyonaka, Osaka 560, Japan

ABSTRACT

Mott-Schottky plots obtained at dark and under weak illumination have shown that the energies of the electronic bands at the surface of an n-GaP electrode are sifted downward, toward more negative, by illumination under anodic polarization. The magnitude of the shift for the (111)-face of the electrode was somewhat smaller than that for the (111)-face. The results are explained by taking account of photoanodically formed surface intermediates, causing a change in the potential difference at the semiconductor-solution interface. These intermediates were found to decay in several minutes at dark under anodic polarization. It is suggested that these intermediates also act as effective surface recombination centers.

The flatband potential (U_{FB}) is the electrode potential of a semiconductor electrode, at which the electrostatic potential inside the semiconductor is flat. The quantity, $-eU_{FB}$, reflects the Fermi level of the semiconductor at the flatband condition, in the sense that the Fermi level of the semiconductor is given with respect to the electron energy (the Fermi energy) of a reference electrode. The lower energy limit of the conduction band of an n-type semiconductor, designated as E_c , is slightly higher (less negative) than the Fermi level. Therefore, at the flatband condition we can express E_c^s , by taking a small value Δ

$$E_c^s = -eU_{FB} + \Delta$$

where E_c^s is the E_c value at the surface of the semiconductor, E_c^s and $-eU_{FB}$ being measured with respect to the same reference electrode.

It is often tacitly assumed that E_c^s is a constant independent of the electrode potential. Under such an assumption, E_c^s is virtually equal to $(-eU_{FB} + \Delta)$. So, U_{FB} can be determined from the so-called Mott-Schottky plots (1, 2). In the case of p-type semiconductors, the upper energy limit of the valence band at the surface, designated as E_v^s , is in a situation similar to E_c^s in the above.

If E_c^s takes different values at electrode potentials (U) different from U_{FB} , it should be distinguished from $(-eU_{FB} + \Delta)$. In this case, we can define U_s as $E_c^s = -eU_s + \Delta$ (Fig. 1). If U_s (or E_c^s) remains nearly constant in a certain range of U , a Mott-Schottky plot should give a straight line in this potential range, from which U_s (or E_c^s) can be determined.

Gerischer and co-workers reported that the "flat-band" potential of an intrinsic germanium electrode changes with either anodic or cathodic prepolarization (3). They explained the result as due to a chemical change at the surface from hydroxide- to hydride-like

structure. This means that the energies of the electronic bands at the surface change with U in an intermediate potential range between the anodic and cathodic polarization.

Measurements of the Mott-Schottky plots under illumination have so far been reported only for a few semiconductors under limited conditions (4, 5). It was reported that the "flatband" potential of an n-TiO₂ electrode was not shifted by illumination (5). For an MoSe₂ electrode in an iodide-containing solution, the shift of the surface band energies by illumination was suggested from capacitive phase-shift measurements (6). The photo-shift of the surface band energies was also suggested from analysis of current-potential curves for a CdS electrode in a low concentration sulfide solution (7). Capacitance changes by illumination were also reported for an SrTiO₃ electrode (8).

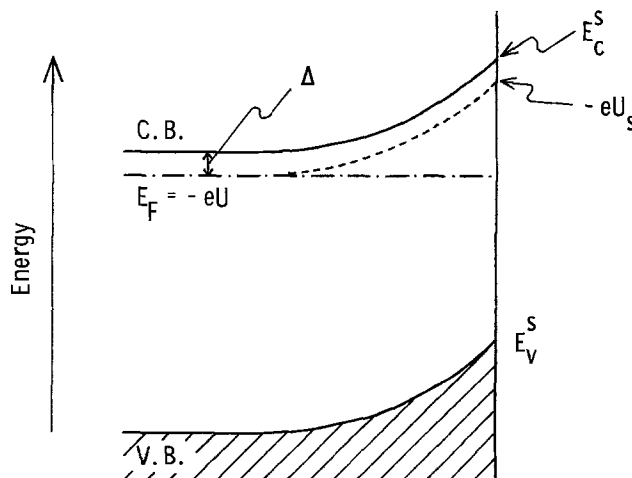


Fig. 1. A schematic figure showing a relation between U_s and E_c^s .

* Electrochemical Society Active Member.

Key words: semiconductor, photoelectrochemistry, reaction intermediate.

It is sometimes found that the onset potentials of anodic photocurrents for n-type semiconductors deviate from the "flatband" potential or above-mentioned U_s at dark to the positive. These results were explained in terms of electron-hole recombination via a pre-existing surface state within the bandgap (9).

We have found that the band energy at the surface of an n-GaP electrode is shifted by weak illumination under anodic polarization. In the present paper, we will report on these experimental results and discuss the effect of electron or hole density at the surface on the surface chemical structure and band energies.

Experimental

The n-type GaP used was a single crystal in the form of wafers, 99.999% pure, doped with sulfur at the concentration of $2-3 \times 10^{17} \text{ cm}^{-3}$ obtained from Yamanaka Chemical Industries Limited. The p-type GaP used was doped with zinc at $3.7 \times 10^{17} \text{ cm}^{-3}$, obtained from Sanyo Electric Company, Limited. Both were cut perpendicular to the [111]-axis. The electrodes were prepared in the same way as reported elsewhere (10). Before the experiment, they were polished and etched with warm aqua regia in order to remove oxide layers at the surface. The (111)-face (Ga face) and the $(\bar{1}\bar{1}\bar{1})$ -face (P face) were distinguishable by microscopic inspection of the etched surfaces, the former very rough and the latter smooth, as reported in the literature (11).

The current-potential curve was obtained with a Hokutodenko HA-101 potentiostat. The differential capacitance was measured mostly with a Yokogawa-Hewlett-Packard Universal Bridge 4265B, having a modulation frequency of 1 kHz and a modulation amplitude of 20 mV (peak to peak). The frequency dependence of Mott-Schottky plots were checked by connecting a function generator with this bridge. The electrode was illuminated through a quartz window, with a 250W high pressure mercury lamp. The light intensity was attenuated by use of neutral density filters made of metal nets.

Solutions were prepared from deionized water by using reagent grade chemicals, in most cases, without further purification. They were deaerated by bubbling nitrogen and stirred with a magnetic stirrer. The pH of the solutions in the range of 3-11 was controlled by using buffer mixtures; acetate, phosphate, borate, or carbonate, each at about 0.01M, where M means mole/dm³. This abbreviation is used throughout the present paper.

Results

Figure 2 shows the current-potential (i - U) curve for the (111)-face of the n-GaP electrode in an alkaline solution. Dark anodic currents were less than $0.1 \mu\text{A}/\text{cm}^2$. The i - U curve under illumination shows hysteresis in the potential range between -2.0 and -1.0V vs. SCE. The hysteresis is quite strong at low illumination intensities or at high potential sweep rates.

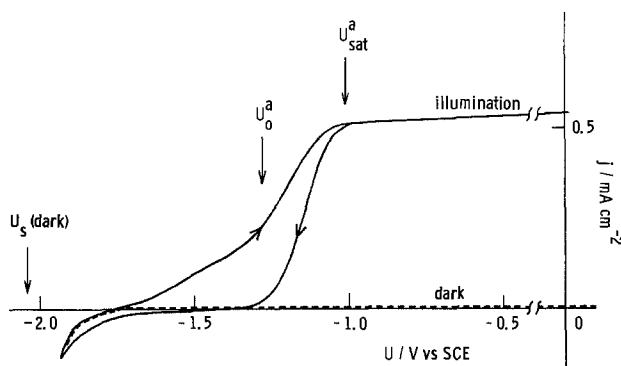


Fig. 2. A current-potential curve for the (111)-face of an n-GaP electrode under illumination. Sweep rate: 120 sec/V. Electrolyte: 0.1M NaOH.

As the cathodic current observed in the range below -2.0V vs. SCE corresponds to hydrogen formation (12, 13), the electrode surface in this range is thought to have a reduced (hydride-like) structure. The photoanodic current in the range above -1.0V corresponds to the oxidative dissolution of the electrode (12-16), and therefore the electrode surface is expected to have an oxidized structure. Accordingly, the anodic and cathodic currents observed in the intermediate potential range can partly be attributed to oxidation of cathodically formed surface hydride and reduction of photoanodically formed surface hydroxide or oxide, respectively (12). Similar hysteresis was reported in the case of Ge and GaAs electrodes (17).

Based on the above interpretation, the i - U curve obtained by scanning from the anodic to the cathodic potential arises from the n-GaP electrode covered with the photoanodically formed surface hydroxide or oxide. Its shape and position can be characterized by two potentials: U_{sat}^a , at which the anodic photocurrent begins to deviate from the saturation value, and U_o^a , at which it is zero, as is shown in Fig. 2. It is to be noted that these potentials shift largely from U_s at dark [U_s (dark)], determined from the Mott-Schottky plot in the present work.

Figure 3 shows the pH dependence of U_o^a and that of U_{sat}^a for the (111)-face of the n-GaP electrode, as compared with that of U_s (dark) described in detail later. U_o^a and U_{sat}^a were measured at a low illumination intensity, with the anodic saturation currents kept at $15 \mu\text{A}/\text{cm}^2$. It is seen that U_{sat}^a and U_o^a shift largely from U_s (dark) in the range of $\text{pH} \geq 4$. The difference between U_o^a and U_{sat}^a increases at around pH 4, conceivably due to the formation of a hydroxide or oxide layer, probably exceeding one-monolayer coverage because of its low solubility around this pH. It is thought that no such thick hydroxide or oxide layer is formed except weakly acidic solutions under weak illumination, because such layers dissolve easily in solution (13, 14).

The large deviations of U_o^a and U_{sat}^a from U_s (dark) suggest that E_c^s (or U_s) of the n-GaP electrode is shifted by illumination. We therefore determined the U_s values under illumination at various pH. Figure 4 shows some examples of Mott-Schottky plots for the n- and p-type GaP electrodes at dark, and Fig. 5 those under illumination. The electrode was illuminated at a low intensity, so as to avoid disturbance in the space charge layer by the flow of photocurrents. Very good straight lines were obtained both at dark and under illumination, showing applicability of the Mott-Schottky method to weakly illuminated electrodes. As

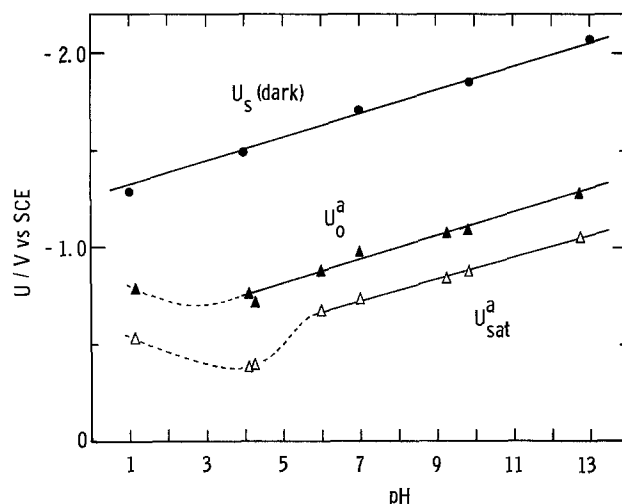


Fig. 3. U_s (dark), U_o^a , and U_{sat}^a for the (111)-face of an n-GaP electrode as functions of pH. Electrolyte: 0.05M H_2SO_4 (pH 1), 0.05M Na_2SO_4 + buffer (pH 4-10), and 0.1M NaOH (pH 13).

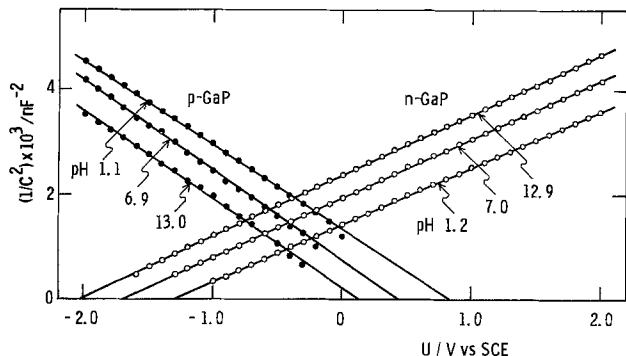


Fig. 4. Mott-Schottky plots for the (111)-face of n- and p-type GaP electrodes at dark. Electrolyte is the same as in Fig. 2. The modulation frequency: 1 kHz.

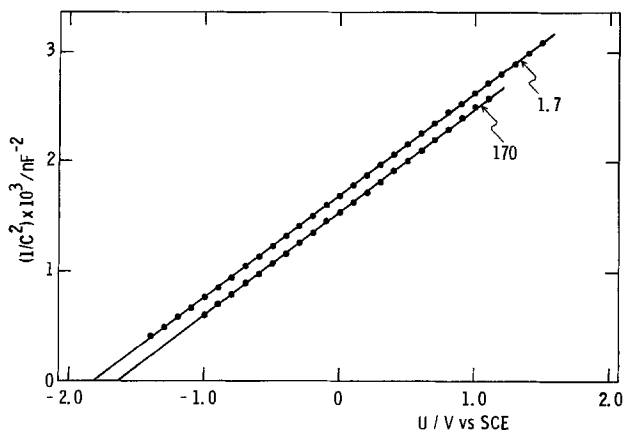


Fig. 5. Mott-Schottky plots for the (111)-face of an n-GaP electrode under illumination. The anodic photocurrents flowing under measurements are shown in unit $\mu\text{A}/\text{cm}^2$. Electrolyte: 0.1M NaOH. The modulation frequency: 1 kHz.

seen in Fig. 4 and 5, the lines have slopes slightly different from each other, due probably to variations in the roughness factor of the electrode surface, caused by the mechanical polishing.

The values of U_s for the (111)-face of the GaP electrodes, determined by extrapolating the inverse square of the differential capacitance to zero, are shown in Fig. 6. Firstly, it is seen that the U_s values of the n- and the p-type GaP electrodes at dark, called U_s^n (dark) and U_s^p (dark), change linearly with pH with a slope of ca. $-60 \text{ mV}/\text{pH}$. The onset potential of the dark cathodic currents changes with pH in parallel with U_s^n , showing the validity of the U_s^n values determined from the Mott-Schottky plots. Secondly, it is seen that the difference between U_s^n (dark) and U_s^p (dark) is about 2.1V throughout the pH range, nearly equal to the bandgap of the GaP semiconductor (2.26 eV). This is a reasonable result, which means that $E_{c,s}$ and $E_{v,s}$ are nearly the same in the n-GaP electrode under anodic polarization and the p-GaP electrode under cathodic polarization. The U_s values in the present work are also in good agreement with the values reported as the "flatband" potential at dark (18), lying very close to the U_s vs. pH lines drawn in Fig. 6.

The values of U_s for the n-GaP electrode under illumination, U_s^n (ill.), shift definitely from U_s^n (dark) to the positive (Fig. 6). The magnitude of the shift increases with the illumination intensity, reaching about 0.4V at the photocurrent density $170 \mu\text{A}/\text{cm}^2$ at pH 13. The values of both U_s (dark) and U_s (ill.) were confirmed to be independent of the modulation frequency in the range of 1-10 kHz for the measurements of the differential capacitance.

Figure 6 also shows that the value of U_s (dark) of the n-GaP electrode at each pH is constant irrespective

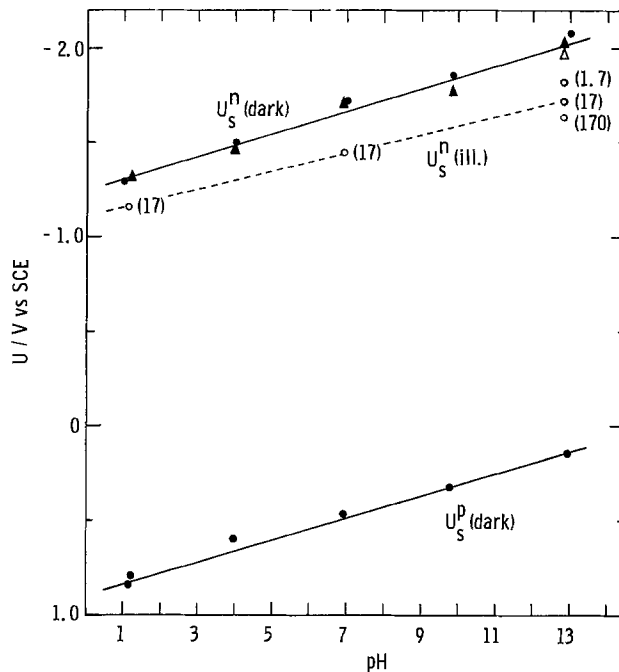


Fig. 6. U_s for the (111)-face of n- and p-GaP electrodes: (●) measured at dark after chemical etching, (▲) at dark in 10 min after the flow of cathodic currents, (△) at dark in 10 min after the flow of anodic photocurrents, and (○) under illumination. The anodic photocurrents flowing under measurements are shown in parenthesis in $\mu\text{A}/\text{cm}^2$. Electrolyte: the same as in Fig. 2.

of whether it was measured after the chemical etching, after the flow of anodic photocurrents, or after the flow of cathodic currents. This means that both the photoanodically formed oxides or hydroxides and the cathodically formed hydrides at the surface disappear at dark under anodic potentials, through reaction with the electrolyte solution. The surface of the n-GaP electrode at dark under anodic polarization is then thought to be in an equilibrium state in the electrolyte solutions, irrespective of pretreatments of the electrode.

We can roughly estimate the average decay rate of the photoanodically formed oxides or hydroxides from the shift of the i - U curve under illumination in a way described below. In Fig. 7, broken lines show the i - U curves under illumination after 10 min preillumination at 0V vs. SCE, while solid lines are those obtained by 10 min preillumination at 0V vs. SCE, followed, after a certain period of dark time, by a potential sweep at 10 sec/V to the negative at dark, and reillumination at -1.0V vs. SCE. Although few examples are shown in Fig. 7 for simplicity, the i - U curve shifts to more negative, the longer the dark period, t_d , and beyond 660 sec no shift was observed. This result shows

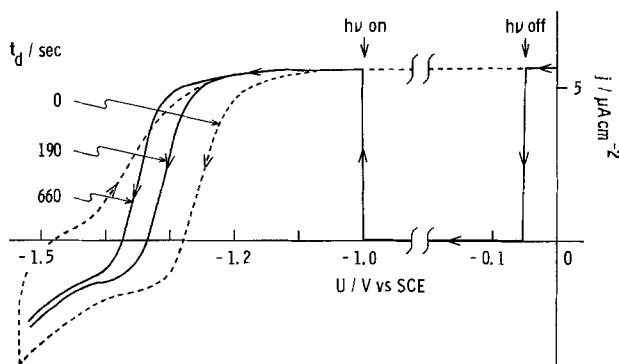


Fig. 7. The i - U curves for the (111)-face of an n-GaP electrode in a 0.1M NaOH solution, obtained under various illumination conditions.

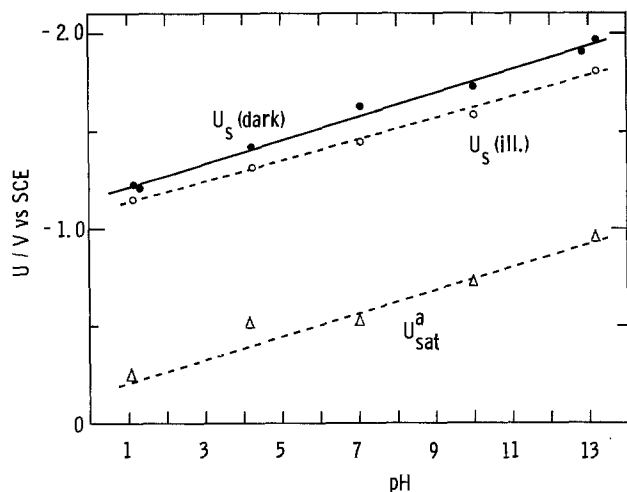


Fig. 8. U_s (dark), U_s (ill.), and U_{sat}^a for the $(\bar{1}\bar{1}\bar{1})$ -face of an n-GaP electrode. U_s (ill.) and U_{sat}^a were obtained at a constant illumination intensity, with the photoanodic saturation currents kept at $17 \mu\text{A}/\text{cm}^2$.

that the photoanodically formed oxides or hydroxides decay at dark in several minutes.

Figure 8 shows U_s (dark), U_s (ill.), and U_{sat}^a for the $(\bar{1}\bar{1}\bar{1})$ -face of the n-GaP electrode. Values of U_s (dark) for this face are in agreement with the reported ones (2), and are nearly equal to (or only slightly more positive than) those for the (111)-face. U_s for the $(\bar{1}\bar{1}\bar{1})$ -face is also shifted to the positive by illumination, similar to the (111)-face, but the magnitude is somewhat smaller than that for the (111)-face.

Discussion

The position of E_c^s and E_v^s of semiconductor electrodes are determined not only by the electron affinity (EA) and the bandgap (E_g) of semiconductors but also by the potential difference (ψ_1) at the semiconductor-solution interface, arising from electric double layers formed by adsorbed ions and/or polar bonds at the surface (19, 20). The change of ψ_1 , designated as $\Delta\psi_1$, should therefore cause the change of U_s equal to $-(\Delta E_c^s/e)$.

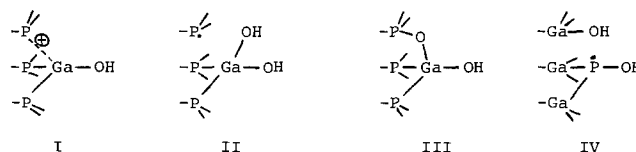
As described before, the Mott-Schottky plots observed at dark showed good straight lines in the range of U where the band bending is large (Fig. 4). This indicates that E_c^s (or U_s) of the GaP electrodes remains unchanged in this potential range. This is understood as follows. For the semiconductors with the size of the bandgap of GaP, the surface densities of electrons in the conduction band and holes in the valence band are both quite small at dark when the band bending is large. Also, the surface intermediates such as oxides or hydrides, which may be formed by the electrons or holes at the surface, decay relatively fast through reactions with the electrolyte solution, as mentioned in the preceding section (Fig. 6 and 7). Therefore, the concentration of such surface intermediates is negligibly small at dark under large band bending. This means that the chemical structure of the electrode surface and therefore ψ_1 are kept nearly the same, independent of U under the above condition. The accumulation of oxide- or hydride-type intermediates (and therefore the change of ψ_1) is expected only when the electrons or the holes come to the surface faster than the decay of these surface intermediates, as can be the case for small band bending or electrode illumination.

From the above consideration, we can also expect that the positions of E_c^s and E_v^s for the n-type GaP electrode under anodic polarization are almost the same as those for the p-type GaP electrode under cathodic polarization. This is really observed experi-

mentally (Fig. 6). The pH dependence of U_s (dark) of the GaP electrodes can be attributed to an acid-base equilibria on the surface, as pointed out in the case of metal oxides (21) or germanium electrodes (3).

On illumination of the n-GaP electrode under anodic polarization, a number of photogenerated holes come to the surface, and induce photoanodic dissolution reaction of the electrode. Many kinds of oxide- or hydroxide-type reaction intermediates may be formed at the surface, but are thought to be in a stationary state in the range of U under which the constant saturation photocurrent is observed. This means that ψ_1 (or U_s) remains constant in this potential range. Very good straight lines observed for the Mott-Schottky plots under illumination (Fig. 5) show that this is actually the case.

It was reported that six holes are consumed per a pair of Ga and P atoms in the photoanodic dissolution reaction at both the (111)- and $(\bar{1}\bar{1}\bar{1})$ -faces, probably producing $\text{Ga}(\text{OH})_3$ and H_3PO_3 or their analogues (11, 13-15). Also, the formation of a layer of hydroxides or oxides of Ga and P is often assumed for explaining quite hysteretic photocurrent-potential curves or production of white films on the electrode surface, especially in the intermediate pH range (10, 13, 14, 16). As to the reaction mechanism, Gerischer proposed that the first step is a nucleophilic attack of bases like OH^- or H_2O on the holes at the surface (1, 22, 23). Therefore, the following reaction intermediates, I, II, III, etc., are expected to exist at the electrode surface under illumination



Then the shift of ψ_1 (or U_s) is expected by the accumulation of either the charged species like I or the highly polar Ga-O or P-O bonds present in II, III, and IV. The latter mechanism is essentially the same as proposed in the case of the Ge electrode (3). The positive shift of U_s can be attributed to the positively polarized Ga or P atom being more or less directed toward the inside of the semiconductor. The magnitude of the shift is thought to depend on the nature and the concentration of the intermediates.

In the discussion made so far, the large deviations of U_o^a and U_{sat}^a from U_s (dark) (Fig. 3 and 8) were mainly attributed to the shift in ψ_1 (or U_s) by illumination. However, as is seen from comparison of Fig. 3 and 6, the differences between U_s (dark) and U_o^a are much larger than those between U_s (dark) and U_s (ill.), that is, U_o^a still deviates considerably from U_s (ill.) to the positive. The photoanodically formed surface intermediates are thought to capture effectively electrons in the conduction band when the band bending is small (12, 17, 24). This means that they act as effective recombination centers for electrons and holes. The large shifts of U_o^a from U_s (ill.) for the n-GaP electrode can therefore be attributed to accumulation of such intermediates at anodic polarization under illumination.

Acknowledgment

The authors wish to express their gratitude to Sanyo Electric Company, Limited for the kind donation of GaP semiconductor single crystals.

Manuscript received Jan. 2, 1980.

Any discussion of this paper will appear in a Discussion Section to be published in the June 1981 JOURNAL. All discussions for the June 1981 Discussion Section should be submitted by Feb. 1, 1981.

Publication costs of this article were assisted by Osaka University.

REFERENCES

- H. Gerischer, *Adv. Electrochem. Electrochem. Eng.*, **1**, 139 (1961).
- F. Cardon and W. P. Gomes, *J. Phys. D: Appl. Phys.*, **11**, L63 (1978).
- H. Gerischer, M. Hoffmann-Perez, and W. Mindt, *Ber. Bunsenges. Phys. Chem.*, **69**, 130 (1965).
- H. Yoneyama, H. Sakamoto, and H. Tamura, *Electrochim. Acta*, **20**, 341 (1975).
- A. J. Nozik, in "Semiconductor Liquid-Junction Solar Cells," A. Heller, Editor, p. 272, The Electrochemical Society Softbound Proceedings Series, Princeton, N.J. (1977).
- H. Tributsch, *This Journal*, **125**, 1086 (1978).
- R. H. Wilson, Extended Abstracts of the 2nd. International Conference on the Photochemical Conversion and Storage of Solar Energy, p. 75, University of Cambridge (1978).
- J. G. Mavroides, in "Semiconductor Liquid-Junction Solar Cells," A. Heller, Editor, p. 84, The Electrochemical Society Softbound Proceedings Series, Princeton, N.J. (1977).
- A. J. Bard and P. A. Kohl, in "Semiconductor Liquid-Junction Solar Cells," A. Heller, Editor, p. 222, The Electrochemical Society Softbound Proceedings Series, Princeton, N.J. (1977).
- Y. Nakato, K. Abe, and H. Tsubomura, *Ber. Bunsenges. Phys. Chem.*, **80**, 1002 (1976); Y. Nakato, S. Tonomura, and H. Tsubomura, *ibid.*, **80**, 1289 (1976).
- R. L. Meek and N. E. Schumaker, *This Journal*, **119**, 1148 (1972).
- M. J. Madou, F. Cardon, and W. P. Gomes, *Ber. Bunsenges. Phys. Chem.*, **82**, 819 (1978).
- R. Memming and G. Schwandt, *Electrochim. Acta*, **13**, 1299 (1968).
- M. J. Madou, F. Cardon, and W. P. Gomes, *Ber. Bunsenges. Phys. Chem.*, **81**, 1186 (1977).
- K. Kohayakawa, A. Fujishima, and K. Honda, *Nippon Kagaku Kaishi*, 780 (1977).
- J. M. Poate, T. M. Buck, and B. Schwartz, *J. Phys. Chem. Solids*, **34**, 779 (1973); Also see B. Schwartz and W. J. Sundburg, *This Journal*, **120**, 576 (1973).
- H. Gerischer, in "Physical Chemistry," Vol. 9A, H. Eyring, Editor, p. 463, Academic Press, New York (1970).
- R. Memming, *This Journal*, **116**, 785 (1969).
- H. Gerischer, *J. Electroanal. Chem. Interfacial Electrochem.*, **58**, 263 (1975).
- M. A. Butler and D. S. Ginley, *This Journal*, **125**, 228 (1978).
- F. Lohmann, *Ber. Bunsenges. Phys. Chem.*, **70**, 428 (1966).
- H. Gerischer and W. Mindt, *Electrochim. Acta*, **13**, 1329 (1968).
- H. Gerischer, *Surf. Sci.*, **13**, 265 (1969).
- S. R. Morrison, *ibid.*, **15**, 363 (1969).

A Mechanistic Study of O₂ Reduction on Water Soluble Phthalocyanines Adsorbed on Graphite Electrodes

J. Zagal,^{*1} P. Bindra,* and E. Yeager*

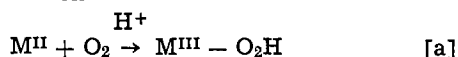
Case Laboratories for Electrochemical Studies and the Chemistry Department,

Case Western Reserve University, Cleveland, Ohio 44106

ABSTRACT

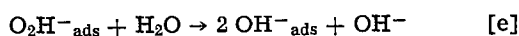
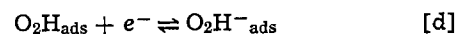
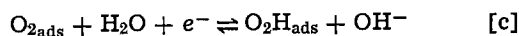
Co and Fe tetrasulfonate phthalocyanines (M-TSP), adsorbed at monolayer levels on graphite surfaces, have been found to have a pronounced catalytic effect on the O₂ reduction process in both acid and alkaline solutions. The kinetics have been examined with the rotating ring-disk electrode technique. Co-TSP promotes the O₂ reduction process via two electrons to give peroxide whereas Fe-TSP promotes a four-electron reduction to give water.

The catalytic properties of metal phthalocyanines for the electroreduction of O₂ have been examined extensively in the literature (see e.g., 1-10, 40). In general, macrocyclic transition metal complexes of this type have been found to have catalytic activity for the O₂ reduction process. A comprehensive review on this field has been published recently (1). Basic kinetic and mechanistic studies of the process, however, are less available. A direct correlation has been found (2-4) between the first oxidation potential of the metal phthalocyanine and its catalytic activity for O₂ reduction. Beck (4) has recently proposed a mechanism for the process based on data for O₂ reduction on Co tetraazaannulene (Co-TAA), which gives Tafel slopes of -60 mV/decade in acid solution. This author proposed that the metal complex reacts with oxygen according to the reaction



where O₂ undergoes partial reduction with simultaneous oxidation of the metal center. The O₂ adduct, according to Beck, then undergoes a two-electron reduction as the rate-determining step, regenerating the catalyst. For a transfer coefficient $\alpha = 0.5$, the Tafel slope could then be -60 mV/decade. Simultaneous two-electron steps, however, are unlikely on energetic grounds.

A mechanism has been recently proposed by Appleby and Savy (5, 8) based on studies of O₂ reduction on Fe phthalocyanines. According to these authors, the rate-determining step is the breaking of the O-O bond and the proposed mechanism in basic media is



Even though this mechanism explains the experimental data, it does not explain the specific involvement of the catalyst and particularly the valency state of the

* Electrochemical Society Active Member.

¹ On leave of absence from Universidad Technica del Estado, Santiago, Chile.

Key words: oxygen electrode, transition metal macrocyclics, oxygen electrocatalysis, phthalocyanines.

transition metal in the reaction sequence. Further, it is unlikely that the superoxide species (O₂H)_{ads} is protonated in alkaline electrolytes in view of the ionization constant ($pK = 4.88$) for the O₂H species in solution (41).

The present work has involved the catalytic properties of water soluble tetrasulfonated phthalocyanines adsorbed on graphite substrates. As previously reported (9, 11), considerable catalytic activity can be achieved by adsorbing these complexes from aqueous solutions. The redox properties of the catalysts can be determined using cyclic voltammetry under the same conditions (pH, solvent) at which the O₂ reduction experiments are carried out. This type of approach is facilitated by use of the basal plane of stress-annealed pyrolytic graphite (SAPG) with x-ray diffraction rocking angles as small as $\Delta\theta_{1/2} = 0.4^\circ$. This material provides a near ideal surface for studying the redox properties of adsorbed species because of its low background currents (22) and very low catalytic activity for the O₂ reduction process (23).

Experimental Procedure

A disk electrode, exposing the basal plane of SAPG² (9-23) with an area of 0.20 cm², was used for most of the rotating disk measurements. For the ring-disk electrode measurements, the disk was constructed with ordinary pyrolytic graphite (OPG)² (radius = 0.250 cm) with gold (99.99% pure) as the ring (inner radius 0.272 cm, outer radius 0.357 cm). The OPG had an x-ray rocking angle of $\Delta\theta_{1/2} = 45^\circ$. Unfortunately the fragile nature of the SAPG prevented its use as the disk in the ring-disk experiments. Unless otherwise indicated, all measurements on SAPG and OPG were on the basal plane.

The ring-disk electrode was calibrated with the ferrous/ferric couple using 10⁻² and 10⁻³M Fe₂(SO₄)₃ in 0.05M H₂SO₄. The value of the collection efficiency,³ N , determined in this manner was 0.382. This value compared favorably with the calculated value of 0.38 obtained from the geometry of the electrodes using the tables of Alberly and Bruckenstein (12). The Teflon cell had separate compartments for the reference [saturated calomel (SCE)] and counterelectrode (Au-foil) with an additional isolation compartment between the working and reference compartments. A Teflon Luggin capillary was used to minimize IR drop with its tip ~3 mm below the center of the rotating disk electrode. The polarization curves for the kinetic measurements were obtained by starting at the open-circuit potential and scanning toward more negative values at a rate of 10 mV/sec. The hysteresis on reverse of sweep was negligible at these scan rates. Small currents (i.e., < 10 μA) were measured point by point by waiting at each potential for the drift rate to become negligible. All measurements were made at 20°-22°C.

The surface of the basal plane of SAPG was renewed by use of the adhesive tape technique with care to avoid contamination of the Teflon mounting with the adhesive of the tape (9, 21, 23). The OPG electrodes were polished using 0.3 μm alumina suspended in water with water on microcloth for the final polish. The M-TSP was adsorbed on the graphite surface by placing a drop of solution of the complex (10⁻⁵M) on the electrode. Similar results were obtained when the adsorbed layer was applied by submerging the electrode in a 10⁻⁵M solution of the complex. The electrode was subsequently washed with purified water (pyrolyzed over Pt/Rh at 800°C). For experiments in acid solution some of this complex was added to the electrolyte to preserve the adsorbed catalyst layer during the measurements. In the other electrolytic solutions the adsorption was sufficiently strong to render the

loss of the adsorbed complex negligible over the duration of the measurements.

Basic (0.1M NaOH) and acid (0.05M H₂SO₄) solutions were prepared as described before (9). Other solutions of various pH were as follows: 1M NaOH, pH = 13.8; 0.1M NaOH, pH = 12.9; 0.1M Na₂CO₃, pH = 11.5; 0.005M Na₂CO₃ + 0.05M Na₂SO₄, pH = 10.8; 0.0015M NaOH + 0.05M H₃BO₃ + 0.05M Na₂SO₄, pH = 8.7; 0.10M NaOH + 0.05M H₃BO₃ + 0.05M Na₂SO₄, pH = 6.3; and 0.1M NaH₂PO₄, pH = 4.4. Special precautions were taken to minimize CO₃⁼ in the alkaline electrolytes. The Co-TSP and Fe-TSP were prepared and purified by the procedures described by Weber and Busch (38).

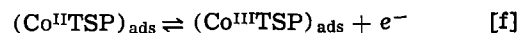
Results

Cyclic voltammetry measurements.—Figure 1 shows the cyclic voltammetry curves obtained at different potential scan rates for Co-TSP pre-adsorbed on the basal plane of SAPG. A Teflon hood, similar to that described by Randin and Yeager (39) was used to eliminate edge effects and leakage of the electrolyte between the Teflon and the side of the disk electrode, which otherwise cause a pronounced slant in the voltammetry curves. The peak currents are directly proportional to the scan rate, which is typical of a Faradaic process involving an adsorbed species. (For the adsorption of a diffusing species the peak currents are directly proportional to the square root of the scan rate.)

From the area under the peak, the charge involved in the process can be estimated. An experimental value of 3 μC/cm² has been determined, which corresponds to a surface concentration of 3×10^{-11} moles/cm² of adsorbed metal complex assuming that a one-electron transfer process is involved. Assuming that the surface redox couple obeys the Nernst equation, the peak current for the voltammetry is given by

$$i_p = \frac{n^2 F^2 \Gamma \nu}{4RT} \quad [1]$$

where Γ is the total surface concentration of the adsorbed complex in moles/cm², ν is the potential scan rate, and n is the number of electrons per adsorbed molecule. The charge under the peak is known and is equal to $Q = nF\Gamma$. Experimental values of Q and i_p give $n = 0.9$ or ~ 1 , indicating that one electron is involved in the surface redox process, which is likely to involve the metal center (13-14); i.e.



The small deviation of n from unity is probably caused by the approximate nature of Eq. [1], which assumes

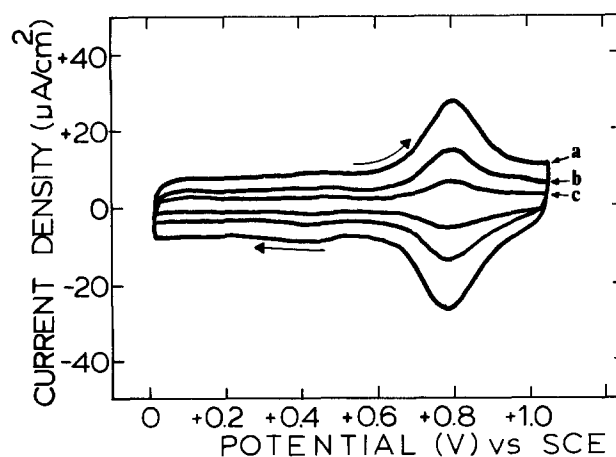


Fig. 1. Cyclic voltammograms at different scan rates for Co-TSP adsorbed on SAPG. Electrolyte: 0.05M H₂SO₄. Sweep rates: (a) 1 V/sec, (b) 0.5 V/sec, (c) 0.2 V/sec. (No Co-TSP in solution; obtained with hood to block electrolyte at edge of disk.)

² The SAPG and OPG were provided by the Union Carbide Corporation through Dr. A. Moore of the Parma Technical Research Center, Parma, Ohio.

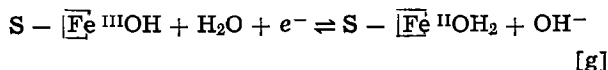
³ $N = I_R/I_D$, where I_R is the ring current and I_D is the disk current.

that the Nernst equation is followed with the activities for the adsorbed species in the two different valence states replaced by the surface concentrations.

Co-TSP readily adsorbs on other carbon substrates including glassy carbon, the edge-orientation of SAPG, and ordinary pyrolytic graphite (OPG). Because of the high background currents of graphite surfaces other than the basal plane of SAPG, however, less well-defined cyclic voltammery curves result. For Co-TSP adsorbed on the basal plane of OPG, the charge estimated from cyclic voltammery is ca. $13 \mu\text{C}/\text{cm}^2$ which is about four times that found on the basal plane of SAPG.

The iron derivative also readily adsorbed on the basal plane of SAPG as evidenced by the voltammery curve shown in Fig. 2. From the scan rate dependence of both peaks 1 and 2, it was established that a one-electron transfer is involved in each case. The charge under each peak, estimated from the area between the solid and the dotted lines in Fig. 2, is $\sim 3.0 \mu\text{C}/\text{cm}^2$, which is the same as found for Co-TSP. This charge is independent of potential scan rate over the range investigated (50-1000 mV/sec). Even though this value is only approximate, it suggests that the surface coverages by Co-TSP and Fe-TSP species are essentially the same. For Fe-TSP adsorbed on the basal plane of OPG, the charge under both peaks 1 and 2 is $13 \mu\text{C}/\text{cm}^2$ each, which is the value found for Co-TSP adsorbed on the same graphite material.

The voltammograms obtained at various pH indicate that the potentials of peaks 1 and 2 shift with pH. Peak 1 appears to involve the process $\text{Fe}^{\text{III}} + e^- \rightarrow \text{Fe}^{\text{II}}$. This process is pH dependent over a range of pH depending on pK_A of the M-TSP. The fact that macrocyclic complexes of transition metals in the oxidation state III undergo hydrolysis in water solutions is a well-known phenomenon [see, e.g., Ref. (15 and 16)]. The redox reaction can be written as



where S represents the graphite substrate.

The potential of the $\text{Fe}^{\text{III}}/\text{Fe}^{\text{II}}$ redox couple, according to reaction [g], should shift with pH as $\Delta E/\Delta \text{pH} = -0.059 \text{ V/pH}$. Figure 3 shows a plot of peak potential (peak 1) vs. pH. The slope of the linear region is -0.057 V/pH , suggesting that a process such as reaction [g] is involved.

The position of peak 2 shifts with pH only at low pH values. It is not clear what type of process is involved in this case. The voltammery curves suggest that the

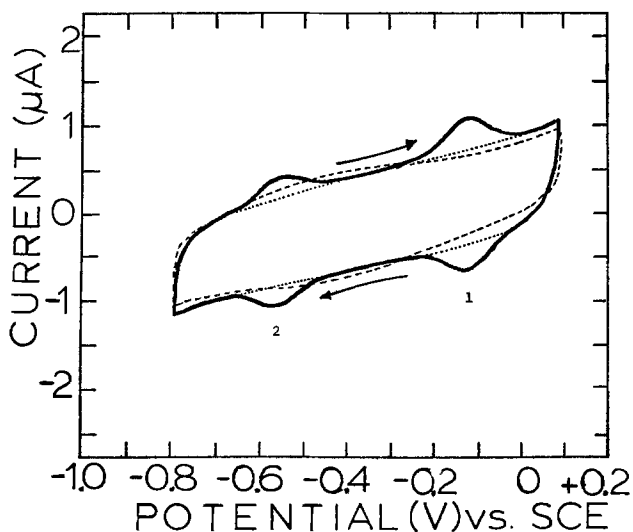


Fig. 2. Cyclic voltammograms with (solid line) and without (dashed line) Fe-TSP pre-adsorbed on SAPG. Supporting electrolyte: 0.1M NaOH, He saturated. Scan rate: 500 mV/sec. (Obtained without hood.)

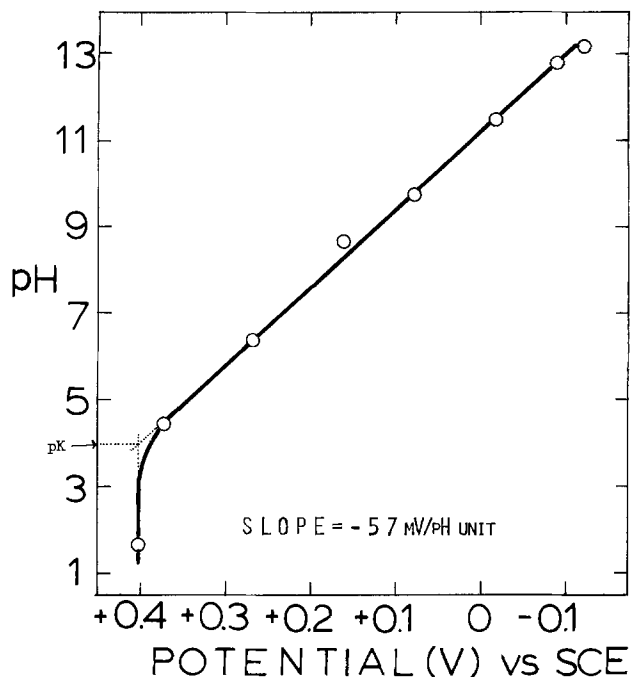


Fig. 3. pH dependence of the potential of peak 1 in the voltammery (see Fig. 2) for Fe-TSP adsorbed on OPG.

process is reversible. Perhaps in the reduced form the transferred electron is delocalized in the π system of the macrocyclic ligand or alternatively the Fe is in the equivalent of the I valent state. Lever and Wilshire (17) have reported that iron (II) phthalocyanine ($\text{Fe}^{\text{II}}\text{Pc}$) can be electrochemically reduced in non-aqueous solvents to give $\text{Fe}^{\text{I}}\text{Pc}$ in which Fe has been shown to be five coordinated on the basis of its electron spin resonance spectrum.

O₂ reduction on graphite with adsorbed Co-TSP.—The O_2 reduction currents on graphite surfaces other than the basal plane of graphite in alkaline solution are large even in the absence of adsorbed transition metal macrocyclics. This makes the interpretation of the electrocatalytic properties of the Co-TSP adsorbed on these surfaces difficult. On all of these surfaces, the presence of the macrocyclic greatly increases the O_2 kinetic reduction current (i_k). The observed current-voltage curves are compared with and without the adsorbed Co-TSP in Fig. 4. The relatively low apparent limiting current for the basal plane of ordinary pyrolytic graphite is the result of combined diffusion and kinetic control with a potential insensitive chemical step (23).

For a process which is first order in a diffusing reactant, the disk current is related to the rotation rate f by the expression (28)

$$1/i = (1/i_k) + 1/(Bf^{1/2}) \quad [2]$$

where B is related to the diffusion limiting current by

$$i_L = Bf^{1/2} \quad [2a]$$

and is given by

$$B = 0.20 (D_{\text{O}_2})^{2/3} \nu^{-1/6} nFA C_{\text{O}_2} \quad [2b]$$

where D_{O_2} and C_{O_2} are the diffusion coefficient and solubility of O_2 , ν is the kinematic viscosity, f is the rotation rate in radians, A is the area, F is the Faraday, and n is the number of electrons transferred per molecule of O_2 diffusing through the Nernst boundary layer. The plot in Fig. 5 for Co-TSP/SAPG in 0.1M NaOH clearly follows Eq. [2], thus confirming first-order dependence of the kinetics on O_2 . Similar behavior has been observed in 0.05M H_2SO_4 . This linearity also provides evidence for reasonable uniformity of the current distribution on the disk even at potentials other than

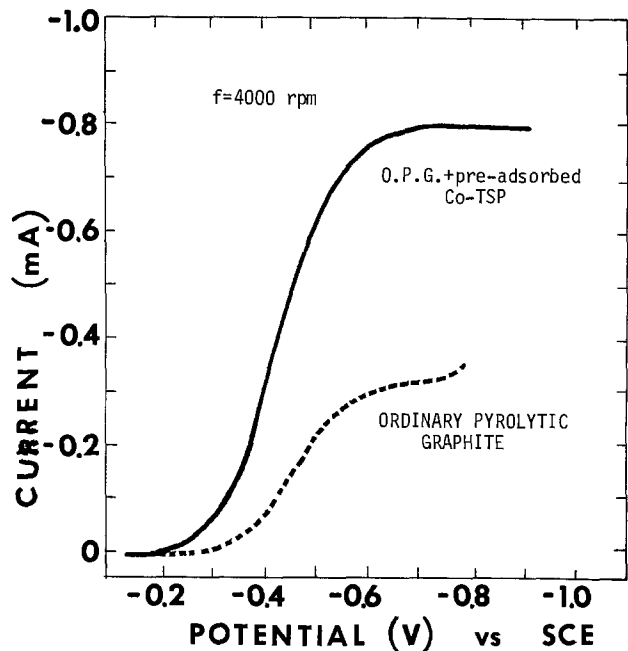


Fig. 4. O₂ reduction in 0.1M NaOH on the rotating disk electrode with (solid line) and without (dashed line) Co-TSP pre-adsorbed on OPG. Rotation rate: 4000 rpm; scan rate: 10 mV/sec.

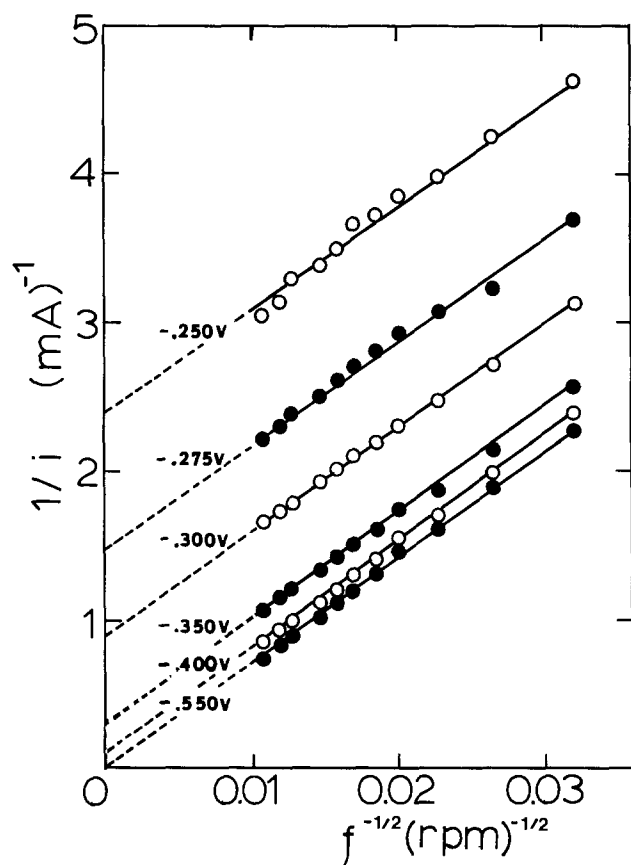


Fig. 5. Plots of $1/i$ vs. $1/f^{1/2}$ for Co-TSP adsorbed on SAPG in 0.1M NaOH + 10^{-6} M Co-TSP.

corresponding to the diffusion limiting value [see discussion in Ref. (29, 32)].

The B values evaluated from the slopes in these plots are 1.47×10^{-2} mA (rpm)^{-1/2}, which compares well with the theoretical value of 1.42×10^{-2} mA (rpm)^{-1/2}, calculated with Eq. [2b] for $n = 2$, using the following values for both 0.05 H₂SO₄ and 0.1M NaOH: $C_{O_2} = 1.38 \times 10^{-6}$ moles/cm³ (24); the diffusion coefficient reported by Gubbins and Walker (25) at 25°C ($D_{O_2} = 1.90 \times 10^{-5}$ cm²/sec) corrected to 20°C

($D_{O_2} = 1.67 \times 10^{-5}$ cm²/sec), using the mean temperature coefficient estimated from the data of Davies, Horvath, and Tobias (26) [$d \ln D_{O_2}/dt = 2.4\%/^{\circ}C$]; $\nu = 9.97 \times 10^{-3}$ cm²/sec, estimated from the viscosity of 1.002×10^{-2} g cm⁻¹ sec⁻¹ and density $\rho = 1.005$ g/cm³ (27); and $A = 0.196$ cm². This agreement confirms that the O₂ reduction catalyzed by adsorbed Co-TSP is the 2e⁻ reduction to the peroxide as the main product.

Kinetic data for O₂ reduction in 0.05M H₂SO₄ with Co-TSP adsorbed on various substrates using the rotating disk technique are summarized in Fig. 6. The kinetic current densities have been corrected for diffusion by multiplying by the factor $i_L/(i_L - i)$ where i_L is the diffusion limiting current density obtained directly from the i vs. E plots. The Tafel plots are essentially identical (-155 mV/decade) for all of the substrates except the basal plane of SAPG with a low rocking angle ($\Delta\theta_{1/2} = 0.4^{\circ}$) for which the slope is -135 mV/decade. The lower slope on this surface may reflect the semiconductor properties (22) which influence the potential distribution at the surface or differences in the ionic double layer for the SAPG basal plane compared to other carbon surfaces.

Figure 7 indicates the Tafel-type plots for O₂ reduction on Co-TSP adsorbed on SAPG of $\Delta\theta_{1/2} = 0.4^{\circ}$

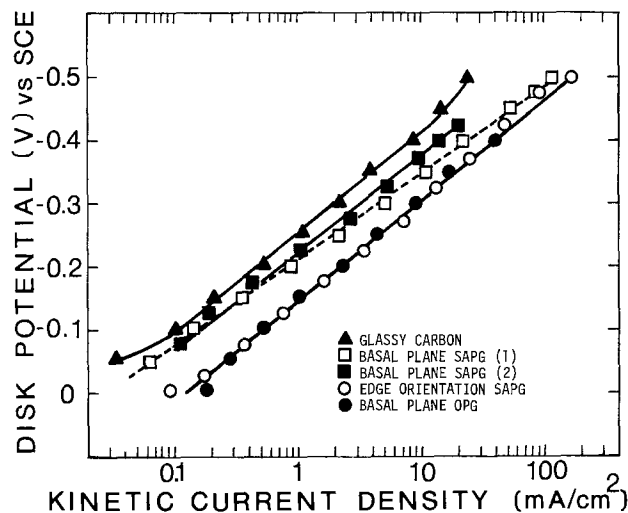


Fig. 6. Tafel plots for O₂ reduction on Co-TSP adsorbed on various carbon surfaces. Kinetic current densities corrected for diffusion. Electrolyte: 0.05M H₂SO₄ + 10^{-5} M Co-TSP; $f = 2600$ rpm.

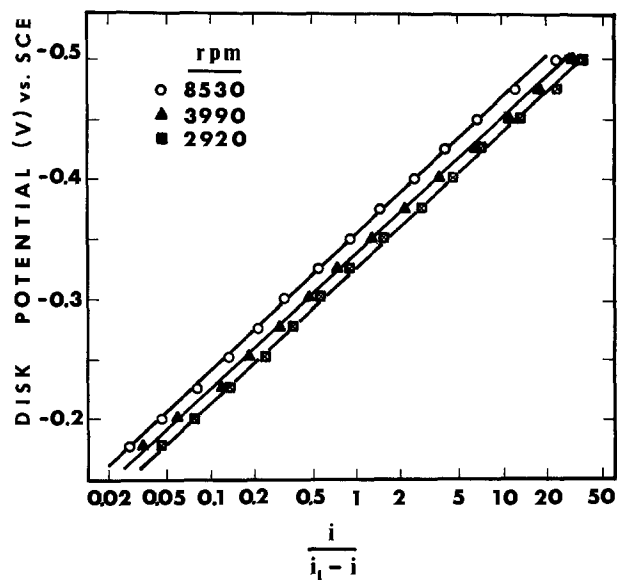
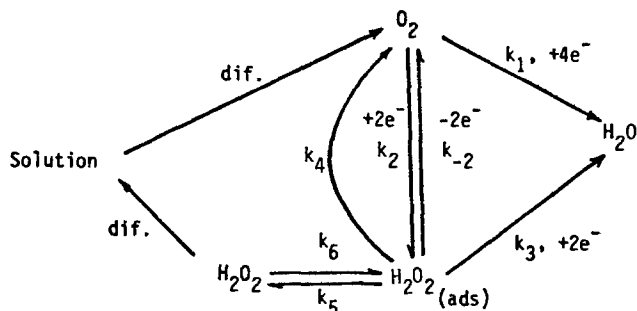


Fig. 7. Tafel plot of $\log [i/i_L - i]$ vs. E for O₂ reduction at various rotation rates for Co-TSP adsorbed on SAPG in 0.1M NaOH.

using the correction factor $(I/I_L - I)$ where I and I_L are the current and diffusion limiting current. This factor has been used rather than $[I_L/I_L - I]$ in order that the data for several rotation rates may be clearly represented. The slope is -120 mV/decade at 25°C , corresponding to an apparent $\alpha = 0.5$.

Rotating ring-disk data for Co-TSP adsorbed on OPG is shown in Fig. 8 for 0.1M NaOH . The gold ring was maintained at a potential in the diffusion limiting current range for the oxidation of peroxide (0.10V vs. SCE). Difficulty was encountered in obtaining well-defined diffusion limiting currents for peroxide oxidation on the Au ring in $0.05\text{M H}_2\text{SO}_4$ and consequently ring-disk experiments are not reported for this electrolyte.

To analyze the rotating ring-disk electrode data (Fig. 8), consider the following series-parallel reaction scheme for O_2 reduction (19)



The disk-ring current ratio for the O_2 reduction process is as follows

$$NI_D/I_R = 1 + (2k_1/k_2) + X + [k_6/(Z_{\text{H}_2\text{O}_2}f^{1/2})]X \quad [3]$$

where

$$X = (2k_1/k_2k_5)(k_{-2} + k_3 + k_4) + [(2k_3 + k_4)/k_5] \quad [3a]$$

and

$$Z_{\text{H}_2\text{O}_2} = 0.62D_{\text{H}_2\text{O}_2}^{2/3}\nu^{-1/6} \quad [3b]$$

If we assume that adsorption equilibrium exists between H_2O_2 on the electrode surface and in the solution, Eq. [3] becomes (18)

$$NI_D/I_R = 1 + (2k_1/k_2) + [1/Z_{\text{H}_2\text{O}_2}f^{1/2}] [2k_3 + k_4 + (2k_1/k_2)(k'_{-2} + k_3 + k_4)] \quad [4]$$

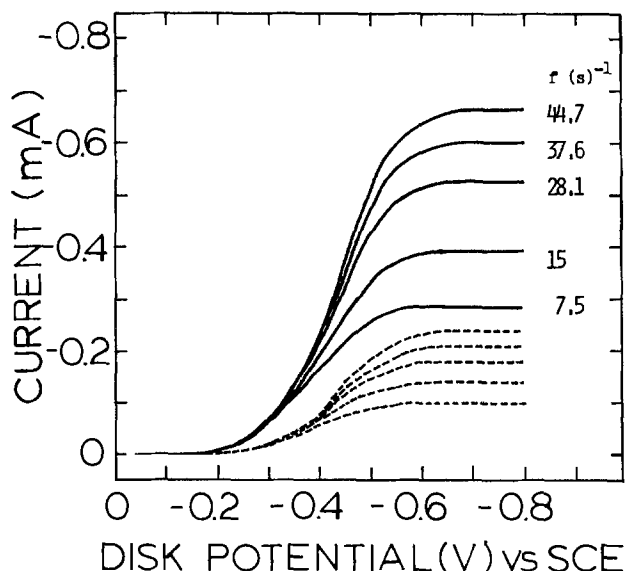


Fig. 8. Rotating ring-disk data for O_2 reduction on Co-TSP pre-adsorbed on OPG in 0.1M NaOH . Disk current indicated by solid lines; ring current by dashed lines. Scan rate: 10 mV/sec. Ring potential: $+0.1\text{V vs. SCE}$. Ring currents are anodic. Collection efficiency: $N = 0.38$.

where

$$k'_{-2} = K_{56}k_{-2}; \quad k'_3 = K_{56}k_3; \quad k'_4 = K_{56}k_4 \quad [4a]$$

with $K_{56} = k_6/k_5$.

The diffusion limiting current for a four-electron reduction of O_2 to yield OH^- or H_2O is given by

$$I'_L = 4AFZ_{\text{O}_2}C_{\text{O}_2}f^{1/2} \quad [5]$$

where

$$Z_{\text{O}_2} = 0.20D_{\text{O}_2}^{2/3}\nu^{-1/6} \quad [5a]$$

It should be noted that I'_L is a theoretical value and not directly observed. Combining Eq. [4] and [5] yields (18), we obtain

$$\frac{(I'_L - I_D)N}{I_R} = 1 + \frac{2(k'_3 + k'_4 + k'_{-2})}{k_2} \cdot \frac{Z_{\text{O}_2}}{Z_{\text{H}_2\text{O}_2}} + \frac{2Z_{\text{O}_2}}{k_2} f^{1/2} \quad [6]$$

A plot of $(I_D/I_R)N$ vs. $f^{-1/2}$ is shown in Fig. 9. The scatter of the points is caused by the expansion of the ordinate, necessary as a result of the surprisingly low slope. This low slope and the closeness of the intercept to unity indicate that very little of the peroxide generated at the electrode is further reduced and that k_1 is small compared to k_2 . Further analysis of the data can be done by plotting $(I'_L - I_D)N/I_R$ vs. $f^{1/2}$. This graph is shown in Fig. 10. The lines are straight as expected from Eq. [6]. From the slopes it is possible to evaluate k_2 . The rate constant k_1 can be evaluated from the intercept in Fig. 9, using Eq. [4]. The scatter of the points in Fig. 9 is too great to permit the independently drawn straight lines through the data to be used to evaluate the intercepts. Consequently all of the lines in Fig. 9 have been drawn through the data with the same slopes. This assumption may not be fully justified and can influence the potential dependence of k_1 .

The Tafel slopes evaluated from the E vs. $\log k$ plots (Fig. 11) are $dE/d \log k_1 = \sim -0.15$ V/decade and $dE/d \log k_2 = \sim -0.12$ V/decade, as compared with an apparent Tafel slope -0.12 V/decade from the E vs. $\log i/(i_L - i)$ plots (Fig. 7). The slope of the $dE/d \log k_1$ plot, however, is based on the assumption that the slopes in Fig. 9 are not potential dependent. In addition, the uncertainties in the intercepts in this figure are substantial even with this assumption. Most likely the potential dependence of k_1 is essentially the same as that of k_2 .

O_2 reduction on adsorbed Fe-TSP.—Figure 12 shows the polarization curves as solid lines obtained at different rotation rates on a ring-disk electrode with a pre-adsorbed layer of Fe-TSP on the OPG disk. The same figure shows the O_2 reduction currents observed on this graphite material without Fe-TSP adsorbed on

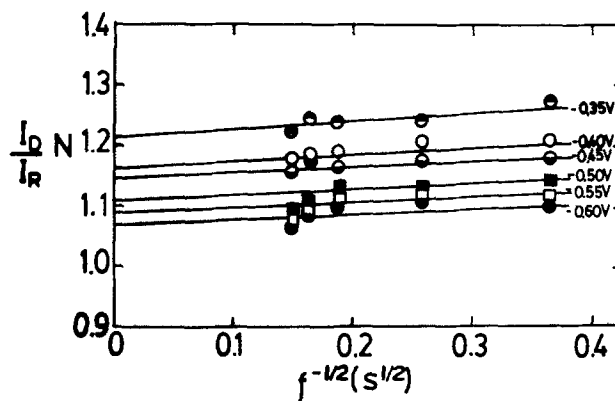


Fig. 9. Plots of $I_D N/I_R$ vs. $1/f^{1/2}$ constructed from ring-disk data in Fig. 8.

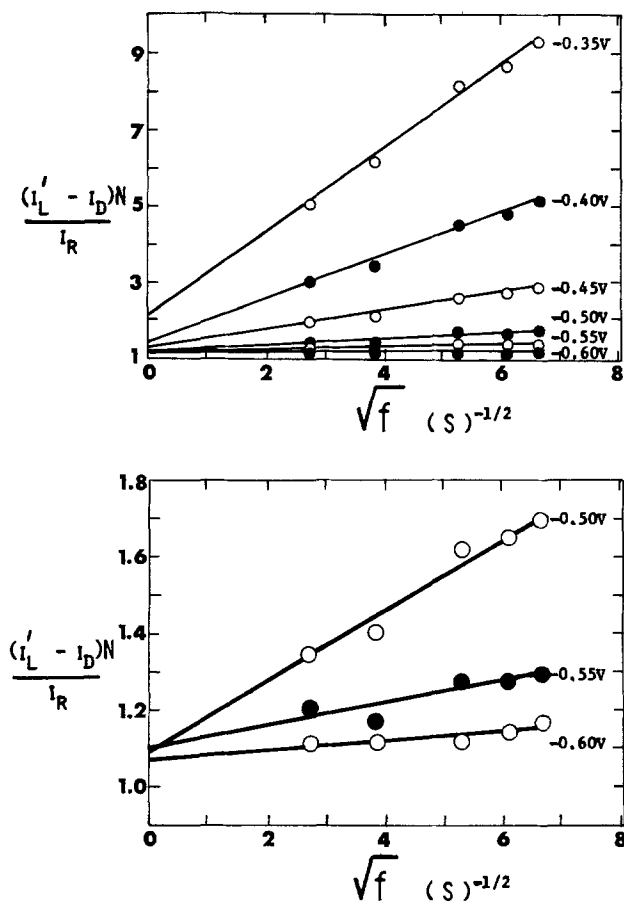


Fig. 10. Plots of $(I_L' - I_D)N/I_R$ vs. $1/f^{1/2}$ constructed from ring-disk data in Fig. 8.

the surface. Also shown is the ring current measured at the diffusion limiting HO₂⁻ peroxide oxidation condition on the Au ring.

The ring currents at disk potentials more positive than $-0.32V$ are zero, which indicates that the O₂ reduction occurs via four-electrons with no detectable amount of peroxide at those potentials. The small amounts of HO₂⁻ detected at higher polarizations may be due in part to the O₂ reduction process on zones of the graphite uncovered by the Fe-TSP. The maximum in I_L for the OPG substrate occurs almost at the same potential as that for the Fe-TSP/OPG. On the other hand, the maximum in I_L for the latter is far too pronounced to be caused just by I_L for the substrate. This

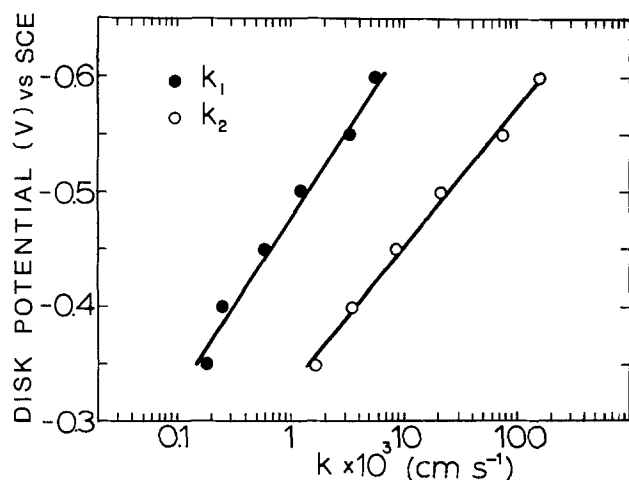


Fig. 11. Potential dependence of the heterogeneous rate constants for the 4e⁻ reduction (k_1) and 2e⁻ reduction (k_2) of O₂ on Co-TSP adsorbed on OPG in 0.1M NaOH.

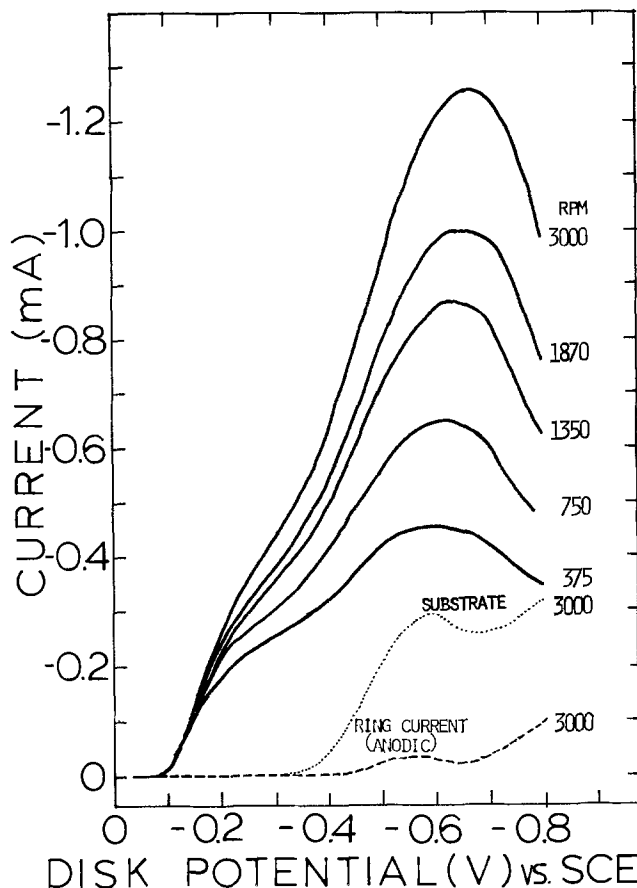


Fig. 12. Rotating ring-disk data for O₂ reduction on Fe-TSP adsorbed on the disk for OPG. Disk currents in solid lines; ring currents in dashed lines; current on OPG disk without Fe-TSP in dotted line. Electrolyte: 0.1M NaOH. Scan rate: 5 mV/sec. Ring potential: $+0.1V$ vs. SCE. Collection efficiency: $N = 0.38$.

maximum in I_L for Fe-TSP/graphite correlates well with the second peak in the voltammetry curve (see Fig. 2).

Plots of $1/I$ vs. $1/f^{1/2}$ (Fig. 13) yield parallel straight lines at potentials anodic to the maximum in Fig. 13 as expected for a first-order process on O₂. The currents at $-0.6V$ correspond to pure diffusion control for the 4e⁻ reduction, based on the intercept and slope in Fig. 14 [$B(\text{exp}) = 2.4 \times 10^{-2} \text{ mA rpm}^{-1/2}$ as compared with $B(\text{theor}) = 2.8 \times 10^{-2} \text{ mA rpm}^{-1/2}$ for $n = 4$]. The deviation of the points at higher rotation rates and more anodic potentials on Fe-TSP/OPG is not fully explained but may be related to a change in rate-controlling step in this potential region as discussed later.

Plots of $1/I$ vs. $1/f^{1/2}$ for potentials cathodic to $-0.6V$ (Fig. 14) have slopes which increase with potential; i.e., B decreases indicating that the 4e⁻ process tends to revert to a 2e⁻ process. This correlates well with the sharp increase in the production of hydrogen peroxide at these potentials as indicated by the ring currents in Fig. 12 and with the second peak in the voltammetry curves (Fig. 2) which indicates a second reduction process at $\sim -0.6V$. This reduced form of the catalyst seems to be less effective for the 4e⁻ reduction process.

Figure 15 shows a plot of NI_D/I_R vs. $1/f^{1/2}$ for the potential range where some peroxide is detected. The marked deviation from linear behavior at low values of $1/f^{1/2}$ may be caused by shaft eccentricity, i.e., wobble. Independent of whether the deviations at low values of $1/f^{1/2}$ are real or an experimental artifact, the data indicate a large potential dependent value of NI_D/I_R at infinite rotation rate. This suggests a parallel mechanism. Such behavior appears reasonable since a portion of the ordinary pyrolytic graph-

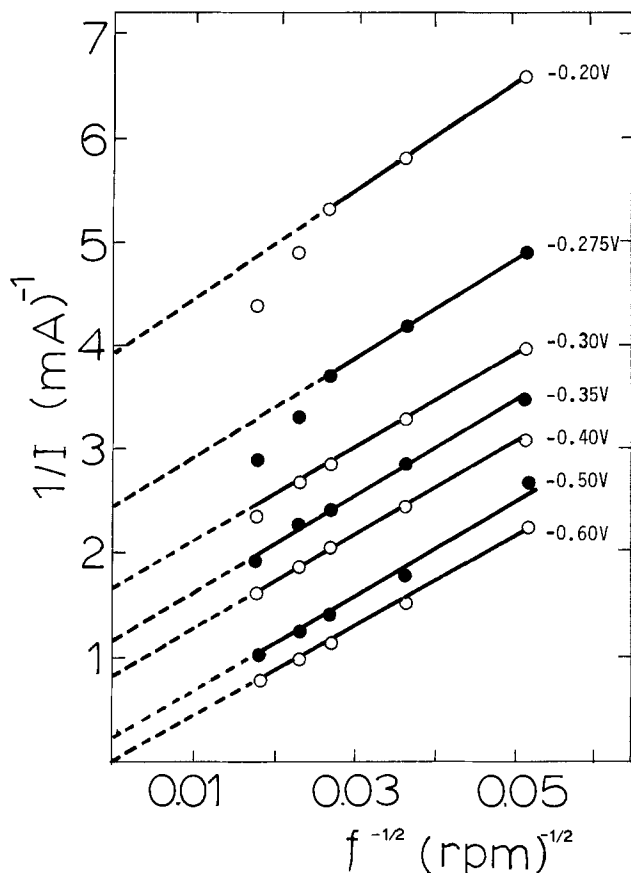


Fig. 13. $1/I$ vs. $1/f^{1/2}$ plot for currents in the potential region more anodic than -600 mV vs. SCE for conditions in Fig. 12.

its surface is probably not blocked by the adsorbed Fe-TSP and will support the O_2 reduction principally to peroxide. The Fe-TSP may still support at least in part the overall $4e^-$ reduction.

The effect of pH on the O_2 reduction currents on Fe-TSP adsorbed on ordinary pyrolytic graphite was studied and the results are summarized in Tafel plots in Fig. 16. The solubility of O_2 in the different solutions varies slightly and is considerably smaller for the 1M NaOH solution according to the different I_L obtained for a given rotation rate. This will give different concentrations of O_2 for the different solutions used, which will be reflected directly in the currents since the process is first order in O_2 . The plots in Fig. 16, however, include a correction for these differences since the parameter $I/(I_L - I)$ is independent of the

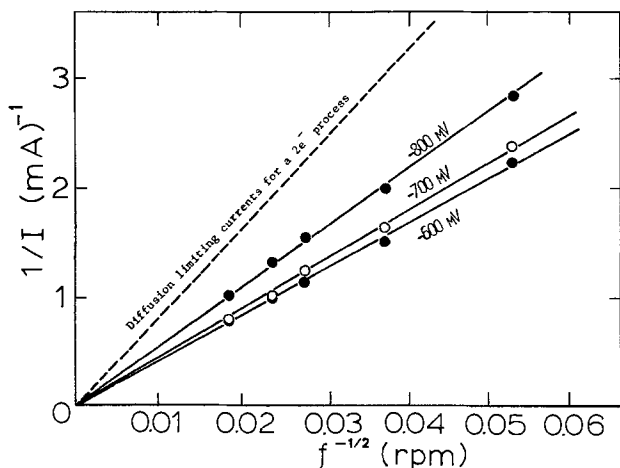


Fig. 14. $1/I$ vs. $1/f^{1/2}$ plot for currents in the potential region more cathodic than -600 mV vs. SCE for condition in Fig. 12.

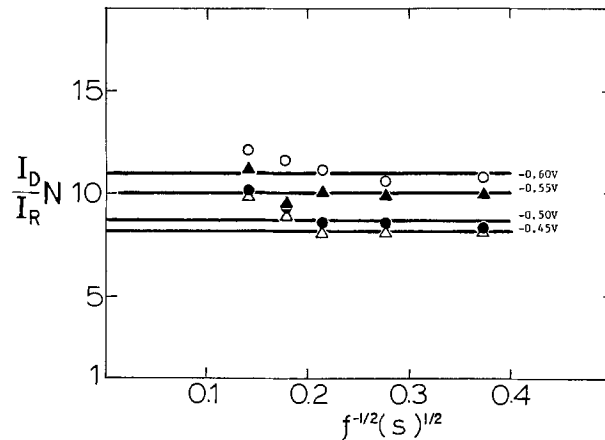


Fig. 15. Plot of $N I_D / I_R$ vs. $1/f^{1/2}$ for various disk potentials for conditions indicated in Fig. 12.

O_2 concentration in solution for first-order kinetics. This is verified in Fig. 17 where data obtained in O_2 and air-saturated solutions also have been plotted in the form $I/(I_L - I)$ vs. E and superimposed.

The linear region of low polarization in Fig. 16 is strongly dependent on pH in contrast to the linear region of high polarization. The slopes of the lines in the pH range 13.8-10.8 are essentially the same and have values in the range -30 to -35 mV/decade. At lower pH values, these slopes increase reaching a value of -65 mV/decade at pH = 4.4. It was not possible to obtain reproducible data at pH values lower than 4.4 since the Fe-TSP complex decomposes when the potential of the electrode is scanned cathodically in acid media. This is accelerated by the presence of O_2 and produces a rapid decrease in activity with time.

Plots of $\log [I/(I_L - I)]$ vs. the overpotential $\eta = E - E_{rev}$ (Fig. 18) show some features which are not clearly evident in Fig. 16. Figure 18 shows that the O_2 reduction process becomes more irreversible with decreasing pH (i.e., the process takes place at higher overpotentials in acid media). This is also observed on other carbon surfaces.

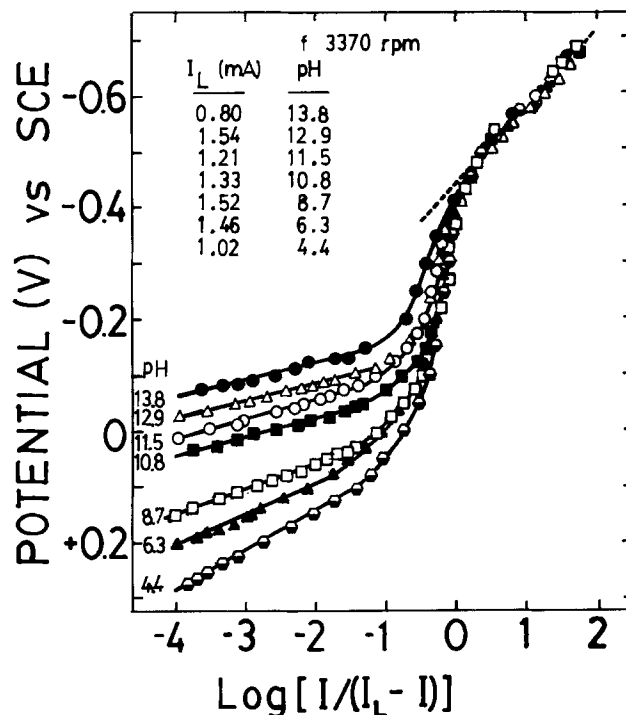


Fig. 16. Tafel plots for O_2 reduction on Fe-TSP adsorbed on OPG in solution of various pH values. Rotation rate: 3370 rpm.

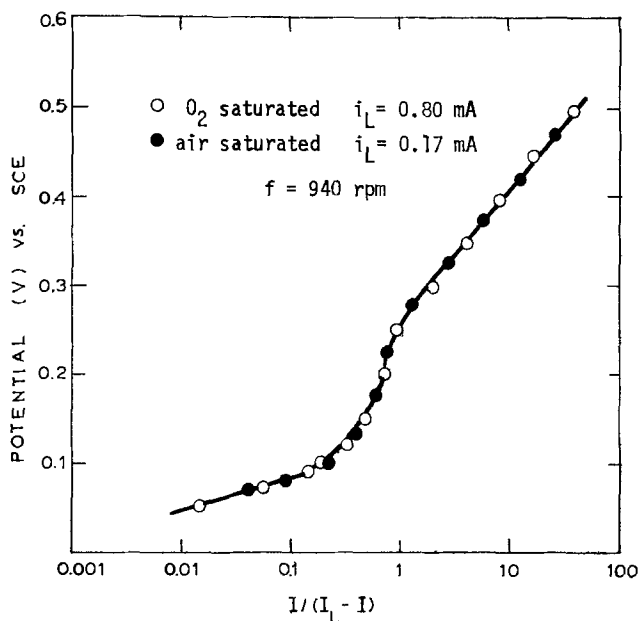


Fig. 17. Tafel plots of $\log [I/(I_L - I)]$ vs. E for O₂ reduction on Fe-TSP on OPG using O₂-saturated and air-saturated 0.1M NaOH.

Another interesting feature that is clearly noted in this figure is that a limiting current is reached at $\log [I/(I_L - I)] = \sim 0.1$. This limiting current is associated with the pre-wave observed in the polarization curves (see Fig. 12). This current is independent of pH for the whole range studied, and independent of potential and first order in O₂ concentrations. A chemical limiting process with essentially potentially independent kinetics appears to be involved.

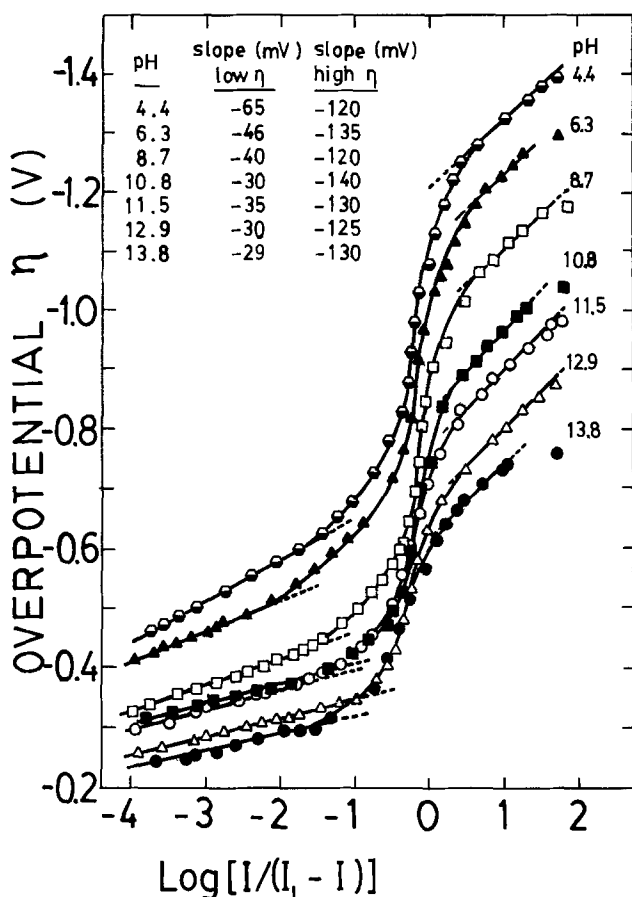


Fig. 18. Tafel plots of overpotential vs. $\log [I/(I_L - I)]$. Conditions are the same as for Fig. 16.

Reaction order in OH⁻ at low polarization on adsorbed Fe-TSP.—Since the reaction is first order in O₂ concentration and the activity of water for the solutions of different pH is essentially constant, the rate of the reaction expressed as a kinetic current is

$$I_k = k[\text{O}_2][\text{OH}^-]^m \quad [7]$$

with the back reaction negligible. From Eq. [7] the reaction order for OH⁻ is

$$m = \left(\frac{\partial \log I_k}{\partial \log [\text{OH}^-]} \right)_E = \left(\frac{\partial \log [I/(I_L - I)]}{\partial \log [\text{OH}^-]} \right)_E \quad [8]$$

where I_k is given by

$$I_k = I_L \frac{I}{(I_L - I)} \quad [9]$$

for a first-order reaction in O₂

The plots of $\log [I/(I_L - I)]$ vs. $\log [\text{OH}^-]$ for the low polarization-Tafel linear region in Fig. 18 yield straight lines in the pH range from 13.8 to 10.8 (Fig. 19). In some instances it was necessary to extrapolate the low polarization-Tafel linear region to lower and higher values of $I/(I_L - I)$ to obtain the data in Fig. 19.

The slopes of the linear portion of the curves in this figure range from -0.87 to -1.1 indicating a reaction order of -1 for OH⁻. For pH values lower than 10.8 the order in OH⁻ decreases numerically. This correlates with an increase of the slope at low pH values in the Tafel plot of Fig. 16.

Plots of the potential vs. pH for constant $I/(I_L - I)$ values in the low polarization-Tafel linear regions yield straight lines for high pH values (13.8-8) with a slope of -30 mV/pH unit. This is compatible with a Tafel slope of -30 mV/decade and $m = -1$.

O₂ reduction on Fe-TSP adsorbed on SAPG.—Essentially the same behavior has been observed for the disk currents for O₂ reduction on Fe-TSP adsorbed on SAPG. On the basis of the observed B values, the O₂ reduction appears to proceed virtually entirely by the overall $4e^-$ process without any peroxide generation at potentials anodic to -0.5 V. The B values indicate that peroxide generation becomes quite substantial at more cathodic potentials. O₂ reduction to peroxide or OH⁻ ion is grossly inhibited on the basal plane in the absence of the adsorbed complexes. Consequently this provides evidence that much of the peroxide is generated on the adsorbed Fe-TSP at more cathodic potentials and not just on the exposed graphite surface.

Tafel plots of $\log [I/(I_L - I)]$ vs. E are given in Fig. 20 for Fe-TSP adsorbed on the basal plane of both SAPG and OPG. The chemical limiting currents are about eight times smaller for the SAPG than for

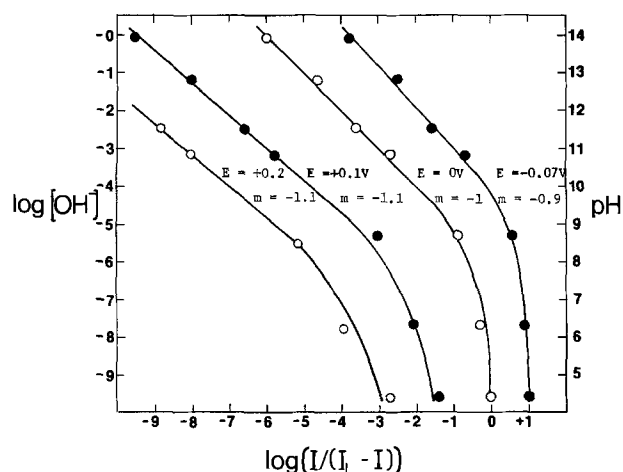


Fig. 19. Plots of $\log [I/(I_L - I)]$ vs. $\log [\text{OH}^-]$ for values of $I/(I_L - I)$ taken from the Tafel linear region of low polarization in Fig. 16, extrapolated, if necessary, at a constant potential.

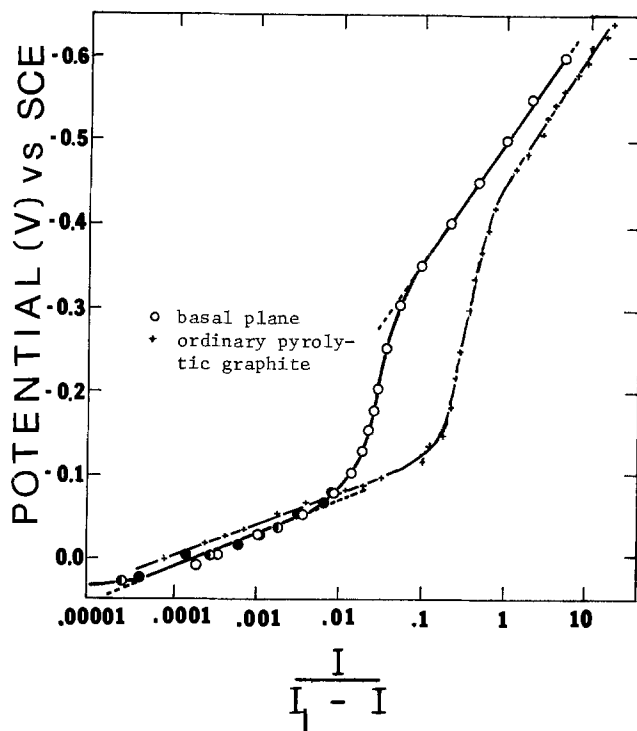


Fig. 20. Tafel plot of $\log [I/(I_L - I)]$ vs. E for O_2 reduction in Fe-TSP adsorbed on SAPG and OPG at $f = 3000$ rpm in 0.1M NaOH.

the ordinary pyrolytic graphite and about twofold smaller for the high polarization-Tafel linear region, but almost the same for the low polarization Tafel linear region.

From the cyclic voltammetry curves for these two surfaces the surface concentration of Fe-TSP on the SAPG is about four to five times smaller than that observed on ordinary pyrolytic graphite, expressed in terms of superficial area.

Discussion

O_2 reduction on Fe-TSP.—On the basis of the experimental results for O_2 reduction on Fe-TSP adsorbed on the basal planes of SAPG and OPG, the mechanisms of O_2 reduction at low and high polarization are not the same. Evidence for this is the different Tafel slopes and pH dependence. The reaction at low polarization is strongly dependent on pH and has an order of -1 in OH^- ions over the pH range 13.8–10.8. In contrast, the process at high polarization is practically pH independent over the entire range studied (13.8–4.4). Both processes are first order in O_2 .

The current potential data can be deconvoluted into two component processes as shown in Fig. 21. The experimental current density i corresponds to the sum of the values for each individual process, i.e., $i(\text{total}) = i_a + i_b$. The process corresponding to i_b has been assumed to follow Tafel linearity only at more cathodic potentials and to approach zero current at potentials negative to the reversible value for the overall $4e^-$ reduction in order to fit the experimental data. Such behavior may occur if process b corresponds to a hydrogen peroxide producing reaction with the bulk peroxide concentration finite but very low (e.g., $10^{-7}M$). Small residual currents were observed on the ring after several cathodic potential sweeps, providing evidence for such peroxide. The curve corresponding to i_b then approaches the reversible potential for the O_2/HO_2^- , OH^- couple for whatever is the bulk concentration of HO_2^- .

Mechanism at low polarization at pH > 8 (mechanism I).—The more anodic peak in the voltammetry curves

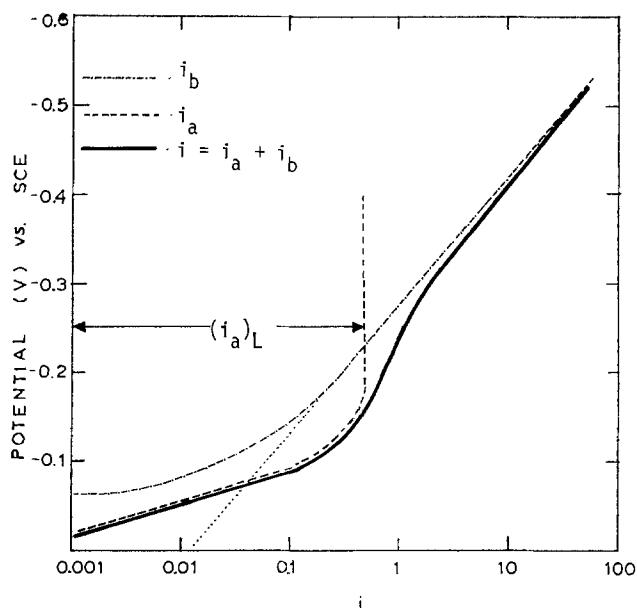
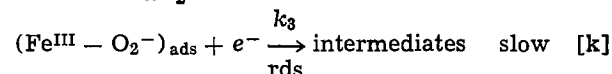
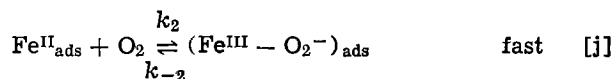
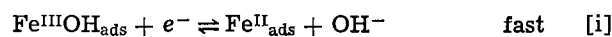


Fig. 21. Graphical representation of the combination of two processes for O_2 reduction on adsorbed Fe-TSP in basic media.

for Fe-TSP in Fig. 2 occurs at potentials in the low polarization region (Fig. 16) where deviations from Tafel linearity become evident. This suggests an involvement of the $[Fe(III)OH\ TSP]_{\text{ads}}/[Fe(II)\ TSP]_{\text{ads}}$ couple in the reaction mechanism responsible for this portion of the polarization curves. The following mechanism explains the O_2 reduction kinetics at $pH > 8$ for the region below the apparent chemical limiting current, corresponding to component i_a in Fig. 21



where the TSP groups have not been shown for simplicity. Reaction [k] would then be followed by further fast steps yielding finally OH^- as the product of the O_2 reduction with a total of $4e^-$ per O_2 consumed. For this reaction scheme, the rate of the reaction expressed as a current density is given by

$$i_a = 4Fk_3[Fe^{III} - O_2^-] \exp \left[-\frac{\alpha F}{RT} (E - E_0) \right] \quad [10]$$

where $[Fe^{III} - O_2^-]$ is the surface concentration of this adsorbed species, α is the symmetry factor, and k_3 is the rate constant at the standard electrode potential for reaction [k]; i.e., at $E = E_0$.

Applying the Nernst equation to reaction [i] and assuming ideal behavior

$$E + E_0 - \frac{RT}{F} \ln \frac{[Fe^{II}](OH^-)}{[Fe^{III}OH]} \quad [11]$$

where $[]$ represents surface concentration and $()$ solution phase concentration. Brown and Anson (20) have called attention to the deviation of adsorbed complexes from Nernst behavior when using concentrations rather than activities or coverage-dependent standard free energies or E_0 values (i.e., non-Langmuir behavior). The deviations, however, should be small in the present work since the concentration of the adsorbed macrocyclic and, hence, the change in charge density are low.

The surface concentration of the Fe species can be expressed in terms of coverage θ , i.e.

$$[\text{Fe}^{\text{II}}] = \theta m; \quad 0 < \theta < 1 \quad [12]$$

$$[\text{Fe}^{\text{III}}\text{OH}] = (1 - \theta)m \quad [13]$$

where m is the total surface concentration of Fe-TSP species. Introducing Eq. [12] and [13] into Eq. [11] and solving for θ

$$\theta = \frac{(\text{OH}^-)^{-1} \exp - \frac{F}{RT} (E - E_0)}{1 + (\text{OH}^-)^{-1} \exp - \frac{F}{RT} (E - E_0)} \quad [14]$$

Assuming steady state for step [j], the concentration of $[\text{Fe}^{\text{III}} - \text{O}_2^-]$ adsorbed species is given by

$$[\text{Fe}^{\text{III}} - \text{O}_2^-] = \frac{\overset{\rightarrow}{k_2}[\text{O}_2]\theta m - i_a}{\overset{\leftarrow}{k_2}} \quad [15]$$

Replacing $[\text{Fe}^{\text{III}}\text{O}_2^-]$ in Eq. [10] with Eq. [15], replacing k_3/k_{-2} by K and rearranging

$$i_a = 4Fk_2(\text{O}_2)\theta m \frac{K \exp - \frac{\alpha F}{RT} (E - E_0)}{1 + K \exp - \frac{\alpha F}{RT} (E - E_0)} \quad [16]$$

When $\theta \rightarrow 1$ and $K \exp - \frac{\alpha F}{RT} (E - E_0) \gg 1$, then i approaches a limiting value, given by

$$(i_a)_L = 4Fk_2(\text{O}_2)m \quad [17]$$

The coverage θ of Fe^{II}-TSP approaches one at potentials cathodic to E_0 , i.e., all Fe-TSP on the surface becomes Fe^{II}-TSP. For example, when $E - E_0 = -0.1\text{V}$, $\theta = 0.93$; and when $E - E_0 = -0.2\text{V}$, $\theta = 0.999$.

Combining Eq. [10]-[16] and rearranging

$$i_a = (i_a)_L \frac{(\text{OH}^-)^{-1} K \exp - \left[(1 + \alpha) \frac{F}{RT} (E - E_0) \right]}{\left[1 + (\text{OH}^-)^{-1} \exp - \frac{F}{RT} (E - E_0) \right] \left[1 + K \exp - \frac{\alpha F}{RT} (E - E_0) \right]} \quad [17a]$$

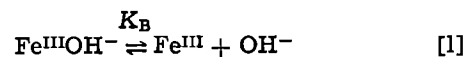
This equation predicts the essential features of the experimental data below the high polarization-Tafel linear region in the pH range from 8.7 to 13.8. The reaction rate is first order in (O₂), -1 in (OH⁻), and predicts a limiting current density $(i_a)_L$ that is directly proportional to O₂ concentration and to Fe-TSP surface concentration and independent of pH. The quantity $(i_a)_L$ is not a diffusing limiting current density, but is due to a potential insensitive chemical process, reaction [j], which becomes rate controlling when the Fe^{II} species approach saturation and the cathodic polarization has increased the rate of reaction [k] to a relatively high value. According to this proposed mechanism, the Tafel slope for the linear Tafel region of i_a should be $-RT/[(1 + \alpha)F]$. The value of the slope will depend on the value of α . For $\alpha = 0.5$ the slope is $-RT/(1.5F)$ or -40 mV/decade and for $\alpha = 1$ is $-RT/(2F)$, or -30 mV/decade as compared with an experimental value of ~ -35 mV/decade. A Tafel linear region of slope $-RT/[(1 + \alpha)F]$ should be observed only if both

terms $(\text{OH}^-)^{-1} \exp - \frac{F}{RT} (E - E_0)$ and $K \exp - \frac{\alpha F}{RT} (E - E_0)$ are small compared to unity. If either term becomes much larger than unity while the other is still very small compared to unity, a second

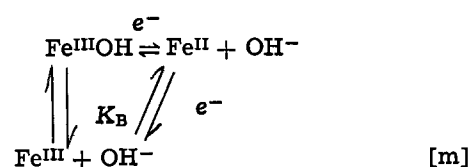
Tafel linear region of higher slope should be observed.

For $(\text{OH}^-)^{-1} \exp - \frac{F}{RT} (E - E_0) \gg 1$ and $K \exp - \frac{\alpha F}{RT} (E - E_0) \ll 1$, then the Tafel slope of $-RT/(\alpha F)$ or ~ -120 mV/decade would be expected while for the reverse situation, the slope should be -60 mV/decade. Neither of these slopes has been observed at high pH. The limiting current $(i_a)_L$ is achieved with a gradual change in the slope and an intermediate linear region is not observed. It is possible that the log linear region occurs only close to the limiting current $(i_a)_L$ over too small a potential range to be evident.

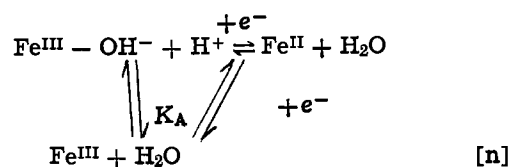
Acid-base equilibrium of Fe-TSP.—At more acid pH it is necessary to consider the acid-base equilibrium



The redox process may be represented as



or alternatively



with

$$K_B = \frac{[\text{Fe}^{\text{III}}](\text{OH}^-)}{[\text{Fe}^{\text{III}}\text{OH}]} = \frac{1 - x}{x} (\text{OH}^-) \quad [18]$$

with x the fraction of the surface adsorbed Fe^{III} complex as Fe^{III}OH. Solving for x

$$x = \frac{(\text{OH}^-)/K_B}{1 + (\text{OH}^-)/K_B} \quad [19]$$

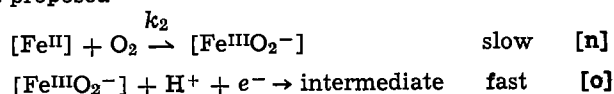
Expressing the concentrations as coverage, the Nernst equation for reaction [m] becomes

$$E = E_0 - \frac{RT}{F} \ln \frac{\theta(\text{OH}^-)}{(1 - \theta)x} \quad [20]$$

Solving Eq. [20] for θ

$$\theta = \frac{x(\text{OH}^-)^{-1} \exp - \frac{F}{RT} (E - E_0)}{1 + x(\text{OH}^-)^{-1} \exp - \frac{F}{RT} (E - E_0)} \quad [21]$$

Mechanism at low polarization in acid media (mechanism II).—It is possible that the uptake of O₂ by Fe^{II} becomes rate controlling when the pH of the solution is lowered. The following mechanism for acid media is proposed



where Fe^{II} is generated by reaction [m]. The rate of the reaction expressed as a current is

$$i_a = 4\text{F}k_2[\text{Fe}^{\text{II}}](\text{O}_2) \quad [22]$$

Expressing $[\text{Fe}^{\text{II}}]$ as coverage, using θ from Eq. [21], and replacing $4\text{F}k_2m(\text{O}_2)$ by $(i_a)_L$ as before, the final expression becomes (21)

$$i_a = (i_a)_L \frac{x(\text{OH}^-)^{-1} \exp - \frac{\text{F}}{RT} (E - E_o)}{1 + x(\text{OH}^-)^{-1} \exp - \frac{\text{F}}{RT} (E - E_o)} \quad [23]$$

This mechanism predicts a Tafel slope of $-\text{F}/RT$ or -60 mV/decade at 25°C . It also predicts a limiting current directly proportional to (O_2) and to the surface concentration of $[\text{Fe-TSP}]$ species. This limiting current is independent of pH.

The terms x and $(\text{OH}^-)^{-1}$ are interdependent according to Eq. [19]. At alkaline pH values, $[\text{OH}^-] \gg K_B$ and x in Eq. [19] becomes unity. At more acid pH values, the behavior of Eq. [19] will depend on the value of K_B . Figure 3 predicts an approximate value for the acid dissociation constant of $K_A \approx 10^{-4}$ and hence $K_B \approx 10^{10}$.

When $(\text{OH}^-) = \sim 10^{-10}\text{M}$, $x = 0.5$ and when $(\text{OH}^-) \ll K_B$, $x = 0$. According to this, at $\text{pH} < 4$ Eq. [20] becomes independent of (OH^-) , and

$$x(\text{OH}^-)^{-1} = \frac{1/K_B}{1 + (\text{OH}^-)/K_B} = 1/K_B \quad [24]$$

Equation [23] becomes

$$i_a = (i_a)_L \frac{K_B^{-1} \exp - \frac{\text{F}}{RT} (E - E_o)}{1 + K_B^{-1} \exp - \frac{\text{F}}{RT} (E - E_o)} \quad [25]$$

Equations [19] and [23] fit the experimental observation (Fig. 19) that, at low pH, i_a has relatively little or no pH dependence.

Mechanism I and II are expected to be competitive in the pH range between 10 and 4. This would explain the gradual change in the Tafel slope over this pH range. Equations [19] and [23] do not include a correction for the mass transport of O_2 to the electrode surface. This correction is small in the current range where i_a is predominant. At high current densities the correction can be made with the equation

$$(\text{O}_2) = \frac{(i_L - i)}{i_L} (\text{O}_2)_{\text{bulk}} \quad [26]$$

where i_L corresponds to the diffusion limiting current density. At more cathodic potentials the fraction of the current corresponding to peroxide generation becomes quite substantial. Since this fraction is potential dependent, i_L also becomes potential dependent. The value at any particular potential can be evaluated from the B values calculated from the $1/I$ vs. $1/f^{1/2}$ plots (Fig. 14).

Mechanism at high cathodic polarization (mechanism III).—Tafel slopes close to -120 mV/decade observed at high polarizations strongly suggest that a first one-electron transfer step becomes rate controlling at those potentials with mechanistic features analogous to those for Co-TSP. The process becomes practically pH independent as shown in the Tafel plots of Fig. 16. The rate of reaction can then be expressed by

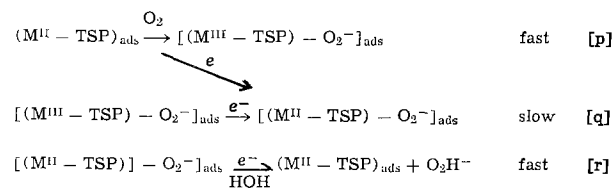
$$i_b = 4\text{F}k_m\theta(\text{O}_2) \exp - \frac{\alpha\text{F}}{RT} (E - E_o) \quad [27]$$

$$i_b = 4\text{F}k_m\theta(\text{O}_2)_{\text{bulk}} \frac{i_L - i}{i_L} \exp - \frac{\alpha\text{F}}{RT} (E - E_o) \quad [27a]$$

where Eq. [27a] contains the correction for mass transport of O_2 from the data.

The pH independence of the process indicates that protons or OH^- ions are not involved before or in the rate-determining step.

A mechanism which explains the behavior at high polarization is as follows



Reactions [p] and [q] may be either separate steps as shown or a single step. This same mechanism probably is also operative for O_2 reduction on $(\text{Co-TSP})_{\text{ads}}$ and is to be preferred to the mechanism suggested earlier (9) since it accounts for the zero reaction order dependence on OH^- ion concentration.

A redox mechanism similar to mechanisms I and II is not observed on the adsorbed Co-TSP. This is probably related to the differences in the redox properties of Fe-TSP and Co-TSP. At pH 1, the $\text{Co}^{\text{II}}/\text{Co}^{\text{III}}$ -TSP couple occurs at $+0.78\text{V vs. SCE}$ and the $\text{Fe}^{\text{II}}/\text{Fe}^{\text{III}}$ couple at $+0.40\text{V}$. Therefore it should be much easier for O_2 in binding to the transition metal of the TSP complex to oxidize Fe^{II} to Fe^{III} than Co^{II} to Co^{III} .

Some caution must be exercised in comparing the behavior of the adsorbed M-TSP at monolayer levels with that of thick layers of the corresponding phthalocyanine on carbon substrates or that of the bulk complex. Nonetheless, the experimental results of the present study may explain the different Tafel slopes found by various authors for O_2 reduction on metal chelates. For example, the Tafel slopes reported for O_2 reduction on iron complexes at $\sim 25^\circ\text{C}$ include -30 (6-8), -45 (30), and -60 (31) mV/decade . For cobalt chelates, slopes of -40 (37), -60 (4), and -120 (9, 10, 30, 33) mV/decade have been found. On the basis of the present work, this distribution of Tafel slopes appears to result from differences in the redox potentials and $\text{p}K$'s of the couples and pH of the electrolytes. Despite the obvious importance of the redox properties of the surface species, relatively few authors have placed much emphasis on them in their studies (see, e.g., 2-4, 34).

Manassen and Bar-Ilan (2) measured the redox potentials of metal phthalocyanines by solubilizing them in tetrabutyl ammonium perchlorate solutions. Randin (3) used the data for the homogeneous couple to rationalize the catalytic behavior of transition metal phthalocyanines in alkaline solutions. Aside from the question of the redox potentials for the heterogeneous vs. homogeneous Fe phthalocyanine couple, the difference in pH is expected to shift the potential very substantially. Similar behavior has been observed for iron porphyrins (35) and vitamin B-12 (36).

Appleby and Savy (6-8) have reported Tafel slopes of -30 mV/decade for O_2 reduction on layers of Fe phthalocyanine on carbon in alkaline media with an OH^- reaction order of -1 . This is similar to the results found in the present work with Fe-TSP on graphite. It is very likely that the potential of the $\text{Fe}^{\text{II}}/\text{Fe}^{\text{III}}$ phthalocyanine couple falls in the same range of potential where these slopes are observed. A recently reported value for the $\text{Fe}^{\text{II}}/\text{Fe}^{\text{III}}$ phthalocyanine couple by Beck (4) at $\text{pH} = 0$ is $+0.7\text{V vs. SHE}$. If we assume that the $\text{p}K_A$ of $\text{Fe}^{\text{III}}\text{Pc-OH}$ is approximately 4, then at $\text{pH} = 14$ the redox potential for iron phthalocyanine

cyanine should be approximately +0.10V, which is in the region of the -30 mV/decade slope.

In summary the present study provides an explanation for the different experimental results reported in the literature in terms of:

1. One mechanism is predominant for alkaline media with a Tafel slope close to $F/2RT$ and another mechanism is predominant in acid media with a Tafel slope close to F/RT . These two mechanisms can become competitive at intermediate pH values. This explains the gradual increase of the slopes at more acid pH values found by several authors (6-8, 37) and in the present work. These two mechanisms are controlled by the M^{II}/M^{III} couples and are only observed when the potential of these redox couples is close to that where O₂ reduction takes place. This is the case for Fe-TSP and on the basis of literature data also for Fe-Pc and Co-TAA (6, 8, 37).

2. At potentials far cathodic to those of the transition metal redox couple, a redox type of mechanism is not operative since all of the catalyst is in the lower valency state and the chemical step $M^{II} + O_2 \rightarrow M^{III}O_2^-$ does not occur because the formation of the M^{III} species is thermodynamically unfavorable even in the O₂ adduction. In this case a first one-electron transfer step becomes rate controlling via a different pathway, and the Tafel slopes are close to $RT/(\alpha F)$ (-120 mV/decade for $\alpha = 0.5$). This is the case for adsorbed Fe-TSP and Co-TSP in the present study and for Co-TAA, Co-Pc, Ni-Pc, and Cu-Pc reported in the literature (30, 33, 37).

Acknowledgment

The authors acknowledge the support of segments of this research by the U.S. Department of Energy, Office of Naval Research, and the Electric Power Research Institute. One author expresses appreciation to the Organization of American States which provided a graduate fellowship to one of the authors (JZ) during 1976-1977.

Manuscript submitted Sept. 21, 1979; revised manuscript received ca. Jan. 21, 1980.

Any discussion of this paper will appear in a Discussion Section to be published in the June 1981 JOURNAL. All discussions for the June 1981 Discussion Section should be submitted by Feb. 1, 1981.

Publication costs of this article were assisted by Case Western Reserve University.

REFERENCES

- H. Jahnke, M. Schonborn, and G. Zimmermann, in "Organic Dyestuffs as Catalysts for Fuel-Cells," Topics in Current Chemistry, **61**, 135 (1976).
- J. Masassen and Bar-Ilan, *J. Catal.*, **17**, 86 (1970).
- J. P. Randin, *Electrochim. Acta*, **19**, 83 (1974).
- F. Beck, *J. Appl. Electrochem.*, **7**, 239 (1977).
- A. J. Appleby and M. Savy, *Nat. Bur. Stand. Spec. Publ.* **455**, 241 (1976).
- A. J. Appleby, J. Fleisch, and M. Savy, *J. Catal.*, **44**, 281 (1976).
- A. J. Appleby and M. Savy, *Electrochim. Acta*, **22**, 1315 (1977).
- A. J. Appleby and M. Savy, in "Proceedings of Symposium on Electrode Materials and Processes for Energy Conversion and Storage," J. D. E. McIntyre, S. Srinivasan, and F. W. Will, Editors, pp. 247-264, The Electrochemical Society Softbound Proceedings Series, Princeton, N.J. (1977).
- J. Zagal, R. Sen, and E. Yeager, *J. Electroanal. Chem. Interfacial Electrochem.*, **83**, 207 (1977), and references therein.
- R. Sen, J. Zagal, and E. Yeager, *Inorg. Chem.*, **16**, 3379 (1977).
- J. Zagal, P. Bindra, and E. Yeager, Paper 539, presented at The Electrochemical Society Meeting, Seattle, Washington, May 21-26, 1978.
- W. J. Albery and S. Bruckenstein, *Trans. Faraday Soc.*, **62**, 1920 (1966).
- F. Beck, *Ber. Bunsenges. Phys. Chem.*, **77**, 353 (1973).
- J. Manassen, *J. Catal.*, **33**, 133 (1974).
- H. Sigel, P. Waldmeir, and B. Prijs, *Inorg. Nucl. Chem. Lett.*, **7**, 161 (1971).
- K. Fenkart and C. H. Brubaker, *J. Inorg. Nucl. Chem.*, 3245 (1968).
- A. B. P. Lever and J. P. Wilshire, *Inorg. Chem.*, **17**, 1145 (1978).
- V. S. Bagotskii, M. R. Tarasevich, and V. Y. Filinovsky, *Electrokhimiya*, **5**, 1218 (1969).
- H. S. Wroblowa, Y. C. Pan, and G. Razumney, *J. Electroanal. Chem. Interfacial Electrochem.*, **69**, 195 (1976).
- A. P. Brown and F. C. Anson, *Anal. Chem.*, **49**, 1589 (1977).
- J. Zagal, Ph.D. Thesis, Case Western Reserve University, 1978.
- J. P. Randin and E. Yeager, *J. Electroanal. Chem. Interfacial Electrochem.*, **36**, 257 (1972).
- I. Morcos and E. Yeager, *Electrochim. Acta*, **15**, 953 (1970).
- W. G. Wilke, "Solubilities of Inorganic and Metal Organic Compounds," Vol. II, 4th ed., p. 1219, American Chemical Society, Washington, D.C. (1969).
- K. Gubbins and R. Walker, *This Journal*, **112**, 469 (1965).
- R. Davies, G. Horvath, and C. W. Tobias, *Electrochim. Acta*, **12**, 287 (1967).
- Handbook of Chemistry and Physics, 54th ed., C. R. C. Press, Cleveland, Oh. (1973).
- V. G. Levich, "Physicochemical Hydrodynamics," English Translation, Prentice Hall, Englewood Cliffs, N.J. (1962).
- J. C. Huang, R. K. Sen, and E. Yeager, *This Journal*, **126**, 786 (1979).
- M. Savy, P. Andro, C. Bernard, and G. Magner, *Electrochim. Acta*, **18**, 191 (1973).
- M. Savy, C. Bernard, and G. Magner, *ibid.*, **20**, 383 (1975).
- J. Newman, *This Journal*, **113**, 1235 (1966).
- E. Yeager, P. Bindra, N. Doddapaneni, J. C. Huang, R. K. Sen, and J. Zagal, Final Report, EPRI E.M.-505, Case Western Reserve University, Cleveland, Ohio (June 1977).
- J. Ulstrup, *J. Electroanal. Chem. Interfacial Electrochem.*, **79**, 171 (1977).
- A. P. Brown, C. Koval, and F. C. Anson, *ibid.*, **72**, 379 (1976).
- D. Lexa and J. M. Saveant, *J. Am. Chem. Soc.*, **98**, 2652 (1976).
- H. Behret, H. Binder, W. Clauberg, and G. Sandstede, in "Proceedings of Symposium on Electrode Materials and Processes for Energy Conversion and Storage," J. D. E. McIntyre, S. Srinivasan, and F. G. Will, Editors, pp. 519-536, The Electrochemical Society Softbound Proceedings Series, Princeton, N.J. (1977).
- J. Weber and D. H. Busch, *Inorg. Chem.*, **4**, 469 (1965).
- J. P. Randin and E. Yeager, *This Journal*, **118**, 711 (1971).
- H. Meier, U. Tschirwitz, E. Zimmerhacki, W. Albrecht, and G. Zeittler, *J. Phys. Chem.*, **81**, 712 (1977).
- D. Behar, G. Czapski, J. Rabani, L. M. Dorfman, and H. A. Schwarz, *ibid.*, **74**, 3209 (1970).

The Nature of Surface States on Chemically Modified TiO₂ Electrodes

Micha Tomkiewicz*¹

Union Carbide Corporation, Tarrytown Technical Center, Tarrytown, New York 10591

ABSTRACT

Two important parameters which strongly influence the flatband potential of a semiconductor in electrolytic solutions are the electron affinity of the semiconductor and the net charge on the surface. An attempt to modify these parameters by chemical derivatization of the surface of the semiconductor will be described. When the surface of TiO₂ is modified with alkylsilanes, impedance and photocurrent measurements indicate that surface states are introduced at the semiconductor-electrolyte interface. These states have broad Gaussian distribution, with a maximum near the bottom of the conduction band. The states act as effective recombination centers for light-generated minority carriers. When the alkylsilane is derivatized with a phosphonate group, the Gaussian distribution of the states is retained but with reduced width, and the maximum is shifted considerably to more positive potentials. These states do not act as recombination centers. An attempt also was made to change the electron affinity of the surface by fluorination. The only measured result was an increase in surface recombination of minority carriers, which resulted in a decrease in the anodic photocurrent.

The position of the flatband potential of a semiconductor in contact with an electrolyte, relative to the oxidation-reduction potential of the solvent, is one of the key parameters determining the solar energy conversion efficiency of a photoelectrolytic cell (1).

According to Butler and Ginley (2) the electron affinity E_e and the flatband potential U_{FB} are related by

$$E_e = E_o - E_{FC} + e(U_{FB} + V_c) \quad [1]$$

where E_o is the difference between the vacuum level and the reference electrode (4.5 eV for SHE), E_{FC} is the energy difference between the Fermi level and the bottom of the conduction band in the bulk of the semiconductor, and V_c is a correction to the flatband potential due to absorption of charges on the surface. The last term vanishes if the measurements can be made at, or corrected to, the zero point of charge (ZPC). Butler and Ginley found very good agreement between the measured flatband potentials for oxides and the values calculated by Eq. [1] from electron affinities and measured ZPC values.

This paper describes our first effort at influencing the potential distribution at the semiconductor-electrolyte interface relative to the potential of the hydrogen electrode in the actual environment in which photoelectrolysis takes place. We chose TiO₂ as the semiconductor because its behavior in photoelectrochemical cells is the best understood; its bulk and surface properties have been extensively studied and its reported flatband potential is only a small fraction of a volt too positive for efficient photoelectrolysis under short-circuit conditions (1, 3). The strategy was to attach chemically functional groups on the surface and to monitor the effects of those groups on the potential distribution and on the light-induced anodic photocurrent.

A detailed study of the potential distribution at the unmodified TiO₂/aqueous electrolyte interface is reported separately (3, 4). For an effective improvement in the performance of a photoelectrolytic cell a modified surface has to meet the following conditions:

1. The modified surface has to be stable in the dark and under photoelectrolytic operation.
2. The oxidation-reduction potential of the attached group has to be significantly more positive than the

potential of the oxygen electrode, so that light-generated holes will tend to oxidize water and not the functional groups.

3. It should not act as a surface recombination center for the light generated minority carriers.

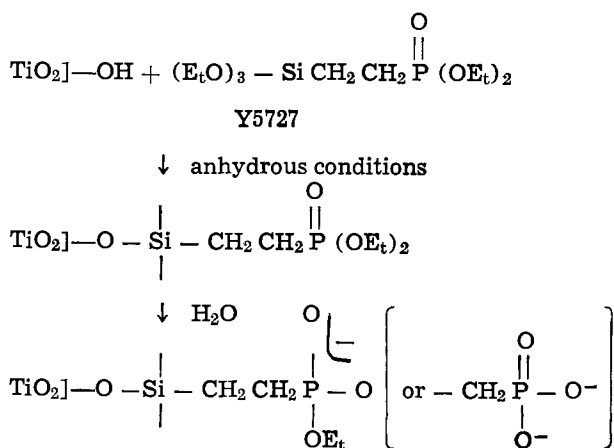
4. The modified surface should not add a potential barrier or a resistive layer to the cell.

5. The modified surface should be negatively charged at a potential more positive than the oxygen potential.

Thus we seek a chemically attached monolayer of acidic groups with the pK much lower than water that will oxidize at potentials more positive than +1.23V vs. SHE and that will not form a recombination center.

Fortunately during the last few years an extensive research effort has been carried out aimed at derivatization of electrode surfaces by chemical modification (5-46). Some of the efforts in this area already have been applied to photoelectrochemical systems (40-46). Based on the expected stability we have limited our choice to silane derivatives (5, 6, 11, 12). A variety of functional groups can be synthesized and attached to the surface.

A demonstrative example of such an attachment is illustrated with the following reaction



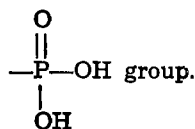
[2]

The net result is the replacement of an —OH group by

* Electrochemical Society Active Member.

¹ Present address: Department of Physics, Brooklyn College of CUNY, Brooklyn, New York 11210.

Key words: solar, impedance, semiconductor, interface.



The ZPC for TiO_2 in the rutile form was reported to be at $\text{pH} = 5.8$ (47). The first pK_a of phosphoric acid is 2.12. If we assume that the ionization constant of phosphoric acid does not change with the substitution of the silane group and the attachment to the surface of the semiconductor, the result should be changed in the ZPC from 5.8 to 2.1 which will result in a negative shift of 225 mV in the flatband potential. Larger shifts can be expected from acidic groups with lower pK attached to semiconductors with a higher ZPC.

Alkylsilanes were used to investigate the interactions of the —Ti—O—Si— functional group with the minority and majority carriers in the semiconductor.

In addition, we will describe an attempt to change the electron affinity of the semiconductor at the surface by surface fluorination.

Experimental

TiO_2 single crystals were purchased from Atomergic and sawed perpendicular to the c axis. The resulting wafers (1 mm thick) were mechanically polished, etched in NaOH at 500°C for 1 hr, rinsed in running distilled water, boiling HCl , and washed again. The wafers were doped with an H_2/Ar mixture at 600°C for 30 min. The alkyl silanes were purchased from Petrarch Systems and distilled in vacuum. Toluene was distilled over Na in benzophenone. The diethyl [$(\beta$ -triethoxysilyl) ethyl] phosphonate (Y5727) was kindly donated by Dr. K. G. Weinberg from the Chemical and Plastic Division of Union Carbide. The samples were reacted with silane derivatives in the apparatus shown in Fig. 1 which is based on a similar design by Cullen *et al.* (32). The procedure for electrode modification is similar to the one used by Murray *et al.* (6). Two samples were introduced into the modification apparatus and soaked in heptane overnight, then heated to 450°C for 4 hr in flowing Ar . One of the samples was soaked in 5% silane in toluene. Both samples were washed extensively with dry toluene, dried in flowing Ar for 30 min at room temperature, washed in distilled water, and dried with forced air.

The samples modified with alkylsilanes changed from hydrophilic to hydrophobic and the contact angle formed between the surface and a small drop of water served as the initial indication of the attachment of the alkylsilane to the surface.

ESCA-Auger analyses of the surfaces were performed using a Physical Electronics Model L 550 SAM-

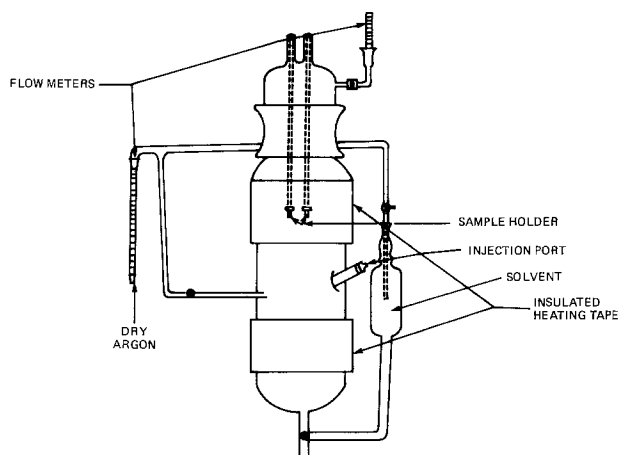


Fig. 1. The apparatus for surface derivatization of the electrodes

ESCA System spectrometer equipped with an Mg x-ray excitation source. All spectra were run at pressures less than 2×10^{-8} Torr. ESCA spectra signal averaging was performed using a Nicolet Model NIC-1072 computer.

Impedance measurements.—The electrochemical cell used for measurements of impedance and light-induced current-potential curves is shown in Fig. 2. Samples were held between two silicon gaskets pressed against the cell wall. The front gaskets had holes with an exposed area of 0.1 cm^2 . The back side of the samples was rubbed with an In/Ga alloy for ohmic contact. A Pt wire attached to a thin Pt disk was pressed against the ohmic contact through a hole in the back gasket and through a hole in a pressure-fit Teflon piston to the outside measuring apparatus. The walls that were not fitted with electrode compartments were fitted with quartz windows. The cell was sealed and purged with N_2 or Ar . The two electrodes were connected to the network analyzer and to a d-c power supply as described previously (3, 4, 48). The potentials of the two electrodes, one modified, the other not, were monitored continuously against the SCE and kept identical. The network analyzer was switched from one sample to the other and the relaxation spectrum analysis, as a function of the electrode potential, was carried out using the same procedure as previously described (3).

The current-potential measurements were made with a PAR Model 173 potentiostat, Model 175 universal programmer, and 150W xenon lamp attenuated with neutral density filter to produce light intensity of 50 mW/cm^2 . The light intensity was kept low to prevent bubble formation.

Surface fluorination.—Samples were fluorinated using a Union Carbide proprietary procedure (49).

Results and Discussion

Electrodes Modified with Alkylsilanes

In a set of preliminary experiments, no noticeable difference was found between alkyltrimethoxysilanes and alkyltrichlorosilanes. A detailed study was performed with methyltrimethoxysilane, hexyltrimethoxysilane, and eicosyltrichlorosilane. All three silane derivatives changed the surface of the electrode from

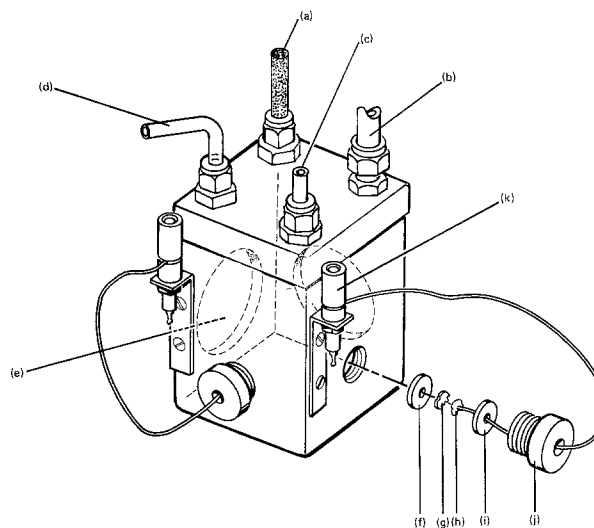


Fig. 2. The photoelectrochemical cell: a, counterelectrode; b, reference electrode (SCE); c and d, inlet and outlet for Ar ; e, optical windows; f and i, silicon rubber gaskets; g, sample; h, platinum disk attached to Pt wire and is pressed against the ohmic contact on the sample; j, Teflon screw; k, electrical connector.

hydrophilic to hydrophobic. The modified surfaces retained their hydrophobic properties after exposure, for as long as 90 hr, to aqueous solution with pH values varying from 1 to 14. The derivatized surface was restored to its unmodified state by boiling the sample in 10M NaOH. ESCA results showed that the silane was attached to the surface. The Si was not present on unmodified surfaces. The Si(2P) peak with a binding energy (BE) of 102 eV was compared to Ti (3P) with a BE of 37 eV. The theoretical cross sections for ionization at these levels are 0.865 and 0.789, respectively (50). Typical molar intensity ratios of these two peaks were 1:1, but this ratio varied nearly 30% between different preparations. Analysis of the LMM and KLL Auger transitions showed that the Si is distributed within a layer of 10Å.

The variations in ESCA and Auger spectra, between various alkylsilane derivatives, were within the scatter for individual silanes.

Impedance and relaxation spectrum analysis (3, 4, 48).—The equivalent circuit of the derivatized TiO₂ was found to be the same as that of underivatized samples (3, 4). Over certain potential ranges, the capacitance values for the modified samples were found to be higher than those for the unmodified surface. Possible explanations that can account for different capacitive values in the derivatized surfaces are:

Formation of an insulating film on the surface.—This will introduce an additional capacitive element, smaller than the space charge capacitance and connected in series with it. This will result in reduction of the observed capacitance in the modified surface which is contrary to observation.

Different surface area and/or different doping level.—In spite of precautionary measures taken to ensure identical surface areas and doping levels, nevertheless these two parameters varied from sample to sample. If the difference in capacitance is due to this variation, the ratio of the two capacitances should be independent of potential, from the following argument:

The unmodified sample obeys the Mott-Schottky relation (51) over the potential range which is being measured

$$\frac{1}{C_u^2} = \frac{2}{A_u^2 \epsilon e N_D^u} \left(U - U_{FB} - \frac{kT}{e} \right) \quad [3]$$

where C_u is the capacitance of the unmodified sample, A_u its area, N_D^u the doping level, ϵ the dielectric constant, e the electronic charge, U the electrode potential, and U_{FB} the flatband potential. A similar expression will hold for the modified sample. If the flatband potential is the same, then

$$\frac{C_m}{C_u} = \frac{A_m}{A_u} \sqrt{\frac{N_D^m}{N_D^u}} \quad [4]$$

which is independent of potential. The experimentally observed potential dependence of the ratio indicates that this is not the primary reason for the difference in capacitance.

Surface states.—If derivatization of the surface does introduce surface states, their capacitance is in parallel with the space charge layer and an increase in the overall capacitance is expected (52). This increase in capacitance should be potential dependent according to the energy and energy distribution of the states, in agreement with our observations.

The ratio of the modified to unmodified capacitance was plotted as a function of potential, as shown in Fig. 3. The region of capacitance ratios which was found to be potential independent was subtracted from the ratio over the entire potential range and the result was multiplied by the capacitance of the unmodified sample. This procedure can be summarized in the

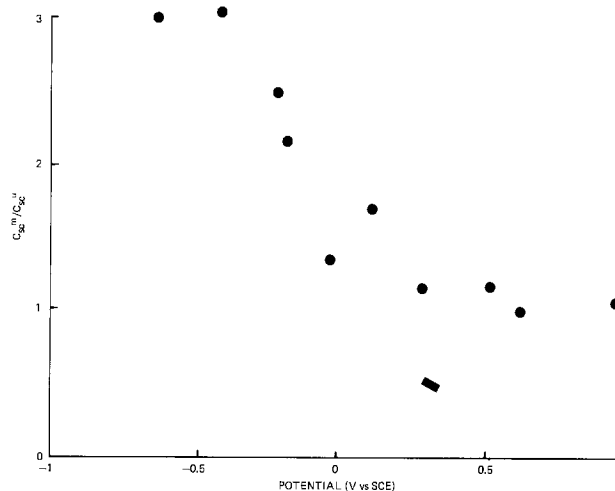


Fig. 3. The ratio of the capacitance of TiO₂ modified with hexyltrimethoxysilane and unmodified TiO₂, as a function of potential. (0.3M phosphate buffer, pH = 6.6.)

following way

$$C_m = C_{sc}^m + C_{ss} \quad [5]$$

$$C_u = C_{sc}^u \quad [6]$$

and therefore

$$C_{ss} = C_{sc}^u \left(\frac{C_m}{C_u} - \frac{A_m}{A_u} \sqrt{\frac{N_D^m}{N_D^u}} \right) \quad [7]$$

The magnitude of C_{ss} as a function of potential, for TiO₂ which was modified with hexyltrimethoxysilane, is presented in Fig. 4.

The surface states are spread over a broad potential range near the bottom of the conduction band. The potential distribution of the capacitance fits a Gaussian line shape with the following parameters

$$C_{ss} = 5.4 \exp(-1.9(U + 0.9)^2) \mu\text{F}/\text{cm}^2 \quad [8]$$

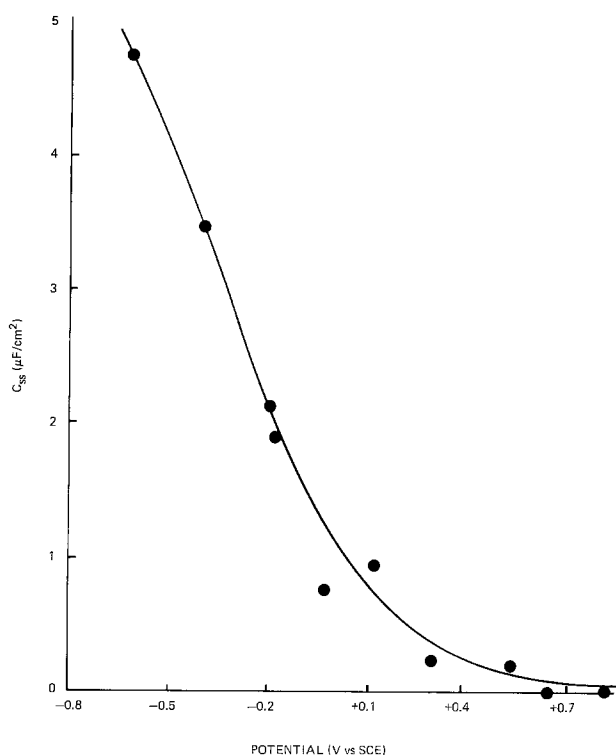


Fig. 4. The surface-states capacitance of TiO₂ which was modified with hexyltrimethoxysilane, as a function of potential. The experimental data were taken from Fig. 3 by using Eq. [7]. The solid line is the theoretical fit to Eq. [8].

This line shape can be interpreted as due to similar distribution of surface states at the semiconductor-electrolyte interface, which can be expressed in the following way

$$N_{ss}(E) = \frac{N_t}{e\sigma\sqrt{2\pi}} \exp[-(E_t - E)^2/2(e\sigma)^2] \quad [9]$$

where E is the energy, E_t is the most probable energy, $e\sigma$ the standard deviation in energy distribution, and N_t the concentration of surface states. Based on equivalent distribution, it was shown (3) that the number of positively charged donor states is given by

$$N_{ss^+}(E) = \frac{N_t}{2} \left\{ \operatorname{erf} \left(\frac{U - U_t}{\sigma\sqrt{2}} \right) - \operatorname{erf} \left(\frac{U_{FB} - U_t}{\sigma\sqrt{2}} \right) \right\} \quad [10]$$

where U is the electrode potential, U_t the potential of the surface states, and U_{FB} the flatband potential.

The differential capacitance due to these states is given by

$$C_{ss} = \frac{e d N_{ss^+}}{d\Delta\phi_s} = \frac{e N_t}{\sigma\sqrt{2\pi}} \exp(-(U - U_t)^2/2\sigma^2) \quad [11]$$

where

$$U = U_{FB} = \Delta\phi_s$$

From Eq. [8] and [11] we obtain the following parameters: $U_t = -0.9V$ vs. SCE; $\sigma = 0.52V$; and $N_t = 4.4 \times 10^{13}/\text{cm}^2$. This surface concentration of impurities corresponds approximately to 5% of a monolayer.

Photoactivity.—The modified semiconductors showed considerably reduced photoactivity compared to unmodified ones. A typical example of the ratio of the light-induced anodic current of an unmodified sample to one which was modified with hexyltrimethoxysilane, as a function of potential, is shown in Fig. 5. The modified and the unmodified electrodes are identical except for their surface composition. Therefore, the difference in the photoinduced anodic current is attributed to surface recombination. As with the surface-state capacitance, the surface recombination takes place in a broad potential range around the flatband.

Understanding these results requires invoking certain assumptions about the origin of the photoinduced anodic current and the mechanism of surface recombination due to the modified surface. The proposed mechanism for the surface recombination reaction is illustrated in Fig. 6. The energy diagram of TiO_2 is

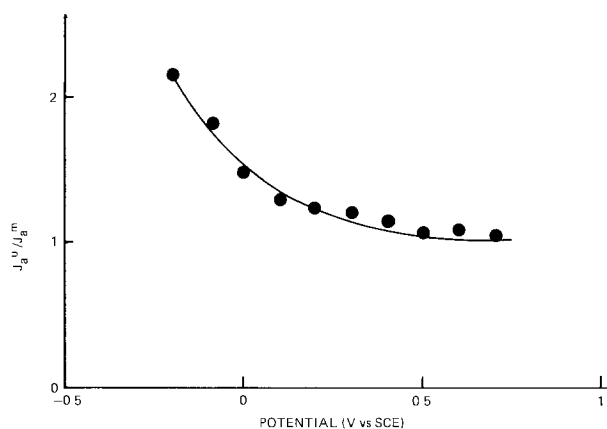


Fig. 5. The ratio of the light-induced anodic current of an unmodified TiO_2 to one which was modified with hexyltrimethoxysilane, as a function of potential. (Phosphate buffer, $\text{pH} = 6.6$.) The photocurrents were normalized to the same light intensity. The solid line is the theoretical fit to Eq. [31] with parameters given in the text.

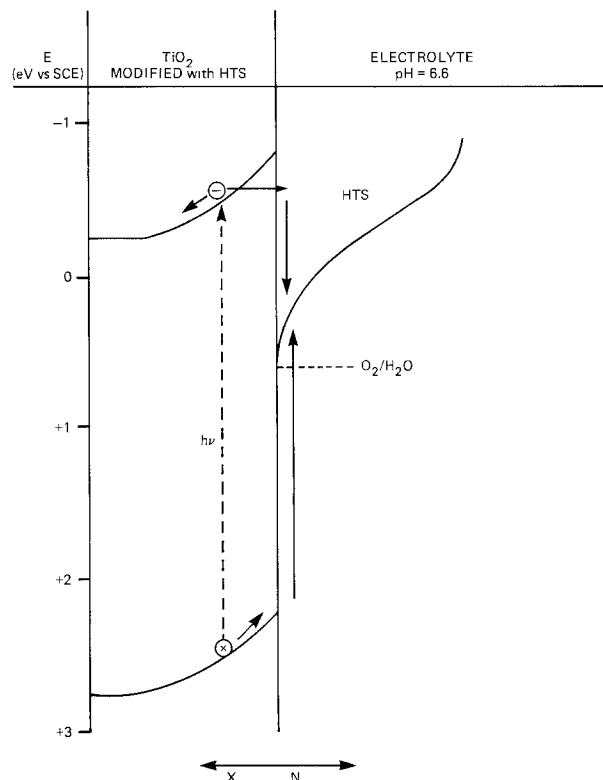


Fig. 6. The proposed mechanism for surface recombination on TiO_2 which was modified with hexyltrimethoxysilane (HTS). The distribution of the surface states was obtained from the capacitance data in Fig. 4.

illustrated together with the normalized distribution of the surface states, obtained from the capacitance data which were described in the previous section. When light is absorbed by the semiconductor, holes in the valence band will be driven to the surface. Either electrons will be driven by the field to the interior of the semiconductor or, at potentials which are not too positive compared to the flatband potential, they will tunnel through the barrier to the surface states. We will assume that this process is very efficient and not rate limiting. The light-induced, minority-carrier current at the surface is given by (1e)

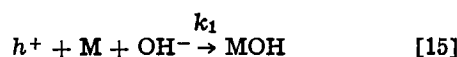
$$J = eF(1 - R) \left[1 - \frac{\exp(-\alpha d)}{\alpha L_p + 1} \right] \quad [12]$$

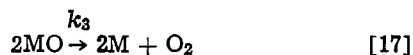
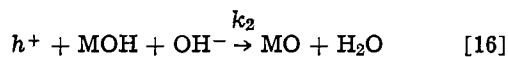
where α is the absorption coefficient, R the reflectivity, F the photon flux, e the electronic charge, d the thickness of the space charge layer, and L_p the minority carrier diffusion length. This current will be divided into the anodic current, J_a , and a current, J_r , due to the recombination processes between the minority carriers and the occupied surface states.

If the anodic oxidation process involves only a single electron or hole the anodic current density may be expressed as (53)

$$J_a = e k p^* C_R \quad [13]$$

where C_R is the concentration of the reduced species that is being oxidized, k is the rate constant, and p^* is the steady-state excess concentration of holes at the surface. The reactions that occur at the anode, resulting in the evolution of oxygen from water, are more complex. Various mechanisms have been suggested (54). One series of reactions that has been proposed is (55)





Reaction [14] represents the surface recombination with a rate constant S . MOH and MO are intermediate radicals involving the electrode material M. Since the anodic reaction is not limited by the dark reversed reaction we will neglect the latter. If reaction [15] is the rate-limiting step we may apply the steady-state method (55), by assuming that the concentrations of the intermediate species do not change with time. The steady-state concentration of the light-generated holes p^* at the surface is found from [12-17] to be

$$p^* = \frac{F(1-R)}{S + 2k_1[\text{OH}^-]} \left[1 - \frac{\exp(-\alpha d)}{\alpha L_p + 1} \right] \quad [18]$$

The anodic current J_a may be expressed as

$$J_a = 4e \frac{d[\text{O}_2]}{dt} = 2ek_1 p^* [\text{OH}^-] \\ = \frac{2ek_1[\text{OH}^-]F(1-R)}{S + 2k_1[\text{OH}^-]} \left[1 - \frac{\exp(-\alpha d)}{\alpha L_p + 1} \right] \quad [19]$$

The ratio of the anodic currents of two identical samples, one with and the other without surface recombination, will be

$$\frac{J_a^o}{J_a} = \frac{S}{2k_1[\text{OH}^-]} + 1 \quad [20]$$

In complete analogy to Eq. [13] the hole recombination current is given by

$$J_{r^h} = ek_r^h p^* n_t^* \quad [21]$$

where n_t^* is the concentration of the occupied surface states given by

$$n_t^* = n_t + \delta n_t \quad [22]$$

where n_t is the equilibrium concentration of the occupied states and δn_t the nonequilibrium increment. The hole recombination current will be compensated by an electron recombination current given by

$$J_{r^e} = ek_r^e p_t^* n_s \quad [23]$$

where p_t^* is the concentration of the unoccupied surface states given by

$$p_t^* = p_t + \delta p_t \quad [24]$$

and n_s is the electron concentration at the surface.

The following relation will also hold

$$p_t^* + n_t^* = p_t + n_t = N_t \quad [25]$$

where N_t is the total surface state concentration.

For surface states with energies close to the flatband potential, the electron exchange between the surface states and the conduction band will be very efficient and the surface recombination current will be limited by the availability of holes, under those conditions

$$\delta n_t \ll n_t \quad [26]$$

and

$$S = k_r^h n_t^* = k_r^h n_t \quad [27]$$

From Eq. [10] we obtain

$$n_t = \frac{N_t}{2} \left\{ \operatorname{erfc} \left(\frac{U - U_t}{\sigma\sqrt{2}} \right) - \operatorname{erfc} \left(\frac{U_{\text{FB}} - U_t}{\sigma\sqrt{2}} \right) \right\} \quad [28]$$

where $\operatorname{erfc}(x) = 1 - \operatorname{erf}(x)$. Substituting Eq. [28] into [27] will result

$$S = \frac{k_r^h N_t}{2} \left\{ \operatorname{erfc} \left(\frac{U - U_t}{\sigma\sqrt{2}} \right) - \operatorname{erfc} \left(\frac{U_{\text{FB}} - U_t}{\sigma\sqrt{2}} \right) \right\} \quad [29]$$

For states which are situated very close to the bottom of the conduction band, such that

$$\frac{k_r^h N_t}{4k_1[\text{OH}^-]} \operatorname{erfc} \left(\frac{U_{\text{FB}} - U_t}{\sigma\sqrt{2}} \right) \ll 1 \quad [30]$$

Equations [20] and [29] will yield

$$\frac{J_a^o}{J_a} \approx 1 - \frac{k_r^h N_t}{4k_1[\text{OH}^-]} \operatorname{erfc} \left(\frac{U - U_t}{\sigma\sqrt{2}} \right) \quad [31]$$

The solid line in Fig. 5 demonstrates the fit of Eq. [31] to the experimental results which are marked by the dark circles. The experimental data were taken from the same samples used to obtain the capacitance data shown in Fig. 4. U_t and σ were taken from the capacitance data and the only adjustable parameter was

$$\frac{k_r^h N_t}{4k_1[\text{OH}^-]} = 6.6 \quad [32]$$

Equation [32] indicates that the minority carriers react with surface states more than six times faster than the rate of reaction of holes with water to evolve oxygen. This interpretation of the parameter which is described by Eq. [32] is as good as the approximation which is described by Eq. [30].

Electrodes Modified with Diethyl [β -(Triethoxysilyl) Ethyl] Phosphonate (Y5727)

Stability and coverage.—ESCA was used for characterization of the surface coverage and stability of the modified surfaces. The P(2P) transitions, with a binding energy of 134 eV, were used in addition to the Si and Ti transitions that were described in the previous section. The P(2P) transitions are close enough in energy to the Ti(3P) and the Si(2P) transitions so that differences in escape depth and geometrical factors can be neglected. The theoretical cross section for the photoionization of the P(2P) level is 1.25 (50). Based on this and the theoretical cross sections of the corresponding Si and Ti peaks, the molar ratio of the elements were calculated. These ratios varied considerably from experiment to experiment, but a few general trends became apparent. Typically, after derivatization the P/Ti ratio was found to be between 0.2-0.4; after exposure of the sample to phosphate buffer for 40 hr, this ratio was reduced by 50%. The ratio of Si/P also varied from experiment to experiment. This ratio was sometimes as high as 6/1 and as low as 1/1. When a sample with initial ratio of Si/P = 1/1 was exposed to 0.1M H_2SO_4 for 24 hr this ratio increased to 2/1. We do not have an explanation for these results. They can be caused by impurities or by chemical reactions on the surface which have yet to be elucidated. It is very probable that the reaction sequence which we described in Eq. [2] will have to be modified. Much more work is needed to understand the reactions which take place on the surface before any definite conclusions could be drawn. The results that will follow will have to be treated with this uncertainty in mind.

Surface state.—The capacitance of the surface states that were introduced due to the surface modification was measured using the same procedure that was described in detail in the section on alkylsilanes. A representative result of these measurements is shown in Fig. 7. The solid line is a theoretical fit of these results to Eq. [11] with the following parameters: $U_t = +0.85\text{V vs. SCE}$; $\sigma = 0.13\text{V}$; and $N_t = 4 \times 10^{12}/\text{cm}^2$. The reproducibility in U_t and σ is much better than that which was obtained with the alkylsilanes but the coverage, as a rule, is order of magnitude smaller.

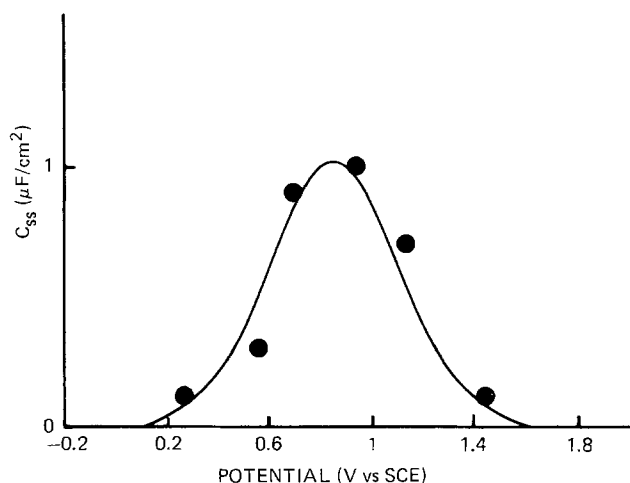


Fig. 7. The surface-states capacitance of TiO_2 which was modified with Y5727, as a function of potential. The solid line is the theoretical fit to Eq. [11] with parameters that are given in the text. (Phosphate buffer, $\text{pH} = 6.6$.)

Based on these results, the normalized distribution of the surface states relative to the position of the TiO_2 bands and the reversible oxygen electrode is shown in Fig. 8. The striking result which is evident in Fig. 8 is that the surface state energies, compared to alkylsilanes, were shifted to potentials even more positive than the reversible oxygen potential. This result indicates that a key requirement of a derivatized electrode was satisfied by the phosphonate derivative. The potential of the surface states ensures that in the competition between water and the silane, light-produced holes will tend to oxidize water. In agreement with this, the photoactivity of derivatized and underivatized electrodes shows no reproducible difference in photocurrent. The potential of zero photocurrent was also the same at both electrodes, under light of equal intensity.

In addition to the large positive shift in the potential of the surface states, compared to the surfaces that were derivatized with alkylsilanes, the energy distri-

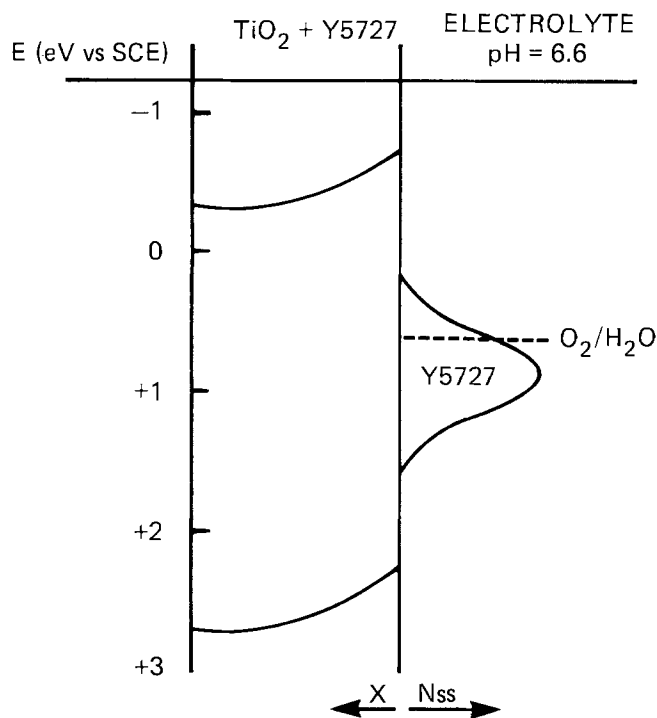


Fig. 8. Combined energy diagram of TiO_2 which was modified with Y5727 in phosphate buffer, $\text{pH} = 6.6$. The energy distribution of the surface states was taken from the data in Fig. 7.

bution of these states is narrowed. In view of the uncertainties in the chemistry of the derivatized surfaces after prolonged exposure to electrolytes, a serious attempt to hydrolyze the phosphonate ester groups was not made. A few preliminary experiments, in which we have tried to hydrolyze the ester groups in various concentrations of H_2SO_4 , resulted in irreproducible changes in coverage, but the potential and energy distribution of the states remained unchanged. Finally, the flatband potential of TiO_2 derivatized with Y-5727 remained unchanged.

Fluorinated Electrodes

To investigate the possibility of altering the flatband potential of TiO_2 by changing the electron affinity of the surface, we have fluorinated the doped TiO_2 . The F (1S) ESCA peak was used for the surface analysis. It was found that the atomic ratio of F/Ti, at the surface, was 3.1. This ratio was reduced to 0.2 upon sputtering to a depth of 10Å and to 0.14 upon sputtering 60Å. Fluorine was observed on the surface after exposure to an electrolyte for a period in excess of 1 week, but in a greatly reduced amount. Only two samples were fluorinated; one was used for the initial ESCA measurement while the other one was used for the electrochemical measurements.

The impedance measurements showed identical behavior for fluorinated and unmodified samples. Both showed the same flatband potential and a linear Mott-Schottky plot over potentials exceeding 2/3 of the bandgap. The fluorinated sample showed considerably reduced photoactivity compared to that of the unmodified sample.

Figure 9 shows the ratio of the photoanodic current of an unmodified to a fluorinated sample, both normalized to the same light intensity. The solid line is a theoretical fit to Eq. [31] with the following parameters: $\sigma = 0.64\text{V}$; $U_t = -0.6\text{V vs. SCE}$; $(k_r^h N_t) / (4k_1[\text{OH}^-]) = 2.7$. These results are qualitatively similar to those obtained with alkylsilanes. This might be due to the close proximity of the semiconductor surface to the groups which directly participate in the electron transfer process. However, in view of the preliminary nature of these results further speculation is premature.

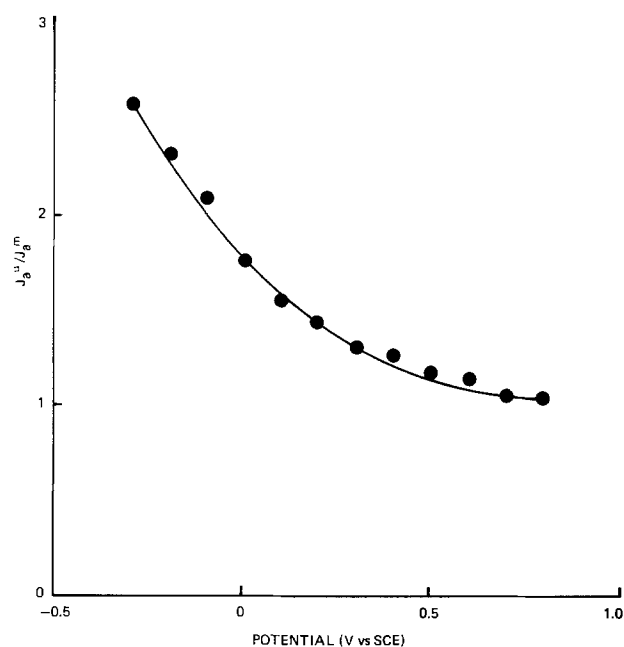


Fig. 9. The ratio of the light-induced anodic current of an unmodified TiO_2 to one which was modified by surface fluorination, as a function of potential. (Phosphate buffer, $\text{pH} = 6.6$.) The solid line is a theoretical fit to Eq. [31] with parameters given in the text.

Reproducibility

The results for the various surface treatments are qualitatively reproducible in the nature of the distribution of the density of states and the potential of these states. Procedures for reproducible coverage of the surface were not achieved and, even more disturbing, there was large irreproducibility in the standard deviation of the Gaussian distribution of the surface states. The standard deviation appears to increase with increasing coverage. The exact nature of this correlation is being further investigated.

Comment on the Origin of the Gaussian Distribution of the Density of Surface States

One possible interpretation of the energy distribution of the surface states is based on changes in the polarization of the solvent molecules near the derivatized surface, upon ionization of the functional groups at the surface. The broadening of surface energy states by this mechanism was described by Morrison (56), as the fluctuating energy level mechanism. According to this model, the probability that the energy levels of the species on the surface will have a value E less than the maximum probability is given by the Boltzmann factor

$$W(E) = (4\pi\lambda kT)^{-1/2} \exp[-(E_t - E)^2/4\lambda kT] \quad [33]$$

where E_t is the most probable energy and λ is the reorganization energy. Comparing this with Eq. [9] will yield

$$e\sigma = (2\lambda kT)^{1/2} \quad [34]$$

Based on this relation, the values of λ for the samples that were evaluated here are: λ hexyltromethoxysilane = 5.2 eV; λ Y5727 = 1.3 eV; and λ_{F_2} = 6.4 eV. These values of λ are larger than any comparable reorganization energies for ions in solution (57). This model also predicts that the standard deviation of the energy distribution will be independent of the coverage.

Based on these arguments we tend to rule out the fluctuating energy levels mechanism as the source of the surface-states line broadening, but we cannot yet offer an alternative model.

Conclusions

The results show no shift in flatband potential of chemically modified TiO₂ surfaces. Perhaps of greater importance is the observation that, in spite of the difficulties in obtaining reproducible surface coverage and the lack of understanding of the chemistry of the modified surface with the electrolyte, we could obtain qualitative and quantitative measurements of the effects of derivatization on the potential and charge distribution at the semiconductor-electrolyte interface and on the photoactivity of photoelectrochemical devices.

Of particular importance is the observation that introduction of a functional group which is removed from the surface can strongly influence the potential and potential distribution of the surface states. This should encourage utilizing organic chemistry in the design of functional groups on silane derivatives or other chemical backbones like phthalocyanines (58) which can be covalently attached with a stable chemical bond to the semiconductor surface in devices which are used either in solar energy conversion or in the semiconductor industry. We believe that, for the first time, methods have been demonstrated, that can tie together the chemistry and physics of surface states, in systems which are not under high vacuum. The methods could help understanding and controlling surface properties of semiconductor devices.

Acknowledgments

The author gratefully acknowledges Mr. R. J. Serino for his valuable technical expertise and dedication in carrying out the experimental part of this work, Dr.

P. H. Kasai and Mr. D. Mcleod, Jr. for the ESCA and Auger measurements, and Dr. M. L. Poutsma for suggesting the use of Y5727.

Manuscript submitted March 13, 1979; revised manuscript received Dec. 24, 1979.

Any discussion of this paper will appear in a Discussion Section to be published in the June 1981 JOURNAL. All discussions for the June 1981 Discussion Section should be submitted by Feb. 1, 1981.

Publication costs of this article were assisted by Union Carbide Corporation.

REFERENCES

- For general up to date review articles see:
 - A. J. Nozik, *Ann. Rev. Phys. Chem.*, **22**, 189 (1978).
 - L. A. Harris and R. H. Wilson, *Ann. Rev. Mater. Sci.*, **8**, 99 (1978).
 - H. P. Maruska and A. K. Ghosh, *Solar Energy*, **20**, 443 (1978).
 - W. A. Gerrard and L. M. Rouse, *J. Vac. Sci. Technol.*, **15**, 1155 (1978).
 - M. Tomkiewicz and H. Fay, *Appl. Phys.*, **18**, 1 (1979).
 - M. S. Wrighton, J. M. Bolts, A. B. Bocarsly, M. C. Palazzotto, and E. G. Walton, *J. Vac. Sci. Technol.*, **15**, 1429 (1978).
- M. A. Butler and D. S. Ginley, *This Journal*, **125**, 228 (1978).
- M. Tomkiewicz, *ibid.*, **126**, 1505 (1979).
- M. Tomkiewicz, *ibid.*, **126**, 2220 (1979).
- P. R. Moses and R. W. Murray, *J. Am. Chem. Soc.*, **98**, 7435 (1976).
- D. F. Untereker, J. C. Lennox, L. M. Wier, P. R. Moses, and R. W. Murray, *J. Electroanal. Chem. Interfacial Electrochem.*, **81**, 309 (1977).
- L. T. Mimmis, M. A. McKnight, and R. W. Murray, *Anal. Chim. Acta*, **89**, 355 (1977).
- D. G. Davis and R. W. Murray, *Anal. Chem.*, **49**, 194 (1977).
- P. R. Moses and R. W. Murray, *J. Electroanal. Chem. Interfacial Electrochem.*, **77**, 393 (1977).
- J. R. Lenhard and R. W. Murray, *ibid.*, **78**, 195 (1977).
- P. R. Moses, L. M. Wier, J. C. Lennox, H. O. Finklea, J. R. Lenhard, and R. W. Murray, *Anal. Chem.*, **50**, 576 (1978).
- J. R. Lenhard, R. R. Rocklin, H. Abruna, K. Willman, K. Kuo, R. Nowak, and R. W. Murray, *J. Am. Chem. Soc.*, **100**, 5213 (1978).
- B. E. Firth and L. L. Miller, *ibid.*, **98**, 8272 (1976).
- L. L. Miller and M. R. Van De Mark, *ibid.*, **100**, 639 (1978).
- J. R. Evans, T. Kuwana, M. T. Henne, and G. P. Royer, *J. Electroanal. Chem. Interfacial Electrochem.*, **80**, 409 (1977).
- D. Chi-Sing Tse and T. Kuwana, *Anal. Chem.*, **50**, 1315 (1978).
- A. P. Brown, C. Koval, and F. C. Anson, *J. Electroanal. Chem. Interfacial Electrochem.*, **72**, 379 (1976).
- A. P. Brown, and F. C. Anson, *Anal. Chem.*, **49**, 1589 (1977).
- C. A. Koval and F. C. Anson, *ibid.*, **50**, 223 (1978).
- N. Oyama, A. P. Brown, and F. C. Anson, *J. Electroanal. Chem. Interfacial Electrochem.*, **87**, 435 (1978).
- K. Itaya and A. J. Bard, *Anal. Chem.*, **50**, 1487 (1978).
- A. Diaz, *J. Am. Chem. Soc.*, **99**, 5838 (1977).
- A. F. Diaz and K. K. Kanazawa, *J. Electroanal. Chem. Interfacial Electrochem.*, **86**, 441 (1978).
- V. S. Srinivasan and W. J. Lamb, *Anal. Chem.*, **49**, 1639 (1977).
- A. N. Voulgaropoulos, R. J. Nowak, W. Kutner, and H. B. Mark, Jr., *J. Chem. Soc., Chem. Commun.*, 244 (1978).
- M. Sharp, *Electrochim. Acta*, **23**, 287 (1978).
- C. P. Andrieux and J. M. Saveant, *J. Electroanal. Chem. Interfacial Electrochem.*, **93**, 163 (1978).
- I. Haller, *J. Am. Chem. Soc.*, **100**, 8050 (1978).
- R. J. Burt, G. J. Leight, and C. J. Pickett, *J. Chem. Soc., Chem. Commun.*, 940 (1976).
- G. T. Cheek and R. F. Nelson, *Anal. Lett.*, **A11**,

- 393 (1978).
31. J. A. Cunningham, L. E. Sharif, and S. S. Baird, *Electrochem. Technol.*, **1**, 242 (1963).
 32. G. W. Cullen, J. A. Amick, and D. Gerlich, *This Journal*, **109**, 124 (1962).
 33. R. F. Lane, A. T. Hubbard, K. Fukunaga, and R. J. Blanchard, *Brain Res.*, **114**, 346 (1976).
 34. H. L. Landrum, R. T. Salmon, and F. M. Hawkridge, *J. Am. Chem. Soc.*, **99**, 3154 (1977).
 35. A. W. C. Lin, P. Yeh, A. M. Yacynch, and T. Kuwana, *J. Electroanal. Chem. Interfacial Electrochem.*, **84**, 411 (1977).
 36. R. F. Lane and A. T. Hubbard, *Anal. Chem.*, **48**, 1287 (1976).
 37. R. F. Lane and A. T. Hubbard, *J. Phys. Chem.*, **81**, 734 (1977).
 38. A. L. Allred, C. Bradley, and T. H. Newman, *J. Am. Chem. Soc.*, **100**, 5081 (1978).
 39. G. J. Leigh and C. J. Pickett, *J. Chem. Soc., Dalton Trans.*, 1797 (1977).
 40. T. Osa and M. Fujihira, *Nature (London)*, **264**, 349 (1976).
 41. M. Fujihira, T. Matsue, and T. Osa, *Chem. Lett.*, 875 (1976).
 42. M. Fujihira, N. Ohishi, and T. Osa; *Nature (London)*, **268**, 226 (1977).
 43. D. D. Hawn and N. R. Armstrong, *J. Phys. Chem.*, **82**, 1288 (1978).
 44. M. S. Wrighton, R. G. Austin, A. B. Bocarsly, J. M. Bolts, O. Hoas, K. D. Legg, L. Nadjo, and M. C. Palazzotto, *J. Am. Chem. Soc.*, **100**, 1602 (1978).
 45. J. M. Bolts and M. S. Wrighton, *ibid.*, **100**, 5257 (1978).
 46. M. S. Wrighton, M. C. Palazzotto, A. B. Bocarsly, J. M. Bolts, A. B. Fischer, and L. Nadjo, *ibid.*, **100**, 7265 (1978).
 47. S. M. Ahmed, in "Oxides and Oxide Films," J. W. Diggle, Editor, Chap. 4, Marcel Dekker, New York (1972).
 48. M. Tomkiewicz, in "Semiconductor Liquid Junction Solar Cells," A. Heller, Editor, p. 92, The Electrochemical Society Softbound Proceedings Series, Princeton, N.J. (1977).
 49. A. W. Hawkins, M. M. O'hara, F. P. Gortsema, and E. Hedaya, U.S. Pat. 4,081,574 (1978).
 50. J. H. Scofield, Lawrence Radiation Laboratory Report No. UCRL-51326 (1974).
 51. a. W. Schottky, *Z. Phys.* **113**, 367 (1939), **118**, 539 (1942). b. N. F. Mott, *Proc. Roy. Soc. London Ser. A*, **171**, 27 (1939).
 52. H. Gerischer, in "Physical Chemistry An Advanced Treatise," Vol. IXA, H. Eyring, Editor, Chap. 5, Academic Press, New York (1970).
 53. A. L. Vanden Berghe, F. Cardon, and W. P. Gomes, *Surf. Sci.*, **39**, 368 (1973).
 54. J. P. Hoare, "The Electrochemistry of Oxygen," Interscience Publishers, New York (1968).
 55. B. E. Conway, "Theory and Principles of Electrode Processes," Chap. 6, Ronald Press Co., New York (1965).
 56. S. R. Morrison, "The Chemical Physics of Surfaces," Chap. 2, Plenum Press, New York (1977).
 57. J. M. Hale, in "Reaction of Molecules at Electrodes," N. S. Hash, Editor, Wiley Interscience, London (1971).
 58. K. G. McGregor, J. W. Otvos, and M. Calvin, 2nd International Conference on the Photochemical Conversion and Storage of Solar Energy, Cambridge, England, Aug. 10-12, 1978.

Polarography of Sn(IV) and Ge(IV) Chloride in Acetonitrile

L. K. Young, M. E. Coles, J. W. Meux, S. D. Sorey, R. J. Williams, and J. W. Rogers

Department of Chemistry, Midwestern State University, Wichita Falls, Texas 76308

ABSTRACT

Spectrophotometric and polarographic data demonstrate that the normal Sn(IV) and Ge(IV) chlorides are nonelectrolytes in the aprotic solvent acetonitrile. Both form the corresponding hexachloro species in the presence of chloride ion. Sn(IV) chloride is quantitatively converted to the hexachlorostannate ion while Ge(IV) chloride behaves as a weaker Lewis acid and exists in an equilibrium with the hexochloro ion in the presence of excess chloride. Each of the normal metal halides acts as a Lewis acceptor toward a test pyridine-N-oxide ligand in acetonitrile. Sn(IV) and Ge(IV) chloride are polarographically reduced in a $4e^-$ step at which the production of the corresponding hexachloro ion, reducible only at higher potentials, controls the plateau current.

Interest in the coordination chemistry of the group IV A metals has increased in recent years. However, this area remains one of the least characterized and understood segments of inorganic chemistry. The metals, germanium, tin, and lead may act as Lewis acids, much like transition metal ions. Examples of this behavior include the formation of halide adducts of tetravalent germanium (1, 2) and tetravalent and divalent tin (3, 4).

Polarographic and spectrophotometric data presented previously show that the two cathodic current plateaus observed in the reduction of Sn(II) chloride in acetonitrile (ACN) solvent containing *tetra*-N-propylammonium perchlorate (TPAP) are attributable to the $2e^-$ reduction of SnCl_2 at the lower potential wave

and to the $2e^-$ reduction of the trichlorostannate ion (SnCl_3^-) at the higher potential (5, 6). The plateau current of the lower potential wave is controlled by the formation of the very stable SnCl_3^- species which is only reducible at potentials of the second wave. Stannous chloride was found also to act as a Lewis acid toward various pyridine-N-oxide ligands; forming 1:1 adducts in ACN (5, 7, 8).

Even though the polarographic reduction of SnCl_2 occurs via irreversible steps, the importance of these data in determining its electrolyte and ligand acceptor properties in low basicity media has prompted similar studies of other chlorides of the group IV metals; specifically Sn and Ge in the +4 oxidation state. A portion of the work presented herein parallels that reported by Thomas and Kolthoff in their survey of the polarographic behavior of the group IV metal halides

Key words: polarography, hexachlorostannate ion, aprotic solvent.

in ACN (9). This work has been expanded with spectrophotometric and additional polarographic investigations. The results are reported herein.

Experimental

Apparatus.—The instrumentation and polarographic cells were of conventional design and have been described elsewhere (4).

Chemicals.—Spectroquality acetonitrile containing less than 0.03% water (Aldrich), polarographic-grade tetramethylammonium chloride (Southwestern Analytical Chemicals), and reagent-grade anhydrous Sn(IV) and Ge(IV) chloride were used. The supporting electrolyte, tetrapropyl-ammonium perchlorate (Eastman Organic Chemicals) was recrystallized from acetonitrile-water solution before use.

All polarographic and spectrophotometric solutions were prepared and transferred under a nitrogen atmosphere.

Results

Polarography.—Tin(IV) chloride, reduced in TPAP supporting electrolyte in ACN, exhibits a polarogram similar in appearance to that of SnCl₂ [Fig. 1(a)] (5). The total current of the two cathodic¹ plateaus appearing at +0.3V and -1.06V vs. saturated calomel (SCE) varies in proportion to the square root of the corrected mercury head height. The individual plateau currents deviate slightly from this behavior and are irreversible.² The current maximum associated with the positive potential plateau has been discussed by Thomas and Kolthoff (9). The diffusion current constants (I_d) measured at 25°C and 1.0 mM concentration are 3.90 and 9.25, respectively, for the positive and negative reduction plateaus.³

The anodic current [not pictured in Fig. 1(a)], apparently a double wave with an ill-defined point of separation, appears at +0.5V vs. SCE. The plateau current deviates from purely diffusion-controlled behavior.

Addition of controlled quantities of tetramethylammonium chloride (TMAC) to the test solution as a source of free (noncomplexed) chloride increases the current of the higher potential wave systematically at the expense of the lower (Fig. 1, Table I). At a ratio of 2/1 TMAC to Sn(IV) chloride a residue of the lower potential plateau remains and a weak anodic current attributable to the oxidation of free chloride is noted. The absence of detectable quantities of free chloride in Sn(IV) chloride or Sn(IV) chloride-chloride solutions of a lower ratio is noted and is a significant observation (5). The $E_{1/2}$ of the lower potential wave is shifted negatively vs. SCE and the higher potential wave positively upon addition of TMAC. The total cathodic current remains approximately constant at all TMAC concentrations (Table I).

Ge(IV) chloride also exhibits two cathodic and one anodic polarographic current plateau in the ACN-TPAP medium [Fig. 2(a)]. Similar to Sn(II) and Sn(IV) chloride behavior, the total cathodic current appears to be diffusion controlled and both cathodic processes are irreversible in nature. The higher potential plateau is extremely broad and the establishment of a reliable $E_{1/2}$ value is consequently difficult. At 1.0 mM concentration of Ge(IV) chloride the I_d of the low and high potential plateaus are 4.80 and 10.02, respectively.

Addition of TMAC to the test solution of Ge(IV) chloride brought about variations in the polarograms qualitatively similar to those noted in the cases of Sn(II) and Sn(IV) chloride. An oxidation current attributable to free chloride is not found in polarograms of 1 mM Ge(IV) chloride [Fig. 2(a)]. Addition of TMAC in a ratio of 0.5/1 TMAC to Ge(IV) chloride

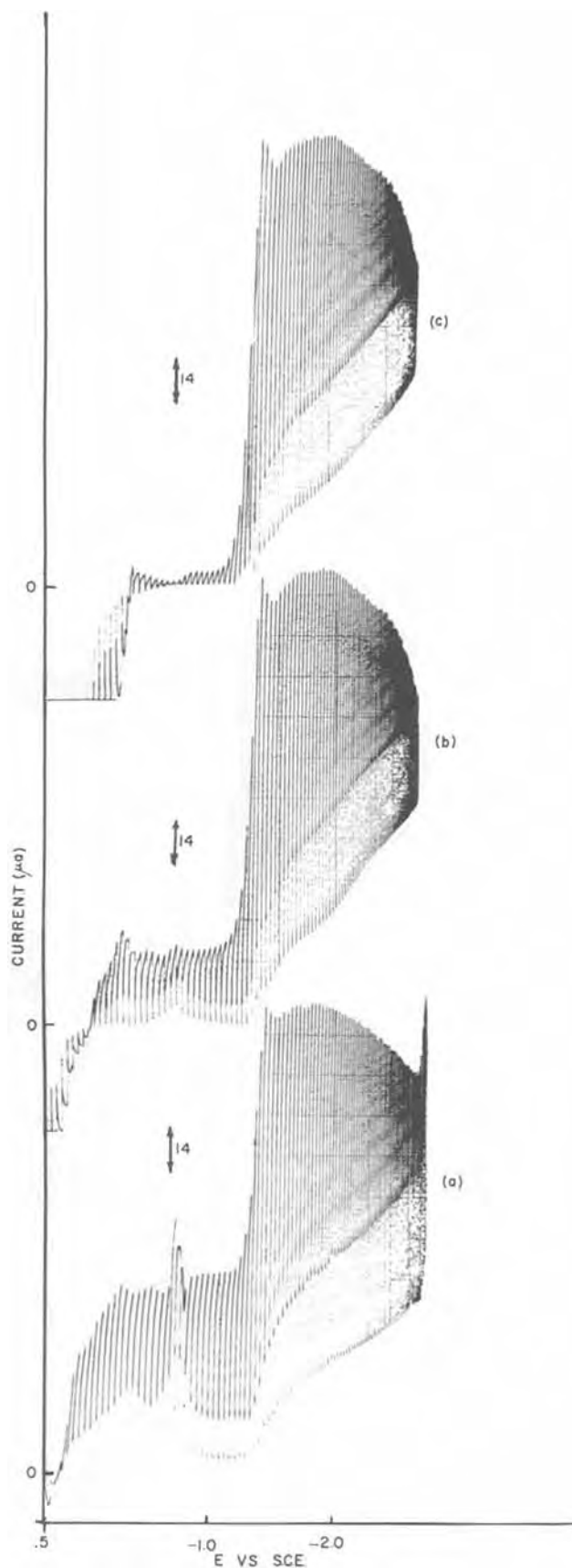


Fig. 1. Polarograms of ACN-TPAP solutions containing (a) 1 mM Sn(IV) chloride, (b) 1 mM Sn(IV) chloride plus 1 mM TMAC, and (c) 1 mM Sn(IV) chloride plus 3 mM TMAC.

diminishes the plateau current at the lower potential cathodic wave (Table I) without affecting the total cathodic current of both plateaus. The addition of TMAC concentrations higher than 2.0 mM to the 1 mM

¹ Cathodic is used throughout to signify a current response consistent with a reduction process.

² Slopes of $\log(i_d - i)/i$ vs. plots are 497 mV and 114 mV, respectively.

³ DME characteristics of open circuit and 50 cm Hg head: $m = 0.993$ mg/sec, $t = 6.42$ sec.

Table I. Polarographic data for reduction of tin(IV) and germanium(IV) chloride in acetonitrile-tetramethylammonium chloride mixtures^a

Tin(IV) Chloride					
[Cl ⁻] ^b (mM)	Cathodic wave		Cathodic wave		Total cathodic current <i>id</i> (μ a)
	<i>E</i> _{1/2} (V)	<i>id</i> (μ a)	<i>E</i> _{1/2} (V)	<i>id</i> (μ a)	
0.00	+0.3	8.77	-1.06	14.96	23.73
0.50	+0.2	8.00	-1.05	16.50	24.50
1.00	0.0	5.70	-1.04	18.79	24.45
2.00 ^c	-0.6	3.70	-1.03	21.25	24.95
3.00	—	0.00	-1.02	24.75	24.75
10.00	—	0.00	-1.00 ^d	24.75	24.75

Germanium(IV) Chloride					
[Cl ⁻] ^b (mM)	Cathodic wave		Cathodic wave		Total cathodic current <i>id</i> (μ a)
	<i>E</i> _{1/2} (V)	<i>id</i> (μ a)	<i>E</i> _{1/2} (V)	<i>id</i> (μ a)	
0.00	-0.24	6.96	— ^e	8.99	15.95
0.50 ^c	-0.30	4.70	— ^e	11.25	15.95
1.00	-0.32	4.50	— ^e	10.60	15.10
2.00	-0.36	3.00	-1.50	12.00	15.00
3.00	-0.38	3.00	-1.50	12.00	15.00
10.00	-0.40	3.00	-1.50	12.00	15.00

^a Tin(IV) and germanium(IV) chloride 1 mM in acetonitrile containing 0.1M TPAP.

^b *tetra-N*-methylammonium perchlorate supporting electrolyte.

^c Oxidation of chloride first detectable at this concentration.

^d *E*_{1/2} corresponds to *tetra-N*-methylammonium hexachlorostannate in ACN containing 0.1M TPAP.

^e Very broad wave.

Ge(IV) chloride solution did not significantly affect the current ratio of the two cathodic plateaus (Table I).

The role of Sn(IV) and Ge(IV) chloride as Lewis acids toward organic ligands in ACN solvent was investigated by adding 4-methoxypyridine-*N*-oxide (MPNO) to the polarographic test solution containing

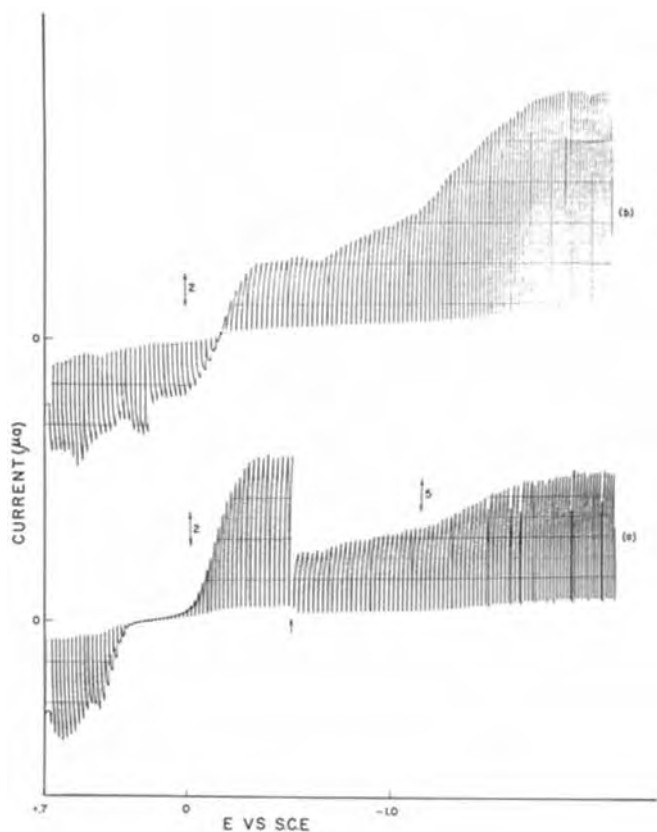


Fig. 2. Polarograms of ACN-TPAP solutions containing (a) 1 mM Ge(IV) chloride and (b) 1 mM Ge(IV) chloride plus 2 mM TMAC.

the metal species. Figure 3 summarizes the effects of increasing concentrations of MPNO on polarograms of Sn(IV) chloride. An irreversible plateau appearing at -0.83 V is attributable to the reduction of an Sn(IV) chloride-MPNO adduct. At concentrations of ligand in twofold excess of Sn(IV) chloride or greater the lower potential plateau is completely replaced by this current. The higher potential plateau is unaltered and the low intensity reduction plateau appearing at -2.08 V in Fig. 3(d) corresponds to the reduction of uncomplexed MPNO. The polarographic behavior of Ge(IV) chloride in the presence of MPNO parallels that of Sn(IV) chloride.

Even though standard quantitative methods cannot be applied to an analysis of the irreversible current plateau, the concentration dependence of the polarographic wave attributed to the reduction of the metal(IV) chloride-MPNO adduct and the low potential reduction wave of the metal(IV) chloride suggests the formation of a neutral complex having the formula $MCl_4 \cdot 2MPNO$.

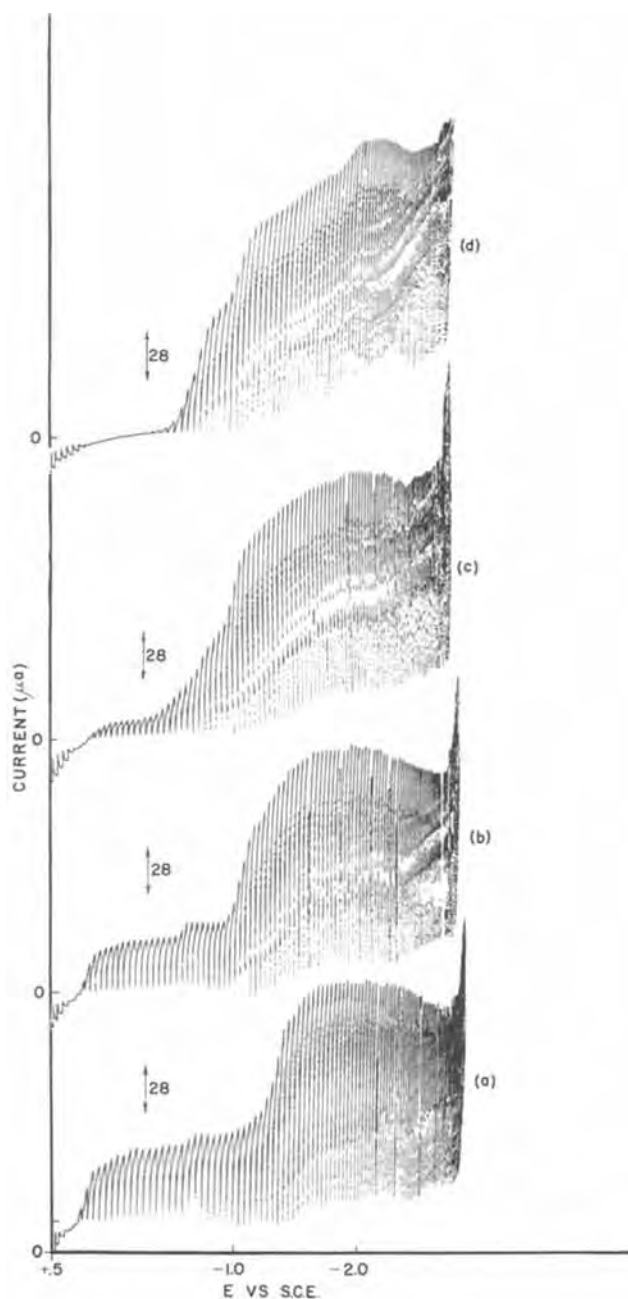


Fig. 3. Polarograms of ACN-TPAP solutions containing 1 mM Sn(IV) chloride plus (a) 0.3 mM MPNO, (b) 0.5 mM MPNO, (c) 1.0 mM MPNO, and (d) 2.0 mM MPNO.

Spectral observations: u.v. spectra of Sn(IV) chloride and Sn(IV) chloride-TMAC mixtures were recorded to establish data relatable to the electrolyte behavior of Sn(IV) chloride in ACN. The spectrum of a 0.8 mM solution of TMAC exhibits one absorption band centered at 198 nm [Fig. 4, curve (a)]. A 0.4 mM solution of Sn(IV) chloride in ACN consists of only one absorption band at 200.4 nm [Fig. 4, curve (b)]. Solutions containing TMAC and Sn(IV) chloride in varying ratios, but at a constant total concentration exhibit one absorption peak which shifts to longer wavelengths with increasing TMAC to Sn(IV) chloride ratios (Fig. 4). A standard continuous variation plot of these data is consistent with the coordination of two chloride ions per metal ion. These data and the absence of a polarographic wave and a u.v. absorption band attributable to chloride ion in Sn(IV) chloride solutions are consistent with the formation of the hexachlorostannate ion (SnCl_6^{-2}) via the complexation of free chloride with the neutral Sn(IV) chloride complex. Neither Ge(IV) chloride nor the products formed upon the addition of TMAC exhibits an absorption maximum detectable in ACN solvent.

The ligand MPNO exhibits absorption maxima at 206.3 and 281.0 nm in ACN solvent, Fig. 5, curve (b). The u.v. spectra of ACN solutions containing Sn(IV) chloride and MPNO exhibit an additional absorption maximum. The maximum appears at 270.4 nm when spectra of solutions containing a 2/1 ratio of ligand to metal are recorded, Fig. 5, curve (c). Continuous variation plots of u.v. data recorded at a total constant concentration (metal chloride plus ligand) of 1.2 mM reveal the formation of an adduct composed of two ligands per metal(IV) chloride.

Similar studies detail the effects of Ge(IV) chloride on the spectra of MPNO in ACN solvent. An absorp-

tion maximum⁴ appearing between the bands associated with pure MPNO may be reasonably attributed to a Ge(IV) chloride-MPNO adduct. Continuous variation studies using the absorbance of this band do not conclusively reveal the presence of a single stable complex.

Discussion

The polarographic and spectrophotometric data show that Sn(IV) and Ge(IV) chloride are nonelectrolytes in ACN solvent. Previous studies have shown that Sn(II) chloride behaves in a similar manner (5). Each of these neutral complexes acts as a ligand acceptor. Data presented herein demonstrate that both metal(IV) chlorides form the hexachloride anion in the presence of free chloride. Tin(IV) chloride forms 2/1 complexes with pyridine-N-oxides in ACN solvent.

Kolthoff considered the first cathodic wave of both Sn(IV) and Ge(IV) to be two-electron reductions since the values of the diffusion current constants of the waves are in the range reported for two-electron reductions in ACN (10). It was noted that the somewhat "suppressed" current of the first reduction wave is analogous to the effect observed in acidic aqueous chloride solutions of Sn(IV) (11). Polarographic and spectrophotometric data presented herein and the similarity of the electrolyte properties and the polarographic behavior of Sn(IV) chloride and Sn(II) chloride in ACN (5, 6) suggest a different reduction mechanism. The polarographic and spectrophotometric behavior of Sn(IV) and Ge(IV) chloride in the presence of added chloride ion demonstrates conclusively that the most negative polarographic wave corresponds to the reduction of the hexachlorostannate ion of each. The direct conversion of the metal(IV) chloride into the hexachloro species by added chloride ion is confirmed by the spectrophotometric and polarographic data. These observations show that the low potential cathodic wave results from the reduction of the neutral tetrachloro species. It seems unlikely that the tetrachloro species would be reduced via a two-electron step and the hexachloro via a single four-electron step. Additionally, the behavior of Sn(II)

⁴ 239.6 nm from solutions containing a 2/1 ratio of ligand to metal.

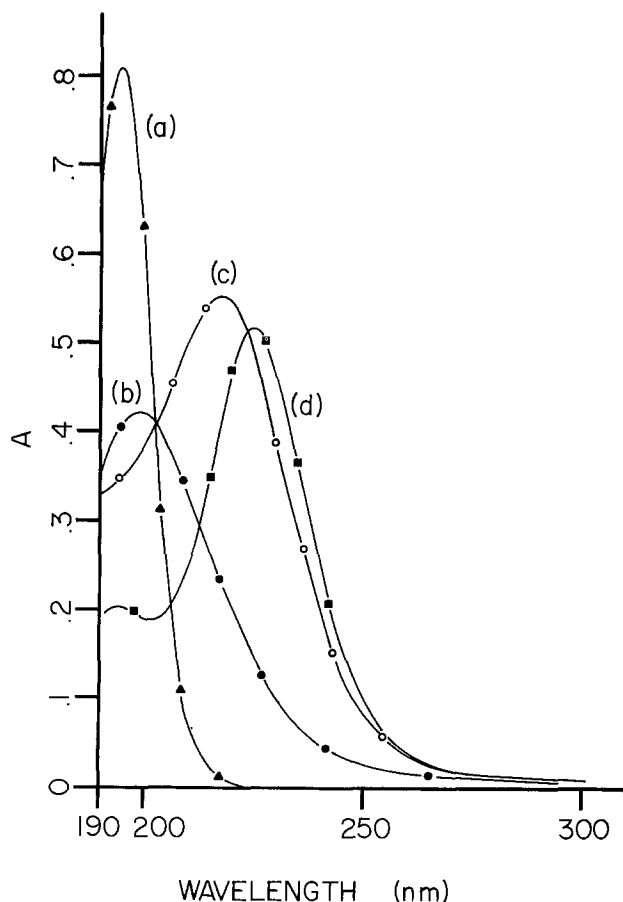


Fig. 4. U.V. spectra of ACN solutions containing: curve (a) 0.8 mM TMAC, curve (b) 0.4 mM Sn(IV) chloride, curve (c) 0.6 mM Sn(IV) chloride plus 0.6 mM TMAC, curve (d) 0.4 mM Sn(IV) chloride plus 0.8 mM TMAC.

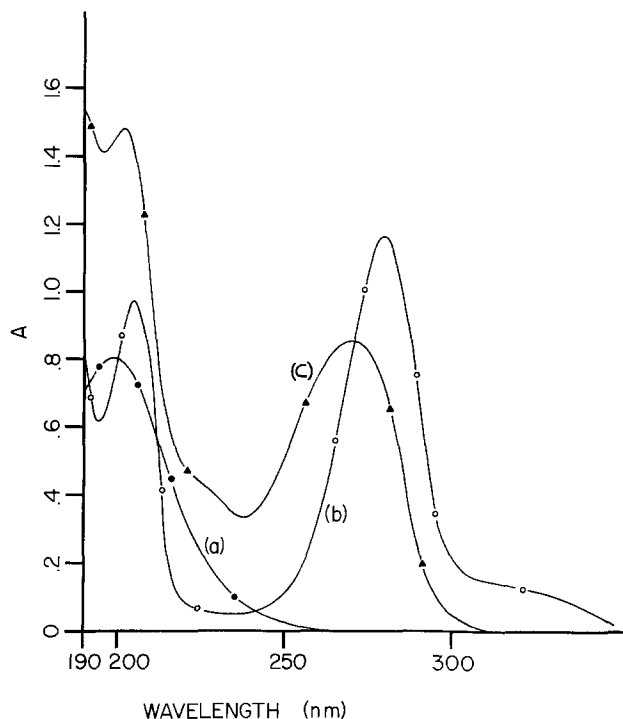
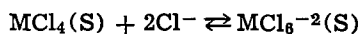
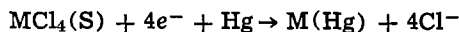


Fig. 5. U.V. spectra of ACB solutions containing: curve (a) 0.4 mM Sn(IV) chloride, curve (b) 0.8 mM MPNO, curve (c) 0.4 mM Sn(IV) chloride plus 0.8 mM MPNO.

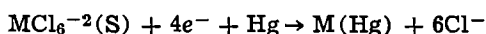
(5, 6) chloride suggest that a two-electron reduction of the tetrachloro species would generate the trichloro-metal(II) anion at the electrode surfaces. No evidence of such species is detected in the polarograms of Sn(IV) and Ge(IV) chloride.

The behavior of the higher potential plateau is exactly analogous to the corresponding wave observed in polarograms of Sn(II) chloride in ACN at which formation of a higher chloride-coordinated species, reducible only at more negative potentials, controls the wave current of the lower potential plateau (5,6). This similarity and data presented herein suggest that the polarographic and complexation behavior of both Sn(IV) and Ge(IV) chloride may be best explained with the following reduction mechanism

First polarographic step

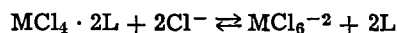
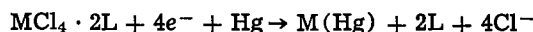


Second polarographic step



In the presence of an organic ligand, the polarographic reduction process may be summarized

First polarographic step



Second polarographic step



Acknowledgments

The authors gratefully acknowledge the financial support of the Robert A. Welch Foundation [R. J. Williams (AO-557), J. W. Rogers (AO-337)].

Manuscript submitted Aug. 27, 1979; revised manuscript received Jan. 21, 1980.

Any discussion of this paper will appear in a Discussion Section to be published in the June 1981 JOURNAL. All discussions for the June 1981 Discussion Section should be submitted by Feb. 1, 1981.

Publication costs of this article were assisted by the Midwestern State University.

REFERENCES

1. R. C. Aggarwal and M. Onyszchuk, *J. Inorg. Nucl. Chem.*, **31**, 3351 (1969).
2. E. N. Belousova, M. M. Bobrovskaya, and L. A. Dashuk, *J. Gen. Chem. (USSR)*, **38**, 2141 (1968).
3. J. D. Donaldson, *Prog. Inorg. Chem.*, **8**, 287 (1967).
4. M. Webster and H. E. Blayden, *J. Chem. Soc.*, (A), 2443, (1969).
5. A. R. Brajer, T. E. Farley, J. W. Kauffman, L. K. Young, R. J. Williams, and J. W. Rogers, *Anal. Chim. Acta*, **91**, 165 (1977).
6. D. Pool, L. K. Young, R. J. Williams, and J. W. Rogers, *ibid.*, **92**, 361 (1977).
7. J. W. Kauffman, D. H. Moor, and R. J. Williams, *J. Inorg. Nucl. Chem.*, **39**, 1165 (1977).
8. P. T. Scott, J. W. Kauffman, J. W. Rogers, and R. J. Williams, *ibid.*, **39**, 2253 (1977).
9. F. G. Thomas and I. M. Kolthoff, *J. Electroanal. Chem. Interfacial Electrochem.*, **31**, 423 (1971).
10. I. M. Kolthoff and J. F. Coetzee, *J. Am. Chem. Soc.*, **79**, 870 (1957).
11. I. M. Kolthoff and J. J. Lingane, "Polarography," Vol. 2, Chapt. XXIII and XXXI, Interscience, New York (1952).

Technical Note



A Preliminary Investigation for an Al/AlCl₃-NaCl/FeS₂ Secondary Cell

N. Koura*

Faculty of Science and Technology, Tokyo University of Science, Yamazaki, Noda, Chiba 278, Japan

A secondary or rechargeable cell is an attractive energy storage device as well as an efficient electrical power source. Wide markets have already been established for several secondary cells, e.g., lead-acid, nickel-cadmium, and nickel-iron. In recent years, according to the rapid growth rate in electric power demand, as well as the projected shortage and rising cost of petroleum, it has become very important to actively consider potential alternative energy sources. Secondary cells, among many potentially promising energy storage devices, are particularly attractive because their technical and economical feasibility appear to be within reach. Of the advanced secondary cells being developed in the world for application to utility load-leveling and electric-vehicle propulsion, major efforts are presently concentrated

on the following five systems: Li-Al/LiCl-KCl/metal sulfide, Na/ β -Al₂O₃/S, Zn/aq.ZnCl₂/Cl₂, Zn/aq.KOH/ β -NiOOH, and so-called lead-acid. In the past several years, significant progress has been made in developing each of these systems, especially Li-Al/FeS₂ or FeS, lead-acid, and Na/S for both load-leveling applications and electric vehicles. However, these systems still possess many technical and economic problems (1).

The objective of this investigation is to develop an Al/AlCl₃-NaCl/FeS₂ cell as a potential candidate for the advanced secondary cells. Aluminum has a considerably negative potential, -2.08V vs. Cl₂/Cl⁻ at 450°C (2), in a molten salts system and a high theoretical capacity, 2.98 A-hr/g. The AlCl₃-NaCl system has a relatively low melting point (the lowest: 107.2°C (3)) and is stable as molten salt not in the presence of air or moisture. Therefore, material corrosion problems are not so severe because of the low operating temperature of the cell. FeS₂ is highly promising as

* Electrochemical Society Active Member.

Key words: Al/FeS₂ cell, high temperature cell, molten salt, secondary cell.

the active material for the positive electrode of a molten salts cell as investigated extensively with the Li-Al/LiCl-KCl/FeS₂ cell (4). Furthermore, FeS₂ as well as Al, AlCl₃, and NaCl are all inexpensive. In addition to these, an investigation for a secondary molten salt cell having an Al negative electrode is scarcely seen except Al/Cl₂ (5) and Al/S or oxidation states of S (6-9) systems.

AlCl₃ was reduced to fine powder in a glove box under an Ar atmosphere, and heated at 180°C for 10 hr *in vacuo*, then mixed in the glove box with NaCl dried at 180°C for 24 hr. The mixture was placed along with Al wire in a Pyrex tube ($\phi 60 \times 200$ mm) and heated at 250°C for 30 hr under a dry N₂ atmosphere in order to remove small amounts of impurities, i.e., Fe²⁺, Pb²⁺, and H₂O. FeS₂ powder of 325 mesh, which has been kindly offered by C. E. Minerals (Pennsylvania) was purified 20 times by a sink-float separation with *s-tetra* bromoethane and the purity was checked by x-ray analysis. An Mo mesh current collector was surrounded with the FeS₂ powder (theoretical capacity: 3 A-hr),¹ covered with a SiO₂ cloth and then Ni mesh, as shown in Fig. 1. The FeS₂ electrode was degassed for 15 min and immersed for 15 min at 200°C in the molten salts bath *in vacuo* to wet both the FeS₂ powder and the current collector completely with the molten salts. The cell, as shown in Fig. 1, which had an Al negative electrode (a disk of 3 mm thick and 50 mm wide, 99.99% purity, theoretical capacity: 15 A-hr)² an AlCl₃ [54.5 mole percent (m/o)]-NaCl (45.5 m/o) molten salts electrolyte, an SiO₂ cloth separator, and an FeS₂ positive electrode (area: 7 cm²), was placed in the thermostated furnace well located in the floor of the Ar atmosphere glove box. Cell performance was observed during repeated cycles of discharge (cutoff: 1.60 V)³-pause (30 min)-charge (cutoff: 0.35V)³-pause (30 min).

Discharge curves at various temperatures are presented in Fig. 2, where the cell voltage (*IR*-free, and so on) is shown as a function of discharge capacity. The cycle was repeated around 20 times. After several cycles the cell performance was steady, therefore, the data of each 10th cycle are presented. Although charge curves are not shown, the coulombic efficiencies were nearly 100%. The *IR* voltage during charge and discharge was 15-40 mV ($R = 0.2-0.6\Omega$).⁴ The cell was first operated at 180°C. The discharge curve showed two plateaus, i.e., a high plateau at about 0.9V and a low plateau (not shown in Fig. 2) at about 0.6V. The operating temperature was then increased to make the high plateau capacity spread. At 300°C it became 0.7 A-hr (including the higher

¹ This capacity corresponds with the change from FeS₂ to FeS as mentioned later.

² The excess Al capacity allows the cell performance to be limited by the positive electrode.

³ *IR* included value.

⁴ The relatively high resistance should be reduced markedly by appropriate modifications of the cell design.

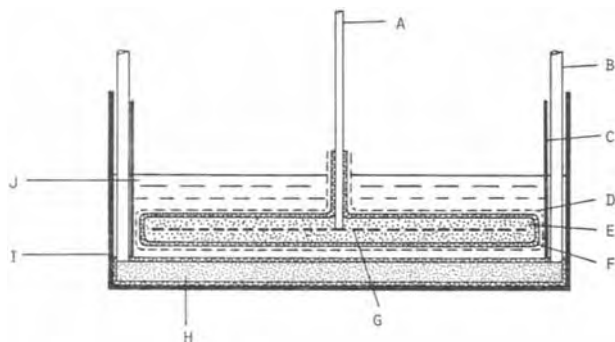


Fig. 1. Schematic diagram of experimental cell. A, positive lead (Mo); B, negative lead (Al); C, Pyrex tube; D, Ni mesh basket; E, FeS₂ electrode; F, SiO₂ cloth; G, Mo mesh current collector; H, Al electrode; I, stainless steel beaker; J, electrolyte (AlCl₃-NaCl).

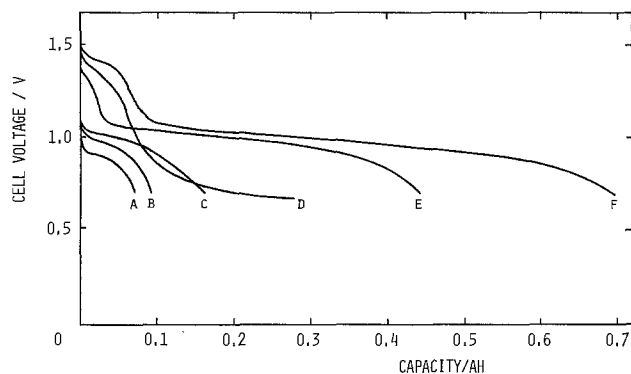


Fig. 2. Discharge curves (*IR*-free) at 10 mA/cm² and various temperatures. Lower cutoff voltage is 0.70V. Curve A, 180°C; curve B, 210°C; curve C, 240°C; curve D, 250°C and 15 mm ϕ Al rod electrode; curve E, 270°C; curve F, 300°C.

plateau capacity), i.e., about 23% of theoretical capacity, where it was assumed that FeS₂ was reduced to FeS. On the other hand, a higher plateau clearly appeared at temperatures above 270°C. The increase in temperature affects not only the reaction rate but also the diffusion rate of Al³⁺ ions in the cell. When the diffusion is slow, it is believed that a passivating salt layer forms at the Al electrode due to enrichment in AlCl₃ upon discharging and that an insoluble passivating salt layer forms due to a decrease in AlCl₃ upon charging (5). It might be the reason why the results in Fig. 2 showed significant effect of temperature on the cell performance. Moreover, when a spiraled Al rod ($\phi 10$ mm, 99.99% purity, 35 cm² area) was used as the negative electrode, the higher plateau capacity increased as seen in Fig. 2 curve D. Improvements of the Al electrode are under way.

Hereafter, data at 240°C will be discussed as a typical example.

Discharge curves at various current densities are shown in Fig. 3. The more the current density increased, the greater was the high plateau capacity. However, the current density could not be increased more than 30 mA/cm² due to a problem involving the Al electrode.

Sn²⁺, Pb²⁺, or Fe²⁺ was added into the molten salts electrolyte in order to improve the quality of Al deposition (10-13). As shown in Fig. 4, SnCl₂ additive showed significant effect on the cell performance. In the case of 1.0 m/o addition both high and low plateau capacities increased about 60%. Effects of the additive on reactions in the FeS₂ electrode are not clear now.

Additives to the FeS₂ electrode (14) were also investigated. It is known from Fig. 5 that an addition of CoS, CuS, or graphite was effective. In the case of CoS the high plateau capacity lengthened about twice.

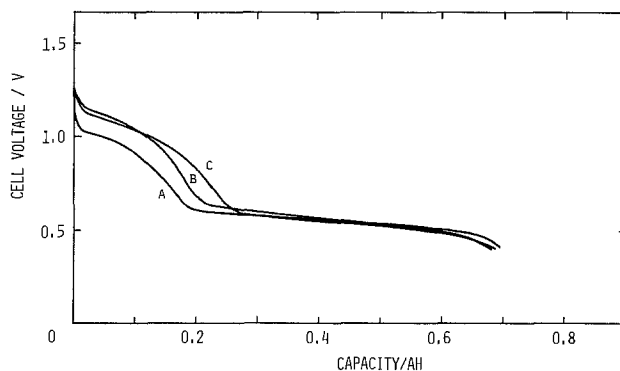


Fig. 3. Discharge curves (*IR*-free) at 240°C and various current densities. Lower cutoff voltage is 0.40V. Curve A, 10 mA/cm²; curve B, 20 mA/cm²; curve C, 30 mA/cm².

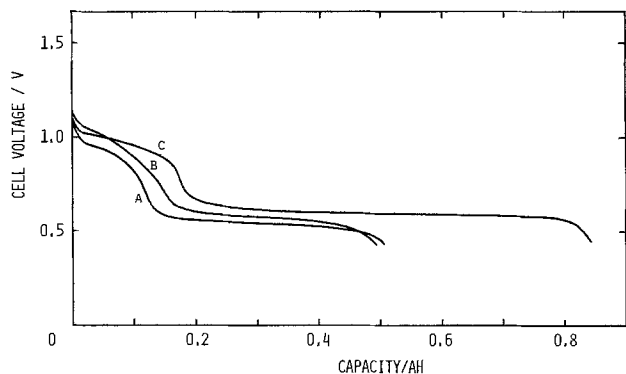


Fig. 4. Discharge curves (IR-free) at 240°C and 7 mA/cm² with SnCl₂ additive. Curve A, none; curve B, 0.4 m/o; curve C, 1.0 m/o.

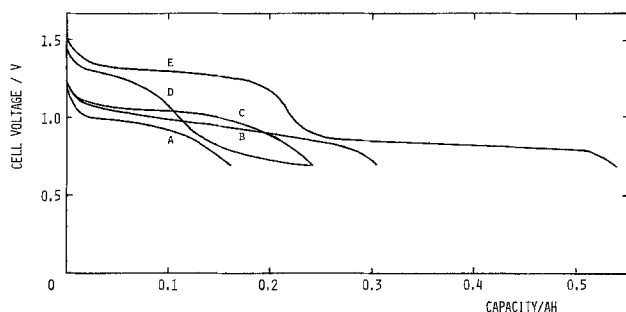
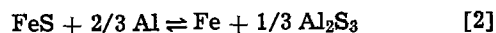
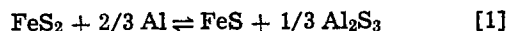


Fig. 5. Discharge curves (IR-free) at 10 mA/cm² and various additives. Lower cutoff voltage is 0.70V. The theoretical capacity value excludes that of additive. Curve A, none, 3.13 A-hr; curve B, 15 m/o CoS, 2.76 A-hr; curve C, 15 m/o CuS, 2.74 A-hr; curve D, 10 w/o graphite, 2.81 A-hr; curve E, 30 w/o graphite, 2.19 A-hr.

Moreover, the graphite additive strongly improved the cell performance at relatively low temperature as like 240°C. On the 30 weight percent (w/o) addition, the higher plateau capacity reached about 10% of theoretical, and the high plateau capacity included the higher capacity also reached about 25%.

On the other hand, three plateaus appeared in the discharge curve as known from above results. A stable compound of Al and S is only Al₂S₃ (15). Cell reactions concerned with FeS₂ and Al₂S₃ are considered to be primarily those shown below



Namely, two plateaus should appear in the discharge (also charge) curve. Although there are few thermodynamic data for Al₂S₃ and these are somewhat indefinite, a theoretical electromotive force for Eq. [1] and [2] can be estimated according to the data of Elliot and Gleiser (16)

$$E_{\text{calc}} [1] = 1.18\text{V (at } 500^\circ\text{K)}$$

$$E_{\text{calc}} [2] = 0.99\text{V (at } 500^\circ\text{K)}$$

In addition to above facts, FeS was detected (but not Al₂S₃) from the FeS₂ electrode discharged up to 0.65V (IR included), while Al₂S₃ was detected up to 0.20V (IR included) by x-ray analysis. Moreover, open-circuit voltage of the cell charged up to 1.60V (IR included) increased strongly with temperature as seen in Fig. 2; however, that estimated from thermodynamic data decreases with temperature. These contradictions as stated above cannot be clearly explained. It should be considered that some complex compounds are formed in the positive electrode by the interaction of Al₂S₃ with iron-sulfur compounds such as in the Li-Al/FeS₂ cell (17).

Acknowledgment

The author would like to acknowledge Dr. H. Shimotake at Argonne National Laboratory for valuable suggestions. The author would also like to thank the active help of Mr. M. Sakka, Mr. T. Inoue, and Miss S. Takahashi in carrying out the experiments.

Manuscript submitted Aug. 15, 1979; revised manuscript received Feb. 20, 1980.

Any discussion of this paper will appear in a Discussion Section to be published in the June 1981 JOURNAL. All discussions for the June 1981 Discussion Section should be submitted by Feb. 1, 1981.

Publication costs of this article were assisted by Tokyo University of Science.

REFERENCES

1. N. P. Yao and I. Ohno, *Denki Kagaku*, **43**, 416 (1975).
2. J. A. Plambeck, *J. Chem. Eng. Data*, **12**, 77 (1967).
3. E. M. Levin, "Phase Diagrams for Ceramists," The American Ceramic Soc., Inc. (1964).
4. For example; D. R. Vissers, Z. Tomczek, and R. K. Steunenberg, *This Journal*, **121**, 665 (1974).
5. J. Giner and G. L. Holleck, *NASA CR-1541* (1970).
6. L. Redey, I. Porubszky, and I. Molnar, *Power Sources 5: Res. Dev. Non-Mech. Electr. Power Sources*, Proc. Int. Symp., 9th, 559 (1974).
7. G. Mamantov, R. Marassi, and J. G. Chambers, U.S. Pat. 3,966,491 (1976), etc.
8. J. Greenberg, U.S. Pat. 3,635,765 (1972).
9. J. Werth, D. A. Crouch, and J. C. Sklarчук, U.S. Pat. 3,960,597 (1976), etc.
10. J. Czochralski and J. Mikolajczyk, *Wiad. Inst. Metalurg. Metaloz.*, **5**, 58 (1938).
11. Y. K. Delimarskii, V. F. Makogon, and V. V. Kuz'movich, *Zashch. Met.*, **4**, 743 (1968).
12. Y. K. Delimarskii and V. F. Makogon, *ibid.*, **5**, 128 (1969).
13. K. Matiasovsky and M. Paucirova, *Povrchove Upravy*, **13**, 10 (1973).
14. W. J. Walsh, C. C. McPheeters, N. P. Yao, and N. Koura, U.S. Pat. 3,992,222 (1976).
15. G. V. Samsonov and S. V. Drozdova, "Sulfidy," Moskva, Metallurgiya (1972).
16. J. F. Elliot and M. Gleiser, "Thermochemistry for Steelmaking," Addison-Wesley Publishing Co., Inc., Reading, Mass. (1960).
17. P. A. Nelson and D. S. Webster, "High-Energy Battery Program at Argonne National Laboratory," ANL-8064, 5 (1974).



Thermodynamics and Kinetics of Chemical Vapor Deposition of Aluminum Nitride Films

Y. Pauleau,* A. Bouteville, J. J. Hantzpergue and J. C. Remy

Laboratoire de Physico-Chimie Minérale et de Thermodynamique, Université d'Angers,

U.E.R. Sciences et Techniques, 49045 Angers, France

and A. Cachard

Département de Physique des Matériaux, Université Claude Bernard, 69621 Villeurbanne, France

ABSTRACT

The thermodynamics of aluminum nitride formation in the $\text{AlCl}_3\text{-NH}_3\text{-H}_2$ and $\text{AlBr}_3\text{-NH}_3\text{-H}_2$ systems have been studied at 1200° and 1400°K. The nature of the condensed phase and the equilibrium gas phase composition have been determined. Aluminum nitride was the only condensed phase formed under the entire range of the gas phase composition investigated. With a gas phase composition in stoichiometric proportions ($P^{\circ}_{\text{AlX}_3} = P^{\circ}_{\text{NH}_3}$), the yield of aluminum nitride decreased rapidly when the halide or ammonia vapor pressure was higher than 10^{-3} atm. At high hydrogen concentration, the formation of monohalides always reduced the yield of aluminum nitride. Aluminum nitride films have been deposited on various substrates between 500° and 900°C, using an initial composition of the $\text{AlBr}_3\text{-NH}_3\text{-H}_2$ system corresponding to a thermodynamic yield of aluminum nitride higher than 90%. The films have been confirmed to be aluminum nitride by x-ray diffraction technique and by Rutherford backscattering spectroscopy. The deposition rate has been investigated with respect to the temperature and the gas phase composition. At an aluminum tribromide vapor pressure of 8×10^{-5} atm, the deposition rate of aluminum nitride decreased with increasing deposition temperature. At an aluminum tribromide vapor pressure of 2.3×10^{-4} atm, the deposition rate increased between 500° and 600°C. Above 600°C, the deposition rate decreased with increasing deposition temperature. A mechanism of the deposition process has been proposed.

Aluminum nitride has chemical, physical, and electrical properties suitable for several applications as active and passive components in semiconductor devices and for the fabrication of surface wave acoustic devices. Preparation, physical and chemical properties of aluminum nitride films have been reviewed lately (1). Aluminum nitride films have been prepared by chemical vapor deposition from the following starting materials: organo-metallic compounds, $\text{Al}(\text{CH}_3)_3$ and $\text{Al}(\text{C}_2\text{H}_5)_3$, adduct compound, $\text{AlCl}_3\cdot\text{NH}_3$, and aluminum chloride, AlCl_3 . The deposition temperatures were always higher than 800°C and the plasma activation of low pressure gas phase did not allow deposition at lower temperature. Hence, the chemical vapor deposition of aluminum nitride films could not be used with many semiconductor substrates unstable in this temperature range. Recently, using the $\text{AlBr}_3\text{-NH}_3\text{-H}_2$ system, aluminum nitride films could be deposited between 500° and 900°C and some properties of these films have been examined (2). A decrease of deposition rate was observed with increasing deposition temperature, and aluminum nitride films could not be deposited above 900°C.

In this work, thermodynamics and kinetics of chemical vapor deposition processes have been investigated in order to determine the origin of the decrease of the

deposition rate. The nature of condensed phases and the equilibrium gas phase compositions have been determined as a function of the initial gas phase compositions at a given temperature for the $\text{AlCl}_3\text{-NH}_3\text{-H}_2$ and $\text{AlBr}_3\text{-NH}_3\text{-H}_2$ systems. The thermodynamic yield of aluminum nitride has been calculated *vs.* the initial gas phase composition, and the domains of formation of aluminum nitride have been determined. Aluminum nitride films have been deposited on various substrates (monocrystalline silicon wafers, nickel and vitreous carbon plates) using an initial composition of the $\text{AlBr}_3\text{-NH}_3\text{-H}_2$ system corresponding to a thermodynamic yield of aluminum nitride higher than 90%. The aluminum nitride deposition rate was investigated with respect to the temperature and the gas phase composition. A mechanism of aluminum nitride film deposition is proposed in this paper.

Thermodynamic Calculations

Procedure.—The computation procedure is based on the minimization of the total Gibbs energy of the system. Assuming that the behavior of the gas phase and the condensed phases is ideal, the free energy of the system is given by the equation

$$\frac{G}{RT} = \sum_{i=1}^N \left[q_i \left(\frac{\mu^{\circ}}{RT} \right)_i + a_i \log_e P_i \right] \quad [1]$$

* Electrochemical Society Active Member.

Key words: equilibrium, film growth insulator, aluminum nitride.

where q_i is the number of moles of the constituent i , μ° is the standard chemical potential of the constituent i , N is the total number of constituents, P_i is the pressure of the gaseous constituent i and a_i is a coefficient ($a_i = 1$ for an ideal gas and $a_i = 0$ for a condensed constituent).

The N chemical constituents considered in the equilibrium computation are given in Table I. The probability of existence of these constituents at equilibrium was estimated by considering the values of their free energy of formation, the temperature, and the pressure. The initial experimental parameters (temperature, total pressure, and initial gas phase composition) and the thermodynamic data (3) (free energy function and standard heat of formation of each constituent) were introduced in the computation program of minimization of Eq. [1] detailed in previous papers (4, 5) and used for other gaseous systems (6-8). The partial vapor pressure of each gaseous compound and the number of moles of each constituent present at equilibrium could be calculated. The equilibrium yield, η , of each aluminum compound (aluminum nitride and aluminum halides) with respect to the initial aluminum trihalide composition could be determined. The aluminum nitride yield is defined by the ratio

$$\eta_{\text{AlN}} = \frac{N_{\text{eq AlN}}}{N^{\circ}_{\text{AlX}_3}} \times 100 \quad [2]$$

where $N_{\text{eq AlN}}$ is the number of moles of aluminum nitride formed at equilibrium and $N^{\circ}_{\text{AlX}_3}$ is the initial number of moles of aluminum trihalide. The yield of aluminum halide is given by an analogous equation.

Results and discussion.—The calculations for the $\text{AlCl}_3\text{-NH}_3\text{-H}_2$ and $\text{AlBr}_3\text{-NH}_3\text{-H}_2$ systems were carried out at 1200° and 1400°K and at a total pressure of 1 atm. These temperatures were chosen in order to compare the results of the theoretical analysis with the experimental data known for the $\text{AlCl}_3\text{-NH}_3\text{-H}_2$ system [using this system, aluminum nitride films were deposited between 1000° and 1600°K (1)]. For a total number of mole close to 1, at equilibrium, a compound can be considered absent when its number of moles is lower than 10^{-7} . That is the accuracy of calculation. The concentration of the constituents preceded by one dot in Table I has been found lower than the accuracy of calculation and, consequently, these constituents are not existing in the system at equilibrium. Aluminum nitride is the only condensed phase formed under the

Table I. Chemical compounds considered in the thermodynamic calculations. The constituents preceded by one dot are not existing in the system at equilibrium

Phase	System	$\text{AlCl}_3\text{-NH}_3\text{-H}_2$	$\text{AlBr}_3\text{-NH}_3\text{-H}_2$
Solid		AlN	AlN
Liquid		.Al	.Al
Gas		H_2	H_2
		NH_3	NH_3
		AlCl_3	AlBr_3
		Al_2Cl_6	Al_2Br_6
		AlCl_2	—
		AlCl	AlBr
		HCl	HBr
		.Cl ₂	.Br ₂
		.Cl	.Br
		N_2	N_2
		.N	.N
		H	H
		.NH	.NH
		.NH ₂	.NH ₂
		.N ₂ H ₂	.N ₂ H ₂
		.N ₂ H ₄	.N ₂ H ₄
		.Al	.Al
		.AlN	.AlN
		.AlH	.AlH

entire range of the gas phase composition investigated. The variation of the yield of aluminum nitride has the same aspect for both systems studied (Fig. 1). For a given initial gas phase composition and temperature, the chloride and bromide systems yielded similar values of the yield of aluminum nitride. The domain of initial compositions corresponding to a yield of aluminum nitride higher than 90% is located between the horizontal axis and curve (A). At 1400°K and at low aluminum trihalide and ammonia concentrations, curve (A) (dashed line) is slightly shifted away from the bisector because of the formation of other aluminum halides (Fig. 2 and 3). At 1200° or 1400°K, using initial concentrations located between curves (A) and (B), the yield of aluminum nitride decreases from 90 to 10%; between curves (B) and (C), the yield decreases from 10 to 1% and beyond curve (C), it is less than 1%.

With a high hydrogen concentration and a low aluminum trihalide concentration in the initial gaseous mixture, the yield of aluminum monohalide is high and increases with increasing temperature. For example, at 1200°K, the yield of aluminum monobromide is higher than 60% when the initial composition is located between the vertical axis and curve (D) in Fig. 1; between curves (D) and (E), this yield decreases down to 5% and beyond curve (E) it is less than 5%. At 1400°K, the surface area of these domains increases; the yield of aluminum monobromide is higher than 60% between the vertical axis and curve (F) and decreases down to 5% between curves (F) and (G).

The initial gas phase compositions of the $\text{AlCl}_3\text{-NH}_3\text{-H}_2$ system used by several investigators are represented in Fig. 1. The initial compositions used by Chu and co-workers (9) (striped area) and by Noreika and Ing (10) (dark area) correspond to a yield of aluminum nitride higher than 90%. The domains of initial compositions of Arnold and co-workers (11) and Bauer and co-workers (12) cannot be located exactly in the diagram because the vapor pressure values were not provided with accuracy. Nevertheless, from these investigators' data it is possible to locate the initial composition domains between curves (A) and (B) where the yield of aluminum nitride is between 90 and 10%. Assuming that the aluminum trichloride vapor pressure is equal to the saturation vapor pres-

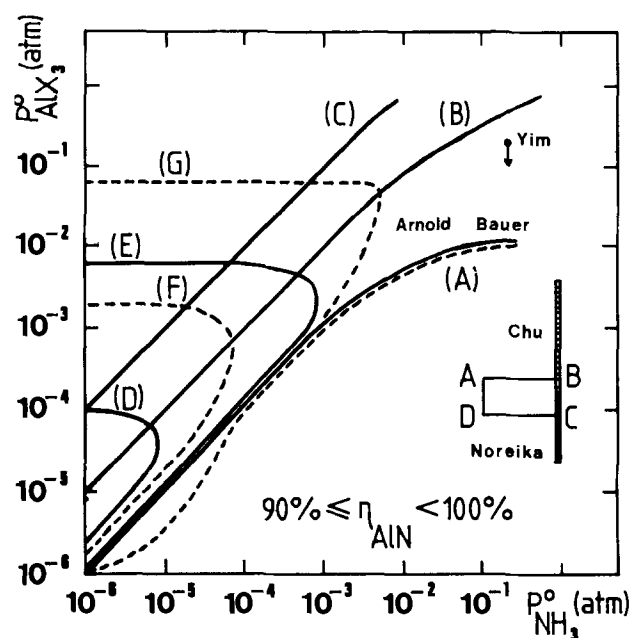


Fig. 1. Deposition domains of aluminum nitride in the initial gas phase composition diagram with the $\text{AlCl}_3\text{-NH}_3\text{-H}_2$ and $\text{AlBr}_3\text{-NH}_3\text{-H}_2$ systems. Solid lines, $T = 1200^\circ\text{K}$; dashed lines, $T = 1400^\circ\text{K}$.

sure, the composition of gaseous mixture used by Yim and co-workers (13) is represented by one point in Fig. 1. The actual halide vapor pressure is certainly lower than the saturation vapor pressure, and then the yield of aluminum nitride is higher than 15%.

The yields of aluminum nitride and aluminum halides as a function of the trihalide vapor pressure or the ammonia vapor pressure are plotted in Fig. 2 and 3. The trihalide and ammonia vapor pressures are equal with an initial gaseous mixture carried out in stoichiometric proportions corresponding to the reaction of aluminum nitride formation. The value of the yield of aluminum monohalide reaches a maximum with an aluminum trihalide vapor pressure of about 10^{-5} atm and this maximum yield increases rapidly with increasing temperature. For chloride system, the abscissa of the maximum yield of aluminum monochloride shifts from about 10^{-5} to 2×10^{-3} atm of aluminum trichloride as the temperature changes from 1200° to 1400°K . The increase of the yield of aluminum monochloride (Fig. 2) or aluminum monobromide (Fig. 3) corresponds to the decrease of the yield of aluminum nitride. The yield of aluminum nitride decreases rapidly at an initial aluminum trihalide vapor pressure higher than 10^{-3} atm when the dissociation of ammonia at equilibrium is important. The yield of dimers (Al_2Cl_6 and Al_2Br_6) is always less than 1%. The yield of aluminum dichloride (Fig. 2) is also very low.

These thermodynamic calculations show that both systems studied are analogous with respect to the yield of aluminum nitride at equilibrium. The prevision of the thermodynamic analysis inserts with the experimental

results obtained for the $\text{AlCl}_3\text{-NH}_3\text{-H}_2$ system (9-13). The thermodynamic estimations can be limited. Indeed, the condensed phases considered are only stoichiometric constituents and the thermodynamic equilibrium is not always established at high gas flow rate. Nevertheless, the thermodynamic calculations give an optimization of deposition conditions from the point of view of yields and condensed phase compositions.

Experimental Procedures

The deposition of aluminum nitride films by chemical reaction in the $\text{AlBr}_3\text{-NH}_3\text{-H}_2$ gas flow system was carried out by using an apparatus described in a previous paper (2). Briefly, the deposition was carried out in a horizontal reaction tube and the substrates (silicon, nickel, or vitreous carbon plate) were supported by a silicon carbide coated graphite susceptor heated by an rf generator. The composition of ammonia-hydrogen mixtures was adjusted and maintained at a constant value by means of flow meters and flow regulators. The total flow rate was always equal to 12 liters/min. The aluminum bromide was contained in a Pyrex evaporator maintained at a constant temperature and the vapor was carried in the reactor by a hydrogen stream at a constant flow rate of $50\text{ cm}^3/\text{min}$. The evaporator was weighed before and after each run. With the evaporator temperatures of 121° and 147°C , the molar flow rate of aluminum tribromide in the reaction tube was 4×10^{-5} and 1.1×10^{-4} mole/min and the aluminum tribromide vapor pressure was 8×10^{-5} and 2.3×10^{-4} atm, respectively. The kinetic study of deposition was carried out with gas

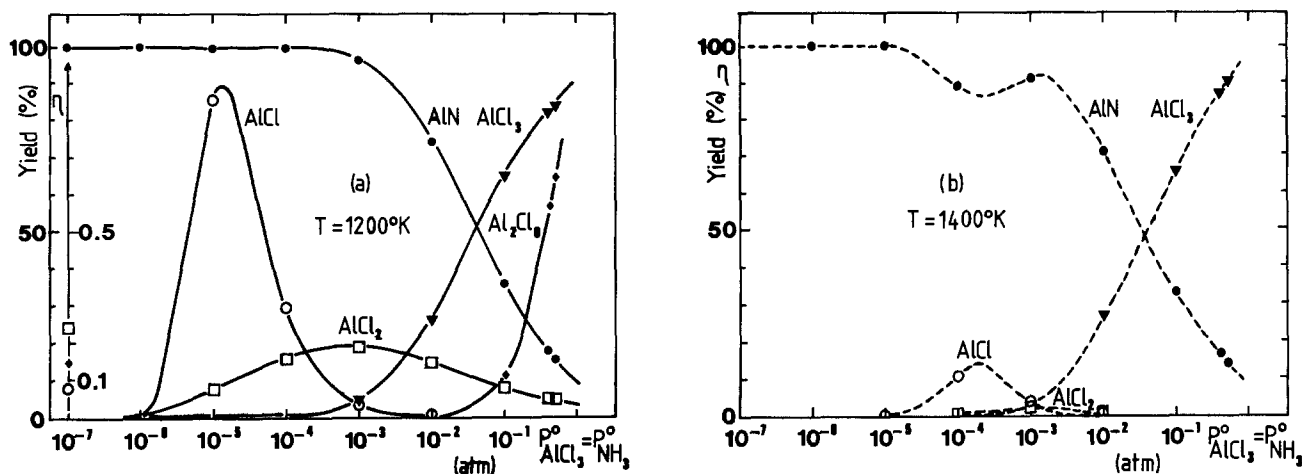


Fig. 2. Variation of equilibrium yields of aluminum nitride and aluminum chlorides using the $\text{AlCl}_3\text{-NH}_3\text{-H}_2$ system in the stoichiometric proportions ($P^{\circ}_{\text{AlCl}_3} = P^{\circ}_{\text{NH}_3}$) (a) at 1200°K and (b) at 1400°K .

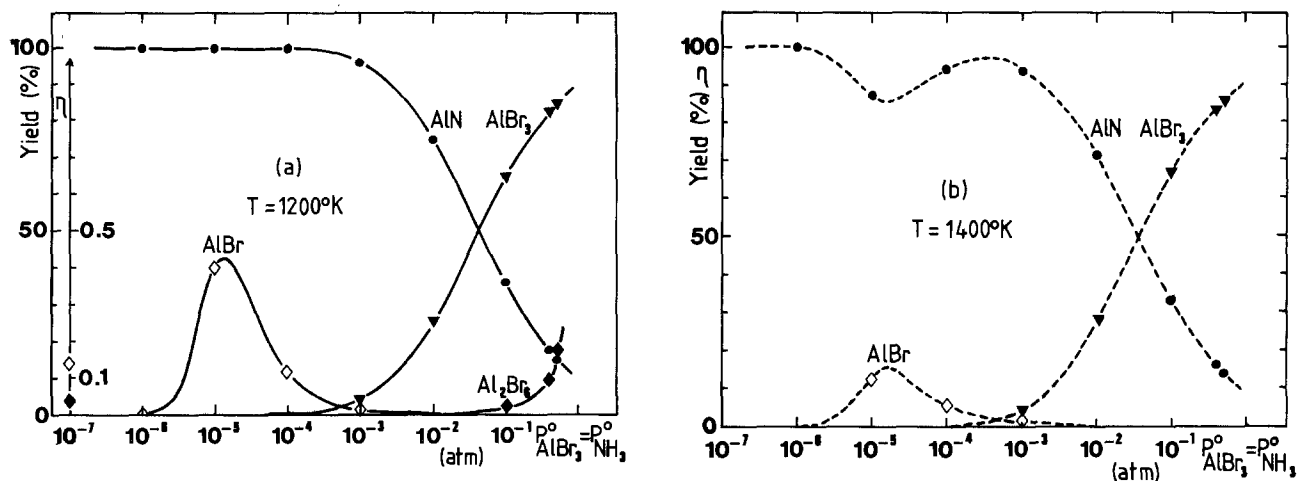


Fig. 3. Variation of equilibrium yields of aluminum nitride and aluminum bromides using the $\text{AlBr}_3\text{-NH}_3\text{-H}_2$ system in the stoichiometric proportions ($P^{\circ}_{\text{AlBr}_3} = P^{\circ}_{\text{NH}_3}$) (a) at 1200°K and (b) at 1400°K .

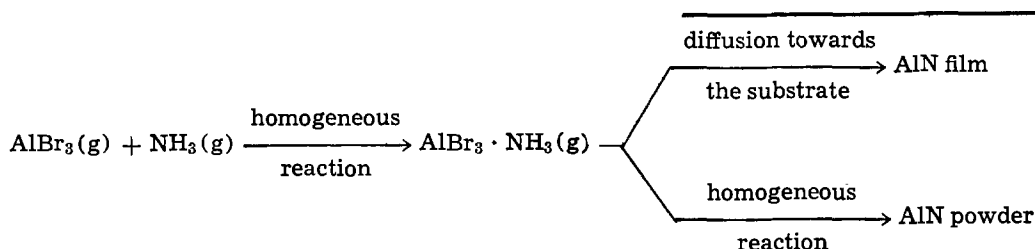
phase compositions located in the rectangle ABCD (Fig. 1) in the initial gas phase composition diagram where the thermodynamic yield of aluminum nitride is about 99%. The mixing zone between ammonia and aluminum bromide vapors was heated at 300°C in order to avoid the formation of solid adduct compounds, $\text{AlBr}_3 \cdot n\text{NH}_3$. Aluminum nitride films were deposited at substrate temperatures in the range 500°-900°C. Above 900°C, the deposition rate was low and the thickness of films was not uniform. The deposition time was determined by the time of hydrogen stream on aluminum bromide.

The crystallographic structure of deposited material was determined by removing the layer from the nickel plate substrate and identifying the x-ray patterns obtained by means of a Debye-Scherrer powder technique. In all the cases, the pattern revealed the presence of polycrystalline aluminum nitride. The films deposited on vitreous carbon substrates were analyzed by Rutherford backscattering spectroscopy (14). The accuracy on the aluminum atom numbers per square centimeter was 0.8%. The deposition rate of aluminum nitride was expressed by the number of aluminum atoms deposited per square centimeter per minute.

Kinetic Study

Results.—At an aluminum bromide vapor pressure of 8×10^{-5} atm, the deposition rate was low and almost independent of the ammonia-hydrogen composition. The measured values fall within the limits of reproducibility of the experiments. The deposition rate decreased with increasing deposition temperature (Fig. 4a). At an aluminum bromide vapor pressure of 2.3×10^{-4} atm, the deposition rate was higher and the reproducibility was better. The rate increased between 500° and 600°C; above 600°C, it decreased with increasing deposition temperature (Fig. 4b). The variation of deposition rate with the ammonia-hydrogen composition was not continuous. The decimal logarithm of the deposition rate vs. the reciprocal absolute temperature is plotted in Fig. 5. Below 600°C, the activation energy was about 9 kcal mole⁻¹. The dashed straight line (Fig. 5) represents the result obtained by Kelm (15) for the deposition of aluminum nitride films by pyrolysis of adduct compound, $\text{AlCl}_3 \cdot \text{NH}_3$. Using the $\text{AlBr}_3\text{-NH}_3\text{-H}_2$ gas flow system, the deposition rate of aluminum nitride films had the same value but in a lower temperature range.

Discussion.—Thermodynamic analysis has shown that the yield of aluminum nitride at equilibrium increased with increasing temperature; this yield was higher than 98% at 1200°K with an initial gas phase composition located in the rectangle ABCD (Fig. 1). Then, the decrease of deposition rate with increasing deposition temperature (Fig. 4) can be only attributed to the kinetic characteristics of the deposition process. This decrease is suggesting of a homogeneous reaction in the gaseous phase and can be analyzed using the model proposed by Sladek (16). Schematically, the deposition process can be represented under the following form



Under our experimental conditions, the gaseous adduct compound, $\text{AlBr}_3 \cdot \text{NH}_3$, was probably formed at 300°C in the mixing zone between ammonia and aluminum bromide vapor. Using the data given by Trusov

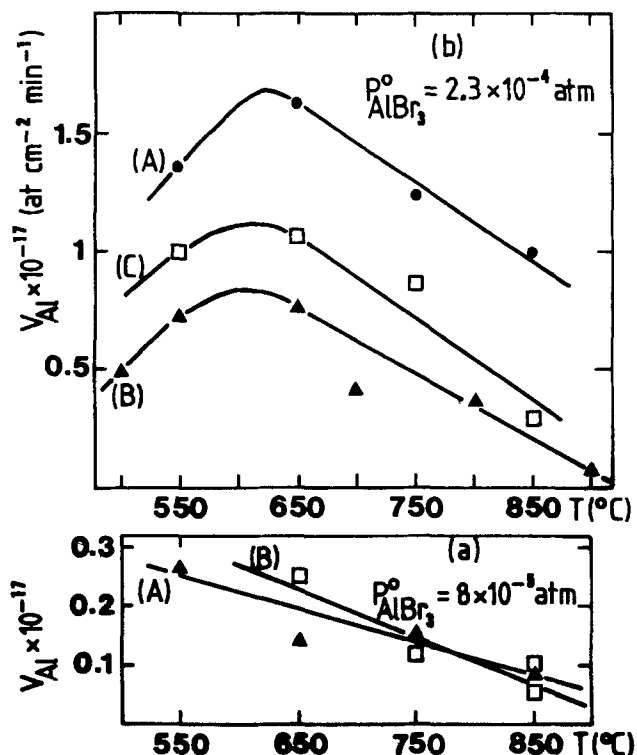


Fig. 4. Variation of AlN deposition rate in the $\text{AlBr}_3\text{-NH}_3\text{-H}_2$ system vs. the deposition temperature.

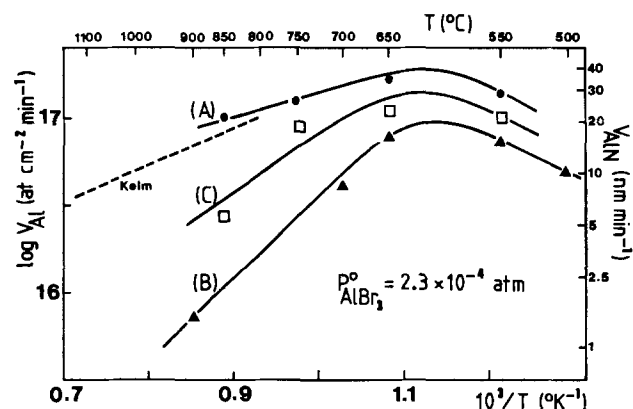
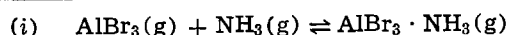


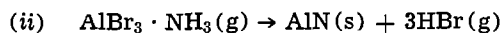
Fig. 5. Variation of the decimal logarithm of aluminum nitride deposition rate vs. the reciprocal absolute temperature at an aluminum bromide vapor pressure of 2.3×10^{-4} atm and an ammonia-hydrogen composition of (A) 1:9, (B) 2:1, and (C) 9:1.

and Suvorov (17), a thermodynamic calculation has shown that the aluminum tribromide vapor introduced into the reactor could be completely transformed into the adduct compound according to the following equilibrium



and the concentration of the adduct compound at equilibrium was independent of the ammonia-hydrogen

composition used. The thermodynamic calculation has also shown that the reverse reaction was possible above 300°C, simultaneously with the reaction of aluminum nitride formation



At low deposition temperature, reaction (ii) occurred in an adsorbed phase on the substrate surface. The activation energy of the surface reaction was low (9 kcal mole⁻¹) probably because of the configuration of the adduct compound; aluminum and nitrogen atoms are already bonded in the molecule $\text{AlBr}_3 \cdot \text{NH}_3$. Simultaneously, a small part of the films could grow by the deposition of aluminum nitride powder formed by nucleation in the gaseous phase.

Under the experimental conditions used, the temperature gradient in the gaseous phase was high and the homogeneous reaction could only occur in a very thin layer located on the substrate surface. The high roughness of films deposited at low temperature [curves (A) and (D), Fig. 6] was probably due to this deposition of powder. The activation energy of homogeneous reaction is higher than that of surface reaction. With increasing temperature, the rate of homogeneous reaction increased more rapidly than the rate of surface reaction and the yield of homogeneous reaction also increased because the volume of gaseous phase where the reaction could occur was larger. At high temperature (above 700°C), the aluminum nitride powder was formed at a large distance from the sub-

strate surface and could not be deposited. The films had a smooth surface [curves (C) and (F), Fig. 6]. The concentration of reactants close to the substrate surface was reduced and the growth rate of film by the surface reaction decreased.

The deposition rate dependence with ammonia-hydrogen composition at the higher aluminum bromide vapor pressure and the independence at the lower vapor pressure cannot be easily interpreted. At an aluminum bromide vapor pressure of 8×10^{-5} atm, the deposition rate (Fig. 4a) and the surface profiles of films [curves (G), (H), and (I), Fig. 6] were not affected by the variation of ammonia concentration in the gaseous phase probably because the concentration of the adduct compound remained constant. The nature of substrate can change some properties of deposit. The effect of the three substrates used (silicon, nickel, and vitreous carbon) could not be investigated because the nature of substrate was appropriated with the property of film studied. Sometimes, the effect of total flow rate might provide insight into the mechanism of deposition. This effect could not be studied because with a total flow rate lower than 10 liters/min, the thickness of films was not uniform and, then, the kinetic study of deposition was not possible.

Summary and Conclusions

The thermodynamics of aluminum nitride formation in the $\text{AlCl}_3\text{-NH}_3\text{-H}_2$ and $\text{AlBr}_3\text{-NH}_3\text{-H}_2$ systems have been studied. The equilibrium gas phase composition and the thermodynamic yield of aluminum nitride have been determined. Aluminum nitride films were deposited in the $\text{AlBr}_3\text{-NH}_3\text{-H}_2$ system between 500° and 900°C. With the higher aluminum bromide vapor pressure (2.3×10^{-4} atm), the deposition rate increased with increasing substrate temperature up to 600°C; above 600°-650°C, the deposition rate decreased. With the lower aluminum bromide vapor pressure (8×10^{-5} atm), the deposition rate was decreasing in the entire temperature range studied. The deposition rate did not depend on the gas phase composition. The roughness of surface of aluminum nitride films deposited at lower temperatures was attributed to the deposition of aluminum nitride powder formed by gas phase nucleation. At higher temperatures, the growth of aluminum nitride films was only due to the adsorbed gas phase reaction on the surface of substrate. A model for the deposition mechanisms of aluminum nitride films was proposed. These results show the influence of homogeneous reactions in a chemical vapor deposition process. Using the $\text{AlCl}_3\text{-NH}_3\text{-H}_2$ system, Arnold and co-workers (18) have shown the effect of the gaseous adduct compound formation, $\text{AlCl}_3 \cdot \text{NH}_3$, on the kinetics of aluminum nitride deposition. The aluminum nitride deposition mechanisms in the $\text{AlCl}_3\text{-NH}_3\text{-H}_2$ and $\text{AlBr}_3\text{-NH}_3\text{-H}_2$ systems are very similar.

Acknowledgments

The authors wish to thank Y. Deniel and A. Jacquot, Thermodata, for their helpful assistances and Dr. T. L. Chu, S.M.U. Electronic Materials Laboratory, for helpful comments on the manuscript. The technical assistance of B. Reignier is greatly appreciated.

Manuscript submitted Dec. 3, 1979; revised manuscript received Feb. 1, 1980.

Any discussion of this paper will appear in a Discussion Section to be published in the June 1981 JOURNAL. All discussions for the June 1981 Discussion Section should be submitted by Feb. 1, 1981.

Publication costs of this article were assisted by the University of Angers.

REFERENCES

1. Y. Pauleau, J. J. Hantzpergue, and J. C. Remy, *Bull. Soc. Chim. Fr.*, **I**(5-6), 199 (1979).
2. Y. Pauleau, A. Bouteville, J. J. Hantzpergue, J. C. Remy, and A. Cachard, *ibid.*, **I**(3-4), 127 (1980).

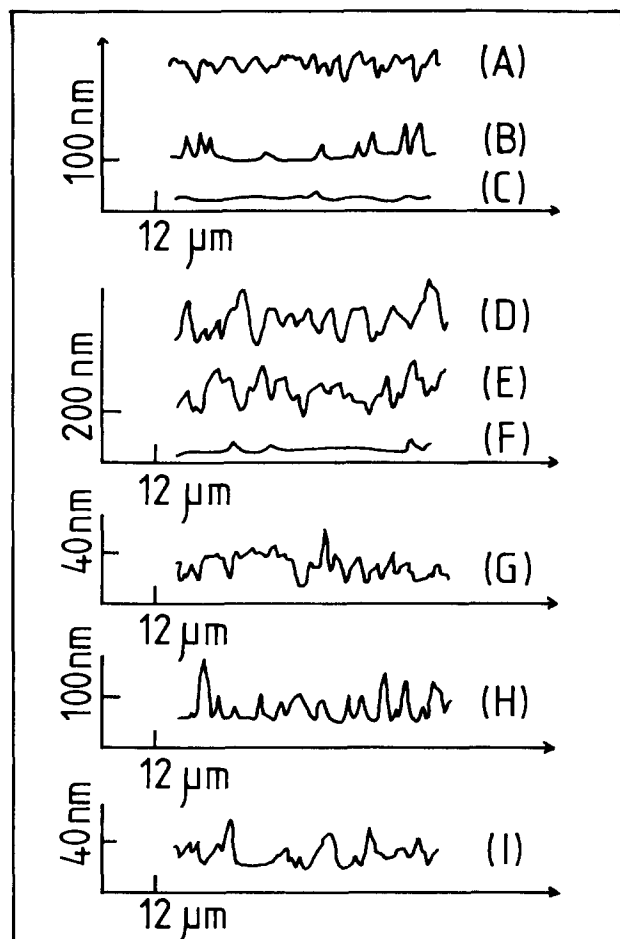


Fig. 6. Surface profiles of aluminum nitride films. Films deposited at (A) 550°C, (B) 750°C, and (C) 850°C with a 2:1 ammonia-hydrogen mixture and an aluminum bromide vapor pressure of 8×10^{-5} atm. Films deposited at (D) 550°C, (E) 750°C, and (F) 850°C with a 2:1 ammonia-hydrogen mixture and an aluminum bromide vapor pressure of 2.3×10^{-4} atm. Films deposited at 650°C with an aluminum bromide vapor pressure of 8×10^{-5} atm and an ammonia-hydrogen composition of (G) 1:9, (H) 2:1, and (I) 9:1.

3. "Thermodata," Bibliothèque Universitaire des Sciences, B.P. 22, 38402 Saint Martin d'Hères, France.
4. C. Bernard, Y. Deniel, A. Jacquot, P. Vay, and M. Ducarroir, *J. Less-Common Met.*, **40**, 165 (1975).
5. M. Ducarroir, M. Jaymes, C. Bernard, and Y. Deniel, *ibid.*, **40**, 173 (1975).
6. M. Ducarroir and C. Bernard, in "Chemical Vapor Deposition, Fifth International Conference," J. M. Blocher, H. E. Hintermann, and L. H. Hall, Editors, p. 72, The Electrochemical Society Softbound Proceedings Series, Princeton, N.J. (1975).
7. F. Teyssandier, M. Ducarroir, and C. Bernard, in "Chemical Vapor Deposition, Seventh International Conference," T. O. Sedgwick and H. Lyd-tin, Editors, p. 398, The Electrochemical Society Softbound Proceedings Series, Princeton, N.J. (1979).
8. F. Christin, R. Naslain, and C. Bernard, *ibid.*, p. 499.
9. T. L. Chu, D. W. Ing and A. J. Noreika, *Solid-State Electron.*, **10**, 1023 (1967).
10. A. J. Noreika and D. W. Ing, *J. Appl. Phys.*, **39**, 5578 (1968).
11. H. Arnold, L. Biste, D. Bolze, and G. Eichhorn, *Krist. Tech.*, **11**, 17 (1976).
12. J. Bauer, L. Biste, and D. Bolze, *Phys. Status Solidi A*, **39**, 173 (1977).
13. W. M. Yim, E. J. Stofko, P. J. Zanzucchi, J. I. Pankove, M. Ettenberg, and S. L. Gilbert, *J. Appl. Phys.*, **44**, 292 (1973).
14. J. Tardy, A. Cachard, J. P. Thomas, and J. Enger-ran, *Le Vide, Les Couches Minces*, **29**, 359 (1974).
15. R. W. Kelm Jr., *Diss. Abstr. Int. B*, **34**, 3791 (1974); Univ. Microfilms, Ann Arbor, Mich., Order N 74-5171, 130 pp.
16. K. J. Sladek, *This Journal*, **118**, 654 (1971).
17. V. I. Trusov and A. V. Suvorov, *Zh. Neorg. Khim.*, **19**, 3253 (1974).
18. H. Arnold, L. Biste, and T. Kaufmann, *Krist. Tech.*, **13**, 929 (1978).

Deformation in Dielectric-Isolated Substrates and Its Control by a Multilayer Polysilicon Support Structure

Takaya Suzuki, Akio Mimura, Tatsuya Kamei, and Takuzo Ogawa

Hitachi Limited, Hitachi Research Laboratory, Hitachi, Ibaraki 319-12, Japan

ABSTRACT

Curved deformations in the dielectric-isolated substrate with a conventional, single polysilicon support structure occur mainly during two processes. One is deposition of the polysilicon support region and the other is thermal oxidation and diffusion for junction formation. The former is concave toward the polysilicon support layer side. The latter, however, has a tendency to bow convexly toward the polysilicon layer side and seems to be caused by expansion stress generated through penetration or diffusion of high concentrations of oxygen into the surface region of the polysilicon support region. These deformations can be successfully controlled by adopting a multilayer polysilicon support structure consisting of alternating polysilicon layers and silicon oxide films for the support region and also by providing a preventive film for oxide diffusion into the surface of the polysilicon support region. During the formation of the multilayer structure, it is proposed that contraction stress, caused by polysilicon deposition, and expansion stress, caused by silicon oxide deposition, are occurring alternately and are compensating each other to form a wafer with little deformation.

Dielectric-isolated (DI) substrates are used in high voltage power IC's and radiation-hardened devices because of their excellent characteristics, including high isolation voltages, isolation capability for an alternating current, diminished parasitic capacitances, and lessened photodiode currents in radiation environments (1, 2). One of the most serious problems in DI manufacture is complicated wafer deformation originating from the use of a relatively thick polysilicon layer as a support structure for single crystal silicon regions (3, 4). The deformation of the DI substrate takes place mainly during the deposition of the polysilicon support region and during the formation of junctions in the single crystal silicon regions, *i.e.*, the processes of thermal oxidation and diffusion. The former kind of deformation has been reported to be caused by the tensile growth stress generated through contraction of the growing polysilicon layer at high temperatures (5, 6). No investigation has apparently been reported as to the latter kind of deformation. These severe macroscopic deformations create undesirable effects in the subsequent grinding process for substrate fabrication and in the photolithography process for junction for-

mation. Therefore, it is very important to control these deformations in order to improve process yield and accuracy. Although it has been reported that doping of a small amount of an impurity, such as oxygen into polysilicon, is effective in minimizing the deformation during polysilicon deposition (7, 8), a successful control method of deformation throughout the whole device fabrication process has not been reported.

This paper first describes the deformations of the DI substrate with a conventional, single polysilicon support structure and then describes a novel method for controlling both kinds of deformation in which a multilayer polysilicon structure consisting of alternating polysilicon layers and silicon oxide films is adopted for use in the support region of the DI substrate.

Experimental

Preparation of DI substrates.—The DI substrates were fabricated by the conventional single poly method (1), as shown in Fig. 1. The single crystal silicon used was CZ type, (100) surface oriented, 50 mm in diameter, about 290 μm in thickness, n-type, and had 10-15 Ωcm resistivity. V-shaped isolation moats were formed by using anisotropic etch with KOH solution (9). Isolation oxide (about 1.7 μm) was grown by thermal

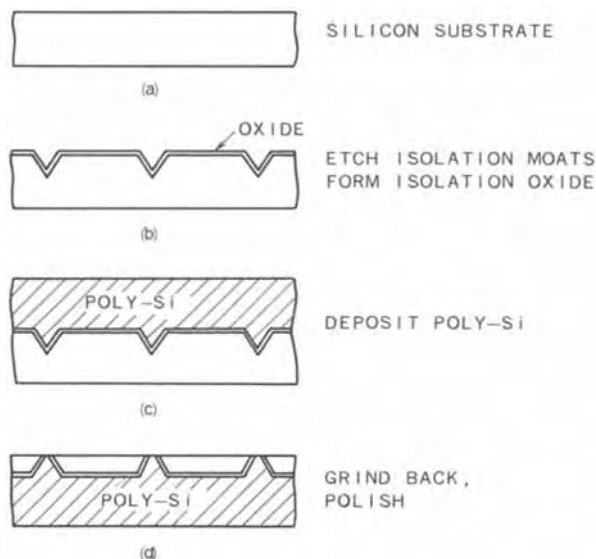


Fig. 1. Fabrication process for DI substrates

oxidation at 1100°C. Two different structures of polysilicon support region were formed in these experiments: a single layer polysilicon structure and a multilayer polysilicon structure. The polysilicon was deposited in a conventional epitaxial reactor with a growth rate of about 6 $\mu\text{m}/\text{min}$ at 1200°-1250°C (optically observed) using a $\text{SiHCl}_3\text{-H}_2$ reduction process. After the polysilicon was deposited, the poly surface was ground. The slice was then inverted and the original single crystal substrate was ground back and polished until the silicon oxide isolation films on the grooves were exposed. The thickness of the single crystal silicon islands ranged between 60-80 μm . After polishing, the substrate was ready for conventional device processing (oxidation and diffusion).

Deposition of multilayer polysilicon structure.—Figure 2 shows cross-sectional examples of the multilayer polysilicon support structure. This support structure consists of an alternating laminate of polysilicon layers and silicon oxide films. The alternating depositions were carried out in a conventional, vertical-type epi-

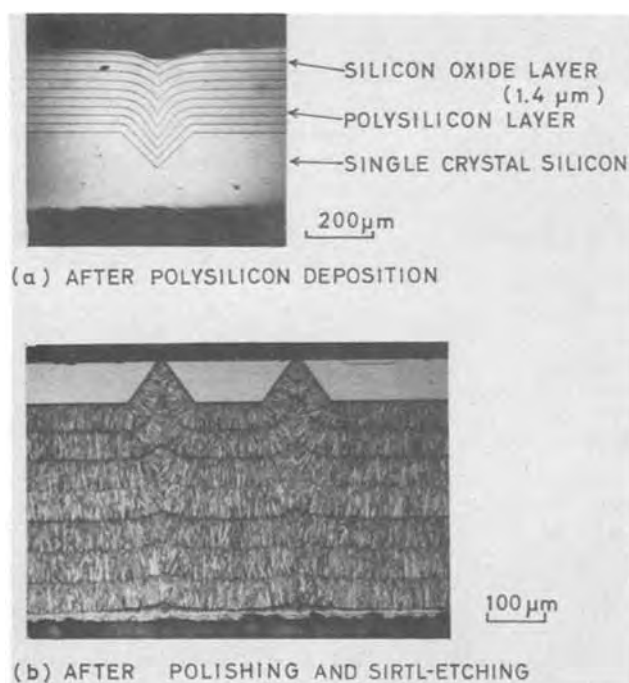


Fig. 2. Cross-sectional views of the multilayer polysilicon support structure.

taxial reactor having a rotating disk 300 mm in diameter. The deposition temperatures were 1200°-1250°C (optically observed). The $\text{SiHCl}_3\text{-H}_2$ reduction process was used for polysilicon and the $\text{SiHCl}_3\text{-CO}_2\text{-H}_2$ process, for silicon oxide. The deposition rates of the polysilicon layers and the silicon oxide films were about 6 and 0.3 $\mu\text{m}/\text{min}$, respectively. The quality of the oxide film was examined and found to be almost the same as that of the oxide film grown by thermal oxidation. The thicknesses of the silicon oxide films were the same through the structure, while various oxide thicknesses ranging from 0.3 to 1.4 μm were used in the experiments. The total thickness of the support region ranged about from 200 to 500 μm .

The steps for producing such multilayer polysilicon support are as follows. Initially, a predetermined thickness of the first polysilicon layer was deposited by introducing trichlorosilane and hydrogen into the reactor. Then, the introduction of trichlorosilane was stopped and the reactor was purged with hydrogen for 5 min. Next, a silicon oxide film was deposited by introducing trichlorosilane and carbon dioxide together with hydrogen. After the deposition of the silicon oxide film, the reactor again was purged with hydrogen and the second polysilicon layer was deposited. In this way, the steps of polysilicon deposition, reactor purge, silicon oxide deposition, and reactor purge were repeated according to the number of layers required.

Degree of wafer bowing.—In the DI process, two types of deformation were observed. One is the type in which the polysilicon support layer side of a wafer is concave while the other is reversed. Therefore, the sign of the bowing direction is defined as "plus" for the former and as "minus" for the latter. The degree of bowing is expressed by the reciprocal of the radius of curvature R calculated from the deviation h from a flat plane 50 mm in length, assuming that the configuration of the deformation is almost spherical (5). The deviation was measured with a surface measuring instrument (Dektak). The value h is the average of the two values measured in the x and y directions on a wafer. The relation between $1/R$ and h is given as $1/R = (2/r^2)h$, where r is the radius of the wafer.

Results and Discussion

Deformation of substrates with single polysilicon support structure.—It was observed that the deformation of wafers took place mainly during the following two processes. One is the deposition of the polysilicon support region and the other is the formation of junctions in the single crystal silicon region, i.e., the processes of thermal oxidation and diffusion.

Figure 3 shows the variation in the degree of deformation (bowing) during the various wafer processes. Results are shown for three different polysilicon thicknesses. The polysilicon deposition temperature was 1230°C. Thermal oxidation was performed at 1200°C in a wet oxygen atmosphere for 5.7 hr. Boron diffusion was carried out at 1200°C for 9 hr after a BN predeposited process at 1000°C. It can be seen that the wafers underwent curved deformations in the plus direction after the deposition of the polysilicon support layer and had a tendency to deform in the minus direction during the thermal oxidation process. The former kind of deformation has been discussed previously (5) and hence will not be described in detail. The degree of bowing after the deposition of the polysilicon layer increases with increasing thickness of the deposited polysilicon layer and tends to increase with lowering of the deposition temperature. It can be considered that this kind of bowing is caused by the tensile growth stress generated through the contraction of the growing polysilicon layer at high temperatures. This contraction of the polysilicon layer may be induced by a mechanism similar to sintering (5). The latter kind of deformation has apparently not been reported previously and hence is examined here in more detail.

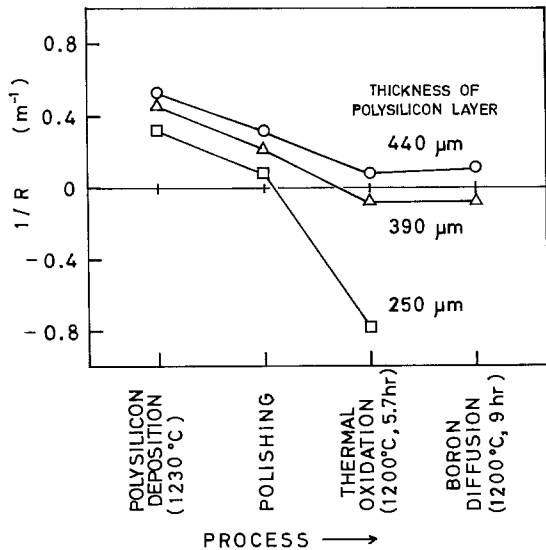


Fig. 3. Effect of process steps on wafer deformations

As seen above, the DI substrate has a tendency to deform convexly toward the side of the polysilicon support layer, i.e., the minus direction, during the subsequent thermal oxidation process. The degree of bowing shows a remarkable change, especially in the case of the substrate with a thinner polysilicon support layer. The change in bowing is smaller as the thickness of the polysilicon support layer increases. It was also observed that the change in bowing during the thermal oxidation process was greater at higher temperature and for longer heat-treatment times. Figure 4 indicates the effect of the time of oxidation t on the amount of the change in the reciprocal of the radius of curvature ($1/R$, where, $\Delta(1/R) = (1/R \text{ before oxidation}) - (1/R \text{ after oxidation})$). It is seen that $\Delta(1/R)$ is approximately proportional to the square root of the oxidation time. This is very similar to the so-called parabolic relationship in the rate of thermal oxide growth. These deformations toward the minus direction did not change even if the oxide film formed on the polysilicon surface was removed by etching. In addition, it was found that this kind of deformation occurred only during the high temperature heat-treatment in an oxygen-containing atmosphere and not in atmospheres such as argon or hydrogen.

From the above results, it appears that the bowing which occurred during thermal oxidation may be caused by the expansion stress generated through penetration or diffusion of high concentrations of oxygen along the grain boundaries of polysilicon into the surface region of the polysilicon support region. The

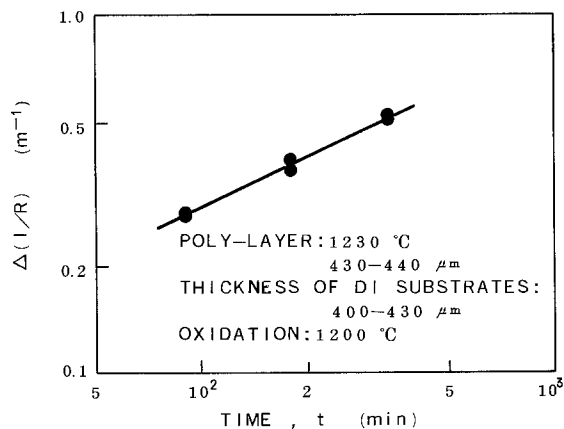


Fig. 4. Dependence of the amount of change in curvature on the time of thermal oxidation, where $\Delta(1/R) = (1/R \text{ before oxidation}) - (1/R \text{ after oxidation})$.

time dependence of $\Delta(1/R)$, see Fig. 4, can be qualitatively explained as follows. The reciprocal of the radius of curvature $1/R$ is proportional to the expansion stress in the polysilicon surface region. This expansion stress can be assumed to be proportional to the amount of oxygen penetrated or diffused into the polysilicon surface. Therefore, since the amount of oxygen which will reach and diffuse into the polysilicon surface region is controlled by the diffusion through the oxide film formed on the polysilicon layer and is proportional to the square root of the oxidation time (10), it may be considered that $\Delta(1/R)$ shows the same time dependence.

Figure 5 shows the profile of oxygen concentration in the polysilicon support layer of the DI substrate which has been subjected to the thermal oxidation process. The oxygen concentration was determined by successively etching the surface and measuring the ratio of $^{44}\text{SiO}^+$ /total ion by secondary ion mass spectroscopy (Hitachi, IMA-2). Although the absolute values of concentration are not known, it can be seen that high concentrations of oxygen exist in the polysilicon support layer ranging from the surface to a depth of about 30-40 μm . Next, the change in bowing of DI substrates which had been deformed by thermal oxidation was measured by successively etching off the surface of the polysilicon layer side. These results are shown in Fig. 6. It was found that, by etching off the polysilicon surface of about 30-40 μm , bowing in the minus direction is almost restored to the initial bowing in the plus direction that had been observed before thermal oxidation. The etched thickness necessary to return to the initial bowing is roughly consistent with the range of high oxygen concentration.

As mentioned above, the DI substrates have a tendency to deform in the minus direction during heat-treatment in an oxygen-containing atmosphere. The change in this bowing can be reduced by increasing the thickness of the polysilicon support layer. However, the degree of bowing during the deposition of the polysilicon support layer becomes larger as the thickness of the polysilicon support layer is increased. Therefore, from the standpoint of practical use, it is necessary to establish a method for controlling deformation, even during thick polysilicon deposition, and also for minimizing deformation during thermal oxidation. In the next section, a novel fabrication method for DI substrates that meets such requirements is described.

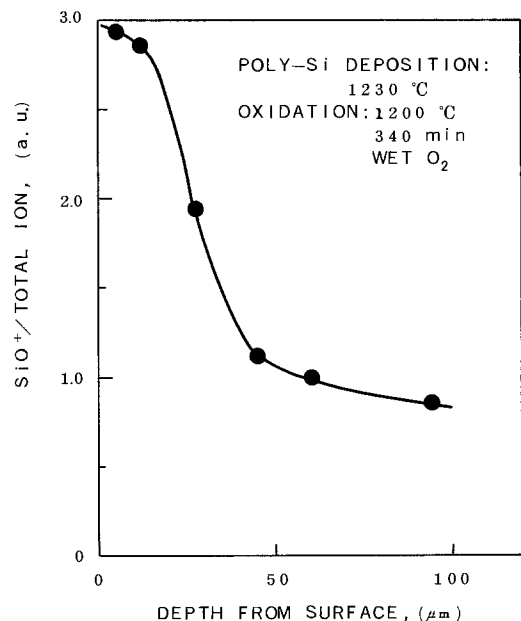


Fig. 5. Profile of oxygen concentration in the polysilicon support region of the DI substrate subjected to thermal oxidation.

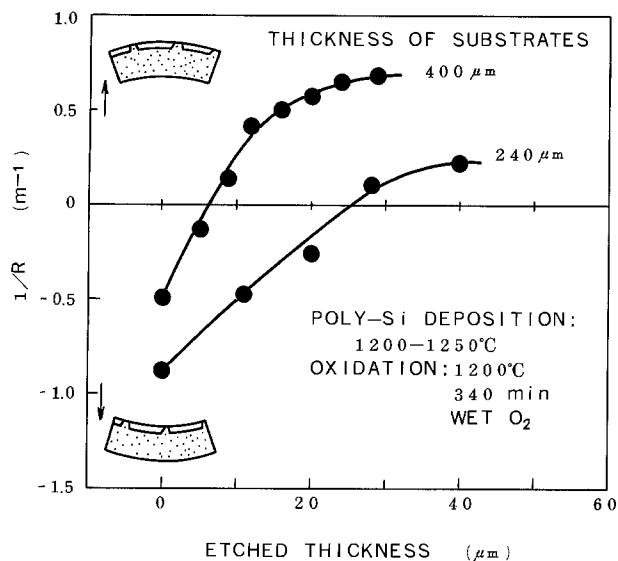


Fig. 6. Bowing recovery of DI substrates deformed by thermal oxidation as measured by successive etching of the surface of the polysilicon layer side.

Control of deformation by a multilayer polysilicon support structure.—Control of deformation during deposition of a polysilicon support structure.—It was found that the magnitude and direction of bowing due to the deposition of a polysilicon support layer can be controlled by applying the multilayer structure consisting of alternating polysilicon layers and silicon oxide films. Figure 7 shows a relation between the number of polysilicon layers in a multilayer structure and the magnitude of bowing of the substrate for two different total thicknesses of the support region. The degree of bowing decreases with increasing numbers of polysilicon layers. Above a certain number of layers, the direction of bowing is inverted so that the polysilicon support region side of the wafer begins to take the form of a convex surface. For the two cases in which the total thicknesses of the support regions are 210–260 and 430–480 μm , the thickness for one polysilicon layer when the degree of bowing is almost zero is about the same, i.e., 40–50 μm . Figure 8 shows typical interference patterns of the deformation for three different numbers of polysilicon layers. The patterns were observed with a commercial flatness tester (Speedlap, Check Flat). The thicknesses of the polysilicon support regions of these samples were 430–460

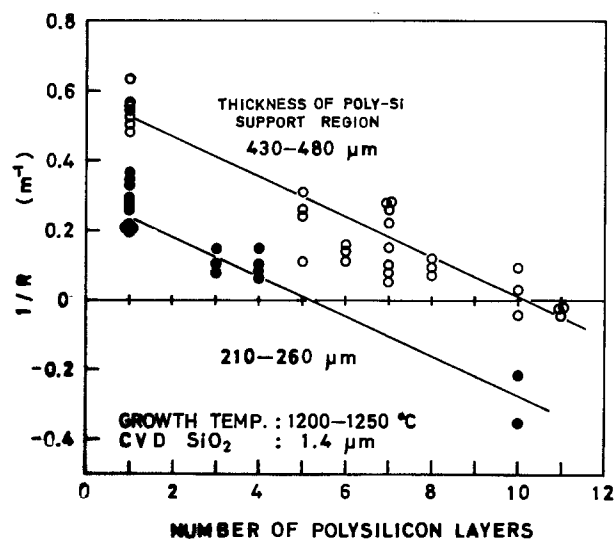


Fig. 7. Relation between the number of polysilicon layers in a multilayer polysilicon support region and the degree of bowing of wafers.

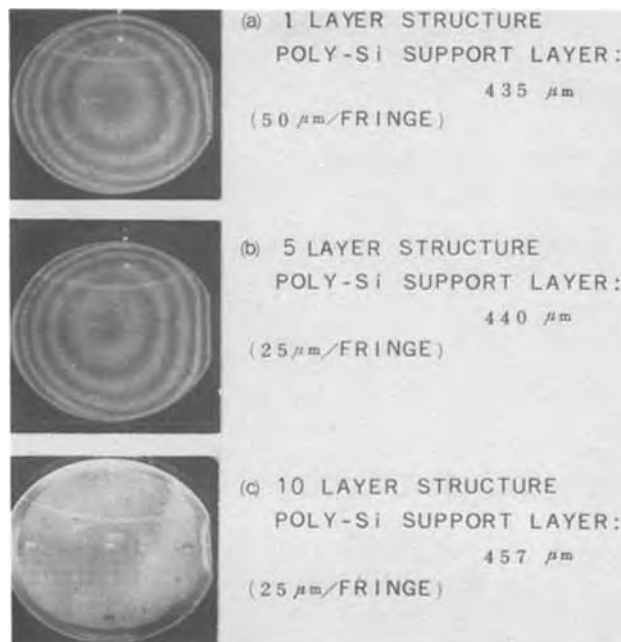


Fig. 8. Typical interference patterns of the deformation for wafers with different numbers of polysilicon layers.

μm . Figure 9 shows the effect of the thickness of the silicon oxide films between the polysilicon layers on the degree of bowing of wafers with a multilayer polysilicon structure. The degree of bowing was hardly affected by the thickness of the silicon oxide films in the range from 0.3 to 1.4 μm .

Next, in order to investigate the cause of the bowing reduction effect by the multilayer structure, the manner of changes in bowing during the deposition of the support region was indirectly observed by measuring the curvature of the wafers when taken out of the reactor at various deposition steps during the multilayer structure fabrication. The results are shown in Fig. 10. The curvature measurements were done at the first, second, fourth, and eighth depositions of polysilicon and silicon oxide. The dashed line indicates an approximation of the bowing variation. It is seen that the degree of bowing which occurred at the first polysilicon layer deposition decreases in the following deposition of the silicon oxide film. Although the magnitude of the bowing increases at the deposition of the second polysilicon layer, it again decreases with the following sili-

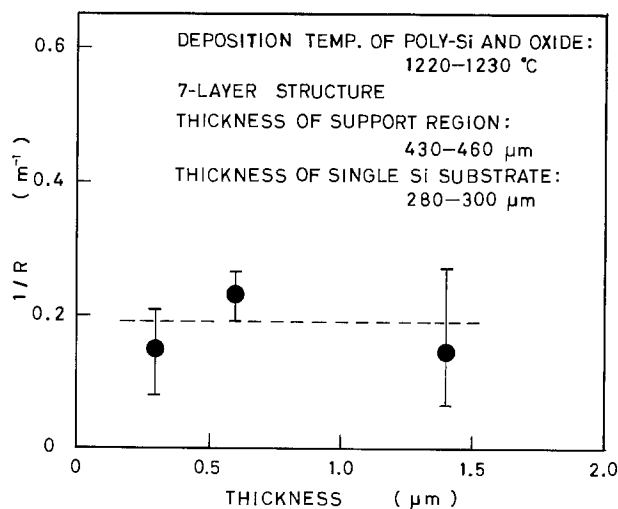


Fig. 9. Effect of the thickness of the silicon oxide films between the polysilicon layers on the degree of bowing of wafers with a multilayer polysilicon structure.

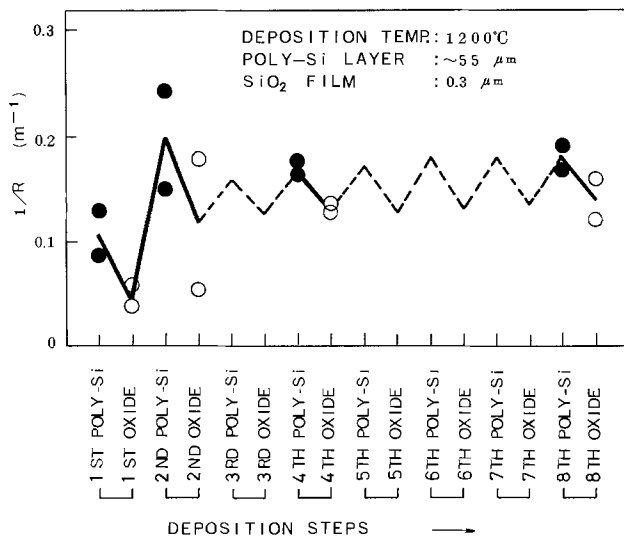


Fig. 10. Curvature variation of the wafers during the formation of a multilayer polysilicon support structure.

con oxide film deposition. The reduction in bowing, however, is somewhat smaller than that of the first deposition step. In this manner, the whole polysilicon support region seems to grow thicker with the repetition of increases and decreases in bowing, according to the alternating polysilicon layer and silicon oxide film depositions. It appears that the penetration or diffusion of high concentrations of oxygen into the polysilicon layer also takes place in the case of the chemical vapor deposition of silicon oxide film at high temperatures just as in the case of thermal oxidation. Therefore, it is proposed that during the formation of the multilayer polysilicon support structure, contraction stress, caused by polysilicon deposition, and expansion stress, caused by silicon oxide deposition, are occurring alternately, and these stresses of opposite direction are successfully compensating each other to form a wafer with little deformation.

Control of deformation during thermal oxidation.—The DI substrate with a multilayer polysilicon support structure was also deformed convexly toward the side of the polysilicon support region, i.e., the minus direction, due to high temperature heat-treatment in an oxygen-containing atmosphere. It was observed, however, that the degree of this kind of deformation was affected by the thickness of the extreme outer polysilicon layer. Therefore, the magnitude of bowing change after thermal oxidation was measured using the sample wafers in which the thickness of the extreme outer polysilicon layer was intentionally varied by lapping. Figure 11 shows a schematic cross-sectional view of such a DI wafer used for the experiments.

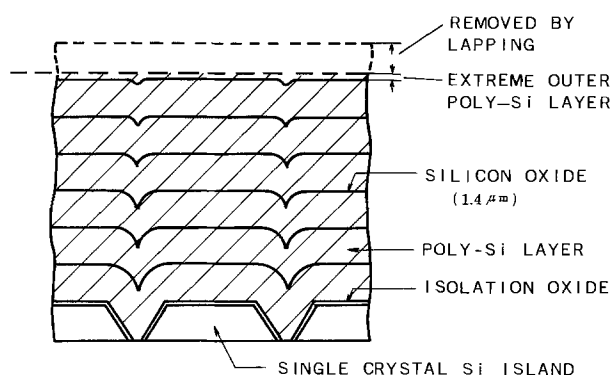


Fig. 11. Schematic cross-sectional view of the multilayer polysilicon support structure in which the thickness of the extreme outer polysilicon layer was thinned.

Figure 12 graphs the experimental results and shows the relation between the ultimate thickness of the extreme outer polysilicon layer after polishing and the change in the magnitude of bowing toward the minus direction, $\Delta(1/R)$, due to thermal oxidation. The thermal oxidation was performed at 1200°C for 340 min in a wet oxygen atmosphere. Although scatter in the measured values is seen, it is evident that the change in the magnitude of bowing $\Delta(1/R)$ decreases as the thickness of the extreme outer polysilicon layer is decreased. The scatter may be due to the uncertainty of the amount of lapping of the extreme outer polysilicon layer, which is caused by wafer bowing after the deposition of the polysilicon support region. Similar experiments, that is, the thermal oxidation of the DI substrates in which the whole extreme outer polysilicon layer was removed by etching and the silicon oxide film was exposed, showed little change in bowing toward the minus direction. Therefore, it is concluded that the deformation of the DI substrate with multilayer polysilicon support structure due to thermal oxidation and diffusion processes is caused by the same mechanism as in the case of the DI substrate with a single layer polysilicon support structure, and that the extreme outer silicon oxide film is acting as the preventive film for oxygen diffusion into the polysilicon support region.

As mentioned above, it is found that the bowing occurring during thermal oxidation or diffusion processes is able to be minimized by providing a film for preventing the penetration or diffusion of oxygen into the surface region of the polysilicon support region. For the DI substrate with a multilayer polysilicon structure, this preventive film is realized by lapping the extreme outer polysilicon layer to a thickness as thin as possible.

Summary

The DI substrate with a single polysilicon support structure is deformed during two processes. One is the deposition of the polysilicon support region and the other is the high temperature heat-treatment in an oxygen-containing atmosphere, i.e., thermal oxidation and diffusion. The deformation after deposition of the polysilicon support region is bowing in a direction such that the polysilicon support region side of the substrate is concave, while the deformation after the thermal oxidation and diffusion is bowing in a direction such that the polysilicon support region side of the substrate tends to become convex. The former bowing seems to be caused by the tensile growth stress gen-

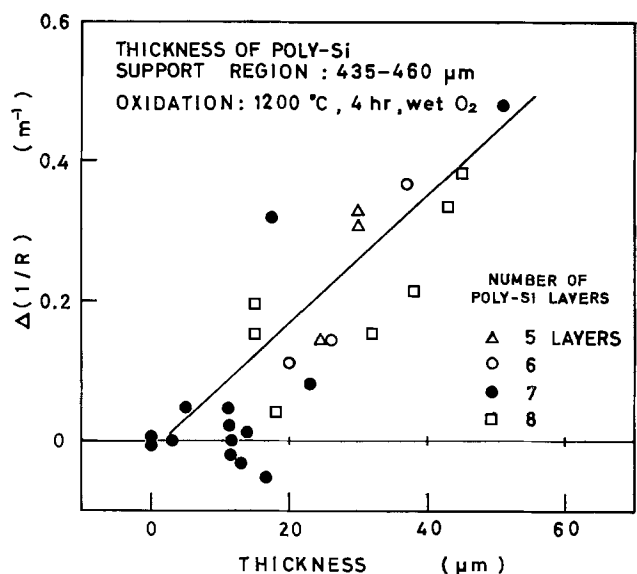


Fig. 12. Relation between the ultimate thickness of the extreme outer polysilicon layer after polishing and the change in the degree of bowing, $\Delta(1/R)$, due to thermal oxidation.

erated through contraction of the growing polysilicon layer at high temperatures. The latter bowing seems to be caused by the expansion stress generated through penetration or diffusion of high concentrations of oxygen into the surface region of the polysilicon support region.

The magnitude and direction of bowing due to the deposition of a polysilicon support layer can be controlled by applying the multilayer structure consisting of alternating polysilicon layers and silicon oxide films. The magnitude of bowing decreases with increasing the number of polysilicon layers for a given total thickness of the support region. The thickness for one polysilicon layer in which the magnitude of bowing is almost zero is about 40–50 μm . It is proposed that during the formation of the multilayer polysilicon support structure, contraction stress, caused by polysilicon deposition, and expansion stress, caused by silicon oxide deposition, are occurring alternately, and these stresses of opposite direction are successfully compensating each other to form a substrate with little deformation.

The DI substrate with a multilayer polysilicon support structure also tends to bow convexly toward the side of the polysilicon support region due to thermal oxidation and diffusion. This type of deformation can be minimized by providing a film for preventing the penetration or diffusion of oxygen into the surface region of the polysilicon support region. This preventive film was realized by lapping the extreme outer polysilicon layer to a thickness as thin as possible.

The deformations which take place during the DI process can be successfully controlled by adopting the multilayer polysilicon support structure and by providing a preventive film for oxygen penetration or diffusion into the surface of the polysilicon support region.

Acknowledgments

The authors wish to express their sincere thanks to Dr. T. Takasuna, Mr. K. Morita, and Mr. M. Tokunaga for their guidance and encouragement in this work.

Manuscript submitted May 2, 1979; revised manuscript received Feb. 5, 1980.

Any discussion of this paper will appear in a Discussion Section to be published in the June 1981 JOURNAL. All discussions for the June 1981 Discussion Section should be submitted by Feb. 1, 1981.

Publication costs of this article were assisted by Hitachi Limited.

REFERENCES

1. K. E. Bean and W. R. Runyan, *This Journal*, **124**, 5C (1977).
2. M. Tokunaga, T. Kamei, I. Ishi, and M. Kawanami, International Switching Symposium 1976, Paper No. 221-4 (1976).
3. R. S. Jacodine and W. A. Schlegel, *J. Appl. Phys.*, **37**, 2429 (1966).
4. U. S. Davidsohn and F. Lee, *Proc. IEEE*, **57**, 1332 (1969).
5. T. Suzuki, A. Mimura, and T. Ogawa, *This Journal*, **124**, 1776 (1977).
6. T. I. Kamins, *ibid.*, **121**, 681 (1974).
7. Japanese Pat. No. 45-32731 (1970).
8. Y. Sumitomo, K. Niwa, H. Sawazaki, and K. Sakai, "Semiconductor Silicon 1973," H. R. Huff and R. R. Burgess, Editors, p. 893, The Electrochemical Society Softbound Proceedings Series, Princeton, N.J. (1973).
9. J. B. Price, *ibid.*, p. 339.
10. A. S. Grove, "Physics and Technology of Semiconductor Devices," p. 22, John Wiley and Sons, Inc., New York (1967).

Electronic States of Ni-Silicides and Its Relation to Metal-Silicide/Si Interfaces

M. Iwami, K. Okuno, S. Kamei, T. Ito, and A. Hiraki

Department of Electrical Engineering, Osaka University, Suita, Osaka 565, Japan

ABSTRACT

Electronic states of Ni-silicides (Ni_2Si , NiSi , and NiSi_2) and potential barrier heights (ϕ_B 's) of Ni-silicide/Si junctions were studied by nuclear magnetic resonance (NMR) and by capacitance-voltage (C-V) measurement, respectively. It was determined that the electronic state of silicon is metallic in all Ni-silicides and that at the site of Si-atom the 3s-electron density with Fermi energy [$\rho_s(E_F, \text{Si})$] becomes larger with increasing Si concentration. From C-V measurements, all of three Ni-silicide/Si junctions showed almost the same barrier height (ϕ_B) of ~ 0.7 eV. These and other experimental results are discussed, and a proposal is made on the nature of the Schottky barrier height at the transition-metal-silicide/Si interfaces.

Many investigations on metal-semiconductor (M-S) interfaces (contacts) have been done for a long period. Above all, so-called contact problems such as the formation of Schottky barriers or ohmic contacts are also practically very important from their role in semiconductor device technology. The metal-semiconductor potential barrier (Schottky barrier) can be classified into two groups whether the barrier height (ϕ_B) is metal dependent or not (1). Although the metal dependent case can be understood very clearly, the metal independent case has stimulated many experimental (2-5) and theoretical studies (6-9); the M-S interface problem is as yet unsettled.

Key words: interfaces, junctions, magnetism.

On the other hand, in transition metal-silicide (tmSi)/Si contact diodes, there is a proposal that the barrier height (ϕ_B) may be determined by the electronic state of tmSi (10). TmSi/Si junctions have been utilized for their reliability owing to the fact that they are formed through the low temperature solid-phase reaction of tm/Si contacts (11) and that the reaction removes impurities and defects existing at the original tm/Si interfaces to form new and clean tmSi/Si junctions. Because of their potential applicability, the mechanism of rectification in tmSi/Si diodes has been studied but has not yet been fully elucidated. However, it is natural to expect that the mechanism of rectification of a tmSi/Si junction depends upon the elec-

tronic state of tmSi. In order to clarify this possibility, including the proposal given in Ref. (10), direct and microscopic information is required on the electronic state of tmSi.

In this respect, we studied the electronic state of silicon in Ni-silicides (Ni_2Si , NiSi , and NiSi_2) and barrier heights (ϕ_B 's) of Ni-silicide (Ni_2Si , NiSi , or NiSi_2)/Si junctions by means of nuclear magnetic resonance (NMR) and by capacitance-voltage (C-V) measurement, respectively.

Experimental

Crystals of Ni-silicides (Ni_2Si , NiSi , and NiSi_2) for NMR measurements were prepared by melting appropriate amounts of nickel powder and polycrystalline silicon in an induction furnace under an argon atmosphere (~ 1 atm). The crystals were identified by the x-ray diffraction method, and then they were filed or crushed into powder. The measurements of T_1 of ^{29}Si in Ni-silicides were carried out by spin-echo technique between 1.4° and 4.2°K at the resonance frequency of 10 MHz.

Schottky diodes of Ni-silicide/Si junctions were prepared as follows. A wafer of n-type silicon, phosphorus-doped with resistivity of $\sim 10 \Omega \cdot \text{cm}$, was cleaned by chemical process, and then an SiO_2 layer left on the surface of the wafer was removed by dipping it in dilute HF. Then an Ni-film ($\sim 1000\text{\AA}$) was deposited on the cleaned Si-substrate under oil-free vacuum ($\sim 10^{-8}$ Torr). Silicides of Ni_2Si , NiSi , and NiSi_2 on Si substrate were formed by heating the Ni(film)/Si(substrate) specimens under conditions given in Table I. Barrier heights (ϕ_B 's) of the Schottky barriers, i.e., Ni-silicide/Si junctions, were deduced from the measurements of diode capacitance as a function of bias voltage.

Results

Spin-lattice relaxation times (T_1 's) of ^{29}Si in three Ni-silicides are shown in Fig. 1 as a function of Si-concentration. Two features are deduced from the figure: (i) T_1 's of ^{29}Si in the silicides fall between 0.7 and 7 sec at 4.2°K , which are very short and comparable with those of pure metals (12); (ii) T_1 of ^{29}Si is shorter in Si-richer silicides— T_1 decreases along with the change of composition from Ni_2Si to NiSi_2 . Another result obtained by NMR measurement which is not shown in the figure is that T_1 's of these Ni-silicides satisfy the relation of $T_1 \cdot T = \text{const.}$ within experimental errors between 1.4° and 4.2°K where T is absolute temperature. In general, T_1 's of metals and nonmetallic semiconductors have characteristics as follows: (i) in metals, T_1 is very short (≤ 1 sec at 4.2°K) due to a high density of conduction electrons and proportional to $[\rho_s(E_F)]^2$ and T^{-1} ; (ii) in nonmetallic semiconductors, T_1 is very long ($\sim 10^6$ sec at 4.2°K) and proportional to N , the density of conduction electrons per unit volume, and $T^{-1/2}$ (13). Therefore, the above results for the Ni-silicides, T_1 is very short and $T_1 \cdot T = \text{const.}$, demonstrate that the local density of 3s-electrons with the Fermi energy at the nucleus of silicon $[\rho_s(E_F, \text{Si})]$ is so high that the electronic state of silicon can be concluded to be metallic.

The second result, T_1 becomes shorter with increasing Si concentration, indicates that $\rho_s(E_F, \text{Si})$ is larger—we term in the present paper this tendency for silicon to be more metallic—in Si-richer silicides.

Table I. Conditions to prepare Ni-silicide/Si junctions by solid phase interfacial reaction

	Temperature ($^\circ\text{C}$)	Time (min)
Ni_2Si	300	10
NiSi	550	10
NiSi_2	800	8

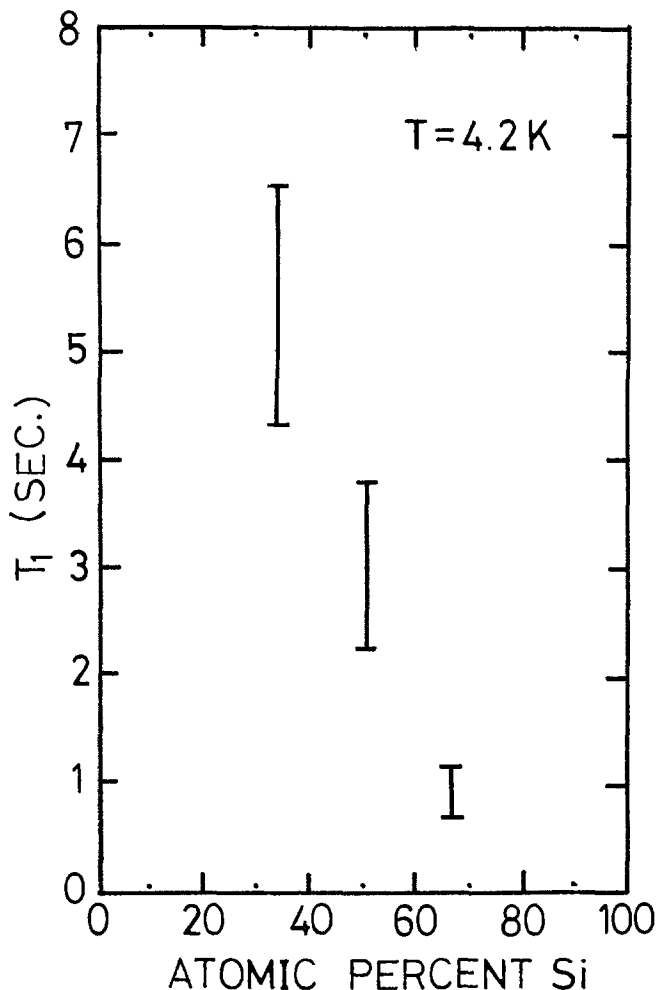


Fig. 1. Spin-lattice relaxation time (T_1) of ^{29}Si in Ni-silicides

As for Schottky barriers, a typical result of a C-V measurement is shown in Fig. 2 for a $\text{Ni}_2\text{Si}/\text{Si}$ junction. ϕ_B 's of Ni-silicide (Ni_2Si , NiSi , or NiSi_2)/Si diodes deduced from the C-V measurement are shown in Fig. 3 as a function of Si-concentration in Ni-silicides; the formation of the corresponding Ni-silicides by the heat-treatment (shown in Table I) was ascertained by

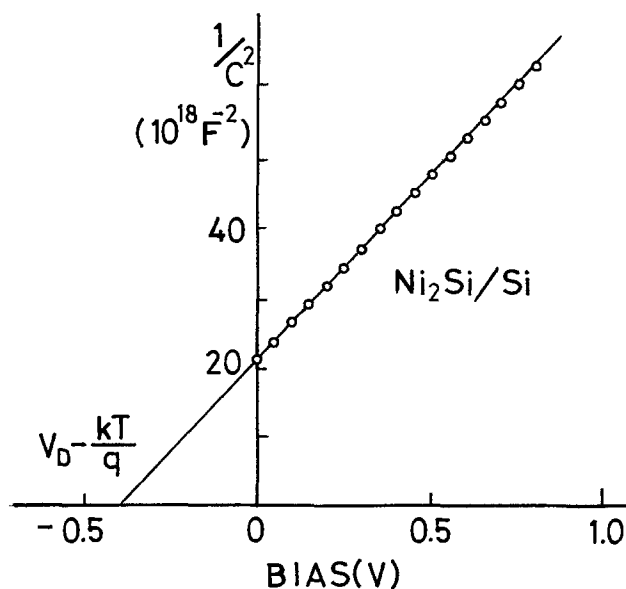


Fig. 2. $1/C^2$ of $\text{Ni}_2\text{Si}/\text{Si}$ Schottky diode as a function of bias voltage.

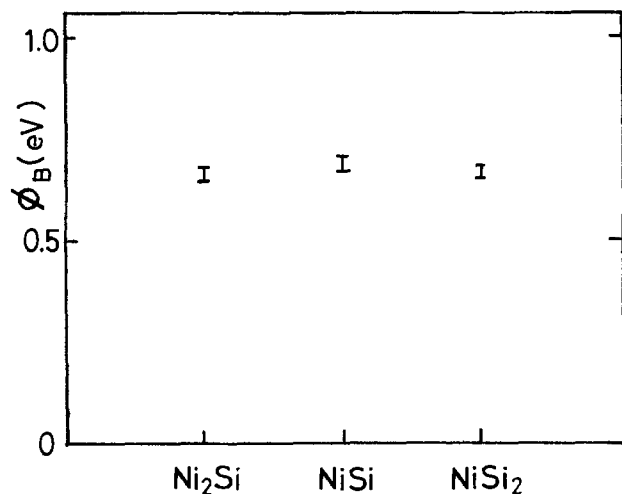


Fig. 3. Schottky barrier height (ϕ_B) in $\text{Ni}_2\text{Si}/\text{Si}$, NiSi/Si , and NiSi_2/Si junctions.

Rutherford backscattering spectroscopy (RBS). An example for NiSi_2 -layer formation on a silicon surface is shown in Fig. 4. The ϕ_B values are distributed around 0.7 eV in all specimens irrespective of the difference in Si concentration in the silicide overlayers. There is no apparent functional relation between ϕ_B and x in $\text{Ni}_{1-x}\text{Si}_x$, which is a clear contrast for the NMR measurement, where T_1 decreases with increasing x .

Discussion

The present results by NMR measurement are summarized in Table II with data of previous works for comparison. Our data show that $\rho_s(E_F, \text{Si})$ is so high compared with that of semiconductor silicon, not only that of pure silicon but also that of degenerate silicon, heavily doped with impurity atoms (14), that Si-atoms are concluded to be making metallic bonding (here we term such silicon as "metallic silicon") in the Ni-silicides. The electronic nature of silicon is metallic when Si atoms are dissolved slightly in the host 3d-metal (the concentration of silicon is so low that an Si atom is considered to be a single impurity), which has been explained theoretically in terms of the redistribution of 3s- and 3p-electrons at silicon sites

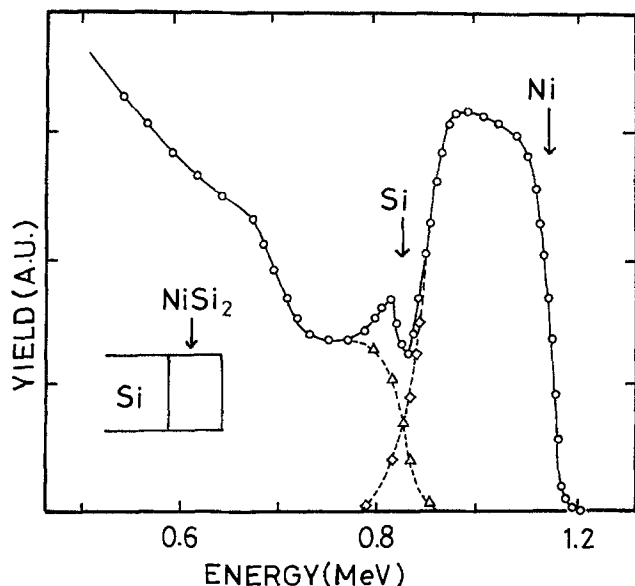


Fig. 4. Rutherford back-scattering examination of the formation of NiSi_2 layer on Si(substrate) by heating a specimen of Ni(film)/Si(substrate) for 8 min at 800°C . Dotted lines show the expected spectra for the distribution of nickel and silicon.

Table II. T_1 values and temperature dependence of T_1 of ^{29}Si in Ni_2Si , NiSi , and NiSi_2 . Those of n-Si crystals doped with donor impurities are also shown for comparison

Specimen	T_1 at 4.2°K (sec)	Temperature dependence of T_1	Reference
Ni_2Si	5.5	T^{-1}	Present study
NiSi	3	T^{-1}	Present study
NiSi_2	0.7	T^{-1}	Present study
n-Si ($n_D = 2.5 \times 10^{19}/\text{cm}^3$)	6×10^2	T^{-1}	(14)
n-Si ($n_D = 4 \times 10^{19}/\text{cm}^3$)	5×10^6	$T^{-1/2}$	(13)

through the hybridization with 3d-electrons of host metals (15). Several experimental results have confirmed the above theory (16, 17). It is plausible that the metallic silicon in Si-deficient-Ni-silicides, for example, in Ni_3Si , is also explained in the same way (17). However, the metallic silicon in Si-richer-Ni-silicides, as in the present study, cannot be explained by the above theory because of extremely high Si concentration. Therefore, it is an interesting question which mechanism metallizes silicon in those Ni-silicides.

For the sake of discussion, we will refer to the data by soft x-ray spectroscopy (SXS) measurements. Figure 5 illustrates measured Si- K_β emission spectra from several Ni-silicides and pure silicon, which provide information on the electronic structure of 3p-electrons of silicon (18). One apparent point to be noted about the silicides is that each spectrum has a finite intensity at the Fermi energy, which indicates that the 3p-electron density of silicon [$\rho_p(E_F, \text{Si})$] is large to show that Si atoms have metallic bonding. Also

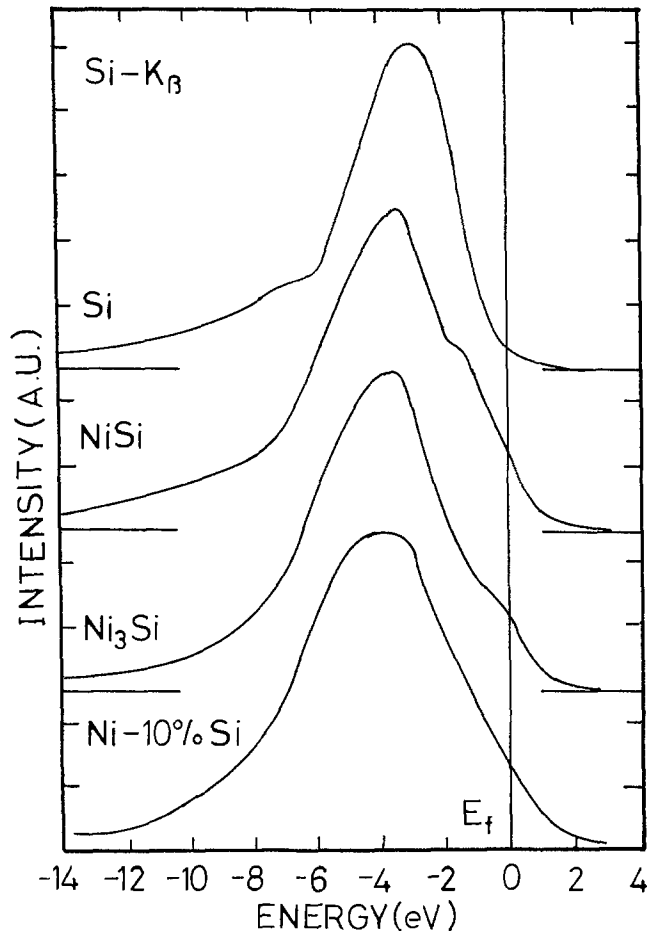


Fig. 5. Si- K_β emission spectra from Ni-silicides and from pure silicon (18). The data for NiSi is unpublished.

the increment of the intensity at E_F , which is roughly proportional to $\rho_p(E_F, \text{Si})$, in Si- K_β emission spectra with increasing Si concentration from Ni_3Si to NiSi is observed to coincide with the results of T_1 measurement in Ni-silicides, i.e., the increment of $\rho_s(E_F, \text{Si})$ with the increase of Si concentration. Another feature of the results (Fig. 5) is that K_β -emission spectra gradually change their shapes from single peaked one of $\text{Ni}_{0.9}\text{Si}_{0.1}$ into the spectrum with a clear shoulder of NiSi . Similar spectral change of K_β -emission was reported for the Ni-Al system as shown in Fig. 6 (18). These results of the Al- K_β emission spectra in the Ni-Al system must be the reflection of the fact that the electronic structure of 3s-electrons of aluminum is approaching that of pure metal aluminum with increasing Al-concentration, i.e., the appearance of the shoulder in NiAl is considered to be an appearance of the free electron nature of pure metal aluminum. The similar change in K_β -emission spectra of Ni-silicides (Fig. 5) to that of Ni-Al system (Fig. 6), i.e., a clear shoulder appears in the spectrum of NiSi , is thought to be an indication of the appearance of metallic silicon, which can be observed only when silicon is either in a liquid state or exposed to an ultrahigh pressure (≥ 200 kb). There is a suggestive report about germanium being metallic, i.e., the radial distribution function of germanium is almost the same as that of liquid (metallic) Ge, in the Ni-Ge system with Ge-rich alloys (19).

Next, we will discuss our present conclusion with the proposal given by Andrews and Phillips (10). They intended to explain the relation between ϕ_B and ΔH_f (heat of formation of tmSi per tm -atom) from the view point of the degree of sp^3 -hybridization of d-electrons of tm -atoms with neighboring Si atoms. Namely, they assumed that tm -atoms in tmSi with higher ΔH_f value would have more sp^3 -like covalent bondings. On

the other hand, the present NMR study clearly indicates that Si-atoms in Ni-silicides have metallic bondings rather than sp^3 -like covalent bondings. Therefore, the present conclusion suggests some different model is necessary for the electronic property of Schottky barriers in tmSi/Si interfaces, especially for Ni-silicide/Si junctions. On this point, the results in Fig. 3 can be a clue. Namely, ϕ_B 's are almost constant for three different diodes, i.e., in $\text{Ni}_2\text{Si/Si}$, NiSi/Si , and $\text{NiSi}_2\text{/Si}$ junctions. Possible explanations for the results on the ϕ_B 's are the existence of some kind of alloy phase at the interface region as with Au/Si contacts (2), the band closure of silicon at the tmSi/Si contact region (6-9), and others (3-5). Further studies will be necessary to decide which mechanism is applicable for Ni-silicide/Si junctions.

Conclusions

NMR measurements of the electronic structure of Ni-silicides (Ni_2Si , NiSi , and NiSi_2) show that Si atoms in the silicides are considered to have metallic bondings with surrounding atoms rather than to have sp^3 -like covalent bondings and that Si-atoms are more metallic in Si-richer-Ni-silicides. Either this fact or the invariance of Schottky barrier heights (ϕ_B 's) shows that some different explanation from previous ones must be considered for the electronic property of Ni-silicide/Si junctions, such as Fermi level pinning due to the band closure of silicon at the M-S contact.

Manuscript received Nov. 12, 1979. This was Paper 347 presented at the Los Angeles, California, Meeting of the Society, Oct. 14-19, 1979.

Any discussion of this paper will appear in a Discussion Section to be published in the June 1981 JOURNAL. All discussions for the June 1981 Discussion Section should be submitted by Feb. 1, 1981.

Publication costs of this article were assisted by Osaka University.

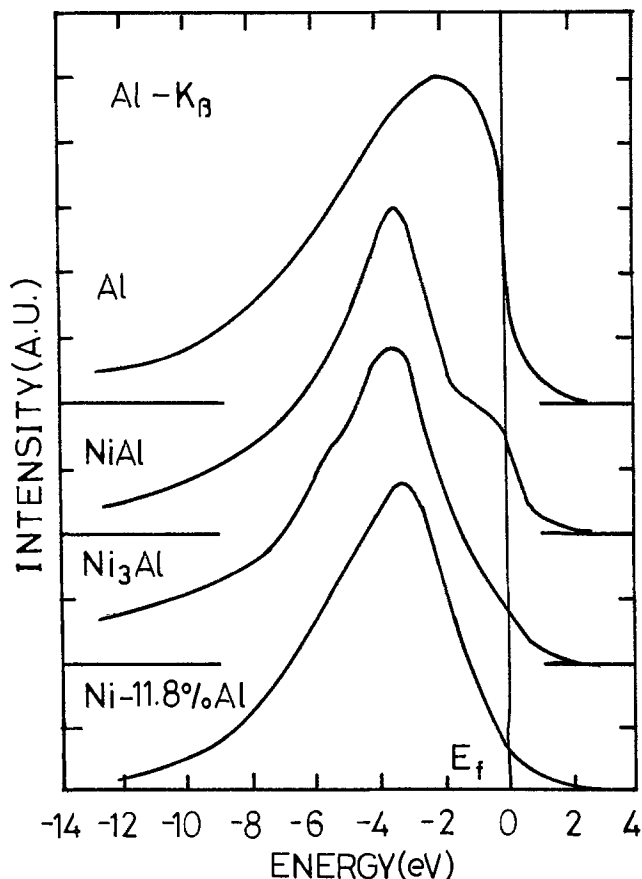


Fig. 6. Al- K_β emission spectra from Al-Ni alloys and from pure aluminum (18).

REFERENCES

1. S. Kurtin, T. C. McGill, and C. A. Mead, *Phys. Rev. Lett.*, **30**, 1433 (1969).
2. A. Hiraki, K. Shuto, S. Kim, W. Kammura, and M. Iwami, *Appl. Phys. Lett.*, **31**, 611 (1977).
3. J. E. Rowe, G. Margaritondo, and S. B. Christman, *Phys. Rev. B*, **15**, 2195 (1977).
4. L. J. Brillson, *ibid.*, **18**, 2431 (1978).
5. I. Lindau, P. W. Chye, C. M. Garner, P. Pianetta, C. Y. Su, and W. E. Spicer, *J. Vac. Sci. Technol.*, **15**, 1332 (1978).
6. V. Heine, *Phys. Rev. A*, **138**, 1685 (1965).
7. J. C. Phillips, *Solid State Commun.*, **12**, 861 (1973).
8. J. C. Inkson, *J. Phys. C*, **6**, 1350 (1973).
9. P. W. Anderson, "Elementary Excitation in Solids, Molecules and Atoms," Part A, Plenum Press, New York (1974).
10. J. M. Andrews and J. C. Phillips, *Phys. Rev. Lett.*, **35**, 56 (1975).
11. K. N. Tu and J. W. Mayer, in "Thin Films—Interdiffusion and Reactions," Chap. 10, J. M. Poate, K. N. Tu, and J. W. Mayer, Editors, A Wiley-Interscience Pub., New York (1978).
12. K. Okuno, M. Iwami, A. Hiraki, M. Matsumura, and K. Asayama, *Solid State Commun.*, To be published.
13. A. Abragam, in "The Principles of Nuclear Magnetism," p. 389, Oxford at the Clarendon Press (1961).
14. W. Sasaki, S. Ikehata, and S. Kobayashi, *J. Phys. Soc. Jpn.*, **36**, 1377 (1974).
15. K. Terakura, *ibid.*, **40**, 450 (1976).
16. K. Tanaka, M. Matsumoto, S. Maruno, and A. Hiraki, *Appl. Phys. Lett.*, **26**, 57 (1975).
17. K. Tanaka and A. Hiraki, *Jpn. J. Appl. Phys.*, **17**, Suppl. 2, 121 (1978).
18. K. Tanaka, *Bull. Jpn. Inst. Metals*, **15**, 753 (1976) (in Japanese).
19. K. Yamada, H. Onodera, and Y. Endo, *J. Phys. Soc. Jpn.*, To be published.

Boron Diffusion into Si from CVD-BN Covered with Si₃N₄ and Application to Master Slice p-MOS IC

Katsufusa Shohno,* Tejin Kim,¹ and Chol Kim

Faculty of Science and Technology, Sophia University, Kioicho-7, Chiyoda-ku, Tokyo, Japan

ABSTRACT

A boron nitride (BN) film was deposited on an n-type Si wafer at about 500°C by the thermal reaction of diborane and ammonia in nitrogen. The boron diffusion into Si was performed in nonoxidizing ambients both during the deposition of the BN on the Si and the subsequent heat-treatment. To obtain the reproducibility of the boron surface concentration at its solid solubility at the diffusion temperature, the BN has to be covered with Si₃N₄, which is deposited at about 750°C in a silane-ammonia-nitrogen system. No silicon-boride formation at the interface of the BN and Si was confirmed. The resistivity of the BN was determined as $\rho = 10^{13}$ - 10^{14} Ω -cm. The BN can be used not only as a boron diffusion source but also as a surface passivation of integrated circuits when the BN and Si₃N₄ remained after the boron diffusion.

Boron diffusion into Si from CVD-BN films as a diffusion source was reported previously (1). The BN had been deposited in a hydrogen carrier gas at a high deposition temperature range of 700°-1250°C. When the BN was used in a practical integrated circuit process, the authors found that less reproducible boron surface concentrations were often observed due to the change of the BN during the boron diffusion heat-treatment in nitrogen. In addition, the writers also found that the low temperature deposition of the BN at about 500°C in nitrogen and the over-coat deposition of Si₃N₄ on the BN were effective in maintaining the reproducibility of the boron surface concentrations at its solid solubility.

Fair summarized the boron diffusion into Si from various diffusion sources (2). When the boron surface concentration exceeds the intrinsic carrier concentration at a diffusion temperature, the effects of electric field enhancement caused by the increase of donor-type vacancies have to be taken into account. Fair's analysis was employed in this work to determine the boron diffusion characteristics from BN in nonoxidizing ambients.

In the final section of this report an application of the BN to master slice p-MOS IC is shown, in which the resistivity of the BN was determined, and the BN was used not only as a diffusion source of boron but also as a surface passivation when it remained after the boron diffusion.

Experimental

The experimental apparatus for the BN and Si₃N₄ deposition has been described previously (1). A quartz reaction chamber used in this work had an internal width of 35 mm, a height of 20 mm, and a length of 400 mm. The reactant gases used for the BN deposition were high purity diborane (B₂H₆) diluted to 5% in nitrogen and ammonia (NH₃), and those gases for the Si₃N₄ deposition were high purity silane (SiH₄) diluted to 5% in nitrogen and ammonia. The carrier gas was high purity nitrogen.

First, the BN was deposited on the n-type (100) Si wafer with a resistivity of 3-5 Ω -cm ($N_D = 0.9$ - 1.5×10^{15} cm⁻³). The deposition conditions were: (i) a wafer temperature of 500°C, and (ii) flow rates of the B₂H₆-N₂, the NH₃, and the N₂ carrier gases of 50, 70, and 2000 cm³/min, respectively. Under those conditions

the average deposition rate of the BN was about 300 Å/min.

The Si₃N₄ was then deposited on the BN after the wafer temperature was increased to 750°C. The flow rates of the SiH₄-N₂, the NH₃, and the N₂ carrier gases were 20, 70, and 2000 cm³/min, respectively, and the average deposition rate of the Si₃N₄ was about 500 Å/min.

With heat-treatment in nitrogen for 10-300 min at 1200°C, the boron diffusion layer was formed in the Si wafer. To measure the diffusion depth and the sheet resistance, the Si₃N₄ was removed by etching in conc HF at room temperature and the BN was removed in hot H₃PO₄ (~160°C). After the complete removal of the films, the hydrophobic or hydrophilic nature of the wafer surface was observed.

The diffusion depth x_j (cm) was measured by spherical drilling and staining (3) and the sheet resistance R_s (Ω/\square) was measured by four-point probe. The boron surface concentration C_s (cm⁻³), the total amount of boron diffusing into Si Q (cm⁻²), and the intrinsic diffusion coefficient D_i (cm²/sec) were all determined by using the following relations given by Fair (2)

$$C_s = \frac{2.78 \times 10^{17}}{R_s x_j} \quad [1]$$

$$Q = 0.4 C_s x_j \quad [2]$$

$$x_j = 2.45 \left(\frac{C_s D_i t}{n_i} \right)^{1/2} \quad [3]$$

The effects of electric-field enhancement caused by the increase of donor-type vacancies were taken into account. The intrinsic carrier density is $n_i = 2 \times 10^{19}$ cm⁻³ at the diffusion temperature of 1200°C.

Results and Discussion

Uniformity and reproducibility.—The uniformity and reproducibility in a run-to-run of a boron diffusion layer in Si become important when the BN is used in a practical Si planar process as a boron diffusion source. After the heat-treatment for boron diffusion from the BN, the Si₃N₄ and the BN were removed, resulting in the hydrophobic nature of the Si surface. To obtain the distribution of the sheet resistance of the boron diffusion layer, a conventional four-point probe was moved from one point to the next at an interval of 2 mm for about 240 points over the entire surface of the Si wafer with a 40 mm diam.

* Electrochemical Society Active Member.

¹ On leave from Faculty of Engineering, Korea University, Kodaira, Japan.

Key words: boron diffusion, CVD-BN, p-MOS IC.

The measurements were repeated five times and the average values were obtained for each of the points. Representative examples of the distribution are shown in Fig. 1 for 29 representative points. The maximum value is 1.70, the minimum one is 1.55, the average is 1.63 Ω/\square , and the distribution is within the range of $\pm 4\%$. The run-to-run distributions are also satisfactory and within the same range.

Characteristics of boron diffusion.—Auger spectroscopic analysis of boron in the BN gives the boron atomic density of about $2-3 \times 10^{22} \text{ cm}^{-3}$. When the thickness of the BN was more than about 500Å, that is, when a sufficient amount of boron was given as a diffusion source, the boron diffusion characteristics are summarized in Fig. 2 for experimentally measured values and in Fig. 3 for calculated values from Eq. [1], [2], and [3].

The junction depth x_j increases in proportion to the square root of the diffusion time and reaches 10 μm for the diffusion time 80 min. The sheet resistance R_s decreases in proportion to the square root of the diffusion time. Consequently, the average resistivity $\bar{\rho}$, which is a product of the junction depth and the sheet resistance, becomes constant for the diffusion time and it is as low approximately as $\bar{\rho} = 1.2 \times 10^{-3} \Omega\text{-cm}$. The constant average resistivity corresponds to a constant boron surface concentration $C_s = 2.7 \times 10^{20} \text{ cm}^{-3}$, which is obtained from Eq. [1] and is almost in agreement with the solid solubility reported by Vick and White (4). The total amount of boron diffusing into Si given by Eq. [2] increases in proportion to the square root of the diffusion time and approaches to about 10^{17} cm^{-2} , with expectation of the continuous supply of a sufficient amount of boron from the BN. The intrinsic diffusion coefficient obtained from Eq. [3] becomes constant for the diffusion time, and the value is $D_i = 1.0 \times 10^{-12} \text{ cm}^2/\text{sec}$, which is almost in agreement with that already reported (4-6).

When the BN with a thickness of about 200Å was used as a boron diffusion source, the supply of boron from the BN becomes apparently poor in relation to the long-time diffusion, as shown in Fig. 4. For a diffusion time of less than 30 min the boron surface concentration is maintained at the solid solubility $C_s \approx 2.7$

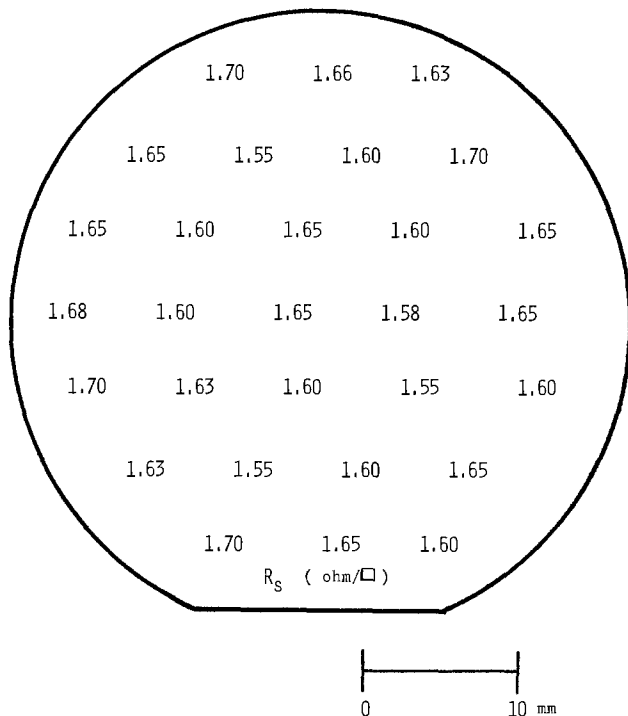


Fig. 1. Sheet resistance of boron diffusion layer. The diffusion temperature was 1200°C and the time was 50 min.

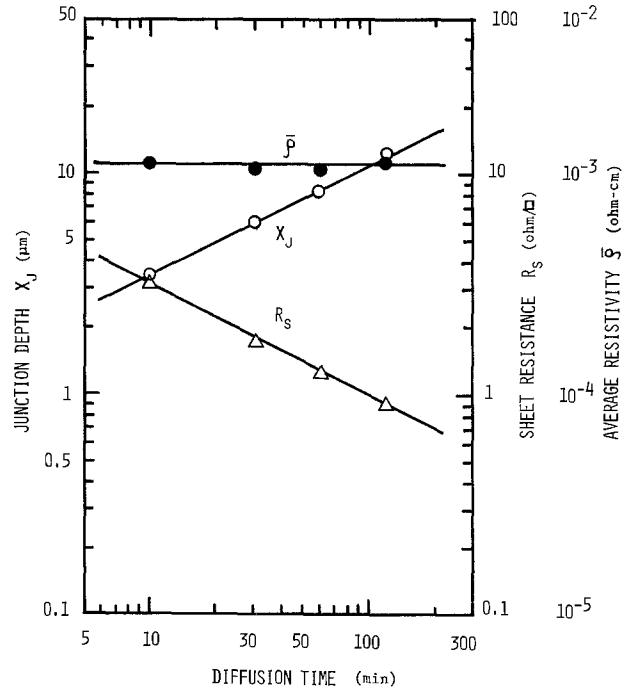


Fig. 2. Junction depth, sheet resistance, and average resistivity of boron diffusion layer of the BN when thicker than about 500Å.

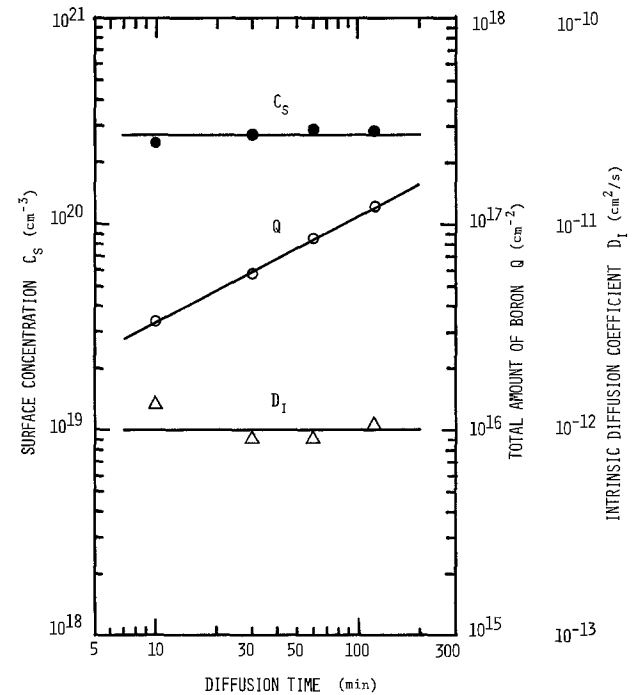


Fig. 3. Surface concentration, total amount, and intrinsic diffusion coefficient of boron diffusing into Si as a function of diffusion time.

$\times 10^{20} \text{ cm}^{-3}$, and the total amount of boron increases in proportion to the square root of the diffusion time. On the other hand, for a diffusion time of more than 30 min the boron surface concentration decreases, and the total amount of boron tends to saturate to $8 \times 10^{16} \text{ cm}^{-2}$.

To determine the boron profile, the change of the sheet resistance is measured by repeated dry plasma etching of the boron diffusion layer. An approximately independent hole mobility of $\mu = 55 \text{ cm}^2/\text{V sec}$ was assumed for a boron concentration larger than $5 \times 10^{19} \text{ cm}^{-3}$. Dry plasma etching was carried out in a gas mixture of CF_4 (98%) and O_2 (2%). The etching rate

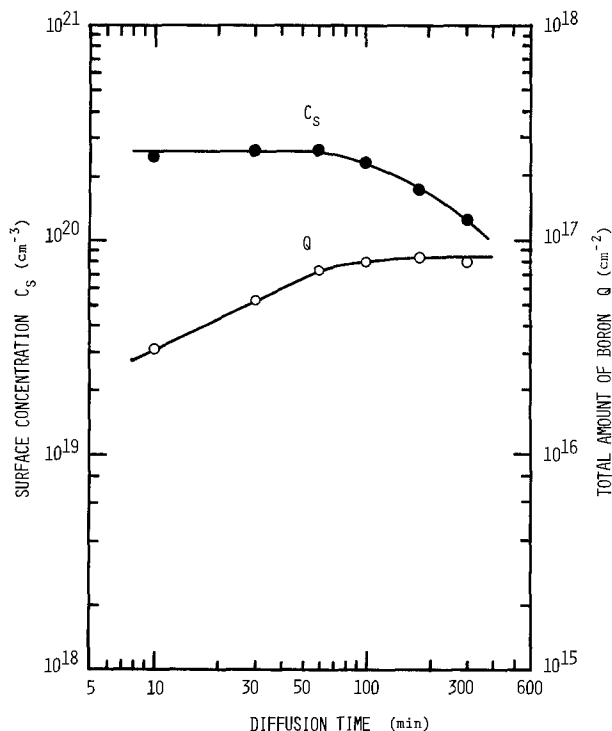


Fig. 4. Surface concentration and total amount of boron diffusing into Si from the BN when thinner than about 200 Å.

was 1000 Å/min, and, after every etching cycle, a measurement was made of the sheet resistance. The thickness of the silicon removed was determined with an interference microscope.

The boron profile obtained is shown in Fig. 5. The black points show experimentally obtained values. For comparison, the well-known error function complement (erfc) curve is shown and the solid line is a curve of the form

$$C(x) = C_s(1 - (x/x_j)^{2/3}) \quad [4]$$

which was given by Fair, and in which the junction

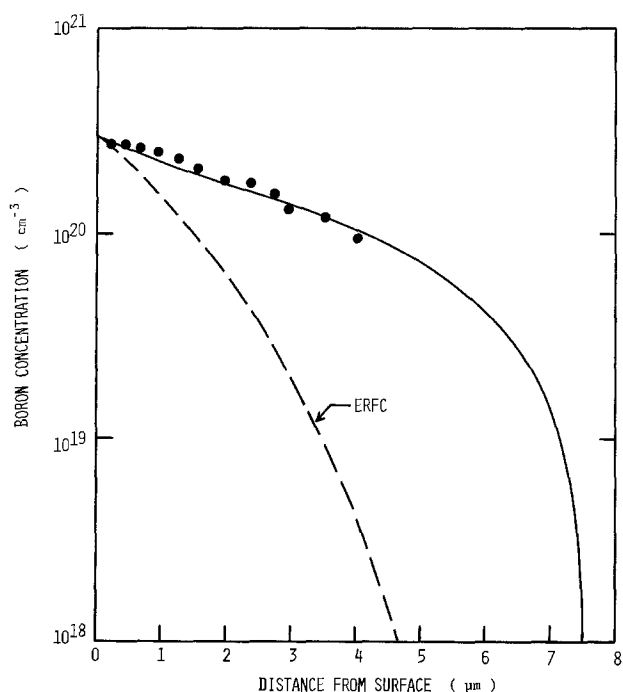


Fig. 5. Boron profile diffused from the BN. The diffusion temperature was 1200°C and the time was 60 min.

depth of 7.5 μm is measured at 10^{15} cm^{-3} . It is clearly seen that the boron diffusion was accelerated due to the effects of electric-field enhancement, compared with the erfc curve.

Interface of BN and Si.—To investigate the interface between BN and Si, diffusions involving two steps were performed. After the deposition of the BN and Si_3N_4 , the prediffusion was done at a temperature between 750° and 1250°C for 10 min. For the samples of the boron diffusion at 750°C, the 10 min prediffusion had to be a total of the Si_3N_4 deposition time at 750°C for 2 min and the prediffusion time for 8 min. In Fig. 6 the solid line is an expected curve of the amount of boron which is calculated by Eq. [2], in which the boron surface concentration C_s is a solid solubility of boron at each of the temperatures (4), and the junction depth x_j is given by Eq. [3].

After the prediffusion, the Si_3N_4 and BN were successively removed. The hydrophobic nature of the Si surface was confirmed.

Before the postdiffusion, the Si surface was newly covered with Si_3N_4 at a deposition temperature of 750°C. The postdiffusion was the heat-treatment for the samples in nitrogen at 1200°C for 30 min. When the prediffusion was done at above 1000°C, the junction depth and sheet resistance could be measured and the amount of boron in Si was determined both after the pre- and postdiffusions. The same amount of boron was obtained for both measurements; the values are shown with black circles in Fig. 6. When the 10 min prediffusion was done below 950°C, the boron diffusion layer was formed of such shallow depth that the direct measurement of the junction depth was difficult. After the shallow boron profiles were extended out by postdiffusion at 1200°C for 30 min, the junction depth and sheet resistance could be measured and the amount of boron determined. The values are shown with white circles in Fig. 6.

The solid line in Fig. 6 is in good agreement with the experimental points, with the result that the amount of boron given in the prediffusion step can be maintained during the postdiffusion step. This result leads to the conclusion that by etching off the BN diffusion source an additional boron diffusion source

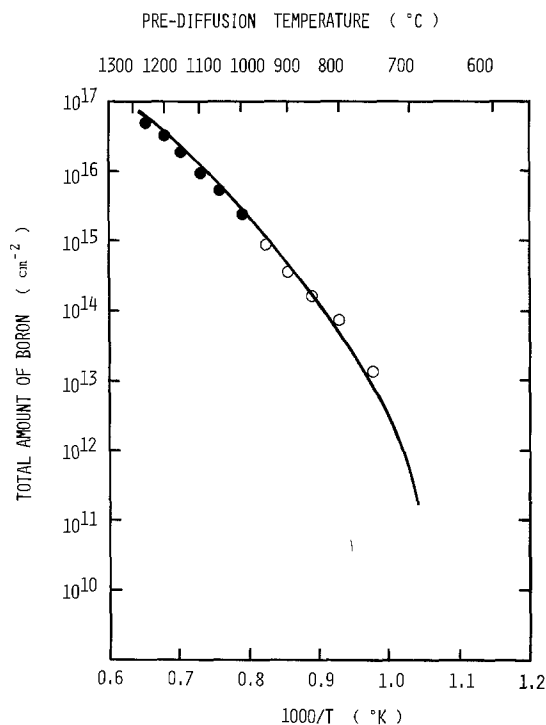


Fig. 6. Conservation of the total amount of boron with two-step diffusions.

did not remain on the Si surface and no silicon-boride (SiB_4) layer was formed at the interface between the BN and Si.

Resistivity of BN and application to master slice p-MOS IC.—The fabrication sequence of the polycrystalline Si-gate self-aligned p-MOS transistor is shown in the cross-sectional view of Fig. 7. The n-type Si wafer with a resistivity of 3-5 $\Omega\text{-cm}$ was thermally oxidized in dry oxygen at 1070°C for 50 min, resulting in a 700Å layer of SiO_2 . A 300Å layer of Si_3N_4 and a 3000Å layer of polycrystalline Si were deposited at 750° and 650°C, respectively. This wafer is the starting material for us (A). The windows of both source and drain were opened in the first photolithographic step by successively etching the polycrystalline Si, the Si_3N_4 , and the SiO_2 layers in a plasma of CF_4 (98%) and O_2 (2%) (B). A 200Å layer of the BN and a 3000Å layer of Si_3N_4 were deposited over the entire surface of the wafer. Boron diffusions in Si to a junction depth of 3 μm and also in polycrystalline Si gate were simultaneously accomplished by an 80 min heat-treatment at 1100°C in nitrogen. The boron surface concentration in Si is $2.5 \times 10^{20} \text{ cm}^{-3}$ and the resistivity of polycrystalline Si is $2.0 \times 10^{-3} \Omega\text{-cm}$ (C). The second photolithographic step is for the opening of the contact windows. Successive dry plasma etching was used to selectively remove the Si_3N_4 and BN layers. Slight attacks on the Si surface and the polycrystalline Si layer make it easy to form the ohmic contacts (D). A 5000Å layer of Al was evaporated over the wafer surface at a wafer temperature of 230°C. The third photolithographic step is for the delineation of the Al (E). The Al is etched in a solution of H_3PO_4 and $\text{DI-H}_2\text{O}$ in equal parts at 55°C (F). In this fabrication process, the BN was used not only as a diffusion source of boron but as a surface passivation of MOS transistors.

The square-type inverter circuits are a unit of the master slice p-MOS IC's, and an overview microphotograph of a part of a chip including six inverter circuits is shown in Fig. 8. The inverter circuit layout has the load transistor at its center, surrounded by the in-

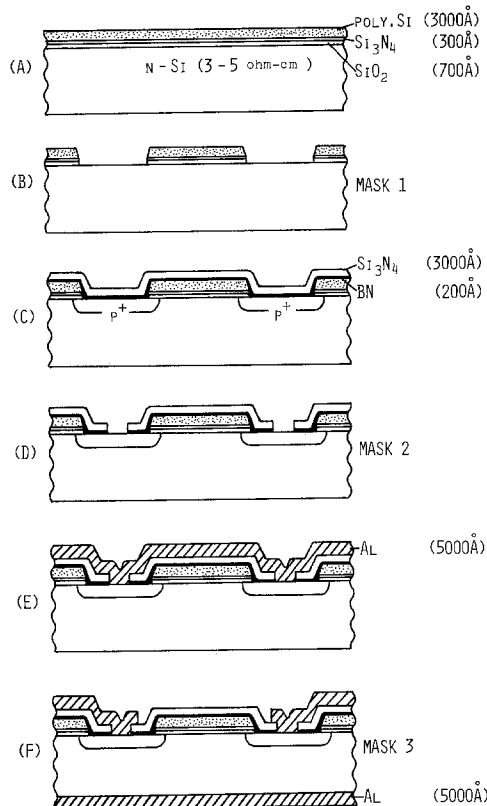


Fig. 7. Fabrication sequence of polycrystalline Si-gate self-aligned p-MOS transistor.

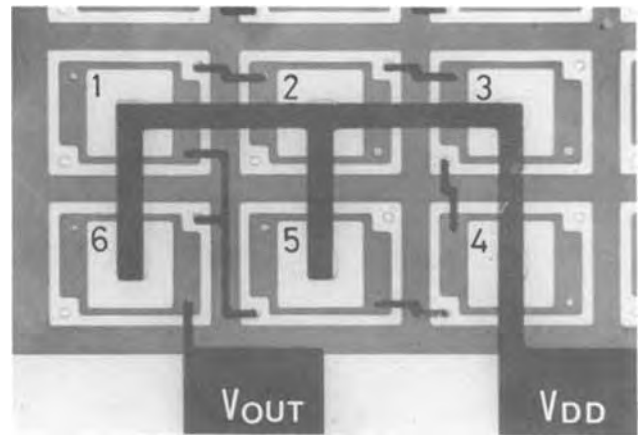


Fig. 8. Overview microphotograph of six inverter circuits. Five inverter circuits, 1-5, are connected to a ring oscillator with a buffer stage, 6.

verter transistor. The source of the load transistor serves as the drain region of the inverter transistor and also as the output of the inverter circuits. The contact windows of Al interconnections are opened at each of the corners. In our practical device fabrication process of the master slice p-MOS IC's, two Al evaporations and delineations are employed. The first Al delineation forms the pads at each of the contact windows to measure the $V_G\text{-}I_D$ characteristics of each of the MOS transistors in advance. The second Al delineation makes Al interconnections for the selected inverter circuits. The photomasks for the Al interconnections are designed for each of the chips using the authors' easy method of photomask fabrication (7).

A cross-sectional view of our fabrication process shown in Fig. 7 (F) has a structure showing that the BN covers the edge wall of the gate insulator, the double layers of SiO_2 , and Si_3N_4 between the polycrystalline Si gate and the source or drain p-region. To determine the resistivity of the BN, once the amount of negative charge was given on the polycrystalline Si gate of the inverter transistors, the gate charge decay time τ was obtained from the decrease of the drain current. The decay time was simply given as

$$\tau = C_1 R = \frac{\epsilon_0 \epsilon_1 l \rho_{\text{BN}}}{2 d_{\text{BN}}} \quad [5]$$

where (i) the gate capacitance is $C_1 = 4\epsilon_0 \epsilon_1 w l / d_i$, (ii) the resistance through the current path is $R = d_i \rho_{\text{BN}} / 8 w d_{\text{BN}}$, (iii) the average dielectric constant of gate SiO_2 and Si_3N_4 layer is $\epsilon_1 = 4.4$, and (iv) the total thickness of gate SiO_2 and Si_3N_4 layer is $d_i = 1000\text{Å}$. The charge decay time and the resistivity of the BN are shown in Fig. 9 as a function of the deposition temperature of the BN. The current path was assumed through the BN along the edge wall of the gate insulator, as shown in the insertions of the figure. The resistivity of the BN was about $10^{13} \Omega\text{-cm}$ for the deposition temperature of the BN at 500°C. This value can be compared with the resistivity of SiO_2 and Si_3N_4 of about $10^{15}\text{-}10^{16} \Omega\text{-cm}$ (8).

An example of the application of the p-MOS IC device using the BN in the fabrication process is a ring oscillator circuit with several inverter stages, as shown in Fig. 8, where the output of the inverter circuit is directly connected to the input of the next inverter circuit stage. The $V_G\text{-}I_D$ curve of each of the MOS load and inverter transistors is measured in advance. The inverter circuits are characterized by the threshold voltage V_T of the gate and the conduction factor k , which has a relation with the surface mobility μ , of each of the load and inverter transistors. The ring

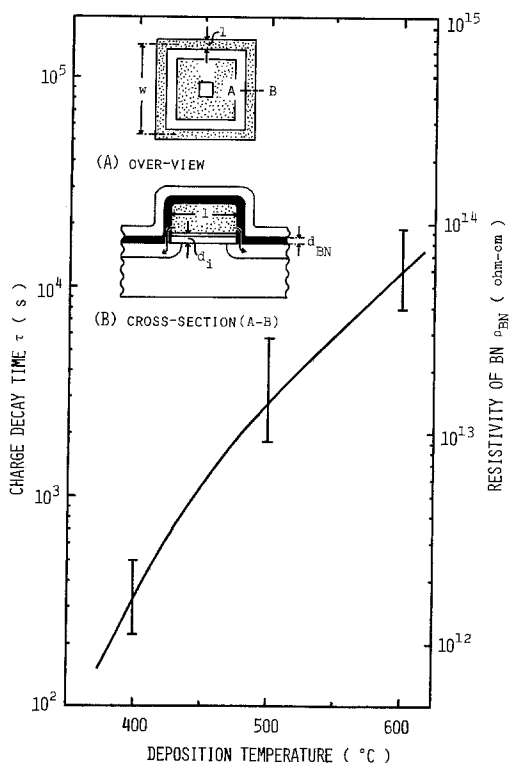


Fig. 9. Charge decay time and resistivity of the BN as a function of the deposition temperature of the BN.

oscillator circuit was formed and connected with the selected number of inverter circuits. Taking into account the load capacitance C_L between each of the inverter circuit stages, the oscillation wave forms are calculated and are compared with the observed ones. The observed frequencies are about 15% less in average than the calculated ones. The leakage current of the inverter transistor through the BN is as small as about 10^{-14} A for the design in Fig. 8, and the drain current under the ring oscillator operation is in the range of from 10^{-5} - 10^{-4} A. No effect of the leakage current through the BN was observed in our practical device application. It can be concluded that the BN

can be used as a surface passivation, except for the special devices which need a long charge holding time, such as the FAMOS memory devices.

Conclusion

The BN deposited at 500°C in the $\text{B}_2\text{H}_6\text{-NH}_3\text{-N}_2$ system and covered with Si_3N_4 acts as a reproducible diffusion source of boron in Si. The boron surface concentration was maintained at its solid solubility, when the BN thickness was above 500Å. After the boron diffusion no silicon-boride formation was observed at the interface of the BN and Si. An application example to the MOS IC device is a master slice polycrystalline Si-gate self-aligned p-MOS IC. The charge decay time on the gate gives the BN resistivity of 10^{13} - 10^{14} $\Omega\text{-cm}$, and the BN can be concluded to be useful as a surface passivation of the devices when the BN remained after the boron diffusion in Si.

Manuscript submitted Dec. 27, 1979; revised manuscript received Feb. 25, 1980. This was Paper 413 presented at the Los Angeles, California, Meeting of the Society, Oct. 14-19, 1979.

Any discussion of this paper will appear in a Discussion Section to be published in the June 1981 JOURNAL. All discussions for the June 1981 Discussion Section should be submitted by Feb. 1, 1981.

Publication costs of this article were assisted by Sophia University.

REFERENCES

1. M. Hirayama and K. Shohno, *This Journal*, **122**, 1671 (1975).
2. R. B. Fair, *ibid.*, **122**, 800 (1975).
3. T. Kinoshita and K. Shohno, *Oyo Buturi*, **39**, 788 (1970) (in Japanese).
4. G. L. Vick and K. M. White, *This Journal*, **116**, 1142 (1969).
5. A. D. Kurtz and R. Yee, *J. Appl. Phys.*, **31**, 303 (1960).
6. S. Wagner, *This Journal*, **119**, 1570 (1972).
7. K. Shohno, in Proceedings of Third Biennial University-Industry-Government Microelectronics Symposium, p. 143 (1979).
8. D. Kuppers, in "Chemical Vapor Deposition," T. O. Sedgwick and H. Lydtin, Editors, p. 159, The Electrochemical Society Softbound Proceedings Series, Princeton, N.J. (1979).

The Systems $\text{Y}_2\text{O}_3\text{-P}_2\text{O}_5$ and $\text{Gd}_2\text{O}_3\text{-P}_2\text{O}_5$

Dinesh Agrawal and F. A. Hummel

Solid State Science Section, Department of Materials Science and Engineering,
The Pennsylvania State University, University Park, Pennsylvania 16802

ABSTRACT

The systems $\text{Y}_2\text{O}_3\text{-P}_2\text{O}_5$ and $\text{Gd}_2\text{O}_3\text{-P}_2\text{O}_5$ each contain six intermediate compounds of 4:1, 3:1, 1:1, 1:2, 1:3, and 1:5 ratios. The systems were investigated by solid-state reactions and also by quenching methods in the glass-forming region between the 1:2 and 1:5 compounds. The 4:1, 1:2, 1:3, and 1:5 compounds in the two systems appear to have identical or similar structures, whereas the 3:1 and 1:1 compounds differ in structure. It was found that the 4:1 and 3:1 compounds in the refractory portion of the systems have lower temperature limits of stability. The newly discovered 1:2 compounds in each system are relatively stable, $\text{Y}_2\text{O}_3 \cdot 2\text{P}_2\text{O}_5$ decomposing to 1:1 and 1:3 near 1450°C and $\text{Gd}_2\text{O}_3 \cdot 2\text{P}_2\text{O}_5$ melting incongruently to 1:1 and liquid near 1305°C . The 1:3 compounds melt congruently and the 1:5 compounds melt incongruently to 1:3 and liquid.

It is already known that YPO_4 , and the ultraphosphates YP_5O_{14} and $\text{GdP}_5\text{O}_{14}$ are of interest for their luminescent behavior when activated by various rare

Key words: inorganic, refraction, phases.

earths, especially Eu^{3+} . Various other compounds in the systems have been reported such as 4:1, 3:1, and 1:3 but neither system has been completely explored and the exact thermal behavior of the known com-

pounds has not been determined. Therefore, the purpose of this study was to determine the phase relationships in both systems, including the refractory portion between the oxide end member and the orthophosphate R³⁺PO₄ and the glass-forming region between R³⁺PO₄ and the 1:5 compound, thus providing a firm basis for further luminescence studies.

Literature

End member rare earth oxides.—The RE₂O₃ rare-earth oxides have been shown to exist in hexagonal (A), monoclinic (B), and cubic (C) forms (1-3). Many detailed studies have been made on the crystal structure, temperature and rate of transformation, and the effect of pressure on the temperature of transformation.

In this study, the cubic form of Y₂O₃ and the cubic and monoclinic forms of Gd₂O₃ were observed in the phase analysis. The high temperature hexagonal and another form of Gd₂O₃ observed by Foex and Traverse (4) above 2360°C were not relevant to this work.

The 4:1 and 3:1 compounds.—Kizilyalli (5) prepared 3Gd₂O₃·P₂O₅ by reaction of GdPO₄ and Gd₂O₃ at 960°C, and claimed the compound to be orthorhombic with *a* = 11.35Å, *b* = 9.75Å, and *c* = 8.80Å. Serra, Coutures, and Rouanut (6) synthesized 3Y₂O₃·P₂O₅ and 3Gd₂O₃·P₂O₅ by heating the oxide and phosphoric acid in air between 800°-1200°C. During further research (7) they prepared the 3:1 and 4:1 compounds of both Y and Gd by reacting the orthophosphates with Y₂O₃ or Gd₂O₃ between 1200°-1400°C.

The orthophosphates.—The natural mineral xenotime (YPO₄) and many other rare earth orthophosphates have been known and examined for many years. Xenotime is structurally related to zircon, ZrSiO₄, which has been synthesized as a gemstone and used as a refractory ceramic material.

YPO₄ is tetragonal and optically positive with *n*_ω = 1.7207 and *n*_o = 1.8155 (8). GdPO₄ is hexagonal and isomorphous with LaPO₄, CePO₄, and NdPO₄. Above 500°C a transformation to a monoclinic form (isostructural with monazite) takes place (in the presence of H₂O). As in the case of the rare-earth oxides, the literature on the orthophosphates is very extensive and easily available, and it need not be repeated here.

The 1:2, 1:3, and 1:5 compounds.—The 1:2 compound was apparently unknown before the present study and therefore no literature was found. Gd(PO₃)₃ was reported (9) to undergo a polymorphic transition between 800°-850°C and melt incongruently to GdPO₄ and liquid.

Bagieu-Beucher and Duc (9) described the preparation of rare earth ultraphosphates of the formula LnP₃O₁₄ (Ln = La - Lu, Y). Mixtures of rare earth oxides and diammonium phosphate were calcined at 500°C for one day. All of the ultraphosphates were reported to melt incongruently to metaphosphate and P₂O₅-rich liquid between 800°-900°C. They claimed that the ultraphosphates existed in three structural types in space groups: (i) P2₁/a, (ii) Cc or C2/c, or (iii) Pc2/n or Pcmn. YP₃O₁₄ existed (9, 10) in orthorhombic and monoclinic forms, but the orthorhombic form was not isolated and occurred only in small quantities with the monoclinic form. GdP₃O₁₄ exists only in the monoclinic form (9, 10).

Materials, Apparatus, and Experimental Procedure

Y₂O₃ (99.99%) from Apache Chemicals, Incorporated, Gd₂O₃ (99.9%) from Ventron ALFA Products, and NH₄H₂PO₄ from Fisher Scientific were used as starting materials. Ten compositions (Table I) in each system were thoroughly mixed in acetone in an agate mortar, heated to 300°-500°C for 24 hr in covered Pt crucibles to eliminate volatiles NH₃ and H₂O, and then given the final heat-treatment as shown. Solid-state reactions were done in SiC Glocal furnaces. In the phosphate-

Table I.

A. Compositions, heat-treatments, and phase analyses for the system Y ₂ O ₃ -P ₂ O ₅			
Mole % P ₂ O ₅	Temperature (°C)	Time (hr)	Phases present
10	1050	160	Y ₂ O ₃ + YPO ₄
	1400	24	Y ₂ O ₃ + Y ₃ P ₂ O ₁₇
20 (4:1)	1050	160	Y ₂ O ₃ + YPO ₄
	1150	60	Y ₂ O ₃ + YPO ₄
	1160	60	Y ₂ O ₃ + YPO ₄
	1180	48	Y ₃ P ₂ O ₁₇ + Y ₂ O ₃
	1400	24	Y ₃ P ₂ O ₁₇
22.5	1500	24	Y ₃ P ₂ O ₁₇ + Y ₃ PO ₇
25 (3:1)	1300	48	Y ₃ P ₂ O ₁₇ + YPO ₄
	1400	50	Y ₃ P ₂ O ₁₇ + YPO ₄
	1430	18	Y ₃ P ₂ O ₁₇ + YPO ₄
	1435	15	Y ₃ P ₂ O ₁₇ + YPO ₄
	1450	18	Y ₃ PO ₇
	1500	10	Y ₃ PO ₇
30	1000	72	Y ₂ O ₃ + YPO ₄
	1400	24	Y ₃ P ₂ O ₁₇ + YPO ₄
40	800	120	Y ₂ O ₃ + YPO ₄
	1000	72	Y ₂ O ₃ + YPO ₄
	1400	24	Y ₃ P ₂ O ₁₇ + YPO ₄
50 (1:1)	1050	48	YPO ₄
	1400	24	YPO ₄
66.66 (1:2)	1200	800	Y ₂ P ₃ O ₁₃
66.66 (1:2)	800	180	Y ₂ P ₃ O ₁₃
(Crystallized from glass)	1250	72	Y ₂ P ₃ O ₁₃
	1335	72	Y ₂ P ₃ O ₁₃
	1395	24	Y ₂ P ₃ O ₁₃
	1430	24	Y ₂ P ₃ O ₁₃
	1470	24	YPO ₄ + Y(PO ₃) ₃
75 (1:3)	1430	24	Y(PO ₃) ₃
	1445	24	Y(PO ₃) ₃
	1480	24	Glass
83.33 (1:5)	800	24	YP ₅ O ₁₄
	850	24	YP ₅ O ₁₄
	870	24	Y(PO ₃) ₃ + glass
	900	24	Y(PO ₃) ₃ + glass
B. Compositions, heat-treatments, and phase analyses for the system Gd ₂ O ₃ -P ₂ O ₅			
Mole % P ₂ O ₅	Temperature (°C)	Time (hr)	Phases present
10	590	20	Gd ₂ O ₃ + GdPO ₄
	1000	75	Gd ₂ O ₃ + Gd ₃ PO ₇
	1400	20	Gd ₂ O ₃ + Gd ₃ P ₂ O ₁₇
20 (4:1)	600	72	Gd ₂ O ₃ + GdPO ₄
	1000	72	Gd ₂ O ₃ + Gd ₃ PO ₇
	1200	80	Gd ₂ O ₃ + Gd ₃ PO ₇
	1280	100	Gd ₂ O ₃ + Gd ₃ PO ₇
	1290	100	Gd ₃ P ₂ O ₁₇ + Gd ₃ PO ₇ + Gd ₂ O ₃
	1300	150	Gd ₃ P ₂ O ₁₇ + Gd ₂ O ₃
	1450	20	Gd ₃ P ₂ O ₁₇
22.5	1350	90	Gd ₃ P ₂ O ₁₇ + Gd ₃ PO ₇
25 (3:1)	600	200	Gd ₃ O ₃ + GdPO ₄
	860	160	Gd ₃ PO ₇ + GdPO ₄ + Gd ₂ O ₃
	880	100	Gd ₃ PO ₇ + Gd ₂ O ₃
	900	140	Gd ₃ PO ₇ + Gd ₂ O ₃ (trace)
	1200	72	Gd ₃ PO ₇
	1450	5	Gd ₃ PO ₇
	1480	10	Gd ₃ PO ₇
30	610	24	Gd ₂ O ₃ + GdPO ₄
	1000	75	Gd ₃ PO ₇ + GdPO ₄
	1200	80	Gd ₃ PO ₇ + GdPO ₄
	1400	24	Gd ₃ PO ₇ + GdPO ₄
40	610	24	GdPO ₄ + Gd ₂ O ₃
	1000	75	GdPO ₄ + Gd ₃ PO ₇
	1200	80	GdPO ₄ + Gd ₃ PO ₇
	1400	24	GdPO ₄ + Gd ₃ PO ₇
50 (1:1)	600	20	GdPO ₄
	1000	75	GdPO ₄
	1200	80	GdPO ₄
	1400	24	GdPO ₄
66.66 (1:2)	1100	40	Gd ₂ P ₃ O ₁₃
(Crystallized from glass)	1200	50	Gd ₂ P ₃ O ₁₃ + GdPO ₄
	1275	60	Gd ₂ P ₃ O ₁₃ + GdPO ₄
	1300	96	Gd ₂ P ₃ O ₁₃
	1315	60	GdPO ₄ + liq.
75 (1:3)	750	400	Unidentified
	800	400	Unidentified
	1100	72	Gd(PO ₃) ₃
	1200	50	Gd(PO ₃) ₃
	1225	65	Gd(PO ₃) ₃
	1250	65	Gd(PO ₃) ₃
	1270	43	Gd(PO ₃) ₃
	1300	65	Glass
83.33 (1:5)	800	155	GdP ₅ O ₁₄
	840	220	GdP ₅ O ₁₄ + liq.

rich, glass forming part of the system, glasses were melted in Pt crucibles for 20 min to avoid loss of P₂O₅ and then quenched to room temperature. The starting materials for preparation of glasses were prereacted crystalline compounds or mixtures of compounds, an-

other technique which was used to minimize or avoid loss of P_2O_5 during melting. A Pt-wound quenching furnace was used not only for quenching of compositions in the glass-forming region, but also for determination of upper and lower temperature limits of stability of compounds in the refractory region of the system. Samples for quenching studies were encapsulated in sealed Pt tubes (2.5 or 5 mm diam) and temperatures of solid-state and quenching studies were measured with Pt/Pt-10% Rh thermocouples.

Phase identification was made with Ni-filtered $CuK\alpha$ radiation from a Norelco diffractometer operated at 40 kV and 15 mA. For routine studies samples were run at $1^\circ 2\theta/\text{min}$, and for standard patterns of the various binary compounds, the speed was reduced at $\frac{1}{4}^\circ 2\theta/\text{min}$. A polarizing microscope was used to measure the refractive indexes of the phosphate-rich glasses using the Becke line method.

Results and Discussion

General.—The phase diagrams shown in Fig. 1 were constructed from the data given in Table I. Both sys-

tems contained six (4:1, 3:1, 1:1, 1:2, 1:3, and 1:5) binary compounds, five of which were previously reported. The 1:2 compound in each system was discovered by careful analysis of compositions which had been prepared by solid-state reaction and by crystallization from glass. Both systems are divided into a refractory portion between the oxide and $REPO_4$ and a glass-forming portion between $REPO_4$ and the ultra-phosphate, which is customary for many systems involving a refractory oxide and P_2O_5 .

In the glass-forming region between the 1:2 and 1:5 compounds, it was easier to prepare the 1:2, 1:3, and 1:5 compounds by crystallization from glass, but they can also be prepared as phase-pure crystalline materials by solid-state reaction if sufficient time is provided at the required temperature levels.

The Y_2O_3 - YPO_4 subsystem.—(i) Y_2O_3 .—Up to $1450^\circ C$, Y_2O_3 was observed to exist only in the cubic form. The monoclinic to cubic transformation at $900^\circ C$ was not observed, probably because yttrium carbonate or oxalate was not used as a starting material or because no H_2O was present during reaction.

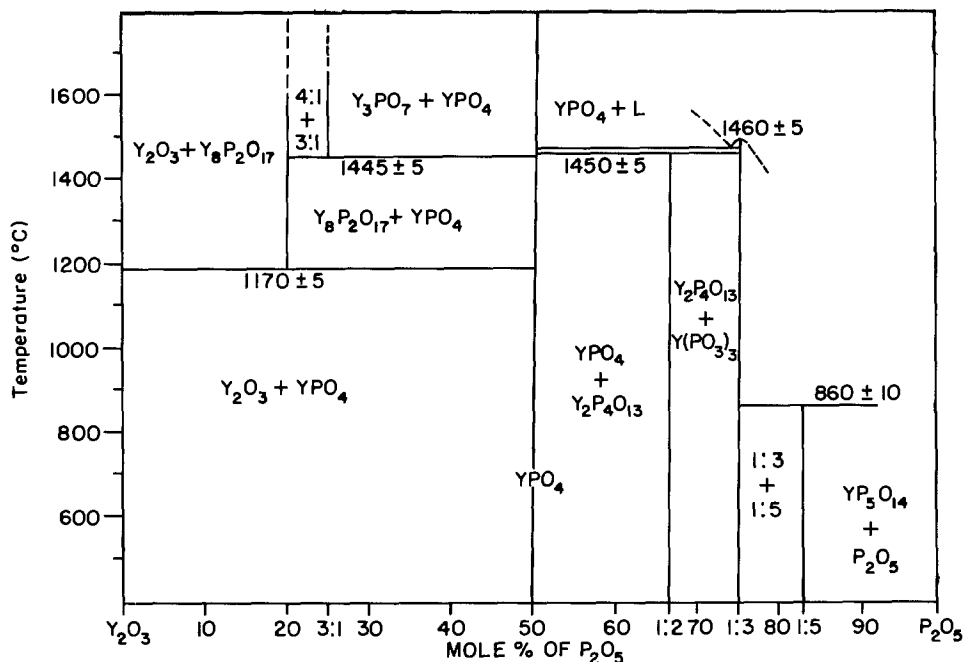
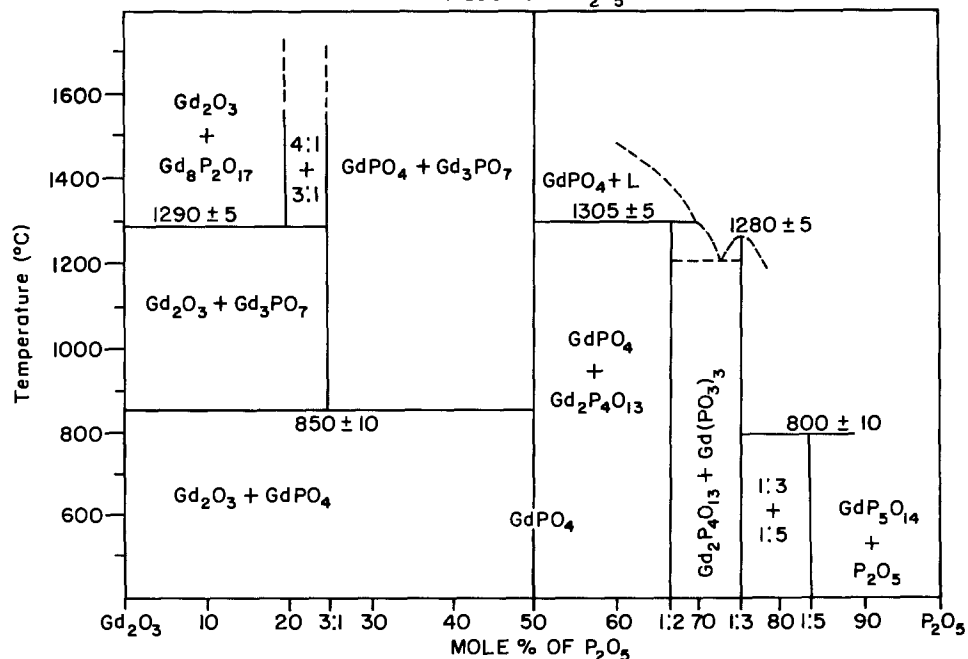


Fig. 1. The systems Y_2O_3 - P_2O_5 and Gd_2O_3 - P_2O_5 .



(ii) Y₃P₂O₁₇ (4:1).—The 4:1 compound was found to have a lower temperature limit of stability at 1170° ± 5°C. When a single phase 4:1 sample prepared at 1300°C was held at 1100° for 72 hr, it decomposed to Y₂O₃ and YPO₄.

(iii) Y₃PO₇ (3:1).—The 3:1 compound has a lower temperature limit of stability at 1445° ± 5°C. Serra *et al.* (6) claimed it could be prepared by reaction of Y₂O₃ and NH₄H₂PO₄ between 1200° and 1400°C, but the present work shows that it would be metastable in that temperature range. A single-phase sample prepared at 1475°C decomposed to 4:1 and YPO₄ when held at 1300°C for 30 hr.

(iv) YPO₄.—The compound existed as the tetragonal zircon type structure from RT to 1400°C.

The YPO₄-P₂O₅ subsystem.—(i) Y₂P₄O₁₃.—Formation of the compound was very difficult by solid-state reaction and its existence could easily be overlooked if sufficient time was not allowed for reaction. It was prepared by holding for 800 hr at 1200°C. However, glass of the 1:2 composition melted at 1550°C crystallized to the 1:2 compound within 72 hr. Using the compound prepared by crystallization from glass, Y₂O₃·2P₂O₅ was found to dissociate to 1:1 and 1:3 at 1450°C.

(ii) Y(PO₃)₃.—The 1:3 compound existed as a single structure from RT to its congruent melting point of 1460° ± 5°C. Earlier it had been reported (9) to melt incongruently to YPO₄ and a P₂O₅-rich liquid.

(iii) YP₅O₁₄.—The 1:5 compound was found to exist only in the monoclinic form and to melt incongruently at 860° ± 10°C to 1:3 and a P₂O₅-rich liquid. No orthorhombic phase was observed as previously reported (9).

The Gd₂O₃-GdPO₄ subsystem.—(i) Gd₂O₃.—The reported (1) polymorphic transformation was briefly investigated. Below 1100°C, only the cubic form could be detected. When heated at 1300°C for 500 hr, the monoclinic phase coexisted with the cubic phase. Perhaps longer times would produce a pure monoclinic phase.

(ii) Gd₃P₂O₁₇ (4:1).—The 4:1 compound was found to have a lower limit of stability at 1290° ± 5°C. When a single phase 4:1 sample prepared at 1350°C was held at 1100°C for 50 hr, it decomposed to Gd₂O₃ and 3:1.

(iii) Gd₃PO₇ (3:1).—The lower temperature limit of stability was 850° ± 10°C. Below 850°C, Gd₂O₃ and GdPO₄ coexist. A phase pure sample of 3:1 prepared at 1100°C for 72 hr decomposed to Gd₂O₃ and GdPO₄ when held at 800°C for 120 hr.

(iv) GdPO₄.—The compound was found to exist only in the monoclinic form and no phase transformation was observed, as had previously been reported (11). Samples were held at 1000°C for 100 hr. Kuznetsev *et al.* (11) reported a change from hexagonal to monoclinic near 500°C when gadolinium chloride and phosphoric acid were used as starting materials in aqueous solution.

The GdPO₄-P₂O₅ subsystem.—(i) Gd₂P₄O₁₃.—The compound behaved in a manner similar to the yttrium analogue as far as reaction rate was concerned. It was prepared by solid-state reaction at 1100°C for 800 hr, and from glass by crystallizing for 60 hr. The glass had been melted at 1500°C. Using the 1:2 compound which had been prepared by crystallization from glass, it was determined that it melted incongruently at 1305° ± 5°C into GdPO₄ and liquid.

(ii) Gd(PO₃)₃.—The 1:3 compound melted congruently at 1280° ± 5°C in contrast to the reported incongruent melting (9). In earlier literature (9), a transition was reported to take place between 800°-850°C. In the

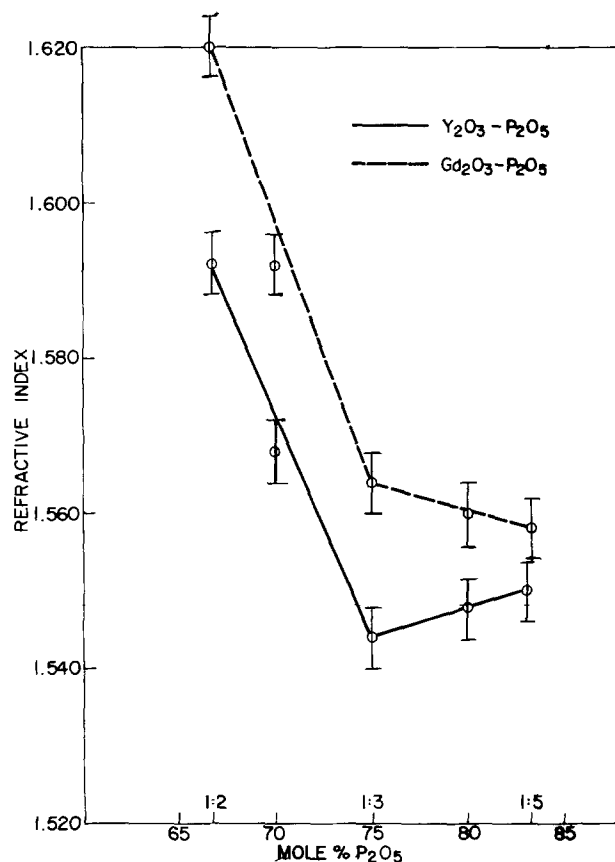


Fig. 2. Refractive indexes of glasses

present work, the transition was detected when the sample was held near 750°C for 400 hr.

(iii) GdP₅O₁₄.—The diffraction pattern agreed well with the monoclinic indexing given in the literature

Table II. X-ray diffraction data for the 1:2 compounds

Gd ₂ O ₃ · 2P ₂ O ₅			Y ₂ O ₃ · 2P ₂ O ₅		
2θ	d, Å	I/I ₀	2θ	d, Å	I/I ₀
14.47	6.118	40	14.36	6.168	25
17.03	5.206	5	16.97	5.223	5
—	—	—	17.61	5.065	2
20.36	4.362	100	20.33	4.368	100
22.35	3.978	10	—	—	—
22.86	3.890	50	22.91	3.882	100
23.02	3.862	18	—	—	—
23.10	3.850	14	—	—	—
24.78	3.593	50	24.77	3.593	90
25.25	3.527	75	25.29	3.522	100
27.74	3.216	12	—	—	—
29.22	3.055	18	29.30	3.048	10
30.34	2.946	6	—	—	—
30.42	2.938	6	—	—	—
30.57	2.924	10	—	—	—
30.74	2.908	25	—	—	—
32.47	2.757	30	—	—	—
32.58	2.748	30	32.74	2.735	20
34.14	2.626	30	34.22	2.620	50
34.33	2.6121	15	34.42	2.605	20
35.49	2.600	20	—	—	—
37.22	2.416	25	37.32	2.409	25
37.55	2.395	6	—	—	—
39.72	2.269	15	39.95	2.257	5
40.10	2.248	12	40.32	2.236	5
41.60	2.171	12	—	—	—
42.19	2.142	6	42.13	2.145	5
42.7	2.117	30	42.97	2.104	20
44.14	2.052	24	44.46	2.038	20
44.21	2.049	24	—	—	—
47.06	1.931	10	47.33	1.921	5
50.15	1.819	25	50.6	1.804	20
50.25	1.816	25	—	—	—
50.38	1.811	25	—	—	—
51.40	1.778	18	—	—	—
51.46	1.776	18	52.20	1.752	10
51.77	1.766	10	—	—	—
52.32	1.748	10	—	—	—
52.65	1.738	10	53.03	1.727	15
53.30	1.719	10	—	—	—
53.52	1.712	10	53.80	1.704	10
54.62	1.680	10	54.56	1.682	10

(9). The 1:5 compound melted incongruently to 1:3 and a P_2O_5 -rich liquid at $800^\circ \pm 10^\circ C$.

Refractive index data.—The RI of the glasses between the 1:2 and 1:5 compositions are shown in Fig. 2. The relatively constant index between the 1:3 and 1:5 compositions is interesting. However, the error in measurement was ± 0.004 and it is unlikely that the index actually increased between the 1:3 and 1:5 compositions in the case of the Y_2O_3 - P_2O_5 system.

X-ray diffraction data.—Patterns for the 1:2 compounds are given in Table II. Analysis of the data indicated that the 4:1, 1:2, 1:3, and 1:5 yttrium and gadolinium compounds had similar structures and would form either complete or partial solid solution systems, whereas the 3:1 compounds had different structures. To further confirm this analysis, 50:50 mixtures of the 4:1, 3:1, 1:2, 1:3, and 1:5 yttrium and gadolinium compounds were prepared and heated at $1400^\circ/24$ hr, $1475^\circ/10$ hr, $1100^\circ/48$ hr, $1100^\circ/48$ hr, and $700^\circ/96$ hr, respectively. The x-ray data confirmed the probable isomorphism of 4:1, 1:2, 1:3, and 1:5 and the coexistence of the $3Y_2O_3 \cdot P_2O_5$ and $3Gd_2O_3 \cdot P_2O_5$ structures.

Manuscript submitted Oct. 10, 1979; revised manuscript received Dec. 27, 1979.

Any discussion of this paper will appear in a Discussion Section to be published in the June 1981 JOURNAL. All discussions for the June 1981 Discussion Section should be submitted by Feb. 1, 1981.

Publication costs of this article were assisted by the Pennsylvania State University.

REFERENCES

1. R. S. Roth and S. J. Schneider, *J. Res. Natl. Bur. Std. Sect. A*, **64**, 309 (1960).
2. M. Foex and J. P. Traverse, *Bull. Soc. Fr. Mineral. Cristallog.*, **89**, 184 (1966).
3. F. Queyroux, A. Harari, and R. Collongues, *Bull. Soc. Fr. Ceram.*, **72**, 37 (1966).
4. M. Foex and J. P. Traverse, *C. R.*, **261**, 149 (1965).
5. M. Kizilyalli, *Middle East Tech. Univ. J. Pure Appl. Sci.*, **8**, 179 (1975).
6. J. J. Serra, J. Coutures, and A. Rouanet, *Proc. Rare Earth Res. Conf.*, **12th**, **2**, 652 (1976).
7. J. J. Serra, J. Coutures, and A. Rouanet, *High Temp. High Pressures*, **8**, 337 (1976).
8. W. R. Foster, *Amer. Mineral.*, **34**, 830 (1949).
9. M. Bagieu-Beucher and Tran Qui Duc, *Bull. Soc. Fr. Mineral. Cristallogr.*, **93**, 505 (1970).
10. A. Durif, *ibid.*, **94**, 314 (1971).
11. G. Kuznetsev, S. M. Petushkova, and I. V. Tanaev, *Zh. Strukt. Khim.*, **5**, 397 (1964).

Sulfur Substitution during Operation of CdSe Photoanodes and Mechanism of Surface Protection

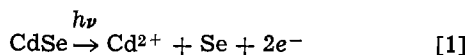
K. T. L. De Silva and D. Haneman

School of Physics, University of New South Wales, Kensington, Australia, 2033

ABSTRACT

The concentrations of S, Se, and Cd during operation of a polycrystalline CdSe photoanode in 1M Na_2S , 1M S, 1M NaOH solutions were measured by x-ray photoelectron spectroscopy as a function of total charge passed. Sulfur had reached half the final concentration in the XPS probed layer after only $5 C cm^{-2}$, although there was little change in cell output. These and other phenomena are analyzed to suggest that the Cd-S layer that forms does not establish a semiconductor heterojunction but merely a chemically protective layer which is of low semiconductor quality and has little barrier to current flow. At high current densities the layer thickens and becomes obstructive, requiring Se in solution to prevent its growth to obtrusive proportions. The XPS results also show that when the electrochemically deposited Cd-Se film is annealed, chemical shifts of the Cd and Se peaks occur, indicating formation of the compound CdSe during annealing, from codeposited but not reacted elements in the initial film.

Sustained, efficient conversion of solar energy to electricity has been demonstrated using photoelectrochemical (PEC) cells based on CdSe photoanodes (1-5). In these PEC cells, photogenerated holes oxidize the reduced component of the redox couple, after which these oxidized species migrate to the cathode to be reduced back again by electrons. The semiconductor CdSe which has many potential advantages as a solar energy conversion photoanode, can be stabilized against photocorrosion by adding sulfur ions to the electrolyte



Key words: solar cells, photoelectrochemical, cadmium selenide, photoanodic protection.

CdSe is oxidized under illumination in the PEC cell, to Cd^{2+} and Se. Cd^{2+} ions probably react to give CdS within a very short time of its formation, because of the high surface concentration of sulfide ions. This means that the surface of the CdSe electrode will be replaced by CdS during illumination. Sulfur was found to depths up to 10 nm from the surface in XPS studies by Cahen *et al.* (6) and by Noufi *et al.* (7). However, the rate at which the surface substitution of Se by S occurs, was not determined. This is of interest in checking the formation of a postulated heterojunction between the CdSe bulk and thin (6-12 nm) CdS layer, and how this affects operation of the electrode.

Experimental

Measurements were made with a Varian IEE-15 photoelectron spectrometer using $MgK\alpha$ radiation

(1253.6 eV), with a resolution of 1.8 eV FWHM (full width half maximum) on gold 4s peaks. The Mg x-ray source was operated at 8 kV and 80 mA. Scanning the spectrum was performed by varying the retarding voltage, with the analyzer set to detect retarded electrons of 100 eV (this gives the above resolution). Preliminary wide scans were carried out over a 90V region (500 channel and 12 sec per scan). The scans were then repeated with 30V scan width (200 channel and 40 sec per scan), so that peak positions could be measured accurately.

Various preparation methods of polycrystalline CdSe are given in the literature (1-4). The polycrystalline CdSe samples (ten) used in this study were prepared by electrolysis of 1M HCl solution containing 1M CdCl₂ and 1M SeO₂. The nickel substrate was cleaned with acetone in the ultrasonic cleaner, then etched in nitric acid and rinsed thoroughly with distilled water. A carbon plate was used as the anode, spaced 1 cm from the Ni substrate. The solution was stirred continuously using a magnetic stirrer. A thick film (about 40 microns) of Cd-Se was formed on the Ni substrate and then annealed in an N₂ atmosphere at 400°C for 1 hr and kept under N₂ until cool. CdSe and CdS single crystals were used as the XPS standards. They were polished and cleaned prior to analysis. Evaporated Se on an Al substrate was also used as a standard.

1M Na₂S, 1M S, and 1M NaOH solutions were used as the electrolyte in the PEC cell. The counterelectrode was prepared by applying aquadag and cobalt acetate on to a stainless steel gauze and subsequently heating it in an N₂ atmosphere. The short-circuit current of this cell, initially 4 mA cm⁻², was measured under illumination by a 250W tungsten filament quartz iodine lamp operated at 16V (rated for 24V). The photoanodes, after photolysis, were washed with 0.5M Na₂S solution, to prevent precipitation of elemental sulfur from the absorbed electrolyte. Then they were washed five times with distilled water to remove physically adsorbed electrolyte, before the analysis.

Results

Prior to annealing, Cd-Se films showed the presence of Cd and Se as shown in Fig. 1, curve I. Scans were made of the Cd-3d region, Se-3p region, S-2p region, and the S Auger peak at ~151 eV kinetic energy. There was no evidence for the presence of sulfur. The positions of Cd, Se, and S peaks obtained from XPS results are given in Table I. Figure 1 shows the spectra obtained from CdS single crystals and CdSe films under various conditions described in the caption. A reduction of the Se concentration on the CdSe surface occurred during the annealing process (curve II). At the same time an increase of the Cd peak intensity was observed. Quantitative analysis showed a reduction of the ratio Se/Cd by ~60%.

As shown in Fig. 1 curve III, after operation as an illuminated photoelectrode, a strong peak at 161.1 eV is observed, due to sulfur (2p_{1/2} and 2p_{3/2}) on the CdSe surface. This peak at 161.1 eV overlaps with the Se peak at 160 eV. The overlapping of the peaks is confirmed by the larger FWHM of this peak (~3.2 eV) compared with the FWHM of the Se-3p_{3/2} peak (~2.6 eV) of a fresh CdSe film. The reduction of the Se-3p_{1/2}

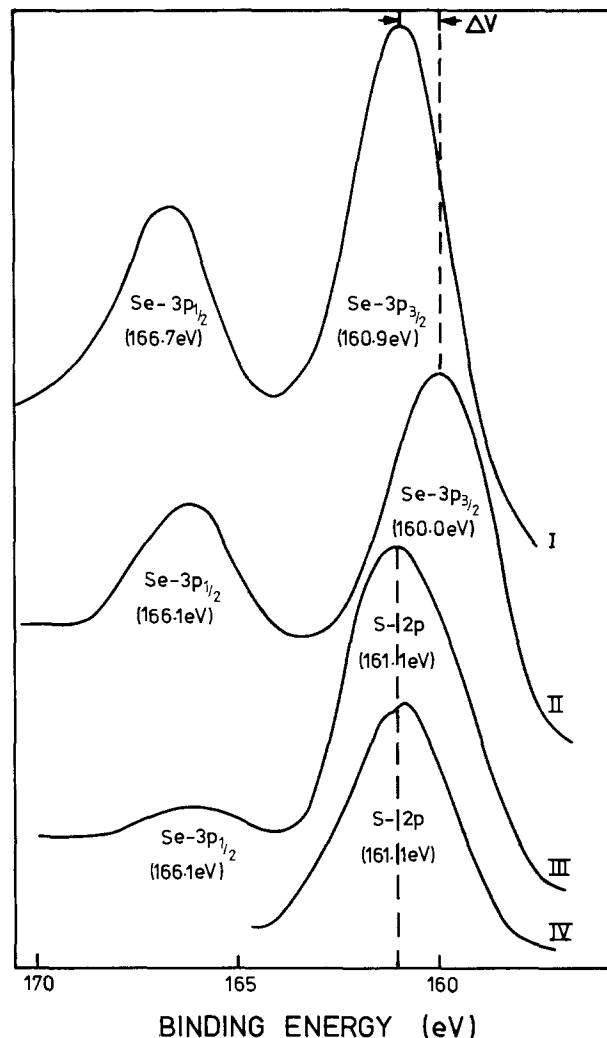


Fig. 1. X-ray photoelectron spectra of CdSe electrode: curve I, before heat-treatment; curve II, same film after heat-treatment; curve III, same film after illuminating as a photoelectrode in PEC cell (after passage of 60 C cm⁻²); curve IV, CdS single crystals. The quantity ΔV represents the difference in position of the Se-3p peaks before and after annealing.

peak at 166.1 eV clearly shows the S/Se substitution. The position of the S-2p peak of CdSe is identical with the S-2p peak of pure CdS, as shown in Fig. 1 curve III and IV. The Cd peaks showed no significant change before and after photolysis.

The ratios of S/Cd and Se/Cd of the electrode surface were measured as a function of charge passed through the photoanode and are shown in Fig. 2. This graph was drawn using the peak heights of Cd-3d, Se-3p, and S-2p. The heights were adjusted for relative XPS sensitivities as given by Berthou and Jorgensen (9). The initial overall efficiency (~2%) of the cell was constant to within 5% during the S/Se substitution.

Table I. Electron binding energies (eV)

	Cd-3d _{3/2}	Cd-3d _{5/2}	Se-3p _{1/2}	Se-3p _{3/2}	S-2p _{1/2} and 2p _{3/2}	K.E. of sulfur L _{2,3} M _{2,3} M _{2,3} Auger peak
CdSe film (unannealed)	411.2	404.5	166.7	160.9	—	—
CdSe film (annealed)	411.7	405.0	166.1	160.0	—	—
CdSe film (after illuminating as a photoelectrode)	411.7	405.0	166.1	—	161.1	151
CdS single crystals	411.7	405.0	—	—	161.1	151
Se film	—	—	167.4	161.5	—	—
Values given in Ref. (8)	411	404	168	162	165	164

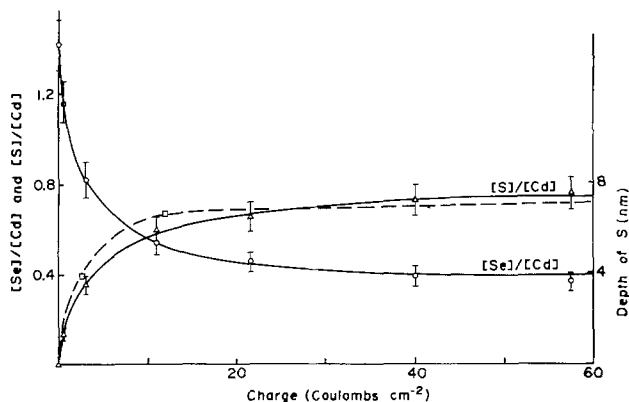


Fig. 2. Dependence of the Se and S concentrations of the CdSe surface on the charge density passed through photoanode. Solid lines are for the ratios Se/Cd and S/Cd; dashed line is for depth of S penetration, drawn using the 2 values in Ref. (7) and, when extrapolated, passing through the value of 10 nm at approximately 540 C cm^{-2} inferred from Ref. (6).

Discussion

After the annealing process we observed (i) a decrease of the ratio Se/Cd, (ii) a negative shift of the Se peak position by 0.9 eV, (iii) a positive shift of the Cd peak position by 0.5 eV. We also observed a very large improvement of the photocurrent after the heat-treatment, by a factor of about 100. Several reasons have been forwarded to explain this improvement (10). These include the liberation of excess Se and formation of crystallites of large sizes. The liberation of excess Se is confirmed by (i) above. The increase of photocurrent may be due to the formation of CdSe from Cd and Se, during the annealing process. A consistent explanation is that the electrolysis process deposits Cd and Se on the substrate but these do not form CdSe. During annealing the two materials react to form Cd-Se complexes. This is supported by the observed chemical shifts after annealing. Also the photocurrent wavelength response is characteristic of CdSe.

The reduction of Se/Cd occurred after a relatively small amount of charge had passed as shown in Fig. 2. The ratio S/Cd was increased at the same time. Because the Cd peak heights did not reduce, the increased sulfur peaks cannot be explained by a deposited sulfur or contaminant over layer (11). Furthermore the binding energy of the sulfur peak is the same as that in CdS (curves III and IV in Fig. 1). Therefore we conclude that the sulfur is present together with Cd, consistent with the conclusions of Heller *et al.* (11) that CdSe in the surface is replaced by CdS. Previous microprobe studies (12) have shown that the S/Se ratio of the CdSe surface, after photolysis for several hours, was about 1:1 in the top micrometer of the layer. Our measurements show that this ratio is about 1.8:1 in the thin layer ($\sim 2\text{-}3 \text{ nm}$) probed by XPS, showing that the sulfur concentration is highest at the surface itself.

An EIS (electrolyte-insulator-semiconductor) band scheme has been proposed by Cahen *et al.* (6) for the $\text{S}^{2-}\text{-CdS-CdSe}$ system, by considering CdS as a thin insulating layer bonded to the CdSe. For insulating layers of $> \sim 2 \text{ nm}$ thickness, a significant increase of series resistance has to be expected (13). The thickness of the CdS layer on the CdSe electrodes is very much larger than 2 nm (11). However, the constancy of photocurrent ($\sim 4 \text{ mA cm}^{-2}$) of our cells during substantial S/Se substitution, does not accord with an increase of such a series resistance, and indeed implies no significant change in mode of operation. Therefore we feel the evidence does not support the growth of an EIS structure over a substantial portion of the surface.

The deterioration of CdSe PEC cells can be prevented by working at low current densities (6, 10). At such densities, ($< 10 \text{ mA cm}^{-2}$) all holes are captured by the redox couple and a decrease in free Cd^{2+} concentration can be obtained because oxidation of CdSe by reaction [1] does not take place. Furthermore at large current densities, ($10\text{-}40 \text{ mA cm}^{-2}$) the rate of deterioration can be decreased with addition of a small amount of Se solution, as shown by Heller *et al.* (10) for polycrystalline hot-pressed and single crystal CdSe photoanodes. This effect is due to the decrease of x in the series of compounds $\text{CdSe}_{1-x}\text{S}_x$ on the surface of CdSe. The barrier to hole transfer to the solution interface is said to be lowered as x decreases. Miller *et al.* (3) and Cahen *et al.* (6) have reported an increase in stability of sintered disk and single crystal CdSe electrodes with increasing S^{2-} concentration in solution. This minimizes the time that free Cd^{2+} can exist by precipitating CdS on the surface.

For electrodeposited polycrystalline electrodes the deactivation is much less (6). According to this explanation, decrease of photocurrent can be prevented by rapid formation of CdS on CdSe. This however appears to contradict the above proposal (10) that CdS causes a barrier to hole transfer and should be reduced by Se addition in order to prevent deterioration at high current densities.

Clearly the situation is complex and all phenomena cannot be accounted for by a single simple explanation. However the results reported here would show that during the initial states of cell operation, S rapidly enters the surface, mostly in the form of Cd-S, without much effect on cell output. We believe this can be accounted for if the Cd-S layer shows substantial leakage through to the underlying CdSe crystals; indeed it is highly unlikely that a high quality hermetic structure could form. A very schematic diagram is shown in Fig. 3. From a topography point of view, scanning microscope pictures of the surface of an electrode after operation show a very uneven surface, as also do those of a CdS electrode (7). The Cd-S layer is presumed to contain many defects and be very conductive, much more than a normal CdS semiconductor. There are impurity and defect levels which are sufficiently closely spaced in the approximately 6 nm Cd-S layer to form impurity bands and hence negligible potential barrier to carriers. Of course carrier recombination will be high, but not necessarily higher than that at the CdSe-electrolyte interface.

At high current densities, the Cd-S structure becomes sufficiently thick and pervasive to cause current obstruction, and also significant light absorption, and hence the addition of Se to the solution would help to keep any such structures to the lesser form that

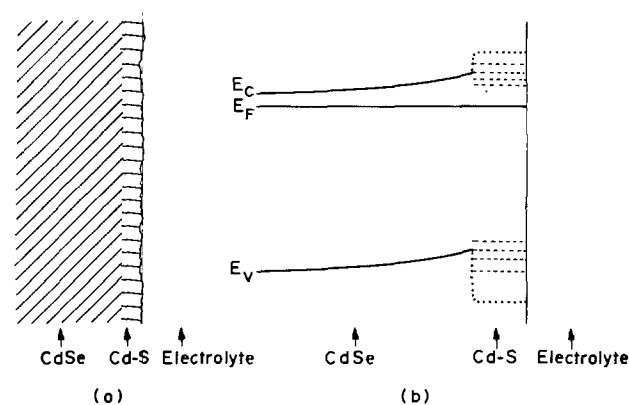


Fig. 3. Schematic diagram showing the CdSe:Cd-S electrolyte interface. The Cd-S layer, about 3-6 nm thick is of poor electrical quality and highly conductive via impurity-defect bands, shown dashed in (b). The "band edges" of the Cd-S are indicated by dotted lines.

develops at lower current densities. This lesser layer does not seal against current flow but reduces corrosion. Although this explanation is necessarily qualitative, it appears to be in accord with a number of phenomena.

Acknowledgment

This work was supported by the Australian Research Grants Committee and by the National Energy Research Development and Demonstration Council.

Manuscript submitted Oct. 30, 1979; revised manuscript received ca. Feb. 6, 1980.

Any discussion of this paper will appear in a Discussion Section to be published in the June 1981 JOURNAL. All discussions for the June 1981 Discussion Section should be submitted by Feb. 1, 1981.

REFERENCES

1. J. Manassen, G. Hodes, and D. Cahen, *This Journal*, **124**, 532 (1977).
2. W. A. Gerrard and J. R. Owen, *Mater. Res. Bull.*, **12**, 677 (1977).
3. B. Miller, A. Heller, M. Robbins, S. Menezes, K. C. Chang, and J. Thomson, Jr., *This Journal*, **124**, 1019 (1977).
4. R. N. Noufi, P. A. Kohl, and A. J. Bard, *ibid.*, **125**, 375 (1978).
5. A. B. Ellis, S. W. Kaiser, and M. S. Wrighton, *J. Am. Chem. Soc.*, **98**, 1635 (1976).
6. D. Cahen, G. Hodes, and J. Manassen, *This Journal*, **125**, 1623 (1978).
7. R. N. Noufi, P. A. Kohl, J. W. Rogers, J. M. White, and A. J. Bard, *ibid.*, **126**, 949 (1979).
8. K. Siegbahn, C. Nordling, A. Fahlman, R. Nordberg, H. Hamrin, J. Hedman, G. Johansson, T. Bergmark, S. Karlsson, I. Lindgren, and B. Lindberg, ESCA Atomic, Molecular and Solid State Structure Studied by Means of Electron Spectroscopy, Appendix 1, (Uppsala 1967).
9. H. Berthou and C. K. Jorgenson, *Anal. Chem.*, **47**, 482 (1975).
10. J. Manassen, G. Hodes and D. Cahen, Abstract 331, p. 851, The Electrochemical Society Extended Abstracts, Philadelphia, Penn., May 8-13, 1977.
11. A. Heller, G. P. Schwartz, R. G. Vadimsky, S. Menezes, and B. Miller, *This Journal*, **125**, 1156 (1978).
12. G. Hodes, J. Manassen, and D. Cahen, *Nature*, **261**, 403 (1976).
13. D. R. Lillington and W. G. Townsend, *Appl. Phys. Lett.*, **28**, 97 (1976).

Electrochemical Sectioning and Surface Finishing of GaAs and GaSb

C. R. Elliott and J. C. Regnault

British Post Office Research Centre, Martlesham Heath, Ipswich IP5 7RE, England

ABSTRACT

The characteristics of a new anodic dissolution process for sectioning and removing damage from monocrystalline GaAs and GaSb are described. Dissolution proceeds in the presence of a solid anodic film, which limits local variations in etch rate, so the flatness and microtopography of initially smooth surfaces are preserved. The high anodic efficiency permits accurate monitoring of material removal. Etch rates may be varied from below $0.01 \mu\text{m hr}^{-1}$ to over $10 \mu\text{m hr}^{-1}$ on GaAs and to $4 \mu\text{m hr}^{-1}$ on GaSb. Applications discussed include epitaxial layer thickness trimming and preparation of substrates for epitaxy and samples for crystallographic defect studies.

Smooth, flat, damage-free surfaces are often required for both growth and characterization of single crystal semiconductor materials. Furthermore, an ability to maintain such surfaces during removal of small, accurately known, thicknesses of material permits profiling and layer thickness trimming to be carried out. Initial flatness in cut slices is best achieved by mechanical lapping and polishing; thereafter, electrochemical polishing is potentially the best process for damage removal and for sectioning, because electrochemical dissolution may be monitored and controlled readily. However, although electropolishing of metals is well established (1) and electropolishing of semiconductors has been reported (2-6), the latter processes are limited in application to low resistivity materials, as relatively high current densities are required. Also, the complication of a scanned jet has been found necessary for producing extended flat areas (7). Compound semiconductor substrates are commonly chemo-mechanically polished (8-11) and then etched chemically to remove the residual damage (12). This process is not well suited to the removal of small, well-defined thicknesses of material and it tends to give beveled edges and "orange peel" type

of surface topography, with the chemical etching quickly degrading surface flatness (13).

Discontinuous processes are employed for profiling semiconductors accurately (14, 15). In these processes material is removed stepwise, by repeated growth and selective dissolution of anodic oxide films, whose thicknesses are determined by the applied voltage. Care is required in order to achieve a reliable thickness/voltage relationship (16) and the maximum thickness of each step is typically limited to a few hundred nanometers.

A novel approach to the problems of surface preparation and controlled removal of material was reported recently by Faktor and Stevenson (17), working on gallium arsenide. By anodizing in an oxide-forming phosphate electrolyte, to which a controlled addition of a chemical complexant (Tiron) had been added, they achieved continuous dissolution of GaAs in the presence of about 100 nm of anodic oxide, which, by transport limitation of the anodic current, ensured a uniform dissolution rate over the semiconductor surface. As the initial surface topography was preserved the process was described as replication etching. We have been concerned with the establishment of improved processes of this type, both for GaAs and for other compound semiconductors, for

Key words: anodization, etching, defects, gallium arsenide, gallium antimonide.

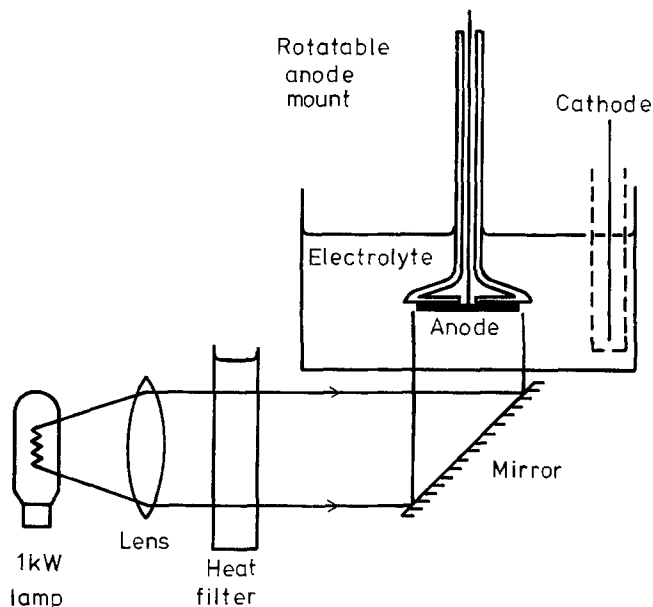


Fig. 1. Apparatus for anodic dissolution of n-type semiconductors of larger area.

the purposes of sectioning epitaxial layers and the removal of damage from mechanically polished slices. We report here the characteristics of a process which is applicable to GaAs and GaSb and has significant practical advantages over that introduced by Faktor and Stevenson for GaAs.

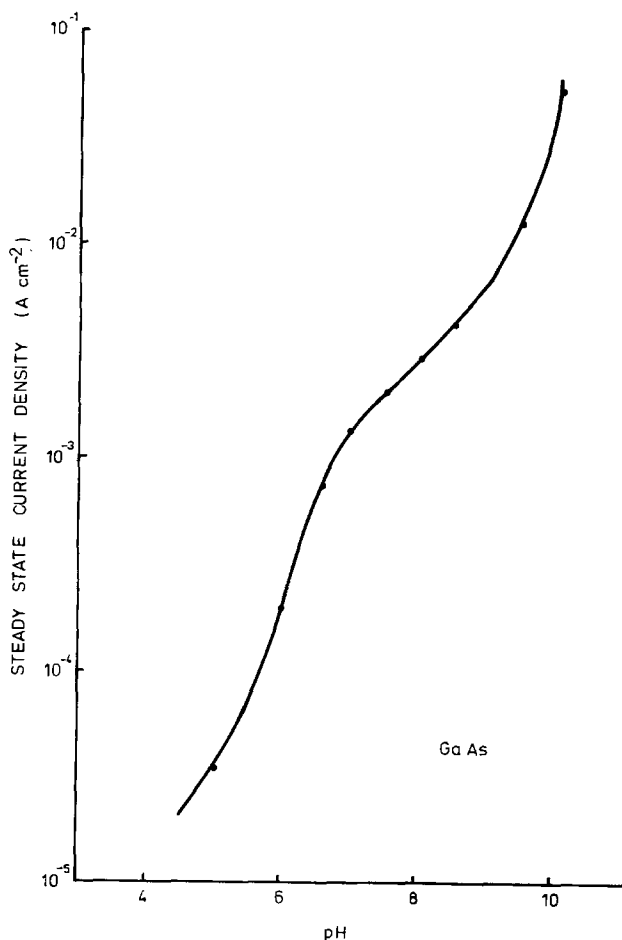


Fig. 2. Variation of steady-state current with pH for a GaAs anode in 0.2M EDTA/ammonium hydroxide.

pH	Charge transferred (C)	Weight loss (mg)	$x + y$
7.2	966	242.9	5.96
9.5	618	151.9	6.10

Experimental

The apparatus of Fig. 1 was employed for larger area specimens, such as substrates for epitaxial growth or whole wafers for microstructural evaluation. Because charge transfer in anodic dissolution of GaAs and GaSb is via holes (18), intense illumination (400 mW cm^{-2}) from a tungsten-halogen lamp was provided for generating a plentiful supply of holes at the surface of n-type materials. The anode was rotated at 50-500 rpm to establish a uniform diffusion layer in the electrolyte at the interface (19). A mercury back contact was usually satisfactory for n- and p-type materials, but any established contacting method may be used. The cathode was platinum foil and a porous membrane prevented any gas bubbles formed at its surface from reaching the anode. Anodizations were carried out at constant voltage, using a stabilized power supply which could provide up to 100V d.c. and had adjustable current limitation. The total charge passed was recorded by means of a digital integrator. The electrolyte consisted of 0.2M ethylene diamine tetraacetic acid disodium salt (EDTA), with ammonium hydroxide added for pH control. Small

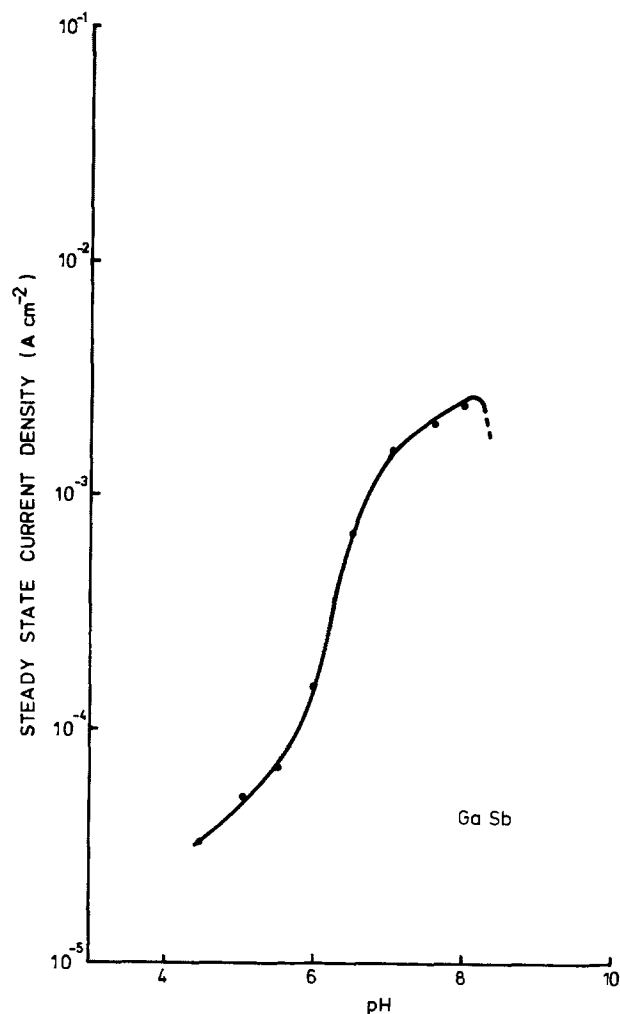
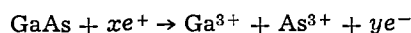


Fig. 3. Variation of steady-state current with pH for a GaSb anode in 0.2M EDTA/ammonium hydroxide.

selected areas were anodized using a microscope-mounted electrochemical cell of the type described by Faktor and Stevenson (17).

Results and Discussion

On applying about 50V between the electrodes a relatively large transient film-forming current flowed. As the thickness of the anodic oxide increased, this current decreased rapidly, reaching a steady value within a few seconds. Figure 2 shows the variation of the steady-state current with pH for a GaAs anode. At pH 4.5, the natural pH of 0.2M EDTA, the low current density of $20 \mu\text{A cm}^{-2}$ indicates negligible oxide solubility. Above pH 10 the current density could reach levels at which limitation by the semiconductor could occur, sometimes resulting in uneven dissolution of the anode. Between these values of pH the correlation of weight loss with charge passed (Table I) confirmed that the anodic reaction was of the form



where $x + y = 6$ and $x \gg y$ (20, 21), corresponding with a dissolution rate of $1.69 \mu\text{m mA}^{-1} \text{cm}^2 \text{hr}^{-1}$. Results for GaSb were similar up to pH 8, with a dissolution rate of $2.1 \mu\text{m mA}^{-1} \text{cm}^2 \text{hr}^{-1}$, but above pH 8 the current density fell, as shown in Fig. 3, and the film became dull in appearance.

At pH values greater than 2.5 EDTA reacts with gallium ions at room temperature to form a strong

complex (formation constant 10^{20}) (22). The increasing solubility of the anodic oxide with pH at near neutral pH's is thus associated with the increasing ionization of the EDTA with pH. At higher pH's the formation of soluble arsenite, antimonite, and gallate species will also be involved. The difference in behavior of GaAs and GaSb above pH 8 probably results from the different solubilities and stability regions of As_2O_3 and Sb_2O_3 (23).

Figures 4a-d are interference contrast micrographs of GaAs and GaSb surfaces before and after anodization in EDTA/ammonium hydroxide. Figure 4a shows a $\frac{1}{4} \mu\text{m}$ diamond polished n-type GaAs (100) surface and 4b the same, after anodic removal of a $20 \mu\text{m}$ thick layer at 2 mA cm^{-2} . Figure 4c shows a bromine/methanol polished GaSb surface and 4d the same, after anodic removal of $10 \mu\text{m}$ at 1 mA cm^{-2} . The topographies of the initial surfaces are still evident after anodization and no new surface structures are present, hence the process fulfills the essential requirements for damage removal and sectioning. Retention of flatness on a macro scale was confirmed by interferometry. Figure 5a shows the interference fringes obtained on a diamond polished GaAs (100) surface and 5b the same after removal of $20 \mu\text{m}$ anodically. Damage removal was confirmed by etching surfaces electrochemically in a defect-sensitive mode (17) before and after anodization in EDTA/ammonium hydroxide. Figures 6a and 6b show, respectively, defect revealed (100) surfaces of GaAs after bromine/methanol polishing and after an-

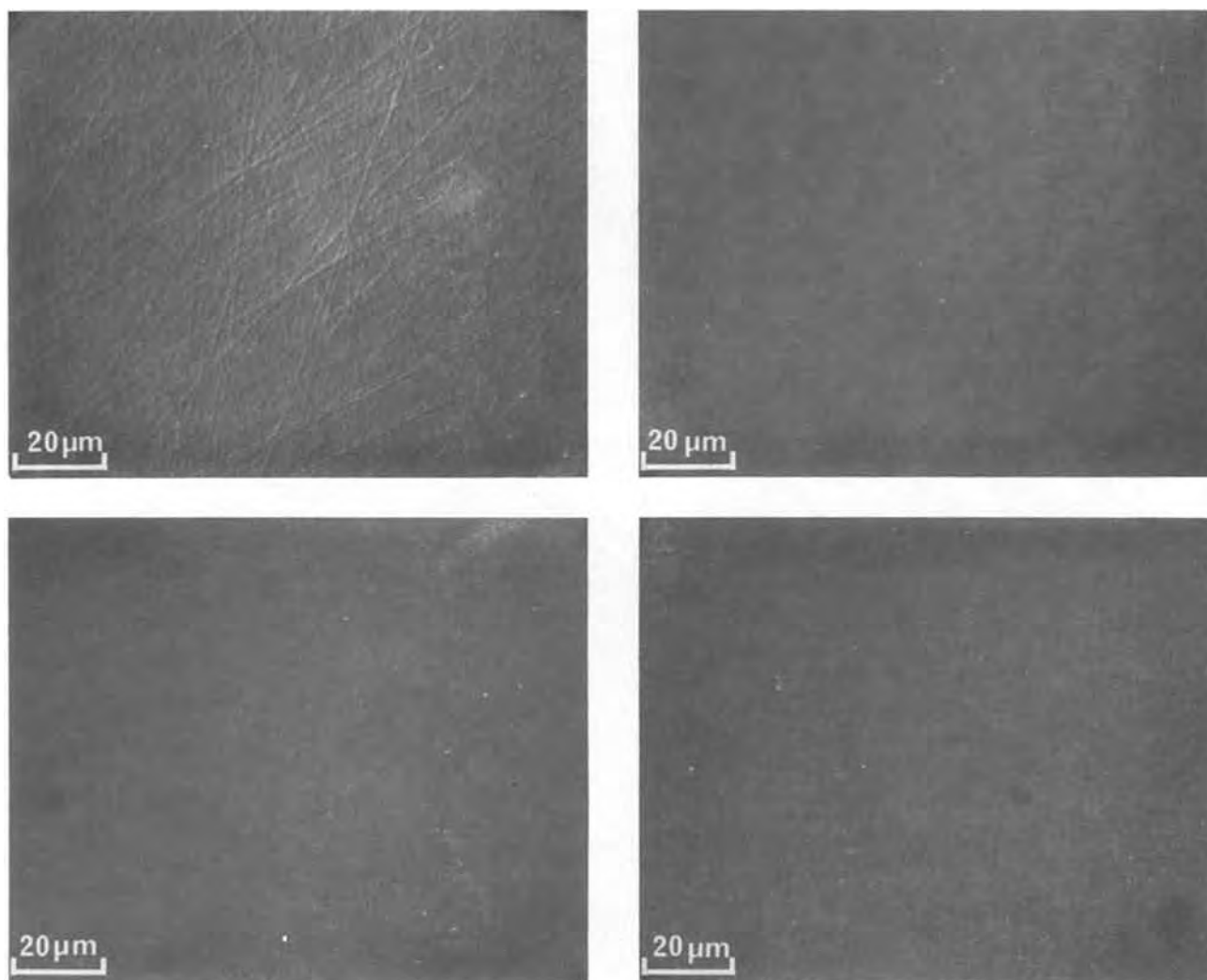


Fig. 4. Interference contrast micrographs of surfaces before and after anodization in EDTA/ammonium hydroxide: (a, top left) $\frac{1}{4} \mu\text{m}$ diamond polished n-type GaAs (100) surface, and (b, top right) the same after removal of $20 \mu\text{m}$ at 2 mA cm^{-2} ; (c, bottom left) bromine/methanol polished undoped GaSb (100) surface, and (d, bottom right) the same after removal of $10 \mu\text{m}$ at 1 mA cm^{-2} .

odic removal of 20 μm from a $\frac{1}{4}$ μm diamond polished surface.

It was noted that the surface of Fig. 4b was slightly smoother than that of 4a. As this implied a possibility of substituting the simple anodization process for one or more of the final stages of mechanical polishing of substrates, which require great care, an additional experiment was undertaken to further evaluate the smoothing effect. A GaAs (100) surface lapped with 25 μm alumina was anodized at 2 mA cm^{-2} until 10 μm had been removed. Figure 7a shows the characteristic "cellular" surface obtained. Within each polygon boundary the surface was smooth and slightly concave. Although the average size of the "cells" increased with anodization time, the structure persisted, even after removal of 105 μm of material, Fig. 7b. An electron channelling pattern, Fig. 8, obtained in the scanning electron microscope, indicated that the surface at this stage was essentially free from damage. Figures 7a and 7b were obtained by interference contrast microscopy, which greatly accentuates the apparent surface irregularity. A Talystep profile, Fig. 9, of the surface shown in Fig. 7b confirmed that the vertical amplitudes of the features were no more than 1 μm , and mostly only $\frac{1}{2}$ μm . The mechanism of formation of this interesting surface structure, under the conditions used here, is not yet understood. Similarly structured surfaces in other semiconductor-

etchant systems have been reported (7, 24), but not investigated in detail. The relationship between anodized surface structure and polishing medium particle sizes between 25 and $\frac{1}{4}$ μm was not pursued in this investigation, but a vapor phase epitaxial layer 20 μm thick was grown on the surface shown in Fig. 7b. The morphology of this layer is shown in Fig. 10.

No electrical breakdown at specimen edges or at surface features was observed during anodization in EDTA/ammonium hydroxide, whereas, in our experience, this does tend to occur in the phosphate/Tiron electrolyte. A further significant practical advantage of the EDTA/ammonium hydroxide system over the latter is its considerably wider range of usable current densities, simply obtained by adjustment of pH.

Applications

The process described has been shown to be satisfactory for preparing diamond polished or chemo-mechanically polished GaAs substrates for liquid phase, vapor phase, and molecular beam epitaxy, no further etching being required before growth (25). Figure 11 is an interference contrast micrograph of an MBE layer 1 μm thick, grown on a GaAs substrate prepared by this process. It has also been used successfully for trimming n-type epitaxial layers to the desired thickness for device fabrication and for preparing surfaces for defect-sensitive etching. In the first of these

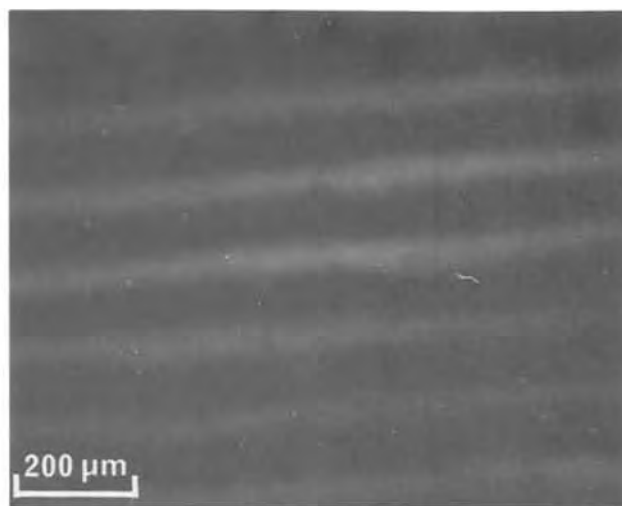
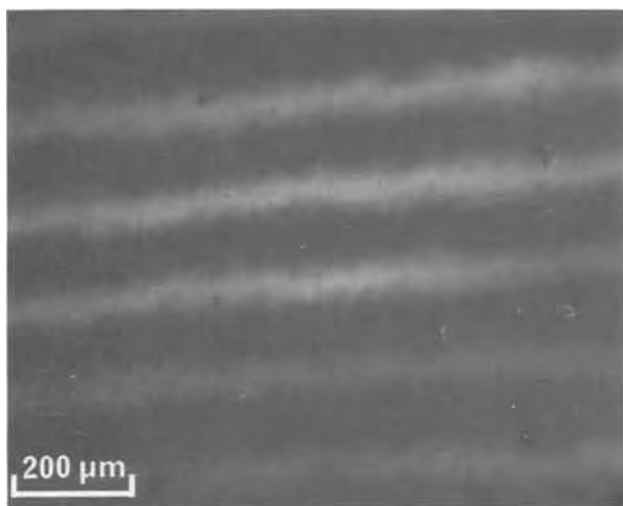


Fig. 5. Interference micrographs of a diamond polished GaAs (100) surface, (a, left) before and (b, right) after removal of 20 μm anodically.

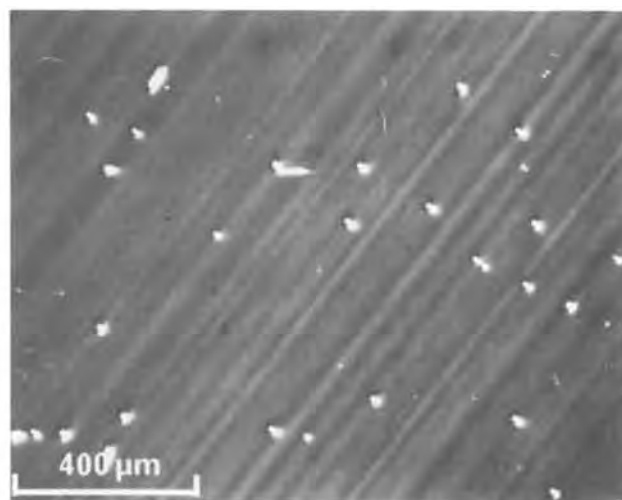
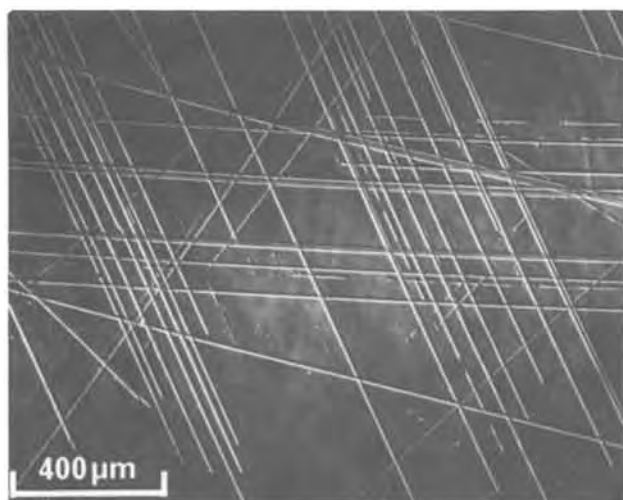


Fig. 6. GaAs (100) surfaces electrochemically etched to reveal defects; (a, left) residual abrasion damage after bromine/methanol polishing delineated, (b, right) damage-free surface after removal of 20 μm anodically following polishing with $\frac{1}{4}$ μm diamond.

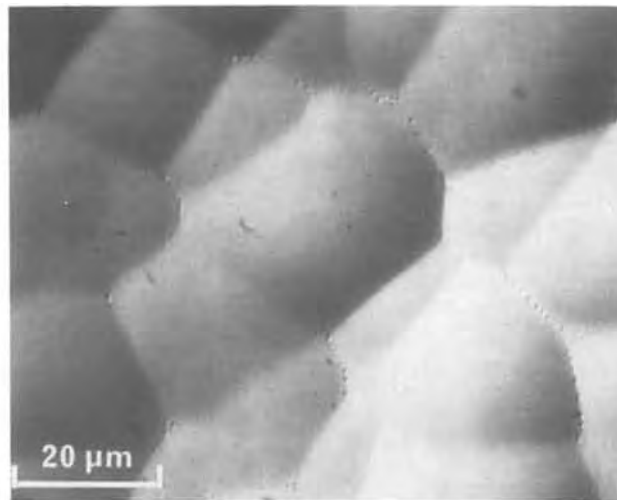
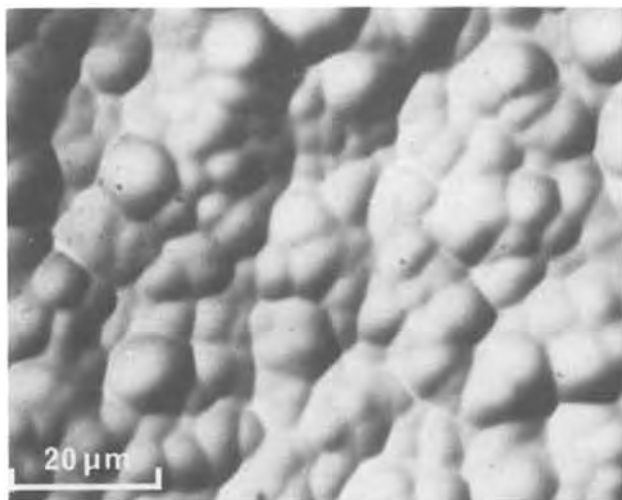


Fig. 7. Interference contrast micrographs of a GaAs (100) surface lapped with 25 μm alumina, after removal of (a, left) 10 μm and (b, right) 105 μm anodically.

applications one advantage of the technique is that the oxide may be left on the substrate as a protective film until immediately before growth. The oxide on GaAs is readily soluble in dilute hydrochloric acid or ammonium hydroxide, and that on GaSb is soluble in 2M aqueous potassium hydroxide. In the case of liquid phase epitaxy, where substrate thicknesses are critical and edge beveling is undesirable, the process has obvious advantages.

Summary

A technique is described for the smooth anodic dissolution of GaAs and GaSb. The process has the advantages of retention of surface flatness, easy and close control over the quantity of material removed, insensitivity to structural defects, and a variable dissolution rate. It has been shown to be satisfactory for trimming epitaxial layer thicknesses accurately

and for preparing damage-free surfaces both for epitaxial growth and for crystallographic defect studies.

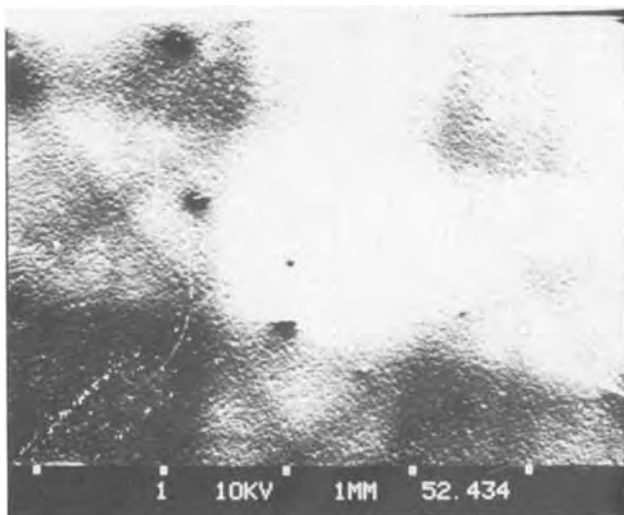


Fig. 8. Electron channeling pattern from the surface of Fig. 7b

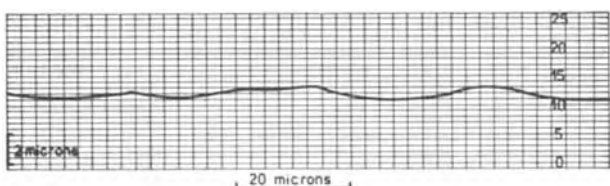


Fig. 9. Talystep profile of the surface of Fig. 7b

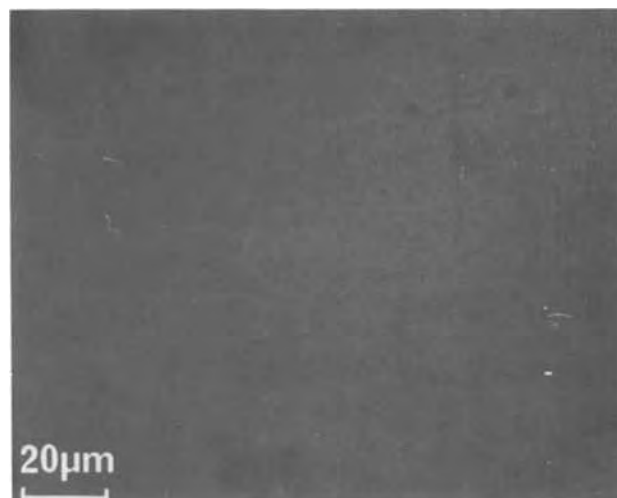


Fig. 10. GaAs layer 20 μm thick, grown by vapor phase epitaxy on the surface shown in Fig. 7b. Interference contrast micrograph.

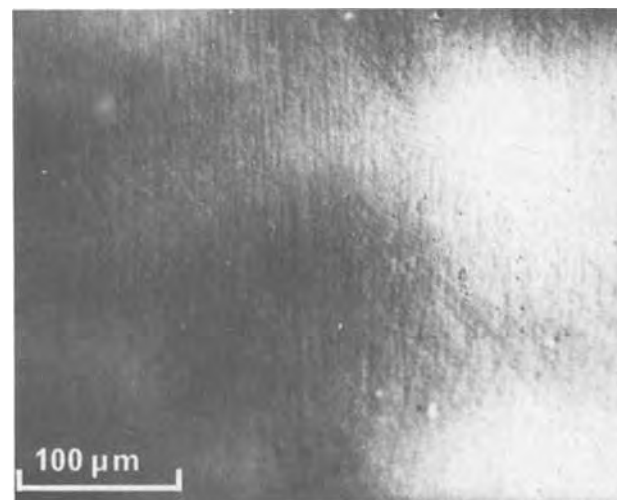


Fig. 11. GaAs layer 1 μm thick, grown by molecular beam epitaxy on a GaAs (100) surface prepared by anodization in EDTA/ammonium hydroxide. Interference contrast micrograph.

Acknowledgments

The authors are grateful for the cooperation of colleagues at the Post Office Research Centre and especially for the advice and encouragement received from M. M. Faktor. Acknowledgment is made to the Director of Research of the British Post Office for permission to publish this paper.

Manuscript received Nov. 2, 1979.

Any discussion of this paper will appear in a Discussion Section to be published in the June 1981 JOURNAL. All discussions for the June 1981 Discussion Section should be submitted by Feb. 1, 1981.

Publication costs of this article were assisted by the Post Office Research Centre.

REFERENCES

1. P. A. Jacquet, *Met Rev.*, **1**, 157 (1956).
2. D. R. Turner, *This Journal*, **105**, 402 (1958).
3. P. F. Schmidt and D. A. Keiper, *ibid.*, **106**, 592 (1959).
4. Yu. V. Pleskov, *Dokl. Akad. Nauk. SSSR*, **143**, 1399 (1962).
5. J. I. Pankove, in "The Electrochemistry of Semiconductors," P. J. Holmes, Editor, Academic Press, London (1962).
6. M. K. Norr, *This Journal*, **109**, 433 (1962).
7. E. J. Thrush, *J. Phys. E: Sci. Instrum.*, **11**, 327 (1978).
8. M. V. Sullivan and G. A. Kolb, *This Journal*, **110**, 585 (1963).
9. M. V. Sullivan and W. R. Bracket, *ibid.*, **114**, 295 (1967).
10. V. L. Rideout, *ibid.*, **119**, 1778 (1972).
11. J. T. Law, *Solid State Technol.*, **14**, 25 (1971).
12. D. J. Stirland and B. W. Straughan, *Thin Solid Films*, **31**, 139 (1976).
13. R. Stickler and G. R. Booker, *This Journal*, **111**, 485 (1964).
14. E. Tannenbaum, *Solid State Electron.*, **2**, 123 (1961).
15. H. Muller, F. H. Eisen, and J. W. Mayer, *This Journal*, **122**, 651 (1975).
16. A. Manara, A. Ostidich, G. Pedroli, and G. Restelli, *Thin Solid Films*, **8**, 359 (1971).
17. M. M. Faktor and J. L. Stevenson, *This Journal*, **125**, 621 (1978).
18. H. Gerischer, *ibid.*, **113**, 1174 (1966).
19. V. G. Levitch, "Physicochemical Hydrodynamics," Prentice Hall, Englewood Cliffs, N. J. (1962).
20. H. Gerischer, *Ber Bunsenges.*, **69**, 578 (1965).
21. H. Gerischer, *Surf. Sci.*, **13**, 265 (1969).
22. F. J. Welcher, "The Analytical Uses of Ethylene Diamine Tetraacetic Acid," Van Nostrand, Princeton, New Jersey (1958).
23. M. J. N. Pourbaix, *Atlas D'Equilibres Electrochimiques a 25°C*, Gauthier-Villars et Cie., Paris (1963).
24. E. Bassous and E. F. Baran, *This Journal*, **125**, 1321 (1978).
25. R. H. Moss, J. Haigh, A. K. Chatterjee, and G. Davies, Unpublished results.

Lateral Definition of Monocrystalline GaAs Prepared by Molecular Beam Epitaxy

S. Hiyamizu, K. Nanbu, T. Fujii, T. Sakurai, H. Hashimoto, and O. Ryuzan

Fujitsu Laboratories Limited, 1015 Kamikodanaka, Nakahara-ku, Kawasaki, Japan

ABSTRACT

Using a thermal oxide of GaAs for masking, excellent planar structures of monocrystalline and polycrystalline GaAs were prepared on GaAs substrates by molecular beam epitaxy. Micron-sized monocrystalline GaAs of device quality with sufficient electrical isolation by semi-insulating polycrystalline regions were obtained. Planar-type MESFET's were successfully fabricated to confirm the application potential of this technique.

Selective epitaxial deposition of GaAs has been long investigated for application to integrated circuits by vapor phase epitaxy (VPE) (1-4), liquid phase epitaxy (LPE) (5-7), and molecular beam epitaxy (MBE) (8-16). MBE has an apparent advantage over VPE and LPE to achieve lateral definition because of its feature of crystal growth in high vacuum. Therefore, many attempts have been made to obtain two- or three-dimensional structures of GaAs and AlGaAs with various techniques, such as deposition with mechanical shadowing using tungsten (8), tantalum (9, 10), and silicon masks (11, 12), deposition on SiO₂ masked substrates (13, 14), and preferentially etched substrates (15, 16). One of the most promising methods among them is planar growth of monocrystalline and polycrystalline GaAs using SiO₂ masking (13, 14), since the well-established and developing technique of lithography can be used to obtain fine patterning with good reproducibility.

In this study we present another promising method, i.e., selective growth of GaAs with the use of a GaAs thermal oxide for masking, which provides a similar, but superior planar structure of monocrystalline and

polycrystalline GaAs. Thermal oxides of GaAs have been extensively investigated (17), but they have not been applied to practical devices due to their poor dielectric properties (18) and poor characteristics for surface passivation of GaAs (19). Notwithstanding, when a thermal oxide was used as a masking film for selective growth by MBE, it exhibited rather favorable features compared with SiO₂ masking, e.g., extremely uniform and thin native oxide with a thickness of about 300Å could be easily obtained with high reproducibility over a large area of GaAs substrates, even up to a 2 in. diam or more, and consequently lateral definition with a micro-sized pattern could be accomplished with superior planar feature.

The electrical properties of high resistivity polycrystalline GaAs grown on the thermal oxide film and those of monocrystalline GaAs isolated by the polycrystalline regions were extensively studied to assess the application potential of this technique. Fabrication of planar-type MESFET's was demonstrated.

Crystal Growth

A (100) oriented, Cr-doped semi-insulating GaAs substrate was chemically etched in a solution of H₂SO₄:H₂O₂:H₂O = 18:1:1 to remove any mechan-

ically damaged layer. After being rinsed in deionized water, the substrate was oxidized in a stream of oxygen (0.5 liter/min) at 550°C for 30 min. An oxide layer with a thickness of about 300Å and exhibiting excellent uniformity up to an area of 2 in. diam or more was formed with good reproducibility. This native oxide was dissolved in HF, but it was hardly attacked by H₂SO₄, HCl, and H₂O₂. The oxide film on areas of the substrate intended for growing monocrystalline GaAs, was removed selectively using a conventional photolithographic technique and HF. Subsequently, the As-rich layer, which inherently exists at the interface of the thermal oxide film and GaAs (20), was also etched off with H₂O₂ to expose the GaAs in the window areas. After photoresist removal the exposed areas of the substrate were lightly etched again with a solution of H₂SO₄:H₂O₂:H₂O = 1:1:125 to remove a ~300Å layer of GaAs and rinsed in deionized water to clean the GaAs surface. The substrate was then loaded in an MBE system described previously (21).

Immediately before MBE growth, the substrates were preheated to about 600°C for a few minutes in an As₄ ambient with 1×10^{-7} Torr. Auger electron spectra of the substrate after preheating are shown in Fig. 1. It can be seen that the exposed surface area [Fig. 1(a)] exhibits the cleanliness of nonmasked GaAs substrates. In a spectrum from a coated area [Fig. 1(b)], we can see large peaks for oxygen and gallium but none for arsenic, which is consistent with that previously reported in GaAs thermal oxides (20, 22). The thermal oxide layer still remained even after the heat-treatment.

GaAs was deposited on such a substrate at growth temperatures between 460° and 530°C. Monocrystalline

and polycrystalline GaAs were deposited simultaneously on exposed GaAs areas and on the thermal oxide coated areas, respectively. Pure graphite cells were used for Ga, As, and Sn evaporation. Effusion cell temperatures were 1050° (Ga), 330° (As), and 800°-950°C (Sn). The growth rate was 0.3-0.5 μm/hr and the background pressure was about 1×10^{-6} Torr during growth.

Results and Discussion

Properties of polycrystalline GaAs.—Figure 2 shows a scanning electron micrograph of a cleaved cross section of a 1 μm thick deposited film, which includes the boundary between the polycrystalline and monocrystalline regions. The film thicknesses were measured with a Talystep. Surfaces of both regions were almost on the same level with each other, that is, the surface was nearly planar. Careful observation, however, revealed that polycrystalline films were about 5% thicker than the monocrystalline GaAs.

An electron micrograph of a platinum-shadowed carbon replica of a 1 μm thick polycrystalline GaAs film deposited at 460°C is shown in Fig. 3(a). The grain size of this film seems to be around 0.5 μm in diam at the surface. Figure 3(b) is a transmission electron micrograph (TEM) observed in the region near the surface of the same sample. Specimens for TEM, which have a 1-1.5 mm diam hole through the substrate and the oxide layer, were prepared by etching with the use of a solution of NH₄OH:H₂O₂ = 1:10 followed by Ar⁺ sputtering. This figure shows that grain size of the film is 0.3-0.5 μm in the region near the surface, which agrees well with that of the carbon replica. The grain size did not depend on the growth temperature in the range of 460°-530°C.

The *I-V* characteristics shown in Fig. 4 were measured through polycrystalline GaAs deposited at 500°C. To measure the electrical resistivity of polycrystalline GaAs, we prepared samples with a planar structure as shown in the inset. The deposited films with 1.1 and 2.3 μm thickness were Sn-doped to a concentration of 1×10^{18} cm⁻³, in which case the resistivity of the monocrystalline region became 2×10^{-3} Ωcm. The doping concentration in polycrystalline GaAs was supposed to be the same as that of monocrystalline regions prepared in the same wafer. Gold-germanium ohmic contacts with 20 μm width were applied to the monocrystalline stripes, and the *I-V* characteristics between these contacts were measured at room temperature (Fig. 4). Assuming that current flows uniformly and only through the polycrystalline film, we obtained resistivities of 2×10^6 Ωcm for the 1.1 μm thick film and 4×10^5 Ωcm for the 2.3 μm thick film from the gradient of the *I-V* curves in the ohmic range (≤ 10 V) and the geometry of the samples. The resistivity decreased by a factor of 5 when the thickness increased from 1.1 to 2.3 μm, suggesting that the films are considerably inhomogeneous in the direction of the thickness.

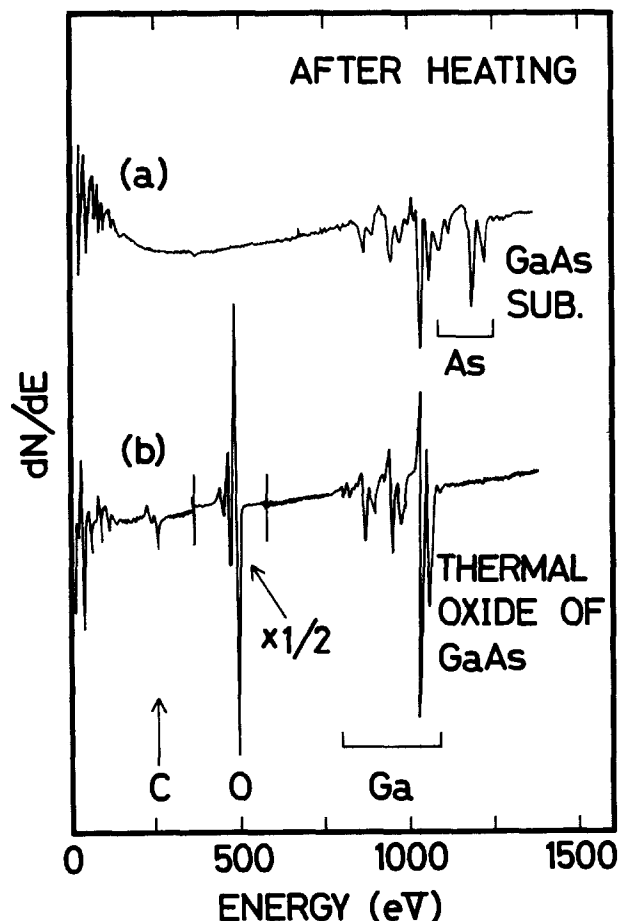


Fig. 1. Auger electron spectra for (a) an exposed-GaAs area and (b) a thermal oxide coated area on a GaAs substrate after preheating to about 600°C in vacuum of 1×10^{-7} Torr just before MBE growth.

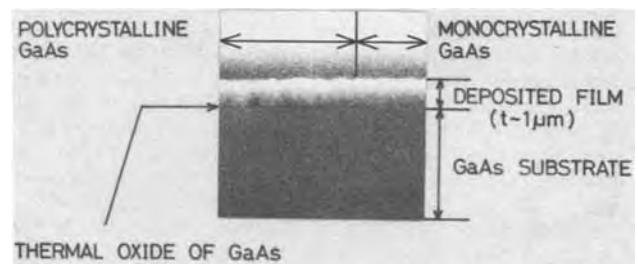


Fig. 2. Scanning electron micrograph of cleaved surface of a 1 μm thick film. The cleaved edge surface was lightly stain-etched. The boundary between polycrystalline and monocrystalline GaAs shows excellent planarity.

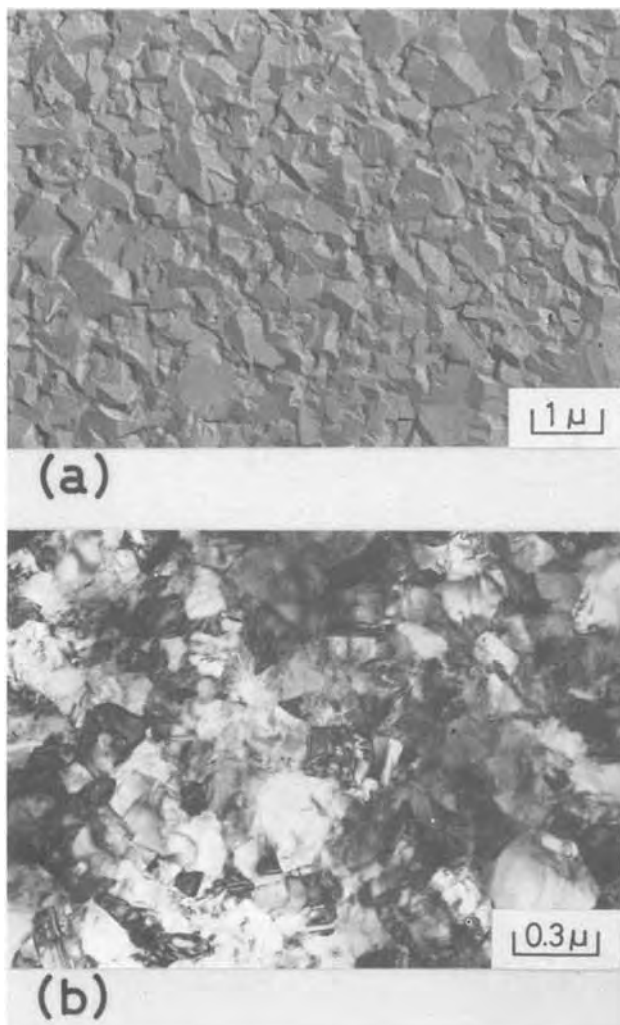


Fig. 3. (a) Electron micrograph of platinum-shadowed carbon replica of a $1 \mu\text{m}$ thick polycrystalline GaAs film deposited on the thermal oxide of GaAs at 460°C , showing grain size of about $0.5 \mu\text{m}$. (b) Transmission electron micrograph of the surface region in the same polycrystalline GaAs, showing grain size of $0.3\text{-}0.5 \mu\text{m}$.

The variation of resistivity in these polycrystalline films was then measured, by step-etching the samples, as a function of d , the distance from the interface of the thermal oxide and polycrystalline film (Fig. 5). In the $2.3 \mu\text{m}$ film the resistivity in the region near the surface ($d \sim 2 \mu\text{m}$) became more than one order of magnitude lower than that in the region within $1 \mu\text{m}$ from the interface. In the latter region, almost constant resistivities, about $2 \times 10^6 \Omega\text{cm}$, were observed in both films. The above assumption on current flow seems to be correct for the $1.1 \mu\text{m}$ film.

Figure 6 shows electron micrographs of platinum-shadowed carbon replicas of the as-grown surfaces for four polycrystalline films with thicknesses of $0.2, 0.5, 1.1,$ and $2.3 \mu\text{m}$ and almost the same doping concentration of about $1 \times 10^{18} \text{cm}^{-3}$. A significant increase in grain size from 0.2 to $1 \mu\text{m}$ can be seen with increasing film thickness from 0.2 to $2.3 \mu\text{m}$. It is likely, therefore, that such a variation in grain size might be realized in the direction of the thickness through the $2.3 \mu\text{m}$ film, and that this is the main cause of the rapid decrease in resistivity with increasing polycrystalline GaAs film thickness as seen in Fig. 5. The resistivity in polycrystalline silicon has been reported (23) to decrease with increasing grain size.

Resistivities at room temperature of about $1 \mu\text{m}$ thick polycrystalline films deposited at $480^\circ\text{-}500^\circ\text{C}$ are plotted as a function of doping concentration

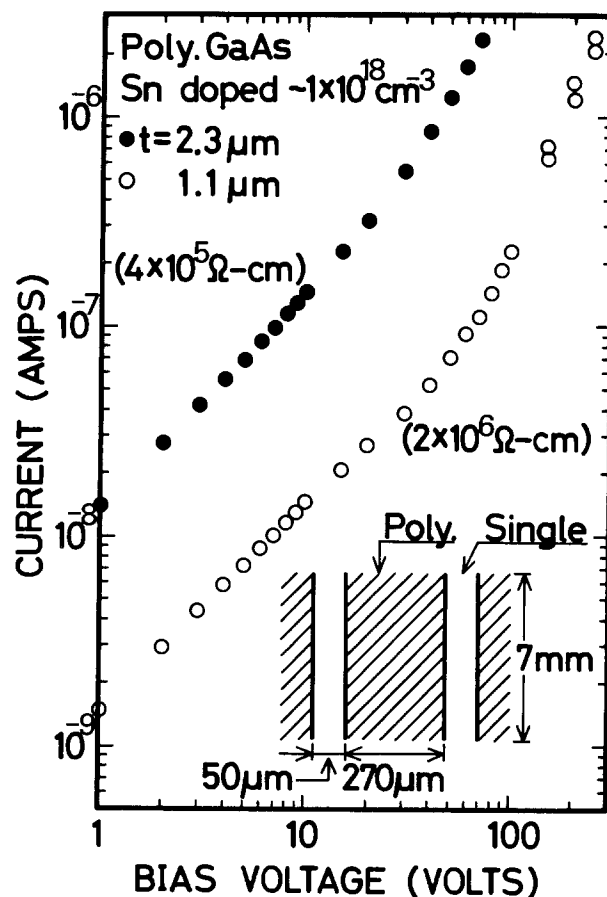


Fig. 4. I - V characteristics of Sn-doped polycrystalline GaAs films with thicknesses of 1.1 and $2.3 \mu\text{m}$ at room temperature. A sample for measurements is schematically illustrated in the inset. Ohmic relation was obtained over the range of bias voltage less than 10V in both films.

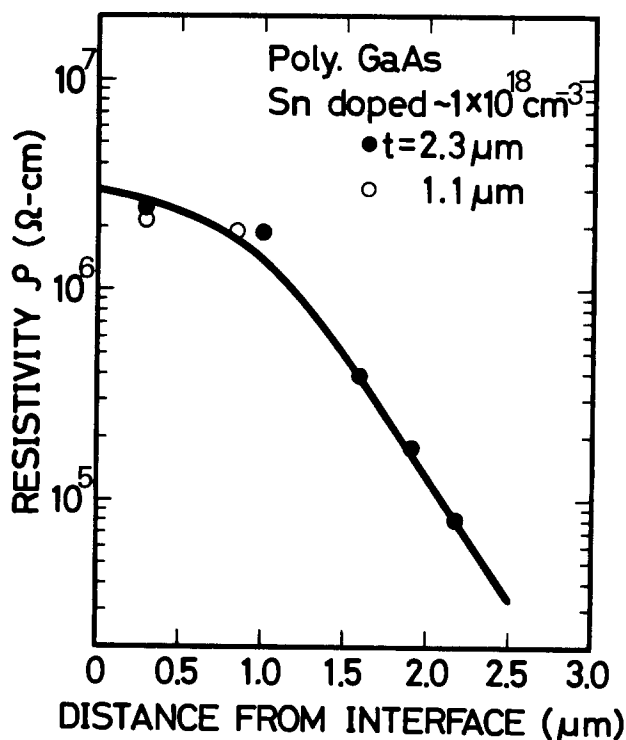


Fig. 5. In-depth profiles of resistivity in 1.1 and $2.3 \mu\text{m}$ thick polycrystalline GaAs with doping concentration of $1 \times 10^{18} \text{cm}^{-3}$, measured by step-etching at room temperature. The resistivity decreases considerably with increasing distance from the interface between thermal oxide and polycrystalline layer.

over a range of 2×10^{17} – 1.2×10^{19} cm^{-3} in Fig. 7. The high resistivity of about 2×10^6 Ωcm was maintained up to the doping level of 4×10^{18} cm^{-3} , and above this point resistivity dropped sharply. This result suggests that this planar growth technique can be applicable for isolation between n^+ contact areas ($n = 3 \times 10^{18}$ cm^{-3}) employed in GaAs power FET's (24). In these films we could not find an appreciable increase in grain size with increasing doping concentration as seen in polycrystalline silicon (25).

Properties of monocrystalline GaAs.—Electrical properties of monocrystalline GaAs in small regions laterally defined by the semi-insulating polycrystalline GaAs were characterized by Hall measurements. A Hall bar-shaped monocrystalline region with a film thickness of $0.5 \mu\text{m}$ (prepared at 500°C) is shown in the inset of Fig. 8. The length of the narrow stripe region was $210 \mu\text{m}$, and the width, w , was varied from 50 to $4 \mu\text{m}$. Hall mobilities and carrier concentrations at room temperature are plotted as a function of stripe width in Fig. 8. Electron mobility remained at a constant $2500 \text{ cm}^2/\text{Vsec}$ ($n \sim 1.4 \times 10^{18} \text{ cm}^{-3}$), even when the stripe width decreased to $4 \mu\text{m}$. This suggests that high quality GaAs can be grown selectively with narrow stripe widths down to $4 \mu\text{m}$. The quality of monocrystalline regions with lower carrier concentration is described in the next section.

Planar-type MESFET's.—In order to test application of this technique, planar-type MESFET's were fabricated. A $0.13 \mu\text{m}$ thick active layer with a carrier

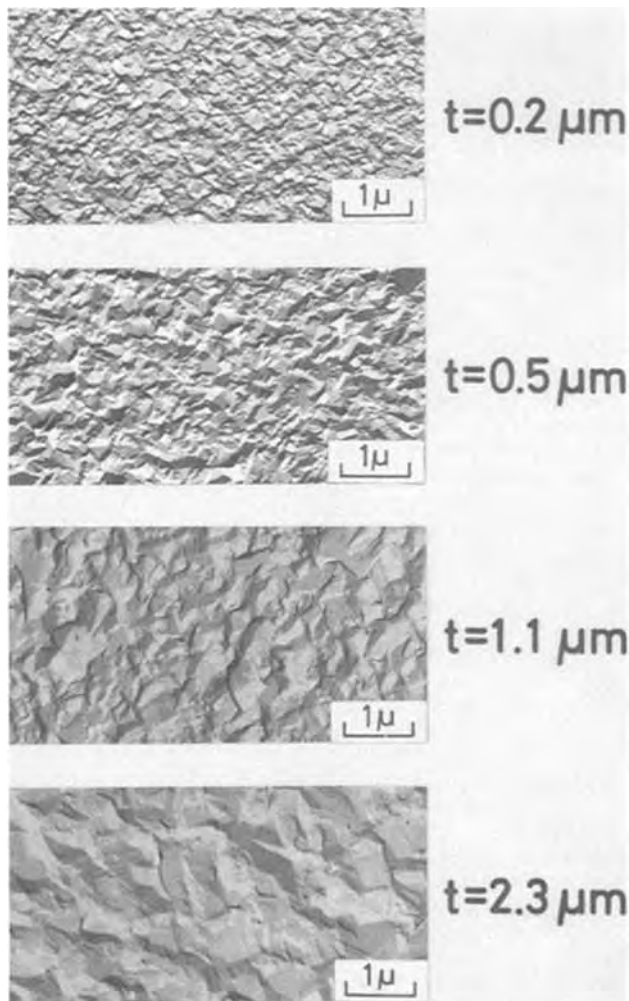


Fig. 6. Electron micrograph of platinum-shadowed carbon replicas of as-grown surface for polycrystalline GaAs films with thicknesses of 0.2 , 0.5 , 1.1 , and $2.3 \mu\text{m}$. The grain size increases with increasing film thickness.

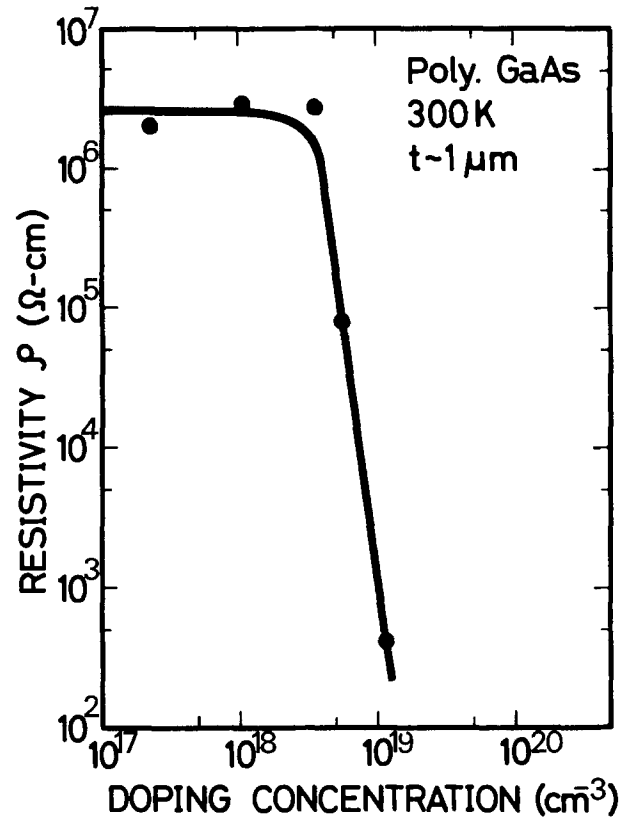


Fig. 7. Resistivity vs. doping concentration in about $1 \mu\text{m}$ thick polycrystalline GaAs films at room temperature.

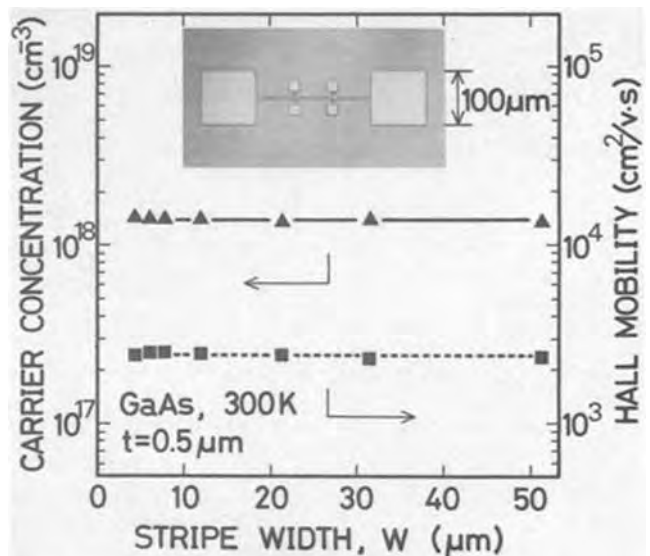


Fig. 8. Carrier concentration and Hall mobility as a function of a stripe width of monocrystalline GaAs region. The inset is a photomicrograph of a Hall-bar-shaped monocrystalline region with a stripe area of $4 \times 210 \mu\text{m}$. The film is $0.5 \mu\text{m}$ thick and Sn doped to a concentration of $1.4 \times 10^{18} \text{ cm}^{-3}$. Electron mobility remained at a constant $2500 \text{ cm}^2/\text{Vsec}$, even when the stripe width decreased to $4 \mu\text{m}$.

concentration of $2.4 \times 10^{17} \text{ cm}^{-3}$ was subsequently deposited on a $1.1 \mu\text{m}$ thick, unintentionally doped buffer layer at 520°C . The unintentionally doped monocrystalline layer showed p-type conduction with resistivity of $4 \times 10^3 \Omega\text{cm}$ at room temperature.

In-depth profiles of electron mobility and carrier concentration in this wafer were measured by a Schottky-barrier Hall technique (26) in a rectangular monocrystalline region with dimensions $400 \times 50 \mu\text{m}$ surrounded by the polycrystalline GaAs (Fig. 9).

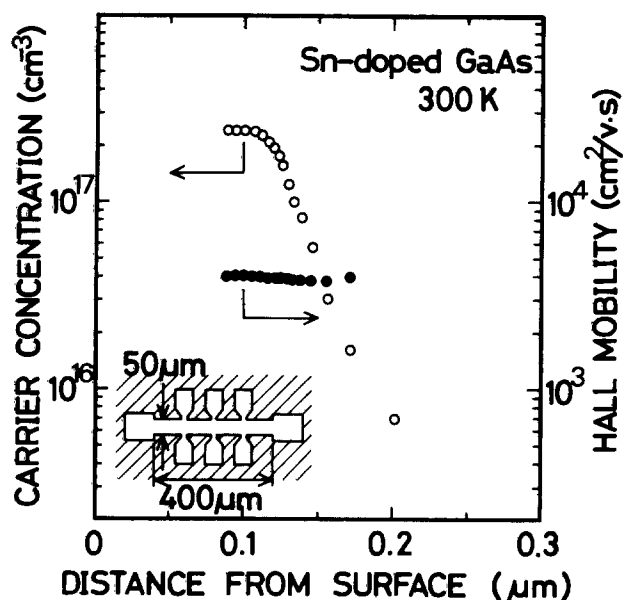


Fig. 9. In-depth profiles of carrier concentration and electron mobility in a rectangular monocrystalline GaAs region ($400 \times 50 \mu\text{m}$), laterally isolated by the polycrystalline GaAs, showing that device quality of monocrystalline GaAs could be obtained in small region. A $0.13 \mu\text{m}$ thick, Sn-doped layer ($n = 2.4 \times 10^{17} \text{cm}^{-3}$) was grown on a $1.1 \mu\text{m}$ thick unintentionally doped, high resistivity buffer layer.

The electron mobility remained almost constant, $4000 \text{cm}^2/\text{Vsec}$ at room temperature, through the active layer and also at the interface between the active and buffer layers.

Figure 10 shows an as-grown surface of an area for preparing MESFET's on the same wafer. Very clear boundaries and featureless surface of monocrystalline regions can be seen. Figure 11(a) shows the same area of the wafer after fabrication of devices. Resistance between two rectangular monocrystalline regions separated by $24 \mu\text{m}$ [Fig. 11(a) lower right], was $1.6 \times 10^9 \Omega$ at room temperature, *i.e.*, sufficient electrical isolation by the polycrystalline region in between them was obtained. Planar-type MESFET's were fabricated in the smallest, rectangular monocrystalline regions with dimensions of $150 \times 18 \mu\text{m}$, which is illustrated with greater magnification in Fig. 11(b). Source (S) and drain (D) contacts (with $5 \mu\text{m}$ separation) were formed by applying gold-germanium and gold. The Schottky gate (G) was made of aluminum. Gate length is $1.5 \mu\text{m}$ and width is $300 \mu\text{m}$.

To test electrical isolation by the polycrystalline regions and their boundaries, over which the Schottky gate crosses, the current-voltage characteristics of the planar-type MESFET [Fig. 11(b)] were compared with those of a conventional ring MESFET, which was fabricated in the largest monocrystalline region [Fig. 11(a) upper left] and did not contain polycrystalline regions. Typical *I-V* characteristics of these FET's are shown in Fig. 12(a) and (b). Both are free from hysteresis. There seems to be no significant difference between them. In the planar-type MESFET, the drain-to-source current was readily controlled by the gate voltage and was pinched off at a gate bias of -3V . There existed no substantial leakage current between the source and drain contacts not only through the polycrystalline regions but also the boundaries. Consequently, we believe that this growth technique could be successfully applied to fabrication of planar-type FET's.

Conclusion

Using a thermal oxide of GaAs for masking, planar-type selective growth of polycrystalline and mono-

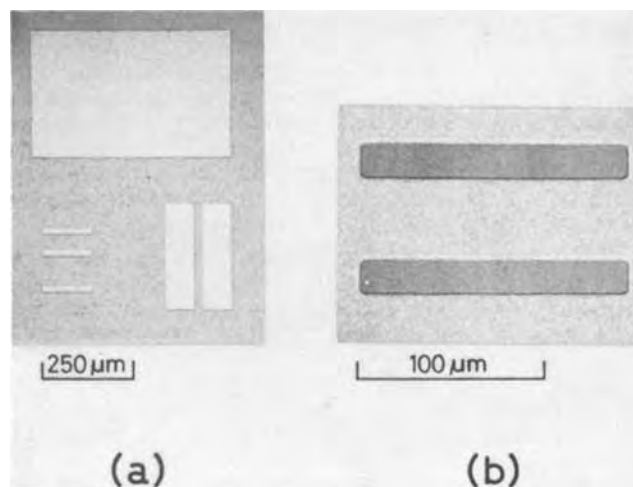


Fig. 10. (a) Photomicrograph of as-grown surface of an area for preparing MESFET's of a selectively grown $1.23 \mu\text{m}$ thick film, showing clearly defined monocrystalline regions with featureless surface. (b) Scanning electron micrograph of the smallest rectangular monocrystalline regions ($150 \times 18 \mu\text{m}$) shown with larger magnification.

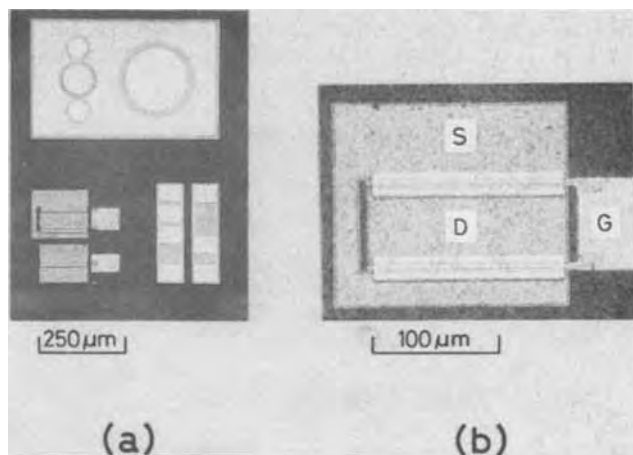


Fig. 11. (a) Photomicrograph of planar-type MESFET's (lower left) and a conventional ring MESFET (upper left). (b) Photomicrograph of a planar-type MESFET. Schottky gate (G) is $1.5 \mu\text{m}$ long and $300 \mu\text{m}$ wide. The distance between source (S) and drain (D) contacts is $5 \mu\text{m}$.

crystalline GaAs has been achieved by MBE. The polycrystalline GaAs was semi-insulating, and exhibited a resistivity of $2 \times 10^6 \Omega\text{cm}$ for $1 \mu\text{m}$ thick film with a doping concentration of less than $4 \times 10^{18} \text{cm}^{-3}$ which is of same order as that of polycrystalline GaAs on SiO_2 mask (13). This resistivity is almost 9 orders of magnitude higher than that of a corresponding monocrystalline film, $2 \times 10^{-3} \Omega\text{cm}$ ($n = 1 \times 10^{18} \text{cm}^{-3}$). It should be noted, however, that the resistivity of the polycrystalline film decreases considerably with increasing film thickness or with increasing dopant concentration above $4 \times 10^{18} \text{cm}^{-3}$. High quality monocrystalline GaAs, *i.e.*, GaAs having high mobilities (2500 and $4000 \text{cm}^2/\text{Vsec}$ for $n = 1 \times 10^{18}$ and $2.4 \times 10^{17} \text{cm}^{-3}$, respectively) were obtained in small regions isolated by the semi-insulating polycrystalline GaAs. In addition, planar-type MESFET's were successfully fabricated by this technique. Consequently, this planar growth by MBE can be considered to have promising features for application to the fabrication of GaAs integrated circuits, *i.e.*, excellent planar structure, sufficient electrical isolation provided by the polycrystalline GaAs, and device quality of monocrystalline regions.

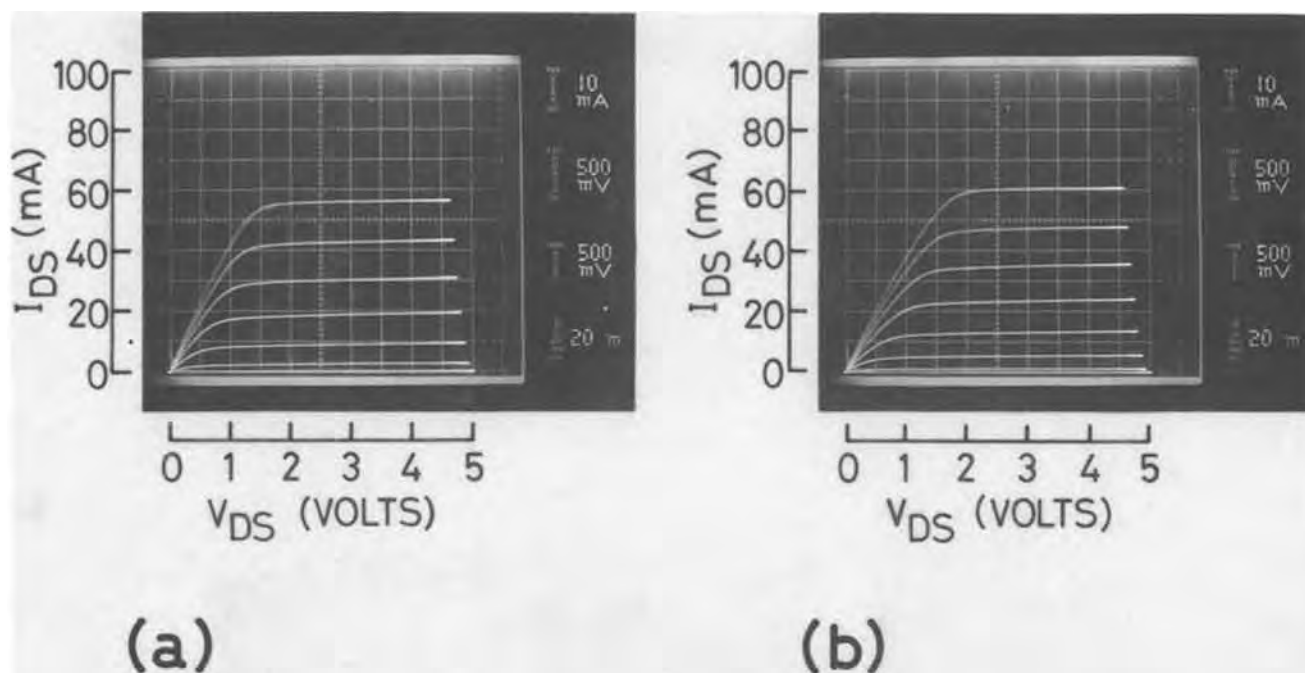


Fig. 12. Current-voltage characteristics of (a) a planar-type MESFET and (b) a ring MESFET.

Acknowledgment

The authors wish to thank K. Odani for his helpful advice on fabrication of MESFET's.

Manuscript submitted Nov. 6, 1979; revised manuscript received Jan. 25, 1980.

Any discussion of this paper will appear in a Discussion Section to be published in the June 1981 JOURNAL. All discussions for the June 1981 Discussion Section should be submitted by Feb. 1, 1981.

Publication costs of this article were assisted by Fujitsu Laboratories Limited.

REFERENCES

1. F. W. Tausch, Jr. and A. G. Lapierre, III, *This Journal*, **112**, 706 (1965).
2. D. W. Shaw, *ibid.*, **113**, 903 (1966); **115**, 777 (1968).
3. Y. Ishibashi and M. Yamaguchi, *Jpn. J. Appl. Phys.*, **9**, 1007 (1970); *ibid.*, **10**, 525 (1971).
4. S. Iida and K. Ito, *J. Crystal Growth*, **13/14**, 336 (1972).
5. K. Sekido, T. Takeuchi, F. Hasegawa, and S. Kikuchi, *Proc. IEEE* **57**, 815 (1969).
6. O. Ishihara, M. Otsubo, and S. Mitsui, *Jpn. J. Appl. Phys.*, **16**, 2109 (1977).
7. M. M. Piskorski and G. D. Stareev, *Solid-State Electron.*, **18**, 859 (1975).
8. A. Y. Cho and F. K. Reinhart, *Appl. Phys. Lett.*, **21**, 355 (1972).
9. J. L. Merz, R. A. Logan, W. Wiegmann, and A. C. Gossard, *ibid.*, **26**, 337 (1975).
10. F. K. Reinhart and A. Y. Cho, *ibid.*, **31**, 457 (1977).
11. W. T. Tsang and M. Ilegems, *ibid.*, **31**, 301 (1977).
12. W. T. Tsang and A. Y. Cho, *ibid.*, **32**, (8), 491 (1978).
13. A. Y. Cho and W. C. Ballamy, *J. Appl. Phys.*, **46**, 783 (1975).
14. W. C. Ballamy and A. Y. Cho, *IEEE Trans. Electron Devices*, **ed-23**, 481 (1976).
15. S. Nagata and T. Tanaka, *J. Appl. Phys.*, **48**, 940 (1977).
16. W. T. Tsang and A. Y. Cho, *Appl. Phys. Lett.*, **30**, 293 (1977).
17. F. Koshiga and T. Sugano, Proc. 8th Conf. Solid State Devices, Tokyo, 1976; *Jpn. J. Appl. Phys.*, **16**, Suppl. 16-1, 465 (1977).
18. D. N. Butcher and B. J. Sealy, *Electron. Lett.*, **13**, 558 (1977).
19. H. T. Minden, *This Journal*, **109**, 733 (1962).
20. K. Watanabe, M. Hashiba, and T. Yamashina, Proc. 9th Conf. Solid State Devices, Tokyo, 1977; *Jpn. J. Appl. Phys.*, **17**, Suppl. 17-1, 335 (1978).
21. S. Hiyamizu, T. Fujii, K. Nanbu, and S. Maekawa, Proc. 9th Conf. Solid State Devices, Tokyo, 1977; *Jpn. J. Appl. Phys.*, **17**, Suppl. 17-1, 79 (1978).
22. I. Shiota, N. Miyamoto, and J. Nishizawa, *This Journal*, **124**, 1405 (1977).
23. T. I. Kamins, *J. Appl. Phys.*, **42**, 4357 (1971).
24. M. Fukuta, K. Suyama, H. Suzuki, Y. Nakayama, and H. Ishikawa, *IEEE Trans. Microwave Theory Tech.*, **mtt-24**, 312 (1976).
25. M. E. Cowher and T. O. Sedgwick, *This Journal*, **119**, 1565 (1972).
26. A. Shibatomi, N. Yokoyama, H. Ishikawa, K. Dazai, and O. Ryuzan, *J. Crystal Growth*, **31**, 240 (1975).

LPE Growth of Misfit Dislocation-Free Thick $\text{In}_{1-x}\text{Ga}_x\text{As}$ Layers on InP

Kazuo Nakajima, Satoshi Komiya, Kenzo Akita, Toyoshi Yamaoka, and Osamu Ryuzan

Fujitsu Laboratories Limited, Semiconductor Materials Laboratory, Nakahara-ku, Kawasaki, 211, Japan

ABSTRACT

The conditions for equilibrium LPE growth of exactly and nearly lattice-matched $\text{In}_{1-x}\text{Ga}_x\text{As}$ epitaxial layers on InP (100) substrates were determined at 650°C by lattice constant measurements. It was found that the half-width of the diffraction peak of the ternary layer was much smaller than that of an $\text{In}_{1-x}\text{Ga}_x\text{As}_{1-y}\text{P}_y$ layer, and that the composition of the ternary layer scarcely varied along the thickness. The threshold region for the formation of misfit dislocations into the ternary layers were experimentally determined by using an x-ray topograph. This region can be displayed by both the lattice misfit and the thickness. It was found that the layers thicker than $10\ \mu\text{m}$ without misfit dislocations could be grown starting from 650°C only when the lattice misfit at room temperature was between -6.5×10^{-4} and -9×10^{-4} . It is most important for the growth of misfit dislocation-free thick layers that the layers should be lattice-matched to the substrates at the growth temperature and that tensile stress should not be incurred at the growth temperature. The relationships between the photoluminescence peak wavelength or solid composition and the lattice misfit were determined experimentally.

The growth of lattice-matched $\text{In}_{0.53}\text{Ga}_{0.47}\text{As}$ on InP substrates has been investigated mainly to fabricate avalanche photodiodes (APD's) for light whose wavelength lies between 1.0 and $1.65\ \mu\text{m}$. Several reports (1-4) were made on the ternary APD's. For the fabrication of optical devices such as APD's, thick and misfit dislocation-free epitaxial layers are required. The thin ternary layers without any misfit dislocations have generally been obtained by exact lattice-matching on the substrates at room temperature. However, we found that misfit dislocations appeared in the exactly lattice-matched thicker $\text{In}_{0.53}\text{Ga}_{0.47}\text{As}$ layers than $4\ \mu\text{m}$, which were grown by liquid phase epitaxial (LPE) method starting from 650°C . These misfit dislocations are introduced by the interfacial stress which is caused by the difference of thermal expansion coefficients between the epitaxial layer and the substrates. Therefore, the conditions for the growth of thick and misfit dislocation-free layers must be studied in order to fabricate APD's of $\text{In}_{0.53}\text{Ga}_{0.47}\text{As}$. Such conditions had ever been determined only for the $\text{Ga}_{1-x}\text{Al}_x\text{As}_{1-y}\text{P}_y$ system on GaAs substrates (5).

In this work, the conditions for the growth of the misfit dislocation-free thick $\text{In}_{0.53}\text{Ga}_{0.47}\text{As}$ layers on InP(100) substrates were experimentally determined. Under these conditions, the misfit dislocation-free layers thicker than $10\ \mu\text{m}$ could be grown. These results were analyzed. In order to determine the accurate wavelength of the exactly lattice-matched $\text{In}_{0.53}\text{Ga}_{0.47}\text{As}$ on InP, the relationship between the photoluminescence peak wavelength and the lattice misfit was measured. The composition variations of the layers with distance from the surface of the substrate were also studied.

Experimental Procedure and Results

LPE growth conditions.—The previously determined liquidus isotherm at 650°C (6) was used to grow $\text{In}_{1-x}\text{Ga}_x\text{As}$ on InP under equilibrium conditions. The conditions for equilibrium LPE growth of exactly and nearly lattice-matched layers on InP (100) substrates were found by lattice constant measurements of these layers grown from melts with compositions on the liquidus isotherms. Supersaturated melts were not used in this growth. Layers were grown starting from 650°C at a constant cooling rate of $0.5^\circ\text{C}/\text{min}$ by the

Key words: misfit dislocation, InGaAs, lattice-matching, photodiode.

ramp cooling technique. Lattice constants were determined from the (400) reflection of the $\text{CuK}\alpha_1$ radiation by the double crystal x-ray diffraction technique. They are lattice constants of the epitaxial lattice perpendicular to the wafer surface.

Figure 1 shows the lattice misfit at room temperature, $\Delta a/a$ as a function of X_{Ga}^1 . Where, Δa is equal to the lattice constant of $\text{In}_{1-x}\text{Ga}_x\text{As}$ minus the lattice constant of InP, $a = 5.86875\text{\AA}$ (7), and X_{Ga}^1 represents the atomic fraction of Ga in the ternary melt. The melt compositions for the growth of layers with various $\Delta a/a$ can be determined from Fig. 1 and previously determined liquidus isotherm (6).

Composition variation along the growth direction.—The existence of composition variations along the growth direction is undesirable because it causes variations of the lattice constant and generates misfit dislocations. Uniform layers without composition variations are also necessary to determine accurately the lattice constant. Figure 2 shows the $\text{CuK}\alpha_1$ rocking curves for the (400) reflection of (curve a) $\text{In}_{0.7}\text{Ga}_{0.3}\text{As}_{0.64}\text{P}_{0.36}$ and (curve b) $\text{In}_{0.53}\text{Ga}_{0.47}\text{As}$ layers grown on InP (100) substrates. These layers were grown

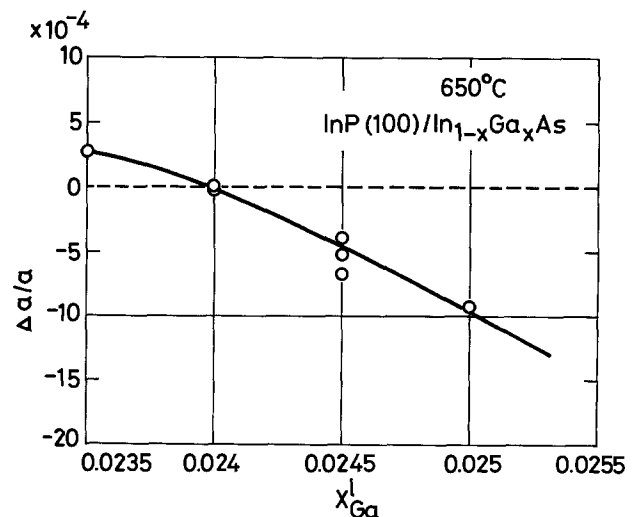


Fig. 1. Lattice misfit $\Delta a/a$ of the $\text{In}_{1-x}\text{Ga}_x\text{As}$ ternary alloys grown on InP (100) substrates at 650°C as a function of X_{Ga}^1 .

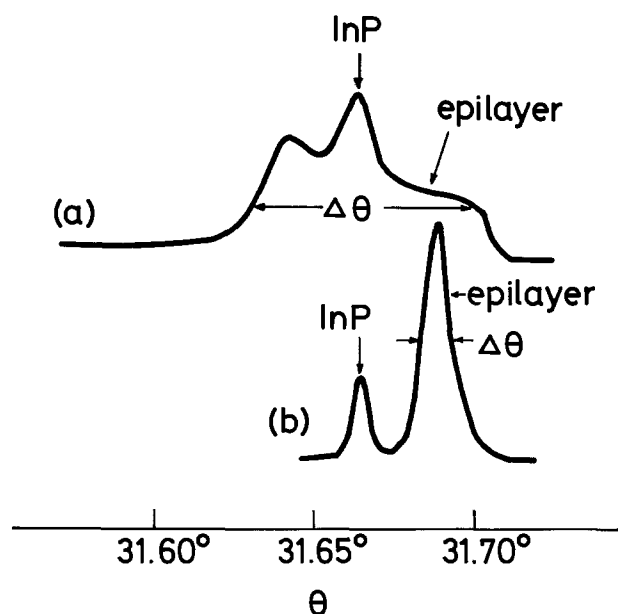


Fig. 2. $\text{CuK}\alpha_1$ rocking curves for the (400) reflection of (curve a) $\text{In}_{0.7}\text{Ga}_{0.3}\text{As}_{0.64}\text{P}_{0.36}$ and (curve b) $\text{In}_{0.53}\text{Ga}_{0.47}\text{As}$ layers grown on InP (100) substrates at 650°C .

starting from 650°C at a constant cooling rate of $0.5^\circ\text{C}/\text{min}$ by using just saturated melts at 650°C . The thicknesses of the ternary and quaternary layers were 4.0 and $4.3\ \mu\text{m}$, respectively. The half-width of the diffraction peak of the ternary layer (about 34 sec) is much smaller than that of the quaternary layer (about 250 sec). This indicates, as also previously pointed out (8, 9), that the composition of the quaternary layer has the gradient of P concentrations as a result of the depletion of P in the quaternary melt near the growing interface, but this also indicates that the ternary layer does not have such a large composition variation. From results shown in Fig. 2, the lattice misfit, $\Delta a/a$ of the ternary layer was found to be -6.85×10^{-4} , but that of the quaternary layer were estimated between 6.2×10^{-4} and -9.9×10^{-4} .

Figure 3 shows how the photoluminescence (PL) peak wavelength of $\text{In}_{0.53}\text{Ga}_{0.47}\text{As}$ and $\text{In}_{0.77}\text{Ga}_{0.23}\text{As}_{0.5}\text{P}_{0.5}$ layers with the distance d (μm) from the interface between the layers and the InP substrate. PL measurements (8) were used to determine wavelengths on step etched surfaces at various distances of

d (μm) from the substrates. The ternary and quaternary layers were grown from 650°C at constant cooling rates of 0.2° and $0.1^\circ\text{C}/\text{min}$, respectively. The thicknesses of the ternary and quaternary layers were 26.5 and $8.5\ \mu\text{m}$, respectively. As shown in Fig. 3, the wavelength of the ternary layer is almost constant with the layer thickness, but that of the quaternary layer varies largely despite its slower cooling rate. This indicates, as also shown in Fig. 2, that the composition of the ternary layer hardly varies with the layer thickness because the ternary system does not include elements like P. Therefore, the lattice constant of $\text{In}_{1-x}\text{Ga}_x\text{As}$ layers can be determined accurately.

Misfit dislocation-free region.—It has been generally expected that thick layers without misfit dislocations can be obtained by exact lattice matching to InP at room temperature. It was found that this idea was not correct. In this work, (422) reflection x-ray topographs using $\text{CuK}\alpha_1$ radiation and double crystals were used to determine whether misfit dislocations are generated or not in epitaxial layers. The generation of interfacial misfit dislocations depends on both the lattice misfit and the layer thickness under a fixed starting growth temperature (10). Therefore, a series of $\text{In}_{1-x}\text{Ga}_x\text{As}$ layers with different $\Delta a/a$ and thicknesses were grown on InP (100) substrates in order to determine the conditions for the growth of misfit dislocation-free layers. In this growth, a constant cooling rate of $0.2^\circ\text{C}/\text{min}$, the starting growth temperature of 650°C , and just saturated melts at 650°C were used. The results are shown in Fig. 4. Open circles show the misfit dislocation-free layers and crosses show the layers with misfit dislocations. The samples are divided into two groups depending on whether misfit dislocations were present or not. Line forming these areas define the threshold for the formation of misfit dislocations. Thus, the area where misfit dislocations do not generate was determined. If the lattice constant of the ternary layer matches that of InP at room temperature, the thickness of the layer without misfit dislocations is less than $3.6\ \mu\text{m}$. In order to obtain misfit dislocation-free layers thicker than $3.6\ \mu\text{m}$, these layers must have a negative lattice misfit. It was found that misfit dislocation-free layers thicker than $10\ \mu\text{m}$ could be grown starting from 650°C only when $\Delta a/a$ was between -6.5×10^{-4} and -9×10^{-4} . The surface morphology of these ternary layers was as good as that of layers with $|\Delta a/a| \leq 1 \times 10^{-4}$.

The maximum attainable thickness in misfit dislocation-free region was not determined in this work. Thicker layers than $11.5\ \mu\text{m}$ were not grown in this

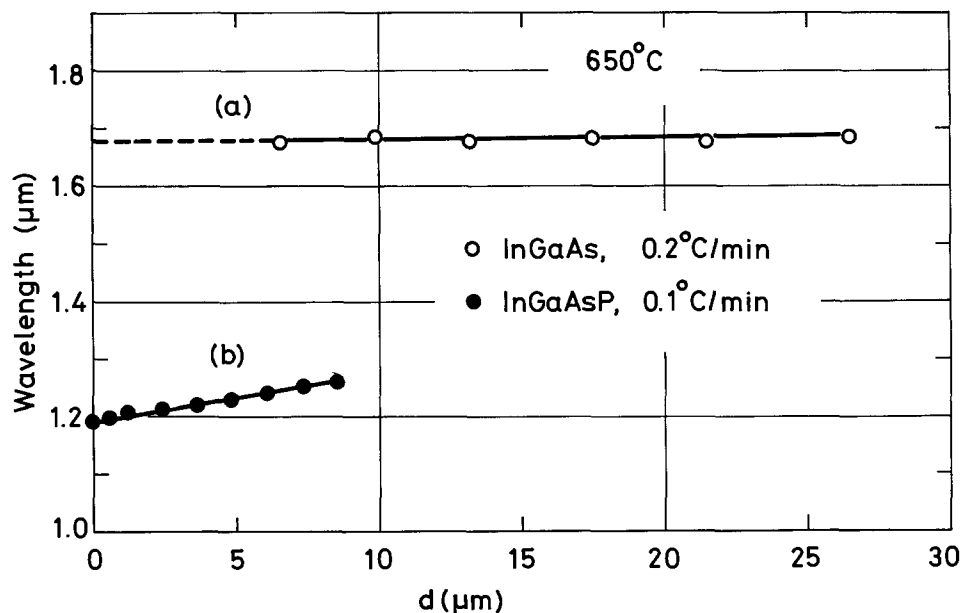


Fig. 3. Wavelength variations of (curve a) $\text{In}_{0.53}\text{Ga}_{0.47}\text{As}$ and (curve b) $\text{In}_{0.77}\text{Ga}_{0.23}\text{As}_{0.5}\text{P}_{0.5}$ layers grown at 650°C with distance d (μm) from the interface between the layers and InP substrates.

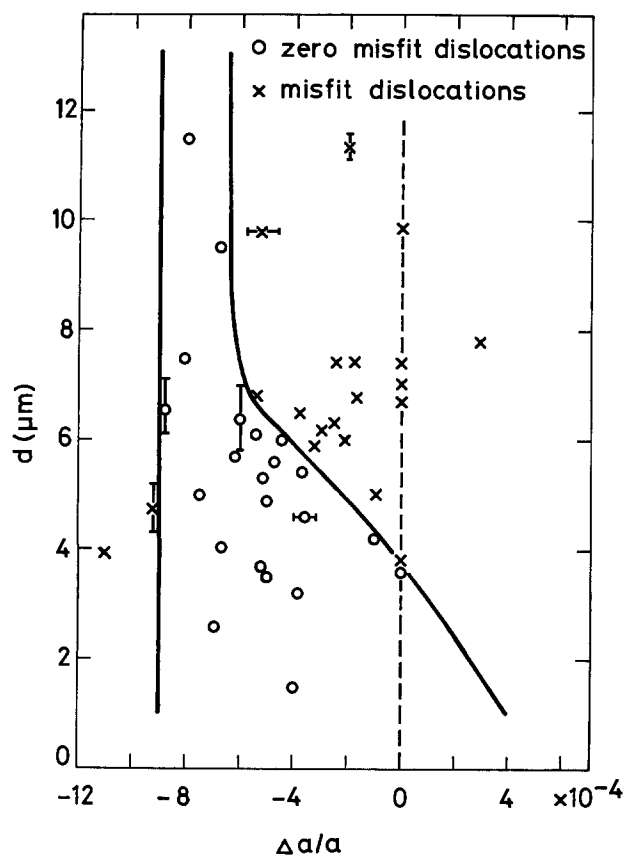


Fig. 4. Threshold region of both the lattice misfit $\Delta a/a$ and the layer thickness d (μm) for initiation of misfit dislocations into $\text{In}_{1-x}\text{Ga}_x\text{As}$ layers on InP. \circ and \times represent samples with no misfit dislocations and with misfit dislocations, respectively.

experiment, but there is a possibility of obtaining misfit dislocation-free and thicker layers than $11.5 \mu\text{m}$. The misfit dislocation-free region for thinner layers than $1 \mu\text{m}$ is not shown in Fig. 4. For thin InGaAsP layers of $0.4 \mu\text{m}$, it was reported that misfit dislocations were not found if $\Delta a/a$ was between 5×10^{-3} and -5×10^{-3} (11).

In ternary layers whose thicknesses are just above the demarcation lines for misfit dislocation generation, it was observed that the density of misfit dislocation was very low and generally less than several hundreds. Most of these misfit dislocations were introduced from edges of wafers in the early stage of their formation and formed unidirectional arrays. As farther from the demarcation lines to the outside of the region, a cross-grid of misfit dislocations was present.

Wavelength and solid composition vs. lattice misfit.—The wavelength and solid composition of $\text{In}_{1-x}\text{Ga}_x\text{As}$ with lattice constants nearly matched to InP were determined. Figure 5 shows the wavelength λ (μm) of ternary layers as a function of the lattice misfit $\Delta a/a$. The wavelength was determined by PL measurements which were previously reported in detail (8). As shown in Fig. 5, the wavelength is approximately $1.685 \mu\text{m}$ when the lattice constant matches that of InP, and the wavelength is approximately $1.65 \mu\text{m}$ when the lattice misfit is -5×10^{-4} . The previously reported wavelengths of the lattice-matched ternary layer on InP were 1.65 (12, 13) and $1.68 \mu\text{m}$ (14, 15). The cause of the difference has not been explained. Degrees of the lattice misfit of samples used for wavelength measurements were not clearly described in most of these reports. In Fig. 5, it can be known that the difference of the reported wavelengths was caused by the difference of degree of lattice matching among them. Pollack *et al.* (13) reported that $\lambda = 1.656 \mu\text{m}$ at $\Delta a/a = -5 \times 10^{-4}$. Their data is consistent with

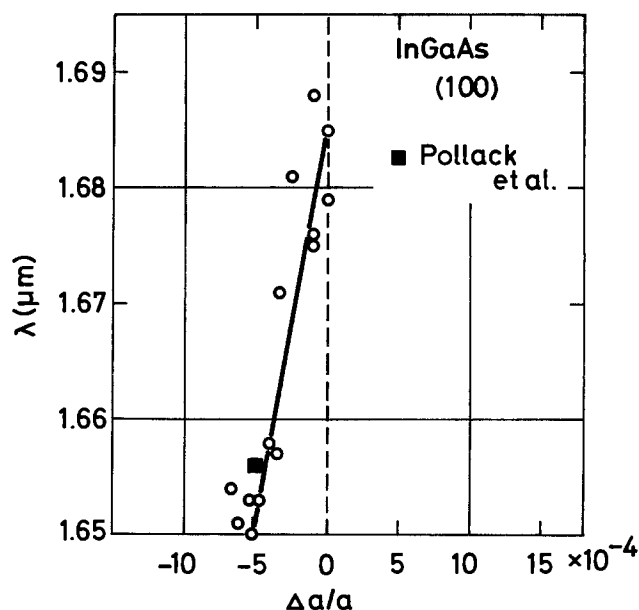


Fig. 5. Wavelength λ (μm) of $\text{In}_{1-x}\text{Ga}_x\text{As}$ layers as a function of the lattice misfit $\Delta a/a$. \blacksquare is the data reported by Pollack *et al.* (13).

present results. Figure 6 shows the solid composition x of $\text{In}_{1-x}\text{Ga}_x\text{As}$ as a function of $\Delta a/a$. The solid composition was determined by electron-probe microanalysis (EPMA) (6, 16) performed on surfaces of $\text{In}_{1-x}\text{Ga}_x\text{As}$ epitaxial layers grown on InP (100) substrates. Just saturated melts at 650°C were used in this growth. x is almost constant in the lattice misfit range from 3×10^{-4} to -1×10^{-3} , and it is about 0.47.

Discussion

The reason why the thickest layer without misfit dislocations have the negative lattice misfit at room temperature as shown in Fig. 4 can be explained by the difference of the thermal expansion coefficients of InP and $\text{In}_{0.53}\text{Ga}_{0.47}\text{As}$. The lattice constants of InP, InAs, and GaAs at 18°C are 5.86875 (7), 6.0584 (7) and 5.6535\AA (17), respectively. The lattice constant of $\text{In}_{0.53}\text{Ga}_{0.47}\text{As}$ can be derived from these values on the

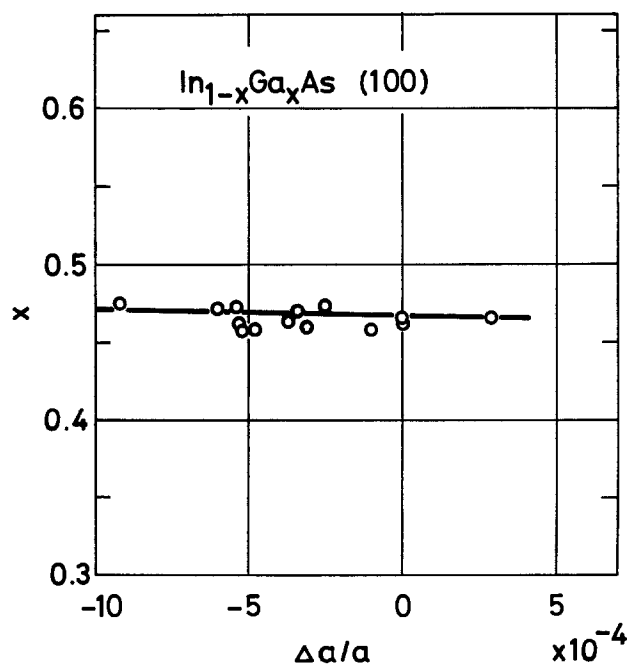


Fig. 6. Solid composition x of $\text{In}_{1-x}\text{Ga}_x\text{As}$ grown on InP (100) substrates as a function of the lattice misfit $\Delta a/a$.

basis of Vegard's law, and it is 5.8681Å. (Strictly speaking, the composition of the ternary alloy which is exactly lattice-matched to InP at 18°C is $\text{In}_{0.5316}\text{Ga}_{0.4684}\text{As}$.) The thermal expansion coefficients of InP and $\text{In}_{0.53}\text{Ga}_{0.47}\text{As}$ reported by Bisaro *et al.* (18) are $(4.56 \pm 0.10) \times 10^{-6}/^\circ\text{C}$ and $(5.66 \pm 0.10) \times 10^{-6}/^\circ\text{C}$, respectively. Assuming the relation between the lattice constant and temperature to be linear, the formula for the thermal expansion is as follows

$$a_T = a_0(1 + \alpha T) \quad [1]$$

where a_T is the lattice constant at any temperature T ($^\circ\text{C}$), a_0 is the lattice constant at 0°C , and α is the thermal expansion coefficient. The calculated lattice constants of InP and $\text{In}_{0.53}\text{Ga}_{0.47}\text{As}$ at 650°C by using this formula are 5.8856 and 5.8891Å, respectively. The temperature dependence of the lattice constants of InP and $\text{In}_{0.53}\text{Ga}_{0.47}\text{As}$ calculated by Eq. [1] is shown by the lines (a) and (b), respectively in Fig. 7. $\text{In}_{0.53}\text{Ga}_{0.47}\text{As}$ has the positive lattice misfit equal to 6×10^{-4} at 650°C . ($\text{In}_{0.5316}\text{Ga}_{0.4684}\text{As}$ exactly lattice-matched to InP at room temperature has the positive lattice misfit equal to 7×10^{-4} at 650°C .) This shows that misfit dislocations are introduced in lattice-matched thick layers by the compressive stress due to the positive lattice misfit at the growth temperature. The thickest layer without misfit dislocations has the negative lattice misfit between 6.5×10^{-4} and -9×10^{-4} at room temperature as shown in Fig. 4, and such a layer almost lattice-matched to InP at the growth temperature, 650°C as shown by the broken line (c) in Fig. 7. Therefore, misfit dislocations are more easily introduced in a lattice-matched layer at room temperature than in a lattice-matched layer at the growth temperature, that is to say, they are easily formed at high temperature.

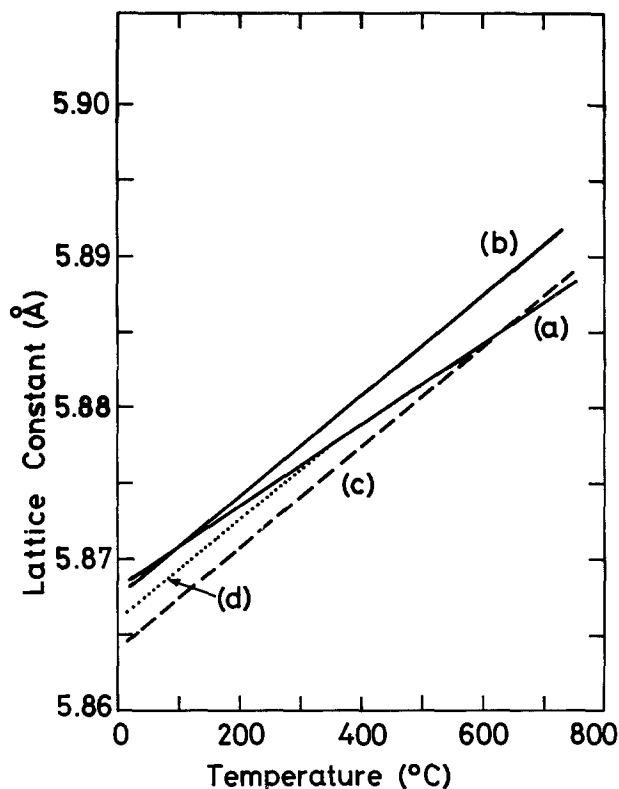


Fig. 7. Temperature dependence of lattice constant for representative heterojunction combinations. Solid lines (a) and (b) are the lattice constants of InP and $\text{In}_{0.53}\text{Ga}_{0.47}\text{As}$. Broken line (c) is a schematic representation of a layer almost lattice-matched to InP at 650°C . Dotted line (d) is a schematic representation of a layer lattice-matched to InP at a lower temperature than 650°C .

For the growth of thin layers within the misfit dislocation-free region shown in Fig. 4, it is desirable that the lattice misfit at room temperature should be as small as possible not to cause the large elastic stress at the interface of the heteroboundary. The line (b) in Fig. 7 shows such a case. As the layer thickness becomes large, the lattice misfit at room temperature must be larger in order to obtain misfit dislocation-free layers, that is to say, the growth condition must approach from the line (b) to (c) in Fig. 7. When the starting growth temperature is changed from 650°C to the lower temperature, the lattice misfit at which the thickest layer without misfit dislocations can be obtained as shown in Fig. 4 becomes smaller. This case is shown by the dotted line (d) in Fig. 7.

Several authors (10, 19) have reported expressions for h_c , the critical epitaxial layer thickness above which misfit dislocations are expected to generate. Jesser and Kuhlmann-Wilsdorf (10) gave the expression for cubic crystals and an infinitely thick substrate in the limit of small strains. For semiquantitative estimate, their rather formidable equation can be replaced by

$$h_c \cong \frac{b}{2|f|} \quad [2]$$

where b is the magnitude of the Burgers vector, and f is the lattice misfit, $\Delta a/a$ (20). This is the simplified equation, but it keeps the essential characteristics of the original expression. h_c was calculated by using Eq. [2] for $b = 4.15\text{Å}$ at room temperature and $b = 4.16\text{Å}$ at 650°C as shown in Fig. 8. The solid line (a) and (b) are the calculated results at room temperature and 650°C , respectively. The line (b) was calculated on the basis of the fact that a layer lattice-matched to InP at 650°C has the negative lattice misfit,

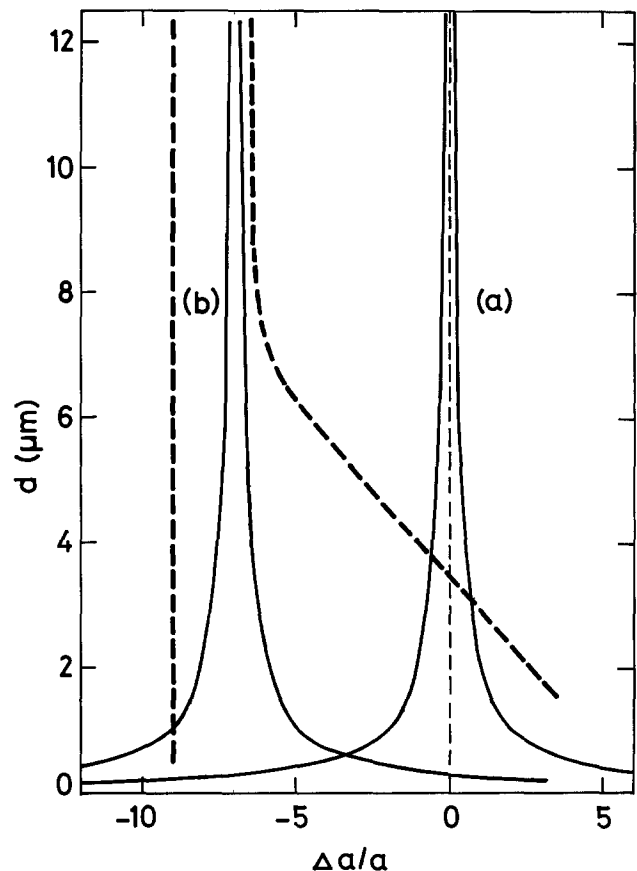


Fig. 8. Calculated threshold region for initiation of misfit dislocations into $\text{In}_{1-x}\text{Ga}_x\text{As}$ layers on InP. Solid lines (a) and (b) are the calculated results at room temperature and 650°C , respectively. Broken line is the experimental threshold region as shown in Fig. 4.

-7×10^{-4} at room temperature. The broken lines are the experimentally determined demarcation lines for misfit dislocation generation as shown in Fig. 4. The experimentally determined region is asymmetric, but the calculated region is symmetric. In all equations to calculate the critical thickness, it was not considered that the mechanism of generation of misfit dislocations in tension and in compression are different from each other.

The experimentally determined misfit dislocation-free region has a perpendicular edge on the negative side as shown in Fig. 4. This shows that at the growth temperature, misfit dislocations were much more easily introduced by tension than by compression. This result is consistent with the previously reported results at room temperature for InGaP/GaAs (21) and InGaAs/InP (22) systems that layers in tension cracked at smaller misfit than those in compression. At room temperature, however, misfit dislocations were not formed in greater tension and the ternary layers yielded elastically even with a negative lattice misfit of -8×10^{-4} . It is most important for the growth of thick and misfit dislocation-free epitaxial layers that at the growth temperature, layers should be lattice-matched to the substrates and that tensile stress should not be incurred at the growth temperature.

Summary

The equilibrium conditions for the LPE growth of exactly and nearly lattice-matched $\text{In}_{1-x}\text{Ga}_x\text{As}$ layers on InP (100) substrates were determined at 650°C by lattice constant measurements. The half-width of the diffraction peak of the ternary layer is much smaller than that of an $\text{In}_{1-x}\text{Ga}_x\text{As}_{1-y}\text{P}_y$ layer, and the composition of the ternary layer scarcely varies along the growth direction. The threshold region for the formation of misfit dislocations into the ternary layers were experimentally determined. The conditions for the growth of misfit dislocation-free layers thicker than 10 μm were found. These layers can be grown starting from 650°C only when the lattice misfit is between -6.5×10^{-4} and -9×10^{-4} at room temperature. It is most important for the growth of thick and misfit dislocation-free epitaxial layers that the layers should be lattice-matched to the substrates and tensile stress should not be incurred at the growth temperature. The relationships between the photoluminescence peak wavelength or composition and the lattice misfit were determined experimentally.

Acknowledgments

The authors wish to acknowledge the crystal growth of Mr. T. Tanahashi and Dr. S. Yamazaki, and the microprobe and photoluminescence measurements of Mrs. T. Furusawa and A. Yamaguchi. We are grate-

ful to Mrs. M. Ito and T. Kotani for their helpful discussions.

Manuscript received Nov. 21, 1979. This was Paper 593 presented at the Los Angeles, California, Meeting of the Society, Oct. 14-19, 1979.

Any discussion of this paper will appear in a Discussion Section to be published in the June 1981 JOURNAL. All discussions for the June 1981 Discussion Section should be submitted by Feb. 1, 1981.

Publication costs of this article were assisted by Fujitsu Laboratories, Limited.

REFERENCES

1. T. P. Pearsall and R. W. Hopson, Jr., *J. Electron. Mater.*, **7**, 133 (1978).
2. K. J. Bachmann and J. L. Shay, *Appl. Phys. Lett.*, **32**, 446 (1978).
3. T. P. Pearsall and M. Papuchon, *ibid.*, **33**, 640 (1978).
4. Y. Matsushima, K. Sakai, S. Akiba, and T. Yamamoto, *ibid.*, **35**, 466 (1979).
5. G. A. Rozgonyi, P. M. Petroff, and M. B. Panish, *J. Cryst. Growth*, **27**, 106 (1974).
6. K. Nakajima, T. Tanahashi, K. Akita, and T. Yamaoka, *J. Appl. Phys.*, **50**, 4975 (1979).
7. G. Giesecke and H. Pfister, *Acta Crystallogr.*, **11**, 369 (1958).
8. K. Nakajima, A. Yamaguchi, K. Akita, and T. Kotani, *J. Appl. Phys.*, **49**, 5944 (1978).
9. J. Matsui, K. Onabe, T. Kamejima, and I. Hayashi, *This Journal*, **126**, 664 (1979).
10. W. A. Jesser and D. Kuhlmann-Wilsdorf, *Phys. Status Solidi*, **19**, 95 (1967).
11. K. Oe, Y. Shinoda, and K. Sugiyama, *Appl. Phys. Lett.*, **33**, 962 (1978).
12. Y. Takeda, A. Sasaki, Y. Imamura, and T. Takagi, *J. Appl. Phys.*, **47**, 5405 (1976).
13. M. A. Pollack, R. E. Nahory, J. C. DeWinter, and A. A. Ballman, *Appl. Phys. Lett.*, **33**, 314 (1978).
14. R. Sankaran, R. L. Moon, and G. A. Antypas, *J. Cryst. Growth*, **33**, 271 (1976).
15. H. Nagai and Y. Noguchi, *Appl. Phys. Lett.*, **32**, 234 (1978).
16. K. Nakajima, T. Kusunoki, K. Akita, and T. Kotani, *This Journal*, **125**, 123 (1978).
17. L. R. Weisberg and J. Blanc, *J. Appl. Phys.*, **34**, 1002 (1963).
18. R. Bisaro, P. Merenda, and T. P. Pearsall, *Appl. Phys. Lett.*, **34**, 100 (1979).
19. J. W. Matthews, S. Mader, and T. B. Light, *J. Appl. Phys.*, **41**, 3800 (1970).
20. J. Blanc, in "Heteroepitaxial Semiconductors for Electronic Devices," G. W. Cullen and C. C. Wang, Editors, p. 282, Springer-Verlag, New York (1978).
21. G. H. Olsen, M. S. Abraham, and T. J. Zamerowski, *This Journal*, **121**, 1650 (1974).
22. H. Nagai and Y. Noguchi, *Appl. Phys. Lett.*, **29**, 740 (1976).

Electrical Defects in Silicon Introduced by Sputtering and Sputter-Etching

E. Grusell, S. Berg, and L. P. Andersson*

Institute of Technology, University of Uppsala, Uppsala, Sweden

ABSTRACT

Sputtering a gold contact on n-silicon or sputter-etching the silicon surface prior to deposition of gold results in a Schottky barrier which shows a barrier height which depends on the sputtering voltage and time, and is lower than a corresponding barrier obtained by evaporation of a gold contact. On p-silicon a sputtered gold contact also shows a barrier height influenced by the sputtering conditions. The modifications of the barrier height are caused by a thin positively charged layer formed in the semiconductor near the metal-semiconductor junction. During sputter etching the silicon surface is subject to bombardment by Ar ions with energies of about the sputtering voltage. If this voltage is high enough charged centers will be introduced. These centers are also observed after sputter deposition at high voltage. We found that damage is caused by etching at 500V but not at 100V. This indicates that the damage found after sputter deposition was caused by rebounded Ar atoms.

It is well known that the properties of a thin film strongly depend on the sputtering or evaporation deposition parameters as well as on the original substrate conditions. However, drastic changes of surface condition of the substrate during deposition may also be important (1-6). During the sputtering process the substrate is bombarded by several kinds of particles: low energy Ar ions from the plasma, sputtered metal atoms with energies up to 20 eV, electrons with energies up to twice the sputtering voltage, and neutral Ar atoms which have been neutralized at the target and backscattered without losing their energy. It has been found that in silicon the sputtering process creates damage which is electrically active at a few nanometers below the surface of the wafer (2, 4, 5). Of the particles mentioned above the electrons are unlikely to produce any damage because of their low mass. It is known that an electron needs more than 250 keV to displace a silicon atom (6). It is shown in this work and by other authors that the sputter-induced damage depends strongly on the sputtering voltage. Of the particles bombarding the substrate during the deposition, only the electrons and the rebounding neutral Ar atoms have energies proportional to the sputtering voltage. The energies of the low energy Ar ions from the plasma and of the sputtered metal atoms depend only weakly on the sputtering voltage. Therefore, we conclude that the rebounding neutral Ar atoms must be mainly responsible for the observed damage. The nature and extent of the defects produced in an n-type or p-type single crystal silicon wafer during deposition of a metal film or sputter-etching followed by deposition of a metal film have been investigated earlier by measuring the electrical characteristics of the resulting metal-silicon junction, *i.e.*, *I-V* (2, 4, 5), *C-V* (2, 3), and temperature activation measurements (4, 5). DLTS (3) (deep level transient spectroscopy) measurements have also been made.

In the DLTS studies of Andersson and Ewvaraye (3) they showed that the sputtering-induced defects formed a band of defect states that are located from $E_c - 0.3$ eV to $E_c - 0.5$ eV. The measured capture cross section for majority carriers was $1.3 \cdot 10^{-19}$ cm². The *C-V* and *I-V* characteristics showed that the defects were donorlike. The concentration $N_t(x)$ of the sputtering-induced traps at a distance x from the surface was shown to be

$$N_t(x) = N_{ts} \exp\left(-\frac{x}{L}\right)$$

where N_{ts} is the trap density at the surface and L is a characteristic length. L and N_{ts} depend on the sputtering voltage and on the sputtering time. As found from the DLTS measurements L is of the order of 160Å and N_{ts} of the order of 10^{18} cm⁻³. When the metal n-silicon contact is reverse biased we assume all the traps to be positively charged. On n-silicon, with L and N_{ts} as stated above this will give a significant probability for electrons to tunnel through the barrier (T-F emission) (7), so that a reduced effective barrier height will be observed. As the sputtering process creates donorlike traps also on p-type silicon, a sputtered metal contact will create a metal contact followed by an n-p junction close to the surface. This will affect the band bending so that the hole barrier will be higher than it would have been if there were no n-type layer. The band bending will also be dependent on the applied voltage so that the reverse current is not expected to saturate.

Experimental

N-type silicon of 50 Ωcm was used. A few samples were made on 350 Ωcm n-type silicon. The p-type silicon used was of 500 Ωcm resistivity. The silicon wafers were etched in CP-6 and on their back sides ohmic contacts were formed. On n-silicon this was done by sputter-etching followed by deposition of Al and Au, and on p-silicon by sputtering of Au at a low voltage. The sputtering was performed in an rf sputtering system using an Ar atmosphere of pressure 0.7 Pa. The target to substrate distance was 7 cm. Before initiating the plasma the vacuum vessel was evacuated to $6 \cdot 10^{-4}$ Pa by an oil diffusion pump. The use of rf sputtering means that the Ar ions have energies up to the peak rf voltage.

The contacts to be investigated were sputtered through a very thin gold-coated stainless steel mask with holes of 3 mm diam. The sputter-etching was also done through this mask. The forward and reverse characteristics of the diodes were measured at different temperatures ranging from -35° to 60° C. *C-V* measurements were made with a capacitance bridge working at 500 kHz. The DLTS spectra were obtained with a setup similar to the one described by Lang (8).

Theory

As first suggested by Mullins and Brunnschweiler (2) and later verified experimentally by Andersson

* Electrochemical Society Active Member.
Key words: defects, sputtering, etching.

and Evararaye (3), we assume the density of the sputtering-induced traps near the surface to be

$$N_t(x) = N_{ts} \exp\left(-\frac{x}{L}\right)$$

where N_{ts} is the trap density at the surface and L a characteristic length. L was estimated to 160Å in Ref. (3). The traps and the ionized donors give a space charge in the depletion region of

$$\rho(x) = q \left(N_{ts} \exp\left(-\frac{x}{L}\right) + N_d \right)$$

where N_d is the doping of the n-type semiconductor. When we integrate the Poisson equation

$$\frac{d^2\phi}{dx^2} = \frac{\rho}{\epsilon\epsilon_0}$$

where ϕ is the position of the conduction band edge, assuming that the true barrier height is ϕ_{B_0} , we get

$$\phi(x) = \frac{qN_{ts}}{\epsilon\epsilon_0} \cdot L^2 \left(\exp\left(-\frac{x}{L}\right) - 1 \right) - \frac{qN_d}{\epsilon\epsilon_0} x \left(w - \frac{x}{2} \right) + \phi_{B_0}$$

where w is the width of the depletion region. For p-type material N_d is of course negative. (See Fig. 1 and 2). The condition

$$\phi(w) = \phi_{B_0} - V_{bi} - V$$

where V is the applied reverse bias and V_{bi} the band bending at zero bias gives

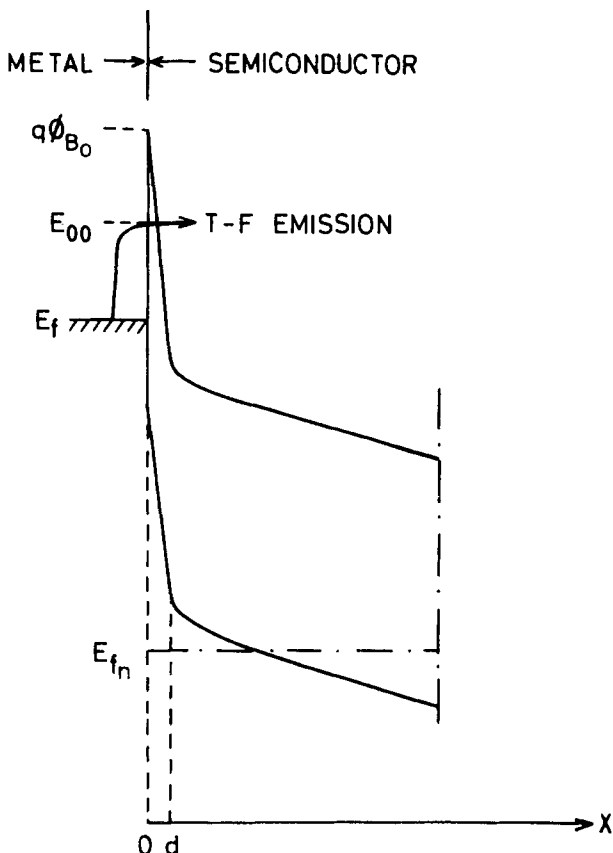


Fig. 1. Schematic energy diagram of a reverse biased sputter-damaged Schottky barrier. The damaged region is $0 < x < d$. The thermionic field emitted electrons are indicated by the arrow. E_f is the Fermi level in the metal and E_{fn} is the quasi-Fermi level for electrons in the semiconductor.

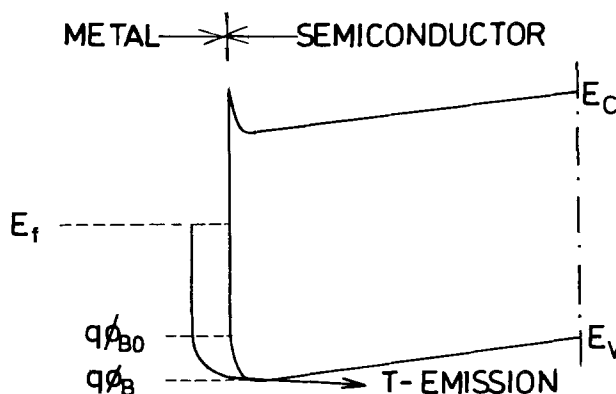


Fig. 2. Schematic energy diagram of a reverse biased sputter-damaged Schottky barrier formed on a p-type semiconductor surface. $q\phi_B - E_f$ is the effective barrier height for holes from the metal to the semiconductor.

$$w = \left\{ \frac{2\epsilon\epsilon_0}{qN_d} \left[V_{bi} + V - \frac{qN_{ts}}{\epsilon\epsilon_0} L^2 \right] \right\}^{1/2}$$

This formula gives the expected value of the junction capacitance C which is

$$C = \frac{A\epsilon\epsilon_0}{w}$$

The barrier height as estimated by plotting $1/C^2$ against V will thus for n-type material be given by

$$\phi_B = \phi_{B_0} - \frac{qN_{ts}}{\epsilon\epsilon_0} \cdot L^2$$

When N_{ts} has a high value there will be tunneling of carriers through the barrier both for reverse and forward bias. In Ref. (4) it is shown that this will give an apparent barrier as estimated from a reverse activation plot lower than ϕ_{B_0} , but not as low as $\phi_{B_0} - \frac{qN_{ts}}{\epsilon\epsilon_0} L^2$. On p-type material ϕ_{B_0} is heightened by $\frac{\epsilon\epsilon_0}{qN_{ts}} L^2$.

Results and Discussion

In Table I and Fig. 3 and 4 we summarize the results from the barrier height measurements. Corresponding measurements on Schottky barriers made by evaporation of Au onto n-type silicon show barrier heights of 0.7-0.8 (10).

It is clear that the contacts which were sputtered at 500V with or without being sputter-etched at 100V show a similar behavior with a barrier height of 0.70 eV. If there is any slight damage in these diodes one can at least say that the etch at 100V did not introduce an appreciable number of extra traps. The substrate temperature was estimated not to exceed 100°C. Depositing at 2.5 kV on the other hand lowers the barrier, and it is interesting to note that the depositing for 2 min results in a lower barrier than does depositing for 30 sec. This means that the particles responsible for creating the damage act through the gold layer which is already deposited after 30 sec. Sputter-etching of the surface at 500V gives a further lowering of the barrier and an increase of the etching voltage gives still lower barriers.

The contacts which were etched for 30 sec at 0.5, 1, and 1.5 kV showed a decreasing barrier height as measured by the forward I - V characteristics. The differences are not very large though. This shows that there is a tendency towards a saturation in the number of active traps.

As shown in the preceding section the expected lowering of the barrier as measured by a C - V plot is

Table I

Sample	Type	Etching voltage and time	Deposition voltage and time	Thermal activation reverse current (eV)	Barrier height I-V forward (eV)	C-V (eV)
1	n	—	500V, 15 min	0.70	0.70	0.70
2	n	—	2.5 kV, 30 sec	0.61	0.61	0.56
3	n	—	500V, 15 min	0.55	0.55	0.52
4	n	100V, 30 sec	2.5 kV, 2 min	0.70	0.71	0.70
5	n	100V, 10 min	500V, 15 min	0.70	0.71	0.68
6	n	500V, 30 sec	500V, 15 min	0.43	0.51	0.45
7	n	1 kV, 30 sec	500V, 15 min	0.47	0.49	0.48
8	n	1.5 kV, 30 sec	500V, 15 min	0.45	0.46	0.35
9	p	—	2.5 kV, 2 min	0.23	0.60	—
10	p	1.5 kV, 30 sec	500V, 15 min	0.23	0.74	—

proportional to $N_{ts}L^2$. This makes it possible to estimate this product, or if a value for L is known, to estimate N_{ts} . For $L = 160\text{\AA}$, for example, a barrier lowering of 0.1 eV is given by

$$N_{ts} = 2.5 \cdot 10^{17} \text{ cm}^{-3}$$

One result from a photoelectric measurement was obtained for a contact which was sputtered at 500V. The result was 0.73 eV, in agreement with the results obtained by the other methods. However, it proved impossible to use this method on the diodes which showed a large lowering of the barrier, because the photoelectric signal was then too small. This indicates a high recombination rate near the surface in these diodes.

The low values found for the thermal activation energies of the reverse currents in the contacts made on p-silicon can be explained by a generation current, which, when the barrier is high, will completely dominate the reverse current. The fact that the sputter etching of the samples at 100V did not give any appreciable damage shows that neither sputtered neutral metal atoms nor Ar ions from the plasma can cause the damage observed when depositing at 2.5 kV. The former have energies below 20 eV, and the latter have energies below 100 eV (9). Among the remaining possibilities are neutral Ar atoms which have been neutralized at the target and which rebound without losing much of their energy, and negative metal ions accelerated by the potential drop in the cathode dark

space. It is not possible to make any conclusive statement about the relative importance of these two mechanisms from the experiments reported here.

The DLTS spectrum of the diode which was sputter-etched at 500V is shown in Fig. 5. There are two peaks near each other, corresponding to energy levels of 0.3 and 0.22 eV below the conduction band. The total concentration is $3 \cdot 10^{17} \text{ cm}^{-3}$ at the surface. These peaks were observed also in spectra from samples 2 and 3, giving concentrations of about $5 \cdot 10^{16} \text{ cm}^{-3}$ at the surface. The concentrations are computed according to the model presented above, i.e., it is assumed that the traps are distributed so that their concentration decreases exponentially near the surface with a characteristic length of 160\AA. The capture cross section was estimated to $6 \cdot 10^{-17} \text{ cm}^2$. These results are similar to the results reported by Andersson and Ewvaraye (3), although the capture cross section reported here is larger.

It was not possible to obtain any DLTS spectra from the diodes which had been etched at higher voltages because of the high leakage currents. The concentrations measured by DLTS are low compared to the concentration of traps estimated from the barrier height data with the aid of the model mentioned above. One possible reason for this is that the traps near the junction can unload themselves by tunnel-

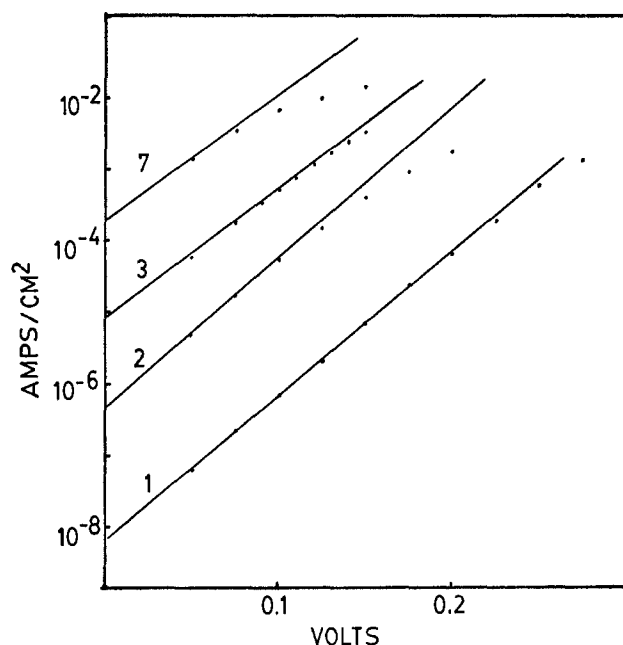


Fig. 3. Forward I-V characteristics of diodes 1, 2, 3, and 7 at -38°C .

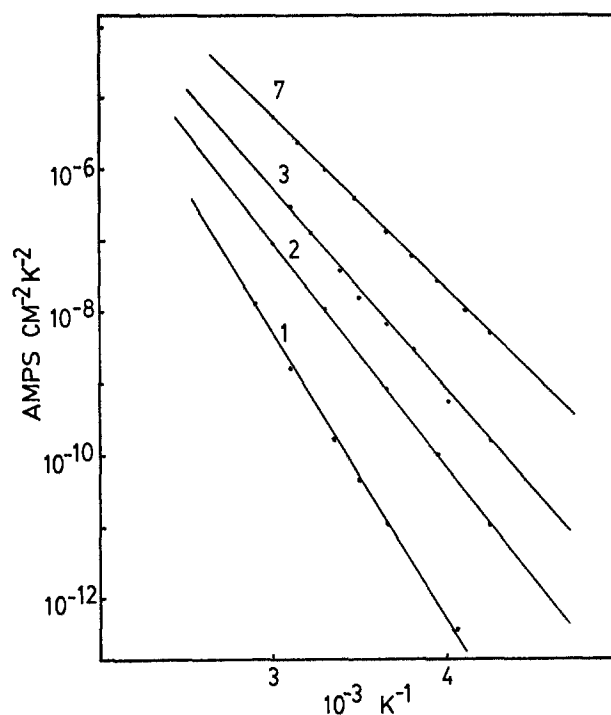


Fig. 4. Temperature activation plots of reverse saturation currents of samples 1, 2, 3, and 7.

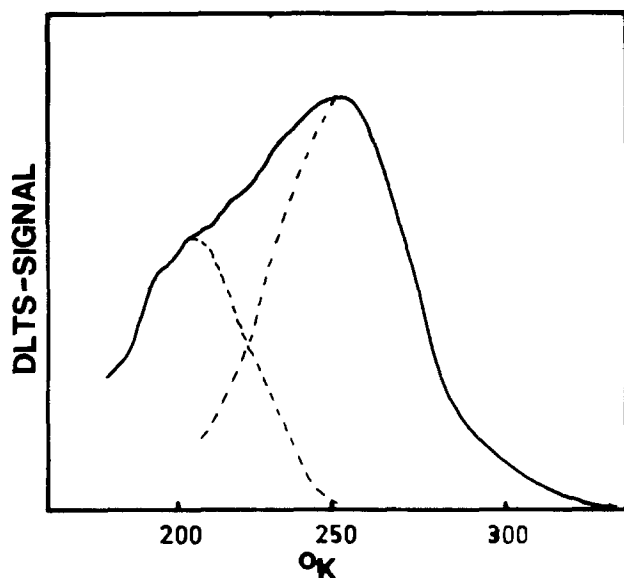


Fig. 5. DLTS spectrum of sample 6 with initial delay equal to 0.2 msec and the rate window equal to 1 msec.

ing, which is a fast process, and they are thus not seen in the DLTS spectrum.

Summary

It is shown that the defects found after sputter deposition of gold on Si at a sputtering voltage of 2.5 kV are not produced during sputter-etching of the Si surface at 100V. From this the conclusion is drawn that the defects are produced by particles more energetic than both the Ar ions accelerated by the plasma potential and the sputtered metal atoms. We suggest that the damage is produced by energetic Ar atoms rebounding from the target. As the difference in barrier

height between the samples etched at 0.5, 1, and 1.5 kV is not very large it is clear that there is a saturation in the number of active traps produced. When the surface is more severely damaged the result is an amorphization of the surface with high generation and recombination rates of the surface. This explains the impossibility of photoelectric measurements on the sputtered contacts and also the insensitivity of DLTS when applied to the contacts made on heavily damaged surfaces.

Manuscript submitted May 31, 1979; revised manuscript received Feb. 25, 1980. This was Paper 148 presented at the Boston, Massachusetts, Meeting of the Society, May 6-11, 1979.

Any discussion of this paper will appear in a Discussion Section to be published in the June 1981 JOURNAL. All discussions for the June 1981 Discussion Section should be submitted by Feb. 1, 1981.

Publication costs of this article were assisted by Uppsala University.

REFERENCES

1. J. W. Mayer and O. J. Marsh, "Applied Solid State Science," Vol. 1, Academic Press, New York (1969).
2. F. H. Mullins and A. Brunnschweiler, *Solid-State Electron.*, **19**, 47 (1976).
3. L. P. Andersson and A. O. Evwaraye, *Vacuum*, **28**, 5 (1978).
4. S. Berg, L. P. Andersson, H. Norström, and E. Grusell, *ibid.*, **27**, 189 (1977).
5. H. Norström, E. Grusell, L. P. Andersson, and S. Berg, *Phys. Scr.*, **18**, 421 (1978).
6. F. Lavin, "Radiation Effects in Semiconductor Devices," John Wiley, New York (1968).
7. F. A. Padovani and R. Stratton, *Solid-State Electron.*, **9**, 695 (1966).
8. D. V. Lang, *J. Appl. Phys.*, **45**, 3014 (1974).
9. J. W. Coburn and E. Kay, *ibid.*, **43**, 4965 (1972).
10. E. H. Rhoderick, "Metal-Semiconductor Contacts," Clarendon Press (1978).

Photoelectrolysis of Water; Photoresponses of Nickel, Chromium and Zinc-Doped Polycrystalline TiO₂ Electrodes

Alain Monnier and Jan Augustynski

Département de Chimie Minérale, Analytique et Appliquée Université de Genève, Geneva, Switzerland

ABSTRACT

The effect of different dopants, chosen among transition elements, on the photoelectrochemical behavior of polycrystalline n-type TiO₂ electrodes was investigated. Except for Cd doping, all other impurities studied are shown to induce a drastic decrease of quantum efficiency of the photoanodes simultaneously with a shift of the photoresponse towards the visible light.

Impurity doping, which is known to induce substantial modifications in the physical properties of semiconductor materials, has been, up to now, only sporadically investigated in connection with semiconducting electrodes for liquid junction solar cells or for photoelectrolysis devices (1-6). The purpose of such studies was essentially to try to extend the photoresponse of some stable, wide bandgap electrode materials to the visible part of the solar spectrum with a view to increase the overall conversion efficiency of the photo-

Key words: photoelectrochemistry, semiconductor electrodes, quantum efficiency.

electrolytic process. This approach was mainly considered with regard to n-type TiO₂ photoanodes employed for the photoelectrolysis of water, which, due to a relatively large bandgap (~ 3.05 eV), can absorb only a small percentage of the solar light.

Thus, doping a single crystal of TiO₂ with tungsten has been found (7) to result in the shift of the photoresponse towards the u.v. region, while the addition of chromium has been reported (8, 9) to extend the absorption spectrum of TiO₂ from the fundamental band-edge at ~ 400 nm to near 550 nm. Recently we have shown (10) that doping polycrystalline TiO₂ electrodes

with several atom percent (a/o) of cadmium extended their photoactive range into the visible light; these electrodes exhibited at the same time high quantum efficiencies in the photoelectrolysis cell.

In the present paper we discuss the effects of doping polycrystalline TiO_2 photoanodes with three different cationic elements: nickel, chromium, and zinc. We also report on results obtained when doping TiO_2 simultaneously with two foreign elements: nickel and beryllium or chromium and beryllium.

Experimental

The electrodes were prepared by depositing a 15-20 μm thick film of doped TiO_2 on the cross section ($\sim 0.28 \text{ cm}^2$) of 99.8% titanium rods obtained from Kobe Steel Limited. The iron content in the titanium was less than 0.024%. The films were formed by applying onto the Ti substrate, layer by layer (usually from 10 to 15 layers), and thermally decomposing in air at 400°-450°C the solutions of the salts of corresponding metals. All these compounds were reagent grade quality: TiCl_4 puriss. (from Fluka, containing less than 0.001% of Fe); $\text{NiCl}_2 \cdot 6 \text{ H}_2\text{O}$, $\text{Cr}(\text{NO}_3)_3 \cdot 9 \text{ H}_2\text{O}$, ZnCl_2 -pro analysi, and $\text{Be}(\text{NO}_3)_2 \cdot 4 \text{ H}_2\text{O}$ extra pure (all from Merck). The solutions of dried salts were prepared with a pro analysi quality ethanol and methanol. In order to induce a partial reduction of the oxide by titanium metal from the substrate all the electrodes were finally heated during 40-60 min in argon at 550°-800°C.

The wavelength response of the electrodes was determined using a 450W xenon lamp (Osram) set in an Oriel Model 6141 housing, and a Jarrell-Ash Model 82-410 monochromator equipped with six Corning filters for the removal of unwanted orders of the spectrum. The absolute intensity of the incident light from the monochromator was measured with a Model 730 A radiometer/photometer from Optronic Laboratories, Incorporated. Photoelectrochemical measurements were performed with a 1M NaOH solution, a platinum counterelectrode, and a mercuric oxide/mercury (HgO/Hg) reference electrode. Photocurrents used to calculate the quantum efficiencies were determined, in all cases, at a potential of $-0.1 \text{ V vs. HgO/Hg}$, i.e., at about 0.4V below the reversible potential for oxygen evolution in the dark.

Results and Discussion

The TiO_2 layers forming the photoanodes contained from 0.4 a/o¹ to 10 a/o of doping elements; these amounts were even higher for TiO_2 -Be-Ni and TiO_2 -Be-Cr electrodes. The choice of dopant concentrations was based on our previous results, particularly on those obtained for TiO_2 -Al (11) and TiO_2 -Be (12) electrodes, which have demonstrated that the optimum doping levels, in the case of the polycrystalline samples, were frequently much larger than equilibrium solubilities of the corresponding oxides. Since the characteristics of the TiO_2 electrodes were strongly dependent not only on the nature and the amount of dopant but also on the temperature of thermal treatment, the samples of a given composition were generally annealed in argon at two different temperatures: $\sim 550^\circ\text{C}$ and $\sim 700^\circ\text{C}$. X-ray diffraction analyses of all the doped samples have shown essentially anatase structure except for the Be-containing electrodes which consisted of a mixture of rutile and anatase.

A perceptible shift of the photoresponse towards the visible light, with respect to the undoped TiO_2 , was mainly observed for moderate doping levels (except, however, for Zn-doped electrodes) and the lower temperature (550°C) heat-treatment. The most pronounced effect was found for TiO_2 -0.4 a/o Cr, TiO_2 -5 a/o Zn, and TiO_2 -0.4 a/o Ni photoelectrodes which displayed a measurable photocurrent up to 500-550 nm (Fig. 1), i.e., 100-150 nm beyond the fundamental absorption edge of TiO_2 . In this sense our results con-

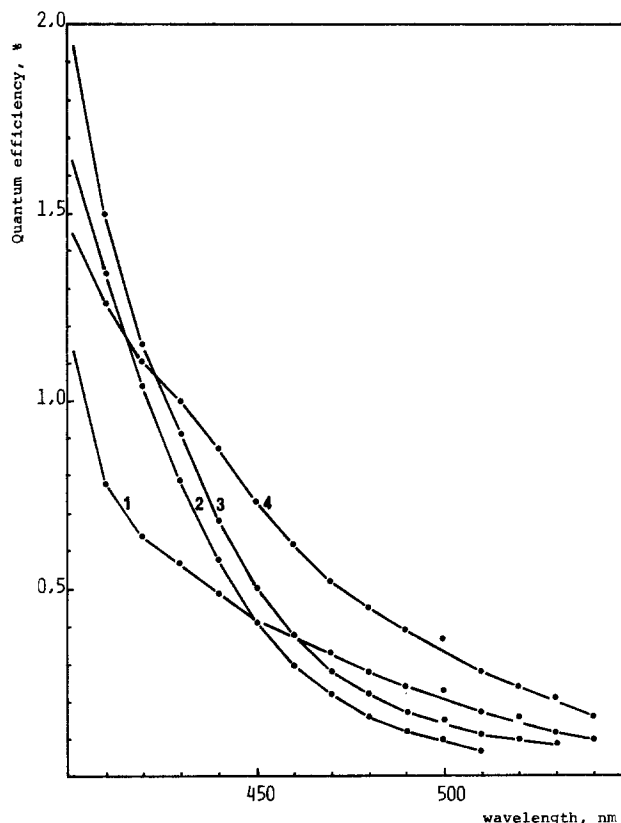


Fig. 1. Quantum efficiency vs. wavelength curves for curve 1, TiO_2 -5 a/o Zn(560°C); curve 2, TiO_2 -4 a/o Ni(560°C); curve 3, TiO_2 -0.4 a/o Ni(560°C); and curve 4, TiO_2 -0.4 a/o Cr(560°C) photoanodes.

firm previous observation of Ghosh and Maruska (8, 9) on the extended photoresponse of the Cr-doped rutile single crystal. However, as visualized by the expanded scale in Fig. 1, quantum efficiencies of the photocurrents corresponding to the wavelengths $>400 \text{ nm}$ were very poor and thus would contribute only in a negligible manner to the overall solar-to-chemical conversion efficiency. Moreover, the presence of dopants affected considerably also the response of the photoelectrodes to the wavelengths $<400 \text{ nm}$, i.e., located in the main part of the TiO_2 absorption spectrum. A particularly drastic decrease of the quantum efficiency was observed (Fig. 2) for heavily Zn and Ni-doped samples, but even for relatively well behaving TiO_2 -0.4 a/o Ni photoanode η_q did not exceed the half of that of the undoped TiO_2 photoanode. In a general way the decrease of quantum efficiency was more pronounced higher the Ni, Cr, and Zn doping level; in the latter case, however, it was attenuated by the heat-treatment in argon at $\sim 700^\circ\text{C}$. These trends are well represented by η_q vs. λ curves for a series of Ni-doped TiO_2 photoelectrodes, shown in Fig. 3. It is also interesting to note that for all the electrodes mentioned above the heat-treatment at $\sim 700^\circ\text{C}$ suppressed practically the photoresponse to the visible light ($\lambda > 400 \text{ nm}$). These observations suggest that a possible interpretation of the effect of extended photosensitivity illustrated in Fig. 1 would involve the structural defects induced by the presence of dopants in TiO_2 . However, since the moderately Ni, Cr, or Zn-doped photoelectrodes (as well as the undoped TiO_2) exhibited essentially anatase structure (12), one could consider at this point the decrease of the quantum efficiency, characterizing the doped samples, as inherent to the above form of TiO_2 . In order to settle this question we have prepared a series of TiO_2 electrodes containing simultaneously two additives: beryllium and nickel or beryllium and chromium. In fact, the Be doping has recently been reported (12) as not only to enhance the quantum

¹ Given with respect to the total amount of metals.

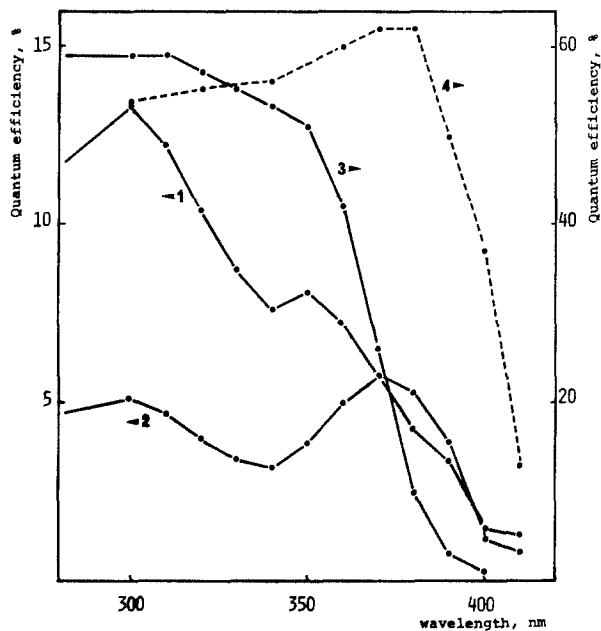


Fig. 2. Effect of the doping on the quantum efficiencies of TiO_2 photoanodes (wavelengths corresponding to the fundamental absorption spectrum of TiO_2): curve 1 TiO_2 -0.4 a/o Cr (560°C); curve 2 TiO_2 -5 a/o Zn (560°C); curve 3 undoped TiO_2 (560°C); and curve 4 TiO_2 -5 a/o Cd (710°C).

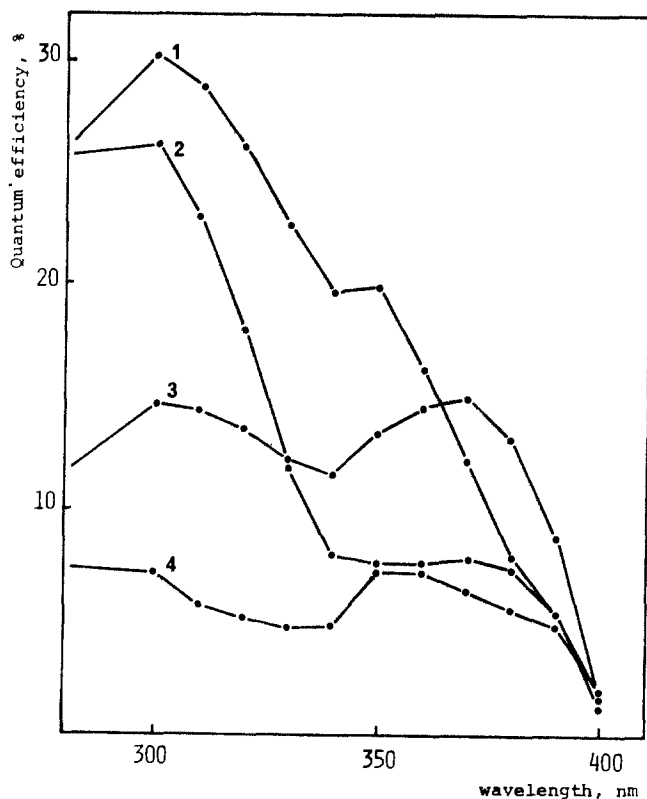


Fig. 3. Effect of the nickel content and of the temperature of the heat-treatment on the quantum efficiencies of TiO_2 -Ni photoanodes: curve 1 TiO_2 -0.4 a/o Ni (560°C); curve 2 TiO_2 -0.4 a/o Ni (700°C); curve 3 TiO_2 -4 a/o Ni (700°C); and curve 4 TiO_2 -4 a/o Ni (560°C).

efficiency of the TiO_2 photoresponse but also to promote the anatase-rutile transformation. For testing the influence of Ni and Cr doping on the behavior of this kind of photoelectrodes we have chosen the optimum (from the point of view of the conversion efficiency) 15 a/o beryllium content. Principal results concerning TiO_2 -Be-Ni electrodes are summarized

in Fig. 4; those for TiO_2 -Be-Cr samples were quite similar and are not shown separately. The only effect practically observed was a general decrease of the quantum efficiency which followed the same trends discussed above.

In conclusion, it appears clearly that the predominant result of doping the polycrystalline TiO_2 photoanodes with nickel, chromium, or zinc is a more or less marked loss of quantum efficiency of the photocurrent relative to the fundamental absorption region of TiO_2 ; this effect overcompensates the gain in overall optical-to-chemical conversion efficiency which would be expected from the extension of the photoresponse towards the visible part of the spectrum. This kind of behavior is very likely consistent with the formation of intermediate levels in the bandgap, which can originate from impurity cations or/and from defects induced by the doping, and which act as recombination centers in the depletion layer. Such effects have, for example, been previously observed for iron-doped TiO_2 photoelectrodes (10) and, in less drastic form, for copper, cobalt, and manganese-doped TiO_2 (13). It is interesting to note that the role played by the above-mentioned dopants is basically different from that of the cadmium addition to TiO_2 . The latter also produces a modification in the spectral photoresponse of TiO_2 , consisting in its extension up to 430 nm and in the appearance of the photocurrent maximum at 390 nm (Fig. 2). Nevertheless, in contrast with other dopants from transition and post-transition series, the Cd doping results in a slight enhancement (instead of the decrease) of quantum efficiency with respect to the undoped TiO_2 . Thus, for TiO_2 -5 a/o Cd photoanode η_q exceeds 60%, the value quite comparable with those

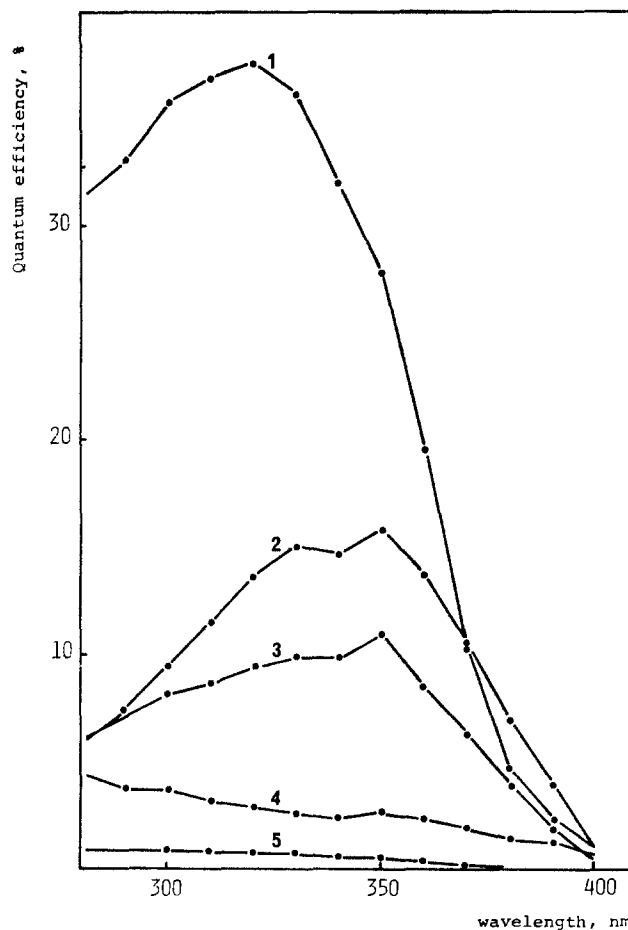


Fig. 4. Quantum efficiency vs. wavelength characteristics of a series of TiO_2 -Be-Ni photoanodes: curve 1 TiO_2 -15 a/o Be-4 a/o Ni (700°C); curve 2 TiO_2 -15 a/o Be-0.4 a/o Ni (700°C); curve 3 TiO_2 -15 a/o Be-10 a/o Ni (700°C); curve 4 TiO_2 -15 a/o Be-0.4 a/o Ni (560°C); and curve 5 TiO_2 -15 a/o Be-4 a/o Ni (560°C).

obtained for the best polycrystalline (Al- or Be-doped) TiO₂ electrodes.

Unfortunately, due to a partial decomposition of the coatings at the temperatures required for annealing, we were unable to prepare the electrodes containing more than 5 a/o of cadmium, and to establish whether the increase of its content in TiO₂ could lead to a further shift of the photoresponse. Actually, although using the TiO₂-Cd photoanode enables only limited improvement of the solar-to-chemical conversion efficiency (which is evaluated as twice that of an undoped TiO₂ photoanode) the qualitative result seems more promising than those obtained with chromium, nickel, and zinc dopants.

Acknowledgment

This work was supported by the Swiss National Science Foundation.

Manuscript submitted June 27, 1979; revised manuscript received Jan. 22, 1980.

Any discussion of this paper will appear in a Discussion Section to be published in the June 1981 JOURNAL. All discussions for the June 1981 Discussion Section should be submitted by Feb. 1, 1981.

Publication costs of this article were assisted by the Université de Genève.

REFERENCES

1. L. A. Harris and R. H. Wilson, *Ann. Rev. Mater. Sci.*, **8**, 99 (1978).
2. H. P. Maruska and A. K. Ghosh, *Sol. Energy*, **20**, 443 (1978).
3. J. G. Mavroides, *Mater. Res. Bull.*, **13**, 1379 (1978).
4. K. Rajeshwar, P. Singh, and J. DuBow, *Electrochim. Acta*, **23**, 1117 (1978).
5. A. J. Nozik, *Ann. Rev. Phys. Chem.*, **29**, 189 (1978).
6. M. Tomkiewicz and H. Fay, *Appl. Phys.*, **18**, 1 (1979).
7. M. S. Wrighton, D. S. Ginley, P. T. Wolczanski, A. B. Ellis, D. L. Morse, and A. Linz, *Proc. Natl. Acad. Sci. U.S.A.*, **72**, 1518 (1975).
8. A. K. Ghosh and H. P. Maruska, in "Solar Energy," J. B. Berkowitz and I. A. Lesk, Editors, p. 92, The Electrochemical Society Softbound Proceedings Series, Princeton, N.J. (1976).
9. A. K. Ghosh and H. P. Maruska, *This Journal*, **124**, 1516 (1977).
10. C. Stalder, A. Monnier, and J. Augustynski, Extended Abstracts of the 2nd International Conference on the Photochemical Conversion and Storage of Solar Energy, p. 81, Cambridge, England, August 10-12, 1978.
11. J. Augustynski, J. Hinden, and C. Stalder, *This Journal*, **124**, 1063 (1977).
12. C. Stalder and J. Augustynski, *ibid.*, **126**, 2007 (1979).
13. A. Monnier, Unpublished results.

Lubrication and Pattern Improvement in Photolithography

D. L. Flowers* and J. N. Smith

Motorola Semiconductor Research and Development Laboratory, Phoenix, Arizona 85008

ABSTRACT

A photoresist overcoat formulation (SLI) has been developed which significantly reduces photolithographic, induced defects and produces improved definition. The overcoat is composed of a surfactant, lubricant, and free radical inhibitor in solvent. The surfactant and lubricant function to decrease photo-mask-photoresist interactions which decreases defect densities. The free radical inhibitor absorbs stray light energy under opaque mask areas. This improves fine line resolution and definition, with particularly beneficial results when used over reflective metal films. The interaction of the overcoat with the mask light energy are discussed and a mechanism is proposed. It was also found that the incidence of scum film formation (smog effect) in developed areas was reduced.

Photolithographic processing is one of the principle areas in semiconductor manufacture where major expense and yield loss occur. Some of these problems have been discussed in considerable detail by Kern and Schnable *et al.* (1, 2). Photodefects caused by mask and resisted wafer sticking due to chemisorption (3, 4) are of prime importance. On separation after exposure, pieces of photoresist are torn from the wafer and adhere to the photomask. This results in pinholes in the substrate when it is later etched. Additionally, opaque pieces of photoresist on the mask are responsible for latent pinholes on further mask use and result in limited useful mask life.

Recently reported work addressed these problems with lubricating mask coatings (5) and a resist protect coat (6) in which longer photomask life and significant pinhole reduction were demonstrated. The above resist protect coat formulation was polyvinyl alcohol-based and hence had to be removed from the exposed, negative photoresist by a water rinse and dry before normal pattern development. As such, it constituted a process inconvenience. Because of these considerations,

attention was turned to developing a resist protect coat that would not change exposure times and would be quickly removable in the normal development cycle and solvent.

Other problems are also important factors controlling acceptable photolithographic processing. Fine line pattern definition with negative photoresist is frequently limited by reflected light closing narrow spaces and enlarging lines. Metal bridging adjacent runners in IC devices is often responsible for rework or low yields. This is due to reflection of incident light by the shiny metal surface. Using resist films as thin as possible has been common practice to solve this problem but film integrity may be compromised so that resist tears and the incidence of pinholes increase unacceptably. Using commonly accepted principles of free radical chemistry, additives to a new protect coat formulation were investigated to absorb the reflected light causing these problems. The same class of additives that can improve definition was expected to be effective in inactivating those ambient materials causing "smog" films periodically plaguing the industry. It is the purpose of this paper to present the results of the resist overcoat approach to minimize the above problems.

* Electrochemical Society Active Member.

Key words: photolithography, resist overcoat, defect reduction, definition improvement, smog film.

Experimental

Materials.—Polished 7.62 cm silicon substrates were used for the definition improvement study. For metal bridging experiments, 1 Knm of Al (Si) was E-beam deposited on the oxide. To evaluate pinhole improvements, a gate circuit, 3.0×3.7 mm with 1 Knm of phosphosilicate glass, PSG, passivation over patterned first layer metal was used. For "smog" film reduction experiments, chips were 3.8×3.8 mm with a 0.25 mm grid. One lot of wafers was patterned for mesa (silicon) etch, one lot was patterned for metal (gold) etch.

The SLI, resist protect coat solution, applied by spinning at 3K rpm for 10 sec, contained a surfactant (S), a lubricant (L), and free radical inhibitor (I) dissolved in electronic grade isopropanol. Film thickness was estimated to be 5-10 nm. Typically, 0.03% w/v Triton X-100 (Rohm and Haas) surfactant, 0.1% w/v glyceryl monostearate (C. P. Hall Company, Illinois), and 0.1% w/v hydroquinone inhibitor were used. One protect coat, SL, containing only the surfactant and lubricant was tested to confirm the effect of the inhibitor.

Photoresist processing and evaluation.—Negative photoresist was applied by spinning to give a thickness of 1 Knm and soft baked for 30 min at $80^\circ \pm 2^\circ\text{C}$ in nitrogen unless otherwise noted. Contact (5-6 psi) exposures were made for times noted in the text. A 20 sec xylene-20 sec butyl acetate spray development cycle was used. This was followed by a 60 min "hard" bake in nitrogen where necessary for subsequent etching.

To evaluate pinhole reduction with the SLI resist coat aluminum metallized wafers with PSG passivation were used. After photolithographic processing of the PSG glass, pinholes in the PSG layer were extended through the metal by etching for 2.5 min at 65°C in a standard, phosphoric acid-nitric acid, aluminum etch. Twenty selected die on each wafer were visually inspected and pinholes counted.

A high resolution test mask was used in the definition improvement experiments to determine the effect of the inhibitor in the SLI coating layer. This mask had a "checkerboard" pattern in the center of each die and ancillary bar and space patterns ranging down to 0.1 mil (2540 nm). Each mask was used for only six contacts. Twenty die per wafer were inspected after development and the percent of bars and spaces defined as a function of width is reported. It was found that a 10 sec exposure at $2500 \mu\text{W}/\text{cm}^2$ was optimum. Exposures ranged from 11-15 sec to increase the amount of reflected light and emphasize the effect of the inhibitor in the SLI protect coat formulation.

Results and Discussion

Defect reduction studies.—Comparative pinhole results as a function of the process step and use of SLI are shown in Table I. Set A shows the pinholes present in the as-deposited PSG passivation. A 95% pinhole-free die yield was achieved on this large chip, one third of which is covered with patterned metal. Set B illustrates the number of pinholes introduced by twice contacting the photomask and photoresisted wafer. After photoresist was removed, the wafers were "aluminum" etched with no prior passivation etch to define pinholes caused by mechanical damage in the glass. This step gives an 87.5% pinhole-free die yield, thus a 10% yield loss is brought about by twice contacting the mask and wafer. In Set C, six photoresisted wafers were each contacted twice, exposed, developed, and given a standard passivation etch simulating normal device processing. After resist strip and aluminum etch to define a reference pinhole yield, the number of pinhole-free die was reduced to 5%. The average number of pinholes in the reject die had more than doubled due to resist damage. Set D shows the im-

Table I. Comparative pinhole formation in processing with and without SLI and 11.1 mm^2 die

Set	Wafer numbers	Pinhole-free die per 20	Average No. pinholes per reject die	Condition
A	1	19	3	PSG glass + "Al" etch, no photoresist
	2	19	1	
B	3	19	10	Resisted, 2 contacts and expose, strip photoresist —no PSG etch, just "Al" etch
	4	16	3	
C	5	2	10	Standard photo processing and etching. No SLI coat
	6	1	7	
	7	1	6	
	8	2	6	
	9	0	6	
	10	0	6	
D	11	5	2	Same as (C) but with SLI spun at 3K rpm.
	12	4	2	
	13	4	2	
	14	2	3	
	15	5	2	
	16	1	2	

provement achieved by using the SLI overcoat on the photoresist. The percentage of pinhole-free die has increased by more than a factor of three to 17.5%. In addition, the average number of pinholes in the reject die has decreased by more than a factor of three. This is a significant improvement compared to the results obtained from standard photolithographic processing.

It should be pointed out that in the SLI formulation, the inhibitor is not necessary for the pinhole reduction achieved with this formulation. It was experimentally verified that only the lubrication composition and concentration in conjunction with the surfactant accomplished this improvement. It was also found during the course of this work that the soft bake cycle dramatically affects the results. That is, if the bake time is shortened or if the bake temperature is lowered residual solvent remains in the resist film and lubrication benefits are not achieved.

Inhibitor effect on resolution over thermal oxide.—The purpose of these experiments was to show that the presence of the inhibitor in the coating formulation does increase resolution limits even at various degrees of overexposure. Six sets of twelve wafers were used for this study. Six wafers from each set were controls and were processed in an identical manner as the experimental wafers except no coating was applied. Three of the experimental sets were coated with SLI and three with SL.

Results of each group of six wafers were averaged to give the values shown in Table II. A significant improvement in resolution is evident after development inspection for the first three experimental sets which were coated with SLI. With an 11 sec exposure, set 1 Expt showed a 13% increase of 0.1 mil spaces open vs. the control set. With a 12 sec exposure a lower overall yield due to overexposure was observed, but with the inhibitor present the percent open spaces

Table II. Effect of SLI on resolution over PSG as a function of exposure time

Set	Exposure time (sec)	Coating formulation	Spaces		
			0.1 mil	0.15 mil	0.2 mil
1 Control	11	None	70	100	100
1 Expt	11	SLI	83	100	100
2 Control	12	None	40	90	100
2 Expt	12	SLI	70	100	100
3 Control	15	None	10	50	80
3 Expt	15	SLI	10	100	100
4 Control	11	None	75	100	100
4 Expt	11	SL	70	90	100
5 Control	12	None	38	96	100
5 Expt	12	SL	39	95	100
6 Control	13	None	32	74	92
6 Expt	13	SL	42	93	99

increased from 40% to 70% for 0.1 mil, and from 90% to 100% for 0.15 mil spaces. In the case of the 5 sec overexposure (15 sec exposure) the inhibitor action was overcome on the 0.1 mil spaces and no improvement was observed. However, in the case of 0.15 mil spaces a 50% increase was observed and with 0.2 mil spaces a 20% increase was observed. The relationship of percent open spaces to the linewidth and overexposure time is a logical one, and is confirmed by the data.

The last three sets of experiments were conducted without the inhibitor in the solution to confirm that the presence of the inhibitor in the coating formulation was indeed responsible for resolution improvement. The results, though scattered show no definition improvement without the inhibitor.

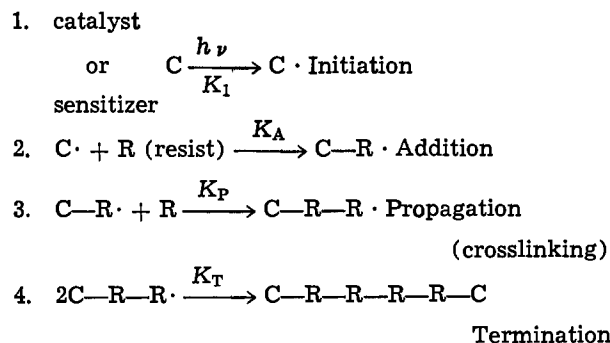
Inhibitor effect on resolution over aluminum.—Because the Al surface is highly reflective, greater problems with definition and "bridging" of fine lines and spaces would be expected. To evaluate the performance of SLI over Al, it was tested on wafers that had 1 Knm of E-beam Al(Si) on them. Variations in the bake cycle were also examined to optimize performance of the overcoat. As shown in Table III, the total bake time of 30 min was held constant while the order of the bake within the process was varied. That is, in Set 2 the overcoat was applied directly after photoresist and both were baked for 30 min, while in Set 4 the photoresist was baked 30 min prior to SLI coating, with no bake after coating; and in Set 3 the bake was split between the two layers. Within the reproducibility of reading the patterns ($\pm 5\%$), Sets 2 and 4 appear to be equivalent. Set 3 with 20 min bake after photoresist spin and a 10 min bake after SLI coating is not quite as satisfactory. Thus, from the results and process efficiency the procedure of Set 2 would be preferred.

Comparison of the control Set 1 to the SLI coated Sets, 2, 3, and 4 shows a very significant improvement in the fine line and space definition due to SLI. For example, considering 0.1 mil geometries with no overcoat, Set 1, all of the photoresist bars were bridged and only 17% of the spaces were open. With SLI overcoat however, Set 2, 26% of the bars and 35.4% of the spaces were clear. This represents an increase of 26% and 19% for 0.1 mil bars and spaces, respectively. The percentage improvement is considerably greater over aluminum than it is over oxide, cf., Set 2, Table II, which is presumably due to the greater reflectivity of the aluminum surface. In general, these data indicate that the greatest improvement occurs in bar patterns which decreases the amount of bridging between adjoining stripes of photoresist. Shrinkage of space openings is also significantly improved, however. Similar but smaller improvements are noted for larger geometries up to 0.2 mil.

Inhibitor mechanism.—The mechanism for improved photoresist definition described above depends on reflected light being much less intense than the incident light and the presence of an inhibitor which absorbs (inactivates) reflected light under the opaque

portions of the photomask. Thus, the presence of the inhibitor eliminates polymerization of photoresist due to reflected light and is not present in high enough concentration to effectively change the intensity of the incident light in the clear areas of the photomask.

The function of the inhibitor is readily explained if one considers the free radical chemistry of polymerization reactions. A general sequence for photochemical crosslinking of negative photoresist may be written



Here, the rate constants K_A and K_P are much larger than K_I or K_T so that Steps 2 and 3 proceed a number of times for each time Step 1 or 4 occurs. Thus, a typical free radical chain reaction is involved. This is the reaction sequence that, in general, occurs when light of the proper energy exposes negative resist. If the light is not perfectly collimated or the underlying surface is not planar, light reflections between the mask and underlying surface are set up. These multi-reflections allow some light energy to reach under the opaque portions of the photomask which will cause crosslinking of photoresist in these areas. Any overexposure of the resist film will of course intensify this effect and cause lines in the pattern to enlarge and spaces to shrink. When the free radical inhibitor is placed as a very thin film on top of the photoresist, attenuation (absorption) of the reflected light can be achieved. That is, the inhibitor has a very high extinction coefficient for the wavelength of light used and does not itself produce active free radicals that produce crosslinking of the resist. Under these conditions, polymerization under opaque areas of the mask is decreased. Among those substances which act as inhibitors are those compounds that, on absorbing light energy form highly resonance stabilized free radicals. Their normal reaction mode is to stabilize by combination with another free radical, i.e.

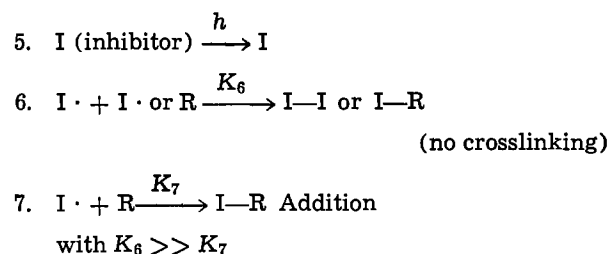


Table III. Effect of SLI on resolution over aluminum as a function of bake cycle

Set	Soft bake cycle (80°C, N ₂)		Percent pattern open					
	After photoresist (min)	After SLI coating (min)	0.10 mil		0.15 mil		0.20 mil	
			Bars	Spaces	Bars	Spaces	Bars	Spaces
1	30	No coating	0	17	20	74	67	93
2	0	30	26	35	54	91	89	100
3	20	10	22	26	43	93	80	100
4	30	0	23	30	59	93	93	100

Exposure time constant at 12 sec.

That is, reaction 6 is much more probable than reaction 7. Some compounds used as free radical inhibitors include: a) hydroquinone, b) pyrocatechol, c) pyrogallol. Also, alkyl or amine substituted compounds of the above type materials may be used, e.g., 2-methyl-4-ethyl hydroquinone or orthoamino phenol.

Summary and Conclusions

This study has resulted in a negative resist overcoat 5-10 nm thick which is readily removed in the develop cycle. The overcoat, composed of a surfactant, a lubricant, and a free radical inhibitor is applied by spinning from an alcohol solution. Use of the overcoat process has resulted in a more than threefold decrease in pinholes and a similar increase in pinhole-free die yields on large, 11.1 mm² chips over those obtained in standard, contact mode photoresist processing. Fine line and space definition, particularly in patterning reflective metal surfaces were significantly improved. A free radical mechanism to explain pattern definition improvement is proposed.

Acknowledgments

The authors wish to thank Mrs. Eileen Uravitch for the careful laboratory work done in these experiments

as well as Drs. H. Hughes and K. Ritchie for many helpful discussions. They are also greatly appreciative to Mrs. Beth Gersitz for preparing the manuscript.

Manuscript submitted May 1, 1979; revised manuscript received Feb. 21, 1980.

Any discussion of this paper will appear in a Discussion Section to be published in the June 1981 JOURNAL. All discussions for the June 1981 Discussion Section should be submitted by Feb. 1, 1981.

Publication costs of this article were assisted by Motorola, Incorporated.

REFERENCES

1. G. S. Schnable, W. Kern, and R. B. Comizolli, *This Journal*, **122**, 1092 (1975).
2. W. Kern, G. L. Schnable, and A. W. Fisher, *RCA Rev.*, **37**, 45 (1976).
3. I. Skeist, "Handbook of Adhesives," p. 7, Reinhold Publishing Corp., London (1962).
4. L. J. Osipow, "Surface Chemistry," ACS Monograph 153, pp. 47, 437, Reinhold Publishing Corp., London (1962).
5. D. L. Flowers and H. G. Hughes, *This Journal*, **124**, 1599 (1977).
6. D. L. Flowers, *ibid.*, **124**, 1608 (1977).

Photoelectrochromic Characteristics of Photoelectrochemical Imaging System with a Semiconductor/Solution (Metallic Ion) Junction

Tooru Inoue, Akira Fujishima,* and Kenichi Honda

Department of Synthetic Chemistry, Faculty of Engineering, The University of Tokyo, Tokyo 113, Japan

ABSTRACT

Photoelectrochemical reactions at semiconductor electrodes in solutions containing metallic ions have been applied to a reversible imaging system. Clearly visible images were formed on the surfaces of TiO₂, SrTiO₃, and ZnO (n-type) and GaP (p-type) semiconductor electrodes in solutions with metallic ions such as Tl⁺, Pb²⁺, Co²⁺, and Ag⁺ as image-forming agents. Image formation occurs under irradiation with light absorbable by the semiconductors, while semiconductor electrodes are polarized either anodically (for n-type) or cathodically (for p-type). Erasing can be accomplished only by polarizing the semiconductor electrodes cathodically (n-type) or anodically (p-type), or the image can be held if desired by opening the circuit after the image formation process. For example, a brown image pattern was formed on a sintered n-type ZnO photoelectrode in an aqueous solution containing Tl⁺ when the electrode was anodically polarized (1.0V vs. SCE) under irradiation with absorbable light. The image was stable for more than 20,000 hr in air, but faded immediately when cathodic polarization of -0.5V vs. SCE was applied at a ZnO electrode. This imaging process has good reversibility during image formation and erasing. Electrochemical characteristics based on the semiconductor photoelectrode reactions were investigated and discussed focusing on charge transfer across the semiconductor/solution junction.

The photoelectrochemistry of semiconductors has been extensively studied in recent years, with the main interest focused on the establishment of heterogeneous charge transfer mechanisms, the development of radiant energy converters to the electrical energy and/or chemical energy, and the development of functional devices. Most recently, electrochemical photocells (EPC's) with a semiconductor/solution junction have been investigated in order to utilize solar energy in chemical and/or electrical form (1-14). The photoelectrocatalytic synthesis of fuels has been also carried

* Electrochemical Society Active Member.

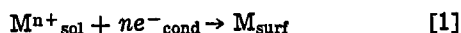
Key words: photoelectrochemistry, semiconductors, photoelectrodes, reproducible imaging, display.

out in semiconductor powder/solution or semiconductor powder/gas systems (15-18).

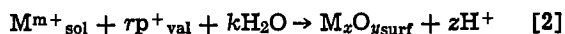
When, in such a photoelectrochemical system with semiconductors, the semiconductor is irradiated with an absorbable light of shorter wavelength than the bandgap frequency, electrons are excited from the valence band to the conduction band while positive holes are generated at the valence band. Thus it follows that these photogenerated carriers (electrons or holes) react with redox agents in solution at the semiconductor/solution interface.

If metallic redox agents (Mⁿ⁺) are oxidized or reduced by the photogenerated carriers (e⁻_{cond}, an elec-

tron in the conduction band or p^+_{val} , a hole in the valence band) and the species produced deposited on the electrode surface, as we have reported previously (19, 20), a photoimage can be obtained by the reaction

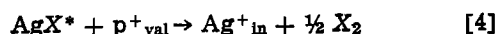
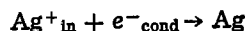
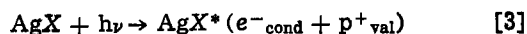


or



where M^{n+}_{sol} and M^{m+}_{sol} denote metallic ions in solution, M_{surf} a metal deposited on the electrode surface, and $M_xO_{y_{surf}}$ a metal oxide deposited on the electrode surface. When the deposited layer of metal or metal oxide is distinguished in color from the semiconductor substrate, a visible image can be recognized.

A variety of new image display methods (21-29) have recently been reported employing nonsilver halides, but silver halides (AgX) continue to be the most widely used as the light sensitive material in photographs. Their initial imaging reactions are (30)



where AgX^* denotes a silver halide excited by light and Ag^+_{in} an interstitial silver ion. These photographic imaging processes are irreversible photochemical reaction, and it is thus impossible to erase an image and to reconstitute the silver halide. One method that gives promise of overcoming the irreversibility of imaging uses a semiconductor electrode/solution system in which one can control the reaction by shifting electrode potential.

McLeod (23) has reported the photographic process by the photocatalytic reduction of metallic ions on nonsilver halide semiconducting materials.

Memming *et al.* (24) have described the electrochemical characteristics on the photographic processes which took place by the action of the photocatalytic deposition of Pb on TiO_2 .

In this report we have investigated semiconductor electrode reactions under light irradiation in the course of imaging processes by means of electrochemical techniques and we discuss them focusing on the charge transfer across the interface of the semiconductor/solution junction.

Experimental

The photosensitive semiconductor materials used in this experiment were n-type TiO_2 (single crystal from Fuji Titan Company, sintered polycrystal with 0.1% Nb as dopant, and evaporated thin film from Mitorika Company) which had donor densities of 10^{17} - 10^{19} cm^{-3} , n-type ZnO (single crystal from 3M Company, sintered polycrystal) with donor density of ca. 10^{18} cm^{-3} , n-type $SrTiO_3$ (single crystal from Fuji Titan Company) with donor density of ca. 10^{18} cm^{-3} , and p-type GaP (single crystal with Zn as dopant from Mitsubishi Kinzoku Kozan Company) which had acceptor density of $3 \cdot 10^{17}$ cm^{-3} . For the ZnO polycrystal electrode, a ZnO substrate was prepared by pressing ZnO powder (1000-2000 mesh) at ca. 1.0 ton/ cm^2 and then heating it at 1300°C for ca. 3 hr in air. Procedures for the preparation of electrodes, such as ohmic contact and connection with the copper lead, are described elsewhere (8-17). A semiconductor electrode was fixed in the aqueous electrolyte solution together with a Pt counterelectrode and a saturated calomel electrode (SCE). Electrode potentials were controlled using a potentiogalvanostat (Nikko Keisoku). Light was irradiated on the electrode surface through the standard test mask (Japan Electronic Photograph Society) from a 500W Xe lamp. Figure 1 is a schematic of the experimental image formation and measuring system. The supporting electrolyte was an aqueous solution of a 0.2 mole/ dm^3 Na_2SO_4 or 0.5 mole/ dm^3 KNO_3 . The metallic ions used as image formation agents were

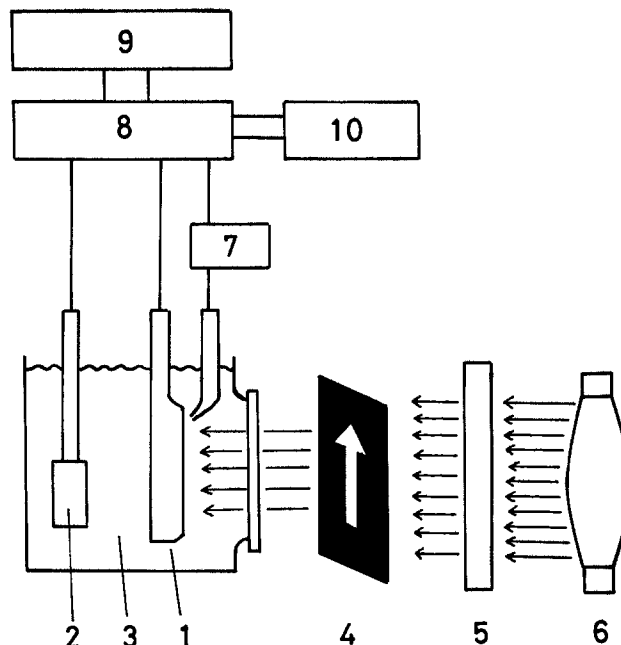


Fig. 1. Schematic of the electrochemical measuring apparatus for photoelectrochemical imaging processes. 1, Semiconductor electrode; 2, Pt electrode; 3, electrolyte; 4, mask; 5, glass filter; 6, light source; 7, saturated calomel electrode (SCE); 8, potentiogalvanostat; 9, potential sweeper; 10, X-Y recorder.

obtained from Tl_2SO_4 , $Pb(CH_3COO)_2$, $MnSO_4$, $CoSO_4$, and $AgNO_3$. Electrolyte solutions were deaerated before measurements by bubbling with purified N_2 gas. Identification of the images formed were carried out by x-ray diffraction.

Results

Figure 2 shows the current-potential characteristics of an n-type TiO_2 electrode in an electrolyte of 0.2 mole/ dm^3 Na_2SO_4 + 0.01 mole/ dm^3 Tl_2SO_4 . When the TiO_2 electrode is set in the supporting electrolyte (0.2 mole/ dm^3 Na_2SO_4) solution, a positive photocurrent appeared under irradiation with wavelengths of 300-400 nm at the anodic polarization at potentials more positive than the flatband potential of TiO_2 , where water in solution was oxidized by photogenerated positive holes (minority carriers) at the valence band, in accordance with equations

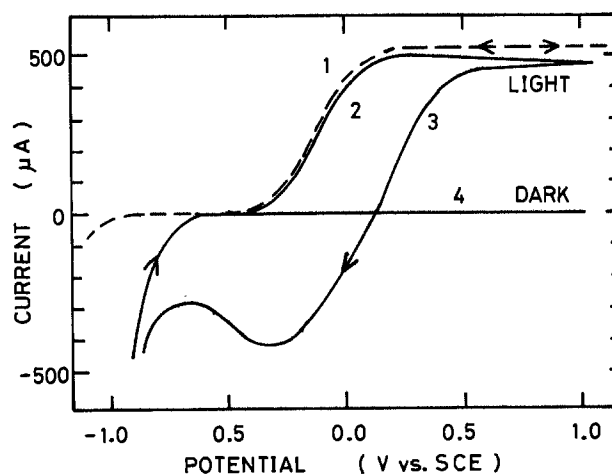
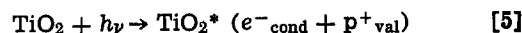
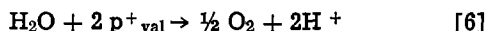
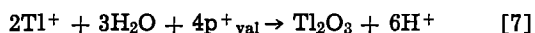


Fig. 2. Current-potential characteristics of an n-type TiO_2 single crystal electrode. 1, In 0.2 mole/ dm^3 Na_2SO_4 aq. soln.; 2, 3, in 0.2 mole/ dm^3 Na_2SO_4 + 0.01 mole/ dm^3 Tl_2SO_4 aq. soln.; 4, in the dark.

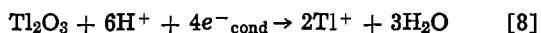


where h denotes the Planck constant, ν the frequency of light, while negligible current flows at TiO_2 during darkness (12, 16) (see 1 in Fig. 2).

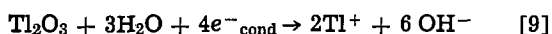
When the metallic ion (Tl^+) was added to the electrolyte an anodic photocurrent (2 in Fig. 2) also appeared at potentials more positive than the flatband potential (the value of which was the same as when there was no Tl^+ in the solution, indicating that adsorptive interaction of Tl^+ against the surface of TiO_2 was very small), and during the appearance of this anodic photocurrent, the portion of the TiO_2 illuminated through the mask turned brown. Hence, it is possible to obtain an image through photo-oxidation at a semiconductor electrode. When after fixation of an image on the electrode surface, the electrode potential was swept to the negative side, cathodic current appeared even at potentials more positive than the flatband potential, and the brown image gradually disappeared with the surface of the TiO_2 electrode returning to the condition before image formation. Therefore, the imaging reactions are reversible and we can write the following equations: for an image formation



and for an image erasing



or



The species oxidized from Tl^+ by the positive holes was identified as thallium oxide (Tl_2O_3) by x-ray diffraction. That is, the imaging step is the formation of a layer of Tl_2O_3 on the TiO_2 surface, and the decoloration step is the erasing of this layer from the TiO_2 substrate.

Figure 3 shows the current-potential characteristics of the ZnO electrode in electrolytes containing PbSO_4 at various concentrations. The ZnO electrode is photo-corrosive in the course of the photoelectrode reaction in the supporting electrolyte (e.g., a 0.2 mole/dm³ Na_2SO_4 aqueous solution), resulting in the reaction

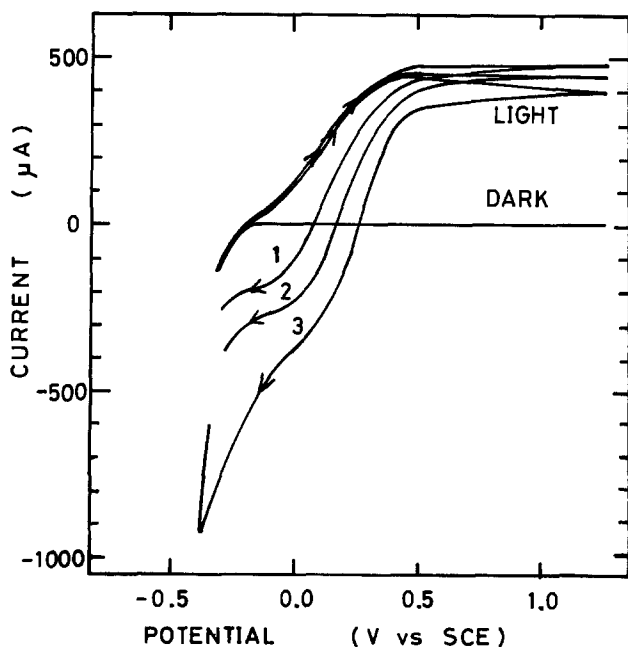
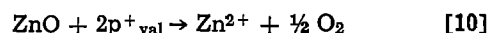
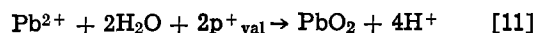


Fig. 3. Current-potential characteristics of an n-type ZnO polycrystal electrode. 1, In 0.2 mole/dm³ Na_2SO_4 + 2×10^{-3} mole/dm³ PbSO_4 aq. soln.; 2, in 0.2 mole/dm³ Na_2SO_4 + 5×10^{-3} mole/dm³ PbSO_4 aq. soln.; 3, in 0.2 mole/dm³ Na_2SO_4 + 10^{-2} mole/dm³ PbSO_4 aq. soln.

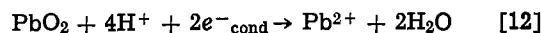
(11, 13)



When the metallic ion (Pb^{2+}) is dissolved in the solution as the imaging agent, both the anodic photocurrent, based on the image formation, and the reduction current, based on the image erasing, are obtained in a way similar to the case of TiO_2 . As shown in Fig. 3, the electrode reactions are: for image formation



and for image erasing



The limiting anodic photocurrent, for image formation, is constant because it is controlled by the supply of photogenerated holes in the valence band of the semiconductor to the electrode surface. The reduction current for the image erasing, on the other hand, varies with the Pb^{2+} concentration, which can be determined on the basis of competitive oxidation at the ZnO electrode. That is, in solutions containing Pb^{2+} , the image formation reaction [11] competes with the photocorrosion reaction of ZnO [10], and the current efficiency (competition ratio) of reaction [11] is enhanced over that of reaction [10] when Pb^{2+} concentration is increased (13). Hence, the quantity of PbO_2 formed on the ZnO electrode determines the total amount of electricity of the reduction current.

Figure 4 shows the current-potential curves when Mn^{2+} or Co^{2+} is dissolved in the solution as the imaging agent. The characteristics obtained were similar to those for Tl^+ and Pb^{2+} , but the reduction behavior of the oxides formed on the semiconductor electrodes

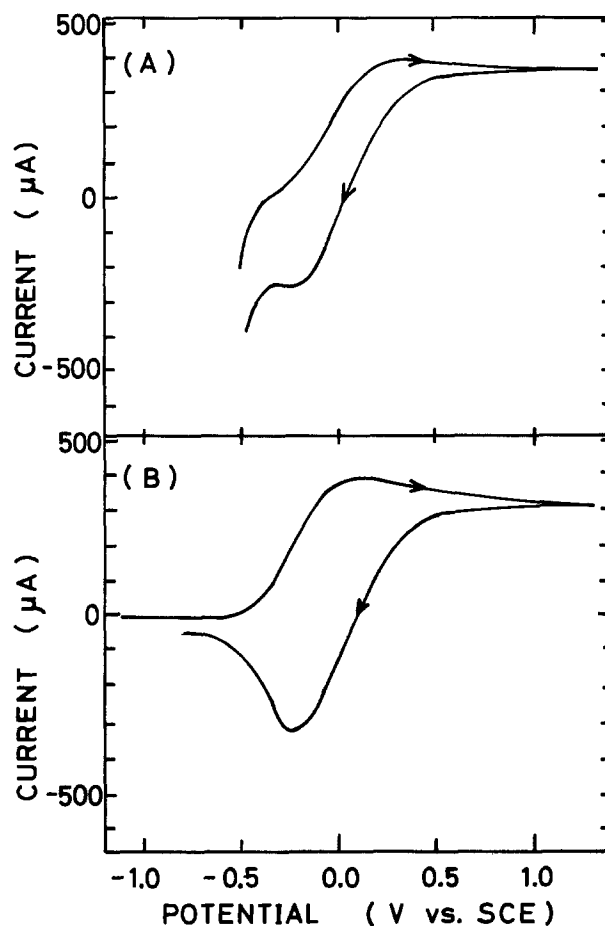
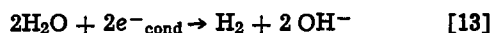


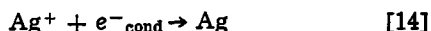
Fig. 4. Current-potential characteristics of an n-type ZnO polycrystal electrode under light irradiation, (A) In 0.2 mole/dm³ Na_2SO_4 + 10^{-2} mole/dm³ CoSO_4 aq. soln.; (B) in 0.2 mole/dm³ Na_2SO_4 + 10^{-2} mole/dm³ MnSO_4 aq. soln.

were slightly different, a fact that may be attributable to a junction of oxide on the semiconductor surface and on the reduction reactivity of the oxide layers.

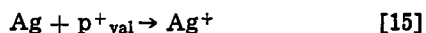
Figure 5 shows the current-potential characteristics at a p-type GaP electrode in an electrolyte solution containing Ag^+ . As this is a p-type semiconductor, the minority carriers are electrons in the conduction band, so that the photoelectrode reaction is reduction electrolysis by photogenerated electrons. In the supporting electrolyte water was reported to be reduced at the GaP electrode, resulting in the evolution of hydrogen



When metallic ions were present in the solution, they were also reduced by electrons during cathodic polarization of an electrode, resulting in metal deposition on p-type semiconductor electrodes. Hence, at a p-type GaP electrode the imaging reaction is



When the image is formed on the surface of the GaP electrode, the illuminated part of the reddish brown GaP substrate turns white based on Ag deposition [14]. To erase the image, the Ag image layer on the GaP is oxidized to Ag^+ by the holes as the majority carrier in the valence band. Thus, the anodic corrosion reaction of Ag is a decoloration reaction



The formation and erasing characteristics and the color are listed in Table I for the images formed in the course of the current-potential measurements.

Figure 6 shows the time dependence of photocurrent at the TiO_2 electrode in solutions containing Tl^+ when the irradiation intensity and Tl^+ concentration is varied, where the electrode potential of TiO_2 is fixed at 1.0V vs. SCE. The phenomena of decreasing photocurrent depend upon the filtering effect that the image layers formed on the TiO_2 surface have against the incident light, and the fact that after sufficient electrolysis the surface is completely covered with image-making oxide. When irradiation intensity is varied and the Tl^+ concentration is kept constant, the photocurrent decreases with time and this decrease is more rapid at higher irradiation intensities [Fig. 6(A)]. And when the Tl^+ concentration is varied and the irradiation intensity is kept constant, the photocurrent again decreases more rapidly at higher concentrations of Tl^+ [Fig. 6(B)]. This indicates that the formation rate ($V(t)$) of an image-making layer becomes the larger under conditions of the increased irradiation intensity and Tl^+ concentration, and thus, we can assume that the initial formation rate ($V_{t=0}$) of an image may be approximately described as a function of the irradiation intensity (Q) and the metallic ion concen-

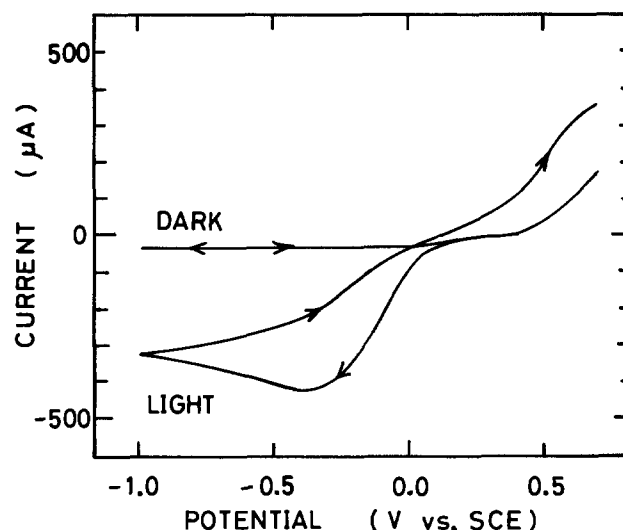


Fig. 5. Current-potential characteristics of a p-type GaP single crystal electrode in a 0.5 mole/dm³ KNO_3 + 10^{-2} mole/dm³ AgNO_3 aq. soln.

tration (C), as follows

$$V_{t=0} = \lim_{t \rightarrow 0} V(t) = \lim_{t \rightarrow 0} r \cdot i(t) = k \cdot Q \cdot C \quad [16]$$

where k denotes the image formation rate constant, $i(t)$ the photocurrent depending on time, and r the competitive ratio of the image formation reaction.

Figure 7 shows the reproducibility of an imaging system with a ZnO electrode/metallic ion (Tl^+) in the solution, where the factors of light intensity, electrode potential (V vs. SCE), optical density (OD), and current are expressed as a function of a common time scale. The hatched areas on the optical density curve indicate the appearance of the image; the positive portions of the current curve correspond to image formation, and the negative portions to image erasing. The results in Fig. 7 for an n-type semiconductor electrode show that image formation requires both anodic polarization of the ZnO electrode and light irradiation, while image erasing needs only cathodic polarization of ZnO. The time response of current in both image formation and erasing is rapid. Image formation requires both cathodic polarization of the electrode and light irradiation, while image erasing needs only anodic polarization of the electrode, if a p-type semiconductor is used. Reversible characteristics analogous to those for an n-type semiconductor are obtained. The image can be held by opening the circuit after the image formation process, or erased by shorting the circuit with a reverse bias against image formation, as desired.

Table I. Imaging characteristics in semiconductor/metallic ion system

Type of semiconductor electrode	Semiconductor substrate	Metallic ions in solution	Color of substrate	Color of image	Formation*	Erasing*	Contrast
TiO_2 (n)	Single crystal	Tl^+ Pb^{2+} Mn^{2+} Co^{2+}	} Gray	Yellow Brown Brown Brown	Good Good Fairly good Fairly good	Good Good Fairly good Fairly good	} Good
	Evaporated film	Tl^+ Tl^+		Green Blue	Yellow Yellow	Good Good	
ZnO (n)	Single crystal	Tl^+ Pb^{2+} Mn^{2+} Co^{2+}	} White	Yellow or brown	} Good	} Good	} Good
	Polycrystal			} Brown to black			
SrTiO_3 (n)	Single crystal	Tl^+	Light gray	Brown	Good	Good	Good
GaP (p)	Single crystal	Ag^+	Reddish brown	White (gray)	Good	Good	Good

* In the course of current-potential measurement with the potential sweep rate of 3 V/min.

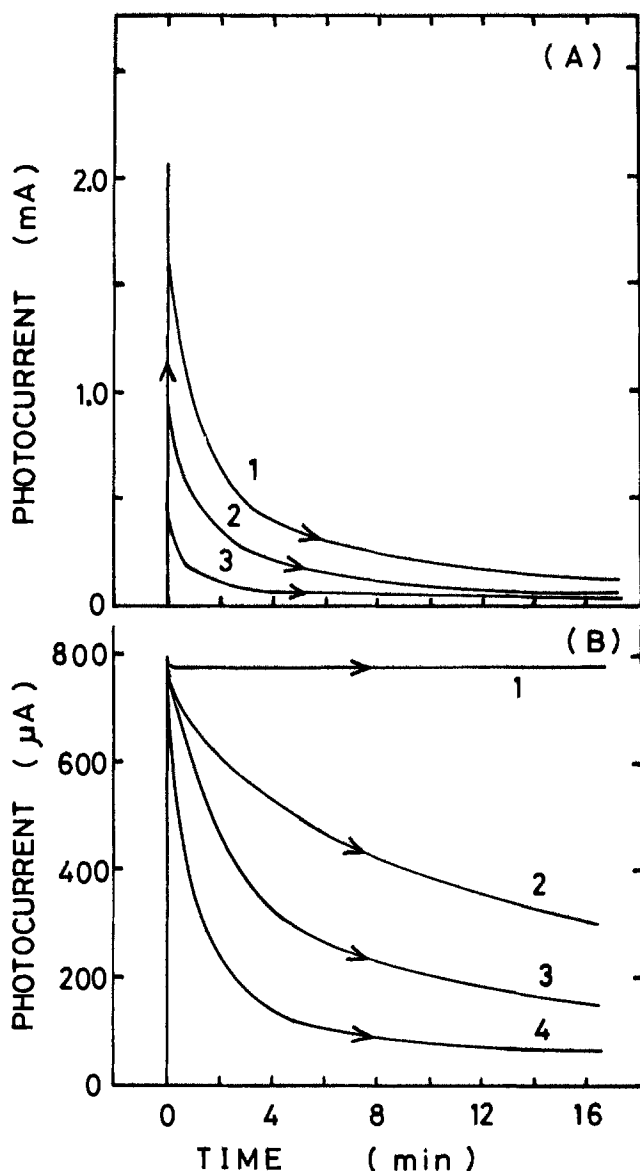


Fig. 6. Time-dependence of photocurrents at an n-type TiO_2 electrode in a $0.2 \text{ mole/dm}^3 \text{ Na}_2\text{SO}_4$ aq. soln. with Ti_2SO_4 . (A) At constant Ti_2SO_4 concentration ($10^{-2} \text{ mole/dm}^3$) and light intensity (a.u.): curve 1 = 4, curve 2 = 2, and curve 3 = 1. (B) At constant irradiated light intensity and Ti_2SO_4 concentration (mole/dm^3): curve 1 = 0, curve 2 = 10^{-4} , curve 3 = 10^{-3} , and curve 4 = 10^{-2} .

Figure 8 shows a photograph of an image obtained on a sintered ZnO electrode with a diameter of 10 cm. The image is negative because the illuminated part of the electrode was colored brown by the formation Ti_2O_3 . Illumination was carried out for 1 min through the standard testing mask with a resolution of ca. 15 lines per mm. As can be seen, a fairly clear image was obtained on the semiconductor substrate and stable for more than 20,000 hr in air, but erased immediately when cathodic polarization of -0.5V vs. SCE was applied at a ZnO electrode.

Discussion

The redox behavior of chemical species in solution at irradiated semiconductor electrodes depends upon the interfacial mode of the semiconductor/solution junction. The reactivity of solution species with photo-generated carriers (electrons and holes) in a semiconductor are due to the correlation between the energy levels of the semiconductor and the redox potentials of the species. Figure 9 shows the energy correlation of the imaging systems employed in this study. As

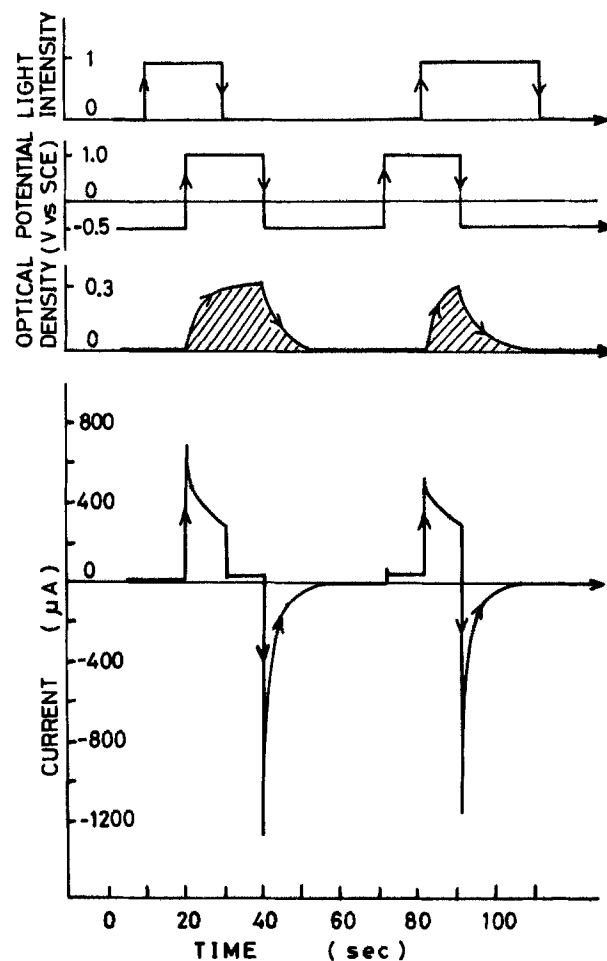


Fig. 7. Dependence of irradiated light intensity and electrode potential on currents at a ZnO electrode in a $0.2 \text{ mole/dm}^3 \text{ Na}_2\text{SO}_4 + 10^{-2} \text{ mole/dm}^3 \text{ Ti}_2\text{SO}_4$ aq. soln. Light intensity and optical density are expressed in arbitrary units. Hatched portions denote the appearance of images.

previously reported in connection with competitive redox reactions at semiconductor photoelectrodes (8-13), the solution species with redox potentials within the bandgap potential region were oxidized at n-type semiconductor electrodes and reduced at p-type electrodes, and the current efficiency of the redox reactions of the solution species depended upon their standard redox potentials. In these imaging systems, the standard redox potentials of oxide-formation for n-type semiconductors, and of metal-deposition for p-type semiconductors lie within the bandgap potential region, analogous to the previous results (8-13), with the result that image-formation (reactions [7], [11], [14], [17], and [18]) proceeds in competition with the decomposition of water or of the electrode itself (reactions [6], [10], and [13]). As for the formation of images with respect to the difference of redox potentials of solution metallic ions, it was qualitatively recognized that an image was formed more favorably in the system with the more negative metallic redox potential than in the system with the more positive metallic redox potential, partly as shown at the term of Formation in Table I, where the systems with Tl^+ and Pb^{2+} have the faster reaction rate for the image formation. In a higher concentration of an imaging agent in a solution, as one can recognize from the result in Fig. 6 (B), when there are imaging agents in higher concentrations in the solution imaging reactions surpass the decomposition reactions. However, when a reducing agent such as hydroquinone (H_2Q) or potassium ferrocyanide ($\text{K}_4\text{Fe}(\text{CN})_6$) was added to imaging systems using an n-type semiconductor, no image could be

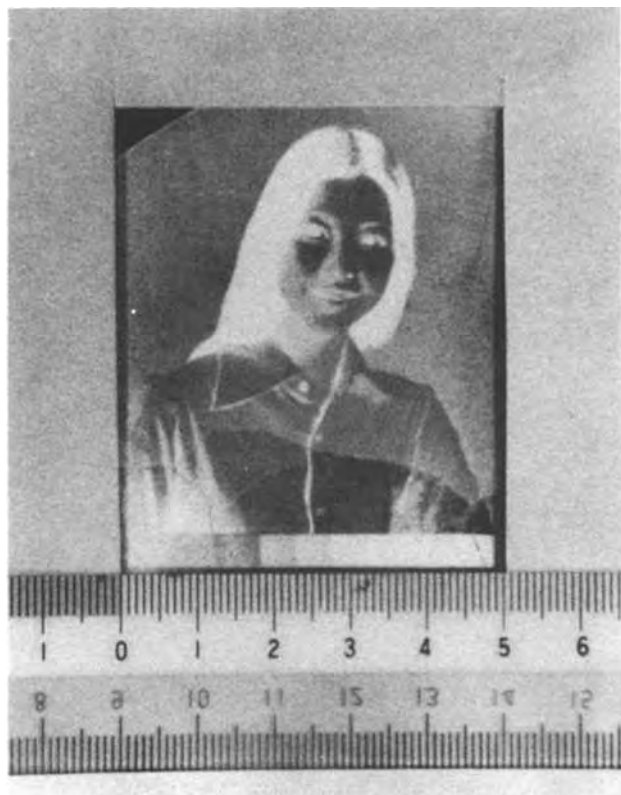


Fig. 8. Photograph of an image formed on a ZnO polycrystal electrode.

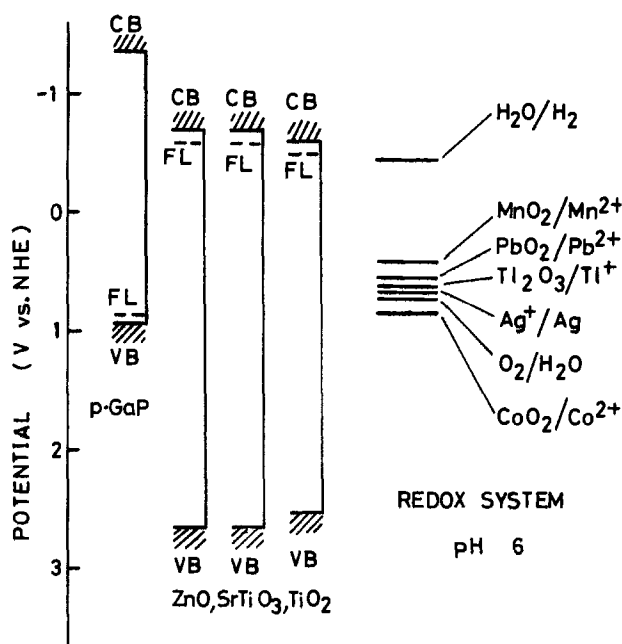


Fig. 9. Schematic correlation of energy levels between semiconductor electrodes and redox couples.

obtained. This can be attributed, with respect to the interfacial redox reactions, to the fact that the redox potentials of the oxidation of H_2Q and $K_4Fe(CN)_6$ are more negative than those of oxide formation reactions and to the fact that the oxidation of reducing agents surpasses any other reactions (imaging or the decomposition of water or the electrode itself), resulting in suppression of imaging reactions (12, 13).

Figure 10 (A) is a schematic presentation of image formation on a typical n-type semiconductor electrode (e.g., ZnO) due to a photoelectrode reaction. The illuminated part alone is covered with an oxide layer.

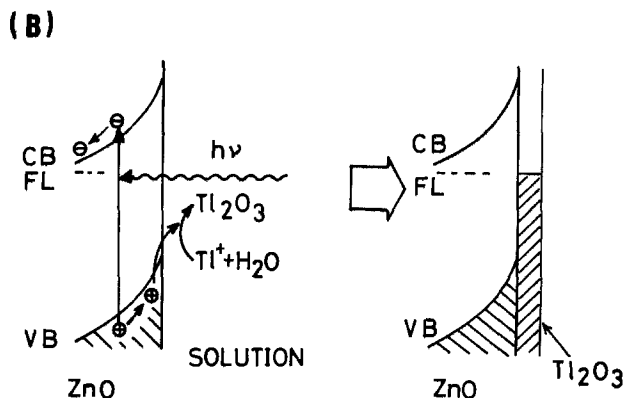
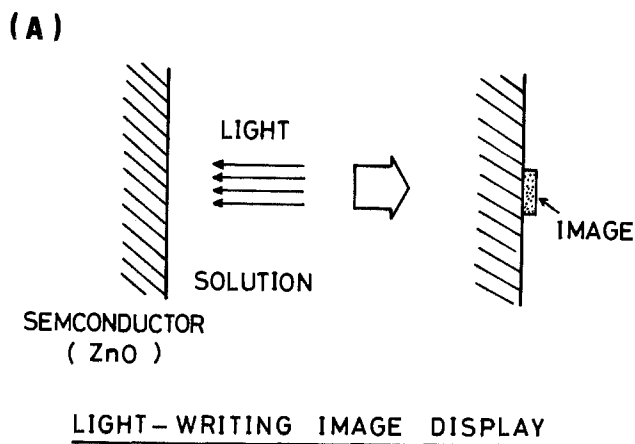


Fig. 10. Schematic of a typical light-writing image display process with a ZnO-Ti⁺ system. An image appears at an irradiated part of the ZnO electrode.

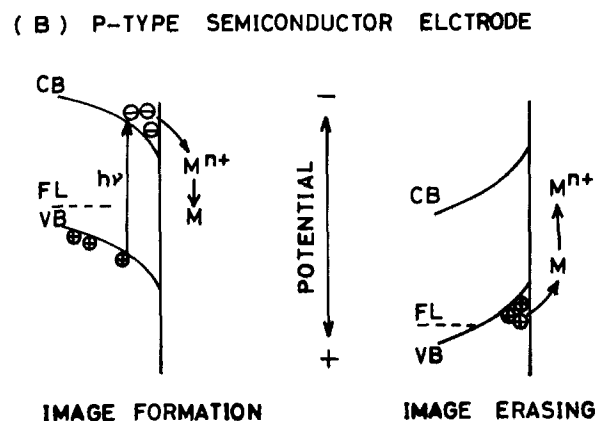
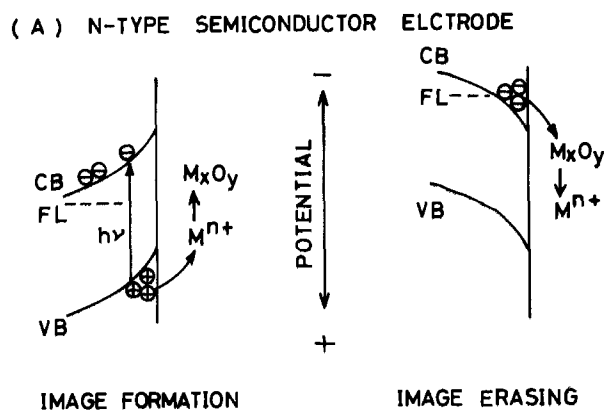


Fig. 11. Schematic of image formation and erasing processes in reversible photoelectrochemical imaging systems with a semiconductor/solution junction. (A) n-type semiconductor electrode, (B) p-type semiconductor electrode.

Figure 10 (B) simply shows the charge transfer across the interface.

Figure 11 is schematic summarizing the reversible photoelectrochemical imaging processes. For an n-type semiconductor electrode, the image formation process is the oxidation of metallic ions by photogenerated positive holes as minority carriers at the valence band under anodic polarization of the semiconductor, and the image erasing process is the reduction of the oxide layer by electrons as majority carriers at the conduction band under cathodic polarization. For a p-type semiconductor electrode, the polarization conditions of image formation and erasing are reversed, i.e., image formation is by the reduction of metallic ions by photogenerated electrons as minority carriers, and erasing is by oxidation of the metal layer by valence band holes as majority carriers.

Image evaluations from the view of displaying points are dealt with in a subsequent report (31).

Acknowledgment

The support of this research by The Toyoto Foundation is gratefully acknowledged.

Manuscript submitted Nov. 14, 1979; revised manuscript received Jan. 21, 1980.

Any discussion of this paper will appear in a Discussion Section to be published in the June 1981 JOURNAL. All discussions for the June 1981 Discussion Section should be submitted by Feb. 1, 1981.

Publication costs of this article were assisted by the University of Tokyo.

REFERENCES

- H. Gerischer, "Physical Chemistry: An Advanced Treatise," H. Eyring *et al.*, Editors, pp. 467-542, Academic Press, New York (1970).
- A. J. Bard, *J. Photochem.*, **10**, 59 (1979).
- A. Fujishima, K. Kohayakawa, and K. Honda, *This Journal*, **122**, 1487 (1975).
- M. S. Wrighton, A. B. Ellis, P. T. Wolczanski, D. L. Morse, H. B. Abrahamson, and D. S. Ginley, *J. Am. Chem. Soc.*, **98**, 2774 (1976).
- A. J. Nozik, *Nature*, **257**, 383 (1975).
- R. H. Wilson, *J. Appl. Phys.*, **48**, 4292 (1977).
- B. A. Parkinson, A. Heller, and B. Miller, *This Journal*, **126**, 954 (1979).
- T. Inoue, T. Watanabe, A. Fujishima, K. Honda, and K. Kohayakawa, *ibid.*, **124**, 719 (1977).
- T. Inoue, T. Watanabe, A. Fujishima, and K. Honda, *Chem. Lett.*, 1073 (1977).
- T. Inoue, T. Watanabe, A. Fujishima, and K. Honda, *Bull. Chem. Soc. Jpn.*, **52**, 1243 (1978).
- A. Fujishima, T. Inoue, T. Watanabe, and K. Honda, *Chem. Lett.*, 357 (1978).
- A. Fujishima, T. Inoue, and K. Honda, *J. Am. Chem. Soc.*, **101**, 5582 (1979).
- T. Inoue, A. Fujishima, and K. Honda, *Bull. Chem. Soc. Jpn.*, **52**, 3217 (1979).
- M. Halman, *Nature*, **275**, 155 (1978).
- H. Reiche and A. F. Bard, *J. Am. Chem. Soc.*, **101**, 157 (1979).
- G. N. Schrauzer and T. D. Guth, *ibid.*, **99**, 7189 (1977).
- J. C. Hemminger, R. Carr, and G. A. Somorjai, *Chem. Phys. Lett.*, **57**, 100 (1978).
- T. Inoue, A. Fujishima, S. Konishi, and K. Honda, *Nature*, **277**, 637 (1979).
- T. Inoue, A. Fujishima, and K. Honda, *Chem. Lett.*, 1197 (1978).
- T. Inoue, A. Fujishima, and K. Honda, *Jpn. J. Appl. Phys.*, **18**, 2177 (1979).
- M. Yamana, *Appl. Phys. Lett.*, **29**, 570 (1976).
- B. Reichman, Fu-Ren F. Fan, and A. J. Bard, *This Journal*, **127**, 333 (1980).
- G. L. McLeod, *Photogr. Sci. Eng.*, **13**, 93 (1979).
- F. Mollers, H. J. Tolle, and R. Memming, *This Journal*, **121**, 1160 (1974).
- S. K. Mohapatra, G. D. Boyd, F. G. Storz, S. Wagner, and F. Wudl, *ibid.*, **126**, 805 (1979).
- S. Gottesfeld and J. D. E. McIntyre, *ibid.*, **126**, 742 (1979).
- B. Reichman and A. F. Bard, *ibid.*, **126**, 583 (1979).
- J. J. Robillard, in "Non-Silver Photographic Processes," R. J. Cox, Editor, Academic Press, New York (1975).
- E. Inoue, H. Kokado, I. Shimizu, H. Kobayashi, and Y. Takahashi, *Bull. Chem. Soc. Jpn.*, **45**, 1951 (1972).
- T. H. James, Editor, "The Theory of the Photographic Process," 4th ed., Macmillan Pub. Co., Inc., New York (1977).
- T. Inoue, A. Fujishima, and K. Honda, *This Journal*, in preparation.

Regrowth Behavior of Three Different Damage Structures in P⁺ Implanted and Subsequently Laser Annealed Si

D. K. Sadana

Lawrence Berkeley Laboratory, University of California, Berkeley, California 94720

M. C. Wilson and G. R. Booker

Department of Metallurgy, University of Oxford, Oxford OX1 3PH, England

and J. Washburn*

Lawrence Berkeley Laboratory, University of California, Berkeley, California 94720

ABSTRACT

The aim of the work was to study the regrowth behavior of three different damage structures, namely, a buried amorphous layer, a continuous amorphous layer extending from the surface of the specimen, and a buried layer of clusters in P⁺ implanted (111) Si. These structures were obtained by implanting P⁺ at 120 keV to doses of 5×10^{14} , 10^{15} , and $5 \times 10^{15}/\text{cm}^2$ at implantation temperatures RT, 150°, and 350°C, respectively. A Q-switched ruby laser with a wavelength of 0.695 nm and at an energy either 0.7 J/cm² or 1.5 J/cm² was used for laser annealing. TEM was used to examine the damage in a 90° "cross-sectional" view. At 0.7 J/cm², two-thirds of the continuous amorphous layer regrew to give a polycrystalline layer. The buried amorphous layer regrew leaving dislocation loops and clusters and the buried layer of clusters remained unaffected. However, at 1.5 J/cm², dislocations and stacking faults extended from the surface for all the structures and were in direct contact with the deeper lying damage containing clusters. The density of dislocations, stacking faults, and deeper lying clusters progressively increased with the dose of the implanted phosphorus.

The potential applications of high energy pulsed laser beams for the regrowth of damage layers in ion-implanted semiconductors has drawn worldwide interest because of the simplicity of the process. By suitable choice of laser parameters, such as the energy, pulse length, etc., epitaxial regrowth of the damaged layers resulting from implantation can, in principle, be carried out either in the solid phase or molten phase (1-3). However, the mechanism of regrowth is not yet fully understood. The present study is therefore aimed at studying the regrowth behavior of three different types of damage structures, namely a buried amorphous layer, a continuous amorphous layer, and a buried layer of damage clusters in P⁺ implanted Si on subsequent pulsed laser annealing at different energies. The origin of the formation of different damage structures has been explained elsewhere (4). For all of the work described here, TEM was used to examine the damage structures in 90° "cross-sectional" and "plan" views before and after the laser annealing. A mechanism for the regrowth has been suggested based on the observations made here.

Experimental

Implantation.—p-Type 17 Ω -cm (111) Si wafers of 5 cm diam were implanted in a nonchanneling direction with 120 keV P⁺ ions using doses of either 5×10^{14} , 10^{15} , or $5 \times 10^{15}/\text{cm}^2$. The implantation energy of 120 keV corresponded to an LSS projected range of $1510 \pm 690\text{Å}$. The implantation time in all instances was 10 min. The implantation temperatures in the three cases were RT, 150°, and 350°C. The increases above RT in the latter two cases being due to ion beam heating.

Laser.—A Q-switched ruby laser operating at a wavelength of 0.695 nm was used. The multiple beam output was passed through a diffusing screen coupled to a light guide in order to achieve a flat and uniform intensity distribution (5). The laser energies of 0.7 and

1.5 J/cm² were used for each specimen. The pulse length for all the specimens was ~ 30 nsec.

TEM.—For TEM studies, 90° "cross-section" and "plan" view specimens were prepared. The "cross-section" specimens were obtained by cleaving the slices and then mechanically polishing followed by low energy ion beam thinning as described previously (6). The micrographs from these specimens correspond to the (110) plane perpendicular to the original (111) specimen surface plane. All of the TEM examinations described here were performed using bright field strong beam diffraction contrast conditions. Transmission electron diffraction (TED) patterns were also obtained to aid in the identification of the damage, using either the standard selected area method or microdiffraction techniques.

Results

Buried amorphous layer.—For the specimen implanted to a dose of $5 \times 10^{14}/\text{cm}^2$, the TEM "cross-section" micrograph showed an $\sim 1150\text{Å}$ wide buried amorphous layer "A" located at a mean depth of $\sim 850\text{Å}$ from the surface (Fig. 1a). The region between the surface and the top edge of damage layer "A" had sparsely distributed clusters.

After the specimen had been laser annealed at 0.7 J/cm², the region between the surface and $\sim 1600\text{Å}$ depth, marked as "B" in Fig. 1b, consisted of dislocation loops (mean diameter $\sim 100\text{Å}$) and clusters. The density of dislocation loops obtained from "plan" view micrograph (not included in the text) was $\sim 6 \times 10^{10}/\text{cm}^2$. The regrown region "B" was followed by a second damage layer "C" $\sim 250\text{Å}$ wide, consisting of dense fine structure and was located at a depth immediately below the bottom edge of layer "A" in the as-implanted specimen (Fig. 1b).

After the specimen had been laser annealed at 1.5 J/cm², the first damage layer "B" in the previous specimen was no longer present. The previous second layer "C" was much less in evidence and consisted mainly of small damage clusters in the layer "D"

* Electrochemical Society Active Member.

Key words: TEM, cross-sectional micrograph, amorphous layer, dislocations, stacking faults.

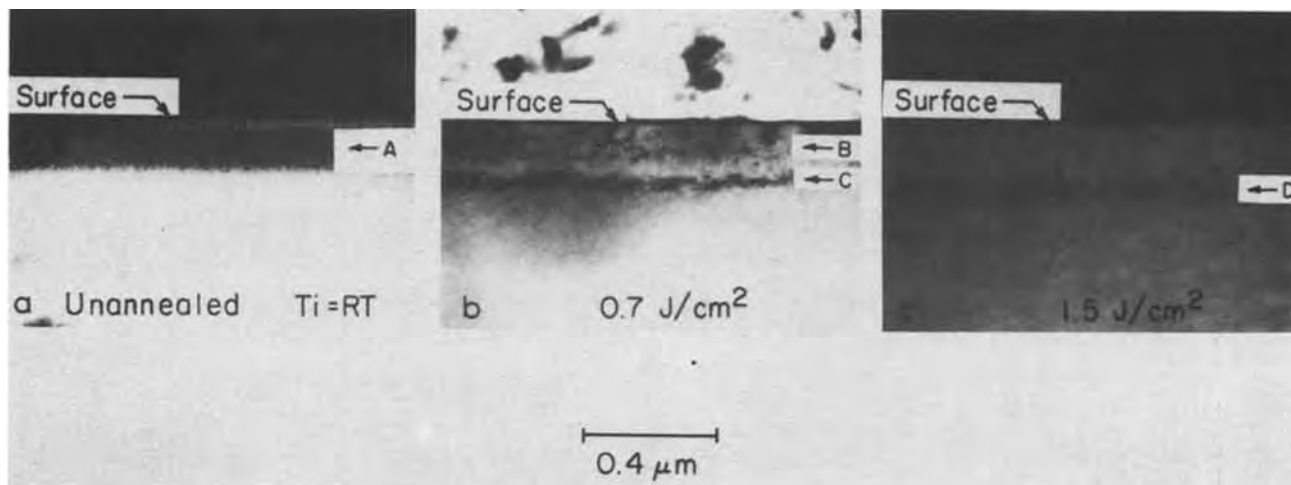


Fig. 1. TEM "cross-section" micrographs showing the laser annealing sequence for P⁺ implanted (111) Si. ($T_i = RT$, $N_{P^+} = 5 \times 10^{14}/\text{cm}^2$, $E_i = 120 \text{ keV}$).

(Fig. 1c). Occasionally, single dislocations extending from the surface to the clusters layer were observed.

Continuous amorphous layer.—For the wafers implanted to a dose of $10^{15}/\text{cm}^2$, the TEM "cross-section" micrographs showed a continuous amorphous layer "E" extending from the surface to a depth of $\sim 1800\text{\AA}$. At the lower edge of this layer there was a narrow irregular zone $\sim 250\text{\AA}$ wide corresponding to heavily damaged but not amorphous material (the narrow dark layer in Fig. 2a).

After the specimen had been annealed at 0.7 J/cm^2 , a first damage layer "F" comprising polycrystalline material with mean grain size $\sim 1000\text{\AA}$ extended from the specimen surface to a depth of 1500\AA (Fig. 2b). A second damage layer "G" consisting of dense fine structure and $\sim 500\text{\AA}$ wide occurred and was in direct contact with the first damage layer (7).

After the specimen had been laser annealed at 1.5 J/cm^2 , a first damage layer "H" comprising single crystal material containing mainly stacking faults but also dislocations extended from the surface to a depth of $\sim 1800\text{\AA}$ (Fig. 2c). The stacking faults density (from "plan" view micrographs) at the surface was $\sim 10^9/\text{cm}^2$. A second damage layer "I" consisting of dense fine structure and $\sim 200\text{\AA}$ wide occurred and was in direct contact with the first damage layer.

Buried clusters layer.—For the specimens implanted to a dose of $5 \times 10^{15}/\text{cm}^2$, the TEM "cross-section" micrographs showed a buried layer of clusters "J," $\sim 1200\text{\AA}$ wide, in single crystal material that was lo-

cated at a mean depth of $\sim 2000\text{\AA}$ (Fig. 3a). There were "visible damage" free regions on either side of layer "J" (the term "visible damage" refers to the damage visible by TEM). After the specimen had been laser annealed at 0.7 J/cm^2 , no noticeable change in the damage structure or distribution occurred (Fig. 3b).

However, for the specimen laser annealed at 1.5 J/cm^2 , the results were similar to that of $10^{15}/\text{cm}^2$ except that the densities of dislocations and stacking faults (from "plan" view micrographs) were now $\sim 10^{10}/\text{cm}^2$ and $\sim 7 \times 10^{11}/\text{cm}^2$, respectively. The first damage layer containing stacking faults and dislocations is marked as "L" and the second damage layer containing small clusters is marked as "M" in Fig. 3c.

Discussion

A striking feature of the laser annealing is that two distinctly different annealing zones are sometimes present within individual specimens (Fig. 2b, 2c, and 3c). We suggest the following mechanism for the formation of the observed regrown structures.

For the as-implanted specimens with buried damage layers (Fig. 1a and Fig. 3a), the near-surface region, although damaged, is still single crystal as shown by TED's (not included in the text). However, for the $10^{15} \text{ P}^+/\text{cm}^2$ specimen, the near-surface region is amorphous. As a result, the energy absorption in the "buried layer" specimens occurred over a larger volume as compared to the "continuous amorphous layer" specimen. This is because of different absorption coefficients for amorphous and single crystal Si. There-

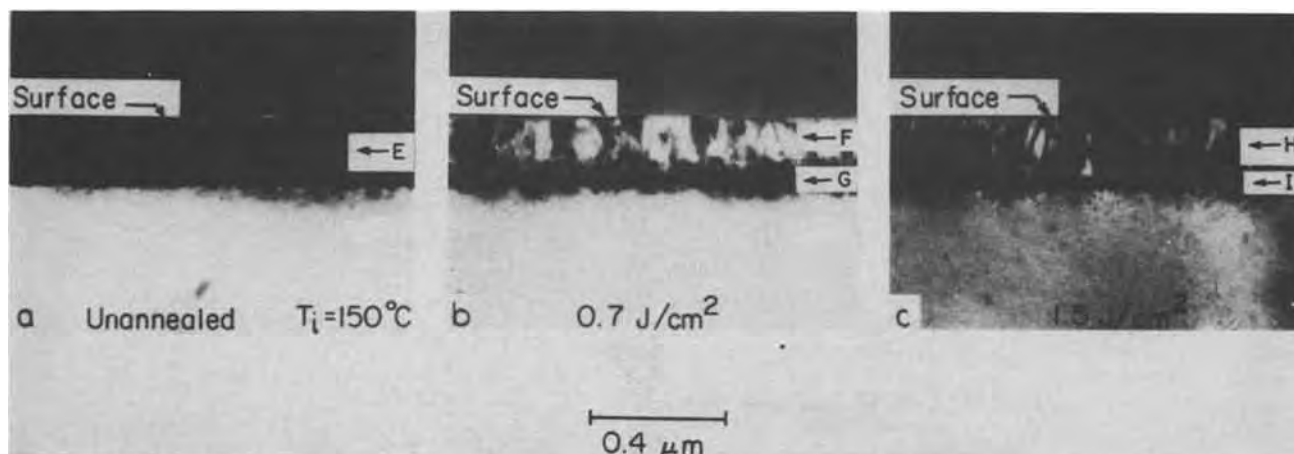


Fig. 2. TEM "cross-section" micrographs showing the laser annealing sequence for P⁺ implanted (111) Si. ($T_i = 150^\circ\text{C}$, $N_{P^+} = 10^{15}/\text{cm}^2$, $E_i = 120 \text{ keV}$).

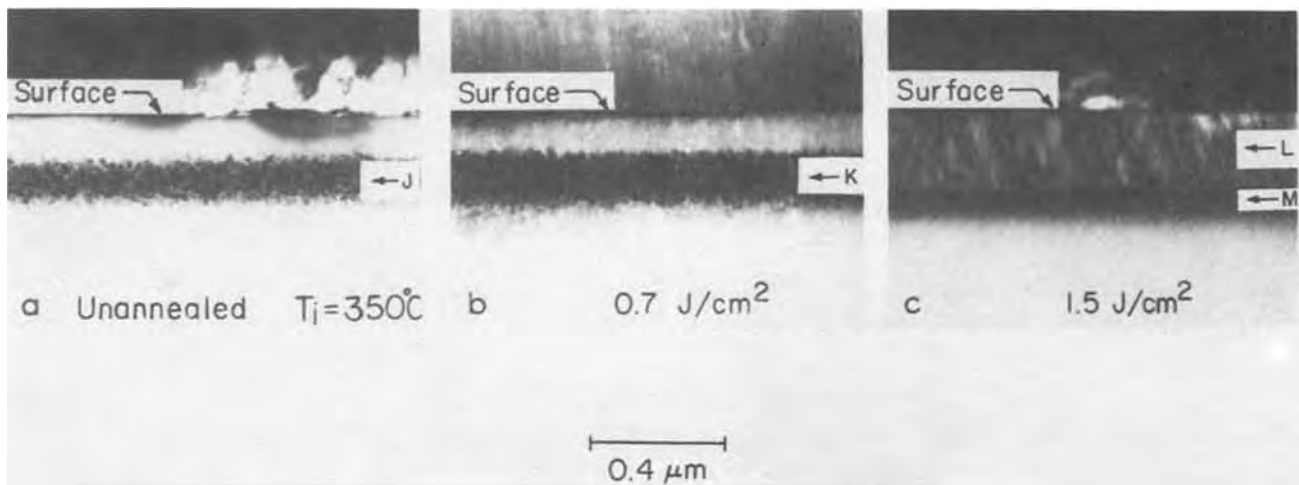


Fig. 3. TEM "cross-section" micrographs showing the laser annealing sequence for P^+ implanted (111) Si. ($T_i = 350^\circ\text{C}$, $N_{P^+} = 5 \times 10^{15}/\text{cm}^2$, $E_i = 120 \text{ keV}$).

fore, at lower energies, *i.e.*, 0.7 J/cm^2 the "buried damage layers" either partially recover (Fig. 1b) or remain unaffected (Fig. 3b) depending on the thickness and the extent of damage in the near-surface region. However, for "continuous amorphous layers" strong absorption of energy nearer to the surface causes melting of the surface layer, but the deeper lying damage still remains amorphous or heavily damaged. The molten upper layer in this case regrows on a heavily damaged or amorphous substrate forming the polycrystalline layer.

At 1.5 J/cm^2 , the laser energy absorption is high enough to melt the main damage layer in all three specimens but the solidification of the molten material on deeper lying clusters still gives rise to the formation of the dislocations and stacking faults. The density of these clusters increases progressively with the dose of the implanted P^+ ions. Consequently, the density of dislocations and stacking faults in the regrown layer also increases.

Conclusions

1. The regrowth structures from damaged layers in P^+ implanted Si resulting from laser annealing at 0.7 J/cm^2 critically depend on the crystallinity of the specimen in the near-surface region.
2. At a laser energy of 1.5 J/cm^2 , the regrowth of the damage layer occurs via melting for all cases. The perfection of the regrown material then depends on the depth of melting relative to the depth of the original implantation damage.

Acknowledgments

The authors would like to thank Dr. A. Cullis of RSRE Malvern (England) for laser annealing the Si

specimens. The authors would also like to acknowledge the financial support of the Department of Energy (USA) through Materials and Molecular Research Division of Lawrence Berkeley Laboratory, Berkeley, California and Science Research Council (UK) through Department of Metallurgy, Oxford.

Manuscript submitted Nov. 8, 1979; revised manuscript received Jan. 30, 1980. This was Paper 512 presented at the Los Angeles, California, Meeting of the Society, Oct. 14-19, 1979.

Any discussion of this paper will appear in a Discussion Section to be published in the June 1981 JOURNAL. All discussions for the June 1981 Discussion Section should be submitted by Feb. 1, 1981.

Publication costs of this article were assisted by the University of California.

Note added in proofs: All the laser energy values reported in this paper have to be multiplied by a factor of 0.8.

REFERENCES

1. G. K. Celler, J. M. Poate, and L. C. Kimerling, *Appl. Phys. Lett.*, **32**, 464 (1978).
2. R. T. Young, C. W. White, G. J. Clark, J. Narayan, W. H. Christie, M. Murakami, P. W. King, and S. D. Kramer, *ibid.*, **32**, 139 (1978).
3. J. S. Williams, Abstract 522, p. 1317, The Electrochemical Society Extended Abstracts, Los Angeles, California, Oct. 14-19, 1979.
4. D. K. Sadana, To be published.
5. A. G. Cullis, H. C. Webber, and P. Bailey, *J. Phys. E.: Sci. Instrum.*, **12**, 688 (1979).
6. H. R. Pettit and G. R. Booker, Proc. 25th Anniv. Meet., EMAG (IOP), London (1971).
7. D. K. Sadana, M. C. Wilson, and G. R. Booker, *J. Microsc.*, **118**, 51 (1980).

The Effect of Phosphorus Doping on Tin Oxide Films Made by the Oxidation of Phosphine and Tetramethyltin

I. Growth and Etching Properties

Yar-Sun Hsu* and Sorab K. Ghandhi*

Electrical and Systems Engineering Department, Rensselaer Polytechnic Institute, Troy, New York 12181

ABSTRACT

This paper describes the growth and etching characteristics of phosphorus-doped tin oxide films, prepared by the simultaneous oxidation of tetramethyltin (TMT) and phosphine gas in the 400°-500°C range. Both the growth and etch rates of these films are found to be relatively constant until the P/Sn ratio exceeds 3.2%, at which point they fall off and eventually become negligible. In addition, films grown by this technique are found to undergo a rapid transition from the polycrystalline to the amorphous state when their P/Sn ratio exceeds 3.2%. Possible mechanisms for this behavior are outlined, based on the relative strength of the P-O and Sn-O bonds and on the network former properties of P₂O₅. It is proposed that the mechanism of film growth and dopant incorporation is the direct (and independent) reaction of phosphine and TMT with oxygen adsorbed on the substrate surface. The transport properties of these films are discussed in a companion paper.

Tin oxide is a promising material for heterojunction solar cells, because it combines the unusual properties of high conductivity and excellent transparency in the visible spectrum. In addition, its large energy gap (~3.5 eV) and its suitable index of refraction (~1.9) make it not only an excellent upper window for solar cells, but also a good antireflection coating. An additional advantage is its durability under harsh environmental conditions. For example, tin oxide is not attacked at room temperature by either concentrated acids or bases.

Many techniques have been developed for its deposition. Among these, chemical vapor deposition or spray hydrolysis of tin tetrachloride-antimony chloride mixtures (1-5) are the commonly used methods. High substrate temperatures ranging from 500° to 750°C are usually required for these processes. In addition films tend to be unstable because of the incorporation of volatile chlorine in them.

In a previous paper (6), we have developed a simple preparation technique for phosphorus-doped tin oxide films formed by the simultaneous oxidation of tetramethyltin (TMT) and phosphine (PH₃), at relatively low temperatures (400°-500°C). TMT is a stable liquid with a relatively high vapor pressure (100 mm Hg) at room temperature. It can be readily transported to the reaction chamber in vapor form by bubbling argon gas through liquid TMT. Because of the absence of volatile chlorine, films made by this technique are more stable than those prepared by alternate methods.

Our past work has emphasized the kinetics of growth of undoped SnO₂ films, and shown that phosphorus doping results in a significant increase in their conductivity. The results were anomalous however, in that the conductivity fell off rapidly once a critical ratio of PH₃/TMT was exceeded.

This paper and its companion extend our work into this regime, and investigate both the growth and transport properties of these films as a function of dopant incorporation. All other process parameters (substrate temperature, argon and oxygen flow rates, and bubbler parameters) were held constant during the course of this work.

* Electrochemical Society Active Member.

Key words: tin oxide, tetramethyltin, chemical vapor deposition.

Experimental

Apparatus.—The deposition of tin oxide films was performed in an open tube vertical reactor. The reactants were introduced into a 130 mm ID, 160 mm long, vertically positioned reaction chamber containing a tungsten susceptor (50 mm diam) which was maintained at the deposition temperature by conventional resistance heating. UHP argon gas¹ was bubbled through the tetramethyltin² (TMT) at room temperature to transport its vapor to the heated substrate. Phosphine³ gas, diluted to 500 ppm in argon, was used to dope these films. A baffle plate was used to mix the TMT vapor with phosphine and argon prior to their reaction with oxygen.⁴ A separate inlet was brought in close to the substrate to introduce oxygen into this chamber, so that the reaction took place near the surface. All depositions were conducted using an argon carrier gas flow of 2.0 liters/min.

Deposition procedures.—Deposition of doped and undoped tin oxide films was carried out on oxidized silicon slices which were positioned on the susceptor. Prior to the deposition, the slices were degreased in trichloroethylene, acetone, and isopropyl alcohol, followed by a thorough rinse in deionized water. The substrates were further cleaned in Caro's etch [1:1 solution of H₂SO₄ (97%) and H₂O₂ (47%)] and given a final rinse in methanol. Subsequently, SiO₂ was grown on the wafer to a thickness of 5000Å in wet oxygen at 1090°C. Next, the chamber was pumped down and flushed with argon gas. Once the deposition temperature was reached, argon gas with flow rate of 16 cm³/min was bubbled through the TMT bubbler at 25°C to transport its vapor to the substrate. At the same time, oxygen was also introduced at a flow rate of 50 cm³/min, followed by phosphine gas. Immediately after SnO₂ growth, a 2000Å layer of SiO₂ was deposited on this film, at the same temperature. This was done by the oxidation of silane⁵ which was used

¹ Ultra High Purity 99.999%, Matheson Gas Products, East Rutherford, New Jersey.

² 5N Electronic grade, Alpha Organometallics, Danvers, Massachusetts.

³ Electronic Grade 99.999% purity, Matheson Gas Products, East Rutherford, New Jersey.

⁴ Research Purity 99.99%, Matheson Gas Products, East Rutherford, New Jersey.

⁵ Semiconductor grade, Matheson Gas Products, East Rutherford, New Jersey.

in a 3% dilution in argon. The silica layer was patterned by conventional photolithographic techniques and used as a mask for etching the tin oxide.

A number of different types of substrates were used in this work. These included microscope cover slides (Corning No. 2940), semi-insulating Cr-doped GaAs, and thermally oxidized silicon. The results for these substrates were virtually identical, but are presented here for the oxidized silicon slices.

Thickness determination.—The silica layer was patterned by conventional photolithography, and served as a mask for the tin oxide film. Electrochemical etching (7) was used to remove exposed regions of highly conductive films. Etching was carried out in a bath of dilute hydrochloric acid [1 part of concentrated HCl (37%) in 5 parts of deionized water] with a platinum anode, and using the tin oxide as the cathode. In this system, nascent hydrogen is generated at the cathode by the passage of current, and probably reduces the SnO_2 to tin, which is continuously dissolved in the electrolyte as etching proceeds.

The electrochemical technique was found to be unsuited for low conductivity films, due to the formation of isolated unetched patches of tin oxide on the substrates. Therefore, an etching solution (8) was prepared by dissolving 1g of chromium metal into dilute HBr [20 ml of concentrated HBr (48%) with 20 ml of deionized water] at 98°C. In this system, it is believed that chromium is first dissolved to chromous ions which can be further converted to chromic ions by reaction with SnO_2 . In this way, the SnO_2 is reduced to Sn which is removed by the hydrobromic acid. This solution was found to be satisfactory for etching the exposed tin oxide, if used as soon as it was prepared. During etching, the addition of extra chromium was sometimes necessary to maintain the chromous ion concentration when the action slowed down.

After etching, the silica mask was removed in hydrofluoric acid. The tin oxide film and substrate were next covered with evaporated aluminum, and the step measured by means of a multiple beam interferometer (Varian Model 980-4012).

X-ray diffraction.—Films were subjected to Cu-K α radiation ($\lambda = 1.5405\text{\AA}$) in a General Electric XRD-7 Diffractometer system, in order to study their crystal structure. The intensity *vs.* 2θ plots were directly obtained in a plotter attachment and compared to standard values available in the literature (9). All of these films were at least 1 μm thick so that the x-ray diffraction signals of sufficient intensity could be obtained.

Results and Discussion

The behavior of tin oxide films as a function of TMT, oxygen flow, and temperature, has been studied earlier (6). Here, we confine ourselves to a study of film behavior as the incorporation of phosphorus is increased. As a result, all data presented here are for films grown at 450°C with 16 cm^3/min flow rate of argon through the TMT bubbler held at 25°C. This corresponds to a partial pressure of 0.7 Torr, assuming that equilibrium transport is achieved. A flow rate of 50 cm^3/min of oxygen was used for these experiments. Film composition was varied by altering the PH_3/TMT mole ratio, while keeping a constant partial pressure of TMT and oxygen.

Composition.—The actual composition of the films was determined by microprobe analysis. Figure 1 shows the oxygen to tin atomic ratio as a function of PH_3/TMT mole ratio in the vapor phase. We note that, for low PH_3 concentration, the film is essentially in the form of SnO_2 with a small oxygen deficit. As the PH_3 concentration is increased, some of the phosphorus replaces the tin, so that there is a small increase of the O/Sn atomic ratio.

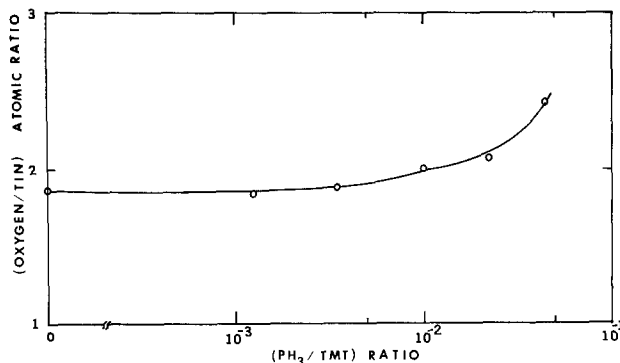


Fig. 1. Oxygen/tin atomic ratio vs. PH_3/TMT mole ratio

The P/Sn atomic ratio in the tin oxide films is plotted in Fig. 2 as a function of the PH_3/TMT mole ratio in the vapor phase, and is seen to be linear over the entire range of interest, with a proportionality factor of 3.2. This type of behavior would be expected if the incorporation of phosphorus and tin into the growing film is both by absorption of oxygen on the surface, and reaction with the incoming tin and phosphorus species at a rate which is directly proportional to their partial pressures. The adsorbed oxygen has a greater affinity for the phosphorus than for the tin, so that its effective sticking coefficient is larger.

Some phosphorus was found to be present in the undoped SnO_2 films. This is believed to be due to the residual impurity in the reaction chamber and the inlet lines.

Morphology.—All films grown with a PH_3/TMT mole ratio less than 0.01 showed x-ray diffraction peaks corresponding to those obtained for polycrystalline SnO_2 . Some differences were observed for films grown under different conditions, as indicated by the change of relative intensity of those peaks. However, peaks were at the same reflection angle, and no new peaks were formed. Thus, the orientation of

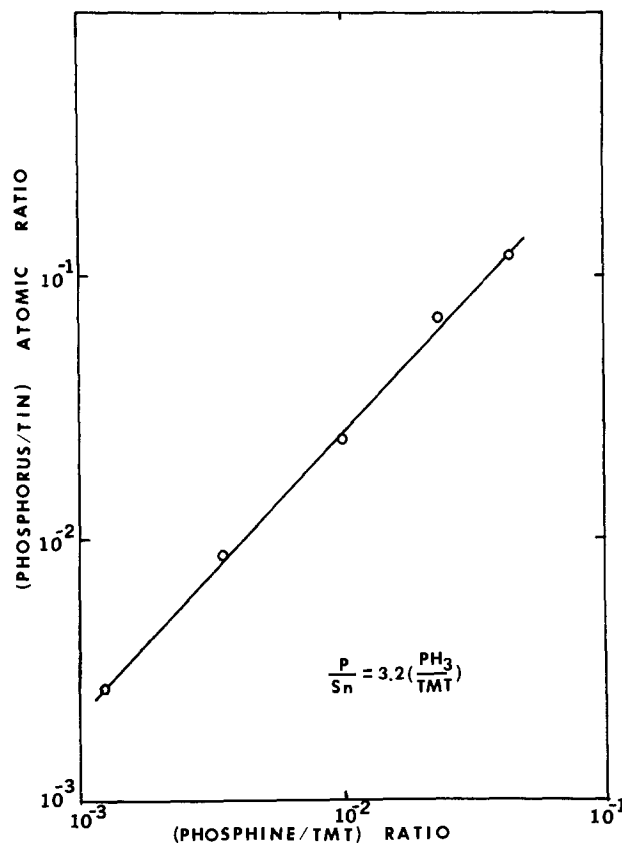


Fig. 2. Phosphorus/tin atomic ratio vs. PH_3/TMT mole ratio

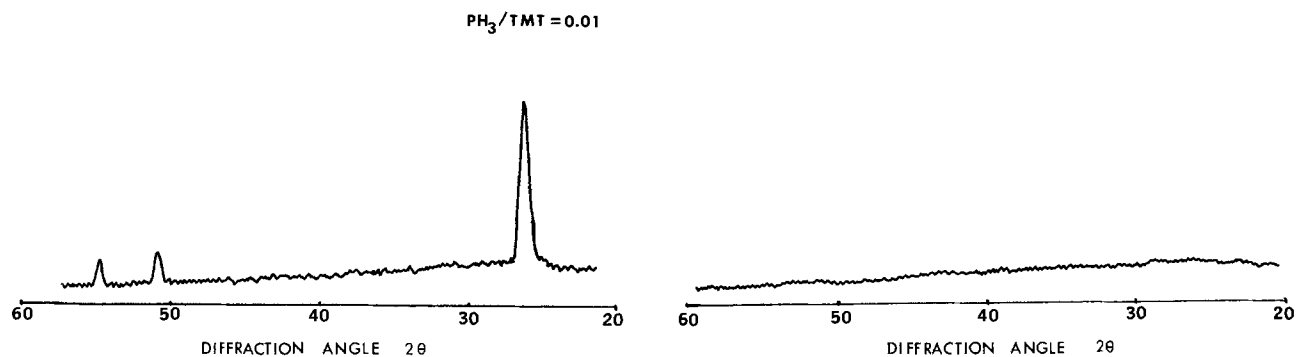


Fig. 3. X-ray diffraction plot for phosphorus-doped films (a, left) $\text{PH}_3/\text{TMT} = 0.01$ (b, right) $\text{PH}_3/\text{TMT} = 0.023$

crystals, as well as the lattice parameters, seemed to be independent of the variation of phosphorus content.

Figure 3a shows a typical diffraction pattern for a film grown with a PH_3/TMT ratio of 0.01. Peaks corresponding to 2θ values of 26.5° (110), 51.7° (211), and 54.7° (220) are clearly seen in this figure. Crystal size could not be resolved by scanning electron microscopy with a magnification of 20,000X. However, calculations based on the broadening of the (110) peak, using Scherer's formula (10) and Jones' conversion curves (11), gave an average grain size of 370Å. This grain size was relatively constant for PH_3/TMT ratios below 0.01, and was independent of the type of substrate used.

Neither SnO nor Sn_2O_4 peaks have been observed. This is in agreement with the result of microprobe analysis, namely that the films are essentially SnO_2 with some oxygen deficit. It is consistently found that the (110) peak was the strongest one. These results are quite different from those obtained for films grown by the pyrolytic decomposition and oxidation of $(\text{CH}_3)_2\text{SnCl}_2$ (5), where the (200) peak was seen to be the strongest. It is interesting to note that this (200) peak was always missing in our samples.

The magnitude of the x-ray diffraction peaks fell off rapidly for PH_3/TMT ratios in excess of 0.01. In fact, no peaks were observed (see Fig. 3b) for $\text{PH}_3/\text{TMT} \geq 0.023$, so that films were essentially amorphous beyond this point. We believe that this comes about because of the large phosphorus-oxygen bond strength (88-111 kcal/mole). As a result, phosphoric oxide is a glass network former (12-13) having the unusual property of high viscosity, which increases rapidly at concentrations in the 1-2% range (14). Its introduction into the tin oxide greatly reduces the mobility of the reactant species on the surface, so that the "critical nucleus" required to form a crystalline film becomes increasingly hard to achieve. This favors the formation of amorphous tin oxide as the phosphorus content increases.

The incorporation of phosphorus and tin into these films remained linear with reactant mole ratios, even though the film structure went through a rapid change from the polycrystalline to the amorphous state. This would indicate that the incorporation mechanism outlined earlier is in effect over this full range, and that chemical compound formation is not the process for initiating the transition to the amorphous state.

Heat-treatment at high temperature was attempted to recover the crystallinity. Annealing the amorphous tin oxide films at 900°C in a nitrogen ambient for 20 hr was found to result in partial recovery as evidenced by the reappearance of x-ray peaks of SnO_2 . However, their intensities were not as strong as those obtained for films grown with PH_3/TMT ratios below 0.01.

Growth rate.—Figure 4 shows the growth rate as a function of PH_3/TMT ratio at the deposition temperature (450°C). This is seen to be relatively constant until a PH_3/TMT ratio of 0.01 is reached, but falls off

with increasing concentration until it becomes essentially zero for a mole ratio of 0.09. Comparable behavior has been noted for arsenic-doped tin oxide films (15), grown by the simultaneous oxidation of arsine gas and tetramethyltin.

A falloff in growth rate of polycrystalline silicon films as a function of arsenic doping has also been noted by other workers (16) and has been explained by using the concept of catalytic poisoning by Group VB elements. We do not believe that this is the case in our films since the high P—O bond strength would favor the presence of phosphorus in the form of tetrahedra where the normally toxic phosphorus atom is shielded by four oxygen atoms (17). We note, however, that the phosphorus is more strongly bound to the adsorbed surface oxygen than the tin (the Sn—O bond strength is 46 kcal/mole). As a result, an increasing phosphorus concentration should increasingly inhibit the attachment of tin to adsorbed oxygen atoms, resulting in the observed falloff in growth rate.

Etch rate.—Figure 5 shows the etch rate of phosphorus-doped films as a function of the PH_3/TMT mole ratio. The same etchant (Cr-HBr system described earlier) was used for all samples as a basis of comparison. Here, we note that the etch rate is relatively constant until a PH_3/TMT ratio of 0.01, and falls beyond this point, becoming essentially zero for a mole ratio of 0.05. This is quite similar to the growth rate behavior, and can also be explained in terms of the large P—O bond strength, as compared to that for the tin-oxygen bond. This is because the etching process essentially involves the rupture of these bonds, and the subsequent dissolution of the reaction products.

Conclusions

The growth and etching properties of phosphorus-doped tin oxide have been described, and explained

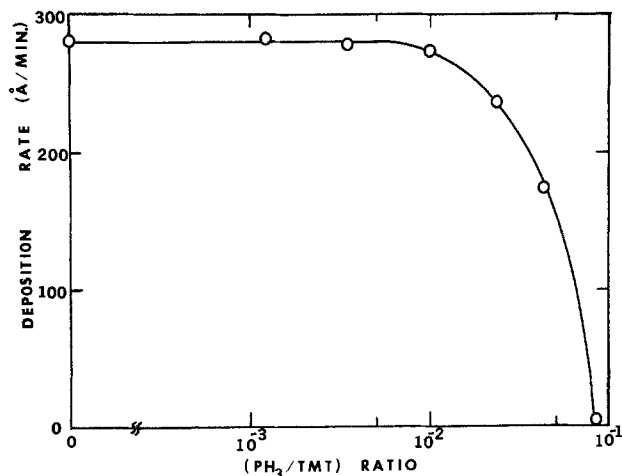


Fig. 4. Deposition rate vs. PH_3/TMT mole ratio

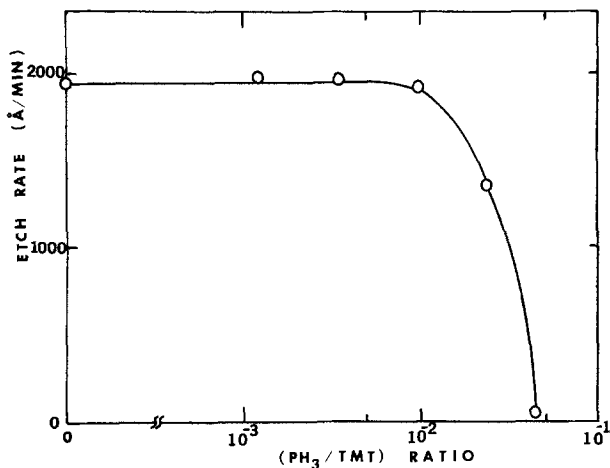


Fig. 5. Etch rate vs. PH₃/TMT mole ratio

on the basis of the relative strengths of the P—O and Sn—O bonds. These arguments also explain the rapid transition of these films from the crystalline to the amorphous state at low phosphorus incorporation levels. Finally, a relatively simple model for the film growth is proposed, based on the direction reaction of the phosphorus and tin species with the surface adsorbed oxygen.

Acknowledgments

The authors wish to thank R. Rafun and A. Hayner for assistance in manuscript preparation. This work was supported by Contract No. XI-9-8000-1 from the Solar Energy Research Institute, Golden, Colorado.

Manuscript submitted Aug. 17, 1979; revised manuscript received Feb. 21, 1980.

Any discussion of this paper will appear in a Discussion Section to be published in the June 1981 JOURNAL. All discussions for the June 1981 Discussion Section should be submitted by Feb. 1, 1981.

Publication costs of this article were assisted by Rensselaer Polytechnic Institute.

REFERENCES

1. K. Ishiguro, T. Sasaki, T. Arai, and I. Imai, *J. Phys. Soc. Jpn.*, **13**, 296 (1958).
2. R. E. Aitchison, *Aust. J. Appl. Sci.*, **5**, 10 (1954).
3. J. A. Aboaf, V. C. Marcotte, and N. J. Chou, *This Journal*, **120**, 701 (1973).
4. V. K. Miloslavskii, *Opt. Spectrosc.*, **7**, 154 (1959).
5. R. Muto and S. Furuuchi, Rept. Res. Lab. Asahi Glass Co., **23**, 27 (1973).
6. B. J. Baliga and S. K. Ghandhi, *This Journal*, **123**, 941 (1976).
7. B. J. Baliga and S. K. Ghandhi, *ibid.*, **124**, 1059 (1977).
8. P. W. Simon, U.S. Pat. 4,009,061 (1977).
9. Joint Committee on Powder Diffraction Standards, "Powder Diffraction File," ASTM, Philadelphia (1969).
10. B. D. Cullity, "Elements of X-ray Diffraction," Addison-Wesley Pub. Co., New York (1956).
11. F. W. Jones, *Proc. Roy. Soc., A*, **166**, 16 (1938).
12. R. H. Doremus, "Glass Science," John Wiley and Sons, New York (1973).
13. W. D. Kingery, "Introduction to Ceramics," 2nd ed., John Wiley and Sons, New York (1976).
14. M. Tomozawa, "Advances in Nucleation and Crystallization in Glasses," American Ceramic Society Special Publication, No. 5 (1972).
15. Y-S Hsu and S. K. Ghandhi, *This Journal*, **126**, 1434 (1979).
16. P. Rai-Choudhury and P. L. Hower, *ibid.*, **120**, 1961 (1973).
17. E. B. Maxted, "Advances in Catalysis," Vol. 3, p. 129, Academic Press, New York (1951).

The Effect of Phosphorus Doping on Tin Oxide Films Made by the Oxidation of Phosphine and Tetramethyltin

II. Electrical Properties

Yar-Sun Hsu* and Sorab K. Ghandhi*

Electrical and Systems Engineering Department, Rensselaer Polytechnic Institute, Troy, New York 12181

ABSTRACT

The electrical properties of tin oxide films have been measured as a function of phosphorus doping. It is shown that the electron concentration increases monotonically with phosphorus doping, with about 7.7% of the incorporated phosphorus being active. An oxygen deficiency is also present in these films, and is found to be about 0.1 eV below the conduction band edge. The mobility increases with phosphorus doping to a maximum of 26 cm²/V sec, and then falls off with further doping, as the film undergoes a crystalline to amorphous transition. Film behavior in these two regimes can be explained by the established theories for current transport in polycrystalline and amorphous films, respectively.

A simple technique for the preparation of tin oxide films by the oxidation of tetramethyltin (TMT) has been reported in a previous paper (1). Although undoped, these films are conducting due to the deficiency of oxygen; typically, their undoped conductivity is

on the order of 1.0 (Ω-cm)⁻¹. This conductivity can be further increased by doping with Group V elements, such as phosphorus (1), antimony (2-6), and arsenic (7).

This paper describes the effect of phosphorus doping upon the conductivity of tin oxide films. An anomalous feature of this doping behavior is that the conductivity

* Electrochemical Society Active Member.
Key words: doping, oxidation, films.

increases with phosphorus content until it reaches a maximum value, and then rapidly falls with further phosphorus doping. Similar behavior has been observed in Sb-doped (6-9) and As-doped SnO_2 (7). However, no detailed explanations have been previously given for this phenomenon.

Here, we show that the change in conductivity behavior of phosphorus-doped tin oxide films is related to their transition from the crystalline to the amorphous state, as demonstrated in a companion paper (10). The separate contributions of mobility and carrier concentration have been determined in this work, and the transport properties of the films related to the change in these parameters with phosphorus concentration.

Experimental

Tin oxide films were prepared on glass microscope slides, oxidized silicon, and on semi-insulating GaAs wafers. The results were essentially the same, and are presented here only with specific reference to films made on oxidized silicon substrates. Films were grown at 450°C with typical gas flow rates of 50 ml/min oxygen and 16 ml/min argon flow through a TMT bubbler. Phosphine gas, diluted in argon, was used to dope the films as described earlier (10).

The mobility and carrier concentration of these films were measured by using bridge samples in a Hall effect apparatus. These samples were obtained by coating the SnO_2 layer with silicon dioxide at 450°C , followed by conventional photolithographic delineation of the oxide. This oxide was used as a mask for etching the SnO_2 layer using either an electrochemical technique (11) or a hot $\text{HBr} + \text{Cr}$ solution (10). Ohmic contacts were made to the arms with silver epoxy, followed by curing at 100°C for 1 hr. The temperature dependence of electrical conductivity, carrier concentration, and Hall mobility were studied between 96° and 373°K . Hall voltages were measured by applying a magnetic field of 4.5 KG.

Results and Discussion

A number of phosphorus-doped tin oxide films were made on this program with a variety of crystalline and amorphous substrates. The results that follow are outlined for one specific set of films, labeled A-H for ease of reference.

Conductivity.—Both undoped and phosphorus-doped tin oxide films were found to be n-type. Undoped SnO_2 with conductivity ranging from 0.5 to 5 $(\Omega\text{-cm})^{-1}$ could be obtained by varying the oxygen to TMT ratio. Increasing the oxygen flow while keeping constant TMT flow results in films with low conductivity. This suggests that conduction of undoped films arises from the lack of stoichiometry, *i.e.*, an oxygen deficiency.

The addition of Group V elements increases the conductivity of SnO_2 films. In this work, phosphine gas was introduced during the growth of SnO_2 for this purpose. Since the ionic radius of P^{5+} (0.35\AA) is different to that of Sn^{4+} (0.71\AA), the introduction of phosphorus into SnO_2 leads to the replacement of some Sn^{4+} ions by P^{5+} ions. This results in the formation of a new donor level, and enhances the conductivity of the films. The rest of the phosphorus is incorporated in the film in inactive form. In all probability, this takes the form of phosphorus-oxygen polyhedra, because of the strength of the P—O bond and the network former character of phosphoric oxide.

Figure 1 shows the change in conductivity as a function of PH_3/TMT mole ratio. The conductivity with no phosphine flow (film A) was 0.9 $(\Omega\text{-cm})^{-1}$. As mentioned in the preceding paper (10), microprobe analysis has indicated the presence of a small amount of residual phosphorus in the undoped films. This was always present, in spite of repeated flushing of the system with argon. Thus, this conductivity

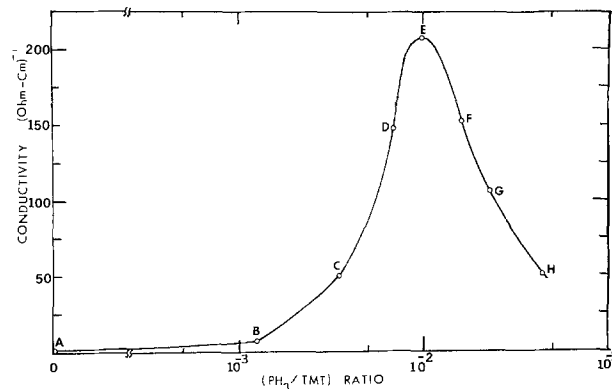


Fig. 1. Conductivity vs. PH_3/TMT mole ratio

value is partly due to the contribution of phosphorus, as well as the oxygen deficiency.

The conductivity of doped films increased with the introduction of phosphorus, reaching a maximum of 210 $(\Omega\text{-cm})^{-1}$ for a PH_3/TMT mole ratio of 0.01 (film E). Increasing the flow rate beyond this point resulted in a rapid drop in conductivity. This is contrary to what is expected from the controlled valency mechanism.

X-ray diffraction data showed that films A-E were polycrystalline, whereas films F-H were amorphous. Thus, the unusual behavior of conductivity is related to this change in film state.

Carrier concentration.—Figure 2 shows the carrier concentration as a function of the amount of phosphorus incorporated in the film. Note that the undoped SnO_2 film already has a high carrier concentration ($\approx 1.5 \times 10^{18}/\text{cm}^3$). This has been attributed to the combined contributions of the residual phosphorus and the oxygen deficiency. The introduction of phosphorus leads to a further increase of this carrier concentration. At high phosphorus concentration, the carrier density approaches saturation. As a result, the rapid drop in conductivity is primarily due to changes in the electron mobility of these films.

It is important to note that a Hall effect measurement of a nonsingle crystalline sample only gives an effective value of carrier concentration, n_{eff} , which is at best a measure of the barrier to current flow through it. Nevertheless, an estimate of the actual carrier concentration can be made by consideration of the theory of current flow in polycrystalline films (12). Films of this type consist of small grains joined together at grain boundaries. These grain boundaries represent a transition region between crystallites of different orientation, and have a large defect density due to incomplete bonding. Current transport between crys-

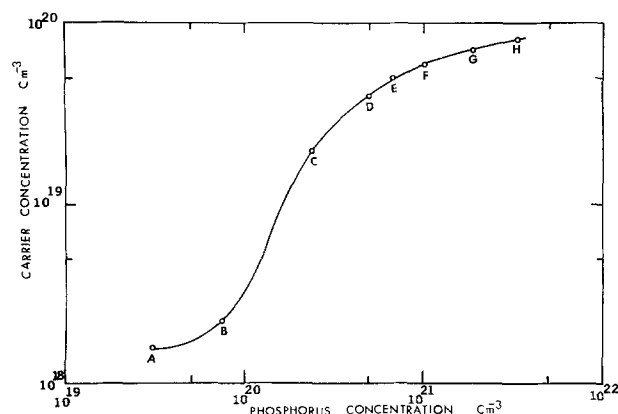


Fig. 2. Effective carrier concentration vs. phosphorus concentration.

tallites is impeded by these defects which capture mobile carriers. This creates a potential barrier between crystallites, and reduces the effective mobility. Using this model, it can be shown that the effective barrier height initially increases with doping concentration until all the traps are filled. Further increase in the doping concentration reduces the potential barrier height and therefore increases the mobility. At very high doping levels there is an additional (apparent) reduction of barrier height due to tunneling effects.

Figure 3 shows the temperature dependence of n_{eff} , from 96° to 373°K. We note that film E is the most heavily doped polycrystalline film and should have the lowest value of barrier height at the grain boundaries. Assigning (for the present) a value of $E_b = 0$ to this film, the actual carrier concentration within the grain is found to be $5 \times 10^{19}/cm^3$. The phosphorus content, however, is $6.5 \times 10^{20}/cm^3$. Thus, approximately 7.7% of this phosphorus is active for this film while the rest is probably incorporated in the form of phosphorus-oxygen polyhedra.

From Fig. 3 it is seen that there are two slopes for the lightly doped SnO₂ films (A and B), and donor levels can be associated with each. One level has been assigned to the oxygen vacancy, and has a slope corresponding to about 0.1 eV below the conduction band. The other level is assigned to the phosphorus impurity, which is at the conduction band edge. As expected, the level attributed to oxygen was not observed in films grown at increasing phosphine flow rates.

Mobility.—Figure 4 shows the room temperature Hall mobility as a function of the phosphorus concentration. This mobility was found to increase as the ratio of PH₃/TMT was increased, while keeping TMT flow constant. The highest mobility value, 26 cm²/Vsec, was observed for a phosphorus concentration of $6.5 \times 10^{20}/cm^3$. Note that films (A-E) were polycrystalline up to this point.

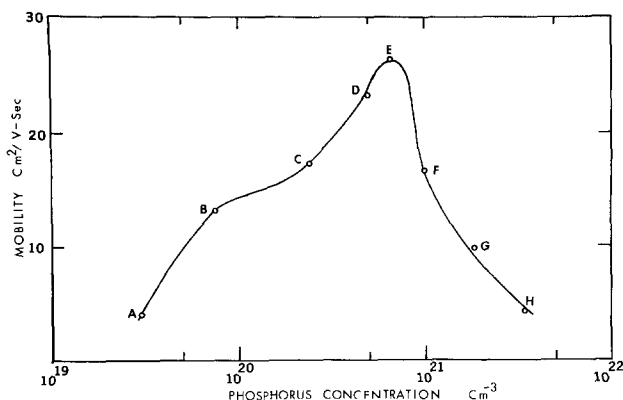


Fig. 4. Effective mobility vs. phosphorus concentration

Further increasing the phosphine flow rate produced a rapid drop in mobility as the films became amorphous (F-H). Since the carrier concentration increases monotonically with increasing phosphine flow rate, the drop in conductivity is primarily due to the fall of this parameter. The mobility behavior of these films can be explained by considering these two types of behavior separately and recognizing that the Hall effect measurements give only an effective value of mobility.

Films A-E.—These are polycrystalline with a grain size of about 370Å. Here, the conductivity increases monotonically with PH₃/TMT mole ratio. This increase is due to the enhancement of both the n_{eff} and μ_{eff} . Again invoking the model for current transport in polycrystalline material, this effective mobility can be expressed as

$$\mu_{eff} = A T^{-1/2} \exp(-E_b/kT)$$

where E_b is the potential barrier height and A is a function of the grain size and the effective electron mass. A plot of $\ln(\mu_{eff} T^{1/2})$ vs. $1/kT$ should yield a straight line with a slope of E_b . Figure 5 shows that our experimental results fit this expression very well. Therefore, it is concluded that grain boundary trapping effects dominate carrier transport in the polycrystalline SnO₂ films.

From this figure, the barrier height for film E is obtained as 7 meV. Thus, the previous assumption that it was negligible is a reasonable one, in view of the crude nature of the calculation.

The model for current transport in polycrystalline films also predicts that

$$E_b = \frac{q N_t^2}{8 \epsilon N}$$

where N is the doping concentration in the grain, and N_t the trap density per unit area at the interface between grains, and $\epsilon \approx 9$ for tin oxide. For highly doped films with low barrier height, $n_{eff} \approx N$. For these films, the $E_b n_{eff}$ product should be constant, and can be used to calculate the trap density per unit area. Results are shown in Table I, where the $E_b n_{eff}$ product is reasonably constant for films C-E, so that these assumptions are justified.

Films F-H.—In this region the films are amorphous and the above model is no longer applicable. We note that the carrier concentration is still high, and that the drop in conductivity at high PH₃/TMT ratio is due to the fall in electron mobility, and results from a transition to the amorphous state.

In noncrystalline material, the lowest states in the conduction band are "localized" because of fluctuations of potential due to disorder (13, 14). There is a con-

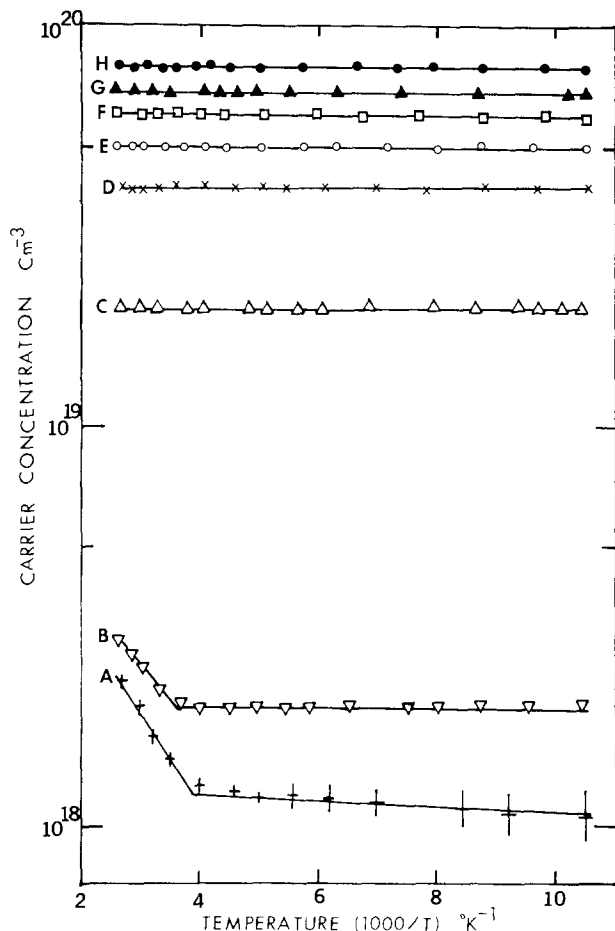
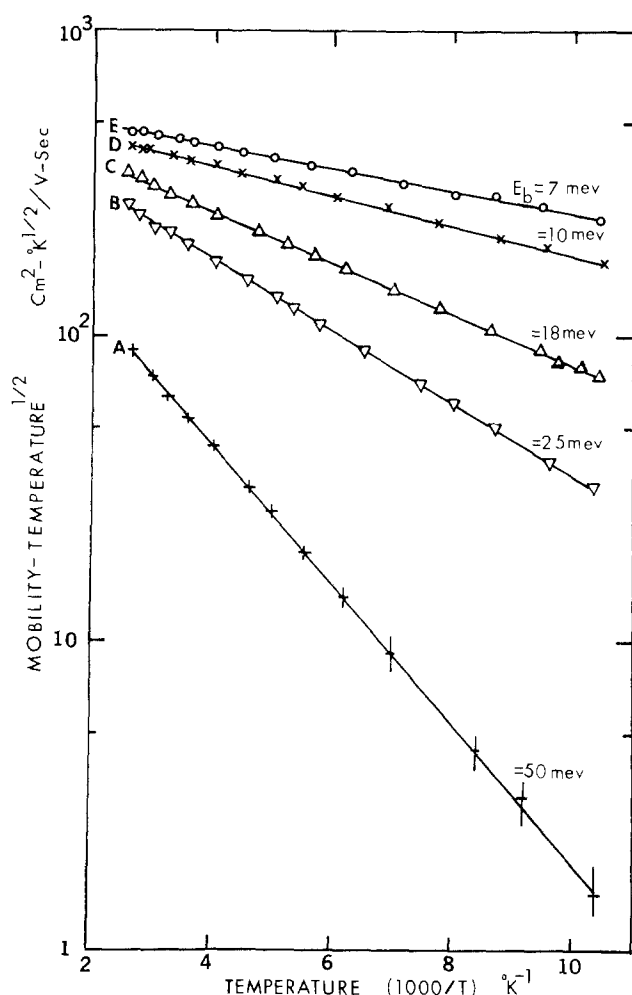


Fig. 3. Effective carrier concentration vs. temperature

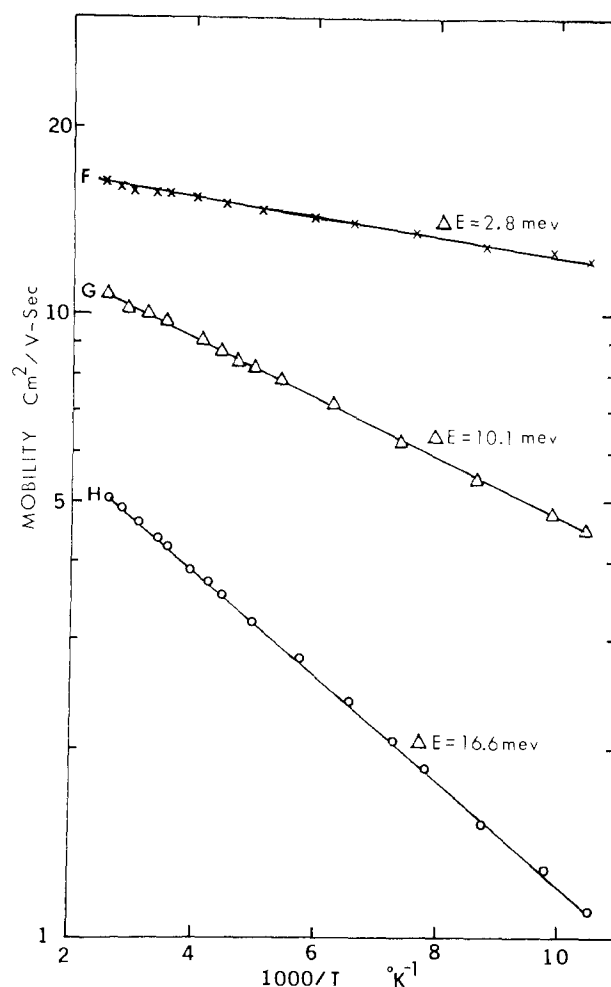
Fig. 5. $\mu_{\text{eff}} T^{1/2}$ vs. temperature

tinuous range of such localized states from the bottom of the band up to a critical energy E_c' (the mobility edge), which separates the high mobility region in the extended states from the low mobility region in the localized states. What one expects for this situation is that charge transport is by "hopping" from one localized state to another at low temperatures. Typically, the range of operation of hopping behavior is between 1° to 20°K. At higher temperatures, current is carried by electrons excited to the mobility edge; to a first order, the effective mobility will vary as $\mu_0 \exp(-\Delta E/kT)$, where ΔE is the difference between E_c' and Fermi level E_F .

This model has been verified for amorphous doped SnO_2 in the higher temperature range. Figure 6 shows the effective mobility from 96°-373°K plotted as a function of $1/T$. The linear relation between $\ln \mu_{\text{eff}}$ and $1/T$ indicates that band conduction of electrons excited above E_c' dominates the contribution to the conductivity over this range.

Conclusions

In a companion paper, we noted that tin oxide films undergo a rapid transition from the polycrystalline to

Fig. 6. μ_{eff} vs. temperature

the amorphous state, once a critical level of phosphorus doping is exceeded. Here, it is shown that the transport properties of these films exhibit a correspondingly abrupt change in behavior. The behavior has been explained in terms of established models for polycrystalline and amorphous films, and is shown to fit these theories quite well. In addition, we have explained the anomalous, abrupt falloff in conductivity at high doping levels, as well as its temperature behavior. The barrier height to current flow has been shown to be small (~ 7 meV), in the heavily doped polycrystalline films, and about 7.7% of the incorporated phosphorus is shown to be electronically active. It is presumed that the rest is in shielded form as phosphorus-oxygen polyhedra.

Acknowledgments

The authors wish to thank R. Rafun and A. Hayner for assistance in manuscript preparation. This work was supported by Contract No. XI-9-8000-1 from the Solar Energy Research Institute, Golden, Colorado.

Manuscript submitted Aug. 17, 1979; revised manuscript received Feb. 21, 1980.

Any discussion of this paper will appear in a Discussion Section to be published in the June 1981 JOURNAL. All discussions for the June 1981 Discussion Section should be submitted by Feb. 1, 1981.

Publication costs of this article were assisted by Rensselaer Polytechnic Institute.

REFERENCES

1. B. J. Baliga and S. K. Ghandhi, *This Journal*, **123**, 941 (1976).
2. K. Ishiguro, T. Sasaki, T. Arai, and I. Imai, *J. Phys.*

Table I

Film	E_b (cm ⁻³)	n_{eff} (cm ⁻³)	$E_b n_{\text{eff}}$	N_t (cm ⁻²)
A	0.05	1.6×10^{18}	8×10^{16}	?
B	0.025	2.3×10^{19}	5.75×10^{17}	?
C	0.018	2×10^{19}	3.6×10^{17}	3.78×10^{12}
D	0.01	4×10^{19}	4×10^{17}	3.99×10^{12}
E	0.007	5×10^{19}	3.5×10^{17}	3.73×10^{12}

- Soc. Jpn.*, **13**, 296 (1958).
 3. R. E. Aitchison, *Aust. J. Appl. Sci.*, **5**, 10 (1954).
 4. J. A. Aboaf, V. C. Marcotte, and N. J. Chou, *This Journal*, **120**, 701 (1973).
 5. V. K. Miloslavskii, *Opt. Spectrosk.*, **7**, 154 (1959).
 6. R. Muto and S. Furuuchi, Rept. Res. Lab. Asahi Glass Co., **23**, 27 (1973).
 7. Y. S. Hsu and S. K. Ghandhi, *This Journal*, **126**, 1434 (1979).
 8. C. A. Vincent, *ibid.*, **119**, 515 (1972).
 9. A. F. Carroll and L. H. Slack, *ibid.*, **123**, 1889 (1976).
 10. Y. S. Hsu and S. K. Ghandhi, *ibid.*, **126**, 1434 (1979).
 11. B. J. Baliga and S. K. Ghandhi, *ibid.*, **124**, 1059 (1977).
 12. J. Y. W. Seto, *J. Appl. Phys.*, **46**, 5247 (1975).
 13. N. F. Mott and E. A. Davis, "Electronic Processes in Non-Crystalline Materials," Clarendon Press, Oxford (1971).
 14. J. Tauc, "Amorphous and Liquid Semiconductors," Plenum Press, New York (1974).

Transient Phenomena in Ion Sensitive Field Effect Transistors

Rosemary L. Smith and Jiří Janata*

Department of Bioengineering, University of Utah, Salt Lake City, Utah 84112

and Robert J. Huber

Department of Electrical Engineering, University of Utah, Salt Lake City, Utah 84112

ABSTRACT

The electrical time response of ion sensitive field effect transistors to an applied step change in bias voltage is examined. The results show that ISFET time response is determined by the ion selective membrane and the conditions at the associated interferences. Lateral charge distribution at the membrane/insulator interface and its effect on time response is discussed. An understanding of the transient characteristics of ISFET's is advantageous in designing systems where bias voltages are switched, i.e., multiplexing and telemetry.

The ion sensitive field effect transistor (ISFET) is one of the family of chemically sensitive semiconductor devices which has been the object of considerable research and development (1). Structurally, the ISFET is an insulated gate field effect transistor (IGFET) in which the metal gate is replaced by an electrochemical structure consisting of a reference electrode, electrolyte solution, and an ion sensitive membrane. A change in the chemical environment to which the membrane is exposed or in the applied electrical voltages will cause a change in the electrical potential at the membrane/transistor interface. This change is directly related to the charge distribution in the semiconductor, which is reflected in a change in current. The time required to reach equilibrium following a change in applied voltage is examined in this study.

The time response of an IGFET is determined by its gate impedance and the transit time of charge carriers in the channel. For a MOSFET, the small values of these factors give typical time constants of 10-100 nsec. The transient characteristics of ISFET's with various membranes depend on four processes: relaxation of the space charge of the membrane at the solution/membrane interface, the bulk impedance of the membrane, the relaxation of space charge at the membrane/insulator (or metal) interface, and the time response of the insulator/semiconductor structure (2). The time constant of the MOSFET indicates that the last impedance is the lowest and can be neglected. Therefore, the time response of an ISFET will be a function of the membrane and its associated interfaces, which can be modeled by a series of parallel combinations of capacitors and resistors.

A series of experiments has been conducted to provide initial data on the relaxation time of different ISFET's. A voltage step method was used in order to obtain a rapid survey of the transient behavior of the

membranes used on our transistors. However, this technique is not readily suitable for the assignment of time constants to the appropriate physical processes. The measurement of the real and imaginary parts of the impedance at various frequencies (Cole-Cole plots) was found to be most suitable for that purpose (3).

The possible effects of potential variation along the channel of an ISFET on charge distribution at the membrane/insulator interface has been suggested by Zemel (4). By making step changes in both the drain and the gate voltages of ISFET devices, these effects were observed.

Experimental

Devices.—The fabrication and principles of operation of ISFET's have been described previously (1). The devices tested in this study can be divided into four groups according to their gate structure. The first type is the MOSFET. Second is the bare gate silicon nitride ISFET which has been shown to be pH sensitive (5, 6). The third group consists of ISFET's with homogeneous polymeric membranes. Calcium ion, K⁺, and H⁺ sensitive membranes of this type were used. The characteristics and method of fabrication of these devices have been reported (7).

The fourth group consists of ISFET's with heterogeneous membranes (8), sensitive to Cl⁻ and I⁻.

The transistors were tested for their chemical response before they were used for transient electrical characteristic studies.

Other equipment.—A Tektronix TM-503/FG-501 function generator was used to produce a symmetrical square wave with variable amplitude, bias, and frequency. The rise time of this signal was on the order of 50 nsec.

A double junction Ag/AgCl (saturated KCl) reference electrode (METROHM EA-437) was used for solution (gate) biasing of the ISFET's. Distilled de-ionized water and reagent grade chemicals were used

* Electrochemical Society Active Member.

Key words: field effect transistors, interface, charge distribution.

in all experiments. All measurements were made at an ambient temperature of $22^\circ \pm 2^\circ\text{C}$.

The drain current was measured by connecting the source lead of the ISFET to the input of an OP AMP electrometer and tracing the output voltage on a Tektronix 7623-A storage oscilloscope. An oscilloscope camera was used to photograph the tracings. The apparatus used to measure transient response is illustrated in Fig. 1.

The Princeton Applied Research Electrochemistry System was used to obtain the steady-state I - V characteristics.

Results

The voltages which are applied to an ISFET device establish the equilibrium charge and potential distribution in the device. This distribution determines the measured drain to source current, I_D . The experimental procedure consisted of making step changes in either of the applied voltages (V_G or V_D) while measuring I_D as a function of time.

The ISFET's were biased as shown in Fig. 1 with the substrate and the source kept at zero volts. The gate voltage was maintained above threshold for all measurements to insure that the time response measured would not include the time required to form an inversion layer in the device. A square wave was used to generate the applied step changes in drain or gate voltage. To measure the response to changes in gate voltage (V_G) a square wave with an amplitude of approximately 500 mV was added to the gate bias voltage while holding the drain voltage constant at 2V. To measure the response to changes in drain voltage (V_D) a square wave with amplitude of approximately 1.5V was added to the drain bias voltage while holding V_G constant. The d-c biasing of the drain and gate were such that the value of I_D was always within the operating range generally used for these devices which is from 0.25 to 1.0 mA.

Typical applied voltage waveforms and the corresponding changes in I_D are shown in Fig. 2 with definitions of the measured parameters: τ_{V_G} , τ_{V_D} , and overshoot. The curves in Fig. 2 show the response to a voltage pulse applied to the drain (a) or to the gate (b), respectively.

As seen in Fig. 2, the current response to a step change in V_G is different than that to a step change in V_D . When V_G is stepwise increased, I_D increases monotonically to its final steady-state value with a time constant of τ_{V_G} . When V_D is increased stepwise, I_D increases to a value greater than its final steady-state value, thus producing an overshoot. It then decays with a time constant of τ_{V_D} . When these two time constants are compared they are found to be nearly identical for any one particular device (see Fig. 3). The time constants of each device are independent of

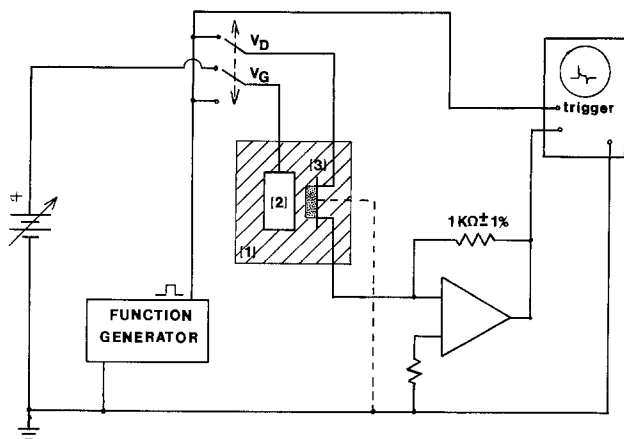


Fig. 1. ISFET biasing and measuring apparatus. (1) ionic solution, (2) reference electrode, (3) ISFET.

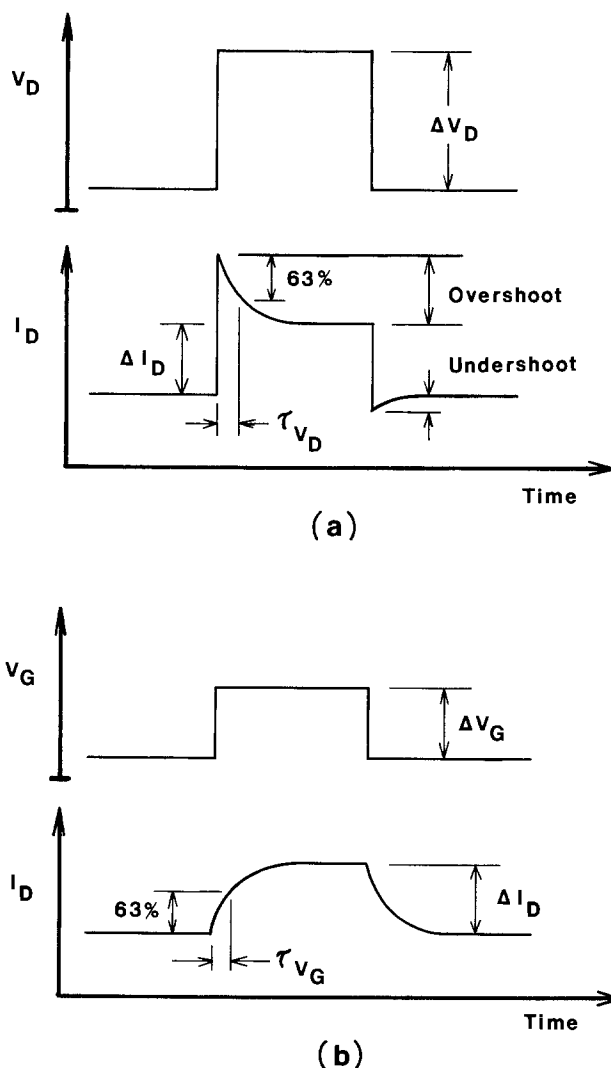


Fig. 2. Definition of terms. (a) ISFET current response to step changes in drain voltage; (b) ISFET current response to step changes in gate voltage.

whether an increasing or decreasing step change in voltage is made. The time response data for all devices is enumerated in Table I.

During the course of study it was found that a symmetrical pulse applied to V_D produced a nonsymmetrical degree of overshoot in comparison to undershoot of I_D . Since I_D is a nonlinear function of V_G and/or V_D , the degree of overshoot will be a function of initial bias, size, and direction of the V_D step. Evidence of this was seen in ISFET's when a train of pulses with increasing pulse height was applied to the drain of a Cl^- ISFET. The resulting I_D showed an increasing degree of overshoot with step size. The applied waveform and resulting drain current are shown in Fig. 4.

The interposition of an electrically floating layer between the insulator and membrane reduced the overshoot for all membranes and affected the time response of most. The results obtained from time response measurements made with gold gate devices provided some insight into the effects of interfacial conditions on the time response of ISFET's. The presence of gold drastically reduces the time response of the heterogeneous membranes (I^- and Cl^-) and slightly increases that of the homogeneous membranes (Ca^{++} , K^+ , and H^+) (Table I).

The time response measured for bare gate and MOSFET devices were three to four orders of magnitude less than that measured for membrane devices. Comparing each type of membrane reveals a time constant hierarchy; the devices with homogeneous PVC

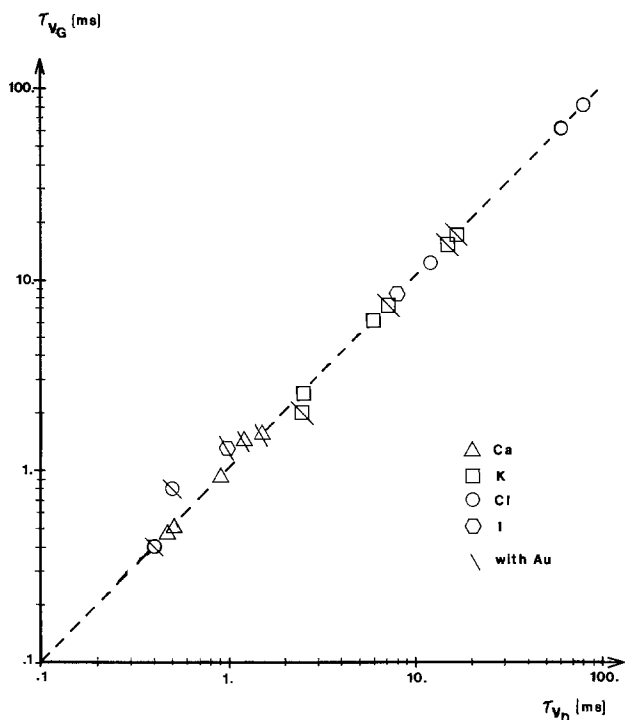


Fig. 3. Log-log plot of the time response to a step change in gate voltage (τ_{V_G}) vs. the time response to a step change in drain voltage (τ_{V_D}) of various ISFET's.

based membranes (Ca^{++} and K^+) were found to have the shortest time constants, followed by those with heterogeneous membranes and finally those with pH membranes.

Discussion

The characteristic current response to pulsed gate or drain voltages of ISFET's can be explained in terms of the lumped parameter model shown in Fig. 5. According to IGFET theory, the drain current is determined by the effective gate voltage (i.e., the voltage at the insulator/membrane interface), the drain voltage, and the geometry of the semiconductor structure (9). The model represents a cross-sectional segment of an ISFET in which the drain voltage is assumed con-

Table I. Time response data for various MOSFET and ISFET gate structures

Device	Device No.	Gold (μm)	$\tau_{\Delta V_G}$ (msec)	$\tau_{\Delta V_D}$ (msec)	Over-shoot (mA)*
MOSFET	1	Aluminum gate	1.0×10^{-4}	1.0×10^{-4}	0.0
	2	Gold gate	1.0×10^{-4}	1.0×10^{-4}	0.0
Bare Si nitride	3	—	1.0×10^{-3}	1.0×10^{-3}	0.0
	4	1.0	1.8×10^{-3}	1.0×10^{-3}	0.0
Calcium membrane	5	—	0.45	0.47	0.75
	6	—	0.5	0.5	0.75
	7	—	0.9	0.9	0.80
	8	1.0	1.4	1.2	0.15
	9	1.0	1.5	1.5	0.20
	10	—	2.5	2.5	0.80
Potassium membrane	11	—	6.0	6.0	0.60
	12	1.0	16.0	16.0	0.40
	13	1.0	15.0	15.0	0.40
	14	10.0	2.0	2.5	0.45
	15	10.0	7.0	7.0	0.45
Iodide membrane	16	—	7.5	7.5	0.75
	17	—	18.0	18.0	0.45
	18	1.0	1.3	1.0	0.20
Chloride membrane	19	—	12.0	12.0	0.40
	20	—	60.0	60.0	0.75
	21	—	80.0	80.0	0.5
	22	1.0	0.4	0.4	0.18
	23	1.0	0.8	0.5	0.24
	24	—	150.0	200.0	0.75
pH membrane	25	1.0	400.0	400.0	0.4
	26	10.0	400.0	400.0	0.38

* For step increase in V_D .

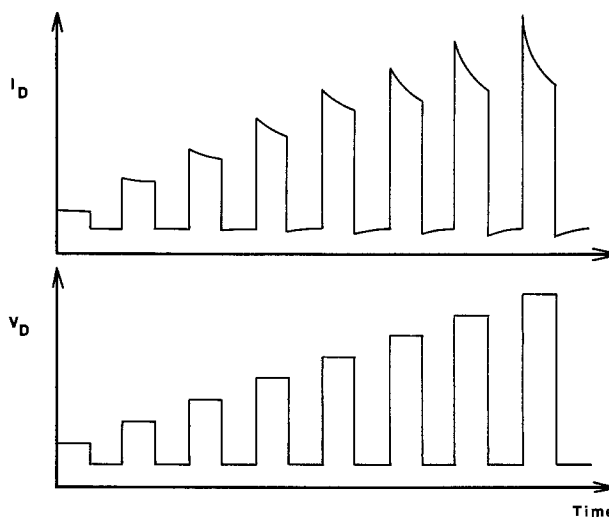


Fig. 4. ISFET current response to consecutively increasing step changes in drain voltage.

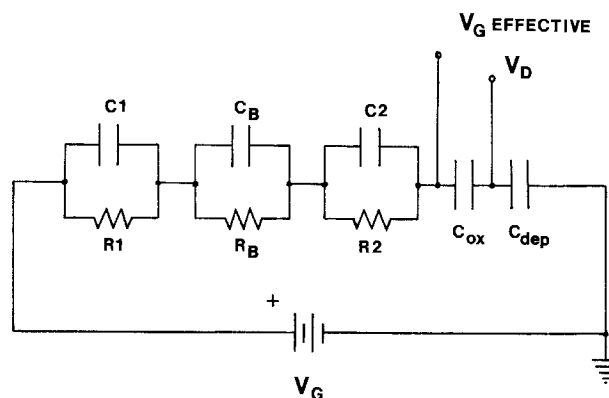


Fig. 5. ISFET lumped parameter model. $R_1 \parallel C_1$ represents the membrane/solution interface impedance; $R_2 \parallel C_2$ represents the membrane/insulator interface impedance; $R_B \parallel C_B$ represents the membrane bulk impedance, where $C_B \gg C_1, C_2$.

stant during steady-state conditions. When the applied gate voltage is increased stepwise, the effective gate voltage is also increased stepwise to a value determined by the capacitor divider network of C_1 , C_2 , and C_{ox} while V_D remains constant. For ISFET's this increase is small due to the large value of C_{ox} compared to C_1 and C_2 . As the voltage across C_1 and C_2 decreases due to R_1 and R_2 , the effective gate voltage continues to increase until the applied gate voltage appears across C_{ox} . In response to the change in effective gate voltage, the drain current increases and reaches its final steady-state value with a time constant characteristic of the membrane and the interfacial impedances. From the V_G-I_D curve of a typical ISFET in Fig. 6(a), the magnitude of change in I_D can be estimated as a function of device parameters. If V_G is stepped from A to B, I_D will increase from A' to B'. The time constant of the response measured was found to be independent of step size or direction which is further evidence that it is determined by the membrane and associated interfaces.

When the drain voltage is pulsed, the response in I_D is more complex. A step increase in V_D will be capacitively coupled through C_{ox} to the gate resulting in a stepwise increase in the effective gate voltage of approximately the same amount. The resulting change in drain current will be a large stepwise increase to a value which can be estimated by the V_D-I_D curves of the device which are shown in Fig. 6(b). If V_D is stepped from C to D, and V_G also initially increases approximately the same amount, I_D will go from C' to D'.

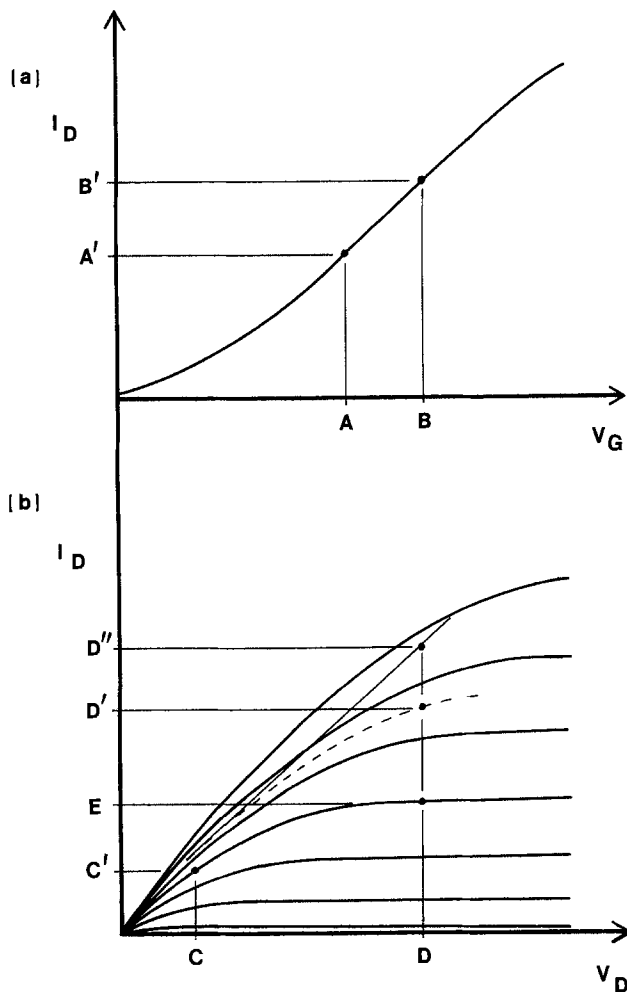


Fig. 6. Typical ISFET I-V characteristics. (a) I_D vs. gate voltage (V_G); (b) I_D vs. drain voltage (V_D).

As the increase in effective gate voltage is dissipated through the membrane model network of R_1C_1 and R_2C_2 , and the effective gate voltage returns to the value of V_G which is applied, I_D decays with a time constant determined again by the membrane impedance. The final value of I_D is determined by the value of V_G applied and the new final value of V_D as indicated by E in Fig. 6(b). The difference between the values of I_D at D' and E is the overshoot defined in Fig. 2 (a).

We have found that interposition of gold between the membrane and the insulator of CHEMFET devices reduces the overshoot of the current response to a step increase in V_D (Table I, devices No. 8, 9, 12-15, 18, 22, 23, 25, and 26). The reduced overshoot of the gold devices cannot be explained solely by the CHEMFET model in Fig. 5. It should be remembered that the model is of an incremental section of the device and does not take into account the fact that V_D varies from drain to source as a function of y or distance from the source. A schematic diagram of the overall channel and the section (dy) considered in the model is shown in Fig. 7. From this figure, it can be seen that in order to represent the entire channel, a series of models could be connected by a lateral impedance with a different V_D at each node. The initial explanation of overshoot assumes an equipotential at the membrane/insulator interface in a lateral direction. This must be true in steady state for equilibrium conditions to be met at the interface. However, if the lateral impedance at the membrane/insulator interface is large, a lateral distribution in potential will be initially formed there in response to a step change in V_D . This potential distribution will match that which is formed along

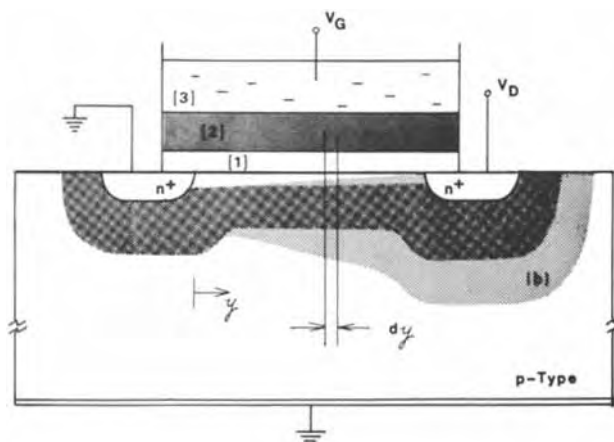


Fig. 7. An ISFET cross section indicating an incremental length along the channel (dy) where V_D may be assumed constant. The space charge and channel geometry for (a) $V_D < V_{Dsat}$ and (b) $V_D \cong V_{Dsat}$ are shown. (1) insulator, (2) membrane, (3) solution.

the insulator/semiconductor interface. During this initial state, the field across the insulator does not change and therefore the channel resistance will remain approximately the same. The expected response in I_D will be a step increase which can be illustrated on the V_D - I_D curves if the slope of the curve is kept constant, as shown in Fig. 6(b) from C' to D". From D" I_D will decay back to E with a decay time determined by the longer of two relaxation times—one in the vertical direction and the other in the lateral direction. Assuming the membrane is an isotropic material, the impedance over any unit length will be the same in all directions. Therefore, the time response measured will be the same as that which was measured for a step change in V_G .

When a layer of gold or any conducting material is placed between the membrane and the insulator, the effect is to short out the lateral interfacial potential distribution. When a step increase is applied to V_D , the effective gate voltage will uniformly increase, independent of position along the channel. The field across the insulator then will not remain constant and the channel resistance will increase. The current overshoot will therefore be less, and can be estimated in the manner described for the sectional model.

This hypothesis was tested using a series of MOSFET's connected as shown in Fig. 8. Two tests were performed. In the first test, R_L was eliminated and the gates were shorted together. This corresponds to the devices with a gold layer as described above. In the second test, R_L was made very large (10 M Ω).

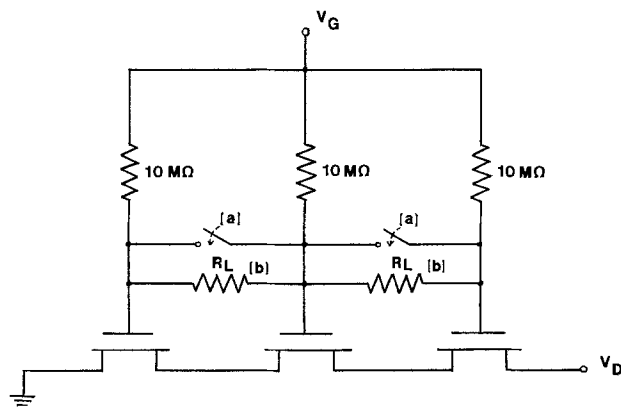


Fig. 8. Electrical circuit used to model effects of lateral potential distribution in the channel on time response of ISFET's (a) with and (b) without gold at the membrane/insulator interface.

When a step increase was made in V_D , an overshoot was observed which was approximately 40% larger than in the first test. This difference in overshoot is comparable to that which was measured on ISFET's (see Table I).

As stated earlier, current overshoot was reduced for all membrane devices when gold was introduced at the membrane/insulator interface. The time response, however, was not always reduced. Instead, it was membrane dependent (see Table I). This suggests that the effect on time response of the gold layer is not due to the change in lateral charge distribution but rather is dominated by the change in the vertical impedance at the interface. This change in impedance is represented by a change in the value of R_2 and C_2 in the lumped parameter model. Whether the impedance increases or decreases will depend on the properties of the gold/membrane interface.

Conclusion

The results of this study show that the time response of an ISFET is determined by membrane and gate structure. There are several applications of ISFET's where electrical time response information is important. Multisensor operation is one example. If several devices were to be operated in the same solution simultaneously, multiplexing of bias voltages may be necessary. The maximum rate of multiplexing would be determined by the number and types of membranes used.

Another application is in ISFET telemetry systems where power consumption is a major concern. To conserve power, switching of bias voltages to low values after sampling may be desired. The time response of the devices will then determine the maximum sampling rate possible.

Acknowledgment

The authors gratefully acknowledge the support for this work from NIGMS Grant Number 22952.

Manuscript submitted Oct. 19, 1979; revised manuscript received Jan. 21, 1980.

Any discussion of this paper will appear in a Discussion Section to be published in the June 1981 JOURNAL. All discussions for the June 1981 Discussion Section should be submitted by Feb. 1, 1981.

Publication costs of this article were assisted by the University of Utah.

REFERENCES

1. J. Janata and R. J. Huber, *Ion-Sel. Electrode Rev.*, **1**, 31 (1979).
2. R. P. Buck, in "Ion-Selective Electrodes in Analytical Chemistry," Vol. 1, H. Freiser, Editor, Chap. 1, Plenum Press, New York (1978).
3. J. Mertens, P. Van Den Winkel, and J. Vereecken, *Bioelectrochem. Bioenerg.*, **5**, 699 (1978).
4. J. N. Zemel, Discussion in "Theory, Design, and Biomedical Applications of Solid State Chemical Sensors," P. W. Cheung, D. G. Fleming, W. H. Ko, and M. R. Neuman, Editors, p. 50, CRC Press, West Palm Beach, Florida (1978).
5. T. Matsuo and K. D. Wise, *IEEE Trans. Bio-Med. Eng.*, **bme-21**, 485 (1974).
6. S. D. Moss, J. B. Smith, P. A. Comte, C. C. Johnson, and L. Astle, *J. Bioeng.*, **1**, 11 (1977).
7. P. T. McBride, J. Janata, P. A. Comte, S. D. Moss, and C. C. Johnson, *Anal. Chim. Acta*, **101**, 239 (1978).
8. B. T. Shiramizu, J. Janata, and S. D. Moss, *ibid.*, **108**, 161 (1979).
9. A. S. Grove, "Physics and Technology of Semiconductor Devices," Wiley, New York (1967).

Conduction Properties of Chemically Deposited Polycrystalline Silicon

T. Yoshihara, A. Yasuoka, and H. Abe

Mitsubishi Electric Corporation, LSI Development Laboratory, Itami, Hyogo 664, Japan

ABSTRACT

The relation between the conduction properties of the polycrystalline silicon films and process parameters such as the dose of implanted impurities, the deposition temperature, and heat-treatment were investigated. The doping concentration in polycrystalline silicon film was precisely controlled by ion implantation techniques. The trapping state density at the grain boundary which was the most important factor for the conduction properties of polycrystalline silicon was calculated using the doping concentration and experimentally obtained potential barrier height. It was found that the trapping state densities were $3.5 \times 10^{12}/\text{cm}^2$ for the boron-implanted polycrystalline silicon deposited at 700°C, and $5.2 \times 10^{12}/\text{cm}^2$ for the phosphorus-implanted polycrystalline silicon, respectively. The trapping state density was found to be reduced by increasing the deposition temperature or by the heat-treatment of the film at high temperature after the deposition of the polycrystalline silicon. It was also revealed that even a very small amount of oxygen caused the increase of the trapping state density.

Pyrolytic polycrystalline silicon has been widely used in silicon technology as gate electrodes, load resistors, and interconnections of silicon gate MOS devices, dielectric isolation, and polycrystalline silicon devices. Kamins (1) measured extensively Hall mobility of polycrystalline silicon films doped by a diffusion method and proposed the grain boundary trapping model in which the electrical conduction

properties of the polycrystalline silicon were determined by the potential barrier of the space charge region originated from the trapping of carriers at the grain boundary of the films. Seto (2) measured the dependence of Hall mobility on temperature and reported the trapping state density of about $3.3 \times 10^{12}/\text{cm}^2$ for the boron-implanted polycrystalline silicon films. In this paper, the relation between the electrical conduction properties of the polycrystalline sili-

Key words: conduction, impurity, deposition.

con films and the dose of implanted impurities, the deposition temperature, heat-treatment and so on, will be described by observing the trapping state density.

Experimental

Polycrystalline silicon films of 0.5 μm in the thickness were deposited on silicon dioxide films thermally grown on silicon wafers by the thermal decomposition of silane diluted in hydrogen ambient at atmospheric pressure at a deposition temperature between 700° and 1050°C. The deposition of the polycrystalline silicon films was carried out using the vertical-type reaction system (Model AMV800), in which an rf heated carbon susceptor was used and gas was injected vertically. Boron (B) or phosphorus (P) impurities whose doses were from $4 \times 10^{13}/\text{cm}^2$ to $1 \times 10^{15}/\text{cm}^2$ were implanted into the as-grown polycrystalline silicon films at 50 keV and 80 keV in energy, respectively. In some experiments, the annealing of the as-grown polycrystalline silicon films was carried out in nitrogen ambient in the temperature range from 700° to 1180°C before ion implantation. B or P-implanted polycrystalline silicon films were annealed to activate these impurities in the films at 1100°C for 30 min in nitrogen ambient. The resistors were fabricated by a process flow shown in Fig. 1. The value of the resistivity was obtained from the Ohm's law region of I - V characteristics of the resistors, because, in the case of lightly doped polycrystalline silicon films, I - V characteristics deviated from the Ohm's law at the region of high electric field (3).

Experimental Results and Discussion

Trapping state density.—In Fig. 2 is shown the activation energy obtained from the slopes of logarithmic plot of resistivity vs. $1/kT$ for B or P-implanted polycrystalline silicon films as a function of the doping concentration N_d , whose value is calculated by dividing the total dose by the thickness of the polycrystalline silicon films. Since the thickness of the polycrystalline silicon is 0.5 μm , the value of the doping concentration N_d is from 8×10^{17} to $2 \times 10^{19}/\text{cm}^3$. It is noticed from Fig. 2 that the activation energy E_a is inversely proportional to the doping concentration N_d .

This experimental result can be interpreted by the grain boundary trapping model proposed by Kamins (1), Seto (2), and other authors (4) as described in the following.

The other model concerning the electrical properties of polycrystalline silicon is the segregation model (5), according to which the grain boundary acts as a sink for impurity atoms due to impurity segregation. It is described by Seto (2) and Baccarani *et al.* (5);

Sample Preparation

- o silicon wafer
- o oxidation (1 μm)
- o polycrystalline silicon deposition (0.5 μm)
- o (heat treatment)
- o ion implantation (B or P)
- o annealing (1,100°C or 1,000°C for 30 min. in N_2)
- o photolithography (polycrystalline silicon)
- o SiO_2 deposition (430°C, 0.8 μm)
- o photolithography (SiO_2 etching for contact window)
- o B or P diffusion (970°C for Ohmic contact)
- o metallization (Al)
- o photolithography (Al)

Fig. 1. Process flow chart of the sample preparation

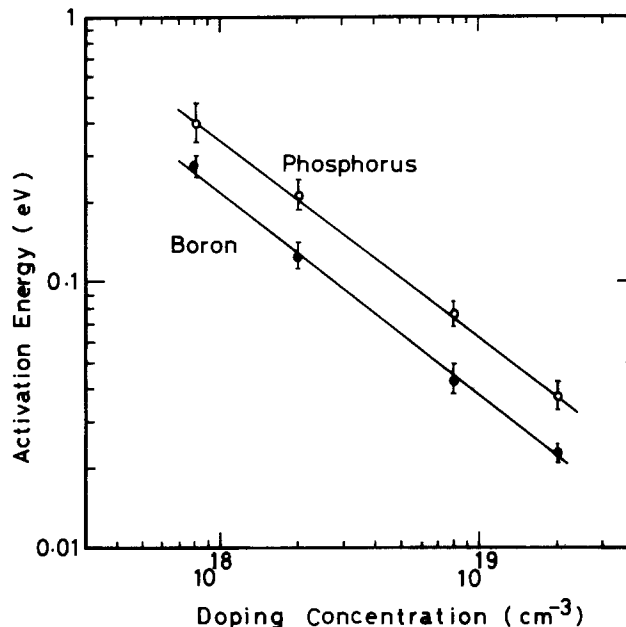


Fig. 2. The relation between the activation energy E_a of the B or P-implanted polycrystalline silicon and doping concentration N_d .

the limitation of this model is that it cannot explain the temperature dependence of resistivity of films which exhibit a negative temperature coefficient.

According to the grain boundary trapping model, there exist a large number of trapping states at the grain boundary in the polycrystalline silicon film. These trapping states are supposed to result from the incomplete atomic bondings. A space charge region is formed in the film by trapping free carriers, then a potential barrier is generated.

The height of this potential barrier can be obtained by solving the Poisson's equation under the appropriate boundary conditions. In our measurement of the resistivity of the films, as the applied voltage to the films is low, most of the measured current that flows across the grain boundary is expected to be caused by the thermionic emission over the potential barrier.

Seto (2) presented two kinds of the expressions for the resistivity due to the thermionic emission current across the grain boundary depending on the doping concentration.

In case I, in which the crystallite is partially depleted, that is, $LN_d > N_t$, where N_d is the doping concentration, N_t is the trapping state density, and L is grain size, the resistivity and the activation energy E_a can be written as follows

$$\rho = \frac{kT}{q^2 L N_d V_c} \exp(E_a/kT) \quad [1]$$

$$E_a = \phi = q^2 N_t^2 / 8 \epsilon N_d \quad [2]$$

where ϕ is the potential barrier height at the grain boundary and equal to the activation energy E_a in this case, V_c is the collective velocity, and ϵ is the permittivity of silicon.

In case II, in which the crystallite is completely depleted the trapping states are partially filled, that is, $LN_d < N_t$, the resistivity ρ and the activation energy E_a are written as follows

$$\rho = \frac{2kT(N_t L N_d)}{q^2 L^2 N_c N_d V_c} \exp(E_a/kT) \quad [3]$$

$$E_a = \frac{1}{2} E_g - E_t \quad [4]$$

where E_t is the energy level of the trapping state referred to the intrinsic Fermi level, N_c is the effective

density of state, and E_g is the bandgap energy. In this case, the potential barrier height ϕ is given by

$$\phi = q^2 L^2 N_d / 8\epsilon \quad [5]$$

which is proportional to the doping concentration N_d .

The experimental result that the resistivity depends exponentially on $1/kT$ can be interpreted by Eq. [1] or [3], because the temperature dependence of the term preceding the exponential term in the equations is small.

The result shown in Fig. 2 that the activation energy is inversely proportional to the doping concentration corresponds to Eq. [2], and then the crystallite is found to be partially depleted for the range of the doping concentration in our experiment. Thereafter, this experimental result is considered to mean that the activation energy E_a is equivalent to the potential barrier height ϕ at the grain boundary in the films.

Among the factors which relate to the potential barrier height as shown in the Eq. [2], the trapping state density is the most important one, because it determines the characteristics of polycrystalline silicon, while the doping concentration can be varied intentionally by changing the ion implantation dose.

The trapping state density at the grain boundary can be obtained from the Eq. [2] using the doping concentration N_d and the measured potential barrier height ϕ . In calculating the trapping state density, the amount of atoms which segregate at the grain boundary is assumed to be small for the range of doping concentration in this experiment (2, 4). The calculated trapping state density N_t are $3.5 \times 10^{12}/\text{cm}^2$ for B-implanted polycrystalline silicon and $5.2 \times 10^{12}/\text{cm}^2$ for the P-implanted one, respectively. The difference of trapping state density between the B and P-implanted polycrystalline silicon is considered due to the difference of the energy level of the trapping state density in the energy band (6). The value of N_t $3.5 \times 10^{12}/\text{cm}^2$ for the B-implanted sample is in good agreement with the value reported by Seto for the B-implanted sample deposited at 650°C (2).

Deposition temperature.—The electrical properties of the polycrystalline silicon film as well as the growth rate depend on the deposition temperature. In this experiment, the deposition temperature was varied from 700°C to 1050°C . Figure 3 shows the dependence of the sheet resistivity on the deposition temperature.

The implanted dose of B is $1 \times 10^{14}/\text{cm}^2$. It is found that the sheet resistivity decreases as the deposition temperature is increased from 700°C to 1050°C (7).

The potential barrier height can be calculated from the dependence of the sheet resistivity on the measuring temperature. In Fig. 4, the relation between the trapping state density N_t obtained by using the Eq. [2] and the deposition temperature is shown. In Fig. 4, the potential barrier height is also shown. It is found from Fig. 4 that the trapping state density N_t decreases when the deposition temperature is increased. In this experiment, the value of trapping state density varies from 3.5×10^{12} to $2.0 \times 10^{12}/\text{cm}^2$ for the range of the deposition temperature from 700°C to 1050°C . These facts suggest that the incompleteness at the grain boundary of the grain boundary of the polycrystalline silicon can be improved by raising the deposition temperature.

It is probable the facts that the grain size becomes large (8) and the deposition rate is limited rather by the diffusion of the reactants than by the surface reaction (9) when the deposition temperature is increased are related to the decrease of the trapping state density.

Effects of heat-treatment.—In this experiment, the effects of the heat-treatment on the electrical characteristics of the polycrystalline silicon before ion implantation were investigated. The temperature of the

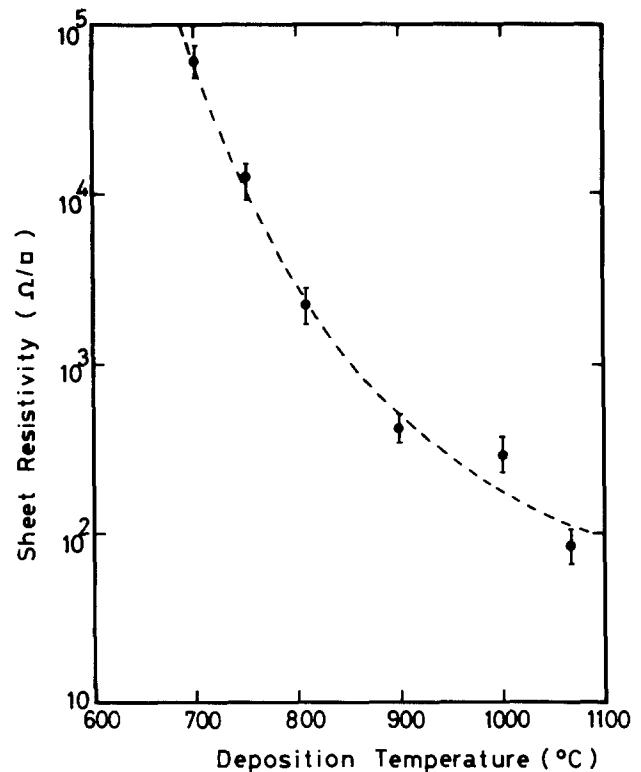


Fig. 3. Sheet resistivity of the B-implanted polycrystalline silicon as a function of deposition temperature. The implanted dose is $1 \times 10^{14}/\text{cm}^2$.

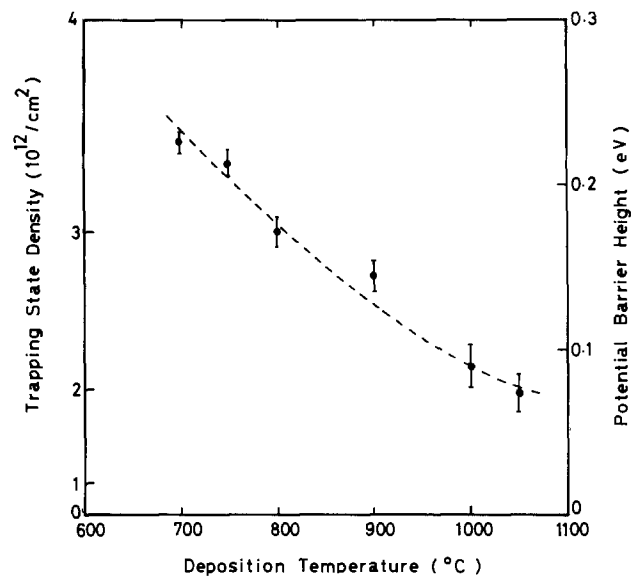


Fig. 4. Trapping state density and potential barrier height of the B-implanted polycrystalline silicon as a function of deposition temperature.

heat-treatment of the polycrystalline silicon films was varied from 700°C (as-grown) to 1180°C .

The annealing after ion implantation was carried out at 1000°C in nitrogen ambient for 30 min to distinguish the effect of the heat-treatment before ion implantation from that of the annealing by lowering the annealing temperature from 1100°C . The implanted dose of B was $1 \times 10^{14}/\text{cm}^2$. Sheet resistivity decreases similarly as in the case of increasing deposition temperature when the temperature of the heat-treatment is increased. The dependence of the trapping state density and the potential barrier height ϕ on the temperature of the heat-treatment of the polycrystalline silicon is illustrated in Fig. 5.

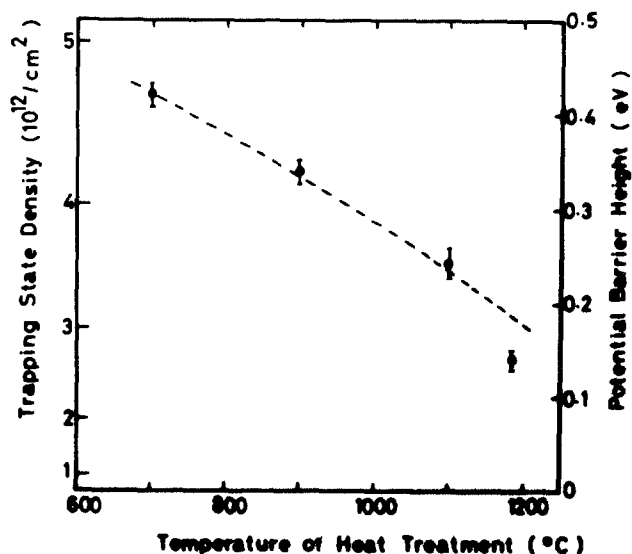


Fig. 5. Trapping state density and potential barrier height of the B-implanted polycrystalline silicon as a function of temperature of heat-treatment before ion implantation. The deposition temperature is 700°C, and the dose is $1 \times 10^{14}/\text{cm}^2$. The annealing is carried out at 1000°C for 30 min in N_2 .

It is observed that the trapping state density N_t decreases from 4.5×10^{12} to $2.6 \times 10^{12}/\text{cm}^2$ with increasing heat-treatment temperature up to 1180°C. It seems that the rearrangement of the polycrystalline silicon at grain boundary occurs and causes the decrease of the trapping state density by heat-treatment before ion implantation as well as in the case of increasing deposition temperature.

Influence of oxygen.—The influence of oxygen on the crystallographical structure (10) and the electrical properties of the oxygen-rich polycrystalline silicon (11, 12) have been reported. In this experiment, CO_2 gas was mixed in reaction gas in order to investigate the influence of oxygen on the trapping state density.

CO_2 gas flow rate was changed up to 425 sccm while the flow rate of 5% silane diluted by Ar was 2500 sccm and that of H_2 carrier gas was 45 slpm, respectively.

In Fig. 6, the sheet resistivity of the B-implanted polycrystalline silicon is plotted as a function of the CO_2 gas flow rate. The dose of B is $1 \times 10^{14}/\text{cm}^2$. It is observed that the existence of a small amount of oxygen causes the abrupt increase of resistivity. In Fig. 7 are shown the relation between the trapping state density and the CO_2 gas flow rate. It can be seen that the trapping state density increases abruptly similarly with the case of sheet resistivity. In the range where CO_2 gas flow rate is small, as the initial state of polycrystalline silicon is pure, so even a very small amount of oxygen has a serious effect on the electrical properties of polycrystalline silicon. When CO_2 gas flow rate is increased, the electrical properties of the polycrystalline silicon is considered to change to that of semi-insulating materials, and then the rate of increase of trapping state is thought to become small.

Conclusions

The electrical conduction properties of the pyrolytic polycrystalline silicon have been investigated by observing the trapping state density at the grain boundary. The doping concentration in the film was precisely controlled by the ion implantation techniques, and its range was from 8×10^{17} to $2 \times 10^{19}/\text{cm}^2$. For this range of the doping concentration, it is revealed that the activation energy E_a obtained from the temperature dependence of resistivity is inversely propor-

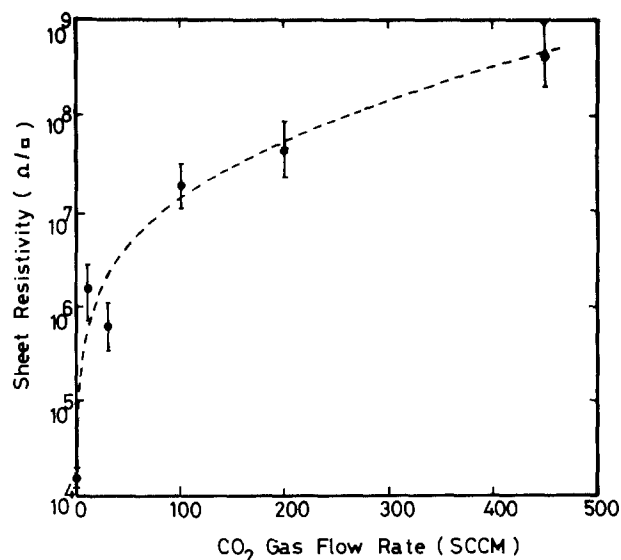


Fig. 6. The relation between sheet resistivity of the B-implanted polycrystalline silicon measured at 70°C and the flow rate of CO_2 gas mixed in reaction gas. The dose is $1 \times 10^{14}/\text{cm}^2$.

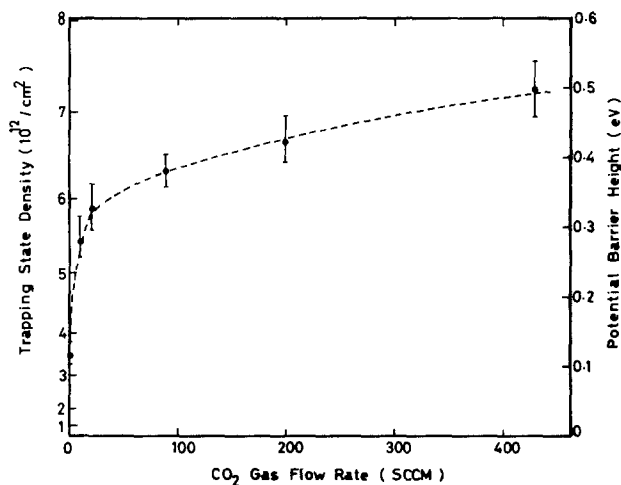


Fig. 7. Trapping state density and potential barrier height of polycrystalline silicon as a function of the flow rate of CO_2 gas.

tional to the doping concentration N_d and therefore the activation energy E_a is found to be equivalent to the potential barrier height ϕ at the grain boundary of the film. The trapping state density estimated from the potential barrier height is about $3.5 \times 10^{12}/\text{cm}^2$ for the B-implanted film and $5.2 \times 10^{12}/\text{cm}^2$ for the P-implanted film, respectively.

The trapping state density is found to be reduced by increasing the deposition temperature of the polycrystalline silicon film or by the heat-treatment of the film after deposition, which seems to be attributed to the decrease of the incompleteness of the bondings of silicon at the grain boundary in the film. It is also found that even a small amount of oxygen caused the increase of the trapping state density. The P-doped polycrystalline silicon films also exhibit the same behavior as the B-doped films as functions of deposition temperature, heat-treatment, and oxygen.

Acknowledgments

The authors would like to thank Drs. T. Nakano and M. Hirose for their encouragement and helpful discussions.

Manuscript submitted June 11, 1979; revised manuscript received Feb. 25, 1980.

Any discussion of this paper will appear in a Discussion Section to be published in the June 1981 JOURNAL. All discussions for the June 1981 Discussion Section should be submitted by Feb. 1, 1981.

Publication costs of this article were assisted by Mitsubishi Electric Corporation.

REFERENCES

1. T. I. Kamins, *J. Appl. Phys.*, **42**, 4357 (1971).
2. J. Y. W. Seto, *ibid.*, **46**, 5247 (1975).
3. G. J. Korsh and R. S. Muller, *Solid State Electron.*, **21**, 1045 (1978).
4. G. Baccarani, B. Ricco, and G. Spadini, *J. Appl. Phys.*, **49**, 5565 (1978).
5. M. E. Cower and T. O. Sedwick, *This Journal*, **119**, 1565 (1972).
6. M. Hirose, M. Taniguchi, and Y. Osaka, *J. Appl. Phys.*, **50**, 377 (1979).
7. F. C. Eversteyn and B. H. Put, *This Journal*, **120**, 106 (1973).
8. Y. Yasuda, M. Yamanaka, T. Moriya, and T. Yoshii, Paper 23 presented at the Electrochemical Society Meeting, Houston, Texas, May 7-11, 1972.
9. B. A. Joyce and R. R. Bradley, *This Journal*, **110**, 1235 (1972).
10. T. I. Kamins, *ibid.*, **121**, 68 (1974).
11. M. Hamasaki, T. Adachi, S. Wakayama, and M. Kikuchi, *Solid State Commun.*, **21**, 591 (1977).
12. M. L. Tarn, *J. Appl. Phys.*, **49**, 4069 (1978).

Infrared Absorption and Microstructure of Li-Saturated Si-Doped GaAs

R. T. Chen* and W. G. Spitzer

Departments of Materials Science and Physics, University of Southern California, Los Angeles, California 90007

ABSTRACT

Infrared absorption, free carrier density, and transmission electron microscopy measurements have been correlated for n-type Si-doped GaAs samples with $1 \times 10^{18} \text{ cm}^{-3} < [\text{Si}] < 5 \times 10^{19} \text{ cm}^{-3}$. The infrared absorption of the

localized vibrational modes was measured after the samples were compensated by e^- irradiation or by ^6Li saturation diffusion. Comparisons of the results of the two compensation methods indicate that: (i) the Li-native defect acceptor complex is responsible in large part for the compensation after a 750°C Li diffusion; (ii) the degree of the Si site transfer from Ga to As lattice sites as a result of the Li saturation diffusion at 950°C is a function of $[\text{Si}]$ and the Li-native defect donor is probably responsible for this transfer; (iii) samples that are heavily Si-doped have Si-rich faulted loops produced by a heat-treatment or Li diffusion at 750°C and this excess Si transfers to As sites if Li is diffused at 950°C ; (iv) absorption cross sections of the Li-native defect donor and acceptor bands can be determined which account for the compensation of the Li-diffused Si-doped samples and also fit previously published data for Li-saturated pure GaAs. There is also the suggestion that, at least in the nondiffused, nonannealed more heavily Si-doped material, not all of the Si shows up in the localized mode measurements even though there is no observable microstructure.

Results are presented here of an investigation of the behavior of Si and Li when they are simultaneously present as impurities in GaAs. This system is a complicated one since the behavior of either Si or Li when individually present as an impurity in GaAs is complex. However, a combination of optical, electrical, and microstructural measurements yields considerable insight into the nature of this double-doped system. In this study one observes clearly the influence of Li saturation diffusions in GaAs:Si at various temperatures on the concentrations of both Li and Si defects for a variety of Si concentrations. The presence of the Si inhibits the formation of certain Li-native defect complexes while the presence of the Li can cause the transfer of Si from one type of lattice site (Ga) to another (As). The measurements of compensated samples permit an estimate of the infrared absorption cross sections of the prominent localized vibrational mode (LVM) bands previously attributed to the two most important electrically active Li-native defect complexes.

The Si site transfer effect in Li-diffused GaAs:Si has been observed previously but was not studied in any detail (1). The present investigation demonstrates that the site redistribution is a function of Si concen-

tration. It also shows that the observed LVM absorption bands produced by Si-related defects in low temperature Li-diffused, heavily Si-doped samples do not account for all the Si. Transmission electron microscope (TEM) measurements of the heavily doped samples after Li diffusion reveal some microstructure which could account for the unobserved Si.

Background

Gallium arsenide doped with Si has been of particular interest in a number of studies because of the amphoteric behavior of the Si. Silicon substitution on a Ga site, Si_{Ga} , is a donor and on an As site, Si_{As} , is an acceptor. The distribution of Si on the two sublattices is known to vary with the Si concentration (2-4), the temperature of growth (2-7), the temperature and time of heat-treatment (8-12), the nature and concentration of other impurities (13-15), and the vacancy concentrations (1, 8-11). Electroluminescent (16) and photoluminescent (8-10) characteristics, LVM absorption band strengths (1-7, 11-15), and transport properties (17) of the GaAs:Si are dependent on the distribution of Si on the two lattice sites. Other Si defects such as $\text{Si}_{\text{Ga}}\text{-Si}_{\text{As}}$ nearest neighbor pairs and Si_{Ga} -native defect complexes have also been proposed and studied.

Lithium is an electrically active impurity in semiconductors and has been the subject of many investiga-

* Electrochemical Society Active Member.

Key words: infrared absorption, microstructure, gallium arsenide, silicon impurity, lithium diffusion.

tions for both technological and scientific reasons. While lithium behaves as an interstitial donor in the elemental semiconductors Si and Ge, it is self-compensating in GaAs. Lithium can form either donor or acceptor defects in GaAs and can be used electrically to compensate either n- or p-type material. The relative concentrations of the different Li defects are controlled by the initial concentrations of electrically active impurities and by the tendency for self-compensation. There has been a considerable volume of literature (2, 18-29) dealing with the detailed behavior of Li in pure and doped GaAs, and as a result of these studies a number of specific defect species involving Li either with native defects or paired with other impurities have been identified.

The earlier studies of the GaAs:Si + Li system arose because of the Li behavior as an electrical compensator. In order to make infrared measurements of the LVM absorption bands in GaAs:Si it is necessary to reduce the free carrier absorption. The free carriers are present because heavily doped GaAs:Si is strongly n-type when grown from a nearly stoichiometric melt. One of the methods used for carrier removal was compensation by Li saturation diffusion at an elevated temperature. For reference Table I summarizes all LVM bands observed in GaAs:Si + Li as deduced from a number of studies (1-7, 11-14, 25, 29-31). Table I gives the peak absorption frequency for each band measured at liquid nitrogen temperature and the defect responsible for the band, where X_A refers to the species X on the A sites. According to the theory of localized vibrational modes the integrated absorption for each band is proportional to the volume concentration of the defect species responsible for the band. We refer to the constant of proportionality as the absorption cross section; $\int_{\text{band}} d\nu/[X_A]$, where α is the absorption coefficient and $[]$ means concentration. The $\nu = 384$ and 399 cm^{-1} bands in Table I are due to Si_{Ga} and Si_{As} and their absorption cross sections have been established (3, 4). The $\nu = 389$ and 406 cm^{-1} bands are attributed to two electrically active ${}^6\text{Li}$ -native defect complexes, and the absorption cross sections for these bands are given in a later section of this work. These latter bands do not involve Si as they occur in Li-diffused undoped GaAs samples. The Si concentration does, however, play a significant role in determining the concentrations of these Li defect species. In Table I the band at $\nu = 367 \text{ cm}^{-1}$ has not been assigned to a specific defect. It was previously assigned to the ${}^{28}\text{Si}_{\text{Ga}}$ - ${}^{28}\text{Si}_{\text{As}}$ nearest neighbor pair defect, however, recent experimental evidence has led to the conclusion that this assignment is not correct (4, 32).

The electrical compensation of GaAs:Si which is necessary for the infrared studies has been accomplished by saturation diffusions of either Li or Cu at elevated temperatures, i.e., $700^\circ\text{C} < T_D < 1000^\circ\text{C}$, or

by penetrating particle irradiation, i.e., 1 to 2 MeV electrons or by neutrons (31). In a few cases partial compensation was achieved (6, 12) by counterdoping with a compensating impurity such as Zn during crystal growth. If one wants to study the distribution of Si among the various defects then a major difficulty of all the above procedures is that the compensation process may alter the Si distribution and even create Si-related defects which were not present in significant concentration prior to the compensation procedure. Ample evidence exists for such changes. Saturation diffusions of Li or Cu result in the formation of $\text{Si}_{\text{Ga}}\text{-Li}_{\text{Ga}}$ or $\text{Si}_{\text{Ga}}\text{-Cu}_{\text{Ga}}$ second neighbor pairs, and Li diffusion at $T_D > 900^\circ\text{C}$ can cause the transfer of substitutional Si from Ga to As sites (1). Also Li and Cu diffusions are done at temperatures, i.e., $T_D \gtrsim 400^\circ\text{C}$, and times for which major aging effects have been observed (11, 33), and these effects are attributed to changes in Si defect concentrations as well as the formation of new defects. The compensation by electron irradiation is frequently done with the sample maintained near liquid nitrogen temperature during the irradiation to reduce thermal annealing. Subsequently the sample is allowed to warm to room temperature. There is the concern that native defects introduced by the irradiation might pair with some of the Si defects and thus alter the defect concentrations (31). In one study (3) the irradiation was continued to fluences approximately five times that necessary to render the samples transparent at frequencies where there is little lattice or LVM absorption. Essentially no changes were observed in the absorption at the Si_{Ga} or $\text{Si}_{\text{Ga}}\text{-Si}_{\text{As}}$ LVM frequencies as a result of this extended irradiation fluence. Further measurements of the removal rate (31) for the Si_{As} band with increases in electron fluence indicate that for the total fluences used in the present study there should be no significant change produced in this band. As will be discussed the present measurements are in accord with this view. From the evidence available the e^- -irradiation method of compensation appears to be the least disturbing to the precompensation distribution of Si defects and in the present work it is assumed that the Si defect concentrations are the same as the precompensated values.

The site transfer of substitutional Si from Ga to As sites in GaAs has been inferred in several studies. Two reports (8, 9) describe thermally related photoluminescence changes introduced in n-type Si-doped GaAs. In one case the change was by heating heavily doped crystals ($n_e \approx 4 \times 10^{18} \text{ cm}^{-3}$) in hydrogen at 1050°C and the other case by heating lightly doped material ($n_e \approx 3 \times 10^{16} \text{ cm}^{-3}$) in evacuated quartz ampuls at 900°C . These two studies indicate that Si atoms may transfer from Ga to As sites via an As vacancy mechanism. One more recent photoluminescence measurement (10) of lightly doped GaAs:Si ($n_e \approx 3.3 \times 10^{16} \text{ cm}^{-3}$) which was annealed in vacuum at a temperature of 800°C has also resulted in the same conclusion. It was also reported (13, 15) that for heavily double-doped crystals of GaAs:Si + Te and GaAs:Si + Se, the effect of the Te or Se is to substantially enhance the fraction of the Si concentration, $[\text{Si}]$, which resides on As sites and thus to reduce the $[\text{Si}_{\text{Ga}}]$. The effect of redistribution of Si between substitutional sites induced by the saturation diffusion of Li at elevated temperatures has been previously observed (1) only for Si-doped GaAs with $n_e \approx 9.0 \times 10^{17} \text{ cm}^{-3}$ and was not studied in any detail.

In the present study a comparison is made of the LVM absorption and microstructure for identically doped samples compensated either by ${}^6\text{Li}$ diffusion or by e^- irradiation as well as comparing the influence of different diffusion temperatures on the degree of Si site transfer. These comparisons are made by using sets of identical samples for the different treatments. Different sets of samples are used to cover a range of values for n_e and $[\text{Si}]$.

Table I. A list of all observed LVM bands in ${}^6\text{Li}$ -diffused Si-doped GaAs

Mode frequency (cm^{-1})	Electrical character	Impurity	Defect
352	Acceptor Donor	${}^6\text{Li}$	${}^6\text{Li}$ -native defect complexes
389			
406			
410			
451			
470		${}^6\text{Li}_{\text{Ga}}$	$\text{Si}_{\text{Ga}}\text{-}{}^6\text{Li}_{\text{Ga}}$
480			
487			
374			
379	Donor	Si_{Ga}	Si_{Ga}
405		Si_{As}	Si_{As}
384	Acceptor	Si_{Ga}	Si_{Ga}
399		Si_{As}	Si_{As}
393		$\text{Si}_{\text{Ga}}\text{-Si}_{\text{As}}$	$\text{Si}_{\text{Ga}}\text{-Si}_{\text{As}}$
464			
367	?	—	Si-related defect

Experimental Method

The samples were taken from several horizontal Bridgman-grown ingots which were doped with different Si concentrations. Some ingots were single crystals while others were polycrystalline but with very large single crystal sections, *i.e.*, typical dimensions of centimeters. The samples were always taken from the single crystal regions. The total Si concentration was $1 \times 10^{18} \text{ cm}^{-3} < [\text{Si}] < 5 \times 10^{19} \text{ cm}^{-3}$ as estimated from the dopant added during crystal growth by using the known segregation coefficient and also from spectrochemical analyses. In a few cases the $[\text{Si}]$ was also measured by using an electron probe micro-analyzer.

All samples were first heat-treated at 1200°C for 1 hr and then quenched to room temperature, a process hereafter called HT + Q. The HT + Q treatment establishes a common thermodynamic background for all samples. It avoids some of the known and previously mentioned lower temperature aging effects for both the free carrier density, n_e and the Si defect concentrations. These aging effects are generally present in the as-grown material because of a cool-down cycle in the growth process. The carrier densities after HT + Q ranged from $1.0 \times 10^{18} \text{ cm}^{-3} < n_e < 8.0$

$\times 10^{18} \text{ cm}^{-3}$. The HT + Q procedure has essentially no effect on the n_e for material with $[\text{Si}] \lesssim 1 \times 10^{18} \text{ cm}^{-3}$ but it substantially increases n_e for samples with $[\text{Si}] \gtrsim 1 \times 10^{19} \text{ cm}^{-3}$. This procedure also significantly improves the microstructural quality of the material, particularly for the heavily Si-doped samples.

After the HT + Q treatment the free electron density of each sample was measured by determining the frequency of the free carrier plasma minimum observed in the infrared reflectivity. This method has been compared previously (34) with Hall measurement results and very good agreement was obtained. Before taking the measured n_e as the bulk value sufficient material was removed from the surfaces, ~ 0.1 mm, that the infrared reflectivity measurements of the plasma frequency indicated that further removal of material did not change the carrier density.

Several samples with nearly the same free carrier density were cut from the same section of each ingot and were divided into two groups. One group was compensated by e^- irradiation while the other group of samples was saturation diffused with ^6Li in an inert atmosphere, some at $T_D = 750^\circ\text{C}$ for 18 hr and others at $T_D = 950^\circ\text{C}$ for 2 hr. The diffusions were done with a "sandwich" arrangement in which the sample of interest was placed between two pure GaAs blocks which had previously been surface alloyed with ^6Li on the outer surfaces, *i.e.*, the surfaces not in contact with the sample to be diffused. This procedure substantially reduced the loss of material which occurs when the sample of interest is surface alloyed with Li directly. The details of the procedure used for the Li diffusions have been reported elsewhere (22). The samples of the first group were compensated by 1.4 MeV e^- irradiation while at temperatures $\lesssim 140^\circ\text{K}$ and with electron fluences of $\sim 1 \times 10^{19} \text{ e}^-/\text{cm}^2$.

The infrared absorption coefficient at liquid nitrogen temperature of the Li-diffused and the e^- -irradiated samples was measured. The spectral range covered was $350 \text{ cm}^{-1} < \nu < 500 \text{ cm}^{-1}$ which contains the frequen-

cies of all the absorption bands of interest in this study. The samples were generally about ~ 0.3 mm thick and had a wedge of $\sim 0.2^\circ$ to eliminate multiple reflection interference fringes. The absorption coefficient α was calculated from the transmission T by using the usual formula

$$T = I_{\text{sample}}/I_0 = (1 - R)^2 \exp(-\alpha x)/1 - R^2 \exp(-2\alpha x)$$

where R is the reflectivity and x is the sample thickness.

After the infrared transmission measurements all Si-doped samples, as well as some pure GaAs samples which had been saturation diffused with ^6Li , were used to prepare specimens for transmission electron microscope measurements (35). The TEM specimens were examined by a Hitachi HU-125C microscope operated at 125 kV. Measurements were also made of the HT + Q, Si-doped materials before Li diffusion as well as undoped samples and they were free of microstructure except for an occasional dislocation loop. In particular the samples showed no stacking faults or precipitates while the Si-doped samples which had not been given the HT + Q treatment, *i.e.*, in the as-grown condition, were found to have frequent extrinsic stacking faults, particularly those samples having the larger $[\text{Si}]$ (36).

Results and Discussion

In this section the results are presented in the following order:

1. The changes introduced by Li diffusion into GaAs: Si at 750°C are examined by comparison with e^- -irradiated samples. Some of the irradiated samples will have no prior annealing while others were thermally aged at 700°C prior to the irradiation.
2. A comparison is made of samples which have been Li-diffused at two different temperatures and the Li-induced Si transfer from Ga to As sites is examined including the $[\text{Si}]$ dependence of the transfer process.
3. The possible role of the known Li-native defect complexes in the Si site transfer process is explored.
4. The LVM absorption measurements of the Li saturation diffused GaAs:Si samples are used with other data to estimate the absorption cross sections of the two bands arising from the two electrically active Li defect complexes. These cross sections are then tested by applying them to previously reported LVM measurements of Li-saturated undoped GaAs.
5. TEM results for the microstructure of the Li-diffused samples are discussed and correlated to the LVM measurements and the Si site transfer observations.

Changes in defect structure and concentration resulting from ^6Li saturation diffusion at 750°C .—One of the primary purposes of the present study is to investigate the site transfer of Si in GaAs:Si which results from ^6Li saturation diffusions at an elevated temperature, *i.e.*, 950°C . This effect is demonstrated by direct comparisons with samples diffused at a lower temperature of 750°C where the transfer process is found to be negligible. However, before reviewing the data for the above comparison it is of interest to inquire first into the changes introduced by Li diffusion at 750°C as compared to the prediffused state. The LVM spectra of the prediffused state is taken to be that of the e^- -irradiated samples. As mentioned previously, the heavily doped GaAs:Si undergoes changes due to thermal aging at temperatures such as 750°C and therefore the effect of the diffusion on Si distribution could be the result of the 750°C diffusion temperature and/or the presence of a large Li concentration.

To demonstrate the changes three absorption curves are used, one for a sample which was Li saturated at 750°C , a second e^- irradiated, and a third annealed near 750°C and then e^- irradiated. These comparisons allow one to attribute the changes as due primarily to Li saturation or due to thermal annealing at the diffusion temperature.

Figure 1 shows the LVM absorption bands for three samples of nearly equivalent $[\text{Si}] \simeq 5 \times 10^{19} \text{ cm}^{-3}$ and $n_e \simeq 8 \times 10^{18} \text{ cm}^{-3}$ after the HT + Q treatment. Sample 7-a, see curve I, was compensated by ^6Li saturation diffusion at 750°C and sample WA-2-3 was electron irradiated, see curve II. The data for these

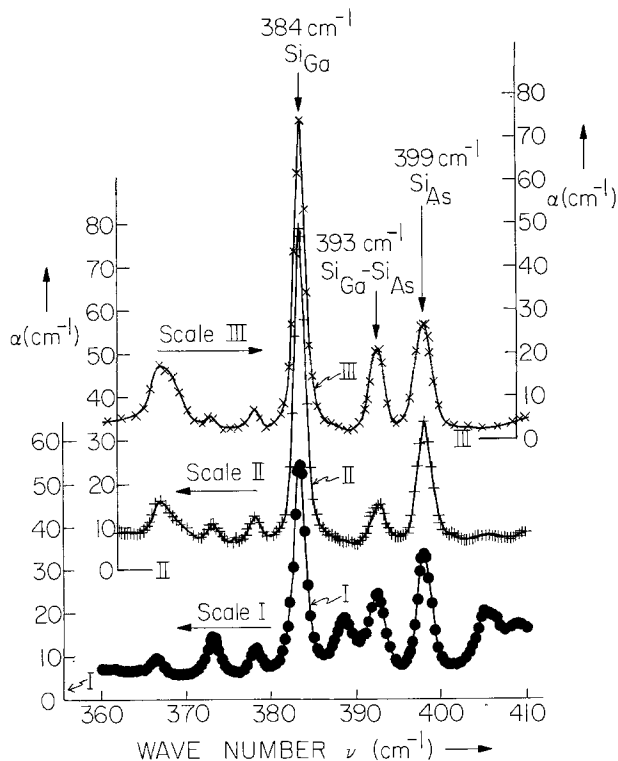


Fig. 1. Infrared absorption spectrum at liquid nitrogen temperature for three GaAs:Si samples having nearly equivalent $[Si] \approx 5 \times 10^{19} \text{ cm}^{-3}$ and with initial $n_e \approx 8 \times 10^{18} \text{ cm}^{-3}$ after $1200^\circ\text{C}/1 \text{ hr} + \text{quench}$ (see Table II). Curve I: sample 7-a, 750°C ^6Li diffused. Curve II: sample WA-2-3, compensated by e^- irradiation. Curve III: sample annealed at 700°C then compensated by e^- irradiation.

two samples including the integrated absorption ($\alpha_p \Delta$) of the LVM are among those of Table II, where α_p is the peak LVM absorption coefficient with the background removed and Δ is the bandwidth at half-maximum. Curve III of Fig. 1 is for the third sample which was annealed at 700°C before being compensated by electron irradiation. The $(\alpha_p \Delta)_{399}$ is the same for the three samples indicating that the $[Si_{As}]$ is independent of the compensation method or thermal aging as long as the temperatures involved are $\sim 750^\circ\text{C}$. The $Si_{Ga}-Si_{As}$ nearest neighbor pair band at 393 cm^{-1} is the same for the annealed sample and the diffused sample but they both are approximately twice the value for the nonannealed, nondiffused sample. This indicates that there is a substantial increase in $[Si_{Ga}-Si_{As}]$ for the diffused and annealed samples, and this increase is clearly a thermal effect rather than the result of the presence of a large $[Li]$. The $(\alpha_p \Delta)_{384}$ for the Si_{Ga} band of the annealed sample is 102.5 cm^{-2} which is below

the 117.3 cm^{-2} of the nonannealed sample, but significantly larger than the 78.3 cm^{-2} of the diffused sample. The decrease of $[Si_{Ga}]$ in the diffused sample therefore appears to be largely a combination of thermal aging and the formation of $(Si_{Ga}-Li_{Ga})$ pairs which give rise to the bands at 374 , 379 , and 405 cm^{-1} , see Table I and Fig. 1-curve I. Several other bands are observed in the absorption spectra of Fig. 1. The weak bands near 374 and 379 cm^{-1} in the nondiffused samples are due to the LVM of the $^{30}Si_{Ga}$ and $^{29}Si_{Ga}$ and they superimpose upon two of the $^{28}Si_{Ga}-Li_{Ga}$ bands, see curve I. The 367 and 369 cm^{-1} bands are poorly resolved and are related to unknown defects involving Si; see Ref. (4) for a discussion of these modes. The 389 cm^{-1} band in the diffused sample is due to a Li-native defect complex which is not Si related, see Table I.

These results necessitate a reinterpretation of some previously published data in which the samples were not given the HT + Q treatment prior to electron irradiation or ^7Li diffusion at 700°C (30). This prior comparison between Li diffusion and e^- irradiation was therefore between samples which had been thermally aged in an unknown temperature profile during the growth process. Therefore, the effective anneal temperature is unknown although a temperature zone of $\sim 800^\circ\text{C}$ was used after the growth zone.

A more complete comparison of the nonannealed, e^- -irradiated, and 750°C ^6Li -diffused cases for different $[Si]$ is given by the data of Table II. In all cases the absorption was measured at liquid nitrogen temperature. The data of Table II were taken from samples such as those in Fig. 1. The data for the irradiated samples were also used in Ref. (4) where they are discussed in detail. From Table II it is seen that the changes observed in Fig. 1 and the conclusions based on those changes appear to apply generally with larger changes being observed at higher $[Si]$. In particular, it can be concluded that the saturation diffusion of Li at 750°C produces no change in the concentration of Si_{As} acceptors, significant increases in the concentration of $Si_{Ga}-Si_{As}$ nearest neighbor pairs, and decreases in the concentration of Si_{Ga} donors with all changes being measured relative to the prediffused state. With this information we may now examine the changes which occur when the saturation temperature is increased.

Si site transfer induced by Li saturation diffusion.— Figure 2 and curve I of Fig. 3 show the absorption coefficient of three samples having different $[Si]$ which were ^6Li diffused at 950°C . Each of these samples is similar to one of those diffused with ^6Li at 750°C . The results of 750° and 950°C saturation diffusions of ^6Li are summarized quantitatively in Table III for pairs of initially similar samples. Comparisons indicate that the 384 and 399 cm^{-1} bands of the Si_{Ga} and Si_{As} , respectively, have changed their relative strengths while the other Si-related bands remain essentially unchanged. The 384 cm^{-1} band is reduced and the 399

Table II. Comparisons of LVM results for e^- irradiation and 750°C ^6Li diffusion

Sample No.	n_e^* (cm^{-3})	Compensation method	$(\alpha_p \Delta)_{384}$ (cm^{-2})	$(\alpha_p \Delta)_{393}$ (cm^{-2})	$(\alpha_p \Delta)_{399}$ (cm^{-2})	$(\alpha_p \Delta)_{369}^\dagger$ (cm^{-2})	$(\alpha_p \Delta)_{377}$ (cm^{-2})	$(\alpha_p \Delta)_{374}$ (cm^{-2})	$(\alpha_p \Delta)_{379}$ (cm^{-2})
KM-26-1	1.07×10^{18}	e^- irradiation	20.8	3.6	0	0	0		
1-a	1.0×10^{18}	$^6\text{Li}^{**}$ diffusion	18.1	5.7	~ 2	—	0	~ 1.2	~ 0.5
KM-16-3	5.4×10^{18}	e^-	79.1	31.2	8.4	1.0	6.4		
4-a	5.3×10^{18}	$^6\text{Li}^{**}$	59.1	30.8	18.5	—	1.8	11.6	8.6
KM-16-4	6.1×10^{18}	e^-	91.0	36.0	8.6	1.0	6.4		
5-a	5.7×10^{18}	$^6\text{Li}^{**}$	61.8	35.6	23.3	—	2.8	11.2	8.0
WA-Si-2-2	7.8×10^{18}	e^-	129.9	57.2	28.4	1.2	8.6		
6-a	7.7×10^{18}	$^6\text{Li}^{**}$	82.5	53.2	45.5	—	7.4	17.1	13.8
WA-Si-2-3	8.0×10^{18}	e^-	117.3	57.4	21.6	7.0	16.4		
7-a	8.0×10^{18}	$^6\text{Li}^{**}$	78.3	55.2	41.2	—	5.3	15.6	11.6

* Measured.

** ^6Li diffusion at 750°C for 18 hr.

† 369 cm^{-1} band only found in e^- -irradiated heavily doped sample.

— Not observed.

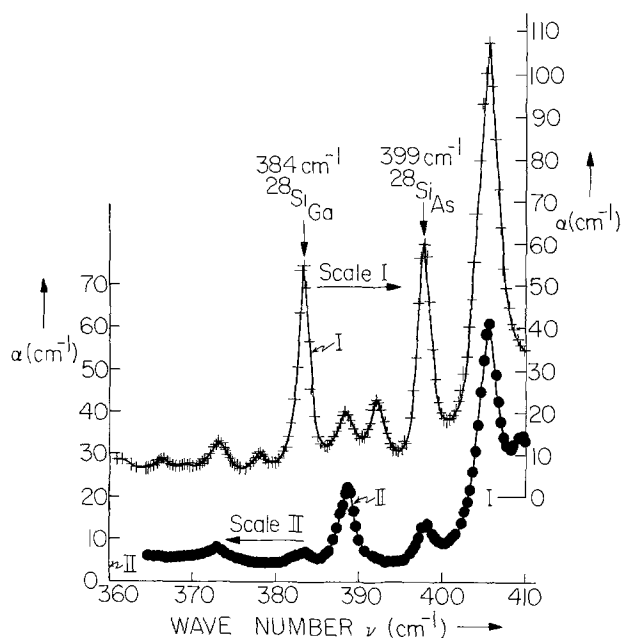


Fig. 2. Infrared absorption spectrum at liquid nitrogen temperature for two GaAs:Si samples having different [Si] and initial n_e ; both ^6Li diffused at 950°C for 2 hr. Curve I: sample 6-b ($n_e \approx 7.7 \times 10^{18} \text{ cm}^{-3}$). Curve II: sample 1-b ($n_e \approx 1.0 \times 10^{18} \text{ cm}^{-3}$).

cm^{-1} band enhanced for the higher diffusion temperature suggesting site transfer of Si from Ga to As sites has been produced. This relative decrease of the 384 cm^{-1} band after the higher temperature diffusion decreases with increasing [Si] while the relative increase for the 399 cm^{-1} band increases. The $\text{Si}_{\text{Ga}}\text{-Si}_{\text{As}}$ pair band strengths at 393 cm^{-1} are almost the same for two diffusion temperatures for each set of samples indicating that the large annealing-induced increase observed at 750°C does not continue with increased Li diffusion temperature. There is no consistent pattern of change and the observed changes are small between the two diffusion temperatures for all other bands.

One can examine site transfer hypothesis quantitatively if the absorption cross sections of the Si defect bands are known. In a recent study (4) the cross sections of Si_{Ga} , Si_{As} , and two other Si-related defect bands were measured for a number of melt-grown Bridgman, HT + Q samples having [Si] and n_e in the range of those used here. All samples were compensated by e^- irradiation. Assuming the $^{28}\text{Si}_{\text{Ga}}$ donor (384 cm^{-1} band), $^{28}\text{Si}_{\text{As}}$ acceptor (399 cm^{-1} band), and two other Si-related defects (367 and 369 cm^{-1} bands) to be electrically active defects then the reciprocal absorption cross sections were determined to be $a = 10.0$

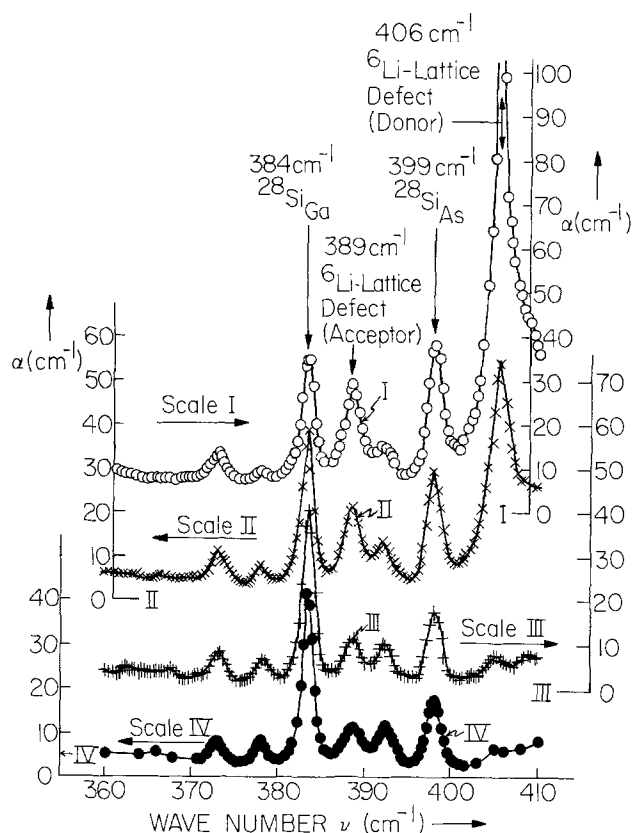


Fig. 3. Infrared absorption spectrum at liquid nitrogen temperature for four GaAs:Si samples having an identical initial $n_e \approx 5.3 \times 10^{18} \text{ cm}^{-3}$. All were ^6Li diffused and in one case subsequently outdiffused. Curve I: sample 4-b, $950^\circ\text{C}/2 \text{ hr}$ ^6Li diffused. Curve II: sample 4-c, $900^\circ\text{C}/3 \text{ hr}$ ^6Li diffused. Curve III: sample 4-a, $750^\circ\text{C}/18 \text{ hr}$ ^6Li diffused. Curve IV: sample 4-c, $900^\circ\text{C}/3 \text{ hr}$ ^6Li diffused + $700^\circ\text{C}/24 \text{ hr}$ ^6Li outdiffused.

$\times 10^{16} \text{ cm}^{-1}$, $b = 12.7 \times 10^{16} \text{ cm}^{-1}$, $c = 25.3 \times 10^{16} \text{ cm}^{-1}$, and $d = 19.0 \times 10^{16} \text{ cm}^{-1}$, where

$$n_e = a(\alpha_p \Delta)_{384} - b(\alpha_p \Delta)_{399} + c(\alpha_p \Delta)_{367} - d(\alpha_p \Delta)_{369} \\ = [\text{Si}_{\text{Ga}}] - [\text{Si}_{\text{As}}] + [\text{Si}]_{367} - [\text{Si}]_{369}$$

As indicated by the signs the charge status found for 367 and 369 cm^{-1} bands are donor and acceptor, respectively. For all of the Li-diffused samples shown in Table III the 369 cm^{-1} band is not observed and the 367 cm^{-1} band is always small and has almost no change in value at different diffusion temperatures. If one assumes that site transfer of Si_{Ga} to Si_{As} is the only mechanism responsible for the changes in the Si

Table III. Comparisons of LVM results of 750° and 950°C ^6Li diffusion measurements

Sample set No.	Sample No./T _D of ^6Li ($^\circ\text{C}$)	n_e^* (cm^{-3})	$(\alpha_p \Delta)_{384}$ (cm^{-2})	$(\alpha_p \Delta)_{399}$ (cm^{-2})	$(\alpha_p \Delta)_{367}$ (cm^{-2})	$(\alpha_p \Delta)_{369}$ (cm^{-2})	$(\alpha_p \Delta)_{374}$ (cm^{-2})	$(\alpha_p \Delta)_{389}$ (cm^{-2})	$(\alpha_p \Delta)_{406}$ (cm^{-2})
1	1-a/750	1.0×10^{18}	18.1	5.7	~2	0	~1.2	9.6	0
	1-b/950	1.0×10^{18}	6.4	17.8	~2	0	5.5	41.9	187.0
2	2-a/750	1.8×10^{18}	34.8	10.5	4.8	0	5.0	15.1	0
	2-b/950	1.8×10^{18}	26.3	20.0	~4.8	0	3.0	15.5	56.1
3	3-a/750	3.1×10^{18}	43.1	18.9	~8.0	0	9.9	21.6	0
	3-b/950	3.1×10^{18}	24.5	41.8	~8.0	0	6.8	44.5	221.7
4	4-a/750	5.3×10^{18}	59.1	30.8	18.5	1.8	11.6	23.0	0
	4-b/950	5.3×10^{18}	44.2	64.0	18.1	0	13.4	54.2	348.2
5	5-a/750	5.7×10^{18}	61.8	35.6	23.3	2.8	11.2	27.6	0
	5-b/950	5.7×10^{18}	47.0	71.4	22.4	0	12.5	54.2	343.2
6	6-a/750	7.7×10^{18}	82.5	53.2	45.5	7.4	17.1	34.6	0
	6-b/950	7.7×10^{18}	73.4	110.7	38.6	3.5	12.6	35.5	317.1
7	7-a/750	8.0×10^{18}	78.3	55.2	41.2	5.3	15.6	34.8	0
	7-b/950	8.0×10^{18}	88.2	92.0	42.0	6.2	15.9	35.0	184.1

* Measured values.

Table IV. The values of β calculated from Table III as a function of initial n_e

Sample set No.	n_e^* (cm ⁻³)	$\delta(\alpha_p\Delta)_{384}^{**}$ (cm ⁻²)	$\delta(\alpha_p\Delta)_{389}^{**}$ (cm ⁻²)	$\beta = \frac{-\delta(\alpha_p\Delta)_{384}}{\delta(\alpha_p\Delta)_{389}}$
1	1.0×10^{18}	-11.7	+12.1	+0.97
2	1.8×10^{18}	-8.5	+9.5	+0.89
3	3.1×10^{18}	-18.6	+22.9	+0.81
4	5.3×10^{18}	-14.9	+33.2	+0.45
5	5.7×10^{18}	-14.8	+35.8	+0.41
6	7.7×10^{18}	-9.1	+57.5	+0.16
7	8.0×10^{18}	+9.9	+36.8	-0.27

* Measured values.

** $\delta(\alpha_p\Delta) = (\alpha_p\Delta)$ at 950°C - $(\alpha_p\Delta)$ at 750°C.

band strengths of the isolated Si species, then one has $\delta[\text{Si}_{\text{Ga}}] = -\delta[\text{Si}_{\text{As}}]$ and thus

$$\beta = \delta(\alpha_p\Delta)_{384}/\delta(\alpha_p\Delta)_{389} = +b/a = +1.27$$

Table IV gives the values for β calculated from Table III and Fig. 4 gives β as a function of n_e . At the lower values of n_e most of the change is indeed accounted for by Si site transfer. However, as n_e and [Si] increase the value of β decreases and the change becomes progressively less due to $\text{Si}_{\text{Ga}} \rightarrow \text{Si}_{\text{As}}$. Since the other Si defect concentrations do not appear to change significantly, the large increases in $(\alpha_p\Delta)_{389}$ must be due to transfer of Si to Si_{As} from some state or states not detected by the LVM measurements made after 750°C Li diffusion. For the samples of largest [Si] this latter process dominates the change. From the TEM measurements mentioned previously it is known that there are no precipitates, inclusions, or extrinsic stacking faults in the pre-diffused samples. Later, TEM measurements will be presented of both 750° and 950°C Li-diffused samples which show that Si-rich loops form at 750°C and disappear at 950°C for the more heavily Si-doped material. Also GaAs:Si samples which were annealed at 900° and 1000°C and then e^- irradiated showed no evidence for the Si site transfer process. The large Li donor concentration present under the conditions of the high temperature saturation diffusion apparently enhances the formation of Si_{As} acceptors. One may thus conclude that site transfer of Si from Ga to As sites is indeed observed for the high temperature Li diffusion. The site transfer is not simply a thermal process, i.e., the presence of the Li is required. Comparisons between low and high tem-

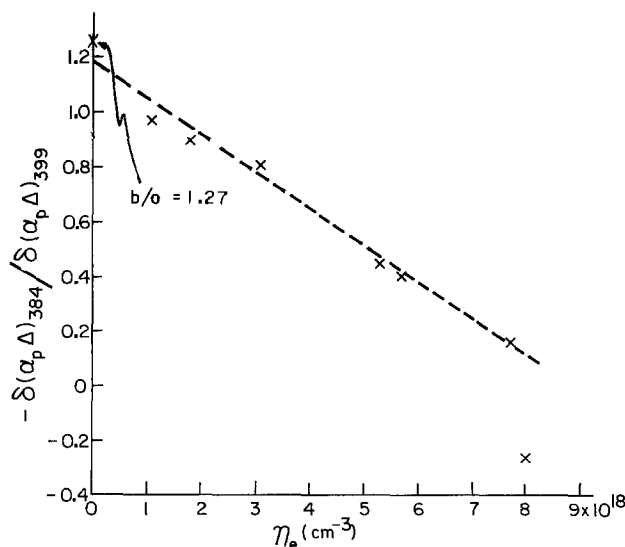


Fig. 4. A plot of $\beta = -\delta(\alpha_p\Delta)_{384}/\delta(\alpha_p\Delta)_{389}$ vs. initial n_e for all of the samples of Table IV. For site transfer only $\beta = 1.27$.

perature Li-saturated samples indicate that at the low [Si] almost all of the $[\text{Si}_{\text{As}}]$ gain for the high temperature case is the result of Si_{Ga} site transfer while at the highest [Si] almost all the $[\text{Si}_{\text{As}}]$ gain results from some other source of Si.

Possible role of Li-native defect complexes in Si site transfer.—From the preceding section we concluded that the presence of the Li was required to produce the site transfer and increase in $[\text{Si}_{\text{As}}]$. It is of interest to inquire whether one can detail in any way how the Li is instrumental in producing this effect and why the higher diffusion temperature is required.

The strengths of the Li-lattice defect complex bands induced by ^6Li diffusion of pure GaAs are very small for a low diffusion temperature (21), i.e., at $T_D \lesssim 750^\circ\text{C}$, and they increase monotonically with T_D . The 389 cm^{-1} (acceptor) and 406 cm^{-1} (donor) bands are known to be the only two bands induced by Li-lattice defect complexes which are electrically active. For pure GaAs the ratio $(\alpha_p)_{406}/(\alpha_p)_{389}$ is approximately 2 at higher diffusion temperatures, $T_D \gtrsim 800^\circ\text{C}$ (21, 22).

Examination of all absorption curves for ^6Li -diffused, Si-doped GaAs samples with different initial n_e and [Si] which were diffused at lower temperatures, i.e., $T_D \lesssim 750^\circ\text{C}$, indicates that the 389 cm^{-1} acceptor band is the only Li-lattice defect band observed with significant strength and it increases in samples with higher n_e and Si values as shown in Table V. This indicates that the growth of the 389 cm^{-1} Li-native defect acceptor band may be a significant factor in the compensation of Si-doped GaAs for the lower temperature diffusions. As a comparison this result is quite different from that of Li-diffused p-type GaAs for a similar diffusion temperature. In this latter case, no Li-lattice defect bands are observed. In particular the 389 cm^{-1} band is absent. The compensation is completely accomplished (28) by forming $\text{Li}_i\text{-Mg}_{\text{Ga}}$ (or $-\text{Zn}_{\text{Ga}}$, or $-\text{Cd}_{\text{Ga}}$, or $-\text{Mn}_{\text{Ga}}$) neutral pairs.

For the high temperature diffusion, $T_D \approx 950^\circ\text{C}$, the Li-lattice defect complex bands in the present samples have increased substantially. To illustrate this Fig. 3 shows the absorption curves for four GaAs:Si samples having a common origin and identical n_e values but ^6Li diffused or outdiffused at different temperatures. Comparisons between these curves indicate that the saturation concentration of Li increases due to a higher diffusion temperature, the 389 and 406 cm^{-1} Li-lattice defect bands both increase, however, the growth rate of 406 cm^{-1} Li-lattice donor band is much larger than that of the 389 cm^{-1} acceptor band. It is this donor formation which likely provides the mechanism producing Si acceptor formation by the transfer of Si to As sites from other defects. When Li is outdiffused at a lower temperature the absorption curve tends to return to the curve it would have if indiffused at that temperature; see curve IV of Fig. 3. In particular, the site transfer produced in a 900°C diffusion has reversed and the 406 cm^{-1} band has disappeared. Furthermore, a 950°C ^6Li rediffusion after a 750°C diffusion produces Si site transfer with similar LVM curves as a sample diffused initially at 950°C .

Table V. Comparison of the $(\alpha_p)_{389}$ values for all 750°C ^6Li -diffused samples

Sample No./ T_D of ^6Li ($^\circ\text{C}$)	n_e^* (cm ⁻³)	$(\alpha_p)_{389}$ (cm ⁻¹)
Pure GaAs/750	—	~2.5
1-a/750	1.0×10^{18}	4.0
2-a/750	1.8×10^{18}	5.8
3-a/750	3.1×10^{18}	9.0
4-a/750	5.3×10^{18}	10.0
5-a/750	5.7×10^{18}	11.5
6-a/750	7.7×10^{18}	14.4
7-a/750	8.0×10^{18}	14.2

* Measured values.

Table VI. Comparison of the $(\alpha_p)_{406}/(\alpha_p)_{389}$ ratios for all 950°C ^6Li -diffused samples

Sample No./ T_D of ^6Li ($^{\circ}\text{C}$)	n_e^* (cm^{-3})	$(\alpha_p)_{389}$ (cm^{-1})	$(\alpha_p)_{406}$ (cm^{-1})	$\frac{(\alpha_p)_{406}}{(\alpha_p)_{389}}$
Pure GaAs/950°C	0	~32	~64	~2
1-b/950	1.0×10^{18}	18.2	55.0	~3
2-b/950	1.8×10^{18}	6.2	17.0	~3
3-b/950	3.1×10^{18}	17.8	65.0	~4
4-b/950	5.3×10^{18}	22.6	105.5	~5
5-b/950	5.7×10^{18}	22.6	104.0	~5
6-b/950	7.7×10^{18}	14.2	99.1	~7
7-b/950	8.0×10^{18}	14.6	53.4	~4

* Measured values.

Table VI shows that the $(\alpha_p)_{406}/(\alpha_p)_{389}$ ratio in general increases with increases of n_e for samples which are ^6Li diffused at 950°C for 2 hr. This observation is consistent with the result that in more heavily doped samples more Si transfers to As sites producing more acceptors.

The conclusion here is that the primary Li defect responsible for the enhancement of the Si_{As} concentration is the Li donor responsible for the LVM band at 406 cm^{-1} (for ^6Li). The increase in the concentration of this Li defect with temperature as measured by the LVM absorption is the reason why the site transfer requires the high diffusion temperature. The concentration of this Li defect and the Si_{As} both increase with the total $[\text{Si}]$.

Absorption cross sections of Li-native defect complex bands.—From the discussion in the previous section we see that the electrically active defects in the Li-saturated samples are the Si_{Ga} donor, the Si_{As} acceptor, the Si-related donor responsible for the 367 cm^{-1} band, the Li donor responsible for the 406 cm^{-1} band, and finally the Li acceptor giving the 389 cm^{-1} band. One can now use this information to obtain the absorption cross sections for the Li bands. For all of the 750° and 950°C ^6Li -diffused samples of Table III one can use the fact that the samples are highly compensated after diffusion to obtain

$$n_e = 0 = a(\alpha_p\Delta)_{384} - b(\alpha_p\Delta)_{389} + c(\alpha_p\Delta)_{367} + E(\alpha_p\Delta)_{389} + F(\alpha_p\Delta)_{406}$$

where a , b , and c have been previously given. If the two Li defects are singly charged then E and F are the reciprocal cross sections for the Li defect bands. If either Li defect is a doubly charged donor or acceptor then the corresponding coefficient contains a factor of 2. For the 389 and 406 cm^{-1} bands our best estimated values of Δ are 2.4 ± 0.2 and $3.4 \pm 0.2 \text{ cm}^{-1}$, respectively. Both of these bands overlap other bands which frequently made determinations of Δ difficult. Figure 5 shows a plot of $(\alpha_p\Delta)_{406}/\eta$ vs. $(\alpha_p\Delta)_{389}/\eta$. Here

$$\eta = -[a(\alpha_p\Delta)_{384} - b(\alpha_p\Delta)_{389} + c(\alpha_p\Delta)_{367}] = E(\alpha_p\Delta)_{389} + F(\alpha_p\Delta)_{406}$$

where all samples of Table III except sample 2-b are included. Sample 2-b was omitted because η was orders of magnitude smaller than for the other samples. Also note that $d(\alpha_p\Delta)_{369}$ is omitted as that band does not occur in Li-diffused samples. The line in Fig. 5 is a least squares fit which gives values for E and F of

$$E = -9.7 \times 10^{16} \text{ cm}^{-1}$$

$$F = +2.8 \times 10^{16} \text{ cm}^{-1}$$

where the signs indicate the 389 cm^{-1} band is an acceptor and the one at 406 cm^{-1} is a donor as expected from previous assignments. Application of these values for E and F and the n_e equation given above to the

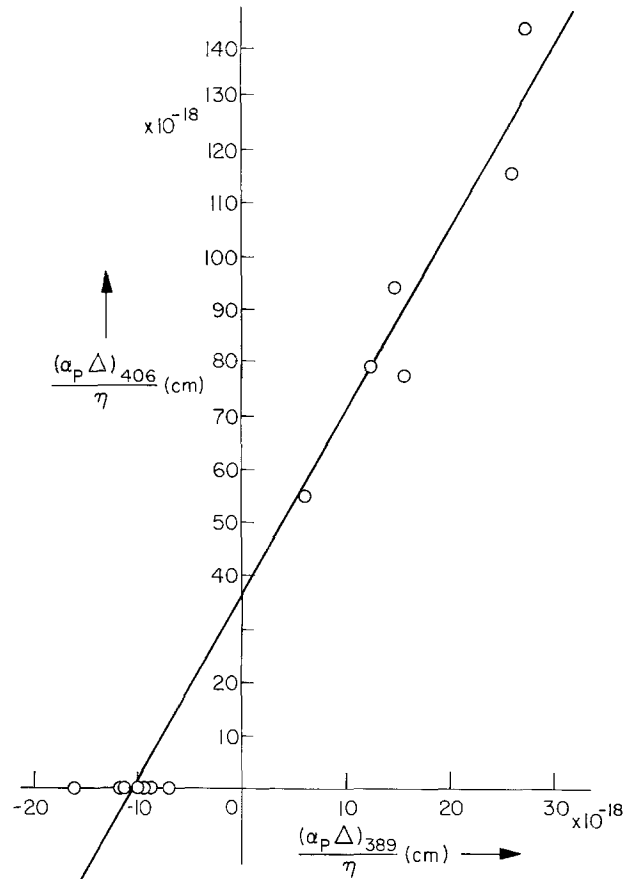


Fig. 5. $(\alpha_p\Delta)_{406}/\eta$ vs. $(\alpha_p\Delta)_{389}/\eta$ for the samples of Table III. The line is a least squares fit which yields values of $E = -9.7 \times 10^{16} \text{ cm}^{-1}$ and $F = +2.8 \times 10^{16} \text{ cm}^{-1}$ (see text).

samples of Table III yields n_e values for all cases save one which are $<6\%$ of the sum of all the defect concentrations used in the n_e equation. The single exception is sample 2-a where the figure is 11%.

When ^7Li is used as the diffusant in place of ^6Li then the Li bands have an isotope shift (22) with the $389 \text{ cm}^{-1} \rightarrow 364 \text{ cm}^{-1}$ and the $406 \text{ cm}^{-1} \rightarrow 379 \text{ cm}^{-1}$. For the same Li concentrations there is also a change in α_p with $(\alpha_p)_{389}/(\alpha_p)_{364} = (\alpha_p)_{406}/(\alpha_p)_{379} = 1.30$. Since the Δ shows almost no change with Li isotope one has

$$E(^7\text{Li}) = 1.30E(^6\text{Li}) = -12.6 \times 10^{16} \text{ cm}^{-1}$$

$$F(^7\text{Li}) = 1.30F(^6\text{Li}) = +3.6 \times 10^{16} \text{ cm}^{-1}$$

As a test of the validity of these values they can be applied to the LVM results previously published (22) for ^7Li saturation diffusion in pure GaAs for $700^{\circ}\text{C} < T_D < 950^{\circ}\text{C}$. Near 700°C the E and F values with the previous data indicate almost exact compensation in agreement with experiment. However, at 900°C the estimated n_e is approximately 10% of the total Li donor and acceptor charge concentration if one still assumes that the 389 (364) and 406 (379) cm^{-1} defects are the only electrically active ones. Experimentally the samples are highly compensated and high resistivity.

One can also use the above values of E and F to estimate the total $[\text{Li}]$ in the saturated pure material. From previous work (22) it is known that the 389 (364) cm^{-1} acceptor complex has 2 Li per defect and the 406 (379) cm^{-1} donor defect has 3 Li. Therefore the total $[\text{Li}]$ due to these two defect centers only is

$$N = 2|E(^7\text{Li})|(\alpha_p\Delta)_{364}/n + 3|F(^7\text{Li})|(\alpha_p\Delta)_{379}/m$$

where n and m are the acceptor and donor defect charge states, respectively. Assuming $n = m = 1$ the calculated values for N are the points in Fig. 6 and they can be compared with the total $[\text{Li}]$ which is

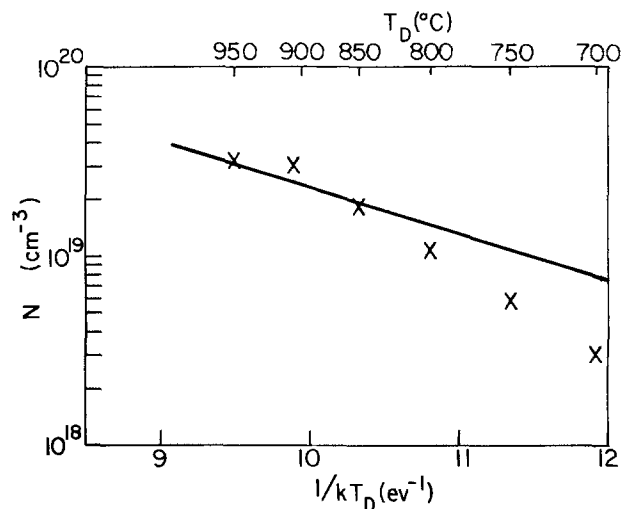


Fig. 6. A plot of $\ln N$ vs. $1/kT_D$ for the ${}^7\text{Li}$ diffused pure GaAs samples in Ref. (22). Here $N = 2 |F({}^7\text{Li})| (\alpha_p \Delta)_{364} + 3 |F({}^7\text{Li})| (\alpha_p \Delta)_{379}$ which is the total $[\text{Li}]$ due to these two defect centers (assuming $n = m = 1$, see text). A straight line is the total $[\text{Li}]$ measured by Fuller and Wolfstein [see Ref. (18)].

given by the straight line determined by the flame spectrophotometric analysis measurements of Fuller and Wolfstirn (18). While there is reasonable agreement between the calculated points and the line there are several difficulties. First, there is no independent evidence that $n = m = 1$. Second, the LVM measurements show additional bands due to the other Li defects and they are not included in the calculated N values. Third, the determination of E and F depends on the prior knowledge of a , b , and c which means that the value of N involves a number of parameters known with only limited accuracy. In view of the uncertainties the qualitative agreement in Fig. 6 is considered to be very satisfactory. Therefore the reciprocal cross sections for the Li-donor and Li-acceptor defects are consistent with the data for the compensation of Li-saturated GaAs:Si, the compensation of Li-saturated pure GaAs and the total $[\text{Li}]$ in the Li-saturated pure GaAs.

Microstructures of ${}^6\text{Li}$ -diffused samples.—The extent and nature of the microstructure of ${}^6\text{Li}$ -diffused samples depend both on the starting material, particularly the $[\text{Si}]$, and on the temperature of the diffusion. It will help to clarify the results if they are discussed by groups of samples as follows:

(i) As previously mentioned nondiffused, nonannealed, HT + Q samples had no significant observable microstructure even for the highest $[\text{Si}]$ used in this study.

(ii) Pure GaAs samples ${}^6\text{Li}$ diffused at $T_D \approx 750^\circ$, 900° , and 950°C were measured and showed Li precipitates and some dislocations which tend to be pinned by the precipitates. Some extrinsic stacking faults on $\{111\}$ planes which may be related to the Li metastable phase were also observed in the 750°C diffusion. The size and density of Li precipitates decrease with decreases in diffusion temperature. In the case of the 950°C diffused samples, the average size of Li precipitates is approximately 1000\AA and their density is approximately 9.5×10^{12} particles/cm 3 . These observations are in agreement with those reported previously (24).

(iii) ${}^6\text{Li}$ -diffused samples at $T_D = 750^\circ\text{C}$ with low $[\text{Si}]$ and $n_e \leq 3.0 \times 10^{18}$ cm $^{-3}$, as in sets No. 1 to 3 of Table III, have a microstructure which is similar for the 750°C ${}^6\text{Li}$ -diffused pure GaAs material described in case (ii). There were however, no extrinsic stacking faults observed. Thermal annealing with $T_D \gtrsim 400^\circ\text{C}$ of

nondiffused samples with $[\text{Si}] \approx 1.5 \times 10^{18}$ cm $^{-3}$, i.e., set No. 1, resulted in no observable microstructure as in the HT + Q state.

(iv) ${}^6\text{Li}$ diffusion at $T_D = 750^\circ\text{C}$ for the samples with high $[\text{Si}] \gtrsim 2 \times 10^{19}$ cm $^{-3}$ and $n_e \gtrsim 5.0 \times 10^{18}$ cm $^{-3}$, as in sets No. 4 to 7 of Table III, induces a high concentration of defects. Samples 4-a and 5-a with $[\text{Si}] \approx 2 \times 10^{19}$ cm $^{-3}$ show a microstructure with primarily triangular-shaped faulted loops, as shown in Fig. 7a. The loops are on four $\{111\}$ planes of a tetra-

hedron and have the displacement vector $\vec{R}_F = a/3 [111]$. To the best of our knowledge this kind of defect has not been reported previously. Similar defects are also observed in the material with similar $[\text{Si}] \approx 2 \times 10^{19}$ cm $^{-3}$ when annealed at 750°C without ${}^6\text{Li}$ diffusion, and their density is similar to that of 750°C ${}^6\text{Li}$ -diffused samples, but they are about three times smaller in linear dimension. By using two different and independent TEM analyses (37, 38) we have established that these triangular loops are extrinsic faults and microanalysis with a scanning electron microscope (SEM) shows that they have a large Si content. We therefore conclude that these triangular loops are due to Si precipitation from GaAs:Si solution, however, the mechanism of their formation is unknown as is the reason for the observed morphology. The microstructure of samples 6-a and 7-a which have the highest $[\text{Si}] \approx 5 \times 10^{19}$ cm $^{-3}$ show primarily circular loops which are also on four $\{111\}$ planes of a tetrahedron as shown in Fig. 7b. The TEM analysis (38) has established that these circular loops are also of the extrinsic type. As seen in Fig. 7b the loops here are much smaller than those in Fig. 7a making the SEM measurement difficult. However it seems reasonable to assume that the circular loops are due to Si precipitation from GaAs:Si solution as in the case of the triangular loops. Typical dimension of these loops is $\sim 2500\text{\AA}$ for the sample with $[\text{Si}] \approx 2 \times 10^{19}$ cm $^{-3}$ (Fig. 7a), decreasing to $\sim 450\text{\AA}$ for the sample with the largest $[\text{Si}] \approx 5 \times 10^{19}$ cm $^{-3}$ (Fig. 7b). The loop density in the former case is $\sim 8.0 \times 10^{12}$ cm $^{-3}$ and is roughly thirty-five times higher or $\sim 2.9 \times 10^{14}$ cm $^{-3}$ in the latter case. This indicates that the amount of Si precipitation through the formation of these triangular or circular loops increases with increasing $[\text{Si}]$ in the 750°C ${}^6\text{Li}$ -diffused samples. Assuming that these extrinsic triangular or circular loops are forming completely by Si with double interstitial layers on $\{111\}$ planes, one can estimate $[\text{Si}] \approx 3.2 \times 10^{18}$ cm $^{-3}$ for the triangular loops observed in sample 4-a (Fig. 7a) and $[\text{Si}] \approx 6.6 \times 10^{18}$ cm $^{-3}$ for the circular loops observed in sample 7-a (Fig. 7b).

(v) ${}^6\text{Li}$ -diffused samples at $T_D = 950^\circ\text{C}$, all sets in Table III, all had similar microstructure, i.e., Li precipitates and some dislocations which tend to be pinned by the precipitates. This is similar to the 950°C ${}^6\text{Li}$ -diffused pure GaAs material. However, the size $\sim 700\text{\AA}$ and density $\leq 3.3 \times 10^{12}$ particles/cm 3 of precipitates is small compared to that of the pure GaAs. One previous study (18) concluded that the solid solubility of Li in doped GaAs is frequently larger than that in pure GaAs which can account for the reduction in precipitates in the Si-doped material. A few large dislocation loops are also observed in samples with high $[\text{Si}] \gtrsim 2 \times 10^{19}$ cm $^{-3}$ as in sets No. 4-7 in Table III. The character of these large loops is not known, however, they would account for only a very small amount of $[\text{Si}]$ even if one assumes their origin is due to Si precipitation. As previously mentioned ${}^6\text{Li}$ re-diffusion at 950°C of sample 7-a after it was ${}^6\text{Li}$ diffused at 750°C , also induces site transfer and shows a similar LVM curve as that of sample 7-b with only 950°C diffusion. After this double diffusion the microstructure does not show the high density of circular loops seen after the first lower temperature diffusion.

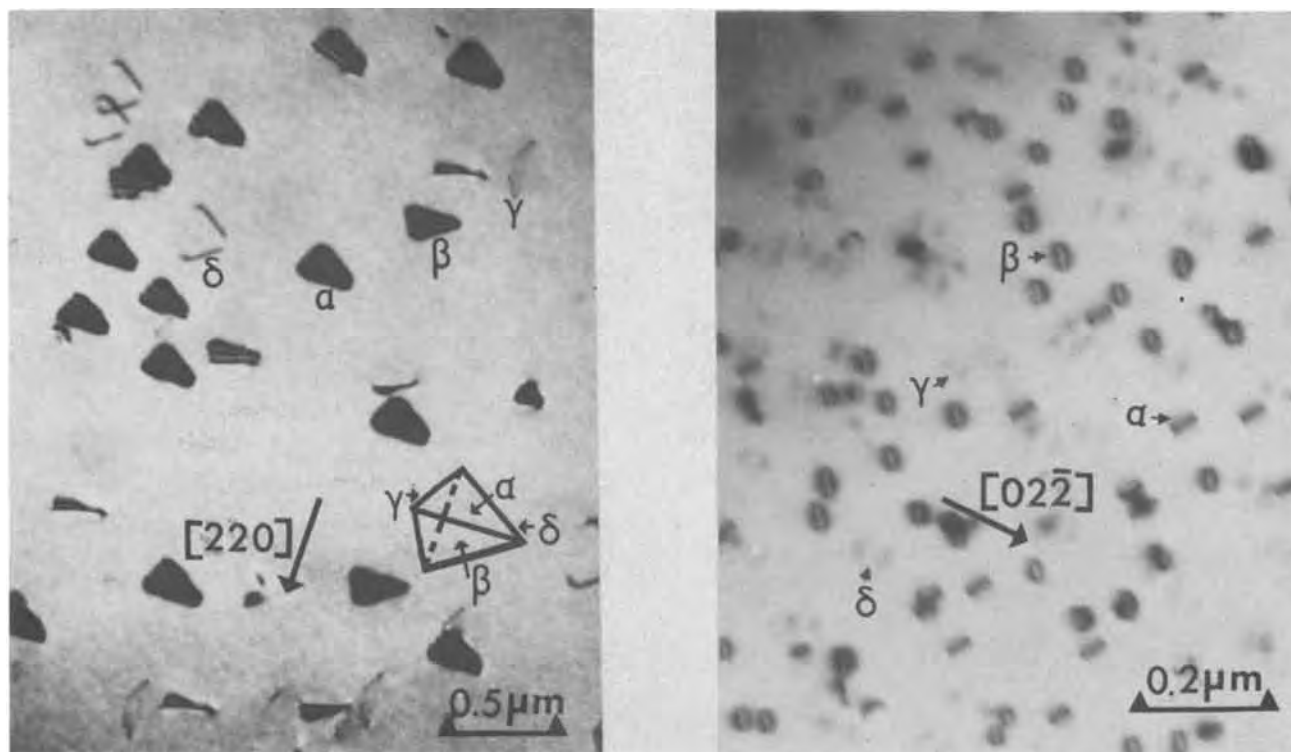


Fig. 7. Bright field micrographs showing the presence of a high concentration of loops which are extrinsic and on four $\{111\}$ planes of a tetrahedron and observed after 750°C ^6Li diffusion. (a, left) Sample 4-a, $n_e \approx 5.3 \times 10^{18} \text{ cm}^{-3}$ shows triangular-shaped faulted loops with density $\sim 8.0 \times 10^{12} \text{ cm}^{-3}$ and the displacement vector $R_F = a/3 [111]$. Half of these triangular faulted loops (γ , δ) do not show fringe contrast under the deflection condition being used here. Foil orientation $\sim \langle \bar{1}14 \rangle$. (b, right) Sample 7-a, initial $n_e \approx 8.0 \times 10^{18} \text{ cm}^{-3}$ shows circular loops with density $\sim 2.9 \times 10^{14} \text{ cm}^{-3}$. Foil orientation $\sim \langle \bar{1}12 \rangle$.

The resulting final microstructure of sample 7-a is very similar to that of sample 7-b.

The microstructural results described above can be correlated with the LVM measurements and some of the results discussed in the four preceding sections. For the samples of lower $[\text{Si}]$ no Si-rich loops are observed at any point in the study and the gain in $(\alpha_p\Delta)$ for the 399 cm^{-1} band for Si_{As} is largely the result of Si site transfer from Si_{Ga} defects, *i.e.*, β values of $+0.97$, $+0.89$, and $+0.81$ for sets No. 1-3 of Table IV as compared to the predicted value of $+1.27$. On the other hand, the higher $[\text{Si}]$ samples show the Si-rich loops after the 750°C diffusion, but essentially none after a 950°C diffusion. These same materials have very low β values indicating that the increases in $[\text{Si}_{\text{As}}]$ come largely from a source other than the Si_{Ga} defect concentration observed at 750°C . Since no other Si-related LVM bands show significant changes between the two temperatures it is reasonable to inquire into the possibility that the Si-rich loops could be the source of the high temperature increases in $[\text{Si}_{\text{As}}]$. By using the reciprocal cross sections a and b given earlier, one can estimate the net changes in $[\text{Si}]$ in the 399 and 384 cm^{-1} band jointly from the data of Table IV. For sample 4-b the increase in $[\text{Si}]$ is $2.7 \times 10^{18} \text{ cm}^{-3}$ and $5.7 \times 10^{18} \text{ cm}^{-3}$ for sample 7-b. These values are quite close to the estimated $[\text{Si}]$ in the loops, $3.2 \times 10^{18} \text{ cm}^{-3}$ and $6.6 \times 10^{18} \text{ cm}^{-3}$, respectively, obtained in the previous section. Therefore we conclude that the Si in the loops formed at 750°C is indeed the source of the additional Si observed after the 950°C diffusion.

There remains the fundamental question of the original source of the Si which appears as the Si-rich loops after a 750°C Li diffusion and as enhanced $[\text{Si}_{\text{As}}]$ after 950°C Li diffusion. We know from the data of Table II that the 750°C Li diffusion causes a reduction of $[\text{Si}_{\text{Ga}}]$, a reduction of both the 367 and 369 cm^{-1} Si-related defects and a substantial increase in the

$[\text{Si}_{\text{Ga-Si}_{\text{As}}}]$. Also the $\text{Si}_{\text{Ga-Li}_{\text{Ga}}}$ bands are created by the diffusion. The $[\text{Si}_{\text{As}}]$ is unaffected. Since the cross sections of the $\text{Si}_{\text{Ga-Si}_{\text{As}}}$ band and the $\text{Si}_{\text{Ga-Li}_{\text{Ga}}}$ bands are not known one cannot quantitatively determine whether the total $[\text{Si}]$ represented by the bands remains constant. It is conceivable that the Si in the loops and the enhanced $[\text{Si}_{\text{As}}]$ comes from net decreases of Si in the Si bands observed in the prediffused samples. If this is the case then the source must be either the Si_{Ga} or the Si-related defects causing the 367 and 369 cm^{-1} bands and cannot be the $\text{Si}_{\text{Ga-Si}_{\text{As}}}$ defect. Also the Si in the loops cannot come from the Si_{As} defects.

An alternate explanation for the original source of the Si in the loops or enhanced $[\text{Si}_{\text{As}}]$ for the more heavily doped samples is the possibility that some of the Si dopant does not give rise to LVM spectra in the prediffused (e^- -irradiated) samples. An indication of this possibility comes from a comparison of the measured total $[\text{Si}]$ with that calculated from LVM spectra by using the known absorption cross sections. It is reasonable to estimate Si concentration by assuming $[\text{Si}]_{\text{calculated}} \approx [\text{Si}_{\text{Ga}}] + [\text{Si}_{\text{As}}] + [\text{Si}_{\text{Ga-Si}_{\text{As}}}] + [\text{Si}]_{367} + [\text{Si}]_{369} \approx a(\alpha_p\Delta)_{384} + b(\alpha_p\Delta)_{399} + 2a(\alpha_p\Delta)_{393} + c(\alpha_p\Delta)_{367} + d(\alpha_p\Delta)_{369}$ for e^- -irradiated samples in Table II. The results for KM-16-3,4 and WA-Si-2-2,3 show that values for $[\text{Si}]_{\text{calculated}}$ account for only 60%-70% of the total $[\text{Si}]$ values measured by electron microprobe analysis which were $2.3 \times 10^{19} \text{ cm}^{-3}$ and $\sim 5 \times 10^{19} \text{ cm}^{-3}$, respectively. In addition, Newman (37) and co-workers have recently studied irradiated samples simultaneously doped with Si and a group VI donor. The $(\alpha_p\Delta)_{384}$ band of Si_{Ga} is about the same as $(\alpha_p\Delta)_{399}$ for Si_{As} . Prolonged irradiation (31) can reduce the $(\alpha_p\Delta)_{399}$. They have found that after such an irradiation and upon annealing, $[\text{Si}_{\text{As}}]$ recovers and $(\alpha_p\Delta)_{399}$ can overshoot its original value by as much as a factor of five even though the $[\text{Si}_{\text{Ga}}]$ does

not change. Furthermore in a most recent communication, they have also observed that annealing Si-doped GaAs samples ($[\text{Si}] \approx 2 \times 10^{18} \text{ cm}^{-3}$) after being irradiated with fast neutrons, the strength of the Si_{As} band also increases and may overshoot its original value by a factor of three but without any measurable change in the strength of other LVM bands involving silicon. They have also concluded that there is some silicon in as-grown crystals which does not give rise to LVM absorption.

Conclusions

The use of measurements of the carrier density, the LVM absorption, and the microstructure of GaAs:Si samples has provided information which allows one to describe in considerable detail the behavior of a number of defects in Li-saturated material. Specifically the conclusions which have been made from the present study are:

1. The effect of a saturation diffusion of Li at a temperature (750°C) which is below that at which Si transfers from Ga to As sites results in significant changes in the Si defect concentrations as compared to the pre-diffused state. These changes are: (i) a decrease in $[\text{Si}_{\text{Ga}}]$; (ii) an increase in $[\text{Si}_{\text{Ga}}-\text{Si}_{\text{As}}]$; and (iii) the creation of $\text{Si}_{\text{Ga}}-\text{Li}_{\text{Ga}}$ defects. There is no change in $[\text{Si}_{\text{As}}]$. The changes increase with increases in $[\text{Si}]$.

2. For samples of lower $[\text{Si}]$, i.e., $[\text{Si}] \lesssim 5 \times 10^{18} \text{ cm}^{-3}$ and $n_e \lesssim 3 \times 10^{18} \text{ cm}^{-3}$, saturation diffusion of Li at a temperature of 950°C does result in $\text{Si}_{\text{Ga}} \rightarrow \text{Si}_{\text{As}}$ and most of the increase in $[\text{Si}_{\text{As}}]$ is attributable to the decrease in $[\text{Si}_{\text{Ga}}]$. The Li defect responsible for inducing the Si site transfer is the Li donor which has an LVM band at 406 cm^{-1} (for ^6Li). The microstructure of these lower $[\text{Si}]$ samples includes some Li precipitates and some dislocations which tend to be pinned by the precipitates. There is no evidence of Si precipitation or extrinsic faults.

3. For samples of higher $[\text{Si}]$, i.e., $[\text{Si}] \gtrsim 2 \times 10^{19} \text{ cm}^{-3}$ and $n_e \gtrsim 5 \times 10^{18} \text{ cm}^{-3}$, the comparisons of Li saturation diffusion at 750° and 950°C are more complicated. The $[\text{Si}_{\text{Ga}}]$ generally decreases and $[\text{Si}_{\text{As}}]$ increases for the higher temperature case, however, $\text{Si}_{\text{Ga}} \rightarrow \text{Si}_{\text{As}}$ site transfer is no longer the dominant process. After the 750°C saturation, TEM measurements show faulted $\{111\}$ extrinsic loops which are Si rich. These loops are not present after a 950°C saturation diffusion. Semiquantitative comparisons indicate that the large increase in $[\text{Si}_{\text{As}}]$ at the higher temperature could come from the Si content of these loops. The question of the origin of the Si in the loops could not be answered unambiguously although two possible sources were identified and discussed.

4. By using the fact that the Li-saturated samples are electrically compensated and using the known values of the absorption cross sections of the electrically active Si defects, the absorption cross sections of the bands for the principal Li-donor and -acceptor defects were determined. These cross sections were used with the knowledge that there are 3 Li per donor defect and 2 Li per acceptor and some previously published data for Li-saturated undoped GaAs to estimate the total $[\text{Li}]$ as a function of saturation temperature. The results are in reasonable agreement with earlier quantitative analysis data.

Acknowledgments

This work was supported by the Air Force Office of Scientific Research (AFSC) under Grant/Contract 76-2990. The authors wish to express their gratitude to Dr. G. H. Narayanan for his helpful advice on the TEM results and to Professor D. B. Wittry for useful discussions during the electron microprobe analysis. The authors would also like to thank L. Lowe and D. Morris for their help with the electron irradiations and their hospitality to one of the authors (W.G.S.) during his

stay at Hanscom Field, Massachusetts. The authors also wish to express their appreciation to Professor R. C. Newman and his co-workers for their comments and communication of their results prior to publication.

Manuscript submitted Oct. 29, 1979; revised manuscript received Feb. 13, 1980. This was Paper 578 presented at the Los Angeles, California, Meeting of the Society, Oct. 14-19, 1979.

Any discussion of this paper will appear in a Discussion Section to be published in the June 1981 JOURNAL. All discussions for the June 1981 Discussion Section should be submitted by Feb. 1, 1981.

Publication costs of this article were assisted by the University of Southern California.

REFERENCES

1. W. G. Spitzer and W. Allred, *Appl. Phys. Lett.*, **12**, 5 (1968).
2. W. G. Spitzer and W. Allred, *J. Appl. Phys.*, **39**, 4999 (1968).
3. K. Laithwaite and R. C. Newman, *J. Phys. C: Solid State Phys.*, **9**, 4503 (1976).
4. R. T. Chen and W. G. Spitzer, Private communication.
5. W. G. Spitzer and M. B. Panish, *J. Appl. Phys.*, **40**, 4200 (1969).
6. A. H. Kachare, W. G. Spitzer, J. M. Whelan, and G. H. Narayanan, *ibid.*, **47**, 5022 (1976).
7. W. G. Spitzer, in "Advances in Solid State Physics," Vol. XI, O. Madelung, Editor, p. 1, Pergamon Press (1971).
8. H. J. Queisser, *J. Appl. Phys.*, **37**, 2909 (1966).
9. C. J. Hwang, *ibid.*, **39**, 3347 (1968).
10. W. Y. Lum and H. H. Wieder, *ibid.*, **49**, 6187 (1978).
11. J. K. Kung and W. G. Spitzer, *ibid.*, **45**, 4477 (1974).
12. L. H. Skolnik, W. G. Spitzer, A. Kahan, F. Eules, and R. G. Hunsperger, *ibid.*, **43**, 2146 (1972).
13. W. P. Allred, G. Cumming, J. Kung, and W. G. Spitzer, in Second International Conference on Gallium Arsenide, Dallas, Texas, p. 66, Institute of Physics and the Physical Society (1968).
14. K. Laithwaite, R. C. Newman, J. F. Angress, and G. A. Gledhill, in Sixth International Symposium on Gallium Arsenide and Related Compound, Edinburgh, Sept. 20, 1976, p. 133, Institute Phys. Conf. 33a, Institute of Physics, London (1977).
15. J. K. Kung and W. G. Spitzer, *J. Appl. Phys.*, **45**, 2254 (1974).
16. H. Rupprecht, J. M. Woodall, K. Konnerth, and D. G. Pettit, *Appl. Phys. Lett.*, **9**, 221 (1966).
17. J. M. Whelan, J. D. Struthers, and J. A. Ditzemberger, in Proceedings of International Conference on Semiconductor Physics, Prague, p. 943 (1960).
18. C. S. Fuller and K. B. Wolfstirn, *J. Appl. Phys.*, **33**, 745 (1962a); *J. Appl. Phys.*, **33**, 2507 (1962b); in Proceedings of International Conference on Physics of Semiconductors, Exeter, p. 745, The Institute of Physics and The Physical Society, London (1962c); *Appl. Phys. Lett.*, **2**, 45 (1963a); *J. Appl. Phys.*, **34**, 1914 (1963b); Radiation Damage in Semiconductors, Report of 7th International Conference on Physics of Semiconductors, Paris, Vol. 3, p. 187, Academic Press, New York (1964).
19. C. S. Fuller and H. W. Allison, *J. Appl. Phys.*, **35**, 1227 (1964).
20. W. Hayes, *Phys. Rev.*, **138**, A1227 (1965).
21. M. Levy, O. Lorimor, and W. G. Spitzer, *J. Appl. Phys.*, **39**, 1914 (1968).
22. M. E. Levy and W. G. Spitzer, *J. Phys. C: Solid State Phys.*, **6**, 3223 (1973).
23. M. E. Levy, Ph.D. Dissertation, University of Southern California, 1973, Unpublished.
24. B. Norris and G. H. Narayanan, *J. Appl. Phys.*, **48**, 2784 (1977).
25. O. G. Lorimor and W. G. Spitzer, *ibid.*, **37**, 3687 (1966).
26. O. G. Lorimor and W. G. Spitzer, *ibid.*, **38**, 2713 (1967).
27. O. G. Lorimor and W. G. Spitzer, *ibid.*, **38**, 3008 (1967).
28. P. C. Leung, L. H. Skolnik, W. P. Allred, and

- W. G. Spitzer, *ibid.*, **43**, 4096 (1972).
29. P. C. Leung, J. Fredrickson, W. G. Spitzer, A. Kahan, and L. Bouthillette, *ibid.*, **45**, 1009 (1974).
30. W. G. Spitzer, A. Kahan, and J. Bouthillette, *ibid.*, **40**, 3398 (1969).
31. K. Laithwaite and R. C. Newman, *Philos. Mag.*, **35**, 1689 (1977).
32. R. C. Newman, Private communication.
33. J. K. Kung and W. G. Spitzer, *J. Appl. Phys.*, **44**, 912 (1973).
34. J. K. Kung and W. G. Spitzer, *This Journal*, **121**, 1482 (1974).
35. G. H. Narayanan and S. M. Copley, *Phys. Status Solidi A*, **23**, 123 (1974).
36. G. H. Narayanan and A. H. Kachare, *ibid.*, **26**, 657 (1974).
37. R. C. Newman, Private communication.
38. R. Gevers, A. Art, and S. Amelinckx, *Phys. Status Solidi*, **3**, 1563 (1963).
39. J. W. Edington, "Practical Electron Microscopy in Materials Science," pp. 134-136, Van Nostrand Reinhold, New York (1976).

AES and PES Studies of Semi-Insulating Polycrystalline Silicon (SIPOS) Films

T. Adachi¹ and C. R. Helms

Stanford Electronics Laboratories, Stanford University, Stanford, California 94305

ABSTRACT

SIPOS (semi-insulating polycrystalline silicon) films with 40 atomic percent oxygen have been studied with Auger electron spectroscopy (AES) and photoelectron spectroscopy (PES). The comparison of the Si LVV Auger spectra with the Si 2p lines suggests that the as-grown SIPOS film contains large amounts of SiO_x ($x < 2$) as well as SiO₂. Annealing at 1100°C causes crystal growth of Si and the change of SiO_x towards SiO₂. An additional peak at 83 eV is found in the Si LVV Auger spectra, which has been reported to exist at the Si-SiO₂ interface, and can be attributed to SiO.

SIPOS (semi-insulating polycrystalline silicon) films have been extensively studied (1-6) because of their practical importance as a passivation layer on silicon devices (7, 8). The SIPOS films, prepared by chemical vapor deposition (CVD), have a macroscopic chemical composition expressed as SiO_x ($0 < x < 2$). The films contain polysilicon grains after annealing at temperatures higher than 850°C, whereas as-deposited films are reported to be amorphous (2).

In the present work, we used Auger electron spectroscopy (AES) and photoelectron spectroscopy (PES) to characterize the SIPOS films with 40 atomic percent (a/o) oxygen. We have found that the as-grown films investigated in this study were composed of SiO_x phases and Si as well as SiO₂ and that annealing at 1100°C induced a change of SiO_x towards SiO₂.

Experimental

SIPOS films were deposited on p-type (100) Si wafers by atmospheric pressure CVD at 650°C (7). The reactant gases and their flow rates were SiH₄ (30 cm³/min), N₂O (93 cm³/min), and N₂ (carrier gas, 25 l/m), which yielded about 40 a/o oxygen concentration. Films 300Å thick were prepared for the measurements reported here in order to prevent any charging effects in the electron spectroscopies used. Annealing effects were also examined for samples annealed in N₂ at 1100°C for 30 min. However, the experimental results indicate that the N₂ gas used for the annealing may have contained enough O₂ for a thin oxide layer to grow on the surface of the annealed films.

We used a Varian Auger microprobe with a cylindrical mirror analyzer (CMA) for AES measurements. A primary electron beam energy of 4.5 keV was employed at a beam current of 2 μA scanned over ~200 μm square area. Both derivative [$d(E \cdot N(E))/dE$] and nonderivative [$E \cdot N(E)$] spectra were examined. Argon ion beam sputtering with 0.5 keV ions at ~10 μA/cm² was used for sputter profiling of the films.

As-grown films were also examined with PES. The radiation source at the Stanford Synchrotron Radiation Laboratory (SSRL) was employed. Photon energies of 180 and 100 eV were used for measurements of Si 2p lines and valence electronic structure, respectively. These photon energies were selected so that photoelectrons would have approximately the same kinetic energy as the Si LVV Auger electrons. Photoelectrons were analyzed with a PHI double-pass CMA, and the energies were referred to the valence band maximum of Si.

Results

Chemical depth profiles.—Figure 1 shows survey Auger spectra of SIPOS films prior to argon ion sputtering. Major elements detected at the surface are Si, O, and C, both for the as-grown and the annealed films. Most of the Si at the surface is so heavily oxidized that the 91 eV peak (in derivative mode) characteristic of pure Si was barely observed in Fig. 1, especially for the annealed film.

Figure 2 shows the chemical depth profiles of the films. Carbon, probably due to surface contamination after deposition, disappears very rapidly. A heavily oxidized surface layer was removed by 5 and 15 min sputtering for the as-grown and the annealed films, respectively. The thicker surface layer of the annealed film may be due to the presence of ppm concentrations of oxygen in the annealing system.

The interface between the SIPOS film and the Si substrate exhibits a peak in oxygen concentration after annealing. This effect may be due to the redistribution of oxygen in the SIPOS film and indicates that the SiO_x in the as-grown film may be unstable at high temperature, with an SiO₂ layer growing both at the Si/SIPOS interface and the SIPOS surface.

Si LVV Auger spectra.—Close examination of the Auger spectra was performed using the nonderivative mode. Figures 3 and 4 show the Si LVV spectra of the as-grown and the annealed films, respectively, at various depths. The positions where these spectra were taken are indicated in Fig. 2. At the surface, Si is almost completely oxidized after annealing [Fig. 4(f)].

¹ Present address: Sony Corporation Research Center, Hodogaya, Yokohama 240, Japan.

Key words: films, interfaces, spectra.

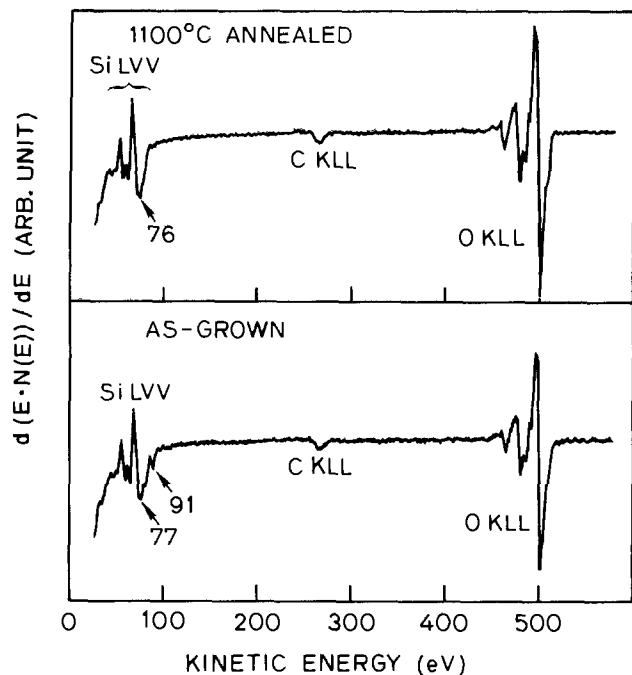


Fig. 1. Auger spectra of as-grown (lower panel) and 1100°C-annealed (upper panel) SIPOS films prior to argon ion sputtering.

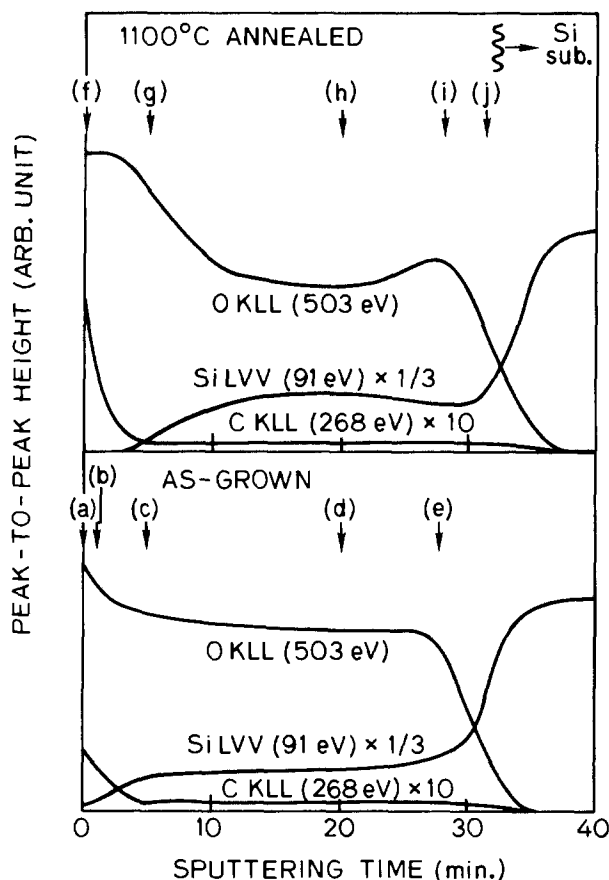


Fig. 2. Chemical depth profiles of as-grown (lower panel) and 1100°C-annealed (upper panel) SIPOS films. The profiles of Si are those of pure Si at ~ 91 eV in the $d(E \cdot N(E))/dE$ mode spectra. Small letters, (a) through (j), in the figure indicate the positions where the Si LVV spectra (Fig. 3 and 4) and/or photoelectron spectra (Fig. 5 and 6) were examined.

Even the as-grown film is heavily oxidized at the surface [Fig. 3(a)], and the Si LVV spectra of both samples are almost identical to that of SiO_2 . A small peak at 88 eV in the as-grown film is probably due to

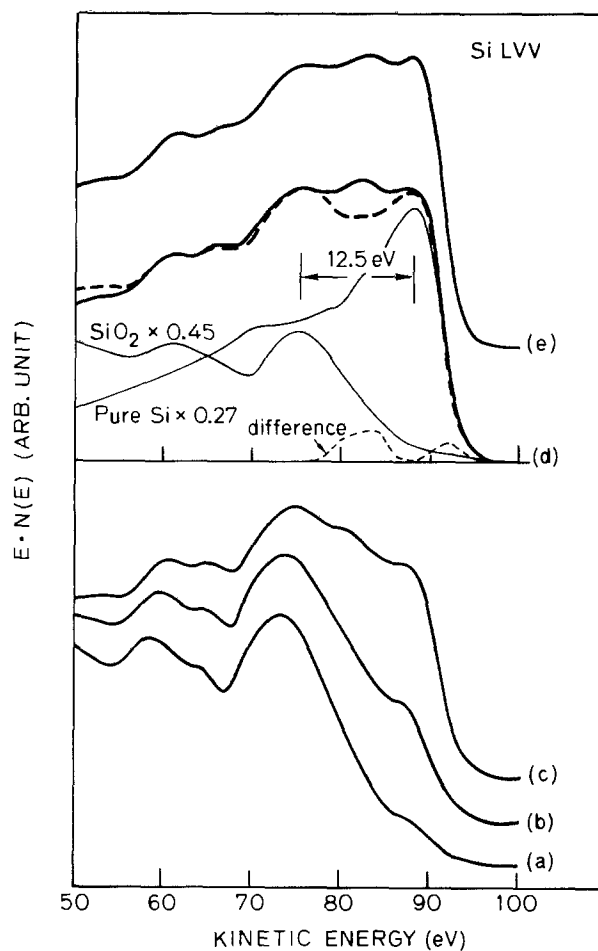


Fig. 3. Si LVV Auger spectra in the $E \cdot N(E)$ mode at various depths of the as-grown SIPOS film. Each spectra corresponds to the position in Fig. 2 indicated by the same letter. The thick solid line in (d) is the measured Si LVV spectra, and the dashed line is the composed spectra using pure Si and (shifted) pure SiO_2 spectra (thin solid lines) as basic components. The dotted line is the difference curve between the measured and the composed spectra. The intensity ratios of the two basic components relative to the intensities of pure spectra are also indicated.

the pure Si which is one of the components of SIPOS film (2, 5).

As shown in Fig. 2, 5 min of argon ion sputtering removes the surface contamination of carbon and the Si LVV spectra at this point [Fig. 3(c) and 4(g)] have at least two components—that is, pure Si and Si in SiO_2 .

In another 15 min of sputtering, spectra were recorded that represent the bulk of the films in an as-sputtered condition [thick solid lines in Fig. 3(d) and 4(h)]. The spectra of the as-grown film [Fig. 3(d)] is quite different from that of the annealed film [Fig. 4(h)]. It shows an Si LVV spectra composed of pure Si and SiO_2 , while the spectra of the as-grown film has an extra peak at 83 eV. Another difference is that only the SiO_2 component in the Si LVV spectra of the as-grown film is shifted towards higher kinetic energy. In order to make these differences clear, we tried a semi-empirical fit of the Si LVV spectra of SIPOS films using spectra of pure Si and thermally grown SiO_2 as basic components. These two spectra were added to get the best fit to measured spectra with proportional coefficients as parameters determined by the least squares method. Since we know, by visual examination, that there is a contribution of the extra peak near 83 eV in the spectra, the data points near this peak were excluded intentionally. As a result, the difference between the measured and the composed spectra gives an estimate of the contribution of the 83 eV peak. Furthermore, to obtain a good fit, the SiO_2 component was

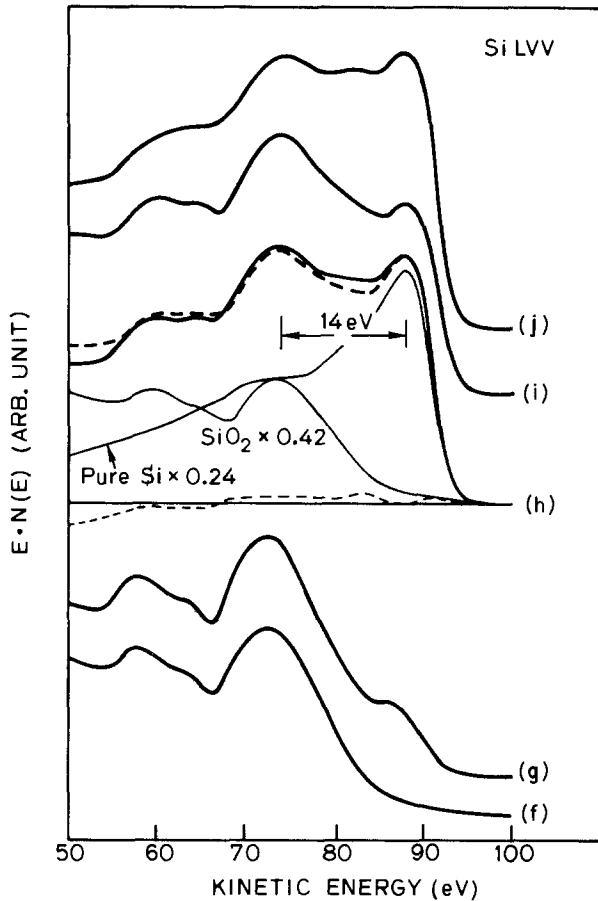


Fig. 4. Si LVV spectra in the $E \cdot N(E)$ mode at various depths of the 1100°C -annealed SIPOS film. Each spectrum corresponds to the positions in Fig. 2 indicated by the same small letter. The thick solid line in (h) is the measured Si LVV spectra, and the dashed line is the composed spectra using pure Si and (shifted) pure SiO_2 spectra (thin solid lines) as basic components. The dotted line is the difference curve between the measured and the composed spectra. The intensity ratios of the two basic components relative to the intensities of pure spectra are also indicated.

shifted towards higher kinetic energy to obtain minimum error. The results are illustrated in Fig. 3(d) and 4(h), where the solid thick lines are the measured spectra of the films, the dashed lines are the composite spectra by the method described above, dotted lines are the differences between the two, and the solid thin lines are the basic components (pure Si and shifted pure SiO_2) used in the calculations. The as-grown film has a large contribution from the 83 eV peak, whereas the 1100°C annealed film has almost none. The shift of the SiO_2 component necessary for the best fit is larger for the as-grown film, and the energy difference between the most prominent peaks of the Si and the SiO_2 components are 12.5 and 14.0 eV for the as-grown and the annealed films, respectively. (Note that the difference is about 15 eV when pure Si and pure thermal SiO_2 are measured separately.) The intensities of the two components are indicated in the figures relative to the intensities of the pure standards.

Another 8 min of sputtering of the annealed film reaches the region where the oxygen concentration is increased with respect to the "bulk value." The spectrum at this point [Fig. 4(i)] contains no new features, but the intensity ratio of the SiO_2 component increases relative to that of the "bulk spectra."

At the interface between the SIPOS film and the Si substrate, the Si LVV spectra of both the as-grown [Fig. 3(e)] and the annealed [Fig. 4(j)] films are similar; that is, the 83 eV peak appears also in the spectra of the annealed film. However, the position of

the SiO_2 component in the spectrum of the annealed film remains at the position found in the bulk spectrum.

Photoelectron spectroscopy.—An as-grown film was examined also with PES. Figures 5 and 6 show the results of the Si 2p spectra and the valence electronic structures, respectively. Although these experiments were done separately from the AES experiments, each spectrum shown in Fig. 5 and 6 were taken at the same depths as the Si LVV Auger spectra in Fig. 3(a), 3(b), and 3(d).

The Si 2p spectrum of the surface prior to sputtering [Fig. 5(a)] has the highest energy peak with the smallest FWHM. About 1 min of sputtering induces a slight shoulder at the right-hand side of the main peak, which is shifted towards lower energy [Fig. 5(b)]. In the bulk of the film, the shoulder observed in the surface region becomes a resolved peak [Fig. 5(d)].

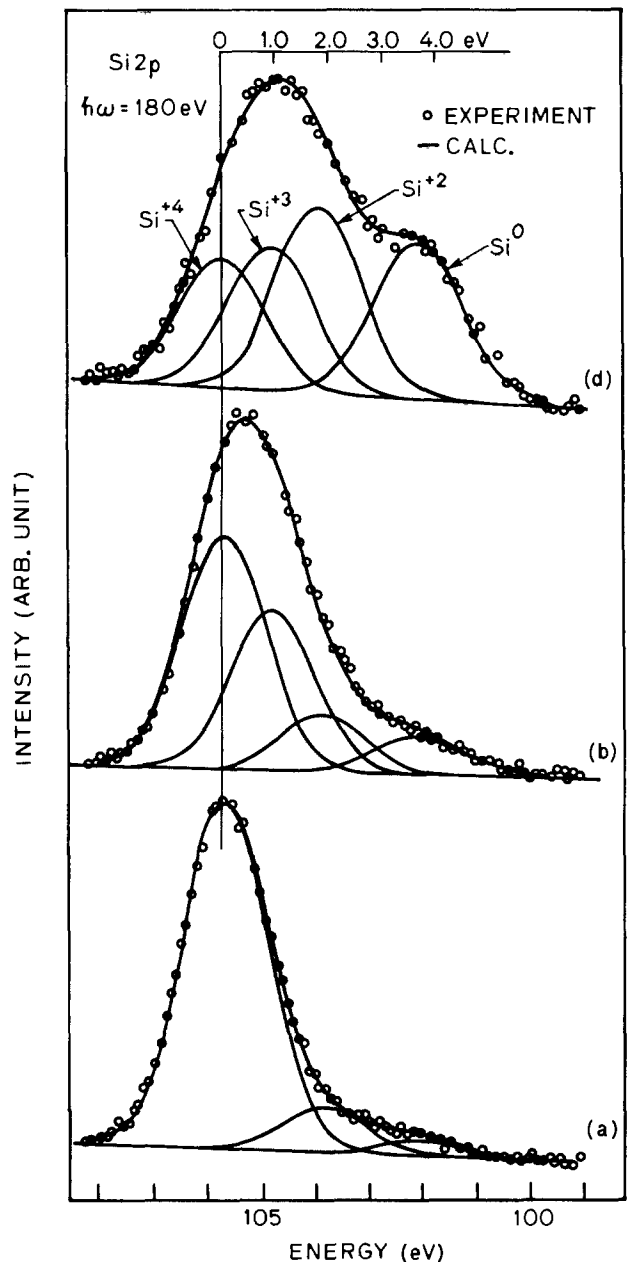


Fig. 5. Si 2p spectra of the as-grown SIPOS film at various depths indicated by the same small letters as in Fig. 2. The measured spectra (dots) are fitted by the five Gaussian peaks (solid lines) corresponding to five possible charge states of Si. Note that some of the five possible Gaussians do not contribute to the spectra. Energy scale refers to the valence band maximum of Si.

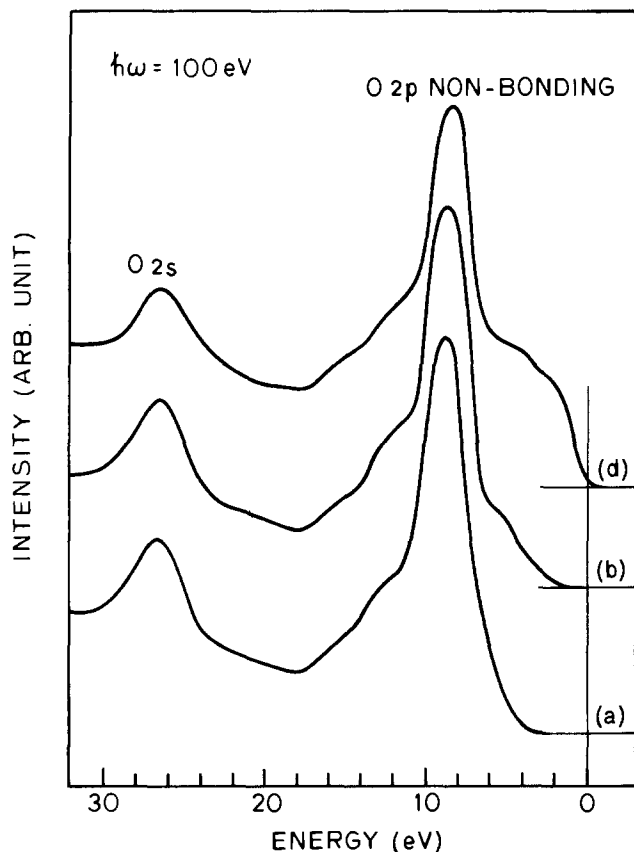


Fig. 6. Valence electronic structure of the As-grown SIPOS film at various depths indicated by the same small letters as in Fig. 2. Energy scale refers to the valence band maximum of Si.

The interpretation of the Si 2p spectra is complicated and a matter of considerable controversy (6, 9, 10, 11). In this paper, we have used a least squares method to fit the measured spectra by five Gaussians corresponding to five possible charge states of Si atoms. The same linewidth was assumed for all five charge states, and the energy differences between adjacent charge states were selected following the bond charge model of Ref. (12). We tried several different values for the chemical shift to minimize the error for all three spectra in Fig. 5. The results are shown with solid lines. We obtained 3.75 eV for the chemical shift of SiO₂ (Si⁴⁺), referred to the energy of the pure Si peak. This value is very close to that reported for thin SiO₂ layers formed in the ultrahigh vacuum on Si surfaces (3.8 eV) (11) and "near interface" SiO₂ as reported by Grunthaler and Maserjian (3.9 eV) (10). One interesting result is that there is no contribution of an Si⁺¹ charge state (corresponding to Si₂O) in any of the three spectra in Fig. 5. The shift and the broadening of the main peak in the bulk spectra are explained by the appearance of Si⁺² and Si⁺³ charge states in addition to the Si⁺⁴ state.

The valence structure at the surface [Fig. 6(a)] is almost identical to that of SiO₂, consistent with the results of the Si 2p and Si LVV Auger spectra. Although 1 min of sputtering induces a shift of the major Si 2p peak, the O 2p nonbonding orbital in the valence band (the peak at ~9 eV in Fig. 6) does not appear to shift. Only the structure near the valence band maximum of SiO₂ appears in addition. In the bulk of the film, the valence structure [Fig. 6(d)] has a contribution from pure Si corresponding to the appearance of the Si⁰ state in the Si 2p spectrum.

Discussion

As shown in Fig. 3(d), the Si LVV spectrum of the as-grown SIPOS film is composed of pure Si, shifted pure SiO₂, and the extra peak near 83 eV. The Si

component in the bulk was found to be about one quarter as intense as pure Si. If the oxide in the film is SiO₂, the intensity of the Si component should be as large as 60% of pure Si since the average oxygen concentration of the film is about 40 a/o. This result indicates that the SiO_x in the film has an average stoichiometry with $x < 2$. In fact, the Si 2p spectra [Fig. 5(d)] indicate that the oxide is a mixture of SiO₂, Si₂O₃, and SiO. The fact that the Si LVV Auger spectra of the film can be fitted with the spectra of shifted pure SiO₂ could be interpreted as that some SiO_x phases give the same spectral shape of the Si LVV spectra as SiO₂, but that spectra is shifted due to the different chemical environment.

The 83 eV peak in the Si LVV Auger spectra has recently been reported at the Si-SiO₂ interface of MOS structures by several researchers (13, 14), and this peak has been attributed to the chemical structure characteristic of the connective layer between Si and SiO₂. The same idea might be applicable to the case of the SIPOS films because both AES and PES data indicate the existence of both Si and SiO₂ in the film, and there must be some connective species between them. Since the appearance of the 83 eV peak in the Si LVV Auger spectra is accompanied by the growth of the SiO peak in the Si 2p spectra, the 83 eV peak can probably be associated with the SiO bonding configuration.

Annealing at 1100°C causes two changes in the Si LVV spectra: disappearance of the 83 eV peak and a reduction in the shift of the SiO₂ component. The latter effect is probably due to the change in the oxide from SiO_x ($x < 2$) towards SiO₂. This is consistent with the recent report by Maxwell and Knoll (15) concerning the change of infrared absorption spectra of SIPOS films by annealing. They observed the shift of the 9 μm absorption band (represents Si-O-Si vibration) by the annealing from the considerably long wavelength position of as-grown SIPOS film towards the shorter wavelength corresponding to SiO₂.

The disappearance of the 83 eV peak by annealing can be understood in terms of the growth of polysilicon grains and larger SiO₂ particles in the film. Since 1100°C annealing causes crystal growth of Si in the film from less than 10 to ~40 Å in diameter (2), the volume fraction of the connective layer between Si and SiO₂ particles in the escape depth of Auger electrons is reduced by annealing and the contribution to the 83 eV peak in the Si LVV spectra is reduced.

The "pile-up" of oxygen near the interface between the SIPOS film and the Si substrate can also be explained by the growth of an SiO₂ film at that interface in which case the intensity of the 83 eV peak in the Si LVV spectra at the SIPOS-Si substrate interface [Fig. 4(j)] would be reduced.

We used an argon ion beam for profiling in these experiments. Ion sputtering has been reported to create an additional peak at ~91 eV in the $dEN(E)/dE$ spectra of SiO₂ (16). Since the position of the peak corresponds to pure Si, the measured spectra of SIPOS films might contain additional contributions from ion-induced components. To minimize these effects, a low ion beam energy (0.5 keV) was used.

Even so, it is surprising that ion beam effects are not more severe than have been observed. For example, Thomas and Goodman (6) have performed profiling experiments both with chemical etches as well as sputter profiling; there are differences in these PES spectra, but the major features are still present. We therefore feel that the ion-induced artifacts in the spectra presented do not alter the conclusions presented.

In their work, Thomas and Goodman (6) studied 900°C annealed SIPOS films with AES and XPS using chemical etching with buffered HF to remove the surface layer. Although their samples were prepared by low pressure CVD, the Si 2p spectra with about the

same oxygen concentration as those reported here have two major peaks separated by 3.7 eV. This is close to the value we derived for the chemical shift of SiO₂. Based on a 4.4 eV for the chemical shift of SiO₂, they interpreted their data as indication of the existence of Si⁺³ and Si⁰ (pure Si), as well as Si⁺¹ as a connective layer.

This interpretation is not consistent with other recent work. Garner *et al.* (11) reported a 3.8 eV shift for a thin SiO₂ layer on the Si surface. Grunthaner and Maserjian (10) have reported that the SiO₂ peak in the Si 2p spectra shifts by 0.45 eV towards lower binding energy as the Si-SiO₂ interface is approached from the bulk SiO₂. They interpreted this effect as due to the change in the Si-O-Si bond angle caused by stress at the interface which is not accompanied by a stoichiometry change. Since it is reasonable to believe that as-grown SIPOS films are a mixture of small Si regions and small SiO_x regions, it is likely that the structure of the SiO₂ in the film is very strongly distorted and that the chemical shift of the SiO₂ phases is much smaller than the value reported for bulk SiO₂. We therefore believe that the major features in the data of Williams and Goodman are not due to Si⁺³ and Si⁰ but Si⁺⁴ (SiO₂) and Si⁰, as in the present work.

One can speculate about the effects of annealing on the SIPOS films using the foregoing arguments. The as-grown film contains very small or amorphous Si grains surrounded with "SiO_x" which is a mixture of SiO₂ and Si₂O₃. These two regions are connected with an SiO bonding configuration. Annealing at 1100°C causes crystal growth of Si, and mixed SiO_x stabilizes to become SiO₂.

Conclusions

40 a/o oxygen SIPOS films have been studied with AES and PES. The Si LVV Auger spectra of the as-grown films were found to be composed of the spectrum of pure Si and SiO₂ and a third peak at ~83 eV. The SiO₂ component was found to be significantly shifted towards higher kinetic energy. The data were interpreted to indicate the existence of an SiO_x phase rather than pure SiO₂ by comparing the Si 2p PES spectra with the Si LVV Auger spectra. The shift of the SiO₂ component is reduced by the 1100°C annealing at the same time the 83 eV peak disappears. These effects are explained by the growth of polysilicon grains and the change in the oxide from SiO_x phases towards stoichiometric SiO₂.

Acknowledgment

This work was supported in part by the Defense Advanced Research Projects Agency (DARPA) pursu-

ant to ARPA Order No. 2985, dated 18 February 1975, Program Code @15p87. The authors would like to thank Mr. H. Yamoto for preparing the samples and Professor E. I. Lindau and Mr. C. Y. Su for assistance with the PES measurements. The authors would also like to thank Professor W. E. Spicer in whose laboratories these studies were performed and one of the referees for extensive editing of the manuscript.

Manuscript submitted Oct. 30, 1979; revised manuscript received Feb. 5, 1980.

Any discussion of this paper will appear in a Discussion Section to be published in the June 1981 JOURNAL. All discussions for the June 1981 Discussion Section should be submitted by Feb. 1, 1981.

Publication costs of this article were assisted by Stanford University.

REFERENCES

1. M. Hamasaki, T. Adachi, S. Wakayama, and M. Kikuchi, *Solid State Commun.*, **21**, 591 (1977).
2. M. Hamasaki, T. Adachi, S. Wakayama, and M. Kikuchi, *J. Appl. Phys.*, **49**, 3987 (1978).
3. M. L. Tarng, *J. Appl. Phys.*, **49**, 4069 (1978).
4. D. Dong, E. A. Irene, and D. R. Young, *This Journal*, **125**, 819 (1978).
5. J. T. McGinn and A. M. Goodman, *Appl. Phys. Lett.*, **34**, 603 (1979).
6. J. H. Thomas III and A. M. Goodman, *This Journal*, **126**, 1766 (1979).
7. T. Aoki, T. Matsushita, H. Yamoto, H. Hayashi, M. Okayama, and Y. Kawana, Abstract 148, p. 352, The Electrochemical Society Extended Abstracts, Toronto, Canada, May 11-16, 1975.
8. T. Matsushita, T. Aoki, T. Otsu, H. Yamoto, H. Hayashi, M. Okayama, and Y. Kawana, *Jpn. J. Appl. Phys. Suppl.*, **15**, 35 (1975).
9. S. I. Raider, R. Flisch, and M. Palmer, *This Journal*, **122**, 413 (1975).
10. F. J. Grunthaner and J. Maserjian, in "The Physics of the SiO₂ and Its Interfaces," P. T. Pantelides, Editor, p. 389, Pergamon Press, New York (1978).
11. C. M. Garner, I. Lindau, C. Y. Su, P. Pianetta, and W. E. Spicer, *Phys. Rev. B*, **19**, 3944 (1979).
12. See, for instance, J. A. Conner, "Handbook of X-Ray and Ultraviolet Photoelectron Spectroscopy," Chap. 5, D. Briggs, Editor, Heyden, New York (1977).
13. C. R. Helms, Y. E. Strausser, and W. E. Spicer, *Appl. Phys. Lett.*, **33**, 767 (1978).
14. J. F. Wagner and C. W. Wilmsen, *J. Appl. Phys.*, **50**, 874 (1979).
15. H. R. Maxwell, Jr. and W. R. Knoll, Abstract 166, p. 441, The Electrochemical Society Extended Abstracts, Boston, Mass., May 6-11, 1979.
16. J. S. Johannessen, W. E. Spicer, and Y. E. Strausser, *J. Appl. Phys.*, **47**, 3028 (1976).

Growth and Microstructure of α -Al₂O₃ on Ni-Al Alloys: Internal Precipitation and Transition to External Scale

H. M. Hindam¹ and W. W. Smeltzer*

Department of Metallurgy and Materials Science, McMaster University, Hamilton, Ontario, Canada L8S 4M1

ABSTRACT

Oxidation properties of Ni-2 and 6 w/o Al alloys were investigated in 1 atm oxygen at temperatures in the range 1273°–1573°K. Ni-2 w/o Al oxidized parabolically, one order of magnitude more rapid than pure nickel, to a duplex scale by metal diffusion consisting of outer and inner layers of Al-doped NiO and NiO-NiAl₂O₄, respectively, and an internal zone of rodlike Al₂O₃ precipitates by oxygen diffusion through the Al-depleted alloy. Oxidation kinetics of Ni-6 w/o Al alloy were irreproducible due to early-stage formation of an imperfect Al₂O₃ scale containing NiO nodules. Impingement of favorably oriented rodlike Al₂O₃ precipitates growing beneath the NiO nodules accompanied with lateral diffusion of aluminum to react with oxygen at the precipitation front eventually led to transition from internal oxidation to development of a multilayered NiO|NiAl₂O₄|Al₂O₃ scale.

Nickel superalloys are used as construction materials for gas turbine engines, combustion furnaces, and high temperature reactors. These alloys, consisting of a Ni-Al γ -solid solution matrix to which several elements are added to impart desirable mechanical properties by solution and precipitation hardening (1), are often protected by nickel aluminide coatings containing Ni₃Al, NiAl, and Ni₂Al₃ intermetallic phases (2). The Ni-Al system, nonetheless, has been the subject of only few oxidation studies (3-9). The conditions under which Al₂O₃² is precipitated internally or is formed as a scale are well established (3), but the growth mechanisms of Al₂O₃ in both cases are not yet understood. The present paper defines the mechanism of internal precipitation and transition to growth of a continuous Al₂O₃ film beneath NiO|NiAl₂O₄ layers.

Experimental

Alloys of nominal compositions 2 and 6 weight percent (w/o) Al were prepared by electric arc melting of nickel (99.99 w/o pure) and aluminum (99.95 w/o pure) in an argon atmosphere gettered of oxygen by titanium chips. Actual compositions of the γ -solid solution phase alloys were 2.1 and 5.9 w/o Al corresponding to 4.4 and 12.0 atomic percent (a/o) Al, respectively. After homogenization at 1473°K for 24 hr in ultrapure grade argon, slices 1 mm thick were electric spark cut from the 1 cm diameter alloy buttons. These slices were subjected to metallographic polishing finishing with 1 μ m diamond paste.

Oxidation runs were carried out in ultrapure flowing oxygen at 1 atm in the temperature range 1273°–1473°K. The reaction kinetics were determined using an assembly equipped with a semiautomatic balance as described elsewhere (10). Several Ni-6 w/o Al specimens were also oxidized in static 1 atm oxygen at 1573°K. Oxide phases were identified by x-ray diffraction powder analyses using Ni filtered Cu-K α radiation. Light and scanning electron microscopy (SEM) were used to study the morphologies of reaction products. Specimens were mounted in room-setting epoxy resin and, whenever etching was difficult, fracture cross-sections were prepared. Electron probe micro-analyses (EPMA) were used to determine composition profiles within the reaction zone. It was necessary to vapor

deposit carbon on the specimens to avoid electrical charge buildup during SEM and EPMA analyses.

Results

Ni-2 w/o Al Alloy

Oxidation kinetics.—These kinetics obeyed a parabolic relation during the intervals investigated (up to 50 hr). Arrhenius plots of the parabolic oxidation rate constants of this alloy and those for pure nickel are shown in Fig. 1. The values of the activation energy for oxidation of the alloy and nickel are 146 and 193 kJ/g mole, respectively.

Scale morphology and structure.—Oxidation led to growth of an internal duplex scale consisting of outer dark gray and inner light green layers and an internal oxide precipitation zone in the alloy. The scale was fractured along the interface between these layers to obtain separate samples for x-ray analyses. The internal precipitates, which were extracted by dissolving the alloy in 10% bromine-methanol, were also subjected to x-ray analyses. According to these determinations, the outer layer was NiO, the inner layer was mainly NiO containing NiAl₂O₄ as a second phase and the internal precipitates were α -Al₂O₃.

Different regions of the duplex scale and internal precipitation zone are shown in Fig. 2. Figure 2 (a) is an overall cross section and (b) is a scale fracture cross section illustrating the coarse grained columnar NiO layer. Well-defined closed pores, 1-5 μ m, were located in the vicinity of its interface with the inner layer. The scale surface adjacent to the gas phase exhibited a terraced structure and grain size of \sim 30 μ m [Fig. 2(c)]. The structure of the inner oxide layer [Fig. 2(d)] consisted of rod-shaped NiAl₂O₄ growths embedded in a NiO matrix. The rods lay parallel to the scale growth direction and extended completely across this inner layer as extensions of the Al₂O₃ rods but their relatively small extension beneath the alloy surface could not be experimentally determined.

Morphologies of Al₂O₃ precipitates were not completely revealed by mechanical polishing [Fig. 2(d)] or chemical etching [Fig. 2(e)], but an appropriate relief was obtained by "deep etching" [Fig. 2(f)]. It is seen here that the precipitates extend across the precipitation zone as cylindrical rods. SEM images in Fig. 3 further document these structural features. Their population and size were relatively uniform through the precipitation zone [Fig. 3(a)] except at alloy

* Electrochemical Society Active Member.

¹ Present address: Lawrence Berkeley Laboratory, University of California, Berkeley, California 94720.

Key words: oxidation Ni-Al alloys, Al₂O₃, NiAl₂O₄, NiO.

² Al₂O₃ is used in the text to designate α -Al₂O₃.

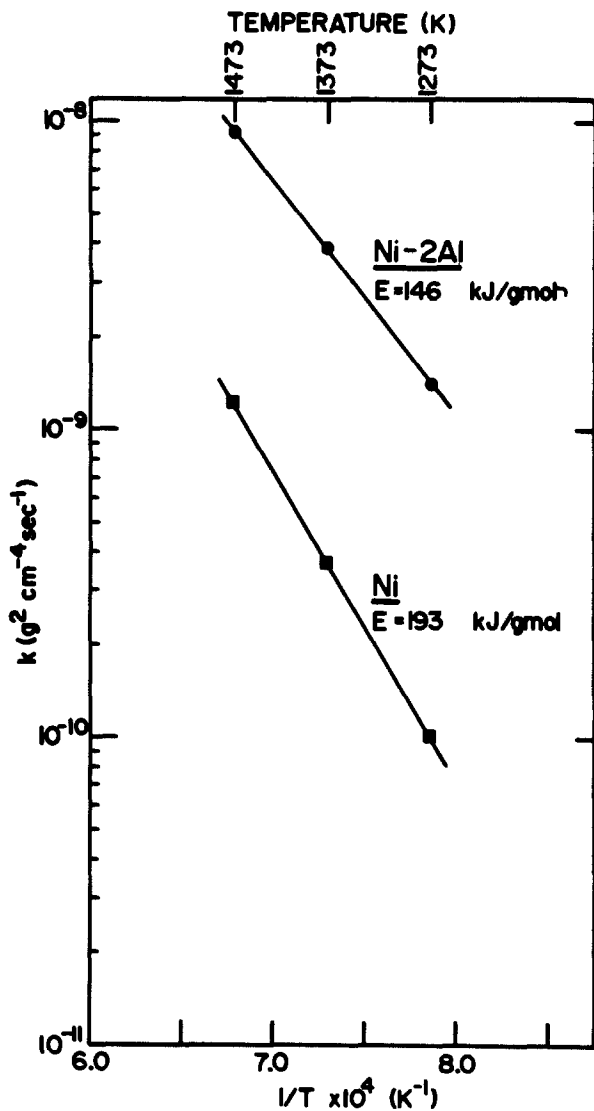


Fig. 1. Arrhenius plot of the parabolic rate constants for Ni and Ni-2 w/o Al oxidation.

grain boundaries where they are more dense without forming a continuous layer [Fig. 3(b)]. These parameters depended on temperature and alloy composition: the precipitates formed at 1473°K were coarser and have a wider spacing, 3 and 10 μm , respectively, than at 1273°K. This former precipitate size and spacing corresponded to a fractional surface coverage of 0.07. The cylindrical shape of the precipitated rods was further ascertained by examining a transverse section [Fig. 3(c)]. It was not possible to establish if a boundary existed at the precipitation front [Fig. 3(d)].

Nickel and Al x-ray scans across the scale and internal oxidation zone are shown in Fig. 4. The alloy was depleted of aluminum ahead of the precipitation front. Amounts of nickel dissolved in Al_2O_3 precipitates or the composition of NiAl_2O_4 growths could not be determined because their lateral dimensions were only $\sim 5 \mu\text{m}$. The outer NiO layer was doped with aluminum but quantitative determination of its amount was not possible because Al x-ray counts were only slightly above those of background.

Layer thickness measurements.—It was possible to determine rates of growth for both oxide layers and penetration of the internal oxidation zone. The latter was measured by optically examining etched cross sections while SEM was used to locate the interface between the two oxide layers by following Al x-ray counts using an energy dispersive analyzer in this instrument. The internal oxidation zone grew most

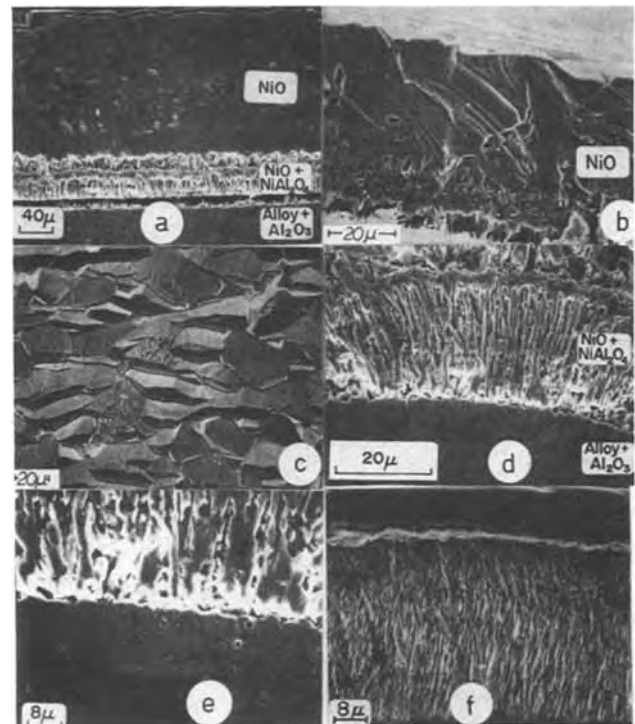


Fig. 2. Ni-2 w/o Al alloy scale structure [SEM images except (e) light microscope image; 1473°K except (f), 1273°K]. (a) Overall cross section, (b) outer NiO layer, (c) outer scale surface, (d) inner NiO-NiAl₂O₄ layer, (e) internal precipitation zone, deeply etched (f).

rapidly and the inner NiO-NiAl₂O₄ two-phase layer grew most slowly. All layers thickened according to a parabolic relation (Fig. 5), and values of the growth rate constants are given in Table I.

Ni-6 w/o Al Alloy

Oxidation kinetics.—These kinetics which were irreproducible due to a phenomenon of nodular growth are shown in Fig. 6. Furthermore, oxygen uptake during initial stages was dependent on alloy surface preparation since specimens polished to 1 μm diamond exhibited smaller uptake and formed fewer nodules than specimens abraded on coarse SiC papers. In this latter case, NiO formed rapidly as an almost complete scale rather than as scattered nodules. The oxidation kinetics when represented by parabolic plots (Fig. 7) exhibited an initial fast stage subsequent to which the kinetics declined to ultimately approach a second slower parabolic rate. At 1473°K, the value of the rate constant during the first parabolic stage was $k_1 = 2.5 \times 10^{-1} \text{ g}^2 \text{ cm}^{-4} \text{ sec}^{-1}$, and its value during the second parabolic stage was $k_2 = 8 \times 10^{-11} \text{ g}^2 \text{ cm}^{-4} \text{ sec}^{-1}$. The balance sensitivity did not permit accurate measurement of reaction kinetics beyond this stage since the specimens oxidized at an extremely low rate.

Scale morphology and structure.—As illustrated in Fig. 8, a thin Al_2O_3 film through which scattered NiO nodules protruded grew in early exposure periods.

Table I. Parabolic rate constants k_o , k_i , and k_p for growth of outer oxide layer, inner oxide layer, and internal oxide precipitation zone, respectively, of Ni-2 w/o Al alloy

T (°K)	$k_o \text{ (}\mu\text{m/hr}^{1/2}\text{)}$ Outer layer	$k_i \text{ (}\mu\text{m/hr}^{1/2}\text{)}$ Inner layer	$k_p \text{ (}\mu\text{m/hr}^{1/2}\text{)}$ Precipitation zone
1273	3.8	1.4	19.8
1373	10.8	4.1	37.8
1473	22.2	11.4	49.8

Fig. 3. Details of the Al_2O_3 precipitation zone [SEM images, (a) and (b) 1273°K, (c) and (d) 1473°K]. (a) Deep-etched longitudinal section, (b) precipitation at grain boundaries, (c) deep-etched transverse section, (d) alloy precipitation front (etched).

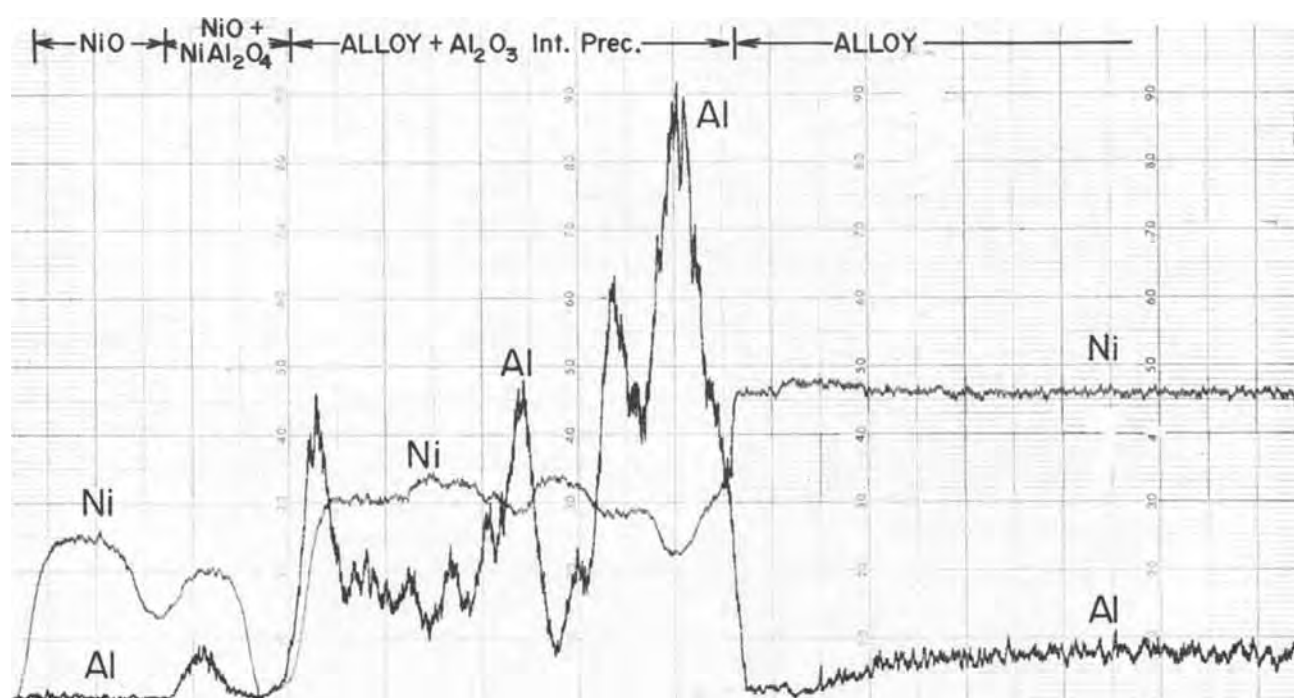
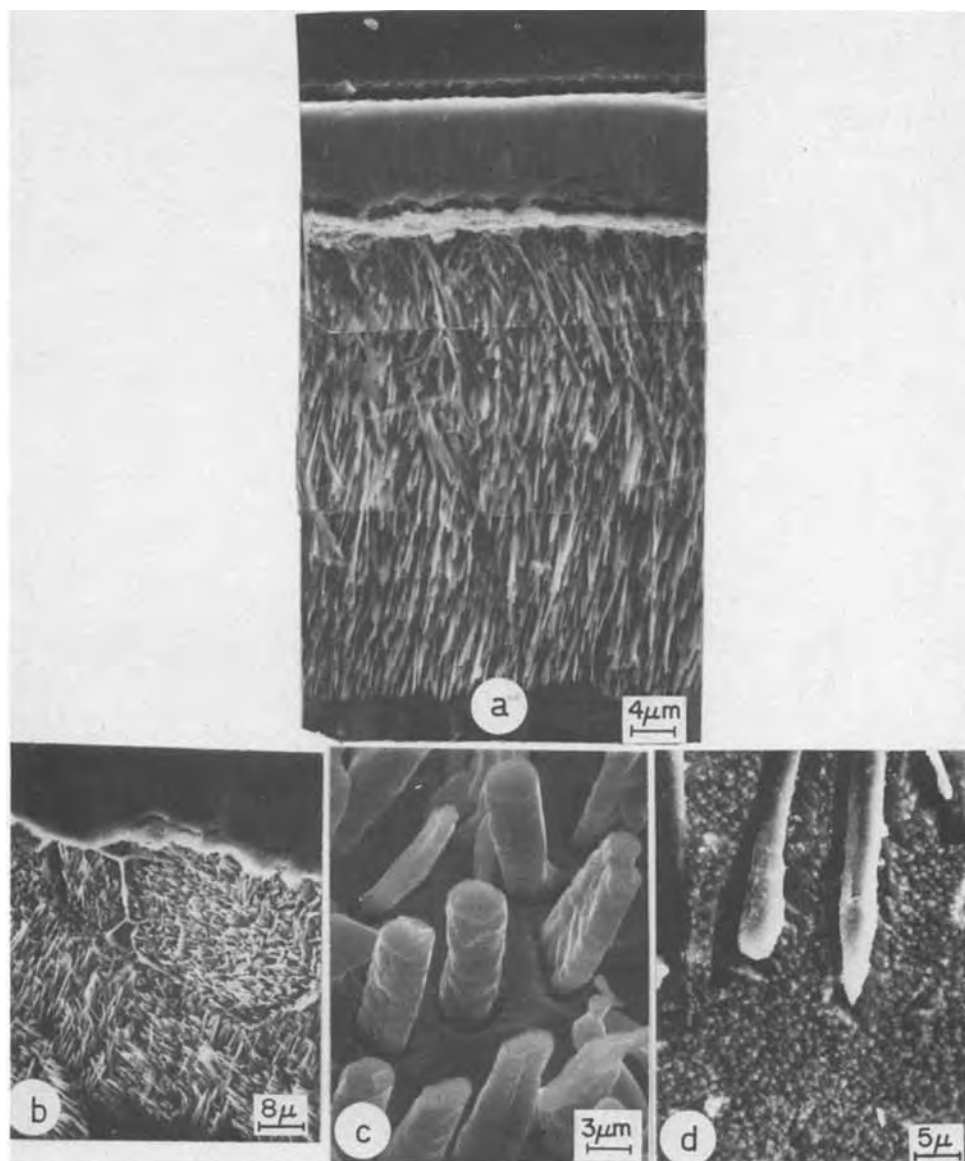


Fig. 4. Ni and Al electron microprobe x-ray scans across a scale formed on Ni-2 w/o Al alloy

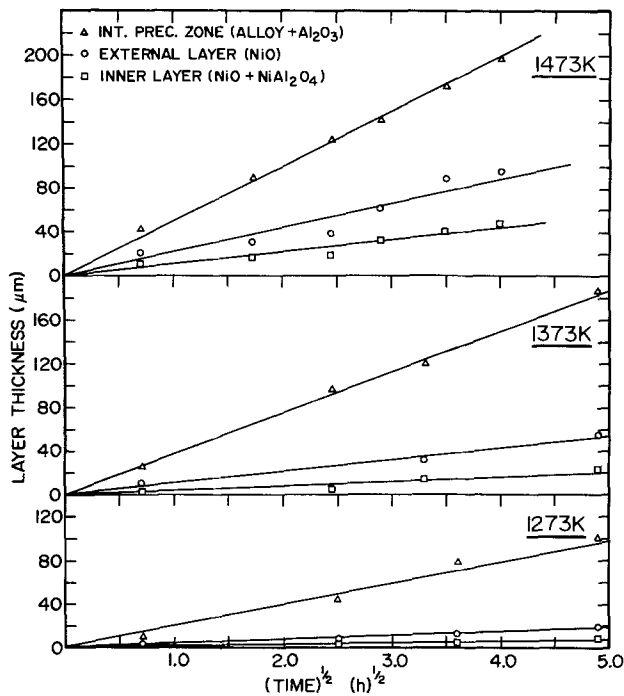


Fig. 5. Parabolic plots of layer growth on Ni-2 w/o Al alloy

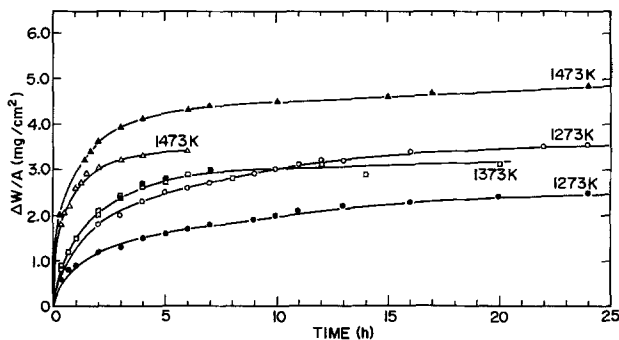


Fig. 6. Ni-6 w/o Al oxidation kinetics: linear presentation of oxygen uptake vs. time.

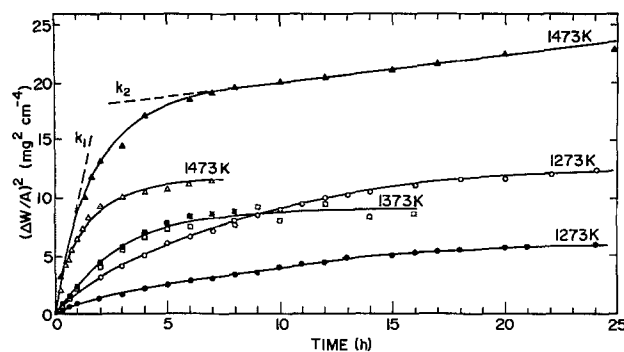


Fig. 7. Ni-6 w/o Al oxidation kinetics: parabolic presentation of the square of oxygen uptake vs. time.

Nodules formed preferentially at alloy grain boundaries [Fig. 8(a) and (b)] and at surface imperfections induced by polishing. In the region of a nodule, the scale was of the morphology observed for the Ni-2 w/o Al alloy consisting of an outer coarse grained NiO layer having a terraced surface, an inner NiO-NiAl₂O₄ layer and an internal Al₂O₃ precipitation zone [Fig. 8(a)-(d)]. Lateral growth of the nodules led to regions of duplex structured scale over an internal oxidation zone. In this alloy, nevertheless, a continuous

Al₂O₃ film developed at the internal oxidation front [Fig. 8(d)].

This alloy underwent a long transient stage extending up to 150 hr during which initially formed reaction products transformed to continuous NiAl₂O₄ and Al₂O₃ layers. Light micrographs in Fig. 9 and SEM images taken from larger areas of specimens in Fig. 10 illustrate oxidation behavior during this transient stage. It can be observed that an Al₂O₃ film was formed at several regions of the precipitation front [Fig. 9(a) and Fig. 10(a)]. Lateral growth of these film sections eventually led to development of a complete film along the highly irregular alloy interface which separated the internal oxidation zone from the alloy substrate [Fig. 9(b) and Fig. 10(b)]. Subsequent reaction within this isolated alloy and Al₂O₃ precipitates resulted initially in formation of an NiO-NiAl₂O₄ conglomerate [Fig. 9(c)-(d), Fig. 10(b)] which was finally converted to a homogeneous NiAl₂O₄ layer laying between the outer NiO and inner Al₂O₃ layers [Fig. 10(c)].

Initiation of continuous Al₂O₃ film formation, which is indicated by arrows in Fig. 9 and 10, occurred at random sites within the alloy grains where the rod-like precipitates impinged. Confirmatory evidence for this mechanism for impingement of particles and lateral growth of Al₂O₃ film at the internal oxidation front is depicted in Fig. 11. Figure 11(a) illustrates that the rodlike precipitates tend to impinge while Fig. 11(b) shows a section of the Al₂O₃ film at the internal oxidation front. Formation of Al₂O₃ depleted the aluminum alloy concentration at precipitate tips but led to insignificant aluminum depletion from the alloy beneath the film since it acted as a diffusion barrier for reactants. This was verified by determining the aluminum profile in these two alloy regions as shown in Fig. 12. It is evident that the alloy is more significantly depleted of aluminum in vicinity of the precipitates (line A-A) than in the region where a continuous film was formed (line B-B). This lateral concentration gradient gave rise to aluminum diffusion in the alloy from beneath the discontinuous film to neighboring precipitates where it reacted with oxygen migrating inward to cause continual lateral film growth [Fig. 11(b)].

A fully developed scale at the highest investigated temperature of 1573°K was of duplex structure consisting of outer and inner NiAl₂O₄ and Al₂O₃ layers, respectively. This scale morphology is illustrated in Fig. 13 in conjunction with the Al and Ni x-ray maps.

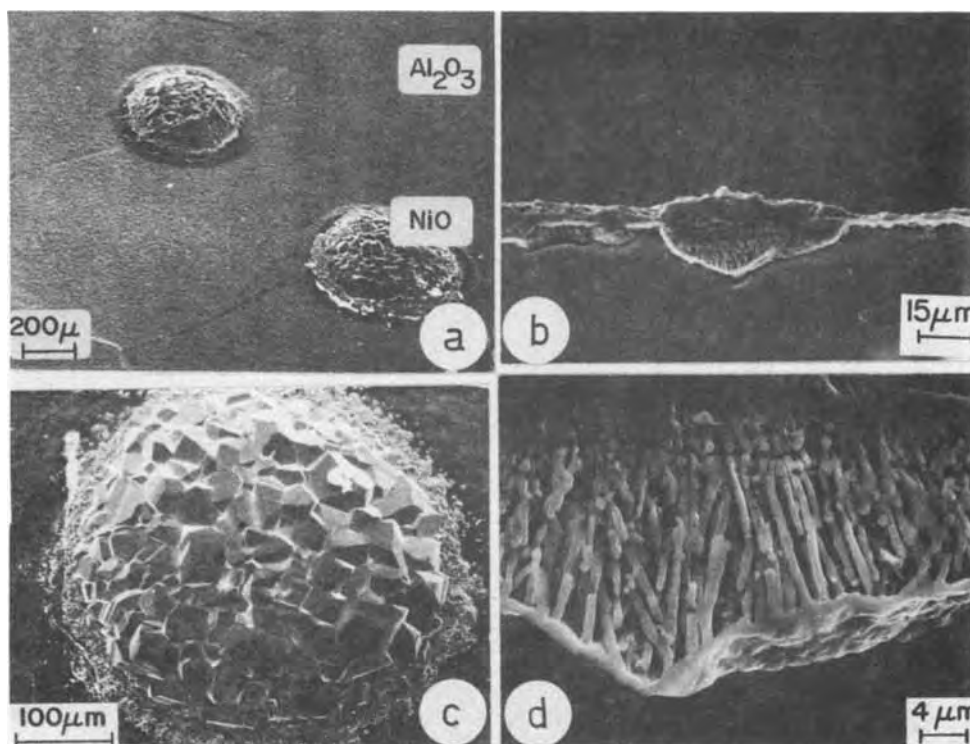
Discussion

Ni-2 w/o Al Alloy

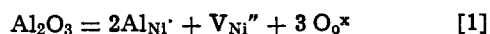
A schematic model depicting parabolic growth of the oxidation products on and in the alloy is illustrated in Fig. 14. The Al₂O₃ rod precipitates beneath the duplex scale are shown to extend perpendicularly to the alloy surface through the internal oxidation zone independent of alloy grain orientation. There is ~7 v/o increase accompanying formation of Al₂O₃ in the alloy and its growth in the form of continuous rods rather than as isolated precipitates decreases the oxide surface area and consequently total interfacial energy.

Growth of the columnar coarse-grained NiO layer is interpreted by predominant outward nickel diffusion since its diffusivity is at least two orders of magnitude larger than the oxygen diffusivity (11). The small density of fine pores found in the intermediate region of the scale [Fig. 2(b)] did not form a continuous network and they are not regarded as effectively contributing to an inward oxidant flux. Formation of these pores possibly arise from ~6 v/o decrease accompanying formation of NiAl₂O₄ from its parent oxides. Partial dissolution of Al₂O₃ into NiO results in alteration of its defect structure according

Fig. 8. Nodular growth on Ni-6 w/o Al alloy (SEM images, 1373°K). (a) Imperfect Al_2O_3 scale containing NiO nodules localized at alloy grain boundaries, (b) nodule outer surface, (c) scale cross section in the vicinity of a nodule, (d) structure of the region beneath a nodule (deeply etched cross section).



to the following equation



where the symbols Al_{Ni}' , V_{Ni}'' , $\text{O}_\text{o}^{\times}$ refer to aluminum dissolved in a nickel site, a nickel vacancy, and oxygen in an oxygen site of NiO, respectively. This increase

in vacancy concentration enhances the nickel diffusivity and combined with the larger oxygen activity gradient across the NiO scale due to the presence of NiAl_2O_4 in its inner region enhances the oxidation rate of the alloy in comparison to pure nickel (Fig. 1). The NiAl_2O_4 particles in the two-phase inner scale

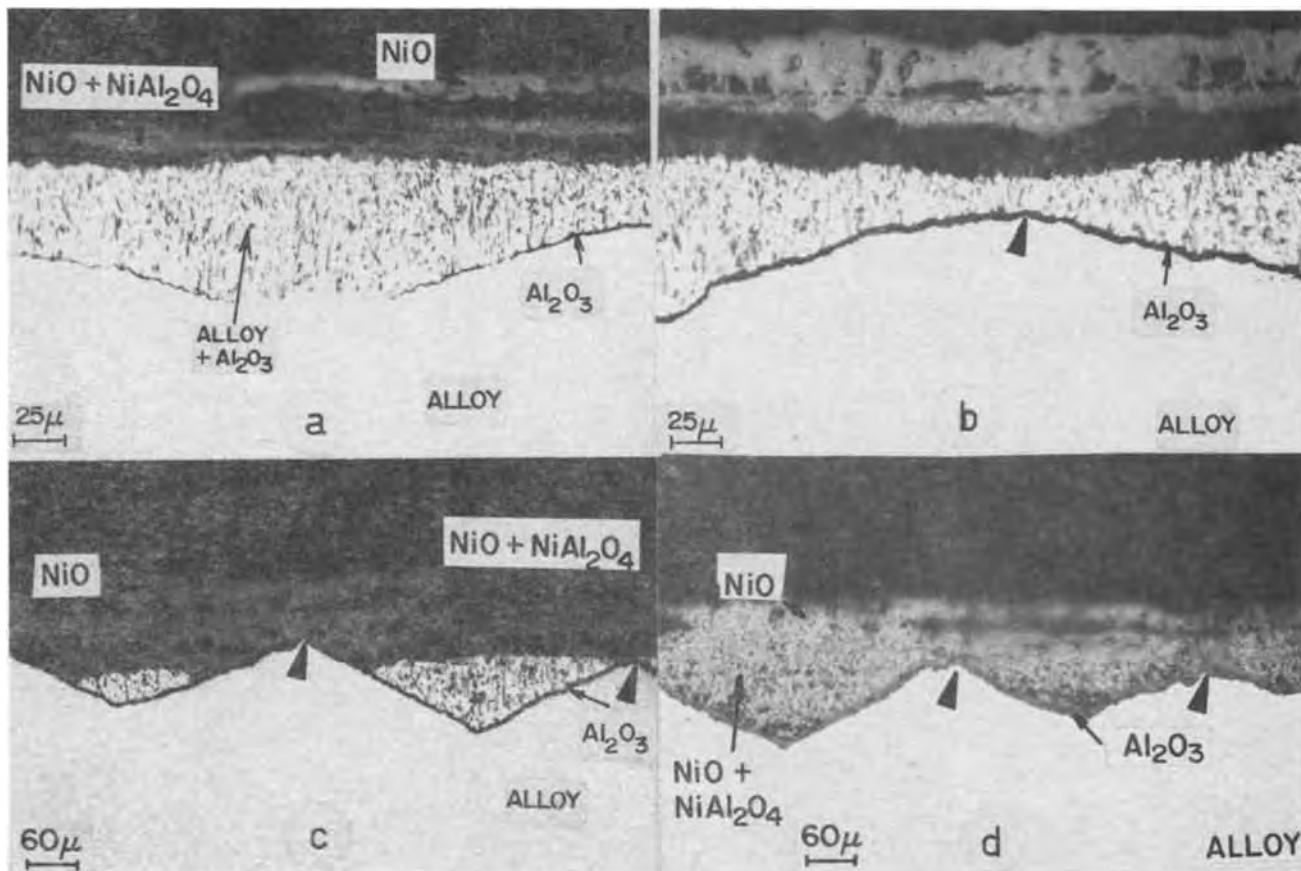


Fig. 9. Ni-6 w/o Al alloy transient oxidation stages (light microscope images, 1473°K). (a) Al_2O_3 internal precipitation and development of a discontinuous Al_2O_3 film, (b) Al_2O_3 continuous film formation, (c) and (d) conversion of the alloy precipitation zone to NiO + NiAl_2O_4 .

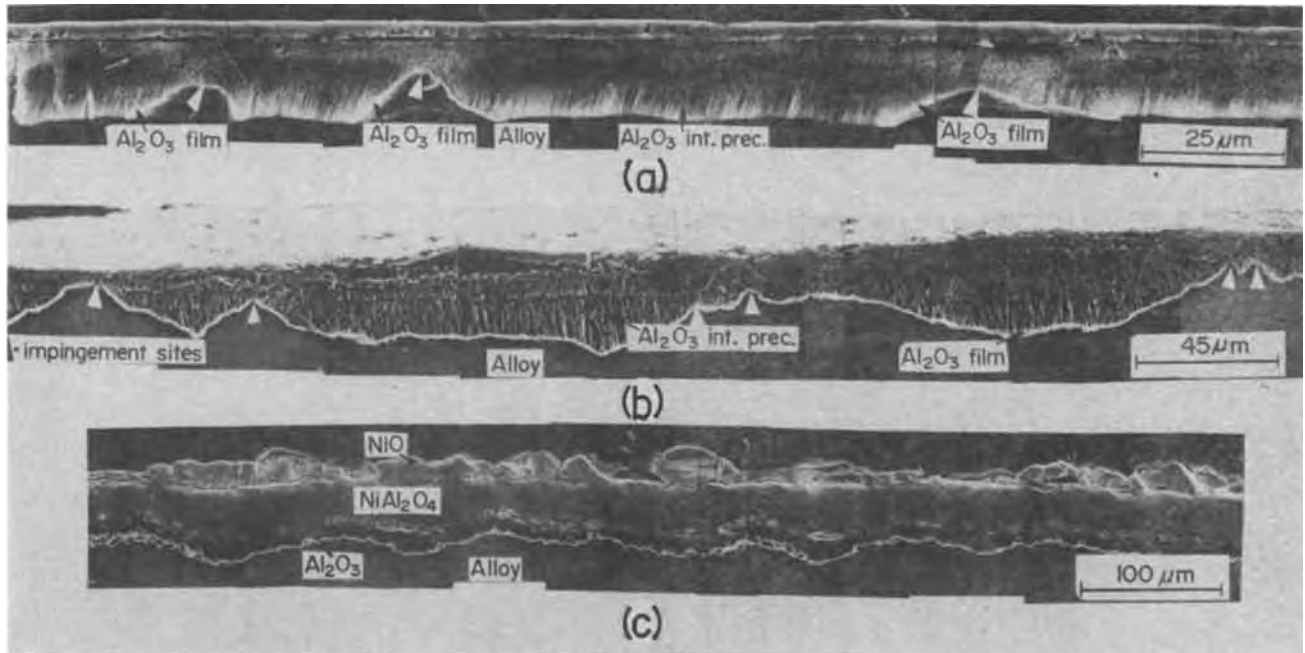
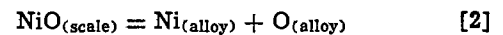


Fig. 10. Ni-6 w/o Al alloy transient oxidation stages (SEM images of deep-etched cross sections, 1373°K). (a) and (b) as Fig. 9(a) and (b), respectively, (c) three-layered morphology.

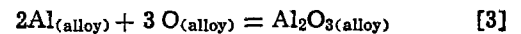
layer, nevertheless, offer a high resistance to outward nickel flux and therefore mask the complete effect of aluminum as a dopant in NiO on scale growth.

Oxygen for growth of Al_2O_3 precipitates resulted from a solid-state displacement reaction between NiO and aluminum present in the alloy since the following equilibrium exists at the two-phase scale/alloy inter-

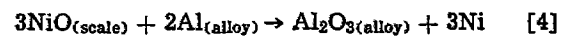
face



Inward oxygen diffusion through the alloy in the internal oxidation zone to react with oxygen at the precipitation front can be represented as



The net displacement reaction then becomes



where the resultant nickel diffuses outward through the scale to react with atmospheric oxygen. If inward growth of the Al_2O_3 rod precipitates was controlled by oxygen diffusion in the aluminum depleted alloy matrix of the internal oxidation zone, the penetration depth, X , of this zone is given to a first approximation by

$$X^2 = 2 \left(\frac{1-f}{f} \right) \left\{ \frac{\text{M.W.}(\text{Al}_2\text{O}_3)}{1.5 \text{ M.W.}(\text{O}_2)} \right\} V_{\text{Al}_2\text{O}_3} D_0 \Delta c_0 t = k_p t \quad [5]$$

where f is the fractional area covered by the Al_2O_3 rods, V is the molar volume, D_0 is the oxygen diffusivity, Δc_0 is the oxygen concentration difference across the alloy precipitation zone, t is time, and k_p is the parabolic penetration rate constant (Table I). Oxygen concentration in the alloy at the alloy/scale interface is assumed equal to its solubility in pure nickel since only trace amounts of aluminum, few ppm, remain in solution upon precipitation of Al_2O_3 (12). Due to the high oxygen affinity for aluminum, the oxygen concentration at the precipitation front is considered as nil. At 1273°K, c_0 in nickel = 0.051 a/o, D_0 in Ni = $4 \times 10^{-9} \text{ cm}^2 \cdot \text{sec}^{-1}$ (14), $f = 0.07$ from measurements in this investigation. Substituting these values in the above equation gives $k_p = 18.7 \mu\text{m} \cdot \text{hr}^{-1/2}$ which is in close agreement with the experimentally determined value, $k_p = 19.8 \mu\text{m} \cdot \text{hr}^{-1/2}$. Based on the temperature dependence of k_p (Table I), the activation energy for oxygen diffusion in the alloy of the internal oxidation zone is 128 kJ/g·mole.

The NiAl_2O_4 part of a rod precipitate was mainly confined to the inner conglomerate layer of the NiO scale. Al_2O_3 in the region of the alloy/scale interface can be converted to NiAl_2O_4 by solid-state reactions.

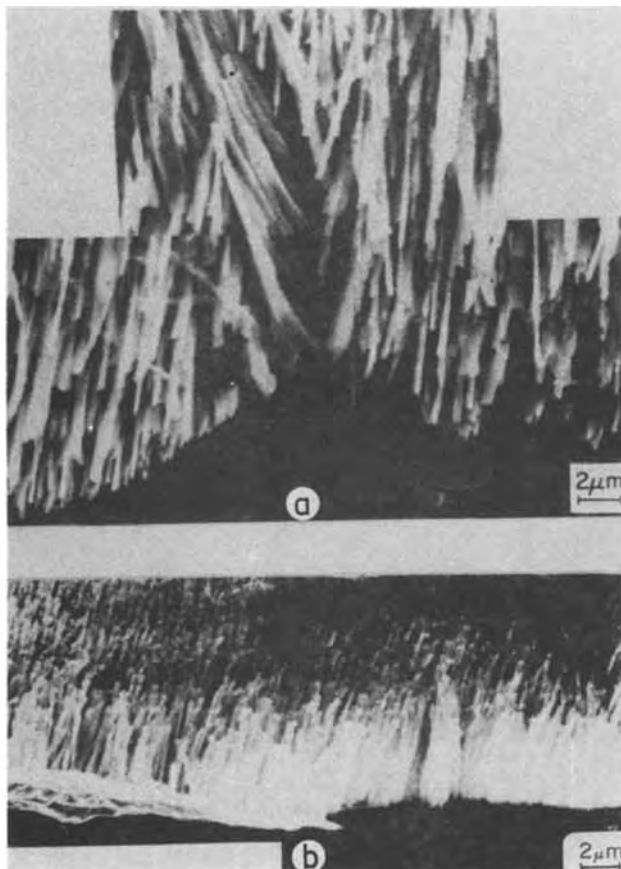


Fig. 11. Development of a continuous Al_2O_3 film on Ni-6 w/o Al alloy. (a) Impingement of Al_2O_3 rodlike precipitates, (b) lateral growth of Al_2O_3 film.

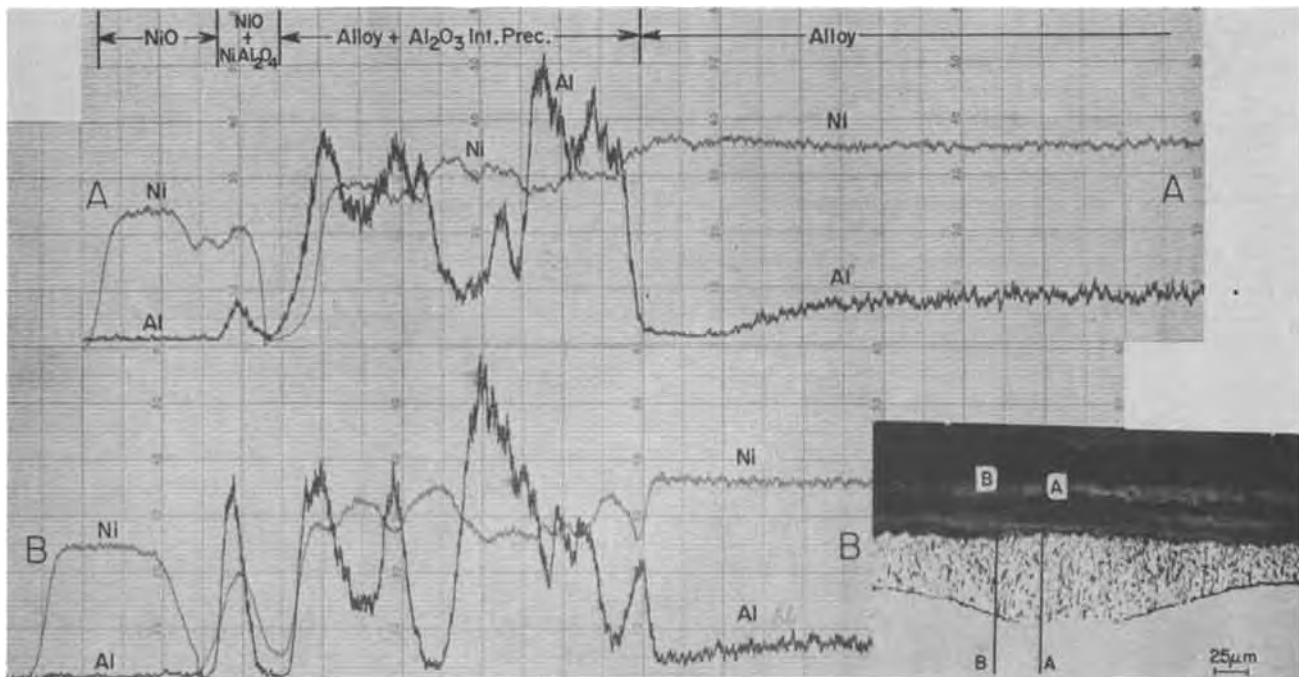


Fig. 12. Ni and Al electron microprobe x-ray scans across a scale formed on Ni-6 w/o Al alloy

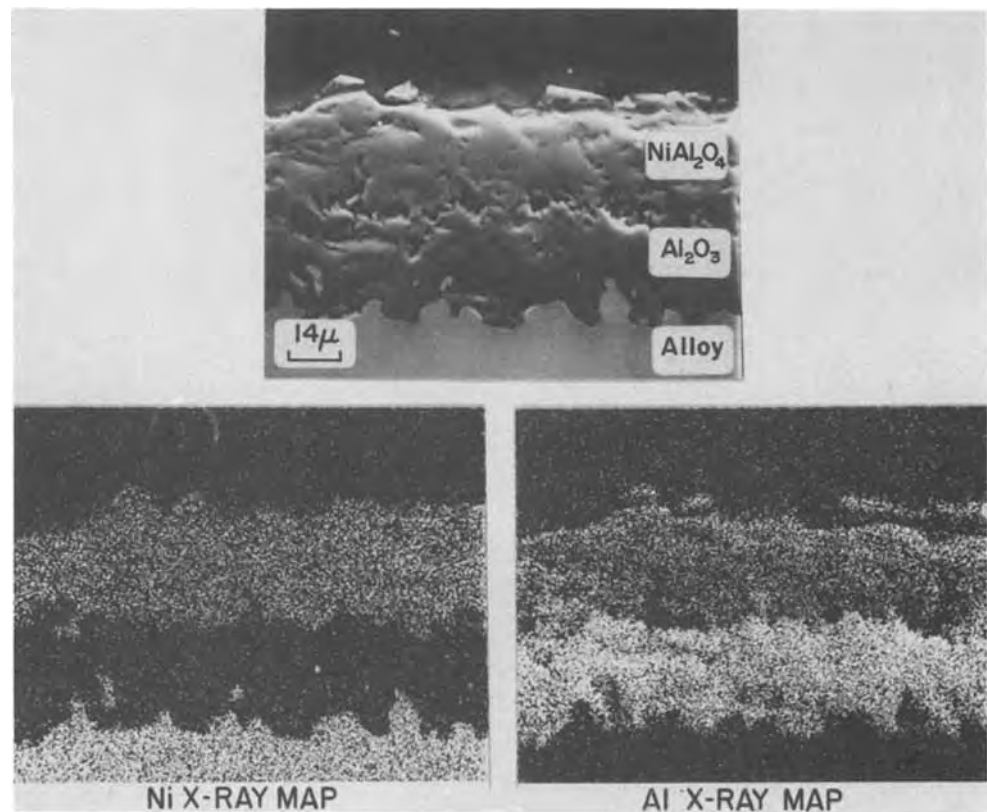
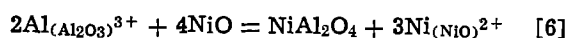


Fig. 13. Ni-6 w/o Al alloy steady-state morphology at 1573°K.

Since the scale retained intimate contact with the receding alloy surface during all stages of oxidation, these reactions involved diffusion processes. In NiO/Al₂O₃ diffusion couples (15), counter diffusion of aluminum and nickel ions give rise to growth of NiAl₂O₄ by means of the following reactions which occur at the NiO/NiAl₂O₄ and NiAl₂O₄/Al₂O₃ interfaces, respectively



For growth of the NiAl₂O₄ rods during the scaling reaction, it would be expected that the Ni²⁺ ions released by reaction [6] would diffuse outward through the scale under the influence of the oxygen activity gradient to form additional NiO. In order, therefore, for the NiAl₂O₄ rods to continually penetrate inward in the absence of a backward Ni²⁺ ionic flux, a solid-state reaction of Al₂O₃ with nickel and dissolved oxygen in the alloy would proceed as follows



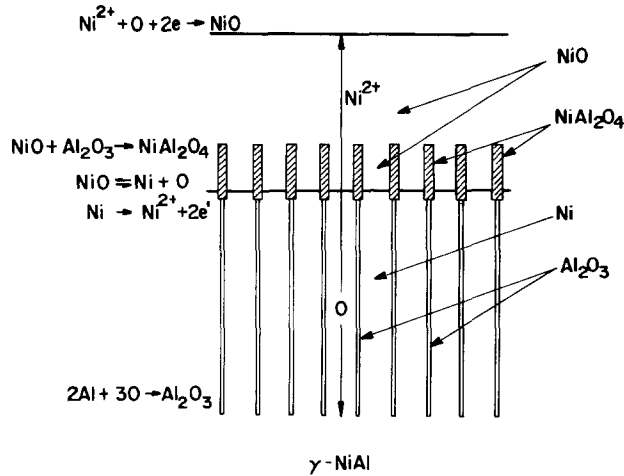


Fig. 14. Schematic model for scale growth on Ni-2 w/o Al alloy

At 1273°K, the NiAl_2O_4 growth rate in a diffusion couple at constant oxygen activity (15) is only ~ 0.1 of the observed advance rate of NiAl_2O_4 in the scale ($k = 0.6$ vs. $11.4 \mu\text{m}\cdot\text{hr}^{-1/2}$). Hence, the growth rate of NiAl_2O_4 as rods in the conglomerate layer of the scale and beneath the alloy surface according to reactions [6] and [8] is probably determined by both boundary and lattice diffusion of the reactants under the influence of the oxygen and metal activity gradients.

Ni-6 w/o Al Alloy

Growth of nodules is a common transient phenomenon of alloy oxidation when large differences exist in diffusion and thermodynamic properties of the oxides. As examples, nodules of less stable and usually less protective oxides have been observed in films of more stable and protective oxides formed on Ni-Al (6,7), Ni-Cr (16,17), Co-Cr-Al (18), Fe-Cr (19,20), Fe-Al (21), and Fe-Si (22) alloys. In the present investigation, the oxidation kinetics decreased continuously with time suggesting that fracture of the oxide film did not occur. The relatively rapid oxygen uptake, however, rather suggests that Al_2O_3 does not form initially as a perfect continuous film but permits NiO to form as a transient phase at alloy grain boundaries and surface imperfections. This oxide subsequently develops as nodules exhibiting a circular base due to isotropic nickel diffusion. As reactant diffusion in NiO (23,24) is several orders of magnitude faster than in Al_2O_3 (25,26), the former overgrows and partially converts the Al_2O_3 film into NiAl_2O_4 .

A mechanism can now be advanced for the transition from scale growth with concurrent internal oxidation to solely external scale growth under these above early stage conditions. This oxidation behavior is interpreted by the schematic model illustrated in Fig. 15. In the region of nodules, the scale grew by a mechanism similar to the case of the Ni-2 w/o Al alloy [Fig. 15(a)]. The value of the parabolic rate constant during this initial oxidation stage, $k_1 = 2.5 \times 10^{-9} \text{ g}^2 \text{ cm}^{-4} \text{ sec}^{-1}$ at 1473°K was the same order of magnitude as that for the latter alloy. As oxidation proceeded, impingement of the Al_2O_3 rod precipitates at random sites of the oxidation front led to the formation of more protective film sections [Fig. 15(b)] and to the observed decline in reaction rate (Fig. 6 and 7). Complete development of an irregular Al_2O_3 film resulting from aluminum lateral diffusion from impingement sites to neighboring precipitates [Fig. 15(c) and (f)] isolated the internal oxidation zone from the alloy substrate. This behavior led to the onset of the second slower parabolic oxidation stage with $k_2 = 8 \times 10^{-11} \text{ g}^2 \text{ cm}^{-4} \text{ sec}^{-1}$ which is one order of magnitude less than $k_1 = 2.5 \times 10^{-9} \text{ g}^2$

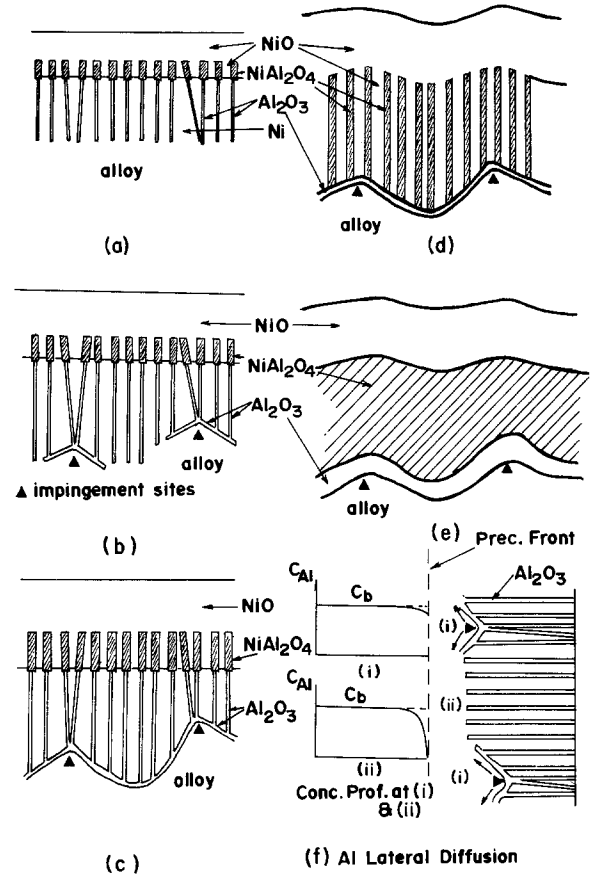


Fig. 15. Schematic model for scale growth on Ni-6 w/o Al alloy

$\text{cm}^{-4} \text{ sec}^{-1}$. During this oxidation stage, nickel from the aluminum depleted alloy in the isolated internal oxidation zone diffused outwards to the scale surface. Simultaneous plastic deformation of the scale and continued incorporation of Al_2O_3 and NiO to form NiAl_2O_4 [Fig. 15(d)] ultimately led to development of the multilayered $\text{NiO}|\text{NiAl}_2\text{O}_4|\text{Al}_2\text{O}_3$ scale [Fig. 15(e) and 10(c)].

Summary

High temperature oxidation properties of dilute Ni-Al alloys were investigated with special interest given to the microstructures and growth kinetics of α - Al_2O_3 .

The alloy of low aluminum concentration, Ni-2 w/o Al, oxidized parabolically. α - Al_2O_3 , which was precipitated internally in the alloy beneath a duplex $\text{NiO}|\text{NiO}-\text{NiAl}_2\text{O}_4$ layered scale, grew as rods extending through the internal oxidation zone parallel to the growth direction and independent of alloy grain orientation. Rod growth, which was controlled by oxygen diffusion in the aluminum depleted alloy of the internal oxidation zone, arose from a displacement reaction between NiO and aluminum in the alloy. A solid-state reaction between NiO and Al_2O_3 accounted for the continual growth of NiAl_2O_4 . A rate-controlling step was not assigned to the reaction because the scale and internal oxidation precipitates grew in a cooperative diffusion mode.

The alloy of higher aluminum concentration, Ni-6 w/o Al, exhibited transient irreproducible oxidation before ultimate development of a $\text{NiO}|\text{NiAl}_2\text{O}_4|\text{Al}_2\text{O}_3$ layered scale. In the early stages of this transient period, $\text{NiO}-\text{NiAl}_2\text{O}_4$ nodules accompanied with an internal oxidation zone of Al_2O_3 precipitates grew through an imperfect Al_2O_3 film. Three distinct reaction stages could be discerned: a stage during which a duplex $\text{NiO}|\text{NiO}-\text{NiAl}_2\text{O}_4$ layered scale and an internal oxidation zone containing Al_2O_3 rod precipitates grew by a mechanism similar to that for the Ni-2

w/o Al alloy, a second and slower stage coinciding with the formation of an Al_2O_3 film at the precipitation front resulting from impingement of the Al_2O_3 rods at random sites and conversion of alloy in the isolated internal oxidation zone to $\text{NiO}|\text{NiAl}_2\text{O}_4$, and a third stage, the kinetics of which are not reported here, controlled by reactant diffusion through the Al_2O_3 film.

Scales formed on both alloys exhibited extraordinary resistance to spalling upon cooling. Scale adherence appeared to be improved by a pinning effect of the rodlike Al_2O_3 precipitates and, in the case of the high aluminum content alloy after long exposures, by the highly irregular inner Al_2O_3 film.

Acknowledgments

This research was completed by H. M. Hindam as part of the requirements for award of the Ph.D. degree at McMaster University. Financial support from the National Research Council of Canada for this research is gratefully acknowledged.

Manuscript submitted July 20, 1980; revised manuscript received Jan. 11, 1980.

Any discussion of this paper will appear in a Discussion Section to be published in the June 1981 JOURNAL. All discussions for the June 1981 Discussion Section should be submitted by Feb. 1, 1981.

Publication costs of this article were assisted by McMaster University.

REFERENCES

1. C. T. Sims, *J. Met.*, **18**, 1119 (1966).
2. S. J. Grisaffe, in "The Superalloys," C. T. Sims and W. C. Hagel, Editors, Chap. 12, John Wiley and Sons, New York (1972).
3. F. S. Pettit, *Trans. Met. Soc. AIME*, **239**, 1296 (1967).
4. J. S. Wolf and E. B. Evans, *Corrosion*, **18**, 129t (1962).
5. F. H. Stott and G. C. Wood, *Corros. Sci.*, **17**, 647 (1977).
6. G. C. Wood and F. H. Stott, *Br. Corros. J.*, **6**, 247 (1971).
7. W. C. Hagel, *Corrosion*, **21**, 316 (1965).
8. J. D. Kuenzly and D. L. Douglass, *Oxid. Met.*, **8**, 139 (1974).
9. J. L. Smialek, *Met. Trans.*, **9A**, 309 (1978).
10. P. Mayer and W. W. Smeltzer, *This Journal*, **121**, 538 (1974).
11. J. S. Choi and W. J. Moore, *J. Phys. Chem.*, **66**, 1308 (1962).
12. F. El Refaie and W. W. Smeltzer, To be published.
13. M. Hansen and K. Anderko, Editors, "Constitution of Binary Alloys," p. 1025, McGraw-Hill Book Co., New York (1958).
14. C. B. Alcock and P. B. Brown, *Met. Sci. J.*, **3**, 116 (1969).
15. F. S. Pettit, E. H. Randklev, and E. J. Felten, *J. Am. Ceram. Soc.*, **49**, 199 (1966).
16. J. Stringer, B. A. Wilcox, and R. I. Jaffee, *Oxid. Met.*, **5**, 11 (1972).
17. D. R. Tenney, C. T. Young, and W. W. Herring, *Met. Trans.*, **5**, 1001 (1974).
18. G. R. Wallwork and Z. Hed, *Oxid. Met.*, **3**, 213 (1971).
19. J. M. Perrow and W. W. Smeltzer, *This Journal*, **109**, 1023 (1962).
20. G. C. Wood and D. P. Whittle, *Corros. Sci.*, **7**, 763 (1967).
21. W. E. Boggs, *This Journal*, **118**, 906 (1971).
22. R. C. Logani and W. W. Smeltzer, *Oxid. Met.*, **3**, 15 (1971).
23. M. T. Shim and W. J. Moore, *J. Chem. Phys.*, **26**, 802 (1957).
24. A. Atkinson and R. I. Taylor, *J. Mater. Sci.*, **13**, 427 (1978).
25. Y. Oishi and W. D. Kingery, *J. Chem. Phys.*, **33**, 480 (1960).
26. A. E. Paladino and W. D. Kingery, *ibid.*, **37**, 957 (1962).

Growth and Microstructure of α - Al_2O_3 on β -NiAl

H. M. Hindam^{*1} and W. W. Smeltzer*

Department of Metallurgy and Materials Science, McMaster University, Hamilton, Ontario, Canada L8S 4M1

ABSTRACT

Growth of α - Al_2O_3 films and scales on β -NiAl (Ni-32 w/o Al) was investigated in oxygen at 1 atm over the temperature range 1273°-1573°K. An initial sub-microcrystalline oxide film recrystallized during its growth to a textured α - Al_2O_3 film containing polycrystalline ridges. Inert marker measurements demonstrated that the initial film grew by inward diffusion of oxygen. Fully developed α - Al_2O_3 scales contained dissolved nickel (0.5 w/o at 1473°K). Metallographic evidence indicated that these scales grew by counter-current aluminum and oxygen boundary diffusion and aluminum lattice diffusion. Cavities, which were generated at the alloy/ Al_2O_3 interface, did not influence scale growth since aluminum was transported at a sufficient sustaining rate by evaporation from the alloy substrate. The square of the average oxide grain size in a growing scale increased proportional to time. The nonparabolic growth kinetics of the α - Al_2O_3 scales were interpreted by a short-circuit diffusion model.

Mechanisms for growth of internal Al_2O_3 precipitates in dilute Ni-Al alloys and transformation of these precipitates to a continuous layer in alloys at intermediate aluminum concentrations were defined

* Electrochemical Society Active Member.

¹ Present address: Lawrence Berkeley Laboratory, University of California, Berkeley, California 94720.

Key words: oxidation, β -NiAl, Al_2O_3 .

in the preceding paper (1). Growth of Al_2O_3 scales on Ni-Al alloys has been the subject of only a few investigations (2-4) but more intensive research has been carried out on the growth mechanisms of these scales on other aluminum-containing alloys (5-12). The purpose of this investigation was to obtain detailed information on the growth kinetics and morpho-

logical development of α -Al₂O₃ on the intermetallic β -NiAl phase at high temperatures in order to advance a growth model.

Experimental Methods and Results

Specimen preparation procedures of the β -NiAl button containing 32.2 weight percent (w/o) Al [50.8 atomic percent (a/o)] were identical to those adopted in the case of alloys with low aluminum contents (1). A horizontal mullite tube furnace closed at one end was used for oxidation runs in static oxygen at 1 atm pressure. Specimens were suspended in a recrystallized alumina boat made by cutting a cylindrical crucible parallel to its axis. Alumina rods resting on grooves in the boat walls were used to support Pt-Rh hooks for the specimens. Oxygen was admitted to the evacuated tube after the furnace was brought to the desired temperature. The boat containing the β -NiAl disk shaped specimens, 1 cm diam and 0.1 cm thick, was then moved from the cold end of the tube to the hot zone by means of a quartz rod sliding through a stainless steel swagelock fixed to the tube by O-ring seals. Thin oxide films were stripped from the alloy substrate using 10% bromine-methanol solution; thick films and scales were fractured from the alloy.

Oxide films formed at exposures less than 5 min at temperatures as high as 1473°K did not exhibit distinct morphological features. Figure 1(a) is a TEM

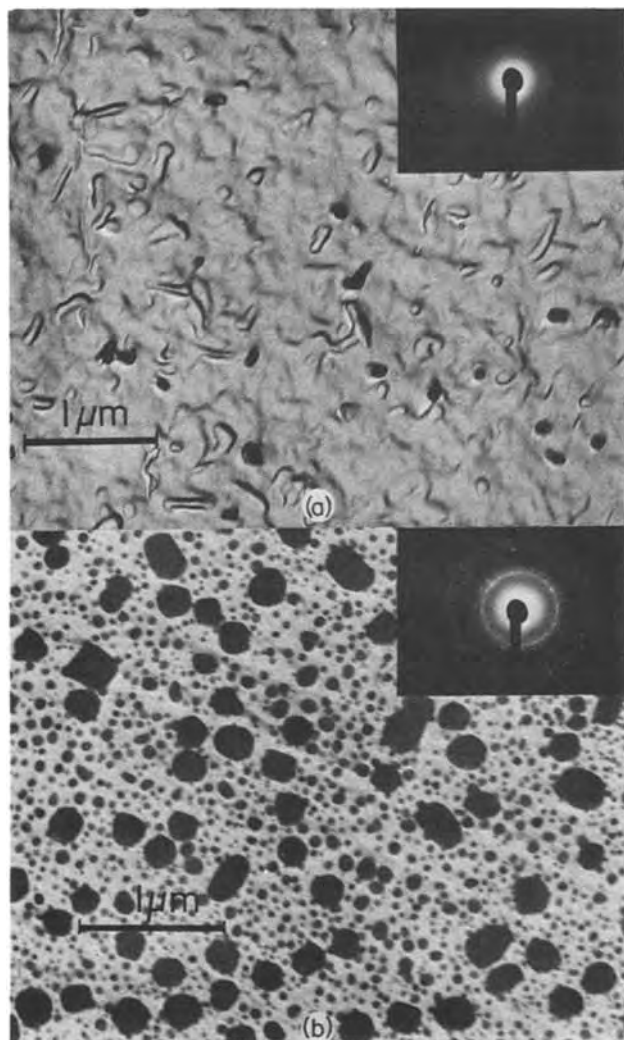


Fig. 1. TEM images and selected area diffraction patterns of oxide films formed on Ni-32 w/o Al alloy: (a) initial sub-microcrystalline film (5 min at 1273°K), (b) film shown in (a) after reheating "in situ" to 1123°K.

image and selected area diffraction pattern of an \sim 120 nm film formed at 1273°K in 5 min. The image exhibits poor contrast and the pattern consists of halos which can arise from sub-microcrystallites $<$ 10 nm in size. Heating this stripped film in the microscope to 1123°K for \sim 30 min led to formation of crystallites having a wide size range, 50-250 nm, as shown in Fig. 2(b). This structure gave rise to a definite electron diffraction ring pattern, which could be indexed as γ -Al₂O₃.

Thicker oxide films became nonuniform due to ridges extending outward and inward at spacing distances dependent on alloy grain orientations. The structure of this type of film (1 μ m thick) formed after 30 min at 1473°K and the corresponding reflection electron diffraction pattern are shown in Fig. 2. The pattern exhibits sharp diffraction rings corresponding to those for α -Al₂O₃, Fig. 2(b). Faceted cavities were consistently observed at the alloy/film interface, Fig. 2(c), which tended to coalesce and form extended troughs between the film and alloy substrate. The oxide film in the vicinity of an alloy grain boundary is shown in Fig. 2(d) where the delineation between ridge spacings is evident.

Thicker scales spalled partially upon cooling which allowed close examination of their structure. Figure 3 illustrates SEM images at different regions of a scale formed after 15 days at 1473°K. It is apparent that the scale fractured intergranularly, Fig. 3(a). Electron probe microanalysis demonstrated that \sim 0.5 w/o Ni was dissolved in this scale. The ridge persisted after this long oxidation period as evidenced by micrographs of the scale outer surface, Fig. 3(b), and underside, Fig. 3(c). The total length of the ridges extending from both interfaces by means of the oxide grain boundaries, nevertheless, accounted for $<$ 10% of the scale thickness. Few whiskers were formed at the scale outer surface, Fig. 3(b). The alloy interface exhibited imprints from the scale corresponding to the ridges in its underside, Fig. 3(c), and oxide-free faceted cavities revealing crystallographic arrangements, Fig. 3(d). Spiral steps on the alloy surface were also evident in some cavities, Fig. 3(e). Though the degree of cavitation varied over different alloy grains, the total volume increased as oxidation was prolonged [compare Fig. 2(c) and 3(d)].

Oxidation kinetics of the recrystallized α -Al₂O₃ scales were determined at 1473° and 1573°K by layer thickness measurements of polished scale cross sections using SEM images at 8000 \times magnification to an accuracy corresponding to 0.1 μ m. The reaction kinetics are shown in Fig. 4; each data point represents the average of 15 readings taken from three samples oxidized in a batch.

In light of the above evidence for reactant transport being dependent on the Al₂O₃ scale structure, the grain size was determined from fracture cross sections of partially spalled scale flakes. The grain diameter was measured parallel to the scale interfaces with the same accuracy as the thickness measurements. In each case, 100 grains chosen at random from different parts of the scale were used to determine the grain size distribution. The average grain size increased with continued oxidation as shown in Fig. 5.

It was feasible to employ inert Pd markers to identify the relative mobilities of the diffusing species during growth of the thin uniform oxide films. As has been described elsewhere (13), AES in combination with depth profiling by Ar ion sputtering can be employed to determine the location of extremely thin (3-5 nm) markers. In this case, a specimen was oxidized at 1273°K for 5 min to form a sub-microcrystalline oxide film. AES analyses of the oxidized specimen prior to and during sputtering of the film are shown in Fig. 6. The Pd marker, which resided at the external film surface, was sputtered completely away in less than 10 min. Disregarding Pd, the film

Fig. 2. Structure of recrystallized α - Al_2O_3 film on Ni-32 w/o Al alloy (SEM images; 30 min at 1473°K): (a) top view, (b) RHEED pattern, (c) fracture cross section, (d) film structure in vicinity of an alloy grain boundary.

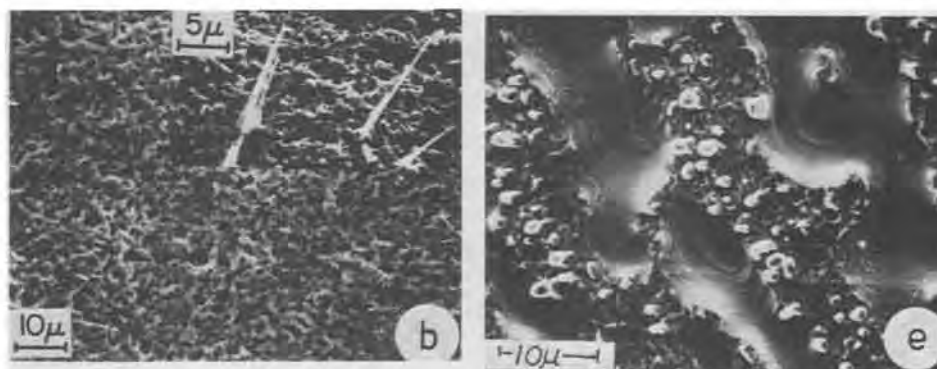
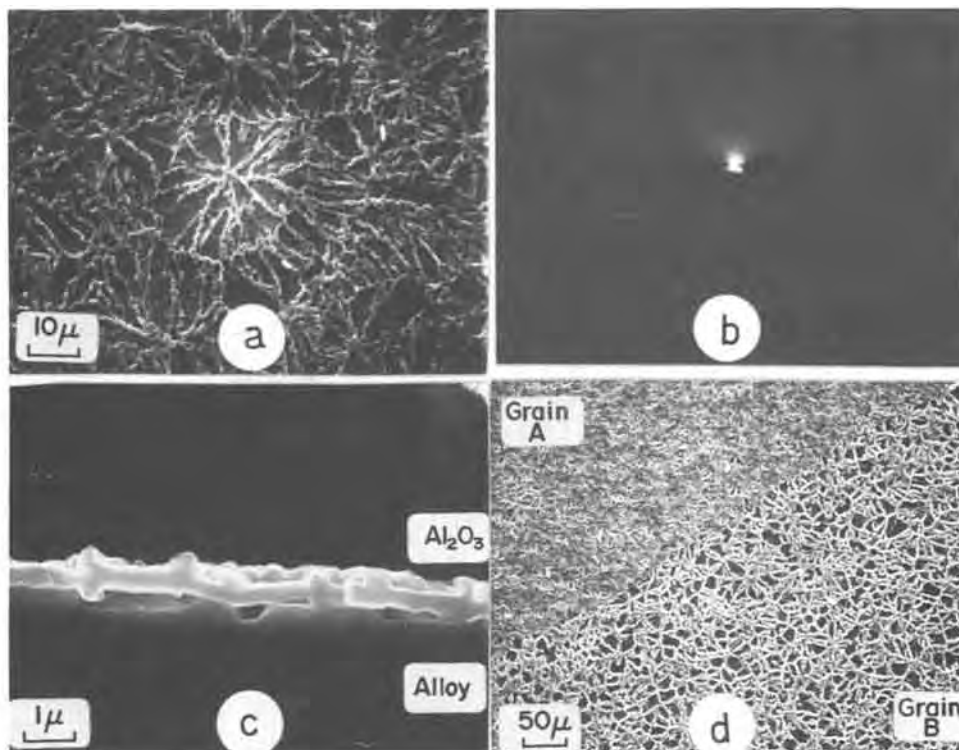


Fig. 3. Structure of thick α - Al_2O_3 scale on Ni-32 w/o Al alloy (SEM images; 15 days at 1473°K): (a) fracture cross section, (b) scale outer surface, (c) scale underside, (d) and (e) alloy/scale interface revealed by scale spalling.



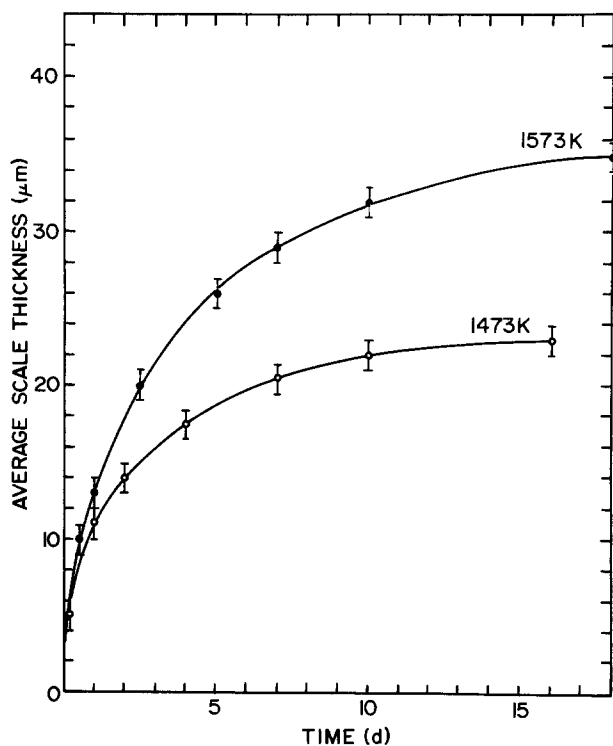


Fig. 4. α - Al_2O_3 scale growth kinetics on Ni-32 w/o Al alloy

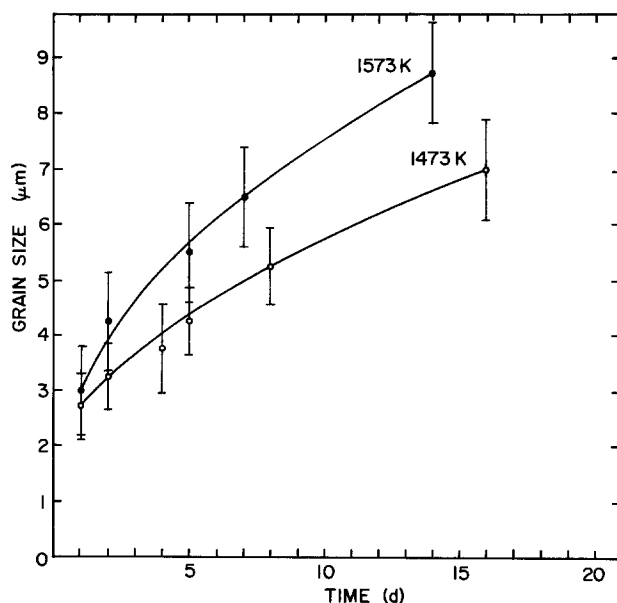


Fig. 5. α - Al_2O_3 scale grain growth

consists of pure Al_2O_3 since Ni could only be detected in the vicinity of the alloy/oxide interface.

Discussion and Conclusions

An initially formed sub-microcrystalline film consisting of Al_2O_3 grew by inward migration of oxygen even at temperatures as high as 1473°K under the conditions of experimentation. Reheating to 1123°K of a stripped film caused its "recrystallization" to γ - Al_2O_3 . It is therefore conceivable that the sub-microcrystalline films, which transformed to α - Al_2O_3 during their growth under isothermal conditions at temperatures exceeding 1273°K, involved the transient formation of the γ - Al_2O_3 allotropic phase. This transformation could lead to the occurrence of faulted regions in the recrystallized film since the conversion of γ to α - Al_2O_3 is accompanied by a reduction of 14.3% in volume (14). The α - Al_2O_3 films were nonuniform

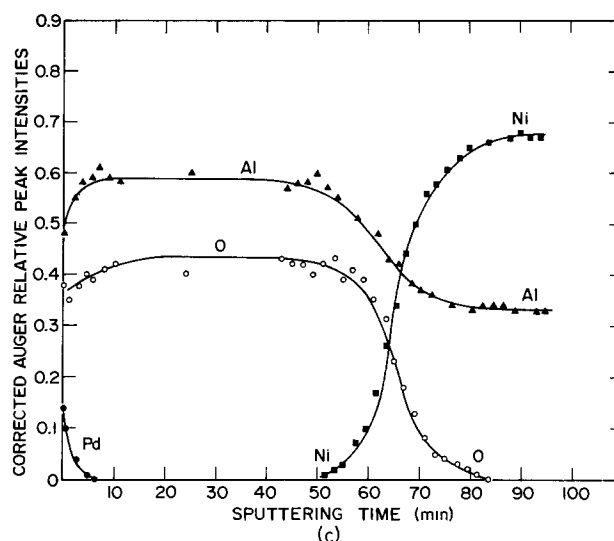
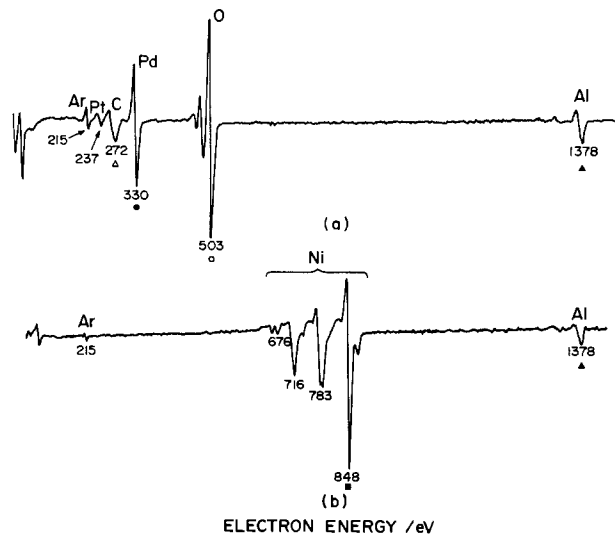


Fig. 6. AES-inert marker results of oxide film shown in Fig. 1(a): (a) and (b) spectrums before and after sputtering oxide film, (c) concentration profile across the film.

exhibiting growth of polycrystalline oxide extending inward and outward which implies that these regions contained a large density of boundaries acting as easy diffusion paths for both reactants. The presence of these polycrystalline ridges between the oriented thinner oxide film regions, Fig. 2(c), could be induced by faults as discussed above or by the influence of the alloy substructure.

Origin of cavities at the alloy/ Al_2O_3 cannot be unequivocally defined. These cavities have also been observed in other investigations on Al_2O_3 forming alloys (2-10, 15). We conjecture that in the presence of a few vacancy sinks, as in the case of coarse-grained alloys or foils having large surface/volume ratio (16-19), the concentration of the vacancies injected to the alloy substrate during oxide growth exceeded the supersaturation limit and led to void formation by vacancy coalescence. Transport of aluminum across the voids by evaporation is given by

$$\frac{dW}{dt} = P_{\text{Al}} \left(\frac{M}{2\pi RT} \right)^{1/2}$$

where P_{Al} and M are the vapor pressure and atomic weight of aluminum, respectively, and R is the gas constant. At $T = 1473^\circ\text{K}$, vapor pressure of pure aluminum = 10^{-5} atm (20) and aluminum activity in β -NiAl = 10^{-3} (21), the calculated aluminum evaporation rate is 0.2×10^{-8} g cm^{-2} sec^{-1} . This rate, which is equivalent to 1.7×10^{-7} gO cm^{-2} sec^{-1} ,

is much larger than the maximum observed oxygen uptake rate by the specimen equal to 1×10^{-9} gO cm $^{-2}$ sec $^{-1}$. An aluminum evaporative mechanism accompanied with outward aluminum migration through the growing scale leads to the conclusion that void formation does not interfere with scale growth and explains the development of relatively uniform thick scales. Aluminum evaporation from the substrate with limited inward boundary oxygen diffusion through the α -Al $_2$ O $_3$ scale can also lead to the observed spiral steps, faceting, and enlargement of voids, Fig. 3(d) and (e).

The experimental evidence offers support to an oxidation mechanism for growth of the α -Al $_2$ O $_3$ scales involving counter diffusion of aluminum and oxygen. Growth of polycrystalline ridges extending inward, Fig. 2(c) and 3(c), indicates that oxygen inward migration is mainly limited to regions of a large density of grain boundaries in the scale. Metallographic observations by previous investigations and those in this investigation suggest outward aluminum diffusion via grain boundaries: outward extension of the above polycrystalline oxide ridges (4, 11), Fig. 2(a), (c), and 3(b); the spacing of these ridges at the scale/gas interface is less than at the scale/alloy interface, Fig. 3(b) and (c), consistent with scale growth predominantly at its outer interface when nucleation of new grains and their subsequent growth are taken into account; growth of Al $_2$ O $_3$ whiskers (3, 5, 10), Fig. 3(b), which can result from metal transport through the scale by a type of line or surface defect (22-24). These considerations are consistent with measurements of tracer diffusivities (25, 26) which demonstrate that at temperatures exceeding 1923°K aluminum diffuses approximately at a rate one order of magnitude higher than oxygen in polycrystalline Al $_2$ O $_3$ and that the ratio of these diffusivities D_{Al}/D_o decreases with decreasing grain size (27). Oxygen diffusion in single crystal Al $_2$ O $_3$ compared to the above aluminum diffusion rate is about two orders of magnitude less. This latter consideration and the continual growth of voids beneath the scales lead to the conclusion that the oriented Al $_2$ O $_3$ grains between the polycrystalline ridges grow by aluminum lattice diffusion to react with oxygen at the external scale surface. The findings from the comprehensive studies on the defect properties of high purity α -Al $_2$ O $_3$ single crystals (28, 29) are consistent with a point defect model involving aluminum interstitial ions and electrons as the major mobile species. This type of aluminum diffusion, moreover, would be enhanced by the doping effect of nickel since the thick scales contained ~ 0.5 w/o Ni. Consequently, enhanced aluminum lattice diffusion accompanied with oxide grain growth led to development of the observed relatively uniform thick scales, Fig. 3(a). As illustrated by the linear plots in Fig. 7, square of oxide average grain size vs. time, the Al $_2$ O $_3$ average grain size during growth of the scales followed a general grain growth relationship. The activation energy for grain growth determined from these measurements at two temperatures is 133 kJ/g mole.

The oxidation kinetics for scale growth can be interpreted to a first approximation by a short-circuit diffusion model similar to that advanced to interpret NiO growth on nickel (30, 31). An effective diffusion coefficient for aluminum and oxygen migration along grain boundaries and aluminum via lattice sites in polycrystalline alumina is expressed as

$$D_{eff} = D_L + f\bar{D}_B$$

where D_L is the aluminum lattice diffusion coefficient, \bar{D}_B is an average diffusion coefficient for counter migration of aluminum and oxygen along grain boundaries in a scale, f is the fraction of grain boundary diffusion sites represented by $f = 2d/D$ where d is

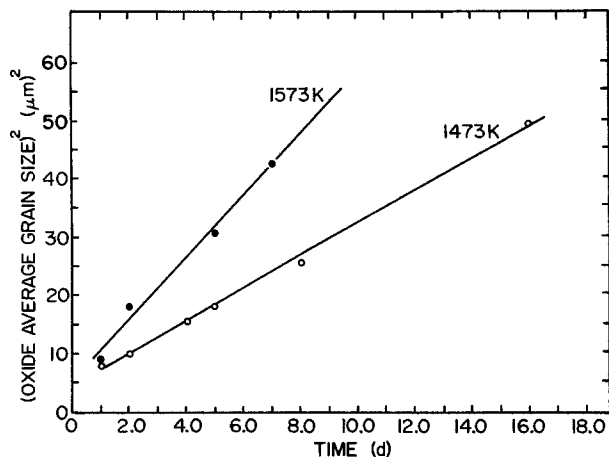


Fig. 7. α -Al $_2$ O $_3$ scale grain growth: parabolic presentation

the grain boundary width and D is the average oxide grain diameter which was shown to obey the relationship $D^2 - D_o^2 = Gt$ where G is the grain growth rate constant. A modified parabolic rate equation

$$x^2 = 2\Omega D_L \Delta c \int_0^t \left(1 + f \frac{D_B}{D_L}\right) dt$$

where Ω is the equivalent volume of alumina represents the oxidation kinetics upon utilizing the approximation of a linear compositional gradient to define the flux of reactants across the oxide layer. This equation is placed on differential form

$$\frac{dx^2}{dt} = k_L + k_B d/D$$

where $k_L = 2\Omega D_L \Delta c$ and $k_B = 2\Omega D_B \Delta c$ to test the obeyance of the oxidation kinetics and alumina grain growth to this simple short-circuit diffusion model. The linear plots of dx^2/dt vs. $1/D$ in Fig. 8 demonstrate the validity of the above relation. Assuming an Arrhenius relationship for k_B and an independence

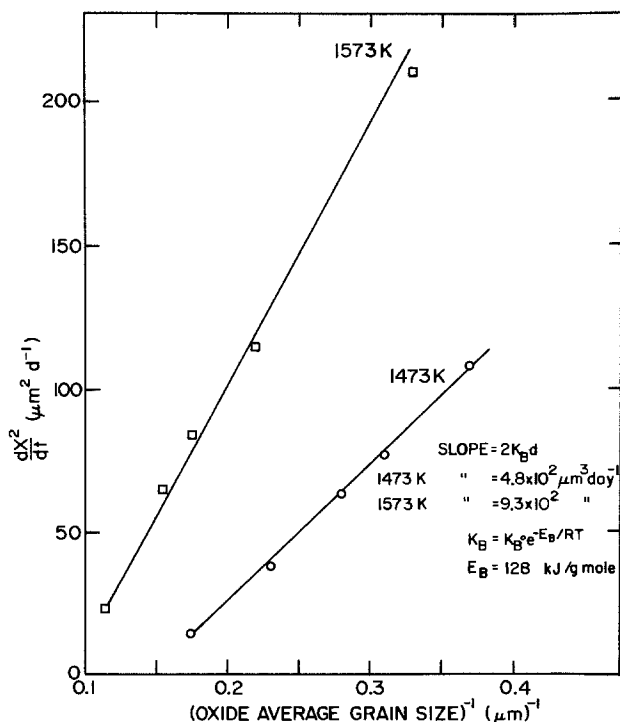


Fig. 8. Verification of short-circuit diffusion model: plot of dx^2/dt vs. D^{-1} .

Table I. Comparison of observed and calculated grain size in the α - Al_2O_3 scale formed at 1573°K

Oxidation time (days)	Average oxidation grain size (μm)	
	Observed	Calculated
2	3.2 ± 0.6	3.8
3	3.6 ± 0.8	4.7
5	4.5 ± 0.6	6.8

of boundary width on temperature, the effective activation energy for aluminum and oxygen boundary diffusion is 128 kJ/g mole. This value is much smaller than the activation energies for aluminum diffusion in high purity polycrystalline (130-200 μm) α - Al_2O_3 , 475 kJ/g mole, and oxygen diffusion in single α - Al_2O_3 crystals, 635 kJ/g mole (25, 26).

Since $k_B \gg k_L$, the scale grain growth rate can be predicted from the above equation using the oxidation kinetic data and knowing the average grain size at a given time. The calculated and measured grain size are given in Table I. The agreement between the observed and calculated values is reasonable when one considers the simple approximations utilized to describe scale growth by a short-circuit diffusion model.

The model schematically represented in Fig. 9 summarizes the present findings for growth of the α - Al_2O_3 scale on β -NiAl. Initially, a submicrocrystalline film was formed containing a large density of boundaries along which oxygen diffused inward. Film recrystallization led to development of an oriented α - Al_2O_3 film containing regions of disarrayed oxide induced by oxide faulting or by the influence of the alloy substructure. Boundaries in this disarrayed oxide for counter diffusion of aluminum and oxygen resulted in the development of ridges extending inward and outward. Based on the recent findings on the defect properties of alumina, it is assumed that oxide within grains grew by outward migration of aluminum ions via an interstitial mechanism. Voids were formed at the NiAl/ Al_2O_3 interface by coalescence of vacancies

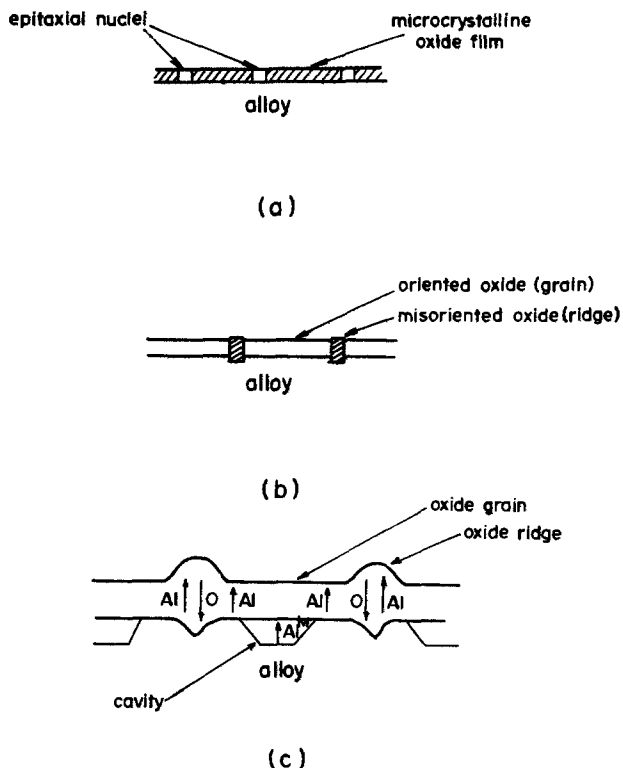


Fig. 9. Schematic model for Al_2O_3 growth on Ni-32 w/o Al alloy

generated by film growth. Aluminum evaporation from these voids in the presence of limited inward boundary oxygen migration in the α - Al_2O_3 scale led to development of faceted cavities. Eventually, counter diffusion of aluminum and oxygen through the boundaries present in the ridge and oxide grain growth coupled with aluminum outward diffusion partially enhanced by nickel doping led to uniform scale growth.

Acknowledgment

This research was completed by H. M. Hindam as part of the requirements for award of the Ph.D. degree at McMaster University. Financial support from the National Research Council of Canada for this research is gratefully acknowledged.

Manuscript submitted July 20, 1979; revised manuscript received Jan. 11, 1980.

Any discussion of this paper will appear in a Discussion Section to be published in the June 1981 JOURNAL. All discussions for the June 1981 Discussion Section should be submitted by Feb. 1, 1981.

Publication costs of this article were assisted by McMaster University.

REFERENCES

- H. M. Hindam and W. W. Smeltzer, *This Journal*, **127**, 1622 (1980).
- G. C. Wood and F. H. Stott, *Br. Corros. J.*, **6**, 247 (1971).
- J. D. Kuenzly and D. L. Douglass, *Oxid. Met.*, **8**, 139 (1974).
- J. L. Smialek, *Metall. Trans.*, **9A**, 309 (1978).
- J. K. Tien and F. S. Pettit, *ibid.*, **3**, 1587 (1972).
- A. Kumar, M. Nasrallah, and D. L. Douglass, *Oxid. Met.*, **8**, 227 (1974).
- C. S. Giggins and F. S. Pettit, Rep. No. ARL 75-0234, United Technologies, Pratt and Whitney Aircraft Group, East Hartford, Connecticut (1975).
- E. J. Felten and F. S. Pettit, *Oxid. Met.*, **10**, 189 (1976).
- F. A. Golightly, F. H. Stott, and G. C. Wood, *ibid.*, **10**, 163 (1976).
- I. M. Allam, D. P. Whittle, and J. Stringer, *ibid.*, **12**, 35 (1978).
- J. S. Sheasby and D. B. Jory, *ibid.*, **12**, 527 (1978).
- F. A. Golightly, F. H. Stott, and G. C. Wood, *This Journal*, **126**, 1035 (1979).
- H. M. Hindam and W. W. Smeltzer, *Oxid. Met.*, In press.
- P. P. Budnikov and A. M. Ginstling, "Principles of Solid State Chemistry," Translated from Russian, K. Shaw, Editor, p. 299, Gordon and Breach Sci. Pub., New York (1968).
- H. L. Fraser, M. H. Loretto, R. E. Smallman, and R. J. Wasilewski, *Philos. Mag.*, **28**, 639 (1973).
- V. R. Howes, *Corros. Sci.*, **8**, 221 (1968).
- V. R. Howes, *ibid.*, **10**, 99 (1970).
- R. Hales and A. C. Hill, *ibid.*, **12**, 843 (1972).
- G. B. Gibbs and R. Hales, *ibid.*, **17**, 487 (1977).
- L. Brewer and A. W. Searcy, *J. Am. Chem. Soc.*, **73**, 5308 (1951).
- A. Steiner and K. L. Komarek, *Trans. Met. Soc. AIME*, **230**, 786 (1964).
- D. J. Barber, *Philos. Mag.*, **10**, 75 (1964).
- E. A. Gulbransen, *Mem. Sci. Rev. Metall.*, **LX11**, 253 (1965).
- R. L. Tallman and E. A. Gulbransen, *This Journal*, **114**, 1227 (1967).
- Y. Oishi and W. D. Kingery, *J. Chem. Phys.*, **33**, 480 (1960).
- A. E. Paladino and W. D. Kingery, *ibid.*, **37**, 957 (1962).
- R. E. Mistler and R. L. Coble, *J. Am. Ceram. Soc.*, **54**, 60 (1971).
- R. J. Brook, J. Yee, and F. A. Kröger, *ibid.*, **54**, 444 (1971).
- J. Yee and F. A. Kröger, *ibid.*, **56**, 189 (1973).
- J. M. Perrow, W. W. Smeltzer, and R. K. Ham, *Acta Metall.*, **15**, 577 (1967).
- J. M. Perrow, W. W. Smeltzer, and J. D. Embury, *ibid.*, **16**, 1209 (1968).

Relationship Between Deposition Conditions and Physical Properties of Sputtered ZnO

James O. Barnes,¹ David J. Leary,* and A. G. Jordan

Department of Electrical Engineering and Center for the Joining of Materials,
Carnegie-Mellon University, Pittsburgh, Pennsylvania 15213

ABSTRACT

Characteristics of the deposition process and properties of the resultant films have been determined for undoped and gallium-doped sputtered zinc oxide. The properties of interest are film growth rate, resistivity of the as-sputtered film, optical transmission, grain size, and carrier concentration and mobility as determined by the Hall effect. The goal of the investigation has been to establish how these properties depend on sputtering conditions, specifically sputtering ambient composition, sputtering power, and substrate temperature. The principal findings are: (i) the dependence of film deposition rate on applied power and ambient composition suggests a complex deposition process involving the transport of several types of aggregates of atoms; (ii) films sputtered in an oxygen-free ambient show strong optical absorption in the visible region and a high concentration of carriers, while films sputtered in a partial pressure of oxygen show absorption similar to that reported for ZnO powder; (iii) substrate temperature has a marked influence on the electrical properties of Ga-doped films, with films sputtered at certain temperatures showing behavior suggesting the existence of intergranular potential barriers.

Past investigations have shown that zinc oxide properties are significantly dependent on sample thermal history and method of preparation, particularly in the case of sintered specimens. The importance of surface effects in this material, due primarily to chemisorbed oxygen, has also been demonstrated. Therefore, measurements of properties of single crystal or sintered samples are not applicable to sputtered films. Because of the recent practical interest in ZnO sputtered thin films for surface acoustic wave (1) and solid-state gas sensing devices (2), and the unavailability of data for these films, the present investigation has been carried out.

Zinc oxide is an n-type ionic wide bandgap semiconductor ($E_g = 3.2$ eV) having a wurtzite crystal structure. It is generally agreed that a nonstoichiometric excess of interstitial zinc which occurs in undoped material is responsible for the free electrons. The temperature dependence of the excess zinc concentration for ZnO in an ambient of air (3) and zinc vapor (4) have been determined by chemical analysis. Early electrical measurements on sintered specimens (5) indicated the importance of heat-treatment in determining conductivity and Hall mobility. Another study of sintered ZnO (6) revealed that a single shallow donor model was unable to describe the temperature dependence of the carrier concentration and suggested the possibility of deep-lying acceptor states. Hutson (7) was the first to report comprehensive single crystal electrical measurements. For most of his zinc-, lithium-, and hydrogen-doped samples, the data could be fitted by a single shallow donor model. The mobility temperature dependence could be described well by a combination of polar optical mode, acoustic mode, and ionized impurity scattering, with the fit being best between 200° and 300°K. Later studies (8) revealed donor band conduction at low temperatures (below about 50°K).

In contrast to the extensive literature for single crystal and sintered specimens, few studies of the electrical properties of sputtered ZnO films have been reported (9, 10). A number of authors have described characteristics of sputtered ZnO films in connection

with surface acoustic wave applications (11). However, the emphasis has been on film morphology, which is important for these devices, and not electrical properties. Of particular interest in the present work have been the influence of applied sputtering power, sputtering ambient composition, and substrate temperature on film properties. Film growth rate, optical transmission, grain size, resistivity, and Hall mobility were examined

Experimental Methods

For gas sensor applications, conductive ZnO films having well-controlled carrier concentration and grain size are required. A number of film deposition techniques, such as vacuum evaporation of ZnO source material, post-deposition oxidation of zinc thin films, and firing of an aqueous suspension of zinc oxide powder have been investigated by us. However, none allows incorporation of dopants and process reproducibility of the radio frequency sputtering process. Targets for this study were fabricated by pressing and sintering high purity powders; both an undoped and gallium-doped target (1% Ga: Zn ratio) were used. Fused quartz substrates were used for electrical measurements, while Pyrex microscope slides were used for optical and growth rate studies. The substrates could be maintained at 500°C during deposition by radiant heating.

Optical measurements were performed with a Cary 14 Double Beam Spectrometer. Film thickness was determined with a commercial stylus profile measuring device. For resistivity and carrier concentration measurements, six-arm Hall specimens were produced by sandblasting through a metal mask. Pressure contacts were then made to evaporated aluminum pads. Measurements at other than room temperature were made in a metal Dewar with the sample surrounded by a vacuum. Except near 100°C, the maximum temperature employed, no changes in electrical properties due to desorption of chemisorbed ions were detected. For Hall effect and conductivity measurements, a conventional d-c technique was used.

Effect of Composition of Sputtering Atmosphere on Growth Rate, Electrical, and Optical Properties

Film growth rate.—The nature of the sputtering process for compound materials has not been well

* Electrochemical Society Student Member.

¹ Present address: Hewlett Packard Company, Fort Collins, Colorado 80525.

Key words: zinc oxide, sputter deposition, electrical properties, optical transmission.

characterized, but it is believed that both individual atoms and aggregates of atoms are sputtered (12). In order to maintain stoichiometry in the deposited film, it has been found necessary to mix a small percentage ($\sim 10\%$) of oxygen with the argon sputtering gas. Properties of films sputtered in less than this percentage of oxygen are sensitive to atmosphere composition, while films sputtered in a greater percentage are not sensitive. The importance of ambient composition in determining film properties has been discussed previously (10).

Figure 1 shows film growth rate *vs.* ambient composition and applied rf power. Addition of 10% oxygen is seen to reduce growth rate by 36%, while further increase to 100% oxygen results in an additional 13% reduction. This behavior is not due simply to the mass difference of the argon and oxygen atom, since a linear relationship between growth rate and percentage oxygen would then be expected. One possible explanation is that, in atmospheres containing less than 10% oxygen, individual zinc and oxygen atoms are sputtered, while in greater than 10% oxygen larger aggregates are sputtered in addition to individual atoms. Ignoring differences in binding energy, the energy transfer from the sputtering ion to the ejected target material is greatest when the mass of the ejected particle equal that of the ion. This would result in a greater sputtering rate in the absence of oxygen.

Figure 1(a) shows the dependence of growth rate on applied rf power. In both 0% and 10% oxygen, an apparent threshold in power is seen below which sputtering does not occur. This behavior has been reported for d-c sputtered SnO_2 (13). Nonlinearity is seen in both curves; however, it is most pronounced in the 10% oxygen curve. This would be expected if (as conjectured above) the 0% sputtering process involved transport only of individual atoms, while the 10% oxygen process involved sputtering of atoms and aggregates in various proportions depending on applied rf power.

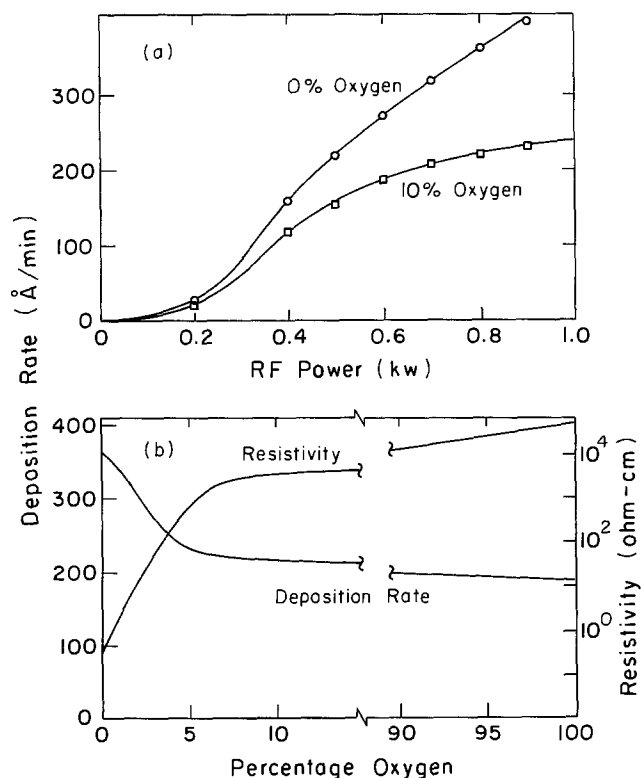


Fig. 1. (a) Dependence of deposition rate of undoped ZnO on applied rf sputtering power; (b) dependence of deposition rate and resistivity of undoped as-sputtered ZnO on argon-oxygen ratio of the sputtering gas. RF deposition power was 0.75 kW.

Resistivity of undoped films.—Films sputtered in less than 10% oxygen contain a high concentration of electrically active defects, as shown in Fig. 1(b). Assuming singly ionized shallow donor defects and a conductivity mobility of $5 \text{ cm}^2/\text{Vsec}$, typical of values found in Hall measurements, films sputtered in pure oxygen have a carrier concentration of about $4 \times 10^{18} \text{ cm}^{-3}$, or 100 ppm atomic. Hagemark and Toren (4) studied the solubility of interstitial zinc for single crystals in equilibrium; the solubility was found to exceed 100 ppm for temperatures in excess of 1050°C . The degree of vibrational disorder of the surface of the growing film should in fact be equivalent to a very high temperature, since the mean energy of the impinging particles is several eV; therefore, the defect density seen in the sputtered films could be of the order of magnitude measured.

The conductivity of as-sputtered undoped films was found to be due in part to defects which annealed rapidly at 400°C . Films sputtered in pure argon and in a partial pressure of oxygen both showed a rapid resistance increase upon heating in air. The high final resistance values made quantitative study of this effect difficult, but an increase of greater than three orders of magnitude occurred for the pure argon films. The rate of diffusion of interstitial zinc at 400°C is too low to account for this annealing; in the solubility study (4), two weeks were required to reach equilibrium between a millimeter size crystal and zinc vapor at 700°C . A more likely explanation for the 400°C resistivity increase is chemisorption of oxygen at surface oxygen vacancies.

Optical transmission.—Figure 2 shows the optical absorption spectrum for single crystal, powder, and sputtered ZnO. The 3700\AA absorption edge for the single crystal corresponds to a bandgap of 3.2 eV. Powder and sputtered samples show absorption at photon energies below the bandgap. Van Craeynest *et al.* (3) attribute the behavior of powder samples to F-centers associated with interstitial Zn, which is singly ionized below 750°C and doubly ionized at higher temperatures. Curve 2 of Ref. (3) represents powder cooled slowly in air from 1100°C and presumably containing a minimal amount of excess Zn. Curve 1 shows a sample quenched from 920°C containing excess Zn^{2+} centers. The sputtered films 1 and 2, sputtered in greater than 10% oxygen, show the same absorption band as powder specimen 1, although stronger in magnitude. The slight shift ($\sim 0.08 \text{ eV}$) to lower photon energies in the curve for the Ga-doped film (No. 2) is due to photo-excitation of carriers to the Ga levels as opposed to the conduction band in the undoped sample. The film sputtered in pure Ar, however, shows a spectrum markedly different from the other sputtered or pow-

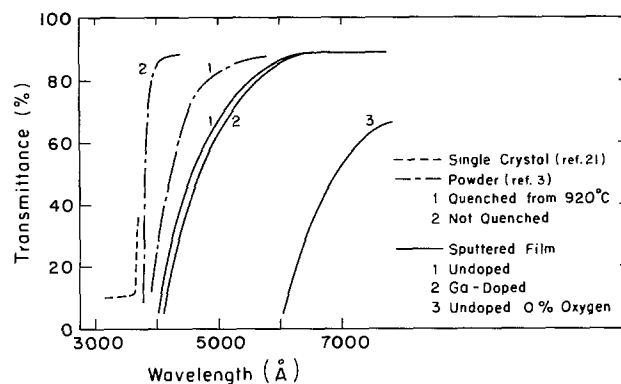


Fig. 2. Optical transmission spectrum of as-sputtered ZnO compared with single crystal and powder ZnO data. Sputtered film thickness is 1000\AA . Data for single crystal and powder samples have been normalized to transmittance of sputtered films 1 and 2 at 7000\AA .

der samples. The absorption edge at 6000Å is associated with the electrically active defects which anneal at 400°C, since the transmittance in the visible is increased with heat-treatment at 400°C. It is reasonable that the surface oxygen vacancy concentration, responsible for the high conductivity and strong optical absorption, should be largest in this film.

Effect of Deposition Temperature on Electrical Properties

The results described in the following section are restricted to Ga-doped films, since these were found to have stable characteristics and resistivities which facilitated measurement of the electrical properties. Substrate temperature can influence electrical characteristics through effects on grain size and doping concentration. Many polycrystalline films, including ZnO, are known to contain a high concentration of acceptor states in the grain boundary region; these states arise from point defects and departures from stoichiometry. In films of small grain diameter, the effective free carrier concentration n_{eff} can become significantly smaller than the doping concentration because of trapping of carriers by grain boundary defects. This behavior has been termed autocompensation (14), and has been modeled by simultaneous solution of Poisson's equation and the charge neutrality relationship in small spherical crystallites (15). The trapped carriers in the grain boundary region give rise to potential barriers and mobility values which are much lower than single crystal values (16, 17). Change in carrier concentration with deposition temperature may be due to loss of volatile dopant during sputtering, as has been reported for Sn_2CdO_4 (18), or annealing of defects during deposition.

Figure 3 shows that both grain size and doping concentration vary with substrate temperature. Grain size is seen to increase fourfold between 120°C (no radiant heating) and 480°C. A decrease in free carrier concentration of almost two orders of magnitude between 270° and 480°C is found. Since the amount of charge trapped in the grain boundary region is smallest at highest deposition temperatures, the loss of dopant at high temperatures is seen to be the predominant effect of substrate heating.

Figure 4 shows the temperature dependence of carrier concentration and mobility in Ga-doped films,

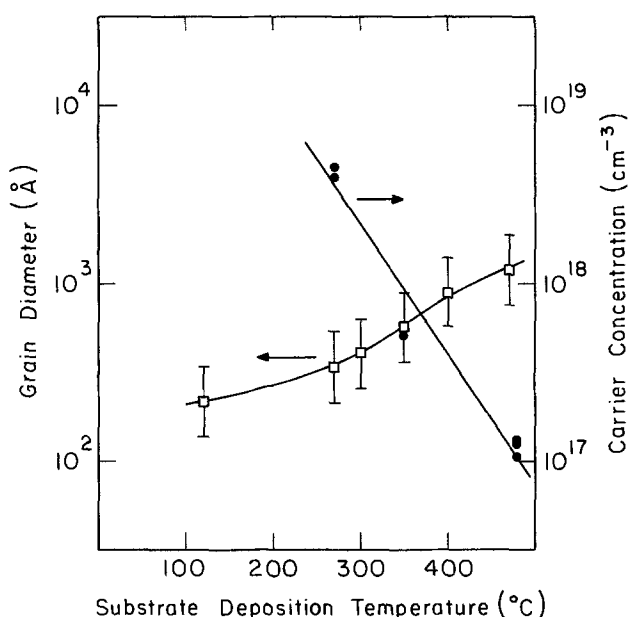


Fig. 3. Grain diameter as determined by scanning electron microscopy and carrier concentration of as-sputtered Ga-doped ZnO vs. substrate deposition temperature.

compared with single crystal and sintered sample measurements. Evidently the variation in doping level and grain size results in quite different behavior for samples deposited at different temperatures. The 270°C sample most closely approximates single crystal behavior in temperature dependence of n_{eff} and μ_{H} , as well as magnitude of mobility in this temperature range.

In Fig. 5, the n_{eff} vs. $1/T$ data are analyzed by plotting

$$\ln \frac{n_{\text{eff}}}{(N_{\text{D}} - n_{\text{eff}})N_{\text{C}}} \quad [1]$$

vs. $1/T$, as was done by Hutson (7). Here N_{C} is the conduction band density of states, calculated using an effective mass of $0.3 m_0$. N_{D} was estimated from the carrier concentration above room temperature. Although previous authors have varied N_{D} from this estimate to produce the best straight line fit to the data, such a procedure is not warranted here. The present discussion is concerned mainly with the slopes of the curves, which are insensitive to order-of-magnitude changes in the value assumed for N_{D} . The heavily doped 270°C sample shows a considerably lower slope than the other two samples and additionally a possible break in slope near room temperature. Although onset of degeneracy can lead to such a slope change, the 270°C sample is at most weakly degenerate. Modification of Eq. [1] to reflect weak degeneracy (19) does not significantly alter the curve. From the data, the level scheme shown in Fig. 5 is inferred, with the Fermi level in this temperature range lying between the upper two donor levels from the 270°C sample and just above the third donor level for the 350° and 480°C samples. One or both of the upper two donor levels is due to Ga. The optical spectra of Fig. 2 indicate a shift toward lower energy of the absorption edge of the Ga-doped sample compared with the undoped sample. The shift could be due to transitions to the middle donor level, since the magnitude (~ 80 meV) is close to the 60 meV donor level measured. Regarding the lower donor level, it is not possible from the present data to establish whether it is due to Ga or is present in the undoped film. The deep-lying acceptor levels which pull the Fermi level down in the less heavily doped samples are probably due to chemisorbed oxygen, which forms acceptor states 0.72 eV below the conduction band (20).

In the mobility plot [Fig. 4(b)], the 270°C sample shows mobility values approaching that of sintered specimens, as well as a decrease with increasing temperature similar to the single crystal and sintered specimens. The mobility fall off near room temperature in single crystal ZnO is due to the predominance of polar optical mode scattering (7). That the mobilities of the sintered and 270°C sputtered samples are similar to the single crystal curves apart from an approximately constant factor suggests that the current flow in the first two is through material having the same electrical behavior as single crystal ZnO. The scaling of the mobility in sintered and 270°C sputtered ZnO implies that the cross-sectional area of the current path in these specimens is smaller than the measured cross-sectional area of the specimen. This would be expected if the current flow is through narrow necks between adjacent grains, with the electrical properties of the necks and material within the grains being essentially the same as single crystal ZnO.

The 350° and 480°C samples have considerably lower mobilities at any temperatures than any of the other samples and moreover have strongly increasing mobilities with temperature. The slope cannot be due to ionized impurity scattering, since this process is of comparable or larger magnitude in the heavily doped sample (270°C). Rather, the slope is indicative of a mobility controlled by intergranular potential barriers due to trapped impurities. From the ther-

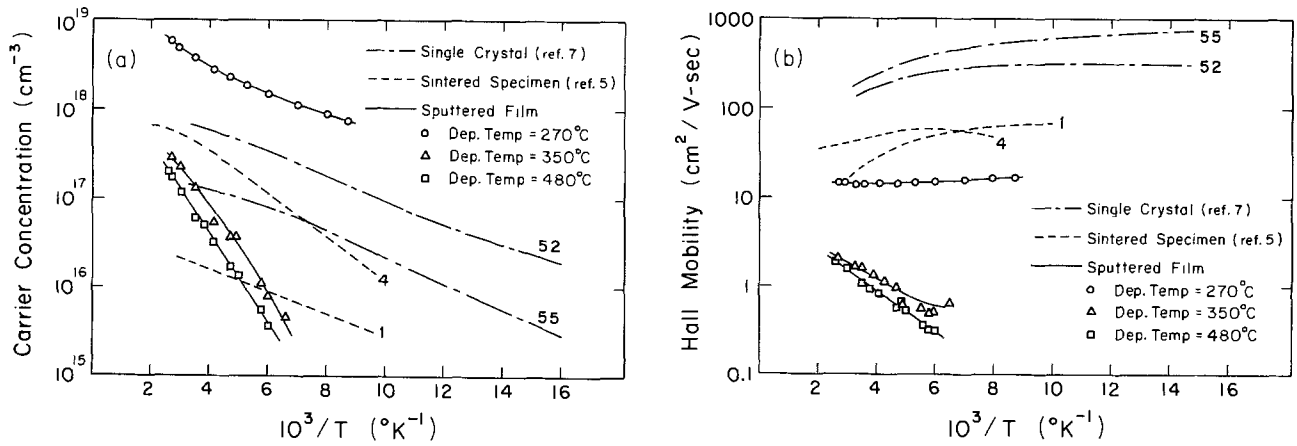


Fig. 4. (a) Carrier concentration of as-sputtered Ga-doped ZnO films vs. reciprocal temperature compared with representative data for single crystal and sintered specimens. Numbers adjacent to curves for the latter two materials correspond to designations of original articles. Sputtered film thickness is 2 μm. (b) Hall mobility for as-sputtered Ga-doped ZnO films compared with representative data for single crystal and sintered specimens.

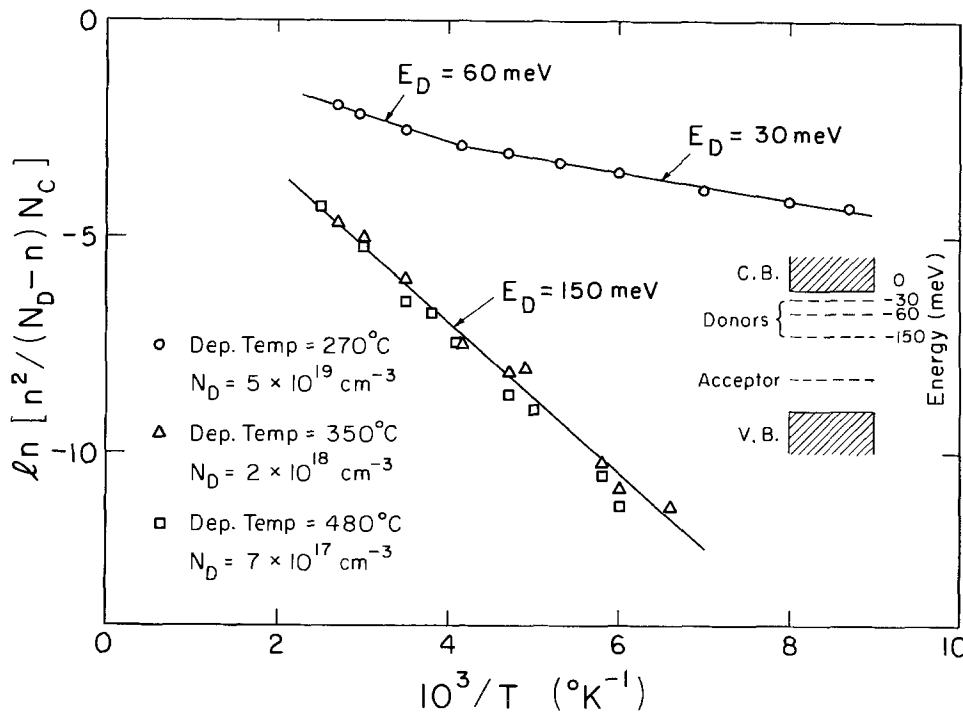


Fig. 5. Analysis of carrier concentration data of Fig. 4(a) after the method of Hutson [Ref (7)].

mionic emission formula, the barrier mobility may be written (16)

$$\mu = \frac{e\langle v \rangle}{N_1 kT} e^{-\phi_b/kT} \quad [2]$$

where $\langle v \rangle$ is the mean thermal velocity of carriers, N_1 is the number of barriers per unit length along the current path, and ϕ_b is the potential barrier height. The exponential temperature dependence of μ_H is seen for both lightly doped samples, the slightly greater slope of the 480°C sample indicating a larger barrier height. Seager and Castner (17) have theoretically and experimentally studied potential barriers in epitaxially grown polysilicon films. It was found that at low doping levels, the barrier height approaches ($E_C - E_A$), the acceptor energy with respect to the conduction bandedge. Above a certain doping level which depends on the trap density, the potential barrier was found to go to zero. This is evidently the case for the 270°C film. The barrier height for the 480°C sample is 0.14 eV, which is considerably less than ($E_C - E_A$) for chemisorbed oxygen. Possible reasons for this difference are: (i) the carrier concentration of the 480°C film is not low enough to

reach the limiting value for ϕ_b ; (ii) the donors are nonuniformly distributed throughout the grains, giving rise to an electric field in opposition to the field due to the grain boundary charge. The latter possibility was avoided in Ref. (17) by doping the silicon through neutron transmutation. Further experiments using less heavily doped films are in progress.

Conclusions

The properties of sputtered zinc oxide films can in certain cases be strongly dependent on deposition conditions. In particular, as-sputtered films deposited in less than 10% oxygen show increased growth rate, markedly increased optical absorption in the visible region, and a higher free carrier density than films sputtered in greater than 10% oxygen. The optical absorption and donor defects which anneal at 400°C in the oxygen-deficient films were attributed to surface oxygen vacancies. Films sputtered in greater than 10% oxygen possess optical absorption similar to that seen in zinc-rich powder ZnO and attributed to F-centers formed by zinc interstitials. For films sputtered in an adequate oxygen concentration, properties are insensitive to precise ambient composition.

Gallium doping was found to produce a slight shift in the absorption edge.

Substrate temperature affects grain size and doping concentration of the Ga-doped films, with the latter effect being of primary significance. Substrate temperature control provides a convenient means for varying the carrier concentration by more than two orders of magnitude for films sputtered from one target. Analysis of the temperature dependence of the carrier concentration revealed at least three donor and one acceptor levels. The trend in the mobility data is similar to that reported for polysilicon. The mobility in samples doped in the range 10^{18} cm $^{-3}$ appears to be controlled by intergranular potential barriers, while samples doped to greater than 10^{19} cm $^{-3}$ do not have barriers. The latter films, as well as sintered samples, show a mobility temperature dependence similar to single crystal ZnO but scaled down by a constant factor.

Acknowledgment

This work was supported in part by the Department of Energy.

Manuscript submitted Aug. 9, 1979; revised manuscript received Jan. 10, 1980.

Any discussion of this paper will appear in a Discussion Section to be published in the June 1981 JOURNAL. All discussions for the June 1981 Discussion Section should be submitted by Feb. 1, 1981.

Publication costs of this article were assisted by Carnegie-Mellon University.

REFERENCES

1. F. S. Hickernell, *Proc. IEEE*, **64**, 631 (1976).
2. D. J. Leary, Thesis, Carnegie-Mellon University, 1978 (unpublished).
3. F. Van Craeynest, W. Maenhout-Van der Vorst, and W. Dekeyser, *Phys. Status Solid.*, **8**, 841 (1965).
4. K. I. Hagemark and P. E. Toren, *This Journal*, **122**, 922 (1975).
5. E. E. Hahn, *J. Appl. Phys.*, **22**, 855 (1951).
6. S. E. Harrison, *Phys. Rev.*, **93**, 52 (1954).
7. A. R. Hutson, *ibid.*, **108**, 222 (1957).
8. P. W. Li and K. I. Hagemark, *J. Solid State Chem.*, **12**, 371 (1975); A. Hausmann and W. Teurle, *Z. Phys.*, **257**, 299 (1972).
9. J. C. Yen, *J. Vac. Sci. Technol.*, **12**, 47 (1975).
10. D. L. Raimondi and E. Kay, *ibid.*, **7**, 96 (1969).
11. For example, H. W. Lehmann and R. Widmer, *Jpn. J. Appl. Phys. Suppl.*, **2**, 741 (1974).
12. G. K. Wehner and G. S. Anderson, in "Handbook of Thin Film Technology," McGraw-Hill, New York (1970).
13. A. G. Sabnis, Thesis, South Dakota School of Mines (1974).
14. J. A. Amick, *RCA Rev.*, **20**, 753 (1959).
15. D. Bernarczyk and J. Bednarczyk, *Thin Solid Films*, **44**, 137 (1977).
16. A. Waxman, V. E. Henrich, F. V. Shallcross, H. Borkan, and P. K. Weiner, *J. Appl. Phys.*, **36**, 168 (1965).
17. C. H. Seager and T. G. Castner, Thirteenth Photo-voltaic Specialist Conference Record, p. 1220, Washington, D.C., June 1978.
18. P. Lloyd, *Thin Solid Films*, **41**, 113 (1977).
19. J. L. Blakemore, "Semiconductor Statistics," Pergamon Press, New York (1962).
20. S. R. Morrison, *Surf. Sci.*, **13**, 85 (1959).
21. N. Y. Liang and A. D. Yoffe, *Phys. Rev. Lett.*, **20**, 59 (1968).

Interpretation of Hall Measurements

R. D. Larrabee

National Bureau of Standards, Washington, D.C. 20234

ABSTRACT

The temperature dependence of the Hall coefficient is the usual parameter measured to determine dopant energy levels and densities in semiconductors. However, this interpretation of Hall measurements is not necessarily unique. An example of current interest is indium-doped silicon, where a new acceptor level has been reported. It was found that the Hall data for an indium-doped silicon sample could be interpreted in two ways: one including, and the other without, the new level. A donor addition experiment was performed that clearly distinguished between these alternative explanations by supporting the new level interpretation and denying the alternative. It is suggested that donor addition is one example of a variety of techniques that can be used to supplement Hall measurements in order to resolve ambiguities of interpretation.

The temperature dependence of the Hall coefficient is the usual parameter measured to determine dopant energy levels and densities in semiconductors. However, the interpretation of Hall measurements in terms of dopant parameters is not necessarily unique. An example of an ambiguity in the interpretation of Hall data is observed with samples of indium-doped silicon. Evidence regarding the existence of a new acceptor level has been reported by some observers (1-4). Since the apparent activation energy of this level (about 0.11 eV) does not correspond to any known elemental dopant or dopant complex, its nature is not immediately apparent, and it has been called the "X"-level. One of the important applications for indium-doped silicon is in monolithic infrared imaging arrays (5);

such arrays can be seriously degraded by the presence of "X"-levels. Therefore, it became important to determine if what is being seen is really due to a new acceptor level, or just an artifact of the measuring techniques used.

Alternative Interpretations of the Same Hall Data

Figure 1 shows the results of some Hall measurements on a sample of Czochralski-grown indium-doped silicon that exhibits the behavior attributed to "X"-levels. The apparent hole density (*i.e.*, $1/qR$, where q is the electronic charge and R is the measured Hall coefficient) is plotted as a function of $1000/T$ on the assumption of equal Hall and drift mobilities [*i.e.*, assuming unity Hall scattering factor (6)]. These experimental points were fitted with a theoretical curve

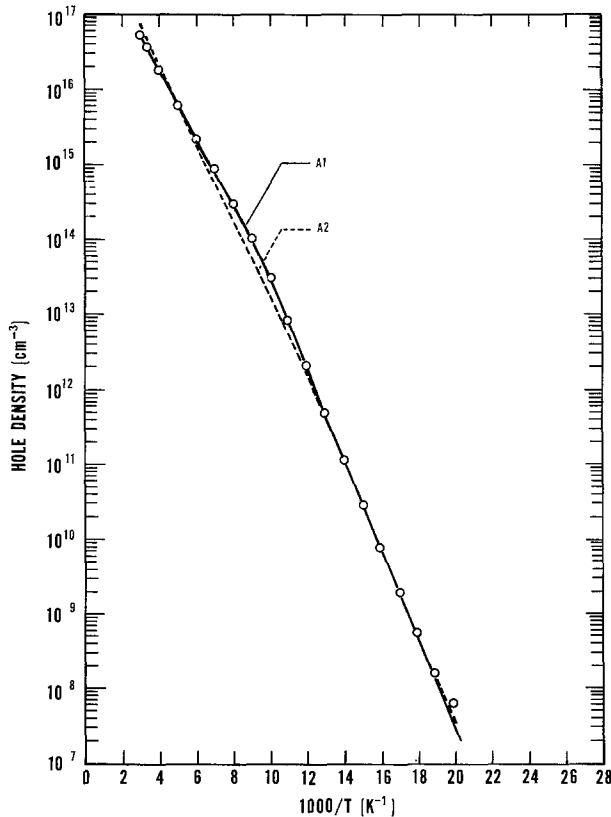


Fig. 1. Hole density vs. $1000/T$ for an indium-doped silicon van der Pauw sample. Points: calculated from the measured Hall coefficients assuming a unity scattering factor. Curve A1: computed curve with "X"-levels. (The five dopant parameters given in Table I were adjusted to fit this curve to these points.) Curve A2: computed curve without "X"-levels. (The two dopant parameters given in Table I were adjusted to fit this curve to these points.)

(A1) derived on the assumption that "X"-levels may be present.¹ The apparent dopant parameters so derived are listed in Table I. These results give the large indium acceptor concentration (expected because the material was intentionally doped with indium), and also indicate the presence of another acceptor level at 0.109 eV above the valence band (*i.e.*, the "X"-level).

There is, however, one other interpretation of these data that does not involve "X"-levels, but requires very close compensation of the omnipresent shallow acceptors (*e.g.*, boron) by donor states. A theoretical curve based on this interpretation was fitted to the experimental points, and the result is shown as curve A2 in Fig. 1 with the corresponding dopant parameters given in Table I. Although this close compensation interpretation does not appear to fit the experimental points quite as well as the new acceptor level interpretation (compare curves A1 and A2 in Fig. 1), it has only two adjustable parameters (see Table I), whereas

¹ The theoretical curves in this paper were generated by computing the carrier density as a function of specimen temperature and the density, energy, and degeneracy of the dopant states assumed to be present. The dopant parameters were determined by a trial-and-error fitting of the computer-generated curves to the experimental data.

Table I. Two possible interpretations of the Hall data in Fig. 1

Curve	Indium density (cm ⁻³)	Indium energy (eV)	"X"-level density (cm ⁻³)	"X"-level energy (eV)	Compensation* (cm ⁻³)
A1	2.3×10^{17}	0.164	1.9×10^{15}	0.109	1.2×10^{14}
A2	5.0×10^{17}	0.176	0	—	—

* Compensation = (Density of donors) - (Density of shallow acceptors). The degeneracy of the indium and "X"-level states was assumed equal to 4 in computing the curves in Fig. 1.

curve A1 has five adjustable parameters. The question then arises whether the better fit of curve A1 is significant, or just an artifact of the larger number of parameters available for fitting it to the experimental data. Further, the measurement of the Hall coefficient is not a direct measure of carrier concentration without *a priori* knowledge of the ratio of Hall-to-drift mobilities as a function of temperature (6). The points in Fig. 1 represent the case where this ratio was taken to be unity at all temperatures. Since this is not strictly true, these points are not really at their correct positions. Finally, the theoretical curves were computed on the assumption that the activation energy of the dopant states relative to the nearest band edge was not a function of temperature. Therefore, the theoretical curves may not truly correspond to the actual dopant situation in the sample. In view of uncertainties of this kind, the curve which appears to fit the points best may not necessarily be based on the correct interpretation.

Identifying Invalid Interpretations

One approach to identifying the invalid interpretation(s) would be to estimate the error of measurement of the Hall coefficient, any additional errors introduced in the computation of carrier density, and the errors introduced by the assumptions made in the computation of the theoretical curves. These errors could then be combined into an estimated rms error of fit between the measured points and the corresponding theoretical curve. A necessary condition for the acceptance of an interpretation would be that its rms error of fit be smaller than this value, and the error of fit of the alternative curve(s) be larger than this value. The fit of curve A1 in Fig. 1 is very good, but the error of the fit of the alternative curve (A2) is not clearly outside the estimated net total error. Therefore, in the present case, the close-compensation interpretation cannot be rejected on this basis alone.

Another approach to resolving this interpretation problem would be to perform some additional measurement that would experimentally resolve the ambiguity. A sensitivity analysis of the two interpretations shows that the close-compensation interpretation is much more sensitive to the introduction of additional donors or shallow acceptors than is the "X"-level interpretation. Donors can be added to silicon samples by several techniques: by neutron transmutation of silicon to phosphorus (2, 7); by indiffusion of interstitial lithium at 300°-500°C (8); or, if sufficient oxygen is present, by annealing in an inert atmosphere at 450°C for a short time (9, 10). Since the material of Fig. 1 had a measured oxygen content of about 2×10^{18} cm⁻³ (deduced from its 9 μ m absorption), the last technique was used to introduce donors. Based on this measured oxygen content, it was estimated that the 450°C anneals would activate oxygen donors at a rate in the low 10^{13} cm⁻³·min⁻¹ range (10). Therefore, annealing times of about 100 min would activate sufficient donors to completely compensate any "X"-level acceptors this sample might contain. The temperature dependence of the Hall coefficient was measured after annealing for 16, 32, 128, and 256 min at 450°C and the results compared with that predicted on the basis of the two alternative interpretations. Prior to these 450°C anneals and the measurement of the initial Hall data in Fig. 1, this sample was annealed at 650°C for 30 min to inactivate any oxygen donors that it might have initially contained (10).

Results of the Oxygen-Donor Addition Experiment

"X"-level interpretation.—Figure 2 shows the experimental points and fitted theoretical curves before annealing (curve A), after annealing for 16, 32, 128, and 256 min at 450°C (curves B through E), and after annealing at 650°C for 30 min to remove the activated oxygen donors to see if the initial preanneal conditions

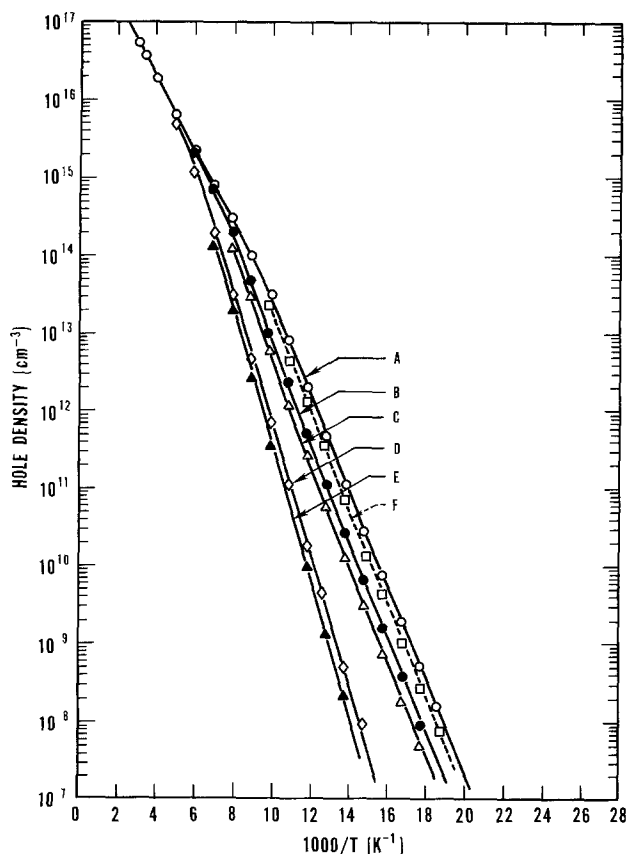


Fig. 2. Donor addition experiment—"X"-level interpretation. Experimental points and fitted theoretical curves of hole density vs. $1000/T$ as the compensation in the sample of Fig. 1 is changed.

could be restored (curve F). Curve A is a copy of curve A1 from Fig. 1 and has the dopant parameters listed for curve A1 in Table I. Each of the other curves in Fig. 2 was fitted by varying only the compensation (i.e., donor concentration), and thus represents a one parameter fit to the corresponding experimental points. The remaining four parameters were held constant at their preanneal values given in Table I for curve A1. The values of compensation deduced in this way are given in Table II and plotted as a function of time in Fig. 3. The initial rate of donor activation agrees with the earlier estimate based on the measured oxygen content of this crystal. The tendency to saturate at the longer annealing times is also expected (10). This, plus the fact that the theoretical curves of Fig. 2 fit the measured points quite well, leads to the conclusion that the "X"-level interpretation provides a satisfactory model for explaining these results with added oxygen donors.

Close-compensation interpretation.—The dominant feature of the original Hall data that suggested "X"-levels was the linear portion of Fig. 1 at low tempera-

Table II. Compensation produced by the anneals of Fig. 2

Curve	450°C annealing time (min)	650°C annealing time (min)	Compensation* (cm ⁻³)
A	0	0	1.2×10^{14}
B	16	0	4.4×10^{14}
C	32	0	8.2×10^{14}
D	128	0	2.4×10^{15}
E	256	0	3.3×10^{15}
F	256	30	3.0×10^{14}

* Determined by fitting curves to the experimental points in Fig. 2.

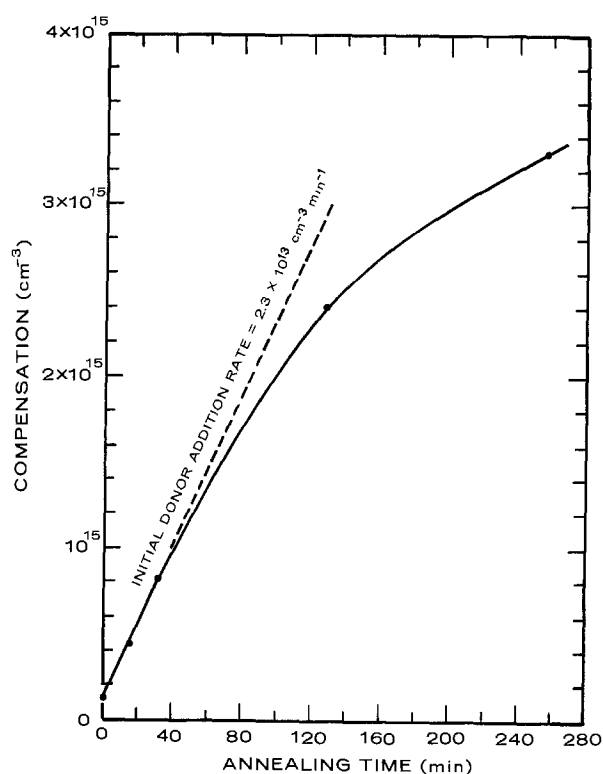


Fig. 3. Addition of donors by 450°C anneals as determined in Fig. 2 and listed in Table II.

tures (i.e., high $1000/T$) that has a slope corresponding to an apparent activation energy of about 0.11 eV. Any alternative explanation without "X"-levels must also be capable of exhibiting a linear region with this slope at these temperatures. The close-compensation interpretation achieves this as a transition between the lower slope of omnipresent shallow acceptors such as boron (undercompensated case) and the larger slope of indium (overcompensated case). Therefore, the close-compensation interpretation would be expected to predict this slope to increase as donors are added to overcompensate the shallow acceptors. The theoretical curves of Fig. 4 illustrate this behavior. Curve A of Fig. 4 is identical to curve A2 of Fig. 1 and has parameters for curve A2 in Table I. Notice that it does exhibit a linear region at low temperatures that agrees well with the experimental data points in this temperature region (open circles). Curves B through E were computed using the same parameters as curve A, but with added compensation levels of 10^{12} , 10^{13} , 10^{14} , and 10^{15} cm⁻³, respectively. Notice that as few as 10^{12} cm⁻³ additional donors are sufficient to change the slope significantly, and that the slope is relatively insensitive to further donor addition. Experimentally, however, the slope did not change for the first two anneals (see Fig. 2), so it becomes impossible to achieve an acceptable fit for these two cases. This is illustrated in Fig. 4 by plotting the 16 min anneal data (solid-circle data points) and noting that they are not well represented by any of the theoretical curves in the family of close-compensation curves of this figure. In addition, based on the measured oxygen content in this crystal, it is expected that 16 min of anneal would add a few times 10^{14} additional donors. This would be equivalent to a curve between curves D and E in Fig. 4. Actually, the change produced by the 16 min anneal was much smaller than this. Consequently, these theoretical curves do not adequately describe the changes or the slopes for short annealing times. Therefore, there seems little doubt that the close-compensation interpretation is unable to explain the observed behavior with added oxygen donors.

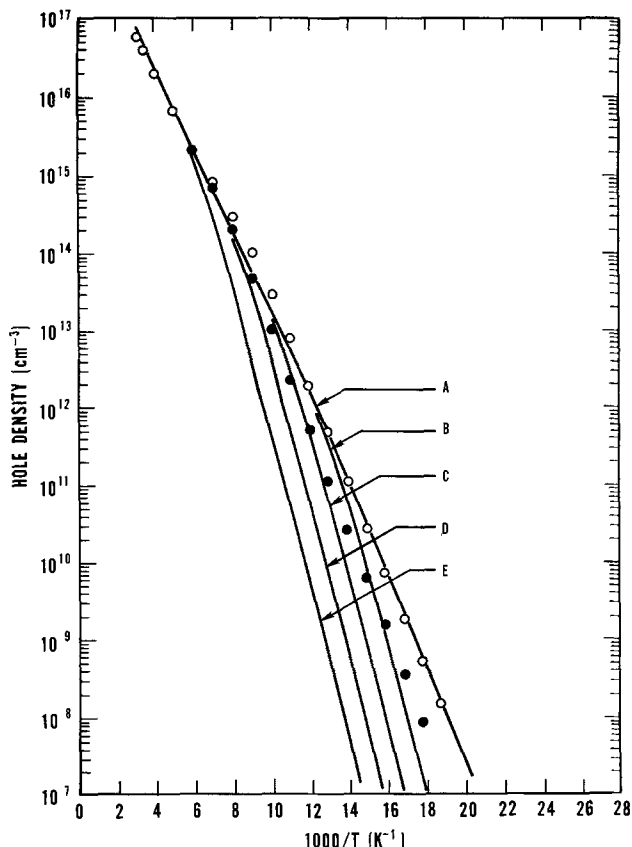


Fig. 4. Donor addition experiment—Close-compensation interpretation. Theoretical curves of hole density vs. $1000/T$ as the compensation in the sample of Fig. 1 is changed. The curve labeled A (and the open data points) correspond to the initial conditions before annealing and are taken from Fig. 1. The theoretical curves labeled B through E correspond to added compensation levels of 10^{12} , 10^{13} , 10^{14} , and 10^{15} cm^{-3} , respectively. The closed circles are the experimental data points after 16 min of anneal at 450°C . Notice that it is impossible to find a value of compensation (*i.e.*, theoretical curve) that will pass through these points.

Conclusions Drawn from the Donor Addition Experiment

The oxygen donor addition experiment has resolved the ambiguity in the interpretation of the Hall data of Fig. 1. As shown in Fig. 2 and 3, this sample exhibits behavior that is well described by the assumption that it contains an acceptor state at about 0.11 eV above the valence band. The only known alternative interpretation that does not involve this new acceptor level was unable to explain the behavior with added oxygen donors (Fig. 4). Therefore, in the absence of any data indicating otherwise, one is forced to accept the "X"-level interpretation of the Hall data for this sample. More fundamentally, however, it has been shown that despite the assumptions made in the analysis of these Hall data, the best fitting curve is based on the correct interpretation. Therefore, the foundation has been laid for a similar treatment of the Hall data from other samples of heavily indium-doped silicon.

Discussion

Donor addition is one example of the variety of ancillary techniques that can be used to supplement Hall measurements in order to resolve ambiguities of interpretation. Annealing to activate oxygen donors is a very convenient and relatively straightforward technique that can utilize the same sample used in the original Hall measurements. However, its use is limited to silicon crystals with comparatively large oxygen content (greater than about 20 ppm atomic), thus ruling out all float-zoned and some Czochralski crystals. Lithium indiffusion and neutron transmutation doping were mentioned earlier as alternative donor addition mechanisms. Looking for the presence (or absence) of infrared absorption or detector spectral response from suspected dopant states provides a fundamentally different type of approach to this interpretation resolution problem. The fields of thermally stimulated current and capacitance or capacitance transient spectroscopy might also be used to resolve interpretation ambiguities. With so many alternative approaches, it is suggested that one first attempt to appreciate the nature of any alternative interpretations and, armed with this insight, devise some simple measurement technique that will distinguish between them.

Acknowledgments

The author would like to thank M. G. Buehler, W. M. Bullis, K. F. Galloway, and W. R. Thurber for many helpful discussions during the course of this work, and Robert Baron, Hughes Aircraft Company, for the suggestion that oxygen donor addition could be used as a test of the validity of the "X"-level interpretation. This work was conducted as part of the Semiconductor Technology Program at NBS. The work was supported by the Defense Advanced Research Projects Agency (Order No. 2397).

Manuscript submitted July 23, 1979; revised manuscript received Jan. 31, 1980.

Any discussion of this paper will appear in a Discussion Section to be published in the June 1981 JOURNAL. All discussions for the June 1981 Discussion Section should be submitted by Feb. 1, 1981.

Publication costs of this article were assisted by the National Bureau of Standards.

REFERENCES

1. R. Baron, M. H. Young, J. K. Neeland, and O. J. Marsh, *Appl. Phys. Lett.*, **30**, 594 (1977).
2. R. N. Thomas, T. T. Braggins, H. M. Hobgood, and W. J. Takei, *J. Appl. Phys.*, **49**, 2811 (1978).
3. M. W. Scott, *Appl. Phys. Lett.*, **32**, 540 (1978).
4. M. C. Ohmer and J. E. Lang, *ibid.*, **34**, 750 (1979).
5. B. Miller, *Aviat. Week Space Technol.*, **104**, 71 (May 3, 1976).
6. E. H. Putley, "The Hall Effect and Related Phenomena," p. 105, Butterworths, London (1960).
7. M. Tanenbaum and A. D. Mills, *This Journal*, **108**, 171 (1961).
8. G. Dearnaly and D. C. Northrop, "Semiconductor Counters for Nuclear Radiations," 2nd ed., p. 150, E. & F. N. Spon, Ltd., London (1966).
9. W. Kaiser, H. L. Frisch, and H. Reiss, *Phys. Rev.*, **112**, 1546 (1958).
10. J. A. Baker, *This Journal*, **120**, 92C (1973).

Method for Determination of Diffusion Coefficients from Carrier Concentration Depth Profiles in Silicon

A. Bakowski

Institute of Electron Technology, 02-668 Warsaw, Poland

ABSTRACT

A method for the determination of diffusion coefficients from carrier concentration depth profiles is presented. Carrier profiles created during diffusion from ion-implanted sources were determined by differential conductivity measurements. The experimentally obtained distribution has been fitted for each sample by a smooth spline function approximation. Then applying the modified version of the Boltzmann transformation, diffusion coefficients of boron, phosphorus, and arsenic in silicon were determined. A full agreement between the measured and the calculated distribution was obtained when the concentration-dependent diffusion coefficient was inserted into the numerical solution of the diffusion equation. The temperature dependence of the diffusion coefficient of boron was also calculated and the activation energy value $E_a = 3.31$ eV was obtained.

For process control, device, and circuit characterization in silicon semiconductors, an accurate knowledge of the diffusion profiles is essential. The use of ion implantation in semiconductor device manufacture makes it possible to achieve the desired impurity distribution with great accuracy (1-6). As the implant concentration profiles of common dopants are fairly well known, knowledge of the diffusion and oxidation process parameters becomes most important. The diffusion coefficient has an especially great influence on impurity profile shape. The exact diffusion process simulation can be made if one knows the concentration-dependent diffusion coefficient (7-14).

Using the Boltzmann-Matano method, an effective diffusion coefficient as a function of carrier concentration can be calculated. This method may be applied when the surface concentration of the diffused impurity is invariant with time. A convenient formula obtained by the Boltzmann transformation has previously been used for determining the diffusion coefficient of phosphorus (15-19) and arsenic (14, 20, 21) as a function of concentration.

When the diffusing dopant of fixed total amount is redistributed, the Boltzmann transformation may not be applied because the surface concentration decreases with time, which implies a time dependence of the concentration separate from the ratio of penetration depth to square root of diffusion time postulated by Boltzmann. In this case the Boltzmann transformation can be replaced by a suitable modification proposed by Ghezzi (22, 23). This modification leads to a dependence of diffusivity on the ratio of concentration to surface concentration. This modified analysis was used by Fair and Tsai (3) for determining the diffusivity of arsenic from implanted, diffused As profiles.

In this paper a simple method of diffusion coefficient determination is presented. Drive-in diffusion occurred from an ion-implanted source. Diffusion coefficients were determined numerically using a modified Boltzmann-Matano transformation. Dependence of the diffusion coefficients on the concentration for boron, phosphorus, and arsenic and on the diffusion temperature for boron were found. Then, using finite difference techniques, the diffusion equation with concentration-dependent diffusivity was solved and a comparison made between experimental and calculated redistributions of the implanted ions.

Key words: ion implantation, diffusion coefficient, diffusion in silicon, spline function.

Experimental

The samples used for electrical measurements were (111) oriented, 4-5 Ω -cm phosphorus-doped silicon wafers for the boron implantations, and 10-12 Ω -cm boron-doped silicon wafers for arsenic and phosphorus implantations. All boron implantations were performed in the energy range 60-100 keV and in the dose range $3.6 \cdot 10^{15}$ - $4.8 \cdot 10^{15}$ cm^{-2} . All P and As implantations were performed in the energy range 60-150 keV and in the dose range $2.5 \cdot 10^{15}$ - $5 \cdot 10^{15}$ cm^{-2} . Wafers were tilted 7° during implantation in order to avoid channeling. Drive-in diffusion was carried out in a dry nitrogen atmosphere. Annealing of B-implanted samples was performed in the temperature range 1000° - 1200°C . Arsenic-implanted samples were annealed at 1070°C and phosphorus-implanted samples at 920°C . Concentration profiles of electrically active impurities were obtained using sheet resistivity measurements combined with an anodic sectioning technique. Anodizations were performed in a mixture of 900 ml of ethylene glycol, 10 ml of water, and 10g of potassium nitride. Oxide layers were stripped in dilute HF and slices were rinsed in deionized water. The sheet resistance was read using a four-point probe with light probe pressure.

After several trials it was found that the variation in thickness of the removed Si layers in the case of different impurity concentrations did not exceed 10%. The concentration profiles were measured by removing $500 \pm 50 \text{ \AA}$ of Si in each step ($300 \pm 30 \text{ \AA}$ in the case of shallow As and P profiles). The distance between the original silicon surface and the stripped region was measured for each sample with a stylus, after the concentration profile measurements had been finished, to check the etching depth.

Resistivity vs. carrier concentration.—Resistivity data from incremental sheet resistivity analysis were converted to impurity concentrations through the use of the expression for carrier concentration dependence of mobility from the work of Coughy and Thomas (24). The hole mobilities given by Wagner (25) and the electron mobilities given by Plunkett, Stone, and Leu (26) were used. The use of these mobility values resulted in calculated dose, Q_{PS} , 5-10% lower than the actual dose Q for boron and 10-20% lower for arsenic and phosphorus. Similar results were obtained for calculated and measured sheet resistances, R_{SPS} and R_s , respectively. The actual and calculated dose as

well as measured and calculated sheet resistances are compared in Tables I, II, and III.

The p-n junction depths were also measured for each sample using groove and stain techniques.

Analysis

Impurity concentration redistribution from an ion-implanted source can be treated as diffusion from a δ function source placed at a depth equal to the projected range of the implanted ions, R_p , from the Si surface. It can be shown that the expression for the determination of the concentration-dependent diffusion coefficient which is applicable to a redistributing impurity of fixed total amount in the case of an ion-implanted source is given (6, 11) by

$$D \left\{ \frac{N(x_0, t)}{N(0, t)} \right\} = - \frac{N(x_0, t) \cdot (x_0 - R_p)}{2 \cdot t \cdot \left. \frac{\partial N}{\partial x} \right|_{x_0}} \quad [1]$$

where D is the diffusivity at a depth x_0 from the surface. It must be emphasized, however, that because the initial profile after ion implantation is Gaussian, Eq. [1] is valid only when

$$\frac{\Delta R_p^2}{2} \ll D_1 \cdot t$$

where ΔR_p is the range straggling of the implanted ions.

Results and Discussion

Spline function and Chebyshev polynomial approximation.—The results of the experimental determinations of carrier concentration depth profiles in Si are shown in Fig. 1-3.

The experimental points for all samples were fitted by a smoothed third degree spline function (27). The way of fitting a smooth spline function to a set of experimental points is shown in the Appendix. Computations were performed using an algorithm published by Reinsch (28, 29). The spline function approximation fidelity was evidenced by comparing the spline function integral Q_{SPLINE} with the experimental points integral Q_{PD} . These integral values are combined in Tables I, II, and III. The spline functions approximating

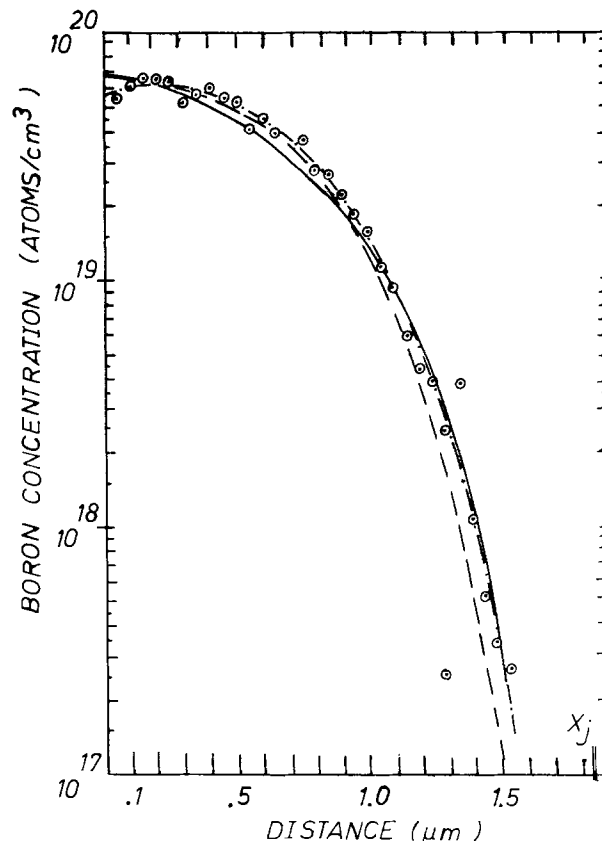


Fig. 1. Carrier concentration depth profile for boron implanted at 60 keV ($4.8 \cdot 10^{15} \text{ cm}^{-2}$) and annealed at 1180°C for 13 min (\odot). Full curve, spline function approximation; dotted curve, Chebyshev polynomial approximation; dashed curve, calculated profile.

experimental carrier concentration profiles are shown in Fig. 1-3. Excellent fitted curves for all samples were obtained.

The carrier concentration profiles were also approximated by Chebyshev polynomials (30). Polynomials

Table I. Calculated and actual boron dose and sheet resistance

	Dose (j/cm ²)				Sheet resistance (Ω/□)		
	Q	Q _{PD}	Q _{SPLINE}	Q _{PS}	R _s	R _{sPD}	R _{sPS}
1	$3.6 \cdot 10^{13}$	$3.21 \cdot 10^{13}$	$3.35 \cdot 10^{13}$	$3.49 \cdot 10^{13}$	1100	1320	
2	$1.5 \cdot 10^{14}$	$1.39 \cdot 10^{14}$	$1.22 \cdot 10^{14}$	$1.44 \cdot 10^{14}$	320	332	310
3	$3.7 \cdot 10^{14}$	$3.25 \cdot 10^{14}$	$3 \cdot 10^{14}$	$3.57 \cdot 10^{14}$	155	177	159.6
4	$6.5 \cdot 10^{14}$	$6.47 \cdot 10^{14}$	$6.1 \cdot 10^{14}$	$6.24 \cdot 10^{14}$	120	120	119.1
5	$2.1 \cdot 10^{15}$	$1.86 \cdot 10^{15}$	$1.97 \cdot 10^{15}$	$1.74 \cdot 10^{15}$	50.5	54.4	
6	$4.8 \cdot 10^{15}$	$4.6 \cdot 10^{15}$	$4.26 \cdot 10^{15}$	$4.66 \cdot 10^{15}$	23.4	24.4	24.1

Table II. Calculated and actual phosphorus dose and sheet resistance

	Dose (j/cm ²)				Sheet resistance (Ω/□)		
	Q	Q _{PD}	Q _{SPLINE}	Q _{PS}	R _s	R _{sPD}	R _{sPS}
1	$2.5 \cdot 10^{15}$	$2.32 \cdot 10^{15}$	$2 \cdot 10^{15}$	$2.46 \cdot 10^{15}$	38	44.3	34.5
2	$5 \cdot 10^{15}$	$4.43 \cdot 10^{15}$	$3.9 \cdot 10^{15}$	$4.9 \cdot 10^{15}$	19	23.9	17.4

Table III. Calculated and actual arsenic dose and sheet resistance

	Dose (j/cm ²)				Sheet resistance (Ω/□)		
	Q	Q _{PD}	Q _{SPLINE}	Q _{PS}	R _s	R _{sPD}	R _{sPS}
1	$2.4 \cdot 10^{15}$	$1.75 \cdot 10^{15}$	$1.61 \cdot 10^{15}$	$2.31 \cdot 10^{15}$	41	50.7	36.7
2	$5 \cdot 10^{15}$	$4.1 \cdot 10^{15}$	$3.5 \cdot 10^{15}$	$4.69 \cdot 10^{15}$	20	24.4	18.6

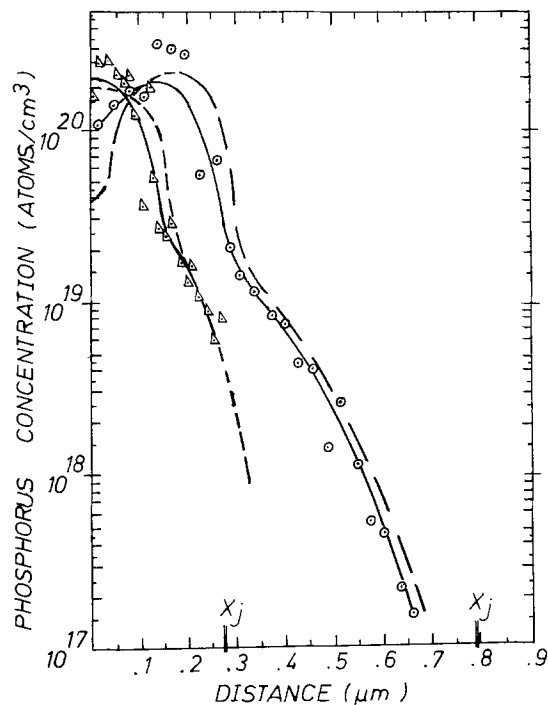


Fig. 2. Carrier concentration depth profiles for phosphorus implanted at 60 keV ($2.5 \cdot 10^{15} \text{ cm}^{-2}$) and annealed at 920°C for 35 min (Δ), and implanted at 150 keV ($5 \cdot 10^{15} \text{ cm}^{-2}$) and annealed at 920°C for 30 min (\odot). Full curves, spline function approximation; dashed curves, calculated profiles.

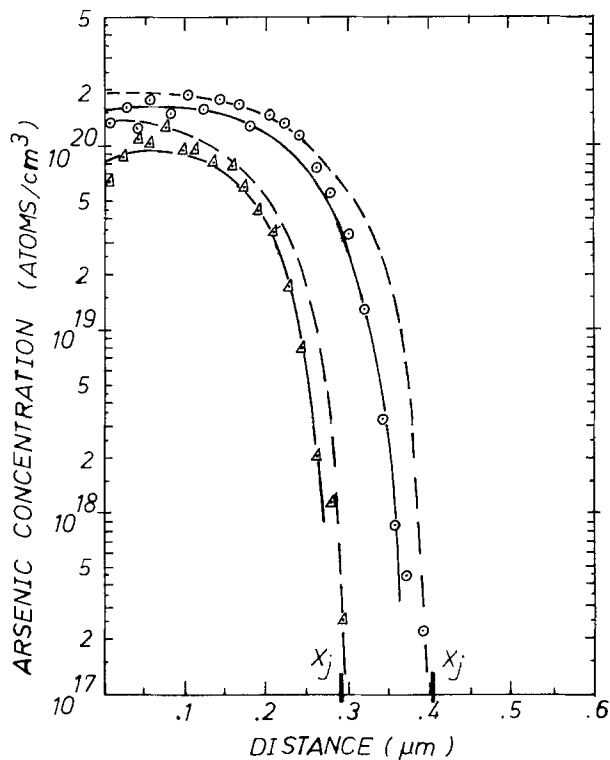


Fig. 3. Carrier concentration depth profiles for arsenic implanted at 60 keV ($2.4 \cdot 10^{15} \text{ cm}^{-2}$) and annealed at 1070°C for 25 min (Δ), and implanted at 150 keV ($5 \cdot 10^{15} \text{ cm}^{-2}$) and annealed at 1070°C for 30 min (\odot). Full curves, spline function approximation; dashed curves, calculated profiles.

from the 2nd to the 10th degree were tried. The best fitted curves were obtained with a fifth degree polynomial. Higher degree polynomials gave better fit but worse smoothness. For some samples the results were not satisfactory, it being impossible to produce smooth

curves that fit the experimental values well. It is a common observation that a polynomial of moderately high degree fitted to a fairly large number of given data points tends to exhibit more numerous and more severe undulations than a curve drawn with a spline.

The Chebyshev polynomial approximation and spline function approximations are compared in Fig. 1.

Diffusion coefficient.—Equation [1] has been used to determine the diffusion coefficient as a function of the carrier concentration from the spline function approximation to the profiles. These results are shown in Fig. 4, 5, and 6. There are two concentration ranges where determined diffusion coefficient values are not confident.

Due to the use of an electrical measurement technique, a large degree of inaccuracy can occur near a p-n junction since the sheet resistance approaches infinity at the junction asymptotically. The drop of boron diffusivity for low concentrations ($< 10^{17} \text{ cm}^{-3}$) probably arises from an experimental error in this region (31). A large error can be also made at depths close to the projected range of implanted ions (i.e., close to the maximum of the carrier distribution).

Two factors in Eq. [1], for $x \rightarrow R_p$, tend to zero simultaneously, $(x - R_p) \rightarrow 0$ and $\partial N/\partial x \rightarrow 0$. Thus, diffusion coefficient values, determined from a Boltzmann-Matano analysis in this region, will show a sharp decrease or increase depending on which factor reaches zero more rapidly.

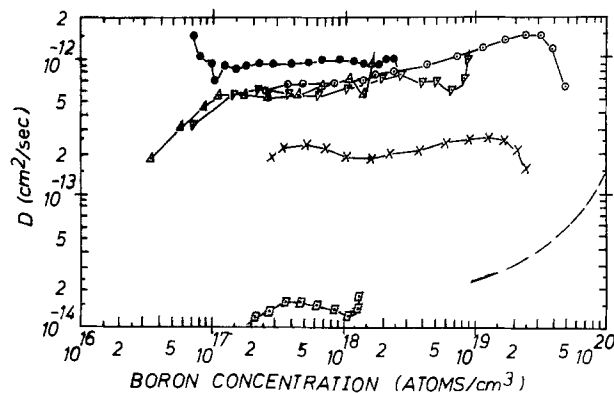


Fig. 4. Boron diffusion coefficient vs. impurity concentration. The data points shown are from this work (1000°C \square), (1100°C \times), (1180°C ∇ Δ \odot), (1200°C \bullet), and the dashed curve for 1000°C is from Crowder et al. (33).

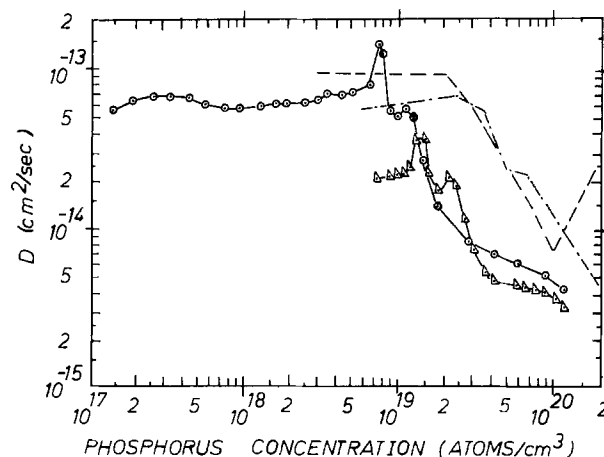


Fig. 5. Phosphorus diffusion coefficient vs. impurity concentration. The data points shown are from this work (920°C , $2.4 \cdot 10^{15} \text{ cm}^{-2}$, 60 keV Δ), (920°C , $5 \cdot 10^{15} \text{ cm}^{-2}$, 150 keV \odot); Lee (900°C \bullet); Ref. (15); and Fair and Tsai (900°C \bullet) Ref. (34).

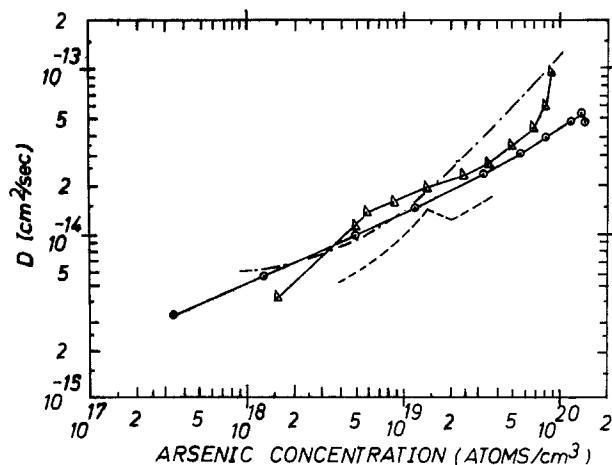


Fig. 6. Arsenic diffusion coefficient vs. impurity concentration. The data points shown are from this work (1070°C, $2.5 \cdot 10^{15}$ cm $^{-2}$, 60 keV Δ), (1070°C, $5 \cdot 10^{15}$ cm $^{-2}$, 150 keV \odot); Fair and Tsai (1050°C - - - -) Ref. (3); and Wang and Ghezzi (1050°C - - - -) (Ref. (20)).

Although the boron diffusion coefficient tends to decrease for high dopant concentrations, as was reported by Brown and Kennicott (32), in our case this effect is a result of analysis error.

It is very difficult to define how reliable are results obtained from a modified Boltzmann-Matano analysis. Only the accuracy of the profile measurements method is known. Because the form of the underlying function is not known *a priori*, accuracy of the spline function approximation and spline function differentiation is almost impossible to estimate.

Thus, the reliability of the technique is demonstrated by the fit of the theoretical profiles to experimental data. Boron, phosphorus, and arsenic concentration-dependent diffusivities are also compared with previously published results (33, 20, 21, 3, 15).

In order to compute the impurity distribution it was necessary to find a function which describes the concentration-dependent diffusivity data for each impurity. It is well known that the diffusivity of phosphorus has three characteristic concentration regions. It was shown that in the high concentration region $D \propto n^2$, in the transition region $D \propto n^{-2}$, and in the low concentration region (tail region), $D = \text{const.}$ (34). Through combination of earlier published results (15, 34) with the results presented in this paper, an empirical function which best describes the experimental points was formed.

In the tail region

$$D = D_{\text{TAIL}} = \text{const.} \quad [2]$$

In the surface and transition region at 920°C

$$D = h \left[3.59 \cdot 10^{-16} + 3.2 \cdot 10^{-18} \left(\frac{N}{n_i} \right)^2 \right] + 3.65 \cdot 10^{-13} \left(\frac{N}{n_i} \right)^{-2} \quad [3]$$

where

$$h = 1 + \frac{N}{2n_i} \left[\left(\frac{N}{2n_i} \right)^2 + 1 \right]^{-1/2} \quad [4]$$

is the electric-field enhancement factor.

A quantitative model of phosphorus diffusion in silicon was proposed by Fair and Tsai (19). But to obtain, based on the Fair and Tsai model, the theoretical dependence of $D(N)$ in the case of phosphorus diffusion from an ion-implanted source required further investigation.

The expression which best describes the concentration-dependent diffusivity of arsenic and boron is

$$D = D_i \cdot h \cdot \left(1 + A \frac{N}{n_i} \right) \quad [5]$$

with $A = 0.1$ for boron and $A = 0.25$ for arsenic

The intrinsic arsenic diffusivity D_i .—From Eq. [5] the value of the intrinsic diffusion coefficient D_i for arsenic was obtained which best describes the data in Fig. 6.

Phosphorus diffusivity in the tail region, D_{TAIL} .—The results obtained from Boltzmann-Matano analysis for phosphorus show the constant tail region diffusivity (see Fig. 5). However, a strong diffusion coefficient dependence on implanted dose is observed in this low concentration region. It was reported that tail diffusivity is influenced by the highly doped region near the surface (34, 35). By the way, the initial impurity concentration profile maximum was almost the same for both implanted samples. The increase in tail diffusivity observed for the high energy (150 keV) implanted P profile is not a result of channeling as could be supposed. A strong increase in phosphorus tail diffusion coefficient was also observed for low energy implanted P profiles in the dose range $2.5 \cdot 10^{15}$ – $7.5 \cdot 10^{15}$ before a rapid decrease for higher dose (36). As can be seen in Fig. 2, the computed and experimental profiles coincide, meaning that a Boltzmann-Matano analysis error is not playing a significant role here either.

To explain the dependence of D_{TAIL} on ion dose, more experiments must be done.

The intrinsic boron diffusivity D_i .—In order to determine values of D_i from boron, experimental $D(N)$ curves of the samples in which the maximum concentration after drive-in dose did not greatly exceed the intrinsic carrier concentration at the diffusion temperature (in this case the factor $\left(1 + A \frac{N}{n_i} \right)$ in Eq. [2] is equal to ~ 1) were approximated by the least squares method as

$$D = D_i \cdot h \quad [6]$$

With D_i values obtained from Eq. [6], Eq. [5] describes the boron diffusivity experimental points very well.

Values of D_i as a function of diffusion temperature are shown in Fig. 7. An activation energy of 3.31 eV with a preexponential factor of 0.205 cm 2 /sec is found to describe boron diffusivity in (111) crystal orientation silicon in the temperature range 1000°–1200°C, in inert ambients. Also shown in Fig. 7 are examples of the boron intrinsic diffusion coefficient as determined by other workers (7, 37–39). The differences are mainly due to different ambient atmospheres. Prince and Schwettmann's diffusion was performed in steam (7). Massetti *et al.* (37) used dry O $_2$.

The results of the present work are in excellent agreement with the data recently published by Antoniadis *et al.* (40). They diffused boron from an ion-implanted source under intrinsic conditions in a non-oxidizing atmosphere. Although their technique of diffusivity determination was quite different from the one presented in this paper, the results over the range of common diffusion temperatures coincide.

Computations of impurity profiles.—The diffusion equation was solved by computer by finite difference techniques using a Crank-Nicolson type approach. The nonlinearity engendered by the concentration dependence of diffusivity required the use of a two-step iterative solution algorithm, the so-called predictor-corrector method of Douglas (7, 41, 42).

The initial implanted profiles were taken to be Gaussian with projected range R_p and range straggling ΔR_p according to earlier calculations (43) based on a method described by Winterbon (44).

The boron segregation coefficient was taken from the Colby and Katz paper (45). Although they used dry O $_2$ oxidations, their data are in general agreement with

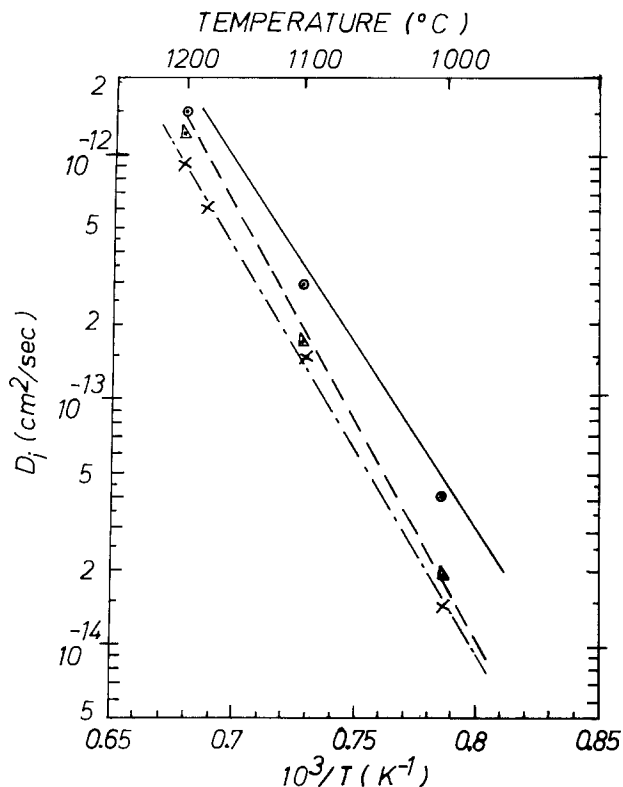


Fig. 7. Boron intrinsic diffusion coefficient vs. inverse temperature. The data points shown are as follows: this work (\times - - - -); Masetti et al. (Δ) Ref. (37); Kurtz and Yee (- - - -) Ref. (38); Prince and Schwettmann (\circ) Ref. (7); and Huang and Wellivier (—) Ref. (39).

our earlier results obtained by a fitting technique (46). When the segregation coefficients of phosphorus and of arsenic were changed during the computations from 0.01 to 0.1, no differences in calculated curves were observed.

The concentration dependence of the diffusion coefficient was assumed for boron and arsenic to be given by Eq. [2] with $A = 0.1$ for boron and $A = 0.25$ for arsenic. Calculated B and As profiles are shown in Fig. 1 and 3. The empirical expression for phosphorus concentration-dependent diffusivity was obtained from the best fit of Eq. [2] and [3] to the experimental data. Calculated P profiles are shown in Fig. 2.

It is shown in Tables I, II, and III that the differences between the dose remaining in the silicon calculated from the experimental points Q_{pp} and the integral of the computed profile Q_{ps} do not exceed 10% for boron and 15% for phosphorus and arsenic. The same differences are observed between the sheet resistance calculated from the experimental points R_{spp} and from the computed profile R_{sps} .

The Boltzmann-Matano analysis presented gives diffusion coefficients that can be successfully used for calculations of impurity diffusion profiles.

Comparing the calculated boron or arsenic or phosphorus profiles to experimental profiles, it is seen that the agreement is satisfactory.

Summary

1. A method was presented for the determination of the diffusion coefficient from the experimental impurity concentration depth profile. This method is valid only when: (i) the total impurity per unit area remains constant during drive-in and (ii) the diffusion length is much longer than the straggling range of the implanted ions.

2. A spline function is most useful for the approximation of measured doping profiles.

3. Activation energy obtained for boron diffusion is $E_a = 3.31$ eV.

4. The diffusion profile from ion-implanted layers after drive-in can be successfully predicted by numerical solution of the diffusion equation when the concentration dependence of the diffusion coefficient is well known. The use of a modified Boltzmann-Matano analysis for diffusivity determination leads to excellent profile calculations.

Acknowledgments

The author wishes to thank Dr. J. Krylow for many valuable discussions and support. Experimental work by Mr. J. Gazda is also acknowledged.

Manuscript submitted Jan. 22, 1979; revised manuscript received Jan. 2, 1980.

Any discussion of this paper will appear in a Discussion Section to be published in the June 1981 JOURNAL. All discussions for the June 1981 Discussion Section should be submitted by Feb. 1, 1981.

APPENDIX

Spline functions.—Spline functions are a class of piecewise polynomial functions that have highly desirable characteristics for approximating, interpolating, and curve-fitting.

Let us define spline functions and natural splines. **Definition of a spline function (27).**—Given a strictly increasing sequence of real numbers, x_1, x_2, \dots, x_n , a spline function $S(x)$ of degree m with the knots x_1, x_2, \dots, x_n is a function defined on the entire real line having the following properties: (i) in each interval (x_i, x_{i+1}) for $i = 0, 1, \dots, n$ (where $x_0 = -\infty$ and $x_{n+1} = +\infty$), $S(x)$ is given by some polynomial degree m or less and (ii) $S(x)$ and its derivatives of orders $1, 2, \dots, m-1$ are continuous everywhere.

Definition of natural splines (27).—A spline $s(x)$ of odd degree $2m-1$ with the knots x_1, x_2, \dots, x_n is called a natural spline if it is given in each of the two intervals $(-\infty, x_1)$, (x_n, ∞) by some polynomial of degree $m-1$ (rather than $2m-1$) or less (in general not the same polynomial in the two intervals).

Thus, a spline function is a piecewise polynomial function satisfying certain conditions regarding continuity of the function and its derivatives.

Smoothing by natural splines (28, 47).—In our problem of fitting a smooth curve to a set of experimental points, (x_i, y_i) $i = 1, \dots, n$, we have to determine the smooth curve $g(x)$ from the condition that

$$\int_{x_1}^{x_n} [g^{(m)}(x)]^2 dx \quad [A-1]$$

is minimized for all $g(x)$ satisfying the smoothing constraint

$$\sum_{i=1}^n w_i [y_i - g(x_i)]^2 \leq S, g \in C^m(x_1, x_n) \quad [A-2]$$

where $w_i > 0$, $i = 1, 2, \dots, n$, and $S \geq 0$ are given numbers.

The choice of $\{w_i\}_1^n$ and S for smoothing depends on the confidence we have in the data $\{y_i\}_1^n$. The S constant is redundant and is introduced only for convenience. It allows for an implicit rescaling of the quantities w_i which control the extent of smoothing. Recommended values for S depend on the relative weights w_i .

It has been suggested (28) that w_i should be chosen as δy_i^{-2} , where δy_i is an estimate of the standard deviation of the ordinate y_i . In this case, natural values of S lie within the confidence interval corresponding to the left-hand side of Eq. [A-2] (28)

$$N - (2N)^{1/2} \leq S \leq N + (2N)^{1/2} \quad N = n + 1$$

Small values of $\{\delta y_i\}_1^n$ and/or S emphasize fidelity to the observed data at the expense of smoothness, while large values do the opposite.

For many problems a choice of a small m is desirable, e.g., $m = 2$ leads to cubic splines. Cubic splines are easily evaluated and give in general satisfactory results. The solution of Eq. [A-1] and Eq. [A-2] may be obtained by the standard method of the calculus of

variations. Thus, by introducing the auxiliary variable z together with the Lagrangian parameter p , we have to look for the minimum of the function

$$\int_{x_1}^{x_n} [g''(x)]^2 dx + p \left\{ \sum_{i=1}^n \left[\frac{y_i - g(x_i)}{\delta y_i} \right]^2 + z^2 - S \right\} \quad [\text{A-3}]$$

It was shown in (28) that the extremal function $g(x)$ is composed of cubic parabolas

$$g(x) = a_i + b_i(x - x_i) + c_i(x - x_i)^2 + d_i(x - x_i)^3 \quad x_i \leq x < x_{i+1} \quad [\text{A-4}]$$

which join at their common endpoints such that g , g' , and g'' are continuous. Hence the solution is a cubic spline. The procedure that permits the computation of the spline coefficients and the evaluation of the splines can be found in Ref. (28, 47, or 18).

LIST OF SYMBOLS

D	diffusion coefficient, $\text{cm}^2 \text{sec}^{-1}$
D_i	intrinsic diffusion coefficient, $\text{cm}^2 \text{sec}^{-1}$
N	impurity concentration, cm^{-3}
E	implantation energy, keV
Q	implanted dose, cm^{-2}
Q_{DP}	implanted dose remaining in Si, calculated from experimental points, cm^{-2}
Q_{SPLINE}	spline function integral, cm^{-2}
Q_{PS}	theoretical profile integral, cm^{-2}
R_s	sheet resistance, measured, Ω/\square
R_{SPD}	sheet resistance calculated from experimental points, Ω/\square
R_{SPS}	sheet resistance calculated from theoretical profiles, Ω/\square
x_j	p-n junction depth, μm
N_B	bulk concentration, cm^{-3}
t	drive-in diffusion time, sec
R_p	projected range of implanted ions, μm
ΔR_p	straggling range of implanted ions, μm
n	free carrier concentration, cm^{-3}
n_i	intrinsic free carrier concentration, cm^{-3}
k	Boltzmann constant, $\text{eV} \cdot \text{K}^{-1}$

REFERENCES

- E. C. Douglas and A. C. F. Dingwall, *IEEE Trans. Electron Devices*, ed-21, 324 (1974).
- S. P. Murarka, *Phys. Rev. B*, **12**, 2502 (1975).
- R. B. Fair and J. C. C. Tsai, *This Journal*, **122**, 1689 (1975).
- H. Muller, H. Kranz, H. Ryssel, and K. Schmid, *Appl. Phys.*, **4**, 115 (1974).
- I. R. Sanders, *Microelectron. Reliab.*, **16**, 75 (1977).
- Y. Wada, S. Nishimatsu, and K. Sato, *Solid-State Electron.*, **21**, 513 (1978).
- J. L. Prince and F. N. Schwettmann, *This Journal*, **121**, 705 (1974).
- R. P. Ricco, J. F. Goldstein, and J. G. Callum *ibid.*, **124**, 276 (1977).
- F. F. Morehead, Paper 194 presented at the New York Meeting of The Electrochemical Society, Oct. 13-17, 1974.
- R. K. Jain and R. Van Overstraeten, Paper 191 presented at the New York Meeting of The Electrochemical Society, Oct. 13-17, 1974.
- T. L. Chiu and H. N. Ghosh, *IBM J. Res. Dev.*, **15**, 472 (1971).
- N. D. Thai, *Solid-State Electron.*, **13**, 165 (1970).
- K. Yokota, M. Iwaki, K. Gamo, K. Masuda, S. Namba, S. Ishihara, and I. Kimura, *Inst. Phys. Conf. Ser.*, No. 28, 6 (1976).
- R. B. Fair and G. R. Weber, *J. Appl. Phys.*, **44**, 273 (1973).
- D. B. Lee, *Philips Res. Rep.*, Supplement No. 5 (1974).
- S. Matsumoto, M. Yoshida, and T. Niimi, *Jpn. J. Appl. Phys.*, **11**, 1386 (1972).
- M. Yoshida, E. Arai, H. Nakamura, and Y. Terunuma, *J. Appl. Phys.*, **45**, 1498 (1974).
- S. Matsumoto, M. Yoshida, and T. Niimi, *Jpn. J. Appl. Phys.*, **13**, 1889 (1974).
- D. Shaw, *Phys. Status Solidi A*, **30**, K139 (1975).
- J. Wong and M. Ghezzi, *This Journal*, **119**, 1413 (1972).
- D. P. Kennedy and P. C. Murley, *Proc. IEEE*, **59**, 335 (1971).
- M. Ghezzi, *This Journal*, **119**, 977 (1972).
- M. Ghezzi, Paper 79 presented at the Chicago, Illinois, meeting of The Electrochemical Society, May 13-18, 1973.
- D. M. Caughy and R. E. Thomas, *Proc. IEEE*, **54**, 2192 (1967).
- S. Wagner, *This Journal*, **119**, 1570 (1972).
- J. C. Plunkett, J. L. Stone, and A. Leu, *Solid-State Electron.*, **20**, 447 (1977).
- "Theory and Applications of Spline Functions," T. N. E. Greville, Editor, Academic Press, New York (1969).
- C. H. Reinsch, *Numer. Math.*, **10**, 177 (1967).
- C. H. Reinsch, *ibid.*, **16**, 451 (1971).
- S. S. Kuo, "Numerical Methods and Computations," Addison-Wesley, Palo Alto (1965).
- P. Kramer and L. J. van Ruyven, *Solid-State Electron.*, **20**, 1011 (1977).
- D. M. Brown and P. R. Kennicott, *This Journal*, **118**, 293 (1971).
- B. L. Crowder, J. F. Ziegler, F. F. Morehead, and G. W. Cole, in "Ion Implantation in Semiconductors and Other Materials," B. L. Crowder, Editor, p. 267, Plenum Press, New York (1973).
- P. B. Fair and J. C. C. Tsai, *This Journal*, **124**, 1107 (1977).
- U. Hartmann, W. Heinze, and H-U. Oberländer, *Phys. Status Solidi A*, **4**, K197 (1971).
- A. Bakowski, Unpublished.
- C. Masetti, S. Solni, and G. Soncini, *Solid-State Electron.*, **19**, 545 (1976).
- A. D. Kurtz and R. Yee, *J. Appl. Phys.*, **31**, 303 (1960).
- J. S. T. Huang and L. C. Wellivier, *This Journal*, **117**, 1577 (1970).
- D. A. Antoniadis, A. G. Gonzalez, and R. W. Dutton, *ibid.*, **125**, 813 (1978).
- D. U. von Rosenberg, "Methods for the Numerical Solution of Partial Differential Equations," American Elsevier Publishing Co., Inc., New York (1969).
- R. M. Krambeck, *This Journal*, **121**, 588 (1974).
- A. Golanski, Private communication.
- B. Winterbon, "Ion Implantation Range and Energy Deposition Distributions," Vol. 2, Plenum Press, New York (1975).
- J. W. Colby and L. E. Katz, *This Journal*, **123**, 409 (1976).
- A. Bakowski and J. Kryłow, "Ion Implantation as Diffusion Source of Boron and Phosphorus in Silicon," Prace ITE, Reports of the Institute of Electron Technology CEMI, Warszawa, Poland, **9**, No. 13, pp. 3-36 (1976), in Polish.
- C. H. Woodford, *BIT*, **10**, 501 (1970).
- T. Lynche and L. L. Schumaker, "ALGOL Procedures for Computing Smoothing and Interpolating Natural Splines," CNA-31, Univ. of Texas, Austin (1971).



Carrier Concentration and Hall Mobility in Heavily Arsenic-Diffused Silicon

Satoru Matsumoto and Tatsuya Niimi

Department of Electrical Engineering, Keio University, Hiyoshi, Yokohama, 223, Japan

and Junichi Murota and Eisuke Arai

Nippon Telegraph and Telephone Public Corporation,

Musashino Electrical Communication Laboratory, Musashino, Tokyo, 180, Japan

The electrical characteristics in high concentration arsenic-diffused silicon layers are an important factor in the design of silicon device structures. It is well known (1, 2) that electrically inactive arsenic atoms such as clusters are formed when arsenic atoms are diffused heavily into silicon and so the total arsenic concentration (C_T) differs from the electron concentration (n) at room temperature for C_T above 10^{20} cm^{-3} . The relationship between C_T and n is usually determined using the data of resistivity (ρ) vs. n , which are varied in many investigations (3-5) for n above 10^{20} cm^{-3} . Assuming that the electrically active arsenic concentration (C_A) at the diffusion temperature is equal to n , the relationship between C_T and C_A has been also discussed (6). However, the diffusion temperature dependence of the ρ - n curve and the relationship between C_A and n are not clear.

In this note, the dependences of Hall mobility μ_H and ρ on n for various diffusion temperatures are obtained from sheet Hall measurements at room temperature, and the relationships among C_T , n , and C_A are also determined.

Heavily arsenic-doped polycrystalline silicon was deposited as a diffusant on p-type silicon wafers of 1-2 Ω -cm with mirror polished (111) surface. The experimental conditions of the deposition of arsenic-doped polycrystalline silicon have been described in detail previously (7). Diffusions were performed at 900°, 950°, and 1000°C in nitrogen atmosphere where the surface of polycrystalline silicon was covered with CVD silicon dioxide. The polycrystalline silicon on the diffusion layer was removed by anodic oxidation in a solution of N-methylacetamide and 0.04N potassium nitrate and HF stripping. To obtain profiles of ρ , n , and μ_H in the diffused layers, measurements of sheet resistivity and sheet Hall coefficient by the van der Pauw method at room temperature and the removal of a thin layer of silicon by anodic oxidation method were repeated (8). The strength of the magnetic field was 6000G and the applied constant current was 1 mA. Also, profiles of total arsenic concentration were obtained by neutron activation analysis (7).

Typical profiles of C_T , n , and μ_H , which were obtained from the sample diffused at 900°C for 2020 min, are shown in Fig. 1. The ρ - n and μ_H - n curves, which are obtained from the data presented in Fig. 1 and the data obtained at the diffusion temperatures of 950° and 1000°C, are shown in Fig. 2. The C_T - n curves for several diffusion temperatures were also obtained simultaneously and are shown in Fig. 3. It is found from Fig. 2 that ρ and μ_H are almost independent of the dif-

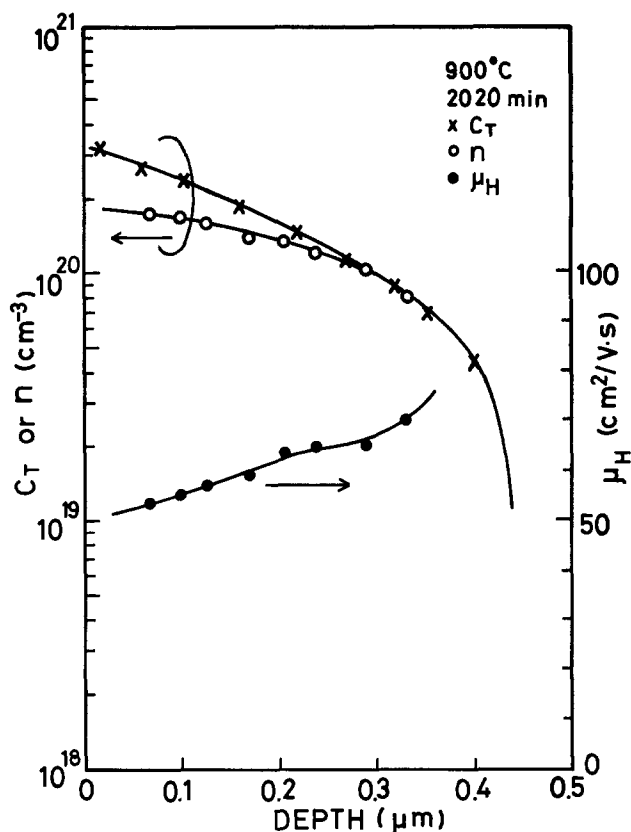


Fig. 1. Typical profiles of C_T , n , and μ_H in diffused layer for 900°C 2020 min diffusion.

fusion temperature for any n specified. On the other hand, the neutral arsenic concentration ($C_T - n$) depends on the diffusion temperature. For example, ($C_T - n$) at $n = 2.6 \times 10^{20}$ cm^{-3} for 950° and 1000°C are 1.3×10^{20} cm^{-3} and 4.5×10^{19} cm^{-3} , respectively, which are estimated from Fig. 3. This fact means that the effect on μ_H of the scattering of carriers due to neutral atoms is negligibly small in the present concentration range. Results of the ρ - n and μ_H - n curves are somewhat different from Irvin's curve and are similar to Fair's and Müller's, which were obtained from the arsenic-implanted samples assuming $C_T = n$. On the other hand, the ρ - C_T and μ_H - C_T curves differ from their data on arsenic-implanted samples because neutral arsenic atoms exist in the present arsenic-diffused sample.

Key words: semiconductor, diffusion, resistivity.

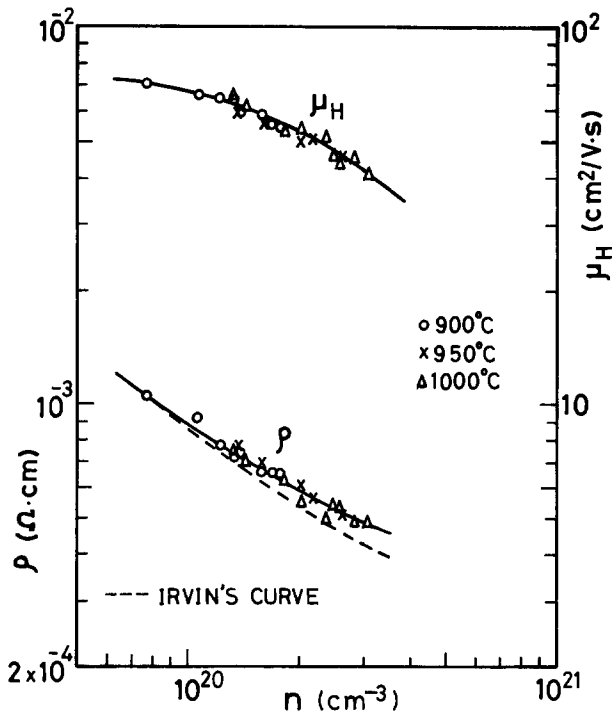


Fig. 2. ρ - n and μ_H - n curves in diffused layer for several diffusion temperatures.

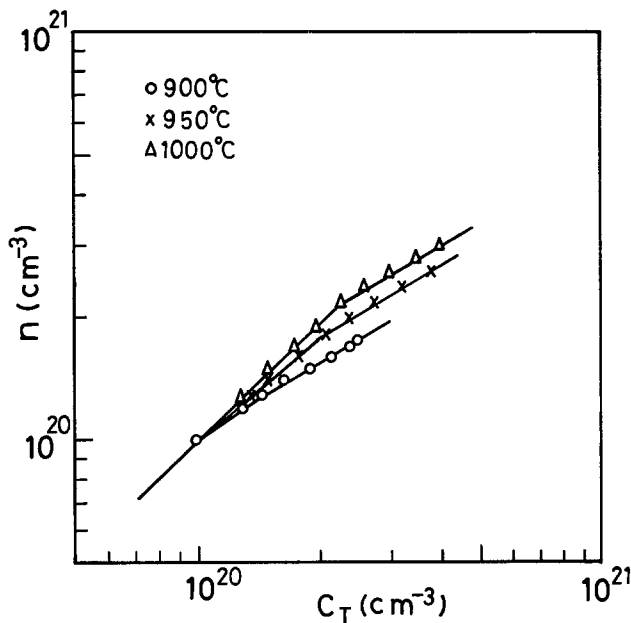


Fig. 3. C_T - n curves for several diffusion temperatures

The relationship between $(C_T - n)/n_i$ and n/n_i , which is obtained from the data presented in Fig. 3, is shown in Fig. 4, where n_i is the intrinsic carrier concentration at the diffusion temperature. From Fig. 4, the relationship between C_T and n for concentrations above 10^{20} cm^{-3} can be approximated by

$$(C_T - n)/n_i = 9.0 \times 10^{-6} (n/n_i)^4 \quad [1]$$

The deviations of experimental values from Eq. [1] are large for n/n_i below about 25.

Usually, the electrically active arsenic concentration at the diffusion temperature (C_A) has been determined by resistivity measurements using the ρ - n curve obtained at room temperature. That is, C_A has been tacitly supposed to be equal to n . On the other hand, Murota *et al.* (7) obtained the relationship between C_T and C_A from the concentration dependence of the

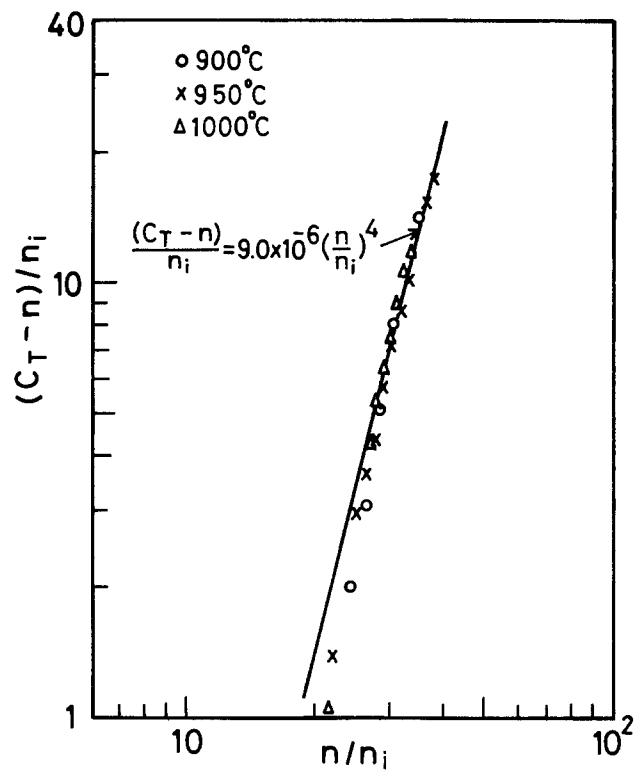


Fig. 4. Relationship between $(C_T - n)/n_i$ and n/n_i obtained from the data presented in Fig. 3.

arsenic diffusion coefficient without using the ρ - n curve

$$(C_T - C_A)/n_i = 3.2 \times 10^{-6} (C_A/n_i)^4 \quad [2]$$

From the comparison between Eq. [1] and Eq. [2], it is found that C_A is not equal to n for concentrations above 10^{20} cm^{-3} . The relationship between C_A and n may be obtained using Eq. [1] and Eq. [2]. However, this method for determining the C_A vs. n amplifies the error, since both Eq. [1] and Eq. [2] are approximate equations. We determined the relationship between C_A and n using the ρ - n curve of Fig. 2 and ρ - C_A curve of Ref. (7). The C_A - n curve thus obtained is shown in Fig. 5. The relationship between C_A and n approxi-

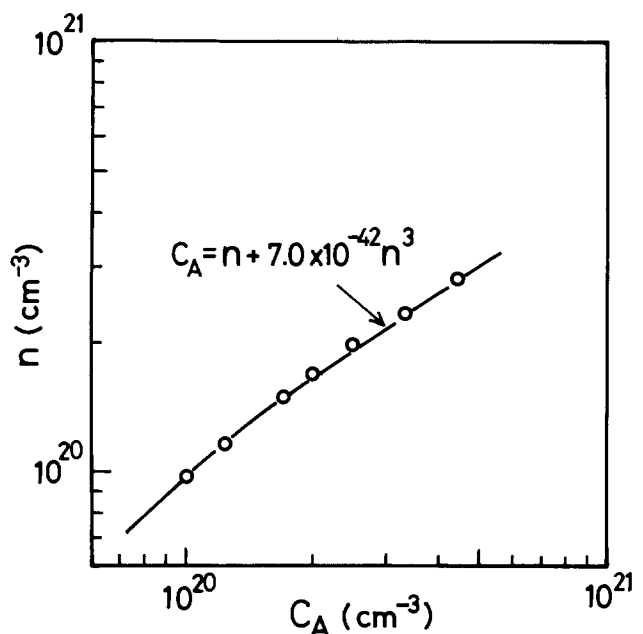


Fig. 5. Relationship between C_A and n obtained from the ρ - n curve of Fig. 2 and the ρ - C_A curve of Ref. (7).

mated by

$$C_A = n + 7.0 \times 10^{-42} n^3 \quad [3]$$

Recently, Fair *et al.* (9) have obtained the relationship between the total phosphorus concentration (C_{TP}) and n in diffused layer. Here, no electrically inactive phosphorus atoms such as cluster in phosphorus-diffused silicon is considered to be formed at diffusion temperature, differing from arsenic-diffused silicon. Replacing C_A with C_{TP} in Eq. [3], the $C_{TP}-n$ curve obtained by Fair *et al.* is approximated within their experimental error by Eq. [3]. It is very interesting for the relationship between electrically active impurity concentration at diffusion temperature and n at room temperature to be given by Eq. [3] in spite of the kind of impurity (As or P). The above result cannot be explained at present. For the analysis of the difference between C_A and n , further investigation should be done.

Acknowledgments

The authors wish to express their gratitude to M. Kondo, F. Yanagawa, and H. Nakamura of Musashino Electrical Communication Laboratory for their encouragement during the course of this work.

Manuscript submitted June 11, 1979; revised manuscript received Feb. 4, 1980. This was Paper 159 pre-

sented at the Boston, Massachusetts, Meeting of the Society, May 6-11, 1979.

Any discussion of this paper will appear in a Discussion Section to be published in the June 1981 JOURNAL. All discussions for the June 1981 Discussion Section should be submitted by Feb. 1, 1981.

Publication costs of this article were assisted by Nippon Telegraph and Telephone Public Corporation.

REFERENCES

1. R. O. Schwenker, E. S. Pan, and R. F. Lever, *J. Appl. Phys.*, **42**, 3195 (1971).
2. S. M. Hu, in "Atomic Diffusion in Semiconductors," D. Shaw, Editor, Chap. 5, Plenum, London (1972).
3. J. C. Irvin, *Bell. Syst. Tech. J.*, **41**, 387 (1962).
4. H. Müller, H. Kranz, H. Ryssel, and K. Schmid, *Appl. Phys.*, **4**, 115 (1974).
5. R. B. Fair and J. C. C. Tsai, *This Journal*, **122**, 1689 (1975).
6. R. B. Fair and G. R. Weber, *J. Appl. Phys.*, **44**, 273 (1973).
7. J. Murota, E. Arai, K. Kobayashi, and K. Kudo, *J. Appl. Phys.*, **50**, 804 (1979).
8. J. W. Mayer, O. J. Marsh, G. A. Shifrin, and R. Baron, *Can. J. Phys.*, **45**, 4073 (1967).
9. R. B. Fair and J. C. C. Tsai, *This Journal*, **124**, 1107 (1977).

Erratum

In the paper "Kinetics of Chemical Vapor Deposition" by J. Subrahmanyam, A. K. Lahiri, and K. P. Abraham, which appeared on pp. 1394-1399 in the June 1980 JOURNAL, Vol. 127, No. 6, it has come to the authors' attention that the free energy of formation of

C_3H_4 (mentioned on p. 1397) taken from Barin (8) is in error. Due to this, the calculated diffusion controlled rates given in Fig. 6 and 7 are in slight error, although no alteration is required in the rest of the text.



Lithium Closoboranes as Electrolytes in Solid Cathode Lithium Cells

Jack W. Johnson and M. Stanley Whittingham*

Exxon Research and Engineering Company, Corporate Research, Linden, New Jersey 07036

Ambient temperature secondary lithium cells are presently limited by low rates and limited lifetimes caused by stability problems at the lithium-electrolyte interface. Often chemical reactions of lithium with the non-aqueous solvent and the electrolyte salt lead to reduced lifetimes of secondary lithium cells. Minimization of these chemical reactions is an important goal in the development of ambient temperature secondary lithium batteries. Herein we report the results of some studies of lithium salts of closoborane anions dissolved in ethereal solvents as electrolytes.

Closoborane anions are closed polyhedra of boron atoms bearing terminal hydrogens or halogens. $B_{10}Cl_{10}^{2-}$ (Fig. 1) is a typical closoborane anion. In contrast to many boron compounds, salts of closoborane anions exhibit an extraordinary degree of kinetic stability to oxidation, reduction, and thermal decomposition. These properties have been exploited for use in electrolytes in Li/SOCl₂ liquid cathode cells (1,2). In preliminary attempts to use Li₂B₁₀H₁₀, Li₂B₁₀Cl₁₀, Li₂B₁₂H₁₂, or Li₂B₁₂Cl₁₂ as electrolyte salts in lithium-solid cathode cells, we were frustrated by problems of low solubility.

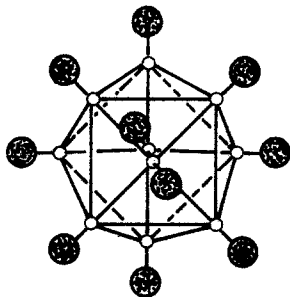


Fig. 1 Structure of $B_{10}Cl_{10}^{2-}$ Anion

The salts are soluble in high polarity solvents such as water, methanol and acetonitrile. These solvents are unsuited for secondary lithium battery applications because of their reaction with lithium metal. The lithium closoborane salts are very poorly soluble in ethereal solvents such as tetrahydrofuran, dimethoxyethane, diglyme, and dioxolane which are more desirable for secondary lithium cell applications. However, by using suitable mixtures containing the chelating ether dimethoxyethane and the cyclic ketal dioxolane, stable solutions containing high concentrations of Li₂B₁₀Cl₁₀ and Li₂B₁₂Cl₁₂ can be formed.

Li₂B₁₀Cl₁₀, obtained by modification (3) of the reported procedures (1,4,5) can be recrystallized from dioxolane/DME mixtures as the solvate Li₂B₁₀Cl₁₀·6DME. This solvate is soluble in pure dioxolane in concentrations from 32 to 50 wt%. At concentrations below this range, two clear liquid layers form, and if dilution is continued, a dioxolane solvate of the salt precipitates. Li₂B₁₂Cl₁₂ behaves in a similar fashion.

When the electrolyte is suitably purified it demonstrates good chemical stability in the presence of both lithium metal and titanium disulfide, a common cathode material. When a shiny piece of lithium metal was sealed in tubes containing Li₂B₁₀Cl₁₀·6DME/dioxolane no visible reaction was observed after one month at 70°C. Similar tests with high purity TiS₂ also demonstrated the electrolyte's inertness. The resistance of the electrolyte to electrochemical oxidation was demonstrated by voltammetric scans on inert electrodes. On a Ta working electrode, scanning positive from a Li reference electrode leads to an oxidation wave at 3.8 V. On a Pt working electrode, there is no significant oxidative current, as the electrode surface passivates at potentials above 4.0 V.

Preliminary cell tests of the lithium closoborane electrolyte in lithium-titanium disulfide cells have demonstrated its

*Electrochemical Society Active Member

Keywords: closoborane, lithium, electrolyte battery

utility. The first discharge curve is shown in Figure 2. It closely resembles that obtained with LiClO_4 in similar cells (6). The total cathode utilization at 2 ma/cm^2 was greater than 85% based on the reaction $\text{Li} + \text{TiS}_2 \rightarrow \text{LiTiS}_2$. On reducing the current to 1 ma/cm^2 , 92% of the theoretical capacity was obtained. The cell was then recharged at 1 ma/cm^2 , followed by discharge at 1 ma/cm^2 . More than 90% of the first discharge capacity was obtained on this second discharge. The charge-discharge cycle could be repeated more than twenty times. In contrast, at electrode concentrations where two liquid phases were present, cathode utilization was low, <10%.

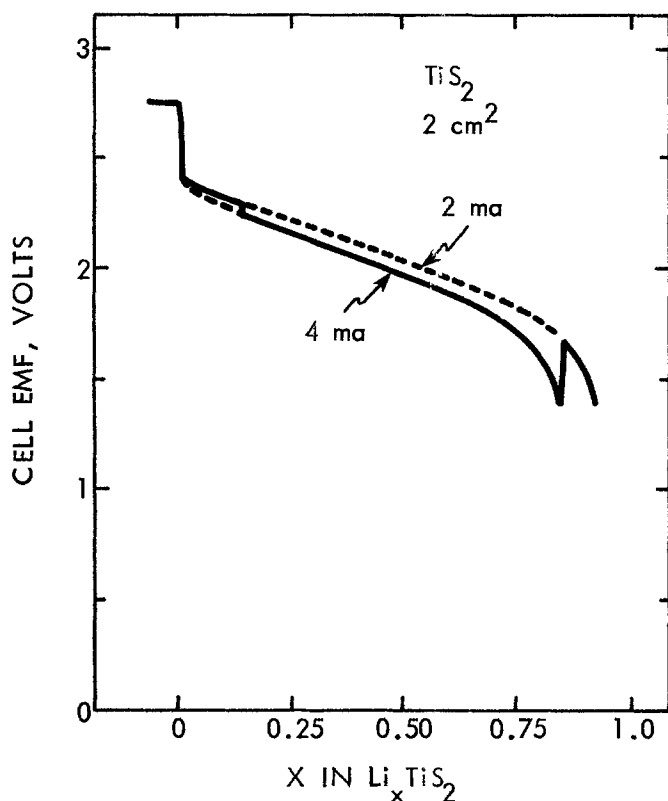


Fig. 2 First discharge curves of Li/TiS_2 cell at 1 and 2 ma/cm^2 . — measured and ---- extrapolated area.

REFERENCES

1. C. R. Schlaikjer, Proceedings of the 28th Power Sources Symposium, p. 241 (1978).
2. A. N. Dey and J. Miller, J. Electrochem. Soc. **126**, 1445 (1979).
3. J. W. Johnson and J. F. Brody, to be published.
4. M. F. Hawthorne and R. L. Pilling, Inorg. Syn **9**, 16 (1967).
5. W. H. Knoth, H. C. Miller, J. C. Sauer, J. H. Salthis, Y. T. Chia, and E. L. Muetterties, Inorg. Chem. **3**, 159 (1964).
6. M. S. Whittingham, Prog. Solid State Chem. **12**, 41 (1978).

Manuscript received March 21, 1980.

Publication costs of this article were steted by Exxon Research & Engineering Company.

In summary, we have found that by use of a suitable mixed ethereal solvent system, lithium closoborane salts can be dissolved to form useful non-aqueous electrolytes that exhibit chemical stability to the components of a lithium titanium disulfide cell and show promise as electrolytes in those cells.



Solubilities of Oxygen and Carbon Monoxide in Carbonate Melts

A. J. Appleby*¹ and C. Van Drunen

Institute of Gas Technology, Chicago, Illinois 60616

ABSTRACT

Physical CO solubilities and total O₂ solubilities (as chemically formed O₂⁻ and O₂⁼ ions) have been determined for a comparatively wide range of carbonate melt compositions, and some restricted data on nitrogen and CO₂ solubilities have also been obtained. In general, the Uhlig-Blander equation in its simple form (without a correction term for gas molecule-melt interaction) does not apply to these melts. Care should be taken in interpreting hydrogen solubilities measured by chemical titration due to the formation of large amounts of chemically bound CO via the shift reaction.

Previous work in this laboratory (1) determined the dissociation pressure of the ternary alkali carbonate melt [43.5 mole percent (m/o) Li, 31.5% Na, 25% K, mp 397°C], both to verify results of previous authors (2), and to establish the minimum pressure to maintain the melt in equilibrium with CO₂, so that gravimetric measurements of the solubility of this gas could be performed using a microbalance. Attempts were made to determine oxygen solubilities at various partial pressures at 700°C, maintaining P_{CO_2} equal to the dissociation pressure of the melt. However, continuous weight losses were experienced, indicating loss of CO₂ (i.e., change of CO₂ dissociation pressure) on absorption of oxygen. This behavior is discussed in detail in this paper. In view of the uncertainty in determining the absolute gas solubility under these conditions, it was decided to use an alternative quenching or melt-chilling method for solubility determination. This method is applied for a variety of carbonate melt compositions for oxygen and carbon monoxide solubility, and for nitrogen and CO₂ solubility in the ternary melt.

Experimental

Since gas solubilities in molten salts increase with temperature, quenching methods may be conveniently used to determine solubility by measurement of the quantity of dissolved gas released on freezing of the melt. Further advantages of such methods include rapid measurements, the possibility of determining solubilities of several gases simultaneously using analytical techniques, and the possibility of absolute measurements if displacement of one gas by another occurs.

The apparatus used is shown in Fig. 1. It was connected to the gas-mixing train and vacuum system described earlier (1), modified by the addition of a low permeability india rubber balloon linked with the main line via a vacuum stopcock to maintain atmospheric pressure during the periods of rapid temperature and gas volume change occurring with melt cooling. All gas mixtures studies were introduced into the apparatus at atmospheric pressure, in the form of nitro-

gen mixtures where necessary. P_{CO_2} was maintained somewhat above the melt dissociation pressure for each measurement (see below).

Melt preparation was as follows: (i) Mixed salts were melted, allowed to solidify, and then were maintained under vacuum at temperatures just below their

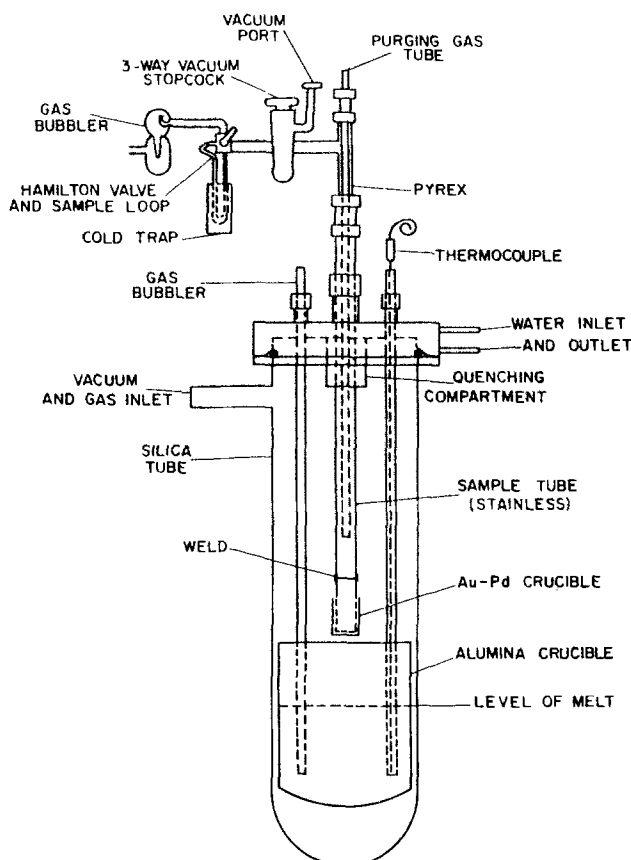


Fig. 1. Apparatus used for solubility measurements

* Electrochemical Society Active Member.

¹ Present address: E.P.R.I., Palo Alto, California 94303.

melting points for approximately 90 hr for preliminary drying and outgassing. (ii) The salt was isolated and slowly heated to about 820°-850°C. (iii) The melt was evacuated until a stable pressure of about 8 mm Hg was obtained. It was then allowed to reach equilibrium at 120 mm pressure with "Mattheson Research Grade" CO₂. This was followed by solidification. (iv) Steps (ii) and (iii) were repeated three times in sequence.

Preliminary experiments showed that saturation of the melt contained in the alumina crucible with each gas mixture was complete after 2-3 hr maximum under bubbling conditions. After saturation, a melt sample was withdrawn in the small Au-Pd crucible shown in Fig. 1 and introduced into the upper quenching compartment by vertical translation of the support tube in its sliding seal attached to the water-cooled stainless steel header. The internal sample tube (an Au-Pd extension of a long stainless steel tube) containing a helium atmosphere, which trapped a prescribed volume of melt, that liberated its dissolved gas on chilling. The quench rate was relatively slow to allow all the gases to escape. This gas was flushed by a stream of helium into the U-tube containing a small amount of activated Linde 5A molecular sieve closed by a Hamilton 4-way gas sample valve. The entire contents of the tube, after being allowed to reach room temperature, were flushed with a stream of carrier gas into a Fisher-Hamilton gas partitioner with Linde 5A column and Katharometer detector for analysis. This gas represented the whole of the solute in the melt aliquot. In earlier work, only a fraction of the atmosphere above the melt was examined (1), which led to some irreproducibility.

Preliminary experiments established that best results were obtained by slowly cooling the sample to 300°C by positioning the melt in the correct part of the upper zone of the furnace. This prevented cracking of the solidified electrolyte and leakage from the remainder of the solid carbonate and the atmosphere above the melt around the end of the sample tube, so that a frozen melt plug seal was produced. Very reproducible results were obtained by maintaining the sampling crucible, which contained a small amount of solid carbonate to isolate the sample tube and external gas systems, in the cooler part of the furnace. This was followed by plunging the crucible into the melt and withdrawing a sample. The volume of carbonate withdrawn was estimated by measuring its upper level with the sliding gas purge tube with a cathetometer. Care was taken to ensure that equilibrium was attained in each case. A number of independent determinations (typically 8-10) were carried out for each gas mixture. Henry constants and standard deviations were thus determined, and Henry's law verified.

Results and Discussion

CO₂ solubilities (ternary melt).—The majority of CO₂ solubility determinations in the ternary melt were carried out using dynamic weighing (1). However, in some cases the quenching method was used to obtain supplemental data to serve as a confirmation of those obtained by weighing. At 700°C, a mean solubility (six separate readings) of 3.60×10^{-3} mole-dm⁻³-atm⁻¹ was obtained by this method in good agreement with the value obtained by weighing [2.84×10^{-3} mole-dm⁻³-atm⁻¹ (1)].

Nitrogen solubilities.—Nitrogen solubilities were determined only in the ternary eutectic. The purpose of these measurements was to allow a standard of comparison with conventional theories (3-5) of solubilities of noninteracting gases in molten salts, since nitrogen may be expected to possess little affinity for the melt and certainly no chemical solubility. Results obtained, including standard deviations, are given in Table I, and these are expressed in the form of an Arrhenius plot in Fig. 2.

According to the so-called Uhlig-Blander theory of gas solubilities in molten salts (4) the free energy of solution is related to the creation of new melt surface in the form of cavities in the liquid, each of which is on the order of the dimensions of a gas molecule. For gases that interact with the melt by physical forces, a further free energy of solution term is required, representing the energy of association of the gas molecule with the surrounding melt ions. Overall, this theory proposes the following relationship

$$\Delta G_s^\circ = 4\pi N r^2 \gamma + \Delta G_a^\circ$$

where ΔG_s° and ΔG_a° are the standard free energies of solution and association, respectively, r is the radius of the gas molecule, γ is the "microscopic" liquid surface tension, and N is Avogadro's number. In general, correlations based on the above equation give a reasonably good agreement (to within about one order of magnitude) with experiment, assuming γ to be equal to the measured value of the melt surface tension. Results often are of a satisfactory order of magnitude agreement for gases of larger molecular radius, but correlations between measured and estimated ΔH_s (heat of solution) values are poor in most cases (5, 6). While modifications of the Uhlig-Blander theory which assume that gas molecules occupy holes already present in the melt rather than create holes for solution (5) may give more consistent agreement between theory and experiment for a wide range of solute radii, the expressions are complex and difficult to use, and they differ from the values given by the Uhlig-Blander expression only by preexponential terms (5).

Table I. Carbon monoxide and nitrogen solubilities in carbonate melts (CO₂ pressures in atm in parentheses)

Composition, m/o	Melting point, °C	Temperature, °C				ΔH_s , kJ mole ⁻¹
		700	750 <i>h.c.</i> × 10 ⁴ , mole-dm ⁻³ -atm ⁻¹	800	850	
Carbon monoxide solubility in carbonate melts						
Li ₂ CO ₃ -Na ₂ CO ₃ -K ₂ CO ₃ (43.5:31.5:25.0)	397	0.86 ± 0.10 (0.50)	1.30 ± 0.10 (0.25)	1.75 ± 0.09 (0.15)	2.82 ± 0.18 (0.15)	69.5
Li ₂ CO ₃ -K ₂ CO ₃ (42.7:57.3)	498		3.25 ± 0.22 (0.25)	4.54 ± 0.39 (0.15)	5.36 ± 0.22 (0.15)	48
Li ₂ CO ₃ -Na ₂ CO ₃ (53.3:46.7)	495		3.04 ± 0.24 (0.25)	3.68 ± 0.2 (0.15)	5.61 ± 0.2 (0.15)	58
Na ₂ CO ₃ -K ₂ CO ₃ (58:42)	710			13.30 ± 0.9 (0.15)	20.10 ± 1.6 (0.15)	~80
Li ₂ CO ₃	726			0.59 ± 0.09 (0.2)	2.25 ± 0.36 (0.4)	~250
Nitrogen solubility in the ternary eutectic						
Li ₂ CO ₃ -Na ₂ CO ₃ -K ₂ CO ₃ (43.5:31.5:15.0)	397	0.69 ± 0.08 (0.026)	1.26 ± 0.07 (0.026)	1.34 ± 0.10 (0.06)	1.71 ± 0.11 (0.10)	51

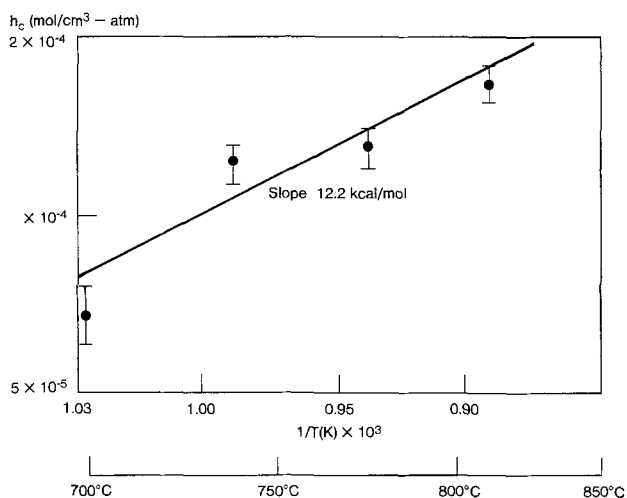


Fig. 2. \log_{10} nitrogen solubility as a function of $1/T(K)$, ternary melt.

Considerations based on the simple Uhlig-Blander theory can still be used in first approximation correlations.

If we use the Uhlig-Blander equation and assume that for nitrogen ΔG_a^0 is equal to zero, then for the ternary eutectic at $1000^\circ K$, $\gamma \sim 0.215 j - m^2$ (7), and using a value of 0.190 nm for the Lennard-Jones radius of N_2 (8), we obtain a calculated solubility of $1 \times 10^{-5} \text{ mole-dm}^{-3} \text{ atm}^{-1}$. This is about a factor of 7 lower than the value obtained experimentally (Table I and Fig. 2). We therefore conclude that the physical solubility of nitrogen in molten carbonates involves a small negative ΔG_a^0 .

Carbon monoxide solubilities.—Carbon monoxide solubilities were obtained for the ternary, binary 42.7: 57.3 m/o Li/K, 53.3: 46.7 m/o Li/Na, 58: 42 m/o Li/Na, 58: 42 m/o Na/K, and pure Li carbonate compositions. Results obtained, indicating standard deviations, are given in Table I. Arrhenius plots for all melts are given in Fig. 3. In all cases, a number of different CO partial pressures were used to determine the Henry constants, nitrogen being used to bring the total pressure to one atmosphere to avoid carbon deposition (8). In the ternary eutectic, the experimental solubilities are close to those of nitrogen. This is reasonable in view of their molecular radii.

An immediate problem observed is that the CO solubilities measured above are appreciably lower than those calculated from potential sweep electrochemical data (9) assuming a reasonable value of the diffusion coefficient ($1 \times 10^{-8} \text{ m}^2\text{-sec}^{-1}$) [cf. Cl^- ion at similar temperatures (10)]. These data showed that two CO species accounted for the total solubility, one corresponding to CO physically dissolved in the melt ($\sim 1.1 \times 10^{-4} \text{ mole-dm}^{-3}$ for 0.318 atm CO/0.682 atm CO_2 at $800^\circ C$ in the ternary eutectic melt), the other being CO in the form of a chemically dissolved species, $CO_2^{=}$ (concentration about 1 times $10^{-3} \text{ mole-dm}^{-3}$ under the above conditions, or ~ 9 times the physically dissolved CO concentration). This implies a Henry constant of $ca. 3 \times 10^{-4} \text{ (mole-dm}^{-3}\text{-atm}^{-1})$ for physically dissolved CO in the ternary melt at $800^\circ C$, in quite good agreement with the data derived from the slow cooling experiments (Table I). Hence, in the method used only physically dissolved CO is detected. Presumably the chemically dissolved part ($CO_2^{=}$) is sufficiently stable to remain in the salt during the chilling and pumping operation. Reducible material has indeed been detected in chilled melts (11). On the basis of the results obtained in the ternary melt it is reasonable to assume that results in other melts also refer to physical solubility.

Some data were obtained, though at only two temperatures, in the Na/K and pure Li melts (see Table

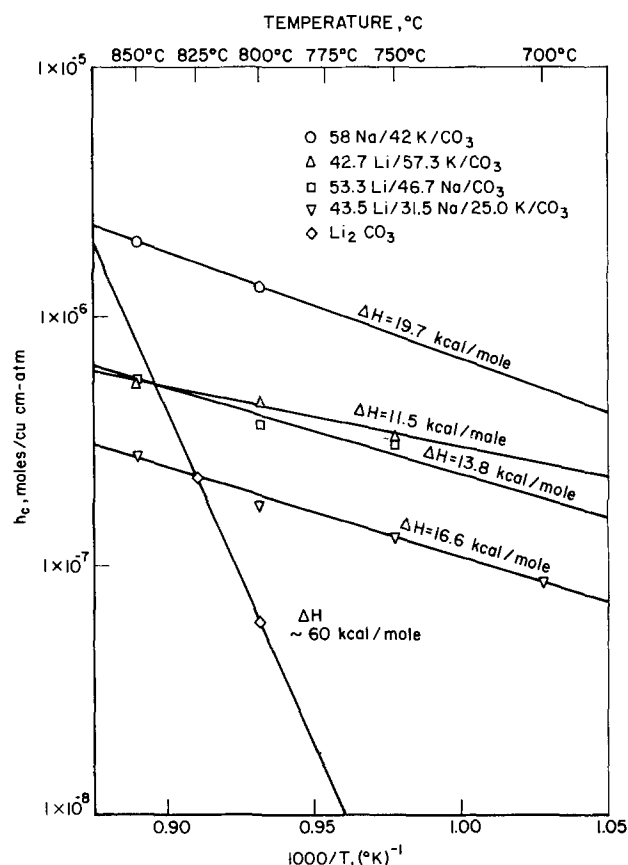


Fig. 3. \log_{10} CO solubility as a function of $1/T(K)$ (Henry constants in $\text{mole-cm}^{-3}\text{-atm}^{-1}$ units. $1 \text{ kcal} = 4.184 \text{ kJ}$).

I). These results appear to be distinctly anomalous. In the Na/K melt, much higher solubilities were recorded than in the lithium-containing melts. This perhaps implies that in the absence of lithium ion the $CO_2^{=}$ ion decomposes during the quenching operation so that both physical and chemical solubilities are detected. In the pure lithium melt the very low solubility detected at $800^\circ C$ and the apparently large temperature coefficient of solubility (cf. that for oxygen, see below) may show that CO solubility detected, like the oxygen solubility, is entirely chemical in this case, with the stability of the $CO_2^{=}$ rapidly increasing with temperature (see discussion of peroxide ion, below). No electrochemical data on CO oxidation are currently available in these two melts, so the above conclusions must be regarded as tentative.

Oxygen solubility.—Determination of O_2 solubility by the weighing method proved unsatisfactory due to displacement of CO_2 during melt saturation. As shown below, this implies chemical solubility of oxygen in the melt, but at the same time introduces a further interpretive difficulty concerning the stability of the compounds formed by association of molecular oxygen and the carbonate melt, so that complete displacement of oxygen is ensured on cooling of the melt to lower temperatures. A comparison of electrochemical and quenching data indicates that reasonable certainty of the relative reversibility of the oxygen dissolution process may be inferred for a number of the carbonate melts, so that the oxygen solubility figures refer to both chemically and physically dissolved oxygen. The nature of the equilibria involved make the chemical species predominant.

Oxygen solubilities were obtained in a number of carbonate compositions by the quenching method (ternary alkali eutectic, 53.3/46.7 m/o Li/Na eutectic, 42.7/57.3 m/o Li/K eutectic, 58/42 m/o Na/K eutectic, pure Li_2CO_3 , and 60 m/o Na_2CO_3 /40 m/o NaCl). Results are given in Table II and Fig. 4. In

Table II. Oxygen solubility in carbonate melts
(CO₂ pressures in atm in parentheses)

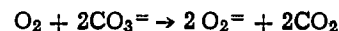
Composition, m/o	Melting point, °C	Temperature, °C				ΔH , kJ mole ⁻¹
		700	750 $h_c \times 10^4$, mole-dm ⁻³ -atm ⁻¹	800	850	
Li ₂ CO ₃ -Na ₂ CO ₃ -K ₂ CO ₃ (43.5:31.5:25.0)	397	2.52 ± 0.24 (0.026)	5.10 ± 0.08 (0.026)	8.47 ± 0.22 (0.06)	15.10 ± 0.53 (0.10)	106.3
Li ₂ CO ₃ -K ₂ CO ₃ (42.7:57.3)	498	4.18 ± 0.35 (0.026)	6.16 ± 0.19 (0.026)	14.00 ± 0.80 (0.06)	25.90 ± 1.60 (0.10)	120.0
Li ₂ CO ₃ -Na ₂ CO ₃ (53.3:46.7)	495		3.57 ± 0.61 (0.026)	5.57 ± 0.27 (0.06)	8.36 ± 0.46 (0.10)	83
Na ₂ CO ₃ -K ₂ CO ₃ (58:42)	710		*13.11 ± 0.60 (0.10)	14.15 ± 0.88 (0.10)	23.53 ± 1.88 (0.10)	79
Li ₂ CO ₃	726		*1.68 ± 0.18 (0.10)	5.92 ± 0.25 (0.20)	†10.30 ± 0.38 (0.40)	206
Na ₂ CO ₃ -NaCl (60:40)	640			20.64 ± 1.31 (0.10)	29.15 ± 1.70 (0.10)	~70

* 775°C.
† 825°C.

all cases, CO₂ partial pressures equal to or somewhat greater than the dissociation pressures were used (Table II). Several oxygen partial pressures in the 0.4-0.8 atm range were examined at each temperature and for each melt, so that apparent Henry constants and standard deviations could be determined.

Electrochemical data in the pure Li and Na/K melts show that oxygen is present as peroxide and superoxide ion in molten carbonates, superoxide being absent in the pure lithium melt (12-14). Calculations assuming a diffusion coefficient of 10⁻⁸ m²-sec⁻¹ using the diffusion peak height/square root sweep rate relationships and data generated in Li (13) and Na/K (14) melts give oxygen solubility (mole-dm⁻³-atm⁻¹) of 7·10⁻⁴ and 1.5·10⁻³, respectively. Comparison of the data indicates good agreement between the electrochemical calculations and the quenching method, which suggests that all the peroxide and superoxide decompose on cooling. Calculations based on the Uhlig-

Blander equation predict physical solubility values at least an order of magnitude lower than the chemical values measured. Attempts to calculate the solubility of oxygen as peroxide and superoxide based on thermodynamic data [JANAF, Ref. (15)] are probably not meaningful due to the approximate nature of the ΔG° values and the probable stabilizing influence of the carbonate ion on O₂⁼ and O₂⁻ [for discussion see Ref. (16)]. The high solubility values in Na₂CO₃-NaCl eutectic (Table II) are of great interest, but no electrochemical data are available at present to confirm the makeup of the species present in the melt. Results in Li₂CO₃ are comparable with those for CO given above, and suggest that the comparative stabilities of CO₂⁼ and O₂⁼ change in the same way with temperature. A very high activation energy for O₂ dissolution (175 kJ-mole⁻¹) was estimated from electrochemical data in a previous paper (13). The present results suggest an even greater value, but it must be pointed out that all the oxygen solubility data given here are for the processes



and



so that ΔH values will contain a component varying from 1.0-0.5 ΔH_d , where ΔH_d is the heat of decomposition of the melt, depending upon which of the above reactions predominates. This results from the fact that the CO₂ pressure above the melt was not held constant, but was maintained slightly over the dissociation value in each case. This effect is most marked for the pure Li melt.

A number of experiments were conducted in the ternary eutectic at 800°C to determine the effect of p_{CO_2} on oxygen solubility. Since the predominant species is superoxide ion in this melt, solubility should be approximately proportional to $p_{CO_2}^{-1/2}$. Changes were difficult to detect on increasing p_{CO_2} , since this required a decrease in p_{O_2} and consequent fall of sensitivity. In addition, it is possible that there is a partial compensation in that physical O₂ solubility may replace chemical solubility as the melt is neutralized; however it is significant that physically dissolved O₂ was not detected experimentally in the previously reported electrochemical sweep work (12-14). Large changes in oxygen content of the melt were only detected at low p_{CO_2} and high p_{O_2} ; these are the conditions of the present work.

Due to the chemical solubility of oxygen, the typical first-order Henry's law should not be obeyed. This was first pointed out by Andresen (17), who determined oxygen solubility in sodium carbonate melts in a higher temperature range than that studied here. In all melts except pure lithium carbonate, the electrochemical results (12-14) indicate that the predominant

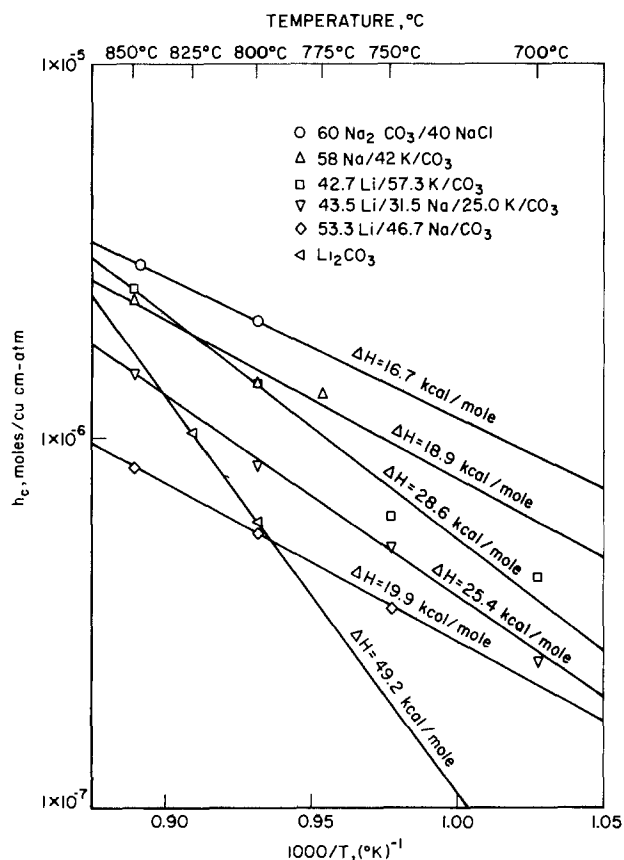


Fig. 4. log₁₀ O₂ solubility as a function of 1/T(K) (units as Fig. 3)

chemical species should be superoxide ion. For this species, the solubility reaction order should be 0.75. The present results do not permit a test of this relationship over only a twofold partial pressure change. In lithium carbonate, the corresponding order should be 0.5, with -1 for p_{CO_2} . Again, these were not detectable within the scatter of the data points at the low solubility levels observed for this melt. However, in calculating oxygen solubilities at other O_2 or CO_2 partial pressures, the reaction orders given above should be used.

It is interesting that results obtained by Broers (18) for oxygen solubility by an amperometric titration method (which will detect both physically and chemically dissolved oxygen) agree well with the values determined here. They are shown for comparison in Fig. 5, which includes total CO value obtained in the ternary eutectic. As expected, this value is several times higher than that for purely physical CO determined in the present work (Table I and Fig. 4). Broers' work (18) shows that hydrogen solubilities may be also high, but he did not distinguish between hydrogen and chemically bonded CO produced via the shift reaction. Work reported in Ref. (9) show that a nonlinear pressure-concentration relationship appears to apply in the case of the chemically bonded CO species. Results for H_2 and CO solubility obtained by amperometric titration therefore require careful interpretation.

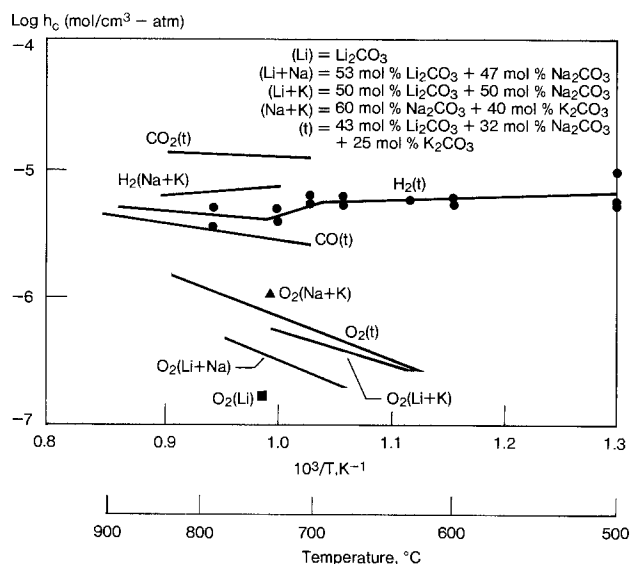


Fig. 5. Data in Ref. (18) (Broers, Schenke, and van Ballegoy) for comparison.

Acknowledgments

This paper is published with the permission of the sponsors of the TARGET Fuel Cell Program and the Power Systems Division of United Technologies Corporation.

Manuscript submitted Dec. 3, 1979; revised manuscript received Jan. 30, 1980.

Any discussion of this paper will appear in a Discussion Section to be published in the June 1981 JOURNAL. All discussions for the June 1981 Discussion Section should be submitted by Feb. 1, 1981.

Publication costs of this article were assisted by EPRI.

REFERENCES

1. A. Borucka, Abstract 5, p. 15, The Electrochemical Society Extended Abstracts, Boston, Massachusetts, May 6-11, 1979.
2. P. L. Spedding and R. Mills. *This Journal*, **112**, 594 (1965).
3. H. H. Uhlig, *J. Phys. Chem.*, **41**, 1215 (1937).
4. M. Blander, W. R. Grimes, N. V. Smith, and G. M. Watson, *ibid.*, **63**, 1164 (1959).
5. A. J. Appleby, *J. Chim. Phys.*, **74**, 447 (1977).
6. F. Paniccia and P. G. Zambonin, *J. Chem. Soc., Faraday Trans. I*, **68**, 2083 (1972).
7. A. T. Ward and G. J. Janz, *Electrochim., Acta*, **10**, 849 (1965).
8. R. A. Svehla, Technical Report R-132 NASA, p. 36, Lewis Research Center, Cleveland, Ohio (1962).
9. A. Borucka and A. J. Appleby, *J. Chem. Soc. Faraday Trans. I*, **73**, 1420 (1977).
10. A. Borucka, J. O'M. Bockris, and J. A. Kitchener, *Proc. Roy. Soc. A*, **241**, 554 (1957).
11. W. M. Vogel, L. Bregoli, and S. W. Smith, Abstract 376, p. 1006, The Electrochemical Society Extended Abstracts, Pittsburgh, Pennsylvania, Oct. 15-20, 1978.
12. A. J. Appleby and S. Nicholson, *J. Electroanal. Chem. Interfacial Electrochem.*, **38**, App. 13 (1972).
13. A. J. Appleby and S. Nicholson, *ibid.*, **53**, 105 (1974).
14. A. J. Appleby and S. Nicholson, *ibid.*, **83**, 309 (1973).
15. JANAF Thermochem. Tables, (1971). 2nd ed., D. R. Stull and H. Prophet, Nat. Bur. Stand., Washington, D.C.
16. B. K. Andersen, "Thermodynamic Properties of Molten Carbonates," Thesis, Technical University of Denmark, Lyngby (1975).
17. R. E. Andresen, *This Journal*, **126**, 328 (1979).
18. G. H. J. Broers, M. Schenke, and H. J. J. van Ballegoy, Extended Abstract No. II77, 20th ISE Meeting Druzha, Bulgaria, Sept. 1977.

Alternate Synthesis of Electrolyte Matrix for Molten Carbonate Fuel Cells

R. H. Arendt* and M. J. Curran

General Electric Company, Corporate Research and Development, Schenectady, New York 12301

ABSTRACT

A process is presented for the preparation of the electrolyte matrix, a poorly bonded assemblage of LiAlO_2 crystallites, based on the use of a fugitive reaction medium, a molten mixture of alkali chlorides. Data on the characteristics of both the reaction and the product are presented.

The electrolyte structure, or tile, used in molten carbonate fuel cells consists of a mixture of liquid alkali metal carbonates retained by capillarity in the interstices of an array of chemically inert inorganic crystallites. At cell operating temperatures, the carbonates form an ionically conducting fluid held in place by capillarity. The selection of the carbonate composition is governed by consideration of, and balance between, proper liquid temperature range, ionic conductivity, reactant/product gas solubilities, volatility, etc. The most commonly used composition is 62 mole percent (m/o) Li_2CO_3 -38 m/o K_2CO_3 , having a liquidus temperature of $\sim 764^\circ\text{K}$, and represents a judicious balance of the critical factors (1). The present matrix material is lithium metaaluminate, LiAlO_2 , which may exist as one, or all, of three crystallographic modifications (2).

The electrolyte- LiAlO_2 matrix composite is most commonly prepared as an intimate mixture using either anhydrous techniques (3) or an initial aqueous solution/slurry of the components (4, 5). It is a characteristic of these preparations that either the electrolyte phase, or its precursor, is present throughout the synthetic sequence. The presence of the electrolyte phase precludes the presence of additional chemical species which could beneficially modify the matrix characteristics during its formation, since the matrix is not separated from these other species. The inclusion of the hygroscopic electrolyte also mandates that care be taken to maintain its chemical composition and purity throughout the required processing operations.

The product of this preparation is a mixture of LiAlO_2 , average spherical equivalent crystallite size ranging from $\sim 0.05 \mu\text{m}$ to more than $1.0 \mu\text{m}$, and the mixed carbonates. It is generally recognized that minimization of the matrix crystallite size will maximize the volume fraction of molten electrolyte that can be properly retained, as well as produce matrix porosity which properly complements that of the fuel cell electrodes. However, the stability of small crystallites in the highly aggressive environment of the molten electrolyte is open to question, and will be more fully addressed in a companion paper.

The electrolyte-matrix composite is fabricated into the electrolyte structure by hot-pressing at temperatures 5° - 15°K below the electrolyte liquidus, and at pressures ranging up to 60 MPa (6). Densities ranging up to 99% of theoretical have been achieved in this fabrication process.

An alternate preparation, the "chloride" synthesis, has been developed for the LiAlO_2 matrix which does not involve the presence of the electrolyte or its precursors. This preparation involves the use of a fugitive molten ionic solvent to promote the formation of the product from the reactants. This approach is predicated on the assumption that the interaction of the reactant and product species with the molten solvent are small

compared with the free energy of the product-forming reaction. Under these circumstances, the product will have a smaller molten solvent solubility than will the reactants. Reaction proceeds by saturation of the solvent by the reactants, resulting in precipitation of the product species until all reactants are consumed to a level consistent with the product's melt solubility. The presence of one reactant in excess will effectively reduce all other reactant final concentrations to zero.

A requirement of the ionic solvent is that it provide a small solubility for the reactants. This solubility need not be great since the reaction "flux" is governed by the high mobility of the dissolved species in ionic melts, coupled with the small diffusion distances required in an intimate mixture of finely particulate reactants. The quantity of solvent required for complete reaction is a function of both the reactant and product crystal sizes. Sufficient solvent is required to provide access of the reactants to each other, providing the required reaction pathways.

A further requirement of the molten solvent is that it can be separated from the products under conditions which do not degrade the product. In general, product compounds of interest are relatively water insoluble. Therefore, water-soluble salts, such as the alkali and alkaline earth halides (except fluorides) are suitable. It has been found that the alkali chlorides, and their mixtures, satisfy these requirements. A number of technologically significant compounds have been prepared in this manner (7, 8).

"Chloride" Synthesis of LiAlO_2

The synthesis of LiAlO_2 was achieved by the reaction of $\text{Al}_2\text{O}_3 \cdot 3\text{H}_2\text{O}$ (ALCOA C-33) with excess $\text{LiOH} \cdot \text{H}_2\text{O}$ (J. T. Baker, reagent grade) in the presence of 50 m/o NaCl-KCl (J. T. Baker reagent grade) at 935° - 945°K . $\text{Al}_2\text{O}_3 \cdot 3\text{H}_2\text{O}$ represents the least expensive, commercial Al^{+3} source available; alpha and gamma- Al_2O_3 were also suitable reactants. The reaction mixture was prepared by briefly ballmilling (α - Al_2O_3 system) together the reactant and solvent components to both homogenize and comminute any large agglomerates present in these materials. A 2 weight percent (w/o) excess of $\text{LiOH} \cdot \text{H}_2\text{O}$ was required to reliably achieve complete $\text{Al}_2\text{O}_3 \cdot 3\text{H}_2\text{O}$ conversion without resorting to extreme homogenization procedures. A solvent content of ≥ 50 w/o was empirically determined as necessary to achieve quantitative conversion of the $\text{Al}_2\text{O}_3 \cdot 3\text{H}_2\text{O}$ used in these experiments.

The homogenized reaction mixture was placed in dense α - Al_2O_3 crucibles and heated to 935° - 945°K at $100^\circ\text{K hr}^{-1}$, maintained at temperature for 1 hr, then cooled to room temperature. An ambient air atmosphere was maintained throughout. The reacted mass was noticeably compacted and hardened, and had lost mass consistent with the appropriate dehydration reactions.

The product LiAlO_2 was retrieved from the chloride solvent and excess $\text{Li}_2\text{O/LiOH}$ by dissolution of the

* Electrochemical Society Active Member.

Key words: electrolyte, fuel cell, fused salts, synthesis.

latter in distilled H_2O , assuming a salt solubility of ~ 250 kg meter $^{-3}$, a process requiring ~ 30 min with constant stirring. The dispersed, small crystallite sized powder was flocculated using an aqueous solution of an organic anionic flocculating agent (Hercocfloc 821, Hercules Chemical Company). The supernatant solution was decanted and retained for chloride solvent recycle. The product was filtered to retrieve the remaining salt solution, washed sparingly with distilled H_2O , then 95 volume percent (v/o) ethanol to facilitate drying, and partially air dried on the filter. After more complete drying in a Teflon vessel at 473°K, the $LiAlO_2$ was briefly heated to 773°-873°K to destroy traces of organic material as well as reverse any hydration that had taken place in previous processing. The mass loss observed during this latter heating was typically 0.70 w/o. It was also determined that $LiAlO_2$ (β -, γ -) possessed an effective H_2O solubility of ~ 1.0 kg meter $^{-3}$ within this processing scheme.

The retained alkali chloride solutions from MSLA-93, . . . , 98, containing the excess $LiOH$ and dissolved $LiAlO_2$, was recycled into the synthesis of MSLA-99 and 100 by simply reducing it to dryness. The crystalline material was briefly comminuted to reduce its crystal size to that of the virgin chloride salts. The proper quantities of $Al_2O_3 \cdot 3H_2O$ and $LiOH \cdot H_2O$ (no excess) were added to the solvent and homogenized. The synthesis was then completed as described above.

Product Characteristics

During the development of "chloride" synthesis for $LiAlO_2$, the effects of maximum reaction temperature and excess concentration of $LiOH \cdot H_2O$ were investigated. Although the binary chloride melt had a liquidus temperature of 931°K, the addition of $LiOH$ (mp = 723°K) to the chloride was anticipated to result in an effectively ternary solvent with liquidus below 931°K. Minimizing the reaction temperature was expected to minimize the product crystal size. The results for a constant composition reaction mixture con-

taining 2 m/o excess $LiOH \cdot H_2O$ are shown in Fig. 1. Similar plots were generated for 6 and 10 m/o excess $LiOH \cdot H_2O$ content mixtures, the curves being displaced toward lower surface areas ($\lesssim 20\%$) with increasing excess $LiOH \cdot H_2O$.

Consider first the circle data, which follow the broken linear relationships indicated. The material corresponding to the highest temperature point was analyzed to be pure γ - $LiAlO_2$. The remaining samples were found to be predominantly β - $LiAlO_2$, with a small amount of α - and γ - $LiAlO_2$. The two lowest temperature samples also showed the presence of poorly crystallized γ - Al_2O_3 . In a separate set of experiments, omitting the $LiOH \cdot H_2O$, γ - Al_2O_3 with a surface area in excess of 120 m 2 g $^{-1}$ resulted. It was concluded from these data that the change in slope, which occurs very near the binary chloride liquidus temperature, resulted from the admixture of small sized, poorly crystalline γ - Al_2O_3 to a predominantly $LiAlO_2$ product. The poor crystallinity of the γ - Al_2O_3 rendered it detectable only at major concentrations.

This conclusion was confirmed with the square data which resulted from samples prepared from a fine $Al_2O_3 \cdot 3H_2O$ reactant, wet mixed with the chlorides and $LiOH \cdot H_2O$. These samples were determined to be predominantly β - $LiAlO_2$, with no γ - Al_2O_3 in evidence. They correspond well with the high temperature segment line. Therefore, to obtain quantitative conversion of $Al_2O_3 \cdot 3H_2O$ to $LiAlO_2$, either special care in reaction mixture preparation was required, or the reaction must be conducted above the chloride liquidus. The latter is the preferred route from an applications point of view. An additional benefit is possible in that the chloride liquidus temperature is very near the fuel cell operating temperature, thereby giving a matrix material more nearly in equilibrium with the conditions expected in operating fuel cells.

Variation of the lithium reactant anion was also explored. The triangle data in Fig. 1 were for samples in which Li_2CO_3 was equivalently substituted for $LiOH \cdot H_2O$. Both samples were composed of α - $LiAlO_2$ and γ - Al_2O_3 . No β - or γ - $LiAlO_2$ were detected. Similar results were obtained with substitution of $LiNO_3$ for $LiOH \cdot H_2O$ in that pure, high surface area α - $LiAlO_2$ resulted, although conversion was apparently complete in that case. These data indicated that the anion species can greatly effect the $LiAlO_2$ allotrope stability in an otherwise constant environment.

The effects of increasing excess of $LiOH \cdot H_2O$ in an otherwise constant composition reaction mixture are shown in Fig. 2. The reaction temperature was in the interval 923°-973°K. All products were predominantly β - $LiAlO_2$, with no unreacted Al_2O_3 detected by x-ray. Although the product surface areas decreased with increasing excess, the effect was relatively minor. Based on these data, it was decided to use a 2 m/o $LiOH \cdot H_2O$ excess in scaled-up preparations of a predominantly β - $LiAlO_2$ matrix material. This was done in order to compensate for expected compositional inhomogeneities in the larger lots of reaction mixture.

Eight 1.5 kg lots of $LiAlO_2$ were prepared using the "chloride" synthesis, the characteristics of which are given in Table I. The first six lots were prepared using virgin chloride solvent components. The last two lots used the recycled chloride solvent and excess $LiOH$ generated by the first six lots. As indicated, there is no difference between the two groupings. The materials are predominantly β - $LiAlO_2$ with an average spherical equivalent crystallite diameter of 0.34 μ m, as determined by BET surface area measurements. The material is, however, composed of crystallites of widely varying morphology and size, as shown in Fig. 3 and 4.

This mixture of crystallite sizes and morphologies was expected to yield matrix compacts which possessed small sized, narrow porosity distributions. It was found, however, that the as-prepared material contains suffi-

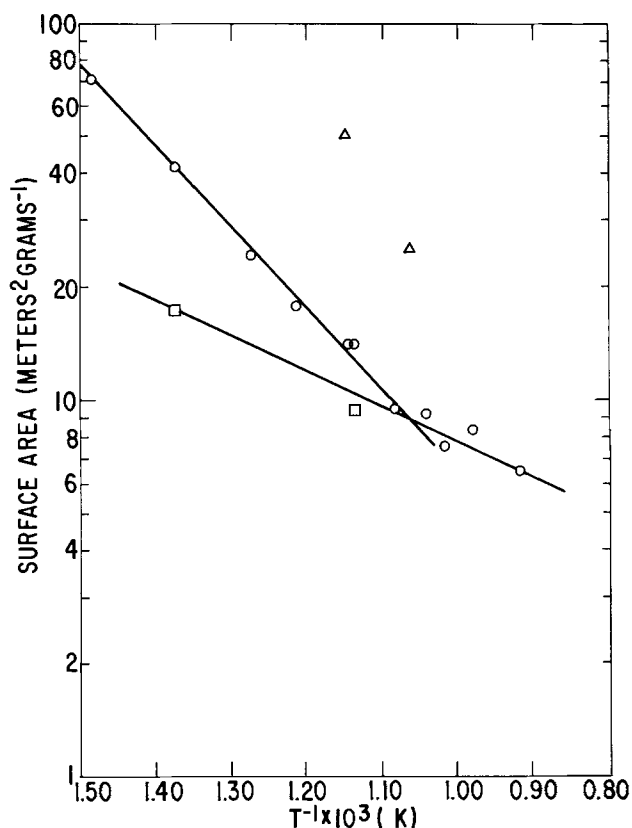


Fig. 1. Product surface area vs. inverse reaction temperature

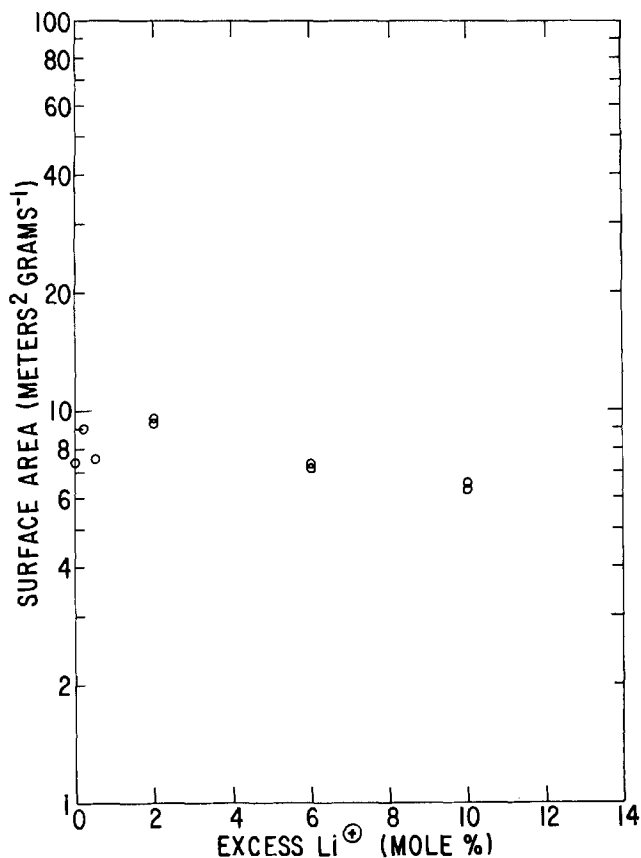


Fig. 2. Product surface area vs. excess LiOH in reaction mixture

cient synthesis-generated agglomerates to yield a broadened, ill-defined porosity distribution. This topic is covered in detail in the companion paper. The appropriate porosity distribution was developed by wet comminuting the as-prepared LiAlO_2 for 8 hr in an $\alpha\text{-Al}_2\text{O}_3$ mill using absolute CH_3OH as the fluid. Although the average spherical equivalent crystal size of the milled sample changes little, from 0.31 to 0.26 μm , the porosity distribution was markedly altered. It became well defined about a maximum in the distribution located at 0.50-0.60 μm . It should be noted that a similar situation probably exists in conventionally prepared matrix-electrolyte composite mixtures. The deagglomeration of such mixtures is, however, made more uncertain by the presence of the relatively soft, hygroscopic electrolyte component.

Conversion to Matrix-Electrolyte Composite

The deagglomerated "chloride" synthesis LiAlO_2 was converted into a matrix-electrolyte composite by simply dry blending the LiAlO_2 with the requisite quantities of Li_2CO_3 and K_2CO_3 . This mixture was heated to 873°K for 1 hr in an air atmosphere using a dense $\alpha\text{-Al}_2\text{O}_3$ crucible. The resultant cake was briefly dry comminuted to produce a powder suitable for fabrication into electrolyte structures by hot-pressing.

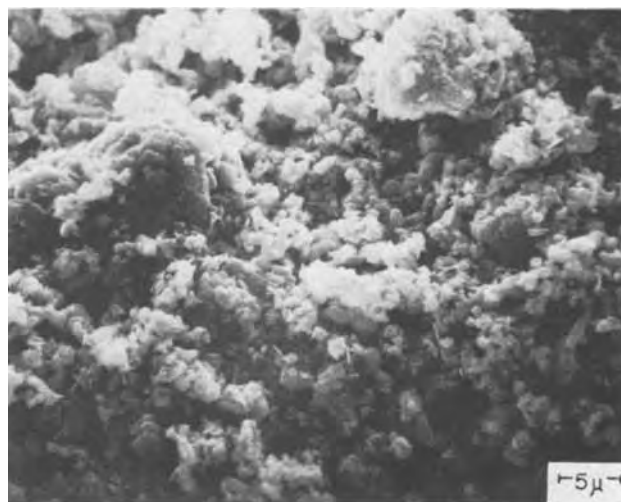


Fig. 3. SEM micrograph of MSLA-95, 2000X



Fig. 4. SEM micrograph of MSLA-95, 10,000X

The behavior of this alternately prepared material during fabrication and subsequent fuel cell evaluation was equivalent to that experienced with conventionally prepared materials.

Conclusions

An alternate, relatively rapid process for the preparation of LiAlO_2 matrix material for molten carbonate fuel cells has been developed. The reaction conditions and processing operations required to generate fuel cell quality material have been defined.

Acknowledgments

The authors wish to acknowledge the contribution of the members of the Materials Characterization Laboratory and the Ceramics Processing Unit, Research and

Table I. Characteristics of "chloride" synthesis LiAlO_2

Sample number	Qualitative x-ray diffraction	BET surface area	$\alpha\text{-LiAlO}_2$	Allotrope composition	
				$\beta\text{-LiAlO}_2$ (volume %)	$\gamma\text{-LiAlO}_2$
MSLA-93	In all cases, major phase	6.11	14	72	14
94	$\beta\text{-LiAlO}_2$, minor to trace	7.38	8	80	12
95	amounts of α - and γ -	6.43	11	72	17
96	LiAlO_2	5.70	12	74	14
97	No α - or $\gamma\text{-Al}_2\text{O}_3$	6.89	10	75	15
98		5.18	10	77	13
99		9.13			
100		7.67			
Average		6.81	11	75	14

Development Laboratory of the General Electric Company, to the completion of this effort. This work was supported in part by the U.S. Department of Energy under Contract DE-AC03-77ET-11319.

Manuscript submitted Dec. 3, 1979; revised manuscript received Feb. 21, 1980. This was Paper 9 presented at the Boston, Massachusetts, Meeting of the Society, May 6-11, 1979.

Any discussion of this paper will appear in a Discussion Section to be published in the June 1981 JOURNAL. All discussions for the June 1981 Discussion Section should be submitted by Feb. 1, 1981.

Publication costs of this article were assisted by the General Electric Company.

REFERENCES

1. "Fuel Cell Research on Second Generation Molten Carbonate Systems, Volume II, Characteristics of

Carbonate Melts. Quarterly Status Report, 1 July-30 Sept, 1976," Institute of Gas Technology for Argonne National Laboratory, Contract 31-109-38-3552, Sept. 1976.

2. K. Kinoshita *et al.*, *Mater. Res. Bull.*, **13**, 445 (1978).
3. D. M. Mason *et al.*, U.S. Pat. 3,998,939 (1976).
4. K. Kinoshita *et al.*, U.S. Pat. 4,115,632 (1978).
5. "Fuel Cell Research on Second Generation Molten Carbonate Systems. Technical Progress Report for 1 April-30 June 1978." Institute of Gas Technology for U.S. Dept. of Energy, SAN-1735-3, July 1978.
6. "Development of Molten Carbonate Fuel Cells for Power Generation. Quarterly Progress Report 15 Nov. 1978-15 Feb. 1979." General Electric Company for U.S. Dept. of Energy, SRD-79-060, March, 1979.
7. R. H. Arendt, *J. Solid State Chem.*, **8**, 339 (1973).
8. R. H. Arendt *et al.*, *Mater. Res. Bull.*, **14**, 703 (1979).

Alternate Fabrication Process for Molten Carbonate Fuel Cell Electrolyte Structures

R. H. Arendt* and M. J. Curran

General Electric Company, Corporate Research and Development, Schenectady, New York 12301

ABSTRACT

A process is presented for the preparation of reinforced molten carbonate fuel cell electrolyte structures which does not involve a hot-pressing operation. This process is based on the use of an electrolyte-free LiAlO_2 matrix material of predetermined, tailored characteristics. The matrix is fabricated into a "blank" using conventional ceramic techniques. The "blank" is subsequently infiltrated under controlled conditions with molten electrolyte.

The electrolyte structure, or tile, used in molten carbonate fuel cells consists of a mixture of alkali metal carbonates contained in the interstices of an array of chemically inert inorganic crystallites. The nature and preparation of the components of the electrolyte structure were discussed in a companion paper (1). The subject of the present paper is an alternate method for the fabrication of the matrix (presently LiAlO_2) and electrolyte (typically 62 mole percent (m/o) Li_2CO_3 -38 m/o K_2CO_3) into the electrolyte structure.

The structure is conventionally fabricated by hot-pressing (2) a finely particulate, intimate, matrix-electrolyte composite mixture. The processing involves heating the die and mixture to temperatures 5° - 15°K below the electrolyte liquidus ($\sim 764^\circ\text{K}$ for the 62:38 composition) and applying pressures of up to 60 MPa for 15-120 min. The entire cycle, including heating and cooling of the apparatus, requires a minimum of 4 hr. Structures in excess of 0.30 m^2 have been successfully prepared in this fashion. However, commercial application of molten carbonate fuel cell will require tens of thousands of square meters of electrolyte structure in unit sizes exceeding 1 m^2 . These size requirements may result in significant lengthening of the unit production time. The capital intensive nature of the present hot-pressing fabrication process indicates a need for an alternate fabrication process.

One possible approach to an alternate fabrication process is to decompose the present simultaneous application of pressure and temperature into two distinct processes. In such an alternate approach, all pressure applications are conducted at ambient temperatures,

while high temperature processing is conducted at ambient pressure. With a process decomposition, it should be possible to both reduce unit process cycle times and introduce continuous processing operations. The development of such a fabrication process is the subject of this paper.

Impregnation Fabrication Process

The alternate process consists of fabricating the matrix material, in the absence of the electrolyte phase, into a particle array of appropriate porosity characteristics at ambient temperatures. This array is then impregnated with molten electrolyte at ambient pressure, using capillarity to draw the molten phase into the matrix interstices. There is, in principle, no limitation on the nature of either the matrix or the electrolyte.

The process was developed using the deagglomerated "chloride" synthesis LiAlO_2 previously reported (1). Any chemically stable matrix source is suitable, provided it contains substantially no second phase content which would preclude the establishment of the appropriate pore size distribution during the matrix fabrication operation. In the present case, cold-pressing of the matrix was used as a matter of convenience. More continuous, high volume fabrication processes, such as tape casting, slip casting, or electrophoretic deposition, are even more attractive. What is required of the matrix forming process is the attainment of a stable, close-packing of the matrix crystallites.

The deagglomerated "chloride" synthesis LiAlO_2 possessed insufficient self-binding character to allow pressing of sufficiently strong thin (~ 1 - 2 mm) slabs to permit handling. This condition was remedied by the addition of an organic compound as a fugitive

* Electrochemical Society Active Member.
Key words. electrolyte, fuel cell, fabrication.

binder. Initial experiments with the aqueous addition of polyvinyl alcohol (du Pont Chemical Company, 51-05) showed that partial hydration of the LiAlO_2 resulted. The hydrate formation led to a detrimental agglomeration of the initially monodispersed crystallites, which in turn resulted in an inappropriate porosity distribution in the pressed body. This point will be considered more fully below.

A suitable binder system was developed based on polyvinyl butyral (Monsanto Chemical Company, BUTVAR B-74 resin) dissolved in absolute methanol. The LiAlO_2 was dispersed in the binder solution [1 weight percent (w/o) resin on a dry basis] using intensive, high-shear blending. The methanol was evaporated by infrared heating, with constant stirring of the mixture to avoid segregation of the binder. The drying process was halted before complete methanol removal, i.e., at a point where a soft, apparently dispersed powder mass resulted. Complete removal of the methanol resulted in a rock-hard mass which could not be pressed into an appropriate porosity body due to binder generated agglomerates of exceptional strength. Such material could, however, be regenerated by the reintroduction of methanol through the vapor phase. The resin:methanol content ratio required is 1:1-1:3 on a mass basis. The binder containing powder was screened -40 mesh before use.

The matrix blanks were cold-pressed in a steel die at 14-35 MPa. The die was loaded with half the required powder charge and leveled. A single layer of pressure-flattened 20 mesh Kanthal® A-1 screen (0.127 mm wire diameter) was placed on the leveled powder and the remaining LiAlO_2 added and leveled. The pressed bodies, reinforced, measuring $165.1 \times 76.2 \times 2.3$ mm, were cut in half to give two blanks suitable for fuel cell experiments in this laboratory. The blanks were transferred to suitable substrates for molten carbonate impregnation.

The nature of the substrate was important to the impregnation process. Since it contacted liquid electrolyte during the process, the substrate had to be chemically inert toward molten carbonate. Another requirement was that the blank-substrate interface be poorly mated to allow atmosphere displaced from the matrix interstices to escape ahead of the advancing liquid electrolyte front which originated at the opposite blank face. Failure to observe these conditions resulted in the generation of liquid envelope-bounded gas bubbles which, in the course of the impregnation, led to physical disruption of the nonbonded matrix crystal array with attendant loss of physical shape and dimension control in the finished electrolyte structure. It was found that porous Al_2O_3 plaques covered with wrinkled, and partially flattened, gold foil satisfied these requirements.

The reinforced matrix blanks were impregnated with molten electrolyte by loading the solid electrolyte, premelted and ground, on top of the blanks in an evenly distributed pattern. The majority of experiments conducted during this development used agglomerated matrix material so that the blanks possessed broad, poorly defined pore size distributions, as will be documented below. These distributions precluded adding the entire electrolyte charge with a single impregnation since no effective, practical means could be devised to throttle the rate of introduction of molten material to the blank. It was found that the rate-controlling step was the absorption and distribution of molten electrolyte within the matrix crystal array. Attempts to introduce the entire electrolyte charge resulted in dilation of the matrix array to the point where the crystallites rearranged themselves physically. This action disrupted the physical shape and dimensions of the blank and rendered the product useless for fuel cell experiments. The problem was eliminated by impregnating with only 50-75% of the required electrolyte. The remaining electrolyte was

added in a second impregnation. Further, it was found necessary to limit the rate of heating to $\leq 40^\circ\text{K hr}^{-1}$ near the electrolyte liquidus temperature. Adherence to these requirements resulted in electrolyte structures which were suitable for fuel cell experiments.

When a deagglomerated matrix material was used, and the reinforcing mesh omitted, the entire electrolyte charge could be added in a single impregnation. Further, there was no limitation on the rate of liquid addition to the blank. The finer porosity present with a deagglomerated matrix, and the attendant uniform capillarity of the array, provided for more rapid and uniform absorption of the liquid phase.

Incorporating a reinforcing mesh into a deagglomerated matrix crystal array resulted in a previously unobserved problem. The pressure-flattened mesh was used without preconditioning it with molten electrolyte since it was felt that such treatment would render the mesh too fragile for the fabrication. When the reinforced blank was impregnated with the entire electrolyte charge, it was observed that the mesh interacted with the molten electrolyte, both oxidizing and "lithiating" of a surface layer on the mesh, generating CO_2 . This gas was trapped in liquid-bounded envelopes at the mesh plane and caused separation of the electrolyte structure at this plane. The problem was not observed using agglomerated matrix since the wide pore size distribution in that case likely provided electrolyte-void channels to vent the gas generated.

The effects of the mesh-molten electrolyte interaction were ameliorated by using two impregnations. The first impregnation added 50% of the required electrolyte. Since uniform, fine porosity was present with the deagglomerated matrix, the liquid electrolyte was substantially restricted to the regions of the blank bounded by the top surface, the point of electrolyte introduction, and the midplane where the mesh resided. The lower half of the blank remained substantially electrolyte-free and provided an escape path for the CO_2 generated during the *in situ* mesh conditioning. The remaining electrolyte was added using a second impregnation, yielding electrolyte structures suitable for fuel cell evaluation.

Fuel Cell Evaluation

The first fuel cell experiment (CRD-027) was conducted using a reinforced electrolyte structure containing agglomerated LiAlO_2 matrix material. The electrochemical performance of this $0.44 \times 10^{-2}\text{m}^2$ active area cell is shown in Fig. 1. This experiment involved more than 20 thermal cycles of the cell between 923°K , the cell operating temperature, and $\sim 650^\circ\text{K}$, a temperature below the electrolyte solidus, at cycle rates of $50^\circ\text{-}75^\circ\text{K hr}^{-1}$. The cell was maintained at the lower temperature for periods randomly

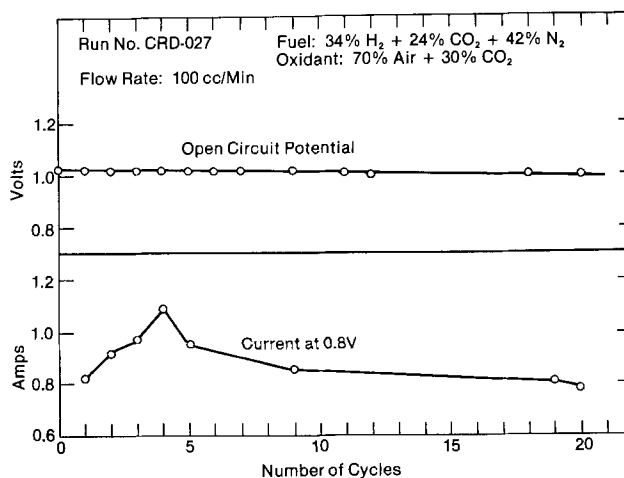


Fig. 1. Electrochemical performance of cell CRD-027

ranging from 2 to 18 hr before returning to the operating temperature. It was assumed that the major impact of thermal cycling was involved with the electrolyte phase transformation. The electrochemical performance of the cell was below (by a factor of 2-3) that achieved in this laboratory using selected, conventionally prepared electrolyte structures in the same hardware. The factors responsible for this behavior are considered below.

The gas management characteristics of this cell are shown in Table I. The wet seal performance was determined from measurement of inlet and outlet gas flow rates. The cross-leakage was determined using an argon-doped cathode stream and mass spectrometric analysis of the anode exit stream. These data indicate excellent anode seal performance from the start of the experiment, while the cathode seal took several days to establish. Both seals maintained integrity over the ~2000 hr of the experiment. The cross-leakage behavior was somewhat more variable. The initial behavior was good. Thermal cycling increased the cross-leakage, and there is indication that the magnitude of leakage is proportional to the frequency of cycling. Further, cessation of cycling, when coupled with steady cell operation, appeared to allow the cycling-induced damage to at least partially reverse itself.

Electrolyte Structure Diagnostics

The maintenance of electrochemical performance is dependent, in part, on the constancy of matrix material characteristics in the functioning electrolyte structure. The effects of cell operating conditions on the matrix were examined by measuring the crystallite surface area, hence average size, before and after use in a fuel cell. Three different electrolyte structures were examined. The first was from the previously discussed experiment (CRD-027). The material used was "chloride" synthesis LiAlO_2 with a surface area of $6.43 \text{ m}^2 \text{ g}^{-1}$, and the experiment duration was more than 2000 hr. The other two structures (DECP-010, CRD-028) were prepared by conventional techniques (3), the matrixes having surface areas of 11.42 and $9.09 \text{ m}^2 \text{ g}^{-1}$, respectively. Their cell environment exposures were ~700 and ~192 hr, respectively. The matrix was separated from the electrolyte by dissolution of the latter in an equal volume mixture of glacial acetic acid-acetic anhydride, followed by filtration, a wash with absolute methanol, and drying at 393°K . The samples analyzed represented quadrants of the electrolyte structures.

The results of this analysis are given in Fig. 2. These data show that the average crystallite size has increased as a result of cell exposure. The initial

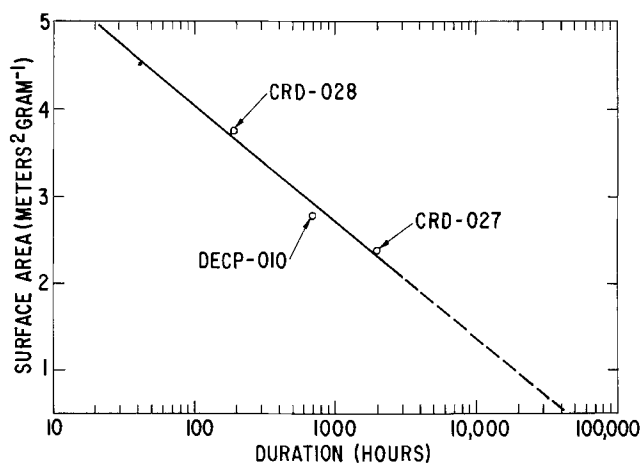


Fig. 2. Matrix crystal growth in fuel cell environment

crystal size difference has given way to one dependent on time of exposure. In addition, there is no indication that the crystal growth process has terminated at 2000 hr. These data indicate an instability of the matrix, hence the electrolyte structure, under cell operating conditions.

Measurement of the matrix crystallite pore size distribution in conventionally prepared materials involves the removal of the electrolyte phase. There is the attendant assumption that the freed material can be reassembled into an array representative of that which would have existed had the electrolyte been present. Such an assumption is unnecessary in impregnation fabrication structure in that measurements can be made directly on the matrix blanks prior to impregnation. Such measurements were made in an effort to determine reasons for the failure of cell CRD-027 to give optimum electrochemical performance.

Figure 3 shows the cumulative pore volume fraction vs. pore diameter, as measured by mercury intrusion porosimetry, for both the matrix blank and the virgin Ni electrode used in the fuel cell experiment. The steepness of the electrode curve is indicative of the well-defined pore size distribution existent in that body. The matrix blank, in contrast, has a shallower slope, indicative of its poorly defined, broad pore size distribution. The distribution overlap between matrix and electrode indicated that at worst ~10% of the electrode pores would be electrolyte-filled. This condition should not have precluded satisfactory electrochemical performance of the cell.

Figure 4 shows that same matrix distribution along with the measured distributions for the anode and

Table I. Gas management in CRD-027

Day	Thermal cycle	Wet seal leakage		Cross leakage (%)
		Anode (%)	Cathode (%)	
1	0	0.00	8.00	0.00
2	0	0.00	5.00	0.00
5	1	—	—	0.00
15	2	—	—	0.50
22	3	—	—	0.25
25	4	—	—	0.25
28	5	—	—	0.40
29	6	—	—	0.25
32	7	—	—	0.25
35	8	—	—	0.25
44	9	—	—	1.8
45	10	—	—	0.75
51	11	—	—	0.00
59	12	—	—	1.00
70	13	—	—	1.00
70	14	—	—	—
71	15	—	—	—
73	16	—	—	—
78	17	—	—	2.75
79	18	—	—	4.50
80	19	—	—	6.50
84	20	0.00	0.00	4.25

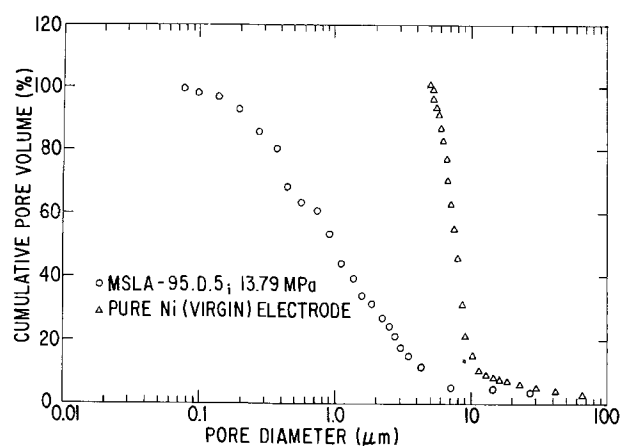


Fig. 3. Porosity distributions of agglomerated matrix and virgin Ni electrode.

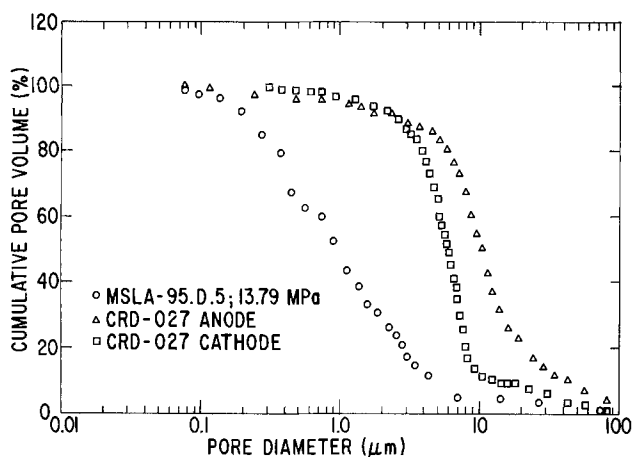


Fig. 4. Porosity distributions of agglomerated matrix and used electrode materials.

cathode retrieved from the cell experiment. The used electrode distributions are somewhat broadened relative to the virgin electrode material, resulting in an increased overlap with the matrix curve. The situation in an operating cell would be worse in that matrix crystal growth would have increased the average pore diameter, thereby further increasing the distributions' overlap. It was concluded from these data that the failure of the cell to perform properly was due in large measure to flooding of the electrodes with molten electrolyte resulting from excessive overlap of the matrix and electrode pore size distributions.

The cause of the poor matrix pore size distribution was determined with the aid of a "reference" material. An alkaline earth titanate, synthesized by a variant of the "chloride" synthesis previously discussed, was pressed into a matrix blank and its pore size distribution measured. This material possessed an average spherical equivalent crystal diameter, as measured through the BET surface area, of $0.31 \mu\text{m}$, compared with $0.36 \mu\text{m}$ for the LiAlO_2 . However, the "reference" material crystallites were more symmetrically shaped and uniformly sized than those of the LiAlO_2 . Further, the "reference" crystallites were known to be substantially monodispersed, a characteristic unevaluated in the LiAlO_2 .

Figure 5 shows the pore volume *vs.* size comparison of the "reference" with the electrodes from the cell experiment. Unlike the LiAlO_2 blank, the "reference" blank had a well-defined pore size distribution which produced only minor overlap with the electrode distributions, a condition which should result in proper electrode wetting. It was concluded from these data that agglomeration in the "chloride" synthesis LiAlO_2 was the source of the poor pore size distribution in the matrix blanks. To assess this conclusion, a sample of "chloride" synthesis LiAlO_2 was deagglomerated, as previously reported (1). The average spherical equivalent diameter was reduced from 0.30 to $0.26 \mu\text{m}$. More strikingly, a blank prepared from the deagglomerated material possessed a pore size distribution indistinguishable from that of the "reference" material, confirming the interpretation.

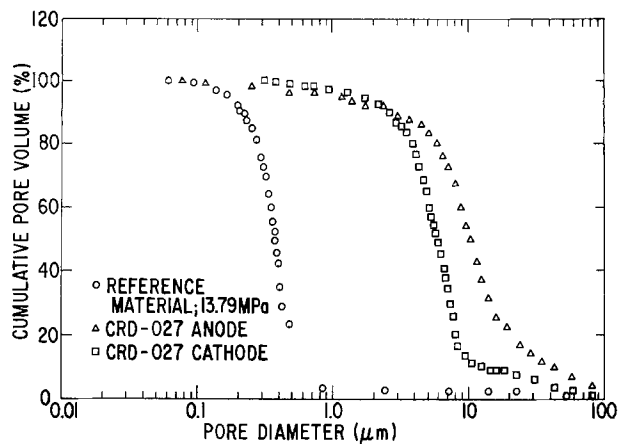


Fig. 5. Porosity distributions of monodispersed "reference" crystalline material and used electrode materials.

The anticipated effect of the documented LiAlO_2 crystal growth under cell operating conditions is to move the pore size distributions of the matrix and electrodes closer together, increasing their overlap. However, the deagglomerated matrix should be more tolerant of this change than was the agglomerated matrix. Experiments are underway to assess the near and long-term performance of cells incorporating deagglomerated "chloride" synthesis LiAlO_2 , both as conventionally and impregnation fabricated electrolyte structures.

Conclusions

A fabrication process for molten carbonate fuel cell electrolyte structures has been developed which eliminates the need for a hot-pressing operation. The requirements and conditions required to prepare structures suitable for fuel cell application have been defined.

Acknowledgments

The authors wish to acknowledge the contributions of M. W. Breiter, J. L. Weininger, K. W. Browall, and E. C. Hayes, Research and Development Laboratory of the General Electric Company, to the completion of this effort. This work was supported in part by the U.S. Department of Energy under Contract DE-ACO3-77ET-11319.

Manuscript submitted Dec. 3, 1979; revised manuscript received Feb. 18, 1980. This was Paper 10 presented at the Boston, Massachusetts, Meeting of the Society, May 6-11, 1979.

Any discussion of this paper will appear in a Discussion Section to be published in the June 1981 JOURNAL. All discussions for the June 1981 Discussion Section should be submitted by Feb. 1, 1981.

Publication costs of this article were assisted by General Electric Company.

REFERENCES

1. R. H. Arendt and M. J. Curran, *This Journal*, **127**, 1660 (1980).
2. "Development of Molten Carbonate Fuel Cells for Power Generation. Quarterly Progress Report, 15 Nov. 1978-15 Feb. 1979," General Electric Company for U.S. Department of Energy, SRD-79-060, March 1979.
3. D. M. Mason *et al.*, U.S. Pat. 3,998,939 (1976).

Alkaline Aqueous Electrolyte Cells for Biomedical Implantable Applications

Paul Ruetschi*

Leclanché S.A., 1400 Yverdon, Switzerland

ABSTRACT

Technological advances, latest state of the art, and ultimate achieved performance of primary mercuric oxide-zinc cells for biomedical implantable applications are reviewed. The data presented in this review should serve as a basis against which long-term performance data of lithium batteries could be compared in the future. The different cell-internal and cell-external self-discharge processes are analyzed as to their relative importance in causing capacity loss. Other aqueous electrolyte, alkaline primary cells, such as the HgO-Cd cell, and secondary NiOOH-Cd batteries are also briefly discussed regarding biomedical implantable applications.

In recent years, more and more cardiac pacemakers have used as a power source a lithium battery of some sort. In the past, however, aqueous electrolyte, alkaline primary batteries of the mercuric oxide-zinc type were used extensively. Fester *et al.* (1) estimate that 99% of the 350,000 cardiac pacemakers implanted during the period 1969 to 1974 were powered by mercuric oxide-zinc cells. By the end of 1976 over 700,000 implanted cardiac pacemakers contained mercuric oxide-zinc cells as the power source (2). The first long-term use of mercuric oxide-zinc cells in pacemakers goes back to about 1960.

The present review describes the improvements made in mercuric oxide-zinc batteries over the past years, ultimate performance reached with this system, and finally some novel means to further optimize the system for long-term use.

The results on long-term testing of mercuric oxide-zinc cells reported in this review should serve as a basis of comparison with performance of various newer lithium batteries.

The major self-discharge processes occurring in HgO-Zn cells are evaluated as a function of temperature, and an estimation of the activation energy is attempted for each individual reaction. In analyzing self-discharge it is of importance to distinguish between cell-internal and cell-external processes.

The two main cell-internal side-reactions leading to capacity loss are: (i) Solubility of mercuric oxide in alkaline electrolytes and diffusion of dissolved mercuric oxide species towards the zinc electrode. (ii) Hydrogen evolution at the zinc electrode. Reactions occurring externally to the cells which may contribute substantially to self-discharge are: (iii) External electrolysis in moisture films on cell surfaces or leads, including anodic oxygen evolution or anodic corrosion of metal parts, and cathodic hydrogen evolution. (iv) External oxygen cycle, due to electrochemical reduction of oxygen on negative terminal parts and oxygen evolution on positive terminal parts.

Reliability, longevity, and uniformity of mercuric oxide-zinc primary batteries are determined by the construction of the inter-electrode separation, in particular the prevention of edge passage ways for mercury droplets, the type of separator material and number of separator layers, the conception of the seal, and the precision of metering anode, cathode, and electrolyte weights.

Besides mercuric oxide-zinc cells, some other aqueous electrolyte alkaline primary battery systems as well as rechargeable types have been proposed for

implantable application, in particular the primary HgO-Cd and the secondary NiOOH-Cd system. So far, these have been of limited practical utilization (3, 4). Their behavior during long-term use is also briefly discussed in the present review.

Mercuric Oxide-Zinc Batteries for Biomedical Application

Primary mercuric oxide-zinc batteries for biomedical use are illustrated in Fig. 1 and 2. The Mallory RM 1 cell, shown to the left of Fig. 1 and 2, was for many years the only available power source (5, 6). It makes use of a cylindrical, ring-shaped electrode structure. The positive mercuric oxide electrode lines the inside can wall. The negative zinc electrode is contained in a centrally located separator tube. With this design it was very difficult to achieve ultimate safety against short circuits around the separator edges.

In the period 1960-1970 pacemakers had to be replaced typically after 18-24 months of service. Since the nominal capacity of RM 1 cells was 1 A-hr, and typical current requirements in a pacemaker at that time were in the order of 30 μ A, only about 50% of the theoretically available capacity could be realized in practice prior to premature failures occurring due to internal short circuits (1, 7).

In order to immobilize the mercury droplets formed during discharge, silver powder was added to the positive electrode mix. The mercury droplets readily form with silver a solid amalgam. However, even though an improvement was noted, the shorting problem was still not solved satisfactorily.



Fig. 1. Medical-grade HgO-Zn cells. Left, Mallory RM1 cell; right, Leclanché MR 81 cell. Dimensions and characteristics are given in Table I.

* Electrochemical Society Active Member.

Key words: alkaline primary cells, mercuric oxide-zinc cells, mercuric oxide-cadmium cells, nickel-cadmium cells, biomedical power source.

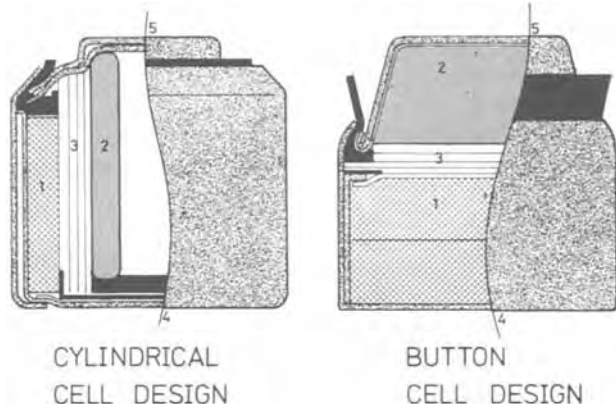


Fig. 2. Construction of RM1 (left) and MR 81 (right) cells. 1, Positive electrode; 2, negative electrode; 3, separators; 4, positive terminal (can); 5, negative terminal (cover) [from Ref. (9)].

In the beginning of the seventies, a further improvement was made by introducing the "double wrap" separator barrier. Better than 5 years longevity has been achieved with cells incorporating this improved separator design (4).

In the MR 81 (Leclanché) button cell design, shown to the right of Fig. 1 and 2, the electrodes are pellets, rather than cylinders (8). The separators are tightly locked at the edge between the grommet seal and a supporting steel ring. This cell construction is characterized by extreme reliability against internal short circuits. Long term performance data achieved with this cell have been reviewed recently (9). MR 81 cells have been available in an absolutely unaltered construction since 1970.

Dimensions and electrical data of RM 1 and MR 81 cells are listed in Table I. Obviously, for modern pacemaker designs, cells of lower height would be desirable. However, the basic design of the MR 81 cell lends itself to the construction of flat button cells, as used, for instance, in watches.

Most pulse generators have used 4 or 5 mercuric oxide-zinc cells of the RM 1 size connected in series. The cells were cast into the epoxy resin together with the electronic circuit. As will be discussed later, cell packaging, and in particular its effectiveness in preventing moisture and oxygen access to the cell surfaces, is of great importance for long-term use. One must remember that the body presents an atmosphere of high humidity and relatively high temperature (37°C).

A third type mercuric oxide-zinc cell, developed for biomedical use, was a relatively large 3.4 A-hr unit (General Electric). Data reported on this cell, (10, 11) indicated a self-discharge rate of about 1.5% per year at 37°C and 15% per year at 65°C. After storage for 24 weeks at 72°C, capacity on an accelerated six months discharge test was 3.0 A-hr, which corresponds to 25%/yr (3). The longest discharge tests reported so far were 5 yr at 37 μ A, that is to only about 50% depletion of cell capacity.

Since internal short circuits tend to occur only when approaching complete exhaustion of anode capacity, it is not yet possible on the basis of the pub-

lished material to judge reliability near the end of discharge.

In the following, life-limiting factors of mercuric oxide-zinc batteries are analyzed by using as a test vehicle the MR 81 cell.

It should be understood that data reported here on this cell could be extended suitably to other mercuric oxide-zinc cells when taking into account relevant geometric and other design features.

Long-Term Performance of Mercuric Oxide-Zinc MR 81 Cells

Typical performance achieved with MR 81 cells are illustrated in Fig. 3-7 and Table II. It should be noted that these data refer to the original MR 81 cell construction, as finalized in 1970.

Mercuric oxide-zinc cells are characterized by their constant discharge voltage (Fig. 3). Initial higher voltage is due to the MnO₂ addition to the positive electrode mix. It may serve as a safety indicator for absence of internal shorts (Fig. 4). Internal impedance remains low to the very end of discharge (Fig. 5). The initial hump in internal resistance, shown in Fig. 3, is due to an electrolyte redistribution phenomenon, which cannot be discussed here in detail. Extremely good uniformity was achieved with this cell by very precise metering of anode material (Fig. 6).

Long-term storage and discharge data are presented in Table II and Fig. 7.

Analysis of the Cell-Internal Self-Discharge Processes Occurring in HgO-Zn Cells

Solubility of mercuric oxide.—A major cause of internal self-discharge is the solubility of mercuric oxide in alkaline electrolytes (12, 13). Solubility may be suppressed, as will be discussed later, by using a very high electrolyte concentration (9). Only scarce data is available concerning dependence of HgO solubility on temperature. From one single literature value, reported for 100°C (14), the heat of dissolution for HgO in water can be estimated approximately at 6 kcal/mole. Solubility of HgO at different temperatures, as evaluated from a 1/T plot, using an integrated Clausius-Clapeyron equation with $\Delta H = 6$ kcal, is listed in Table III. Mercuric oxide dissolves in alkaline electrolytes probably in form of undissociated Hg(OH)₂ (9).

Self-discharge caused by mercuric oxide solubility may be measured experimentally by analyzing the amount of mercury present in the anode after known periods of storage at a given temperature. For such studies, it is preferable to use HgO-Cd cells, rather than HgO-Zn cells. The cadmium sponge anode is initially mercury-free, and its mercury content can be determined with good precision whereas with amalgamated zinc anodes, the diffused mercury must be determined as the difference between two large numbers.

Mercuric oxide diffusion may be expressed in terms of a self-discharge current. The surface available for diffusion is determined by the separator interface between positive and negative electrode. In

Table I

	Mallory RM 1	Leclanche MR 81
Average discharge voltage, V/cell	1.35	1.35
Diameter, mm	15.8	15.8
Height, mm	16.4	16.4
Volume (by displacement), cm ³	3.0	3.0
Weight, g	13.8	14.2
Anode capacity, A-hr	1.19	1.25
Energy density, W-hr/cm ³	0.54	0.56
Internal resistance 20°C, Ω	~2	~5

Table II. Discharge of MR 81 HgO-Zn cells at 37°C

(Epoxy encapsulated units) Lot size for each load resistance: 50 cells			
Load resistance (Ω)	Discharge time (average) (hr)	Capacity (average) (mA-hr)	Standard deviation (mA-hr)
1,200	1,135	1,230	22
4,700	4,400	1,230	25
10,000	9,170	1,230	12
20,000	18,000	1,215	16
47,000	41,800	1,200	19

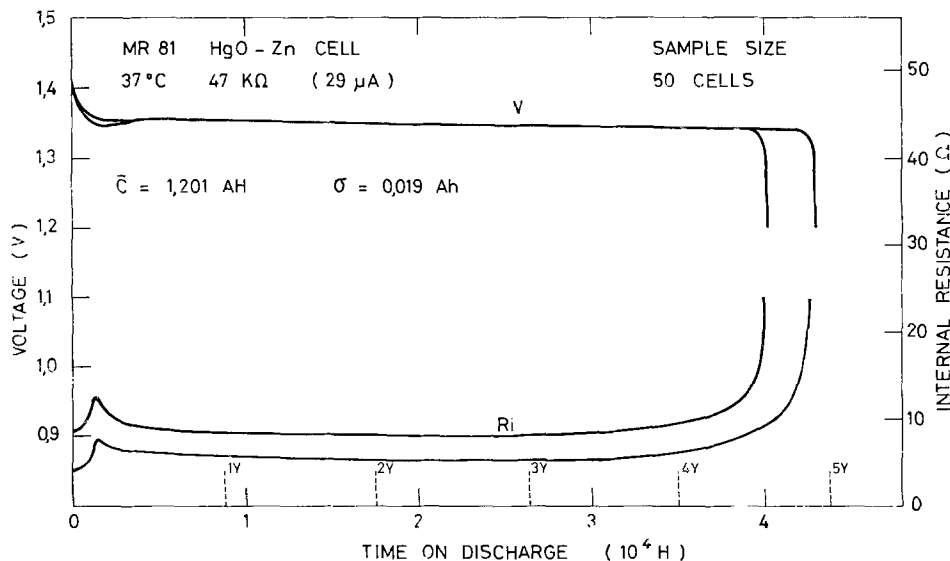


Fig. 3. Voltage (V) and internal resistance (R_i) spread of a typical test-lot of MR 81 cells, as a function of discharge time under 47 kΩ load. Capacity standard deviation (19 mA-hr) includes variation of discharge resistors.

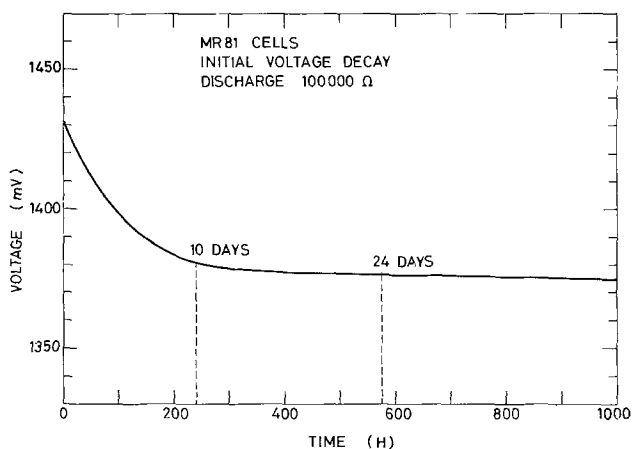


Fig. 4. Initial voltage decay of MR 81 cells during 100 kΩ discharge.

RM 1 cells, this surface amounts to about 2.4 cm². In the MR 81 cell it is restricted to the opening in the sealing grommet and amounts to only 0.8 cm². Rate of Hg(OH)₂ diffusion depends also on the type of separator, number of separator layers (distance between electrode surfaces) and on quantity and concentration of alkaline electrolyte in the cell.

Self-discharge current densities in the order of 0.1-0.3 μA/cm² at 22°C have been reported (15) for cells with radiation-grafted and cross-linked polyethylene (Permion® 2291-40/60) and an electrolyte of 30% KOH.

Self-discharge due to Hg(OH)₂ diffusion increases rapidly with temperature. At 71°C, for two layers of Permion®, a value of 2.4 μA/cm² has been reported (16). Measurements, carried out in our laboratories using HgO-Cd cells, are included in Table III. Using these values one can calculate the theoretical self-discharge due to Hg(OH)₂ diffusion in an MR 81 cell (theoretical anode capacity 1230 mA-hr, diffusional area 0.8 cm²). Results are given in the last column of Table III. An Arrhenius plot with these values indicates an activation energy of 12 kcal/mole (Fig. 8, curve A). Self-discharge due to Hg(OH)₂ diffusion is particularly low in cells of the MR 81 design because of the restricted diffusional area, the wide electrode separation, and the high electrolyte concentration used in these cells. Various novel means to reduce mercuric oxide diffusion are discussed in a later chapter.

Hydrogen-evolution.—Hydrogen evolution on zinc in alkaline electrolytes according to $Zn + H_2O \rightarrow ZnO + H_2$ may be decreased to extremely small values by careful amalgamation and by using very pure zinc.

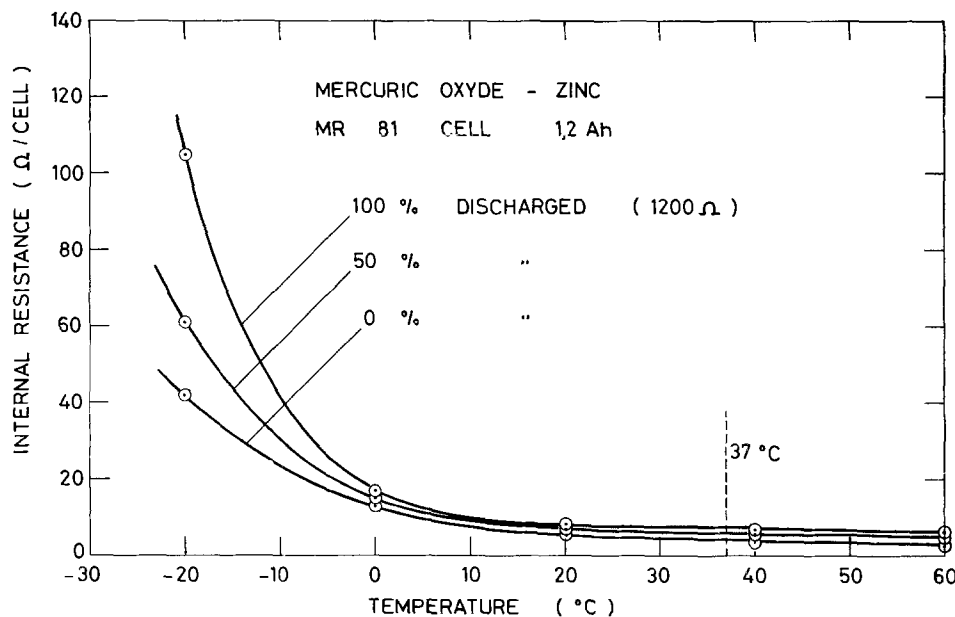


Fig. 5. Dependence of internal impedance (as measured at 40 Hz with a Keithley Milliohm-Meter) on temperature and depth of discharge. (Each point average of 5 cells)

Fig. 6. Capacity distribution for discharge of 50 MR 81 cells at 47 k Ω .

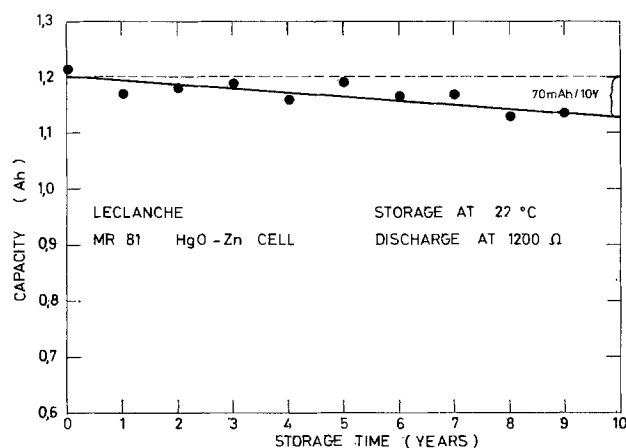
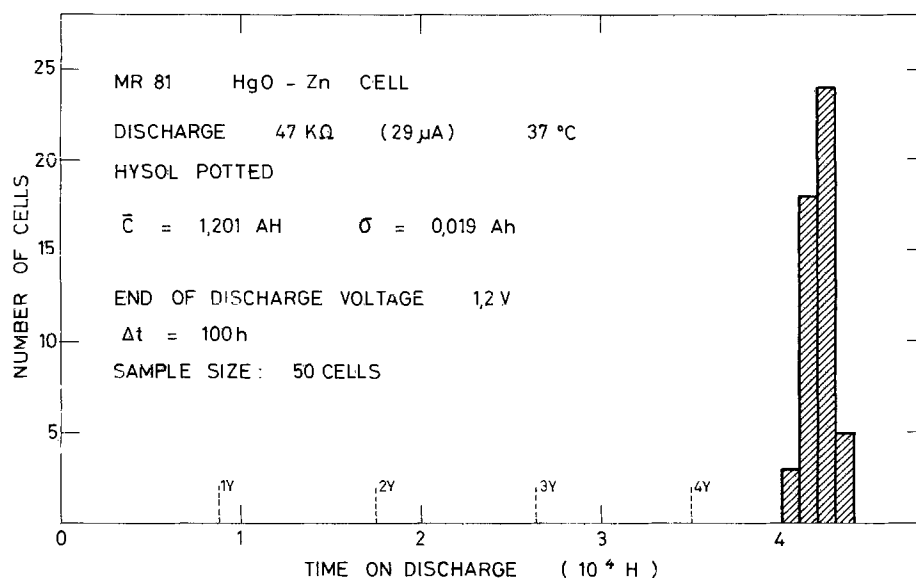


Fig. 7. Capacity of MR 81 cells, measured under 1200 Ω load, as a function of storage time at 22°C. Each point average of 5 cells. (Cells stem from several different lots manufactured in 1970.)

Gassing rates of zinc powder containing 10% Hg, as measured in a Pyrex glass cell in 50% KOH, are given in Table IV. From a plot of $\log H_2$ evolution rate vs. $1/T$ an activation energy of 19 kcal/mole is derived (Fig. 8, curve B). It is apparent from a comparison of the data in Table III and Table IV and from Fig. 8 that self-discharge due to H_2 evolution becomes increasingly important in relation to self-discharge by $Hg(OH)_2$ diffusion as the temperature increases.

In the MR 81 cell the zinc powder is in contact with an amalgamated copper or bronze surface, lining the inside of the cover (Fig. 2). It may be shown experimentally that the presence of a clean amalgamated copper or bronze surface, in contact with zinc powder, does not increase H_2 evolution significantly. On the other hand, if impurities, which would lower the hydrogen overvoltage, are present within the cell, self-discharge due to H_2 evolution may be increased drastically.

Table III. Solubility of HgO in 30% KOH (estimated) and self-discharge due to $Hg(OH)_2$ diffusion

Temperature (°C)	Solubility (mole/liter)	Hg(OH) ₂ diffusion current (μA/cm ²)	Self-discharge due to Hg(OH) ₂ diff. (%/yr)
22	$2.3 \cdot 10^{-4}$	0.26	0.15
37	$3.3 \cdot 10^{-4}$	0.7	0.40
75	$9.8 \cdot 10^{-4}$	5.5	3.1
100	$1.7 \cdot 10^{-3}$	17.2	9.8

In the RM 1 cell (Fig. 2), the inside wall of the cover consists of tin plated steel. H_2 evolution in RM 1 cells, particularly when partly discharged, appears to be considerably larger than in MR 81 cells. Gassing is increased in partly discharged cells if the zinc anode has insufficient porosity such that electrolyte depletion occurs locally within certain sections of the electrode (17). The amount of hydrogen escaping through the seal of RM 1 cells at 37°C has been reported to be 7.3 cm³ per cell and per yr (2). This would represent 1.5% self-discharge per year.

In RM 1 cells the seal is constructed as to allow hydrogen venting. Means to increase hydrogen venting through the neoprene seal have also been proposed (18). In this latter reference, H_2 evolution in RM 1 cells is reported to be about 5.5 cm³/yr. For aged and partly discharged RM 1 cells gassing rates of up to 17 cm³/yr at 37°C have been measured (9).

The MR 81 seal does not provide for H_2 venting. The only way of escape is by diffusion through the nylon grommets. Hydrogen escape from MR 81 cells, measured with an apparatus as shown in Fig. 10, is only 0.35 cm³/H₂/yr at 37°C (9), representing only 0.07% self-discharge per year. (To avoid effects of Pyrex leachants on gassing, it is of advantage to repeatedly clean the cell with hot conc. KOH solution for several days.) However, actual H_2 production within the cell is probably higher, as discussed below, with a large portion of the hydrogen being re-absorbed (oxidized) in the positive electrode.

Total cell-internal self-discharge.—Self-discharge of MR 81 HgO-Zn cells was measured experimentally by long-term storage tests (2-9 yr, depending on temperature) at different constant storage temperatures (22°-75°C). After storage, the cells were discharged at low rates (1.2 k Ω load, 40 day test, or 10 k Ω load, 360 day test). Results are shown in Fig. 9 and Table V. Plotting \log of percent capacity loss per year against $1/T$ yields a straight line (Fig. 8 curve C), from which a formal activation energy for the

Table IV. Gassing rate of amalgamated zinc powder (10.3% Hg), *in vitro*

(Average of five tests at each temperature)		
Temperature (°C)	(cm ³ H ₂ STP/g/yr)	Self-discharge Zn + H ₂ O → ZnO + H ₂ (%/yr)
37	0.31	0.1
45	0.62	0.2
60	2.1	0.7
75	8.2	2.7

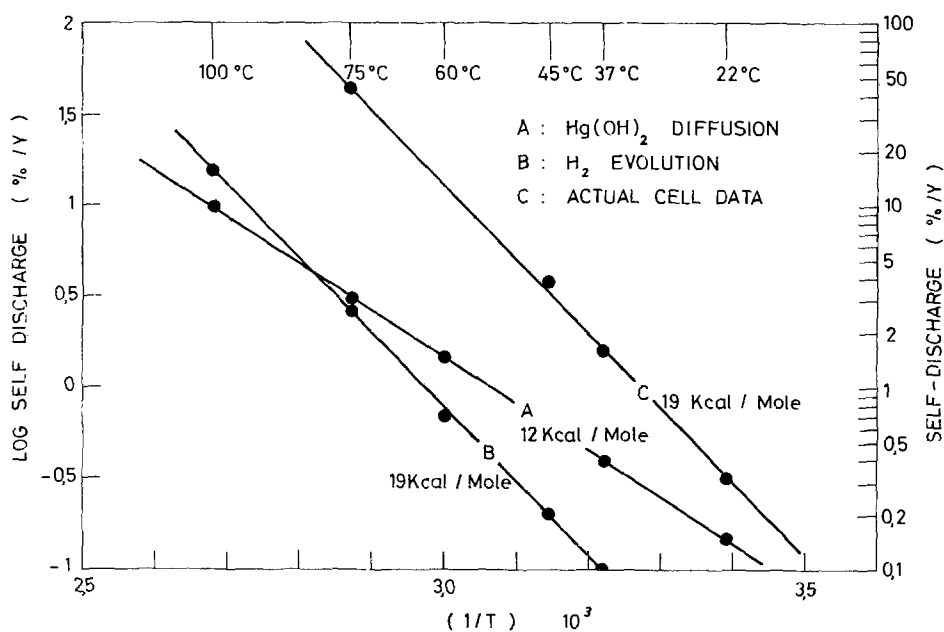


Fig. 8. Log self-discharge rate (%/yr) against $1/T$ plots for A, loss by $\text{Hg}(\text{OH})_2$ diffusion; B, H_2 evolution *in vitro*; and C, total self-discharge as determined from storage tests (Fig. 9).

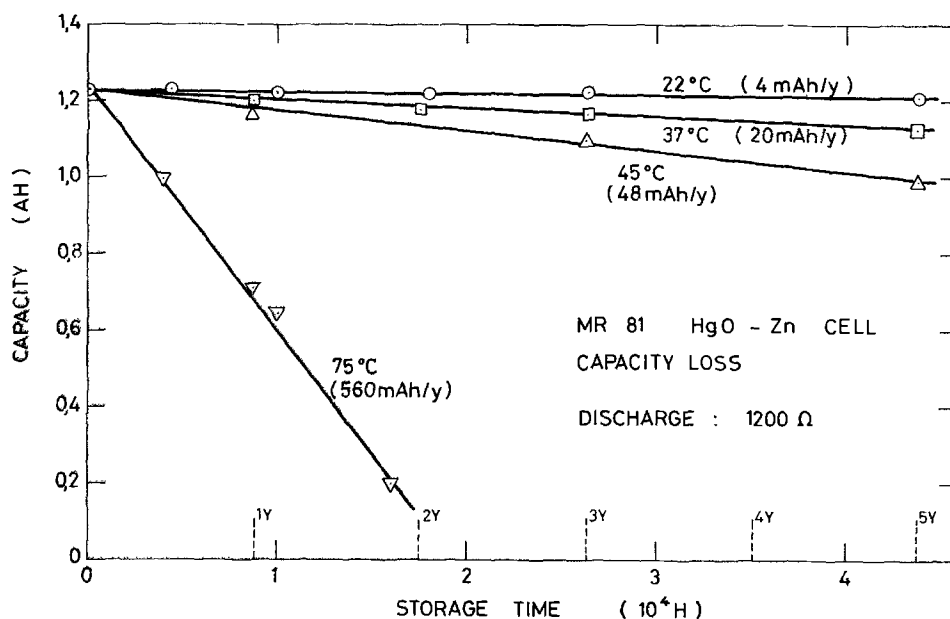


Fig. 9. Capacity loss of MR 81 HgO-Zn cells during storage at different temperatures. Each point average of 5 cells. (All cells stem from the same lot, manufactured in 1970).

overall self-discharge process of 19 kcal/mole may be calculated.

This value is very close to the value found for H_2 evolution *in vitro* (curve B), which suggests that H_2 production in the actual cell is strongly enhanced over that measured in a glass cell, and is actually a major, if not dominant, cause of cell-internal self-discharge (catalyzed H_2).

The fact that self-discharge follows a simple Arrhenius equation was also found for HgO-Cd cells (19). From the data reported in this latter reference a formal activation energy of 12 kcal/mole may be derived, indicating that $\text{Hg}(\text{OH})_2$ diffusion is the only self-discharge process of importance in this type of cell.

Table V. Total cell-internal self-discharge of MR 81 HgO-Zn cells

Temperature (°C)	Self-discharge from capacity loss after storage of MR 81 cells (%/yr)	Microcalorimetry literature data on RM1 cells (%/yr)
22	0.3	—
37	1.6	4 (22); 3 (21)
45	3.9	—
75	45	—

Cataldi (11) has reported an activation energy of 15 kcal/mole for the self-discharge process in HgO-Zn cells. However, his self-discharge rates are somewhat questionable since they were based on the assumption that capacity loss per unit time is proportional to remaining capacity. Experimentally, one finds that self-discharge rates tend to be constant over very long periods of time and are finally increasing rather than decreasing, due to separator and seal degradation (9).

Cataldi's results indicate that at low temperatures a process of lower activation energy (9 kcal/mole) becomes dominant. This is in agreement with Fig. 8.

Microcalorimetric measurements.—Recently, the use of microcalorimeters has been proposed to determine self discharge of batteries for biomedical implantable applications (20-22). Using this technique, Untereker (22) estimated self-discharge loss of an RM 1 cell at $7 \mu\text{W}$, which would correspond to a self-discharge current of $5 \mu\text{A}$, or about 4% capacity loss/year. It should be pointed out that microcalorimetric measurements are not easy to interpret, mostly because true steady-state conditions in a cell are difficult to achieve, even on open circuit, and still more so during discharge. Many very slow processes take place in the cell which are not directly related to ca-

capacity, such as electrolyte equilibration in micropores of anode, cathode, and separators, buildup of soluble zincate concentration gradients, nucleation, crystallization and growth of ZnO crystals, and so on. Probably the largest unknown side reactions producing or absorbing heat are due to the addition of MnO₂ in the HgO cathode. Electrolyte penetration into micropores of MnO₂, uptake of K⁺ or Na⁺ ions into the lattice (23) dehydration, recrystallization and equilibration of its oxidation state, are slow, capacity-unrelated processes. Furthermore, it is known that for all chemical reactions involving solids of high surface area, the surface free energy can contribute noticeably to the overall free enthalpy change (24).

All the above-mentioned phenomena are more or less unrelated to cell capacity, but will contribute thermal effect. For this reason one must be careful in making any predictions on self-discharge, based on microcalorimetric measurements, carried out over periods of days or weeks only.

Cell-External Processes Influencing Self-Discharge

External electrolysis.—Electrolysis in moisture films surrounding the cells and bridging the grommet area becomes theoretically possible at cell voltages above about 1.23V.

In most pacemakers, used in the past, mercuric oxide-zinc cells were potted in epoxy resin. Moisture films could form between the epoxy casting and external cell walls. Considerable concern existed with manufacturers and users as to the possible effect of the presence of such moisture films, particularly when these latter would contain KOH, stemming from a defect seal (25, 26). However, Fester *et al.* have shown (27) that with properly encapsulated cells (Hysol or Scotchcast No. 15) external electrolysis does not contribute significantly to self-discharge.

In order to study the maximum self-discharge external electrolysis could possibly provoke, MR 81 HgO-Zn cells were placed into a volumetric glass apparatus (Fig. 10) which was then filled with 50% KOH solution (oxygen-free). Groups of 2 cells each were separated by insulating Teflon spacers, in order to avoid series connection of cells. Gas evolution, could be measured to a precision of 0.001 cm³ by observing the displacement of the meniscus in the capillary. Gas evolution rates, measured at different temperatures, are given in Table VI. Assuming that external electrolysis produced O₂ and H₂ in stoichiometric ratios, the corresponding self-discharge was calculated. (Hydrogen stemming from the cell interior is negligible with respect to gassing by external electrolysis). As seen from Table VI, self-discharge due to external electrolysis even under these extreme conditions, is still surprisingly small. This must be due to passivation phenomena on pure nickel surfaces

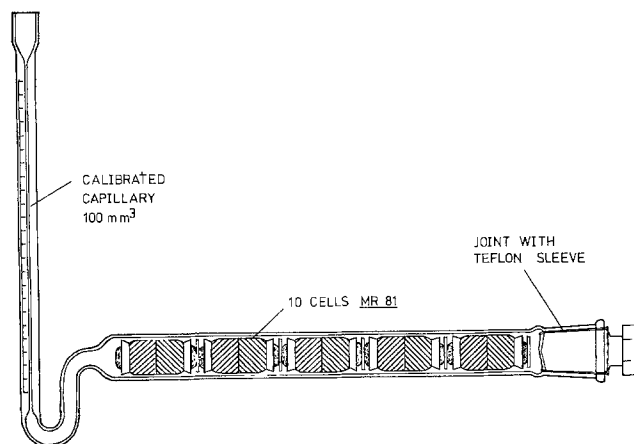


Fig. 10. Volumetric apparatus for measuring external electrolysis on HgO-Zn cells when submerged in KOH solution [from Ref. (9)].

Table VI. External electrolysis on MR 81 HgO-Zn cells submerged in 50% KOH solution

(Average of 10 cells at each temperature)		
Temperature (°C)	Gas from electrolysis (cm ³ STP/yr/cell)	Capacity loss H ₂ O → H ₂ + ½ O ₂ (%/yr)
37	5.5	0.7
47	8.9	1.1
57	27	3.5
75	102	13

in 50% KOH solution, causing a high overvoltage for O₂ evolution.

With epoxy-encapsulated cells only very thin bridging films could be present, and the resulting self-discharge from external electrolysis should be smaller than that given in Table VI due to higher electrolytic resistance.

External electrolysis is enhanced, however, when a continuous liquid film forms over the surface of two or more cells, connected in series. A voltage of 2.7 or more volts is then available for electrolysis. In a pacemaker package, individual cells should therefore be separated from each other by long, well-embedded, welded connections, having surfaces which inhibit electrolyte creepage. (See section on cell-packaging.)

Finally, it should be mentioned that the presence of liquid films of NaCl solution, rather than KOH, provokes severe can corrosion, accompanied by a correspondingly increased capacity loss (9).

External oxygen cycle.—This type of self-discharge mechanism was described for the first time only very recently (9). It involves oxygen reduction on the negative cell terminal or lead, and oxygen evolution on the positive cell terminal or lead.

For this mechanism to take place, a liquid medium film, surrounding the cell, and oxygen must both be present.

The magnitude of self-discharge due to this process depends on the rate of oxygen diffusion to the negative terminal, as given by the geometry of the liquid medium surrounding the cell, by the solubility of oxygen in this medium, and by oxygen access to the medium. Even the low voltage of an HgO-Cd cell (0.9V) would be sufficient to drive an "oxygen cycle."

Oxygen diffusion at 37°C through a 2 mm thick epoxy encapsulation may not be entirely negligible (neither is H₂O diffusion). Only in hermetically sealed pacemakers could, of course, the described "oxygen cycle" not occur.

In order to study the contribution of the "oxygen cycle" to self-discharge, MR 81 cells were submerged in air-saturated KOH solution. The electrolyte level was 1 cm above the cell covers. Capacity loss, as measured by discharge tests after given storage times under these conditions, is shown in Fig. 11. After deduction of the loss due to external electrolysis, assumed independent of KOH concentration (Table VI) and total internal self-discharge (Table V), the approximate contribution due to the oxygen cycle was estimated in Table VII.

With increasing KOH concentration, oxygen solubility decreases strongly due to salting-out (28) which explains why the contribution of the "oxygen cycle" to self-discharge decreases with increasing KOH concentrations.

Long-lasting cell-seals.—Much progress has been realized over the past years in sealing alkaline cells. The use of a one-piece cover, (Fig. 1 and 2, right-hand side) in place of the earlier double-top construction (Fig. 1 and 2, left-hand side), which was spurred by the development of miniature cells for watches, has resulted in a more reliable long-term

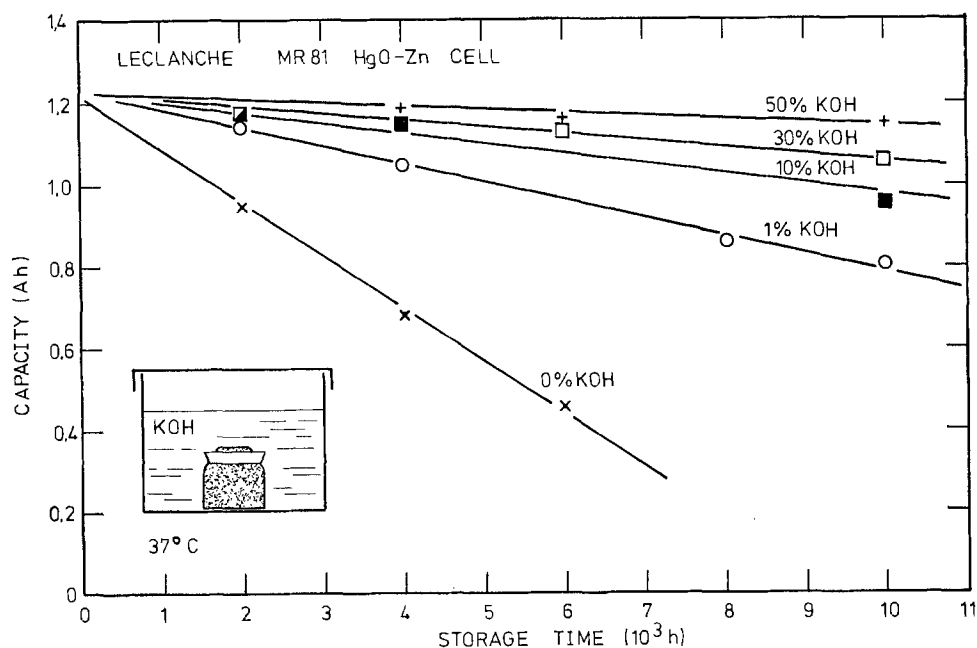


Fig. 11. Self-discharge of MR 81 cells submerged in KOH solutions of different concentrations at 37°C. Each point average of 5 cells [from Ref. (9)].

seal, based on the resiliency of the cover material (29).

Factors affecting the creepage of alkaline electrolytes along metallic parts have been the subject of several recent investigations (30-32). The presence of moisture and oxygen accelerate creepage and must thus be excluded from the cells as much as possible. Electrolyte concentration and viscosity, the nature of the metallic surface and the electric potential applied thereto are other factors affecting creepage rate.

The seal of MR 81 HgO-Zn medical grade cells, as shown in Fig. 2, is constructed in a manner such as to take into account these parameters.

Separators for long-life cells.—Separator degradation has in the past been of concern as a life limiting factor. A recent investigation (9) has shown, however, that cellophane separators become extremely stable against hydrolysis and oxidation when highly concentrated alkaline electrolytes are used. (See below under "Water-starved Cells.")

In addition to cellophane, radiation-grafted and cross-linked methacrylic acid polyethylene (33, 34) and Teflon-based separators (35) are available which show very good stability in highly concentrated alkaline solutions. The results of Fig. 9 indicate that no deterioration of (cellophane) separators leading to accelerated self-discharge, is taking place in MR 81 cells even after prolonged storage at elevated temperatures.

In MR 81 cells the multilayer cellophane separator package is protected against the positive electrode by a nonwoven polypropylene fabric. The separators are tightly clamped at the edge between supporting steel ring and grommet (Fig. 12), which assures that no internal short circuit can occur.

The relative importance of the cell-external self-discharge processes as measured under the extreme

conditions shown in Fig. 10 and 11, are compared to cell-internal self-discharge in Fig. 13.

Importance of cell packaging.—In spite of the fact that external self-discharge processes appear to be of little importance in properly engineered pacemakers, many failures have occurred in the past precisely because of cell-external electrochemical phenomena, in particular electrochemical corrosion processes occurring in moisture films. It is interesting to note that not the cells themselves, but primarily electronic components in proximity thereto, had to suffer from such electrochemical corrosion processes.

In some early pacemaker designs thin liquid films, present between epoxy encapsulation and cell components, became exposed to excessive voltage gradients. Corrosion processes then would occur in these films, causing destruction of electronic components, or producing shorts (current interruptions).

Figure 14 shows a pacemaker (Vitatron) in which the print plate touched three mercury cells in series. Moisture films present on the print plate were ex-

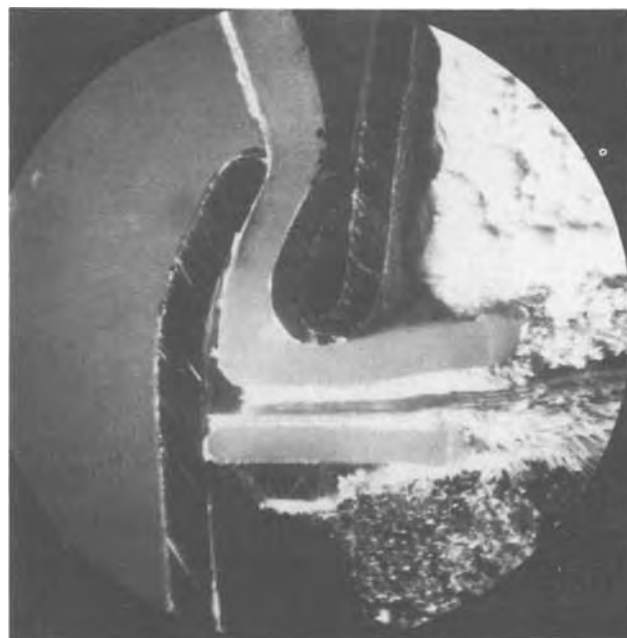


Fig. 12. Separator arrangement in MR 81 cells

Table VII. External oxygen cycle on MR 81 HgO-Zn cells at 37°C

Surrounding KOH concentration (%)	"Oxygen cycle" self-discharge (%/yr)
1	29
10	15.5
30	9.8
50	3.4

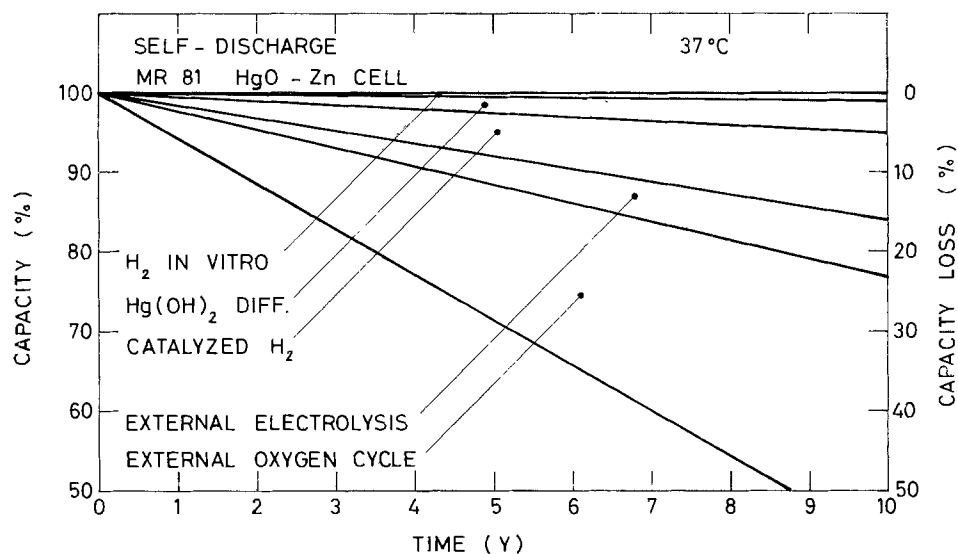


Fig. 13. Relative importance of cell-internal and cell-external self-discharge processes.

posed to high voltage (4.6V), causing severe corrosion of electronic components. The fact that this phenomenon occurred only in pacemakers exposed to high humidity (implanted or water-bath tested units) makes it likely that the moisture film stemmed from body fluid. Had the cells been separated from the print plate, early failures due to corrosion would not have occurred. It is unfortunate that in this instance the mercury cells were made the scapegoat for the failure, rather than packaging design.

Another corrosion phenomena, known under the name of "dendrite formation" also occurs as the result of moisture films creeping along electronic circuit parts and voltage drops occurring therein. An electrostatic field present in the film provokes anodic dissolution at the positively polarized part, and cathodic deposition of metal at the negatively polarized part of the interface. A critical area, where this can occur, is for instance at the lead exit.

An important observation concerning corrosion in thin water films on electronic components was made recently by Koelmans and Kretschman (36). These authors found that, in the presence of sodium ions at impurity levels, concentrated sodium hydroxide would form at the negatively polarized portion of the film, causing heavy corrosion. This proved for the first time very clearly that alkalinity in the moisture film does not need to stem from the cells, but could form *in situ* by electrolysis.

These examples show that the electronic circuit must be protected as much as possible against water

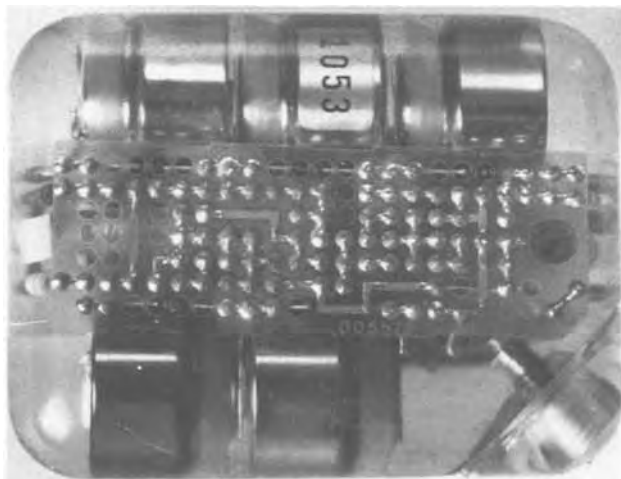


Fig. 14. Pacemaker package with epoxy-encapsulated print-plate touching three (plus 2) MR 81 cells in series.

intrusion. Hermetically sealed packaging of the circuit is thus a necessity. Moisture does more harm to electronic parts than it does to electrochemical cells. It should be mentioned in this connection that the good start lithium batteries have been able to make in pacemaker application was probably aided by the fact that the pacemakers were hermetically sealed and their electronic circuits better protected against moisture effects.

Also mercuric oxide-zinc batteries could be hermetically encapsulated, as shown in the experimental model of Fig. 15. For safety reasons, the hermetic enclosure should also contain a hydrogen absorber capsule, along with the cells. The hydrogen absorber can consist for instance of silver oxide (37) or manganese dioxide (38).

Newest Innovations in Mercuric Oxide-Zinc Batteries for Long-Term Use

Cells with "filter electrodes."—Under the term "filter electrode" is understood a porous, electronically conducting layer placed on top of the positive electrode surface in contact with the separator layers (9). The filter electrode may, for instance, consist of a bed of graphite particles or of a sintered nickel matrix. Filter electrodes should have a thickness of at least 0.1 mm and should have a high tortuosity factor.

The purpose of the "filter electrode" is to decrease $\text{Hg}(\text{OH})_2$ diffusion to the negative electrode by prolonging the diffusion path. The electronically conducting material in the filter electrode should be chemically inert and corrosion resistant in alkaline electrolytes at the potential of the positive electrode. It has been found to be of advantage to incorporate into the filter electrode finely divided substances of

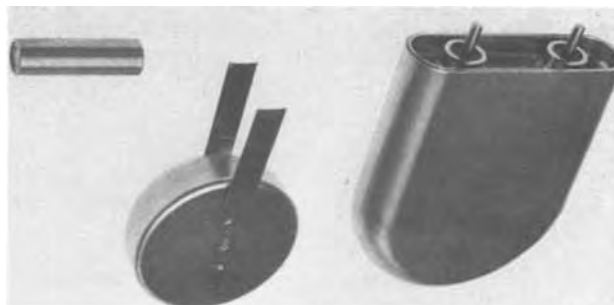


Fig. 15. Hermetically double-sealed HgO-Zn cell with glass feed-throughs. The cell package contains a round button cell and a small cylindrical H₂ absorber.

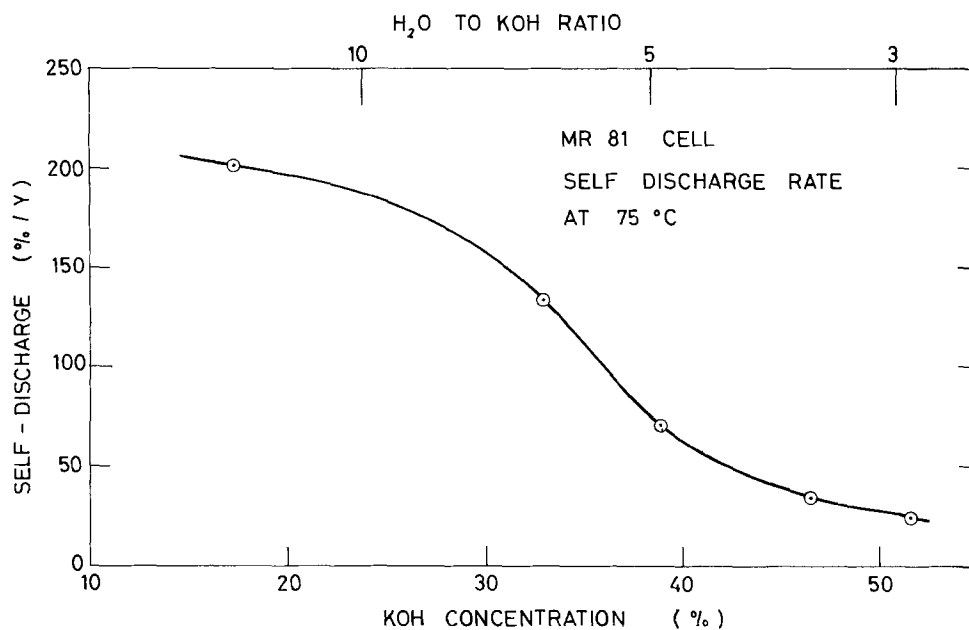


Fig. 16. Self-discharge of MR 81 HgO-Zn cells as a function of cell electrolyte concentration. Each point average of 50 cells.

high surface area which are insoluble in alkaline electrolytes. One substance of this type which has been found to be effective is, for instance, manganese dioxide. In addition, the filter electrode may contain inert binders and thickening agents for the alkaline electrolyte.

In spite of the fact that in MR 81 cells the dominant cell-internal self-discharge process is apparently due to H_2 evolution (Fig. 12), filter electrodes have been found to have a noticeable effect in reducing self-discharge (9). The reason for this could be, that not only the self-discharge loss by $Hg(OH)_2$ diffusion, but also "catalyzed H_2 evolution" (due to "impurities" or "local action cells") is decreased in presence of a filter electrode.

Diffusion of $Hg(OH)_2$ probably leads to localized discharge of the Zn electrode, just as partial high-rate discharge does. It is known that under such conditions hydrogen evolution (17) and associated self-discharge (39) is increased.

"Water-starved" cells.—With increasing NaOH or KOH concentration more and more water is tightly held in the inner ionic hydration shells. Once a molar ratio of water to alkali hydroxide of about 3 is reached, all the water molecules are bonded directly to the solute (40). Concentrated electrolytes have a very low water vapor pressure (41), which is of advantage when it comes to reducing the humidity level in a package containing also electronic components.

Solubility of HgO does not decrease as strongly with increasing electrolyte concentration as one would expect for completely nonionic solutes, such as H_2 (42), or O_2 (28), where the salting-out effect is very pronounced. Due to increased viscosity and decreased swelling of the cellophane or Permion barrier membranes, less $Hg(OH)_2$ will, nevertheless, diffuse to the Zn electrode at high electrolyte concentration.

Experimentally, one finds that self-discharge of HgO-Zn cells decreases drastically with increasing KOH concentration (Fig. 16). This decrease cannot be explained solely by a decrease in $Hg(OH)_2$ diffusion. Rather, at very high electrolyte concentration "catalytic H_2 evolution" on the zinc electrode must also be decreased. One of the reasons why the self-discharge of RM 1 cells is higher than that of MR 81 cells must also be the more dilute electrolyte used in the former. Capacity of RM 1 cells begins to decrease for discharge times greater than 10^4 hr (42).

"Catalytic hydrogen evolution" is apparently occurring when Zn electrodes are being locally and nonuniformly discharged by the reaction $Zn +$

$Hg(OH)_2 \rightarrow ZnO + Hg + H_2O$ leading to a local dilution of the electrolyte. This then results in $H_2O + Zn \rightarrow ZnO + H_2$. At high electrolyte concentration this reaction mechanism is suppressed.

In order to take full advantage of the principle of a "water-starved" cell, separators, positive electrode, and grommet must be dried prior to cell assembly in order to avoid possible dilution of the electrolyte with water contained in these components.

"Water-starved" cells have a somewhat higher internal impedance than standard cells. For "water-starved" MR 81 cells internal resistance at $37^\circ C$ was found to be about 20Ω . It should be remembered, however, that "water-starved" cells cannot be utilized at low temperatures, because of the high freezing point of the electrolyte.

"Punctured membrane" current focusing.—Another approach to reduce diffusion of mercuric oxide is depicted in Fig. 17. A very thin, inert membrane is tightly clamped at the edge, between grommet and support, but contains centrally one or more mechanically produced pinholes of controlled diameter. All the ionic current flow is focused across the pinholes.

At first sight it appears that such an extreme compartmentalization would drastically increase internal resistance of a cell.

However, when using an ultrathin "punctured membrane" this is not the case. For a membrane thickness of $l = 0.005$ cm, a pinhole diameter of $r_1 = 0.01$ cm, and a specific electrolyte resistance of $\rho = 2 \Omega\text{-cm}$, one calculates, for instance, a pinhole electrolyte resistance of

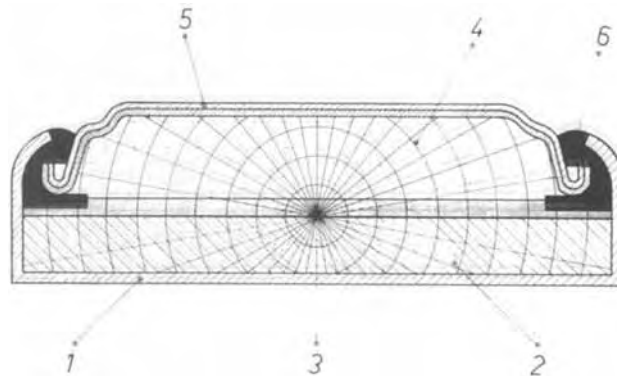


Fig. 17. Schematic illustration of current distribution in a cell with "punctured membrane."

$$R_1 = \frac{\rho \cdot l}{\pi r_1^2} = 32\Omega$$

Electrolyte resistance outside the pinhole may be estimated at

$$R_e = \rho \int_{r_e=0.01}^{r_e=\infty} \frac{d(r_e)}{4\pi r_e^2} = 16\Omega$$

Thus, total electrolyte resistance associated with the use of the "punctured membrane" would still be below 50 Ω .

"Mechanically punctured membranes" are reproducible means to prolong the average length of the diffusion path of dissolved $\text{Hg}(\text{OH})_2$. On the other hand, reproducible manufacture of microporous membranes of very low porosity are technologically much more difficult to achieve. Mercuric oxide diffusion measured experimentally in cells having membranes with mechanically punctured holes of different diameters are shown in Fig. 18. These results were obtained with HgO -Cd cells, containing Permion 2291 40/60 separators in addition to the punctured membrane. Increase of mercury content of the Cd anode during storage at 75°C was determined by atomic absorption. The results are expressed in terms of anode capacity loss per year (mA-hr/yr). Capacity loss is not exactly proportional to diffusion surface probably because of edge effects (spherical diffusion).

Obviously, capacity loss through $\text{Hg}(\text{OH})_2$ diffusion is greatly minimized in presence of a "punctured membrane."

Other Aqueous Alkaline Electrolyte Systems for Biomedical Implantable Applications

Primary batteries.—Mercuric oxide-cadmium primary batteries have been of interest for some time as ultrastable power sources for long-term military applications, because of their capability to perform well at low temperature even after prolonged hot storage.

Cadmium electrodes are entirely stable in alkaline electrolytes and do not evolve hydrogen. This is of importance when it comes to storage of cells at very high temperatures. On the other hand, at low temperatures and for cell designs with a large separator interface between positive and negative electrode, self-discharge of HgO -Zn and HgO -Cd cells become rather similar.

That diffusion of dissolved $\text{Hg}(\text{OH})_2$ is the only self-discharge process of importance in HgO -Cd cells is demonstrated in Fig. 19. Capacity loss as determined from mercury analysis of the anode, and as determined from discharge tests after storage, agree within the experimental error limits.

Boden (44) and Weiss and Pearlman (19) report for HgO -Cd cells at 21.1°C (70°F) a self-discharge rate of 1.3%/yr. Klein and Eisenberg (45) give for

Fig. 18. Capacity loss (mA-hr/yr) due to $\text{Hg}(\text{OH})_2$ diffusion at 75°C, as measured experimentally with HgO -Cd cells by Hg analysis of the anode, as a function of diffusion surface. Each point average of min. 5 determination.

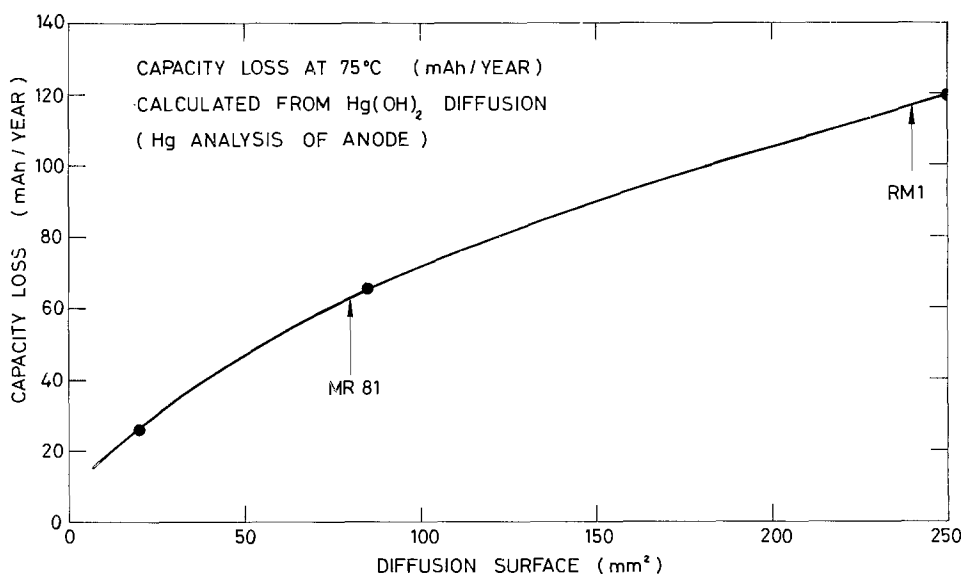
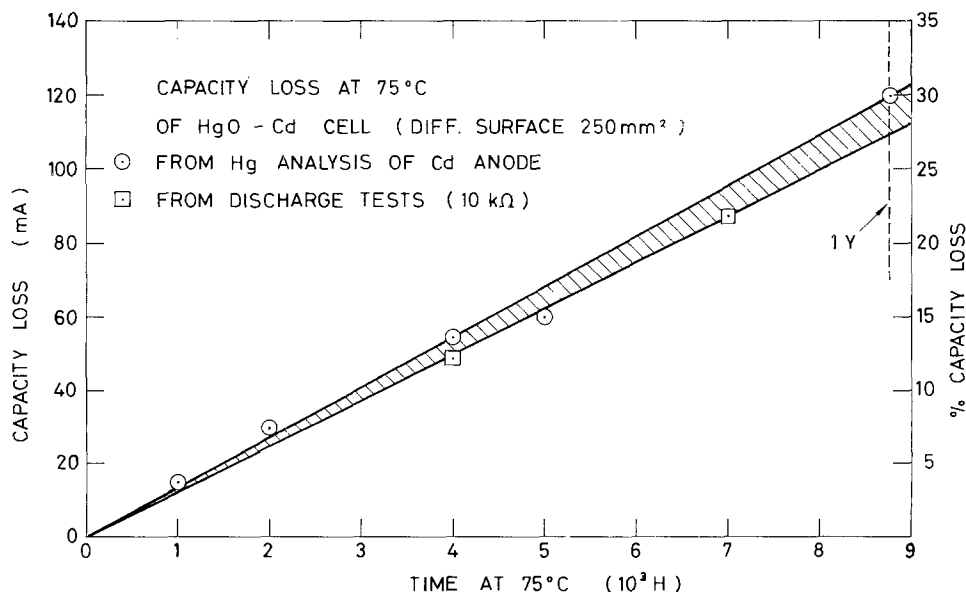


Fig. 19. Self-discharge of HgO -Cd cells (initial cell capacity 400 mA-hr) at 75°C. Each point average of 5 cells.



74°C (165°F) a figure of 21%/yr. Self-discharge depends strongly on design (interelectrode area) and could be kept extremely small for cells requiring only low discharge rates.

Performance data of HgO-Zn and HgO-Cd cells are compared in Table VIII. The lower self-discharge rate of HgO-Cd cells does not offset the advantage of the higher initial energy density for the HgO-Zn cells, when it comes to long-term use at 37°C.

Silver oxide-zinc and manganese-dioxide zinc cells, optimized for long-term use at 37°C, would have similar self-discharge rates as HgO-Zn cells. Their volumetric energy density would, however, be inferior.

Silver oxide-cadmium and manganese dioxide-cadmium cells would have very low self-discharge rates, but again much smaller energy densities. One argument in favor of these cells could be that their safety is higher since no internal or external electrolysis is possible.

Rechargeable cells.—Nickel-cadmium secondary batteries have made their appearance in implantable devices for some time (46). In recent years, the space programs have spurred technical progress in nickel-cadmium batteries.

The nickel-cadmium battery used in the Johns Hopkins Pacemaker resembles a standard 225 mA-hr button cell (diameter 25 mm, height 8.6 mm). Deliverable capacity at the 6 hr rate was 280 mA-hr (3). Self-discharge was found to be 50 mA-hr/week at 37°C (3). Normally, the battery would be recharged 1 hr a week (4). The capacity of the battery is potentially sufficient to operate the pacemaker approximately 8 weeks. It is hoped that it will be possible to develop the system further and that, eventually, it will be possible to charge the cells at less frequent intervals (47). By the end of 1977, about 3100 "Pacemaker" units had been implanted (48, 49).

One problem, which must be given careful consideration when using nickel-cadmium batteries in a mode, involving relatively quick charge and subsequent slow discharge at 37°C, is growth of large Cd and Cd(OH)₂ crystallites (Fig. 20) and resulting charge and discharge inefficiency. Cd(OH)₂ crystallites can also grow into the separator, causing short-circuit failures (50-55).

It has been suggested that a Teflon treatment could retard migration. Pressed-powder type cadmium electrodes appear to resist the described crystallization phenomena somewhat better than sintered electrodes. Many additives have been studied to decrease crystal growth, without entire success, however.

The so-called "memory effect" in nickel-cadmium batteries is also a phenomenon related to the negative electrode. With repetitive partial discharge cycling, the same portion of the electrode keeps being called to work all the time while the rest of the (active)Cd becomes slowly insulated by resistive Cd(OH)₂ layers. These latter can only be broken down again by deep-discharge cycling with heavy overcharge. The relatively shallow cycling, at relatively high temperature, present in pacemaker application, would be ideally suited for causing a strong "memory effect" which could reduce reserve capacity to an unacceptably low level. It appears that more progress is needed in this area to improve long-term

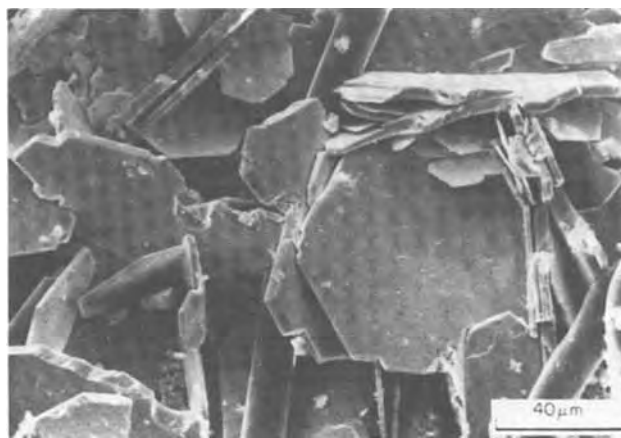


Fig. 20. Surface of a cadmium electrode in a Ni-Cd battery after aging for 5 years at 20°C [from Ref. (53)].

use of nickel-cadmium cells in a rechargeable pacemaker.

Rechargeable nickel-cadmium batteries will thus have to fight a long uphill battle if large-scale use should ever become a reality.

Rechargeable mercuric oxide-zinc batteries (56) would have the advantage of very low self-discharge. This would hopefully necessitate recharge only once every few years. However, zinc electrodes are, after deep discharge, notoriously difficult to recharge. It also appears with this system that considerable technological advance is still needed. Present resistance to the use of rechargeable battery systems could possibly be overcome some day if recharge were carried out at the hospital, and not by the patient, at intervals of several years.

Summary

Self-discharge of alkaline primary HgO-Zn batteries is reduced to 1-2 %/yr at 37°C, when using an appropriate design. It appears that operating life spans of 10 years at 37°C are possible, with total cell-internal self-discharge of less than 20%. Cell-external self-discharge by electrolysis and oxygen cycle must be avoided by careful, hermetic packaging.

Acknowledgments

Permission from Academic Press to reproduce Figures 2, 10, 11, and 20 is gratefully acknowledged.

Manuscript submitted Oct. 5, 1979; revised manuscript received Jan. 28, 1980. This was Paper 66 presented at the Los Angeles, California, Meeting of the Society, Oct. 14-19, 1979.

Any discussion of this paper will appear in a Discussion Section to be published in the June 1981 JOURNAL. All discussions for the June 1981 Discussion Section should be submitted by Feb. 1, 1981.

Publication costs of this article were assisted by Leclanche S.A.

REFERENCES

1. K. Fester, R. L. Doty, and R. J. Vander Velden, Abstract 9, p. 26, The Electrochemical Society Extended Abstracts, Vol. 74-2, New York, N.Y., Oct. 13-17, 1974.
2. W. G. Howard, E. O. Jurva, and K. Fester, Abstract 60, p. 159, The Electrochemical Society Extended Abstracts, Vol. 76-2, Las Vegas, Nev., Oct. 17-22, 1976.
3. K. Fester, R. L. Doty, and R. Vander Velden, 16th Annual American Society of Mechanical Engineers Symposium on Energy Alternatives, Albuquerque, New Mexico, Feb. 1976.
4. V. Parsonnet, *Am. Heart J.*, **94**, 517 (1977); *Chest*, **61**, (Feb. 1972).
5. S. Ruben, *Ann. N.Y. Acad. Sci.*, **000**, 627 (1969).
6. S. J. Angelovich and T. C. O'Nan, in Proceedings of the Pacemaker Colloquium, J. Normann

Table VIII. Comparison of HgO-Zn and HgO-Cd long-life batteries

Property	HgO-Zn	HgO-Cd
Discharge voltage (V)	1.35	0.90
A-hr/cm ³	0.4	0.2
W-hr/cm ³	0.55	0.18
Self-discharge (37°C)		
%/yr	2	0.2
Available energy during 10 years (W-hr/cm ³)	0.440	0.176

- and A. Rickards, Editors, p. 91, Tamminga b.v., Arnhem (1975).
7. K. A. Gasper and K. Fester, in Proc. Intersociety Energy Conversion Engineering Conf., pp. 1205-1213, Newark (1975).
 8. R. Goldson, *Med. Electr. Data*, pp. 60-63 (May-June, 1974).
 9. P. Ruetschi, in Proceedings of 11th International Power Sources Symposium, J. Thompson, Editor, p. 533, Academic Press, London (1979).
 10. H. Cataldi, 10th AAMI Meeting, Boston, Mass. (1975).
 11. H. Cataldi, in Proceedings of the 27th Power Sources Symposium, p. 138, Atlantic City (1976).
 12. A. B. Garrett and A. E. Hirschler, *J. Am. Chem. Soc.*, **60**, 299 (1938).
 13. G. Fuseya, *ibid.*, **42**, 368 (1920).
 14. K. Schick, *Z. Phys. Chem.*, **42**, 155 (1903).
 15. R. A. Griffin, Abstract 10, p. 29, The Electrochemical Society Extended Abstracts, Vol. 74-2, New York, N.Y., Oct. 13-17, 1974.
 16. F. J. Przybyla, G. R. Ramsay, and J. Scandariato, Proceedings of the 26th Power Sources Symposium, p. 166, Atlantic City (1974).
 17. P. Ruetschi, in Proceedings of the 8th International Power Sources Symposium, D. Collins, Editor, p. 381, Oriel Press, Newcastle-upon-Tyne (1973).
 18. W. L. King, U.S. Pat. 3,970,479 (1976).
 19. D. Weiss and E. Pearlman, Abstract 11, p. 31, The Electrochemical Society Extended Abstracts, Vol. 74-2, New York, N.Y., Oct. 13-17, 1974.
 20. E. J. Prosen and J. C. Colbert, *Nat. Bur. Stand. U.S. Spec. Publ.*, **400-42** (August 1977).
 21. L. D. Hansen and R. M. Hart, *This Journal*, **125**, 842 (1978).
 22. D. F. Untereker, *ibid.*, **125**, 1907 (1978).
 23. P. Ruetschi, *ibid.*, **123**, 495 (1976).
 24. P. Schindler, in "Advances in Chemistry," No. 67, p. 196, American Chemical Society (1967).
 25. G. G. Wickham and T. B. Cartmill, *Med. J. Aust.*, **2**, 138 (1971).
 26. H. J. Th. Thalen, "The Artificial Cardiac Pacemaker," pp. 232-235, Royal Van Gorcum Publishers (1969).
 27. K. Fester and R. L. Doty, 8th Annual AAMI Meeting, Washington, D.C., March 1973.
 28. R. E. Davis, G. L. Horvath, and C. W. Tobias, *Electrochim. Acta*, **12**, 287 (1967).
 29. P. Ruetschi, U.S. Pat. 3,657,018 (1972).
 30. M. N. Hull and H. I. James, *This Journal*, **124**, 332 (1977).
 31. L. M. Baugh, J. A. Cook, and J. A. Lee, *J. Appl. Electrochem.*, **8**, 253 (1978).
 32. J. M. Davis and M. N. Hull, *This Journal*, **125**, 1918 (1978).
 33. V. D'Agostino, J. Lee, and G. Orban, in "Zinc-Silver Oxide Batteries," A. Fleischer and J. J. Lander, Editors, pp. 271-281, Wiley and Sons, New York (1971).
 34. V. D'Agostino, J. Lee, and R. Coyle, in Proceedings of the 27th Annual Power Sources Conference, p. 87, Atlantic City (1976).
 35. J. Lee, V. D'Agostino, J. Santisi, and C. Perini, Abstract 47, p. 130, The Electrochemical Society Extended Abstracts, Vol. 78-2, Pittsburgh, Pa., Oct. 15-20, 1978.
 36. H. Koelmans and H. J. Kretschman, *This Journal*, **125**, 1715 (1978).
 37. P. Ruetschi, in "Zinc-Silver Oxide Batteries," p. 117, A. Fleischer and J. J. Lander, Editors, p. 117, John Wiley and Sons, New York (1971).
 38. C. S. Brooks, *J. Catal.*, **4**, 535 (1965).
 39. J. J. Lander, Abstract 26, p. 68, The Electrochemical Society Extended Abstracts, Vol. 73-2, Boston, Mass., Oct. 7-11, 1973.
 40. G. Yagil and M. Anbar, *J. Am. Chem. Soc.*, **85**, 2376 (1963).
 41. P. Bro and H. Y. Kang, *This Journal*, **118**, 1430 (1971).
 42. H. Matschiner, K. B. Otte, S. Rudolf, and K. Wiesener, *J. Power Sources*, **3**, 359 (1978).
 43. P. Ruetschi and R. F. Amlie, *J. Phys. Chem.*, **70**, 718 (1966).
 44. D. P. Boden, "Proceedings of the Intersociety Energy Conversion Engineering Conference," p. 529 (1971).
 45. M. G. Klein and M. Eisenberg, *Electrochem. Technol.*, **3**, 58 (1965).
 46. J. Love, K. Lewis, and R. Fischell, *JAMA*, **234**, 64 (1975).
 47. Pacesetters Systems Inc., Manufacturer's Report, 1976.
 48. S. H. Stertzer, N. P. De Pasquale, M. Bruno, and L. I. Cohn, *J. Electrocardiol.*, **9**, 391 (1976).
 49. R. Lev, J. Lev, P. Niemeyer, A. Rubinsky, and F. Lev, 5th International Symposium on Cardiac Pacing, Tokyo, 1976.
 50. J. P. Harivel, B. Morignat, and J. Migeon, in Proceedings of the 4th International Power Sources Symposium, D. H. Collins, Editor, p. 107, Pergamon Press, Elmsford, N.Y. (1964).
 51. P. Bro and H. V. Kang, *This Journal*, **118**, 519 (1971).
 52. R. Barnard, J. A. Lee, A. H. Rafinski, and F. L. Tye, in Proceedings of the 9th International Power Sources Symposium, D. H. Collins, Editors, p. 183, Academic Press, New York (1975).
 53. R. W. Bramham, R. J. Doran, S. E. A. Pomroy, and J. Thompson, Proceedings of the 10th International Power Sources Symposium, D. H. Collins, Editor, p. 129, Academic Press, New York (1976).
 54. D. F. Pickett, J. J. Lander, I. F. Luke, J. W. Logsdon, and U. D. Martin, Abstract 10, p. 36, The Electrochemical Society Extended Abstracts, Vol. 78-2, Pittsburgh, Pa., Oct. 15-20, 1978.
 55. R. Barnard, G. S. Edwards, and F. L. Tye, *J. Power Sources*, **3**, 175 (1978).
 56. G. W. O. Tyers, H. C. Hughes, R. Brownslee, N. J. Manley, and I. N. Gorman, *Am. J. Cardiol.*, **38**, 607 (1976).

Lead-Acid Battery Expander

I. Electrochemical Evaluation Techniques

B. K. Mahato*

Globe-Union Incorporated, Milwaukee, Wisconsin 53201

ABSTRACT

The role of lignosulfonate constituent of the lead-acid battery expander on the negative electrode performance is analyzed. Two quantitative electrochemical techniques have been developed to monitor the expander activities on constant current discharge and capacity maintenance behavior of the electrode during cycling. Both these techniques are based on small electrodes and proved effective in evaluating expander candidate materials outside the test battery. Test results agree closely with the reported expander's influence on the pasted electrode. The plausible mechanisms of expander action during high rate discharge and deep discharge cycling are elucidated.

The lead-acid battery is presently being considered for the near term electric vehicle application. Its future dominance in the EV market in relation to the newly developing high energy systems such as Ni-Zn, Na/S, Li-Al/FeS₂, and Zn/Cl₂ will depend upon significant performance improvement while maintaining a relatively low cost per kilowatt hour. An effort is underway to improve energy density of the lead-acid battery by optimization of structural parameters and improved faradaic efficiency of the active materials (1). Under deep discharge cyclic operation the cycle life of this system is largely controlled by the active material shedding and the grid corrosion of the positive electrode (2, 3). However the lead or negative electrode represents a potentially significant area for improvement in specific energy of the system due to its relative small decline in capacity with cycling and underutilized active mass.

The material utilization of the lead electrode which has to date been greatly influenced by the expander incorporated in the paste during electrode preparation (2-16) has remained close to 40% at the 3 hr rate (1). This leaves behind 60% unutilized mass of this electrode to account for, at least partly, the low energy density of the lead-acid system. Any reduction of this nonutilized (or underutilized) mass without a loss in existing performance requires a proportionate increase in the effective surface area of the electroactive mass. The inclusion of expander in the paste is noted to increase the active mass surface area from 0.23 m²/g to 0.50 m²/g (7). This suggests that an additional increase in the active material surface area and its material utilization is possible by improving the quality of expander material.

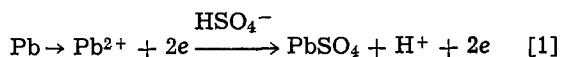
The conventional expander is a mixture of a lignin compound, barium sulfate, and carbon black (2, 3). Out of these the lignin compound brings out the most beneficial influence (or expander action) to the lead active mass by altering its structure during formation (4-6) and by suppressing the growth of large lead crystals during repeated charge/discharge cycling (7); the barium sulfate and carbon black have very limited and sometimes questionable influence on the electrode characteristics (4-6). Thus the improvement in expander quality relies heavily on obtaining an improved lignin compound. The word "expander" is used here (as elsewhere in the paper) to mean the lignin constituent of the expander.

A significant difficulty exists in improving the quality of the expander. This is primarily due to its ill-defined chemical nature, lack of analytical means in monitoring its concentration, and our limited knowledge of the expander action, i.e., how the presence of

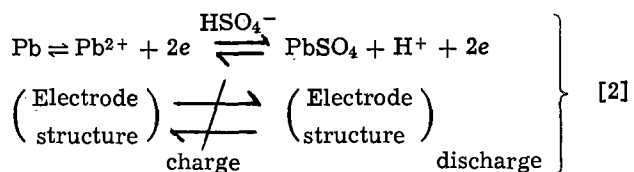
expander modifies the electrode performance. To date the expander evaluation has been attempted by measuring its influence on the overall electrochemical performance of a pasted plate or the battery (4-13, 15, 16). These test results being influenced by the electrode preparation parameters have rendered very limited understanding of the expander action. It is therefore suggested that a mechanistic understanding of the expander action and means of quantitative measurement of expander activity be developed to aid in the selective evaluation of expander candidates. The objective of this work has been to define expander activity and develop techniques for quantitative determination of expander type and concentration.

Mechanism of Expander Action

The negative electrode of a lead-acid battery consists of a high surface area reactive lead mass and is characterized by its material utilization during discharge (Eq. [1]) and the maintenance of the electrode structure or the capacity during repeated charge/discharge cycling (Eq. [2])



(PbSO₄ deposits on lead surface)



The discharge process of the lead electrode in sulfuric acid solution is controlled by the formation of a lead sulfate passivating layer on the electrode surface (2, 3, 17-19). During repeated charge/discharge cycling the lead electrode active mass, i.e., the high surface area lead particles, experiences a tendency to coalesce and thereby lose its specific surface area. This in turn reduces cycling ability of the electrode. Presence of expander in the system influences both the discharge behavior (Eq. [1]) as well as the capacity maintenance behavior of the electrode during cycling (Eq. [2]). No significant difference in electrode performance was observed with the mode of inclusion of expander in the system (9). The mechanistic understanding of expander action on the electrode performance has to date remained highly speculative.

The conventional expander is a lignosulfonate, a naturally occurring polymer with ill-defined structure (20). Its molecular weight varies from a few hundreds to several thousands. It is anionic and has surfactant properties (21). It adsorbs on solids (lead

* Electrochemical Society Active Member.

Key words: lead electrode, voltammetry, additive.

and lead sulfate) (22, 23) and has decreased solubility with increasing acid concentration (7). A reasonable understanding of the expander action is anticipated from a greater understanding of the expander material and its influence on the basic electrode kinetics (Eq. [1] and [2]).

Expander action on discharge.—The discharge process of the lead electrode as represented by Eq. [1] involves the dissolution of lead metal to Pb^{2+} ion controlled by the gradual coverage of the electroactive surface by resistive lead sulfate film. The anodic passivation of the lead electrode by the formation of a permselective lead sulfate membrane which limits the transport of reacting species and changes the interfacial pH has been discussed by Pavlov (17), Ruetschi (18), and Winsel *et al.* (19). The kinetics of this passivation process, *i.e.*, the dissolution process ($Pb \rightarrow Pb^{2+} + 2e$) as well as the lead sulfate precipitation (resistive film formation) process are affected by the presence of the expander, either in the electrode matrix or in the surrounding electrolyte.

The expander adsorbs on lead (22) as well as on lead sulfate (23). During anodic dissolution, besides the concentration of dissolved species, the pH of the interfacial layer increases (17, 18). This brings the adsorbed expander into solution, promotes the formation of $Pb(II)$ or "lead-lignin" complex intermediate, and possibly alters the saturation concentration of Pb^{2+} ion at the interface. The adsorption of the expander on the freshly precipitated lead sulfate affects the particle size and the ion permeability of the product layer. The decomposition of transient $Pb(II)$ intermediate upon the termination of discharge and acid diffusion provides a mechanism of formation of a compact lead sulfate layer as well as occlusion of the expander in the discharge product matrix. The presence of a labile quinoid structure in the expander molecule (24) also indicates a possibility that it might act as an electron transfer medium when adsorbed in the lead sulfate matrix. All the above-mentioned effects of the expander on the oxidation behavior of the lead electrode result in an increased intensity of discharge or the longer constant current discharge period. The delayed passivation of the lead electrode in the presence of the expander has been reported (2, 3, 5, 7, 9-13, 15, 16) and explained in terms of the expanders contribution in decreasing the resistivity of the lead sulfate layer (10), in altering the morphology of the passivating discharge product matrix (5, 6, 10-12, 15, 16), in commencing the solid-phase reaction between the Pb and SO_4^{2-} or HSO_4^- anions under the influence of anodic potential (7, 12), and in the formation of $Pb(II)$ soluble intermediate (25).

Expander action on charge.—The charging or the cathodic reduction of the lead electrode involves the electroreduction of the lead sulfate to a metallic lead. The conventional reduction process occurs through the chemical dissolution of $PbSO_4$ to Pb^{2+} ions followed by the electroreduction of Pb^{2+} to a metallic lead. The observation of Popova and Kabanov (26) that the lead electrode has limiting current close to 2000 A/cm² in 3-5.5M H_2SO_4 solution suggests that the dissolution process may not be rate limiting. The electroreduction of lead is very efficient, particularly in a pure system, due to high hydrogen overpotential on lead. For the same reason, the cathodic reduction of the pasted-type lead electrode is known to progress from the external surface to the interior of the plate matrix (17).

The obvious disadvantages of the high electroreduction efficiency are the tendency of the highly energized, freshly deposited lead particles to coalesce forming a low surface area deposit and to cause incomplete conversion of lead sulfate particles to metallic lead by sheathing the lead sulfate particles with

impervious metallic lead (3). The latter is occasionally observed at high temperature formation and/or in a highly sulfated electrode (2).

The presence of the expander in the lead electrode matrix or in the surrounding electrolyte influences the overall electroreduction kinetics. This is caused by adsorptive surface coverage of lead sulfate and the lead deposition sites by expander molecules. The former controls the dissolution of $PbSO_4$, inhibits the complete sheathing of lead sulfate particles by electrodeposited lead, and helps the overall electroconversion efficiency. The latter, by blocking coverage of activation sites, prevents the sintering of the electrodeposited lead mass and helps to maintain or increase the surface area of the electrode after charging operation. Mahato (7) has noted that the expander present in the pasted lead electrode increases the specific surface area of the active mass and 150A, 0°F capacity after formation and hinders the agglomeration of the lead active mass during SAE-J240 type cycling. Expander in the paste has also been shown to alter the lead crystal structure after formation and to improve the cycle life behavior of the lead electrode (4-7).

Definition of Expander Activity and Evaluation Techniques

It has previously been noted that the expander influences both the discharge and the charge behavior of the lead electrode. During discharge it alters the morphology of the lead sulfate film and the interfacial electrode kinetics. During charge it restricts the lead adatom deposition sites and the lead sulfate dissolution process. Upon cycling the integral influence of expander on both discharge and charge will dominate the electrode behavior. Considering the complex functioning of the expander on the electrode performance an unambiguous definition of the expander activity which could truly reflect its influence on the electrode performance has been extremely difficult. However, as the intensity of discharge and the maintenance of the electrode structure are dominantly influenced by the expander, a quantitative estimation of expander effect is possible by determining its effect on the electrode performance, *i.e.*, the discharge behavior and the capacity maintenance characteristics during repeated charge/discharge cycling.

The dischargeability of a well-defined lead electrode under constant temperature and acid concentration can be expressed in terms of the effective capacity, K_o as shown in Eq. [3]

$$I t_o = K_o \quad [3]$$

Where I , t_o , and n are current density, duration of discharge, and an empirical constant, respectively. In the presence of the expander in the system the duration of discharge (t) and effective capacity (K) will change and the expander activity can be monitored by following the absolute value of K and its relative change as defined in Eq. [4]

$$\eta_{\text{disch}} = \left(\frac{K - K_o}{K_o} \right)_{T,C} \quad [4]$$

T and C being temperature and acid concentration, respectively. The η_{disch} can be termed as high rate index also.

Likewise the cycling ability or the cycle life index of the expander (η_{cycle}) can be defined as the relative capacity change of the electrode cycled in acid electrolyte with and without the expander as shown in Eq. [5]

$$\eta_{\text{cycle}} = \left(\frac{Q_f - Q_o}{Q_o} \right)_{T,C,S,\phi,m} \quad [5]$$

where Q_o is initial electrode capacity, Q_f is electrode capacity at m th cycle, C is electrolyte concentration,

S is concentration of expander in the electrolyte, T is temperature, and ϕ is mode of cycling.

The precise determination of the expander activities (K , η_{disch} , η_{cycle}) primarily depends upon the reliability of the electrode preparation. The conventional pasted electrodes as used in the lead-acid battery has a high degree of uncertainty of being reproducible because of the complexities associated in its preparation. The expander activity evaluation by such pasted electrodes as used by Ritchie (8), Willhnganz (10), Pierson *et al.* (4, 5, 6), Mahato (7), Simon (9), Zachlin (11), and Gillibrand *et al.* (15, 16) has remained highly qualitative. These observations suggest that the precise expander activity determination must involve a well-defined electrode and should preferably be carried out outside the test battery. For simplicity we have selected small electrodes with surface areas close to 1.57 cm² for high rate index determination. For cycle life index determination we felt the need of having a geometrically well-defined porous high surface area electrode at the start. This we have achieved by cycling the well-defined lead electrode in low gravity sulfuric acid solution similar to "Plante-type electrode" preparation as will be outlined in the experimental section. To simulate the conditions which approximate the expander action in a practical battery operation the electrode potential range for anodic process of -960 to -500 mV (*vs.* Hg/Hg₂SO₄) was selected. For cyclic operation the potential range between 100 mV anodic and 200 mV cathodic overpotential was selected.

Experimental

The test electrodes were made out of 2-2.2 mm diam cast wire of 99.999% pure lead (Cominco). The electrode length was 2 cm made from a 4 cm long section of the cast wire by isolating remainder with a coating of hot wax followed by two layers of heat-shrinkable Teflon tubing. An electric connection was made to this end. A 1.27 cm diam cast rod was made from 99.999% pure lead and used as the counter-electrode. The electrodes were degreased by rubbing with acetone soaked tissue paper followed by chemical cleaning in glacial acetic acid/hydrogen peroxide mixture as outlined by Burbank (27). The test electrode, counterelectrode, and an Hg/Hg₂SO₄/"m" H₂SO₄ reference electrode were assembled in a test cell with 50 ml of "m" sulfuric acid electrolyte. The reference electrode was isolated from the bulk electrolyte by establishing a small crack at the capillary of the reference compartment through a soft glass bead melted in it. This was very effective in maintaining the electrolyte purity and the reliability of the reference potential. The sulfuric acid electrolyte was prepared from reagent grade sulfuric acid and deionized distilled water. The test expander was Reax 80C lignosulfonate obtained from Westvaco Incorporated, Charleston, South Carolina. This was prepared from Kraft lignin and had a wide molecular size distribution. The exact composition of this polymeric material was not known. Limited evaluation and information obtained from Westvaco suggested that it contains 11.4% Na, 33.7% ash, 2.9% organic sulfur, and 92% sodium sulfonated lignin.

A "Precision Current Source, Model CS-120, North Hill Electronics, Incorporated" with $\pm 0.1 \mu\text{A}$ precision was used to determine the constant current oxidation behavior of the lead electrode. The discharge time to -500 mV (*vs.* reference) was monitored by an electric timer and the half-cell potential was monitored by a Soltec recorder, Model VP-6232S in conjunction with a Keithley electrometer Model 616. The cycle life index determination was carried out by cycling a test electrode using a linear potential sweep cycling described elsewhere (28). The sweep was regulated by a function generator (PARTM 175/99) at 0.5 mV/sec between -1160 to -860 mV (*vs.*

reference). The current was supplied to the electrode by a PARTM 173 potentiostat equipped with a Model 179 digital coulometer. During cycling, the peak cathodic current, peak anodic current, cathodic charge, and anodic charge were monitored by interfacing the Model 179 digital coulometer output to a PDP-11 data acquisition system (Digital Equipment Corporation) through a KIM-I microprocessor. The PDP-11 was also interfaced with the Honeywell 66/40 and a "graphic display system" for graphic print out. The duration of the experiment for cycle life index determination was four days involving approximately 290 cycles. Initially the electrode was cycled in 1.050 sp gr H₂SO₄ for 2 days (~145 cycles), in order to prepare a porous electrode. This was followed by cycling the electrode in test solution, acid electrolyte with or without the expander, for 145 cycles. The current and electrode potentials were also monitored by an Esterline Angus Model L1102S two channel recorder. The voltammograms during cycling were recorded by a Hewlett Packard/Moseley Autograph Model 7000AM X-Y recorder.

Results and Discussion

The effect of lignosulfonate expander in sulfuric acid solution on the constant current discharge profile of a lead electrode is shown in Fig. 1. It is in every respect similar to the constant current discharge profile of the pasted electrode (7, 10, 15, 16) and substantiates the fact that barium sulfate and carbon black present in the conventional expander contributes very little on the discharge behavior of the lead electrode. Nonetheless, the long term stabilizing effect of barium sulfate and/or carbon black on the lead electrode, particularly in the industrial-type cell which uses an appreciable amount of barium sulfate and a small amount of expander may be significant but has not been thoroughly investigated. The presence of the expander in the system has caused higher polarization at the start, but a greater depth of discharge. The latter is noted from the longer discharge time. The adsorption of expander on the lead electrode surface is responsible for higher electrode polarization (22). The delay in the passivation process in the presence of expander is associated in part with its ability to modify the morphology and resistivity of the discharge product layer and in part to its influence on the interfacial electrode kinetics.

Figure 2 exemplifies the influence of expander on the morphology or the particle size of the lead sulfate layer. The lead sulfate particle size is significantly smaller in presence of expander than that obtained in

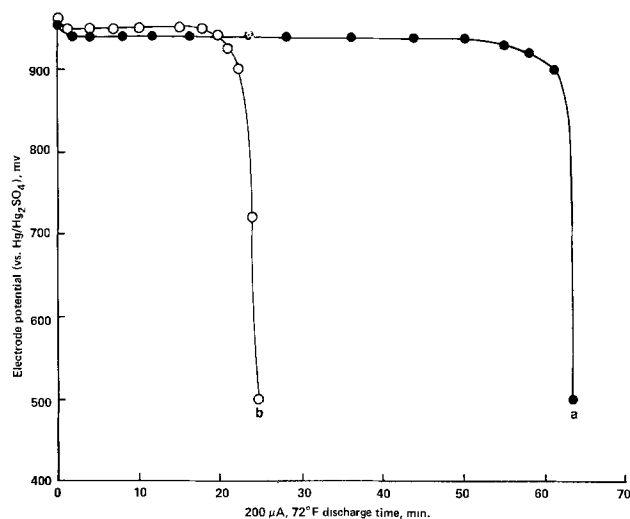


Fig. 1. Discharge characteristics of a lead microelectrode in 1.250 sp gr H₂SO₄ with (a) and without 10 ppm Reax 80C lignosulfonate (b) at 200 μA .

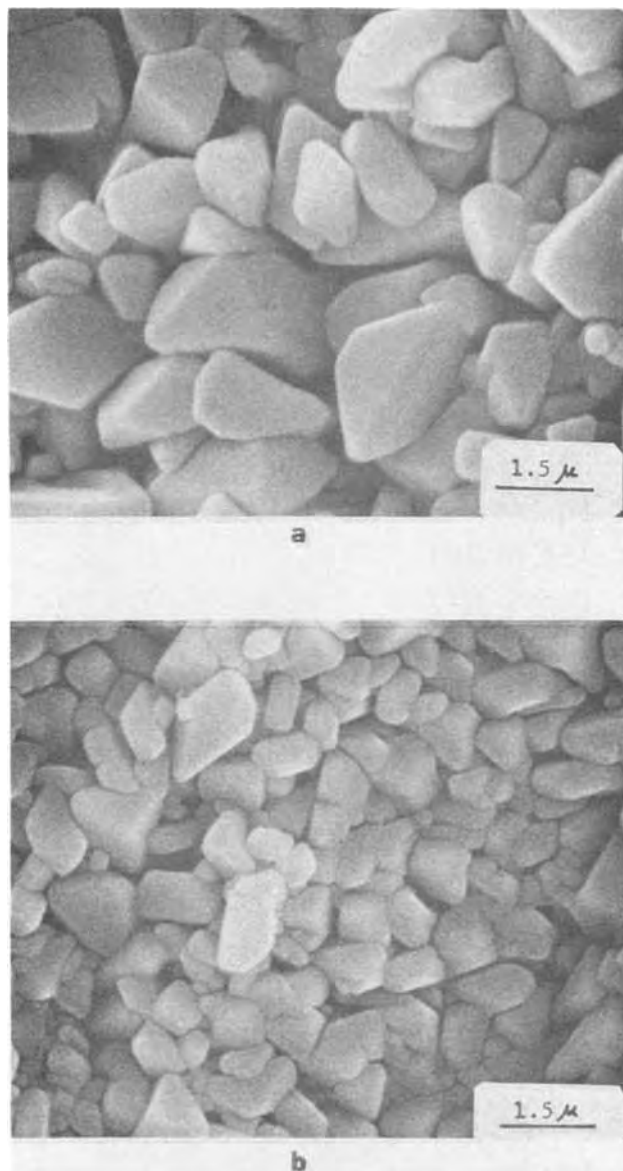


Fig. 2. Influence of expander on the discharge product morphology. 1.57 cm^2 lead electrode was discharged at $200 \mu\text{A}$ in $1.250 \text{ sp gr H}_2\text{SO}_4$ without (a) and with 10 ppm Reax 80C expander (b).

absence. The smaller particle size is the result of the surface adsorption of expander on the growing lead sulfate crystals. In the absence of the expander the growth of lead sulfate crystals remains unhindered and results in a larger size (Fig. 2). This is in agreement with Yampol'skaya *et al.* (29) who observed the chemically precipitated lead sulfate to be long and coarse, but in the presence of lignin fine leaflets were formed. The decreased resistivity of the lead sulfate product layer as observed by Willihnganz by the polarization measurement appears to be related to the increased ionic permeability of the lead sulfate matrix in presence of expander. The presence of a labile quinoid structure in the expander molecule (20) indicates a possibility that it might act as an electron transfer medium (24) when present in the lead sulfate matrix and reduce its electronic resistivity.

The lead electrode voltammograms in sulfuric acid solution without additive (Fig. 3) show a normal behavior, namely the oxidation at potential $> -960 \text{ mV}$, passivation at $\sim -860 \text{ mV}$, and reduction at $< -960 \text{ mV}$, all with respect to the $\text{Hg}/\text{Hg}_2\text{SO}_4/\text{m H}_2\text{SO}_4$ reference electrode. These voltammograms indicate that

the oxidation kinetics of this electrode is influenced by the dynamic growth of the passivating lead sulfate layer on the reacting surface whereas the reduction kinetics is controlled by the dissolution of lead sulfate and the lead adatom deposition sites. In the presence of the expander in solution (dotted line in Fig. 3) the conventional electrode kinetics is altered due to its affinity to adsorb on both the metallic lead and lead sulfate surface of the electrode. During anodic sweep or discharge an increase in the discharge overpotential is caused by the surface blocking effect of the expander; the increased intensity is caused by the expander's influence on the lead sulfate product morphology and on the nature of the reactive interface. On reverse scan the expander in solution severely inhibits the cathodic reaction as indicated by a reduction in cathodic peak current and by maintaining a considerable reduction rate at higher cathodic potential (long tail between -1100 to -1160 mV). The reduction in cathodic peak current is associated with the lack of deposition sites controlled by adsorptivity of expander on the lead surface whereas the reduction process at the extended potential range is controlled by the availability of Pb^{2+} species or the dissolution kinetic of the lead sulfate. The overall influence of expander on the cyclic voltammogram agrees well with the recent observation of Barradas *et al.* (30) who reported the effect of lignosol C-16 (Lignosol Chemical Limited, Quebec) on the cyclic voltammogram of Pb-Hg amalgam in PbCl_2 solution. In agreement with the present observation, a decreased charge acceptance of the lead electrode in the presence of the expander has been reported (2, 3, 31).

Figure 4 shows that the presence of the expander in the test solution influences the morphology of the lead electrode deposit and increases the reactive surface area after charge. This agrees with the reported increased surface area of the lead electrode in the presence of the expander (5, 7). This increase, as hypothesized earlier, results from the blocking coverage of deposition sites and dynamic adsorptive behavior of the expander on the electrode surface. Figure 5 shows that the capacity and peak discharge current buildup of the lead electrode is faster when cycled in the presence of expander than in absence. Both the capacity and the peak discharge current reflect the increased electrode surface area upon cycling and suggest that the electrode capacity would be better maintained in the presence of expander in the electrode in agreement with the reported observation (7).

Table I shows the reproducibility of the lead electrode discharge data obtained at varied acid concentration with and without 10 ppm Reax 80C expander. A good repeatability of the test data is apparent. The value of effective capacity, K , and exponential, " n ", as obtained from the curve fitting of test data in $I^{nt} = K$ equation as well as the value of K' equivalent to $I^{1.5t}$ are included in the table. The exponential " n " is seen to vary from 1.45 to 1.64 with no apparent dependency to either acid concentration or the expander content in it. The K' values agree fairly well with the K indicating the possible use of K' for the design of the application-oriented cell. Further correspondence of the K' to the test data is shown in Fig. 6 in which the solid line is drawn based on $n = 1.5$. It notes that the presence of the expander in solution shifts the $\log t - \log I$ line upwards and increases the K' value almost twice that of the control electrode. It also suggests the use of either K' or its relative ratio (Eq. [4]) as a quantitative measure of the expander activity on discharge.

The discharge activity of the lead electrode decreases almost linearly with increasing acid concentration and nonlinearly in the presence of expander in the electrolyte are also shown in Table I. The expander activity on discharge is highly pronounced in $1.050 \text{ sp gr H}_2\text{SO}_4$ but not so in $1.350 \text{ sp gr H}_2\text{SO}_4$.

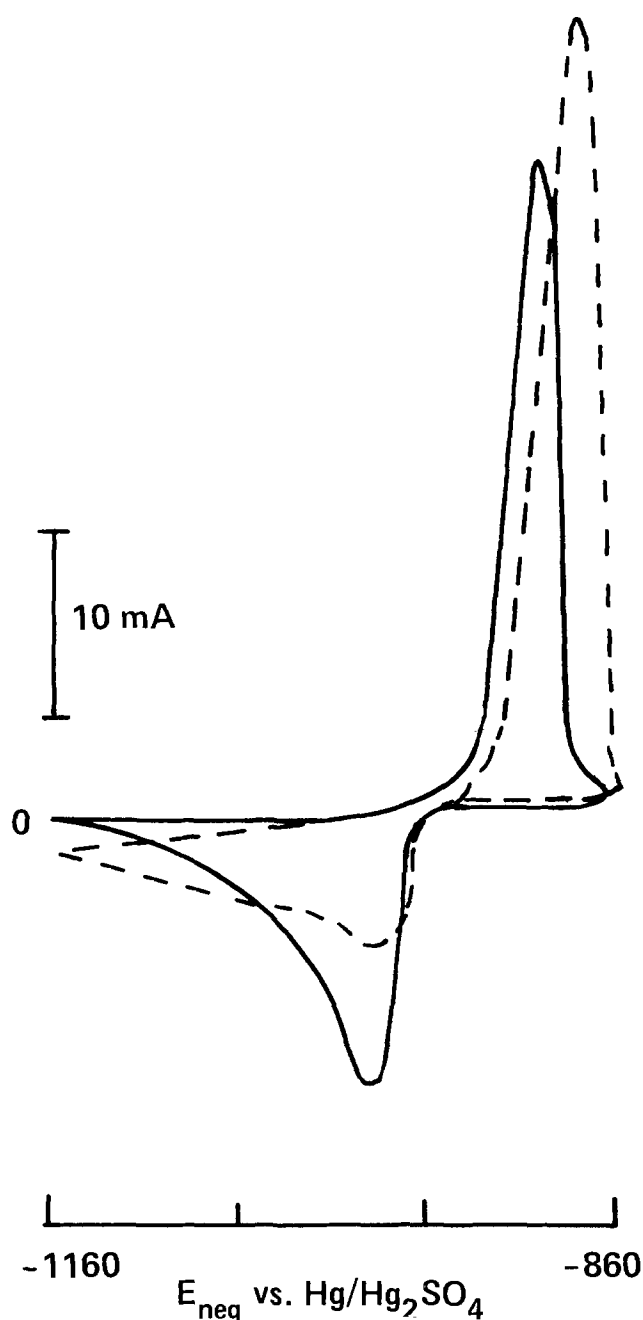


Fig. 3. Effect of 10 ppm lignosulfonate expander on the lead electrode voltammogram between -1160 to -860 mV (vs. $\text{Hg}/\text{Hg}_2\text{SO}_4$) in 1.250 sp gr H_2SO_4 . — pure H_2SO_4 ; --- H_2SO_4 solution with expander.

The K' values were found to increase over the no expander in solution by factors of 3.24, 1.97, 1.94, and 1.18 for 1.050, 1.150, 1.250, and 1.350 sp gr H_2SO_4 , respectively. The exact cause of the decreased expander activity on the electrode dischargeability with increasing acid concentration is not known. It might be related to the acid concentration dependent precipitation kinetics of the lead sulfate and the adsorption-desorption behavior of the lignosulfonate on the lead and lead sulfate particles. Furthermore, Table I shows a continuous increase in K' values with increasing expander concentration up to 10 ppm with no significant changes between 10 and 40 ppm concentration in the test solution. The lack of increased expander activity with increasing expander concentration appears to be caused by supersaturation and/or by the formation of partial inactive electrode surface by multilayer surface adsorption.

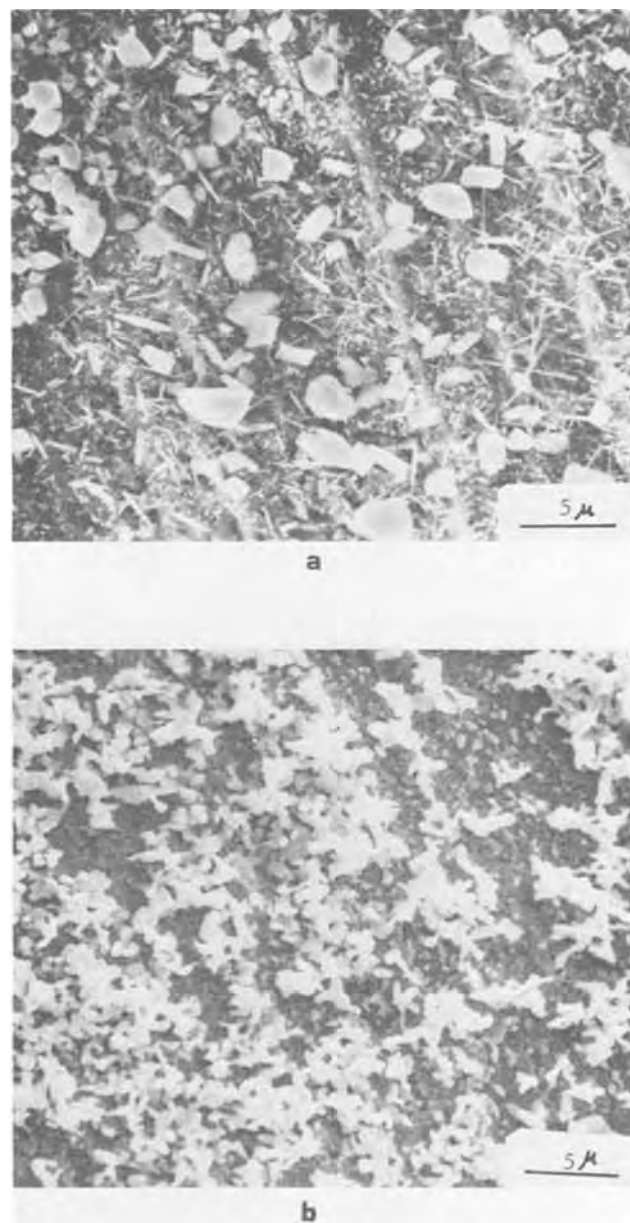


Fig. 4. Morphology of electrodeposited lead on the lead electrode at -1160 mV (vs. $\text{Hg}/\text{Hg}_2\text{SO}_4$) in 1.250 sp gr H_2SO_4 without (a) and with 10 ppm Reax 80C expander (b). Deposition period was 4 hr.

Table II shows the reproducibility of the cycle life test data. It indicates a poor reproducibility of the initial capacity of the test electrode obtained after 2 days cycling in 1.050 sp gr acid and a good reproducibility of the cycle life index value as defined in Eq. [5] and noted in the last column of Table II. The variation in initial capacity is associated with electrode preparation, i.e., our inability to control the initial electrode surface area which is influenced by the microroughness and the precision of the length of the cast lead wire electrode. However, this variation in initial capacity does not affect the sensitivity of this technique in determining the capacity maintenance behavior of the electrode during cycling. This is evident from the reproducibility of the cycle life index data. This table also notes a decreased electrode capacity when cycled in pure acid but increased electrode capacity when cycled in electrolyte with 10 ppm expander. This closely agrees with the reported observation of the expander's influence on the cycle life of the pasted negatives (5,7) and validates the use of cycle life index as determined here in quanti-

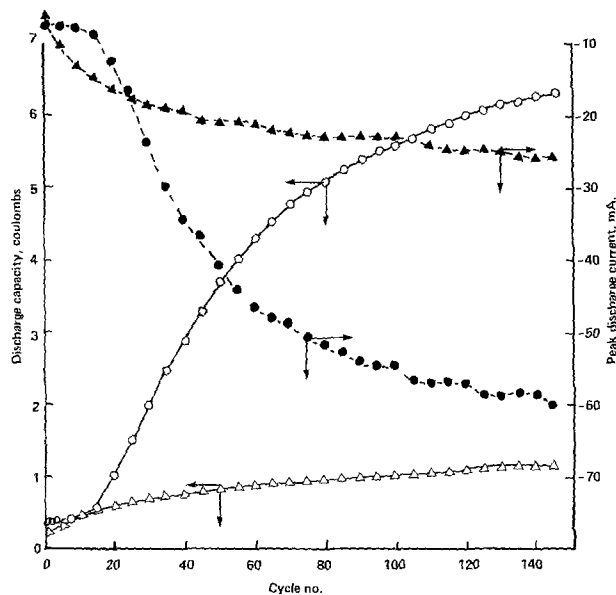


Fig. 5. Capacity and anodic peak current behavior of the lead electrode during linear potential sweep cycling between -1160 to -860 mV (vs. $\text{Hg}/\text{Hg}_2\text{SO}_4$) at 0.5 mV/sec in 1.050 sulfuric acid solution without (Δ - \blacktriangle) and with 10 ppm expander (\circ , \bullet).

tative monitoring the expander activity on the cyclic performance of the lead electrode. It appears that this technique, being free from the complexities of the pasted electrode preparation, will offer unbiased information on the quality of expander in altering the lead electrode cyclic performance.

The effects of acid concentration and the influence of 10 ppm expander in an acid solution on the cycling ability of the lead electrode are illustrated in Fig. 7. It indicates that the capacity maintenance behavior of the lead electrode significantly decreases with increasing acid concentration. However, in the presence of 10 ppm expander in 1.250 sp gr H_2SO_4 , a threefold increase in capacity is observed. The cycle life index (CLI) values for 1.050 , 1.150 , 1.250 , and 1.350 sp gr H_2SO_4 are 0.25 , 0.10 , -0.30 , and -0.68 , respectively (Fig. 7). The presence of 10 ppm Reax 80C lignosulfonate in 1.250 sp gr has increased the CLI from -0.30 to $+0.69$. The decreased cycle life index with increasing acid concentration appears to be the result of an increasing tendency of the electrode for

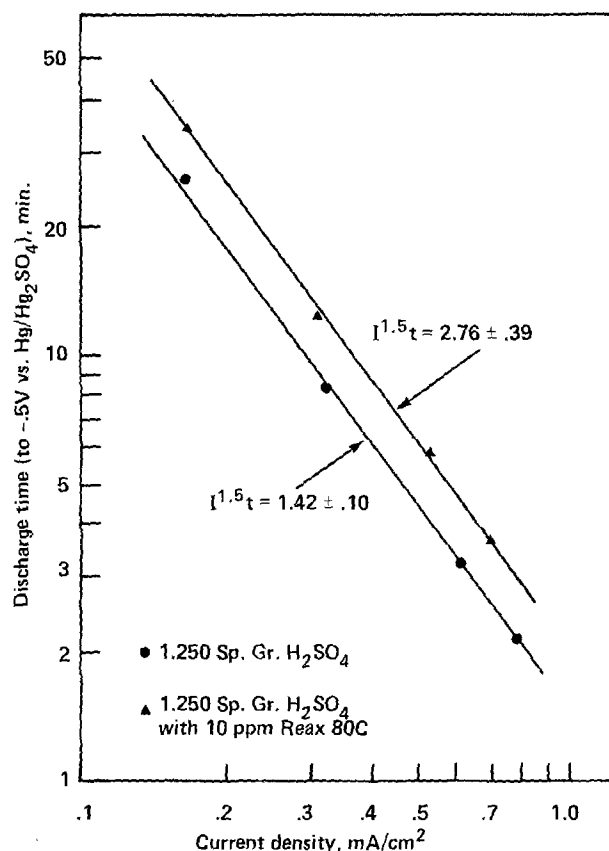


Fig. 6. Effect of 10 ppm Reax 80C lignosulfonate in 1.250 sp gr H_2SO_4 on the log-log relationship between discharge time and current density.

lead sulfate passivation and the greater loss of surface area caused by sintering of lead particles during electroconversion of lead sulfate to metallic lead. This is illustrated from the linear potential sweep voltammograms taken at the end of the test cycles (Fig. 8). The gradual diminishing pattern of the voltammograms reflects the change in passivation behavior and/or the loss of effective surface area with increasing acid concentration during cycling. In the presence of the expander in the test solution, however, the shape of the voltammogram is changed as

Table I. Forced discharge of lead electrodes in sulfuric acid solution with and without expander at 72°F

Electrolyte composition		Discharge time (to -0.5V vs. $\text{Hg}/\text{Hg}_2\text{SO}_4$) in minutes at current (μA)				Values obtained from curve fitting ($K = I^n t$)		$\left(\frac{K'}{\text{cm}^2}\right)^{1.5}$ min
Specific gravity	Concentration of Reax 80C expander (ppm)	1000	750	400	200	K	n	
1.050	0	3.30	6.38	18.40	43.60	2.46	1.54	2.58 ± 0.31
		3.60	6.29	18.50	39.30			
		3.37	6.31	18.02				
1.150	0	2.75	5.17	14.75	35.89	2.16	1.49	2.15 ± 0.26
		2.75	5.50	14.75	32.50			
		2.95	5.00					
1.250	0	1.91	3.30	8.51	27.56	1.34	1.55	1.42 ± 0.10
		2.10	3.40	7.50	26.50			
		1.91	3.35	7.70	24.50			
1.350	0	2.38	—	—	—	0.66	1.53	0.68 ± 0.02
		1.00	1.60	3.93	12.10			
		1.10	1.60	4.10	12.00			
1.050	10	11.93	19.47	45.40	149.90	8.19	1.52	8.37 ± 0.54
		12.83	21.50	46.80	150.00			
		6.13	9.53	25.30	73.00			
1.150	10	6.63	9.47	25.30	77.00	4.07	1.54	4.23 ± 0.15
		4.70	6.60	16.60	60.75			
		4.30	6.40	18.30	63.50			
1.250	10	4.37	5.97	—	64.97	2.36	1.64	2.76 ± 0.40
		4.87	—	—	—			
		1.32	1.95	4.47	13.20			
1.350	10	1.31	1.85	4.47	13.25	0.83	1.45	0.80 ± 0.04
		1.22	—	—	—			
		—	—	—	—			

Table II. Reproducibility of cycle life index data

System	Initial capacity, Q_0 (coulombs)	Final capacity, Q_f (coulombs)	Cycle life index $Q_f/Q_0 - 1$
1.250 sp gr H_2SO_4	1.934	1.362	-0.296
	1.953	1.371	-0.298
	1.562	1.110	-0.289
1.250 sp gr H_2SO_4 with 10 ppm Reax 80/C lignosulfonate	1.389	2.335	0.681
	1.654	2.729	0.650
	1.681	2.624	0.680

shown in Fig. 9. This indicates the expander's influence on the overall charge and discharge kinetics

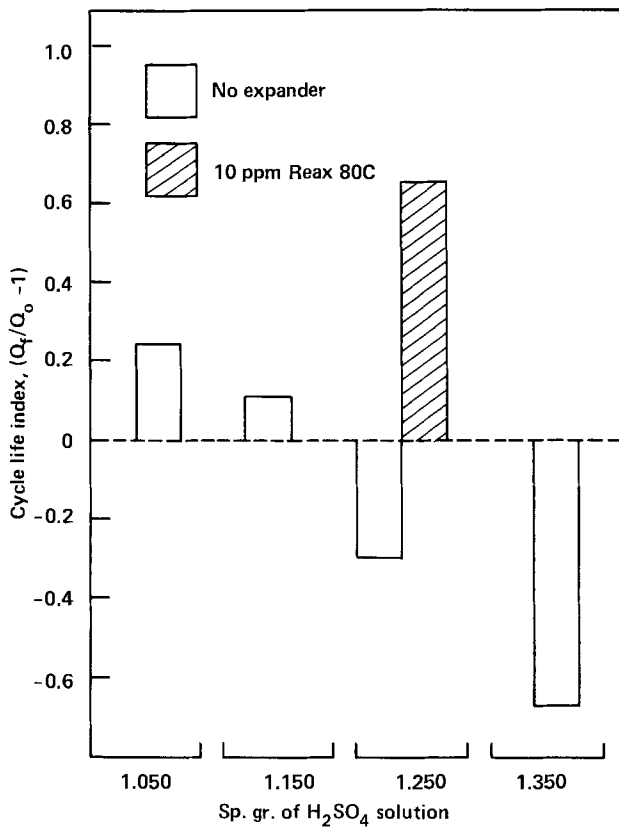


Fig. 7. Effect of sulfuric acid concentration and expander content in the acid electrolyte on the capacity maintenance behavior of the lead electrode.

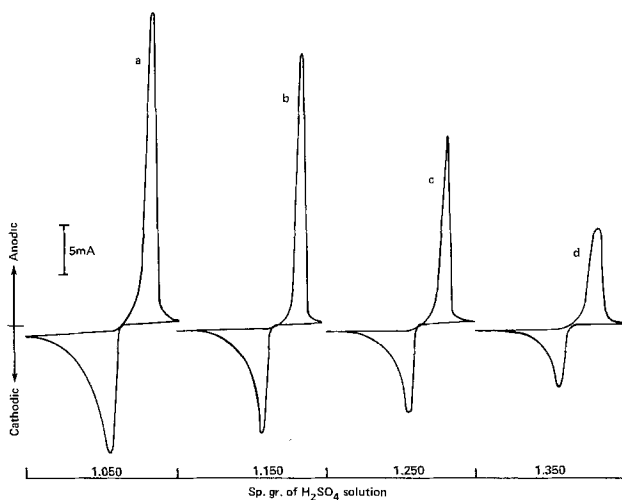


Fig. 8. Effect of sulfuric acid concentration on the lead electrode voltammograms carried out at 0.5 mV/sec between -1160 to -860 mV (vs. Hg/Hg₂SO₄) after 145 cycles. (a) 1.050 sp gr, (b) 1.150 sp gr, (c) 1.250 sp gr, and (d) 1.350 sp gr.

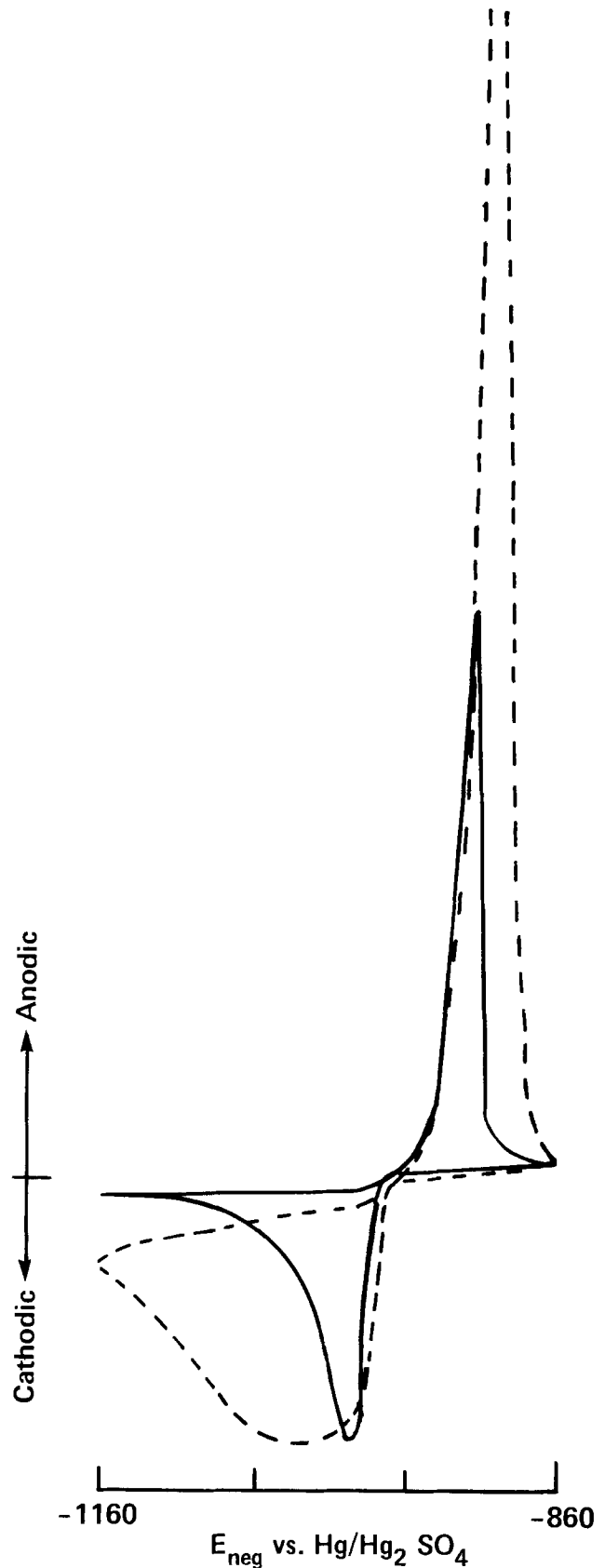


Fig. 9. Lead electrode voltammograms taken at 145th test cycle in 1.250 sp gr H_2SO_4 without (—) and with (---) 10 ppm Reax 80C lignosulfonate illustrate the role of expander on the cyclic performance.

which in turn has resulted in a significant gain in capacity and in mode of cathodic reduction behavior.

Expander added to the test solution causes charge inhibition during cathodic reduction (Fig. 3). This is

caused primarily by blocking of the lead adatom deposition sites through dynamic adsorptive coverage. Such electrodeposition hindrance favors the formation of an electrodeposit with increased surface area (Fig. 4). During repetitive charge/discharge cycling the growth of surface area and subsequent discharge behavior intensify and result in an electrode as typified in Fig. 9.

SEM micrographs of electrodes cycled in 1.250 sp gr H_2SO_4 with and without 10 ppm expander are shown in Fig. 10. The formation and maintenance of the high surface area electrode in the presence of expander is exemplified here. The size of the lead particles of the test electrode are much finer compared to the control electrode cycled in pure acid solution. This micrographic observation agrees well with the reported expander's influence on the pasted electrode morphology after electroformation and to a limited extent after cycling (4-7) and signifies the pertinence of the present technique in quantifying the expander activity on the electrode performance during cycling service.

The effect of expander concentration in 1.250 sp gr H_2SO_4 on the lead electrode cycle life index is shown in Fig. 11. It notes a continuous increase in CLI with increasing expander concentration up to 10 ppm; no

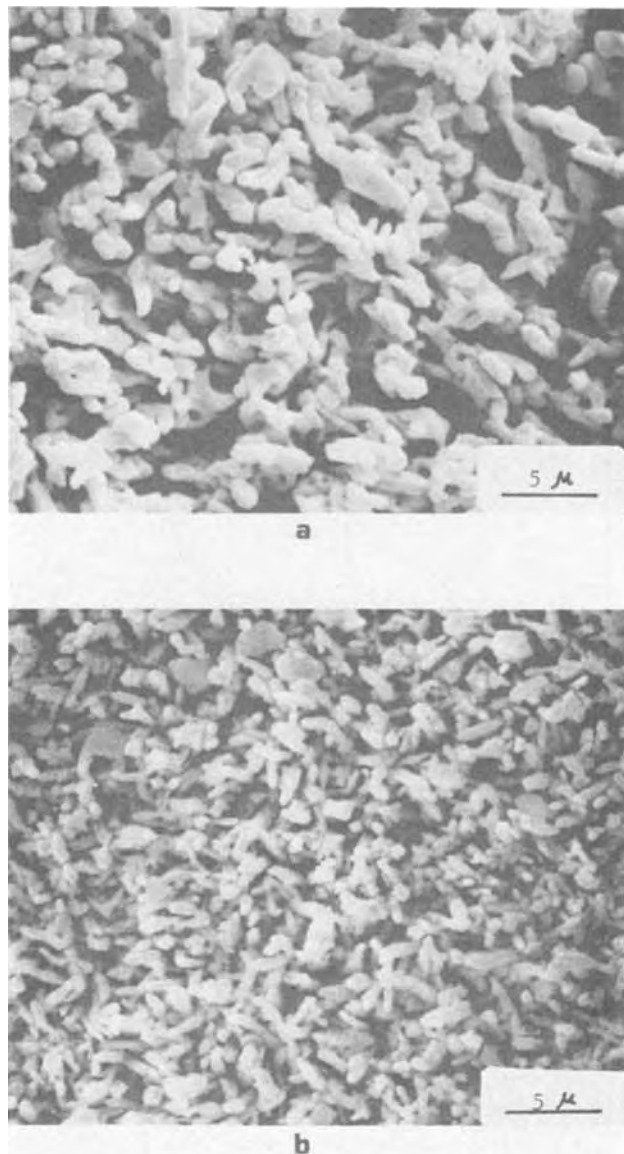


Fig. 10. Morphology of the linear potential sweep cycled lead electrode at 145th cycle in 1.250 sp gr H_2SO_4 without (a) and with 10 ppm Reax 80C (b).

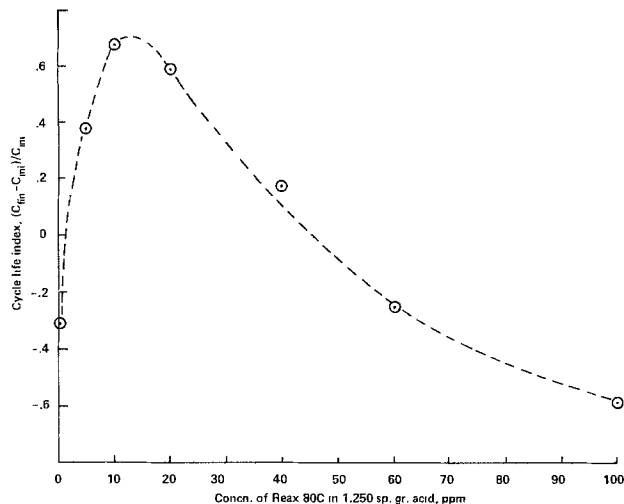


Fig. 11. Effect of Reax 80C lignosulfonate concentration in 1.250 sp gr H_2SO_4 on the lead electrode cycle life index.

significant difference between 10 and 20 ppm; and concentration in excess of 20 ppm decreases sharply the CLI values. The apparent presence of an optimum expander concentration in test solution for a maximum cyclic electrode performance indicates the sensitivity of the overall electrode kinetics on the expander concentration in the test solution. The expander when present in test solution at concentration >20 ppm loses its effectiveness in rendering beneficial influence and starts degrading the electrode performance. This is apparently related to the excessive adsorption of the expander on the electrode surface causing a significant deviation in the normal electrochemical behavior of the electrode. This is clearly illustrated from the voltammograms of the test electrodes cycled in 1.250 sp gr H_2SO_4 solution with 40, 60, and 100 ppm expander as shown in Fig. 12. The critical examination of voltammograms given in Fig. 9 and 12 indicates that the higher expander concentration in the test electrolyte primarily dominates the reduction kinetics of the lead electrode. This reduction process is in part controlled by the available deposition sites and in part by the Pb^{2+} concentration or the dissolution rate of lead sulfate particles. The greater adsorption of expander on lead rather than on the surface of lead sulfate (22) suggests that the overall cathodic process is to be solely controlled by the availability of the deposition sites. The gradual decrease of the deposition site area of the lead elec-

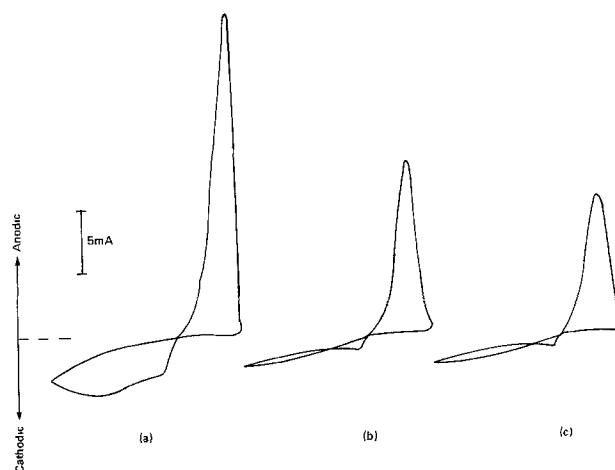


Fig. 12. The effect of higher Reax 80C lignosulfonate concentration in 1.250 sp gr H_2SO_4 on the lead electrode voltammograms obtained at 145th cycle point. (a) 40 ppm, (b) 60 ppm, and (c) 100 ppm.

trode with increasing expander concentration in test solution is qualitatively noted from the decrease in cathodic peak current at the onset of the cathodic sweep (Fig. 9 and 12). The follow up cathodic process is complex and appears to be controlled by the generation of lead nuclei, coverage of the freshly formed nuclei with expander, and possibly the potential dependent adsorption-desorption process of the expander on the electrode material.

In view of the limited information on the physical and chemical nature of the expander material which is known to have a highly complex polymeric structure, more work is needed for a thorough definition of the structure-dependent expander action on the charge and discharge processes of the lead-acid battery negative.

Conclusions

1. The expander action on the lead electrode performance has been defined in terms of its influence on the high rate discharge and capacity maintenance behavior during cycling.

2. Two electrochemical techniques have been developed for measuring expander activities outside the test battery. These techniques based on small electrodes are simple, free from the complexities of the pasted electrode, and provide unbiased information of expander activities. The test results agree well with the reported expander's influence on the pasted electrode performance.

3. Expander influences the high rate discharge of the lead electrode by modifying the lead sulfate passivating layer which decreases with increasing acid concentration.

4. The capacity maintenance behavior of the lead electrode is influenced by the presence of expander as it prevents the sintering of the lead mass during repeated charge/discharge cycling process. An optimum expander concentration exists for a maximum cyclic performance of the lead electrode.

5. The charge inhibition of the lead electrode in the presence of expander is caused by the blocking coverage of lead adatom deposition sites.

6. In view of the structural complexities of the expander material, a considerable difficulty exists in correlating the electrochemical activities of the expander to that of the molecular structure of this polymeric material.

Acknowledgments

The author would like to thank Globe-Union Incorporated for permission to publish this work, W. Tiedemann for helpful contribution and suggestions during the course of the work, M. Fallgatter for microprocessor based data acquisition software development and data management system, S. Hanna, K. Bullock, and G. Wierschem for helpful discussion, L. Ellzey for electrode preparation and high rate discharge experiments, and H. Moorer of Westvaco, Incorporated for the Reax 80C sample. This research was sponsored by Argonne National Laboratory under Contract No. 31-109-38-4205.

Manuscript submitted Dec. 17, 1979; revised manuscript received Feb. 19, 1980. This was Paper 57 presented at the Los Angeles, California, Meeting of the Society, Oct. 14-19, 1979.

Any discussion of this paper will appear in a Discussion Section to be published in the June 1981

JOURNAL. All discussions for the June 1981 Discussion Section should be submitted by Feb. 1, 1981.

Publication costs of this article were assisted by Globe-Union Incorporated.

REFERENCES

1. D. A. J. Rand, *J. Power Sources*, **4**, 101 (1979).
2. H. Bode, "Lead Acid Batteries," John Wiley & Sons, Inc., New York (1977).
3. J. Burbank, A. C. Simon, and E. Willihnganz, in "Advances in Electrochemistry and Electrochemical Engineering," Vol. 8, P. Delahay and C. W. Tobias, Editors, John Wiley & Sons, Inc., New York (1970).
4. J. R. Pierson, P. J. Gurlusky, A. C. Simon, and S. M. Caulder, *This Journal*, **117**, 1463 (1970).
5. A. C. Simon, S. M. Caulder, P. J. Gurlusky, and J. R. Pierson, *ibid.*, **121**, 463 (1974).
6. A. C. Simon, S. M. Caulder, P. J. Gurlusky, and J. R. Pierson, *Electrochim. Acta*, **19**, 739 (1974).
7. B. K. Mahato, *This Journal*, **124**, 1663 (1977).
8. E. J. Ritchie, *Trans. Electrochem. Soc.*, **92**, 229 (1947); *This Journal*, **100**, 53 (1953).
9. W. Simon, *Bosch Technische Berichte*, **1**, 234 (1966).
10. E. Willihnganz, *Trans. Electrochem. Soc.*, **92**, 281 (1947).
11. A. C. Zachlin, *This Journal*, **98**, 325 (1951).
12. M. P. J. Brennan and N. A. Hampson, *J. Electroanal. Chem. Interfacial Electrochem.*, **48**, 465 (1973); **52**, 1 (1974); **54**, 263 (1976).
13. A. A. Abdul Azim and A. A. Ismail, *J. Appl. Electrochem.*, **4**, 351 (1974).
14. T. Chiku and K. Nakajima, *This Journal*, **118**, 1395 (1971).
15. P. E. Baikal, M. I. Gillibrand, and K. Peters, *Electrochim. Acta*, **17**, 839 (1972).
16. M. I. Gillibrand and G. R. Lomax, *ibid.*, **8**, 693 (1963).
17. D. Pavlov, *Ber. Bunsenges.*, **71**, 398 (1967); D. Pavlov and N. Iordanov, *This Journal*, **117**, 1103 (1970); D. Pavlov and R. Popova, *Electrochim. Acta*, **15**, 1483 (1970); D. Pavlov, S. Zanova, and G. Paparov, *This Journal*, **125**, 1522 (1977).
18. P. Ruetschi, *This Journal*, **120**, 331 (1973).
19. A. Winsel, U. Hullmeine, and E. Voss, *J. Power Sources*, **2**, 369 (1977/78).
20. D. A. I. Goring in "Lignins," K. V. Sarkanen and C. H. Ludwig, Editors, Chap. 17, pp. 695-761, Wiley-Interscience, New York (1971); J. M. Harkin in "Oxidative Coupling of Phenols," W. I. Taylor and A. R. Battersby, Editors, Chap. 6, pp. 243-321, Marcel Dekker, Inc., New York (1967).
21. M. J. Rosen, "Surfactants and Interfacial Phenomena," John Wiley & Sons, Inc., New York (1978).
22. T. Sharpe, *Electrochim. Acta.*, **1**, 635 (1969).
23. B. K. Mahato, Unpublished work.
24. A. N. Bloch, in "Energy and Charge Transfer in Organic Semiconductors," K. Masuda and M. Silver, Editors, Plenum, New York (1974).
25. A. LeMehaute, *J. Appl. Electrochem.*, **6**, 543 (1976).
26. T. J. Popova and B. N. Kabanov, *Zh. Prikl. Khim.*, **32**, 326 (1959).
27. J. Burbank, *This Journal*, **103**, 87 (1956).
28. B. K. Mahato, *ibid.*, **126**, 365 (1979).
29. E. G. Yampol'skaya, M. I. Ershova, V. V. Surikov, I. I. Astakov, and B. N. Kabanov, *Sov. Electrochem. (Engl. Trans.)*, **8**, 1209 (1972); E. G. Yampol'skaya, I. A. Smirnova, M. I. Ershova, S. A. Sapotnitskii, and L. I. Kryukova, *ibid.*, **8**, 1289 (1972).
30. R. G. Barradas, S. Fletcher, and J. D. Portar, *J. Power Sources*, **2**, 137 (1977/78).
31. E. Willihnganz, "Power Sources 6," D. H. Collins, Editor, Academic Press, London (1977).

Effect of Helium, Iron, and Platinum Implantation on the Absorption of Hydrogen by Iron

M. Zamanzadeh, A. Allam, and H. W. Pickering*

*Metallurgy Section, Department of Materials Science and Engineering,
The Pennsylvania State University, University Park, Pennsylvania 16802*

and G. K. Hubler

Naval Research Laboratory, Washington, D. C. 20375

ABSTRACT

A preliminary study was made of the effect of certain elements implanted in iron on the absorption of hydrogen by Ferrovac-E iron. Using the permeation technique, it was found that the location of implanted Pt, as modified by selective dissolution of iron from the surface, affects the kinetics of the hydrogen evolution reaction and, hence, of the hydrogen absorption process. The rate of hydrogen absorption decreased with increase in Pt concentration on the surface in both 0.1N NaOH and 0.1N H₂SO₄. A catalytic mechanism is proposed to explain the marked reduction in hydrogen permeation. There are no significant differences in the permeation behavior of unimplanted and helium- or iron-implanted iron membranes in 0.1N NaOH. The experimentally observed Tafel slope, the permeation-(charging) potential relationship, and the permeation-(charging) current relationship indicate a coupled discharge-recombination mechanism of hydrogen evolution on He-, Fe-, or Pt-implanted iron. At higher cathodic overpotentials in 0.1N NaOH, corresponding to potentials more negative than -1.0V (SHE), another mechanism of hydrogen evolution is indicated. Selective dissolution of iron from the Pt-implanted Fe surface layer may involve some platinum and iron interdiffusion according to Rutherford backscattering analyses.

Hydrogen absorption greatly reduces the mechanical properties of structural alloys. A number of investigators have studied the possibility of reducing hydrogen absorption by coatings (1-4). Besides functioning as barriers to hydrogen entry, coatings may also reduce hydrogen absorption through their effect on the kinetics of the hydrogen evolution reaction and, hence, of the hydrogen absorption process. Chatterjee *et al.* (4) provided experimental evidence for the catalytic mechanism of decreasing hydrogen entry into iron. They found that discontinuous electrodeposited coatings of Pt, Ni, or Cu on iron are effective in reducing hydrogen entry into the membrane. The ion implantation technique is another method for altering the surface chemically and, thus, the mechanism and kinetics of the hydrogen evolution reaction, without affecting bulk physical or mechanical properties.

Ashworth and co-workers (5) were among the first to report the effect of implantation on the polarization behavior of iron. They found that there are no significant differences between the polarization behavior of unimplanted and argon-implanted iron beyond that due to changes in surface roughness associated with the implantation process. Other implanted elements in iron, such as chromium and lead, were shown to influence the polarization behavior (6, 7).

This paper reports the results of initial studies directed at evaluating the effect of implantation on hydrogen permeation. No other studies of hydrogen permeation of implanted membranes are known to be reported in the literature. Specifically, the results provide insight on:

1. Whether, and to what extent, implanted platinum, helium, or iron reduce hydrogen permeation through iron.

2. The effect of the nature and proximity to the surface of the implanted species on the mechanism and kinetics of the hydrogen evolution reaction and, hence, of the hydrogen absorption process.

3. The effect of implantation on (effective) hydrogen diffusivity which may be related to trapping characteristics.

The rationale behind choosing Pt for implantation is that Pt is one of the best electrocatalysts for the hydrogen evolution reaction. In order to sort out any effects due to the implantation process, itself, the inert element, He, and the substrate element, Fe, were also chosen for comparison.

Experimental Procedure

The hydrogen permeation measurements were carried out on Ferrovac-E iron. The Fe membranes were prepared by cold-rolling wafers cut from a master ingot to the required thickness (0.365 mm). After polishing to 600 grit, they were degreased using benzene and methanol in a soxhlet apparatus, and then annealed for 2 hr at 1273°K (1000°C) in an argon-filled silica capsule. The latter treatment produced an etched surface. One side of some of these membranes was exposed to beams of Fe⁺, He⁺, or Pt⁺ ions at fluences and energies given in Table I. The samples were implanted in a vacuum of 10⁻⁴ Pa (10⁻⁶ Torr) and were in close proximity to a cold surface at liquid nitrogen temperatures (77°K) which minimized carbon contamination. The temperature of the samples during implantation did not exceed 323°K. The implanted samples were stored in an evacuated desiccator. Prior to the permeation runs, the Pt content on the surface of the Pt-implanted membranes was increased by selective dissolution of iron via immersion in 1M H₂SO₄ for 20 sec. This amount of etching produced no change in surface morphology observable by light or

Table I. Energies and fluences of implanted ions in iron membranes

Ion	Energy, keV	Fluence, ions/cm ²
Fe	150	1 × 10 ¹⁷
Pt	100	1.5 × 10 ¹⁸
He	25	1.6 × 10 ¹⁷

* Electrochemical Society Active Member.

Key words: ion implantation, hydrogen evolution, Fe-Pt, Tafel slope, catalyst.

scanning electron microscopy. Permeation measurements were also made after subsequent 10 sec immersions in 0.1N H₂SO₄. Sulfuric acid is known to selectively remove iron from a Fe-Pt solid solution (8).

Electrolyte solutions were prepared from conductivity water (doubly distilled) prepared by the method of Powers (9) and reagent grade chemicals. Final purification was made by pre-electrolyzing the solutions in an external cell prior to admitting them to the permeation cell.

The technique of Devanathan and Stachurski (10) was used to measure the permeability of hydrogen through a membrane while evolving hydrogen off the implanted surface. In this method, a thin metallic membrane is electrolytically charged with hydrogen on the implanted side, while on the other exit side the hydrogen, which has diffused through the membrane, is anodically oxidized. The orifice of the cell and, thus, the charging area was 0.785 cm². The measured anodic current is a direct measure of the hydrogen flux through the membrane for conditions at the exit surface, which included a thin palladium coating and an oxidizing potential of 0.018V (SHE). These are the same conditions found previously to be suitable for oxidizing all of the hydrogen arriving at the anodically polarized surface (4). The reported values are the measured values after correction for the residual current which is typically less than 1 μA cm⁻². The potential of the charging surface was measured using an Hg/Hg₂SO₄ reference electrode in 0.1N H₂SO₄ and an Hg/HgO reference electrode in 0.1N NaOH, and that of the exit surface using an Hg/HgO reference electrode in 0.1N NaOH. Both chambers of the cell were de-aerated by bubbling oxygen-free nitrogen through the solutions. The permeation measurements were performed under conditions of cathodic protection. Details of the cell and circuitry are reported elsewhere (4).

The permeation data were obtained as follows. The Fe- and He-implanted iron membranes were pre-charged at $i_c = 0.10 \text{ mA cm}^{-2}$ for 45 min by which time a quasi-stationary permeation current was established. The Pt-implanted membranes were similarly precharged at 1 mA cm^{-2} (~15 min in 0.1N NaOH and ~7 min in 0.1N H₂SO₄). The membranes were then charged galvanostatically in 0.02 mA cm⁻² steps in 0.1N NaOH or in 0.2 mA cm⁻² steps in 0.1N H₂SO₄ in descending and then ascending directions. Each charging current was maintained for about 4 min by which time a quasi-stationary permeation current was established. This procedure has been found to give constant and reproducible permeation transients dependent only on the charging conditions for a given specimen.

Some of the concentration profiles after implantation were measured by means of high resolution Rutherford backscattering of alpha particles with a depth resolution of 4 nm. For this measurement, the surface to be implanted was first polished to a mirror finish with 6 μm diamond paste. Details of this method may be found elsewhere (11, 12).

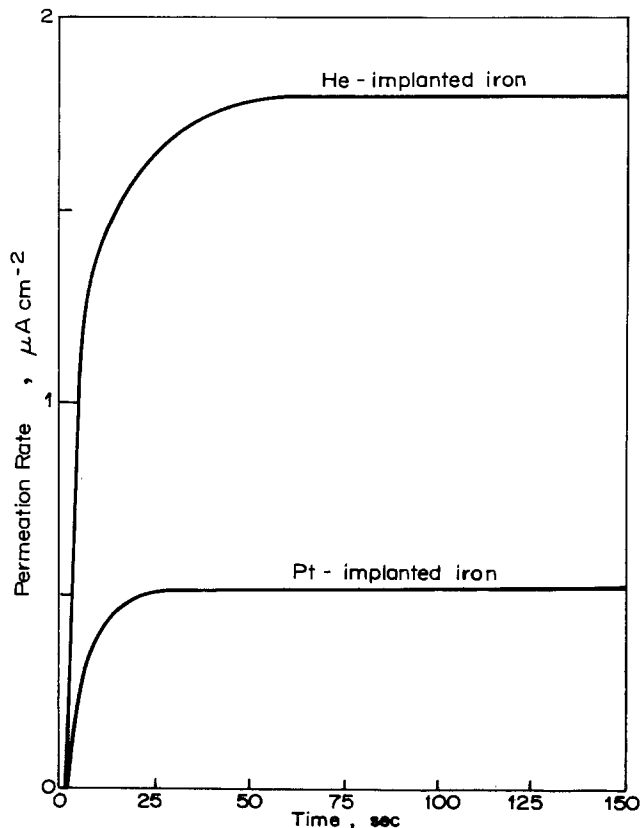


Fig. 1. Hydrogen permeation transients for an He-implanted Fe membrane and for a Pt-implanted Fe membrane after a 20 sec dissolution in 1M H₂SO₄. $i_c = 0.1 \text{ mA cm}^{-2}$ in 0.1N NaOH.

Results

Table II shows that the steady-state hydrogen permeation fluxes, i_s , and electrode potentials at the charging side, E , in 0.1N NaOH are the same for unimplanted Fe membranes and identical membranes implanted with He or Fe. These values and the transients themselves are also typical for these samples after various periods of immersion in sulfuric acid.

The permeation transients prior to steady state were also the same within the experimental error for these membranes; the half-rise time ($t_{1/2}$) was 5.5 ± 1.0 sec. Typical permeation transients are shown in Fig. 1. The effective diffusivity, calculated using the expression (13, 14)

$$D = \frac{0.138 L^2}{t_{1/2}}$$

where L is the membrane thickness, is $D = 3 \times 10^{-5} \text{ cm}^2 \text{ sec}^{-1}$. This value is in good agreement with literature values for well-annealed iron (15) and is also essentially the value obtained by extrapolation of high temperature diffusion data to room temperature (16). The experimentally observed Tafel slope is $-122 \pm 5 \text{ mV}$ (Fig. 4). This value is the same as that re-

Table II. Variation of the steady-state hydrogen permeation flux and of the electrode potential at the charging side with the charging current density for an unimplanted Fe membrane and for an identical membrane implanted with He or Fe. Charging solution was 0.1N NaOH

Charging current density, mA/cm ²	Steady-state permeation rate and electrode potential of the charging side					
	Unimplanted iron		He-implanted iron		Fe-implanted iron	
	i_s , μA/cm ²	$-E_c$, V (SHE)	i_s , μA/cm ²	$-E_c$, V (SHE)	i_s , μA/cm ²	$-E_c$, V (SHE)
0.1	1.77	1.005	1.78	1.005	1.65	1.00
0.08	1.50	0.990	1.46	0.989	1.45	0.990
0.06	1.32	0.975	1.27	0.974	1.27	0.975
0.04	1.02	0.950	1.02	0.950	1.01	0.950
0.02	0.70	0.910	0.74	0.910	0.67	0.910

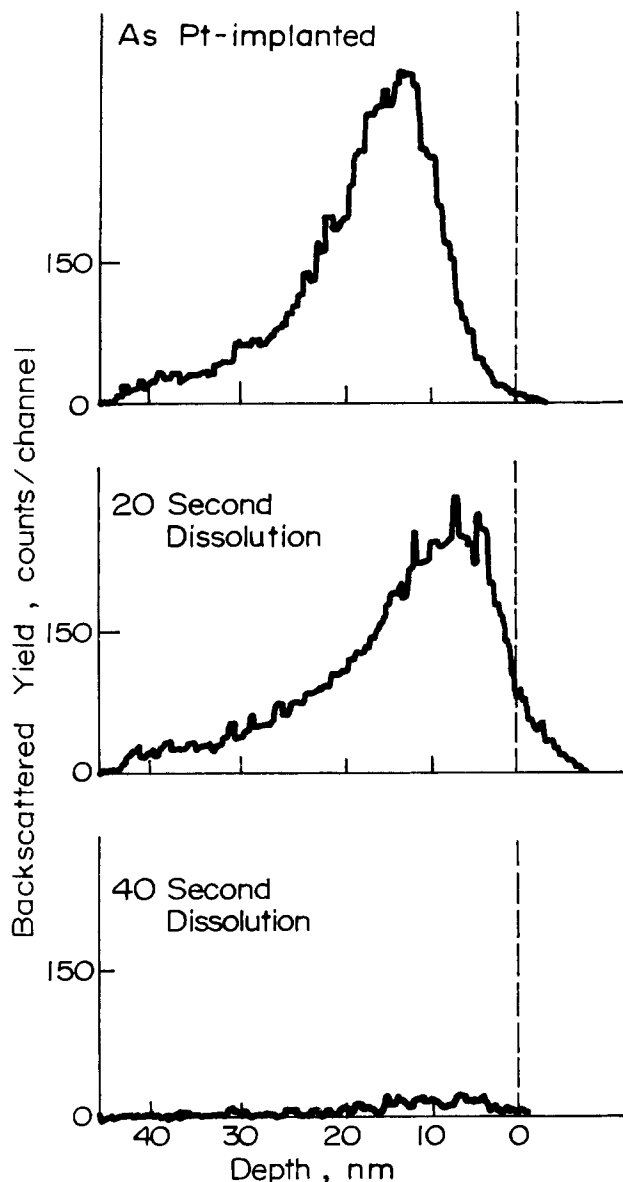


Fig. 2. Rutherford backscattering profiles of implanted Pt in Fe as a function of time of immersion of the implanted sample in 1M H_2SO_4 at room temperature. Depth of resolution is 4 nm (40\AA).

ported for hydrogen evolution on Fe in 0.1N NaOH (17).

Figure 2 shows distribution profiles of Pt implanted in Fe after different amounts of dissolution in 1M H_2SO_4 at room temperature. After 20 sec immersion in the acid, the peak concentration of Pt is closer to the surface and the area under the curve is essentially unchanged, indicating that only iron is dissolved during this initial dissolution period; and the tail of the profile extends further into the alloy as measured from either the peak or the original surface position (not shown), suggesting Pt diffused into the alloy (during and/or following dissolution) to a distance roughly equal to the distance the surface has receded.¹ The (average) Pt concentration within a surface region of about 4 nm thickness as measured by Rutherford backscattering is significantly higher ($\sim 3\%$ by weight) than in the as-implanted case ($\sim 0.1\%$).

Profiles obtained after a second 20 sec dissolution period in 1M H_2SO_4 show that the Pt content is much less and nearly at background levels (Fig. 2), which indicates that most of the Pt is lost from the mem-

¹ This follows since the profile width is about the same before and after the initial 20 sec immersion. An estimate is 10 nm after 20 sec based on published corrosion rates ($>10^{-3} \text{ A cm}^{-2}$ at 298°K) of steel in sulfuric acid (18).

brane during this second dissolution process. Permeation measurements were mainly done, therefore, after an initial 20 sec exposure of the Pt-implanted membranes to 1M H_2SO_4 .

Figure 3 shows a linear dependence of the steady-state permeation current density on the square root of the charging current density with the curve passing through the origin for an unimplanted Fe membrane and for a Pt-implanted Fe membrane following a 20 sec immersion in 1M H_2SO_4 . This is taken as an indication of a diffusion-controlled hydrogen permeation process (17, 19). The permeation transient for the latter membrane is shown in Fig. 1. The hydrogen permeability is less at all charging currents for the Pt-implanted, than for the unimplanted, iron membranes. Pt profiles which were not modified by selective iron dissolution were found to have an insignificant effect on the hydrogen evolution and permeation kinetics.

The electrode potentials for hydrogen evolution on the Pt-implanted membrane (after immersion in acid) are invariably more noble than those on the unimplanted membrane, Fig. 4. The Tafel slope is $-122 \pm 5 \text{ mV}$ for both unimplanted and Pt-implanted iron. The relations between permeation and the electrode potential of the charging surface for unimplanted and Pt-implanted Fe membranes are given in Fig. 5 for the 0.1N NaOH charging solution. The slopes of the straight segments of the curves of both the unimplanted Fe and Pt-implanted Fe membranes are $-255 \pm 5 \text{ mV}$. About the same slope is also obtained in the 0.1N H_2SO_4 charging solution over a wide range of overpotential for both charging surfaces, Table III.

As with the Pt content of the surface (Fig. 2), both the measured electrode potential of the Pt-implanted surface and the permeation rate of hydrogen through the Pt-implanted membrane during hydrogen charging are functions of the pretreatment immersion time in, and concentration of, sulfuric acid. Figure 6 shows variations in potential and permeation as a function of additional 10 sec immersion periods (following the initial 20 sec immersion) in a diluted sulfuric acid. The trends of i_s decreasing and E increasing in a more oxidizing direction hold for an additional 40 sec immersion in 0.1N H_2SO_4 . Then, a reversal of the electrochemical parameters occurs.

Discussion

The electrocatalytic activity of a surface for the hydrogen evolution reaction can be estimated from the overpotential required to evolve hydrogen at a given current density—the lower the overpotential or the more noble the electrode potential, the more catalytic the surface. Figure 4 and Table III show the electrode potentials measured in alkaline- and acid-charging solutions. It is seen that the electrode potential for the hydrogen evolution reaction is more noble on Pt-implanted than on unimplanted surfaces. It follows

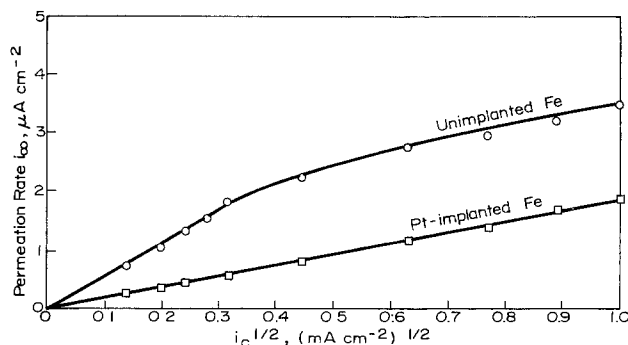


Fig. 3. Steady-state permeation rate i_s as a function of the square root of the charging current density i_c for an unimplanted Fe membrane and a Pt-implanted and acid-treated Fe membrane. Charging solution was 0.1N NaOH.

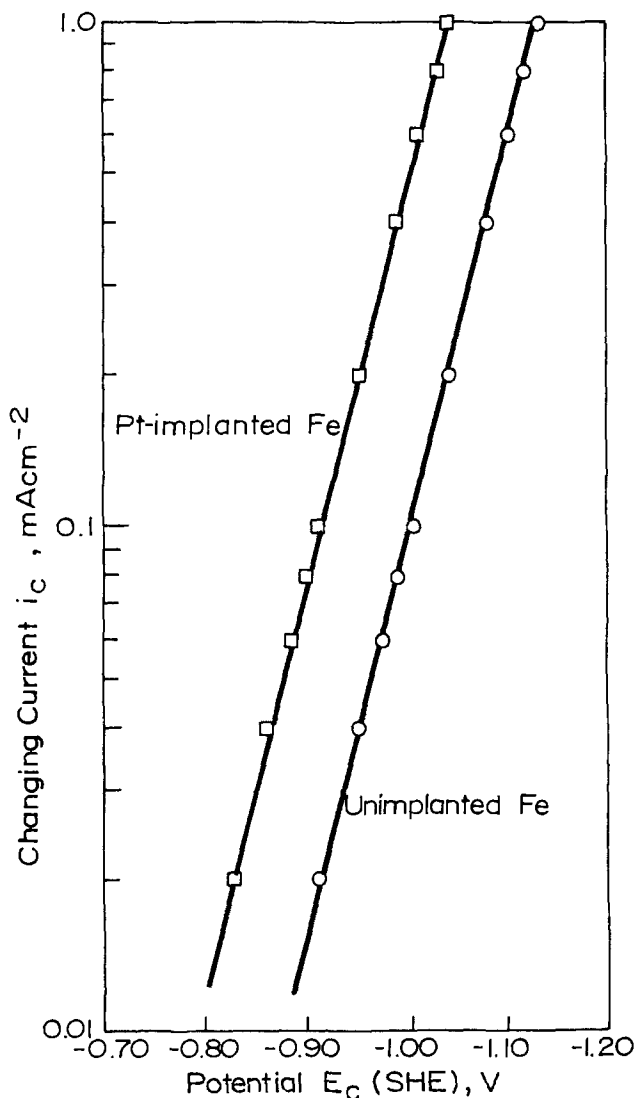


Fig. 4. The polarization curve in the Tafel region for hydrogen evolution in 0.1N NaOH on an unimplanted iron (O) and a Pt-implanted Fe membrane following a 20 sec immersion in 1M H₂SO₄ (□).

that the degree of hydrogen coverage, θ , and the permeability of hydrogen should be less for Pt-implanted, than for unimplanted, iron membranes (20, 13, 4) in accord with the permeation results in Fig. 3 and 5.

The above reasoning also explains the decrease of the steady-state permeation and the more positive electrode potential with increasing pretreatment immersion time (Fig. 6), i.e., acid attack initially increases the Pt content of the surface as was shown by

Table III. Variation of the steady-state hydrogen permeation flux and of the electrode potential of the charging side with the charging current density for an unimplanted Fe membrane and for a Pt-implanted Fe membrane. Charging solution was 0.1N H₂SO₄

Charging current density, mA/cm ²	Steady-state permeation rate and electrode potential of the charging side			
	Unimplanted iron		Pt-implanted iron	
	i_{zs} , $\mu\text{A}/\text{cm}^2$	$-E_c$, V (SHE)	i_{zs} , $\mu\text{A}/\text{cm}^2$	$-E_c$, V (SHE)
1.0	22.0	0.425	16.2	0.407
0.8	20.0	0.415	14.5	0.395
0.6	17.5	0.400	12.5	0.380
0.4	14.2	0.380	10.5	0.360
0.2	10.2	0.345	7.5	0.325
0.1	7.3	0.310	5.5	0.290

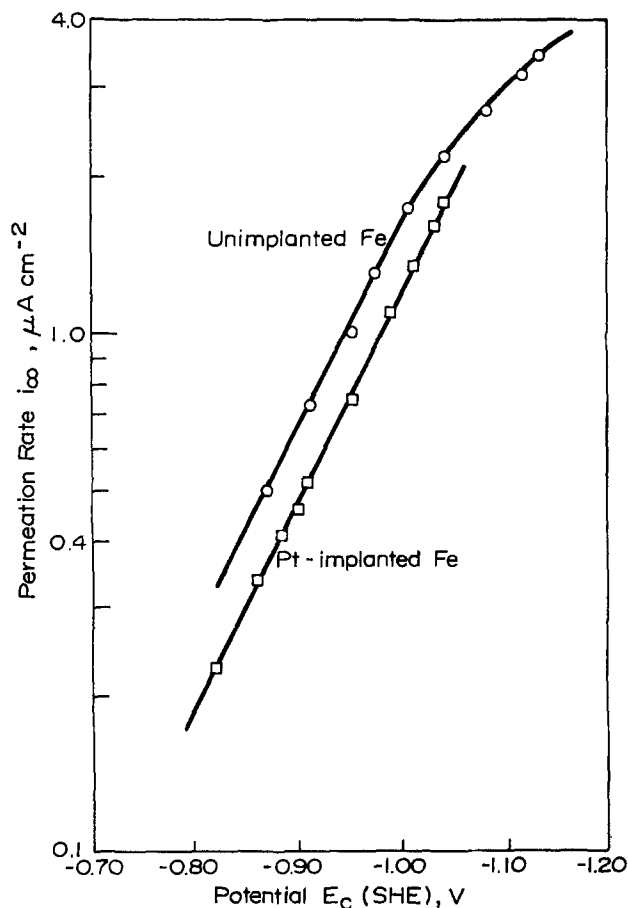


Fig. 5. Steady-state permeation rate i_s as a function of the potential of the charging surface of the membrane, E_c . Charging solution was 0.1N NaOH.

Rutherford backscattering (Fig. 2). A correspondence of the electrochemical and the backscattering data also holds at longer pretreatment immersion times when a reversal in the trends of E_c and i_s corresponds to a loss of Pt from the surface. Thus, it would seem

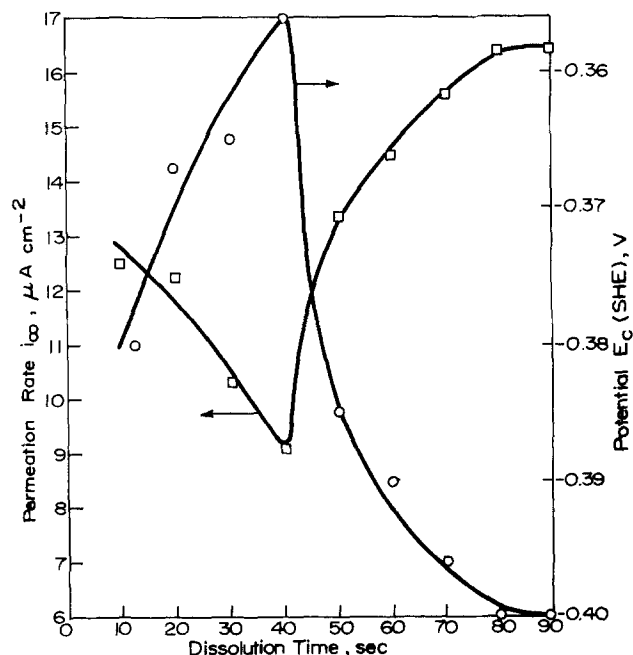


Fig. 6. Steady-state permeation rate (□) and charging potential (O) as a function of additional immersion periods in 0.1N H₂SO₄ beyond the initial 20 sec immersion in 1M H₂SO₄ of the Pt-implanted surface. Charging current was 0.6 mA cm⁻² in 0.1N H₂SO₄.

that as the surface recedes and overtakes the Pt profile, the Pt concentration on the surface reaches a level for which accumulation of Pt into particles, followed by detachment, occurs. Such is known to happen when an alloy contains low percentages ($\sim 1\%$) of a noble metal in solid solution (21), and is in accord with industrial experience, especially during electrolytic refining of copper containing small amounts of gold. The reversal in the trends of E_c and i_{∞} occurs at shorter immersion times for higher concentrations of sulfuric acid (Fig. 2 vs. Fig. 6). This is in accord with a faster rate of attack in the more concentrated acid, and thus a faster rate of recession of the surface. That continued dissolution of the membrane eventually leads to Pt loss from the surface (Fig. 2) is supported by the approach after long times of the i_{∞} and E_c values to those for unimplanted Fe membranes.

In summary, the mechanism by which implanted Pt reduces hydrogen absorption by iron is related to the different catalytic tendencies of Pt and Fe for the hydrogen evolution reaction. In this case, the hydrogen evolution reaction occurs more readily (lower overvoltage required) on Pt than on Fe (sites); thus, the coverage of hydrogen on the composite Pt-Fe surface is lower and, consequently, so also is the absorption rate. Thus, these results indicate that for implantation in iron to be effective for reducing hydrogen absorption, implants should have a higher exchange current density for hydrogen evolution than that for the substrate metal. The data also show for Pt implants that modifications of the implantation profile, which increase the concentration of the implant in the outermost surface layer, increase evolution and decrease absorption of hydrogen.

The Rutherford backscattering data here and elsewhere (11) give some indication that a limited amount of interdiffusion of the alloy components occurs during (and/or after) selective dissolution (of the iron). While this has yet to be shown to be the actual explanation of the backscattering profiles obtained before and after the initial (20 sec) dissolution period (Fig. 2), the explanation itself is reasonable for certain conditions of anodic dissolution which generate vacancies as analyzed elsewhere (21-25).

The data in Table II for He- and Fe-implanted iron show that there are no significant differences in the polarization or permeation behavior between unimplanted and He- or Fe-implanted iron. Furthermore, the Tafel slopes are also the same. Thus, the implantation process, itself, does not modify the mechanism of, or the catalytic character of the surface for, the hydrogen evolution reaction. Ashworth *et al.* (5), also found that once the air-formed oxide is removed, the polarization behavior of unimplanted and argon-implanted iron is nearly the same. A delay in the permeation-kinetics, on the other hand, might have been expected for the implanted membrane since the implantation process, itself, introduces defects to about the depth of the profile. In recent ion beam studies of deuterium-implanted iron, Myers *et al.* (26) found that the activation energy of a deuterium trap produced by the implantation process is 0.81 eV, that slow release from the traps occurs between 300° and 400°K, and that either implanted deuterium or iron creates the traps. The presence of effective hydrogen traps can, in principle, be indicated by a comparison of the permeation rise times for unimplanted and implanted membranes. That the half-rise times in the present measurements were the same within the experimental error may be attributed to (i) modifications of the nature or density of the traps during the long (~ 9 month) delay between the implantation process and the permeation measurements, (ii) filling of the traps with hydrogen from other sources during the above-mentioned delay, and/or (iii) a lack of sensitivity in the measurement. Experiments are currently underway in an attempt to resolve this issue.

Some of the data obtained in this work are of the type normally used for evaluation of the mechanism of the hydrogen evolution reaction. It has been shown elsewhere (13, 19, 20) that if hydrogen evolution occurs via a coupled discharge-recombination mechanism, as is the case for iron, the following relations are obtained at low hydrogen coverages, θ , for rate-controlling diffusion through the membrane

$$i_{\infty} \propto i_c^{1/2} \quad [1]$$

$$\frac{\partial \eta}{\partial \ln i_c} = -\frac{2RT}{F} = -120 \text{ mV} \quad [2]$$

$$\frac{\partial \eta}{\partial \ln i_{\infty}} = \frac{\partial \eta}{\partial \ln \theta} = -\frac{4RT}{F} = -240 \text{ mV} \quad [3]$$

where η is the overpotential for hydrogen evolution, F the Faraday, R the gas constant, and T the temperature. In this investigation it was found that the steady-state permeation current is directly proportional to the square root of the charging current density (Fig. 3 and Table II) for Fe-implanted, He-implanted, and unimplanted iron membranes in accord with Eq. [1]. Furthermore, the Tafel slope (Fig. 4) is -122 ± 5 mV and $\partial \eta / \partial \ln i_{\infty} = -255 \pm 5$ mV (Fig. 5) in reasonably good agreement with Eq. [2] and [3], respectively. At higher cathodic overpotentials in 0.1N NaOH, corresponding to potentials more negative than $-1.0V$ (SHE), there appears to be a change in the mechanism of hydrogen evolution for the unimplanted and Fe- and He-implanted membranes to slow discharge-fast electrochemical desorption, as indicated by an increase in $\partial \eta / \partial \ln i_{\infty}$, Fig. 5 (17, 20).

For Pt-implanted Fe, as modified by the 20 sec acid immersion the Tafel slope is -122 ± 5 mV and $\partial \eta / \partial \ln i_{\infty} = -255 \pm 5$ mV, and the steady-state permeation varies linearly through the origin with the square root of the charging current density. Thus, it is concluded that the mechanism of hydrogen evolution for Pt-implanted Fe is also coupled discharge-chemical desorption in both the 0.1N NaOH and 0.1N H_2SO_4 solutions within the overpotential range studied. The Tafel slope reported in the literature for hydrogen evolution on Pt surfaces is in two different ranges, either -110 to -130 mV in NaOH solutions (27-30) or about -30 mV in H_2SO_4 solutions (29) for ultra-clean systems. Tafel slopes greater than -30 mV in H_2SO_4 have, however, been observed in the presence of impurities (31).

Conclusions

Implantation by the ion beam technique can be used to reduce hydrogen entry into iron. This was shown using the (model) system of Pt implanted into Fe. Pt is known to greatly reduce hydrogen entry into iron via a catalytic effect of the hydrogen evolution reaction when the Pt is present on the surface (4). The effectiveness of implanted Pt was greatly increased by controlled selective dissolution of iron which increased the surface concentration of Pt. There are no significant differences in the permeation behavior of unimplanted and He- or Fe-implanted Fe specimens.

The experimentally observed Tafel slope, the permeation-charging potential relationship, and the permeation-charging current relationship indicate a coupled discharge-recombination mechanism of hydrogen evolution on Fe-, He-, or Pt-implanted Fe surfaces in 0.1N NaOH or 0.1N H_2SO_4 charging solutions.

Acknowledgment

This work was partially supported by the Metallurgy Branch of the Office of Naval Research under Contract N000-14-75-C-0264.

Manuscript submitted Sept. 27, 1979; revised manuscript received Feb. 26, 1980.

Any discussion of this paper will appear in a Discussion Section to be published in the June 1981

JOURNAL. All discussions for the June 1981 Discussion Section should be submitted by Feb. 1, 1981.

Publication costs of this article were assisted by The Pennsylvania State University.

REFERENCES

- M. A. Figelman and A. V. Shreider, *J. Appl. Chem. (USSR)*, **31**, 1175 (1958).
- T. Matsushima and H. H. Uhlig, *This Journal*, **113**, 555 (1966).
- H. P. Tadrif and H. Marquis, *Can. Metall. Q.*, **1**, 153 (1962).
- S. S. Chatterjee, B. G. Ateya, and H. W. Pickering, *Metall. Trans.*, **9A**, 389 (1978).
- V. Ashworth, W. A. Grant, R. P. M. Procter, and T. C. Wellington, *Corros. Sci.*, **16**, 393 (1976).
- V. Ashworth, D. Baxter, W. A. Grant, and R. P. M. Procter, *ibid.*, **16**, 775 (1976).
- V. Ashworth, W. A. Grant, R. P. M. Procter, and E. J. Wright, *ibid.*, **18**, 681 (1978).
- H. W. Pickering and P. J. Byrne, *This Journal*, **120**, 608 (1973).
- R. W. Powers, *Electrochem. Technol.*, **2**, 163 (1969).
- M. A. V. Devanathan and Z. Stachurski, *Proc. Roy. Soc. A*, **270**, 90 (1962).
- G. K. Hubler and E. McCafferty, *Corros. Sci.*, To be published.
- J. K. Hirronen and G. K. Hubler, "Ion Beam Surface Layer Analysis," Vol. 1, O. Meyer, G. Linker, and F. Käppeler, Editors, p. 457, Plenum, New York (1976).
- J. McBreen, L. Nanis, and W. Beck, *This Journal*, **113**, 1218 (1966).
- J. O'M. Bockris, in "Proceedings of International Conference on Stress Corrosion Cracking and Hydrogen Embrittlement of Iron Base Alloys," p. 286, Firminy, France, June 1973.
- T. R. Radhakrishnan and L. L. Shreir, *Electrochim. Acta*, **12**, 889 (1967).
- O. D. Gonzalez, *Trans. Met. Soc. AIME*, **239**, 229 (1967).
- J. O'M. Bockris, J. McBreen, and L. Nanis, *This Journal*, **112**, 1025 (1965).
- W. Whitman, R. Russel, C. Welling, and J. Cochran, *Ind. Eng. Chem.*, **15**, 672 (1923).
- J. McBreen and M. A. Genshaw, in "Proceedings of the International Conference on Fundamental Aspects of Stress Corrosion Cracking," R. W. Staehle, A. J. Forty, and D. van Rooyan, Editors, p. 51, NACE (1969).
- M. A. V. Devanathan and Z. Stachurski, *This Journal*, **111**, 619 (1964).
- H. W. Pickering, *ibid.*, **117**, 8 (1970).
- H. W. Pickering and C. Wagner, *This Journal*, **114**, 698 (1967).
- H. W. Pickering, *ibid.*, **115**, 143 (1968).
- J. E. Holliday and H. W. Pickering, *ibid.*, **120**, 470 (1973).
- H. W. Pickering, "Darken Conference: Physical Chemistry in Metallurgy," R. M. Fisher, R. A. Oriani, and E. T. Turkdogan, Editors, pp. 353-373, U.S. Steel Corporation, Pittsburgh, Pa. (1976).
- S. M. Myers, S. T. Picraux, and R. E. Stoltz, *J. Appl. Phys.*, To be published.
- S. Schuldiner, *This Journal*, **107**, 426 (1954).
- I. A. Ammar and S. Darwich, *J. Phys. Chem.*, **63**, 983 (1959).
- J. O'M. Bockris and S. Srinivasan, *Electrochim. Acta*, **9**, 31 (1964).
- C. M. Shepherd and S. Schuldiner, *This Journal*, **115**, 1124 (1968).
- J. O'M. Bockris, I. A. Ammar, and A. K. M. S. Huq, *J. Phys. Chem.*, **61**, 879 (1957).

Impedance Measurements of the Anodic Iron Dissolution

H. Schweickert and W. J. Lorenz

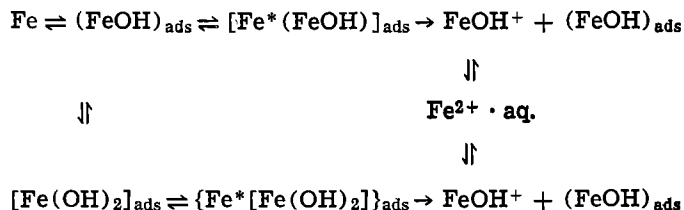
Institute of Physical Chemistry and Electrochemistry, University of Karlsruhe, Karlsruhe, Germany

and H. Friedburg

Institute of Microwave-Technics and Electronics, University of Karlsruhe, Karlsruhe, Germany

ABSTRACT

The kinetics of the Fe/Fe²⁺ electrode have previously been explained on the basis of either a consecutive or a catalytic charge transfer mechanism including adsorbed intermediates. In order to obtain more exact kinetic information, pulse and frequency response measurements on polycrystalline Fe in acidic sulfate solutions at *T* = 298°K have been carried out. The stationary current density-potential curves already allow a preselection of the proposed reaction models. Dynamic parameters were calculated from the measured electrode impedance. It is shown that the existing reaction models do not agree with the measured impedance behavior. However, the experimental results can be explained assuming a potential-dependent relaxation of the surface combined with a catalyzed dissolution mechanism. The mechanism of the iron electrode in the active, transition, and prepassive ranges can be described by the reaction scheme



The kinetic data of the anodic iron dissolution in acid solutions free of oxygen and surface active substances have been interpreted for the active range

Key words: iron dissolution kinetics, impedance measurements, surface structure, surface relaxation.

assuming a consecutive mechanism [Bockris (1)] or a catalyzed mechanism [Heusler (2)] which depend on the substructure of the electrode, i.e., the surface activity (3-5). The kinetics of the iron dissolution processes in the transition, prepassive, and passive

layer formation ranges have been explained taking into account different intermediates, $[\text{Fe}(\text{OH})_n]_{\text{ads}}$ with $n = 1, 2, 3$, which are potential-dependently adsorbed at the metal surface (6-11). The proposed mechanism of iron dissolution in the different ranges is shown in Table I.

Nonstationary methods have been used to further clarify the electrode reaction mechanism, e.g., pulse techniques or sine wave measurements (12-15). Single pulse measurements have been performed on the iron electrode (2, 16, 17). The galvanostatic double pulse (GDP) method has been applied only on the consecutive charge transfer reaction of the Cu/Cu^{2+} electrode (18). Impedance measurements of iron dissolution have been carried out extensively by Epelboin *et al.* (19-28).

Transfer Function Measuring Methods

The dynamic electrochemical electrode properties, i.e., the transfer function or the two-pole function,¹ can be determined by analyzing the system response which can be measured either directly as a function of time (time domain) or as a function of the frequencies of the applied test signal (frequency domain). The system responses in both domains are connected by the Laplace transformation. The analysis of the system response is often more difficult in the time domain than in the frequency domain (29). Moreover, a greater resolution of the system response in the frequency domain can be achieved. Therefore, in many cases measurements in the frequency domain are more precise.

For frequency response measurements on electrochemical systems a large frequency range from mHz up to MHz may be necessary and the correlation technique² appears to be the most convenient one (23, 29).

Neglecting transport phenomena, the measured impedance of the system, as well as that calculated for the reaction model, can be represented by a broken rational function

$$Z(s) = \frac{\sum_{i=0}^m p_i s^i}{\sum_{i=0}^n q_i s^i} = k \frac{\prod_{i=1}^m (s - s_{oi})}{\prod_{i=1}^n (s - s_{zi})} \quad [1]$$

where p_i and q_i are the coefficients, while s denotes the Laplace variable and s_{oi} and s_{zi} represent the zeros and poles of this function.

The impedance Z corresponds to a two-pole function and, therefore, the relation

$$m - 1 \leq n \leq m + 1 \quad [2]$$

must be valid. Moreover, the two-pole function must be stable having no singularities under both potentiostatic and galvanostatic control (30). The two-pole function can be determined graphically or analytically. In the case of more complicated electrode properties, analytical methods are to be preferred (29).

Experimental

The investigations were carried out in the systems $\text{Fe}(\text{polycrystalline})/x \cdot \text{M H}_2\text{SO}_4 + y \cdot \text{M Na}_2\text{SO}_4$ ($x + y = 0.5$), $0.3 \leq \text{pH} \leq 6$ at $T = 298^\circ\text{K}$ using conventional three-electrode techniques. Additionally, a platinum probe was connected in parallel with the reference electrode ($\text{Hg}/\text{Hg}_2\text{Cl}_2/\text{KCl sat.}$) by a capacitor in order to achieve a reference system of low re-

¹ The transfer function generally represents the correlation between input and output variables. In the case of electrochemical systems, the interest is mostly directed to the correlation between the current flux and the voltage across the electrode/electrolyte interphase. This special type of transfer function is called the two-pole function.

² The correlation technique gives directly the real and imaginary parts of the transfer function calculated via the cross-correlation functions between the test signal and the system response.

Table I. Mechanism of anodic iron dissolution and passivation in electrolytes free of oxygen and surface active substances at $0 < \text{pH} < 6$

Active range	
$\text{Fe} + \text{H}_2\text{O} \rightleftharpoons (\text{FeOH})_{\text{ads}} + \text{H}^+ + e^-$	[11]
Catalyzed charge transfer	Noncatalyzed charge transfer
$\text{Fe} + (\text{FeOH})_{\text{ads}} \rightleftharpoons [\text{Fe}(\text{FeOH})]_{\text{ads}}$	$(\text{FeOH})_{\text{ads}} \xrightarrow{\text{rds}} \text{FeOH}^+ + e^-$ [2]
$[\text{Fe}(\text{FeOH})]_{\text{ads}} + \text{OH}^- \xrightarrow{\text{rds}}$	[3]
$\text{FeOH}^+ + (\text{FeOH})_{\text{ads}} + 2e^-$	[4]
$\text{FeOH}^+ + \text{H}^+ \rightleftharpoons \text{Fe}^{2+} \cdot \text{aq.} + \text{H}_2\text{O}$	[5]
Transition range	
$(\text{FeOH})_{\text{ads}} + \text{H}_2\text{O} \rightleftharpoons [\text{Fe}(\text{OH})_2]_{\text{ads}} + \text{H}^+ + e^-$	[6]
Prepassive range	
$\text{Fe} + [\text{Fe}(\text{OH})_2]_{\text{ads}} \xrightarrow{\text{rds}} \text{FeOH}^+ + (\text{FeOH})_{\text{ads}} + e^-$	[7]
$[\text{Fe}(\text{OH})_2]_{\text{ads}} + \text{H}_2\text{O} \rightleftharpoons \text{Fe}(\text{OH})_3 - \text{oxide phase} + \text{H}^+ + e^-$	[8]
Passive layer formation range	
$2\text{Fe}(\text{OH})_3 - \text{oxide phase} \rightleftharpoons \text{Fe}_2\text{O}_3 + 3\text{H}_2\text{O}$	[9]
$[\text{Fe}(\text{OH})_2]_{\text{ads}} + \text{Fe}_2\text{O}_3 \rightleftharpoons \text{Fe}_3\text{O}_4 + \text{H}_2\text{O}$	[10]

sistance which is important for avoiding phase shifts at high frequencies.

A rotating disk electrode was used as the working electrode, the rotational speed could be varied between $5 \cdot \text{sec}^{-1} \leq \nu \leq 160 \cdot \text{sec}^{-1}$. The polycrystalline, highly pure iron samples³ were recrystallized under vacuum ($p < 10^{-8}$ bar) at $T = 1400^\circ\text{K}$ for 2 hr. The electrode was then embedded in polyethylene holders with an epoxy resin. After polishing and cleaning with acetone, the electrode was dipped in 0.5M H_2SO_4 for 10 min. Prior to each experiment, the electrode was polarized anodically by a current density of $i = 70 \text{ mA} \cdot \text{cm}^{-2}$ for 5 min in the measuring cell in order to provide a reproducible initial state of the electrode surface.

The electrolytes with constant ionic strength of $c_{\text{SO}_4^{2-}} = 0.5\text{M}$ were prepared of sulfuric acid,⁴ sodium sulfate,⁴ and bidistilled water. The system was maintained under hydrogen atmosphere.

The experiments were carried out under potentiostatic as well as under galvanostatic conditions using a Wenking potentiostat, Type PCA 72 L, and a Megaphysik multichannel pulse galvanostat system MPI-IM 400, respectively. A Solartron Frequency Response Analyser 1172 was applied for transfer locus measurements. The pulse responses were registered by a Tektronix storage oscilloscope, Type 549 with plug-in unit W.

In the transition range, the iron dissolution is characterized by nonmonotonous current density-potential curves (7-9). Therefore, only potentiostatic measurements can be performed in this range in order to get defined stationary conditions.

Further experimental details are published elsewhere (31).

Results

The basic requirements of nonstationary low signal measurements is the stability of operating points of the system under investigation. First information about the reaction kinetics can be obtained by analyzing the stationary current density-potential curves.

Stationary measurements.—The stationary current density-potential curves were registered point by point. Under galvanostatic control, the stationarity was assumed when the condition $|\Delta e/\Delta t| < 1 \text{ mV} \cdot \text{min}^{-1}$ was fulfilled. Under potentiostatic control, a variation of the current less than $1\% \cdot \text{min}^{-1}$ and an asymptotic current-time transient were required.

³ Marz grade iron (Materials Research Corporation).

⁴ Suprapur grade (Merck).

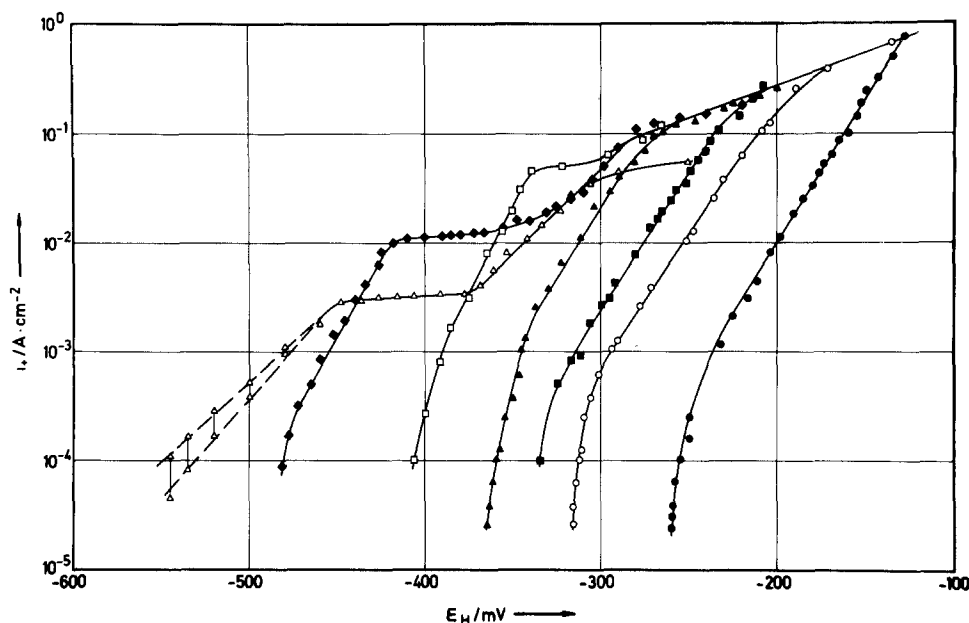


Fig. 1. Stationary anodic current density-potential curves of the systems Fe(polycrystalline, recrystallized)/ $x \cdot M \text{Na}_2\text{SO}_4 + y \cdot M \text{H}_2\text{SO}_4$ ($c_{\text{SO}_4^{2-}} = 0.5M$); $T = 298^\circ\text{K}$, galvanostatic and potentiostatic measurements. $\nu = 70 \text{ sec}^{-1}$: \bullet , pH = 0.3; \circ , pH = 1.45; \blacksquare , pH = 2; \blacktriangle , pH = 2.9; \square , pH = 4; \blacklozenge , pH = 5. $\nu = 70\text{-}150 \text{ sec}^{-1}$: \triangle , pH = 6.

Longer waiting periods caused no significant changes of the stationary values. At higher pH values, the waiting time for stationarity in transition and prepassive ranges ($i > 10 \text{ mA} \cdot \text{cm}^{-2}$) was about 15 min.

Figure 1 shows the measured stationary current density-potential curves in the active, transition, and prepassive ranges. The given potentials are corrected for the ohmic drop, IR_Ω . The current density is related to the geometrical surface area.

In general, the rotational speed of the rotating disk electrode does not influence the anodic results (16, 17). Only at pH > 5.0 the current density in the active range decreased slightly with increasing rotational speed at constant electrode potential.

As can be seen from Fig. 1, the active range of iron dissolution at $0 < \text{pH} < 3$ is characterized by Tafel slopes of $b_+ = (\partial \epsilon / \partial \log i_+)_{a_i} = +40 \pm 2 \text{ mV}$. The index a_i denotes constant activities of all species i , except $a_{\text{Fe}^{2+}}$ in the electrolyte. The iron dissolution kinetics, however, is independent of $a_{\text{Fe}^{2+}}$ (3). The standard deviation of the Tafel slopes was determined by averaging different current density-potential measurements at each constant pH value.

The pH dependence of the iron dissolution kinetics is characterized by the electrochemical reaction order

$$n_{+, \text{pH}} = \left(\frac{\partial \log i_+}{\partial \text{pH}} \right)_{\epsilon, a_i} \quad [3]$$

where the index a_i denotes constant activities of all species i except $a_{\text{Fe}^{2+}}$ and a_{H^+} in the electrolyte. It can be shown using the Jacobian representation of the partial derivatives that

$$n_{+, \text{pH}} = - \left(\frac{\partial \log i_+}{\partial \epsilon} \right)_{a_i, \text{pH}} \cdot \left(\frac{\partial \epsilon}{\partial \text{pH}} \right)_{i_+, a_i} \\ = - \frac{1}{b_+} \cdot \left(\frac{\partial \epsilon}{\partial \text{pH}} \right)_{i_+, a_i} \quad [4]$$

Inserting the experimental results given in Fig. 2 and the measured Tafel slope of $b_+ = +40 \pm 2 \text{ mV}$ into Eq. [4], one obtains an electrochemical reaction order of $n_{+, \text{pH}} = 1.1 \pm 0.1$.

In contrast to earlier findings (7, 9), the transition range is characterized by a current density plateau I instead of the previously reported current density maximum I (7, 9-11). It can be shown that the current maximum I appears only under potentiodynamic polarization conditions using sweep rates $|d\epsilon/dt| \gtrsim 0.1 \text{ mV} \cdot \text{sec}^{-1}$. Obviously, the time constants of the reaction kinetics in the transition range are rela-

tively high. The pH dependence of the current density plateau I (Fig. 3) was found to be

$$\left(\frac{\partial \log i_{+, \text{pl } I}}{\partial \text{pH}} \right)_{a_j} = -0.6 \pm 0.05 \quad [5]$$

The adjacent prepassive range is characterized by a Tafel slope of $b_+ = 60 \pm 8 \text{ mV}$ (Fig. 1) and a reaction order of $n_{+, \text{pH}} = 0 \pm 0.1$. This Tafel slope of about 60 mV contradicts previous results of $b_+ = +120 \text{ mV}$ (7-10). It can be shown clearly that this discrepancy is caused by the influence of the sweep rate on the anodic current density-potential measurements. A steady state of the iron electrode in the prepassive range can be achieved only at sweep rates $|d\epsilon/dt| \lesssim 0.1 \text{ mV} \cdot \text{sec}^{-1}$. However, this lower Tafel slope in the beginning of the prepassive range violates the reaction model given in Table I. In this model, the prepassive range is characterized by a dominating electrochemical equilibrium (step [8], Table I) and

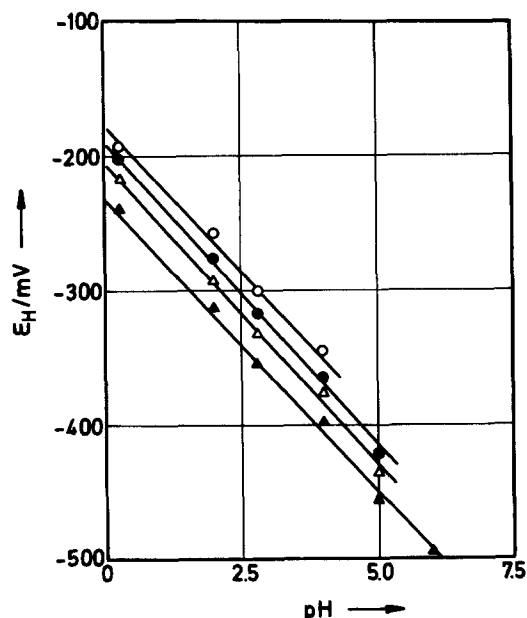


Fig. 2. pH dependence of the stationary anodic current density-potential curves in the active range of the system Fe/ $x \cdot M \text{Na}_2\text{SO}_4 + y \cdot M \text{H}_2\text{SO}_4$ ($c_{\text{SO}_4^{2-}} = 0.5M$); $T = 298^\circ\text{K}$; $\nu = 70 \text{ sec}^{-1}$. \blacktriangle , $1 \text{ mA} \cdot \text{cm}^{-2}$; \triangle , $4 \text{ mA} \cdot \text{cm}^{-2}$; \bullet , $10 \text{ mA} \cdot \text{cm}^{-2}$; \circ , $30 \text{ mA} \cdot \text{cm}^{-2}$.

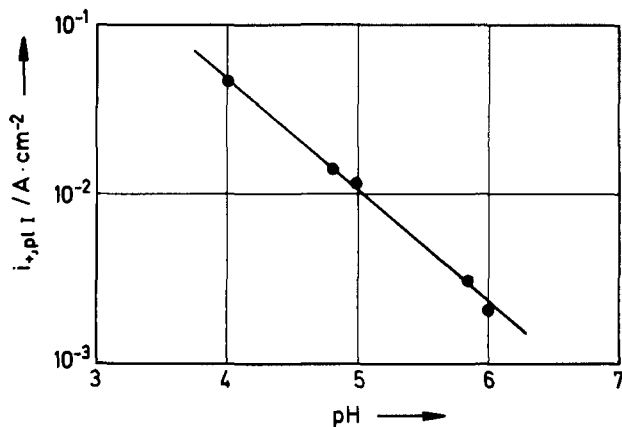


Fig. 3. pH dependence of the current density $i_{+,pl} I$ at plateau I. System: $\text{Fe}/x \cdot \text{M Na}_2\text{SO}_4 + y \cdot \text{M H}_2\text{SO}_4$ ($c_{\text{SO}_4^{2-}} = 0.5\text{M}$); $T = 298^\circ\text{K}$; $\nu = 70 \text{ sec}^{-1}$.

by a rate-determining charge transfer reaction (step [7], Table I) which occur in parallel. The degree of coverage of the electrode surface with $[\text{Fe}(\text{OH})_2]_{\text{ads}} \equiv \theta_2$ has been assumed to be nearly unity and constant. Under these conditions, the reaction model in Table I leads to a Tafel slope of $b_+ = 2.303RT/\alpha_7F$ and an electrochemical reaction order $n_{+,pH} = 0$ for the prepassive range (8-10).

Impedance measurements.—Frequency response measurements have been carried out in the frequency range $5 \cdot 10^{-3} \leq f \leq 10^4 \text{ Hz}$. In order to get quantities independent of the geometrical surface area, a normalized and dimensionless impedance

$$Z_N = (Z_m - R_\Omega) \cdot \frac{I_s}{U_N} = R_N + jX_N \quad [6]$$

is used, where Z_m denotes the measured impedance, I_s is the stationary d-c current in the outer circuit, and the normalization voltage U_N is taken as 1 mV.

Normalized reaction impedances Z_N of the systems $\text{Fe}(\text{polycrystalline})/x \cdot \text{M H}_2\text{SO}_4 + y \cdot \text{M Na}_2\text{SO}_4$ ($c_{\text{SO}_4^{2-}} = 0.5\text{M}$) are shown in Fig. 4-6 for the active, transition, and prepassive ranges. The impedance diagrams agree qualitatively with the results previously published by Epelboin *et al.* (19, 20, 22, 27, 28).

The steady-state value $Z_N(f = 0)$, which is identical with the polarization resistance R_{pN} , was calculated from the stationary current density-potential curves by

$$R_{pN} = R_p \cdot I_s / U_N \quad [7]$$

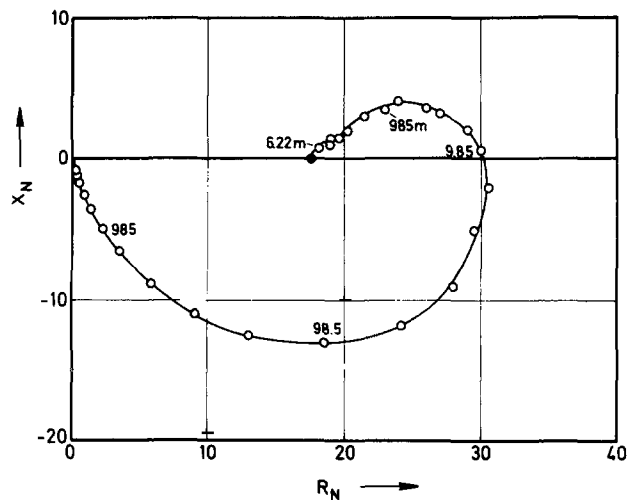
where

$$R_p \cdot I_s = \frac{d\epsilon}{dI_s} \cdot I_s = b_+ \cdot \frac{1}{2.303} \quad [8]$$

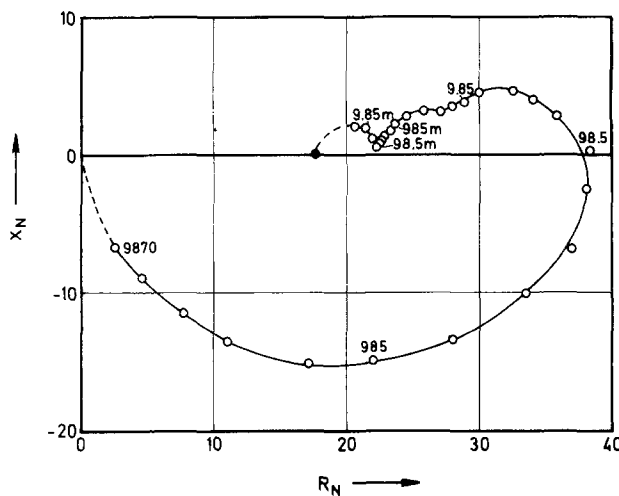
The transfer resistance R_t is defined as the real part of the impedance Z at infinite frequency after subtraction of the impedance arising from the double layer capacity C_D .

From the impedance diagrams, the following facts can be derived: (i) Several time constants exist in the inductive part. (ii) The capacitive part differs from a semicircle, i.e., the frequency response in the capacitive half-plane is determined by more than one time constant. (iii) In the transition range, negative real parts of the electrode impedance were found. (iv) In the prepassive range, the extrapolation of the transfer locus $f \rightarrow 0$ yields a polarization resistance R_{pN} which corresponds to a Tafel slope of $b_+ = 60 \text{ mV}$. This finding agrees well with the results of the stationary measurements.

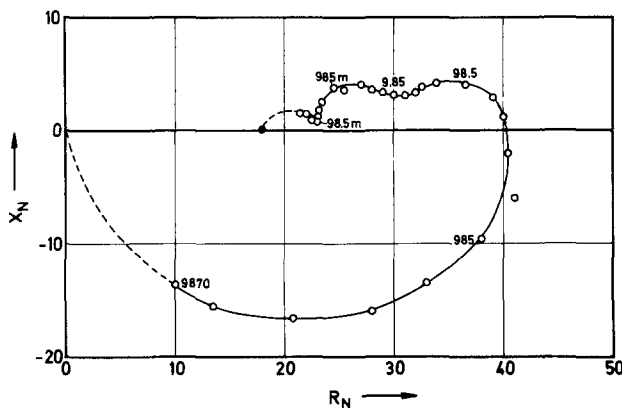
The broken rational function Eq. [1] under the restriction of Eq. [2] was fitted to the normalized impedance diagrams obtained for the iron dissolution in the active range at different pH values. A satisfactory fit



a. $\epsilon_H = -225 \text{ mV}$; $i_s = 2 \text{ mA} \cdot \text{cm}^{-2}$



b. $\epsilon_H = -203 \text{ mV}$; $i_s = 8 \text{ mA} \cdot \text{cm}^{-2}$



c. $\epsilon_H = -160 \text{ mV}$; $i_s = 100 \text{ mA} \cdot \text{cm}^{-2}$

Fig. 4. Transfer loci of the electrode impedance in the active range of iron dissolution. System: $\text{Fe}/0.5\text{M H}_2\text{SO}_4$; $\text{pH} = 0.3$; $T = 298^\circ\text{K}$; $\nu = 70 \text{ sec}^{-1}$; frequencies in Hz. ●, Stationary value Z ($f \rightarrow 0$) calculated from the Tafel slope.

for the degree $m/n = 4/5$ was obtained corresponding to the solid lines in Fig. 3. This result shows that one has to expect five time constants for the system studied in the active range. Two of these time constants determine the capacitive part of the transfer locus and three of them the inductive part. Obviously, one of the time constants in the capacitive part of the transfer locus represents the influence of the double layer capacity C_D .

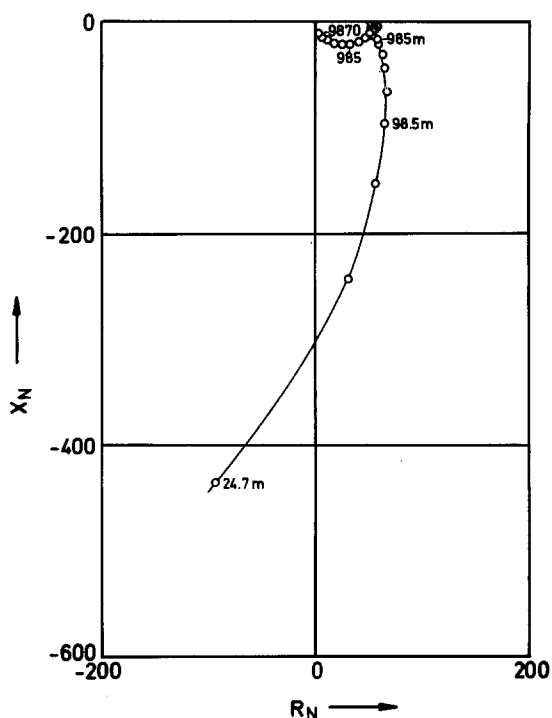


Fig. 5. Transfer locus of the electrode impedance in the transition range of iron dissolution. System: $\text{Fe}/x \cdot \text{M Na}_2\text{SO}_4 + y \cdot \text{M H}_2\text{SO}_4$ ($c_{\text{SO}_4^{2-}} = 0.5 \text{ M}$); $\text{pH} = 5$; $T = 298^\circ\text{K}$; $\nu = 70 \text{ sec}^{-1}$; $\epsilon_{\text{H}} = -313 \text{ mV}$; $i_s = 28 \text{ mA} \cdot \text{cm}^{-2}$; frequencies in Hz.

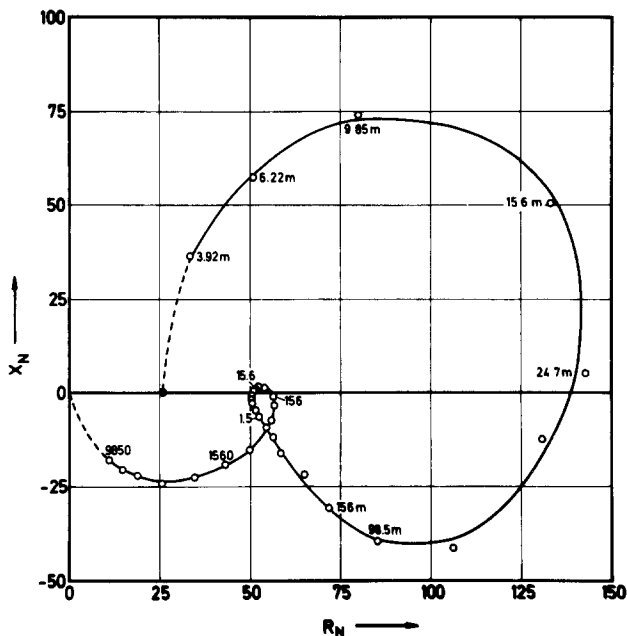


Fig. 6. Transfer locus of the electrode impedance in the 60 mV Tafel region of the prepulsive range of iron dissolution. System: $\text{Fe}/x \cdot \text{M Na}_2\text{SO}_4 + y \cdot \text{M H}_2\text{SO}_4$ ($c_{\text{SO}_4^{2-}} = 0.5 \text{ M}$); $\text{pH} = 5$; $T = 298^\circ\text{K}$; $\nu = 70 \text{ sec}^{-1}$; $\epsilon_{\text{H}} = -293 \text{ mV}$; $i_s = 63 \text{ mA} \cdot \text{cm}^{-2}$; frequencies in Hz. ●, Stationary value $Z(f \rightarrow 0)$; calculated from the Tafel slope.

Under the assumption that the double layer capacity is in parallel with the faradaic impedance Z_f , the values of C_D and $R_t \cdot I_s$ have been determined from the coefficients of the fitted broken rational function Eq. [1]) as well as by graphical analysis of the transfer loci after transformation of the impedance diagrams into the admittance plane (31). Both, C_D and R_t have been obtained additionally applying the GDP method (18).

Figures 7 and 8 show the results for the active dissolution of iron. At relatively low overvoltages, an apparent Tafel slope of

$$b_t = \left(\frac{\partial \epsilon}{\partial \log (R_t \cdot I_s)} \right)_{a_i} = 56 \pm 5 \text{ mV} \quad [9]$$

and a reaction order related to the pH value

$$n_{t,\text{pH}} = \left(\frac{\partial \log (R_t \cdot I_s)}{\partial \text{pH}} \right)_{\epsilon, a_i} = 0.81 \pm 0.05 \quad [10]$$

can be estimated from the results in Fig. 8. At relatively high overvoltages, $R_t I_s$ becomes constant at about $30 \pm 5 \text{ mV}$ and the reaction order $n_{t,\text{pH}}$ reaches zero (Fig. 8).

Discussion

Kinetics with regard to previous models.—The experimental results of the iron dissolution in the active range are usually explained on the basis of the consecutive (Bockris) mechanism, corresponding to the reaction steps [1], [2], and [5] in Table I. Under the conditions (i) step [1] is in equilibrium, (ii) step [2] is the rate-determining one, and (iii) Langmuir adsorption behavior of the intermediate $(\text{FeOH})_{\text{ads}}$ is valid at relatively low degree of coverage, a theoretical treatment of the consecutive mechanism yields a steady-state Tafel slope of $b_+ = 2.303RT/(1 + \alpha_2)F = +40 \text{ mV}$ at $\alpha_2 = 0.5$, $T = 298^\circ\text{K}$, and an electrochemical reaction order of $n_{+, \text{pH}} = +1$ (32). These theoretical values agree well with the present data. For this mechanism, the theoretical frequency response of the electrode impedance must be capacitive in the whole frequency range (31, 33). However, this prediction is contradicted by the experimental inductive impedance characteristics of the iron electrode in the active range at lower frequencies [cf. Fig. 3, (19, 20, 22, 27, 28)].

Impedance measurements on active iron electrodes showing inductive parts were interpreted by Epelboin

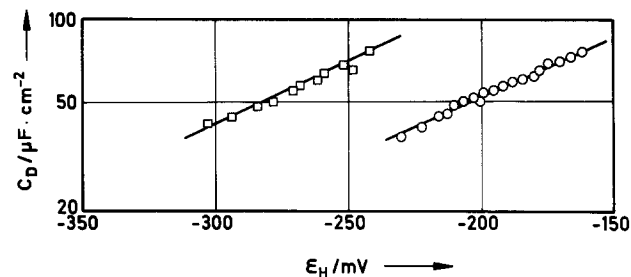


Fig. 7. Potential dependence of the double layer capacity as a function of pH. System: $\text{Fe}/x \cdot \text{M Na}_2\text{SO}_4 + y \cdot \text{M H}_2\text{SO}_4$ ($c_{\text{SO}_4^{2-}} = 0.5 \text{ M}$); $T = 298^\circ\text{K}$; $\nu = 70 \text{ sec}^{-1}$. ○, $\text{pH} = 0.3$; □, $\text{pH} = 2$.

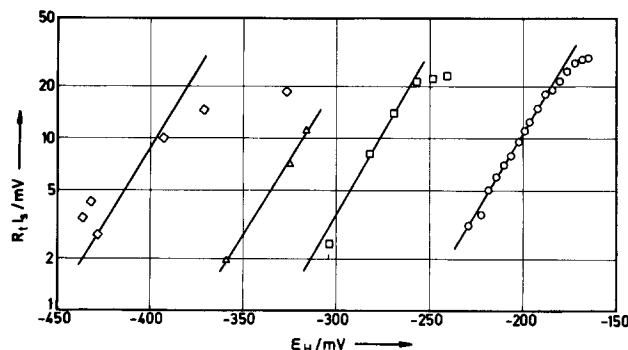


Fig. 8. Potential dependence of $R_t \cdot I_s$ as a function of pH. System: $\text{Fe}/x \cdot \text{M Na}_2\text{SO}_4 + y \cdot \text{M H}_2\text{SO}_4$ ($c_{\text{SO}_4^{2-}} = 0.5 \text{ M}$); $T = 298^\circ\text{K}$; $\nu = 70 \text{ sec}^{-1}$; ○, $\text{pH} = 0.3$; □, $\text{pH} = 2$; △, $\text{pH} = 2.9$; ◇, $\text{pH} = 5$.

et al. (22, 27, 28) using a modified consecutive Bockris mechanism. Their theoretical considerations are based on experimental steady-state Tafel slopes of $b_+ = 63$ mV at low overvoltages and $b_+ = 220$ mV at high overvoltages with corresponding electrochemical reaction orders of $n_{+,pH} = 1$ and $n_{+,pH} = 0$, respectively. In the reaction model proposed, the reaction step [1] is assumed to be irreversible. This model is only able to explain anodic steady-state Tafel slopes of $b_+ \geq 60$ mV at $T = 298^\circ\text{K}$, leading to asymmetric charge transfer coefficients of $\alpha_1 = 0.96-0.99$ and $\alpha_2 = 0.18-0.27$, respectively. Obviously, the relatively high b_+ and α_1 values do not agree with the usual results and interpretations (3, 32-36).

Furthermore, because of the occurrence of capacitive reaction impedances, the disregard of all capacitive parts, as done by Epelboin *et al.* (22, 27, 28), seems rather doubtful.

Lorenz *et al.* (4, 5) had previously suggested iron dissolution to be caused by the simultaneous transfer reactions of the consecutive and the catalyzed mechanisms given in Table I. On the basis of this concept, the measured steady-state values $b_+ = 40$ mV and $n_{+,pH} = 1$ in the active range can only be explained by a dominating consecutive dissolution mechanism. However, a theoretical analysis of the corresponding impedance behavior (31) leads to the additional conditions $b_t = 60$ mV and $R_t \cdot I_s < 5.2$ mV. The experimental $R_t \cdot I_s$ values (Fig. 7) were much greater than 5.2 mV showing that the reaction cannot be described by a dominating Bockris mechanism only.

Consequently, all theoretical models including a consecutive Bockris mechanism are not appropriate to explain both the steady-state kinetic data and the dynamic electrode behavior.

Kinetics with regard to the surface state.—The existing reaction models have been based on the uniformity and potential independence of the electrode surface. However, it is well known that a polycrystalline metal surface is inhomogeneous and contains discontinuities such as grain boundaries, atomic step lines, etc. Such a surface is subdivided in different microregions with different electrochemical behavior depending on the crystal orientation, microroughness, and dislocation density. For this reason, the anodic metal dissolution process will take place preferentially at active surface sites. It has been demonstrated that kink sites are mainly responsible as active centers for the charge transfer process of metal ions (34, 37-47). Obviously, surface diffusion processes do not play an important role in the kinetics (40, 48). Kink sites are localized at monoatomic steps which can be produced by 2-D nucleation and growth processes as well as via screw dislocations. Emergency points of edge dislocations at the metal surface are inactive for the metal deposition processes, while they represent active centers for metal dissolution (49).

Recently, Harrison *et al.* (50, 51) assumed that structural surface effects have to be taken into account for explaining the time dependence of copper and gold electrode kinetics. Furthermore, morphological and electrochemical investigations on single crystal faces of iron electrodes showed a significant influence of the surface structure and the density of kink sites on the anodic dissolution process (44-47).

Consequently, a reaction model of the iron dissolution, the charge transfer of which is catalyzed by surface active Fe^* centers, is proposed for the active, transition, and prepassive ranges. A relatively simple reaction scheme for a polycrystalline iron surface is given in Table II. Moreover, a time dependence, as well as a potential dependence, of the surface state may be assumed. This surface relaxation process will change both the number N of the adsorption sites and the number N^* of the active centers. The catalysts $\{\text{Fe}^*(\text{FeOH})\}_{\text{ads}}$ and $\{\text{Fe}^*[\text{Fe}(\text{OH})_2]\}_{\text{ads}}$ are assumed to be formed at N^* sites, only.

Table II. Modified mechanism of anodic iron dissolution

Active range	
$\text{Fe} + \text{H}_2\text{O} \rightleftharpoons (\text{FeOH})_{\text{ads}} + \text{H}^+ + e^-$	[1]
$\text{Fe}^* + (\text{FeOH})_{\text{ads}} \rightleftharpoons [\text{Fe}^*(\text{FeOH})]_{\text{ads}}$	[3]
$[\text{Fe}^*(\text{FeOH})]_{\text{ads}} + \text{OH}^- \xrightarrow{\text{rds}} \text{FeOH}^+ + (\text{FeOH})_{\text{ads}} + 2e^-$	[4]
Transition range and the beginning of prepassive range†	
$(\text{FeOH})_{\text{ads}} + \text{H}_2\text{O} \rightleftharpoons [\text{Fe}(\text{OH})_2]_{\text{ads}} + \text{H}^+ + e^-$	[6]
$\text{Fe}^* + [\text{Fe}(\text{OH})_2]_{\text{ads}} \rightleftharpoons \{\text{Fe}^*[\text{Fe}(\text{OH})_2]\}_{\text{ads}}$	[7a]
$\{\text{Fe}^*[\text{Fe}(\text{OH})_2]\}_{\text{ads}} \xrightarrow{\text{rds}} \text{FeOH}^+ + (\text{FeOH})_{\text{ads}} + e^-$	[7b]
$\text{FeOH}^+ + \text{H}^+ \rightleftharpoons \text{Fe}^{2+} \cdot \text{aq.} + \text{H}_2\text{O}$	[5]

† At higher overvoltages in the prepassive range, the increasing formation of $\text{Fe}(\text{OH})_3$ -oxide phase (Eq. [8] in Table I) causes the maximum II in the current density-potential curves (8-11). The present investigation does not regard this extended prepassive range.

Next, the following notations will be used

$$N_1 = \text{number of adsorbed species } (\text{FeOH})_{\text{ads}} \quad [11]$$

$$N_2 = \text{number of adsorbed species } [\text{Fe}(\text{OH})_2]_{\text{ads}} \quad [12]$$

$$N_{k1} = \text{number of adsorbed species } [\text{Fe}^*(\text{FeOH})]_{\text{ads}} \quad [13]$$

$$N_{k2} = \text{number of adsorbed species } \{\text{Fe}^*[\text{Fe}(\text{OH})_2]\}_{\text{ads}} \quad [14]$$

Clearly, the number of the free adsorption places on the electrode surface is given by $N - N_1 - N_2 - N_{k1} - N_{k2}$. Normalizing the different N values with respect to the corresponding equilibrium values, leads to

$$\frac{N}{N_o} \equiv \Phi \equiv \text{roughness coefficient} \quad [15]$$

$$\frac{N^*}{N_o^*} \equiv \Psi \equiv \text{active center coefficient} \quad [16]$$

$$\frac{N_1}{N_o} \equiv \theta_1 \equiv \text{degree of coverage with } (\text{FeOH})_{\text{ads}} \text{ or } [\text{Fe}(\text{OH})_2]_{\text{ads}}, \text{ respectively} \quad [17]$$

$$\frac{N_{ki}}{N_o} \equiv \theta_{ki} \equiv \text{degree of coverage with } [\text{Fe}^*(\text{FeOH})]_{\text{ads}} \text{ or } \{\text{Fe}^*[\text{Fe}(\text{OH})_2]\}_{\text{ads}}, \text{ respectively} \quad [18]$$

The index o indicates the values at the equilibrium potential ϵ_o of the Fe/Fe^{2+} electrode.

Assuming (i) Langmuir adsorption behavior and (ii) the reverse reaction of the rate-determining steps [4] and [7b] in Table II to be negligible, the following reaction equations can be derived using the exchange flux densities, $v_{o,i}$ (cf. Table II)

$$v_1 = v_{o,1} \left\{ \frac{\Phi - \theta_1 - \theta_{k1} - \theta_2 - \theta_{k2}}{1 - \theta_{10} - \theta_{k10} - \theta_{20} - \theta_{k20}} E_1 - \frac{\theta_1}{\theta_{10}} E_{-1} \right\} \quad [19]$$

$$v_3 = v_{o,3} \left\{ \frac{\theta_1}{\theta_{10}} \Psi - \frac{\theta_{k1}}{\theta_{k10}} \right\} \quad [20]$$

$$v_4 = v_{o,4} \frac{\theta_{k1}}{\theta_{k10}} E_4 \quad [21]$$

$$v_6 = v_{o,6} \left\{ \frac{\theta_1}{\theta_{10}} E_6 - \frac{\theta_2}{\theta_{20}} E_{-6} \right\} \quad [22]$$

$$v_{7a} = v_{o,7a} \left\{ \frac{\theta_2}{\theta_{20}} \Psi - \frac{\theta_{k2}}{\theta_{k20}} \right\} \quad [23]$$

$$v_{7b} = v_{o,7b} \frac{\theta_{k2}}{\theta_{k20}} E_7 \quad [24]$$

with

$$E_1 = \exp \left(\frac{z_1 \alpha_1 F}{RT} \eta \right) \quad [25]$$

and

$$E_{-1} = \exp \left(\frac{-z_1(1 - \alpha_1) F}{RT} \eta \right) \quad [26]$$

where z_1 = electrochemical valency and $\eta = e - e_0$.
The flux balances yield

$$N_o \left| \frac{d\theta_1}{dt} = v_1 - v_3 + v_4 - v_6 + v_{7b} \right. \quad [27]$$

$$N_o \frac{d\theta_{k1}}{dt} = v_3 - v_4 \quad [28]$$

$$N_o \frac{d\theta_2}{dt} = v_6 - v_{7a} \quad [29]$$

$$N_o \left| \frac{d\theta_{k2}}{dt} = v_{7a} - v_{7b} \right. \quad [30]$$

The surface functions Φ and Ψ are assumed to be simple exponential functions

$$\Phi = \exp \left(\frac{\alpha_\Phi F \eta}{RT} \right) \quad [31]$$

$$\Psi = \exp \left(\frac{\alpha_\Psi F \eta}{RT} \right) \quad [32]$$

where α_Φ and α_Ψ are formal parameters.

From Eq. [19-32], a general stationary current density-potential relation of the iron dissolution reaction in the active, transition, and prepassive ranges results

$$i_s = 2F\Phi\Psi \frac{v_{o,4}E_4W_3 + v_{o,7b}E_7W_4}{\{(W_1K + \theta_{10})W_4 + \theta_{k10}\Psi\}W_3 + W_4(\theta_{20}W_2 + \theta_{k20}\Psi)} \quad [33]$$

where

$$K \equiv \exp \left(-\frac{F}{RT} \eta \right) \quad [34]$$

$$W_1 \equiv 1 - \theta_{10} - \theta_{20} - \theta_{k10} - \theta_{k20} \quad [35]$$

$$W_2 \equiv 1 + \frac{v_{o,7b}}{v_{o,7a}} E_7 \quad [36]$$

$$W_3 \equiv K \cdot W_2 + \frac{v_{o,7b}}{v_{o,6}} \Psi \exp \left[\frac{(\alpha_7 - \alpha_6) F}{RT} \eta \right] \quad [37]$$

$$W_4 \equiv 1 + \frac{v_{o,4}}{v_{o,3}} E_4 \quad [38]$$

From the Faraday admittance only, the general relation

$$R_t \cdot I_s = \frac{RT}{F} \cdot \frac{2\Psi[v_{o,4}E_4W_3 - v_{o,7b}E_7W_4]}{[v_{o,1}E_{-1}W_4 + 4v_{o,4}\alpha_4E_4\Psi]W_3 + v_{o,6} \left[E_{-6} \cdot W_2 + (\alpha_6 + \alpha_7) \frac{v_{o,7b}}{v_{o,6}} \Psi E_7 \right]} \quad [39]$$

can be calculated (31).

Restricting the iron dissolution reaction to the active range and assuming

$$v_{o,3} \ll v_{o,4}E_4 \quad [40]$$

one obtains the steady-state current density-potential relation

$$i_s = 2F\Phi E_1 \cdot \frac{v_{o,4}E_4\Psi}{[(1 - \theta_{10} - \theta_{k10})E_{-1} + \theta_{10}E_1] \frac{v_{o,4}}{v_{o,3}} E_4 + \theta_{k10}E_1\Psi} \quad [41]$$

and

$$R_t \cdot I_s = \frac{RT}{F} \cdot \frac{2\Psi}{\frac{v_{o,1}}{v_{o,3}} E_{-1} + 4\alpha_4\Psi} \quad [42]$$

Equations [41] and [42] can be compared with the experimental results of both the steady-state polarization measurements ($b_+ = +40$ mV and $n_{+,pH} \approx 1.1$) and the impedance measurements ($b_t = 56$ mV and $n_{t,pH} = 0.81$ at low overvoltages as well as $R_t \cdot I_s \approx 30$ mV and $n_{t,pH} \approx 0$ at high overvoltages) in the active range of iron dissolution. From this comparison result the values $\alpha_1 = 0.4$, $\alpha_4 = 0.4$, $\alpha_\Psi = 0.5$, and $\alpha_\Phi = 0^5$. A complete correspondence of all experimental results with the model proposed can be achieved for this set of parameters only. These adjusted α parameters seems to be more reasonable than those derived from the model by Epelboin *et al.* (22, 27, 28) as mentioned above. Therefore, the presented model is suitable for the interpretation of the steady-state as well as the dynamic electrode behavior for iron dissolution in the active range.

Furthermore, a fitting of the relation [33] to the steady-state current density-potential curve in the active, transition, and prepassive ranges at $0.3 \leq pH \leq 6$ was performed assuming (i) $v_{o,3} \ll v_{o,4}E_4$, (ii) $v_{o,7a} \gg v_{o,7b}E_7$, and (iii) $e_{o,Fe/Fe^{2+}} = -560$ mV⁶ and using the adjusted α values for the active range.

The computer simulation is demonstrated in Fig. 9. The simulation results agree well with the measured current density-potential curves in the overall poten-

tial range depending on the pH of the electrolyte as can be seen by comparing Fig. 1 and 9. At $pH > 5$, the measured Tafel slope in the active range of iron dissolution increases due to lateral interactions between the adsorbed intermediates at higher degrees of coverages, where the conditions for a simple Langmuir behavior are no longer valid (32). The general agreement between the simulated and the measured current density-potential curves shows that the model proposed does not contradict the experimental findings. It should be mentioned, however, that the computer simulation was carried out using several fitting parameters included in the kinetic Eq. [19-26]. Therefore, the agreement between simulation and experiment is only of qualitative nature.

A relaxation behavior of the active centers can be described by

$$\Delta\Psi(s) = \Delta e(s) \frac{\left(\frac{\partial\Psi}{\partial e} \right)}{1 + s \cdot \tau} \quad [43]$$

where τ represents the relaxation time constant.

⁵ $\alpha_\Psi = 0$ implies the potential independence of the surface roughness.
⁶ Assuming $a_{Fe^{2+}} \approx 10^{-7}$ in the electrolyte.

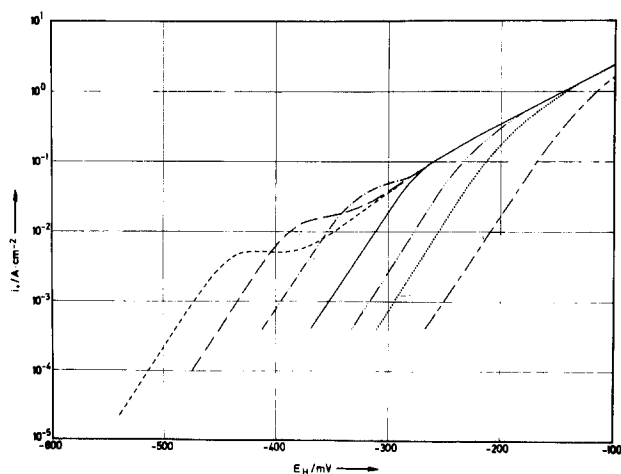


Fig. 9. Simulated current density-potential curves of anodic iron dissolution. —●— pH = 0.3; . . . pH = 1.45; — · — pH = 2; — pH = 2.9; — · · — pH = 4; — — — pH = 5; - - - - - pH = 6.

For the reaction model proposed in Table II, the normalized impedance is a function of many variables

$$Z_{fN} = Z_{fN} \left(\eta, \alpha_1, \alpha_4, \alpha_\psi, \frac{v_{o,4}}{v_{o,3}}, \theta_{10}, \theta_{k10}, \frac{v_{o,3}}{v_{o,1}}, \frac{N_o}{v_{o,3}}, \tau \right) \quad [44]$$

The values of α_1 , α_4 , α_ψ , $v_{o,3}$, $v_{o,4}$, θ_{10} , and θ_{k10} , estimated above, and $v_{o,3}/v_{o,1} = 10^{-7}$, obtained by the analysis of $R_t \cdot I_s$, can be used for an impedance simulation in the active range of iron dissolution. Assuming $N_o/v_{o,3} = 10^8$ sec and $\tau = 1$ sec, the simulated transfer loci of the Faraday impedance are shown in Fig. 10 as a function of the overpotential $\eta = \epsilon - \epsilon_{o,Fe/Fe^{2+}}$.

This simple model of a surface relaxation and the proposed reaction mechanism given in Table II yield a Faradaic impedance with two time constants in the inductive region of the transfer locus and one time constant in the capacitive one. Taking into account the double layer capacity, the simulated curves in Fig. 10 are in reasonable agreement with the measured curves in Fig. 4. The additionally observed fifth time constant may be caused by cosorption phenomena and/or by surface nucleation and growth processes. However, a more precise analysis of such a complex dynamic electrode behavior requires the use of single crystal electrode surfaces.

Recently, Heusler and Allgaier (44-47) carried out electrochemical measurements on iron single crystal surfaces, assuming a catalyzed iron dissolution mechanism which is very similar to that in Table II. However, in order to explain the observed steady-state kinetic data $b_+ = 30$ mV and $n_{+,pH} \approx 2$ for the iron dissolution in the active range, the surface concentration of the kink sites was postulated by a different potential dependence of $\psi = \exp(F\eta/RT)$. The deviations of the present experimental results and the modified theoretical assumption in Eq. [32] may be explained by a different crystal imperfection density of the electrode material used (3-5, 44-47). The kink sites at the iron surface are assumed to be preferentially covered by adsorbed OH^- ions which arise in acid solutions by deprotonation of adsorbed water dipoles (3). Thus, an energetically nonfavored two-electron charge transfer process starting from such covered kink sites seems to be possible in the active range of iron dissolution (52). On this basis, the electrochemical reaction order related to the bulk pH reflects the degree of "stabilization" of the kink site density at the electrode surface which may depend on the crystal imperfection density of the bulk metal.

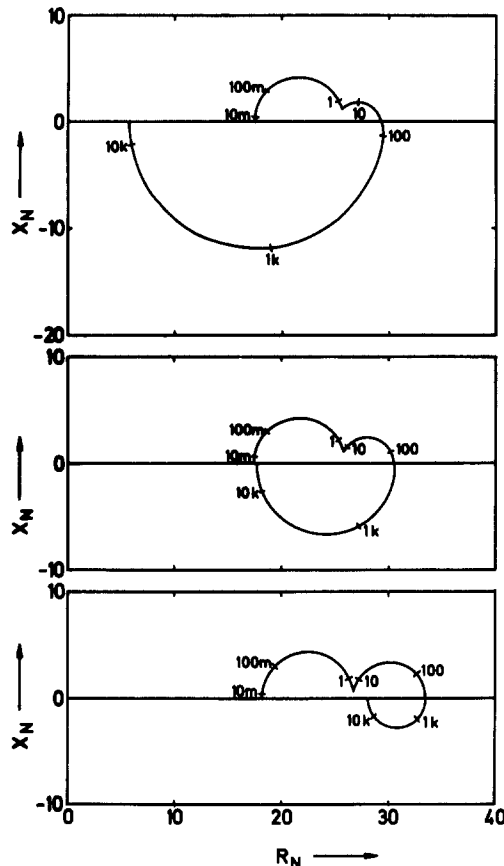


Fig. 10. Simulated transfer loci of the Faraday impedance of anodic iron dissolution (frequencies in Hz). (a, top) $\eta = 330$ mV; (b, center) $\eta = 370$ mV; (c, bottom) $\eta = 410$ mV (values of parameters cf. text).

Conclusions

The impedance measurements of the anodic iron dissolution reaction show clearly that the electrode behavior is determined not only by charge transfer steps including different adsorbed intermediates, but also by the influences of electrocrystallization steps and surface relaxation phenomena. The number of kink sites, which are responsible for the catalyzed dissolution reaction, were found to be strongly dependent on the electrode potential. Moreover, the time behavior of the electrode kinetics at low frequencies can be explained assuming surface relaxation processes. Both effects produce the observed impedance characteristics.

So far, the kinetics of cathodic metal deposition, as well as anodic metal dissolution of polycrystalline metal substrates containing a relatively high density of crystal imperfections, has been interpreted by charge transfer mechanisms only, disregarding electrocrystallization and surface relaxation processes as rate-determining steps. The present investigation shows, however, that these assumptions do not hold in the system studied. At this stage of the investigations, a reconsideration of the theory of polycrystalline Me/Me^{z+} -electrode kinetics with regard to electrocrystallization and surface relaxation processes seems to be necessary.

Manuscript submitted Sept. 4, 1979; revised manuscript received Feb. 26, 1980.

Any discussion of this paper will appear in a Discussion Section to be published in the June 1981 JOURNAL. All discussions for the June 1981 Discussion Section should be submitted by Feb. 1, 1981.

REFERENCES

1. J. O'M. Bockris, D. Drazic, and A. R. Despic, *Electrochim. Acta*, **4**, 325 (1961).

2. K. E. Heusler, Habilitation Thesis, University of Stuttgart, 1966.
3. F. Hilbert, Y. Miyoshi, G. Eichkorn, and W. J. Lorenz, *This Journal*, **118**, 1919, 1927 (1971).
4. G. Eichkorn and W. J. Lorenz, *Ber. Bunsenges. Phys. Chem.*, **70**, 99 (1966).
5. H. Rosswag, G. Eichkorn, and W. J. Lorenz, *Werkst. Korros.*, **25**, 86 (1974).
6. G. Bech-Nielsen, *Electrochim. Acta*, **21**, 627 (1976).
7. D. Geana, A. A. El Miligy, and W. J. Lorenz, *Corros. Sci.*, **13**, 505 (1973).
8. A. A. El Miligy, D. Geana, and W. J. Lorenz, *Electrochim. Acta*, **20**, 273 (1975).
9. J. Bessone, L. Karakaya, P. Lorbeer, and W. J. Lorenz, *ibid.*, **22**, 1147 (1977).
10. P. Lorbeer, Doctoral Thesis, University of Karlsruhe, 1978.
11. P. Lorbeer and W. J. Lorenz, *Corros. Sci.*, In press.
12. D. D. Macdonald, "Transient Techniques in Electrochemistry," Plenum Press, New York (1977).
13. M. Sluyters-Rehbach and J. H. Sluyters, in "Electroanalytical Chemistry," Vol. 4, A. J. Bard, Editor, Marcel Dekker, New York (1970).
14. R. D. Armstrong, M. F. Bell, and A. A. Metcalfe, in "Specialist Periodical Reports—Electrochemistry," Vol. 6, The Chemical Society, London (1978).
15. R. D. Armstrong and M. Henderson, *J. Electroanal. Chem. Interfacial Electrochem.*, **39**, 81 (1972).
16. G. J. Bignold and M. Fleischmann, *Electrochim. Acta*, **19**, 363 (1974).
17. J. A. Harrison and W. J. Lorenz, *ibid.*, **22**, 205 (1977).
18. H. Schweickert, A. A. El Miligy, A. Melendez, and W. J. Lorenz, *J. Electroanal. Chem. Interfacial Electrochem.*, **68**, 19 (1976).
19. I. Epelboin and M. Keddam, *This Journal*, **117**, 1052 (1970).
20. I. Epelboin, M. Keddam, and H. Takenouti, *J. Appl. Electrochem.*, **2**, 71 (1972).
21. I. Epelboin, *Metalloberfläche-Angew. Elektrochem.*, **27**, 113 (1973).
22. I. Epelboin, M. Keddam, and J.-C. Lestrade, *Faraday Discuss. Chem. Soc.*, **56**, 264 (1973).
23. C. Gabrielli and M. Keddam, *Electrochim. Acta*, **19**, 355 (1974).
24. I. Epelboin, Ph. Morel, and H. Takenouti, *This Journal*, **118**, 1282 (1971).
25. G. Blanc, I. Epelboin, C. Gabrielli, and M. Keddam, *Electrochim. Acta*, **20**, 599 (1975).
26. I. Epelboin, C. Gabrielli, M. Keddam, J.-C. Lestrade, and H. Takenouti, *This Journal*, **119**, 1632 (1972).
27. I. Epelboin, C. Gabrielli, M. Keddam, and H. Takenouti, *Electrochim. Acta*, **20**, 913 (1975).
28. B. Bechet, I. Epelboin, and M. Keddam, *J. Electroanal. Chem. Interfacial Electrochem.*, **76**, 129 (1977).
29. H. Strobel, "Systemanalyse mit determinierten Testsignalen," Verlag Technik, Berlin (1968).
30. H. Wolf, "Lineare Systeme und Netzwerke," Springer Verlag, Berlin-Heidelberg-New York (1978).
31. H. Schweickert, Doctoral Thesis, University of Karlsruhe, 1978.
32. J. R. Vilche and W. J. Lorenz, *Z. Phys. Chem. NF*, **96**, 251 (1975).
33. A. Rahmel and W. Schwenk, "Korrosion und Korrosionsschutz von Stählen," Verlag Chemie, Weinheim (1977).
34. K. J. Vetter, "Electrochemical Kinetics," Academic Press, New York-London (1967).
35. W. J. Plieth, *Z. Phys. Chem. NF*, **67**, 178 (1969).
36. J. R. Vilche, H. C. Albaya, F. Hilbert, and W. J. Lorenz, *ibid.*, **82**, 277 (1972).
37. M. Fleischmann and H. R. Thirsk, in "Advances in Electrochemistry and Electrochemical Engineering," Vol. 3, p. 123, John Wiley & Sons, Inc., New York-London (1963).
38. J. O'M. Bockris and G. A. Razumney, "Fundamental Aspects of Electrocrystallization," Plenum Press, New York (1967).
39. J. A. Harrison and H. R. Thirsk, in "Electroanalytical Chemistry," Vol. 5, Marcel Dekker, New York (1971).
40. H. Gerischer, in Proceedings of "Surface 66," p. 11, Forster-Verlag, Zürich (1967).
41. T. Vitanov, A. Popov, and E. Budevski, *This Journal*, **121**, 207 (1974).
42. E. Budevski, in "Progress in Surface and Membrane Science," Vol. 11, p. 71, Academic Press, New York-San Francisco-London (1976).
43. E. Budevski, V. Bostanov, and G. Staikov, *Electrocrystallization, Material Sci.*, In print.
44. W. Allgaier, Doctoral Thesis, University of Clausthal, 1975.
45. W. Allgaier and K. E. Heusler, *Z. Phys. Chem. NF*, **98**, 161 (1975).
46. W. Allgaier and K. E. Heusler, *Z. Metallkd.*, **67**, 766 (1976).
47. W. Allgaier and K. E. Heusler, *J. Appl. Electrochem.*, **9**, 155 (1979).
48. M. Fleischmann, S. K. Rangarajan, and H. R. Thirsk, *Trans. Faraday Soc.*, **63**, 1240 (1967).
49. Ch. Nanev, D. Vladikova, and R. Kaishev, Paper presented at the 28th ISE Meeting, Varna, Bulgaria, 1977.
50. I. R. Burrows, J. A. Harrison, and J. Thompson, *J. Electroanal. Chem. Interfacial Electrochem.*, **58**, 241 (1975).
51. I. R. Burrows, J. A. Harrison, and J. Thompson, *ibid.*, **53**, 283 (1974).
52. J. G. Dash, "Films on Solid Surfaces," Academic Press, New York-San Francisco-London (1975).

Raman and Infrared Spectroscopy of Aqueous Corrosion Films on Lead in 0.1M Chloride Solutions

Richard J. Thibeau and Chris W. Brown

Department of Chemistry, University of Rhode Island, Kingston, Rhode Island 02881

Arnold Z. Goldfarb and Robert H. Heidersbach*

Department of Ocean Engineering, University of Rhode Island, Kingston, Rhode Island 02881

ABSTRACT

The Pb-H₂O-Cl Pourbaix diagram was investigated by examining potentiostatically oxidized lead samples using Raman and infrared spectroscopy. The surface films formed in 0.1M HCl solution were those predicted by the potential-pH diagram. In neutral and basic solutions, the film compositions were not as predicted by thermodynamic calculations, although potentiostatic results agreed very well with potentiodynamic polarization curves. Two polymorphs of PbO were found at different potentials in pH7 solutions, the orthorhombic form at low potentials and the tetragonal form above +0.18V vs. NHE. Infrared spectra gave indications that orthorhombic PbO is formed by deposition from solution while tetragonal PbO forms from the reaction of water with the metallic lead surface.

Laser Raman spectroscopy is an effective technique for analysis of aqueous corrosion product films on metal surfaces. It can identify insoluble aqueous corrosion products *in situ*, without removing a sample from its corrosive environment (1).

Raman spectra of relatively thin surface films (50Å) on metals can be observed (2). Since water is a very weak Raman scatterer, there is little difference between spectra of dry samples and of those immersed in a reactive aqueous solution (1, 3). Metal samples can be examined undisturbed in an electrochemical cell while oxidation proceeds under controlled conditions in different regions of a Pourbaix diagram. *In situ* Raman spectroscopy, in combination with the complementary and more sensitive technique, infrared reflection-absorption spectroscopy, can unambiguously identify insoluble films formed at specific conditions of potential and pH.

A previous report discussed investigations of the Pourbaix diagram for the Pb-H₂O system (1). The present report describes spectroscopic results from exposures of lead under similar conditions with 0.1M chloride ions added to the solutions in order to identify the effect of the chloride ion on lead oxide surface films.

Experimental

Raman spectra were recorded with a Spex Industries Model 1401 double monochromator using a photon counting detection system. A Coherent Radiation Laboratories Model CR-3 argon ion laser was used as the excitation source. Both the 488.0 and 514.5 nm wavelength laser lines were used and the power at the sample was approximately 500 mW.

Infrared reflection-absorption spectra were obtained with a Wilks Scientific Corporation Model 9 multiple specular reflection attachment in both the sample and reference beams of a Perkin-Elmer Model 521 infrared spectrophotometer equipped with a grating polarizer. The reflection apparatus was adjusted to give 2-4 reflections and a 65° angle of incidence of the infrared beam. Details of the exposure apparatus and instrumentation used in this research are contained in a previous report (1).

Lead foil (1.6 mm thick) supplied by Alfa Products, Incorporated, at greater than 99.9% purity was used for the investigation. It was cut into 2.8 × 5.7 cm rectangles to fit the sample holder of the electrochemical cell. This size was also required for the infrared reflection attachment. Prior to placing a lead sample in solution, it was immersed in warm, concentrated ammonium acetate solution for 5 min to dissolve the outer layer, leaving a clean, silvery surface. The clean sample was washed with distilled water and immediately placed in the exposure solution.

The solutions were sparged with dry nitrogen for 30 min before and throughout the electrochemical exposures. The potential of the working electrode, lead, was held constant relative to the saturated calomel reference electrode by a Wenking Model LT73 potentiostat for periods ranging from 1 to 24 hr. Upon completion of an exposure period, an *in situ* Raman spectrum was recorded. The sample was then removed from the cell, washed thoroughly with distilled water, and allowed to dry in air. The dry sample was returned to the Raman spectrometer for examination and then analyzed by the infrared spectrophotometer.

The solutions used were made from reagent grade compounds. The acid solution was 0.1M HCl. The pH7 buffer was KH₂PO₄-NaOH solution and that for pH10 was a NaHCO₃-NaOH mixture, both with KCl added to make the solution 0.1M in Cl⁻. Buffer solutions were desired to maintain pH constant throughout periods of exposure as long as 24 hr, but no suitable buffer was available in the strongly acidic region.

Results and Discussion

The Pourbaix diagram for the Pb-H₂O-Cl system was calculated in the manner used by Appelt (4) but employing more recent thermodynamic data for some species (5). The newer free energy values used in the calculations are given in Table I. The positions of equilibria between species on the diagram depend strongly on the chloride concentration. A concentration of 0.1M was chosen for the exposures as a reasonable ionic concentration which should affect oxide film formation. The 0.1M Cl⁻ concentration was used in construction of the potential-pH diagram shown in Fig. 1.

In order to provide an experimental basis for choosing exposure potentials, as well as the theoretical,

* Electrochemical Society Active Member.
Key words: spectroscopy, corrosion, films.

Table I. Revised free energy values used to calculate Pourbaix diagram

Substance	NBS (5)	ΔG_f° (cal/mole) Used by Appelt (5)
OH ⁻	-37,594	-37,595
Cl ⁻	-31,372	-31,350
PbCl ₂	-75,080	-75,040
3PbO · PbCl ₂	-224,686	-225,000

thermodynamic basis (the Pourbaix diagram), potentiodynamic polarization curves were recorded for lead in the three solutions selected for exposures. The polarization curves were run with a slowly changing potential, 40 mV/min, to allow the formation of a relatively thick oxide film, as would be encountered in potentiostatic oxidation.

It can be seen from the polarization curves, Fig. 2, that there is a definite relation between these curves and the Pourbaix diagram. The lower oxidative wave occurs at the approximate potential of the predicted Pb/PbCl₂ or Pb/3PbO · PbCl₂ transitions and the wave at +0.96V (vs. NHE) in pH10 corresponds roughly to the 3PbO · PbCl₂/PbO₂ transition. The Pourbaix diagram offers no reason for the waves found at +0.17V in pH7 or at -0.07V in pH10, however.

Potentials to be used for lead exposures were chosen so that at least one was located in each region of the theoretical Pourbaix diagram and in all potential regions where the polarization curves indicated the possible formation of different species. The exposure conditions selected and the resulting spectra obtained from these potentiostatic oxidations are

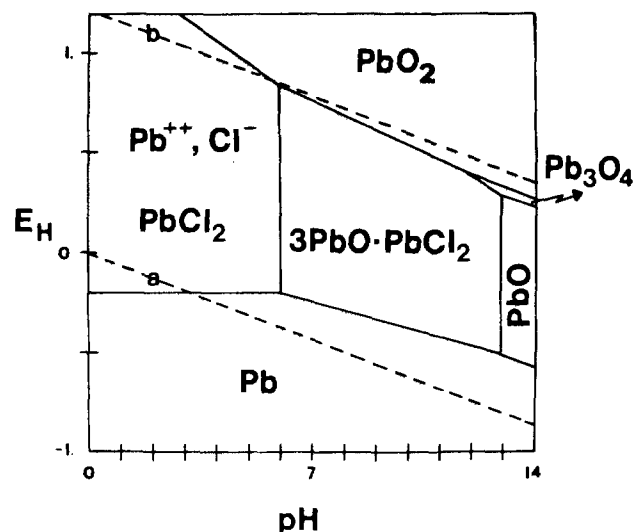
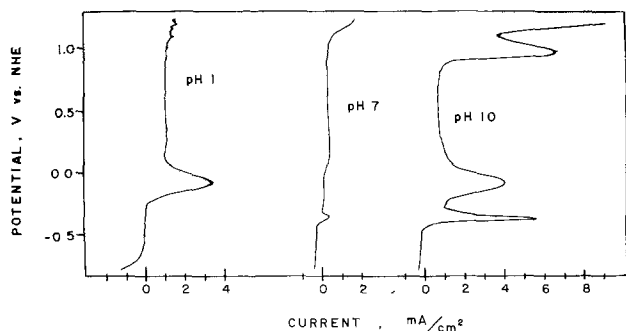
Fig. 1. Potential-pH diagram of the system Pb-H₂O-Cl at 25°C for $a_{Cl} = 0.1$.

Fig. 2. Potentiodynamic polarization curves for lead, scan rate 40 mV/min.

Table II. Potentiostatic exposures conducted in 0.1M chloride solutions

Solution pH	Potential, V vs. SHE	Current, $\mu\text{A}/\text{cm}^2$	Surface film spectrum
1	-0.46	11.2 ^a	None ^b
1	-0.30	120 ^a	None ^b
1	+0.14	7300	PbCl ₂
1	+0.69	6800	PbCl ₂
1	+1.09	10,000	PbCl ₂
7	-0.62		None
7	-0.11	20	PbO (o)
7	-0.01	22	PbO (o)
7	+0.18	19	PbO (o + +)
7	+0.49		PbO (+)
7	+0.68	12	PbO (+)
7	+0.99	22	PbO (+)
10	-0.42		None
10	-0.26	6.5	(PbCO ₃) ₂ · Pb(OH) ₂
10	-0.01	14	PbO (+)
10	+0.08	12	PbO (+)
10	+0.49		PbO (+)
10	+0.74	34	PbO (+)
10	+1.07	28	Pb ₃ O ₄

^a Current flow in reducing direction.

^b Some orthorhombic PbO found on dried sample; (o) indicates orthorhombic structure, (+) indicates tetragonal structure.

summarized in Table II. The current densities listed are those recorded after current became steady.

pH1 exposures.—In 0.1M HCl solution, lead is stable at low potentials while it is oxidized to PbCl₂ at higher potentials (3, 6). The Raman spectra of lead oxidized at potentials of +0.14V and higher indicated the presence of a PbCl₂ surface layer as shown in Fig. 3. The spectrum of the surface film is identical to that of a powder sample of pure PbCl₂ with bands at 62, 88, 126, 156, and 178 cm⁻¹ (7, 8). No infrared spectra of these samples were obtained because lead chloride has no absorption bands in the infrared region examined by the spectrophotometer, 1500-250 cm⁻¹ (9). Current densities for these samples were extremely high and the lead quickly became covered with a light gray crystalline coating.

In the region where immunity is predicted, net current flow was in the reducing direction and samples remained clean in appearance. *In situ* Raman spectra gave no indication of film formation but upon drying both Raman and infrared spectra indicated the presence of orthorhombic PbO on the lead surface. It is unlikely that the PbO was formed by oxidation of the lead under generally reducing conditions, but it is probably the result of dissolved lead being re-

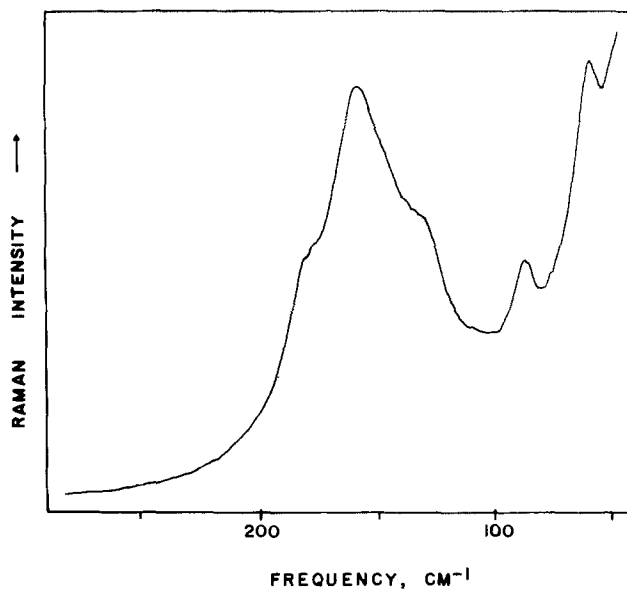
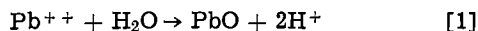


Fig. 3. Raman spectrum of the surface film on lead exposed to 0.1M HCl at +0.69V vs. SHE for 2.5 hr.

deposited from the solution as the oxide. It has been suggested (10) that orthorhombic PbO is formed from the plumbous ion by the reaction



Due to the solubility of lead in 1.0M hydrochloric acid, sufficient quantities of Pb^{++} are present to form orthorhombic PbO films on lead undergoing exposure for several hours.

In the potential region where PbCl_2 was formed, a gray coating was deposited on the platinum cathode. After drying, the material gave the Raman spectrum of orthorhombic PbO. Apparently the oxide on the auxiliary electrode was formed by the same dissolution-deposition mechanism as that found on the working electrode.

Raman spectra of the dried cathode coating were recorded in two ways: as a powder in a glass capillary tube, or pressed into a KBr pellet. As shown in Fig. 4, the spectra are slightly different for the different sample preparation techniques. While both are spectra of orthorhombic PbO, the pellet spectrum shows impurity bands at 84, 149, and 344 cm^{-1} , the three strong bands of tetragonal PbO, litharge. The same results were obtained with spectra of reagent grade orthorhombic PbO. The grinding required to make a pellet transforms some of the orthorhombic PbO to the lower energy, tetragonal form. The crystal structures of the two oxides are very similar (11) and at room temperature the tetragonal structure is thermodynamically stable. Orthorhombic PbO is known to be stabilized by the presence of small quantities of various impurity anions (12), which allow it to remain indefinitely without reverting to the tetragonal structure. It is likely the the presence of chloride or some other ion in the solution stabilizes orthorhombic PbO so that it can remain in that form until intensive grinding brings about the transformation.

pH7 exposures.—According to the Pourbaix diagram in Fig. 1, controlled potential oxidations of lead in a pH7, 0.1M chloride solution should show immunity at potentials below -0.26V vs. NHE, formation of $3\text{PbO} \cdot \text{PbCl}_2$ between -0.26V and $+0.75\text{V}$, and formation of PbO_2 at higher potentials. The predicted compounds were not found experimentally.

In the region where immunity is predicted, i.e., below -0.26V , the Pourbaix diagram, polarization curve, and spectroscopic results all agree. Potentiostatic ex-

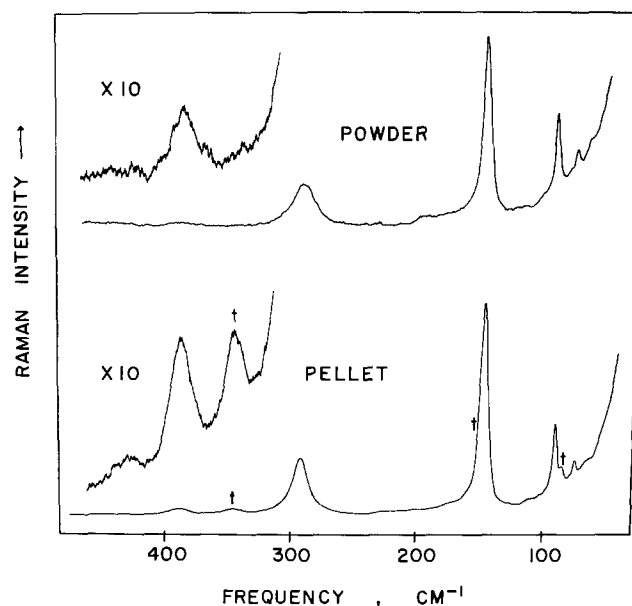


Fig. 4. Raman spectra of dried material from the Pt cathode after lead exposure at $+1.09\text{V}$ in 0.1M HCl for 17 hr. Bands marked "t" are due to tetragonal PbO.

posure resulted in a reducing current, the sample remained shiny and silver in color, and no infrared or Raman bands could be observed.

Above the potential where Pb is the stable species, i.e., -0.34V according to the polarization curve of Fig. 2, an insoluble oxidation product film was formed. Current flow, although small, was in the oxidizing direction. The sample surface darkened and, after a few hours, became dull gray in color. *In situ* Raman spectra and infrared reflection spectra of sample surfaces indicated that, at potentials between -0.11V and $+0.18\text{V}$, orthorhombic PbO was formed. At potentials above $+0.18\text{V}$, the film consists entirely of tetragonal PbO, whereas exposures at $+0.18\text{V}$ showed both types present, as spectra show in Fig. 5. There was no difficulty in identifying which PbO polymorph was present. While the structures are similar, infrared and Raman spectra of the two polymorphs are markedly different (13, 14).

We have no explanation why the two types of PbO should be found at different potentials. The tetragonal form is thermodynamically favored under all conditions at room temperature. It is likely that the weak wave at approximately $+0.16\text{V}$ on the polarization curve indicates a $\text{PbO}(0)$ to $\text{PbO}(+)$ transition, but such a transition is not reflected in the Pourbaix diagram which is based solely on thermodynamic equilibria.

Infrared spectra indicate that the orthorhombic PbO films may be formed by deposition from the solution. Reflection spectra of orthorhombic PbO films recorded using two different polarizations of the infrared beam were very similar, differing only in intensity (15). However, spectra of tetragonal PbO films had differing

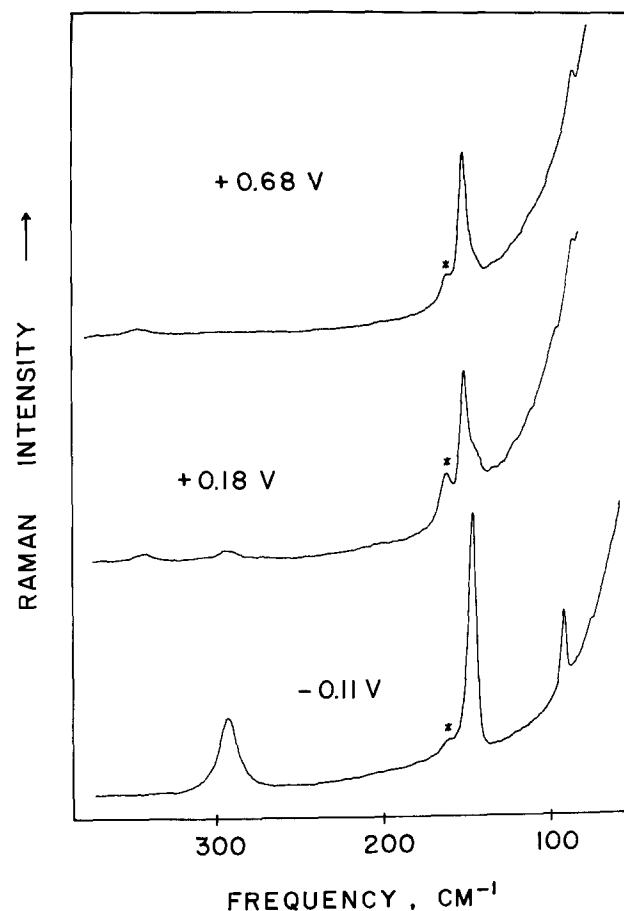
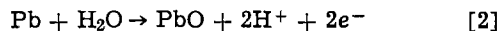


Fig. 5. *In situ* Raman spectra of lead surfaces exposed to pH 7, 0.1M chloride solutions for 18 hr at 0.68V, $+0.18\text{V}$, and -0.11V vs. SHE. The spectra indicate tetragonal, tetragonal plus orthorhombic, and orthorhombic PbO films, respectively. The feature marked with an asterisk is a grating ghost.

relative peak heights depending on polarization. This is shown in Fig. 6. This indicates that, while orientation of orthorhombic PbO crystals is probably random, there is probably some long-range order to the tetragonal films. Long-range order may be expected if the oxide is formed directly on the lead surface by the reaction



Thus the tetragonal PbO layer may be aligned with the grain structure of the underlying metal while orthorhombic PbO, formed by a dissolution-deposition route, is random in orientation.

The effect of chloride ions was investigated by conducting exposures at -0.01V in pH7 solutions of different KCl concentrations: 0.01M and 0.1M. In 0.01M Cl^- solution, the oxidation product detected was tetragonal PbO, the same compound observed in nil chloride exposures (1). In 0.1M Cl^- orthorhombic PbO was formed. These results indicate that it is indeed the chloride present in solution which allows the formation of the thermodynamically unstable orthorhombic PbO layer.

pH10 exposures.—According to the Pourbaix diagram the results of potentiostatic exposures should be the same in pH10 solutions as in pH7 but, experimentally, they are not. The differences are due, in part, to the composition of the pH10 buffer used. They are also due to the behavior of soluble lead species in basic solutions.

The pH10 buffer, a bicarbonate solution, gave slightly different results from those predicted in the immunity region. As in nil chloride exposures (1), potentials in the region of Pb stability in the potential-pH diagram, but above -0.42V , gave oxidizing currents and a thin film of basic lead carbonate. The oxidation wave at -0.35V apparently corresponds to the Pb to $(\text{PbCO}_3)_2 \cdot \text{Pb}(\text{OH})_2$ transition.

At potentials higher than the carbonate region, tetragonal PbO was found, between -0.07V and $+0.96\text{V}$. No trace of the orthorhombic form was detected. The dissolved lead species, Pb^{++} and HPbO_2^- , are in

equilibrium at a pH of 9.34 (16). In more basic solutions only HPbO_2^- is present, the Pb^{++} needed to make orthorhombic PbO according to the mechanism of reaction [1] is not present.

Although the transition to a higher oxidation state predicted by the Pourbaix diagram would give PbO_2 , none could be detected. Instead a thick, nonprotective film of Pb_3O_4 was formed at potentials above the $+0.96\text{V}$ wave. The Raman spectrum of this compound has not previously been reported but the composition of the film was confirmed by comparison of its Raman spectrum with that of the pure compound, as shown in Fig. 7, and by its infrared spectrum which agrees with a previously reported infrared spectrum of Pb_3O_4 (17).

Conclusions

In situ Raman spectroscopy and infrared reflection-absorption spectroscopy are excellent methods for the experimental investigation of Pourbaix diagrams. Examining two different potential-pH diagrams, we have found considerable difference in the oxidation of lead between nil chloride and 0.1M chloride solutions. Orthorhombic PbO and Pb_3O_4 were formed only in the presence of chlorides. The relationship between the tetragonal and orthorhombic PbO polymorphs is not well understood. Some potentials and chloride concentrations result in formation of one type while other potentials or concentrations give the other.

The experimental results of potentiostatic oxidations agree very well with slow potentiodynamic polarization curves but only partially with the calculated Pourbaix diagram. The major difference is that, where $3\text{PbO} \cdot \text{PbCl}_2$ is predicted, PbO was found. The compound $3\text{PbO} \cdot \text{PbCl}_2$, which probably exists as $3\text{Pb}(\text{OH})_2 \cdot \text{PbCl}_2$ or $(\text{Pb}_8(\text{OH})_{12})_n \text{Cl}_{4n}$, has a somewhat different spectrum (3) and should have been easily detected. In calculating the regions of the diagram, the presence of dissolved substances other than lead or chloride species was not considered. The presence of the buffer solutions may account for the discrepancies between experimental results and those predicted by the Pourbaix diagram. In 1.0M HCl, a simpler solution where no unaccounted for compounds were present, the Pourbaix diagram, polarization curve, and potentiostatic exposures all agreed.

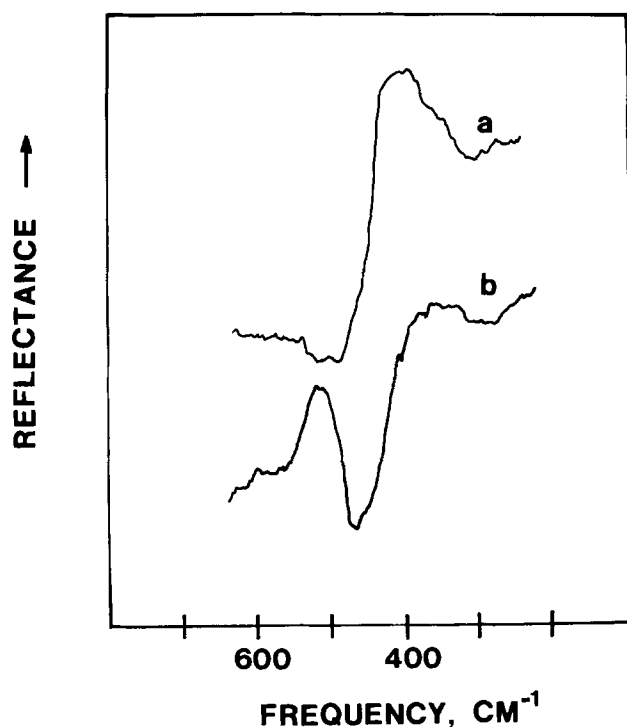


Fig. 6. Infrared reflection spectra of a tetragonal PbO surface film with two different polarizations of the incident beam. The PbO was formed by exposure of lead in pH 10, 0.1M chloride solution at $+0.49\text{V}$ for 17 hr.

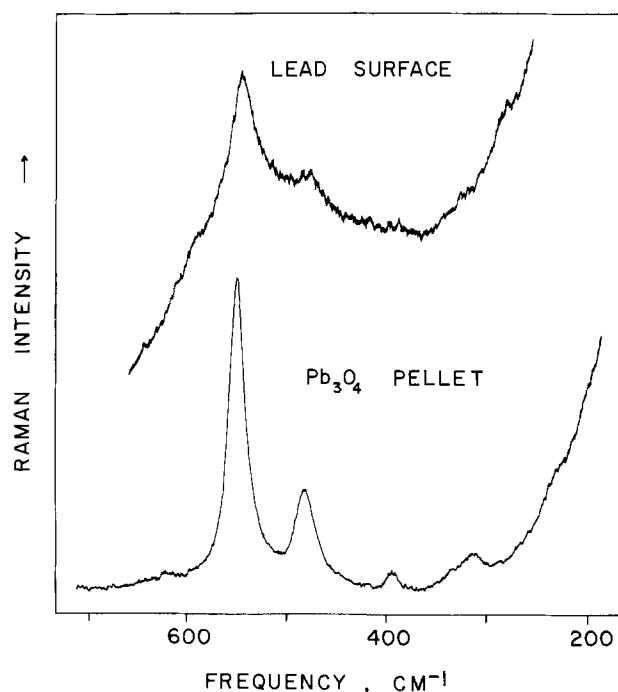


Fig. 7. Raman spectra of a KBr pellet of Pb_3O_4 and of the surface of lead after exposure in pH 10, 0.1M chloride solution at $+0.97\text{V}$ for 18 hr.

Acknowledgment

The authors thank the Department of the Navy, Office of Naval Research, for support of this research under Contract N0014-76-C-0889.

Manuscript submitted Aug. 23, 1978; revised manuscript received June 25, 1979.

Any discussion of this paper will appear in a Discussion Section to be published in the June 1981 JOURNAL. All discussions for the June 1981 Discussion Section should be submitted by Feb. 1, 1981.

REFERENCES

1. R. J. Thibeau, C. W. Brown, A. Z. Goldfarb, and R. H. Heidersbach, *This Journal*, **127**, 37 (1980).
2. R. G. Greenler and T. L. Slager, *Spectrochim. Acta*, **29A**, 193 (1973).
3. E. S. Reid, R. P. Cooney, P. J. Hendra, and M. Fleischmann, *J. Electroanal. Chem. Interfacial Electrochem.*, **80**, 405 (1977).
4. K. Appelt, *Electrochim. Acta*, **13**, 1521 (1968).
5. D. D. Wagman, W. H. Evans, V. B. Parker, I. Halow, S. M. Bailey, and R. H. Schumm, NBS

- Technical Note 270-3, U.S. Government Printing Office, 1975.
6. R. G. Barradas, K. Belinko, and J. Ambrose, *Can. J. Chem.*, **53**, 389 (1975).
 7. L. A. Isupova and E. V. Sobolev, *Zh. Strukt. Khim.*, **9**, 324 (1968).
 8. G. A. Ozin, *Can. J. Chem.*, **48**, 2931 (1976).
 9. T. S. Moss and A. G. Peacock, *Infrared Phys.*, **1**, 104 (1961).
 10. J. Burbank, *This Journal*, **106**, 369 (1959).
 11. E. W. Abel, in "Comprehensive Inorganic Chemistry," Vol. 2, J. C. Bailar, H. J. Emeleus, R. Nyholm, and A. F. Trotman-Dickenson, Editors, p. 119, Pergamon, New York (1973).
 12. W. Kwestroo, J. DeJonge, and P. H. G. M. Vromans, *J. Inorg. Nucl. Chem.*, **29**, 39 (1967).
 13. J. D. Donaldson, M. T. Donoghue, and S. D. Ross, *Spectrochim. Acta*, **30A**, 1967 (1974).
 14. D. M. Adams and D. C. Stevens, *J. C. S. Dalton*, **1977**, 1096 (1977).
 15. R. G. Greenler, *J. Chem. Phys.*, **44**, 310 (1966).
 16. M. Pourbaix, "Atlas of Electrochemical Equilibria," pp. 485-492, Pergamon, New York (1966).
 17. N. T. McDevitt and W. L. Baun, *Spectrochim. Acta*, **20**, 799 (1964).

Automatic Corrosion Rate Monitoring of Metals in Solution

Lindsay F. G. Williams

Materials Research Laboratories, Department of Defence, Ascot Vale, Victoria, 3032, Australia

ABSTRACT

The paper describes a versatile computerized method for automatic corrosion rate monitoring of metals in solution. Potentiostatic pulses of varying amplitude are applied to the metal and the current sampled after the initial decay has finished. These data are then computer fitted to the general equation for corrosion of metals in solution and the corrosion current calculated together with the anodic and cathodic Tafel parameters. The corrosion of zinc in an aerated ethylenediaminetetra-acetic acid solution at a pH of 8.5 has been used to demonstrate the method.

Previously, the corrosion rate of metals in solution has been monitored using potentiostatic pulse methods such as those described recently (1-3). The advances in microcomputer technology have enabled the economic extension of computer methods to the control of the potentiostat and data acquisition. This, together with computer fitting methods of calculating corrosion rates (4-6), opens up the possibility of automated corrosion rate measurements.

This paper describes a microcomputer system for automating electrochemical corrosion rate measurements. The system is fitted with two digital to analogue converters and one analogue to digital converter, and is programmed to produce a polarization curve around the corrosion potential and then fit the data to the equation originally derived by Wagner and Traud (7). The curve fitting programs are similar to those published by Mansfeld (4) and yield both the Tafel parameters and the corrosion current.

The corrosion of zinc in an ethylenediaminetetra-acetic acid solution at a pH of 8.5 was chosen to demonstrate the computerized method for two reasons. The cathodic process is diffusion-controlled oxygen reduction as confirmed by rotating disk studies (8) and the current response to short duration potentiostatic pulses is ideally suited to these experiments (1).

Key words: corrosion, zinc, nonlinear polarization, microcomputer.

Experimental

Computerized system.—A block diagram of the system is shown in Fig. 1. The microcomputer was an Intel Microdevelopment system fitted with 32 kbits of memory, and an Input-Output Board (SPC 732) with one twelve bit analogue to digital (A/D) and two twelve bit digital to analogue (D/A) converters. The other peripherals were an Intel Double Density Disc system, a Tektronix Oscilloscope, a Princeton Applied Research Model 174 Polarographic Analyzer (PAR 174), and a Teletype Model 43. The output from the

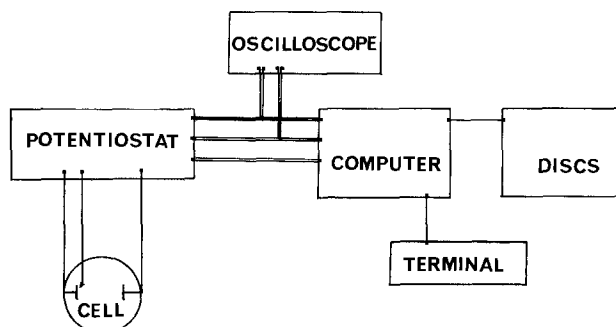


Fig. 1. Schematic diagram of the computerized system

D/A converters was reduced to ± 50 mV and fed into the d-c external input on the PAR 174 while the current output on the PAR 174 was read by the A/D converter every 2 msec. The converters were calibrated according to the manual prior to use. After roughly setting the potentiostat at the corrosion potential, one of the D/A converters was used to adjust the current to as close as possible to zero. The second converter was then used to apply the pulses.

To check the system a dummy circuit consisting of a $100 \mu\text{F}$ capacitor across a 47Ω resistor in series with a further 100Ω resistor was connected across the working electrode terminal and both the auxiliary and reference terminals of the PAR 174. The current response to pulses of ± 2 , ± 4 etc. mV can be seen in the oscilloscope traces in Fig. 2 and gave the expected values within 1%.

Programming.—Subroutines in assembly language for applying single pulses of varying amplitude were developed for each pulse length (60 msec to 10 sec). Control of the experiment was achieved from a Basic Program as shown in Fig. 3. After setting the system to the corrosion potential by zeroing the current output, pulses of ± 2 , ± 4 , ± 6 etc. mV were applied to the corroding metal. In all experiments, the 10 current readings over the final 20 msec of each pulse were averaged and this was used in subsequent calculations. In this way 30 points on a polarization curve within ± 30 mV of the corrosion potential were obtained.

Computer fitting of the polarization curves was achieved by the methods previously described (4), resulting in both Tafel parameters and the corrosion current. The program fits the polarization data to the equation

$$2.3 R_p I = \frac{b_a b_c}{b_a + b_c} \left\{ \exp \left(\frac{2.3 \Delta E}{b_a} \right) - \exp - \left(\frac{2.3 \Delta E}{b_c} \right) \right\} \quad [1]$$

where R_p is the polarization resistance, I the current at a potential ΔE from the corrosion potential, and b_a and b_c are the anodic and cathodic Tafel parameters, respectively. This equation can be reduced to a linear equation which enables a linear regression calculation. Programs were checked on theoretical data and on data obtained manually.

Cell and electrodes.—The cell was similar to that used in previous experiments (1) with a saturated calomel reference electrode (SCE) fitted in a Luggin probe. Cylindrical specimens of zinc (99.999%) with an exposed area 3.66 cm^2 were mounted in a standard holder and immersed in the solution at 20°C .

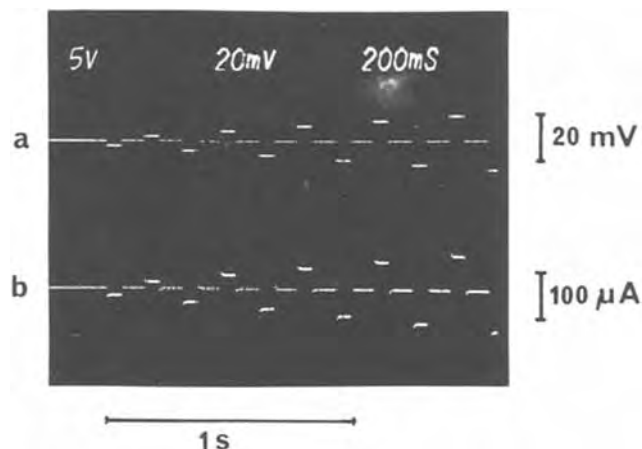


Fig. 2. Oscilloscope traces showing (a) the 60 msec pulses of ± 2 mV, ± 4 mV etc., and (b) the current response of the equivalent circuit described in the text.

PROGRAMS

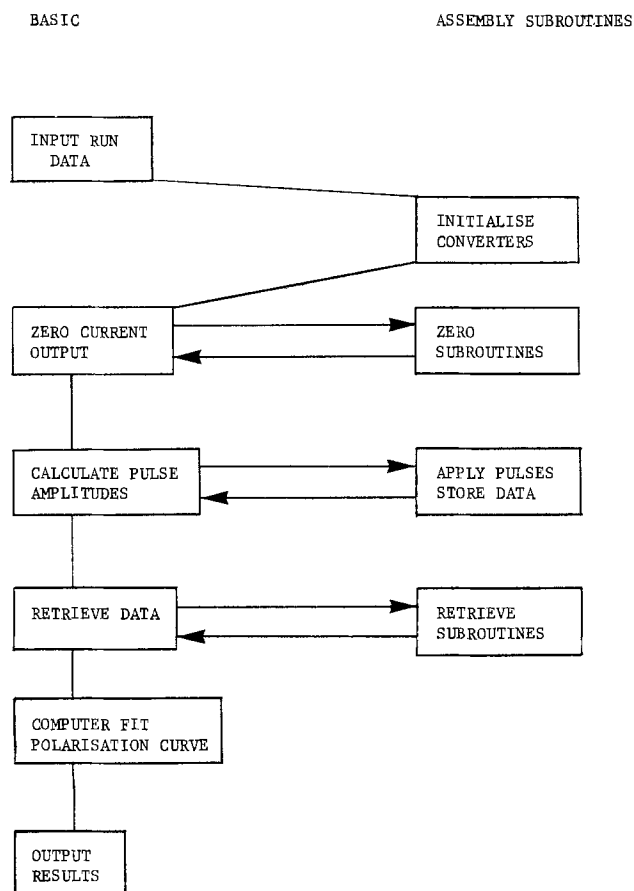


Fig. 3. Flow chart for the computer program

The solution contained 0.1 mole/liter ethylenediaminetetra-acetic acid (EDTA) (R grade) and adjusted to a pH of 8.5 by additions of NaOH (AR grade). Air was passed over the solution to avoid the slight changes in E_{corr} caused by bubbling through the solution.

Results

The current responses to the potential pulses were similar to those previously published (1). The polarization curves obtained using 60 msec pulses and averaging the currents over the final 20 msec of each pulse are shown in Fig. 4. The points are the experimental results while the line is the curve fit calculated by the computer. In all instances the percentage fit of the regression was greater than 99% and the mean square deviation of the individual points was typically 1%. For example, the percentage fit and the mean square deviation for the data in Fig. 4 were curve (i) 99.2% and 1.2%, curve (ii) 99.7% and 0.7%, curve (iii) 99.6% and 1.0%, and curve (iv) 99.9% and 0.2%, respectively.

Table I compares the anodic Tafel parameters with previously published experiments. A value of 80 ± 2 mV has been obtained from an IR compensated Tafel plot (1). However, values could be calculated from the previous work (1) by LeRoy's method (9) and assuming a diffusion-controlled cathodic process (8). These previous results for the first 9 hr of each experiment are compared with the present results in the table. The calculated error in the b_a in the present work was less than 1 mV. The cathodic Tafel parameter was always greater than 300 mV as would be expected for a diffusion-controlled process.

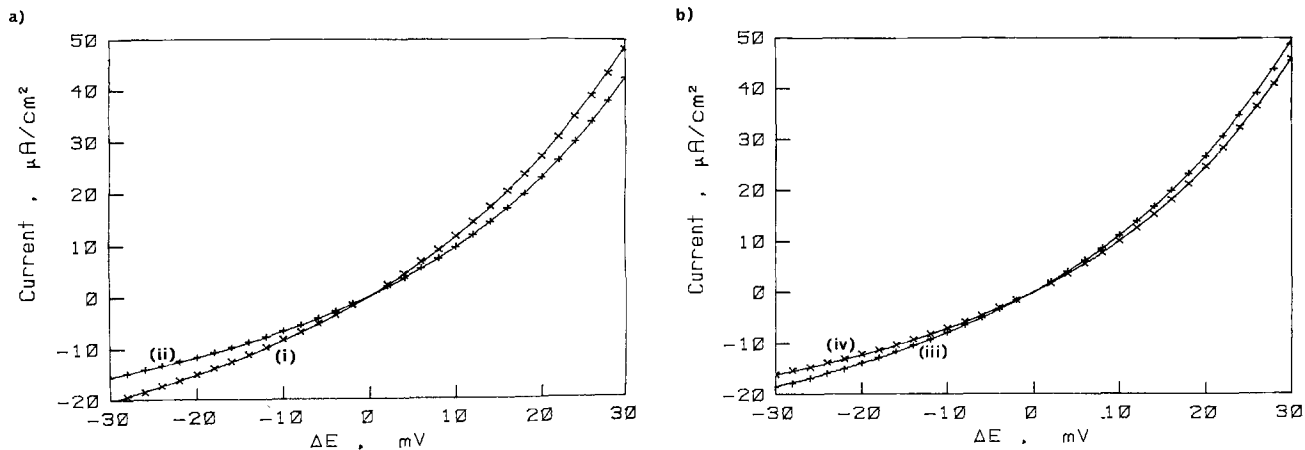


Fig. 4. Polarization data obtained at potentials ΔE mV from the corrosion potential for a zinc electrode after curve (i) 10 min, curve (ii) 1.5 hr, curve (iii) 10 min, and curve (iv) 2.5 hr immersion in a 0.1 mole/liter EDTA solution at pH 8.5; (a) from the first experiment and (b) from a duplicate run.

A plot of the calculated corrosion currents against time for duplicate experiments is shown in Fig. 5. The error calculated from the regression fit was less than $1 \mu\text{A}/\text{cm}^2$ but results obtained 2 min apart gave values of 16.8 and $14.8 \mu\text{A}/\text{cm}^2$ in the worst instance. Since this corrosion reaction is diffusion controlled (8), the current would be expected to remain fairly constant. Therefore, differences of $2 \mu\text{A}/\text{cm}^2$ probably reflect the experimental errors rather than real changes in corrosion rates.

Discussion

Computerization of the method for obtaining polarization data has enabled a polarization curve to be generated very rapidly. The use of a 12 bit A/D converter means the currents are obtained very accurately and similarly the potential pulses are accurate to 0.03 mV. After the pulse is applied, the time at which the current is recorded can be altered to suit the type of current decay for individual experiments. For example, in the latest experiments on steel (10) pulses between 60 msec and 10 sec have been used. When the current is sampled, 10 consecutive readings are averaged to give one data point.

Once the data are obtained, curve fitting can be used to calculate the corrosion current and the electrochemical parameters. The microcomputer can also be programmed to plot the results as shown in Fig. 4. Automatic recording of corrosion rates over a period of time is now possible using appropriate timing subroutines or interrupts. The automation of data collection will improve the efficiency of experiments in the laboratory and can be used commercially to monitor the corrosion rates of metals in solution.

The present results for zinc in an EDTA solution at pH 8.5 confirm that the cathodic reaction is diffusion controlled as evidenced by the large cathodic Tafel

parameters calculated from the curve fit. The b_a values as shown in the table are similar to those calculated at similar times from previous experiments where the values tend to a minimum value after 3-7 hr immersion and, thereafter, tend to increase. Slightly different b_a values result from only small, subtle changes in the shape of the polarization curve and these small changes in the curves are responsible for the spread of results observed in the I_{corr} values calculated (see Fig. 5). As mentioned above, two consecutive experiments 2 min apart resulted in a $2 \mu\text{A}/\text{cm}^2$ difference between the I_{corr} values calculated. The R_p values, however, remained fairly constant at 1353 and $1317 \Omega\text{-cm}^2$ for the two sets of data but b_a varied from 57.0 to 60.2 mV. Thus, variations observed in the calculated corrosion current largely resulted from small variations in the shape of the polarization curve. The computer fitting method seems to be sensitive to small changes in shape which produce significant changes in b_a and b_c calculated from the current fit.

The effect of random and systematic errors on the calculated Tafel slopes and the I_{corr} values will be the subject of a later paper. In some instances, the b_c values were large negative numbers and this resulted from a very small uncompensated resistance overvoltage (IR drop). As the ohmic resistance was small compared with R_p it would not have affected the I_{corr} calculated.

Table I. The anodic Tafel slopes for zinc in an EDTA solution at pH 8.5; (a) and (b) duplicate results calculated from previous experiments (1) using LeRoy's method (9); (c) and (d) duplicate results from these experiments

Time of immersion (hr)	Anodic Tafel slope (mV)			
	a	b	c	d
0.25	63	91	58	65
1	66	67	56	55
2	74	69	56	56
3	61	67	54	57
4	63	79	55	56
5	67	77	54	51
6	59	91	58	50
7	54	116	62	56
8	110	95	61	54
9	126	96		

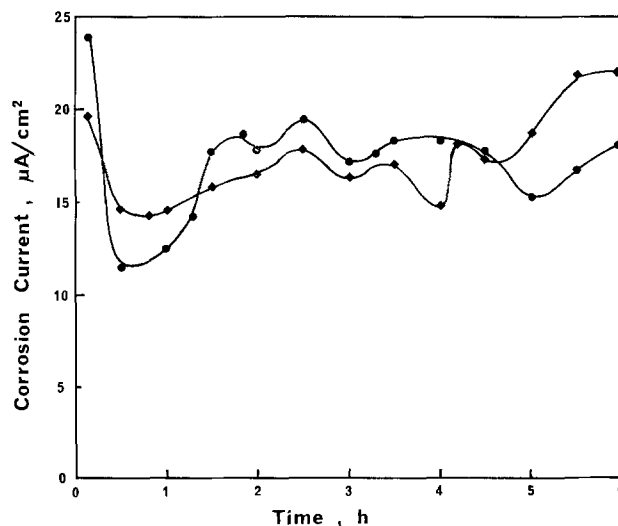


Fig. 5. Plots of corrosion current densities from duplicate runs for a zinc electrode immersed in an aerated 0.1 mole/liter EDTA solution at pH 8.5.

Conclusions

Full computerization of electrochemical corrosion rate measurements by potentiostatic pulsing methods enables automatic monitoring not only of the corrosion rate but also the Tafel parameters which give kinetic information on the corrosion reactions. The corrosion of zinc in an aerated EDTA solution has been used to demonstrate the capabilities of the system.

Acknowledgments

The author is very grateful to Messrs H. Kellock and G. Thege of these laboratories for their assistance with the microdevelopment system.

Manuscript submitted Sept. 11, 1978; revised manuscript received May 22, 1979.

Any discussion of this paper will appear in a Discussion Section to be published in the June 1981 JOURNAL. All discussions for the June 1981 Discussion Section should be submitted by Feb. 1, 1981.

Publication costs of this article were assisted by the Department of Defence.

REFERENCES

1. K. G. Boto and L. F. G. Williams, *This Journal*, **124**, 656 (1977); *Corros. Sci.*, **17**, 917 (1977).
2. F. Mansfeld, *Werkst. Korros.*, **28**, 6 (1977).
3. S. Brunet, G. Pinard-Legry, G. Plante, and G. Turliver, 6th European Congress of Metallic Corrosion, London, p. 357 (1977).
4. F. Mansfeld, *Corrosion*, **29**, 397 (1973).
5. F. Mansfeld, in "Advances in Corrosion Science and Technology," Vol. 6, M. G. Fontana and R. W. Staehle, Editors, Chap. 3, Plenum, New York (1976).
6. G. W. Walter, *Corros. Sci.*, **16**, 573 (1976).
7. C. Wagner and W. Traud, *Z. Elektrochem.*, **44**, 391 (1938).
8. K. G. Boto and L. F. G. Williams, *J. Electroanal. Chem. Interfacial Electrochem.*, **77**, 1 (1977).
9. R. L. LeRoy, *This Journal*, **124**, 1006 (1977).
10. R. J. Taylor and L. F. G. Williams, *Corrosion*, **36**, 41 (1980).

High Speed Electrodeposition of Chromium from Low Concentration Chromic Acid Solutions

Mitchell A. LaBoda,* Arnold H. Holden, and James P. Hoare*

General Motors Research Laboratories, Electrochemistry Department, Warren, Michigan 48090

ABSTRACT

The presence of trichromate ions in the chromic acid solution is required to obtain a cathodic film from which metallic Cr may be deposited. With a high flow rate plating system, it was predicted from this proposed mechanism that bright, smooth, adherent deposits of Cr can be laid down on Cu or Fe substrates from solutions as dilute as 25 g/liter CrO_3 but no deposit from 1 g/liter CrO_3 . A high speed plating process (HSP), based on an air pressure flow system (APFS) propulsion of electrolyte through a narrow gap between the cathode and anode separated by about 4 mm, was used to plate chromium metal on copper samples at rates up to 50 times faster from solutions 5 times as dilute as conventional chromium plating techniques. The HSP system, the APFS descriptions, and some selected results are presented.

During the conventional electrodeposition of chromium, the part to be plated is immersed in a properly catalyzed chromic acid bath under a low, d-c, applied voltage with a Pb anode, and the deposit is laid down at current densities ranging between 0.16 and 0.3 A/cm². Because of poor cathode current efficiency (12-15%), the process is slow, varying between 10 and 100 $\mu\text{m/hr}$. In most cases, particularly decorative plating applications, this system is satisfactory since it provides the required coating at a reasonable cost.

For industrial "hard" chromium used for wear and corrosion protection, the thickness of the coating may be about 25 μm . It is desirable, consequently, to develop a method to improve the efficiency, and hence, the rate of deposition of chromium.

A high rate process for the electrodeposition of chromium has been reported by Safranek and Layer (1) which indicated that both the limiting current and the deposition rate could be increased by increasing the rate of ion transport and reducing diffusion layer thickness by rapid flow of solution. No description of the cells or devices used for achieving the fast solution flow was given, however. Chin (2) has also studied the deposition of Cr at current densities from 1 to 70 A/cm² in a small flow cell using steel cathodes and a Pt anode at a flow rate of 2 liters/min ($\text{Re} = 9000$).

* Electrochemical Society Active Member.

Key words: coatings, cathode, current efficiency, kinetics.

A high speed plating (HSP) process consisting essentially of passing a stream of electrolyte under high air pressure (by reciprocating the flow between two tanks acting alternately as a reservoir and a sink) through the narrow gap (~ 4 mm) between the anode and cathode has been developed by LaBoda (3). With this air pressure flow system (APFS) (4), it is possible to deposit hard Cr from chromic acid solutions ranging from 1/10 to 1/25 of the conventional concentrations (250-300 g/liter). It is the purpose of this report to discuss the results of the deposition of hard Cr from dilute chromic acid solutions using APFS.

Theory

From an analysis of steady-state, galvanostatic, and potentiostatic polarization curves obtained (5) on Pt-bead cathodes in a Teflon cell in various chromate and chromic acid solutions, it was concluded for conventional Cr-plating: (i) that metallic Cr is deposited from a cathodic film without which a deposit is not formed, (ii) that a cathodic film is detected only if a polychromate is present, (iii) that polychromates are formed in strong solutions of chromic acid at low values of pH, (iv) that the cathodic film is required to protect the Cr^{+3} ion from forming the very stable complex with water, $\text{Cr}(\text{H}_2\text{O})_6^{+3}$, from which metallic Cr cannot be deposited, (v) that the cathodic film is decomposed by an acid catalyzed hydrolysis, (vi) that the discharge of the chromous ion decomposition prod-

uct to metallic Cr is catalyzed by the HSO_4^- ion, and (vii) that the HSO_4^- also acts as a blocking agent so that the proper cathodic film is generated.

According to this model for conventional Cr plating, the cathodic film is composed of a mixture of various complexes between HSO_4^- ions and complex polychromates. Since these complexes can bond to one another by hydrogen bonding through water molecules, a viscous layer of hydrated complex polychromates is formed in the Nernst diffusion layer next to the cathode surface. This viscous layer may be identified with the blocking film of Müller (6), the colloidal film of the Russian workers (7-9), and the viscous film of Saiddington and Hoey (10, 11).

Because the complex trichromate ions from which metallic Cr is eventually deposited must diffuse through this viscous layer, the solution must be stirred well to reduce the thickness of the layer, and hence, shorten the diffusion path for high rate deposition of chromium. To reach HSP rates (high current densities) stirring alone is not enough because of the large IR-drop over the solution path between the anode and cathode (12). Consequently, this solution path between anode and cathode is reduced (to 3.8 mm, typically) permitting very high current densities (up to 15.5 A/cm^2 or 100 A/in.^2) to be passed. At such high current densities, the solution must be passed through the gap at very high rates (up to 6.3 m/sec) to (i) reduce the temperature of the solution in the gap (otherwise the solution would boil away); (ii) sweep out the viscous film so that the diffusion layer will be as thin as possible; and (iii) bring fresh solution into the gap so that depletion of the active material will not occur. To obtain this high solution flow the APFS system was invented (4).

With the APFS plating system, the viscous layer is made very thin and large quantities of fresh solution are transported to the cathode surface continuously. Successful high rate plating of hard Cr should be possible from solutions with concentrations of CrO_3 as low as 50 or 25 g/liter, since these solutions are red showing the presence of trichromate ion. Also, polarization studies show that cathodic films are formed in these solutions.

As a strong solution of chromic acid is diluted, the color of the solution changes, passing from deep red (250 g/liter) through red (100 g/liter) and orange (10 g/liter) to yellow (1 g/liter). From the polarization studies (5), it was found that the electrochemical behavior of the 10 g/liter solution of CrO_3 (orange) is similar to that of a solution of $1\text{M Na}_2\text{Cr}_2\text{O}_7$. Here, the orange color is associated with the dichromate ion and a cathodic film was detected.

Similar behavior between the yellow solutions of CrO_3 (1 g/liter) and $1\text{M Na}_2\text{CrO}_4$ was found. In these cases, the yellow color is associated with the monomer, HCrO_4^- ion, and the presence of cathodic films on the electrode surface was not observed.

According to this mechanism, one should expect only a very thin deposit of metallic Cr to be laid down on the cathode from the 10 g/liter solution in the APFS system under the same experimental conditions used in the 50 g/liter case. Even though cathodic films are detected at cathodes in orange solutions of CrO_3 , this behavior is predicted because the concentration of trichromate ions must be very low.

Since cathodic films were not detected at the electrode surface in the yellow 1 g/liter solution of CrO_3 and since the concentration of trichromate most likely is negligible, one should not expect to obtain a deposit of Cr metal under this given set of experimental conditions.

Experimental

The samples to be plated were copper tubes 7.6 cm long with an OD of 3.8 cm and a wall thickness of 0.17 cm (cathode area is 83.6 cm^2). Preparation of the Cu samples included polishing, buffing electroclean-

ing, acid dipping, and drying. Seventy-five liters of electrolyte were placed in tank No. 1 of the APFS plating system shown in Fig. 1 and the Cu sample was clamped into position in the fixture presented in Fig. 2. A detailed account of the operation of the APFS system may be found elsewhere (3). The electrolyte was heated by a steam heat exchanger. Samples were plated for 1 min.

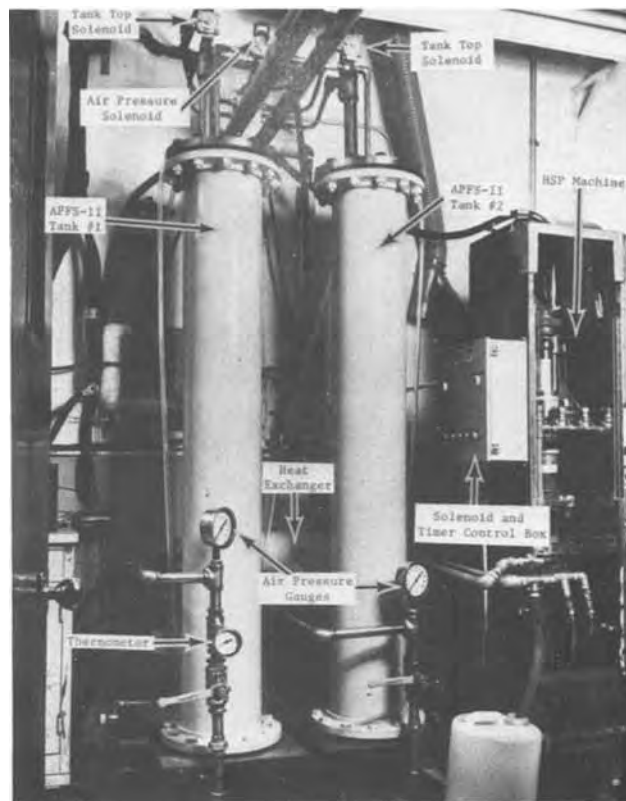


Fig. 1. HSP installation including APFS

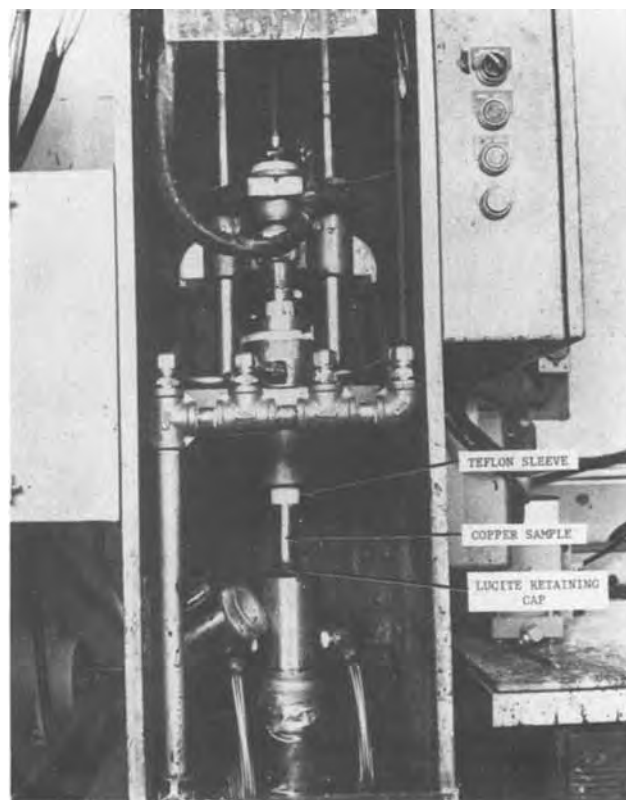


Fig. 2. HSP plating fixture open to load-unload position

Current efficiency measurements were obtained from weight-gain determinations of the sample and the total current passed which was determined by integrating under the current-time trace recorded on a strip chart. Integration was accomplished by cutting out the chart trace, weighing, and comparing that weight with the weight of a unit area of chart paper.

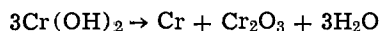
The outside surfaces of the Cu-tube samples were plated with Cr against a concentric 95% Pb-Sn alloy anode at temperatures ranging between 41° and 91°C with applied voltages ranging from 5 to 15V and solution flow rates up to 6.15 m/sec. In all cases, the chromic acid electrolyte was made up so that the ratio of $\text{CrO}_3/\text{H}_2\text{SO}_4$ was 100/1 since uncatalyzed CrO_3 electrolytes did not give deposits of metallic Cr.

Results and Discussion

According to the proposed model (5), bright Cr deposits should be obtained from solutions as dilute as 25 g/liter of CrO_3 . In Fig. 3, typical results of Cr deposition on Cu tubes from a solution of 25 g/liter of CrO_3 and 0.25 g/liter of H_2SO_4 are given.

At this temperature and flow rate, the deposits were bright, smooth, and adherent between applied voltage of 7.5 and 12.5V (see Fig. 3B-D). Above 12.5V (Fig. 3E), the deposits became dull and were often blistered. In addition, a thin, adherent, yellow film was deposited along with partial coverage with bright Cr. This film was analyzed with the electron probe, Auger electron spectroscopy (AES), x-ray photoelectron spectroscopy (XPS), and the scanning electron microscope (SEM). The AES, XPS, and electron probe results indicate that the yellow film is almost completely composed of Cr_2O_3 . SEM micrographs of the bright Cr surface are shown in Fig. 4 A-C and of the yellow film in Fig. 4 D-F at three different magnifications.

The proposed model states that the cathodic film from which Cr is eventually deposited, is a hydrated complex of HSO_4^- ion hydrogen bonded to a chromous dichromate species. By an acid catalyzed hydrolysis, this film is decomposed to form chromous hydroxide which complexes with HSO_4^- ion (5). The chromous bisulfate complex may then be discharged to metallic Cr with the transfer of two electrons. The result is the deposit shown in Fig. 4A. For very high deposition rates (Fig. 3E, 9 $\mu\text{m}/\text{min}$), some hydroxide may be codeposited with the metallic Cr. When the sample is removed from the plating machine and dried, the dehydrated hydroxide film decomposes to Cr and Cr_2O_3



as detected in Fig. 4D.

The highest plating rate obtained in the 25 g/liter electrolyte was 12 $\mu\text{m}/\text{min}$ but was whitish gray; bright deposits were obtained only in the 3-5 $\mu\text{m}/\text{min}$ range.

A plot of the cathodic current efficiencies as a function of the current density for three temperatures is given in Fig. 5. As the temperature is increased the current efficiency for Cr deposition decreases for a given current density. The reason for this is the fact that a parallel reaction, the reduction of H^+ , can occur. Although the rate of Cr deposition increases with

temperature, the rate of H_2 evolution also increases but at a higher rate of increase (Fig. 6). As a result, the current efficiency for Cr deposition falls off even though the actual amount of Cr deposited per unit time at a given current density may be greater at the higher temperature.

The voltage range over which bright Cr may be obtained is extended with higher temperatures. The deposit in Fig. 3E obtained at 79°C was greatly improved when deposited under the same conditions at 91°C.

To determine the optimum electrolyte for plating from low concentration chromic acid electrolytes, a 50 g/liter CrO_3 solution containing 0.5 g/liter H_2SO_4 was investigated. The deposition rate for bright deposits in this electrolyte ranged from 6 to 12 $\mu\text{m}/\text{min}$, over twice the rate obtained in the 25 g/liter solution. From the 50 g/liter electrolyte, deposit thicknesses of 18-20 μm were routinely achieved in 1.5 min, a thickness which is the present-day industrial specification for the chromium plating of MacPherson struts. Deposits up to about 12 μm were adherent, bright, and smooth (similar to Fig. 3B or C).

As a further test of the predictions made from the proposed model, Cu tubes were plated in the APFS system from very dilute electrolytes composed of 10 g/liter CrO_3 + 0.1 g/liter H_2SO_4 and 1 g/liter CrO_3 + 0.01 g/liter H_2SO_4 .

Three copper samples plated in the 10 g/liter CrO_3 electrolyte at 85°C are shown in Fig. 7, since the best results were obtained at this temperature. At the high applied voltages (above 10V) the samples were covered with the yellow film. Although the deposits were thin (about 1 μm) they were smooth, and at the higher applied voltages, were bright. Since the concentration of trichromate ion from which the cathodic film is formed is very low in this electrolyte, one would expect to find the observed low deposition rate.

At a concentration of 1 g/liter CrO_3 , Cr metal deposits were not detected at low applied voltages. Even at higher applied voltages, virtually no Cr deposits were observed as noted by a slight loss in weight of the copper sample indicating some dissolution of the copper tube in this electrolyte. This observation agrees well with the polarization curves obtained (5) in this solution showing no evidence for cathodic film formation. Consequently, a Cr deposit should not be expected.

Use of the 50 g/liter CrO_3 electrolyte in the APFS, HSP system offers one the opportunity of plating metallic Cr 30-40 times faster than that in conventional Cr plating (25 $\mu\text{m}/\text{hr}$ from 250 g/liter CrO_3) from solutions containing only 20% of the CrO_3 . Not only does the HSP have an obvious economic advantage, but since it is a closed loop system (opened only for load and unload), the chromic acid misting is contained in the APFS system providing a reduction in the corrosion of ventilating systems and in environmental pollution control.

Manuscript submitted Sept. 28, 1979; revised manuscript received Feb. 18, 1980.

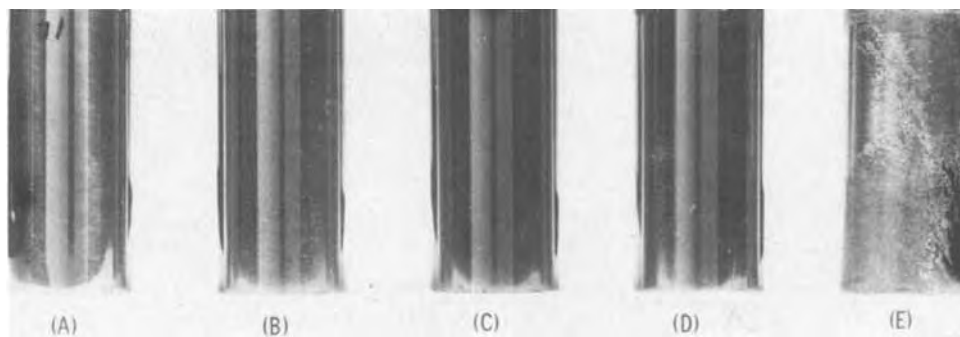


Fig. 3. HSP of Cu-tube samples in a solution of 25 g/liter CrO_3 + 0.25 g/liter H_2SO_4 for 1 min at 79°C with a flow rate of 6.15 m/sec and applied voltages; (A) 5V, (B) 7.5V, (C) 10V, (D) 12.5V, and (E) 15V. Deposit thicknesses are: (A) >1 μm , (B) 3 μm , (C) 5 μm , (D) 8 μm , and (E) 9 μm .

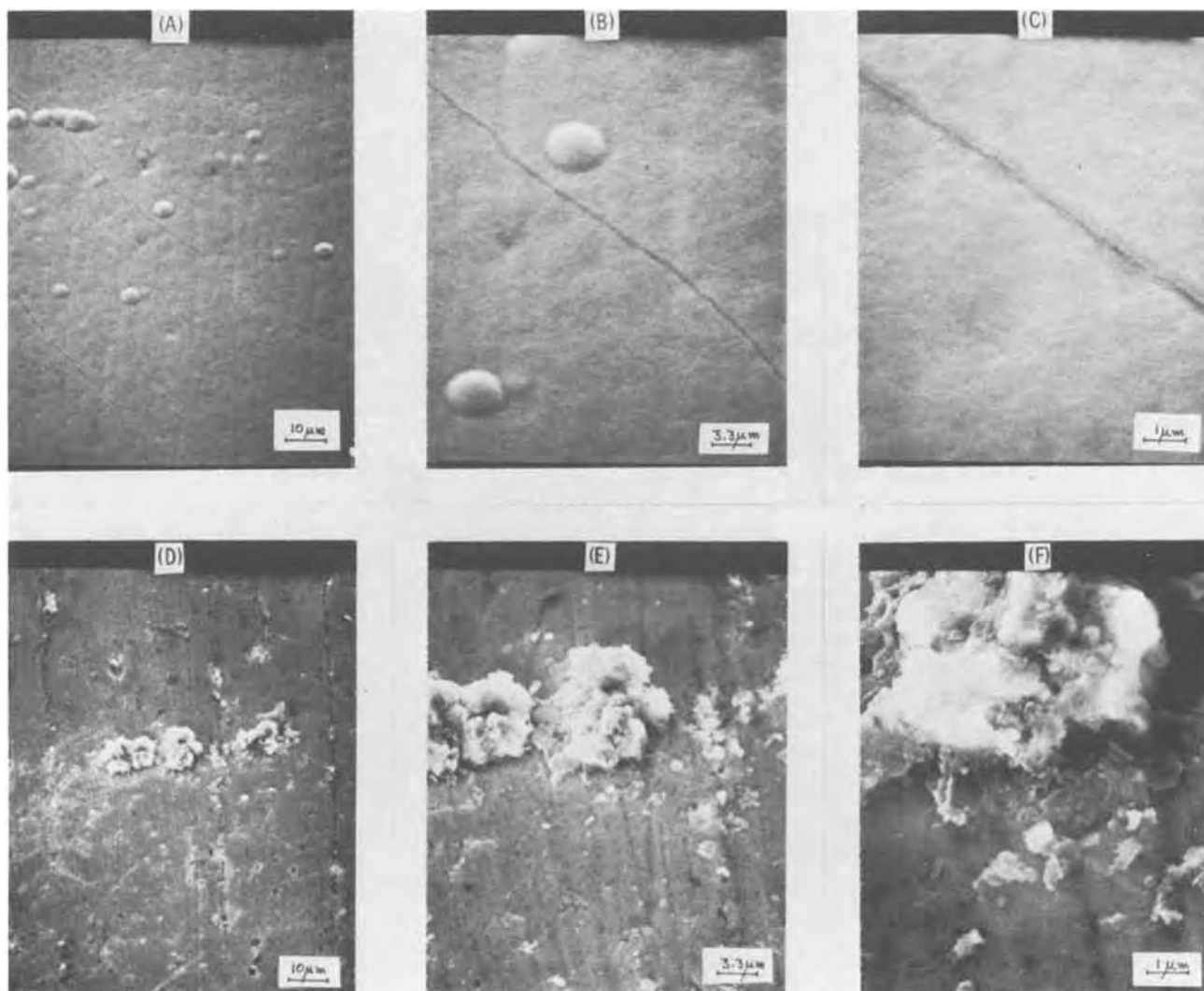


Fig. 4. Scanning electron micrographs at three magnifications of a bright Cr deposit (A, B, C) and of a bright Cr deposit with the yellow film (D, E, F).

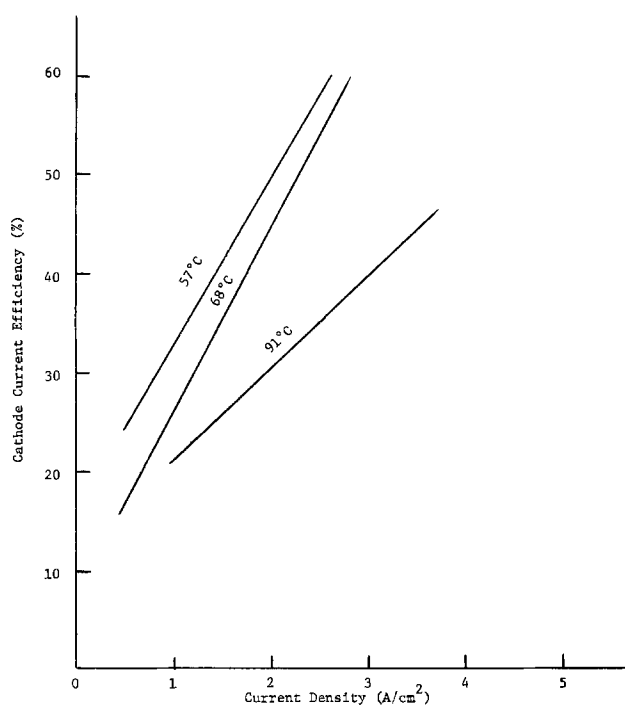


Fig. 5. Cathode efficiency as a function of the current density for Cr plating from 25 g/liter $\text{CrO}_3 + 0.25$ g/liter H_2SO_4 at 3 temperatures and a flow rate of 4.2 m/sec.

Any discussion of this paper will appear in a Discussion Section to be published in the June 1981 JOURNAL. All discussions for the June 1981 Discussion Section should be submitted by Feb. 1, 1981.

Publication costs of this article were assisted by General Motors Research Laboratories.

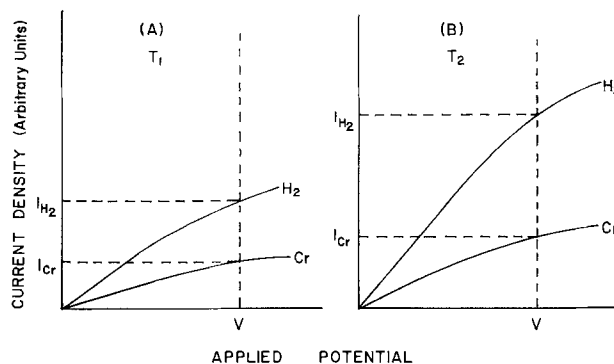


Fig. 6. Idealized polarization curves for the deposition of Cr and evolution of hydrogen at two temperatures, T_1 in A and T_2 in B where $T_2 > T_1$; total current is $i_{\text{Cr}} + i_{\text{H}_2}$ at the given potential V . Using arbitrary units, i_{Cr} is assigned 0.80 A/cm² in A and 1.2 A/cm² in B. Then the current efficiency for Cr deposition decreases from 31.0% in A to 26.8% in B but the rate of Cr deposition increases from 0.80 C/sec in A to 1.2 C/sec in B per unit area.

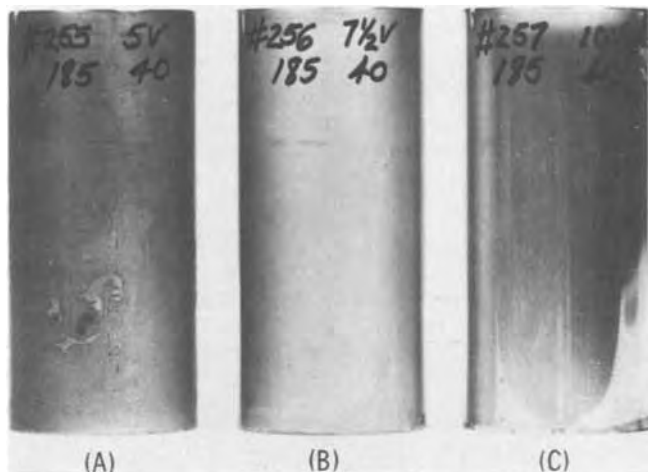


Fig. 7. HSP of Cr on Cu-tube samples from a solution of 10 g/liter CrO_3 + 0.10 g/liter H_2SO_4 for 1 min at 85°C with a flow rate of 4.2 m/sec and applied voltages; (A) 5V, (B) 7.5V, and (C) 10V. Deposit thicknesses are: (A) $<1 \mu\text{m}$, (B) $1 \mu\text{m}$, and (C) $1.5 \mu\text{m}$.

REFERENCES

1. W. H. Safranek and C. H. Layer, *Trans. Inst. Met. Finish.*, **53**, 121 (1975).
2. D. T. Chin, *Plating Surf. Finish.*, **64**, (9), 57 (1977).
3. M. A. LaBoda, *Surf. Technol.*, In press.
4. M. A. LaBoda, U.S. Pat. 4,111,761 (1978).
5. J. P. Hoare, *This Journal*, **126**, 190 (1979).
6. E. Müller, *Trans. Faraday Soc.*, **31**, 1194 (1935).
7. M. A. Shluger and V. A. Kasakov, *Zhur. Prikl. Khim.*, **33**, 644 (1960).
8. A. T. Vagramyan and D. N. Usachev, *ibid.*, **32**, 1900 (1958).
9. A. T. Vagramyan and M. K. Zhamagortsyants, "Electrodeposition of Metals and Inhibiting Adsorption," Nauka, Moscow, USSR (1969); NBS Transl., p. 194, (1974).
10. J. C. Saiddington and G. R. Hoey, *This Journal*, **117**, 1011 (1970); **120**, 1475 (1973).
11. M. H. Jones and J. C. Saiddington, *Plating*, **52**, 39 (1956).
12. S. Suzuki, K. Yoda, H. Suzuki, I. Yaguchi, and H. Karasawa, U.S. Pat. 4,080,268 (1978).

Photoelectrochemical Investigation on Trigonal Selenium Film Electrodes

W. Gissler

Commission of the European Communities, Joint Research Centre, Ispra Establishment, 21020 Ispra (Varese), Italy

ABSTRACT

The photoelectrochemical properties of trigonal selenium films were investigated in view of a possible application in semiconductor liquid junction photo cells. A photo decomposition reaction of Se into hydrogen selenide was observed in acidic solutions. Only redox couples with a relatively anodic standard potential can prevent the decomposition process. The results are interpreted by a charge transfer process via interband states. Possible applications of Se-film electrodes are discussed.

The conversion of solar energy into electrical and storable chemical energy by semiconductor liquid junction solar cells is a potential low cost technique provided that cheap semiconductor materials of suitable photoelectrochemical properties can be found [see, e.g., Ref. (1)]. So far only relatively few semiconductors have been investigated (2, 3) and an investigation of less known materials seems to be warranted. In this paper results of an investigation on photoelectrochemical properties of trigonal selenium are reported. Formerly selenium has been used for the production of solid-state photoelements and current rectifiers (4), but so far no attempts have been made to use it in semiconductor liquid junction solar cells. Measurements of the electrochemical behavior with and without illumination have been reported earlier (5).

In the solid state, selenium has several allotropic forms. At room temperature the only stable phase is that of trigonal selenium which is a p-type semiconductor with a bandgap energy of $E_g = 1.9 \text{ eV}$ (6) exhibiting a direct optical transition with a correspondingly high absorption coefficient. Polycrystalline selenium films can be easily produced either by evaporation or by dipping metallic substrates in the liquid phase (melting point 220°C). These properties make selenium an interesting candidate as photoelectrode for solar energy conversion.

Key words: semiconductor electrolyte, photocorrosion, electrode.

Experimental

Selenium film electrodes were made either by evaporation or from commercially available rectifiers. Evaporation was performed with 99.999 atomic percent (a/o) Se at 240°C onto a gold film covered aluminum substrate which was kept at 150°C . After the evaporation process the layers were annealed at 100°C for a period of 24 hr in order to assure a complete transformation of the film into the crystalline state. The gold selenium contact showed a pure ohmic behavior. The selenium film electrodes from rectifiers were made by removing the Cd film by etching. The thickness of both film electrodes was between 5 and $10 \mu\text{m}$.

The electrodes were mounted in single compartment cells with a calomel reference and platinum counter-electrodes. An aqueous solution of 1F H_2SO_4 was used as an electrolyte. Potentiostatic measurements were performed with a PAR Model 173 potentiostat in conjunction with a PAR Model 175 Universal Programmer. For the measurement of the transient current behavior a PAR Model 4202 signal averager was used. Illumination was from a 500W xenon lamp filtered by 10 cm of water, and the light was interrupted by either a PAR Model 192 chopper or a Spindler and Hoyer rapid manual shutter. As monochromator, a Spex Model Minimate was used. Capacity measurements were made by superimposing on the potentiostatically controlled d-c voltage an a-c volt-

age of approximately 100 mV amplitude at 20-100 kHz. The a-c amplitude and phase angle were measured in a circuit in which the cell was placed in series with a resistance (7). Gas analysis was performed with a Balzers quadrupol residual gas analyzer Type QMG 111 B.

Results

The photocurrent wavelength dependence of selenium was measured at an electrode potential of $U = -0.5V$ (SCE) and compared with the light source spectrum, from which the photoresponse spectrum (photocurrent/photon flux) was derived (Fig. 1). The spectrum is consistent with a direct optical transition for a bandgap energy of $E_g = 1.9$ eV.

Space charge capacity (C_{SC}) measurements were performed in a potential range U of -0.5 - $0.25V$ (SCE) where the electrodes showed only a small dark current ($i_d < 20 \mu A/cm^2$). Frequency dispersion was observed below 50 kHz, indicating the existence of "slow" energy states (e.g., surface states). Linear Mott-Schottky plots ($1/C_{SC}^2$ vs. U) were only obtained with the electrodes made from selenium rectifiers. Figure 2 shows such a plot at 100 kHz for a dark and an illuminated electrode (intensity ~ 2 sun AM2). From the slope of the plot for the dark electrode an acceptor density of $2.3 \cdot 10^{17} cm^{-3}$ is obtained assuming a value of 13 (8) for the dielectric constant. For the flatband potential a value of $U_{FB} = 0.84V$ (SCE) is obtained by extrapolation of $1/C_{SC}^2 \rightarrow 0$. For the illuminated electrode, U_{FB} is only slightly increased. The obtained capacity values are about 2 times larger than for the dark electrode.

Current-potential (i vs. U) curves were measured with intermittent light (frequency ≈ 1 Hz) using a

scan speed of 20 mV/sec. Figure 3a depicts normal behavior of p-type rotating disk semiconductor. The appearance potential of the photocurrent, however, is about 0.6V more cathodic than the flatband potential. Such a discrepancy has been observed also with other p-type semiconductors (9,10). Measurements on a stationary electrode (Fig. 3b) revealed a quite anomalous behavior: with a positive potential scan direction and for potentials $U > 0.4V$ (SCE) an anodic photocurrent superimposed on a relatively large dark current was observed. The fact that this anomalous behavior could be observed only with the stationary electrode suggests that it is due to an electrochemical reaction of the product of the cathodic photo reaction. This hypothesis is also supported by the observation that the anomalous behavior disappears with reversed scan direction. Cyclic voltammograms (Fig. 4) elucidated this effect further.

The time response of the photocurrent to a trapezoidal light pulse has been measured with the stationary and the rotating electrode in the potential range $0.4 < U < 0.8V$ (SCE) (Fig. 5). Before every measurement the electrode was kept for 1 min at a potential of $-0.5V$ (SCE) and illuminated. Interestingly the rotating electrode, which does not exhibit a stationary photocurrent in this potential region, responds like a capacitor to a potential step. The photocurrent response of the stationary electrode resembles the response of a system where diffusion enters the kinetics.

The cathodic photocurrent causes a decomposition of the electrode. It is accomplished by a visible evolution of a gas of a strong unpleasant smell. A mass-spectrometric investigation revealed hydrogen selenide as decomposition product. It is therefore assumed that in acidic solutions the cathodic photocurrent is due to the reaction

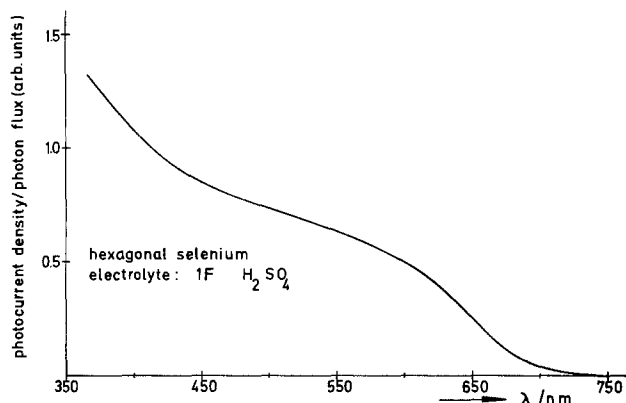


Fig. 1. Photoresponse spectrum of an Se/0.1F H_2SO_4 junction measured at a potential of $-0.5V$ (SCE).

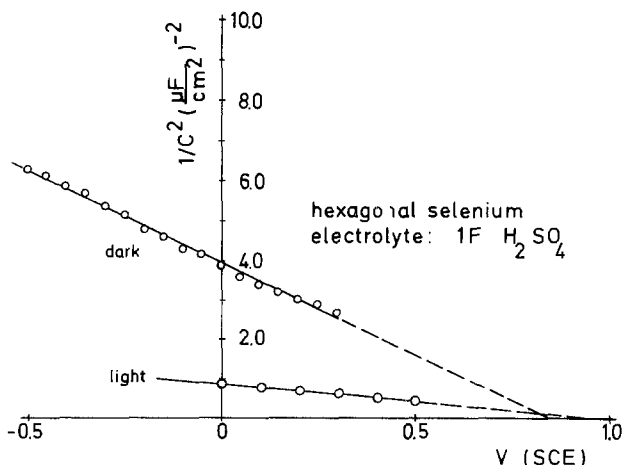


Fig. 2. Mott-Schottky plot of an Se/0.1F H_2SO_4 junction in the dark and under illumination with $2 \times AM_2$. The selenium electrode was made from an Se rectifier. Frequency 100 kHz.

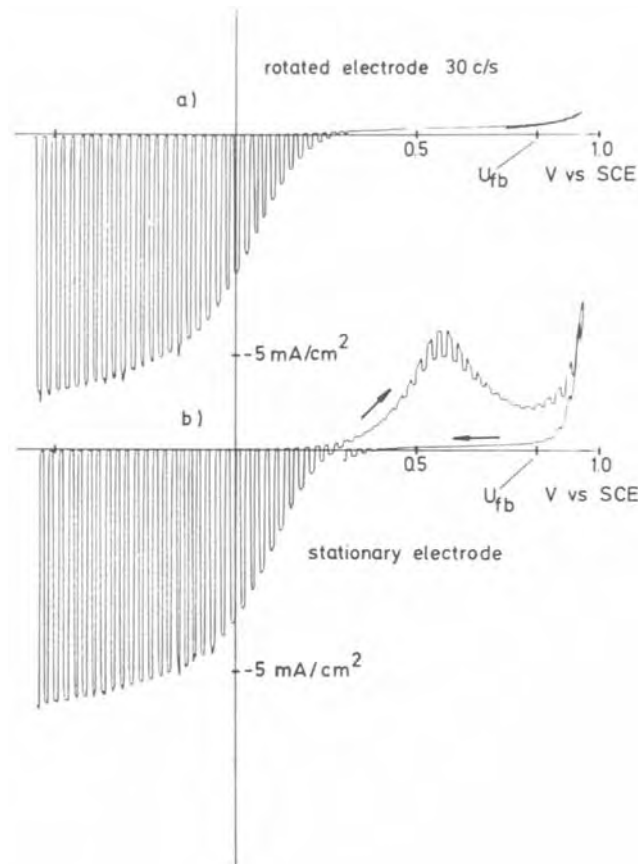


Fig. 3. Current-potential dependence measured with intermittent light of a xenon lamp. (a) Electrode rotated with 30 C/sec; (b) stationary electrode.

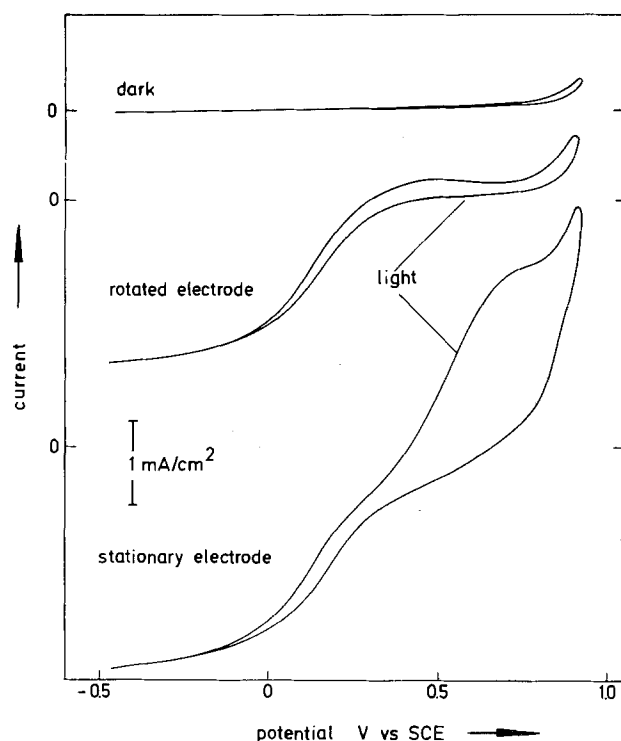


Fig. 4. Cyclic voltammograms of Se, scan rate 2 V/sec

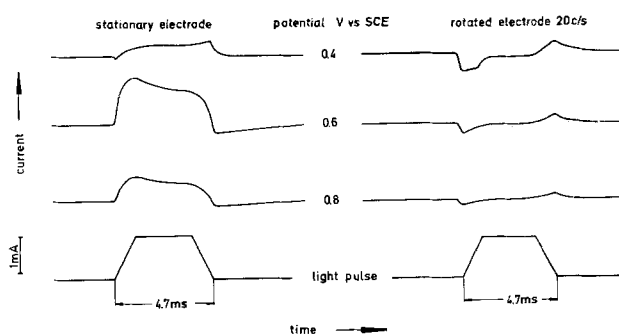
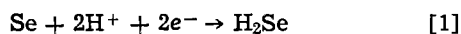


Fig. 5. Photocurrent response of a stationary and rotated (30 C/sec) electrode on a trapezoidal light pulse.



From thermodynamic considerations (11) Se is expected to be decomposed into H_2Se for potential $U < -0.46\text{V}$ (NHE) and into H_2SeO_3 for potentials $U > 0.69\text{V}$ (NHE) at pH 1.

Experiments to stabilize the electrode by adding redox systems as $\text{Eu}^{2+/3+}$ and $\text{Cr}^{2+/3+}$ failed. The standard potentials of both couples are slightly more positive than the potential of the decomposition reaction [1], and the unoccupied levels of both couples can be assumed to overlap well with the conduction bandedge. Also the hydrogen evolution reaction can evidently not compete with the photodecomposition, although it cannot be completely excluded. With other p-type semiconductors, e.g., GaP and GaAs, a photocurrent stabilization due to hydrogen evolution has been obtained (9).

Using redox systems of relatively positive standard potentials such as $\text{Fe}(\text{CN})_6^{4-/3-}$, $\text{Fe}^{2+/3+}$, and $\text{Ce}^{3+/4+}$ the odor of H_2Se could no longer be detected and the photocurrent became stable within $\pm 5\%$ over the measurement period of 2 hr. Figure 6 shows the $i-U$ curves in the dark (full line) and under illumination (broken line) obtained with a rotating electrode (30 C/sec) for the pure electrolyte of 1F H_2SO_4 (curve 1) and for solutions to which the following redox systems have been added: 0.1M $\text{K}_3\text{Fe}(\text{CN})_6 + 0.01\text{M}$ $\text{K}_4\text{Fe}(\text{CN})_6$ (curve 2), $+0.05\text{M}$ $\text{Fe}_2(\text{SO}_4)_3 + 0.01\text{M}$

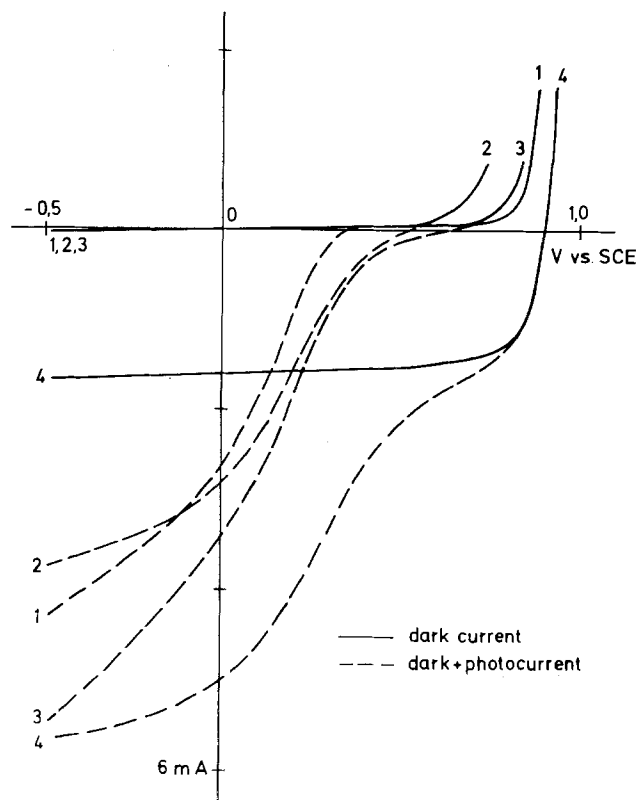


Fig. 6. Current-potential dependence of a dark (full) and illuminated (dashed) Se electrode for different redox electrolytes. Curve 1: 1F H_2SO_4 ; curve 2: 1F $\text{H}_2\text{SO}_4 + 0.1\text{M}$ $\text{Fe}(\text{CN})_6^{3-} + 0.01\text{M}$ $\text{Fe}(\text{CN})_6^{4-}$; curve 3: 1F $\text{H}_2\text{SO}_4 + 0.1\text{M}$ $\text{Fe}^{3+} + 0.01\text{M}$ Fe^{2+} ; curve 4: 1F $\text{H}_2\text{SO}_4 + 0.1\text{M}$ $\text{Ce}^{4+} + 0.01\text{M}$ Ce^{3+} .

FeSO_4 (curve 3), and 0.1M $\text{Ce}(\text{SO}_4)_2 + 0.01\text{M}$ $\text{Ce}_2(\text{SO}_4)_3$ (curve 4). It is interesting to note that the more anodic the redox potential of the couple the more the appearance potential U_{AP} of the photocurrent is shifted towards the flatband potential. The cathodic dark current is large only in the case of the $\text{Ce}^{3+/4+}$ redox couple which is probably due to a direct charge transfer from the valence band. An estimation from the rearrangement energy (12) shows that the unoccupied levels overlap well with the valence band. Also an anodic dark current is observed. This is to be expected for $U > U_{\text{FB}}$. However, for the $\text{Fe}(\text{CN})_6^{4-/3-}$ and $\text{Fe}^{2+/3+}$ redox couples an anodic dark current is also observed for $U < U_{\text{FB}}$.

Discussion

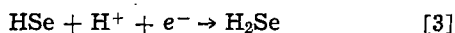
From thermodynamic considerations (14), it is expected that only those redox reactions can successfully compete with the photodecomposition of p-type semiconductors having more positive standard redox potentials. This is the case for all redox couples used in our experiments. However, only the redox couples with very anodic standard potentials seem to compete with the photodecomposition, although the oxidation levels in all cases are located within the bandgap of selenium [as estimated from the rearrangement energies (12)]. Corresponding observations have been made on n-type semiconductors (15). Whether the direct electron transfer model is an adequate description or surface states are involved is still an open question.

The observed difference between standard redox potential and appearance potential of the photocurrent can be understood by both types of transitions if large surface recombination rates (in comparison to the rate of charge exchange between semiconductor and solution) are assumed (13, 16).

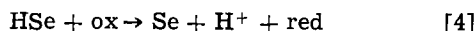
It is difficult to estimate the kinetics of the charge transfer process via surface states for the redox couples

used in this experiment. However, the observed large values of $(U_{FB} - U_{ap})$ for the photodecomposition reaction might be indicative of slow kinetics for this reaction, compared to simple redox reactions.

Recently for n-type semiconductors it has been assumed that the decomposition proceeds in different steps and that the energy levels of the intermediate states are located within the bandgap (17). Only the last step is the virtual decomposition reaction, which can be prevented if suitable redox reactions can compete with it. If such a model is applied to selenium the decomposition might be assumed to consist of the two steps



It is reasonable to assume that the rate constant for reaction [3] is smaller than for a competing redox reaction of the type



because the decomposition process according to [3] probably also involves some geometrical restraints in contrast to the redox reaction [4]. If the standard potential for reaction [3] is more positive than the reversible hydrogen electrode it also becomes clear that only the redox couples with more positive standard potentials prevent the decomposition process. The existence of interband states in hexagonal Se has been observed earlier by capacitance relaxation measurements (18).

The observation of an anodic dark current (Fig. 3a and Fig. 6) at electrode potentials $U < U_{FB}$ suggests either a tunnel mechanism or an avalanche breakdown (19). An estimation using the expression for the tunnel probability T given in (20) shows that this process is fairly probable even for the relatively low charge carrier density of $2.3 \cdot 10^{17} \text{ cm}^{-3}$ if it is assumed that the occupied states are located only a few tenths of an electron volt above the valence bandedge. The anodic dark current assumes large values only during the anodic potential scan direction at the illuminated stationary electrode (Fig. 3b and Fig. 4). It might therefore be due to the product of the cathodic reaction which should be a solution species to be detected in the anodic reaction. A possible reaction is the back reaction of [3] which, however, can occur at $U < U_{FB}$ only assuming a hole injection process via tunneling.

The anomalous anodic photocurrent is always accompanied by a large anodic dark current. It might therefore be due to an increase of the tunneling probability under illumination; this is actually to be expected because the observed capacity increase under illumination (Fig. 2) can only be explained in a potentiostatic experiment by a reduction of the space charge layer, leading to an increase in the tunneling probability. In the absence of a reactant, a pure charging and discharging current of the space charge capacity should be observed. This is actually the case (Fig. 5).

Due to the fact that a stabilization can be reached only with redox couples of relative positive standard potentials, selenium electrodes seem to be unsuitable for use in regenerative solar cells: a large part of the energy which has been gained by band-band excitation is lost by transitions from the conduction band into the lower interband levels, and correspondingly, only small cell voltages can be obtained.

However, selenium photocathodes might be used in a novel way for hydrogen production: in contrast to direct photolysis, in a first step hydrogen selenide is produced by utilizing the photodecomposition reaction [1], and then in a subsequent reaction step hydrogen selenide is thermally dissociated in hydrogen and selenium, which has to be, however, regenerated for use as electrode. Since the fabrication of selenium electrodes from the melt is a well-established low

cost technique (4) and the dissociation reaction occurs at relatively low temperatures (21) a more detailed investigation of the feasibility of such a cycle would seem to be worthwhile.

Acknowledgments

The author wishes to express his thanks to Dr. J. S. Curran and Dr. G. Schütz for valuable suggestions and discussions and to Messrs. A. Hoffmann and R. Schubert for very helpful technical assistance. The very stimulating discussions with Dr. R. Memming are particularly acknowledged.

Manuscript submitted Dec. 3, 1979; revised manuscript received Feb. 29, 1980. This was Paper 638 presented at the Los Angeles, California, Meeting of the Society, Oct. 14-19, 1979.

Any discussion of this paper will appear in a Discussion Section to be published in the June 1981 JOURNAL. All discussions for the June 1981 Discussion Section should be submitted by Feb. 1, 1981.

Publication costs of this article were assisted by the Commission of the European Communities.

REFERENCES

1. "Semiconductor Liquid-Junction Solar Cells," A. Heller, Editor, The Electrochemical Society Softbound Proceedings Series, Princeton, N.J. (1977).
2. H. P. Maruska and A. K. Gosh, *Solar Energy*, **20**, 443 (1978).
3. K. Rajeshwar, P. Singh, and J. DuBow, *Electrochim. Acta*, **23**, 1117 (1978).
4. G. Mierde and J. Kroczeck, "Selengleichrichter," Ed. VEB Verlag Technik Berlin, Berlin (1959).
5. D. Popov, *Nauchn. Fr. Plovdivski Univ., Mat., Fiz., Khim., Biol.*, **11**, (2) 107 (1973) (Bulg.).
6. W. Henrion in "The Physics of Selenium and Tellurium," Proceedings of the Int. Symposium held at Montreal, Canada, Oct. 12-13, 1967, W. Charles Cooper, Editor, p. 75, New York (1969).
7. W. Gissler, EUR-Report No. 6214 EN (1978).
8. T. Salo, T. Stubb, and E. Suosara, in "The Physics of Selenium and Tellurium," Proceedings of the Int. Symposium held at Montreal, Canada, Oct. 12-13, 1967, W. Charles Cooper, Editor, p. 335, New York (1969).
9. R. Memming and G. Schwandt, *Electrochim. Acta*, **13**, 1299 (1968).
10. J. O'M. Bockris and K. Uosaki, *This Journal*, **124**, 1348 (1977).
11. M. Pourbaix, "Atlas of Electrochemical Equilibria in Aqueous Solutions," Pergamon Press, London (1966).
12. R. Memming and F. Möller, *Ber. Bunsenges. Phys. Chem.*, **76**, 475 (1972).
13. R. H. Wilson, in "Semiconductor Liquid Junction Solar Cells," A. Heller, Editor, p. 67, The Electrochemical Society Softbound Proceedings Series, Princeton, N.J. (1977).
14. H. Gerischer, *J. Electroanal. Chem. Interfacial Electrochem.*, **82**, 133 (1977); R. Memming in "Semiconductor Liquid-Junction Solar Cells," A. Heller, Editor, p. 38, The Electrochemical Society Softbound Proceedings Series, Princeton, N.J. (1977); A. J. Bard and M. S. Wrighton, *ibid.*, p. 195.
15. W. P. Gomes, Paper 602 presented at The Electrochemical Society Meeting, Los Angeles, California, Oct. 14-19, 1979.
16. D. Laser, *This Journal*, **126**, 1011 (1979).
17. R. Memming, *Electrochim. Acta*, In press.
18. H. P. D. Lanyon and R. N. Krambeck, in "The Physics of Selenium and Tellurium," Proceedings of the Int. Symposium held at Montreal, Canada, Oct. 12-13, 1967, W. Charles Cooper, Editor, p. 59, New York (1969).
19. J. C. Tranchart, L. Hollan, and R. Memming, *This Journal*, **125**, 1185 (1978).
20. B. Pettinger, H.-R. Schöppel, and H. Gerischer, *Ber. Bunsenges. Phys. Chem.*, **78**, 451 (1974).
21. O. H. Krikovian and H. H. Otsuki, Preprint UCRL-80282 (1977).

The Measurement of Sulfur Chemical Potential Differences Using a Calcium Fluoride Solid Electrolyte

T. A. Ramanarayanan^{*1} and W. L. Worrell*

Department of Materials Science and Engineering, University of Pennsylvania, Philadelphia, Pennsylvania 19104

ABSTRACT

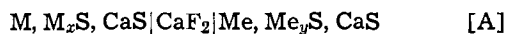
Calcium fluoride has been conventionally used as a solid electrolyte to measure fluorine chemical potentials in high temperature systems. However in this investigation, this electrolyte has been used as a sulfur sensor. Open-circuit emf measurements have been carried out with the following four galvanic cells



The cells were investigated in the temperature range, 500°-900°C. Using Richardson and Antill's data for the standard Gibbs energy of formation of Cu₂S, the standard Gibbs energies of formation of FeS, Ag₂S, MnS, and CrS have been determined.

Several investigators have used a calcium fluoride solid electrolyte to determine the Gibbs energies of formation of metal fluorides (1, 2). This electrolyte has also been used to obtain Gibbs energy data for carbides and silicates (3, 4). Recently, calcium fluoride has been used to measure oxygen chemical potentials (5, 6). This paper reports measurements of the sulfur chemical potentials of solid electrodes using a CaF₂ solid electrolyte. Moriyama and co-workers (7, 8) and Jacob, Rao, and Nelson (9) have also used the CaF₂ solid electrolyte for sulfur chemical potential measurements at high temperatures.

Consider the electrochemical cell



where M and Me are different metals. The equilibrium of the reaction



establishes a sulfur chemical potential, μ_{S_2}' , at the left-hand electrode of cell [A]. Further, consider the equilibrium



The equilibrium constant, K_2 , of this reaction is given by

$$K_2 = p_{\text{F}_2}/p_{\text{S}_2}^{1/2} \quad [3]$$

where p_{F_2} and p_{S_2} denote partial pressures of fluorine and sulfur, respectively. Since the chemical potential, μ_{S_2}' , at the left-hand electrode is fixed, the fluorine chemical potential, μ_{F_2}' , is also fixed in accordance with Eq. [3]. In a similar manner, the chemical potentials, μ_{F_2}'' and μ_{S_2}'' are fixed at the right-hand electrode.

Calcium fluoride is a solid electrolyte having anionic Frenkel disorder. Under conditions of negligible electronic conduction, the transport number of fluorine ions is unity. The open-circuit emf of cell [A] is then given by

$$E = \frac{1}{2F} [\mu_{\text{F}_2}'' - \mu_{\text{F}_2}'] = \frac{RT}{2F} \ln \frac{p_{\text{F}_2}''}{p_{\text{F}_2}'} \quad [4]$$

with $\mu_{\text{F}_2}'' > \mu_{\text{F}_2}'$. According to Hinze and Patterson (10), electronic conduction in CaF₂ is negligible even at unit activity of calcium. Delcet, Heus, and Egan (11) have recently reported that at temperatures between 800° and 950°C n-type electronic conduction is present in single crystalline calcium fluoride at calcium activities higher than 10⁻³. Combining this value with data for the Gibbs energy of formation of CaS (12) one calculates a value of 3.6 × 10⁻³⁶ atm for the low p_{S_2} limit for predominant ionic conduction ($t_{\text{ion}} \cong 0.99$) in CaF₂ at 1100°K. The lowest p_{S_2} investigated in the present work was only 4.3 × 10⁻²⁰ atm at 1100°K. Thus no electronic contribution to the conductivity is expected. On combining Eq. [3] and [4]

$$E = \frac{RT}{4F} \ln \frac{p_{\text{S}_2}''}{p_{\text{S}_2}'} \quad [5]$$

If p_{S_2}' is known, then p_{S_2}'' may be calculated from the measured open-circuit cell emf's using Eq. [5]. The standard Gibbs energy of formation of Me_yS is related to p_{S_2}'' through

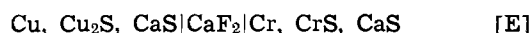
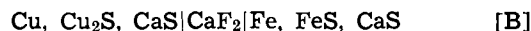
$$p_{\text{S}_2}'' = \exp \left(\frac{2\Delta G_f^\circ(\text{Me}_y\text{S})}{RT} \right) \quad [6]$$

Similarly, p_{S_2}' is given by

$$p_{\text{S}_2}' = \exp \left(\frac{2\Delta G_f^\circ(\text{M}_x\text{S})}{RT} \right) \quad [7]$$

Thus if the standard Gibbs energy of formation of M_xS is known, then that of Me_yS may be determined.

In the present study, the standard Gibbs energies of formation of FeS, Ag₂S, MnS, and CrS were determined using the cells



Materials and Experimental Procedure

Metal and sulfide powders of 99.99% purity were obtained from Cerac Incorporated. Optical grade high purity single crystals of CaF₂ (½ in. diam and 1 in. length) grown along the <111> axis were obtained

* Electrochemical Society Active Member.

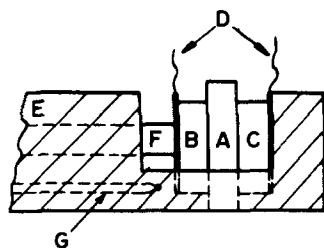
¹ Present address: Exxon Research and Engineering Company, Corporate Research Laboratory, Linden, New Jersey 07036.

Key words: solid electrolyte, sulfur sensor, emf measurements.

from Harshaw Chemical Company. The electrolyte was cut into disks of $\frac{1}{8}$ in. in thickness with a diamond wheel. The electrolyte faces were finely ground and polished with $1 \mu\text{m}$ diamond paste. The metal, metal sulfide, and calcium sulfide powders were mixed in roughly equal amounts by volume. The mixed powders were pressed in a 1 cm diam die into electrode pellets of approximately $\frac{1}{4}$ in. thickness at about 12 tsi. The electrodes were not presintered. The cell was assembled in an alumina cell holder as shown in Fig. 1. Light spring pressure was exerted to keep the electrode and electrolyte in intimate contact. Platinum disks spot-welded to Pt wires were used as electrical leads. A Pt-Pt(10% Rh) thermocouple, placed within $\frac{1}{2}$ cm of the cell, was used to measure temperatures. The cell was placed in the constant temperature zone ($\pm 1^\circ$) of a Pt-Rh wound resistance furnace. A flowing inert atmosphere of purified argon was maintained around the cell. The argon was purified by first passing through anhydrous calcium sulfate, then through activated copper (BASF) maintained at 200°C and then through titanium sponge maintained at 800°C . Any final traces of oxygen were removed by having a tantalum foil around the alumina cell holder upstream from the cell.

After the cell was heated to the experimental temperature, the open-circuit emf was measured using a high impedance digital electronic voltmeter. The cell emf was considered steady if the random variation was within ± 0.5 mV over a 5 hr period. The emf's were independent of the argon flow rate. Cell reversibility was confirmed by passing a small current (10-20 μA) for a few minutes. After the current passage, the open-circuit emf's returned to the original values within 0.5 mV.

Cell [B] was assembled and heated in purified argon atmosphere to a temperature of 550°C . The cell emf reached the equilibrium value in about 15 hr. The cell temperature was then raised by 50° increments. After changing the temperature, the attainment of the new equilibrium cell emf took approximately 5 hr. The highest temperature used was 850°C . Open-circuit emf readings were also taken upon cooling at 50° intervals. Equilibration times for cell [C] were similar to those for cell [B]. The cell was investigated over the temperature range, 500° - 750°C . Above 750°C , the silver-sulfide showed a tendency to decompose. Cell [D] was investigated in the temperature range, 700° - 900°C . After heating the cell to 700°C , the initial equilibration took ~ 48 hr. Upon changing the cell temperature, equilibrium at the new temperature was attained in about 15 hr. The attainment of equilibrium was too slow at temperatures below 700°C . The initial equilibration with cell [E] occurred within 15 hr at



- A CaF_2 ELECTROLYTE
- B,C METAL-METAL SULPHIDE - CaS ELECTRODES
- D PT LEADS CONNECTED TO PT DISCS
- E ALUMINA CELL HOLDER
- F ALUMINA PUSHROD
- G THERMOCOUPLE

Fig. 1. Experimental cell arrangement

727°C ; subsequent equilibrations occurred within 3 hr.

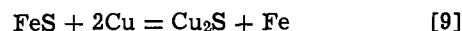
X-ray diffraction patterns of the electrode pellets were taken before and after the experiments. In all cases, only the metal, metal sulfide, and calcium sulfide phases were observed. No mutual solubility between calcium sulfide and the other metal sulfides was detected.

Results and Discussion

The open-circuit emf values obtained using cell [B] are shown in Fig. 2, in which the solid line fits the least squares expression

$$E \text{ (mV)} = -128.29 + 0.159T (\pm 5 \text{ mV}) \quad [8]$$

The uncertainty indicated in brackets is twice the standard deviation of E about the regression line. Emf's calculated using Richardson and Antill's data (13) for the Gibbs energy of formation of Cu_2S and Rosenqvist's data (14) for the Gibbs energy of formation of FeS are also shown in Fig. 2. The uncertainty in this calculated line is estimated to be ± 14 mV, which corresponds to about 650 cal in the standard Gibbs energy change for the reaction



The agreement between the two lines is excellent, within 5 mV at the lower temperatures and within 9 mV at the higher temperatures.

In the four cells investigated in the present study, the $\text{Cu-Cu}_2\text{S-CaS}$ electrode was used as the reference electrode. The $\text{Cu-Cu}_2\text{S}$ equilibrium has been investigated by Richardson and Antill (13) over the temperature range 800° - 1313°K . The uncertainty in their data is ± 300 cal, and their data are in good agreement with other results in the literature (12, 15). The standard Gibbs energy of formation of Cu_2S according to Richardson and Antill is given by the expression

$$\Delta G_f^\circ (\text{Cu}_2\text{S}) = -31,390 + 7.33T (\pm 300) \text{ cal/mole} \quad [10]$$

Using the Gibbs energy of formation for Cu_2S , the free energy of formation of FeS can be calculated using Eq. [5]-[7]. Such a calculation yields the following expression for the standard Gibbs energy of formation of FeS at temperatures between 550° and 850°C

$$\Delta G_f^\circ (\text{FeS}) = -37,310 + 14.66T (\pm 500) \text{ cal/mole} \quad [11]$$

The standard Gibbs energy of formation of FeS obtained by various investigators are compared in Fig. 3. The data of Alcock and Richardson (16) and of Rosenqvist (14) were obtained from gas-equilibration

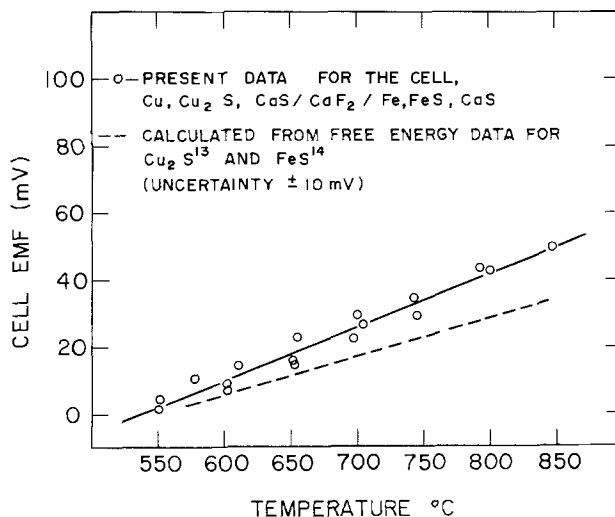


Fig. 2. Temperature variation of the open-circuit emf for cell [B].

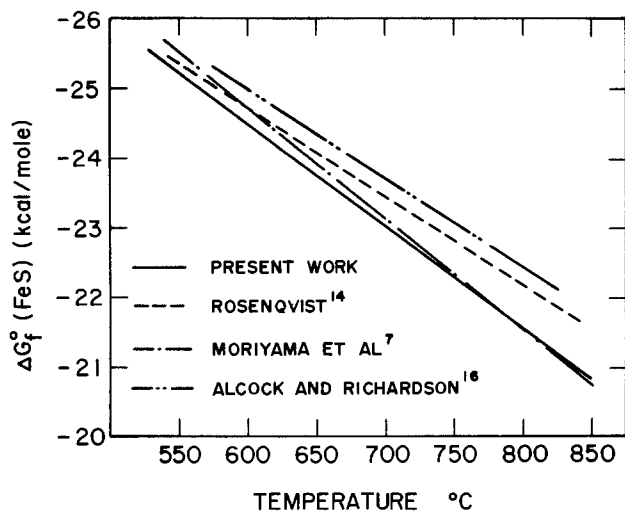


Fig. 3. Comparison of the standard Gibbs energy of formation of FeS determined in this study with results from earlier investigations.

studies using H_2 - H_2S mixtures. Moriyama and co-workers (7) used an electrochemical cell based on a calcium fluoride solid electrolyte. Our values are in good agreement with those of Moriyama *et al.*, but are less negative than those of Rosenqvist by 200-500 cal and those of Alcock and Richardson by 500-800 cal.

The emf values obtained using cell [C] are plotted as a function of temperature in Fig. 4. Also shown in Fig. 4 is the line calculated from the data of Richardson and Antill (13) for the Cu-Cu₂S equilibrium and of Rosenqvist (17) for the Ag-Ag₂S equilibrium. The solid line in Fig. 4 fits the least squares expression

$$E \text{ (mV)} = 231.75 + 0.0126T (\pm 4 \text{ mV}) \quad [12]$$

On combining Eq. [10] and [12], the standard Gibbs energy of formation of Ag₂S at temperature between 500° and 750°C is calculated to be

$$\Delta G_f^\circ (\text{Ag}_2\text{S}) = -20,700 + 7.91T (\pm 500) \text{ cal/mole} \quad [13]$$

The standard Gibbs energy of formation of Ag₂S has been plotted as a function of temperature in Fig. 5. Also shown in Fig. 5 are the results of Rosenqvist (17) and of Thompson and Flengas (18). Rosenqvist used a gas equilibration technique involving H_2 - H_2S gas mixtures for his investigations whereas Thompson and Flengas used an electrochemical technique based on a KCl-NaCl molten salt containing AgCl and Ag₂S. Our results are in excellent agreement with those of Rosenqvist and agree with those of Thompson and Flengas within 500 cal.

The emf results of cell [D] are shown as a function of temperature in Fig. 6. The upper dotted line in

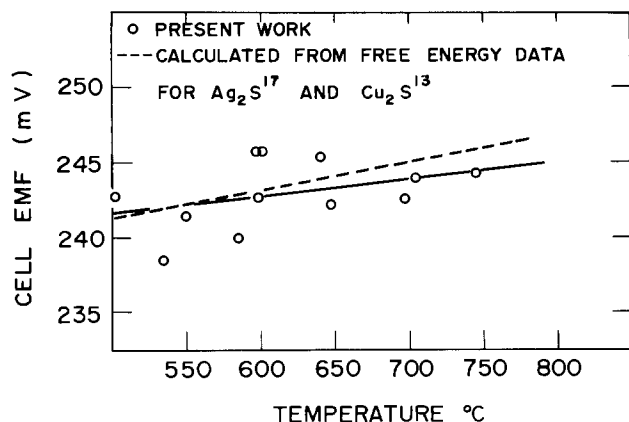


Fig. 4. Temperature variation of the open-circuit emf for cell [C]

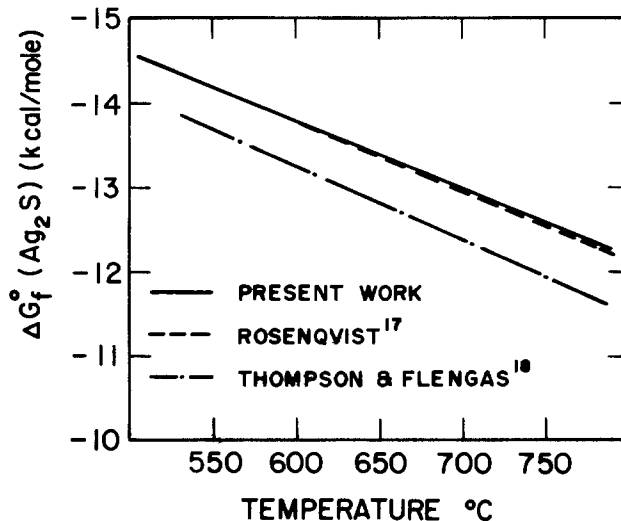


Fig. 5. Comparison of the standard Gibbs energy of formation of Ag₂S determined in this study with results from earlier investigations.

Fig. 6 is based on the Mn-MnS equilibrium data of Larson and Elliott (19). The lower line comes from the Mn-MnS equilibrium data reported by Richardson and Jeffes (20). Our data points in Fig. 6 fit the least squares expression

$$E \text{ (mV)} = 720.65 - 0.155T (\pm 12 \text{ mV}) \quad [14]$$

On combining Eq. [10] and [14], one calculates for the standard Gibbs energy of formation of MnS at temperatures between 700° and 900°C

$$\Delta G_f^\circ (\text{MnS}) = -64,635 + 14.46T (\pm 900) \text{ cal/mole} \quad [15]$$

The standard Gibbs energy of formation of MnS has been plotted as a function of temperature in Fig. 7. Shown also in Fig. 7 are the results of Larson and Elliott (19), of Moriyama *et al.* (8), of Richardson and Jeffes (20), and of Turkdogan *et al.* (21). Richardson and Jeffes quote an uncertainty of ± 1500 cal in their estimate for the free energy of formation of MnS. Larson and Elliott's values are based on electrochemical measurements of the MnO-MnS-SO₂ equilibrium using a stabilized zirconia solid electrolyte. Moriyama *et al.* (8) used an electrochemical technique based on a CaF₂ solid electrolyte. The values reported by Turkdogan and co-workers are derived from measurements of the MnO-MnS-H₂O-H₂S equilibrium. Our free energy values are less negative than those of Larson and Elliott by 500-900 cal, and of Turkdogan *et al.* by 1700-2500 cal and more negative than those of Moriyama *et al.* by 400-600 cal.

The emf values obtained using cell [E] at temperatures between 500° and 950°C are shown in Fig.

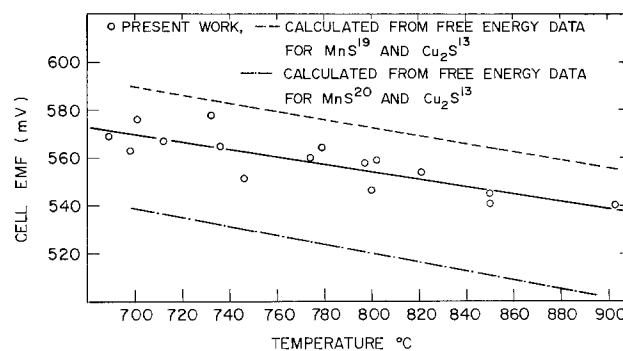


Fig. 6. Temperature variation of the open-circuit emf for cell [D].

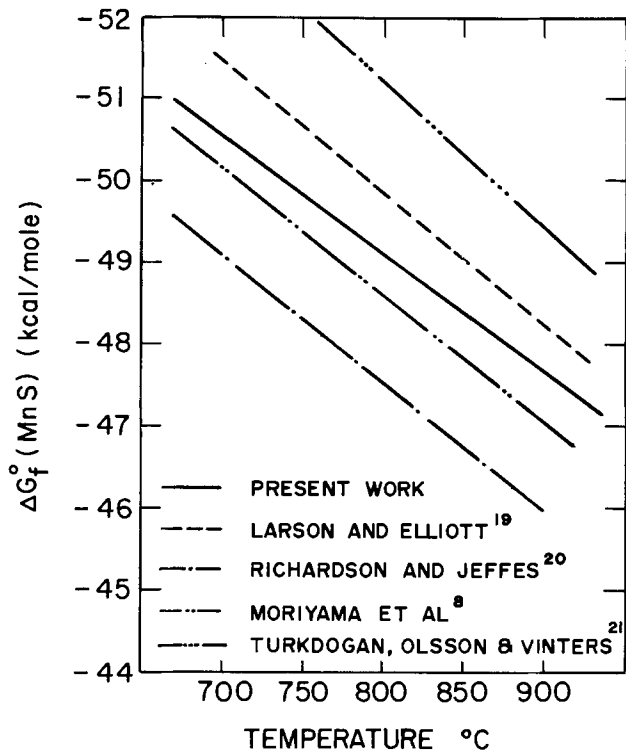


Fig. 7. Comparison of the standard Gibbs energy of formation of MnS determined in this study with results from earlier investigations.

8. The solid line in Fig. 8 fits the least squares expression

$$E \text{ (mV)} = 368.72 - 0.13T (\pm 2 \text{ mV}) \quad [16]$$

On combining Eq. [10] and [16], one calculates for the standard Gibbs energy of formation of CrS at temperatures between 550° and 950°C

$$\Delta G_f^\circ (\text{CrS}) = -48,400 + 13.3T (\pm 400) \quad [17]$$

As shown in Fig. 9, the results for ΔG_f° of CrS are in excellent agreement (within 100 cal) with the extrapolated results of Hager and Elliott (22), who used an $\text{H}_2/\text{H}_2\text{S}$ gas-equilibration technique at 1100°-1300°C. Our results are also within the quoted uncertainty (± 2000 cal) of a single gas-equilibration measurement at 700°C by Young *et al.* (23).

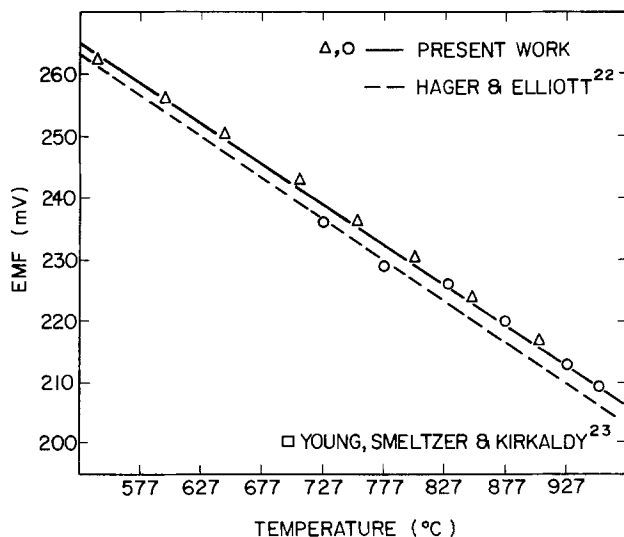


Fig. 8. Temperature variation of the open-circuit emf for cell [E].

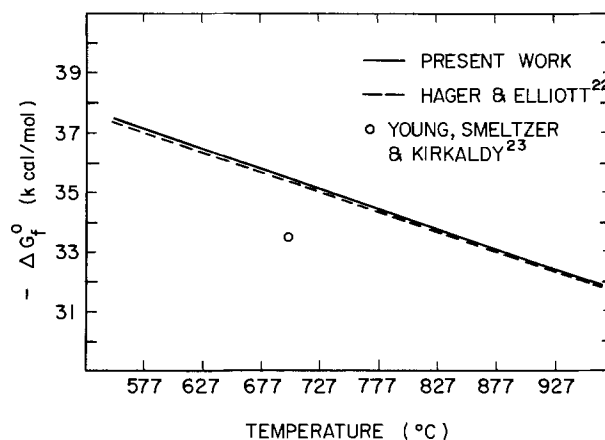


Fig. 9. Comparison of the standard Gibbs energy of formation of CrS determined in this study with results from earlier investigations.

Conclusions

The CaF_2 solid electrolyte is suitable for the measurement of sulfur chemical potentials in solid electrodes at temperatures between 500° and 950°C. Measurements with metal-metal sulfide electrodes have been used to determine the standard Gibbs energy of formation of FeS, Ag_2S , MnS, and CrS. The CaF_2 electrolyte has also been used to measure sulfur potentials in gaseous atmospheres (9). Further experimentation with this electrolyte in the measurement and control of sulfur potentials in melts seems worthwhile. However, the influence of dissolved oxygen in the melt would need to be established.

Acknowledgment

The support of this research by the National Science Foundation through the Division of Materials Research is gratefully acknowledged.

Manuscript submitted Oct. 24, 1978, revised manuscript received Feb. 27, 1980.

Any discussion of this paper will appear in a Discussion Section to be published in the June 1981 JOURNAL. All discussions for the June 1981 Discussion Section should be submitted by Feb. 1, 1981.

Publication costs of this article were assisted by the University of Pennsylvania.

REFERENCES

- W. H. Skelton and J. W. Patterson, *J. Less-Common Met.*, **31**, 47 (1973).
- T. L. Markin, in "Emf Measurements in High Temperature Systems," C. B. Alcock, Editor, p. 91, Inst. Mining and Met. Pub., London (1968).
- J. J. Egan, *J. Phys. Chem.*, **68**, 978 (1964).
- R. Benz and C. Wagner, *ibid.*, **65**, 1308 (1961).
- S. F. Chou and R. A. Rapp, in "High Temperature Metal Halide Chemistry," D. L. Hildenbrand and D. D. Cubicciotti, Editors, p. 392, The Electrochemical Society Softbound Proceedings Series, Princeton, N.J. (1978).
- T. A. Ramanarayanan, M. L. Narula, and W. L. Worrell, *This Journal*, **126**, 1360 (1979).
- J. Moriyama, T. Oishi, K. Ogino, and A. Egami, in "Proceedings of the Fourth Int. Conf. on Thermal Analysis," p. 869, Budapest, Hungary (1974).
- T. Oishi, T. Fujimura, K. Ogura, and J. Moriyama, *Nippon Kinzoku Gakkaishi*, **40**, 969 (1976).
- K. T. Jacob, D. B. Rao, and H. G. Nelson, *This Journal*, **125**, 758 (1978).
- J. W. Hinze and J. W. Patterson, *ibid.*, **120**, 96 (1973).
- J. Delcet, R. J. Heus, and J. J. Egan, *This Journal*, **125**, 755 (1978).
- O. Kubaschewski, E. L. Evans, and C. B. Alcock, "Metallurgical Thermochemistry," Pergamon Press, New York (1967).

13. F. D. Richardson and J. E. Antill, *Trans. Faraday Soc.*, **51**, 22 (1955).
14. T. Rosenqvist, *J. Iron Steel Inst.*, **176**, 37 (1954).
15. K. Sudo, *Sc. Rep. Res. Inst., Tohoku Univ. Ser. A*, **2**, 519 (1950).
16. C. B. Alcock and F. D. Richardson, *Nature*, **168**, 661 (1951).
17. T. Rosenqvist, *J. Metals*, **185**, 451 (1949).
18. W. T. Thompson and S. N. Flengas, *This Journal*, **118**, 420 (1971).
19. H. R. Larson and J. F. Elliott, *Trans. TMS AIME*, **239**, 1713 (1967).
20. F. D. Richardson and J. H. E. Jeffes, *J. Iron Steel Inst.*, **171**, 165 (1952).
21. E. T. Turkdogan, R. G. Olsson, and J. V. Vinters, *Metall. Trans. B*, **8B**, 59 (1977).
22. J. P. Hager and J. F. Elliott, *Trans. TMS AIME*, **239**, 513 (1967).
23. D. J. Young, W. W. Smeltzer, and J. S. Kirkaldy, *This Journal*, **120**, 1221 (1973).

EMF and Vapor Pressure Measurements of Cadmium Activities over Dilute Solutions of Palladium in Cadmium

Donald R. Conant

Los Alamos Consultants, Los Alamos, New Mexico 87544

and Barton L. Houseman¹

University of California, Los Alamos Scientific Laboratory, Los Alamos, New Mexico 87545

ABSTRACT

The activities of cadmium over alloys containing 0.0007-0.1454 mole fraction of palladium at 776°K have been determined from emf and from vapor pressure measurements. In the range of $N_{Cd} = 1$ to $N_{Cd} = 0.9648$ the equation

$$a_{Cd} = 1 - N_{Pd} - 2.538N_{Pd}^2$$

fits the combined emf and vapor pressure results with a standard deviation of 0.00043. In the range of $N_{Cd} = 0.9648$ to $N_{Cd} = 0.8546$ a constant value of 0.9616 is observed for the activity, indicating the presence of a solid phase together with a saturated liquid phase.

This work forms part of a continuing investigation at this laboratory into the behavior of solvent activities in dilute alloys (1-11); it was undertaken in order to compare the activity of cadmium in dilute palladium-cadmium solutions as measured by emf with the same activity determined by vapor pressure measurements.

Cadmium activities were determined from stirred H-cell measurements using molten cadmium iodide as the electrolyte with cadmium and cadmium alloy electrodes. Earlier work has indicated that the value of n in the equation $-nF(dE) = RT(d \ln a_{Cd})$ is non-integral for the Cd-CdI₂ system (10, 16); this comparison of emf activity with vapor pressure activity, using Pd as the solute, verifies the earlier work.

Vapor pressure measurements of cadmium activity in solutions of the same concentration range were made using the isopiestic balance (1, 3, 4, 6, 7), which measures the temperature difference needed to establish a condition of zero transfer of vapor between pure cadmium and a cadmium alloy.

Procedures and Calculations

EMF measurements.—The H-cell shown in Fig. 1 has been described (8). The lower portion of the cell was attached to a Pt/Pt-10%Rh thermocouple and lowered into a furnace (2) designed to minimize temperature fluctuations and gradients. Cadmium of 99.999% purity, as analyzed by the United Mineral and Chemical Corporation, was melted and boiled, at 10⁻⁷ atm pressure, in intimate contact with cadmium iodide, so that any traces of electrochemically interfering elements (e.g., zinc) would be oxidized by the CdI₂.

Small, conveniently sized beads of Pd were created by melting the metal (99.95% pure by manufacturer's

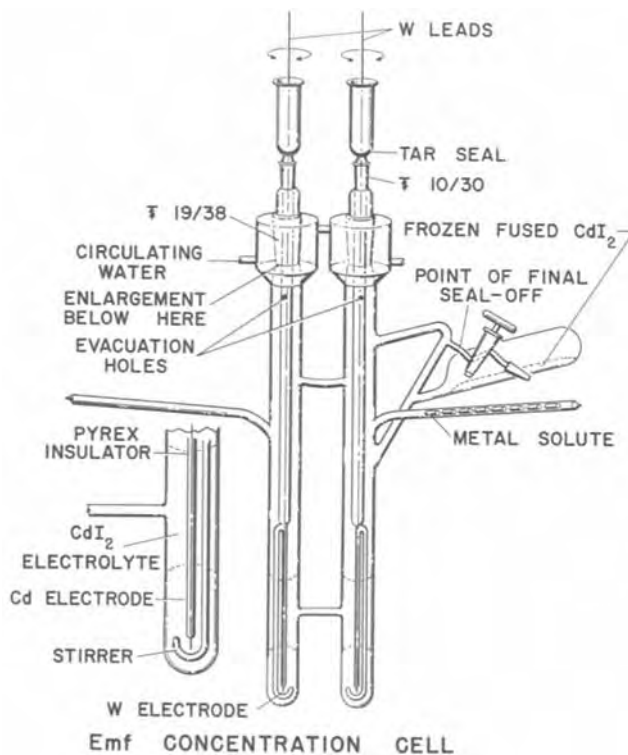


Fig. 1. EMF concentration cell

¹ Present address: Department of Chemistry, Goucher College, Towson, Maryland 21204.
Key words: metals, electrode, potential, activity coefficient.

analysis) in an rf-furnace. The tungsten electrodes were cleaned by using them as electrodes to pass alternating current through concentrated NaOH solution (thereby removing the tungsten oxide layer) and washing them with distilled water. Reagent grade CdI_2 was loaded into the side tube shown in Fig. 1, boiled under vacuum until the molten CdI_2 caused no higher pressure than 10^{-5} Torr to be registered on the pump side of the liquid nitrogen cold trap, then cooled. This was necessary to remove the substantial amounts of adsorbed gas in the commercially available CdI_2 . The cell was backfilled to a pressure of 0.5 atm with argon which had been purified by distillation. The cell was loaded into the furnace, the cadmium in the legs melted, and the CdI_2 fused by torch and allowed to run into the H-cell legs and cross arm.

The liquid metal in each leg of the cell are relatively good thermal conductors compared with the glass of the cell, and the conduction area of the metal was large, relative to the cross-sectional area of the cell walls. Therefore, one can expect good temperature uniformity in each of the cell legs. However, because of the small diameter of the cross arm of the H-cell, thermal conductance between the two legs was not as good, and, in spite of the careful design of the furnace, evidence of a small temperature gradient between the two electrodes could be observed.

Thermodynamically, the emf arising from this cell may be considered as the sum of two emf's, one arising from $\text{Cd}(T_2)$ vs. $\text{Cd}(T_1)$, and the other arising from $\text{Cd}(T_1)$ vs. alloy(T_1). The second emf is required for determining the activity of the Cd at temperature T_1 . Since initially no solute had been added to the alloy side, the second emf was initially zero, and the first was just the measured emf before the addition of the first piece of Pd. This value, which remains essentially constant, must be subtracted from emf readings obtained for the alloys to obtain that value which arises from the cell $\text{Cd}(T_1)$ vs. alloy(T_1).

After the cell was allowed to equilibrate for two days with occasional stirring, an initial emf bias between the two pure cadmium legs was recorded. For run 1 the cell was then tipped so that when the side-arm was tapped, a piece of palladium would slide down into the alloy leg. For run 2 a ground glass joint allowed the leg to be rotated to obtain the angle necessary for tapping a solute piece into the alloy leg. During run 2 the main cell body was fixed rigidly to the furnace so that the bias would remain more nearly constant.

After each piece was added, both legs of the cell were stirred and the emf was observed until no further change occurred. The thermocouple and cell emf's were then recorded.

For run 1, cell emf's were recorded to the nearest $0.1 \mu\text{V}$ and thermocouple emf's to the nearest μV . For run 2, cell emf's and thermocouple emf's were both recorded to the nearest $0.01 \mu\text{V}$ although the uncertainty in absolute temperatures was probably as much as $\pm 0.1^\circ\text{K}$. A correction factor of $1.37 \mu\text{V}$ was subtracted from the measured thermocouple emf to bring the equation (12)

$$E = -309.17 + 8.29558 t + 0.00144103 t^2 + 0.0000001634 t^3 \quad [1]$$

into agreement with more recent reference tables (13). For Eq. [1], E is in microvolts and t is in degrees Celsius.

Cadmium was weighed to the nearest 0.1 mg and palladium to the nearest 0.01 mg. The CdI_2 over each leg was estimated to be about 35g. The uncertainty in cadmium added was less than one part in 100,000. For the most dilute palladium piece added, the uncertainty was approximately one part in 2000.

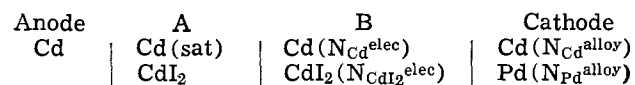
The experimental values of cell emf, temperature, and material added are known to a high degree of ac-

curacy as well as precision. The calculated values for alloy composition, electrolyte composition, and activity are subject to further uncertainties, however, which result from the significant solubility of cadmium in CdI_2 .

For cells containing cadmium alloys in the presence of molten CdI_2 electrolyte, the evaluation of cadmium activities from the emf data depends upon the value assigned to n in the equation $-nF dE = Rt d \ln a_{\text{Cd}}$. The value of n , the average charge per mole of cadmium transferred, depends upon the solubility of cadmium in its iodide and upon the types, concentrations, and mobilities of the various chemical species present in the electrolyte.

When the solubility of cadmium in its iodide at 775°K is assumed to be 6.5 mole percent consistent with the cooling curve measurements of Topol and Landis (14) and when the mobilities of the various cadmium ion species are assumed to be about the same as is true for the chloride system investigated by Herzog and Klemm (15), emf data taken on the Ni-Cd system yield activities which agree with Raoult's limiting law (10). The value estimated for n from these assumptions is 1.87 at the limit of infinite dilution. This value agrees with a direct experimental determination of n by Houseman (16).

Consistent with these results, the cadmium activities for the cell



were calculated using the equation (10, 17)

$$\ln a_{\text{Cd}} = -\frac{2F}{R} \int_0^{E/T} N_{\text{CdI}_2}^{\text{elec}} d \frac{E}{T} \quad [2]$$

where it was assumed for dilute alloy solutions that $N_{\text{Cd}}^{\text{elec}} = 0.065 N_{\text{Cd}}^{\text{alloy}}$. A change in the coefficient 0.065 by an amount 0.001 will cause a change in the slope of the cadmium activity with concentration by approximately one part per thousand. The variation of $N_{\text{CdI}_2}^{\text{elec}}$ with E/T is so slight over the range of the measurements that the trapezoid rule may be employed between the actual experimental points instead of drawing a smooth curve through the data. As a consequence, the experimental uncertainty is essentially retained in the calculated activities.

Vapor pressure measurements.—The isopiestic balance (Fig. 2) consists of a quartz tube with two legs, one of which contains the alloy and the other pure cadmium condensate. When vapor equilibrium is established between the alloy and pure cadmium, measurement of the temperature difference between the two legs allows the reduction of cadmium activity over the alloy from that for pure cadmium to be determined.

The tube is suspended by a balance system and surrounded by a furnace. The leg and cross arm temperatures are separately controlled.

Palladium and cadmium of the same purities as used in the emf measurements were cleaned in the same manner as previously described except that the cadmium was not boiled with CdI_2 .

The palladium metal was introduced directly into the balance tube. However, the cadmium was vaporized into the tube under an initial vacuum of 10^{-5} Torr from an attached U-tube. Half of the cadmium originally loaded into the U-tube remained in the tube after completing the evaporation.

The run started with all of the cadmium in the alloy leg. Lowering the temperature of the other leg then allowed cadmium to condense while simultaneously increasing the solute concentration of the alloy. The temperatures for equilibrium between a particular alloy and the reservoir were determined by slowly shifting the reservoir temperature until cadmium

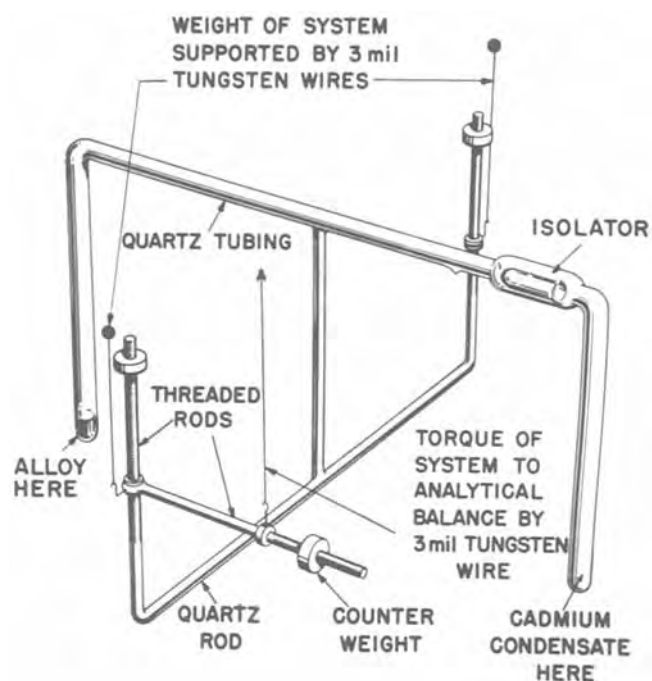


Fig. 2. Isopiestic balance (schematic)

transfer ceased, then reversed. Reversal points were approached from both higher and lower temperatures relative to the equilibrium temperature.

The balance system was adjusted to a sensitivity sufficient to detect weight shifts of 0.02 mg at the analytical balance for reversal detection. However, the accuracy of the analytical balance with its weights was probably only ± 0.2 mg or less. Since the balance factor (the ratio between weight shift read at the analytical balance and weight shift occurring in the balance tube) is approximately six, the uncertainty in the weight of cadmium transferred is ± 0.03 mg. For a 1g sample this gives an uncertainty of three parts in 100,000. The metals were weighed to 0.01 mg before introduction into and after removal from the balance tube.

A Leeds and Northrup galvanometer and Wenner potentiometer combination which had a sensitivity of $0.01 \mu\text{V}$ was used to measure the Pt/Pt-10% Rh ther-

mocouple emf's. Temperatures were calculated in the same manner as for the H-cell measurements.

Because the thermocouple junctions below the legs of the tube are not at exactly the same temperatures as the tube legs, a correction factor must be added to the measured emf. This bias correction also varies with weight of cadmium transferred in the tube due to the fact that a small temperature gradient is present along the legs. When the amount of metal in a given reservoir increases, its height increases, changing the average metal temperature relative to the thermocouple junction below. This effect has been measured (9) to be

$$\Delta \text{emf} = -(0.075 \pm 0.007) \times \text{bal. shift} + \text{const.} \quad [3]$$

where the emf is in μV and the balance shift is in grams. The additive constant is determined for a given run by extrapolating an activity vs. mole fraction plot to infinite dilution.

The activities are determined by dividing the solvent vapor pressure over the alloy by the vapor pressure of pure solvent at the same temperature. Activity is used because it varies slowly with alloy temperature and is determined by the temperature difference between the alloy and pure solvent reservoirs.

The vapor pressure over pure cadmium was calculated using the equation

$$P_{\text{Cd}}^{\circ} = \exp[(-13119/T) + 19.950 - 1.05676 \ln T] \quad [4]$$

which is consistent with Hultgren's values (18). The 150 cal-per-mole uncertainty in $\Delta H_{v, 298-K}$ indicated by Hultgren corresponds to an uncertainty of one part in 200 in the slope of activity vs. mole fraction (1).

More extensive descriptions of the experimental apparatus, techniques, and uncertainties are available (1, 3, 4, 7, 9).

Results

For the palladium-cadmium systems, the results taken by emf are listed in Table I and those taken by vapor pressure are listed in Table II. Figure 3 is a plot of cadmium activity vs. cadmium mole fraction. In the range of $N_{\text{Cd}} = 1$ to $N_{\text{Cd}} = 0.9648$ the equation

$$a_{\text{Cd}} = 1 - N_{\text{Pd}} - 2.538 N_{\text{Pd}}^2 \quad [5]$$

fits the combined emf and vapor pressure results with a standard deviation of ± 0.00043 . In the range of N_{Cd}

Table I. Activity of cadmium alloyed with palladium, emf measurements

Point No.	Palladium (moles)	Cell emf ^a (μV)	Temp. ^b ($^{\circ}\text{K}$)	Cadmium alloy (mole fraction) ^c	Cadmium activity	Deviation from calc.
Run 1						
1	0.0010699	119.9	776.43	0.99652	0.99665	0.00016
2	0.0021391	245.1	777.64	0.99307	0.99318	0.00023
3	0.0033650	388.5	777.64	0.98914	0.98921	0.00037
4	0.0051782	619.6	778.96	0.98339	0.98287	0.00018
5	0.0075274	920.0	778.15	0.97604	0.97464	0.00006
6	0.0102651	1278.0	777.24	0.96762	0.96490	-0.00006
7	0.0137152	1384.8	777.74	0.95721	0.96204	0.00047
8	0.0184210	1385.0	777.34	0.94337	0.96202	0.00045
Run 2						
9	0.0002182	25.42	778.12	0.99927	0.99929	0.00002
10	0.0008631	101.59	778.14	0.99712	0.99717	0.00008
11	0.0016235	191.89	778.13	0.99460	0.99466	0.00013
12	0.0026736	318.26	778.17	0.99113	0.99116	0.00023
13	0.0038837	465.15	778.18	0.98717	0.98710	0.00035
14	0.0052654	634.32	778.09	0.98269	0.98245	0.00052
15	0.0066071	801.65	778.17	0.97838	0.97787	0.00068
16	0.0080556	985.42	778.28	0.97377	0.97287	0.00085
17	0.0095367	1177.99	778.20	0.96910	0.96764	0.00096
18	0.0117167	1420.50	778.27	0.96230	0.96111	-0.00046

^a All cell emf values reduced by $0 \mu\text{V}$ for run 1 and by $13.17 \mu\text{V}$ for run 2 due to initial bias arising from slight temperature differences between two legs.

^b Measured with Pt/Pt-10% Rh thermocouple against ice junction.

^c For run 1, 0.313125 mole of Cd and 0.0956 mole of CdI_2 were added to alloy leg. For run 2, 0.305494 mole of Cd and 0.0956 mole of CdI_2 were added to alloy leg. The solubility of Cd in CdI_2 was assumed to be $N_{\text{Cd}}^{\text{elec}} = 0.065 N_{\text{Cd}}^{\text{alloy}}$.

Table II. Activity of cadmium alloyed with palladium, vapor pressure measurements

Point No.	Balance shift (g)	Cadmium mole fraction ^a	Temperature (°K) ^b				ΔT (°K) ^c	Cadmium activity ^d	Deviation from calculation ^e
			Alloy	Cadmium	Alloy cross arm	Cadmium cross arm			
1	6.8499	0.99555	775.8	775.6	795.4	795.5	0.222	0.99548	-0.00002
2	7.5304	0.99503	775.8	775.6	794.6	795.3	0.230	0.99531	0.00034
3	8.6246	0.99388	775.1	774.8	792.8	794.7	0.304	0.99379	-0.00000
4	9.5826	0.99233	777.0	776.6	794.4	796.5	0.394	0.99200	-0.00018
5	10.1712	0.99092	776.9	776.4	794.2	796.1	0.476	0.99034	-0.00037
6	10.6090	0.98948	776.8	776.2	794.0	796.2	0.560	0.98864	-0.00056
7	11.0179	0.98765	776.9	776.3	794.4	796.4	0.650	0.98683	-0.00043
8	11.1782	0.98674	776.4	775.7	793.6	795.9	0.698	0.98584	-0.00045
9	11.7072	0.98252	777.2	776.3	794.3	796.3	0.899	0.98184	0.00010
10	11.9364	0.97972	777.4	776.4	794.1	796.2	1.069	0.97845	-0.00023
11	12.2630	0.97372	776.1	774.7	792.9	794.8	1.404	0.97169	-0.00028
12	12.4297	0.96905	776.6	774.9	793.3	795.4	1.708	0.96569	-0.00093
13	12.5274	0.96545	776.9	775.0	793.9	795.6	1.907	0.96179	-0.00063
14	12.7375	0.95393	776.5	774.6	793.2	795.0	1.909	0.96172	0.00015
15	12.7290	0.95454	776.5	774.6	792.9	795.0	1.906	0.96177	0.00020
16	12.8641	0.94234	776.5	774.6	792.8	795.0	1.918	0.96154	-0.00003
17	12.9164	0.93566	776.7	774.8	792.9	794.8	1.936	0.96120	-0.00037
18	13.1468	0.86850	776.7	774.8	793.1	795.0	1.859	0.96272	—
19	13.1679	0.85460	776.6	774.8	792.9	794.9	1.810	0.96369	—
20	12.9805	0.92500	776.7	774.7	792.5	795.0	1.937	0.96117	-0.00040

^a 6.0650g balance shift = 1.00000g cadmium shift. Initial cadmium 2.19926g, palladium 0.00453g.

^b Measured with Pt/Pt-10% Rh thermocouple against ice junction to nearest 0.1°K.

^c Measured with Pt/Pt-10% Rh thermocouple to 0.001°K temperature difference between alloy and pure cadmium. Distinct reversal of cadmium transfer observed 0.010°-0.015°K beyond equilibrium values. ΔT calculated from millivolts using equation of Roeser and Wenzel, after subtracting a bias correction of $[0.00266-0.000075 \times \text{balance shift (grams)}]$ millivolts. The first constant is established by finding that correction necessary to make the data extrapolate to unit activity at pure solvent; the second constant is determined from measurements on pure cadmium runs.

^d Vapor activity relative to that over pure liquid cadmium, using equation consistent with Hultgren's (17) value, namely $P_{Ca}^{\circ} = \exp [(-13\ 119/T) + 19.950 - 1.05676 \ln T]$.

^e Calculated using equations in text.

= 0.9648 to $N_{Cd} = 0.925$ the cadmium activity is 0.96157 with a standard deviation of ± 0.00035 . Better fits can, of course, be obtained if the emf and vapor pressure results are each fitted individually to separate curves. In this case the separate curves do not agree. However, the discrepancy between the two curves is less than the absolute uncertainties associated with various aspects of the two methods of measurement.

Although the least squares fit to the three runs gives an indication of the accuracy of the results, the precision associated with the individual emf runs is much higher than is indicated by the above fit. However, because saturation occurs at such dilute concentrations, the palladium dissolved very slowly in the cadmium. As a result, days rather than hours were involved in obtaining individual emf measurements. Consequently, the emf results for the Pd-Cd system are less precise and less accurate than those obtained for the Ni-Cd (10) or Au-Cd (19) systems.

The scatter in the data for the vapor pressure measurements tends to remain constant with solute concentration whereas the emf scatter tends to be proportional to solute concentration due to the nature of the measurements taken.

The solution is evidently saturated at a composition corresponding approximately to $PdCd_{27}$ or $N_{Cd} = 0.9643$.

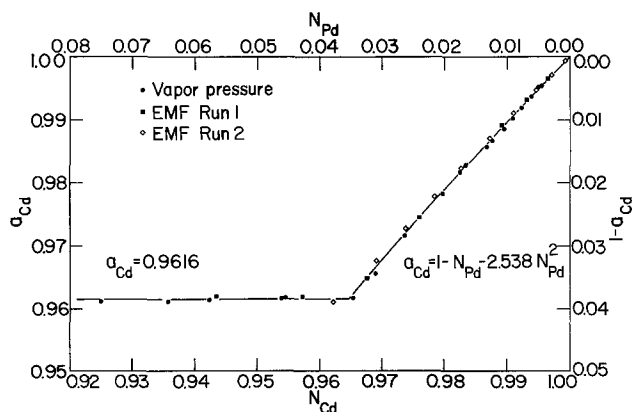


Fig. 3. Cadmium activities for solutions containing small amounts of palladium.

From the form of Eq. [5] it is apparent that the dilute palladium-cadmium solutions are in agreement with Raoult's limiting law within the uncertainty of the data. As a consequence, we have obtained further evidence that the assumption of 1.87 for the value of n at the limit of infinite dilution is justified.

Acknowledgment

This work was done under the auspices of the U.S. Department of Energy.

Manuscript submitted Jan. 22, 1979; revised manuscript received Oct. 15, 1979.

Any discussion of this paper will appear in a Discussion Section to be published in the June 1981 JOURNAL. All discussions for the June 1981 Discussion Section should be submitted by Feb. 1, 1981.

Publication costs of this article were assisted by the University of California.

REFERENCES

- G. R. B. Elliott, J. F. Lemons, and H. S. Swofford, Jr., *J. Phys. Chem.*, **69**, 933 (1965).
- G. R. B. Elliott and J. F. Lemons, *This Journal*, **114**, 935 (1967).
- H. S. Swofford, Jr. and G. R. B. Elliott, *Inorg. Chem.*, **7**, 666 (1968).
- D. R. Conant and G. R. B. Elliott, *J. Chem. Eng. Data*, **13**, 354 (1968).
- G. R. B. Elliott, *This Journal*, **115**, 1143 (1968).
- D. R. Conant, *J. Chem. Eng. Data*, **14**, 9 (1969).
- D. R. Conant and H. S. Swofford, *ibid.*, **14**, 369 (1969).
- B. L. Houseman and G. R. B. Elliott, *This Journal*, **116**, 1363 (1969).
- D. R. Conant and H. S. Swofford, Jr., *J. Chem. Eng. Data*, **15**, 539 (1970).
- D. R. Conant, *ibid.*, **16**, 430 (1971).
- B. L. Houseman and D. R. Conant, *J. Phys. Chem.*, Submitted for publication.
- W. F. Roeser and H. T. Wenzel, *Nat. Bur. Stand. J. Res.*, **10**, 276 (1933).
- H. Schenker, J. I. Lauritzen, Jr., R. J. Corruccini, and S. T. Lonberger, "Reference Tables for Thermocouples," *Nat. Bur. Stand. Circ.*, 561 (1955).
- L. E. Topol and A. L. Landis, *J. Am. Chem. Soc.*, **82**, 6291 (1960).
- V. W. Herzog and A. Klemm, *Z. Naturforsch.*, **15a**, 1100 (1960).
- B. L. Houseman, *J. High Temp. Sci.*, **8**, 25 (1976).

17. G. A. Crawford and J. W. Tomlinson, *Trans. Faraday Soc.*, **62**, 3046 (1966).
 18. R. Hultgren, R. L. Orr, P. D. Anderson, and K. K. Kelley, "Selected Values of Thermodynamic

- Properties of Metals and Alloys," p. 62-65, John Wiley & Sons, Inc., New York (1963).
 19. D. R. Conant and G. R. B. Elliott, *J. High Temp. Sci.*, Submitted for publication.

The Coulostatic Method: Analysis of Error and Computation of Parameters

H. Reller and E. Kirowa-Eisner

Institute of Chemistry, Tel-Aviv University, Ramat-Aviv, Israel

ABSTRACT

Analysis of error has been carried out for the coulostatic method. The optimal time scale for the determination of i_0 has been shown to be equal to $2\tau_c$. The determination of i_0 is based on the computer curve-fitting of a set of points on the transients to the analytical equation of potential decay. The uncertainty in the determination of i_0 depends only on the ratio τ_c/τ_d . Highest accuracy is obtained for $\tau_c/\tau_d > 500$, where the uncertainty in the determination of i_0 is 3.3 times that for the measurement of the potential. Reasonable accuracy can be obtained for values of τ_c/τ_d not less than 0.5. An iteration method for the simultaneous determination of i_0 and C_{dl} has been outlined.

The state of the art of the coulostatic method has been recently reviewed by van Leeuwen (1). Although the strength of this method is suited well for the study of fast electrode reactions, its use is rather limited.

In this work we have addressed ourselves to three problems encountered in the study of fast electrode reactions by the coulostatic method.

1. The optimal experimental conditions for undertaking coulostatic measurements and the estimation of the accuracy and the limits of the method must be determined. Some data on this subject are given in the work of Kooijman and Sluyters (2).

2. The common methods for determination of C_{dl} are not operative for fast electrode processes, where the faradaic current plays an important role from the very beginning of the measurements. However, it is necessary to know C_{dl} for the determination of i_0 when diffusion corrections have to be made. In this work, we propose an iteration method for the simultaneous determination of i_0 and C_{dl} based on measurements at different parts of the decay curve.

3. The complex form of the mathematical expressions impose difficulties on the evaluation of the experimental data. Methods based on approximation (3), nomograms (2), and transformation of the transients data into an impedance plane (4) have been proposed. Our approach is based on the use of a computer parameter fitting program, which permits straightforward evaluation of the kinetic parameters from Eq. [2], without the need to use any approximation other than those made in the derivation of the basic Eq. [2].

Discussion

Fast electrode processes are controlled by charge transfer and mass transfer simultaneously. Delahay (5) and Reinmuth (6) derived a potential-time expression for single step reactions, taking the diffusion into consideration (Eq. [2]). Reller and Kirowa-Eisner (7) treated the case of multi-step reactions of the type



where the stoichiometric coefficients ν_0 and ν_R are different than unity.

The equation of the potential decay at small perturbations from equilibrium ($|\eta| \ll RT/\alpha F$) is gen-

eral for single step and multi-step reactions (7)

$$\eta = \eta_0 \frac{1}{\gamma - \beta} \{ \gamma \exp(\beta^2 t) \operatorname{erfc}(\beta t^{1/2}) - \beta \exp(\gamma^2 t) \operatorname{erfc}(\gamma t^{1/2}) \} \quad [2]$$

where η_0 is the overpotential at the completion of the charge injection, and

$$\beta = \frac{\tau_d^{1/2} + (\tau_d - 4\tau_c)^{1/2}}{2\tau_c} \quad [3]$$

$$\gamma = \frac{\tau_d^{1/2} - (\tau_d - 4\tau_c)^{1/2}}{2\tau_c} \quad [4]$$

The parameters ν_0 , ν_R , and ν (stoichiometric coefficients and stoichiometric number) which alone characterize multi-step reactions at small perturbations from equilibrium are incorporated in τ_c and τ_d

$$\tau_c = \frac{\nu}{n} \frac{RT}{F} \frac{C_{dl}}{i_0} \quad [5]$$

$$\tau_d^{1/2} = \frac{RTC_{dl}}{n^2 F^2} \left[\frac{\nu_0^2}{C_0^0 D_0^{1/2}} + \frac{\nu_R^2}{C_R^0 D_R^{1/2}} \right] \quad [6]$$

τ_c and τ_d are the time constants for the charge-transfer and the diffusional relaxation, respectively.

Equation [2] is derived on the assumption that no faradaic current is flowing during the charging step.

The parameters i_0 and C_{dl} are determined on the basis of Eq. [2]. The complexity of the equation has usually involved the use of approximations which introduce systematic errors. To avoid this type of error, we use a parameter-fitting program, in which equally weighted points along the transient are fitted into Eq. [2] (details at end of paper).

Optimal time scale and accuracy in the determination of i_0 .—It is important to analyze the potential-time Eq. [2] in terms of the level of information and the accuracy in the determination of i_0 as a function of the kinetic parameters of the reaction and the time scale on which the transient is observed.

The kinetic information content along the decay curve can be expressed by the absolute value of the first derivative of the potential $\partial\eta/\partial i_0$. The level of in-

formation is dependent on the kinetic parameters of the electrode reaction and on the time elapsed from the start of the transient. We define the instantaneous information content, I , as

$$I = \frac{i_o}{\eta_o} \left| \frac{\partial \eta}{\partial i_o} \right| \quad [7]$$

Zero value for I means that the measured parameter η is independent of i_o or in other words it does not provide information about i_o . Unity value for I indicates maximum information content in respect to a linear relationship between both parameters.

The expression for I , which is too long to be presented here, was analytically derived on the basis of Eq. [2] and calculated for specific values of exchange currents, concentrations, and time by a computer program. The instantaneous information content, I , is independent of η_o , while $\partial \eta / \partial i_o$ is proportional to η_o (Eq. [2]). The variations of the instantaneous information content with time, for different values of τ_c / τ_d are shown in Fig. 1. The potential decays for the conditions presented in Fig. 1 are given in Fig. 2.¹

Three regions can be distinguished on the curves (Fig. 1): (i) for $t < \tau_c$, where the capacitance contribution is high, there is little instantaneous information, in spite of the small degree of diffusion control; (ii) for $t \sim \tau_c$, maximum instantaneous information; (iii) for $t > \tau_c$, where the measured signal has fallen to low values and where, in the case of fast reactions, the transient is largely controlled by diffusion, again little instantaneous information.

The shape of the information curve is similar to the one derived for discharge of a condenser through a constant resistance ($I = t/RC \exp[-t/RC]$). The maximum in this case is reached at a time equal to $RC \times 1$ or in terms of the charge-transfer time constant to $\tau_c \times 1$. The value of I at the maximum is

¹The presentation of the potential decays in a scale of t/τ_c gives the wrong impression that the slowest decay belongs to the largest exchange current.

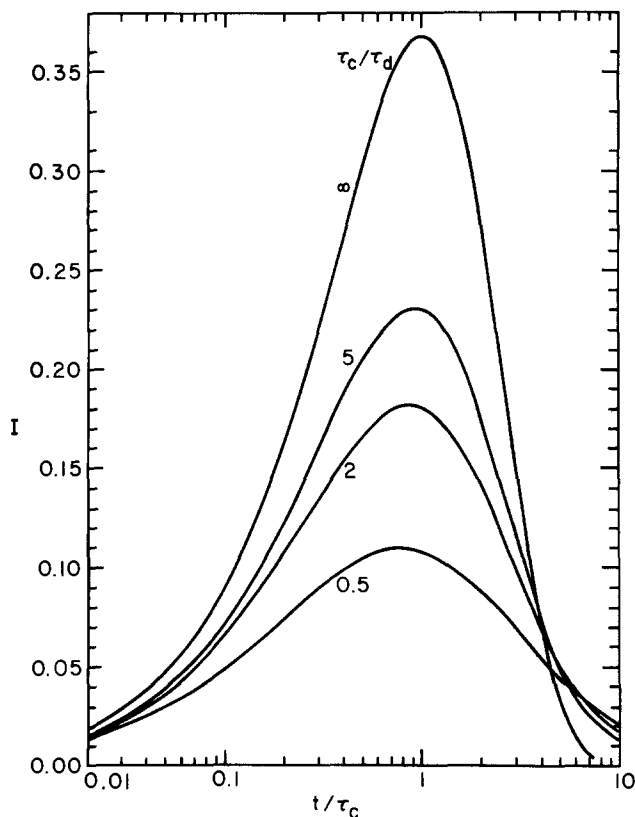


Fig. 1. Instantaneous information in respect to exchange current density, $I(i_o)$ along the potential transient, for a set of electrode reactions with different τ_c / τ_d .

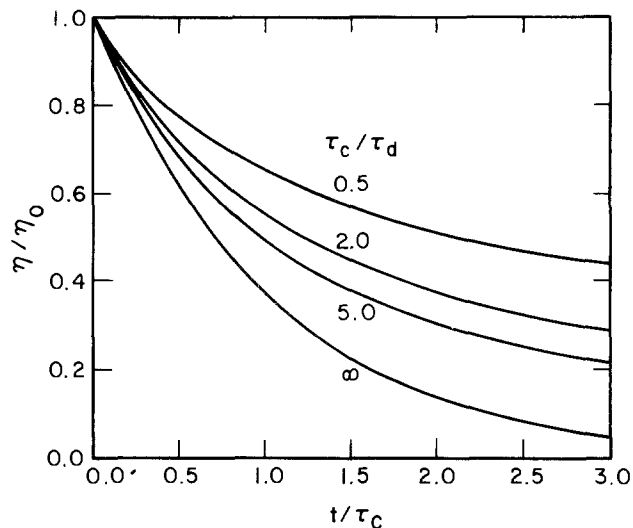


Fig. 2. Potential decays for a set of electrode reactions. Conditions as in Fig. 1.

e^{-1} (0.37). That will be the limiting value reached in an electrochemical system with negligible diffusion control. The higher the contribution of diffusion (lower τ_c / τ_d), the lower the maximal value for I (see Fig. 1).

This approach of presenting the instantaneous information content is similar to that used by Kooijman and Sluyters (2).

The aim of our work is to estimate the average information content over a certain measuring-time interval. This is of practical importance in computing parameters from a considerable section of the transient, rather than from a single point on it. The optimal time scale does not necessarily coincide with the occurrence of a maximum in the instantaneous information curve. For the method of determination of i_o we propose, based on fitting a set of points from the transient into Eq. [2], the average value of the information along the transient is of interest.

The average information \bar{I} is expressed as

$$\bar{I} = \frac{1}{T} \int_0^T I dt = \left| \frac{i_o}{\eta_o T} \int_0^T \frac{\partial \eta}{\partial i_o} dt \right| \quad [8]$$

where T is the full time-scale reading at which the transient is observed.

The average information varies along different parts of the transient. The time scale at which the potential decay provides the highest value of average information is the optimal time scale from which data have to be used.

Curves with average information along the transient are shown in Fig. 3 (the data correspond to the potential decays shown in Fig. 2). For the purpose of determining the optimal time scale, the maximum in these curves is searched. Characteristic to all curves, the maximum is found at $t/\tau_c = 1.8$. Thus the time at which the maximum of the average information content is reached is about twice as long compared to the value for the instantaneous information content. This stems from the need to compensate for the low instantaneous information content at short times. The optimal time scale is determined solely by the value of the exchange current and the capacity as would be for a simple system of a capacitor discharged through a resistor. The diffusion rate has no effect on the optimal time scale. This was confirmed by determining the optimal scale for a large set of systems in which i_o was varied in the range of 10^{-4} -2 A/cm² and the concentration in the range of 0.1-100 mM.

One can further optimize the average information by limiting the time scale at its lower extreme (up to $0.2 \tau_c$) as well as at the upper end (near $2 \tau_c$), since

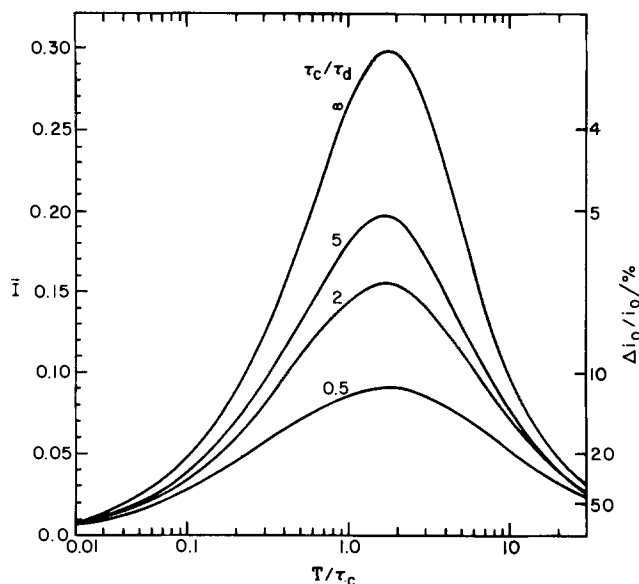


Fig. 3. Average information in respect to exchange current density, $\bar{I}(i_0)$, along the potential transient. Conditions as in Fig. 1. Right-hand axis is calibrated as $\Delta i_0/i_0$, calculated for $\Delta\eta/\eta_0 N^{1/2} = 0.01$.

the data up to $0.2 \tau_c$ contain a low level of instantaneous information (Fig. 1). This modification brings about some improvement in the value of the average information, \bar{I} (\bar{I} is increased by about 10%).

It is important to compute the accuracy by which i_0 can be determined and to study the factors which determine it. Thus the potentiality and the limits of the coulostatic method can be estimated.

The accuracy in the determination of i_0 is proportional to the average information content, \bar{I} . The error, Δi_0 , is proportional to the reciprocal value of \bar{I} ; before using this relationship, one has to ensure that the error, Δi_0 , is determined solely by the first order derivative $\partial i_0/\partial\eta$. The error in the exchange current as a function of the uncertainty in the overpotential can be expressed by expanding the function $i_0 = F(\eta)$ into Taylor's series

$$\Delta i_0 = \frac{\partial i_0}{\partial \eta} \Delta \eta + \frac{\partial^2 i_0}{\partial \eta^2} \frac{\Delta \eta^2}{2!} + \dots \quad [9]$$

We have calculated and compared the values of the first and second derivatives along the decay curve for a large set of systems in which τ_c/τ_d was varied between 10^{+2} - 10^{-3} . In all cases, for a typical value of $\Delta\eta = 10^{-4}$ V, the second term on the rhs of Eq. [9] was found to be only 7% of the first term. However, the simplified equation $\Delta i_0 = \frac{\partial i_0}{\partial \eta} \Delta \eta$ cannot be used in its present form because (i) $\partial i_0/\partial \eta$ varies along the part of the transient used for the computation of i_0 ; its average value $\frac{1}{T} \int_0^T \frac{\partial i_0}{\partial \eta} dt$ has to be used instead; (ii) $\Delta\eta$, which is the uncertainty in the determination of a single point has to be replaced by its mean value over the set of N points used for computation of i_0 , which is $\Delta\eta/N^{1/2}$.

The relative error $\Delta i_0/i_0$ is estimated by

$$\frac{\Delta i_0}{i_0} = \frac{\Delta \eta}{N^{1/2} T} \left| \int_0^T \frac{\partial i_0}{\partial \eta} dt \right| = \frac{\Delta \eta}{\eta_0 N^{1/2} \bar{I}} \quad [10]$$

The relative error can be estimated from Fig. 3, where the right-hand side of the y-axis is calibrated in $\Delta i_0/i_0$ units for a typical case of $\eta_0 = 5$ mV, $\Delta\eta = 0.15$ mV, and $N = 10$. The error decreases with the decrease of the exchange current (or the increase

of τ_c/τ_d). This naturally is expected as kinetic control predominated with the decrease of i_0 . The relative error, at the optimal time scale $T = 2\tau_c$, is shown in Fig. 4 and 5 as function of exchange current and concentration. The y-axis in these figures are calibrated as $1/\bar{I}$ and $\Delta i_0/i_0$.

The maximal value of the average information \bar{I} , has been computed for different combinations of i_0 , C , and C_{dl} , for the purpose of correlating the error $\Delta i_0/i_0$ with the parameters of an electrode reaction. Large sets of systems have been tested (over a concentration range 0.1-100 mM; capacity range 5-40 $\mu\text{F}/\text{cm}^2$ and exchange current range 10^{-4} -5 A/cm^2). It was found that systems with the same value for the ratio τ_c/τ_d (or C^2D/i_0C_{dl} in the case $C_0^o = C_R^o = C$ and $D_0 = D_R = D$) provide the same average information, \bar{I} , at the optimal time scale. Kooijman and Sluyters (3) have pointed out (by expanding Eq. [2] in the form of power series) that the value τ_c/τ_d , and not i_0 itself, determines the capability of the method. This knowledge permits us to generalize in a useful way, the dependence of the error on the parameters characterizing the system. An empirical equation, relating \bar{I} with τ_c/τ_d , has been formulated (Eq. [11])

$$\ln \frac{\tau_c}{\tau_d} = 0.64 - 1.5 \ln \frac{\bar{I}_{lim} - \bar{I}}{\bar{I}} \quad [11]$$

The relative error for any system complying with Eq. [2], can be calculated on the basis of Eq. [10].

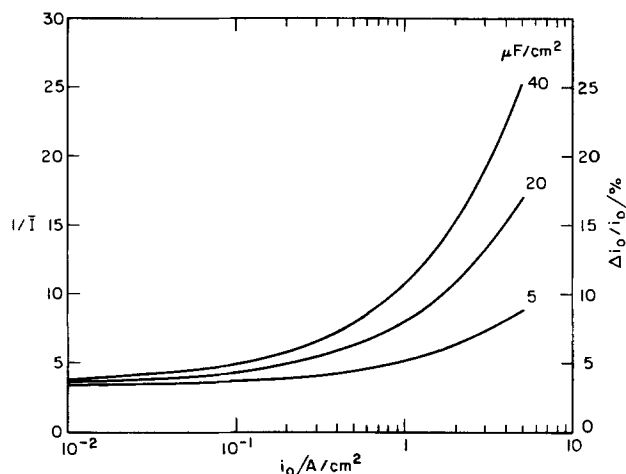


Fig. 4. Error curves as function of exchange current. Y-axis calibrated as $1/\bar{I}$ and $\Delta i_0/i_0$. $C_0^o = C_R^o = 5$ mM; $D_0 = D_R = 10^{-5}$ cm^2/sec ; $T = 2\tau_c$; $\Delta\eta/\eta_0 N^{1/2} = 0.01$.

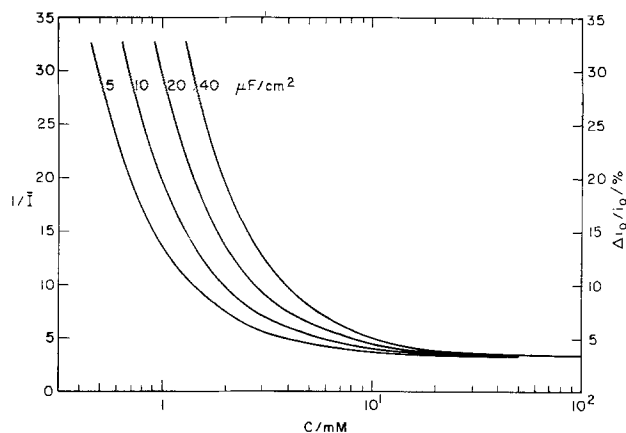


Fig. 5. Error curves as function of concentration. Y-axis calibrated as $1/\bar{I}$ and $\Delta i_0/i_0$. $i_0 = 0.5$ A/cm^2 ; $C_0^o = C_R^o$; $D_0 = D_R = 10^{-5}$ cm^2/sec ; $T = 2\tau_c$; $\Delta\eta/\eta_0 N^{1/2} = 0.01$.

\bar{I}_{lim} is the value of the average instantaneous information, \bar{I} , reached for $\tau_c/\tau_d > 10^3$. Its numerical value is 0.30, which is identical to the average information calculated for discharge of a condenser through a resistor.

Equation [11] can also be expressed in terms of i_o , C_{dl} , and C , in view of Eq. [5] and [6]. For the simple case of $C_{O^0} = C_{R^0} = C$ and $D_{O^0} = D_R = 1.1 \times 10^{-5}$ cm²/sec, $\tau_c/\tau_d = C^2/i_o C_{dl}$ (C in mM, i_o in A/cm², and D_{dl} in $\mu\text{F}/\text{cm}^2$). The equation describes faithfully the correlation between \bar{I} and the parameters τ_c and τ_d . This is demonstrated in Fig. 6, where the solid line of the \bar{I} curve corresponds to the empirical Eq. [11] and the points are calculated according to Eq. [8]. The correlation coefficient of the individual points in relation to the line fitted to these points is -0.9996 .

The error curve (calculated on the basis of \bar{I} and Eq. [11] for $\frac{\Delta\eta}{\eta_0} \frac{1}{N^{1/2}} = 0.01$) is presented in Fig. 6, alongside the average information curve. Good accuracy can be reached only for values of τ_c/τ_d larger than unity; below unity the error strongly increases, although satisfactory results can be obtained for $\tau_c/\tau_d = 0.5$. Highest accuracy is obtained for $\tau_c/\tau_d > 500$, where the uncertainty in the determination of i_o is 3.3 times that for the measurement of the potential (Eq. [11]).

In addition, Eq. [11] was used to estimate the largest value of the exchange current that can be measured at a given concentration of reaction species within the limits of a predetermined error. These data are summarized in Table I.

Practically, the upper limit of the obtainable exchange current density is determined by (i) the instrumental problems of observing the potential decay at short time scale [$T_{min} \sim 0.5 \mu\text{sec}$ (8)]; (ii) the limitations dictated by Eq. [2], which requires that no faradaic current flows during the charging step. To fulfill this requirement the charge injection should be completed at a time shorter than $0.1 \tau_c$. Injection time of 50 nsec have been used (8). Thus, the smallest value of τ_c that can be experimentally determined is about $0.5 \mu\text{sec}$, which in terms of i_o is $0.5\text{-}2$ A/cm² (for C_{dl} $10\text{-}40 \mu\text{F}/\text{cm}^2$).

An increase in the concentration of reacting species causes an increase in τ_c/τ_d (decrease of $\Delta i_o/i_o$), while simultaneously decreasing τ_c . Thus, there is an upper concentration limit imposed by the experimental requirement of $\tau_c > 0.5 \mu\text{sec}$.

If the maximum values of i_o estimated above are combined with a value of $\tau_c/\tau_d = 0.5$, for which rea-

Table I. Maximal values of i_o measured with a predetermined error of 10% and 20%. $\Delta\eta/\eta_0 N^{1/2} = 0.01$; $C_{O^0} = C_{R^0}$

C/mM	$C_{dl}/\mu\text{F}/\text{cm}^2$	$\Delta i_o/i_o = 10\%$		$\Delta i_o/i_o = 20\%$	
		$10 \mu\text{F}/\text{cm}^2$	$40 \mu\text{F}/\text{cm}^2$	$10 \mu\text{F}/\text{cm}^2$	$40 \mu\text{F}/\text{cm}^2$
0.5		0.03	0.01	0.1	0.3
1		0.1	0.03	0.5	0.1
5		3	0.8	5	3
20		>5	>5		>5

sonable accuracy in the determination of i_o can be achieved, it turns out that a standard rate constant, k_s , up to 3 cm/sec can be measured. (In the calculation of k_s we refer to a simple electrode reaction for which $k_s = i_o [\eta\text{F}(C_{O^0})^{\alpha_c}(C_{R^0})^{\alpha_a}]^{-1}$, $C_{O^0} = C_{R^0}$ and $\alpha_a = \alpha_c = 0.5$.)

It should be stressed that the above treatment considers only the error resulting from the measurement of the potential. It gives a general information of the factors on which the accuracy of the method is dependent. It can be used only when the exchange current is the only parameter that has to be determined (C_{dl} is known from some other independent method).

Analysis of error for the single step and double step galvanostatic method is in preparation.

Simultaneous determination of i_o and C_{dl} .—In some cases there is no previous information about C_{dl} and its value has to be determined simultaneously with the exchange current density. But even when C_{dl} is known from some independent method, it is important to confirm that its value is constant along the coulostatic transient.

For the sake of simplicity, we shall consider first the hypothetical case in which C_{dl} is the only variable to be determined, while i_o is known without error. The error, $\Delta C_{dl}/C_{dl}$, is determined on the basis of Eq. [12] analogous to Eq. [10]. Only first derivatives are used in view of Eq. [9] (terms with higher derivatives have been found negligible)

$$\frac{\Delta C_{dl}}{C_{dl}} = \frac{1}{N^{1/2}} \frac{\Delta\eta}{T} \left| \int_0^T \frac{\partial C_{dl}}{\partial \eta} dt \right| = \frac{\Delta\eta}{\eta_0 N^{1/2}} \frac{|1|}{\bar{I}(C_{dl})} \quad [12]$$

The variation of the average information, $\bar{I}(C_{dl})$, as a function of time scale T is given in Fig. 7. For pure kinetic control ($\tau_c/\tau_d \rightarrow \infty$), $\bar{I}(C_{dl}) = \exp(-t/\tau_c)$. When the time scale is short, $T \ll \tau_c$, the average in-

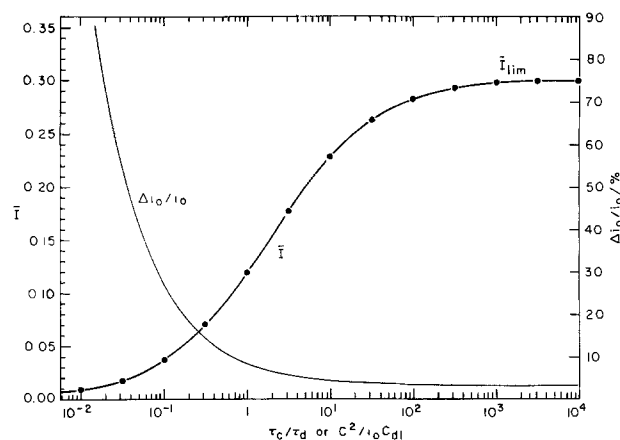


Fig. 6. Average information in respect to exchange current as function of τ_c/τ_d . Relative error as a function of τ_c/τ_d (calculated for $\Delta\eta/\eta_0 N^{1/2} = 0.01$) X-axis calibrated also as $C/i_o C_{dl}$ ($\tau_c/\tau_d = C/i_o C_{dl}$ for $C_{O^0} = C_{R^0} = C$; $D_{O^0} = D_R = 1.1 \times 10^{-5}$ cm²/sec; C [mM]; C_{dl} [$\mu\text{F}/\text{cm}^2$]; i_o [A/cm²]).

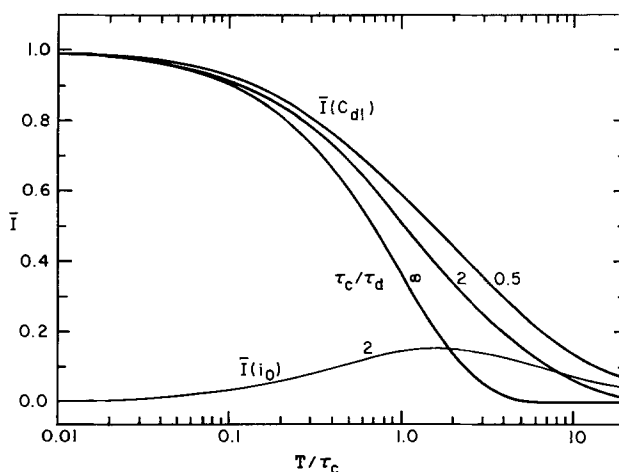


Fig. 7. Average information curves in respect to double layer capacity at different τ_c/τ_d . A curve with average information in respect to exchange current density is given for comparison purposes.

formation approaches unity, independently of τ_c/τ_d . For longer time scales, the information decreases with the rate of decrease depending on τ_c/τ_d .

Since the optimal time scales for the determination of the individual parameters differ appreciably, the simultaneous determination of i_0 and C_{dl} for a particular time scale will entail a large error. Our approach to this problem is the use of an iteration method, combined with the parameter-fitting program. In principle, the complex-plane analysis used by Sluyters *et al.* (4) is another solution to the problem.

1. Preliminary computation of i_0 and C_{dl} . Potential decays are recorded on several time scales. From the data of each decay the parameters i_0 and C_{dl} are computed (with the use of the computer curve-fitting program). The mean and standard deviation of the two parameters are calculated.

2. Computation of C_{dl} as single parameter. The data from the shortest experimentally attainable time scale are used for the determination of C_{dl} with the predetermined value of i_0 , obtained from 1. (At short times, the high value of $\bar{I}(C_{dl})/\bar{I}(i_0)$ ensures that C_{dl} can be determined quite accurately in the presence of large error in i_0 .)

3. Computation of i_0 as single parameter. Data from the optimal time scale, $T = 2\tau_c$, for the determination of i_0 , are used (τ_c is estimated from step 1). i_0 is computed with the predetermined value of C_{dl} , obtained from step 2.

4. Steps 2 and 3 are repeated until i_0 and C_{dl} remain unchanged within the expected errors (estimated from the value of τ_c/τ_d).

The efficiency of the iteration method is demonstrated in Table II by a simulated experiment of a system with a large diffusion contribution ($\tau_c/\tau_d = 0.5$). The data in Table II were obtained as follows.

Potential decays with an initial potential of 5 mV were calculated according to Eq. [2]. Four time scales have been used. At each time scale six experiments have been simulated with different sequences of random errors. Sets of data for each decay, were constructed as follows: 10 points were selected at equal time intervals, the first point at 0.1T and the last at T. A normally distributed random error with zero mean value and a standard deviation of 0.15 mV was added to the calculated value of the potential at each point.

We shall add that a two-indicator electrode cell proposed by Sluyters *et al.* (10) is suitable for the above outlined experiment. The cell provides an excellent solution for most of the nonlinearity problems which may arise when the initial potential is larger than 1 mV.

The value of i_0 and C_{dl} were calculated according to the iteration method outlined above. The steps followed by the simulated experiment are summarized in Table II. First, i_0 and C_{dl} were determined by two-parameter curve-fitting. The standard derivatives were large [$\sigma(i_0) = 50\%$ from the mean of i_0 and $\sigma(C_{dl}) = 7\%$ from the mean of C_{dl} , both at $T \sim 2\tau_c$]. At sub-

sequent recalculation i_0 and C_{dl} according to the iteration procedure, the standard deviations decrease to 8% and 1%, respectively, in good agreement with the expected values as calculated from $\bar{I}(i_0)$ and $\bar{I}(C_{dl})$ at the respective time scales ($\sim 2\tau_c$ for i_0 and $\sim 0.3\tau_c$ for C_{dl}).

The proposed method for computation of parameters is applicable to reactions controlled by charge transfer and by mass transfer. If a simple scheme is not operative, the use of complex-plane method (4) is advised.

Computation of parameters.—The evaluation of the parameters i_0 and C_{dl} from the potential decay curves cannot be performed by a direct approach using Eq. [2]. Berzins and Delahay (3) proposed an approximation method. Kooijman and Sluyters (2) developed a numerical analysis based on the use of nomograms and van Leeuwen *et al.* (4) introduced a method based on transformation of the experimental relaxation curve into the impedance plane.

Our approach is based on the use of a parameter-fitting program [library program MINUIT (11)], in which the data from the experimental relaxation curve has been fitted to the analytical expression of the η -t curve (Eq. [2]). The kinetic parameters are computed on the basis of searching minimum for the chi-square, χ^2

$$\chi^2 = \sum_{i=1}^n \left(\frac{\eta_{i(\text{calc})} - \eta_{i(\text{exp})}}{\Delta\eta} \right)^2 \quad [13]$$

where $\eta_{i(\text{exp})}$ is the measured potential at point i ; $\eta_{i(\text{calc})}$ is the calculated value obtained from the curve-fitted parameters; and $\Delta\eta$ is the standard deviation of the measured potential.

The computer program supplies the following information: i_0 , C_{dl} , τ_c , τ_d , $\eta_{i(\text{calc})}$; graphic comparison of experimental decay curve with calculated curve. A program for calculating the derivative $(\partial\eta/\partial i_0)_{\tau_c, \tau_d}$ is included for enabling the estimation of the error $\Delta i_0/i_0$. The input data are: the experimental points along the decay curve, the value of the injected charge, the concentration and diffusion coefficients of species O and R, and the value of n .

In respect to the output, it is suggested to perform a χ^2 -test for the goodness of fit and to check if the experimental points of the decay curve are randomly distributed along the calculated potential decay curve.

The computer program is written in Fortran IV. The program is available upon request from the authors.

Acknowledgments

This work was supported by The Israel National Academy of Sciences. The authors wish to express their thanks to Prof. E. Gileadi, Dr. J. Penciner, and Mr. A. Zaloziecki for their interest in the work.

Manuscript submitted Aug. 1, 1979; revised manuscript received Jan. 28, 1980.

Table II. Simulated experiment for the determination of i_0 and C_{dl}

Parameters of the investigated reaction: $i_0 = 0.25 \text{ A/cm}^2$; $C_{dl} = 30 \text{ } \mu\text{F/cm}^2$; ($\tau_c = 3 \text{ } \mu\text{sec}$); $\tau_c/\tau_d = 0.5$ ($C_O^0 = C_R^0 = 1.94 \text{ mM}$; $D_O = D_R = 1.1 \times 10^{-5} \text{ cm}^2/\text{sec}$)

Parameters of the decay curves: $\eta_0 = 5 \text{ mV}$; $\Delta\eta = 0.15 \text{ mV}$; $N = 10$; No. of simulated decays at each time scale: 6

T (μsec)	Potential at first and last point of the decay, mV		Two-parameter curve-fitting		Single-parameter curve-fitting	
	η_1	η_{10}	$i_0 \pm \text{st. dev.}$	$C_{dl} \pm \text{st. dev.}$	Fixed parameter	Fitted parameter
1	4.7	4.0	0.29 ± 0.12	29.7 ± 0.9	$i_0 = 0.30^b$	$C_{dl} = 29.5 \pm 0.3$
2	4.6	3.8	0.32 ± 0.10	29.6 ± 1.1		
5	4.3	2.9	0.33 ± 0.15	29.4 ± 2.0	$C_{dl} = 29.5^c$	$i_0 = 0.26 \pm 0.02$
20 ^a	3.8	1.6	0.24 ± 0.25	31.1 ± 3.2		

^a One of the six decays did not converge in the two-parameter curve-fitting.

^b i_0 , as determined from the two-parameter curve-fitting at all scales.

^c C_{dl} , as determined from the single-parameter curve-fitting at the shortest time scale.

Any discussion of this paper will appear in a Discussion Section to be published in the June 1981 JOURNAL. All discussions for the June 1981 Discussion Section should be submitted by Feb. 1, 1981.

LIST OF SYMBOLS

C_{dl}	double layer capacity
$C_{O^0}, (C_{R^0})$	bulk concentration of oxidized (reduced) form in bulk of solution
$D_O, (D_R)$	diffusion coefficient of oxidized (reduced) form
I	instantaneous information
$\bar{I}(\bar{I}(C_{dl}))$	average information in respect to the exchange current density (double layer capacity)
\bar{I}_{lim}	\bar{I} at $\tau_c/\tau_d > 10^3$
i_o	exchange current density
Δi_o	error in the determination of i_o
N	number of points along the transient used for the computation of i_o
O, (R)	oxidized (reduced) form of reactive species
T	full time scale reading
t	time elapsed from the start of the potential transient
$\beta(\gamma)$	defined by Eq. [3] (4)
η	overpotential
η_o	the overpotential at the completion of the charge injection (at $t = 0$).

ν	stoichiometric number
$\nu_O(\nu_R)$	stoichiometric coefficient of O(R) in the overall electrode reaction
τ_c	charge-transfer relaxation constant
τ_d	diffusional relaxation constant

REFERENCES

- H. P. van Leeuwen, *Electrochim. Acta*, **23**, 207 (1978).
- D. J. Kooijman and J. H. Sluyters, *ibid.*, **12**, 1579 (1967).
- T. Berzins and P. Delahay, *J. Am. Chem. Soc.*, **77**, 6448 (1955).
- H. P. van Leeuwen, D. J. Kooijman, M. Sluyters-Rehbach, and J. H. Sluyters, *J. Electroanal. Chem. Interfacial Electrochem.*, **23**, 475 (1969).
- P. Delahay, *J. Phys. Chem.*, **66**, 2204 (1962).
- W. H. Reinmuth, *Anal. Chem.*, **34**, 2204 (1962).
- H. Reller and E. Kirowa-Eisner, *J. Electroanal. Chem. Interfacial Electrochem.*, **103**, 335 (1979).
- H. Reller, M.Sc. Thesis, Tel-Aviv University (1977).
- M. Sluyters-Rehbach and J. H. Sluyters, in "Electroanalytical Chemistry," Vol. 4, A. J. Bard, Editor, Marcel Dekker, New York (1970).
- D. J. Kooijman, M. Sluyters-Rehbach, and J. H. Sluyters, *Electrochim. Acta*, **11**, 1197 (1966).
- F. James and M. Roos, *Comp. Phys. Commun.*, **10**, 343 (1975).

Electrochemical Analysis of Copper Oxides Present in Cuprous Sulfide

J. Vedel* and M. Soubeyrand†

Laboratoire d'Electrochimie Analytique et Appliquée (associé au CNRS), E.N.S.C.P., 75005, Paris, France

ABSTRACT

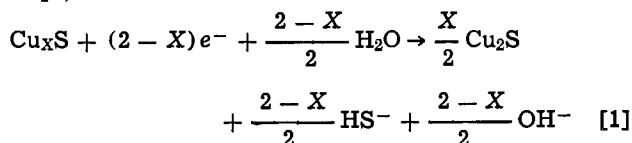
A titration method permitting the determination of the products of air oxidation of thin layers of cuprous sulfide containing copper or not is described. It consists of a cathodic reduction at constant current with potentiometric determination of the equivalent point (current density, 2 A m^{-2} ; electrolyte, 0.1M aqueous solution of sodium acetate). Nonstoichiometric cuprous sulfide (Cu_xS) is reduced to Cu_2S at -0.7V (vs. Ag/AgCl/KCl 1M electrode) and Cu_2S to copper at -1.0V . When cuprous sulfide is heated in air, cupric oxide is formed which is reduced at -0.16V . If an excess of metallic copper is present, cuprous oxide is formed and reduced at -0.45V . The titration method may be used to characterize the cuprous sulfide from CdS- Cu_2S solar cells.

The active element in CdS- Cu_2S solar cells is the heterojunction which exists between the cadmium sulfide and a layer of cuprous sulfide formed on its surface. Most of the light is absorbed by the cuprous sulfide, whose properties strongly influence the output of photocells. The properties of cuprous sulfide are governed by its composition or, more precisely, the departure from the stoichiometric composition Cu_2S which is thus a very important parameter (1, 2).

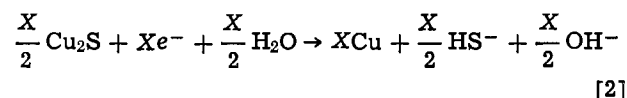
A few years ago we developed a method of analyzing cuprous sulfide, which permitted the determination of the stoichiometric ratio, X, of Cu_xS (3), and which contributed to the manufacture of rather efficient CdS- Cu_2S solar cells (7.2%) (4).

This method consists of the cathodic reduction of the sulfide layer at constant current. The progress of the reduction is followed by recording the variation over time of the potential of the electrode formed by the layer of sulfide. With samples of sulfide which do not contain oxide, titration curves like the curve in Fig. 1 were obtained. These curves show two equi-

valent points. Analysis of layers of controlled composition and the determination, by chemical analysis, of the total quantity of copper involved has shown (3) that the first step in reduction corresponds to the reduction of nonstoichiometric cuprous sulfide, Cu_xS , to Cu_2S , thus



The second step corresponds to the total reduction of cuprous sulfide to copper



Finally the reduction of the water is observed.

This total reduction of thin layers of cuprous sulfide (the thickness existing on solar cells never exceeds $1 \mu\text{m}$) is due to the great mobility of Cu^+ ions in the Cu_2S lattice as observed by Etienne (5). He studied

* Electrochemical Society Active Member.

† Present address: Photon Power, Incorporated, El Paso, Texas 79935.

Key words: copper, oxide, sulfide, titration, solar cells.

the growth of copper sulfides on a copper anode in a saturated acidic solution of H_2S at constant current.

If t_1 and $t_1 + t_2$ are the values of time at the two equivalent points, the deviation from stoichiometry δ is given by

$$\delta = 2 - X = \frac{2t_1}{t_1 + t_2} \quad [3]$$

Certain treatments of solar cells involve heating the layers of Cu_xS , which can be overlaid with copper, in air (6). Upon analysis, the titration curves of the layers which are thus treated show new plateaus, no doubt linked to the presence of oxide. The aim of this work is to study the influence of these treatments on the form of the titration curves and to deduce from them a method for the determination of the quantities formed. Thus, samples of air-oxidized cuprous sulfide were analyzed. The quantities of oxide formed are very slight and cannot be identified by physical methods. In order to characterize the oxidation products, the samples were put in contact with solutions containing appropriate reagents and the titration curves obtained with the samples thus treated were compared with those of the untreated samples.

Experimental Section

The cathode reduction is carried out in a closed glass cell permitting the liberation of gas released from the electrolyte (0.1M sodium acetate solution). The auxiliary electrode, which serves as the anode, is a platinum wire placed in a separate compartment. The current density used is $200 \mu A cm^{-2}$. The reference electrode is an Ag/AgCl/KClM electrode. The titration curves are obtained by means of a recording voltmeter with high input impedance.

The samples are obtained by depositing a layer of electrolytic copper on a platinum disk. This layer is then anodically oxidized in an aqueous solution of sodium sulfide. The sulfide obtained is generally non-stoichiometric. The samples are equilibrated by cathodically reducing the excess Cu(II). They are, for this purpose, placed in the titration cell and reduced, as in the analysis, until point A (Fig. 1) is attained. A known quantity of copper can be deposited on the sulfide by continuing the electrolysis beyond point A, for example point B (Fig. 1).

The oxidation consists of heating, in air, at $100^\circ C$, for 120 min. The quantities of oxide formed are reproducible at better than 1%. Layers of pure oxide were

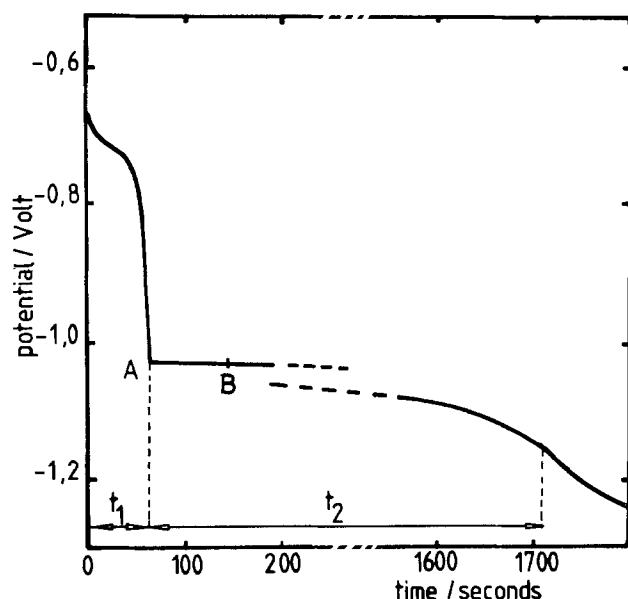


Fig. 1. Potentiometric titration curve at constant current of a layer of nonstoichiometric cuprous sulfide.

prepared by heating, the copper layer in air under the same conditions as above, for the cuprous oxide and by anodic oxidation of copper in an N solution of sodium hydroxide for the cupric oxide (7) (current density, $2A m^{-2}$).

The solutions used to characterize the products formed are a $10^{-3}M$ sodium sulfide solution (solution of sulfide) and a dilute perchloric acid solution, $pH = 3.5$ (acidic solution).

Results

Figure 2 summarizes the influence of oxygen on cuprous sulfide. Only the first part of the titration curve has been presented; the plateau at $-1.0V$ corresponds to the potential observed during the reduction of Cu_2S to copper (reaction [2]). Equilibration gives the Cu_xS stoichiometric (curve 1). Upon treating in air again a plateau appears at a higher potential ($-0.16V$ vs. Ag/AgCl) than that corresponding to reaction [1] ($-0.70V$ vs. Ag/AgCl) (curve 2, Fig. 2). After immersion in the sulfide solution, a plateau of the same length as the preceding one is observed, but at the level of reaction [1] ($-0.70V$). Finally the reaction of the acid solution leads to a plateau at the same potential as the preceding one but half the length. The reduction of pure cupric oxide occurs at a different potential ($-0.65V$ vs. Ag/AgCl) (curve 5, Fig. 2).

If a layer of copper-enriched cuprous sulfide is treated in the same way, the titration curves shown in Fig. 3 are obtained. For a sample which is only air-oxidized (curve 2), a plateau is observed at $-0.45V$, next to the plateau at $-0.16V$ already observed after the heating, in air, of the cuprous sulfide alone, whose length is exactly equal to the time of reduction during which the reduction of equilibrated Cu_2S was carried out. The action of the sulfide solution (curve 3) and the action of the acid solution (curve 4) eliminate this plateau and the previous behavior as is observed. Cuprous oxide alone is reduced at $-0.75V$. When the proportion of reduced copper is increased, there is a decrease of reduction potential of the supplementary wave, which tends toward this same value of $-0.75V$. (Fig. 4).

Finally, Fig. 5 represents titration curves recorded during the analysis of a copper sulfide obtained by ion exchange on a layer of vacuum deposited CdS [Shirland method (8)]. Curve 1 was obtained by

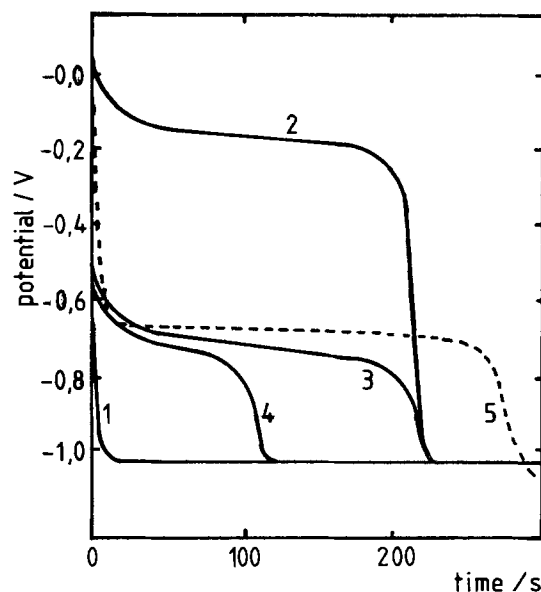


Fig. 2. Potentiometric titration curve at constant current of a layer of equilibrated cuprous sulfide. 1, After equilibration; 2, 3, and 4, after air oxidation. 2, Without treatment; 3, after contact with the sulfide solution; 4, after contact with the acid solution; 5, reduction of a CuO layer.

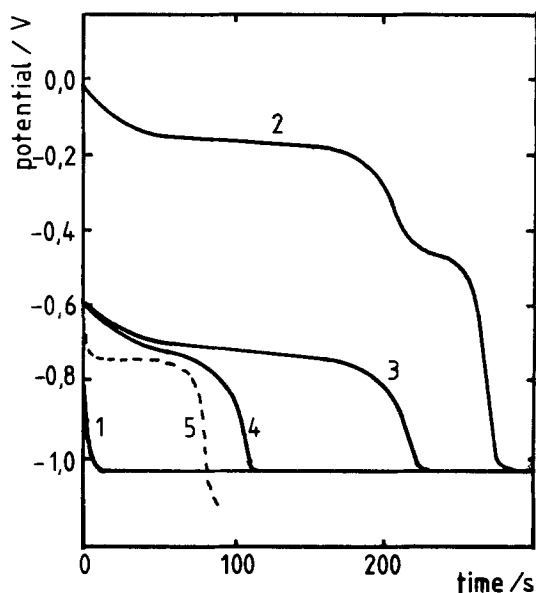


Fig. 3. Potentiometric titration curve at constant current of a layer of equilibrated cuprous sulfide containing an excess of copper. 1, After equilibration; 2, 3, and 4, after air oxidation. 2, Without treatment; 3, after contact with a sulfide solution; 4, after contact with an acid solution; 5, reduction of a Cu_2O layer.

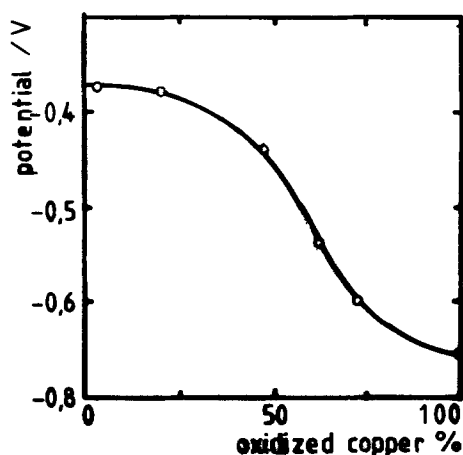
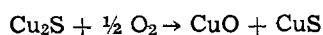


Fig. 4. Variation of reduction potential of the oxidation product of the excess copper (cf. Fig. 4) as a function of the proportion of transformed copper (oxidized copper/transformed copper/total copper).

carrying out the analysis just after the formation, and curve 2 after treatment in the sulfide solution. Curve 1 shows three plateaus, a, b, and c, of which the latter, which corresponds to reaction [2], is situated at a potential more negative than on the curve in Fig. 1. Likewise, plateau b, which corresponds to reaction [1], is displaced toward the more negative potentials. This variation of potentials of plateaus is frequently observed with samples of different origins and can be attributed to modifications of ohmic drop in the underlying layers.

Discussion

The action of oxygen on cuprous sulfide leads to the formation of cupric oxide and cupric sulfide



For low ratios of oxidation, this transformation can be accounted for by writing the reaction of the insertion of oxygen in the cuprous sulfide. As a result of its electronegativity, oxygen is fixed to a sulfur site, by the reaction

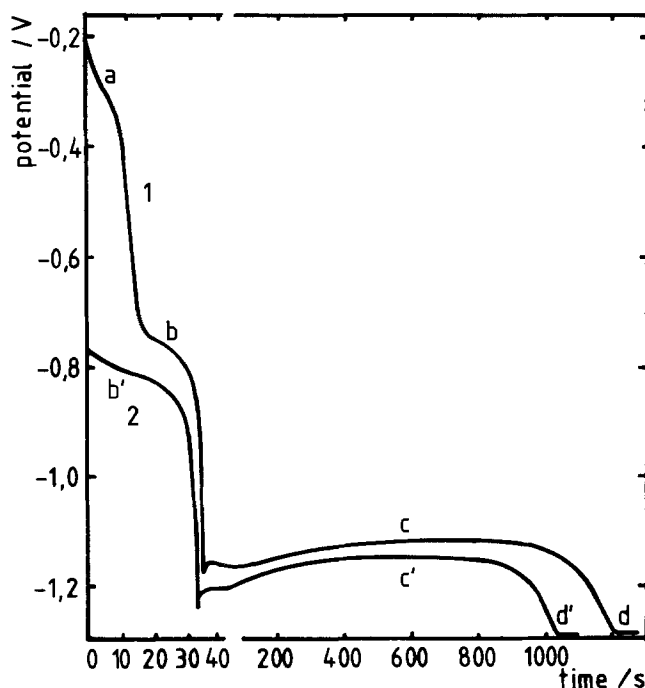
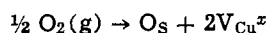
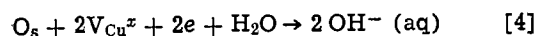
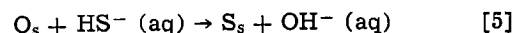


Fig. 5. Titration curve of a layer of cuprous sulfide obtained by ion exchange between a layer of vacuum-deposited CdS and a solution of cuprous salt. 1, After ion exchange; 2, after ion exchange and contact with the sulfide solution.

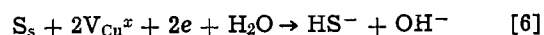
where, following the notation of Kröger, O_s represents an oxide ion occupying a sulfur site, and $\text{V}_{\text{Cu}^\times}$, the neutral vacancy of copper which, as in the case of Cu_2O (9), can be considered as the association between a Cu^{2+} ion at a place normally occupied by a Cu^+ ion (Cu_{Cu}') and a copper ion vacancy V_{Cu}' (i.e., a Cu^+ ion is missing). Upon oxidation by an atom of oxygen two Cu^{2+} ions and two copper ion vacancies appear in the solid. The reduction reaction for $(\text{O}_\text{s} + 2\text{V}_{\text{Cu}^\times})$ is written



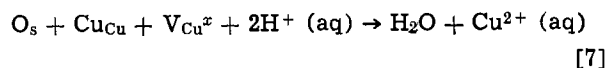
The copper sulfides are more insoluble than the corresponding oxides. The action of the sulfide solution thus leads to an exchange between the O^{2-} ions and the S^{2-} ions by the reaction



which leaves the copper ion vacancy $\text{V}_{\text{Cu}^\times}$ unchanged and available for a later reduction



This is another way of writing reaction [1]. The action of the acid solution is written



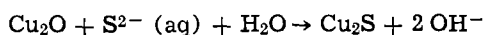
Reaction [7] consumes half the $\text{V}_{\text{Cu}^\times}$ vacancies formed during the oxidation by oxygen. Their subsequent reduction thus requires only half the amount of charge as was previously necessary. Thus, the plateau at -0.16 (vs. Ag/AgCl) is attributed to reduction of cupric oxide introduced into the cuprous oxide structure during the air-oxidation.

The oxidation of excess copper leads to the formation of cuprous oxide. Indeed, (i) as much electricity is necessary to reduce the oxidation product to copper as was necessary in preparing the copper from cuprous sulfide; (ii) when the proportion of Cu_2S in the analyzed mixture is decreased, the reduction potential of the material formed tends toward the reduction potential of pure Cu_2O ; and (iii) the action of the sulfide solution and the action of the acid solution eliminate

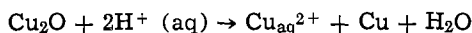
Table I. Reduction potential of materials obtained after air-oxidation of copper-enriched cuprous sulfide

Material being reduced	Reduction potential (V)	
	vs. Ag/AgCl	vs. Cu ₂ S/Cu
CuO (in Cu ₂ S)	-0.16	+0.84
Cu ₂ O (in Cu ₂ S)	-0.45	+0.55
CuS (in Cu ₂ S, i.e., Cu ₂ S)	-0.70	+0.30
Cu ₂ S	-1.00	0
H ₂ O	-1.21	-0.21

the formation of the compounds formed by the following reactions



and



To summarize, the reduction potentials of various materials present in cuprous sulfide are assembled in Table I. In order to eliminate the variations in potentials observed during the study of various samples, the table includes the values obtained by taking, as the reference potential, the potential corresponding to the reduction of Cu₂S to Cu for the sample being considered.

The potentials of the plateaus a, b, c, and d of the titration curve No. 1 in Fig. 5 are 0.84, 0.38, 0, and -0.14V, respectively. Comparing these values with those in Table I, the first plateau, a, can be attributed to the reduction of cupric oxide, the second to the reduction of Cu_xS to Cu₂S (reaction [1]) and the third

to the reduction of Cu₂S to Cu (reaction [2]). This conclusion is confirmed by curve 2, Fig. 5, which was obtained after immersion of the sample in the sulfide solution. The first plateau disappeared following reaction [5] and a plateau b' appears whose length is equal to the sum of the lengths of plateaus a and b. If t₀, t₁, and t₂ are the times corresponding to the lengths of plateaus a, b, and c, it is shown, according to reactions [1], [2], and [4] that the fraction of cupric oxide present in the sample, in relation to the total quantity of sulfur, equals t₀/(t₁ + t₂). The fraction of cuprous oxide would be calculated in a similar way.

Manuscript submitted April 2, 1979; revised manuscript received Dec. 12, 1979.

Publication costs of this article were assisted by Centre National de la Recherche Scientifique.

REFERENCES

1. W. Palz, J. Besson, T. N'Guyen Duy, and J. Vedel, 9th IEEE Photovoltaic Specialists Conference, Maryland (1972).
2. T. S. Te Velde and J. Dieleman, *Philips Res. Rep.*, **28**, 573 (1973).
3. E. Castel and J. Vedel, *Analysis*, **3**, 487 (1972).
4. W. Palz, J. Besson, T. N'Guyen Duy, and J. Vedel, 10th IEEE Photovoltaic Specialists Conference, Palo Alto, California (1973).
5. A. Etienne, *This Journal*, **117**, 870 (1970).
6. F. Pfisterer, H. W. Schock, and W. H. Bloss, 12th IEEE Photovoltaic Specialists Conference, Baton Rouge, Louisiana (1976).
7. L. De Brouckere, F. Bouillon, and Y. Bouillon-Nyssen, *Bull. Soc. Chim. Belg.*, **60**, 26 (1956).
8. F. A. Shirland, *Adv. Energy Convers.*, **6**, 201, (1966).
9. H. Dunwald and C. Wagner, *Z. Phys. Chem. Abt. (B)*, **17**, 467 (1933).

Periodic Phenomena during Anodic Dissolution of Copper at High Current Densities

John F. Cooper,*¹ Rolf H. Muller,* and Charles W. Tobias*

Materials and Molecular Research Division, Lawrence Berkeley Laboratory, and Department of Chemical Engineering, University of California, Berkeley, California 94720

ABSTRACT

Uniform and sustained anode potential oscillations (amplitude, 10-20V) have been observed in galvanostatic dissolution of copper in chlorate electrolyte. The oscillations occur in the current density range of 0.3-150 A/cm². Frequency increases with current density in this range from 10⁻³ to 10³ Hz. Increases in electrolyte temperature, acidity, and flow rate were found to result in a decrease of oscillation frequency. Large amplitude oscillations were also observed in a narrower current density range and with less cycle uniformity, in a variety of mixed electrolytes containing small concentrations of halides. The rise and fall of potential reflects an alternate growth and destruction of an adherent cuprous oxide surface layer. A model for the oscillations is proposed based on resistive switching transitions within the anode surface film.

The anodic dissolution of copper in sodium chlorate electrolyte gives rise to a remarkable phenomenon. On applying a constant current to the cell, the anode potential fails to reach a steady level; rather, the potential undergoes a periodic rise and fall of about 10V, as shown by the sample oscillograph recording (Fig. 1). The individual cycles are impressively uniform in period and amplitude. Oscillations are found with galvanostatically controlled current densities in the range of 0.3 to over 150 A/cm². Above approximately 180 A/cm², random fluctuations accompanied by gassing and sparking were observed. Frequency increases with

current density within this range from 0.003 Hz to over 1000 Hz. In a narrower current density range and with less cycle uniformity, large amplitude oscillations may also be produced with a variety of mixed electrolytes containing small concentrations of halide ions. In addition, the anodic dissolution of iron in the chlorate electrolyte occurs with similar potential oscillations.

The oscillations associated with the copper/chlorate system (1, 2) were first encountered during a study of electrolytes commonly used in electrochemical machining, the technique which employs anodic dissolution at current densities from 5 to 500 A/cm² to cut, shape, and polish metals (3, 4). The possibility that the oscillations were connected with the favorable results obtainable with the chlorate electrolyte (5)

* Electrochemical Society Active Member.

¹ Present address: University of California, Lawrence Livermore Laboratory, Livermore, California 94550.

Key words: oscillations, copper dissolution, electrochemical machining.

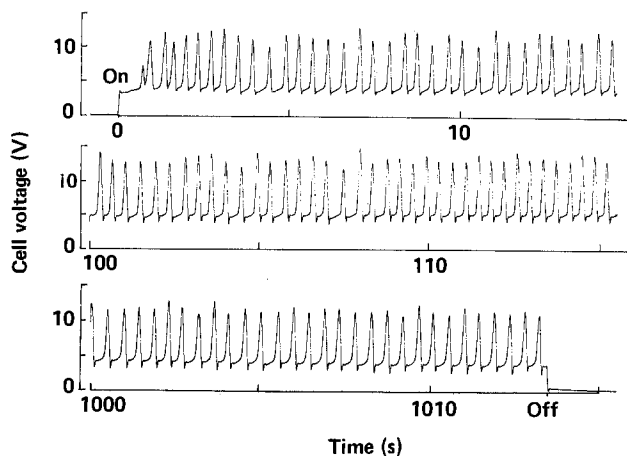


Fig. 1. Sustained cell voltage oscillations. Cell voltage recorded at three intervals during a dissolution experiment lasting over 1000 sec. Electrolyte composition, 2M NaClO_3 ; current density, 3 A/cm^2 ; electrode area, 0.32 cm^2 ; ambient temperature; stationary electrode, stirred electrolyte.

prompted the thorough investigation reported here. Large amplitude oscillations reflect the alternate growth and decline of the electrical resistance of passive or transpassive surface layers. An understanding of the periodic growth and breakdown of such layers should lead to a better general understanding of passive and transpassive electrode states.

Earlier Interpretations of Periodicity

Electrode reactions taking place with periodic changes in current or potential are by no means uncommon. A wealth of descriptive literature dates from the early nineteenth century. The preponderance of the over one hundred cases reported involves active-passive or active-transpassive transitions occurring during the anodic polarization of metals. The older literature has been reviewed by Hedges and Meyers (6) and by Indira *et al.* (7). Wojtowicz reviewed recent experimental work with emphasis on the relatively few cases where attempts at rational interpretations were made (8).

Numerous schemes have been proposed for the periodic growth and breakdown of electrode resistance. The models fall into perhaps five general categories: (i) Changes in local anolyte pH brought about by electrode reactions coupled with diffusion may shift the Flade potential for active/passive transitions. Franck developed a general theory along these lines (9, 10) and applied it to the $\text{Fe}/\text{H}_2\text{SO}_4$ system (11). (ii) The sequential deposition, oxidation, and chemical dissolution of a salt or oxide layer may induce the transitions (12). (iii) Active-passive transitions may reflect the exhaustion, followed by the diffusion-controlled replenishment, of an acceptor anion necessary for active dissolution (13, 14). (iv) Dielectric or mechanical disruption of the resistive layer may alternate with periods of film growth and repair (15, 16). (v) Changes in electrode state may reflect solid-state transformations within the resistive layer, such as recrystallization, transport, and accumulation of aggressive anions within the lattice, insulator-to-conductor "switching" transitions, etc.

In this last category, Indira and co-workers proposed that oscillations in certain instances may arise from subtle changes in the stoichiometry of solid anodically formed layers (7, 17). The gradual and uniform growth of the layer (by ionic conduction) was said to terminate in a nondestructive dielectric breakdown, which leaves behind a number of discrete filaments of highly defective and hence highly conductive material. The repair and buildup of the film then begins anew. The mechanism for restoring the high resistance state was not identified by the authors,

nor was the existence of the filaments verified experimentally. Nevertheless, field-induced insulator-to-conductor transitions are known to occur in a wide variety of materials (18) including cuprous oxide (19, 20).

A theory of periodicity must first of all identify the individual processes dominant in each phase of the cycle. The models described above present reasonable mechanisms for the growth and destruction of current-restricting layers. As pointed out by Wojtowicz, however, many authors have assumed that (rather than explained why) growth and breakdown should occur in sequence and in phase over an extended electrode surface. The possibility must be ruled out that the same processes could occur simultaneously (but out of phase) on discrete sites on the electrode surface. With a sufficiently large number of such sites, the electrode potential might approach steady levels which reflect the mixed potential of a large number of sites in different stages of the growth/breakdown cycle. Thus, a second requirement of a theoretical model is that the processes involved must occur in phase over the electrode surface.

This paper reports an investigation into the potential oscillations associated with the copper/sodium chlorate system, which is treated as a model for a wider range of high amplitude, sawtooth oscillations observed in certain halide-containing electrolytes at high anodic current densities. For purposes of comparison, data on these other systems are reported in Appendix A.

Experimental Apparatus and Materials

The potential oscillations in the chlorate electrolyte occur over a broad and elevated range of current densities: 0.3-150 A/cm^2 . Experimental studies under these conditions presented technical difficulties in the design of electrolysis cells. In our investigation (1), the primary factors considered were: (i) the provision of high rates of solution-side mass transfer under reproducible and reasonably well-defined hydrodynamic conditions, (ii) prevention of excessive ohmic heating of the electrolyte, and (iii) a reasonably constant cell geometry despite the rapid changes in the position and topography of the electrode surface during dissolution. No single experimental system met all of these requirements. At the lower end of the current density range a rotating disk electrode was employed. The disk was formed by casting an epoxy cylinder of diameter 3.5 cm around a 0.56 cm diam copper rod. The 0.25 cm^2 disk electrode was ground flush with the surface of the epoxy between experiments.

In an intermediate current density range (up to about 30 A/cm^2), a rectangular duct flow channel system was used. The flow system was designed for use under reproducible hydrodynamic conditions at Reynolds numbers up to 10,000. The copper electrodes, 3 mm square, were positioned opposite each other and flush with the horizontal walls of the flow channel. Electrode separation was 0.1 cm. The entrance length of 30 cm (200 hydraulic diameters) was sufficient to establish stable fluid velocity profiles in the vicinity of the electrodes. Electrode potentials were measured against a saturated calomel electrode by means of capillary openings drilled into the horizontal channel walls just 0.01 cm upstream of the leading edge of the electrodes.

An electrolyte jet apparatus provided the high rates of heat and mass transport needed for investigations in the high current density range. A 0.32 cm diam jet of electrolyte was directed against the anode surface; the circular end of a 1.6 mm diam copper wire was held in a Teflon plug. The electrolyte flows radially outward over the surface of the anode and plug and thence over a concentric cathode ring (area, 10 cm^2). The wire was periodically advanced such that the electrode surface remained flush with the floor of the cell.

We have chosen to investigate the oscillatory phenomena under galvanostatic conditions, thereby allowing an important experimental parameter to be fixed and accurately determined. The galvanostat (Electronics Measurements Power Supply, Model C618) delivered a maximum of 3A at 200V, with a rise time of 1 msec. Electrical measurements (cell or anode potential, current) were recorded either on a light beam oscillograph with a frequency response of 1 kHz or, when necessary, on an oscilloscope.

For the jet electrode system, zone-refined high purity copper (99.999+%) was used. Impurities quoted by the manufacturer (Materials Research Incorporated, Orangeburg, New York) were as follows (ppm, weight): Zn < 5; Sn < 1; Ni, P, Pb, < 1; O < 2; Mo < 5; rare earths < 1; Cl < 0.01. In all other experimental systems, oxygen-free, high conductivity copper (OFHC, 99.99+%) was used. Solutions were prepared from reagent grade sodium chlorate and doubly distilled water.

Experimental Results

Electrical properties of the oscillations.—Waveform, cycle uniformity, and persistence.—By separate measurements of anode and cathode potential against a reference electrode, it was determined that the oscillatory phenomena are associated with the anode. Once it had been established that polarization of the copper cathodes used in all three experimental systems was low and independent of time, the oscillations in anode potential could conveniently be monitored by measurements of cell voltage.

The oscillations are characteristically of a sawtooth waveform: an upward-sweeping potential terminates in a relatively sharp peak, followed by an abrupt fall to lowest potential of the cycle, *i.e.*, the trough (see Fig. 1-4). Considerable detail appears within each cycle at the lower end of the current density range for oscillations. Figure 2 depicts the first oscillation obtained following the start of dissolution of a rotating disk electrode. A low potential phase (V_1) and a high potential phase and peak (V_2-V_p) are evident and are separated by a short interval of random potential fluctuations of low (0.2-0.3V) amplitudes. For reasons which will become clear later (see discussion of morphology below), we shall refer to the low and high potential phases as, respectively, "active" and "transpassive" dissolution.

Below the minimum current density at which the peaks are observed (for given conditions of flow rate, temperature, etc.), the electrode potential fluctuates randomly between the active and transpassive levels (Fig. 3a). As the current density is raised in the

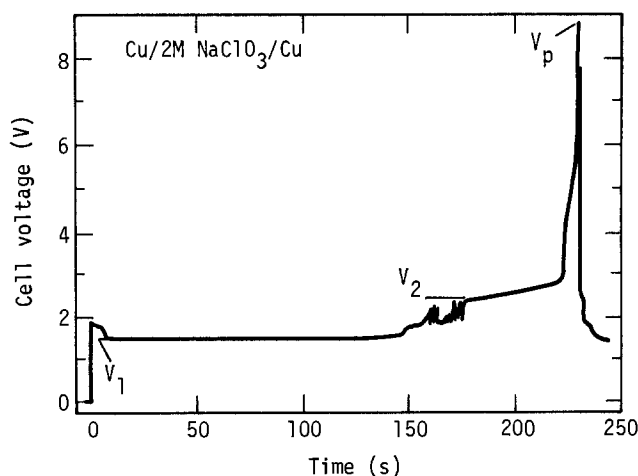


Fig. 2. Details of oscillation waveform produced at low current density. Rotating disk electrode system, 360 rpm, current density = 0.32 A/cm². V_1 = potential of active phase; V_2 = potential at onset of transpassive dissolution; V_p = peak potential.

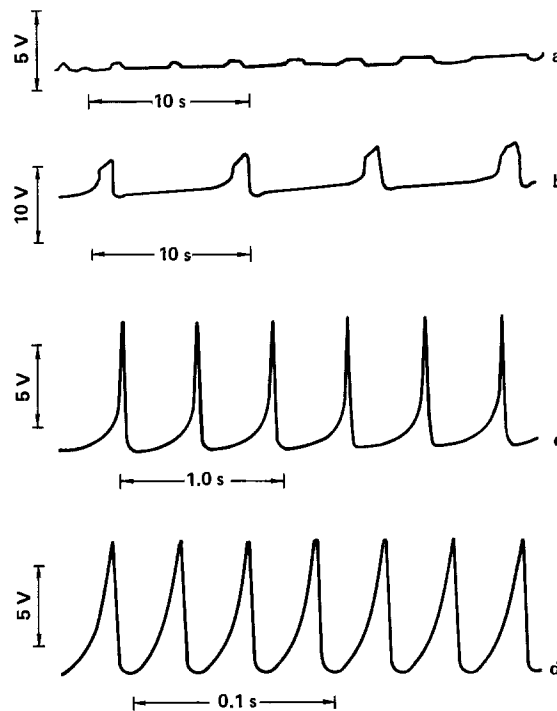


Fig. 3. Waveforms characteristic of different current density ranges. Channel flow system. 2M NaClO₃ electrolyte. (a) Low current density extreme, no potential peaks; $i = 0.61$ A/cm²; $Re = 425$; (b) active and transpassive dissolution, showing potential peaks; 1.83 A/cm², $Re = 6810$; (c) transpassive dissolution only; 6.57 A/cm², $Re = 6810$; (d) 33.4 A/cm², $Re = 6810$.

range 1-5 A/cm², however, the peaks appear and the duration of the transpassive phase increases at the expense of the active phase. Above approximately 5 A/cm², discrete active phase of the potential cycle is no longer evident, and the cycles assume the characteristic waveforms shown in Fig. 3c and d. Above about 100 A/cm², another waveform is found, which has the appearance of a spike of about 20V superimposed on the more rounded peaks as shown in the insets of Fig. 10.

The oscillations observed in the chlorate electrolyte represent a sustained mode of dissolution and persist essentially unchanged as long as the experimental conditions (flow rate, current, cell geometry) are maintained. Recordings of potential against time in various intervals of single dissolution experiments are shown in Fig. 1 and 4. If the surface of the electrode is disturbed during dissolution (for example, with a glass pick), the oscillations first become disordered, then rapidly revert to a uniform period and amplitude (see Fig. 4a). The cycling shows no tendency to dampen permanently even after as many as 2500 cycles. The standard deviation in both peak amplitude and period over twenty consecutive oscillation cycles was less than 2%.

Dependence of period length on experimental parameters.—Period length shows a strong dependence on current density. This is shown in the composite plot of data (Fig. 5) taken with the rotating disk, channel flow, and jet systems over the entire range of mass transport conditions under which the phenomenon occurs. The relationship between period length and current density is linear on the double-logarithmic plot, with a change in slope from -2.5 to -1.5 occurring in the range 3-10 A/cm².

To a much lower extent than can be depicted on the scale of Fig. 5, the oscillation period also depends on flow rate. Below about 5 A/cm², the period is proportional to the 0.3 power of flow rate ($450 < Re < 1500$) in the flow channel (Fig. 6). In the higher current density range investigated with the jet (above

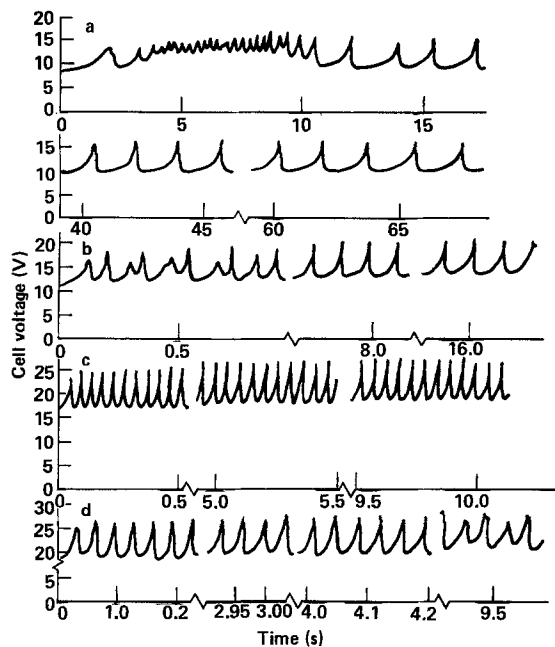


Fig. 4. Oscillation waveforms at different intervals of dissolution, showing persistence of phenomenon. Electrolyte, 2M NaClO₃. Channel flow, Re = 6810. (a) $i = 8.3$ A/cm²; (b) 12.2 A/cm²; (c) 17.3 A/cm²; (d) 19.9 A/cm².

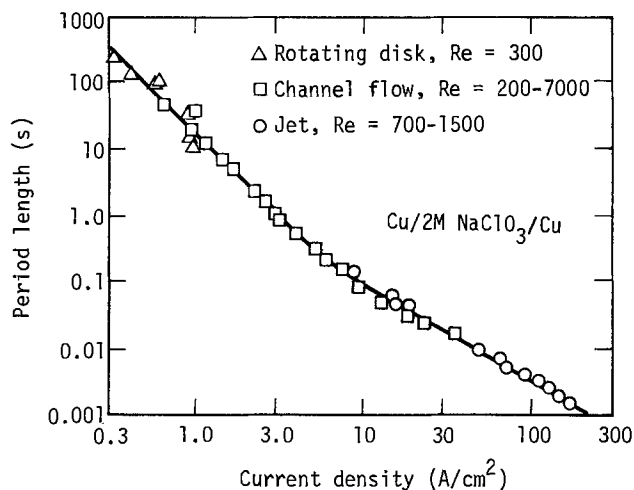


Fig. 5. Inverse relation between period length and current density. Composite of data from three different hydrodynamic systems.

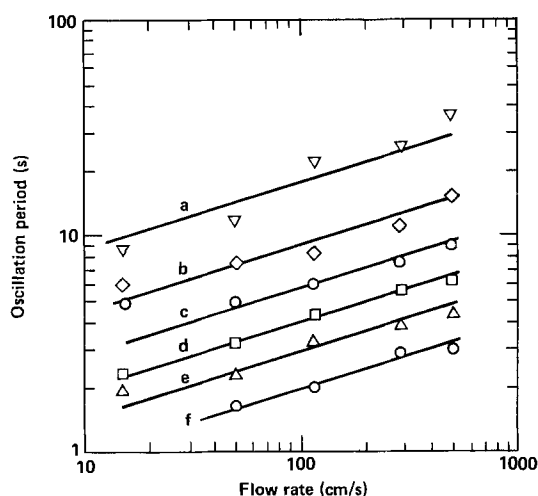


Fig. 6. Increase of period length with average linear flow rate. Channel flow system. Electrolyte 2M NaClO₃. (a) Current density = 1.2 A/cm²; (b) 1.51; (c) 1.84; (d) 2.14; (e) 2.45; (f) 3.05. Range of flow rates correspond to Re = 450-15,000.

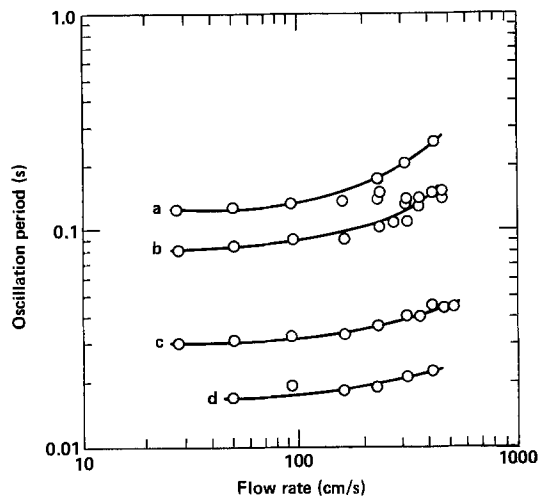


Fig. 7. Increase of period length with flow rate. Jet electrolyte flow system. Electrolyte, 2M NaClO₃. (a) Current density = 8.5 A/cm²; (b) 10.9; (c) 21; (d) 31.5.

10 A/cm²), the dependence of period on flow rate is comparatively weak (Fig. 7). Generally, the oscillation period increases with increasing electrolyte flow rate, and the effect of flow rate decreases at current densities above 10 A/cm².

The oscillation period increases with electrolyte temperature (Fig. 8) in the range of 4°-80°C. The effect of electrolyte pH was investigated using solutions of 2M NaClO₃ containing additions of sodium hydroxide or perchloric acid. The oscillation period increases with solution acidity over a pH range of 11.2-1.4, the influence of acidity being greatest at the lowest current densities (Fig. 9).

Dependence of oscillation amplitude and trough potentials on current density.—While the oscillation period length showed a strong dependence on current density, the oscillation amplitude was relatively independent of current density as shown in the plots of cell peak and trough voltages against current (Fig. 10). The right-hand inset in Fig. 10 indicates the high current density waveform found above about 100 A/cm². This waveform, having the appearance of a spike superimposed on the waveform of lower current densities, is probably the result of the formation of a thin gas layer on the electrode surface followed

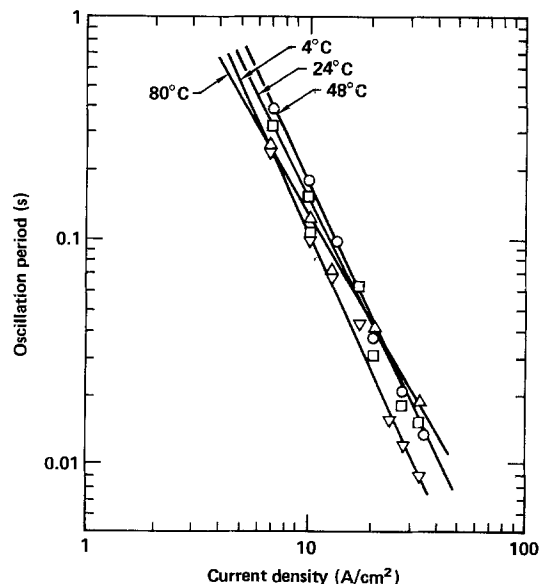


Fig. 8. Effect of temperature on period length. Channel flow, Re = 400; electrolyte, 2M NaClO₃.

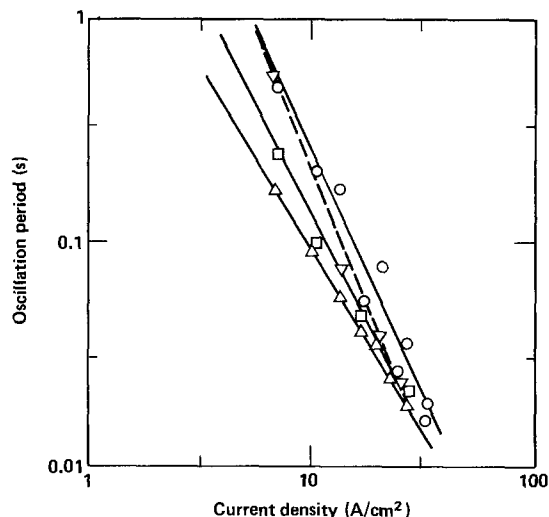


Fig. 9. Dependence of oscillation period on bulk electrolyte pH. Channel flow system, $Re = 400$. ∇ , $pH = 1.4$; \circ , 2.4 ; \square , 4.6 ; \triangle , 11.2 . Electrolyte, $2M NaClO_3$.

by an electrical discharge through it. Sparking and gas evolution are clearly evident whenever this waveform occurs. After falling from the peak, the potential pauses at the level extrapolated from the peaks of lower current density waveforms (indicated by triangle data points in Fig. (10)). The potential spikes are probably unrelated to the periodic phenomena of interest and are not treated further in this paper.

The trough potentials (i.e., the lowest potential of the cycle) plotted against current density in the range of $40\text{--}150 A/cm^2$ extrapolate to $10V$ at zero current. This possibly indicates that the electrode is still covered with a resistive film, the resistance of which has a nonlinear dependence on current.

Chemical aspects of the copper/chlorate system. Apparent valence.—At the electrode potentials observed in this system, mono-, di-, and even trivalent copper oxidation states may be produced (21). The average apparent valence, \bar{n}_a , was determined from anode weight loss measurements using the following equation

$$\bar{n}_a = (It/F)/(\Delta W/M) \quad [1]$$

Here, I is current, t is dissolution time (at least ten times the period length, F is Faraday's constant, ΔW is weight loss, and M is the atomic weight of copper. Average apparent valence is plotted against current

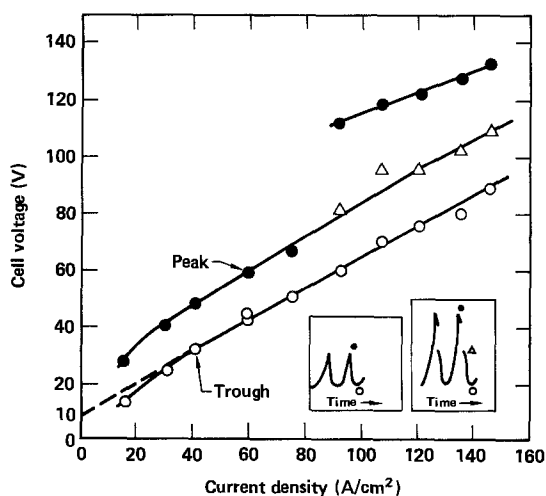


Fig. 10. Increase of trough and peak potentials with current density and appearance of potential spikes above $100 A/cm^2$. Jet electrolyte system, $Re = 1500$. Anomalous waveform shown in inset. Electrolyte, $2M NaClO_3$.

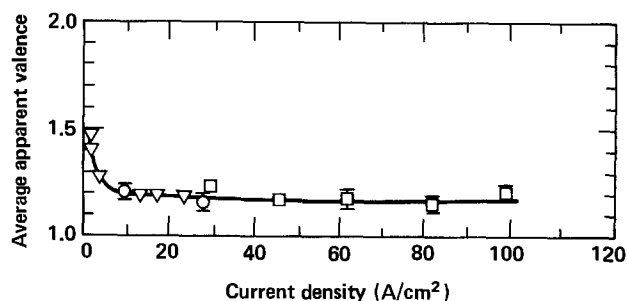


Fig. 11. Average apparent valence. Channel flow: ∇ , $Re = 700$; jet electrolyte flow: \circ , $Re = 700$; \square , $Re = 1500$. Electrolyte, $2M NaClO_3$.

density in Fig. 11 and is shown to approach a nearly constant level of 1.2 ± 0.04 above $10 A/cm^2$.

The possibility that the stoichiometry of dissolution might change periodically made it necessary to measure the instantaneous apparent valence within a single cycle. To determine instantaneous apparent valence, a copper disk ($9.6 cm^2$) was anodically dissolved with the electrode surface facing upward in a stationary electrolyte cell of low volume ($20 ml$). A number of experiments, conducted at $0.54 A/cm^2$, were interrupted at successive points within the first cycle. Weight loss during each experiment was plotted against the quantity of charge passed through the cell, as shown in Fig. 12. The derivative of the curve obtained may be related to the apparent valence, n_a

$$d\Delta W/dQ = (M/n_a) \quad [2]$$

where Q is the quantity of charge passed (in equivalents). Although the precision of the technique is insufficient to allow detection of changes within intervals of less than 10^{-5} equiv./ cm^2 , it is apparent that the stoichiometry of dissolution is constant within both the active and the passive phase. The same result was obtained for dissolution at $1.33 A/cm^2$.

Production of chloride.—In each instantaneous apparent valence determination at 0.54 and $1.33 A/cm^2$, the anolyte was collected, filtered, and analyzed for chloride by means of potentiometric titration with a standardized solution of silver nitrate. The quantity of chloride in the anolyte was found to be proportional to the quantity of charge passed. The chloride is the product of the reduction of chlorate by the cuprous ion according to the net reaction

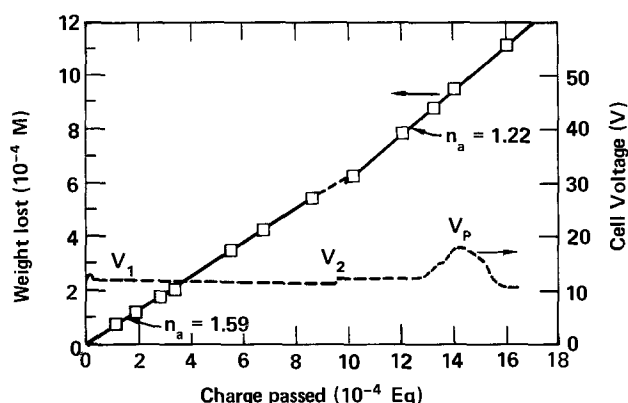
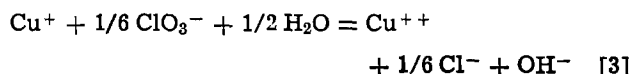


Fig. 12. Total copper dissolved as a function of charge passed. Stationary copper disk, $9.6 cm^2$; $i = 0.54 A/cm^2$; instantaneous apparent valence indicated, showing distinct values for active and transpassive phases. Cell voltage is plotted against charge passed, with active (V_1), transpassive (V_2), and peak (V_p) cell voltages indicated.

Taking into account the nonintegral apparent valence, the quantity of chloride produced corresponded to roughly 60% of the quantity of monovalent copper produced. These results are consistent with those of Royer *et al.* (22), who studied the dissolution of copper in 1.2M NaClO₃ (at 15 mA/cm²) and found an apparent valence of 1.0 at temperatures above 70°C and a quantitative reduction of ClO₃⁻ to Cl⁻. It may be concluded that the electrolyte adjacent to the anode surface and within any pores in the solid surface layer contains a high concentration of the chloride ion.

Analysis of solid reaction products.—Solid reaction products adhering to the surface of the anode following dissolution were analyzed by x-ray diffraction. The copper substrate served as an internal reference. The water-insoluble phases of products resulting from active dissolution, as well as transpassive dissolution, showed only diffraction lines for cuprous oxide. Extraneous lines were absent, including those for other possible products such as Cu(OH)₂, CuCl, CuO, etc.

Morphological changes occurring within the potential cycle.—As shown in Fig. 2, the oscillation cycle at low current densities can be resolved into a succession of distinct potential plateaus and a potential peak. During the low potential phase of the cycle, the copper substrate becomes etched and in places pitted, while

an adherent layer of a red-orange substance (identified as cuprous oxide) accumulates on the metal surface. The appearance of the electrode during the active phase with dissolution at 0.3 A/cm² is clearly shown in the photomicrograph of Fig. 13a. The term "active phase" has been given to this portion of the cycle because of the etched appearance of the substrate and the low overpotentials for dissolution. Active dissolution involves the passage of the metal cation directly from the metal lattice to an aqueous complex. Continued removal of cations from sites of lower free energy of dissolution gives rise to the formation of fine pits, the walls of which often consist of planes of low index numbers (23). Light scattered from the pitted surface accounts for the dull, matt appearance. A fraction of the cuprous ion precipitates from the aqueous complex to form the thick (10-20 μm) porous layer of cuprous oxide.

Beginning with the onset of transpassive dissolution, the copper substrate becomes progressively smoothed and polished and attains a nearly specular appearance as peak potentials are approached. Solid reaction products in this low current density range are found in two distinct layers: (i) a thin adherent layer of sub-micron thickness, found to consist of cuprous oxide; and (ii) a thick (10-100 μm) loosely adherent layer consisting of cuprous oxide and water-soluble copper

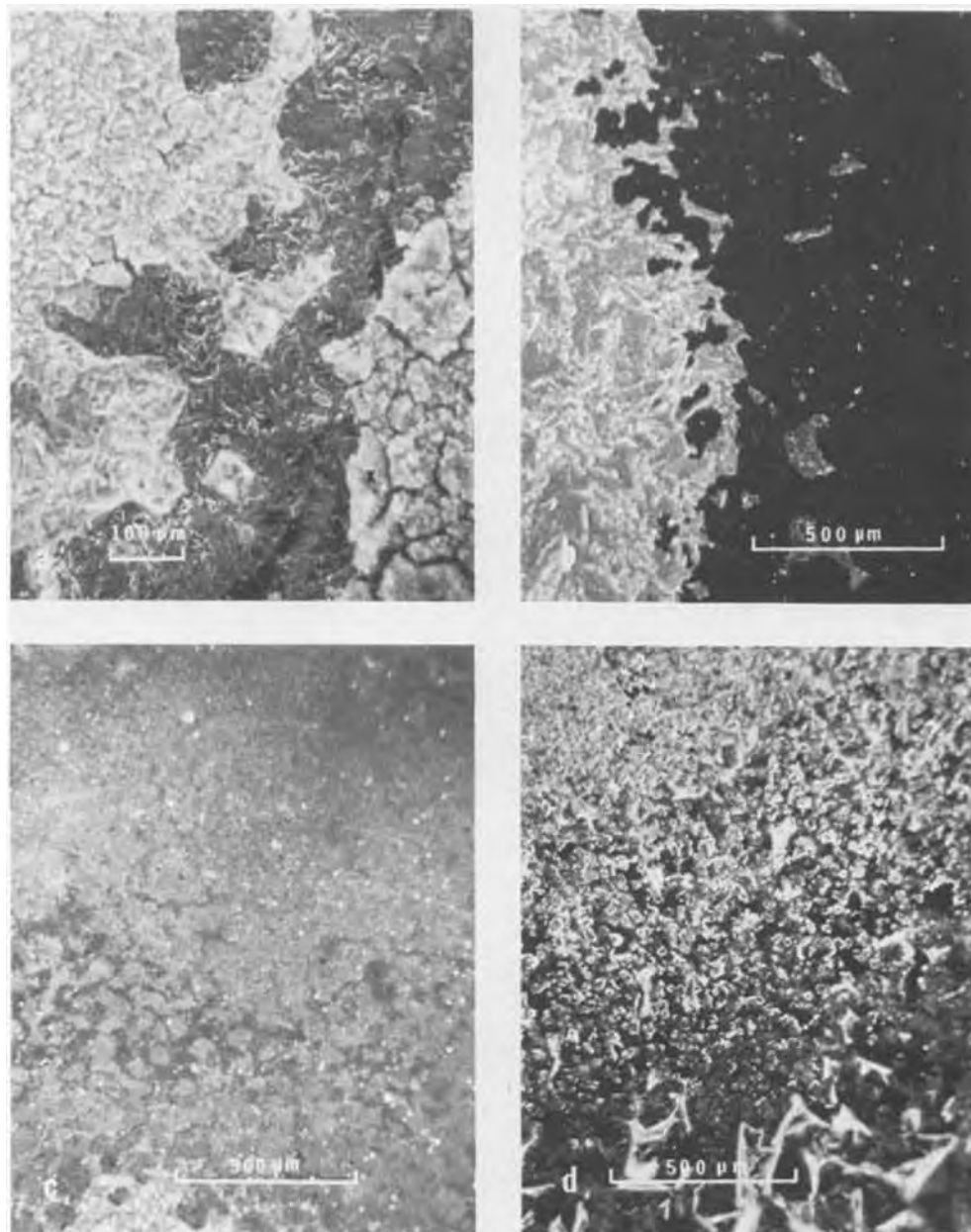


Fig. 13. Sequence of changes of surface morphology during a potential cycle. Rotating disk electrode, $i = 0.32$ A/cm², 360 rpm. (a) Appearance of active phase electrode showing thick Cu₂O layer (x) and roughened substrate (bright field illumination). (b) Progression (right to left) of transpassive film; thick film has been removed; dark field illumination. (c) Electrode surface at peak potential (bright field). (d) Beginning of active phase of second cycle (dark field).

oxychlorides. The formation of the thin layer begins at the periphery of the electrode and spreads progressively inward, undermining and dislodging the porous layer formed during the active phase. The advance of the transpassive layer is shown in the dark field photograph of Fig. 13b.

Immediately before the fall from peak potentials, the electrode surface loses its polished appearance, becoming dull and relatively uniform under intense bright field illumination (Fig. 13c). At the beginning of the active phase of the succeeding cycle, the thin film peels away from the surface (Fig. 13d), while crystals of a new thick phase of cuprous oxide are beginning to form.

The alternating periods of film growth and rupture/removal were recorded using motion picture photography for dissolution experiments at 3 A/cm². The rupture of the film and a rapid outward movement of solid reaction products were shown to coincide with the fall from peak potential within a time interval of less than 0.03 sec.

Observations of resistive switching transitions in the transpassive film.—Many electronic insulators and semiconductors are known to show an abrupt decrease in resistance on being subjected to a critical electric field strength. When the transition is accompanied by the destruction of the material (through spark discharge and local vaporization), the term "breakdown transition" is used. In other cases, called "resistive switching transitions," no readily perceptible change occurs in sample morphology as a result of the transition. Materials showing the latter behavior have been used in both monostable and bistable electronic switches. The subject of switching transitions has been reviewed by Klein (24).

Resistive switching transitions have been observed in samples of cuprous oxide produced by the high temperature oxidation of copper in air (19, 20, 25, 26). The schematic steady-state electrical characteristic is shown in Fig. 14A. The current-voltage plot consists of a stable high resistance, low current branch (H) and a low resistance, high current branch (L). The voltage (V_s) and resistance of the external circuit (represented by a load line) determine currents before and after transition. Although a low resistance state is formed immediately on the collapse of voltage, the stable, reproducible characteristic (L) is established only with the continued passage of charge. This

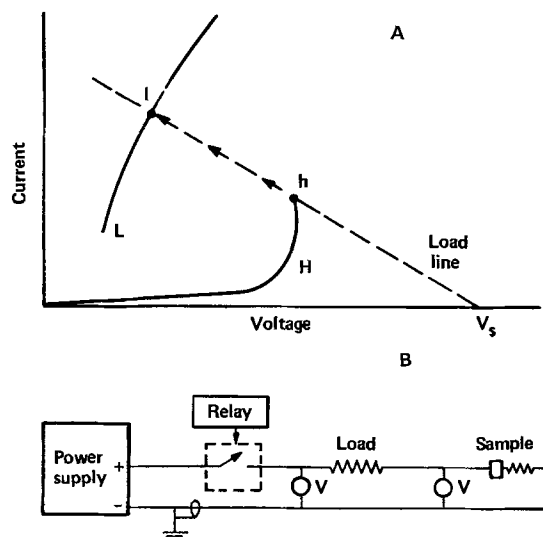


Fig. 14. (A) Current-voltage characteristics of materials showing resistive-switching transitions. H, high resistance state; L, low resistance state. V_s , voltage of power supply. (B) Testing circuit used in the study of electrical breakdown in transpassive surface films. A mercury-wetted relay and a dual beam oscilloscope (V, V) were used with a decade resistance load.

phenomenon has been called "electroforming" (25). The threshold field strength for such transitions was found to be about $2 \times (10)^5$ V/cm by Morgan and Howes for 10^{-5} cm thick samples of Cu_2O (25). Resistive switching in cuprous oxide results in the formation of discrete channels of a low resistivity copper oxide which, when formed at sufficiently high currents, contains filaments of elemental copper (26).

Experiments were undertaken to determine whether the thin cuprous oxide films formed during transpassive dissolution could undergo resistive switching transitions at voltages comparable to the oscillation amplitudes. Sample electrodes were anodized at various points within the transpassive region. The electrodes were then removed from the cell, washed in distilled water, and dried in vacuum. Breakdowns were detected with a movable copper whisker probe using the electrical circuit depicted in Fig. 14B. The probe was brought to rest on the electrode surface and a potential step (1-10V) was then applied.

Resistive switching transitions occurred during which the resistance of the probe-electrode assembly fell from 10^7 - 10^8 to 1 - 10Ω within less than a microsecond. The observed time lag between voltage application and collapse (Fig. 15) depended inversely on the applied voltage. The time lag varied widely from point to point on the electrode surface; an order of magnitude spread in the data is consistent with the statistical nature of the phenomenon (25). Electroforming of the low resistance state was also observed. There is little doubt that the transitions observed are similar to those reported earlier (19). In addition, the applied voltages required for transitions in the dried samples are comparable to voltages occurring during transpassive dissolution.

Interpretation of Experimental Results

In this section we first use the results of solid-state ionic conduction theory to interpret the potential-time behavior during the growth phase of the cycle. Next, we offer an explanation for the near-constancy of the

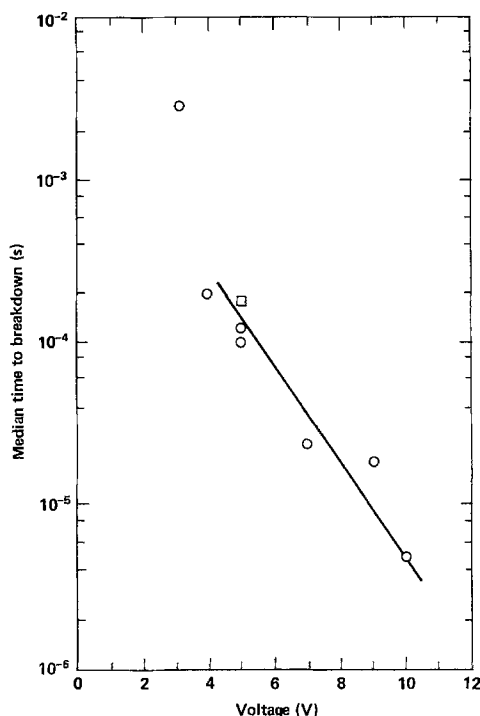


Fig. 15. Dependence of lag time for resistive switching transitions on applied voltage. Lag time is the interval between the application of voltage to the sample and voltage collapse. Transpassive film produced at 0.8 A/cm². Dissolution interrupted at a voltage of 5.9V above trough potential. Peak potential for these conditions is roughly 9V.

amplitude over a wide range of current densities, based on the assumption that the probability for a switching transition is proportional to the thickness of the film and to the field strength. Then a model is presented which attributes the oscillatory nature to the alternation of periods of film growth by high field ionic conduction and field breakdown resulting from switching transitions. A permanent mixed electrode state, allowing simultaneous ionic conduction through the film and electronic conduction through breakdown channels, is shown to be impossible because of the widely different field strengths required for the two processes. Finally, the possible roles of the chloride and chlorate ions are discussed.

Ionic conduction in transpassive surface films.—The copper substrate becomes progressively polished during the interval in which the potential rises from the lowest level to the highest level of the cycle. We refer to this interval as the "potential growth phase." As suggested by Hoar (23) and Novak (27), such electropolishing of copper results from (i) the generation of vacancies in the copper sublattice of the anodic oxide film at the film/electrolyte interface, (ii) the transport of vacancies through the film to the metal surface, and (iii) the annihilation of the vacancies by combination with cations from the metal phase. The flattening and polishing of the anode substrate during this phase is a consequence of the large resistance of the thin film to ionic conduction. With the onset of transpassive dissolution, the resistance of the thin film controls the distribution of current on a microscopic scale. If the thin film is of uniform properties (ionic conductivity and thickness), the current density will be uniform on the surface of any asperity having dimensions which are large compared to the thickness of the film. Continued dissolution under these circumstances will lead to a smoothing of an initially rough surface. The mechanism described here is similar to that which is widely held responsible for the electropolishing of copper in, for example, orthophosphoric acid solutions.

The vacancies reflect the nonstoichiometric nature of cuprous oxide. The material is a cation-deficient, p-type semiconductor, and the vacancies migrate within an electrostatic field as if they were negatively charged. The cation deficiency, indicated by y in the formula, Cu_{2-y}O , varies widely with sample preparation. [Values of $y = 10^{-3}$ (28), 0.5 (29), and 0.76 (30) have been reported for samples showing the same unit cell structure.] It is therefore not possible to predict *a priori* the properties of the surface film during high rate dissolution. Nevertheless, it is reasonable to conclude that the primary mode of ionic conduction during the transpassive phase of the oscillation cycle is the migration of negatively charged cation vacancies from the electrolyte to the metal substrate.

We can test the hypothesis of vacancy migration with the use of high field strength ionic conduction theory, as presented by Dignam (31). When diffusion can be neglected, and for a sufficiently high field strength, the current density i may be expressed as a function of field strength, E

$$i = 2A \sinh (BE) \quad [4]$$

$$\sim A \exp (BE) \quad [5]$$

where the approximation [5] is valid for $BE > 1$. A is proportional to the concentration of charged vacancies, while B is proportional to the width of the potential energy barrier encountered by the defect during migration through the periodic field. The physical meanings of A and B are discussed further in Appendix B.

In Fig. 16, we have plotted $\log(i)$ against the mean field strength, \bar{E} , estimated for the growth phase of the cycle. Mean field strength was obtained without an independent measurement of film thickness using the following equations

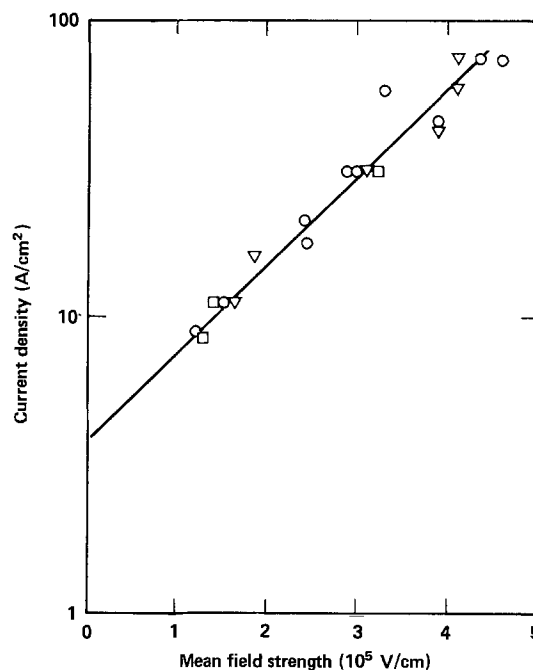


Fig. 16. Dependence of current density on mean field strength. Jet electrolyte flow system. Electrolyte, 2M NaClO_3 . Flow rates: \circ , 93; \square , 160; ∇ , 193 cm/sec.

$$\bar{E} = (V_p - V_2)/S \quad [6]$$

where V_p and V_2 are peak and trough potentials and S is the corresponding change in film thickness

$$S = \left[\frac{2 - \bar{n}_a}{\bar{n}_a} \right] \frac{i\tau M_{\text{Cu}_2\text{O}}}{2Fd} \quad [7]$$

Here τ is the oscillation period, and $M_{\text{Cu}_2\text{O}}$ and d are the formula weight and density of cuprous oxide, respectively. The quantity in brackets is the fraction of current producing monovalent copper, if only Cu^+ and Cu^{2+} are produced. Equation [7] results from the assumptions that all monovalent copper formed during dissolution is retained within the film as Cu_2O and that the film is pore free. The plot of $\log(i)$ against \bar{E} shown in Fig. 16 is linear, with a slope of 6.8×10^6 cm/V for field strengths, 1.5×10^5 – 4.5×10^5 V/cm. This linearity and the greater-than-unity values of $B\bar{E}$ tend to support the high field strength ionic conduction mechanism proposed for the growth phase of the potential cycle. The slope is the same (6.8×10^6 cm/V) as that estimated by Kojima (32) from impedance data and a film thickness value of 60Å estimated by ellipsometry (27) for electropolishing films produced in the copper/phosphoric acid system. The proposed mechanism is further supported by the relative magnitudes of field strength, slope, and intercept, as discussed in Appendix B. We conclude that the predominant mode of charge transfer during the film growth phase is ionic conduction through a thin solid film.

The occurrence of resistive breakdown transitions.—The observations of voltage breakdowns in the dry films suggest that these can also occur in the transpassive films during anodic dissolution. In addition, the breakdowns occur at approximately the same voltage (or field strength) on dry and on immersed electrodes.

In general, resistive switching transitions begin to occur when the field strength is raised above a critical threshold. The threshold is inversely related to the sample thickness, measured in the direction of the applied field. The thickness dependence is said to arise from the increase in probability that an electron ini-

tiating an avalanche of a critical magnitude will be situated along a line of breakdown (24). The probability for a breakdown should then be proportional to sample thickness.

Assuming that it is the acceleration of an electron by the field that causes the critical avalanche, the probability for a transition should be proportional to field strength. The net probability of the breakdown should then be proportional to the product of film thickness and field strength, *i.e.*, the voltage drop across the film. We have already noted the weak dependence of amplitude on experimental parameters.

The experimentally established dependence of film thickness at breakdown field strength is shown in Fig. 17. The relation between S and E is given by

$$S \exp(K_1 \bar{E}) = K_2$$

where $K_1 = 3.2 \times 10^{-6}$ cm/V and $K_2 = 1.4 \times 10^{-4}$ cm. During the growth of the film, both S and maximum field strength (*i.e.*, as indicated by the slope of the potential-time curves) increase very rapidly as the peak potential is approached; therefore, the incidence of breakdown transitions should also increase.

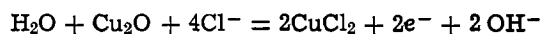
A Model for the Potential Oscillations

The model presented below is based on three assumptions: (i) During the potential growth phase of the cycle, charge is passed through a growing nonporous film by ionic conduction. (ii) Channels of low electronic resistance exist in the film after the peak potential is reached. (iii) The passage of current through these channels causes the removal of adjacent film material such that the film becomes porous. The following sequence of film growth, channel formation, and partial or complete film removal is proposed.

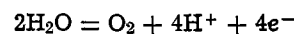
During the potential growth phase of the cycle, a uniform, nonporous film increases in thickness and the charge carriers are predominately ionic. Above a threshold voltage (*i.e.*, above a critical product of field strength and thickness), resistive switching transitions begin to occur in parallel with film growth. These transitions result in the formation of channels of low electronic resistivity and provide alternate paths for the current. As film growth continues, the voltage rises and the incidence of such transitions increases. The accumulation of parallel current paths of low resistance causes a progressive decrease in electrode resistance and an eventual drop in voltage at constant current. With the drop in voltage, the flow of ionic current and the growth rate of the

film is greatly reduced because of the exponential dependence of current on voltage at constant film thickness (see Eq. [4]). The formation of channels ultimately results in a shift of current from the bulk of the film to the channels and a change in charge carriers from ionic to electronic species. The continued flow of electronic current through the channels results in the removal of the channels and adjacent cuprous oxide by a mechanism described below. Following the complete removal of the low resistivity channels, the high field strengths can again be achieved as required for growth of a new nonporous film or for the repair of the existing film.

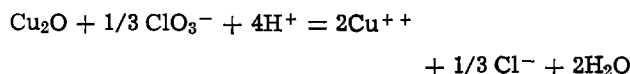
It is an assumption of this model that the flow of electronic current in the channels effects the removal of the channels and the adjacent cuprous oxide. There are several likely mechanisms for promoting partial or complete film removal. With a means for electron transfer supplied, the film might undergo localized anodic oxidation in the presence of acceptor anions (Cl^- or ClO_3^-)



Water could be oxidized at the trough potentials, producing a local drop in pH



The lowering of pH could accelerate the chemical oxidation and dissolution of Cu_2O



It is also possible that during the potential growth phase of the cycle space charge accumulates near to the film/electrolyte interface and that the capacitor thus formed is rapidly discharged through newly formed channels causing the channels to be vaporized, as in dielectric breakdown. The upward sweeping potentials (*i.e.*, $d^2V/dt^2 > 0$) which are observed during film growth at constant current are supporting evidence for the existence of such space charge. Such a catastrophic breakdown, however, is not required by the model.

Once the channels are removed from the film, a process of film repair or film growth can resume. It is necessary to remove all of the conductive channels in order to polarize the film of a given thickness to the field strengths required for ionic conduction. At low current densities, the removal of the cuprous oxide film is complete, as evidenced by the resumption of active dissolution potentials, the restoration of an etched substrate, and the observed undermining and removal of the film. At current densities above about 10 A/cm², the removal of the film is partial, and the lowest potentials of the cycle (trough potentials) are roughly 10V above the potential for active dissolution.

The Inability of the Anode to Reach a Stable Potential

The widely different field strengths required for the two modes of current flow (ionic conduction through the bulk of the film and electronic conduction through channels) preclude the possibility that both mechanisms can occur simultaneously over extended periods of time on the same electrode surface to produce a steady state. As long as the field strength and thickness have exceeded a critical combination allowing the transitions, the transitions will occur and tend to lower the effective resistance of the electrode and ionic current will be effectively terminated. Nor can electronic current flow alone result in a stable state: the cuprous oxide film can only conduct electrons through electrochemical mechanisms which tend to destroy the film. Finally, no stable electrode state can be reached through ionic conduction mechanisms; as long as cuprous oxide is produced at a rate greater than it dissolves in the electrolyte, the film would

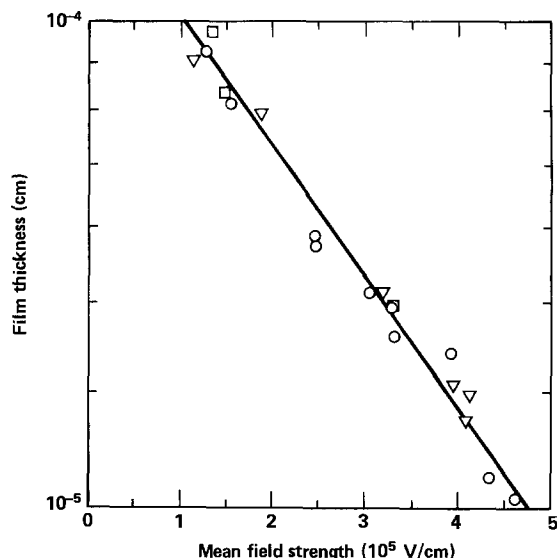


Fig. 17. Inverse relation between film thickness and mean field strength jet electrolyte flow system. Electrolyte, 2M NaClO_3 . Flow rates: \circ , 93; \square , 160; ∇ , 193 cm/sec.

continue to thicken and the potential would increase without limit.

This model differs fundamentally from those citing dielectric breakdown and repair as mechanisms for potential oscillations in anodically formed films. Unlike the resistive transitions, the dielectric breakdown leaves behind no permanently conducting channels. Breakdown is followed by immediate field restoration and film repair. In this case, a stable potential is reached when the rate of film growth just equals the rate of film destruction.

The Role of Chloride and Chlorate Anions

Anode potential oscillations of the nature discussed here may be produced in various electrolytes by the addition of halide ions. The oscillations are particularly uniform and occur over an exceptionally wide range of current densities only in the chlorate electrolyte, which contains some chloride as a result of *in situ* reduction of chlorate. To understand the role of the chlorate or chloride we first examine two conditions of ionic conduction in thin cuprous oxide films: with the chlorate electrolyte and in phosphoric acid solutions. On the basis of impedance data collected from numerous publications, Kojima (32) showed that the thickness of cuprous oxide films in orthophosphoric acid was in the range of 15-125Å, with a most probable thickness of 60Å as determined by ellipsometry (27). For the typical voltage drop through such films of 1.0V, field strengths are in the range of 10^6 - 10^7 V/cm and, therefore, the high field ionic conduction Eq. [5] should apply. Parameters BE and A of the equation can be derived from experimental polarization curves. The experimentally accessible parameters for the two systems are compared in Table I.

The most striking difference between the polarization equations of the two cuprous oxide films is in the pre-exponential factor, A . As this factor is proportional to the concentration of mobile ionic defects, the difference between two electrolyte systems is the concentration of vacancies. Chloride and other "aggressive" anions have long been known to alter the resistance to corrosion of anodic oxide films, and incorporation of the anions into the crystal lattice of the film is a mechanism proposed to account for the phenomenon. If chloride displaces an oxygen ion from the lattice, the difference in the valences requires the removal of cation (formation of a vacancy) to maintain charge neutrality. The chlorate ion might contribute to an increase in vacancy concentration by the partial (non-stoichiometric) oxidation of cuprous oxide at the film electrolyte interface to form the divalent ion. Electro-neutrality requires the formation of a vacancy in the copper sublattice for this mechanism as well.

For the chlorate system, the large value of A allows current densities of up to 150 A/cm² to be achieved with moderate field strengths (5×10^5 V/cm); above 150 A/cm², the increased field strength begins to effect

Table I. Comparison of parameters of high field ionic conduction for cuprous oxide films formed in chlorate and phosphoric acid electrolytes

	Cu/ClO ₃ ⁻	Cu/H ₂ PO ₄
Film thickness, S (cm)	10^{-5} - 10^{-4}	$1.3(10^{-7})$ - $1.2(10^{-8})$; $6(10^{-7})$ *
Field strength, E (V/cm)	10^5 - 5×10^5	10^6 - 10^7
Exponential term, B (cm/V)	$6.8(10^{-6})$	$(1.5-14) \times 10^{-6}$; $6.8(10^{-6})$ *
Exponential term, BE	0.7-3.4	11†
Pre-exponential factor, A (A/cm ²)	4	$2(10^{-7})$

* Most probable film thickness, based on ellipsometric measurements (27).

† Based on experimental data using an equation derived from [5]

$$BE = V_p / i(dV/di)_i$$

where V_p is voltage drop through the film and V is electrode potential (32).

destructive breakdown of the films. For the phosphoric acid electrolyte, not even current densities of 10 A/cm² can be achieved below field strengths of approximately 2.5×10^6 V/cm, at which level destructive breakdowns and stable mixed-electrode processes are encountered

The high current density oscillations in the halide-containing electrolytes are apparently the result of dissolution through thin films at field strengths which promote switching rather than destructive breakdown.

Conclusions

The anode potential oscillations in the chlorate electrolyte are interpreted as sequential periods of film growth (by a high field ionic conduction mechanism), field collapse (following the onset of resistive switching transitions), and partial dissolution and removal of film material (at discrete sites adjacent to the breakdown channels). A stable electrode state with a constant potential is inaccessible in this model, because of the large differences in field strengths required for the separate processes of film growth and conduction through channels, and because each process acting alone results in conditions favoring the opposite process.

The role of the chlorate or chloride ion has not been firmly established. Comparisons of the dissolution of copper in phosphoric acid and in chlorate electrolytes leads to the conclusion that the latter electrolyte promotes a high concentration of mobile vacancies in the copper sublattice. Consequently, the conductivity of the film is higher, and dissolution at current densities from 10 to 150 A/cm² requires field strengths in the range giving rise to resistive switching transitions as opposed to dielectric breakdown. Although this hypothesis is consistent with the experimental results obtained, firm proof of its validity will require more detailed knowledge of the effects of chloride ions on the properties of growing oxide surface layers.

Acknowledgment

This work was supported by the Division of Materials Sciences, Office of Basic Energy Sciences, U.S. Department of Energy under contract No. W-7405-Eng-48.

Manuscript submitted July 16, 1979; revised manuscript received Feb. 29, 1980.

Any discussion of this paper will appear in a Discussion Section to be published in the June 1981 JOURNAL. All discussions for the June 1981 Discussion Section should be submitted by Feb. 1, 1981.

Publication costs of this article were assisted by the University of California.

APPENDIX A

Large-Amplitude Anode Potential Oscillations in Electrolytes Containing Halide Ions

Large-amplitude oscillations in potential were found during the constant current dissolution of copper in a number of mixed electrolytes containing halide ions. In these electrolytes, the range of current densities over which the oscillations were observed was narrower than in the chlorate electrolyte. Also, the cycles tended to lack uniformity of amplitude and period length. Oscillation parameters are summarized in Table A-1, and sample oscillographs of the more uniform oscillations are shown in Fig. A-1 and A-2.

The anodic dissolution of iron in pure sodium chlorate electrolytes gave rise to uniform oscillations having the same waveform and uniformity as in the copper/chlorate system.

APPENDIX B

Ionic Transport and Space Charge in Crystalline Solids

Fundamental equations of ionic transport.—In crystalline solids, ionic conduction occurs through the movement of charge point defects: anion or cation vacancies and interstitial anions or cations. With a simple kinetic model, a transport equation may be derived which expresses the flux of a defect species

Table A-1. Large-amplitude anode potential oscillations in electrolytes containing halide ions*

Electrode/ electrolyte	Current density (A/cm ²)	Period (sec)	Ampli- tude (V)	Comments
Cu/5M NaNO ₃ , 0.1M NaCl	20	0.025	20-25	Irregular waveform
Cu/2M KNO ₃ , 0.03M KCl	3.1	0.54	8-10	Nearly sinusoidal waveform
Cu/2M KNO ₃ , 1M KI	3.2	0.24	5	Nearly sinusoidal waveform
Cu/1M K ₂ SO ₄ , 1M KCl	9	0.33	25-30	Sharp peaks; O ₂ evo- lution
Cu/2.5M H ₃ PO ₄ , 0.03M NaCl	19.6	0.01	25	Spark discharge ob- served during dis- solution
Cu/2M HCl	20	0.088	>50	
	25	0.050		
	30	0.032		
	35	0.020		
	40	0.016		
45	0.021			
50	0.009			
Cu/4M NaOH, 1M KCl	9.5	0.046	30-50	Continuous O ₂ evo- lution, spark dis- charge
Fe/5M NaClO ₃	19	0.014	5	Waveform similar to Cu/5M NaClO ₃ sys- tem. Anode metal was SAE-1018 steel

* Investigations conducted by these authors.

as a function of field strength and certain physical constants. A simplified derivation is given below. Detailed derivations and fuller discussion of transport theory in solids are found in Young [Chap. II, Ref. (33)] and Dignam (31).

For a solid free of any externally applied field, charged defects are pictured to diffuse through a field of identical potential energy barriers of height W and width $2a$. A defect will surmount a barrier if sufficient thermal energy is acquired. From Boltzmann statistics, the probability of a defect possessing a kinetic energy greater than W is proportional to $\exp(-W/kT)$. When an electrostatic field is applied to the sample in direction x , the energy of the defect will be the sum of thermal energy and energy acquired by movement in the field. This situation gives rise to a skewing of the periodic potential profile such that the effective barrier height for a defect at x with charge q and in a field strength E , will be $(W + qaE)$ for diffusion with or against the direction of the applied field.

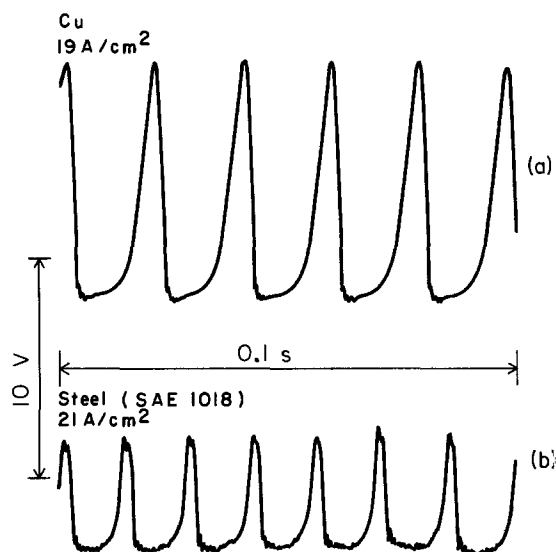


Fig. A-1. Oscillation waveforms for dissolution of Cu and Fe: cell voltage tracings. Current density = 19 A/cm²; stationary electrolyte. (a) Cu/5M NaClO₃; (b) Fe/5M NaClO₃; anode metal, SAE 1018 steel.

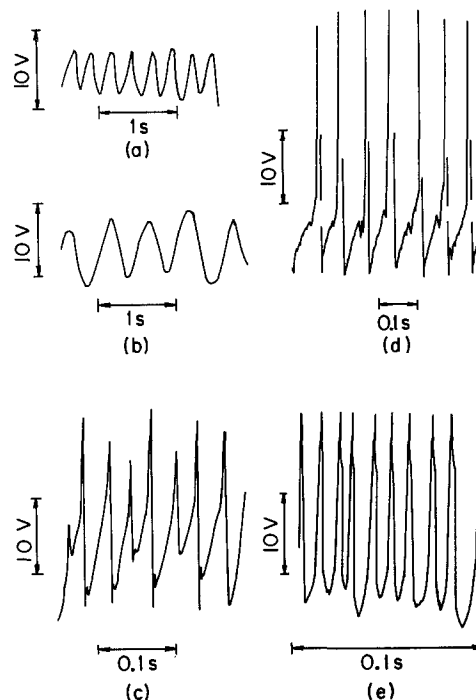


Fig. A-2. Oscillation waveforms in halide-containing electrolytes; stationary electrolyte; copper anodes. (a) 2M KNO₃, 1M KI; 3.2 A/cm²; (b) 2M KNO₃, 0.3 MKCl; 3.1 A/cm²; (c) 5M NaNO₃, 0.1M NaCl; 20 A/cm²; (d) 4M NaOH, 1M KCl; 9.5 A/cm²; (e) 2.5M H₃PO₄, 0.03M NaCl; 19.6 A/cm².

From elementary rate theory, the flux in the direction of the field (increasing x) is given by (30)

$$\vec{j} = 2ac\nu \exp(-W - qaE)/kT \quad [\text{B-1}]$$

The flux against the field is given by

$$\leftarrow j = 2a(c + 2a(dc/dx))\nu \exp(-W + qaE)/kT \quad [\text{B-2}]$$

The net flux in the direction of the field is

$$j = \vec{j} - \leftarrow j \quad [\text{B-3}]$$

$$j = 4ac\nu \exp(-W/kT) \sinh(qaE/kT) - 4a^2\nu(dc/dx)\exp(-W + qaE)/kT$$

High field approximation.—As shown by Dignam [p. 142, Ref. (31)], the diffusion term may be neglected for space charge densities less than about $5 \times (10^9) e/cm^3$ provided $qaE/kT \geq 1$. Under these conditions, Eq. (B-3) takes the simple form

$$j = 2ac\nu \exp(-W/kT) \exp(qaE/kT) \quad [\text{B-4}]$$

To convert the above expression into units of A/cm², we multiply by the factor, qF/N_a

$$I = A \exp(qBE) \quad (\text{A/cm}^2)$$

$$A \equiv qc(2a\nu F/N_a) \exp(-W/kT)$$

$$B \equiv a/kT \quad [\text{B-5}]$$

Despite the simplicity of the model, the exponential dependence of current on field strength is well established by experiment with anodic oxide films formed on a variety of metals (23, 33, 34).

LIST OF SYMBOLS

a	activation distance, cm
c	concentration of mobile defects, cm ⁻³
d	density, g/cm ³
i	current density, A/cm ²
j	ionic flux, cm ⁻² sec ⁻¹
k	Boltzmann constant, eV/°K
n_a	apparent valence
q	charge number on mobile defect
t	time, sec

A	area, cm ²
A	pre-exponential factor in Eq. [4] and [5], A/cm ²
B	coefficient of field strength in Eq. [4] and [5], cm/V
E	field strength, V/cm
\bar{E}	mean field strength, V/cm
F	Faraday constant, C/equiv.
I	current, A
M	atomic weight, g/g-mole
N _a	Avogadro's number, equiv. ⁻¹
Q	charge, C
Re	Reynolds number
S	thickness of transpassive film, cm
T	absolute temperature, °K
V ₁ , V ₂ , V _p	active, initial-transpassive, and peak potentials, V
W	activation energy, eV
W	weight, g
ν	characteristic vibration frequency of mobile lattice effect, sec ⁻¹
τ	oscillation period length, sec

REFERENCES

- J. F. Cooper, Ph.D. Thesis, University of California, Berkeley, California, LBL-2730, April 1975.
- J. F. Cooper, R. H. Muller, and C. W. Tobias, in "Fundamentals of Electrochemical Machining," C. L. Faust, Editor, The Electrochemical Society Softbound Proceedings Series, Princeton, N.J. (1971).
- K. Kinoshita, Ph.D. Thesis, University of California, Berkeley, September 1969 (Lawrence Berkeley Laboratory Report No. UCRL-19051).
- "Electrochemical Machining," A. E. de Barr and D. A. Oliver, Editors, American Elsevier (1968).
- M. A. LaBoda and M. L. McMillan, *Electrochem. Technol.*, **5**, 340 (1967).
- E. S. Hedges and J. E. Meyers, *J. Chem. Soc. (L)*, 1013 (1925).
- K. Indira, S. Rangarajan, and K. Doss, *J. Electroanal. Chem. Interfacial Electrochem.*, **21**, 49 (1969).
- J. Wojtowicz, in "Modern Aspects of Electrochemistry," Vol. 8, J. O'M. Bockris and B. Conway, Editors, Chap. 1, Plenum Press, New York (1972).
- U. F. Franck, *Z. Phys. Chem. N.F.*, **3**, 183 (1955).
- U. F. Franck, *Z. Elektrochem.*, **62**, 649 (1958).
- U. F. Franck and R. Fitzhugh, *ibid.*, **65**, 156 (1961).
- A. Shams el Din and F. Abd el Wahab, *Electrochim. Acta*, **9**, 883 (1964).
- M. T. Francis and W. H. Colmer, *This Journal*, **97**, 237 (1950).
- R. Cooper and J. Bartlett, *ibid.*, **105**, 109 (1958).
- B. Pointu, *Electrochim. Acta*, **14**, 1207 (1969).
- H. Lal, H. R. Thirsk, and W. F. K. Wynne-Jones, *Trans. Faraday Soc.*, **47**, 70, 999 (1951).
- K. S. Indira and K. S. G. Doss, *Proc. Indian Acad. Sci. A*, **66**, 69 (1967).
- N. Klein, *J. Thin Solid Films*, **7**, 149 (1971).
- E. L. Cook, *J. Appl. Phys.*, **41**, 551 (1970).
- K. H. Batner, *Kristall Technik*, **9**, 1315 (1974).
- B. Miller, *This Journal*, **116**, 1675 (1969).
- D. Royer, J. Kleinberg, and A. Davidson, *J. Inorg. Nucl. Chem.*, **4**, 115 (1957).
- T. P. Hoar, in "Modern Aspect of Electrochemistry," Vol. 2, J. O'M. Bockris, Editor, chap. 4, Plenum Press, New York (1959).
- N. Klein, in "Advances in Electronics and Electron Physics," Vol. 26, p. 309, Academic Press, New York (1969).
- D. V. Morgan and M. J. Howes, *Phys. Status Solidi A*, **21** (1), 191 (1974).
- M. J. Zarabi and M. Satyam, *J. Appl. Phys.*, **45**, 775 (1974).
- M. Novak, A. K. N. Reddy, and H. Wroblowa, *This Journal*, **117**, 733 (1970).
- M. O'Keeffe and W. J. Moore, *J. Chem. Phys.*, **36**, 3009 (1962).
- H. Wieder and A. W. Czanderna, *J. Phys. Chem.*, **66**, 816 (1962).
- R. M. King, *J. Am. Ceram. Soc.*, **54**, 361 (1971).
- M. J. Dignam, in "The Anodic Behavior of Metals and Semiconductors Series—Oxides and Oxide Films," Vol. 1, J. Diggle, Editor, chap. 2, Marcel Dekker, New York (1972).
- K. Kojima, Ph.D. Thesis, University of California, Berkeley, California, 1972, pp. 168-171; K. Kojima and C. W. Tobias, *This Journal*, **120**, 1202 (1973).
- L. Young, "Anodic Oxide Films," Academic Press, London (1961).
- D. A. Vermilyea, in "Advances in Electrochemistry and Electrochemical Engineering, Vol. 3, C. W. Tobias, Editor, chap. 4, p. 211 (1963).

The Measurement of pH in Aqueous Systems at Elevated Temperatures Using Palladium Hydride Electrodes

Digby D. Macdonald,^{*1} Paul R. Wentrcek, and Arthur C. Scott

SRI International, Materials Research Laboratory, Menlo Park, California 94025

ABSTRACT

The use of palladium hydride electrodes (Pd black on Pd, Pt, and Au) for the measurement of pH in high temperature aqueous systems (298°-548°K) is described. The electrodes were calibrated against boric acid/lithium hydroxide buffer solutions, whose pH_T vs. temperature profiles have been calculated using known dissociation constants for the components. Linear potential vs. pH correlations are observed for all temperatures studied. However, the gradients of the correlations deviate from the predicted Nernstian values. Furthermore, thermodynamic analyses of the systems demonstrate that above 373°K the observed potential deviates significantly from the equilibrium values calculated on the supposition that the potential-determining reaction is $H^+ + e^- \rightleftharpoons H(Pd, \alpha + \beta)$. Possible reasons for the observed deviation from ideal behavior are identified.

A major obstacle to the study of physicochemical processes in aqueous systems at elevated temperatures is the lack of a reliable and generally applicable method for measuring the activity of hydrogen ion in this hostile environment. Previous studies involving precise pH measurements in high temperature aqueous systems have employed concentration cells with transport to compare the activity of H^+ in the solution of interest with that in a standard solution for which the pH can be calculated. This technique has been used extensively by Mesmer *et al.* (1-4) and by Macdonald and co-workers (5-7) to study various hydrolysis reactions and transport processes in high temperature solution. Although the technique is very precise, it suffers two restrictive requirements: First, an overpressure of hydrogen is required for the proper operation of the cell. Accordingly, the technique is applicable only to those systems that are stable to reduction by molecular hydrogen. Second, due to a lack of reliable transport data for various ions in high temperature aqueous solution, it is usually necessary to suppress the isothermal liquid junction potential between the two electrode compartments. This has been accomplished by use of KCl as the supporting electrolyte in both the working and reference compartments, although it should be noted that the problem of junction potential is common to most electrometric techniques for the determination of pH.

In this paper we describe the use of palladium hydride electrodes for the measurement of pH ($= -\log a_{H^+}$) in aqueous systems at temperatures as high as 275°C. Previous work by Dobson and co-workers (8-11) on this system has indicated that palladium hydride electrodes exhibit Nernstian pH responses at elevated temperatures. However, their work was restricted to highly acidic and highly basic systems, and no data were obtained for the technologically important pH range from ~5 to ~13. In the present work, we have analyzed the pH response of palladized palladium, palladized platinum, and palladized gold electrodes in various lithium hydroxide-boric acid buffer solutions ranging in pH (25°C) between 5 and 13.

Experimental

Apparatus.—The high temperature recirculating loop used for these studies will be described elsewhere

* Electrochemical Society Active Member.

¹ Present address: Fontana Corrosion Center, Department of Metallurgical Engineering, The Ohio State University, Columbus, Ohio 43210.

Key words: pH, acidity measurements, aqueous solution, elevated temperatures, palladium hydride electrodes.

(12). Briefly, the aqueous solution was pumped from a reservoir through a preheater and into the measuring cell using a positive displacement diaphragm pump. The exiting solution was heat-exchanged with the input and then discharged back to the reservoir via a pressure control valve. The pressure in the circuit was maintained at 74.3 kPa (1100 psig) to maintain a single (liquid) phase within the loop. Both the preheater and the measurement cell were thermostated with electrical heaters and controllers. Adjustment of these heaters permitted the cell temperature to be controlled to within $\pm 2^\circ K$ at temperatures as high as 548°K (275°C).

Details of the measurement cell used in this study are shown in Fig. 1. The solution enters the bottom of the cell and passes over the three pH probes that protrude into the stream from insulated lead-troughs. The porous zirconia liquid junction of the reference electrode is located immediately downstream (~0.5 cm) from the three pH probes. The stainless steel

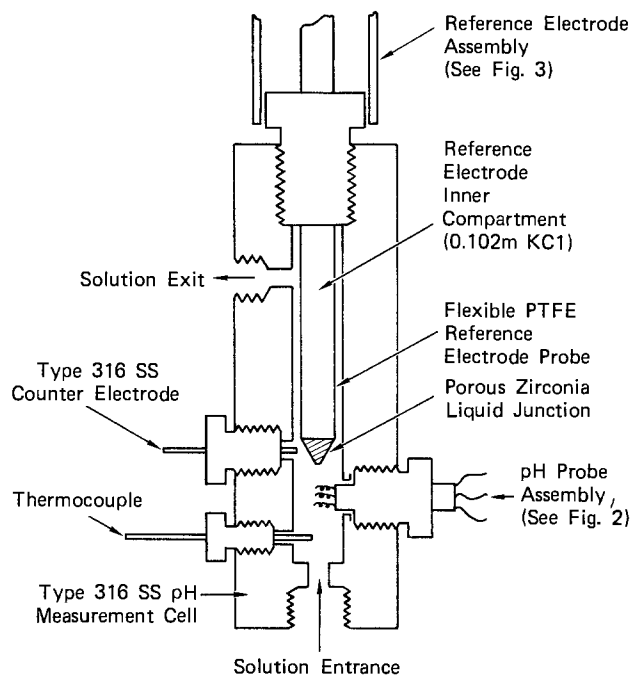


Fig. 1. Design of cell used for the measurement of pH in aqueous solution at elevated temperatures (25°-275°C).

counter-electrode is also located in this region so that electrolysis products generated at this electrode will not interfere with the operation of the pH probes. A thermocouple for temperature control and measurement also protrudes into the fluid stream.

The design of the pH probe assembly is shown in detail in Fig. 2. The fine wire pH probes (1 cm long \times 0.0254 cm diam), were sealed between two PTFE sleeves that had been heat-shrunk onto a roughened central steel shaft. The shaft was then inserted through a standard CONAX fitting in the normal manner.

The palladium, platinum, and gold pH probes were initially cleaned in concentrated nitric acid and were then palladized cathodically in acidified PdCl_2 solution (2 weight percent PdCl_2 in 1M HCl) at a current of 23 mA for 60 sec. Microscopic examination of the surfaces showed that the palladium deposit was highly porous and had the characteristic structure of palladium "black." The probes were cleaned and repalladized prior to each run.

A major problem in any electrochemical study involving high temperature aqueous systems is choosing a suitable reference electrode as reviewed by Macdonald (13). In this work we have used a pressure-balanced external reference electrode, rather than the traditionally employed internal reference electrodes. The design of the external reference electrode is shown in Fig. 3; details of the construction and operation of the electrode have been given recently by Macdonald, Scott, and Wentreck (14). Briefly, the external silver-silver chloride electrode (25°C) was calibrated against an identical internal electrode in various KCl solutions ranging in concentration from 0.005 to 0.505M. Thermodynamic analyses then permitted the evaluation of the correction parameter $\Delta E_{\text{SHE}}(T) - \Delta E_{\text{obs}}(T)$, where $\Delta E_{\text{obs}}(T)$ is the observed potential of the pH probe *vs.* the external reference electrode and $\Delta E_{\text{SHE}}(T)$ is the corresponding potential *vs.* the hypothetical standard hydrogen electrode at temperature T . Numerical values for this correction parameter for an internal 0.102M KCl solution in the reference electrode were found to be 0.287, 0.237, 0.185, 0.130, 0.069, and -0.001V for ΔT values of 0, 50°, 100°, 150°, 200°, and 250°K, respectively, where $\Delta T = T - 298.15^\circ\text{K}$.

Method.—At the start of each run, the solution in the reservoir was purged with 99.99% nitrogen overnight to remove traces of oxygen. After pressurization and steady flow had been achieved, each of the pH probes was charged cathodically at a total current of 0.8 mA (1.6 A/cm² apparent surface area) for various times between 5 and 15 min; for most experiments, however, a standard cathodic charging time of 5 min was adopted, except for the Pd (black)-Pd system. In this case, the substrate also absorbs hydrogen so that a longer charging time of 15 min was adopted. We also found that brief anodization (15 sec for Pd (black)-Pd, 5 sec for Pd-Pt and Pd-Au at 0.8 mA) immediately after cathodization, or after the potential had decayed

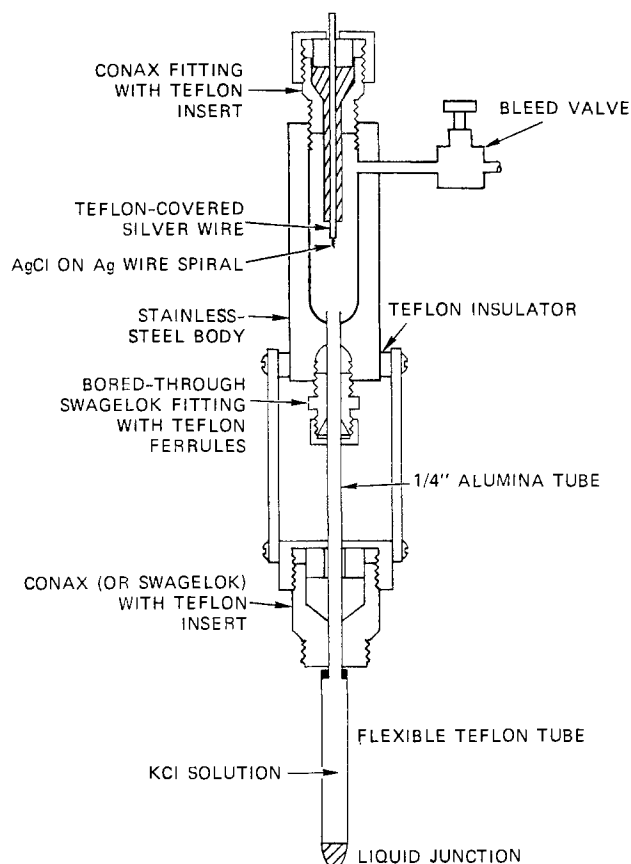


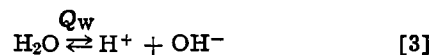
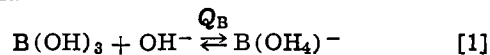
Fig. 3. Reference electrode assembly

to an approximate steady state, frequently reduced the response time for the electrode, particularly if anodization was carried out without delay on interruption of cathodic deposition of hydrogen.

Results and Discussion

Potential decay.—Typical potential decay curves for Pd-Pd, Pd-Pt, and Pd-Au electrodes in 0.1M LiOH at 298° and 548°K after cathodization and subsequent anodization are shown in Fig. 4. In all cases shown, the potential eventually decayed to a steady value that was found to be independent of the brief anodization that was applied after the initial decay to the plateau observed on cessation of cathodization. However, the decay times were generally much shorter at 298°K than they were at 548°K, and the plateau lifetimes were much greater at the lower temperature. Also, plateau lifetimes were found to be dependent on the pH of the solution. For example, in 0.1M LiOH at 548°K plateau lifetimes of several hours were observed, whereas in 0.1M $\text{B}(\text{OH})_3$ the plateaus endured for generally less than 1 hr.

System composition.—The calibration of pH probes for the use in high temperature aqueous solutions requires calculation of the composition of the system and in particular the activity of hydrogen ion at the temperature of interest. For the system $\text{B}(\text{OH})_3/\text{LiOH}/\text{H}_2\text{O}$, the composition of a dilute solution ($<0.1\text{M}$) can be calculated by considering the following equilibria



where Q_B , Q_L , and Q_W are the ionic products for reactions [1], [2], and [3], respectively. Thus

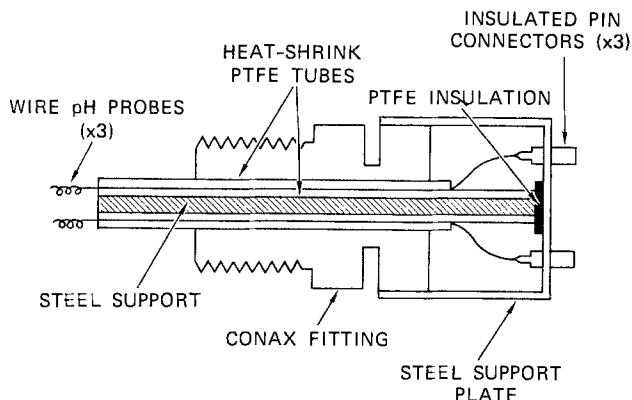


Fig. 2. pH probe assembly

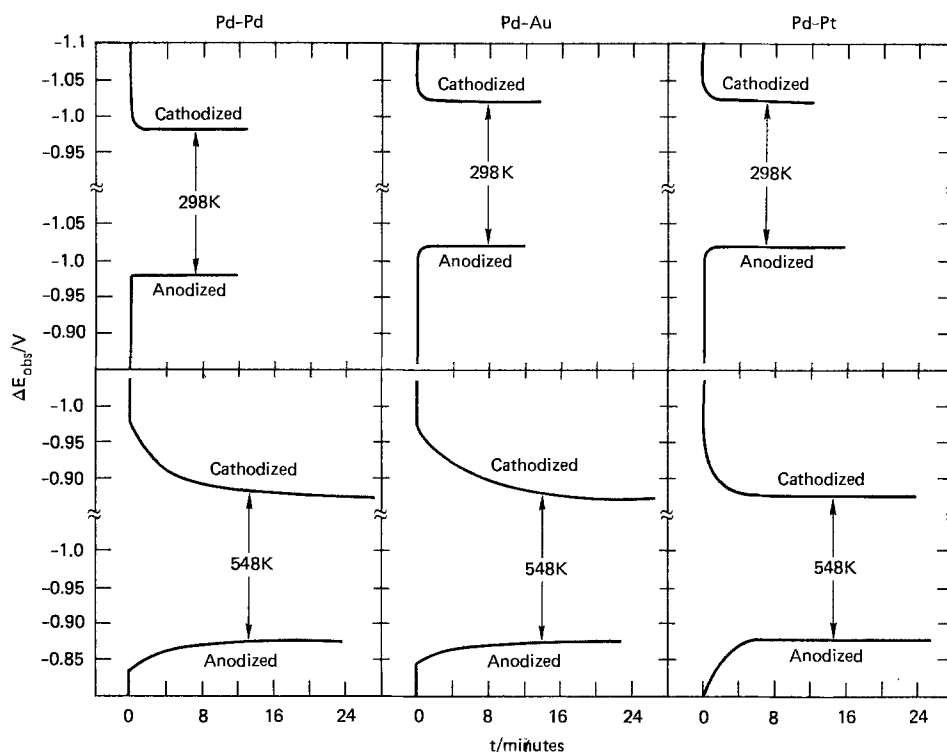


Fig. 4. Potential decay curves for bimetallic Pd-Pd, Pd-Au, Pd-Pt hydride electrodes in 0.1M LiOH at 298° and 548°K after cathodic deposition of hydrogen and subsequent anodization. ΔE_{obs} is the observed potential vs. the external Ag/AgCl, 0.102M KCl electrode (298°K). Cathodization and anodization parameters are given in the text.

$$Q_B = M_{B(OH)_4^-} / M_{B(OH)_3} \cdot M_{OH^-} \quad [4]$$

$$Q_L = M_{LiOH} / M_{Li^+} \cdot M_{OH^-} \quad [5]$$

$$Q_W = M \cdot M_{OH^-} \quad [6]$$

Mass and charge balance constraints provide three additional relationships

$$M_{B(OH)_4^-} = M^{\circ}_B - M_{B(OH)_3} \quad [7]$$

$$M_{Li^+} = M^{\circ}_{Li} - M_{LiOH} \quad [8]$$

$$M + M_{Li^+} - M_{OH^-} - M_{B(OH)_4^-} = 0 \quad [9]$$

where M°_x is the total molality of element x and M is the molality of hydrogen ions in the system. From Eq. [4] and [9] we obtain

$$M^4 + AM^3 + BM^2 - CM - D = 0 \quad [10]$$

where

$$A = Q_W(Q_L + Q_B) + M^{\circ}_{Li} \quad [11]$$

$$B = Q_W(Q_L Q_B Q_W + M^{\circ}_{Li} Q_B - 1 - M^{\circ}_B Q_B) \quad [12]$$

$$C = Q_W(Q_L Q_W + Q_B Q_W + M^{\circ}_B Q_L Q_B Q_W) \quad [13]$$

$$D = Q_L Q_B Q_W^3 \quad [14]$$

Equation [10] was solved iteratively using the Newton-Raphson technique. Data for Q_B , Q_W , and Q_L were taken from the work of Mesmer, Baes, and Sweeton (3), Sweeton, Mesmer, and Baes (15), and Tremaine (16), respectively. The first two quantities are given as functions of both temperature and ionic strength. Accordingly, a double iterative technique about both M and $I = \sum M_i Z_i^2$ ($Z_i =$ ionic charge)

was employed. Satisfactory convergence of both M and I (ΔM and ΔI per iteration $< 0.01\%$) was generally obtained in less than ten iterations for I . Satisfactory convergence was also judged from the value for the

This quantity was found to be always less than 10^{-7} , thereby indicating excellent convergence for the solution of Eq. [10].

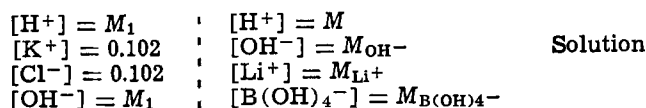
The activity coefficient for H^+ was calculated using Debye-Huckel theory

$$\ln \gamma_1 = -AZ_1^2 \sqrt{I} / (1 + Ba_0 \sqrt{I}) \quad [16]$$

where A and B are the Debye-Huckel coefficients and a_0 is the so-called "distance of closest approach." A value of 4.5×10^{-8} cm was adopted for a_0 in accordance with the recommendation of Naumov *et al.* (17). Calculated activity coefficients for univalent ions in the systems employed are summarized in Table I. Combining these data with the calculated values for the concentration of hydrogen ion yields the pH data summarized in Table II.

The accuracy of these calculations is difficult to assess since the input data (Q_W , Q_L , and Q_B) were taken from three different sources (two laboratories) and complete statistical information on the precision of the data is not available. However, the data for Q_B and Q_W were obtained using highly precise pH titrations employing concentration cells with transference. Furthermore, errors in the parameter of lowest precision (Q_L) do not have a major effect on the computed values for M , at least for the relatively dilute systems ($< 0.1M$ LiOH) of interest here. Finally, the calculated and measured pH values at 298°K agreed to within ± 0.05 , and it is believed that this level of precision is typical for all temperatures considered.

Liquid junction potentials.—A complete thermodynamic analysis of the potentiometric data reported in this paper requires estimation of the liquid junction potential between the internal KCl solution of the reference electrode and the $B(OH)_3/LiOH/H_2O$ system at each composition and temperature. Formally, the junction can be represented as



where M_1 is taken as $\sqrt{Q_W}$; that is the solution in the reference electrode is assumed to be neutral. According to the Planck-Henderson theory (18), the liquid

excess charge, defined here as

$$Z_{\text{ex}} = \sum M_i Z_i / \sum M_i |Z_i| \quad [15]$$

Table I. Single ion activity coefficient for various B(OH)₃/LiOH/H₂O systems as a function of temperature and composition

M ^o _B	M ^o _{Li}	T (°K)					
		298	373	473	498	523	548
0.1	—	0.997	0.995	0.994	0.994	0.993	0.993
0.01	—	0.998	0.997	0.996	0.996	0.996	0.995
0.001	—	0.999	0.998	0.997	0.997	0.996	0.996
0.01	0.0001	0.989	0.986	0.981	0.979	0.977	0.974
0.01	0.001	0.965	0.959	0.944	0.938	0.931	0.922
0.01	0.01	0.903	0.886	0.848	0.834	0.817	0.795
—	0.01	0.904	0.887	0.849	0.835	0.817	0.795
—	0.1	0.786	0.752	0.681	0.656	0.626	0.589

Table II. Calculated pH values for various B(OH)₃/LiOH/H₂O systems as a function of temperature and composition

M ^o _B	M ^o _{Li}	T (°K)					
		298	373	473	498	523	548
0.1	—	5.11	4.96	4.99	5.03	5.08	5.15
0.01	—	5.60	5.45	5.41	5.42	5.46	5.49
0.001	—	6.10	5.88	5.60	5.57	5.57	5.60
0.01	0.0001	7.22	6.92	6.83	6.85	6.90	6.99
0.01	0.001	8.27	7.96	7.86	7.88	7.93	8.02
0.01	0.01	10.62	9.59	9.06	9.04	9.06	9.14
—	0.01	12.00	10.29	9.34	9.27	9.26	9.32
—	0.1	13.02	11.33	10.42	10.37	10.38	10.46

junction potential is given by

$$E_J \approx \left(\frac{2.303RT}{F} \right) \left\{ \frac{\sum \lambda_i^o (M_{iS} - M_{iR})}{\sum \lambda_i^o Z_i (M_{iS} - M_{iR})} \right\} \log \left\{ \frac{\sum \lambda_i Z_i M_{iR}}{\sum \lambda_i^o Z_i M_{iS}} \right\} \quad [17]$$

where λ_i^o is the limiting equivalent conductance for ion *i*, and subscripts R and S designate the reference electrode and solution side of the junction, respectively.

Limiting equivalent conductances for the ions of interest at temperatures to 548°K (275°C) were interpolated from the estimated values given by Quist and Marshall (19). No data are available for B(OH)₄⁻; instead values listed by Quist and Marshall (19) for bisulfate ion were assigned to this species.

Calculated liquid junction potentials for the reference electrode/solution interface for various solution compositions as a function of temperature are listed in Table III. The liquid junction potentials become significant from a practical viewpoint (*i.e.*, $E_J > 0.010V$) only at temperatures above 373°K (100°C), particularly for pure boric acid and pure lithium hydroxide solutions. Also, the sign of the liquid junction potential changes as the concentration of lithium hydroxide is increased. This change in sign reflects a change in the dominant charge carrier from H⁺ for boric acid solutions to OH⁻ for the alkaline systems. Finally, it should be noted that the Planck-Henderson equation is derived assuming a uniform variation in concentration across the liquid junction. Since no techniques are currently available to examine the concentration profiles at the junction, particularly for high temperature systems, the values listed in Table III must be regarded as approximate only.

Table III. Calculated liquid junction potentials (volts) for the reference electrode/solution interface

M ^o _B	M ^o _{Li}	T (°K)					
		298	373	473	498	523	548
0.1	—	0.004	0.011	0.013	0.016	0.019	0.022
0.01	—	0.005	0.012	0.014	0.018	0.020	0.024
0.001	—	0.005	0.013	0.015	0.018	0.021	0.024
0.01	0.0001	0.004	0.009	0.010	0.012	0.014	0.016
0.01	0.001	0.003	0.006	0.007	0.008	0.009	0.011
0.01	0.01	0.0006	0.003	0.001	0.002	0.003	0.004
—	0.01	-0.005	-0.002	-0.001	0.000	0.001	0.002
—	0.1	-0.019	-0.017	-0.015	-0.013	-0.012	-0.010

Potential-pH correlations.—Plots of the observed potential of the three palladized pH probes corrected for the calculated liquid junction potential against pH are presented in Fig. 5a and 5b. Correction of the observed potentials to the SHE scale using the calibration factors discussed earlier yields the $E_{SHE} + E_J$ vs. pH_T correlations summarized in Table IV. The least squares fits have been performed for each probe separately and for the combined set of data for a given temperature. The fitting coefficients, which are a measure of the success of the linear correlations, are also given in Table IV.

Both the data plotted in Fig. 5a and 5b and the correlations reported in Table IV demonstrate that the plateau potentials observed during desorption of hydrogen from palladium vary linearly with pH over the range of acidity considered in this study. Assuming that the potential-determining reaction is a one-electron

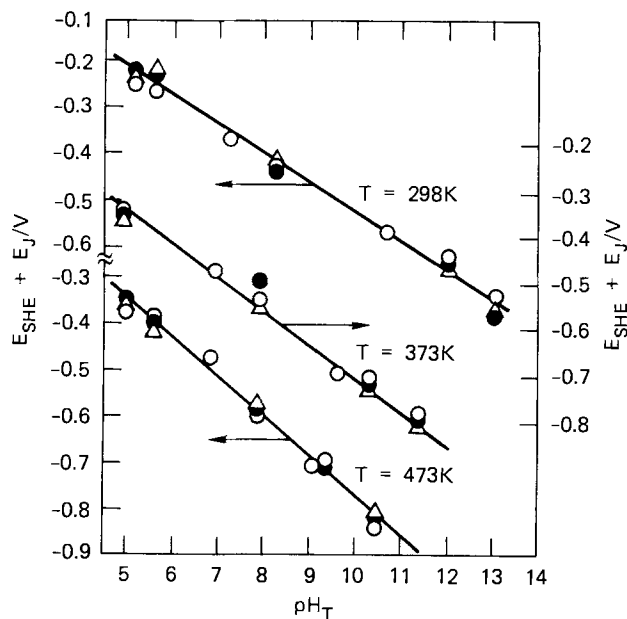


Fig. 5a. Potential pH correlations for Pd-Pd (O), Pd-Pt (Δ), and Pd-Au (●) hydride electrodes at 298°, 373°, and 473°K.

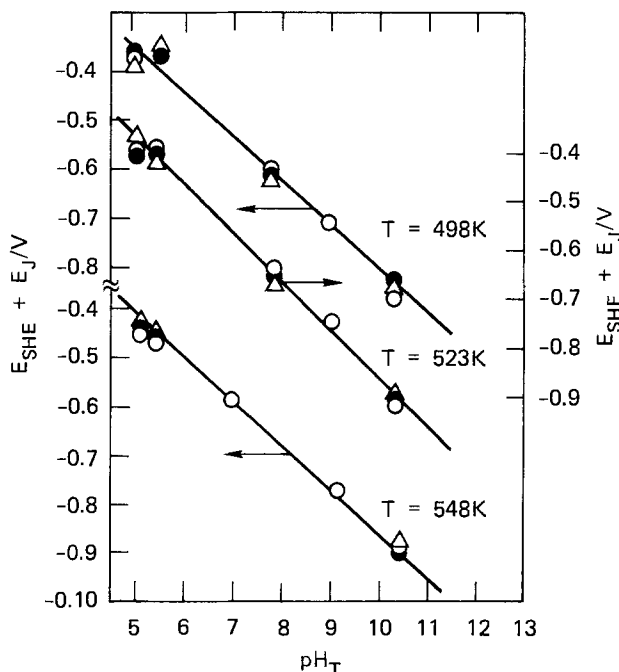


Fig. 5b. Potential pH correlations for Pd-Pd (O), Pd-Pt (Δ), and Pd-Au (●) hydride electrodes at 498°, 523°, and 548°K.

Table IV. Experimental potential-pH correlations for various palladium hydride electrodes as a function of temperature

Electrode	$\Delta E_{SHE} + E_J = a + b pH_T$			r^2
	N	a	b	
$T = 298^\circ\text{K} (25^\circ\text{C})$				
Pd on Pd	7	0.063	-0.059	0.998
Pd on Pt	5	0.138	-0.067	0.989
Pd on Au	5	0.123	-0.065	0.991
Σ^*	17	0.106	-0.064	0.989
$T = 373^\circ\text{K} (100^\circ\text{C})$				
Pd on Pd	6	0.024	-0.073	0.994
Pd on Pt	4	-0.006	-0.070	0.995
Pd on Au	4	0.029	-0.072	0.978
Σ	14	0.016	-0.072	0.988
$T = 473^\circ\text{K} (200^\circ\text{C})$				
Pd on Pd	8	0.080	-0.090	0.978
Pd on Pt	5	0.093	-0.087	0.947
Pd on Au	6	0.067	-0.090	0.979
Σ	19	0.079	-0.090	0.970
$T = 498^\circ\text{K} (225^\circ\text{C})$				
Pd on Pd	4	0.040	-0.092	0.994
Pd on Pt	5	-0.008	-0.095	0.980
Pd on Au	5	0.006	-0.095	0.980
Σ	14	0.015	-0.093	0.982
$T = 523^\circ\text{K} (250^\circ\text{C})$				
Pd on Pd	5	-0.031	-0.095	0.996
Pd on Pt	4	-0.061	-0.099	0.998
Pd on Au	4	-0.021	-0.094	0.995
Σ	13	-0.037	-0.096	0.996
$T = 548^\circ\text{K} (275^\circ\text{C})$				
Pd on Pd	5	0.001	-0.085	0.999
Pd on Pt	3	0.008	-0.088	1.000
Pd on Au	3	0.027	-0.085	0.999
Σ	11	0.012	-0.086	0.999

* Correlation for the complete data set at each temperature.

tron process, then the slope of the $E_{SHE} + E_J$ vs. pH correlation should be equal to $2.303 RT/F$. Comparisons of the observed and theoretical slopes are given in Fig. 6. Reasonable agreement between theory and experiment is observed, except at 548°K (275°C) where the difference between the theoretical and observed slopes is ~ 20 mV/pH. This is considered to be well outside the estimated error in the experimental data.

From a practical viewpoint, the correlations given in Table IV can be used to measure the pH of a solution at elevated temperatures, provided that the approximate composition is known so that the liquid junction potential can be estimated. Reproducibility of the measured plateau potentials from run to run was found to be better than ± 10 mV which indicates that at

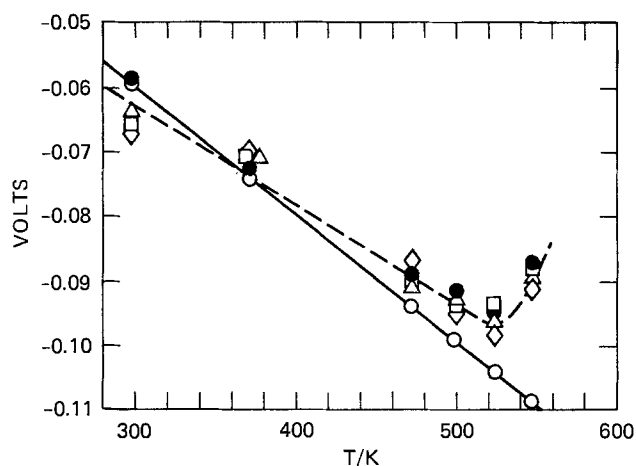
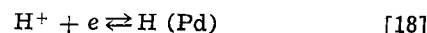


Fig. 6. Comparison of the measured dE/dpH values for the Pd-Pd (\bullet), Pd-Pt (\diamond), and Pd-Au (\square) hydride electrodes and for the total data set (\triangle) with the theoretical value for a one-electron equilibrium. $2.303 RT/F$ (\circ).

548°K (275°C) the pH of the solution can be determined to within ± 0.1 . This level of precision is sufficient for all but the most accurate acid-base titration work and is only slightly less than that available at ambient temperature using glass membrane potentiometry unless precautions are taken to ensure electrode stability and to compensate for "alkaline error."

Thermodynamic considerations.—It has been suggested (20) that the potential of the palladium hydride electrode in aqueous solution is due to the equilibrium



It is clear, therefore, that an understanding of the origin of the potential requires a brief analysis of the thermodynamic properties of the palladium hydride system.

The phase diagram for the Pd-H system as given by Lewis (21) is shown in Fig. 7. Each isotherm for $T < 310^\circ\text{C}$ exhibits a plateau over which equilibrium exists between the α (solid solution of hydrogen in palladium) and the β (Pd_xH , \bar{x} given by the boundary between the $\alpha + \beta$ and β regions) phases. By definition, the activity of Pd_xH is unity so that the activity of hydrogen in the lattice in the $\alpha + \beta$ region is given by

$$\ln a_{\text{H},\alpha+\beta} = (\mu^\circ_{\text{Pd}_x\text{H}} - x\mu^\circ_{\text{Pd}} - \bar{\mu}^\circ_{\text{H}})/RT \quad [19]$$

where $\mu^\circ_{\text{Pd}_x\text{H}}$, μ°_{Pd} , are the Gibbs energies per mole of Pd_xH and Pd, and $\bar{\mu}^\circ_{\text{H}}$ is the standard partial molal Gibbs energy for hydrogen in the lattice. These quantities are functions of temperature only (at constant pressure), so that the activity of hydrogen in the lattice is fixed for a given value of T .

In the present study, hydrogen was discharged cathodically onto the palladium surface such that the surface of the metal attains a composition that is assumed to lie well into the β region of the phase diagram. Following brief anodization that presumably oxidizes some of the hydrogen from the lattice and also oxidizes metal impurities that may have been electrodeposited during cathodization, the current is interrupted and hydrogen is allowed to desorb spontaneously into the solution (note that p_{H_2} in solution $\ll p_{\beta\alpha}$). Consequently, the composition of the surface layer passes through the $\alpha + \beta$ region, during

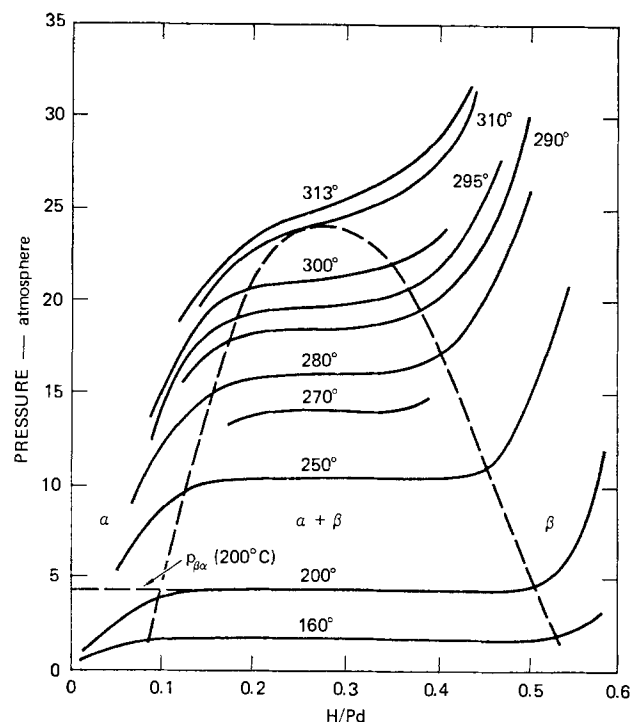
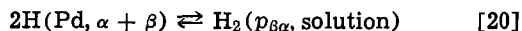


Fig. 7. Phase diagram for the palladium-hydrogen system

which time the potential should remain constant. This is precisely what is observed (Fig. 4).

Previous work (20) has shown that at 298°K the potential of the palladium hydride electrode is about 50 mV more positive than that for the hydrogen electrode $H_2(p_{H_2} = 1 \text{ atm})/H^+$ in the same solution. In the present work at $pH = 8$ this difference is found to be ~ 67 mV. The origin of this difference between the palladium hydride and the hydrogen electrode has been discussed by a number of authors (8-11, 20), and it is generally attributed to the difference in the "nature of the potential-determining reaction." However, if the palladium-hydride electrode were at equilibrium, the chemical potential of hydrogen in the lattice would be equal to the chemical potential of hydrogen in solution. That is, for the equilibrium



the activity of hydrogen in the lattice is given by

$$\ln a_{H,\alpha+\beta} = [\bar{\mu}_{H_2,\text{soln}} + RT \ln p_{\beta\alpha}] / 2 - \bar{\mu}_{H,\alpha+\beta} / RT \quad [21]$$

where $p_{\beta\alpha}$ is the partial pressure of hydrogen for the appropriate isotherm in the plateau region (see Fig. 7). Since the potential of the palladium hydride electrode is given by (see reaction [18])

$$E_{\text{Pd-H}} = - (\bar{\mu}_{H,\alpha+\beta} - \bar{\mu}_{H^+,\text{soln}}) / F - (RT/F) \ln a_{H,\alpha+\beta} - (2.303RT/F) pH \quad [22]$$

then substitution of Eq. [21] for $\ln a_{H,\alpha+\beta}$ yields

$$E_{\text{Pd-H}} = - (\bar{\mu}_{H_2,\text{soln}} / 2 - \bar{\mu}_{H^+,\text{soln}}) / F - (RT/2F) \ln p_{\beta\alpha} - (2.303RT/F) pH \quad [23]$$

which is, of course, the expression for the hydrogen electrode for a hydrogen partial pressure equal to $p_{\beta\alpha}$ (by definition the first term is zero). The important point is simply that any meaningful thermodynamic comparison between the palladium hydride and hydrogen electrodes must be made at equivalent hydrogen partial pressures.

Data for the equilibrium partial pressure of hydrogen in the plateau region of the isotherm for the Pd-H system are not in good agreement; indeed, the values quoted by various works (21, 22) appear to be somewhat dependent on the technique employed for their determination. Furthermore, hysteresis is frequently observed between the absorption and desorption isotherms and values for $p_{\alpha\beta}$ (absorption) and $p_{\beta\alpha}$ (desorption) frequently differ by as much as 50%. In the present study the plateau potentials were measured during desorption of hydrogen from the β phase so that the analysis given below employs values for $p_{\beta\alpha}$ as quoted by Mueller *et al.* (22)

$$\log p_{\beta\alpha} = 4.44698 - 1835.4/T \quad (0^\circ\text{C} < T < 180^\circ\text{C}) \quad [24]$$

$$\log p_{\beta\alpha} = 4.602186 - 1877.82/T \quad (200^\circ\text{C} < T < 300^\circ\text{C}) \quad [25]$$

Using the data for $p_{\beta\alpha}$ given above and Eq. [23] with our experimentally determined $E_{\text{Pd-H}}$ we have calculated values for the potential difference between the palladium hydride electrode and the hydrogen electrode at equivalent partial pressures of hydrogen ($p_{\beta\alpha}$) at $pH_T = 5, 8,$ and 11 , as a function of temperature (Fig. 8). For temperatures below 373°K (100°C), the potential difference is small indicating that the measured potentials are consistent with reaction [18] being the potential-determining process for the palladium hydride electrode. However, at higher temperatures, the difference is substantial and furthermore depends on the pH of the medium.

A number of hypotheses can be advanced to explain the apparent discrepancy between the observed po-

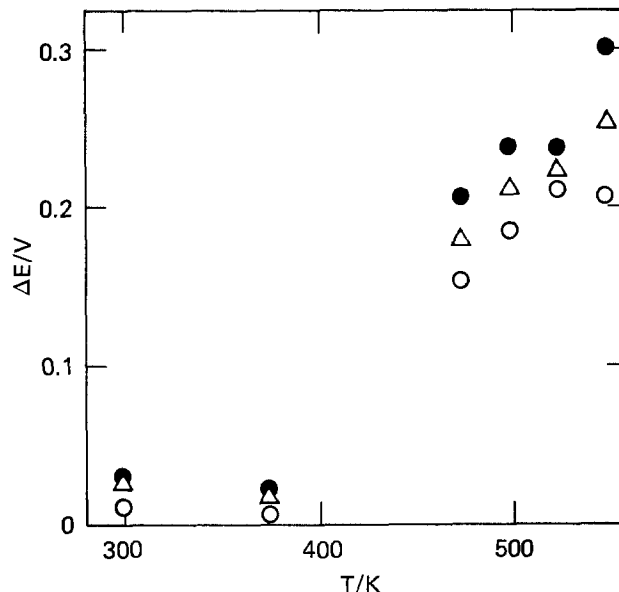


Fig. 8. Plot of $\Delta E = E[\text{Pd}/\text{Pd}_x\text{H}] - E[\text{H}_2(p_{\beta\alpha})/\text{H}^+]$ vs. T for pH values of 5 (\circ), 8 (Δ), and 11 (\bullet).

tentials and those predicted at equilibrium for the palladium hydride system. First, it could be argued that the potential of the reference electrode deviates from that computed in a previous publication (14). For that to be so, the potentials for the thermocell (298) $\text{Ag}/\text{AgCl}, \text{KCl}; \text{KCl}, \text{AgCl}/\text{Ag}(T)$ and/or the isothermal potential for the cell $\text{H}_2/\text{HCl}, \text{AgCl}/\text{Ag}$ at $373^\circ\text{K} < T < 548^\circ\text{K}$ would have to be in error by as much as 0.2-0.3V. However, the potentials of both cells have been substantiated by a number of workers [see Ref. (14) and (23)], so that we do not believe that this is a realistic explanation for the observed behavior. Furthermore, this hypothesis does not offer an explanation for the lack of Nernstian behavior shown in Fig. 6 (at least at 548°K) or the pH dependence of the potential deviation shown in Fig. 8. A second hypothesis can be advanced to the effect that the brief anodization employed after the cathodic deposition of hydrogen results in the formation of surface oxide phases, and hence the establishment of a mixed potential. However, anodization appeared to merely result in a more distinct plateau and did not appear to shift the plateau potential itself significantly. Finally, it must be recognized that, overall, the electrode is irreversible in that hydrogen is continually being desorbed from the palladium lattice. Thus, the potential of an irreversible or quasi-reversible electrode is expected to be less negative than that for the reversible system (as observed), and the difference should become more apparent as the rate of desorption increases due to increasing temperature. Clearly, this explanation must be regarded as speculative in nature, and it is apparent that additional work is required if the potential-determining processes for the palladium hydride electrode in aqueous solution at elevated temperatures are to be understood.

Acknowledgments

The authors wish to thank the Electric Power Research Institute, Palo Alto, California, Dr. Thomas O. Passell, Project Manager, for financial support of this work under Contract RP1168-1.

Manuscript submitted Oct. 5, 1979; revised manuscript received Dec. 28, 1979.

Any discussion of this paper will appear in a Discussion Section to be published in the June 1981 JOURNAL. All discussions for the June 1981 Discussion Section should be submitted by Feb. 1, 1981.

Publication costs of this article were assisted by SRI International.

REFERENCES

1. R. E. Mesmer, C. F. Baes, and F. H. Sweeton, *J. Phys. Chem.*, **74**, 1937 (1970).
2. R. E. Mesmer and C. F. Baes, *Inorg. Chem.*, **10**, 2290 (1971).
3. R. E. Mesmer, C. F. Baes, and F. H. Sweeton, *ibid.*, **11**, 537 (1972).
4. R. E. Mesmer and C. F. Baes, *J. Soln. Chem.*, **3**, 307 (1974).
5. D. D. Macdonald, P. Butler, and D. Owen, *Can. J. Chem.*, **51**, 2590 (1973).
6. D. D. Macdonald, P. Butler, and D. Owen, *J. Phys. Chem.*, **77**, 2474 (1973).
7. D. D. Macdonald and D. Owen, *Can. J. Chem.*, **51**, 2747 (1973).
8. J. V. Dobson, M. N. Dagless, and H. R. Thirsk, *J. Chem. Soc., Faraday Trans. I*, **68**, 749 (1972).
9. J. V. Dobson, M. N. Dagless, and H. R. Thirsk, *ibid.*, **68**, 764 (1972).
10. J. V. Dobson, B. R. Chapman, and H. R. Thirsk, in "High Temperature High Pressure Electrochemistry in Aqueous Solutions," R. W. Staehle, D. de G. Jones, and J. E. Slater, Editors, p. 341, National Association of Corrosion Engineers, Houston, NACE-4 (1976).
11. J. V. Dobson, *J. Electroanal. Chem.*, **35**, 129 (1972).
12. D. D. Macdonald, A. Scott, and P. Wentrcck, To be published.
13. D. D. Macdonald, *Corrosion (Houston)*, **34**, 75 (1978).
14. D. D. Macdonald, A. C. Scott, and P. Wentrcck, *This Journal*, **126**, 908 (1979).
15. F. H. Sweeton, R. E. Mesmer, and C. F. Baes, *J. Soln. Chem.*, **3**, 191 (1974).
16. P. Tremaine, R. Von Massow, and G. Shierman, *Thermochim. Acta*, **19**, 287 (1977).
17. G. B. Naumov, B. N. Ryzhenko, and I. L. Khodakovskiy, "Handbook of Thermodynamic Data," USGS Transl. USGS-WRD-74-001 (1974).
18. P. Henderson, *Z. Phys. Chem.*, **59**, 118 (1907); *ibid.*, **63**, 325 (1908).
19. A. S. Quist and W. L. Marshall, *J. Phys. Chem.*, **69**, 2984 (1965).
20. D. J. G. Ives and G. J. Janz, "Reference Electrodes. Theory and Practice," Academic Press, New York (1961).
21. F. A. Lewis, "The Palladium-Hydrogen System," Academic Press, London (1967).
22. W. Mueller, J. P. Blackledge, and G. G. Libowitz, "Metal Hydrides," Academic Press, New York (1968).
23. D. D. Macdonald, in "Modern Aspects of Electrochemistry," Vol. 11, B. E. Conway and J. O'M. Bockris, Editors, chap. 4, Plenum Press, New York (1975).

Photoelectrochemical Compatibility of n-WSe₂ and n-MoSe₂ with Various Redox Systems

S. Menezes,* F. J. DiSalvo, and B. Miller*

Bell Laboratories, Murray Hill, New Jersey 07974

ABSTRACT

Photoelectrochemical reactions at n-WSe₂ and n-MoSe₂ in several redox electrolytes have been resolved into hole transfer and photocorrosion components by hydrodynamically modulated rotating disk and ring disk electrode methods. Different n-WSe₂ specimens show a range of current-potential behavior, although parallel chemistry, with the better examples exceeding n-MoSe₂ in photopotential. Both semiconductors show the same selectivity to redox couples with optimum photoelectrochemical output in I⁻/I₂ solutions. Surfaces exposed to I⁻/I₂ have catalytic activity for Br⁻ oxidation. The rotating disk methods show examples (I⁻, Fe(CN)₆⁻⁴) of efficient solution hole transfer, mixed solution oxidation-photocorrosion (Cu(I)-NH₃, Br⁻), and photocorrosion (Ti⁺³, Fe⁺², Ce⁺³) at these semiconductors. The photopotential-current characteristics indicate specific surface interactions strongly modify redox potential ordering.

A limiting problem with regenerative semiconductor-liquid junction cells is the extent of the competitive photodecomposition of the semiconductor surface. One of the more satisfactory efforts at surface stabilization, due to Tributsch, involves using transition metal dichalcogenides in which d-d photoexcitation does not break bonds (1). An extensive selection process for these compounds considering specific properties, such as maximum d-d splitting and smallest metal-metal distances, yielded MoS₂, WS₂, MoSe₂, and WSe₂ as the most promising (1).

In addition to bandgaps near the optimum for solar conversion, increased stability in these materials permits use of redox systems with more positive potentials. Photoelectrochemical cells so far developed are generally dependent on specific redox systems for stabilization (2-5) and are therefore affected by the restrictions of the solutions such as light absorption, toxicity, and air sensitivity. A wider range of redox couples

with less limited properties would be expected to be open to inherently more stable semiconductors, if their flatband positions are also advantageous. These materials also allow investigating the influence of several redox systems on a particular semiconductor.

From photoelectrochemical studies on the transition metal dichalcogenides, the most efficient systems reported so far are based on the n-MoSe₂ or n-WSe₂/I⁻/I₂ junctions, but the results are very sensitive to crystal selection and orientation (6-10). In the present work we have examined the photoelectrochemical reactions of n-MoSe₂ and n-WSe₂ in these and other electrolytes for a variety of specimens to gain further information on the factors which determine photoefficiency and stability in these systems.

Successful regenerative operation of a semiconductor-liquid junction solar cell requires no net change in either the electrolyte composition or the semiconductor surface. Thus in an n-type semiconductor, the light separated holes should oxidize the solution species rather than the crystal surface. The resolution of the various reaction paths occurring at photoanodes can

* Electrochemical Society Active Member.

Key words: photovoltaic, energy conversion, voltammetry, semiconductor.

be usefully studied with rotating disk electrode (RDE) methodology, particularly in its two extensions of the rotating ring-disk electrode (RRDE) technique (11-15), and sinusoidal hydrodynamic modulation (SHM) at the RDE (14, 15). The former provides quantitative and qualitative identification of the various reactants and products involved in photochemical reactions and the latter may be used to separate solution (e.g., regenerative redox reactions) from surface processes (e.g., photocorrosion). We utilize these methods to investigate compatibility of n-WSe₂ and n-MoSe₂ with several redox systems.

Experimental

WSe₂ and MoSe₂ crystals were grown by Cl₂ or TeCl₄ transport at temperatures ranging from 850°-1000°C (16). Approximately 0.1 cm² disks were punched out from thin crystals isolated from as-grown clusters and fabricated into RDE and RRDE (17) using silver-epoxy for electrical contact. Surface preparation or renewal involved peeling off the damaged and disrupted layers with an adhesive tape. Surface orientation is \perp to the C axis (van der Waals plane facing the electrolyte).

The RRDE's were provided with a Pt ring with inner radius of 0.24 cm and outer radius of 0.31 cm. Circuitry for RRDE voltammetry and SHM experiments has been previously described (17, 18). Electrochemical experiments were performed potentiostatically under an N₂ atmosphere in a three-electrode cell equipped with an optical flat window. Carbon rod counterelectrodes were used with either a saturated calomel electrode (SCE) or another carbon rod as reference electrodes. The disk was illuminated with a 100W tungsten-halogen lamp. Electrolytes were prepared with reagent grade chemicals and triply distilled water. Photocurrent spectra were taken as before (19).

A center rotation speed of 1600 rpm and scan rate of 5 mV/sec were maintained in all experiments except for spectra (stationary electrode). Peak to peak modulation $\Delta\omega^{1/2} = 2 \text{ rpm}^{1/2}$ was superimposed on the rotation speed at a frequency of 1 Hz in SHM experiments.

Results

RDE voltammetry and photocurrent spectra.—Current-voltage curves for I⁻/I₂ solution were recorded on several samples of n-doped WSe₂, with and without illumination. These crystals generally showed a negative shift in potential at open circuit when illuminated (n-type response) but the magnitude varied and that of the currents at different biases even more so. The current-voltage curves of the two samples shown in Fig. 1 illustrate the two extremes of photoresponse found in the n-WSe₂ crystals, labeled Types I and II. The anodic photocurrent and open-circuit photovoltage for the Type I electrodes of Fig. 1 exceeded 24 mA/cm² and 0.6V, respectively, under the circumstances for which Type II behavior included both n- and p-type photocurrents and as low as 0.1V photovoltage. Anodic dark current is virtually nil in Type I electrodes and the cathodic behavior is essentially independent of illumination, as expected for ideal n-type electrodes. Intermediate behavior variously includes lower photocurrents and photovoltage than Type I values, as well as more poorly defined steps for mass transport limited (MTL) reactions (observed when millimolar concentrations of electroactive species were employed with high light fluxes). At some specimens grouped into Type II, cathodic currents which decrease under illumination (n-direction) were seen, opposite to the Fig. 1 Type II behavior.

Current-voltage characteristics of different n-MoSe₂ crystals under Fig. 1 conditions were all similar and qualitatively like that of Type I n-WSe₂. The definition of the anodic steps for solution species on n-MoSe₂ was generally better than that of WSe₂. However,

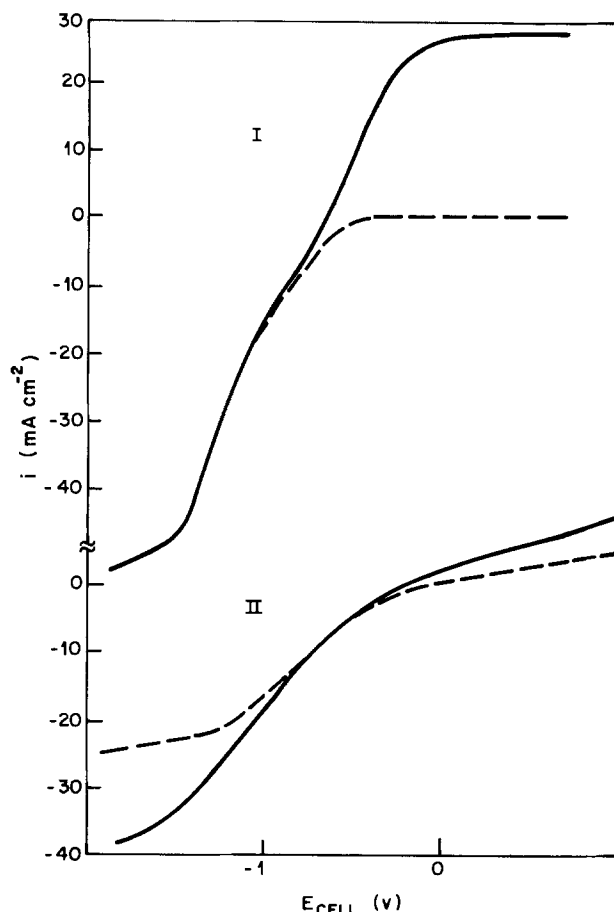


Fig. 1. Current-voltage characteristics of Type I and II n-WSe₂ in 1M I⁻ + 0.25M I₂ under illumination (—) and in dark (---). Potentials referred to carbon electrode measuring the solution redox potential.

high dark currents in the anodic direction for MoSe₂ were sometimes observed.

In Fig. 1 with bias negative of the flatband condition, the cathodic current step ought to be limited by iodine mass transfer to the disk, unaffected by light, as is the case for the Type I sample. In this Type II specimen the step increases on illumination. Figure 2 contains Levich plots for a Type I (independent of illumination) and such a Type II electrode (with and without illumination) in the same iodine-containing electrolyte. The $i_D - \omega^{1/2}$ traces for Type I are linear with a slope of 45 $\mu\text{A} \cdot \text{rpm}^{-1/2}$. With Type II, apparent Levich behavior is still attained, but the slope increases from 18 to 40 $\mu\text{A} \cdot \text{rpm}^{-1/2}$ on illumination. The latter value is in accord with that of the Type I electrode, within experimental electrode geometry matching.

The photocurrent spectra of Types I and II n-WSe₂ in 1M iodide solution are shown in Fig. 3 [MoSe₂ spectra are available elsewhere (6)]. Type I has a normal response near the bandedge whereas phase shifts and oscillations occur in that region for Type II, and the output and sign above 850 nm are phase setting dependent. The apparent bandgap is otherwise the same for both types, 1.4 eV, in agreement with other measurements (20).

RRDE and SHM Measurements.—RRDE data on these materials have not previously been given. We present studies on n-MoSe₂, which resembles Type I WSe₂, and on Type II WSe₂, as representative of the range of chemical behavior that was encountered.

Redox processes in I⁻/I₂ solution at an illuminated MoSe₂ disk with Pt ring are displayed in Fig. 4 for the disk potential range of -0.3 to +0.2V vs. SCE. Two separate scans with different fixed ring potentials, E_R^+

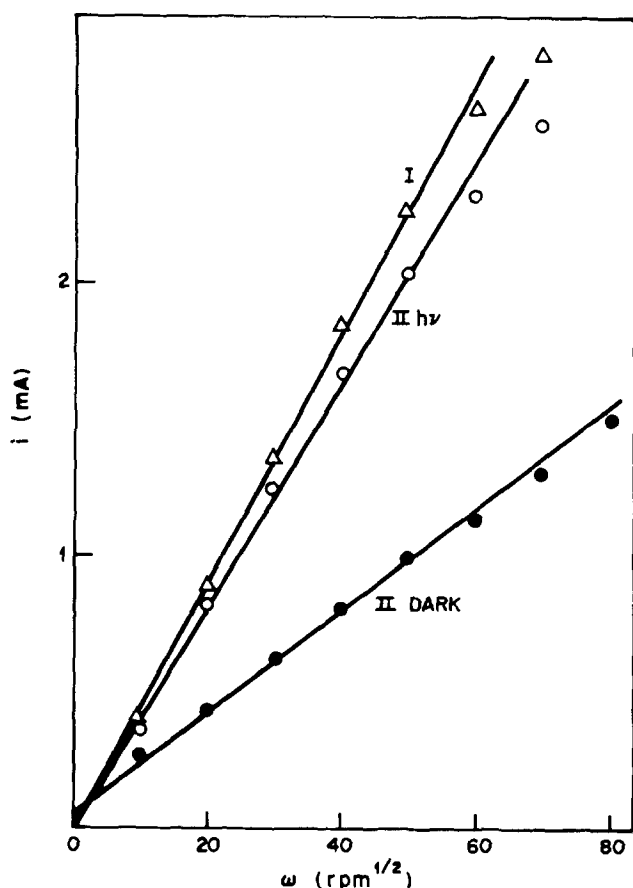


Fig. 2. Cathodic currents at -1.25V vs. carbon/ I^-/I_2 at Type I (Δ), illuminated Type II (\circ) and unilluminated Type II (\bullet) WSe_2 crystals in $1\text{M I}^- + 0.01\text{M I}_2$ as a function of rotation speed.

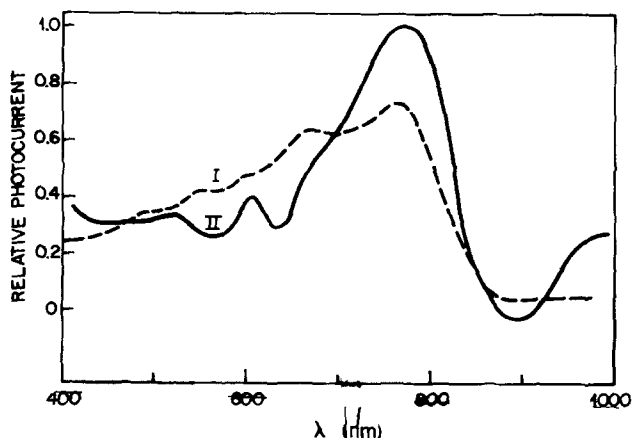


Fig. 3. Photocurrent spectrum under short-circuit conditions of Type I (---) and Type II (—) $n\text{-WSe}_2$ in 1M I^- .

and E_{R}^- , adjusted to oxidize I^- and reduce I_2 , respectively, at MTL rates were used to construct the figure; the disk trace is reproducible. The disk and ring currents are i_{D} and i_{R}^+ and i_{R}^- , the latter corresponding to E_{R}^+ and E_{R}^- , respectively. Disk oxidation of I^- to I_2 causes an increase in i_{R}^- , Δi_{R}^- , and a concomitant decrease in i_{R}^+ , Δi_{R}^+ , as measured from the ring values at zero disk current and at the ring current plateaus at the positive extreme of the disk scan. In a similar fashion the changes in ring currents due to the cathodic reduction of iodine at the disk can be derived from the figure. In either anodic or cathodic case the disk current corresponding to the ring flux change is related by the collection efficiency, N (21). Since a conventional, perfectly circular, and concentric RRDE

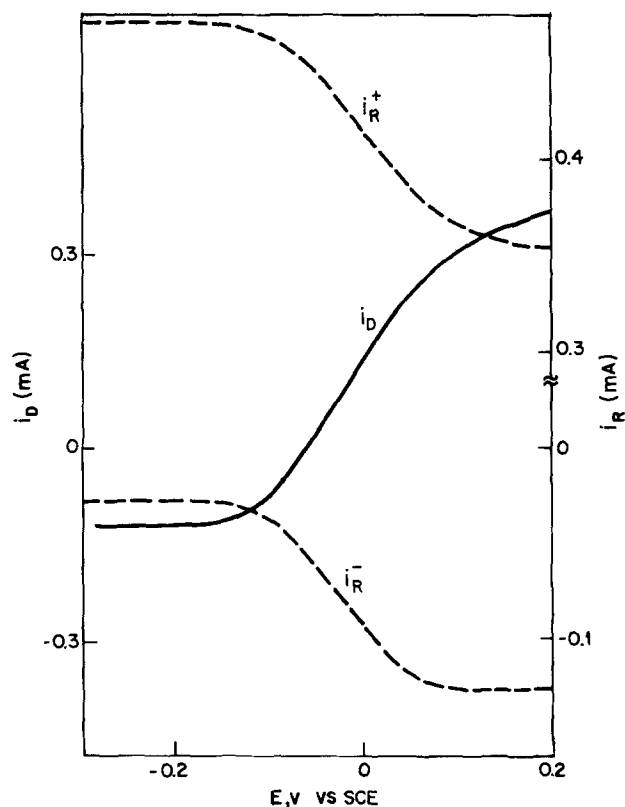


Fig. 4. Disk current i_{D} , ring oxidation i_{R}^+ , and ring reduction i_{R}^- , for MoSe_2 disk potential scan in $2\text{ mM I}^- + 0.5\text{ mM I}_2 + \text{acetate buffer (pH 5)}$ under illumination. $E_{\text{R}}^+ = 0.6\text{V}$ and $E_{\text{R}}^- = 0.0\text{V}$ vs. SCE.

was difficult to fabricate from the punched out disks of the layered crystals, N cannot be accurately calculated. This factor was internally calibrated from the disk cathodic branch of the plot which was assumed to be totally due to iodine reduction.

Ring and disk current data from Fig. 4 are tabulated in the MoSe_2 column in Table I. The four values for N obtained from each of the Δi_{R}^+ and Δi_{R}^- pairs for the cathodic and anodic disk processes are identical and verify that the photoassisted oxidation of I^- at MoSe_2 proceeds quantitatively within the accuracy limits, estimated as ± 0.02 in N .

Analogous experiments with a Type II WSe_2 disk-Pt ring electrode are displayed in Fig. 5 and the WSe_2 column in Table I. Because the waves are less well defined, the potential scale is wider than in Fig. 4. The disk current shows an inflection consonant with a transport limited current for I^- oxidation, and then increases sharply. The ring in either monitoring mode tracks the I^-/I_2 disk processes up to the inflection in i_{D} in a manner, from Fig. 5 and the Table I calculations, which leads to conclusions parallel to those given for MoSe_2 . During the sharp increase in anodic current at the positive extremes of the disk scan, the levels of i_{R}^+ and i_{R}^- remain unchanged, thus implying that the additional disk current arises from surface processes occurring simultaneously with iodide oxidation. [Oxygen evolution would not be detected at the cathodic ring because of iodide poisoning of its reduction at Pt surfaces but there is no visible gassing or other evidence (1) for such occurring.] It is to be

Table I

	MoSe_2		WSe_2	
	I^-	I_2	I^-	I_2
i_{D} , mA	0.33	0.12	0.70	0.20
Δi_{R}^+ , mA	0.09	0.03	0.17	0.05
Δi_{R}^- , mA	0.08	0.03	0.20	0.06
N^+	0.27	0.25	0.24	0.25
N^-	0.24	0.25	0.28	0.30

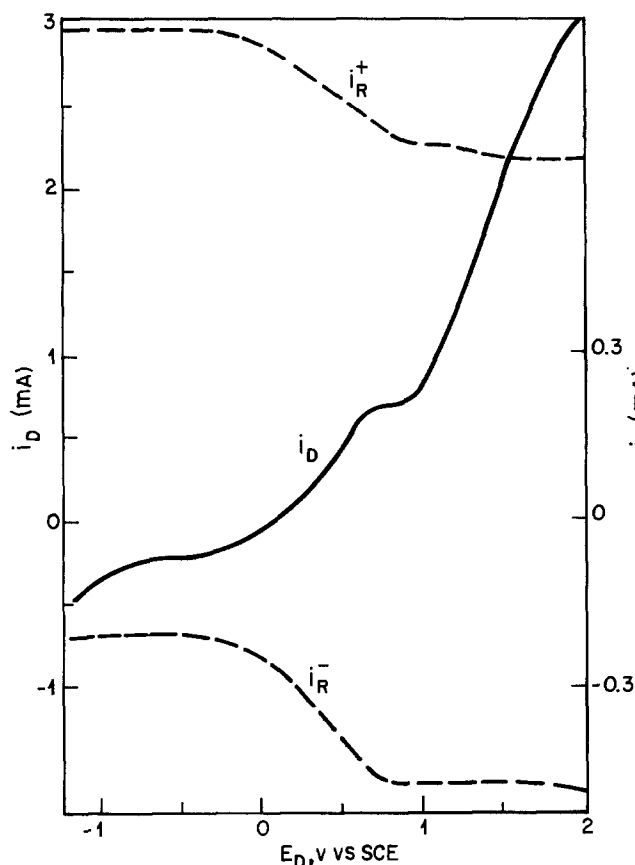


Fig. 5. Experiment of Fig. 4 at WSe_2 (II) RRDE in 10 mM I^- + 1 mM I_2 + 1M $HClO_4$.

noted that the apparent complication in the WSe_2 Type II case of light sensitivity in both directions (Fig. 1) will not affect the ring calibration for N since the mechanistic origin of I^- cathodic generation does not alter the ring collection characteristics as long as the only flux changing process at the disk is iodine reduction at 100% current efficiency.

Further data to distinguish among the processes occurring in the WSe_2 and $MoSe_2$ electrodes in I^-/I_2 solution was obtained with sinusoidal hydrodynamic modulation at the respective disk electrodes in Fig. 6. For the WSe_2 electrode the modulated current com-

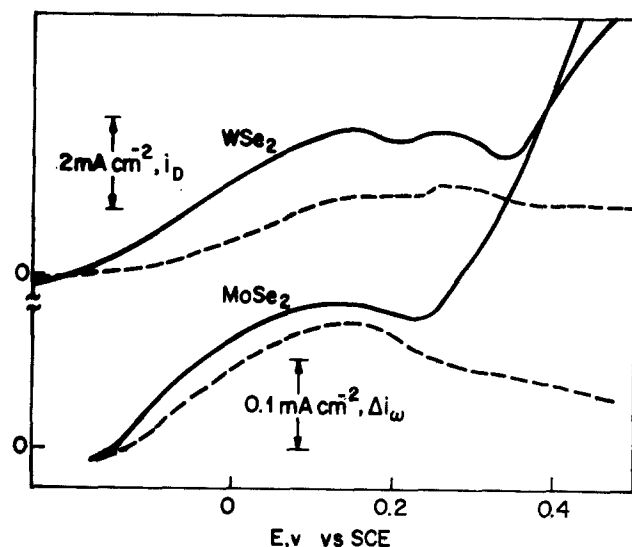


Fig. 6. Average current i_D (—) and modulated current Δi_ω (---), for potential scan in 5 mM I^- + 0.5 mM I_2 + acetate buffer for WSe_2 and $MoSe_2$. Rotation speed of 1600 rpm, $\Delta\omega^{1/2} = 2 \text{ rpm}^{1/2}$, modulation frequency of 1 Hz.

ponent, Δi_ω , wave shape resembles that of the ring responses in Fig. 5 in that it does not drop to zero level in the photocorrosion region as long as the total current, i_D , is not limited by photon flux (15); slight decrease in Δi_ω at positive potentials occurs as the disk current approaches light flux control. (The difference in the potentials for the Fig. 5 and 6 transitions arises from the use of a Type I crystal in the latter.) In these systems, noise and spurious responses at center speed related frequencies, caused by the imperfect circular symmetry of the disks rotating in a partially focused beam, are of more than usual significance. The $MoSe_2$ results are, however, closer to mass transfer control theory for which the Fig. 6 i_D and $\Delta i_\omega \times \omega^{1/2}/\Delta\omega^{1/2}$ traces would be coincident, within the small frequency effects (22) and electronic gain errors (18) which reduce the modulated part of the signal by about 5%.

Potential scan derived plots of i_D and Δi_ω in Fig. 7 from n- $MoSe_2$ and WSe_2 disks in Br^-/Br_2 solution show the expected behavior for the dark Br_2 reduction (well-defined waves) but an absence of anodic SHM response until high levels of total disk current, i_D . The anodic disk current shows no plateau for either semiconductor and must be dominated by surface corrosion above 0.4V. Although the anodic Δi_ω response is initially nil, it becomes evident positive of corrosion current appearance. Its magnitude, however, is much less than that seen for comparable iodide concentrations. A slightly narrower potential region of no SHM response is obtained with $MoSe_2$ under the same conditions, but corrosion is still the dominant process for the latter at any significant anodic current. Modulated response at both electrodes at the high anodic current appears not to be an artifact, as it is found experimentally to be a linear function of $\Delta\omega^{1/2}$ at the anodic SHM plateau. Additional confirmation that part of the disk current at $MoSe_2$ proceeds to Br^- oxidation was provided by RRDE experiments of Fig. 8 parallel to the one shown in Fig. 4. The ring traces in the Br^- case of Fig. 8 are similar to those for iodide in terms of their indications of halide/halogen flux change during the cathodic and anodic steps. The additional disk current component

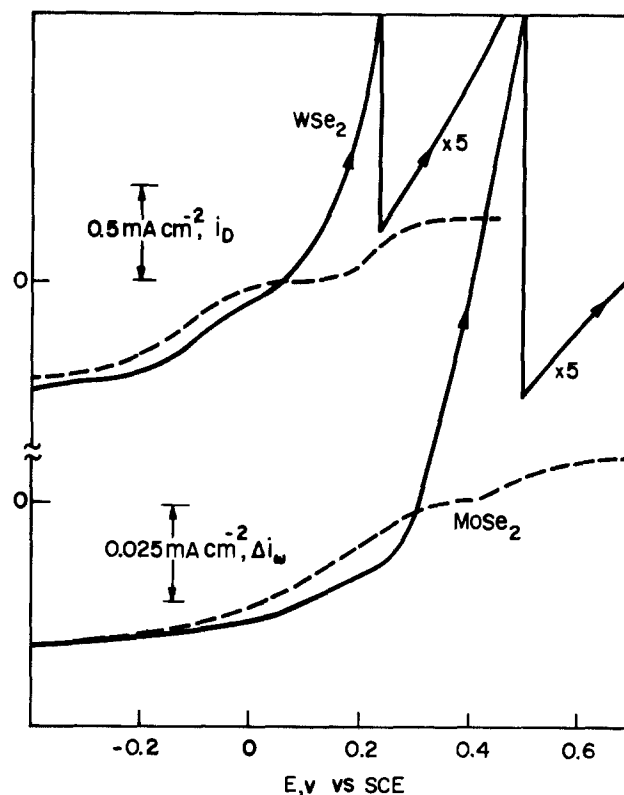


Fig. 7. SHM experiment of Fig. 5 at WSe_2 and $MoSe_2$ in 2 mM Br^- + 0.5 mM Br_2 + acetate buffer.

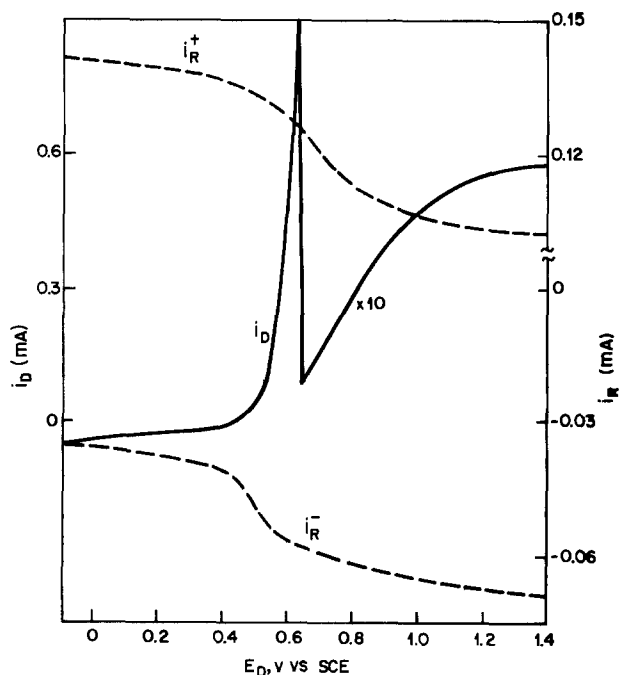


Fig. 8. RRD experiment of Fig. 4 in 1 mM $\text{Br}^- + 0.25 \text{ mM Br}_2 +$ acetate buffer. $E_{R^+} = 1.2\text{V}$ and $E_{R^-} = 0.1\text{V}$ vs. SCE.

at positive potentials is not accounted for by the bromide oxidation and thus is attributed to surface corrosion.

The power output characteristics of the n-MoSe₂-I⁻/I₂ based cell have been ascribed to specific interaction between these solution species and the MoSe₂ surface layers (6). To test whether such effects can be used to activate the surface for other reactions, an MoSe₂ electrode was initially cycled in I⁻/I₂ solution and the Fig. 7 scans repeated. The result is shown in Fig. 9. The iodide or iodine species adsorbed by n-MoSe₂ are still effective in Br⁻ solution as seen by the distinctly improved Br⁻ oxidation step and its separation from the surface photocorrosion. That the current in the region 0-0.2V is due to Br⁻ and not adsorbed I⁻ oxidation is shown by the SHM response and the fact that the current can be maintained for prolonged periods of time. However, scanning the electrode potential positive of the point of active corrosion destroys the catalysis due to the I⁻/I₂ exposure, as indicated by a rapid decrease in SHM response above 0.4V vs. SCE in Fig. 9, not here due to photon flux

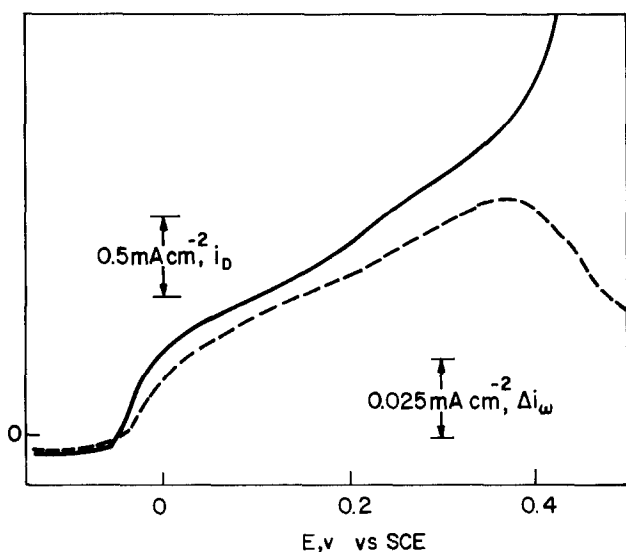


Fig. 9. Experiment of Fig. 7 at MoSe₂ prepilled in I⁻/I₂ solution

control. The catalytic properties are completely lost after a few Fig. 9 scans (behavior reverts to that of Fig. 7) and can only be recovered by another immersion into I⁻/I₂ solution.

Figure 10 shows i_D and Δi_ω plots as a function of linearly scanned disk potential at n-WSe₂ and n-MoSe₂ in an acidified Fe(CN)₆⁻⁴ solution. The scaled SHM current follows the total current wave in the mass transfer controlled region and continues unchanged during the corrosion process at the sharp rise in i_D , until the light limited current region is approached in both cases. The onset of photocurrent is at a more positive potential for MoSe₂. Similar data, not shown, are obtained for the redox system Cu(I)-Cu(II)-NH₃ at these electrodes.

The results with three other redox couples in acid solution, Ti(III)-Ti(IV), Fe(II)-Fe(III), and Ce(III)-Ce(IV), were clearly different from those above. No evidence of Ti(III) or Fe(II) oxidation at n-WSe₂ was detected from SHM behavior, although such reaction was reported for p-WSe₂ (23). Cathodic reduction of Fe(III) gives the expected MTL current step and SHM response, whereas no anodic current appears until photocorrosion occurs. Large photocurrents and open-circuit photovoltage are observed with the Ce(III)-Ce(IV) couple at n-WSe₂, but no SHM response could be extracted on the anodic side indicating that the current was due to corrosion. In that case a dark open-circuit voltage exists, already reflecting a mixed corrosion process.

Redox potentials and photovoltages.—The relation of redox potentials to photovoltages in the above acid systems was investigated. A higher concentration (up to 1M) of redox species than in SHM experiments (low millimolar) was used. A set of four crystals each of n-WSe₂ and n-MoSe₂ were employed to average the cell potentials. The photopotentials, E_{cell} , are plotted vs. the measured redox potentials at a carbon electrode. No dark potentials were observed in any of the solutions outside of Ce(III)-Ce(IV), which had about 0.15V.

The photopotential plot in Fig. 11 is obviously not a smooth function of redox potentials, but the direction of scatter is consistent for both semiconductors, and suggests other systematic factors are of influence. To examine this more closely, current-voltage curves with n-WSe₂ and MoSe₂ in all these redox systems under illumination are shown in Fig. 12 and 13, respectively. (The slopes of the individual curves reflect the ap-

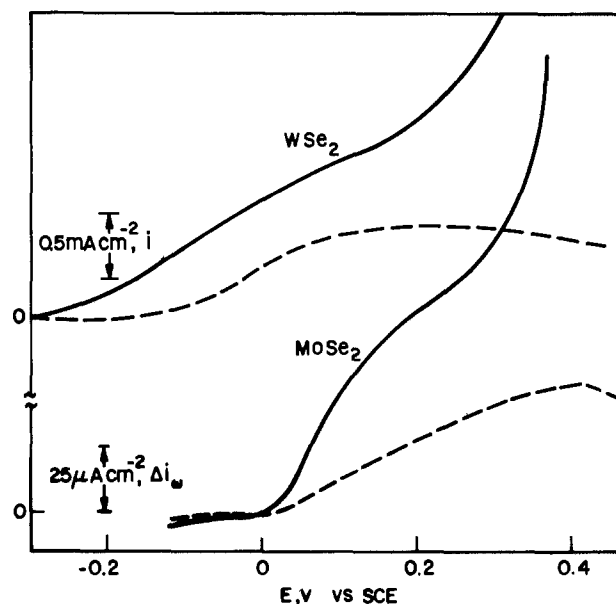


Fig. 10. Modulation experiments as in Fig. 6 in 10 mM Fe(CN)₆⁻⁴ + 1M HClO₄.

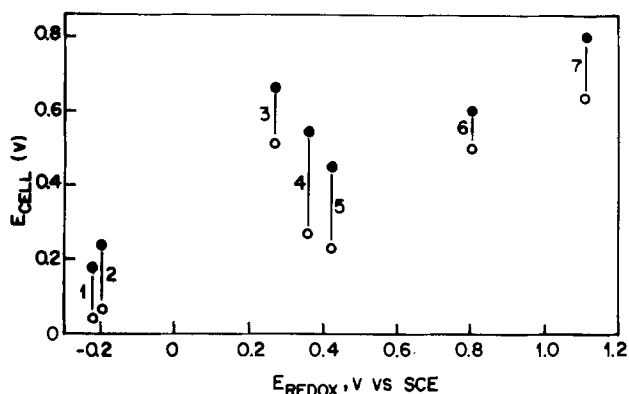


Fig. 11. Cell voltage under illumination at WSe_2 (●) and $MoSe_2$ (○) in (1) $Cu(I)-Cu(II)-NH_3$, (2) $Ti^{3+/4}(1M HCl)$, (3) I^-/I_2 , (4) $Fe(CN)_6^{-3/-4}$ (pH 5), (5) $Fe^{2+/3}(1M H_2SO_4)$, (6) Br^-/Br_2 , and (7) $Ce^{3+/4}(1M H_2SO_4)$.

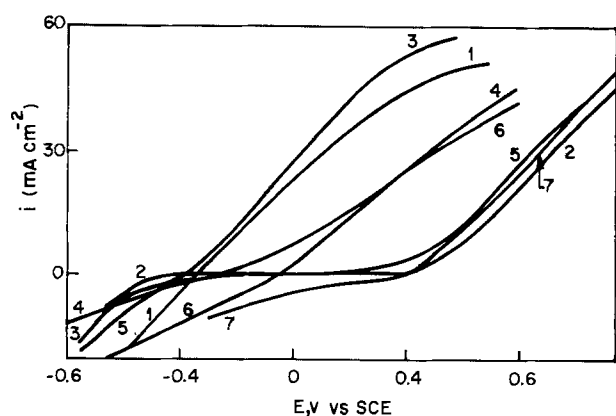


Fig. 12. Current voltage curves at WSe_2 in redox solutions of Fig. 11.

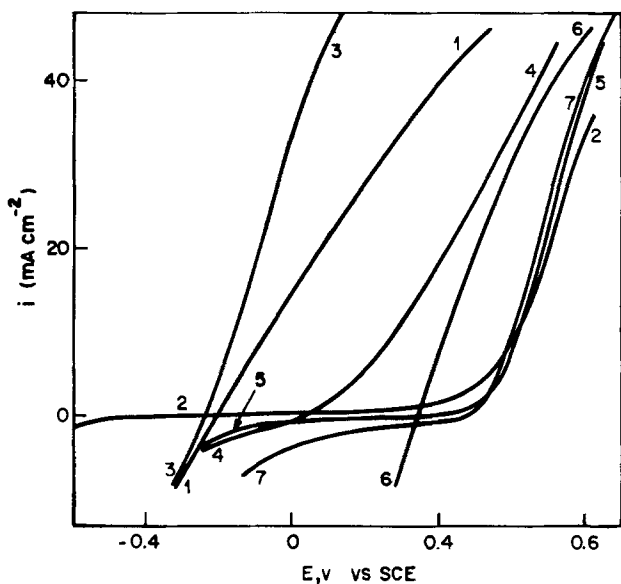


Fig. 13. Experiment of Fig. 12 at $MoSe_2$

parent resistance, charge transfer, and otherwise, of the particular samples selected and are not important for the present purpose.) If the onset of the photocurrent is an approximate measure of the flatband potential and contributions of surface states thus ignored, the shift to most negative onset potentials is observed for the I^-/I_2 redox couple, in agreement with the high photovoltage in Fig. 11 and the other exceptional behavior earlier noted for this system. Correspondingly smaller shifts were observed in $Fe(CN)_6^{-3/-4}$, $Cu(I)-$

$Cu(II)-NH_3$, and Br_2/Br^- solutions, all of which are less readily oxidizable to the extent earlier indicated by the respective SHM and RRDE results.

Anodic current for the $Ti(III)$, $Fe(II)$, and $Ce(III)$ ions is essentially absent in the potential range of $-0.4-0.4V$ vs. SCE. A sharp rise in current is common to all three at essentially the same potential when the semiconductor corrosion actively proceeds. This is consistent with SHM results where modulated current output was detected only for the (light or dark) cathodic processes of $Fe(III)$ and $Ce(IV)$.

Discussion and Conclusions

In general this examination of a range of $n-WSe_2$ and $n-MoSe_2$ samples suggests that crystal surface quality determines the quantitative current-voltage characteristics but not the fundamental occurrence of given electrochemical processes. For example, our data show that photo-oxidation of I^- proceeds in an identical manner at both Type I and Type II WSe_2 . Thus physical imperfections of Type II crystals which limit their power conversion outputs do not alter the attainable interfacial chemical reactions but rather the potentials at which they occur at given rates.

From the RRDE and SHM data for WSe_2 and $MoSe_2$ in the seven redox couples investigated, the voltammetric characteristics can be classified into regions of potential dominated by the following:

- Cathodic MTL reduction wave
- Anodic MTL oxidation wave
- Anodic MTL oxidation and surface corrosion, in parallel
- Surface corrosion

The sequence a-b-c has been quantitatively identified for the systems I^-/I_2 , $Fe(CN)_6^{-3/-4}$ and I^- surface-catalyzed- Br^-/Br_2 . In the cases of Br^-/Br_2 and $Cu(I)-Cu(II)-NH_3$, the reactions basically proceed from a to c since, for the first, no MTL oxidation step and, for the second, only partial separation of such a step were observed. For the three multivalent cations only d is detectable in the anodic region.

Figure 6 shows a distinct photo-oxidation step in I^-/I_2 before the onset of corrosion. The wider region of stability is consistent with its correlation to the most negative current onset potential shift, as estimate of flatband position, observed in Fig. 11-13, as well as the optimum photoconversion characteristics observed with this system for both semiconductors.

RRDE and SHM response at positive potentials in Fig. 5 and 6 illustrate that photo-oxidation and corrosion can occur competitively and concurrent surface dissolution of the electrode does not necessarily suppress its role in the hole transfer process even at high relative levels of corrosion. This feature complements the foregoing observations that diffusion-controlled photo-oxidation of I^- can still occur at Type II samples.

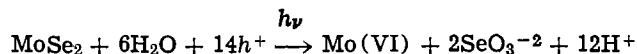
The redox potentials of Br^-/Br_2 appear too positive to restrain photocorrosion in the absence of a specific surface interaction reflected in a large negative flatband shift. Thus i_D-E_D curves of Fig. 7 and 8 show no diffusion-limited wave for oxidation of Br^- . Modulation and ring current response resemble the processes occurring positive of decomposition (indicated by the sharp rise in i_D) in Fig. 5 and 6, where surface corrosion and oxidation of I^- proceed simultaneously.

However, Fig. 9 shows that it is possible to attain well-defined separation of solution and surface processes in Br^-/Br_2 when the surface has been exposed to I^-/I_2 and has acquired the flatband shift characteristic of that medium. The loss of this activity after forced surface corrosion indicates that only surface layers undergo changes, possibly by I^- adsorption on Mo at the more reactive exposed edges (6).

Specific surface interaction can also occur in the larger, multiply charged $\text{Fe}(\text{CN})_6^{-3/-4}$ ions which have redox potential close to that of the I^-/I_2 couple, and also a well-defined oxidation step, but less of a flatband potential shift at the solar equivalent levels investigated here.

Absence of photo-oxidation and flatband shifts in $\text{Ti}(\text{III})-\text{Ti}(\text{IV})$, $\text{Fe}(\text{II})-\text{Fe}(\text{III})$, and $\text{Ce}(\text{III})-\text{Ce}(\text{IV})$ suggest that these multivalent cations do not participate in any type of complex formation or intercalation with either W or Mo selenides. In the case of the $\text{Cu}(\text{I})-\text{Cu}(\text{II})-\text{NH}_3$ couple, which is as negative in potential vs. SCE as $\text{Ti}(\text{III})-\text{Ti}(\text{IV})$, but in alkaline medium, oxidation occurs at both WSe_2 and MoSe_2 . However, the low photoactivity and nearly degenerate behavior of WSe_2 and MoSe_2 , respectively, with this system implies that band bending is minimal with either crystal. Therefore the redox potential must be nearly coincident with the flatband level of MoSe_2 and only slightly positive of that of WSe_2 .

It is well understood that 100% current efficiency for solution process b is essential for regenerative operation of a power conversion cell. Evidence of substantial photovoltages or photocurrents is of course possible with mixed corrosion/oxidation or exclusively corrosion. The overall corrosion reaction at MoSe_2 (as WSe_2) probably occurs via



or other closely related multiple electron reactions which involve passage of a large number of coulombs before signs of crystal deterioration are evident (6, 7). Stability over long periods observed at MoSe_2 in redox systems such as Br^-/Br_2 may be misleading as the RDE methodologies show; 100% current efficiency in the uncatalyzed surface condition is unlikely.

Negative potential shifts of anodic current onset have been observed with the three anions investigated but the location of Br^-/Br_2 bandedges is not sufficiently favorable. The flatband shifts in I^-/I_2 and $\text{Fe}(\text{CN})_6^{-3/-4}$ are large enough to produce a distinct oxidation wave before the onset of corrosion. Cell response curves with I^-/I_2 , however show definite superiority to $\text{Fe}(\text{CN})_6^{-3/-4}$ for power conversion efficiencies.

All experimental results indicate that semiconductor-electrolyte interfacial chemistry is similar for MoSe_2 and WSe_2 . Two differences between the semiconductors are (i) negative potential shift of about 0.15V for WSe_2 relative to MoSe_2 under similar conditions, and (ii) voltammetric curves with steeper slopes and higher dark currents for MoSe_2 . The former is consistent for all the redox couples investigated and implies that the conduction bandedges in WSe_2 are situated higher (negative) than MoSe_2 . The second feature may relate to doping levels and morphological differences not well enough known in the individual exposed surfaces.

Photoelectrochemical performance of W and Mo dichalcogenides has already been shown to depend on the orientation of the crystal surface (8-10); rates of electron transfer vary for surfaces \parallel and \perp to the C-axis. Exposed edges have surface states that provide recombination sites for minority carriers and reduce photoresponse. The range of photoactivity observed at WSe_2 specimens (8) of the same origin as those examined here can be correlated to surface morphology of the crystals. The extent of Type II character is probably dependent on the fraction of the surface comprising exposed edges as opposed to the smooth van der Waals surfaces which ought to exhibit Type I behavior.

Surface orientation, however, does not account for the p and n character of Type II samples. To interpret these results we assume that inhomogeneous doping and occlusions (24), originating from the arbitrary growth process, result in crystals with p conducting

areas interspread on a surface with dimensions \cong diffusion layer thickness. In the absence of illumination, the p areas of the electrode are inactive under cathodic bias. Cathodic current contribution to the diffusion limited I_2 reduction is exclusively from the n area with $\omega^{1/2}$ dependence still dominant (25). Illumination photoactivates the p areas and the entire surface of the electrode then participates in the reduction process, yielding the expected geometric area diffusion-controlled currents. The latter is confirmed by Fig. 2 where the value of Levich slope at a Type II crystal under illumination, about twice as much as in the dark, is equivalent to that of a Type I crystal of comparable area.

Crystals with both types of carriers in low concentration have been found among naturally occurring MoS_2 samples (26). In the present synthetic procedure, the transport agent used empirically determines the carrier type (16), along with the stoichiometry of W(Mo) and Se. Although it may be possible to alter growth of n- WSe_2 to more reproducible Type I behavior of wafer segments, it is difficult to conceive of also attaining high area coverage quality electrodes for the purpose of solar conversion with these materials.

Manuscript submitted Feb. 4, 1980; revised manuscript received March 15, 1980.

Any discussion of this paper will appear in a Discussion Section to be published in the June 1981 JOURNAL. All discussions for the June 1981 Discussion Section should be submitted by Feb. 1, 1981.

Publication costs of this article were assisted by Bell Laboratories.

REFERENCES

- H. Tributsch, *Z. Naturforsch., Teil. A*, **32**, 972 (1977).
- A. B. Ellis, S. W. Kaiser, and M. S. Wrighton, *J. Am. Chem. Soc.*, **98**, 1645 (1976).
- K. C. Chang, A. Heller, B. Schwartz, S. Menezes, and B. Miller, *Science*, **196**, 1097 (1977).
- A. Heller, G. P. Schwartz, R. A. Vadimsky, S. Menezes, and B. Miller, *This Journal*, **125**, 1156 (1978).
- G. Hodes, J. Manassen, and D. Cahen, *Nature (London)*, **261**, 403 (1976).
- H. Tributsch, *Ber. Bunsenges. Phys. Chem.*, **82**, 169 (1978).
- J. Gobrecht, H. Tributsch, and H. Gerischer, *This Journal*, **125**, 2085 (1978).
- H. J. Lewerenz, A. Heller, and F. J. DiSalvo, *J. Am. Chem. Soc.*, **102**, 1817 (1980).
- S. M. Ahmed and H. Gerischer, *Electrochim. Acta*, **24**, 705 (1979).
- W. Kautek, H. Gerischer, and H. Tributsch, *Ber. Bunsenges. Phys. Chem.*, **83**, 1000 (1979).
- A. Fujishima, E. Sugiyama, and K. Honda, *Bull. Chem. Soc. Jpn.*, **44**, 304 (1971).
- T. Inone, T. Watanabe, A. Fujishima, K. Honda, and K. Kohayakawa, *This Journal*, **124**, 719 (1977).
- R. Memming, *Ber. Bunsenges. Phys. Chem.*, **81**, 732 (1977).
- B. Miller, S. Menezes, and A. Heller, in "Semiconductor Liquid Junction Solar Cells," A. Heller, Editor, p. 186, The Electrochemical Society Soft-bound Proceedings Series, Princeton, N.J. (1977).
- B. Miller, S. Menezes, and A. Heller, *This Journal*, **126**, 1483 (1979).
- H. Schafer, in "Chemical Transport Reactions," p. 57, Academic Press, New York (1964).
- B. Miller, *This Journal*, **116**, 1117 (1969).
- B. Miller and S. Bruckenstein, *Anal. Chem.*, **46**, 2026 (1974).
- A. Heller, K. C. Chang, and B. Miller, *This Journal*, **124**, 1019 (1977).
- L. C. Upadhyayula, J. J. Loferski, A. Wold, W. Giriat, and R. Kershaw, *J. Appl. Phys.*, **39**, 4736 (1968).
- W. J. Albery and S. Bruckenstein, *Trans. Faraday Soc.*, **62**, 1920 (1966).
- K. Tokuda, S. Bruckenstein, and B. Miller, *This Journal*, **122**, 1316 (1975).

23. J. Gobrecht, H. Gerischer, and H. Tributsch, *Ber. Bunsenges. Phys. Chem.*, **82**, 1331 (1978).
24. W. D. Sproul and M. H. Richman, *Appl. Phys. Lett.*, **23**, 460 (1973).
25. J. Landsberg and R. Thiele, *Electrochim. Acta*, **11**, 1243 (1966).
26. H. Tributsch and J. C. Bennett, *J. Electroanal. Chem. Interfacial Electrochem.*, **81**, 97 (1977).

A Determination of the Oxygen-Content of Platinum-Oxygen Alloys

James P. Hoare

General Motors Research Laboratories, Electrochemistry Department, Warren, Michigan 48090

ABSTRACT

Samples of Pt (99.97% pure) foil were converted to a Pt-O alloy either by anodizing at 16 mA/cm² (~2.0V) in 1M H₂SO₄ or by soaking in concentrated HNO₃. The gain in weight during the conversion process, determined gravimetrically with corrections for the amount of dissolved oxygen, corresponds to an O/Pt atomic ratio of about 0.03 in agreement with AES depth profile values, both of which are less by an order of magnitude than the value expected for a saturated Pt-O alloy. The results are discussed in terms of two absorption sites for dissolved oxygen: intergranular oxygen and interstitial oxygen in octahedral sites of an fcc lattice.

There is good evidence in the literature (1-9) that oxygen can be dissolved in bulk platinum. According to the model proposed (10) for a Pt/O₂ electrode at rest, a local cell is set up at the electrode surface such that oxygen is dissolved in the Pt by the driving force of the local cell potential. Consequently, the reversible potential cannot be observed because of the presence of this local cell. If, however, the Pt sample could be charged to saturation with dissolved oxygen, the adsorbed oxygen layer generated by the local cell would grow to a complete monolayer, the local cell would be eliminated, and the reversible oxygen potential would be observed (10-13).

Two ways to charge Pt with dissolved oxygen are: (i) strong anodization (~2.0V) for several hours (11, 12) and (ii) treatment with concentrated nitric acid (7, 13). Of these two methods, treatment with HNO₃ charges the Pt with dissolved oxygen to a greater extent (7, 11-13). Platinum charged with dissolved oxygen is referred to as a Pt-O alloy. When a Pt-O alloy diaphragm was formed by treating a Pt foil on the back side with HNO₃, the reversible oxygen potential was observed on the front side (13) and the foil was bulged by lattice expansion.

If enough oxygen can be dissolved in Pt to cause the Pt foil to bulge due to lattice expansion, it would seem possible that the dissolved oxygen could be detected by an increase in weight of the Pt sample. In this report, Pt-O alloys were made both by anodization and by immersion in concentrated HNO₃, and the oxygen content of the alloys was determined gravimetrically.

Experimental

Early work was carried out in Teflon cells but later work was done in glass beakers. In both cases the results were the same. All measurements reported here were obtained in cleaned 30 ml glass beakers over which inverted 150 ml beakers were placed. Platinum samples were cut from the same piece of Pt foil (0.0127 cm thick and 99.97% pure). To each of the 1 × 1 cm square Pt samples, a Pt lead wire was spot welded for handling. Each sample plus lead wire was weighed on an analytical balance (to ±50 μg). These samples were cleaned by heating to a white heat in a burning jet of H₂ gas and quenching

in concentrated HNO₃. This procedure was repeated until the H₂ flame was colorless after which the white hot Pt was allowed to cool down in air.

In one 30 ml beaker, exactly 10 ml of 1M H₂SO₄ solution was pipetted, and in another, exactly 10 ml of concentrated HNO₃. The lead wires were bent into the form of a hook so that the Pt foil was suspended 1 cm below the surface of the electrolyte. The sample in 1M H₂SO₄ was anodized at 16 mA/cm² and ~2.0V against a large Pt gauze counterelectrode, and that in the HNO₃ was soaked in the air-saturated concentrated HNO₃ under open-circuit conditions. Each day the Pt samples were removed from the beakers, washed with triply distilled water, blotted with filter paper, and dried in a vessel with air drawn over the sample by a vacuum pump for at least 30 min. After the samples had been weighed again and the 10 ml solution samples collected in sample vials, the Pt samples were treated as before newly pipetted 10 ml portions of H₂SO₄ and HNO₃. This procedure was repeated each day until seven determinations were made (8 day run). The 14 electrolyte samples were analyzed for Pt in solution by atomic adsorption spectroscopy using a graphite furnace (flameless) (to ±0.5 μg).

Results

Nearly all of the change in weight occurred in the HNO₃-treated sample in the first 50-70 hr of treatment. During the first 48 hr, 0.8 × 10⁻⁶g of Pt went into solution, but with further time of exposure to HNO₃, additional Pt was not detected in solution. In contrast to this behavior, the weight of the anodized sample changed each day and about equal amounts of Pt were found in solution. Over the 8 day period, 4.0 × 10⁻⁶g of Pt went into solution.

The increase in weight of the sample had to be corrected for Pt dissolution by subtracting the weight of dissolved Pt from the initial sample weight to obtain a corrected weight gain value. As seen in Table I, this correction is negligibly small and affects only the estimated figures of the corrected values. It is of interest to note that very little Pt is dissolved in the HNO₃ because the Pt surface becomes passivated, whereas Pt is continuously dissolved during anodization. The weight of the initial sample must be corrected by subtracting the weight of the lead wire above the solution. It is assumed that the Pt lead

Table I. Determination of O-content in two samples of Pt-O alloys

	Anodized sample	HNO ₃ -treated samples
Initial wt	0.2295 ₀ g	0.2323 ₀ g
Final wt	0.2296 ₀ g	0.2325 ₀ g
Weight gain	0.0001 ₀ g	0.0002 ₅ g
Total Pt in soln	0.00000 ₄₀ g	0.00000 ₀ g
Corrected gain in wt	0.0001 ₀ g	0.0002 ₅₀ g
Pt lead wire wt	0.1336 ₀ g	0.1140 ₀ g
Corrected initial Pt wt	0.0959 ₀ g	0.1183 ₀ g
O/Pt atomic ratio	0.013 ₂	0.025 ₇

* Estimated figures are distinguished from significant figures by displaying them as subscripts.

wire above the solution level contributes negligibly to the determination of dissolved oxygen. Using 16.00 and 195.09 for the atomic weights of oxygen and platinum, respectively, the oxygen/platinum ratio in the anodized Pt sample was found to be 0.013, and in the HNO₃-treated Pt, 0.026 as outlined in Table I.

It is valid to assume that the increase in weight is due only to oxygen dissolved in the Pt metal since oxygen adsorbed on the surface contributes negligibly as demonstrated by the following calculations. The volume of Pt in the foil samples is 0.0127 cm³ and the total area of the samples is 2.051 cm². Using values of 21.45 g/cm³ and 195.09g for the density and molecular weight of Pt, one finds that there are 8.40×10^{20} atoms of Pt. Noting that a unit cell of face centered cubic (fcc) Pt contains 4 Pt atoms, one calculates that there are 2.10×10^{20} atoms of O atoms dissolved in the Pt metal at saturation if each oxygen occupies the octahedral hole of the unit cell. Assuming that 420 $\mu\text{C}/\text{cm}^2$ of adsorbed oxygen constitute a complete monolayer of adsorbed oxygen, one determines that this value represents 1.31×10^{15} O atoms/cm² (5, 11, 14). The number of oxygen atoms adsorbed on the surface of the Pt foil sample is 2.69×10^{15} atoms. The O/Pt ratio for dissolved oxygen is 0.25 and for adsorbed oxygen 0.37×10^{-5} . Whether the adsorbed layer is PtO or PtO₂, adsorbed oxygen is less by 4 orders of magnitude than the dissolved oxygen found in Table I.

Discussion

Since the Pt crystal is face centered cubic (fcc), there exists one octahedral hole in the center of each unit cube. It is possible for a dissolved oxygen atom to reside in the octahedral hole and produce the observed lattice expansion.

Since the O/Pt atomic ratio at saturation is 0.25, it is an order of magnitude larger than that found in the Pt-O alloy formed from HNO₃ passivation in Table I. To account for this observation, one concludes that O atoms dissolved interstitially in the octahedral holes are unstable in the dehydrated state. Consequently, when the Pt-O alloy sample is removed from the cell, washed, and dried for analysis, this interstitial oxygen escapes to the surroundings.

It was observed (7, 15) that the electrocatalytic properties of HNO₃-treated Pt-O alloys were retained even after application of strong reducing conditions to the alloy electrode (such as strong cathodization in a hydrogen atmosphere) if a source of oxygen dissolved in the electrolyte was restored to the system. An x-ray diffraction analysis of a Pt-O alloy shows (16) that the lattice is expanded compared to untreated Pt by shifts in the diffraction lines even though Auger (AES) spectroscopy depth profiling shows that only about 3 atomic percent oxygen is present in the interior of the sample (16). This oxygen concentration corresponds to an O/Pt atomic ratio of 0.031 which is in good agreement with the gravimetric analysis reported in this work. These observations indicate that oxygen can enter the expanded lattice of an HNO₃-treated Pt-O alloy interstitially from the oxygen-

saturated electrolyte as easily as interstitial oxygen can escape from the dehydrated alloy without a collapse of the expanded lattice. To return the expanded Pt lattice to its original state, the sample must be heated white hot causing the collapse of the lattice (15).

Another absorption site for dissolved oxygen is in the grain boundaries. In a differential thermal analysis (DTA) study of Pt-O alloys (17), the data were interpreted in terms of two types of dissolved oxygen, intergranular oxygen occupying sites in the grain boundaries and interstitial oxygen occupying octahedral sites in the lattice. In the case of Pt-O alloys formed by moderate anodization, most of the dissolved oxygen is intergranular without expansion of the Pt lattice. Lattice expansion (interstitial oxygen) of anodized Pt-O alloys has been observed (18, 19) only in those instances where the Pt was anodized severely for extended periods of time.

Another source of evidence for intergranular oxygen is obtained from studies of the diffusion of oxygen through Pt foils. By anodizing Pt diaphragms on one side and detecting oxygen on the other, the diffusion coefficient for oxygen through Pt was determined (5, 18) to be about 10^{-11} cm² sec⁻¹. Such a value appears to be too high (20) for the diffusion of O atoms through lattice sites of bulk Pt. It is more likely that oxygen diffuses at these high rates along the grain boundaries of these anodized Pt foils.

The difference between Pt-O alloys made by anodization and by HNO₃ treatment rests in the amount and location of oxygen dissolved in Pt. This situation arises from the fact that anodization produces only general corrosion of the Pt surface whereas treatment with HNO₃ causes preferred etching of the Pt surface as seen in Fig. 1. This etched Pt surface approximates the stepped surfaces investigated by Somorjai and co-workers (21) which expose high index planes where oxygen can easily penetrate to the Pt lattice. As a result, the HNO₃-treated Pt-O alloy can dissolve more oxygen per unit time than the anodized Pt-O alloy which in the absence of exposed high index planes must dissolve oxygen by the slower place-exchange mechanism (22-24). It seems, then, that oxygen dissolves in Pt intergranularly without lattice expansion first, and after reaching a certain concentration, oxygen is dissolved interstitially accompanied by lattice expansion. It follows, therefore, that intergranular oxygen is more stable than interstitial oxygen. The oxygen-content of Pt-O alloys determined gravimetrically (Table I) and by AES depth profiling analysis (16) is probably mostly intergranular oxygen.

It is surprising that the expanded lattice of the HNO₃-treated Pt-O alloy does not collapse with the loss of interstitial oxygen. Yet, because it does not and because the surface is preferentially etched, the electrode can regain its catalytic activity by replacing it in the cell in contact with oxygen-saturated electrolyte. On the contrary, when dissolved oxygen is removed from an anodized Pt-O alloy by strong cathodization (11), the catalytic activity is not regained by exposure to O₂-saturated electrolyte, but must be reanodized.

This observation is in agreement with that of a number of electroanalytical chemists (25-28) who noted that the catalytic activity of Pt indicator electrodes for certain reduction processes was greater for freshly anodized Pt electrodes.

Acknowledgments

The author is pleased to recognize Noel Potter of the Analytical Chemistry Department of GMR for obtaining the atomic adsorption analyses of the Pt-containing solutions.

Manuscript submitted Dec. 26, 1979; revised manuscript received Feb. 27, 1980. This was Paper 42 pre-

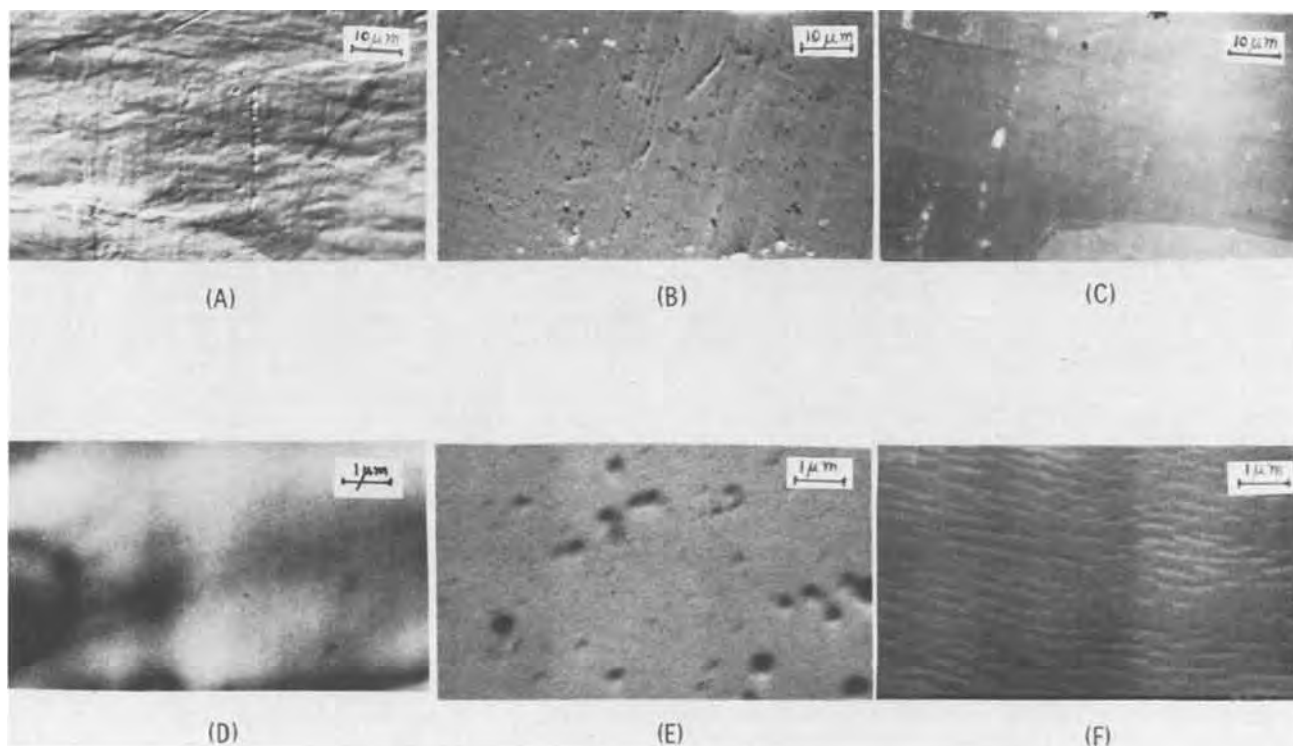


Fig. 1. Scanning electron micrographs of Pt foils at two magnifications, 1000 \times and 10,000 \times ; (A, D) untreated Pt, (B, E) HNO₃ passivated Pt, and (C, F) anodized Pt.

sented at the St. Louis, Missouri, Meeting of the Society, May 11-16, 1980.

Any discussion of this paper will appear in a Discussion Section to be published in the June 1981 JOURNAL. All discussions for the June 1981 Discussion Section should be submitted by Feb. 1, 1981.

Publication costs of this article were assisted by General Motors Research Laboratories.

REFERENCES

1. A. Hickling, *Trans. Faraday Soc.*, **41**, 333 (1945).
2. T. V. Kalish and R. Kh. Burshtein, *Dokl. Akad. Nauk SSSR*, **81**, 1093 (1951); **88**, 863 (1953).
3. A. D. Obrucheveva, *Zhur. Fiz. Khim.*, **26**, 1448 (1952).
4. V. I. Luk'yanyacheva and V. S. Bagotskii, *Dokl. Akad. Nauk. SSSR*, **155**, 160 (1964).
5. J. P. Hoare, *This Journal*, **116**, 612, 1390 (1969).
6. H. Shimizu, *Electrochim. Acta*, **14**, 55 (1969).
7. J. P. Hoare, R. Thacker, and C. R. Wiese, *J. Electroanal. Chem. Interfacial Electrochem.*, **30**, 15 (1971).
8. P. R. Nadebaum and T. Z. Fahidy, *Electrochim. Acta*, **17**, 1659 (1972).
9. J. Balij and O. Spalek, *Czech. Chem. Comm.*, **37**, 499 (1972); **38**, 29 (1973).
10. J. P. Hoare, *J. Phys. Chem.*, **79**, 2175 (1975).
11. R. Thacker and J. P. Hoare, *J. Electroanal. Chem. Interfacial Electrochem.*, **30**, 1 (1971).
12. J. P. Hoare, *This Journal*, **125**, 1768 (1978).
13. J. P. Hoare, *ibid.*, **126**, 1518 (1979).
14. S. Trasatti, *Electrochim. Metall.*, **2**, 12 (1967).
15. J. P. Hoare, S. G. Meibuhr, and R. Thacker, *This Journal*, **113**, 1078 (1966).
16. J. P. Hoare, *Electrochim. Acta*, In press.
17. J. P. Hoare, R. F. Paluch, and S. G. Meibuhr, *This Journal*, **123**, 1821 (1976).
18. J. P. Hoare, *ibid.*, **121**, 872 (1974).
19. J. P. Hoare, *Electrochim. Acta*, **20**, 267 (1975).
20. R. J. Brook, W. L. Pelzmann, and F. A. Kroger, *This Journal*, **118**, 185 (1971).
21. B. Lang, R. W. Joyner, and G. A. Somorjai, *Surf. Sci.*, **30**, 440, 454 (1972).
22. N. Sato and M. Cohen, *This Journal*, **111**, 512 (1964).
23. A. K. N. Reddy, M. A. Genshaw, and J. O'M Bockris, *J. Chem. Phys.*, **48**, 671 (1968).
24. K. J. Vetter and J. W. Schultze, *J. Electroanal. Chem. Interfacial Electrochem.*, **34**, 141 (1972).
25. F. C. Anson and J. J. Lingane, *J. Am. Chem. Soc.*, **79**, 1015, 4901 (1957).
26. D. G. Davis, *J. Electroanal. Chem.*, **1**, 73 (1959); *Talanta*, **3**, 335 (1960).
27. I. M. Kolthoff and E. R. Nightingale, *Anal. Chim. Acta*, **17**, 329 (1957).
28. S. S. Lord and L. B. Rogers, *Anal. Chem.*, **26**, 284 (1954).

Cation Effects on the Electrode Reduction of Molten Nitrates

M. H. Miles* and A. N. Fletcher*

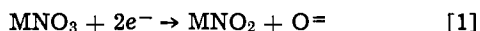
Naval Weapons Center, Chemistry Division, China Lake, California 93555

ABSTRACT

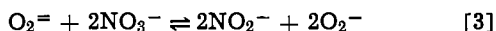
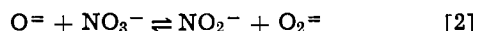
Cyclic voltammetric, potentiostatic, and galvanostatic methods were used to investigate the electroreduction of molten alkali metal nitrates at 350°C on a platinum electrode. The cation of the nitrate salt plays a major role in the reduction reaction as well as in determining the ultimate fate of the oxide ion produced. Nitrate reduction occurs most readily in LiNO₃ melts, and the Li₂O formed appears to be relatively stable. Overvoltages for nitrate reduction increase with increasing size of the metal cation involved and the oxide ions produced by the reaction become more prone to oxidation to form peroxides or superoxides. The rate of water removal by purging the nitrate melt with helium gas was monitored by the water-wave on platinum. Surprisingly, no water-wave was detected using a nickel electrode. The solubilities of several substances were determined in LiNO₃ and KNO₃ and compared with ideal solubility calculations.

The chemistry of alkali metal compounds depends greatly upon the nature of the metal cation involved. For example, the alkali metals burn in air to yield lithium monoxide, sodium peroxide, and potassium, rubidium, and cesium superoxides (1). The strong, positive electric field around the small lithium ion restricts the spread of negative charge from the oxygen anion towards another oxygen atom, making the formation of higher oxides difficult. The weaker electric field around the larger unipositive ions allows the formation of the peroxide, O₂⁼, or superoxide, O₂⁻, to take place.

Oxide ions are produced by the electrochemical reduction of molten alkali metal nitrates (2-5)



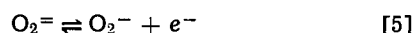
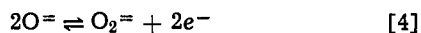
The role of the oxide ion produced by this reaction has been a controversial ghost which has haunted the chemistry of fused nitrates (6, 7). A variety of studies (8-17), however, support the conclusions that the oxide ion in nitrate melts is an unstable species due to the following reactions



in which the oxide is converted to peroxide or superoxide (6, 18, 19).

Most of the previous studies were conducted in molten NaNO₃-KNO₃ mixtures at about 230°C with very little consideration given to the role of the metal cation. By considering the strength of the electric field of the cation, it seems that the electrochemical reduction of molten alkali metal nitrates would produce Li₂O, Na₂O₂, KO₂, RbO₂, and CsO₂ as stable products in molten LiNO₃, NaNO₃, KNO₃, RbNO₃, and CsNO₃, respectively. Thermodynamical data predict both solid Na₂O₂ and KO₂ to be stable in equimolar NaNO₃-KNO₃ and that with increasing K⁺ content the formation of O₂⁻ ions will be favored at the cost of O₂⁼ ions (14, 20). Studies in individual nitrate melts show the preferential formation of peroxide in NaNO₃ and superoxide in KNO₃ (21).

Just as the positive electric field of a cation near a reacting species can make it more difficult to remove electrons in anodic reactions such as



* Electrochemical Society Active Member.

Key words: kinetics, solubility, voltammetry, water, molten nitrates.

the cation field can also make it less difficult to add electrons in cathodic reactions such as in Eq. [1]. The rate of the electrochemical reduction of molten nitrates is strongly dependent upon the cation radii and decreases in the order LiNO₃ > NaNO₃ > KNO₃ ~ RbNO₃ (22). Hills and Johnson (2) also noted that the presence of lithium ions facilitates the reduction of nitrates. The thermal stability of the nitrates themselves with regard to decomposition into nitrites and oxygen decreases with decreasing cation radius (20). Catalytic effects produced by small cations having large electric fields have also been observed for other electron transfer reactions (23, 24).

Our interest in molten nitrates is related to their possible use as an oxidizing electrolyte in thermal batteries (25-27). A previous "open-pan" study of thin Ca/MNO₃ cells exposed to the atmosphere reports the effect of varying temperature upon the cathodic potential during cell discharge at constant currents (22). The present study reports half-cell investigations of nitrate reduction at fixed temperatures under a dry helium atmosphere. In addition to individual investigations of molten LiNO₃, NaNO₃, KNO₃, and RbNO₃, studies were also made on the LiNO₃-LiCl-KCl system [50-25-25 mole percent (m/o), mp = 160°C] found to be promising in thermal battery cell tests (27).

Experimental

The electrochemical cell and electrodes were similar to a previous study of the calcium anode (25) except that platinum or nickel disks were used as the working electrode in place of calcium. Uncompensated solution resistance was minimized by positioning the working electrode within 1-2 mm of the Luggin capillary tip. A glass tube for bubbling helium gas through the nitrate melt to remove water was added to the cell. The helium gas was passed through tubes of anhydrous calcium sulfate (indicating Drierite) and P₂O₅ prior to entering the cell. During all studies in this cell, a blanket of flowing helium gas was maintained above the melt. An Ag/AgNO₃ (0.1M) reference electrode in KNO₃-NaNO₃ was used as before. Temperature control was maintained within ±5°C by the use of a fluidized sand bath (Tecam).

All electrochemical measurements were obtained with a PAR Model 173 potentiostat/galvanostat. For cyclic voltammetric measurements, a PAR Model 175 programmer was also used and results were recorded with an X-Y recorder (Houston 2000 or Hewlett-Packard 7047A). Results for potentiostatic and galvanostatic

static experiments were recorded using a strip chart recorder (HP 7100B).

Approximate values for the solubilities of several oxides, peroxides, and superoxides were obtained using the method of successive additions. Solutions were generally equilibrated overnight to insure that true saturation limits were obtained. These measurements were made in a glass tube equipped for helium bubbling through the melt to remove any water and to provide stirring action.

All of the nitrate salts used were reagent grade except for rubidium nitrate (from Pfaltz and Bauer). The cyclic voltammograms for this salt suggested considerable nitrite was present, and its melting point (291°-298°C) also indicated impurities. Since most studies showed that the cathodic behavior of RbNO_3 was quite similar to KNO_3 , results for this salt will generally not be shown. All salts were used without further purification except for drying in a vacuum oven overnight at 130°C.

Results

The presence of dissolved water in nitrate melts can be readily detected on a platinum electrode using cyclic voltammetry. Figure 1 (solid line) shows the water-wave that occurs just prior to the main nitrate reduction wave in molten LiNO_3 despite using LiNO_3 that had been oven-dried as described above. This water-wave has been reported by other authors (3, 8, 28-31) and is not due to trivial electrolysis of water since no hydrogen or oxygen is formed (8). Preliminary studies indicate that the water-wave can also be detected in LiNO_3 on iridium, silver, and gold electrodes at about the same potential as on platinum.

Surprisingly, no water-wave was detected when a nickel electrode was substituted for the platinum electrode as shown by the dashed line in Fig. 1. In addition, the anodic peak at -0.36V due to the oxidation of insoluble Li_2O to Li_2O_2 became much more clearly

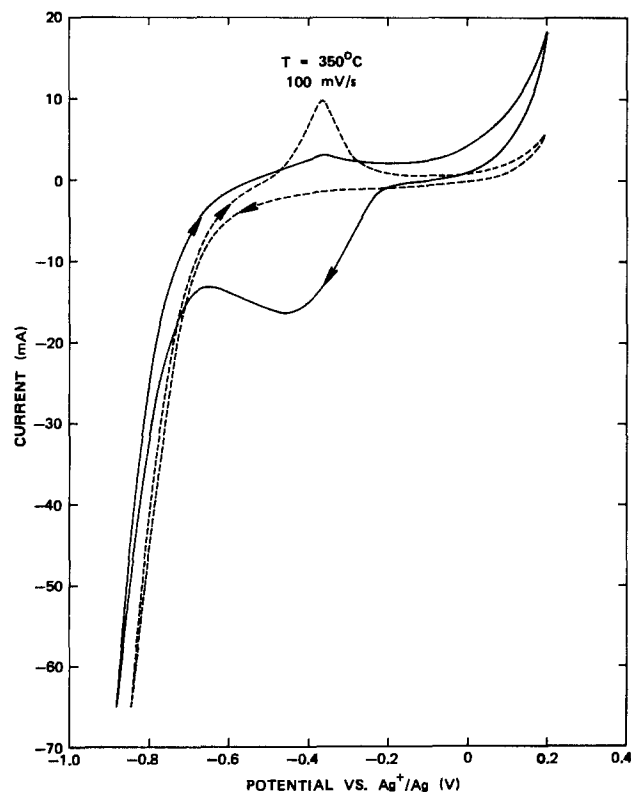
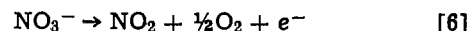


Fig. 1. Cyclic voltammograms showing the difference in the water-wave on platinum and nickel in molten LiNO_3 at 350°C. The solid line is the trace using a platinum electrode while the dashed line is the trace with a nickel electrode. Potential sweep rate was 100 mV/sec. Electrode area was 0.32 cm^2 .

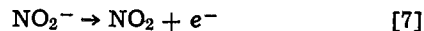
defined on nickel. The absence of this water-wave on nickel greatly simplified the analysis of the "open-pan" studies reported previously (22).

Studies of the water-wave on platinum at 350°C showed that the bubbling of dried helium gas through the molten LiNO_3 for about 1 hr was required to remove the water retained by this salt, whereupon the cyclic voltammogram became practically identical to the results shown for nickel in Fig. 1 (dashed line). In other alkali metal nitrates, the water-wave is smaller and tends to shift to more negative potentials as the size of the cation increases. The retention of water by the molten salt is much less a problem with NaNO_3 and KNO_3 , since the small amounts of water present in these salts at 350°C can be removed within 5-10 min by purging the melt with the dried helium gas.

Figure 2 shows typical cyclic voltammograms for water-free melts of LiNO_3 , NaNO_3 , and KNO_3 obtained at 350°C using a platinum electrode and a potential sweep rate of 100 mV/sec. These results were obtained in quiet solutions (no stirring) under a helium atmosphere. The cathodic wave clearly shows the cation effect on the electrochemical reduction of molten nitrates. At 100 mV/sec, this major reduction wave represented by Eq. [1] reaches 70 mA (220 mA/cm^2) at potentials of -0.90V , -1.36V , and -1.82V for LiNO_3 , NaNO_3 , and KNO_3 , respectively. Neither the main anodic wave at about 1.1V resulting from nitrate oxidation (32-39)



nor the anodic process having a peak potential of about $+0.5\text{V}$ reflecting nitrite oxidation (8, 18, 19, 38, 40, 41)



appear to be greatly affected by the nature of the cation. For LiNO_3 , the anodic peak due to the oxidation of Li_2O to Li_2O_2 is again observed at -0.36V . Other peaks in Fig. 2 are more difficult to define, but they likely involve reactions of peroxides or superoxides (15, 19, 21). The addition of KO_2 to KNO_3 produced a large increase in the anodic current beginning at about -0.5V ; however, gas evolution indicates that some decomposition of the KO_2 occurs at 350°C.

Cyclic voltammetric studies provide a means of detecting the presence of insoluble oxide on the electrode surface by use of the anodic reaction

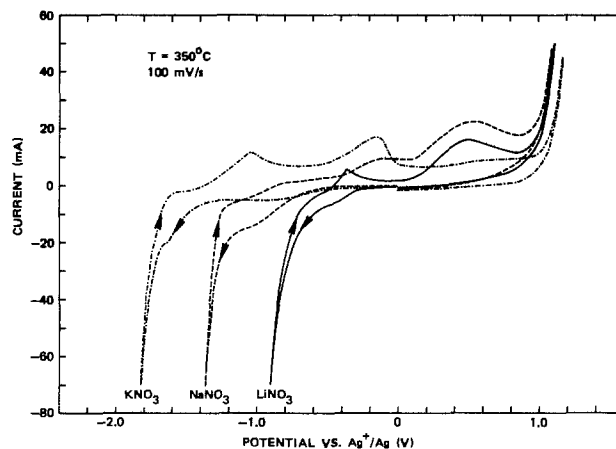
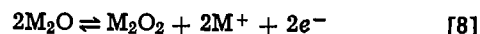


Fig. 2. Cyclic voltammograms for molten LiNO_3 , NaNO_3 , and KNO_3 obtained at 350°C in a helium atmosphere using a platinum electrode ($A = 0.32 \text{ cm}^2$). Potential sweep was begun at 0.0V and swept first cathodically, then anodically, and finally cathodically to the starting potential. Potential sweep rate was 100 mV/sec.

wherein the precipitated oxide is electrochemically oxidized to the more soluble peroxide. By gradually increasing the cathodic sweep limit, anodic peaks corresponding to this reaction are first observed at about -0.35V in LiNO_3 and at about -1.2V in NaNO_3 . Fleeting evidence was also obtained for a slight anodic peak at about -1.6V in KNO_3 . These results are consistent with the decreasing stability of the oxide with increasing radius of the alkali metal cation. In a voltammetric study on platinum using a thin Ca/LiNO_3 cell that generates Ca^{++} ions, a new anodic peak develops at about -0.1V indicating the oxidation of insoluble calcium oxide. Due to its higher charge, the electric field about the small Ca^{++} ion is even stronger than that about the Li^+ ion, hence a more stable oxide is to be expected. Cyclic voltammetric studies of the electrochemical reduction of LiNO_3 , NaNO_3 , RbNO_3 , $\text{Ca}(\text{NO}_3)_2$, and $\text{Sr}(\text{NO}_3)_2$ mixtures with KNO_3 indicate that insoluble oxides form in the presence of all cations except K^+ and Rb^+ ions. These experiments suggest that the catalytic effect of the cation on nitrate reduction decreases in the order $\text{Ca}^{++} > \text{Sr}^{++} \sim \text{Li}^+ > \text{Na}^+ > \text{K}^+ \sim \text{Rb}^+$.

Cyclic voltammograms of LiNO_3 and NaNO_3 obtained using a small platinum working electrode ($A = 0.006\text{ cm}^2$) to minimize uncompensated IR effects are shown in Fig. 3. The usual relationship between peak current (I_p) and potential sweep rate (ν) was observed, i.e., $I_p \propto \nu^{1/2}$, while the peak potential (E_p) tended to vary with the rate of potential change. The greater stability of Li_2O compared with Na_2O is reflected by the more positive potential required for Li_2O oxidation. Despite the shorter potential excursions in NaNO_3 , most of the Na_2O formed is apparently lost during the sweep cycle. At the slower sweep rates, the anodic peak in NaNO_3 disappears entirely. It is also interesting to note that the residual current following the cathodic peak is smaller in LiNO_3 where the more stable Li_2O is formed. The cyclic voltammograms in molten KNO_3 and RbNO_3 at 350°C do not show such interrelated peaks involving nitrate reduction.

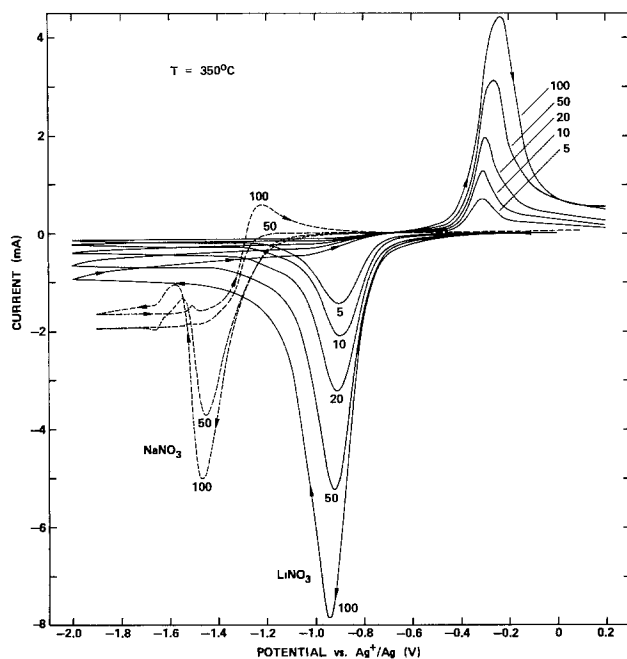


Fig. 3. Effect of the potential sweep rate on the cyclic voltammograms for molten LiNO_3 at sweep rates of 5, 10, 20, 50, and 100 mV/sec . Voltammograms for NaNO_3 at 50 and 100 mV/sec are shown for comparison (dashed lines). Results were obtained at 350°C in a helium atmosphere using a small platinum electrode ($A = 0.006\text{ cm}^2$). Potential sweep was begun at 0.0V and swept cathodically to -2.0V then anodically to 0.2V .

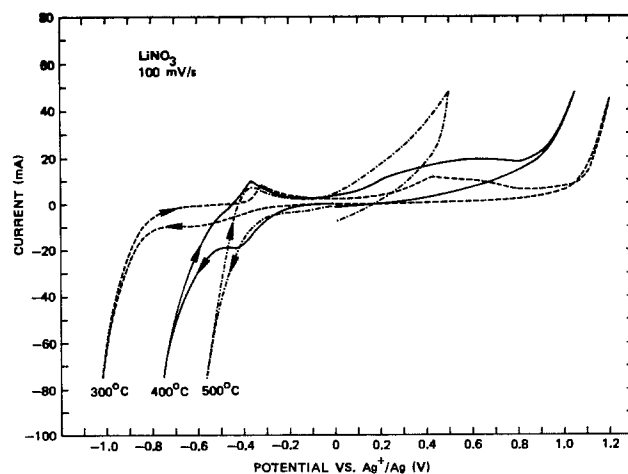
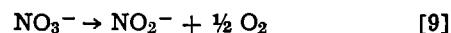


Fig. 4. Effect of the temperature upon the cyclic voltammograms in molten LiNO_3 under a helium atmosphere. Results were obtained at 300° , 400° , and 500°C using a platinum electrode ($A = 0.32\text{ cm}^2$).

Figure 4 shows the effect of temperature upon the cyclic voltammogram obtained in LiNO_3 . In addition to the 300° , 400° , and 500°C results shown, experiments were also conducted at 350° and 450°C . The large shifts in potential for the nitrate reduction wave reflect the improved kinetics for this reaction at the higher temperatures. At a selected constant current of 50 mA for this reduction reaction, the potential, E , varies linearly with the temperature (correlation coefficient = 0.988) with $\partial E/\partial T = 2.31 \times 10^{-3}\text{ V/K}$. This shows good agreement with previous "open-pan" cathode studies obtained with Ca/LiNO_3 cells under conditions of varying temperature and constant current (22). The nitrate oxidation wave (Eq. [6]) also shows a large shift in potential between 300° and 400°C . The nitrite oxidation peak (Eq. [7]) increases with temperature such that it dominates the anodic reactions at 500°C . This is likely due to the nitrite formed by the increasing thermal decomposition



with increasing temperature (7, 20, 42-44).

Chronopotentiometric studies of nitrate reduction on platinum in unstirred solutions are shown in Fig. 5. Sharp transition times were always observed in the LiNO_3 and NaNO_3 melts as well as in the mixed salt solution. The observed transition times are much shorter than expected for a reaction controlled by the diffusion and migration of nitrate ions, hence the

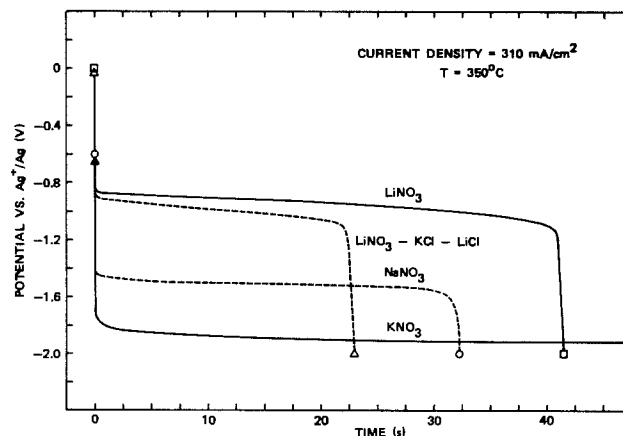


Fig. 5. Chronopotentiometric studies of nitrate reduction using a constant current of 310 mA/cm^2 . Results were obtained at 350°C in a helium atmosphere using a platinum electrode ($A = 0.32\text{ cm}^2$).

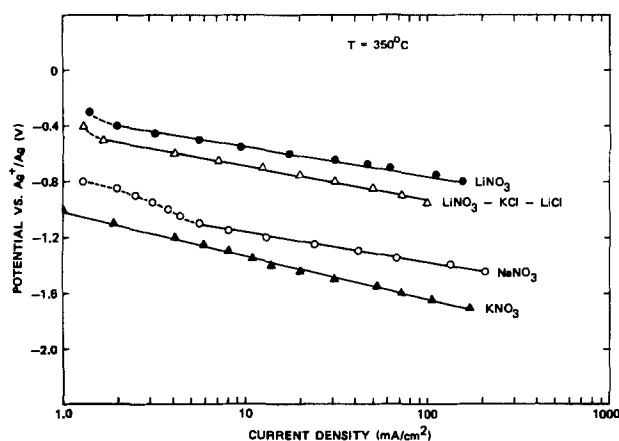


Fig. 6. Potentiostatic studies of the electrochemical reduction of molten nitrates at 350°C in a helium atmosphere using a platinum electrode ($A = 0.32 \text{ cm}^2$).

abrupt changes in potentials are likely caused by blocking effects of insoluble oxides. There were no abrupt changes in potential during the constant current reduction of KNO_3 even for time periods exceeding 100 sec.

Potentiostatic studies of nitrate reduction on platinum at 350°C are shown in Fig. 6. Measurements were made under conditions of a steady stirring action produced by bubbling helium through the melt. The experimental currents dropped when the stirring was stopped, suggesting concentration polarization due to the buildup of reaction products (13). Linear Tafel behavior was usually observed between about 2-100 mA/cm^2 . Tafel and kinetic parameters calculated from these studies are given in Table I. Experimental current densities generally reached limiting values between 100-200 mA/cm^2 ; even the studies in molten KNO_3 showed this limiting current effect under potentiostatic conditions. The limiting current is likely caused by blockage of the electrode surface by insoluble reaction products. A potentiostatic study of the reduction of molten LiNO_3 on nickel gave results very similar to those obtained with a platinum electrode.

Since oxides, peroxides, and superoxides are so entwined with the electrochemistry of molten nitrates, approximate values for the solubilities of a few of these compounds were measured. Results are given in Table II where solubility measurements of KCl are also included and show good agreement with published values. Data on solubility values in fused alkali metal nitrates reported in the literature are sparse (7, 45), hence in the absence of experimental data, ideal solubility calculations provide rough approximations for the solubility of substances that do not react with the molten nitrate. The ideal solubility given by

$$\ln X = \frac{\Delta H_{fus}}{R} \left(\frac{1}{T_M} - \frac{1}{T} \right) \quad [10]$$

Table I. Tafel and kinetic parameters for the electrochemical reduction of molten nitrate on platinum at 350°C under a helium atmosphere

Salt	a^*/V	b/V	α_c	$i_0^*/A \text{ cm}^{-2}$
LiNO_3	-0.98	-0.22	0.57	3.5×10^{-5}
$\text{LiNO}_3\text{-KCl-}$ LiCl^{**}	-1.17	-0.25	0.50	2.1×10^{-5}
NaNO_3	-1.60	-0.22	0.57	5.3×10^{-8}
KNO_3	-1.96	-0.32	0.40	7.5×10^{-7}

* Assuming an equilibrium potential of 0.0V vs. Ag^+/Ag for the nitrate reduction reaction (22).

** 50-25-25 m/o.

Table II. Solubilities in molten nitrates at 350°C in an atmosphere of helium

Substance added	Solubility in LiNO_3 (m/o)	Solubility in KNO_3 (m/o)	Ideal solubility* (m/o)
CaO	0.1	0.005	0.04
Li_2O	0.1	0.005	0.06
Na_2O	0.4	0.2,r	0.60
Li_2O_2	0.25,r	0.5,r	—
KO_2	1.6,r	1.0,r†	46
KCl	55	14‡	10

* Reacts. Gas evolution was visible in each reaction except for Na_2O which forms a yellow product (probably KO_2).

* Calculated from $\ln X = \frac{\Delta H_{fus}}{R} \left(\frac{1}{T_M} - \frac{1}{T} \right)$.

† Phase diagram value is 58 m/o (48).

‡ Phase diagram value is 13.8 m/o (55).

demonstrates that the lower the melting point, T_M , and the lower the heat of fusion, ΔH_{fus} , of the substance concerned, the greater will be its ideal solubility in mole fraction, X , at any given temperature, T (46, 47). The phase diagram of the $\text{KNO}_3\text{-KO}_2$ system (20, 48) shows a high solubility for KO_2 as indicated by the ideal solubility calculated. The low experimental values shown in Table II suggest a low solubility for some reaction product formed. Insufficient oxygen concentration may cause KO_2 to decompose into K_2O_2 or even K_2O (17, 48). A decreasing stability of superoxide ions with rising temperature has been predicted (20). Experimental solubilities in molten KNO_3 are generally closer to ideal solubility values than are the measured solubilities in LiNO_3 . Ideality in a solution requires uniformity of the intermolecular forces between the various components. In LiNO_3 , interactions involving the small Li^+ ion are likely much stronger than interactions involving the NO_3^- ion whereas in KNO_3 the interactions involving K^+ and NO_3^- are more equal.

Discussion

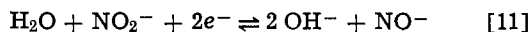
The experimental transfer coefficient of about 0.5 found for the electrochemical reduction of molten nitrates (Table I) is in agreement with a previous study where the addition of the first electron to undissociated MNO_3 and breakage of the N-O bond was postulated to be the slow step (22). Cation effects for this reduction arise from the interaction of the positive metal ion with the nitrate ion that weakens the N-O bond and aids the electron transfer. The lack of obvious cation effects on the electrochemical oxidation of NO_3^- and NO_2^- (Fig. 2) could result from reaction mechanisms that do not involve bond rupture in the slow step. Nitrite oxidation may simply involve an electron transfer to form NO_2 as represented by Eq. [7].

Results shown in Fig. 2, 5, and 6 show a strong correlation between the experimental potential, E , for nitrate reduction and the radius, r , of the cation. Theoretically, the electric field of the cation acts to reduce the free energy of activation such that E will vary with r^{-1} of the cation (22). Using potentials taken at 100 mA/cm^2 in Fig. 2 and 6 and potentials taken at 10 sec in Fig. 5, $\partial E/\partial(r^{-1}) = 1.30, 1.24,$ and $1.36 \text{ V}\cdot\text{\AA}$, respectively. The correlation coefficient is better than 0.99 in each case.

The rather low i_0 values as well as the large temperature effect (Fig. 4) suggest the need for catalyzing the nitrate reduction reaction even at elevated temperatures. Open-pan cyclic voltammetric studies of molten LiNO_3 at 350°C on various metals suggest a catalytic order for nitrate reduction of $\text{Ag} \sim \text{Au} \sim \text{Ir} \sim \text{Ni} \sim \text{Pt} > \text{Mo} > \text{Ti} \gg \text{Ta}$. For many metals, nitrate reduction for a given melt occurs at about the same potential (2, 3, 22). The large concentration

of added chloride in the $\text{LiNO}_3\text{-KCl-LiCl}$ mixture (Table I) does not appear to greatly affect the reduction of LiNO_3 .

Lovering *et al.* (31) propose that the electroreduction of water in nitrate melts is coupled with nitrite reduction



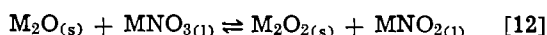
In agreement with their study, we found the water-wave to be smaller on the initial cathodic sweep but quickly increased as nitrite is produced by the main nitrate reduction wave. Cyclic voltammetric studies of the water-wave on platinum showed that $I_{pav}^{1/2}$ while E_p is not dependent on either the sweep rate or the concentration of water. This is the expected behavior for a diffusion-controlled reversible reaction with soluble reactants and products (49, 50) and is consistent with Eq. [11]. The fact that Lovering's reaction does not yield measurable currents on nickel electrodes could be related to the observed tendency of dark oxide films to form on nickel in molten nitrates. Such films could greatly restrict the involvement of chemisorbed water or hydrogen in the reaction mechanism. The dissolution of Li_2O by water adsorbed on platinum could also explain the smaller anodic peaks observed with this electrode in melts containing water.

The residual currents following the nitrate reduction peaks (Fig. 3) have been noted by other workers who propose that the limiting process is the rate of dissolution of the oxide precipitate (2, 13, 19) or that this current depends upon the permeability of the solid deposit (20). We suggest that the after-peak current may result from the oxidation of the metal oxide by the molten nitrate (Eq. [2]) followed by the electrochemical reduction of the peroxide formed. The smaller after-peak currents in LiNO_3 can then be correlated with the fact that Li_2O is more stable than Na_2O with respect to oxidation to the peroxide.

The lack of an observed reduction peak in molten KNO_3 is likely related to the rapid conversion of the unstable K_2O to K_2O_2 and KO_2 (19). In cyclic voltammetric experiments at high current densities, the current-potential trace becomes quite irregular suggesting rate-control by surface processes. The electrochemical reduction of the higher oxides formed on the surface helps to sustain the high cathodic currents observed when the potential is allowed to vary.

Other experimental results also show the important role of the cation in the electrochemistry of molten nitrates. During the cathodic reduction of nitrate melts on platinum, multilayer oxide films grow rapidly in KNO_3 , slowly in NaNO_3 , and not at all in LiNO_3 (13). We also observed a corrosive attack on platinum and nickel with the formation of black particles during the electroreduction of KNO_3 whereas any such attack was much less evident in NaNO_3 and LiNO_3 . These results are consistent with the oxide stability order of $\text{Li}_2\text{O} > \text{Na}_2\text{O} > \text{K}_2\text{O}$ in the corresponding nitrate. Conversion of the oxide to peroxide and superoxide in NaNO_3 and KNO_3 gives remarkable oxidizing power and reactivity to the molten nitrate (8, 13) such that even corrosive attack of platinum can occur (13, 51). Cation effects were also readily apparent in the rate of attack of the nitrate melts upon the Pyrex glass cell used. Crazing and etching of the glass surface contacting the melt was much more rapid with LiNO_3 than with NaNO_3 or KNO_3 .

Thermodynamic calculations support the conclusions regarding the important role of the cation in reactions involving molten nitrates. Considering, for example, the reaction



the standard free-energy change, ΔG° , at 350°C is estimated to be about 10.2 kcal/mole in LiNO_3 , 1.8

kcal/mole in NaNO_3 , and -3.4 kcal/mole in KNO_3 from available data (14, 52-54). These values show that Li_2O is quite stable, thermodynamically, in LiNO_3 at 350°C , and that the stability of the metal oxide in its corresponding nitrate melt decreases with increasing size of the cation involved. Observations during solubility measurements (Table II) also support these cation effects. Li_2O appeared to be stable in both LiNO_3 and KNO_3 while Na_2O was stable in LiNO_3 but reacts in the KNO_3 melt.

Manuscript submitted Sept. 4, 1979; revised manuscript received Feb. 8, 1980.

Any discussion of this paper will appear in a Discussion Section to be published in the June 1981 JOURNAL. All discussions for the June 1981 Discussion Section should be submitted by Feb. 1, 1981.

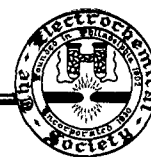
Publication costs of this article were assisted by the Naval Weapons Center.

REFERENCES

1. R. B. Helsop and P. L. Robinson, "Inorganic Chemistry," pp. 245-246, Elsevier Publishing Co., New York (1960).
2. G. J. Hills and K. E. Johnson, in "Advances in Polarography," Vol. 3, I. S. Longmuir, Editor, pp. 974-981, Pergamon Press, New York (1960).
3. H. S. Swofford, Jr. and H. A. Laitinen, *This Journal*, **110**, 814 (1963).
4. G. G. Bombi and M. Fiorani, *Talanta*, **12**, 1053 (1965).
5. H. E. Bartlett and K. E. Johnson, *This Journal*, **114**, 64 (1967).
6. P. G. Zambonin and J. Jordan, *J. Am. Chem. Soc.*, **91**, 2225 (1969).
7. D. H. Kerridge, in "Inorganic Chemistry: Main Group Elements, Groups V and VI," Series 1, Vol. 2, C. C. Addison and D. B. Sowerby, Editors, pp. 30-34, Butterworths, London (1972).
8. J. Jordan, *J. Electroanal. Chem. Interfacial Electrochem.*, **29**, 127 (1971).
9. J. M. Schlegel and D. Priore, *J. Phys. Chem.*, **76**, 2841 (1972).
10. P. G. Zambonin, *J. Electroanal. Chem. Interfacial Electrochem.*, **45**, 451 (1973).
11. P. G. Zambonin, *J. Phys. Chem.*, **78**, 1294 (1974).
12. J. D. Burke and D. H. Kerridge, *Electrochim. Acta*, **19**, 251 (1974).
13. S. Shibata and M. P. Sumino, *ibid.*, **20**, 871 (1975).
14. J. M. de Jong and G. H. J. Broers, *ibid.*, **21**, 605 (1976).
15. J. M. de Jong and G. H. J. Broers, *ibid.*, **21**, 893 (1976).
16. K. H. Stern and R. Panayappan, *This Journal*, **124**, 641 (1977).
17. P. G. Zambonin, *J. Electroanal. Chem. Interfacial Electrochem.*, **33**, 243 (1971).
18. P. G. Zambonin and J. Jordan, *J. Am. Chem. Soc.*, **89**, 6365 (1967).
19. P. G. Zambonin, *J. Electroanal. Chem. Interfacial Electrochem.*, **24**, 365 (1970).
20. J. M. de Jong and G. H. J. Broers, *Electrochim. Acta*, **22**, 565 (1977).
21. K. E. Johnson and P. S. Zacharias, *This Journal*, **124**, 448 (1977).
22. A. N. Fletcher, M. H. Miles, and M. L. Chan, *This Journal*, **126**, 1512 (1979).
23. J. L. Copeland, A. S. Metcalf, and B. R. Hubble, *J. Phys. Chem.*, **80**, 236 (1976).
24. A. Soffer and E. Yeager, Paper 547 presented at The Electrochemical Society Meeting, Seattle, Washington, May 21-26, 1978.
25. M. H. Miles, D. A. Fine, and A. N. Fletcher, *This Journal*, **125**, 1209 (1978).
26. A. N. Fletcher and D. A. Fine, Proceedings, 28th Power Sources Symposium, pp. 92-94 (1978).
27. M. H. Miles and A. N. Fletcher, *J. Appl. Electrochem.*, **10**, 251 (1980).
28. M. Peleg, *J. Phys. Chem.*, **71**, 4553 (1967).
29. P. G. Zambonin, V. L. Cardetta, and G. Signorile, *J. Electroanal. Chem. Interfacial Electrochem.*, **28**, 237 (1970).
30. S. B. Aganesova, P. Ladani, V. P. Yurinskii, and A. G. Morachevskii, *Zh. Prikl. Khim. (Lenin-*

- grad), 48, 1164 (1975); C.A., 83, 104091k (1975).
31. D. G. Lovering, R. M. Oblath, and A. K. Turner, *Chem. Commun.*, 673 (1976).
 32. S. Karpatschiff and W. Patzugi, *Z. Phys. Chem.*, **A173**, 383 (1935).
 33. J. Jordon, K. A. Romberger, and M. W. Young, *Angew. Chem.*, **75**, 1031 (1963).
 34. J. A. A. Ketelaar and A. Dammers-de Klerk, *Rec. Trav. Chim.*, **83**, 322 (1964).
 35. W. E. Triaca and A. J. Arvia, *Electrochim. Acta*, **10**, 409 (1965).
 36. N. Gupta and B. R. Sundheim, *This Journal*, **112**, 836 (1965).
 37. A. J. Arvia, A. J. Calandra, and M. E. Martins, *Electrochim. Acta*, **11**, 963 (1966).
 38. A. F. J. Goeting and J. A. A. Ketelaar, *Electrochim. Acta*, **19**, 267 (1974).
 39. T. Yoshimori, H. Kawahara, T. Hara, and A. Ikeda, *Anal. Chim. Acta*, **98**, 171 (1978).
 40. L. E. Topol, R. A. Osteryoung, and J. H. Christie, *J. Phys. Chem.*, **70**, 2857 (1966).
 41. P. G. McCormick and H. S. Swofford, Jr., *Anal. Chem.*, **41**, 146 (1969).
 42. A. A. El Hosary and A. M. Shams El Din, *Electrochim. Acta*, **16**, 143 (1971).
 43. R. N. Kust and J. D. Burke, *Inorg. Nucl. Chem. Lett.*, **6**, 333 (1970).
 44. M. Fredericks, R. B. Temple, and G. W. Thickett, *J. Electroanal. Chem. Interfacial Electrochem.*, **38**, App. 5 (1972).
 45. J. Brough and D. H. Kerridge, *J. Chem. Eng. Data*, **11**, 260 (1966).
 46. G. N. Lewis and M. Randall, "Thermodynamics," revised by K. S. Pitzer and L. Brewer, 2nd ed., pp. 224-230, McGraw-Hill Book Co., New York (1961).
 47. L. K. Nash, "Elements of Classical and Statistical Thermodynamics," Book One, pp. 119-122, Addison-Wesley Publishing Co., Reading, Mass. (1970).
 48. J. M. de Jong and G. H. J. Broers, *J. Chem. Thermodyn.*, **8**, 367 (1976).
 49. M. H. Miles and P. M. Kellett, *This Journal*, **117**, 60 (1970).
 50. E. Gileadi, E. Kirowa-Eisner, and J. Penciner, "Interfacial Electrochemistry," pp. 370-375, Addison-Wesley Publishing Co., Reading, Mass. (1975).
 51. L. Sabbatini, F. Palmisano, P. Zambonin, and B. De Angelis, *Ann. Chim. (Rome)*, **67**, 525 (1977).
 52. "JANEF Thermochemical Tables," 2nd ed., Nat. Stand. Ref. Data Ser., Nat. Bur. Stand. (U.S.), **37** (June 1971).
 53. F. D. Rossini, D. D. Wagman, W. H. Evans, S. Levine, and J. Jaffe, "Selected Values of Chemical Thermodynamic Properties," Nat. Bur. Stand. Circular 500 (February 1952).
 54. W. M. Latimer, "Oxidation Potentials," 2nd ed., pp. 328-337, Prentice-Hall, Inc., Englewood Cliffs, N.J. (1952).
 55. E. M. Levin, C. R. Robbins, and H. F. McMurdie, "Phase Diagrams for Ceramists, 1969 Supplement," M. K. Reser, Editor, p. 464, The American Ceramic Society, Columbus, Ohio (1969).

Technical Notes



Testing of Sintered LiAlO₂ Structures in Molten Carbonate Fuel Cells

J. W. Sim,* R. N. Singh, and K. Kinoshita¹

Argonne National Laboratory, Argonne, Illinois 60439

Molten carbonate fuel cells are under development for use in generating electricity for utility networks (1). The operating cycle of such cells will inevitably require that they be thermally cycled from the operating temperature (650°C) to ambient temperature. The electrolyte component of the cell must withstand the thermal cycling without developing large cracks, which would permit cross-mixing of the fuel and oxidant and lead to decreased operating efficiency. This note describes work on electrolyte structures containing sintered LiAlO₂; these structures resist cracking during thermal cycling and prevent cross-mixing of reactant gases.

Porous sintered structures of MgO infused with molten alkali carbonates were previously used by many investigators (2-6) as the electrolyte component in experimental fuel cells. Use of such structures was discontinued because the low porosities and coarse pores of the sintered bodies gave rise to high cell resistance and poor retention of the molten carbonates. Paste electrolytes formed by hot-pressing finely divided MgO powder and alkali carbonates were then

used to overcome the problems associated with sintered MgO structures. The use of MgO in paste structures was subsequently abandoned in favor of LiAlO₂ because MgO proved to be soluble in the carbonate melt. In this study, electrolyte structures were fabricated by sintering LiAlO₂ powders and impregnating the resultant porous bodies with molten carbonates. One structure of this type was tested in a cell and sustained five thermal cycles with no cross-mixing of reactant gases. The high porosities (64%) and low mean pore size (0.1 μm) obtained with some sintered LiAlO₂ bodies suggest that the problems associated with sintered MgO structures can be minimized by using sintered LiAlO₂ structures instead.

The LiAlO₂ powders used to fabricate the sintered structures were prepared by heating mixtures of Li₂CO₃ and Al₂O₃, first at 600°C for 66-82 hr to form α-LiAlO₂, then at 900°C for 16-20 hr to convert the α-LiAlO₂ to γ-LiAlO₂. Porous bodies of γ-LiAlO₂ were formed by pressing the powders at 6895 kPa and firing the compacted powders at 1000°-1200°C for 0.5-4 hr. A screen (20 mesh) of Kanthal² wire (Type Al, 0.13 mm diam) was incorporated into some of the structures at midplane. A typical pore-size distribution

* Electrochemical Society Active Member.

¹ Present address: SRI International, Menlo Park, California 94025.

Key words: electrolyte, cracking, failure, ceramics.

² The Kanthal Corporation, Bethel, Connecticut.

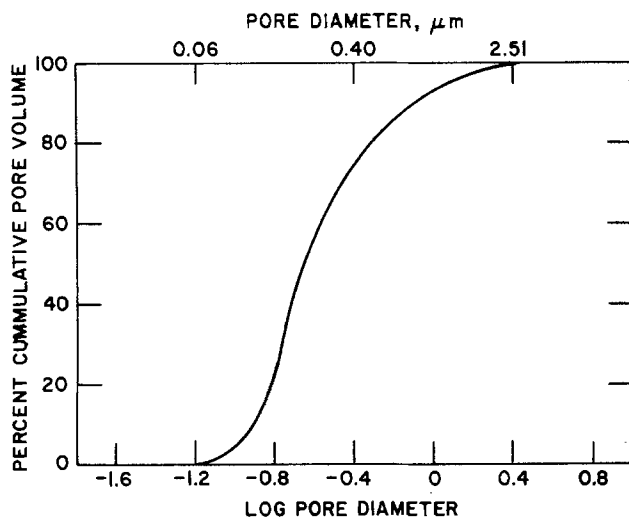


Fig. 1. Pore size distribution of sintered LiAlO_2

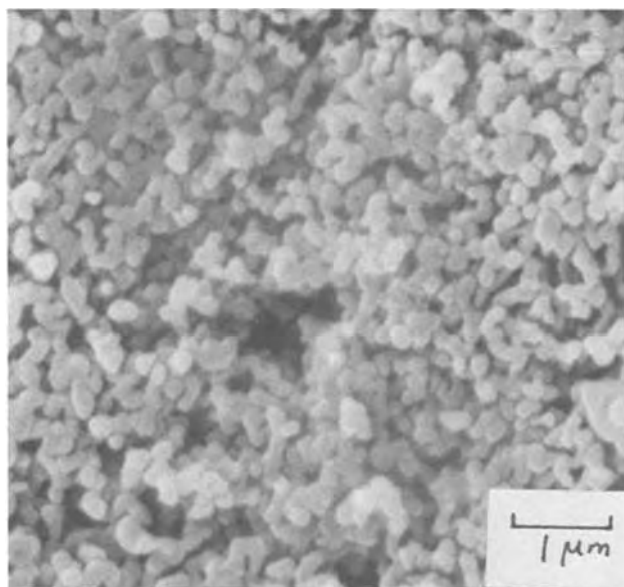


Fig. 2. Microstructure of porous sintered LiAlO_2

(determined by mercury porosimetry) for a structure prepared by this method is shown in Fig. 1, and a typical microstructure is shown in Fig. 2. The porosities of the structures tested in cells ranged from 52 to 57%, but porosities up to 64% were obtained in some specimens which were too small for cell testing. Impregnation by the carbonates was accomplished by evacuating the porous structures, and then dipping them into the molten carbonate eutectic [62 mole percent (m/o) Li_2CO_3 -38 m/o K_2CO_3]. The entire fabrication process is described in more detail elsewhere (7).

The impregnated structures (nominally $70 \times 70 \times 1.8$ mm) were examined for defects by x-ray radiography before cell testing. The cell hardware and reactant gases used are described elsewhere (8). Cross-leakage of reactant gases through the electrolyte structures was monitored by measuring the amount of nitrogen in the anode exhaust while varying the differential pressure between the cathode and the anode. Because the cathode gas contained ~ 57 volume percent nitrogen while the anode gas was pure helium during the cross-leakage measurement, any increase in nitrogen in the anode exhaust with increasing differential pressure was taken as an indication of cross-leakage. When the level of nitrogen did not increase with differential pressure, the nitrogen that was detected was caused by diffusion of air through imperfections in the "wet-seal" (8) formed between the

anode housing and the electrolyte structure. This was verified by maintaining a constant differential pressure between the cathode and the anode while increasing the anode pressure; the level of nitrogen decreased with increasing anode pressure. Each thermal cycle consisted of cooling the cell from 650° to 25°C at a rate of $\sim 3^\circ\text{C}/\text{min}$ and reheating to 650°C at the same approximate rate.

Three structures were tested: two were reinforced with a Kanthal screen and one was not reinforced. One of the reinforced structures, which had no detectable flaws under radiographic examination, underwent five thermal cycles. After the second thermal cycle, 0.5% nitrogen was detected in the anode exhaust, with and without 6.9 kPa differential pressure between the cathode and the anode, clearly indicating the absence of cross-leakage. The anode wet-seal efficiency during these measurements was 99%, which is consistent with the low level of nitrogen detected. After the third and subsequent thermal cycles, the anode wet-seal efficiency increased to 100%, and the nitrogen levels, with and without 6.9 kPa differential pressure, were less than 0.03%. Thus, no cross-leakage was detected after five thermal cycles, when the cell was voluntarily terminated to inspect the cell components.

The second reinforced structure, which contained two small cracks (~ 0.01 mm wide) prior to cell assembly, was tested to determine whether such small cracks would permit cross-leakage. Two thermal cycles were performed before the cell was terminated, due to obstruction of the anode inlet tube. The level of nitrogen in the anode exhaust after the first thermal cycle increased from 1.2 to 2.7% when the differential pressure between the cathode and the anode was increased from 0 to 2.5 kPa, clearly indicating cross-leakage. The anode wet-seal efficiency was 96%. Similar levels of nitrogen (1.4 and 2.7% at 0 and 2.5 kPa, respectively) were detected after the second thermal cycle, indicating that the amount of cross-leakage was essentially unaffected by the second cycle. Thus, cross-leakage was detected with the second reinforced structure, possibly due to the small cracks observed under radiographic inspection prior to cell assembly.

The nonreinforced structure, which contained four larger cracks (~ 0.03 - 0.06 mm wide) before cell assembly, showed cross-leakage upon startup. At 0 and 2.0 kPa differential pressure, the nitrogen level was 0.3 and 1.4%, respectively, and the wet-seal efficiency was 99%. After two thermal cycles, however, severe failure of the structure occurred, as indicated by a drop in open-circuit voltage to less than 1V (1.096V theoretical). Examination of the sintered structure after cell testing indicated that the failure was caused by enlargement of one of the cracks present before testing.

In summary, this study demonstrated one of the advantages of using a sintered LiAlO_2 structure impregnated with carbonates as an electrolyte component in fuel cells. When the structure contained no cracks prior to cell assembly, cross-leakage of reactant gases through the structure was not detected, even at a differential pressure of 6.9 kPa and after five thermal cycles. When cracks were present in the structures before testing began, cross-leakage occurred during cell operation. Additional testing is necessary to fully demonstrate the feasibility of utilizing sintered LiAlO_2 structures in molten carbonate fuel cells, however.

Manuscript submitted Nov. 26, 1979; revised manuscript received Feb. 15, 1980.

Any discussion of this paper will appear in a Discussion Section to be published in the June 1981 JOURNAL. All discussions for the June 1981 Discussion Section should be submitted by Feb. 1, 1981.

Publication costs of this article were assisted by Argonne National Laboratory.

REFERENCES

1. J. P. Ackerman and S. S. Borys, Paper 136 presented at The Electrochemical Society Meeting, Los Angeles, California, Oct. 14-19, 1979.
2. A. N. Webb, W. B. Mather, Jr., and R. M. Suggit, *This Journal*, **112**, 1059 (1965).
3. Isaac Trachtenberg, *ibid.*, **111**, 110 (1964).
4. Y. L. Sandler, *ibid.*, **109**, 1115 (1962).
5. M. L. Kronenberg, *ibid.*, **109**, 753 (1962).
6. G. H. J. Broers and M. Schenke, in "Fuel Cells, Volume II," G. J. Young, Editor, pp. 6-23, Reinhold Publishing Co., New York (1963); E. B. Shultz, Jr., K. S. Vorres, L. G. Marianowski, and H. R. Linden, *ibid.*, pp. 24-36.
7. R. N. Singh and J. T. Dusek, *J. Am. Ceram. Soc.*, To be submitted.
8. R. B. Swaroop, J. W. Sim, and K. Kinoshita, *This Journal*, **125**, 1799 (1978).

Spectroelectrochemistry in Melts: Applications to Molten Chloroaluminates

G. Mamantov and V. E. Norvell

Department of Chemistry, The University of Tennessee, Knoxville, Tennessee 37916

and L. Klatt

Oak Ridge National Laboratory, Analytical Chemistry Division, Oak Ridge, Tennessee 37830

The use of spectroelectrochemistry as a tool for studying redox chemistry in solutions has developed rapidly over the last several years (1). This technique yields simultaneous spectral and electrochemical information useful in the elucidation of mechanisms of redox reactions. By using appropriate experimental designs, short-lived intermediate species, which may be undetectable electrochemically, can be studied.

The transmission mode spectroelectrochemical experiment involves the use of an optically transparent electrode (OTE), *i.e.*, an electrode which is transparent in the spectral region of interest. Radiation of the desired wavelengths is passed through the solution and the OTE where a portion is absorbed by the solute species. The attenuated radiation is then measured to give a spectrum. Spectroelectrochemistry most commonly involves the u.v.-visible-IR spectral regions, but it has been applied to ESR, NMR, and mass spectrometry as well (1).

We are currently developing u.v.-visible spectroelectrochemical techniques for studying redox systems in molten chloroaluminates (mixtures of AlCl_3 and alkali halides). Solute chemistry in these melts is quite dependent on the melt acidity (2-4). The acid-base properties of the chloroaluminate melts near the 1:1 AlCl_3 -NaCl mole ratio can be described by the equilibrium (5-9)



AlCl_4^- is the predominant anion in the equimolar AlCl_3 -NaCl melt. As the acidity is increased, Al_2Cl_7^- becomes more abundant (5-9).

To date we have examined by spectroelectrochemistry the reduction of niobium (V) and the oxidation of sulfur in chloroaluminate melts. The use of OTE's to study species in melts spectroelectrochemically has not been reported previously.

Experimental

A block diagram of the spectrometer/data acquisition system used to carry out spectroelectrochemical experiments is shown in Fig. 1. The spectrometer is a silicon-vidicon based rapid-scan spectrometer (RSS) which is controlled by the PDP-8/I minicomputer. To obtain an absorption spectrum of a sample, white light is passed through the sample and into a polychromator where it is dispersed by a grating. A 400 nm wide segment of this spectrum is directed across the face of the

vidicon detector, where it is read as light intensity *vs.* wavelength by an electron beam. The sweep frequency of this beam can be adjusted so that spectra may be acquired at time intervals varying from 50 msec to 5 sec. Since the spectrometer operates in a single-beam mode, a 100% transmission spectrum (with no sample in the beam) is also acquired and the absorbance spectrum is calculated using the computer. Spectra are stored either on disk or cassette tape. An absorption spectrum can be viewed either on a CRT display, or displayed on an X-Y recorder. A potentiostat is also interfaced to the system; this makes it possible to synchronize the start of spectral data acquisition with the initiation of the electrochemical experiment as well as to simultaneously acquire and store both spectral and electrochemical data. A more detailed description of the spectrometer and the computer interface system is available (10).

A typical cell used to carry out molten salt spectroelectrochemical experiments is illustrated in Fig. 2. The optically transparent electrode consists of a piece of reticulated vitreous carbon (11) (RVC-4, 80 or 100 pores per inch porosity, the Fluorocarbon Company, Anaheim, California), a tungsten grid (Buckbee Mears Company, St. Paul, Minnesota), or a piece of 80 mesh platinum screen. The electrical contact to the tungsten

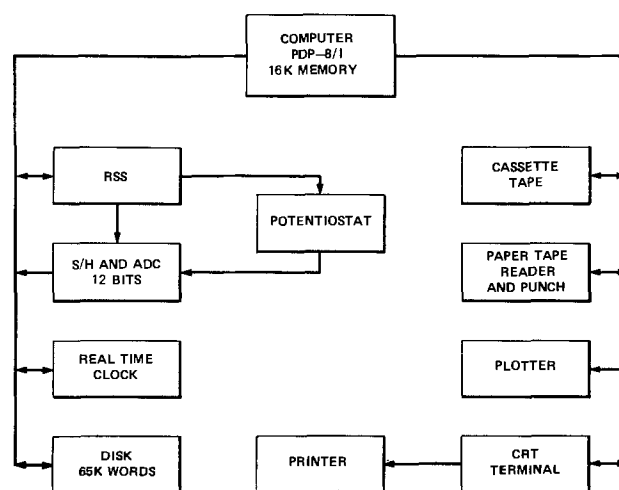


Fig. 1. Block diagram of the system used for spectroelectrochemical experiments.

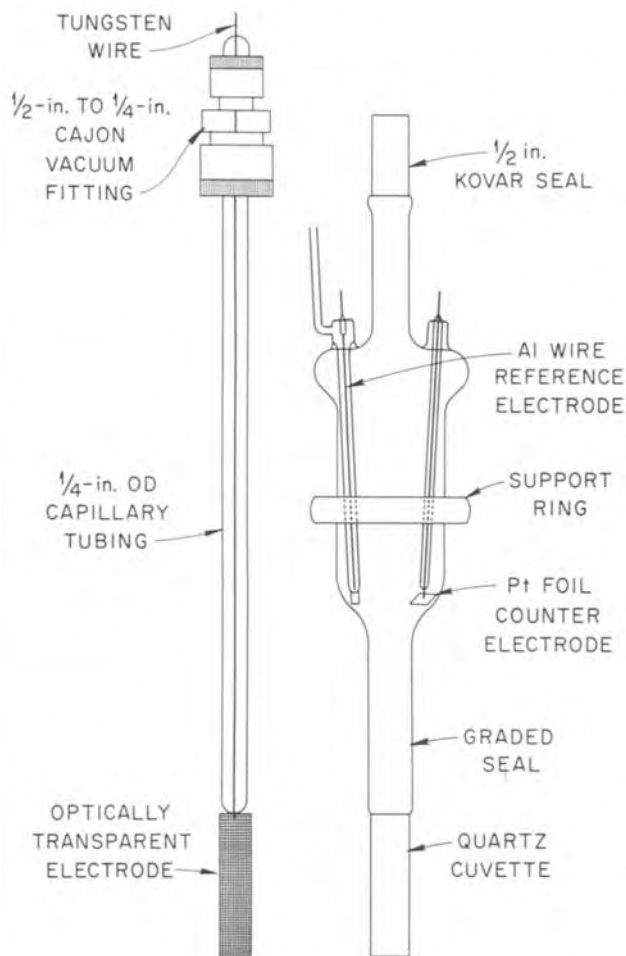


Fig. 2. Typical spectroelectrochemical cell used in the molten salt studies. The reference electrode is isolated from the bulk melt by a porous ceramic frit.

or platinum electrodes is made by spot welding to a platinum or tungsten wire which was previously sealed into $\frac{1}{4}$ in. OD capillary tubing. Electrical contact to the reticulated vitreous carbon electrode is accomplished by inserting a platinum wire approximately 1 cm into the top of the electrode and cementing it in place with carbon cement (UCAR C-34, Union Carbide Corporation, New York). The cement connection is carbonized by heating to approximately 900°C under vacuum. The platinum wire is then spot welded to a tungsten wire sealed in capillary tubing as described above. The OTE is inserted into the quartz cuvette, the pathlength of which ranges from 0.25 mm (for platinum or tungsten OTE's) to 2.00 mm (for reticulated vitreous carbon OTE's). The completed OTE assembly is held in place by a Cajon vacuum fitting. The counterelectrode is a platinum foil electrode and the reference electrode is an aluminum wire in a separate fritted compartment.

Other electrodes, not shown for clarity, include a platinum or tungsten wire working electrode for cyclic voltammetry, and an extra platinum foil electrode. The melt is added via a filling tube (not shown) in the top of the cell which is then sealed under vacuum. The cell is mounted in a suspension assembly by means of the support ring, and this assembly is then lowered into an optical furnace. The furnace consists of a glass tube wrapped with a Nichrome heating element, and contains two quartz windows through which spectra are taken. The furnace temperature is controlled by using a variable voltage transformer. A tungsten lamp and a xenon arc lamp serve as light sources.

Spectroelectrochemical Study of the Reduction of Niobium (V)

The redox chemistry of transition metals in Groups IVB-VIB in chloroaluminate melts is unusual because of the tendency to form metal clusters in which the metal exists in an unusually low oxidation state (2, 4, 12-14). The electrochemical reduction of Nb(V) in both acidic [mole percent (m/o) $\text{AlCl}_3 > 50$] and basic (m/o $\text{AlCl}_3 < 50$) chloroaluminates has been previously reported (4). Potentiometric and spectroscopic studies of Nb(V) in AlCl_3 -KCl melts have also been performed (15). In basic melts the first step of the reduction of the bright-yellow Nb(V) results in the formation of purple Nb(IV). The spectroelectrochemistry of this reduction was studied at a Pt screen OTE in an NaCl-saturated (basic) melt at 225°C . Figure 3 illustrates the spectra obtained during the course of the reduction. At $t = 0$ sec, an absorption band at 300 nm due to Nb(V) is observed. Following a potential step to the diffusion plateau of the first reduction wave, two new absorption bands appear at 275 and ~ 350 nm. Previous spectra of Nb(IV) obtained in this melt (14), in solid phase (16), and in another solvent (17) show bands near 285 and 325 nm, plus other lower wavelength bands. The reported band positions vary by as much as 10-15 nm. Figure 4 shows a thin-layer coulogram of this reduction calculated from chronoamperometric data obtained simultaneously with spectral data. The charge value obtained from this curve yields an n value of 0.99, thus confirming a simple electrochemical reduction.

In acidic melts, the reduction of Nb(V) proceeds through an ECE mechanism to produce an Nb(III) species (4) as shown below

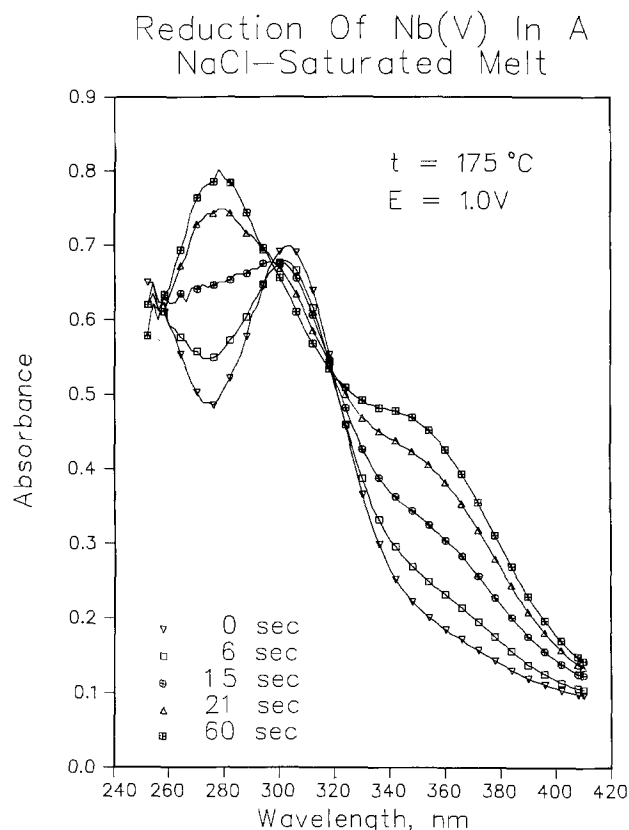
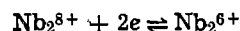
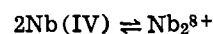
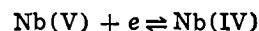


Fig. 3. Spectra obtained during the reduction of Nb(V) in the NaCl-saturated chloroaluminate melt. Potential stepped from 1.5V to 1.0V vs. the Al(III)/Al reference electrode in the NaCl-saturated melt. OTE: Pt screen; pathlength: 0.25 mm; conc. Nb(V): 0.0015M.

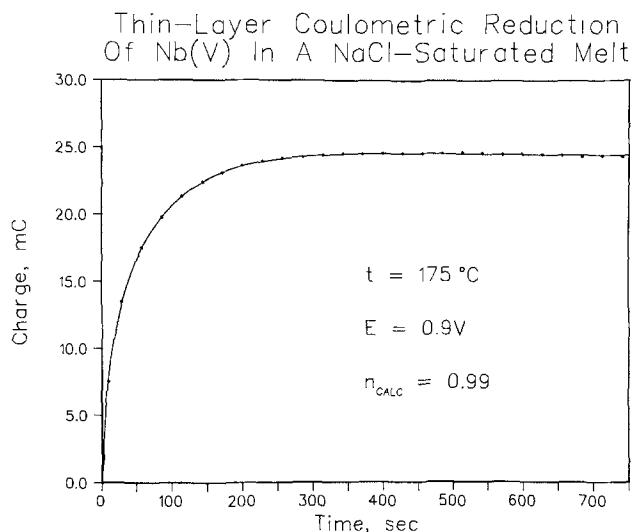


Fig. 4. Charge vs. time plot for the thin-layer coulometric reduction of Nb(V) in the NaCl-saturated chloroaluminate melt. Potential stepped from 1.5 to 0.9V vs. the Al(III)/Al reference electrode in the NaCl-saturated melt. OTE: Pt screen.

This reduction was studied spectroelectrochemically in an acidic melt (AlCl₃-NaCl 63-37 m/o) at 225°C, and the resulting spectra are shown in Fig. 5. The Nb(V) band at 300 nm disappears as the reduction is carried out, and no new bands are observed. The slight increase in absorbance seen at the longer wavelengths is probably due to the formation of a precipitate containing Nb(III) (14). Because this precipitate apparently was deposited on the screen OTE, it could be reoxidized completely to Nb(V), as indicated by the reappearance of the band at 300 nm. Thin-layer coulometry carried out simultaneously with spectral acquisition gave an n value of 2.2. Although this value

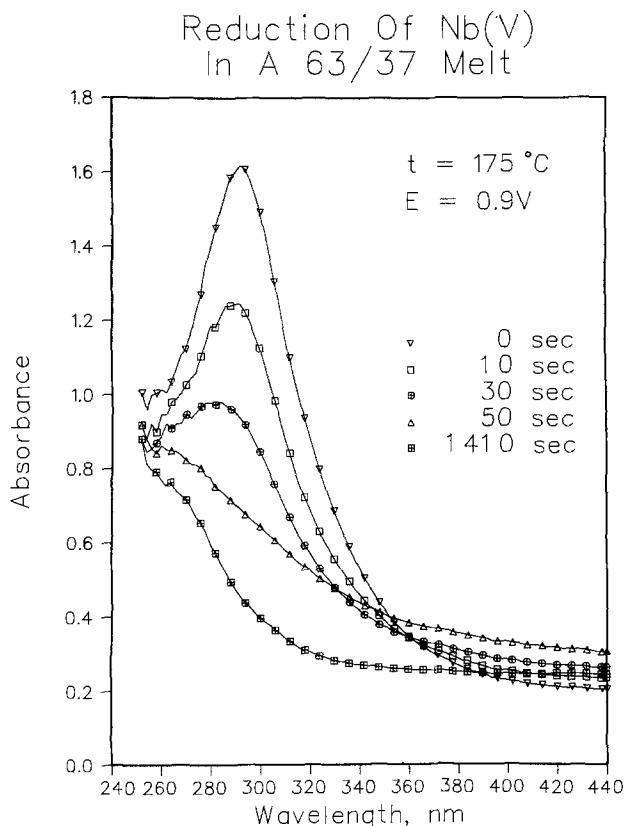


Fig. 5. Spectra obtained during the reduction of Nb(V) in AlCl₃-NaCl (63-37 m/o) melt. Potential stepped from 1.5 to 0.9V vs. the Al(III)/Al reference electrode in the 63-37 melt. OTE: Pt screen; pathlength: 0.25 mm; Conc. Nb(V): 0.0036M.

deviates from the expected value of 2.0, it should be considered as a preliminary result because an exhaustive coulometric study of this system has not been undertaken.

Spectroelectrochemical Study of Sulfur Oxidation

The electrochemistry of sulfur in molten chloroaluminates is of considerable importance to the development of a molten salt battery using a sodium anode and positive oxidation states of sulfur as the cathode (18, 19); it has been investigated in both basic and acidic melts (20-22). Because sulfur can be oxidized to higher oxidation states in acidic melts, its chemistry in these melts is of greater importance to the battery work. In acidic AlCl₃-NaCl melts sulfur is oxidized in three steps, the final product being S(IV) as indicated by voltammetry and controlled-potential coulometry (22). Both Raman (23) and potentiometric (24, 25) studies have indicated that S(IV) is present as SCl₃⁺.

We are using spectroelectrochemistry to study further the mechanism of the oxidation of sulfur in acidic chloroaluminates. By oxidizing elemental sulfur in the melt to S(IV), at least five intermediate oxidation states can be produced (24, 25). Several of these species have characteristic absorption maxima which can be used to ascertain the species present as a function of the potential applied to the OTE.

Elemental sulfur was dissolved in an acidic chloroaluminate melt (AlCl₃-NaCl 63-37 m/o); this solution was studied spectroelectrochemically at platinum and carbon OTE's at 225°C. Thin-layer coulometry was carried out on the first oxidation wave by holding the potential of a Pt OTE at +1.65V. N values ranging from 0.14 to 0.16 were obtained. These results agree with those obtained through exhaustive bulk coulometry (22). An n value of 0.125 would correspond to the formation of S₁₆²⁺ (or S₈⁺), while an n value of 0.25 would indicate formation of S₈²⁺. The intermediate value suggests that a mixture of these species is formed. The spectra shown in Fig. 6, obtained at a

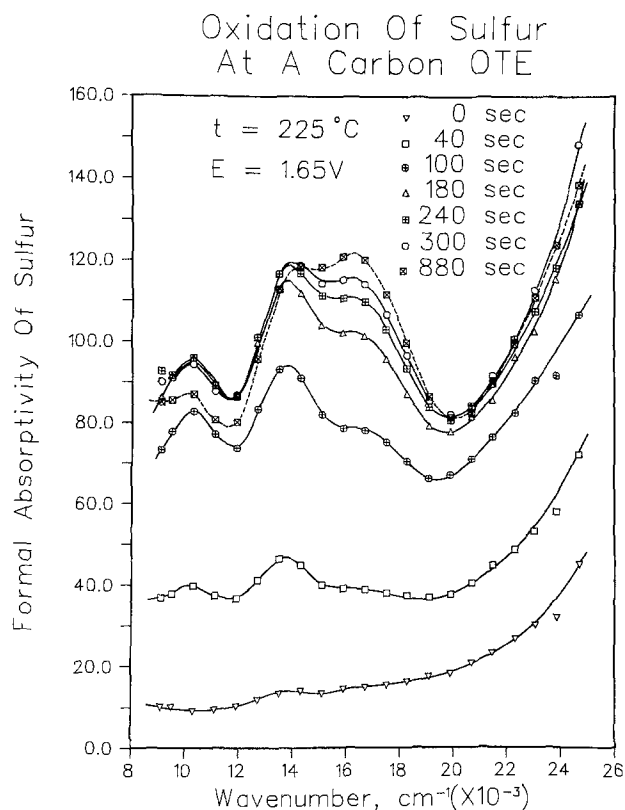


Fig. 6. Spectra obtained during the oxidation of sulfur at a glassy carbon OTE in the AlCl₃-NaCl (63-37 m/o) melt. Potential stepped from 1.3 to 1.65V vs. the Al(III)/Al reference electrode in the 63-37 melt. Conc. S: 0.013M.

A vs. T At Absorbance Maxima For The First Sulfur Oxidation Wave

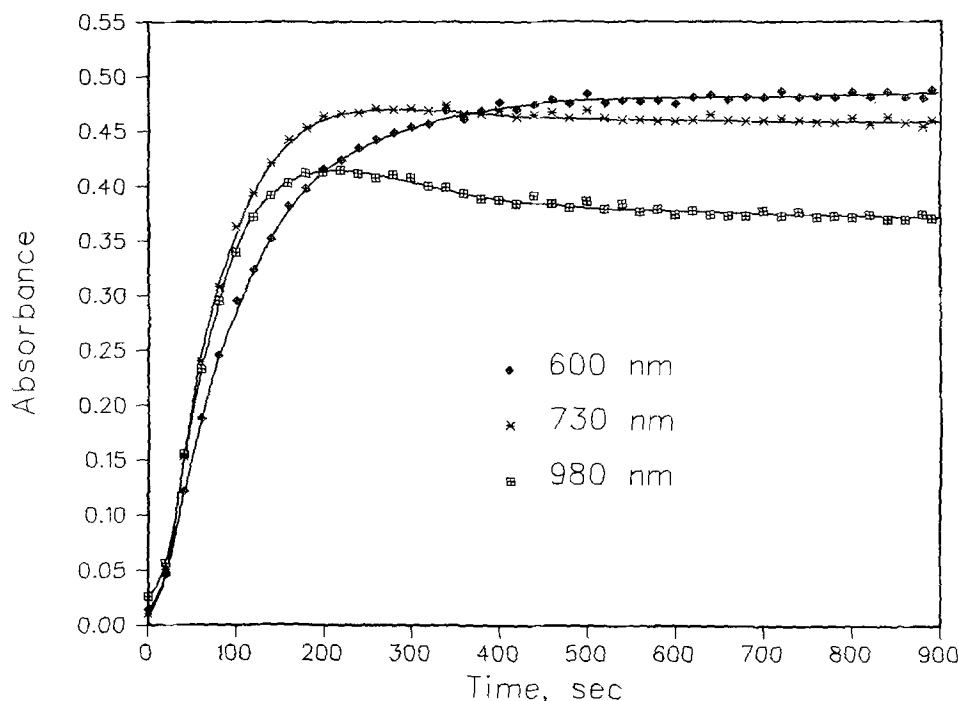


Fig. 7. Absorbance vs. time plots for the three absorbance bands shown in Fig. 6. Path-length: 2.0 mm.

carbon OTE, substantiate this supposition. As the oxidation takes place, three absorption bands appear approximately simultaneously at $16,600\text{ cm}^{-1}$ (600 nm), $13,700\text{ cm}^{-1}$ (730 nm), and $10,200\text{ cm}^{-1}$ (980 nm). The latter two bands achieve a maximum absorbance after about 4 min and begin to decrease as the first band continues to increase. This can be seen clearly from the absorbance-time profiles illustrated in Fig. 7. According to previously published work (24, 25), it is reasonable to attribute the 600 nm band to S_8^{2+} and the 730 and 980 nm bands to S_{16}^{2+} . This first oxidation step then produces a mixture of S_{16}^{2+} (or S_8^+) and S_8^{2+} . Marassi *et al.* (22) have proposed mechanisms involving chemical reactions which could account for these results.

The spectra shown in Fig. 8 were obtained by stepping the potential of the carbon OTE from 1.65V (plateau of the first wave) to 1.85V (just past the plateau of the second wave). The band at $13,700\text{ cm}^{-1}$, due to S_{16}^{2+} (or S_8^+) immediately vanishes while the band at $16,600\text{ cm}^{-1}$ (S_8^{2+}) initially increases. This band then slowly disappears as S_8^{2+} is oxidized to S(I). In a similar experiment carried out at a Pt screen OTE, but recording spectral data at shorter wavelengths, bands at ca. $26,300\text{ cm}^{-1}$ (380 nm) and $\sim 31,000\text{ cm}^{-1}$ (323 nm) appeared as the oxidation proceeded. At least one and perhaps both of these bands can be attributed to the formation of S(I) (as S_2^{2+}) (25). The third sulfur oxidation wave is not very interesting for spectroelectrochemical study because the S(IV) product does not exhibit any absorption in the visible region (25).

Conclusion

We have demonstrated that spectroelectrochemistry can be carried out successfully in melts using optically transparent electrodes. The correlation of the spectral data with the electrochemical results has proved very helpful in determining what species are formed during the reduction or oxidation, thereby yielding insight into the mechanisms of the electrochemical processes in melts.

Acknowledgments

Molten salt research at the University of Tennessee is supported by the National Science Foundation Grant

CHE 77-21370, and the Department of Energy, Contract EY-76-S-05-5053. V. E. Norvell acknowledges the receipt of an Oak Ridge Associated Universities Fellowship.

Manuscript submitted Dec. 21, 1979; revised manuscript received March 5, 1980. This was Paper 357 pre-

Oxidation Of Sulfur At A Carbon OTE

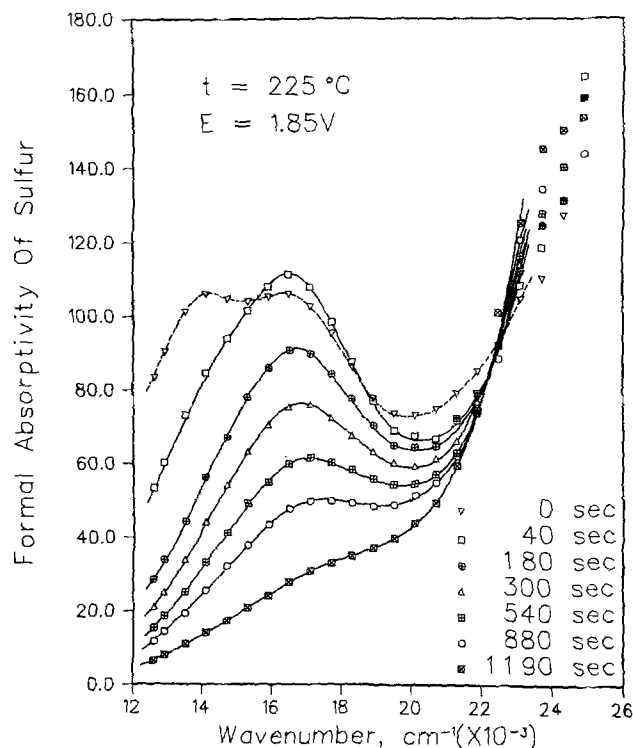


Fig. 8. Spectra obtained during the oxidation of sulfur at a glassy carbon OTE in the $\text{AlCl}_3\text{-NaCl}$ (63-37 m/o) melt. Potential stepped from 1.65 to 1.85V vs. the Al(III)/Al reference electrode in the 63-37 melt. Conc. S: 0.013M.

sented at the Pittsburgh, Pennsylvania, Meeting of the Society, Oct. 15-20, 1978.

Any discussion of this paper will appear in a Discussion Section to be published in the June 1981 JOURNAL. All discussions for the June 1981 Discussion Section should be submitted by Feb. 1, 1981.

Publication costs of this article were assisted by the University of Tennessee.

REFERENCES

- W. R. Heineman, *Anal. Chem.*, **50**, 390A (1978), and references therein.
- G. Mamantov and R. A. Osteryoung, in "Characterization of Solutes in Nonaqueous Solvents," G. Mamantov, Editor, pp. 223-249, Plenum Press, New York, (1978).
- G. Torsi, K. W. Fung, G. M. Begun, and G. Mamantov, *Inorg. Chem.*, **10**, 2285 (1971).
- G. Ting, K. W. Fung, and G. Mamantov, *This Journal*, **123**, 624 (1976).
- B. Tremillon and G. Letisse, *J. Electroanal. Chem. Interfacial Electrochem.*, **17**, 371 (1968).
- G. Torsi and G. Mamantov, *Inorg. Chem.*, **10**, 1900 (1971).
- G. Torsi and G. Mamantov, *ibid.*, **11**, 1439 (1972).
- A. A. Fannin, L. A. King, and T. W. Seegmiller, *This Journal*, **119**, 801 (1972).
- L. G. Boxall, H. L. Jones, and R. A. Osteryoung, *ibid.*, **120**, 223 (1973).
- L. N. Klatt, *J. Chromatogr. Sci.*, **17**, 225 (1979).
- V. E. Norvell and G. Mamantov, *Anal. Chem.*, **49**, 1470 (1977).
- D. L. Brotherton, Ph.D. Dissertation, University of Tennessee (1974).
- L. E. McCurry, G. Mamantov, N. J. Bjerrum, F. W. Poulsen, and J. H. von Barner, in "High Temperature Metal Halide Chemistry," D. L. Hildebrand and D. D. Cubicciotti, Editors, pp. 421-425, The Electrochemical Society Softbound Proceedings Series, Princeton, N.J. (1978).
- L. E. McCurry, Ph.D. Dissertation, University of Tennessee (1978).
- J. H. von Barner, N. J. Bjerrum, and G. P. Smith, *Acta Chem. Scand.*, **A32**, 837 (1978).
- G. W. A. Fowles, D. J. Tidmarsh, and R. A. Walton, *Inorg. Chem.*, **8**, 631 (1969).
- S. M. Horner and S. Y. Tyree, *Inorg. Nucl. Chem. Lett.*, **1**, 43 (1965).
- G. Mamantov and R. Marassi, U.S. Pat. 4,063,005 (1977).
- G. Mamantov, R. Marassi, J. P. Wiaux, S. E. Springer, and E. J. Frazer, in "Load Leveling," N. P. Yao and J. R. Selman, Editors, pp. 379-383, The Electrochemical Society Softbound Proceedings Series, Princeton, N.J. (1977).
- R. Marassi, G. Mamantov, and J. Q. Chambers, *This Journal*, **123**, 1128 (1976).
- K. A. Paulsen and R. A. Osteryoung, *J. Am. Chem. Soc.*, **98**, 6686 (1976).
- R. Marassi, G. Mamantov, M. Matsunaga, S. E. Springer, and J. P. Wiaux, *This Journal*, **126**, 231 (1979).
- F. W. Poulsen, R. Huglen, and G. Mamantov, Unpublished work.
- N. J. Bjerrum, in "Characterization of Solutes in Nonaqueous Solvents," G. Mamantov, Editor, pp. 251-271, Plenum Press, New York (1978).
- R. Fehrmann, N. J. Bjerrum, and F. W. Poulsen, *Inorg. Chem.*, **17**, 1195 (1978).

Erratum

In the paper "Primary Current Distribution on a Sinusoidal Profile" by Peter Fedkiw which appeared on pp. 1304-1308 in the June 1980 JOURNAL, Vol. 127,

No. 6, Eq. [16] should read as follows

$$\Phi(X, Y) = -Y + A [(1 - e^{-2\pi Y}) \cos 2\pi X] \dots$$



Oxidation Behavior of Two-Phase Alloy Fe-44 w/o Cu

F. Gesmundo and P. Nanni

Centro Studi di Chimica e Chimica Fisica Applicata alle Caratteristiche di Impiego dei Materiali del Consiglio Nazionale delle Ricerche, Genoa, Fiera del Mare-Pad. D, Italy

and D. P. Whittle*

*Materials and Molecular Research Division,
Lawrence Berkeley Laboratory, University of California, Berkeley, California 94720*

ABSTRACT

The oxidation of a two-phase iron-copper alloy has been studied as an example of the behavior of multiphase systems with simple compositions of the component single phases. The alloy oxidizes more slowly than either of the pure metals, particularly iron, and the scale contains both components, copper being particularly accumulated close to the scale-gas interface. A deep region of internal oxidation is also present, where the iron-rich particles have been converted into FeO. Possible reasons for the observed reduction of the oxidation rate in comparison with pure iron are examined: by means of an approximate calculation based on the theory of the growth of multilayer scales it is concluded that a major fact is the thermodynamic destabilization of the fast growing wustite phase, due to the low iron activity at the alloy-scale interface. No particular effect of growth stresses, due to the anticipated differences in oxidation rate of the component phases, has been observed. Instead, in agreement with the observation that the scale composition is rather uniform laterally and shows the largest changes perpendicularly to the alloy surface, the two-phase nature of the alloy does not seem to exert a strong influence on the overall oxidation behavior.

During the high temperature oxidation of alloys the scales that form often contain a number of different phases, each of which may contain more than one alloy component. Thus, the ratio of the metals in the scale is different from their ratio in the alloy because the various components have different affinities for oxygen, and the rate of transport in the scale is different for each cation and in each phase. The composition of the scale may also vary with position due to these differing diffusivities. Some success has been achieved in attempts to correlate the theories of alloy oxidation kinetics with diffusional, structural, and compositional parameters of the metal oxides in systems in which a solid solution scale is formed (1-4). This paper continues that theme in attempting to analyze the behavior of the Fe-Cu alloys where the oxides of the constituent metals are virtually immiscible, and clearly the overall oxidation rate will depend heavily on the distribution of the various oxide phases in the scale. In addition, Fe and Cu are relatively immiscible in the metallic phase and large compositional changes in the alloy due to any preferential oxidation are therefore precluded even though there are considerable differences in stabilities between iron and copper oxides. Thus, some internal oxidation is anticipated.

There are also substantial differences in oxidation rate of two pure metals and, hence, presumably between the two constituent phases in the alloy. Originally, it was anticipated that this could give rise to

complex growth stress development in the growing scale: this does not seem to be the case, as will be seen later.

Experimental

The alloy used in the present study was prepared by melting 99.998% Fe and 99.9996% Cu in a high frequency induction furnace and casting into a water-cooled mold. Analysis gave an average composition of 44.1 weight percent (w/o) Cu. The ingot was mechanically worked into a cylindrical shape and samples in the form of disks about 0.8 mm thick were cut from it. The disks were subsequently polished on SiC papers and were then annealed for 24 hr at 850°C in vacuo ($\approx 10^{-5}$ Torr). Immediately prior to oxidation they were lightly re-abraded on 6/0 emery paper to remove the tarnish film produced during the annealing process.

Oxidation tests were performed in pure, dry oxygen at 760 Torr pressure under static conditions in a Mettler thermoanalyzer; weight gain was continuously recorded. At the end of the experiments the samples were cooled down in vacuo in the balance chamber; no further changes in weight were detected.

Cross sections of oxidized specimens were examined by standard methods of optical and electron microscopy. Concentration profiles were measured by an EDAX attachment to a JEOL SEM. Phases were identified by x-ray diffraction.

Results

Alloy microstructure.—Figure 1 shows the microstructure of the alloy after annealing: essentially the

* Electrochemical Society Active Member.

Key words: two-phase alloy, iron-copper, oxidation.

1555

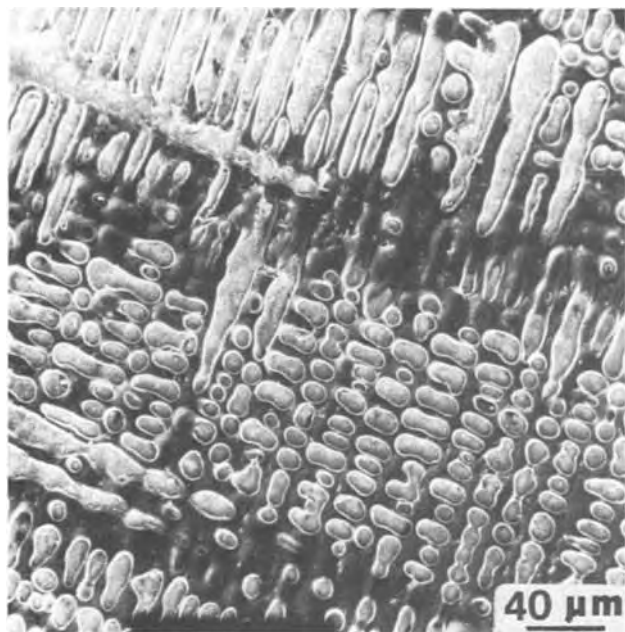


Fig. 1. Microstructure of the alloy

as-cast dendritic structure is maintained. The dendrites are the iron-rich phase which according to the phase diagram contains 5.81 w/o Cu; the copper-rich matrix contains 2.06 w/o Fe at 1000°C (5). The average size of the iron-rich phase particles is around 20-30 μm.

Kinetics.—Plots of squared weight gains per unit area vs. time are reported in Fig. 2 for the different temperatures (one individual curve for each T). They show that oxidation of this alloy follows, to a reasonable approximation, a parabolic rate law, especially if the complex nature of the alloy and the scale is considered. This is particularly true for relatively short reaction times (6 hr), with a scatter of K_p values of $\pm 10\%$ at 800°C and $\pm 2\%$ at the other temperatures. For longer times increasing deviations are observed,

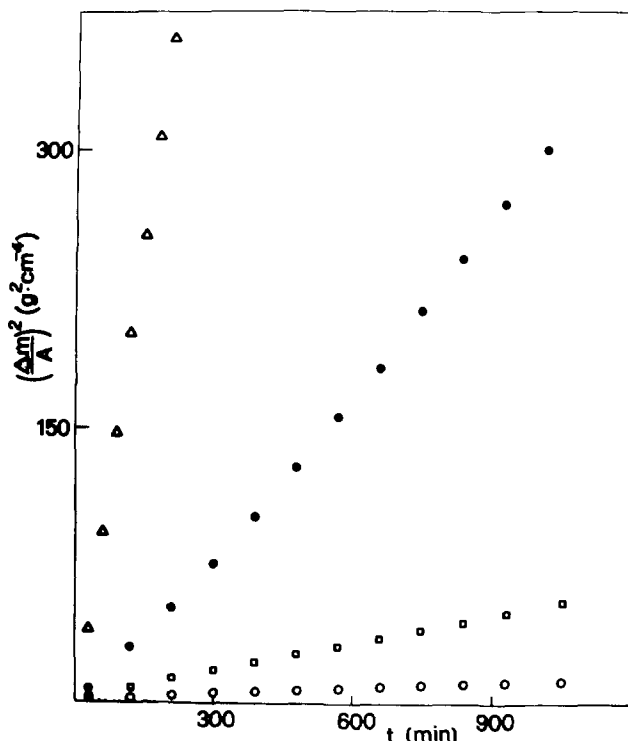


Fig. 2. Parabolic plot of the weight gain as a function of time: ○ 700°C, □ 800°C, ● 900°C, △ 1000°C.

Table I.

T (°C)	Parabolic rate constants ($g^2 cm^{-4} sec^{-1}$)			k_{Cu}	k_{Fe}
	Cu	Fe (8)	Alloy	k_{all}	k_{all}
700	1.72×10^{-9} (6)	6.0×10^{-9}	2.61×10^{-10}	6.6	23
800	5.53×10^{-9} (6)	5.7×10^{-9}	8.61×10^{-10}	6.4	66
900	2.80×10^{-8} (7)	2.5×10^{-7}	4.73×10^{-9}	5.9	53
1000	8.1×10^{-8} (7)	1.1×10^{-6}	$\sim 3.11 \times 10^{-8}$	2.6	35

the rate constant up to 18 hr showing on the average an increase with time at 900° and 1000°C and a decrease at 700°C; there is no definite trend at 800°C. Average values of the parabolic rate constant calculated for 6 hr oxidation are reported in Table I ($g^2 cm^{-4} sec^{-1}$).

A comparison of the alloy oxidation kinetic constants with those of the pure base metals (Table I) shows an improved resistance of the alloy to oxidation; the alloy oxidizes marginally more slowly than pure copper, but substantially more slowly than iron. The ratio between alloy and pure copper parabolic rate constants remains almost constant up to 900°C and then decreases sharply, whereas for a similar ratio between the alloy and iron a maximum is observed at 800°C.

Identification of scale products.—X-ray diffraction analysis of the scale still adherent to the alloy reveals the presence of CuO and two iron oxides (FeO and Fe_3O_4): sometimes also other lines are observed which can be attributed to a mixed oxide $CuFeO_2$ (delafossite). Although this compound is well known (9) and its x-ray diffraction pattern established (10), more recent studies (11) throw some doubts on its existence, a conclusion which is probably related to the instability of this compound under high oxygen pressures. In the scale examined in the present work, the mixed oxide is always present under an outer CuO layer and therefore can be stabilized by the relatively low oxygen potential at that location. Point microanalysis always gives a copper/iron molar ratio very close to that expected for this phase.

The distribution of the different phases in the scale can be found by a combined use of different techniques, such as observations under the optical microscope, the electron microscope in the backscattered

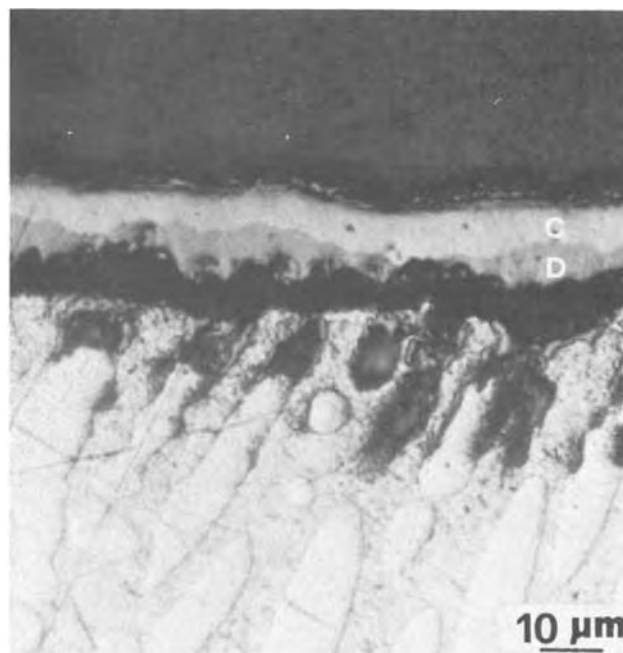
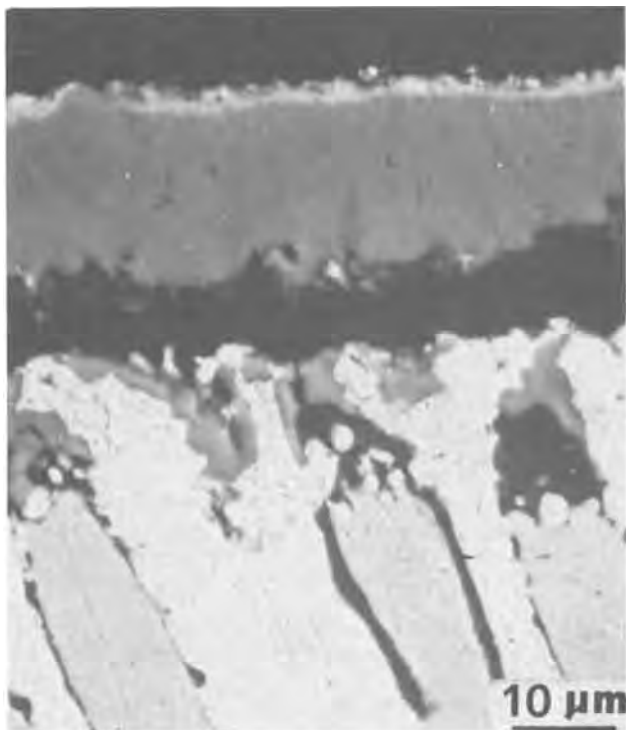


Fig. 3. Cross section of the scale formed on the alloy oxidized for 18 hr at 700°C, optical micrograph. C: Fe_3O_4 ; D: FeO.

electron-image mode which is sensitive to composition (BEI), and by the use of x-ray maps. The two iron oxides are clearly differentiated under optical observation, while copper oxide and the mixed oxide are very similar in appearance and can be distinguished from iron oxides only under very favorable conditions. BEI micrographs, on the other hand, do not differentiate between the iron oxides, but clearly show the differences between copper oxide (light gray), mixed oxide (intermediate gray), and the iron oxides (dark gray): this is confirmed by the corresponding x-ray maps and by point microanalysis performed in the various phases.

Scale microstructure and composition.—700°C.—The essential features of the scale formed at this temperature are independent of exposure time and are shown in Fig. 3 and 4. The outermost scale layer is primarily CuO; in many cases it becomes detached from the remainder of the scale, and also its thickness varies irregularly around the sample section. Quantitatively the Fe content is difficult to measure, because of the limited thickness of the layers; it appears to be quite low. Beneath this outer layer is a layer containing a light intermediate zone (Fe_3O_4) and an inner darker zone (FeO), although these differences are not detected in the BEI image of Fig. 4 as indicated earlier. In a



a. BEI

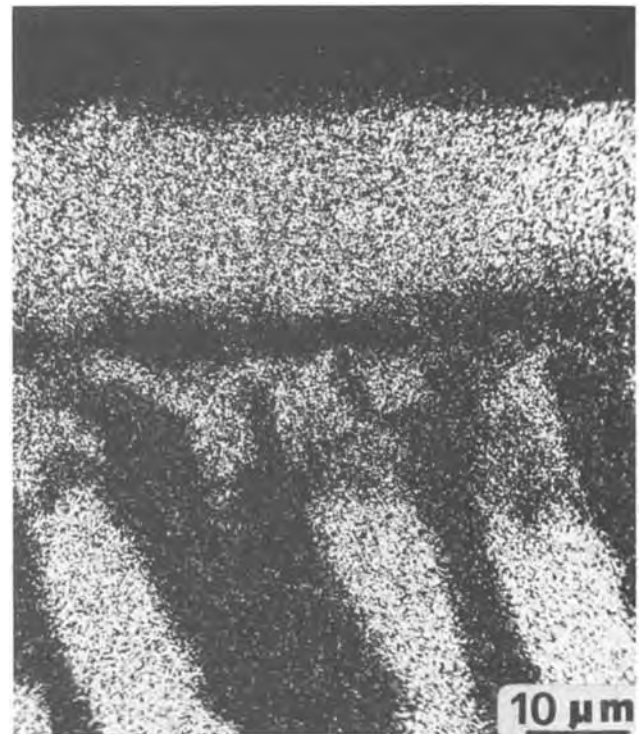
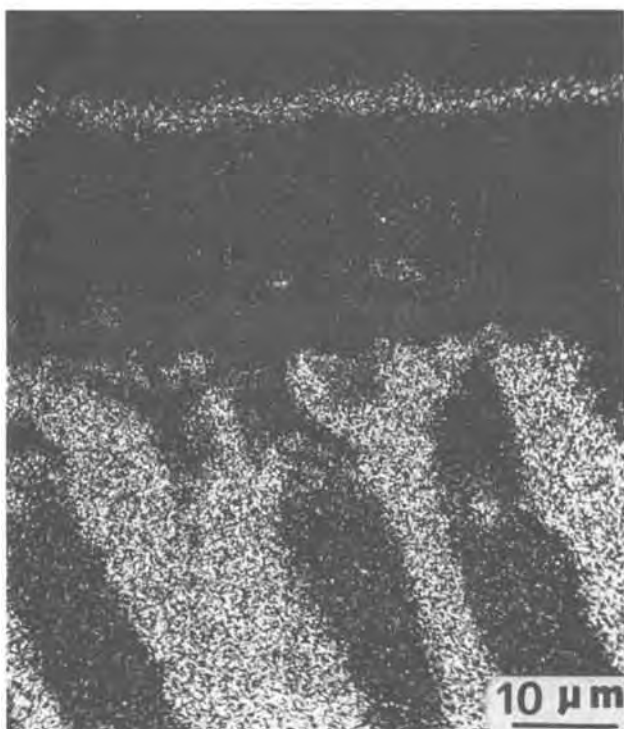
c. FeK α imageb. CuK α image

Fig. 4. Cross section of the scale formed on the alloy oxidized for 18 hr at 700°C.

few locations the magnetite phase appears to extend right up to the alloy/scale interface; normally it is separated from the alloy by an intervening FeO layer (Fig. 3). Point analysis of the Fe_3O_4 layer indicates a low solubility of Cu, 0.5 w/o Cu in Fe_3O_4 .

The interface between the scale and the alloy is very undulating due to the preferential oxidation of the Fe-rich islands in the alloy; the Cu grains remain intact up to the scale/alloy interface and can even be incorporated unoxidized into the scale. The oxidation of the Fe-rich grains in the alloy completely encircles the unoxidized Cu grains, and these can extend up to half-way across the scale before they are converted to oxide.

800°C.—The scales formed at 800°C are similar in many aspects to those formed at 700°C, except for the appearance of an additional phase sometimes between the FeO and Fe_3O_4 layers, but more normally between the outer CuO layer and the underlying Fe_3O_4 phase; Fig. 5 and 6 show typical examples. Microanalysis identifies this phase as the mixed oxide CuFeO_2 , referred to earlier. It appears as an intermediate shade of gray in the optical micrograph, Fig. 5, and more clearly in the BEI image and x-ray images of Fig. 6.

In the optical micrograph of Fig. 5, in which the various oxides of iron can be distinguished [FeO (dark), Fe_3O_4 (light)], it seems that FeO separates the magnetite layer from the alloy along much of the interface and is also formed within the Fe-rich grains of the alloy. However, where the mixed oxide CuFeO_2 forms below the magnetite, then this can extend up to the alloy surface. The numerous voids at and under the alloy/scale interface appear to be a result of scale pull-out during polishing. Finally, the outer CuO layer tends to vary in thickness around the sample section as observed at lower temperatures; generally however it is thicker.

At longer oxidation times, the mixed oxide appears to be largely confined to a region immediately below the outer CuO layer. In addition, FeO is mainly present only in the internally oxidized region and most of the iron in the outer scale is present as magnetite. Otherwise the scale morphology changes little with time.

It was possible to measure the Fe content of the outer CuO layer at this temperature and EPMA gave a value of 8-9 w/o. The solubility of Cu was around

0.75 w/o in the magnetite, but up to 2.5 w/o in the inner FeO layer.

900°C.—Figure 7 shows a typical scale cross section at 900°C enabling the four principal scale layers to be identified: outer CuO, a layer of CuFeO_2 or magnetite layer, and an inner wustite layer. In addition, as at the lower temperatures, there is a form of internal oxidation of the Fe islands within the alloy. After longer oxidation times, 18 hr, at this temperature, the outer CuO zone develops considerable porosity, which tends to be elongated in the growth direction and is shown in Fig. 8. The amount of Fe dissolved in this layer is about 7 w/o and the Cu concentration in the inner layers is 3.5 and 1.0 w/o in FeO and Fe_3O_4 , respectively.

1000°C.—A distinctive feature of the scale present on the alloy at this temperature and not at the lower temperatures is the porosity which has developed in the outer CuO layer. Some of the porosity is clearly accentuated during metallographic preparation, but nevertheless a large portion of it is inherent. The pores are elongated in the growth direction and seem to initiate at the inside of this layer. In most locations the CuO layer is completely detached from the underlying scale. This is illustrated in Fig. 9 and 10. The accompanying x-ray maps also indicate the layer of mixed oxide, CuFeO_2 , immediately below the outer CuO layer, and also the presence of this phase as elongated precipitates within the inner Fe-rich oxides, mainly FeO. At some positions an intermediate layer of Fe_3O_4 is also observed, formed inside the FeO layer, probably as a consequence of scale cracking, not evident in the micrograph. After 18 hr oxidation the scale structure is rather similar although internal oxidation of the Fe-rich phase of the alloy is very pronounced; Fig. 11 and 12. Surprisingly most of the internal oxide has been lost, presumably during metallographic preparation. Where the oxide does remain near to the alloy/scale interface, it is primarily FeO. Cu solubilities in Fe_3O_4 and FeO at this temperature were 2.5 and 8.0 w/o, respectively; Fe solubility in the CuO was not measurable using EPMA because of the high porosity.

Discussion

Although the scale structures described in the previous section are rather complex, they essentially consist of an outer layer of CuO, containing a small concentration of dissolved Fe, and inner layers of magnetite and wustite, both containing Cu in solution, whose concentration increases with increasing temperature. In particular the wustite layer, with the exception of samples oxidized at 1000°C, has a smaller relative thickness than in the oxidation of pure iron, where it amounts to about 0.95 of the entire scale from 700° to 1200°C (12). In addition, at the higher temperatures a layer of the compound oxide CuFeO_2 forms between the CuO and magnetite layers and as a precipitate within the magnetite. Beneath the scale there is a region of internal oxidation, having a thickness comparable to that of the external scale, and where the Fe-rich dendrites in the alloy have been oxidized to FeO.

The outer layer of CuO presumably formed in the early transient stages of oxidation (13) when on initial exposure of the alloy both alloy components will form their respective oxides. However, because of its higher relative affinity for oxygen, iron is eventually selectively oxidized from the alloy and continuous layers of magnetite and wustite will develop at the alloy/scale interface. In effect, the copper oxide is then cut off from its direct supply of Cu ions from the alloy, although there may be a reduced continuing flux of copper through the scale, since it is soluble in the iron oxides.

Below the outer CuO region the scale contains principally iron oxides. Magnetite is not stable, however,

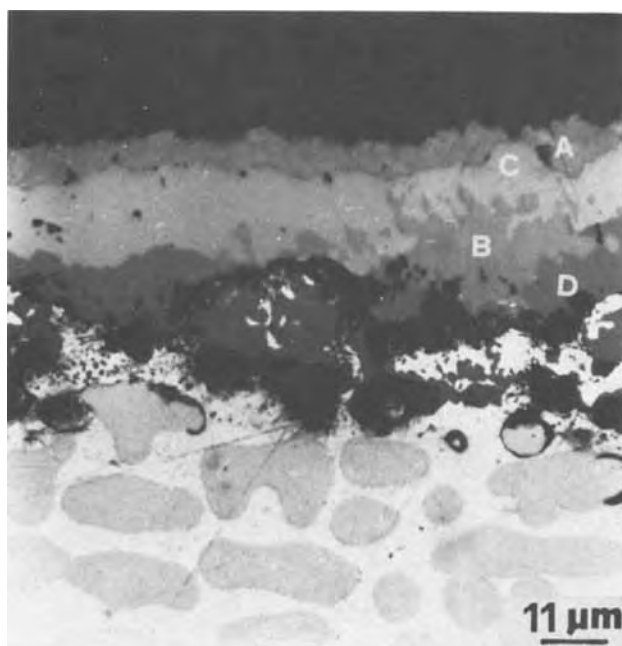
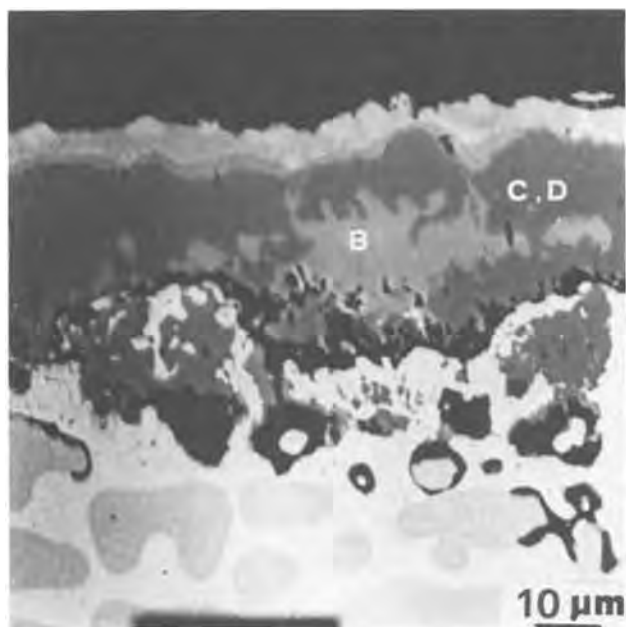
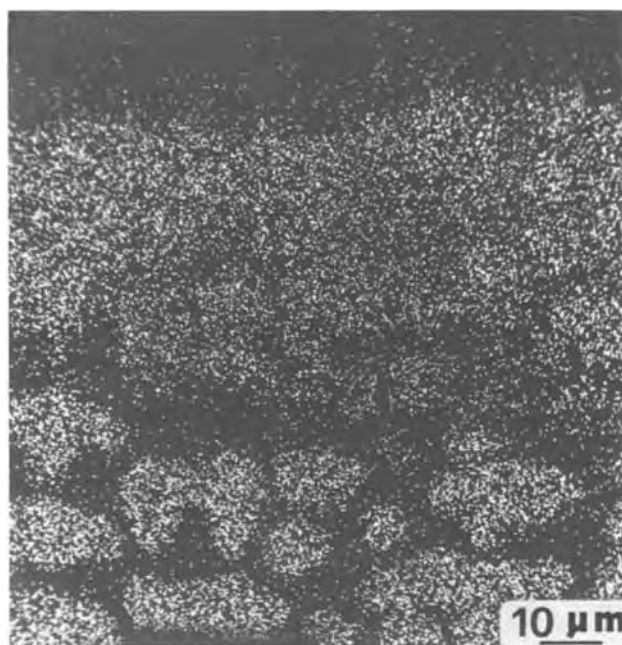


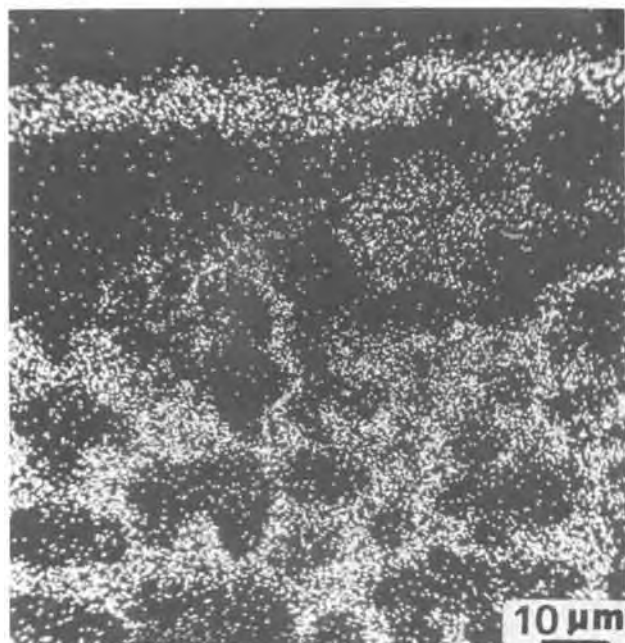
Fig. 5. Cross section of the scale formed on the alloy oxidized for 6 hr at 800°C, optical micrograph. A, CuO; B, CuFeO_2 ; C, Fe_3O_4 ; D, FeO.



a. BEI: A, CuO; B, CuFeO₂; C, Fe₃O₄; D, FeO (C and D not differentiated).



c. FeK α image



b. CuK α image

Fig. 6. Cross section of the scale formed on the alloy oxidized for 6 hr at 800°C.

in contact with CuO since the lowest value of the oxygen activity at the inner interface of CuO corresponds to the CuO/Cu₂O equilibrium and amounts of 5.88×10^{-3} at 700°C and to 0.374 at 1000°C, while the highest activity of oxygen at the outer interface of magnetite is much smaller, amounting to 2.85×10^{-6} at 700°C and to 2.62×10^{-3} at 1000°C. Therefore, the two phases must be separated by either Cu₂O or Fe₂O₃ or both. These compounds are never observed, however, either because CuO and magnetite are separated by an intervening layer of the mixed oxide CuFeO₂ formed by chemical interaction between copper oxide and iron oxide, as it occurs at high temperatures, or even because the effective thickness of these layers is too small to be detected.

In any case oxygen is supplied to the inner iron oxides from the outer CuO layer either directly or through the intermediate mixed oxide, producing an outward flux of copper in the CuO layer. At high temperatures the corresponding inward flux of vacancies

through CuO is not completely incorporated into the underlying mixed oxide and can condense out in a porous region at the interface. Eventually the CuO layer may become completely detached and a dissociative-type mechanism for the supply of oxygen to the inner scale region can take over. An extreme situation of this kind would correspond to the formation of a continuous porous network in the outer layer, with oxygen being supplied directly from the gas phase to the inner scale regions. This seems particularly likely at 1000°C in view of the high porosity in CuO.

At the alloy/scale interface oxygen is supplied by partial dissociation of the scale and dissolves into the alloy. In view of the very large difference between the thermodynamic stability of the oxides of the two metals, iron is preferentially oxidized producing FeO, while copper cannot be oxidized due to the low oxygen potential established there, and the network of copper-rich grains remains relatively intact. As the scale grows and encroaches into the alloy, copper particles

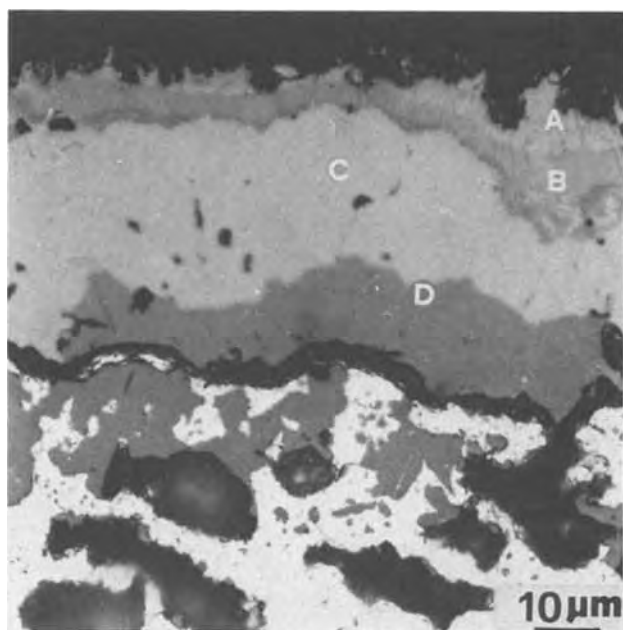


Fig. 7. Cross section of the scale formed on the alloy oxidized for 6 hr at 900°C, optical micrograph. A, CuO; B, CuFeO₂; C, Fe₃O₄; D, FeO.

are incorporated into it and are subsequently oxidized when exposed to a sufficiently high oxygen activity. Copper is oxidized in the scale mainly to CuFeO₂ which partly dissolves into the surrounding iron oxides and partly remains as isolated particles.

It is appropriate at this point to consider how the features of the scale formed on this alloy, reported above, would affect the overall oxidation rate, which at any temperature is smaller than for either of the pure metals. The reduction in rate in comparison with that of pure Fe is especially significant since the scale consists mainly of the oxides of Fe. Undoubtedly it is due to many concurrent effects in view of the complexity of the structure of the alloy and also of the scale. These are now considered individually.

The absence of an outer hematite layer should not have a great influence, since it grows rather slowly, even on pure iron. The reduction of the relative thickness of the wustite layer could instead have a marked effect, since this oxide has a large defect concentration and a correspondingly high cation diffusivity. The effect of this on the reaction kinetics has been discussed in greater detail in a study of the oxidation of an iron-rich monophase Fe-Cu alloy published elsewhere (14), which has a simpler scale composition, where it is shown that the reaction rate can be strongly decreased in this way. The situation of the two-phase alloy is more complex, however, not only because of the presence of CuO and the mixed oxide in the outer region of the scale, but also because the interface between FeO and Fe₃O₄ is often very irregular. Moreover from 700° to 900°C the wustite layer is even discontinuous, since at some positions magnetite reaches the scale interface, while at 1000°C a continuous thick layer of FeO is developed.

A rough estimate of the influence of this aspect of the scale structure on the scaling constant can be obtained by ignoring the presence of FeO and evaluating the growth rate expected in presence of magnetite alone. The rate constant for the direct formation of magnetite on an iron alloy having a metal activity at the alloy/scale interface corresponding to the equilibrium FeO/Fe₃O₄ and an oxygen activity at the outer magnetite interface as required for the equilibrium Fe₃O₄/Fe₂O₃ is one-fourth of the so-called third-kind rate constant for the magnetite growth (15), as shown in the Appendix. The latter has been calculated from

the experimental results on the oxidation of iron and has been reported in an earlier paper (16). Unfortunately there was an error in the quoted value and the correct value is given as a function of temperature as (17)

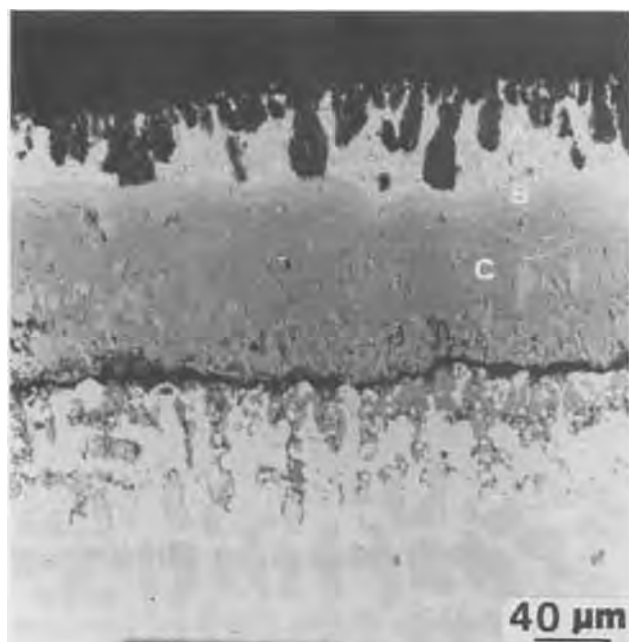
$$k_p(\text{Fe}_3\text{O}_4) = 2.08 \exp(-40.8/RT)$$

Thus, the required rate constant $k' = k_p/4$ amounts to ($\text{g}^2 \text{cm}^{-4} \text{sec}^{-1}$) 3.517×10^{-10} at 700°C, 2.517×10^{-9} at 800°C, 1.288×10^{-8} at 900°C and 5.097×10^{-8} at 1000°C. These values are somewhat higher than the experimental rate constant for this alloy, in spite of the presence of some FeO, particularly at 1000°C, in the scales. The presence of FeO should imply that the above calculated rate constants represent minimum values, and the other factors are presumably involved. In particular, the oxygen activity at the outer magnetite interface could be lower than that for the Fe₃O₄/Fe₂O₃ equilibrium as assumed above. Indeed, Fe₂O₃ is not observed in the scale. This situation would lead to a decrease of the rate constant for the growth of magnetite and thereby of the overall rate constant.

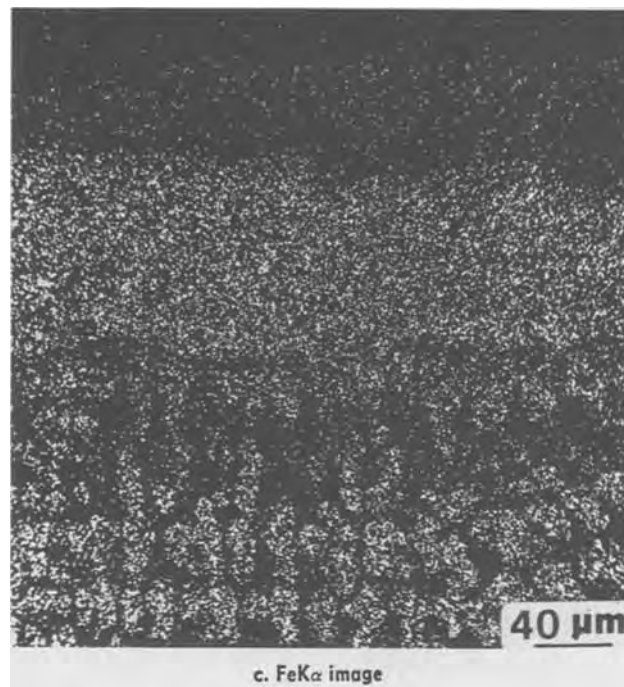
A contribution to the decrease of the scaling rate can also come from the dissolution of copper in iron oxides. In fact FeO, in spite of the large deviations from stoichiometry and the complex nature of its defects, is essentially a p-type semiconductor, so that the presence of copper, most probably in the form of Cu⁺ ions owing to the low oxygen activity, should produce a decrease of the vacancy concentration and hence slow down the diffusion of iron. Actually large additions would be thought necessary for this effect due to the high concentration of native defects in FeO as compared to similar oxides like NiO or CoO (18): observations on the influence of Li₂O on the rate of formation of FeO (19) and on the rate of oxidation of Fe-Cr alloys (20) are in substantial agreement with this prediction, even if the effect is small. In addition, the presence of foreign ions in magnetite is known to produce a strong decrease of the iron mobility (21).

The two-phase alloy oxidizes more slowly even than the monophase iron-rich alloy, since the reduction factor of the parabolic rate constant with respect to iron for the latter system ranges from 4 to 9 according to the temperature (14), so that additional factors are operating to reduce the reaction rate further in this alloy. The main differences between the scale structure of the mono- and two-phase alloys are the absence of the outer layers of CuO and mixed oxide, the greater relative thickness of the FeO layer, except at 1000°C, and the absence of the internal oxidation region in the former system. In addition the copper concentration in the iron oxides is much larger for the two-phase alloy. All these aspects can affect the oxidation rate, but in view of the previous discussion the destabilization of wustite and copper dissolution in iron oxides seem to be the most important factors.

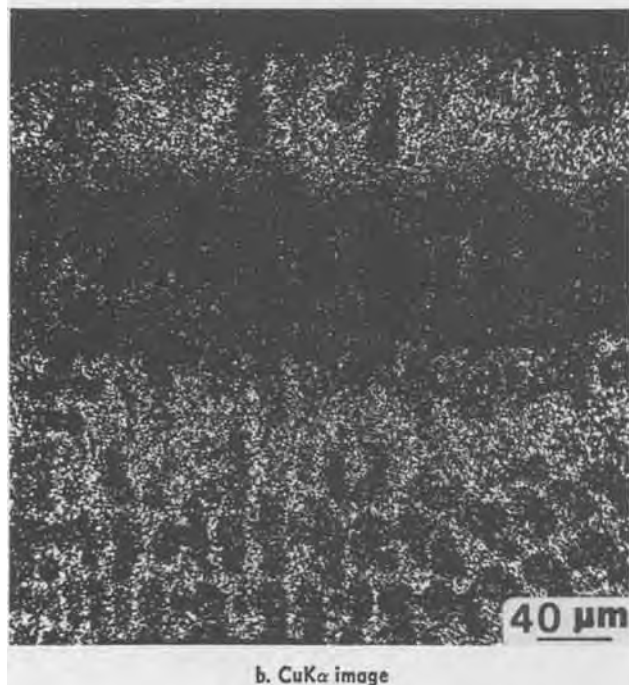
Possible stress effects associated with the development of different oxides growing at different rates on the alloy seem to be absent from this system. In fact, the scale appears compact and of uniform thickness and shows no lateral variations in structure or composition, at least none which can be directly associated with the two-phase structure of the alloy only. The thickness of the wustite layer sometimes shows large variations around the surface of the sample where at some positions it is confined to the internal oxidation region while in others it extends far into the scale. The relative uniformity of the scale structure is possibly related to the small grain size of the alloy, so that Cu-rich and Fe-rich regions in the alloy alternate frequently at the alloy/oxide interface and lateral diffusion is sufficiently rapid to even out these fluctuations: differences in the scale structure are in fact confined mainly in a direction perpendicular to the alloy surface rather than parallel to it.



a. BEI: A, CuO; B, CuFeO₂; C, Fe₃O₄



c. FeK α image



b. CuK α image

Fig. 8. Cross section of the scale formed on the alloy oxidized for 18 hr at 900°C.

Conclusions

The results obtained in this study on the oxidation of a two-phase alloy lead to the following conclusions.

1. The alloy oxidizes more slowly than the constituent pure metals, especially, Fe, at all temperatures in the range 700°–1000°C.

2. A number of factors are involved in the reduction in rate but that of particular importance is the partial destabilization of wustite due to a large decrease in the iron activity at the alloy/scale interface.

3. The inner regions of the scale contains mainly iron-rich oxides and the outer scale layer is CuO. This CuO layer is virtually cut off from the alloy after the initial transient stages. Porosity, more pronounced at 1000°C, develops between the outer CuO and Fe₃O₄ layers, as a result of an exchange reaction at that interface and the continued flux of copper through the outer CuO layer. This can lead to complete detachment of the outer layer and a dissociative-type mechanism.

4. Internal oxidation of the iron-rich phase in the alloy is always observed to a thickness comparable with that of the external scale. This also produces a depletion of iron in the surrounding Cu-rich matrix, as evidenced by the destabilization of FeO and the concomitant reduction in the relative thickness of the FeO layer in the scale in comparison with the oxide scales formed on pure Fe.

5. The two-phase nature of the alloy does not seem to have any particular effect on the scale properties. This is presumably related to the rather regular and closely spaced distribution of the two phases in the alloy. Certainly, stress development due to the accommodation within the scale of two phases oxidizing at different rates are not evident.

Acknowledgments

Thanks are due to Mr. M. Piazza for his help in the experimental part of this work.

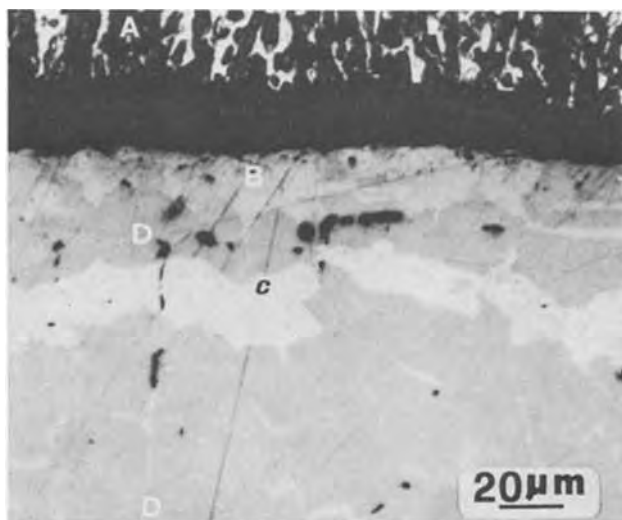
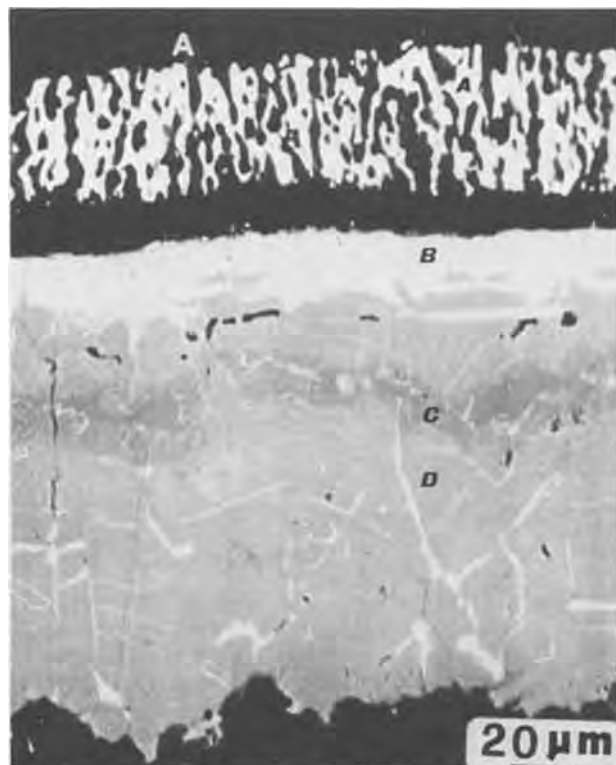
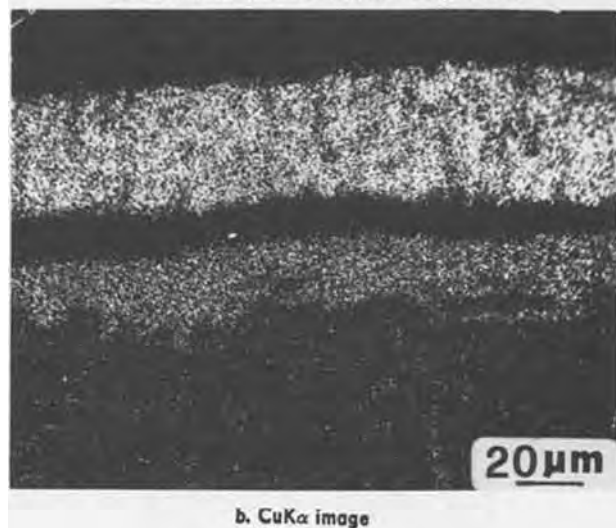


Fig. 9. Cross section of the scale formed on the alloy oxidized for 6 hr at 1000°C, optical micrograph. A, CuO; B, CuFeO₂; C, Fe₃O₄; D, FeO.



a. BEI: A, CuO; B, CuFeO₂; C, Fe₃O₄; D, FeO



b. CuKα image

Manuscript submitted Sept. 28, 1979; revised manuscript received Feb. 25, 1980.

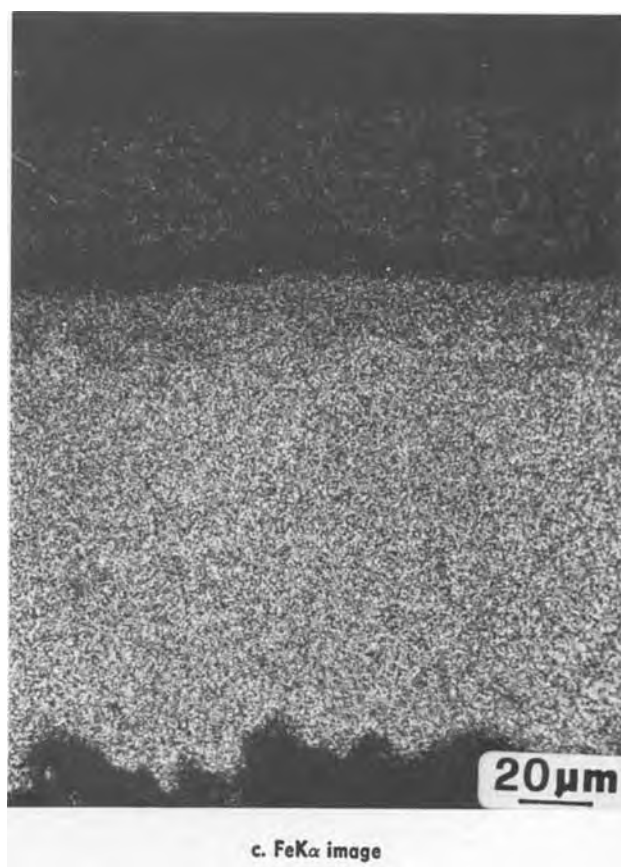
Any discussion of this paper will appear in a Discussion Section to be published in the June 1981 JOURNAL. All discussions for the June 1981 Discussion Section should be submitted by Feb. 1, 1981.

Publication costs of this article were assisted by Centro Studi di Chimica e Chimica Fisica Applicata alle Caratteristiche di Impiego dei Materiali del Consiglio Nazionale delle Ricerche.

APPENDIX

The relationship between the rate constant for the direct growth of magnetite on an iron alloy at a surface iron activity corresponding to the equilibrium FeO/Fe₃O₄ and an oxygen activity at the outer surface corresponding to the equilibrium Fe₃O₄/Fe₂O₃ and the rate constant of third kind for magnetite growth (15) is obtained as follows.

The systems to be considered are referred to as A and B and are schematized below



c. FeKα image

Fig. 10. Cross section of the scale formed on the alloy oxidized for 6 hr at 1000°C.

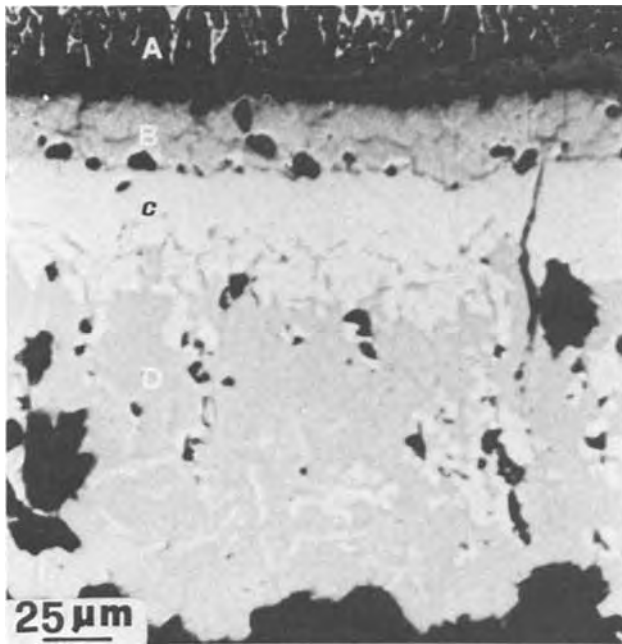
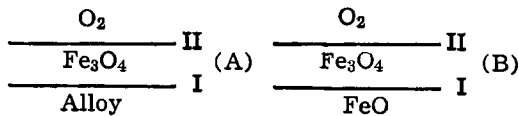


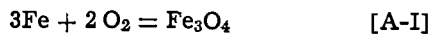
Fig. 11. Cross section of the scale formed on the alloy oxidized for 18 hr at 1000°C, optical micrograph. A, CuO; B, CuFeO₂; C, Fe₃O₄; D, FeO.



The oxygen activity in the gas phase is assumed to correspond to the magnetite/hematite equilibrium in both cases, while the iron activity at the interface I corresponds to the equilibrium FeO/Fe₃O₄, so that FeO is completely destabilized in system A. If the oxidation rate is controlled by diffusion through the magnetite layer, the flux of iron ions J for both systems is related to the parabolic rate constant k_t (molecules cm⁻¹ sec⁻¹) by (22)

$$\frac{J}{3} = \frac{dn}{dt} = \frac{k_t}{x} \quad [\text{A-1}]$$

where dn is the number of Fe₃O₄ formula units formed in the time dt per unit area at the interface II by the reaction



and x is the instantaneous thickness of the magnetite layer. For an exclusive cation diffusion in an oxide M_aO_b, one has (23)

$$k_t = \frac{c_0}{a} \int_{a_0^i}^{a_0^e} D_M d \ln a_0 \quad [\text{A-2}]$$

The relationship between the weight of oxygen of the magnetite layer per unit area q , the corresponding number of moles n , and the thickness x are

$$q = \frac{4M(\text{O})}{N_A} n = \frac{4dM(\text{O})}{M(\text{Fe}_3\text{O}_4)} x \quad [\text{A-3}]$$

(N_A = Avogadro's number, d = oxide density, $M(\text{O})$ = atomic weight of oxygen, $M(\text{Fe}_3\text{O}_4)$ = molecular weight of magnetite). Deriving Eq. [A-3] with respect to t and using Eq. [A-3], [A-9], and [A-10] results in, the system A

$$\begin{aligned} \frac{dq(\text{A})}{dt} &= \frac{k(\text{A})}{2q(\text{A})} = \frac{4M(\text{O})}{N_A} \frac{dn(\text{A})}{dt} \\ &= \frac{4M(\text{O})}{N_A} \frac{k_t}{x(\text{A})} = \frac{16dM^2(\text{O})}{N_A M(\text{Fe}_3\text{O}_4)} \frac{k_t}{q(\text{A})} \end{aligned} \quad [\text{A-4}]$$

or

$$k(\text{A}) = 16 \frac{2dM^2(\text{O})}{N_A M(\text{Fe}_3\text{O}_4)} k_t \quad [\text{A-5}]$$

On the contrary, deriving Eq. [A-3] with respect to t and using Eq. [A-3], [A-9], and [A-13] results in the system B

$$\begin{aligned} \frac{dq(\text{B})}{dt} &= \frac{k(\text{B})}{2q(\text{B})} = \frac{4M(\text{O})}{N_A} \frac{dn(\text{B})}{dt} \\ &= 4 \frac{4M(\text{O})}{N_A} \frac{k_t}{x(\text{B})} = 4 \frac{16dM^2(\text{O})}{N_A M(\text{Fe}_3\text{O}_4)} \frac{k_t}{q(\text{B})} \end{aligned} \quad [\text{A-6}]$$

or

$$k(\text{B}) = 64 \frac{2dM^2(\text{O})}{N_A M(\text{Fe}_3\text{O}_4)} k_t \quad [\text{A-7}]$$

Comparing Eq. [A-5] and [A-7] gives finally

$$k(\text{A}) = k(\text{B})/4 \quad [\text{A-8}]$$

where D_M is the self-diffusion coefficient of the metal ions in the oxide, c_0 the concentration of oxygen in the oxide (ions cm⁻³), and a_0^i and a_0^e are the oxygen activities at the metal/scale and scale/gas interfaces, respectively.

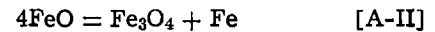
If a_0^i and a_0^e are the same for the two systems, as assumed here, k_t will be the same in both, since D_M depends on a_0 in the same way. However, in spite of the equality of k_t , the parabolic rate constants as functions of the weight of oxygen in magnetite per unit area for the two systems, defined by

$$q^2(\text{A}) = k(\text{A})t \quad \text{and} \quad q^2(\text{B}) = k(\text{B})t \quad [\text{A-9}]$$

differ. In fact, for the system A Fe₃O₄ forms only at the interface II with the rate defined by Eq. [A-1] and controlled by the iron flux J in the form

$$\frac{dn(\text{A})}{dt} = \frac{J}{3} = \frac{k_t}{x(\text{A})} \quad [\text{A-10}]$$

while in the system B Fe₃O₄ forms at the interface I by the reaction



creating the flux J diffusing through the magnetite layer and oxidized at the interface II according to reaction [A-1]. Reaction [A-II] requires however, that one formula unit of magnetite forms at the interface I for every Fe ion diffusing in magnetite. The rate of formation at the two interfaces are

$$\frac{dn(\text{B})(\text{II})}{dt} = \frac{J}{3} = \frac{k_t}{x(\text{B})} \quad [\text{A-11}]$$

and

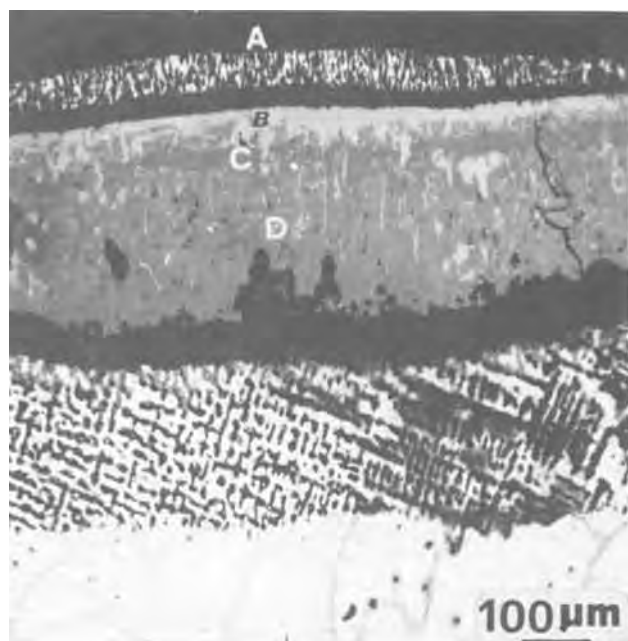
$$\frac{dn(\text{B})(\text{I})}{dt} = 3 \frac{J}{3} = 3 \frac{k_t}{x(\text{B})} \quad [\text{A-12}]$$

and the overall rate of formation of magnetite results

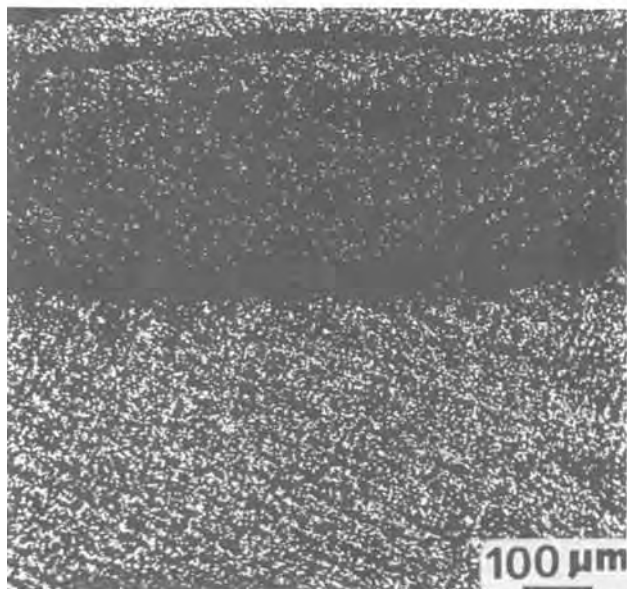
$$\frac{dn(\text{B})}{dt} = \frac{dn(\text{B})(\text{I})}{dt} + \frac{dn(\text{B})(\text{II})}{dt} = \frac{4}{3} J = 4 \frac{k_t}{x(\text{B})} \quad [\text{A-13}]$$

REFERENCES

1. C. Wagner, *Corros. Sci.*, **9**, 9 (1969).
2. D. E. Coates and A. D. Dalvi, *Oxid. Met.*, **2**, 331 (1970).
3. B. D. Bastow, D. P. Whittle, and G. C. Wood, *Corros. Sci.*, **16**, 57 (1976).
4. B. D. Bastow, D. P. Whittle, and G. C. Wood, *Proc. R. Soc. London, Ser. A*, **356**, 177 (1977).
5. G. Salje and M. Feller-Kniepmeier, *Z. Metallkd.*, **69**, 167 (1978).
6. D. W. Bridges, J. P. Baur, G. P. Baur, and W. M. Fassel, Jr., *This Journal*, **103**, 475 (1956).
7. S. Mrowec and A. Stoklosa, *Oxid. Met.*, **3**, 291 (1971).
8. M. H. Davies, M. T. Simnad, and C. E. Birchenall, *Trans. AIME*, **191**, 889 (1951).



a. BEI: A, CuO; B, CuFeO₂; C, Fe₃O₄; D, FeO



b. CuK α image



c. FeK α image

Fig. 12. Cross section of the scale formed on the alloy oxidized for 18 hr at 1000°C.

9. R. A. Yund and G. Kellerud, *Am. Mineral.*, **49**, 689 (1964)
10. W. Saller and A. J. Thompson, *Phys. Rev.*, **47**, 644 (1935).
11. A. M. M. Gadalla and J. White, *Trans. Br. Ceram. Soc.*, **65**, 1 (1966).
12. J. Paidassi, *Acta Metall.*, **6**, 184 (1958).
13. B. Chattopadhyay and G. C. Wood, *Oxid. Met.*, **2**, 373 (1970).
14. P. Nanni and F. Gesmundo, *Corrosion (Houston)*, **36**, 119 (1980).
15. F. Gesmundo and F. Viani, *Corros. Sci.*, **18**, 217 (1978).
16. F. Gesmundo and F. Viani, *ibid.*, **18**, 231 (1978).
17. F. Gesmundo and F. Viani, *ibid.*, **18**, 437 (1978).
18. G. C. Wood, I. G. Wright, T. Hodgkiess, and D. P. Whittle, *Werkst. Korros.*, **21**, 900 (1970).
19. E. Brauns and A. Rahmel, *ibid.*, **7**, 448 (1956).
20. C. S. Tedmon Jr., *Corros. Sci.*, **7**, 525 (1967).
21. C. E. Birchenall, in "Oxidation of Metals and Alloys," D. L. Douglass, Editor, ASM, Metals Park, Ohio (1970).
22. P. Kofstad, "High-Temperature Oxidation of Metals," p. 116, John Wiley & Sons, Inc., New York (1966).
23. P. Kofstad, *ibid.*, p. 119.

Reversal of Relative Oxidation Rates of $\langle 111 \rangle$ and $\langle 100 \rangle$ Oriented Silicon Substrates at Low Oxygen Partial Pressures

S. I. Raider¹ and L. E. Forget

IBM System Products Division, East Fishkill Facility, Hopewell Junction, New York 12533

ABSTRACT

Crystalline Si wafers oriented in the $\langle 100 \rangle$ and $\langle 111 \rangle$ planes were oxidized in ambients containing low oxygen partial pressures to examine the role played by oxidant pressure on relative oxidation rates. The grown oxide films were formed at temperatures between 850° and 1050°C and were less than 300Å thick. Substrates with $\langle 111 \rangle$ oriented surfaces are generally oxidized more readily than substrates with $\langle 100 \rangle$ orientations at the same oxidation temperature and oxidant pressure. However, a reversal in the relative oxidation rates of these crystalline Si substrates was observed at low oxygen partial pressures. This reversal was nearly independent of oxidation temperature and also of oxidant diluent gas. A qualitative model is proposed to account for these results.

Thermal growth of SiO₂ films on Si substrates in an oxygen ambient takes place at an SiO₂-Si interface (1) after oxygen is diffused to the substrate. The oxidation reaction occurs at the substrate and goes to completion in the partially oxidized transition region located between the crystalline substrate and the amorphous SiO₂ film. Oxygen reacts with accessible, nonoxidized Si-Si bonds to form siloxane groups. At a fixed temperature, the Si oxidation rate is altered by changes in the partial pressure of oxygen, p_{O_2} (1-4), in oxide film thickness, and in the crystalline substrate orientation (2, 5, 6).

Si oxidation rates are rate-controlled by the crystalline substrate surface orientation in the thin (<300Å) film thickness region. The oxidation rate within the interfacial reaction zone is dependent upon the oxygen concentration in this region. The oxygen concentration in this zone is directly proportional to the oxygen partial pressure in the oxidizing ambient (1, 7, 8).

The dependence of Si oxidation kinetics upon substrate orientation has been observed in the thin film range at temperatures below, but not at, 1200°C (2-6). At a given oxidation temperature and oxidant pressure, single crystal Si substrates with $\langle 111 \rangle$ oriented surfaces (2, 5, 6) generally oxidize more readily in oxygen and in water vapor ambients than substrates with $\langle 100 \rangle$ orientations. The number of accessible, nonoxidized Si-Si bonds at the substrate surface and within the SiO₂-Si transition regions is greater on $\langle 111 \rangle$ Si than on $\langle 100 \rangle$ Si (5, 9-11). As a consequence of this difference in observed oxidation kinetics at a constant p_{O_2} for substrates with $\langle 100 \rangle$ and $\langle 111 \rangle$ orientations, a relationship between thermal oxide growth rates and the accessible Si-Si bond concentration at the interface was proposed (5, 11).

Si oxidation kinetics in this thin film range are often approximated by linear growth. The linear rate constant, k_{lin} , for oxidation of $\langle 111 \rangle$ and $\langle 100 \rangle$ oriented Si decrease with p_{O_2} at 850°C and at 1000°C in O₂/N₂ ambients (2). At a given oxidation temperature, straight line plots of k_{lin} vs. p_{O_2} indicate a stronger pressure dependence on oxidation of $\langle 111 \rangle$ oriented substrates than on oxidation of $\langle 100 \rangle$ oriented substrates. The plots are not parallel but intersect at a nonzero value of p_{O_2} . The relative magnitudes of $\ln k_{lin}\langle 111 \rangle$ and of $\ln k_{lin}\langle 100 \rangle$ reverse when one extrapolates to low oxygen partial pressures.

Cabrera and Mott (12) have proposed a steric argument in which the order of increasing oxidation rates is the same as the density of decreasing atoms on the crystalline faces. This model predicts that the $\langle 100 \rangle$ face of Si should oxidize faster than the $\langle 111 \rangle$ face. Kamigaki and Itoh (13) have fit their Si oxidation rate data to the Cabrera-Mott oxidation equation for oxide films $\leq 200\text{Å}$ thick and $p_{O_2} \leq 10^{-2}$ atm. They have observed pressure-dependent reversals in relative oxidation rates of oriented Si substrates after oxidizing at 1100°C in O₂/N₂ ambients. Much of their data is obtained at O₂ pressures at which the N₂ diluent, which can react with Si (14, 15), may affect the Si oxidation kinetics.

The extent to which nitrogen interaction with Si alters the oxidation kinetics at low oxygen partial pressures is unknown. Nitridation reactions are known to occur at the SiO₂-Si interface provided that the oxidant concentration is sufficiently low (14, 15). In order to determine whether a reversal in oriented Si oxidation kinetics will occur in ambients free of nitrogen, oxidation kinetics of $\langle 111 \rangle$ and $\langle 100 \rangle$ oriented Si substrates at low p_{O_2} were examined in O₂/Ar, O₂/He, and O₂/N₂ ambients in this thin Si oxide growth range.

Experimental

Si single crystal wafers that were chem-mech polished, p or n-type, 1-2 Ω-cm, $\langle 100 \rangle$ and $\langle 111 \rangle$ oriented, were used in this investigation. They were cleaned in (i) NH₄OH, H₂O₂, H₂O (1:1:5) at 65°C, (ii) H₂O, (iii) HCl, H₂O₂, H₂O (1:1:5) at 65°C, (iv) H₂O, and (v) etched in HF:H₂O (1:1) followed by a (vi) deionized water rinse. In some cases, the wafers were subjected to a clean-up oxidation step. An SiO₂ film about 2000Å thick was first grown at 1050°C in dry oxygen and then removed by etching. This step was later discontinued since no difference in oxidation kinetics was detected as a result of its omission.

Oxidations were carried out at atmospheric pressure in furnaces containing single walled, high purity, fused silica tubes at temperatures of 850°-1050°C. Total gas flow velocities were 1-3 cm sec⁻¹. High purity nitrogen, argon, and helium gases with < 2 ppm H₂O were used as diluents to reduce the oxidant partial pressures. The oxidant was generally dry O₂ (< 2 ppm H₂O) but some experiments were performed using H₂O vapor as the oxidant by bubbling a fraction of the N₂ carrier gas through H₂O kept at 25°C. The water vapor content of the N₂ carrier gas

¹ Present address: Thomas J. Watson Research Center, Yorktown Heights, New York 10598.

Key words: silicon, silicon dioxide, thermal oxidation, oxidation kinetics, pressure dependence.

in the latter experiments was estimated (16) to be about 750 ppm and about 2000 ppm.

During oxidation, the wafers were vertically arranged on a quartz carrier with $\langle 100 \rangle$ and $\langle 111 \rangle$ oriented wafers symmetrically positioned. Several wafers with each orientation were oxidized at a given time. Positions of oriented wafers were often reversed to eliminate errors in oxide film thickness due to small gradients in temperature in the oxidation zone within the furnace tube. Wafers were warmed to temperature in the diluent gas and then oxidized for a desired length of time at a fixed oxidant partial pressure, p_{O_2} .

Oxide film thickness was generally measured by ellipsometry at the center of each wafer after aligning the ellipsometer. All data points were measured in 2 zones at a wavelength of 5461 Å and with an angle of incidence of 70.00°. In some cases, oxide film thicknesses were derived from x-ray photoelectron spectroscopy (XPS) intensity data and were compared with corresponding ellipsometric measurements.

Results

In Fig. 1, changes in oxide film thickness of $\langle 111 \rangle$ and $\langle 100 \rangle$ oriented Si substrates oxidized at 850° and 1050°C for 10 min intervals are plotted vs. oxygen partial pressures, p_{O_2} . The oxygen is diluted with nitrogen gas. At $p_{O_2} \sim 0.07$ atm, the $\langle 100 \rangle$ and $\langle 111 \rangle$ oriented substrates are oxidized at the same rates independent of oxidation temperature. At higher p_{O_2} values, the commonly observed orientation dependence occurs with $\langle 111 \rangle$ oriented substrates oxidizing faster than $\langle 100 \rangle$ oriented substrates. At lower p_{O_2} , this orientation dependence on oxidation rates is reversed.

N_2 gas interacts with Si at the SiO_2 -Si interface when the oxygen concentration is low (14, 15). The

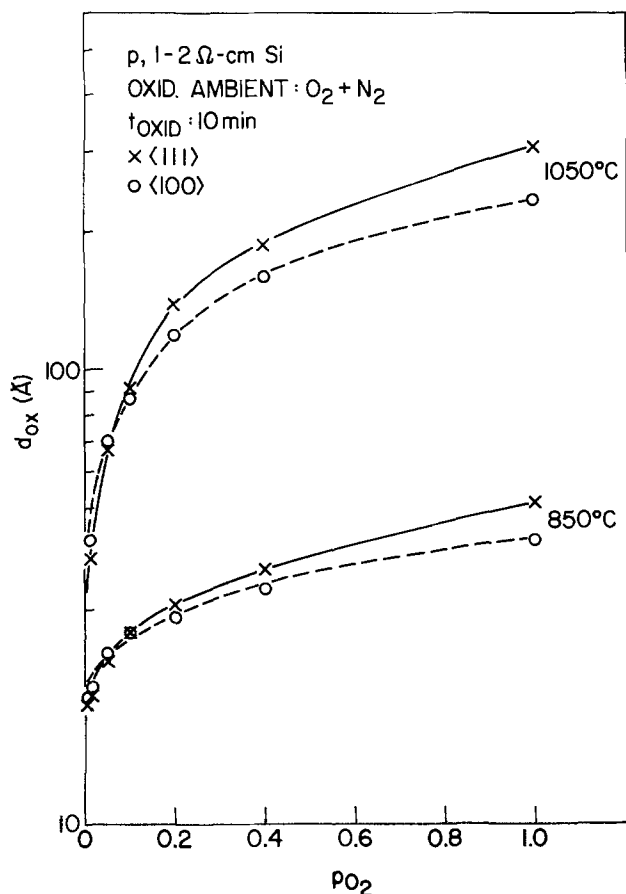


Fig. 1. The effect of O_2 partial pressure on SiO_2 film thickness after thermally oxidizing $\langle 100 \rangle$ and $\langle 111 \rangle$ oriented substrates for 10 min at 850° and 1050°C in O_2/N_2 mixtures.

Table I. Effect of diluent gas on Si oxide growth

Diluent gas	T (°C)	Substrate	d_{oxide} (Å)			
			0.5% O_2	1% O_2	5% O_2	10% O_2
N_2	850	$\langle 111 \rangle$	16.2	19.0	22.0	25.8
	850	$\langle 100 \rangle$	19.5	20.1	22.7	25.8
N_2	1050	$\langle 111 \rangle$	—	33.8	65.7	96.6
	1050	$\langle 100 \rangle$	—	37.9	69.3	92.0
Ar	1050	$\langle 111 \rangle$	—	37.9	69.8	—
	1050	$\langle 100 \rangle$	—	42.4	69.9	—
He	1050	$\langle 111 \rangle$	—	41.2	83.5	—
	1050	$\langle 100 \rangle$	—	47.4	84.0	—

1-2 Ω -cm, n-Si.
 t_{oxid} : 10 min.

reversal in relative oxidation rate of the two crystalline Si surfaces was reexamined at 1050°C with respect to diluent gas used in the oxidation ambient. Film thicknesses are given in Table I for $\langle 111 \rangle$ and $\langle 100 \rangle$ oriented substrates oxidized for 10 min intervals in ambients containing either N_2 , Ar, or He with p_{O_2} ranging from 0.01 to 0.1 atm. A reversal in orientation dependence is detected for $p_{O_2} = 0.05$ to 0.1 atm for O_2/N_2 mixtures and at $p_{O_2} \sim 0.05$ atm for O_2/Ar or O_2/He mixtures.

In Fig. 2, thicknesses of oxide films on $\langle 111 \rangle$ and $\langle 100 \rangle$ oriented substrates formed at 1050°C are plotted vs. oxidation time with $p_{O_2} = 0.01$ atm in N_2 , Ar, and He diluents. With each diluent, the oxide formed on the $\langle 100 \rangle$ oriented substrate is thicker than the oxide formed on the $\langle 111 \rangle$ oriented substrate. Small differences in film thickness are observed with change of diluent gas but these differences are likely to be associated with small experimental errors in mixing

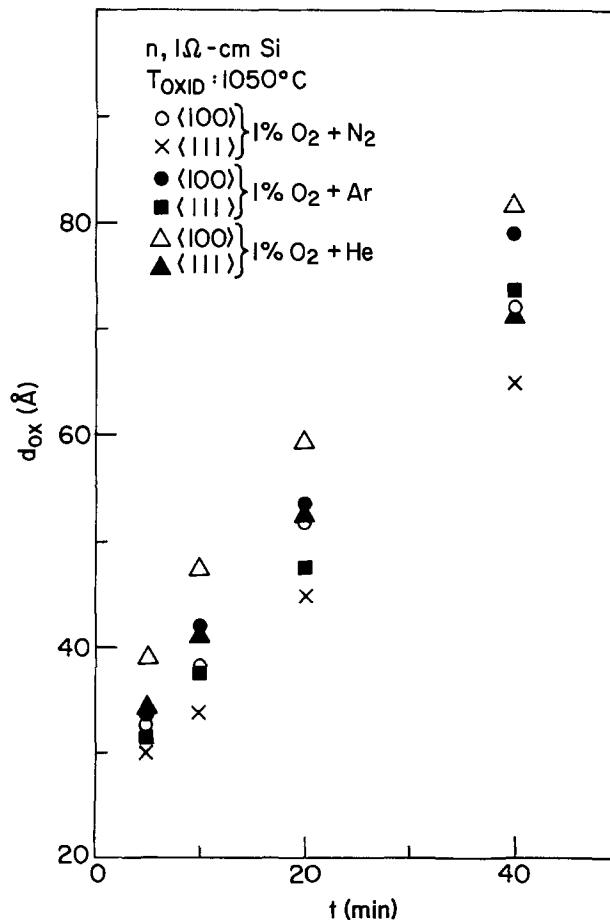


Fig. 2. The effect of change in oxygen ambient diluent at $p_{O_2} = 0.01$ atm on SiO_2 film growth at 1050°C on $\langle 100 \rangle$ and $\langle 111 \rangle$ oriented substrates.

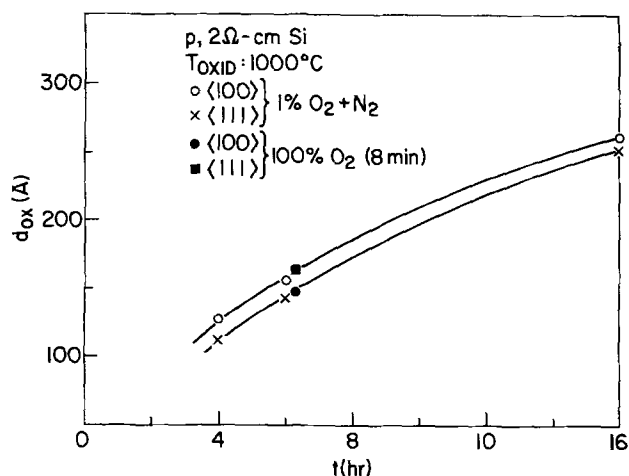


Fig. 3. Long-term Si oxidation of <100> and <111> oriented substrates at $p_{O_2} = 0.01$ atm and at an oxidation temperature of 1000°C compared with corresponding 8 min oxidation at $p_{O_2} = 1.0$ atm.

of the gases. From this comparison of oxidation rates in different diluent ambients, no evidence of N₂ reactivity with Si are apparent at oxygen partial pressures as low as 0.01 atm. However, as the oxygen partial pressure is decreased further, competition between the nitrogen reaction and the oxygen reaction with Si may complicate the oxidation kinetics.

In Fig. 3, thicknesses of oxide films on <111> and <100> oriented substrates formed at 1000°C are plotted vs. oxidation time with $p_{O_2} = 0.01$ atm in an N₂ diluent. Oxidation times are from 4 to 16 hr and yield film thicknesses in the 100-300Å range. Again, oxide films formed on <100> oriented substrates are thicker than the films formed on <111> oriented substrates. Changes in film thickness for oxides formed on <100> and <111> oriented substrates with $p_{O_2} = 0.01$ atm are summarized in Table II. Oxidation rates decrease with time indicating that the reaction has progressed beyond a linear oxidation range. After oxidation at $p_{O_2} = 0.01$ atm in an N₂ diluent for 10 min at 850°C, ellipsometric thickness measurements show oxide films on <100> oriented substrates to be 0.5-2Å thicker than oxides formed on <111> oriented substrates. XPS intensity measurements of Si 2p photoelectrons from the oxide film yield oxide film thickness data consistent with those obtained from the ellipsometric measurements.

Oxide films were also formed by oxidizing <111> and <100> oriented Si substrates in H₂O/N₂ mixtures at 850° and 1050°C. The N₂ stream was partially diverted and bubbled through deionized water at 25°C. In the first experiment, about 750 ppm of water vapor was added to the N₂ stream. In the second experiment, about 2000 ppm of water vapor was added to the N₂ stream. The water vapor oxidation results are illustrated in Fig. 4. After oxidation had occurred for 10 min at 850°C and at 1050°C, a reversal in the relative oxidation rates of <111> and <100> Si is ob-

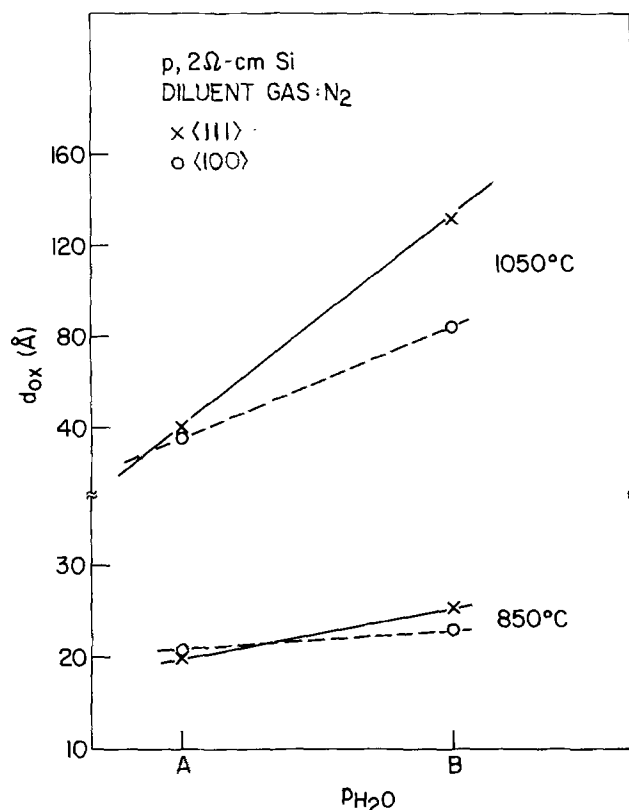


Fig. 4. Effect of low partial pressures of water vapor on relative oxidation kinetics of <111> and <100> Si.

served that is dependent upon the partial pressure of water vapor. At the low water vapor partial pressures, <100> Si is oxidized more rapidly than <111> Si.

Discussion

The <111> and <100> Si surfaces exhibit different dependencies upon oxidant partial pressure in the thin Si oxide film range. A consequence of this difference is that the relative oxidation rates of <111> and <100> oriented Si substrates reverse at $p_{O_2} < 0.1$ atm. The partial pressure of O₂ at which this reversal is observed is unaffected by change in diluent gas from N₂ to Ar to He. This reversal is only weakly affected by change in temperature from 850° to 1050°C. A similar reversal is observed in our preliminary oxidation studies with low water vapor partial pressures. Changes in the relative oxidation rates of <111> and <100> oriented Si surfaces are associated with changes in the partial pressure of the oxidant (O₂ or H₂O).

Other chemical reactions that are faster on <100> than on <111> Si surfaces have previously been observed. Addition of 10% HCl to an O₂ oxidizing ambient appears to alter the relative oxidation rates of <100> and <111> oriented Si substrates (17). The <111> surface is less chemically reactive when etched in wet ambients (18), but is more reactive when oxidized in water vapor. The chemistry affecting the relative reaction rates on these substrate orientations requires further clarification for the different reactions.

The pressure-dependent reversal in oxidation kinetics on Si substrates with different surface orientations are neither accounted for by comparison with Si-Si bond accessibility in the transition region (5, 11) nor by a steric argument proposed by Cabrera and Mott (12). These models can be fit to separate portions of the oxidation rate- p_{O_2} or $-p_{H_2O}$ data. Neither model explains the observed dependence of the relative oxidation rates of the crystalline Si surfaces upon oxygen pressure.

Table II. Comparison of oxide growth on <100> and <111> oriented Si surfaces at $p_{O_2} = 0.01$ atm

t	T (°C)	$d_{ox<100>} - d_{ox<111>} (Å)$		
		N ₂	Ar	He
5 min	1050	2.9	2	4.5
10		3.8	4.2	6.5
20		7	6	7.2
40		7	6.5	10
4 hr	1000	14	—	—
6		12	—	—
16		10	—	—

The oxygen transported to the SiO₂-Si transition regions is determined by the oxygen partial pressure in the ambient. The ratio of Si-Si bond densities within the transition regions of <111> and <100> oriented substrates is expected to remain nearly constant during the oxidation process, particularly as p_{O_2} is decreased. Oxygen transport through an amorphous oxide film to the transition region is either totally independent of the substrate orientation or differs by a small, constant rate. The reversal in oxidation rates of the differently oriented substrates presumably occurs without significant change in the relative concentrations of either accessible Si-Si bonds or of oxidant at the transition regions. The observed oxidation kinetics, i.e., the stronger dependence of oxidation rate with oxygen partial pressure of a <111> than a <100> oriented surface, are associated with differences in intrinsic properties of the two oriented substrates and are made visible by changes in transition region oxidant concentrations.

To account for the oxidation kinetics, the chemical environment of the partially oxidized transition region in which the oxidation reaction occurs must be considered. This region is a three-dimensional structure where Si-Si bonds are converted to siloxane (Si-O-Si) groups during oxidation. A volume change occurs upon oxidation in which the Si atom surface density in an oriented substrate is decreased by more than 50% when SiO₂ is formed. Greater than 50% of this transition to SiO₂ occurs within 2-3Å from the substrate (9, 10).

Despite the higher Si atom density on <111> Si than on <100> Si, the first transition region oxide layer appears to be less completely oxidized on <111> Si than on <100> Si substrates (9, 10). The transition region width between crystalline Si and SiO₂ is greater on <111> Si than on <100> Si. The estimated number of nonoxidized Si-Si bonds located within the transition regions are equivalent to 1-2 layers of Si substrate atoms. XPS studies of the SiO₂-Si interface (9, 10) indicate, within detection limits, that the composition and width of the transition regions of a given crystalline orientation are independent of the oxidation conditions (e.g., oxidation temperature, oxygen partial pressure, oxide film thickness, etc.) for oxide films formed at temperatures $\leq 1050^\circ\text{C}$. The dependence of transition region width on substrate orientation represents the different volume over which the two substrates convert Si into SiO₂ and suggests the possibility that oxidation of crystalline Si is occurring layer by layer.

The microscopic details of the interfacial Si oxidation reaction are not known. A multistep Si oxidation reaction has been proposed (19) in which oxygen initially reacts with and breaks Si-Si covalent bonds. A thermally activated reaction step follows in which siloxane groups form. The initial reaction between nonoxidized Si and oxygen depends upon their concentrations as reactants within the transition region. Since the oxygen concentration is significantly lower than the Si-Si bond concentration, the rate of this initial reaction is proportional to the oxidant concentration within the transition region and, therefore, to the oxidant partial pressure.

Formation of siloxane groups requires insertion of an oxygen atom between chemically bound Si atoms at the Si surface and within the transition region. Nonoxidized substrate Si atoms accessible to oxidant are primarily constrained by tetrahedral bonding to the crystalline substrate. These constraints are reduced for nonoxidized, or partially oxidized, Si atoms within the transition region. For oxidation to proceed, siloxane formation requires displacement of those Si substrate atoms at which reaction is occurring as well as of the neighboring lattice atoms (20). Completion of the reaction requires a reduction in the substrate lattice constraints that act to prevent the

required volume expansion upon oxidation. This is accomplished by breaking of Si-Si covalent bonds at the substrate surface. The oxidation rate depends upon the local density of broken Si-Si bonds and is directly dependent upon the oxygen partial pressure. Oxidation is thus a cooperative phenomena involving several oxygen atoms. Synchrotron radiation studies indicate that the initial oxidation process on <111> oriented Si occurs about 2Å below the free Si surface (21). Subsurface oxidation can detach Si surface atoms from the substrate thereby lifting the lattice constraints for oxidation at a substrate surface.

Substrate lattice constraints cause oxidation at a crystalline Si surface to be anisotropic. Si-Si bonds perpendicular to the surface are readily oxidized whereas Si-Si bonds parallel to the surface are constrained by the crystal lattice. Oxidation is rate limited by the oxidation rate in the plane of the substrate. The kinetics of reaction on the two oriented Si surfaces are related to, but have different dependencies upon, the oxygen partial pressure. Three subsurface Si-Si bonds must be broken at a <111> substrate compared with two Si-Si bonds at a <100> surface. Nonoxidized Si-Si bonds at <111> surfaces, oriented primarily in the plane of the substrate surface, are accessible to the oxidant whereas Si-Si bonds at <100> substrate surfaces are directed in a more inclined direction to the substrate (5). The molecularity for oxidation of Si atoms in the plane of a <111> surface is higher than for oxidation of Si atoms in a <100> Si plane. As a consequence, there is a stronger dependence upon the oxygen pressure for <111> oxidation. At low p_{O_2} , this results in a reversal of the commonly observed relative oxidation rates of the crystalline substrate surfaces. As p_{O_2} is increased, the greater accessibility of nonoxidized Si-Si bonds at the <111> surface and the relatively high oxygen concentration at the interface cause the <111> oxidation rate to be higher than that for <100> Si. A strong dependence upon oxidation temperature in the range considered or upon diluent gas is not expected and is consistent with the experimentally obtained results.

Acknowledgments

Discussions with J. W. Matthews were of significant help in both formulating and clarifying our ideas concerning this work and are greatly appreciated. We thank the Divisional Editor, Prof. J. B. Wagner, Jr., for his patience and interest and thank R. A. Ghez, W. A. Pliskin, and J. A. VanVechten for helpful comments. R. Flitsch is gratefully acknowledged for the ESCA measurements.

Manuscript submitted Oct. 7, 1977; revised manuscript received March 31, 1980.

Any discussion of this paper will appear in a Discussion Section to be published in the June 1981 JOURNAL. All discussions for the June 1981 Discussion Section should be submitted by Feb. 1, 1981.

Publication costs of this article were assisted by IBM Corporation.

REFERENCES

1. B. E. Deal and A. S. Grove, *J. Appl. Phys.*, **36**, 3770 (1965).
2. Y. J. van der Meulen, *This Journal*, **119**, 530 (1972).
3. M. A. Hopper, R. A. Clarke, and L. Young, *ibid.*, **122**, 1216 (1975).
4. D. W. Hess and B. E. Deal, *ibid.*, **122**, 579 (1975).
5. J. R. Ligenza, *J. Phys. Chem.*, **65**, 2011 (1961).
6. W. A. Pliskin, *IBM J. Res. Dev.*, **10**, 198 (1966).
7. R. H. Doremus, *J. Phys. Chem.*, **80**, 1773 (1976).
8. D. O. Raleigh, *This Journal*, **113**, 782 (1966).
9. S. I. Raider and R. Flitsch, *IBM J. Res. Dev.*, **22**, 294 (1978).
- 10a. S. I. Raider and R. Flitsch, in "Proceedings of the International Conference on The Physics of SiO₂ and Its Interfaces," S. T. Pantelides, Editor,

- p. 384, Pergamon Press, New York (1978); b. S. I. Raider, R. Flitsch, and R. Rosenberg, *This Journal*, To be published.
11. R. Ghez and Y. J. van der Meulen, *This Journal*, **119**, 1100 (1972).
 12. N. Cabrera and N. F. Mott, *Rep. Prog. Phys.*, **12**, 163 (1948).
 13. Y. Kamigaki and Y. Itoh, *J. Appl. Phys.*, **48**, 2891 (1977).
 14. S. I. Raider, R. A. Gdula, and J. F. Petrak, *Appl. Phys. Lett.*, **27**, 150 (1975).
 15. J. K. Howard, R. Flitsch, and S. I. Raider, *J. Vac. Sci. Technol.*, **14**, 69 (1977).
 - 16a. E. A. Irene, Private communication; b. E. A. Irene and R. Ghez, *This Journal*, **124**, 1757 (1977).
 17. K. Hirabayashi and J. Iwamura, *This Journal*, **120**, 1595 (1973).
 18. K. E. Bean and P. S. Gleim, *Proc. IEEE*, **57**, 1469 (1969).
 19. S. I. Raider and A. Berman, *This Journal*, **125**, 629 (1978).
 20. P. D. Dankov, *C. R. Acad. Sci. URSS*, **L1**, 453 (1946).
 21. R. S. Bauer, J. C. McMnamin, H. Petersen, and A. Bianconi, in "Proceedings of the International Conference on The Physics of SiO₂ and Its Interfaces," S. T. Pantelides, Editor, p. 401, Pergamon Press, New York, (1978).

The Growth and Characterization of Very Thin Silicon Dioxide Films

A. C. Adams, T. E. Smith, and C. C. Chang

Bell Laboratories, Murray Hill, New Jersey 07974

ABSTRACT

Very thin oxides (30-140Å) have been prepared by oxidizing silicon at 900°-1000°C at reduced pressure (0.25-2.0 Torr). The oxidation rate is parabolic. The oxides have been characterized by ellipsometry, infrared spectroscopy, Auger spectroscopy, etch rate variation, and breakdown voltages. The thin, low pressure oxides have properties similar to those of thicker oxides prepared at atmospheric pressure. The intrinsic breakdown fields are high (10-13 MV/cm) and distributed over a very narrow range. The ellipsometric, etch rate, and Auger data indicate a thin interfacial region <15Å thick, but such a region is not detected in the infrared spectra.

Very thin silicon dioxide films, in the range of 40-100Å, are being investigated for applications in several types of silicon devices. These thin oxides are usually prepared by oxidation of silicon with oxygen or steam at low temperatures (400°-800°C) (1, 2) or by oxidation at higher temperatures with the oxygen or steam diluted with an inert gas (3-5). Alternative methods for the oxidation of silicon to produce very thin films have used nitric oxide and hydrogen at 950°-1140°C (6); hot nitric acid (7); boiling water (8); and room temperature air (9, 10). Except for the oxidations with nitric oxide and hydrogen, these alternative methods produce maximum film thicknesses of only 20-40Å and thus are too thin for many device applications. Oxidations at reduced pressure have been reported (11, 12), but these oxidations have used specialized experimental equipment rather than furnaces suitable for device fabrication. In this paper, we describe the growth of thin (30-140Å) oxides at temperatures of 900°-1000°C in a furnace maintained at low pressure (0.25-2.0 Torr oxygen).

The very thin oxides described in this paper have been characterized by ellipsometry, infrared spectroscopy, Auger electron spectroscopy, etch rate determination, and electrical measurements. Thicker oxide films on silicon have been analyzed by many techniques. Much of this work, which has been recently summarized (13-15), has been directed at determining the thickness and composition of the interfacial region between the oxide and the silicon. The results tend to support a very thin interfacial region with a maximum thickness of <30Å and a composition that is silicon-rich, SiO_x where $x < 2$; however, other interpretations for the data have been suggested (13, 14, 16). The nature of the interface structure is relevant to the present work since the thicknesses

of the oxides considered in this paper are comparable to some of the thicknesses proposed in the literature for the interfacial transition layer.

Electrical characterizations of oxide films have been reported (4, 17), and it has been suggested that oxides grown in dry oxygen may have an increased defect density caused by micropores in the oxide (17). Again, an alternative interpretation of the data has been suggested (18). In this paper, electrical, physical, and chemical data have been used to compare the very thin oxides grown at reduced pressure with thicker oxides grown at atmospheric pressure.

Experimental

The thin oxides are grown in a low pressure chemical vapor deposition reactor (19, 20). The oxidation takes place in an 11.5 cm diam quartz tube heated by a 3-zone furnace. Temperatures are uniform within ±0.5°C over the central 55 cm zone. The furnace has a capacity of 110 wafers. The reduced pressure is obtained with a Roots blower backed by a mechanical pump. Ultrahigh purity oxygen is metered through a calibrated flowmeter. The pressure is measured with a capacitance manometer.

Unless stated otherwise, the silicon substrates are 75 mm in diameter, 20 mils thick, (100) orientation, boron-doped, with a resistivity of 8-30 Ω-cm. The substrates are chemically etched on the back to reduce roughness and polished on the front surface to give a mirror finish. Prior to oxidation, the substrates are cleaned in a sequence of acidic and basic hydrogen peroxide solutions (21), etched in dilute hydrofluoric acid (100:1 H₂O:49% HF), rinsed in deionized water, and spun dry. The samples are loaded into the furnace in a nitrogen ambient and the furnace evacuated to 0.002 Torr for 15 min while thermal equilibrium is reached. The oxidation is started by admitting oxygen, and the pressure maintained by adjusting the oxygen

flow. At the end of the oxidation, the furnace is evacuated to 0.002 Torr for 5 min and then backfilled to atmospheric pressure with nitrogen. The samples are removed from the hot zone in nitrogen and unloaded after cooling.

Several control oxidations have been performed by leaving samples in the furnace under vacuum (0.001-0.002 Torr) for 4 hr or under 2 Torr nitrogen for 4 hr. These samples have 25-27Å of oxide after treatment. This small amount of oxidation may result from oxygen or water vapor introduced during loading, from impurities in the nitrogen, or from small leaks in the system.

The ellipsometer measurements are made with a Rudolph Model 43603-200E ellipsometer at an angle of incidence of 70.00° and a wavelength of 0.5461 μm . The instrument is aligned using standard procedures (22) and checked by making measurements on fused silica (23). Psi and delta are obtained from measurements made in two zones (24). The reported data are averages of at least two measurements per sample. The reproducibility is generally within $\pm 0.02^\circ$ for psi and $\pm 0.05^\circ$ for delta.

Infrared measurements are made with a Perkin-Elmer Model 580 spectrophotometer using an ordinate expansion of 5, 10, or 20 \times . Samples are cleaved and the oxide removed from one part by etching in dilute hydrofluoric acid. The resulting bare silicon is used in the reference beam. This procedure gives exact compensation for the substrate. Some spectra have been obtained using thicker silicon substrates (30 mils thick) polished on both sides. These spectra are complicated by interference fringes which are evident at the high ordinate expansions. The best data are obtained by using silicon substrates that are polished on the front and etched on the back to reduce roughness. Apparently the scattering from the back is large enough to eliminate the interference fringes but still small enough so that spectra can be measured.

The experimental procedure for the Auger analysis has been described previously (25). The initial analysis measures the contamination, if any, on the surface and in the film. The oxide thickness is determined using the chemically shifted silicon peaks, and the interface chemistry is examined utilizing ion-mill depth profiling. Etch rates are measured at 25°C using dilute hydrofluoric acid (100:1 H₂O:49% HF).

Samples are prepared for electrical measurements by evaporating 7000Å of aluminum on the oxide and using standard photolithography and etching techniques to form dots with a 0.076 cm (30 mil) diameter. The oxide is removed from the back of the sample by etching and aluminum is evaporated for a back contact. The samples are not annealed after metallization. Two hundred measurements of the breakdown voltage are made for each sample. The measurements are made with the top aluminum dot biased negatively so the p-type silicon substrates are in accumulation. The breakdown is indicated by a current $> 10 \mu\text{A}$.

Oxidation Kinetics

The oxidation rate at 953°C and 1.0 Torr oxygen has been determined by measuring the film thickness on 34 samples oxidized for different times (0.5-24 hr). Seven rate laws, all of which have been previously suggested to describe the oxidation of silicon to form very thin oxides, have been considered.

$$\text{linear-parabolic } t = A_0 + A_1 d + A_2 d^2$$

$$\text{linear } t = A_0 + A_1 d$$

$$\text{parabolic } t = A_0 + A_1 d^2$$

$$\text{logarithmic } d = A_0 + A_1 \ln t$$

$$\text{inverse logarithmic } 1/d = A_0 + A_1 \ln t$$

$$\text{variable power } d = A_0 t^{A_1}$$

$$\text{cubic } d = A_0 + A_1 t^{1/3}$$

Table I. Coefficients for seven rate laws^a

	A_0	A_1	A_2
Linear-parabolic	-1440	-184	8.47
Parabolic	-7630	7.25	
Linear	-42,800	1070	
Logarithmic	-154	22.6	
Inverse logarithmic	0.0721	-0.00562	
Variable power	2.20	0.342	
Cubic	-5.24	2.59	

^a Thickness measured in Å and times in sec; for oxidations at 953°C and 1.0 Torr oxygen.

where d is the oxide thickness, t is the oxidation time, and the A 's are coefficients which are determined by linear least squares and are given in Table I for oxide thicknesses measured in angstroms and times measured in seconds.

Plots of thickness vs. time show that the linear and the logarithmic rate laws give a very poor fit to the data (Fig. 1). The remaining five rate laws are all much better (Fig. 2 and 3). The parabolic and linear-parabolic laws are almost identical except at very short times where the parabolic law overestimates the oxide thickness (Fig. 2). The inverse logarithmic law overestimates the thickness at long times, while the variable power law and the cubic law give fairly good fits for all times (Fig. 3).

The rate laws have been further evaluated by examining the residuals (the calculated thicknesses minus the measured thickness for each sample). The residuals are compared using four parameters: the range, the midspread, the median absolute deviation (mad), and the standard deviation, which are given in Table II. The residuals for the linear and the logarithmic laws are very large, agreeing with the poor fit observed graphically. The residuals for the other five laws are smaller showing better agreement between the experimental and predicted thicknesses. The rate laws in Table II have been ordered; the laws giving the best fit are listed first. It must be remembered that the linear-parabolic law has three adjustable co-

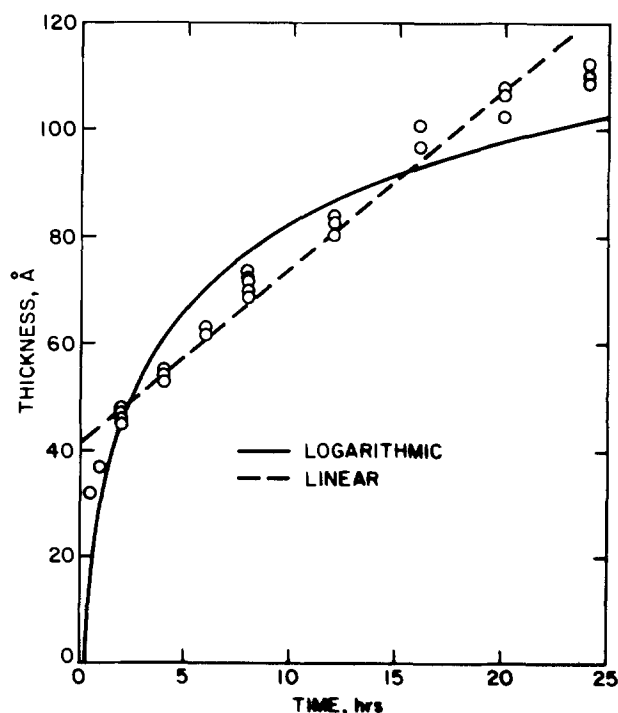


Fig. 1. Film thickness vs. oxidation time; the lines are calculated for the logarithmic and the linear rate laws.

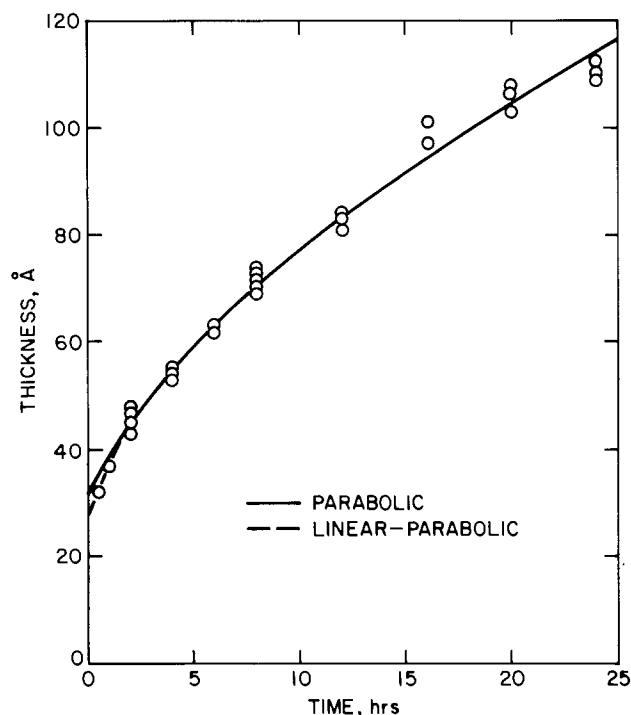


Fig. 2. Film thickness vs. oxidation time; the lines are calculated for the parabolic and the linear-parabolic rate laws.

efficients and the improvement observed with this law is due in part to the additional coefficient.

Previous work has described the oxidation of silicon at high temperature to form very thin oxides as following a linear (17), a linear-parabolic (11), or an inverse logarithmic rate law (4, 5). For the conditions used in this work, the rate is clearly not linear. The linear-parabolic law gives a negative linear rate constant (agreeing with previous work) (4, 5), but as discussed by others the determination of the linear rate constant is very difficult, especially when the oxidation is predominantly parabolic (11, 26). Also, calculation

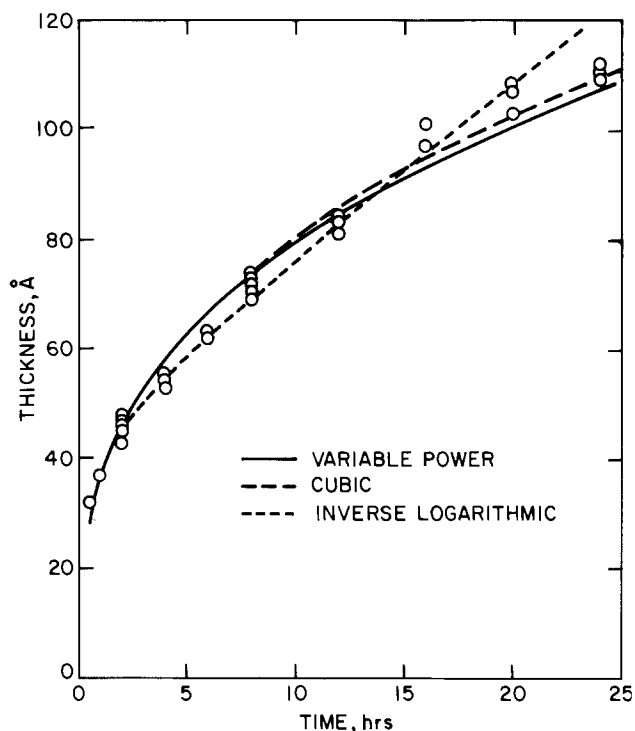


Fig. 3. Film thickness vs. oxidation time; the lines are calculated for the variable power, the cubic, and the inverse logarithmic rate laws.

Table II. Analysis of residuals for seven rate laws^a

	Range	Std. dev.	Mid-spread	Mad
Linear-parabolic	10	2.2	4	2
Parabolic	11	2.4	4	2
Cubic	11	3.5	6	3
Variable power	13	3.6	6	3
Inverse logarithmic	19	4.1	3	2
Linear	19	5.0	6	3
Logarithmic	26	6.8	14	6

^a Residuals are measured in Å.

of a negative linear rate constant is not justification for rejecting the parabolic rate law. Calculation of the parabolic rate constant from the least squares coefficients gives $0.12 \text{ Å}^2/\text{sec}$ ($1/A_2$) for the linear-parabolic law and $0.14 \text{ Å}^2/\text{sec}$ ($1/A_1$) for the parabolic growth.

Comparison of these rate constants with published values is difficult because of differences in oxidation conditions. Parabolic rate constants calculated from published data for oxidations at 953°C and 1.0 Torr oxygen, assuming a linear pressure dependence (12, 27), are given in Table III. The value measured in this work is near the middle of the published data extrapolated to 1.0 Torr.

Since a parabolic rate law implies that diffusion through the oxide is the rate-limiting step, the rate constant should be independent of substrate effects (27, 28). Experimentally determined parabolic rate constants for oxidations at 1.0 Torr oxygen are given in Table IV for different substrates. No variation is observed for different dopants, doping levels, or orientations. This is additional evidence for believing that the parabolic rate law is valid.

An inverse logarithmic law results if oxidation occurs by cation migration in a strong field caused by the potential difference between the silicon and absorbed oxygen (1, 31). This rate law has been used to describe the oxidation of silicon to form very thin oxides (1, 4, 5, 7); however, an upper temperature limit of 500°C has been estimated for inverse logarithmic growth. (1) In view of this temperature limitation it is unlikely that the inverse logarithmic law is valid for oxidations at 953°C , in spite of the fairly good empirical agreement shown in Fig. 3. As a further check, values for the potential difference can be calculated from the least squares coefficients (1). Assuming that the migrating silicon has a charge of plus four, and that the jump distance is 5 Å , then the calculated potential is about 2V. This is about an order of magnitude larger than values observed for silicon oxidations at low temperatures (1) and observed for germanium oxidation (32). This large calculated potential also makes the inverse logarithmic law (cation migration in a strong potential field) unlikely.

Detailed models for silicon oxidation leading to the cubic or the variable power laws have not been devel-

Table III. Parabolic rate constants for oxidations at 953°C and 1.0 Torr oxygen

Pressure (Torr)	Ambient	Temperature ($^\circ\text{C}$)	k ($\text{Å}^2/\text{sec}$)	Reference
760	O_2	900-1150	0.08	(12)
50-1200	O_2	700-950	0.10	(11)
20-400	O_2	950-1100	0.11	(12)
760	$\text{N}_2\text{-O}_2$	700-1100	0.13	(4)
1	O_2	953	0.14	This work
760	O_2	900-1300	0.19	(28)
760	O_2	800-1000	0.20	(29) ^a
760	$\text{N}_2\text{-O}_2$	780-980	0.22	(30)
760	O_2	700-1300	0.25	(27)

^a k is calculated from data reported in Ref. (30).

Table IV. Parabolic rate constants for different substrates

Dopant	Resistivity (Ω -cm)	Orientation	Rate constant ($\text{Å}^2/\text{sec}$)
As	4-6	1-0-0	0.14
As	6-12	1-0-0	0.16
P	1-2	1-0-0	0.15
P	5-30	1-0-0	0.15
Sb	0.01-0.03	1-0-0	0.14
B	8-30	1-0-0	0.14
B	8-20	1-1-1	0.16

oped. However, it has been suggested that the variable power law may result if a reversible reaction occurs between the diffusing species and the oxide (12), and the cubic law may result for room temperature oxidations after very long times (33).

The best description for the oxidation kinetics at low pressure to form very thin oxides is provided by the parabolic rate law (or the linear-parabolic law with the parabolic term dominating). The parabolic rate constants agree with those observed for a variety of oxidation conditions. Difficulties exist for the remaining rate laws. Cation migration (inverse logarithmic growth) is unlikely at high temperatures; mechanisms leading to the variable power law and the cubic law have not been developed; and, the linear and logarithmic laws give a very poor fit to the data.

Oxide Characterization

Ellipsometry.—Although ellipsometry is a well-established technique for measuring the thickness and the refractive index of transparent films, there are limitations when the films are very thin. The measured values for the thickness and the refractive index of very thin films are strongly influenced by the choice of optical constants for the substrate and by the model of the interface structure (3, 34, 35). The procedure we have used to minimize these effects is similar to that described by van der Meulen (3). Briefly, the interface is assumed to be abrupt, so there are only five quantities that must be known or measured: the complex refractive index of the silicon substrate, $n_{Si}-ik_{Si}$; the complex refractive index of the film, n_F-ik_F ; and the film thickness, d . These quantities are determined as follows. It is assumed that the film is nonabsorbing (the imaginary part of the film refractive index, k_F , is zero). The imaginary part of the silicon refractive index, k_{Si} , is obtained from optical transmission measurements and has a value of 0.031 at a wavelength of $0.5461 \mu\text{m}$ (23, 36). The value for the real part of the silicon refractive index, n_{Si} , is obtained using ellipsometric measurements from samples with very thin films ($d < 50 \text{Å}$). The refractive index of the oxide film is calculated using samples containing thicker films ($d > 100 \text{Å}$). Once the optical constants of the silicon substrate and the oxide film are known, the film thickness can be calculated for each sample. This procedure assumes that the optical constants are the same for all samples, and that the only sample variable is the film thickness.

This procedure is illustrated in Fig. 4 and 5. Values of the measured quantities, psi and delta, are shown in Fig. 4 for samples oxidized at 900°C to form very thin films ($d < 70 \text{Å}$). The solid lines are calculated for different film thicknesses and different values for n_{Si} assuming that the film refractive index is 1.50. The average value for n_{Si} calculated from 28 samples with $d < 50 \text{Å}$ is 4.040; the standard deviation is 0.0022. No variation with oxidation temperature is observed. The complex refractive index for the silicon samples used in these experiments is taken as $4.040-0.031i$. Data from samples with thicker films are shown in Fig. 5. The lines are calculated for different values for the film refractive index using $4.040-0.031i$ for the silicon substrate. The average value for the film refractive index

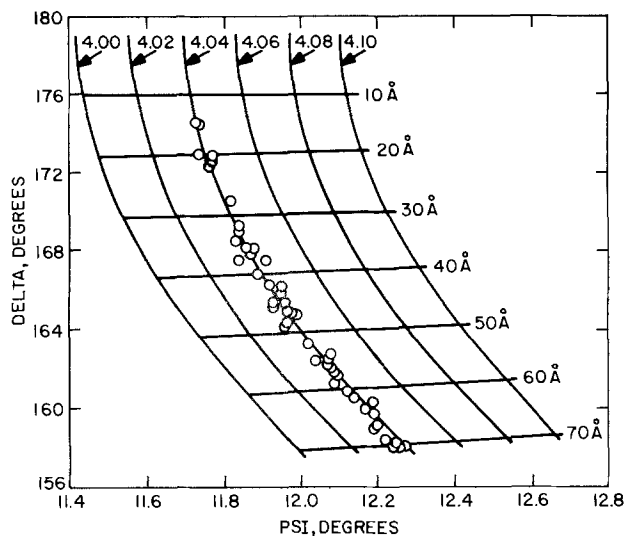


Fig. 4. Ellipsometric data for thin ($d < 70 \text{Å}$) oxides; the lines are calculated for different values of n_{Si} and d assuming that $k_{Si} = 0.031$ and $n_F = 1.50$; the samples have been oxidized at 902° , 953° , and 999°C .

from 19 samples with thicknesses between 100 and 140Å is 1.55; the standard deviation is 0.063. The film thickness can be calculated for each sample using the average refractive index of 1.55.

The value for the silicon refractive index, $4.040-0.031i$, is similar to reported values for etched silicon, approximately $4.05-0.028i$ (24, 37, 38) or $4.08-0.028i$ (3, 23, 39). Mechanisms for variations in n_{Si} have been proposed and invoke a thin layer at the silicon surface with optical properties different from bulk silicon (40). The value for the film refractive index is considerably higher than expected; oxide films usually have an index of 1.46 (24, 37-39). However, slightly higher values (1.47-1.48) have been reported (3, 23). Recent ellipsometric (34, 35), XPS (16), and Auger (15) data indicate an interfacial layer approximately 6Å thick (with an effective refractive index of about 2.8) be-

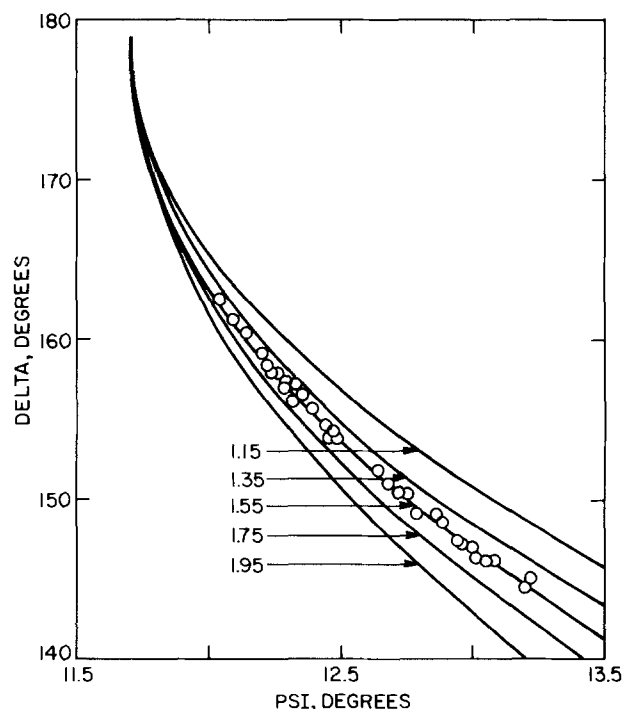


Fig. 5. Ellipsometric data for thicker ($50 \text{Å} < d < 140 \text{Å}$) oxides; the lines are calculated for different n_F assuming that the complex refractive index of Si is $4.040-0.031i$; the samples have been oxidized at 902° , 953° , and 999°C .

tween the silicon substrate and the thermal oxide. If the ellipsometric data in Fig. 5 are recalculated using a similar interfacial layer, the refractive indexes for the oxide films are reduced to 1.460-1.465, in good agreement with the reported values.

Etch rates.—The etch rate of an oxide film is strongly dependent on the oxide composition and structure (41). In general, strain or porosity causes an increase in etch rate, while an oxygen deficiency (a silicon-rich film) causes the etch rate to decrease. Comparing the etch rate of the thin oxides with thicker oxides prepared by oxidation at atmospheric pressure provides information on the composition of the thin oxides. In addition, changes in etch rate with film thickness may indicate the presence of surface or interfacial layers.

Film thicknesses are shown vs. etch times in Fig. 6 for three samples etched at 25°C in dilute hydrofluoric acid (100:1 H₂O:49% HF). The solid points show the thicknesses measured after the samples become hydrophobic; the samples are hydrophilic for all other points. The average etch rate determined from the slopes is 25.6 Å/min. For comparison, samples of thermal oxide, approximately 1000Å thick, prepared by oxidation at 950°C in dry oxygen at atmospheric pressure have an etch rate of 25.3 Å/min. The similar etch rates show that both oxides have similar structure and composition. There is no indication of increased porosity in the thin, low pressure oxides.

The samples in Fig. 6 show a decrease in etch rate starting at 15-20Å. This may represent the beginning of an Si-rich interfacial layer. Such a layer is in good agreement with results obtained by other methods (16, 42). However, the decrease in etch rate may also result from an abrupt interface with a nonuniformly thick oxide, as has been suggested (13). If this is the case, the silicon surface starts to be exposed when the average film thickness is about 15Å. As etching continues, more of the surface becomes exposed causing an apparent decrease in etch rate.

Infrared spectra.—An infrared spectrum for a film 110Å thick is shown in Fig. 7. Since the spectrum is measured in transmission, through the silicon substrate, the total film thickness is assumed to be 220Å (110Å on the front and also on the back). The spectrum

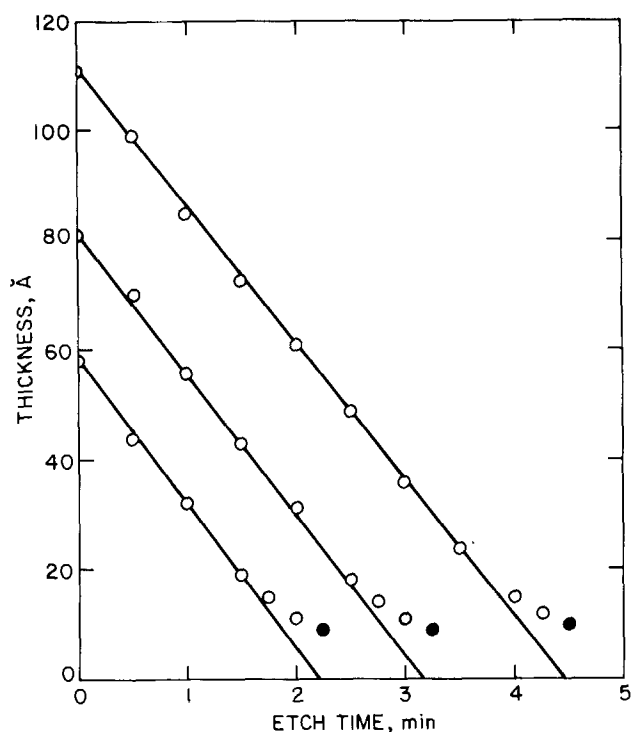


Fig. 6. Thickness vs. etch time for three samples oxidized at 953°C and 2.0 Torr.

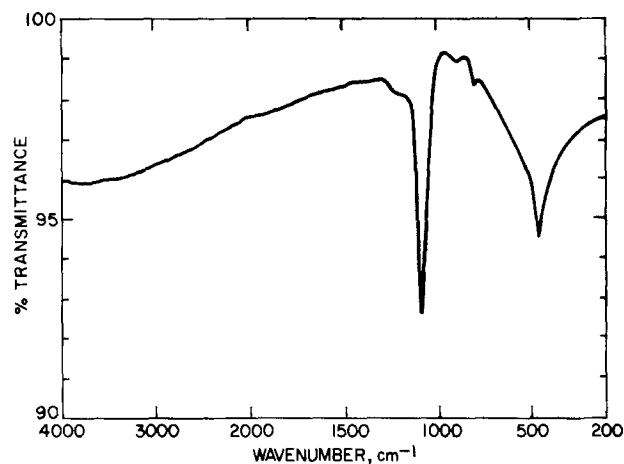


Fig. 7. Infrared spectrum for an oxide 110Å thick; the ordinate expansions is 10X.

shows the three SiO₂ lattice absorptions at approximately 1080, 800, and 450 cm⁻¹ (43). A small peak at 880 cm⁻¹ is observed for most samples. This peak is also observed when clean silicon is placed in the sample and the reference beams, and is probably caused by slight differences in the incident angles for the sample and reference beams. Absorptions associated with OH or with SiH have not been observed (44, 45).

The absorbance at 1080 cm⁻¹ is plotted against the total film thickness (front and back) in Fig. 8. The solid points are measured from samples with oxide on the front and the back. The total film thickness is assumed to be twice the thickness measured on the front surface. The open points are measured from samples with the film removed from the back by etching in dilute hydrofluoric acid. For these samples the film thickness is the thickness measured for the front surface plus 10Å (the thickness of the native oxide on a silicon surface after etching, rinsing, and drying). The straight line is calculated by least squares assuming the Lambert-Bouguer law

$$A = 0.434\alpha(d - d_0)$$

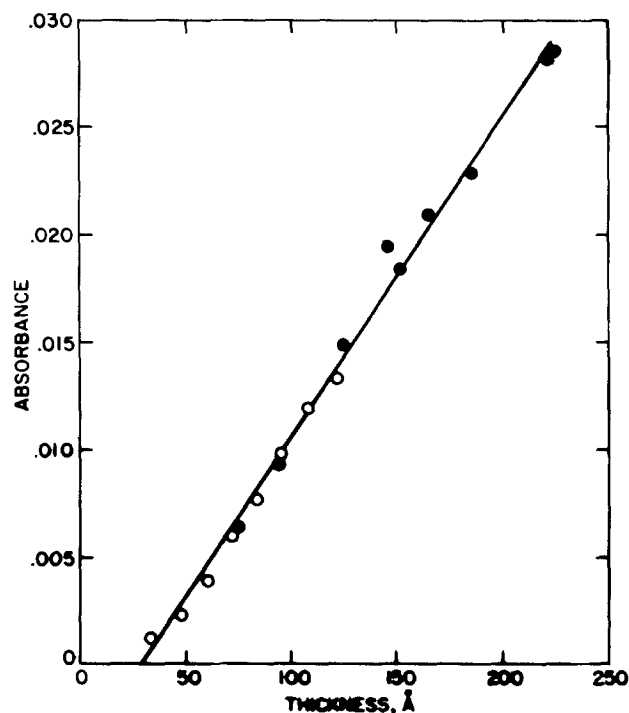


Fig. 8. Absorbance at 1080 cm⁻¹ vs. the total oxide thickness; the samples have been oxidized at 902°, 953°, and 999°C.

where A is the absorbance, α is the apparent absorption coefficient, d is the total film thickness, and d_0 is the total oxide thickness on the silicon sample in the reference beam. The values for α and d_0 obtained from the least squares fit are $3.4 \times 10^4 \text{ cm}^{-1}$ and 19\AA . The value of α is identical to values reported for much thicker oxide films: $3.3\text{--}3.7 \times 10^4 \text{ cm}^{-1}$ (43, 46-48). The value for d_0 is also in very good agreement with experimental values. Film thicknesses measured on silicon wafers immediately after cleaning, rinsing, and drying range between 8 and 11\AA , giving values for d_0 between 16 and 22\AA .

The infrared spectra show no indication of an interfacial layer. Absorption peaks for spectra other than SiO_2 are not observed; in addition, there is no tendency for the absorption peaks to shift with film thickness. However, spectra of the interfacial layer will be canceled if the two samples (reference beam and sample beam) contain identical interfaces.

Auger analysis.—Three samples have been examined by Auger spectroscopy in combination with *in situ* ion-milling to provide depth information. All three samples have carbon on the surface; the amount of carbon is estimated at about 0.5\AA . This is only slightly higher than for clean samples exposed to air (0.3\AA) and probably represents contamination of the samples after oxidation. No other impurities are observed on the surface, and no impurities are observed within the film. The Auger spectra are essentially identical to spectra obtained from thicker thermal oxides grown at atmospheric pressure. Oxide thicknesses have been calculated from the chemically shifted Auger spectra (25) and are about 10\AA less than the thicknesses measured by ellipsometry. A large part of this discrepancy can be explained by the existence of an interface layer containing mostly SiO . The chemical depth profiles at the silicon interface have been obtained and are essentially the same as those obtained from thermal oxides grown at atmospheric pressure. Based on the Auger, infrared, and etch rate data, we conclude that these very thin, low pressure oxides contain no detectable impurities and are essentially identical to much thicker thermal oxides.

Dielectric breakdown.—Breakdown measurements have been made on several samples with oxide thicknesses between 30 and 140\AA . Representative results are shown in the histogram in Fig. 9 showing data for a sample with 93\AA of oxide, and in the cumulative distribution plots in Fig. 10 showing data from three samples with oxide thicknesses of 56, 73, and 94\AA . Several features are apparent from these figures.

Most breakdowns occur at high fields and within a very narrow range. Except for one sample 56\AA thick (shown in Fig. 10), more than 75% of the breakdowns occur at fields between 11-13 MV/cm. One sample, 69\AA thick, has more than 90% of the breakdowns between 11.6 and 12.2 MV/cm showing a very narrow distribution. The high fields and narrow distributions indicate an extremely uniform and homogeneous oxide (49). The distribution of intrinsic (high field) breakdowns is neither Gaussian nor log-normal (50), but there are insufficient data from the present samples to determine the actual distribution. The median breakdown fields are dependent on the oxide thickness (51). The observed breakdown fields are $10.5\text{--}11.0 \text{ MV/cm}$ for oxides about 100\AA thick; $11.5\text{--}12.0 \text{ MV/cm}$ for oxides 75\AA thick; and $12\text{--}13 \text{ MV/cm}$ for 50\AA oxides. The so-called secondary breakdowns (at fields of $1\text{--}3 \text{ MV/cm}$), believed to be caused by small crystalline regions in the amorphous oxide (52) are not observed. These secondary breakdowns are not expected since the samples have not been heated to high enough temperatures to cause crystallization.

Low field breakdowns, caused by structural defects such as pinholes or particulate contamination (the oxide samples are not prepared in a clean environment)

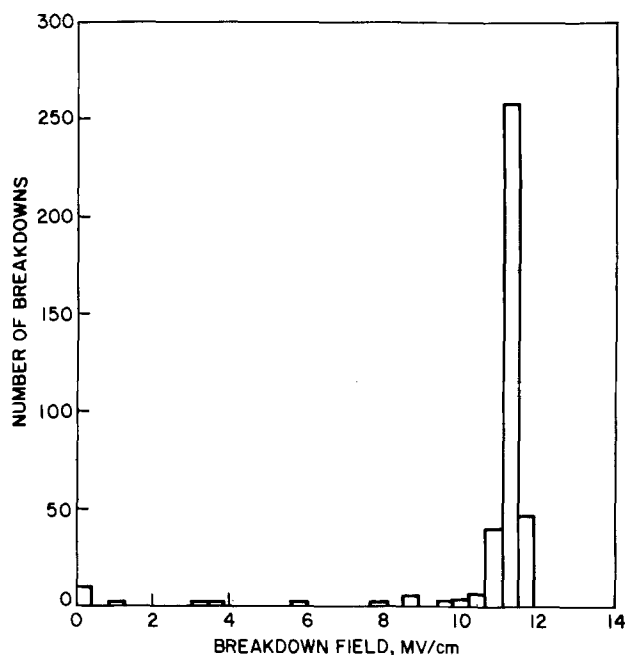


Fig. 9. Histogram showing breakdown fields for an oxide 93\AA thick; the sample has been oxidized at 953°C and 2.0 Torr.

are observed for all samples. Between 1 and 30% of the breakdowns for each sample occur at fields less than 0.5 MV/cm . These low field breakdowns have a very strong (exponential) dependence on oxide thickness as shown in Fig. 11. The point at 150\AA is taken from Ref. (17) for oxides prepared at atmospheric pressure.

Comparisons with oxides prepared at atmospheric pressure are difficult because of differences in oxide thickness. Data have been reported for samples 150\AA thick prepared with dry oxygen and no postoxidation anneal; a maximum in the breakdown distribution occurs at about 9 MV/cm , but with the breakdowns ranging between 6 and 15 MV/cm , and with about 20% of the breakdowns occurring below 6.5 MV/cm (17). Samples prepared with steam are much better with the breakdowns occurring between 8 and 14 MV/cm (17). The thin low pressure oxides reported in this paper are comparable to the thicker steam oxides. The percent of intrinsic (high field) breakdowns for silicon oxidized in oxygen at atmospheric pressure is reported to decrease with decreasing thickness, and less than 30% of the breakdowns are intrinsic for oxides less

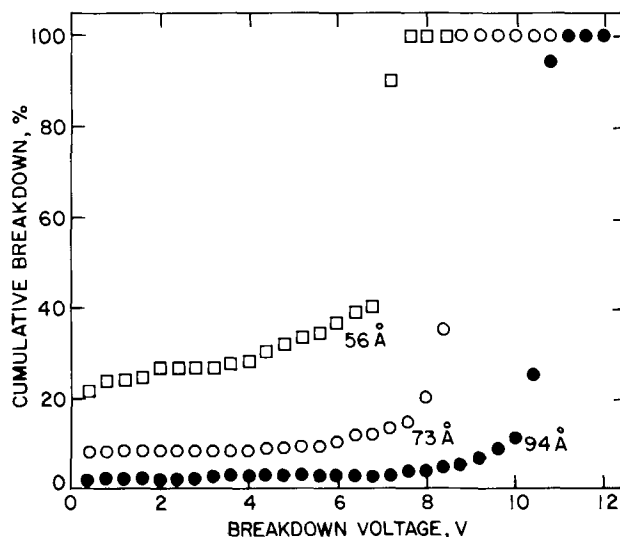


Fig. 10. Cumulative distribution plot showing breakdown voltages for three samples oxidized at 953°C and 2.0 Torr.

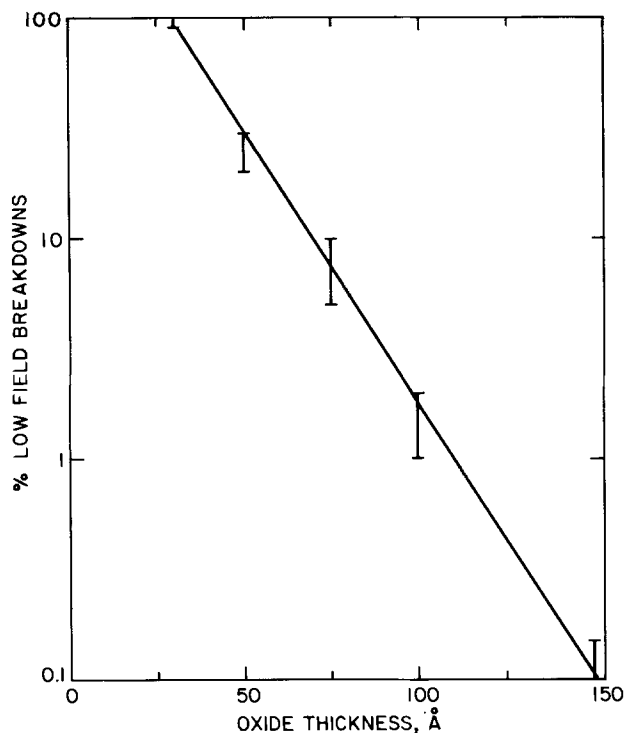


Fig. 11. The % low field breakdowns vs. oxide thickness; the point at 150Å is taken from Ref. (17) for an oxide prepared at atmospheric pressure.

than 200Å thick (49). As already stated, the low pressure oxides have a much higher percent of intrinsic breakdowns even though the films are very thin. The very narrow distribution, high breakdown fields, and high percent of intrinsic breakdowns observed for the present samples indicate that the very thin low pressure oxides are high quality, low porosity films and are more homogeneous than thicker samples oxidized at atmospheric pressure.

Capacitance-voltage measurements have been made on several samples. No attempt has been made to investigate the effects of oxide thickness or of processing parameters (annealing and cleaning) on the MOS properties. Typical values are: fixed charge, $1-5 \times 10^{11} \text{ cm}^{-2}$; mobile charge, $<2 \times 10^{10} \text{ cm}^{-2}$; fast state density at midgap, $4-6 \times 10^{10} \text{ cm}^{-2} \text{ V}^{-1}$.

Summary and Conclusions

Silicon samples have been oxidized at 900°-1000°C using oxygen at reduced pressure (0.25-2.0 Torr) to give films 30-140Å thick. The growth of these very thin films is easily controlled because of the low oxidation rate. The low pressure oxidation follows the parabolic rate law (or the linear-parabolic law with the parabolic term dominating). The parabolic rate constants calculated for the reduced pressure oxidation are in good agreement with values extrapolated from atmospheric pressure. Other rate laws have been evaluated but are not as suitable as the parabolic law.

The very thin oxides have been characterized by infrared spectroscopy, Auger spectroscopy, etch rate variation, ellipsometry, and breakdown voltage. The film properties are independent of the oxidation temperature over the range studied. Auger spectroscopy shows a small amount of carbon on the oxide surface, which is only slightly higher than observed for typical oxidations at atmospheric pressure. No impurities are detected within the film. The infrared spectra have three absorptions due to the SiO_2 lattice; absorptions caused by SiH or OH are not observed. The absorbance at 1080 cm^{-1} is a linear function of the oxide thickness and agrees with values obtained from thicker samples. The infrared data show no indication of an interfacial

region. The effective film refractive index, determined by ellipsometry, is high, 1.55. This high value may be caused by a thin interfacial layer with a high refractive index (34, 35). The etch rate (in dilute hydrofluoric acid) of the thin, low pressure oxides is identical to that of thicker oxides prepared at atmospheric pressure. The etch rates are uniform throughout the film, indicating a homogeneous oxide, except for a decrease in etch rate about 15Å from the silicon interface. This decrease may be caused by a silicon-rich interfacial layer. The distribution of breakdown voltages is characterized by high breakdown fields (10-13 MV/cm), a narrow range, and a high percent of intrinsic breakdowns, indicating a very uniform, homogeneous oxide. The percent of low field breakdowns (probably caused by pinholes or particulate contamination) increases exponentially with decreasing thickness; however, the percent of low field breakdowns may be reduced by oxidizing the samples in a cleaner environment. The chemical, physical, and electrical data indicate that the very thin oxides prepared at low pressure are very similar to thicker oxides prepared at atmospheric pressure.

Acknowledgment

The authors would like to thank H. J. Levinstein for his many comments and suggestions.

Manuscript submitted Dec. 20, 1979, revised manuscript received March 27, 1980.

Any discussion of this paper will appear in a Discussion Section to be published in the June 1981 JOURNAL. All discussions for the June 1981 Discussion Section should be submitted by Feb. 1, 1981.

Publication costs of this article were assisted by Bell Laboratories.

REFERENCES

1. F. P. Fehlner, *This Journal*, **119**, 1723 (1972).
2. A. M. Goodman and J. M. Breece, *ibid.*, **117**, 982 (1970).
3. Y. J. van der Meulen, *ibid.*, **119**, 530 (1972).
4. M. Horiuchi, Y. Kamigaki, and T. Hagiwara, *ibid.*, **125**, 766 (1978).
5. Y. Kamigaki and Y. Itoh, *J. Appl. Phys.*, **48**, 2891 (1977).
6. J. A. Aboaf, *This Journal*, **118**, 1370 (1971).
7. R. E. Oakley and G. A. Godber, *Thin Solid Films*, **9**, 287 (1972).
8. W. Przyborski, J. Roed, J. Lippert, and L. Sarholt-Kristensen, *Radiat. Eff.*, **1**, 33 (1969).
9. R. J. Archer, *This Journal*, **104**, 619 (1957).
10. S. I. Raider, R. Flitsch, and M. J. Palmer, *ibid.*, **122**, 413 (1975).
11. M. A. Hopper, R. A. Clarke, and L. Young, *ibid.*, **122**, 1216 (1975).
12. P. J. Burkhardt and L. V. Gregor, *Trans. Metall. Soc. AIME*, **236**, 299 (1966).
13. J. F. Wagner and C. W. Wilmsen, *J. Appl. Phys.*, **50**, 874 (1979).
14. C. R. Helms, *J. Vac. Sci. Technol.*, **16**, 608 (1979).
15. C. C. Chang in "Semiconductor Characterization Techniques," P. A. Barnes and G. A. Rozgonyi, Editors, p. 106, The Electrochemical Society Softbound Proceedings Series, Princeton, N.J. (1978).
16. F. J. Grunthner and J. Maserjian, *IEEE Trans. Nucl. Sci.*, **ns-24**, 2108 (1977).
17. E. A. Irene, *This Journal*, **125**, 1708 (1978).
18. A. G. Revesz, *ibid.*, **126**, 502 (1978).
19. A. C. Adams and C. D. Capio, *ibid.*, **126**, 1042 (1979).
20. A. C. Adams and C. D. Capio, *ibid.*, **127**, 399 (1980).
21. W. Kern and D. A. Puotinen, *RCA Rev.*, **31**, 187 (1970).
22. F. L. McCrackin, E. Passaglia, R. R. Stromberg, and H. L. Steinberg, *J. Res. Nat. Bur. Stand.*, **67A**, 363 (1963).
23. E. A. Taft, *This Journal*, **125**, 968 (1978).
24. R. J. Archer, *J. Opt. Soc. Am.*, **52**, 970 (1962).
25. C. C. Chang and D. M. Boulton, *Surf. Sci.*, **69**, 385 (1977).

26. W. A. Pliskin, *IBM J. Res. Dev.*, **10**, 198 (1966).
27. B. E. Deal and A. S. Grove, *J. Appl. Phys.*, **36**, 3770 (1965).
28. A. G. Revesz and R. J. Evans, *J. Phys. Chem. Solids*, **30**, 551 (1969).
29. E. A. Irene, *This Journal*, **121**, 1613 (1974).
30. E. A. Irene and Y. J. van der Meulen, *ibid.*, **123**, 1380 (1976).
31. N. Cabrera and N. F. Mott, *Rep. Prog. Phys.*, **12**, 163 (1948).
32. J. R. Ligenza, *J. Phys. Chem.*, **64**, 1017 (1960).
33. F. Lukes, *Surf. Sci.*, **30**, 91 (1972).
34. D. E. Aspnes and J. B. Theeten, *Phys. Rev. Lett.*, **43**, 1046 (1979).
35. E. Taft and L. Cordes, *This Journal*, **126**, 131 (1979).
36. W. C. Dash and R. Newman, *Phys. Rev.*, **99**, 1151 (1955).
37. S. S. So and K. Vedam, *J. Opt. Soc. Am.*, **62**, 596 (1972).
38. K. Vedam, W. Knausenberger, and F. Lukes, *ibid.*, **59**, 64 (1969).
39. T. Smith and A. J. Carlin, *J. Appl. Phys.*, **43**, 2455 (1972).
40. F. Meyer, E. E. De Kluizenaar, and G. A. Bootsma, *Surf. Sci.*, **27**, 88 (1971).
41. W. A. Pliskin and H. S. Lehman, *This Journal*, **112**, 1013 (1965).
42. R. A. Clarke, R. L. Tapping, M. A. Hopper, and L. Young, *ibid.*, **122**, 1347 (1975).
43. J. Wong, *J. Appl. Phys.*, **44**, 5629 (1973).
44. K. H. Beckmann and N. J. Harrick, *This Journal*, **118**, 614 (1971).
45. A. G. Revesz, *ibid.*, **124**, 1811 (1977).
46. T. Nakayama and F. C. Collins, *ibid.*, **113**, 706 (1966).
47. W. A. Pliskin and R. P. Esch, *Appl. Phys. Lett.*, **11**, 257 (1967).
48. J. E. Dial, R. E. Gong, and J. N. Fordemwalt, *This Journal*, **115**, 326 (1968).
49. N. J. Chou and J. M. Eldridge, *ibid.*, **117**, 1287 (1970).
50. C. M. Osburn and D. W. Ormond, *ibid.*, **119**, 591 (1972).
51. N. Klein, *IEEE Trans. Electron Devices*, **ed-13**, 281 (1966).
52. C. Fritzsche, *Z. Angew. Phys.*, **24**, 48 (1967).

Behavior of Phosphors under Low Voltage Cathode Ray Excitation

Kinichiro Narita, Akiyasu Kagami, and Yoshiyuki Mimura

Kasei Optonix, Limited, Odawara 250, Japan

ABSTRACT

The behavior of phosphors under low voltage (less than 100V) cathode ray excitation is investigated. A phosphor coated on an anode plate is excited by low voltage cathode rays from two line cathodes. Brightness increases as the distance between the anode and the cathodes decreases. Most phosphors used here show high brightness when mixed with conductive materials such as In_2O_3 or SnO_2 . The smaller diameter of In_2O_3 mixed with $\text{Y}_2\text{O}_3\text{S:Eu}$, the lower added amount of In_2O_3 necessary for maximum brightness. ZnS:Cu,Al coated with SnO_2 shows maximum brightness when the added amount of SnCl_4 is 100 w/o and the sample is fired at 700°C . $(\text{La}_x\text{Lu}_{1-x})\text{InO}_3\text{:Eu}$ shows spectrum variations according to the change of x and Eu concentration. The peak wavelength of $\text{LaInO}_3\text{:Eu}$ changes to longer wavelength when the phosphor is sulfurized into $\text{LaInO}_3\text{S:Eu}$, which is a similar phenomenon to that shown by $\text{Y}_2\text{O}_3\text{:Eu}$ and sulfurized $\text{Y}_2\text{O}_3\text{S:Eu}$ under conventional high voltage cathode ray excitation.

Currently, various display devices are being actively studied. Among them fluorescent display tubes (1), in which phosphors are excited by cathode rays of several tens of volts, are one of the best display devices and are widely used for hand or desk top calculators and other digital display applications. However the only emission color is bluish green, peaked at 520 nm, because only ZnO:Zn has been available for low voltage cathode ray tubes. Multi-color fluorescent tubes are needed for further development, for example, panel meters, flat television sets, and large area display devices. Phosphors for the tubes were first reported by Hiraki, Kagami, Hase, Narita, and Mimura in 1976. The phosphors were mixed with conductive materials such as ZnO or In_2O_3 to lower threshold voltage for emission (2). Nitta, Matsuoka, Tohda, Wasa, and Hayakawa reported on $\text{SnO}_2\text{:Eu}$. This phosphor shows 60 f-L at 20V without any conductive materials (3). Kukimoto, Oda, and Nakayama reported on ZnS and ZnSe activated by Cu or Ag together with Al. They used single crystals subjected to the Zn-extraction treatment (4).

However, there are few reports about other phosphors, the relation between brightness and applied

voltage or current, and the luminescent mechanism under low voltage cathode ray excitation. In this paper the behavior of phosphors under low voltage excitation is reported.

Experimental

The apparatus for phosphor evaluation under low voltage cathode ray excitation is demountable. Eight anode plates ($2 \times 2 \text{ cm}^2$) coated with phosphors can be mounted on a ceramic disk. Two line cathodes are used for electron sources. The distance between the plate and the cathodes is variable. In operation, the anode voltage is applied to only one anode just below the cathodes thus preventing electrons from diverging. Evacuation is carried out by a rotary pump with trap and a noble pump (Nichiden-Varian). The phosphors are coated on the anode plates by the sedimentation method. Brightness is measured by a photometer (Pritchard). The emission spectrum and CIE chromaticity coordinates are obtained by a grating monochromator, an optical multi-channel analyzer (OMA-Princeton Applied Research), a micro-computer, and a four color plotter (Yokogawa-Hewlett Packard). Figure 1 shows the block diagram. A synchroscope is used for a spectrum monitor. In order to

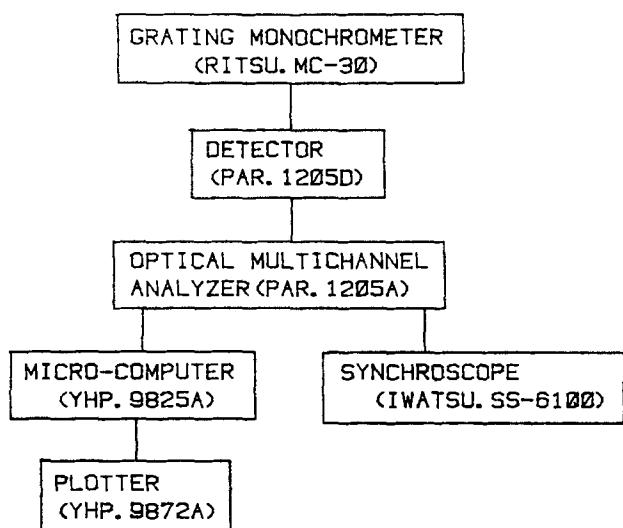


Fig. 1. Block diagram to obtain emission spectrum and CIE chromaticity. Synchroscope is used for a spectrum monitor.

measure the resistivity, phosphors are pressed into disks of 17.5 mm in diameter and 0.5 mm thick at a pressure of 200 kg/cm². The measurement is carried in the evacuated vessel at a pressure of 10⁻⁸ Torr.

Results and Discussion

Figure 2 shows brightness vs. applied voltage. The parameter is distance between an anode plate with a phosphor and the two line cathodes in mm. The phosphor used here is ZnO:Zn. These curves show that the brightness is more strongly dependent on the applied voltage and that the threshold voltage for emission goes down when the plate and the cathodes are closer. Figure 3 shows brightness (solid line) and anode current density (dotted line) vs. distance between electrodes in mm. These curves show that brightness and current density increase rapidly as the distance narrows. The density is three orders of magnitude higher than that of conventional high voltage cathode ray excitation. Anode-cathode diode characteristics in

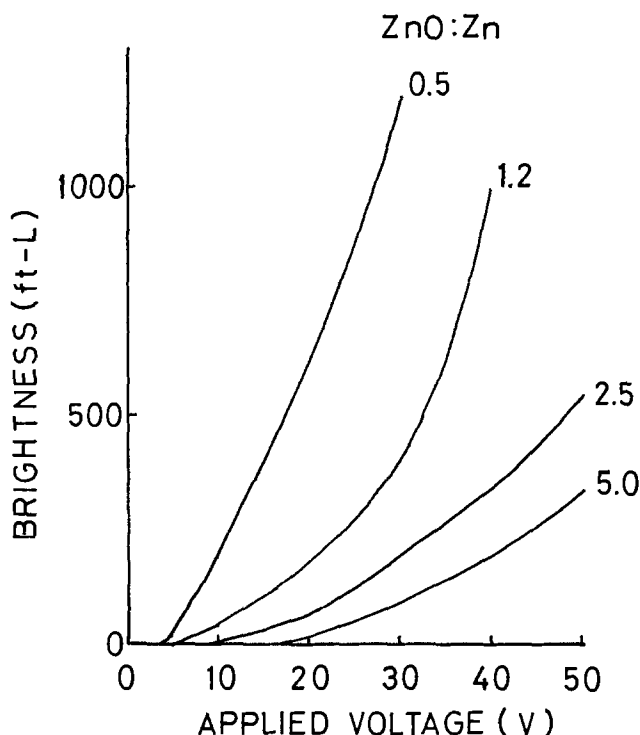


Fig. 2. Brightness vs. applied anode voltage. Parameter is distance between the anode and the cathodes in mm.

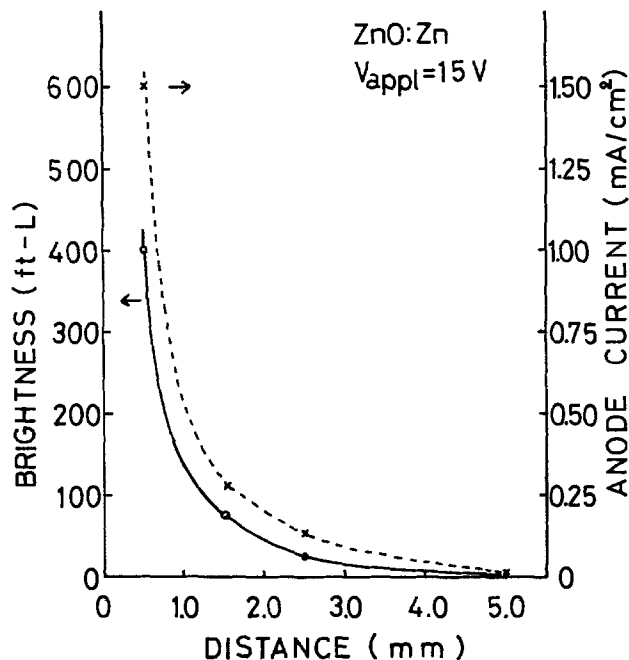


Fig. 3. Brightness and anode current vs. distance between electrodes. Applied anode voltage is 15V.

vacuum usually show $I = K \cdot V^{3/2} \cdot d^{-2}$ (I : current, K : constant, V : applied voltage, and d : distance between electrodes) because current is space charge limited. In this experiment, the power of V from a log-log plot (not shown here) is not 3/2 but 5/2. This difference seems to be due to the fact that the anode plate is coated with a phosphor, and so the current flows through the limited area at low voltage region (below 10V) and at large distances (above 3.0 mm), resulting in the fact that the phosphor emission is not uniform. In commercial tubes a mesh grid for the diffusion and the drawing of the current is placed between the cathode and the anode to get uniform phosphor emission. It may be said, however, that in this diode construction space charge limited current flows and the brightness depends largely on the current through the phosphor.

Phosphors generally have high resistivity (for example, 10¹³ Ω·cm orders of magnitude in Y₂O₃S:Eu disk), so that under conventional high voltage cathode ray excitation the phosphor screen of television tubes is metal-backed to prevent charge-up. On the other hand certain phosphors with relatively low resistivity, for example, ZnO:Zn, SnO:Eu, and (Zn,Cd)S:Cu or Ag, emit brightly under low voltage cathode ray excitation. Some phosphors can also show high brightness when mixed with conductive materials such as ZnO, In₂O₃, or SnO₂. Figure 4 shows brightness vs. In₂O₃ content. The phosphor used here is Y₂O₃S:Eu, the particle diameter being 8 μm. The parameter is the diameter of the In₂O₃ conductive material. The curves show that the content for maximum brightness decreases as the diameter of In₂O₃ becomes smaller, and that the maximum brightness is nearly constant. Figure 5 shows brightness vs. applied voltage, in which the parameter is the diameter of Y₂O₃S:Eu. Mixture ratio of Y₂O₃S:Eu to In₂O₃ is 1.0. The brightness of 4 μm Y₂O₃S:Eu is much higher than that of 8 μm.

Figure 6 shows brightness vs. diameter ratio of ZnS:Cu,Al to In₂O₃. The parameter is the phosphor diameter. Curves in this figure also show that the mixture of the phosphor and the conductive material with small diameter can show higher brightness than that with large diameter, and that the mixture of a phosphor and a conductive material with the same diameter emits more brightly than that with different diameters. The penetration depth of electrons into

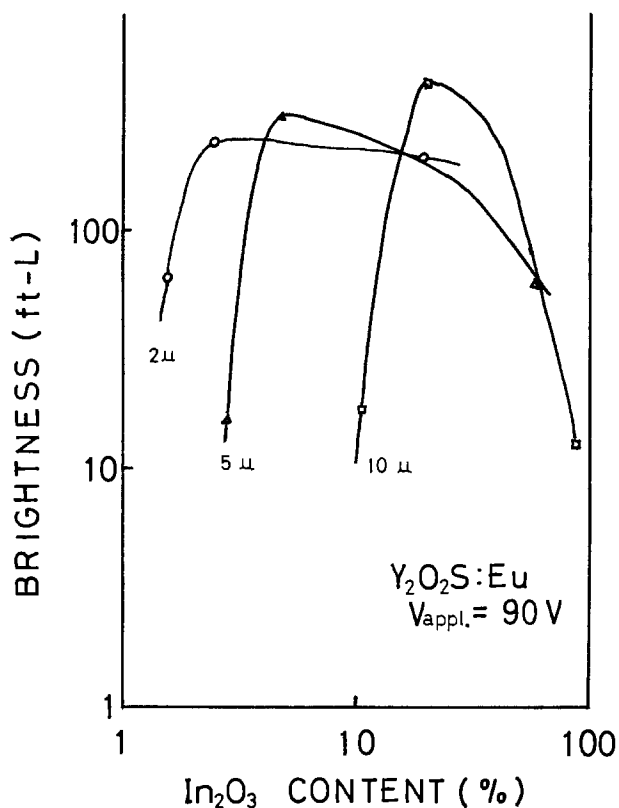


Fig. 4. Brightness vs. In₂O₃ content. Parameter is the diameter of Y₂O₂S:Eu. Applied anode voltage is 90V.

phosphors, according to Leverenz (5), Young (6), and Feldman (7), is less than a few tens of angstroms at 100V anode voltage. This shows that the phosphors preferred for low voltage cathode ray tubes should

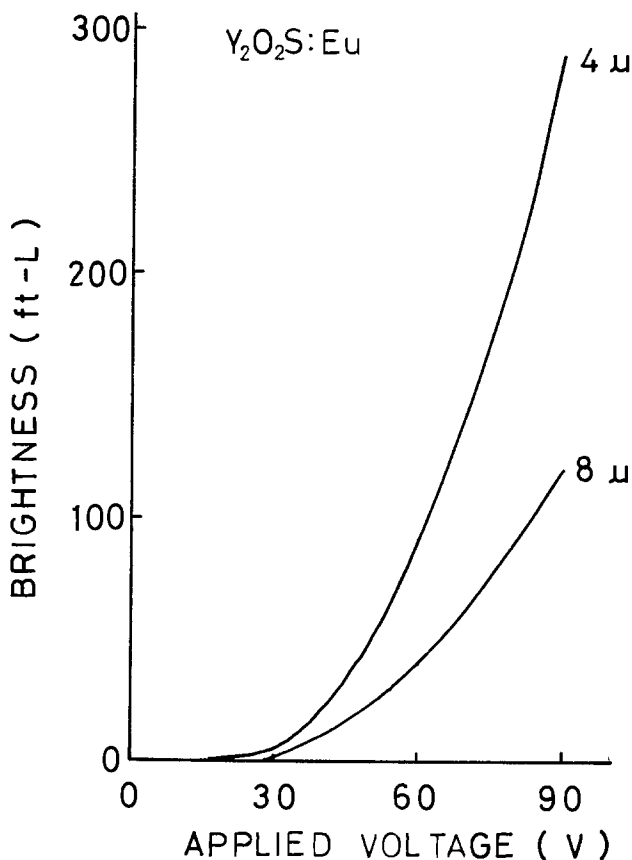


Fig. 5. Brightness vs. applied anode voltage. Parameter is the diameter of Y₂O₂S:Eu.

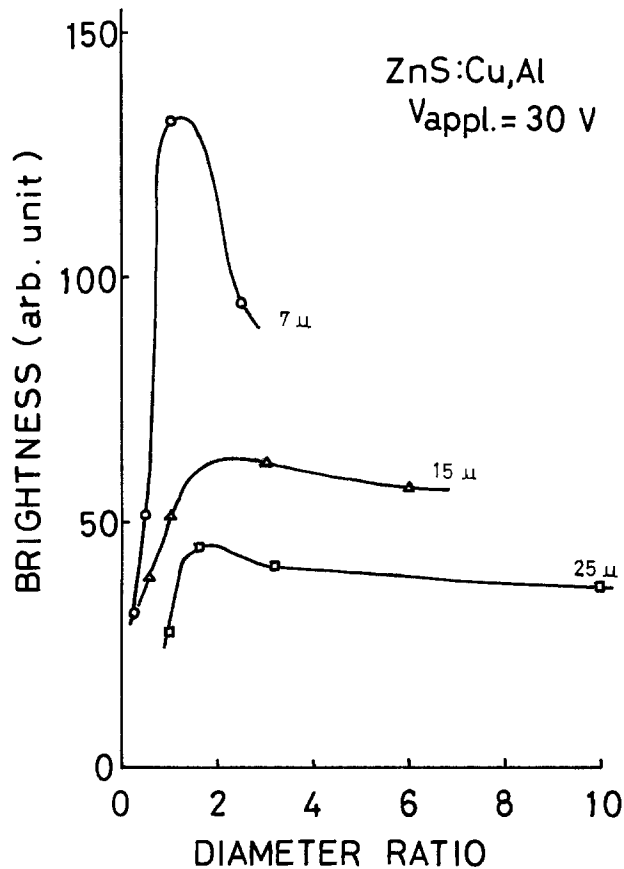


Fig. 6. Brightness vs. diameter ratio. The ratio is the diameter of ZnS:Cu,Al to that of In₂O₃. Parameter is the diameter of ZnS:Cu,Al.

be of small diameter in order to obtain large surface emitting area and thin and uniform to obtain high brightness. Furthermore, it can be said that the same small diameter is generally preferred for maximum brightness of settled powder screens.

Figure 7 shows brightness and anode current density vs. SnCl₄ content for conductively coated ZnS:Cu,Al. The phosphor is dipped in a solution containing SnCl₄ and then baked at 700°C for 10 min in air. This results in an SnO₂ coating on the phosphor. Maximum brightness is obtained at 100 weight percent (w/o) of SnCl₄, while the current continues to increase as the

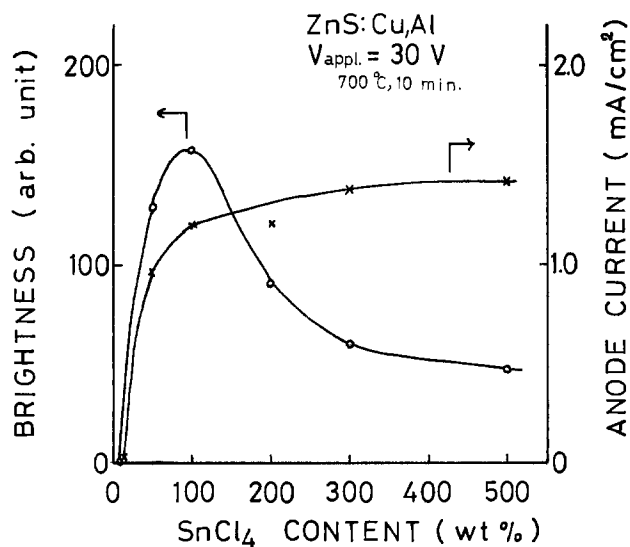


Fig. 7. Brightness vs. SnCl₄ content. ZnS:Cu,Al is dipped in SnCl₄ and fired at 700°C for 10 min in air. Applied anode voltage is 30V.

SnCl₄ content increases. This result shows that there is an optimum conductivity for maximum brightness under low voltage cathode ray excitation, and that any additional increase in conductivity is only effective to draw space charge limited current without excitation of the phosphor itself.

Most oxides including phosphors have generally very high resistivity, so that Y₂O₃:Eu is not as bright as Y₂O₂S:Eu under low voltage cathode ray excitation, even if In₂O₃ is added. But (La_xLu_{1-x})InO₃:Eu is a compound already containing In₂O₃. Hence it shows bright emission (see the spectra of Fig. 8) when it is mixed with In₂O₃. Curves 1, 2, 3, and 4 are for $x = 0.75, 0.50, 0.25,$ and $0.00,$ respectively. The intensity of the 610 nm peak increases as x decreases. This fact shows that LaInO₃ and LuInO₃ form a solid solution and the transition probability of Eu levels changes corresponding to the mixture ratio of La and Lu ions. Figure 9 shows the dependence of emission spectrum on Eu concentration in LaInO₃. An increase of Eu concentration from 2 mole percent (m/o) (curve 1) to 6 m/o (curve 2) decreases the intensity of the 550 nm subpeak. According to this spectral change the CIE chromaticity coordinates change from $x = 0.570$ and $y = 0.389$ to $x = 0.621$ and $y = 0.364$. This spectral change is also observed for Y₂O₂S:Eu under conventional high voltage cathode ray excitation, as is well known. Similar spectral change is also observed when the phosphor is fired at different temperatures, even if

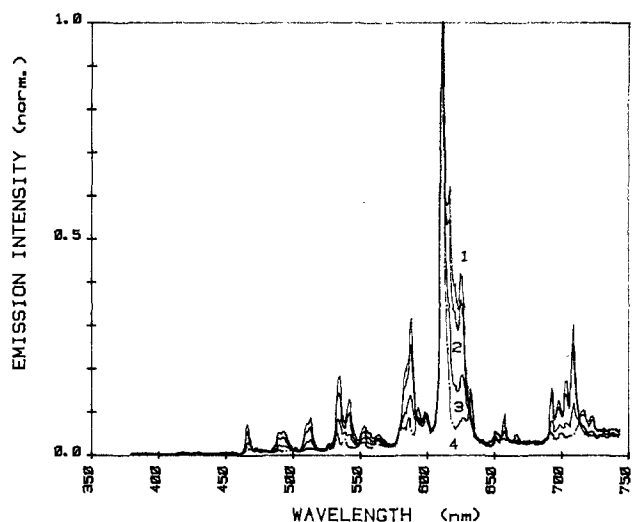


Fig. 8. Emission spectra of (La_x, Lu_{1-x})InO₃:Eu. Curves 1, 2, 3, and 4 are of $x = 0.75, 0.50, 0.25,$ and $0.00,$ respectively.

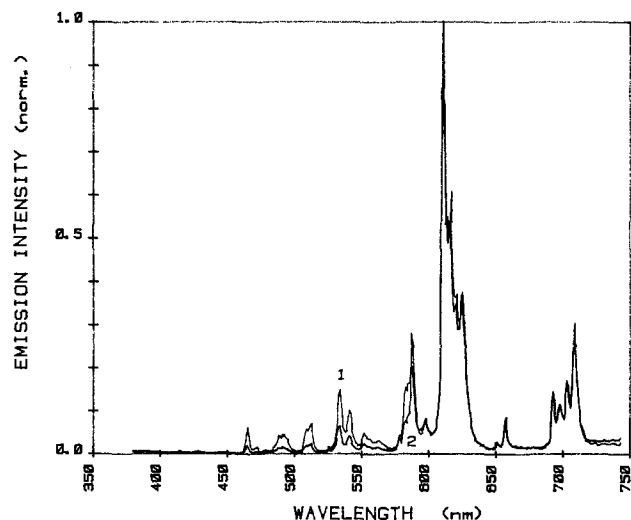


Fig. 9. Emission spectra of LaInO₃:Eu. Curves 1 and 2 are of 2 and 6 m/o of Eu concentration, respectively.

the Eu concentration is not changed. The subpeak is higher when the phosphor is fired at 1000°C than when fired at 1400°C, not shown here. This is due to the fact that Eu ions are introduced more effectively at 1400°C than at 1000°C, the effect similar to that of adding excess Eu.

Figure 10 shows the difference of spectra between LaInO₃:Eu (curve 1) and LaInO₂S:Eu (curve 2). The latter shows a main peak at longer wavelength than the former. The same relation exists between the spectrum of Y₂O₃:Eu and that of Y₂O₂S:Eu under conventional high voltage cathode ray excitation, as is well known.

Conclusion

In the case of low voltage (less than 100V) cathode ray luminescence, that which is produced by a phosphor coated on an anode and subjected to electron shower from line cathodes, the current through the phosphor strongly affects the brightness. Since the current is space charge limited, the high current density for high brightness is obtained with the lowering of the threshold voltage by narrowing the distance between the anode and the cathode. Experiments show that phosphors for fluorescent tubes should be of small diameter, a fact which can be explained using the electron range equations. The emission spectrum of (La_xLu_{1-x})InO₃:Eu varies according to x value and Eu concentration. The relation of the spectral change between LaInO₃:Eu and sulfurized LaO₂S:Eu under low voltage cathode ray excitation is the same as that between Y₂O₃:Eu and Y₂O₂S:Eu under conventional high voltage excitation.

Acknowledgments

The authors thank Prof. N. Mikoshiba of Tohoku University, Dr. S. Gonda of Electrotechnical Laboratory, and Mr. T. Kojima of NHK for their encouraging and fruitful discussions. The authors also thank Mr. N. Furuya and Dr. T. Toryu of Dai Nippon Toryo Company, Limited and Dr. Y. Kodera of Toyohashi Institute of Technology for their valuable discussions.

This work was supported, in part, by Japan Electric Industry Development Association, by Dai Nippon Toryo Company, Limited, and by Kasei Optonix, Limited, respectively.

Manuscript submitted Dec. 26, 1979. Revised manuscript received March 3, 1980.

Any discussion of this paper will appear in a Discussion Section to be published in the June 1981 JOURNAL. All discussions for the June 1981 Discussion Section should be submitted by Feb. 1, 1981.

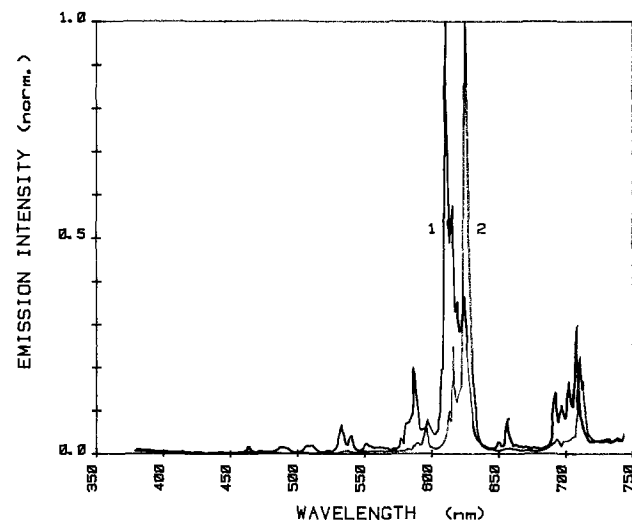


Fig. 10. Emission spectra of LaInO₃:Eu (curve 1) and LaInO₂S:Eu (curve 2).

Publication costs of this article were assisted by Kasei Optonix, Limited.

REFERENCES

1. K. Tanji, U.S. Pat. 3,508,101 (1970).
2. M. Hiraki, A. Kagami, T. Hase, K. Narita, and Y. Mimura, *J. Lumin.*, **12/13**, 941 (1976).
3. T. Nitta, T. Mastuoka, T. Tohda, K. Wasa, and

- S. Hayakawa, Abstract 336, p. 836, The Electrochemical Society Extended Abstracts, Seattle, Washington, May 21-26, 1978.
4. H. Kukimoto, S. Oda, and T. Nakayama, *J. Lumin.*, **18/19**, 365 (1979).
5. H. W. Leverenz, *J. Opt. Soc. Am.*, **27**, 25 (1937).
6. J. R. Young, *Phys. Rev.*, **103**, 292 (1960).
7. C. Feldman, *Phys. Rev.*, **117**, 455 (1960).

Annealing Technique for LEC Grown Twin-Free InP Crystals

W. A. Bonner

Bell Laboratories, Murray Hill, New Jersey 07974

ABSTRACT

An *in situ*, postgrowth annealing technique for liquid encapsulated Czochralski (LEC) grown twin-free InP crystals is reported. The procedure described minimizes the effects of both growth-induced stress and that resulting from differential thermal contraction between the InP crystal and the B₂O₃ skin adhering to it after growth.

A systematic study and control of crystalline defects and growth related problems associated with InP substrate preparation has until recently been difficult due to the limited availability of constant quality twin-free InP crystals. A new liquid encapsulated Czochralski (LEC) growth technique which limits the rate of diameter enlargement while a nearly planar crystal-melt interface is maintained has essentially eliminated the problems related to twinning and polycrystalline growth (1). Using the apparatus employed in Ref. (1, 2), ~100g InP single crystals, (30 mm diam × ~80 mm long) of constant quality suitable for quaternary alloy device studies can be routinely grown. Twin-free crystals so grown, however, have been found to exhibit evidence of somewhat greater internal stress than previously observed in twinned crystals. In this paper, an *in situ*, postgrowth annealing technique is reported, which has been found effective in minimizing the effects of both growth-induced strain and that resulting from differential thermal contraction between the InP crystal and the B₂O₃ skin adhering to it after growth.

Experimental and Results

LEC growth of InP crystals is accomplished using an inert gas pressure of ~38 atm to prevent dissociation of the compound at the melting point and molten B₂O₃ as the encapsulant to seal the melt. As the crystal is pulled through the encapsulant layer a thin skin of B₂O₃ adheres to the boule surface. Differential thermal contraction between this B₂O₃ skin ($1.5 \times 10^{-5} \text{ }^\circ\text{C}^{-1}$) (3) and the InP crystal ($5.3 \times 10^{-6} \text{ }^\circ\text{C}^{-1}$) (4) during cooling can introduce mechanical strain as well as impede the relief of growth-induced stress unless properly annealed as discussed below.

Previous conventional procedures suggest, at the conclusion of growth, InP crystals be cooled without decreasing pressure in the growth chamber to prevent decomposition. Prior to the growth technique reported in Ref. (1), most InP "single" crystals contained twins which appear as a sequence of closely spaced parallel (111) planes. For crystals grown in a <111> direction, three geometrically similar (111) planes occur at 70.32° to the growth direction symmetrically spaced 120° apart.

Recent studies (1) have shown that if the rate of diameter enlargement is such that the angle the growing crystal makes with the <111> growth direction exceeds ~19.68° twins form which are parallel to the <111> surfaces expected at 19.68°. However, if the rate of diameter enlargement results in an angle less than 19.68° so (111) surfaces are avoided, initial twin formation is prevented. So limiting the rate of diameter enlargement while employing growth parameters which result in a nearly planar crystal melt interface reproducibly yields twin-free crystals.

An example of a typical, twinned, crystal is shown in Fig. 1. The surface of this crystal has been sandblasted using 3 μm alumina to produce a uniform matte finish and subsequently etched with concentrated HCl to reveal twins. Conventional cooling procedures alluded to above appear to have been sufficient to prevent strain in crystals of this morphology as stress relief can occur primarily through deformation twinning and slip.

Evidence for the presence of internal stress in twin-free InP crystals was the observation that crystals cooled prior to decreasing the pressure exhibit a greater tendency to crack during wafering.

Twin-free InP crystals (example shown in Fig. 2) cooled to room temperature while a pressure of 38 atm is maintained in the chamber show a rough and



Fig. 1. InP so-called "single" crystal showing <111> parallel twin planes.

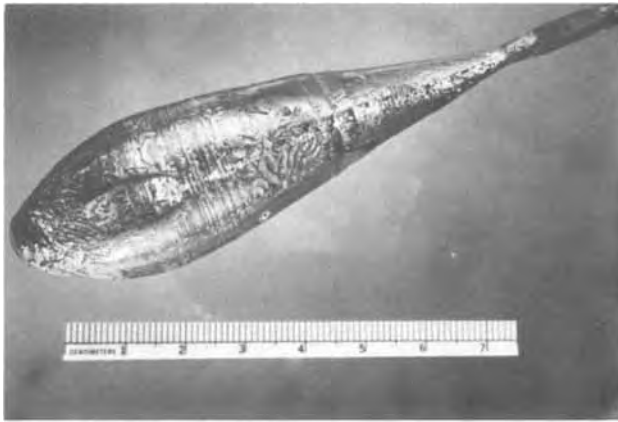


Fig. 2. Surface feature typical of twin-free InP crystal cooled at 38 atm pressure.

mottled surface. It is a result of spalling of the B_2O_3 skin remaining on the crystal after growth. Spalling of the crystal surface also occurs due to the development of surface microcracks caused by differential thermal contraction and adhesion of the B_2O_3 . A $\langle 111 \rangle$ slice through such a crystal is shown in Fig. 3, and reveals the extent to which surface damage can occur. Further, failure to relieve growth-induced strain causes cracking during wafering. Nominally, 15% of the wafers cut from twin-free crystals improperly annealed crack.

Figure 4 shows a twin-free crystal cooled at the same rate as that in Fig. 3, after the pressure was reduced to 1 atm. In contrast, the surface does not spall and is smooth and free of surface cracks. The B_2O_3 skin remaining on crystals annealed in this manner was also smooth and continuous. In the example shown the B_2O_3 has been removed by washing. Twin-free crystals so annealed show no tendency to crack during



Fig. 3. $\langle 111 \rangle$ slice through twin-free InP boule cooled at 38 atm pressure, $5\times$ showing extent to which surface damage can occur.



Fig. 4. Surface feature typical of twin-free InP crystal cooled at 1 atm pressure.

wafering, quaternary alloy devices prepared on substrates from these crystals exhibit less variability in device characteristics (5), and substrate cleavage is sharper and cleaner (6).

Growth-induced internal stress responsible for cracking can be relieved and strain prevented in twin-free crystals provided the temperature of the grown crystal is maintained sufficiently high so that the B_2O_3 skin remains somewhat fluid while the ambient pressure is gradually reduced. This is easily accomplished in our apparatus without the use of auxiliary after-heaters by proper positioning of the crystals above the crucible and maintaining rf power to the susceptor. In this regard, it is essential that the entire InP melt be extracted from the crucible during crystal growth, as material remaining in the crucible will decompose at the decreased pressure. Heating of the crystal then occurs by radiation and conduction by the inert gas atmosphere. Strain annealing is accomplished when the inert gas pressure is gradually decreased to 1 atm and the crystal subsequently cooled by decreasing power to the susceptor. The rate of pressure decrease is unimportant. In these studies approximately 1 atm/min was found convenient. Slower rates did not improve the final crystal quality. Cooling rates between $40^\circ\text{C}/\text{min}$ and $2^\circ\text{C}/\text{min}$ were examined. Qualitatively, stress relief appeared complete if rates $20^\circ\text{C}/\text{min}$ or slower were used.

A temperature profile of the growth chamber at 38 atm and 1 atm are shown in Fig. 5. R-f power to the susceptor was maintained at the same level during crystal growth. The position of the crystal and crucible (susceptor) during annealing is indicated. Although a significant thermal gradient exists along the crystal length it has not been found detrimental.

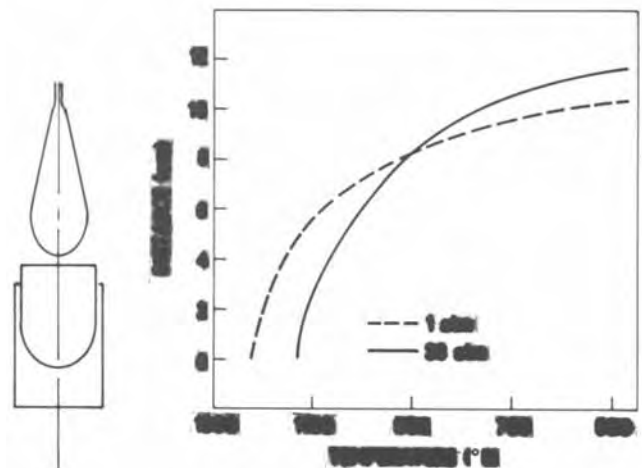


Fig. 5. Temperature profile of growth chamber for 38 atm and 1 atm pressure prior to cooling.

Discussion

In the case of twinned "single" crystals (Fig. 1), differential thermal contraction between InP and the B_2O_3 skin does not present a serious problem. The effects are manifested primarily in the rough surface texture due to spalling, surface cracks, and the formation of above average dislocations near the surface. A plot depicting typical dislocation densities, as revealed by etch pitting on (100) surfaces, for crystals cooled while at 38 atm and cooled after the pressure was reduced to 1 atm, is shown in Fig. 6. The (100) wafers were cut from twin-free crystals grown in a $\langle 111 \rangle$ direction. Although the density of dislocations is quite similar for the bulk of material the density near the surface is about ten times greater for crystals cooled prior to decreasing the chamber pressure. TEM studies by Mahajan (7) indicate some of the dislocations near the surface are slip generated.

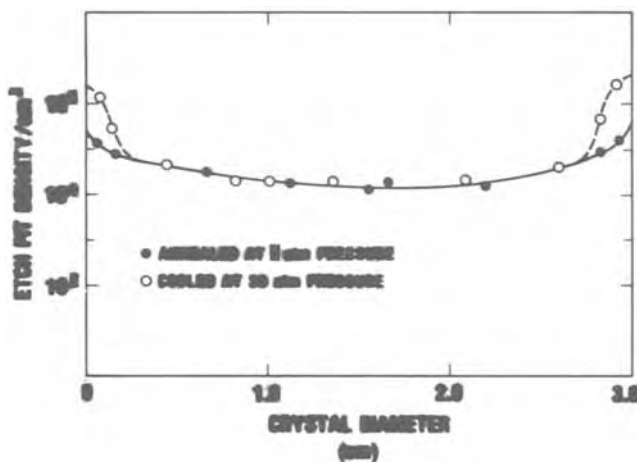


Fig. 6. Idealized plot of dislocation density across (100) InP wafers from crystals cooled at 38 atm and 1 atm.

No attempt has been made to measure the magnitude of the stresses due to differential thermal contraction. A smooth, continuous B_2O_3 skin has, however, been observed on twin-free InP crystals cooled prior to lowering the pressure provided very slow cooling rates ($<1^\circ\text{C}/\text{min}$) were used. However, in such cases, the B_2O_3 skin and crystal surface decrepitate with some degree of violence upon simply touching or washing. Crystals annealed in this manner also crack severely during wafering, suggesting relief of growth-induced strain was restricted. It is apparent then that cooling of twin-free InP crystals at low ambient pressure in the growth chamber is essential in order to minimize the effects of growth-induced stress and prevent surface deformation resulting from differential thermal contraction of the encapsulant.

Acknowledgments

I wish to thank E. Berry for technical assistance and J. H. Wernick for valuable discussions.

Manuscript submitted Jan. 4, 1980; revised manuscript received March 12, 1980. This was Paper 249 presented at the Los Angeles, California, Meeting of the Society, Oct. 14-19, 1979.

Any discussion of this paper will appear in a Discussion Section to be published in the June 1981 JOURNAL. All discussions for the June 1981 Discussion Section should be submitted by Feb. 1, 1981.

Publication costs of this article were assisted by Bell Laboratories.

REFERENCES

1. W. A. Bonner, *Mater. Res. Bull.*, **15**, 63 (1980).
2. E. Buehler, *J. Cryst. Growth*, **43**, 584 (1968).
3. K. J. Bachmann, E. Buehler, J. L. Shay, and D. L. Malm, *Inst. Phys. Conf. Ser. No. 24*, Chapter 3 (1975).
4. A. Cousen and W. E. S. Turner, *J. Soc. Glass Technol.*, **12**, 169 (1928).
5. R. Logan, Private communication.
6. J. C. De Winter, Private communication.
7. S. Mahajan, Unpublished data.

Epitaxial Growth of Cubic ZnS_xSe_{1-x} by Vapor Phase Transport

D. Etienne, L. Soonckindt, and G. Bougnot

Centre d'Etudes d'Electronique des Solides (associé au C.N.R.S.),

Université des Sciences et Techniques du Languedoc, 34060 Montpellier Cedex, France

ABSTRACT

Films of cubic ZnS_xSe_{1-x} have been grown epitaxially on cleaved CaF_2 substrates by vapor phase transport in flowing hydrogen and the conditions to obtain epitaxial deposits of these compounds have been determined. The effects of gas flow rates and both source and substrate temperatures on the composition x have been investigated. The composition dependence of the bandgap was determined by photovoltage measurements.

II-VI compound semiconductors and their alloys cover a wide range of electrical and optical properties which make them potentially useful for a variety of practical applications. These include luminescence, photoconductive, acoustoelectric properties and p-n junction light emitting diodes. Unfortunately, the synthesis of these materials is frequently complicated by the combination of high melting temperatures and dissociation pressures. However, many of the diffi-

Key words: chemical vapor deposition, semiconductors, electronics.

culties associated with these complications are minimized when vapor phase crystal growth methods are employed, primarily because of the low growth temperatures involved with this technique.

Among the different possible approaches to the vapor deposition of II-VI compounds, only open-tube flow methods offer the flexibility and control needed to prepare compounds or alloys, with widely varying composition, doping, and geometries.

For ZnSe, ZnS, the literature describes many methods dealing with the growth of ZnSe (1-5) or ZnS

(6-9), but information on the zinc sulfoselenide system, however, is rather sketchy (4, 10-12) and the crystals obtained are reported to be inhomogeneous.

Recently a method has been developed (13) for growing $\text{ZnS}_x\text{Se}_{1-x}$ boules with uniform composition and consisting in several grains, using the iodine vapor transport technique in a sealed ampul.

In a previous paper, we had briefly described the application of an open-tube system for the preparation of $\text{ZnS}_x\text{Se}_{1-x}$ (14). In that system, deposition of epitaxial films of $\text{ZnS}_x\text{Se}_{1-x}$ composition in the range $0 \leq x \leq 1$ was carried out on calcium fluoride (CaF_2) substrates by reaction of hydrogen with the compound in powdered form. In the present paper, we wish to give more details on the results thus obtained.

Growth Procedure

The growth apparatus previously described for ZnS and ZnSe (15, 16) was modified for growing $\text{ZnS}_x\text{Se}_{1-x}$ by flowing H_2 over two independent sources (Fig. 1).

The reaction chamber consisted of a 30 mm inner diameter, 1m long quartz tube. It was positioned in a horizontal two-zone furnace which provided the temperature profile needed for the sources and for the epitaxial deposition.

The CaF_2 substrates ($1 \times 1 \text{ cm}^2$ area) were cleaved in a (111) plane, mechanically polished to a mirror-smooth finish and etched with a HCl-HNO_3 (1:1) solution. The operation of the system may be summarized as follows: the tube is first flushed with hydrogen, then the sources and deposition zone are brought to the required temperatures, and by means of a quartz push rod, the substrate is moved into the deposition zone and etched *in situ* in flowing H_2 . The hydrogen flow and deposition is commenced when the temperature of the substrate is reasonably stable.

Growth times were between 1 and 8 hr, yielding films between 5 and 40 μm thick. At the end of the run the furnace was slowly cooled (100°C/hr) to room temperature in order to avoid cracks arising from the difference in the thermal expansion coefficients. This difference is one of the most important factors to be considered in selecting suitable substrate materials in addition to the room temperature lattice constant. In fact, CaF_2 , in spite of its good lattice match (5.482Å for CaF_2 , 5.6687Å and 5.4093Å for ZnSe and ZnS) shows a relatively large difference in the thermal expansion coefficients ($19 \cdot 10^{-6} \text{ }^\circ\text{C}^{-1}$ for CaF_2 , $6.7 \cdot 10^{-6} \text{ }^\circ\text{C}^{-1}$ for ZnSe and ZnS at room temperature). The epitaxial deposition was carried out at a source temperature within the $800^\circ\text{-}950^\circ\text{C}$ range (usually 850°C for both ZnS and ZnSe sources), total hydrogen flow rates of about $100\text{-}300 \text{ cm}^3 \text{ min}^{-1}$, and substrate temperatures within the $630^\circ\text{-}780^\circ\text{C}$ range. The linear velocity (defined as the ratio of the carrier gas flow rate to the cross section of the reaction tube) of the system depends on the flow rate over the two sources.

Theoretical Determination of Composition in $\text{ZnS}_x\text{Se}_{1-x}$

The composition x was determined by a simple formula, based on the thermodynamics of the equilibria.

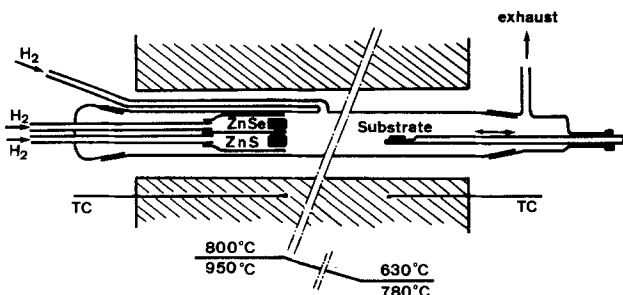
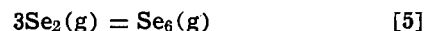
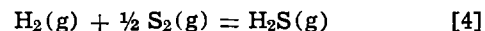
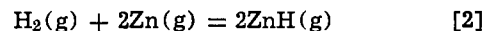
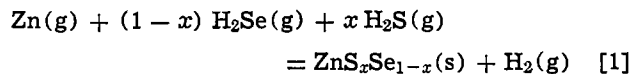
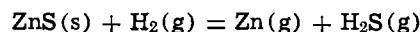
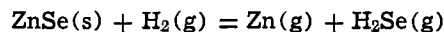


Fig. 1. $\text{ZnS}_x\text{Se}_{1-x}$ vapor growth system: experimental arrangement and temperature profile during growth.

The mechanism for the $\text{ZnS}_x\text{Se}_{1-x}$ formation involves six chemical reactions



Equation [1] may be considered as the superposition of two chemical reactions due to hydrogen over two independent solid sources



Lever's principle (17) of resolution, which is based on Gibb's phase rule and which was improved by Hurle and Mullin (18) was used (19) for the determination of the equilibria constant K_p .

The values of the partial pressures are calculated for each chemical substance able to exist in a vapor state on the basis of a thermodynamical equilibrium between solid and vapor phase. If " p_j " represents the partial pressure of the gaseous species " j ", and if " n_i " stands for the total number of atoms per unit volume of the constituent " i " in an elemental or compound form in the gaseous mixture at the output of the two sources, the equations enabling us to give an overall description of the system are:

The six relations between partial pressures corresponding to the chemical equilibria [1]-[6].

The constancy of the total pressure

$$P_0 = \sum p_j \text{ with } P_0 = 1 \text{ atm.}$$

The stoichiometry conservation

$$P_{\text{Zn}} + P_{\text{ZnH}} = 2P_{\text{Se}_2} + 6P_{\text{Se}_6} + P_{\text{SeH}_2} + P_{\text{SH}_2} + 2P_{\text{S}_2} + 8P_{\text{S}_8}$$

The concentration x in zinc sulfide in the vapor phase with source at temperature T_1 , given by

$$\frac{x}{1-x} = \frac{n_s}{n_{\text{Se}}} = \frac{2P_{\text{S}_2} + 8P_{\text{S}_8} + P_{\text{SH}_2}}{2P_{\text{Se}_2} + 6P_{\text{Se}_6} + P_{\text{SeH}_2}}$$

From these conditions, the partial pressures of each gaseous species are calculated in all the range of temperature and composition (Fig. 2, 3).

One concludes that the main gaseous species are Zn, H_2Se , H_2S , and to a less extent, S_2 , Se_2 , and ZnH.

Let $\gamma = (D^{\circ}\text{H}_2)_{\text{ZnS}} / (D^{\circ}\text{H}_2)_{\text{ZnSe}}$, where $(D^{\circ}\text{H}_2)_{\text{ZnS}}$, $(D^{\circ}\text{H}_2)_{\text{ZnSe}}$ are, respectively, the hydrogen flow rates over the ZnS and ZnSe sources, as measured at room temperature.

At the source temperature T_1

$$\gamma \simeq \frac{(D^{\circ}\text{H}_2)_{\text{ZnS}}}{(D^{\circ}\text{H}_2)_{\text{ZnSe}}} = \frac{V_{\text{ZnS}}}{V_{\text{ZnSe}}}$$

V_{ZnS} and V_{ZnSe} are the linear velocities over the separate sources, $(D^{\circ}\text{H}_2)_{\text{ZnS}}$ and $(D^{\circ}\text{H}_2)_{\text{ZnSe}}$ the H_2 flow rate at T_1 . Atomic fluxes leaving the sources regions are given by

$$J_i = N_i \cdot V_{\text{ZnS or ZnSe}}, \text{ with } N_i = \sum_{j=1}^{j=m} \lambda_{ij} \frac{P_j}{RT_1}$$

N_i is the total number of " i " atoms over each source and λ_{ij} is the stoichiometric coefficient of the i th element in the j th specie. For the ZnS and ZnSe sources

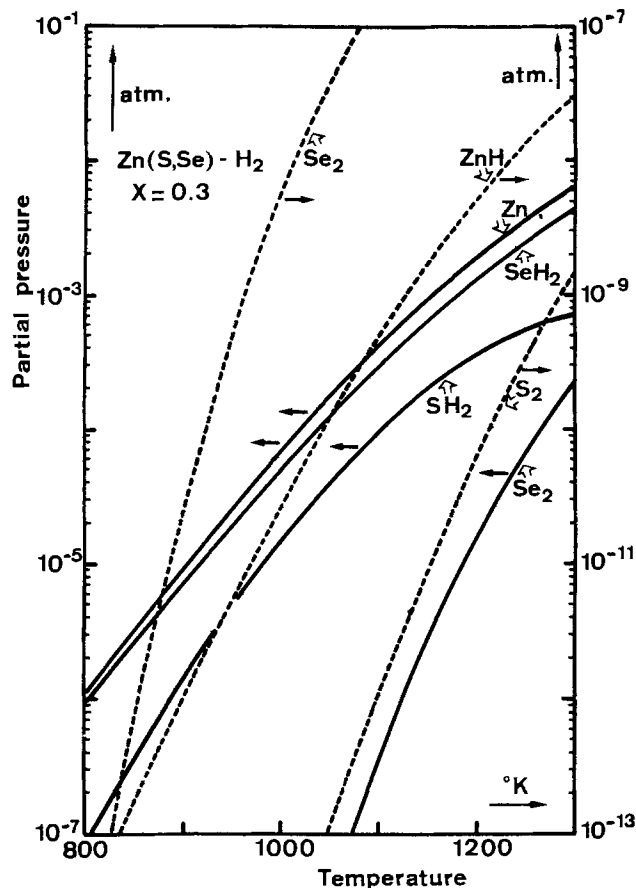


Fig. 2. Partial pressure in the system $\text{ZnS}_x\text{Se}_{1-x}\text{-H}_2$ as a function of temperature for $x = 0.3$.

$$J_S = \frac{V_{\text{ZnS}}}{RT_1} [2P_{\text{S}_2} + P_{\text{SH}_2}]_{T_1/\text{ZnS}}$$

$$J_{\text{Se}} = \frac{V_{\text{ZnSe}}}{RT_1} [2P_{\text{Se}_2} + P_{\text{SeH}_2}]_{T_1/\text{ZnSe}}$$

$$= \frac{1}{\gamma} \cdot \frac{V_{\text{ZnS}}}{RT_1} [2P_{\text{Se}_2} + P_{\text{SeH}_2}]_{T_1/\text{ZnSe}}$$

where the partial pressures are now calculated in the systems ZnS/H_2 and ZnSe/H_2 , separately considered at temperature T_1 . Then, the composition x is determined by

$$\frac{x}{1-x} = \frac{J_S}{J_{\text{Se}}} = \gamma \cdot \frac{[2P_{\text{S}_2} + P_{\text{H}_2\text{S}}]_{T_1/\text{ZnS}}}{[2P_{\text{Se}_2} + P_{\text{H}_2\text{Se}}]_{T_1/\text{ZnSe}}} \quad [7]$$

So, it is possible to calculate the theoretical composi-

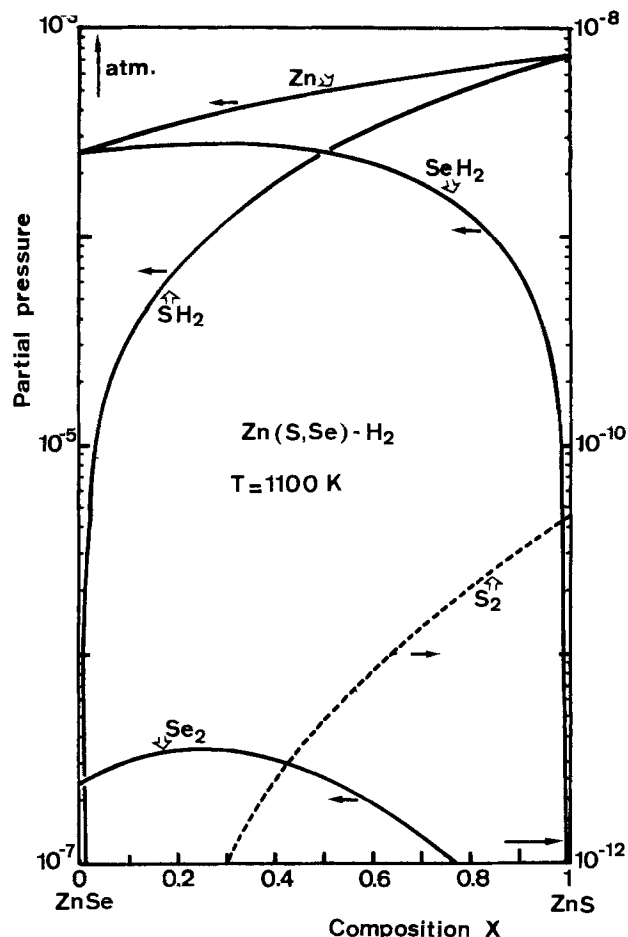


Fig. 3. Partial pressure in the system $\text{ZnS}_x\text{Se}_{1-x}\text{-H}_2$ as a function of composition x for $T = 1100^\circ\text{K}$.

tion x , in terms of the ratio γ of the hydrogen flow rates over the ZnSe and ZnS sources and with variation of sources temperature T_1 .

Experimental Results

Morphology and crystal structure.—The growth temperature is one of the important parameters which determine the crystal quality and morphology. The epitaxial quality of the individual films was evaluated primarily by means of microscopic studies of the film surfaces. These studies were initially checked against x-ray and electron diffraction results.

Figure 4a and b are photomicrographs of the as-grown surfaces of two $\text{ZnS}_x\text{Se}_{1-x}$ films, with various parameters. In both cases, the layers deposited di-

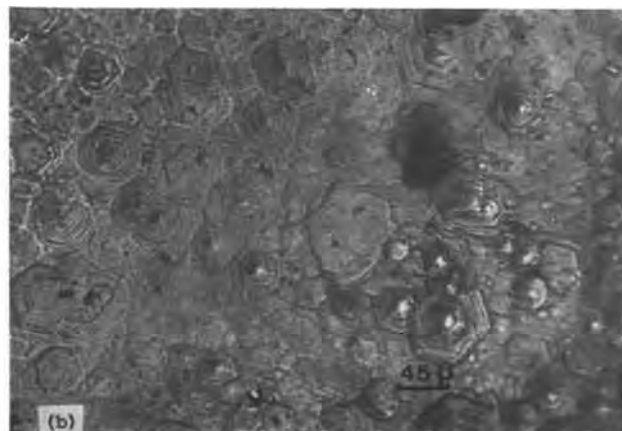


Fig. 4. Photomicrographs of $\text{ZnS}_x\text{Se}_{1-x}$ layers grown on (111) CaF_2 substrates: (a) $x = 0.22$, source temperature 850°C , substrate temperature 780°C , $\gamma = 0.1$; (b) $x = 0.86$, source temperature 850°C , substrate temperature 730°C , $\gamma = 2$.

rectly on (111)-CaF₂ substrates showed well-defined microstructure, and revealed well-oriented triangular growth pattern, characteristic of the (111) epitaxy.

Reflection electron diffraction was used to determine the crystalline quality of the layers. The investigations give structural information about highly localized areas of the deposited layers. Figure 5 shows reflection electron diffraction patterns of the alloy layer with various composition and various growth temperatures. The diffraction pattern consists in strong spots which indicates a good crystalline structure. The alloy layers were single crystals with the same orientation as the substrate.

In some cases (substrate temperature < 650°C), the diffraction pattern indicates a good single crystal structure although the superimposed satellite spots do suggest the inclusion of structural defects such as twins or stacking faults. For substrate temperature of 630°C, the diffraction pattern shows so-called Debye rings; this indicates a polycrystalline structure. Figure 6 shows x-ray (CuK α) diffraction patterns from the films deposited on CaF₂ substrate. The layers investigated were between 5 and 15 μ m thick and were not etched before the measurements. It shows only a reflection from the (111) planes. By using this growth method, ZnS, ZnSe, and ZnS_xSe_{1-x} high quality films are obtained with high reproducibility and these x-ray diffractometer scans proved the results of the reflection electron diffraction.

Results on the x variation.—Figure 7 shows the variation of composition x vs. the ratio γ for the same source temperature 850°C and for two substrate temperatures 730° and 780°C. It is possible, at a substrate temperature $T_2 = 730^\circ\text{C}$, to obtain a composition x in the range $0 < x < 0.5$; with the temperature $T_2 = 780^\circ\text{C}$, the composition range is $0.5 < x < 1$.

The composition x was determined from lattice-constant measurements on the basis of Vegard's law or by electron probe microanalyzer. The solid curves represent the theoretical variations of x , in function

of γ , which were obtained from calculations using Eq. [7]. Good agreement is found with the experimental values, it confirms that the S content in the vapor phase is increasing with increasing flow over the ZnS source (high γ values).

With the source temperature T_1 , the variation of composition x is shown on Fig. 8 for different substrate temperatures and different values of γ . The solid curves represent the theoretical values of x (Eq. [7]), and good agreement is found with the experimental values. We observe that a wide range of x values may be obtained by varying γ , but these x values are rather insensitive to the sources temperatures.

Figure 9 shows the variation of composition x with substrate temperature T_2 . Such a variation is not expected from the theory; the composition x should depend only on T_1 and not on T_2 , since from the equation of continuity, the concentration of ZnS must be the same at the source and substrate temperatures. This variation of composition x with T_2 can be explained by the nucleation on the wall of the reaction chamber. At high temperature, the Se is the first deposit experimentally observed, and at low temperature the S concentration is higher than the Se one. In this case the composition x is a function of the substrate temperature and the composition x decreases with the increasing of T_2 . However, these experimental results show that the composition remains constant with the substrate temperature for two ranges of temperature. For $\gamma < 0.5$, the composition is constant with $T_2 > 750^\circ\text{C}$, and for $T_2 < 750^\circ\text{C}$ the composition is varying in function of T_2 . The same results are observed for $T_2 < 750^\circ\text{C}$ and $\gamma > 0.5$. In this range of temperature, the composition for different γ remains constant vs. T_2 .

This result is consistent with the curve of Fig. 7. For $T_2 = 780^\circ\text{C}$ ($T_2 > 750^\circ\text{C}$), the composition is well defined and any variation occurs with the substrate temperature according to the theory. For $T_2 = 730^\circ\text{C}$ ($T_2 < 750^\circ\text{C}$), in the range $0.5 < \gamma < 4$, any influence of substrate temperature occurs.

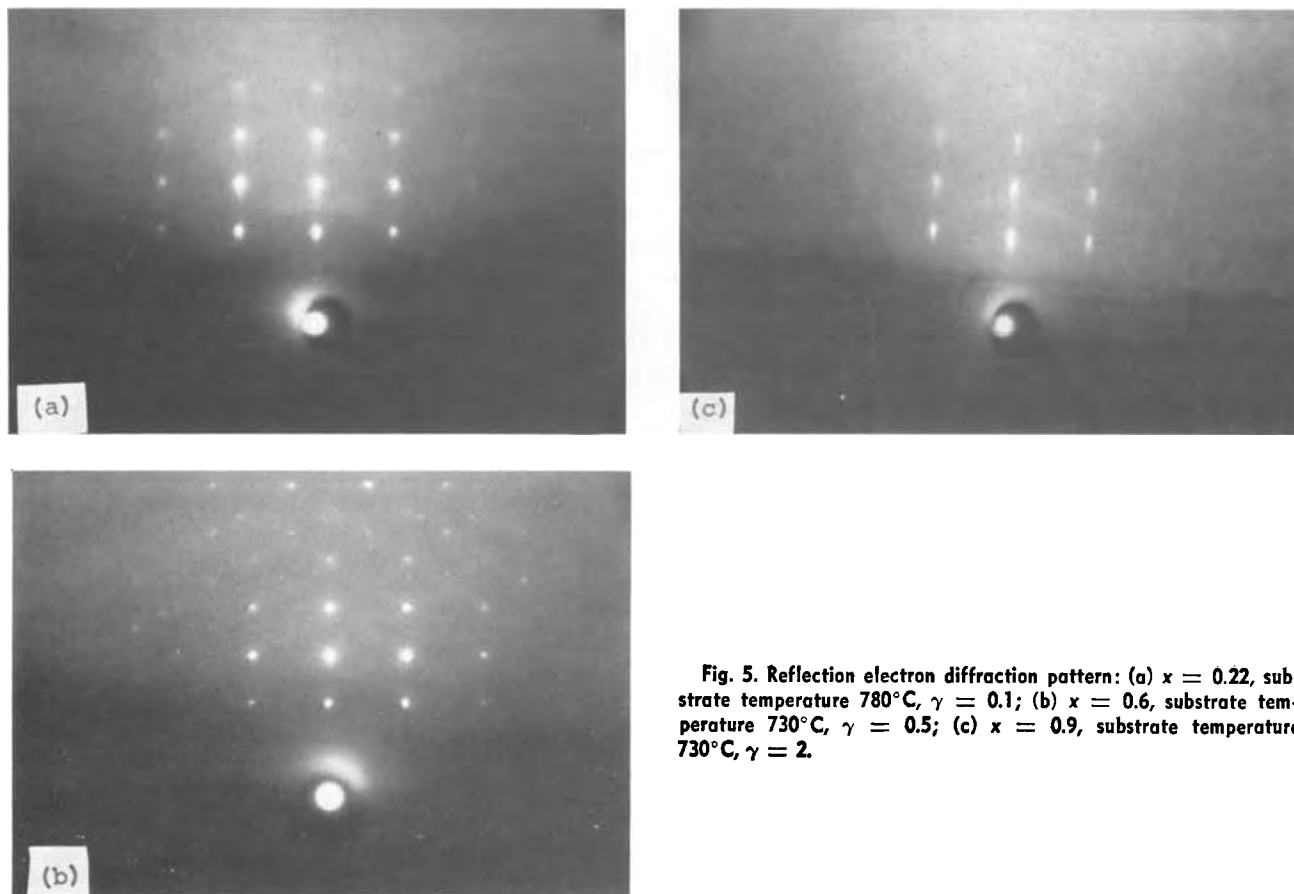


Fig. 5. Reflection electron diffraction pattern: (a) $x = 0.22$, substrate temperature 780°C , $\gamma = 0.1$; (b) $x = 0.6$, substrate temperature 730°C , $\gamma = 0.5$; (c) $x = 0.9$, substrate temperature 730°C , $\gamma = 2$.

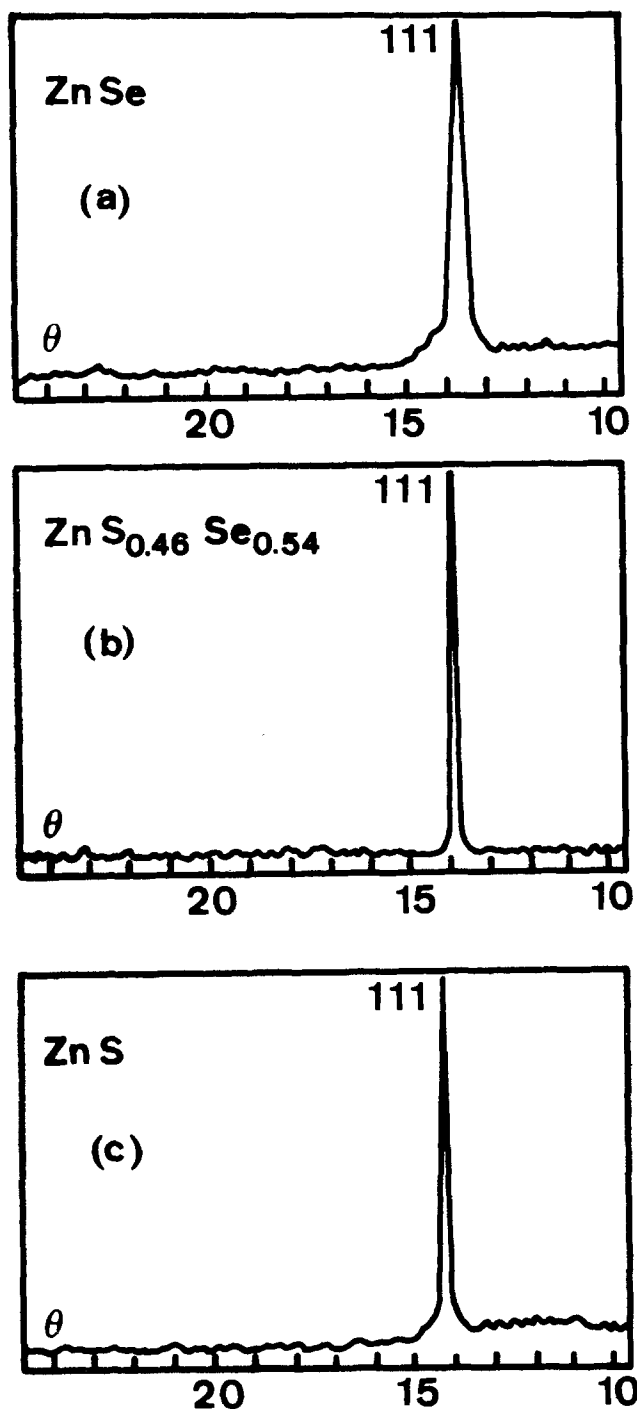


Fig. 6. X-ray diffraction scan: (a) ZnSe layer, substrate temperature 730°C; (b) ZnS_{0.46}Se_{0.54} layer, substrate temperature 780°C, $\gamma = 0.3$; (c) ZnS layer, substrate temperature 750°C.

Electro-Optical Characterization of the Samples

Method of measurement.—The technique used is based on the Kelvin method (20). It consists in measuring the contact potential V_{cp} between the surface and a reference electrode. From the variation of V_{cp} it is possible to obtain the variation of the surface potential V_s . To increase the sensitivity of the systems, we used a wavelength modulation technique (21), so as to get directly the derivative $dV_{cp}/d\lambda = dV_s/d\lambda$ of the signal with respect to the wavelength. The measurement cell is a capacitance constituted by the sample in front of which a semitransparent electrode is placed parallel to the semiconductor surface, about 0.2 mm away. In series with the capacitance is a high input impedance amplifier. The illumination of the sample with pulsed radiation of energy $h\nu > E_c - E_v$ gives variations of dV_s of the barrier potential V_s . In

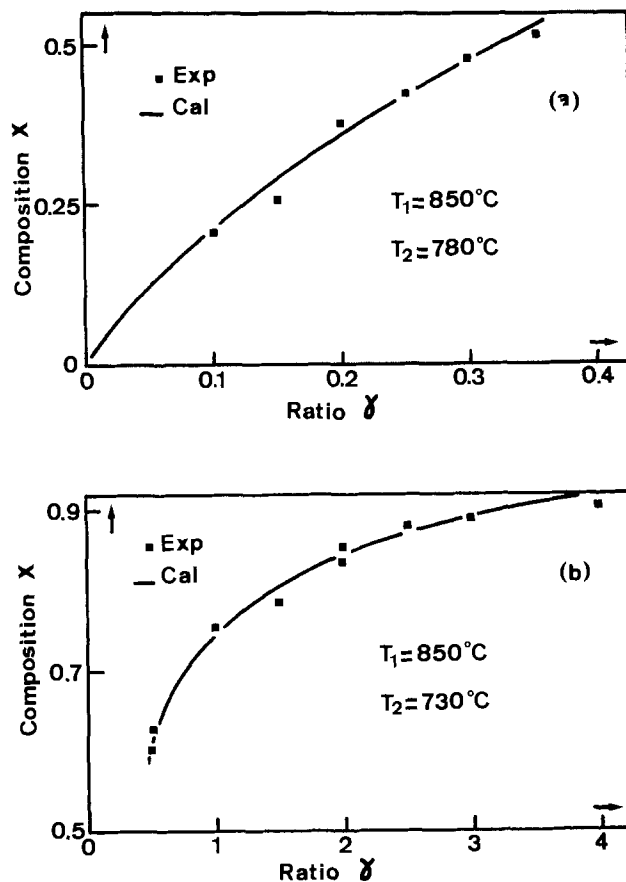


Fig. 7. Variation of the composition with the ratio γ : (a) source temperature 850°C, substrate temperature 780°C; (b) source temperature 850°C, substrate temperature 730°C.

the circuit then appears a pulsed current whose amplitude is proportional to dV_s .

The method can be used over a wide temperature range and does not need any contact or evaporation of a semitransparent electrode on the sample. It does not require the measurement of the incident or reflected light intensity and any optical detector is not required for the measurement of $dV_{cp}/d\lambda$. The sensitivity is good and the signal-to-noise ratio is better than the field electroreflectance for the same conditions of surface states.

Experimental results.—The composition dependence of the fundamental bandgap at 300°K is given on Fig. 10. Our results fit with good approximation the quadratic expression in x

$$E_o(x) \text{ eV} = 2.721 + 0.352x + 0.630x^2$$

given by Ebina *et al.* (11) from reflectivity measurements on cleaved single crystals. We have studied the variation of the fundamental bandgap with temperature on samples of different composition.

Figure 11 shows the wavelength modulated surface photovoltage spectra of zinc selenide epitaxial layers near the fundamental edge for different temperatures; the width of the curve at midheight is close to 35–40 meV.

The variations of the fundamental bandgap were studied on samples of composition $x = 0; 0.4; 0.6; 1$. Figure 12 shows this variation for zinc selenide and zinc sulfo-selenide epitaxial layers with $x = 0.4$. The variations are found to be linear in the temperature range studied. The values of the variation of the gap are listed on Table I.

Conclusion

The investigations carried out indicate that the technique described can be successfully used for obtaining

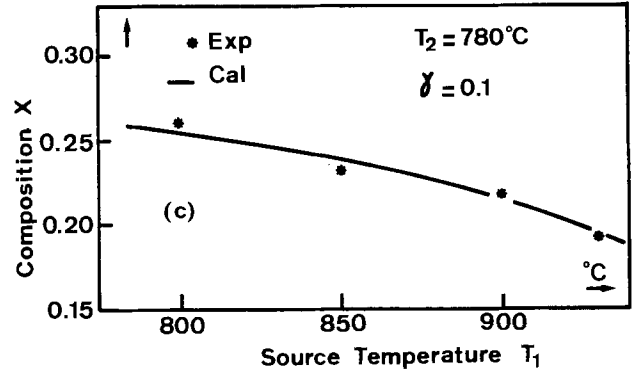
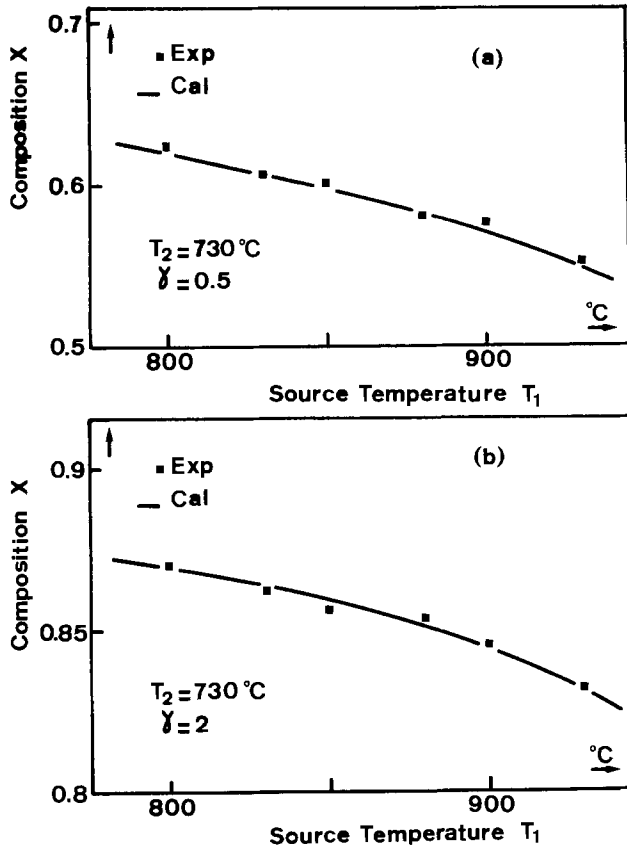


Fig. 8. The composition of layers as a function of the source temperature T_1 : (a) substrate temperature 730°C , $\gamma = 0.5$; (b) substrate temperature 730°C , $\gamma = 2$; (c) substrate temperature 780°C , $\gamma = 0.1$.

ZnSe, ZnS, and $\text{ZnS}_x\text{Se}_{1-x}$ epitaxial layers on CaF_2 substrate.

It is possible by this method to get monocrystalline epitaxial films with controlled composition x by variation of the ratio γ of the hydrogen flow rates over the ZnS and ZnSe sources, and by variation of the

source temperature T_1 . The experimental results show good agreement with the theoretical values calculated on the basis of a thermodynamic analysis. The results of the energy bandgap variation obtained by a new

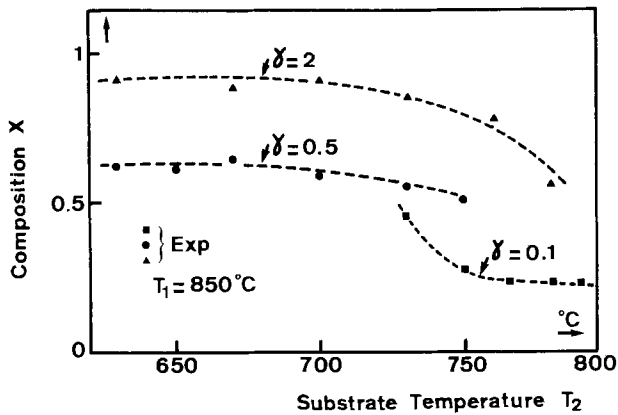


Fig. 9. The composition of layers as a function of the substrate temperature T_2 , with source temperature 850°C and various ratio γ .

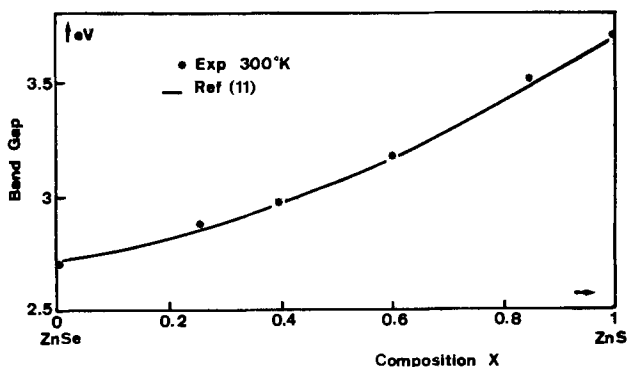


Fig. 10. Variation of the fundamental bandgap at 300°K as a function of composition x .

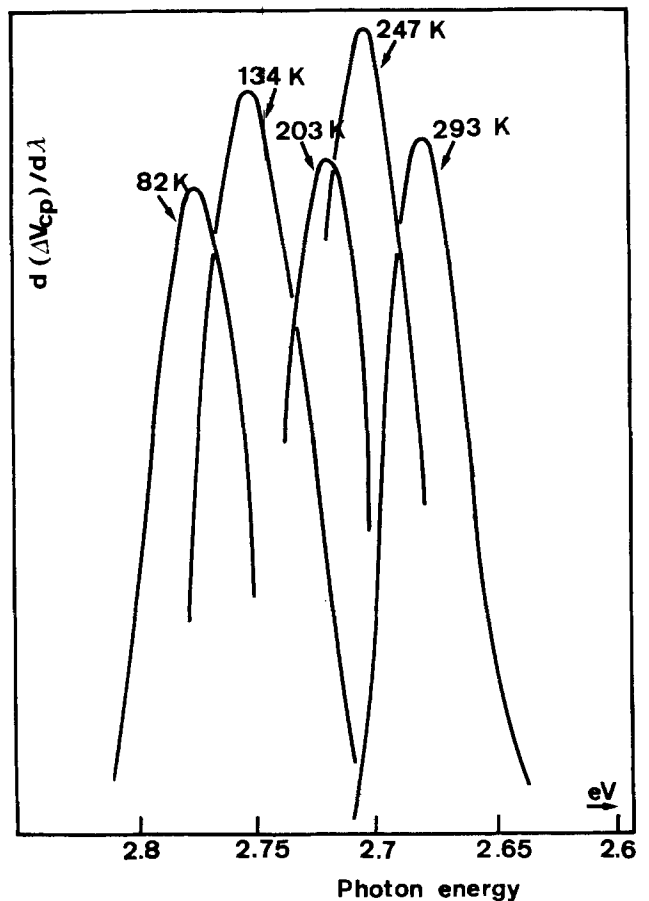


Fig. 11. Variation of the wavelength modulated surface photo-voltage spectra of ZnSe epitaxial layer.

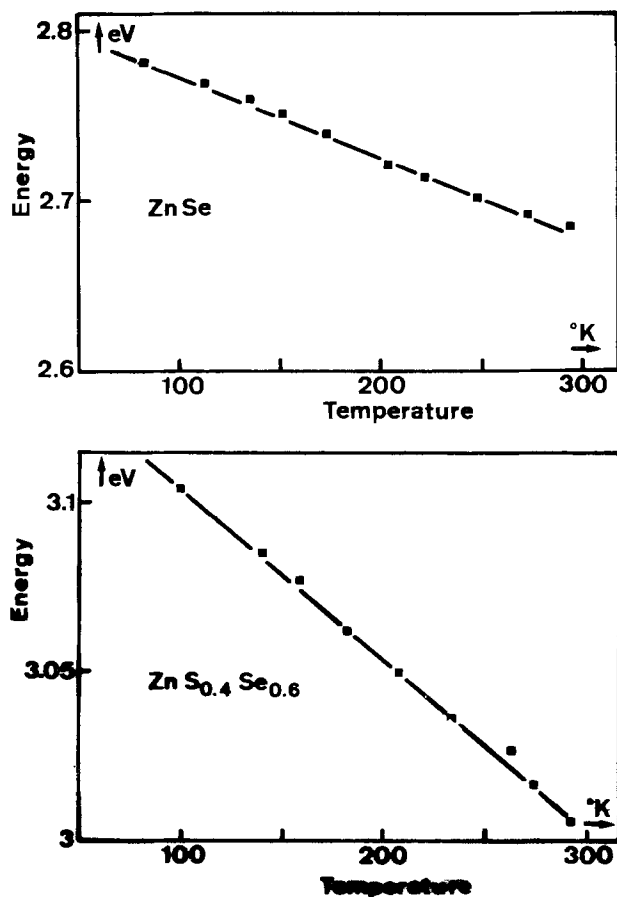


Fig. 12. Variation of the fundamental bandgap as a function of temperature: (a, top) ZnSe layer; (b, bottom) ZnS_{0.4}Se_{0.6} layer.

method are compared with similar ones obtained by previous methods.

Manuscript submitted Nov. 12, 1979; revised manuscript received March 1, 1980.

Any discussion of this paper will appear in a Discussion Section to be published in the June 1981

Table I.

$x = 0$	$-(4.8 \pm 0.2) \cdot 10^{-4} \text{ eV/}^\circ\text{K}$
$x = 0.4$	$-(5.1 \pm 0.2) \cdot 10^{-4} \text{ eV/}^\circ\text{K}$
$x = 0.6$	$-(5.2 \pm 0.2) \cdot 10^{-4} \text{ eV/}^\circ\text{K}$
$x = 1$	$-(5 \pm 0.2) \cdot 10^{-4} \text{ eV/}^\circ\text{K}$

JOURNAL. All discussions for the June 1981 Discussion Section should be submitted by Feb. 1, 1981.

Publication costs of this article were assisted by the Université des Sciences et Techniques du Languedoc.

REFERENCES

1. E. Kaldis, *J. Phys. Chem. Solids*, **26**, 1701 (1965).
2. E. Kaldis, *J. Cryst. Growth*, **5**, 376 (1969).
3. W. C. Holton, R. K. Watts, and R. D. Stinedurf, *ibid.*, **6**, 97 (1969).
4. S. G. Parker and J. E. Pinnell, *Trans. Metall. Soc. AIME*, **245**, 451 (1969).
5. K. F. Burr and J. Woods, *J. Cryst. Growth*, **9**, 183 (1971).
6. P. N. Dangel and B. J. Wuensch, *ibid.*, **19**, 1 (1973).
7. P. Wohl, W. R. Buchan, and J. E. Genthe, *This Journal*, **118**, 1842 (1971).
8. P. Lilley, P. L. Jones, and C. N. W. Litting, *J. Cryst. Growth*, **13/14**, 371 (1972).
9. W. M. Yim and E. J. Stofko, *This Journal*, **119**, 381 (1972).
10. T. S. Wagner, G. H. Heckelmann, and H. Belkowski, *Phys. Status Solidi B*, **65**, K75 (1974).
11. A. Ebina, E. Fukunaga, and T. Takahashi, *Phys. Rev. B*, **10**, 2495 (1974).
12. M. E. Ozsan and J. Woods, *Appl. Phys. Lett.*, **25**, 489 (1974).
13. A. Catano and Z. K. Kun, *J. Cryst. Growth*, **33**, 324 (1976).
14. D. Etienne, J. Chevrier, and G. Bougnot, *ibid.*, **37**, 147 (1977).
15. G. Bougnot, D. Etienne, J. Chevrier, and C. Bohe, *Mat. Res. Bull.*, **6**, 145 (1971).
16. J. Chevrier, D. Etienne, G. Galibert, and G. Bougnot, *J. Cryst. Growth*, **28**, 109 (1975).
17. R. F. Lever, *IBM J. Res. Dev.*, **8**, 460 (1964).
18. D. T. J. Hurle and J. B. Mullin, *J. Phys. Chem. Solids, Suppl.* **1**, 241 (1967).
19. J. Chevrier, D. Etienne, and G. Bougnot, *Rev. Phys. Appl.*, **9**, 315 (1974).
20. L. Kelvin, *Philos. Mag.*, **46**, 82 (1898).
21. L. Lassabatere, C. Alibert, J. Bonnet, and L. Soonckindt, *J. Phys. E.: Sci. Instrum.*, **9**, 773 (1976).

Resistivity-Dopant Density Relationship for Phosphorus-Doped Silicon

W. R. Thurber, R. L. Mattis, and Y. M. Liu*

National Bureau of Standards, Electron Devices Division, Washington, D. C. 20234

and J. J. Filliben

National Bureau of Standards, Statistical Engineering Division, Washington, D. C. 20234

ABSTRACT

New data for the resistivity-dopant density relationship for phosphorus-doped silicon have been obtained for phosphorus densities between 10^{13} and 10^{20} cm^{-3} and temperatures of 296°K (23°C) and 300°K. For dopant densities less than 10^{18} cm^{-3} , results were calculated from resistivity and junction capacitance-voltage measurements on processed wafers. For more heavily doped material, data were obtained from Hall effect and resistivity measurements on specimens cut from bulk silicon slices. The results differ by 5-15% from the commonly used Irvin curve, always in the direction of lower dopant density for a given resistivity. For comparison with the electrical measurements, phosphorus densities were also obtained by neutron activation analysis and the photometric technique. The values from these methods were within 10% of the electrical results. Analytical fits were determined for the resistivity-dopant density product as a function of resistivity and dopant density for temperatures of 23°C and 300°K. Similar fits were obtained for the calculated electron mobility as a function of resistivity and electron density.

The conversion between resistivity and dopant density of silicon is widely used in the semiconductor industry. In device design, the calculation of various parameters such as breakdown voltage involves relating resistivity, which can be readily measured, to dopant density, which is the desired quantity but very difficult to measure directly. Applications using the conversion over many decades of dopant density include the calculation of the surface dopant density of a diffused layer from the sheet resistance-junction depth product and the determination of a dopant density profile from anodic oxidation/incremental sheet resistance measurements. Significant error in the results of these measurements occurs when incorrect expressions are used to relate resistivity and dopant density.

During the past decade, the most frequently used conversion curves for both n- and p-type silicon are those formulated by Caughey and Thomas (1) based on the curves of Irvin (2). Irvin's curve for n-type material includes measurements on silicon doped with arsenic, antimony, and phosphorus. More recently Baccarani and Ostojic (3) published a conversion for phosphorus-doped silicon which agrees with that of Irvin at low phosphorus densities but departs at high densities with a difference of 30% at 10^{20} cm^{-3} . This paper describes the results of a comprehensive redetermination of the resistivity-dopant density relationship for phosphorus-doped silicon. Differences of 5-15% from the n-type Irvin curve were found, always in the direction of lower dopant density for a given resistivity. A preliminary report on this work was presented earlier (4).

Electrical Measurements

For dopant densities of 10^{18} cm^{-3} or less, data were obtained from test structures fabricated on silicon slices. The resistivity was measured directly on planar four-probe square array structures described in detail elsewhere (5). A cross-sectional view of this structure is shown in Fig. 1. The dopant density was determined from capacitance-voltage (C-V) measurements (6) on p+n junction diodes. These test structures and other

diagnostic structures were assembled on microelectronic test patterns NBS-3 (7) and NBS-4 (8) which were prepared especially for this work.

The starting material, in both ingot and slice form, was obtained from several different suppliers and was selected for minimum resistivity gradients by mechanical four-probe measurements prior to fabrication of the test patterns by bipolar processing (9). The difference between center and half radius resistivity

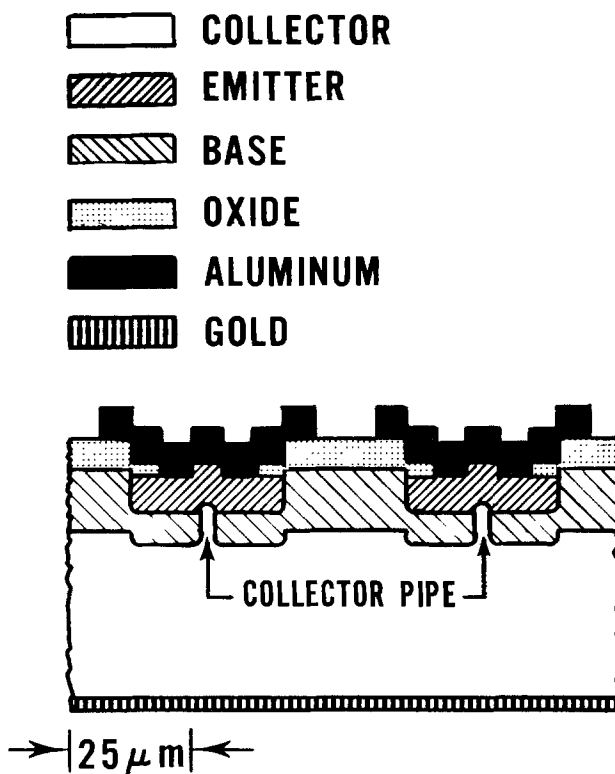


Fig. 1. Schematic cross-sectional view of the four-probe resistor test structure. The pipes are arranged in a square configuration with a center-to-center spacing of 57.2 μm (2.25 mil).

* Electrochemical Society Active Member.

Key words: electron mobility, Hall effect, neutron activation analysis, photometric technique, semiconductor.

values ranged from -3% to $+7\%$ with an average absolute difference of $+2.5\%$ for the material used in this study. The resistivity data obtained from the square array structures after processing agreed to within a few percent with the mechanical four-probe measurements prior to fabrication. Most of the results on high resistivity material were obtained on neutron transmutation doped silicon which was much more uniform than material doped by conventional techniques. Leakage current measurements were made on the processed wafers to verify the fabrication and to assure proper operation of the test structures.

The dopant density of the collector region was obtained by the junction C-V method (6) on the gated base-collector diode structure shown schematically in Fig. 2. This method gives the net dopant density, i.e., the number of dopant atoms in excess of any compensating atoms. For the C-V measurements, the gate was biased at the flatband voltage which was determined from C_{\min} - C_{\max} measurements on an MOS capacitor structure on the test pattern (10). The dopant density calculated from the C-V method is sensitive to the value used for the diameter of the diode as the diameter enters as the fourth power. The diameters (nominally $432 \mu\text{m}$) of several diodes were measured by a scanning interferometer (11). These results were then used as a calibration for determining from photomicrographs the diameters of other diodes from each processing run of wafers. The uncertainty in the diameter is estimated to be less than $1 \mu\text{m}$. The base junction depth, used in the analysis of the C-V data, was measured by the groove and stain technique (12) with an estimated error of $\pm 0.1 \mu\text{m}$.

Dopant density values were calculated from the C-V data pairs using a computer program which includes corrections for peripheral effects and for back depletion into the diffused base region (13). A fitting procedure (14) was incorporated into the program in which a Gaussian shape is assumed for the base diffusion near the junction, and the surface concentration of the diffusion and the background dopant density are adjusted to give a best fit to all the C-V data. The fitting procedure made it possible to obtain results on wafers with dopant densities greater than 10^{17}cm^{-3} which otherwise could not be measured because of compensation by the diffusion tail within the obtainable depletion depth. Errors in the dopant density due to uncertainties in the surface dopant density of the diffusion, junction depth, and random measurement error were examined in idealized data studies (14). Based on these studies, the errors caused by uncertainties in these parameters for the wafers in this work are expected to be less than 1%. In the calculations, a value of 11.7 (15) was used for the relative dielectric constant of silicon. For a few of the lightly doped wafers, it was not necessary to use the fitting procedure for reducing the C-V data to dopant density.

The square array resistivity results were corrected to 23°C and 300°K from the actual measurement temperatures using published coefficients (16). The C-V measurements were made at room temperature; no correction for temperature is required because the dopant is completely ionized in the depletion layer.

The procedure used for correlating the resistivity and dopant density values was slightly different for the two test patterns. On test pattern NBS-3, the



Fig. 2. Cross-sectional view of the base-collector diode used for the junction C-V measurements of dopant density.

one four-probe resistor structure on the pattern, which is repeated over the entire wafer, is located about 2.5 mm from the diode used for the dopant density measurements. In order to minimize the influence of resistivity variations over the wafer, the average of the resistivities measured on the two four-probe resistors on either side of the diode was taken as the resistivity corresponding to the dopant density at that diode site. On test pattern NBS-4, there are three four-probe resistor structures (with different collector pipe sizes for measuring a wide range of resistivities) located within 1.2 mm of the base-collector diode. On this pattern, an average resistivity was obtained from measurements on two or more of these structures for correlation with the dopant density determined from C-V measurements on the diode. Typically, for wafers fabricated with either test pattern, data were collected for six sites near the center of each wafer and the results averaged. Mobility values calculated for a small number of the wafers were judged significantly below those from other wafers with similar dopant densities. Data from these wafers were omitted from the analysis so that the curves would represent good material without compensation or other problems.

For dopant densities greater than 10^{19}cm^{-3} , Hall effect and resistivity measurements were made on van der Pauw specimens ultrasonically cut from bulk silicon slices. The shape of the specimens is shown in Fig. 3. The measurements were made at controlled temperatures of 23°C and 300°K for a magnetic flux density of 0.6 T (6 kG) following standard procedures (17). The commercial Hall probe for measuring the flux density was calibrated using an NMR gaussmeter. The integrating digital voltmeter used for all the voltage measurements was calibrated using a standard voltage source and a standard cell. The standard resistors used for the determination of the current through the specimens were calibrated against other standard resistors with known values.

The electron density, n , was calculated from the expression $n = -r/qR_H$, where q is the electronic charge, R_H is the Hall coefficient, and r is the Hall scattering factor which is unity for heavily doped material. The Hall effect was not used for material

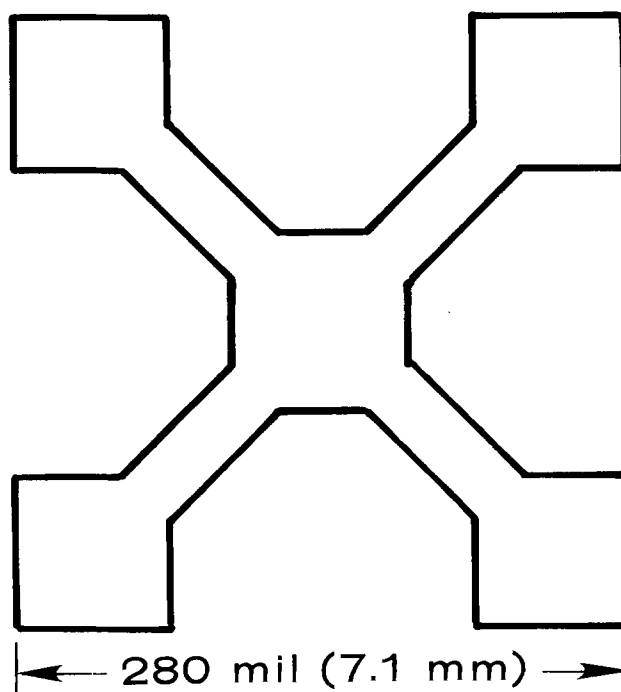


Fig. 3. Shape of van der Pauw specimens ultrasonically cut from bulk silicon slices.

doped less than 10^{19} cm^{-3} because of the unknown value of the Hall scattering factor.

Chemical Techniques

Chemical measurements of phosphorus density were made for comparison with the electrical data as a check on systematic errors and to determine the agreement between total and electrically active densities. The chemical techniques were also used for confirmation of the curve fit in the region between the Hall effect and C-V measurements.

Neutron activation analysis.¹—Neutron activation analysis was used to determine the phosphorus content in about 20 silicon slices with phosphorus densities between 10^{15} and 10^{20} cm^{-3} (18). The majority of these slices were cut from ingots used for the other measurements. The slices and suitable phosphorus monitors were irradiated for 14 hr at a nominal flux of 1×10^{13} $n \cdot \text{cm}^{-2} \cdot \text{sec}^{-1}$ in the Texas A&M reactor. After removal from the reactor, the slices were cleaned and placed on x-ray film to check the dopant uniformity by autoradiography. Using the autoradiograms as guides, a uniformly doped region about 2 cm square was scribed from the center of each slice for beta counting, and the specimens were dissolved in 1:3 HF:HNO₃. Three or four aliquots of the solution were dried on filter paper and counted for each slice. The monitors, NH₄H₂PO₄, were dissolved in deionized water and aliquots were pipetted onto filter paper for counting by the same method used for the slices. The samples were allowed to decay for either 17 or 21 days after irradiation before beta counting to decrease the considerable ³¹Si activity. Gamma ray surveys during the decay period did not detect any major interferences. Half-life determinations ($T_{1/2} = 14.4$ days) were made for positive identification of the ³²P isotope. Phosphorus counts from both the slices and monitors were corrected for background and decay over the counting time. The phosphorus concentrations in atoms/cm³ were calculated from the weights of the samples counted and the ratios of the ³²P activity from slices and monitors.

Photometric technique.²—The photometric technique (19), also known as the colorimetric method, was used to analyze nine silicon slices with phosphorus densities from 2×10^{17} to 5×10^{19} cm^{-3} . The slices were dissolved in platinum dishes in nitric acid with the addition of small amounts of hydrofluoric acid. The solutions were diluted with perchloric acid and heated to evaporate the nitric and hydrofluoric acids. They were then diluted with water, reduced by heating with bisulfite, and the phosphorus color was developed by the successive addition of bismuth sulfate, ammonium molybdate, and ascorbic acid solutions. Spectrophotometric measurements were made in a 1 cm cell. For the smaller amounts of phosphorus, the phosphomolybdate complex was extracted into 10 ml of iso-butyl alcohol and the absorbance measured against synthetic standards which went through all steps of the procedure including the extraction part. Each dissolved slice was divided into at least two and sometimes three or four portions for analysis. For heavily doped material, individual values had a spread of less than 2%. At the lightly doped end, the spread increased to 10%. For two slices, additional phosphorus was added to the solution for one portion of each slice. The added phosphorus was deducted from the final result which was in excellent agreement with that from the unadulterated portions of each slice.

Results

Figure 4 is a graph of the product of resistivity and dopant density as a function of resistivity at

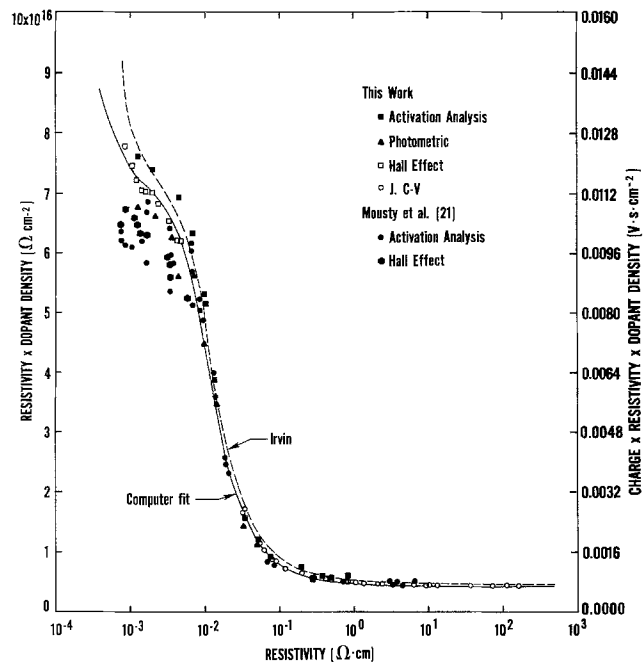


Fig. 4. Resistivity-dopant density product for phosphorus-doped silicon at 300°K. Results of this work are compared with those of Mousty *et al.* (21) and Irvin (2). Values of the $q\rho N$ product are on the right ordinate.

300°K. Since to the first approximation resistivity is inversely proportional to dopant density, a plot of the product allows deviations from this relationship to be seen, particularly for low resistivities where the product is large. As seen in Fig. 4, there is a systematic difference between the results from neutron activation analysis and those from the photometric technique. The data points from the Hall effect, which measures only electrically active phosphorus, lie between the two chemical techniques. Even though the chemical techniques are less sensitive for low dopant densities, the data from these techniques are in good agreement with the junction C-V results. A more detailed comparison of the chemical and electrical results is available elsewhere (20). The data of Mousty *et al.* (21), obtained from resistivity measurements and either neutron activation analysis or Hall effect for phosphorus density, are also plotted in Fig. 4. Their results are in reasonable agreement with this work except at the low resistivity end where differences are as large as 15%. Both the Irvin (2) curve and the computer fit to the data of this work are also shown in Fig. 4. Throughout the resistivity range the fit to the data presented here is displaced from the Irvin curve in the direction of lower dopant density for a given resistivity. The difference varies between 5 and 15% over the resistivity range with somewhat larger deviations below 1 $\Omega \cdot \text{cm}$ than above.

Figure 5 is a graph of electron mobility at 300°K as a function of electron density. The junction C-V results of the present work were converted to electron density using the percent ionization calculations of Li and Thurber (22). For example, at a dopant density of 10^{18} cm^{-3} about 10% of the phosphorus atoms are not ionized in equilibrium but they are counted by the C-V method as all atoms are ionized in the depletion layer. Consequently, the dopant density measured by C-V must be reduced by the fraction of atoms not ionized to obtain the electron density before the carrier mobility is calculated. No such reduction is needed for results from Hall effect measurements as the Hall effect is a transport phenomenon for which equilibrium conditions exist. In addition, for heavily doped material, conduction is metallic-like and each dopant atom contributes an electron for conduction.

¹ Work performed under the direction of Dr. Joseph A. Keenan at Texas Instruments, Incorporated, Dallas, Texas.

² Work done by Ledoux and Company, Teaneck, New Jersey.

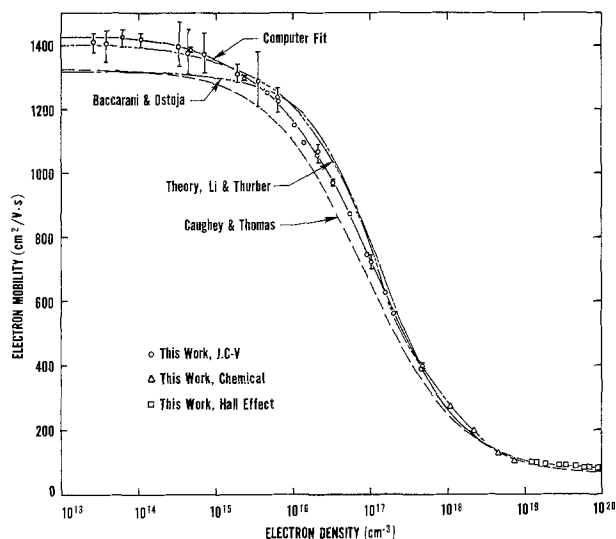


Fig. 5. Electron mobility as a function of electron density for phosphorus-doped silicon at 300°K. The junction C-V data have been corrected for deionization using the calculations of Li and Thurber (22). The error bars are the standard deviation in the individual mobility values for that wafer. When not shown, the error bars lie within the plotted symbol. Shown for comparison with the computer fit to the data are the mobility expressions of Caughey and Thomas (1), Baccarani and Ostoja (3), and the theoretical calculation of Li and Thurber (22).

The theoretical curve of Li and Thurber (22) in Fig. 5 is in good agreement with the experimental results. The Caughey and Thomas mobility expression for n-type silicon (1) gives significantly lower mobility at low electron density as shown in Fig. 5. The Caughey and Thomas expression is a fit to the Irvin curve with the assumption that the electron density equals the dopant density. This is true except for moderately doped material prior to the onset of metallic conduction at about $3 \times 10^{18} \text{ cm}^{-3}$. For phosphorus densities greater than about $5 \times 10^{19} \text{ cm}^{-3}$, the formation of phosphorus-vacancy pairs gives rise to electrically inactive atoms (23).

Also shown in Fig. 5 is the mobility expression of Baccarani and Ostoja (3) based on the data of Mousty *et al.* (21) with the assumption that electron and dopant densities are equal. For comparison with the other curves, the Baccarani and Ostoja expression has been corrected to 300°K since the Mousty data were taken at 23°C. At low dopant densities, the Baccarani and Ostoja curve is about 7% below the data of this work. In the range 10^{16} to $5 \times 10^{17} \text{ cm}^{-3}$, their curve is parallel to, but about 5% above, the results of this work. At high dopant densities, the Baccarani and Ostoja curve gives values between 10 and 20% larger than those obtained in this work as is seen more clearly in Fig. 6.

For detailed comparison with the results of other workers, the electron mobility for densities greater than 10^{19} cm^{-3} is plotted in Fig. 6. All of the results shown were obtained by Hall effect and resistivity measurements with the assumption that the Hall scattering factor was unity. In this dopant range, the Caughey and Thomas curve is lower and the Baccarani and Ostoja curve is higher than the results of this work. The modification of the Caughey and Thomas expression shown in the figure consists of multiplying the constant μ_{min} by a term which decreases μ_{min} at high electron densities (24). The computer fit to the data, discussed in the next section, is also shown in Fig. 6.

With the exception of the data point of Fair and Tsai (25), all of the results in Fig. 6 were obtained on silicon doped during crystal growth. Recently Masetti and Solmi (26) have made extensive measure-

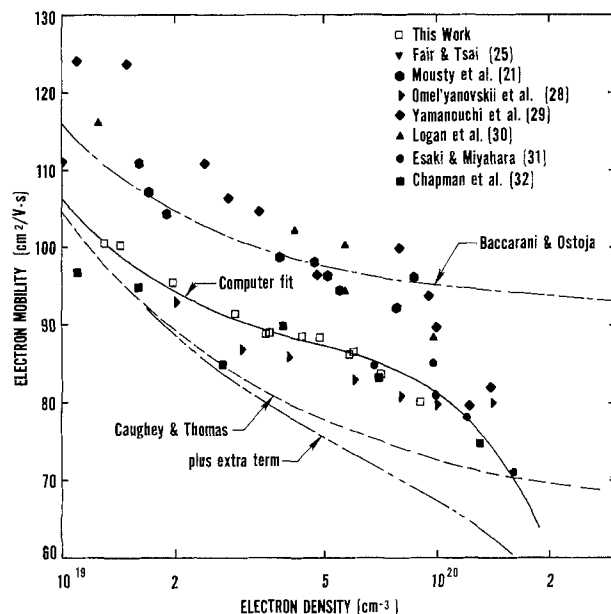


Fig. 6. Electron mobility determined from Hall effect measurements for electron densities greater than 10^{19} cm^{-3} . The computer fit to the data of this work lies between the mobility expressions of Caughey and Thomas (1) and Baccarani and Ostoja (3). The extra term in the modified Caughey and Thomas expression is given by Plunkett *et al.* (24).

ments on silicon heavily doped by thermal diffusion. Their mobility values obtained from incremental sheet resistance and Hall effect measurements are in good agreement with those of this work. They concluded, from a comparison of their data with those of Mousty *et al.*, that the mobility in diffused phosphorus-doped silicon is always lower than that in uniformly doped silicon for $n > 10^{19} \text{ cm}^{-3}$. However, when the results of Masetti and Solmi are compared with those of this work, the conclusion is that the mobility is the same in diffused and uniformly doped silicon.

Computer Curve Fits

The curve fits of the data were done using the DATAPLOT language (27) for the nonlinear least squares fitting. The simplest expression which gave a fit of the same precision as the uncertainty in the experimental data was a third degree polynomial divided by a third degree polynomial. The equation for fitting the resistivity-dopant density product is of the form

$$\log_{10}(P/P_0) = \frac{A_0 + A_1X + A_2X^2 + A_3X^3}{1 + B_1X + B_2X^2 + B_3X^3} \quad [1]$$

with $P = q\rho N$ where q is the electronic charge, ρ is the resistivity, and N is the electrically active dopant density. The normalization factor, P_0 , was taken equal to $1 \text{ V}\cdot\text{sec}/\text{cm}^2$. Fits were made for both $X = \log_{10}(\rho/\rho_0)$ and $X = \log_{10}(N/N_0)$ with $\rho_0 = 1 \text{ }\Omega\cdot\text{cm}$ and $N_0 = 10^{18} \text{ cm}^{-3}$. With the use of these normalizing values, the magnitude of X is usually less than 4. This is better from a computational standpoint because the computation is much less sensitive to the number of significant figures retained for the coefficients.

The data used for the fits consisted of 26 points obtained from the C-V measurements, four points based on the photometric and NAA results, twelve points determined from the Hall effect measurements, two points from Esaki and Miyahara (31) at 1.2×10^{20} and $1.6 \times 10^{20} \text{ cm}^{-3}$, and one point from Fair and Tsai (25) at $3 \times 10^{20} \text{ cm}^{-3}$. The latter three points are shown in Fig. 6 and were included to increase the range of the fit at the high density end beyond that justified by the data of this work alone.

In addition, a point was added at $N = 1 \times 10^{12} \text{ cm}^{-3}$ to improve the fit for calculating values in the low dopant density range. This point was taken equal to the average of the four lowest dopant density data points since the ρN product is essentially constant in this region. Also, the inclusion of this point helps insure that the fits as a function of $\log_{10}(\rho/\rho_0)$ and $\log_{10}(N/N_0)$ both give essentially the same calculated values in this region. All seven coefficients as determined by the fit are given in Table I for 23°C and 300°K. The approximate standard deviation is given for each coefficient and the residual standard deviation (R.S.D.) for the fit is listed in units of $\text{V}\cdot\text{sec}/\text{cm}^2$. The R.S.D. is the square root of the quotient of the sum of the squared residuals divided by the number of degrees of freedom.

The plot of the data used for the curve fit, with the exception of the point at 10^{12} cm^{-3} , and the least squares fit of the $q\rho N$ product vs. N for 300°K are shown in Fig. 7. This figure clearly shows that the "min-max" expressions of Caughey and Thomas (1) are not suitable for this data as there is no plateau or maximum at high dopant densities. The curve obtained for the product as a function of resistivity is plotted in Fig. 4 along with the experimental data of this work and other results.

The two expressions, one a function of $\log_{10}(\rho/\rho_0)$ and the other a function of $\log_{10}(N/N_0)$, have a worst case self-consistency of 8% for all values of N (and corresponding values of ρ) within the range 1×10^{12} to $4 \times 10^{20} \text{ cm}^{-3}$. That is, when the product $q\rho N$ is calculated for a given N , a ρ is derived which can be used in the $q\rho N$ vs. ρ expression to again calculate the product. The latter product will be within 8% of the former. The maximum difference occurs only in the low 10^{18} cm^{-3} range and elsewhere the fits are consistent within 4%. When the self-consistency is calculated starting with a given ρ , the fits have a maximum difference of 4% for resistivities from 2×10^{-4} to $3 \times 10^3 \Omega\cdot\text{cm}$.

Fits were also obtained for electron mobility as a function of both electron density, n , and resistivity. It was found that better and more self-consistent fits were possible if the data point at $3 \times 10^{20} \text{ cm}^{-3}$ were omitted. Otherwise the data used for the mobility fits corresponded to that used for the product fits. As mentioned previously, the percent ionization calculations of Li and Thurber (22) were used to obtain the electron density from the measured dopant density

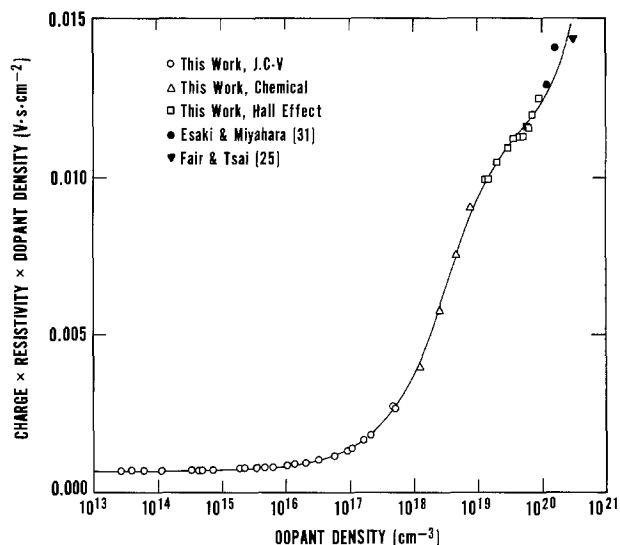


Fig. 7. Graph of the $q\rho N$ product as a function of N for 300°K. The curve is the least squares fit to the data.

prior to the computation of mobility. The expression for calculating the electron mobility is of the form

$$\log_{10}(\mu/\mu_0) = \frac{A_0 + A_1X + A_2X^2 + A_3X^3}{1 + B_1X + B_2X^2 + B_3X^3} \quad [2]$$

where μ is the mobility and $\mu_0 = 1 \text{ cm}^2/\text{V}\cdot\text{sec}$. As before, fits were made for both $X = \log_{10}(\rho/\rho_0)$ and $X = \log_{10}(n/n_0)$ for temperatures of 23°C and 300°K. Values for the coefficients are given in Table II. The plot of the mobility data and fitted curve as a function of resistivity for 300°K is given in Fig. 8. The fit of mobility vs. electron density is shown in Fig. 5 and 6 for comparison with experimental data. An expression of the form suggested by Mosetti and Solmi (26) was also tried for the mobility fits, but the percent residuals in the low mobility range were significantly larger than with Eq. [2], particularly for the fit as a function of resistivity.

The mobility fits are self-consistent within 6% for electron densities in the range 10^{12} - 10^{20} cm^{-3} . The expressions rapidly diverge for densities greater than $2 \times 10^{20} \text{ cm}^{-3}$. The fit as a function of resistivity is the better choice for approximating mobility values beyond the range of the fitted data. When the self-

Table I. Coefficients and residual standard deviation (R.S.D.) for the fit of the product $q\rho N$ using Eq. [1]

Temp. X	23°C	23°C	300°K	300°K
	$\log_{10}(\rho/\rho_0)$	$\log_{10}(N/N_0)$	$\log_{10}(\rho/\rho_0)$	$\log_{10}(N/N_0)$
A_0	-3.1083 ± 0.0038	-3.0769 ± 0.0027	-3.0951 ± 0.0037	-3.0652 ± 0.0026
A_1	-3.2626 ± 0.0952	2.2108 ± 0.0392	-3.2303 ± 0.0909	2.1853 ± 0.0415
A_2	-1.2196 ± 0.0341	-0.62272 ± 0.0159	-1.2024 ± 0.0325	-0.61080 ± 0.0170
A_3	-0.13923 ± 0.00468	0.057501 ± 0.00287	-0.13679 ± 0.00466	0.056189 ± 0.00327
B_1	1.0265 ± 0.0318	-0.68157 ± 0.0134	1.0205 ± 0.0305	-0.67642 ± 0.0141
B_2	0.38755 ± 0.0109	0.19833 ± 0.00507	0.38382 ± 0.0105	0.19542 ± 0.00541
B_3	0.041833 ± 0.00168	-0.018376 ± 0.000986	0.041338 ± 0.00169	-0.018100 ± 0.00112
R.S.D.	2.78×10^{-4}	2.21×10^{-4}	2.67×10^{-4}	2.09×10^{-4}

Table II. Coefficients and residual standard deviation (R.S.D.) for the fit of electron mobility using Eq. [2]

Temp. X	23°C	23°C	300°K	300°K
	$\log_{10}(\rho/\rho_0)$	$\log_{10}(n/n_0)$	$\log_{10}(\rho/\rho_0)$	$\log_{10}(n/n_0)$
A_0	3.1122 ± 0.0034	3.0746 ± 0.0025	3.0985 ± 0.0037	3.0629 ± 0.0025
A_1	3.3347 ± 0.0951	-2.2679 ± 0.0076	3.3257 ± 0.0923	-2.2522 ± 0.0077
A_2	1.2610 ± 0.0511	0.62998 ± 0.00245	1.2581 ± 0.0481	0.62327 ± 0.00249
A_3	0.15701 ± 0.0198	-0.061285 ± 0.00087	0.15679 ± 0.0189	-0.060415 ± 0.00087
B_1	1.0463 ± 0.0324	-0.70017 ± 0.00290	1.0485 ± 0.0317	-0.69851 ± 0.00292
B_2	0.39941 ± 0.0167	0.19839 ± 0.00113	0.40020 ± 0.0156	0.19716 ± 0.00114
B_3	0.049746 ± 0.00547	-0.020150 ± 0.00041	0.049883 ± 0.00512	-0.019950 ± 0.00041
R.S.D.	14.9	11.6	14.8	11.2

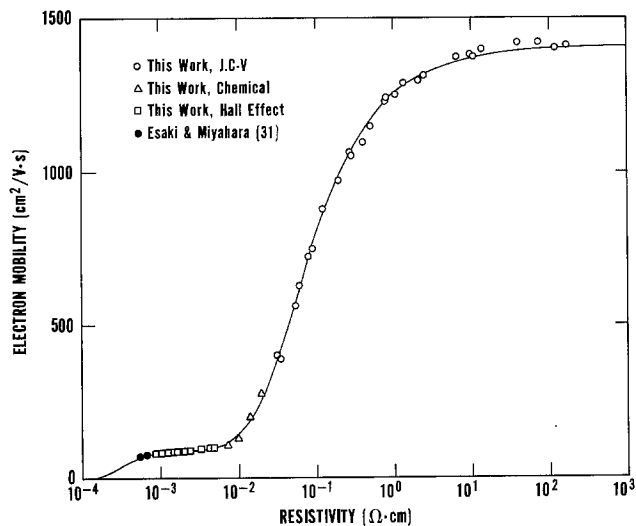


Fig. 8. Graph of electron mobility as a function of resistivity for 300°K. The curve is the least squares fit to the points.

consistency is calculated starting with a given resistivity, the fits have a maximum difference of 3% for resistivities from 6×10^{-4} to $10^4 \Omega \cdot \text{cm}$. Graphs showing the self-consistency and other details of the curve fitting will be included in a forthcoming NBS Special Publication on this work.

Conclusions

The relationship between resistivity and dopant density has been determined for phosphorus-doped silicon for densities between 10^{13} and 10^{20} cm^{-3} . The results differ from the n-type Irvin curve by 5-15%, always in the direction of lower dopant density for a given resistivity. The work is in agreement with the mobility curve of Baccarani and Ostojia in the 10^{15} - 10^{18} cm^{-3} range but differences exist for lower and for higher doping levels. The phosphorus densities measured by neutron activation analysis and the photometric technique were within $\pm 10\%$ of those obtained from the electrical methods on the same crystals. Using a model convenient for engineering calculations, analytical fits were determined for the resistivity-dopant density data as a function of resistivity and dopant density for temperatures of 23°C and 300°K. Similar fits were obtained for the calculated electron mobility as a function of resistivity and electron density.

Acknowledgments

The authors are indebted to D. R. Ricks for the mechanical four-probe resistivity measurements, to J. S. Beers for the measurements of diode diameter using the line-standard interferometer, to F. H. Brewer for the Hall effect measurements, and to J. Krawczyk and L. A. Robinson for specimen preparation. Special thanks are due Dr. M. G. Buehler for designing the test structures used in this work. This work was conducted as part of the Semiconductor Technology Program at NBS and was supported by the Defense Advanced Research Projects Agency (Order No. 2397).

Manuscript submitted May 4, 1979; revised manuscript received April 16, 1980.

Any discussion of this paper will appear in a Discussion Section to be published in the June 1981

JOURNAL. All discussions for the June 1981 Discussion Section should be submitted by Feb. 1, 1981.

Publication costs of this article were assisted by the National Bureau of Standards.

REFERENCES

1. D. M. Caughey and R. E. Thomas, *Proc. IEEE*, **55**, 2192 (1967).
2. J. C. Irvin, *Bell System Tech. J.*, **41**, 387 (1962).
3. G. Baccarani and P. Ostojia, *Solid-State Electron.*, **18**, 579 (1975).
4. W. R. Thurber, R. L. Mattis, and Y. M. Liu, in "Semiconductor Characterization Techniques," P. A. Barnes and G. A. Rozgonyi, Editors, pp. 81-92, The Electrochemical Society Softbound Proceedings Series, Princeton, N.J. (1978).
5. M. G. Buehler and W. R. Thurber, *IEEE Trans. Electron Devices*, **ed-23**, 968 (1976).
6. R. L. Mattis and M. G. Buehler, *Nat. Bur. Stand. Spec. Publ.*, 400-17, 27 (November 1975).
7. M. G. Buehler, *Nat. Bur. Stand. Spec. Publ.*, 400-22 (June 1976).
8. W. R. Thurber and M. G. Buehler, *Nat. Bur. Stand. Spec. Publ.*, 400-32 (April 1978).
9. T. F. Leedy and Y. M. Liu, *Nat. Bur. Stand. Spec. Publ.*, 400-53 (December 1978).
10. A. S. Grove, "Physics and Technology of Semiconductor Devices," pp. 278-285, John Wiley and Sons, Inc., New York (1967).
11. K. E. Gilliland, H. D. Cook, K. D. Mielenz, and R. B. Stephens, *Metrologia*, **2**, 95 (1966).
12. B. McDonald and A. Goetzberger, *This Journal*, **109**, 141 (1962).
13. R. L. Mattis and M. G. Buehler, *Nat. Bur. Stand. Spec. Publ.*, 400-11 (June 1975).
14. R. L. Mattis and M. G. Buehler, *This Journal*, **124**, 1918 (1977).
15. W. C. Dunlap and R. L. Watters, *Phys. Rev.*, **92**, 1396 (1953).
16. Standard Method for Measuring Resistivity of Silicon Slices with a Collinear Four-Probe Array, ASTM Method F 84, Annual Book of ASTM Standards, Part 43 (November 1979).
17. Measuring Hall Mobility and Hall Coefficient in Extrinsic Semiconductor Single Crystals, ASTM Method F 76, Annual Book of ASTM Standards, Part 43 (November 1979).
18. K. G. Heinen and G. Larrabee, *Anal. Chem.*, **38**, 1853 (1966).
19. C. L. Luke and S. S. Flaschen, *ibid.*, **30**, 1406 (1958).
20. W. R. Thurber, *J. Electron. Mater.*, **9**, 551 (1980).
21. F. Mousty, P. Ostojia, and L. Passari, *J. Appl. Phys.*, **45**, 4576 (1974).
22. S. S. Li and W. R. Thurber, *Solid-State Electron.*, **20**, 609 (1977).
23. R. B. Fair, *This Journal*, **125**, 323 (1978).
24. J. C. Plunkett, J. L. Stone, and A. Leu, *Solid-State Electron.*, **20**, 447 (1977).
25. R. B. Fair and J. C. C. Tsai, *This Journal*, **124**, 1107 (1977).
26. G. Mosetti and S. Solmi, *Solid-State Electron Devices*, **3**, 65 (1979).
27. J. J. Filliben, in "Proceedings of the Statistical Computing Section of the American Statistical Association," pp. 344-353, 1978 Annual Meeting, San Diego, California.
28. E. M. Omel'yanovskii, V. I. Fistul', and M. G. Mil'vidskii, *Sov. Phys.-Solid State*, **5**, 676 (1963).
29. C. Yamanouchi, K. Mizuguchi, and W. Sasaki, *J. Phys. Soc. Jpn.*, **22**, 859 (1967).
30. R. A. Logan, J. F. Gilbert, and F. A. Trumbore, *J. Appl. Phys.*, **32**, 131 (1961).
31. L. Esaki and Y. Miyahara, *Solid-State Electron.*, **1**, 13 (1960).
32. P. W. Chapman, O. N. Tufte, J. D. Zook, and D. Long, *J. Appl. Phys.*, **34**, 3291 (1963).

Enhanced Diffusion of Implanted Arsenic and Boron in Silicon by Low-Temperature Heat-Treatment

G. J. van Gorp, J. W. Slotboom, F. J. B. Smolders, W. T. Stacy,¹ and Y. Tamminga²

Philips Research Laboratories, Eindhoven, The Netherlands

ABSTRACT

The parameters of high frequency transistors with implanted arsenic emitter and boron base were found to change significantly on annealing at temperatures between 600° and 900°C with a maximum change at about 700°C. The change can be interpreted as a decrease of boron concentration in the base and of the donor concentration gradient at the emitter-base junction. Determination of the concentration profiles by secondary ion mass spectrometry and by Rutherford backscattering spectrometry (RBS) showed that these decreases were due to enhanced diffusion of both arsenic and boron. Electron microscopy showed precipitation which was probably preceded by arsenic clustering, in agreement with RBS channeling results. These showed that the substitutional fraction of arsenic, which was between 95% and 98%, decreased by a few percent on annealing at 700°C. The enhanced diffusion is thought to be caused by vacancy generation by either one of two precipitation-induced processes: dissociation of As-vacancy complexes or growth of interstitial defects.

Implanted arsenic is now widely used as a donor-type impurity in silicon. For example, bipolar transistors are made with implanted boron base and arsenic emitter. After implantation the As and B are electrically activated by an appropriate heat-treatment around 1000°C. In a process which involved a subsequent annealing at 650°C, we found that the parameters of high frequency transistors with shallow As emitter (0.2 μm) and B base (0.35 μm) were drastically affected by this annealing. The current gain, for example, was greatly increased.

The effects of low temperature heat-treatments on Si with As diffused into it have been studied earlier. Osvenskii *et al.* (1) found interstitial dislocation loops by transmission electron microscopy on As-doped Si crystals which had been annealed at 800°C in vacuum after quenching from 1250°C. The loops were attributed to As precipitation. Schwenker *et al.* (2) found for As diffused at 1050° and 1100°C to a depth of 6-9 μm into Si that heat-treatment between 500° and 970°C in argon caused the sheet resistance to increase. Around 750°C this increase was maximum, being a factor of 2 at a surface concentration of $1.2 \times 10^{21} \text{ cm}^{-3}$ and less at lower concentrations. Transmission electron microscopy showed dark spots and interstitial hexagonal Frank dislocation loops. The effects on sheet resistance were ascribed to As clustering or vacancy-complex formation. An increase in sheet resistance due to heat-treatment between 500° and 800°C in vacuum was also found by Miyamoto *et al.* (3) who observed an increase of the lattice constant, which was supposed to be due to SiAs formation. Haskell *et al.* (4) studied Rutherford backscattering on As in Si and found from channeling that 90% to 95% of the As was on lattice sites. Heat-treatment between 650° and 900°C in argon increased the aligned As yield, showing As to be displaced from substitutional lattice sites. Shibayama *et al.* (5) observed an enhancement of both B and As diffusion in Si for As surface concentrations above about 10^{20} cm^{-3} , due to heat-treatment between 500° and 800°C in nitrogen. The effects were ascribed to As precipitation and subsequent vacancy generation.

All this previous work was carried out on Si with chemically deposited As. In the present paper we re-

port a study on the effect of low temperature heat-treatment on the electrical parameters of high frequency transistors with shallow As emitter and B base both made by ion implantation. These effects are correlated with changes in the chemical As and B profiles as measured by secondary ion mass spectrometry (SIMS) and by Rutherford backscattering spectrometry (RBS) and with precipitation effects as studied by transmission electron microscopy (TEM) and by the RBS channeling technique.

Experimental Procedures

Electrical measurements were carried out on npn test transistors made in epitaxial N-type Si (3.3 μm , phosphorus $3 \times 10^{15} \text{ cm}^{-3}$) grown on N⁺-Si <100> wafers ($10^{-2} \Omega\text{-cm}$). The base (65 \times 65 μm) was made by B implantation (25 keV, dose $1.3 \times 10^{14} \text{ cm}^{-2}$), followed by 40 min annealing at 950°C in dry N₂. Two emitters (4 \times 32 μm) were made by As implantation (60 keV, dose $6.5 \times 10^{15} \text{ cm}^{-2}$), followed by 12 min annealing at 990°C in dry N₂. In both cases the annealing was followed by fast cooling (pulling out of the furnace). The process yielded an emitter, with a sheet resistance of about 30 Ω and a depth of 0.2 μm , and a base, with a sheet resistance of about 600 Ω and a depth of 0.35 μm .

For the measurement of the As and B profiles and for the TEM observations two types of wafers were used. One series had had a treatment identical to that of the wafers in which transistors were grown, except for the masking operations (type I). The other series (type II) were N-type <100> Si, 1 $\Omega\text{-cm}$ ($2\text{-}3 \times 10^{15} \text{ cm}^{-3}$ phosphorus) substrates without an epitaxial layer. These received two B implantations: 20-25 keV, dose $1.3 \times 10^{14} \text{ cm}^{-2}$ and a lower dose with 60 or 80 keV. The implantation was followed by annealing for 30 min at 875°C in dry N₂. Subsequently As was implanted at 60 keV, dose 10^{16} cm^{-2} , followed by annealing for 24 min at 990°C in dry N₂ and fast cooling. The implantation and annealing treatments are summarized in Table I. These standard treatments were given to all samples.

The effect of a low temperature heat-treatment was studied by an additional annealing in dry N₂ at a temperature between 500° and 1000°C. On the test transistors this treatment was carried out after opening of the contact windows, but before metallization.

SIMS profiles were determined with the CAMECA IMS 300 using a 5.5 keV, 1 μA , 60° incident O₂⁺ pri-

¹ Present address: Philips Research Laboratories, Sunnyvale, California 94086.

² Permanent address: Philips Research Laboratories, Amsterdam, Netherlands.

Key words: clustering, precipitation, impurity profiles in silicon, vacancy diffusion.

Table I. Implantation and standard annealing treatments

Type-I
B: $1.3 \times 10^{14} \text{ cm}^{-2}$, 25 keV; 40 min 950°C N ₂
As: $6.5 \times 10^{15} \text{ cm}^{-2}$, 60 keV; 12 min 990°C N ₂
Type-II
B: $1.3 \times 10^{14} \text{ cm}^{-2}$, 20 keV + $1.6 \times 10^{14} \text{ cm}^{-2}$, 60 keV (sample A)
$1.25 \times 10^{14} \text{ cm}^{-2}$, 25 keV + $1.1 \times 10^{14} \text{ cm}^{-2}$, 80 keV (sample B)
30 min 875°C, N ₂
As: 10^{16} cm^{-2} , 60 keV, 24 min 990°C N ₂

mary beam. Oxygen gas was introduced into the sample chamber at a pressure of about 3×10^{-5} Torr, except for one arsenic profile, which was measured in the 10^{-7} Torr residual vacuum. The primary beam was rastered over 1.5×1.5 mm, leading to an erosion rate of about 5 Å/sec. Secondary ion acceptance was restricted by a 300 μm field aperture to the center of the sputtered crater. Signals monitored were ¹¹B⁺ and ⁷⁵As⁺, the latter with a target potential shift of typically 50V to minimize the contribution from Si₂O⁺ at mass number 75. The boron and arsenic profiles were measured in separate runs at different sample locations. The secondary ion currents were converted into concentrations (accuracy ±12%) via calibration from standard implants, and the depth scale was obtained by linear extrapolation from the final crater depth measured with a mechanical stylus instrument. The detection limit was determined by the 3 decades dynamical range. Uncertainties in crater depth determination are caused by curvature of the crater bottom (i.e., nonuniform primary ion current density) and nonplanarity of the sample surface.

Arsenic profiles were also measured with RBS using the Van de Graaff accelerator at Philips Research Laboratories, Amsterdam, with 2 MeV He⁺ ions and using a scattering angle of 170° and target angles between 0 and 65°. The detector resolution was 15 keV. Depth determination was done using published values of stopping cross sections (6). These are accurate to within a few percent. With channeling in <100> and <110> directions the same values were used as for a random direction. The number of arsenic atoms per square centimeter was determined from the area of the As peak and the height of the Si signal for scattering in a random direction. The concentration was then obtained from the number of counts per channel and the channel width (7). The accuracy of this determination is a few percent.

TEM observations were made using a Philips EM 400 or the high voltage microscope at the T.N.O., Apeldoorn, on samples that were wet-chemically thinned from the back.

Electrical Measurements

We measured the sheet resistance, R_b , of the base underneath the emitter, and the current gain on the transistor, h_{FE} , as a function of the time of annealing at 700°C. The results are shown in Fig. 1, which shows a change of both parameters by an order of magnitude after 16 hr. Even relatively short annealing times had a strong effect. The ratio between h_{FE} and R_b remained constant.

The base sheet resistance is given by

$$R_b^{-1} = \int q\mu_p N_B dx \quad [1]$$

where μ_p is the hole mobility in the base, N_B is the acceptor concentration, and the integration is taken over the base. The current gain $h_{FE} = I_c/I_b$, where the collector current I_c is given by

$$I_c = \frac{A_e q n_{i0}^2}{G_b} \exp(qV_{eb}/kT) \quad [2]$$

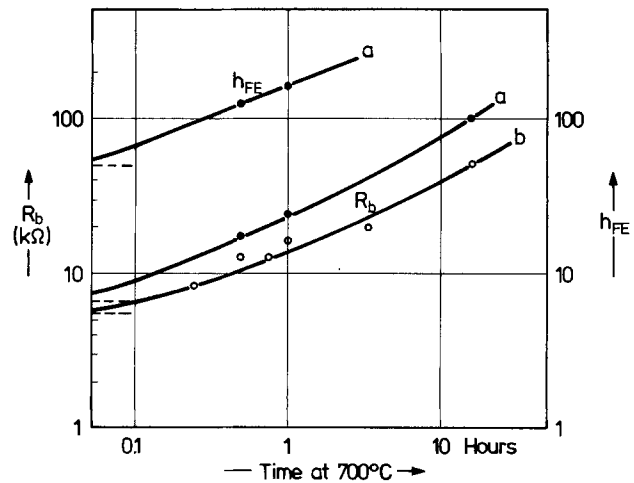


Fig. 1. Buried base sheet resistance R_b and current gain h_{FE} for two transistors (a and b) as a function of annealing time at 700°C. The values before annealing are indicated by broken lines.

and I_b is the base current. In Eq. [2] A_e is the emitter area, n_{i0} is the intrinsic carrier concentration for low impurity concentrations, V_{eb} is the applied emitter-base voltage, and G_b is the Gummel number of the base. This is given by

$$G_b = \int \frac{N_B}{D_n} \left(\frac{n_{i0}}{n_i} \right)^2 dx \quad [3]$$

where D_n is the diffusion coefficient for electrons in the base, n_i is the dope-dependent intrinsic carrier concentration, and the integration is carried out over the base (8). G_b can be derived from the I_c (V_{eb}) characteristics at low currents.

Figure 2 shows the dependence of h_{FE} , R_b , and G_b on the temperature of the additional heat-treatment at constant annealing time. It appears that h_{FE} and R_b are maximum after annealing at 700°C, while G_b is minimum at the same annealing temperature. It was found that the base current was not significantly affected by the annealing treatment, so that the change of h_{FE} is only caused by a change in I_c . For

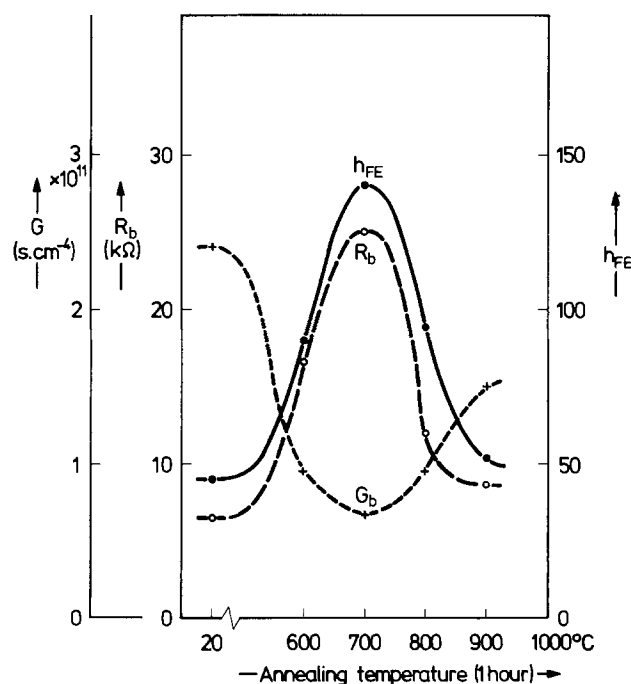


Fig. 2. Buried base sheet resistance R_b , current gain h_{FE} , and base Gummel number G_b as a function of annealing temperature (1 hr annealing).

constant base current h_{FE} is inversely proportional to G_b , according to Eq. [2]. This was also found experimentally. The fact that h_{FE} and R_b go through a maximum while G_b goes through a minimum strongly suggests that the total number of acceptors in the base is a minimum on annealing at 700°C, as follows from Eq. [1] and [3]. A rough estimate, using Eq. [3] and taking into account the dope dependence of D_n and n_i , gives for the integrated base impurity concentration $\int N_B dx$ a value of about $6 \times 10^{12} \text{ cm}^{-2}$ before annealing and about $2 \times 10^{12} \text{ cm}^{-2}$ after annealing at 700°C.

We also made measurements of the emitter-base capacitance and the cut-off frequency f_T , in order to investigate the annealing effect on the behavior of the impurity distribution in the junction region. As can be seen in Fig. 3, the capacitance C at $V_{eb} = 0$ changes by a factor of two, whereas the cut-off frequency hardly changes. These results may be interpreted in terms of a change of the impurity concentration gradient at the emitter-base junction, dN/dx . This can be calculated from the emitter-base capacitance C using the expression for a linear doping profile (9)

$$C^{-3} = \frac{12(V_g - V_{eb})A_e^{-3}}{qa\epsilon^2\epsilon_0^2} \quad [4]$$

where V_g is the so called built-in gradient voltage and $a = dN/dx$, which can thus be derived from a C^{-3} - (V_{eb}) plot. This is the usual procedure for determining the impurity gradient in the emitter-base junction. This gradient is also shown in Fig. 3. We learned from numerical simulations that for steep arsenic-boron profiles the gradient so obtained may differ by a factor of up to 3 from the actual gradient. However, we think that the large variation of the slope of the C^{-3} - (V_{eb}) plots that we measured indicates a similar change in the impurity gradient.

The insensitivity of f_T on low temperature annealing may be explained by a rather long and constant collector delay time, which is not affected by annealing, and by the fact that the influence of the varying gradient on the charge storage in the emitter-base junction

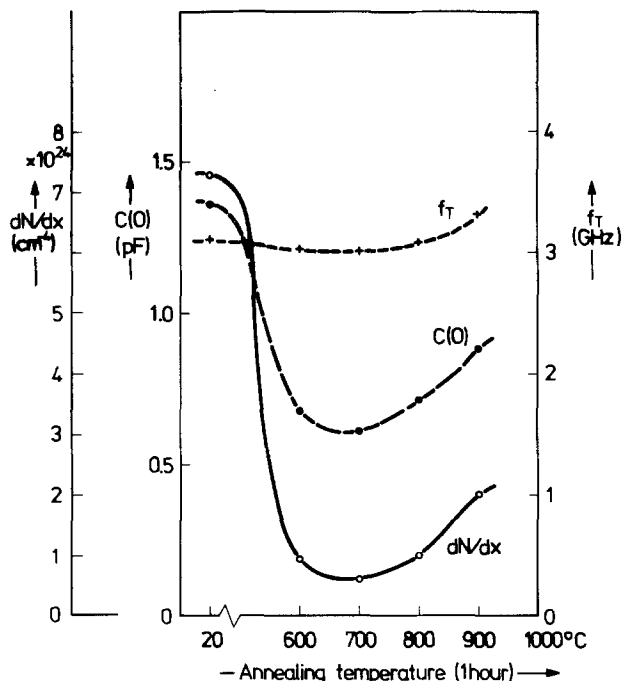


Fig. 3. Emitter-base capacitance at zero voltage $C(0)$, cut-off frequency f_T , and donor concentration gradient at the emitter-base junction dN/dx , as a function of annealing temperature (1 hr annealing).

[the neutral charge capacitance (10, 11)] is partly compensated by the variation of the Gummel number.

Profiles

Type I wafers.—Boron profiles were measured with SIMS before and after low temperature annealing between 600° and 1000°C. Profiles as measured before and after annealing for 1 hr at 700° and 800°C are shown in Fig. 4. The boron concentrations in the profiles were equalized at the value at 500Å depth. This involved shifts of the order of 10% or less, which is within the accuracy of the concentration determination. The maximum in the boron concentration at about 850Å is a remainder of the implantation maximum. The minimum around 0.2 μm is likely to be located at the p-n junction. Because of the electric field at this junction, ionized boron is driven toward the N-type area and this causes a minimum in the boron concentration (12, 13). This provides a means of determining the depth of the p-n junction. The effect of annealing is much larger at 700° than at 800°C. The profile has shifted to greater depth. As the minimum in the profile is located at the p-n junction, this means that the arsenic profile has also shifted. We measured the location of the minimum d and also the location where the boron concentration had decreased to $3 \times 10^{16} \text{ cm}^{-3}$, which is about the lower limit of boron detection, d^1 , as a measure of the base-collector junction depth. Figure 5 shows the dependence of d and d^1 on annealing temperature. The curves are similar and exhibit a maximum at 700°C and a minimum between 800° and 900°C.

The integrated dopant concentration in the base is an important parameter, as was discussed in the previous section. Assuming the p-n junction to be situated at the boron minimum, we determined the value of the integrated boron concentration below the minimum in the profile, Q_B , which is approximately equal to

$\int N_B dx$. The result is also shown in Fig. 5, where the

value of Q_B , expressed as a fraction of the total boron density Q_0 , measured on the same profile, is drawn as a function of annealing temperature. Q_B goes through a minimum at 700°C, in agreement with the electrical measurements. It can be seen from the difference between d and d^1 , which has a more or less constant value of about 0.22 μm at most annealing temperatures,

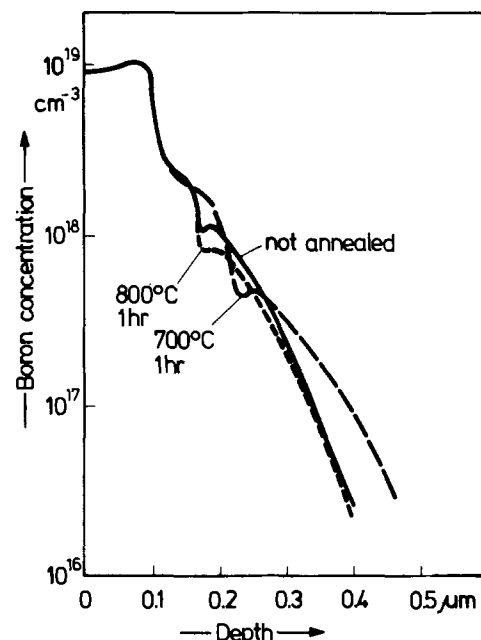


Fig. 4. Boron profiles as measured with SIMS on type I samples without additional annealing and annealed for 1 hr at 700°C and at 800°C.

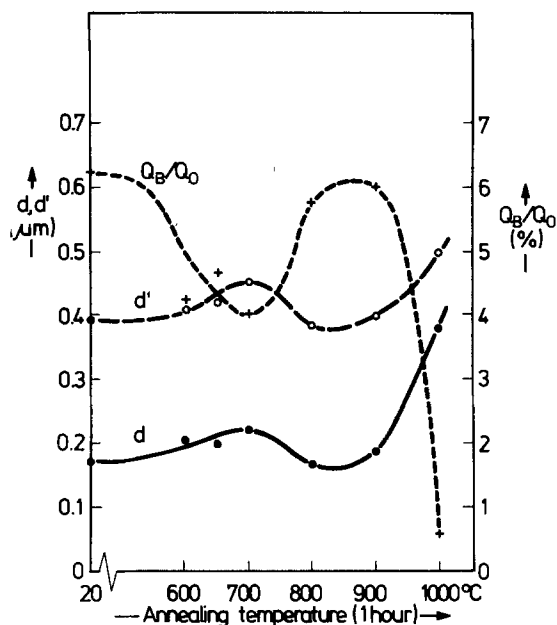


Fig. 5. Depth of the minimum in the boron profile, d , and of the boron concentration of $3 \times 10^{16} \text{ cm}^{-3}$, d' , and the boron density below the minimum Q_B , as related to the total boron density Q_0 as a function of annealing temperature (1 hr annealing).

that the change in Q_B is not due to a smaller base width, but mainly to a lower boron concentration. The value of Q_B after 1 hr at 700°C is a factor of 1.5 smaller than that before annealing, which is about $8 \times 10^{12} \text{ cm}^{-2}$.

The effect of annealing time at 700°C is shown in Fig. 6, where d is seen to increase and Q_B/Q_0 is seen to decrease with time.

The values of d and d' and of Q_B/Q_0 show some scatter. This is partly caused by the possible error in the depth determination in SIMS experiments, which is about 5%. Other possible causes of scatter are real differences between the samples owing to variations in, for example, temperature during implantation, dislocation density, and cooling rate after annealing. The results of measurements made on samples that were all cut from the same wafer are shown in Fig. 6 by open symbols.

Arsenic profiles were also determined with SIMS. Figure 7 shows the profile for a sample that had not undergone low temperature annealing. The profiles

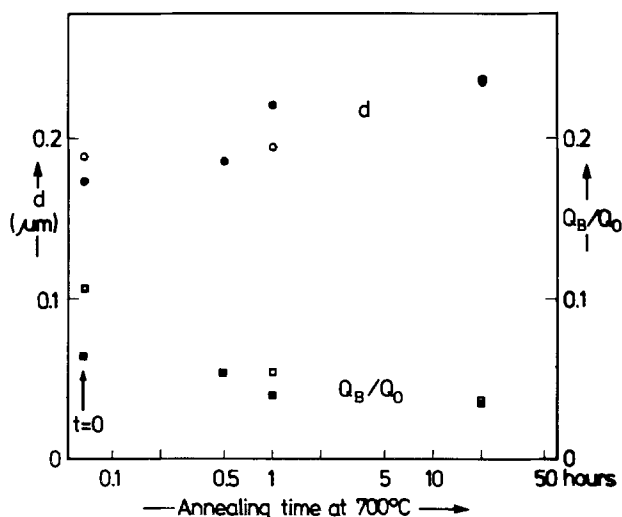


Fig. 6. d and Q_B/Q_0 , as defined in Fig. 5, as a function of the time of annealing at 700°C . The open symbols correspond to measurements on one wafer.

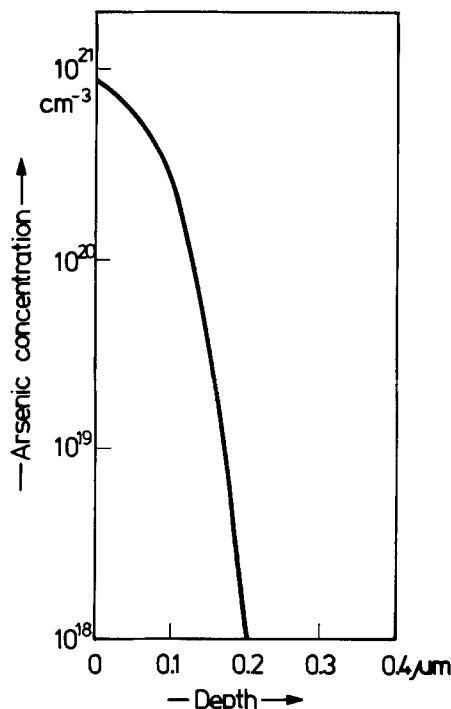


Fig. 7. Arsenic profile as measured with SIMS on a type I sample

taken on samples annealed at various temperatures exhibited little difference. However, for these samples the uncertainty in the depth determination due to asymmetric sputter effects or samples that were not sufficiently flat, was about 8%. Therefore, it could not be shown that the minimum in the boron profile was indeed at the depth where As and B concentrations were equal. Other uncertainties are caused by the fact that the arsenic and boron profiles were measured on different sites.

Arsenic profiles as determined by RBS do not suffer from uncertainty in depth determination as caused by sputter etching. Figure 8 shows As profiles measured by RBS on samples before and after annealing at 700°C and 800°C . The measurements show that after annealing a tail is found at concentrations below about $8 \times 10^{19} \text{ cm}^{-3}$. The shift of the profile due to the annealing at 700°C is of the order of 300\AA . The appearance of a tail means that after annealing the profile is less steep than before annealing. This causes a decrease

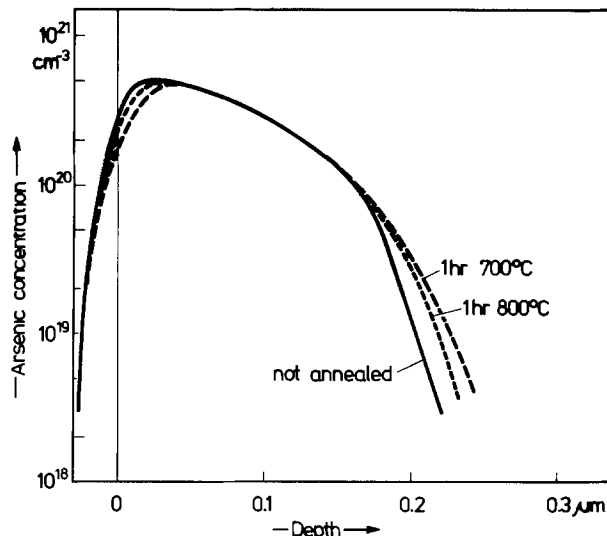


Fig. 8. The effect of an additional annealing treatment (1 hr at 700° and at 800°C) on arsenic profiles, as measured with RBS on type I samples.

of the impurity gradient at the p-n junction, as was also found by electrical measurements. The effect of annealing at 800°C is smaller than at 700°C, in qualitative agreement with the boron profiles.

Our results on the shift of As and B profiles are similar to those of Shibayama *et al.* (5) from electrical measurements. However, they found a maximum at a lower annealing temperature around 600°C.

Type II wafers.—Boron profiles were also measured on type II wafers, where the profile is deeper than in type I wafers. They are shown in Fig. 9 for no low temperature annealing and annealing for 1 hr at 650° and 800°C on sample A (see Table I). Figure 10 shows profiles before and after annealing for 17.5 hr at 700°C on sample B (see Table I). Again, the minima in the boron concentration are found to shift on annealing at 650° and 700°C and less so at 800°C. They are also deeper than for type I wafers. The value of Q_B/Q_0 decreases from 3.6% before annealing to 1.6% after annealing for 1 hr at 650°C for sample A and from 4.6% before annealing to 0.6% after annealing for 17.5 hr at 700°C for sample B.

Arsenic profiles were measured on sample B with the same annealing treatment using SIMS, as also shown in Fig. 10. The arsenic profile of the annealed sample was measured in vacuum. The shift of the As profile on annealing is larger than for type I wafers and is in agreement with the shift of the boron minimum. The uncertainty in the depth determination for both arsenic and boron was about 3%.

Transmission Electron Microscopy

Type I wafers were found to contain dislocations with density of about 10^8 cm^{-2} , as shown in Fig. 11. These may have originated as a result of implantation damage. From the number of extinction fringes at the edge of the crystal, it was found that they were located at about 0.3 μm below the surface. Annealing at temperatures between 600° and 800°C did not change the dislocation density and also no precipitates were found, when using the weak-beam technique (14) which set an upper limit to precipitate diameters of about 50Å.

The effect of annealing at various temperatures was also investigated on type II wafers. On sample B

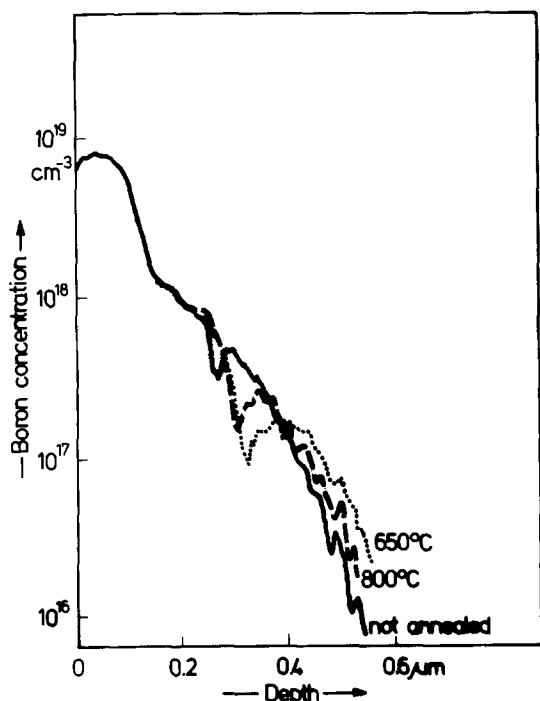


Fig. 9. The effect of an additional annealing treatment (1 hr at 650° and at 800°C) on boron profiles, as measured with SIMS on type II samples (A).

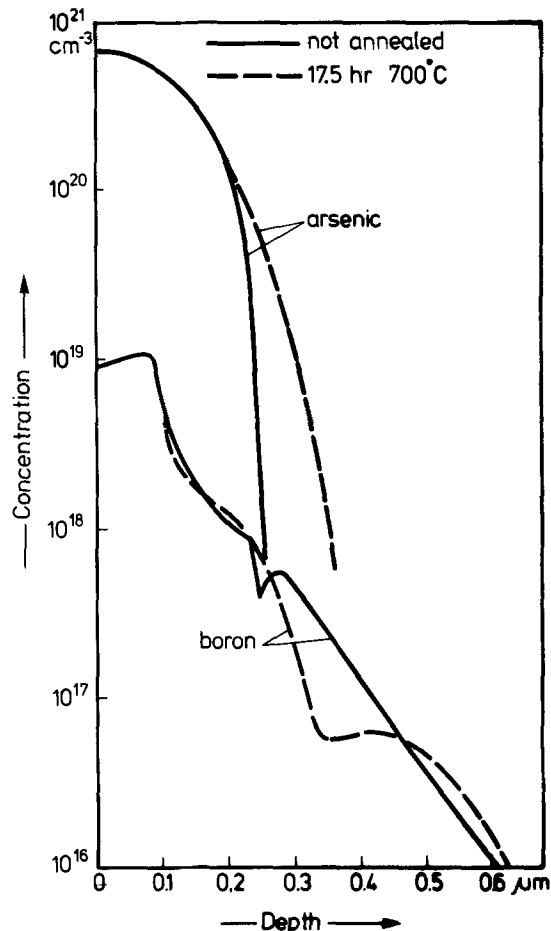


Fig. 10. The effect of an additional annealing treatment (17.5 hr at 700°C) on arsenic and boron profiles as measured with SIMS on type II samples (B).

which was annealed for 18 hr at 700°C, rod-shaped defects were present as shown in Fig. 12. This type of defect has been reported to be associated with boron implantation and is probably of an interstitial type (15, 16). Also particles of about 100-200Å in diameter, as well as dislocation segments between particles, were observed. No defects were found on an unannealed sample.

On sample A no defects were seen before annealing and after annealing for 1 hr at 800°C, but extensive defect formation had occurred after annealing for 1 hr at 650°C. The micrograph is shown in Fig. 13. The annealing produced small defects, about 200Å in diameter which were too small to determine unambiguously whether they were precipitates or dislocation loops and a smaller number of precipitates between 400Å and 1500Å in diameter. Annealing at 700° produced similar precipitates but fewer than at 650°C. The micrograph also shows dislocation segments between some of the particles.

Assuming the composition of the precipitates to be SiAs and assuming that the contrast in the micrographs is caused entirely by the particle, thus neglecting the strain field of the precipitate, the densities of the larger precipitates at 650° and 700°C correspond to densities of about 10^{15} and 3×10^{14} As atoms/cm², respectively. If the strain field of the precipitates was taken into account, smaller densities would be obtained.

The results on sample A are in qualitative agreement with the change in electrical parameters and in the profiles, which is maximum after annealing around 700°C.

The main differences compared with sample B, which exhibited the rod-shaped defects, are the higher

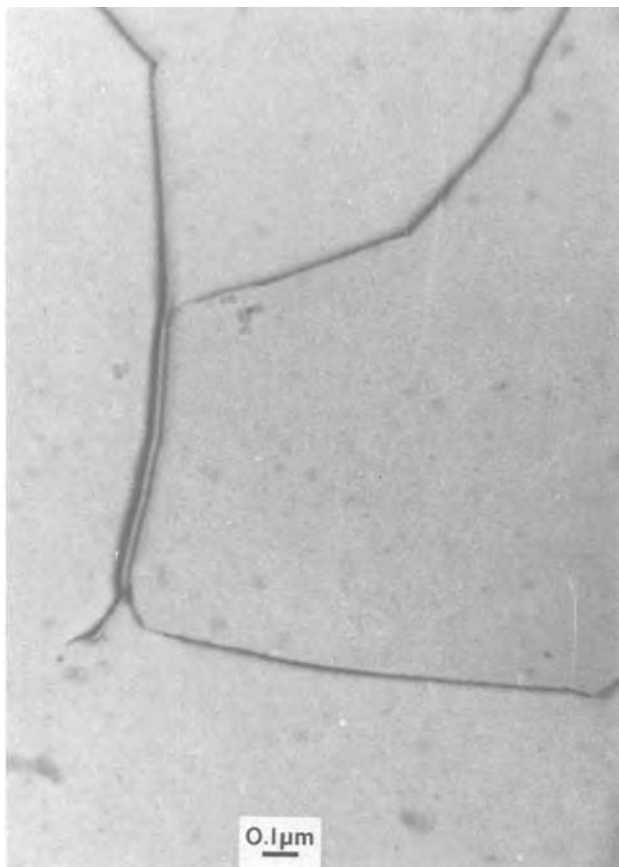


Fig. 11. Transmission electron micrograph of a type I sample after annealing for 1 hr at 650°C.

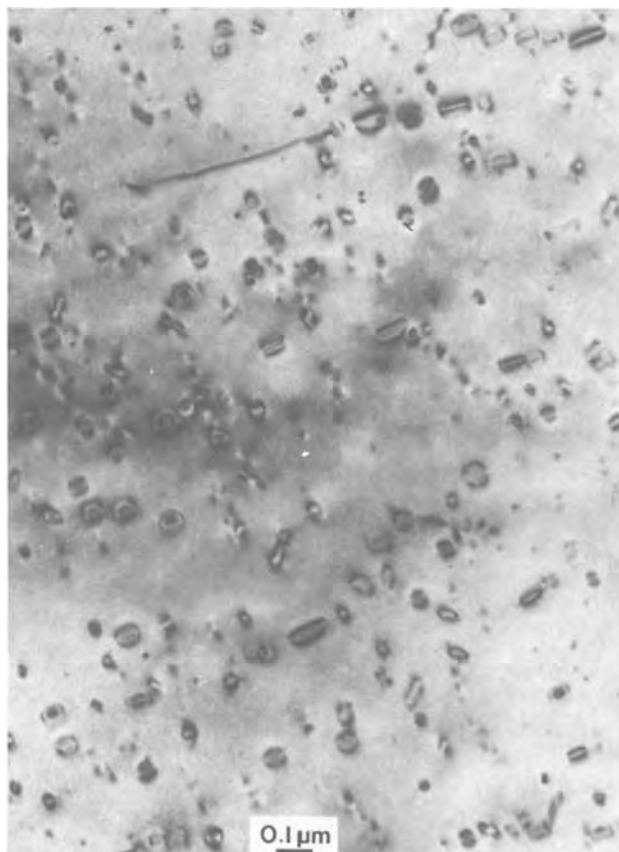


Fig. 12. Transmission electron micrograph of a type II sample (B) after annealing for 18 hr at 700°C.

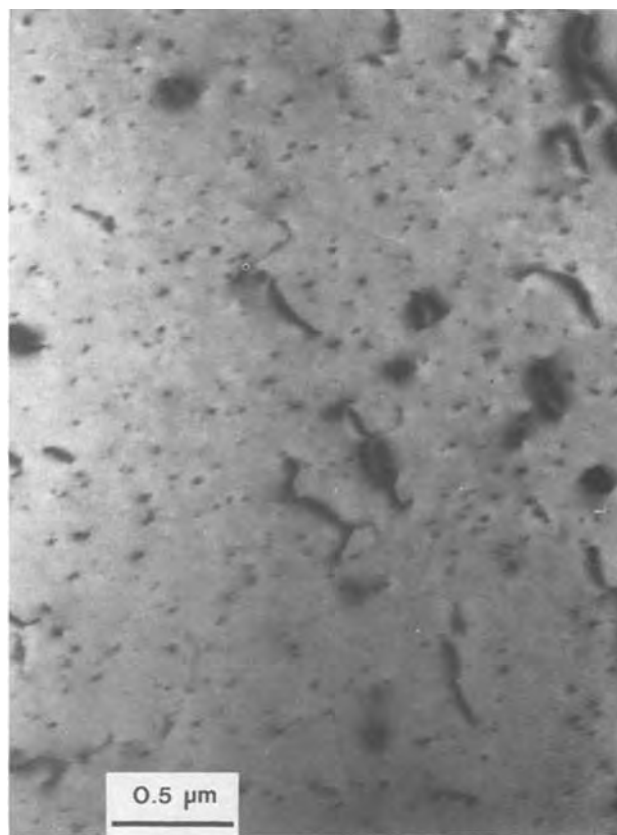


Fig. 13. Transmission electron micrographs of a type II sample (A) after annealing for 1 hr at 650°C.

boron implantation energies and the longer annealing time for sample B.

The absence of precipitates in type I wafers may be caused by the presence of dislocations, which may act as nucleation sites for very small precipitates.

Channeling

The fraction of As not on lattice sites f_{ns} was determined by RBS with the primary ion beam aligned in the $\langle 100 \rangle$ or the $\langle 110 \rangle$ direction (channeling). This can be calculated from the minimum backscattering yield related to the yield in a random direction x_{As} for As and x_{Si} for Si (7)

$$f_{ns} = \frac{x_{As} - x_{Si}}{1 - x_{Si}}$$

The values of x_{As} and x_{Si} were determined from the integrated yields in an interval 500-2000Å below the surface. This interval was based on the stopping cross section for the beam in a random direction. As the stopping cross section for perfectly aligned He ions is less than that for nonaligned particles by about 20% (7), this may introduce an error in the calculated values of x_{Si} , x_{As} , and f_{ns} . However, since we are mainly interested in the change of these quantities by annealing, we may neglect this error.

In the experiments the beam was aligned with the proper crystalline direction to give a minimum yield and the sample was then displaced in order to make the measurements on a nonirradiated spot. This was done to minimize As displacement by the ion beam (17). For each measurement this was carried out a number of times until subsequent measurements yielded approximately the same value of x_{As} .

Table II gives values of x_{Si} and f_{ns} , averaged over 2 to 4 measurements in which the spread was about 20%. For type I wafers the nonsubstitutional fraction of As, which was 5.1% in the $\langle 100 \rangle$ direction and 2.0% in the $\langle 110 \rangle$ direction, increased by about 2% on annealing at 700°C, corresponding to an As dose

Table II. RBS channeling results in two directions

	<100>		<110>	
	x_{Si}^* (%)	f_{ns}^\dagger (%)	x_{Si}^* (%)	f_{ns}^\dagger (%)
Type I				
Not annealed	3.7	5.1	2.2	2.0
1 hr 700°C	3.6	5.1	2.2	4.1
20 hr 700°C	3.5	6.5	2.2	4.1
Type II (sample B)				
Not annealed	3.8	2.6	2.1	2.3
17.5 hr 700°C	5.1	5.6	2.8	5.2

* x_{Si} = minimum yield for Si.

† f_{ns} = nonsubstitutional fraction of As.

of $1.3 \times 10^{14} \text{ cm}^{-2}$. Table II also shows that for type II wafers (sample B) annealing at 700°C changed the values of f_{ns} , which were 2.6% in the <100> direction and 2.3% in the <110> direction, by about 3%, corresponding to an As dose of $3 \times 10^{14} \text{ cm}^{-2}$. This is about a factor of 3 less than the maximum amount of precipitated arsenic obtained from TEM micrographs, assuming the contrast to be due completely to precipitate particles. As the strain field of these particles also causes contrast, a better agreement would be obtained between the two methods, if this were taken into account. These results show that most of the As is on substitutional lattice sites. The change that is observed on annealing is in agreement with earlier work by Haskell *et al.* (4) and is ascribed to precipitation.

There is a difference between type I and type II wafers, as regards the variation of x_{Si} on annealing. It increases only for type II wafers. This is presumably caused by lattice defects introduced by precipitation. In type I wafers precipitation may have taken place on dislocations already present before the heat-treatment.

Discussion

The measurements on the As and B profiles have shown that low temperature annealing gives rise to a shift of these profiles to greater depths, which is maximum for annealing around 700°C. These results are in qualitative agreement with those of Shibayama *et al.* (5) on chemically deposited As and B, for which a maximum in the shift was found around 600°C. The shift of the profiles can be correlated with the change of electrical parameters. These were shown to be due to two effects, both of which were maximum after annealing at 700°C: a decrease of the total number of impurities in the base and a decrease of the impurity gradient at the emitter-base junction. The profile measurements indeed showed that the shifts led to such changes, although there is some discrepancy between the values of the chemical impurity density in the base Q_B , as measured with SIMS, and the carrier density $\int N_B dx$, as calculated from the Gummel number. For example, after 1 hr at 700°C Q_B has changed by about a factor of 1.5 and $\int N_B dx$ by a factor of 3.

We ascribe this discrepancy to the scatter in the measurements, to uncertainty in the values of D_n and n_i in Eq. [3], and to the fact that in electrical measurements the effective base width is determined by the depletion layers on either side of the base. These are wider at lower impurity concentrations, so that they extend further into the base after annealing. The fact that the buried base resistance changes by a factor of 10 on annealing for 16 hr at 700°C, but the boron density only by a factor of 2, can only partly be explained by the above-mentioned causes. Perhaps there are differences between the chemical profile, as measured by SIMS, and the electrical profile.

The question that remains is what causes the shift of the As and B profiles. In agreement with Shiba-

yama's proposition, our TEM and RBS results support a mechanism of enhanced diffusion due to generation of point defects caused by precipitation of As. The number of precipitates as found by TEM, assuming them to be SiAs, corresponded reasonably well with the number of As atoms not on lattice sites, as determined with RBS. The number of precipitates was maximum around 650°C. This can be understood qualitatively from the phase diagram in Fig. 14, which shows the total and the electrically active As solubilities (18). The As solubility at the temperature at which the wafers were annealed after implantation, 990°C, is about 10^{21} cm^{-3} . Due to the relatively fast cooling to room temperature, most of the implanted As remains in solution (approximately 95-98%, according to RBS measurements). Since the solubility at room temperature is negligible, the As is in supersaturation. By subsequent annealing at a temperature, where diffusion is possible, the equilibrium situation can be restored by precipitation.

The rate of precipitation is the product of the nucleation rate and the growth rate. For homogeneous precipitation, the energy barrier that must be overcome to nucleate a precipitate is proportional to $\gamma^3/\Delta F_v^2$, where γ is the interface free energy per unit area between particle and matrix and ΔF_v is the bulk free energy change per unit volume on precipitation (19). This is to a first approximation proportional to the degree of undercooling and, therefore, the nucleation rate increases with the amount of undercooling, i.e., with decreasing temperature. On the other hand, the growth rate is limited by diffusion and therefore decreases with decreasing temperature. So the precipitation rate will have a maximum at some intermediate temperature.

In the case of precipitation on dislocations the nucleation rate will be larger than with homogeneous precipitation and the temperature of maximum precipitation will be higher. This may have caused the precipitation rate in type II wafers to be maximum at a lower temperature than in type I wafers. In the latter case, the shift of the profiles was indeed maximum at a somewhat higher temperature. The absence of visible precipitation in type I wafers and the fact that the minimum yield of Si changed little on annealing could be related to very small precipitates on dislocations.

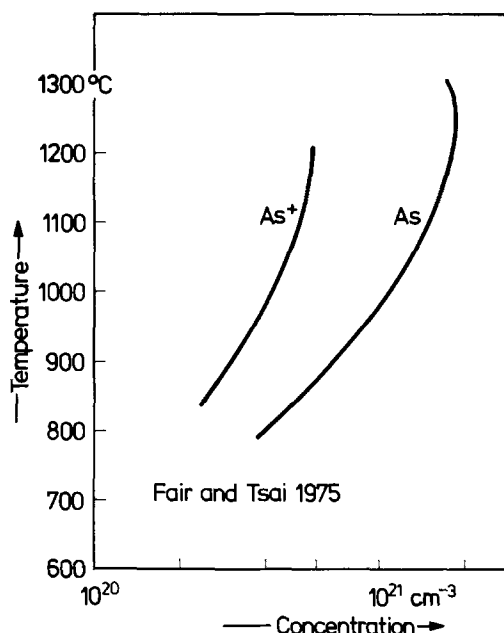


Fig. 14. Solid solubility of As in Si (As) and electrically active As concentration (As^+) for implanted As as a function of diffusion temperature. After Fair and Tsai (18).

If the precipitation is diffusion limited, the As diffusion length should be large enough to reach the dislocations or the precipitation nuclei. From extrapolation of the values reported by Masters and Fairfield (20) for the diffusion coefficient of As in Si at concentrations between 10^{20} and 10^{21} cm⁻³ we find for the diffusion length in 1 hr at 700°C a value of the order of 10Å, which is much too low to provide a diffusion current for precipitation both in type I and in type II wafers. It is therefore likely that there is a first stage in the precipitation where As clustering occurs or small coherent precipitates are formed, too small to be observed in TEM. With these clusters or precipitates a very small interface energy and thus a small energy barrier for formation are associated. The formation of As₄Si clusters with As on Si lattice sites was earlier proposed by Hu (21) and evidence for cluster formation was presented by Chu and Masters (22). Formation of such clusters would not change f_{ns} significantly. If cluster of coherent precipitate formation gives rise to generation of point defects, then diffusion is enhanced and precipitation is speeded.

A shift of As profiles over a distance of the order of 300Å corresponds to a diffusion coefficient of about 3×10^{15} cm²/sec, which is a factor of about 3×10^3 larger than the value at 700°C, obtained from extrapolation of high temperature values.

Enhanced diffusion of various elements in Si has also been obtained by radiation with protons (23, 24). This radiation probably generates lattice vacancies at a depth comparable to the proton range. The profiles acquire a tail by such treatment.

Since at low temperatures diffusion of As in Si probably takes place by a lattice vacancy mechanism (25), it is plausible to assume that the point defects generated by cluster formation or precipitation, are lattice vacancies. The fact that the atomic size of As is very similar to that of Si and the high degree of substitutionality of both Si and As show that a supersaturation of self-interstitials is unlikely.

Two mechanisms of vacancy generation by As clustering and precipitation may be active: dissociation of arsenic-vacancy complexes and the growth of interstitial defects.

Arsenic-vacancy complexes were first postulated by Schwenker *et al.* (2) to explain the fast conductivity change during low temperature annealing on samples that had been quenched from a high temperature and the difference between the electrically active and the total As concentrations. These complexes would presumably involve two arsenic atoms and a vacancy. RBS showed the atoms to be on lattice sites. This model was worked out by Fair and Weber (26) for chemically deposited and diffused As. Fair and Tsai (18) believed that this model was not true for ion-implanted As, because at not too high concentrations, maximum activation of As could be obtained in that case. However, the solubility of As⁺ is still much lower than that of As and the RBS results show that here too most of the As is on lattice sites. Dissociation of arsenic-vacancy complexes, caused by As clustering and precipitation, gives rise to vacancy generation. These highly mobile vacancies will diffuse both toward the surface and into the bulk. Some of these vacancies will be available to enhance As and B diffusion. Since dislocations will trap some vacancies, the effects of enhanced diffusion may be somewhat larger in dislocation-free Si.

An alternative mechanism of vacancy generation is the growth of interstitial defects. These may be small interstitial dislocation loops as found earlier in transmission electron microscopy (1, 2). Also a climbing dislocation is a source of vacancies by the growth of the extra half-plane.

The rate-limiting step in the successive processes: clustering and precipitation-vacancy generation-As diffusion may be determined from the time dependence. In three-dimensional diffusion-limited precipita-

tion the amount of impurity precipitated is initially proportional to t^n , with n depending on the shape of the precipitates, in general $n \geq 1$ (19). A simple one-dimensional diffusion has a $t^{1/2}$ time dependence. A plot of the increase of the buried base sheet resistance with annealing time gives a time dependence with $n \approx 0.55$, as can be deduced from Fig. 1. This suggests that the As diffusion is rate limiting. The shift of the boron minimum d with annealing time exhibits too much scatter for its time dependence to be determined, but Fig. 6 shows it to be sublinear.

The relatively large amount of scatter in d , Q_B/Q_0 , and f_{ns} between different wafers may be due to various causes: variation of precipitation nucleation rate by variation of dislocation density, variation of cooling rate from 990°C and thus of the amount of As and vacancy supersaturation, and variations in temperature during implantation, which may cause variations of the profile (27).

The effect of low temperature treatment on diffusion of As is very similar to the same process with phosphorus where the increase of the base resistance and the change of the P and B profiles can be correlated. The effect is ascribed to dissociation of P-vacancy complexes (*E* centers) (28, 29).

Our results suggest that the base push-out effect that is sometimes observed with arsenic emitters (30) is related to the precipitation of arsenic.

Conclusions

1. Annealing at temperatures between 600° and 900°C changed the parameters of high frequency transistors with implanted arsenic emitter and boron base, with a maximum change at 700°C. The buried base resistance and the current gain increased, the base Gummel number, the donor concentration gradient at the emitter-base junction and the emitter-base capacitance decreased, and the cut-off frequency did not change. These changes are interpreted as a decrease of the boron concentration in the base and the donor concentration gradient at the emitter-base junction.

2. Arsenic and boron profiles as measured with SIMS or RBS indeed showed these effects by shifts of the profiles to greater depth.

3. TEM observations showed precipitation in dislocation-free material, but not in dislocated Si.

4. RBS channeling in $\langle 100 \rangle$ and $\langle 110 \rangle$ directions showed that the substitutional fraction of As, which was between about 95% and 98%, decreased by a few percent on annealing.

5. The results are explained in terms of arsenic clustering and precipitation causing vacancy generation and thus enhanced diffusion. Precipitation is maximum at about 700°C. At higher temperatures the supersaturation is too small and at lower temperatures the diffusion is too slow. Vacancy generation is assumed to be due to dissociation of arsenic-vacancy complexes or to growth of interstitial defects.

Acknowledgments

The measurement of the many SIMS profiles by H. W. P. Akerboom is gratefully acknowledged. Thanks are also due to Mrs. J. R. M. Gijsbers and M. P. A. Vieggers for help with the electron microscopy, to J. H. Rector for help with the RBS, and to A. E. Morgan for discussions on SIMS.

Manuscript submitted Oct. 30, 1979; revised manuscript received Feb. 25, 1980. This was Paper 216 presented at the Pittsburgh, Pennsylvania, Meeting of the Society, Oct. 15-20, 1978.

Any discussion of this paper will appear in a Discussion Section to be published in the June 1981 JOURNAL. All discussions for the June 1981 Discussion Section should be submitted by Feb. 1, 1981.

Publication costs of this article were assisted by Philips Research Laboratories.

LIST OF SYMBOLS

a	donor concentration gradient at emitter-base junction, cm^{-4}
A_e	emitter area, cm^2
C	emitter-base capacitance, F
d	depth at minimum in boron concentration, cm
d'	depth at boron concentration of $3 \times 10^{16} \text{ cm}^{-3}$, cm
D_n	diffusion coefficient of electrons in the base, $\text{cm}^2 \text{ sec}^{-1}$
f_{ns}	nonsubstitutional fraction of As in Si
f_T	cut-off frequency ($h_{FE} = 1$), Hz
G_b	Gummel number of the base, $\text{cm}^{-4} \text{ sec}$
h_{FE}	current gain of transistor (I_c/I_b)
I_b	base current, A
I_c	collector current, A
k	Boltzmann's constant, $\text{cal } ^\circ\text{K}^{-1}$
n_i	dope-dependent intrinsic carrier concentration, cm^{-3}
n_{io}	intrinsic carrier concentration for low impurity concentration, cm^{-3}
N	donor concentration, cm^{-3}
N_B	acceptor concentration, cm^{-3}
q	electronic charge, C
Q_B	boron density in the base, cm^{-2}
Q_o	total boron density, cm^{-2}
R_b	sheet resistance of the base underneath the emitter, Ω
T	absolute temperature, $^\circ\text{K}$
V_{eb}	emitter-base voltage, V
V_g	built-in voltage at e-b junction, V
x	distance perpendicular to the surface, cm
γ	interface free energy per unit area between precipitate and matrix, cal cm^{-2}
ϵ	dielectric constant
ϵ_o	permittivity of free space, F cm^{-1}
ΔF_v	bulk free energy change per unit volume on precipitation, cal cm^{-3}
μ_p	hole mobility in the base, $\text{cm}^2 \text{ V}^{-1} \text{ sec}^{-1}$
x_{As}	minimum aligned RBS yield of As
x_{Si}	minimum aligned RBS yield of Si

REFERENCES

- V. B. Osvenskii, L. M. Morgulis, S. P. Grishina, and N. M. Klimova, *Fiz. Tverd. Tela*, **11**, 1314 (1969); English translation: *Soviet Phys.-Solid State*, **11**, 1064 (1969).
- R. O. Schwenker, E. S. Pan, and R. F. Lever, *J. Appl. Phys.*, **42**, 3195 (1971).
- N. Miyamoto, E. Kuroda, and S. Yoshida, *Suppl. Jpn. J. Appl. Phys.*, **43**, 408 (1974).
- J. Haskell, E. Rimini, and J. W. Mayer, *J. Appl. Phys.*, **43**, 3425 (1972).
- H. Shibayama, H. Masaki, H. Ishikawa, and H. Hashimoto, *This Journal*, **123**, 742 (1976).
- J. F. Ziegler, "The Stopping and Ranges of Ions in Matter," Vol. 4, Pergamon, New York (1977).
- W. K. Chu, J. W. Mayer, and M. A. Nicolet, "Backscattering Spectrometry," Academic Press, New York (1978).
- J. W. Slotboom and H. C. de Graaff, *Solid-State Electron.*, **19**, 857 (1976).
- B. R. Chawla and H. K. Gummel, *IEEE Trans. Electron Devices*, ed-18, 178 (1971).
- J. A. Kerr and F. Berz, *ibid.*, ed-22, 15 (1975).
- A. S. Wang, Paper 15.5, Proceedings of International Electron Devices Meeting, Washington, D.C., 1976.
- S. M. Hu and S. Schmidt, *J. Appl. Phys.*, **39**, 4272 (1968).
- R. B. Fair, *ibid.*, **44**, 283 (1973).
- D. J. H. Cockayne, in "Diffraction and Imaging Techniques in Material Science," Vol. I, S. Amelinckx, R. Gevers, and J. van Landuyt, Editors, p. 153, North Holland Publishing Co., Amsterdam (1978).
- P. K. Madden and J. M. Davidson, *Radiat. Eff.*, **14**, 271 (1972).
- J. A. Lambert and P. S. Dobson, *Philos. Mag.*, **37**, 441 (1978).
- L. W. Wiggers and F. W. Saris, *Radiat. Eff.*, **41**, 149 (1979).
- R. B. Fair and J. C. C. Tsai, *This Journal*, **122**, 1689 (1975).
- See e.g., A. H. Cottrell, "Theoretical Structural Metallurgy," Edward Arnold, London (1965).
- B. J. Masters and J. M. Fairfield, *J. Appl. Phys.*, **40**, 2390 (1969).
- S. M. Hu, in "Atomic Diffusion in Semiconductors," D. Shaw, Editor, chap. 5, Plenum Press, London (1973).
- W. K. Chu and B. J. Masters, in "Laser-Solid Interactions and Laser Processing," S. D. Ferris, H. J. Leamy, and J. M. Poate, Editors, p. 305, American Institute of Physics Conference Series 50 (1979).
- H. Ryssel, H. Kranz, K. Schmid, and I. Ruge, in "Ion Implantation in Semiconductors," S. Namba, Editor, p. 169, Plenum Press, New York (1975); H. Ryssel, H. Kranz, and P. Eichinger, in "Applications of Ion Beams to Materials," p. 1, Institute of Physics Conference Series 28, London (1976); H. Ryssel and I. Ruge, "Ionen-Implantation," p. 96, B. G. Teubner, Stuttgart (1978).
- B. J. Masters and E. F. Gorey, *J. Appl. Phys.*, **49**, 2717 (1978).
- A. Seeger, *Radiat. Eff.*, **9**, 15 (1971); A. Seeger, W. Frank, and U. Gösele, in "Defects and Radiation Effects in Semiconductors," p. 148, Institute of Physics Conference Series 46, London (1978).
- R. B. Fair and G. R. Weber, *J. Appl. Phys.*, **44**, 273 (1973).
- W. K. Hofker, W. J. M. J. Josquin, D. P. Oosthoek, and J. R. M. Gijsbers, in International Conference on Ion Beam Modification of Materials, Budapest, 1978.
- F. N. Schwetmann and D. L. Kendall, *Appl. Phys. Lett.*, **19**, 218 (1971); *ibid.*, **21**, 2 (1972); J. G. Aiken and F. N. Schwetmann, in "Semiconductor Silicon 1973," H. R. Huff and R. R. Burgess, Editors, p. 717, The Electrochemical Society Softbound Proceedings Series, Princeton, N.J. (1973).
- M. Aceves and D. L. Kendall, *Electron. Lett.*, **15**, 282 (1979).
- For a review, see, A. F. W. Willoughby, *J. Phys. D.*, **10**, 455 (1977).

Photocurrent Spectroscopy of Interface States at a Semiconductor-Electrolyte Junction

by J.-N. Chazalviel

Laboratoire de Physique de la Matière Condensée, Groupe de Recherche
du Centre National de la Recherche Scientifique, Ecole Polytechnique, 91128 Palaiseau, France

ABSTRACT

We have investigated the photocurrent induced by subbandgap light irradiation at the n-Si-aqueous electrolyte junction. The observed effect is shown to arise from optical processes involving interface states, and mainly from electron transitions from the filled interface states to the conduction band. The dependence of the photocurrent upon anodic voltage is accounted for quantitatively by considering the Schottky barrier lowering effect, already measured from the dark I - V characteristics. The dependence of the photocurrent upon photon energy enables us to extract a density of states curve for the occupied interface states. It suggests that these states are bound states on the semiconductor side, due to the coulomb potential of adsorbed ions. Complementary observations on oxidized and bandgap irradiated junctions are discussed and are found to fit well in the above picture.

Experimental evidence for the role of interface states at the semiconductor-electrolyte junction has been brought in many instances, mostly through capacitance and recombination studies (1, 2). These techniques however, hardly permit a systematic investigation of interface states through the semiconductor gap. A true spectroscopy of these states might rather be obtained by observing the photocurrent induced by subbandgap optical transitions between these levels and the semiconductor bands (3, 4). This technique however, suffers from two drawbacks: (i) the expected effects are rather small; (ii) larger effects may be present in the same photon energy range, for example onset of bandgap absorption, transitions involving deep levels in the bulk or the space charge region, and also thermal effects (5). We present here the results of an investigation of the photocurrent induced by subbandgap light at the n-silicon-aqueous electrolyte junction, where interface states are known to be present (2, 6). We show that they are indeed responsible for the observed effect and their energy distribution can be attained from the experimental data.

Experimental

The electrochemical cell was similar to a previously described one, allowing transient measurements when the sample is put into contact with the electrolyte (6). The optical arrangement is shown in Fig. 1. The design had to provide a maximum subbandgap light intensity, together with rigorous exclusion of bandgap light, because the investigated subbandgap signal can be very small and any parasitic bandgap light might obscure it because of the large associated photoelectrochemical current. The light source was a 250W tungsten lamp and the monochromator was single beam, 1:5 aperture, equipped with a 2 μ m blazed grating. All the light from the output slit was focused onto the sample with an elliptical mirror. The sample was shaped as a Weierstrass sphere, to provide reliable concentration of the light on the small Si-electrolyte interface area. Rigorous exclusion of bandgap light was obtained by inserting an 8 mm thick pure silicon filter in the light path; this material was heated at 100°-200°C to increase slightly its cutoff wavelength (7). With this arrangement the light intensity on the sample was a few milliwatts for a typical 50 nm resolution and rejection of bandgap light was about

10⁵. Additional filters were used to measure the weakest signals at wavelengths larger than 1.5 μ m. The light was chopped at a typical frequency of 30 Hz and the small photocurrent was measured by using a standard three-electrode potentiostatic arrangement and a lock-in amplifier.

The minimum detectable photocurrent is limited by the background noise current I_N , which is due to the shotnoise fluctuations of the dark current I . This gives for a frequency interval $\Delta\nu$ (8)

$$\langle I_N^2 \rangle = 2 I e \Delta\nu$$

with $\Delta\nu \sim 1$ Hz and $I \sim 10^{-6}$ A, this gives a minimum detectable signal $\sqrt{2 I e \Delta\nu} \sim 10^{-12}$ A which corresponds to a quantum yield (number of detected electrons per incident photon) $\eta \sim 10^{-9}$. In practice for carefully prepared surfaces the sensitivity was indeed close to this theoretical limit but any defects left on the surface upon polishing were found to increase the noise drastically (flicker noise), due to localized avalanche breakdown near the defects.

The sample was cut from a dislocation-free single crystal doped with $N_D = 2.4 \times 10^{16}$ cm⁻³ phosphorus. This doping was chosen as a compromise to allow a small concentration of bulk defects, together with a thin space charge layer, in order to minimize the unwanted photocurrents that might arise from photoionization of traps in the bulk or the space charge region. The flat surface of the sample was prepared using the mechanochemical procedure described earlier (6) in order to obtain a defect-free surface. [111] and [100] surfaces were investigated and were found to give similar results. The electrolytes used were aqueous solutions of 1M HCl or 1M buffered KCl. As reported earlier (6) there is no evidence for anion adsorption on n-Si either with Cl⁻ or with the various 0.05M buffer anions.

Results and Discussion

The observed photocurrent is independent of the frequency of light chopping in the investigated 10-100 Hz range. This rules out thermal effects as the explanation for the effect (5). The effect, expressed as a quantum yield, is plotted in Fig. 2 as a function of photon energy for a fixed electrode potential $V = 1V_{SCE}$. The sharp rise around 1 eV corresponds to the onset of bandgap absorption and the associated large photocurrent. The change of slope near 0.95 eV indicates that the observed effect between 0.6 and 0.9 eV is of a different nature. This conclusion is further supported by

Key words: photoelectrodes, surface states, semiconductor electrochemistry.

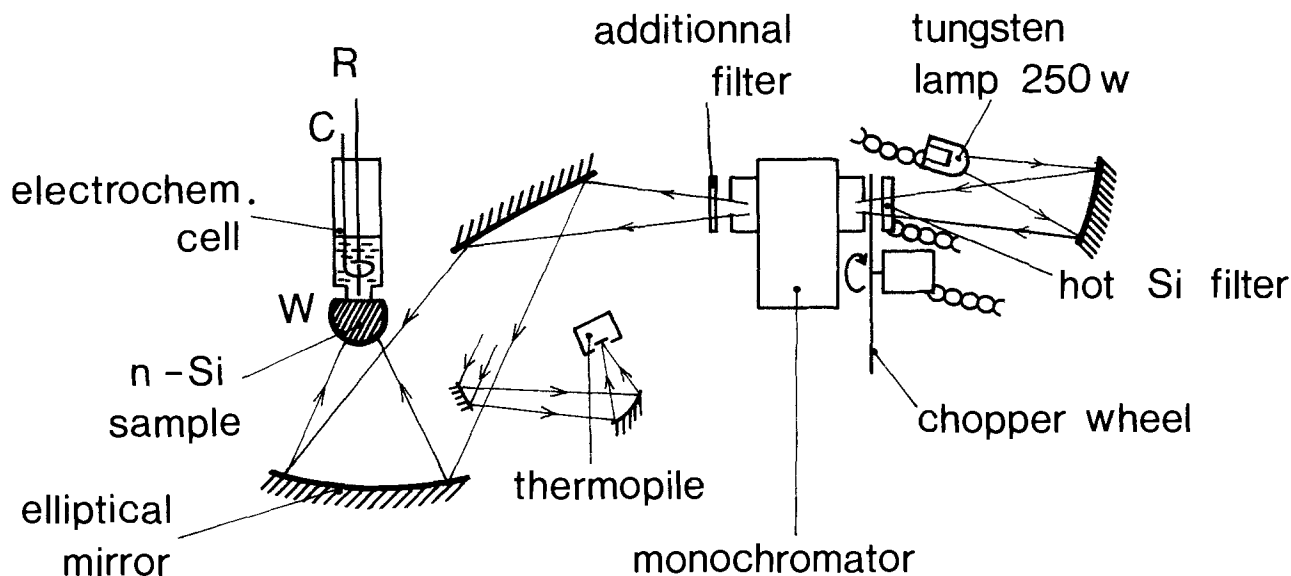


Fig. 1. Scheme of the optical arrangement (see text)

the dependence of the effect upon electrode potential, which shows a different behavior for $h\nu = 1$ eV and 0.8 eV, see Fig. 3. When pH is changed the bandgap effect remains the same, except for a trivial shift of the voltage scale (Nernst law) (6) but the subbandgap effect is found to increase by about a factor of 5 when going from pH = 0.1 to pH = 4.7. This large sensitivity of the subbandgap effect to pH is taken as marked evidence for a surface process.

One can imagine two elementary processes involving interface states (4); these processes are sketched as (a) and (b) in Fig. 4. Process (a) is electron excitation from the valence band into empty interface states; process (b) is electron excitation from occupied interface states into the conduction band (similar to internal photoemission in metal-semiconductor junctions). Whether the observed effect is due to process (a) or (b) can be tentatively answered on the basis of the model we have used previously to account for the dark I - V and C - V characteristics (6). According to

this model, charge transport through the interface proceeds via two serial steps, also sketched in Fig. 4: step 1 electrochemical transfer from the electrolyte to the interface states and step 2 electron transfer from the interface states to the semiconductor bulk. Step 2 has been shown to proceed via thermal activation of the electrons over the Schottky barrier (6); although our understanding of step 1 is far less advanced one may think of it as an ionic transfer (*e.g.*, OH^- ions) through the Helmholtz layer and eventually the oxide layer created as the net result of the two steps. The associated overvoltages for 1 and 2 are, respectively, of the form (6)

$$\delta V_1 = (kT/\beta e) \ln(I/I_{ex}) \quad [1]$$

$$\delta V_2 = -(kT/e) \ln(1 - I/I_1) \quad [2]$$

where I_{ex} and I_1 are two constant currents, and $\beta \sim 0.2$. In the framework of this model, the effect of illumination is to provide an alternative pathway for step 1 [process (a)] or for step 2 [process (b)]. Since the total overvoltage is fixed and the two steps are in series, illumination may induce a new repartition of the overvoltage between steps 1 and 2. This effect is summarized in Fig. 5; the net result is that the photocurrent (a) associated with step 1 will be

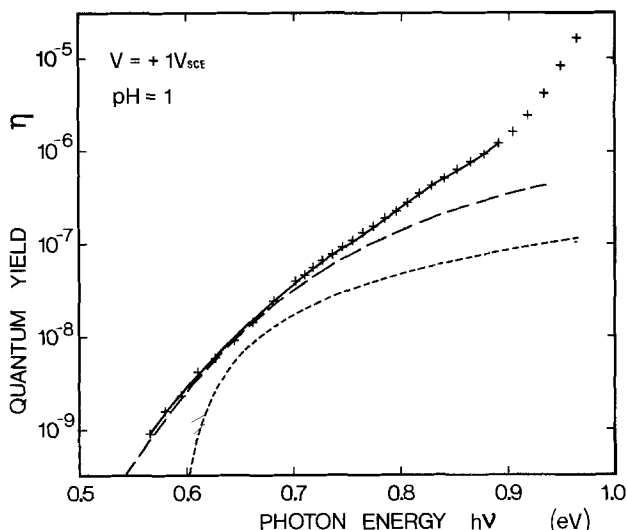


Fig. 2. Quantum yield as a function of photon energy. The points are experimental and the full curve is a fit with the energy distribution of interface states (see text). The fast increase of η near $h\nu = 0.95$ eV is due to the onset of bandgap transitions. The dotted curve is the expected yield from a single type of surface states at energy $E_C - 0.6$ and the dashed curve is for a constant density of surface states through the gap with $E_F = E_C - 0.6$ and $T = 297^\circ\text{K}$.

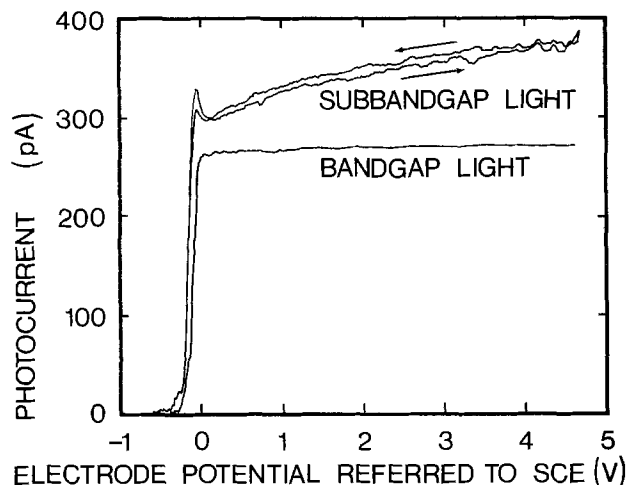
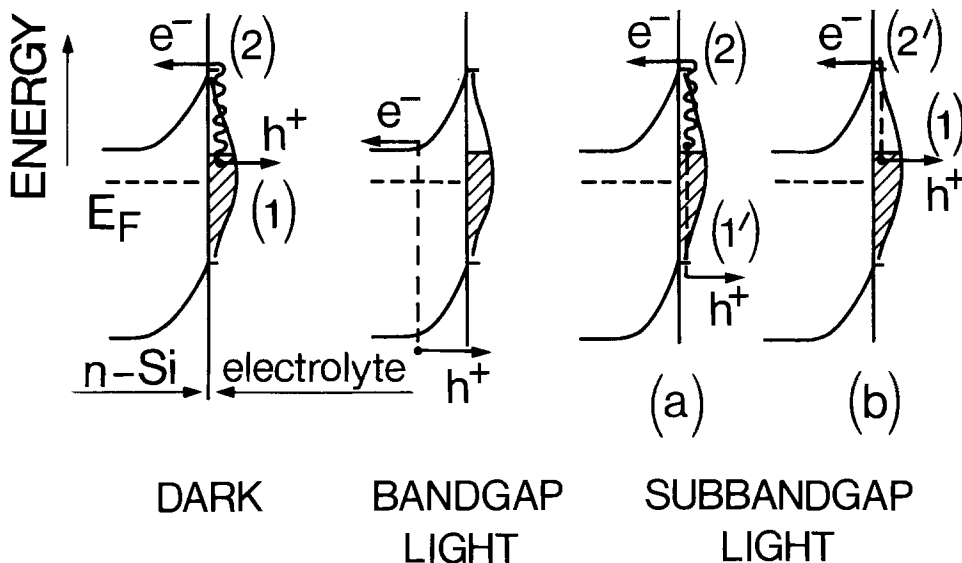


Fig. 3. Photocurrent as a function of electrode potential. Subbandgap light is $h\nu = 0.8$ eV, intensity $\sim 10^{-3}\text{W}$; bandgap light is $h\nu = 1.0$ eV, intensity $\sim 10^{-4}\text{W}$ (vertical sensitivity is 10^2 times smaller). Notice the different shape of the two curves.

Fig. 4. Scheme for anodic current flow at the n-Si-electrolyte junction in the dark, with band-gap light, and with subbandgap light. The curve near the semiconductor surface schematizes the energy distribution of interface states and the hatched area is for the occupied ones. The dotted line is the bulk Fermi level. The vertical wiggly and dashed lines are for thermal excitation and light excitation, respectively. Steps 1 and 2 are the two steps for dark current from Ref. (6) (see text).



affected by a factor $R_1/(R_1 + R_2)$ and the photocurrent (b) by $R_2/(R_1 + R_2)$, where R_1 and R_2 are the differential resistances associated with step 1 and 2, respectively. In the anodic region the current reaches its limiting value and R_2 is orders of magnitude larger than R_1 so that process (a) should have a much smaller efficiency than (b) (in other terms, the relevant process will be that associated with the limiting step). For electrode potentials less anodic than a certain potential V_0 , (6) step 2 is no more the limiting step, R_1 and R_2 are of comparable magnitude, and processes (a) and (b) may both participate in the photoeffect. A quantitative analysis of the data in Fig. 3 is however difficult in this region, because the band curvature gets small and the photoeffect (bandgap as well as subbandgap) subsequently decreases to zero. We will therefore limit our quantitative analysis to the strongly anodic region ($V > V_0$).

Effect of anodic voltage.—As Fig. 3 shows, the band-gap photoeffect is nearly independent of electrode potential through the anodic range; in contrast the subbandgap photoeffect appreciably increases with anodic voltage. This can be understood as a consequence of

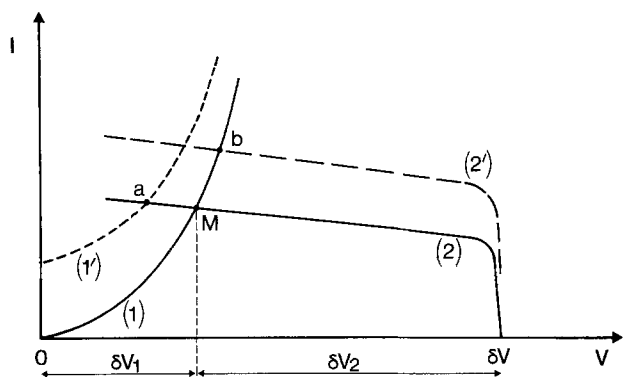


Fig. 5. Graphical discussion of processes (a) and (b) of Fig. 4. According to Ref. (6) the dark current flows through two serial steps. Here curve 1 is the I - V characteristic for step 1 and curve 2 is that for step 2; this last curve is plotted backwards starting from δV so that the current for a given overpotential δV is given by the ordinate of the intersect M of curves 1 and 2. In the presence of subbandgap light, process (a) enhances step 1 and curve 1 must be replaced by curve 1' (upwards shift by I_{ph}^a). The new current is given by the ordinate of the intersect a of 1' and 2. The current increase is seen to be much smaller than the initial I_{ph}^a . The effect on process (b) is similar: curve 2 is replaced by 2' and M by b. The current increases are related to the inverse slopes of curves 1 and 2 at point M, i.e., the differential resistances for processes 1 and 2 (see text).

Schottky barrier lowering: it has been previously deduced (6) from the dark-current characteristics that the Schottky barrier height ϕ_B decreases with anodic voltage V following the law

$$\phi_B = \phi_B^0 - \Delta\phi_B = \phi_B^0 - [2(V - V_{FB} - kT/e) eN_D/\epsilon\epsilon_0]^{1/2} ed \quad [3]$$

where $\Delta\phi_B$ is the barrier lowering, V_{FB} is the flatband potential, ϵ is the dielectric constant of silicon, N_D is the donor concentration, and $d \approx 13\text{\AA}$ (6). If the subbandgap photoeffect is due to process (b), decreasing the barrier height will result in enhancing the photocurrent I_{ph} ; i.e., to the first order in $\Delta\phi_B$

$$\Delta I_{ph} = \frac{\partial I_{ph}}{\partial \phi_B} (-\Delta\phi_B) \approx \frac{\partial I_{ph}}{\partial (h\nu)} \Delta\phi_B \quad [4]$$

where we have made the reasonable assumption that I_{ph} depends on ϕ_B only through the photon energy above threshold ($h\nu - \phi_B$). Since the quantity $\partial I_{ph}/\partial (h\nu)$ can be measured separately, Eq. [4] provides a good checkpoint for the above explanation of the dependence of I_{ph} upon V . Figure 6 shows I_{ph} plotted as a function of $\Delta\phi_B$, as given by Eq. [3], for typical experimental conditions. In spite of the 30% variation of I_{ph} the linear approximation (Eq. [4]) is well obeyed and the slope is in good agreement with the measured $\partial I_{ph}/\partial (h\nu)$ (see the dashed line in Fig. 6). As a further verification we have investigated the photoeffect in a sample with a smaller donor concentration $N_D = 1.8 \times 10^{15} \text{ cm}^{-3}$. Due to this smaller doping the barrier lowering effect was nearly four times smaller for this sample and the dependence of I_{ph} upon V was found to be reduced accordingly. This good agreement of the results with Eq. [4] gives a verification that the photoeffect in the anodic region is due to process (b) as process (a) would not give such a voltage dependence.

Effect of photon energy.—A typical dependence of the photocurrent I_{ph} vs. photon energy $h\nu$ is shown in Fig. 2. If a single type of interface state, at a well-defined energy E_t in the bandgap, were responsible for the photoeffect, one would expect for the photocurrent near threshold a dependence

$$I_{ph} \propto (h\nu + E_t - E_C)^\alpha \quad [5]$$

where E_C is conduction band energy. The most appropriate value for the exponent should be $\alpha = 3/2$.¹

¹ The choice $\alpha = 3/2$ can be briefly justified as follows: the final density of states is that of the conduction band $[(h\nu + E_t - E_C)^{3/2}]$ but the matrix element for the transition probability introduces a further factor $(h\nu + E_t - E_C)$ because a conduction band wavefunction has to fall to zero near the interface, hence the amplitude will be at most $\sim k_1 a$ at a distance a from the surface, if k_1 is the normal component of the wavevector; this leads to the factor $k^2 \propto (h\nu + E_t - E_C)$ in the transition probability. The final α is therefore $1/2 + 1 = 3/2$.

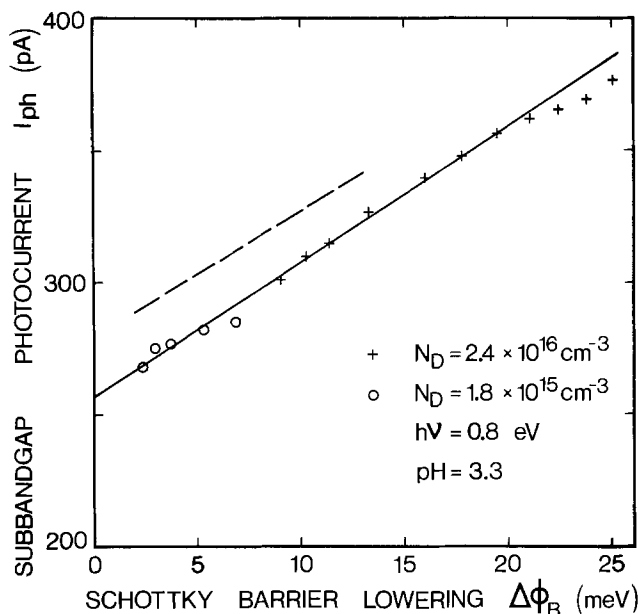


Fig. 6. Effect of barrier lowering on the photocurrent. The crosses represent the data of Fig. 3 ($pH = 3.3$; $N_D = 2.4 \times 10^{16} \text{ cm}^{-3}$; $h\nu = 0.8 \text{ eV}$) plotted as a function of barrier lowering $\Delta\phi_B$, calculated from Eq. [3]. The full line has been drawn through the experimental points. The dashed line is the calculated slope, from Eq. [4] and the measured $\partial I_{ph}/\partial(h\nu)$. The circles are data from a sample with $N_D = 1.8 \times 10^{15} \text{ cm}^{-3}$ (the vertical scale has been adjusted to the same extrapolated photocurrent at $\Delta\phi_B = 0$).

However the observed dependence cannot be fitted with Eq. [5] whatever the value given to α . The observed behavior is more suggestive of a broad energy distribution of surface states; if such is the case, then one expects

$$I_{ph} \propto \int_{E_V}^{E_0} g(E_t) (h\nu + E_t - E_C)^\alpha dE_t \quad [6]$$

where E_V is valence band energy. We have tried to determine the distribution $g(E_t)$ by fitting the experimental data in Fig. 2 with Eq. [6]. The interface state energy distribution was taken as a histogram and the amplitudes of the histogram were used as the parameters for the fit. It was found that the $I_{ph}(h\nu)$ curve is not very sensitive to the details of the $g(E_t)$ distribution, and the cell for the histogram can hardly be taken smaller than 50 meV. A typical result for $g(E_t)$ is shown in Fig. 7. An exponent $\alpha = 3/2$ was assumed for Eq. [6] but values of α ranging between 1 and 2 yield very similar shapes for $g(E_t)$. The quantity $g(E_t)$ corresponds to the density of occupied states per unit energy interval and as expected goes to zero for $E_C - E_t \gtrsim \phi_B \approx 0.60 \text{ eV}$. The most prominent feature of $g(E_t)$ is its increase near the valence bandedge; this feature may be somewhat exaggerated by matrix element effects that we do not consider here; however, this behavior is very similar to that reported from field effect data for the dry Si-SiO₂ interface (9). The interface states there have been attributed to localized states inside the semiconductor due to the coulomb potential of charged impurities in the oxide. With regard to our problem, this may suggest a synthetic picture for the anodic process: if, e.g., OH⁻ ions are adsorbed onto the surface upon step 1, such localized states will result in the silicon. These, after being emptied via step 2, will be left with localized holes, allowing neutralization of the OH⁻ with formation of Si-OH bonds.

Effect of the oxide.—The effect of oxidation on the dark current I has been investigated earlier by using a transient technique (6). The same technique has

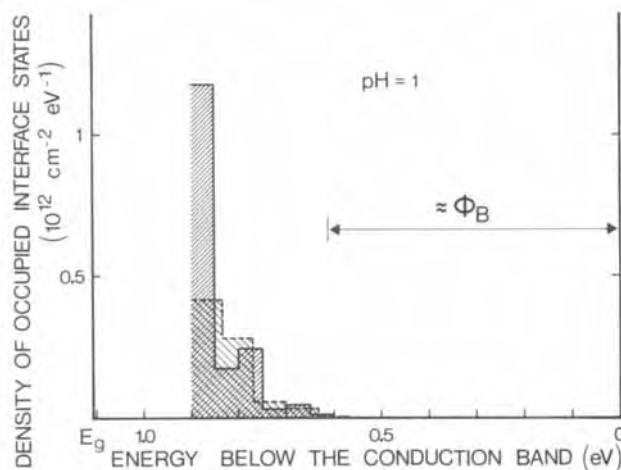


Fig. 7. Density of occupied interface states as deduced from the fit in Fig. 2. The vertical scale is only given as an order of magnitude; assuming a cross section $\sigma = \sigma_0[(h\nu - E_C + E_t)/E_g]^{3/2}$ with $\sigma_0 = 10^{-15} \text{ cm}^2$. The two curves are obtained from fits with two different meshes.

been used here in the presence of chopped light, allowing in principle the separate recording of I and I_{ph} during the oxide growth. We have been able to measure I_{ph} in this way for bandgap photon energies. The effect of oxide growth is found to be much smaller than for the dark current: in the first minute the decay for I_{ph} is less than a factor of two, while for I it is more than one order of magnitude; and only at larger oxide thicknesses (for example after anodic oxidation under strong illumination) is the bandgap photocurrent drastically reduced. The same technique could not be applied to the measurement of the sub-bandgap photocurrent because it is a small effect and a lock-in detection is necessary; this makes transient measurements impossible, at least for times shorter than a few seconds. Recordings of the lock-in output for times between a few seconds and a few minutes seem to show that the decay of the subbandgap effect is intermediate between the large decay of the dark current and the small decay of the bandgap current.² No significant change of shape of the $I_{ph}(h\nu)$ curve was observed with time, so that the role of the oxide seems to be unessential and the measurements shown in Fig. 2 are thought to be representative of the oxide-free surface, within a scale factor of a few units.

An interesting point is the time evolution of the shape of the $I_{ph}(V)$ curves for the subbandgap effect. While the anodic photocurrent decreases a peak develops near V_0 after a few minutes (see Fig. 8) and slowly increases with oxide growth. We think this peak can be accounted for by an increase of process (a) in Fig. 4, due to the increase of the resistance R_1 associated with step 1 under the influence of the oxide. This peak exhibits about the same dependence upon $h\nu$ as the anodic photocurrent; this possibly implies that the distribution of empty surface states has a shape similar to the symmetric of Fig. 7 around midgap. We think this qualitative information is the most we can obtain from such strongly oxidized interfaces.

Effect of double illumination.—We have been looking for crossed effects between bandgap and subbandgap illumination. The subbandgap photocurrent is orders of magnitudes smaller than the dark current and therefore constitutes a negligible disturbance for the system, but the bandgap photocurrent can be very large and may affect the population of the interface states, thereby changing the subbandgap effect. A

² All these observations are consistent with the simple expectation that the deeper in energy is the hole created at the interface, the more easily will the resulting reaction take place, i.e., the weaker is the effect of oxidation.

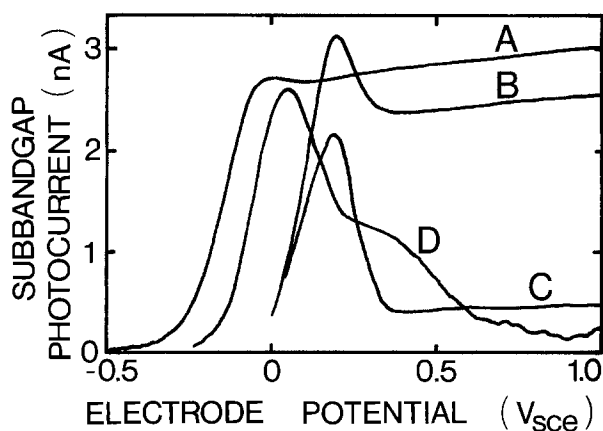


Fig. 8. Voltage dependence of the subbandgap photocurrent. Curve A: freshly immersed surface; curve B: oxidized surface (1 hr immersion); curve C: oxidized surface in the presence of bandgap light; curve D: surface with defects; the signal decrease correlates with avalanche breakdown; notice the associated increase of the noise. The anodic shift of curves B and C (and possibly D) relative to A is due to the large oxide thickness. $\text{pH} = 3.3$; $h\nu = 0.85 \text{ eV}$.

small 0.5W lamp was added to the experimental setup a few centimeters below the sample, allowing a small continuous bandgap irradiation. The corresponding bandgap photocurrent ($\approx 1 \mu\text{A}$ for a useful surface of $\sim 1 \text{ mm}^2$) is found to decrease the subbandgap photocurrent, weakly ($\sim 10\%$) for a freshly immersed surface, but with increasing effectiveness as oxide is growing; after 30 min the subbandgap effect in the anodic region is almost completely quenched ($\sim 90\%$) by a bandgap photocurrent as small as $0.1 \mu\text{A}$. In contrast the peak near V_0 attributed to process (a) is unaffected by bandgap irradiation.

These observations are quite consistent with our interpretation of the photocurrent: the main effect of bandgap irradiation is to create holes near the surface; instead of being directly transferred to the electrolyte, these holes will have some probability of being trapped on the occupied surface states, thereby decreasing their density and quenching process (b). The same detrimental influence of holes on the subbandgap photocurrent has been verified when holes are created by avalanche breakdown near surface defects (see Fig. 8). A thick oxide layer hinders hole transfer to solution and favors hole trapping, hence the increased quenching effect in the presence of oxide. On the other hand, the insensitivity of the peak near V_0 to these holes is not surprising, since this peak has

been attributed to process (a), which should not be affected by hole trapping.

Conclusion

We have measured the photocurrent arising from subbandgap light irradiation of the n-Si-electrolyte junction. The measured effect is shown to arise from interface states and processes involving transitions to the conduction band and from the valence band are separately identified. The dependence of the photocurrent upon anodic voltage is accounted for quantitatively by the Schottky barrier lowering effect. The spectral dependence of the photoeffect allows us to deduce the energy distribution of the occupied interface states. The result suggests that these states are localized states on the semiconductor side, bound by the coulomb potential of adsorbed ions.

Acknowledgments

The author is very much indebted to Dr. G. Lampel for help in designing and setting up the optical apparatus and especially for his ingenious idea of the hot silicon filter. He also enjoyed many invaluable discussions on the experimental results with Dr. T. B. Truong.

Manuscript submitted Nov. 20, 1979; revised manuscript received March 11, 1980.

Any discussion of this paper will appear in a Discussion Section to be published in the June 1981 JOURNAL. All discussions for the June 1981 Discussion Section should be submitted by Feb. 1, 1981.

Publication costs of this article were assisted by Ecole Polytechnique.

REFERENCES

1. P. J. Boddy and W. H. Brattain, *This Journal*, **110**, 570 (1963).
2. R. Memming and G. Schwandt, *Surf. Sci.*, **5**, 97 (1966).
3. H. Morisaki, M. Hariya, and K. Yazawa, *Appl. Phys. Lett.*, **30**, 7 (1977).
4. D. Laser and S. Gottesfeld, *This Journal*, **126**, 475 (1979).
5. F. Decker, J. F. Julião, and M. Abramovich, *Appl. Phys. Lett.*, **35**, 397 (1979).
6. J.-N. Chazalviel, *Surf. Sci.*, **88**, 204 (1979).
7. W. L. Wolfe, in "Handbook of Optics," W. G. Driscoll and M. Vaughan, Editors, pp. 7-50, McGraw-Hill, New York (1978).
8. A. Van der Ziel, "Noise," pp. 88-98, Prentice Hall, Englewood Cliffs, N.J. (1956).
9. A. Goetzberger, V. Heine, and E. H. Nicollian, *Appl. Phys. Lett.*, **12**, 95 (1968).

Electron Microscope Study of Annealed SiH_2^+ Implanted InP

J. J. Comer, D. Eirug Davies, and J. P. Lorenzo

Rome Air Development Center, Solid State Sciences Division, Hanscom Air Force Base, Massachusetts 01731

ABSTRACT

Transmission electron microscopy was used to characterize structural defects in annealed InP implanted both at room temperature and at 200°C with 10^{14} SiH_2^+ /cm² at 150 keV. During implantation at room temperature an amorphous layer was formed to a depth of $\sim 1850\text{\AA}$, whereas no such layer was formed on the specimen implanted at 200°C. Upon recrystallization of the amorphous layer at 650°C or higher shear dislocations were observed as well as loop structures up to 2000Å in diameter on {111} and {110} planes within that region. Smaller, interstitial loops were present on {110} planes throughout the implanted region. The specimens implanted at 200°C did not go through a recrystallization stage. Therefore, no shear dislocations were formed in this case. However, these specimens when annealed to 650°C or higher contained loops under 100Å in size. The structural differences observed between the room temperature and 200°C implants may account for the higher carrier mobility measured for the 200°C implant.

Structural damage resulting from ion implantation in elemental semiconductors such as silicon (1-5) and the III-V semiconductors, notably GaAs (6), has been studied extensively by transmission electron microscopy. A correlation was sometimes found between the extent of damage formed and the electrical behavior of the material after postimplantation annealing to obtain maximum electrical activity.

In ion implantation, damage results from displacement of atoms in the crystal lattice, causing the introduction of interstitial atoms and vacancy sites. When the specimen is annealed these defects aggregate to form dislocation loops. At high fluences, the damage may be severe enough to form an amorphous layer near the surface of the specimen. When this occurs, the postanneal temperature must be sufficiently high to bring about epitaxial regrowth of the layer. Earlier work on Si-implanted InP in which the substrate was heated to 200°C during the implantation suggested that an amorphous layer does not form under these conditions (7). The present work shows that, for room temperature implants, not only does an amorphous layer form at the surface but, also, that following post-implantation annealing the loop structures for these implants are much larger than the defects found in the hot implants under similar annealing conditions.

Whether the ion implantation method is used to form semi-insulating regions in InP or for conventional doping it is important to know the structural damage that occurs because of the effect it may have on device performance. To this end, transmission electron microscope studies were made of annealed InP implanted at room temperature and at 200°C. Defects formed under various annealing conditions have been characterized and the results of electrical measurements are presented to show how they may be affected by the defects.

Experimental

The InP used in these experiments was grown in these laboratories by the Czochralski encapsulation method and was doped with 10^{16} Fe/cm³. Wafers were cut and polished to obtain specimens oriented 3° from the (001) plane. The concentration of grown-in dislocations was $\sim 10^4$ /cm². Extreme care was exercised in handling the specimens because of the room temperature plasticity exhibited by the material (8, 9). Specimens were implanted with SiH_2^+ at room tem-

perature or at 200°C. The fluence was 10^{14} ions/cm² at 150 keV. Postannealing was done isothermally in a PH_3/H_2 ambient to prevent deterioration of the InP surface (10). Anodic oxidation and stripping of the oxide layer was carried out on some specimens to obtain an estimate of the depth of the amorphous layer formed during the room temperature implant (11). Final thinning of the specimen for electron microscopy was done by the jet-etching method of Booker and Stickler (12) using 0.5% bromine in methanol for the solvent.

Specimens were examined in a JEM-100CX/ASID transmission electron microscope equipped with a $\pm 60^\circ$ goniometer and a $\pm 45^\circ$ tilting stage. The instrument was operated at 100 kV. All micrographs were printed with the emulsion side up. Kikuchi patterns were used to establish beam directions and diffracting vectors. Extensive use of stereomicrographs was made to determine loop planes or sense of tilt, and to measure distance of defects from the top or bottom surfaces of the specimen. To aid in these determinations, a 5Å thick layer of gold was evaporated onto the top or bottom surface for identification, and to establish a reference point for the measurements. The angle and direction of tilt was controlled by using Kikuchi patterns.

Results and Discussions

Room Temperature Implants

At a fluence of 10^{14} SiH_2^+ /cm² at 150 keV an amorphous layer forms near the surface of the specimens. This layer was detected by both reflection electron diffraction and selected area diffraction. Similar amorphous layers have been reported for ion-implanted Si, Ge, and GaAs. They are derived from overlapping disordered zones in the crystal caused by atomic displacements (1-6, 13). An oxidation and stripping technique (11) was applied to the present specimens to remove from 100 to 750Å of material in each of several successive steps. After each step, the specimen was examined by reflection electron diffraction at 100 keV and electron channeling patterns at 20 kV. From these, it was estimated that the amorphous region extended to a depth of $\sim 1850\text{\AA}$.

Recrystallization of the amorphous layer.—Some recrystallization of the amorphous layer occurred as the result of specimen heating caused by the electron beam during examination in the electron microscope. This was seen in the selected area diffraction mode where the diffuse rings, characteristic of the amorphous ma-

Key words: InP, ion implantation, transmission electron microscopy.

terial, gradually changed to sharp ring patterns showing some preferred orientation but no epitaxial regrowth. Other specimens were examined after annealing isothermally at temperatures ranging from 400° to 750°C for periods of 15 min. Although recrystallization occurs well below 400°C, epitaxial regrowth is not observed until the specimen is heated to 650°C or higher. Below 640°C, the recrystallized material was poorly oriented and the electron micrographs exhibited Moiré fringe patterns. Diffraction patterns contained "extra" spots due to double diffraction; streaking through the spots indicated the presence of thin platelets. A micrograph of material recrystallized at 600°C is shown in Fig. 1.

Dislocations associated with epitaxial regrowth.—Several examples of imperfect epitaxial recrystallization have been reported in the literature for ion-implanted Si and GaAs (3, 6, 13). Davidson and Booker (3) observed a dislocation network in annealed N⁺ implanted Si which they believe formed at the interface between crystals of very slightly different lattice spacings resulting from the simultaneous recrystallization of two amorphous/crystalline interfaces on either side of a buried amorphous layer. They suggest that improper matching of the lattice could be due to varying impurity concentrations. In the present study, specimens annealed up to 650°C often contained regions where epitaxial regrowth was not complete. Contrast within these regions was different than in the surrounding epitaxially recrystallized material and Moiré fringes were observed. Some of these regions were present as islands within the epitaxially regrown material. While it is probable that the Moiré fringes are due to rotation of one lattice with respect to another identical one, this has not been proved. Therefore, the possibility that they are caused by slight differences in unit cell dimensions resulting from non-stoichiometric conditions cannot be ruled out. It is certain, however, that on heating to 700°C or higher no Moiré fringes remain and electron diffraction shows good epitaxial regrowth. Before this stage is reached, at 650°C or below, line dislocations extend from the poorly oriented material into the epitaxially regrown regions as shown in Fig. 2. Some of the dislocations are aligned along $\langle 110 \rangle$ directions. Where islands of incomplete epitaxial growth exist, as in Fig. 3, the dislocations spread out radially. Often these islands, which are sources of dislocations, were removed by preferential etching while thinning the specimen for electron microscopy. In all cases, the dislocations have Burgers vectors of the type $\bar{b} = a/2 \langle 110 \rangle$ inclined to the (001) specimen plane. A determination of the Burgers vectors of dislocation segments A and B is illustrated in Fig. 3. Segment A is out of contrast for

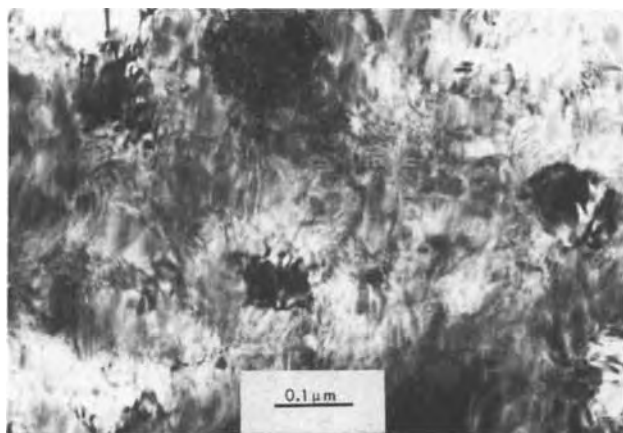


Fig. 1. Bright field electron micrograph illustrating a recrystallized amorphous layer after annealing at 600°C. Moiré fringes and other contrast effects are due to incomplete epitaxial regrowth.

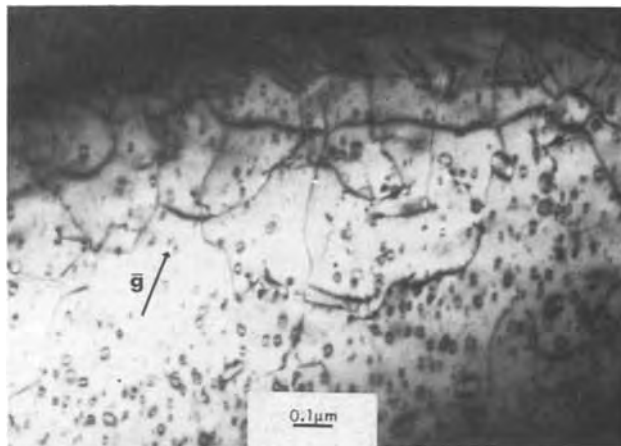


Fig. 2. This micrograph of a specimen annealed to 650°C shows regions of complete and incomplete epitaxial regrowth. The dislocations introduced at this stage have Burgers vectors of the type $a/2 \langle 110 \rangle$ inclined to the (001) plane of the specimen.

$\bar{g} = 040$ and $\bar{g} = \bar{1}3\bar{1}$ (Fig. 3c and 3e) but is in contrast for all other reflections. Applying the invisibility criterion for $\bar{g} \cdot \bar{b} = 0$, it was determined that $\bar{b} = \pm a/2 [101]$ for this segment. Similarly, the Burgers vector of segment B which is out of contrast for $\bar{g} = \bar{4}00$ and $\bar{g} = \bar{3}1\bar{1}$ (Fig. 3d and 3f) was determined to be $\bar{b} = \pm a/2 [011]$. The depth of these dislocations was $\sim 700\text{Å}$ below the surface, or within the region recrystallized from the amorphous state. Within the island are Moiré fringes, one set of which is shown in Fig. 3b.

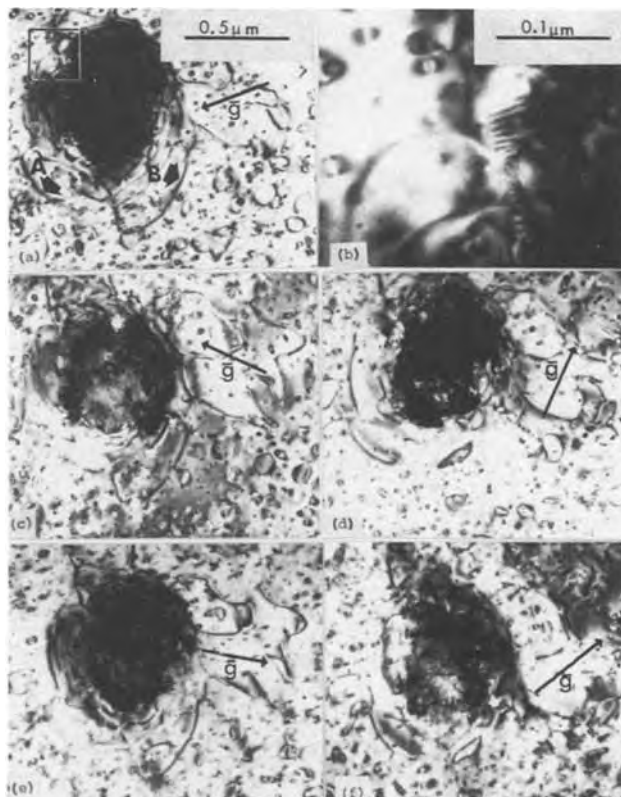


Fig. 3. Electron micrographs illustrating Burgers vectors determination of dislocations emitted from circular "islands" of poorly oriented regrown material. (a) $\bar{g} = \bar{2}20$; (b) enlargement of area within box in (a); (c) $\bar{g} = 040$; (d) $\bar{g} = 400$; (e) $\bar{g} = \bar{1}3\bar{1}$; and (f) $\bar{g} = \bar{3}1\bar{1}$. Beam directions were close to [001] for (a), (b), (c), and (f), and close to $[\bar{1}\bar{1}4]$ and $[\bar{1}\bar{1}4]$ for (e) and (d).

Loop structures.—Half-loops were found in some specimens annealed at 650°C. In Fig. 4 the loop in the center of the field was found by stereomicroscopy to lie on the $(\bar{1}\bar{1}1)$ plane. It goes out of contrast when the diffracting vectors are $\bar{g} = 400$ or $3\bar{1}\bar{1}$ and is in contrast for the vectors $\bar{2}\bar{2}0$, 040 , $\bar{2}\bar{2}0$, and $\bar{1}3\bar{1}$. From these observations, it was determined that $\bar{b} = \pm a/2 [011]$, with \bar{b} parallel to the loop plane. This is a shear loop containing both screw and 60° dislocation segments.

Other dislocation structures resulting from the recrystallization consist of large loops with meandering dislocations lines about 500-1000Å below the specimen surface. These loops, some of which are shown in Fig. 5, are not confined to a particular plane. An area of interest in Fig. 5 contains segments labeled A, B, and C. Points where the dislocation line rises sharply to the surface are shown by the arrows. In comparing images of the three segments for the operating reflections $\bar{2}\bar{2}0$, $\bar{1}3\bar{1}$, 400 , and $\bar{2}\bar{2}2$ (Fig. 5a-5d), loop A is out of contrast only for the $\bar{1}3\bar{1}$ reflection, B is out for the 400 and $\bar{2}\bar{2}2$ reflections only, and C is out for $\bar{1}3\bar{1}$. From this, the Burgers vectors are found to be $\pm a/2 [101]$, $\pm a/2 [011]$, and $\pm a/2 [101]$, respectively.

In a specimen annealed to 750°, shown in Fig. 6, the larger loops, 500-2000Å in diameter, lie on both $\{111\}$ and $\{110\}$ planes. These loops lie closer to the surface than the small loops which are uniformly dispersed throughout the specimen thickness. Intersecting loops on $\{111\}$ planes share a common dislocation segment shown by the arrow in Fig. 6a. Stereomicroscopy shows that the loops are in a "butterfly" configuration with A on the $(\bar{1}\bar{1}1)$ and B on the (111) plane. Images were formed with the reflections $\bar{2}\bar{2}0$, $\bar{2}\bar{2}0$, 040 , $\bar{2}\bar{2}2$, $\bar{4}00$, and $\bar{3}\bar{1}\bar{1}$. Since loop A is out of contrast only for the $\bar{4}00$ reflection, the Burgers vector is $\pm a/2 [0\bar{1}1]$. Loop B is out of contrast for 040 and $\bar{2}\bar{2}2$, therefore $\bar{b} = \pm a/2 [10\bar{1}]$. The shared dislocation segment is a screw type with $\bar{b} = \pm a/2 [1\bar{1}0]$ and is out of contrast only for the $\bar{2}\bar{2}0$ reflection. Similar results were obtained for other pairs of intersecting loops on $\{111\}$ planes. The Burgers vector of loop A on the $(\bar{1}\bar{1}1)$ plane does not lie on the loop plane, whereas that of loop B on the (111) is parallel to the loop plane. Thus, A is a prismatic loop, and B is a glissile loop. The probable reaction between the two dislocations is: $a/2 [10\bar{1}] + a/2 [0\bar{1}1] = a/2 [1\bar{1}0]$. The vector of this screw dislocation is parallel to the (001) specimen plane.

In Fig. 2-5 it is clear that many of the loops are under 500Å in diameter, and are uniformly distributed from top to bottom of the region of the specimen under examination. The concentration is $\sim 2 \times 10^{10}/\text{cm}^2$.

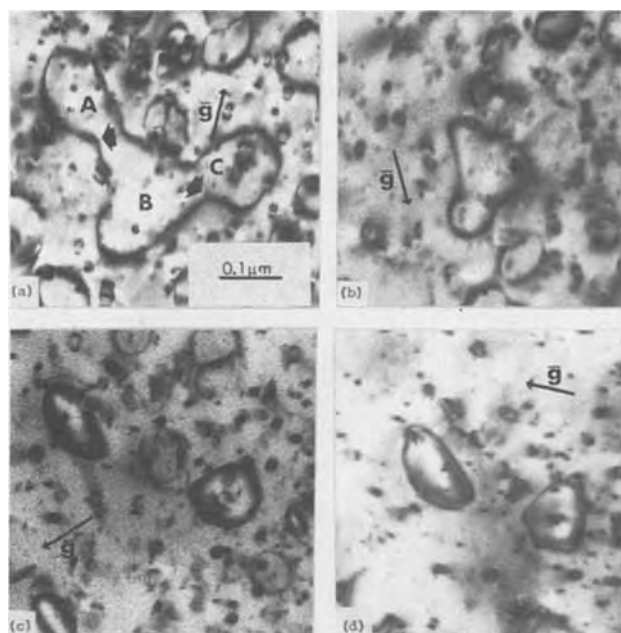


Fig. 5. Micrograph showing meandering loops in specimen annealed at 650°C. Segments A, B, and C are all in contrast for $\bar{g} = \bar{2}\bar{2}0$ in (a). Other reflections are: (b) $\bar{g} = \bar{1}3\bar{1}$; (c) $\bar{g} = 400$; and (d) $\bar{g} = \bar{2}\bar{2}2$. Beam directions are close to $[001]$ for (a) and (c), and close to $[\bar{1}\bar{1}2]$ for (b) and (d). The dislocation line bends up sharply at points indicated by the arrows.

These loops form on annealing by aggregation of point defects. Unlike the larger loops associated with strain introduced by the recrystallization of the amorphous region, they lie mainly in $\{110\}$ planes and are prismatic. The loops shown in Fig. 7 are all under 500Å except for the ones labeled A. These lie on the (101) plane, and the Burgers vector is $\bar{b} = \pm a/2 [101]$. Smaller loops, B and C, on the $(1\bar{1}0)$ and (110) planes, have Burgers vectors of $\bar{b} = a/2 [1\bar{1}0]$ and $\bar{b} = \pm a/2 [110]$.

Nature of loops.—Analyses were made to determine whether the prismatic loops were of the interstitial or vacancy type. The method used was that applied by Groves and Kelly to the analysis of loops in MgO (14). For the product $(\bar{g} \cdot \bar{b})s > 0$, where s is the deviation parameter, the loop exhibits outside contrast and for $(\bar{g} \cdot \bar{b})s < 0$ it exhibits inside contrast. In applying this method the sense of inclination of the loop was first determined by stereomicroscopy to establish the direc-

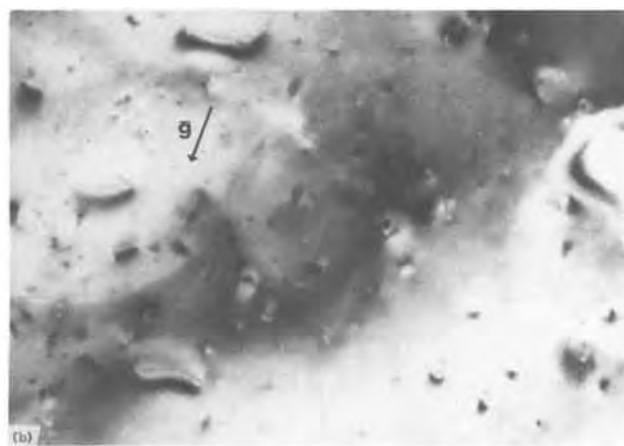
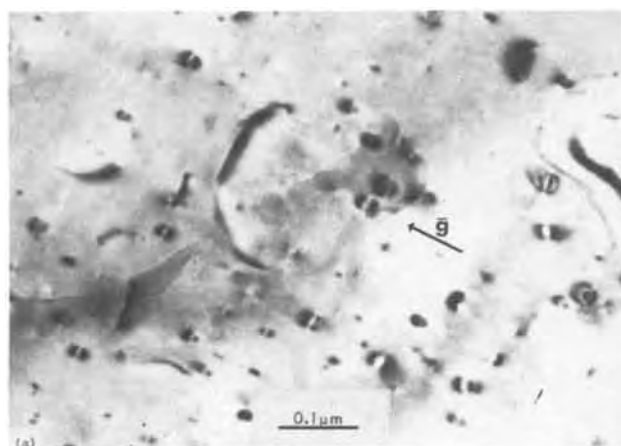


Fig. 4. Half-loop on (111) in contrast for $\bar{g} = \bar{2}\bar{2}0$ in (a), and out of contrast for $\bar{g} = 3\bar{1}\bar{1}$ in (b)

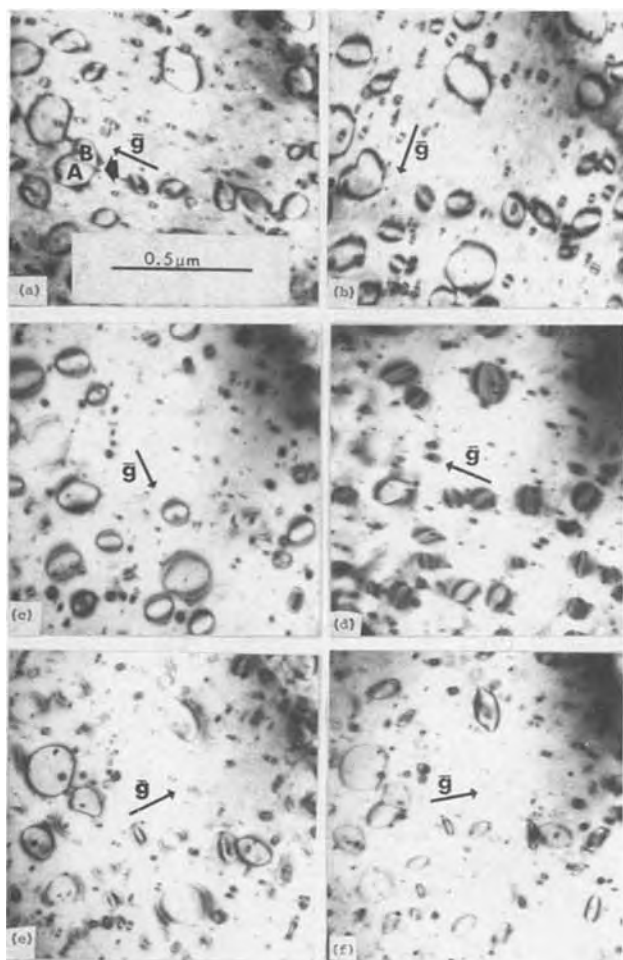


Fig. 6. Electron micrographs showing interaction between loop A on the $(\bar{1}\bar{1}1)$ plane and loop B on the $(11\bar{1})$ plane. The following diffracting vectors were used: (a) $\bar{g} = 2\bar{2}0$; (b) $\bar{g} = 2\bar{2}0$; (c) $\bar{g} = 040$; (d) $\bar{g} = 2\bar{2}2$; (e) $\bar{g} = 400$, and (f) $\bar{g} = 3\bar{1}\bar{1}$. Beam directions were close to $[001]$ for (a), (b), (c), and (e) and were $[\bar{1}\bar{1}2]$ and $[\bar{1}\bar{1}4]$ for (d) and (f).

tion of \bar{n} , the upward-drawn normal to the loop. Then, images were obtained for $+\bar{g}$ and $-\bar{g}$ conditions while keeping $s > 0$. By noting whether the image exhibited outside or inside contrast the sense of \bar{b} was determined. When \bar{b} is in the same sense as that of the upward-drawn normal to the loop, $(\bar{n} \cdot \bar{b})$ is greater than

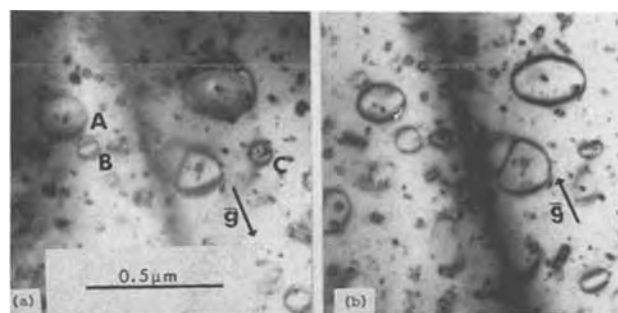


Fig. 8. Effect on loop size of tilting from $\bar{g} = 040, s > 0$ in (a) to $\bar{g} = 040, s > 0$ in (b). Loops A and C shrink. Loop B expands.

0 and the loop is interstitial in nature; if it is opposite in sense, the loop is of the vacancy type. In Fig. 8, loops A, B, and C were found by stereomicroscopy to lie on the (011) , $(0\bar{1}1)$, and $(01\bar{1})$ planes and have Burgers vectors of $\pm a/2 [011]$, $\pm a/2 [0\bar{1}1]$, and $\pm a/2 [01\bar{1}]$. In Table I the results obtained on imaging the layers with $\bar{g} = 040$ and 040 are summarized. The results indicate that the Burgers vectors are in the same upward direction as the loop normals and by definition are interstitial in nature. Similar results were obtained on other specimens annealed in the same manner.

Implants at 200°C

When the specimen was held at 200°C during the implantation no detectable amorphous layer formed. On annealing at 650°C the only defects found were "black spots," considered to be unresolved loops, and a few defects recognized as loops. The concentration of these defects was of the same order of magnitude as those for the room temperature implants. However, even after annealing at 750°C the average size of the defects was only 50-100Å in diameter as shown in Fig. 9 whereas loops above 2000Å in diameter were found in room temperature implants. A detailed analysis of the spots was not attempted. However, an estimate of the nature of the defects was made by applying a technique described by Wilkens (15). The bottom, or etched surface, of the specimen was coated with 5Å of evaporated gold so that it could be identified in stereomicrographs. Stereo pairs of micrographs were obtained using Kikuchi patterns to guide the tilting around a $\langle 220 \rangle$ axis, and to obtain accurate measurements of the tilt angle. Images of stereo pairs were obtained with a 220 reflection. A stereometer was used to measure the height of defects above the bottom surface so that those defects under 60Å in diameter lying between 0-100Å from the bottom could be selected for

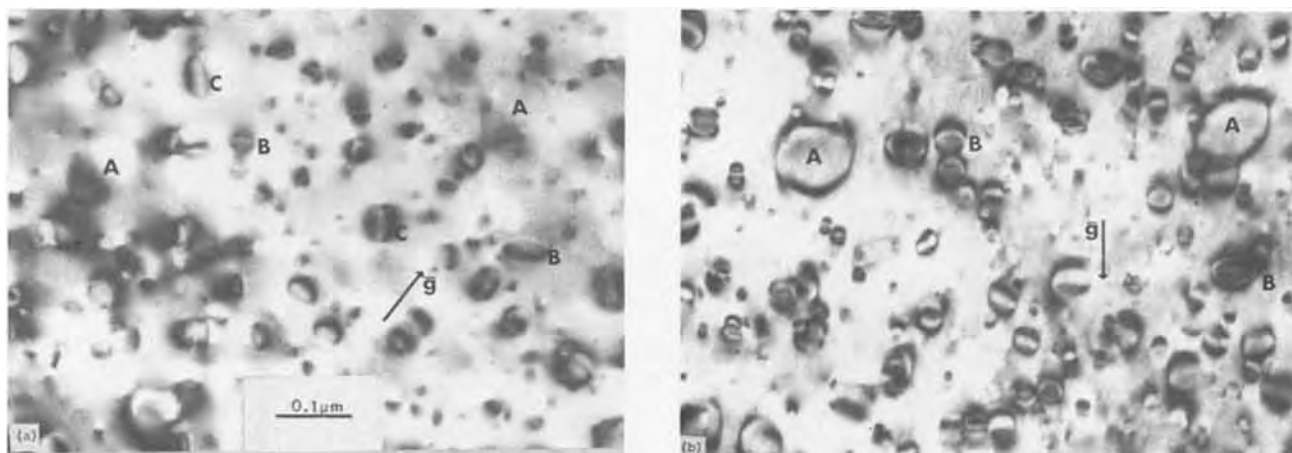


Fig. 7. Bright field micrographs of specimen annealed to 700°C showing loops on $\{110\}$ planes derived from aggregation of point defects. Diffracting vectors are: (a) $\bar{g} = 040$; and (b) $\bar{g} = 220$. Loops A, B, and C lie on the (101) , $(1\bar{1}0)$, and (110) planes, respectively.

Table I. Nature of prismatic loops on {110} planes

Loop	Loop plane	Loop contrast on changing from $\bar{g} = 040$, $s > 0$ to $\bar{g} = 040$, $s > 0$	Sign of $n \cdot b$	Loop nature
A	(011)	Inside, $(\bar{g} \cdot b)s < 0$	> 0	Interstitial
B	($\bar{0}11$)	Outside, $(\bar{g} \cdot b)s > 0$	> 0	Interstitial
C	(011)	Inside, $(\bar{g} \cdot b)s < 0$	> 0	Interstitial

observation. For these defects, the direction of black-to-white contrast on positive prints made from micrographs under bright-field conditions pointed in the same direction as the \bar{g} vector. This type of contrast is expected for interstitial defects where the distance of the defect is less than one-third of the extinction distance from the bottom of the specimen.

Effect of implantation temperature on carrier mobility.—The difference in the physical structure of the material is also reflected in the electrical properties. In some recent work with 1 MeV Si^+ implants into InP, it was shown that the electron mobility was greater by a factor of ~ 2 on implanting at 200°C rather than at room temperature (7). This applied after annealing at the temperatures ranging from 650° to 800°C. While measurements on lower energy implants are less extensive, the same appears to hold in this case as well. For $4 \times 10^{14} \text{Si}^+ \text{cm}^{-2}$, 200 keV implants at RT and 200°C, the corresponding sheet mobilities were 1130 and 860 cm^2/Vsec . This was after annealing to 750°C in a PH_3/H_2 ambient without encapsulation and where the active sheet carrier concentrations were $1.91 \times 10^{14} \text{cm}^{-2}$ and $1.96 \times 10^{14} \text{cm}^{-2}$. Other similar concentration room temperature implants at 100 and 200 keV have yielded mobilities ranging from 500 to 740 cm^2/Vsec . The peak concentrations within such layers are $\sim 10^{19} \text{cm}^{-3}$. As similarly doped epitaxial layers yield mobilities $\sim 1000 \text{cm}^2/\text{Vsec}$, it is apparent that factors other than dopant impurity scattering again limits the mobility within room temperature implanted layers at these lower energies.

Summary and Conclusions

When InP is implanted with 10^{14}SiH_2^+ at room temperature at an energy of 150 keV an amorphous layer is formed near the surface to a depth of $\sim 1850 \text{Å}$. However, similar implants into specimens at 200°C do not produce this layer.

For room temperature implants, epitaxial regrowth of the amorphous layer at $\sim 650^\circ\text{C}$ introduces shear dislocations generated at the interface between single crystal and poorly oriented material. These form closed

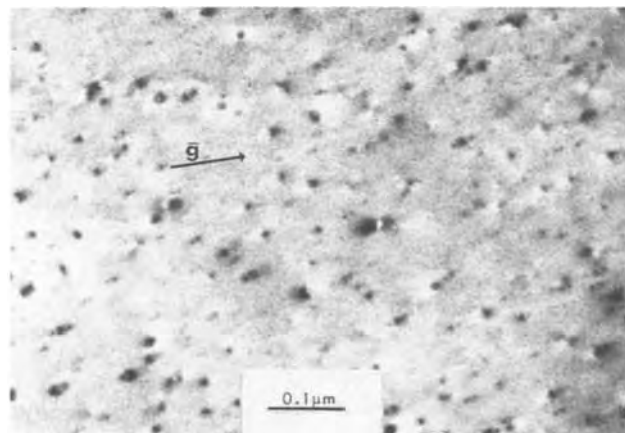


Fig. 9. Black-white contrast of defects in specimen implanted at 200° and annealed at 750°C. Defect concentration is $4 \times 10^{10}/\text{cm}^2$. Grainy background is from evaporated gold film.

loops about 500-100Å below the specimen surface. The dislocation line enclosing the loops meanders and does not lie in any particular plane. At 700°-750°C the larger loops are replaced by smaller ones, still over 500Å in diameter, lying on both {111} and {110} planes. Both prismatic and shear loops were found on the {111} planes. Interaction between two such loops results in the formation of a screw dislocation common to both loops. The Burgers vector was of the type $\bar{b} = a/2 <110>$ parallel to the (001) specimen plane. The other important defects observed first at 650° along with the shear dislocations were prismatic loops of an interstitial nature lying on {110} planes. These were mainly under 500Å in diameter and were uniformly dispersed throughout the depth of the region under examination. Their concentration was $\sim 2 \times 10^{10}/\text{cm}^2$. These loops are believed to be formed by aggregation of point defects.

The specimen implanted at 200°C did not have to go through a recrystallization stage upon postannealing. Therefore, shear dislocations, as observed in the room temperature implants, were not formed. On annealing, damage resulting from the implantation appeared as black spots, some of which could be recognized as loops. These are believed to form by aggregation of point defects. The concentration of these defects was of the same order of magnitude as the loops found in the room temperature implants. The size of the loops, even after a 750°C anneal, was only 50-100Å in diameter. These defects also appear to be interstitial in nature.

That dislocations can affect the electrical properties of semiconductors has been known for some time (16), and recent papers by Booyens, Vermaak, and Proto (17, 18), and Esquivel, Sen, and Lin (19) have discussed the electrical anisotropy of α and β dislocations in III-V compounds as they affect carrier mobility. In the present case, an increase in electrical carrier mobility by a factor ~ 1.3 was demonstrated for hot implants at 150-200 keV and, earlier, an increase by a factor of ~ 2 (7) for 1 MeV implants. From these results, we conclude that the reduction in structural damage observed for the high temperature implants may account in part for the increase in carrier mobility.

Acknowledgment

The authors are indebted to John K. Kennedy for supplying the specimens of InP, and to William D. Potter for technical assistance.

Manuscript received Dec. 11, 1979.

Any discussion of this paper will appear in a Discussion Section to be published in the June 1981 JOURNAL. All discussions for the June 1981 Discussion Section should be submitted by Feb. 1, 1981.

Publication costs of this article were assisted by the Rome Air Development Center.

REFERENCES

1. L. T. Chadderton and F. H. Eisen, *Radiat. Eff.*, **7**, 129 (1971).
2. D. J. Mazey, R. S. Nelson, and R. S. Barnes, *Philos. Mag.*, **17**, 1145 (1968).
3. S. M. Davidson and G. R. Booker, *Radiat. Eff.*, **6**, 33 (1970).
4. W.-K. Wu and J. Washburn, *J. Appl. Phys.*, **48**, 3747 (1977).
5. J. J. Comer, *Radiat. Eff.*, **36**, 57 (1978).
6. D. J. Mazey and R. S. Nelson, *ibid.*, **1**, 229 (1969).
7. D. Eirug Davies, J. J. Comer, J. P. Lorenzo, and T. G. Ryan, *J. Appl. Phys. Lett.*, **35**, 192 (1979).
8. H. Gottschalk, G. Patzer, and H. Alexander, *Phys. Status Solidi A*, **45**, 207 (1978).
9. J. J. Comer, *J. Appl. Phys.*, **50**, 6003 (1979).
10. D. Eirug Davies, W. D. Potter, and J. P. Lorenzo, *This Journal*, **125**, 1845 (1978).
11. J. P. Lorenzo, D. Eirug Davies, and T. G. Ryan, *ibid.*, **126**, 118 (1979).

12. G. R. Booker and R. Stickler, *Br. J. Appl. Phys.*, **13**, 446 (1962).
13. M. D. Matthews, *Radiat. Eff.*, **11**, 167 (1971).
14. G. W. Groves and A. Kelly, *Philos. Mag.*, **6**, 1527 (1961).
15. M. Wilkins in "Modern Diffraction and Imaging Techniques in Material Science," S. Amelinckx, R. Gevers, G. Remaut, and J. Van Landuyt, Editors, p. 233, North Holland Pub. Co., Amsterdam (1970).
16. G. H. Schwuttke, Report No. AFCRL-70-0110, Air Force Cambridge Research Laboratories (March 1970).
17. H. Booyens, J. S. Vermaak, and G. R. Proto, *J. Appl. Phys.*, **48**, 3008 (1977).
18. H. Booyens, J. S. Vermaak, and G. R. Proto, *ibid.*, **49**, 1173 (1978).
19. A. L. Esquivel, S. Sen, and W. N. Lin, *J. Appl. Phys.*, **47**, 2588 (1976).

The Phase Transition Phenomenon in Metal Phthalocyanine Crystals

M. Sakaguchi,* M. Ohta,* and T. Nozawa

Department of Applied Chemistry, Faculty of Engineering, Niigata University, Niigata, Japan

and M. Takada

Toyo Ink Manufacturing Company, Limited, Research and Development Laboratories, Itabashi, Tokyo, Japan

ABSTRACT

The study was carried out on the gas adsorption and the $\alpha \rightarrow \beta$ phase transition in metal phthalocyanine (Pc) crystals at different degrees of purity. The uptake of NH_3 , O_2 , or H_2S on CuPc crystals decreased remarkably with the degree of purification, but the uptake of HCl did not change. The $\alpha \rightarrow \beta$ phase transition of CuPc crystals was accelerated by purifying, and it was considerably affected by the ambient gases in the low purity crystal, and hardly at all affected in the high purity crystal. The $\alpha \rightarrow \beta$ phase transition of ZnPc crystals in NH_3 gas began upon decomposition of the NH_3 -ZnPc addition complex (near 220°C) which formed readily at 25°C . The results of NiPc crystals were mostly similar to that of CuPc crystals.

The phase transition phenomenon in metal phthalocyanine (Pc) crystals has been extensively investigated, since the crystals are used as organic semiconductors exhibiting different properties due to crystallographic modification (1-3).

The dependence of some properties of metal Pc crystals on impurity presence is still an open question because of the difficulty in obtaining the high purity crystals in spite of purification by combined procedures of vacuum sublimation, acid washing, and extraction by organic solvents (3-7). Recently, Kiryukhin *et al.* (6) and Sadaoka *et al.* (7) reported the dependence of electrical conductivity of CuPc crystals on crystal purity. Also Sakaguchi *et al.* (8) observed the $\alpha \rightarrow \beta$ phase transition in CuPc crystals to be appreciably affected by chemisorption of ambient gases on the crystal.

In the present work, we report a study on gas adsorption and the $\alpha \rightarrow \beta$ phase transition in CuPc crystals at different degrees of purity. Similar examinations are reported for ZnPc and NiPc crystals.

Experimental

Materials.—Commercial β -CuPc crystals¹ (supplied by Toyo Ink Manufacturing Company, Limited) were pretreated by washing with sulfuric acid [2 weight percent (w/o)] and NaOH aqueous solution (2 w/o), and followed by washing with pure water (deionized and distilled), then the crystals were vacuum dried and ground; this is our source sample A. This source sample A was further purified by extraction with organic solvents and by vacuum sublimation; the details

* Electrochemical Society Active Member.

Key words: phase transformation, phthalocyanine, adsorption, semiconductor.

¹IR spectroscopic analysis indicated that commercial β -CuPc crystals contained as impurities the synthesis raw materials and by-products.

are given in Table I. Sample B (α -CuPc) was prepared by recrystallization from concentrated sulfuric acid solution using source sample A followed by washing successively in pure water, NH_4OH (2 w/o), and pure water; then the residue was vacuum dried for 2 hr at 110°C and ground (200 mesh through). Sample C was purified by Soxhlet extraction with methyl alcohol (MeOH). Samples D, E, and F were purified by repeated consecutive Soxhlet extractions with dimethylformamide (DMF) and MeOH, and sublimation *in vacuo* (10^{-3} mm Hg at 480°C); each sample was further subjected to similar recrystallization process as for sample B. α -ZnPc and α -NiPc crystals (supplied by Eastman Kodak Company) were prepared by a similar pretreatment as sample F. In the highest purity sample F, the high pure α -ZnPc, and the high pure α -NiPc, no organic impurity was detected by gas chromatographic and liquid chromatographic analyses, and the total amount of the foreign metals did not exceed 15 ppm according to atomic absorption spectrometry.

The reagents (DMF, MeOH, sulfuric acid, aqueous ammonia) used in these experiments were guaranteed reagent grade (supplied by Junsei Chemical Company, Limited).

The gases used for the adsorption and the heating atmosphere of phase transition reaction were prepared as follows: high purity He was further purified by passage through a glass tube containing the molecular sieve 5A at -196°C ; high purity HCl, H_2S , and NH_3 were further purified by vacuum distillation using both Dry Ice-alcohol and liquid O_2 baths; O_2 was prepared by evaporation of pure liquid O_2 .

Apparatus.—The apparatus used for heat-treatment and adsorption measurements in various ambient gases and BET surface area measurements was of the static

Table I. Purification of CuPc crystal

Sample*	Treatment time (hr)									
	Extraction 1		Vacuum sublim. 1	Vacuum sublim. 2	Extraction 2		Vacuum sublim. 3	Extraction 3		
	DMF	MeOH			DMF	MeOH		DMF	MeOH	
B	—	—	—	—	—	—	—	—	—	
C	—	10	—	—	—	—	—	—	—	
D	5	1.3	7	7	5	1.3	—	—	—	
E	10	2.5	30	5	10	2.5	5	10	2.5	
F	20	5	30	10	20	5	10	20	5	

* All samples are transformed into α -form crystal.

type constructed of borosilicate glass. The system dead space was ~ 100 ml. The sample chamber was protected from mercury and grease contamination by presence of cold trap (0°C).

Procedure.—(a) *Gas adsorption.*—The weighed sample (2.0g), after preliminary evacuation at 25°C for 1 hr, was further evacuated under high vacuum at 250°C for 1 hr. The adsorbate gas (initial pressure: 100 mm Hg, i.e., $5.2 \times 10^2 \mu\text{mole}$) was then admitted to the sample. The surface area of each sample was determined by BET method using N_2 as adsorbing gas at -196°C . The uptake of gases (NH_3 , O_2 , H_2S , HCl) by all metal Pc crystals was irreversible under the present experimental conditions, i.e., these gases were sorbed on the crystals.

(b) *Phase transition.*—The sample (1.0g) was heated at $200^\circ \sim 300^\circ\text{C}$ for 1 hr in various gases (1 atm) after evacuating under high vacuum for 1 hr at 25°C . The time interval required to reach the heating temperature was 20 min in all cases. After heating the sample was rapidly cooled at the rate of about $50^\circ\text{C}/\text{min}$. The x-ray powder diffraction pattern of each heated sample was obtained using $\text{Cu}(\text{Ni})\text{K}\alpha$ radiation, and the β -form content was determined by the method reported by Suito *et al.* (9). The rate of the $\alpha \rightarrow \beta$ phase transition of metal Pc crystals during heating in various gases was determined by using an apparatus which enabled simultaneous measurement of high temperature x-ray diffraction and differential thermal analysis (DTA) (Rigaku Denki Company, Limited).

Results

The sorption characteristics of various gases on sample B are shown in Fig. 1. The lower initial uptake of O_2 is in striking contrast to HCl and NH_3 sorption.

The sorption characteristics of NH_3 on each α -CuPc crystal (samples B \sim F) of varying purity are shown in Fig. 2. The uptake of NH_3 decreased considerably with the purity.

The sorption characteristics of various gases on the highest purity crystal, sample F, are shown in Fig. 3. The uptake of HCl with time is in striking contrast to NH_3 , H_2S , O_2 .

The effect of the ambient gases on the $\alpha \rightarrow \beta$ phase transition in samples B and F at different temperatures is given in Fig. 4. The noticeable effect of the ambient gas on the transition is evident for sample B whereas for the highest purity sample F the effect of the gas is barely discernible. It was reported by Takahashi (10) that the transition temperature in air was at $250^\circ \sim 300^\circ\text{C}$. It is noteworthy that in the most pure crystal, the phase transition was least affected by the sorption of HCl , nevertheless the crystal sorbed HCl gas readily.

The ambient gas phase transition effect on samples B and F in NH_3 , O_2 , and He was examined in more detail² by using simultaneous high temperature x-ray diffraction and DTA as shown in Fig. 5 and 6. The temperature for $\alpha \rightarrow \beta$ conversion (intersection of α and β line intensities) in sample B decreases in the

² HCl and H_2S gases were not included because of corrosive action on instrument.

order $\text{O}_2 > \text{He} > \text{NH}_3$ whereas no such order is recognizable in sample F; these results are consistent with Fig. 4. In the case of heating sample F in O_2 , the diffraction peaks characteristic of β -form crystals disappeared near 300°C with the simultaneous increase in exothermicity on the DTA curve; these results are in direct contrast to sample B heated in O_2 . We interpret these results to indicate that sample F is more reactive

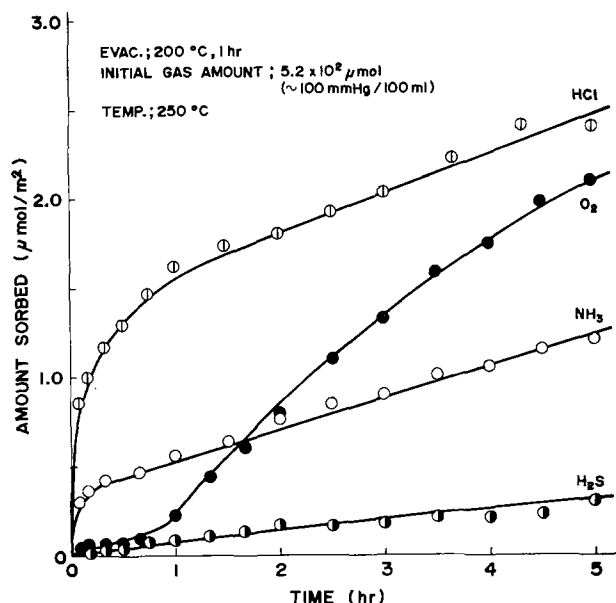


Fig. 1. Sorption of various gases on sample B

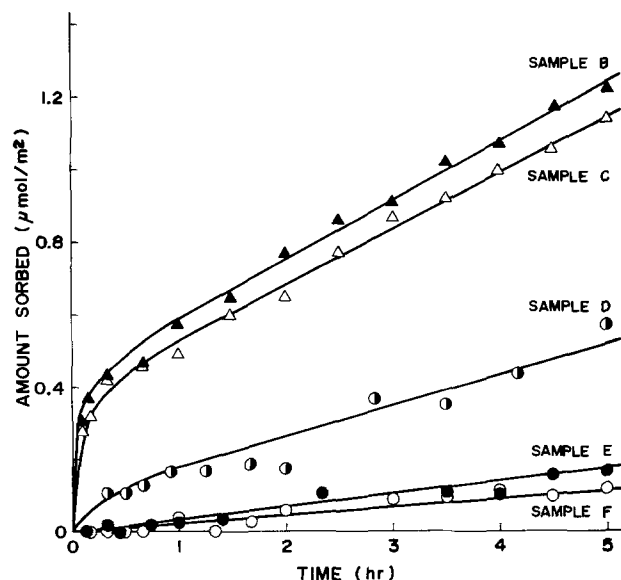


Fig. 2. Sorption of NH_3 on each α -CuPc crystal of varying purity (the reaction condition is the same as Fig. 1).

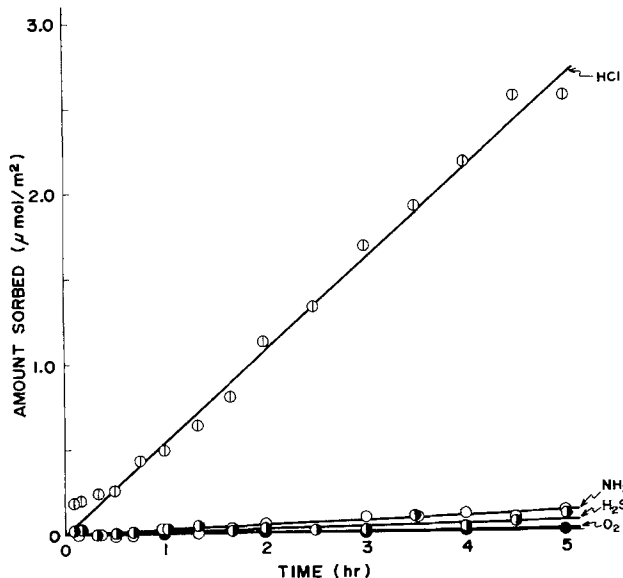


Fig. 3. Sorption of various gases on sample F (the reaction condition is the same as Fig. 1).

than sample B in an oxidizing atmosphere at 300°C. For comparison purposes, we examined two other commercially available CuPc crystals³ (Eastman Kodak Company, Tokyo Kasei Industrial Company) and we obtained similar results.

Parallel experiments carried out on the high purity α -ZnPc and α -NiPc crystals obtained using the purification procedure detailed for sample F gave the results shown in Fig. 7. In view of the high sorption for NH₃ on α -ZnPc crystals it was desirable to extend the study of gas sorption (NH₃, O₂, He) on α -ZnPc crystals by simultaneous high temperature x-ray diffraction and DTA; the curves are presented in Fig. 8. He and O₂ presence show no effect on the characteristic

³The data for the impurity contained in these commercial CuPc crystals was similar to that of the CuPc crystal supplied by Toyo Ink Manufacturing Company, Limited.

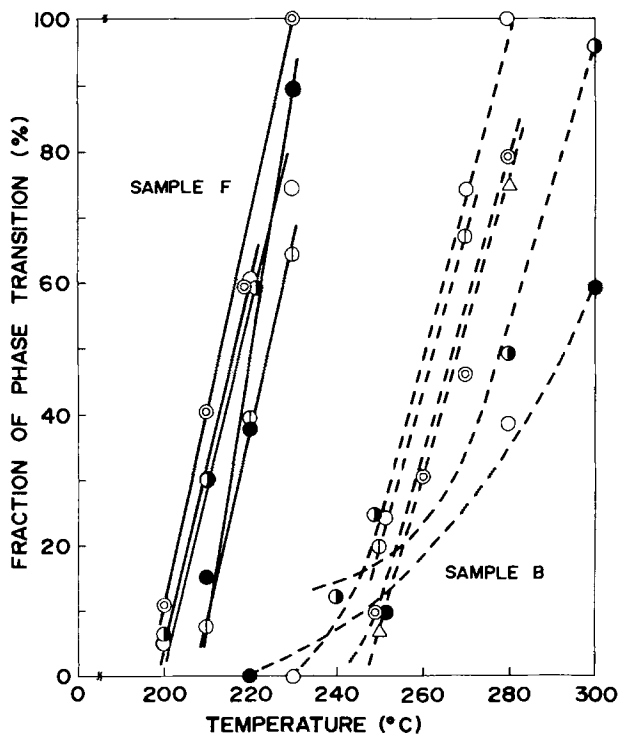


Fig. 4. The $\alpha \rightarrow \beta$ phase transition of CuPc crystals heated for 1 hr at various temperatures: \circ , in NH₃; \bullet , in O₂; \circ , in H₂S; \circ , in HCl; \bullet , in He; Δ , in vacuo.

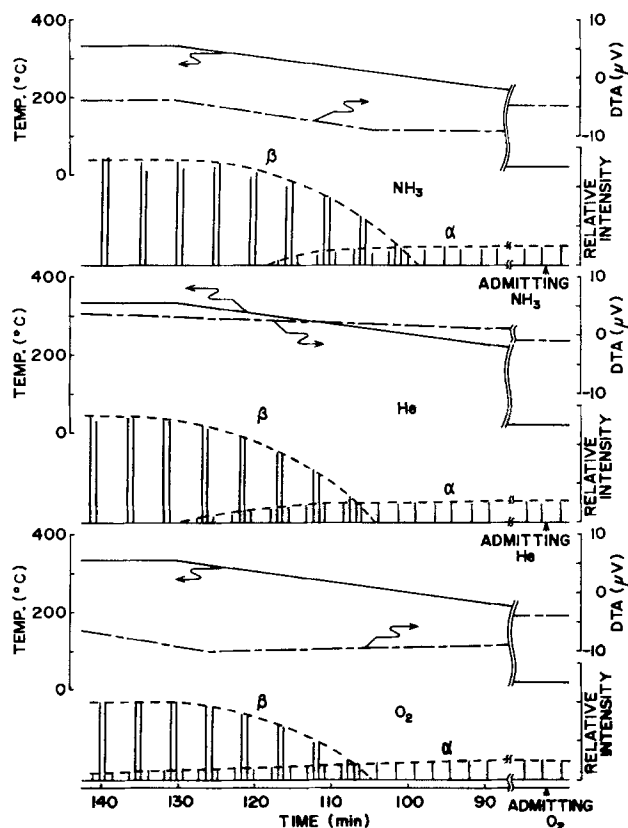


Fig. 5. The $\alpha \rightarrow \beta$ phase transition of sample B by high temperature x-ray diffractometry-differential thermal analysis in various ambient gases (flow of 100 ml/min) at 2θ region of 23.0° ~ 27.0°, and at a heating rate of 2.5°C/min.

peak height of α -ZnPc crystals up to 220°C at which temperature a slight rise in diffraction peak intensity and weak endotherm is observed. On the other hand, the presence of NH₃ on α -ZnPc affects an immediate disappearance of α -ZnPc diffraction peak and appearance of a high diffraction peak at a lower angle with a

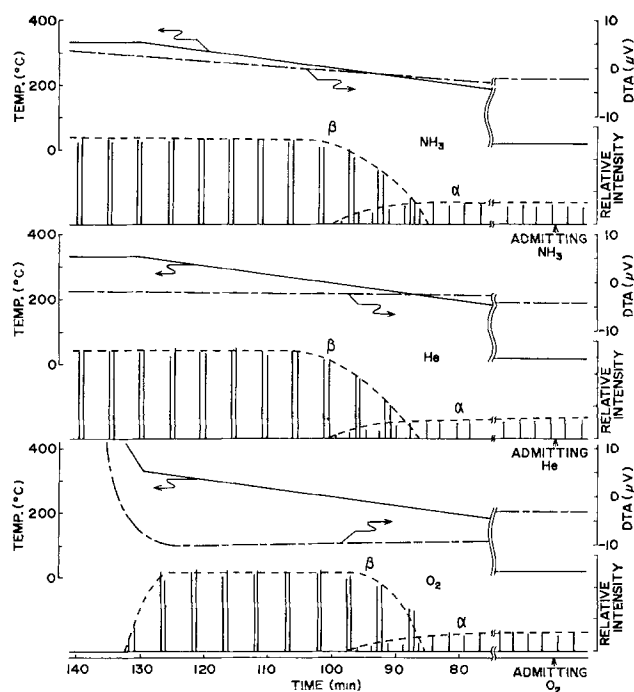


Fig. 6. The $\alpha \rightarrow \beta$ phase transition of sample F by high temperature x-ray diffractometry-differential thermal analysis (the reaction condition is the same as Fig. 5).

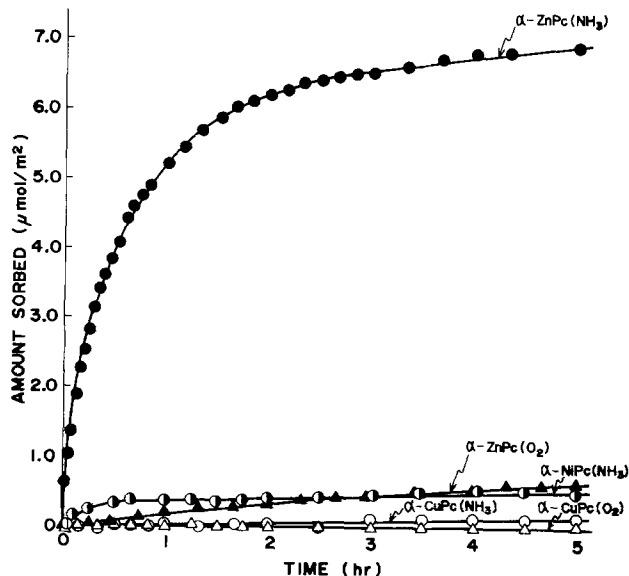


Fig. 7. Sorption of NH_3 or O_2 on high purity α -metal Pc crystals (the reaction condition is the same as Fig. 1).

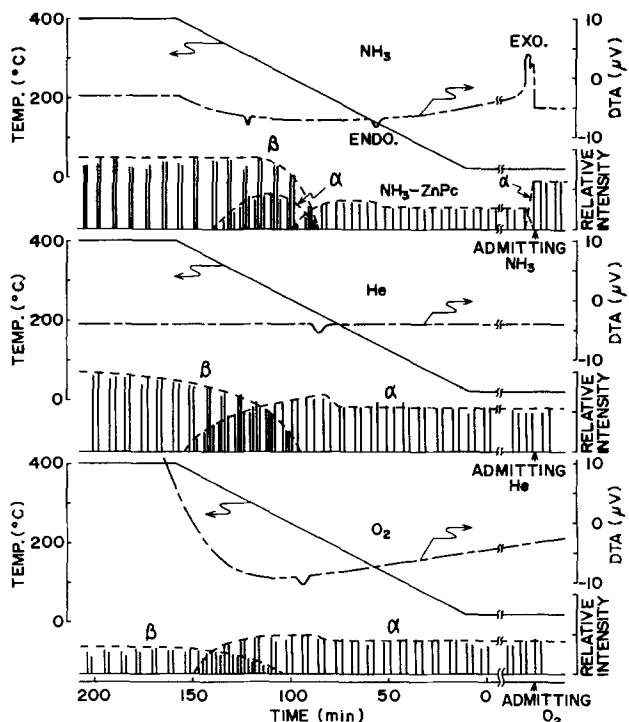


Fig. 8. The $\alpha \rightarrow \beta$ phase transition of high purity ZnPC crystals by high temperature x-ray diffractometry-differential thermal analysis (the reaction condition is the same as Fig. 5).

simultaneous exothermic effect on the DTA curve. The characteristic features of the assumed NH_3 -ZnPC addition complex disappeared at 220°C followed by the reappearance of the α -ZnPC peak and the onset of $\alpha \rightarrow \beta$ phase transition which is almost complete at 350°C . The endotherm at 320°C is attributed to a recrystallization or sintering effect. The effects of ambient gases on the initial and final temperatures of the phase transition in α -ZnPC crystals showed a similar trend to sample F.

The results of the phase transition study on the α -NiPC crystals using the same method did not follow the pattern of behavior in α -ZnPC crystals, but were similar to that of the highest purity sample F.

Discussion

The impurities present in CuPC crystals are interpreted to be bound as a complex or some stable configuration because the impurities resisted extraction by normal procedures (cf. Table I and Fig. 2). As shown in Fig. 2, the high purity CuPC crystals did not exhibit the sorption capacity for NH_3 , but the low purity CuPC crystal complex showed an increased ability for gas sorption. Steinbach *et al.* (11) pointed out that the enhanced gas sorption ability of the complex must result from the change of electron density of the Cu atom in the CuPC molecule due to the strong interaction of π electron between the CuPC molecule and incorporated impurities.

In the case of O_2 sorption, the slight initial increase of O_2 uptake reflects a net effect resulting from generation of volatile products from the oxidized surface, i.e., surface cleansing action. The subsequent O_2 uptake is enhanced by surface oxide layer.

Because of its highly ionic polar character HCl would be expected to be sorbed not only on the Cu atom but also on the edge benzene group in CuPC molecule as shown by Shigemitsu (13). Accordingly, the sorption ability of HCl should not be affected by the purity of the crystals (Fig. 3).

The phase transition in sample B was promoted by NH_3 or HCl, but inhibited by O_2 or H_2S exhibited an inhibiting effect in comparison with He or vacuum. These results suggest that the sorbed gas affects the intermolecular force within the CuPC crystal. That is, the intermolecular force of CuPC crystals would be weakened by the sorption of NH_3 or HCl and strengthened by the sorption of O_2 or H_2S . Accordingly, the rate of phase transition with negligible gas sorption on sample F, except for HCl was similar in all ambient gases (Fig. 4); HCl would not be expected to be as effective on the phase transition of sample F even if it were taken up by sample F. Furthermore, the phase transition in highest purity sample F occurred at lower temperatures than in sample B since the stabilizing effect due to bound impurities in the CuPC crystal was absent. The negligible effect of ambient gas on the phase transition temperature for sample F, is consistent with this fact.

The result that the high sorption of NH_3 was instantaneous on the high purity α -ZnPC crystal is attributed to the formation of NH_3 -ZnPC complex (Fig. 8). This interpretation is supported by x-ray diffraction pattern and DTA thermal peaks along with the parallel formation of the n-hexylamine complex of ZnPC crystal as reported by Kobayashi *et al.* (14).

The basis for NH_3 -metal Pc complex formation in ZnPC crystal only might be found in the character of divalent zinc ion to adopt a tetrahedral configuration by use of sp^3 hybrid orbitals, but the details must await further work.

Acknowledgment

The authors are grateful to Professor E. A. Secco of St. Francis Xavier University for helpful suggestions and Mr. K. Uematsu of Niigata University for his assistance in x-ray analysis work.

Manuscript submitted Aug. 20, 1979; revised manuscript received March 4, 1980.

Any discussion of this paper will appear in a Discussion Section to be published in the June 1981 JOURNAL. All discussions for the June 1981 Discussion Section should be submitted by Feb. 1, 1981.

Publication costs of this article were assisted by Niigata University.

REFERENCES

1. K. Wihksne and A. E. Newkirk, *J. Chem. Phys.*, **34**, 2184 (1961).
2. Y. Sakai, Y. Sadaoka, and H. Yokouchi, *Bull. Chem. Soc. Jpn.*, **47**, 1886 (1974).

3. E. Suito and N. Uyeda, *Kolloid Z.*, **193**, 97 (1963).
4. O. K. Krutoyarova, M. I. Al'yanov, Ya. I. Yashin, V. F. Vorodkin, V. A. Benderskii, and Yu. I. Khoinov, *Izv. Vyssh. Uchebn. Zaved., Khim. Khim. Tekhnol.*, **14**, 1379 (1971).
5. J. Luczak and J. Budzisy, *Barwniki-Srodki Pomocnicze*, **19**, 268 (1975).
6. I. A. Kiryukhin, K. N. Lobanova, Yu. A. Popov, Yu. Kh. Shaulov, and V. A. Benderskii, *Zh. Fiz. Khim.*, **50**, 649 (1976).
7. Y. Sadaoka and Y. Sakai, *J. Chem. Soc., Faraday Trans. 2*, **72**, 379 (1976).
8. M. Sakaguchi, T. Hirabayashi, and T. Koyama, *Nippon Kagaku Kaishi*, **1975**, 1428.
9. E. Suito and N. Uyeda, *Nippon Kagaku Zasshi*, **86**, 969 (1965).
10. H. Takahashi, *Shikizai*, **36**, 550 (1963).
11. F. Steinbach, H. H. Schmidt, and M. Zobel, in "Proc. Int. Symp. on Relations between Heterogeneous and Homogeneous Catalytic Phenomena," Brussels, 1974, p. 417, Elsevier, Amsterdam (1975).
12. T. Sekiguchi, E. Yamazaki, and Y. Bansyo, *Kogyo Kagaku Zasshi*, **70**, 503 (1967).
13. M. Shigemitsu, *Bull. Chem. Soc. Jpn.*, **32**, 607 (1959).
14. T. Kobayashi, T. Ashida, N. Uyeda, E. Suito, and M. Kakudo, *Bull. Chem. Soc. Jpn.*, **44**, 2095 (1971).

The Nucleation of CVD Silicon on SiO₂ and Si₃N₄ Substrates

II. The SiH₂Cl₂-H₂-N₂ System

W. A. P. Claassen and J. Bloem*

Philips Research Laboratories, Eindhoven, The Netherlands

ABSTRACT

A description is given of nucleation experiments with silicon on SiO₂ and Si₃N₄ substrates in the SiH₂Cl₂-H₂-N₂ system, performed at temperatures between 800° and 1100°C. The saturation cluster densities were determined for different mixtures as a function of temperature and could be varied between 10⁵-10¹⁰ cm⁻². A reaction scheme is proposed in which silicon adatoms reach a steady-state concentration before nucleation occurs. Comparison of the experimental data with existing nucleation theories gives approximate values for the size of the critical cluster. A strong adsorption of atomic hydrogen, especially on SiO₂ surfaces, may explain the substantial differences in nucleation on SiO₂ and Si₃N₄ surfaces at temperatures below 1000°C.

Polycrystalline silicon layers are finding extensive application in the fabrication of integrated circuits, e.g., as gate material in MOS (metal-oxide-silicon) field effect transistors (1). For this purpose CVD with SiH₄ as input gas is most widely used, but chlorosilanes too, such as SiHCl₃ and SiCl₄ and recently SiH₂Cl₂, are becoming increasingly important as starting materials for the deposition of silicon layers (2). Reports of nucleation experiments with silicon on amorphous, polycrystalline, and monocrystalline substrates are relatively scarce. The present authors discussed such experiments in a previous paper dealing with nucleation of silicon on SiO₂ and Si₃N₄ substrates in the SiH₄-HCl-H₂ system (3). The present paper deals with nucleation in the SiH₂Cl₂-H₂-N₂ system on SiO₂ and Si₃N₄ substrates. The experimental results are described and compared with existing nucleation theories.

Experimental

The nucleation experiments were performed in a horizontal rf heated reactor, consisting of a rectangular air-cooled fused silica tube, provided with a pyrographite-coated carbon susceptor covered with a thin layer of silicon. Nucleation of silicon was performed on silicon slices (wafer 0.5 in. square) covered with an amorphous 1500Å thick LP-CVD SiO₂ or Si₃N₄ layer. The effective cross section of the reactor tube was about 11 cm². The gas system was provided with automatic mass flow controllers for the hydrogen and nitrogen carrier gas and the SiH₂Cl₂ source. Some experiments were performed with SiHCl₃, in which case the input concentrations were controlled by passing a

flow of hydrogen, monitored by means of an automatic mass flow controller, through a bubbler filled with SiHCl₃ at a constant temperature. The carrier gas was purified; both water vapor and oxygen concentrations were below 1 ppm. The slices were cleaned prior to a deposition experiment in an H₂SO₄-H₂O₂ mixture followed by rinsing in water of ultrahigh purity. After spin drying, the slices were further cleaned in the reactor tube with 0.2 volume percent (v/o) HCl in hydrogen at 1000°C for 5 min. After this, the reactor was purged by a hydrogen flow, while the substrate temperature was brought to the desired nucleation temperature. Prior to deposition the reactor was flushed with the particular H₂-N₂ mixture, which is also used during the nucleation experiment for about 5 min. During the nucleation experiment the H₂-N₂ mixture loaded with SiH₂Cl₂ was passed over the slices. In order to obtain stable gas flow conditions a room temperature gas velocity of about 60 cm/sec was chosen. The temperature of the slices was measured with an optical pyrometer focused on the surface of an uncoated silicon slice, and the values were corrected for the emissivity of silicon and the absorption and reflection of the system. After termination of the experiment the substrates were cooled without SiH₂Cl₂ addition and inspected at room temperature. The density of the nuclei formed was determined from either SEM or TEM photomicrographs.

Experimental Results

A series of short depositions was carried out with different concentrations of SiH₂Cl₂ in H₂, N₂, or mixtures of H₂ and N₂ at temperatures between 800° and 1100°C. As in the SiH₄-HCl-H₂ system (3), it was

* Electrochemical Society Active Member.
Key words: polysilicon, nucleation, CVD.

found that after an incubation period the density of stable clusters very quickly reached a saturation density of nuclei with respect to exposure time. After this period the clusters merely increased in size until coalescence occurred. The existing clusters showed a very narrow size distribution, from which it may be concluded that the clusters are formed in a very short period of time.

Nucleation on an SiO₂ substrate.—The experimentally observed saturation densities of Si clusters in the SiH₂Cl₂-H₂-N₂ system have been collected in Table I. In Fig. 1 the saturation densities of silicon clusters on SiO₂ substrates at 1000°C are plotted for 0.1 v/o SiH₂Cl₂ for some H₂-N₂ mixtures, the latter expressed as $p_{H_2}/(p_{H_2} + p_{N_2})$. The highest saturation density can be observed for pure nitrogen, while the introduction of hydrogen strongly reduces the saturation density of Si clusters on SiO₂ substrates. Figure 2 gives a plot of the saturation density of nuclei vs. the reciprocal temperature in the temperature region 925°-1100°C (with the exception of nitrogen, where results at 800°C are also given). For nitrogen the formation process is barely a function of temperature. If hydrogen is added to the mixture the temperature dependence of the formation process increases with increasing hydrogen concentrations. Figure 3 shows photomicrographs of nucleations on SiO₂ substrates at 1000°C, for an input concentration of 0.1 v/o SiH₂Cl₂ in pure H₂ (a) and pure N₂ (b).

It is shown below that the experimental data on saturation densities of nuclei (N_s) on an SiO₂ substrate at 1100°C as a function of gas phase composition can be described by

$$N_s = \frac{A p_{SiH_2Cl_2}(b)}{1 + B p_{H_2}^{1/2}} \quad [1]$$

where $p_{SiH_2Cl_2}(b)$ is the input concentration of SiH₂Cl₂ and A and B are constants. For $B p_{H_2}^{1/2} > 1$ a plot of $\log [N_s/p_{SiH_2Cl_2}(b)]$ vs. $\log (p_{H_2})$ should show a linear dependence, as indicated in Fig. 4. For temperatures below 1100°C the tangent in Fig. 4 differs from $1/2$ for high hydrogen pressures. In this figure the points at p_{H_2} around 10^{-3} represent the saturation densities of nuclei for the SiH₂Cl₂-N₂ system (no hydrogen added). As described later, in a nitrogen medium SiH₂Cl₂ decomposes almost completely in the gas phase

to SiCl₂ and H₂. This means that an input concentration of 0.1 v/o SiH₂Cl₂ gives $p_{H_2} \approx 10^{-3}$ bar.

Nucleation on an Si₃N₄ substrate: difference compared with an SiO₂ substrate.—Table II gives the experimental data for the saturation densities of stable clusters on Si₃N₄ substrates in the SiH₂Cl₂-H₂-N₂ system. Figure 1 also shows saturation densities of silicon clusters for Si₃N₄ substrates as a function of $p_{H_2}/(p_{H_2} + p_{N_2})$ at 1000°C. The difference between SiO₂ and Si₃N₄ substrates is remarkable. Introduction of hydrogen to the system reduces the saturation density of nuclei for the Si₃N₄ substrate, but for the SiO₂ substrate the variation is much stronger. In Fig. 5 saturation densities of nuclei on Si₃N₄ substrates are given for 0.1 v/o SiH₂Cl₂ in hydrogen and nitrogen as a function of temperature. As for the SiO₂ system (Fig. 2) the experiments in hydrogen give the lowest saturation density of nuclei and the strongest temperature dependence of the formation process. It appears that if the hydrogen content is very low there is hardly any difference between an SiO₂ and an Si₃N₄ substrate. The experimentally found expression for the saturation density of stable clusters (Eq. [1]) as a function of temperature and gas phase composition could also be used for Si₃N₄ substrates. In Fig. 6 $\log (N_s/p_{SiH_2Cl_2})$ vs. $\log (p_{H_2})$ is plotted at 1000°C for Si on Si₃N₄, giving a linear dependence between the two parameters. Further it can be observed that the tangent in this figure is smaller than $1/2$, indicating that the assumption $B p_{H_2}^{1/2} > 1$ is not acceptable in this case.

Nucleation of Si on SiO₂ and Si₃N₄ substrates: comparison of the SiH₂Cl₂-H₂ system with other silicon-containing compounds in hydrogen.—Figures 7 and 8 give saturation densities of silicon clusters for SiO₂ and Si₃N₄ substrates, respectively, as a function of temperature for SiH₄ (3), SiH₂Cl₂, and SiHCl₃ (all concentrations about 0.1 v/o) in hydrogen as a carrier gas. The difference in the saturation nucleus density between SiH₄ and SiH₂Cl₂ as the silicon-containing compounds for both substrates is remarkable. The saturation density of nuclei in the SiH₄-H₂ system increases with decreasing temperatures, whereas for the other systems the opposite occurs. On SiO₂ substrates SiHCl₃ behaves in much the same way as SiH₂Cl₂, whereas on Si₃N₄ substrates this is only true at high temperatures (Fig. 8).

Table I. Saturation nucleus density (cm⁻²) for the SiH₂Cl₂-H₂-N₂ system on SiO₂ substrates between 800° and 1100°C. t is the exposure time.

Partial pressure (bar)			Temperature (°C)									
			1100		1000		925		900		800	
$p_{SiH_2Cl_2}$	p_{H_2}	p_{N_2}	t (sec)	N_s (cm ⁻²)	t (sec)	N_s (cm ⁻²)	t (sec)	N_s (cm ⁻²)	t (sec)	N_s (cm ⁻²)	t (sec)	N_s (cm ⁻²)
1×10^{-3}	1	—	10	4×10^8	10	5×10^7	120	8×10^6	—	—	—	—
2×10^{-3}	1	—	3	9×10^8	5	1.1×10^8	15	2.5×10^7	—	—	—	—
4×10^{-3}	1	—	—	—	5	1.8×10^8	15	5×10^7	—	—	—	—
1×10^{-3}	0.76	0.24	—	—	5	7×10^7	—	—	—	—	—	—
1×10^{-3}	0.44	0.56	—	—	5	4×10^8	—	—	—	—	—	—
1×10^{-3}	0.18	0.82	3	1.4×10^9	5	6×10^8	15	4×10^8	—	—	—	—
1×10^{-3}	0.03	0.97	3	4×10^9	5	3×10^9	15	2×10^9	—	—	—	—
2×10^{-4}	—	1	—	—	10	4×10^9	—	—	—	—	—	—
5×10^{-4}	—	1	5	1.1×10^{10}	5	1.1×10^{10}	30	1.2×10^{10}	—	—	—	—
1×10^{-3}	—	1	3	1.2×10^{10}	5	1.5×10^{10}	—	—	15	1.3×10^{10}	60	1.7×10^{10}

Table II. Saturation nucleus density (cm⁻²) for the SiH₂Cl₂-H₂-N₂ system on Si₃N₄ substrates between 800° and 1100°C. t is the exposure time.

Partial pressure (bar)			Temperature (°C)							
			1100		1000		900		800	
$p_{SiH_2Cl_2}$	p_{H_2}	p_{N_2}	t (sec)	N_s (cm ⁻²)	t (sec)	N_s (cm ⁻²)	t (sec)	N_s (cm ⁻²)	t (sec)	N_s (cm ⁻²)
1×10^{-3}	1	—	5	6×10^9	10	4×10^9	15	1.4×10^9	120	7×10^8
1×10^{-3}	0.18	0.82	—	—	5	4×10^9	—	—	—	—
1×10^{-3}	0.03	0.97	—	—	5	7×10^9	—	—	—	—
5×10^{-4}	—	1	5	1.1×10^{10}	5	1.1×10^{10}	—	—	—	—
1×10^{-3}	—	1	3	1.1×10^{10}	5	1.2×10^{10}	15	1.6×10^{10}	60	1.7×10^{10}

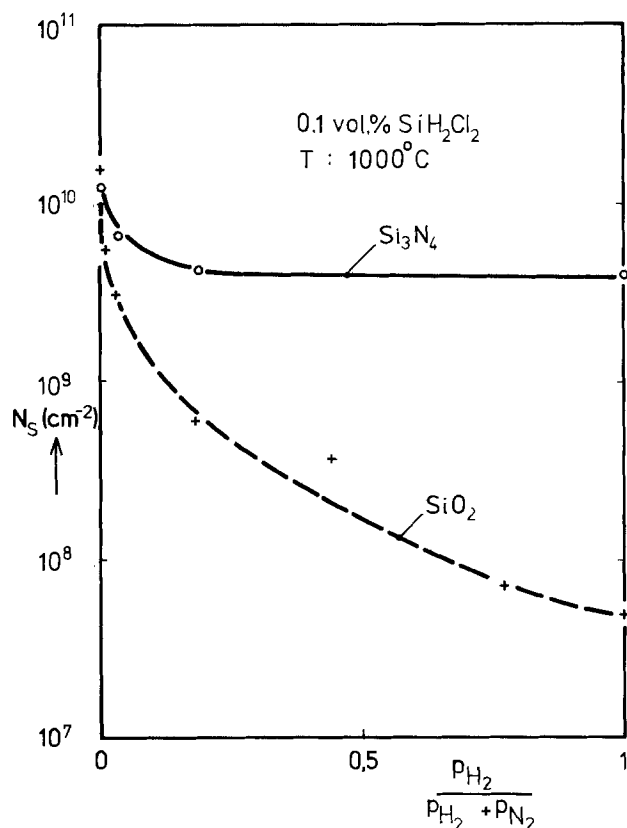


Fig. 1. The saturation nucleus density for some H_2 - N_2 mixtures and 0.1 v/o SiH_2Cl_2 on SiO_2 and Si_3N_4 substrates at $1000^\circ C$.

It was observed that the growth rate of silicon on silicon for a mixture of 0.1 v/o SiH_4 and 0.2 v/o HCl is almost equal to that of 0.1 v/o SiH_2Cl_2 , both systems having hydrogen as a carrier gas and a temperature of $1000^\circ C$ (4). It is therefore interesting to compare the saturation densities of nuclei on SiO_2 and Si_3N_4 substrates in the SiH_2Cl_2 - H_2 system with the results of nucleation experiments in the SiH_4 - HCl - H_2 system. In Fig. 9 saturation densities of silicon clusters are given for SiO_2 and Si_3N_4 substrates as a function of temperature for 0.1 v/o SiH_2Cl_2 and a mixture of 0.1 v/o SiH_4 and 0.2 v/o HCl (4), both systems in a hy-

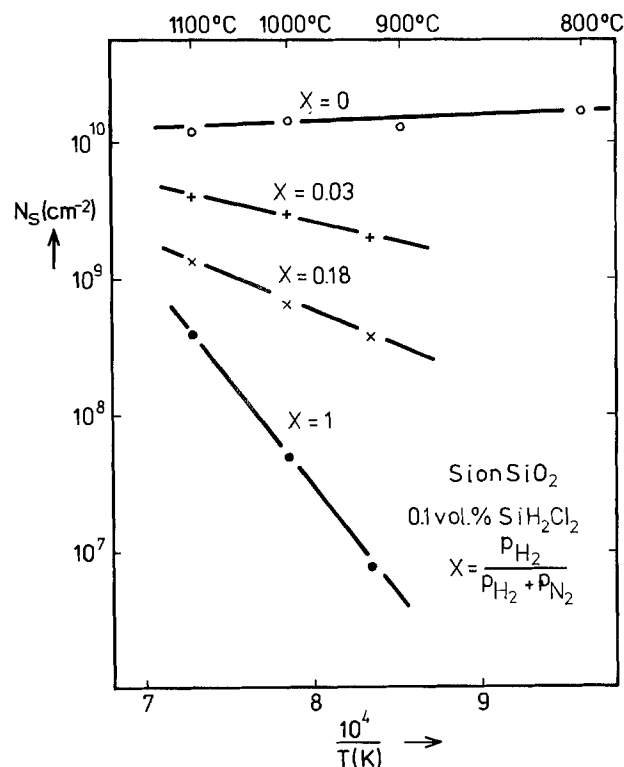


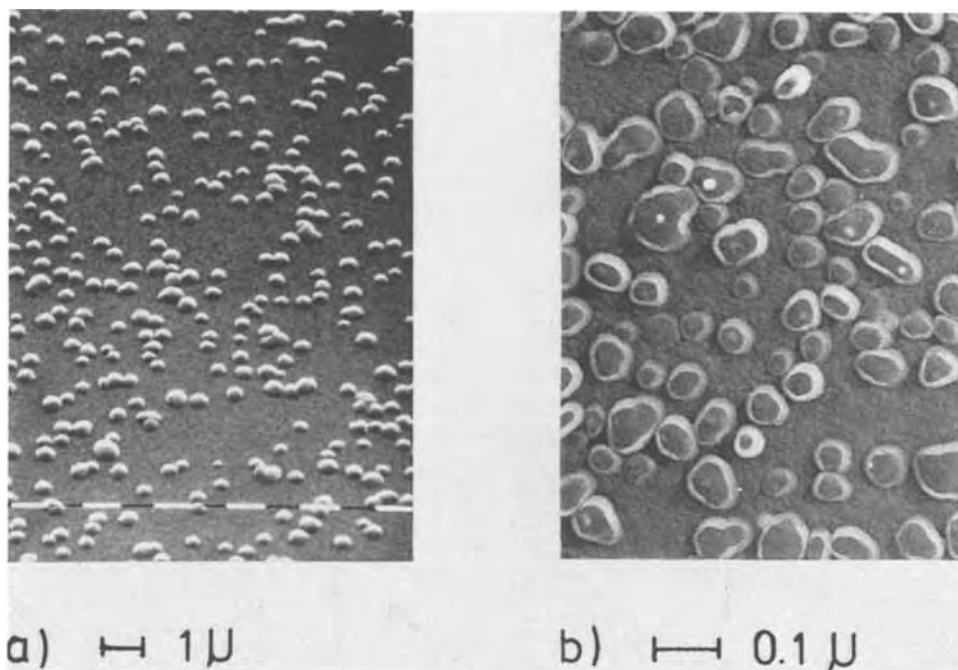
Fig. 2. The saturation nucleus density as a function of temperature on SiO_2 substrates for some H_2 - N_2 mixtures and 0.1 v/o SiH_2Cl_2 .

drogen medium. It can be observed on both substrates that for the SiH_2Cl_2 - H_2 mixture the saturation density of nuclei decreases with decreasing temperature, whereas for the SiH_4 - HCl - H_2 mixture the opposite occurs.

Discussion

Adatom concentration and surface coverage.—In order to arrive at an expression describing the adatom concentration of silicon on the substrate it would be very helpful to have thermochemical data of the Si - H - N - Cl system. With this in view thermochemical data of the Si - H - Cl and Si - N - Cl systems have been calculated for $Cl/H_2 = 10^{-3}$ and $Cl/N_2 = 10^{-3}$, respec-

Fig. 3. Photomicrographs of the nucleus density for 0.1 v/o SiH_2Cl_2 in pure H_2 (a) and pure N_2 (b).



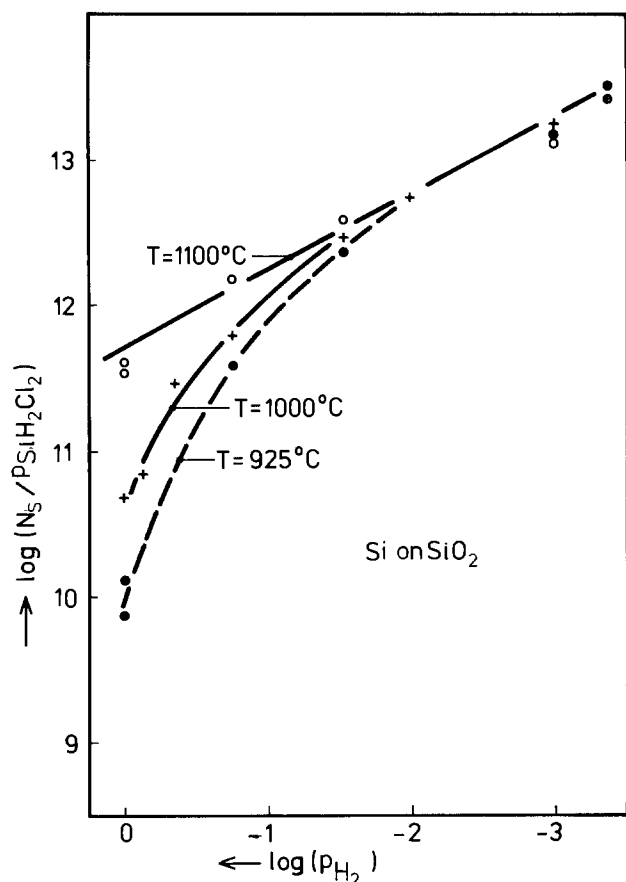


Fig. 4. The saturation nucleus density at 925°-1000°C and 1100°C for different mixtures of SiH_2Cl_2 - H_2 - N_2 , expressed as $\log(N_s/p_{\text{SiH}_2\text{Cl}_2})$ vs. $\log(p_{\text{H}_2})$, on SiO_2 substrates.

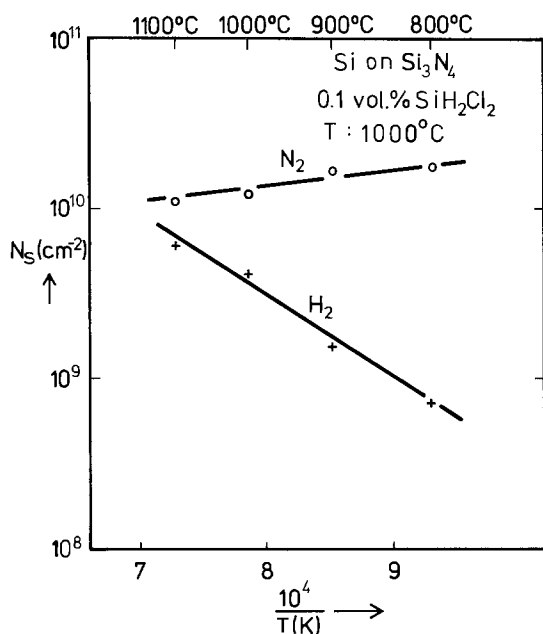


Fig. 5. The saturation nucleus density on Si_3N_4 substrates for 0.1 v/o SiH_2Cl_2 in pure H_2 (+) and pure N_2 (○) as a function of temperature.

tively, in the temperature range of 900°-1400°K, using the procedure reported by Van der Putte *et al.* [5] (Fig. 10). In equilibrium with solid silicon the most abundant species are H_2 , HCl , SiCl_2 , SiH_2Cl_2 , SiCl_4 , and SiHCl_3 , in accordance with mass spectrometric analysis results reported by Ban and Gilbert (6). With the aid of thermochemical data a number of reactions that can take place on or near the substrate are sum-

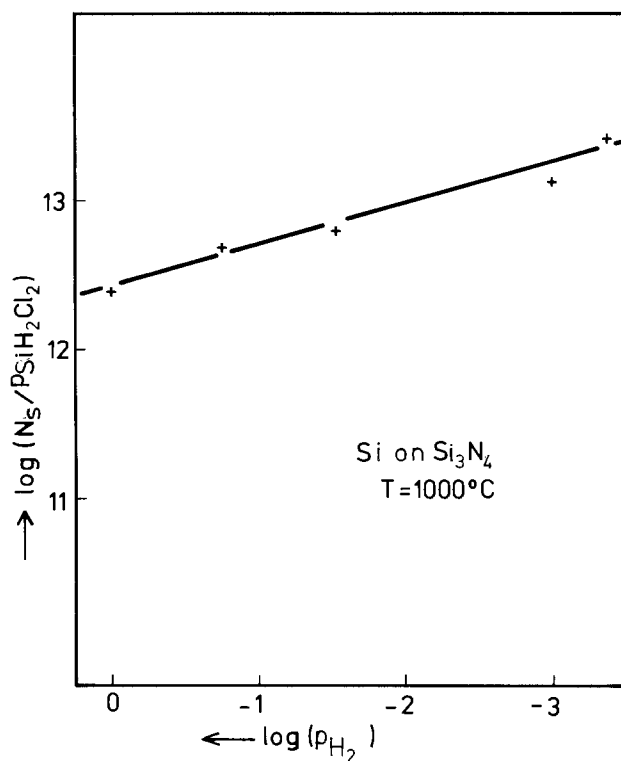


Fig. 6. $\log(N_s/p_{\text{SiH}_2\text{Cl}_2})$ vs. $\log(p_{\text{H}_2})$ at 1000°C for Si on Si_3N_4 .

marized in the Appendix. As discussed in the Appendix, reasonable assumptions could be made for the initial states of nucleation, leading to an expression for the silicon adatom concentration [A-15]

$$\frac{n_1}{n_0} = \frac{K_3 p_{\text{SiCl}_2}}{k_8 (1 + K_3 p_{\text{SiCl}_2} + K_{10} p_{\text{H}_2}^{1/2})} \quad [2]$$

The dissociation of SiH_2Cl_2 to SiCl_2 and H_2 [A-1] followed by a very strong adsorption of SiCl_2 compared to SiH_2Cl_2 plays an important role in obtaining this expression. The decomposition parameter α of reaction [A-1] can be defined by

$$p_{\text{SiH}_2\text{Cl}_2} = (1 - \alpha) p_{\text{SiH}_2\text{Cl}_2}(b) \\ p_{\text{SiCl}_2} = \alpha p_{\text{SiH}_2\text{Cl}_2}(b) \quad [3]$$

where $p_{\text{SiH}_2\text{Cl}_2}(b)$ is the input concentration of SiH_2Cl_2 . If the equilibrium partial pressure of SiCl_2 is much higher than that of SiH_2Cl_2 it can be assumed that the decomposition of SiH_2Cl_2 into SiCl_2 and H_2 is almost complete ($\alpha \cong 1$) (Fig. 10). For an H_2 - N_2 mixture we obtain, by introducing the decomposition parameter α into Eq. [2]

$$\frac{n_1}{n_0} = \frac{A \alpha p_{\text{SiH}_2\text{Cl}_2}(b)}{(1 + K_3 \alpha p_{\text{SiH}_2\text{Cl}_2}(b) + K_{10} p_{\text{H}_2}^{1/2})} \quad [4]$$

where $A = K_3/k_8$. Equation [4] for the silicon adatom concentration can also be used if no H_2 is added deliberately. In that case p_{H_2} is given by the equilibrium partial pressure of H_2 (proportional to $\alpha p_{\text{SiH}_2\text{Cl}_2}(b)$).

Interpretation of results.—The SiH_2Cl_2 - H_2 - N_2 system.—It was concluded that expressions given by Venables (3, 7) can be used to characterize the saturation density of stable clusters (N_s) in the present case where incomplete condensation of silicon has to be assumed. Because of the existence of an incubation period before the actual nucleation starts, it is thought probable that an equilibrium concentration of silicon adatoms can build up prior to the first nucleation. In this period, therefore, a strong incomplete condensation regime applies. For this situation the relevant expression given by Venables can be rewritten as

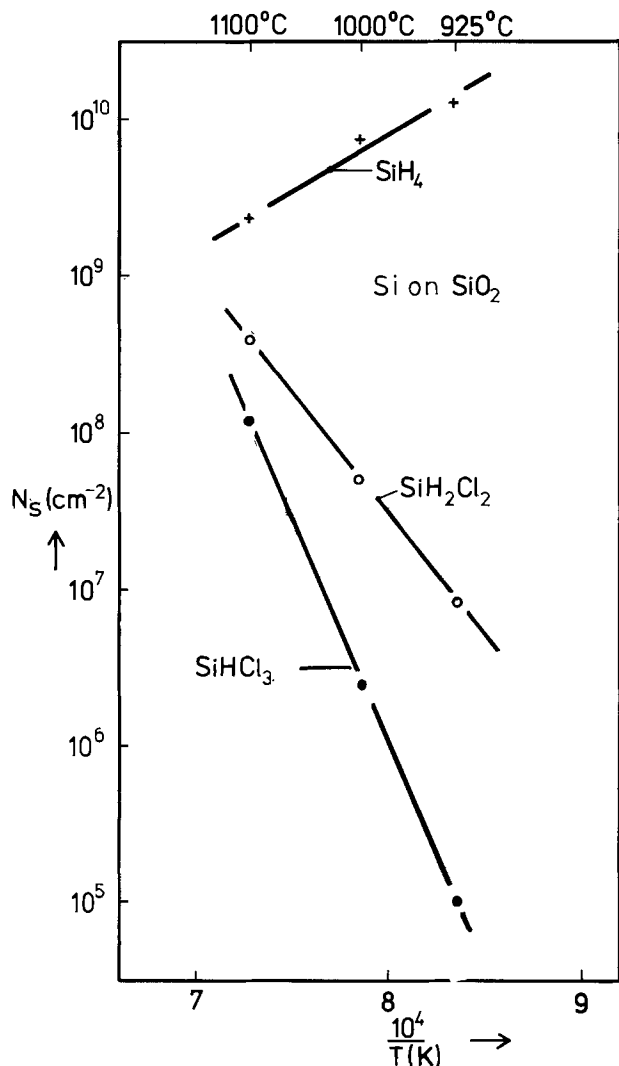


Fig. 7. Saturation densities on SiO_2 substrates as a function of temperature for SiH_4 , SiH_2Cl_2 , and SiHCl_3 (all concentrations about 0.1 v/o) in H_2 as a carrier gas.

$$\frac{N_s}{n_0} \cong \left(\frac{n_1}{n_0} \right)^{\frac{i+1}{2}} \exp [(E_i + E_m - E_d)/2kT] \quad [5]$$

where i is the number of atoms in the initial cluster, n_1 the monomer or adatom concentration, and n_0 denotes the number of surface sites ($\cong 10^{14} \text{ cm}^{-2}$). E_i is the heat of formation of a cluster consisting of i atoms, E_m is the activation energy for surface diffusion of mobile clusters, and E_d is the activation energy for surface diffusion of adatoms. As discussed above n_1/n_0 can be given as a first approximation by Eq. [4], leading to

$$\frac{N_s}{n_0} = \left\{ \frac{A\alpha p_{\text{SiH}_2\text{Cl}_2}(b)}{(1 + K_{3\alpha} p_{\text{SiH}_2\text{Cl}_2}(b) + K_{10} p_{\text{H}_2}^{1/2})} \right\}^{\frac{i+1}{2}} \exp [(E_i + E_m - E_d)/2kT] \quad [6]$$

where A is a constant, α is the decomposition parameter, and $p_{\text{SiH}_2\text{Cl}_2}(b)$ is the input concentration of SiH_2Cl_2 , the other parameters being as defined before (Eq. [5]).

Starting with the experiments done on SiO_2 substrates, it can be observed in Table I that N_s in the SiH_2Cl_2 - H_2 system is almost proportional to $p_{\text{SiH}_2\text{Cl}_2}(b)$. It can thus be concluded that in Eq. [6] $K_{3\alpha} p_{\text{SiH}_2\text{Cl}_2}(b) < (1 + K_{10} p_{\text{H}_2}^{1/2})$, and moreover $i = 1$ for the temperature range between 925° and 1100°C. If $i = 1$ for

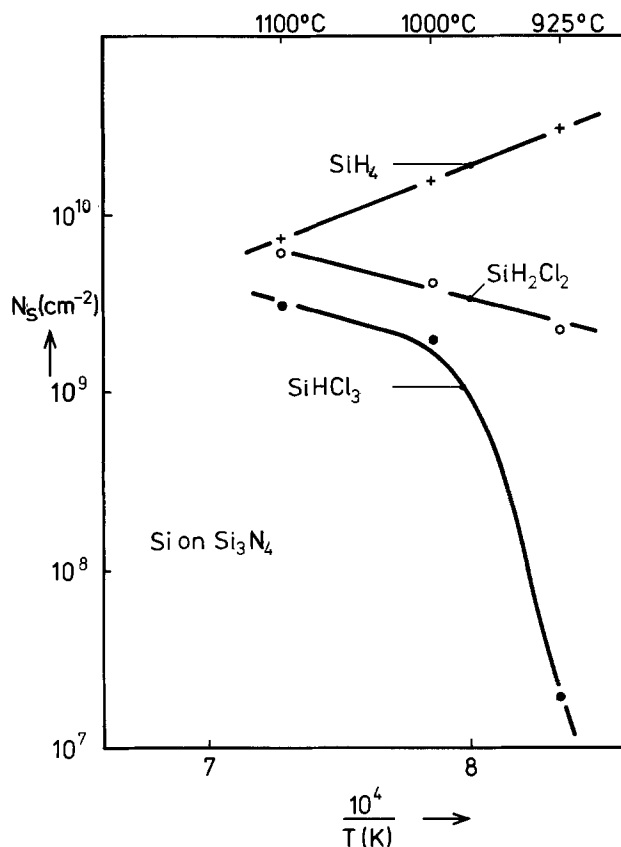


Fig. 8. Saturation densities on Si_3N_4 substrates for SiH_4 , SiH_2Cl_2 , and SiHCl_3 in H_2 as a carrier gas (all concentrations about 0.1 v/o) as a function of temperature.

the SiH_2Cl_2 - H_2 system, it is acceptable that in all other cases where the saturation nucleus density is higher one will also have $i = 1$. If, furthermore, $K_{3\alpha} p_{\text{SiH}_2\text{Cl}_2}(b) < (1 + K_{10} p_{\text{H}_2}^{1/2})$ for all H_2 - N_2 mixtures, we obtain, from Eq. [6], for a fixed temperature

$$\frac{N_s}{n_0} = \frac{A\alpha p_{\text{SiH}_2\text{Cl}_2}(b)}{1 + K_{10} p_{\text{H}_2}^{1/2}} \quad [7]$$

The experimental data given in Fig. 4 by plotting $\log [N_s/p_{\text{SiH}_2\text{Cl}_2}(b)]$ vs. $\log (p_{\text{H}_2})$ can now be analyzed. At 1100°C we observe a tangent which is almost $1/2$ for all H_2 - N_2 mixtures, from which it may be concluded that adsorption of atomic hydrogen plays an important role in nucleation kinetics on SiO_2 substrates ($K_{10} p_{\text{H}_2}^{1/2} > 1$). Equation [7] can be used for the SiH_2Cl_2 - N_2 system by introducing the equilibrium partial pressure of H_2 . This is done in Fig. 4, and the results show that α is close to unity in accordance with the thermochemical data in Fig. 10 [$p_{\text{H}_2} \cong p_{\text{SiH}_2\text{Cl}_2}(b)$]. At lower temperatures the tangent in Fig. 4 is only $1/2$ for the lowest hydrogen pressures and the deviation from the slope $1/2$ is strongest at 925°C. Especially at the lower temperatures the assumption $K_{10} p_{\text{H}_2}^{1/2} > [1 + K_{3\alpha} p_{\text{SiH}_2\text{Cl}_2}(b)]$ remains acceptable. For SiO_2 substrates an additional decrease in N_s then has to be found in a lower value of α .

At lower temperatures and the highest hydrogen pressures, therefore, hydrogen adsorption is no longer the only factor that determines the saturation density. According to Fig. 10, the dissociation of SiH_2Cl_2 into SiCl_2 and H_2 becomes more difficult under these experimental conditions, leading to the smaller value of α . If the decrease in saturation density is only caused by a decrease in α and if $\alpha \cong 1$ at 1100°C, we calculate an effective value of $\alpha = 10^{-2}$ at 925°C using Fig. 4.

For the Si_3N_4 substrates Eq. [6] can also describe the experimental data given in Fig. 1, 5, and 6. If we compare Fig. 2 and 5, where the saturation nucleus

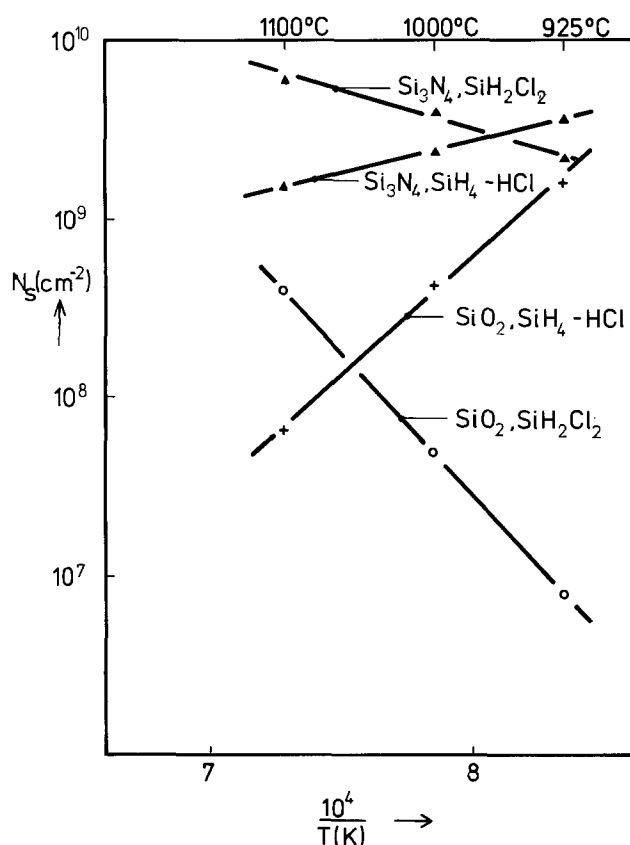


Fig. 9. Saturation nucleus densities on SiO_2 and Si_3N_4 substrates as a function of temperature for 0.1 v/o SiH_2Cl_2 and a mixture of 0.1 v/o SiH_4 and 0.2 v/o HCl .

density is plotted for hydrogen and nitrogen as a carrier gas, on SiO_2 and Si_3N_4 substrates, it can be observed that hydrogen adsorption on Si_3N_4 substrates could play a role, but to a lesser degree than on SiO_2 substrates. By plotting $\log [N_s/p_{\text{SiH}_2\text{Cl}_2}(b)]$ vs. $\log (p_{\text{H}_2})$ (Fig. 6) we observe that the tangent in this figure is less than $\frac{1}{2}$ at 1000°C , leading to the conclusion that the assumption $K_{10}p_{\text{H}_2}^{1/2} > [1 + K_3\alpha p_{\text{SiH}_2\text{Cl}_2}(b)]$ is not acceptable in this case, adsorption of SiCl_2 thus cannot be neglected.

It may be concluded that the difference in saturation nucleus densities between SiO_2 and Si_3N_4 substrates in a hydrogen medium is caused by strong adsorption of atomic hydrogen, especially on SiO_2 substrates. According to the JANAF tables (8) the OH bond energy is stronger than the NH bond by about 20 kcal/mole. This difference in bond energy is sufficient to explain the experimental data.

Comparison between different silicon-containing compounds in an H_2 medium.—Figures 7 and 8 give saturation nucleus densities of silicon clusters for SiO_2 and Si_3N_4 substrates, respectively, for SiH_4 , SiH_2Cl_2 , and SiHCl_3 (all concentrations about 0.1 v/o) in hydrogen as a carrier gas. If we start with the SiO_2 substrate a remarkable difference between the SiH_4 - H_2 and the SiH_2Cl_2 - H_2 system is observed. As discussed above, the presence of hydrogen hampers the dissociation of SiH_2Cl_2 , and moreover adsorption of atomic hydrogen on SiO_2 blocks the adsorption for silicon species, as a consequence of which the saturation density decreases with decreasing temperature. In the SiH_4 - H_2 system, hydrogen adsorption does not determine nucleation kinetics in the temperature range under discussion. At temperatures below 900°C hydrogen adsorption also becomes important for SiH_4 on SiO_2 substrates, which results in a decrease of the saturation density with decreasing temperatures for the SiH_4 - H_2 system as well (3). The SiHCl_3 - H_2 system behaves like the SiH_2Cl_2 system, but shows a lower saturation nucleus

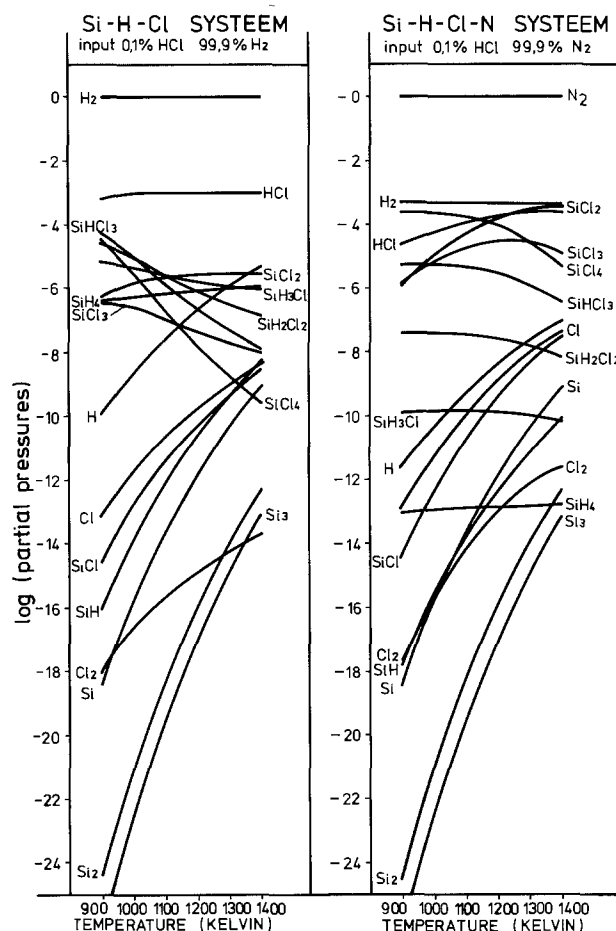


Fig. 10. Thermodynamic data for the Si-H-Cl and the Si-N-H-Cl systems as a function of temperature and an input of 0.1 v/o HCl .

density than the former system. Nucleation is more difficult than for the SiH_2Cl_2 - H_2 system, probably because of a lower SiCl_2 concentration in the gas phase due to a smaller decomposition parameter. For Si_3N_4 substrates the difference between the SiH_2Cl_2 - H_2 system and the SiH_4 - H_2 system is smaller than for the SiO_2 substrates (Fig. 8). This can be understood because we have seen that hydrogen adsorption plays a less important role on Si_3N_4 substrates in the SiH_2Cl_2 - H_2 system, and in the SiH_4 - H_2 system hydrogen adsorption does not come into play. The strong decrease of the saturation density at temperatures below 1000°C in the SiHCl_3 - H_2 system also has to be explained by a decrease of the SiCl_2 concentration in the gas phase.

Introduction of HCl to the SiH_4 - H_2 system decreases the saturation nucleus density, but down to 900°C this density still increases with decreasing temperature (Fig. 9). In the SiH_4 - HCl - H_2 system etching of Si adatoms by HCl occurs, whereas, in the SiH_2Cl_2 - H_2 system as discussed in the Appendix hardly any free HCl is present before the onset of nucleation. The greater critical cluster size, which varies from 1 to approximately 4 for the SiH_4 - HCl - H_2 system, could also be explained in terms of the etching of Si adatoms by HCl , giving SiCl_2 (3). The differences in nucleation on SiO_2 and Si_3N_4 substrates in the SiH_4 - HCl - H_2 and SiH_2Cl_2 systems are ultimately traced back to the difference in the steady-state concentration of silicon adatoms on the substrates prior to the actual nucleation.

Conclusions

In an attempt to understand and be able to monitor the crystallite size of polycrystalline silicon layers we have studied the nucleation of silicon on various substrates for different silicon-containing compounds as a function of gas phase composition and tempera-

ture. Experiments with nucleation of silicon on SiO₂ and Si₃N₄ substrates were reported for the SiH₂Cl₂-H₂-N₂ system in the temperature range of 800°-1100°C. The differences and conformities between the SiH₄-H₂-HCl, SiHCl₃-H₂, and the SiH₂Cl₂-H₂ systems were also discussed. As far as the SiH₂Cl₂-H₂-N₂ system is concerned it is observed that the saturation nucleus densities on SiO₂ and Si₃N₄ substrates are almost the same for nitrogen as a carrier gas, and these densities are barely a function of temperature. Introduction of hydrogen strongly reduces the saturation nucleus density and this decrease is much stronger for SiO₂ than for Si₃N₄ substrates, resulting in a decrease of the saturation nucleus density with decreasing temperatures. Further the temperature dependence of the formation process increases with increasing hydrogen pressures. The experimental data can be explained from an analysis of the silicon adatom concentration on the surface as a function of gas phase composition and temperature. Application of an expression for the saturation nucleus density as obtained by Venables gives an indication of the size of the critical cluster, which seems to be 1 for all SiH₂Cl₂ mixtures under discussion. The differences between the SiH₄-H₂-HCl, the SiH₄-H₂, the SiHCl₃-H₂, and the SiH₂Cl₂-H₂ systems are remarkable. For SiHCl₃ and SiH₂Cl₂ the saturation density of silicon clusters decreases with decreasing temperature, whereas for the SiH₄-HCl-H₂ and SiH₄-H₂ systems the opposite occurs. Formation of SiCl₂ by dissociation of SiH₂Cl₂ or SiHCl₃ becomes more difficult at decreasing temperatures, leading to a smaller steady-state concentration of silicon adatoms at lower temperatures.

Acknowledgments

The authors wish to thank H. Haanstra and members of his group for the SEM and TEM photomicrographs.

Manuscript submitted Jan. 22, 1980; revised manuscript received March 25, 1980.

Any discussion of this paper will appear in a Discussion Section to be published in the June 1981 JOURNAL. All discussions for the June 1981 Discussion Section should be submitted by Feb. 1, 1981.

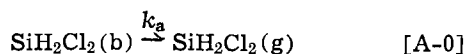
Publication costs of this article were assisted by Philips Research Laboratory.

APPENDIX

Reaction Scheme for the SiH₂Cl₂-H₂-N₂ System

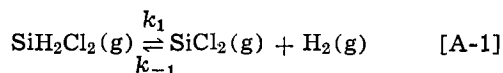
According to the thermochemical data in Fig. 10 the main processes which take place on or near the surface can be summarized as follows:

Supply of SiH₂Cl₂ by means of gas phase diffusion

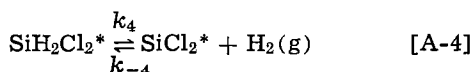
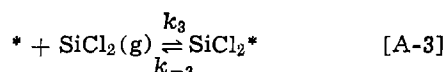
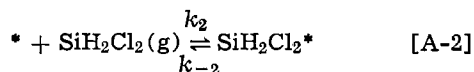


SiH₂Cl₂(b) is the input concentration of SiH₂Cl₂ and SiH₂Cl₂(g) the concentration of SiH₂Cl₂ near the surface.

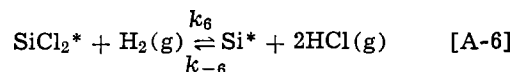
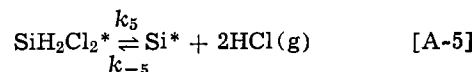
Dissociation of SiH₂Cl₂ in the gas phase



Adsorption of SiH₂Cl₂ and SiCl₂ on a free surface site (denoted by an asterisk) and dissociation of SiH₂Cl₂*



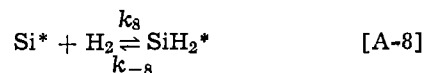
Formation of Si adatoms on the surface



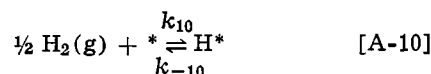
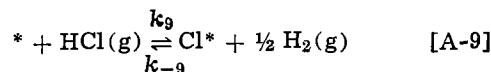
Formation of stable silicon clusters by diffusion of Si adatoms on the surface



Reaction of Si adatoms with hydrogen



Adsorption of hydrogen and chlorine



Formation of chlorosilanes other than SiCl₂, such as SiHCl₃ and SiCl₄, can be left out of consideration, at least in the initial stage of nucleation, where practically no HCl is present. The notation (g) will only be used when comparison with bulk values of the vapor pressure is made.

The total number of reactions can be decreased by judging the various parameters in view of experimental results and thermochemical data. The following assumptions can be made:

Because hardly any HCl is present in the initial stage of nucleation, the back reaction k_{-5} and k_{-6} can be neglected and also [Cl*] can be treated as small.

Nucleation and growth experiments in the SiH₄-HCl-H₂ system lead to the conclusion that silicon adatoms [Si*] are needed to arrive at nucleation (3).

Gas phase dissociation of SiH₂Cl₂ to SiCl₂ and H₂ occurs at temperatures above 800°C. This is according to Smith and Sedwick (9) who performed *in situ* measurements using inelastic light scattering and obtained spectra of SiCl₂ in an rf heated reactor in the SiH₂Cl₂-H₂ system.

The nucleation starts via the adsorption of SiCl₂ or via adsorption of SiH₂Cl₂.

In order to discriminate between adsorption of SiH₂Cl₂ and SiCl₂ we have to notice that SiH₂Cl₂ is a fully coordinated molecule with four atoms bonded in a tetrahedral configuration. If SiH₂Cl₂ adsorbs without dissociation, then a peripheral hydrogen or chlorine atom has to come into contact with the surface. In the nonlinear SiCl₂ molecule the silicon atom is not sterically blocked from the surface of the substrate, and the presence of the unbonded electrons on the silicon greatly enhances its adsorption by interaction with the dangling bonds on the surface (10). It can therefore be concluded that the adsorption energy of SiH₂Cl₂ is much smaller than that of SiCl₂. This means that [A-2], [A-4], and [A-5] can be left out of consideration. With the above approximations the steady-state concentrations of [Si*] and [SiCl₂*] will be given by

$$n_1 = [\text{Si}^*] = \frac{k_6[\text{SiCl}_2^*]p_{\text{H}_2} + k_{-8}[\text{SiH}_2^*]}{k_7 + k_8p_{\text{H}_2}} \quad [\text{A-11}]$$

$$[\text{SiCl}_2^*] = \frac{k_3p_{\text{SiCl}_2}[*]}{k_{-3} + k_6p_{\text{H}_2}} \quad [\text{A-12}]$$

As for the SiH₄-HCl-H₂ system (3) the nucleus density very quickly reaches a saturation density, with respect to exposure time, after an incubation period. On the basis of these experiments it was assumed that the time needed to attain the population of adatoms is small, giving a constant value of n_1 before nucleation occurs. This means that k_7 can be omitted until nucleation takes place. The second term in the nominator, the indirect formation of Si*, can be assumed to be small

compared to the first term and can be neglected. The silicon adatom concentration will be much smaller than the concentration of adsorbed SiCl_2 molecules, therefore, it can be assumed that $k_{-3} > k_6 p_{\text{H}_2}$. With these approximations one obtains.

$$n_1 = \frac{k_6 K_3 p_{\text{SiCl}_2} [*]}{k_8} \quad [\text{A-13}]$$

For the concentration of free surface sites we can write

$$[*] = n_0 - [\text{Si}^*] - [\text{SiCl}_2^*] - [\text{H}^*] - [\text{SiH}_2^*]$$

where n_0 is the total number of sites per unit area. With $[\text{H}^*] = K_{10} p_{\text{H}_2}^{1/2} [*]$; $K_{10} = k_{10}/k_{-10}$, $[\text{SiCl}_2^*] = K_3 p_{\text{SiCl}_2} [*]$; $K_3 = k_3/k_{-3}$ and $[\text{Si}^*]$, $[\text{SiH}_2^*] \ll [\text{SiCl}_2^*]$, this leads to

$$[*] = \frac{n_0}{(1 + K_3 p_{\text{SiCl}_2} + K_{10} p_{\text{H}_2}^{1/2})} \quad [\text{A-14}]$$

The silicon adatom concentration can now be given by

$$\frac{n_1}{n_0} = \frac{K_3 k_6 p_{\text{SiCl}_2}}{k_8 (1 + K_3 p_{\text{SiCl}_2} + K_{10} p_{\text{H}_2}^{1/2})} \quad [\text{A-15}]$$

REFERENCES

1. See, for example: T. I. Kamins, *IEEE Trans. Parts, Hybrids, Packag.*, **10**, 221 (1974).
2. P. H. Robinson and N. Goldsmith, *J. Electron. Mater.*, **4**, 313 (1975); V. S. Ban, *This Journal*, **122**, 1398 (1975).
3. W. A. P. Claassen and J. Bloem, *This Journal*, **128**, 194 (1980).
4. J. Bloem and W. A. P. Claassen, *J. Cryst. Growth*, In press.
5. P. van der Putte, L. J. Giling, and J. Bloem, *ibid.*, **41**, 133 (1977).
6. V. S. Ban and S. L. Gilbert, *This Journal*, **122**, 1382 (1975).
7. J. A. Venables, *Philos. Mag.*, **27**, 697 (1973).
8. JANAF Thermochemical Tables, 2nd ed., June 1971, NSRDS-NBS-37.
9. J. E. Smith, Jr. and T. O. Sedgwick, *Thin Solid Films*, **40**, 1 (1977).
10. A. A. Chernov, *J. Cryst. Growth*, **42**, 55 (1977).

Growth of Epitaxial ZnO Thin Films by Organometallic Chemical Vapor Deposition

Chi Kwan Lau,* Shibani K. Tiku,* and K. M. Lakin

University of Southern California, Los Angeles, California 90007

ABSTRACT

Organometallic chemical vapor deposition of ZnO on sapphire, using the reaction of diethylzinc with $\text{H}_2\text{O}/\text{H}_2$, $\text{N}_2\text{O}/\text{N}_2$, and CO_2/H_2 oxidizing gas systems, has been studied. Epitaxial films have been achieved at temperatures of 400° and 730°C, respectively, in the first two systems. The films have been characterized using scanning electron microscopy (SEM), reflection electron diffraction (RED), and surface acoustic wave techniques.

ZnO is one of the most versatile and useful thin film materials for acoustoelectric, acousto-optic, electro-optic, and photoconductive device applications (1). The heteroepitaxial system, (11 $\bar{2}$ 0) ZnO/(01 $\bar{1}$ 2) Al_2O_3 with the c-axis of ZnO in the plane of the R-plane sapphire, is highly desirable for surface acoustic wave (SAW) device applications because of the high electromechanical coupling coefficient of ZnO and low acoustic wave propagation loss of sapphire. Furthermore, R-plane sapphire is the orientation used in silicon-on-sapphire (SOS) technology and for the growth of many III-V and II-VI compounds, implying the potential for integrating ZnO and semiconductor devices on a single substrate. Finally, substrates with good epitaxial quality surfaces are available commercially.

Growth methods.—RF sputtering is the most popular technique for ZnO thin film fabrication and recently planar magnetron sputtering has been successful in producing 5-10 micron thick films on glass substrates in an hours growth time (2, 3). These sputtered films have a tendency of growing with c-axis perpendicular to the substrate surface and only at very low growth rates (100 Å/min) and high substrate temperatures (~450°C) have (11 $\bar{2}$ 0) ZnO films on R-plane sapphire been achieved by sputtering (4). Growth of ZnO from the vapor phase has also been widely investigated. Most of the methods reported to date are essentially based on ZnO transport using the transport agents H_2/HCl (5) and $\text{H}_2/\text{H}_2\text{O}$ (6) or con-

trolled oxidation of zinc vapor. Growth rates of about 1.2 $\mu\text{m}/\text{min}$ have been achieved at substrate temperatures around 775°C. However, because of the nucleation problems associated with the use of zinc vapor, film growth is nonuniform and nonreproducible. This problem can be solved by the introduction of a pre-sputtered layer of ZnO on the substrate. Using this technique with the $\text{ZnO}/\text{H}_2\text{O}/\text{O}_2/\text{H}_2$ transport system, Ohnishi *et al.* (7) have grown films with excellent uniformity and surface finish. Growth rates of 1 $\mu\text{m}/\text{min}$ were achieved at a rather high substrate temperature of 975°C. However, extensive corrosion of the quartzware takes place in all these transport systems. The corrosion problem has been mitigated by employing the reaction of zinc vapor and H_2O (8).

ZnO films grown by any of the vapor phase techniques show low resistivity, making postgrowth compensation necessary. Diffusion of lithium (and polishing to remove the damage due to etching by the lithium source) must be done before the films can be used for piezoelectric applications. Since the resistivity of ZnO films has been seen to increase in the presence of CO_2 (1), the Zn(v)/ CO_2 reaction was recently investigated for the growth of ZnO films on sapphire (9). Here an as-grown resistivity of $10^6 \Omega\text{-cm}$ resulted, but degraded on further process handling and exposure to the atmosphere.

Organometallic growth.—In recent years, the organometallic process for semiconductor thin film growth has received increasing attention, because of certain distinct advantages largely associated with the ease of handling the metal sources (10). Growth of compound

* Electrochemical Society Active Member.

Key words: organometallic, CVD of ZnO, ZnO for SAW devices, ZnO thin films.

semiconductor films using organometallic reactions has been reviewed by Manasevit (11) and the heteroepitaxial growth has been successful for a number of III-V semiconductor materials on various oxide substrates (10). The successful growth of II-VI compounds based on zinc has been reported by Manasevit and Simpson (12). The only organometallic growth method reported for the deposition of ZnO is by the decomposition of zinc propionate and zinc acetyl-acetonate (13). Oriented films were obtained at extremely low growth rates (27 Å/min) on mica substrates.

In this paper, we report the results on the growth of ZnO thin films in R-plane sapphire, using the oxidation of diethylzinc, $(C_2H_5)_2Zn$ (DEZ), by the three oxidizing gas mixtures, H_2O/H_2 , CO_2/H_2 , and NO_2/N_2 (14). Hydrogen, which plays a dominant role in the growth process, was used as the carrier for the H_2O and CO_2 reaction systems and N_2 was used for the DEZ/ N_2O system.

Experiment

Growth system.—Both horizontal and vertical quartz tube reactors were used in the present study as shown schematically in Fig. 1. The vertical gas flow system with substrate rotation proved to be advantageous in the DEZ/ N_2O growth system, as more uniform films could be grown. In the case of the DEZ/ H_2O reaction system, solid ZnO particles were formed on the inside walls of the injection tube. In the vertical geometry, these particles can be blown by the carrier gas onto the substrate, causing spurious growth problems. The horizontal growth system gave better quality films due to the absence of this problem. In both geometries the gas flow was at near normal incidence to the substrate surface. The temperature was monitored by a thermocouple with its tip placed inside a small hole in the susceptor. The injection tube-to-substrate distance was adjustable. The exhaust was connected to a scrubber through a rotary vacuum pump maintaining a pressure of about 400 Torr inside the reaction chamber.

The entire gas flow system for both the horizontal and the vertical reactors was assembled using stainless steel tubing, stainless steel bubblers for DEZ and deionized H_2O , and with provisions made for purging the system with nitrogen. The quartz reaction cham-

ber is 40 mm ID, 40 cm long tube. The susceptors used were 30 mm diam graphite disks capable of holding 20 mm square substrates.

Nitrogen gas was obtained directly from liquid nitrogen boil-off, and H_2 , N_2O , and CO_2 were of four-nine purity. Electronic grade DEZ was chilled with melting ice to get better control over its flow rate. (The vapor pressure of DEZ at 20°C is 15 Torr.)

Substrate preparation.—R-plane sapphire (3.8 cm diam and 1.23 mm thick) of epitaxial surface quality was purchased from Union Carbide. A standard polishing and cleaning procedure consisted of Syton (Monsanto) polishing for 10 min followed by cleaning with trichloroethylene, acetone, and methanol. Deionized water was used for the final wash before the dry nitrogen blow-off.

Experimental procedure.—To start a growth run, the reactor was evacuated and the carrier gas was admitted. The preparatory sequence continued by heating the substrate to the deposition temperature, followed by introduction of the oxidizing gas. After about 5 min, growth was initiated by introduction of DEZ and continued for a specified time. After the growth run, the substrate was cooled slowly.

As-grown films were examined visually under an optical microscope and a small portion of the film was etched away with dilute HCl and the remaining film thickness measured across the etched step using a stylus-type profile meter (Dektak). Further physical characterization was carried out using SEM and RED.

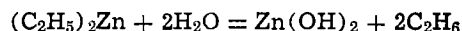
Electrical characterization consisted of a four-point probe resistivity measurement followed by capacitance and electromechanical coupling coefficient measurements using a surface acoustic wave interdigital electrode transducer.

Results and Discussion

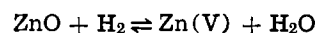
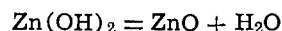
Reactions.—DEZ is an electron deficient compound with two vacant orbitals. The presence of these vacant orbitals available for bonding explains its high chemical reactivity. Thus, DEZ forms complexes easily with compounds containing free electron pairs. DEZ forms complexes at temperatures near ambient or higher with H_2O , CO_2 , and N_2O (15). The reactions of interest in the present study are:

1. DEZ/ H_2O/H_2 system (15)

At room temperature, in the gas stream

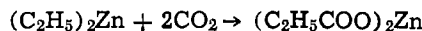


At the surface at high temperature (400°C)

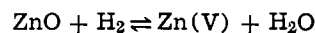
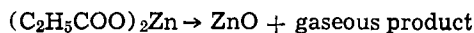


2. DEZ/ CO_2/H_2 system (16)

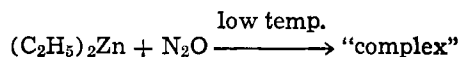
At 150°C, in the gas stream



At high temperature, on the substrate (500°C)



3. DEZ/ N_2O/N_2 system (15)



Growth kinetics.—Because of the formation of organo-zinc complexes [or $Zn(OH)_2$ in the DEZ/ H_2O system] at low temperature, it is necessary to keep the reactants separate until they are a short distance

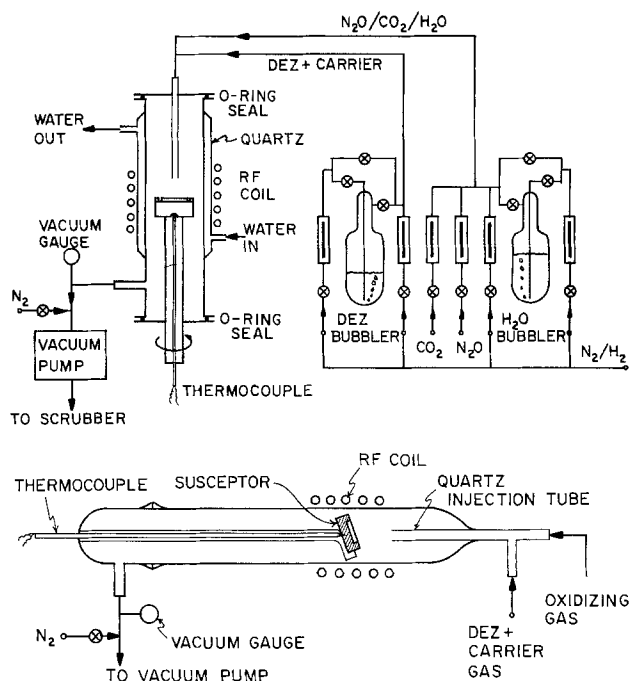


Fig. 1. Schematic diagram of the growth system used for ZnO, OM-CVD growth, (a, top) vertical geometry, (b, bottom) horizontal geometry.

Table I. Growth parameters and properties of ZnO films grown by OM-CVD

Process	Optimum growth temperature, °C	Growth rate, Å/min	Optimum gas flow rates, l/min			
			H ₂	N ₂	DEZ	Oxidizing gas
DEZ/H ₂ O/H ₂	400	300-850	2.7	—	0.015	H ₂ O = 0.02
DEZ/CO ₂ /H ₂	500	300-500	2.5	—	0.015	CO ₂ = 0.05
DEZ/N ₂ O/N ₂	730	80-120	—	2.5	0.021	N ₂ O = 0.05

Reactor pressure: 400 Torr.

away from the substrate. Homogeneity of mixing and delivery of the reactants uniformly to the substrate is difficult to achieve. The reactor must be geometrically optimized to achieve growth uniformity and low pressure must be used in order to accelerate complex dissociation and removal of reaction products from the growth surface.

Table I shows the growth parameters for the three reaction systems. The rate of growth as a function of

temperature (with all other parameters being constant and equal to the optimum values given in Table I) is shown in Fig. 2. The optimum temperatures for the three systems are 400°C for the H₂O/H₂, 500°C for the CO₂/H₂, and 730°C for the N₂O/N₂ process. The shapes of the curves indicate that the growth is kinetically controlled at low temperature because of the activation energy needed to dissociate Zn(OH)₂ or the complexes. At high temperatures, the growth rate drops due to thermodynamic factors, including the instability of ZnO in the presence of hydrogen. In addition, the growth rate was observed to decrease as the DEZ/oxidizing gas ratio was increased and at very high DEZ concentration growth stopped in all the three reaction systems. This indicated poisoning of the growth surface by excess complex molecules. Thus, the desorption of large organic species may be the rate-limiting step under such conditions. Figure 3 shows the dependence of the growth rate on the oxidizing gas flow rate with constant flow rates of other gases (equal to the optimum values of Table I). Maxima are observed in each case. Thus adsorption of H₂O, CO₂, and N₂O by the ZnO surface may also lead to a drop in the growth rate.

Growth morphology.—Films obtained with the DEZ/H₂O/H₂ process were pale white translucent with a rough surface. The SEM micrograph for a typical film, shown in Fig. 4, does not reveal any obvious

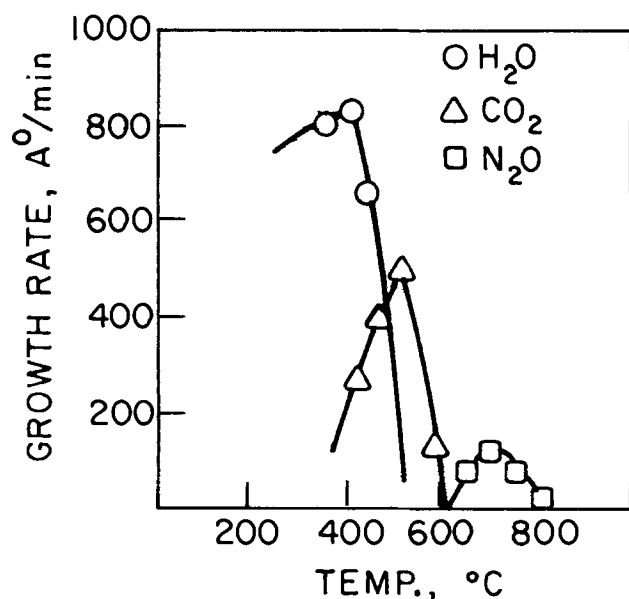


Fig. 2. Growth rate as a function of temperature, with other parameters constant at the optimum values given in Table I.

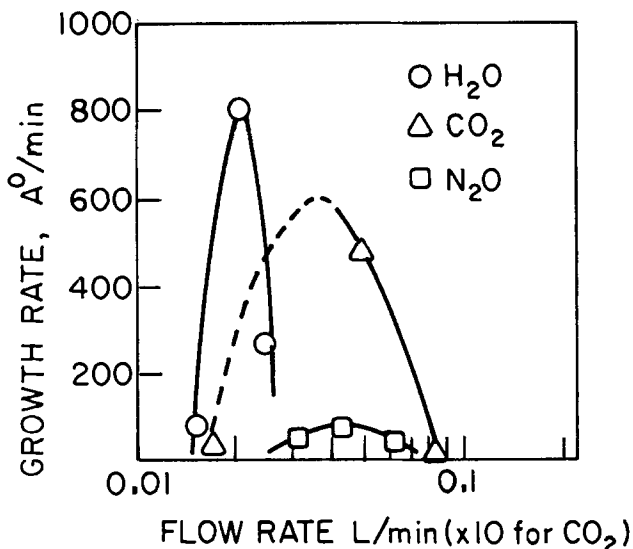


Fig. 3. Growth rate as a function of the flow rate of H₂O, CO₂, and N₂O (other parameters at their optimum values given in Table I).

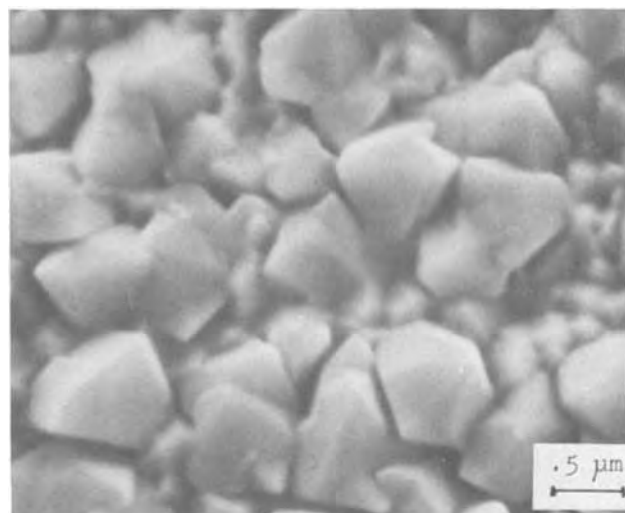


Fig. 4. SEM/RED for a 2 μm thick ZnO film grown at 400°C by the DEZ/H₂O/H₂ growth process.

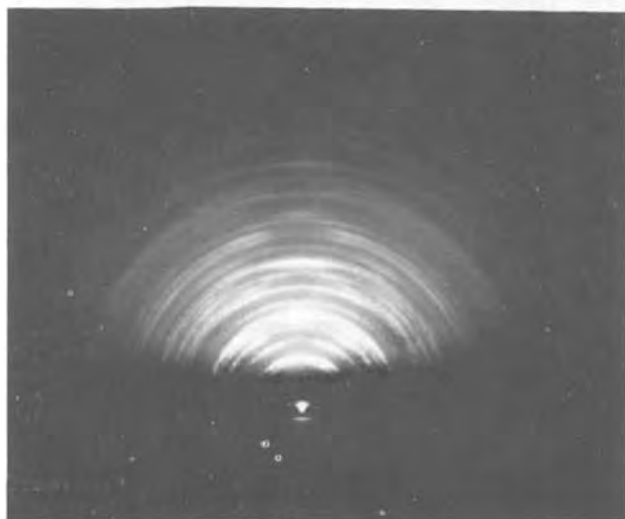
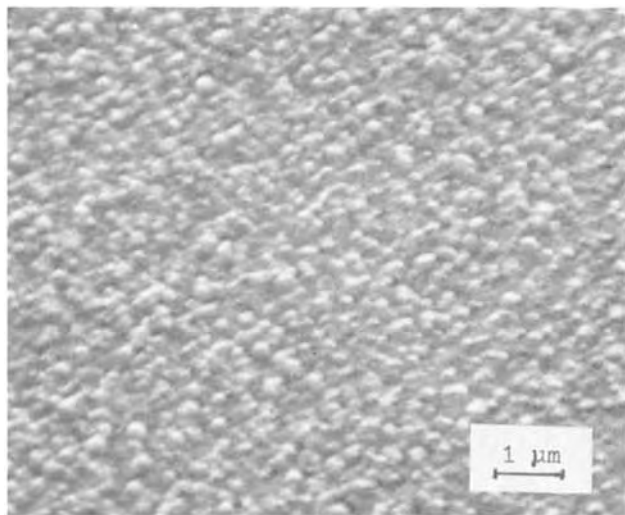


Fig. 5. SEM/RED for a 2 μm thick ZnO film grown at 500°C by the DEZ/ CO_2/H_2 growth system.

alignment of crystallites, although the RED confirms an oriented film. Films grown by the DEZ/ CO_2/H_2 system were polycrystalline (Fig. 5). Films grown by the $\text{N}_2\text{O}/\text{N}_2$ process were transparent with very smooth surfaces and the SEM/RED data, Fig. 6, show that the crystallites are aligned along the c-axis of ZnO crystallites in the R-plane sapphire. ZnO has a marked tendency of growing fast along the c-axis and it appears that in the presence of H_2 any needles that are not in the growth plane become unstable. In the DEZ/ $\text{N}_2\text{O}/\text{N}_2$ system, because of the absence of hydrogen, spurious growth can become important. Thus, if the arrival rate of the complex is increased by reducing the distance between the injection tube and the substrate, growth rate increases and spurious growth, with hexagonal needles growing out of the plane, results as shown in Fig. 7. Thus, the growth rates must remain low in order to retain epitaxy.

Electrical characterization.—Resistivity of the films was measured by the four-point probe method. The results are listed in Table II. Films grown by using CO_2 have a high resistivity of $10^6 \Omega\text{-cm}$ and those grown by H_2O and N_2O reactions exhibit low resistivity. For SAW applications, a resistivity of greater than $10^6 \Omega\text{-cm}$ is necessary. Lithium diffusion for increasing the resistivity was carried out for some films, by coating the film with Li_2CO_3 solution and heating them in air at 700°C for 12 hr. The film had to be polished after the diffusion to remove the surface damage due to the etching of Li_2CO_3 .

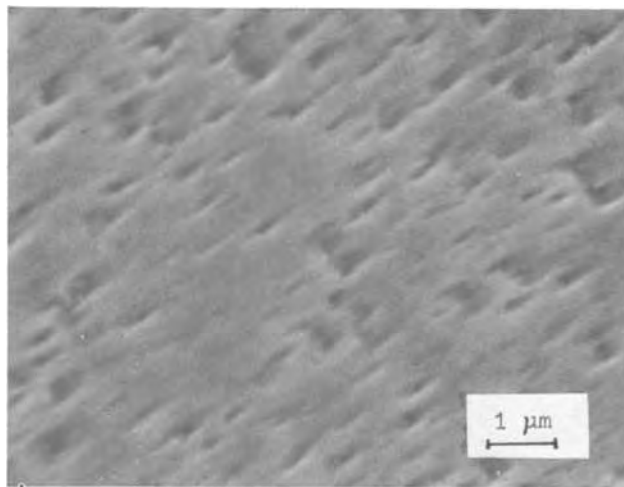


Fig. 6. SEM/RED for a 1.5 μm thick ZnO film grown at 730°C by the DEZ/ $\text{N}_2\text{O}/\text{N}_2$ growth system.

Aluminum interdigital transducers (IDT) of 15 μm wavelength were fabricated on the film surface using the "lift-off" technique (17). The impedance of the IDT was then measured as a function of frequency using an HP8410 network analyzer. The SAW electro-mechanical coupling coefficient (K^2) for the c-axis propagating ZnO/ Al_2O_3 structure was then calculated using the expression (18)

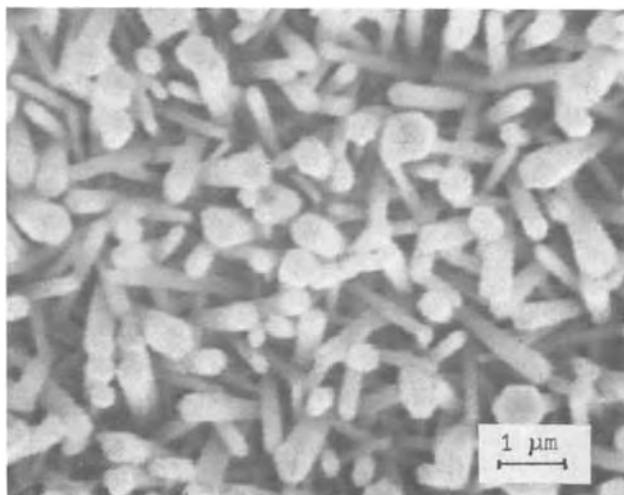


Fig. 7. SEM picture of film grown by the $\text{N}_2\text{O}/\text{N}_2$ process under high flux conditions, showing spurious growth.

Table II. Properties of ZnO films grown by OM-CVD

Process	Electrical resistivity, $\Omega\text{-cm}$		SAW properties			
	As-grown	After Li diffusion	Film thickness, μm	Resonant freq., MHz	t/λ	Coupling coef. K^2
DEZ/H ₂ O/H ₂	1-10	>10 ⁶	1.0	351.17	0.067	0.22%
DEZ/N ₂ O/N ₂	10 ²	>10 ⁶	1.2	343.43	0.08	0.61%

* After polishing, the film thickness was uniform within $\pm 0.1 \mu\text{m}$ over an area of $1 \times 2 \text{ cm}$.

$$K^2 = \pi^2 f_0 R_a C_s / 2$$

where f_0 = resonant frequency, R_a = radiation resistance, and C_s = capacitance/finger pair.

The coupling coefficient and other relevant parameters are tabulated in Table II. The films grown by the H₂O and N₂O reaction systems were found to be piezoelectric as expected from the RED data. The films grown by the CO₂ process were found to be of poor quality, and several attempts to measure the SAW properties were unsuccessful. For the DEZ/N₂O/N₂ process, a K^2 value of 0.61% at a thickness to wavelength ratio (t/λ) of 0.08 was determined which is better than the value obtained by Pizzarello using the ZnO/HCl/H₂ closed-space transport process (19), and is comparable to the theoretical value obtained by Lakin and Penunuri (20). The coupling coefficient for films grown by the DEZ/H₂O/H₂ process is lower (0.22% at $t/\lambda = 0.067$), but reasonable for a low growth temperature of 400°C.

Conclusion

The organometallic reaction systems using the reaction of DEZ with H₂O/H₂, CO₂/H₂, and N₂O/N₂ were investigated and these show promise as low temperature growth techniques for epitaxial ZnO thin films. The films were evaluated by SEM, RED, and by surface acoustic wave measurements. The films grown by the H₂O and N₂O reactions at temperatures of 400° and 730°C showed electromechanical coupling coefficients of 0.22% and 0.61% at $t/\lambda = 0.08$, respectively.

Methods to increase the growth rate and the resistivity are under investigation.

Acknowledgment

This work was supported by the Air Force Office of Scientific Research under Contract F49620-79-C-0138.

Manuscript submitted Dec. 7, 1979; revised manuscript received March 6, 1980. This was Paper 596

presented at the Los Angeles, California, Meeting of the Society, Oct. 14-19, 1979.

Any discussion of this paper will appear in a Discussion Section to be published in the June 1981 JOURNAL. All discussions for the June 1981 Discussion Section should be submitted by Feb. 1, 1981.

Publication costs of this article were assisted by the University of Southern California.

REFERENCES

1. M. T. Duffy, in "Heteroepitaxial Semiconductors for Electronic Devices," G. W. Cullen and C. C. Wang Editors, Chap. 4, p. 150, Springer-Verlag, New York (1977).
2. T. Shiosaki, IEEE Ultrasonics Symposium Proceedings, p. 100 (1978).
3. T. Hata, T. Minamikawa, O. Morimoto, and T. Hada, *J. Cryst. Growth*, **47**, 171 (1979).
4. E. L. Paradis and A. J. Shuskus, *Thin Solid Films*, **38**, 131 (1976).
5. G. Galli and J. E. Coker, *Appl. Phys. Lett.*, **16**, 439 (1970).
6. A. Reisman, M. Berkenblit, R. Ghez, and S. A. Chan, *J. Electron. Mater.*, **1**, 395 (1972).
7. S. Ohnishi, Y. Hirokawa, T. Shiosaki, and A. Kawabata, *Jpn. J. Appl. Phys.*, **17**, 773 (1978).
8. A. Reisman, M. Berkenblit, S. A. Chan, and J. Angilello, *J. Electron. Mater.*, **2**, 177 (1973).
9. S. Tikku, C. K. Lau, and K. M. Lakin, *Appl. Phys. Lett.*, To be published.
10. C. C. Wang, in "Heteroepitaxial Semiconductors for Electronic Devices," G. W. Cullen and C. C. Wang, Editors, Chap. 3, p. 106, Springer-Verlag, New York (1977).
11. H. M. Manasevit, *J. Cryst. Growth*, **13/14**, 306 (1972) and **22**, 125 (1974).
12. H. M. Manasevit and W. I. Simpson, *This Journal*, **118**, 644 (1971).
13. L. A. Ryabova, Ya. S. Savitskaya, and R. N. Sheftal, *Izv. Akad. Nauk SSSR Neorg. Mater.*, **4**, 602 (1968).
14. C. K. Lau, S. K. Tikku, and K. M. Lakin, Paper 596 presented at The Electrochemical Society Meeting, Los Angeles, California, Oct. 14-19, 1979.
15. J. G. Noltes, in "Zinc Chemicals," M. Farnsworth and C. H. Kline, Editors, p. 212-214, Zinc Institute Inc., New York (1973).
16. M. E. Volpin and I. S. Kolomnikov, in "Organometallic Reactions," Vol. 5, E. I. Becker and M. Tsutsui, Editors, p. 313, Wiley-Interscience, New York (1975).
17. H. I. Smith, in "Surface Wave Filters," H. Mathews, Editor, p. 188, Wiley, New York (1977).
18. W. R. Smith, H. M. Gerard, J. H. Collins, T. M. Reeder, and H. J. Shaw, *IEEE-MTT*, **17**, 856 (1969).
19. F. Pizzarello, *J. Appl. Phys.*, **43**, 3627 (1972).
20. K. M. Lakin and D. Penunuri, IEEE Ultrasonic Symposium, Miami Beach, Paper D-7 (1971) unpublished.

Silicon Oxidation in Fluoride Solutions

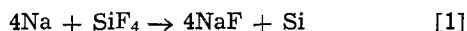
Kenneth M. Sancier and Vijay Kapur*¹

SRI International, Menlo Park, California 94025

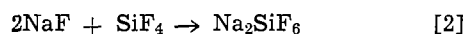
ABSTRACT

Silicon is produced in a NaF, Na₂SiF₆, and Na matrix when SiF₄ is reduced by metallic sodium. Hydrogen is evolved during acid leaching to separate the silicon from the accompanying reaction products, NaF and Na₂SiF₆. The hydrogen evolution reaction was studied under conditions simulating leaching conditions by making suspensions of the dry silicon powder in aqueous fluoride solutions. The mechanism for the hydrogen evolution is discussed in terms of spontaneous oxidation of silicon resulting from the cooperative effects of (i) elemental sodium in the silicon that reacts with water to remove a protective silica layer, leaving clean reactive silicon, and (ii) fluoride in solution that complexes with the oxidized silicon in solution and retards formation of a protective hydrous oxide gel.

A process for producing silicon has been developed at SRI International and is based on the reaction between sodium and silicon tetrafluoride

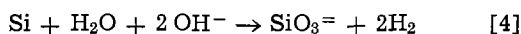
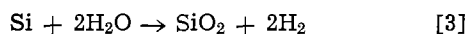


The reaction is initiated at temperatures above 500°K and is highly exothermic. Reaction temperatures lower than 900°K favor formation of some sodium fluosilicate according to the reaction



The reaction product from the SiF₄-Na reaction is a solid mixture of Si, NaF, Na₂SiF₆, and, occasionally, unreacted sodium.

The silicon can be recovered from the reaction product mixture by aqueous leaching of the soluble NaF, Na₂SiF₆, and unreacted Na. Acidic solutions are used for leaching to neutralize unreacted sodium and to avoid the spontaneous oxidation of silicon that occurs rapidly in alkaline solutions



However, even when a strong acid solution is used for leaching, hydrogen evolution may continue for several days. In this paper we discuss the conditions under which hydrogen evolution occurs when silicon powder that is recovered by leaching is added to fluoride solutions to simulate additional leaching.

Experimental Details

Three types of silicon powder were used to study hydrogen evolution. Most of the experiments were performed with silicon that had been recovered by rapid leaching of the soluble fluoride salts from the SiF₄-Na reaction products and then dried. Typically, a 100g batch of the reaction products of the SiF₄-Na reaction was suspended in 4 liters of 1.2N H₂SO₄, agitated for 30 min, and then centrifuged. Eight successive leach-centrifuge steps requiring a total of about 4 hr were sufficient to decrease the fluoride ion concentration in the wash solution to less than 10⁻⁴N. The silicon was then washed with deionized water, dried at 380°K for 1 hr, and stored in a capped polyethylene bottle; in the following discussion this material is referred to as SRI silicon. The average particle diameter was 0.1 μm, as indicated by a measurement of surface area by the BET method. Some of the above reaction products were stored in a plastic bottle, and 122 days later the silicon was recovered by leaching.

* Electrochemical Society Active Member.

¹ Present address: AkCo Solar, Chatsworth, California 91311.

Key words: silicon, silicon oxidation, fluoride, sodium.

Silicon produced by Union Carbide Company by pyrolysis of SiH₄ (with a particle diameter of 0.1 μm) and silicon obtained from Alfa Products (99.5% pure with a particle diameter of less than 44 μm) were also used.

To study hydrogen evolution, we added silicon powder to solutions that were similar to those used during leaching of the reaction products. Typically, 1.0g of silicon powder was added to 100 ml of solution containing H₂SO₄, NaF, or Na₂SiF₆ (Baker, reagent grade). The suspension was contained in a 125 ml plastic bottle that was capped and connected by tubing to an inverted graduated cylinder so that hydrogen gas could be collected by water displacement. The room temperature solubility of hydrogen in the water was neglected. The fluoride ion concentration of the suspension was measured with a fluoride ion-specific electrode (Orion).

The gas evolved from the SRI silicon-fluoride suspension was identified to be hydrogen by mass spectrometry. The SRI silicon was also examined by mass spectrometry at temperatures of up to 1070°K to determine if elemental sodium was present in the silicon.

Results

The SRI silicon powder used in the main part of the study was recovered by rapidly leaching reaction products which had been stored in air for approximately 30 days after the SiF₄-Na reaction was performed. Because gas evolution occurs during leaching, the leaching process was carried out as rapidly as possible to minimize loss of silicon by oxidation (e.g., within 4 hr). Gas evolution studies were first made after the SRI silicon had been stored in a capped bottle for 7 days. The rate of hydrogen evolution increased with increasing the concentration of NaF in the suspension containing SRI silicon and 1.2N H₂SO₄, as shown in Fig. 1. The hydrogen evolution behavior of a suspension containing 0.060M NaF and 1.2N H₂SO₄ was remarkably similar to that containing water saturated with Na₂SiF₆ for which the fluoride ion concentration is comparable. In all cases, the rate of hydrogen evolution decreased with time. The percentage of silicon oxidized, as calculated from the amount of hydrogen evolved (reaction [3]), is indicated on the right-hand ordinate of Fig. 1.

Table I gives, as a function of solution composition, the initial rate of hydrogen evolution indicating that fluoride ions are required in the mechanism of hydrogen evolution.

The hydrogen evolution characteristics of the SRI silicon stored 7 days in air were essentially independent of pH in the range of -0.08 to 9.7 for solutions containing 0.60N NaF, as shown in Fig. 2. However, when this silicon was introduced into 1N NaOH, the rate of

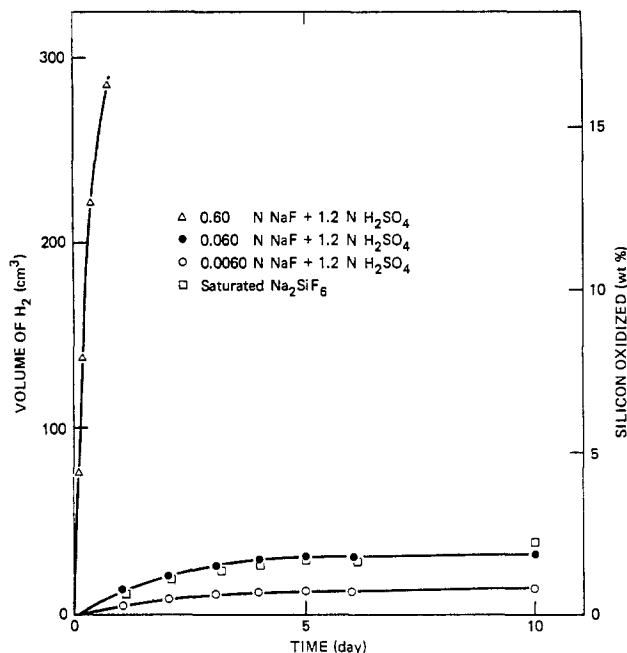


Fig. 1. Hydrogen evolved by SRI silicon in NaF solutions containing 1.2N H₂SO₄ and in water saturated with Na₂SiF₆. Si stored in air 7 days after recovery by leaching, then 1.0g Si added to 100 ml solutions containing a fluoride salt.

hydrogen evolution was 100 times greater than the highest rate observed in acid fluoride solutions.

The evolution rate of hydrogen from SRI silicon in an acid fluoride solution decreased with the storage time of the silicon powder in air (in capped plastic bottle) following leaching. This result is illustrated in Fig. 3 for a given sample of silicon powder that was stored for 7, 94, and 154 days before the hydrogen evolution measurement in a solution containing 0.60N NaF and 1.2N H₂SO₄. To determine whether a protective silicon oxide layer was inhibiting the hydrogen evolution, the 154-day-old sample (Fig. 3) was treated with 50% HF for 1 hr to remove surface silica. The hydrogen evolution behavior was again measured in a solution containing 0.60N NaF and 1.2N H₂SO₄ and was comparable to that originally observed for the 154-day-old sample before the HF treatment. This result shows that the decreased hydrogen evolution rate of aged silicon was not the result of a thick protective silicon oxide layer.

A sample of SRI silicon was also recovered by leaching the products of the SiF₄-Na reaction which had been stored for 122 days. The hydrogen evolution rate of this silicon powder was about the same as that of the 94-day-old silicon (Fig. 3). This result suggests that in silicon that is stored over a given period of time, similar chemical changes occur, either in the reaction products or in the dried silicon powder that is recovered by leaching.

Table I. Initial rate of hydrogen evolution from aqueous suspensions of SRI silicon¹

Fluoride salt		H ₂ SO ₄ concentration (N)	Fluoride ion concentration ² (M)	Initial rate of H ₂ evolution ³ (cm ³ /min)
Salt	Concentration (M)			
NaF	0.60	1.2	2.00×10^{-3}	0.50
	0.060	1.2	1.02×10^{-4}	0.014
	0.0060	1.2	1.05×10^{-5}	0.0060
	0.000	1.2	—	0.000
Na ₂ SiF ₆	Saturated	0	8.00×10^{-5}	0.0015

¹ 1.00g SRI silicon powder in 100 ml solution.

² Measured with a specific ion electrode.

³ Determined from the slopes of the curves 1 hr after mixing the suspension.

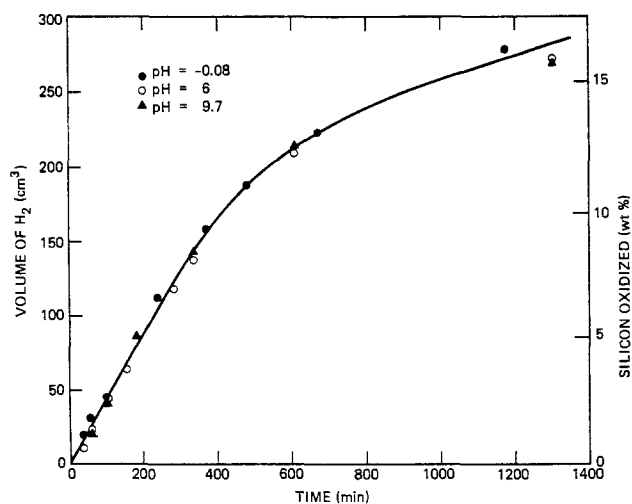


Fig. 2. Hydrogen evolved from reaction between SRI silicon powder and solutions containing 0.60N NaF at 20°C. Si stored in air 7 days after recovery by leaching, then 1.0g Si added to 100 ml of solution.

The results in Fig. 1 through 3 demonstrate that oxidation of the silicon can be appreciable in acid fluoride solutions, for example, at least 16 weight percent (w/o) per day. If the silicon is in continuous contact with such acid fluoride solutions for 8-10 days, 90 w/o of the silicon can be lost by oxidation.

When the other two silicon samples (nonfluoride process) were introduced separately into solutions containing 0.60N NaF and 1.2N H₂SO₄, the rate of gas evolution, presumed to be hydrogen but not analyzed, was much less than that for the SRI silicon. The Alfa Products silicon produced 11 cm³ of gas in the first hour, and evolution then ceased over a monitoring period of 5 days. The Union Carbide silicon produced 44 cm³ of gas slowly over a period of 5 days, and thereafter evolution ceased.

The SRI silicon contained 0.75 w/o sodium (by emission spectroscopy), part of which could be Na, NaF, or Na₂SiF₆ that was not completely removed by leaching. The SRI silicon that had been stored 154 days was examined by high temperature mass spectrometry. At sample temperatures above 575°K, the evolved gases contained sodium atoms, as indicated from the peak at mass 23 and the low appearance potential of 5.5 eV, in agreement with the reported value of 5.1 eV for sodium (2). Above a sample temperature of 650°K, SiF₄ molecules were detected in the gas, indicating that Na₂SiF₆ was present in the silicon. The mass spectrometric

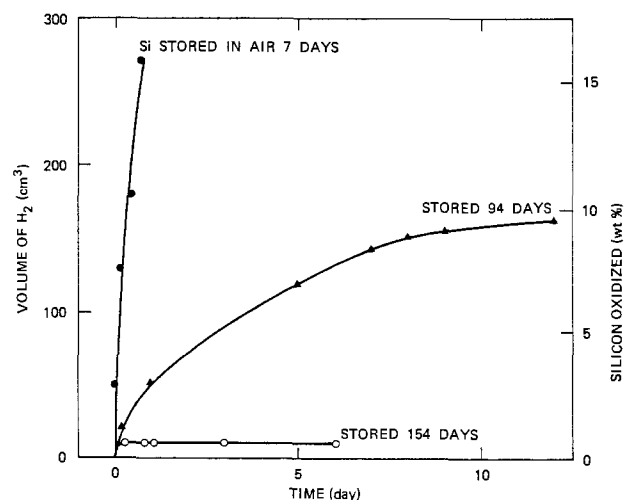


Fig. 3. Hydrogen evolved by SRI silicon powder in acid fluoride solution after storing silicon in air. 1.0g Si in 100 ml solution of 0.60N NaF and 1.2N H₂SO₄.

measurements indicated semiquantitatively that the amount of Na_2SiF_6 in the silicon was greater than that of the elemental sodium.

When the SiF_4 -Na reaction is carried out so that the reaction products contain no unreacted sodium, hydrogen evolution is not observed when the reaction products are immersed in acid fluoride solutions.

Discussion

Hydrogen evolution is known to occur spontaneously when silicon is placed in a strongly alkaline solution, but such evolution has not been observed in acid solutions (3). The evidence discussed here indicates that the SRI silicon is oxidized by the combined effects of sodium in the silicon and high concentrations of fluoride in solution.

The high temperature mass spectroscopy measurements demonstrate that the elemental sodium was driven off from the SRI silicon. These sodium atoms could have originated either from metallic sodium or from sodium silicide. Sodium in the elemental state would be expected to appear in the gas phase at sample temperatures as low as 425°K (4). Although sodium silicide is reported to decompose significantly at temperatures greater than 675°K (5), vapor pressure data are unavailable. In the present discussion the term sodium refers either to the elemental form or to sodium silicide. It should be noted that the sodium atoms observed by high temperature mass spectroscopy could not arise from thermal decomposition of the Na_2SiF_6 impurity in the silicon since the products are SiF_4 and NaF, which is very stable thermally and would have an appearance potential much higher than that of Na.

Hydrogen evolved during simulated leaching did not originate solely from the reaction between sodium and water. If all the sodium in the sample (0.75 w/o by emission spectroscopy) was present as elemental sodium and reacted with water to produce hydrogen, the maximum amount of hydrogen would be about 8 cm^3 or about 3% of the greatest amount shown in Fig. 1.

The mechanism for hydrogen evolution by the SRI silicon in fluoride solutions should take into account the evidence that the rate of hydrogen evolution is related to (i) the presence of sodium in the silicon, (ii) the fluoride ion concentration, and (iii) the age of the silicon after preparation. We propose that a small amount of sodium is incorporated in the silicon, either dissolved in the silicon or trapped in a microporous structure resulting from sintering of small crystallites of silicon. When this sodium reacts with water, hydroxyl ions and hydrogen are produced, and these species can remove the protective surface oxide from the silicon: hydroxyl ions will dissolve silica and will react with silicon to produce more hydrogen. Also, some silica may be dislodged from the surface by the bubbling action of hydrogen evolution, especially in restricted volumes within the microporous structure. The role of sodium in hydrogen evolution is further supported by results from studies with reaction products containing no unreacted sodium, since upon leaching no hydrogen evolution is observed from those reaction products.

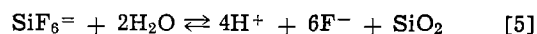
One explanation for a high, local alkalinity in the solution, even though the main solution may be strongly acid, is that the sodium reaction occurs in restricted volumes. For example, the reaction may occur in the microporous structure of silicon crystallites, where the diffusion rate of acid from the solution is small. The generation of hydrogen by reaction [4] can proceed only to the extent that sodium was originally present to produce the local alkaline environment. However, hydrogen evolution by reaction [3] will proceed with clean silicon without consuming hydroxyl ions. We believe that the role of the fluoride is to prevent a passivating layer from forming on the clean and

reactive silicon in the restricted volumes. For example, when the solution near the silicon surface becomes neutral (e.g., as acid diffuses into the microporous structure), silicic acid that results from silicon oxidation will tend to polymerize and form a passivating layer on the silicon. However, fluoride ions at sufficiently high concentration will probably complex with the silicic acid to form species such as $\text{Si}(\text{OH})_3\text{F}^-$, and thus retard formation of a passivating layer. Eventually, enough acid will diffuse into the microporous structure to neutralize the local alkalinity produced by the sodium, and hydrogen evolution will cease.

The protective silicon oxide layer on the outermost surface of silicon may initially be removed by HF which is present in acid fluoride solutions. The dissolution rate of SiO_2 films on silicon is reported to be linearly dependent on the HF concentration (6). Indeed, we observed that the hydrogen evolution produced by SRI silicon is roughly linearly proportional to the HF concentration which is essentially equal to the NaF concentration in acid solutions (Table I). However, the mechanism for removal of the protective oxide layer on silicon by HF cannot apply when the pH of the solution is high enough ($\text{pH} > 5$) to completely hydrolyze the HF to F^- ions. Figure 2 shows that hydrogen evolution characteristics are the same for acid, neutral, and basic fluoride solutions, indicating that HF is not necessarily involved in the hydrogen evolution reaction. Therefore in neutral and basic solutions, F^- ions, rather than HF, must be the active fluoride species. However, fluoride species (HF or F^-) alone are insufficient to cause hydrogen evolution, as indicated for the 154-day-old silicon in Fig. 3. Therefore, the results shown in Fig. 2 support a hypothesis that some common reactive species is responsible for the hydrogen evolution. We suggest that this species is sodium in the silicon and that hydrogen is generated mostly by spontaneous oxidization of silicon by reaction [3].

The decrease in the hydrogen evolution rate with time (Fig. 1 and 2) suggests that a rate-limited process is occurring. First-order kinetics is suggested from the data on the 94-day-old silicon (Fig. 3) when we assume that the limiting amount of hydrogen evolved (175 cm^3) is proportional to some reactant, such as sodium in the silicon that maintains a high local pH. The data for the other two curves in Fig. 3 are inadequate to test for first-order kinetics. Alternatively, the rate-limiting process may be diffusion controlled, as suggested from the linear relationship obtained by replotting the data for the 7-day- and 94-day-old silicon in Fig. 3 according to the parabolic rate law, that is, hydrogen volume *vs.* square root of time. The data for the 154-day-old silicon are inadequate for this analysis. It is possible to account for a diffusion-controlled process in two ways: the sodium is dissolved in silicon and diffuses through the silicon to react with solution, or the sodium metal is trapped in the microporous structure of the silicon and the solution diffuses through this structure to reach the sodium.

To account for the decreased rate of hydrogen evolution that was observed after the SRI silicon was stored for extended periods of time (Fig. 3), we suggest that some water was adsorbed on the silicon or on NaOH resulting from partial Na oxidation. The adsorbed water will hydrolyze sodium fluosilicate, shown to be present in the SRI silicon; thus, weakly acidic products are produced, according to the equilibrium



for which the equilibrium constant is $K_a = 10^{-26}$ (6, 7). Ultimately, if there is sufficient water and fluosilicate, the fluosilicate will completely neutralize the local alkaline regions due to sodium and NaOH that promote spontaneous oxidation of silicon. Subsequent exposure of such silicon to a fluoride solution will not result in

hydrogen evolution, such as in the case of the SRI silicon stored 154 days (Fig. 3).

The mechanism for evolution of the relatively small quantities of gas from aqueous suspensions of the other two silicon samples clearly cannot involve the sodium mechanism discussed above, since sodium was not used in producing these silicon samples. However in the case of the Union Carbide sample, the gas evolved could be due to hydrogen that was incorporated in the silicon during its production by thermal decomposition of SiH_4 to Si and H_2 and that was either attached to defect sites (8) or present as Si-H alloy (9).

Acknowledgments

The authors acknowledge support from the Jet Propulsion Laboratory under Contract No. 954471, NAS 7-100. We also acknowledge contributions of SRI staff valuable discussions with Dr. Leonard Nanis and Dr. Angel Sanjurjo, and high temperature mass spectrographic analyses by Dr. Kai Lau.

Manuscript submitted Dec. 17, 1979; revised manuscript received March 10, 1980.

Any discussion of this paper will appear in a Discussion Section to be published in the June 1981

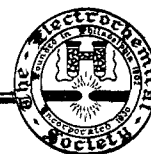
JOURNAL. All discussions for the June 1981 Discussion Section should be submitted by Feb. 1, 1981.

Publication costs of this article were assisted by SRI International.

REFERENCES

1. V. K. Kapur, L. Nanis, and A. Sanjurjo, Submitted to *This Journal*.
2. H. M. Rosenstock, K. Draxl, B. W. Steiner, and J. T. Herron, *J. Phys. Chem. Ref. Data*, **6**, Suppl. 1 (1977).
3. S. O. Izidinov, T. I. Borisova, and V. I. Veselovskii, *Russ. J. Phys. Chem.*, **36**, 659 (1962).
4. D. R. Stull and H. Prophet, Editors, "JANAF Thermodynamical Tables," 2nd ed., NSRDS-NBS-37, U.S. Govt. Printing Office, Washington (1971).
5. M. Hansen and K. Anderlo, Editors, "Constitution of Binary Alloys," McGraw Hill Book Co., Inc. (1958); First Supplement, 1965.
6. J. S. Judge, *This Journal*, **118**, 1772 (1971).
7. J. H. Simon, Editor, "Fluorine Chemistry," Vol. II, p. 127, Academic Press, New York (1954).
8. W. Paul, A. J. Lewis, G. A. N. Connell, and T. D. Moustakas, *Solid State Commun.*, **20**, 969 (1976).
9. E. C. Freeman and W. Paul, *Phys. Rev. B*, **23**, 4288 (1978).

Technical Notes



Modified Poly-Paraxylylene Coatings and Films with Improved Oxidation Resistance

T. E. Baker,* G. L. Fix, and J. S. Judge*

Raytheon Company, Sudbury, Massachusetts 01776

Many studies have been performed on the physical and chemical properties of poly-paraxylylene (2-5). [Parylene is the generic name for members of this well-known polymer series. (1.)] Films of poly-paraxylylene which are produced by vapor phase polymerization are approved as a conformal coating for military electronic assemblies. Although the electrical and physical properties of these films are generally superior to spray applied epoxy or urethane conformal coatings, one inherent shortcoming is their oxidation resistance. The work which is reported in this paper deals specifically with improving the oxidation resistance of films which are produced from the dichloro-di-paraxylylene dimer (6). The techniques and chemistry involved, however, are easily applied to the other poly-paraxylylene polymers as well.

Experimental

The films utilized in this study were produced from dichloro-di-paraxylylene dimer which was obtained from Union Carbide. A Union Carbide Model No. 10C coater was used to produce polymeric films approximately 18 μm in thickness. In all instances the standard processing parameters and temperatures were employed. These conditions are described in detail elsewhere (5) and will not be reiterated here.

For this investigation two separate coating deposi-

tions were performed. In each instance 4×6 aluminum foil panels were employed as the coating substrates. The first deposition was conventional and was produced from 57g of dichloro-di-paraxylylene dimer. The total substrate area was 2320 cm^2 . The second deposition was produced from a homogenous mixture of 21g of dichloro-di-paraxylylene dimer and 0.21g of a sterically hindered phenol, 4,4'-methylene-bis-(2,6-di-tert-butylphenol). The total substrate area was 970 cm^2 .

Oxidative degradation of the polymer films was performed at 140°, 180°, and 200°C in a forced air oven. The relative degree of oxidation was monitored periodically by infrared spectroscopy. The infrared technique of monitoring the oxidation of a material is accomplished by measuring the absorbance intensity of the peak at 1700 cm^{-1} . This absorption peak can be attributed to the organic acid ($-\text{COOH}$) functionality which is formed by oxidative attack. This absorption is not present in either film initially. Its intensity is observed to monotonically increase as a function of time and temperature.

Results

Figure 1 shows the infrared absorption intensity of the 1700 cm^{-1} peak for both films. The data of the figure clearly illustrate that the addition of the antioxidant successfully prevents the oxidation of the poly-paraxylylene polymer for more than 250 hr at 140°C.

* Electrochemical Society Active Member.
Key words: coatings, films, oxidation.

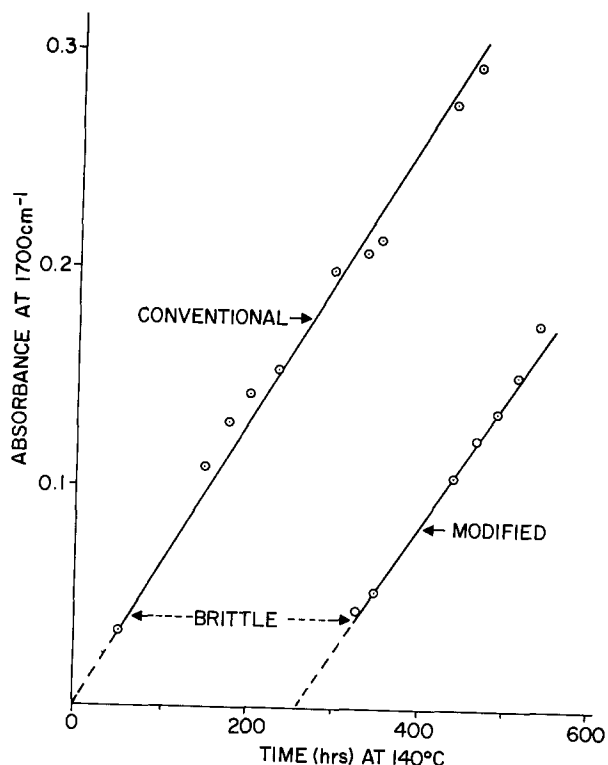


Fig. 1. Plot of absorbance at 1700 cm^{-1} as a function of time at 140°C for conventional and modified poly-paraxylylene films.

The oxidation of the conventional films is seen to be spontaneous. The point on each curve marked "brittle" is the point where the films failed to sustain a 180° bend test. This point corresponds to a peak intensity at 1700 cm^{-1} of 0.04 absorbance units. Similar testing at 180° and 200°C showed that the presence of the antioxidant inhibits oxidation for approximately 5 hr at 180°C and 1 hr at 200°C . Figure 1 also shows that once oxidation is initiated in the modified film the rate of degradation is comparable to that of conventional parylene C. This indicates that the antioxidant activity of the additive is finite and is consumed as a function of time and temperature. Once it is consumed the oxidative mechanisms for both films are identical.

Figure 2 is a plot of the log of the time required to embrittle the two films as a function of the recip-

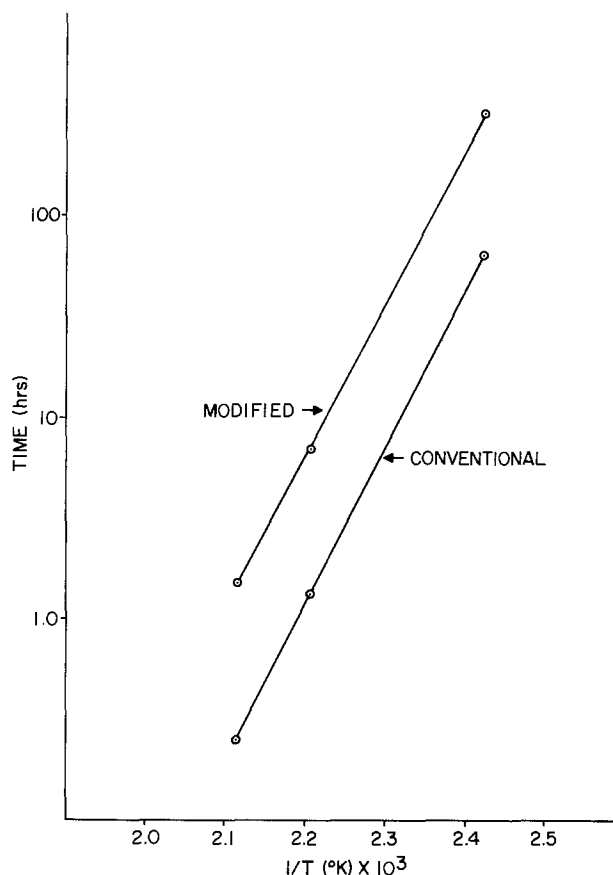


Fig. 2. Plot of the log of the time required to embrittle conventional and modified poly-paraxylylene films as a function of reciprocal absolute temperature.

cal of the absolute temperature ($^\circ\text{K}$). The difference between the two lines at any one temperature is the period of time over which the antioxidant effectively prevents degradation of the film. Table I lists some extrapolated values of the time required to embrittle the two films at lower temperatures.

Summary

Oxidation resistant poly-paraxylylene conformal coatings can easily be produced by incorporating an appropriate antioxidant material into the starting dimer. The resultant polymeric films exhibit greater than five times the service life of conventional unmodified films.

Manuscript received Dec. 11, 1979.

Any discussion of this paper will appear in a Discussion Section to be published in the June 1981 JOURNAL. All discussions for the June 1981 Discussion Section should be submitted by Feb. 1, 1981.

Publication costs of this article were assisted by Raytheon Company.

REFERENCES

1. U.S. Pat. 3,221,068; 3,288,728; and 3,342,754.
2. M. H. Kaufman, H. F. Mark, and R. B. Mesrobian, *J. Polym. Sci.*, **XIII**, 3 (1954).
3. H. H. G. Jellinek and S. H. Ronel, *ibid.*, **9**, 2605 (1971).
4. S. Kubo and B. Wunderlich, *J. Appl. Phys.*, **42**, 4565 (1971).
5. T. E. Baker, S. L. Bagdasarian, G. L. Fix, and J. S. Judge, *This Journal*, **124**, 897 (1977).
6. U.S. Pat. 4,176,209 (1979).

Table I. Comparative service life of conventional and modified poly-paraxylylene films

SERVICE LIFE		
Temperature, $^\circ\text{C}$	Conventional	Modified
80	11 yrs.	58 yrs.
90	1.5 yrs.	8 yrs.
100	10 mos.	55 mos.
115	42 days	250 days
150	22 hrs.	130 hrs.

Analysis of Hydrogen Content in Plasma Silicon Nitride Film

Takeo Yoshimi, Hideo Sakai, and Keizo Tanaka

Computer Development Laboratories, Limited, Kodaira, Tokyo, Japan

Plasma-activated silicon nitride (P-SiN) films (1-7) are widely applied as final chip passivation films for silicon devices. It is important to control the hydrogen content, H_2 , and the atomic ratio, Si/N, in the P-SiN film in order to obtain good mechanical properties, such as film stress and crack resistance, and electrical and optical properties. Both the H_2 and the Si/N in the P-SiN film deposited by an SiH_4-NH_3 reaction are affected by various deposition parameters such as temperature, rf-power input for plasma activation, pressure, and reactant ratios, SiH_4/NH_3 . In this work, composition of the H_2 in the P-SiN film was performed by using a quadrupole mass analyzer (8) during high temperature annealing. The ratio, Si/N, in the P-SiN film was determined by Auger electron spectroscopy (AES) and electron spectroscopy for chemical analysis (ESCA) for various deposition conditions. From these measurements, film compositions, $Si_xN_yH_z$, of the P-SiN film, were determined.

Experimental and Results

The production of P-SiN film was carried out through reaction of SiH_4 , NH_3 , and N_2 mixtures in the plasma-activated reactor. The reactor design consisted of two parallel electrodes with one electrode connected to a 2 kW, 50 kHz rf power supply (9) and the other grounded. Conditions for the P-SiN film deposition were as follows: deposition temperature 130°-350°C, total gas flow 1200 ml/min, rf input power 250-800W, and pressure 0.2 Torr (0.27×10^2 Pa). The system for quadrupole mass analysis of the H_2 in the P-SiN film is schematically shown in Fig. 1. A silica tube was 2 cm in inner diameter, 40 cm long, and the hot zone was 20 cm long. Film thickness of a sample deposited in the plasma-activated reactor was measured with a Talystep. The sample was put into the silica tube and evacuated to 1.3×10^{-4} Pa. The hydrogen content in the P-SiN film was measured in the annealing temperatures ranging from 400° to 900°C. The duration of heat-treatment in the quadrupole mass analysis was 20 min for temperatures of 400°, 500°, 600°, 700°, 800°, and 900°C, as shown in Fig. 2. The Si/N ratio was measured as a function of deposition temperature by AES and ESCA.

Key words: hydrogen content, quadrupole mass analysis, step coverage, crack resistance, protection film.

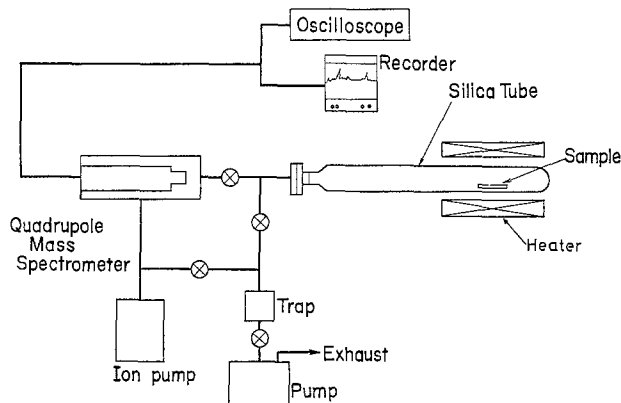


Fig. 1. System of quadrupole mass analyzer used for analysis of hydrogen content in P-SiN film.

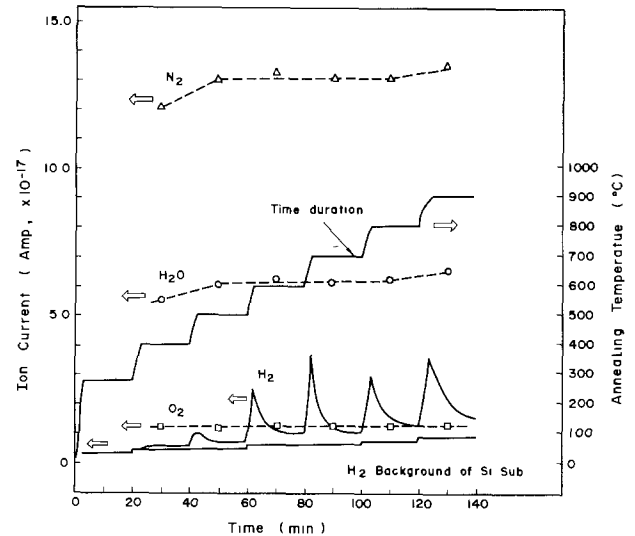


Fig. 2. Time duration for hydrogen content measurement with quadrupole mass analyzer.

The relationship between H_2 and rf power is shown as a parameter of deposition temperature, 270°, 310°, and 350°C, in Fig. 3. The H_2 obtained by annealing

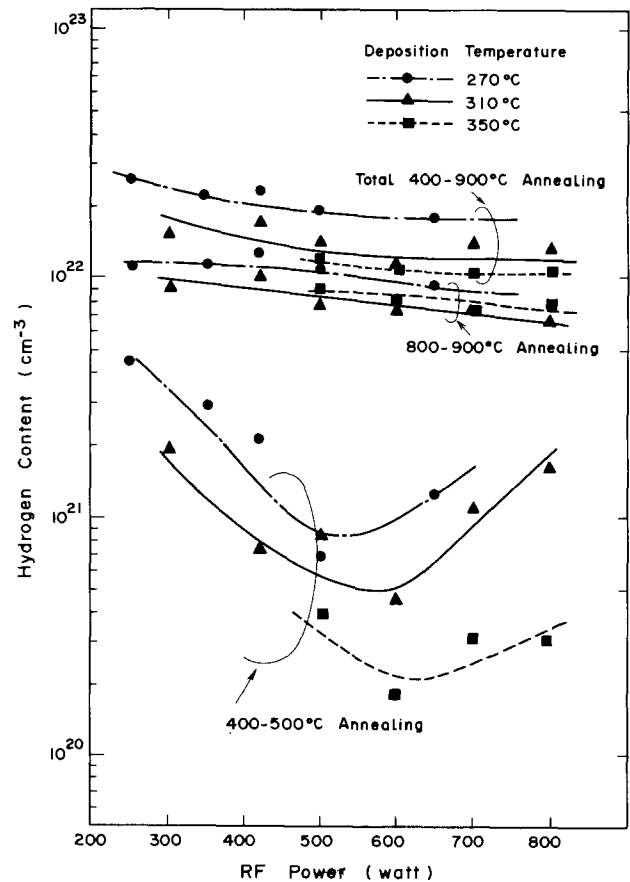


Fig. 3. Variation of hydrogen content with rf power

at 400°-500°C, was clearly a function of rf power. The total amount of hydrogen dissociated from the P-SiN film through the annealing temperature range, 400°-900°C, was about $1-3 \times 10^{22} \text{ cm}^{-3}$ at each deposition temperature and rf power 250-800W. The deposition temperature dependences of the H_2 are shown in Fig. 4 at rf power of 420W. At lower annealing temperatures (400°-600°C), H_2 was influenced strongly by the deposition temperature. When the P-SiN film was deposited at 305°C, the H_2 was $1 \times 10^{20} \text{ cm}^{-3}$, or approximately 10 times less than that obtained at a deposition temperature of 130°C. The total H_2 obtained at annealing temperature decreased gradually with increasing deposition temperature.

An SiH_4 flow rate of 120-150 ml/min and an NH_3 flow rate of 150-350 ml/min had little effect on the H_2 and the dependence of H_2 on pressure, 0.1-0.4 Torr, was even less.

The quantitative technique of quadrupole mass analysis was useful and sensitive for the measurement of hydrogen content in the P-SiN film. The H_2 was $3.6, 3.1, 2.8,$ and $2.0 \times 10^{22} \text{ cm}^{-3}$ for deposition temperatures of 130°, 220°, 270°, and 305°C, respectively. H_2 removed by annealing until 900°C was 80-85% of total H_2 included in the P-SiN film. The dependence on higher frequency (MHz) of the H_2 was not investigated in the same deposition system.

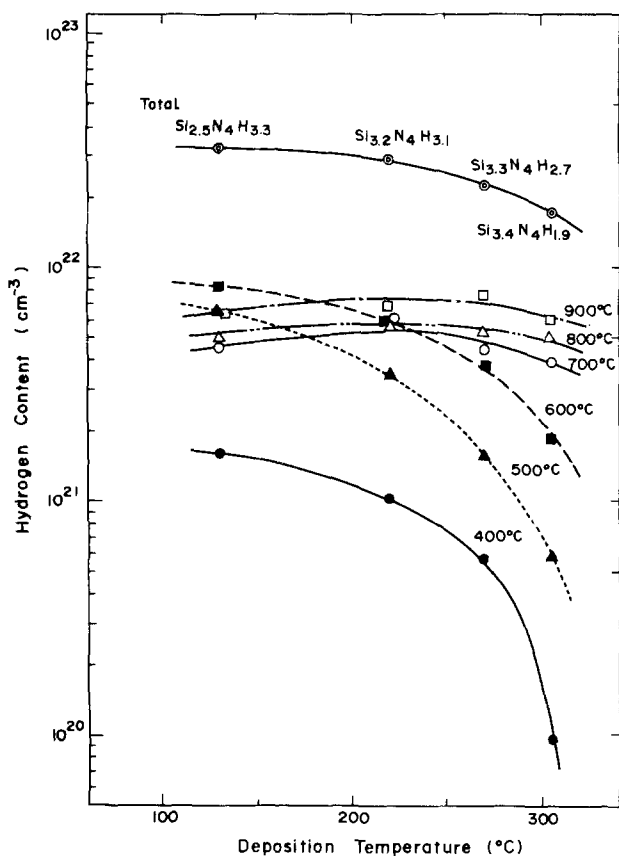


Fig. 4. Variation of hydrogen content with deposition temperature.

Table I. Hydrogen content and composition in P-SiN film

Measurements					Calculation	
depo temp	ref index	density	H content	Si/N ^{**}	wt % of H	Si _x N _y H _z ^{***}
(°C)		(gr/cm ³)	($\times 10^{22} \text{ cm}^{-3}$)			
130	1.95	2.3	3.6	0.62	2.6	Si _{2.5} N ₄ H _{3.3}
220	2.03	2.5	3.1	0.81	2.1	Si _{3.2} N ₄ H _{3.1}
270	2.07	2.6	2.8	0.83	1.8	Si _{3.3} N ₄ H _{2.7}
305	2.11	2.7	2.0	0.86	1.2	Si _{3.4} N ₄ H _{1.9}

* Quadrupole mass analysis

** Auger electron spectroscopy and electron spectroscopy for chemical analysis

*** A composition of nitrogen, N_y, is normalized of 40.

The Si/N in the P-SiN film was determined from an integral spectrum, produced by computer from a differential spectrum. It is considered that the atomic ratio, Si/N, and the H_2 affect characteristics on Si devices, such as resistivity and crack resistance. A summary of these results is shown in Table I. Hydrogen content was found at a concentration of about $1-4 \times 10^{22} \text{ cm}^{-3}$ in the P-SiN film deposited under the various deposition conditions, such as reactant ratio $\text{SiH}_4/\text{NH}_3 = 0.50$, pressure 0.20 Torr, rf power 250-800W, deposition temperature 130°-305°C, and an electrode spacing of 2 in. (5 cm). The film composition of the P-SiN film deposited at 305°C and 420W was $\text{Si}_{3.4}\text{N}_{4.0}\text{H}_{1.9}$, corresponding to 1.2 weight percent of hydrogen. P-SiN film should be deposited by higher deposition temperature to reduce the H_2 .

Acknowledgments

The authors would like to thank Mrs. M. Shibata for quadrupole mass analysis. Special thanks to Dr. K. Sugawara and Mr. M. Ohno for the discussions and encouragements in this work.

Manuscript submitted Nov. 26, 1979; revised manuscript received March 13, 1980.

Any discussion of this paper will appear in a Discussion Section to be published in the June 1981 JOURNAL. All discussions for the June 1981 Discussion Section should be submitted by Feb. 1, 1981.

Publication costs of this article were assisted by Computer Development Laboratories, Limited.

REFERENCES

1. R. C. G. Swann, R. R. Mehta, and T. P. Cauge, *This Journal*, **114**, 713 (1967).
2. R. J. Joyce, H. F. Sterling, and J. A. Alexander, *Thin Solid Films*, **1**, 481 (1967).
3. Y. Kuwano, *Jpn. J. Appl. Phys.*, **7**, 88 (1968).
4. Y. Kuwano, *ibid.*, **8**, 867 (1969).
5. R. Greth and W. Scherber, *This Journal*, **117**, 1248 (1972).
6. A. K. Sinha, H. J. Levinstein, T. E. Smith, G. Quintana, and S. E. Haszko, *ibid.*, **125**, 601 (1978).
7. M. J. Helix, K. V. Vaidyanathan, and B. G. Streetman, *Thin Solid Films*, **55**, 143 (1978).
8. T. Yoshimi, H. Sakai, and K. Sugawara, *This Journal*, **123**, 1140 (1976).
9. W. Kern and R. S. Rosler, *J. Vac. Sci. Technol.*, **14**, 1082 (1977).

Determination of the Diffusion Coefficient of Thallium in KCl Crystal by Electron Irradiation

K. Goswami, S. Chaudhuri, D. P. Banerjee, and A. Chaudhury

Department of Physics, Jadavpur University, Calcutta—700032, India

Thallium-doped ionic crystals are important for their application as detectors for ionizing radiations. The Tl atoms are usually incorporated into the crystal during growth from its melt and the product is known as phosphor. Phosphors can also be made by the process of thermal diffusion of Tl in alkali halide crystals. Although a lot of work (1, 2) has accumulated on the diffusion phenomenon in solids, limited attention (3) has been applied to diffusion of Tl in alkali halide crystals.

The incorporation of Tl atoms in the KCl lattice is found to create luminescent centers in the host crystal. For constant external conditions of excess Tl atoms at the crystal surface in equilibrium with an external vapor, the distribution is well described by a complementary error function (4). The luminescence yield under electron irradiation from successive depths of the activated crystal is related to the Tl penetration into the crystal and can be used to obtain information on the diffusion process in alkali halide phosphors. If a solid is exposed to a volume of metal vapor having a uniform concentration N_0 atoms per unit volume, these atoms will diffuse into the solid medium following an equation (4)

$$N(x, t) \approx N_0 \left(1 - \operatorname{erf} \frac{x}{2\sqrt{Dt}} \right) = N \operatorname{erfc} \frac{x}{2\sqrt{Dt}} \quad [1]$$

When a KCl crystal is doped with Tl atoms, it becomes a phosphor. If it is assumed that the luminescence yield is linearly proportional to the concentration of Tl atoms in the host crystal the ratio $N(x, t)/N_0$ in Eq. [1] may be replaced by $L(x, t)/L_0$, where $L(x, t)$ is the luminescence yield due to Tl atoms as a function of the distance x from the surface, t is the period of heat-treatment, and L_0 is the yield from the surface. Equation [1] takes the form

$$\frac{L(x, t)}{L_0} \approx \operatorname{erfc} \left(\frac{x}{2\sqrt{Dt}} \right) \quad [2]$$

An experimental determination of $L(x, t)/L_0$ as a function of x may lead to the evaluation of the diffusion coefficient D . The activation energy of diffusion (E) may also be estimated using an equation

$$D = D_0 \exp(-E/kT) \quad [3]$$

Experimental

A block of cleaved KCl $\langle 100 \rangle$ crystal (Harshaw Chemical) and properly distilled thallium metal of known weight were put in a glass tube. The glass tube had two intercommunicating sections separated by a constriction to avoid direct contact between the sample and the metallic Tl. The tubes were sealed under vacuum, heated at diffusion temperatures for a period of 4 hr, and quenched to room temperature. Four such KCl samples were doped with Tl at four different temperatures, 573°, 623°, 673°, and 723°K. The time and other conditions for the doping process were kept the same in all the cases.

The doped crystals were inserted into an electron accelerator tube and irradiated with normally incident 5 keV electrons. Beam current was $0.5 \mu\text{A cm}^{-2}$.

Key words: potassium chloride, thallium diffusion, luminescence.

The intensity of luminescence was measured by an RCA IP21 photomultiplier. All doped samples showed luminescence spectra under electron irradiation peaking at 3050 and 4750Å while no luminescence was detected in the case of pure KCl crystal. The diffusion of Tl was followed by measuring the intensity of luminescence at the surface of the specimen and at various depths along $\langle 100 \rangle$ direction by successive removal of surface layers.

Results and Discussion

The luminescence spectrum peaking at 4750Å at room temperature is in conformity with that of others (5, 6). The depth of Tl diffusion has been measured from luminescence yield observed under 5 keV electron irradiation. At such an energy (5 keV) the electron penetration is very low (less than $1 \mu\text{m}$) and the observed luminescence is primarily due to doped atoms present in a shallow surface layer of the specimen. In the present experiment the Tl concentration had been sufficiently low and accordingly (7) the luminescence yield may be considered to be proportional to the number of atoms and the ratio $L(x, t)/L_0$ between the luminescence yields at a depth x and at the surface should be equal to $N(x, t)/N_0$ as assumed in Eq. [2]. The ratio of luminescence yields $L(x, t)/L_0$ is determined for different values of x shown in Table I.

The values of $y = x/2\sqrt{Dt}$ for various observed values of $L(x, t)/L_0$ are computed from the graphical solution of Eq. [2].

A graph between y and x is plotted in Fig. 1 for different temperatures of heat-treatment. The straight line plots passing through the origin support the conclusion that the complementary error function solution is valid in this case of vapor to solid phase diffusion. From the slope of the curve of Fig. 1 the values of the diffusion coefficient for different temperatures of doping have been determined and are also shown in Table I.

The values of the diffusion coefficient increase as the temperature of diffusion rises. A plot of $\log_{10} D$ vs. $1/T$ is shown in Fig. 2. The plot is a straight line satisfying the relation as stated in Eq. [3]. From the slope of the straight line (Fig. 2), the activation energy of diffusion is estimated and found to be

Table I. Measured $L(x, t)/L_0$ at various depths of KCl:Tl and diffusion coefficient for different temperatures of heat-treatment, period of heat-treatment 4 hr. Electron energy 5 keV and beam current $0.5 \mu\text{A cm}^{-2}$

Depth in microns	Ratio $\frac{L(x, t)}{L_0}$ for			
	573°K	623°K	673°K	723°K
5	0.733	—	—	—
10	0.556	0.600	0.674	0.692
15	0.289	0.444	0.533	0.582
20	0.156	0.300	0.440	0.462
25	—	0.178	0.315	—
30	—	0.100	0.212	0.297
35	—	0.044	—	—
40	—	—	0.098	0.187
50	—	—	—	0.082
D in $\text{cm}^2 \text{sec}^{-1}$	0.8×10^{-10}	1.2×10^{-10}	2.0×10^{-10}	2.8×10^{-10}

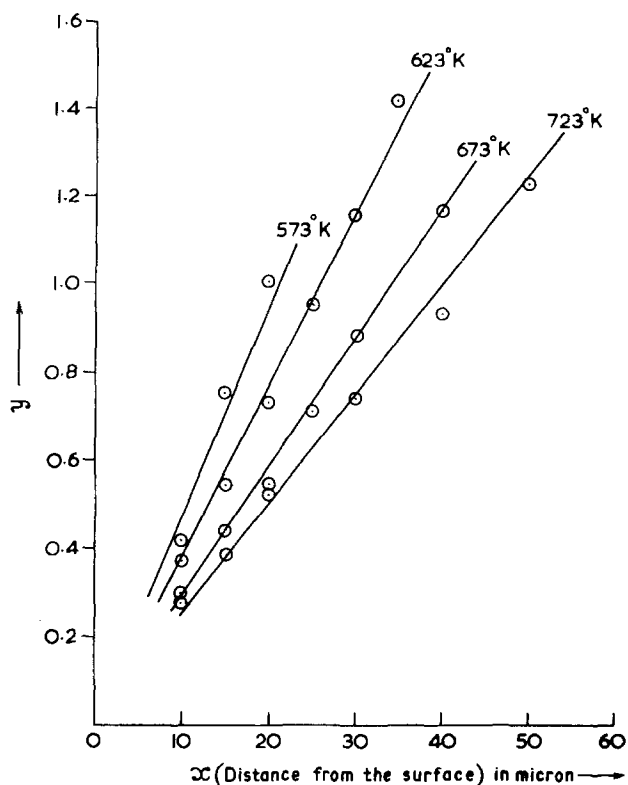


Fig. 1. Computed values of y as a function of distance (x) from the surface for different temperatures of heat-treatment.

$E = 0.32$ eV (temperature of heat-treatment between 573° and 723°K). The value of activation energy (E) is quite low but is in reasonable agreement with the work of Tierman and Wuensch (3).

Manuscript submitted Dec. 11, 1978; revised manuscript received March 2, 1979.

Any discussion of this paper will appear in a Discussion Section to be published in the June 1981 JOURNAL. All discussions for the June 1981 Discussion Section should be submitted by Feb. 1, 1981.

REFERENCES

1. W. Jost, "Diffusion in Solids, Liquids and Gases," Academic Press, New York (1955).

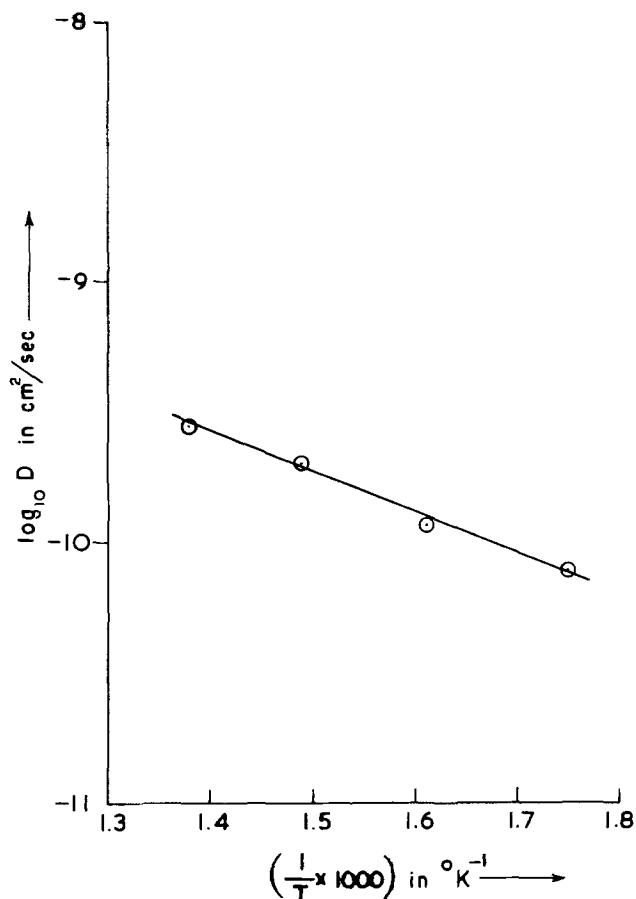


Fig. 2. Variation of $\log_{10} D$ with reciprocal of temperature of doping for KCl:Ti.

2. A. B. Lidiard, *J. Phys. Chem. Solids*, **6**, 298 (1958).
3. R. J. Tierman and B. J. Wuensch, *J. Chem. Phys.*, **55**, 4996 (1971).
4. H. S. Carslaw and J. C. Jaeger, "Conduction of Heat in Solids," Clarendon Press, Oxford (1959).
5. P. D. Johnson and F. E. Williams, *J. Chem. Phys.*, **20**, 124 (1952).
6. A. Ranfagni, G. P. Pazzi, P. Fabeni, C. Villani, and M. P. Fontanne, *Phys. Rev. Lett.*, **28**, 1035 (1972).
7. P. D. Johnson and F. E. Williams, *J. Chem. Phys.*, **18**, 1477 (1950).



A Chemical Method for the Deposition of Thin Films of Bi_2Se_3

P. Pramanik, R. N. Bhattacharya, and A. Mondal

Department of Chemistry, Indian Institute of Technology, Kharagpur 721302, India

Thin film formation of selenide of Pb^{2+} by chemical deposition is a very well known process (1,2,3), but chemical methods of deposition of thin films of bismuth selenide have not yet been reported. This brief communication describes a chemical method for the deposition of Bi_2Se_3 thin films.

A sodium selenosulfate solution was prepared by refluxing 5g selenium powder with 12g of sodium sulfite (anhydrous) in 100ml of water for about 5 hours. It was cooled and kept overnight, since on cooling a little selenium separated out from the solution. It was then filtered to obtain a clear solution.

One gram of $\text{Bi}(\text{NO}_3)_3 \cdot 5\text{H}_2\text{O}$ was triturated with 10ml of triethanolamine and then 50ml of water was added to it. The resulting solution was continuously stirred till a nearly clear solution was obtained, which was then filtered.

Ten millilitre of the Bi^{3+} solution was taken in a glass beaker. To it 4ml of 0.65(M) NH_4OH and 10ml of the sodium selenosulfate solution were added and the volume was made upto 100ml with water. It was then poured into another glass beaker containing two cleaned glass slides, which were clamped vertically. It was kept at room temperature (30°C) for about two hours. Uniform films of Bi_2Se_3 were obtained on the glass substrates. They were then taken out, washed with water and dried in air. When the solution contained 2ml of hydrazine hydrate, the films had more metallic lustre and better electrical conductivity, but the deposition time was reduced to 30 minutes since on longer staying the films became brittle. The Bi_2Se_3 films were about 0.1 - 0.2 microns thick.

NH_4OH was added to slow down the formation of Bi_2Se_3 and to increase the adherence of it on the glass substrate.

X-ray diffraction data showed that the film deposited from the solution which was free of hydrazine hydrate contained traces of elemental selenium. Selenium deposition was due to atmospheric oxidation of Se^{2-} .

X-ray diffraction data in both the cases, with hydrazine hydrate and without hydrazine hydrate, showed distinct d-lines of Bi_2Se_3 . Scanning electron microscopy showed that films contained random distribution of small crystallites shown in figures (1) and (2). Specific resistance of the film obtained from the solution without hydrazine hydrate was 2.4×10^5 ohm-cm. and that of the film obtained from the solution with hydrazine hydrate was 4.5×10^2 ohm-cm. Optical band-gap was found to be 1.15eV for the first case and 1.03eV for the second case, as shown in figure (3). All the films were photoconductive in nature. More detailed studies are in progress.

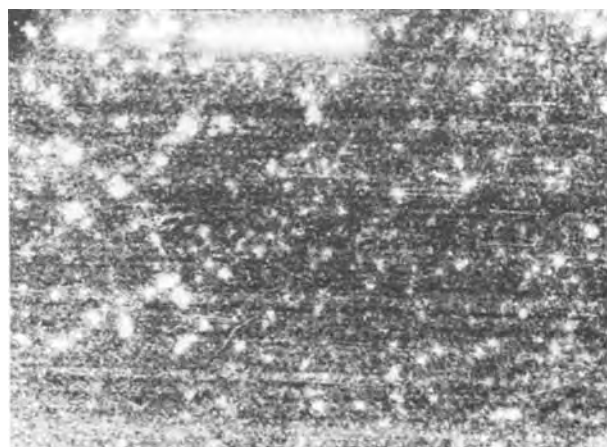


Fig. 1: Scanning electron micrograph of Bi_2Se_3 (in presence of hydrazine hydrate), (Secondary Electron; 1090X)

Key words: thin film, chemical deposition, bismuth selenide.

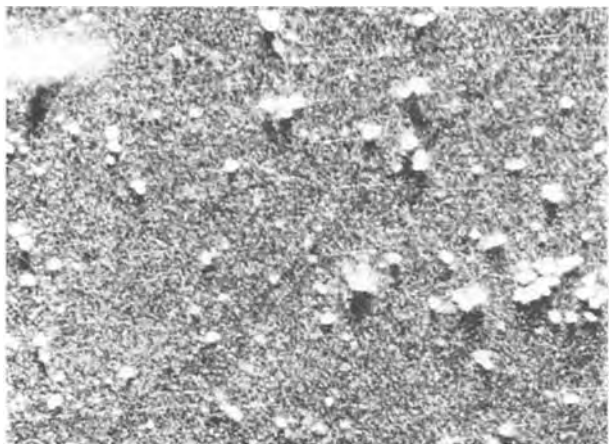


Fig. 2: Scanning electron micrograph of Bi_2Se_3 (without hydrazine hydrate), (Back scattered Electron; 1210X)

REFERENCES

1. T.S. Moss, Proc. IRE **43**, 1869 (1955).
2. J. Bloem, App. Sci. Res. **6B**, 92 (1956).
3. D.H. Roberts and J.E. Baines, J. Phys. Chem. Solids **6**, 184 (1958).

Manuscript submitted March 24, 1980;
revised manuscript received May 13, 1980.

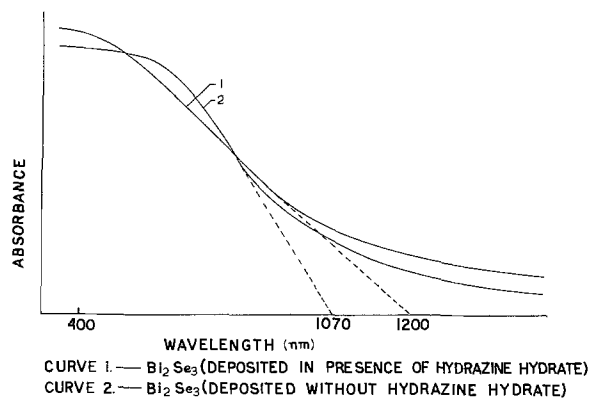


Fig. 3: Electronic absorption spectra

A Dry Etching Technique Using Electron Beam Resist-PBS

T. Yamazaki, Y. Watakabe, Y. Suzuki,* and H. Nakata

Mitsubishi Electric Corporation LSI Research and Development Laboratory 4-1 Mizuhara, Itami, Hyogo, Japan

The technology of electron beam lithography is of great importance for the fabrication of devices directly on silicon, and for the patterning of photomasks. Although electron beam resists such as PMMA, PBS and others have already been used for many experiments, the acceptance of these resists in the manufacturing environment has been very slow due to the uncertainties associated with processing of these materials.

Among the many electron beam resists, PBS has the best combination of resolution, sensitivity, and adhesion. The main limitation to PBS is its poor resistance to dry etching environments which attributed to plasma depolymerization which enhances the rate of film loss.

The purpose of this paper is to demonstrate a new technique of gas plasma etching of chromium photomask films using PBS. Figure 1 shows the etching resistance of PBS to the gas plasma environment for chromium photomask etching, together with other

electron beam resists and AZ-1350. In this experiment, gas plasma etching was carried out in a barrel type plasma reactor, in which the gas plasma was generated by RF discharge at 13.56 MHz. The pressure in the reactor was maintained at 0.2 torr. and the RF power was kept at 240 W. The etching gas was a mixture of CCl_4 , N_2 , and O_2 .

From Fig. 1, it is apparent that the loss rate of PBS is high compared with AZ-1350 or the electron beam resists COP and FMR. Since the etch rate of the chromium film is $50 \text{ \AA}/\text{min.}$ in this gas plasma condition and the loss rate of PBS film is $1140 \text{ \AA}/\text{min.}$, it would be necessary to use more than 14000 \AA of PBS film for a 600 \AA chromium film.

In a previous paper, we reported on the reversal gas plasma etching technique for chromium films using AZ-1350 (1). In this paper, in order to obtain fine patterns with an electron beam exposure technique, we have used PBS instead of AZ-1350 in the

* Present address; Computer Development Laboratories Limited,
4-1, Mizuhara, Itami, Hyogo, Japan

Key words; Gas Plasma, Photomask, Electron Beam Resist.

reversal gas plasma etching of chromium photomasks. Figure 2 shows photographs at different stages of the reversal plasma etching process where PBS was used as the patterning film.

The photomasks used in this experiment consisted of an anti-reflective chromium film, comprised of a chromium oxide film on a chromium film all deposited on a glass substrate. The thickness of the chromium oxide film and the chromium film were 200 Å and 600 Å, respectively. The photomask size was 4 x 4 inches. The chromium oxide film was deposited by resistance heating and the chromium film was deposited by flash evaporation. The PBS processing was the same as the one described by Bowden (2). The thickness of PBS films were 4000 Å, measured by a Talystep. An AES analysis of the chromium oxide film showed that tungsten impurities are included in the surface of the chromium oxide film. These impurities are assumed to be caused by evaporation of the tungsten boat during heating. The elemental concentration ratio of tungsten to chromium at the surface layer was 0.6 as determined by AES analysis.

As we described in the previous paper, in reversal gas plasma etching, a naturally grown WO_3 layer in the surface of a chromium oxide film works as a masking layer for the gas plasma environment and the decomposed species of the resist film react with the WO_3

masking layer to remove it while the resist film is decomposing. PBS, which is very weak to the gas plasma environment, can be used as a patterning resist for reversal gas plasma etching if its decomposition time is long enough for the decomposed species to react with WO_3 masking layer. In the case of AZ-1350 which has high resistivity to the plasma environment, a long time is required to decompose all of the resist film. Accordingly, the decomposed species react with WO_3 near a photoresist pattern and make it difficult to control pattern widths precisely. In the case of a PBS film, as the decomposition of the film occurs quickly, the decomposed species can react with WO_3 layer just underneath the patterning film and sharp edged patterns can be obtained. Figure 3 shows an example of a photomask which was prepared by the reversal gas plasma etching, and demonstrates good edge profiles for minimum 2 μm line width.

In summary, a new gas plasma etching technique using the electron beam resist PBS, which is known as a very weak resist for dry etching environments, has been demonstrated. With this new technique, 2 μm line widths were obtained with chromium photomasks.

ACKNOWLEDGEMENT

The authors express their appreciation to Dr. Oka for his encouragement.

REFERENCES

- (1) T. Yamazaki, Y. Suzuki, J. Uno and H. Nakata, *This Journal*, **126**, 1794 (1979).
- (2) M. J. Bowden, L. F. Thompson and J. P. Ballantyne, *J. Vac. Sci. Technol.*, **12**, 1294 (1975).

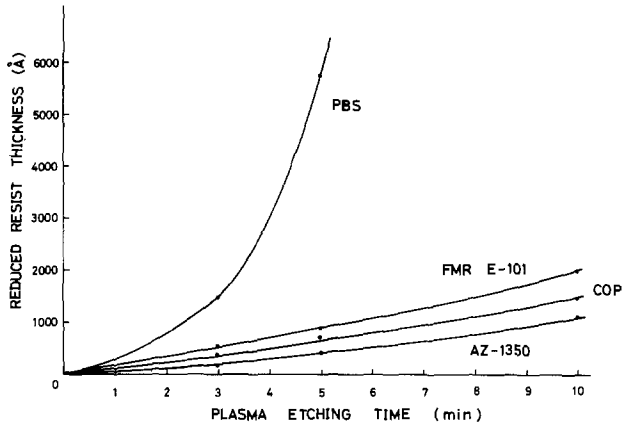


Fig. 1. The relation between plasma etching time and resist thickness reduction.

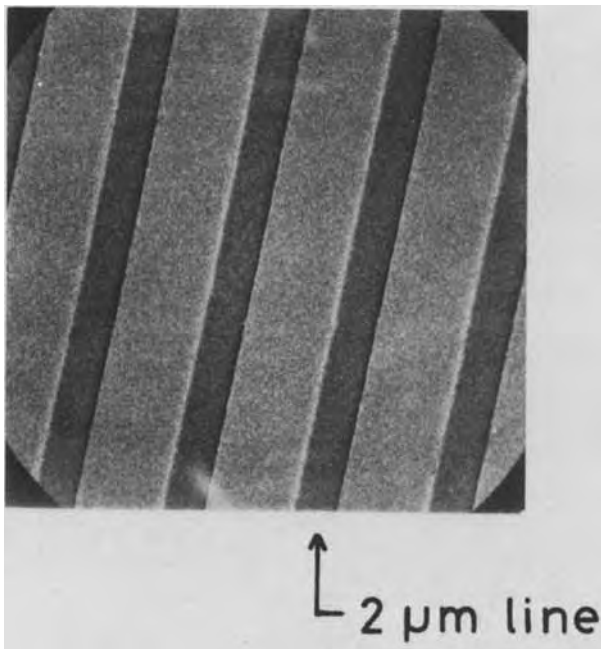


Fig. 3. An SEM photograph of a mask prepared by PBS reverse gas plasma etching.

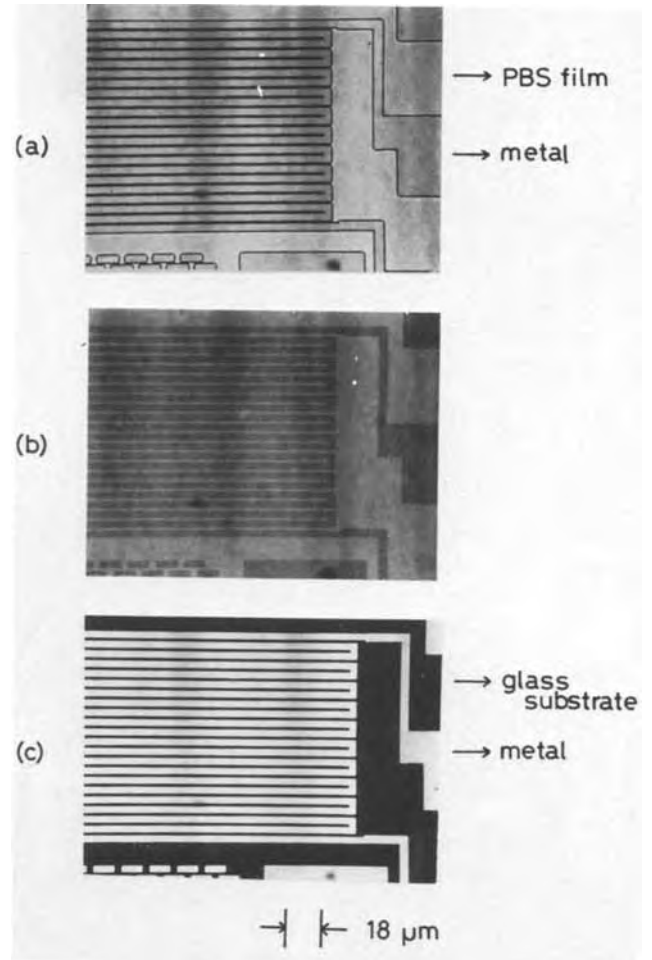


Fig. 2. Photographs at different stages during reverse gas plasma etching. (a) Reflection photograph of a sample before etching. (b) Reflection photograph of a sample after 10 min etching. (c) Reflection photograph of a sample after 15 min etching.

Manuscript received March 27, 1980.

Publication costs of this article were assisted by Mitsubishi Electric Corporation.

Radiation Damage Estimates and Control in Ion-Beam Lithography

K. F. Galloway*

National Bureau of Standards, Electron Devices Division, Washington, DC 20234

The purpose of this note is to present estimates of the radiation dose absorbed in critical device dielectric layers during the application of ion-beam lithography (IBL). Ion-beam lithography has been demonstrated as a technique providing sub-micrometer resolution with the capability of large throughput in work recently reported by Rensch et al. (1) and by Seliger and Sullivan (2). These estimates should facilitate the comparison of this technique with other techniques delivering a radiation dose to device structures during processing.

Device structures fabricated with x-ray or electron-beam lithographic techniques receive absorbed radiation doses in critical dielectric layers in excess of 1 Mrad(SiO₂) (3). This process-related radiation exposure may affect the ultimate reliability and radiation hardness of devices so fabricated (3,4,5). In fact, the radiation hardness of devices fabricated using x-ray lithography has been shown to be diminished even though the damage due to the lithography was apparently annealed out (5).

In order to arrive at the desired estimate for radiation dose due to IBL, a description of the behavior of an ion beam passing through multiple thin films is required. The technique of Bernstein and Kolodny (6) has been used to obtain such a description. Consider the schematic illustration of Fig. 1. ϕ_0 and E_0 are the incident fluence (ions/cm²) and incident ion energy (keV) impinging on the layered film structure. ϕ_1 and E_1 are the fluence and average ion energy passing from film one into film two and so on. The number of ions stopped in any film is indepen-

dent of the following films. Assuming the distribution to be Gaussian, the number of ions stopped in film one is found by integrating the ion density distribution

$$n(x_p) = \frac{\phi_0}{\phi_p \sqrt{2\pi}} \exp \left\{ \frac{-(x_p - R_p)^2}{2\sigma_p^2} \right\}$$

over the film thickness using R_p (projected range) and σ_p (straggle) from the tabulated values for ion-film-energy combinations (7); x_p is measured along the direction of incidence of the beam. The fluence into film two (ϕ_1) is found by subtracting the number stopped in film one from ϕ_0 . This procedure is then followed for each subsequent film. The increase in straggle as the ions pass

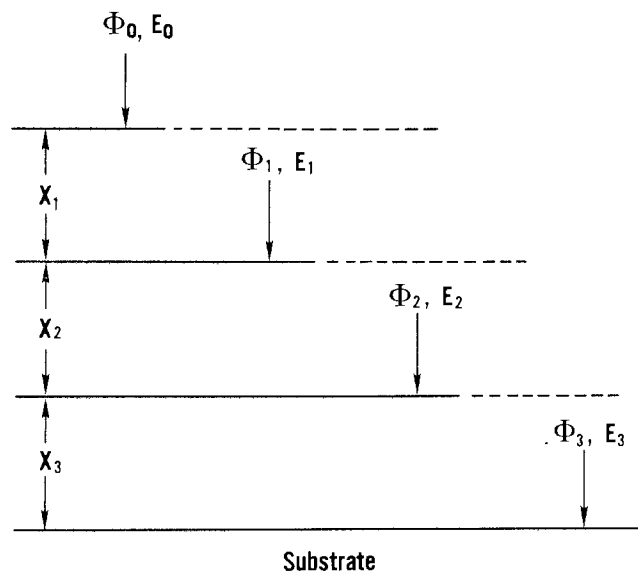


Fig. 1. Schematic illustration of three films of thickness x_1 , x_2 , and x_3 , respectively, on a semi-infinite substrate with the ion fluence and average ion energy entering each film indicated.

through the several films has been ignored as have such subtleties as ion backscattering at film interfaces and the departures of the ion penetration distribution from a Gaussian due to higher order moments in the solution of the range equation. E_1 , the average ion energy entering film two after passing through film one, is found using the tables (7) as follows:

1. Find $R_p(E_0, \text{film one})$, the projected range that the ion beam of energy E_0 would have in film one if the film were infinitely thick.
2. Subtract the thickness of film one, x_1 , from $R_p(E_0, \text{film one})$.
3. If $R_p(E_0, \text{film one}) < x_1$, the ion beam is essentially stopped in film one and E_1 is approximately zero.
4. Otherwise, find E_1 as the energy required for an ion to have a range $R_p(E_1, \text{film one}) = R_p(E_0, \text{film one}) - x_1$.

This procedure for obtaining the average ion energy (6) is then repeatedly applied as the ions pass through each film in the layered structure.

Consider the application of the procedure discussed in the preceding paragraph to a structure where a silicon substrate is covered by a 0.05- μm thick film of silicon dioxide which is covered by a 1.0- μm thick film of aluminum metallization which is in turn covered with a 1.0- μm thick film of photoresist to be patterned by IBL. Since AZ11 is the only resist considered in the tables (7), its tabulated parameters were used; the estimates based on these parameters are expected to be typical of other resists. The average energy per ion deposited in the oxide layer is calculated as $E_2 - E_3$ (see Fig. 1), and using ϕ_2 , the total energy deposited and the dose can be calcu-

lated. In the ion-energy regimes considered here, electronic interaction processes dominate possible nuclear interaction processes (7). Typical values of the ion beam parameters have been selected from the work of Rensch et al. (1). If E_0 is 200 keV and the incident ions are protons, $E_2 - E_3$ is 8 keV and $\phi_2 \sim \phi_1 \sim \phi_0$ for the structure considered. For ϕ_0 of $2 \times 10^{13}/\text{cm}^2$, the radiation-absorbed dose in the silicon dioxide layer is approximately 220 Mrad(SiO_2).* If E_0 were 58 keV, the proton projected range in the aluminum film would be 0.8 μm , and the projected standard deviation would be 0.187 μm . Thus, the proton beam would be stopped in the aluminum film and there would be no absorbed dose in the oxide layer (ignoring beam straggle beyond a standard deviation, possible x-ray production, and secondary electrons).

If the aluminum film in the material configuration above is replaced by a 1.0- μm thick film of polysilicon, there are differences in radiation-absorbed dose in the oxide layer because of differences in the projected range for ions in polysilicon as compared to that for ions in aluminum. The radiation-absorbed dose in the silicon dioxide layer under the polysilicon film is approximately 200 Mrad(SiO_2) for a proton beam with an E_0 of 200 keV and a ϕ_0 of $2 \times 10^{13}/\text{cm}^2$. If E_0 were 93 keV, the proton projected range in the polysilicon film would be 0.8 μm and the projected standard deviation would be 0.111 μm . If beam straggle beyond a standard deviation, possible x-ray production, and secondary electrons are ignored, there will no radiation-absorbed dose in the oxide film for proton beams with energy less than 93 keV.

If the aluminum or polysilicon represents the gate metallization of an MOS device, a positive resist and an etch-back process (plasma or ion etching) will probably be utilized. In this case, no ions will be inci-

* The SI unit for absorbed dose is the gray (Gy) in units of J/kg. One rad equals 1×10^{-2} Gy.

dent on the gate oxide layer. However, laterally scattered radiation might be expected to yield significant radiation exposures in the vicinity of the gate metallization edges.

The estimates presented here indicate that the radiation-absorbed dose in device oxide layers when applying ion-beam lithography can be substantial. It has been shown that annealing temperatures higher than 550°C are required to remove both the positive and neutral traps generated by ionizing radiation from the oxide layers (8). Also, it should be noted that the implantation of protons in device oxides has been suggested as a technique for advantageously tailoring device interface states (9). The estimates also indicate that by carefully matching the ion beam energy to the material configuration, the radiation-absorbed dose in critical oxide layers can be essentially eliminated. In general, this means operating with a beam energy which is as low as practicable after accounting for mask membrane penetration (1) and allowing for loss of resolution due to beam scattering and which is high enough to achieve uniform exposure and minimize lateral scattering in the resist. This ability to reduce the radiation-absorbed dose in the oxide is perhaps a significant advantage over electron-beam or x-ray lithography (3).

ACKNOWLEDGMENT

The author would like to thank D. R. Myers and J. H. Albers for useful discussions and the authors of references (1) and (2) for preprints of their work.

*Electrochemical Society Active Member.

Manuscript received May 5, 1980.

Publication costs of this article were assisted by the National Bureau of Standards.

REFERENCES

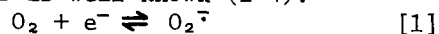
1. D. B. Rensch, R. L. Seliger, G. Csanky, R. D. Olney, and H. L. Stover, *J. Vac. Sci. and Technol.* 16, 1897 (1979).
2. R. L. Seliger and P. A. Sullivan, *Electronics* 53, No. 7, 142 (1980).
3. K. F. Galloway, S. Mayo, and P. Roitman, *This Journal* 126, 2245 (1979).
4. K. F. Galloway, *IEEE Trans. Nucl. Sci.* NS-25, 1469 (1978).
5. H. L. Hughes, *IEEE Trans. Nucl. Sci.* NS-26, 5053 (1979).
6. T. Bernstein and A. Kolodny, *IEEE Trans. Electron Devices* ED-24, 1365 (1977).
7. J. E. Gibbons, W. S. Johnson, and S. W. Mylorie, *Projected Range Statistics*, 2nd ed. (Dowden, Hutchinson and Ross, Inc., 1975. Distributed by Halsted Press.)
8. J. M. Aitken, *IEEE Trans. Electron Devices* ED-26, 372 (1979).
9. G. W. Arnold, *IEEE Trans. Nucl. Sci.* NS-20, No. 6, 220 (1970).

Observations on the Mechanism of the Reaction of Electrogenerated Superoxide Ion with 2-Phenylenediamine

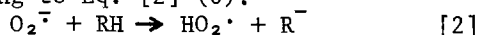
C. L. Hussey,* T. M. Laher, and J. M. Achord

Department of Chemistry, The University of Mississippi, University, Mississippi 38677

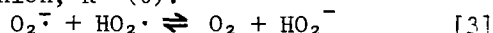
The one-electron quasireversible reduction of oxygen to superoxide ion, O_2^- , in aprotic solvents is well known (1-4).



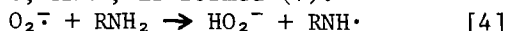
Superoxide ion has been shown to function as a base, nucleophile and reductant in reactions with organic compounds (5). It also possesses the enigmatic ability to act as an oxidizing agent toward certain organic compounds under conditions which appear thermodynamically unfavorable for it to do so (6). This property of O_2^- is of considerable interest to workers studying the role of O_2^- in biological systems. It is generally believed that the first step in these oxidations involves proton transfer from the substrate to O_2^- , according to Eq. [2] (6).



Actual oxidation of the substrate is postulated to result from the reaction of $HO_2\cdot$ or O_2 , the latter produced by the disproportionation reaction depicted in Eq. [3], with the substrate anion, R^- (6).



Recent synthetic explorations of the reaction of O_2^- with phenylenediamines, employing KO_2 , resulted in the isolation of oxidation products, e.g., nitrosoanilines, nitroanilines, and diaminoazobenzenes (7, 8). On the basis of these products, the oxidation of phenylenediamine by O_2^- was postulated to entail an initial hydrogen abstraction process in which a phenylenediamino radical intermediate, $RNH\cdot$, is formed (7).



We wish to communicate electrochemical data concerning the reaction of electrogenerated O_2^- with 2-phenylenediamine (2-PDA) which contributes to further understanding of the involvement of proton transfer in these reactions.

EXPERIMENTAL

Electrochemical experiments were carried out in N,N-dimethylformamide, DMF, (Burdick and Jackson) with a specified water content of

0.004%. The supporting electrolyte, tetra-n-butylammonium perchlorate, TBAP, was synthesized according to standard procedures and dried at 100°C in a vacuum for several days. The 2-phenylenediamine (Eastman) was recrystallized twice from chloroform and dried in a vacuum for 24 hrs. The cell and electrodes, electrochemical instrumentation, and experimental procedure are detailed in a companion publication (9).

RESULTS AND DISCUSSION

Cyclic voltammograms, corresponding to the process represented in Eq. [1], at a glassy carbon electrode in O_2 saturated DMF containing 0.1 M TBAP are shown in Fig. 1. In the presence of 2-PDA the O_2^- reoxidation peak at -0.82 V in Fig. 1 is diminished, and peaks representing the oxidation of products are apparent. As shown in Table I, the cyclic voltammetric peak current ratio, i_p^a/i_p^c , for the O_2/O_2^- electrode process is less than 1.0 in the presence of 2-PDA, but increases toward 1.0 as the scan rate, ν , is increased. Values of the voltammetric current function, $i_p^c/\nu^{1/2}$, for oxygen reduction given in Table I are the same within experimental error at each scan rate tested regardless of whether 2-PDA is added. The cyclic voltammetric data given in Table I for the O_2/O_2^- process in the presence of 2-PDA match diagnostic criteria presented by Nicholson and Shain (10) for a charge transfer process followed by an irreversible chemical reaction, i.e., an EC mechanism.

Table I. Cyclic Voltammetric Data for the O_2/O_2^- Electrode Reaction at 40.0°C.

ν (V/s)	i_p^a/i_p^c		$i_p^c/\nu^{1/2}$ (mA s ^{1/2} /V ^{1/2})	
	O_2	$O_2 + 2-PDA^1$	O_2	$O_2 + 2-PDA^1$
0.02	1.00	0.58	2.1	2.2
0.05	1.00	0.73	2.0	2.0
0.10	1.01	0.80	1.9	1.9
0.20	1.02	0.87	1.8	1.8
0.50	1.00	0.90	1.7	1.6
1.00	1.03	0.92	1.6	1.5

¹The concentration of 2-PDA was 0.1 M.

*Electrochemical Society Active Member

Key words: free radicals, organic, kinetics

Further indication of an EC mechanism was obtained using chronopotentiometry. Figure 2 shows a chronopotentiogram with current reversal for the process represented by Eq. [1] in oxygen saturated solutions with and without added 2-PDA. The reverse transition time, τ_r , for reoxidation of O_2^- is decreased considerably in the solution containing 2-PDA and additional waves representing the oxidation of products are apparent. The ratio, τ_r/t_f , where t_f is the forward electrolysis time, is 0.3 for the oxygen reduction-reoxidation process without added 2-PDA but decreases to 0.1 when 2-PDA is added to the solution. Behavior of this nature can be attributed to an EC process (11).

These electrochemical data suggest that the reduction of O_2 in solutions containing 2-PDA involves a charge-transfer process to form O_2^- followed by homogeneous irreversible chemical reactions in which O_2^- attacks 2-PDA. The overall process appears complex, since both cyclic voltammograms and chronopotentiograms exhibit waves due to the oxidation of numerous products. Furthermore, the O_2 reduction process in the presence of 2-PDA involves the same number of electrons as the O_2 reduction process without added 2-PDA, since data for $i_p^c/\nu^{1/2}$ in the last two columns of Table I are virtually identical. Additional support for this conclusion is obtained from chronoamperometric experiments in which a potential step from 0 to -1.25 V was applied to the working electrode in O_2 saturated solvent and the resulting current was recorded as a function of time. Values of $it^{1/2}$ for the O_2 reduction process obtained from these experiments are shown in Table II. No significant increase in $it^{1/2}$ is evident for O_2 reduction in the presence of 2-PDA compared to $it^{1/2}$ for O_2 reduction without added 2-PDA.

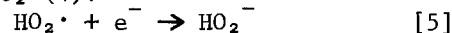
Table II. Chronoamperometric Data for the Oxygen Reduction Process at 40.0°C

t (s)	$it^{1/2}$ (mA s ^{1/2})	
	O_2	$O_2 + 2-PDA^1$
2.0	0.51	0.56
4.0	0.52	0.57
6.0	0.53	0.58
8.0	0.53	0.59
10.0	0.54	0.61
12.0	0.55	0.62

¹The concentration of 2-PDA was 0.1 M.

If proton transfer from the phenylenediamine to O_2^- were a significant step in the overall mechanism, whereby the organic substrate is oxidized, then it should be possible to observe the reduction of HO_2^* produced by proton transfer to O_2^- . This process would be

concurrent with the reduction of O_2 according to Eq. [5], since HO_2^* is more readily reduced than O_2 (4).



An overall reduction sequence represented by Eqs. [1], [2], and [5] should produce a voltammetric response indicative of an ECE process (12). In addition, O_2 produced by the reaction represented in Eq. [3] would also contribute to the initial O_2 reduction current (13). In any case, if proton transfer to O_2 by 2-PDA were a significant process, the reduction of O_2 in the presence of 2-PDA would involve more than one electron and both $i_p^c/\nu^{1/2}$ and $it^{1/2}$ would be enhanced. This response would be similar to that reported for the reaction of electrogenerated O_2^- with proton donors, when O_2^- is electrogenerated in the presence of acidic organic or inorganic substrates and course of its existence is followed electrochemically (4, 9, 14, 15). We also observed this behavior experimentally for the reduction of O_2 in the presence of ascorbic acid which is known to undergo net oxidation in the presence of O_2^- (16).

The preliminary electrochemical data presented in this communication suggest that O_2^- attacks 2-PDA via a pathway which circumvents an initial proton transfer step. Thus, proton transfer does not appear to be important in all cases for which net oxidation of an organic substrate by O_2^- is reported. Our results appear consistent with a process involving Eqs. [1] and [4], although the overall mechanism may be complex. Further nonelectrochemical studies will be required to delineate the exact pathway by which these reactions take place.

ACKNOWLEDGMENT

This work was supported by Lawrence Livermore Laboratories through Subcontract No. 4288309 and through a University of Mississippi Faculty Research Grant.

REFERENCES

1. D. L. Maricle and W. G. Hodgson, *Anal. Chem.*, **37**, 1562 (1965).
2. D. T. Sawyer and J. L. Roberts, Jr., *J. Electroanal. Chem.*, **12**, 90 (1966).
3. E. L. Johnson, K. H. Pool, and R. E. Hamm, *Anal. Chem.*, **38**, 183 (1966).
4. M. E. Peover and B. S. White, *Electrochim. Acta.*, **11**, 1061 (1966).
5. E. Lee-Ruff, *Chem. Soc. Rev.*, **6**, 195 (1977).
6. D. T. Sawyer, M. J. Gibian, M. M. Morrison and E. T. Seo, *J. Am. Chem. Soc.*, **100**, 627 (1978).
7. G. Crank and M. I. H. Makin, *Tett. Lett.*, 2169 (1979).

8. E. Balogh-Hergovich, G. Speier, and E. Winkelmann, *ibid.*, 3541 (1979).
9. C. L. Hussey, T. M. Laher, and J. M. Achord, *This Journal*, in press.
10. R. S. Nicholson and I. Shain, *Anal. Chem.*, **36**, 706 (1964).
11. A. C. Testa and W. H. Reinmuth, *ibid.*, **32** 1512 (1960).
12. R. S. Nicholson and I. Shain, *ibid.*, **37** 178 (1965).
13. M. D. Hawley and S. W. Feldberg, *J. Phys. Chem.*, **70**, 3459 (1966).
14. J. E. A. Toni, *This Journal*, **116**, 212 (1969).
15. H. J. James and R. F. Broman, *J. Phys. Chem.*, **75**, 4019 (1971).
16. E. F. Elstner and R. Kramer, *Biochim. Biophys. Acta*, **314**, 340 (1973).

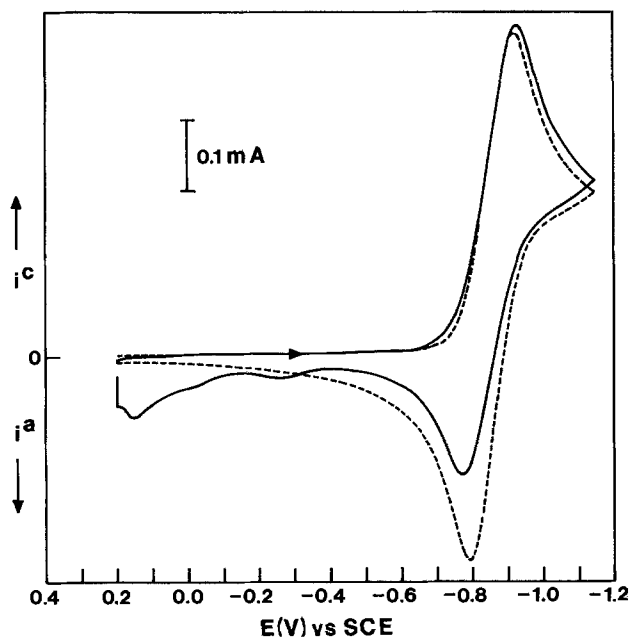


Figure 1. Cyclic voltammograms at a glassy carbon electrode (area = 0.22 cm²) in DMF + 0.1 M TBAP at 40.0°C, (dashed line) saturated with O₂ at 1 atm., (solid line) saturated with O₂ at 1 atm. and 0.1 M in 2-PDA. Sweep rates were 0.050 V/sec.

Manuscript submitted March 1, 1980;
revised manuscript received May 20, 1980.

Publication costs of this article were
assisted by The University of Mississippi.

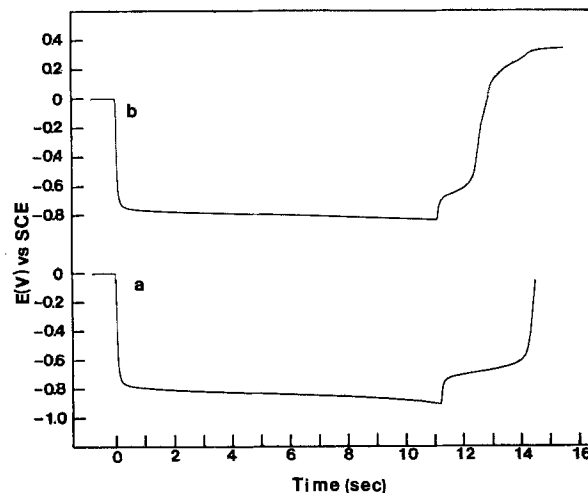
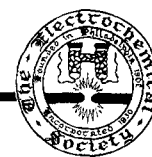


Figure 2. Current reversal chronopotentiograms at a glassy carbon electrode (area = 0.22 cm²) in DMF + 0.1 M TBAP at 40.0°C, a. saturated with O₂ at 1 atm., b. saturated with O₂ at 1 atm. and 0.1 M in 2-PDA. Current was 225 μA.



Properties of Lead Dioxide Doped with Antimony

F. Caldara, A. Delmastro, G. Fracchia, and M. Maja*

Istituto di Elettrochimica, Politecnico di Torino, Torino, Italy

ABSTRACT

The effects of antimony on the electrocrystallization and on the electrochemical behavior of α and β lead dioxide were investigated by scanning electron microscopy, x-ray diffraction, and chemical analysis. Galvanostatic reduction tests in alkaline solutions were also performed. Antimony drastically modifies the crystal morphology of α lead dioxide and, up to a concentration of 0.2%, changes the O/Pb ratio by filling lattice vacancies. On β PbO_2 , on the contrary, antimony does not seem to have any significant influence. The reduction tests on lead dioxide showed that the cathodic process occurs in a homogeneous system until the O/Pb ratio reaches a value depending on the dioxide allotropic form and on the antimony content. The O/Pb ratio of intermediate oxide increases from pure α PbO_2 (1.33) to Sb-doped β PbO_2 (1.65).

For many years the most relevant effects of antimony on the performance of lead acid batteries have been known (1-4). Antimony, which is present in the grids as an alloying element to improve mechanical properties and castability of lead alloys, dissolves in the electrolyte and then reacts with the active material.

On negative plates, antimony has a detrimental influence poisoning the sponge lead and inducing local electrochemical action which causes self-discharge. In addition the presence of antimony affects the charge efficiency. The increase of the amount of antimony on the sponge lead is partially avoided by stibine formation during charge periods.

For positive plates, some studies (5-9) have shown a different behavior of the plates with antimonial lead grids compared to those without antimony; there is evidence that antimony improves some properties of the positive active material.

Burbank (5) characterizing positive active material with SEM and x-ray diffraction, showed that antimony modifies the crystal size and habit of lead dioxide and promotes α PbO_2 formation. Ritchie and Burbank (6) examined the behavior of lead acid cells with pure and antimonial lead grids, concluding that cells with pure lead grids were losing slow discharge capacity more rapidly than the antimonial cells.

Antimony appears to act as an inhibitor for the growth of dioxide crystals or as a nucleating catalyst, thus reducing average crystal size.

Swets (7) suggested that the increase of α PbO_2 in the active material during the life of the batteries with antimonial lead grids is due to the formation of meta-antimonate. This compound, identified by x-ray diffraction, should passivate the dioxide during the discharge of the plates and should help the nucleation of α PbO_2 during the recharge period. Dawson (8) studied the chemical reaction involving solvated antimony ions in lead acid batteries and the adsorption of antimony on lead dioxide.

Maskalick (9) measured antimony adsorption on positive active material during accelerated life tests

* Electrochemical Society Active Member.

Key words: lead acid cell, electrocrystallization, photoeffects, lead dioxide reduction.

showing the buildup of a greater concentration in positive active material compared with the negative

Simon (10) showed another phenomenon directly related to antimony: the formation (when Sb_2O_3 is added during paste mixing) of acicular crystals, precursors of PbO_2 crystals. Recently Abdularim and Asmail (11) reported that the addition of Sb_2O_3 to positive active material enhances the capacity of positive plates.

The mode of influence of Sb on the morphology of positive active material is still not clear. Ritchie and Burbank (6) suggested that antimony in the form of pentavalent ions, according to the positive plate potential, could both enter the lead dioxide lattice, occupying Pb^{4+} positions, and be absorbed at growth sites on the lead dioxide crystal surface.

The present work concerns the effect of antimony on the properties and electrocrystallization of lead dioxide. For this purpose various samples of Sb-doped lead dioxide were prepared by electrolyzing plumbous salt solutions to which different quantities of antimony were added. The samples were analyzed to determine antimony concentration and the oxygen/metal atomic ratio (O/Pb). The semiconducting properties and the electrochemical characteristics of Sb-doped lead dioxide were also determined. These semiconducting properties were investigated by means of photoeffect measurements; the electrochemical characteristics were studied by analyzing the linear sweep voltammetry (LSV) curves traced during the reduction of the samples in alkaline solutions. The effect of antimony on the structure of lead dioxide was investigated using x-ray diffraction and scanning electron microscopy.

The effect of antimony on the reactivity of α and β PbO_2 was recently reported by Brenet (12) and co-workers. From galvanostatic reduction curves, traced in 8N H_2SO_4 , 10^{-4} N Sb_2O_3 solution, these authors deduced an influence of antimony on the electrochemical reactivity of lead dioxide.

With regard to semiconducting properties, Mindt (13) investigated resistivity, Hall effect, and optical absorption of electrodeposited α and β PbO_2 and stated that the n-semiconduction of PbO_2 could be due to deviation from stoichiometry or to incorporation of hydrogen in the lattice.

Other lead oxides (14) present semiconducting properties and clearly display photoconductivity in the visible region of the light spectrum.

Pavlov (15) studied the photoeffects on PbO_x formed on the lead and its photo-activation. Lyamina (16) evaluated the semiconducting properties of partially reduced PbO_2 by studying the dioxide behavior in a redox system concluding that there is an inhibition of the reduction processes.

Concerning dioxide reduction in alkaline solutions, Jones (17) and Glickman (18) observed, during galvanostatic reduction of lead anodically oxidized, two potential arrests on the voltage-time curves corresponding to the couples PbO_2/PbO and PbO/Pb . Ezerskii (19) showed that during dioxide reduction in hot concentrated alkaline solutions, at high current density ($i > 100 \text{ mA/cm}^2$), Pb_3O_4 is formed by reaction of HPbO_2^- ions with the PbO_2 layer. Lyamina (20, 21), in contrast to the previous results, found that the dioxide reduction proceeds in a homogeneous system until the O/Pb ratio reaches a value near 1.3, then lead formation begins to occur. Moreover, this author (20) pointed out that the process limiting the cathodic current is oxygen diffusion in the solid phase.

Chartier (22) traced potentiodynamic and galvanostatic curves for α and β PbO_2 reduction in dilute alkaline solutions and showed that lead dioxide passivates at a potential below PbO formation. From galvanostatic curves this author deduced also that the reduction mechanism of the two allotropic lead dioxide forms is different.

Carr and Hampson (23) studied α PbO_2 reduction by fast linear voltammetry and they observed two cathodic peaks at potentials corresponding to the reduction of α PbO_2 to PbO and PbO to Pb . The β PbO_2 reduction seems to be complicated by a transformation of β PbO_2 to α PbO_2 which occurs at the electrode surface.

Experimental

Anodic layers of α and β PbO_2 were electrodeposited on a gold substrate according to methods described in the literature (24). α PbO_2 was deposited at 30°C from a 2N KOH solution saturated with PbO at a current density of 10 mA/cm^2 . β PbO_2 was obtained at 25°C from 0.15N $\text{Pb}(\text{NO}_3)_2$, 0.15N HNO_3 solution at a current density of 100 mA/cm^2 . The nitric acid solution was also used to deposit mixtures of α and β PbO_2 which were analyzed by x-ray technique considering reflection lines from (111) plane for the α PbO_2 and from (110) plane for β PbO_2 .

To obtain antimony-doped lead dioxide, Sb_2O_3 dissolved in KOH was added to the solution used to deposit lead dioxide. The concentration of trivalent antimony ions was in the range 0–100 ppm.

Some of the anodic deposit of pure and doped lead dioxide were finely ground, washed in 1M KOH or in 10% HNO_3 solution, rinsed in doubly distilled water, and analyzed to determine the O/Me ratio and the antimony amount. The O/Me ratio was determined by means of iodometric titration (25). This analytical technique was previously tested by measuring the O/Mn ratio for Mn_2O_3 samples prepared by calcining pure MnCO_3 at 700°C . The standard deviation of these measures was smaller than 0.01%. The antimony amount in the anodic deposit was determined by means of an atomic absorption technique.

The reduction of pure and doped lead dioxide was carried out in pure 1M and 5M KOH solutions at a temperature of 22°C . For this purpose linear sweep voltammetry (LSV) curves were traced with a low scan rate ($200 \mu\text{V}/\text{sec}$). During the reduction, the amount of charge required by the cathodic process was measured with an electronic integrator; the amount of charge and the current intensity were recorded vs. the electrode potential.

The working electrode, made of gold covered with lead dioxide layers 2–8 μm thick, had a surface area of

0.8 cm^2 . The reference half-cell was an Hg/HgO electrode and the counterelectrode was a Pt foil. To determine the change of lead dioxide structure and the appearance of new phases during the cathodic processes, some reductions were interrupted at various electrode potential. Subsequently the partially reduced samples, rapidly removed from the cell, rinsed with water and dried with acetone, were analyzed by x-ray diffraction and were observed at the SEM.

To determine the effects induced by light on the electrochemical cathodic processes the working electrode was illuminated with a chopped (13 Hz) white light of a mercury lamp (OSRAM HBO-200) during the slow potentiodynamic reductions, and the photocurrents were detected by means of a lock-in amplifier.

Results and Discussion

Pure lead dioxide.—X-ray diffraction patterns of anodic layers showed that crystals are strongly oriented. α PbO_2 layers displayed a very very strong line from (200) plane ($d = 2.48 \text{ nm}$) in agreement with literature data (26, 27). β PbO_2 layers, on the contrary, gave a strong line from (031) plane ($d = 1.486 \text{ nm}$). In both cases the remaining lines were very weak or absent. The diffraction patterns recorded from finely ground anodic layers displayed the characteristic peaks, reported in ASTM cards (No. 11-549 and 25-447).

Concerning the O/Me ratio measurements, the results obtained by analyzing 50 samples, by iodometric technique, showed that lead dioxide has a chemical composition corresponding to $\text{PbO}_{1.87}$ for the α allotropic form and corresponding to $\text{PbO}_{1.92}$ for the β form. In Fig. 1 and 2 are represented the electron micrographs of both allotropic forms of electrodeposited lead dioxide.

Sb effect on the structure.—When α PbO_2 is deposited from solutions containing trivalent antimony ions, it can be observed that x-ray reflection lines from powdered samples are weakly shifted toward lower angles; this shift is particularly evident (0.05°) for the reflection lines from (110) and (111) plane when the antimony concentration in the electrolyte is greater than 60 ppm.

Small modifications seem to occur in the diffraction patterns of powdered β PbO_2 samples; only a slight broadening of the peaks can be observed. X-ray analysis of α and β mixtures codeposited showed that antimony favors α PbO_2 formation. The increase of α form has been about 20% when Sb concentration in the solution is 100 ppm and the α/β ratio for pure PbO_2 is 1.

Chemical analysis.—Chemical analysis showed that antimony concentration in the anodic deposits in-

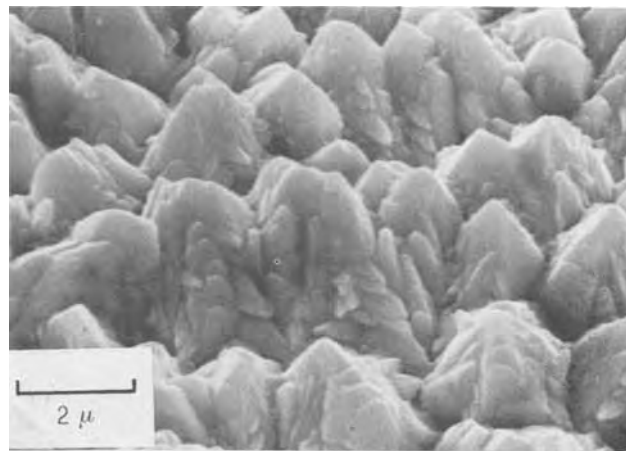


Fig. 1. SEM micrograph of pure α PbO_2 electrodeposited from 2N KOH saturated with PbO ; $i_{\text{dep}} = 10 \text{ mA/cm}^2$, $T = 30^\circ\text{C}$.

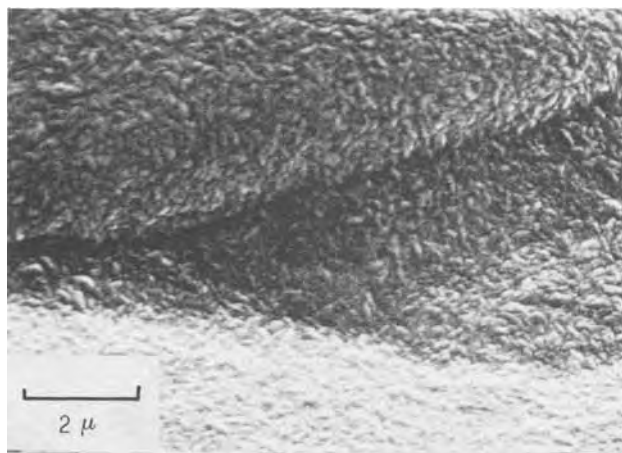


Fig. 2. SEM micrograph of pure β PbO_2 electrodeposited from $0.5\text{M Pb}(\text{NO}_3)_2$ and 0.15M HNO_3 ; $i_{\text{dep}} = 100 \text{ mA/cm}^2$, $T = 30^\circ\text{C}$.

creases with increasing antimony content in the electrolyte, as reported in Fig. 3. It can be seen that antimony content in α PbO_2 is higher than in β PbO_2 . In Fig. 3 the values of the O/Pb ratio are also reported.

As can be easily seen, the O/Pb ratio in the α lead dioxide increases markedly with increasing antimony content in the electrolyte, until the antimony concentration in the anodic layer reaches the value of 0.02%, corresponding to 40 ppm of antimony in the electrolyte. Above this value the O/Pb ratio reaches a constant value. On the other hand, antimony does not seem to change the O/Pb ratio in the β lead dioxide.

Considering that antimony pentavalent ions behave, with respect to iodometric analysis, as tetravalent lead ions, both oxidizing two equivalents of iodine, the Sb^{5+} substitution for Pb^{4+} does not modify the O/Me ratio of lead dioxide. Instead, this ratio is changed if

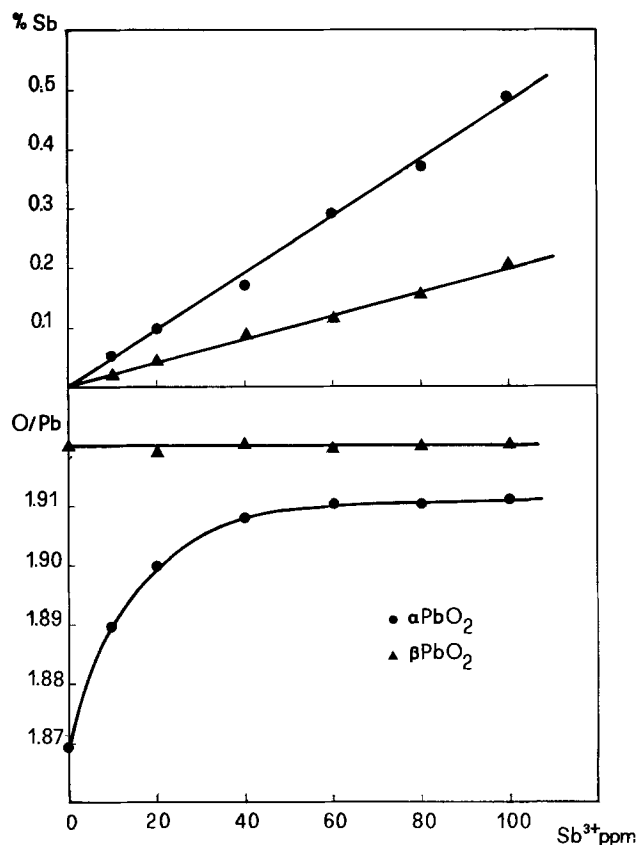


Fig. 3. Antimony content in the anodic deposits of α (●) and β (▲) PbO_2 (upper diagram), and O/Pb ratio (lower diagram) vs. antimony content in the electrolyte.

antimony fills lattice vacancies or substitutes divalent lead ions.

Antimony decreases the number of lattice defects (26) thus contributing to the growth of a more regular structure. This latter effect is outstanding because the observed O/Pb ratio is surprisingly greater than that one would expect from the introduction of small quantities of Sb in the PbO_2 lattice. From Fig. 3 it can also be deduced that for antimony concentration greater than 0.2% the O/Pb ratio increases no more and the Sb^{5+} enters the lattice by substituting tetravalent lead ions.

The greater solubility of antimony in $x\text{PbO}_2$ could explain the increasing amount of that allotropic form in the positive active material of lead acid cell with antimonial lead grids.

Effect of Sb on crystal habit.—When antimony is present in the α PbO_2 lattice, the crystal habit of the dioxide changes drastically. Comparing Fig. 1 with Fig. 4a and Fig. 4b with Fig. 4c, it appears clearly that antimony reduces the crystal size. Its influence is so relevant as to cause a change in the crystal morphology when the antimony amount in the dioxide is greater than 0.2%.

With increasing antimony amount, the crystal size becomes smaller and its surface energy increases until "soap bubble" forms can grow. The crystal size reduction is already apparent when, on the oxide surface, for about 20 lead ions there is one antimony ion. That seems in better agreement with the assumption of an influence of antimony on crystal growth rate, based on the adsorption, rather than an influence on the nucleation rate.

With regard to β PbO_2 , for which the crystal size is already very small, antimony does not seem to have any influence. But a slight broadening of the peaks observed in the diffraction patterns could reveal that also for the β form there is a crystal size reduction. Moreover for both allotropic forms of lead dioxide it was observed that electrodeposition occurs with greater difficulty if the antimony concentration in the solution is greater than 100 ppm.

α PbO_2 : reduction tests.—An LSV curve for the α PbO_2 reduction in 0.1N KOH solution is reported in Fig. 5. The curves in 0.1N KOH solutions show two main peaks. The first main peak appears at a potential of -170 mV (NHE) and it is preceded by a lower peak [$V = 140 \text{ mV (NHE)}$] which appears as a shoulder if the scanning rate is greater than $50 \mu\text{V/sec}$.

The second main peak is observed at about $V = -700 \text{ mV (NHE)}$ and it is followed by a lower peak or by a shoulder at $V = -900 \text{ mV (NHE)}$ before hydrogen evolution.

The values of the amount of charge measured during the reduction permitted calculation from the initial O/Pb ratio of the mean value of the reduction degree of lead dioxide, at various points on the LSV curves.

The mean O/Me ratio calculated according to the cathodic reaction



is also reported vs. the electrode potential in Fig. 5.

In this way it is possible to verify that the first main peak corresponds to the formation of an oxide having a composition near to that of Pb_3O_4 , and the second main peak corresponds to a simultaneous formation of PbO and Pb . During the first lower peak, lead dioxide apparently reduces to $\text{PbO}_{1.8}$. The shoulder, which appears before hydrogen evolution, should correspond to lead formation from residual PbO .

If pure lead dioxide is reduced in 5N KOH solution, the voltammetric curves show only the first main peak. In this case the oxide dissolves completely in the electrolyte and the charge required for the reduction corresponds to PbO formation.

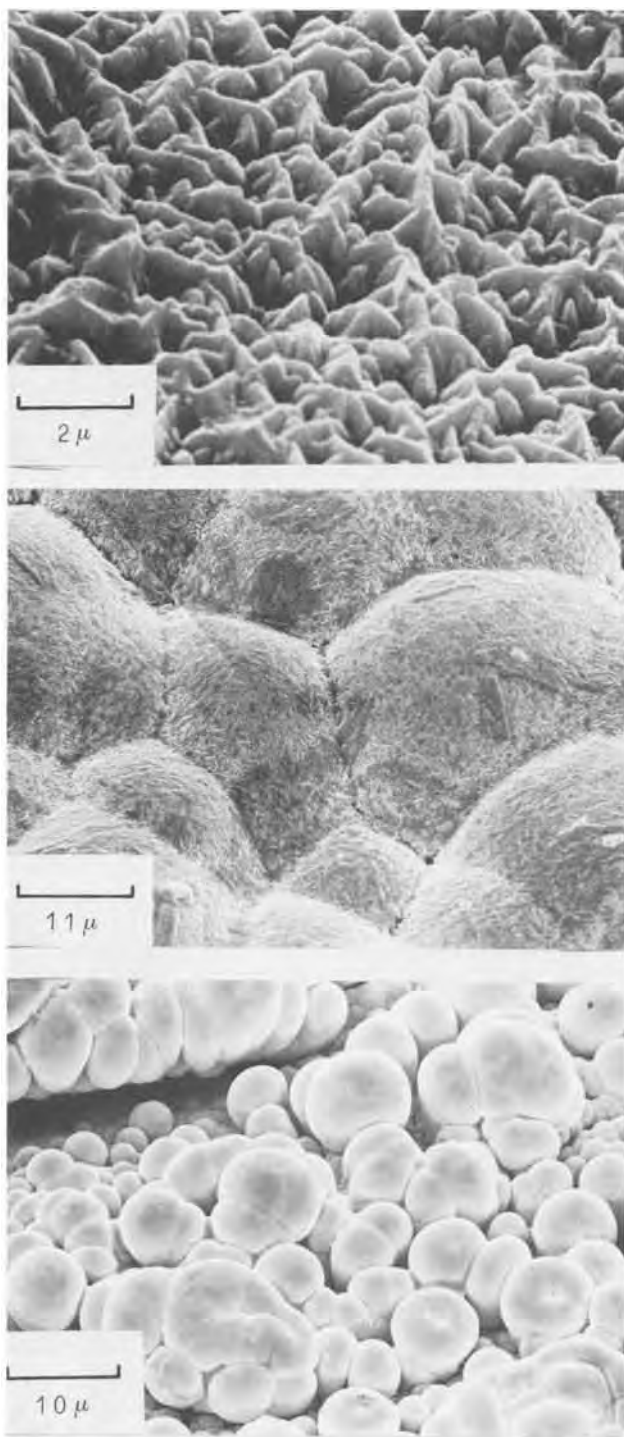


Fig. 4. SEM micrographs showing the effect of antimony on α PbO_2 morphology. Sb^{3+} concentration in the electrolyte: (a, top) 25 ppm, (b, center) 60 ppm, (c, bottom) 100 ppm.

When the lead dioxide is doped with antimony, some change in the LSV curves occurs. An example is reported in Fig. 6 which shows the curves referring to reduction in 0.1N KOH solution of α PbO_2 electrodeposited from a solution containing 100 ppm of Sb. It can be observed that the first main peak appears at a potential of 100 mV (NHE), the intermediate oxide has a composition near that of $\text{PbO}_{1.57}$, and the intensity of the second main peak, which appears at a potential of -700 mV (NHE), is very small.

In addition a third peak appears at a potential of -980 mV (NHE) before the lead peak [$V = -1150$ mV (NHE)], and hydrogen evolution begins when the O/Pb ratio is greater than one. The reduction tests

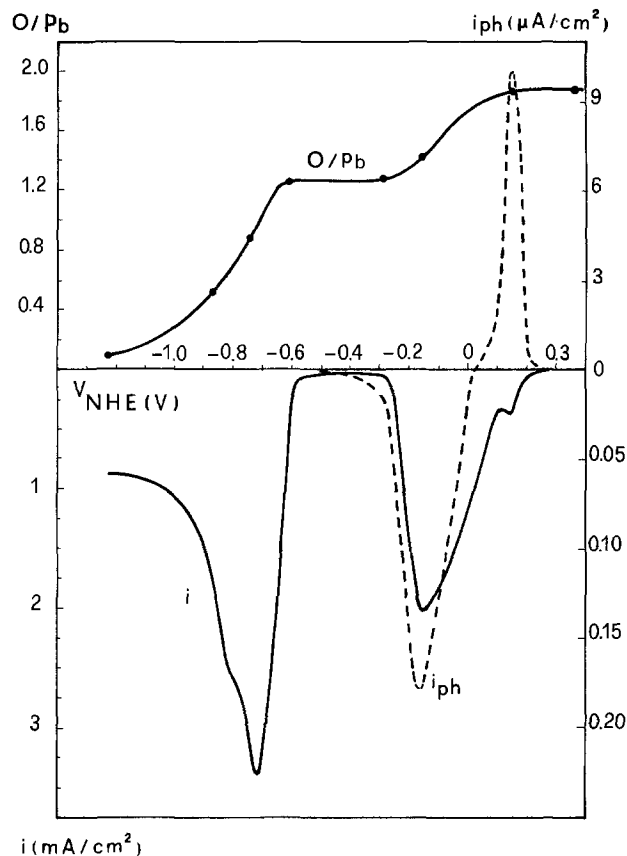


Fig. 5. Linear sweep voltammetry curve (full line), photocurrent intensity (dotted line), and O/Pb mean ratio (●) for α PbO_2 reduction in 0.1N KOH.

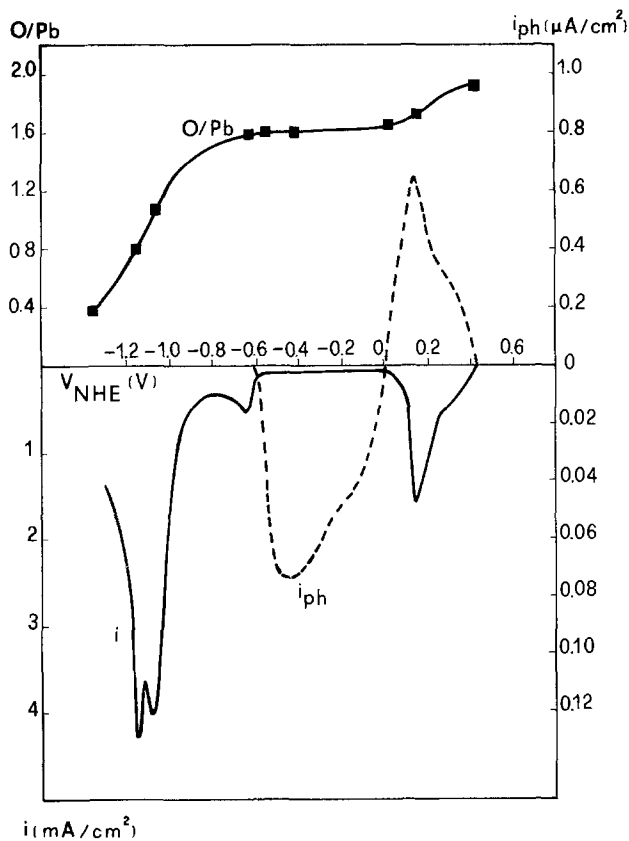


Fig. 6. Linear sweep voltammetry curve (full line), photocurrent intensity (dotted line), and O/Pb mean ratio (■) for α PbO_2 reduction in 0.1N KOH solution containing 100 ppm of Sb.

carried out in 5N KOH solutions showed that the oxide layer does not dissolve in the electrolyte and the

LSV curves display the peaks corresponding to PbO and Pb formation. The reductive dissolution appears more difficult and some areas of the electrode remain covered with partially reduced lead dioxide and metallic lead also at the end of the voltammetric curves.

The x-ray diffraction analysis and the SEM observations of the anodic layers partially reduced showed that the cathodic process occurs in the solid state. For an O/Pb ratio greater than 1.33, the diffraction patterns clearly show only one reflection line from (200) plane of PbO₂, the intensity of which decreases with decreasing the O/Pb ratio.

Moreover the background noise of the diffraction patterns and some very, very weak lines appear. These lines correspond to reflection from (211), (112), and (310) planes of Pb₃O₄, when the O/Pb ratio is near 1.33. When the O/Pb ratio is smaller than 1.1, a line corresponding to reflection from (111) plane of lead appears. The tests carried out with Sb-doped α lead dioxide show that the lead line appears when the O/Me ratio is close to 1.57.

The SEM observations of the electrode surface after partial reduction, some of which are shown in Fig. 7-10, are in good agreement with x-ray results. Moreover it can be seen that the crystal habit of lead dioxide is maintained during the reduction until lead and lead oxide appear at the same time. As Gourbonova pointed out (20), the reduction takes place in a homogeneous system.

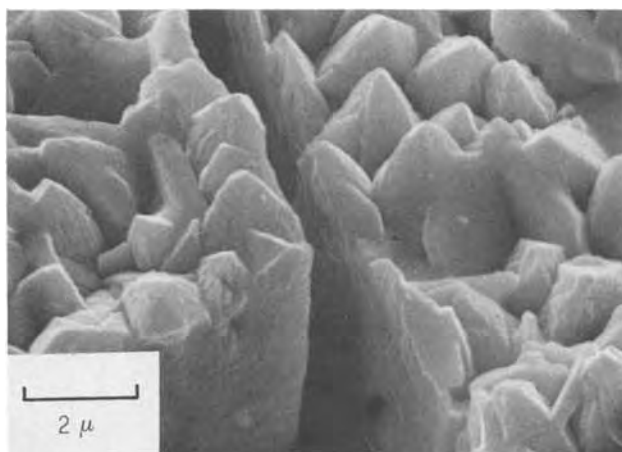


Fig. 7. SEM micrograph of α PbO₂ electrodeposited from 2N KOH saturated with PbO ($i_{\text{dep}} = 10 \text{ mA/cm}^2$, $T = 30^\circ\text{C}$) and reduced until PbO_{1.33} in 0.1N KOH.

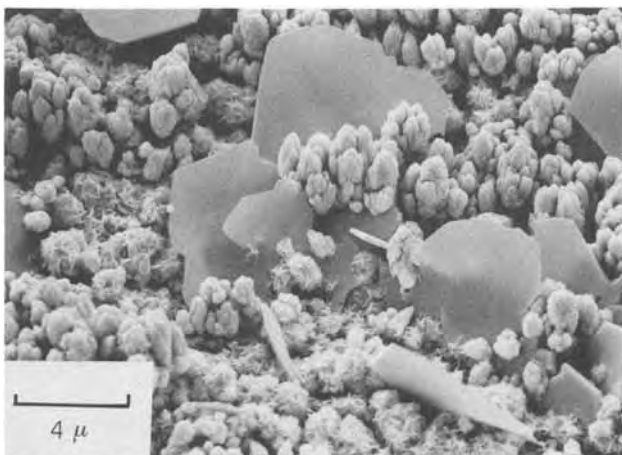


Fig. 8. SEM micrograph of α PbO₂ electrodeposited from KOH ($\text{pH} > 14$) saturated with PbO ($i_{\text{dep}} = 10 \text{ mA/cm}^2$, $T = 30^\circ\text{C}$) and reduced until PbO_{0.8} in 0.1N KOH.

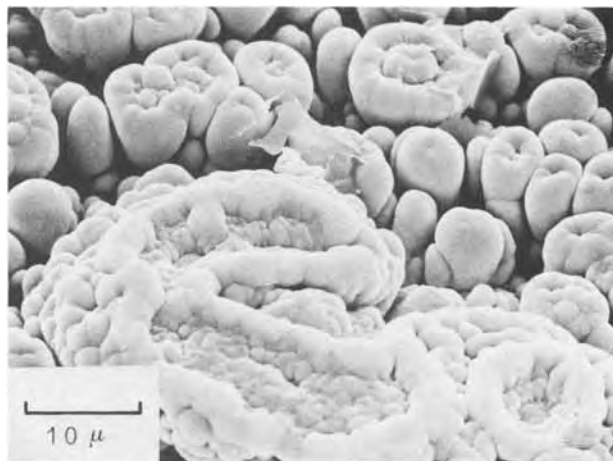


Fig. 9. SEM micrograph of α PbO₂ electrodeposited from KOH ($\text{pH} > 14$) saturated with PbO, containing 100 ppm of antimony ($i_{\text{dep}} = 10 \text{ mA/cm}^2$) and reduced until PbO_{1.48} in 0.1N KOH.

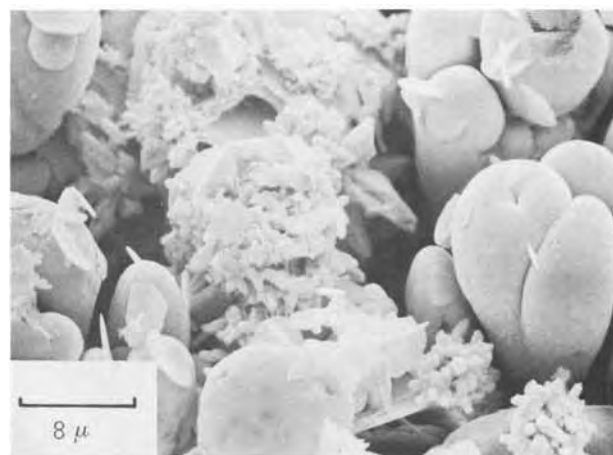
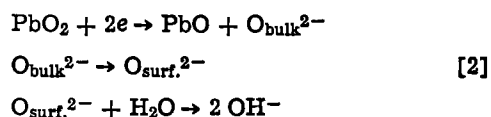


Fig. 10. SEM micrograph of α PbO₂ electrodeposited from KOH ($\text{pH} > 14$) saturated with PbO, containing 100 ppm of Sb ($i_{\text{dep}} = 10 \text{ mA/cm}^2$, $T = 30^\circ\text{C}$) and reduced until PbO_{1.66} in 0.1N KOH.

Thus the cathodic process occurs by removal of oxygen ions from the dioxide lattice. Initially the process takes place at the oxide-solution interface where the electrons are available and Pb⁴⁺ ions can be reduced to Pb²⁺. The oxygen, so released, reacts with the adsorbed water molecules to form hydroxide ions. In this way, a concentration gradient of oxygen ions and an opposite gradient of Pb²⁺ ions are set up in the oxide. Subsequently the reduction of Pb⁴⁺ ions takes place far from the oxide-solution interface, and oxygen ions released in the bulk of the oxide move toward the solution under the action of the diffusion gradient and of the electric field. In this condition the cathodic process includes the following three consecutive steps



The removal of oxygen from the dioxide lattice causes nonstoichiometric PbO_x oxide formation. The known stable PbO_x oxides are solid solutions having a composition in the range PbO_{1.33}-PbO_{1.57} (28-29). Their solubility in alkaline solutions (30) is very small, decreasing from PbO_{1.33} to PbO_{1.57}. Since the reduction tests, carried out in 5N KOH solutions, showed that the oxide layer dissolves quickly during the first main peak of LSV curves, we can suppose

that the reduction process initially causes, at the oxide-solution interface, a decreasing of the O/Pb ratio until this ratio reaches a value near one.

In 5N KOH solutions while the reduction of Pb^{4+} occurs in the solid state, PbO dissolution at the oxide-solution interface can take place. In dilute alkaline solutions a little dissolution of PbO can also occur because, owing to cathodic process, OH^- ions are formed at the oxide-electrolyte interface.

The $HPbO_2^-$ ions, so formed, can hydrolyze where the local $HPbO_2^-/OH^-$ ratio is greater than the equilibrium constant value for the PbO dissolution reaction. This clearly appears from the electron micrograph, Fig. 11, referring to a reduction carried out without stirring the solution to enhance the phenomenon. In this case PbO appears on the electrode surface, during the first main peak of the LSV curves, in the shape of platelets coming out from PbO_x crystals. The x-ray diffraction patterns do not display a strong line of this compound. It can be deduced that PbO hydrolyzes in amorphous form.

However in dilute alkaline solutions the PbO dissolution is a secondary process. In fact all the tests carried out with dioxide layers having different thickness (2–8 μm) showed, for the intermediate oxide, the same value of the above-mentioned O/Pb mean ratio. When the entire layer is reduced to PbO_x , the reduction process stops since PbO_x is a poor conductor. This is confirmed by some oxidation tests of the intermediate oxide. These tests showed that the electrode seems passivated and PbO_x is oxidized only if the electrode potential is greater than 550 mV (NHE). Moreover the SEM observations show that lead dioxide is subjected, during the reduction, to internal stresses which produce some cracks in the layer (Fig. 13). The crack formation can explain the presence on the LSV curves of the first lower peak. This peak should indicate when, on the electrode surface, the O/Pb ratio becomes one and cracks begin to form. The cracks explain also why PbO_x can still be reduced when the electrode potential reaches more negative values (3rd and 4th peak on LSV curves). The reduction begins to take place near the crack edges at substrate-oxide-electrolyte contact.

With regard to Sb-doped lead dioxide, it was observed that during the reduction in concentrated alkaline solutions the intermediate oxide does not dissolve in the electrolyte. From this behavior we can deduce that the O/Pb ratio, at the oxide surface, decreases only to 1.5. In these conditions, owing to greater conductivity of the intermediate oxide, the further reduction to form PbO and Pb can go on also by a reductive dissolution-precipitation mechanism. Moreover

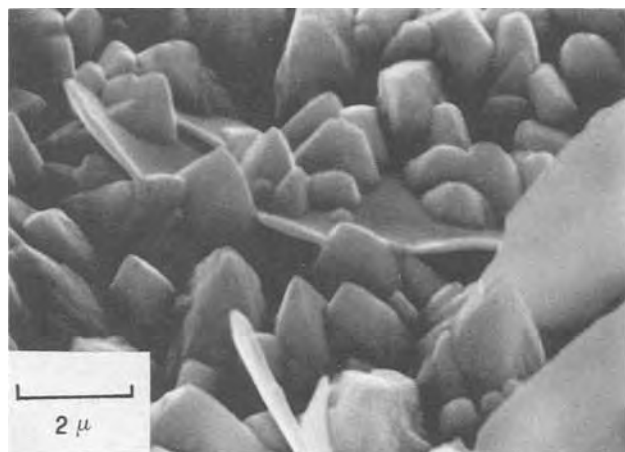


Fig. 11. SEM micrograph of α PbO_2 electrodeposited from 2N KOH saturated with PbO ($i_{dep} = 10 \text{ mA/cm}^2$, $T = 30^\circ\text{C}$) and reduced until $PbO_{1.33}$ (crystals) with some blades of PbO in 0.1N KOH.

the peak at $V = -980 \text{ mV}$ (NHE) on the LSV curves reveals that there are two paths for PbO formation perhaps corresponding to two areas with different Sb amount.

The previous discussion agrees with the conclusions by Rickert *et al.* (31,32) referring to the electrochemical behavior of the PbO_2 electrode. In lead dioxide the values of chemical potential of lead and oxygen seem to vary within a wide range according to the electrode polarization. The corresponding change of stoichiometry is related to the change in the number of free electrons. Thus, lead dioxide can acquire semiconducting properties exhibiting n-type behavior. For this reason photoelectrochemical measurements are a useful tool for investigating lead dioxide electrodes.

Photoeffects on α PbO_2 electrodes.—The results of photocurrent measurements are also reported in Fig. 5 and 6. The anodic photocurrents appear when the reduction begins; later the photocurrents become cathodic and their intensity reaches a maximum value when $PbO_{1.33}$ forms. When Pb and PbO begin to form the photocurrents disappear.

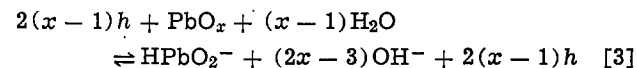
With regard to Sb-doped PbO_2 the photocurrents are smaller and the cathodic ones reach a maximum when PbO appears. The effects induced by light confirm the proposed reduction mechanism.

The anodic photocurrent can be explained by supposing that light produces Pb^{4+} centers in the oxide which hinder the reduction according to a mechanism similar to that proposed by Pavlov (15) for the photoactivation of PbO to PbO_2 . In the first stage of the reduction, a concentration gradient of Pb^{2+} , Pb^{4+} , and oxygen ions is set up in the oxide near the electrolyte. Under these conditions, owing to photon absorption, some electrons jump from the valence to the conduction band of the semiconducting oxide. The holes are captured by divalent lead ions while the electrons move, according to band bending, toward the bulk of the oxide. As a result, some tetravalent lead ions are created in the oxide near the solution, trapping the oxygen ions. In this way the oxygen ion migration is hindered. Thus light decreases the cathodic process rate and this influence is revealed as an anodic photocurrent.

Continuing the reduction, a thin layer of intermediate oxide is formed near the solution and the bands of semiconducting oxide are bent downward. That is due not only to a potential shift toward the cathodic direction but also to a change of the oxide composition. The intermediate oxides are poor electrical conductors and the cathodic potential tends to localize in a thin surface layer of the oxide near the solution.

In this condition, the light can promote the PbO_x photocomposition according to the mechanism proposed by Williams (33). It is known that $PbO_{1.33}$ is a photosensitive material (30) and its solution rate in KOH increases when the oxide is illuminated.

The photon absorption produces electrons and holes which are separated by the electric field. The electrons go toward the oxide-solution interface where they are available for the reaction



The photoeffects disappear when the reduction process begins to occur at the substrate-oxide interface, as it has been supposed above.

The effect of antimony on the semiconducting properties of lead dioxide is revealed by the decrease of photocurrent intensity during the reduction. This also indicates a decrease in the number of lattice defects in the intermediate oxides.

β PbO_2 reduction test and photoeffects.—The LSV curves referring to β PbO_2 reduction in 0.1N KOH

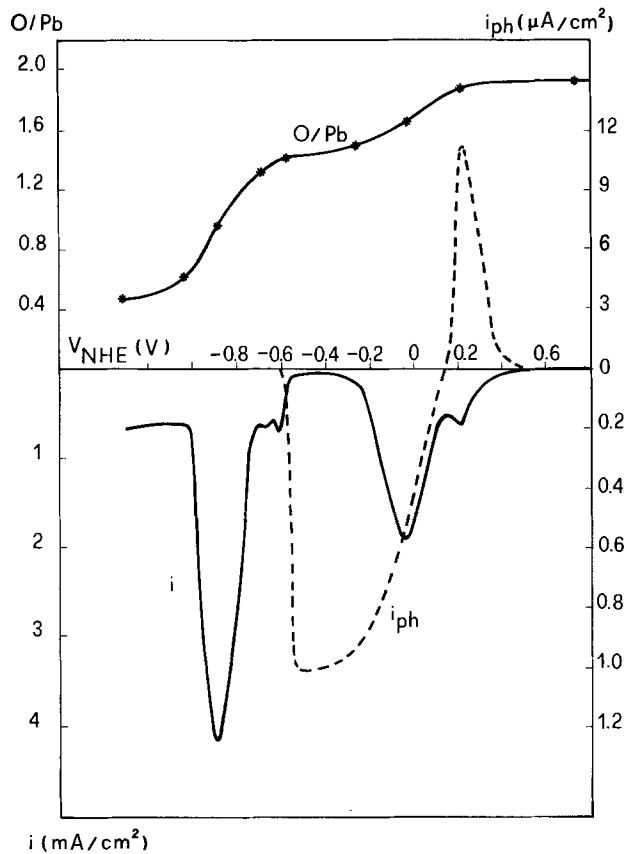


Fig. 12. Linear sweep voltammetry curve (full line), photocurrent intensity (dotted line), and O/Pb mean ratio (*) for β PbO_2 reduction in 0.1N KOH.

solution present two main peaks, Fig. 12, which appear at $V = -50$ mV (NHE) and $V = -880$ mV (NHE), respectively. Each of these peaks is preceded by a lower peak at $V = 200$ mV (NHE) and at $V = -600$ mV (NHE). The intermediate oxide formed after the first main peak has a composition very close to that of $\text{PbO}_{1.57}$.

Antimony shifts the first peak toward positive values of the electrode potential as reported in Table I, where the potential of the first peak and the calculated O/Pb ratio for the initial and intermediate oxide are listed for pure and doped lead dioxide.

As it appears from the electron micrograph reported in Fig. 13, which refers to partially reduced lead dioxide, the cathodic process for the reduction of β PbO_2 in alkaline solution is similar to that of the α form; i.e., the reduction takes place initially in a homogeneous system. The photocurrent measurements and the effect of antimony are in agreement with previous discussion concerning α PbO_2 reduction.

The most remarkable effect of antimony, as it is shown in Table I, concerns the O/Pb ratio value of intermediate oxide. The amount of charge required to form PbO_x increases from Sb-doped β PbO_2 to pure α PbO_2 . The galvanostatic reduction curves confirm the above reported results as shown in Fig. 14. We can deduce from these curves the different amount of

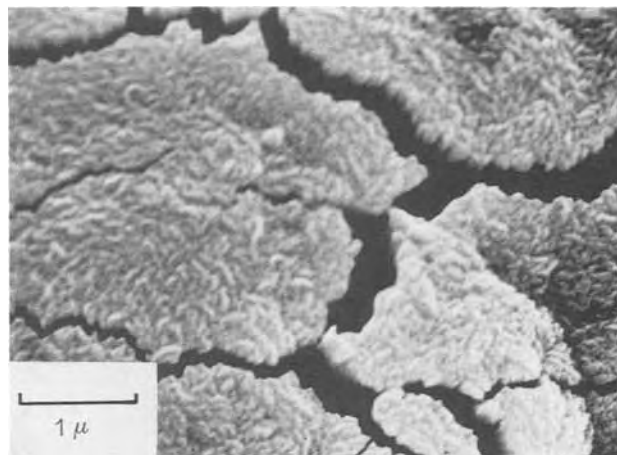


Fig. 13. SEM micrograph of β PbO_2 electrodeposited from 0.15M HNO_3 and 0.5M $\text{Pb}(\text{NO}_3)_2$ ($i_{\text{dep}} = 100$ mA/cm², $T = 30^\circ\text{C}$) and reduced until $\text{PbO}_{1.5}$ in 0.1N KOH.

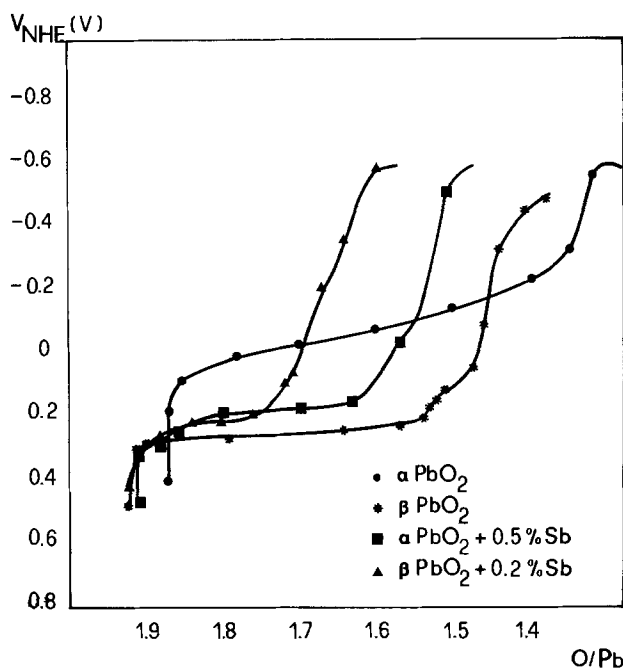


Fig. 14. Electrode potential vs. O/Pb ratio during the galvanostatic reductions of α and β lead dioxide with different Sb content.

charge required by the various lead dioxides to reach the PbO/Pb potential and also the different reducibilities of these dioxides.

In agreement with previous findings (22), the kinetics of reduction for the α and β allotropic form of lead dioxide seem to be different. By considering reaction [2], if oxygen transfer through the oxide-solution interface is faster than oxygen ion migration within the oxide, diffusion polarization sets up in the oxide. In this case, under galvanostatic condition the overpotential increases during the cathodic process.

Table I. Potential values of the first and second peak on voltammetric curves and O/Pb ratio for the initial and intermediate oxide obtained on pure and doped lead dioxide

Oxide	V_{NHE} (mV) (1st peak)	V_{NHE} (mV) (2nd peak)	(O/Me) _{PbO₂}	(O/Me) _{PbO₂}
Sb-doped β PbO_2 Sb 0.2%	320	140	1.92	1.65
Sb-doped α PbO_2 Sb 0.5%	280	100	1.91	1.57
β PbO_2	250	-20	1.91	1.50
α PbO_2	140	-170	1.87	1.33

From Fig. 14 it seems that α PbO_2 reduction is really controlled by oxygen migration in the oxide. On the contrary, under the same conditions the overpotential during the galvanostatic reduction of β PbO_2 is constant. Then we can imagine that the reaction is controlled by oxygen transfer from the oxide to the solution. The effect of antimony is to change the kinetic mechanism of α PbO_2 reduction by making it similar to that of β PbO_2 . Further investigation is necessary to explain the different shape of the galvanostatic reduction curves, and this will be matter for further work.

Conclusions

Antimony enters the lattice of lead dioxide changing the morphology and the electrochemical behavior. Sb dissolution is greater in the α than in the β form. Sb, up to a concentration of 0.2%, fills the lattice vacancies of α PbO_2 and promotes more regular structure. As for β PbO_2 , Sb^{5+} simply substitutes Pb^{4+} ions. The crystal size of α PbO_2 reduces by increasing the antimony content. The β PbO_2 crystal size apparently is not modified.

The greater solubility of antimony in α PbO_2 can explain the increase of this form in the lead acid cell with antimonial lead grids and the different performance of positive plates with respect to lead calcium grids.

The reduction of lead proceeds initially in a homogeneous system until lead dioxide is converted to PbO_x with $1.33 < x < 1.65$. The effect of antimony is particularly on the electrochemical reactivity of the dioxide, the O/Pb ratio of intermediate oxide, and PbO formation.

Acknowledgments

This work was supported by the Battery Division of Magneti Marelli Spa and by Fiat Research Centre Spa. The authors wish to thank Dr. G. Clerici (M. Marelli) for useful discussions.

Manuscript submitted Sept. 26, 1979; revised manuscript received ca. March 31, 1980.

Any discussion of this paper will appear in a Discussion Section to be published in the June 1981 JOURNAL. All discussions for the June 1981 Discussion Section should be submitted by Feb. 1, 1981.

Publication costs of this article were assisted by the Politecnico di Torino.

REFERENCES

- J. T. Crennel and A. G. Milligan, *Trans. Faraday Soc.*, **27**, 103 (1931).
- H. E. Haring and U. B. Thomas, *This Journal*, **68**, 293 (1935).
- J. W. R. Byfield, *ibid.*, **79**, 259 (1941).
- W. Herrmann and G. Pröpste, *Z. Elektrochem.* **61**, 1154 (1957).
- J. Burbank, *This Journal*, **111**, 1112 (1964).
- E. J. Ritchie and J. Burbank, *ibid.*, **117**, 299 (1970).
- D. E. Swets, *ibid.*, **120**, 925 (1973).
- J. L. Dawson, M. I. Gillibrand, and J. Wilkinson, in "Power Sources 3," D. H. Collins, Editor, p. 1, (1971), Proceedings of 7th International Symposium, Brighton (1970).
- N. J. Maskalick, *This Journal*, **122**, 19 (1975).
- A. C. Simon, S. M. Caulder, and E. J. Ritchie, *ibid.*, **117**, 1264 (1970).
- A. A. Abdularim and A. A. Ismail, *J. Appl. Electrochem.*, **7**, 119 (1977).
- A. Ejjenne, H. Nguyen Cong, J. Brenet, and P. Faber, *C. R. Acad. Sci., Ser. C*, **395**, t288 (1979).
- W. Mindt, *This Journal*, **116**, 1076 (1969).
- P. Kofstad, "Nonstoichiometry, Diffusion and Electrical Conductivity in Binary Metal Oxides," Wiley-Interscience, New York (1972).
- D. Pavlov, S. Zanova, and G. Papazov, *This Journal*, **124**, 1522 (1977).
- L. I. Lyamina, N. I. Tarasova, and K. M. Gorbounova, *Elektrokhimiya*, **11**, 238 (1976).
- P. Jones, H. R. Thrisk, and W. F. K. Wynne Jones, *Trans. Faraday Soc.*, **52**, 1003 (1956).
- R. Glicksman and C. K. Morehouse, *This Journal*, **104**, 589 (1957).
- M. L. Ezerskii, *Elektrokhimiya*, **2**, 1037 (1966).
- L. I. Lyamina, N. I. Korol'Kova, and K. M. Gorbounova, *ibid.*, **6**, 389 (1970).
- L. I. Lyamina, N. I. Korol'Kova, and K. M. Gorbounova, *ibid.*, **6**, 633 (1972).
- P. Chartier, *Bull. Soc. Chim.*, No. 7, 2250 (1969).
- J. P. Carr and N. A. Hampson, *This Journal*, **118**, 1262 (1971).
- T. S. Sharpe, in "Encyclopedia of Electrochemistry of the Elements," Vol. 1, A. J. Bard, Editor, p. 305, Marcel Dekker, New York (1973).
- "Scott's Standard Methods of Chemical Analysis," N. H. Furman, Editor, p. 675, D. Van Nostrand, New York (1950).
- N. E. Bagshaw, R. L. Clarke, and B. Halliwell, *J. Appl. Chem.*, **16**, 180 (1966).
- A. I. Zaslavsky, Y. D. Kondrashev, and S. S. Tol'kachev, *Dokl. Akad. Nauk SSSR*, **75**, 559 (1950).
- P. Pascal, *Nouveau Traité de Chimie Minérales*, Tome IX, Masson ed. (1958).
- Th. Katz, *Ann. Chim.*, **5**, 5 (1950).
- P. Chartier, *Bull. Soc. Chim.*, No. 8, 2706 (1967).
- W. Fischer and H. Rickert, *Ber. Bunsenges. Phys. Chem.*, **77**, 975 (1973).
- J. P. Pohl and H. Rickert, in "Power Sources 5," Collins, Editor, p. 15 (1975), Proceedings of 9th International Symposium, Brighton (1974).
- R. Williams, *J. Chem. Phys.*, **32**, 1505 (1960).

Safety Studies on Li/SO₂ Cells

IV. Investigations of Alternate Organic Electrolytes for Improved Safety

A. N. Dey* and R. W. Holmes

Duracell International, Incorporated, Laboratory for Physical Science, Burlington, Massachusetts 01803

ABSTRACT

The lithium reactivity of a variety of organic solvents and their mixtures was determined by measuring the exotherm initiation temperature of the organic solvents with Li using DTA. The least reactive solvent and mixtures were used to prepare electrolytes comprising 1M LiBr and 70% liquid SO₂ and the electrical conductivities of these electrolytes were measured at various temperatures. Eight electrolytes were found to have equivalent or better conductivities and significantly less reactivity towards Li compared to the state-of-the-art electrolyte comprising LiBr, acetonitrile, and SO₂. Some of the electrolytes showed a reduction in conductivity on storage.

Li/SO₂ organic electrolyte cells consisting of Li anode, porous carbon cathode, and LiBr-acetonitrile-liquid SO₂ electrolyte were demonstrated (1-5) to be an excellent power source for various military applications requiring high current drains, long shelf life, and exceptionally cold temperatures. Although the battery system was found (3) to be quite abuse resistant for a variety of abuse conditions, the object of this ongoing investigation was to improve the abuse resistance of the cells even further so that the cells are safe under all reasonable abuse conditions. We have shown earlier (6) that the reaction most responsible for initiating a thermal runaway was the exothermic reaction between the Li and the organic solvent, acetonitrile (AN), that may work on deep discharging an Li/SO₂ cell when almost all the SO₂ has been consumed. We have also shown by kinetic studies (7) that the above reaction may be mitigated by the addition of other less reactive solvents. As an extension of these studies it is of interest (i) to determine the optimum concentration of the additive solvent required for suppressing the Li-AN reaction, and (ii) to determine the electrical conductivity of the LiBr-SO₂ electrolytes made with the above solvent mixtures. Our objective is to develop the least reactive electrolytes that has an adequate conductivity for the applications of interest.

We have chosen to use the exotherm initiation temperature (defined as the temperature at which the Li-solvent reaction exotherm starts) as a measure of the Li-solvent reactivity. The higher the exotherm initiation temperature, the lower the reactivity and conversely. We measured the Li-solvent exotherm initiation temperature as a function of the organic solvent concentrations at a fixed heating rate using DTA and we determined the electrical conductivities of the electrolytes consisting of approximately 70% liquid SO₂, 1M LiBr, and the promising organic solvent mixtures selected from the above studies. The experimental details and the results are described in this paper.

Experimental

The Mettler TA2000 DTA system was used with the Nemonic crucibles. 20 μ l of the solvents of interest were run with 0.00029g Li disks at the 5.0°C/min heating rate. The resulting thermograms were interpreted as follows: the programmed temperature, T_p , was determined where the steepest slope of the Li-solvent reaction exotherm intersected the projected baseline. The exotherm initiation temperature was determined by subtracting the thermal lag of the sample crucible, ΔT_{LAG} , from the intersect temperature. Fig-

ure 1 shows the DTA thermogram at 5°C/min for two samples and the typical determination of the exotherm initiation temperature.

For the effort centering on the use of AN with an additive we generally used 5% (volume) additive and 95% AN. Promising solvent systems were studied in more detail by determining the exotherm initiation temperature at various additive concentrations.

The electrical conductivity of the electrolytes was measured with a high pressure conductivity cell, shown in Fig. 2. Pressurized SO₂ electrolytes were

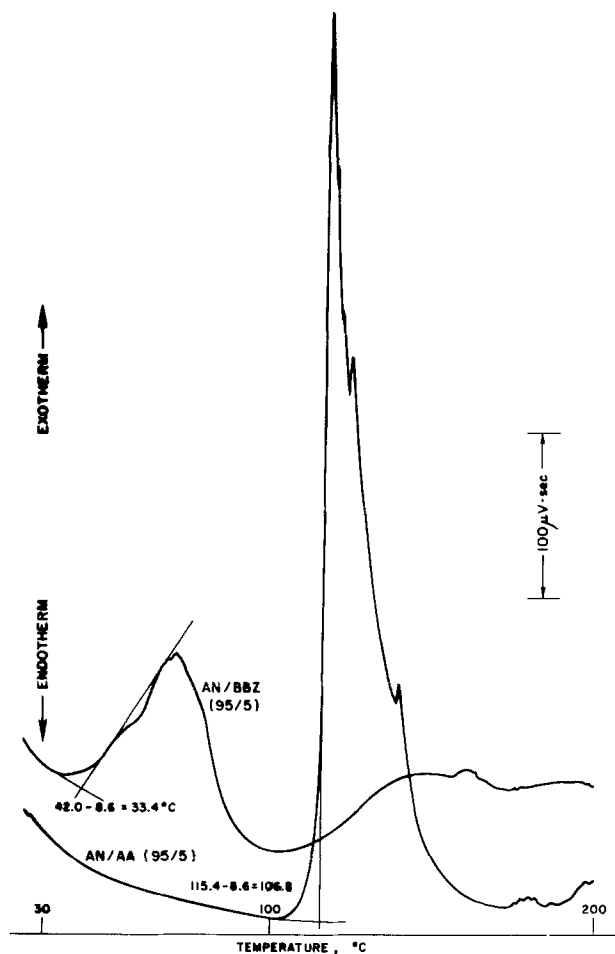


Fig. 1. Thermograms at 5°C/min showing the determination of the exotherm initiation temperature: (1) Li + AN/bromobenzene (95/5), (2) Li + AN/acetic anhydride (95/5).

* Electrochemical Society Active Member.

Key words: battery, DTA, organic, electrolyte.

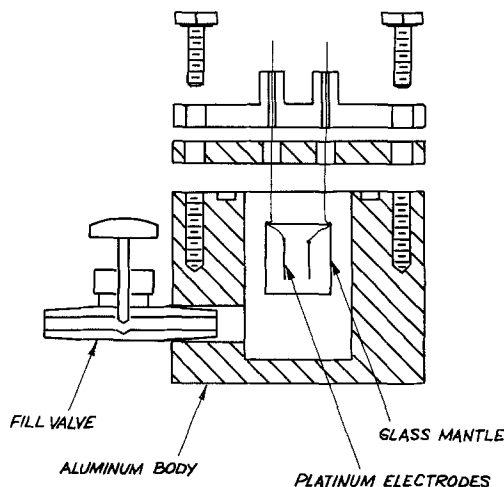


Fig. 2. High pressure conductivity cell

made up in 115 ml polypropylene cylinders fitted with polypropylene ball valves on each end and an additional three-way stainless steel valve on one end. Vacuum-dried LiBr and appropriate distilled solvents (except acetic anhydride) were introduced into the polypropylene electrolyte cylinder and SO₂ was condensed into the chilled cylinder through the three-way valve. The conductivity cell was filled with argon and then connected to the electrolyte filling station via the fill valve. At the filling station the conductivity cells were evacuated to facilitate the introduction of electrolyte which was introduced through the fill valve. The filled cells were equilibrated at various temperatures between -40° and 98°C. At thermal equilibrium, the solution resistances were measured with a GenRad GS1657 Digibridge at 1 kHz (0.3V rms maximum) and the series equivalent circuit was used.

All the solvents except PC, DME, BL, and dioxolane were used as received from Eastman Kodak. PC and BL were vacuum distilled over Li. Water content of AN was less than 0.01%.

Results and Discussion

Exotherm initiation temperature of Li and organic solvent.—The effect of a variety of organic solvents as additives on the exotherm initiation temperatures of Li + AN was determined by the method described above and are tabulated in Table I, in the code of ascending exotherm initiation temperature; the ternary mixtures are listed separately at the bottom of the table. The organic compounds and additives investigated include the following functional groups: alcohol, aldehyde, ketone, acetate, anhydride, amide, amine, carboxylic acid, carbonate, glycol, and sulfoxide. The exotherm initiation temperature of Li + AN varied from 25° to 50°C depending upon the condition of the surface of the lithium specimen, as discussed later.

The results in Table I show that the organic solvent additives in items numbering 1-17 had exotherm initiation temperatures below 50°C, and as seen these provide no reductions in the reactivity of Li with acetonitrile. Item 18, contained acrylonitrile, an impurity of AN, which had a negligible effect on the exotherm initiation temperature of Li + AN. Similarly items 19 through 27 were only marginally beneficial. Items 28 through 37 indicated a significant increase in the exotherm initiation temperature. The organic solvents involved are propylene carbonate (PC), butyrolactone (BL), acetic anhydride (AA), and methyl formate (MF). Of these, methyl formate is known (8) to decompose in presence of moisture to form CO. Also, H₂ may form by a side reaction with Li. Both of these are flammable and would increase the internal pressure of the Li/SO₂ cells.

Table I. Chemical reactivity of solvent systems DTA at 5°C/min. 0.00029g Li + 20 μl of indicated solution

Item No.	Solution	Initiation temp (°C)
1	AN	25-50
2	AN/DME (95/5)	25
3	AN/carbon tetrachloride (95/5)	25
4	AN/diglyme (95/5)	25
5	AN/THF (95/5)	26
6	AN/bromobenzene (95/5)	33
7	AN/pyridine (95/5)	37
8	AN/allyl alcohol (95/5)	38
9	AN/diethylamine (95/5)	42
10	AN/diethyl carbonate (95/5)	42
11	AN/butyl acetate (95/5)	43
12	AN/acetamide (0.0v43 g/ml)	44
13	AN/Triton surfactant, 0.5%	45
14	AN/dioxolane (95/5)	46
15	AN/oleic acid (95/5)	47
16	AN/benzaldehyde (95/5)	47
17	AN/methanol (95/5)	49
18	AN/acrylonitrile (95/5)	52
19	AN/ethyl acetate (95/5)	55
20	AN/di-tert butyl dicarbonate	55
21	AN/N, N, -dimethyl formamide (95/5)	58
22	AN/acetone (95/5)	60
23	AN/methyl ethyl ketone (95/5)	62
24	AN/dimethyl sulfoxide (95/5)	63
25	AN/ethylene glycol (95/5)	64
26	AN/naphthalene (0.015 g/ml)	67
27	AN/MF (95/5)	71
28	AN/PC (95/5)	96
29	AN/BL (95/5)	98
30	AN/acetic anhydride (95/5)	107
31	AN/BL (80/20)	130
32	AN/MF (50/50)	140
33	BL	168
34	MF/PC (50/50)	171
35	MF	173
36	PC	244
37	DME	425
38	AN/PC/methanol (86/9/5)	48
39	AN/BL/methanol (86/9/5)	63
40	AN/DME/acetic anhydride (90/5/5)	92
41	AN/PC/acetic anhydride (90/5/5)	101
42	AN/PC/DME (90/5/5)	104
43	AN/BL/acetic anhydride (90/5/5)	111
44	AN/PC/BL (90/5/5)	111

Note: PC, BL, and dioxolane were distilled.

The reactivity of dimethoxyethane (DME) and other ethers towards Li were investigated earlier using the activation energy method (7). The measurement of exotherm initiation temperatures of the above ether with Li verified our earlier findings that Li is very unreactive with ether but ethers do not suppress the Li + AN reaction when used as an additive, they enhance it. Compare the results of item 37 with items 2, 4, and 5 in Table I.

In the ternary mixture (item 42, Table I) AN/PC/DME(90/5/5), the exotherm initiation temperature is increased to 104°C, indicating that the tenacious protective film formed in the presence of PC is insoluble in DME, thus providing continued protection to Li in the presence of AN. Ethers therefore may be useful in certain ternary solvent systems.

In view of the excellent protection of Li by PC, we studied a few more ternary solvent systems and found (items 38 and 39, Table I) that neither PC nor BL could protect Li adequately in AN containing methanol (5%), which itself reacts with Li. We had included methanol in the hope of finding electrolytes with increased conductivity. The ternary mixtures consisting of two of the three "protective" solvents (*viz.* PC, BL, and AA) with AN, showed no beneficial synergistic effects (items 41, 43, 44, Table I).

For the more promising solvent systems, we determined the optimal concentrations of the additive solvent by measuring the exotherm initiation temperature as a function of the concentrations of the additive solvent. The effect of addition of PC and AA to AN on the exotherm initiation temperature is shown in Fig. 3. Note that the exotherm initiation temperature of Li + AN increases with addition of PC and AA from 50°C to approximately 110°C up to a concentration of 10% of PC and AA and then levels off.

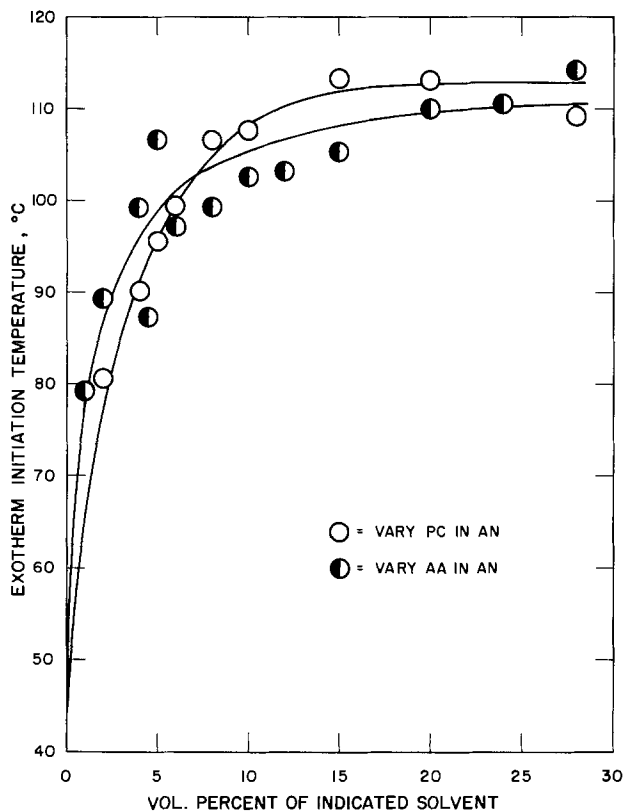


Fig. 3. Exotherm initiation temperature of Li + AN reaction as a function of the concentration of additive solvents, PC and AA.

Therefore, the optimal concentrations of PC and AA are about 10%.

We examined the ternary solvent system, AN/PC/DME, in the above manner. The results are shown in Fig. 4. In these experiments in one case, we started

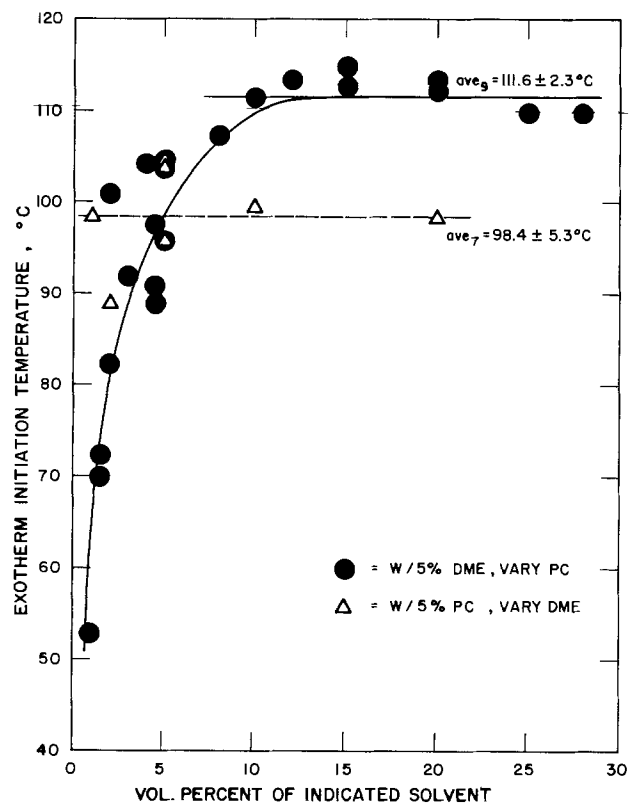


Fig. 4. Exotherm initiation temperature of (1) Li + AN + 5% DME with addition of PC and (2) Li + AN + 5% PC with addition of DME.

out with a mixture of 95% AN and 5% DME and determined the exotherm initiation temperature with Li as a function of the concentration of added PC. The addition of PC resulted in the increase of the exotherm initiation temperature from 50° to 110°C up to a concentration of approximately 10% of PC; no further increase in the exotherm initiation temperature occurred at higher concentrations of PC. In another case, we started out with a mixture of 95% AN and 5% PC and measured the exotherm initiation temperature as a function of the concentration of added DME. In this case, the exotherm initiation temperature started out at 100°C, as expected and remained unchanged with the addition of DME. This confirmed our earlier observation in regard to the level of protection of Li by DME in conjunction with AN. PC is the only "protective" solvent in this mixture.

We examined the AN + BL binary solvent systems as well and found that the data had great scatter as shown in Fig. 5. Despite the scatter, BL appears to effectively inhibit the Li + AN reaction as evidenced by the increase in the exotherm initiation temperature.

We have also studied the effect of SO₂ on the exotherm initiation temperature of Li + AN in order to determine the minimum amount of SO₂ needed to provide protection. We carried out these experiments on the Li disks as well as with Li powder. We also examined the effect of moisture (1%). The results are shown in Fig. 6. Note that the exotherm initiation temperature increases rapidly from 50° to over 150°C with the addition of 3-5% SO₂. Moisture of up to 1% does not appear to have a significant effect on the exotherm initiation temperature. However, Li powder was found to be considerably more reactive as evidenced by the lower exotherm initiation temperature compared to the Li disks.

It is interesting to note that the exotherm initiation temperature of Li + AN with 20% SO₂ was above 400°C. This is considerably higher than the exotherm initiation temperature of 180°C (6) of Li + SO₂ elec-

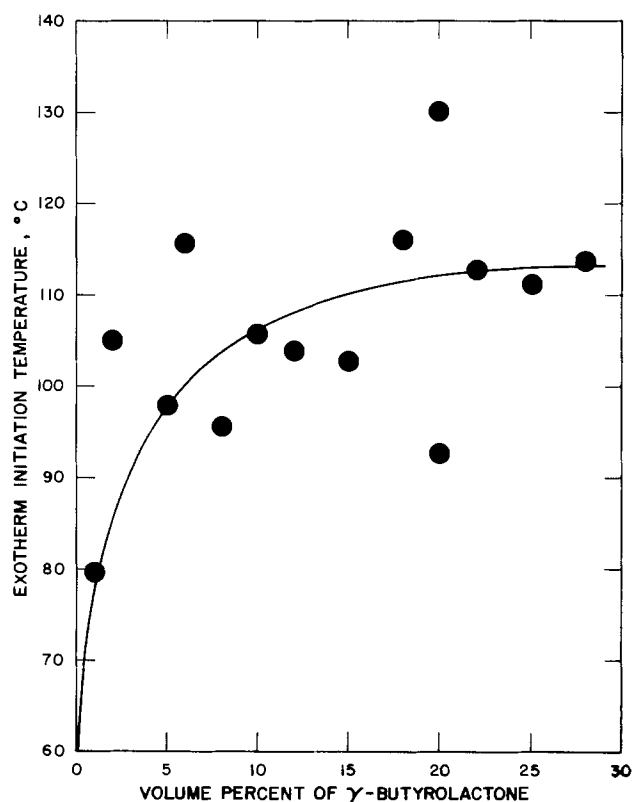


Fig. 5. Exotherm initiation temperature of Li + AN as a function of addition of concentration of BL.

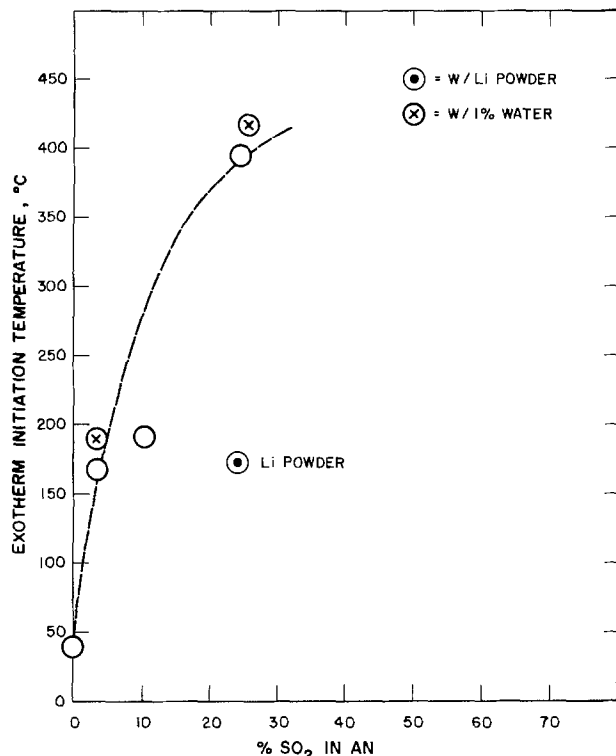


Fig. 6. Exotherm initiation temperature of the Li + AN reaction as a function of SO_2 concentration.

trolyte containing LiBr + AN. This lowering of exotherm initiation temperature indicates a possible catalytic effect of LiBr in promoting the Li + AN reaction. Similar catalysis of the Li-solvent reaction by salts such as LiClO_4 has been reported by others (9).

Based on the above studies, we selected sixteen SO_2 organic electrolytes all containing 70% SO_2 and 5-6% LiBr for further evaluations based on electrical conductivity.

Electrical conductivity.—The exact composition of the 16 electrolytes selected for conductivity studies are shown in Table II. The plots of the specific conductance vs. temperature of the various electrolytes are shown in Fig. 7. The electrolytes were ranked in order of decreasing conductivity and are listed in Table III. All but the last seven electrolytes had conductivities equal to or greater than the standard electrolyte containing AN. We rated the conductivity of the electrolyte containing BL as marginal since its specific conductance plot was within the variability of the specific conductance of standard electrolyte which showed a reduction of conductivity (25-30%) on storage at 72°C for a few days. Electrolytes 4 containing AN/BL(90/10) and 7 containing AN/PC/

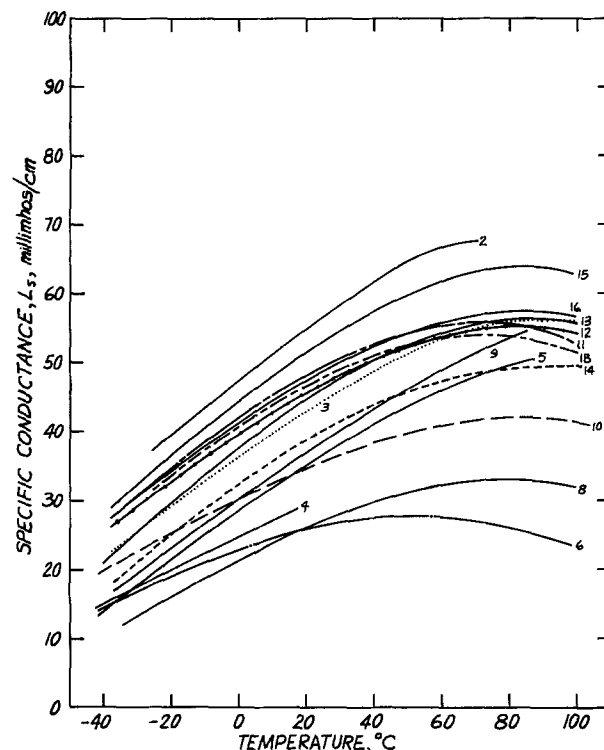


Fig. 7. Specific conductance vs. temperature for several SO_2 electrolytes, the compositions of which are described in Table II.

DME(95/10/5) had good conductivities when fresh, but the conductivities dropped considerably on storage for a few days at room temperature as shown in Fig. 8. The conductivity of electrolyte 7 dropped from $5.1 \times 10^{-2} \Omega^{-1} \text{cm}^{-1}$ to $1.1 \times 10^{-2} \Omega^{-1} \text{cm}^{-1}$ on storage at 25°C for a week. The decrease of conductivity was accompanied by the salting out of an unknown white precipitate containing bromine and sulfur as determined by KEVEX (SEM). The x-ray diffraction indicated that the precipitate was a crystalline compound. The exact chemical formula is not known as yet.

Conclusions

Based on the chemical reactivity of the organic solvents and solvent mixtures towards Li as determined by the exotherm initiation temperature, we selected approximately 16 solvent systems for further evaluation based on their electrical conductivities in SO_2 -LiBr containing electrolytes. We included a solvent system containing methanol in spite of its relatively high reactivity, in order to determine the contribu-

Table II. SO_2 electrolyte compositions for conductivity study (the number refers to weight percent)

Electrolyte No.	Solute (%)	Solvents (solvent ratio)	SO_2 (%)
1A	LiBr 6.1	AN 18.0%, AA 2.8% (90/10)	73.2
1B	LiBr 5.8	AN 20.9, AA 3.2 (90/10)	70.1
2	LiBr 5.9	AN 20.8, PC 3.6 (90/10)	69.7
3	LiBr 6.3	AN 24.5	69.2
4	LiBr 5.9	AN 21.0, BL 3.4 (90/10)	69.7
5	LiBr 5.2	PC 31.3	63.5
6	LiBr 5.7	THF 25.1	69.2
7	LiBr 5.7	AN 19.1, PC 3.5, DME 1.2 (85/10/5)	70.5
8	LiBr 5.7	DME 24.8	69.5
9	LiBr 5.3	BL 30.0	64.7
10	LiBr 5.3	MF 13.0, PC 16.1 (50/50)	65.6
11	LiBr 5.7	AN 11.1, MF 13.8 (50/50)	69.4
12	LiBr 5.7	AN 20.3, PC 1.7, BL 1.6 (90/5/5)	70.6
13	LiBr 5.4	PC 1.63, DME 11.7 (50/50)	68.7
14	LiBr 5.7	BL 18.1, DME 12.3 (50/50)	66.0
15	LiBr 5.8	AN 19.2, PC 3.5, MeOH 1.1 (85/10/5)	70.4
16	LiBr 5.7	AN 19.2 BL 3.2, DME 1.2 (85/10/5)	70.6

Table III. Conductivity of SO_2 electrolytes in order of higher to lower conductivities. (SO_2 and LiBr were common to all.)

Electrolyte No.	Solvents	Specific conductivity at 25°C ($10^{-3} \Omega^{-1} \text{cm}^{-1}$)	Notes
2	AN/PC (90/10)	57	Conductivity acceptable ↑ Marginal ↓ Conductivity too low ↑
1A	AN/AA (90/10)	57	
15	AN/PC/MeOH (85/10/5)	53	
16	AN/BL/DME (85/10/5)	49	
11	AN/MF (50/50)	49	
12	AN/PC/BL (90/5/5)	47	
1B	AN/AA (90/10)	48	
13	PC/DME (50/50)	46	
3	AN (standard electrolyte)	45	
14	BL/DME (50/50)	40	
9	BL	39	
5	PC	37	
10	MF/PC (50/50)	36	
7	AN/PC/DME (95/10/5)	51 (11) (unstable)	
8	DME	27	
6	THF	26	
4	AN/BL (90/10)	31	

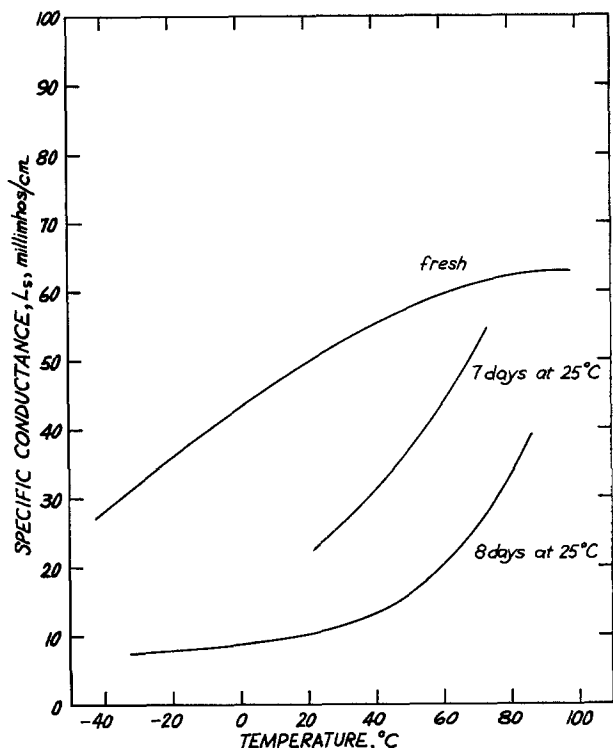


Fig. 8. Specific conductance vs. temperature for electrolyte 7: LiBr, AN/PC/DME (85/10/5), SO₂.

tion of highly polar solvents such as methanol on the conductivity. Based on the conductivity data, it is clear that there are at least 8 or 9 solvent systems with electrical conductivities superior or comparable to the standard electrolytes and having significantly lower reactivity towards Li than the standard electrolyte containing AN. Of these there are at least two or three solvent systems, as shown in Table III which

do not contain any AN at all, and as such are the most suitable for improving the safety of the Li/SO₂ cells without any significant performance penalty.

Acknowledgment

The work was carried out under a contract from U.S. Army, ERADCOM, contract No. DAAB07-77-C-0472.

Manuscript submitted Jan. 25, 1980; revised manuscript received April 7, 1980.

Any discussion of this paper will appear in a Discussion Section to be published in the June 1981 JOURNAL. All discussions for the June 1981 Discussion Section should be submitted by Feb. 1, 1981.

Publication costs of this article were assisted by Duracell International Incorporated.

REFERENCES

1. P. Bro, R. Holmes, N. Marincic, and H. Taylor, Paper No. 45, "Proc. Intl. Power Sources Symposium," Brighton, England (1974).
2. P. Bro, H. Y. Kang, C. Schlaikjer, and H. Taylor, Tenth Intersociety Energy Conversion Engineering Conference, Newark, Delaware, p. 432 (1975).
3. H. Taylor and B. McDonald, "Proc. 27th Power Sources Symposium," p. 66, Atlantic City, N.J. (1976).
4. E. S. Brooks, "Proc. 26th Power Sources Symposium," p. 42, Atlantic City, N.J. (1974); G. DiMain, "Proc. 27th Power Sources Symposium," p. 75, Atlantic City, N.J. (1976).
5. H. F. Hunger and J. A. Christopoulos, R&D Technical Report ECOM-4292, February 1975.
6. A. N. Dey and R. W. Holmes, *This Journal*, **126**, 1637 (1979).
7. A. N. Dey and R. W. Holmes, *ibid.*, **127**, 775 (1980).
8. F. Dampier *et al.*, Final Report; Wright Patterson Air Force Base; AFAPL-TR-74-63 (1964); ESB Inc.
9. A. Soffer and E. Yeager, Abstract No. 547, p. 1367, The Electrochemical Society Extended Abstracts, Seattle, Wash., May 21-26, 1978.

Evaluation of High Temperature LiAl/TiS₂ Cells

Z. Tomczuk,* K. E. Anderson, D. R. Vissers,* and M. F. Roche*

Argonne National Laboratory, Chemical Engineering Division, Argonne, Illinois 60439

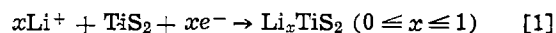
ABSTRACT

The electrochemistry of the TiS₂ electrode of Li/TiS₂ cells in molten LiCl-KCl was found to be similar to that in room temperature cells. The emf curve for Li_xTiS₂ (0 ≤ x ≤ 1) was nonlinear and could be treated in terms of a regular solution model. The effect of TiS₂ electrode thickness was investigated, and the results indicated that good utilization (~70%) could be obtained with thick (0.66 cm) TiS₂ electrodes. The performance of engineering-scale LiAl/TiS₂ cells (77-142 A-hr capacities) was investigated.

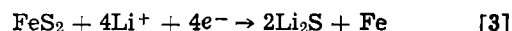
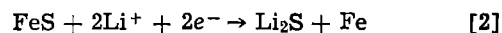
A variety of transition-metal sulfides (1-3) are used as positive electrode materials in high temperature (~400°C) cells. These cells employ molten LiCl-KCl as the electrolyte and Li-Al or Li-Si alloys as the negative electrode materials. The metal sulfides that have received the greatest attention are FeS and FeS₂ (4). However, recent studies of Whittingham (5-7) and others (8,9) have shown that TiS₂ is an excellent positive electrode material for ambient temperature Li/TiS₂ cells, and, therefore, we have decided to evaluate the performance of TiS₂ cells with a molten LiCl-KCl electrolyte.

* Electrochemical Society Active Member.
Key words: cell, fused salt, emf.

The discharge mechanism of TiS₂ in the ambient temperature cells is different from that of iron sulfide in high temperature cells. The reaction of TiS₂ in ambient temperature cells is



The overall reactions of FeS and FeS₂ electrodes in high temperature cells are, respectively



Reaction [1] involves a single phase intercalation process, while reactions [2] and [3] typically involve three phases.

To study the performance capabilities and the reaction mechanism of TiS_2 electrodes, we operated a variety of small (1-5 A-hr) LiAl (or Li)/LiCl-KCl/ TiS_2 cells and examined the TiS_2 electrode products at various states of discharge. Based upon the favorable results obtained with these small-scale cells, we then tested engineering-scale cells (77-142 A-hr capacities) to evaluate the LiAl/ TiS_2 system on a practical level.

Experimental

A total of 14 small cells were operated. The cells were of an open design described earlier (1), and were operated at temperatures of 375°-445°C in furnace wells located in helium-atmosphere glove boxes. The cell chemicals were LiCl-KCl electrolyte of eutectic composition from Lithcoa (Lithium Corporation of America), TiS_2 from Great Western Inorganic, Li from Lithcoa, and Li-Al [48 atomic percent (a/o)] from Kawecki-Berylco Industries. When lithium was used, the negative electrode consisted of a 5 cm² × 0.6 cm disk of Type 302 stainless steel Feltmetal¹ (90% porosity, 27 μm pore size) that had been wet with 1g (4 A-hr) of liquid lithium. When the lithium-aluminum alloy was used, the negative electrode was prepared by vibrating 12g (10 A-hr) of the alloy (-40 +140 mesh) into an iron Retimet² disk which was contained in a 1008 mild-steel cylinder (15.6 cm² × 0.7 cm deep). The Li-Al particles were retained in the cylinder by a stainless steel (-325 mesh) screen and zirconia cloth. The positive electrode was prepared by placing either a compressed TiS_2 pellet (65-75% theoretical density) or TiS_2 powder in a cylindrical cup of ATJ graphite. The cup opening was covered by either a PG-60 porous graphite diffusion barrier (0.63 cm thick) or by zirconia cloth and molybdenum screen (-70 mesh). The area of the positive electrodes was generally 5 cm², but for some tests the area was 11.4 cm². The electrode leads were iron (negative lead) and either carbon or molybdenum (positive lead). The electrodes and the electrolyte (~150g) were contained in an alumina beaker. Boron nitride cloth, which was impregnated with electrolyte, was used in some of the cells as an electrode separator; otherwise, the electrodes were separated by approximately 1 cm of molten salt.

The prismatic design of the engineering cells is shown in Fig. 1, and the cell components are listed in Table I. The cell construction is similar to that reported for Li-Al/LiCl-KCl/ FeS_2 cells (10). The TiS_2 electrodes were prepared by cold pressing the TiS_2 (without electrolyte) onto a molybdenum current collector at 43 MPa to a density of 2.05 g/cm³ (64% of theoretical). The Li-Al electrodes were prepared in a similar manner, but with small amounts (10g) of electrolyte added.

The cells were cycled at constant current using automatic cyclers that switched polarity at pre-selected voltage limits of 1.0V (discharge) and 2.2-2.3V (charge). The current densities employed during cycling ranged from 16 to 140 mA/cm². Both the current density and voltage were monitored using strip-chart recorders and digital voltmeters. After the cycling tests had been completed, the positive electrodes of small cells were examined by metallography, x-ray diffraction, and, in one case, by ESCA; the engineering cells were cross-sectioned and examined by metallography.

A special cell was constructed for the purpose of making emf measurements. It was a small cell identical in design to the small cells described above. The cell employed polarographic-grade LiCl-KCl electrolyte of eutectic composition (from Anderson Physics Laboratory), a compressed TiS_2 pellet (2.10g; 5 cm² × 0.6 cm) electrode, and an Li-Al electrode to which Al powder was added to make the final com-

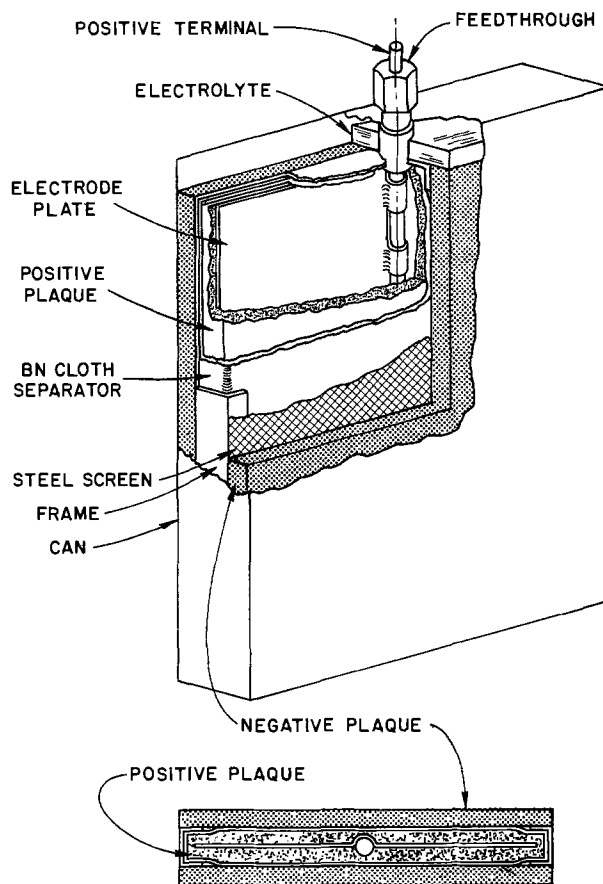


Fig. 1. Cell design used for engineering-scale cell tests

position 42 a/o lithium. The cell was discharged to successively larger voltage values of x (see Eq. [1]) and the open-circuit voltage was monitored with a Model 5330 Dana digital voltmeter. The time on open circuit was at least one-half hour for each emf measurement, although most measurements were made for periods in excess of 20 hr. Measurements for values of x near zero were made after first taper charging the cell at a low current density (1 mA/cm²) to a voltage of 2.4V and then making measurements after small increments of discharge. The values of x

Table I. Components of engineering-scale Li-Al/ TiS_2 cells

Cell designation	DK-52	TiSp1 ^a	TiSp2 ^a
Positive electrode^b			
TiS ₂ , g	594	500	322
Capacity, A-hr	142	120	77
Area, cm ²	155	155	155
Thickness, cm	2.0	1.35	0.89
Density, % theoretical	60	75	72
Negative electrode^b (2 of each required)			
LiAl, g	115	115	50
Theor. capacity, A-hr	85	85	37
Area, cm ²	139	155	155
Thickness, cm	0.70	0.63	0.30
Density, % theoretical	70	70	65
Cell dimensions, cm	16 × 13 × 3.8	16 × 13 × 3.8	16 × 13 × 2.5
Cell temperature, °C	430	411	407
Cell weight, ° kg	1.97	1.935	1.372

^a Fabricated by Eagle-Picher Industries, Incorporated, Joplin, Missouri.

^b Mild steel and molybdenum honeycomb were the negative and positive current collectors, respectively. Electrode enclosures were stainless steel frames and screens. Zirconia cloth was the particle retainer, and BN fabric was the separator.

^c Weight of electrolyte required to fill cell is included.

¹ A product of the Brunswick Corporation.

² A product of Dunlop, Limited.

The emf data from the high temperature and ambient temperature cells are compared in Fig. 4 with the model curves which were generated using Eq. [6]. The molar free energy changes for the cell reactions were obtained by integrating Eq. [6] were calculated from the ratio of the capacity discharged to the theoretical capacity of the TiS₂ electrode.

Results and Discussion

Typical discharge and charge data for a small Li/TiS₂ cell are shown in Fig. 2; the utilization of the TiS₂ was 100% at a current density of 98 mA/cm². These data show that TiS₂ has rate capabilities that are comparable to FeS and FeS₂ in LiCl-KCl electrolyte (1). Equivalent utilizations of TiS₂ in ambient temperature cells were obtained at current densities below 10 mA/cm² (5). The above data were obtained for a cell having an unpressed TiS₂ electrode of relatively low capacity density, 50 mA-hr/cm². Because higher electrode loadings are required in a practical cell, another cell with a pellet TiS₂ electrode having a capacity density of 200 mA/cm² (4.2g TiS₂, 5 cm² × 0.4 cm, ~65% theoretical density) was cycled. The utilization of this positive electrode was again high, 97% at 98 mA/cm², and the voltage curve at a current density of 98 mA/cm² was nearly identical to that of the previous cell (see lowest curve in Fig. 2).

The shapes of the discharge curves in Fig. 2 are similar to those observed in ambient temperature cells (5, 8, 9). This finding suggests that the reaction mechanism is the same (i.e., intercalation) for both cell types. An x-ray diffraction examination was conducted on the positive electrode materials obtained from five cells operated between $0 \leq x \leq 1$ (see Eq. [1]). These examinations showed that the electrode materials had lattice parameters that were in excellent agreement with those reported by Whittingham for Li_xTiS₂ (3). An ESCA examination of the LiTiS₂ showed the presence of Ti³⁺, which is consistent with the formation of LiTiS₂. These results show that the reaction mechanism is intercalation in the high temperature cell.

Three small cells having LiAl negative electrodes and pelletized TiS₂ positive electrodes were used to evaluate the effect of TiS₂ electrode thickness on the performance of LiAl/TiS₂ cells. These cells had positive electrode thicknesses of 0.20, 0.40, and 0.66 cm

and were cycled at various current densities. The results, summarized in Table II, indicated that good utilization (~70%) can be obtained with thick (0.66 cm) TiS₂ electrodes and that the utilization decreases only slightly with increasing current densities. The voltage curves from these tests were similar to those shown in Fig. 2, but were ~0.3V lower because Li-Al is ~0.3V less anodic than Li at these temperatures (11). These tests show that the LiAl/TiS₂ cell should achieve an acceptable capacity density at the high electrode loadings required in engineering-scale cells.

Voltage vs. current-density data for a small Li/TiS₂ cell,³ using 15 sec current pulses, are shown in Fig. 3 for three temperatures. Peak power densities calculated from these curves were 0.55, 0.47, and 0.40 W/cm² at 457°, 428°, and 382°C, respectively. These data compare favorably with the earlier power data for Li/FeS₂ cells (1). However, the data for the TiS₂ system showed a slight temperature dependence and are nonlinear, whereas the data for the FeS₂ system did not. Further study will be required to resolve these differences.

Owing to the excellent performance of the small cells, we decided to test three engineering cells. The performance results for these cells are summarized in Table III. The best achieved capacities were obtained at approximately the 10 hr rate and were 90 A-hr (specific energy 54 W-hr/kg) for cell DK-52, 61 A-hr (54 W-hr/kg) for cell TiSp1, and 52 A-hr (67 W-hr/kg) for cell TiSp2. These specific energies are approximately equal to those of similarly constructed Li-Al/FeS cells (12). Since a specific energy of 90-100 W-hr/kg has been achieved in LiAl/FeS cells of a more advanced design (12), we believe that, with further development, the Li-Al/TiS₂ cell will also achieve 90-100 W-hr/kg.

The cycle life of the Li-Al/TiS₂ engineering cells was limited to less than 20 cycles by various mechanical failures, as determined by the post-test metallographic examinations. In one case, for example, the cell failure was a result of penetration of the separator by the molybdenum honeycomb current collector; this caused a short circuit. The ultimate cycle life of improved engineering cells is expected, however, to be high, as the small scale cells were cycled in some cases to 200 cycles without any signs of failure. (The coulombic efficiencies of the laboratory cells and the engineering cells, in their early cycles, were greater than 95%.)

The above results showed that the kinetics of the high temperature Li-Al/TiS₂ system were satisfac-

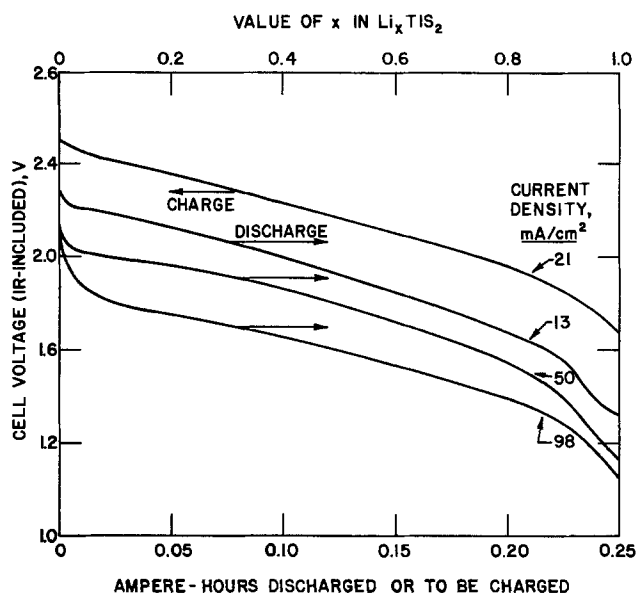


Fig. 2. Performance of Li/TiS₂ cell at 420°C (all discharges preceded by 21 mA/cm² charges).

³ The cell had a pellet TiS₂ electrode (3.75g, 4.5 cm × 0.4 cm, 200 mA-hr/cm²).

Table II. Effect of electrode thickness on LiAl/TiS₂ cell performance

Electrode thickness, cm	Charge rate, A/cm ²	Discharge rate, A/cm ²	Capacity density, A-hr/cm ²	Sulfur utilization, % of theoretical
0.20	0.035	0.035	0.099	85.6
	0.035	0.070	0.097	83.8
	0.035	0.140	0.098	84.6
	0.070	0.035	0.089	74.9
	0.070	0.070	0.090	77.7
	0.070	0.140	0.087	75.1
0.40	0.035	0.035	0.195	84.7
	0.035	0.070	0.193	83.9
	0.035	0.140	0.192	83.4
	0.070	0.035	0.189	82.1
	0.070	0.070	0.182	79.1
	0.070	0.140	0.154	68.9
0.66	0.035	0.035	0.272	79.3
	0.035	0.070	0.277	80.8
	0.035	0.140	0.229	66.8
	0.070	0.035	0.247	72.0
	0.070	0.070	0.237	69.1
	0.070	0.140	0.239	69.7

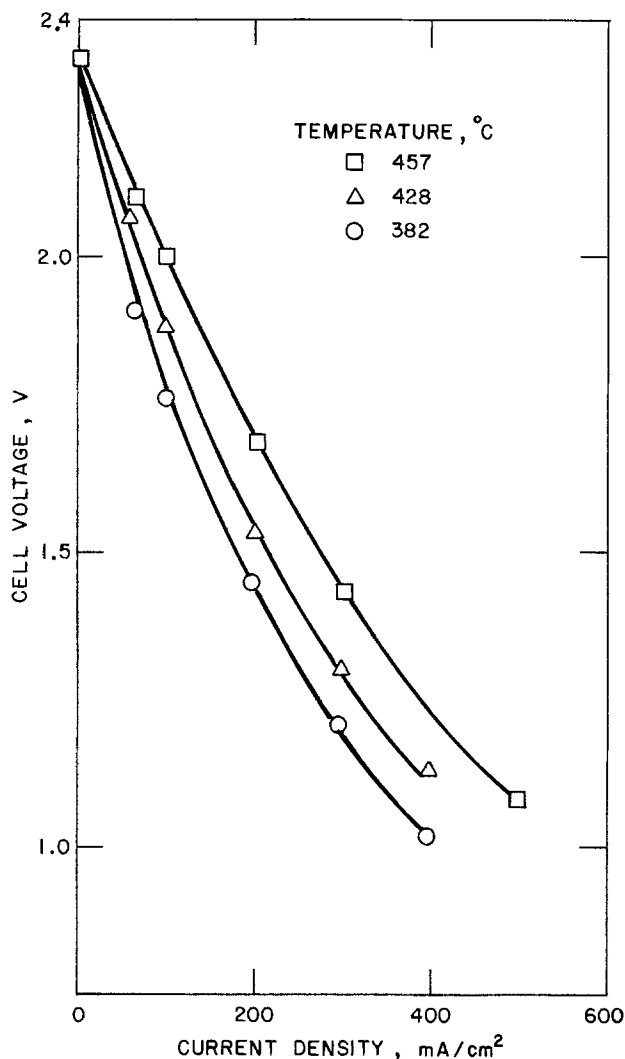


Fig. 3. Voltage vs. current density data for an Li/TiS₂ cell

tory, and that, with further development, a system having high specific energy and cycle life could be developed. To determine the theoretical specific energy of the high temperature cell, we measured its emf.

The emf data for the Li-Al/TiS₂ cell at 431°C are given in Table IV. This emf, like that for the ambient temperature cell (3) decreases with increasing values of *x*. Winn *et al.* (8) have noted that the essential features of the emf curve for the ambient temperature cell could be reproduced by a relatively simple interaction model; however, no details of this model were given. We found that the emf data in Table IV and the emf data for the ambient temperature cell can be satisfactorily reproduced by a regular solution model (13) in which the positive electrode, Li_xTiS₂ is treated as a solution of *x* moles of LiTiS₂ in (1 - *x*) moles of TiS₂. The regular solution model leads to the following equations for the activity coefficients, γ

$$RT \ln \gamma_{LiTiS_2} = k(1 - x)^2 \quad [4]$$

Table III. Summary of engineering cell performance

Cell designation	DK-52	TiSp1	TiSp2
Cycles	17	20	16
Current, A	10, 20	5	5, 10
TiS ₂ electrode utilization, % of theoretical (current, A)	63 (10), 49 (20)	49	69 (5), 49 (10)
Max. W-hr/kg (at the 10 hr rate)	54	54	67

Table IV. Emf of Li-Al/TiS₂ cell at 431°C

<i>x</i> ¹	Emf, volts
0.016	2.254
0.034	2.202
0.050	2.155
0.066	2.118
0.082	2.093
0.100	2.074
0.160	2.080
0.210	2.042
0.310	1.975
0.420	1.910
0.460	1.875
0.688	1.682
0.742	1.655
0.752	1.634
0.860	1.529
0.970	1.325

¹ Value of *x* in Li_xTiS₂.

$$RT \ln \gamma_{TiS_2} = kx^2 \quad [5]$$

where *k* is an interaction parameter. These equations, when combined with the Nernst equation, yield the following emf equation

$$E = E_m + \frac{RT}{F} \ln \left(\frac{1-x}{x} \right) - \frac{k}{F} (1-2x) \quad [6]$$

where *E_m* is the voltage at *x* = 0.5. The values of *E_m* and *k/F* were found by plotting

$$E - \frac{RT}{F} \ln \left(\frac{1-x}{x} \right) \text{ vs. } x$$

The values for the high temperature Li-Al/TiS₂ cell were 1.80 and - 0.214V, respectively, while those for the ambient temperature Li/TiS₂ cells were 2.22 and - 0.181V, respectively. The fairly close agreement of the *k/F* values indicates that the behavior of the system is reasonably consistent with the regular solution model, which requires that *k* be temperature independent, or nearly so (13).

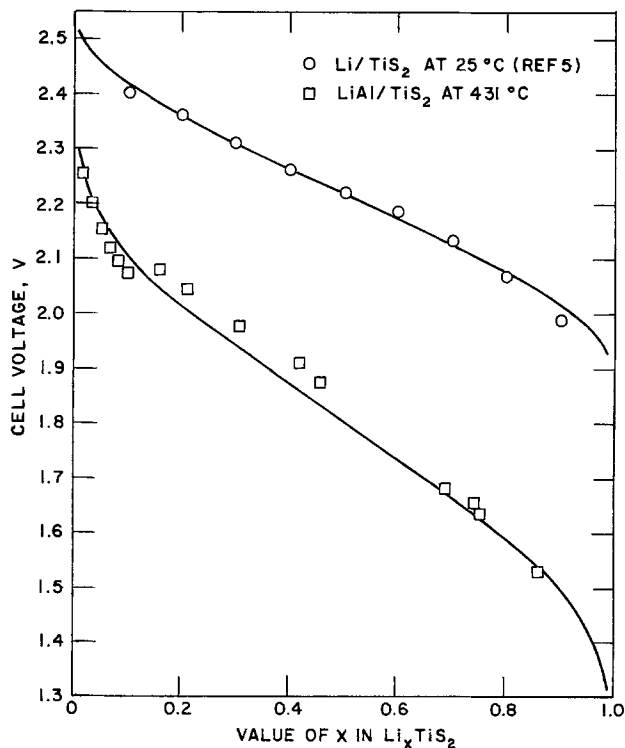


Fig. 4. Emf vs. composition for Li/TiS₂ cell based on regular solution model.

$$\Delta G = -F \int_0^1 E dx \quad [7]$$

$$= -FE_m$$

Thus, ΔG is -174 kJ (-41.66 cal) for the Li-Al/TiS₂ cell at 431°C and is -214 kJ (-51.2 kcal) for the Li/TiS₂ cell at 25°C . The theoretical specific energies of these cells are 331 and 500 W-hr/kg, respectively. The relatively large difference in specific energies is due to the use of Li-Al which has a higher equivalent weight and is less anodic than lithium. Because of technical problems with the use of liquid lithium in high temperature cells, solid lithium alloys are preferred (14).

Although we have employed a regular solution model to treat the emf of the Li/TiS₂ cell for values of $x \leq 1$, others (15,16) have employed emf equations that vary linearly with x for other cells (Na/TaS₂ and Li/TaS₂) that also operate by an intercalation reaction. Thus, the regular solution model is not always applicable to intercalation reactions.

Continued discharge of the LiAl/TiS₂ cell to cutoff voltages below those normally used (1V vs. Li-Al) yielded voltage plateaus having an emf of 0.86 and 0.4V. The length of the plateau at 0.86V was approximately one-half that necessary to form LiTiS₂. The constant emf obtained on this plateau suggests a two-phase region between LiTiS₂ and perhaps Li₂TiS₂, which has been recently reported as forming in room temperature cells (17). However, in the high temperature cell, Li₂TiS₂ is not likely to have formed because the overall TiS₂ electrode composition at the end of the plateau is equivalent to Li_{1.5}TiS₂. We did not determine the full length of the 0.4V plateau, but the electrode reaction must involve three phases, since lithium sulfide and some other sulfide of titanium, not identified, were found in the electrode by x-ray diffraction.

Conclusions

These experiments indicate that the electrochemistry of the TiS₂ electrode in high temperature Li-Al/TiS₂ cells is similar to that observed in ambient temperature Li/TiS₂ cells. However, the performance capability of the high temperature cell was considerably better, as the cell could be cycled at current densities a factor of 10 greater than could be used in ambient temperature cells. The engineering test results suggest that, with further development, the LiAl/TiS₂ system should achieve a performance comparable to the lithium-aluminum/iron sulfide system. The emf curves of the TiS₂ cells could be reproduced using a regular solution model.

Acknowledgments

The authors are grateful to B. Tani and A. E. Martin who did the x-ray and metallographic examination of the laboratory-scale TiS₂ electrodes. Thanks are extended to F. Mrazek and J. Battles for metal-

lographic examination of the engineering-scale cells. Special thanks are extended to S. Siegel who provided the ESCA results, and to J. Harmon for editorial assistance. This work was performed under the auspices of the Department of Energy.

Manuscript submitted Nov. 16, 1979; revised manuscript received March 31, 1980.

Any discussion of this paper will appear in a Discussion Section to be published in the June 1981 JOURNAL. All discussions for the June 1981 Discussion Section should be submitted by Feb. 1, 1981.

Publication costs of this article were assisted by Argonne National Laboratory.

REFERENCES

1. D. R. Vissers, Z. Tomczuk, and R. K. Steunenberg, *This Journal*, **121**, 665 (1974).
2. Z. Tomczuk, A. E. Martin, and R. K. Steunenberg, Abstract 53, p. 130, The Electrochemical Society Extended Abstracts, New York, N.Y., Oct. 13-17, 1974.
3. L. A. Heredy *et al.*, in "Metal Sulfide Electrodes for Secondary Lithium Batteries," New Uses of Sulfur, J. R. West, Editor, pp. 203-215, *Adv. Chem. Ser.*, **140**, ACS, Washington (1975).
4. Summary Report for 1978, ANL-79-64, Argonne National Laboratory, July 1979.
5. M. S. Whittingham, *This Journal*, **123**, 315 (1976).
6. M. S. Whittingham, *Science*, **11**, 1127 (1976).
7. M. S. Whittingham, in "Electrode Processes for Energy Conversion and Storage," J. D. E. McIntyre, S. Srinivasan, and F. G. Will, Editors, pp. 784-798, The Electrochemical Society Softbound Proceedings Series, Princeton, N.J. (1977).
8. D. A. Winn, J. M. Shemilt, and B. C. Steele, *Mater. Res. Bull.*, **11**, 559 (1976).
9. G. L. Holleck, and J. R. Driscoll, *Electrochim. Acta*, **22**, 674 (1977).
10. H. Shimotake and L. G. Bartholme, Argonne National Laboratory Report No. 76-8, B-210 (1976).
11. N. P. Yao, L. Heredy, and R. C. Saunders, *This Journal*, **118**, 1039 (1971).
12. High Performance Batteries for Electric-Vehicle Propulsion and Stationary Energy Storage, Progress Report for the Period October 1978-March 1979, ANL-79-39, Argonne National Laboratory (1979).
13. J. Lumsden, "Thermodynamics of Molten Salt Mixtures," Academic Press, London (1966).
14. E. Gay *et al.*, *This Journal*, **123**, 1591 (1976).
15. A. Nagelbert and W. Worrel, in "Electrode Processes for Energy Conversion and Storage," J. D. E. McIntyre, S. Srinivasan, and F. G. Will, Editors, pp. 847-860, The Electrochemical Society Softbound Proceedings Series, Princeton, N.J. (1977).
16. S. Basu and W. Worrel, in "Electrode Processes for Energy Conversion and Storage," J. D. E. McIntyre, S. Srinivasan, and F. G. Will, Editors, pp. 861-868, The Electrochemical Society Softbound Proceedings Series, Princeton, N.J. (1977).
17. D. W. Murphy and J. N. Carides, *This Journal*, **126**, 359 (1979).

Safety Studies on Li/SO₂ Cells

V. Effect of Design Variables on the Abuse Resistance of Hermetic D Cells

A. N. Dey

Duracell International, Incorporated, Laboratory for Physical Science, Burlington, Massachusetts 01803

ABSTRACT

The effect of cell design variables such as stoichiometric ratios of Li:SO₂, electrode area, electrolyte salt, SO₂ content of the electrolyte, etc. on the abuse resistance of the hermetic Li/SO₂ D cells on force-discharge, especially at -30°C at a current of 2A, was evaluated. Both the Li:SO₂ ratio and the current density of operation were found to be important design parameters from the safety standpoint. Lithium-limited cell designs were found to be safer than the lithium-rich cell designs for a given current density of operation.

In the study of intrinsic abuse resistance of Li/SO₂ cells, we have pursued two approaches: (i) A causative approach involving the identification of chemical and/or electrochemical reactions occurring during use and abuse of Li/SO₂ cells, that are responsible for unsafe behavior and the development of possible ways of quenching these reactions for increased safety, and (ii) an empirical approach involving the construction and testing of D size hermetic Li/SO₂ cells made with several design modifications for increased abuse resistance.

The former approach involving DTA of Li/SO₂ cell constituents was pursued separately and the results are reported elsewhere (1). The latter approach has been pursued in this paper. The empirical approach involved the construction and abuse testing of hermetic D cells according to twelve different designs which included the following cell construction variables: (i) electrode area (moderate rate and high rate); (ii) electrode thickness; (iii) SO₂ content in the electrolyte (70% and 80%); (iv) organic solvent in the electrolyte (AN, PC + AN); and (v) electrolyte salt (LiBr, LiAsF₆).

The details of the twelve selected cell designs incorporating the above variables are shown in Table I. A major variable, shown earlier (2) to have signifi-

cant impact on the safety, is the stoichiometric ratio of Li:SO₂ which was varied in the cell designs by varying the thickness of Li and the SO₂ content of the electrolyte. We showed earlier (1) from the DTA studies of the Li/SO₂ cell constituents that the exothermic reaction between Li and AN (in the absence of SO₂) which occurs at room temperature is a major cause of hazardous behavior of cells on force-discharge, that may be encountered by individual cells in a series connected multi-cell battery. The presence of SO₂ prevents the Li + AN exothermic reaction from occurring at room temperature. Therefore, the starting stoichiometric ratio of Li:SO₂ is important since the cell discharge results in the consumption of Li and SO₂ is according to the reaction



and depending upon the initial Li:SO₂ ratio, the cells may end up with either Li and AN, or only AN or SO₂ and AN (assuming 100% utilization of Li and SO₂), as shown in the cell reaction trajectories I, II, and III in Fig. 1. According to the earlier studies (1, 2), the latter two conditions are more desirable from a safety standpoint.

The main objective of this program is to establish the dependence of the cell performance and cell safety on the cell composition and design; so that

* Electrochemical Society Active Member.

Key words: organic, electrolyte, battery, stoichiometry.

Table I. Details of the selected cell designs^{1,2}

Design	Li anode		Stoichiometric capacity of Li (A-hr)	Cathode length (in.)	Electrolyte	Stoichiometric capacity of SO ₂ (A-hr)	Li:SO ₂ stoich. ratio	Type of roll
	Length (in.)	Thickness (in.)						
1(a)	21.0	0.008	9.2	23.5	34.2g (70% SO ₂) LiBr + AN (std)	10.0	1:1.08	Exterior cathode
1(a)'	21.0	0.008	9.2	23.5	36.5g (70% SO ₂) LiBr + AN (std)	10.7	1:1.16	Exterior cathode
2(a)	22.5	0.008	9.9	21.0	36.5g (70% SO ₂) LiBr + AN (std)	10.7	1:1.08	Exterior anode
3(a)	21.0	0.01	11.5	23.5	34.2g (70% SO ₂) LiBr + AN (std)	10.0	1.15:1	Exterior cathode
1(b)	21.0	0.008	9.2	23.5	34.2g (LiAsF ₆) AN + 70% SO ₂	10.0	1:1.08	Exterior cathode
1(c)	21.0	0.008	9.2	23.5	34.2g (PC + AN 1:9) LiBr + 70% SO ₂	10.0	1:1.08	Exterior cathode
1(g)	21.0	0.008	9.2	23.5	34.2g (80% SO ₂) LiBr + AN	11.4	1:1.24	Exterior cathode
2(g)	22.5	0.008	9.9	21.0	34.2g (80% SO ₂) LiBr + AN	11.4	1:1.15	Exterior anode
3(g)	21.0	0.01	11.5	23.5	34.2g (80% SO ₂) LiBr + AN	11.4	1:1	Exterior cathode
8(a)	32.0	0.006	10.0	30	33g (70% SO ₂) LiBr + AN (std)	10.0	1:1	Exterior anode
8(b)	32.0	0.006	10.0	30	33g (LiAsF ₆) AN + 70% SO ₂	10.0	1:1	Exterior anode
10(a)	32.0	0.008	14.0	30	31g (70% SO ₂) LiBr + AN (std)	9.0	1.56:1	Exterior anode

¹ The electrode width: 1.625 in.

² The following cell designs were selected from a Design Matrix consisting of 144 possible designs.

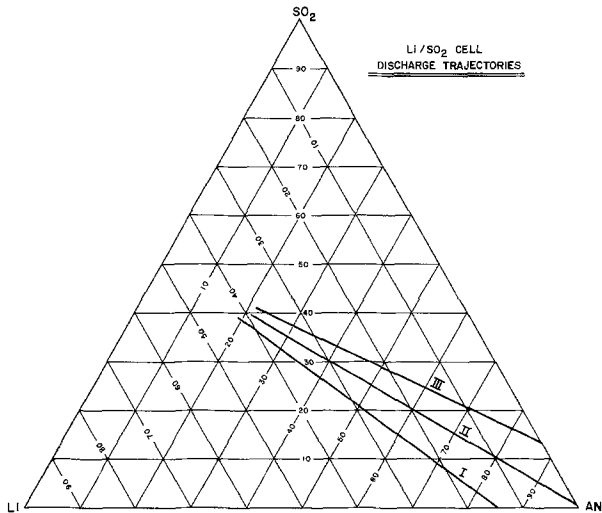


Fig. 1. Li/SO₂ cell discharge trajectories

an optimum cell design can be developed with respect to both the cell performance and the safety. The underlying assumption is that the electrical performance can be traded for an increased abuse resistance (safety) and our objective is to optimize this tradeoff.

Experimental

State-of-the-art hermetic Li/SO₂ D cells were made by winding the Li anode and the carbon cathode of appropriate lengths and thicknesses according to the twelve different designs specified in Table I. Porous polypropylene separators were used in-between the anode and the cathode layers. The cells were filled with appropriate electrolytes and were tested as follows: (i) capacity test at various loads at ambient temperature, and (ii) abuse test on constant current (2A) discharge and reversal at -30°C.

Both the voltage and the wall temperature of the cells were monitored during the latter tests. The abuse resistance of the cells was determined by examining the cells visually after the test and photographically recording the condition of the cell.

Results and Discussion

Capacity-rate characteristics.—The capacity-rate characteristics of the D cells of the twelve types are shown in Fig. 2, 3, and 4. Note that the maximum capacity of the D cells of type 1a, 1a', 2a, 1b, 1c, 1g, and 2g is approximately 7 A-hr whereas the maximum capacity of the D cells of type 3a and 3g is approximately 10 A-hr. Considering the fact that the

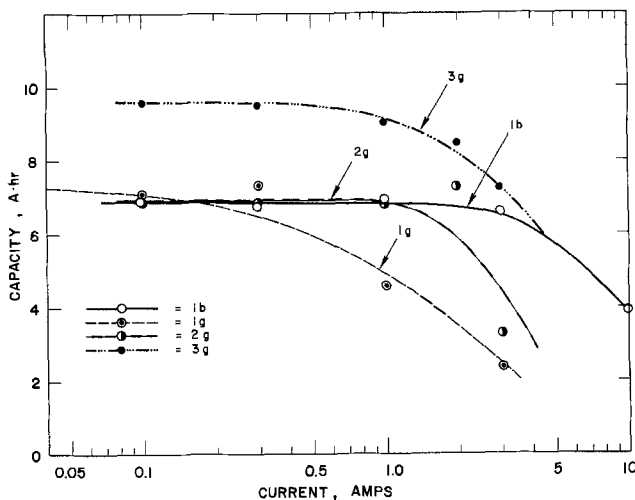


Fig. 2. Capacity-rate characteristics of Li/SO₂ D cells of type 1b, 1g, 2g, and 3g.

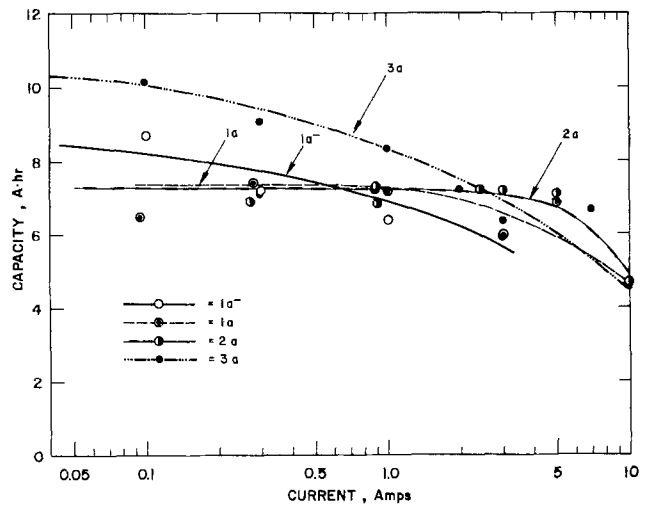


Fig. 3. Capacity-rate characteristics of Li/SO₂ D cells of type 1a, 1a', 2a, and 3a.

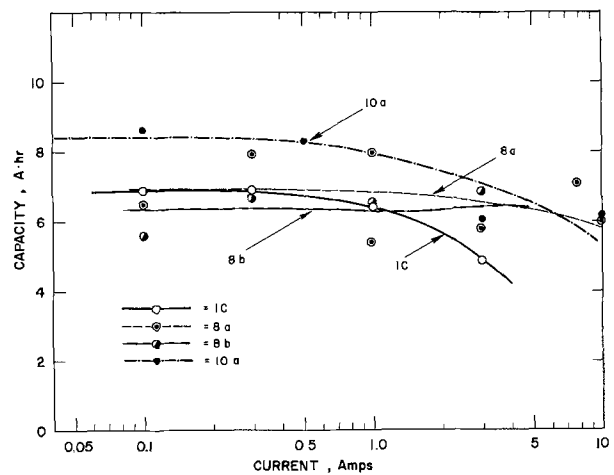


Fig. 4. Capacity-rate characteristics of Li/SO₂ D cells of type 1c, 8a, 8b, and 10a.

stoichiometric capacity of SO₂, based on reaction [1], is approximately 10-11 A-hr (Table I) for all the cell types, the low capacity of the D cells of type 1a, 1a', 2a, 1b, 1c, 1g, and 2g indicate that these cells are lithium anode limited. The stoichiometric capacity of Li for these latter types of cells varied from 9.2 to 9.9 A-hr thus giving rise to lithium utilization efficiencies of 70-76%. This indicates that the so-called lithium-limited cells must contain excess unused Li at the end of the low current discharge. The amount of excess Li remained varied from 2.2 to 2.9 A-hr whereas the amount of excess SO₂ varied from 3 to 4.4 A-hr for the D cells of type 1a, 1a', 2a, 1b, 1c, 1g, and 2g. In contrast, the D cells of type 3a and 3g are cathode and/or SO₂ limited; the utilization of SO₂ based on reaction [1] was 90-100%. Thus there was virtually no SO₂ left at the end of the low current discharge of the D cells of type 3a and 3g. The amount of excess Li left was approximately 1.5 A-hr.

The type of electrode configuration, viz. exterior cathode vs. interior cathode does not appear to have any effect on the capacity-rate characteristics of the cells. D cells of type 1g appear to be an exception in that the rate capability of this group of cells is quite poor.

The effect of the electrolyte variables such as LiAsF₆ salt on the capacity-rate characteristics of the cells at ambient temperature does not appear to be very significant. The rate capability of the cells with 80% SO₂ appears to be marginally lower than the standard.

The capacity penalty of the D cells of type 1a, 1a', 2a, 1b, and 1c compared to 3a and 3g is significant at low rates (0.1-1.0A), but insignificant at high rates (2-10A).

The addition of PC (1c) appears to lower the rate capability of the cell somewhat.

Constant current (2A) discharge and reversal at -30°C.—We tested six cells from each type of D cells under this condition. Typical voltage and temperature profiles of the cells of type 1a are shown in Fig. 5. Simplified qualitative voltage profiles of all types of D cells on 2A discharge and reversal at -30°C are shown in Fig. 6.

In general the cell wall temperature changed with the cell voltage in approximately a mirror image fashion indicating that the cell heating was due to the cell polarization. The most rapid cell heating occurred at the point where the cell experienced deep reversal towards the end of the test. This was the point where venting and/or fire and explosion occurred. We define this point as the "trigger point." We did not see any spontaneous cell heating after the completion of the test leading to a venting and/or fire. Whatever happened, happened at this trigger point. There are several instances when neither venting nor explosion occurred even at the trigger point.

The cell voltage reflects primarily the potential of the cathode since the Li anode potential remains

constant throughout the discharge because of its high exchange current. This is demonstrated by discharging a D cell with an Li reference electrode as shown in Fig. 7. The electrochemical reactions occurring in the cell up to the zero volt result in the formation of Li salts according to reaction [1] (primarily $\text{Li}_2\text{S}_2\text{O}_4$ and possibly others), and the consumption primarily of Li and SO_2 . These reactions may be viewed as deactivating processes which reduce the amount of active materials such as Li which can initiate and/or propagate a combusive and/or explosive process. The electrochemical reactions occurring below zero volt result in the formation of active materials such as Li on the cathode. This Li may spontaneously alloy (3) with the Al grid of the cathode or may be in a very active form to initiate and/or propagate a fire and/or an explosion.

Based on the above analysis, the voltage profiles of the D cells of the various types can be grouped into four different classes, as shown in Fig. 6. The voltage profiles of D cells of type 1a, 1a', 2a and 1c, and 2g belong to class I. The class I voltage profile has a plateau above 2V and a stepwise decline to zero volt followed by an immediate deep reversal corresponding to the trigger point. The deep reversal occurs because of the consumption and/or disconnection of the Li anode which does not have a current collector. The interval between the zero volt and the deep reversal is very small indicating very little or no formation of active form of Li on the cathode. Consequently, the cells did not exhibit explosion or fire at the trigger point; only venting occurred. The amount of SO_2 consumed up to zero volt was approximately 7-8 A-hr which meant that there was 2-3 A-hr of SO_2 still left at the trigger point to cool the cell sufficiently on venting. The cells exhibiting this type of voltage profile had excellent abuse resistance on 2A reversal at -30°C. It should be noted

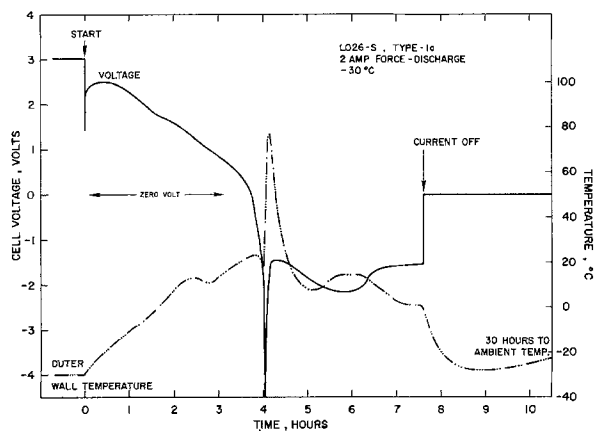


Fig. 5. Typical voltage and temperature profiles of Li/SO₂ D cell of type 1a on 2A discharge and force-discharge at -30°C.

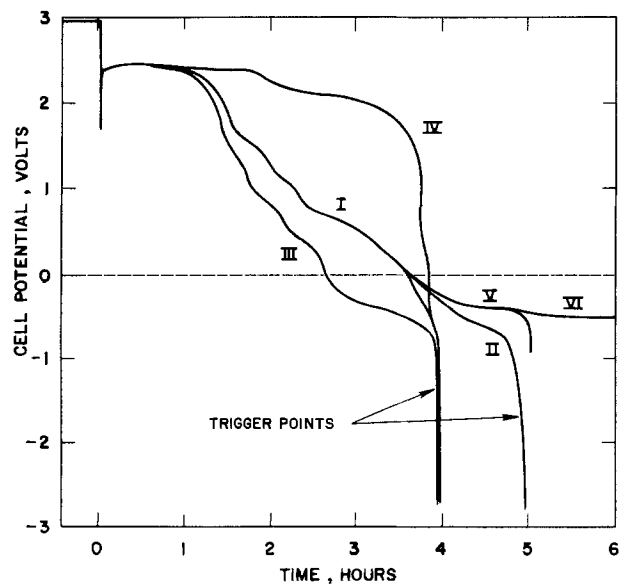


Fig. 6. Classification of voltage profiles of D cells of various types on 2A discharge and force-discharge at -30°C.

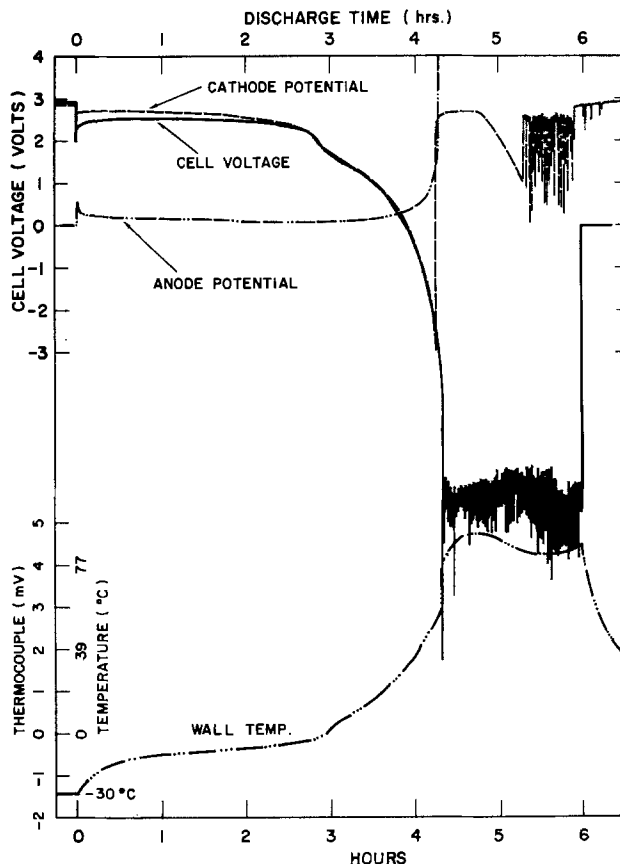


Fig. 7. Cell voltage, individual electrode potential (vs. Li reference), and temperature profiles of Li/SO₂ D cell of type 1a on 2A discharge and force-discharge at -30°C.

that for a given current and temperature the amount of Li and the anode design determines the trigger point; the carbon cathode and the electrolyte composition determines the time to zero volt. For a safe cell the interval between the above two must be as close to zero as possible; also the stoichiometric amount (A-hr) of SO₂ must be higher than the capacity up to zero volt to ensure excess SO₂ at the trigger point.

The class II voltage profile is very similar to class I profile except that the cell voltage lingers below zero volt quite a bit longer prior to the trigger point. The above analysis conforms to the observed explosion and fire of the D cells of type 3a and 3g whose voltage profiles on reversal belong to class II. The interval between zero volt and the trigger point of these cells was 1 hr (2 A-hr) or more thus resulting in the formation of significant amounts of active forms of Li on the cathode which caught fire at the trigger point. This was because the anode had excess Li which made the time to trigger point much longer.

The voltage profiles of D cells of type 1g belongs to class III, where although the stoichiometric amount of Li was the same as in 1a, 1a', 2a, 1c, and 2g, the poor performance of the cathode resulted in the increase of the interval between the zero volt and the trigger point and the consequent unsafe behavior at the trigger point.

The voltage profiles of D cells of type 1b was quite exceptional and belongs to class IV. This is very similar to class I except that the cell voltage remains at a relatively high level prior to reaching zero volt and the immediate deep reversal at the trigger point. These cells were also safe on 2A reversal at -30°C, since there was no chance of lithium deposition on the cathode. The higher operating voltage of this type of cell gives them a longer useful life to a given cut-off voltage. These cells have LiAsF₆ salt as the electrolyte.

The voltage profiles of D cells of type 8a and 8b belong to class V. This is very similar to class II except that the trigger point is very shallow and the voltage drop was insufficient to cause any appreciable cell heating. There was no venting or explosion on force-discharge. This was due to the higher (50%) electrode area of these cells compared to the cells of general type 1, 2, or 3. Accordingly, the current density of operation at 2A was 50% lower in these cells than the others.

The voltage profiles of D cells of type 10a belong to class VI and the cells do not reach the trigger point during the test since the Li content of these cells was far in excess of the others. Furthermore, the current density of operation at 2A is also 50% lower than the other cells. None of the cells of this type vented or exploded on 2A force-discharge at -30°C in spite of high Li:SO₂ ratio.

The above results indicate that the abuse resistance of D cells on constant current reversals at -30°C depends on (i) the absence of lithium deposition on the cathode prior to the exhaustion of Li on the anode (trigger point), (ii) the availability of excess SO₂ at the trigger point, and (iii) the low current density of operation.

There was no dramatic effect of the addition of PC on the abuse resistance of the cells of type 1c since the cells contained excess SO₂. The effect of current density on the abuse resistance of D cells was further evaluated by testing D cells of type 1a and 2a on force-discharge at currents of 0.5A and 3.0A at -30°C. The typical voltage and temperature profiles of D cells of type 1a on 0.5A and 3.0A tests at -30°C are shown in Fig. 8 and 9, respectively. While the cells did not vent on 0.5A force-discharge, the cells vented, some violently, on 3A force-discharge. Note that at 0.5A test (Fig. 8) the capacity between the zero volt and the deep reversal (trigger point) was insignificant, whereas at 3.0A test, the capacity was suffi-

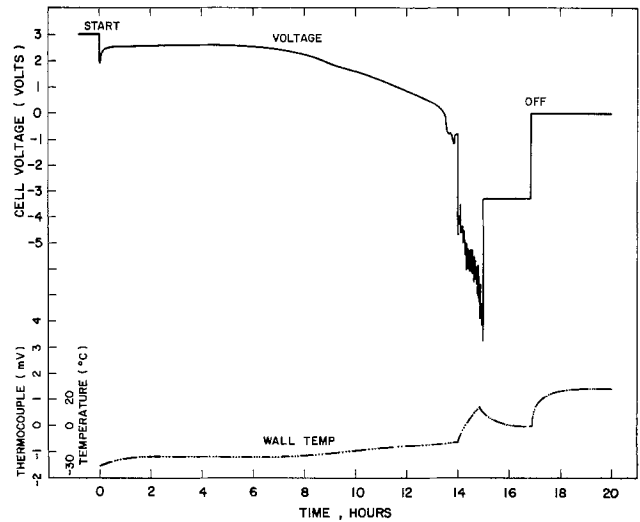


Fig. 8. Voltage and temperature profiles of D cells of type 1a on 0.5A discharge and force-discharge at -30°C.

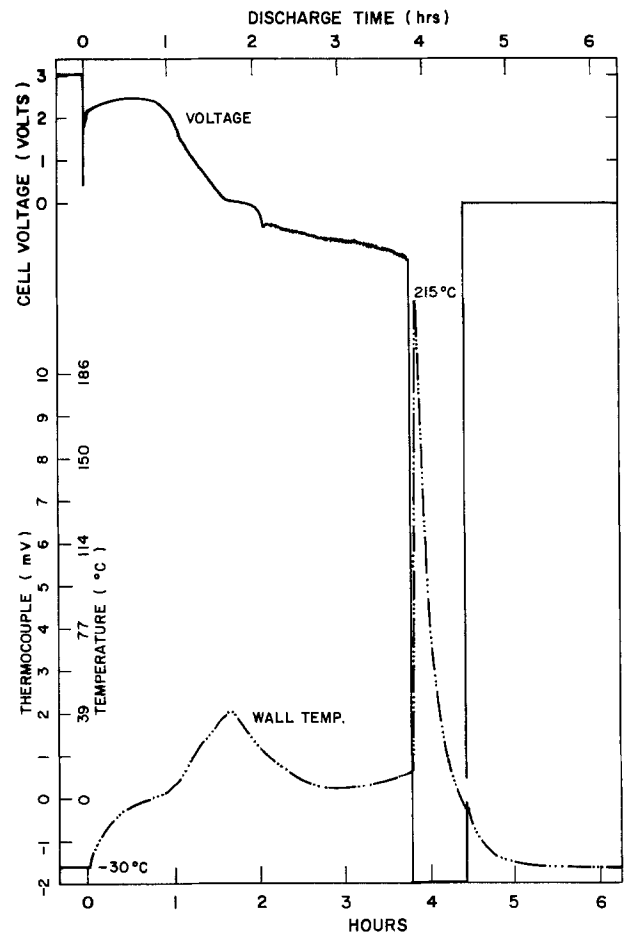


Fig. 9. Voltage and temperature profiles of D cells of type 1a on 3A discharge and force-discharge at -30°C.

ciently significant to cause the unsafe behavior. The D cells of type 2a behaved similarly and showed no venting on 0.5A test and venting (some violently) on 3.0A test.

Conclusions

The Li:SO₂ ratio was found to be an important parameter affecting the safety of the Li/SO₂ cells, and the lithium-limited cell designs were found to be safer than the lithium-rich cell designs. Furthermore, the high rate D cells having a higher rate capability were found to be safe under a 2A force-discharge at -30°C with a larger Li:SO₂ ratio. The abuse re-

sistance of the cells appears to depend markedly on the current (current density) of the abusive discharge. The cells which were found to be safe on 2A force-discharge became unsafe on 3A force-discharge. It should be possible, therefore, for any given abuse, to design cells capable of tolerating that abuse with impunity, provided we know how to construct truly high rate cells.

The importance of the stoichiometric ratio of Li:SO₂ in a cell in determining the safety on reversal is only applicable when both Li and SO₂ are utilized efficiently. Whereas the Li electrode is inherently efficient at high current densities provided there is electrical continuity, the efficiency of the carbon cathode depends on the current density and the current distribution in the cell, as well as on the cathode fabrication process. Assuming that the latter is kept invariant, the importance of Li:SO₂ stoichiometric ratio is valid up to a limiting current density of operation. At higher current densities the cathode may polarize prematurely leading to Li deposition in the cathode prior to the exhaustion of Li anode. This deposited Li is very active towards AN and may lead to an unsafe situation.

Acknowledgments

The author wishes to thank Gabriel DiMasi for helpful discussions and P. Witalis for experimental assistance.

The work was carried out under contracts from ERADCOM DAAB07-77-C-0458 and DAAB07-78-C-0535.

Manuscript submitted Nov. 30, 1979; revised manuscript received March 21, 1980. This was Paper 47 presented at the Los Angeles, California, Meeting of the Society, Oct. 14-19, 1979.

Any discussion of this paper will appear in a Discussion Section to be published in the June 1981 JOURNAL. All discussions for the June 1981 Discussion Section should be submitted by Feb. 1, 1981.

Publication costs of this article were assisted by Duracell International, Incorporated.

REFERENCES

1. A. N. Dey and R. W. Holmes, *This Journal*, **126**, 1637 (1979).
2. G. DiMasi, in "Proc. 27th Power Sources Symposium," p. 75, Atlantic City, N.J. (1976).
3. A. N. Dey, *This Journal*, **118**, 1547 (1971).

On the Mechanism of Corrosion of Cu-9.4Ni-1.7Fe Alloy in Air Saturated Aqueous NaCl Solution

I. Kinetic Investigations

C. Kato, B. G. Ateya,*¹ J. E. Castle,² and H. W. Pickering*

Metallurgy Section, Department of Materials Science and Engineering, The Pennsylvania State University, University Park, Pennsylvania 16802

ABSTRACT

The mechanism of formation of the protective layer on commercial Cu-9.4Ni-1.7Fe alloy in aerated 3.4 weight percent NaCl solution at room temperature was investigated for various times up to 191 days. The weight of the sample, the weight of the corrosion product layer, and the anodic and cathodic polarization curves were measured before and after the corrosion periods. Results of these experiments show that the decrease in the overall corrosion rate by formation of the protective layer is due mainly to a decrease in the oxygen reduction rate and only slightly to a decrease in the metal dissolution rate. They indicate that to a large degree, if not entirely, the location of the oxygen reduction reaction is the surface of a thin, strongly adherent inner layer which is in contact with electrolyte as a result of the porous nature of the much thicker outer layer. The rate-determining step of this reaction was found to be the transport of electrons through the inner layer, which increases in thickness according to the parabolic law. The results further show that the (modest) decrease in the anodic reaction during open-circuit corrosion is due entirely to the porous outer layer.

The commercial Cu-9.4Ni-1.7Fe alloy (CDA 706) has been used successfully as condenser tubes in saline environments. It is generally believed that this corrosion resistant alloy is protected by the films developed on its surface in seawater. The effect of minor Fe additions is to improve the corrosion resistance of Cu-Ni alloys (1-4) with, however, some accompanying loss of ductility at room temperature (5). Stewart and LaQue (2) found that the alloy with Fe in solid solution (solutionized) was more corrosion resistant than the alloy containing Fe precipitates, in agreement with Swartzendruber and Bennet (4).

Room temperature anodic polarization curves over a limited potential range have been determined for this alloy in aqueous NaCl solution by several investigators (6-8). The curves exhibit a sharply increasing rate of anodic dissolution with increase in electrode potential. Ijsseling and Kroughman (9) investigated cathodic polarization curves on the uncorroded and pre-corroded (protected by corrosion products) samples in seawater. They found the cathodic reaction to be more highly polarized the longer the corrosion periods, confirming earlier results by North and Pryor (6), who also observed the same for anodic polarization. Thus, the presence of the film retards both the cathodic and anodic reaction and, hence, the overall reaction.

The purpose of this paper is to investigate the corrosion of commercial (solutionized) Cu-9.4Ni-1.7 Fe alloy in aerated 3.4 weight percent (w/o) NaCl

* Electrochemical Society Active Member.

¹ Present address: Chemistry Department, Cairo University, Cairo, Egypt.

² Permanent address: Department of Metallurgy and Materials Technology, University of Surrey, Guildford, GU2 5XH, England.

Key words: marine corrosion, polarization, condenser tubes, protective films, oxygen reduction.

aqueous solution at room temperature $23^\circ \pm 3^\circ\text{C}$. Following the procedures of Wagner and Traud (10), the mechanism of the corrosion process in the presence and absence of a protective corrosion-product layer is determined from the individual anodic and cathodic polarization curves. Anodic and cathodic polarization curves were determined after different periods of corrosion and for various conditions and amounts of the protective film on the sample.

Experimental

Materials and specimen preparation.—The composition and mechanical properties of the Cu-9.4Ni-1.7Fe alloy sheet material (0.17 cm thick) in the solutionized condition (850°C for 30 min, water quench), are given in Tables I and II, respectively. Specimens (0.17 × 1.5 × 2.5 cm) were cut from the master sheet and polished successively down to 600 grit. The samples were then immersed in deaerated 10 volume percent (v/o) H₂SO₄ for 10 min to remove the air-formed oxide. This was followed by degreasing in 50 v/o acetone-benzene mixture with ultrasonic surface cleaner for 10 min and finally rinsing in a methanol solution and drying in a desiccator for 25 hr. The electrolyte used throughout this work was 3.4 w/o NaCl.

Weight loss under open-circuit corrosion conditions.—Open-circuit corrosion tests were always run using duplicate specimens which were suspended in a 1 liter beaker by glass hooks through holes in the corners of the specimens. The specimens were weighed and their thickness measured before immersion. Each pair was allowed to corrode for varying lengths of time, i.e., 1, 2, 12, and 24 hr; and 2, 3, 5, 10, 30, and 191 days at room temperature. The solutions were changed weekly. At the end of a run, the specimen was removed from the solution, rinsed with distilled water, dried, and weighed. One of the two specimens was analyzed by ESCA (XPS), Auger electron spectroscopy, and/or x-ray diffraction (11). The other specimen was immersed in deaerated 15 v/o H₂SO₄ for 2 hr to dissolve the corrosion products. This was followed by rinsing with distilled water, drying with hot air, and weighing. An identical noncorroded sample treated similarly gave no detectable weight loss indicating that the deaerated sulfuric acid treatment did not attack the alloy itself. From the first and third, and the second and third weighings, the weight loss of the sample due to metal oxidation and the weight of the corrosion-produced layers were determined, respectively.

Table I. Composition of the Cu-Ni-Fe alloy

Element	Cu	Ni	Fe	Mn	Zn	Pb	P	S	Ag	O
Weight per-cent*	Balance	9.4	1.7	0.32	0.15	0.02	0.02	0.02	N.D.**	N.D.
Weight per-cent†		9.4	1.9							

* Hussey Metal Company, Leetsdale, Pennsylvania.

** None detectable.

† Mineral Constitution Laboratory, The Pennsylvania State University.

Table II. Mechanical properties of solutionized (850°C) Cu-Ni-Fe alloy*

Tensile strength	42,000-43,000 (psi)
0.5% Extension yield point	7,350-8,000 (psi)
Elongation in 2 in.	39.0-42.5 (%)
Hardness (Rockwell)	35† (B scale)
Bend	180 (degrees without fracture)

* Hussey Metal Company, Leetsdale, Pennsylvania.

† Measured by the authors.

Polarization measurements.—Current-potential curves were obtained on fresh and corroded samples using an Aardvark potentiostat (Model V) and a Honeywell chart recorder (Electronic 193). The electrochemical cell includes a saturated calomel reference electrode (SCE), a working alloy disk (1.35 cm diam) electrode, an auxiliary electrode (Cu wire or carbon rod), and a gas disperser. These were arranged in a beaker containing 300 ml electrolyte (pH adjusted with NaOH to 8). A Cu wire covered with an acrylic plastic sleeve was soldered to the top (back side) of the disk. The sleeve end and back side of the disk were shielded from the electrolyte by cold mount, such that only the (bottom) disk surface was exposed to the electrolyte. This surface was abraded, as above. Anodic and cathodic polarization curves were obtained on these samples after periods of open-circuit corrosion, in some cases following stripping of the corrosion product with tape. The electrode was immersed in the electrolyte and the gas flowed (either prepurified nitrogen or air) for 30 min before measurements were started. All potentials are reported vs. the standard hydrogen electrode (SHE).

Anodic polarization curves were measured on the 0, 5, 10, 15, and 191 day corroded samples. The surface films were formed by the method described in the weight-loss measurements. The corroded specimens at the completion of their open-circuit exposure were immediately transferred to the electrochemical test cell. Measurements were taken at various potential scanning rates in the range of 45-545 mV (SHE) as follows: (i) high scanning rate (75 mV min⁻¹), (ii) low scanning rate (1.5 mV min⁻¹), (iii) manual stepping of the potential by 10 or 20 mV steps and allowing the current to reach a steady value before the next potential step, and (iv) direct immersion of a fresh sample at each of the following potentials: 145, 170, 245, 320, 345, 445 mV (SHE).

The cathodic polarization curves were measured potentiostatically by stepping the potential 20 or 50 mV over the range of 45 to -455 mV (SHE). The current was measured after 10 min at each potential. Though quasi-stationary currents were obtained by this time, some of the current was due to reduction of the oxide films. The amount of film reduction was obtained by measuring the cathodic polarization curves on the 30 day precorroded specimen with nitrogen gas bubbling through the cell.

In order to assess the roles of electronic resistance of the corrosion-product layer and/or the catalytic nature of the corrosion-product surfaces, some specimens were coated with the electrocatalyst Pd in the following manner: (i) The specimen surface (fresh, corroded or corroded and stripped) was dried thoroughly. (ii) A few drops of 0.5% of Pallamers solution (Technic Incorporated, Chicago, Illinois) was placed on the whole area of the specimen surface. (iii) After 5 min, the excess Pallamers solution was removed with tissue paper and air dried.

Other samples in the corroded but not stripped condition were coated with another electrocatalyst,³ Pt, by sputtering Pt on the corrosion-product surface.

Results and Discussion

Corrosion and film growth rates.—Figure 1a is a plot of the weight of the solid corrosion product layer (film) and of the overall weight loss vs. time of immersion of the sample in aerated solution under free corrosion conditions. Figure 1b shows the variation of the average corrosion rate with time. Note that film weight refers to the compounds Cu₂(OH)₃Cl, Cu₂O, and possibly others (11), and consequently the weight of the metal included in forming the film is less than the film weight. On the other hand, the overall weight loss and corrosion rate refer to metal.

³ The exchange current density of oxygen reduction is about one order of magnitude greater on Pd than on Pt (12).

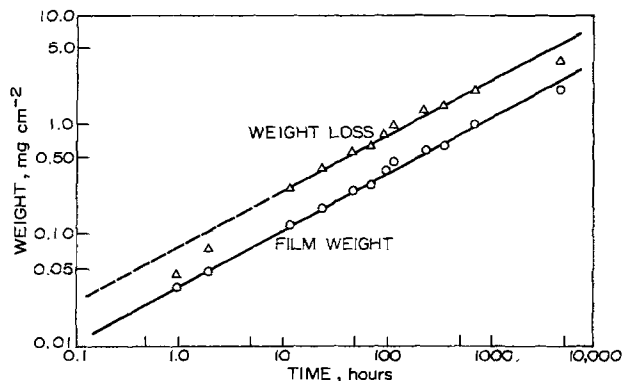


Fig. 1a. Time variations of film weight and total weight loss of the Cu-Ni alloy in the 3.4 w/o NaCl solution.

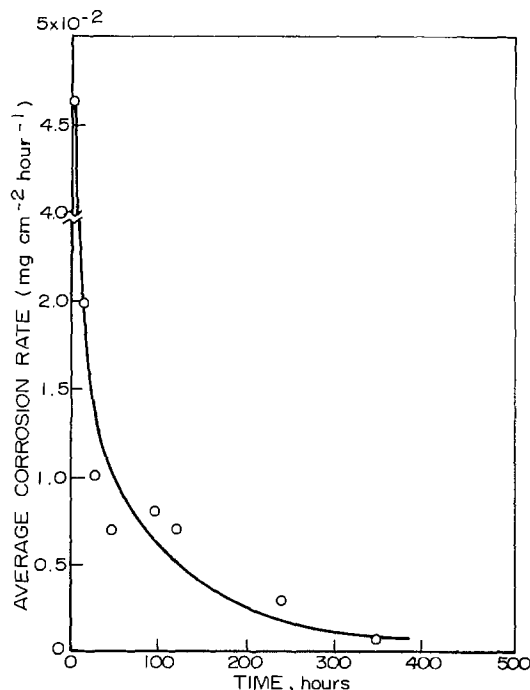


Fig. 1b. Time variation of the average corrosion rate of the alloy, i.e., weight loss rate.

This shows that, at all times, only a fraction of the metal ions resulting from the corrosion reaction are present in the solid corrosion product. The corrosion rate of the alloy (Fig. 1b) decreases with time of immersion; the most pronounced rate-of-decrease being at shorter times. This has been attributed to the protective effect of the corrosion product layer on the limiting corrosion process.

The weight of the film per unit area is taken as a measure of its thickness, with the solid line representing the least squares correlation of the data points (all except the last one which shows the most deviation; about 25% lower than predicted by the correlation). The slope of the straight film line in Fig. 1a is 0.51 and the correlation coefficient is 0.995. Thus

$$WF = 3.5 \times 10^{-2} t^{0.51} \quad 1 < t < 1000 \text{ hr} \quad [1]$$

where WF is the weight of the film in mg cm^{-2} of alloy surface area, and t is the time of free corrosion in hours. This parabolic relation indicates that the growth of the film follows a transport-limited mechanism. The above correlation applies for at least 1000 hr (42 days); the film weight for the one datum point at >1000 hr is lower than that obtained by extrapolation.

The variation of the overall weight loss with time is more complex than that of the film weight. The

parabolic rate law is closely approximated in the 10-1000 hr period. Even at short times, however, the slope is closer to one-half than to unity, i.e., closer to parabolic than to linear-law behavior. During this initial period the film appears to undergo substantial change, both in composition and in structure, as reported in Part II of this series (11).

The solution pH was initially 7.5, increased to 8.0 within a day, and increased more gradually thereafter to 8.1 after one week.⁴ The open-circuit corrosion potential varied with time, starting out at about 65 mV (SHE) and drifting to about -10 mV by 48 hr.

Anodic polarization measurements.—Figure 2 shows the effect of potential scan rate on the anodic current-potential curves. While the low scan rate (1.5 mV min^{-1}) gives nearly steady-state behavior, the high scan rates, typical of many previous studies, $\lesssim 300 \text{ mV min}^{-1}$ (6-8), give quite different results at potentials beyond the Tafel region. The maximum and minimum currents in the 1.5 mV min^{-1} curve are reproducible, but are not observed using the fast scan rate for determining the polarization curve. The time to reach a steady-state current is relatively long, e.g., $> 60 \text{ min}$ at 345 mV (insert in Fig. 2). The decrease of current with time at 345 mV is consistent with the formation and thickening of a protective layer. In the Tafel region shorter times are required consistent with the establishment of stable Cl^- and CuCl_2^- ion profiles in the solution boundary layer as discussed below.

The steady-state anodic current-potential curves were also measured on precorroded specimens (for times up to 191 days), Fig. 3. A current peak was always observed, at around 200 mV, for the alloy

⁴Buffered solutions were not used because of their effect on the anodic polarization behavior (Fig. 6).

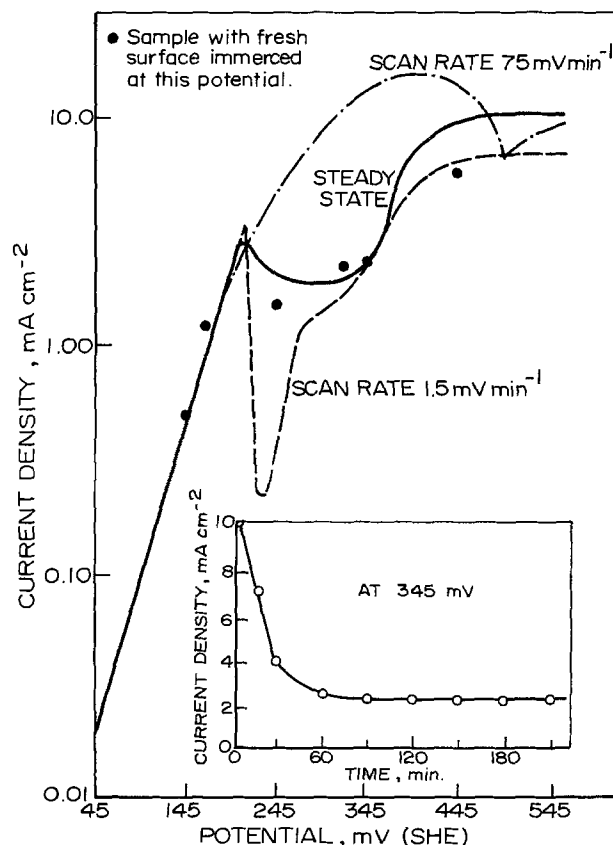


Fig. 2. Effect of potential scanning rate on the anodic polarization curves of the alloy in deaerated 3.4 w/o NaCl solution. Insert: anodic current vs. time behavior of the alloy in deaerated 3.4 w/o NaCl solution at 345 mV (SHE).

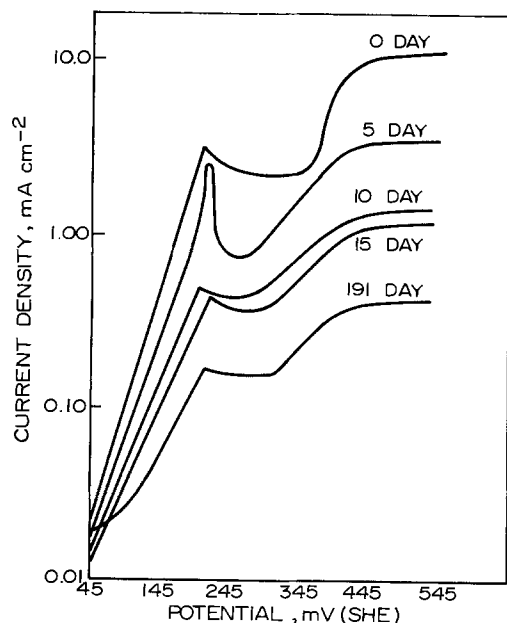


Fig. 3. Anodic polarization curves of the Cu-Ni alloy after various periods of free corrosion.

in different stages of protective film formation. The corrosion product layer restricts the anodic current at any given potential; the decrease is greater the longer the free-corrosion period. The decrease in current is rather large at high anodic potentials, but is small near the corrosion potential compared to the decrease in corrosion rate shown in Fig. 1b.

The curves of Fig. 2 and 3 can be divided into three regions: (i) Linear E -log i or Tafel region extending from 45 to 200 mV. (ii) Passivation region extending from 200 to 325 mV. This, more appropriately, may be labeled brightening region in view of the relatively high currents of 1-2 mA cm⁻² (13). Results for pure Cu are compared with those for Cu-Ni in Fig. 4. Since both pure Cu and Cu-Ni alloy show a brightening

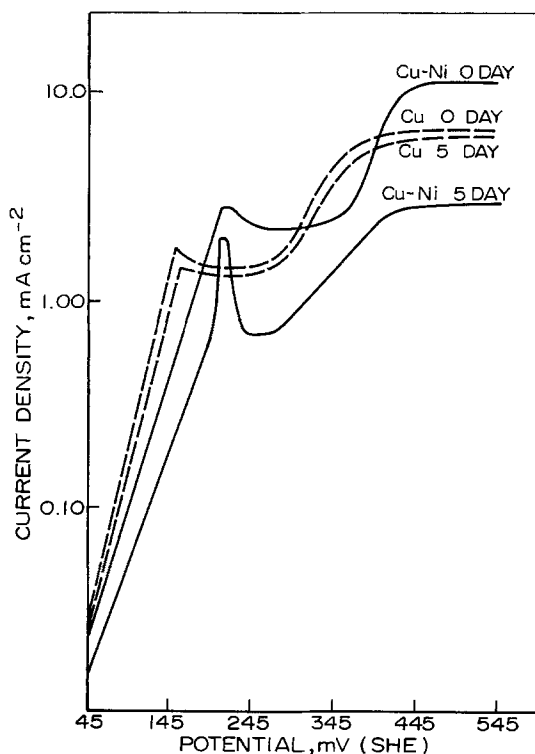
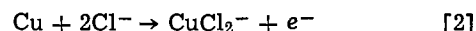


Fig. 4. Anodic polarization curves of pure Cu and Cu-Ni alloy after 5 days of free corrosion.

region, Cu-rich reaction product, seemingly CuCl or Cu₂(OH)₃Cl (11) may be responsible for the brightening effect. (iii) "Transpassive" region extending above 325 mV. CuCl and Cu₂(OH)₃Cl were detected on the sample in this potential region by x-ray diffraction (11).

Kinetics of anodic dissolution in the Tafel region.—The Tafel slope, $dE/d \log i$, on the pure Cu surface is 60 mV for both the zero and 5 day corroded samples (Fig. 4). A Tafel slope of 60 mV (at room temperature) can be readily attributed to a one-electron transfer reaction, with diffusion of a reactant or product in the aqueous phase being the rate-determining step (14-17). Thus, if



is the predominant anodic dissolution reaction in the Tafel region, as has been suggested (8, 14, 16, 18), transport of Cl⁻ to, or of CuCl₂⁻ away from, the surface is the rate-determining step.

The Tafel slope obtained on the fresh Cu-Ni surface is 70 mV per current decade, and the open-circuit corrosion potential is about 10 mV more noble for the alloy than for pure copper, with both values varying somewhat with time. Reaction [2] may also be one of the anodic dissolution reactions for the alloy. The greater polarization of the alloy compared to pure copper may be due to various causes. A thin (10Å thick) NiO layer has been shown by ESCA to cover the air-exposed surface of Cu-10Ni (19). The Tafel slope increases with the length of the open-circuit corrosion period, being 70, 75, 100, 110, and 120 mV per current decade for the 0, 5, 10, 15, and 191 day exposure, respectively (Fig. 3).

Effect of the loosely adherent surface layer.—Figure 5 shows the E -log i relations on the following specimens: zero day corroded specimen, 10 day corroded specimens with the surface in the wet and the dry conditions, and 10 day precorroded specimens after the film has been stripped with tape. The stripped film has been identified by x-ray diffraction as Cu₂(OH)₃Cl (11). The 10 day stripped specimens gave the same Tafel line as the fresh specimens. This indicates that transport through the outer por-

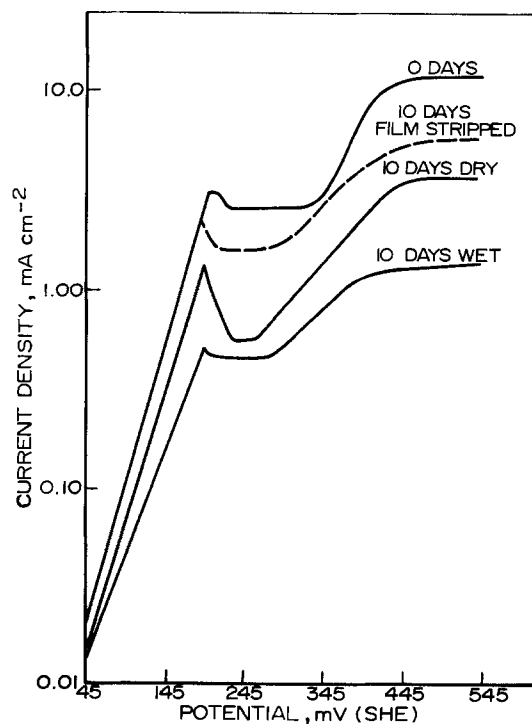
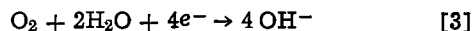


Fig. 5. Effect of the corrosion-product layer on the anodic polarization curves of the alloy precorroded for various lengths of time.

ous layer (probably Cl^- or CuCl_2^- diffusing through electrolyte within the pores) is responsible for the (modest) decrease of the anodic reaction rate in the Tafel region, and that the underlying adherent layer is not a hindrance in the Tafel region to the anodic dissolution reaction or the transport of Cu^+ ions (and presumably Ni^{++} and Fe^{++} ions) through it. The polarization curves also show that the dried surface scale is less protective than the nondried one. This may be attributed to cracking and/or flaking of the loosely adherent film on drying.

Effect of some buffers on the passive current.—It has been found that under free corrosion conditions the pH of the solution changes from 7.5 to 8 in the first day and then levels off becoming 8.1 after a week. Since the measured pH refers to the overall electrolyte, it suggests that there is a considerable local increase in pH to even higher values near the corroding surface. The most likely source of OH^- will be the reduction of oxygen at the corroding alloy surface according to the reaction



In order to minimize the effect of these pH variations on the corrosion process, it would be necessary to corrode the specimen in buffered solutions. However, the effect of the anions of the buffer on the anodic dissolution reaction is significant. Figure 6 shows the anodic E -log i relations in several buffer solutions which are all 3.4 w/o NaCl. The lower currents obtained in the passive region with borate and phosphate buffers, and the higher currents obtained with ammonia buffers, can be readily correlated to the solubilities of their respective Cu salts. Furthermore, copper gives a stable Cu-ammonia complex which would explain the higher currents obtainable in the Tafel region.

Cathodic polarization measurements.—**Oxygen transfer in the aqueous phase.**—Figure 7 shows the effect of air-stirring rate on the cathodic E -log i curves of specimens with freshly prepared surfaces. The well-defined diffusion-limiting currents show clearly that for the alloy in the starting condition oxygen

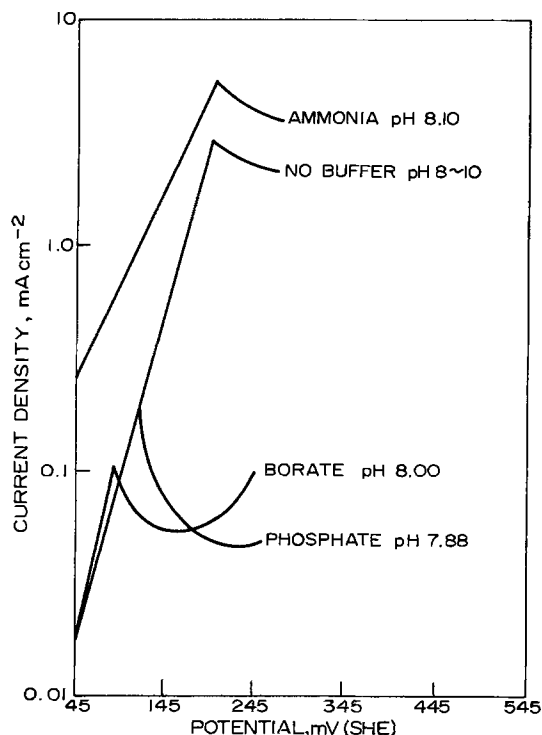


Fig. 6. Effect of different buffers on the anodic polarization curves of the alloy.

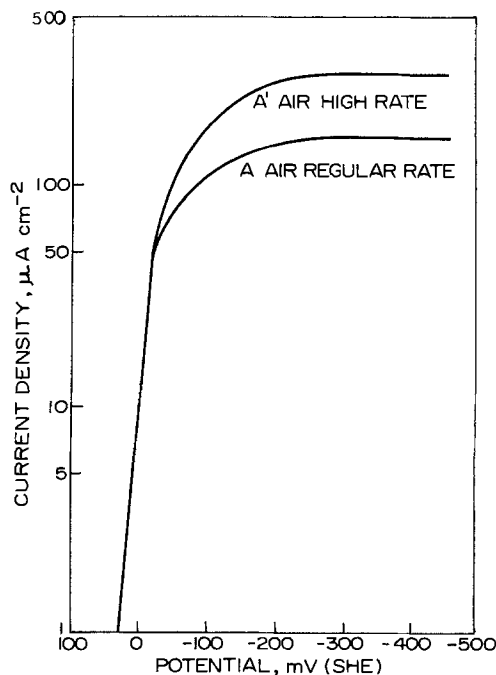


Fig. 7. Effect of stirring on the oxygen reduction rate on fresh alloy surfaces.

reduction is the predominant cathodic reaction, see reaction [3]. Since these limiting currents are an order of magnitude (or more) higher than the currents obtainable on the pre-corroded samples, it is concluded that, in the latter case, reasons other than transport of oxygen through the diffusion boundary layer are responsible for the reduced corrosion current. Nor is transfer of dissolved oxygen in the porous, corrosion-product layer likely to be the slow step responsible for the reduced corrosion rate brought about by the corrosion-product layer. This is supported by two other observations: (i) the thickness of the porous layer ($1\ \mu\text{m}$) is very small compared to the thickness of the diffusion boundary layer, and (ii) the observations in Fig. 8 and below. Consequently, it follows that oxygen was not depleted inside the pores of the corrosion product layer during the open-circuit corrosion experiments.

Effect and location of the electron transfer step.—Figure 8 shows that the corrosion product layer at a rather advanced stage of development causes a substantial decrease in the rate of the oxygen reduction reaction. Clearly, this reaction, at potentials near the corrosion potential, is much more affected by the corrosion product than is the anodic reaction, Fig. 3, 8, and 9; hence, oxygen reduction may be projected as the more important reaction in determining the overall corrosion rate in the presence of the corrosion product (protective) layer.

Figure 8 also shows the effect of the adherent (thin) and detachable (thick) layers of the corrosion product on the kinetics of oxygen reduction. Stripping of the corrosion product with tape causes little (e.g., curves E and F in Fig. 8) or no difference (see the conditions of curve D) in the oxygen reduction rate. These results suggest for a well-developed protective layer that oxygen reduction occurs at the interface (fracture plane) between a porous detachable outer, and an adherent thin inner, layer. This interface supports much lower oxygen reduction currents compared to the fresh alloy surface. The extent of this decrease increases with immersion time at open circuit (i.e., the inner layer becomes more of a hindrance to the cathodic reaction and, hence, more protective against corrosion), as shown by comparing curves D and F.

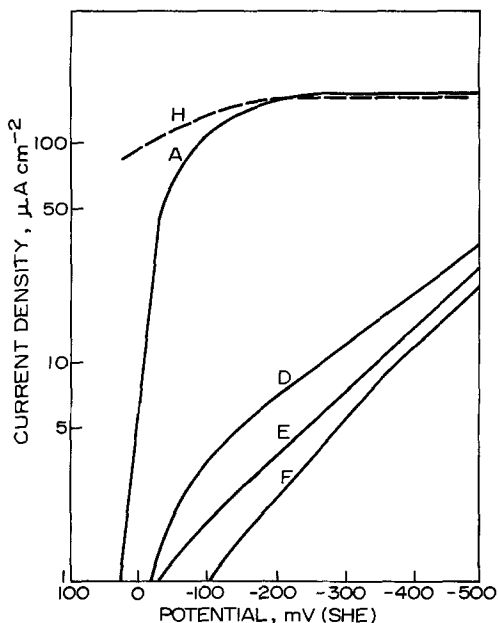


Fig. 8. Effect of the adherent (thin) corrosion-product layer and of the detachable (thick) layer on the current potential relations for oxygen reduction. Curve A, fresh surface; curve D, 10 day corroded with or without stripping detachable layer; curve E, 30 day corroded and stripped; curve F, 30 day corroded; curve H, Pd deposit on 10 or 30 day corroded samples after stripping.

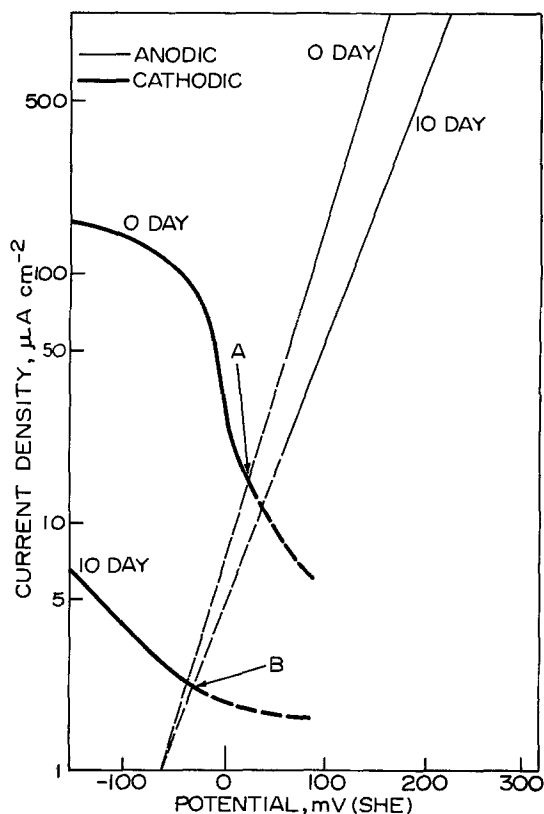


Fig. 9. Superposition of the anodic (Fig. 3) and cathodic (Fig. 8) polarization curves near the corrosion potential of zero day (A) and 10 day (B) corroded samples.

This decrease in the O_2 -reduction current is likely due to a lack of electrons at the interface because of a high electronic resistivity of the adherent layer, as is discussed next.

Mechanism of open-circuit corrosion.—Let us consider what happens when copper is heated in air at 1273°K. A dense layer of solid cuprous oxide forms

on the copper surface. At the Cu/Cu_2O interface, copper ions and electrons form (anodic reaction) and both migrate through the Cu_2O layer toward the outer surface where formation of oxygen ions occurs by the (cathodic) reduction of oxygen gas. This is a somewhat different process than is usually discussed during aqueous corrosion of metals, i.e., that the electrons which form at the anodic site move through the metal to the cathodic site where they are consumed by the cathodic reaction. The latter situation (only) is generally referred to as a local cell (corrosion) process.

In the present experiments, the open-circuit aqueous corrosion of Cu-Ni specimens which are covered with a well-developed protective corrosion-product layer, is like the oxidation of copper at elevated temperatures. Cu^+ (Ni^{++} and Fe^{++}) ions and electrons form at the alloy/oxide interface and both migrate through the (inner) oxide layer, Fig. 10a. At the inner oxide/outer oxide interface, reduction of oxygen occurs and the cations enter the aqueous phase or form the porous outer layer (accompanied by oxidation to the plus two state in the case of copper ions). The outer layer provides some hindrance to the anodic reaction (Tafel region of Fig. 5) and thus provides a (small) contribution of anodic control (as compared to the much larger contribution of the inner layer to cathodic control) of the overall corrosion process (Fig. 9).

The rate-determining step (rds) for the reduction of oxygen is electronic conductance through the inner oxide layer. Identification of a transport process through the inner layer as the rds, coupled with the finding that the overall film thickness increases according to the parabolic law (Fig. 1), establishes that the inner layer also thickens according to the parabolic rate law. It also follows for these conditions that, in addition to a flux of cations arriving at the inner oxide/outer oxide interface given by the parabolic rate law, the ratio of cations which enter the aqueous solution to those which participate in the formation of the outer porous layer is fixed.⁵ The rds for the less important (from the point of view of reducing the rate of the overall corrosion process) anodic reaction is the diffusion of cations through (probably the aqueous phase of) the porous structure

⁵ This ratio may be partly established by the greater tendency of one component(s) of the alloy to participate in formation of the outer film (e.g., Ni and Fe) than another (Cu), as is shown in Part II of this series.

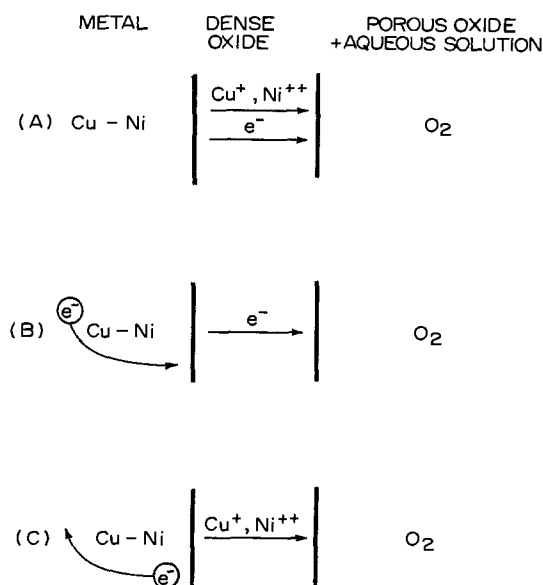


Fig. 10. Schematic of the transport processes in the reaction product during (a) open-circuit corrosion, (b) cathodic polarization (oxygen reduction), and (c) anodic polarization (metal dissolution).

of the outer layer. Only these rds can be rationalized with all of the experimental observations as follows:

Weight loss data.—The rate of metal oxidation and of thickening of the solid reaction product follow the parabolic rate law (Fig. 1a). Hence, transport through the reaction product layer essentially determines the overall corrosion rate.

Oxygen reduction kinetics.—The significant decrease in oxygen reduction rate in going from a fresh to a reaction-product covered Cu-Ni surface during cathodic polarization (Fig. 8) indicates that electron transport through the oxide is difficult. This follows since oxygen reduction during cathodic polarization requires only the transport of electrons through the reaction product layer (Fig. 10b). When the same low rate was observed after stripping away the outer porous layer, the inner (dense) reaction product layer was identified as the actual barrier for transport of the electrons from anodic to cathodic sites.

Metal oxidation kinetics.—There is no reduction in alloy dissolution rate (in the Tafel region) in going from a fresh Cu-Ni surface to one covered only with the thin inner layer (Fig. 5). Since only cation diffusion through the reaction product layer is involved during anodic polarization in oxygen-free solution (Fig. 10c), this result indicates that cation transport through the inner layer is relatively fast. Cation transport through the outer layer, on the other hand, is a (small) hindrance to the anodic reaction in the Tafel region (Fig. 5).

Pd-covered oxide layer.—When Pd was electrodeposited on the inner layer the oxygen reduction rate during cathodic polarization increased (significantly) to that of a fresh Cu-Ni surface (Fig. 8). This is consistent with the formation of a palladium short circuit through the dense oxide layer, thereby providing a metallic conductor for the electrons. The Pd is envisioned to have penetrated the inner layer during electrodeposition along a crack in the oxide or along the specimen edge. A similar result was obtained for an analogous experiment using platinum.

This result is also significant in that it rules out any possibility that either cation or oxygen ion transport is important, since their transport requires an ionic, not metallic conductor. Another function of the palladium or platinum is to increase the rate of Eq. [3] since these metals are excellent catalysts for the oxygen reduction reaction (12). However, in view of a shortage of electrons at the cathodic sites, consistent with electron transfer through the inner layer as the rds, the rate of Eq. [3] increases in the presence of Pd or Pt seemingly due to an increase in electronic conductance, rather than due to an increased catalytic nature of the cathodic site.

Conclusions

The results of the corrosion rate and polarization studies on commercial Cu-9.4Ni-1.7Fe alloy in 3.4 w/o NaCl solution at room temperature show that (i) the corrosion-product layer is composed of a thin adherent inner layer, and a much thicker, porous outer layer which can be easily removed by tape; (ii) the cathodic half-cell reaction, which is

oxygen reduction, is more polarized than the anodic reaction in the presence of this layer and, hence, is more important in controlling the rate of the corrosion process; (iii) the inner and the outer corrosion product layers both thicken during the first 1000 hr of their formation in accord with the parabolic rate law; (iv) the weight loss, which is the sum of metal oxidized to solid corrosion product and to soluble ions in the aqueous phase, also follows the parabolic rate law during most of this period; and (v) transport of oxygen through the aqueous-solution boundary layer and through the electrolyte within the porous outer layer is more than adequate to maintain the relatively slow oxygen reduction rate which is determined by the transport rate of electrons across the inner layer.

Acknowledgments

The Office of Naval Research under Contract No. N00014-75-C-0264 provided financial support.

Manuscript submitted Nov. 19, 1979; revised manuscript received March 20, 1980. This was Paper 126 presented at the Pittsburgh, Pennsylvania, Meeting of the Society, Oct. 15-20, 1978.

Any discussion of this paper will appear in a Discussion Section to be published in the June 1981 JOURNAL. All discussions for the June 1981 Discussion Section should be submitted by Feb. 1, 1981.

Publication costs of this article were assisted by The Pennsylvania State University.

REFERENCES

1. G. L. Bailey, *J. Inst. Metals*, **79**, 243 (1951).
2. W. C. Stewart and F. L. LaQue, *Corrosion (Houston)*, **8**, 259 (1952).
3. J. M. Popplewell, R. J. Hart, and J. A. Ford, *Corros. Sci.*, **13**, 295 (1973).
4. L. J. Swartzendruber and L. H. Bennett, *Scr. Metal.*, **2**, 93 (1968).
5. J. P. Chubb, J. Billingham, P. Hancock, C. Dimbylous, and G. Newcombe, *J. Metals* (March 1978).
6. R. F. North and M. J. Pryor, *Corros. Sci.*, **10**, 297 (1970).
7. K. D. Efrid, *Corrosion (Houston)*, **31**, 77 (1975).
8. M. E. Walton and P. A. Brook, *Corros. Sci.*, **17**, 317 (1977).
9. F. P. Ijsseling and J. M. Kroughman, Unpublished.
10. C. Wagner and W. Traud, *Z. Elektrochem.*, **44**, 391 (1938).
11. C. Kato, J. E. Castle, B. G. Ateya, and H. W. Pickering, *This Journal*, **127**, 1897 (1980).
12. J. Hoare, in "Encyclopedia of Electrochemistry of the Elements," Vol. 2, A. J. Bard, Editor, p. 209, Marcel Dekker, New York (1974).
13. T. P. Hoar, D. C. Mears, and G. P. Rothwell, *Corros. Sci.*, **5**, 279 (1965).
14. C. H. Bonfiglio, A. C. Albaya, and O. A. Cobo, *ibid.*, **13**, 717 (1973).
15. J. O'M. Bockris, B. T. Rubin, A. Despic, and B. Lovrecek, *Electrochim. Acta*, **17**, 973 (1972).
16. A. L. Bacarella and J. C. Griess, Jr., *This Journal*, **120**, 459 (1973).
17. L. H. Jenkins, *ibid.*, **117**, 630 (1970).
18. M. E. Walton and P. A. Brook, *Corros. Sci.*, **17**, 593 (1977).
19. J. E. Castle, *Nature (London), Phys. Sci.*, **234**, 93 (1971).

On the Mechanism of Corrosion of Cu-9.4Ni-1.7Fe Alloy in Air Saturated Aqueous NaCl Solution

II. Composition of the Protective Surface Layer

C. Kato, J. E. Castle,¹ B. G. Ateya,^{*2} and H. W. Pickering*

*Metallurgy Section, Department of Materials Science and Engineering,
The Pennsylvania State University, University Park, Pennsylvania 16802*

ABSTRACT

The formation of protective layers on Cu-9.4Ni-1.7Fe alloy in air-saturated, aqueous 3.4 weight percent NaCl solution, both under natural corrosion and under potentiostatic conditions, has been studied by ESCA (XPS), SEM, and x-ray diffraction. It was concluded that the protective film formed under open-circuit corrosion conditions has the following features: (i) is comprised of a relatively thick outer layer, mainly $\text{Cu}_2(\text{OH})_3\text{Cl}$, and an inner thin layer containing appreciable chloride, oxygen, and copper, and some nickel, (ii) is rich in chloride throughout the film with a maximum concentration along a plane located within the inner layer near the inner layer/outer layer interface, (iii) is relatively poor in Ni and Fe in the inner layer compared to levels in the outer layer, and (iv) has, in early stages of growth, an outer surface consisting of a cuprous (probably Cu_2O) compound which with time gives way to a carbonate and finally to a cupric ($\text{Cu}_2(\text{OH})_3\text{Cl}$) compound. The transition in Cl, Fe, Cu, and Ni concentrations is sharply confined to the interface region between the thin inner and thick porous outer layers. The thin inner layer is mainly responsible for the good corrosion resistance of the alloy according to electrochemical results reported in Part I of this series.

In Part I of this series (1) the mechanism of corrosion and of protective layer formation on solutionized (850°C, 30 min, W.Q.) Cu-9.4Ni-1.7Fe alloy in air-saturated, aqueous NaCl solution at $23^\circ \pm 3^\circ\text{C}$ is examined by well-established polarization methods and by special electrochemical tests designed to identify the rate-determining step. It was found that samples containing the protective layer exhibited a much increased cathodic polarization and a marginally increased anodic polarization compared to samples without the free-corrosion-grown protective layer. This tended to support the view that a much reduced rate of the cathodic reaction (oxygen reduction) is mainly responsible for the good corrosion resistance of the Cu-Ni alloys in seawater. The corrosion product which was responsible for the high cathodic polarization was shown to be in the region of the metal/oxide interface and to remain adherent after the bulk of the corrosion-product layer was stripped with tape. An adherent layer of this type is well suited for chemical analysis with the surface-sensitive techniques of x-ray photoelectron spectroscopy, XPS (also known as ESCA) (2), or Auger electron spectroscopy (3). Such analyses are reported herein and are augmented by x-ray diffraction examination of the corrosion-product layer.

The material which can be removed by tape has, in the vicinity of the corrosion potential, a modest influence on the rate of the anodic reaction, and little or no effect on the rate of the cathodic reaction (1). However, its composition, structure, and chronological sequence of formation are important for an improved understanding of the mechanism of formation of the underlying protective layer. Structural and compositional analyses of such films on cupronickel alloys have been conducted by several investigators (4-8). The presence of Cu_2O and $\text{Cu}_2(\text{OH})_3\text{Cl}$ as major components, in amounts which vary with

temperature (4) and flow velocity of the solution (6, 8), has been revealed by x-ray diffraction. North and Pryor (4) based an explanation of the protective behavior on the electronic and ionic resistance of a defective form of Cu_2O inner layer. Ijsseling (6) showed that the total concentration of iron and nickel was at its highest in the interface region between the inner and outer layer, and it would follow that a discrete layer could be of importance in determining corrosion resistance.

Experimental

The corrosion system is the same as described in Part I of this series (1), where the specimen preparations and arrangements for open-circuit and polarization experiments and procedures are also given. X-ray diffraction, SEM, and ESCA analyses of the corrosion products formed during the open-circuit (corrosion) tests were done on one of two (duplicate) samples immersed for varying lengths of time; weight change data were obtained from the other sample of each pair (1).

X-ray diffraction examination.—X-ray diffraction examination of samples after the open-circuit corrosion periods were performed by placing a sample (5×5 mm), carefully cut from the corroded sample, in a Debye-Scherrer camera at an angle of about 8° to the x-ray beam, in order to increase the path length of the x-rays in the sample.

In the case of the anodically polarized samples the corrosion product films were scraped off with a knife, and the resulting powder was utilized for the x-ray diffraction analysis. Corrosion products which become detached and dispersed throughout the solution during anodic polarization were also gathered, rinsed with water, dried, and then analyzed as above.

XPS (ESCA) studies.—Samples (6×6 mm), cut from the corrosion test coupons taking care to avoid handling the faces to be examined, were mounted in batches of five on the probe of the XPS spectrometer and examined with $\text{AlK}\alpha$ radiation. The heights and areas of the principal peaks of the elements Cl, C, O, Cu, Fe, and Ni were obtained using a computer-based

* Electrochemical Society Active Member.

¹ Permanent address: Department of Metallurgy and Materials Technology, University of Surrey, Guildford, GU2 5XH, England.

² Present address: Chemistry Department, Cairo University, Cairo, Egypt.

Key words: ESCA analysis, thin films, composition profile, cupronickel, oxidation.

data acquisition system (V. G. Datasystems Limited, England). In addition, survey scans covering the binding energy range 0-1000 eV were taken from each sample. Individual peaks could be obtained to an accuracy of ± 0.2 eV from the computer display. Values obtained in this way, corrected the reference levels of $\text{Cu}2p_{3/2} = 932.8$ eV (10) or $\text{C}_{1s} = 285$ eV (10), are quoted in the text where appropriate for the identification of bonding state. Cupric compounds are readily recognized by the presence of the shake-up satellite (Fig. 1). Analyses in all cases were corrected, using relative sensitivity factors based on those published by Jorgenson and Berthou (9) and normalized to 100 atom percent excluding carbon, which in most cases was merely present as a surface contaminant. The analysis so obtained is a surface-weighted mean with about 70% of the signal obtained from the top 1 nm.

The outer surfaces of samples exposed to the test solution for 12 hr, 1, 3, 5, and 10 days were examined in order to establish the chronological order in which new phases appeared on the surface. This was found to be the period of corrosion activity necessary to develop the underlying protective film (1). The samples were examined prior to ion etching since ion etching is known to alter valence states, in particular cupric ions are always transformed to the cuprous state (11). The adsorbed film on these samples will reduce slightly the intensity of low kinetic energy peaks, such as copper, with respect to those of high energy, such as chloride, but not to an extent which would warrant ion etching.

Information relating to the distribution in depth of the phases within the reaction product layer was obtained using samples exposed separately for 5 days. For these studies, the visible corrosion product was removed using tape and both the fractured material remaining on the metal substrate and that adhering to the tape were subjected to detailed analysis. Ion beam etching was used sequentially with XPS analysis after initial examination in order to obtain the direction of concentration gradients in the region of the fracture. An ion current of 10 μA and a beam energy of 8 keV was used. The etch rate so obtained was of the order of 0.02 nm sec^{-1} .

Because of an overlap between the $\text{Fe}2p_{3/2}$ photoelectron peak and a prominent copper Auger line, the presence of Fe in the region of the interface had to be confirmed using Auger electron spectroscopy. In this case the surface film was stripped from a 5 day test sample using indium foil. Auger analysis of the fracture surface was, however, only possible on the substrate side because of problems associated with electrostatic charging of the stripped material.

Results

X-ray diffraction analysis.—The x-ray diffraction results on (corroded) samples immersed more than 5 days indicate that the corrosion product is mainly $\text{Cu}_2(\text{OH})_3\text{Cl}$ and contains much less Cu_2O ; d-spacings are shown in Table I. Samples immersed less than 5 days exhibited only Cu-Ni diffraction lines, indicating insufficient oxide thickness ($\ll 1$ μm). The loosely adherent film on the 30 day corroded sample (stripped with double-face tape) showed only $\text{Cu}_2(\text{OH})_3\text{Cl}$. Tables II-IV show the identity of reaction products formed during anodic polarization of the Cu-Ni alloy at potentials more noble than the Tafel region (labeled brightening region in Part I).

Surface analysis.—Figure 1 shows wide scan (1000 eV) spectra obtained from the outer surface of the 0.5, 1, 3, 5, and 10 day samples. The lack of a shake-up satellite (12) on the copper 2p peaks at 0.5 and 1 day shows this element to be metallic or in the cuprous form; the Cu LMN peak position (917.0 eV) shows it to be cuprous (12). At 3 days and after, the

Table I. X-ray diffraction analysis of the corrosion products developed on Cu-Ni alloy. Measured d-spacing (\AA) after 191 and 10 days of open-circuit corrosion

Compound	d-spacings (\AA) on file*	Measured d-spacing**	
		191 days	10 days
$\text{Cu}_2(\text{OH})_3\text{Cl}$	5.45	5.507	5.617
$\text{Cu}_2(\text{OH})_3\text{Cl}$	4.70	4.715	4.825
$\text{Cu}_2(\text{OH})_3\text{Cl}$	4.55	4.550	
$\text{Cu}_2(\text{OH})_3\text{Cl}$	3.41	3.439	
Cu_2O	3.02	3.031	
$\text{Cu}_2(\text{OH})_3\text{Cl}$	2.90	2.915	2.982
$\text{Cu}_2(\text{OH})_3\text{Cl}$	2.75	2.771	
Cu_2O	2.47	2.482	2.464
$\text{Cu}_2(\text{OH})_3\text{Cl}$	2.33	2.352	2.333
$\text{Cu}_2(\text{OH})_3\text{Cl}$	2.26	2.269	
Cu-Ni	2.09†	2.085	2.097
Cu-Ni	1.94†	1.937	1.950
Cu-Ni	1.82†	1.809	1.830
$\text{Cu}_2(\text{OH})_3\text{Cl}$	1.70	1.716	
Cu_2O	1.51	1.512	1.514

* Joint Committee for Powder Diffraction File (JCPDF).

** These were the only lines that were observed.

† The average d-spacings of Cu-9.4Ni-1.7Fe.

Table II. X-ray diffraction analysis of the corrosion products developed on the Cu-Ni surface after anodic polarization for 5 hr at 245 mV (SHE)

Compound	d-spacings on file (\AA)	Measured d-spacing* (\AA)
NiO · OH	7.70	7.664
$\text{Cu}_2(\text{OH})_3\text{Cl}$	5.31	5.381
$\text{Cu}_2(\text{OH})_3\text{Cl}$	4.70	4.976
NiO · OH	3.85	3.828
CuCl	3.13	3.095
$\text{Cu}_2(\text{OH})_3\text{Cl}$	2.90	2.805
$\text{Cu}_2(\text{OH})_3\text{Cl}$	2.75	2.704
NiO · OH	2.56	2.548
$\text{Cu}_2(\text{OH})_3\text{Cl}$	2.33	2.329
Cu-Ni	2.09†	2.063
Cu-Ni	1.94†	1.964
CuCl	1.92	1.895
Cu-Ni	1.82†	1.785
CuCl	1.63	1.616

* These were the only lines that were observed.

† The average d-spacings of Cu-9.4Ni-1.7Fe (alloy particles were also identified in the scrapings by their lustrous metallic appearance).

Table III. X-ray diffraction analysis of the corrosion products which fell to the bottom of the cell during anodic polarization [245 mV (SHE)]

Compound	d-spacings on file (\AA)	Measured d-spacings* (\AA)
$\text{Cu}_2(\text{OH})_3\text{Cl}$	5.31	5.433
$\text{Cu}_2(\text{OH})_3\text{Cl}$	2.75	2.705
Cu_2O	2.47	2.455
$\text{Cu}_2(\text{OH})_3\text{Cl}$	2.33	2.244
Cu_2O	2.13	2.122
Cu_2O	1.74	1.735
Cu_2O	1.51	1.503

* These were the only lines that were observed.

Table IV. Compounds identified by x-ray diffraction analysis which developed on pure Cu and/or Cu-Ni alloy during anodic polarization*

Material	Location	Potential range mV (SHE)	Compounds identified
Cu-Ni	On the alloy surface	245-545	CuCl , $\text{Cu}_2(\text{OH})_3\text{Cl}$, NiO · OH
Cu	In the electrolyte	205-545	Cu_2O , $\text{Cu}_2(\text{OH})_3\text{Cl}$
Cu	On the alloy surface	245-545	CuCl , $\text{Cu}_2(\text{OH})_3\text{Cl}$
Cu	In the electrolyte	205-545	Cu_2O , $\text{Cu}_2(\text{OH})_3\text{Cl}$

* Reaction products obtained below +245 mV (SHE) on the alloy surface were too thin to be identified by x-ray diffraction.

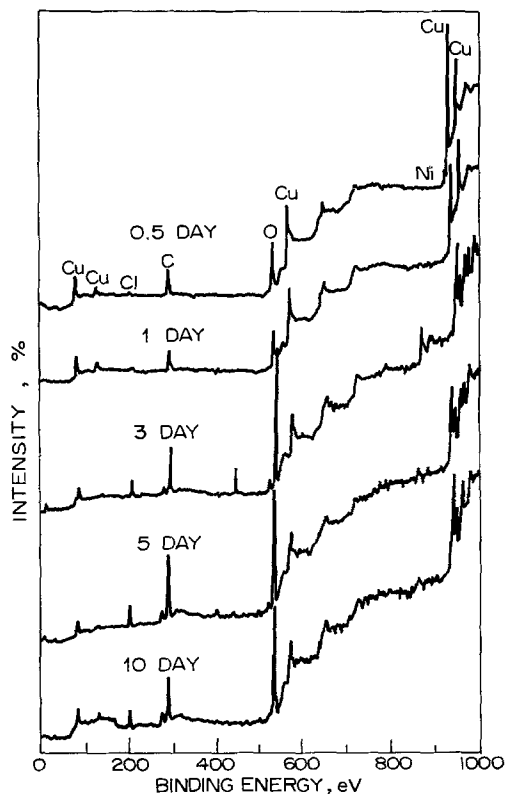


Fig. 1. ESCA spectrums of the outer surface of the corrosion product after 0.5, 1, 3, 5, and 10 days immersion of the Cu-Ni-Fe samples in the aerated aqueous NaCl solution.

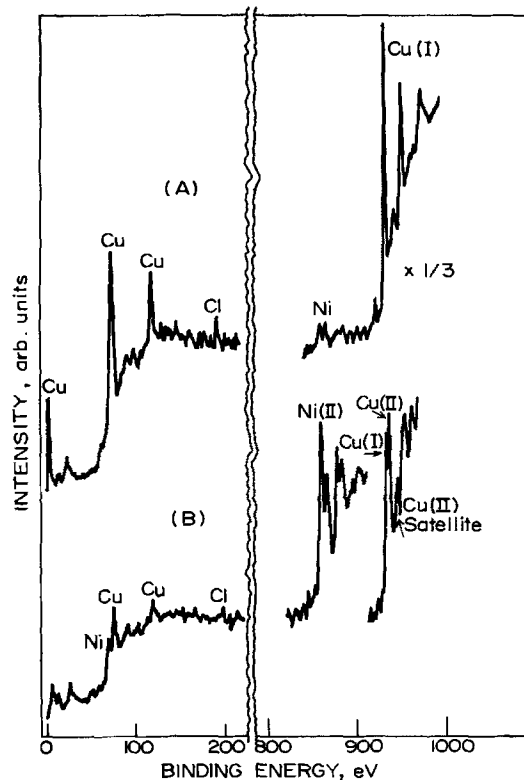


Fig. 2. ESCA spectrums of the outer surface of the corrosion product after 1 day immersion. (a) Bright area, (b) visible corrosion product area.

presence of a satellite shows the surface film to be entirely in the cupric form. There is also a marked increase in the chloride peak, first noted in the 3 day spectrum (Fig. 1). Both the nickel and sodium signals are negligible on these samples while, after correction for charging, the oxygen peak is entirely in the position (531 eV) usually ascribed to OH^- ion (13) (Fig. 1). Thus, the analyses would be consistent with the presence of cuprous oxide, having perhaps a hydrated surface, at 12 hr and of basic cupric chloride at 3 days and after. The sample exposed for 1 day was the first which showed the visible corrosion product that covered subsequent samples. At 1 day the film covered one-third to one-half of the surface; it appeared to start at an edge and grow laterally over the surface. Analysis of this filmed region showed copper to be in the cupric form, unlike the bright half which remained in the cuprous state, Fig. 2. However, the transition in valence state did not coincide with the pickup of chloride ion, since there was very little present, even on the discolored half of the 1 day specimen (Fig. 2).

Both the oxygen and carbon signals obtained from a scan of the 1 day specimen, which included both halves, show prominent shoulders (Fig. 3a and 3b). Separate spectra from the filmed and unfiled areas show that the high energy shoulders for both elements are uniquely found on the tarnished half, on which they form a major part of the signal. One possible reason for this unusual observation is that the filmed and unfiled areas of the specimen were electrostatically charged relative to each other. Thus, care was taken to reference the position of the carbon signal on the unfiled half to the cuprous position and on the filmed half to the cupric position (using $\text{Cu(II)} 2p_{3/2} = 934.4$ obtained from laboratory standards). This procedure confirmed the carbon 1s position to be 285.0 eV on the unfiled material and 288.0 eV on the filmed material. The equivalent oxygen positions are 531.3 and 534 eV, respectively. A similar procedure applied to the single carbon and oxygen

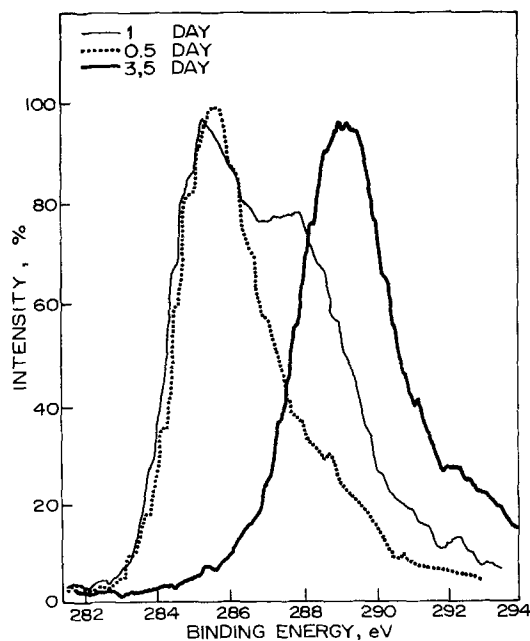


Fig. 3a. Carbon peaks in ESCA spectra of the outer surface of corrosion products after 0.5, 1, 3, and 5 days immersion.

peaks on the 3 and 5 day specimens fully accounted for the observed shift in terms of electrostatic charging. Nickel ions are only present to a trivial extent in the 12 hr, 1 day (bright), and 5 and 10 day surfaces. However, they are prominent in the spectra from the filmed half of the 1 day sample and from the 3 day sample (Fig. 1c). The composition of the outer surface based on the above analysis and individual peak intensities is plotted as a function of corrosion time in Fig. 4. Also shown are some likely compounds containing the identified elements at the various stages of dissolution.

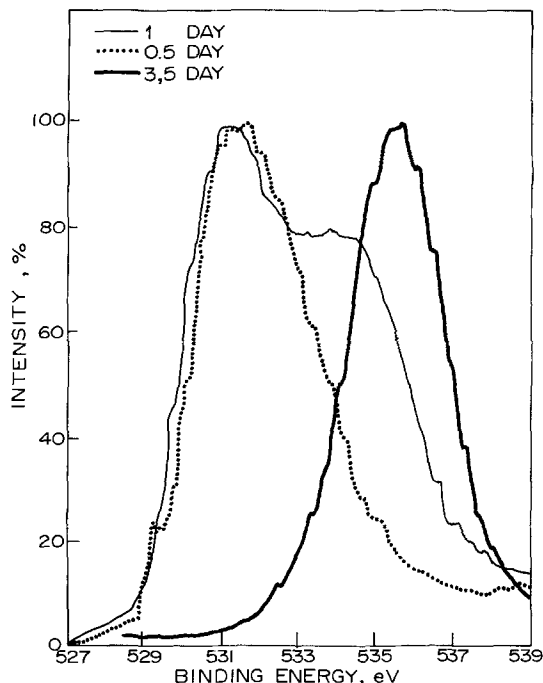


Fig. 3b. Oxygen peaks in ESCA spectrums of the outer surface of corrosion products after 0.5, 1, 3, and 5 days immersion.

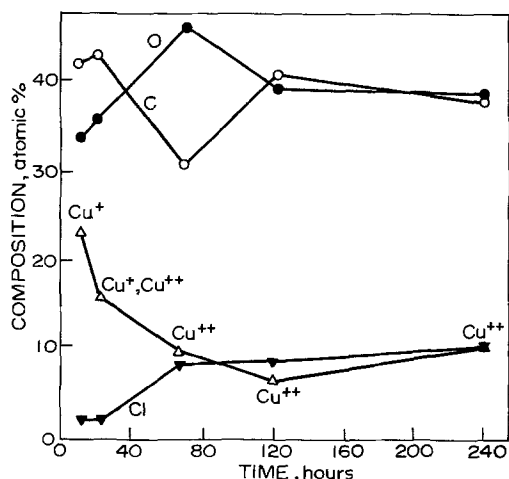


Fig. 4. ESCA semiquantitative analysis of the outer surface for different corrosion periods.

Interface analysis, 5 day samples.—The analyses obtained from the fracture surface of the stripped substrates of the 5 day samples are given in Table V. These give the relative proportions of Cu, Ni, Fe, and Cl only; oxygen and carbon are excluded because of the different behavior of adsorbed gases in the XPS and AES spectrometers. The high Ni content in three of the samples in Table V appears to be associated with reaction product characteristic of the stripped side of the fracture surface rather than that on the substrate side (Table VI and Fig. 5). Sample 3, on the other hand, was repeatedly stripped prior to analysis and showed a lower Ni level. Results in Table V,

Table V. Analysis (%) of the fracture surface (substrate side, no etching) of three 5 day specimens by ESCA and one 5 day specimen by Auger

Sample	1 (XPS)	2 (XPS)	3 (XPS)	1 (AES)
Cu	32	22	34	30
Ni	26	39	10	26
Fe	ND	9	<2	8
Cl	42	31	56	36

Table VI. ESCA analysis (%) of the outer surface of the reaction product and both sides of the fracture interface (see key, Fig. 5)

	Fracture surface,* outer layer	Fracture surface,* inner layer	Surface†
Cu	10	32	20 (30)
Ni	18	4	1 (2)
Fe	15	0	0 (0)
Cl	11	24	16 (24)
O	45	40	62 (40)

* Analyses after 2 min (10 nm) etching.
† Experience shows that the oxygen value would be reduced to ca. 40% by removal of adsorbed gas; the adjusted values are shown in parentheses.

furthermore, show a high concentration of chloride ions and a low concentration of iron. After ion etching (Table VI) the iron level is not detectable in the substrate side and much higher in the stripped material. Conversely, chlorine is much lower in the stripped material. These results, coupled with about 1 nm resolution (in the absence of ion etching), indicate a very sharp change of the iron and chloride contents along the plane separating the material which can be stripped from the sample from that which cannot. Nickel and copper similarly exhibit sharp concentration gradients along this plane. An ion etch profile obtained by XPS from the matching surfaces of sample 3 of Table V is given in Fig. 5. Comparing matching values in the plane of fracture (i.e., before ion etching) one observes the mentioned sharp composition changes across the fracture plane for Cl, Fe, Cu, and Ni, and that whereas the phase which is stripped away is enriched in nickel and iron, the adherent reaction product on the substrate side of the fracture plane contains mainly Cu and some Ni with the Cu:Ni ratio the same as that of the bulk alloy. The chloride content of the reaction product, furthermore, is a maximum along a plane located within the inner layer near the fracture plane itself. Thus, it appears that the thin inner and thick porous outer layers are distinctly different reaction product phases.

Metallographic examination.—SEM examination of the outer surface at different stages of film formation is shown in Fig. 6. The corrosion product is easily recognizable by tarnish colors in less than 1 hr (Table VII) and appears porous and discontinuous by one day. After 5 days, it is more compact. After stripping, the substrate appears metallic with some

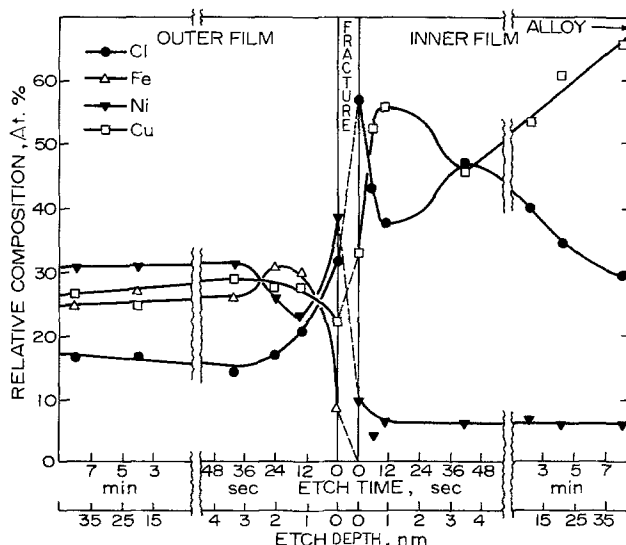


Fig. 5. An etch profile obtained by ESCA of the fracture surfaces after 5 days immersion. Oxygen and carbon are not included. (Approximate etching speed of 50 Å/min.)

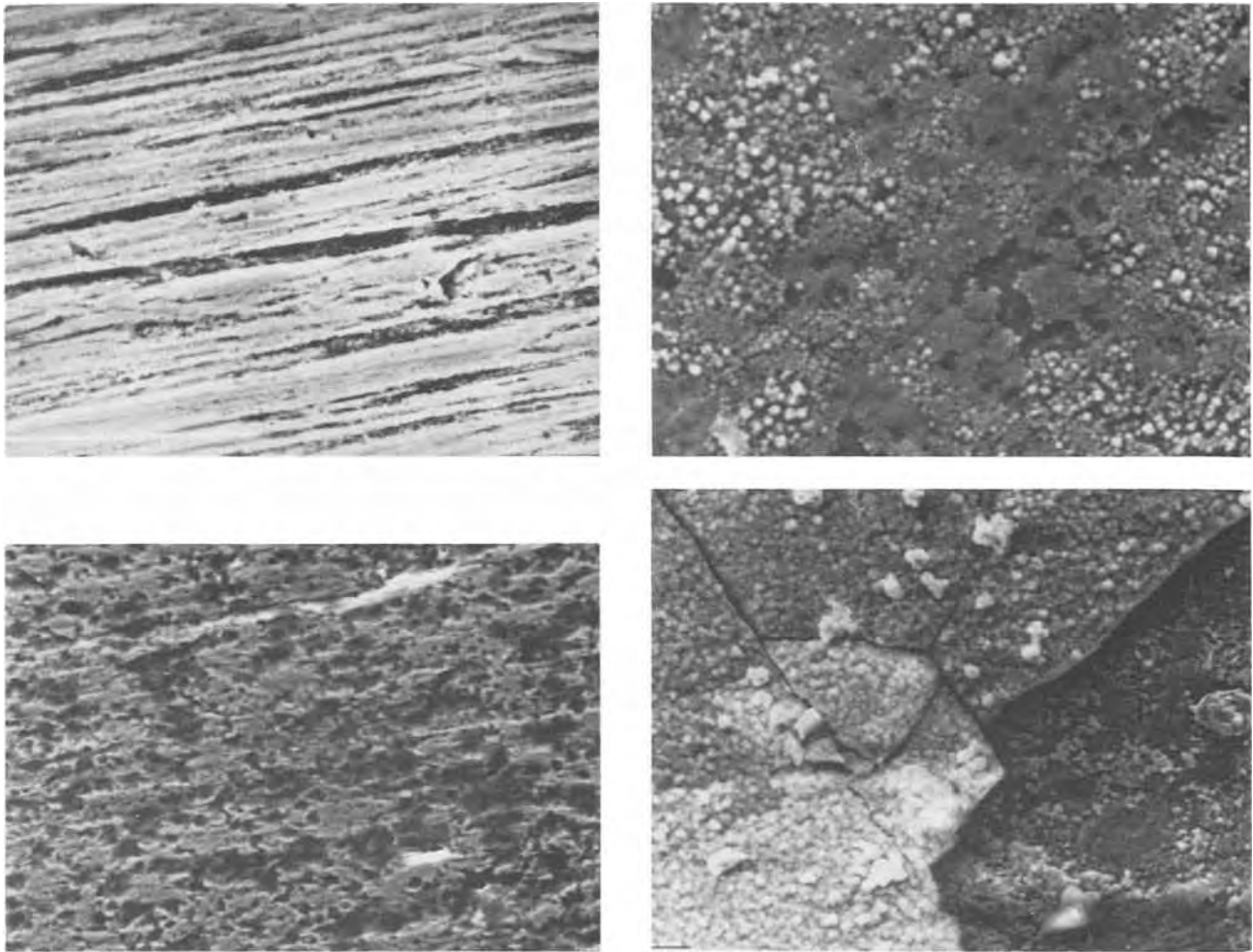


Fig. 6. SEM photomicrographs of the outer surface after (a, top left) 2 hr (1150 \times), (b, bottom left) 1 day (1150 \times), (c, top right) 5 days (1150 \times), and (d, bottom right) 191 days (575 \times) immersion.

locations still covered with reaction product. This is consistent with the ESCA results which show a high Cl concentration on the substrate side of the fracture plane. The corrosion product adhering to the tape had a greenish hue.

Discussion

The results presented above provide a chronological sequence of the phases appearing on the outer surface of the test pieces and a structural sequence of some of the compositions found in the thick corrosion product. Because of the shallow depth of analysis, the chronological sequence is important as an indicator of the direction of chemical reactions with the environment such as hydrolysis or oxidation at different times of exposure. Similarly the structural sequence provides analyses close to interfaces in the hierarchy. Each series of analyses must be supplemented with the bulk analyses for a full picture of the surface processes.

Table VII. Color changes of the Cu-Ni alloy during immersion in the 3.4 w/o NaCl solution at room temperature

Time	Color
8 min	Shiny reddish brown
10 min	Shiny dark reddish brown
15 min	Shiny light reddish brown
25 min	Shiny blue-green
35 min	Shiny tan
24 hr	Shiny tan and dull tan areas
48 hr	Shiny tan and dull tan areas
72 hr	Dull tan
96 hr	Dull tan

Early stages of protective layer formation.—The chronological sequence for the appearance of copper compounds at the corrosion product/bulk solution interface shows that by 3 days, cuprous oxide has transformed to basic cupric chloride, paratacamite. The basic chloride is clearly the stable product, as evidenced by the diffraction patterns of long-term test pieces and the SEM observation of clusters of crystals growing into rafts, which, after about 3 days, cover the whole of the surface. In the initial transient period cuprous oxide was present over the whole specimen surface for 12 hr and remained on some areas for over a day which is a surprisingly long time in a well-aerated solution. Although the cuprous oxide was probably generated in the first place during preparation and subsequent air exposure, XPS analysis has been shown to be quite capable of detecting progressive changes in the air-formed film as it equilibrates with water, e.g., on stainless steel changes are observed within 10 min of exposure to pure water (14). The longevity of cuprous oxide as the surface phase probably is due mostly to an activated step in the nucleation of cupric compounds and, particularly, of the stable basic chloride. This is in accord with the observation that nucleation of cupric compounds starts first at an edge and moves across the surface as a front.

The identity of the first precipitate of cupric material remains to some extent uncertain. Examination of the 1 day spectrum in detail reveals no possible anions, other than carbon and oxygen, on the part of the specimen which returned a strong cupric signal. The carbon peak at 288 eV could arise from an unusual quirk of electrostatic charging but this seems unlikely. It

would require an organic contaminant on the surface to have charged relative to the cupric phase on this sample, whereas it does not charge relative to either the thin cuprous oxide phase at shorter times or to the thick cupric, paratacamite phase at longer times. An alternative possibility is that the first cupric precipitate is the basic carbonate, malachite, $\text{CuCO}_3\text{Cu}(\text{OH})_2$. The position of the carbon peak in sodium carbonate is 289.6 eV, but the binding energy could be lower in a less strongly ionic compound or in a poorly oriented surface compound. The formation of a carbonate as first precipitate in a chloride-rich environment may arise from the nucleation difficulties of the chloride, or because the necessary thermodynamic conditions exist as a brief transient. Bianchi and Longhi (15) have provided a diagram giving the stability ranges of $\text{Cu}_2(\text{OH})_3\text{Cl}$ and $\text{CuCO}_3\text{Cu}(\text{OH})_2$ as a function of the pH value and the total inorganic carbon content of the solution. Maximum stability occurs at a pH of about 7.5, where approximately 2.5×10^{-3} g-at/liter of carbon is required to enter the stability field of malachite. While they show that this is reached in many natural seawaters, it seems unlikely that it could have been reached in the aerated sodium chloride solutions used in this study. Furthermore, the movement of pH toward a value of 8, as recorded during the exposure (1), would tend to move that part of the surface supporting the oxygen reduction reaction (Eq. [3] in Part I) away from a carbonate stability field and ensure that any such deposit had only a transient existence. Pourbaix (16), discussing behavior in natural waters, also indicates the basic carbonates to have only a transient existence at anodic sites because of a shift in pH to lower values due to hydrolysis reactions. Thus, a carbonate could have a prolonged life, although its appearance probably arises only because of its preferred nucleation as a surface phase.

The copper spectrum from the tarnished half of the 1 day specimen contains both cupric and cuprous (or copper) components. The appearance, Fig. 2, of very strong nickel (II) signals, coupled with the lack of evidence for the diffusion of nickel ions through an air-formed cuprous oxide film at room temperature (17), indicates that the underlying cuprous oxide has undergone modification during the course of precipitation of the cupric compound. This is supported by evidence which was obtained at a later stage of the film formation and is presented in Part I of this series (1) that cations diffuse readily through the inner layer and only slightly less so through the outer layer. Again, because of the almost total lack of chloride ions in the film during its early stage of formation, we presume the nickel to be present primarily as $\text{Ni}(\text{OH})_2$, which is known to be the preferred surface phase on nickel in humid conditions (18). It is noticeable that the cuprous spectrum on the bright half remains identical to that found after 12 hr. Thus the nucleation of the cupric phase on one part of the surface does not result in modification of the cuprous oxide over a large area.

The developed protective layer.—Turning to the sequential analyses carried out on the specimen immersed for 5 days we find two important results: (i) the layer removed by use of adhesive tape included the corrosion product layer enriched in iron and nickel, which other authors have reported to be important for the good corrosion resistance of cupro-nickel alloys (4); (ii) the layer remaining adherent to the substrate was not enriched in iron and nickel but contained the highest concentrations of chloride ions found in any part of the film. It is this adherent layer which was identified in Part I to be primarily responsible for protection (1).

The analytical results (i) and (ii) taken together with the finding reported in Part I, that mechanical removal of the visible corrosion product caused the

anodic polarization curve in the Tafel region to revert to the polarization curve found without prior exposure, indicate some resistance to cation transport through the thick porous outer layer. These data are, on the one hand, consistent with Popplewell *et al.*'s (5) conclusion that the thick porous outer layer offers a resistance to the corrosion reaction, but, on the other hand, inconsistent with their view that this film is the primary source of protection. Furthermore, the underlying adherent layer is not simply a defective form of cuprous oxide as found by these authors since it is very highly enriched in chloride and contains nickel. This is important since the inner layer is mainly responsible for the good corrosion resistance of the alloy. The latter is a result of its poor electronic conductivity as shown in Part I, thereby restricting the oxygen reduction reaction (1).

Ion beam profiling results show that the high chloride level in the inner layer is not present as an adsorbed monolayer, but is a layer extending over several tens of nanometers. It is not possible to say whether the material *in situ* is in the cuprous or cupric form, because of its ready interconversion by air oxidation in the one direction and by ion etching in the other. However, the high chloride content remains closer to Pourbaix's description of residual layers formed on copper covered with paratacamite than to Popplewell's presumption of cuprous oxide inner layers.

Although Cu and Cl are in the approximate mole ratio of 1:1 in a part of the inner layer near the inner/outer layer interface, Fig. 5, CuCl is usually associated with nonprotective, rather than protective, layers, such as form at the bottom of pits in copper (16) and in the brightening region in this work, Table II. Furthermore, other elements are present in the inner layer, in particular, much oxygen (Table VI) and Ni, so that the nature of the inner layer remains partly unresolved. CuCl , itself, is stable at $\text{pH} \lesssim 4$ for the conditions reported here (16), and, if present, would be evidence that the pH in electrolyte within the porous layer is in this range. It is not clear, however, that the pH should be lower in the porous structure, since the hydrolysis reaction which is expected to occur at anodic sites and the oxygen reduction reaction which occurs at the cathodic sites (1) shift the pH in opposite directions. No evidence was found on the freely corroded samples of the $\text{Ni}(\text{OH})_2$ layer formed as a passivating layer at high anodic potentials (19), see also Table IV.

In general the analyses are in good accord with the dynamic view of the nature of corrosion in NaCl solutions expressed by Popplewell *et al.* The outer composition is close to that required for paratacamite, considered to be back deposited by a continuous process of dissolution and precipitation. This covers an intermediate zone enriched in the oxides or hydroxy oxides of iron and nickel, which have enriched because of greater Cu ion solubility in the aqueous phase. To this we now add the finding of an innermost layer, rich in chloride and possessing a high cationic and low electronic conductivity, the latter of which controls its rate of formation and to very large degree the overall corrosion rate.

Conclusions

1. The chronological sequence of results suggests that the stable outer phase of basic copper chloride ($\text{Cu}_2(\text{OH})_3\text{Cl}$, paratacamite, was identified by x-ray diffraction) is formed early in the film formation process by a reconstitution of the initial cuprous oxide phase with involvement of a transient carbonate phase.

2. During the transition period (1-3 days) oxidized nickel is visible in the spectrum obtained from the reaction-product surface. A nickel oxide phase would normally underlie the cuprous oxide (17), and

its appearance in an analysis having such a shallow depth of penetration means that the growing cupric phase is forming as isolated nuclei on or within a mixed cuprous/nickel oxide/hydroxide layer.

3. SEM micrographs reveal a porous, discontinuous reaction product, particularly for the 1 and 5 day samples (Fig. 6a-d), consistent with the conclusion in 2.

4. After 5 days the cupric compound outer layer covers the entire surface, but it is highly enriched in nickel and iron on the substrate side of the layer. This thick, porous layer is responsible for the (relatively small) contribution of anodic control to the overall corrosion rate.

5. The inner layer (that which cannot be removed by stripping) associated with strong cathodic control of the overall reaction is not selectively enriched in either iron or nickel, but does contain the greatest concentration of chloride, about equal to that of copper near the inner/outer layer interface, found in any part of the corrosion product structure and a Cu:Ni ratio which is the same as in the bulk alloy.

6. The strongly protective nature of the inner layer arises from its low electronic conductivity which thereby restricts the rate of cathodic reduction of oxygen at the inner layer/outer layer interface, according to electrochemical experiments in Part I of this series (1). The electrochemical data also show that the inner layer is highly permeable to Cu, Ni, and Fe ions.

Acknowledgments

Mr. R. H. West of the University of Surrey performed the ESCA analysis under INCRA Project No. 254. The Office of Naval Research under Contract No. N00014-75-C-0264 provided financial support.

Manuscript submitted Nov. 19, 1979; revised manuscript received March 20, 1980. This was Paper 127 presented at the Pittsburgh, Pennsylvania, Meeting of the Society, Oct. 15-20, 1978.

Any discussion of this paper will appear in a Discussion Section to be published in the June 1981

JOURNAL. All discussions for the June 1981 Discussion Section should be submitted by Feb. 1, 1981.

Publication costs of this article were assisted by The Pennsylvania State University.

REFERENCES

1. C. Kato, B. G. Ateya, J. E. Castle, and H. W. Pickering, *This Journal*, **127**, 1890 (1980).
2. J. E. Castle, *Surf. Sci.*, **68**, 583 (1977).
3. J. C. Riviere, *Contemp. Phys.*, **14**, 513 (1973).
4. R. F. North and M. J. Pryor, *Corros. Sci.*, **10**, 297 (1970).
5. J. M. Popplewell, R. J. Hart, and J. A. Ford, *ibid.*, **13**, 295 (1973).
6. F. P. Ijsseling and J. M. Kroughman, in Proceedings of 6th European Congress on Metallic Corrosion, p. 181, Society of Chemical Industry, London (1977).
7. R. G. Blundy and M. J. Pryor, *Corros. Sci.*, **12**, 65 (1972).
8. T. Ozake and Y. Ishikawa, MERL technical brief, Hitachi Mechanical Engineering Research Laboratory, p. 23 (1977).
9. C. K. Jorgensen and H. Berthou, *Discuss. Faraday Soc.*, **54**, 269 (1972).
10. G. Johansson, J. Hedman, A. Berndtsson, M. Klasson, and R. Nilson, *J. Electron Spectrosc. Relat. Phenom.*, **2**, 293 (1973).
11. K. J. Kim, W. E. Baitinger, I. W. Amy, and N. Winograd, *ibid.*, **5**, 351 (1974).
12. J. E. Castle and D. C. Epler, *Proc. R. Soc. London, Ser. A*, **339**, 49 (1974).
13. C. R. Brundle, T. J. Chuang, and K. Wandelt, *Surf. Sci.*, **68**, 459 (1977).
14. J. E. Castle and C. R. Clayton, *Corros. Sci.*, **17**, 7 (1977).
15. G. Bianchi and P. Longhi, *ibid.*, **13**, 853 (1973).
16. M. B. Pourbaix, *This Journal*, **123**, 25C (1976).
17. J. E. Castle and M. Nasserian-Riabi, *Corros. Sci.*, **15**, 537 (1975).
18. P. R. Norton, R. L. Topping, and J. W. Goodale, *Surf. Sci.*, **65**, 13 (1977).
19. G. E. McQuire, A. L. Bacarella, J. C. Griess, Jr., R. E. Clausing, and L. D. Hulett, *This Journal*, **125**, 1801 (1978).

The Nature of Anodic Films on Nickel and Single Phase Nickel-Molybdenum Alloys

V. Mitrovic-Scepanovic and M. B. Ives

Institute for Materials Research, McMaster University, Hamilton, Ontario, Canada L8S 4M1

ABSTRACT

The decay of potential after anodization at a passive potential has been followed for a series of nickel-molybdenum alloys and the observations used to speculate on the effects of molybdenum alloying additives on the nature of the passivating films formed on nickel in 0.15N Na₂SO₄ at a pH of 2.8. It is concluded that small quantities (<5 w/o) of molybdenum causes considerable defectiveness to passive films, decreasing their stability. It is proposed that at higher alloy levels, but levels which do not produce a two-phase alloy, a mixed oxide (Mo³⁺, Mo⁶⁺)_xO_y is produced along with a much less stable defective NiO.

Whenever a passivated metal or alloy is subjected to an environment which tends to dissolve the surface film which maintains passivity, it has been found instructive to follow the potential with time as it tends towards the equilibrium open-circuit potential of the metal/electrolyte system. The decay curves invari-

ably show a structure represented by arrests at characteristic potentials which may sometimes be related to redox potentials for the appropriate species existing in the passivating film (1-3). The application of the open-circuit potential decay technique to films formed on nickel in sulfate solutions by MacDougall and Cohen (4-6) has, however, shown that potential arrests may also be related to the presence of regions

Key words: potential, anodization, passivation.

of defective film and not necessarily different phase oxides.

The potential decay technique has been applied to the study of passive films on nickel and on single phase nickel-molybdenum alloys in an attempt to elucidate the manner in which molybdenum changes the structure and properties of passive films formed on nickel in aqueous sulfate solutions.

Experimental

The electrochemical studies were carried out in a cylindrical cell with a working volume of approximately 200 ml. Alloy specimens were fixed in a Teflon holder which fitted snugly into one arm of the cell providing a constant relative position with a Luggin capillary and connected to a saturated calomel electrode (SCE) by an agar/ Na_2SO_4 salt bridge. Two inlets for nitrogen were provided both above and below the electrolyte surface.

Electrolyte solution was supplied to the cell from a storage vessel with a capacity of approximately 4 liters, which was kept under a stream of purified nitrogen. Deaeration of all solutions was performed for a minimum of 48 hr prior to each experimental run. Pure nitrogen¹ was further purified by passing it over copper wool at 450°C, cooled in a coiled glass water column, and dried by passing through silica gel, anhydrous CaSO_4 , and a molecular sieve.

All experiments were performed in 0.15N Na_2SO_4 solution prepared from ultrapure Na_2SO_4 .² The pH of the solution was adjusted with conc H_2SO_4 to pH = 2.7-2.8. Oxygen dissolved in the solution was removed by prolonged bubbling with purified nitrogen. The pH of the solution was checked before each experimental run by means of a pH-meter (Fisher Acumet 140).

Electrical measurements were performed using a potentiostat (Wenking 70HC3), a digital multimeter, and a two-pen potentiometric recorder provided with an integrating facility.

The electrode geometry in the cell is dictated primarily by the need to establish a symmetric electric field at the working electrodes. By using a platinum gauze counterelectrode with an area more than 20 times that of the working electrode, the dimensions of the working electrode can be varied over a wide range as also can its position, thus improving the flexibility of measurement and comparison between samples.

Samples were prepared of nickel and nickel-molybdenum alloys containing 1, 3, 5, 10, and 15 weight percent (w/o) Mo. The nickel samples were prepared from "low oxygen" material received as cold-rolled sheets prepared from refined cathode material, containing typically a maximum of 15 ppm carbon. The analysis of the pure nickel is given in Table I. The alloys were prepared from 99.9% nickel and 99% molybdenum. Qualitative spectrographic analysis of the base metals used in the preparation of the alloys is given in Table II. All the alloys are known to be single phase alloys in the nickel-molybdenum system (7). Samples were cut from sheets rolled from arc-melted buttons, heat-treated in accordance with the schedules noted in Table III under a vacuum of 10^{-5} Torr. These heat-treatments produced average grain sizes of approximately 0.02-0.04 mm.

Samples with surface areas ranging from 0.25 to 0.5 cm^2 were attached to tin-coated copper wires on the back surface and mounted in epoxy resin, such that only one face was exposed for polishing. This assembly fitted snugly into a Teflon holder. Samples were mechanically polished to 1 μm diamond polish following which they were ultrasonically degreased in acetone and electropolished. Electropolishing was performed

¹ Canada Liquid Air Limited, "Certified Grade" purity 99.99%, oxygen 20 ppm max, moisture <10 ppm.

² Obtained from Alfa Division, Ventnor Corporation, Danvers, Massachusetts.

Table I. Analysis of the cold-rolled sheets of Ni prepared directly from cathode material

Element	Analysis in ppm by weight
Al	<1
Ca	3
C	15
Cr	<0.6
Co	6
Cu	8
Fe	4
Pb	8
Mg	<1
Mn	<0.7
P	<2
Si	5
S	5
Ti	<1
H	1.5
N	2
O	1.4

Table II. Qualitative spectrographic analysis of Ni and Mo used for preparation of Ni-Mo alloys

Element	Range in w/o	
	Ni	Mo
Al	0.01-0.10	0.003-0.03
Ca	0.0003-0.003	0.001-0.01
Cr	—	0.001-0.01
Co	0.001-0.01	0.003-0.03
Cu	0.0001-0.001	—
Fe	0.003-0.03	0.01-0.1
Mg	0.001-0.01	0.001-0.01
Mo	—	MC
Ni	MC	0.1-1
Si	0.001-0.01	0.003-0.03

MC — main component.

Table III. Heat-treatment schedule for Ni and Ni-Mo alloys

Material	Conditions of heat-treatment
Ni	900°C × 1 hr FC
Ni-Mo	800°C × 1.5 hr FC
Ni-3 Mo	800°C × 1.5 hr FC
Ni-5 Mo	800°C × 1.5 hr FC
Ni-10 Mo	800°C × 7.5 hr FC
Ni-15 Mo	850°C × 57 hr FC

FC — furnace cooled.

immediately before each experimental run in ice-cooled 60 volume percent H_2SO_4 at a current density of 0.1 A/ cm^2 for 1 min.

Specimens were washed immediately after electropolishing with double-distilled water and transferred to the cell, where they were cathodically polarized at -2V for 10 min, in the absence of nitrogen bubbling to avoid the possibility of the deposition of impurities (8). The conditions for appropriate cathodic reduction were established from the behavior of pure nickel in the active region during subsequent potentiostatic polarization. The active dissolution peak at the active-passive transition was found to increase with decreasing potential of cathodic reduction. Cathodic reduction carried out at potentials more negative than -2V did not cause any further change in the active dissolution peak and consequently, -2V was adopted as the cathodic polarization practice. The Ni-Mo alloy were also subjected to the same cathodic reduction even though there is some possibility of hydrogen production and absorption which has been ignored in this investigation, but may well affect the detailed potential decay characteristics.

Anodic potentiostatic curves were obtained in 50 mV steps made at 2 min intervals, starting from -600 mV. Moderate nitrogen bubbling was introduced after the current polarity changed from negative to positive. Polarization at fixed potentials in the passive

region was performed by stepping the potential from -600 mV to the desired value. The potential decay curves were recorded by switching the potentiostat off after anodic polarization at a potential in the passive region for certain periods of time.

Specimens were routinely checked by optical metallographic examination to ensure that localized attack at grain boundaries (indicating possible segregation effects during sample preparation) or due to crevice attack at the sample edges have been avoided. Results from samples exhibiting such attack were always discarded.

"Surface reactivity" measurements (5) were performed in order to determine relative activity of the surface after a time on the open circuit. When a metal electrode is directly subjected to a potential in the passive region after the cathodic pretreatment, the amount of charge consumed during the formation of a steady-state film, Q_0 , can be considered as the amount of charge needed for film formation on a "clean" surface. If, however, the film were formed under the same conditions (potential and time of anodization) but starting with a surface not completely film-free, the charge consumed, Q , would be less than in the former case. The ratio $Q/Q_0 \times 100\%$ can be defined as surface reactivity, R_s , since a film-free surface would be 100% active. The surface reactivity was measured after different elapsed times on open circuit by stepping the potential back to the value at which the film had been previously grown. Conclusions on the stability of film coverages can be made on the basis of such results.

All potential data reported here are referred to the saturated calomel electrode. Both change of current with time during anodic oxidation and change of potential with time during open-circuit potential decay were followed by the chart recorder. For all experiments the curves presented here are the record of particular experimental runs, but are typical for the given conditions. Potentiostatic polarization measurements were reproducible to within $\pm 5\%$ in the active region. The maximum scatter in the potential decay measurements was ± 10 mV.

Results and Discussion

Polarization Characteristics of Ni and Ni-Mo Alloys

The anodic potentiostatic polarization behavior of Ni and Ni-Mo alloys was investigated first in order to determine the potential range of passivity. The results are given in Fig. 1 and 2. Although the passivation behavior will not be discussed in detail here, it is worth observing that (i) the 1% and 3% Mo alloys do not show ability to completely passivate, exhibiting two narrow "passive" regions. (ii) The passivation current and potential do not show any trend with molybdenum content. The current increases

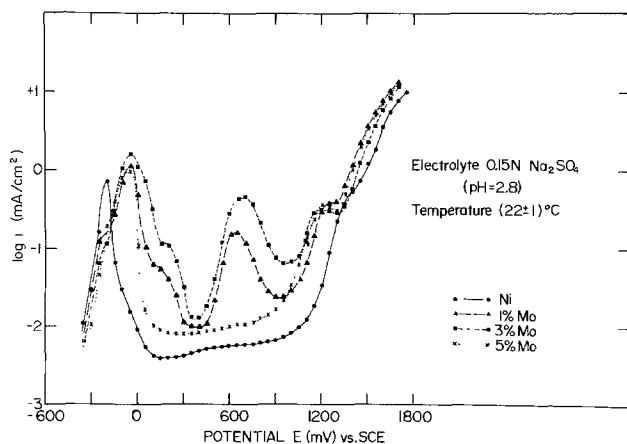


Fig. 1. Anodic potentiostatic polarization of nickel and nickel-low molybdenum alloys.

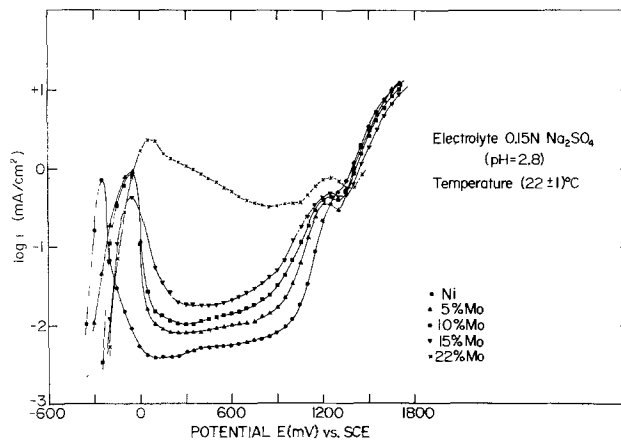


Fig. 2. Anodic potentiostatic polarization of nickel and single phase nickel-higher molybdenum alloys.

and then decreases with increasing molybdenum content, the passivating potential being shifted 200 mV in the positive direction with respect to that of pure Ni for all the alloys. (iii) The current density in the passive region increases monotonically with Mo content.

The observed behavior indicates a negative effect of molybdenum on the corrosion resistance of Ni and a significant difference in anodic polarization behavior between the alloys low and high in molybdenum. Similar observations were reported by Greene (9) and Tachibana and Ives (10).

Potential Decay and Surface Reactivity Measurements

Pure Ni.—Open-circuit potential decay and surface reactivity measurements were performed so that the effect of two variables could be studied: anodization potential and time (Fig. 3, 4, 5). All decay profiles show an abrupt change of potential (a "spike") at approximately -300 mV which appears after times which depend on the potential and time of anodization. The decay time elapsed before the spike, t_s , is longer for higher potentials and longer times of film formation. The surface reactivity was estimated at t_s and ($t_s + 10$ min) (labeled R_s and $R_{s'}$, respectively).

All decay curves, except those for electropolished nickel, also exhibit well-resolved potential arrests (Fig. 5). The characteristic potential plateaus occur close to -150 and -200 mV. Polarization at $+800$ mV brings out an additional arrest at approximately -10 mV. However, none of these potential arrests corresponds to the redox potentials of nickel oxides (Table IV) which should appear in the experimentally observed potential region.

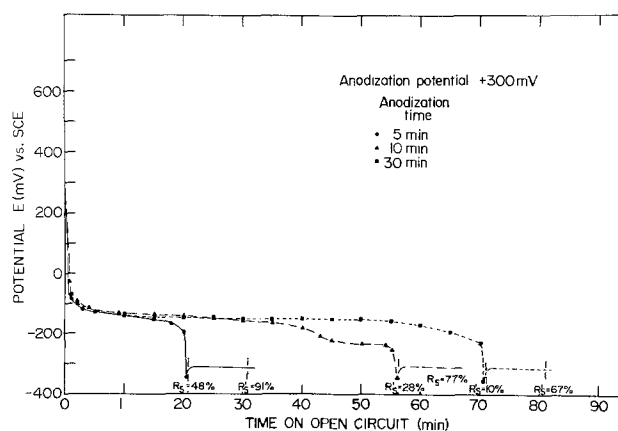


Fig. 3. Effect of anodization time at a fixed potential of $+300$ mV (SCE) on open-circuit potential decay of nickel.

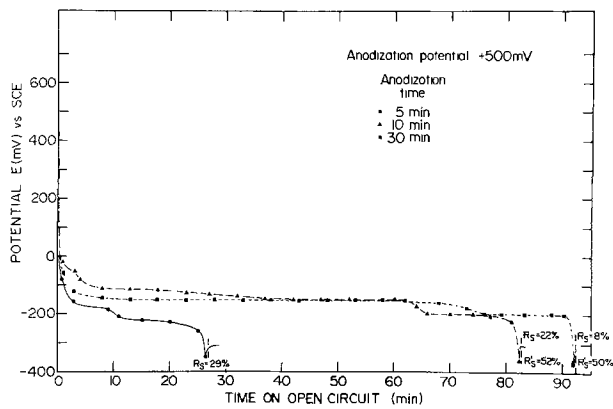


Fig. 4. Effect of anodization time at a fixed potential of +500 mV (SCE) on open-circuit decay of nickel.

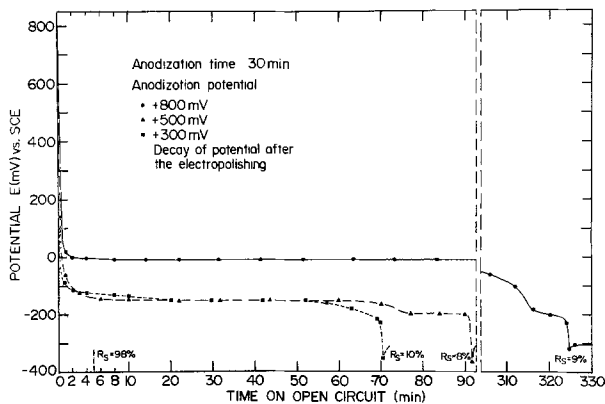


Fig. 5. Effect of anodization potential on open-circuit potential decay of nickel.

The potential spike at -300 mV is close to the equilibrium potential of a Ni/NiO electrode, suggesting it is NiO which is present on the anodized Ni under these experimental conditions, in agreement with the observations of MacDougall and Cohen (6). The other potential arrests could be explained in terms of a defective NiO which covers a part of the surface, the remainder being covered with stoichiometric NiO. The structure of the decay curve of electropolished nickel (Fig. 5) suggests the same type of oxide coverage, probably formed due to air exposure after electropolishing, but being much thinner than that formed by polarization at a potential in the passive region. Surface reactivity measurements suggest that prior to the spike only a relatively small fraction of defective film is susceptible to dissolution. After the potential shift to -300 mV, the ($t_s + 10$ min) values indicate that the surface reactivity increases rapidly. It appears that the oxide is removed quickly from the surface once the potential reaches -300 mV, perhaps by the process of undermining (6).

Ni-Mo alloys.—The open-circuit behavior and surface reactivity measurements made on the Ni-Mo alloys are shown in Fig. 6-10. The corresponding results for nickel are also given for comparison. Surface reactivities were estimated after different times at open circuit (dotted vertical lines on the decay curves).

Table IV. Equilibrium potentials of Ni and Mo oxides calculated for the electrolyte of pH = 2.8 with respect to SCE (mV)

Ni/NiO	-299.4	Mo/MoO ₂	-479.5
NiO/Ni ₂ O ₃	+489.5	Mo/MoO ₃	-339.5
NiO/Ni ₂ O ₃	+624.5	MoO ₂ /MoO ₃	-87.5
Ni ₂ O ₃ /Ni ₂ O ₃	+897.5		

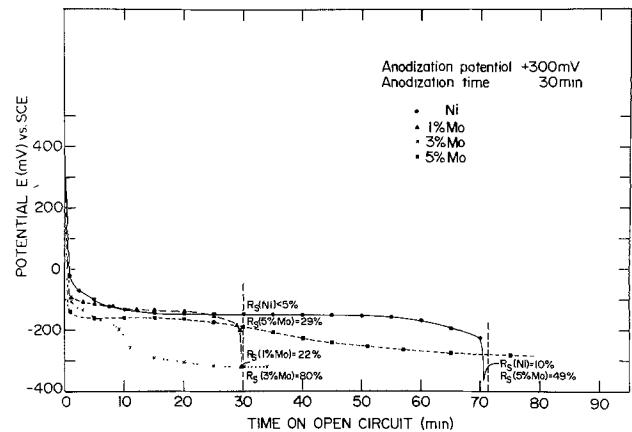


Fig. 6. Open-circuit potential decay of nickel-molybdenum alloys anodized at +300 mV (SCE) for 30 min.

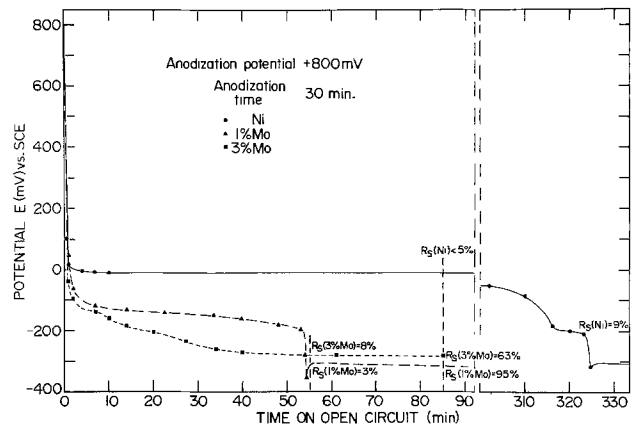


Fig. 7. Open-circuit potential decay of nickel-molybdenum alloys anodized at +800 mV (SCE) for 30 min.

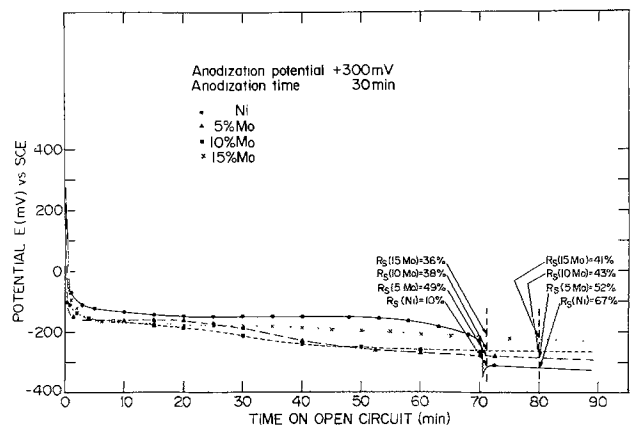


Fig. 8. Open-circuit potential decay of nickel-molybdenum alloys anodized at +300 mV (SCE) for 30 min.

The decay profiles and surface reactivity measurements may be summarized as follows: (i) only the 1% Mo alloy shows the potential spike characteristic of Ni, t_s being much smaller however, and depending on the conditions of film formation. (ii) The 3% Mo alloy shows a faster decay of potential than the 1% Mo alloy for which the surface reactivity measurements indicate that the oxide coverage on the 3% Mo alloy is the least stable of any of pure Ni, 1% Mo, and 3% Mo alloys. It appears that small amounts of molybdenum markedly affect the stability of the anodic film (Fig. 6, 7). (iii) Films formed on higher Mo alloys are less stable than NiO within the period t_s , but are more stable than nickel at longer times (Fig. 8, 9, 10).

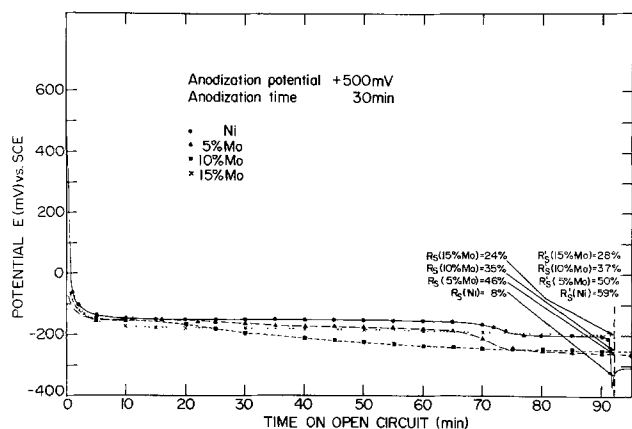


Fig. 9. Open-circuit potential decay of nickel-molybdenum alloys anodized at +500 mV (SCE) for 30 min.

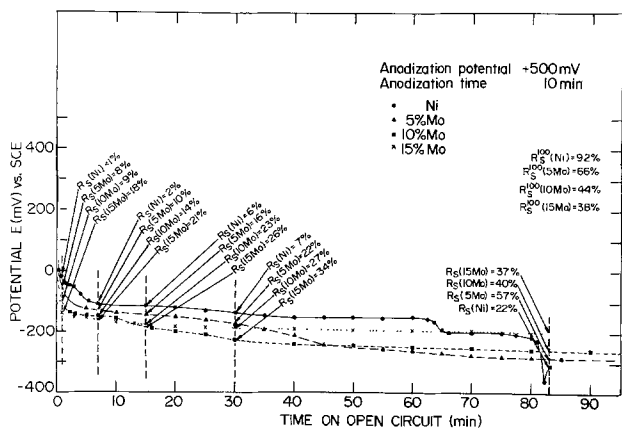


Fig. 10. Open-circuit potential decay of nickel-molybdenum alloys anodized at +500 mV (SCE) for 10 min. [R_s^{100} -surface reactivity measured after 102 min on open circuit.]

The above observations suggest that anodic films formed on the alloys low in Mo differ from those formed on alloys with higher Mo content. The effect of Mo content on the potential of the arrest at ~ -150 mV, the one in common for all the alloys, is summarized by a set of "inverse rate curves" in Fig. 11. It can be seen that the arrest at ~ -150 mV is shifted to a more positive potential for 1% Mo and to more negative potentials for 5, 10, and 15% Mo alloys. The potential decay of 3% Mo alloy occurs very quickly, so that the corresponding potential arrest is relatively poorly resolved (Fig. 6). Open-circuit behavior does not give any indication of the presence of MoO_2 and MoO_3 on the surface (Table IV).

In general the potential of a metal immersed in a conducting solution is that of either a single oxidation-reduction process or of a mixed potential of several redox reactions. In the absence of electrode reactions involving hydrogen or oxygen it may be assumed that the potential of the metal specimen is determined by some redox reaction involving the metal and/or the surface film. The simplest approach is to assume the arrest exhibited on the potential decay curves to be the equilibrium potentials of the surface oxides present (3).

In these studies more than one potential arrest has been observed for both pure nickel and the nickel molybdenum alloys. In addition, an abrupt change of potential appears consistent with the observations on nickel by MacDougall and Cohen (5).

Comparison of the observed arrests with the expected equilibrium potentials (Table IV) shows no correlation with any arrest except for the nickel "spike" at -300 mV, suggesting that the passive film on nickel is NiO . The nature of the other potential

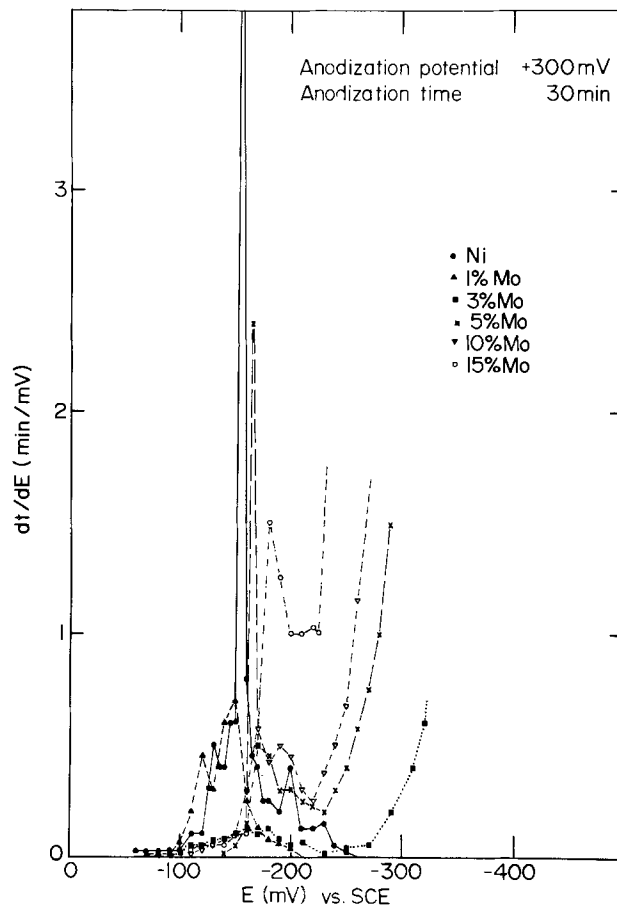


Fig. 11. Inverse rate curves constructed from potential decay data following anodization at +300 mV (SCE) for 30 min.

arrests could have a variety of origins most of which require the concept of defective oxide film. It is most likely that such films have regions of varying defectiveness and/or composition and the corresponding arrest potentials should probably therefore be considered as mixed potentials corresponding to the phases currently reacting with the solution. If the surface is mostly covered with stoichiometric NiO , the defective oxide could control the open-circuit potential if its exchange current were significantly high.

Considering the behavior of anodized nickel one could suppose that each potential arrest corresponds to a particular degree of imperfection of nickel oxide. The difference in potential $\Delta\epsilon$ between the arrest and the Ni/NiO potential would give an estimate of the excess free energy, ΔG , from the simple relationship $\Delta G = 2F\Delta\epsilon$, where $F = 96.5$ kC.

NiO is a metal deficit oxide, so that each potential arrest might be thought of as the equilibrium potential of $\text{Ni}/(\text{NiO})_{\text{def}}$. Defective NiO would be an oxide with a definite concentration of point defects (Ni -vacancies) associated with each potential plateau. The atom fraction of vacancies which could contribute to the observed ΔG range from 0.08 for the arrest at -200 mV to 0.24 for the arrest at -10 mV as shown in Fig. 5. Such large defect concentrations are difficult to rationalize and suggest other causes for some of the observed potential arrests.

It is, however, interesting to note that recent data (11) provide evidence for the influence of oxygen on the position of the lowest potential arrest (-200 mV): it is shifted towards more positive potentials in the presence of oxygen. The defect equation $\frac{1}{2} \text{O}_2 \rightarrow \text{O}_{\text{O}}^* + V_{\text{Ni}} + 2h^+$ implies that concentration of vacancies increases with increasing oxygen concentration

$$K = \frac{[V_{Ni''}][h^\circ]^2}{P_{O_2}^{1/2}} = \frac{4[V_{Ni''}]^3}{P_{O_2}^{1/2}}$$

where $[V_{Ni''}]$ denotes the concentration of negatively charged nickel vacancies and $[h^\circ]$ the concentration of positive holes in the structure of the nickel oxide. Since

$$[V_{Ni''}] = \frac{1}{2} [h^\circ]$$

then

$$[V_{Ni''}] = \left(\frac{k}{4}\right)^{1/3} P_{O_2}^{1/6}$$

which supports the assumption of nonstoichiometry.

The open-circuit behavior of nickel could also be interpreted in terms of other types of imperfection. The films could be strained or cracked and porous so that the estimated energies, ΔG , could represent strain energy and/or surface energy, but these would be excessive.

The behavior of low Mo alloys might be considered to be a consequence of doping nickel oxide with molybdenum, resulting in a higher concentration of defective sites more susceptible to dissolution. The shift of the arrest potential for 1% Mo alloy to a more positive value would be consistent with this conclusion, since a higher concentration of defects would correspond to a more positive potential arrest. The thermodynamic stabilities of oxides possibly present in the film suggest the existence of Mo-oxides as separate phases rather than as solutions of molybdenum in NiO, after some critical content of Mo is reached (probably between 3 and 5% Mo).

Pozdeeva *et al.* (12) have studied the electrochemical behavior of all the oxides of molybdenum and their results permit one to assume a mixed oxide phase of the type $(Mo^{4+}, Mo^{6+})_xO_y$, which could be present in the films on the higher Mo alloys, due to its much higher thermodynamic stability.

The amount of charge consumed for film formation (Table V) indicates that the steady-state film thickness increases with increased molybdenum content of the alloy, if 100% current efficiency is assumed. This would support the assumption of a Mo enrichment of the film. Tachibana and Ives (10) reported enrichment of the film in Mo on the basis of solution analysis. When the alloy film breaks down, the NiO phase probably dissolves first, leaving a surface covered mostly with a mixed Ni-Mo oxide. The surface reactivity data are in agreement with this conclusion; the films on the 5, 10, and 15% Mo alloys are only slowly removed from the surface, and are much more stable than NiO at longer dissolution times. The fact

Table V. Charge consumed for 10 min anodization at +500 mV

w/o Mo	$Q \frac{mC}{[cm^2]}$
0	8.7
5	10.3
10	16.5
15	19.4

that surface reactivity for these alloys increases faster than that for Ni for $t < t_s$ and slower at longer times could also indicate that the film on the alloys breaks down much faster at open circuit than does the film on nickel. Once the film breaks down, its removal involves active metal dissolution from oxide-free (or defective) areas and a cathodic reaction, such as hydrogen evolution on the remaining oxide-covered surface. The effect of molybdenum then might be such that (i) it increases the polarization associated with the active metal dissolution (by decreasing the exchange current density) which leads to a slower rate of oxide undermining, compared to that on pure nickel after t_s ; and/or (ii) the cathodic reaction might be slowed down with resulting decrease of metal dissolution and a corresponding lower rate of reactivation after t_s . Moreover, it is possible that the amount of bare surface after the spike is much higher for the alloys and, since the undermining is probably under cathodic control, the surface reactivity should increase more slowly.

Any further elucidation of a nature of films formed on nickel and nickel molybdenum alloys in these solutions must now be provided by other than purely electrochemical measurements. To this end, it is planned to perform additional chemical analysis of the solutions following anodic dissolution, and also to initiate studies of the structure and composition of surface films using physical surface analysis techniques.

Manuscript submitted June 4, 1979; revised manuscript received March 12, 1980.

Any discussion of this paper will appear in a Discussion Section to be published in the June 1981 JOURNAL. All discussions for the June 1981 Discussion Section should be submitted by Feb. 1, 1981.

Publication costs of this article were assisted by McMaster University.

REFERENCES

- G. Okamoto and N. Sato, *J. Electrochem. Soc. Jpn.* (Overseas Ed.), **27**, No. 4-6, E125 (1959).
- G. Okamoto and N. Sato, *Trans. Jpn. Inst. Met.*, **1**, 16 (1960).
- N. Sato and G. Okamoto, *This Journal*, **110**, 605 (1963).
- B. MacDougall and M. Cohen, *ibid.*, **123**, 191 (1976).
- B. MacDougall and M. Cohen, *ibid.*, **123**, 1783 (1976).
- B. MacDougall and M. Cohen, *ibid.*, **124**, 1185 (1977).
- P. V. Guthrie and E. E. Stansbury, Rept. ORNL-3078, Oak Ridge National Laboratory, Oak Ridge, Tennessee (July 1961).
- B. MacDougall and M. Cohen, *This Journal*, **122**, 383 (1975).
- N. D. Greene, in "Proc. 1st Int. Conf. Met. Corros.," p. 113, Butterworths, London (1962).
- K. Tachibana and M. B. Ives, in "Passivity of Metals," R. P. Frankenthal and J. Kruger, Editors, p. 878, The Electrochemical Society, Inc., Princeton, N.J. (1978).
- B. MacDougall, *This Journal*, **125**, 1883 (1978).
- A. Pozdeeva, E. I. Antonovskaya, and A. M. Suhotkin, *Corros. Sci.*, **6**, 149 (1966).

Ellipsometry and Auger Analysis of Chromium Surfaces Passivated in Acidic and Neutral Aqueous Solutions

Masahiro Seo

Corrosion Research Group, Faculty of Engineering, Hokkaido University, Sapporo, 060 Japan

Ryuichi Saito

Ishikawajima Harima Heavy Industries Company, Limited, Tokyo, 100 Japan

and Norio Sato*

Corrosion Research Group, Faculty of Engineering, Hokkaido University, Sapporo, 060 Japan

ABSTRACT

Ellipsometry and Auger electron spectroscopy (AES) were applied in order to elucidate the state and composition of chromium surfaces in deaerated 0.15M H_3PO_4 (pH 1.55), 0.15M NaH_2PO_4 (pH 4.38), and borate (pH 6.48 and 8.42) solutions. The cathodic reduction of chromium at -1.19V (HESS) for 15 min in 0.15M NaH_2PO_4 (pH 4.38) solution gives a good reproducible bare surface whose refractive index N_s is 4.35-4.15. The refractive index of the passive film formed on chromium for 1 hr at constant potential in the passive region is 1.80-(0.0 ~ 0.20)i, independent of the film thickness. In the case of pH 6.48 and 8.42 solutions the film thickness obtained ellipsometrically is in good agreement with that obtained coulometrically. The thickness (0.3 ~ 2.0 nm) of passive films increases linearly with increasing anodic potential and becomes smaller in the solution of the higher pH. The quantitative Auger analysis reveals that the average composition in depth of the passive film is nearly equal to Cr_2O_3 and that only the uppermost surface is hydrated.

Chromium is the most beneficial alloying element for improving the corrosion resistance of iron-base alloys. Recently surface analytical techniques such as Auger electron spectroscopy (AES) and x-ray photoelectron spectroscopy (XPS) have revealed that chromium is enriched in passive films formed on stainless steels (1, 2). The high corrosion resistance of stainless steels is mainly attributed to the chromium enrichment in passive films. Numerous studies (3-8) concerning the passivity of chromium have been undertaken in relation to the corrosion resistance of iron-chromium alloys. No clear information, however, has been obtained on the state and composition of chromium surfaces passivated in aqueous solutions.

In the present study, ellipsometry combined with electrochemical measurements was applied to throw light onto the passivation of chromium surfaces in aqueous solutions. Furthermore, the chromium surfaces after passivation were quantitatively analyzed by means of AES and ellipsometry.

Experimental

Specimen and electrolyte solution.—A zone-refined polycrystalline chromium lump (purity > 99.9%) was machined to plates ($0.2 \times 1.0 \times 2.0$ cm), vacuum annealed for 30 min at 873°K , and cooled gradually to room temperature. Further, the specimen was polished with emery paper, finally polished with $\alpha\text{-Al}_2\text{O}_3$ abrasives ($0.05 \mu\text{m}$), and washed with a mixture of methanol and acetone using an ultrasonic technique. The electrolyte solutions used were 0.15M H_3PO_4 (pH 1.55), 0.15M NaH_2PO_4 (pH 4.38), and boric acid-sodium borate (pH 6.48 and 8.42) solutions, which were completely deaerated in solution reservoirs by purified nitrogen gas before introduction into an electrolytic cell.

* Electrochemical Society Active Member.

Key words: ellipsometry, Auger analysis, passive film, chromium.

Ellipsometry and electrochemical measurement.

The ellipsometer used was of the horizontal type with a compensator placed on the side of incident beam and a mercury arc lamp (546.1 nm) with an interference filter as a light source. An electrolytic cell with two optical-glass windows was used for simultaneous measurements of ellipsometry and electrochemical polarization. The details of ellipsometer and electrolytic cell are described elsewhere (9). The specimen in the cell was first cathodically reduced in different electrolyte solutions to obtain a bare surface which was used as an optical reference plane. After cathodic reduction, the electrolyte solution was renewed and the specimen was passivated potentiostatically at a desired anodic potential for 1 hr. The ellipsometric and coulometric measurements were simultaneously conducted with respect to the passivated surfaces of the specimen. The amount of chromium ion dissolved into the electrolyte solutions during cathodic reduction and passivation of the specimen was measured by colorimetry (diphenyl-carbazide method). The measurements were carried out at a constant temperature of $298^\circ \pm 0.1^\circ\text{K}$. The electrode potential of the specimen was referred to a hydrogen electrode in the same solution (HESS).

AES measurement.—After passivation, the specimen was rapidly washed with doubly distilled water and dried with a jet of nitrogen gas. The specimen was set on a sample holder in the Auger chamber (PHI, 540A), which was evacuated to a vacuum better than 2.7×10^{-7} Pa, and then Auger spectra of the specimen surface were taken by using a primary electron beam (2 kV, $40 \mu\text{A}$) with a diameter of about $50 \mu\text{m}$ and a modulation amplitude of 4V at a frequency of 30 kHz.

Results and Discussion

Cathodic reduction of chromium in strongly acidic solutions (6, 10) has frequently been employed to ob-

tain a bare surface without films. This procedure, however, gives rise to a significant dissolution of chromium substrate producing a rough surface which is not suitable for ellipsometer measurements. In the present study, therefore, potentiostatic cathodic reduction of the specimen in 0.15M NaH₂PO₄ (pH 4.38) solution was tentatively conducted to obtain an optically flat surface without films. It was eventually found that potentiostatic cathodic reduction of the specimen at -1.19V (HESS) for 15 min in 0.15M NaH₂PO₄ (pH 4.38) gave a good reproducible surface without films.

Figure 1 shows the measured values of two ellipsometer reading, P and A for a number of specimens cathodically reduced at -1.19V (HESS) for 15 min in 0.15M NaH₂PO₄ (pH 4.38) solution. In Fig. 1, the computed P-A grid for a bare substrate of varied refractive indexes ($N = n - ik$) is superimposed on the measured values. It appears that all the experimental P-A values are located within a limited region of the computed grid with n ranging from 4.2 to 4.5 and k from 4.0 to 4.4. An average value of complex refractive index N_s for the cathodically reduced chromium surface, is determined to be $N_s = 4.35 - 4.15i$, which is in good agreement with that ($N_s = 4.17 - 5.19i$) obtained by Genshaw and Sirohi (10).

Anodic oxidation of chromium.—The stationary anodic polarization curves of chromium obtained after 1 hr of anodic oxidation at constant potential in 0.15M H₃PO₄ (pH 1.55), 0.15M NaH₂PO₄ (pH 4.38), and boric acid-sodium borate (pH 6.48 and 8.42) solutions are shown in Fig. 2. The transpassive dissolution of chromium proceeds at anodic potentials higher than 1.10V (HESS) in all solutions studied. The total amount of electric charge passed Q_T (C · m⁻²) and the amount of chromium dissolved into solutions W_D (mg · m⁻²) during 1 hr of anodic oxidation are plotted vs. anodic potential E_{HESS} in Fig. 3. The value of W_D in the passive region is negligibly small so that Q_T in the passive region is equal to the amount of electric charge required for film formation Q_F . The results in Fig. 3 indicate that the thickness of the passive film increases linearly with increasing anodic potential.

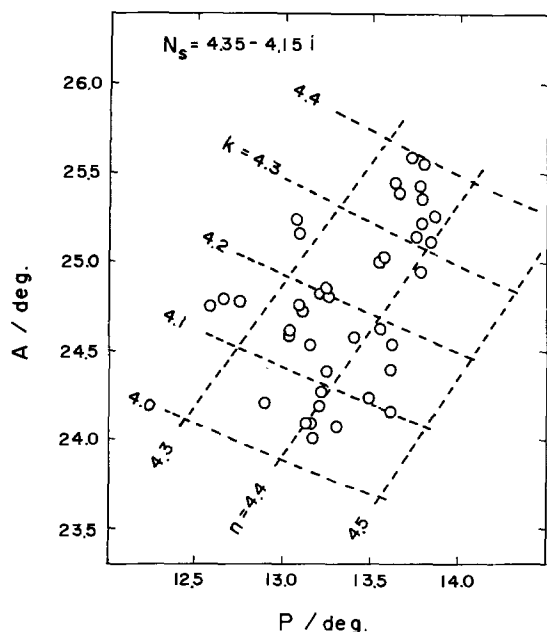


Fig. 1. Two ellipsometer readings, P and A, experimentally obtained for a number of chromium surfaces cathodically reduced at -1.19V (HESS) for 15 min in 0.15M NaH₂PO₄ (pH 4.38) solution. Dashed lines show a computed P-A grid for a bare substrate of various refractive indexes ($N_s = n - ik$).

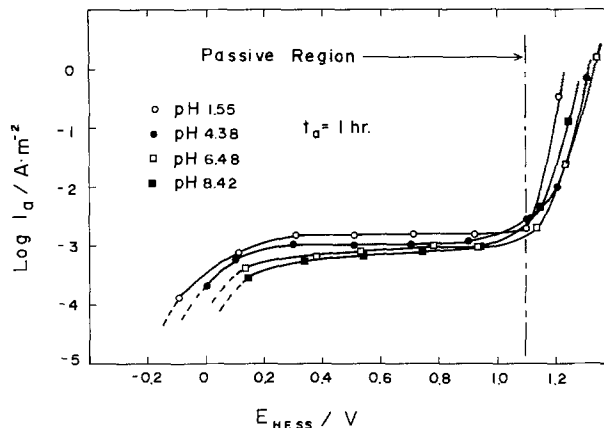


Fig. 2. Stationary anodic polarization curves of chromium obtained after 1 hr of anodic oxidation at constant potential in 0.15M H₃PO₄ (pH 1.55), 0.15M NaH₂PO₄ (pH 4.38), and boric acid-sodium borate (pH 6.48 and 8.42) solutions.

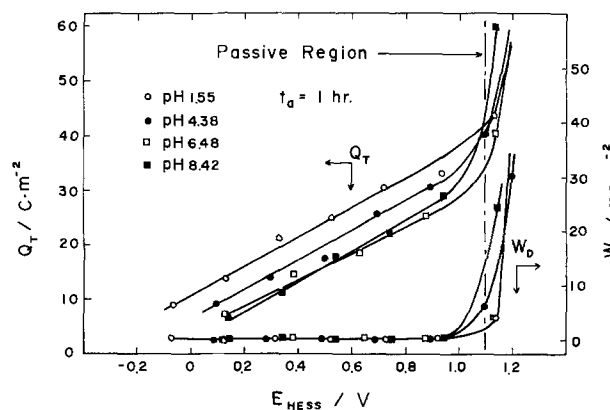


Fig. 3. Total amount of electric charge passed Q_T and amount of chromium dissolved into solutions W_D during 1 hr of anodic oxidation at constant potential E_{HESS} .

Figure 4 shows the pair-values of P and A observed after 1 hr oxidation at constant potential, the values being referred to P_0 and A_0 of the bare chromium surface. From a linear relationship observed between δP and δA in the passive region, it is suggested that the passive film on chromium consists of a single layer, the refractive index of which is constant, independent of potential (and hence of thickness), although slightly dependent on the solution pH. Theoretical computation for a film having a constant refractive index and increasing thickness leads to a linear re-

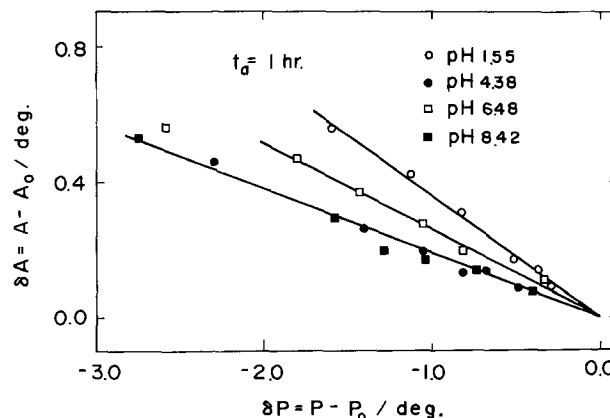


Fig. 4. Two ellipsometer readings P and A observed for chromium surfaces passivated at constant potential for 1 hr in solutions of different pH values, δP and δA being referred to P_0 and A_0 for the bare surface.

relationship between δP and δA . The refractive index of the passive film can be evaluated by comparing the experimental values of δP and δA for a growing film with the computed values for various refractive indexes and thicknesses. The refractive indexes ($N_f = n - ik$) of the passive films thus obtained, are $1.80 - 0.0i$ for the solution of pH 1.55, $1.80 - 0.15i$ for the solution of pH 6.48, and $1.80 - 0.20i$ for the solutions of pH 4.38 and 8.42.

Once the refractive index of the film is determined, the film thickness L_f can be computed as a function of either δP or δA . Figure 5 shows the film thickness computed as a function of δP for surface films on chromium with three different refractive indexes. The film thickness for certain experimental values of δP in Fig. 4 can be obtained from the relation between L_f and δP shown in Fig. 5. The thickness thus obtained for the passive film formed on chromium is plotted as a function of anodic potential in Fig. 6. Figure 7 shows the film thickness calculated coulometrically from the values of Q_F in Fig. 3, assuming that the passive film consists of Cr_2O_3 . In the case of pH 6.48 and 8.42 solutions, the film thickness obtained ellipsometrically is in good agreement with that obtained coulometrically. In the case of pH 1.55 and 4.38 solutions, the agreement between the film thickness obtained ellipsometrically and coulometrically is not satisfactory probably because of the surface roughening in acid solution.

Composition of passive film.—Figure 8 shows the Auger spectra of chromium anodically oxidized at +0.71V (HESS) for 1 hr in 0.15M NaH_2PO_4 (pH 4.38) solution. The Auger peaks of P (120 eV) and C (272 eV) as well as the main peaks of Cr (529 eV) and O (510 eV) were observed for the passivated chro-

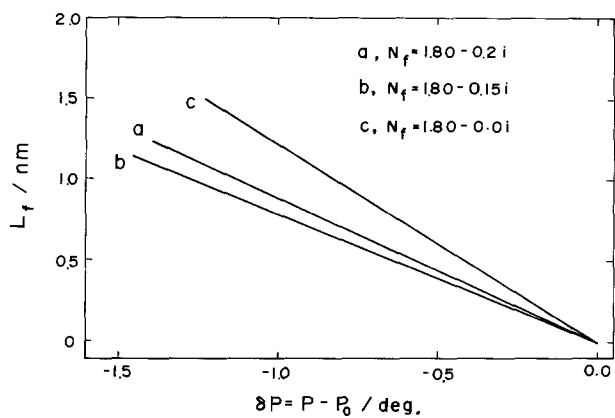


Fig. 5. Film thickness L_f computed as a function of δP for surface films on chromium with three different refractive indexes.

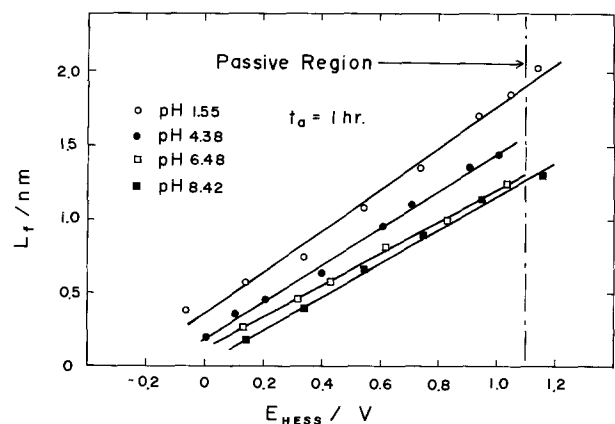


Fig. 6. Film thickness L_f obtained ellipsometrically as a function of anodic potential E_{HESS} .

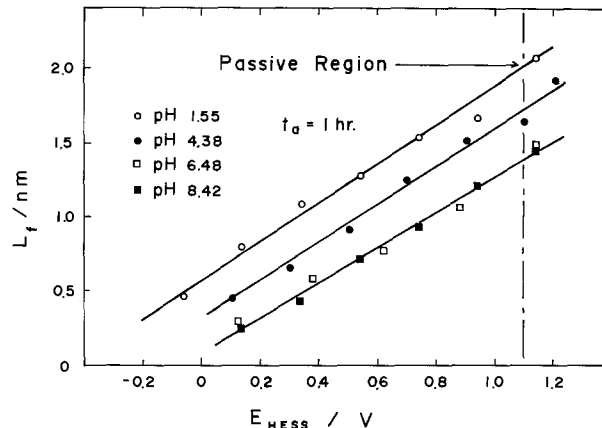


Fig. 7. Film thickness L_f obtained coulometrically as a function of anodic potential E_{HESS} .

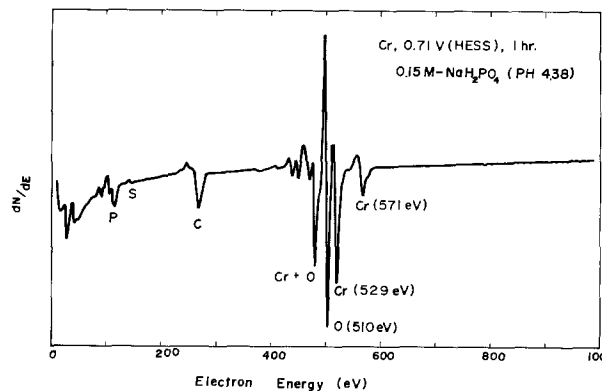


Fig. 8. Auger spectra of chromium anodically oxidized at +0.71V (HESS) for 1 hr in 0.15M NaH_2PO_4 (pH 4.38) solution.

mium surface. For the quantitative analysis of the passive film on chromium, it is necessary to separate the pure Auger peak of Cr (529 eV) from the overlapped peaks of Cr (529 eV) and O (510 eV). In the present study, separation of the pure Auger peak of Cr (529 eV) was accomplished by subtracting the pure Auger peak of O (510 eV), observed with an Fe_2O_3 film on iron, from the overlapped peaks of Cr (529 eV) and O (510 eV), assuming that the shape of O (510 eV) peak is the same for both Fe_2O_3 and Cr_2O_3 films. The justification of this method has been verified by Frankenthal and Thompson (11). The Auger peak-to-peak height ratio of O (510 eV) to Cr (529 eV), H_O/H_{Cr} , thus obtained is plotted vs. the film thickness obtained ellipsometrically in Fig. 9. The value of H_O/H_{Cr} increases with increasing film thickness.

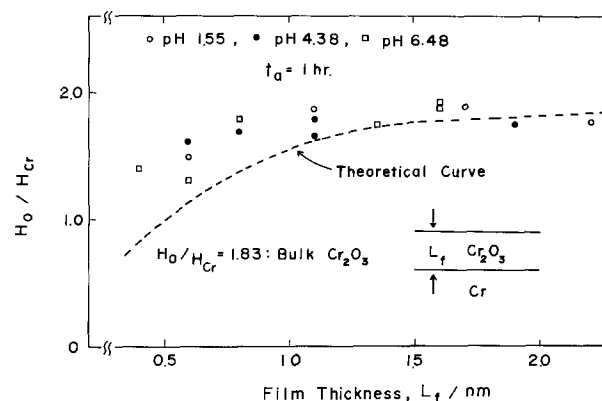


Fig. 9. Auger peak to peak height ratio H_O/H_{Cr} vs. film thickness L_f obtained ellipsometrically. Dashed line shows a theoretical curve for a single layer of Cr_2O_3 .

For determination of the composition of passive films from the value of H_O/H_{Cr} , the contribution of chromium substrate for the total Auger peak-to-peak height of chromium must be taken into account, because the escape depth (0.8 nm) of Auger electrons of Cr (529 eV) is the same order of magnitude as the film thickness. The Auger peak-to-peak heights of Cr (529 eV) and O (510 eV), H_{Cr} and H_O , are given by

$$H_{Cr} = \alpha_{Cr} n_{Cr}^f \sum_{i=1}^{i=l} e^{-k(i-1)d} + \alpha_{Cr} n_{Cr}^b \sum_{i=l+1}^{i=\infty} e^{-k(i-1)d} \quad [1]$$

$$H_O = \alpha_O n_O^f \sum_{i=1}^{i=l} e^{-k(i-1)d} \quad [2]$$

where α_{Cr} and α_O are the sensitivity coefficients of chromium and oxygen atoms, n_{Cr}^f and n_O^f the atomic densities of chromium and oxygen in the passive film, n_{Cr}^b the atomic density of chromium in the substrate, l the number of surface atomic layers in the passive film, d the thickness of surface monolayer, and k the attenuation coefficient per unit length of Auger electrons of chromium or oxygen. In Eq. [1] and [2], it is assumed that both n_{Cr}^f and n_O^f are uniform in depth up to the film/substrate interface. Further, the attenuation coefficient k is given (12) by

$$k = \frac{1}{\lambda_1 \cos \theta_1} + \frac{1}{\lambda_p \cos \theta_2} \quad [3]$$

where λ_1 is the escape depth of Auger electrons of chromium or oxygen λ_p the mean free path of primary electron in the specimen, θ_1 the acceptance angle of Auger electrons in the CMA, and θ_2 the incidence angle of primary electrons to the specimen measured from the normal direction. As previously reported elsewhere (13), the value of k was determined as 2.36 nm^{-1} by substituting the reasonable values of $\lambda_{Cr} = \lambda_O = 0.8 \text{ nm}$, $\lambda_p = 3.0 \text{ nm}$, $\theta_1 = 42^\circ$, and $\theta_2 = 60^\circ$ into Eq. [3]. The sensitivity coefficient ratio of oxygen to chromium α_O/α_{Cr} was determined as 1.22 from the Auger results (14) of an $\alpha\text{-Cr}_2\text{O}_3$ film which was prepared by dry oxidation of chromium in the air for 15 min at 873°K . Assuming that the passive film on chromium consists of Cr_2O_3 and that the monolayer thickness is 0.3 nm (13), the values of $d = 0.3 \text{ nm}$, $n_O^f/n_{Cr}^f = 1.5$ and $n_{Cr}^f/n_{Cr}^b = 0.5$ are obtained for the calculation of H_O/H_{Cr} as a function of film thickness, using Eq. [1] and [2].

The dashed curve in Fig. 9 shows the relation between the value of H_O/H_{Cr} thus calculated and the film thickness. The experimental value of H_O/H_{Cr} exceeds slightly the theoretical curve of Cr_2O_3 (dashed curve), revealing that the average composition of passive film in depth is nearly equal to Cr_2O_3 . The deviation of experimental value from the theoretical curve, however, increases with decreasing film thickness. The XPS study (15) by Bouyssoux *et al.* showed that only the uppermost surface of the passive film on chromium is hydrated. The increasing deviation of the experimental value of H_O/H_{Cr} from the theoretical curve with decreasing film thickness can be attributed to the presence of a hydrated layer localized in the uppermost part of the surface film. The results of quantitative Auger analysis for the passive films on chromium are consistent with those obtained by ellipsometry and coulometry.

Conclusion

Ellipsometry combined with electrochemical measurements was applied to elucidate the state and

composition of chromium surfaces passivated in deaerated 0.15M H_3PO_4 (pH 1.55, 0.15M NaH_2PO_4 (pH 4.38), and boric acid-sodium borate (pH 6.48 and 8.42) solutions. Furthermore, quantitative Auger analysis was performed on the chromium surfaces after 1 hr passivation, by taking the escape depth of Auger electrons and the film thickness obtained ellipsometrically into account. The following conclusions were drawn:

1. The cathodic reduction of chromium at -1.19V (HESS) for 15 min in 0.15M NaH_2PO_4 (pH 4.38) solution gives a good reproducible bare surface whose refractive index N_s is 4.35-4.15i.

2. The refractive index N_f of the passive film formed on chromium for 1 hr at constant potential in the passive region is 1.80-(0.0 ~ 0.20)i, independent of the film thickness. In the case of pH 6.48 and 8.42 solutions, the film thickness obtained ellipsometrically is in good agreement with that obtained coulometrically, assuming that the passive film consists of a single layer of Cr_2O_3 .

3. The thickness (0.3-2.0 nm) of passive films increases linearly with increasing anodic potential. The thickness of passive film formed at the same anodic potential (HESS) becomes smaller in the solution of the higher pH.

4. The Auger analysis reveals that the average composition in depth of the passive film is nearly equal to Cr_2O_3 and that only the uppermost surface is hydrated.

Manuscript submitted Dec. 28, 1979; revised manuscript received March 17, 1980.

Any discussion of this paper will appear in a Discussion Section to be published in the June 1981 JOURNAL. All discussions for the June 1981 Discussion Section should be submitted by Feb. 1, 1981.

Publication costs of this article were assisted by Hokkaido University.

REFERENCES

1. J. B. Lumsden and R. W. Staehle, *Scr. Metall.*, **6**, 1205 (1972).
2. I. Olefjord and H. Fischmeister, *Corros. Sci.*, **16**, 697 (1975).
3. V. M. Knyazheva and Ya. M. Kolotyarkin, *Dokl. Akad. Nauk SSSR*, **114**, 1265 (1957).
4. P. F. King and H. H. Uhlig, *J. Phys. Chem.*, **63**, 2020 (1959).
5. T. Heumann and F. W. Diekotter, *Ber. Bunsenges. Phys. Chem.*, **67**, 671 (1963).
6. V. V. Andreeva, *Corrosion*, **20**, 35t (1964).
7. H. W. Pickering and R. P. Frankenthal, *This Journal*, **112**, 761 (1965).
8. R. P. Frankenthal, *ibid.*, **114**, 542 (1967); **116**, 580 (1969).
9. N. Sato and G. Okamoto, "Structure and Properties of Metal Surfaces," Honda Memorial Series on Material Science, No. 1, p. 438, Maruzen Co. Ltd., Tokyo (1973).
10. M. A. Genshaw and R. S. Sirohi, *This Journal*, **118**, 1558 (1971).
11. R. P. Frankenthal and D. E. Thompson, in "Passivity of Metals," R. P. Frankenthal and J. Kruger, Editors, p. 262, The Electrochemical Society, Inc., Princeton, N.J. (1978).
12. F. Pons, J. Le Héricy, and J. P. Langeron, *Surf. Sci.*, **69**, 547, 565 (1977).
13. M. Seo and N. Sato, *ibid.*, **86**, 601 (1979); *Trans. ISIJ*, **19**, 504 (1979).
14. M. Seo and N. Sato. Unpublished data.
15. G. Bouyssoux, M. Romand, H. D. Polaschegg, and J. T. Calow, *J. Electron Spectrosc. Relat. Phenom.*, **11**, 185 (1977).

Raman and Infrared Spectroscopy of Aqueous Corrosion Films on Lead in 0.1M Sulfate Solutions

Richard J. Thibau¹ and Chris W. Brown

Department of Chemistry, University of Rhode Island, Kingston, Rhode Island 02881

and Arnon Z. Goldfarb² and Robert H. Heidersbach*

Department of Ocean Engineering, University of Rhode Island, Kingston, Rhode Island 02881

ABSTRACT

The Pb-H₂O-SO₄ Pourbaix diagram was investigated by examining potentiostatically oxidized lead samples using Raman and infrared spectroscopy. In 0.1M sulfate solutions surface film compositions were not in complete agreement with predictions of the calculated potential-pH diagram. The Pourbaix diagram did not predict the formation of PbO under any conditions; however, spectra indicated the presence of the oxide at certain potentials in acid and neutral solutions and at all potentials above the immunity region in basic solutions. Spectroscopic identification of insoluble surface species was in agreement with potentiodynamic polarization curves.

Laser Raman spectroscopy can unambiguously identify the compounds present in aqueous corrosion product films on metal surfaces. It can be used to analyze insoluble surface layers *in situ* without removing a metal sample from the corrosive solution with which it is reacting (1-3). The ability to identify surface species without changing the environment makes this technique ideal for experimental confirmation of theoretical Pourbaix diagrams, which identify the lowest energy species for any given set of conditions.

In situ Raman spectroscopy, in combination with the complementary technique, reflection-absorption infrared spectroscopy, has been used to study the Pourbaix diagrams for the Pb-H₂O and Pb-H₂O-Cl systems (1, 2). Potentiostatic exposures of lead electrodes were conducted in buffer solutions and the resulting surface films were analyzed spectroscopically. The compounds comprising the surface corrosion product films were only in partial agreement with Pourbaix diagram predictions, and reasons for these differences were discussed. In the present research simple, unbuffered solutions were used for electrochemical exposures to find if experimental results would be closer to those predicted by thermodynamics if the solutions did not contain the extra dissolved species of the buffer systems used previously.

The behavior of lead in sulfate solutions has been studied extensively due to the widespread use of lead-acid storage batteries. For this reason, the preponderance of experimental work has involved the reactions of lead with sulfuric acid, and very little research on lead in neutral or basic sulfate solutions has been conducted. Pourbaix diagrams for lead in aqueous sulfate solutions have been calculated (4-6). Some efforts have been made to verify the theoretical predictions experimentally, although experimental sulfate exposures have been confined to the acid and neutral regions of the diagram (4, 7). The present report describes infrared and Raman spectroscopic results from systematic exposure of lead samples in 0.1M sulfate solutions under conditions covering a large part of the Pourbaix diagram.

Experimental

Raman spectra were recorded with a Spex Industries Model 1401 double monochromator using a photon

* Electrochemical Society Active Member.

¹ Present address: Sperry Research Center, Sudbury, Massachusetts 01776.

² Present address: Tel Aviv, Israel.

Key words: corrosion, spectra, infrared.

counting detection system. A Coherent Radiation Laboratories Model CR-3 argon ion laser was used as the excitation source. Both the 488.0 and 514.5 nm wavelength laser lines were used. Additional details are contained in previous reports (1-2).

Infrared reflection-absorption spectra were obtained with a Wilks Scientific Corporation Model 9 multiple specular reflection attachment in both the sample and reference beams of Perkin-Elmer Model 521 infrared spectrophotometer equipped with a grating polarizer. Details of the special electrochemical cell and instrumentation used for controlled potential sample exposures are contained in a previous report (1).

Lead foil (1.6 mm thick) supplied by Alfa Products, Incorporated, at greater than 99% purity was used for this investigation. It was cut into 2.8 × 5.7 cm rectangles to fit the sample holder of the electrochemical cell. This size was also required for the infrared reflection attachment. Prior to placing a lead sample in solution, it was immersed in warm, concentrated ammonium acetate solution for 5 min to dissolve the surface layer, leaving a clean, silvery sample. The clean lead sample was washed with distilled water and immediately placed in the exposure solution.

The three solutions used were made from reagent grade compounds. The acid solution was 0.1M H₂SO₄. The neutral solution chosen was 0.1M K₂SO₄ which has a pH of approximately 6.5, and for exposure in basic solution, a solution of 0.1M K₂SO₄ and 0.004M KOH, giving an approximate pH of 11, was used.

The electrochemical cell filled with solution was purged with dry nitrogen for 30 min before and throughout the controlled potential exposures. The potential of the lead working electrode was held constant relative to the saturated calomel reference electrode by a Wenking Model LT73 potentiostat for periods ranging from ¼ to 21 hr. Upon completion of an exposure period, an *in situ* Raman spectrum was recorded. The sample was then removed from the cell, washed thoroughly with distilled water, and allowed to dry in air. The dry sample was returned to the Raman spectrometer for examination and then analyzed by the infrared spectrophotometer.

Some exposures were conducted on lead films which were vapor deposited onto gold substrates on glass microscope slides. These samples allowed the lead to be completely oxidized leaving a nonreacted gold mirror substrate. The approximate thickness of oxidized lead films on such samples was measured by a Taly-step-1 stylus-type profile instrument.

Results and Discussion

The Pourbaix diagram for the lead-water-sulfate system was calculated using the relationships used by Ruetschi and Angstadt (4) but employing more recent values for the free energy of formation of some species (8). The newer thermodynamic data, summarized in Table I, caused only small changes in the positions of the PbO·PbSO₄ equilibria lines. A sulfate ion activity of 0.1 was used for the calculations resulting in the Pourbaix diagram shown in Fig. 1.

Electrochemical exposures were carried out in solutions of the desired pH which were 0.1M in sulfate. The solutions used gave pH values of approximately 1, 6.5, and 11 to allow observation of the reactions of lead over a wide portion of the Pourbaix diagram. Measurement of solution pH before and after potentiostatic exposures showed that the pH remained fairly constant, i.e., it did not change by more than 0.6 after as long as 24 hr.

In order to provide an experimental basis for choosing exposure potentials, potentiodynamic polarization curves were recorded for lead in the three solutions selected for exposures. Polarization curves were recorded with a relatively slowly changing potential of 40 mV/min to allow the formation of a relatively thick oxidation product film, as would be encountered in potentiostatic oxidation.

The polarization curves are shown in Fig. 2. They are rather similar, each has a strong wave at approximately -0.25V (vs. NHE) as its major feature. These waves mark the transition from reduction to oxidation, i.e., the upper limit of the immunity region. In accordance with the Pourbaix diagram, the potential of such

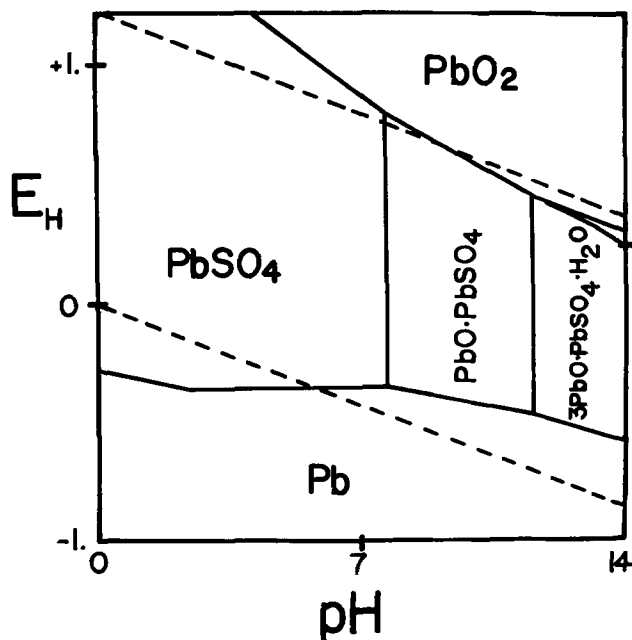


Fig. 1. Pourbaix diagram for the Pb-H₂O-SO₄ system at 25°C for a_{SO₄} = 0.1.

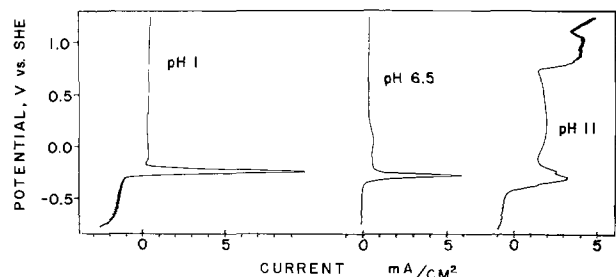


Fig. 2. Potentiodynamic polarization curves for lead in 0.1M sulfate solutions, scan rate 40 mV/min.

Table I. Free energy data used to calculate the lead-water-sulfate Pourbaix diagram

Species	Standard free energy of formation (cal/mole)	
	NBS (8)	Ruetschi and Angstadt (4)
SO ₄ ²⁻	-177,970	-177,340
HSO ₄ ⁻	-180,690	-179,940
H ₂ O	-56,690	-56,690
P ₂ O ₅	-143,700	-147,600
Pb ₂ O ₃	-98,417	-98,417
α-PbO ₂	-51,940	-51,940
β-PbO ₂	-52,340	-52,340
PbSO ₄	-194,360	-193,890
PbO · PbSO ₄	-246,700	-243,200
3PbO · PbSO ₄ · H ₂ O	-397,300	-397,300
5PbO · 2H ₂ O	-336,350	-336,350
PbO	-45,050	-45,050

a transition decreases as pH increases. The oxidative wave was observed at -0.23V in pH 1, -0.27V in pH 6.5, and -0.30V in pH 11 solution. The positions of these waves are in general agreement with the Pb to PbSO₄ and Pb to PbO·PbSO₄ transitions of the Pourbaix diagram.

Potentials used for lead exposures were chosen so that at least one was located in each region of the theoretical Pourbaix diagram and in all potential regions where the polarization curves indicated the possible formation of different species. The exposure conditions selected and the resulting spectra obtained from these potentiostatic oxidations are summarized in Table II.

pH 1 exposures.—In the 0.1M H₂SO₄ solutions used to attain acidic conditions, lead is stable at low potentials, but it is oxidized to lead sulfate at higher potentials (4, 9, 10). After formation of a surface sulfate film thick enough to hinder reactions of lead with solution species, layers of PbO or basic lead sulfates develop under the sulfate film at potentials of +0.32V and higher (4, 9, 11). Although the formation of underlying oxide layers was not considered in the calculation of the Pourbaix diagram, the very weak wave at +0.34V on the pH 1 polarization curve may indicate the commencement of formation of another compound beneath the sulfate film.

Potentiostatic exposures of lead in 0.1M sulfuric acid formed surface films whose compositions agreed well with x-ray diffraction work by Pavlov and

Table II. Results of potentiostatic exposures in 0.1M sulfate solutions

Solution, pH	Volts vs. SHE	Exposure period, hr	Current, μA/cm ^{2(a)}	Spectrum observed
1	-0.46	19.5	73 ^(b)	None ^(c)
1	-0.26	18	19.7	PbSO ₄
1	-0.02	4	13.3	PbSO ₄
1	+0.48	17.5	15.7	Tetr. PbO and PbSO ₄
1	+0.80	20	12.8	Tetr. PbO and PbSO ₄
1	+1.24	2.5	48.4	Tetr. PbO and PbSO ₄
6.5	-0.46	21	9.4 ^(b)	None
6.5	-0.16	19	1.7	PbSO ₄ ^(d)
6.5	+0.24	1.7	4.2	PbSO ₄ ^(d)
6.5	+0.84	20	6.3	Tetr. PbO
6.5	+0.94	3	19.6	Tetr. PbO
11	-0.51	18		None
11	-0.34	18.5	24.2	Tetr. PbO
11	-0.25	2.2	109	Tetr. PbO
11	-0.08	3.5	121	Tetr. PbO
11	+0.34	1.7	256	Tetr. PbO
11	+0.74	2.5	125	Tetr. PbO
11	+1.09	2	243	Tetr. PbO

(a) Final or steady current.

(b) Current flow in reducing direction.

(c) Dry sample spectrum indicated lead sulfate and orthorhombic PbO.

(d) Band at 451 cm⁻¹ abnormally intense.

Jordanov (11). Raman and infrared spectroscopic results indicate three ranges of potential: immunity, lead sulfate, and a lead sulfate-lead monoxide region.

At potentials below -0.26V , lead appeared to be immune to oxidation. An insoluble surface layer was not detected by *in situ* Raman spectroscopy, samples remained clean and shiny, and current flow was in the reducing direction. Previous reports show the lack of Raman spectra for PbO (1, 2). Thus if PbO were formed on the surface, none could be detected by *in situ* Raman spectroscopy. When samples exposed in this region were washed and allowed to dry, a non-uniform, light gray surface coating appeared. Infrared spectra identified the surface layer composition as lead sulfate and orthorhombic PbO . Raman spectra of dry sample surfaces confirmed this finding but showed that the sulfate and oxide were not found together but were occupying separate parts of the sample surface. The appearance of these compounds probably results from precipitation of dissolved lead compounds after removal of the applied potential (2). In the generally reducing conditions of this region, it is unlikely that any lead would be directly oxidized at the electrode surface during the potentiostatic exposure. The formation of PbO and lead sulfate is probably a result of the sample removal, washing, and drying process.

At potentials higher than the -0.23V wave of the polarization curve, net current flow was in the oxidizing direction and spectra showed that lead sulfate was formed. Oxidation at -0.26 and -0.02V resulted in PbSO_4 films.

Exposure at potentials higher than the wave at $+0.34\text{V}$ gave surface films identified as tetragonal PbO and PbSO_4 , in agreement with the findings of earlier research (11, 12). A Raman spectrum of the film in this potential region is compared with one of a purely PbSO_4 film and with the spectrum of reagent grade PbSO_4 powder in Fig. 3.

It was not possible to measure the relative amounts of PbO and PbSO_4 in the surface films from their spectra; just as it is impossible to measure film thickness. However, observation of strong tetragonal PbO spectra gave an indication of the thickness of films analyzed by these techniques. Ruetschi (9) developed a model for the PbO/PbSO_4 two-phase film formed by oxidation of lead in sulfuric acid solutions. He assumed that a surface film with a thickness on the order of a micron was needed before any underlying tetragonal PbO could form (4). Electrochemical measurements and calculations based on ion diffusivity in the films determined that a 24 hr exposure of lead in 4.2M H_2SO_4 in the range of $+0.2$ – $+1.1\text{V}$ would give a film consisting of 1 micron of lead sulfate covering 1 micron of tetragonal PbO . The ability to record strong spectra of the underlying layer of PbO gives indication that Raman and infrared spectroscopy can examine the entirety of films with thicknesses on the order of a micron.

pH 6.5 exposures.—The lead-water-sulfate Pourbaix diagram predicts that in a pH 6.5, 0.1M sulfate solution lead should be stable at potentials below -0.3V , PbO_2 should form above $+0.9\text{V}$, and PbSO_4 should be found at potentials in between. The lower transition was observed in the polarization curve for lead in the 0.1M K_2SO_4 solution used, but the transition to PbO_2 was not observed. The polarization curve shows a weak wave at $+0.06\text{V}$ which does not correspond to any feature of the Pourbaix diagram.

Potentiostatic exposures resulted in films with compositions which were in better agreement with the polarization curve than with the Pourbaix diagram. Exposure at potentials below the -0.27V wave resulted in immunity. Current flow was in the reducing direction, the surface remained clean and shiny, and no spectra were obtained in solution or in air. Higher potentials resulted in oxidation of the lead electrode and formation of insoluble surface films. Films con-

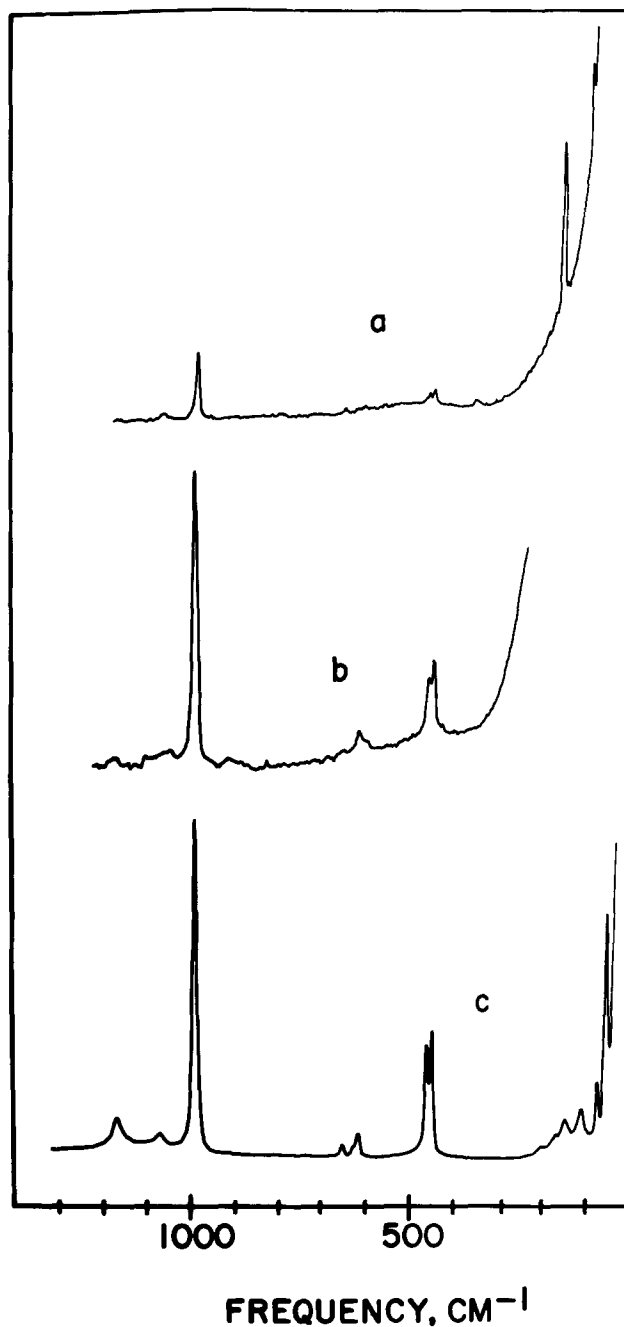


Fig. 3. Raman spectra of (a) lead in 0.1M H_2SO_4 after 20 hr at $+0.80\text{V}$, (b) lead in 0.1M H_2SO_4 after 18 hr at -0.26V , (c) PbSO_4 powder.

sisted of lead sulfate up to $+0.24\text{V}$ and, above that, tetragonal PbO covered the sample surfaces.

The formation of lead sulfate was in agreement with the Pourbaix diagram, but the PbSO_4 gave slightly different spectra from the sulfates examined previously. As shown in Fig. 4, the sulfate film gave an exceptionally strong 451 cm^{-1} Raman band, the band associated with the O-S-O bending vibration (13). Infrared reflection spectra also had a sharp band at 451 cm^{-1} as shown in Fig. 5. Such a vibration is not infrared active in normal sulfate compounds. The unusual intensity of the 451 cm^{-1} band is assumed to be due to a distortion of the normal lead sulfate lattice.

The broad wave at $+0.06\text{V}$ is near the potential where film composition changed from lead sulfate to tetragonal PbO , and it may be due to such a transition. Lead monoxide films were black in color and gave no evidence of the presence of sulfate. The transition from sulfate to PbO was not considered in cal-

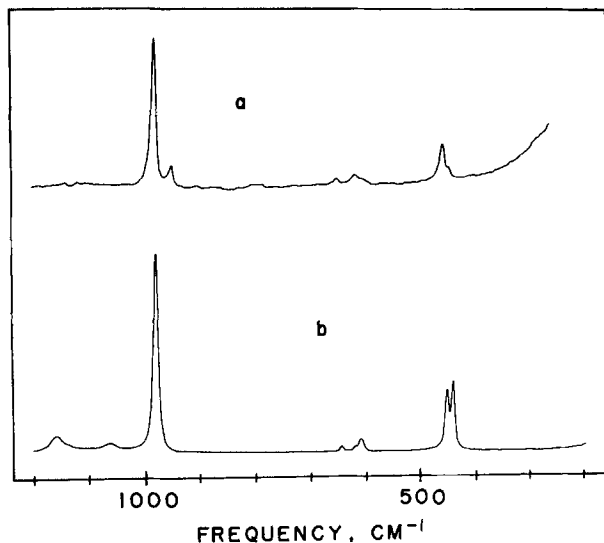


Fig. 4. Raman spectra of (a) lead surface after 19 hr at $-0.16V$ in $0.1M K_2SO_4$, (b) $PbSO_4$ powder.

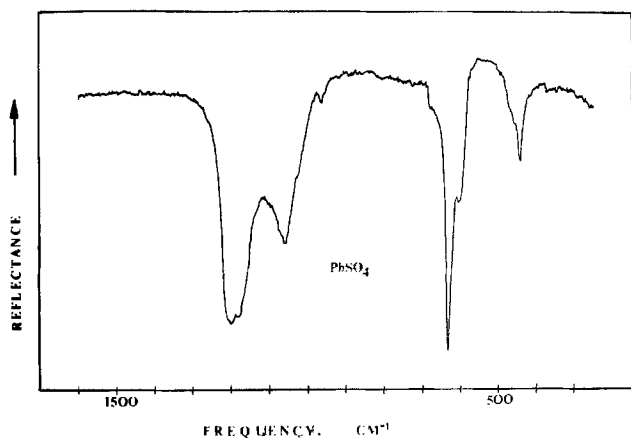


Fig. 5. Infrared reflection spectra obtained from lead exposed in $0.1M$ sulfuric acid, $pH = 0.9$, at $0.80V$ NHE for 20.5 hr (a) parallel polarization, (b) perpendicular polarization.

culating the Pourbaix diagram, since this reaction was not anticipated. No waves were observed at higher potentials and spectra did not indicate a change to the PbO_2 predicted by the Pourbaix diagram.

pH 11 exposures.—Oxidation of lead at a pH of 11 was predicted to form a basic lead sulfate, $PbO \cdot PbSO_4$, at potentials between -0.45 and $+0.50V$ and PbO_2 at higher potentials. The solution used, $0.1M K_2SO_4$ with enough KOH added to make the initial pH 11, resulted in a polarization curve with only one clear oxidation feature. The experimentally observed wave, or group of waves, at approximately $-0.30V$ represents the transition from lead stability to the formation of an oxidized species. The oxidative change seen above $+0.80V$ in Fig. 2 could represent a transition to a higher oxidation state, but it is probably due to the decomposition of water to evolve oxygen.

Potentiostatic exposures were conducted throughout the potential range where water is stable. As expected, exposure at low potentials gave extremely low current flow in the reducing direction, and no Raman bands were observed. Lead is immune to oxidation below the $-0.30V$ wave of the polarization curve.

All exposures at higher potentials resulted in the formation of tetragonal PbO surface films. An oxidation at $-0.34V$, a potential higher than the first lobe of the oxidative wave, resulted in a film which gave a strong tetragonal PbO spectrum. Although the wave

at $-0.30V$ seems to be made up of three separate waves, all exposures at potentials above $-0.45V$, where the current recorded in the polarization curve first became oxidative, formed tetragonal PbO .

Although the composition of the films was identified as PbO , Raman spectra recorded in solution were somewhat misleading. *In situ* spectra, as shown in Fig. 6, contained the strong bands of tetragonal PbO but also the $980 cm^{-1}$ band characteristic of the SO_4 symmetric stretching vibration and a broad band in the $450 cm^{-1}$ region. Except for the broadness of the $450 cm^{-1}$ band, these spectra look like a mixture of PbO and $PbSO_4$. Upon washing the samples thoroughly, however, those bands characteristic of sulfate disappeared. Dry sample spectra indicated only tetragonal PbO . The sulfate bands, which can be distinguished from those of $PbSO_4$ by the broad $450 cm^{-1}$ band (lead sulfate has two sharp bands in that region, at 439 and $451 cm^{-1}$), are due to the sulfate of the solution. The bulk sulfate solution gave the same sulfate spectrum. The change in the spectrum caused by washing the samples was evidence that spectra of both wet

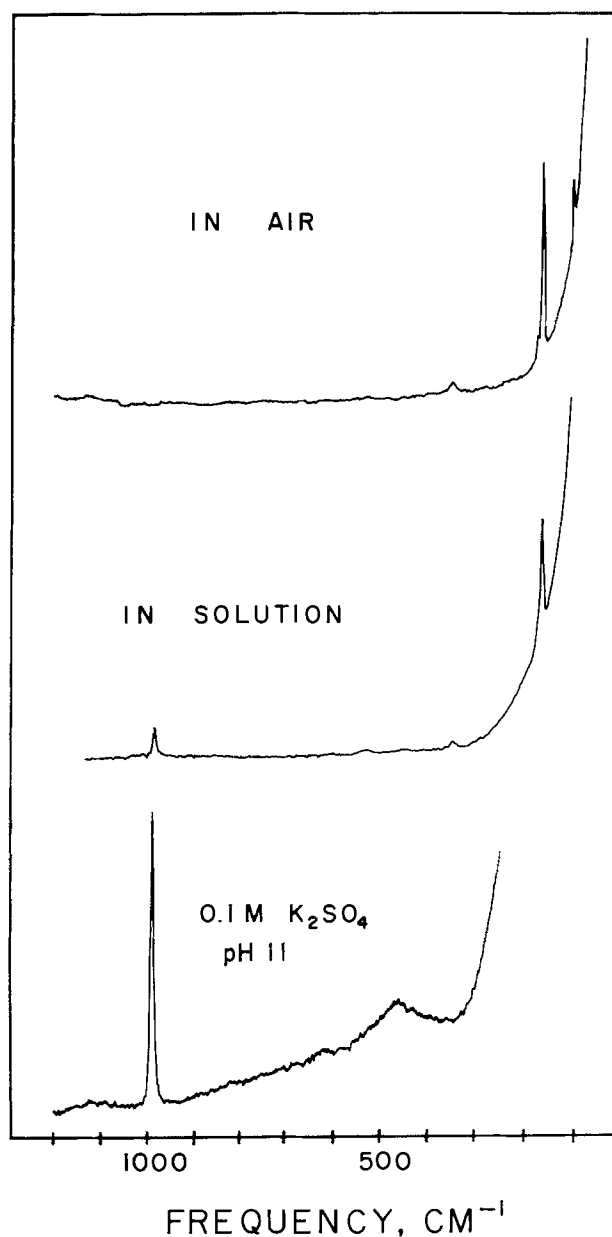


Fig. 6. Raman spectra of lead exposed to pH 11, $0.1M$ sulfate solution for 18.5 hr at $-0.34V$ recorded with the sample in solution and, after washing, in air; and the Raman spectrum of the pH 11, $0.1M$ sulfate solution.

and dry samples are needed to distinguish solution or adsorbed species from those compounds which were actually part of an insoluble surface film.

The possibility that the surface layer might consist of $\text{PbO}\cdot\text{PbSO}_4$ as predicted by the Pourbaix diagram calculations was investigated. Although spectra of the sample surfaces identified tetragonal PbO , Raman spectra of the basic sulfate are not available for comparison. Infrared reflection spectra confirmed that tetragonal PbO was the compound present. Comparison with published infrared spectra of $\text{PbO}\cdot\text{PbSO}_4$ (14) indicated that this compound was not present.

The oxidation currents recorded during potentiostatic exposures and potentiodynamic polarization curve measurements confirmed that lead sulfate forms more protective surface films than does PbO . In 0.1M sulfate solutions, all of which had approximately the same conductivity and ionic strength, conditions which caused the formation of PbO resulted in net current flow 5-10 times greater than that observed when PbSO_4 was formed. The smallest differences were noted in pH 6.5 exposures, a pH near the minimum of PbO solubility (15), but even in those conditions oxide films allowed measurably higher current flow than sulfate films. The ability of sulfates to form an insoluble, passivating film on lead is well known.

Film thickness.—Potentiostatic oxidation of vapor-deposited lead samples was conducted so that the thickness of the resulting films could be measured and their spectra recorded. While films of organic compounds on silver mirrors have shown that Raman spectra of films as thin as 50Å can be recorded (16, 17) and infrared spectra of oxide layers as thin as 10Å have been reported (18), the minimum detectable film thickness varies widely with the composition of a thin film.

A lead sulfate film, measured to be $2140 \pm 60\text{Å}$ thick, was formed by oxidation at +0.80V in 0.1M H_2SO_4 for 15 min. The Raman spectrum in Fig. 7 shows that the strong sulfate bands are clearly visible. The infrared spectrum of the same sample, shown in Fig. 8, is an excellent lead sulfate spectrum. Exposure of solid lead electrodes under identical conditions formed a film which consisted of both PbSO_4 and

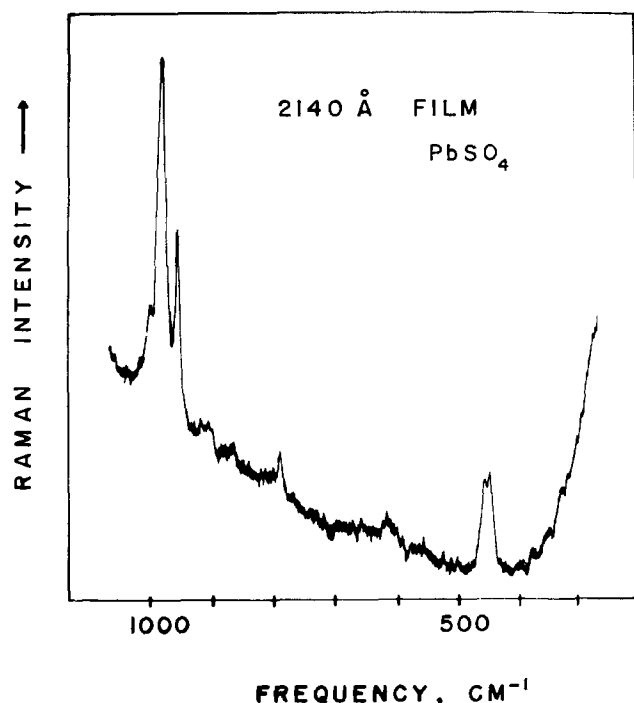


Fig. 7. Raman spectrum of a 2140Å thick film of PbSO_4 made from a vapor-deposited lead sample by exposure at +0.80V for 15 min in 0.1M H_2SO_4 . The features at 790 and 920 cm^{-1} are grating ghosts.

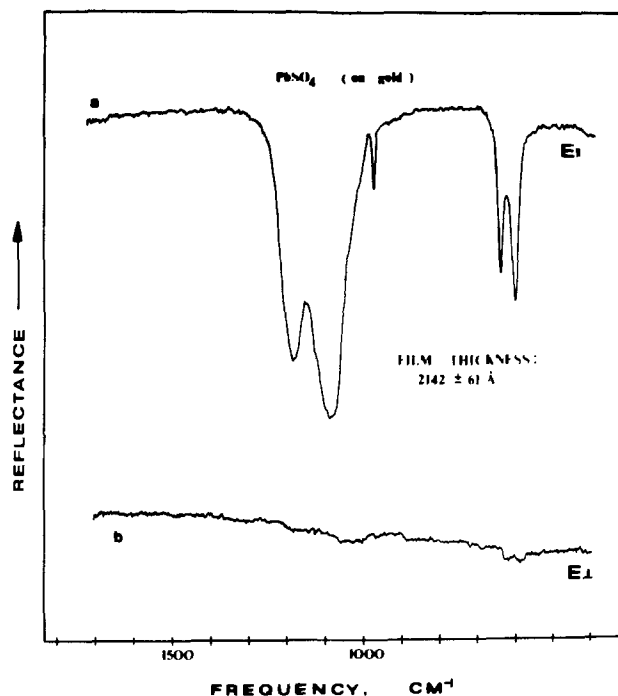


Fig. 8. Infrared reflection-absorption spectra of a 2140Å thick PbSO_4 film made from a vapor-deposited lead sample. The two spectra were recorded with two different polarizations of the infrared beam. For thin films only light with its electric vector parallel to the plane of incidence interacts with the surface species.

tetragonal PbO , but the vapor-deposited sample showed no trace of PbO . Presumably the thin sulfate film was not thick enough to provide the diffusion barrier necessary to allow formation of an underlying PbO layer (19).

It is estimated that a lead sulfate film approximately one-tenth of the 2140Å thickness would still give spectra with signal to noise ratios of two or more, the ratio considered necessary for observation of a band. Films as thin as 200Å should be identifiable by Raman and infrared spectroscopy with very little difficulty. Single spectrometer scans were used to record all spectra. Greater sensitivity to very thin films could be achieved by averaging the results of multiple scans. Signal averaging of more than one scan of the spectral region of interest would increase the signal to noise ratio observed and reduce the minimum detectable thickness (20).

Conclusions

In situ Raman spectroscopy and reflection-absorption infrared spectroscopy can conclusively identify the compounds present in thin corrosion product films on metal surfaces. Using these techniques, the Pourbaix diagram for lead in 0.1M sulfate solutions was examined and the surface species observed showed only partial agreement with predictions based on thermodynamic equilibria. Spectroscopic analysis of surface films during and after potentiostatic exposure in sulfate solutions was in excellent agreement with potentiodynamic polarization curves but the oxides and sulfates frequently formed were not those predicted in the Pourbaix diagram. The major difference was that tetragonal PbO was found experimentally in neutral and basic solutions and $\text{PbO}\cdot\text{PbSO}_4$, the compound predicted to be stable under such conditions, was not.

It has been shown that spectra of sample surfaces in solution and after drying are both needed to distinguish between spectral features due to solution species and those from compounds comprising insoluble surface films, just as they are both needed to determine if changes occur when samples are removed from solution. Measurement and estimation of film thicknesses

have shown that the Raman and infrared techniques can identify components in films as thin as 200Å and analyze the entirety of films as thick as 1 micron.

Acknowledgment

This work was sponsored by the Office of Naval Research.

Manuscript submitted Aug. 17, 1979; revised manuscript received Feb. 6, 1980.

Any discussion of this paper will appear in a Discussion Section to be published in the June 1981 JOURNAL. All discussions for the June 1981 Discussion Section should be submitted by Feb. 1, 1981.

Publication costs of this article were assisted by the University of Rhode Island.

REFERENCES

1. R. J. Thibeau, C. W. Brown, A. Z. Goldfarb, and R. H. Heidersbach, *This Journal*, **127**, 37 (1980).
2. R. J. Thibeau, C. W. Brown, A. Z. Goldfarb, and R. H. Heidersbach, *ibid.*, **127**, 1702 (1980).
3. E. S. Reid, R. P. Cooney, P. J. Hendra, and M. Fleischmann, *J. Electroanal. Chem. Interfacial Electrochem.*, **80**, 405 (1977).
4. P. Ruetschi and R. T. Angstadt, *This Journal*, **111**, 1323 (1964).
5. P. Delahay, M. Pourbaix, and P. Van Rysselberghe,

- ibid.*, **98**, 57 (1951).
6. P. Ness, *Electrochim. Acta*, **12**, 161 (1967).
7. J. Burbank, *This Journal*, **106**, 369 (1959).
8. D. D. Wagman, W. H. Evans, V. B. Parker, I. Halow, S. M. Bailey, and R. H. Schumm, NBS Technical Note 270-3, U.S. Government Printing Office (1975).
9. P. Ruetschi, *This Journal*, **120**, 331 (1973).
10. A. N. Fleming and J. A. Harrison, *Electrochim. Acta*, **21**, 905 (1977).
11. D. Pavlov and N. Iordanov, *This Journal*, **117**, 1103 (1970).
12. D. Pavlov, C. N. Poulieff, E. Klaja, and N. Iordanov, *ibid.*, **116**, 316 (1969).
13. K. Nakamoto, "Infrared Spectra of Inorganic and Coordination Compounds," p. 111, Wiley-Interscience, New York (1970).
14. H. W. Billhardt, *This Journal*, **117**, 690 (1970).
15. M. Pourbaix, "Atlas of Electrochemical Equilibria in Aqueous Solutions," NACE, Houston (1974).
16. R. G. Greenler and T. L. Slager, *Spectrochim. Acta*, **29A**, 193 (1973).
17. M. L. Howe, K. L. Watters, and R. G. Greenler, *J. Phys. Chem.*, **80**, 382 (1976).
18. R. W. Hannah, *Appl. Spectrosc.*, **17**, 23 (1963).
19. A. Z. Goldfarb, M. S. Thesis, University of Rhode Island (1978).
20. C. H. Warren and L. Ramaley, *Appl. Opt.*, **12**, 1976 (1973).

The Electrolyte-Silicon Interface; Anodic Dissolution and Carrier Concentration Profiling

C. D. Sharpe and P. Lilley

Electrical Engineering Laboratories, The University of Manchester, Manchester, M13 9PL, England

ABSTRACT

The electrical behavior of the NaF:H₂SO₄ electrolyte-silicon interface has been investigated. *I-V*, *C-V*, and anodic dissolution phenomena are discussed in relation to the feasibility of using the interface for the determination of carrier concentration profiles in silicon structures; specimen electrochemical profiles are presented and compared with corresponding spreading resistance profiles.

The object of the work described here was to establish the feasibility of measuring carrier concentration profiles of epitaxial silicon structures, with minimal restriction on the range of carrier concentration and depth, by the electrochemical capacitance-voltage technique (1); conventional *C-V* profiling is limited in depth by dielectric breakdown and, as for resistivity techniques, deep profiles require etch or angle lapping procedures.

The electrolyte-semiconductor interface includes a space charge region within the semiconductor surface adjacent to the electrolyte (2), and for certain overpotentials the interface approximates to a Schottky barrier. Recently *C-V* characterization of such a barrier, involving a GaAs electrode, has been combined with anodic dissolution of the semiconductor to yield semicontinuous carrier concentration profiles (1); an automated system is commercially available for profiling this compound.¹ In the case of silicon, Pham *et al.* have reported capacitance-depth profiles for shallow ion-implanted layers (3); a different measurement technique was used and the conversion factor relating capacitance and carrier concentration could not be established.

We have applied the basic measurement principles used for GaAs, namely simultaneous dissolution and *C-V* analysis, to semiconducting n-type silicon; the problem being to establish an electrolyte and suitable

operating potentials for (i) smooth and flat dissolution to depths in excess of 20 microns, and (ii) interface conditions approximating to a Schottky barrier, such that overall interface capacitance is given by

$$C = A (\epsilon\epsilon_0 n q / 2V)^{1/2} \quad [1]$$

where A is the interface area, and n the carrier concentration in the semiconductor at a distance W_D from the interface equal to the depletion width; the equation

$$W_D = \epsilon\epsilon_0 A / C \quad [2]$$

yields the depletion width.

To produce a carrier concentration profile, the dissolution depth W_R must be added to W_D . The dissolution current is integrated, to yield W_R by the Faraday relation

$$W_R = \frac{M}{DANF} \int Idt \quad [3]$$

where M and D are the molecular weight and density of the semiconductor, and N is an empirical number representing the electronic charge passing through the external circuit per molecule of semiconductor liberated.

Experimental Arrangement

The electrochemical cell included a silicon anode, carbon cathode, saturated calomel reference, and platinum (capacitance) electrodes. The silicon slice was

Key words: interfaces, electrolyte, semiconductors.
¹ Polaron Equipment, Limited, Watford, England.

held against the exterior wall of the cell, via a Teflon sealing ring, by a spring-loaded plunger; twin antimony-doped gold wires were incorporated in the plunger and gave low resistance ($\sim 10\Omega$) back-contacts to high doped material following a short 30V, 50 Hz pulse across them. Anodic dissolution was confined to an area A ($\sim 0.1\text{ cm}^2$) defined by the sealing ring. The SCE reference electrode was linked to the electrolyte in the vicinity of the silicon surface by a salt bridge and a fine capillary, the potential of the silicon electrode (cell potential) being measured by a high impedance differential amplifier connected between the second back-contact and the reference electrode. Potentiostatic control was achieved by comparing the cell potential with a reference voltage (variable), the error signal changing the current accordingly.

Illumination, necessary for n-type semiconductor dissolution, was provided by a 150W tungsten halogen lamp, via a copper sulfate infrared filter and short light pipe. Capacitance measurements were made with a Wayne-Kerr "Autobalance" bridge (1.5 kHz), a.c. coupled to the silicon and to the platinum electrode near the silicon surface. Both C-V and I-V characteristics of the silicon electrode were obtained dynamically, by ramping the reference voltage. A computed "best fit" to the C^{-2} -V information was used to obtain carrier concentration. The system was not fully automated, unlike the Post Office apparatus for GaAs (1) (which uses a two-frequency technique for increased resolution); for the purpose of this feasibility study an automated system was undesirable, tending to mask the detailed nature of the interface.

Electrolyte.—The criteria governing choice of electrolyte for an electrochemical profiling system are:

1. The C-V characteristic of the semiconductor-electrolyte interface must correspond to that of the space charge layer, i.e., effects due to Guoy and Helmholtz capacitance, and to surface states on the semiconductor, should be negligible. In practice, the former can be satisfied by using a concentrated electrolyte ($> 0.1M$).

2. The etched surface should be (a), smooth and (b), flat. If these criteria are not satisfied, errors are introduced into the profiles due to the averaging of depth information and consequent uncertainty in carrier concentration, particularly in the region of junctions. Similarly, gassing at the silicon electrode must be minimized.

3. The electrolyte should give a dissolution rate $> 1\ \mu\text{m/hr}$, to achieve profiles in a reasonable time.

The characteristics of several electrolytes interfaced with Si have been investigated; sodium fluoride/sulfuric acid has to a large extent satisfied the above criteria.

Experimental Results

Anodic V-I characteristics of the Si-H₂SO₄/NaF system.—For all specimens the dark rest potential was $-0.45 \pm 0.1V$ (relative to SCE) and photopotentials were -70 mV for n-type and 150 mV for p-type Si. Anodic V-I characteristics, obtained by scanning the cell voltage at a rate of 400 sec/V in the anodic direction, show a saturation current for both p- and n-type silicon. Figure 1 illustrates the effect of increasing fluoride content on the V-I characteristics of p-type silicon ($0.01\ \Omega\text{ cm}$). $0.05M$ sulfuric acid alone produced an approximately linear $V\text{-log } I$ characteristic, the high Tafel slope ($\sim 0.725\text{ V/decade}$) indicating that current was controlled neither by carrier supply nor reaction rate; rather, it was suggestive of current limitation by an oxide film at the interface, through which electrolyte ions must travel to reach the silicon surface. Small concentrations of sodium fluoride changed the characteristic to one with a slope tending to 60 mV/decade at low current, and caused the appearance of a well-defined peak in the current. As the NaF content was increased, the near exponential low current

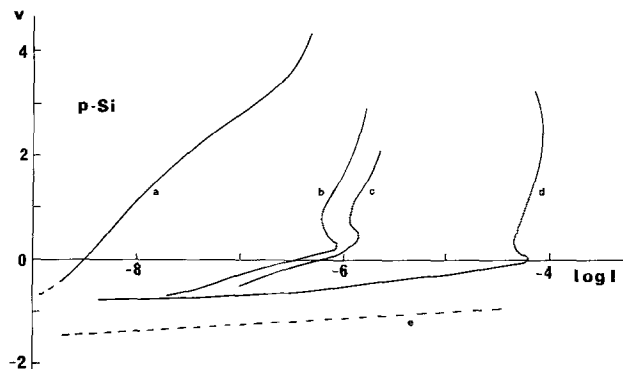


Fig. 1. The effects of increasing fluoride concentration on the V-I characteristics of the p-Si: NaF/H₂SO₄ interface (a) 0.05M H₂SO₄, (b) 0.05M H₂SO₄/0.05M NaF, (c) 0.05M H₂SO₄/0.1M NaF, (d) 0.05M H₂SO₄/0.2M NaF. ---- (e) represents a slope of 60 mV/decade .

region extended and approached $10^{-4}A$ at $0.2M$ concentration (a current level indicating a reasonable dissolution rate). Current levels below the peak were little affected by acid concentration, whereas above the peak, current increased with acid content.

As expected, illumination of the p-type electrode caused virtually no change in current; holes for dissolution being in plentiful supply. Illumination of low doped n-type Si, caused a large increase in current, due to increased hole concentration at the surface, whereas the behavior of heavily doped n-type silicon was characterized by a large dark current; such currents have been observed by Meek (4) for the Si-HF system.

Gas evolution was observed at both n- and p-type Si electrodes under anodic bias, reaching a maximum at or near the current peak. Although diminishing at higher voltage, evolution of gas continued at a slow rate even at $2V$ overpotential (bubbles noticeable on the surface after a period of several minutes).

Anodic dissolution of n-type silicon.—Currents below the saturation region gave a pitted etch, together with traces of a dark film, [as noted by Uhler (5) and others] which in some cases changed appearance after removal from the solution, finally resembling a dust on the surface. Samples etched in the current saturation region were considerably smoother, particularly under strong illumination, electrolytes with the higher acid content giving the smoothest etches, with few pits or spikes on the surfaces; however it was apparent that electrolytes with a high sodium fluoride content gave flatter etched surfaces in terms of gross uniformity over the whole of the exposed area. The $1M$ NaF: $0.05M$ H₂SO₄ electrolyte has been found to be a reasonable compromise and was used for the remaining experiments to be described, although deep etches ($> 10\ \mu\text{m}$) left a pronounced slope in one quadrant of the etched area (recently this problem has been overcome by pulsating the electrolyte near the Si electrode, a technique similar to jet etching generally used to improve the flatness of chemically etched pits).

A detailed discussion on the electrode reaction and transport kinetics is not appropriate in this paper. However two experimental observations, (i) that deep etched surfaces were nonplanar and (ii) that stirring increased the dissolution rate, leads us to suggest the mass transport in the electrolyte, in the vicinity of the Si electrode, plays an important role in the dissolution process.

The dissolution valence N has been estimated to be 3.50 ± 0.3 (by weight loss measurements on epitaxial n-type material) for the "standard" cell condition used for dissolution (cell potential $1.0V$, $0.05M$ H₂SO₄ + $1M$ NaF). This value has been used to establish profiles, irrespective of doping level and type. Recent work by Arita (6) has shown that for HF electrolyte/silicon the

dissolution valence is dependent on carrier concentration and type, in addition to illumination and current levels, varying over a range $2 < N < 4$. We are carrying out a corresponding investigation for the NaF: H₂SO₄ electrolyte, and intend to include the effects of crystallographic orientation on dissolution.

C-V characteristics for n-type silicon.—C-V graphs were obtained by scanning the cell potential between 0 and -0.6V at rate of 20 sec V⁻¹, about 10 sec after illumination was removed. The fast sweep rate, relative to that used for V-I plots, was preferable for two reasons. Firstly, the technique depends upon a 1:1 relationship between change in cell potential ΔV, and change in semiconductor space charge potential Δφ_s; a change in Helmholtz potential drop Δφ_H would distort this relationship. Since processes occurring in the Helmholtz layer are considerably slower than the relaxation time of carriers in the space charge region, Δφ_H is reduced by a fast change in cell potential. It would have been preferable to use a much faster rate than 20 sec V⁻¹; this figure represents a compromise between the above considerations and the response time of the measurement system (capacitance bridge and X-Y recorder). Secondly, it is important to minimize dark dissolution, in the case of n-type material, as this generally results in a pitted surface, particularly on heavily doped specimens.

The C-V data obtained from low doped n-type material was found to yield either inaccurate or ambiguous values for carrier concentration. Consider the C⁻²-V plot of Fig. 2(a). The data is a reasonable fit to the Schottky function with carrier concentration $n = 1.0 \times 10^{16} \text{ cm}^{-3}$ which, although the result was obtained from an encouragingly linear C⁻²-V plot, indicates a large error when compared with a quoted value of $4.5 \times 10^{15} \text{ cm}^{-3}$ for this specimen. In some cases, particularly at or close to the original surface, a well-defined "hump" appeared in the C-V curves (Fig. 3) being most pronounced at the original surface, and diminishing with dissolution depth; the C⁻²-V plot, corresponding to a dissolved depth of ~ 0.5 μm, shows two distinct slopes (Fig. 3). In other cases, although no definite hump in the C-V plot existed, two (or more) straight lines could be drawn through the C⁻²-V data; again this could occur at the surface or in the bulk of a layer. Figure 2(b) shows C⁻²-V results for which this phenomenon was particularly well defined (the steeper slope corresponds to a carrier concentration n of 8.6×10^{15} ; the shallower slope giving $n = 2.5 \times 10^{16}$; these are to be compared with a spreading resistance result corresponding to $1.2 \times 10^{16} \text{ cm}^{-3}$).

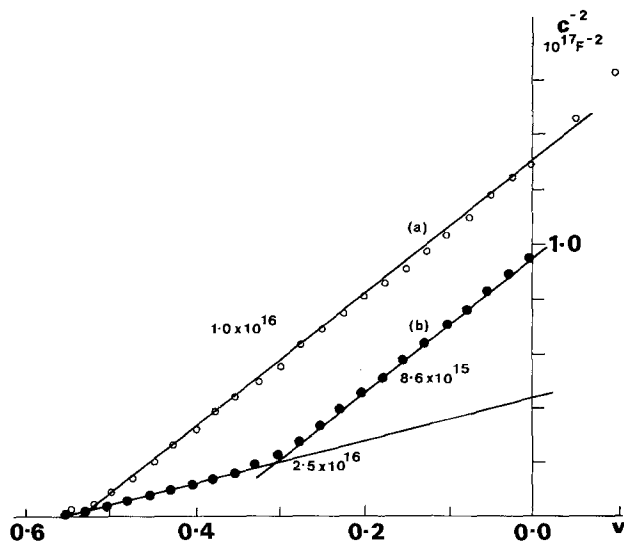


Fig. 2. C-V data and Schottky function best fit for two low doped silicon specimens, (a) quoted as $4.5 \times 10^{15} \text{ cm}^{-3}$, (b) spreading resistance estimate $1.2 \times 10^{16} \text{ cm}^{-3}$.

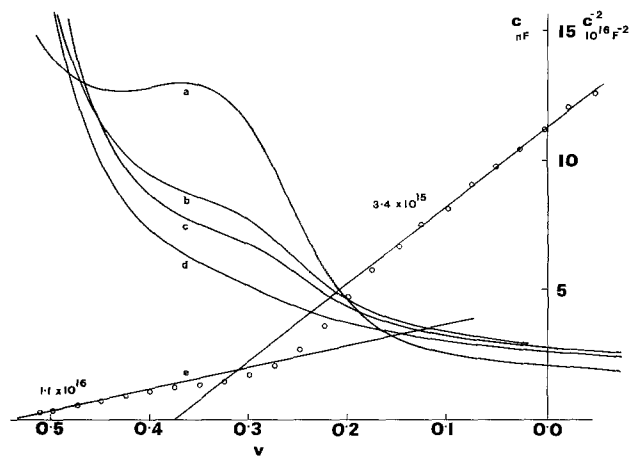


Fig. 3. C-V data from a low doped specimen at depths of (a) 0.0, (b) 0.05, (c) 1.5, (d) 3.5 microns, and C⁻²-V plot at 0.5 microns, ($N = 2.5 \times 10^{15} \text{ cm}^{-3}$ from spreading resistance).

In contrast, the C⁻²-V plots from highly doped material were usually linear, and gave values for carrier concentration in close agreement with those obtained from spreading resistance. Generally, high doped material did not provide the extensive problems associated with low doped material. A phenomenon related to this, is the difference in apparent flatband potential between high and low doped material; Dewald (7) reported a similar effect, both in magnitude and direction, for the ZnO electrode, and attributed the phenomenon to a change in metal-semiconductor (back contact) potential. This variation in flatband potential appears somewhat anomalous, since any shift in metal semiconductor contact potential should be balanced by an equal and opposite change in semiconductor-electrolyte contact potential, as the cell potential is not a function of Fermi level (8).

Generally, in the case of highly doped n-type silicon, the electrochemical result for carrier concentration was slightly lower than that obtained from spreading resistance measurement, this in contrast to the situation at low doping levels, where the electrochemical result was substantially higher. Ambridge and Faktor (9) noted a difference between resistivity measurements and electrochemical results on low doped GaAs. They attributed the differences to the presence of deep traps in the material. Under strong reverse bias (during anodic dissolution) the Fermi level may fall below such levels causing ionization of the traps. The space charge is then that due to both uncompensated donor atoms and ionized trap states. If the traps have long relaxation times, a measurement of the C-V characteristic is interrupted (as was the practice here) would show a Schottky curve corresponding to concentration $n' = n + N_t$, where N_t is the trap concentration. If however, the system was left at the equilibrium potential (low reverse bias, in the present case) for some time in the dark following dissolution, then the trap states could be neutralized by recombining electrons. A subsequent measurement of the C-V characteristic would therefore be expected to correspond to the "true" carrier concentration. This has been observed to be the case; a sample left at rest potential in the dark for 10 min following dissolution resulted in a value of $n = 2.4 \times 10^{15} \text{ cm}^{-3}$ for a specimen quoted as $2.5 \times 10^{15} \text{ cm}^{-3}$.

In some case, particularly on low doped material but not exclusively so, the C⁻²-V plots gave two parallel linear regions, suggesting a shift in potential distribution at the interface during the voltage sweep, which can be attributed to (i) a distinct fast surface state and/or (ii) a shift in Helmholtz region potential drop. Since it is unlikely that the surface state charge density is comparable with the space charge

density at high doping levels, it is suggested that the potential shift has origins primarily in the electrolyte side of the interface (i.e., the Helmholtz region). This is a very tentative explanation and it is important to note that a fast space-charge modulation technique (such as used in the gallium arsenide profiler) for determination of C-V data would be expected to exclude most of the effects due to the Helmholtz region potential change; though it might not exclude the effects of fast surface states, if such exist.

Profiling.—Profiling conditions for silicon, using the H_2SO_4/NaF electrolyte were: (i) a dissolution cell potential of 1.0V, (ii) C-V characteristics taken 10-15 sec after dissolution and illumination terminated, (iii) cell potential scanned at 20 sec/V in the cathodic direction, over a range 0.0 to $-0.6V$, to obtain a C-V characteristic. Investigation of C-V characteristics taken throughout single epitaxial layers indicated that consistent values for the carrier concentration could be obtained from the slope of the C^{-2} -V graphs at $-0.45V$ (relative to the SCE); although, as shown in the previous section, yielding excessive values for low doped material, this slope was used for the feasibility study, which also involved profiling multi-epitaxial structures.

A profile of a uniformly doped low resistivity substrate wafer is shown in Fig. 4(a); for depths to about 10 μm the measured values of carrier concentration are in close agreement with those obtained from spreading resistance, whereas at greater depths the uncertainty of the measured value increases due to excessive nonlinearity of the C^{-2} -V graphs. This problem was found to be associated with material crystallizing from the solution in the vicinity of the silicon electrode (x-ray fluorescence spectra indicated the deposit to be Na_2SiF_6); furthermore, slow gas evolution at the interface over long periods of time (hours) used for deep dissolution caused the formation of bubbles on the silicon electrode. Recently we have found that pulsating the electrolyte in the vicinity of the silicon electrode, at about 10 sec intervals, solves the deep dissolution problems.

One example of an epitaxial silicon structure profiled as described above (without pulsation) is shown in Fig. 4(b). The corresponding spreading resistance profile is also given for comparison; this clearly shows the large error at the low doping levels.

Recent investigation of G-V (shunt conductance-voltage) characteristics of the interface over the range of voltage used for the C-V characteristics has shown that in the region of $-0.45V$ the shunt conductance is changing rapidly with voltage (Fig. 5) whereas at

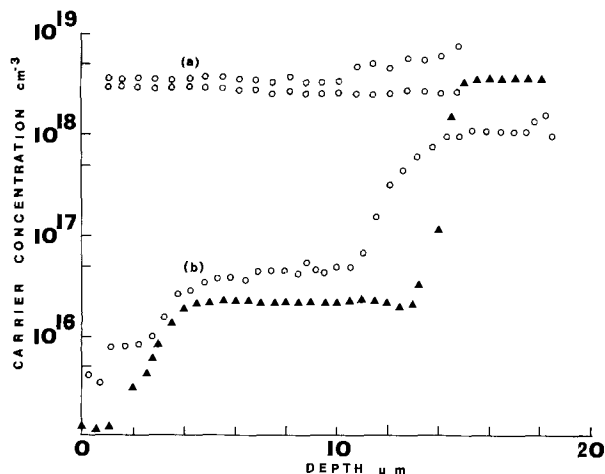


Fig. 4. Electrochemical carrier concentration profile of (a) uniformly doped silicon wafer (quoted as $3 \times 10^{18} cm^{-3}$), and (b) of a multi-epi wafer; experimental values (\circ) taken from C^{-2} -V plots with $-0.6 < V < 0.0V$. The triangles (\blacktriangle) represent the corresponding profile from spreading resistance.

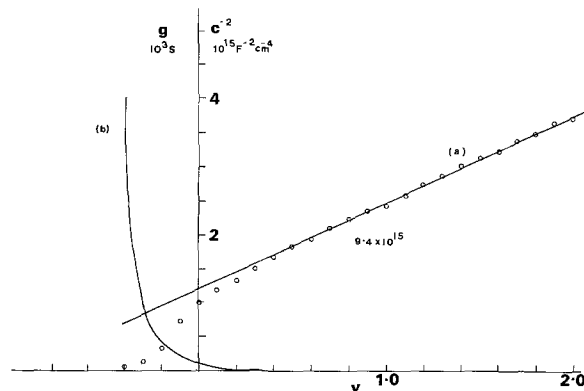


Fig. 5. (a) C^{-2} -V, and (b) G-V plots over a large voltage range $-0.5 < V < 2.0V$ for low doped silicon quoted as $1.2 \times 10^{16} cm^{-3}$.

potentials $> 0.0V$ the G-V characteristics are generally flat, the conductance being negligible (this may well be associated with a recombination current due to traps in the surface region, as discussed earlier). It became clear that detailed C-V characteristics were required at more positive cell potentials—the bridge quoted was unsuitable for this range of capacitance, and investigations were carried out on a Post Office plotter suitably modified for our cell configuration. Figure 5 shows a C^{-2} -V plot for the low doped specimen quoted as $1.2 \times 10^{16} cm^{-3}$; the trend towards lower estimates of carrier concentration as cell voltage approached zero continued into the positive region, finally giving close agreement with spreading resistance measurements.

Electrochemical profiles have been taken with a pulsed electrolyte and cell potential of $+ 1.0V$, using the two-frequency automated facility of the Post Office plotter (10); an example is shown in Fig. 6 along with a corresponding profile obtained from spreading resistance measurements, and indicates close agreement over a wide range of carrier concentration.

Conclusion

An investigation of I-V, G-V, and C-V characteristics of the silicon: H_2SO_4/NaF interface has shown that certain cell potentials can be used for deep dissolution and carrier concentration measurements. To obtain meaningful estimates of carrier concentration, ranging over several orders of magnitude, C-V measurements should be taken with the depleted surface heavily ($> 1V$) reverse biased. In that way we have

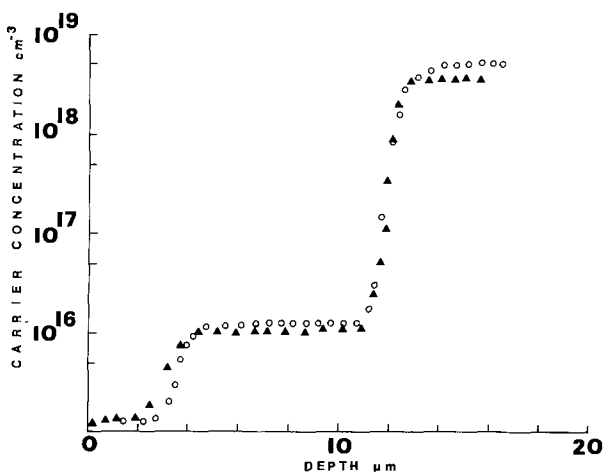


Fig. 6. Electrochemical profile of a multi-epitaxial silicon structure, taken by the Post Office Semiconductor Plotter, at a cell voltage of 1.0V, using pulsed NaF/H_2SO_4 electrolyte.

shown that it is possible to profile n-type silicon structures (10). The technique also appears to be suitable for p-type silicon structures, for which the conventional mercury probe C-V technique presents problems due to an inherently low barrier height. One of the most useful application areas has been found to be that of ion implantation, complimenting other (comparatively expensive) systems such as SIMS.

Acknowledgments

The authors would like to thank The Post Office Research Establishment, Ipswich, England for funds and facilities associated with this work, in addition to advice and encouragement from Drs. M. M. Faktor, T. Ambridge, and P. Arrowsmith of that organization.

Manuscript submitted Nov. 14, 1979; revised manuscript received Feb. 25, 1980.

Any discussion of this paper will appear in a Discussion Section to be published in the June 1981

JOURNAL. All discussions for the June 1981 Discussion Section should be submitted by Feb. 1, 1981.

REFERENCES

1. T. Ambridge and M. M. Faktor, *Inst. Phys. Conf. Ser.*, **24**, 320 (1975).
2. P. J. Holmes, Editor, "Electrochemistry of Semiconductors," Academic Press, London (1972).
3. M. T. Pham, *Phys. Status Solidi A*, **37**, 439 (1976).
4. R. L. Meek, *This Journal*, **118**, 437 (1971).
5. A. Uhlir, *Bell Syst. Tech. J.*, **35**, 333 (1956).
6. Y. Arita, *J. Cryst. Growth*, **45**, 383 (1978).
7. J. F. Dewald, *Bell Syst. Tech. J.*, **39**, 615 (1960).
8. J. I. Carasso and M. M. Faktor, in "Electrochemistry of Semiconductors," P. J. Holmes, Editor, Chap. 5, Academic Press, London (1972).
9. T. Ambridge and M. M. Faktor, *J. Appl. Electrochem.*, **4**, 135 (1973).
10. C. D. Sharpe, P. Lilley, C. R. Elliott, and T. Ambridge, *Electron. Lett.*, **15**, 622 (1979).

Faradaic Processes at the Ir/Ir Oxide Electrode

S. Gottesfeld*¹

Bell Laboratories, Murray Hill, New Jersey 07974

ABSTRACT

Faradaic reactions at the Ir/Ir oxide electrode provide information on the energy levels and the nature of electronic states in the electrochromic oxide. The rate of carrier injection and transport is found to depend strongly on the distribution of electronic levels in the oxide film and in the electrolyte. Conclusions can be drawn on the mechanism of charge injection and transport during electrochromic transients under small and large potential perturbations.

The electrochromic reaction in anodic iridium oxide (1-4) as well as rhodium oxide (5) films has been described recently. The anodic iridium oxide film exhibits a strong increase in light absorption (coloration) under anodic applied potentials in aqueous solutions and is reversibly bleached under cathodic applied potentials. Such reactions involve double ejection or injection of electrons and protons during the anodic or cathodic half-cycles, respectively (2). The kinetics depend, in principle, on the interfacial transfer and bulk transport of both electrons and protons through the oxide layer. Recent a-c impedance studies of the oxide-covered iridium electrode in acid solutions (6) showed that, for small potential perturbations ($\Delta V \sim 1$ mV), transport through the film is rate-controlling in the reversible charging process and the apparent conductance of the film (per unit area), $G_{a.c.}$, increases exponentially with the applied d-c bias. For an Ir oxide film with an ellipsometrically determined thickness of 1500 Å (7), $G_{a.c.}$ changes from $<10^{-2} \Omega^{-1} \text{cm}^{-2}$ for the completely bleached form at $V < 0.4V_{SCE}$ up to $10^2 \Omega^{-1} \text{cm}^{-2}$ for the colored form at $V = 1.0V_{SCE}$ (6). In an attempt to resolve the contribution of electron transfer and transport (ETR) to the total impedance in the electrochromic process, the faradaic reactions of some redox couples were examined at a rotating-disk (RDE) oxide-covered iridium electrode. Such reactions require only ETR through the film with no coupled ionic transfer or transport. Since these tests are conducted with the electrode immersed in the aqueous electrolyte, they reflect the properties of the unmodified active hydrous form of the electrochromic oxide film.

Results and Discussion

Figure 1 shows the current-potential curves for the $\text{Fe}(\text{CN})_6^{3-}/\text{Fe}(\text{CN})_6^{4-}$ couple obtained at the bare and at the oxide-covered iridium RDE in acid solutions. The oxide layer was grown to a thickness of ca. 1500 Å in a separate cell containing 0.5M H_2SO_4 , by the potential multipulsing technique described elsewhere

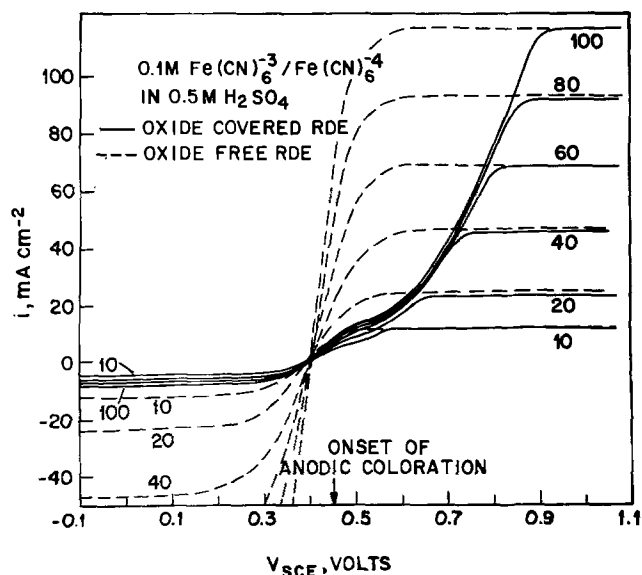


Fig. 1. Current-potential curves obtained at the Ir and the Ir/Ir oxide RDE with the $\text{Fe}(\text{CN})_6^{3-}/\text{Fe}(\text{CN})_6^{4-}$ in acid solutions. Scan rate -5 mV sec^{-1} . The square root of the rotational speed is designated in $(\text{rpm})^{1/2}$.

* Electrochemical Society Active Member.

¹ On leave from the Department of Chemistry, University of Tel Aviv, Tel Aviv, Israel. Present address for correspondence.

Key words: films, semiconductor, mobility, transport.

(2). The behavior of the redox couple at the bare RDE was regular (Fig. 1), exhibiting anodic and cathodic limiting currents directly proportional to the respective concentrations and also to $\omega^{1/2}$ up to $\omega = 10,000$ rpm. In the voltammograms obtained at the oxide-covered RDE three potential regions can be clearly distinguished in Fig. 1: At $V < 0.5V_{SCE}$ the limiting currents, i_L , in both the cathodic and anodic faradaic processes are "blocked," i.e., much lower than those obtained at the "bare" RDE. On the other hand, at $V > 0.9V_{SCE}$ the values of i_L obtained at the oxide-covered RDE are practically equal to those measured at the metal RDE for ω up to 10,000 rpm. The gradual transition of the film from a blocking to a nonblocking layer occurs in the intermediate potential range of 0.5–0.9 V_{SCE} . The onset of this transition coincides with the onset of anodic coloration. [The potential of the early anodic peak in the Ir oxide voltammogram (1) was chosen to designate the coloration onset in Fig. 1 and 2.] This coincidence demonstrates that the rate of ETR through the film increases in this case significantly with coloration. At $V > 0.9V_{SCE}$, where the oxide is strongly colored, charge exchange with the ferrocyanide ions occurs at the oxide-electrolyte interface and the high rate of ETR through the films allows bulk diffusion-controlled oxidation currents at bulk concentrations higher than 0.1M. On the other hand, the limiting currents in the blocking region at $V < 0.4V_{SCE}$ are not proportional to $\omega^{1/2}$ as expected for bulk diffusion-controlled currents, but rather converge upon a saturation level $i_{L,SAT}$ at high ω , as shown in Fig. 1. $i_{L,SAT}$ was found to be proportional to the bulk concentration and inversely proportional to film thickness. These results suggest that the current in the blocking region is limited by diffusion through the oxide film. The diffusing species may be the ferricyanide and ferrocyanide ions, which diffuse from solution through a pore network or through pinholes in the film, while the charge-transfer takes place at the metal substrate. The rate of the reactions of the ferri- or ferrocyanide ions at the bleached oxide in acid solutions is thus limited by ionic transport through pores in the film.

In contrast to the case presented in Fig. 1, high faradaic reduction rates were monitored at the bleached form of the oxide when redox couples with a higher oxidizing power (relative to that of the pH-dependent Ir couple) were employed. This behavior was found for the reduction of ceric ions in sulfuric acid solutions and for the reduction of the ferricyanide ion in alkaline solutions. In both cases there was no detectable difference between limiting reduction currents measured at the metal RDE and at the RDE covered with the bleached form of the oxide. The case of $Fe(CN)_6^{3-}$ reduction in 0.1M KOH is shown in Fig. 2.

The results of Fig. 1 and 2 demonstrate that the rate of ETR through the bleached film depends strongly

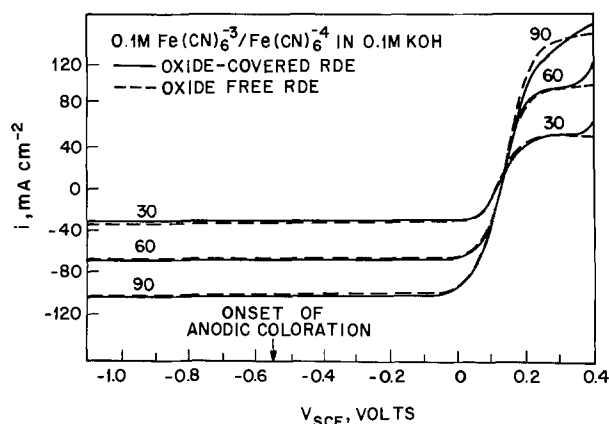


Fig. 2. Same as Fig. 1, in 0.1M KOH

on the relative positions of the electron energy levels in solution and in the oxide. Such a dependence, which was found before in many cases for semiconducting or insulating electrode materials (8), may serve as a source of information on the energy distribution and on the nature of electronic states in the oxide film. A schematic diagram of electronic states in the oxide in the relevant energy region, as suggested by the results of the ETR measurements, is given in Fig. 3. The basic features of this diagram are: (i) all the electronic states in the oxide which lie below (anodic to) the potential of the main current peak in the cyclic voltammogram ($E_p = 0.7V_{SCE}$ in 0.5M H_2SO_4 and $-0.35V_{SCE}$ in 0.1M KOH) belong to a band of extended states. This is most probably a metal-oxygen $d-\pi^*$ band, as proposed by Rogers *et al.* (9) for IrO_2 and identified by XPS measurements on pressed-powder IrO_2 samples (10). In the colored form these are the highest occupied electronic levels and the band is partially filled as in IrO_2 (9), allowing fast carrier transport through the colored oxide. (ii) During bleaching higher levels are gradually occupied, the band is filled, and the Fermi level in the oxide, $E_{F,OX}$, is shifted to more cathodic potentials, (higher electron energies). The density of the last levels which are occupied in the cathodic bleaching process, e.g., at $V < 0.6V_{SCE}$ in acid, is small, and their associated mobility is low as expected in a disordered solid for electronic states located close to a bandedge or in the bandgap (11). The fine-grained microcrystalline structure reported for anodic Ir oxide from x-ray diffraction measurements (12) suggests that the electronic structure of the colored form may be indeed related to that of crystalline IrO_2 (9), with modifications due to some loss of long-range order. In IrO_2 a complete

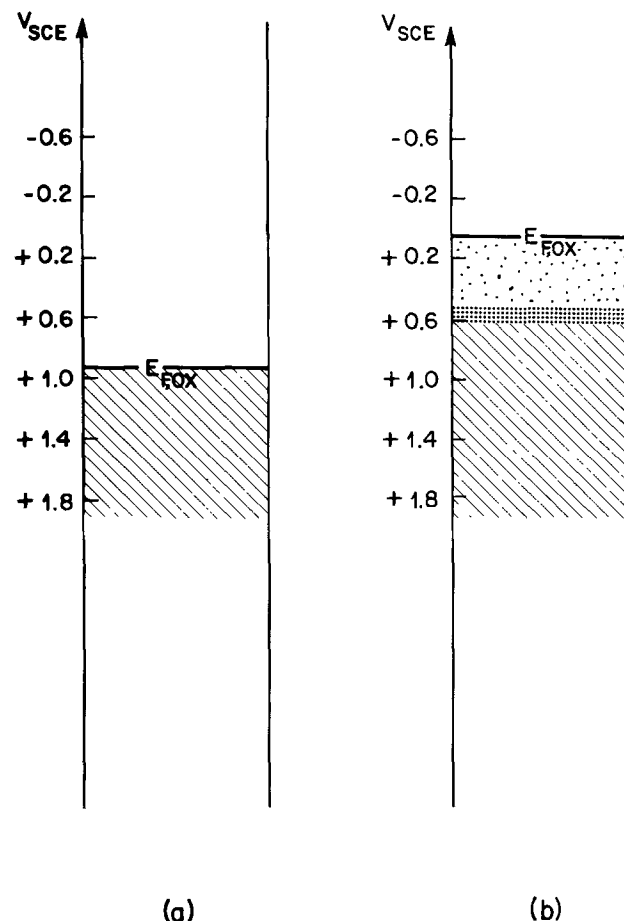


Fig. 3. Occupation of electronic levels in the colored (a) and in the bleached (b) forms of the Ir oxide electrochromic film. The hatched region designates occupied states in a band. The dotted region designates occupied states of lower densities and mobilities, located near the bandedge and in the bandgap.

filling of the $d-\pi^*$ band is expected when one extra electron is added per Ir atom, *i.e.*, when the formal oxidation state is lowered from IV to III (9). The assumption that bleaching involves only the filling of unoccupied levels with no accompanying variations of band structure may be an oversimplification, since the protons injected into the oxide during bleaching may, for example, split-off levels from the $d-\pi^*$ band to form a separate narrow band of localized states near $E_{F,OX}$. However, even according to the simple diagram in Fig. 3 it is possible to see why the states near $E_{F,OX}$ in the bleached film may be less dense and more localized, while the deeper states may still be forming a band associated with a higher mobility.

The results obtained for faradaic reductions at the bleached form of the oxide can be now understood in terms of the schematic diagrams in Fig. 3: when E_{Redox} is close to $E_{F,OX}$, charge injection has to take place at an energy level where the density of states in the bleached oxide is small and the mobility is low. Hence, low rates of both charge-injection at the oxide-electrolyte interface and charge transport through the bulk of the oxide are expected. This seems to be the situation for the reduction of $Fe(CN)_6^{-3}$ at the bleached oxide in acid solutions [see Fig. 4(a)]. If, on the other hand, the energy difference $E_{Redox}-E_{F,OX}$ is sufficiently large, holes can be injected into the lower lying more extended occupied electronic levels in the oxide. The density of states and the mobility in the band are higher and, therefore, the rates of both hole injection and hole transport through the bleached oxide are significantly enhanced. This is demonstrated schematically for the reduction of Ce^{+4} in acid in Fig. 4(b) and for the reduction of $Fe(CN)_6^{-3}$ in 0.1M KOH in Fig. 4(c). It is easy to see that the "hot hole" transport mode depicted in Fig. 4(b) and 4(c) requires that the hole trapping time in the bleached film be much longer than L/v , where L is film thickness and v the hole velocity in the band. A significant effect of trapping could not be detected even for films 10,000Å thick, at which the same unaltered diffusion-controlled currents were still recorded for the reduction of Ce^{+4} .

Optical measurements showed that the Ir oxide film was maintained in its bleached form in the presence of a stirred 0.1M Ce^{+4}/Ce^{+3} acid solution when subjected to potentials more cathodic than $0V_{SCE}$, *i.e.*, that the Fermi level in the oxide is determined by the potential applied to the metal. This means that high rates of hole injection and transport are indeed observed through the bleached film (Fig. 2), and that under the strong nonequilibrium conditions imposed the large potential drop is located in a narrow region at the oxide-electrolyte interface as assumed in Fig. 4, al-

lowing hole-injection into the lower lying levels in the bleached oxide.

The corrosion of the oxide during these hole injection processes was checked and found to be negligible during the short times required to record the current-potential curves. This is not very surprising considering that hole injection occurs into a d -band which has a relatively minor role in the bonding in this oxide (13), and that the oxide was kept under cathodic applied potentials during the measurement.

The faster ETR observed through the bleached film under strong nonequilibrium conditions may be significant in the mechanism of the electrochromic process: a high rate of charge transport is expected through the bleached form of the oxide at the onset of the coloration process, in spite of the low a-c conductance of the film, provided a large anodic perturbation, *e.g.*, a pulse of $1V_{SCE}$ in acid is applied. Under these conditions the rate of anodic coloration will be determined by the higher rates of injection and transport via lower lying extended states. This is shown in Fig. 5(a), which demonstrates hole-injection from the colored region of the film adjacent to the metal to the bleached part of the film adjacent to the solution following an anodic pulse. (This form of color gradient in the film is expected if the rate of electron transport is lower than that of proton transport.) Since $G_{a.c.}$ is measured at small perturbations, the low conductance obtained for the bleached form (6) is apparently due to the low density and mobility of states near $E_{F,OX}$, as demonstrated in Fig. 5(b). Comparison of Fig. 5(a) and (b) elucidates the lack of a unique correspondence between large and small signal measurements, as noted before (6).

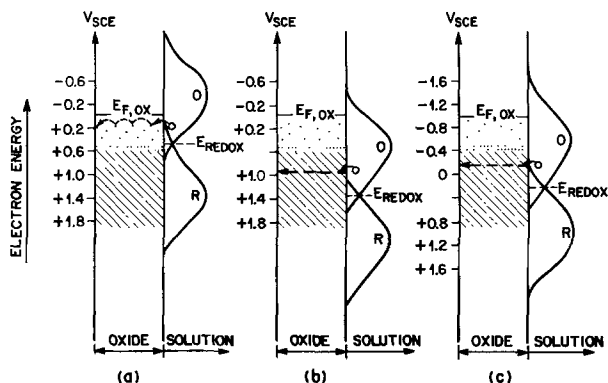


Fig. 4. Schematic electron energy diagram for the bleached oxide film and the redox couples in solution. Case (a) depicts the relative positions of electronic levels for $Fe(CN)_6^{-3}$ reduction in acid. Cases (b) and (c) describe the relative positions for Ce^{+4} reduction (in acid) and for $Fe(CN)_6^{-3}$ reduction in 0.1M KOH, respectively.

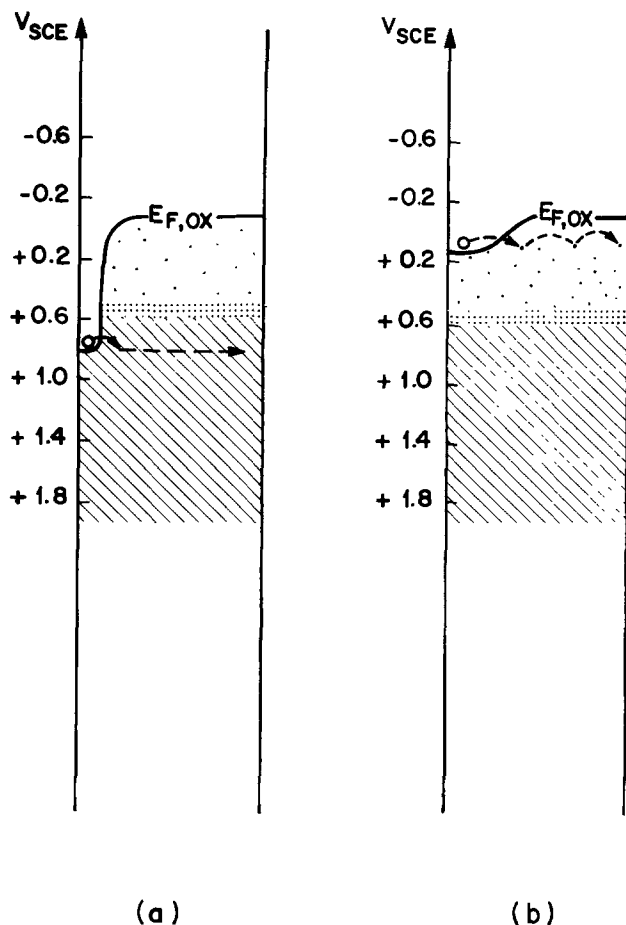


Fig. 5. Part (a) describes conditions for fast hole transport through lower levels in the bleached oxide during a coloration transient under large anodic perturbations. Part (b) describes the slower transport expected during a coloration transient under small anodic perturbations.

Acknowledgment

The author wishes to thank Barry Miller, D. E. Aspnes, and S. H. Glarum for valuable discussions.

Manuscript submitted Dec. 31, 1979; revised manuscript received March 14, 1980.

Any discussion of this paper will appear in a Discussion Section to be published in the June 1981 JOURNAL. All discussions for the June 1981 Discussion Section should be submitted by Feb. 1, 1981.

Publication costs of this article were assisted by Bell Laboratories.

REFERENCES

1. S. Gottesfeld, J. D. E. McIntyre, G. Beni, and J. L. Shay, *Appl. Phys. Lett.*, **33**, 208 (1978).
2. S. Gottesfeld and J. D. E. McIntyre, *This Journal*, **126**, 742 (1979).
3. G. Beni and J. L. Shay, *Appl. Phys. Lett.*, **33**, 567 (1978).
4. J. L. Shay, G. Beni, and L. Schiavone, *ibid.*, **33**, 942 (1978).

5. S. Gottesfeld, *This Journal*, **127**, 272 (1980).
6. S. H. Glarum and J. H. Marshall, *This Journal*, **127**, 1467 (1980).
7. S. Gottesfeld and S. Srinivasan, *J. Electroanal. Chem. Interfacial Electrochem.*, **86**, 89 (1978).
8. See, for example, S. N. Frank and A. J. Bard, *J. Am. Chem. Soc.*, **97**, 7427 (1975); W. P. Gomes and F. Cardon, *Z. Phys. Chem.*, **86**, 330 (1973); W. Mehl, J. M. Hale, and F. Lohman, *This Journal*, **113**, 1166 (1966).
9. D. B. Rogers, R. D. Shannon, A. W. Sleight, and J. L. Gillson, *Inorg. Chem.*, **8**, 841 (1968). For the evaluation of detailed band profiles and density of states in IrO_2 see L. F. Mattheis, *Phys. Rev. B*, **13**, 2433 (1976).
10. J. Riga, C. Ternet-Noel, J. J. Pieraux, R. Candano, and J. J. Verbist, *Phys. Scr.*, **16**, 351 (1977).
11. See, for example, M. H. Cohen, *J. Noncryst. Solids*, **2**, 4321 (1970).
12. D. Michell, D. A. J. Rand, and R. Woods, *J. Electroanal. Chem. Interfacial Electrochem.*, **84**, 117 (1977).
13. H. Tributsch, *This Journal*, **125**, 1086 (1978).

Anodic Etching of Defects in P-Type Silicon

H. Föll

IBM Thomas J. Watson Research Center, Yorktown Heights, New York 10598

ABSTRACT

A new etching technique for p-type Si has been developed which combines the advantages of chemical etching and EBIC. The method is electrochemical in nature and the silicon sample is biased as the anode in an electrochemical cell. The etching behavior of defects is governed by the magnitude of the applied voltage. At low voltages only electronically active defects are etched and the etching pattern corresponds to an EBIC image of the same area. At higher voltages all defects are etched and the etching behavior resembles chemical etching. The method offers considerable advantages as compared to EBIC and chemical etching.

Preferential chemical etching of defects in Si crystals with special chemical solutions ("etches") has been the most important technique for revealing defects in crystalline Si. An etching solution based on the HF-CrO_3 system which was first introduced by Sirtl and Adler (1) has been widely used in its original form or in modified versions (2-4) but etches based on the HF-HNO_3 system are also used (5, 6).

Despite the widespread use of these etches, it is not understood exactly how they work, *i.e.*, why, under certain circumstances, they attack certain defects with an etching rate different from that of the perfect crystal. This is illustrated, *e.g.*, by the remarkable difference in the etching behavior of the Sirtl-, Secco-, and Seiter-etch (1, 2, 4), all of which are based on the HF-CrO_3 system: whereas Sirtl etch works best on $\{111\}$ planes and not on $\{100\}$ planes, the Seiter etch is sensitive to all crystal planes except the $\{111\}$ plane. Finally, the Secco etch works on all crystal planes.

This lack of universality of most etches is no major drawback for the purpose of defect delineation in single crystals of Si because the crystal orientation and the kinds of defects which might be present usually are known. Thus the proper etch can be chosen and fine-tuned to the specific application without major problems [see Ref. (7) for an example].

The situation has changed with the advent of polycrystalline Si for photovoltaic applications in recent years. Neither the orientation of various grains nor the nature of defects to be expected is known: all kinds of dislocations, stacking faults, low- and high-

angle grain boundaries, and precipitates of impurities may be present simultaneously. Application of standard etching procedures thus may leave defects undetected or give different responses in different grains. Moreover, the response of grain boundaries to the various etches is not known.

Chemical etching gives information about the presence of certain defects, but no information about their electronic activity. Because the latter is the most interesting property of defects with respect to photovoltaics, additional experimental methods such as scanning microscopy in the electron-beam induced current (EBIC) mode have to be employed if electronic properties are to be studied.

This paper proposes a new etching method for p-type silicon which is based on electrochemical methods. It exploits the difference between the electrochemical potential of defects and the silicon matrix. Therefore, etching features can be related to electronic properties of defects. The same information about defects as obtained in EBIC measurements can be derived, making this method especially suited for the evaluation of polycrystalline Si. The method can be easily extended to all kinds of p-type Si crystals and possibly to other semiconductors.

Background: Electrochemistry of Silicon

If Si is anodically biased in an electrochemical cell and a suitable electrolyte is used, it will dissolve with a rate proportional to the current density (8-10). It has been shown that the dissolution process requires holes, therefore only p-type Si will dissolve anodically with ease. The silicon-electrolyte interface behaves in

many respects like a Schottky diode which is forwardly biased for p-type Si and reversely biased for n-type Si. Consequently, even with a rather high voltage applied to the electrochemical cell, n-type Si will not dissolve rapidly and the current density will be small (corresponding to the leakage current of a reversely biased diode). A space-charge region is built up at the Si-electrolyte interface and any defects present in this layer which are able to generate holes, may locally enhance the current density and thus the etching rate. This effect is known to provide a valuable tool for etching "electronically active" defects and has already been mentioned by Turner (8). Anodic etching of n-type GaAs has indeed been used for some time for defect detection and was shown to offer considerable advantages over chemical etching (11-13), but not until recently was it applied to the characterization of defects in n-type Si (14).

Anodic etching of defects in p-type semiconductors has not been attempted so far. Since holes are the majority carriers in this case, no influence of defects on the current density was expected. Moreover, a layer of so-called porous Si (8, 15) is frequently formed on the etched surface and this was believed to mask possible preferential etching of defects (14). While this is true for bias voltages larger than a few volts, it will be shown in this paper that at low bias voltages a very pronounced etching of defects occurs. In this case the silicon half-cell is operated around or below the threshold voltage for current flow in the forward direction (in the diode picture of the half-cell) and the presence of defects can substantially alter the current-voltage characteristic of the Si-electrolyte "diode." Moreover, the etching rate for a given defect is very sensitive to changes in the applied voltage and it is different for defects with different electronic properties. Therefore, by varying the applied voltage it is possible to probe the specimen for defects with different electronic activities.

Experimental

A very simple experimental setup was used for the present work. The electrolytic cell consisted of a plastic beaker, and a Pt wire was used as the cathode of the system. The solution was agitated by a magnetic stirrer and etching was usually performed at room temperature in the dark. No reference electrodes were used and measurements of currents and voltages were made with typical (low impedance) laboratory instruments.

The specimens used were polycrystalline silicon obtained by unidirectional solidification (16) with a resistivity of ~ 10 -20 Ωcm and silicon ribbons (17) with a resistivity of ~ 1 -2 Ωcm . The specimens were mounted on a metal stick and the back side contact was made by a drop of liquid Ga-In alloy. A good back side contact was found to be essential; earlier experiments using carbon- or silver-paste yielded irreproducible results. The specimen holder and the edges of the specimen were then covered with wax so that only the surface of the specimen was exposed to the electrolyte. The electrolyte was HF [49%] diluted with a 50:50 mixture of distilled water and absolute ethanol so that the HF concentration was typically 1-10%. If water alone was used as a dilutant, the etching was often inhomogeneous and spotty in appearance, probably because of wetting problems. A constant voltage power supply was used and the voltage applied ranged from -0.5 to $+20\text{V}$. The small negative voltages still biased the silicon anodically because the built-in voltage of the Pt-Si cell was around 0.7V.

Some of the specimens were subjected to electron-beam induced current (EBIC) measurements in a scanning electron microscope (18). The Schottky contact necessary to apply this technique was made by

evaporating 40-50 nm of Ti on the carefully cleaned sample surface.

Results

General observations.—The open-circuit voltage of the Pt-HF [5%]-Si system is about 0.7V; the silicon electrode is the positive terminal of the cell. A typical current-voltage curve is shown in Fig. 1 for poly-Si. Preferential etching of defects can be achieved in the region between -0.7 and $\sim 2\text{V}$. Figure 2 shows an example to illustrate the etching quality. The poly-Si specimen was etched ~ 40 min at 0V bias voltage (short-circuited cell); the current density was ~ 1.3 mA/cm² and ~ 3 μm of Si was removed during etching. Dislocations and grain boundaries are clearly visible; the dislocation etch pits are usually round or elliptical and can be very extended for dislocations running nearly parallel to the surface. Any surface damage is also revealed because only the top layer of the crystal was removed.

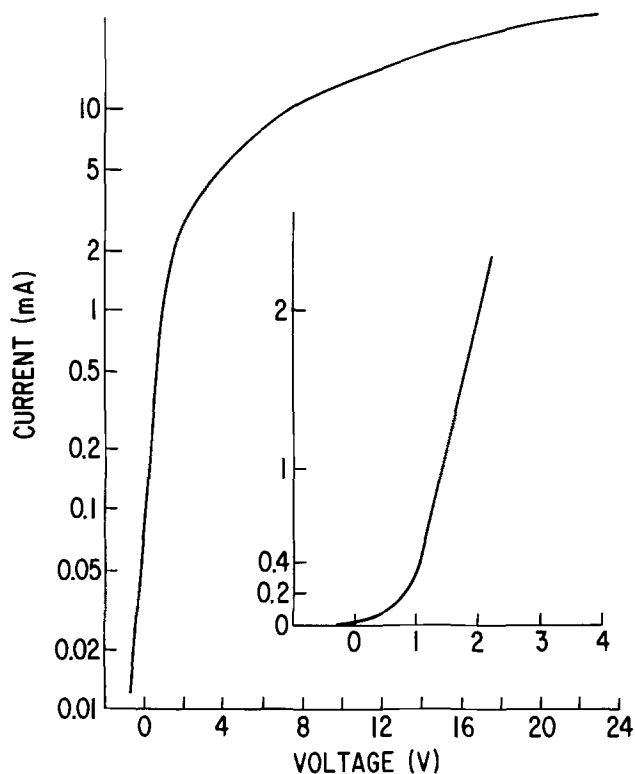


Fig. 1. Current-voltage characteristic for poly-Si in 5% HF. The inset shows the current-voltage characteristic for small voltages on a linear scale.

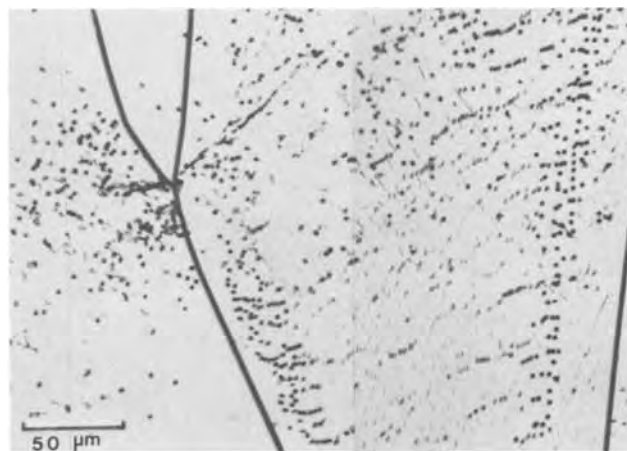


Fig. 2. Example of anodically etched poly-Si (40 min at 0V bias)

If a positive voltage $>2V$ is applied, only grain boundaries are revealed (Fig. 3). If the voltage is further increased, electro-polishing will eventually begin (around 15V, *e.g.*, for poly-Si in a 5% HF solution) and the surface appears to be structureless.

The voltage regions within which these characteristic features are observed depend somewhat on the HF concentration and on the resistivity of the samples. Higher HF concentrations and lower resistivities tend to shift the "critical" voltages to higher values.

It is important to note that grain boundaries may be visible after etching (including purely chemical etching) for two unrelated reasons: they may be preferentially etched, *i.e.*, a groove is formed (Fig. 4a) or they may be outlined as a step between two grains because the etching rate in the two grains was different (Fig. 4b). In general, a mixture between groove and step will prevail (Fig. 4c). It is only when an etch groove is formed that the boundary can be considered to be truly etched. It is not always possible to distinguish between the three cases but a decision can frequently be made if the etch pattern is sufficiently developed and a microscope with interference or Nomarski contrast is used at moderate magnifications ($\sim 200\text{-}800\times$).

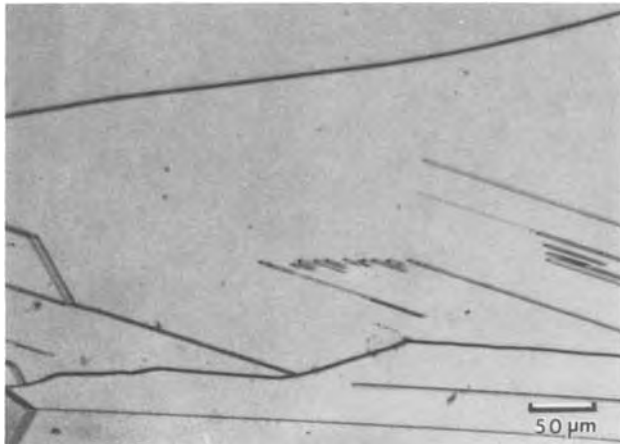


Fig. 3. Example of anodically etched poly-Si (1 min at 5V bias voltage).

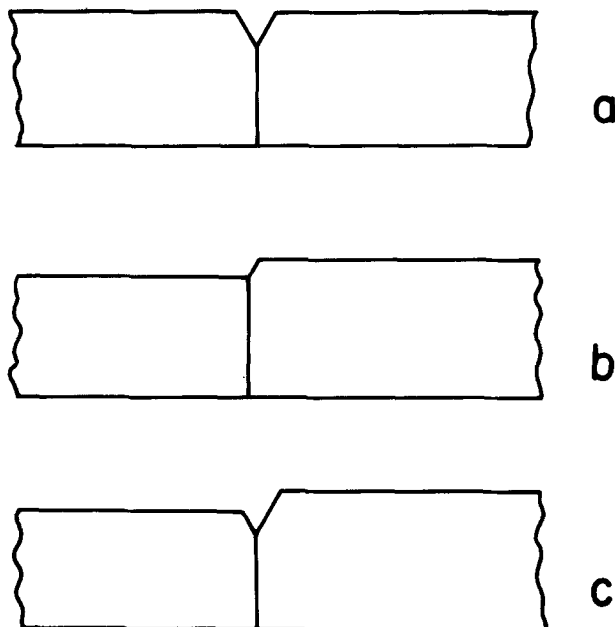


Fig. 4. Schematic outline of possible etching features at grain boundaries.

At low voltages the silicon surface is always covered with a thin layer of so-called porous Si (8, 15). This film mostly appears as a homogeneous layer displaying bright interference colors. Grains with different orientations may be outlined distinctly by this film because they appear in different colors due to a different film thickness. The etch pattern is visible through this film; it is however advantageous to remove it by transferring the specimen to a 1% solution of HF and by applying a voltage of $\sim 7V$ for 1-2 min. This treatment will always remove the colored layer without changing the etching pattern as has been ascertained in numerous cases. Other methods for removing the porous silicon layer are mentioned in Ref. (15) and may work as well, although they have not been tried in this case. Sometimes, particularly at very low or negative bias voltages, a rough-looking brownish surface appears instead of the colored film. This film could not be completely removed by the above treatment and the surface remains somewhat rough and covered with many small pits. This can be disturbing but does not seriously interfere with the defect etching pattern.

The voltage dependence of preferential etching.— In the low voltage region ($-0.7\text{-}\sim 2V$) the etching behavior of defects is strongly voltage dependent. Figure 5 shows directly neighboring parts of a silicon ribbon etched at 0V (Fig. 5a), $-0.4V$ (Fig. 5b), and $+0.5V$ (Fig. 5c) for 10, 20, and 5 min, respectively. Whereas it is safe to say that the nature and spatial distribution of defects did not change considerably in those parts of the sample probed at the three different voltages, the etching patterns look quite different. Especially if a small negative voltage is applied to the silicon electrode (in order to reduce the open-circuit voltage) many of the (twin) boundaries which were etched at 0 and $+0.5V$ are no longer revealed. Dislocations, however, are still preferentially etched and their density and distribution in Fig. 5b corresponds perfectly to those in Fig. 5a and c. Etching at 0 and $+0.5V$ produces similar patterns but dislocations running nearly parallel to the specimen surface are better revealed at $+0.5V$ than at 0V. These dislocations are also etched quite nicely in Fig. 5b. They are shorter, however, because in this case only $\sim 0.4\ \mu\text{m}$ of Si has been removed as compared to $\sim 2.1\ \mu\text{m}$ at 0V and $\sim 1.4\ \mu\text{m}$ at $+0.5V$. The sensitivity of the preferential etching, *i.e.*, the ratio between the etch-pit size and the amount of silicon which was dissolved, decreases with increasing voltage. At a voltage of

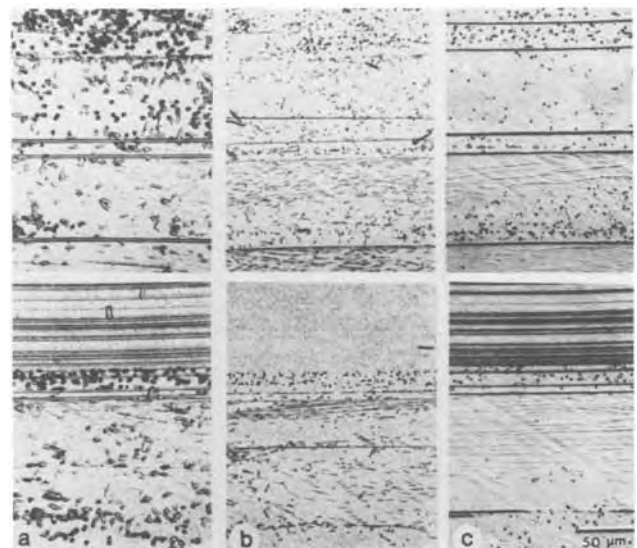


Fig. 5. Anodically etched Si-ribbon at (a) $+0.5V$, (b) 0V, and (c) $-0.4V$.

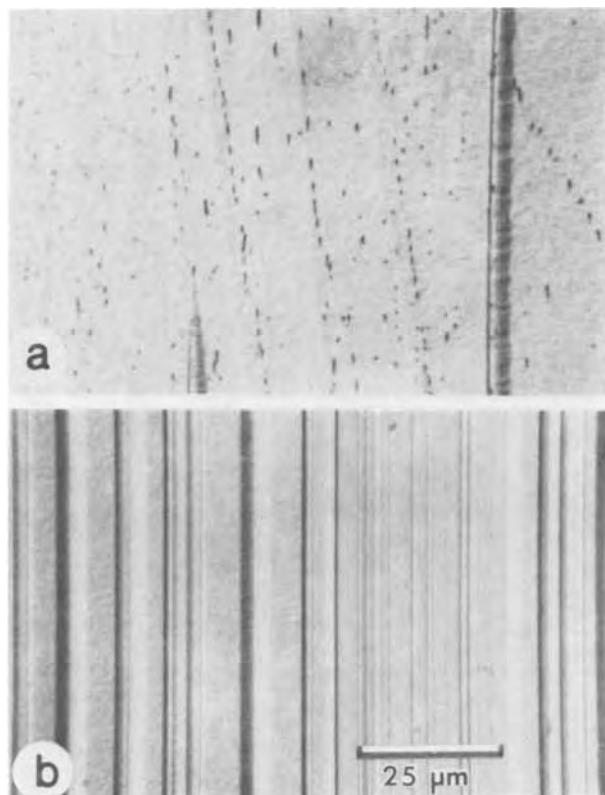


Fig. 6. Si ribbon etched at 5V. In (a) dislocation etch pits are still visible whereas in a neighboring area dislocations are no longer revealed.

5V only steps at grain boundaries are left. Figure 6a shows an intermediate case: pronounced steps have been formed at the boundaries but dislocations are only revealed as very small pits. In neighboring grains dislocations are no longer etched at all, showing that the changeover is somewhat orientation dependent (Fig. 6b).

Geometrically shaped etch pits [as found, e.g., with Sirtl (1) or Wright (3) etch] have never been observed, indicating that etching occurs on all crystallographic planes with comparable etching rates.

Comparison with chemical etching and EBIC.—Figure 7 shows the same area of a poly-Si sample anodically etched at $-0.4V$ (Fig. 7a), $+0.4V$ (Fig. 7b), and with Sirtl etch (Fig. 7c). Although more spectacular examples could have been chosen, these pictures demonstrate several points: (i) Sirtl etch did not attack all the twin boundaries present, whereas anodic etching does. (ii) Although the etch-pit patterns

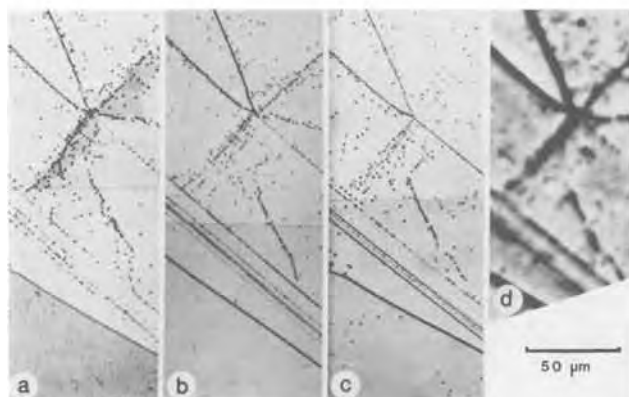


Fig. 7. Comparison between anodic etching, Sirtl etching, and EBIC in poly-Si. For details see text.

for dislocations seem to correlate fairly well between Fig. 7a-c (allowing for unavoidable changes in the distribution because several microns of the surface had to be removed between successive etching steps) there are differences: Fig. 7a shows that dislocations are present in the outermost twin boundary which are missing in Fig. 7b and which are only poorly resolved in Fig. 7c. This may indicate that the etching properties of dislocations depend on their type. (iii) In Fig. 7a the colored layer has not been completely removed; it can be seen that it does not interfere with the observation of the etching pattern. (iv) The EBIC picture of the same area (Fig. 7d) corresponds better to Fig. 7a than to Fig. 7b and c.

Similar behavior can be observed for Si ribbons. Figure 8 shows a Sirtl-etched area next to an anodically etched one. With one exception the twin boundaries are not visible in the anodically etched part of the sample.

Secco-etched samples may show a better correlation to anodically etched ones because dislocations on all crystal planes are revealed. With respect to boundaries it appears to work similar to Sirtl etch. Interestingly, Secco etch applied to ribbons sometimes left a rough surface full of small pits very similar to the rough surface sometimes obtained with anodic etching.

It has been shown that twin boundaries, especially coherent twin boundaries in Si ribbons, often do not significantly influence the electronic properties of the crystal, e.g., the carrier collection efficiency of a solar cell (19). Because twin boundaries can be made to disappear completely in anodic etching there seems to be a correlation between their electrical activity in solar cells and their anodic etching behavior. Both ribbon and poly-Si samples were therefore subjected to a test of the electrical activity of their defects using a scanning microscope in the EBIC mode. Figures 9 and 10 show some results, another example was already given in Fig. 7. The correspondence between the EBIC pictures and the anodic etching pictures is one-to-one for a negative bias voltage of the sample. This has been observed in many more cases than can be shown here. It is particularly interesting that the few twin boundaries out of a whole bundle which show electrical activity in EBIC are also revealed in the anodic etching whereas the electrically inactive twin boundaries appear only at higher etching voltages. Figures 9 and 10 show that the etch pattern is much clearer than the EBIC picture thus allowing a more detailed interpretation of the electrically active defects.

Discussion

Enhanced dissolution rate of defects.—The dissolution rate of a given area of Si is proportional to the current passing through it, i.e., the current density.

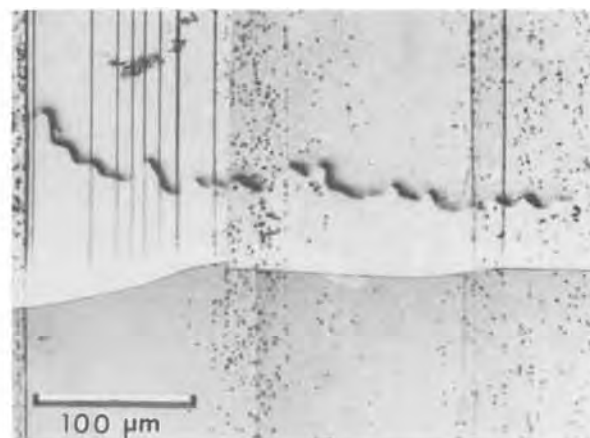


Fig. 8. Comparison between anodic etching and Sirtl etching in ribbon Si.

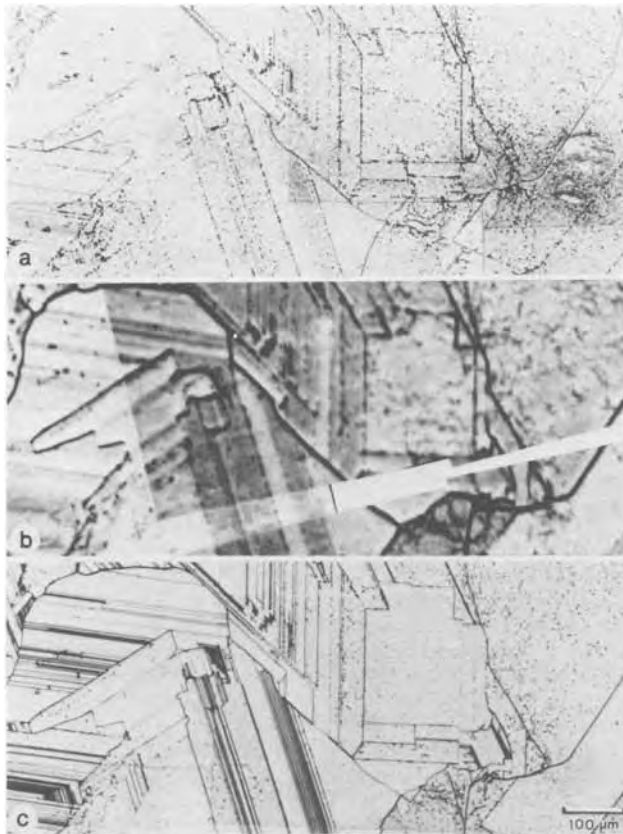


Fig. 9. Poly-Si etched anodically at $-0.4V$ (a) and with Sirtl etch (c). Figure 9(b) shows the EBIC image of this area.

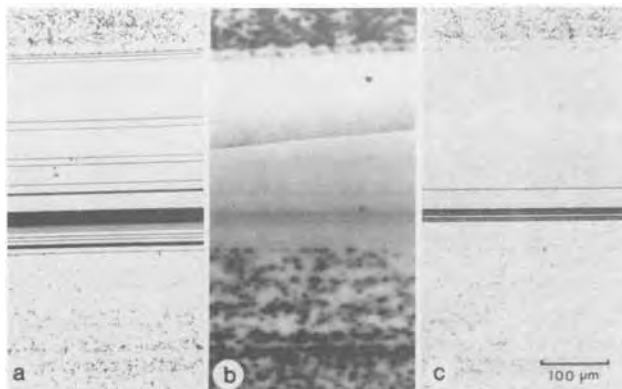


Fig. 10. Comparison between anodic etching at $+0.5V$ (a), EBIC (b), and anodic etching at $-0.4V$ (c) in ribbon-Si.

Preferential etching of defects thus requires higher current densities at the intersection of defect and surface as compared to the undisturbed surface. The current density at a given voltage depends on several factors; the most important ones are the resistance of the electrolyte, the generation and transfer of charge at the silicon-electrolyte interface, and the bulk properties of the silicon.

At high voltages the current density is limited by the resistance of the electrolyte only and practically does not depend on any specific interface or bulk properties of the silicon. The current density across the interface is governed by the HF concentration, thus electropolishing will occur.

At intermediate voltage ranges pronouncedly different etching rates are observed for different surface orientations. This demonstrates that surface properties are dominating the current density in this voltage

region. This is in general agreement with the observation that the holes required for the dissolution process are generated in the near-surface regions rather than in the bulk of the Si (9). This is in contrast to Ge where holes from the bulk are diffusing to the interface. The concentration of holes generated near the surface is related to the bulk concentration and their flow across the interface is not inhibited since the band-bending introduced by the applied voltage favors the flow of current.

At very low or negative applied voltages the bulk concentration of holes (and the surface concentration related to it) is no longer important. This is demonstrated by the fact that the potential current curves for p- and n-type Si are almost identical for small applied voltages, i.e., for small overpotentials (15). The current density for n-type Si of low overpotentials can be even higher than that of p-type Si (15), indicating a possible surface inversion-layer. Thus it appears that not the availability of holes but their transport across the interface is rate determining. In other words, potential barriers between hole states in the semiconductor and in the electrolyte may exist, making current flow difficult. Defects may introduce additional transition possibilities for holes to the electrolyte.

A full understanding of the current-potential curves of semiconductors with and without defects requires a sophisticated theory which is beyond the scope of this paper. Phenomenologically, the difference in etching rates for defects and for perfect material can be described by appropriately chosen voltage-current characteristics. From the limited number of experiments performed so far a rough idea of these characteristics can be derived; this is shown in Fig. 11. Comparing these curves to characteristics given in (15), it is clear that defected areas in p-type Si behave as p⁺-type Si. In other words, defects in p-type Si behave like p⁺-type material; this is in accordance with the general view of the electronic properties of defects in Si, cf. various papers given in Ref. (20).

Dislocations and grain boundaries other than twin related boundaries appear to be etched under most conditions although they may show some voltage dependence as illustrated in Fig. 7. Thus they are strongly electronically active and this is related to the states in the bandgap introduced by them (20, 21). Most twin boundaries, on the other hand, are not etched at small negative voltages. This may indicate that no electronic states in the bandgap are associated with them. However, the fact that they are preferen-

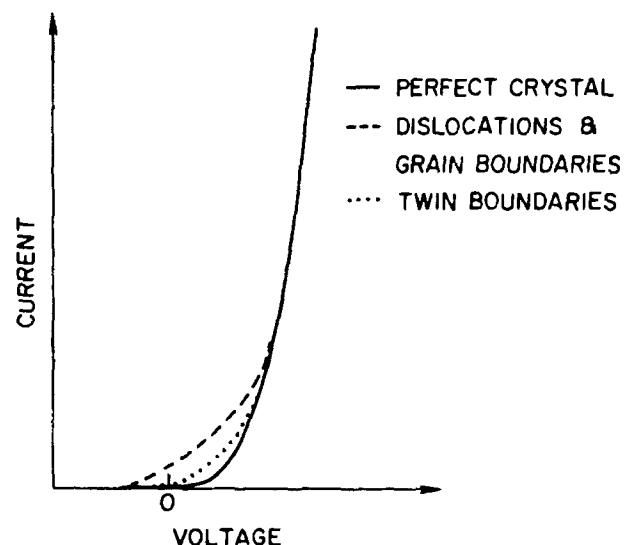


Fig. 11. Tentative current-voltage curves for various defects

tially etched at small positive voltages [scanning electron microscopy showed that true etch grooves and not steps were formed (Fig. 12)] indicates that they do influence the electronic structure of the semiconductor to some extent. This might be due to a change in the surface states around the twin boundaries rather than to states in the bandgap. It may also explain why chemical etching usually does attack twin boundaries and stacking faults (which are closely related defects) although these defects do not have an appreciable strain field or electrical (bulk) activity and cannot always be assumed to be decorated with impurities.

The correspondence between EBIC and anodic etching at negative voltages is striking, even for fine details. This indicates that anodic etching essentially probes the same properties of the defects as EBIC does, namely their ability to act as carrier recombination or generation centers. Of particular interest here is the observation that certain twin boundaries may be electronically active while others are not. This was attributed to the presence of dislocations in these boundaries (17) but this could not be confirmed in the present work.

Chemically etched specimens looked similar to specimens etched anodically at a certain voltage. It appears that Secco etch corresponds roughly to anodic etching at ~ 0 -1V and Sirtl etch to somewhat higher voltages. Since chemical etching is also an electrochemical reaction, the present experiments may lead to a better understanding of their operation.

Some remarks on the applicability of the method.—Anodic etching offers a simple and elegant way to obtain defect information about defects in Si which usually would require EBIC and chemical etching. It has considerable advantages compared to EBIC, the setup and the preparation is simple as compared to the rather complex specimen preparation and equipment needed for EBIC. The resolution is much better for anodic etching and large areas can be etched and inspected in a short time. On the other hand, EBIC is nondestructive and can be made quantitative whereas anodic etching requires the dissolution of a thin surface layer ($\leq 1 \mu\text{m}$) and is as yet not quantitative.

Anodic etching can replace chemical etching if the correct voltage is chosen. The sensitivity seems to be better than that of most chemical etches and there is no ambiguity about the selectivity of the etching with respect to certain surface orientations or certain defects.

It is important to note that the method is not restricted to p-type Si; n-type Si can be anodically

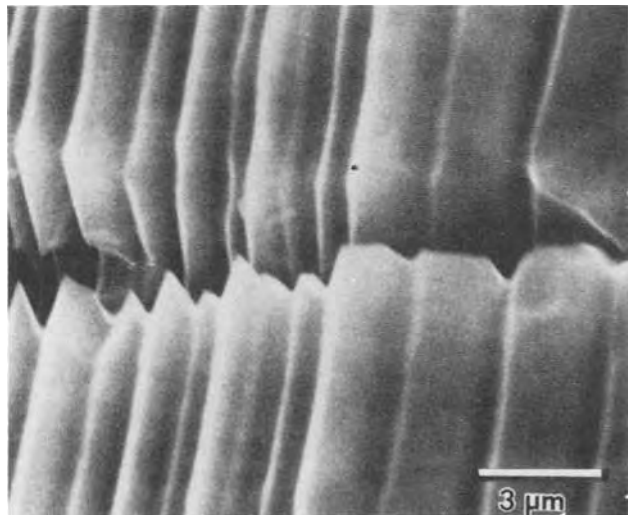


Fig. 12. SEM picture of etch-grooves at twin boundaries crossing a scratch-mark in ribbon Si after anodic etching at +0.5V.

etched in much the same way as was already demonstrated in Ref. (14). Moreover, the method very likely can be applied to any semiconductor if a suitable electrolyte can be found. This might be difficult, but certainly it is less so than the development of a chemical etch.

It is felt that the method could be made quantitative if a better theoretical understanding of the basic process could be achieved and if quantitative experimental results could be supplied. The latter would involve precise measurements of the Si-potential-current relationship rather than simple voltage-current characteristics and should also define the role of the resistivity of the Si.

Conclusions

1. Defects in p-type Si can be etched anodically and their etching behavior depends on the applied voltage.
2. At very low potentials only defects are etched which would be classified as "electrically active" by EBIC.
3. At somewhat higher potentials the etching is similar to chemical etching but is more sensitive and free of ambiguities.
4. Anodic etching has the potential to develop into a powerful technique for defect characterization in many semiconductors for both p- and n-type and can widely replace EBIC and chemical etching.

Acknowledgments

Thanks are due to C. F. Aliotta who was of great help during the EBIC investigations, to S. H. Libertini who helped make the EBIC samples, and to G. H. Schwuttke who supplied the Si samples used in this study. J. L. Deines provided unpublished details of his study; this is gratefully acknowledged.

Manuscript received Jan. 23, 1980.

Any discussion of this paper will appear in a Discussion Section to be published in the June 1981 JOURNAL. All discussions for the June 1981 Discussion Section should be submitted by Feb. 1, 1981.

Publication costs of this article were assisted by IBM Corporation.

REFERENCES

1. E. Sirtl and A. Adler, *Z. Metall.*, **52**, 529 (1961).
2. F. Secco d'Aragona, *This Journal*, **119**, 948 (1972).
3. M. Wright Jenkins, *ibid.*, **124**, 757 (1977).
4. H. Seiter, in "Semiconductor Silicon 1977," H. R. Huff and E. Sirtl, Editors, p. 187, The Electrochemical Society Softbound Proceedings Series, Princeton, N.J. (1977).
5. D. G. Schimmel, *This Journal*, **123**, 734 (1976).
6. W. C. Dash, *J. Appl. Phys.*, **27**, 1193 (1956).
7. L. I. Bernewitz and K. R. Mayer, *Phys. Status Solidi A*, **16**, 579 (1973).
8. D. R. Turner, in "The Electrochemistry of Semiconductors," P. J. Holmes, Editor, p. 155, Academic Press, London and New York (1962).
9. E. A. Limou and I. G. Erusalimchik, "Electrochemistry of Ge and Si," Translated by A. Peiperl, The Sigma Press (1963).
10. A. K. Vijh, in "Encyclopedia of Electrochemistry of the Elements," A. J. Bard, Editor, p. 287, Marcel Dekker, Inc., New York and Basel (1976).
11. H. M. Faktor and J. L. Stevenson, *This Journal*, **125**, 621 (1978).
12. R. M. Redstall, J. C. Reguault, and J. L. Stevenson, in "Semiconductor Characterization Techniques," P. A. Barnes and G. A. Rozgonyi, Editors, p. 296, The Electrochemical Society Softbound Proceedings Series, Princeton, N.J. (1978).
13. K. Takahashi, *Jpn. J. Appl. Phys.*, **18**, 1741 (1979).
14. J. L. Deines, J. W. Philbrick, M. R. Poponiak, and D. B. Dove, *Appl. Phys. Lett.*, **34**, 746 (1979).
15. Y. Arita and Y. Sunohara, *This Journal*, **124**, 285 (1977).
16. H. Fischer, in "Festkörperprobleme XVIII," p. 19 (1978).
17. G. H. Schwuttke, *Phys. Status Solidi A*, **43**, (1977).

18. H. J. Leamy, L. C. Kimerling, and S. K. Ferris, in "Scanning Electron Microscopy 1976," Part IV, p. 529, IIT Res. Insd., Chicago (1976).
19. G. H. Schwuttke, K. Yang, and T. F. Cizek, *J. Cryst. Growth*, **43**, 329 (1978).
20. Journal de Physique, Colloque C-6, supplement au No. 6, International Symp. on Dislocations in Tetrahedrally Coordinated Semiconductors (1978).
21. H. F. Mataré, *Solid State Electron.*, **22**, 651 (1979).

Applications of a Low Noise Potentiostat in Electrochemical Measurements

Ugo Bertocci*

National Bureau of Standards, Chemical Stability and Corrosion Division, Washington, D.C. 20234

ABSTRACT

Measurements on two electrochemical systems, copper in copper sulfate and aluminum in boric acid/tetraborate buffer, have been carried out by recording the amplitude spectrum of the fluctuations in the current density. For these measurements, a low noise potentiostat developed and built at NBS was employed. In the case of copper, the current spectra are found to be the deterministic response of the electrode to the noise voltage generated by the potentiostat. The electrode characteristics for charge-transfer and for diffusion could be obtained from the impedance plots derived from the measurements when the level of the applied signal was of the order of 10^{-7} V. In the case of aluminum, the deterministic response observed in the absence of pitting gave way to random fluctuations in the current in conditions leading to pitting. It is shown that the onset of pit formation can be detected from noise measurements. The significance of the information obtained in electrochemical noise measurements is briefly discussed.

The study of random fluctuations in current and potential of electrodes, usually known as electrochemical noise, is receiving increasing attention, and interesting applications are being envisaged in the field of corrosion (1). In these studies, it is often necessary to detect and measure very low amplitude signals, and it is therefore very important to reduce the noise generated by the measuring instruments. Since in most electrochemical studies it is desirable to control the electrode potential, a low noise potentiostat is a particularly useful device (2).

Elsewhere (3), the circuit and performance of a potentiostat designed and built at NBS have been described. The purpose of this communication is to report on measurements carried out on some electrochemical cells, taking advantage of the characteristics of such a potentiostat. These measurements are not restricted to the detection of noise, but concern also the observation of the current response to very small voltage signals.

Experimental Procedures

The measurements were carried out with the apparatus shown schematically in Fig. 1. All the instruments inside the dot-dashed enclosure are battery operated, and the enclosure represents electromagnetic shielding as well as some protection from mechanical vibrations. The potentiostat provides for a low noise d-c control voltage and for the measurement of the d-c current. A built-in a-c amplifier is employed for the detection of the fluctuations in the current in the frequency range approximately between 0.1 Hz and 2 kHz. The cell is provided with two reference electrodes, a low impedance one, which is used as a sensor for the potentiostat and for the measurement of the voltage noise, and a second one, often an SCE, employed for the monitoring of the d-c electrode potential. The values of the d-c voltage and current are recorded on a two-channel recorder.

* Electrochemical Society Active Member.

Key words: aluminum, copper, impedance measurements, pitting, potentiostat.

An additional voltage signal can be added to the d-c control voltage. In this work, the superimposed voltage consisted of a constant amplitude, swept frequency signal, sweeping linearly over a factor of ten. The repetition rate was slightly less than the time of acquisition of a spectrum by the spectrum analyzer.

The frequency analysis of the output signal, either the current or the electrode potential, depending on the position of the switch shown in Fig. 1, was carried out by a spectrum analyzer with a frequency resolution of 1/200 of the range. In the 50 Hz range, for example, the spectrum consisted of 200 values at intervals of 0.25 Hz. The acquisition time for one spectrum is equal to one period at the lowest frequency, that is, 4 sec for the range mentioned above.

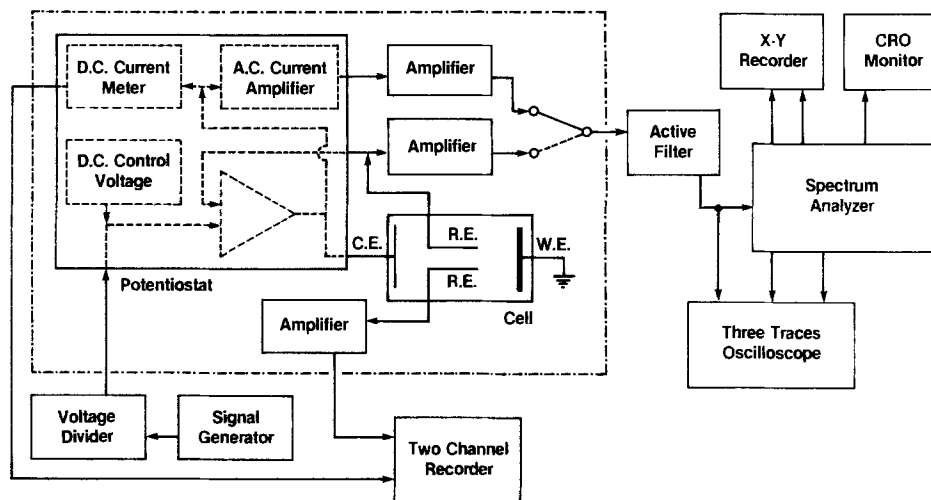
The input waveform to the spectrum analyzer as well as the instantaneous and average spectra were observed continuously on the oscilloscope. Average spectra were then recorded on an X-Y recorder, either on a linear or on a logarithmic scale.

The time involved in acquiring the average spectra in the low frequency ranges can be considerable. In the 5 Hz range each spectrum requires 40 sec so that for an average over 64 spectra the acquisition time is of the order of 40 min.

Experimental Results

The results presented here concern two quite different electrode systems, one having low and the other high resistance to the faradaic current. As a low impedance system, the reaction between Cu metal and a 0.5 mole/liter $\text{CuSO}_4 + 0.1$ mole/liter H_2SO_4 solution was examined. Figure 2 and 3 show the voltage and current spectra, respectively. The reference electrode was also copper, and the data were taken in conditions of zero d-c current. The spectra were also taken when a swept frequency signal was added to the d-c control voltage. The amplitude of the signal as shown in Fig. 2 was about 10-100 times the background noise but never larger than about 2 μV . Figure 3 shows the current response with and without the superimposed voltage signal.

Fig. 1. Experimental circuit for the recording of current and voltage spectra under potentiostatic conditions.



The impedance of the electrode $|Z|$ can be obtained as the ratio of voltage to the current at every frequency, and the results are shown in Fig. 4. These ratios were calculated after subtracting from each

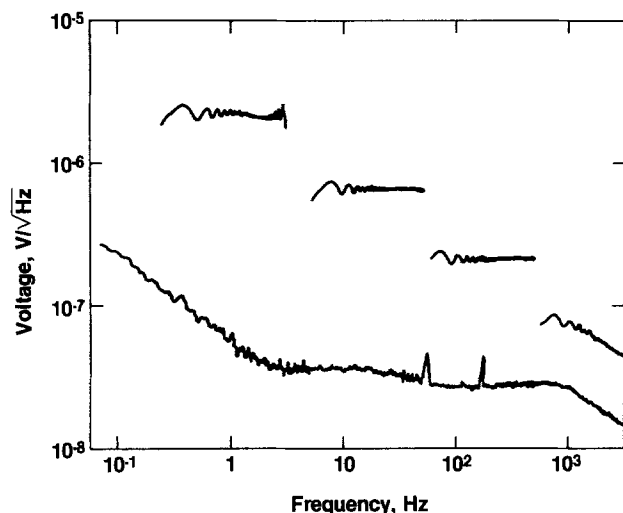


Fig. 2. Voltage spectra recorded under potentiostatic conditions ($i_{dc} = 0$) on Cu in 0.5 mole/liter CuSO_4 + 0.1 mole/liter H_2SO_4 . The four segments are the swept frequency signal superimposed to the d-c control voltage.

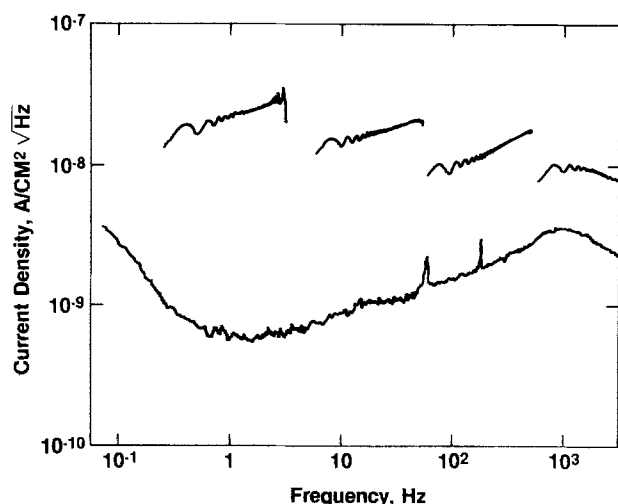


Fig. 3. Current spectra recorded under potentiostatic conditions ($i_{dc} = 0$) on Cu in 0.5 mole/liter CuSO_4 + 0.1 mole/liter H_2SO_4 . The four segments are the current response to the swept frequency signal shown in Fig. 2.

value the instrumental noise, which had been previously measured (3). For the voltage, the instrumental noise is less than $10^{-8} \text{ V}/\sqrt{\text{Hz}}$ above 8 Hz and for the current it is equivalent to $3 \cdot 10^{-11} \text{ A}/\sqrt{\text{Hz}}$ above 1 Hz. The points in Fig. 4 obtained with and without the superimposed voltage signal are very close. This is because the electrode impedance is rather small, and therefore the instrumental noise in the current density data is small compared with the recorded value of the current. The increased signal-to-noise ratio obtained by a larger voltage signal has little effect on the accuracy of the results.

The results have been fitted to an equivalent circuit (shown in the inset in Fig. 4). The line drawn in Fig. 4 shows $|Z|$ as calculated from this circuit, using the following values: ohmic drop resistance $R_\Omega = 5\Omega$, charge-transfer resistance $R_{ct} = 15\Omega$, equivalent to an exchange current i_0 for the rate-determining step (4) $\text{Cu}^{++} + e^- \rightleftharpoons \text{Cu}^+$ of $0.42 \text{ mA}/\text{cm}^2$; double layer capacitance $C = 35 \mu\text{F}/\text{cm}^2$.

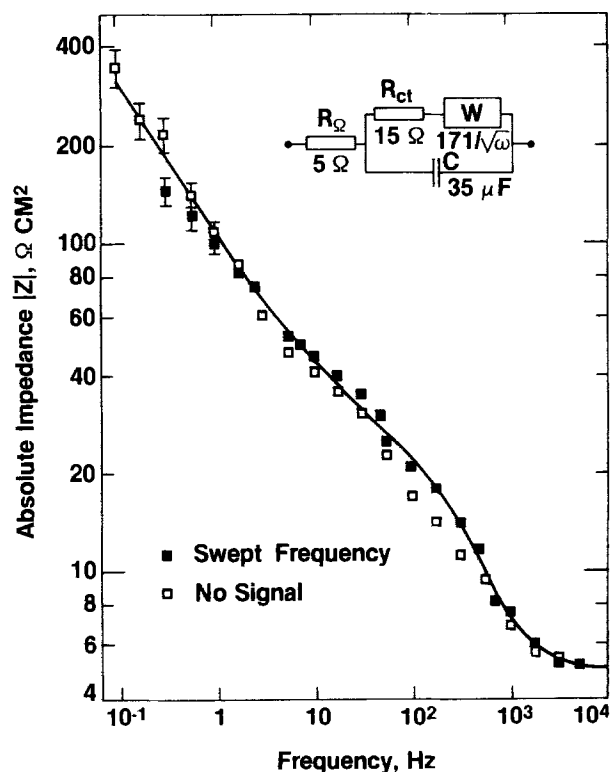


Fig. 4. Absolute impedance $|Z|$ vs. frequency for Cu in 0.5 mole/liter CuSO_4 + 0.1 mole/liter H_2SO_4 obtained from current and voltage spectra. Solid line calculated for circuit shown.

Since one of the species involved in the rate-determining step, Cu^+ , is present only in low concentrations, a significant Warburg impedance is present at low frequencies. The value of the Warburg impedance

$$W = \frac{RT}{z^2 F^2 (\text{Cu}^+) \sqrt{2\omega D_{\text{Cu}^+}}}$$

was calculated choosing $D_{\text{Cu}^+} = 1.38 \cdot 10^{-5} \text{ cm}^2/\text{sec}$ and $\text{Cu}^+ = 2.9 \cdot 10^{-4} \text{ mole/liter}$. Most of these values are in excellent agreement with the literature; for instance, the exchange density (5) and the diffusion coefficient of Cu^+ (6). The Cu^+ concentration that gives the best fit is about 80% larger than that calculated from the reaction



whose equilibrium constant is $7 \cdot 10^{-4}$ (6, 7), and taking the activity coefficient of 0.5 mole/liter CuSO_4 as 0.062 (8). The value of the Cu^+ concentration affects the magnitude of the Warburg impedance and therefore that of $|Z|$ only at low frequencies, where the reliability of the experimental points, as shown by the error bars in Fig. 4, is not as good as at higher frequencies.

The second system examined was 6061 aluminum in a 1:1 mixture of saturated H_3BO_3 and $\text{Na}_2\text{B}_4\text{O}_7$ with and without addition of 0.05M NaCl. The current and voltage spectra in the solution not containing chlorides are as given in Fig. 5.

In the chloride-containing solution, which is known to cause pitting if the potential is raised approximately above $-700 \pm 50 \text{ mV vs. SCE}$ (9), the current spectra obtained below and at the pitting potential are reported in Fig. 6 together with the voltage spectrum. During the recording of the spectra, the d-c current was about $10 \mu\text{A}/\text{cm}^2$ cathodic at -800 mV , while at -650 mV , it became anodic, increasing slowly to about $50 \mu\text{A}/\text{cm}^2$.

The impedance plots for this system are given in Fig. 7. Here again the onset of pitting is marked by a fundamental change in the impedance plot up to 1 kHz.

Discussion

The results shown for the Cu/CuSO_4 electrode indicate that random fluctuations in electrode characteristics are so low that they do not affect significantly the current response to the broadband noise voltage signal. For this reason, the impedance plot shown in Fig. 4 can be accounted for satisfactorily by the deterministic response of the circuit drawn, from which reliable values concerning the kinetics of the electrode can be obtained. Therefore, although the intrinsic noise of the control voltage is still too large in

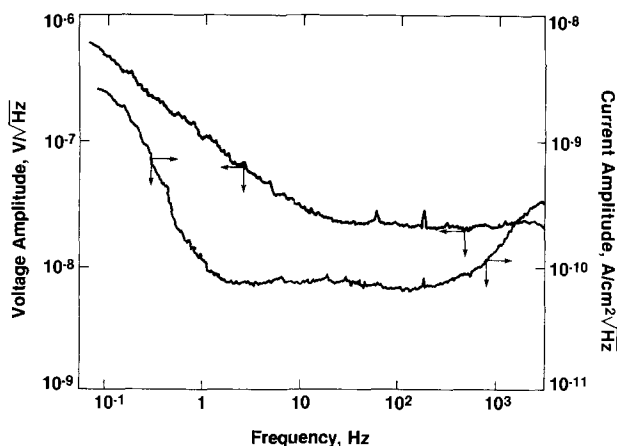


Fig. 5. Current and voltage spectra recorded in potentiostatic conditions ($E = -320 \text{ mV vs. SCE}$) on Al in $\text{H}_3\text{BO}_3:\text{Na}_2\text{B}_4\text{O}_7$ solution.

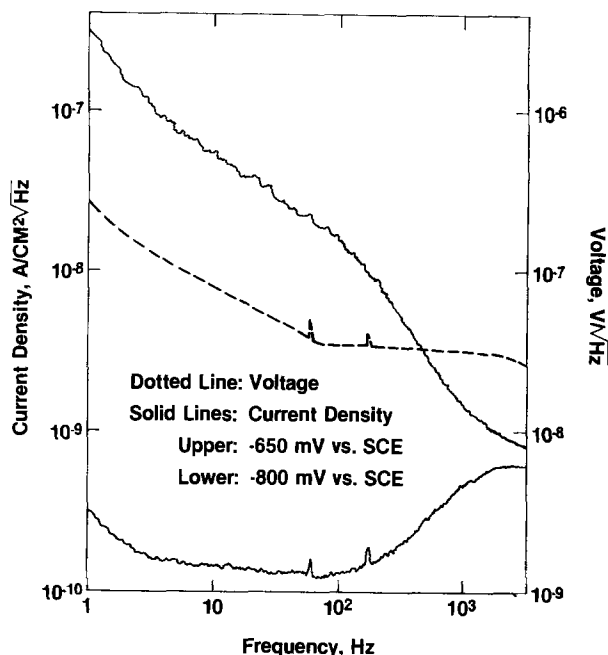


Fig. 6. Current and voltage spectra recorded under potentiostatic conditions below and at the pitting potential on Al in $\text{H}_3\text{BO}_3:\text{Na}_2\text{B}_4\text{O}_7 + 0.05 \text{ mole/liter NaCl}$.

this case for the detection of random processes at the electrode, good measurements can be carried out even for signals below $0.1 \mu\text{V}$, detecting currents in the nA range.

In the case of aluminum in boric/borate solution, when pitting does not occur, random current fluctuations are below the limits of detection, and the electrode response is largely that of a capacitor of about $0.3 \mu\text{F}/\text{cm}^2$. The data of Fig. 7 seem to indicate a larger capacitance in chloride containing solution, where thinning of the film can occur (10). Above the pitting potential, the noise current increases more than two orders of magnitude, and the impedance plot in Fig. 7

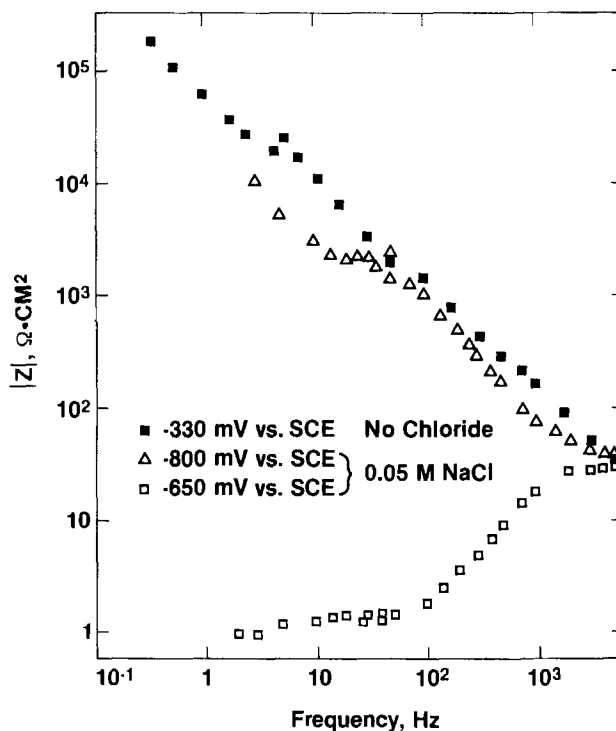


Fig. 7. Absolute impedance $|Z|$ vs. frequency for Al in $\text{H}_3\text{BO}_3:\text{Na}_2\text{B}_4\text{O}_7$ with and without chloride added.

cannot be explained other than as caused by random fluctuations of the electrode current, independently of the voltage signal applied.

The detection of this current noise is a good indication of the beginning of pitting, and the large fluctuations are probably due to hydrogen evolution from the pits (11). The onset of the large current noise has shown to be reproducible within a range of 10–20 mV.

The noise current observed is the sum of several contributions since the fluctuations of the control voltage interact with the random variations of the electrode resistance and capacitance causing intermodulation terms. These terms are, however, much smaller than the contributions due to the fluctuations of the d-c current, which are independent of the control voltage noise. Since the d-c current, upon pitting, increases to several $\mu\text{A}/\text{cm}^2$, the noise current observed can be accounted for by oscillations of the order of a few percent of the average d-c current.

It is more difficult to estimate the possible contribution of fluctuations in the double layer capacitance; they can be caused by changes in surface area as well as changes in the thickness of the protecting film, a more likely case for Al in neutral solution. The current generated is

$$i_c = (E - E_{zc}) \frac{dC}{dt}$$

where E_{zc} is the potential of zero charge. If the capacitance varies by a fraction k at angular frequency ω , that is

$$C = C_0(1 + k \sin \omega t)$$

the current at that frequency is

$$i_c = (E - E_{zc}) \omega C_0 k \cos \omega t$$

The potential of zero charge for Al is at about -0.75V vs. SCE (12), therefore $|E - E_{zc}|$ can be estimated to be of the order of $0.1 \pm 0.2\text{V}$. Since $C_0 \simeq 0.3 \mu\text{F}/\text{cm}^2$, for $k = 1$, the rms value of the capacitive noise current would be about $1.3 \cdot 10^{-7}\text{A}$ at 1 Hz and 100 times larger at 100 Hz. Since the experimental value of the current decreases with frequency and is about 10^{-8}A at 100 Hz, it is safe to conclude that the higher frequency fluctuations of the capacitance are very small, but it is not possible to assign the noise observed unambiguously to variations in the faradaic rather than in the capacitive current.

The results presented show that reduction of the instrumental noise is essential for the study of random fluctuations and that it can be quite useful in all circumstances, allowing measurements with very little perturbation of the systems under investigation. The fact that deterministic measurements can be done using the almost white noise in the control

voltage (13) has, however, important implications for a proper understanding of the current spectra when "noise" measurements are attempted. Only in electrochemical systems where the data cannot be explained by assigning constant values to the components of the equivalent circuit is it appropriate to describe the signal observed as electrochemical noise.

Manuscript submitted Jan. 21, 1980; revised manuscript received April 8, 1980.

Any discussion of this paper will appear in a Discussion Section to be published in the June 1981 JOURNAL. All discussions for the June 1981 Discussion Section should be submitted by Feb. 1, 1981.

Publication costs of this article were assisted by the National Bureau of Standards.

REFERENCES

1. W. P. Iverson, *This Journal*, **115**, 617 (1968); G. Okamoto, T. Sugita, S. Nishiyama, and K. Tachibana, *Boshoku Gijutsu*, **23**, 439, 445 (1974); G. Blanc, I. Epelboin, C. Gabrielli, and M. Keddam, *J. Electroanal. Chem. Interfacial Electrochem.*, **75**, 97 (1977); U. Bertocci, in 7th International Congress on Metallic Corrosion, p. 2010, Rio de Janeiro, 1978, ABRACO (1979).
2. I. Epelboin, C. Gabrielli, M. Keddam, and L. Railton, *J. Electroanal. Chem. Interfacial Electrochem.*, **93**, 155 (1978).
3. U. Bertocci and R. W. Schideler, *Nat. Bur. Stand. J. Res.*, **85**, 211 (1980).
4. E. Mattsson and J. O'M. Bockris, *Trans. Faraday Soc.*, **55**, 1586 (1959).
5. A. Damjanovic, T. H. V. Setty, and J. O'M. Bockris, *This Journal*, **113**, 429 (1966); U. Bertocci, C. Bertocci, and B. C. Larson, *J. Cryst. Growth*, **13/14**, 427 (1972); D. Postl, G. Eichkorn, and H. Fischer, *Z. Phys. Chem. (NF)*, **77**, 138 (1972).
6. L. M. Gedansky, E. M. Woolley, and L. G. Hepler, *J. Chem. Thermodyn.*, **2**, 561 (1970).
7. CODATA Bulletin 28, Internat. Council of Scientific Unions (1977); U. Bertocci and D. R. Turner, in "Encyclopedia of Electrochemistry of the Elements," A. T. Bard, Editor, Vol. II, p. 387, M. Dekker, New York (1974).
8. R. A. Robinson and J. H. Jones, *J. Am. Chem. Soc.*, **58**, 959 (1936).
9. M. Pourbaix, *Corrosion*, **26**, 431 (1970); J. R. Galvele and S. M. de DeMicheli, *Corros. Sci.*, **10**, 795 (1970); K. Nisancioglu and H. Holtan, *ibid.*, **18**, 835 (1978).
10. M. A. Heine, D. S. Keir, and M. J. Pryor, *This Journal*, **112**, 24 (1965).
11. C. B. Bergeron and R. B. Givens, *ibid.*, **124**, 1845 (1977); Corrosion Res. Conf., NACE, Atlanta (1979).
12. S. Trasatti, *J. Electroanal. Chem. Interfacial Electrochem.*, **33**, 351 (1971).
13. G. Blanc, I. Epelboin, C. Gabrielli, and M. Keddam, *Electrochim. Acta*, **20**, 599 (1975).

Electroless Gold Plating on III-V Compound Crystals

L. A. D'Asaro, S. Nakahara, and Y. Okinaka

Bell Laboratories, Murray Hill, New Jersey 07974

ABSTRACT

Electroless gold plating in an alkaline bath containing potassium borohydride as the reducing agent has been found to produce tightly adherent plated films on GaAs, $\text{Al}_x\text{Ga}_{1-x}\text{As}$, GaP, and InP. In this process, the substrate is activated in an acidified solution of palladium chloride prior to plating. The same process applied to Si or Ge produces poorly adherent films. A transmission electron microscope study of activated GaAs and Si surfaces revealed markedly different morphology and distribution of Pd grains on these two substrates. The adhesion of the subsequently plated electroless gold is discussed in terms of these observations and a model involving atomic interactions at interfaces.

An electroless (autocatalytic) gold plating process utilizing potassium borohydride as the reducing agent has been previously described (1) and used for plating on noble metals such as Pd, Pt, Rh, or Au, or on active metals such as Cu and its alloys (2). The noble metals catalyze the plating reaction, and this fact has led to a method of activating certain metallic surfaces, such as tantalum. An activator solution for that purpose was developed by DeAngelo, *et al.* (3), using acidified palladium chloride containing HF and acetic acid. The HF removes oxide from the surface, allowing activation of the freshly cleaned surface *in situ*. We have found that treatment in similar solutions will induce electroless gold plating on a variety of III-V compound crystals. Comparisons of the electroless gold films (about 1 μm thick) plated by this method with evaporated films of Cr-Au or Ti-Pt-Au indicate that the electroless gold is more tightly adherent, more reproducible, and less expensive to prepare than the evaporated films. These films pass the "Scotch tape test" and cannot be removed by rubbing or scratching with a metal point.

It is shown in this paper that the activation with the PdCl_2 -containing solution involves the reduction of Pd^{2+} ions to metallic Pd by galvanic displacement. With this activation mechanism one can easily imagine that the overall adhesion of the subsequently plated electroless gold layer will be influenced by the adhesion of the catalyst to the substrate. In fact, there are substrates to which electroless gold adheres poorly. An example is silicon activated by the same process as is used for GaAs. In order to obtain insight into the difference in adhesion on different semiconductor substrates, the morphology and distribution of the Pd catalyst on the substrates were studied using a transmission electron microscope (TEM). The results will be discussed in relation to the mechanism of catalyst deposition. A model involving atomic interactions at various interfaces is presented to explain the observed strong adherence of electroless gold to the III-V compounds.

Solution Preparation and Plating Procedure

In the procedures described here, the plating bath was held constant. The bath composition is given in Appendix 1 (2). We have found that it is convenient to prepare a 5 \times concentrated solution for storage. It is important to avoid organic contaminants in the water to obtain good results.

The activator solution was modified somewhat for each III-V compound as a result of empirical tests. The preparation of the activator for GaAs and $\text{Al}_x\text{Ga}_{1-x}\text{As}$ is given in Appendix 2 (3).

The adherence of gold film is strongly dependent on the cleaning procedures which should therefore be made as stringent as possible. We have used an

HCl rinse on chemically polished surfaces followed by rf plasma cleaning to remove traces of organic contaminants.

The plating procedure consisted of activation for at least 1 min (longer time when plating is nonuniform) followed by rinse in distilled deionized water, and immersion in the plating bath held at 70°C. It is essential to supply agitation to the sample in the bath in order to obtain uniform and rapid plating (2). A typical plating rate was 1 μm in 40 min in the present conditions.

A useful technique to insure uniform plating is to inspect the sample after 10 or 15 min and replate if any spots are unplated. The sample will then plate everywhere, unless contamination is present.

The plating proceeds equally rapidly on n-type, p-type, or semi-insulating crystals, on crystals containing p-n junctions, and on crystals where noble metals are bonded to the surface. Details for each III-V compound are as follows

1. GaAs and $\text{Al}_x\text{Ga}_{1-x}\text{As}$ —The procedure is as described above. Various compositions of $\text{Al}_x\text{Ga}_{1-x}\text{As}$ were plated, with the largest $x = 0.4$.

2. GaP—The acetic acid was omitted from the activator.

3. InP—The activator was modified by omitting acetic acid and adding 5 times the normal HF. It was necessary to heat the activator to 50°C and immerse the InP wafers for 2 min in order to obtain satisfactory plating.

In cases where contamination is present, modification of the activator bath to higher fluoride ion concentration and/or higher activation temperature will usually enable plating.

Photoresist Masking

Masking with negative photoresist is useful for producing patterns of electroless gold. An example of a masked pattern formed on the back of a GaAs metal epitaxy Schottky field effect transistor (MESFET) is shown in Fig. 1.

TEM Observation of Activated GaAs and Si

Sample preparation.—The substrates used in this study were (110) GaAs and (111) Si. Annealed OFHC copper was used for comparison. In order to compare the surface structures of the same specimen before and after activation, thin foil TEM specimens were used as substrates. Gallium arsenide foils were prepared by first mechanically polishing a 3 mm disk which had been ultrasonically cut out of a (110) wafer, to a thickness of about 50 μm , and then thinning down further by ion milling. Thin foils of Si were obtained by chemically etching the sample in a solution prepared by mixing 100 ml of conc HNO_3 and 140 ml of glacial acetic acid (4). Copper foils

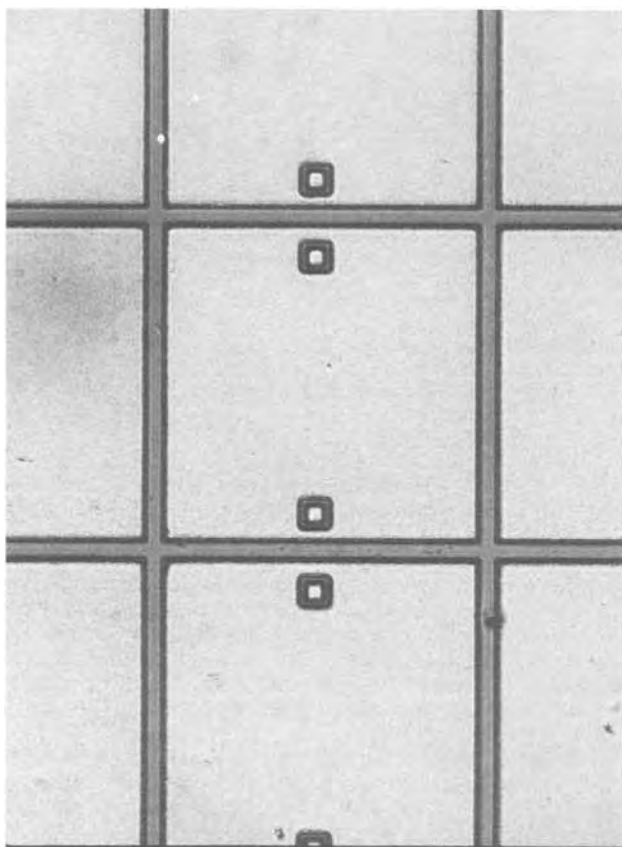


Fig. 1. Bonding pads formed by electroless gold plating through a photoresist mask on the back of a wafer of GaAs MESFET's. The pad dimensions are $500 \mu\text{m}$ square. The small squares are alignment marks.

were prepared by electropolishing an annealed sheet in a mixture of 2 parts methanol and 1 part conc HNO_3 at dry ice temperature.

Transmission electron micrographs were taken with a JEM 200 electron microscope operated at 200 kV.

TEM results.—The two TEM micrographs (a) and (b) shown in Fig. 2 compare the structures of (110) GaAs foils before and after activation, respectively. It is seen in Fig. 2(b) that a high density of small "dark" particles has grown on the top and bottom surfaces of the foil upon activation. The particle density has been determined to be $(1 \sim 2) \times 10^{12}/\text{cm}^2$. An electron diffraction analysis identified these particles as metallic palladium (see Table I). Appreciable etching of GaAs in the activator solution is also indicated by the presence of large "white" holes shown in Fig. 2(b). In order to measure the size of the palladium particles, a dark-field micrograph was taken using a portion of (111) Pd diffraction ring (see Fig. 3). The bright spots represent the images of individual Pd grains measuring 50-100Å. Furthermore, these Pd grains are randomly oriented without any epitaxial relationship to the (110) GaAs substrate. This randomness is indicated by the continuous diffraction rings of Pd grains as shown in Fig. 4. From the size and density of Pd grains, the surface coverage can be calculated to be about 75-85%.

Figure 5 shows a TEM micrograph of an activated (111) Si foil. A large number of round particles are seen to have grown with a smaller density and coverage than those on GaAs. Electron diffraction analysis revealed that these particles also consist of grains of metallic Pd (see Table I). The morphology and distribution of the particles are, however, markedly different from those on activated GaAs substrate (see Fig. 2). Substrate etching appeared to be less on Si than on GaAs. In order to compare the particle

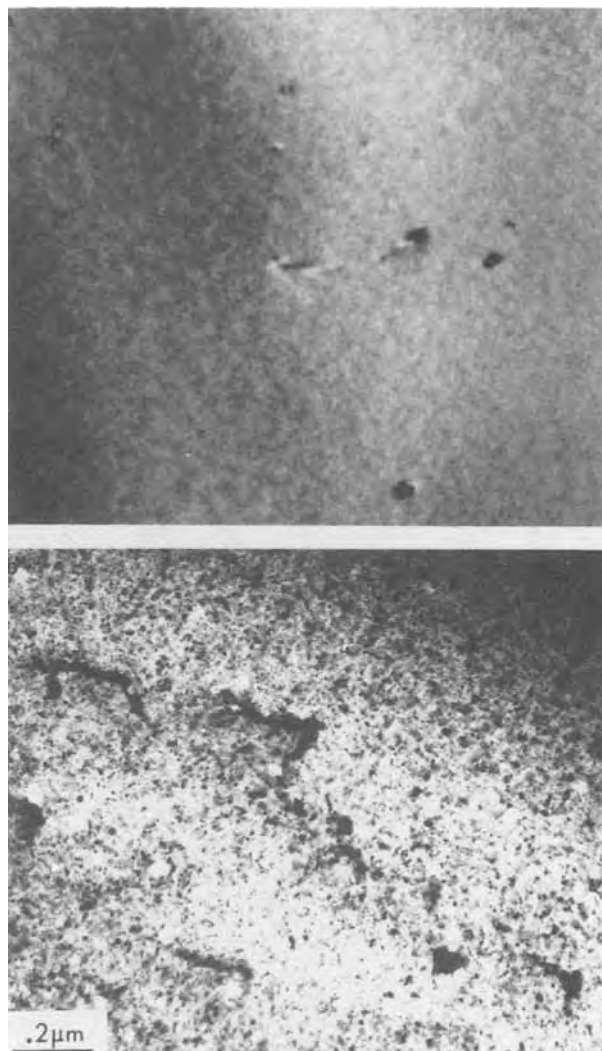


Fig. 2. TEM micrographs of (110) GaAs foils (a) before and (b) after activation. Fine Pd grains are seen to be uniformly distributed on surface. Dark linear features indicate regions containing closely grown Pd grains at the surface steps.

size and distribution at the same magnification, a part of the area in Fig. 5(a) taken at a slightly higher magnification is shown in Fig. 5(b). It is seen that each particle measuring 500-2000Å, in fact, consists of smaller grains ($\sim 100\text{Å}$) and the particle shape resembles that of spherulites in polymer crystals (5). These hemispherical particles were distributed non-uniformly over the substrate with a density of $\sim 1 \times 10^{10}/\text{cm}^2$. An image taken using the high-resolution defocus contrast technique (6) revealed that these spherulite particles contain pores along their radial direction. The particle morphology can be best described as spongy sphere and hemisphere (Fig. 6). The electron diffraction pattern is shown in Fig. 7. The Pd rings are not as continuous as those found with activated GaAs (Fig. 4). This discontinuity is a primary indication of the nonuniform distribution of Pd grains.

Electroless gold plating on copper does not require an activation step because an initial layer of gold is formed as a result of a galvanic displacement reaction, and this layer was previously found to serve as the catalyst for the initial deposition of electroless gold (7). Nevertheless, the surface of copper treated in the activating solution was examined for comparison with the semiconductor substrates. A TEM micrograph of an activated copper foil is shown in Fig. 8. The growth of needle-shaped crystals is noted. From electron diffraction analysis these crystals were

Table I. Electron diffraction analysis of activated GaAs, Si, and Cu

Deposit on GaAs substrate		Deposit on Si substrate		Pd metal*	
$d_{\text{obs.}}$ (Å)	Intensity	$d_{\text{obs.}}$ (Å)	Intensity	d (hkl) (Å)	I/I_{max}
2.274	VS	2.249	VS	2.240 (111)	100
1.947	S	1.945	S	1.945 (200)	42
1.376	S	1.366	S	1.376 (220)	25
1.178	S	1.163	S	1.173 (311)	24
Deposit on Cu surface					
$d_{\text{obs.}}$ (Å)	Intensity	d (hkl) (Å)	I/I_{max}	Cu_2O^{**}	
3.039	S	3.020 (110)	9		
2.518	S	2.465 (111)	100		
2.189	S	2.135 (200)	37		
1.510	S	1.510 (220)	27		

VS = very strong.

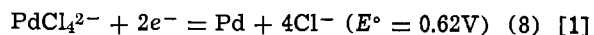
S = strong.

* From JCPDS diffraction file 5-0681.

** From JCPDS diffraction file 5-0667.

found to be cuprous oxide (Cu_2O) rather than metallic palladium (see Table I). This result is of interest because it shows that metallic palladium, which undoubtedly forms, does not adhere to the copper surface under the conditions of this experiment. The formation of metallic palladium is indicated by the appearance of finely dispersed black particles during the activation treatment in conjunction with the consideration of electrochemical potentials involved. The nonadherence of metallic palladium on copper is attributed to the stability of Cu_2O on copper and the more favorable nucleation in the solution phase than on Cu_2O or copper. Undercutting may also be responsible. It should be noted that the Cu_2O needles did not result from air oxidation of copper; the air-oxide is known to grow epitaxially in the form of cubes. The Cu_2O needles must be the product of oxidation of copper by palladium ions.

Discussion of TEM results.—Before the morphology and adhesion of palladium particles can be considered, it is instructive to discuss the mechanism of chemical reactions leading to the nucleation and growth of metallic palladium. The activator solution contains excess HCl which serves to dissolve PdCl_2 by complexing it to form PdCl_4^{2-} . The deposition of metallic palladium from this species occurs according to the reaction



The required electrons must be supplied by the sub-

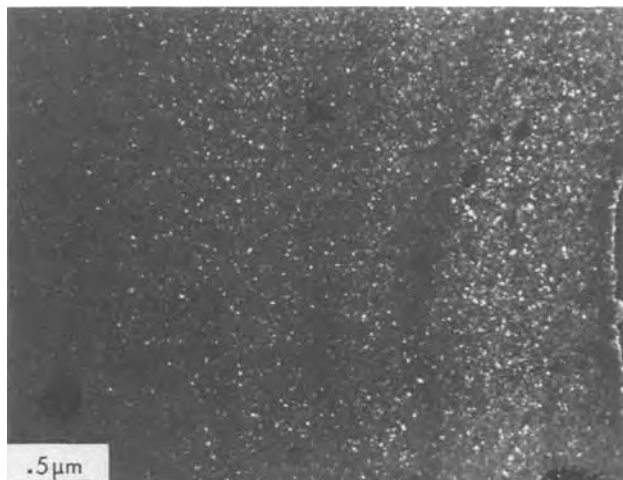


Fig. 3. Dark-field TEM micrograph corresponding to Fig. 2(b), taken from a portion of a (111) Pd diffraction ring. Bright spots indicate finely distributed Pd grains grown on activated (110) GaAs foil.

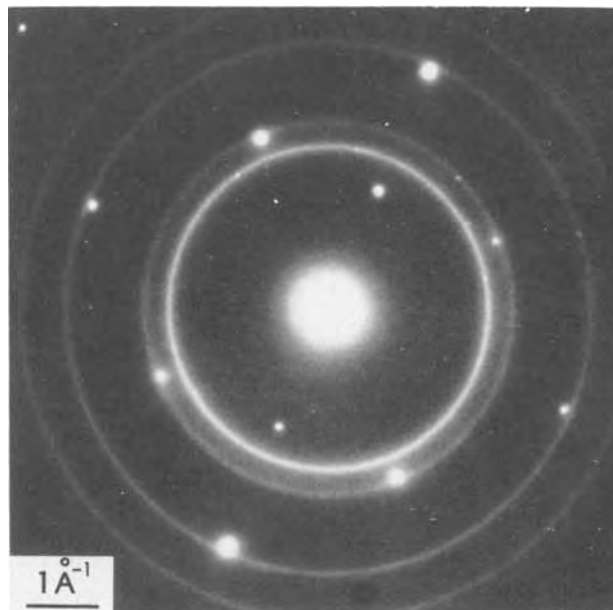


Fig. 4. Electron diffraction pattern from activated (110) GaAs foil. The continuous rings originate from finely distributed Pd grains, whereas the spots result from single crystal (110) GaAs.

strate. In the case of GaAs¹ the following reactions

¹ The ionicity of the Ga-As bond is estimated to be only 5-10% (9), which may be ignored for the purpose of the present discussion.

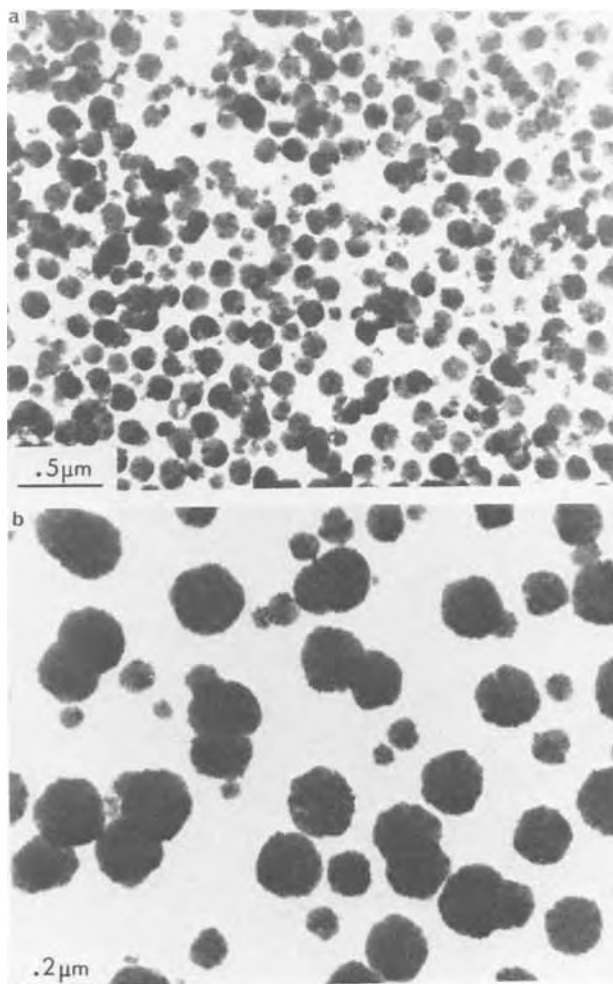


Fig. 5. Morphology and distribution of Pd deposits grown on activated (111) Si foil. Part of the region in (a) was taken at a slightly higher magnification to give (b).



Fig. 6. TEM micrograph showing spongy Pd deposits grown at the edge of activated (111) Si foil. To reveal porous regions in the deposit, the image was taken in a slightly underfocused condition.

may proceed from right to left

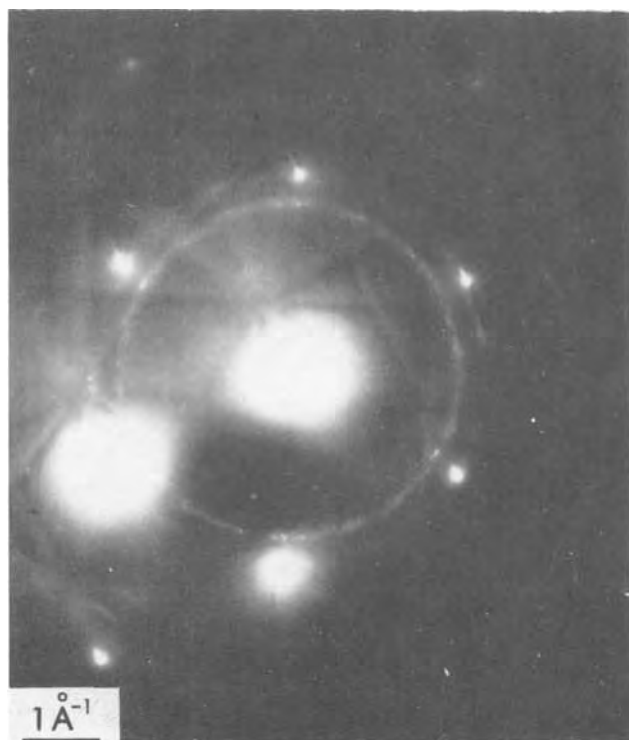
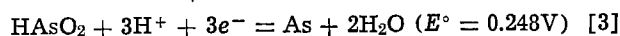
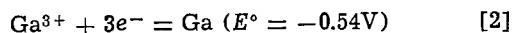


Fig. 7. Electron diffraction pattern from activated (111) Si. The rings are from Pd grains; the spots are from (111) Si. The discontinuity in the rings indicates that Pd grains are not uniformly distributed over the Si surface.

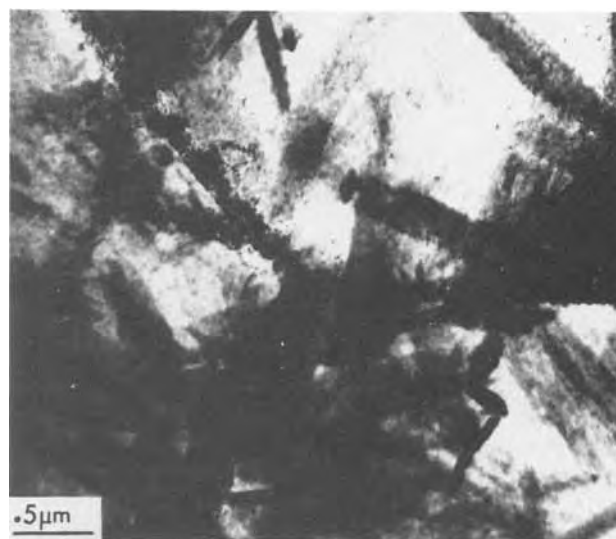
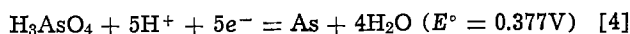
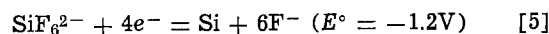


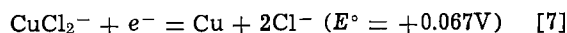
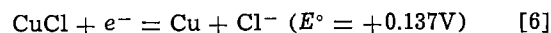
Fig. 8. Needles of copper oxide (Cu_2O) grown on activated copper foil.



The relevance of these reactions was inferred from the predominance diagram for GaAs recently published by Park and Barber (10). The values of E° indicate that both Ga and As may be oxidized by PdCl_4^{2-} . For Si in the presence of F^- , the relevant oxidation will be the reverse of the following reaction



For Cu in the presence of Cl^- ,² the corresponding reactions are



Comparison of these E° values with the value for reaction [1] indicates the thermodynamic possibility for the formation of Pd metal by galvanic displacement in all cases. Based on the above considerations and the experimental results, we conclude that the metallic palladium particles observed were formed as a result of galvanic displacement.

We shall now consider why metallic Pd thus formed give rise to different morphologies depending on the substrate. A galvanic displacement reaction can be considered as a mixed potential reaction consisting of cathodic and anodic half-reactions in much the same way as a corrosion reaction. At any instant during the reaction, then, cathodic and anodic sites must be distributed side by side on a microscopic scale on the substrate surface. Palladium will deposit at the cathodic sites, while substrate oxidation (dissolution) will take place at the anodic sites. The deposition of palladium will involve nucleation and growth as in conventional electrodeposition processes. The uniform distribution of very small Pd grains observed on GaAs indicates that nucleation is highly promoted on this substrate. On the other hand, the morphology observed on Si indicates that after the initial nucleation took place on the relatively small number of cathodic sites, further nucleation occurred preferentially on the already existing palladium particles rather than directly on the substrate, thus resulting in the formation of the spherulite particles. It is generally recognized (12) that for any metal deposition systems a strong atom-to-surface interaction will result in the formation of a high density of nuclei while a weak interaction will give widely spaced nuclei. The observed high density of Pd nuclei

² F^- forms only a very weak complex with Cu (11).

grown on GaAs, therefore, indicates that there is a strong interaction at the interface between Pd and GaAs. The observation with Si, on the other hand, indicates a much weaker interaction. The nature of the atom-to-surface interaction will be discussed later. The manner in which electroless gold deposition progresses on a substrate only partially covered with discrete Pd catalyst particles can be depicted as follows. Immediately after the substrate is placed in the electroless plating bath, gold begins to nucleate on Pd and to grow in all directions. The growth of gold in the lateral direction results in coalescence of adjacent particles and eventually in the formation of a continuous layer of gold. The thickness of this layer continues to grow indefinitely because of the autocatalytic nature of the process. The adherence of the gold film formed in this manner must depend on adherent interactions at three different interfaces: (i) Pd/substrate, (ii) Au/Pd, and (iii) Au/substrate in the regions between Pd catalyst sites.

Pd/substrate interface.—As already discussed, the microscopic observations indicate that a strong interaction exists between Pd and GaAs, while the interaction between Pd and Si is weak. The binary phase diagram for Pd-Ga (13) shows that Ga has a significant solubility at room temperature in Pd. Also, Pd forms intermetallic compounds with Ga (and other Group IIIA elements). On the other hand, Pd and Si have no mutual solubility according to the phase diagram of this system (13). Intermetallic compounds are known, but if formed, these are ineffective in promoting adherence of the electroless gold.

Au/Pd interface.—The adhesion of electroless gold to evaporated or sputtered Pd films or to bulk Pd metal has previously been shown to be extremely strong regardless of the surface roughness (1), and thus the adherence of electroless gold to Pd catalyst particles is expected to be strong on both GaAs and Si.

Au/substrate interface.—The phase diagrams (13) again show significant solubilities of Au in Ga and other Group IIIA elements and possibilities of the formation of intermetallic compounds. There is independent evidence showing that evaporated gold reacts chemically with GaAs at room temperature (14). On the other hand, no evidence is found for room temperature chemical interaction between Au and Si. Hence the bonding of Au to Si at room temperature can be expected to be weak. In the case of GaAs it is not expected that the Au/substrate interface plays a major role in determining the overall adhesion because of the high Pd coverage (~80%) of the substrate. Nevertheless, the expected strong interaction between Au and GaAs certainly should reinforce the overall adhesion. For Si the lack of chemical interaction with Au in conjunction with the low Pd coverage seems decisively responsible for the poor overall adhesion observed.

From the analysis of the model consisting of three interfaces presented above, it is concluded that the strong adhesion of electroless gold to GaAs and other III-V semiconductors is due to the favorable situation at all three component interfaces.

Finally, it is of interest to mention that the adherence of electroless gold on Pd-activated germanium was found to be as poor as for Si. This result is also consistent with the expected lack of chemical interaction at room temperature, as inferred from the corresponding phase diagram.

Summary and Conclusions

A range of III-V compounds can be electroless gold plated if appropriate activation is used. The films, about 1 μm thick, are tightly adherent as judged by scratching with a sharp metal point and pulling with "Scotch tape."

The activation of GaAs, Si, and Cu by the activator containing HCl, HF, and acetic acid was studied using TEM. It was shown that metallic Pd forms on GaAs and Si by galvanic displacement, while on Cu only Cu_2O was observed. On GaAs, grains of Pd measuring 5-100A are uniformly and densely distributed [$(1 \sim 2) \times 10^{12}/\text{cm}^2$] so that they cover ~80% of the surface, whereas on Si these grains form large agglomerates (500-2000A) which are distributed with large separation (~1000A). These differences in morphology and distribution of Pd grains were discussed in relation to the difference in surface-to-Pd atom interaction. The strong adherence of electroless gold to Pd-activated GaAs and other III-V compounds and the weak adherence to Si (and Ge) can be explained using a model based on atomic interaction at three component interfaces: Pd/substrate, Au/Pd, and Au/substrate.

These results indicate that electroless gold plating can be usefully applied to a variety of III-V compound devices where pure, soft gold is required. In a recent application, via-connections on GaAs MESFET's were plated (15). We believe that other III-V compounds than those reported here could also be electroless gold plated using suitable modifications of the process.

Acknowledgments

The assistance of C. Wolowodiuk and D. T. Lassota is gratefully acknowledged. We thank J. V. DiLorenzo and D. R. Turner for their encouragement during this investigation.

Manuscript submitted Jan. 21, 1980; revised manuscript received March 19, 1980.

Any discussion of this paper will appear in a Discussion Section to be published in the June 1981 JOURNAL. All discussions for the June 1981 Discussion Section should be submitted by Feb. 1, 1981.

Publication costs of this article were assisted by Bell Laboratories.

APPENDIX 1

Plating Solution

		5 X conc. (g/liter)
KAu(CN) ₂	0.003M (0.864 g/liter)	4.3
KOH	0.2M (11.2 g/liter)	56.0
KCN	0.1M (6.5 g/liter)	32.5
KBH ₄	0.2M (10.8 g/liter)	54.0

To make 5 X concentrate:

1. Dissolve KOH in 500 ml of H₂O. Add KBH₄ and stir until dissolved.
2. Dissolve KCN in 200 ml of H₂O in a volumetric flask. Add KAu(CN)₂ and stir until dissolved.
3. Add solution 1 to solution 2 in a volumetric flask and make up to volume with distilled H₂O. Filter through a filter paper. Store in a Teflon or polypropylene bottle. Do not close tightly because the solution liberates hydrogen slowly during storage.

APPENDIX 2

Activator Solution

Dissolve 0.3g PdCl₂ in 9 ml conc. HCl and dilute it with 9 ml H₂O. Add this mixture to 864 ml glacial acetic acid; then add 18 ml HF(49%) and mix.

REFERENCES

1. Y. Okinaka, *Plating*, **57**, 914 (1970).
2. Y. Okinaka, R. Sard, C. Wolowodiuk, W. H. Craft, and T. F. Retajczyk, *This Journal*, **121**, 56 (1974).
3. M. A. DeAngelo, H. Square, M. W. Sagal, and D. J. Sharp, U.S. Pat. 3,485,665.
4. P. B. Hirsch, A. Howie, R. B. Nicholson, D. W. Pashley, and M. J. Whelan, "Transmission Electron Microscopy of Thin Crystals," Butterworths, London (1965).
5. F. P. Price, *J. Am. Chem. Soc.*, **74**, 311 (1958).

6. S. Nakahara and Y. Okinaka, in "Properties of Electrodeposits—Their Measurement and Significance," R. Sard, H. Leidheiser, and F. Ogburn, Editors, Chap. 3, The Electrochemical Society Softbound Proceedings Series, Princeton, N.J. (1975).
7. R. Sard, *This Journal*, **117**, 1156 (1970).
8. W. M. Latimer, "Oxidation Potential," 2nd ed., Prentice-Hall, Englewood Cliffs, N.J. (1952).
9. J. M. Whelan, in "Semiconductors," N. B. Hannay, Editor, Chap. 9, Reinhold Publishing Co., New York (1959).
10. S. M. Park and M. E. Barber, *J. Electroanal. Chem. Interfacial Electrochem.*, **99**, 67 (1979).
11. "Stability Constants of Metal-Ion Complexes," Special Publication No. 17, p. 263, The Chemical Society, London (1964).
12. D. M. Mattox, in "Adhesion Measurement of Thin Films, Thick Films, and Bulk Coatings," K. L. Mittal, Editor, ASTM, Philadelphia, Pa. (1978).
13. M. Hansen, "Constitution of Binary Alloys," Second Ed., McGraw-Hill, New York (1958); R. P. Elliott, "Constitution of Binary Alloys," First Supplement, McGraw-Hill, New York (1965); F. A. Shunk, "Constitution of Binary Alloys," Second Supplement, McGraw-Hill, New York (1969).
14. J. R. Waldrop and R. W. Grant, *Appl. Phys. Lett.*, **34**, 630 (1979).
15. L. A. D'Asaro, J. V. DiLorenzo, and H. Fukui, *IEEE Trans. Electron Devices*, **ed-25**, 1218 (1978).

Electrowinning of Silicon from K_2SiF_6 -Molten Fluoride Systems

Gopalakrishna M. Rao,* Dennis Elwell,* and Robert S. Feigelson

Center for Materials Research, Stanford University, Stanford, California 94305

ABSTRACT

The electrowinning of silicon from solutions of K_2SiF_6 in fluoride melts at 745°C has been achieved. Electrolysis close to the deposition potential gave dense, coherent, and well-adherent deposits. Up to 3 mm thick films were grown using a K_2SiF_6 concentration of 4-6 m/o. The polycrystalline silicon has a columnar structure with grain size up to 100 μ m. The morphology of the electrodeposited silicon onto silver substrates and its dependence on the deposition parameters is discussed. The purity of the deposits is substantially higher than that previously reported for electrodeposited silicon.

The availability, low toxicity, and high degree of technological development make silicon the most likely material to be used in terrestrial solar cells. The cost of silicon solar cells is still too high, however, for economic energy production, and the cost of pure elemental silicon is itself a major problem in achieving the cost objective of \$100-300 per peak kW by 2000 (1). Electrowinning is, in principle, a very attractive process for production of elemental silicon since it allows direct, single-stage production from some source material. The process can be operated at relatively low temperatures in comparison with those which involve molten silicon, and can yield a product which is substantially lower in impurity concentration than the source material.

The electrodeposition of silicon was first reported in 1854 (2) but there have been relatively few systematic studies reported in the literature. The most detailed investigation to date has probably been that of Monnier *et al.* (3, 4), who showed that silicon of 99.99% purity could be produced in a two-stage winning and refining process. Their deposits were, however, apparently powdery and incoherent and required subsequent separation from entrapped solvent. Cohen *et al.* (5-7) in our laboratory showed that single crystal epitaxial layers could be electrodeposited from solutions of K_2SiF_6 in a KF/LiF eutectic and that continuous films could be produced by electrorefining using a dissolving silicon anode.

The objective of the present study was to electrowin high purity silicon, in bulk form or as films with large grain size, from an inexpensive source. The morphology of the polycrystalline silicon films produced and their dependence on the electrodeposition conditions is discussed. A preliminary report of this investigation has been presented previously (8).

* Electrochemical Society Active Member.

Key words: polycrystalline silicon, electrocrystallization, semiconductor, solar cell.

Experimental

The apparatus used in this investigation was similar to that reported by De Mattei *et al.* (9), except that silica tubes were used to electrically insulate the electrode leads from the top flange. The nickel leads were fixed into the silica tubes using a low vapor pressure epoxy cement. The tubes were replaced after several experiments when devitrification was evident.

Potassium fluorosilicate was chosen as the source of silicon because of the large number of successful silicon and silicide depositions using this material (2-8). Fluorosilicic acid is a by-product of phosphate fertilizer manufacture and has at present no useful application, so that fluorosilicates are an inexpensive source of silicon. The potassium salt has the lowest volatility and material of 99% purity was obtained commercially (Alfa Ventron).

The solvent used was the ternary LiF/NaF/KF eutectic "Flinak" (mp 459°C) or the binary LiF/KF eutectic (mp 492°C). These solvents have the advantages of high conductivity, low viscosity, high decomposition voltage, and high solubility for oxides which tend to form on the electrode surfaces. LiF of 99.5% purity, NaF of 99% purity, and 99-99.5% KF were used in this investigation. These anhydrous materials were mixed and dried first under vacuum at 200°C and then under flowing argon for several hours prior to fusion. The argon was purified by passing it over titanium chips at 650°C. After cooling the fused solvent, K_2SiF_6 was added and the resulting solution was purified by pre-electrolysis for 12-24 hr under conditions similar to those used for deposition but at a substantially higher potential and current density.

Electrodeposition of silicon was performed at 745°C \pm 10°C in a two- or three-electrode configuration with the melt contained in a vitreous carbon crucible. After graphite, niobium, and nickel had been tried

in preliminary experiments, silver was selected as the cathode material because of its low reactivity with silicon. Graphite was found to be unsuitable as an anode material because it reacts and tends to disintegrate. Platinum was therefore used both as anode and reference electrode. Electrodes were ultrasonically cleaned in ethanol prior to use. Voltammetry and electrolysis at constant current or potential were carried out using a potentiostat/programmer and the charge passed was measured with a coulometer.

Salts adhering to the deposit were removed by digesting in hot distilled water for about 12 hr followed by ultrasonic cleaning in water, then ethanol, for about 15 min.

The morphology of the deposits was investigated by scanning electron microscopy and optical microscopy. The samples were analyzed for impurities by x-ray, electron microprobe, and emission spectrographic analysis.

Results

Morphology.—A major aim of this investigation was to determine the conditions for the deposition of inclusion-free, coherent layers of uniform thickness. Initial studies were made using K_2SiF_6 concentrations from 0.5 to 2.5 mole percent (m/o) in the two-electrode configuration and a typical cyclic voltammogram for a 1 m/o solution at 750°C is shown in Fig. 1. Deposition potentials extrapolated from linear regions of current-voltage plots for graphite, nickel, niobium, and silver are listed in Table I. Silicon is highly reactive at 750°C and only in the case of silver was the reaction between the deposit and the substrate found to be negligible.

Cell voltages above $-2V$ vs. Pt and corresponding current densities above 20 mA cm^{-2} were found to result in very nonuniform powdery or dendritic deposits on top of a thin, coherent layer about $2 \mu\text{m}$ thick. Reducing the deposition potential to $-1.9V$ was found to give coherent and strongly adherent deposits. Figure 2 shows a typical sample of about 20

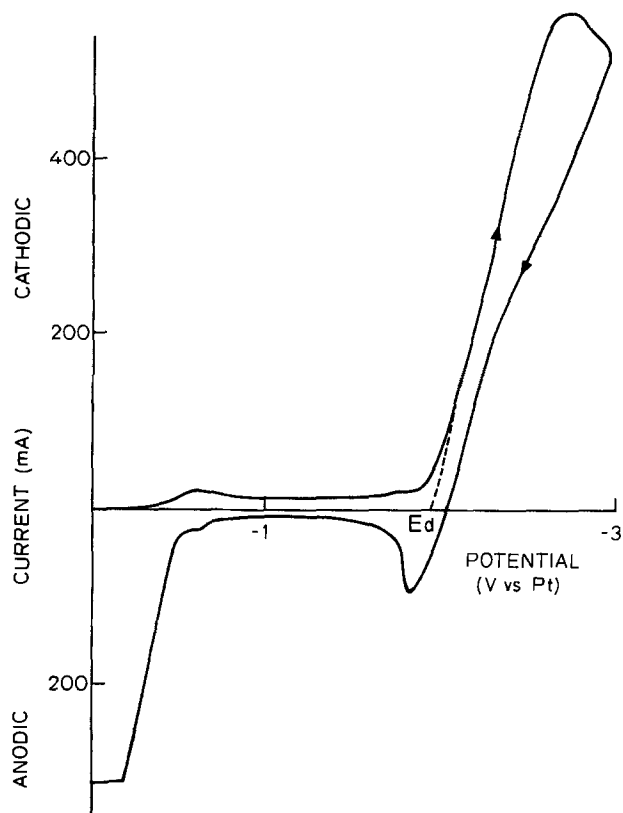


Fig. 1. Cyclic voltammogram of 1 m/o solution of K_2SiF_6 in Flinkak eutectic at 750°C, $v = 1 \text{ V/sec}$, silver cathode area $\sim 1.56 \text{ cm}^2$.

Table I. Deposition potentials extrapolated from linear regions of current-voltage plots

Substrate	Deposition potential (V)	Remarks
Graphite	-0.75 ± 0.1 (vs. graphite)	No identifiable deposit
Nickel	-1.26 ± 0.01 (vs. graphite)	Powdery deposit—mainly nickel silicides
Niobium	-1.45 ± 0.05 (vs. graphite)	Powdery deposit—mainly niobium silicides
Silver	-1.96 ± 0.03 (vs. platinum)	Dense, coherent, and well-adherent silicon

μm thickness which was deposited at a constant potential and the current density was 3.9 mA cm^{-2} with a total charge passed of 208 C cm^{-2} . The average grain size is about $16 \mu\text{m}$. A similar deposit at a constant current of 3.2 mA cm^{-2} is shown in Fig. 3 and 4. The measured potential was about $-1.95V$ vs. Pt and the total charge passed was 514 C cm^{-2} . The cross section demonstrates that the deposit is free from inclusions but also shows the irregularity in the thickness.

It was found possible to deposit reproducibly coherent, well-adherent films of about $50 \mu\text{m}$ average thickness using a cell potential of $-1.88 \pm 0.02V$ vs. Pt with current densities of $2\text{--}13 \text{ mA cm}^{-2}$ depending on the solute concentration. The current efficiency

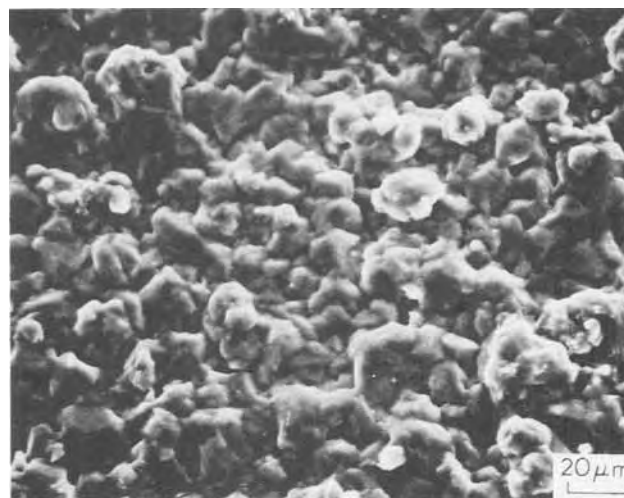


Fig. 2. Scanning electron micrograph of a deposit plated at constant cell potential of $-1.9V$ vs. Pt at 750°C, the K_2SiF_6 concentration $\sim 1 \text{ m/o}$.

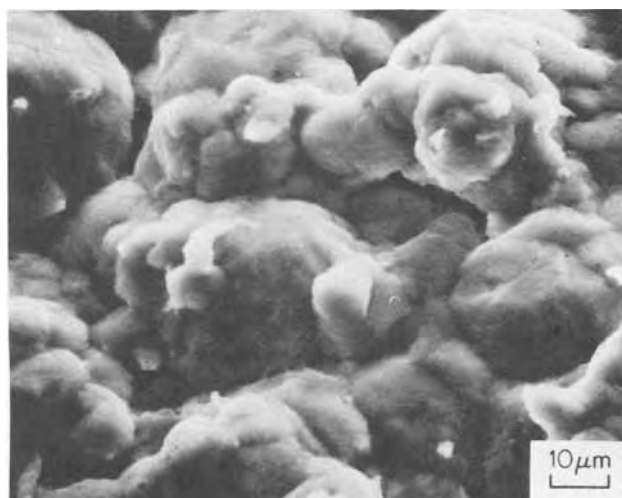


Fig. 3. Scanning electron micrograph of a deposit plated at constant current density of 3.2 mA cm^{-2} at 735°C, the K_2SiF_6 concentration $\sim 1.5 \text{ m/o}$.

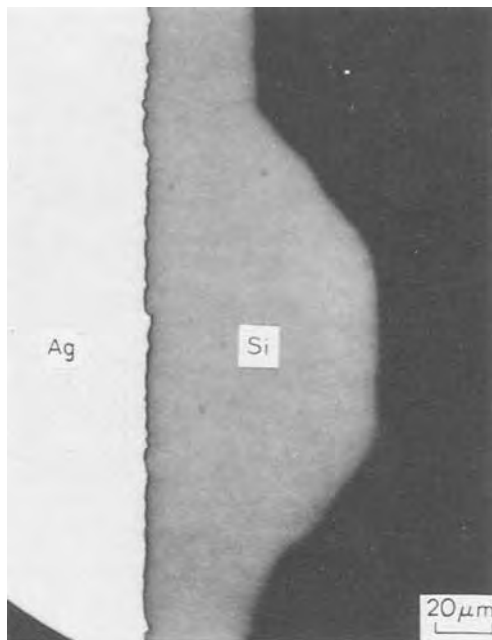


Fig. 4. Cross-sectional view of silicon, electrodepositing conditions same as in Fig. 3.

was normally 35-50% and the grain size up to 60 μm on top of an initial layer of 8-14 μm average grain size.

Attempts were made to deposit relatively thick layers at these low current densities. Figure 5 shows the result of prolonged electrolysis at $-1.90 \pm 0.02\text{V}$ vs. Pt over two days (2945 C cm^{-2} charge), at current densities in the range from 4 to 12 mA cm^{-2} . The deposit was 2 mm in thickness but a cross section (Fig. 6) shows that there was a very high concentration of fluoride inclusions trapped between grains. A surprising feature of this experiment is that the inclusion concentration is rather high even during the early stages of growth, but the deterioration in the later stages is severe.

Since thick, inclusion-free layers could not be electrodeposited from the dilute solutions used, the K_2SiF_6 solute concentration was increased to 4-6 m/o in subsequent investigations. In addition, a three-electrode arrangement was introduced since in principle this gives better control over the deposition rate. Although boron nitride compartmented metal/metal ion (e.g., Ni/Ni^{2+}) and the hazardous fluorine reference cells have been used (10), a platinum foil pseudo-



Fig. 5. General view of thick deposit plated at constant cell potential of -1.9V vs. Pt at 750°C , the K_2SiF_6 concentration ~ 2.5 m/o.

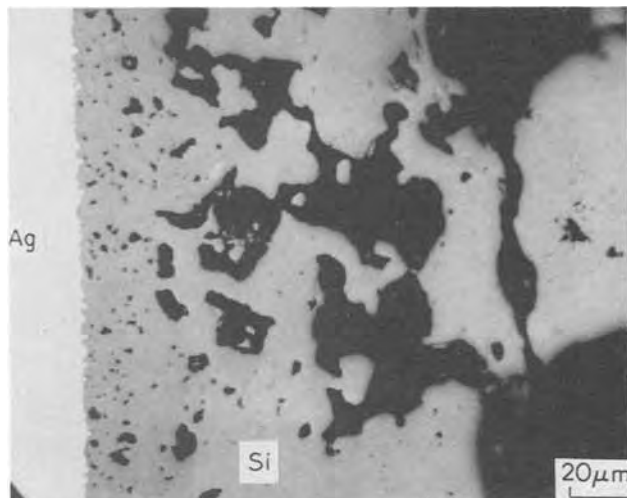


Fig. 6. Cross-sectional view of silicon, electrodepositing conditions same as in Fig. 5.

reference electrode was preferred in this study because of its simplicity. The measured deposition potential against a Pt reference electrode was found to be $-0.74 \pm 0.03\text{V}$. However, variations by as much as 0.10V were observed in a few experiments. These variations may be due to changes in electrode separation or to small changes in electrode surface structure, or to the inherent uncertainties in the determination of deposition potential (11). The deposition potential was therefore determined prior to each electrodeposition experiment.

Well-adherent, inclusion-free deposits up to 3 mm in thickness were found possible using applied potentials in the vicinity of the deposition potential (Table II). The corresponding current density was from 10 to 60 mA cm^{-2} and the efficiency was from 35 to 70%. Figure 7 shows a typical example of a deposit plated at -0.75V vs. Pt for about four days (total charge 12,890 C cm^{-2}). The cross section of this deposit at the silver-silicon interface is shown in Fig. 8. With the exception of a few cracks introduced either during cooling or mounting, the deposits are substantially coherent; the wedge shape of Fig. 7 is an end effect and is characteristic of the small samples currently prepared.

Figure 9 shows the grain structure of a typical deposit as revealed by an HNO_3/HF etch. Growth is columnar with a grain size up to 100 μm , the grain size increasing with increasing thickness of the deposit as is usual for electrodeposits from aqueous solutions without complexing agents (12). Grain orientation has not yet been studied in detail but a columnar structure might be advantageous for the direct use of polycrystalline films in solar cells.

Purity.—As mentioned earlier, starting materials were of 99-99.5% purity and were not given any purification treatment apart from pre-electrolysis. This latter procedure is expected to remove from the

Table II. Experimental parameters and results for thicker deposits in three-electrode configuration

Experiment No.	Cathode potential vs. Pt (V)	Approximate current density (mA cm^{-2})	Total charge (C cm^{-2})	Thickness of the deposit (mm)	Efficiency
1	-0.74	44	2450	0.9	50
2	-0.75	33	12,889	2.5	44
3	-0.74	19	6884	1	34
4	-0.75	10	6822	2	41
5	-0.85	60	4100	1.2	69
6	-0.86	50	1749	0.4	49
7	-0.64	20	4015	1.1	38

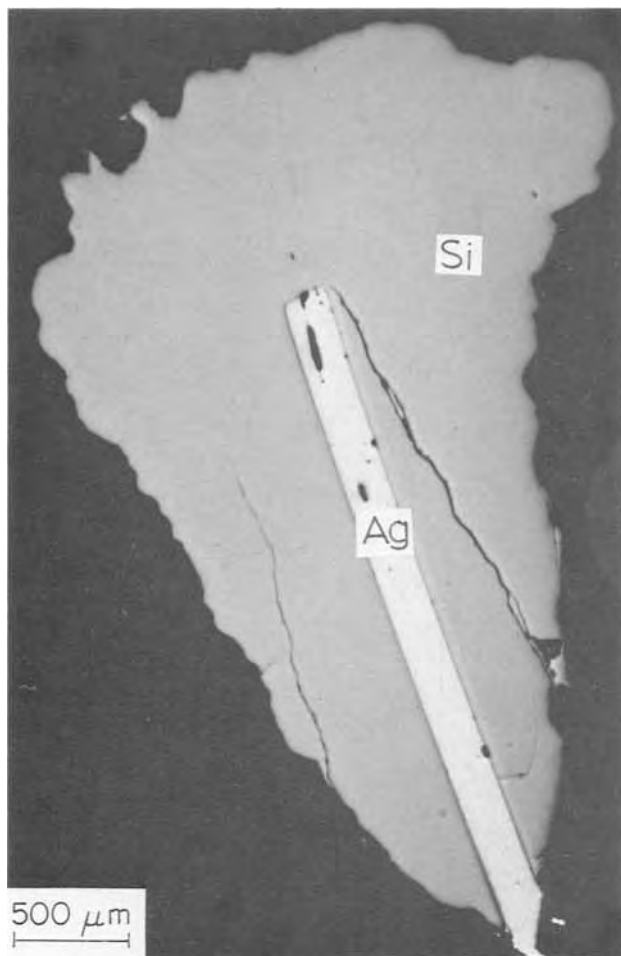


Fig. 7. Micrograph of silicon, deposited at constant cathodic potential of $-0.75V$ vs. Pt at $746^{\circ}C$, the K_2SiF_6 concentration ~ 5 m/o.

solution those impurities which deposit at lower potentials than silicon. Impurities with a higher deposition potential than that used for subsequent electrodeposits should remain in solution. This idealized situation rarely occurs in practice since co-deposition tends effectively to reduce differences in deposition potentials between individual elements. An additional factor to be considered is that normal segregation of impurities is expected to depend upon the morphology of the deposit, and also on the grain size.

The increase in impurity concentration in irregular deposits at higher potentials was confirmed by analysis of highly dendritic films. These showed 2-20% of Li,

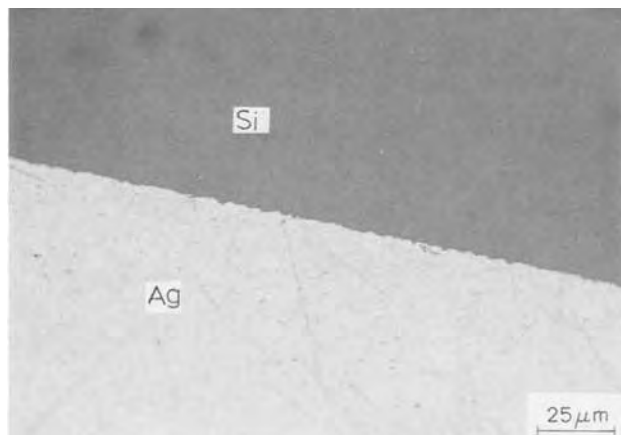


Fig. 8. Micrograph of silicon-silver interface of the deposit in Fig. 7.



Fig. 9. Micrograph of etched silicon surface of the deposit plated at constant cathodic potential of $-0.74V$ vs. Pt at $747^{\circ}C$, the K_2SiF_6 concentration ~ 4 m/o.

presumably as inclusions of LiF, together with about 2% of other impurities, mainly Al, Cr, and Fe with traces of B, Cu, Mg, and Ni.

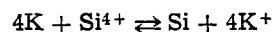
When deposits were made at potential close to the deposition potential, the impurity concentration was reduced to typically about 200 ppm of Al, B, Cr, Fe, Mg, and Ni. The best electrodeposits, however, showed only 10 ppm of total impurity (2 ppm B, 5 ppm Cr, 0.6 ppm Cu, 0.3 ppm Pt, and 1 ppm Ag). This material appears to be the highest purity silicon to be prepared by electrodeposition to date, since the best material previously reported is that of Monnier *et al.* (3, 4) with 99.99% purity.

The thicker inclusion-free deposits were sometimes found to contain 0.01-0.1% of Cr and Fe. These deposits require a period of several days of electrolysis during which fluoride vapor or anodically liberated fluorine can attack the Inconel atmosphere tube and produce transition metal fluorides. These may be transported to the melt via the vapor phase and result in the transition metal contamination. Microprobe analysis of the reacted scales on the furnace wall indicated a Cr-rich phase instead of normal Ni-rich Inconel 600. Such a Cr-rich surface film formation upon aqueous oxidation of Inconel 600 even at $300^{\circ}C$ was demonstrated recently by McIntyre *et al.* (13). This source of contamination can clearly be eliminated by the use of an alternative furnace design with an internal graphite element and water-cooled stainless steel jacket. However the 99.999% pure material was produced as thick deposits.

Discussion and Conclusions

Reproducible deposits of silicon onto silver have been obtained by the electrolysis of K_2SiF_6 -fluoride systems at $745^{\circ}C$ and conditions have been determined for the deposition of inclusion-free and well-adherent layers. Although silicon has been deposited previously from fluoride melts, the present experiments appear to be the first in which electrowinning of silicon gave coherent deposits up to 3 mm in thickness.

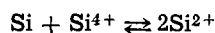
The powdery deposits at high potentials and the spongy or dendritic deposits on prolonged electrolysis of dilute K_2SiF_6 solutions at the deposition potential could be explained in terms of a secondary reaction between alkali metal deposited by the primary deposition as observed by Dodero (14)



No evidence for electrodeposition of potassium was observed in our system and this is considered unlikely in view of the large difference in deposition potential between alkali metals and silicon. Dodero used very high depositional potentials and so the primary elec-

trodeposition of alkali metals was to be expected in his experiments.

The noncoherent deposits may also be explained in terms of a secondary reaction between the deposited silicon and the melt



Dissolution of silicon has been observed when wafers were held in contact with the melt in the absence of an applied potential. However this does not necessarily imply that disproportionation occurs under the conditions of deposition, and it is difficult to understand how this effect can explain the major improvement in morphology on increasing the solute concentration.

It appears likely that polynuclear complexes are present in the solution and that these may have a strong influence on the deposition process. Complexes such as $\text{Mo}_2\text{Cl}_9^{3-}$ (15) in alkali chloride melts and $\text{U}_2\text{O}_4^{3-}$ in perchlorate solutions (16) are formed when the concentrations of MoCl_3 and uranyl ions, respectively, are increased. Compounds of structure $\text{Si}_n\text{F}_{2n+2}$ are known to exist, and both Si_3F_8 and Si_4F_8 have been isolated (17). It is suggested that a slow chemical step involving dissociation of a polynuclear complex precedes the electron-transfer reaction and that this dissociation step is rate controlling and favors the deposition of coherent films. Further study is required before this postulate can be confirmed, but we believe that it is important to determine the rate-controlling step in the silicon deposition reaction.

The purity of the best deposits is good in comparison with the starting materials and indicates that the single stage electropurification process is effective. Since the solvent phase is reusable, high purity alkali metal fluorides can be used reducing the initial impurity content in the melt. Improved furnace design to eliminate high temperature reactions between fluoride vapors and Inconel 600 should lead to the deposition of "solar cell" grade material as either thin or thick films in a single step.

Thick films have a columnar structure of relatively large grain size as is required of the deposited material is to be used directly for solar cell fabrication. The power required to deposit 1 kg of silicon is about 16 kW-hr plus the cost of maintaining the melt at 745°C. In large scale plants, joule heating from the deposition current is adequate to maintain temperatures of this order, so that we believe that electro-deposition has the potential to yield silicon of adequate purity for solar cells at about \$1 per kg. Silver is clearly too expensive a material for use on a large scale but the substrates could be reused if bulk silicon were stripped from the cathode after deposition. Alternatively a 20-100 μm coating on a cheap substrate would be sufficient in a process to produce thin film solar cells directly using this method.

Acknowledgments

This work was supported by the Division of Basic Energy Studies of the U.S. Department of Energy under contract No. EY-76-5-03-0326. It has greatly benefitted from facilities and equipment made available to the Center for Materials Research at Stanford University through the NSF-MRL program.

Manuscript submitted Jan. 21, 1980; revised manuscript received March 31, 1980. This was Paper 451 presented at the Los Angeles, California, Meeting of the Society, Oct. 14-19, 1979.

Any discussion of this paper will appear in a Discussion Section to be published in the June 1981 JOURNAL. All discussions for the June 1981 Discussion Section should be submitted by Feb. 1, 1981.

Publication costs of this article were assisted by Stanford University.

REFERENCES

1. L. M. Magid, in "Proc. Nat. Workshop on Low Cost Polycrystalline Silicon Solar Cells," T. L. Chu and S. S. Chu, Editors, p. 4., May 18-19 (1976), Southern Methodist University, Dallas, Texas.
2. H. St. C. Deville, *Ann. Chim. Phys.*, **43**, 31 (1854).
3. R. Monnier and J. G. Giacometti, *Helv. Chim. Acta*, **47**, 345 (1964).
4. R. Monnier and D. Barakat, U.S. Pat. 3,219,561 (1965); 3,254,010 (1966).
5. U. Cohen and R. A. Huggins, *This Journal*, **123**, 381 (1976).
6. U. Cohen, U.S. Pat. 3,983,012 (1976); 4,142,947 (1977).
7. U. Cohen, *J. Electron. Mater.*, **6**, 607 (1977).
8. G. M. Rao, D. Elwell, and R. S. Feigelson, Abstract 451, p. 1125, The Electrochemical Society Extended Abstracts, Los Angeles, Calif., Oct. 14-19, 1979.
9. R. C. De Mattei, D. Elwell, and R. S. Feigelson, *J. Cryst. Growth*, **44**, 545 (1978).
10. J. A. Plambeck, in "Encyclopedia of Electrochemistry of Elements—Fused Salt Systems," Vol. X, A. J. Bard, Editor, Marcel Dekker, New York (1976).
11. Iu. K. Delimarskii and B. F. Markov, "Electrochemistry of Fused Salts," Sigma Press, Washington (1961).
12. R. S. Sethi, in "Adv. Surface Coating Tech.—Int'l Conf.," p. 153, London (1978).
13. N. S. McIntyre, D. G. Zetaruk, and D. Owen, *This Journal*, **126**, 750 (1979).
14. M. Doderio, *Bull. Soc. Chim. Fr.*, **6**, 209 (1939).
15. D. Inman and S. H. White, *J. Appl. Electrochem.*, **8**, 375 (1978).
16. M. Mastragostino and J. M. Saveant, *Electrochim. Acta*, **13**, 751 (1968).
17. G. C. Demitras, C. S. Russ, J. F. Salmon, J. H. Weber, and G. S. Weiss, "Inorganic Chemistry," Prentice Hall, London (1972).

Formation of Oxide Films at Platinum Anodes in Alkaline Solutions

I. Question of Kinetics and Mechanisms

A. Damjanovic,* L.-S. R. Yeh,* and James F. Wolf

Allied Chemical Corporation, Corporate Research Center, Morristown, New Jersey 07960

ABSTRACT

The kinetics of growth of anodic oxide films at platinum electrodes was determined in 1M KOH solutions at room temperature using linear potential sweep and galvanostatic charging techniques. Irrespective of the mode or rate of growth, the same oxide film forms at potentials anodic to 1.0V vs. RHE. Oxygen initially adsorbed at prereduced electrodes at potentials below 1.0V is used at higher potentials for the film formation. The rate equation for the growth in alkaline solutions has the same general form as in acid solutions. Growth proceeds according to the model of high field assisted formation of ions at the metal/oxide interface (first step) and their migration through the oxide phase (second step). The exchange current density for the growth in alkaline solutions is, however, significantly higher, about 10^3 times, than in acid solutions. This is not expected for the proposed model of growth with either the first or the second step as rate determining.

In acid solutions, an oxide film grows over platinum electrodes at potentials above about 1.0V vs. RHE according to (1-4)

$$i = i_0 \exp \left[\frac{\alpha(V - V_0)}{d} \right] \quad [1]$$

where α and i_0 are constants independent of pH, V_0 is a parameter that changes with pH, and d is the thickness of the oxide film equal to τq . Factor τ converts charge density q into thickness. This equation describes the formation of the film irrespective of the mode or rate of growth, e.g., irrespective of whether the film grows galvanostatically, potentiostatically, or potentiodynamically (4). The physical model of the growth is that of the high field, $(V - V_0)/d$, assisted formation of ions at the metal/oxide interface (the first reaction step) and their migration in the field through the oxide film (the second reaction step). Kinetic data of growth appears to be compatible with the first step as rate determining (5, 6).

No similar study was found in the literature on kinetics and mechanisms of formation of anodic films at platinum in alkaline solutions. This is surprising in view of the role platinum plays as an electrocatalyst in alkaline solutions. For, whenever an electrode is covered by a thin anodic film, no meaningful analysis of kinetics, mechanism, or electrocatalysis of an electrochemical reaction can be made unless the properties of the film, including its thickness, are first known. Recent studies of oxygen evolution illustrate this (7-8).

To determine if an oxide film forms according to the same model of growth in alkaline as in acid solutions, we examined the kinetics of film formation at platinum in alkaline solutions.

Experimental

The experimental procedure was the same as described previously (4-6, 9). Two series of experiments were carried out in 1M KOH solutions saturated at room temperature with either O_2 or N_2 . In the first series, the potentiodynamic technique was used to examine the buildup of anodic films. A linear potential sweep was applied to a polished disk electrode (0.33 cm^2) which was initially prereduced at a potential just before hydrogen evolution ($\sim 0.2 \text{ V vs. RHE}$). In a few experiments, the starting potential of the

sweep was set in an N_2 -saturated solution at 0.65V vs. RHE ($\sim -0.4 \text{ V vs. SCE}$), and the anodic and cathodic branches of the sweep were recorded. For most of the experiments, the starting potential was set at the rest potential in O_2 -saturated solutions ($\sim 0.95 \text{ V vs. RHE}$). Currents for different rates of potential sweeps, S , were followed with time either with an oscilloscope or an X-Y recorder.

In the second series of experiments, the galvanostatic technique was used. A constant current was applied to a prereduced electrode starting from the rest potential in O_2 -saturated solutions and the potential was recorded with time.

Potentiodynamic Formation of Oxide Films

Asymmetry of the i - V traces.—A typical potentiodynamic i - V trace in an N_2 -saturated solution is shown in Fig. 1. It is similar to those reported in acid and alkaline solutions for the same potential region [cf. Ref. (4, 10-15)]. The similarity of the traces in acid and alkaline solutions suggests that the same processes control the anodic film formation and their reduction in both solutions [e.g., Ref. (10-17)].

As in acid solutions, a current plateau appears at potentials above about 0.95V vs. RHE. Following the initial adsorption stage at lower potentials, an anodic film of few monolayers is formed in the plateau region (4, 13, 17). If similar processes control the

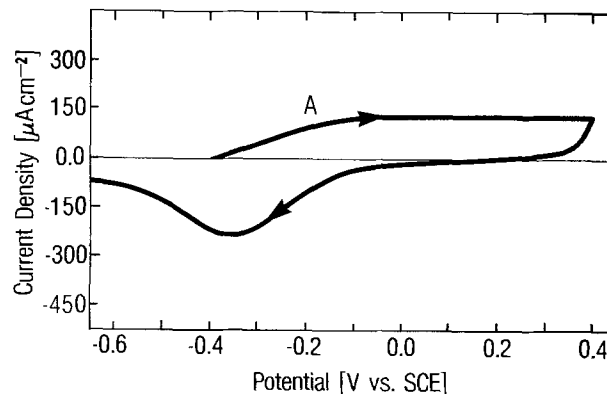


Fig. 1. Typical i - V profile in 1M KOH solution. The scan rate 0.05 V/sec. Current density not corrected for the roughness of electrode surface ($RF = 1.6$).

* Electrochemical Society Active Member.

Key words: platinum anodic films, anodic oxide growth.

formation of films both in acid and alkaline solutions, then the film in alkaline solutions, too, is an oxide phase [cf. Ref. (3, 15)].

On the reversal of the potential scan, a cathodic peak for the film reduction is observed at potentials negative to those of the anodic scan in the plateau region. This asymmetry of current traces in the anodic and cathodic scans is a general characteristic of i - V profiles in acid and alkaline solutions. It is a consequence of the diametrically different mechanisms that must hold for the anodic formation and cathodic reduction of oxide films (18). According to the model of high field assisted growth, only an oxide film of uniform thickness can grow. The model itself, however, precludes any possibility that the reduction of the oxide film can occur according to the same mechanism. Not only is the uniform reduction of an oxide film precluded, but the reduction cannot be completed by the action of a simple mechanism. This is because any point on the oxide film at which the reduction is randomly initiated must become a "weak" point that will dissolve preferentially due to the locally increased field (now in the opposite direction). When a pit in the oxide phase, which is formed in this initial process, reaches the surface of the metal itself, lateral reduction of the oxide film along the metal surface is an easy alternative process for further rapid reduction. The overall process is therefore a reversed nucleation and growth process and should lead to a current peak rather than to a plateau [cf. Ref. (16, 18)].

Analysis of the i - V traces in the plateau region.— If a unique relationship exists between current density, potential, and film thickness during the growth of oxide films in the plateau region, *i.e.*, if

$$i = i(V, q) \quad [2]$$

the following analysis of the i - V profiles, originally suggested by Harris for the growth of films in acid solutions (4), can be made. Taking V as an independent variable, differentiation gives

$$\frac{di}{dV} \equiv \left(\frac{\partial i}{\partial V} \right)_q + \left(\frac{\partial i}{\partial q} \right)_V \frac{dq}{dV} \quad [3]$$

which, with the identity

$$\left(\frac{\partial i}{\partial q} \right)_V = - \left(\frac{\partial i}{\partial V} \right)_q \left(\frac{\partial V}{\partial q} \right)_i \quad [4]$$

transforms to

$$\frac{di}{dV} = \left(\frac{\partial i}{\partial V} \right)_q \left[1 - \left(\frac{\partial V}{\partial q} \right)_i \frac{dq}{dV} \right] \quad [5]$$

Now, since

$$\frac{dV}{dq} = \frac{dV}{dt} / \frac{dq}{dt} \equiv \frac{S}{i} \quad [6]$$

Eq. [5] can be rewritten in the form (4)

$$\frac{di}{dV} = \left(\frac{\partial i}{\partial V} \right)_q \left[1 - i \left(\frac{\partial V}{\partial q} \right)_i / S \right] \quad [7]$$

This equation, which is independent of a model or mechanism of anodic film growth, shows that as the potential increases current density may in principle either increase, remain constant, or even decrease depending on the relative values of the terms in the brackets.

When i remains constant during the potential scan, as in the plateau region, the following condition must be satisfied (4)

$$i_s = \left[\left(\frac{\partial V}{\partial q} \right)_{i_s} \right]^{-1} S \quad [8]$$

Here, i_s is the current density in the plateau region

for a given scan rate, S . From Eq. [8], i_s is either exactly proportional to S , *i.e.*, $(\partial V/\partial q)_{i_s} = \text{const.} \neq f(S)$, or i_s increases either faster or less rapidly with S than required by the proportionality, *i.e.*, $(\partial V/\partial q)_{i_s} = f(S) \neq \text{const.}$

With i_s obtained from i - V profiles such as that in Fig. 1, $\log i_s$ is plotted *vs.* $\log S$ in Fig. 2. A nearly linear relationship with a slope close to one is observed. This can lead to the conclusion that $(\partial V/\partial q)_{i_s} = \text{const.} \neq f(S)$. However, for the proportionality, the slope should be equal to one. The proportionality is indicated in Fig. 2 with two lines drawn close to the experimental points. The deviation from linearity is now evident. It is a consequence of the change of $(\partial V/\partial q)_{i_s}$ with S . It indicates that i_s increases less rapidly with S than required by the proportionality, *i.e.*, $(\partial V/\partial q)_{i_s}$ increases with S and hence also with i_s . A more sensitive check is a plot of S/i_s against S (4). Clearly, S/i_s is not constant, but is an increasing function of $\log S$ (cf. Fig. 3). Whether i_s is proportional to S or not depends, of course, on the mechanism of film formation. Suppose that the film formation is described by an equation of the form

$$i = i(\alpha V - \beta q) \quad [9]$$

where α and β are constants. Since from Eq. [9]

$$\left(\frac{\partial V}{\partial q} \right)_i = \frac{\beta}{\alpha} = \text{const.} \quad [10]$$

it follows from Eq. [6] and [8] that in the plateau region

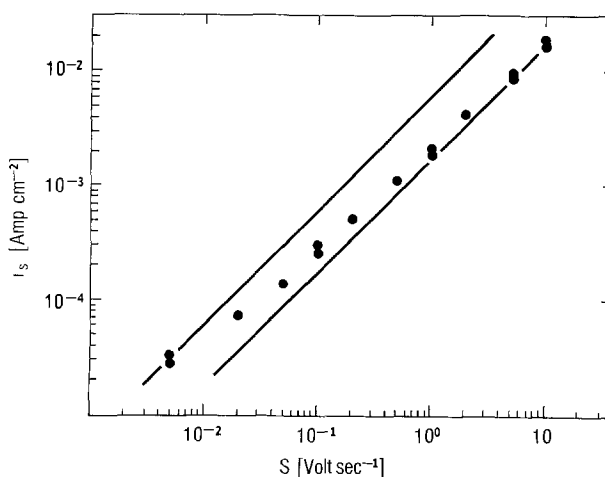


Fig. 2. Variation of anodic plateau current density with potential scan rates. Current density not corrected for the roughness of electrode surface.

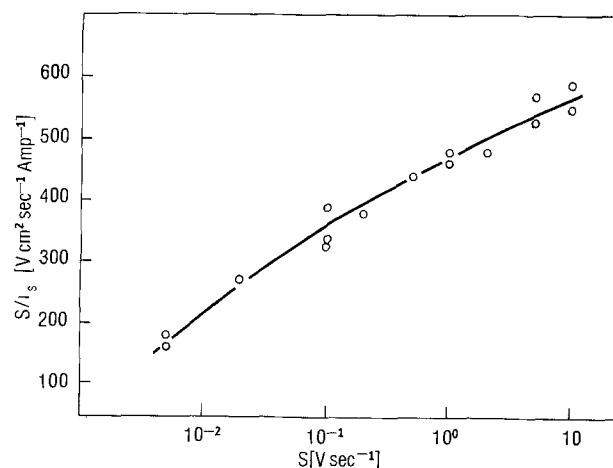


Fig. 3. Ratio of scan rate to plateau current density as function of scan rate from Fig. 2.

$$\frac{S}{i_s} = \left(\frac{\partial V}{\partial q} \right)_{i_s} = \frac{\beta}{\alpha} = \text{const.} \neq f(S) \quad [11]$$

Equation [9], therefore, describes a process of growth for which $S/i_s = \text{constant}$, i.e., the process for which i_s increases linearly with S [c.f. Ref. (10, 15)]. Since present experiments show that $S/i_s = f(S) \neq \text{const.}$, any mechanism for film formation leading to a rate equation of the form of Eq. [9] does not represent the formation of an anodic film in the plateau region. This analysis eliminates, for example, any mechanism that leads to a rate equation of the form

$$i = i_0 \exp(\alpha V - \beta q) \quad [12]$$

Such an equation can describe the buildup of adsorbed oxygen films at anodes under Temkin conditions of adsorption. This analysis illustrates how, on the basis of the quasi-linear dependence of i_s on S with the slope close to one, an incorrect conclusion can be reached regarding the rate equation and the mechanism of film formation.

Rate equation for oxide growth.—What is the form of the rate equation that satisfies condition [8] and can this equation be derived from the potentiodynamic data alone? An equation such as [1], that describes the growth of oxide films in acid solutions, would, for instance, satisfy this condition, e.g.

$$\left(\frac{\partial V}{\partial q} \right)_{i_s} = \frac{S}{i_s} = \frac{1}{\alpha} \ln \frac{i_s}{i_0} = f(i) \neq \text{const.} \quad [13]$$

Whether the potentiodynamic data in alkaline solutions follow this relationship can be checked by plotting S/i_s vs. $\log i_s$. It is clear from Fig. 4 that $(\partial V/\partial q)_i$ depends strongly on $\log i_s$. It is, however, not so clear if the dependence is linear as it should be to satisfy Eq. [13]. It may be noted that the condition [8] does not itself require linearity. Apparently, present potentiodynamic data are not sensitive enough for this test. It will be shown later from galvanostatic data that $(\partial V/\partial q)_i$ does change linearly with $\log i$. This dependence is indicated in Fig. 4 by the broken line.

If instead of Eq. [2] one writes $V = V(i, q)$ and takes i as an independent variable, then

$$\frac{dV}{di} = \left(\frac{\partial V}{\partial i} \right)_q + \left(\frac{\partial V}{\partial q} \right)_i \frac{dq}{di} \quad [14]$$

Now, $(\partial V/\partial q)_i$ can be obtained from data in Fig. 4 using Eq. [13]. Since a linear dependence of $(\partial V/\partial q)_i$ on $\log i_s$ is indicated in the figure, we can take for this dependence the analytical expression given by Eq. [13]. $(\partial V/\partial i)_q$ can be obtained from the i - V data at different S . For instance, contours of constant q ,

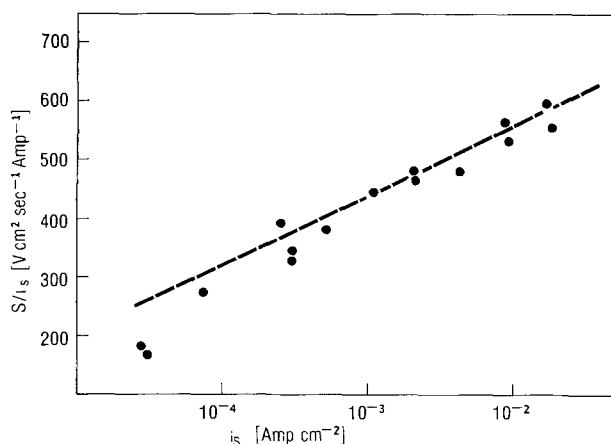


Fig. 4. Ratio of scan rate to plateau current density as function of plateau current density.

obtained by integration along any single i - V profile from a suitable starting point, e.g., from A in Fig. 1, can be superimposed over i - V contours and then the $(\partial V/\partial i)_q$ evaluated along such contours. It is, therefore, possible to determine the rate equation from the potentiodynamic data alone providing analytical expressions can be derived both for $(\partial V/\partial \ln i)_q$ and for $(\partial V/\partial q)_i$ dependence. Since the plot of S/i_s vs. $\log i_s$ indicates that an equation similar to [1] can describe the growth under potentiodynamic conditions, it is convenient to examine $V = V(\ln i, q)$ instead of $V = V(i, q)$ and to rearrange Eq. [14] accordingly. If Eq. [1] is valid also for growth in alkaline solutions, then $(\partial V/\partial \ln i)_q$ should be equal to q/α and Eq. [14] can be integrated. Unfortunately, as in the case of $(\partial V/\partial q)_i$ the potentiodynamic data are not accurate enough to allow an analytical expression for $(\partial V/\partial \ln i)_q$ to be determined.

Galvanostatic Formation of Oxide Films

Constant current charging curves.—In a series of experiments a constant current was applied to an initially prerduced electrode starting from the rest potential in oxygen-saturated solutions. Under these conditions, a rest potential was established in a few minutes. In Fig. 5, galvanostatic charging curves are reproduced from a photograph of an oscilloscope storage screen (Tektronix, 7623A) for 3×10^{-5} , 3×10^{-4} , 3×10^{-3} , and 3×10^{-2} A/cm². Time scales on the scope were adjusted to represent charge density, q .

At all current densities, the potential after an initial short, steep, and nonlinear rise increased nearly linearly with charge density. The linear region was followed by a potential "plateau." In the plateau region, the potential, however, was not constant; it continued to increase with time but much slower than in the linear region. Using a rotating ring-disk electrode it was shown that O₂ does not evolve in the linear region. It starts to evolve in the plateau region and soon becomes the predominant reaction (Fig. 6). In the linear region, therefore, the current is used almost entirely for forming an anodic film (except for a small part used for charging the double layer).

The most significant feature of the linear V - q traces is that the $(\partial V/\partial q)_i$ slopes increase linearly with the logarithm of applied current density, i.e.

$$\begin{aligned} \left(\frac{\partial V}{\partial q} \right)_i &= f(i) = c' \log i + b \\ &= c \ln(i/i_0) \end{aligned} \quad [15]$$

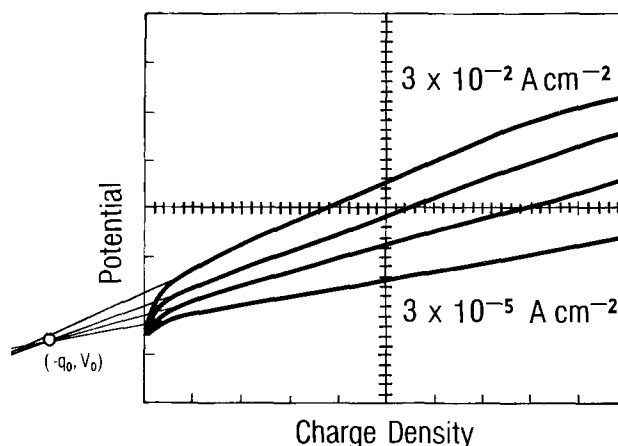


Fig. 5. Galvanostatic charging curves at various current densities. Charge density: 150 $\mu\text{C cm}^{-2}$ per division. Potential: 0.2V per division. Data are not corrected for the roughness of electrode surface.

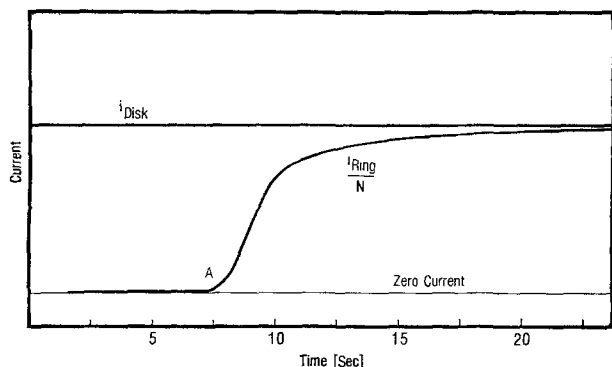


Fig. 6. The ring current for reduction of oxygen after correction for the collection efficiency. Constant current of 10^{-4} A was applied to the Pt disk electrode (area 0.49 cm^2).

This is shown in Fig. 7. The slope of this relationship is given by the constant c' ($=2.3c$), i.e.

$$\frac{\partial^2 V}{\partial q \partial \ln i} = c [=52 \text{ VC}^{-1} \text{ cm}^2] \quad [16]$$

Parameter b is the value of $\partial V/\partial q$ at $\log i = 0$. It is approximately equal to $800 \text{ VC}^{-1} \text{ cm}^2$. Here, neither b nor c is corrected for the roughness of the electrode surface. Constant i_0 is the exchange current density for the growth (see below); $i_0 = \exp(-b/c)$, i.e., it is equal to $1.3 \times 10^{-7} \text{ A cm}^{-2}$ when corrected for the roughness of the electrode surface ($RF = 1.6$).

The linearity of the $(\partial V/\partial q)_i$ vs. $\log i$ extends for four decades of the current densities used in this work. This is possible only when the same mechanism of growth holds for a wide range of growth rates. A similar relationship has been observed for the anodic oxide film formation in acid solutions (3, 9).

Returning now to Eq. [13] and Fig. 4, the galvanostatic $(\partial V/\partial q)_i$ data agree reasonably well with the potentiodynamic S/i_s data, particularly at high current densities. The deviation of S/i_s from linearity at low current densities is perhaps due to an experimental error in the potentiodynamic data rather than to any change in the mechanism of film formation. Evidently, the same film forms at platinum anodes irrespective of the mode of growth.

The second significant feature of the galvanostatic data is that the extrapolated V - q traces for various constant current densities intercept at the same potential, $V_0 = 0.94 \text{ V vs. RHE}$ and at the same negative value of charge density, $-q_0 \sim -260 \mu\text{C cm}^{-2}$ (cf. Fig. 5). Following the same discussion as in case of growth of anodic films in acid solutions (3, 9), it can be shown

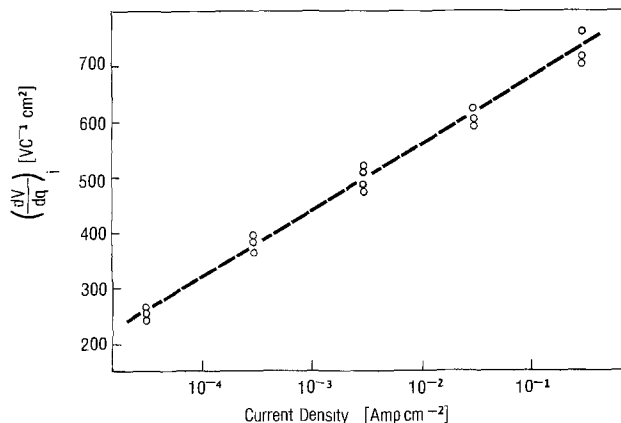


Fig. 7. Slopes of galvanostatic charging curves at various constant current densities. Data are not corrected for the roughness of electrode surface.

that V_0 is related to the potential at which an oxide film would initiate and grow at zero field with the rate equal to the exchange current density i_0 (cf., Eq. [1]). V_0 is not necessarily equal to the potential from which a constant current is applied, e.g., to the rest potential in O_2 -saturated solutions, V_R . The negative charge density is related to the oxygen adsorbed at electrodes prior to the application of a constant anodic current (9).

Since V - q traces at different current densities all intercept in extrapolation at the same point ($\sim q_0, V_0$), the linear dependence for any given current density is given by (6)

$$V - V_0 = (q + q_0)f(\log i) \quad [17]$$

$$= (q + q_0) \left(\frac{\partial V}{\partial q} \right)_i$$

or, with Eq. [15], by

$$V - V_0 = c(q + q_0) \ln(i/i_0) \quad [18]$$

Here, the constants c and i_0 have the same significance as in Eq. [15]. The rate Eq. [18] can be rearranged to the more familiar form

$$i = i_0 \exp \frac{V - V_0}{c(q + q_0)} \quad [19]$$

that can now be compared with the rate Eq. [1] for the growth in acid solutions.

Returning to Fig. 5, the dependence of the potential on current density at any constant q can be graphically determined. This is shown in Fig. 8. From the separation of the Tafel lines at any constant current density it follows, as expected from Eq. [19], that $(\partial V/\partial \log i)_q$ is a linear function of q , i.e.

$$\left(\frac{\partial V}{\partial \ln i} \right)_q = f(q) = a(q + q_0) \quad [20]$$

Constant a is found to be equal to $55 \text{ VC}^{-1} \text{ cm}^2$. It should be equal to c (cf. Eq. [18]) if $V = V(\ln i, q)$. Rate Eq. [19] can be obtained also from Eq. [15] and [20] using [14]. It can be concluded, therefore, that a rate equation of the same form as in acid solutions describes the growth of anodic films above 1.0 V vs. RHE in alkaline solutions.

Initial adsorption.—In this study, before a constant anodic current was applied to the test electrode, the electrode was cathodically prerduced at a potential just short of hydrogen evolution and then allowed to reach its rest potential, V_R , in O_2 -saturated solutions. Under these conditions, the coverage with oxygen at V_R , expressed as charge density, is (19) about $200 \mu\text{C cm}^{-2}$ (not corrected for electrode roughness). As in acid solutions, the extrapolated charge

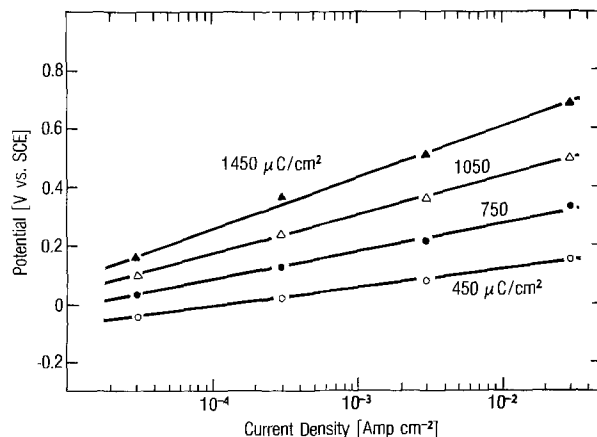


Fig. 8. Tafel slopes for oxide growth at constant thicknesses of oxide films.

density q_0 in Fig. 5 was identified with the adsorbed oxygen at oxide free electrodes at the rest (or starting) potential (9).

Though no evidence regarding the nature of the anodic film in alkaline solutions is available from ellipsometric, electron diffraction, or spectroscopic studies, it is taken here that the film is an oxide phase rather than an adsorbed oxygen layer. The following evidence supports this view. First, the rate equation for anodic film formation has the same form as the rate equation for the growth of anodic oxide films under the influence of a high field within oxide films. A rate equation of the same form normally does not describe an adsorption process. For an adsorption process and intermediate coverages, an equation of the form of Eq. [12] rather than [19] is expected (11, 15). Second, the similarity of the kinetic data in acid and alkaline solutions suggests that the nature of the films is the same in both solutions. In acid solutions, ellipsometry and other techniques have shown that the film is an oxide phase (20-22). Third, total charge density in the formation of the anodic film at the end of the linear region at 3×10^{-4} A cm $^{-2}$ is about 1800 μ C cm $^{-2}$ (cf. Fig. 5 and 6). This charge density already includes the density q_0 equivalent to oxygen initially adsorbed at electrodes. However, immediately following the linear region, in the plateau region, a substantial part of the current is still being used for film formation. In Fig. 6, integration of $i_{\text{disk}}-i_{\text{ring}}$ shows that beyond the linear region, which ends at point A in Fig. 5, the film continues to grow an additional 30-35% for the same period of time it grew in the linear region. Total charge density for the film formation is, therefore, at least 2400 μ C cm $^{-2}$. This coverage is not corrected for the roughness of the electrode surface. The roughness factor was determined in N $_2$ -saturated 1M KOH solution by capacitance measurements in the "polarizable" region. Taking the capacitance of an ideal surface to be 16 μ F cm $^{-2}$, RF is calculated to be 1.6. The total charge density for the anodic film formation is then about 1500 μ C cm $^{-2}$. This coverage is too high to be accounted for in terms of adsorption. Fourth, in the case of adsorption, the desorption process is expected to occur by the same mechanism as the adsorption process though in reverse direction. A symmetry of the i - V anodic and cathodic profiles in potentiodynamic experiments, or of the V - t traces in galvanostatic experiments, should then be observed. Such a symmetry has been observed by Conway and co-workers (12, 23), but only when the upper potential limit of a potential sweep is below a potential at which an oxide phase is formed. Once an oxide film had been initiated, an asymmetry in the V - i profiles develops. All the evidence, therefore, points toward the formation of an oxide film at potentials above about 1.0V vs. RHE. Of course, adsorption at least up to the level of q_0 always precedes oxide film formation (9, 13).

Because the linear V - q dependences for different current densities intercept in extrapolation at $(-q_0, V_0)$, and because q_0 is identified as the coverage with oxygen before the application of a constant current, it follows that in the process of anodic film formation initially adsorbed oxygen is almost entirely used for the formation of the oxide film. Further, because the linearity is established soon after the current is applied, the adsorbed oxygen is used for oxide formation during the very early stages of growth upon the application of a constant current. Coverage with adsorbed oxygen, or OH $^-$, over the oxide surface must, therefore, be fairly low. In acid solutions, this coverage has been determined by Vetter and Schultze (2) to be only about 0.02-0.03. It is necessary, therefore, to add q_0 to q ($= it$) in Eq. [19]. Writing

$$q_T = q_0 + it = q_0 + q \quad [21]$$

the rate Eq. [19] becomes

$$i = i_0 \exp \frac{V - V_0}{cq_T} \quad [22]$$

This is equivalent to shifting the origin of the coordinate V - q system from $(0, V_0)$ to $(-q_0, V_0)$.

Analysis of the rate equation.—For the model of the high field assisted growth of anodic oxide films with the potential barrier at the metal/oxide interface as the rate-determining step (the Cabrera-Mott mechanism), the following rate equation has been derived [e.g., Ref. (18)]

$$i = zeN\nu \exp \left[-\frac{W}{RT} \right] \exp \left[\frac{ze\lambda(V - V_0)}{dkT} \right] \\ = i_0 \exp \left[\frac{\alpha \Delta V_{\text{of}}}{d} \right] \quad [23]$$

Here, N is the density of metal ions in the metal surface, ν is their vibrational frequency, ze is the charge of the migrating ion, λ is the half-jump distance, and W is the activation energy. ΔV_{of} is the potential difference across the oxide film and d is the thickness of the film such that $\Delta V_{\text{of}}/d$ is the electric field within the film.

Comparison of Eq. [21] and [22] gives

$$\alpha = \frac{ze\lambda}{kT} = \frac{r}{c} \quad [24]$$

This relationship allows the product $z\lambda$ to be determined from experimental parameters and hence a check to be made regarding the validity of the model for anodic film formation in alkaline solutions. For anodic film formation in acid solutions, r is calculated to be 9×10^3 $\text{\AA} \text{ C}^{-1} \text{ cm}^2$ (3). With the same factor for alkaline solutions and with $c = 83 \text{ VC}^{-1} \text{ cm}^2$ when corrected for the roughness of the electrode surface, α and $z\lambda$ are respectively equal to 108 $\text{\AA} \text{ V}^{-1}$ and 2.8 \AA . Were z equal to 1, i.e., were Pt $^+$ a migrating species, which is improbable, the half-jump distance would be quite high, 2.8 \AA . For $z = 2$, i.e., for a divalent cation as the migrating species, such as in Pt(OH) $_2$, $\lambda = 1.4\text{\AA}$. This is a reasonable value for the half-jump distance. A similar value for the half-jump distance, $\lambda = 2\text{\AA}$, was reported for the growth in acid solutions (3). The agreement is satisfactory and provides additional support for the hypothesis that the same mechanism of growth controls the formation of anodic films and that the same oxide phase is formed both in acid and in alkaline solutions.

The exchange current density.—Difficulties arise, however, when the exchange current densities, i_0 's, for growths in acid and alkaline solutions are compared and analyzed. In acid solutions, $i_0 = 2 \times 10^{-10}$ A cm $^{-2}$, whereas in 1M KOH solution it is 1.3×10^{-7} A cm $^{-2}$ (see above).

The exchange current density according to Eq. [23] is given by

$$i_0 = N\nu ze \exp \left[\frac{-W}{RT} \right] \quad [25]$$

For the process at the metal/oxide interface as the rate-determining step, i.e., for the Cabrera-Mott model of growth, N , ν , z , and W should all be independent of the conditions in solution or at the oxide/solution interface. Hence, i_0 should be the same both in acid and in alkaline solutions. The observed difference in i_0 's would then, in general, indicate a different rate-determining step for the growth in alkaline solutions.

If N is the only parameter that is responsible for the observed difference in i_0 's, its value in alkaline solutions (1M KOH) should be 10^8 times higher than in acid solutions. In acid solutions, N has been determined from a temperature study to be closely equal to the density of atoms in the metal surface (5, 6).

In general, N in alkaline solutions can only be equal to or less than N in acid solutions. Hence, the observed difference in i_0 's cannot be accounted for in terms of N alone. If W is responsible for the observed difference in i_0 's, then W for the growth in alkaline solutions should be about 4 kcal/mole lower than W (~ 25 kcal/mole) in acid solutions. Present data do not provide any clue whether W or N , or both, change from acid to alkaline solutions. However, both for the first and for the second step as rate determining, no solution effect on either W or N is expected.

The observed difference in i_0 's cannot be accounted for with the same model of growth but with the second step as rate determining in alkaline solutions. For the second step to become rate determining, its activation energy should increase over that for the process at the metal/oxide interface rather than decrease. However, a decrease is indicated by the higher value of i_0 in alkaline solutions.

In a following paper, the kinetics of film formation is determined at different temperatures and N and W are evaluated and correlated to the possible rate-determining steps.

Manuscript received Nov. 5, 1979.

Any discussion of this paper will appear in a Discussion Section to be published in the June 1981 JOURNAL. All discussions for the June 1981 Discussion Section should be submitted by Feb. 1, 1981.

Publication costs of this article were assisted by the Allied Chemical Corporation.

REFERENCES

1. J. L. Ord and F. C. Ho, *This Journal*, **118**, 46 (1971).
2. K. J. Vetter and J. W. Schultze, *J. Electroanal. Chem.*, **34**, 131, 141 (1972).
3. A. Damjanovic, A. T. Ward, B. Ulrick, and M. O'Jea, *This Journal*, **122**, 471 (1975).
4. L. B. Harris and A. Damjanovic, *ibid.*, **122**, 539 (1975).
5. A. Damjanovic, in "Proceedings of the Workshop on Electrocatalysis on Non-Metallic Surfaces," National Bureau of Standards Special Publication, No. 455, p. 259 (1976).
6. A. Damjanovic and L. S. R. Yeh, *This Journal*, **126**, 555 (1979).
7. A. Damjanovic and B. Jovanovic, *ibid.*, **123**, 374 (1976).
8. A. Damjanovic, A. T. Ward, and M. O'Jea, *ibid.*, **121**, 1186 (1974).
9. A. Damjanovic, L.-S. R. Yeh, and J. F. Wolf, *ibid.*, **127**, 874 (1980).
10. W. Böld and M. Breiter, *Electrochim. Acta*, **5**, 145 (1961).
11. M. W. Breiter, *ibid.*, **8**, 925 (1963).
12. R. Woods, in "Electroanalytical Chemistry," Vol. 9, A. J. Bard, Editor, p. 1, Marcel Dekker, Inc., New York (1976).
13. H. Angerstein-Kozłowska, B. E. Conway, and W. B. A. Sharp, *J. Electroanal. Chem.*, **43**, 9 (1973).
14. P. Stonehart, H. A. Kozłowska, and B. E. Conway, *Proc. R. Soc. London, Ser. A*, **310**, 541 (1969).
15. S. Gilman, *J. Electroanal. Chem.*, **2**, 111 (1967).
16. H. Angerstein-Kozłowska, B. E. Conway, and J. Klinger, *ibid.*, **87**, 301, 321 (1978).
17. B. E. Conway and H. Angerstein-Kozłowska, in "Proceedings of the Workshop on Electrocatalysis on Non-Metallic Surfaces," National Bureau of Standards Special Publication, No. 455, p. 107 (1976).
18. A. Damjanovic and A. T. Ward, *MTP Int. Review Sci., Phys. Chem., Ser. II*, p. 103 (1976).
19. M. L. B. Rao, A. Damjanovic, and J. O'M. Bockris, *J. Phys. Chem.*, **67**, 2508 (1963).
20. A. K. N. Reddy, M. A. Genshaw, and J. O'M. Bockris, *J. Chem. Phys.*, **48**, 671 (1968).
21. W. Visscher, *Optic*, **26**, 402 (1967).
22. S. H. Kim, W.-K. Paik, and J. O'M. Bockris, *Surf. Sci.*, **33**, 617 (1972).
23. B. E. Conway and Sh. Gottesfeld, *J. Chem. Soc. Faraday Trans. I*, **69**, 1090 (1973).

Formation of Oxide Films at Platinum Anodes in Alkaline Solutions

II. Temperature Study

A. Damjanovic,* L.-S. R. Yeh,* and James F. Wolf

Allied Chemical Corporation, Corporate Research Center, Morristown, New Jersey 07960

ABSTRACT

The kinetics of growth of oxide films at platinum anodes in 1M KOH solution is determined at different temperatures using the galvanostatic charging technique. The growth of the oxide film at potentials above about 1.0V vs. RHE follows the model of high field assisted formation of ions at the metal/oxide interface and their migration within the oxide film. The activation energy and preexponential factor are determined as 18.5 kcal/mole and 10^{13} cm⁻², respectively. These parameters differ significantly from the respective values reported for the growth in acid solutions. Comparison of the growth kinetics in acid and alkaline solutions leads to a serious difficulty. Neither the process of ion formation at the metal/oxide interface, nor the process of ion migration through the oxide phase as the rate-determining step, can account for the growth kinetics in alkaline solutions, unless it is assumed that different oxide phases form in acid and alkaline solutions. This is, however, an unlikely assumption.

It is shown in a preceding paper (1) that at platinum in alkaline solutions an anodic oxide film grows above about 1.0V vs. RHE according to

$$i = i_0 \exp \left[\frac{V - V_0}{cq_T} \right] \quad [1]$$

$$= i_0 \exp \left[\frac{\Delta V_{of}}{cq_T} \right]$$

where q_T , when corrected for the roughness of the electrode surface [$RF = 1.6$ (1)], represents the thickness of the oxide film expressed in C cm⁻² and $\Delta V_{of}/(rq_T)$ is the electric field within the growing oxide phase. Factor r converts charge density into thickness. V_0 is the potential at which an oxide film would grow without the accelerating effect of the field with a rate equal to the exchange current density i_0 [cf. Ref. (1)]. A rate equation of the same form was observed also for anodic growth in acid solutions (2-5). Evidently, the rate equations for growth in both acid and alkaline solutions, considered independently of each other, obey the formalism of the well-known model of the high field assisted formation of oxide films (6, 7). For this model, the following rate equation has been derived (6, 8)

$$i = N_{\nu}ze \exp \left[\frac{-W}{kT} \right] \exp \left[\frac{ze\lambda\Delta V_{of}}{kTd} \right] \quad [2]$$

$$= i_0 \exp \left[\frac{\alpha\Delta V_{of}}{rq} \right]$$

Meanings of the various parameters are given in the preceding paper (1). There is, however, a significant difference in i_0 's in acid (2×10^{-10} A cm⁻²) and alkaline (1.3×10^{-7} A cm⁻²) solutions. As discussed in the preceding paper, this difference cannot be accounted for by the model with the suggested rate-determining steps.

In order for the significance of the observed difference in i_0 's to be appreciated, it is helpful to analyze briefly the meanings of various parameters in the rate equation. Parameter α is defined by

$$\alpha = \frac{ze\lambda}{kT} \left(= \frac{r}{c} \right) \quad [3]$$

with ze being the charge of the ions that migrate across the metal/oxide interface and through the oxide phase, and λ their half-jump distance. Both in acid and alkaline solutions it was determined that $z = 2$. In acid solutions, λ is close to 2Å, while in alkaline solutions it is close to 1.4Å. This is only a minor and perhaps insignificant difference which may, at least partially, be due to uncertainty in the determinations of the roughness factors in these two solutions. The agreement indicates that the same oxide phase forms in both solutions and that Pt⁺⁺ is the most likely species migrating in the process of growth.

V_0 in 1M alkaline solutions is about 800 mV more negative than in 1M H₂SO₄ when both are referred to a pH-independent reference electrode. This difference is, however, expected. In acid solutions V_0 decreases about 60 mV as the pH increases for one unit (9). If the same dependence holds over the entire pH range, this will account for the observed difference in V_0 . Though Eq. [2] does not explicitly predict such a dependence, it is not contrary to the model. V_0 is related to the critical field in the metal/solution double layer which is just sufficient to pull metal ions from their positions in the surface lattice and place them over the metal surface. This field, however, depends on pH in a similar way as does the potential of zero charge (9). Neither α (through z) nor V_0 is expected to affect the exchange current density.

The exchange current density is given by

$$i_0 = N_{\nu}ze \exp \left[\frac{-W}{kT} \right] \quad [4]$$

Only two parameters, N and W , can be responsible for the observed difference in the exchange current densities. Both parameters, however, will depend on the rate-determining step. Two variations of the model, or different rate-determining steps, have been suggested [cf. Ref. (1, 6-8)]. According to the first variation, the Cabrera-Mott mechanism of growth (6), the first reaction step, i.e., the process of formation of ions at the metal/oxide film interface, is rate determining. For this step, the preexponential factor N

* Electrochemical Society Active Member.
Key words: platinum oxide films, anodic film formation.

should be closely equal to the density of atoms in the metal surface, N_s . According to the second variation, the Verwey mechanism of growth (7), the second reaction step, *i.e.*, the process of ion migration from one to an adjacent interstitial position within the oxide phase, is rate determining. For this step, the factor N should be equal to the density of the interstitial cations in a reaction plane within the oxide phase, N_i . Then, N_i should be less than N_s by a few orders of magnitude. Factor N for either of these two rate-determining steps, however, is not expected to depend on the conditions in solution, specifically on pH. Similarly, W for the same rate-determining step should not depend on the conditions in solution, *i.e.*, on pH. Of course, W will change with the rate-determining step. Now, factor N for the growth in acid solutions has already reached the maximum possible value, *i.e.*, $N_s = 10^{15} \text{ cm}^{-2}$ (10, 11). It is difficult to visualize any reaction step in the model for which N would be higher than N_s . For the growth in alkaline solutions, therefore, N is expected to be either equal to or less than N_s , *i.e.*

$$N_{\text{alk}} \leq N_{\text{acid}} = N_s \quad [5]$$

But, if N for the growth in alkaline solutions is equal to or less than N_s , then, considering N only, the exchange current density in alkaline solutions should be either equal to or less than the exchange current density in acid solutions, rather than higher as observed. Since

$$(i_0)_{\text{alk}} \gg (i_0)_{\text{acid}} \quad [6]$$

it would appear that the activation energy, W , for the growth in alkaline solutions should be substantially lower than the activation energy in acid solutions. But why should the activation energy change at all?

An objective of this study is to evaluate N and W in alkaline solutions and correlate them to the corresponding parameters in acid solutions and rate-determining steps.

Results and Discussion

Galvanostatic charging curves.—In 1M KOH solutions at different temperatures, 1°, 22°, and 45°C, V - q dependencies are determined galvanostatically for various current densities. The experimental procedure is the same as in previous studies (1, 9). In Fig. 1, V - q traces at 45°C for 3×10^{-5} , 3×10^{-4} , 3×10^{-3} , and $3 \times 10^{-2} \text{ A cm}^{-2}$ are reproduced from an oscilloscope storage screen. Evidently, general shapes of these traces are similar to those previously reported for room (22°C) temperature [cf. Fig. 5 in Ref. (1)]. In Fig. 2, V - q traces for the same current density,

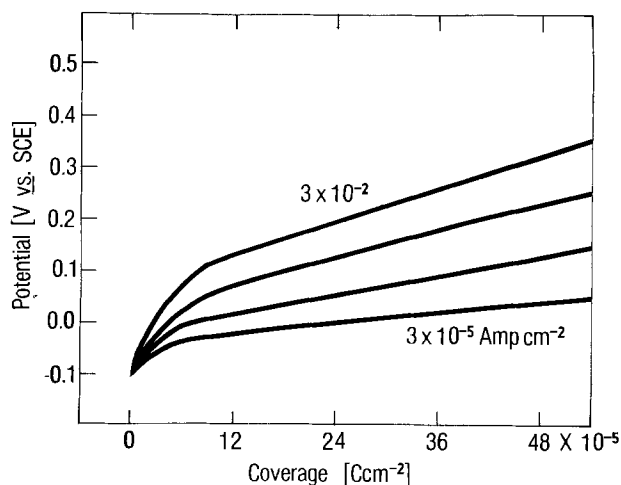


Fig. 1. Potential-charge density relationships for 3×10^{-5} , 3×10^{-4} , 3×10^{-3} , and $3 \times 10^{-2} \text{ A cm}^{-2}$. Temperature 45°C. Data not corrected for RF.

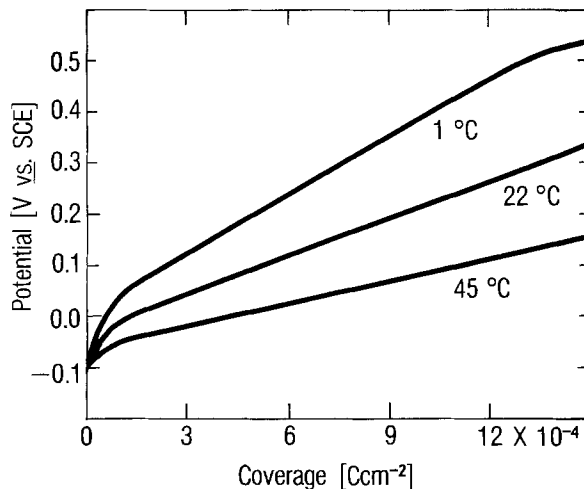


Fig. 2. Potential-charge density relationships for $3 \times 10^{-5} \text{ A cm}^{-2}$ at 1°, 22°, and 45°C. Data not corrected for RF.

$3 \times 10^{-5} \text{ A cm}^{-2}$, are shown for the three temperatures. From Fig. 1 and 2, and other data, plots $(\partial V / \partial q)_{i,T}$ vs. $\log i$ are constructed for each temperature. They are shown in Fig. 3. These plots, which are linear at all temperatures, show the same basic features as the plots for the anodic oxide growth at different temperatures in acid solutions [cf. Fig. 2 in Ref. (11)]. They are used here to evaluate N and W .

For the suggested model of growth, irrespective of the rate-determining step, the slopes of $(\partial V / \partial q)_i$ vs. $\log i$ should increase with temperature according to (cf. Eq. [1] and [2])

$$\begin{aligned} \frac{\partial^2 V}{\partial q \partial \log i} &= 2.3c(T) = \frac{2.3r}{\alpha} \\ &= \frac{2.3rRT}{zF\lambda} \end{aligned} \quad [7]$$

Parameters α and $z\lambda$ can be determined from measurements at room temperature only. They are respectively equal to 108 \AA V^{-1} and 2.8 \AA . If λ does not change in the narrow range of temperature in the present study, then $c(T)$, or the slopes of the plots of $\partial V / \partial q$ vs. $\log i$, should increase with temperature according to Eq. [7]. It is evident from Fig. 4 that $c(T)$ does change linearly with temperature. The slope of $c(T)$ vs. T is about $0.3 \text{ V \AA}^{-1} \text{ }^\circ\text{C}^{-1}$, and this is in accordance with the analysis of α from the data at room temperature. Temperature study, therefore, provides an additional confirmation for the proposed model of growth.

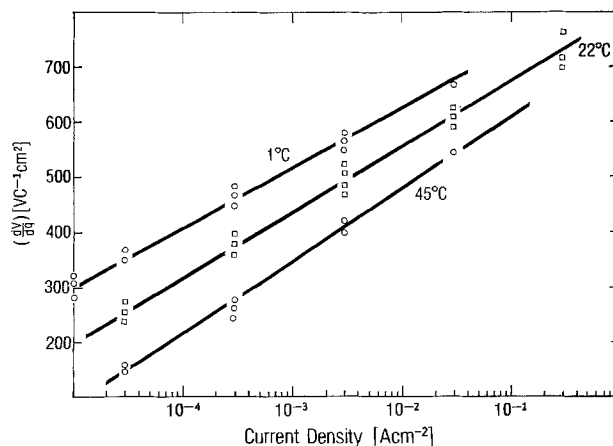


Fig. 3. The characteristic $\partial V / \partial q$ vs. $\log i$ plots at different temperatures. Data not corrected for RF.

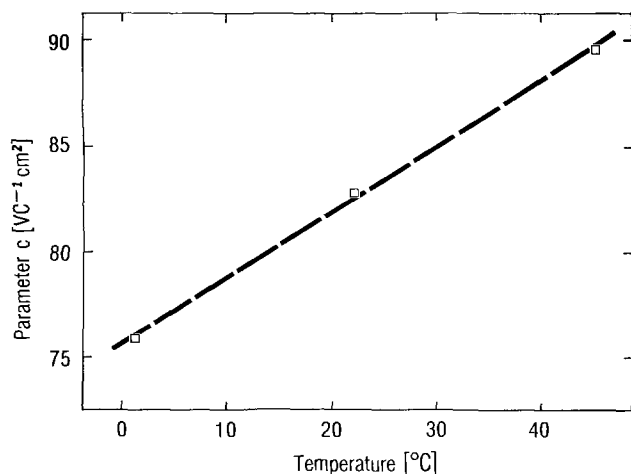


Fig. 4. Slopes from Fig. 3 plotted against temperature. Slopes are corrected for $RF = 1.6$ (1).

The exchange current density, activation energy, and frequency factor N .—From Eq. [1] it follows that

$$\left(\frac{\Delta V}{\Delta q}\right)_T = 2.3c(T) \log i - 2.3c(T) \log i_0 \quad [8]$$

From here, the exchange current density can be calculated for any given temperature, e.g., with the known value of $c(T)$ and the value of $(\Delta V/\Delta q)_T$ extrapolated to $i = 1 \text{ A cm}^{-2}$. In Fig. 5, i_0 is plotted against reciprocal temperature. At all temperatures, i_0 in alkaline solutions is substantially higher than i_0 in acid solutions ($2 \times 10^{-10} \text{ A cm}^{-2}$), for instance, 800 times at room temperature. The activation energy is now calculated from this plot using the relationship (cf. Eq. [4])

$$W = -2.3R \frac{d \log i_0}{d(1/T)} \quad [9]$$

It is $18.5 \text{ kcal/mole}^{-1}$.

The activation energy in alkaline solutions is, therefore, significantly lower than the activation energy in acid solutions previously determined to be $25 \text{ kcal mole}^{-1}$ (11). This difference in the activation energies alone would increase i_0 in alkaline solutions at room temperature over i_0 in acid solution by about 9×10^4 . Since at room temperature $i_{0,\text{alk}} \approx 800i_{0,\text{acid}}$, it follows that the activation energy is not the only factor affecting the change of i_0 in alkaline solutions. The preexponential factor, too, must change from acid to alkaline solution; N must be at least 100 times less than the same factor in acid solutions. From Eq. [4], N can now be obtained; it is about 1.5×10^{13} , i.e.,

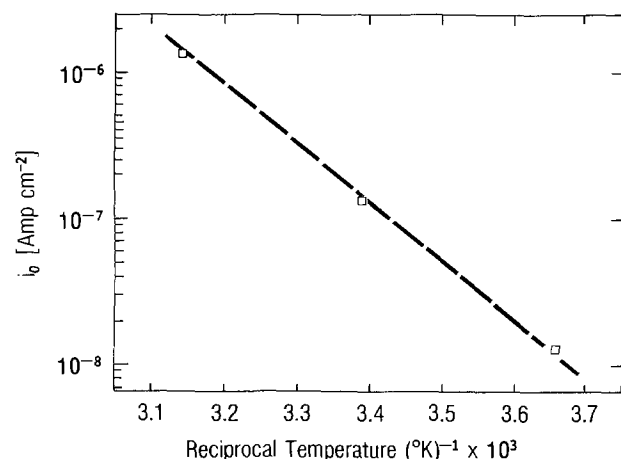


Fig. 5. Exchange current density vs. $1/T$. Current densities are corrected for RF .

it is indeed significantly less than observed in acid solutions ($\sim 1 \times 10^{15} \text{ cm}^{-2}$).

Comparison of growth kinetics in acid and alkaline solutions.—This study shows that both W and N differ from the corresponding parameters in acid solutions. At first sight, the difference in both W and N would indicate that in alkaline solutions the rate-determining step is different from that suggested for the growth in acid solutions. Since N for the growth in acid solutions is close to 10^{15} cm^{-2} , i.e., close to the density of surface sites, it was suggested (10, 11) that the formation of ions at the metal/oxide interface is the rate-determining step. For alkaline solutions, then, the second reaction step, i.e., the process of migration of ions within the oxide phase, would be expected to be the rate-determining step. This interpretation would then formally account for the observed changes both in W and N . It is difficult, however, to understand why the rate-determining step should change from acid to alkaline solutions and why, in alkaline solutions, W for the second step should become higher than for the first step. N is certainly expected to be less for the second step as rate determining. However, for the second step, N still appears to be too high. It would require the concentration of interstitial cations in the oxide phase to be about 1%.

The real difficulty in the interpretation of the kinetic data arises when W for the growth in alkaline solutions is compared with that in acid solutions. For instance, if one assumes that the process of ion formation at the metal/oxide interface is the rate-determining step in acid, but not in alkaline solutions, then why should W for this step change and become, in alkaline solutions, even less than W for the second step, particularly since, as suggested, the same oxide phase forms in both solutions? Activation energy for the first step should not at all depend on the conditions in solutions. Further, if the process of cation migration through the oxide phase is rate determining in alkaline solutions, then why should the process within the oxide phase become slower than the same process in acid solutions? For, the process of ion migration through the oxide phase is also not expected to be affected by the conditions in solutions.

A modified picture regarding the mechanism of growth in both solutions will, however, emerge and this difficulty will disappear once the present temperature study is complemented with the study of pH dependence of growth in alkaline solutions. This will be discussed in the next paper. It will be shown that, though the same basic model of growth is still valid, neither of the reaction steps discussed in this and previous papers is rate determining, certainly not in alkaline and most probably not in acid solutions.

Manuscript received Nov. 5, 1979.

Any discussion of this paper will appear in a Discussion Section to be published in the June 1981 JOURNAL. All discussions for the June 1981 Discussion Section should be submitted by Feb. 1, 1981.

Publication costs of this article were assisted by the Allied Chemical Corporation.

REFERENCES

1. A. Damjanovic, L.-S. R. Yeh, and J. F. Wolf, *This Journal*, **127**, 1945 (1980).
2. K. J. Vetter and J. W. Schultze, *J. Electroanal. Chem.*, **34**, 131 (1972).
3. K. J. Vetter and J. W. Schultze, *ibid.*, **34**, 141 (1972).
4. A. Damjanovic, A. T. Ward, B. Ulrick, and M. O'Jea, *This Journal*, **122**, 471 (1975).
5. L. B. Harris and A. Damjanovic, *ibid.*, **122**, 593 (1975).
6. N. Cabrera and N. F. Mott, *Rep. Prog. Phys.*, **12**, 163 (1949).
7. E. J. W. Verway, *Physica*, **2**, 1059 (1935).

8. A. Damjanovic and A. T. Ward, *MTP International Review of Science, Physical Chemistry, Series Two*, p. 103, Butterworths, University Park Press (1976).
9. A. Damjanovic and L.-S. R. Yeh, *This Journal*, **126**, 555 (1979).
10. A. Damjanovic, in "Proceedings Workshop Electro-catalysis Non-Metallic Surfaces," National Bureau of Standards Special Publication, No. 455, 259 (1976).
11. A. Damjanovic, L.-S. R. Yeh, and J. F. Wolf, *This Journal*, **127**, 874 (1980).

The Thermodynamics of Aqueous Water Electrolysis

Rodney L. LeRoy* and Christopher T. Bowen

Electrolyser Incorporated, Etobicoke, Ontario, Canada M9C 1B9

and

Noranda Research Centre, Pointe Claire, Québec, Canada H9R 1G5

and Donald J. LeRoy

Science Council of Canada, Ottawa, Ontario, Canada K1P 5M1

ABSTRACT

Precise definitions are given of three thermodynamic parameters which characterize the water-electrolysis reaction: the enthalpic voltage, the higher-heating-value voltage, and the thermoneutral voltage. Expressions are derived for these parameters and for the reversible potential, as functions of temperature between 25° and 250°C, and of pressure between 1 and 100 atm. Heat losses due to radiation, convection, and conduction are also considered, and a thermal-balance voltage is defined; representative values are calculated. Electrical-energy efficiency is related to the characteristic parameters, and thermodynamic limitations on its value are discussed.

Although hydrogen production by the electrolysis of water has been practiced for over a hundred years, this technique has been receiving special prominence in recent years because of its potential role in the energy economy. A substantial effort is being devoted to the problem of minimizing the energy requirements of the electrolytic process. This requires a two-pronged approach. Firstly, an attempt is made to reduce or eliminate internal energy losses, such as those arising from the electrode overvoltages and ohmic-resistance. Secondly, a choice is made of the optimum operating conditions for the electrolysis: the temperature, the pressure and, in the case of aqueous water electrolysis, the concentration of the electrolyte.

In present commercial water electrolyzers, electrical-energy efficiency is limited by the internal energy losses; cooling water is normally required to remove excess heat. However, technical advances now being made promise to reduce these losses to the point where efficiency will be limited instead by the requirement that sufficient heat be generated internally to maintain the electrolyte temperature. This latter limitation relates to the energy balance around the electrolyzer cell, and it can be calculated from thermodynamics. In fact, the ultimate limitations on the energy requirements of the electrolytic process are thermodynamic.

Although one might think that the calculation of the values of the relevant thermodynamic parameters for various operating conditions would be a relatively straightforward matter, serious errors have crept into the literature and have led to a considerable amount of confusion. The present examination of the thermodynamics of water electrolysis has been undertaken for this reason. Consideration is given primarily to aqueous water electrolysis using KOH as the electrolyte. However, many of the considerations are also applicable to the case of solid electrolytes.

* Electrochemical Society Active Member.

Key words: electrolysis, hydrogen, reversible potential energy efficiency.

Energy Requirements for an Ideal Electrolysis Cell

In examining the thermodynamics of the electrolytic process, it is convenient to consider an "ideal" electrolysis cell, consisting of a reversible hydrogen electrode and a reversible oxygen electrode immersed in a solution of potassium hydroxide of molality m at a total pressure of p atm and maintained at a temperature $T^\circ\text{K}$ or $t^\circ\text{C}$ by means of a thermostat. The hydrogen and oxygen in contact with the reversible electrodes are assumed to be "wet," in the sense of containing water vapor in equilibrium with the water in the KOH solution.

Calculations will be made using one of the following two sets of assumptions: (i) hydrogen, oxygen, and water vapor are ideal gases and the first two form ideal binary gaseous solutions with the third; and (ii) the individual gases are not ideal but the two binary gaseous solutions are. In either case the partial pressure of water vapor in each of the wet gases will be equal to p_w , the aqueous vapor pressure of the KOH solution. Thus $p = p_w + p_{\text{H}_2} = p_w + p_{\text{O}_2}$.

The continuous production of hydrogen and oxygen would require addition of reagent water in the amount of $[1 + 1.5p_w/(p - p_w)]$ moles per mole of hydrogen produced. The products of the process would consist of one mole of hydrogen mixed with $p_w/(p - p_w)$ moles of water vapor at a total pressure p , and 0.5 mole of oxygen mixed with $0.5p_w/(p - p_w)$ moles of water vapor, also at a total pressure p .

The total energy required per mole of hydrogen produced would be made up of electrical energy plus heat energy removed from the thermostat. It can be defined in terms of an enthalpy change, ΔH , with the value of ΔH being expressed in terms of the enthalpies of the three phases concerned

$$\Delta H = H(\text{wet hydrogen}) + H(\text{wet oxygen}) - H(\text{reagent water}) \quad [1]$$

The enthalpies of the two gaseous solutions can be

expressed in terms of the partial molar enthalpies of the components¹

$$H(\text{wet hydrogen}) = [\bar{H}_{\text{hy}} + (p_w/(p - p_w))\bar{H}_{\text{w(g)}}]_{t,p} \quad [2]$$

$$H(\text{wet oxygen}) = 0.5[\bar{H}_{\text{ox}} + (p_w/(p - p_w))\bar{H}_{\text{w(g)}}]_{t,p} \quad [3]$$

The enthalpy of the reagent water can be expressed in terms of the molar enthalpy of liquid water. If this is supplied at $t^\circ\text{C}$ and p atm then²

$$H(\text{reagent water}) = [1 + 1.5p_w/(p - p_w)]\tilde{H}_{\text{w(1),t,p}} \quad [4]$$

The enthalpy change defined by Eq. [1]-[4] is clearly equal to the minimum amount of energy that would be required, per mole of hydrogen, to produce wet hydrogen and wet oxygen on a continuous basis using as the feedwater liquid water at the temperature and pressure of the electrolysis.

If the electrolysis is conducted at a temperature $t > 25^\circ\text{C}$ and a pressure $p > 1$ atm, the total energy requirement must include the amount of energy required to heat the feedwater from 25° to $t^\circ\text{C}$ and to increase its pressure from 1 to p atm, namely³ $[1 +$

$1.5p_w/(p - p_w)] [\tilde{H}_{t,p} - \tilde{H}^{\circ 25}_{\text{w(1)}}]$. The total energy can be expressed either in terms of energy units (joules or calories) or as a voltage, using the conversion factor $nF = 192973\text{J mole}^{-1}\text{V}^{-1} = 46122\text{cal mole}^{-1}\text{V}^{-1}$. When expressed as a voltage it will be called the thermoneutral voltage, in keeping with the practice of a number of authors, and given the symbol V_{tn} . Rearranging terms, nFV_{tn} may be written as the sum of three terms

$$nFV_{\text{tn}} = [\bar{H}_{\text{hy}} + 0.5\bar{H}_{\text{ox}} - \tilde{H}_{\text{w(1)}}]_{t,p} + \Phi[\langle \bar{H}_{\text{w(g)}} \rangle - \tilde{H}_{\text{w(1)}}]_{t,p} + [1 + \Phi][\tilde{H}_{t,p} - \tilde{H}^{\circ 25}_{\text{w(1)}}] \quad [5]$$

where

$$\Phi = 1.5p_w/(p - p_w) \quad [6]$$

and $\langle \bar{H}_{\text{w(g)}} \rangle$ is a weighted average of the partial molar enthalpies of water in wet hydrogen and wet oxygen gases

$$\langle \bar{H}_{\text{w(g)}} \rangle = \frac{1}{1.5} [(\partial H/\partial n_{\text{w(g)}})_{\text{nh}_2} + 0.5(\partial H/\partial n_{\text{w(g)}})_{\text{nox}}]$$

The calculation of accurate values of V_{tn} at various temperatures and pressures is a matter of some importance. However, it is usually sufficient to simplify the calculation by making either of the two sets of assumptions referred to above. On the basis of set (i), the chemical potentials of the three gases can be expressed in the form

$$\mu_i = \tilde{G}^{\circ}_i + RT \ln p_i \quad [7]$$

where the first term on the right-hand side is the molar free energy of the pure component as an ideal gas at 1 atm pressure, and p_i is its partial pressure in

¹ \bar{H}_i denotes the partial molar enthalpy of component i , $(\partial H/\partial n_i)_{T,p}$.

² \tilde{H}_i denotes the molar enthalpy of component i , H_i/n_i .

³ It is assumed in all calculations in this paper that water fed to electrolyzers for water decomposition, and to replace the water carried off as vapor with the product gases, has a temperature of 25°C . In fact, this water comes from two sources in some electrolyzer designs: condensate returned from gas coolers or scrubbers, and make-up water added from an external source at the ambient temperature. These two streams can be at different temperatures, both of them different from 25°C . This can be accounted for in a straightforward manner in the detailed calculations, although the effect on derived values of the characteristic voltages is small for representative operating conditions.

the gaseous solution. Partial molar enthalpies are related to chemical potentials by the expression

$$\bar{H}_i = \mu_i - T\partial\mu_i/\partial T \quad [8]$$

Substitution of Eq. [7] into Eq. [8] demonstrates that, in this case, the partial molar enthalpy is equal to the molar enthalpy of the pure component as an ideal gas at 1 atm pressure and $t^\circ\text{C}$

$$\bar{H}_i = \tilde{G}^{\circ}_i - T\partial\tilde{G}^{\circ}_i/\partial T = \tilde{G}^{\circ}_i + T\tilde{S}^{\circ}_i = \tilde{H}^{\circ}_i \quad [9]$$

Equation [5] can then be written

$$nFV_{\text{tn}} = [\tilde{H}^{\circ}_{\text{hy}} + 0.5\tilde{H}^{\circ}_{\text{ox}} - \tilde{H}_{\text{w(1),t,p}}]_{t,p} + \Phi[\tilde{H}^{\circ}_{\text{w(g)}} - \tilde{H}_{\text{w(1),t,p}}]_{t,p} + [1 + \Phi][\tilde{H}_{t,p} - \tilde{H}^{\circ 25}_{\text{w(1)}}]_{t,p} \quad [10]$$

It is clear from Eq. [10] that if the gases and their solutions were ideal then an increase in the pressure at which the electrolysis takes place would have no effect on the thermoneutral voltage, except for the quite minor influence of pressure on the enthalpy of liquid water and on p_w . Unfortunately, a number of authors engaged in water-electrolysis research who, for simplicity, have assumed gas ideality, have come to a quite different conclusion (1-4). As the result, thermoneutral voltages calculated by them are in error by an amount of the order of 90 mV for a cell operating at 120°C and 35 atm pressure.

The effect of pressure on the enthalpy of any phase is determined by the relation

$$\partial H/\partial p = V - T\partial V/\partial T \quad [11]$$

The error appears to have arisen through the neglect of the second term on the right of Eq. [11] which, for an ideal gas, exactly cancels the first. The error in calculating the enthalpy of one mole of H_2 plus 0.5 mole of O_2 at a pressure of p atm from its value at 1 atm would be $1.5RT \ln p/nF$ V. For 120°C and 35 atm this is approximately 90 mV.

The set of assumptions (ii) is somewhat less "ideal" than set (i) used above, in that none of the individual gases is ideal but the binary solutions of wet gases are. In this case the chemical potential of a component i in one of the gaseous solutions would be equal to the molar free energy of that component as a pure gas at

the pressure p_i , namely \tilde{G}_{i,p_i} . Thus, in view of Eq. [8]

$$\bar{H}_{i,p} = \tilde{G}_{i,p_i} - T\partial\tilde{G}_{i,p_i}/\partial T = \tilde{G}_{i,p_i} + T\tilde{S}_{i,p_i} = \tilde{H}_{i,p_i} \quad [12]$$

and the thermoneutral voltage may be written

$$nFV_{\text{tn}} = [\tilde{H}_{\text{hy}} + 0.5\tilde{H}_{\text{ox}} - \tilde{H}_{\text{w(1)}}]_{t,p-p_w} - [\tilde{H}_p - \tilde{H}_{p-p_w}]_{\text{w(1),t}} + \Phi[\tilde{H}_{\text{w(g),p_w}} - \tilde{H}_{\text{w(1),p}}]_{t,p} + [1 + \Phi][\tilde{H}_{t,p} - \tilde{H}^{\circ 25}_{\text{w(1)}}]_{t,p} \quad [13]$$

The first of the four terms in Eq. [13] can be seen to be the negative of the molar enthalpy of formation of liquid water at $t^\circ\text{C}$ and $p - p_w$ atm; it can be written $-\Delta\tilde{H}_f[\text{H}_2\text{O}(1)]_{t,p-p_w}$. The second term will be very small; it is the increase in enthalpy on isothermally compressing liquid water from $p - p_w$ to p atm. The third term is the energy required to evaporate the water that is carried off with the evolved gases at $t^\circ\text{C}$. The last term is the energy required to heat and compress the feedwater from 25°C and 1 atm to $t^\circ\text{C}$ and p atm.

It should be noted that as the total pressure is increased at constant temperature the mole fraction of water vapor in the wet gases, p_w/p will get smaller

and the validity of Eq. [12] will be improved. The quantity Φ will tend toward zero and the difference between p and $p - p_w$ can be neglected. The expression for $n\mathbf{F}V_{tn}$ given by Eq. [5] will tend toward the limiting expression

$$n\mathbf{F}V_{tn} \rightarrow \Delta\tilde{H}_{t,p} + [\tilde{H}_{t,p} - \tilde{H}^{\circ}_{25}]_{w(1)} \text{ as } p/p_w \rightarrow \infty \quad [14]$$

in which $\Delta\tilde{H}_{t,p}$ is a convenient expression for $-\Delta\tilde{H}_f[\text{H}_2\text{O}(1)]_{t,p}$.

Since $\Delta\tilde{H}_{t,p}$ is the negative of the enthalpy of formation of liquid water from the elements at t and p , the quantity $\Delta\tilde{H}_{t,p}/n\mathbf{F}$ will be called the enthalpic voltage $V_{t,p}$. The quantity $\{\Delta\tilde{H}_{t,p} + [\tilde{H}_{t,p} - \tilde{H}^{\circ}_{25}]_{w(1)}\}/n\mathbf{F}$ will be called the higher-heating-value voltage and given the symbol V_{HHV} . The relation [13] can then be written

$$n\mathbf{F}V_{tn} = n\mathbf{F}V_{HHV} + \Phi[\tilde{H}_{w(g),t,pw} - \tilde{H}^{\circ}_{w(1),25}] \quad [15]$$

where V_{HHV} is evaluated at the pressure $(p - p_w)$.

The Effect of Temperature and Pressure on the Enthalpy of Formation of Water; The Enthalpic Voltage

Since the enthalpy of formation of liquid water is a negative quantity, we will deal with the positive quantity $\Delta\tilde{H}_{t,p}$. Its evaluation is most easily effected in two steps, starting with the value $\Delta\tilde{H}^{\circ}_{25} = 2.85840 \times 10^5$ J/mole obtained from the JANAF tables (5)

$$\Delta\tilde{H}_{t,p} - \Delta\tilde{H}^{\circ}_{25} = [\Delta\tilde{H}^{\circ}_t - \Delta\tilde{H}^{\circ}_{25}] + [\Delta\tilde{H}_{t,p} - \Delta\tilde{H}^{\circ}_t] \quad [16]$$

where

$$\begin{aligned} \Delta\tilde{H}^{\circ}_t - \Delta\tilde{H}^{\circ}_{25} &= [\tilde{H}^{\circ}_t - \tilde{H}^{\circ}_{25}]_{hy} + 0.5[\tilde{H}^{\circ}_t - \tilde{H}^{\circ}_{25}]_{ox} \\ &\quad - [\tilde{H}^{\circ}_t - \tilde{H}^{\circ}_{25}]_{w(1)} \quad [17] \end{aligned}$$

and

$$\begin{aligned} \Delta\tilde{H}_{t,p} - \Delta\tilde{H}^{\circ}_t &= [\tilde{H}_{t,p} - \tilde{H}^{\circ}_t]_{hy} + 0.5[\tilde{H}_{t,p} - \tilde{H}^{\circ}_t]_{ox} \\ &\quad - [\tilde{H}_{t,p} - \tilde{H}^{\circ}_t]_{w(1)} \quad [18] \end{aligned}$$

The effect of temperature on $\Delta\tilde{H}^{\circ}$.—($\tilde{H}^{\circ}_t - \tilde{H}^{\circ}_{25}$) is reported as a function of temperature for hydrogen and oxygen gases in the JANAF tables (5). Data covering the temperature range $25^{\circ}\text{C} \leq t \leq 327^{\circ}\text{C}$ for one mole of hydrogen plus one-half mole of oxygen were fitted to the expression $-1087.4 + 43.472t + 2.940 \times 10^{-3}t^2$ J, where t is the temperature in $^{\circ}\text{C}$. The average deviation of this expression from the JANAF data at 25° , 26.8° , 126.8° , and 326.8°C was 0.8J. The enthalpy of liquid water at 1 atm pressure was interpolated from the Steam tables (6). Data for temperatures above 100°C were theoretical, calculated using the fundamental equation of Keenan *et al.*

Values of $(\Delta\tilde{H}^{\circ}_t - \Delta\tilde{H}^{\circ}_{25})$ (Eq. [17]) were derived at 20°C intervals between 25° and 250°C , and were fitted by the method of least squares with the expression

$$\Delta\tilde{H}^{\circ}_t - \Delta\tilde{H}^{\circ}_{25} = 730.68 - 28.752t - 0.01898t^2 \quad [19]$$

where units are J/mole of water. The corresponding expression for the enthalpic voltage $\Delta\tilde{H}^{\circ}_t/n\mathbf{F} = V^{\circ}_t$ is⁴

⁴ Because of the nonideality of hydrogen and oxygen gases, $\Delta\tilde{H}_{t,p=1}$ is not equal to $\Delta\tilde{H}^{\circ}_t$, and the corresponding voltage differs slightly (by a maximum of 15 μV) from the value calculated for V°_t using Eq. [20]; see Table I.

$$V^{\circ}_t = 1.4850 - 1.490 \times 10^{-4}t - 9.84 \times 10^{-8}t^2 \text{ V} \quad [20]$$

This expression is drawn as the bottom curve in Fig. 1. It is in approximate agreement with predictions

based on $\Delta\tilde{H}^{\circ}_t$ values reported by Wicks and Block (7) for temperatures up to 100°C , but predicts lower values at higher temperatures.

The value of V°_t decreases significantly with rising electrolyte temperature, from 1.4812V at 25°C to 1.4416V at 250°C . An earlier result for V°_t erroneously showed it to increase with increasing temperature (8).

The effect of pressure on $\Delta\tilde{H}_t$.—The effect of pressure on enthalpy is given by Eq. [11], and hence for each of the three phases involved in the expression for $\Delta\tilde{H}_t$ there will be a relation of the form

$$\tilde{H}_{t,p_2} - \tilde{H}_{t,p_1} = \int_{p_1}^{p_2} (\tilde{V} - T\partial\tilde{V}/\partial T) dp \quad [21]$$

In the case of hydrogen and oxygen the value of the integral in [21] is nonzero only because of the non-ideality of the two gases.

The equations of state for hydrogen and oxygen gases are conveniently represented by the modified Virial equation of the form

$$\frac{p\tilde{V}}{RT} = 1 + B'p + C'p^2 + \dots \quad [22]$$

where R is the gas constant. Substitution in Eq. [21] gives

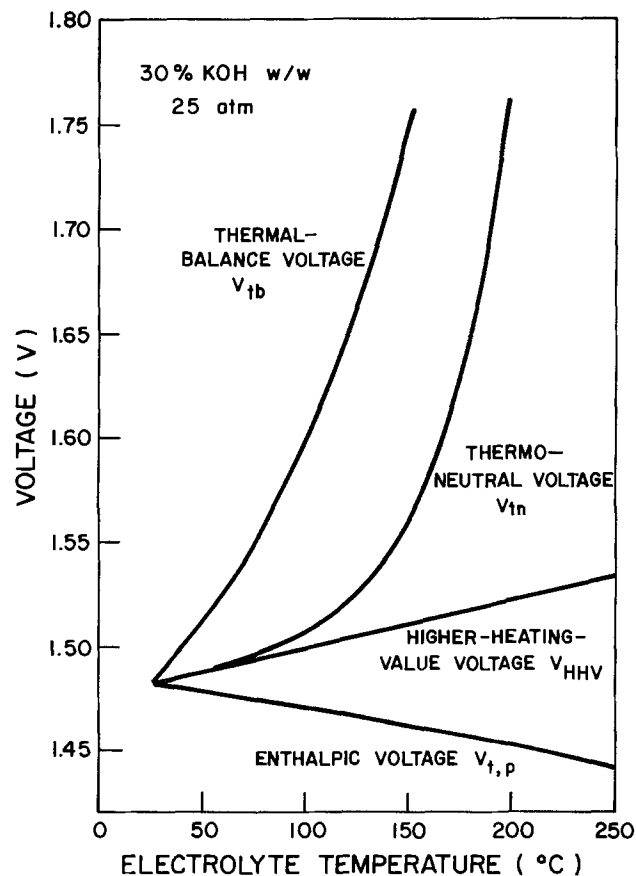


Fig. 1. Variation of the principle voltage parameters of a water electrolyzer with temperature, for representative operating conditions. The contribution V_{rc} of radiation and convection to the thermal-balance voltage is calculated assuming an electrolyzer surface area of $0.1 \text{ m}^2/\text{kA}$, and a surface emissivity of 0.8.

$$\tilde{H}_{t,p_2} - \tilde{H}_{t,p_1} = RT^2 \int_{p_1}^{p_2} \left(\frac{\partial B'}{\partial T} + p \frac{\partial C'}{\partial T} + \dots \right) dp \quad [23]$$

Values of the coefficients B' , C' , ... of the modified Virial equation are not normally provided, and must be derived from coefficients B , C , ... of the standard Virial equation

$$\frac{p\tilde{V}}{RT} = 1 + B/\tilde{V} + C/\tilde{V}^2 + \dots \quad [24]$$

The two sets of parameters can be shown to be related through the expressions

$$B' = B/RT \quad [25]$$

and

$$C' = (C - B^2)/(RT)^2 \quad [26]$$

These results are substituted in Eq. [23] to express the pressure dependence of the enthalpy of a non-ideal gas in terms of known quantities⁵

$$\tilde{H}_{t,p} = \tilde{H}^{\circ}_t + \left(B - T \frac{\partial B}{\partial T} \right) p + \frac{C - B^2 - \frac{1}{2} T \left(\frac{\partial C}{\partial T} - 2B \frac{\partial B}{\partial T} \right)}{RT} p^2 + \dots \quad [27]$$

Virial-coefficient data for hydrogen and oxygen are plotted against linearizing functions of temperature in Fig. 2 and 3, respectively. The data are taken from critical compilations by Dymond and Smith (9), and by Sengers *et al.* (10), and the temperature functions

⁵The enthalpy of the gases in their standard state is evaluated by setting $p = 0$, since real gases approach ideality at zero pressure, and the enthalpy of an ideal gas is independent of pressure.

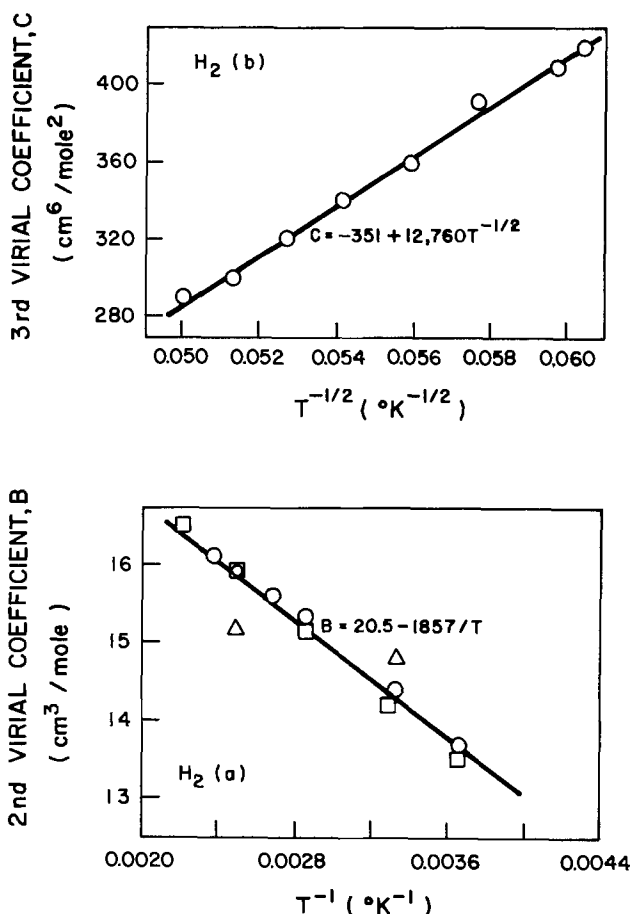


Fig. 2. Virial coefficient data for hydrogen gas

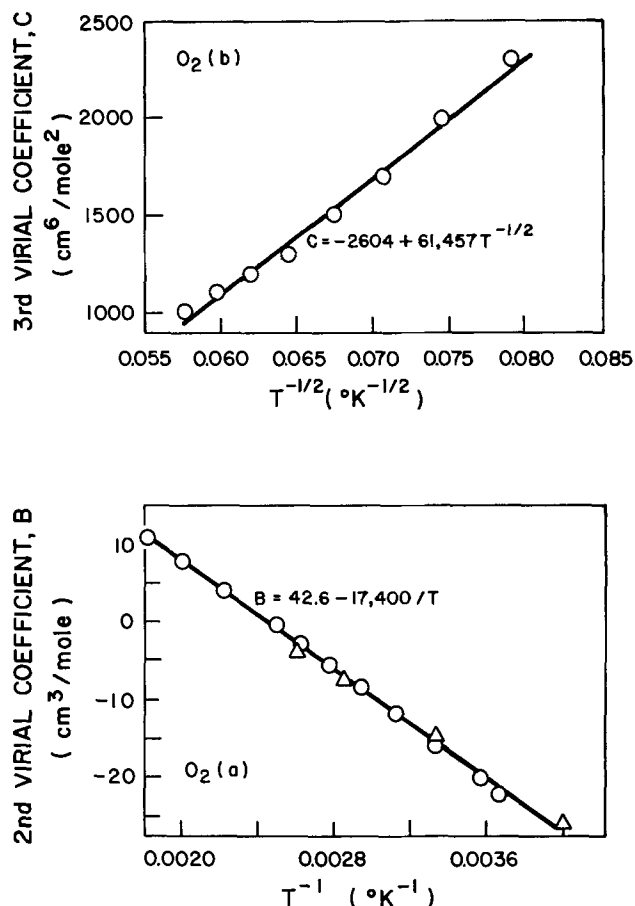


Fig. 3. Virial coefficient data for oxygen gas

were suggested by the work of Goodwin *et al.* (11). The data for both gases are well represented between 25° and 250°C by the expressions

$$B = b_1 + b_2/T \quad [28]$$

and

$$C = c_1 + c_2/T^{1/2} \quad [29]$$

where values of the coefficients are indicated in the figures. Substituting these expressions, Eq. [27] can be written

$$\tilde{H}_{t,p} - \tilde{H}^{\circ}_t = (b_1 + 2b_2/T)p + \left(c_1 + \frac{1.25c_2}{T^{1/2}} - [b_1 + 2b_2/T]B \right) p^2/RT \quad [30]$$

The first term on the right of Eq. [30] dominates, so that portion of $\Delta\tilde{H}_{t,p}$ relating to the product gases varies roughly linearly with pressure.

To complete the calculation of $\Delta\tilde{H}_{t,p} - \Delta\tilde{H}^{\circ}_t$ values of $\tilde{H}_{t,p} - \tilde{H}^{\circ}_t$ for pure liquid water were obtained from the Steam Tables (6). The pressure dependence of the enthalpic voltage expressed as $(\Delta\tilde{H}_{t,p} - \Delta\tilde{H}^{\circ}_t)/nF$, in millivolts, is given in Table I for a range of temperatures and pressures. It is apparent from this table that the pressure dependence of the enthalpic voltage is very small over the temperature and pressure range of interest.

The Higher-Heating-Value Voltage

As shown by Eq. [19], $\Delta\tilde{H}^{\circ}_t < \Delta\tilde{H}^{\circ}_{25}$ for $t > 25^\circ\text{C}$. However, to heat the reagent water from 25° to $t^\circ\text{C}$ requires $(\tilde{H}^{\circ}_t - \tilde{H}^{\circ}_{25})_{w(l)}$ J/mole at 1 atm pressure. The total corresponding energy requirement per mole of hydrogen produced, expressed as a voltage, is

Table I. Pressure dependence of the enthalpic voltage*

$$(V_{t,p} - V^{\circ}) = (\Delta\tilde{H}_{t,p} - \Delta\tilde{H}^{\circ}_{t})/nF \text{ (mV)}$$

t (°C)	p = 1 atm	25 atm	50 atm	75 atm	100 atm
25	-0.0152	-0.578	-1.143	-1.686	-2.208
100	-0.0078	-0.354	-0.694	-1.018	-1.320
200	(-0.0015)	-0.121	-0.242	-0.342	-0.439
250	(+0.0008)	(+0.041)	+0.083	+0.125	+0.167

* Bracketed values are theoretical only; liquid water would not exist under these conditions.

the higher-heating-value voltage, $V^{\circ}_{HHV,t}$, and is defined by the equation

$$V^{\circ}_{HHV,t} = V^{\circ}_t + (\tilde{H}^{\circ}_t - \tilde{H}^{\circ}_{25})_{w(1)}/nF \quad [31]$$

Values of V°_t given by [20], together with values of $(\tilde{H}^{\circ}_t - \tilde{H}^{\circ}_{25})_{w(1)}$ obtained from the Steam tables (6), yield the equation

$$V^{\circ}_{HHV,t} = 1.4756 + 2.252 \times 10^{-4}t + 1.52 \times 10^{-8}t^2 \quad [32]$$

This expression is plotted in Fig. 1.

For a pressure of p atm we can write

$$nFV_{HHV,t,p} = (\tilde{H}_{t,p})_{hy} + 0.5(\tilde{H}_{t,p})_{ox} - (\tilde{H}^{\circ}_{25})_{w(1)} \quad [33]$$

The pressure dependence of the higher-heating-value voltage can then be expressed as

$$V_{HHV,t,p} - V^{\circ}_{HHV,t} = [(\tilde{H}_{t,p} - \tilde{H}^{\circ}_t)_{hy} + 0.5(\tilde{H}_{t,p} - \tilde{H}^{\circ}_t)_{ox}]/nF \quad [34]$$

Representative values of the quantity defined by Eq. [34] are recorded in Table II. It should be noted that they differ from zero solely because of the deviations of the two gases from ideality, and that they differ from the corresponding data in Table I by the omission of the term $(\tilde{H}_{t,p} - \tilde{H}^{\circ}_t)_{w(1)}/nF$.

The Thermoneutral Voltage

Within the limitations implied by the validity of Eq. [12] for wet hydrogen and wet oxygen, the thermoneutral voltage can be expressed by Eq. [15], where V_{HHV} is evaluated for the pressure $p - p_w$. As indicated by Table II, the effect of pressure on V_{HHV} is quite small. We will, therefore, drop the distinction between p and $p - p_w$ and write

$$nFV_{tn} = nFV_{HHV} + \Phi[\tilde{H}_{w(g),t,p_w} - \tilde{H}^{\circ}_{w(1),25}] \quad [35]$$

where V_{HHV} is evaluated at t and p .

The quantity Φ is defined by Eq. [6]. For any given value of the total pressure p , values of Φ can be calculated provided p_w , the vapor pressure of the KOH solution, is known. Values of p_w at various temperatures and concentrations were obtained from the International Critical Tables (12) and fitted to the equation

$$\ln p_w = 0.01621 - 0.1380m + 0.1933m^{1/2} + 1.024 \ln p_w^* \quad [36]$$

Table II. Pressure dependence of the higher-heating-value potential

$$(V_{HHV,t,p} - V^{\circ}_{HHV,t}) \text{ (mV)}$$

t (°C)	p = 1 atm	25 atm	50 atm	75 atm	100 atm
25	-0.0152	-0.370	-0.720	-1.048	-1.354
100	-0.0078	-0.185	-0.350	-0.497	-0.624
200	-0.0015	-0.031	-0.050	-0.057	-0.051
250	+0.0008	+0.023	+0.056	+0.098	+0.149

The vapor pressure of pure water, p_w^* , can be obtained from, for instance, the Handbook of Chemistry and Physics (13) or can be calculated with an error of less than 1% over the range 25°-250°C using the relation

$$\ln p_w^* = 37.04 - 6276/T - 3.416 \ln T \quad [37]$$

The quantity $[\tilde{H}_{w(g),t,p_w} - \tilde{H}^{\circ}_{w(1),25}]$ in the second term of Eq. [35] may be approximated by $[\tilde{H}_{w(g),t,p_w^*} - \tilde{H}^{\circ}_{w(1),25}]$, values of which can be obtained from

Steam tables (6). $\tilde{H}_{w(g),t,p_w}$ is the molar enthalpy of steam at $t^{\circ}\text{C}$ and at the pressure p_w equal to the vapor pressure of water over the KOH solution. This pressure will be less than the vapor pressure of pure water, p_w^* , at $t^{\circ}\text{C}$. However, the molar enthalpy of water vapor at p_w^* will differ from that at p_w only because of deviations from ideal-gas behavior. The corrections can be calculated in the same way as they were for hydrogen and oxygen, but in view of the fact that they will be smaller than the errors in Φ arising through uncertainties in p_w it was not considered worthwhile to prepare a table of corrections. One calculation, made for a 30% w/w solution of KOH ($m = 7.64$) at 150°C and a total pressure $p = 10$ atm, gave $p_w = 2.34$ atm, $p_w^* = 4.70$ atm, and a correction,

$\Phi[\tilde{H}_{p_w} - \tilde{H}_{p_w^*}]_{w(g),150}$ equal to 32 J mole⁻¹ or 0.17 mV. This value was calculated using van der Waal's constants for water vapor (13).

The expression for the thermoneutral voltage may then be written

$$nFV_{tn} = nFV_{HHV} + \Phi Y \quad [38]$$

where, for simplicity, $[\tilde{H}_{w(g),t,p_w^*} - \tilde{H}^{\circ}_{w(1),25}]$ is given the symbol Y . This quantity depends only on the temperature, and can be represented within 0.02% by the equation

$$Y = 42960 + 40.762t - 0.06682t^2 \text{ J mole}^{-1} \quad [39]$$

over the temperature range 25°C $\leq t \leq$ 220°C.

Values of V_{tn} calculated from Eq. [38] (using [32], [36], [37], and [39]) are plotted in Fig. 1 for a 30% w/w solution of KOH and a total pressure of 25 atm. The rapid increase of V_{tn} with temperature, as compared to the relatively modest increase of V_{HHV} , occurs because of the rapid increase with temperature of the amount of water vapor that is carried off with the hydrogen and oxygen. The quantity Y does not increase very strongly with temperature, but Φ does. The quantity Φ decreases with increasing total pressure p , and, as shown by Fig. 4, this causes V_{tn} to decrease with increasing pressure. As noted in Eq. [14], V_{tn} approaches V_{HHV} asymptotically as $p \rightarrow \infty$.

The designation "thermoneutral voltage" has been used previously in water-electrolyzer literature, although without a clear definition. Numerous authors (14-17) have reproduced a curve which originated with Gregory (18), which shows what is identified as the thermoneutral voltage to increase weakly with increasing temperature. Absolute values were between the curves drawn in Fig. 1 for the enthalpic and higher-heating-value voltages. Thus the earlier result must be considered to be an approximation to these quantities, which do not include the unavoidable energy requirements of water evaporation.

The Efficiency of a Water Electrolyzer

In discussing the efficiency of a real electrolyzer which is operating with an observed voltage V_{obs} , it is convenient to think of a black box into which water at 25°C and 1 atm pressure is fed together with energy in the amount nFV_{obs} , and out of which comes wet hydrogen and wet oxygen together with waste energy in the form of radiation, convection, and conduction. These waste-energy terms can be grouped

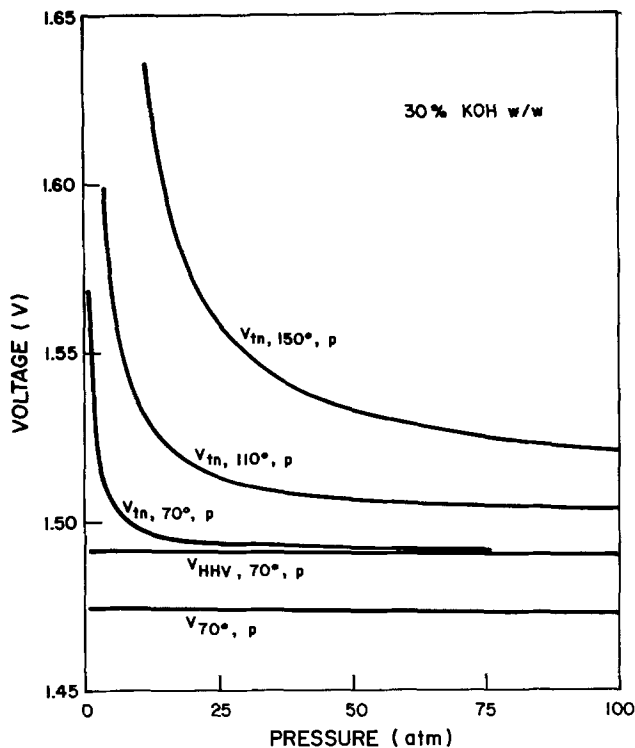


Fig. 4. Variation of the thermoneutral voltage with total pressure for three representative electrolyte temperatures. The enthalpic and high-heating-value voltages are indicated at 70°C.

together and defined as Q J/mole of hydrogen produced.⁶ Since energy is conserved

$$nFV_{\text{obs}} = H(\text{wet hydrogen})_{t,p} + H(\text{wet oxygen})_{t,p} - H(\text{feed water})_{25,1 \text{ atm}} + Q = nFV_{\text{tn}} + Q \quad [40]$$

Within the accuracy implied by the use of Eq. [38]

$$nFV_{\text{obs}} = nFV_{\text{HHV}} + \Phi Y + Q \quad [41]$$

The useful output from the expenditure of nFV_{obs} J is usually considered to be the energy equivalent to the higher-heating value of the product hydrogen, represented by the term nFV_{HHV} . It is customary, then, to define the electrical-energy efficiency of an electrolyzer as η , where

$$\eta = V_{\text{HHV}}/V_{\text{obs}} \quad [42]$$

This definition of efficiency has become widely accepted, in spite of the fact that it would never be possible to recover the full higher heating value of hydrogen in an energy application. Nevertheless, a uniform basis for comparison is required. The use of V_{HHV} has the strong advantage that it is a thermodynamic quantity, whose value is independent of the way in which the product gases are subsequently treated or used. The efficiency with which the heat content of the product gases can be transformed into useful energy in a particular application can then be analyzed as a separate issue.

As an example of efficiency calculation, it follows from Eq. [32] that the value of V_{HHV} at 100°C is 1.4983V. Using Table II, the value of V_{HHV} at 100°C and 50 atm is $1.4983 - 0.350 \times 10^{-3} = 1.4980$ V. The electrical energy efficiency of an electrolyzer operating at 1.750V at this temperature and pressure would then be $1.4980/1.750 = 85.6\%$. It is interesting to note that if the pressure dependence of V_{HHV} had been calculated by the method of neglecting the second term in Eq. [11] (1-4), the calculated value of V_{HHV} would have been $1.4983 + 0.0944 = 1.5925$ V, and the efficiency η of an electrolyzer operating at

⁶ Q will, of course, depend on the electrolyzer and its operating conditions, including the current.

1.750V at 100°C and 50 atm would have been calculated to be 91.0%.

The enthalpic voltage ($V_{t,p}$), the higher-heating-value voltage (V_{HHV}) and the thermoneutral voltage (V_{tn}) are thermodynamic state functions, depending only on the temperature and pressure of the electrolyzer and, in the case of V_{tn} , on the concentration of the KOH electrolyte. In particular, they are quite independent of the magnitude of the electrolyzing current, which determines the rate of production of hydrogen. On the other hand, the net energy losses due to radiation, convection, and conduction usually manifest themselves as a power loss of, say P_{QW} or P_{Q} J/sec. For an electrolysis current of I amp the rate of production of hydrogen would be I/nF moles/sec. The energy loss per mole of hydrogen produced, the quantity Q in Eq. [40] and [41], would then be given by

$$Q = nFP_{\text{Q}}/I \text{ J mole}^{-1} \quad [43]$$

It can also be expressed as a voltage

$$V_{\text{Q}} = Q/nF = P_{\text{Q}}/I \quad [44]$$

It is evident from Eq. [40] that if V_{tn} can be calculated, then V_{Q} can be obtained by subtracting V_{tn} from V_{obs}

$$V_{\text{obs}} = V_{\text{tn}} + V_{\text{Q}} \quad [45]$$

The Thermal-Balance Voltage

It should be noted that if cooling water is used to remove heat from the electrolyzer this will make a positive contribution to V_{Q} ; if heat has to be supplied to the electrolyzer in order to maintain its temperature at $t^\circ\text{C}$ then this will make a negative contribution to V_{Q} . The latter situation would arise if the energy dissipation in the electrolyzer represented by overvoltages and ohmic-resistance losses were not sufficient to raise nFV_{obs} to a value large enough to exceed nFV_{tn} by enough to supply the energy losses from radiation and convection.

It follows from these considerations that if the operating conditions of an electrolytic cell, including the temperature, pressure, KOH concentration, and current, were such that V_{obs} was equal to $V_{\text{tn}} + V_{\text{rad}} + V_{\text{conv}}$ then separate heating or cooling of the cell would not be required. That particular value of V_{obs} would be the thermal-balance voltage V_{tb}

$$V_{\text{tb}} = V_{\text{tn}} + V_{\text{rad}} + V_{\text{conv}}$$

or

$$V_{\text{tb}} = V_{\text{tn}} + V_{\text{rc}} \quad [46]$$

where $V_{\text{rad}} + V_{\text{conv}} = V_{\text{rc}}$.

It should be noted that V_{tb} is not a thermodynamic state function because neither V_{rad} nor V_{conv} is a state function. Nevertheless, an estimate of the magnitude of both of the latter two quantities can be made.

The radiation loss can be estimated using the well-known fourth-power law of radiation

$$P_{\text{rad}} = A\epsilon\sigma(T^4 - T_a^4) \quad [47]$$

where A is the radiating area, ϵ is its emissivity, σ is the Stefan-Boltzmann constant, $5.67 \times 10^{-8} \text{ W m}^{-2} \text{ deg}^{-4}$, and T_a is the ambient temperature. As an example, consider a cell operating at the temperature $T = 373.2^\circ\text{K}$ with the ambient temperature $T_a = 298.2^\circ\text{K}$. Suppose that the emissivity is 0.8 and the area of the radiating surface is 0.1 m^2 per kA of current passing through the cell. The heat loss by radiation would be 52.1W per kA, corresponding to $V_{\text{rad}} = 52.1 \text{ mV}$.

It is also possible to make an estimate of the heat loss by convection, using an expression taken from Perry (19)

$$P_{\text{conv}} = 1.77A(T - T_a)^{1.25} \text{ W} \quad [48]$$

Using the same values of T , T_a , and A as before, P_{conv} per kA would be 39.1W, and V_{conv} would be equal to 39.1 mV. V_{rc} would then be 91.2 mV.

It is evident from Eq. [47], [48], and [44] that for fixed operating and ambient temperatures, V_{rad} and V_{conv} are inversely proportional to the electrolyzing current for any particular electrolyzer. This effect has been noted previously (20).

In Fig. 1 values of the thermal-balance voltage V_{tb} , defined by Eq. [46], are plotted as a function of temperature for an electrolyzer operating at 25 atm total pressure, using a 30% KOH electrolyte and having the area and emissivity referred to above. At 150°C and 25 atm, V_{tb} is 1.743V. Operation below this voltage would require input of heat from an external source. Under these conditions, V_{HHV} is 1.510V. Thus the energy efficiency of an electrolyzer operating at V_{tb} would be $1.510/1.743 = 86.6\%$. If the cell were perfectly insulated V_{tb} would be equal to V_{tn} , and the efficiency for operation at the thermal-balance voltage would be 96.8%.

The value of the thermal-balance voltage represents a limitation on the maximum electrical-energy efficiency which can be achieved in an electrolyzer, if a supplementary source of heat is not available to maintain the temperature. These limitations are particularly onerous for high operating temperatures and modest pressures. Kunstreich's group has given the first systematic attention to this problem, proposing energy recovery from gas driers as an essential component of efficient high temperature electrolysis systems (1, 2).

As has been noted by many authors, it is possible for the electrical efficiency of a water electrolyzer, as defined by Eq. [42], to exceed 100%. In terms of the present discussion such a situation implies that energy release internal to the electrolyzer (from electrode overvoltages and resistive losses) is so low that energy input by conduction must exceed the difference between V_{tb} and V_{HHV} .

Dependence of the Thermal-Balance Voltage on Pressure and Electrolyte Concentration

As indicated by Eq. [46], the thermal-balance voltage can be calculated from a knowledge of the thermoneutral voltage, V_{tn} , which is a state function depending only on the temperature, the pressure, and the concentration of the electrolyte, and of the value of V_{re} , which depends on the electrolyzer and its operating conditions, including current. The value of V_{re} can be estimated, for example, by using Eq. [47] and [48]. It can also be estimated by subtracting V_{tn} from V_{obs} to get V_q , using Eq. [45], and then subtracting from V_q the contribution (positive or negative) made by external cooling or heating other than by radiation and convection. If the electrolyzer were perfectly insulated, then V_{re} would be equal to zero and V_{tb} would be equal to V_{tn} . In view of these considerations the dependence of the thermoneutral voltage on pressure and electrolyte concentration is illustrated in Fig. 4 and 5.

In Fig. 4 values of the thermoneutral voltage for 30% w/w KOH are plotted as a function of pressure for three representative electrolyte temperatures. In addition, values of the enthalpic and the higher-heating-value voltages at 70°C are plotted. The slight decreases in the values of these latter quantities with increasing pressure were calculated using linear interpolation of the data in Tables I and II. As a result of the rapid decrease in the quantity $\Phi [= 1.5p_w / (p - p_w)]$ with increasing total pressure, V_{tn} approaches V_{HHV} at high pressures. This is illustrated quite clearly by the data for 70°C. It should be noted that the curves in Fig. 4 are substantially different from the results reported by Kunstreich *et al.* (1, 2) for comparable conditions.

Figure 5 illustrates the dependence of the thermoneutral voltage on electrolyte concentration for various operating temperatures at a total pressure of 5 atm. The rapid decrease in V_{tn} with increasing concentra-

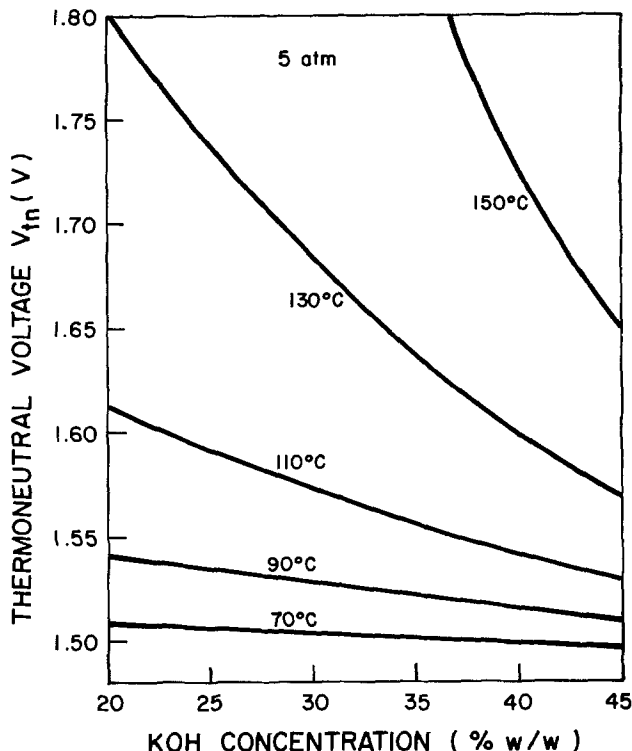


Fig. 5. Dependence of the thermoneutral voltage on concentration of the KOH electrolyte for representative temperatures.

tion of electrolyte, particularly at the higher temperatures, arises because of the strong dependence of the vapor pressure on electrolyte concentration, and the even stronger dependence of the quantity Φ . For example, at 130°C the vapor pressure over a 45% solution of KOH is only about 34% of that over a 20% solution; the value of Φ is about 22% of that for the weaker solution.

The Reversible Potential

In the course of developing expressions for $V_{t,p}$, V_{HHV} , and V_{tn} it was convenient to consider an imaginary electrolytic cell immersed in a thermostat at temperature $t^\circ\text{C}$ with reversible electrodes, one of which was in contact with wet hydrogen, the other with wet oxygen, the whole being at a pressure of p atm. The emf of such a cell would be the so-called reversible potential, E_{rev} , where

$$nFE_{rev,t,p} = -\Delta G_{t,p} = \mu_{hy} + 0.5\mu_{ox} - \mu_{w(soln)} \quad [49]$$

in which μ_{hy} is the chemical potential of hydrogen in the gaseous solution of hydrogen and water vapor, μ_{ox} is the chemical potential of oxygen in the gaseous solution of oxygen and water vapor, and $\mu_{w(soln)}$ is the chemical potential of water in the electrolyte.

If, as has been assumed, the water in each of the gaseous solutions is in equilibrium with the water in the electrolyte, then $\mu_{w(soln)}$ will be equal to $\mu_{w(g)}$, the chemical potential of water in either of the two gaseous solutions. To simplify the development it will be assumed that the gaseous solutions are ideal and that the individual pure gases are also ideal. In this case Eq. [7] would apply and Eq. [49] can be written

$$nFE_{rev,t,p} = [\tilde{G}^{\circ}_{hy} + 0.5\tilde{G}^{\circ}_{ox} - \tilde{G}^{\circ}_{w(g)}]_t + RT \ln [(p - p_w)^{1.5}/p_w] \quad [50]$$

The first term in square brackets is the negative of the standard free energy of formation of gaseous water at $t^\circ\text{C}$. This can be expressed in terms of the negative of the standard free energy of formation of

liquid water by obtaining a relation between $\tilde{G}_{w(g)}^\circ$ and $\tilde{G}_{w(l)}^\circ$.

For pure liquid water in equilibrium with its vapor at a pressure of p_w^* atm

$$[\tilde{G}_{w(l)}]_{p_w^*} = [\tilde{G}_{w(g)}]_{p_w^*} \quad [51]$$

If the vapor can be considered as an ideal gas, Eq. [51] may be expanded as

$$\tilde{G}_{w(l)}^\circ + \int_1^{p_w^*} \tilde{V}_{w(l)} dp = \tilde{G}_{w(g)}^\circ + RT \ln p_w^* \quad [52]$$

The value of the integral in Eq. [52] is zero at 100°C, negative below 100°C, and positive above; expressed in terms of a voltage by dividing by nF , its absolute value is less than 10 μ V at 25°C and less than 1 mV at 250°C. Dropping the integral and substituting for $\tilde{G}_{w(g)}^\circ$ in Eq. [50]

$$nFE_{rev,t,p} = nFE_{rev,t}^\circ + RT \ln [(p - p_w)^{1.5} p_w^* / p_w] \quad [53]$$

where

$$\begin{aligned} nFE_{rev,t}^\circ &= [\tilde{G}_{hy}^\circ + 0.5 \tilde{G}_{ox}^\circ - \tilde{G}_{w(l)}^\circ]_t \\ &= -\Delta\tilde{G}_f^\circ [H_2O(l)]_t \quad [54] \end{aligned}$$

The value of the standard free energy of formation of liquid water at 25°C is $-56\,690.2$ cal (21) and so the value of $E_{rev,25}^\circ$ is equal to 1.2291V.

In developing the expressions for the enthalpic voltage and the higher-heating-value voltage, corrections arising as a result of the nonideality of the individual gases were evaluated and tabulated in Tables I and II. Analogous corrections to E_{rev} are not made in this paper; although this could be done in a fairly straightforward manner. Instead of using Eq. [7] in derivation of the expression for $E_{rev,t,p}$ (Eq. [50]), the molar free energy of a gas i at pressure p would be written

$$\tilde{G}_i = \tilde{G}_i^\circ + RT [(\ln p_i + B'p_i + C'p_i^2/2 + \dots)] \quad [55]$$

in which B' and C' are the second and third virial coefficients defined previously.

In examining the effect of temperature on the reversible potential, the coefficient of RT in Eq. [53] can be evaluated with the aid of Eq. [36] and [37]. Also, in view of the thermodynamic relation

$$\partial(G/T)/\partial T = -(H/T^2) \quad [56]$$

it follows that

$$\partial(E_{rev,t}^\circ/T)/\partial T = -(V_t^\circ/T^2) \quad [57]$$

where V_t° is given by Eq. [20]. After integration and rearrangement $E_{rev,t}^\circ$ is given by the expression

$$\begin{aligned} E_{rev,t}^\circ &= 1.5184 - 1.5421 \times 10^{-3}T + 9.523 \\ &\quad \times 10^{-5}T \ln T + 9.84 \times 10^{-5}T^2 \quad [58] \end{aligned}$$

E_{rev}° decreases with increasing temperature in an almost linear fashion, as shown in Fig. 6. In the same figure values of E_{rev} are plotted for a total pressure of 25 atm and a 30% KOH electrolyte.

It is interesting to compare the values of E_{rev} and V_{th} for this pressure and electrolyte concentration and for the same temperature, say 100°C. The values of E_{rev} and V_{th} are 1.2522 and 1.5070V, respectively. The amount of electrical energy required per mole of hydrogen produced in an ideal electrolyzer having no overvoltages and no ohmic-resistance losses would be nFE_{rev} . The balance of the energy required for the chemical process, 0.2548 nF or 49,170J, together with any energy required to cover losses through radiation

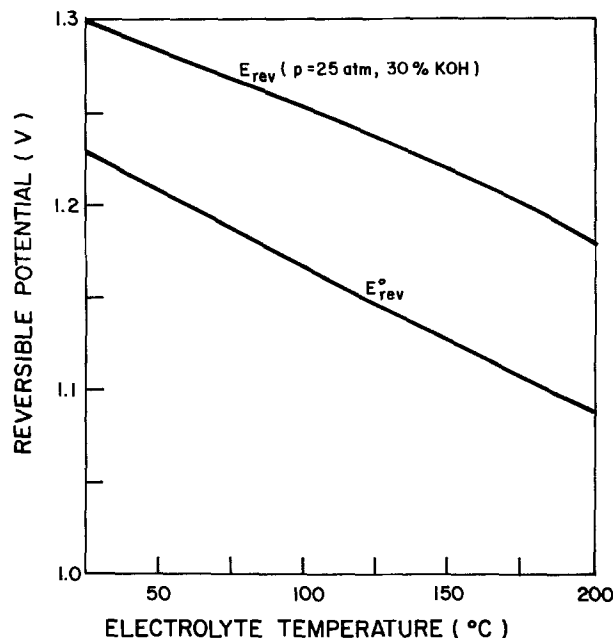


Fig. 6. Dependence of the reversible potential on electrolyte temperature, under standard conditions, and for 30% w/w KOH electrolyte at 25 atm pressure.

and convection, could, in principle, be supplied as heat. The value of V_{obs} for the cell would be 1.2522V. Since V_{HHV} for these conditions is 1.4981V, the electrical efficiency of the cell would be $1.4981/1.2522 = 119.6\%$.

Acknowledgments

We are indebted to Mr. A. Hufnagl whose energy-balance analyses of advanced water-electrolyzer designs prompted the calculations reported here, as well as to Professor R. Aziz of the University of Waterloo and Dr. G. Kell of the National Research Council of Canada who assisted in critical evaluation of thermodynamic data for hydrogen, oxygen, and water.

Manuscript submitted Nov. 6, 1978; revised manuscript received March 10, 1980.

Any discussion of this paper will appear in a Discussion Section to be published in the June 1981 JOURNAL. All discussions for the June 1981 Discussion Section should be submitted by Feb. 1, 1981.

Publication costs of this article were assisted by Noranda Research Centre.

REFERENCES

1. S. Kunstreich and J. Sterlini, in "Hydrogen Energy System," Vol. 5, T. N. Veziroglu and W. Seifritz, Editors, p. 2413, Pergamon Press, Oxford (1979).
2. S. Kunstreich, M. C. Murillo, and J. Sterlini, in "Seminar on Hydrogen as an Energy Vector: Its Production, Use and Transportation," EEC Report EUR 6085, Brussels, October 1978.
3. P. W. T. Lu and S. Srinivasan, *J. Appl. Electrochem.*, **9**, 269 (1979).
4. A. J. Appleby and G. Crépy, in "Hydrogen Energy System," Vol. 1, T. N. Veziroglu and W. Seifritz, Editors, p. 227, Pergamon Press, Oxford (1978).
5. JANAF Thermochemical Tables, 2nd Ed., D. R. Stull and H. Prophet, Project Directors, National Standard Reference Data System, NBS-37, Washington, June 1971.
6. J. H. Keenan, F. G. Keyes, P. G. Hill, and J. G. Moore, "Steam Tables: Thermodynamic Properties of Water Including Vapour, Liquid, and Solid Phases (SI units)," J. Wiley and Sons, New York (1978).
7. C. E. Wicks and F. E. Block, "Thermodynamic Properties of 65 Elements—Their Oxides, Halides, Carbides, and Nitrides," U.S. Bureau of Mines

- Bulletin 605 (1963).
8. J. Evangelista, B. Phillips, and L. Gordon, "Electrolytic Hydrogen Production: An Analysis and Review," NASA Technical Memorandum TM X-71856, December 1975.
 9. J. H. Dymond and E. B. Smith, "The Virial Coefficients of Gases: A Critical Compilation," Clarendon Press, Oxford (1969).
 10. J. M. H. L. Sengers, M. Klein, and J. S. Gallagher, "Pressure-Volume-Temperature Relationships of Gases: Virial Coefficients," Arnold Engineering Development Center Report TR-71-39, March 1971.
 11. R. D. Goodwin, D. E. Diller, H. M. Roder, and L. A. Weber, *J. Res. Nat. B. Stand.*, **68A**, 121 (1964).
 12. "International Critical Tables," Vol. 3, E. W. Washburn, Editor, McGraw-Hill Book Co., Inc., New York (1928).
 13. "Handbook of Physics and Chemistry," 50th Ed., R. C. Weast, Editor, Chemical Rubber Company, Cleveland (1969).
 14. "Hydrogen Manufacture by Electrolysis, Thermal Decomposition, and Unusual Techniques," M. S. Caspar, Editor, Noyes Data Corporation, Park Ridge, New Jersey (1978).
 15. J. C. Gillis, D. P. Gregory, and J. B. Pangborn, "Survey of Hydrogen Production and Utilization Methods," Vol. 2, Institute of Gas Technology, Chicago, August 1975.
 16. A. J. Konopka and D. P. Gregory, "Hydrogen Production by Electrolysis: Present and Future," p. 1184, 10th Inter-society Energy Conversion Engineering Conference, Newark, Delaware, August 18-22, 1975.
 17. A. P. Fickett and F. R. Kalhammer, in "Hydrogen: Its Technology and Implications," Vol. 1, K. E. Cox and K. D. Williamson, Editors, CRC Press, Cleveland (1977).
 18. D. P. Gregory, "A Hydrogen-Energy System," report prepared for the American Gas Association, Institute of Gas Technology, Chicago, August 1972.
 19. J. H. Perry, "Chemical Engineers' Handbook," 3rd Ed., McGraw-Hill, New York (1950).
 20. *Nitrogen*, **97**, 35 (1975).
 21. F. D. Rossini, D. D. Wagman, W. H. Evans, S. Levine, and I. Jaffe, "Selected Values of Chemical Thermodynamic Properties," National Bureau of Standards Circular 500 (1952).

Gold Passivation in Aqueous Alkaline Cyanide

D. W. Kirk,* F. R. Foulkes,* and W. F. Graydon

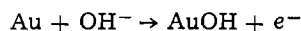
*Department of Chemical Engineering and Applied Chemistry,
University of Toronto, Toronto, Ontario, Canada M5S 1A4*

ABSTRACT

The behavior of gold electrodes in alkaline cyanide solution was studied using potentiostatic and potentiodynamic techniques. The results showed that the three anodic current peaks found in both steady-state and potential sweep experiments resulted from passivation of the gold cyanide dissolution reaction

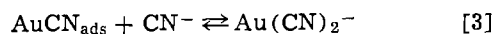


Potential pH measurements showed that the passivating reactions were dependent on the hydroxyl ion concentration. The potentials at which passivation occurred closely corresponded to the formation potentials of gold oxide and suboxide surface species. It was concluded that the most anodic dissolution reaction (peak 3) was passivated by the formation of gold (III) oxide. The less anodic gold dissolution peaks, peaks 1 and 2, were passivated by the formation of gold (I) hydroxide according to



From the remarkable similarity between the location of the gold dissolution peak in alkaline cyanide solution and the location of the oxide and suboxide peaks in cyanide-free alkaline solution, it was concluded that peaks 1 and 2 corresponded to gold dissolution and subsequent passivation predominantly on the (100) and (111) crystal planes, respectively; whereas peak 3 corresponds to gold dissolution and subsequent passivation over the complete electrode surface.

Gold displays a complex anodic behavior in aqueous alkaline cyanide solutions. Potentiostatic (1-3) and slow potential sweep measurements (1) have shown the presence of three peaks in the anodic potential profile. These three peaks have been identified with a gold dissolution process (1). The electron stoichiometry of the dissolution process has been measured and shown to be unity for each of the three peak regions (4). The dissolution process in each peak region has been shown to follow the reaction sequence



The rate-determining step has been identified for each of the peak regions (1, 5).

* Electrochemical Society Active Member.
Key words: metals, electrode, passivity, dissolution.

There have been several attempts made to explain the origin of the peaks. Cathro and Koch (2) suggested that the formation of basic cyanide films anodic of peaks 1 and 2 caused the passivation of these peaks. Later, MacArthur (6) questioned the formation of the basic cyanide films and suggested that the reaction mechanism and not passivation was the cause of peak 1. Peak 1 was identified by MacArthur with a charge transfer reaction followed by a chemical reaction mechanism in which the chemical reaction is rate determining and the surface intermediate interferes with the charge transfer reaction. Peak 2 was not separated from peak 3 in MacArthur's work and was not identified.

In a more recent paper by Eisenmann (3), the formation of peaks 1 and 2 was said to be the result of diffusion limitation of the cyanide ion. Our own work (1) on the anodic behavior of gold indicated that the formation of passivating surface films was

the cause of the peaks, although the nature of these films was not determined.

Knowledge of the electrochemical reactions of gold in alkaline cyanide is important for the development of electrolytic processing of industrial gold liquors. Although it is generally agreed (1-3, 14) that the peak 3 reaction is passivated by the formation of gold (III) oxide, the cause of the formation of the other peaks has not been explained satisfactorily. Therefore work was carried out to investigate the process of peak formation in potentiostatic and potentiodynamic measurements on gold in alkaline cyanide solutions.

Experimental Section

The equipment consisted of a Wenking potentiostat (Model 70TS1) and voltage scan generator (Model VSG72). The potential sweep measurements were recorded with a Hewlett-Packard Model 70004Bx4 recorder for slow sweep rates, and a Tektronics Model 5113 dual beam storage oscilloscope for fast sweep rates.

Gold electrodes (99.99% purity) were used for both working and counterelectrodes in a Pyrex cell. The working electrode was a gold wire 0.0381 cm in diam. The counterelectrode consisted of 2 gold foil sheets (each 1.6 cm²) set 1.25 cm to either side of the working electrode and contained in glass fritted tubes. The reference electrode was a saturated calomel electrode.¹ The cell configuration has been described previously (1, 7).

The surface area of the electrode was determined from potential scan measurements using the linear relation between the current peak height and the square root of the voltage scan rate for the oxidation of Fe(CN)₆⁴⁻. The relation given by Nicholson and Shain (8) is

$$\frac{i_p}{nFA C_o D_o} \frac{nFv^{1/2}}{RT} = 0.4463$$

where C_o is the concentration of Fe(CN)₆⁴⁻ (mole · cm⁻³), D_o is the diffusion coefficient of Fe(CN)₆⁴⁻ (cm² · sec⁻¹), i_p is the peak current (A), A is the area (cm²), n is the number of electrons transferred in the oxidation, v is the scan rate (Vsec⁻¹), and F , R , and T have their usual meanings.

Solutions prepared from analytical grade reagents and doubly distilled water were deoxygenated by bubbling with oxygen-free nitrogen.

A standard pretreatment of the gold electrode was necessary to achieve reproducibility in the voltage scans. The electrode was first heated to redness in air, then etched in hot aqua regia for 10 sec, then washed in doubly distilled water and dried. It was immediately given a further treatment consisting of a 5 min reduction period in the electrolyte at -1.2V.

Results and Discussion

A typical single sweep potential profile is shown in Fig. 1 for gold in 0.1M KOH + 0.1M KCN at a sweep rate of 1.0 mV · sec⁻¹. For the anodic sweep direction there are three current peaks, labeled peak 1, peak 2, and peak 3. The reaction in each of these peak regions has been shown to be a one electron transfer process (4) following the reaction sequence [1], [2], and [3] (1,5). The current peaks in the potential scan represent the rate of gold dissolution in alkaline cyanide under the given experimental conditions. The fact that the dissolution rate does not increase monotonically or reach a plateau with increase in potential suggests that the surface may become partially passivated during the potential sweep by the formation of either nonreactive or slowly reactive surface species.

¹ All potentials in this work are reported vs. the saturated calomel electrode.

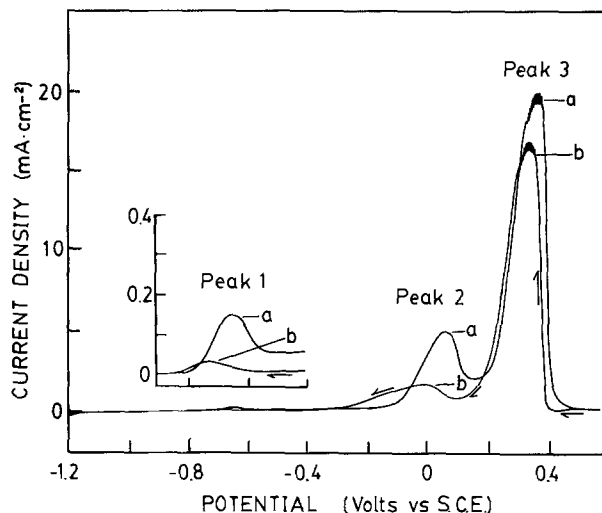


Fig. 1. Single sweep potential profile in aqueous alkaline cyanide: 0.1M KOH + 0.1M KCN; sweep rate = 1.0 mV · sec⁻¹; initial potential = -1.2V; temperature = 23.5°C. a) anodic scan, b) cathodic scan.

The current maximum measured in the region of peak 3 can be seen to be unstable. This current instability, which is observed in both the anodic and cathodic sweep directions, is typical of a phenomenon known as periodic oxidation (9-12). In most cases, this type of oscillation or current variation has been found to be the result of two competing reactions, one of which involves dissolution and the other passivation. The dissolution reaction is believed to undermine the passivating layer, causing the collapse of the passivated surface and resulting in the exposure of fresh surface. This process ceases when the passivating layer has completely covered the surface of the electrode.

In the case of the peak 3 cyanide reaction, the passivating species is the gold (III) oxide, which is thermodynamically stable at these potentials. Without cyanide present, the oxidation and reduction peak of the gold (III) oxide species easily can be observed near the potential of peak 3 (1, 6). In alkaline cyanide solutions, the competing dissolution reaction is the gold dissolution reaction via sequence [1], [2], and [3].

The cathodic scan of gold in alkaline cyanide solutions has received very little attention in the literature. The single sweep profile shown in Fig. 1 reveals several interesting features in the cathodic portion of the scan. Although the sweep is in the cathodic direction, there are multiple anodic current peaks in the profile. This behavior is not common in potential sweep or cyclic sweep experiments, but is very significant. The first small cathodic current peak (~0.42V) in the cathodic scan is associated with the start of the reduction of the gold (III) oxide. Once sufficient oxide has been reduced, the anodic reaction recommences. The cathodic reduction peak will be discussed in greater detail later. The first anodic current maximum in the cathodic scan is very similar to that of peak 3 in the anodic scan and must correspond to the same anodic dissolution reaction. As the potential becomes more negative during the cathodic scan, the rate of gold dissolution decreases in the fashion of a normal faradaic reaction. An arrest in the current decrease occurs at about +0.15V, after which an anodic current increase again takes place. This second anodic current increase may reasonably be associated with the anodic reaction at peak 2, since it is in the same potential region. The arrest and second anodic current increase strongly suggest that the reaction at peak 2 is blocked by the formation of a passivating layer during the anodic scan, and that the

reduction of this passivating layer during the cathodic scan (at $\approx +0.15\text{V}$) allows the anodic dissolution reaction to recommence. A cathodic peak indicating the presence of a reducible species would be expected only if the magnitude of the cathodic reaction was greater than that of the competing anodic reaction.

The continuation of the cathodic scan from peak 2 in Fig. 1 shows that the current remains anodic, but decreases with potential. From the inset in Fig. 1 it can be seen that a third anodic increase takes place in the peak 1 region. Although the peak 1 reaction is weak at these potentials, it is clear that the behavior of the gold electrode in this region is very similar to that observed for the peak 2 and peak 3 regions. The reduction of a passivating species (at $\approx -0.6\text{V}$) would allow the anodic dissolution reaction to recommence.

Thus the cathodic scan in Fig. 1 is consistent with the proposal that the anodic current peaks are the result of a dissolution reaction which is blocked by the formation of passivating surface species.

The effect of the extent of the sweep range is shown in Fig. 2. The range of the potential sweep was varied from 0.06 to 0.5V past peak 3. When the anodic sweep extent was just sufficient to cause the passivation of peak 3 (curve 1), the cathodic scan revealed almost complete reversibility of the peak 3 reaction. However, with greater potential scan ranges, the reversibility of the peak 3 reaction decreased (curves 2, 3, and 4). When the extent of the potential sweep exceeds $+0.8\text{V}$ (curve 4), little or no evidence of the peak 3 reaction can be seen on the cathodic sweep. The thickness of the oxide may increase with oxidation time and the nature of the oxide may change with increase in oxidation potential. Either phenomenon could account for the progressive decrease of anodic current in the cathodic scan in Fig. 2.

Figure 3 shows the effect of varying the sweep rate for a fixed sweep range. At sweep rates of 1Vsec^{-1} , peak 2 is no longer distinct from peak 3 in the anodic scan. In the cathodic scan, the cathodic reduction peak of the gold (III) oxide is more readily observed. Thus at the faster sweep rates, the gold (III) oxide reduction reaction is more readily separated from the anodic dissolution reaction. By holding the potential at the end of the anodic scan for various times, then performing the cathodic scan at 1Vsec^{-1} , the change in the oxide buildup can be estimated. This change can be seen in Fig. 4. The magnitude of the reduction peak increases with the time held at the end of the

²The theoretical monolayer coverage was calculated using an atomic density of $1.15 \times 10^{15}\text{ atoms}\cdot\text{cm}^{-2}$ (7) based on the average of the atomic density of the three crystal planes (100), (110), and (111).

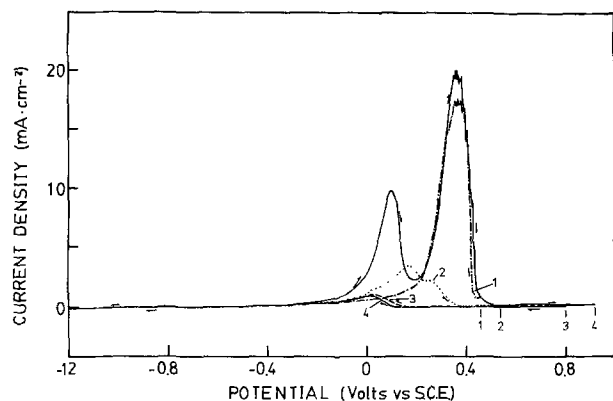


Fig. 2. Effect of potential scan range on single sweep potential profile in aqueous alkaline cyanide: 0.1M KOH + 0.1M KCN; sweep rate = $10\text{ mV}\cdot\text{sec}^{-1}$; initial potential = -1.2V ; temperature = 19.8°C . Sweep extent: curve 1, $+0.46\text{V}$; curve 2, $+0.54\text{V}$; curve 3, $+0.80\text{V}$; curve 4, $+0.92\text{V}$.

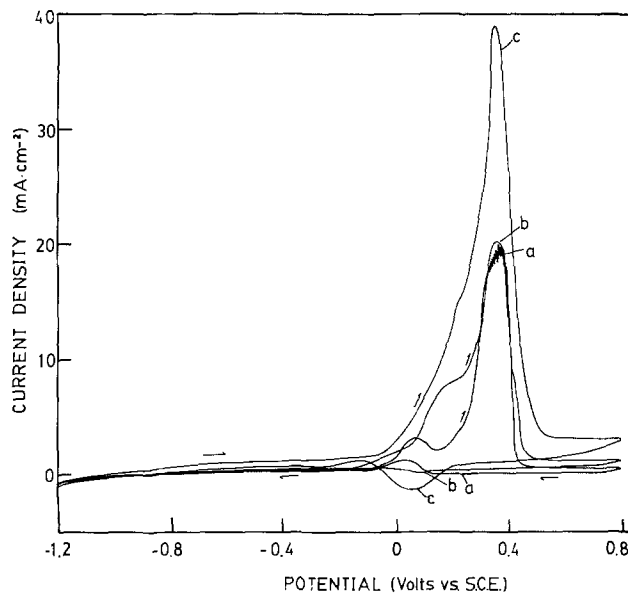


Fig. 3. Effect of sweep rate on single sweep potential profile in aqueous alkaline cyanide: 0.1M KOH + 0.1M KCN; initial potential = -1.2V ; temperature = 22.3°C . Sweep rate: a, $10\text{ mV}\cdot\text{sec}^{-1}$; b, $100\text{ mV}\cdot\text{sec}^{-1}$; c, $1.0\text{ V}\cdot\text{sec}^{-1}$.

anodic sweep, although a limiting value is reached after approximately 2 min (see insert). This limiting value in the 0.1M KOH + 0.1M KCN electrolyte corresponds to approximately 75% coverage with an Au^{+3} monolayer. Under conditions more favorable to the oxide formation (increased hydroxide concentration, 1.0M), the limiting value was achieved more rapidly ($<1\text{ min}$) and was higher, corresponding to 100% coverage of a monolayer of Au^{+3} oxide. The lower values in the 0.1M KOH + 0.1M KCN may simply reflect a greater proportion of the anodic dissolution reaction in the measurements. There is evidence in Fig. 4 that the cathodic oxide reduction reaction is not completely separated from the anodic dissolution reaction. The tail of the reduction peak from -0.1 to -0.3V becomes anodic, indicating that the anodic process dominates for this region and obscures a portion of the reduction peak, thereby yielding lower apparent values of oxide coverage. These data support the theory that gold (III) oxide passivates the peak 3 cyanide reaction. The presence of cyanide in solution appears to limit the oxide growth

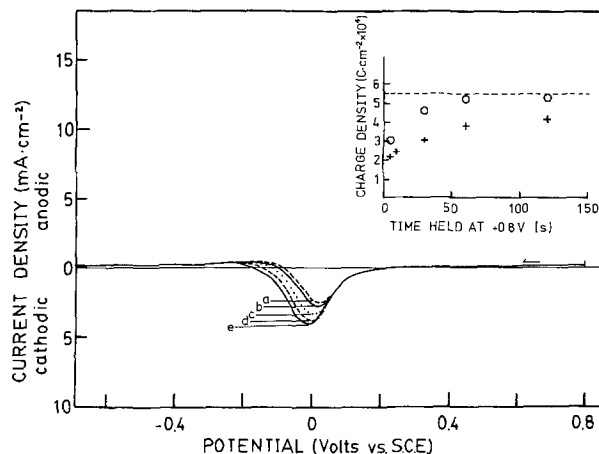


Fig. 4. Cathodic single sweep potential profile after holding electrode potential at $+0.8\text{V}$ in aqueous alkaline cyanide: 0.1M KOH + 0.1M KCN; sweep rate = $1.0\text{ V}\cdot\text{sec}^{-1}$; temperature = 22.8°C . Holding time: a, 5 sec; b, 10 sec; c, 30 sec; d, 60 sec; e, 20 sec. Insert shows total charge for cathodic currents during run. Dotted line indicates charge required for reduction of an Au^{+3} monolayer. +: measurements from curves a, b, c, d, and e; o: measurements from similar runs in 1.0M KOH + 0.1M KCN.

to about a monolayer. In alkaline solutions without cyanide, multilayer oxide formation does take place (7). It is clear in the cathodic scans in Fig. 2 that when the extent of the potential scan is small (curve 1), the oxide layer is either incomplete or does not have time to rearrange to form a more stable layer (13) and the reduction is relatively easy, allowing the anodic reaction to recommence. For greater scan ranges (curve 4), the oxide layer is more complete or more stable and the reduction of this oxide layer may occur at more cathodic potentials. This effect can be seen in the shift of cathodic reduction peak potential with increase in oxidation time in Fig. 4. A more complete or more stable oxide would also take longer to reduce and thus the potential may pass the peak 3 region in the cathodic scan before the oxide is removed (curve 4, Fig. 2).

By stopping the potential sweep at the anodic peak potential on the cathodic sweep, it can be seen that, given sufficient time, the oxide reduction can take place at that potential. Shown in Fig. 5b is the current-time behavior of a gold electrode after an anodic sweep to +0.70V and a cathodic sweep back to +0.38V. Figure 5a shows the single sweep profile without the hold at +0.38V vs. SCE. The single sweep profile of Fig. 5a shows that in the cathodic sweep the anodic reaction would not be observed until a potential of +0.13V. By holding the potential at +0.38V,

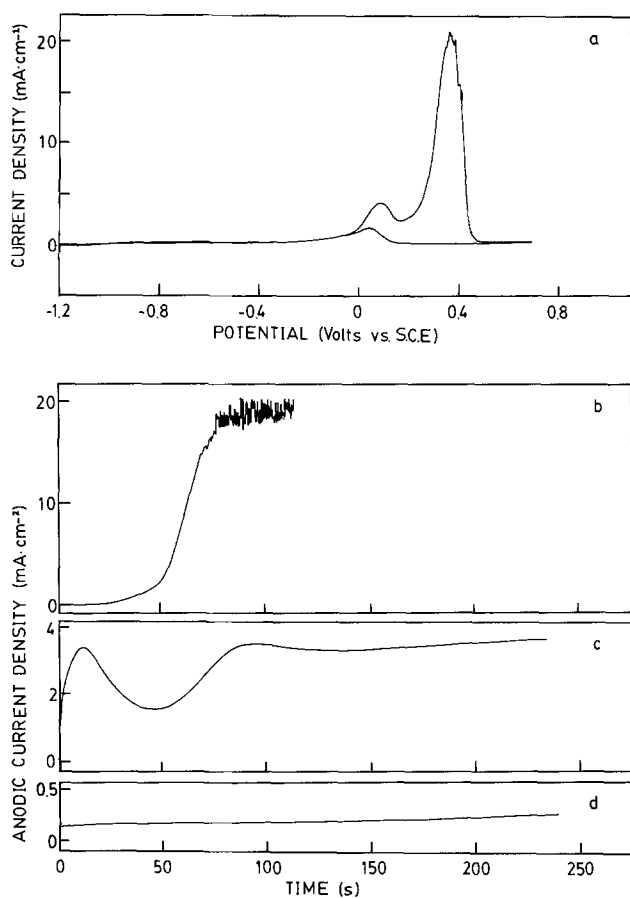


Fig. 5. Anodic recovery behavior of a gold electrode in aqueous alkaline cyanide after passivation: 0.1M KOH + 0.1M KCN; temperature = 22.3°C. a) single sweep potential profile: sweep rate = 10 mV · sec⁻¹. b) current-time behavior at peak 3 after passivation by a single potential sweep as in 5a except that the potential was stopped and held at +0.38V in the cathodic sweep. c) current-time behavior at peak 2 after passivation by a single potential sweep to +0.2V. The potential was stopped and held at +0.1V during the cathodic sweep. d) current-time behavior at peak 1 after passivation by a single potential sweep to -0.4V. The potential was stopped and held at -0.62V during the cathodic sweep.

the steady-state dissolution rate of peak 3 is achieved in about 90 sec. This represents the time required to reduce the oxide from full surface coverage to the steady-state coverage at +0.38V. The oscillation in the steady-state current at +0.38V can be observed easily in Fig. 5b. This instability, as noted earlier, appears to be the result of the inability of the gold (II) oxide reaction to dominate and passivate the surface at this potential.

The nature of the passivating layer for peak 2 may also be examined by measuring the recovery time of the anodic reaction after passivation. Potential scans were carried out in which the potential was stopped in the passivation region of peak 2 (+0.2V), then returned to a potential at the peak value (+0.1V). A current-time curve after the potential sweep is shown in Fig. 5c. It is clear from this figure that the passivation is not complete for peak 2 and that the anodic recovery begins immediately. However, the time required to reach the steady-state anodic dissolution rate is longer than that required for peak 3 recovery. In addition, it can be seen that the steady-state value is not reached in a monotonic fashion. This transient behavior is believed to be related to the dark film formation which is observed in the peak 2 region. This dark film, which has been reported in earlier works, (1, 2), has not yet been identified. The film does not seem to be the passivating layer, since the anodic reaction proceeds despite its formation. The film may, however, cause an increase in the effective surface area and hence cause a temporarily high anodic dissolution rate. The measurement of the surface area of an electrode held at peak 2 (+0.1V) for 5 min revealed that the area increased by about 26% as a result of the film formation. This area increase is sufficient to cause the current "overshoot" in the current-time behavior observed in Fig. 5c. Despite this added feature, the recovery behavior is consistent with that expected for a reaction which has been blocked by the formation of a passivating film.

The recovery time of the anodic reaction in the peak 1 region also was studied. After an anodic scan to -0.40V, the cathodic potential scan was stopped at a value of -0.62V in the cathodic leg of the scan. The current-time profile was then recorded and is shown in Fig. 5d. In this profile, the current slowly returns to its steady-state level. This slow return is partly the result of the slow rate of reaction of the cyanide reaction at this potential.

It is clear that the formation of intermediates during the dissolution reaction could cause peaks in the potential scans if the rate of reaction was dependent on either the diffusion of the reactants forming the intermediate or the diffusion of the products of the intermediate. In either case, however, steady-state measurements would show limiting current plateaus and not current peaks. In earlier works (1-3), steady-state measurements have shown potential-current profiles which have three peaks, and not three current plateaus. It is unlikely, therefore, that the passivating species is a reaction intermediate in the dissolution process. The formation of the gold (III) oxide species does passivate the reaction at the peak 3 region. Thus one might expect that if lower valence oxides could form, they might also be able to passivate the cyanide reaction. Recently it has been shown (7) that lower valence oxides may be found in alkaline solutions at potentials cathodic of the gold (III) oxide potential. In three different potential regions, distinct hydroxide-gold reactions were found. These reactions, identified by current peaks found in fast potential sweep profiles in potassium hydroxide solutions, were the result of monolayer hydroxide adsorption on the gold surface via the reaction



The three potential regions where the current peaks were found were labeled peaks A, B, and C and were from -1.2 to -0.7 V, -0.7 to -0.3 V, and -0.3 to $+0.2$ V, respectively.

In Fig. 6, a single anodic potential sweep profile is shown for gold in 0.1 M KCN + 0.1 M KOH. The potentials of formation of the gold hydroxide species at peaks A, B, and C, corrected for these pH conditions, are indicated. The potential regions indicated for peaks A, B, and C are the 95% confidence limits of the peak maxima for the data presented in Ref. (7). Peaks B and C were not found to shift with sweep rate, hence the potentials for a sweep rate of $1 \text{ mV} \cdot \text{sec}^{-1}$ are directly available from the potential-pH diagram [Fig. 5 in Ref. (7)]. Peak A, however, was shown to behave irreversibly with a potential shift of $+0.053$ V per decade of increasing sweep rate. Direct extrapolation of the peak potential measured at 1 Vsec^{-1} in the earlier work to $1 \text{ mV} \cdot \text{sec}^{-1}$ in this work is not advisable since the reaction may not remain irreversible at slow sweep rates (15). Therefore the "reversible" potential of peak A obtained using
$$\left(\frac{E_{p \text{ cathodic}} + E_{p \text{ anodic}}}{2} \right)$$

(16) was used to indicate the formation potential of peak A. Direct measurement of the peak formation potentials at a sweep rate of $1 \text{ mV} \cdot \text{sec}^{-1}$ is not possible because the small number of coulombs required to complete the reactions is obscured by the background current. The potential of formation of the gold (III) oxide (peak D), which is found in the solution without cyanide, is also shown.

As can be seen from Fig. 6, gold (III) oxide is formed just anodic of the peak 3 cyanide reaction. Thus, it is clear that the buildup of the oxide on the surface is the cause of the termination of the cyanide reaction. The oxide layer has been shown to be passive in potassium hydroxide solutions (7), and the variation of the current near the peak is the result of the competition between the passivation and anodic dissolution reactions as discussed earlier.

It can also be seen from the figure that the formation of the hydroxide adsorption peak C coincides with the minimum between the cyanide reactions of peak 2 and peak 3, and is anodic of peak 2. This is the region in which the formation of a passivating film would be expected in order to account for the decrease in the cyanide reaction at peak 2. The hy-

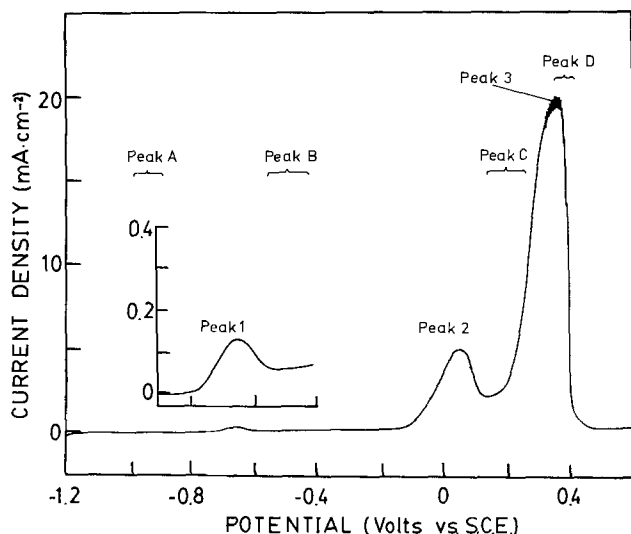


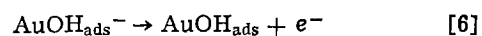
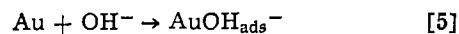
Fig. 6. Comparison of peaks in alkaline and alkaline cyanide electrolytes: anodic single sweep potential profile: 0.1 M KOH + 0.1 M KCN; sweep rate = $1.0 \text{ mV} \cdot \text{sec}^{-1}$; temperature = 23.5°C ; potential ranges of peaks A, B, and C represent 95% confidence limits for peak potentials at this sweep rate.

droxide adsorption peak C has been shown to be passive (7). Thus it is reasonable to associate the formation of the adsorbed hydroxide layer of peak C with the passivating surface species of the peak 2 cyanide reaction.

From Fig. 6 it can also be seen that the formation of the adsorbed hydroxide species at peak B is anodic of the cyanide reaction of peak 1, and is approximately at -0.5 V. This is the region in which the formation of a passivating film would be expected in order to account for the decrease in the cyanide reaction at peak 1. The hydroxide adsorption peak B has been shown to be passive (7), and it is reasonable to associate the formation of the adsorbed hydroxide layer of peak B with the passivating surface species of the peak 1 cyanide reaction.

If the passivation reaction involves the hydroxyl ion, then the potential of formation of the hydroxide species may be shifted by altering the concentration of the hydroxyl ion in the solution. This would then change the peak potential of the cyanide reaction because passivation would be either advanced or retarded. The change of cyanide peak potential with hydroxide concentration is shown in Fig. 7. The earlier results of Cathro and Koch are also shown in the figure. The change of peak potential with hydroxide concentration for both peaks 1 and 3 is approximately -0.06 V/decade , while peak 2 does not appear to shift over the hydroxide concentration range 10^{-3} to 1 M. In the case of the peak 3 passivation, the theoretical potential of formation of the gold (III) oxide decreases linearly at the rate of 0.059 V per tenfold increase in hydroxide concentration. This is in good agreement with the measured cathodic shift of 0.063 V per tenfold increase in hydroxide concentration for the peak 3 cyanide reaction.

In the case of peaks 1 and 2, passivation, via reaction [4], would be expected to cause the cyanide peak to shift cathodically at the rate of 0.059 V per tenfold increase in hydroxide concentration. The measured cathodic shift of 0.057 V per tenfold increase in hydroxide concentration for peak 1 is in good agreement with the theoretical value. The potential at peak 2, however, does not show any change for concentrations above 10^{-3} M KOH. Despite the lack of potential shift of peak 2, the concentration of hydroxide does affect the rate of reaction in the peak 2 region. In Ref. (1) (Fig. 7), the rate of dissolution was shown to decrease with increase in hydroxide concentration. This effect was greatest for changes in hydroxide concentration above 10^{-2} M. From these data it appears that the $\text{AuOH}_{\text{ads}}^-$ species may have a significant concentration at the surface in the peak 2 region. By using the data presented in Ref. (1), it is possible to model the hydroxide adsorption isotherm and estimate the coverage of $\text{AuOH}_{\text{ads}}^-$ on the surface. The details are given in the Appendix and show that, even for concentrations of hydroxide as low as 10^{-3} M, the surface coverage of the $\text{AuOH}_{\text{ads}}^-$ species could be 48%. As a result of the relatively high surface coverage of the $\text{AuOH}_{\text{ads}}^-$ species in the region of peak 2, it is necessary to consider the formation of AuOH_{ads} in a two stage reaction



The reversible potential of formation of AuOH_{ads} can be seen to depend on the concentration of the $\text{AuOH}_{\text{ads}}^-$ species via the relation

$$\Delta\phi_s = \Delta\phi_e^\circ + \frac{RT}{F} \ln \frac{a_{\text{AuOH}_{\text{ads}}}}{a_{\text{AuOH}_{\text{ads}}^-}} \quad [7]$$

From the adsorption data, the concentration of $\text{AuOH}_{\text{ads}}^-$ is relatively high for hydroxide concentrations above 10^{-3} M. If the activities of the two sur-

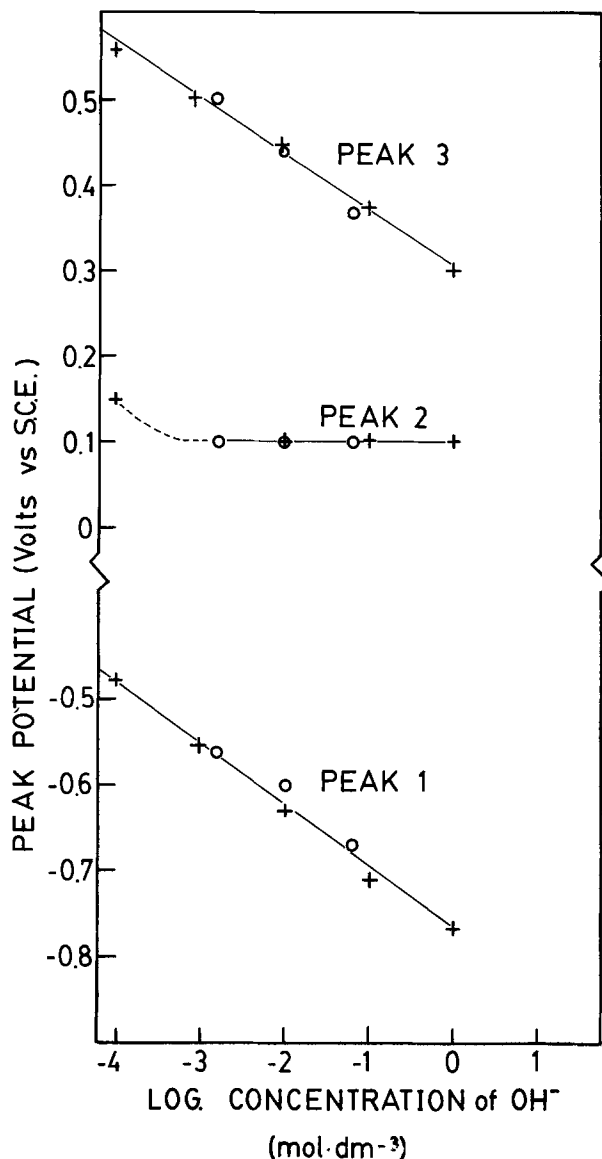
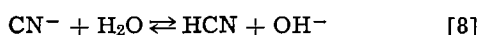


Fig. 7. Effect of hydroxide concentration on peak potentials in aqueous alkaline cyanide: free cyanide concentration = 0.1M; temperature = 23°C. +, data from this work; ○, data from Cathro and Koch (2).

face species AuOH_{ads} and $\text{AuOH}_{\text{ads}}^-$ remain approximately constant for bulk hydroxide concentrations greater than 10^{-3}M , then $\Delta\phi_e$, the potential of formation, will remain constant. Under these conditions, the passivation of peak 2 would not shift with changing hydroxide concentration. For lower hydroxide concentrations ($<10^{-3}\text{M}$), the formation of the AuOH_{ads} should become dependent on the hydroxide concentration in the bulk solution and a potential shift of -0.059V per tenfold increase in hydroxide concentration would be expected. As can be seen in Fig. 7, the peak 2 potential for the 10^{-4}M concentration is shifted from the 0.1V value. For lower pH values, buffering is required. Although it is not known what effect the buffering ions will have on the adsorption of hydroxide ions, an anodic potential shift of the passivation would be expected with a decrease in hydroxide concentration.

A potassium phosphate buffering system was used to lower the pH. Sufficient potassium cyanide was dissolved in the solution to set the free cyanide ion concentration at 0.1M despite the formation of undissociated hydrocyanic acid via the reaction



Very slow sweep rates ($0.1 \text{ mV} \cdot \text{sec}^{-1}$) were used so that the passivation reactions could still take place despite the reduced hydroxide concentration. The results showed that from pH 10-7.8, peak 2 shifted in the anodic direction at the rate of 0.065 ± 0.010 (95% confidence) V per pH unit. This value agrees favorably with the theoretical value of 0.059V per pH unit. As a result of the anodic potential shift with decrease in pH the peak 3 cyanide reaction begins to obscure the passivation of the peak 2 reaction to the extent that peak 2 appears to be only a shoulder of the peak 3 reaction. Potential scans in the buffered solutions ($\text{pH} \leq 10$) appear to be more complex than in those of high alkalinity. Multiple peak formation is observed in these solutions. Since several new species are present in the buffered solutions (HCN , PO_4^{3-} , HPO_4^{2-} , H_2PO_4^- , H_3PO_4) it is not clear whether these species may be contributing to the complexity of the potential scans. Despite these new features in the potential scans, it is clear that the passivation of the peak 2 cyanide reaction is affected by the hydroxyl ion. In addition, the model for the hydroxide adsorption phenomenon presented in the Appendix is consistent with both the earlier findings (1) that the dissolution rate decreased linearly with $\log [\text{OH}^-]$ and with the potential-pH behavior of peak 2 in this work.

It is clear that the hydroxyl ion is involved with the passivation of the cyanide reactions and that the oxide formation potentials occur just anodic of the cyanide peaks. Therefore, it is reasonable to associate the passivation of the cyanide reactions at peaks 1 and 2 with the formation of the adsorbed hydroxide species indicated by peaks B and C as shown in Fig. 6. The passivation of the cyanide reaction at peak 3 is the result of the formation of gold (III) oxide indicated by peak D.

The linking of the passivation of peaks 1 and 2 with the species identified at peaks B and C in alkaline solutions has interesting consequences. The passivating species formed at peaks B and C were shown to be the result of monolayer hydroxide adsorption on distinct crystal planes (7). This would then explain why the same dissolution reaction sequence was indicated for peaks 1 and 2. Peak C was identified with hydroxide adsorption on the (111) gold crystal plane. Thus, if the peak C reaction is the cause of the passivation of the peak 2 cyanide reaction, then the peak 2 cyanide reaction must occur predominantly on the (111) crystal plane. Peak B was identified with the monolayer hydroxide adsorption on the (100) crystal plane. By similar reasoning, the peak 1 cyanide reaction should occur predominantly on the (100) crystal plane. Thus the same dissolution reaction sequence would be found for peaks 1 and 2. After peak C in alkaline solutions, the surface is predicted (7) to have complete coverage of adsorbed hydroxide. Thus the cyanide reaction at peak 3 which is anodic of peak C must take place despite the hydroxide coverage. As a result of the reaction proceeding in spite of the hydroxide coverage, the hydroxide concentration should not affect the peak 3 cyanide reaction rate. This is indeed the case. In Fig. 5 of Ref. (1), the concentration of the hydroxide ion was shown to have no effect on the gold dissolution rate at peak 3 over the concentration range 10^{-3} to 1M. From the data presented, it is clear that the gold oxide and suboxide reactions can provide an explanation for the complex behavior of gold in alkaline cyanide solutions.

The effect of the peak A hydroxide adsorption reaction on the cyanide dissolution reaction has not yet been discussed, although it is likely that the blockage of the (110) crystal plane may simply prevent reaction from occurring on that plane until the peak 3 region.

Summary

The results of this work indicate clearly that the three anodic current peaks found in potentiostatic and potentiodynamic profiles for alkaline cyanide solutions are the result of passivation of the active gold surface. That the various passivation species are gold hydroxides, was shown by the hydroxyl ion dependence measurements. Passivation potentials correspond closely to the formation potentials of gold oxide and suboxide species.

The most anodic dissolution peak for the cyanide dissolution is passivated by the formation of gold (III) oxide. The more cathodic peaks are subject to passivation by hydroxide adsorption on various crystal planes to form a gold (I) surface species. These various dissolution and passivation phenomena are illustrated in the schematic representation of the anodic behavior of gold in alkaline cyanide solution shown in Fig. 8.

Manuscript received Dec. 20, 1979.

Any discussion of this paper will appear in a Discussion Section to be published in the June 1981 JOURNAL. All discussions for the June 1981 Discussion Section should be submitted by Feb. 1, 1981.

Publication costs of this article were assisted by the University of Toronto

APPENDIX

Calculation of an isotherm for hydroxide adsorption on gold in the region of peak 2 (+0.1V) in aqueous alkaline cyanide

From Ref. (1), Fig. 7, the following data are obtained

Table IA. The effect of hydroxide concentration on the dissolution rate of gold at peak 2 (+0.1V)

Dissolution rate (mg · m ⁻² · sec ⁻¹)	Concentration of [OH ⁻] (mole · dm ⁻³)	Current density* (A · m ⁻²)
25	1.0	12.2
42	0.1	20.6
62	0.01	30.4
77	0.001	37.7

[CN⁻] = 0.05M

* The current density is calculated by converting the dissolution rate to mole · m⁻² · sec⁻¹, then by noting that the dissolution reaction is a one-electron transfer process (1), multiplication by 96,489 c/mole gives current density (A · m⁻²).

In Ref. (1), step [2] was shown to be the rate-determining step in the dissolution sequence [1], [2], and [3] in the region of peak 2. The theoretical reaction rate for step [2] was shown to be

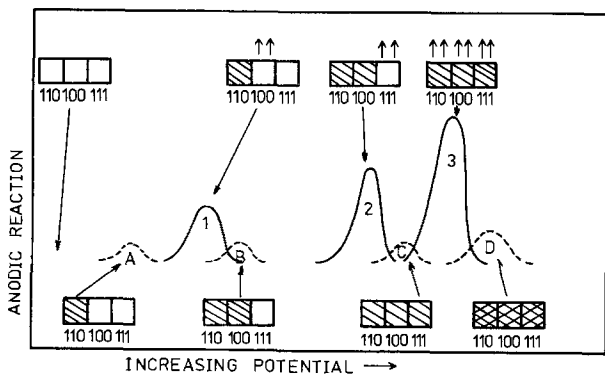


Fig. 8. A schematic representation of the anodic behavior of gold in aqueous alkaline cyanide. □ bare Au; ↑ Au dissolving; ▨ OH covered; ▩ Au₂O₃ covered. — reaction in alkaline cyanide solution, - - - reaction in cyanide-free alkaline solution. The numbers refer to the crystal planes involved in the reactions.

$$i = \frac{\overset{\rightarrow}{k_1} \overset{\rightarrow}{k_2} (1 - \theta'') [\text{CN}^-]}{\overset{\rightarrow}{k_1} + \overset{\rightarrow}{k_1} [\text{CN}^-]} \exp\left(\frac{\beta F \Delta \phi}{RT}\right) \quad \text{[A-1]}$$

where $\overset{\leftarrow}{k_i}$, $\overset{\rightarrow}{k_i}$ are the partial electrochemical rate constants, θ'' is the surface coverage by AuOH_{ads}⁻, β is the symmetry factor of the rds, $\Delta\phi$ is the electrode potential, i is the reaction rate expressed as current density, and F , R , T , have their usual meanings.

For constant potential and constant cyanide concentration this expression reduces to

$$i = K(1 - \theta'') \quad \text{[A-2]}$$

where K is the constant $\frac{\overset{\rightarrow}{k_1} \overset{\rightarrow}{k_2} [\text{CN}^-]}{\overset{\rightarrow}{k_1} + \overset{\rightarrow}{k_1} [\text{CN}^-]} \exp\left(\frac{\beta F \Delta \phi}{RT}\right)$

It is clear from Table IA that an increase in the concentration of hydroxide causes a decrease in the dissolution rate. A plot of current density vs. log [OH⁻] in Fig. A-1 shows that $i \propto \log [\text{OH}^-]$.

Using linear regression the relationship can be found to be

$$i = 12.28 - 8.63 \log [\text{OH}^-] \quad \text{[A-3]}$$

As a consequence of the similarity between Eq. [A-2] and [A-3] it is reasonable to assume that $\theta'' \propto \log [\text{OH}^-]$. Furthermore if the concentration of the surface species AuOH_{ads}⁻ is assumed to be ≈ 0 for a concentration of [OH⁻] = 10⁻⁷M, then

$$\theta'' = \frac{7 + \log [\text{OH}^-]}{8.42}$$

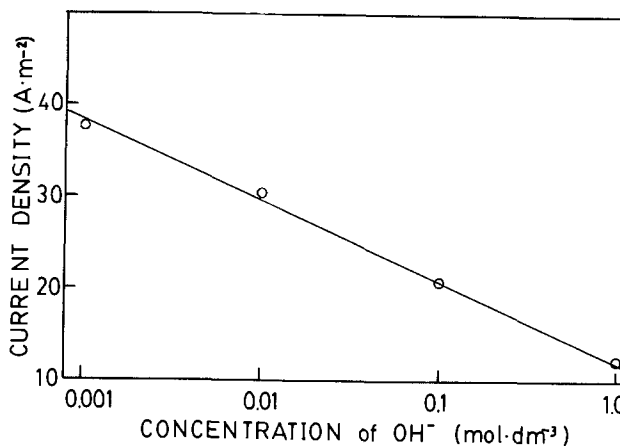


Fig. A-1. Effect of hydroxide concentration on the dissolution rate of gold in aqueous alkaline cyanide: temperature = 23.5°C; 0.05M [CN⁻]. Data from Fig. 7, Ref. (1).

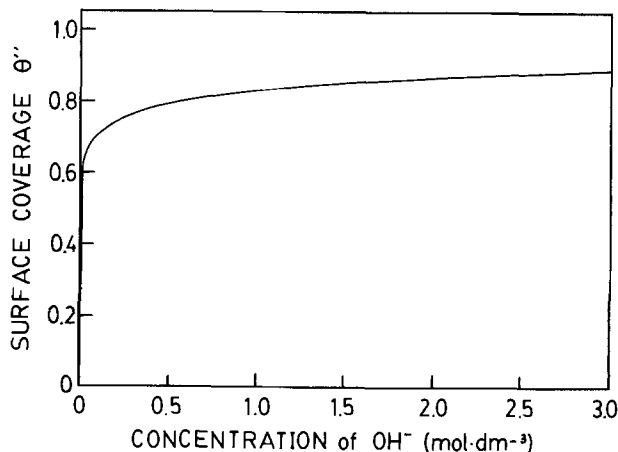


Fig. A-2. Surface coverage (θ'') of AuOH_{ads}⁻ vs. concentration of hydroxide for the adsorption isotherm $\theta'' = 7 + \log [\text{OH}^-] / 8.42$.

This relationship has been plotted in Fig. A-2. From this isotherm the coverage of the gold by $\text{AuOH}_{\text{ads}}^-$ at $[\text{OH}^-] = 10^{-3}\text{M}$ is about 48%.

From Fig. A-2 it can be seen that at concentrations $> 10^{-3}\text{M}$ KOH the surface concentration of $\text{AuOH}_{\text{ads}}^-$ remains relatively constant.

REFERENCES

1. D. W. Kirk, F. R. Foulkes, and W. F. Graydon, *This Journal*, **125**, 1436 (1978).
2. K. J. Cathro and D. F. A. Koch, *ibid.*, **111**, 1416 (1964).
3. E. T. Eisenmann, *ibid.*, **125**, 717 (1978).
4. D. W. Kirk, F. R. Foulkes, and W. F. Graydon, *ibid.*, In press.
5. D. W. Kirk and F. R. Foulkes, *ibid.*, In press.
6. D. M. MacArthur, *ibid.*, **119**, 672 (1972).
7. D. W. Kirk, F. R. Foulkes, and W. F. Graydon, *ibid.*, **127**, 1069 (1980).
8. R. S. Nicholson and I. Shain, *Anal. Chem.*, **36**, 706 (1964).
9. U. F. Franck, *Z. Phys. Chem.*, **3**, 183 (1955).
10. T. Bak, *Adv. Chem. Phys.*, **3**, 33 (1961).
11. J. Wojtowicz, N. Marincic, and B. E. Conway, *J. Chem. Phys.*, **48**, 4333 (1968).
12. J. Wojtowicz and B. E. Conway, *ibid.*, **52**, 1407 (1970).
13. R. Córdova O., M. E. Martins, and A. J. Arviá, *This Journal*, **126**, 1172 (1979).
14. J. D. E. McIntyre and W. F. Peck Jr., *ibid.*, **123**, 1800 (1976).
15. H. Angerstein-Kozłowska, J. Klinger, and B. E. Conway, *J. Electroanal. Chem. Interfacial Electrochem.*, **75**, 45 (1977).
16. H. Angerstein-Kozłowska, J. Klinger, and B. E. Conway, *ibid.*, **75**, 61 (1977).

Models for the Photoelectrolytic Decomposition of Water at Semiconducting Oxide Anodes

J. M. Kowalski,* K. H. Johnson, and H. L. Tuller**

Department of Materials Science and Engineering,
Massachusetts Institute of Technology, Cambridge, Massachusetts 02139

ABSTRACT

Surface states at semiconducting TiO_2 /electrolyte interfaces are believed to play an important role in charge transfer and thereby the efficiency of photoelectrochemical processes at such interfaces. Theoretical calculations were therefore performed using the SCF- X_α -SW method to determine the position and character of surface states at various characteristic interfaces. At the TiO_2 /water interface, antibonding surface states were found which when occupied would explain the experimentally observed dissociation of water into hydroxyl groups at n-type semiconducting TiO_2 surfaces. Similarly, antibonding surface states were found at the TiO_2 / OH^- interface which when occupied would tend to destabilize the OH bond. A likely mechanism for the dissociation of water and decomposition of certain photoanodes in photoelectrochemical cells based on the above results is presented. The effects of surface reconstruction at heavily reduced TiO_2 surfaces on the validity of our calculations are also discussed.

The present fuel shortage has stimulated much research concerning the production of hydrogen gas by the photoelectrolysis of water on semiconductor electrode surfaces. To date, only a few semiconducting oxides, including titanium dioxide and some perovskites, have been shown to remain inert in cell operation and decompose water. In all cases surface states at the electrode-electrolyte interface are believed to play an important role in the charge transfer process and thereby the overall efficiency of such cells (1, 2). Little is known, however, concerning the source of these surface states and the manner in which they assist the photoelectrolytic process. In the following, SCF- X_α -SW calculations are presented which serve to clarify some of these issues.

The catalytic behavior of a surface often depends on its ability to interact electronically with the adsorbate. The determination of the electronic structure of the surface perturbed by the chemisorbed species may, therefore, provide a basis for understanding charge transfer catalysis. In order to understand the electronic interaction between water and a TiO_2 surface, cluster molecular-orbital calculations were performed using the self-consistent-field- X_α -scattered wave (SCF- X_α -SW) method (3). This technique is based on the com-

bined use of the X_α density-functional approximation to electron-electron exchange and correlation and the multiple-scattered-wave method of solving Schrödinger's equation. Details of the technique, including computational procedure, and previous applications are described in Ref. (3). The SCF- X_α -SW method was chosen over the conventional Hartree-Fock self-consistent-field linear-combination-of-atomic orbitals (HF SCF-LCAO) method since the former is less laborious and costly in computer time and leads to a more reliable description of electronic structure (3). Molecular orbital methods were chosen over band theory since it offers a more appropriate description of local interactions and chemical bonding.

Previous SCF- X_α -SW studies (4) have shown that the local electronic structure of bulk TiO_2 (rutile) can be realistically modeled in terms of a $(\text{TiO}_6)^{8-}$ cluster, yielding results in good agreement with measured photoemission and optical absorption spectra. In the same manner, the chemisorption of H_2O on a titanium dioxide surface can be modeled by the combination of a TiO_2 surface cluster and an adsorbed H_2O molecule. In the remainder of this paper, results for the clean, water-chemisorbed, and OH^- -chemisorbed surfaces are presented and compared with recently measured photoemission spectra. With these results, a possible mechanism is suggested for the dissociation of water in the photoelectrochemical cell.

* Electrochemical Society Student Member.

** Electrochemical Society Active Member.

Key words: photoelectrolysis, catalysis, titanium dioxide, perovskite titanates.

Results of Calculations

Figure 1(a) shows the schematic energy level diagram for "bulk" TiO_2 as calculated by the SCF- X_α -SW method along with those for the free oxygen and titanium atoms. Only the $\text{Ti}3d$ and $\text{O}2p$ levels are shown since they are the only ones involved in bonding on this energy scale. One observes that the titanium $3d$ level splits into the antibonding e_g^* and t_{2g}^* levels which represent the conduction band of bulk TiO_2 . The valence band is composed mainly of oxygen bonding and nonbonding $2p$ character and lies approximately 3 eV below the conduction band.

Clean surfaces.—The simplest model for the clean (110) titanium dioxide surface is the $(\text{TiO}_5)^{6-}$ cluster which consists of a slightly distorted and truncated octahedron in which a titanium atom is surrounded by five nearest neighbor oxygen atoms. These slight distortions are ignored in our analysis to simplify calculations. Furthermore, since this is nearly the same local environment of a titanium atom in the perovskite structure, this cluster also represents the (100) active surface site of SrTiO_3 . The charge on the cluster is chosen such that the valencies of the atoms sum to zero. This simulates charge transfer with neighboring titanium atoms in the solid.

The calculated energy levels for the $(\text{TiO}_5)^{6-}$ surface cluster are shown in Fig. 1(b). Here the $3d$ levels split further due to the lower symmetry near the surface. Since the cluster method does not correctly treat the Madelung constant, the resultant energy levels are only on a relative scale and must be aligned with the absolute scale. This is usually done by choosing a nonbonding level and aligning it with that of the free atom, since nonbonding levels are not expected to shift much upon bonding. The diagrams are aligned using the $\text{O}2p$ nonbonding level, which lies at the top of the valence band.

The splitting of the t_{2g}^* and e_g^* levels in the surface cluster results in the d_{yz}^* and d_{xz}^* states extending into the energy gap. These bandgap surface states are simply due to the truncation of the lattice. In the intrinsic material, only levels to the top of the valence band are filled while these bandgap surface states are empty. If the material is made n -type, however, these surface states become occupied.

Similar calculations were performed for the $(\text{TiO}_4)^{4-}$ cluster, which represents the oxygen deficient (001) surface. The resultant energy level diagram shown in

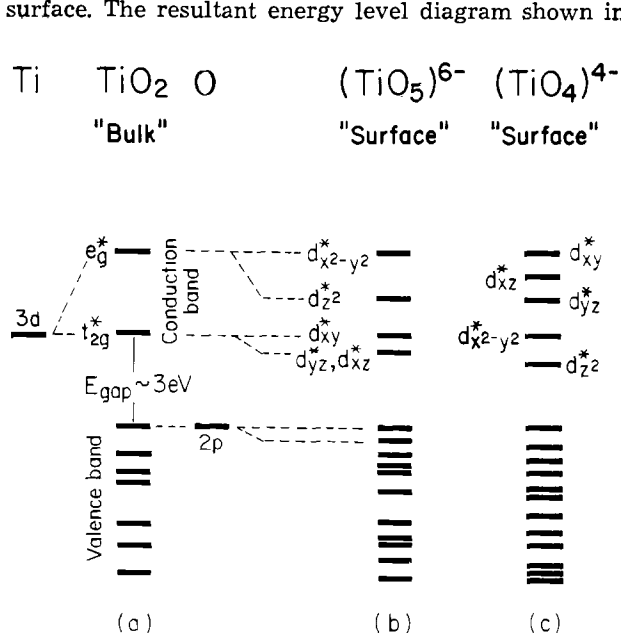


Fig. 1. (a) Energy level diagrams of bulk TiO_2 and the free titanium and oxygen atoms, (b) energy levels for the clean (110) TiO_2 and (100) SrTiO_3 surface modeled by the $(\text{TiO}_5)^{6-}$ cluster, or (c) the $(\text{TiO}_4)^{4-}$ cluster.

Fig. 1(c) reveals that the d levels are further split by the reduced symmetry of this surface. A new characteristic surface state, designated by d_{2z}^* , is generated at this surface.

Surface clusters with chemisorbed water.—To study the interaction of water with a TiO_2 surface, calculations for both surface clusters were extended to include a chemisorbed water molecule. The resultant energy diagrams for both surfaces are largely a superposition of those for the separated clean surfaces and H_2O molecule.

The electronic structure of the $(\text{TiO}_5)^{6-}\text{H}_2\text{O}$ cluster is shown in Fig. 2, along with that for the clean surface and that for the H_2O molecule. The figures are aligned such that the oxygen $2p$ nonbonding levels coincide, which is the top of the valence band for the surface clusters and the b_1 level for the water molecule. The a_1^* and b_2^* water levels are normally empty and lie about 5 eV above the filled b_1 level. Although the a_1^* and b_2^* levels of water are traditionally viewed as corresponding to "Rydberg orbitals," they have significant antibonding character which increases through the interaction with TiO_2 d orbitals discussed below. In the $(\text{TiO}_5)^{6-}\text{H}_2\text{O}$ cluster, the water valence levels are still identifiable (mixing very little with the TiO_2 valence band) and are pulled down almost uniformly in energy. The a_1 level does, however, shift more to tighter binding energy and bonds more with titanium than the b_1 and b_2 levels. This suggests that water is chemisorbed onto the surface as an intact molecule and bonds to the surface through the a_1 orbital. The antibonding a_1^* and b_2^* water levels are also pulled down in energy but mix more strongly with the TiO_2 $3d$ levels. These states, normally unoccupied in the intrinsic material could, however, become filled if the material were made n -type by reduction or doping.

Photoemission data of Henrich (5) for water chemisorbed on annealed (110) TiO_2 and (100) SrTiO_3 surfaces show the H_2O levels displaced uniformly about 2 eV below the top of the valence band with the a_1 orbital shifting more to tighter binding energies, in agreement with our calculations. This suggests non-dissociative water chemisorption on the annealed surface. Our calculations however predict a larger shift for the water levels of about 4 eV . This discrepancy

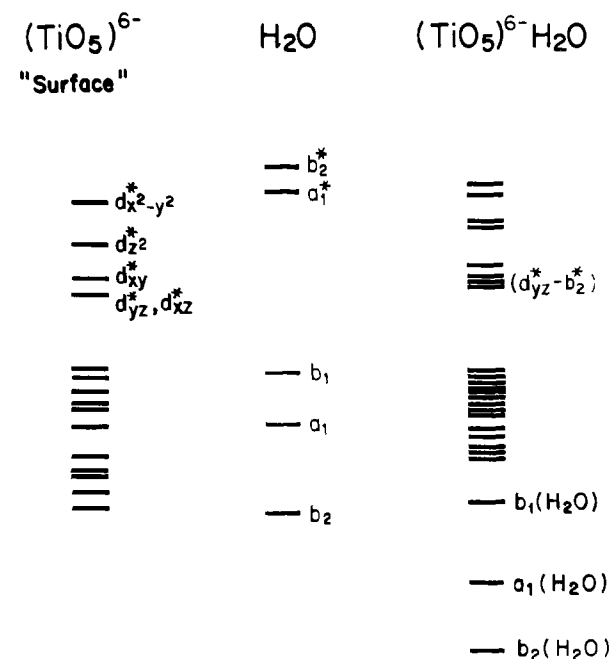


Fig. 2. Calculated energy levels for the $(\text{TiO}_5)^{6-}$, H_2O , and $(\text{TiO}_5)^{6-}\text{H}_2\text{O}$ clusters representing the clean TiO_2 surface, the water molecule, and the water chemisorbed surface.

may be due to the short bonding distance between the surface and the H_2O molecule chosen for the calculation. The bonding distance between the surface titanium atom and the water oxygen atom may very well be greater than the bulk Ti-O bond length of 1.94\AA chosen. A larger value would have the effect of lowering the attraction between the surface and the water molecule, thereby lessening the perturbation on the H_2O molecule.

Lo, Chung, and Somarjai (2) likewise conclude on the basis of their photoemission studies that water molecules chemisorbed on stoichiometric TiO_2 surfaces remain undissociated. On the other hand, for surfaces reduced by heating to above 800°C or by argon bombardment, they obtained evidence for the existence of dissociated water in the form of hydroxyl groups. We later show that dissociation of water molecules on reduced surfaces of TiO_2 can be explained by considering the destabilizing effects that occupation of the $d_{yz}^* - b_2^*$ antibonding states have on the stability of the H_2O molecule.

Surface clusters with adsorbed OH radicals.—As a simple model for the TiO_2 -electrolyte interface in a photoelectrochemical cell, the $(\text{TiO}_5)^{6-}\text{OH}^-$ and $(\text{TiO}_4)^{4-}\text{OH}^-$ clusters were chosen to represent the local electronic interaction between the titanium dioxide surface and basic electrolyte. The resultant energy levels are a superposition of those for the clean surfaces and the OH^- ion, with some mixing. The results for the $(\text{TiO}_5)^{6-}\text{OH}^-$ cluster are shown in Fig. 3 along with the energy levels of the OH radical and clean surface cluster. Again the diagrams are aligned at the nonbonding oxygen 2p level, which is the filled π level for the OH^- ion. The π and σ OH^- levels appear to remain relatively unperturbed upon chemisorption, but the antibonding σ^* and π^* levels are pulled far down in energy to interact with TiO_2 d levels resulting in additional surface states within the bandgap. In the next section these states will be shown to play a potentially important role in the photoelectrolytic decomposition of water.

Discussion

As a result of our calculations we have been able to predict the relative positions of surface states generated at TiO_2 -vacuum, $-\text{H}_2\text{O}$, and $-\text{OH}^-$ interfaces as well as the character of these states. It should be noted that the adsorbate itself has a strong influence on the position, character, and number of surface states that exist at a given interface. In the following we consider the consequences that occupa-

tion of these surface states have on water dissociation and photoelectrolysis and compare these predictions with experimental evidence.

Clean surfaces.—A number of investigators have recently studied the surface electron structure of TiO_2 by ultraviolet photoemission spectroscopy (UPS), low-energy-electron diffraction (LEED), and Auger electron spectroscopy (AES). Henrich *et al.* (6) observed a UPS peak at about 2.5 eV above the bottom of the valence band for annealed TiO_2 surfaces which they attributed to surface defect states. This peak increased by more than a factor of 10 under argon-ion bombardment which was shown to result in the formation of Ti^{3+} ions at the surface (6). Lo *et al.* (2) observed similar absorption peaks which were sensitive to annealing and Ar bombardment treatments. Both studies are consistent with our calculations which indicate the existence of normally empty surface states which become occupied upon reduction of the surface resulting in the formation of Ti^{3+} ions. Subsequent exposure of the surface to oxygen results in a sharp decrease in the emission peak indicating a reversible depopulation of the Ti-like surface states.

Water dissociation.—In investigating the chemisorption of water on variously treated TiO_2 surfaces by photoemission (UPS), Lo *et al.* (2) discovered that whereas water is adsorbed as an intact molecule on oxidized TiO_2 surfaces, it appears to dissociate on reduced surfaces leaving behind $(\text{OH})^-$ molecules adsorbed on the surface. Henrich *et al.* (5) observed similar results for argon bombarded (110) TiO_2 surfaces upon exposure of up to 10 liters H_2O .

Since existence of Ti^{3+} ions at the surface appears to be critical in determining the manner in which water molecules adsorb on the surface we examine the consequences of surface state occupation on bonding between TiO_2 and adsorbed water molecules.

Reduction of the TiO_2 surface by argon bombardment or annealing in hydrogen should result in occupation of the $d_{yz}^* - b_2^*$ levels of the TiO_2 - H_2O interface (see Fig. 2). The contour diagrams for these orbitals are shown in Fig. 4. The d_{yz}^* orbital is antibonding between the titanium 3d and oxygen 2p levels; this is revealed by opposite signs in the overlapping lobes between the titanium and oxygen. In the diagrams, the lobes are shrunken in size and are not shown as overlapping for clarity. The sign inside the lobes represents the phase of the wave-function: overlapping

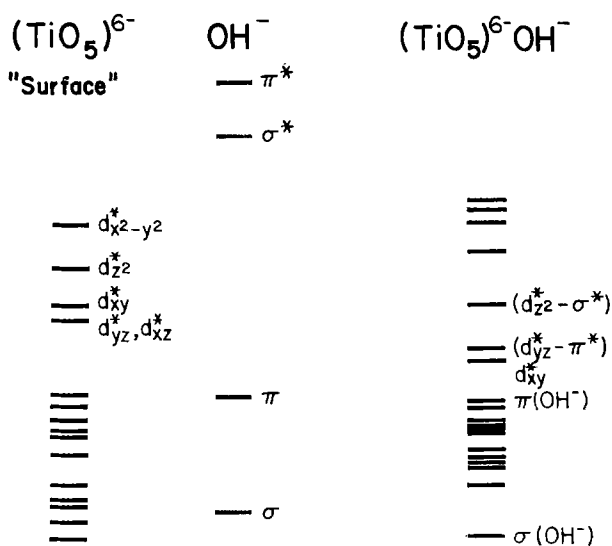


Fig. 3. Calculated energy levels for the clean TiO_2 surface, the OH^- ion, and the OH^- chemisorbed surface.

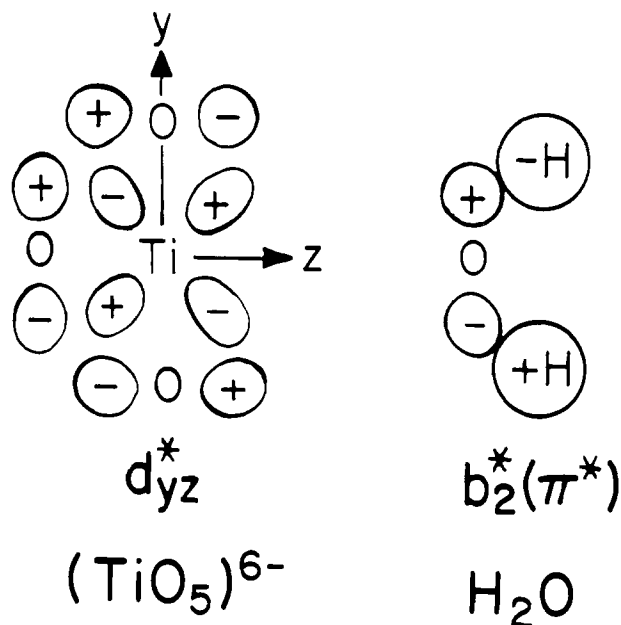
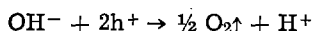


Fig. 4. Contour diagrams of the d_{yz}^* and $b_2^*(\pi^*)$ antibonding orbitals before mixing in the $(\text{TiO}_5)^{6-}\text{H}_2\text{O}$ cluster.

lobes of the same sign signify bonding. When the d_{yz}^* and b_2^* orbitals mix, the titanium d lobes and the oxygen 2p lobe (of H_2O) overlap in a bonding fashion as do the oxygen 2p lobes (of the lattice) and the hydrogen lobe. When the $d_{yz}^*-b_2^*$ orbital is occupied, as it is in the bombarded TiO_2 surface with chemisorbed water, bonding between the titanium d and oxygen 2p (of H_2O) and the surface oxygen 2p and hydrogen orbitals will be strengthened; the OH bonding within the water molecule will be weakened since the overlapping orbitals have opposite phase. Thus, a plausible mechanism exists for the break up of chemisorbed water into OH radicals on the surface if and only if the surface states with antibonding character are occupied as they are in reduced TiO_2 . Similar results are also obtained for the $(TiO_4)^{4-}H_2O$ cluster.

Photoelectrolytic decomposition of water.—When n-type photoanodes such as TiO_2 or $SrTiO_3$ are immersed in liquid electrolytes and are illuminated with band-gap light, oxygen gas (O_2) is known to be released (7). This process of oxygen evolution has been modeled assuming that a Schottky barrier is formed at the solid liquid interface at which electron-hole pairs are formed during illumination. The built-in space-charge field is then believed to cause the photogenerated holes to be swept towards the interface while the electrons are swept away from the interface towards the platinum counterelectrode. The OH^- ions adsorbed at the interface are now believed to lose their electrons to the semiconductor valence band via surface states (1) producing oxygen by the reaction



Because the energy of the electrons associated with the OH^- ions (commonly referred to as the OH^-/O_2 redox level) lies considerably above the semiconductor valence band in energy, direct charge transfer is highly unlikely. The existence of surface states nearly de-

generate with the OH^-/O_2 level would, however, exhibit the high tunneling probabilities necessary for efficient charge transfer across the interface. Although such surface states are believed to play an important role in photoelectrolysis, little is now known concerning their identity.

Examining again the energy levels for the $(TiO_5)^{6-}OH^-$ cluster, we find that the states labeled d_{xy}^* , $d_{yz}^*-\pi^*$, and $d_{z^2}^*-\sigma^*$ lie within the bandgap. Since the TiO_2 anodes used for photoelectrolysis are n-type with a Fermi level near the bottom of the conduction band, these levels have a high probability of being occupied, and therefore, may be viewed as representing one possible surface state configuration. Recent surface photocurrent spectroscopy data of Mavroides *et al.* (1) for reduced $SrTiO_3$ operating in an electrolytic cell with basic electrolytic, support the occupation of bandgap surface states in this energy range.

To explain the observed O_2 gas released from the semiconductor surface according to the proposed equation above, one must first show a mechanism for splitting the O-H bond in the OH radical. In general, bonds are broken by occupying antibonding orbitals or by depopulating bonding orbitals. The $(TiO_5)^{6-}OH^-$ results show the top valence level to be mainly of $OH-\pi$ character. Under illumination in the electrochemical cell, this state would most probably be depopulated. However, since it is a nonbonding O_2p level, it does not bond with hydrogen so its depopulation would not be expected to destabilize the OH bond. On the other hand, the occupation of antibonding orbitals may lead to destabilization of the O-H bond.

If we consider the lowest antibonding orbital, d_{xy}^* , we observe that it does not mix with the OH^- orbital due to symmetry conservation and thus contains no OH^- character. Similarly, examination of the contour map of the $d_{yz}^*-\pi^*$ orbital in Fig. 5(a) shows that no OH breakup is expected since the π^* orbital contains no H bonding.

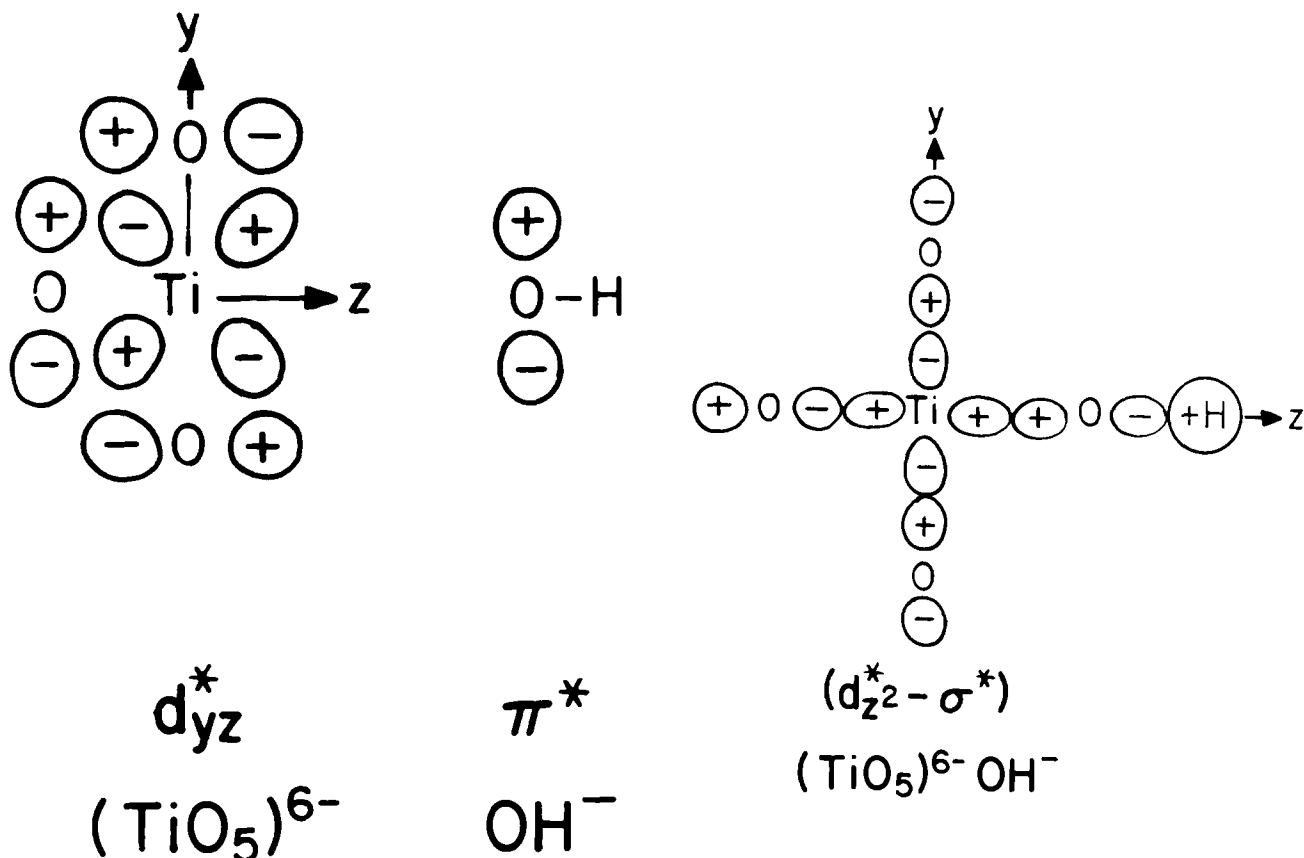


Fig. 5. (a, left) Contour diagram of the antibonding d_{yz}^* and π^* orbitals for the $(TiO_5)^{6-} OH^-$ cluster; (b, right) contour diagram of the antibonding $d_{z^2}^*$ and σ^* orbitals for the $(TiO_5)^{6-} OH^-$ cluster.

Occupation of the $d_{2z^2}-\sigma^*$ orbital would, however, tend to destabilize the O-H bond since the σ^* orbital is antibonding between the oxygen and hydrogen. Occupation of the $d_{2z^2}-\sigma^*$ orbital would also tend to promote bonding between the Ti atom and the oxygen atom of the OH⁻ ion since their wavefunctions are in-phase. Thus occupation of the $d_{2z^2}-\sigma^*$ orbital would provide a mechanism for breaking the O-H bond, while leaving the O of OH bonded to the surface.

Other antibonding states higher in energy on the (TiO₂)⁶⁻OH⁻ energy diagram also contain some σ^* character, though not as much as the $d_{2z^2}-\sigma^*$ level (i.e., less mixing between the d^* and σ^* orbitals). For this reason, occupation of the $d_{2z^2}-\sigma^*$ orbital is expected to be, in large part, responsible for splitting the O-H bond, although higher states may contribute to some extent.

The contour diagram of the $d_{2z^2}-\sigma^*$ orbital [Fig. 5(b)] shows the oxygen atom of the OH radical to be more strongly bonded to the Ti atom than the oxygen atoms of the lattice (which are antibonding with respect to the Ti atom). This suggests that the observed O₂ gas released from the oxide surface during photoelectrolysis may originate from the lattice. Oxygen atoms leaving the surface layer would thereby create vacancies which might then be occupied in turn by oxygen ions originating with the adsorbed OH⁻ ions.

The possibility suggested above that surface oxygen ions may be released preferentially from TiO₂ surfaces during illumination, might explain their relative stability to photodecomposition. For nonoxide electrodes, regeneration of the lost surface anions from the adsorbed OH⁻ ions would not be possible and might therefore explain their propensity to decompose under illumination.

Extension of Calculations

The above calculations have been performed using the simplest models possible to represent the ideal clean TiO₂ surface interacting with adsorbed species. A major simplification made in our calculations was to assume that the n-type TiO₂ and SrTiO₃ surfaces differed from the stoichiometric (annealed) surfaces only by the occupation of the bandgap states. Both Henrich *et al.* (6) and Lo *et al.* (2) report, however, that argon-bombarded surfaces and highly reduced (oxygen deficient) surfaces become disordered and show a succession of different surface-defect phases depending on the degree of reduction. In fact, extensive bombardment on the TiO₂ surface results in the formation of a different compound, Ti₂O₃, on the surface. Similar phenomena are known to occur in bulk TiO₂ upon reduction. A whole range of closely spaced intermediate compounds are formed related to the parent rutile structure by a series of "shear" transformations in which planes of oxygen ions are removed from the lattice resulting in modified Ti-Ti bond lengths and reduced symmetry (8).

Such structural transformations are not believed to occur in TiO₂ or the perovskite titanates made "n-type" by virtue of doping rather than by creation of oxygen deficiency. Consequently, our calculations should be more directly applicable to such surfaces. On the other hand, since similar photoelectrolytic response has been observed for both reduced and doped samples, the implication exists that models pre-

sented above are at least qualitatively correct in either case.

Recent studies by Subbarao *et al.* (9) on TiO_{2-x} and TiO_{2-x}F_x showed that the fluorine-doped TiO₂ exhibited a different spectral response than reduced TiO₂. This difference was characterized by a greater sensitivity to longer wavelengths and generation of higher photocurrent with the fluorine-doped material. Similar studies by Kowalski and Tuller (10) on reduced and Nb-doped BaTiO₃ showed the doped material to exhibit much enhanced photocurrents under similar conditions.

The above results are consistent with the expectation that the reduced surfaces will possess surface states with different character and at different energies than the surface states calculated here which are more characteristic of the doped materials. Further work is underway to determine whether surfaces with Ti₂O₃ character can explain the differences in photoresponse observed for the two types of surfaces.

Acknowledgment

The authors thank the Office of Naval Research for sponsoring this work under contract numbers: N00014-78-C-0366 (JMK and HLT) and N00014-75-C-0970 (JMK and KHJ).

Manuscript submitted Dec. 4, 1979; revised manuscript received March 13, 1980. This was Paper 346 presented at the Boston, Massachusetts, Meeting of the Society, May 6-11, 1979.

Any discussion of this paper will appear in a Discussion Section to be published in the June 1981 JOURNAL. All discussions for the June 1981 Discussion Section should be submitted by Feb. 1, 1981.

Publication costs of this article were assisted by the Massachusetts Institute of Technology.

REFERENCES

1. J. G. Mavroides, V. E. Henrich, H. J. Zeiger, G. Dresselhaus, J. A. Kafalas, and D. F. Kolesar, in "Electrode Materials and Processes for Energy Conversion and Storage," J. D. E. McIntyre, S. Srinivasan, and F. G. Will, Editors, p. 45, The Electrochemical Society Softbound Proceedings Series, Princeton, N.J. (1977).
2. W. J. Lo, Y. M. Chung, and G. A. Somorjai, *Surf. Sci.*, **71**, 199 (1978).
3. K. H. Johnson, in "Advances in Quantum Chemistry," Vol. 7, P. O. Löwden, Editor, p. 143, Academic Press, New York (1973); J. C. Slater, "Quantum Theory of Molecules and Solids," Vol. 4, McGraw-Hill, New York (1974).
4. J. A. Horsley, *J. Am. Chem. Soc.*, **101**, 2870 (1979).
5. V. E. Henrich, G. Dresselhaus, and H. J. Zeiger, *Solid State Commun.*, **24**, 623 (1977).
6. V. E. Henrich, G. Dresselhaus, and H. J. Zeiger, *Phys. Rev. Lett.*, **36**, 1335 (1976).
7. M. S. Wrighton, D. S. Ginley, P. T. Wolczanski, A. B. Ellis, D. L. Morse, and A. Linz, *Proc. Natl. Acad. Sci. U.S.A.*, **72**, 1518 (1975).
8. L. A. Bursill, B. G. Hyde, and M. O'Keeffe, in "Solid State Chemistry," N.B.S. Special Publ. 364, R. S. Roth and S. J. Schneider, Editors, p. 197, U.S. Gov't Printing Office, Washington, D.C. (1972).
9. S. N. Subbarao, Y. H. Yun, R. Kershaw, K. Dwight, and A. Wold, *Mater. Res. Bull.*, **13**, 1461 (1978).
10. J. M. Kowalski and H. L. Tuller, *Ceramurgia Int.*, To be published.

O₂ Electrocatalysis on Thin Film Metallic Oxide Electrodes with the Delafossite Structure

P. F. Carcia,* R. D. Shannon, P. E. Bierstedt, and R. B. Flippen

E. I. du Pont de Nemours and Company, Central Research and Development Department, Experimental Station, Wilmington, Delaware 19898

ABSTRACT

Thin film electrodes of PtCoO₂, PdCoO₂, PdRhO₂, and PdCrO₂ delafossite-type oxides are good electrocatalysts for O₂ reduction and O₂ evolution in NaOH. O₂ reduction activity correlates with the noble metal cation (Pt > Pd), while O₂ evolution activity correlates with the transition metal cation (Co > Rh > Cr). Electrodes were prepared by rf sputtering from metal alloy targets. The as-sputtered films are amorphous. The delafossite phase forms on annealing in air or O₂ at 700°-850°C. Thin films are metallic with $\rho \sim 10^{-4} \Omega\text{-cm}$.

The current interest in O₂ electrocatalysis is motivated by the potential for energy applications. For example, an improved O₂ reduction electrode would increase the electrical power output of fuel cells (1), making them more attractive for electric power generation. The efficiency for H₂ production from H₂O electrolysis would also be improved by a better O₂ anode (2). In the chlor-alkali industry, which annually consumes ~\$1 billion in energy (3), an O₂ reduction cathode instead of the H₂ evolving cathode could reduce the voltage for brine electrolysis by as much as 1V (a savings of ~ 1/3).

In this paper we discuss O₂ electrocatalysis on thin film electrodes with delafossite structure (4). Noble metal delafossites, PdCoO₂, PdCrO₂, PdRhO₂, and PtCoO₂, are interesting electrode candidates because they are excellent metallic conductors and allow investigation of specific cation effects of both a noble metal and a transition metal in the same compound. We report for the first time their activity for O₂ reduction and O₂ evolution in NaOH.

Experimental

Thin film preparation.—Thin films were prepared by rf sputtering in a commercial system (Materials Research Corporation SEM-8620) and by subsequently annealing the films. The sputtering targets were arc-melted buttons (e.g., PdCo) which had been remelted several times to insure homogeneity. The 3/8 in. diam buttons were Ag-epoxied to a 1/4 in. diam Cu rod threaded into an H₂O-cooled backing plate, which was shielded from sputtering by a grounded adapter plate. The sputtering was done in various partial pressures of O₂ and Ar; substrates were Al₂O₃ and Pt or Pd foils. The sputtering power was ~200W, which gave deposition rates of ~150 Å/min. Annealing was done overnight in a box furnace in air or O₂ at 700°-850°C.

Characterization.—Films were routinely characterized by x-ray diffraction. Some were also examined by scanning electron microscopy (SEM), electron spectroscopy for chemical analysis (ESCA), and x-ray microprobe analysis. Four-probe electrical resistivity measurements from 300° to 4.2°K were made for films on Al₂O₃ substrates. Film thicknesses were determined from a fractured edge by SEM.

Electrochemical measurements.—Measurement of O₂ reduction and evolution was made potentiostatically by slowly sweeping a PAR (Princeton Applied Research) 173 Potentiostat with a triangular waveform from a PAR 175 programmed source. The cell was a single compartment. The measured IR corrections were

negligible. Electrolytes were made with reagent grade NaOH and triply-distilled H₂O. The reference electrode was a dynamic hydrogen electrode (DHE) (5) brought close to the working electrode surface with a glass capillary. The auxiliary electrode was a 2 cm² Au or Pt foil. Thin film electrodes were Pd or Pt foils coated on both sides with 3-5 μm of the delafossite phase. Electrical connection was made with a Pd or Pt wire previously welded to the foil. Relative electrochemical surface areas were estimated from capacitances measured by a low frequency (10 Hz) impedance (6) or a transient technique (7).

Results

The delafossite structure is indicated in Fig. 1 for PtCoO₂. It consists of alternating layers of Pt and Co atoms. The platinum atoms are linearly coordinated with two oxygen atoms and the cobalt atoms are octahedrally coordinated by oxygen atoms. Each platinum atom in the plane is coordinated hexagonally by other platinum atoms.

The fact that these noble metal delafossites could be prepared by sputtering and annealing of the thin films

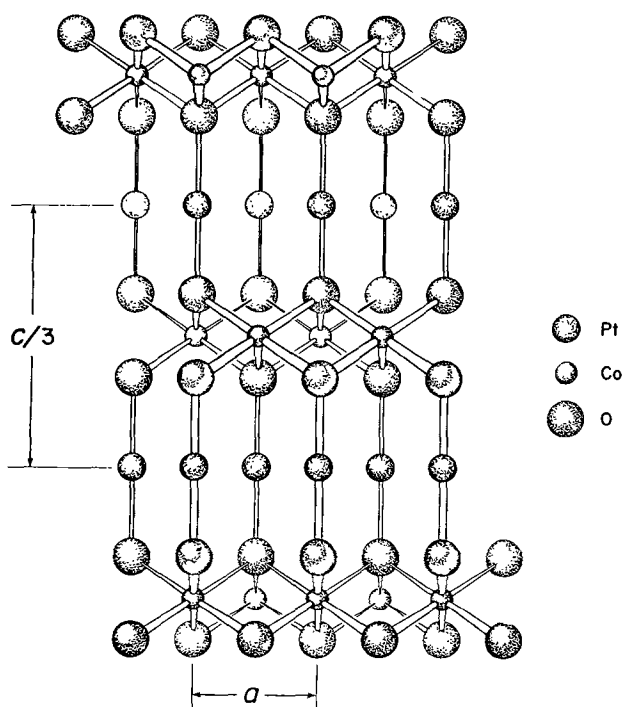


Fig. 1. PtCoO₂ (delafossite) structure

* Electrochemical Society Active Member.

Key words: films, electrodes, catalysis, sputtering.

Table I. Synthesis conditions and cell dimensions of delafossite-type oxide thin films

	$P_{(Ar)}$ (mTorr)	$P_{(O_2)}$ (mTorr)	T_A (°C)	a (Å)	c (Å)
PtCoO ₂	20	1	700	2.827	17.84
PdCoO ₂	20	1	700-725	2.830	17.75
PdRhO ₂	20	0.1	750	3.028	18.08
PdCrO ₂	20	0.1	800-850	2.929	18.10

is novel. Previous syntheses have used solid-state reactions, metathesis, high pressure, and hydrothermal methods (8, 9).

Table I summarizes the optimum sputtering pressures, the 16 hr annealing temperatures, and cell dimensions found for these phases. The films were either annealed in air or in a low stream of O₂.

Initially, the sputtered films are amorphous to x-rays. It is possible that oxygen is incorporated in the films, disordering the alloy which would form with only Ar as the sputtering gas. PdRhO₂ and PdCrO₂ required a lower O₂ partial pressure during sputtering; otherwise, annealing produced only the binary oxides plus some noble metal product. These same products were also obtained in all preparations where annealing was done under high O₂ flow rates. Once the binary oxides are produced, they do not readily react to form the delafossite phase.

The annealed films are nearly single phase by x-ray diffraction for the Co-containing oxides. Free Pt in PtCoO₂ and Pd or PdO in PdCoO₂ is usually <1%. In some PdCrO₂ and PdRhO₂ films, which must be annealed close to the decomposition temperature, PdO or Pd levels are sometimes higher (~5%). For many of the films, x-ray data indicate a high degree of preferred orientation, the plane of the film being perpendicular to the c-axis. Cell dimensions of the delafossite-type oxides given in Table I agree well with those in Ref. (8).

We examined the surface of a PtCoO₂ and a PdCoO₂ thin film on Al₂O₃ by ESCA using a du Pont 650B Spectrometer. Figure 2 shows the photoelectron spectra for Pt 4f and Co 2p photoelectrons in PtCoO₂. Table II compares the Pt 4f binding energies of PtCoO₂ to those of Pt metal and its oxides. The energies are charge corrected to the O 1s peak at 531.6 eV.

The Pt sample was a bright foil, α -PtO₂ was a commercial grade obtained from Engelhard Industries, and the preparation of β -PtO₂ has previously been described (10). Binding energies for PtO were taken from the literature (11). From these data, we conclude that the formal valence of Pt at the surface of the PtCoO₂ thin film is +1. Both the lack of a definite shakeup satellite structure in the Co 2p spectra of PtCoO₂ and the Co photoelectron binding energies are consistent with accepted ESCA interpretations (12, 13) for low spin Co³⁺. These oxidation states, Pt(I) and Co(III), at the surface of the PtCoO₂ thin film are the same as found for powder samples (8). The same oxidation states were also found (ESCA) for a thin film of PdCoO₂, i.e., Pd(I) and Co(III).

Electron microprobe analysis¹ of the PtCoO₂ film showed that both Pt and Co were distributed evenly with no apparent segregation effects at 500 \times magnifi-

¹ Microprobe analysis was performed by Micron Incorporated, Wilmington, Delaware 19807.

Table II. Photoelectron binding energies for Pt and Pt oxide surfaces

	Pt		Co	
	4f 5/2	4f 7/2	2p 1/2	2p 3/2
Pt	74.3 eV	71.1 eV	—	—
PtCoO ₂ (film)	75.7	72.2	795.4 eV	780.5 eV
PtO	76.6	73.3	—	—
β -PtO ₂	78.3	75.0	—	—
α -PtO ₂	78.6	75.3	—	—

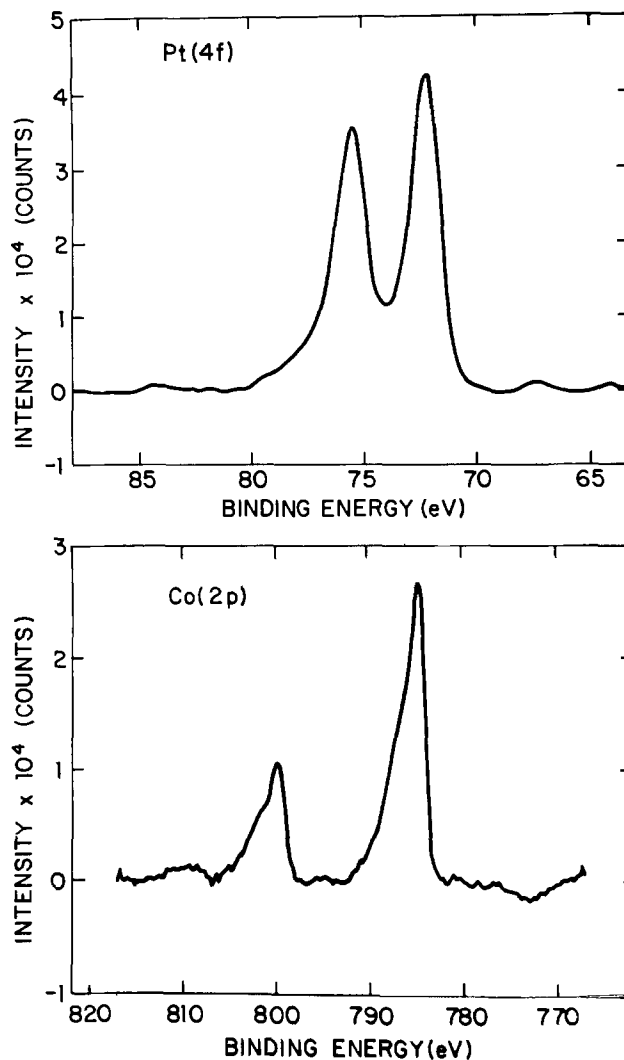


Fig. 2. Photoelectron spectra for Pt and Co in PtCoO₂

cation. Quantitative Pt and Co analysis for three separate areas gave a Pt:Co ratio of 1.003 with 65.46% Pt and 19.72% Co. These values are 4% lower than the calculated values of 68.3% and 20.6% for Pt and Co, respectively, in PtCoO₂. The measured values would give a composition Pt_{0.72}Co_{0.72}O₂. This is close to Pt_{0.8}Co_{0.8}O₂, a nonstoichiometric delafossite phase previously prepared by Shannon *et al.* (8). However, the Pt(II) oxidation state of this phase is not consistent with monovalent Pt found at the surface of the films by ESCA. The lower values may instead result from the rough surface of the film. A number of cracks extend to the Al₂O₃ substrate and thus may reduce the total x-ray fluorescence. The composition, Pt_{1.0}Co_{1.0}O₂, is consistent with the Pt:Co ratio of 1.0 and the oxidation states from ESCA.

Scanning electron micrographs of PtCoO₂, PdCoO₂, and PdRhO₂ thin film surfaces on Al₂O₃ substrates are shown in Fig. 3. PtCoO₂ and PdCoO₂ have "mud-crack" surfaces. Thin films of PdCrO₂, not shown, show similar morphology. The PdRhO₂ films are, however, denser. All films have large grains, 5-10 μ m. We measured the (BET) surface area of a PtCoO₂ thin film on smooth Pt by Kr physisorption. The surface area was ~10 m²/g which corresponds to a surface roughness of ~200 \times . The capacitance measured for the same film was 3.6 mF which corresponds to an electrochemical surface roughness of 40-80 \times if we assume that 1 cm² is equivalent to 20-40 μ F of capacitance. Similarly obtained electrochemical surface roughness for PdCoO₂ and PdCrO₂ thin films were within a factor of 2 \times that of PtCoO₂ films, while the denser PdRhO₂ film has smaller surface roughness.

Fig. 3. 3000 \times magnification, scanning electron micrographs of (a, left) PtCoO₂, (b, middle) PdCoO₂, and (c, right) PdRhO₂ thin films on Al₂O₃.

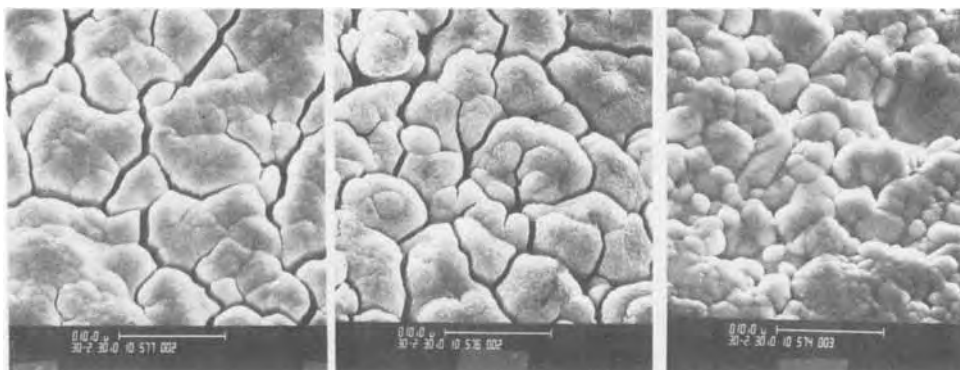


Figure 4 shows the temperature dependence of resistivity for the thin film delafossites. The positive temperature coefficients indicate metallic conductivity with resistivities of $\sim 10^{-4}$ Ω -cm at 300 $^{\circ}$ K for all films. The resistivities for PdRhO₂ and PdCrO₂ had not been previously measured, but metallic conductivity was predicted from a one-electron band model (8). The resistivity for the PtCoO₂ films is considerably higher than for a single crystal (8), but nearly the same as for polycrystalline PtCoO₂ prepared in our laboratory. The contribution to resistance from grain boundaries likely accounts for the higher resistance of the thin film and polycrystalline samples.

Figure 5 shows the current-voltage characteristic for thin film PtCoO₂ in 0.1N NaOH. We swept the voltage at 0.1 mV/sec from the open-circuit value to 0.8 V/DHE, and then swept back to near the open-circuit voltage. We obtained data in the same way for PdCoO₂, PdRhO₂, and PdCrO₂ between the open-circuit voltage and a lower limit ~ 0.75 V/DHE. The current-voltage curves swept in opposite directions are within 10 mV over most of the current range. The Tafel regions are linear and at least two decades wide. The limiting current (I_L) in 0.1N NaOH is ~ 2 mA, the same for all electrodes. Currents in O₂-saturated electrolytes are $>100\times$ those in N₂, confirming O₂ reduction activity.

Table III compares O₂-reduction current densities at $E = 0.9$ V/DHE, Tafel slopes (b), and open-circuit

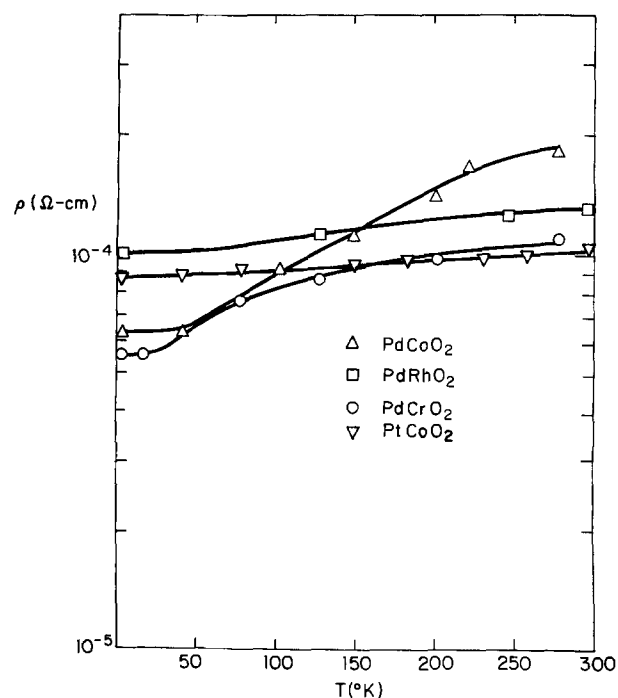


Fig. 4. Resistivity vs. temperature for the thin film oxides

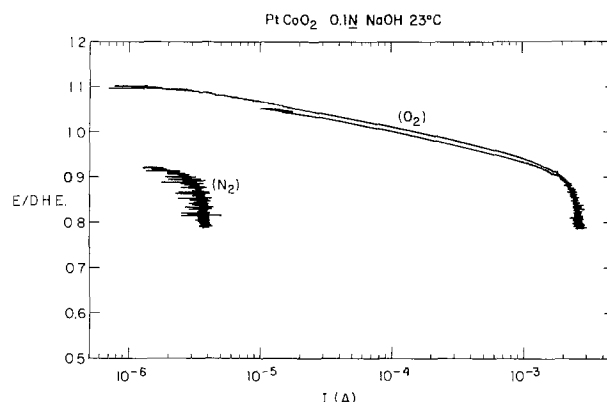


Fig. 5. O₂ reduction current vs. potential for thin film electrode of PtCoO₂ in 0.1N NaOH taken at sweep rate 0.1 mV/sec.

voltages ($E_{o.c.}$) for the oxides from these sweep experiments. It also includes data obtained in the same way for smooth Pt and Pd electrodes. Current densities are all based on geometric areas, and the data represent the average values measured for at least two different electrodes of each oxide.

PtCoO₂ has the highest O₂ reduction current density, $\sim 10\times$ that for the Pd oxides. PtCoO₂ also has the highest open cell potential. PdCoO₂, PdCrO₂, and PdRhO₂ have approximately the same current density, 10^{-4} A/cm², and nearly the same Tafel slope, $b \sim 45$ mV, which is different than for PtCoO₂, $b \sim 60$ mV. Since the capacitance-determined surface areas for the oxides only differ by $\sim 2\times$, we conclude that the O₂ reduction activity correlates with the noble metal cation, Pt > Pd, and is nearly independent of the transition metal cation in Pd oxides.

Because of their larger surface roughness, the oxides have higher current densities than either smooth Pt or Pd. If we use the BET surface roughness ($\sim 200\times$) for PtCoO₂ and assume a roughness $\sim 1.5\times$ for smooth Pt, the current density of PtCoO₂ is approximately half that of Pt. But they have approximately equal current densities if we use the surface roughness for PtCoO₂ from capacitance data.

Table III. O₂ reduction activity in 0.1N NaOH at 23 $^{\circ}$ C

	$E_{o.c.}^{\dagger}$ (V/DHE) [*]	i at 0.9 V/DHE [*] (μ A/cm ²)	b (mV)
PtCoO ₂	1.09	1900	58
PdCoO ₂	1.00	150	43
PdCrO ₂	1.01	85	47
PdRhO ₂	1.00	75	43
Pt (smooth)	1.02	25	65
Pd (smooth)	1.00	20	40

[†] $E_{o.c.}$ = open-circuit voltage in O₂-saturated 0.1N NaOH.

^{*} DHE = dynamic hydrogen reference electrode.

To further study the influence of the noble metal on oxygen reduction activity, we synthesized thin films with compositions intermediate to PtCoO_2 and PdCoO_2 . This was done by simultaneously sputtering from a PdCo and a PtCo target, spaced ~ 25 mm apart. Al_2O_3 substrates were placed underneath and between the targets. Scanning electron micrographs show that all films have the same "mud-crack" morphology of PtCoO_2 and PdCoO_2 films shown in Fig. 2.

Electrochemical measurements were only made on single phase materials (x-ray diffraction). Electrical contact for electrochemical measurements was made in the plane of films at one end of the Al_2O_3 substrate by a thin gold foil strip, welded to a gold wire and clamped to the film between two planar sections of a holder of Teflon.

PtCoO_2 and PdCoO_2 are isostructural with nearly identical lattice dimension. We can distinguish them by x-ray diffraction since the 003 diffracted peak is twice as strong for PtCoO_2 as for PdCoO_2 . The normalized 003 peak intensities were 29, 11, and 6 from the Pt-rich to Pd-rich end of the (Pt, Pd) CoO_2 series.

Table IV gives (Pt, Pd) CoO_2 film compositions from electron microprobe analysis. The composition is close to " $\text{A}_{1.0}\text{B}_{1.0}\text{O}_2$ " for the Pd-rich film, but is closer to " $\text{A}_{0.8}\text{B}_{0.8}\text{O}_2$ " for the Pt-rich film, as was observed for PtCoO_2 . (To confirm whether this nonstoichiometric effect in Pt-oxides and mixed Pt-rich oxides is real and not an artifact of the rough thin film surfaces, we must characterize these films further.)

The O_2 reduction current densities are higher for these three mixed oxides (Table IV) than for PdCoO_2 (Table III). The oxide with intermediate Pt concentration (Pt/Pd = 0.54) has the highest current density. However, its electrochemical area, estimated by capacitance, is $2\times$ higher than for the other films (2.5 mF for Pt/Pd = 0.54 compared to 1.3 mF for Pt/Pd = 0.34 and 1.2). A thickness gradient for films on substrates between targets probably causes these surface area differences. If we normalize for this, then higher O_2 reduction current correlates with higher Pt/Pd ratio. This is consistent with the higher activity measured for PtCoO_2 than PdCoO_2 .

The Tafel slopes for mixed oxides are intermediate to those of the end member compositions. It seems plausible to us that O_2 reduction on mixed oxides proceeds by a combination of rate-determining steps that are the same as for PtCoO_2 and PdCoO_2 .

We have also studied O_2 evolution for these oxides. The current densities were measured by sweeping the electrodes at 10 mV/sec with negligible hysteresis between 1.2 and 1.8 V/DHE in 1N NaOH at 23°C. Figures 6 and 7 summarize O_2 evolution currents from sweeping experiments for the oxides and smooth Pt and Pd. Prior to O_2 evolution sweeps, Pt and Pd electrodes were preanodized at 10 mA for 3 min to form stable oxide surfaces. For consistency the delafossite electrodes were identically preconditioned. In contrast to O_2 reduction, O_2 evolution activity is strongly dependent on the transition metal, $\text{Co} > \text{Rh} > \text{Cr}$. Figure 7 highlights differences in potential for O_2 evolution at $I = 5$ mA.

One of the PtCoO_2 electrodes was tested galvanostatically for ~ 30 hr at 5 mA. Initially, the potential was 1.58V. After 30 hr, it increased to 1.68 V/DHE. X-ray diffraction of this film showed $\sim 10\%$ Pt not

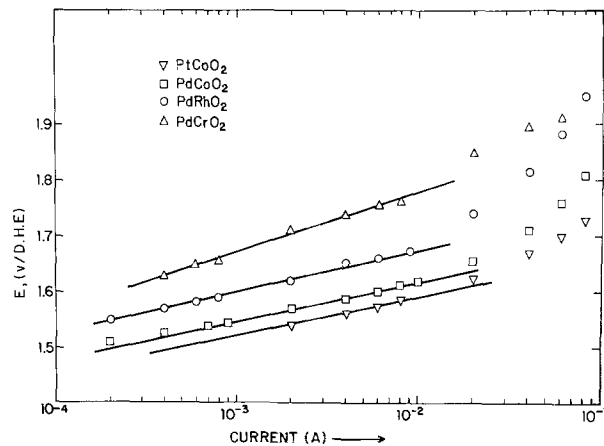


Fig. 6. O_2 evolution current vs. potential for thin film oxide electrodes obtained at 10 mV/sec in 1N NaOH at 23°C.

initially present. It is likely, therefore, that some decomposition to Pt occurred and is responsible for the higher overpotential.

Discussion

Oxygen reduction necessarily involves oxygen adsorption as the first step (14, 15); but little is known about the nature and distribution of atoms which would be potential adsorption sites at the surface of complex oxides in solutions, especially under the influence of oxidizing potentials. However, it seems reasonable to assume that at potentials > 0.7 V/DHE, the surfaces of PtCoO_2 would consist of $\text{O}^=$ or OH^- ions bonded to either Co^{3+} or Pt^+ ions. Although t_{2g} orbitals of Co III LS, in the center of the CoO_6 octahedral face, point in the 001 direction, these orbitals are filled and would not allow the possibility of bond formation. However, surface oxygen vacancies or Co III HS at the surface would allow the possibilities of adsorption sites for O_2 in the Co layer. Oxygen vacancies have been proposed to take part in the oxygen reduction mechanism on perovskite oxides such as LaNiO_3 (16) and $\text{Nd}_{1-x}\text{Sr}_x\text{CoO}_3$ (17), but neither the presence of oxygen vacancies nor Co III HS in delafossite-type oxides has been demonstrated.

As noted earlier, our electrochemical data show that the O_2 reduction activity on the delafossites is high,

O_2 -EVOLUTION 1.0N NaOH 23°C S=10mV/S. I=5mA

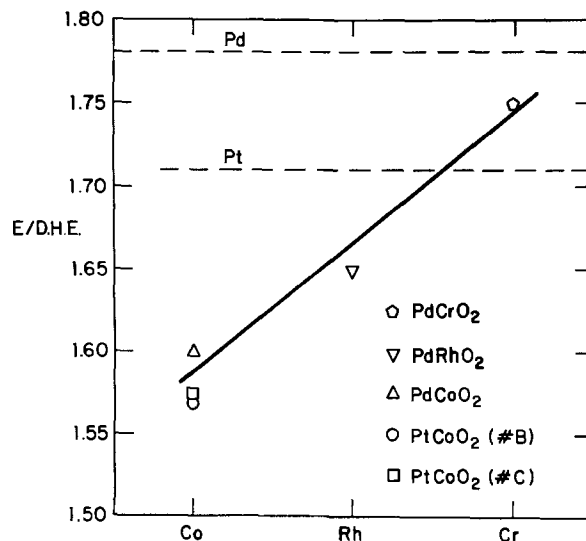


Fig. 7. Potential for O_2 evolution at $I = 5$ mA vs. transition metal cation in thin film oxide electrodes. Data obtained from sweep experiments at 10 mV/sec.

Table IV. O_2 reduction activity of (Pt, Pd) CoO_2 in 0.1N NaOH at 23°C

	Pt/Pd	i^* at 0.9 V/DHE ($\mu\text{A}/\text{cm}^2$)	b (mV)
$\text{Pt}_{0.72}\text{Pd}_{0.35}\text{Co}_{0.51}\text{O}_2$	1.2	772	52
$\text{Pt}_{0.31}\text{Pd}_{0.57}\text{Co}_{0.9}\text{O}_2$	0.54	968	50
$\text{Pt}_{0.25}\text{Pd}_{0.73}\text{Co}_{0.93}\text{O}_2$	0.34	312	53

and correlates with the noble metal ($\text{Pt} > \text{Pd}$), but in PdMO_2 is nearly independent of the transition metal ($\text{Co} \sim \text{Cr} \sim \text{Rh}$). A possible explanation for the relative insensitivity of the PdMO_2 to the transition metal ion in O_2 reduction is that these ions are all remarkably similar, i.e., all are strongly stabilized in an octahedral crystal field with d^3 (Cr^{3+}) and low spin d^6 (Rh^{3+} , Co^{3+}) electron configurations. Bonding of O_2 to these sites is either sterically hindered, or in the case of an anion vacancy, too strong to be effective for reduction to H_2O .

Furthermore, to our knowledge, high O_2 reduction activity has never before been observed on an oxide electrocatalyst containing either Rh^{3+} or Cr^{3+} . The high activity on Co-oxides is frequently correlated with Co^{2+} or high spin Co^{3+} as in Co-chelates (18) and $\text{La}_{1-x}\text{Sr}_x\text{CoO}_3$ (19), respectively.

Therefore, most of the O_2 reduction likely occurs on noble metal sites, and the transition metal contributes little to the overall activity. Pt atoms, in contrast to Co atoms, have O neighbors oriented only along the c-axis. Crystal surfaces 100 and 110 which contain Pt distances in PtCoO_2 of 2.83Å are comparable to those in Pt metal of 2.77Å. These short distances might allow "side-on" O_2 adsorption and a mechanism similar to that on Pt metal. Furthermore, even the 001 oxygen layers are probably not strongly bonded to Pt (ΔF_f for PtO_2 is -19 kcal/mole compared to -60 kcal/mole for Co_3O_4). Thus, these O atoms might be stripped off in solution at potentials for oxygen reduction creating even more Pt atoms for bonding with O_2 molecules. Similar crystallographic and thermodynamic arguments can be made for PdCoO_2 , PdCrO_2 , and PdRhO_2 . In support of this view, the Tafel slopes appear to reflect Pt-like and Pd-like character. The slope is $\sim RT/F$ for PtCoO_2 and $\sim 2RT/3F$ for the Pd delafossites. These are the same slopes observed for O_2 reduction on Pt and Pd electrodes in alkaline electrolytes (20).

The analogy with Pt and Pd cannot be carried too far, however, because the noble metal atoms and molecular orbitals available for adsorption in PtCoO_2 and PdMO_2 with formally Pt(I) and Pd(I), will be different than those in Pt and Pd metals. Indeed, Pt and Pd have roughly the same O_2 -reduction activity measured at 0.9 V/DHE in contrast to the higher activity for PtCoO_2 than PdMO_2 . Further, the open-cell potential for PtCoO_2 is higher than is normally observed for Pt in alkaline electrolytes. We ruled out the possibility that the activity differences are due to a larger PtCoO_2 surface area which we accounted for. The capacitance of PtCoO_2 electrodes is larger, but is less than $2\times$ that for PdCoO_2 , much smaller than the $10\times$ difference in their O_2 reduction currents. Further experimental and theoretical work is thus needed to explain the O_2 reduction activity of these materials.

In O_2 evolution, the activity in delafossite-type oxides correlates with the transition metal ($\text{Co} > \text{Rh} > \text{Cr}$), and is nearly independent of the noble metal ($\text{Pd} \sim \text{Pt}$). For metals, the highest activities occur for those whose oxides are also good electrical conductors, e.g., RuO_2 and IrO_2 (21). This would seem reasonable, particularly if the rate-determining step involves an electron transfer as suggested by O'Grady *et al.* (15). Pt and Pd, whose surfaces are necessarily covered with an oxide at O_2 evolution potentials, have low activity. This correlates with poor conductivity in PtO_2 ($\rho \sim 10^6 \Omega\text{-cm}$) and PdO ($\rho \sim 10^2 \Omega\text{-cm}$) (22). If the noble metal planes of the delafossites are also oxide covered, their specific contribution to O_2 evolution may be low. It is not surprising then that the experimental results correlate with the transition metal cation. Intuitively, the negative hydroxyls should be attracted to the trivalent cations making these the most likely adsorption sites. The results are also correlated with those of Miles *et al.* (23) who found that Cr oxide electrodes have much lower electrocatalytic activity for oxygen

evolution than either Co or Rh oxide electrodes. Furthermore, there are several examples (24, 25) of Co-oxides with low overpotential for O_2 evolution and recently Burke (26) has observed high O_2 evolution activity on an oxidized surface of Rh.

Acknowledgments

We would like to thank H. A. Selz for assistance with the sputtering experiments, D. J. Jones and P. R. Spring for the electrochemical measurements, J. F. Whitney for assistance with x-ray diffraction, M. L. Van Kavelaar for the SEM photographs, and R. J. Bouchard for helpful discussions and review of the manuscript.

Manuscript submitted Dec. 4, 1979; revised manuscript received April 11, 1980.

Any discussion of this paper will appear in a Discussion Section to be published in the June 1981 JOURNAL. All discussions for the June 1981 Discussion Section should be submitted by Feb. 1, 1981.

Publication costs of this article were assisted by E. I. du Pont de Nemours and Company.

REFERENCES

1. A. P. Fickett, *Sci. Am.*, **236**, 70 (1978).
2. S. Srinivasan and R. H. Wiswall, in "Energy Storage," J. B. Berkowitz and H. P. Silverman, Editors, p. 82, The Electrochemical Society Softbound Proceedings Series, Princeton, N.J. (1976).
3. K. Hass and P. Schmittinger, *Electrochim. Acta*, **21**, 1115 (1976).
4. R. D. Shannon, U.S. Pat. 3,498,931 (1970).
5. J. Giner, *This Journal*, **111**, 376 (1964).
6. J. McHardy, J. M. Baris, and P. Stonehart, *J. Appl. Electrochem.*, **6**, 371 (1976).
7. B. V. Tilak, C. G. Rader, and S. K. Rangarajan, *This Journal*, **124**, 1879 (1977).
8. R. D. Shannon, D. B. Rogers, and C. T. Prewitt, *Inorg. Chem.*, **10**, 713 (1971); C. T. Prewitt, R. D. Shannon, and D. B. Rogers, *ibid.*, **10**, 719 (1971); D. B. Rogers, R. D. Shannon, C. T. Prewitt, and J. L. Gillson, *ibid.*, **10**, 723 (1971).
9. D. Cahen, Ph.D. Thesis, Northwestern University, (1973).
10. R. D. Shannon, *Solid State Commun.*, **6**, 139 (1968).
11. K. S. Kim, N. Winograd, and R. E. Davis, *J. Am. Chem. Soc.*, **93**, 6296 (1971).
12. N. S. McIntyre and M. G. Cooke, *Anal. Chem.*, **47**, 2208 (1975).
13. D. C. Frost, C. A. McDowell, and I. S. Woosely, *Chem. Phys. Lett.*, **17**, 320 (1972).
14. J. Huang, R. K. Sen, and E. Yeager, *This Journal*, **126**, 786 (1979).
15. W. O'Grady, C. Iwakura, J. Huang, and E. Yeager, in "Electrocatalysis," M. W. Breiter, Editor, p. 286. The Electrochemical Society Softbound Proceedings Series, Princeton, N.J. (1974).
16. Y. Matsumoto, H. Yoneyama, and H. Tamura, *Bull. Chem. Soc. Jpn.*, **51**, 1927 (1978).
17. T. Kudo, H. Obayashi, and T. Gejo, *This Journal*, **122**, 159 (1975).
18. H. Alt, H. Binder, and G. Sandstede, *J. Catal.*, **28**, 8 (1973).
19. A. C. C. Tseung and H. L. Bevan, *J. Electroanal. Chem. Interfacial Electrochem.*, **45**, 429 (1973).
20. D. S. Gnanamuthu and J. V. Petrocelli, *ibid.*, **114**, 1036 (1967).
21. M. H. Miles, E. A. Klaus, B. P. Gunn, J. R. Locker, W. E. Serafin, and S. Srinivasan, *Electrochim. Acta*, **23**, 521 (1978).
22. D. B. Rogers, R. D. Shannon, and J. L. Gillson, *J. Solid State Chem.*, **3**, 314 (1971).
23. M. H. Miles, Y. H. Huang, and S. Srinivasan, *This Journal*, **125**, 1931 (1978).
24. A. G. C. Kobussen, F. R. Van Buren, T. G. M. Van Den Belt, and H. J. A. Van Wees, *J. Electroanal. Chem. Interfacial Electrochem.*, **96**, 123 (1979).
25. A. C. C. Tseung and S. Jasem, *Electrochim. Acta*, **22**, 31 (1977).
26. L. D. Burke and E. J. M. O'Sullivan, *J. Electroanal. Chem. Interfacial Electrochem.*, **97**, 123 (1979).

Electron Transfer and Axial Coordination Reactions of Cobalt Tetra(Aminophenyl)Porphyrins Covalently Bonded to Carbon Electrodes

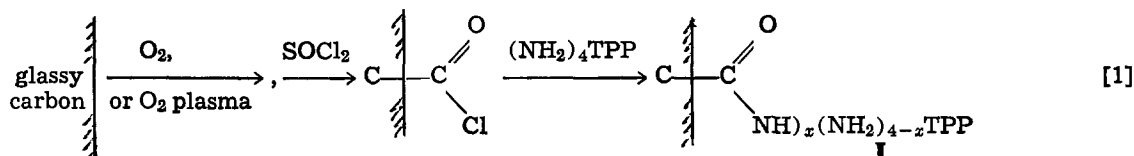
Colleen P. Jester,¹ Roy D. Rocklin,* and Royce W. Murray

Kenan Laboratories of Chemistry, University of North Carolina, Chapel Hill, North Carolina 27514

ABSTRACT

Electrochemistry of tetra(aminophenyl)porphyrin covalently attached to glassy carbon and then cobalt-metallated, was investigated in DMSO and CH₃CN solvents in the presence of pyridine. Shifts in formal potential were used to measure complex stability constants and coordination number for the pyridine complexes of the immobilized metalloporphyrin. Unusually slow electrochemistry of the Co(III/II) reaction was also studied by cyclic voltammetry and by reflectance spectroelectrochemistry. It is proposed that coordination of cobalt by surface carboxylate groups causes extraordinarily slow electron transfer for the Co(III/II) step.

This laboratory has in previous reports (1-3) described the covalent immobilization of tetrakis(p-aminophenyl)porphyrin, (p-NH₂)₄TPP, on glassy carbon electrodes by the reaction sequence



The number of amine bonds formed to the surface was determined by x-ray photoelectron spectroscopy, XPS, to be two, on the average (2). The surface porphyrin I can be metallated *in situ* with first row transition elements such as Fe and Co (1-3). All these immobilized species exhibit electron transfer reactions with the carbon electrode with formal potentials E_{surf}° near those of their unattached molecular analogs (4).

It is well known (5) that metalloporphyrins immobilized within the framework of biological macromolecules can exhibit special chemistry associated with proximity of axially coordinating ligands attached to the framework or with steric restrictions imposed by the framework on the axial coordination of otherwise potent ligands. Inasmuch as some analogies between the circumstances of biological macromolecular and electrode immobilization can be envisioned, a better understanding of the axial coordination chemistry of metalloporphyrins prepared from structure I was of interest. With this in mind, a further study of the cobalt-metallated form of structure I, C/ \sim Co(NH₂)₄TPP, in contact with solutions containing the ligand pyridine, has been carried out and is described here. Results are also given for the monoamine tetraphenylporphyrin, C/ \sim Co(NH₂)TPP. Of interest was how the coordination number of axially bound pyridine depends on the oxidation state of the immobilized cobalt porphyrin and its complex stability constants. A base of comparative electrochemical data for the interaction of pyridine with dissolved cobalt tetraphenylporphyrin is available (6-8). Also of interest was a better understanding of the previously noted (2) abnormally small electrochemical surface wave for reduction of immobilized C/ \sim Co(III)(NH₂)₄TPP as compared to C/ \sim Co(II)(NH₂)₄TPP.

Experimental

Immobilization.—Glassy carbon electrodes (Atomergic Chemetals Corporation, Plainview, New York,

Grade V10-50, 3-4 mm diam) with freshly polished ends were oxidized *in vacuo* at ca. 400°C for 1 hr or in an rf plasma (9) chamber at ca. 200 mTorr O₂ and

5W for 30 min. Lower background currents were observed with plasma-oxidized electrodes. The oxidized electrodes were refluxed in ca. 2 ml freshly distilled SOCl₂ in 15 ml of sodium dried toluene for 1 hr, briefly rinsed with dry toluene, and refluxed for 3 hr in a hot solution of ca. 1 mg of (NH₂)₄TPP or (NH₂)TPP porphyrin in 15 ml of dry toluene. Thorough rinses with dry toluene and reagent grade methanol were used to remove adsorbed porphyrin. The immobilized porphyrins were metallated by refluxing the air-dried electrodes in a solution of ca. 0.5g of CoCl₂ in 20-30 ml CH₃CN followed by washing with CH₃CN. The electrodes were mounted for electrochemical experiments in a cylinder of heat-shrinkable Teflon, leaving the cylinder end exposed. Cobalt metallation was ordinarily complete as indicated by the absence of electrochemical waves for residual-free base.

Electrochemistry.—Electrochemical experiments were carried out in dimethylsulfoxide (DMSO) and acetonitrile solvents predried over molecular sieves and containing 0.1M Et₄NClO₄ supporting electrolyte and various concentrations of pyridine ligand. The solutions were degassed with N₂ presaturated with vapor of a pyridine/solvent mixture identical to that in the electrochemical cell. The pyridine had been distilled and stored over molecular sieves.

The electrochemical cell was conventional, with a Luggin capillary to the NaCl-saturated calomel reference electrode (SSCE). To ascertain that junction potential effects at the Luggin tip were unimportant as the pyridine concentration was varied over a wide range, the formal potential of the ferrocene/ferricenium couple was measured as a function of [Py]. Its potential was constant, +0.496 ± 0.006V vs. SSCE.

Electrochemical equipment was a Princeton Applied Research Model 174 as potentiostat for cyclic voltammetry and differential pulse voltammetry with a locally designed triangular wave generator (10) as signal source for the former. A freshly prepared electrode was first inspected by cyclic voltammetry, then volt-

* Electrochemical Society Student Member.

¹ Present address: Dionex Corporation, Sunnyvale, California.

Key words: modified electrodes, ligand, surface, interfaces.

ammograms were determined at a series of [Py] with differential pulse voltammetry, whose application to immobilized electrode reactants has been described by Brown and Anson (11). E_{surf}° is the average of the potentials for current peaks observed on cathodic and anodic-going scans. The differential pulse experiment allowed accurate determination of peak potentials even at the very slow potential scan rates desirable for E_{surf}° measurements.

Chemicals.—Tetrakis(p-aminophenyl)porphyrin, $(\text{NH}_2)_4\text{TPP}$, and mono(p-amino)-tetraphenylporphyrin, $(\text{NH}_2)_2\text{TPP}$, were prepared as previously (2,3) and generously supplied by C. M. Elliott (Stanford University), respectively. Cobalt tetraphenylporphyrin (Man-Win Chemicals, Washington, D.C.) was used as received.

Determination of x in reaction [1].—The dangling amine groups remaining on the immobilized porphyrin in reaction [1] were coupled to 3,5-dinitro-benzoyl chloride and the relative XPS N 1s band intensities for nitro and porphyrin nitrogens determined as described previously (2). This measurement was carried out on electrodes prior to metallation and also on electrodes after cobalt insertion. XPS spectra were obtained with a du Pont Model 650B Electron Spectrometer with the assistance of Dr. M. Umaña.

Results and Discussion

Some general characteristics of the cyclic voltammetry of tetra(p-aminophenyl)porphyrin attached to carbon as in Eq. [1] and then cobalt metallated, $C/m\text{Co}(\text{NH}_2)_4\text{TPP}$, and of its monoamine analog, $C/m\text{Co}(\text{NH}_2)_2\text{TPP}$, are illustrated by Fig. 1-3. In both DMSO and CH_3CN solvents, the Co(III/II) and Co(II/I) porphyrin reactions occur at potentials similar to the E° values for unattached CoTPP (+0.12 and -0.82V vs. SSCE in DMSO), typical of modified electrodes (3,4). The voltammograms in DMSO and CH_3CN are unusual however, in that in the absence of added pyridine ligand (Fig. 1A, 2A), the Co(III/II) wave is typically only 1-5% as large as the Co(II/I) wave. When pyridine is added (compare Fig. 1A, 1B), and for $C/m\text{Co}(\text{NH}_2)_2\text{TPP}$ as compared to $C/m\text{Co}(\text{NH}_2)_4\text{TPP}$ (compare Fig. 1A, 2B), the Co(III/II) wave is enhanced, but remains $< 1:1$ in relation to the Co(II/I) step. Voltammetry of $C/m\text{Co}(\text{NH}_2)_4\text{TPP}$ in pyridine as solvent is similar to that in $>1\text{M}$ solutions of pyridine in DMSO.

The cathodic Co(II/I) wave in both DMSO ($E^{\circ} = -0.87\text{V vs. SSCE}$) and CH_3CN ($E^{\circ} = -0.87\text{V vs. SSCE}$) exhibits an irreversible prewave whose definition varies from electrode to electrode (Fig. 1A, 3A),

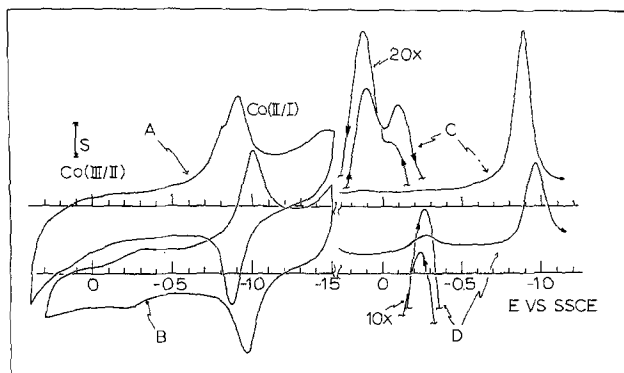


Fig. 1. Cyclic voltammetry at 100 mV/sec of 6×10^{-10} mole/cm² $C/m\text{Co}(\text{NH}_2)_4\text{TPP}$ in DMSO (curve A) and in 3.47M pyridine in DMSO (curve B). Differential pulse voltammetry (2 mV/sec scan rate, 0.5 sec/cycle, 25 mV modulation) of 5.7×10^{-10} mole/cm² $C/m\text{Co}(\text{NH}_2)_4\text{TPP}$ in DMSO (curve C) and in 3.47M pyridine in DMSO (curve D). $S = 13.8 \mu\text{A}/\text{cm}^2$ (curves A, B); $27.6 \mu\text{A}/\text{cm}^2$ (curves C, D). Insets are Co(III/II) DPV responses of curves C and D amplified as indicated for precise measurement of E_{peak} .

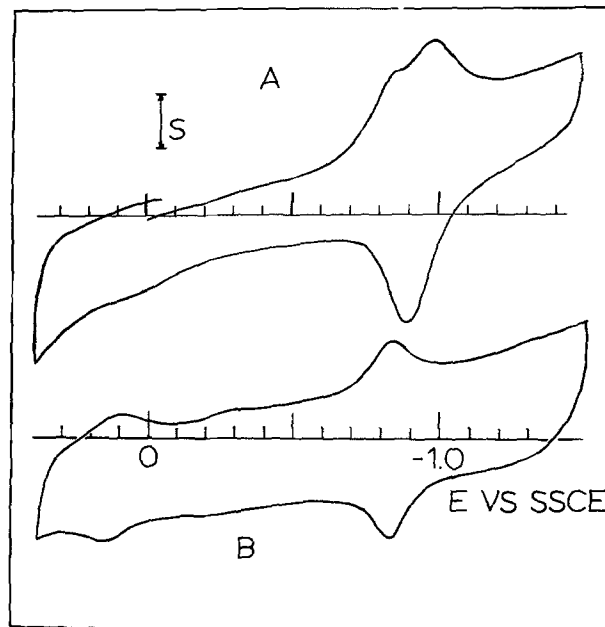


Fig. 2. Cyclic voltammetry at 100 mV/sec of 1.1×10^{-9} mole/cm² $C/m\text{Co}(\text{NH}_2)_4\text{TPP}$ in CH_3CN (curve A) and of 3.2×10^{-10} mole/cm² $C/m\text{Co}(\text{NH}_2)_4\text{TPP}$ in DMSO (curve B). $S = 27.6 \mu\text{A}/\text{cm}^2$ (curve A); $2.8 \mu\text{A}/\text{cm}^2$ (curve B).

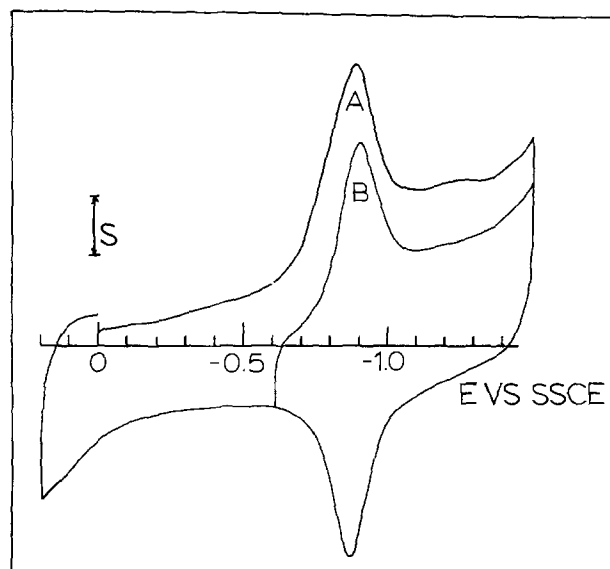


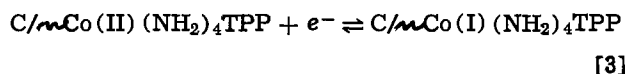
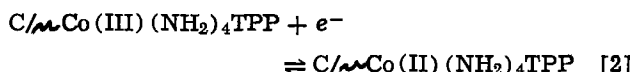
Fig. 3. Cyclic voltammetry at 100 mV/sec of $C/m\text{Co}(\text{NH}_2)_4\text{TPP}$ in DMSO. Curve A: potential scan after potentiostating at 0V for ca. 1 min, $Q_{\text{cath}}/Q_{\text{anod}} \approx 1.38$; curve B: steady-state scan between -0.6 and -1.5V vs. SSCE , $Q_{\text{cath}}/Q_{\text{anod}} = 1.02$.

and which has no anodic counterpart. If the potential scanning region is restricted (Fig. 3B) or if the electrode is prepotentiostated at -0.4V for a few minutes, the cathodic prewave is largely eliminated.

From these general observations it seems that only a fraction of the immobilized metalloporphyrin population undergoes the Co(III/II) reaction at its reversible potential, but that most if not all of the Co(II/I) reaction proceeds normally especially if the electrode is prepotentiostated as described above. We will return to this point after considering the axial ligation properties as deduced from the reversible Co(III/II) sites and the Co(II/I) reaction.

Coordination with pyridine.—Theory for the shift in reversible redox potential of an electrode immobilized metal complex caused by a change in coordination has not been discussed previously. It is formally similar to

the conventional solution relations, replacing solution concentrations by surface excess Γ (moles/cm²). We will assume that $r_0 = r_R$ for the surface interaction terms (11). Thus for the reactions of $C/mCo(NH_2)_4TPP$

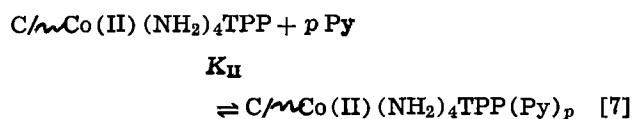
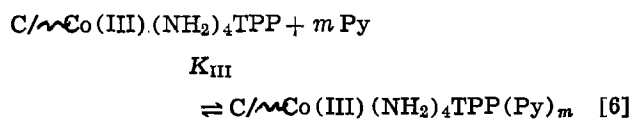


the reversible potentials in the absence of pyridine are

$$E = E_{surf(III/II)}^{\circ'} - 0.059 \log [\Gamma_{Co(II)}/\Gamma_{Co(III)}] \quad [4]$$

$$E = E_{surf(II/I)}^{\circ'} - 0.059 \log [\Gamma_{Co(I)}/\Gamma_{Co(II)}] \quad [5]$$

and after addition of pyridine generating the equilibria



we obtain

$$E_{surf/complx(III/II)}^{\circ'} = E_{surf(III/II)}^{\circ'} - 0.059 \log [K_{III}/K_{II}] - 0.059(m-p) \log [Py] \quad [8]$$

$$E_{surf/complx(II/I)}^{\circ'} = E_{surf(II/I)}^{\circ'} - 0.059 \log [K_{II}] - 0.059(p) \log [Py] \quad [9]$$

Measurement of $E_{surf/complx}^{\circ'}$ as a function of $[Py]$ yields p [the number of pyridine axially coordinated to Co(II)] and K_{II} from Eq. [9] and thence m [the number of axially coordinated pyridines for Co(III)] and K_{III} from Eq. [8]. These values depend on solvent since solvent coordinates competitively with pyridine.

To accurately measure peak potentials for the Co(III/II) and Co(II/I) waves, differential pulse voltammetry produces sharply defined waves at the slow potential scan rates desirable to ensure Nernstian charge transfer equilibrium for reactions. Also, the small Co(III/II) wave, detected with difficulty by cyclic voltammetry is easily seen (Fig. 1) in the DPV experiment. $E^{\circ'}$ was taken as the average of E_{peak} negative and positive-going potential sweeps (see Fig. 1C, 1D insets). Table I shows that DPV peak potential separations (ΔE_p) are small, with differences between the Co(III/II) and Co(II/I) steps and between $C/mCo(NH_2)_4TPP$ and $C/mCo(NH_2)TPP$. In DMSO, a spurious wave at $-0.10V$ (Fig. 1C), which disappears when a small concentration (2 mM) of pyridine is added, is thought to arise via adventitious ligands such as trace water. The potential of the more positive wave is taken as $E_{surf(III/II)}^{\circ'}$, $+0.124V$ vs. SSCE.

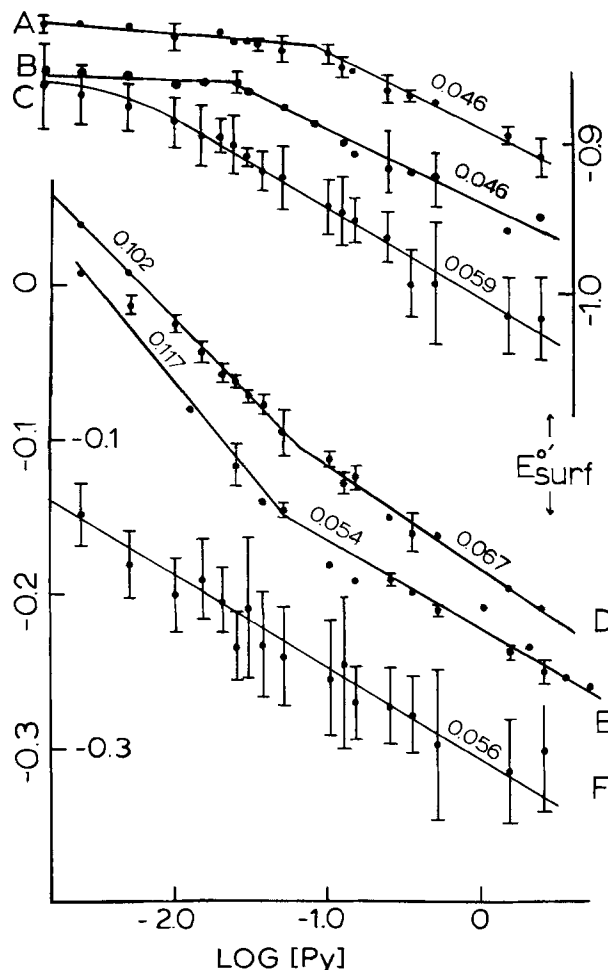


Fig. 4. Formal potential $E_{surf}^{\circ'}$ (average of E_{peak} of positive and negative DPV sweeps) as a function of $\log [Py]$. Curves A, B, C are Co(II/I) wave, curves D, E, F are Co(III/II) wave. Curves A, D: $C/mCo(NH_2)_4TPP$ in DMSO; curves B, E: $C/mCo(NH_2)_4TPP$ in DMSO; curves C, F: $C/mCo(NH_2)_4TPP$ in CH_3CN . Numbers by curves are least squares slopes.

Data for $E_{surf}^{\circ'}$ as a function of $[Py]$ are displayed in Fig. 4. Results for different experiments are overlaid. The potential becomes more negative as pyridine is added, since the Co(III) state is more stabilized by pyridine coordination than the Co(II) state. In DMSO, clearly defined changes in slope for both $C/mCo(NH_2)_4TPP$ and $C/mCo(NH_2)TPP$ occur at $[Py] \sim 0.05M$ and the slopes are approximate multiples of 0.059. At low $[Py]$, $m - p$ for the Co(III/II) reaction is for both porphyrins near two and p for Co(II/I) is zero. At these concentrations, both axial sites on $C/mCo(III)(NH_2)_4TPP$ and $C/mCo(III)(NH_2)TPP$ are occupied by pyridine, and these are both displaced upon reduction to $C/mCo(II)TPP$. At high $[Py]$, we

Table I. Stability constants^a for complexation of pyridine by immobilized cobalt aminotetraphenylporphyrins

Solvent	Porphyrin	Log K_{III}	Log K_{II}	$E_{surf}^{\circ'}$		$\Delta E_{peak},^c$ mV	
				III,II ^b	II,I ^b	III,II	II,I
DMSO	$C/mCo(NH_2)_4TPP$	7.26 ± 0.15	1.44 ± 0.18	+0.124	-0.868	43 ± 22	5 ± 7
CH_3CN	$C/mCo(NH_2)_4TPP$	8.51 ± 0.19	2.25 ± 0.11	+0.060	-0.869	50 ± 22	9 ± 7
DMSO	$C/mCo(NH_2)TPP$	6.32 ± 0.13	1.25 ± 0.12	+0.115	-0.821	12 ± 6	11 ± 6
DMSO	CoTPP	$5.86,^d 6.41^e$	$2.15,^d 1.32^e$				
PrCN	CoTPP	9.10^f	2.60^f				

^a Stability constants were calculated for integral m and p , using Eq. [8] and [9] and $E_{surf}^{\circ'}$ listed in Table.

^b Average of cathodic and anodic peak potential from DPV.

^c Difference between cathodic and anodic peak potential in DPV at 2 mV/sec, 25 mV modulation amplitude.

^d Ref. (6).

^e Ref. (7).

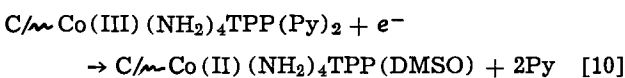
^f Ref. (20).

find $m - p = 1$, so only one of the two initially present pyridines becomes displaced in $C/mCo(II)TPP$, the second being lost upon reduction to $C/mCo(I)TPP$.

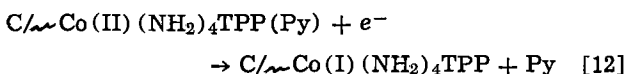
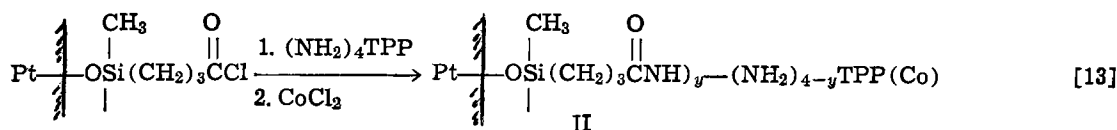
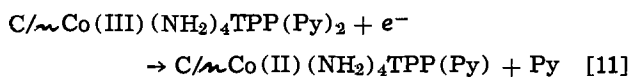
Acetonitrile is a less strongly coordinating solvent and so it is not surprising that Fig. 4 shows that only one pyridine is dissociated upon reduction to $C/mCo(II)TPP$, over the entire range of $[Py]$. As before, the second pyridine is lost upon further reduction to $C/mCo(I)TPP$. The data from different determinations in acetonitrile show greater scatter than in DMSO; the weaker ligand CH_3CN probably allows greater coordinative interference from impurity ligands such as water.

These results are summarized in the reactions

In DMSO, at $[Py] < 0.05M$



In DMSO at $[Py] > 0.05M$, and in CH_3CN



Reactions [10]-[12] for immobilized cobalt porphyrin are consistent with previous electrochemical information on solutions of cobalt porphyrin (6, 7). In structural studies of cobalt porphyrins (12-16), Co(III) is generally six coordinate (two axial ligands), Co(II) is generally five coordinate, and square pyramidal with the metal displaced 0.1-0.2Å out of the plane of the porphyrin ring, and Co(I) is four coordinate (no or very weak axial ligation). The data of Fig. 4 for all cases, show six coordinate Co(III), i.e., $C/mCo(III)-(NH_2)_4TPP(Py)_2$, at most one pyridine coordinated to Co(II), and overall dissociation of two pyridines upon complete reduction of Co(III) to Co(I). Similar results for axial coordination of pyridine in solutions of CoTPP in DMSO and propionitrile solvents were reported by Davis (5). In DMSO, Kadish and co-workers (7) reported an additional reduction wave at intermediate $[Py]$ which we did not observe for the immobilized cobalt porphyrins.

Stability constants for Eq. [6] and [7] calculated using Eq. [8] and [9] are summarized in Table I. Except for K_{III} for $C/mCo(III)(NH_2)_4TPP$, which is notably larger, K_{III} and K_{II} agree fairly well with the values cited by Kadish (7) for solutions of CoTPP in DMSO. K_{III} and K_{II} are larger in the less coordinating acetonitrile solvent, consistent with coordination number results in Fig. 4, and in good agreement with results in propionitrile (6).

Aspects of surface binding and the Co(III/II) reaction.—The above results show that the axial coordination numbers and stability constants for the reversibly reacting $C/mCo(NH_2)_4TPP$ and $C/mCo(NH_2)TPP$ are little different from that for solutions of CoTPP. However, we have also observed that only a small fraction of the total immobilized cobalt porphyrin population seems to react at the reversible Co(III/II). Associated with this effect is the appearance of a prewave of the Co(II/I) wave (Fig. 1A, 2A, 3A). The combined charge of this prewave and the Co(II/I) wave, Q_{cath} , relative to that of the subsequent Co(I/II) wave, Q_{anod} , as shown for $C/mCo(NH_2)_4TPP$ in DMSO in Table

II, depends upon the potential scanning history of the electrode. On a fresh electrode, Q_{cath}/Q_{anod} is nearly 2/1. This value drops upon succeeding potential scans, especially for continuous scanning, and falls to 1.02 if the potential scan is restricted to the vicinity of the Co(II/I) wave. The value of Q_{cath}/Q_{anod} which is observed after brief potentiostating at 0V especially increases if pyridine is present since the reversible Co(III/II) potential is then more negative than 0V.

The strong implication of this behavior is that immobilized Co(III) porphyrin which does not react in the small, reversible Co(III/II) wave, reacts as the prewave of the Co(II/I) wave. The electron transfer rate for this "slow Co(III) porphyrin" must be very slow. Further, the overlap of the "slow Co(III/II)" wave (the prewave) and the reversible Co(II/I) wave suggests that the onset of the latter catalyzes the former, perhaps through generation of some Co(I) sites from the reversibly reacting Co(III/II) population.

To observe the slow Co(III/II) reaction by a different method, we have conducted reflectance spectroelectrochemistry on the same porphyrin system attached to Pt electrodes using organosilane chemistry

As shown in Fig. 5, voltammetry of the silane-bound cobalt porphyrin, II is similar to that seen on glassy carbon, i.e., an abnormally small Co(III/II) wave and a prewave to the Co(II/I) reaction. Reflectance spectra taken *in situ*, acquisition time ca. 15 sec) with the surface II potentiostatted at +0.4, -0.4, -1.1, -0.4, and +0.4V vs. SSCE in DMSO are shown in the figure. Details of the reflectance experiment are given elsewhere (17). The +0.4V spectrum (curve a) should correspond to the Co(III) state, and its 452 nm λ_{max} is in good agreement with the 450 nm value obtained for a solution of Co(III)(NH₂)₄TPP in DMSO in an optically transparent thin layer electrochemical cell (17). When the potential is changed to -0.4V, appropriate for the Co(II) state, a spectral change commences (curves b, c, d), but this is very slow; even after 10 min there is only a 3 nm shift in λ_{max} . In contrast, changing the applied potential to -1.1V is accompanied by an immediate change of the reflectance spectrum to that of Co(I) as shown in Fig. 5, curve e. Likewise, return of the potential to -0.4 immediately results in a Co(II) porphyrin spectrum (curve f) with $\lambda_{max} = 435$ nm (the corresponding solution value is 433 nm). Finally, return of the potential to +0.4V vs. SSCE also restores the Co(III) spectrum (curve g); the Co(II/III) spectral change occurs much more rapidly than that for the Co(III/II) reaction. These

Table II. Ratio of cathodic charge for Co(II/I) wave plus prewave to anodic charge for Co(I/II) wave

DMSO, $C/mCo(NH_2)_4TPP$	Q_{cath}/Q_{anod}
Virgin scan	1.89 ± 0.44
Continuous scanning +0.3V ⇌ -1.5V	1.26 ± 0.11
Continuous scanning -0.6V ⇌ -1.5V	1.02
After potentiostat (~ 1 min) at 0.0V, ^a $[Py] = 0$	1.38 ± 0.24
After potentiostat (~ 1 min) at 0.0V, ^a $[Py] > 0.005$	1.71 ± 0.51
CH_3CN , $C/mCo(NH_2)_4TPP$	
After potentiostat (~ 20 sec) at 0.0V, $[Py] > 0.02$	1.89 ± 0.65
DMSO, $C/mCo(NH_2)TPP$	
After potentiostat (~ 20 sec) at 0.0V	1.20 ± 0.31

^a Following previous potential scan +0.3V → 1.5V → +0.3V → 0.0V, stop.

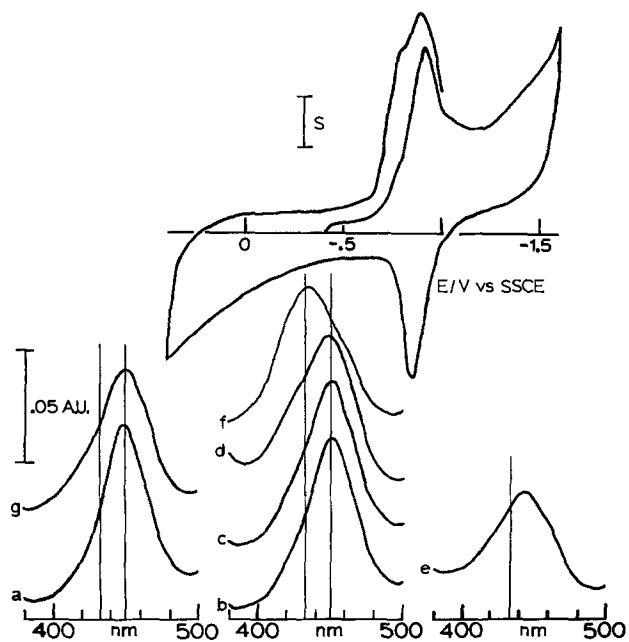


Fig. 5. Reflectance spectroelectrochemistry of structure II (3.3×10^{-10} mole/cm²) in DMSO. Spectra are taken successively curves a to g. Curve a: potential applied to +0.4V vs. SSCE; curve b: after ca. 30 sec at -0.4V; curve c: after ca. 1 min at -0.4V; curve d: after ca. 10 min at -0.4V; curve e: after ca. 30 sec at -1.1V; curve F: after ca. 30 sec at -0.4V; curve g: after ca. 1 min at +0.4V.

spectral results confirm the extraordinarily slow Co(III/II) electrochemistry, and also indicate that the reversible potential for the "slow Co(III/II)" species is more positive than -0.4V.

To verify the absence of artifacts in our solutions, cyclic voltammetry of unattached Co(III)TPPCl in DMSO solution was reexamined at glassy carbon electrodes. The Co(III/II) wave is indeed fully developed (with $i_p/v^{1/2} = \text{constant}$ for $v = 0.05\text{--}0.2$ V/sec) as compared to the Co(II/I) wave as shown in Fig. 6.

We propose that the slow electron transfer in the "slow Co(III/II)" species involves an axial coordination effect, in which a potent ligand X axially binds to one axial side of the immobilized $C/\sim\text{Co(III)(NH}_2)_4\text{TPP}$, leaving the other side open to coordination by solvent or pyridine. Thus, in DMSO

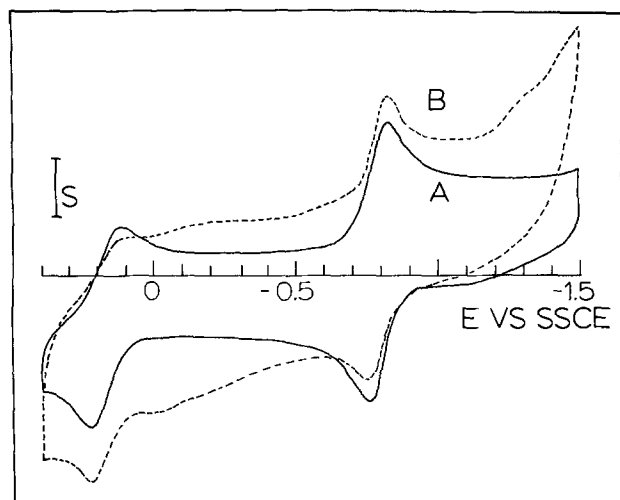
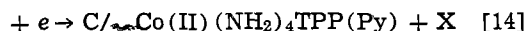
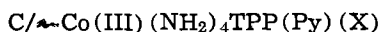


Fig. 6. Cyclic voltammograms at 100 mV/sec of a 0.4 mM solution of cobalt tetraphenylporphyrin in DMSO (curve A) with 0.4M tetraethylammonium benzoate added (curve B). $S = 27.6 \mu\text{A}/\text{cm}^2$.

containing $[\text{Py}] > 0.05\text{M}$, a small population of $C/\sim\text{Co(NH}_2)_4\text{TPP}$ is not coordinated by X at all and undergoes reaction [11] at the reversible potential as found in Fig. 4, whereas most of the immobilized metalloporphyrin undergoes a very slow electron transfer from the electrode or a faster one from neighbor Co(I) sites according to the reaction



In Eq. [14], X becomes dissociated rather than pyridine as attested by the results of Fig. 4 (i.e., $p = 1$). The Co(II) product of both Eq. [11] and [14] thereafter undergo the expected Co(II/I) reaction [12].

Intervention of ligand X in the electrochemistry of $C/\sim\text{Co(NH}_2)_4\text{TPP}$ is supported by several experimental results. First, we expect that to some extent X should be displaced by added ligands, with an associated increase in the magnitude of the reversible Co(III/II) wave. Figure 1 shows that indeed the reversible Co(III/II) wave is enhanced in the presence of added pyridine, i.e., a larger proportion of the porphyrin reacts as in Eq. [11] rather than Eq. [14]. Secondly, a sterically small, hard ligand such as chloride produces a similar effect as shown in Fig. 7. A large excess of chloride both attenuates the prewave and enhances the reversible Co(III/II) wave which in the case of $C/\sim\text{Co(NH}_2)_4\text{TPP}$ (curve d) exhibits a charge nearly equal now to that of the Co(II/I) wave, suggesting nearly complete replacement of X by chloride.

Whatever X is, it has the property of being stably bound (competes well with large excess of pyridine) and of dramatically slowing the electron transfer for

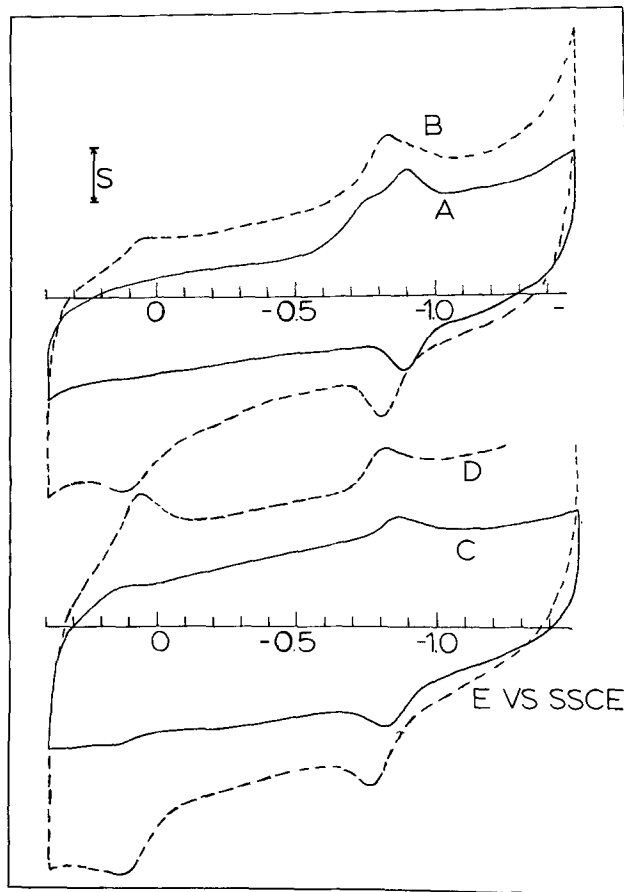
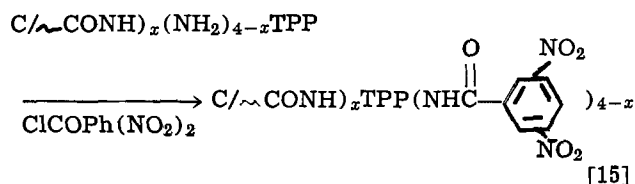


Fig. 7. Cyclic voltammograms at 100 mV/sec in DMSO of 2.2×10^{-10} mole/cm² $C/\sim\text{Co(NH}_2)_4\text{TPP}$ (curve A) with excess tetraethylammonium chloride added (curve B), and of 6.2×10^{-10} mole/cm² $C/\sim\text{Co(NH}_2)_4\text{TPP}$ (curve C) with excess $\text{Et}_4\text{N}^+\text{Cl}^-$ added (curve D). $S = 13.8 \mu\text{A}/\text{cm}^2$ (curves A, B); $55.5 \mu\text{A}/\text{cm}^2$ (curves C, D).

the Co(III/II) reaction. We must consider X as being either a trace constituent of the solvent-electrolyte system contacting the electrode, or a chemical functionality which is attached to the surface molecular framework. For some time we suspected that traces of dioxygen in the solvent might coordinate to the cobalt porphyrin. In aqueous acid, immobilized $C/\sim\text{Co}(\text{NH}_2)_4\text{TPP}$ does catalyze dioxygen reduction, at potentials suggesting H_2O_2 as product, and with eventual deactivation of the porphyrin. Also, deliberately added small amounts of dioxygen in DMSO and CH_3CN enhance current at the potential of the prewave. Scrupulous degassing, however, neither eliminates the prewave nor restores the Co(III/II) wave to a normal magnitude. We do not have satisfying evidence for the involvement of dioxygen and propose instead that X is a ligand constituent of the surface itself.

Immobilized ligands on surfaces I and II include dangling amine functionalities of $(\text{NH}_2)_4\text{TPP}$ which did not couple to the surface acid chloride groups, and carboxylic acid groups which are eventual hydrolytic products of the latter. The dangling amine groups can be investigated by the amidization reaction



by measuring the relative intensities of the x-ray photoelectron N 1s spectral bands for the nitro groups and for the overlapping porphyrin plus amide nitrogens as we have earlier described (2). For unmetallated porphyrin, we redetermined $4 - x$ as 1.85 ± 0.28 , in agreement with the earlier result from which we concluded that an average of two amide bonds formed between each $(\text{NH}_2)_4\text{TPP}$ and the carbon surface. In a new experiment, the porphyrin was metallated with cobalt prior to reaction [15]; the result was again $4 - x = 1.82 \pm 0.54$ (average of three measurements). Thus, cobalt does not change the number of dangling amines with the implication that such amines are not pre-empted from reaction [15] by axial coordination to cobalt. Also cobalt-metallated electrodes still exhibit small Co(III/II) waves after reaction [15]. Finally, neighbor amine donors should not be possible on $C/\sim\text{Co}(\text{NH}_2)_4\text{TPP}$ surfaces, which exhibit the "slow Co(III/II)" effect, albeit to a lesser degree (Fig. 2B, 7C).

The second surface ligand model, in which X is a carboxylate function of the glassy carbon lattice which centrally underlies $C/\sim\text{Co}(\text{NH}_2)_4\text{TPP}$ sites and coordinates axially with the cobalt from the electrode side of the porphyrin ring, is thought to be a stronger possibility. Since carboxylate groupings on glassy carbon occur with sufficient surface density to permit two groups to fall into register with an amide bond to (on the average) two amine sites on each porphyrin, it is therefore plausible that many axial porphyrin sites should also achieve a register with a third carboxylic acid surface group. On surface II, there is of course a large population of dangling carboxylic acid groups not consumed by the amide bonding reaction but still attached by the silane linkage to the Pt electrode.

Figure 6B shows a cyclic voltammogram of unattached CoTPP in the presence of a 10^2 -fold excess of benzoate ion (a molecular analog of a graphite carboxylate edge site). The Co(III/II) wave is split. A diminished solvent-coordinated Co(III/II)TPP wave remains visible and so the stability constant for benzoate coordination is small. A diffuse, second Co(III/II)TPP wave with large ΔE_p is seen at more negative potentials. This behavior shows that benzoate coordination by itself retards the electron transfer

rate for the Co(III/II) reaction.

In six coordinate Co(III)TPP complexes, the low spin Co(III) lies in the plane of the four porphyrin nitrogens (12, 18). In five coordinate Co(II)TPP, on the other hand, the usual cobalt coordination geometry is square pyramidal with the low spin Co(II) protruding from the porphyrin plane toward the axial ligand by 0.1-0.2 Å (12, 13, 19) or more. Thus reduction of Co(III) in Eq. [11] and [14] is accompanied by an adjustment of the metal site geometry as well as loss of one axial ligand. To the extent that the rate of electron transfer depends on either or both of these events, and it is likely that it does, involvement of a ligand X which is affixed indirectly to the porphyrin itself (via the surface) could cause severe constraints on the electron transfer rate. Neither the proposed X, carboxylate groups, or the $\text{Co}(\text{NH}_2)_4\text{TPP}$, attached as they are to the surface, have unrestricted motion on the surface, especially relative to one another. The mobility of $C/\sim\text{Co}(\text{NH}_2)_4\text{TPP}$ should be greater than that of $C/\sim\text{Co}(\text{NH}_2)_4\text{TPP}$, being attached by one amide bond rather than two, and correspondingly $\text{Co}/\sim\text{Co}(\text{NH}_2)_4\text{TPP}$ exhibits prewave and small Co(III/II) wave effects less pronounced than for $C/\sim\text{Co}(\text{NH}_2)_4\text{TPP}$.

The above model of the axial ligand X as carboxylate groups attached to surfaces I and II, while consistent with the available experimental results, is nonetheless admittedly speculative. The evidence for some interfering ligand X is strong, but we have no direct, only circumstantial evidence identifying X as carboxylate. Precedent for our model is found, however, in a prior proposal by Kuwana and co-workers (21) that carbon surface oxides can axially bind to and induce the adsorption of cobalt tetrapyrrolylporphyrin from aqueous acid.

Acknowledgment

This research was supported in part by a grant from the Office of Naval Research. This is Part XXIII of a series on Chemically Modified Electrodes.

Manuscript submitted Jan. 24, 1980; revised manuscript received April 7, 1980.

Any discussion of this paper will appear in a Discussion Section to be published in the June 1981 JOURNAL. All discussions for the June 1981 Discussion Section should be submitted by Feb. 1, 1981.

Publication costs of this article were assisted by the University of North Carolina.

REFERENCES

1. J. C. Lennox and R. W. Murray, *J. Electroanal. Chem. Interfacial Electrochem.*, **78**, 395 (1977).
2. J. C. Lennox and R. W. Murray, *J. Am. Chem. Soc.*, **100**, 3710 (1978).
3. R. D. Rocklin and R. W. Murray, *J. Electroanal. Chem. Interfacial Electrochem.*, **100**, 271 (1979).
4. J. R. Lenhard, R. Rocklin, H. Abruna, K. Willman, K. Kuo, R. Nowak, and R. W. Murray, *J. Am. Chem. Soc.*, **100**, 5213 (1978).
5. J. P. Collman, *Acc. Chem. Res.*, **10**, 265 (1977).
6. L. A. Truxillo and D. G. Davis, *Anal. Chem.*, **47**, 2260 (1975).
7. K. M. Kadish, L. A. Bottomley, and D. Beroiz, *Inorg. Chem.*, **17**, 1124 (1978).
8. K. M. Kadish, L. K. Thompson, D. Beroiz, and L. A. Bottomley, "Electrochemical Studies of Biological Systems," ACS Sympos. No. 38, D. T. Sawyer, Editor, p. 65 (1977).
9. J. F. Evans and T. Kuwana, *Anal. Chem.*, **49**, 1632 (1977).
10. W. S. Woodward, R. D. Rocklin, and R. W. Murray, *Chem. Instr.*, **9**, 95 (1979).
11. A. P. Brown and F. C. Anson, *Anal. Chem.*, **49**, 1559 (1977).
12. W. R. Scheidt, *Acc. Chem. Res.*, **10**, 339 (1977).
13. F. A. Walker, *J. Am. Chem. Soc.*, **95**, 1150 (1973).
14. P. N. Dwyer, P. Madura, and W. R. Scheidt, *J. Am. Chem. Soc.*, **96**, 4815 (1974).
15. W. R. Scheidt, *ibid.*, **96**, 84 (1974).

16. W. R. Scheidt, *ibid.*, **96**, 90 (1974).
 17. R. D. Rocklin, K. Willman, R. Nowak, K. Kuo, F. A. Schultz, and R. W. Murray, *J. Am. Chem. Soc.*, **102** (1980).
 18. W. R. Scheidt, J. A. Cunningham, and J. L. Hoard, *J. Am. Chem. Soc.*, **95**, 8289 (1973).
 19. R. G. Little and J. A. Ibers, *J. Am. Chem. Soc.*, **96**, 4440 (1974).
 20. L. A. Truxillo and D. G. Davis, *Anal. Chem.*, **48**, 456 (1976).
 21. A. Bettelheim, R. J. H. Chan, and T. Kuwana, *J. Electroanal. Chem. Interfacial Electrochem.*, **99**, 391 (1979).

Anodic Photocurrents at Silver Electrodes in Halide Solutions

M. A. Butler*

Sandia Laboratories, Albuquerque, New Mexico 87185

ABSTRACT

Enhanced anodic photocurrents are observed at silver electrodes when the electrolyte contains halide ions. The potential behavior of this effect suggests the formation of a silver halide surface layer. This surface layer then enhances the photocurrent by reducing the back-reaction at the electrode surface. Considerable structure is observed in the photocurrent as a function of photon energy. This structure is related to the electronic structure of the surface film. These kinds of measurements appear to be a promising technique for studying films on metal electrodes such as might occur in corrosion or passivation processes.

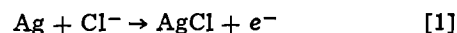
Photocurrents at metal electrodes have been studied for a number of years. Both cathodic and anodic currents have been observed and attributed to photoemission processes and photoinduced surface reactions. A number of good reviews have been written on the subject (1, 2).

In this paper, we discuss anodic photocurrents at silver electrodes and the effects of adding halide ions to the electrolyte. Anodic photocurrents at silver electrodes have been observed previously (3). We observe that the addition of halide ions to the electrolyte greatly enhances these anodic photocurrents when the electrode is positive of some potential, E_0 , or has recently been at a potential positive of E_0 . With Cl^- ions in solution there is a hysteresis in the enhancement effect about E_0 . As the potential is scanned in a positive direction, there is no enhancement until after E_0 is passed. If the potential is then scanned in a negative direction, the enhancement persists to potentials negative to E_0 . This hysteresis in the enhancement of the anodic photocurrent suggests growth of a surface layer. Formation of this layer and its removal would take time and thus would give a hysteretic effect. From the value of E_0 we have identified this layer as AgCl . The corresponding behavior with appropriate shift in E_0 is observed with Br^- ions in solution. The structure observed in the spectral response will be discussed in terms of the electronic structure of the surface.

The experimental apparatus consisted of a Schoeffel 500W xenon lamp and high intensity monochromator. The monochromatic light is modulated with a PAR chopper at 13.6 Hz before being incident upon a three-electrode electrochemical cell with quartz windows. The silver electrodes are nominally 99.99% pure, polycrystalline foils, which are etched in aqua regia diluted 1:5 and rinsed in distilled water. This procedure is not essential as the enhancement effect is not very sensitive to electrode preparation procedures. The electrolytes are reagent grade with no additional purification. The potential of the Ag electrode is controlled by a PAR Model 173 potentiostat. The output of the potentiostat goes into a PAR Model 124A lock-in amplifier and the photoresponse is detected at the chopping frequency. By scanning the wavelength of the incident

light a spectral response curve is produced such as shown in Fig. 1. The cutoff at short wavelengths is due to a loss of light intensity.

Both spectra in Fig. 1 are taken at the same potential +0.1V (SCE). As can be seen spectrum (B) shows a strong photoresponse while spectrum (A) shows negligible photoresponse. The difference between these two measurements is that the electrode was biased to a more positive potential, +0.15V (SCE), for 10 min before spectrum (B) was taken at +0.1V (SCE). This illustrates hysteresis in the photoresponse and suggests chemical modification of the Ag surface. For a $2 \times 10^{-3}\text{M}$ KCl electrolyte the reaction (4)



occurs at a potential of +0.14V (SCE), which suggests the growth of an AgCl layer on the silver electrode surface. For our silver electrodes 10 min at +0.15V (SCE) corresponds to growth of a film $\sim 400\text{\AA}$ thick. We believe that the enhancement effect arises from the growth of this surface layer. Previous experiments to

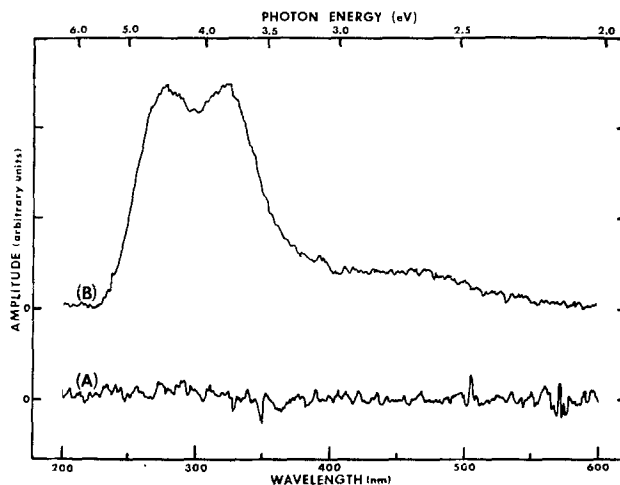


Fig. 1. The spectral response uncorrected for light intensity of an Ag electrode in $2\text{M H}_2\text{SO}_4$ with $2 \times 10^{-3}\text{M}$ KCl electrolyte. Spectrum (A) is taken at +0.1V (SCE) and spectrum (B) at +0.1V (SCE) after being at +0.15V (SCE) for 10 min. The sensitivity in spectrum (A) is ten times greater than in spectrum (B).

* Electrochemical Society Active Member.
 Key words: electrolyte, films, surfaces.

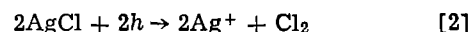
observe the effects of Cl^- ions on photocurrents at Pt and Au electrodes did not show significant enhancement effects (5). This is because the potential was always negative of the potential for formation of platinum and gold chlorides.

Photoemission of electrons from a metal electrode into an aqueous electrolyte is another example of internal photoemission (6). The electrolyte may be considered an amorphous semiconductor (7) and the electron is photoemitted into the empty conduction band [see Fig. 2(a)]. Thus, all metals show the same threshold for photoemission into aqueous electrolytes (2). Conversely, anodic photocurrents may arise from emission of photoexcited holes into the valence band of the aqueous electrolyte [see Fig. 2(a)], although this interpretation of anodic photocurrents is still subject to some controversy (8).

The magnitude of the photoemitted currents is determined by a number of factors. The amorphous nature of the aqueous electrolyte suggests considerable scattering and indeed the range of photoemitted electrons is observed (9) to be 20-30Å. At such a distance from the metal surface, back reactions on the electrode surface are highly likely. For electron emission the back reaction can be reduced by a suitable choice of scavenger in the electrolyte (2). A good scavenger for holes has not yet been found. The net observed photocurrent is the difference between the photoemission and back-reaction currents.

Although the morphology of our films is not known and undoubtedly is not simple, we will assume for purposes of analysis a uniform surface layer. Then the energy level diagram is as shown in Fig. 2(b). The light is incident through the electrolyte and can cause photoexcitation at various depths in the surface layer structure. For photons of energy less than the silver halide bandgap, internal photoemission from the silver into the silver halide will be observed. The transport of the photoexcited electron or hole in the silver halide will depend on trap sites and the electric field in the halide layer. The actual character and composition of this layer is complex because ionic conduction of the Ag^+ ion is expected at room temperature (10). An excess of Ag^+ ions in the layer may be a source of traps for any photoexcited electrons. At the interface with the electrolyte, the photoexcited charge carriers will cause an electrochemical reaction to take place, probably relating to decomposition of the AgCl . The only requirement is that the electron-driven electro-

chemical reactions have redox potentials below the conduction band and the hole-driven electrochemical reactions have redox potentials above the valence band. For electrons which reach this interface a possible reaction is the reverse of that given in Eq. [1]. For holes we may speculate that the following reaction is possible



since the standard potential is +1.4V (SCE) and the valence band edge occurs at +2.3V (SCE) for AgCl . At any given photon energy the net photocurrent observed is the sum of electron and hole currents.

For photons with energy larger than the bandgap of the silver halide we expect additional excitations across the bandgap in the halide layer. Again the disposition of these photoexcited carriers will depend on trapping and the electric fields in the surface layer.

The magnitude of the photocurrents observed for such a surface layer structure should be different than for the bare metal electrode. For any electron or hole which reaches the electrolyte and reacts to form some charged species in solution, the back reaction will be drastically reduced. A number of factors contribute to this effect. Most important, an electron or hole which reacts with the electrolyte must lose energy equal to the difference between the relevant redox potential and the appropriate band edge. Thus, the halide layer creates a potential barrier on the order of 1 eV which must be overcome for the back reaction to occur.

Some information about the electronic structure of the surface may be obtained by examining the spectral response curves. The yield curves for $\text{Ag}:\text{AgCl}$ and $\text{Ag}:\text{AgBr}$ are shown, respectively, in Fig. 3 and 4. We see that for these anodic photocurrents, considerable structure exists in the yield curves. It does not

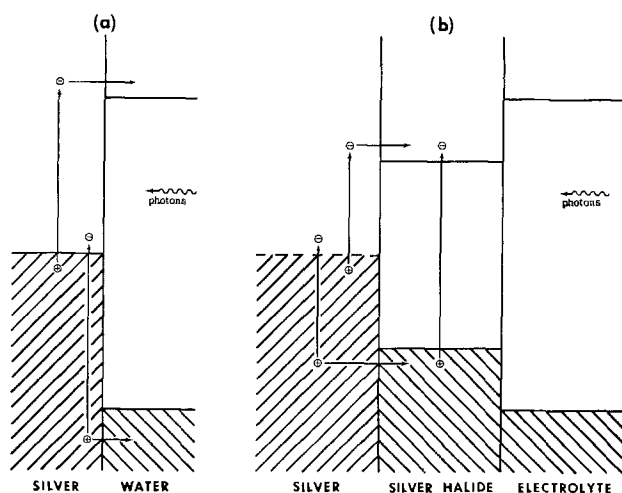


Fig. 2. The energy level diagram for the silver electrode with and without a silver halide layer on the surface. (a) The excitations for electron and hole photoemission from silver into water considered as an amorphous semiconductor. (b) The photoexcitation processes from silver into the silver halide layer and within the silver halide layer. At the surface of the electrolyte, the excited carriers react to form some unknown species in the electrolyte.

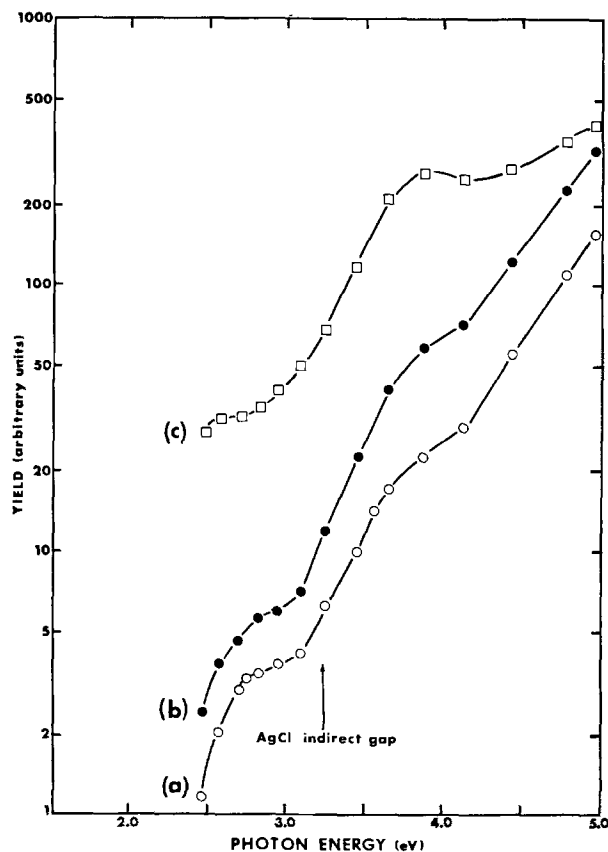


Fig. 3. The spectral response curves, corrected for light intensity, for an AgCl layer on an Ag electrode at +0.1V (SCE). The layer thickness is on the order of 500Å and varies from (a) to (c) with increasing thickness. The bandgap of silver chloride is indicated.

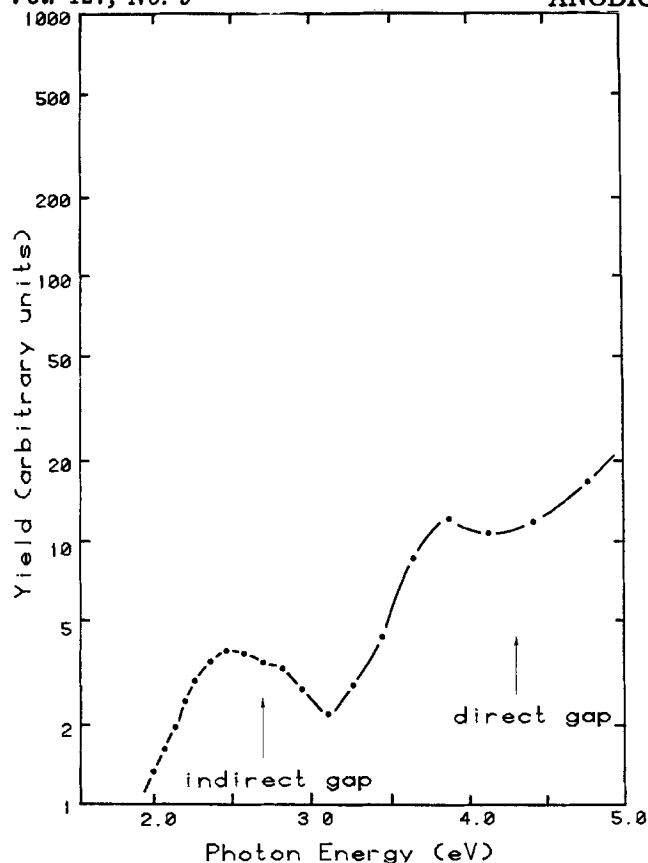


Fig. 4. The spectral response curve, corrected for light intensity, for an AgBr layer on an Ag electrode at 0.0V (SCE). Both the indirect and direct bandgaps of AgBr are indicated.

appear that this structure correlates with the known bandgaps of the halide layers.

For a clean Ag metal electrode a peak is sometimes observed in the yield spectrum due to surface plasmons (3). These surface excitations can result in generation of excess excited holes and electrons near the electrode surface which can then result in photoanodic or photocathodic currents depending on the electrode potential (3). Such a surface plasmon should exist at the Ag:Ag halide interface and will occur at a photon energy given by (11)

$$\epsilon_1(\hbar\nu_{sp}) = -\epsilon_d \quad [3]$$

where ϵ_1 is the dielectric constant of Ag (12) and ϵ_d the dielectric constant of the halide film (13). If the interface is sufficiently rough to allow the photons to couple to this plasmon, we would expect structure in the yield spectra at 3.2 eV for both AgCl layers and AgBr layers. From Fig. 3 and 4, we see that dips occur in the photoanodic current which would correspond to the surface plasmon contributing a photocathode component to the current. Considering the potentials at which these spectra were taken, this is consistent with the observations in Ref. (3).

While one would normally expect a yield curve to be a monotonically increasing function, there appears to be a peak in both the AgBr and AgCl data at about 3.8 eV. The common nature of this peak to both halides suggests that it is a feature of the silver rather than specifically the halide layer. A peak at this energy has been previously identified as the excitation of a longitudinal volume plasmon which then decays into single particle excitations which contribute to the photoemission current (14). While excitation of this plasmon required p-polarized light and in our experiment the light was incident normal to the surface, the polycrystalline nature of the electrode and its rough surface would make excitation of this plasmon possible. Whether such an excitation should contribute an

anodic or cathodic component to the photocurrent will depend on potential, relative lifetime of photoexcited holes and electrons, and other factors. Thus, it is not clear that it should exhibit the same sign as the surface plasmon effect since the excitation mechanism is different in the two cases. The observation of this peak suggests the possibility of a very rough halide layer on the surface where the underlying silver is sufficiently exposed to the electrolyte to allow direct photoemission without influence of the halide layer.

For photon energies below the bandgap of the halide and the threshold for photoemission into the electrolyte, we still see a contribution to the yield curve. This is attributed to internal hole photoemission from the Ag into the Ag halide followed by a reaction at the silver halide surface. This hypothesis is best explored by analyzing the thresholds of the yield curves. In Fig. 5, we show Fowler plots for two examples of chloride ion and one of bromide ion in solution. Whether $Y^{0.5}$ should be plotted rather than $Y^{0.4}$ is still an unsettled question relating to shielding of the photoemitted electron charge by ions in the electrolyte (1). Since our data do not cover a sufficient range to differentiate these two behaviors, we use the form we believe to be correct. Note that for the chloride example, a shift in potential of the Ag electrode is reflected in a corresponding shift in the photocurrent threshold. This suggests that the additional potential is dropped across the Ag:Ag halide interface and not in the Ag halide layer or at the Ag halide:electrolyte interface. This behavior is not typical of conventional metal-semiconductor junctions and arises because of the unique properties of the silver halides.

This interface is a blocking junction for electronic conduction since the Fermi level of Ag is in the bandgap of the silver halide (see Fig. 2). However, the

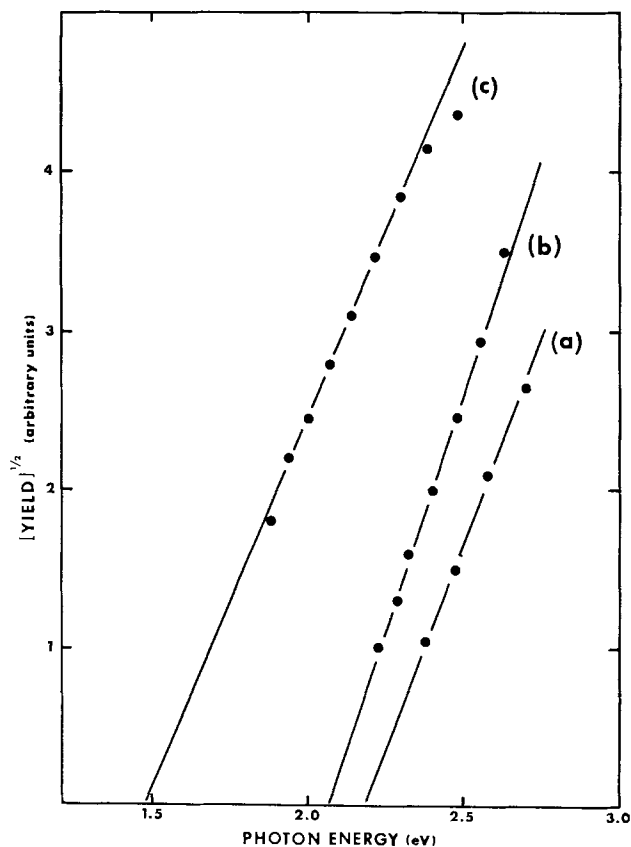


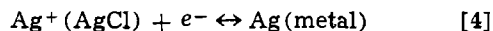
Fig. 5. Fowler plots for anodic photocurrents on a silver electrode. The potentials and halide ion concentrations are: (a) 0.1V (SCE) 2×10^{-3} M KCl, (b) 0.2V (SCE) 5×10^{-5} M KCl, and (c) 0.0V (SCE) 2×10^{-3} M KBr. The threshold energies are: (a) 2.18 eV, (b) 2.07 eV, and (c) 1.48 eV.

silver halides are also Ag^+ ion conductors at room temperature with a conductivity for polycrystalline (AgBr) of about $(15) 10^{-5} (\Omega\text{-cm})^{-1}$. Our halide layers are estimated from measurements of total charge used in growing the layers to be $\lesssim 10^3 \text{\AA}$ thick. Thus, they would have a resistance for a 1 cm^2 sample of about 1Ω . Since the d-c currents flowing when the photoresponse measurements are made are at most 10^{-4} A/cm^2 , we would expect at most a voltage drop across the halide layer of $\sim 0.1 \text{ mV}$. Thus, the film cannot support a potential drop of any size.

The electrochemical reaction which results in transport of Ag^+ ions across the $\text{Ag}:\text{Ag}$ halide interface is one for which the exchange current density at room temperature is quite small ($\ll 10^{-6} \text{ A/cm}^2$) (16). Thus, it could support a considerable overpotential. We believe that the shift in the photocurrent threshold in Fig. 5 for the two AgCl layers is evidence for this overpotential.

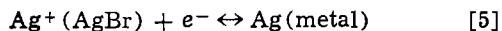
The indirect bandgap of AgCl is 3.25 eV (17). Internal photoemission of electrons from Ag into AgCl was observed previously (18) to have a threshold of 1.1 eV at low temperature. At these temperatures, the ionic conduction is frozen out and the major part of the applied potential will be dropped across the AgCl . Thus, we would expect the threshold for hole photoemission, with little or no potential drop across the $\text{Ag}:\text{AgCl}$ interface, to be at $\sim 2.15 \text{ eV}$. This is in reasonable agreement with the thresholds that we observe.

An important question to ask is why the Fermi level in the Ag occurs $\sim 1.1 \text{ eV}$ below the conduction band of the AgCl . For conventional metal:electrolyte interfaces at equilibrium we expect the Fermi level in the metal to be pinned at the redox level in the electrolyte. If AgCl is considered as an electrolyte then a similar argument can be made. The Fermi level in the Ag must be pinned at the electrochemical reaction potential for



otherwise considerable current will be flowing across the interface. This concept of equilization of electrochemical potentials may be relevant to the determination of barrier heights at other semiconductor-metal interfaces.

For the AgBr layer the bandgap is smaller, 2.68 eV (17). The threshold for electron emission has not been measured but we would expect it to be similar to that for AgCl , since the Ag^+ ion transfer reaction



should occur at a similar electrochemical potential to the transfer reaction at the $\text{Ag}:\text{AgCl}$ interface. Thus, the hole photoemission threshold should decrease approximately the same amount as the bandgap decreases or to about 1.5 eV . This is in reasonable agreement with the measured threshold of 1.48 V , since overpotentials of a few tenths of a volt are possible at the $\text{Ag}:\text{AgBr}$ interface.

These results for AgCl and AgBr films on silver electrodes illustrate the sensitivity of this technique to the films. Drastic changes in the spectral response of these electrodes are observed. The potential for

the onset of enhanced photocurrents identifies the surface reaction taking place and thus the chemical nature of the surface film. The spectral response of these electrodes gives considerable information about the electronic structure of the surface as illustrated by the data. The photoresponse of electrodes appears to be one of the most promising techniques for examining solid-liquid interfaces and should find useful application for studying corrosion and passivation processes.

Acknowledgment

This work was supported by the Materials Sciences Program, Division of Basic Energy Sciences, U.S. Department of Energy, under Contract DE-ACO4-76-DP00789.

Manuscript submitted Dec. 10, 1979; revised manuscript received March 17, 1980. This was Paper 357 presented at the Boston, Massachusetts, Meeting of the Society, May 6-11, 1979.

Any discussion of this paper will appear in a Discussion Section to be published in the June 1981 *JOURNAL*. All discussions for the June 1981 Discussion Section should be submitted by Feb. 1, 1981.

Publication costs of this article were assisted by Sandia Laboratories.

REFERENCES

1. A. M. Brodsky and Y. V. Pleskov, in "Progress in Surface Science," Sidney G. Davison, Editor, pp. 1-73, Pergamon, New York (1972).
2. H. Gerischer, D. M. Kolb, and J. K. Sass, *Adv. Phys.*, **27**, 437 (1978).
3. J. K. Sass, R. K. Sen, E. Meyer, and H. Gerischer, *Surf. Sci.*, **44**, 515 (1974).
4. D. Dobos, "Electrochemical Data," p. 250, Elsevier, New York (1975).
5. H. Gerischer, E. Meyer, and J. K. Sass, *Ber. Bunsenges.*, **76**, 1191 (1972).
6. R. Williams, in "Semiconductors and Semimetals," Vol. 6, R. K. Willardson, Editor, Chap. 2, Academic Press, New York (1970).
7. F. Williams, S. P. Varma, and S. Hillenius, *J. Chem. Phys.*, **64**, 1549 (1976).
8. J. K. Sass, in "Topics in Surface Chemistry," E. Kay and P. S. Bagus, Editors, p. 41, Plenum, New York (1978).
9. Z. A. Rotenberg and Yu. Ya. Gurevich, *J. Electroanal. Chem. Interfacial Electrochem.*, **66**, 165 (1975).
10. C. P. Flynn, "Point Defects and Diffusion," p. 379, Clarendon Press, Oxford (1972).
11. E. A. Stern and R. A. Ferrell, *Phys. Rev.*, **120**, 130 (1960).
12. D. C. Skillman, *J. Opt. Soc. Am.*, **61**, 1264 (1971).
13. N. J. Carrera and F. C. Brown, *Phys. Rev. B*, **4**, 3651 (1971).
14. J. K. Sass, H. Laucht, and K. L. Kliever, *Phys. Rev. Lett.*, **35**, 1461 (1975).
15. J. H. Kennedy, in "Physics of Electrolysis," J. Hladik, Editor, p. 933, Academic Press, New York (1972).
16. D. O. Raleigh, in "Electroanalytical Chemistry," Vol. 6, A. J. Bard, Editor, p. 144, Dekker, New York (1973).
17. W. H. Strehlow and E. L. Cook, *J. Phys. Chem. Ref. Data*, **2**, 163 (1973).
18. M. A. Gilleo, *Phys. Rev.*, **91**, 534 (1953).

A Thermodynamic Theory of Dissolution Potential and Further Tests of the Theory

R. P. Rastogi and S. A. Kahn¹

Department of Chemistry, Gorakhpur University, Gorakhpur, U.P. India

ABSTRACT

A theory of dissolution potential of electrolytes has been developed on the basis of the thermodynamics of irreversible processes. The theory is found to be in agreement with the available experimental data. In order to provide further tests of the theory, the diffusion and dissolution potentials of KI in dimethylformamide-water mixtures and of KCl in KCl-HCl aqueous solutions have also been measured. The sign of diffusion potential and dissolution potential are found to be the same in the former case, in conformity with the predictions of the theory. The measurements of dissolution potential of KCl in KCl-HCl aqueous solutions further confirm the theory. Although the dissolution potential of KCl in water alone is negative, it is positive in aqueous KCl-HCl mixtures.

The phenomenon of dissolution and precipitation potential was discovered by Rastogi, Dass, and Batra (1) in 1961. Comprehensive studies of these potentials have been reported by Rastogi and co-workers (2-5). They have explained the development of these potentials on the basis of unequal mobilities of anions and cations. It has been postulated by these workers that the precipitation potential develops due to a difference in the rate of attachment of cations and anions during crystallization, and dissolution potential develops due to a difference in the rate of detachment of cations and anions during dissolution. In the light of this mechanism Rastogi, Shukla, and Bhagat (4) could explain the sign and magnitude of precipitation and dissolution potentials in a large number of cases.

Recently Girdhar and co-workers (8, 9) have studied the precipitation and dissolution potentials of a number of electrolytes in aqueous medium. They have tried to explain the development of these potentials on the basis of a solvation mechanism (8, 10).

Ibl *et al.* (6, 7) have recently reported studies on crystallization and dissolution potentials using single crystals. They have tried to explain the phenomenon in terms of a "corrosion" model based on the difference in the kinetics of the dissolution of cations and anions.

More intensive studies are necessary in order to have a clear picture of the phenomenon and hence the present investigation was undertaken. In this communication an attempt has been made to develop a theory of dissolution potential on the basis of the thermodynamics of irreversible processes. It is found that the theory gives a satisfactory explanation of the observed facts.

In order to have a sensitive check of the theory measurements of the following quantities can be made.

(i) Diffusion potential and dissolution potential of a number of electrolytes in solvents in which ($U_{+}^{\circ} - U_{-}^{\circ}$) may have different signs, where U_{+}° and U_{-}° are the ionic mobilities of cations and anions, respectively.

(ii) Diffusion potential and dissolution potential of an electrolyte in a mixture of solvents in which ($U_{+}^{\circ} - U_{-}^{\circ}$) may change sign with change in composition.

(iii) Diffusion and dissolution potential of KCl in KCl-HCl aqueous solutions in which ($U_{K^{+}}^{\circ} - U_{Cl^{-}}^{\circ}$) can be very large (15).

Measurements of type (i) have been reported by Rastogi, Shukla, and Bhagat (4) and Vishnu, Khan,

and Jahan (13). Thermodynamic theory is found to be in accord with their findings. Experimental data of type (ii) and (iii) are reported in this communication. The results are striking and confirm the underlying hypothesis of the thermodynamic theory.

Thermodynamic Theory of Dissolution Potential

The physics of dissolution potential can be understood from the schematic diagram given in Fig. (1). When a platinum electrode loaded with the crystals of an electrolyte (α -phase) is introduced into the solvent, dissolution starts immediately. Ions detach from the surface of the crystal and a narrow zone of high concentration is set up in its vicinity. We shall call it β -phase for convenience. From the kinetics of dissolution it has been found that the process of dissolution is diffusion controlled and the crystal maintains a state of near saturation in the liquid film adjacent to it (14). The justification of the existence of β -phase is further provided by the fact that the phase potential is a reality. In the steady state the rate at which ions become detached from the crystal surface is equal to the rate at which they diffuse away from the liquid film (β -phase) adjacent to the surface of the crystal. The concentration of the electrolyte in the β -phase would vary with time but we shall assume that at a particular instant a steady concentration is attained. The ions diffuse away from β -phase and go into the bulk of the solvent, where a concentration gradient is set up. We shall call it as δ -phase for convenience.

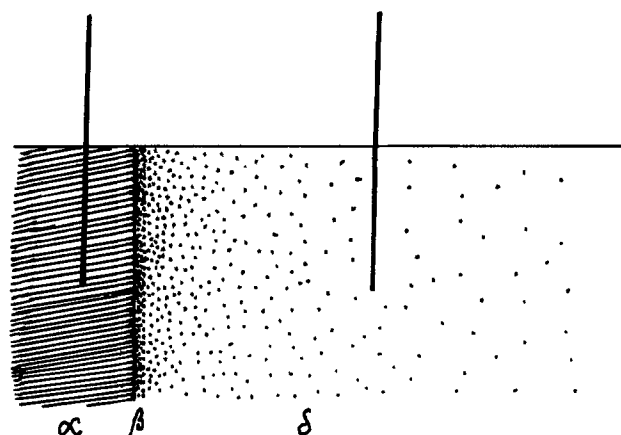


Fig. 1. Schematic diagram of dissolution cell

¹ Present address: Chemistry Department, St. Andrew's College, Gorakhpur, India.

Key words: thermodynamics, dissolution, potential.

Thus the above system comprises a discontinuous system involving α - and β -phases and a continuous system involving δ -phase. We use the terms "continuous" and "discontinuous" as they are understood in the terminology of irreversible thermodynamics. It should be noted that such a combined system has not been examined from the viewpoint of nonequilibrium thermodynamics so far. We present below a formal treatment of such a system.

The total entropy of the system would be given by the equation

$$TdS = TdS^\alpha + TdS^\beta + TdS^\delta \quad [1]$$

where dS^α , dS^β , and dS^δ are the entropy changes for the three sub-systems.

The Gibbs equation for the sub-systems α and β would be given by

$$TdS^\alpha = dU^\alpha + PdV^\alpha$$

$$- \sum_{i=1,2} (\mu_i^\alpha + e_i\phi^\alpha) dM_i^\alpha - \frac{2\gamma}{\rho r} dM^\alpha \quad [2]$$

$$TdS^\beta = dU^\beta + PdV^\beta - \sum_{i=1,2} (\mu_i^\beta + e_i\phi^\beta) dM_i^\beta \quad [3]$$

where μ_i^α = chemical potential of component i in the phase α , e_i = the charge carried by i , ϕ^α = electrical potential of phase α , dM_i^α = change of mass of component i in phase α , γ = surface energy at α - β interface, ρ = density, r = radius, and M = molecular weight. The terms with β suffix have similar meaning in β -phase.

Thus from Eq. [1], [2], and [3] we get

$$TdS = dU^\alpha + PdV^\alpha$$

$$- \sum_{i=1,2} (\mu_i^\alpha + e_i\phi^\alpha) dM_i^\alpha - \frac{2\gamma}{\rho r} dM^\alpha$$

$$+ dU^\beta + PdV^\beta - \sum_{i=1,2} (\mu_i^\beta + e_i\phi^\beta) dM_i^\beta + TdS^\delta \quad [4]$$

Thus,

$$T \frac{dS}{dt} = \frac{dQ^{\alpha,\beta}}{dt} - \sum_{i=1,2} (\mu_i^\alpha + e_i\phi^\alpha) \frac{dM_i^\alpha}{dt} - \sum_{i=1,2} (\mu_i^\beta + e_i\phi^\beta) \frac{dM_i^\beta}{dt} - \frac{2\gamma}{\rho r} \frac{dM^\alpha}{dt} - T \frac{dS^\delta}{dt} \quad [5]$$

Now putting

$$- \frac{dM_i^\alpha}{dt} = \frac{dM_i^\beta}{dt} = J_i \quad [6]$$

$$\frac{dM^\alpha}{dt} = J_c \quad [7]$$

$$- \frac{2\gamma}{\rho r} = J_c \quad [8]$$

$$S^\delta = sM \quad [9]$$

where s = specific entropy of the phase δ and M = total mass of the phase δ we write Eq. [5] as

$$T \frac{dS}{dt} = \frac{dQ^{\alpha,\beta}}{dt} + \sum_{i=1,2} J_i (\Delta\mu_i^{\alpha,\beta} + e_i\Delta\phi^{\alpha,\beta}) + J_c X_c + TM \frac{ds}{dt} \quad [10]$$

Using the results of irreversible thermodynamics of continuous processes (11), we get

$$T \frac{ds}{dt} = \frac{1}{\rho} \left[-\text{div} \left(J_q^\delta - \sum \mu_i^\delta J_i^\delta \right) + \sum J_i^\delta X_i^\delta \right] \quad [11]$$

where J_i^δ = mass of the component i flowing per unit area per unit time across β - δ interface. μ_i^δ = chemical

potential of the component i in the δ -phase. And

$$X_i^\delta = e_i \text{grad } \phi^\delta + \text{grad } \mu_i^\delta \quad [12]$$

Now if A is the area of β - δ interface and the mass flowing per unit area per unit time from phase β to the phase δ is the same all along the interface

$$J_i = AJ_i^\delta \quad [13]$$

Using Eq. [10] and [11] we get

$$T \frac{dS}{dt} = \frac{dQ^{\alpha,\beta}}{dt} + \sum_{i=1,2} J_i (\Delta\mu_i^{\alpha,\beta} + e_i\Delta\phi^{\alpha,\beta}) + J_c X_c + \frac{M}{\rho} \left[-\text{div} \left(J_q^\delta - \frac{1}{A} \sum \mu_i^\delta J_i \right) + \frac{1}{A} \sum J_i X_i^\delta \right] \quad [14]$$

Or

$$T \frac{dS}{dt} = \left[\frac{dQ^{\alpha,\beta}}{dt} - \frac{M}{\rho} \text{div} \left(J_q^\delta - \frac{1}{A} \sum \mu_i^\delta J_i \right) \right] + \sum_{i=1,2} J_i [(\Delta\mu_i^{\alpha,\beta} + e_i\Delta\phi^{\alpha,\beta}) + 1X_i^\delta] + J_c X_c \quad [15]$$

When we consider the gradient along the x -axis to be uniform, Eq. [12] yields

$$X_i^\delta \int_{x=0}^{x=1} dx = e_i \int_{\phi_0}^{\phi_1} d\phi^\delta + \int_{\mu(\text{sat})}^{\mu(\text{soln.})} d\mu^\delta$$

or

$$1X_i^\delta = e_i\Delta\phi^\delta + \Delta\mu_i^\delta \quad [16]$$

Thus from Eq. [15] and [16] we get

$$T \frac{dS}{dt} = \left[\frac{dQ^{\alpha,\beta}}{dt} - \frac{M}{\rho} \text{div} \left(J_q^\delta - \frac{1}{A} \sum \mu_i^\delta J_i \right) \right] + \sum_{i=1,2} J_i [(\Delta\mu_i^{\alpha,\beta} + e_i\Delta\phi^{\alpha,\beta}) + (e_i\Delta\phi^\delta + \Delta\mu_i^\delta)] + J_c X_c \quad [17]$$

Hence from Eq. [17] we find

$$\sigma = \sum_{i=1,2} J_i [(\Delta\mu_i^{\alpha,\beta} + e_i\Delta\phi^{\alpha,\beta}) + (e_i\Delta\phi^\delta + \Delta\mu_i^\delta)] + J_c X_c \quad [18]$$

Or

$$\sigma = \sum_{i=1,2} J_i x_i + J_c X_c \quad [19]$$

where

$$x_i = [(\Delta\mu_i^{\alpha,\beta} + e_i\Delta\phi^{\alpha,\beta}) + (e_i\Delta\phi^\delta + \Delta\mu_i^\delta)] \quad [20]$$

Thus flux-force equations will be given by

$$J_1 = L_{11}x_1 + L_{12}x_2 \quad [21]$$

$$J_2 = L_{21}x_1 + L_{22}x_2 \quad [22]$$

The current I flowing through the system would be given by

$$I = (e_1J_1 + e_2J_2) \quad [23]$$

Since we measure the potential when $I = 0$, we get from Eq. [23], [22], and [21]

$$l_1x_1 + l_2x_2 = 0 \quad [24]$$

where

$$l_1 = e_1L_{11} + e_2L_{22} \quad [25]$$

$$l_2 = e_1L_{12} + e_2L_{22} \quad [26]$$

From Eq. [20] and [24] we get

$$l_1 [(\Delta\mu_1^{\alpha,\beta} + e_1\Delta\phi^{\alpha,\beta}) + (e_1\Delta\phi^\delta + \Delta\mu_1^\delta)] + l_2 [(\Delta\mu_2^{\alpha,\beta} + e_2\Delta\phi^{\alpha,\beta}) + (e_2\Delta\phi^\delta + \Delta\mu_2^\delta)] = 0 \quad [27]$$

Therefore

$$\begin{aligned}
 -(\Delta\phi^{\alpha,\beta} + \Delta\phi^\delta) &= \frac{l_1}{e_1 l_1 + e_2 l_2} \Delta\mu_1^{\alpha,\beta} \\
 &+ \frac{l_2}{e_1 l_1 + e_2 l_2} \Delta\mu_2^{\alpha,\beta} + \frac{l_1}{e_1 l_1 + e_2 l_2} \Delta\mu_1^\delta \\
 &+ \frac{l_2}{e_1 l_1 + e_2 l_2} \Delta\mu_2^\delta \quad [28]
 \end{aligned}$$

Using Onsager reciprocal relation

$$L_{12} = L_{21}$$

it can be easily proved that

$$\left(\frac{t_1}{e_1}\right)_{\Delta\mu_1=0, \Delta\mu_2=0} = \frac{l_1}{e_1 l_1 + e_2 l_2} \quad [29]$$

$$\left(\frac{t_2}{e_2}\right)_{\Delta\mu_1=0, \Delta\mu_2=0} = \frac{l_2}{e_1 l_1 + e_2 l_2} \quad [30]$$

where t_1 and t_2 are effective transport numbers. Thus from Eq. [28], [29], and [30] we get

$$\begin{aligned}
 -(\Delta\phi^{\alpha,\beta} + \Delta\phi^\delta) &= \left[\frac{t_1}{e_1} \Delta\mu_1^{\alpha,\beta} + \frac{t_2}{e_2} \Delta\mu_2^{\alpha,\beta} \right] \\
 &+ \left[\frac{t_1}{e_1} \Delta\mu_1^\delta + \frac{t_2}{e_2} \Delta\mu_2^\delta \right] \quad [31]
 \end{aligned}$$

There are two terms on the right side of Eq. [31]. Let us denote them as $(\Delta\phi)_I$ and $(\Delta\phi)_{II}$ for convenience. Thus we get

$$(\Delta\phi)_I = \frac{t_1}{e_1} \Delta\mu_1^{\alpha,\beta} + \frac{t_2}{e_2} \Delta\mu_2^{\alpha,\beta} \quad [32]$$

$$(\Delta\phi)_{II} = \frac{t_1}{e_1} \Delta\mu_1^\delta + \frac{t_2}{e_2} \Delta\mu_2^\delta \quad [33]$$

The right-hand side of Eq. [33] is the well-known equation for the diffusion potential. In terms of activity and mobility it is given by

$$(\phi\Delta)_{II} = (\Delta\phi)_{\text{Diff}} = -\frac{RT}{F} \left(\frac{U^+ - U^-}{U^+ + U^-} \right) \ln \frac{a^\delta}{a^\beta} \quad [34]$$

where it has been supposed that

$$\frac{a_1^\delta}{a_1^\beta} = \frac{a_2^\delta}{a_2^\beta} = \frac{a^\delta}{a^\beta} \quad [35]$$

for uni-univalent electrolytes.

From Eq. [32] we have

$$(\Delta\phi)_I = \frac{t_1}{F} (\mu_1^\alpha - \mu_1^\beta) - \frac{t_2}{F} (\mu_2^\alpha - \mu_2^\beta) \quad [36]$$

where

$$e_1 = -e_2 = F$$

The chemical potentials in α and β phases are given by

$$\mu_i^\alpha = \mu_i^{0(s)} + RT \ln a_i^{(s)} \quad [37]$$

$$\mu_i^\beta = \mu_i^0 + RT \ln a_i^\beta \quad [38]$$

where $\mu_i^{0(s)}$ and μ_i^0 are the standard chemical potentials in solid and solution, respectively. Further $a_i^{(s)}$ is the activity of the component i in solid phase α , which will be equal to unity, and a_i^β is the activity of component i in the liquid phase β .

Thus from Eq. [36], [37], and [38] we get

$$\begin{aligned}
 F(\Delta\phi)_I &= [t_1\{\mu_1^{0(s)} - \mu_1^0 - RT \ln a_1^{(s)}\} \\
 &- t_2\{\mu_2^{0(s)} - \mu_2^0 - RT \ln a_2^{(s)}\}] \\
 &+ RT \left[t_1 \ln \frac{a_1^{(s)}}{a_1^\beta} - t_2 \ln \frac{a_2^{(s)}}{a_2^\beta} \right] \quad [40]
 \end{aligned}$$

where $a_1^{(s)}$ and $a_2^{(s)}$ denote the activities of ions

1 and 2 in the saturated solution. If $(\Delta\phi)_{\text{Phase}}$ denotes the phase potential, it can be easily shown (12) that

$$\mu_1^{0(s)} - \mu_1^0 - RT \ln a_1^{(s)} = -F(\Delta\phi)_{\text{Phase}} \quad [41]$$

$$\mu_2^{0(s)} - \mu_2^0 - RT \ln a_2^{(s)} = +F(\Delta\phi)_{\text{Phase}} \quad [42]$$

where 1 denotes cation and 2 denotes anion. Hence from Eq. [40], [41], and [42] we get

$$\begin{aligned}
 F(\Delta\phi)_I &= -F(t_1 + t_2) (\Delta\phi)_{\text{Phase}} \\
 &- RT(t_1 - t_2) \ln \frac{a^\beta}{a^{(s)}} \quad [43]
 \end{aligned}$$

where we have supposed that

$$\frac{a_1^{(s)}}{a_1^\beta} = \frac{a_1^{(s)}}{a_2^\beta} = \frac{a^{(s)}}{a^\beta} \quad [44]$$

As

$$(t_1 + t_2) = 1$$

and

$$(t_1 - t_2) = \frac{U^+ - U^-}{U^+ + U^-}$$

we get from Eq. [43]

$$(\Delta\phi)_I = -(\Delta\phi)_{\text{Phase}} - \frac{RT}{F} \left(\frac{U^+ - U^-}{U^+ + U^-} \right) \ln \frac{a^\beta}{a^{(s)}} \quad [45]^2$$

The second term on the right side of Eq. [45] denotes the dissolution potential. The crystal dissolves while $a^\beta/a^{(s)} < 1$. When the ratio becomes equal to unity dissolution stops.

Thus $(\Delta\phi)_{\text{Diss}}$ is given by

$$(\Delta\phi)_{\text{Diss}} = -\frac{RT}{F} \left(\frac{U^+ - U^-}{U^+ + U^-} \right) \ln \frac{a^\beta}{a^{(s)}} \quad [46]$$

Thus from Eq. [31], [34], [44], and [45] we find that the observed dissolution potential would be given by

$$(\Delta\phi)_{\text{Observed}} = (\Delta\phi)_{\text{Phase}} + (\Delta\phi)_{\text{Diss}} + (\Delta\phi)_{\text{Diff}} \quad [47]$$

where the first, second, and third terms of Eq. [47] have already been defined by Eq. [41], [42], [46], and [34], respectively.

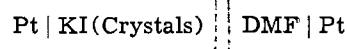
Experimental

Materials

B.D.H. chemicals (AR grade) were used without further purification. The specific conductivity of the DMF used as $1.95 \times 10^{-6} \Omega^{-1} \text{cm}^{-1}$. Platinum electrodes fused in Pyrex glass tubes were welded to copper wire in order to avoid electrical contacts through mercury which might form unsuspected secondary cells. Coaxial cables were used which are unaffected by stray external fields. The platinum electrodes were thoroughly cleaned by boiling in nitric acid and then by heating in a flame before each experiment. The experiments were performed as described earlier (4).

Potentials were recorded with the help of a Lindemann Quadrant Electrometer. All parts of the experimental circuits were properly insulated. In order to avoid electrical disturbances, additional stabilizers were introduced into the circuit of electrometer mains.

Measurement of dissolution potential.—The dissolution potential was measured with the following cell

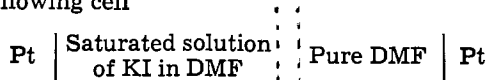


Two bare platinum electrodes were introduced in the dissolution cell containing the solvent and asymmetry potential was recorded between them. It was minimized as far as possible by a proper adjustment of electrical contacts and cleaning of electrodes once

² It should be noted that U^+ and U^- in Eq. [45] are the mobilities of the cations and anions at the crystal interface. However, these would be equivalent to ionic mobilities.

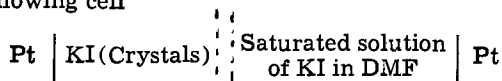
again if necessary. A uniform thick layer of the salt was deposited on one of the electrodes by controlled crystallization from a solution of the salt saturated at 75°C. The electrode loaded with the crystals of the salt was mechanically dipped in the dissolution cell. The potential thus generated was recorded as a function of time. The asymmetry potential was checked once again. The actual dissolution potential was determined by taking the asymmetry potential into account. Dissolution potentials of KI in various dimethylformamide-water compositions and those of KCl in aqueous KCl-HCl solutions were measured.

Measurement of diffusion potential.—The apparent diffusion potential was determined with the help of the following cell



The experimental setup for the measurement of apparent diffusion potential was similar to that of Rastogi and Shukla (4). The buildup and decay of apparent diffusion potential was recorded.

Measurement of phase potential.—The phase potential, which is the potential difference arising from an electrical double layer developed at the liquid-crystal interface as a result of the dynamic equilibrium of ion migration from the crystal phase to the liquid phase and vice versa, was determined with the help of following cell



A uniform thick layer of the salt was deposited on a platinum electrode by controlled crystallization from a saturated solution of the salt at 75°C. The electrode loaded with the crystals was mechanically dipped in a cell filled with the saturated solution of the salt.

The phase potential was measured with reference to the potential of another bare platinum electrode dipping in the above saturated solution. The asymmetry potential existing between the two platinum electrodes was taken into account in order to determine the phase potential. The potential difference was measured electrostatically by means of the electrometer.

Comparison with the experimental data.—Equations [46] and [47] are in general agreement with the available experimental data. These equations predict that (i) the sign of dissolution potential should depend on the sign ($U^+ - U^-$) for an electrolyte, (ii) the magnitude of $(\Delta\phi)_{\text{Diss}}$ should be directly proportional to the magnitude of $\frac{U^+ - U^-}{U^+ + U^-}$,

and (iii) the decay of observed dissolution potential with time should be similar to that observed in case of diffusion potential. The signs of the true dissolution potentials of alkali halides in acetone (4), form-

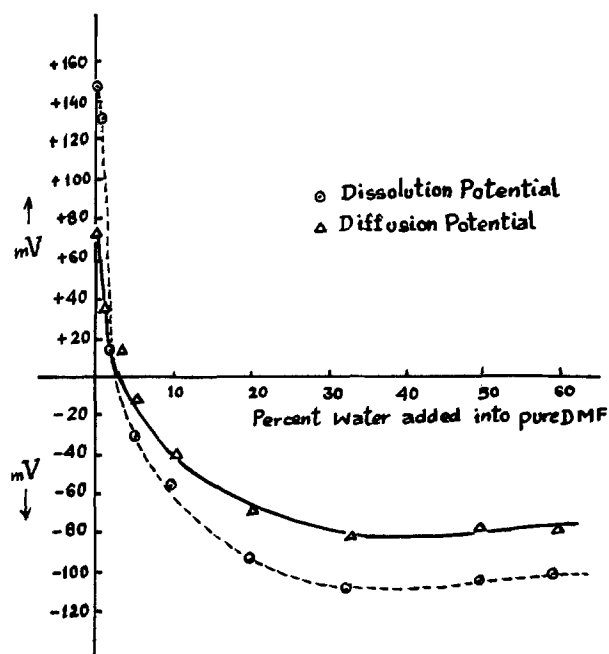


Fig. 2. Dissolution and diffusion potential of KI in DMF + H₂O mixtures.

amide (4), and DMF (13) are in agreement with the first prediction. The experimental data reported by Rastogi, Shukla, and Bhagat (4) are in accord with the second prediction. The decay experiments on dissolution potential made by Rastogi *et al.* (3, 4), Girdhar *et al.* (9, 10), and Vishnu, Khan, and Jahan (13) are in agreement with the third prediction.

The effect of temperature and concentration can also be predicted from Eq. [46]. These effects will be similar to those observed in case of diffusion potential. The experimental results of Rastogi and co-workers, and those of Girdhar and co-workers are once again in agreement with the theory.

The theory developed in the section "Thermodynamic Theory of Dissolution Potential" is also in agreement with the data reported in this communication.

The dissolution potential measured at various DMF-water compositions are given in Table I. The true dissolution potential was calculated from Eq. [47], i.e.

$$\begin{aligned} \text{True dissolution potential} &= \text{observed dissolution potential} \\ &\quad - \text{diffusion potential} \\ &\quad - \text{phase potential} \end{aligned}$$

Results reported in Table I and plotted in Fig. 2 show that the sign of diffusion potential of KI in DMF-water mixtures exactly matches the sign of the dissolution potential of KI in the same solvent medium. From Eq. [34] and [46] we observe that the sign of both the diffusion potential and dissolution potential would depend upon the difference of the mobilities of cations and anions. Hence, according to the theory the sign of diffusion and dissolution potentials should match, and this is confirmed by the experimental data.

Results reported in Table II provide another strong confirmation of the thermodynamic theory of dissolution potential. Experiments on the dissolution potential of KCl in the aqueous KCl-HCl mixtures show that, whereas in pure water the dissolution potential is negative, it assumes positive values when HCl is added. This is understandable since the transport number of Cl⁻ is much greater than that of K⁺ in the system. Accordingly Cl⁻ leaves the lattice much faster, making it positively charged. The diffusion potential and dissolution potential of KCl in

Table I. Dissolution potential of KI in DMF/H₂O mixtures

Medium	Obs. diss. pot. (mV)	Phase pot. (mV)	Diff. pot. (mV)	True Diss. pot. (mV)
Pure DMF	+264 ± 6	+42 ± 3	+75 ± 3	+147 ± 6
DMF + 1% H ₂ O	+196 ± 3	+28 ± 1	+36 ± 1	+132 ± 3
DMF + 2% H ₂ O	+52 ± 3	+12 ± 1	+26 ± 1	+14 ± 3
DMF + 3% H ₂ O	+45 ± 1	+27 ± 1	+15 ± 1	+3 ± 1
DMF + 5% H ₂ O	-58 ± 3	-18 ± 1	-10 ± 1	-30 ± 3
DMF + 10% H ₂ O	-120 ± 3	-27 ± 1	-38 ± 3	-55 ± 6
DMF + 20% H ₂ O	-196 ± 6	-35 ± 1	-68 ± 3	-93 ± 6
DMF + 33% H ₂ O	-222 ± 6	-32 ± 1	-81 ± 3	-109 ± 6
DMF + 50% H ₂ O	-216 ± 6	-48 ± 3	-75 ± 3	-93 ± 6
DMF + 75% H ₂ O	-228 ± 6	-28 ± 1	-84 ± 3	-116 ± 6
DMF + 90% H ₂ O	-210 ± 6	-35 ± 1	-72 ± 3	-103 ± 6
DMF + 99% H ₂ O	-204 ± 6	-42 ± 3	-72 ± 3	-90 ± 6
DMF 0%				
Cond. water pure.	-204 ± 6	-42 ± 3	-69 ± 3	-93 ± 6

Table II. Dissolution potential of KCl-HCl aqueous solutions

Medium	t_{H^+}	t_{K^+}	t_{Cl^-}	Diff. pot. (mV)	Phase pot. (mV)	Obs. diss. pot. (mV)	True diss. (mV)
Cond. H ₂ O	—	0.4906	0.5094	-73 ± 3	-25 ± 1	-197 ± 3	-99 ± 7
0.075M HCl + 0.025M HCl	0.7456	0.0503	0.2041	-131 ± 3	-26 ± 1	-19 ± 1	+138 ± 5
0.05M + 0.05M KCl	0.6198	0.1242	0.2560	-66 ± 3	-26 ± 1	-82 ± 3	+174 ± 7
0.25M HCl + 0.075M KCl	0.4109	0.2477	0.3414	-33 ± 1	-23 ± 1	+92 ± 3	+148 ± 5

the aqueous KCl-HCl mixtures do not have the same sign (Table II), since the former is determined by the transport numbers of H⁺, K⁺, and Cl⁻ ions, and the latter is determined by the transport numbers of K⁺ and Cl⁻ ions only.

Acknowledgment

The authors are extremely grateful to Professor Graham Hills of Southhamton University for helpful comments. S. A. Khan is thankful to U.G.C. for providing financial assistance. He is also thankful to Dr. Y. B. Singh, Principal, St. Andrew's College, Gorakhpur, for providing necessary facilities.

Manuscript submitted Jan. 9, 1980; revised manuscript received March 27, 1980.

Any discussion of this paper will appear in a Discussion Section to be published in the June 1981 JOURNAL. All discussions for the June 1981 Discussion Section should be submitted by Feb. 1, 1981.

REFERENCES

1. R. P. Rastogi, R. K. Dass, and B. P. Batra, *Nature*, **191**, 765 (1961).
2. R. P. Rastogi, R. K. Dass, and B. P. Batra, *Bull. Natl. Inst. Sci. India*, **19**, 231 (1961).

3. R. P. Rastogi and R. D. Shukla, *J. Appl. Phys.*, **41**, 2787 (1970).
4. R. P. Rastogi, R. D. Shukla, and S. Bhagat, *This Journal*, **121**, 1564 (1974).
5. R. P. Rastogi and R. D. Shukla, *Indian J. Chem.*, **6**, 611 (1968).
6. N. Ibl, W. Richarz, and H. Wederkehr, *Z. Phys. Chem.*, **98s**, 123 (1975).
7. N. Ibl *et al.*, "Topics in Pure and Applied Electrochemistry," SAEST (1975).
8. H. L. Girdhar and R. P. Matta, *Electrochim. Acta*, **22**, 373 (1976).
9. H. L. Girdhar and R. P. Matta, *Indian J. Chem.*, **4**, 344 (1977).
10. H. L. Girdhar, S. F. Ahmad, and R. P. Matta, *J. Electroanal. Chem. Interfacial Electrochem.*, **89**, 407 (1978).
11. de Groot, "Thermodynamics of Irreversible Processes," p. 98, North Holland Publishing Company, Amsterdam (1966).
12. Butler, "Electrical Phenomena at Interfaces," p. 15, Methuen and Co. Ltd., London (1951).
13. Vishnu, S. A. Khan and E. Jahan, *Electrochim. Acta*, **24**, 387 (1979).
14. C. W. Davies, "Electrochemistry," p. 96, George Newnes Ltd., London (1967).
15. D. A. MacInnes, "The Principles of Electrochemistry," p. 87, Dover Publications Inc., New York (1961).

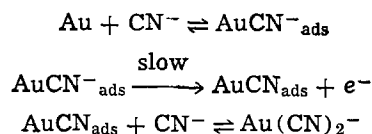
Anodic Dissolution of Gold in Aqueous Alkaline Cyanide Solutions at Low Overpotentials

D. W. Kirk* and F. R. Foulkes*

Department of Chemical Engineering and Applied Chemistry,
University of Toronto, Toronto, Ontario, Canada M5S 1A4

ABSTRACT

Potentiodynamic and potentiostatic methods were used to study the anodic dissolution of gold in aqueous alkaline cyanide at low overpotentials (in the region of -0.65 vs. SCE). The effect of cyanide and hydroxide concentration on the anodic dissolution rate at -0.65 V vs. SCE was determined from weight loss measurements. The variation of the potential sweep profile with sweep rate and stirring rate was determined and Tafel parameters were measured. The steady-state gold dissolution was shown to follow the sequence



in which the second step is the rate-determining step. Measurements at sweep rates > 20 mV · sec⁻¹ revealed various aspects of the reaction sequence which helped to reconcile conflicting statements found in the literature regarding the reaction mechanism.

Although the alkaline cyanide medium has been used extensively for the processing of gold, the basic electrochemical reactions of gold in this medium are not yet fully understood. In particular some confusion still exists concerning the anodic dissolution process at

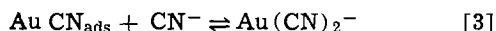
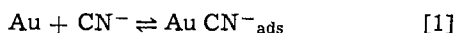
low overpotentials. In an earlier paper (1) the anodic dissolution of gold in aqueous alkaline cyanide was studied for a wide potential range (-0.9 to $+0.8$ V¹). Three current peaks found in potential sweep measurements were shown to be the result of a gold dis-

* Electrochemical Society Active Member.
Key words: anode, dissolution, kinetics, metals.

¹ All potentials are reported vs. the saturated calomel electrode.

solution process. The electron stoichiometry of the reaction in each of the regions was identified and indicated that $n = 0.85, 0.95,$ and 1.05 for peaks 1 (-0.9 to $-0.6V$), 2 (-0.1 to $+0.15V$), and 3 ($+0.2$ to $+0.38V$), respectively. Later it was shown (2) that when competing chemical dissolution was taken into account, the n values became 1 for each of the three peaks.

A single reaction scheme



was shown to account for the reaction at the three peaks. The rate-determining steps for the dissolution process in the regions of peak 2 and peak 3 were identified. There is general agreement (1, 3-5) that the dissolution of gold in the region of peak 1 proceeds via the reaction sequence [1], [2], and [3], although in two cases (3, 4) the steps [1] and [2] have been combined. However, these studies do not all predict the same rate-determining step, hence the limiting step is still uncertain for the peak 1 region. MacArthur (3) used cyclic voltammetry and galvanostatic transients to study the process and concluded that step [3] was the rate-determining step. Cathro and Koch (4) used potentiostatic and galvanostatic methods and reported that



was the rate-determining step. Eisenmann (5), using steady-state and relaxation methods with a rotating disk electrode, reported that step [2] was the rate-determining step. As a result of the discrepancies in the reported rate-determining step it was apparent that additional data were needed to clarify the dissolution process in the peak 1 region.

Experimental Methods

Solutions, prepared from analytical grade reagents and doubly distilled water were deoxygenated by bubbling with oxygen-free nitrogen gas for at least 30 min before an experiment. In experiments for which no stirring rate is reported the nitrogen gas was passed over the electrolyte during the measurements. Gold foil electrodes ($>99.99\%$ purity) were used for both the working and counterelectrodes. The reference electrode was a saturated calomel electrode. A Luggin capillary, housing the reference electrode, was positioned with the 0.1 cm diam capillary tip located 0.17 cm from the electrode. This configuration has been shown to distort the current density at the point of measurement by less than 1% (6-8). Because the maximum IR -drop for peak 1 was only 0.3 mV, the data were not corrected for IR -drop. Details of the cell and electronic equipment have been given in Ref. (1). Gold dissolution rates were determined from weight losses and electrode surface areas. Each experimental run was continued for a sufficient time to allow a minimum weight loss of 200 μg , which was measured using a semimicro balance with an accuracy of $\pm 10 \mu\text{g}$. The longest run was 2 hr. The surface area of the electrode was determined from potential scan measurements, using the linear relation between the current peak and the square root of the voltage scan rate for the oxidation of $\text{Fe}(\text{CN})_6^{4-}$. This relationship has been given by Nicholson and Shain (9). A standard electrode pretreatment was necessary to achieve reproducibility. The electrode was first heated to redness in air, then etched for 10 sec in hot aqua regia, washed in doubly distilled water, dried, and weighed. It was immediately given a further treatment consisting of a 5 min reduction period in the electrolyte at $-1.2V$. This latter pretreatment was found to improve the reproducibility of the potentiodynamic measurements but did not affect the measured

weight of the electrode. At the end of an experiment, the electrode was thoroughly washed in doubly distilled water, dried, and weighed.

Results and Discussion

The effect of cyanide and hydroxide concentration on the dissolution rate for the reaction at peak 1 was studied using six levels of cyanide and three levels of hydroxide. The results shown in Fig. 1 demonstrate that, for low cyanide concentrations ($<0.2M$), the dissolution rate is linear with cyanide concentration, and that the dissolution rate decreases with increasing hydroxide concentration.

The potential sweep rate dependence of the reaction at peak 1 is shown in Fig. 2. The peak current decreases with an increase in sweep rate, (v), and at sweep rates faster than $2 \text{ mV}\cdot\text{sec}^{-1}$, a new peak (1a) appears. This new peak begins to dominate for sweep rates $\geq 10 \text{ mV}\cdot\text{sec}^{-1}$. Therefore, two different peaks, and possibly two different mechanisms, may be studied, depending on the range of sweep rate employed. Indeed, the Tafel slope for sweep rates of 0.5 and $1.0 \text{ mV}\cdot\text{sec}^{-1}$ (peak 1) was found to be $0.12 \pm 0.01 \text{ V/decade}$, while at $20 \text{ mV}\cdot\text{sec}^{-1}$, Tafel slopes of $0.36 \pm 0.01 \text{ V/decade}$ for peak 1 and $0.06 \pm 0.01 \text{ V/decade}$

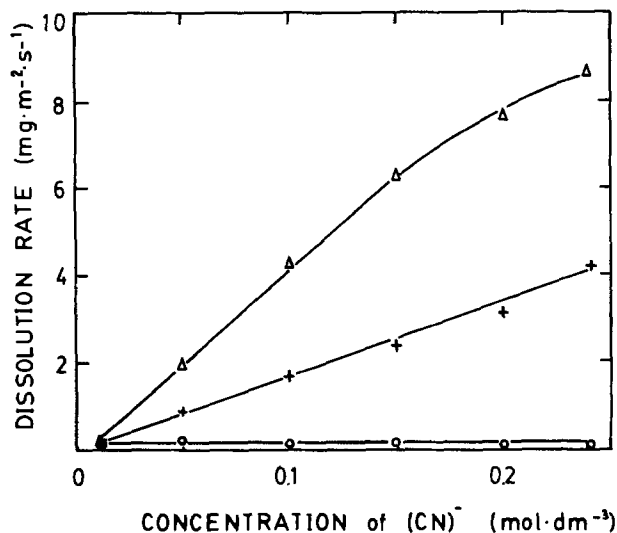


Fig. 1. Dependence of dissolution rate on free-cyanide and hydroxide concentration for peak 1 ($-0.65V$ vs. SCE); \circ , $1.0M$ KOH; $+$, $0.1M$ KOH; Δ , $0.01M$ KOH; temperature = 23.5°C .

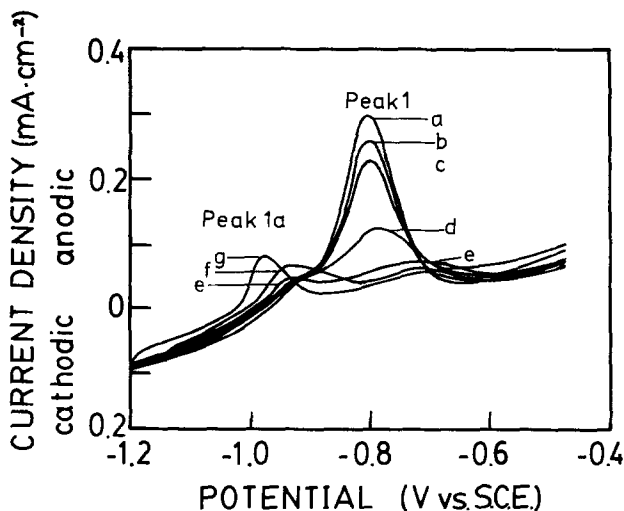


Fig. 2. Dependence of anodic single sweep profile on sweep rate for the region of peak 1: $1.0M$ KOH + $0.1M$ KCN; a) $v = 0.1 \text{ mV}\cdot\text{sec}^{-1}$; b) $v = 0.2 \text{ mV}\cdot\text{sec}^{-1}$; c) $v = 0.5 \text{ mV}\cdot\text{sec}^{-1}$; d) $v = 1.0 \text{ mV}\cdot\text{sec}^{-1}$; e) $v = 2.0 \text{ mV}\cdot\text{sec}^{-1}$; f) $v = 10 \text{ mV}\cdot\text{sec}^{-1}$; g) $v = 100 \text{ mV}\cdot\text{sec}^{-1}$; temperature = 23.3°C .

for peak 1a were measured. At $100 \text{ mV} \cdot \text{sec}^{-1}$ no Tafel region was found. Some caution must be exercised in interpreting Tafel data from potential sweep measurements since the Tafel equation applies to steady-state conditions. The measurements for the slow sweep rates of 0.5 and $1.0 \text{ mV} \cdot \text{sec}^{-1}$ safely can be assumed to be at steady state since the slope was unchanged for either sweep rate. While the steady-state condition may not strictly apply to the measurements at $20 \text{ mV} \cdot \text{sec}^{-1}$, it appears that the Tafel slope parameter increases with sweep rate. The Tafel slope for peak 1a at $20 \text{ mV} \cdot \text{sec}^{-1}$ would be valid if the reaction for this peak is sufficiently rapid to achieve steady-state conditions during the potential sweep. Typical sets of data for these measurements are shown in Fig. 3. Since measurements taken using different potential sweep rates yield different Tafel parameters, some of the discrepancy found in the literature for the rate-determining step for the initial cyanidation reaction may be understood.

Cathro and Koch (4) reported a Tafel slope of 0.13 V/decade for peak 1 from steady-state measurements. More recent measurements by Eisenmann (5) using steady-state current potential measurements with a rotating gold disk electrode in $0.1\text{M KCN} + 0.01\text{M KOH}$ electrolyte can be shown to yield a Tafel value of 0.11 V/decade . Both these values compare favorably with the measured Tafel slope of $0.12 \pm 0.01 \text{ V/decade}$ obtained in this work for the slow sweep measurements.

MacArthur (3), who used potential sweep measurements with sweep rates greater than $40 \text{ mV} \cdot \text{sec}^{-1}$, reported a rate-determining step (step 3) which would theoretically yield a Tafel value of 0.059 V/decade .² This value is within the experimental limits for that found for peak 1a in this work ($0.06 \pm 0.01 \text{ V/decade}$) for sweep rates of $20 \text{ mV} \cdot \text{sec}^{-1}$.

The reaction scheme [1], [2], [3] presented earlier can account for the reaction at peak 1 since, for steady-state measurements (or very slow scan measurements), step [2] has a theoretical Tafel value of 0.12 V/decade .² In addition, step [2] theoretically should show a linear dependence on cyanide concentration for low cyanide concentration, and the rate of dissolution should decrease with increase in hydroxide concentration (1). This behavior is observed for the steady-state dissolution reaction in the region of peak 1, as shown in Fig. 1.

Since step [2] does not directly involve the reaction with the cyanide in the solution, stirring rate would be expected to have little effect. At a sweep rate of $1 \text{ mV} \cdot \text{sec}^{-1}$ no stirring rate dependence is found for peak 1 (see Fig. 4a). Therefore, although the rate-

² See Appendix for derivation of theoretical Tafel slopes.

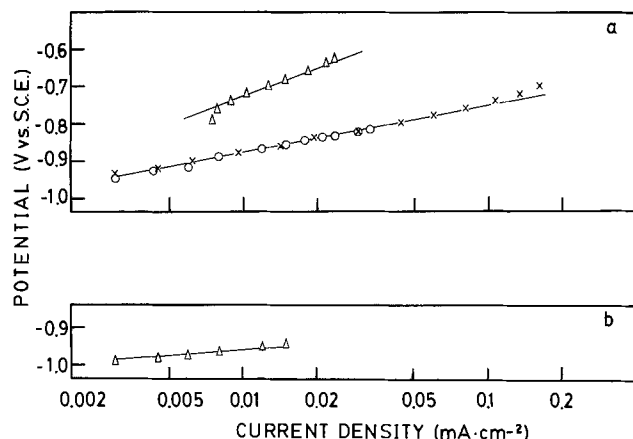


Fig. 3. Typical data for Tafel slopes in the potential region -1.2 to -0.6 V at various sweep rates (temperature = 23.5°C , electrolyte $0.1\text{M KOH} + 0.1\text{M KCN}$). a) Peak 1: \circ — $0.5 \text{ mV} \cdot \text{sec}^{-1}$; \times — $1.0 \text{ mV} \cdot \text{sec}^{-1}$; \triangle — $20 \text{ mV} \cdot \text{sec}^{-1}$. b) Peak 1a: \triangle — $20 \text{ mV} \cdot \text{sec}^{-1}$.

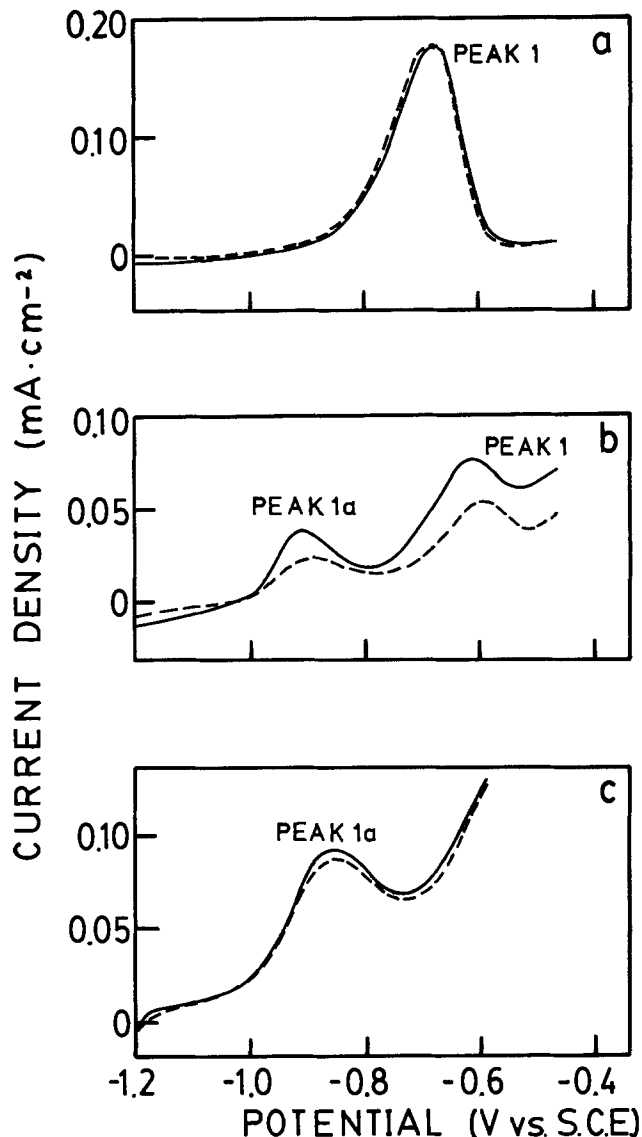
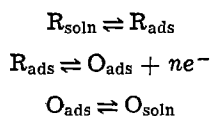


Fig. 4. Effect of stirring on the reaction in the region of peak 1: electrolyte $0.1\text{M KOH} + 0.1\text{M KCN}$, temperature = 23.5°C . a) $v = 1.0 \text{ mV} \cdot \text{sec}^{-1}$; b) $v = 20 \text{ mV} \cdot \text{sec}^{-1}$; c) $v = 100 \text{ mV} \cdot \text{sec}^{-1}$. — electrolyte well stirred; - - - electrolyte unstirred.

determining step [4] proposed by Cathro and Koch correctly predicts the measured Tafel slope, the reaction does not account for the lack of dependence on the stirring rate. Thus the complete reaction sequence [1], [2], and [3], in which the adsorption of the cyanide species is considered, is necessary to model the dissolution process. The Tafel slope and the lack of stirring-rate dependence show that step [2] is the rate-determining step. This rate-determining step is in agreement with that proposed by Eisenmann (5) who had also used steady-state measurements. The variation of the potential sweep profile with sweep rate can yield information about the reaction mechanism. The decrease in the height of peak 1 with increase in sweep rate (Fig. 2) indicates that the reaction rate of the rate-determining step (step 2) is slow relative to these sweep rates. Therefore, the extent of reaction 2 is decreased by increase in sweep rate. As the extent of this reaction is decreased, the previous stage (step 1) should become important. Thus the measured Tafel parameter for peak 1 is larger at $20 \text{ mV} \cdot \text{sec}^{-1}$ and reflects the contribution of step [1] which has a theoretical Tafel slope of ∞ . In addition, stirring rate would affect step [1]; therefore stirring rate should start to influence peak 1 at the faster sweep rates, as observed in Fig. 4b.

In contrast, the behavior of peak 1a shows that as the sweep rate increases the peak current also increases. This behavior is typical for fast electrochemical reactions such as adsorption reactions (10, 11). For a kinetically fast adsorption process the amount of charge passed during a single potential sweep remains constant regardless of sweep rate and therefore as the measurement time is decreased the peak size is correspondingly increased. Although the analysis of reactions where both adsorption and diffusion are important is difficult, it has been shown that when adsorption of either the products or reactants of a reaction occurs, then linear scan voltammetry can give rise to the formation of pre-peaks or post-peaks. This type of phenomenon has been discussed by several workers (12-14). Although the exact behavior of the adsorption peak depends on the type of adsorption and the free energy of the bonding process, the effect of strong adsorption of the product of the reaction most closely resembles peak 1a behavior. For the reaction sequence (12) given below the effect of sweep rate on the potential profile for the case of strong product adsorption is shown in Fig. 5



where O is the oxidized species and R is the reduced species.

This is the behavior of peak 1a shown in Fig. 2. Since peak 1a begins to dominate the potential sweep profile for sweep rates greater than $20 \text{ mV}\cdot\text{sec}^{-1}$ and since peak 1a appears to be related to the adsorption of the product of the reaction [1], [2], and [3], one would expect the final step in the reaction (step [3]) and the subsequent diffusion of the product to characterize the reaction process at these sweep rates.

It is evident therefore that electrochemical measurements taken at sweep rates above $20 \text{ mV}/\text{sec}$ might reflect the desorption of the $\text{Au}(\text{CN})_2^-$ species from the electrode surface. The Tafel parameter measured in this work for peak 1a at $20 \text{ mV}\cdot\text{sec}^{-1}$ was $0.06 \text{ V}/\text{decade}$ and corresponds to the theoretical value of $0.059 \text{ V}/\text{decade}$ for step [3]. This is in agreement with the rate-determining step reported by MacArthur who used potentiodynamic methods with sweep rates greater than $40 \text{ mV}/\text{sec}$. Step [3] theoretically should show a dependence on stirring rate (1) as would the desorption of the product. In Fig. 4 at $20 \text{ mV}\cdot\text{sec}^{-1}$ it can be seen that stirring rate does increase the peak 1a size. However, at $100 \text{ mV}\cdot\text{sec}^{-1}$, little or no stirring rate dependence is found. This is probably the consequence of insufficient transfer of reactants or products through the boundary layer to be influenced by bulk stirring, at this sweep rate. Thus the behavior of gold in aqueous alkaline cyanide at low overpotentials

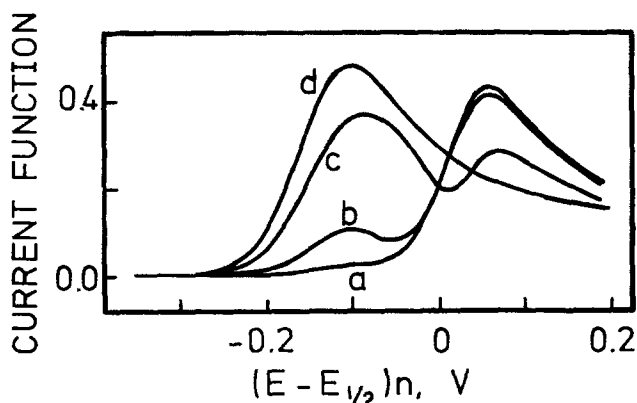


Fig. 5. Theoretical variation of potential sweep profile with sweep rate for product strongly adsorbed. From Ref. (9). Relative scan rates: a, 1; b, 25; c, 625; d, 2500.

is consistent with the reaction scheme [1], [2], and [3] with step [2] limiting the steady-state dissolution rate. Potentiodynamic measurements at sweep rates of $20 \text{ mV}\cdot\text{sec}^{-1}$ reflect effects attributable to the slow kinetics of step [2]. Therefore it appears that some of the discrepancy found in the literature for the reported rate-determining step is a result of the different measurement techniques. The slow scan or steady-state methods show that the rate of dissolution is controlled by step [2]. At sweep rates greater than $20 \text{ mV}\cdot\text{sec}^{-1}$ the potential sweep profile measurements suggest that the adsorption of the product of the reaction dominates the measurements.

Conclusions

1. The dissolution rate of gold in aqueous alkaline cyanide was found to increase linearly with increase in cyanide concentration ($< 0.20 \text{ M}$) and decrease in hydroxide concentration at low overpotentials (-0.65 V vs. SCE).

2. Tafel parameters from slow potential sweep measurements ($\leq 1.0 \text{ mV}\cdot\text{sec}^{-1}$) and the lack of variation of the potential sweep profile with stirring rate demonstrate that step [2] is the rate-determining step for the anodic steady-state dissolution of gold at low overpotentials.

3. The formation of peak 1a at sweep rates $\geq 20 \text{ mV}\cdot\text{sec}^{-1}$ appears to be the result of product adsorption. The potentiodynamic behavior of peak 1a, the measured Tafel parameter at $20 \text{ mV}\cdot\text{sec}^{-1}$, and the stirring rate dependence indicate that step [3] dominates the process at these sweep rates. This agrees with the rate-determining step reported by MacArthur for fast ($> 40 \text{ mV}\cdot\text{sec}^{-1}$) potential sweep measurements.

4. The variation in the reported rate-determining step for the anodic dissolution of gold resulted in one study (4) because the adsorption and electrochemical charge transfer steps were combined, and, although the combined step correctly predicted the observed Tafel parameter, it did not predict the observed lack of stirring rate dependence of the potential sweep profile. In the other study (3), measurements taken at sweep rates $> 20 \text{ mV}\cdot\text{sec}^{-1}$ reflected the limitations of the kinetics of the reaction process under those conditions but do not necessarily apply to the steady-state process.

Acknowledgment

Financial assistance from National Research Council of Canada is gratefully acknowledged.

Manuscript submitted June 15, 1979; revised manuscript received Oct. 29, 1979.

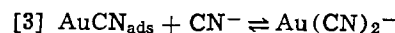
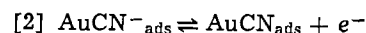
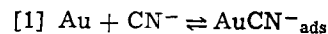
Any discussion of this paper will appear in a Discussion Section to be published in the June 1981 JOURNAL. All discussions for the June 1981 Discussion Section should be submitted by Feb. 1, 1981.

Publication costs of this article were assisted by the University of Toronto.

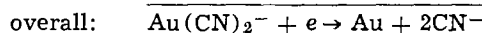
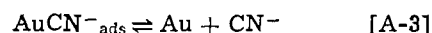
APPENDIX

Tafel Parameters

Reaction scheme: Anodic



Cathodic:



Using $\alpha_{\text{anodic}} = n - \gamma/\nu - r\beta'$ derived by Bockris (15)

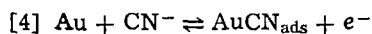
from the generalized Butler-Volmer equation for the cathodic reaction, the following is obtained

rds	n	γ	ν	τ	β'	α_B	b_A
[A-1]	1	0	1	0	—	1	0.059
[A-2]	1	0	1	1	0.5	0.5	0.118
[A-3]	1	1	1	0	—	0	∞

where n = number of electrons transformed per unit act of the overall reaction, γ = number of electrons transferred before the rate-determining step, ν = number of times the rate-determining step occurs per unit act of the overall reaction, $\tau = 1$ for a rate-determining step with an electron transfer and $= 0$ for a rate-determining step without an electron transfer, β' = symmetry factor (usually assumed to be ≈ 0.5) for the rate-determining step, α_A = anodic transfer coefficient, and b_A = Tarel slope for anodic reaction.

From the table, if [A-1] is rds, $b = \infty$ V/decade; if [A-2] is rds, $b = 0.118$ V/decade; if [A-3] is rds, $b = 0.059$ V/decade.

For the mechanism presented by MacArthur and Cathro and Koch



Following the same procedure as above, if [4] is rds, then $b = 0.118$ V/decade; if [3] is rds, then $b = 0.059$ V/decade.

LIST OF SYMBOLS

A	surface area of electrode cm^2
C_o^+	concentration of oxidized species in bulk of solution ($\text{moles} \cdot \text{cm}^{-3}$)
D_o	diffusion coefficient of oxidized species ($\text{cm}^2 \cdot \text{sec}^{-1}$)
D_R	diffusion coefficient of reduced species ($\text{cm}^2 \cdot \text{sec}^{-1}$)
E	potential (V)

$E_{1/2}$	polarographic half-wave potential (V)
F	Faraday
$i(t)$	instantaneous current (A)
n	number of electrons involved in overall reaction
R	universal gas constant
t	time, sec
T	temperature ($^\circ\text{K}$)
v	sweep rate ($\text{V} \cdot \text{sec}^{-1}$)

$$\text{current function} = \frac{i(t)}{nFA C_o^+ \sqrt{D_o n F V / RT}}$$

REFERENCES

- D. W. Kirk, F. R. Foulkes, and W. F. Graydon, *This Journal*, **125**, 1436 (1978).
- D. W. Kirk, F. R. Foulkes, and W. F. Graydon, *ibid.*, **127** (1980).
- D. M. MacArthur, *ibid.*, **119**, 672 (1972).
- K. J. Cathro and D. F. A. Koch, *ibid.*, **111**, 1416 (1964).
- E. T. Eisenmann, *ibid.*, **125**, 717 (1978).
- E. Gileadi, E. Kirowa-Eisner, and T. Penciner, "Interfacial Electrochemistry," p. 210, Addison-Wesley Publ., Reading, Mass. (1975).
- S. Barnartt, *This Journal*, **99**, 549 (1952).
- S. Barnartt, *ibid.*, **108**, 102 (1961).
- R. S. Nicholson and I. Shain, *Anal. Chem.*, **36**, 706 (1964).
- S. Srinivasan and E. Gileadi, *Electrochim. Acta*, **11**, 321 (1966).
- H. Angenstein-Kozłowska, J. Klinger, and B. E. Conway, *J. Electroanal. Chem. Interfacial Electrochem.*, **75**, 45 (1977); *ibid.*, **75**, 61 (1977).
- R. H. Wopschall and I. Shain, *Anal. Chem.*, **39**, 1514 (1967).
- M. Sluyters-Rehbach and J. H. Sluyters, *J. Electroanal. Chem. Interfacial Electrochem.*, **65**, 831 (1975).
- R. Guidelli and F. Pergola, *ibid.*, **84**, 225 (1977).
- J. O'M. Bockris and A. K. N. Reddy, "Modern Electrochemistry," Vol. 2, pp. 1004-1008, Plenum Press, New York (1970).

The Influence of Water on the Ni(II)/Ni(Hg) Electrode Process in Molten LiNO_3 - KNO_3 Eutectic

David G. Lovering* and Richard M. Oblath¹

Chemistry and Metallurgy Department, Royal Military College of Science, Shrivvenham, Swindon SN6 8LA, England

ABSTRACT

D-C, pulse, differential pulse, and linear sweep polarographic methods have been used to characterize the Ni(II)/Ni(Hg) reduction as a function of water content in the LiNO_3 - KNO_3 eutectic melt at 145°C . For very small concentrations of water added to the anhydrous melt, anodic shifts were observed in the Ni(II) polarographic wave. This was accompanied by changes in the kinetic shape parameter, αn_a . At higher water concentrations cathodic shifts occurred in the half-wave potentials and the waves became irreversible. These effects are attributed to dramatic changes in the coordination of the Ni(II) ion, especially the initial cleavage of the bidentate nitrate rings, rather than to adsorption of water molecules at the interface or catalytic acceleration of the reduction.

The interaction of water with molten salts is of interest and importance for both technological (1) and theoretical reasons. Surprisingly, the electroactivity of water itself, dissolved in nitrate melts is still not fully comprehended (2), in spite of a number of studies spanning more than twenty years (3-9). Few investi-

gations (10-17) have been carried out in the experimentally difficult regime between aqueous melts and anhydrous molten salts; of these, only a small number have been concerned with the influence of water, per se, on electrode processes in nitrate melts.

Polarographic methods are suitable for monitoring electrode processes in aqueous melts (12) and low melting nitrate eutectics (18). In this investigation, the effect of small, controlled additions of water on the Ni(II)/Ni(Hg) electroreduction in anhydrous mol-

* Electrochemical Society Active Member.

¹ Present address: Goodyear International Tire Technical Centre, COLMAR-BERG, Luxembourg.

Key words: fused salts, water, polarography, reduction.

ten $\text{LiNO}_3\text{-KNO}_3$ at 145°C during the initial hydration stages has been studied. The small, highly polarizing Ni(II) ion is particularly sensitive to the water content of the medium, both in aqueous (19) as well as molten systems (10, 13), being wholly irreversibly reduced in the former, but apparently completely reversibly reduced in anhydrous nitrate melts (10, 18). In $\text{Ca(NO}_3)_2 \cdot 4\text{H}_2\text{O} + 46$ mole percent (m/o) KNO_3 , $\text{LiNO}_3 \cdot 3\text{H}_2\text{O}$, and $\text{Ca(NO}_3)_2 \cdot 4\text{D}_2\text{O}$ aqueous melts the reduction is also substantially irreversible, while in $\text{CaCl}_2 \cdot 6\text{H}_2\text{O}$ and $\text{MgCl}_2 \cdot 6\text{H}_2\text{O}$ it appears to be reversible (13). Furthermore, both diffusion data (18) and spectroscopic measurements (20-22) indicate that Ni(II) ions are complexed by nitrate ions in anhydrous nitrate melts; these species are reduced at half-wave potentials, $E_{1/2}$, close to the theoretical standard electrode potential (10, 18, 23) unlike the behavior of hexaquo-nickelate(II) complexes which predominate in aqueous environments (19). Moreover, coordinating aquo-ligands are not significantly displaced until the water content is reduced well beyond that in aqueous melts (13). In contrast, considerable cathodic $E_{1/2}$ shifts can be observed (13) when a solution of Cd(II) ions in $\text{Ca(NO}_3)_2 \cdot 4\text{H}_2\text{O} + 56$ m/o KNO_3 is titrated with water, indicating that nitrate-water substitution reactions are still occurring for the Cd(II) ion within this concentration regime.

The surprising effects observed in this work for the Ni(II)/Ni(Hg) reaction upon addition of water to the melt precluded the calculation of aquo-nickelate(II) stability constants, since unusual shifts in $E_{1/2}$ occurred. In order to explain certain aspects of the present results, the Pb(II)/Pb(Hg) and Tl(I)/Tl(Hg) electroreductions were also monitored under similar conditions.

Experimental

The experimental equipment and procedures have been described in detail elsewhere (24). Pyrex glass cells incorporating electrodes, gas inlet/outlet, and entry facilities either attached to sliding glass tubes through a Pyrex cell head or passing directly through a p.t.f.e. cell head via "O"-ring seals were used. The assembly was thermostatted in an heated aluminum block to $\pm 0.1^\circ\text{C}$; visual observation and magnetic stirring facilities were provided.

Two straight-sided Pyrex dropping mercury electrodes, DME's, having m.t. products of 9.17 mg and 4.80 mg and a Radiometer hanging mercury drop electrode, HMDE, Type 958B at a fixed area of 0.0235 cm^2 were employed throughout. Mercury pool counter-electrodes and Ag/Ag(I) in melt asbestos wick, reference electrodes were used.

All equipment and materials were stored, assembled, and/or handled in the dry box prior to experimental work. Salts were of analytical grade from B.D.H. and (LiNO_3) Alfa Ventron, with the exception of the anhydrous $\text{Ni(NO}_3)_2$ prepared from N_2O_5 and kindly supplied by B. O. Field, City University. Mercury was of "polarographic grade" from Belgrave (Mercury) Limited, dried and used only once.

Water contents $> 1.8 \times 10^{-1}\text{m}$ were introduced directly into the sealed cell via a neoprene septum and microlitre syringe. Equilibration with known water vapor pressures monitored by M.K.S. Baratron equipment was employed for lower water concentrations. Henry's law was adopted for calculating the precise concentration of water dissolved in the melt (24).

A PAR 174A polarographic analyzer, with 174/170 drop timer, 175 programmer, Bryans xy/t 25000 chart recorder, and Datalab DL 905 transient recorder were utilized for monitoring d.c., normal pulse, differential pulse, and fast linear sweep polarograms.

Results

D-C polarograms for Ni(II) , Pb(II) , and Ti(I) at low concentrations, were regular sigmoidal-shaped when corrected for residual current, in the anhydrous

$\text{LiNO}_3\text{-KNO}_3$ melt (24). Plots according to the Heyrovsky-Ilkovic equation, H.I.E., were linear, having $E_{1/2}$ intercepts of -560 mV, -652 mV, and -816 mV vs. Ag/Ag(I) , 10^{-3}m reference electrode, and slopes of 45.4, 42.8, and 83.0 mV, respectively. Diffusion coefficients, D , calculated through the Ilkovic equation [see Ref. (12) and (18) for discussion of applicability] from limiting currents were $2.25 \times 10^{-7} \text{cm}^2 \text{sec}^{-1}$, $9.3 \times 10^{-7} \text{cm}^2 \text{sec}^{-1}$, and $8.3 \times 10^{-7} \text{cm}^2 \text{sec}^{-1}$, respectively. In some cases $E_{1/2}$ values and slopes, and, in each case, D values may be compared with tabulated values from the literature for similar melts (18, 24); no new or major departures from previous determinations are evident.

Interestingly, this most recent and precise evaluation of the H.I.E. slope leads to a value of $\alpha n_a = 1.83$ for the Ni(II)/Ni(Hg) reaction, i.e., the process is less than wholly reversible in the classical sense, when determined in this pseudo-steady state manner. This is in agreement with the evidence of a square-wave polarographic study (25), but not other workers (10, 18, 23). In the former case (25), wave asymmetry was ascribed to traces of water (vide infra), although large amounts of KCl were also present in the melt. In another case (18), polarograms were constructed from true, point-by-point, steady-state measurements.

Normal pulse and differential pulse polarograms, (d.p.p.'s), for the Ni(II) reduction were also of regular shape (24); values for $E_{1/2}$ and D were coincident with d-c polarographic determinations. Wave analysis for normal pulse polarograms indicated $\alpha n_a = 1.86$. The peak potential of d.p.p.'s was -555 mV vs. Ref. [$\equiv -557.5$ mV for $E_{1/2}$ (26)] and their half-peak width was 82.5 mV compared with a theoretical value (27) of 63.4 mV for a totally reversible process; pulse amplitudes were 5 mV.

Typical linear sweep voltammograms for the nickel ion reduction at the HMDE are shown in Fig. 1(a); peak currents, i_p , were a linear function of Ni(II) concentrations ($0.4\text{-}2.8 \times 10^{-3}\text{m}$) for sweep rates, ν , between 0.1 to 10V sec^{-1} . Curvature in the i_p vs. $\nu^{1/2}$ plots, shown in Fig. 1(b), confirms the Ni(II)/Ni(Hg) electroreduction as "quasi-reversible" (28-29). Differences between the peak potential, E_p , and half-peak potential, $E_{p/2}$ are tabulated in Table I for various sweep rates and enable the values of αn_a to be evaluated according to (29, 30)

$$E_p - E_{p/2} = -1.857 \frac{RT}{\alpha n_a F}$$

Values for the ratio $\Delta E_p / \Delta \log \nu$, determined between sweep rates in the range $0.1\text{-}10 \text{V sec}^{-1}$, were ~ -13 compared with $-30/n$ for a classically irreversible process (29).

When very small amounts of water were added to the melt, the d-c polarograms were initially shifted in the anodic direction. As the water content was raised above $\sim 5 \times 10^{-3}\text{m}$ this shift reverted to the cath-

Table I. Typical values of peak potential (E_p) and half-peak potential ($E_{p/2}$), vs. Ag/Ag(I) 10^{-3}m reference electrode, for the Ni(II)/Ni(Hg) reduction in anhydrous $\text{LiNO}_3\text{-KNO}_3$ eutectic at 145°C , obtained from linear sweep voltammetry at a hanging mercury drop electrode (surface area of drop = 0.0235cm^2), at various potential sweep rates (ν)

ν , Vsec^{-1}	E_p , mV	$E_{p/2}$, mV	$E_p - E_{p/2}$, mV	Apparent αn_a
10	-604	-555	-49	1.36
5	-600	-552	-48	1.38
1	-591	-545	-46	1.45
0.5	-587	-542	-45	1.48
0.1	-579	-536	-43	1.56

αn_a was determined from

$$E_p - E_{p/2} = -1.857 \frac{RT}{\alpha n_a F} \quad (29, 30)$$

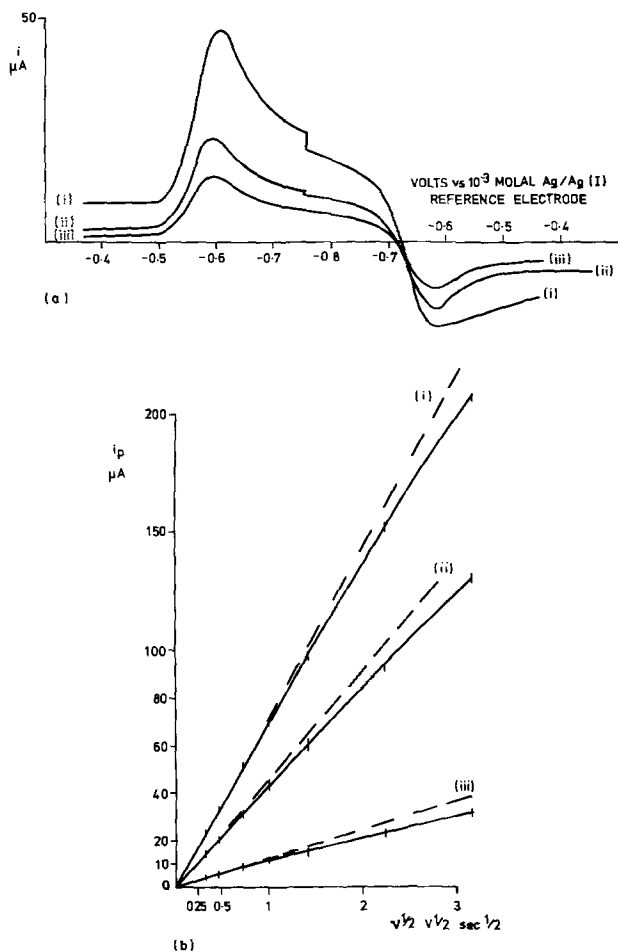


Fig. 1. (a) Typical linear sweep polarograms for the Ni(II)/Ni(Hg) reduction in LiNO₃-KNO₃ eutectic melt at 145°C, at the hmde (area = 0.0235 cm²) for sweep rates: (i) 5 V sec⁻¹ (ii) 1 V sec⁻¹. (b) *i_p* vs. *v*^{1/2} for linear sweep polarograms at (a), except larger range of data points for sweep rate and concentrations of Ni(II): (i) 2.8 × 10⁻³m (ii) 1.72 × 10⁻³m (iii) 0.45m, with linear extrapolation shown as broken line.

odic direction, i.e., that normally expected on the basis of the formation of more stable aquo complexes. Figure 2 shows the relevant d-c polarograms; corresponding *E*_{1/2} shifts, wave shapes, and mean diffusion coefficients are given in Table II. Notably, the value of *αn_a* increases sharply from 1.83 to the totally reversible value of 2.0 at a water content of 4.5 × 10⁻³m before falling again to only 1.35 at 3.36m H₂O, i.e., approaching the totally irreversible behavior familiar in non-

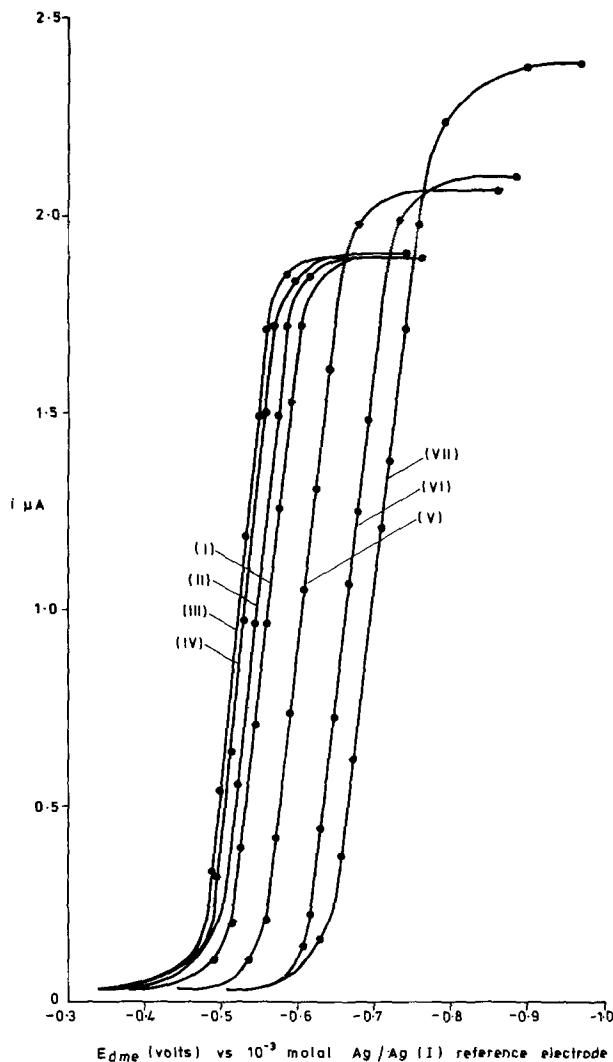


Fig. 2. Effect of water additions on the d-c polarograms for the Ni(II)/Ni(Hg) reduction in LiNO₃-KNO₃ eutectic melt at 145°C: Ni(II) concentration 8.35 × 10⁻⁴m, water concentration, molal (i) 0, (ii) 2.25 × 10⁻³, (iii) 4.5 × 10⁻³, (iv) 1.8 × 10⁻², (v) 0.89, (vi) 1.74, (vii) 3.36. Capillary m.t. product = 4.80 mg.

Table II. D-C polarographic data for the Ni(II)/Ni(Hg) reduction in LiNO₃-KNO₃ eutectic at 145°C containing 8.35 × 10⁻⁴m Ni²⁺ (concentration in anhydrous melts)

Conc. H ₂ O, m	<i>E</i> _{1/2} , mV vs. Ag(I) 10 ⁻³ m	Δ <i>E</i> _{1/2} , mV	<i>αn_a</i>	<i>i</i> _{max} , μA	<i>D</i> , cm ² sec ⁻¹ × 10 ⁶
0	-560	—	1.83	1.86	0.22 (5)
2.25 × 10 ⁻³	-540	+20	1.91	1.86	0.22 (5)
4.5 × 10 ⁻³	-521	+39	2.0	1.86	0.22 (5)
9.0 × 10 ⁻³	-525	+35	2.0	1.87	0.22 (6)
1.8 × 10 ⁻²	-530	+30	1.96	1.87	0.22 (6)
2.7 × 10 ⁻²	-533	+27	1.92	1.88	0.22 (7)
0.45	-576	-16	1.79	1.94	0.25 (4)
0.89	-609	-49	1.71	2.03	0.28 (6)
1.32	-640	-80	1.65	2.04	0.30
1.74	-668	-108	1.60	2.06 (5)	0.31 (7)
2.16	-686	-126	1.52	2.13	0.34 (8)
2.57	-695	-135	1.46	2.25	0.40 (1)
2.97	-704	-144	1.40	2.31	0.43 (1)
3.36	-709	-149	1.35	2.34	0.45 (6)

The values for the half-wave potentials (*E*_{1/2}) and *αn_a* were obtained from Heyrovsky-Ikovic equation plots.

complexing aqueous media (19). Plots of the Ni(II) reduction half-wave potential as a function of water concentration are shown in Fig. 3; the gap in data collection between ~ 3 × 10⁻²m to ~ 4 × 10⁻¹m H₂O corresponds to the changeover in method of introducing water into the cell, although the inset and main figure suggest that this is not a region of crucial importance in this case. Virtually coincident plots result from the pulse polarographic data (24).

In order to further assess the kinetic effect of water additions on the electrode process suggested by the d-c polarographic data, fast linear sweep polarograms were recorded both as a function of sweep rate and water content of the melt. Some typical analyses for a sweep rate of 10 V sec⁻¹ are compared with d-c polarographic data in Table III.

Using (30)

$$E_p = -1.14 \frac{RT}{\alpha n_a F} + \frac{RT}{\alpha n_a F} \ln \left\{ \frac{k_{ofn}}{D^{1/2}} \right\} - \frac{RT}{2\alpha n_a F} \ln \alpha n_a \nu$$

and

$$k_s = k_{ofn} \exp \cdot \left\{ \frac{-\alpha n_a F E^\circ}{RT} \right\}$$

values of the standard rate constant, *k_s*, were estimated

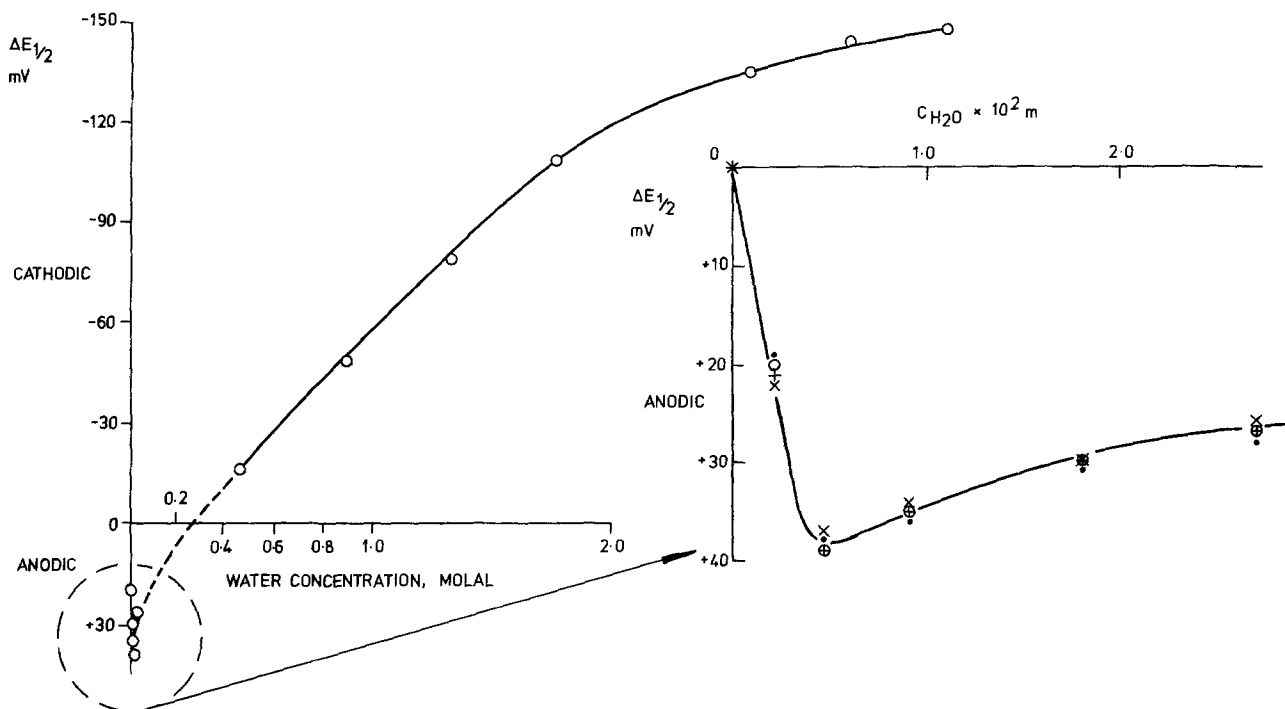


Fig. 3. Effect of water additions on the half-wave potential for the Ni(II)/Ni(Hg) reduction in LiNO₃-KNO₃ eutectic melt at 145°C. Initial concentrations of Ni(II): ×, 6.73 × 10⁻⁴m; +, 7.83 × 10⁻⁴m; ○, 8.35 × 10⁻⁴m; ·, 1.07 × 10⁻⁴m.

at each half-wave potential (equated to E°) for the various water concentrations. These values were fully corrected for the variation in melt density² (which affects the diffusion coefficient) and for the shifts in $E_{1/2}$; lack of data precluded these corrections in the earlier study (10), whose results are compared with the present ones in Fig. 4. The importance of these corrections may be gauged by examining their (10) third data point, for example, at ~ 0.175 mole fraction of water for which the actual density² of the melt would be ~ 1.90 g ml⁻¹, the viscosity² ~ 11½ cp, and $E_{1/2}$ ~ -0.83V vs. their ref. compared with ~ 1.99 g ml⁻¹, ~ 21½ cp, and ~ -0.70V in the completely anhydrous system.

Discussion

A number of features of the present study are surprising and in conflict with earlier reports. First and most importantly, the anodic $E_{1/2}$ shifts (Fig. 3) for the Ni(II)/Ni(Hg) reaction at very low water concentrations in the melt are unexpected. Anodic shifts for

²We thank Professor P. Claes and his colleagues of Louvain University for the provision of density and viscosity data prior to publication.

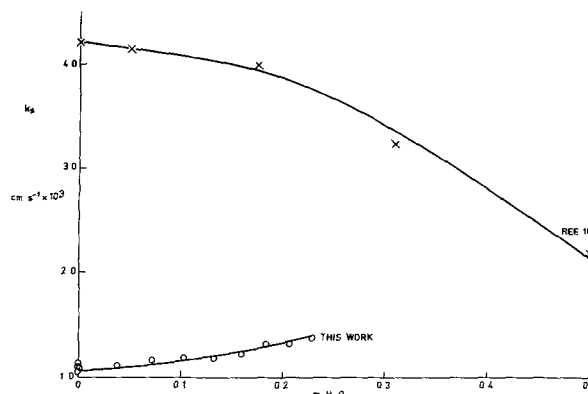


Fig. 4. Comparison of the variation in standard rate constant, k_s , with mole fraction of water in LiNO₃-KNO₃ melts: ×—uncorrected impedance data (10) at 140°C; ○—present work at 145°C.

Ni(II) ions are well known, especially in aqueous complexing media but invariably occur as a consequence of very large increases in the electrolyte con-

Table III. Analysis of the Ni(II)/Ni(Hg) reduction in LiNO₃-KNO₃ eutectic at 145°C obtained from (a) d-c polarography and (b) linear sweep voltammetry (10 V sec⁻¹)

Data obtained from	b		a		b		a	
	E_p , mV vs. 10 ⁻³ m Ag(I)	$E_{1/2}$, mV vs. 10 ⁻³ m Ag(I)	Apparent value $\alpha\eta_{1a}$ at 10 V sec ⁻¹	D_s , × 10 ⁵ cm ² sec ⁻¹	k_{ofb} , × 10 ¹⁰ cm sec ⁻¹	k_s , × 10 ³ cm sec ⁻¹	k_s , × 10 ³ cm sec ⁻¹	
0	-604	-560	1.36	0.22 (5)	7	1.0		
2.25 × 10 ⁻³	-583	-540	1.38	0.22 (5)	11	1.1		
4.5 × 10 ⁻³	-563	-521	1.40	0.22 (5)	17	1.1		
9.0 × 10 ⁻³	-567	-525	1.40	0.22 (6)	15	1.1		
1.8 × 10 ⁻²	-572	-530	1.39	0.22 (6)	14	1.1		
2.7 × 10 ⁻²	-576	-533	1.38	0.22 (7)	14	1.1		
0.45	-620	-576	1.35	0.25 (4)	4.7	1.1		
0.89	-654	-609	1.34	0.28 (6)	1.7	1.2		
1.32	-685	-640	1.33	0.30	0.6	1.2		
1.74	-714	-668	1.32	0.31 (7)	0.3	1.2		
2.16	-733	-686	1.30	0.34 (8)	0.2	1.2		
2.57	-742	-695	1.29	0.40 (1)	0.2	1.3		
2.97	-752	-704	1.28	0.43 (1)	0.2	1.3		
3.36	-757	-709	1.27	0.45 (6)	0.2	1.4		

centration, *i.e.*, large decreases in the water content of the system. In the present case the formation of more stable aquo-complexes in the bulk melt, which must occur to a certain extent, is evidently eclipsed by an overlying factor. Liquid junction potentials arising from slight cell asymmetry during water additions were eliminated as a possible cause of the anodic shift by making simultaneous additions of water to both the main cell and reference electrode compartments: no additional changes in $E_{1/2}$ were evident. Neither could the $E_{1/2}$ shifts be caused by bulk structural changes in the melt at such low water concentrations (14, 16). Furthermore, it seems unlikely that very small additions of water could significantly change the gross structure of the electrical double layer (10, 11) and thereby affect the reduction potential. Nevertheless in order to affirm the latter contention, experiments were carried out under the same conditions using Pb(II) and Tl(I) ions as depolarizers in place of Ni(II). The Pb(II) ion is relatively large, exerts a weak field, is rarely specifically adsorbed at most electrodes, and being a nontransition metal ion of low polarizing power is only weakly solvated or complexed in most oxyanionic media. Indeed, both the half-wave potential of -652 mV *vs.* ref. and the value of $\alpha n_a = 1.94$ for the Pb(II)/Pb(Hg) reduction in the melt were invariant over the range of water concentrations 0-3.36m. Moreover, such changes as were observed in the diffusion coefficient could be attributed almost entirely to viscosity changes in the solvent, as shown in Table IV. The faster diffusion rate of the Pb(II) ion as compared to the Ni(II) ion is also consistent with the latter being extensively coordinated (18, 20-22), (*vide infra*).

The Tl(I) ion is also a large, weak field species of low polarizing power, but unlike Pb(II) (and Ni(II)) ions is frequently adsorbed at electrode interfaces from dilute solution. Adsorption behavior is generally manifested as a maximum in polarographic waves, and these did appear in the present work at concentrations $\geq 1.12 \times 10^{-3}$ m. Initially, polarograms were recorded for the Tl(I)/Tl(Hg) reduction over a range of water concentrations 0-1.74m at depolarizer concentrations $< 10^{-3}$ m. Polarographic maxima were always absent and again the values of $E_{1/2} = -816$ mV *vs.* ref. and $\alpha n_a = 1.0$ were unaffected by the presence or absence of water; the variation of the diffusion coefficient was wholly accounted for in terms of viscosity changes (Table IV). However, in order to better probe the electrode/melt interface for possible direct interference by dissolved water molecules, polarograms for Tl(I) were also recorded at higher depolarizer concentrations $\sim 4 \times 10^{-3}$ m, *i.e.*, in the range where maxima were clearly evident. The peak current at the maximum was then compared to the post-maximum diffusion-limited current (to eliminate viscosity effects) over the same range of water contents: this ratio remained constant at 1.2. Hence, there seems to be no evidence that small, (or even quite large!)

amounts of water present in the melt significantly influences these polarographic reduction processes at the interphasial level. This conclusion would seem to be at variance either directly (19) or indirectly (10) with previous contentions, although Eriksrud has recently indicated (31) that charge-transfer rather than diffuse-layer effects might be responsible for the medium effect observed for Co(II) and Ni(II) (19) reductions.

Intuitively, it might be thought that very small quantities of water in the melt could dissociate and subsequently catalyze the reduction of Ni(II) ions; both temperature and entropy considerations would favor such a mechanism. The position of the Ni(II) polarographic wave in nitrate melts certainly resembles the catalytic prewave reported for aqueous environments in the presence of strongly complexing ligands (32). Moreover, any second wave (32) would be obscured by the onset of the nitrate ion reduction in the melt. Additionally, low apparent polarographic diffusion currents for Ni(II) ions in nitrate melts might be held to support this notion. Nevertheless, both the dielectric constant of the medium together with all previous experimental evidence (4, 8, 11, 13-17) firmly argue against even the slightest dissociation of water molecules in nitrate melts, especially at low concentrations. Since the earliest investigation (23), there has never been any indication that the observable polarogram for Ni(II) in nitrate melts is other than a normal, diffusion-controlled wave (10, 18, 25); in this work, wave analysis responded to all the usual criteria identifying the polarographic wave as such. Furthermore, the evidence of the Pb(II)/Pb(Hg) and Tl(I)/Tl(Hg) reductions provides no support for catalytic involvement by water either. The fact that the fully corrected standard rate constant, k_s , for the Ni(II)/Ni(Hg) reduction varies comparatively little from the anhydrous melt up to water concentrations of ~ 3 m, also detracts from any catalytic scheme. The invariance of k_s in the presence of nitric acid (10), which would suppress hydrolysis, seems to eliminate this line of approach.

The variation in the value of αn_a with water concentration perhaps provides the best clue as to why anodic shifts are initially observed for the Ni(II) half-wave potential. Most probably changes in the structure of the diffusing species, which occur as water is added to the anhydrous system, best account for the experimental facts and concur with Eriksrud's reasoning (31).

According to the spectroscopic evidence, Ni(II) ions in nitrate melts are substantially coordinated by bidentate nitrate ions with ligand numbers of three (20, 22) or four (21), probably in an octahedral complex. The known chemistry (33) of anhydrous nitrate compounds emphasizes the extreme susceptibility of bidentate linkages to hydrolysis. Consequently ring opening may reasonably be assumed as the first stage in the hydration displacement equilibrium for the

Table IV. Variation of diffusion coefficients, viscosities,² and Stokes-Einstein equation quotients for dissolved Ni(II), Pb(II), and Tl(I) ions in molten, eutectic LiNO₃-KNO₃ at 145°C with added water (0-3.36 m)

Concentration H ₂ O, m	0	9.0 × 10 ⁻³	2.7 × 10 ⁻²	0.45	0.89	1.32	1.74	2.16	2.57	2.97	3.36
η , cp ²	19.30	19.25	19.20	17.45	15.65	14.15	12.85	11.55	10.35	9.45	8.88 (5)
Diffusion coefficient, × 10 ⁹ cm ² sec ⁻¹											
Ni(II)	0.225	0.226	0.227	0.254	0.286	0.300	0.317	0.348	0.401	0.431	0.456
$D\eta$, g cm sec ⁻³ × 10 ⁸	4.34	4.35	4.36	4.43	4.48	4.25	4.07	4.02	4.15	4.07	4.00
Pb(II)	0.933	—	—	1.02	1.13	1.24	1.37	1.48	1.60	1.73	1.86
$D\eta$, g cm sec ⁻³ × 10 ⁹	18.01	—	—	17.80	17.68	17.55	17.60	17.09	16.56	16.35	16.32
Tl(I)	0.833	—	—	0.913	1.02	1.13	1.24	—	—	—	—
$D\eta$, g cm sec ⁻³ × 10 ⁹	16.08	—	—	15.93	15.96	15.98	15.95	—	—	—	—
$D\eta$		Ni(II)	4.23	Pb(II)	17.22	Tl(I)	15.98				
σn_a		Ni(II)	0.17	Pb(II)	0.66	Tl(I)	0.06				

² See footnote 2, previous page.

Ni(II) ion in the melt. At the lowest concentrations, the change from bidentate nitrate ligands to monodentate nitrate and water ligands necessarily increases the ligand number. The thermodynamic consequences for the diffusing particles are most profound. There will be a sharp entropy decrease in the system due to the "loss" of the extra water ligand, and the complex will be somewhat destabilized (i.e., lability increased) by an "inverse chelate effect." While this need not affect the rate of reduction of the Ni(II) species, it must affect the transfer coefficient for the process since this reflects the shape of the potential energy functions during the initial stages of ion desolvation prior to discharge. Furthermore, additional destabilization may occur as a result of "trans effect" labilization of other ligands. Thus, the partially substituted, mixed aquo-nitrato-nickelate(II) complex may more readily pass through the desolvation steps and lead to the appearance of classically reversible polarograms. The simultaneous sharpening of the polarographic wave may then account for the net anodic shift of $E_{1/2}$. Second order thermodynamic effects (not influencing reduction kinetics directly), include favorable enthalpy changes resulting from relief of steric ring-strain in the bidentate nitrate ions, and an increase in translational entropy arising from ring scission. Ligand rearrangement, homogeneous ligand exchange, and an enhanced statistical probability of ligand substitution constitute additional features complicating the initial ion hydration phase and are best studied, per se, by spectroscopy.

As the water content of the melt is increased beyond 10 millimolar, $E_{1/2}$ shifts revert to the cathodic direction, signaling the steady, step-wise formation of more stable aquo-complexes. At the same time, the polarographic wave becomes progressively less reversible, until at 3m in water it more closely resembles the wave obtained in aqueous media.

The near constancy of the $D\eta$ product, with varying water content, for all three ions is shown in Table IV. It provides an interestingly unique case of the apparent applicability of the Stokes-Einstein equation in molten salts; unlike previous examples, the medium, rather than the ion (34) is varying here. These results indicate that the approximate size and extent of interaction of each ion or complex with the surrounding medium is little changed whether or not the entity itself is undergoing substitutional modification. Clearly, bridged or polynuclear entities are not involved even as intermediates. Moreover, if all three ions are assumed six coordinate, Pb(II) and Tl(I) are assumed uncomplexed and unsolvated to a first approximation, then using Shannon and Prewitt (35) effective ionic radii, the $D \cdot \eta \cdot r$ products for Pb(II), Tl(I), and Ni(II) ($(\text{NO}_3)_2$) in the anhydrous melt are sensibly comparable at 21.3, 24.1, and 19.8, respectively, in $\text{g cm}^2 \text{sec}^{-2} \times 10^{-16}$ units, when a radius of 1.93Å is taken for the nitrate ion (34). Notwithstanding these sweeping assumptions, perhaps the trend of the $D\eta$ product for Pb(II) suggests that the bare ion does acquire an aquo ligand at the highest water concentration.

Unfortunately, the initial complications in the hydration equilibria for the Ni(II) ion, manifested by the change in direction of $E_{1/2}$ shifts, the variation in αm_a values together with the continuously varying viscosity and density of the melt, preclude calculation of either formation constants or \bar{n}_{max} for the aquo complexes formed. Nevertheless, a simplistic approach can be adopted to estimate the range in which the primary coordination sphere of the Ni(II) ion becomes substantially substituted with water molecules. The "associated radius" of the nickel nitrate complex in the anhydrous melt will be (34) 4.56Å, while that for the nickel aquo complex (regardless of structure or ligand number) will be 3.48Å, if $r_{\text{NO}_3^-} = 1.93\text{\AA}$, $r_{\text{H}_2\text{O}} = 1.39\text{\AA}$ (34), and $r_{\text{Ni(II)}} = 0.7\text{\AA}$ (34). Ignoring consequential changes in the interaction of the diffus-

ing particles with the medium, the diffusion coefficient of the nickel aquo complex will be approximately $0.295 \times 10^{-6} \text{ cm}^2 \text{ sec}^{-1}$ in proportion to the associated radii. If this value is then multiplied by the appropriate melt viscosity for each experimental water concentration employed in Table IV, when $D\eta \approx 4.4 \times 10^{-8} \text{ g cm sec}^{-2}$ the value so calculated coincides with that experimentally observed, i.e. at $\sim 1\text{m}$ in water. Such an elementary derivation makes many assumptions concerning the transport process and fails to account for the stepwise nature of the association equilibrium indicated by the $\Delta E_{1/2}$ vs. water concentration plot. However, the Ni(II) ion appears to be essentially coordinated by water molecules at the relatively dilute water concentration $\sim 1\text{m}$ [cf. Cd(II) ions (34)].

Evidently many complicated factors may be involved in the initial hydration of transition metal ions in molten salts. A complete and quantitative treatment remains elusive; polarization forces between all the ions in the melt have also been conveniently ignored. However, in any Li-containing melt, the highly polarizing Li^+ ion must be considered a competitor for water molecules present. This competition may not be particularly effective compared to the field exerted by Ni(II) ions, but any attempt to quantify this conjecture, whether or not the Born equation is invoked, seems hazardous at present.

Conclusions

Polarographic studies of the Ni(II)/Ni(Hg) reduction in the $\text{LiNO}_3\text{-KNO}_3$ eutectic melt at 145°C illustrate some rather unusual electrochemical effects which occur during the initial stages of ion hydration. Apparently, the consequences of adding very small amounts of water to the anhydrous system cause no important changes either in the electrode/melt interface or in the overall transport behavior of the diffusing species. Such changes as do occur seem to alter the shape of the energy barriers for reduction rather than the overall rate for the process. This probably arises from changes in the nature of the diffusing entity, in this case an increase in ligand number arising from the disruption of bidentate nitrate bonds coordinating the Ni(II) ion with the incorporation of aquo ligands into a mixed ligand complex. The most profound electrochemical consequences, namely anodic shifting of the polarographic wave and an increase in the apparent reversibility, are dramatically sharp at extremely low levels of water. In view of the variable degree of dryness of, especially, LiNO_3 -containing melts employed by previous workers, previous conclusions may need reviewing particularly where transition metal ions are involved. The roles of such thermodynamic and kinetic factors as have been discussed here could usefully be examined with respect to the highly concentrated aqueous electrolytes that are employed in industrial electrochemical devices and processes. Apart from parallel spectroscopic investigations, these studies need to be extended to other molten systems, other transition metal ions [especially Co(II)] and to be conducted over a wide range of temperatures using additional transient techniques in order to gain a better insight into the initial hydration of ions.

Acknowledgments

We thank the Science Research Council for a Research Grant and Dr. D. Inman of Imperial College for valuable discussions.

Manuscript submitted Nov. 26, 1979; revised manuscript received March 4, 1980. This was Paper 362 presented at the Pittsburgh, Pennsylvania, Meeting of the Society, Oct. 15-20, 1978.

Any discussion of this paper will appear in a Discussion Section to be published in the June 1981 JOURNAL. All discussions for the June 1981 Discussion Section should be submitted by Feb. 1, 1981.

REFERENCES

1. D. G. Lovering and R. M. Oblath in "Ionic Liquids," D. G. Lovering and D. Inman, Editors, Plenum Press, New York (1981).
2. D. G. Lovering, R. M. Oblath, and A. K. Turner, *J. Chem. Soc. Chem. Commun.*, 673 (1976).
3. H. S. Swofford and H. A. Laitinen, *This Journal*, **110**, 814 (1962).
4. T. E. Geckle, Thesis, Penn. State University (1964); U.S.A.E.C., TID21511 (1964).
5. M. Peleg, *J. Phys. Chem.*, **71**, 4553 (1967).
6. G. J. Hills and P. D. Power, *J. Polarogr. Soc.*, **13**, 71 (1967).
7. P. G. Zambonin, V. L. Cardetta, and G. Signorile, *J. Electroanal. Chem. Interfacial Electrochem.*, **28**, 237 (1970); *Anal. Chem.*, **43**, 1571 (1971).
8. J. Jordan, *J. Electroanal. Chem. Interfacial Electrochem.*, **29**, 127 (1971).
9. A. Espinola and J. Jordan, in "Proceedings A.C.S. Symposium," San Francisco, August (1976).
10. J. E. B. Randles and W. White, *Z. Electrochem.*, **59**, 666 (1955).
11. V. Sh. Palanker, A. M. Skundin, and V. S. Bagot-skii, *Elektrokhim.*, **2**, 640 (1966).
12. D. G. Lovering, Thesis, City University (1969); Extended Abstracts, p. 340, 23rd Meeting I.S.E., Stockholm (1972).
13. D. G. Lovering, *Collect. Czech. Chem. Commun.*, **37**, 3697 (1972).
14. J. P. Frame, E. Rhodes, and A. R. Ubbelohde, *Trans. Faraday Soc.*, **57**, 1075 (1961).
15. J. Braunstein, *Inorg. Chim. Acta Rev.*, **2**, 19 (1968).
16. T. B. Tripp and J. Braunstein, *J. Phys. Chem.*, **73**, 1984 (1969).
17. P. G. Zambonin, *J. Electroanal. Chem. Interfacial Electrochem.*, **24**, 365 (1970) et seq.
18. D. Inman, D. G. Lovering, and R. Narayan, *Trans. Faraday Soc.*, **63**, 3017 (1967).
19. J. Dandoy and L. Gierst, *J. Electroanal. Chem.*, **2**, 116 (1961).
20. C. J. Liu, J. Hasson, and G. Pedro Smith, *Inorg. Chem.*, **7**, 2244 (1968).
21. S. V. Volkov and N. I. Buryak, *Zh. Neorg. Khim.*, **17**, 1045 (1972).
22. T. R. Griffiths and P. J. Potts, *Inorg. Chem.*, **14**, 1039 (1975).
23. M. Steinberg and N. Nachtrieb, *J. Am. Chem. Soc.*, **72**, 3558 (1950).
24. R. M. Oblath, Thesis, C.N.A.A. (R.M.C.S., Shrivensham) (1978).
25. G. C. Barket and R. L. Faircloth, A.E.R.E. Report C/R 2032 (1956).
26. E. P. Parry and R. A. Osteryoung, *Anal. Chem.*, **40**, 65 (1968).
27. G. C. Barker and A. W. Gardener, *Z. Anal. Chem.*, **173**, 79 (1960).
28. H. Matsuda and Y. Ayabe, *Z. Electrochem.*, **59**, 494 (1955).
29. R. S. Nicholson and I. Shain, *Anal. Chem.*, **36**, 706 (1964).
30. Z. Galus, "Fundamentals of Electrochemical Analysis," Ellis Horwood, Chichester (1976).
31. E. Eriksrud, *J. Electroanal. Chem. Interfacial Electrochem.*, **90**, 347 (1978).
32. L. R. McCoy, H. B. Mark, Jr., and L. Gierst, *J. Phys. Chem.*, **72**, 4637 (1968), et seq.
33. B. O. Field and C. J. Hardy, *Q. Rev.*, **18**, 361 (1964); C. C. Addison, *Q. Rev.*, **25**, 289 (1971).
34. See D. G. Lovering, *Collect. Czech. Chem. Commun.*, **38**, 1719 (1973), for discussion and further references.
35. R. D. Shannon and C. T. Prewitt, *Acta Crystallogr. Sect. B*, **25**, 925 (1969); *ibid.*, **26**, 1076 (1970).

Hydrogen Peroxide as an Intermediate in Electrocatalytic Reduction of Oxygen. A New Method for the Determination of Rate Constants

F. van den Brink, E. Barendrecht,* and W. Visscher

Laboratory for Electrochemistry, University of Technology, 5600 MB Eindhoven, The Netherlands

ABSTRACT

On most electrocatalysts H_2O_2 is an intermediate in the electroreduction of oxygen. H_2O_2 can decompose either chemically or electrochemically and in assessing the performance of the electrocatalyst it is crucial to distinguish between these reaction paths. A simple method is proposed to determine whether or not the chemical path is followed.

For the electrochemical reduction of oxygen a general scheme of reactions can be given as in Fig. 1. Whether the reduction of oxygen to water will follow the direct path 1 or the consecutive path 2-3, or both these paths in parallel, is determined by the electrocatalytic properties of the electrode which are also critical for the further reaction of H_2O_2 : electrochemical reduction (reaction 3) and/or chemical decomposition (reaction 4).

With the introduction of the rotating ring-disk electrode technique it became possible to distinguish between the consecutive and parallel pathways (1-4). Here, the disk current is measured at various potentials and rotation frequencies, while simultaneously the ring current is measured at a potential at which

hydrogen peroxide is oxidized quantitatively. Several methods have been proposed to analyze the data obtained from these experiments; these methods have been reviewed by Pleskov and Filinovskii (5), while Wroblowa (6) has added a general criterion for distinguishing between the parallel and consecutive pathway. These analyses show that, in principle, only four (combinations) of the five rate constants in the general scheme can be obtained.

A problem which remains to be solved is that of the fate of the hydrogen peroxide, produced by reactor 2 in Fig. 1: H_2O_2 can be either reduced electrochemically (reaction 3) or chemically decomposed (reaction 4). Moreover, the solution of this problem is of vital importance in the evaluation of the performance of electrocatalysts for the oxygen electrode, since reaction 4 involves no net electron transfer and is

* Electrochemical Society Active Member.

Key words: electrocatalysts, reduction, decomposition.

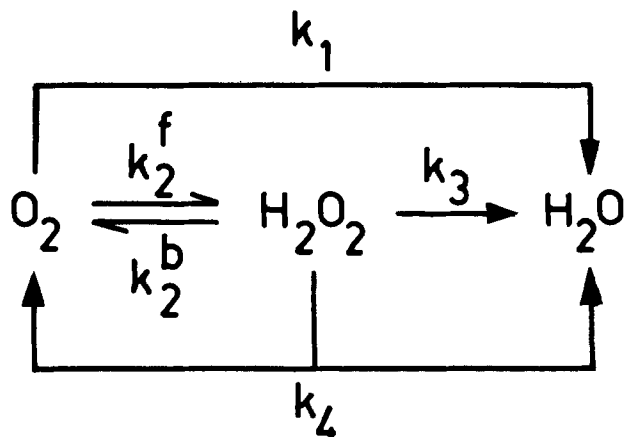


Fig. 1. Scheme of reactions for reduction of oxygen

electrochemically wholly unproductive. In this paper we will present a simple method to determine the rate constant of reaction 4, so that, in principle, it becomes possible to calculate all five individual rate constants of Fig. 1.

Theory

In the ring-disk electrode (RRDE) experiment, referred to in the introduction, sets of disk currents (I_D) and limiting ring currents (I_R) are obtained as functions of rotation frequency (ω) and disk potential, E_D . These data are analyzed by plotting at constant E_D according to (5)

$$-N_o I_D / I_R = A + B / \sqrt{\omega} \quad [1]$$

and

$$-N_o (I_{D, \text{lim}}^{\text{H}_2\text{O}_2} - I_D) / I_R = C + D \sqrt{\omega} \quad [2]$$

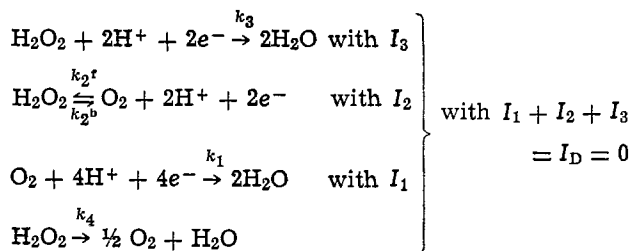
where $I_{D, \text{lim}}^{\text{H}_2\text{O}_2}$ is the limiting current at the disk for the reduction of oxygen to water and N_o is the RRDE's collection efficiency (7). A , B , C , and D are functions of the five rate constants, from which k_1 , k_2^f , $2k_2^b + k_4$, and $2k_3 + k_4$ can be obtained (5).

We wish to point out that the value of k_4 can be found in many practical cases by measuring ring currents in a solution containing only H_2O_2 and no O_2 , while the disk current is kept zero.

Relations between currents and rotation frequencies in H_2O_2 containing solutions have been derived by Bagotskii (1). From his equations the combinations $2k_2^b + k_4$, $2k_3 + k_4$, and $k_2^f - k_3$ can be obtained. A further extension of this method was given by Tarasevich and Radyushkina (8) who applied Bagotskii's equations under the condition that $I_D = 0$. They, again, found k_1 , k_2^f , $2k_2^b + k_4$ (describing the rate with which H_2O_2 gives O_2), and $2k_3 + k_4$ (describing the rate with which H_2O_2 gives H_2O). We will show that they lost valuable information, *viz.*, that obtained from the value of the disk's open-circuit potential, by substituting the zero current condition ($I_D = 0$) only in Bagotskii's resulting equations (1).

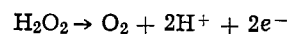
In a solution containing hydrogen peroxide, but no oxygen, the hydrogen peroxide will react electrochemically (reactions 2 and 3) and chemically (reaction 4), giving oxygen and/or water; oxygen may react further (reactions 1 and 2). The quantities of formed oxygen and of decomposed hydrogen peroxide can be determined by measuring the anodic and cathodic limiting currents on the ring electrode. If, moreover, the disk current is zero, the net amount of oxygen formed by the electrochemical reaction is known if the ratio of the rates of production and of consumption of O_2 by the electrochemical reactions, *i.e.*, $k_2^b - k_3/2k_1 + k_2^f$ is known at the disk's rest-potential. This means that the amount of oxygen formed by reaction 4 can be found, *i.e.*, that the value of k_4 can be determined.

Thus, on the disk electrode

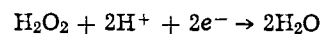


The assumptions are that reaction 4 is potential independent, that the pertinent reactions are first order in O_2 or in H_2O_2 , and that adsorption to and desorption from the electrocatalyst of O_2 and H_2O_2 are fast.

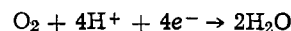
On the ring electrode the anodic limiting current is $I_{R, \text{lim}}^a$ for the reaction



and $I_{R, \text{lim}}^c$ the cathodic limiting current for the reactions



and



At the disk we have the mass balances, for hydrogen peroxide

$$\gamma_2 \sqrt{\omega} (c_2^s - c_2^o) = (k_{2,r}^b + k_{3,r} + k_4) c_2^o - k_{2,r}^f c_1^o \quad [3]$$

and for oxygen

$$\gamma_1 \sqrt{\omega} c_1^o = (k_{2,r}^b + \frac{1}{2} k_4) c_2^o - (k_{1,r} + k_{2,r}^f) c_1^o \quad [4]$$

Because of the zero current condition

$$\frac{I_D}{2FA} = (k_{2,r}^b - k_{3,r}) c_2^o - (2k_{1,r} + k_{2,r}^f) c_1^o = 0 \quad [5]$$

where the c 's are the concentrations of O_2 (subscript 1) and of H_2O_2 (subscript 2). The superscripts o and s on the c 's denote the electrode surface and the bulk of the solution, respectively, while a subscript r is attached to k_1 , k_2^f , k_2^b , and k_3 because the disk electrode is at its rest potential. Further, $\gamma \sqrt{\omega} = 0.62D^{2/3} \nu^{-1/6} \sqrt{\omega}$ is the rate constant for diffusion and A the disk area.

At the ring we have the limiting currents

cathodic

$$-\frac{I_{R, \text{lim}}^c}{N_o A F} = 4\gamma_1 \sqrt{\omega} c_1^o - 2k_4 c_2^o + \frac{\beta^{2/3}}{N_o A F} I_{D, \text{lim}}^{\text{H}_2\text{O}_2} \quad [6]$$

anodic

$$\frac{I_{R, \text{lim}}^a}{N_o A F} = -2k_4 c_2^o + \frac{\beta^{2/3}}{N_o A F} I_{D, \text{lim}}^{\text{H}_2\text{O}_2} \quad [7]$$

where $I_{D, \text{lim}}^{\text{H}_2\text{O}_2}$ is the absolute value of the limiting current at the disk for the oxidation of H_2O_2 to O_2 and $\beta^{2/3}$ is a geometrical factor, defining the shielding factor $(1 - N_o \beta^{-2/3})$ of the RRDE (7).

Elimination of c_1^o and c_2^o between the sets of Eq. [3], [4], and [6], and [3], [4], and [7], respectively, together with the condition [5] gives

$$\frac{I_{R, \text{lim}}^c}{2N_o A F c_2^s} = \frac{k_4}{1 + K} - \left(\frac{K}{1 + K} + \frac{\beta^{2/3}}{N_o} \right) \gamma_2 \sqrt{\omega} \quad [8]$$

and

$$\frac{-I_{R, \text{lim}}^a}{2N_o A F c_2^s} = \frac{k_4}{1 + K} - \frac{\beta^{2/3}}{N_o} \gamma_2 \sqrt{\omega} \quad [9]$$

where

$$K = \frac{2\gamma_1}{\gamma_2} \frac{k_{2,r}^b - k_{3,r}}{2k_{1,r} + k_{2,r}^f}$$

The pseudo constant k can be obtained by extrapolation of the values for the k 's found with Eq. [1] and [2] to the rest potential at each rotation frequency.

If we may assume that the rest potential will not vary strongly with the RRDE's rotation frequency, K will be a constant. Then the plots of the limiting ring currents *vs.* $\sqrt{\omega}$ will give straight lines. Two limiting cases can be considered (Fig. 2). First $K \ll 1$, i.e., H_2O_2 is, electrochemically, much less reactive than O_2 at the disk electrode. Therefore the anodic and cathodic limiting ring currents become equal, while reaction 4 is responsible for extra shielding of the ring current by the disk electrode. The second case $K \gg 1$, i.e., H_2O_2 is electrochemically more reactive. O_2 formed on the disk diffuses away, thereby increasing the cathodic limiting ring current. Now the influence of reaction 4 is much less than in the first case, because of the low H_2O_2 concentration near the disk surface. In Fig. 2, schematic diagrams are given for these two cases.

In general, by plotting $I_{R,\text{lim}} \text{ vs. } \sqrt{\omega}$, or, more precisely, $(1 + K)I_{R,\text{lim}} \text{ vs. } (1 + K)\sqrt{\omega}$ (Eq. [9]), c_2^s can be found. Then k_4 can be calculated at each value of ω from

$$k_4 = (1 + K) \left[\frac{I_{R,\text{lim}}^c}{2N_o A F c_2^s} + \left(\frac{K}{1 + K} + \frac{\beta^{2/3}}{N_o} \right) \gamma_2 \sqrt{\omega} \right] \quad [10a]$$

$$= (1 + K) \left[\frac{-I_{R,\text{lim}}^a}{2N_o A F c_2^s} + \frac{\beta^{2/3}}{N_o} \gamma_2 \sqrt{\omega} \right] \quad [10b]$$

The results can be averaged to give a final value of k_4 . Alternatively, k_4 can be determined from the intercepts of $(1 + K)I_{R,\text{lim}}^c/2N_o A F c_2^s$ and $-(1 + K)I_{R,\text{lim}}^a/2N_o A F c_2^s \text{ vs. } (1 + K)\gamma_2 \sqrt{\omega}$. The resulting value of k_4 is then subtracted from $2k_2^b + k_4$ and $2k_3 + k_4$, obtained from Eq. [1] and [2], to give the separate values for all five rate constants at each potential for which ring and disk currents are available.

Experimental

As an example, an experiment according to the line of reasoning described above was carried out, using an RRDE with an Au disk and a Pt ring in 1M KOH at 298°K. The construction of the RRDE was as described before (9). Its dimensions were such that $A = 51.5 \times 10^{-6} \text{ m}^2$, $N_o = 0.1437$, and $\beta = 0.1515$ (as calculated from the radii $r_{10} = 4.047 \text{ mm}$, $r_{20} = 4.260 \text{ mm}$, and $r_{30} = 4.437 \text{ mm}$). A standard electrochemical cell was used, with a reversible hydrogen electrode (RHE) as reference and a platinum wire as counter-electrode. The Pt ring was slightly platinized ($5 \times$

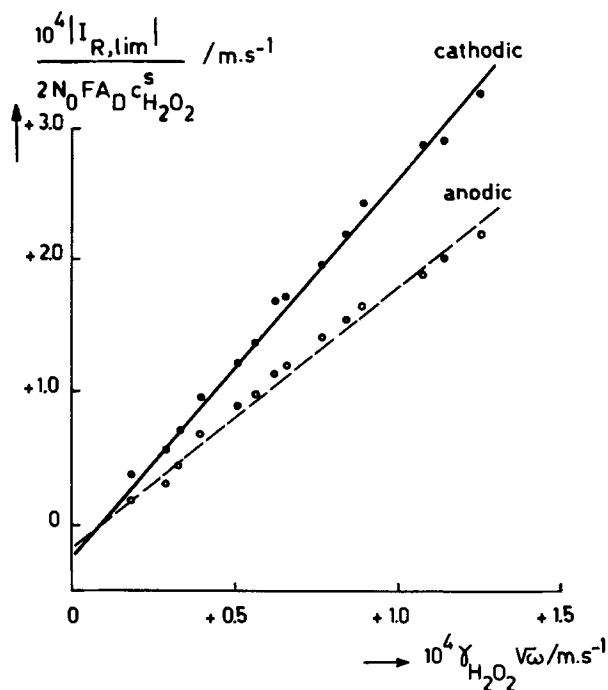


Fig. 3. Limiting ring currents *vs.* $\sqrt{\omega}$; for an Au/Pt-RRDE in 1N KOH at 298°K, plotted according to Eq. [8] and [9]. a = anodic, c = cathodic.

$10^{-6} \text{ mole} \cdot \text{m}^{-2}$). The measurements were carried out using a Tacussel bipotentiostat, Type BIPAD.

The KOH solution (prepared with p.a. quality KOH and doubly distilled water) was purified by preelectrolysis, made oxygen-free, and kept in Ar atmosphere. Hydrogen peroxide was added¹ and anodic and cathodic limiting currents at the ring were measured while the disk current was zero. To avoid poisoning of the ring by the stabilizer from the H_2O_2 solution used, the currents were measured by cyclic voltammetry with scan rates of 100-500 $\text{mV} \cdot \text{sec}^{-1}$. The rest potential at the disk was measured to be 889 mV *vs.* a reversible hydrogen electrode in the same solution and was independent of the rotation frequency. Therefore it was possible to obtain the H_2O_2 concentration from a $I_{R,\text{lim}}^a \text{ vs. } \sqrt{\omega}$ -plot. The slope of this plot gave $c_2^s = 5.3 \text{ mM}$, which value was verified by titration with KMnO_4 . The results, plotted as $I_{R,\text{lim}}/2N_o A F c_2^s \text{ vs. } \gamma_2 \sqrt{\omega}$, are given in Fig. 3. The

¹ Brocacef, 30% v/w, Ph. Eur.

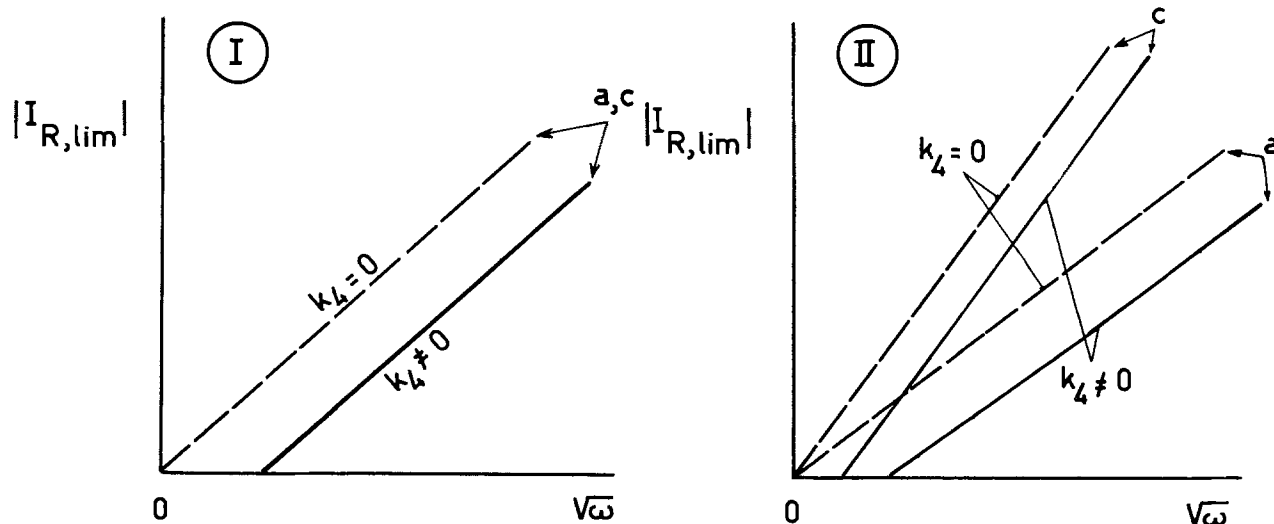


Fig. 2. Limiting cases of Eq. [8] and [9] (arbitrary units). I: $K \ll 1$; II: $K \gg 1$; a = anodic; c = cathodic limiting current; - - - for $k_4 = 0$; — for $k_4 \neq 0$.

slope of the anodic branch is calculated to be 1.98 ± 0.06 , in very good agreement with the theoretical value of

$$\frac{\beta^{2/3}}{N_0} = 1.978$$

From the slope of the cathodic branch (2.89 ± 0.07), the value of $K = 10.1$ can be calculated. This means that H_2O_2 is, electrochemically approximately five times more reactive at a gold electrode than O_2 .

The intercepts of the anodic and cathodic branches are, respectively, $-0.12 \times 10^{-4} \text{ msec}^{-1}$ and $-0.17 \times 10^{-4} \text{ msec}^{-1}$. This gives, by application of Eq. [8] and [9], $k_4 = (1.6 \pm 0.3) \times 10^{-4} \text{ msec}^{-1}$. Calculation according to Eq. [10] gives $k_4 = (1.6 \pm 0.2) \times 10^{-4} \text{ msec}^{-1}$.

Conclusion

As shown in the introduction, there are two nodal points in the scheme of reactions for O_2 reduction where a distinction is to be made between possible paths. The first is where oxygen can give either H_2O or H_2O_2 . Here, RRDE experiments in O_2 -containing solutions enable us to make the distinction. The second is where hydrogen peroxide can react either electrochemically or chemically. The method proposed here makes it possible to determine whether or not H_2O_2 decomposes chemically. In those cases where it may be assumed that k_4 does not depend on the disk electrode potential, it is even possible to calculate the magnitude of k_4 . This assumption is valid as long as the catalytic properties of the electrode surface for the decomposition of H_2O_2 do not change significantly when the electrode potential is changed from the rest potential.

Furthermore, the method described here is simpler than that given recently by Appleby and Savy (10). They use an RRDE with a pyrolytic graphite ring, at which H_2O_2 is stable, to find k_4 . This means that they need two different RRDE's, one to find k_1 , k_2^f , k_2^b , and k_3 in oxygen-containing solutions and another one for use in solutions containing H_2O_2 to find k_4 .

Acknowledgment

This work has been carried out with financial support from the Netherlands Organization for the Advancement of Pure Research (ZWO).

Manuscript received Nov. 7, 1979.

Any discussion of this paper will appear in a Discussion Section to be published in the June 1981 JOURNAL. All discussions for the June 1981 Discussion Section should be submitted by Feb. 1, 1981.

Publication costs of this article were assisted by the University of Technology.

LIST OF SYMBOLS

A	disk area (m^2)
c^0	concentration near disk surface (mole m^{-3} = mM)
c^s	concentration in solution (mole m^{-3} = mM)
D	diffusion coefficient ($\text{m}^2 \text{ sec}^{-1}$)
E_D	disk potential (V)
F	Faraday constant
I_D	disk current (A)
$I_{D,\text{lim}}^{\text{H}_2\text{O}}$	limiting disk current for reaction $\text{O}_2 \rightarrow \text{H}_2\text{O}$ (A)
$I_{D,\text{lim}}^{\text{H}_2\text{O}_2}$	limiting disk current for reaction $\text{H}_2\text{O}_2 \rightarrow \text{O}_2$ or $\text{H}_2\text{O}_2 \rightarrow \text{H}_2\text{O}$ (A)
I_R	ring current
$I_{R,\text{lim}}$	limiting current (A)
k	reaction rate constant (see Fig. 1) (msec^{-1})
K	pseudo constant, defined in formula [9]
N_0	collection efficiency of RRDE
β	geometric factor of RRDE
γ	$0.62 D^{2/3} \nu^{-1/6}$ ($\text{msec}^{-1/2}$)
ν	kinematic viscosity ($\text{m}^2 \text{ sec}^{-1}$)
ω	angular rotation frequency of RRDE (sec^{-1})

Superscripts

a	anodic
c	cathodic

Subscripts

1	O_2
2	H_2O_2
r	refers to rest potential

REFERENCES

- V. S. Bagotskii *et al.*, *Sov. J. Electrochem.*, **4**, 1129 (1968); *ibid.*, **5**, 1158 (1969).
- A. Damjanovic, M. A. Genshaw, and J. O'M Bockris, *J. Chem. Phys.*, **45**, 4057 (1966).
- J. D. E. McIntyre, *J. Phys. Chem.*, **73**, 411 (1969).
- M. R. Tarasevich, *Sov. J. Electrochem.*, **4**, 182 (1967); *ibid.*, **6**, 1468 (1970).
- Yu. V. Pleskov and V. Yu. Filinovskii, "The Rotating Disc Electrode," Consultants Bureau, New York/London (1976).
- H. S. Wroblowa, Yen-Chi-Pan, and G. Razumney, *J. Electroanal. Chem. Interfacial Electrochem.*, **69**, 195 (1976).
- W. J. Albery and M. L. Hitchman, "Ring Disc Electrodes," Clarendon Press, Oxford (1971).
- M. R. Tarasevich and K. A. Radyushkina, *Sov. J. Electrochem.*, **6**, 370 (1970).
- J. F. van der Plas and E. Barendrecht, *Rec. Trav. Chim. Pays Bas*, **96**, 133 (1977).
- A. J. Appleby and M. Savy, *J. Electroanal. Chem. Interfacial Electrochem.*, **92**, 15 (1978).

Transient and Failure Analyses of the Porous Zinc Electrode

I. Theoretical

W. G. Sunu^{*,1} and D. N. Bennion^{*,2}

School of Engineering and Applied Sciences, University of California, Los Angeles, California 90024

ABSTRACT

A mathematical model which describes the transient behavior of porous zinc electrodes has been developed on the basis of concentrated ternary electrolyte theory. The model predicts the current distribution, potentials in the solution, concentrations of hydroxide ion and zincate ion, porosity, and volume fractions of zinc and zinc oxide as a function of time and position perpendicular to the surface of the electrode. Numerical techniques were used to predict zinc electrode behavior during galvanostatic operation of the cell with and without a membrane. During discharge of the cell without a membrane, much of the discharge product, zincate ions, are lost into the counter-electrode compartment. For the cell with a membrane, this zincate loss is effectively restricted, but the utilization of zinc is severely limited by depletion of hydroxide ions within the zinc electrode compartment. In both cases, the reaction profiles are highly nonuniform and the reaction zone, located near the electrode surface, is very thin. This highly nonuniform reaction distribution accentuates the failure due to electrolyte depletion in the interior of the porous electrode, resulting in the low discharge capacity. On repeated cycling, the difference in anodic and cathodic reaction distribution causes the redistribution of solid zinc and zinc oxide species.

The zinc electrode has been commonly used as a negative electrode in primary cells such as Leclanché dry cells and alkaline zinc manganese dioxide cell. It also has received considerable attention, during the last decade, as a negative plate in secondary batteries, *e.g.*, zinc-nickel, zinc-silver oxide, zinc-bromine, and zinc-chlorine cells. The use of zinc electrodes in secondary batteries is attractive because of its availability, its low cost, and its ability to deliver high energy and power density. However, secondary batteries using zinc electrodes have poor cycle life, limited by zinc electrode failure. Any improvements on the cycle life of the alkaline zinc electrode can be applicable to its use in Zn-NiOOH or Zn-AgO rechargeable batteries, which are potential systems for use in electric vehicle propulsion or aerospace.

Failure of the zinc electrode can be attributed to a variety of causes. Two major causes of failure are zinc dendrite formation and shape change. The zinc dendrites which are formed during charge penetrate the separator and cause short circuits to the counter-electrode. Much of the work to date on improving zinc electrode behavior during charge has been associated with zinc deposit morphology, deposit adherency, and mechanism of dendrite growth (1-5). These studies have suggested that the use of low charge rate, pulse charging, and metallic or organic additives have some beneficial effects on preventing the formation of dendritic zinc deposits. The detrimental dendrite penetration, however, has been successfully reduced by use of an appropriate membrane material (6) such as commercially available grafted polyethylene ion exchange membrane.

Another failure known as shape change is the redistribution of solid zinc species over the electrode surface during cycling, which eventually decreases the effective surface area and thus cell capacity of the zinc electrode. Previous investigators (7-9) have

indicated that the solid species moves from the top and sides to the bottom and center of the zinc electrode during cycling and that loose packing, compared to tight packing, of the cell promotes more rapid redistribution of zinc.

A mechanism based on gravitational effects has been proposed (10), but this mechanism is not consistent with the fact that shape change is independent of cell orientation. Other investigators (7, 9, 11) suggested concentration cell effects as a mechanism of shape change. McBreen (7) has suggested that a concentration cell is generated by the difference in the current distribution during charge and discharge. Recently, Choi *et al.* (12, 13) have proposed that the main reason for the shape change is the concentration cell caused by the difference in the convective flow pattern during cycling, *i.e.*, flow of supersaturated zincate solution toward the zinc electrode center during discharge and flow of unsaturated zincate solution toward the electrode edge or solution reservoir during charge. They confirmed that sealing or tight packing of the cell, preventing convection, successfully eliminated the shape change.

The simple approaches mentioned above have been effective in extending cycle life, but the resulting cycle life appears still to be limited by other factors. Initial loss of cell capacity as well as rapid decrease in cell capacity with continued cycling were observed even for the sealed cells for which chemical analysis for the zinc species confirmed no shape change (13). This indicates that there are further reasons for cell failure to be explained and minimized in order to gain further cycle improvements. The first step towards disclosing other failure modes and mechanism is to understand and be able to predict the zinc behavior within the porous electrode.

Various mathematical models have been proposed to describe the behavior of porous electrodes as summarized by Newman and Tiedemann (14). Winsel (15) described battery discharge by considering a single pore electrode of constant porosity and uniform concentration. Newman and Tobias (16) included the effects of a matrix resistance and concentration changes in their steady-state analysis of a

* Electrochemical Society Active Member.

¹ Present address: Gould Incorporated, Gould Laboratories—Energy Research, Rolling Meadows, Illinois 60008.

² Present address: Chemical Engineering Department, Brigham Young University, Provo, Utah 84602.

Key words: porous zinc electrodes, mathematical modeling, current distribution, failure mechanism.

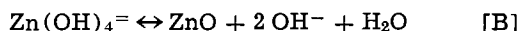
one-dimensional, homogeneous mixture model. An attempt to consider structural changes in the pores was initiated by Alkire *et al.* (17). Dunning *et al.* (18) proposed a mathematical model which predicted discharge and cycling behavior of an Ag/AgCl electrode in NaCl solution. Recently, Gu *et al.* (19) extended the model of Dunning *et al.* to include surface diffusion of the adsorbed complex ion and realistic active surface area based on their experimental measurements. Simonsson (20,21) applied his model to predict the failure mode of the positive electrode of the lead-acid battery. He showed that the discharge of the positive lead dioxide electrode at high current load failed by the severe depletion of sulfuric acid at the pore mouth, while Gidaspow and Baker (22) emphasized the pore plugging as a major cause of discharge failure.

In the present work, a mathematical model is developed to describe the transient behavior of the porous zinc electrode on the basis of concentrated ternary electrolyte theory. The discharge product ZnO is highly soluble in KOH solution, resulting in the potassium hydroxide-potassium zincate-water ternary mixture. It was also reported that the solution near the discharging zinc surface could become supersaturated with zincate (23). Therefore, fundamental equations developed for describing the concentrated ternary solution (24) were applied to the present model.

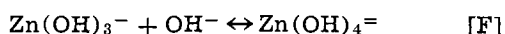
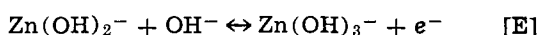
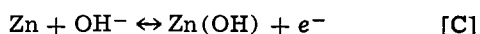
The model presented here consists of Ohm's law in the solution phase, Ohm's law in the matrix phase, kinetic rate expression, conservation of charge, and conservation equations of OH⁻ ion, zincate ion, water, and solid species. The effect of local mass transfer between the electrode active surface and the bulk solution in the pores, changes in porosity, variations of active surface area, and convection arising from the difference in molar volumes of reactants and products were included. The effect of the membrane separator and the solution reservoir on the zinc electrode performance was also included in the model to predict mathematically behavior under conditions similar to a practical battery system. The results of the numerical solution were used to suggest certain modes of failure and performance limitations of the zinc electrode.

The Mathematical Model

Zinc electrode reaction.—The process occurring in the zinc electrode in alkaline solution has been described by a dissolution-precipitation mechanism (25, 26)



Discharge of the zinc electrode produces supersaturated zincate solution by electrochemical reaction [A], from which ZnO precipitates by a chemical reaction [B]. The reverse process occurs during charge. Previous investigators (26, 27) have attempted to determine the rate of the precipitation reaction. However, values of rate constants are not precisely known. The kinetic mechanism of reaction [A] has been studied in alkaline media using both zinc amalgam electrodes (28-30) and pure solid zinc electrodes (31-34). The mechanism proposed by Bockris *et al.* (34) was considered in the present work to estimate kinetic parameters



where reaction step [E] is the rate-controlling step.

In a concentrated KOH solution saturated with ZnO, it is possible for the following complexes of zinc species to be present as intermediate compounds: Zn²⁺, Zn(OH)⁺, Zn(OH)₂, Zn(OH)₃⁻, Zn(OH)₄²⁻, . . . Zn(OH)_n²⁻ⁿ. Based on the equilibrium constants reported by Butler (35), Boden *et al.* (36) concluded that the only species present to any appreciable extent in KOH solution was Zn(OH)₄²⁻ ion. Other workers (37-39) also confirmed that the predominant species was zincate ion. Therefore, in the present work, the electrolytic solution was considered as a four component system containing K⁺, OH⁻, Zn(OH)₄²⁻, and H₂O.

Description of the model.—A one-dimensional mathematical model of a porous zinc electrode has been proposed which predicts OH⁻ concentration c_3 , Zn(OH)₄²⁻ concentration c_2 , superficial current density j , porosity ϵ , superficial volume average velocity v , potential in the solution ϕ_2 , and potentials in the matrix ϕ_1 , as a function of time and position perpendicular to the electrode surface. The geometric feature of the model is quite similar to that of previous studies (16, 19). A backing plate is located at $x = 0$ and the membrane or boundary layer at $x = L$. The porous electrode is treated as a homogeneous mixture of ionically conducting solution phase and electrically conducting matrix phase. The solid matrix might contain zinc, ZnO, and inert conducting materials (e.g., graphite) or any combination of the three.

The macroscopic averaging technique (14, 40) was applied to the present model by disregarding the actual geometric details of the pores. For example, consider c_i as the concentration of species i averaged over the volume of solution in the pores. Then the superficial concentration, averaged over the unit volume of the electrode, is ϵc_i where ϵ is the porosity of the electrode. If N_i is defined by the superficial flux based on the unit cross-sectional area of the electrode, N_i/ϵ represents the flux through the unit area of solution phase in the pores. Similarly, v/ϵ is the velocity in the solution phase if v is a superficial bulk fluid velocity.

With these average quantities (N_i/ϵ , i_2/ϵ , and v/ϵ), transport equations developed for the concentrated ternary solution (24) were applied to the present four component system on the basis of reaction mechanism [A] and [B]. The results are written as

$$\frac{N_2}{v_2A} = -D_{AA}\epsilon^{1+t} \frac{dc_A}{dx} - D_{AB}\epsilon^{1+t} \frac{dc_B}{dx} + \frac{t_2}{z_2v_2A\mathbf{F}} i_2 + c_A v \quad [1]$$

$$\frac{N_3}{v_3B} = -D_{BA}\epsilon^{1+t} \frac{dc_A}{dx} - D_{BB}\epsilon^{1+t} \frac{dc_B}{dx} + \frac{t_3}{z_3v_3B\mathbf{F}} i_2 + c_B v \quad [2]$$

$$N_o = D_{OA}\epsilon^{1+t} \frac{dc_A}{dx} + D_{OB}\epsilon^{1+t} \frac{dc_B}{dx} + c_o v \quad [3]$$

where

$$\left. \begin{aligned} D_{ij} &= (D_{ij})^o - D_{Oj}(c_i/c_o) & ; i, j = A, B \\ D_{Oj} &= \sum_k c_o \bar{V}_k (D_{kj})^o & ; j, k = A, B \\ t_i &= (t_i)^o - z_i c_i t_o & ; i = 1, 2, 3 \\ t_o &= \frac{\bar{V}_1(t_1)^o}{z_1} + \frac{\bar{V}_2(t_2)^o}{z_2} + \frac{\bar{V}_3(t_3)^o}{z_3} \end{aligned} \right\} \quad [4]$$

where subscripts 1, 2, 3, A, B, and o represent K⁺ ion, Zn(OH)₄²⁻ ion, OH⁻ ion, potassium zincate, potassium hydroxide, and water, respectively, N_i is the flux of species i , \bar{V}_i is the partial molar volume of species i , c_i is the concentration of species i , z_i is the charge number of species i , i_2 is the current density

in the solution phase, t is the tortuosity factor, and v is the volume average velocity. The diffusion coefficients D_{ij} ($i, j = A, B$) and the transference numbers t_i ($i = 1, 2, 3$) are defined with respect to the volume average velocity v , while those with superscripts "o" are referred to the solvent reference velocity v_o . The ν_{ij} is the number of ionic species i per molecule of electrolyte "j."

Electroneutrality requires $z_1\nu_{1A} + z_2\nu_{2A} = 0$, $z_1\nu_{1B} + z_3\nu_{3B} = 0$, and $z_1c_1 + z_2c_2 + z_3c_3 = 0$. For the solvent velocity reference frame, the parameters D_{OA} , D_{OB} , and t_o disappear from the above equations. The parameters D_{ij} , t_i , and v should be replaced with $(D_{ij})^o$, $(t_i)^o$, and v_o , respectively, to represent the flux equations referred to the solvent velocity v_o . The effective diffusion coefficients $D_{ij}e^{1+t}$ account for the tortuosity correction. Schofield and Dakshinamurti (41) have suggested that the effective diffusion coefficients are proportional to $e^{1.5}$ (or $t = 0.5$). The parameter t_o was taken as zero (or $t_i = t_i^o$) by definition [see Ref. (24)].

Ohm's law in the solution phase.—A modified Ohm's law applied to the ternary electrolyte solution is given by the following equation

$$i_2 = -\kappa e^{1+t} \frac{d\phi_2}{dx} - \frac{\kappa e^{1+t}}{nF} \left(\frac{s_2}{\nu_{2A}} + \frac{nt_2}{z_2\nu_{2A}} - \frac{s_o}{c_o} c_A \right) \frac{d\mu_A}{dx} - \frac{\kappa e^{1+t}}{nF} \left(\frac{s_3}{\nu_{3B}} + \frac{nt_3}{z_3\nu_{3B}} - \frac{s_o}{c_o} c_B \right) \frac{d\mu_B}{dx} \quad [5]$$

where ϕ_2 is the potential of a reference electrode of the same kind as the working electrode placed in the bulk solution within the pores of the porous electrode, κ is the conductivity of solution at concentration c_i , and μ_i is the chemical potential of species i . The s_i is the stoichiometric coefficient of species i for the electrode reaction given by

$$\sum_i s_i M_i^{z_i} = ne^- \quad [6]$$

where M_i is the symbol representing the chemical formula of species i , z_i is the charge number of species i , and n is the number of electrons transferred by the electrode reaction.

The effective solution conductivity corrected for tortuosity is represented by κe^{1+t} . Meredith and Tobias (42) and Gagnon (43) suggested t as 0.5, while $t = 2$ was observed by Ksenzhek *et al.* (44). Simonsson (20) and Romanova and Selitsky (45) observed an effective conductivity which was only one-tenth of the conductivity of the free electrolytic solution. They attributed this large reduction to the gas generated in the pores.

Redox electrochemical rate expression.—The rate of charge transfer reaction [A] at the solid-solution interface and the conservation of charge can be represented by the following equation

$$j = \frac{1}{a_m} \left(\frac{di_2}{dx} \right) = i_o^o \left(\frac{c_{2s}}{c_{2r}} \right)^\gamma \left(\frac{c_{3s}}{c_{3r}} \right)^\zeta \left(\frac{\alpha_a F}{e RT} (\phi_1 - \phi_{2s}) - \frac{\alpha_c F}{RT} (\phi_1 - \phi_{2s}) \right) \quad [7]$$

where α_a and α_c are the effective anodic and cathodic transfer coefficients, respectively, j is the local transfer current per unit area of active zinc surface which acts as active sites for reaction (A), i_o^o is the exchange current density evaluated at reference concentrations c_{2r} and c_{3r} , γ and ζ are the orders of dependence of the exchange current density on zincate and hydroxide concentrations, respectively, ϕ_1 is the potential of the matrix phase, ϕ_{2s} is the potential of the reference electrode of the same kind as the working electrode located just outside the double layer, a_m is the solid-

solution interface area per unit volume of electrode which acts as active sites for reaction [A]. The transfer current j was related to the gradient of the current density i_2 by the charge conservation equation.

The concentration of zincate ion (c_{2s}) and hydroxide ion (c_{3s}) at the reacting metal surface can be determined from the following equations

$$\frac{di_2}{dx} = -\frac{nF}{s_2} ak_A (c_{2s} - c_2) \quad [8]$$

$$\frac{di_2}{dx} = -\frac{nF}{s_3} ak_B (c_{3s} - c_3) \quad [9]$$

where a is the solid-solution interface area per unit volume of the electrode and k_i is the mass transfer coefficient of species i transferring from the bulk solution in the pores to the reaction sites which are active for charge transfer reaction [A] or vice versa.

The potential at the metal surface, ϕ_{2s} , was assumed to be the same as the potential of the bulk solution in the pores, ϕ_2 . The mass transfer coefficients k_A and k_B and the active surface area a_m change with time and the state of charge. True values of these parameters are difficult to determine. Consequently, the mathematical forms described in Appendix B were assumed in this work. The constants γ , ζ , α_a , and α_c , corresponding to the reaction mechanism of Bockris *et al.* (34), are 0.75, 0, 1.5, and 0.5, respectively. The exchange current density, i_o^o , reported by previous investigators (29, 31, 34, 46) has values in the range of 10-300 mA/cm².

Species conservation equation.—The use of appropriate averaging quantities yields the following conservation equation

$$\frac{\partial \epsilon c_1}{\partial t} = -\frac{dN_1}{dx} + R_1 \quad [10]$$

where R_1 represents production or consumption of species i due to the electrode reaction. During discharge, zincate ion is produced by charge transfer reaction [A] and consumed by precipitation reaction [B]. On the other hand, hydroxide ion is consumed by reaction [A] and produced by reaction [B]. The reaction source term R_i can be written as

$$R_1 = -\frac{s_1}{nF} \frac{di_2}{dx} + s_1^* ak_{s^*} (c_2 - c_{2e}) \quad [11]$$

where k_{s^*} , during discharge, is defined by the rate constant combining mass transfer of zincate ions from bulk solution in the pores to the reaction sites with chemical rate constant for precipitation of ZnO, c_{2e} is the equilibrium or saturation concentration of zincate ion at the solid-solution interface which is active for reaction [B], and s_1 and s_1^* are the stoichiometric coefficients of species i for the reaction [A] and for the reaction [B], respectively, defined by Eq. [6]. Substitution of Eq. [11] into Eq. [10] yields

$$\frac{\partial \epsilon c_2}{\partial t} = -\frac{dN_2}{dx} + \frac{1}{nF} \frac{di_2}{dx} - ak_{s^*} (c_2 - c_{2e}) \quad [12]$$

$$\frac{\partial \epsilon c_3}{\partial t} = -\frac{dN_3}{dx} - \frac{4}{nF} \frac{di_2}{dx} + 2ak_{s^*} (c_2 - c_{2e}) \quad [13]$$

$$\frac{\partial \epsilon c_o}{\partial t} = -\frac{dN_o}{dx} + ak_{s^*} (c_2 - c_{2e}) \quad [14]$$

where $s_2 = -s_2^* = -1$, $s_3 = 4$, $s_3^* = -2$, $s_o = 0$, and $s_o^* = -1$ have been substituted.

Overall conservation equation.—The porosity of the electrode will increase as zinc dissolves and decrease as ZnO precipitates. A material balance on the solid species shows how the porosity varies with time as

$$\frac{\partial \epsilon}{\partial t} = \frac{1}{nF} \sum_i \bar{V}_i s_i \frac{di_2}{dx} + \sum_i \bar{V}_i s_i^* a k_s^* (c_2 - c_{2e}) \quad [15]$$

where \bar{V}_i is the partial molar volume of species i and the species i represents the solid species, namely, zinc and ZnO.

Similarly, a material balance on the ionic species leads to the following electrolyte continuity equation

$$\frac{\partial \epsilon}{\partial t} + \frac{dv}{dx} = - \left(\frac{\bar{V}_A t_2}{z_2 \nu_{2A}} + \frac{\bar{V}_B t_3}{z_3 \nu_{3B}} + \frac{\bar{V}_A s_2}{\nu_{2A}} + \frac{\bar{V}_B s_3}{\nu_{3B}} + \frac{\bar{V}_o s_o}{n} \right) \frac{di_2}{F dx} - a k_s^* \left(\frac{s_2^* \bar{V}_A}{\nu_{2A}} + \frac{s_3^* \bar{V}_B}{\nu_{3B}} + \bar{V}_o s_o^* \right) (c_2 - c_{2e}) \quad [16]$$

This equation is obtained by adding Eq. [12], [13], and [14] which have been multiplied by \bar{V}_A/ν_{2A} , \bar{V}_B/ν_{3B} , and \bar{V}_o , respectively, and using the relations of $c_A \bar{V}_A + c_B \bar{V}_B + c_o \bar{V}_o = 1$, $\bar{V}_A D_{AA} + \bar{V}_B D_{BA} - \bar{V}_o D_{OA} = 0$, and $\bar{V}_A D_{AB} + \bar{V}_B D_{BB} - \bar{V}_o D_{OB} = 0$. The last two relations for D_{OA} and D_{OB} can be derived from Eq. [4].

From Eq. [15] and [16], the convective bulk flow motion in the porous electrode can be described by the following overall continuity equation

$$\frac{dv}{dx} = - \frac{1}{nF} \left[\bar{V}_{Zn} + 4\bar{V}_B - \bar{V}_A - 2 \left(\frac{t_2 \bar{V}_A}{\nu_{1A}} + \frac{t_3 \bar{V}_B}{\nu_{1B}} \right) \right] \frac{di_2}{dx} + a k_s^* [\bar{V}_{ZnO} + \bar{V}_o + 2\bar{V}_B - \bar{V}_A] (c_2 - c_{2e}) \quad [17]$$

The second bracket term is the volume change of reaction [B]. The first bracket term represents the volume change of reaction [A], i.e., $(t_2 \bar{V}_A/\nu_{1A} + t_3 \bar{V}_B/\nu_{1B}) = \bar{V}_1$, if the transference number t_o , defined in Eq. [4], is chosen as zero.

Ohm's law in the solid matrix.—Ohm's law in the solid matrix can be written as

$$i_1 = I - i_2 = -\sigma_{em} \frac{d\phi_1}{dx} \quad [18]$$

where ϕ_1 is the potential of the solid matrix and ϵ_m is the volume of conducting material per unit volume of the electrode (not necessarily equal to $1 - \epsilon$). The superficial current density in the solid phase i_1 and that in the solution phase i_2 are related to the total applied current density I as $i_1 + i_2 = I$. The conductivity of the solid matrix is approximated by

$$\sigma = \sigma_{Zn}(\epsilon_{Zn})^{t^*} + \sigma_{ZnO}(\epsilon_{ZnO})^{t^*} + \sigma_I(\epsilon_I)^{t^*} \quad [19]$$

where σ_{Zn} , σ_{ZnO} , and σ_I are the conductivities of the zinc metal, zinc oxide, and inert material in the pure solid phase, respectively, and ϵ_{Zn} , ϵ_{ZnO} , and ϵ_I are the volume fractions of the corresponding solid species.

Computation procedures.—The six equations; two second-order equations [12] and [13] and four first-order equations [5], [7], [17], and [18]; form a set of nonlinear coupled differential equations. The six unknown variables are i_2 , ϕ_2 , c_2 , c_3 , v , and ϕ_1 , which are functions of time and position. The six equations can be solved by use of a numerical technique with the following initial and boundary conditions.

Initial conditions at time = 0 are

$$c_2 = c_{2o}, \quad c_3 = c_{3o}, \quad v = 0 \quad [20]$$

For the other variables, the following approximate equations were solved to estimate the initial profiles of i_2 , ϕ_1 , and ϕ_2

$$\left. \begin{aligned} i_2 &= -\kappa \epsilon^{1+t} \frac{d\phi_2}{dx} = -\kappa_e \frac{d\phi_2}{dx} \\ \frac{di_2}{dx} &= a_m t_o \frac{(\alpha_a + \alpha_c) F}{RT} (\phi_1 - \phi_2) = R_e (\phi_1 - \phi_2) \\ i_1 &= I - i_2 = -\sigma_{em} \frac{d\phi_1}{dx} = -\sigma_e \frac{d\phi_1}{dx} \end{aligned} \right\} \quad [21]$$

The solution of Eq. [21] becomes as follows, e.g., for current distribution

$$\frac{di_2}{dy} = \frac{IQ}{\kappa_e + \sigma_e} \left[\sigma_e \frac{\cosh Qy}{\sinh Q} + \kappa_e \frac{\cosh Q(1-y)}{\sinh Q} \right]; \quad Q = L \sqrt{R_e \left(\frac{1}{\kappa_e} + \frac{1}{\sigma_e} \right)} \quad [22]$$

where y is the dimensionless distance from the backing plate (x/L); L is the electrode thickness.

The boundary conditions at $x = 0$ are as follows

$$\frac{d\phi_2}{dx} = 0 \text{ (or } i_2 = 0), \quad \frac{dc_2}{dx} = 0, \quad \frac{dc_3}{dx} = 0, \quad v = 0, \quad \phi_1 = 0 \quad [23]$$

The boundary conditions at $x = L$ are

$$\left. \begin{aligned} i_2 &= I \\ \frac{\partial(Vc_i)}{\partial t} &= A(N_i)_L - A(N_i)_m; \quad i = 2, 3 \end{aligned} \right\} \quad [24]$$

where I is the applied current density, A is the cross-sectional area of the electrode, and V is the volume of the solution reservoir located between the electrode surface and the membrane. The $(N_i)_L$ and $(N_i)_m$ represent fluxes of species i across the boundary $x = L$ and across the membrane, respectively. If a solution reservoir is absent (i.e., $V = 0$), the above boundary conditions simply represent the conservation of fluxes at the boundary, i.e., $(N_2)_L = (N_2)_m$ and $(N_3)_L = (N_3)_m$.

The fluxes $(N_2)_L$ and $(N_3)_L$ are Eq. [1] and [2], applied to the boundary $x = L$, respectively. The fluxes $(N_2)_m$ and $(N_3)_m$ are written as

$$\left. \begin{aligned} \frac{(N_2)_m}{\nu_{2A}} &= \frac{(D_{AA})_m}{d} (c_{2L} - c_{2o}) + \frac{(t_2)_m}{z_2 \nu_{2A} F} I + c_{2m} v_m \\ \frac{(N_3)_m}{\nu_{3B}} &= \frac{(D_{BB})_m}{d} (c_{3L} - c_{3o}) + \frac{(t_3)_m}{z_3 \nu_{3B} F} I + c_{3m} v_m \end{aligned} \right\} \quad [25]$$

where d is the thickness of the membrane and subscripts "m", "L", and "o" represent values taken at the membrane, reservoir solution, and the counter-electrode compartment, respectively.

The six equations were linearized about a trial solution, put into finite difference forms, and solved by the numerical technique developed by Newman (47) subject to the initial conditions [20] and [21] and the boundary conditions [23] through [25]. The Crank-Nicolson implicit method (48) was used for averaging time derivatives in Eq. [12] and [13]. The resulting six finite difference equations are correct to second order, h^2 and $(\Delta t)^2$, where h and Δt are the mesh sizes of distance and time. The convergence criterion used was 10^{-5} which is defined by the ratio of the difference between the two successive solutions to the present solution. The details of the numerical procedures as well as the computer program have been described by Sunu (49). The physical and chemical parameters used for numerical calculations are summarized in Appendix A. The numerical calculations

were carried out in double precision using an IBM 360/91 computer.

Result

The mathematical model described in the previous section was solved under the following conditions; the initial solution of 8M KOH - 0.66M $K_2Zn(OH)_4$ and the electrode initially composed of 40% void volume, 50% zinc, and 10% ZnO by volume ($\epsilon = 0.4$, $\epsilon_{Zn} = 0.5$, $\epsilon_{ZnO} = 0.1$, and $\epsilon_I = 0$). The total capacity of this electrode estimated from the amount of zinc is 17.6 A-min and corresponds to a discharge for 352 min at 50 mA/cm². This capacity is referred to as "100% depth of discharge" or as "100% utilization" throughout this paper. The capacity equivalent to the hydroxide ions of the pore solution is only 1.03 A-min or 5.85% utilization. This number is surprisingly small. Three boundary cases were considered using the parameters shown in Table I. They include the type I membrane boundary (second column), solution boundary (third column), and type II membrane boundary which is equivalent to the use of one layer of RAI P2291 cation exchange membrane. The results on discharge are shown in Fig. 1 to 5 and those on cycling are summarized in Fig. 6 and 7.

Figure 1 shows how concentrations of KOH (top curves) and potassium zincate (bottom curves) vary with time during discharge. Initial concentration was shown by dotted lines. After 1 min polarization, hydroxide concentration decreases to 7.6M, a value averaged over the entire pore solution, and zincate becomes supersaturated (curve A). On further discharge, hydroxide concentration drops rather slowly because a large amount of hydroxide ions which are transferring from the counterelectrode also participate in the electrode reaction. For example, at 30% depth of discharge (or 5.28 A-min), only 0.43 A-min is corresponding to the decrease of OH⁻ concentration of pore solution from 8M to 4.7M, and the remaining 4.85 A-min is resulting from the hydroxide ions supplied from the counterelectrode compartment. This indicates that the membrane affects significantly the utilization of active zinc particularly of the cell having a limited amount of electrolyte. Equilibrium concentration of zincate decreases with KOH concentration and therefore zincate concentration also decreases as discharge continues. However, there is always some degree of supersaturation with a maximum being located near the electrode face.

The effect of the membrane is clearly shown in Fig. 2 where profiles of KOH concentration obtained with three types of boundaries are presented. The average KOH concentration obtained after 10% depth of discharge was 7.5M for the solution boundary, 5.3M for the type I membrane boundary, and 2M for the type II membrane boundary. A similar calculation showed that a cell with two layers of type II (RAI P2291 cation exchange) membrane was completely depleted of hydroxide ions after only 8% depth of discharge. Clearly, discharge of the cell having a type II membrane as a separator could fail due to KOH depletion.

Table I. Transport parameters applied to the various boundary layers

	Type I membrane boundary	Solution boundary	Type II membrane (RAI P2291)*
$(t_1)_m$	0.5	0.23	0.5
$(t_2)_m$	0.0	0.05	0.0
$(t_3)_m$	0.5	0.72	0.5
$(D_{AA})_m$ (cm ² /sec)	2.5×10^{-6}	6.0×10^{-6}	1.0×10^{-8}
$(D_{BB})_m$ (cm ² /sec)	2.5×10^{-7}	2.0×10^{-3}	7.5×10^{-8}
d (cm)	0.0025	0.005	0.0025
$(L_{AA})_m$ (cm/sec)	1.0×10^{-5}	0.0012	4.0×10^{-6}
$(L_{BB})_m$ (cm/sec)	1.0×10^{-4}	0.004	3.0×10^{-5}

* Transport parameters for RAI P2291 membrane were taken from the data of Sinha and Bennion (50). The parameter $(L_{11})_m$ is defined by $(D_{11})_m/d$ (refer to Eq. [25]).

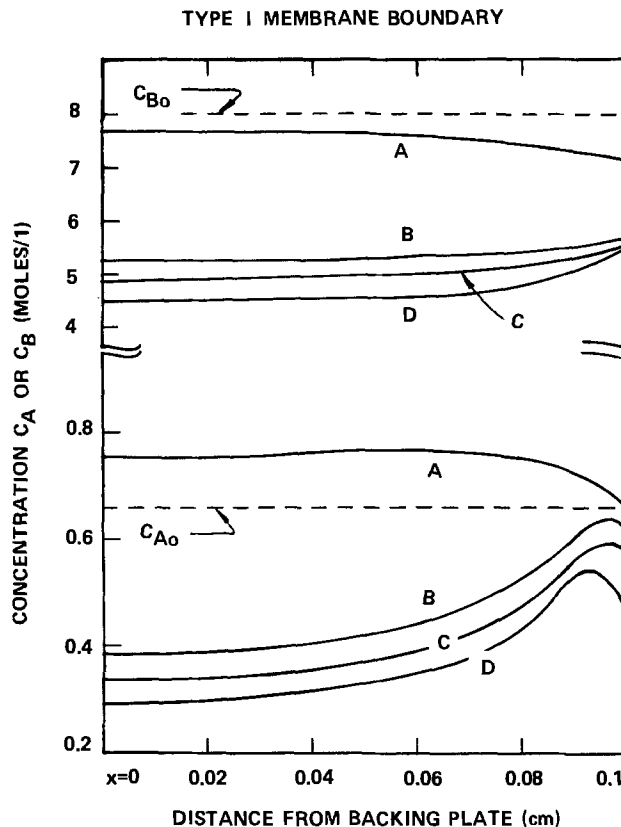


Fig. 1. Concentration profiles during constant current discharge for type I membrane boundary ($i = 50$ mA/cm², A for 1 min polarization and B, C, and D for 10%, 20%, and 30% depth of discharge, respectively).

The charge transfer current, j (mA/cm²), is plotted as a function of distance in Fig. 3. Initially, the reaction distribution is shown as curve A, having a maximum at the face of the electrode. As discharge continues to 10% depth, KOH concentration, porosity, and therefore the conductivity of the solution decreases. This effect shifts the reaction toward the front face

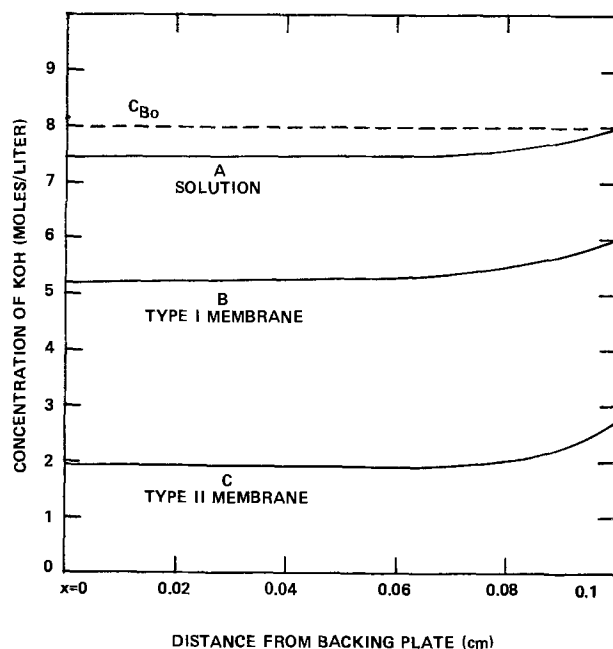


Fig. 2. Profiles of KOH concentration after 10% depth of discharge ($i = 50$ mA/cm² and A, B, and C for solution boundary, type I membrane boundary, and type II membrane boundary, respectively).

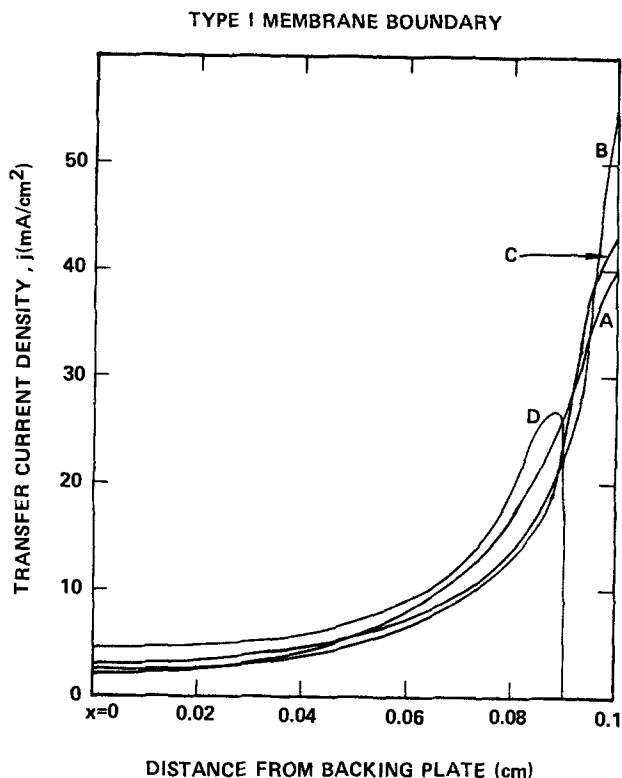


Fig. 3. Distribution of local charge transfer current, j (mA/cm²), for type I membrane boundary ($I = 50$ mA/cm², $L = 0.1$ cm, and A, B, C, and D represent 0%, 10%, 20%, and 40% depth of discharge, respectively).

and the reaction profile becomes less uniform as shown in curve B. When the electrode is discharged further beyond 20% depth, the reaction at the electrode face starts decreasing due to the depleted active zinc metal (curve C). After 40% depth of discharge, all the zinc near the front face is used up as shown in curve D. The overpotentials rose substantially when only 40% of the initial zinc metal was utilized. The reaction profile is highly nonuniform and the effective reaction zone moves step by step from the face of the electrode toward the backing plate. Similar trends were obtained with the other two boundaries.

The distribution of solid zinc and ZnO, in terms of volume fractions, is plotted in Fig. 4 for the type I membrane and in Fig. 5 for the solution boundary. The total amount of zinc dissolution into zincate at a specified time, i.e., the integrated area between the dotted line denoted by $(\epsilon_{Zn})_0$ and the curve ϵ_{Zn} at time t , are the same for both cases. However, the total amount of ZnO precipitated, i.e., the integrated area of ZnO profiles, is smaller for the solution case than for the membrane case. For example, after 40% depth of discharge, the amount of precipitated ZnO obtained from Fig. 4 and 5 are 95% and 55%, respectively, of the total amount of the zinc consumed during the same period of 141 min. The missing zinc oxide is lost into the counterelectrode compartment as a soluble species, zincate ion, before precipitation occurs.

The electrode initially composed of 40% liquid filled pores, 50% zinc, and 10% ZnO by volume was cycled numerically with a constant current density of 50 mA/cm². Each cycle consisted of 20% depth of discharge and 20% depth of charge. The current distribution predicted during one cycle is presented in Fig. 6 for the type I membrane case. It shows that current distribution becomes more uniform on charging than on discharging, in particular, near the beginning of charge (curve A). When charge starts, the solid-solution interfacial area near the electrode face contains mainly the area of ZnO precipitates and a very small

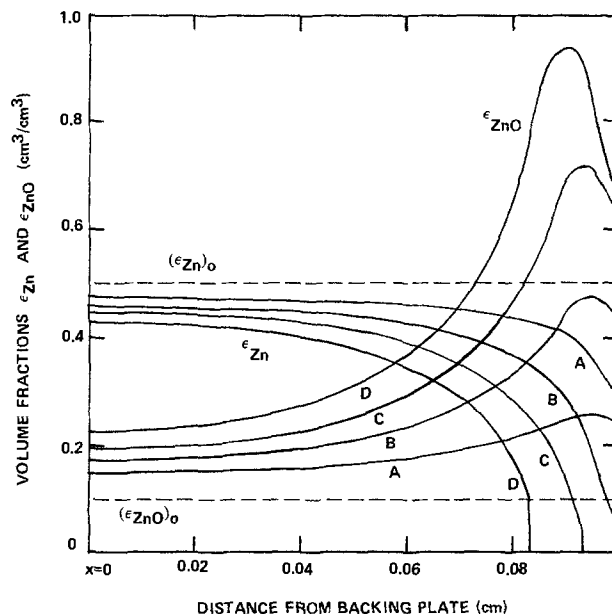


Fig. 4. Distribution of Zn and ZnO plotted as volume fractions for type I membrane boundary ($I = 50$ mA/cm², and A, B, C, and D represent 10%, 20%, 30%, and 40% depth of discharge, respectively).

active zinc area (see curves B of Fig. 4). This reduced zinc area at the electrode face prohibits the transfer reaction on charge and shifts the reaction toward the backing plate, resulting in curve A. If sufficient amount of zinc forms and serves as nucleation sites for further zinc deposition reaction, current distribution which is similar in shape to that of discharge will result (curves B and C).

In Fig. 7, the volume fractions of zinc and zinc oxide during two cycles are plotted as a function of the distance from the backing plate. After each complete cycling, the solid zinc species (Zn and ZnO) have not reformed in their original positions. This is due to the difference in the current distribution during discharge and charge. The redistribution of zinc and zinc oxide becomes less uniform as cycling continues. Numerical predictions obtained with a cell having no membrane

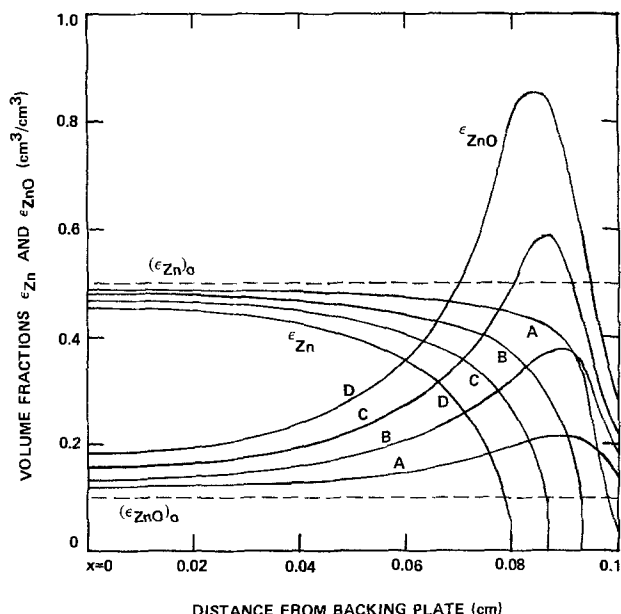


Fig. 5. Distribution of Zn and ZnO plotted as volume fractions for solution boundary ($I = 50$ mA/cm², and A, B, C, and D represent 10%, 20%, 30%, and 40% depth of discharge, respectively).

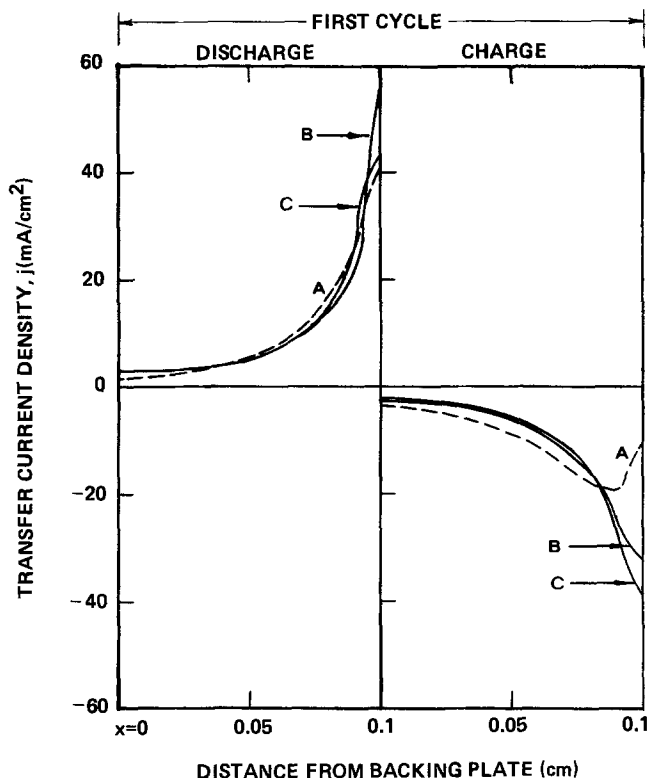


Fig. 6. Distribution of local charge transfer current density, j (mA/cm²), during the first cycle for type I membrane boundary ($I = 50$ mA/cm², $L = 0.1$ cm, and A, B, and C represent 0%, 10%, and 20% depth of discharge or charge, respectively).

showed greater degree of redistribution of solid species (49).

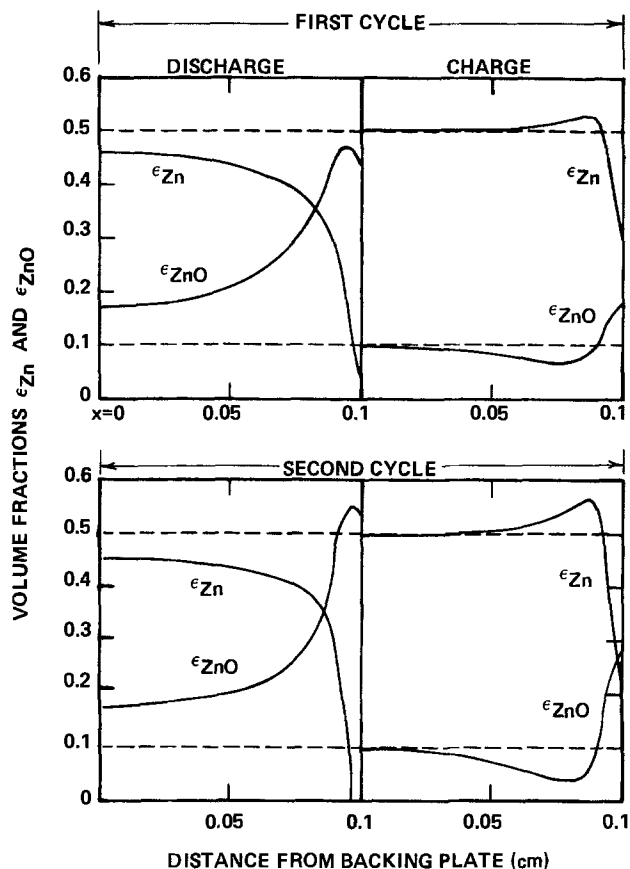


Fig. 7. Distribution of Zn and ZnO plotted as volume fractions during two cycles for type I membrane boundary ($I = 50$ mA/cm², $L = 0.1$ cm, $\epsilon_0 = 0.4$, $(\epsilon_{Zn})_0 = 0.5$, $(\epsilon_{ZnO})_0 = 0.1$).

Discussion

Failure during discharge.—Zinc electrode behavior occurring during discharge has been predicted by a mathematical model. The model predicts that discharge of the zinc electrode having a porosity of 0.4 and one layer of type I membrane could fail after only 40% utilization due to the decrease in pore size (blockage of the first kind) as shown in Fig. 4. The primary effect of the decreased pore size is, as in the lead positive electrode (20), the restricted diffusion of electrolytes into the interior of the porous electrode, causing electrolyte depletion at the reaction sites. If the porosity falls below a certain limit, the resistance across the pore solution rises substantially and serves as a factor in limiting further utilization.

The model predicts that the reaction distribution is highly nonuniform, and the effective reaction zone is very thin (Fig. 3). The reaction distribution or the penetration depth has been characterized by certain dimensionless parameters (14). In the case of uniform concentration and low activation polarization, two parameters, σ_e/κ_e and Q of Eq. [22], could determine the shape of distribution. The reaction distribution becomes less uniform as the parameter Q increases. The ratio σ_e/κ_e determines the shape of distribution curves, namely, the position having a maximum utilization. Maximum utilization would occur at the electrode face for $\sigma_e > \kappa_e$ and at the backing plate for $\kappa_e > \sigma_e$. Concentration polarization and the decrease of pore size have an effect of increasing the effective resistance of pore solution and thus promoting the degree of nonuniformity. This effect was illustrated in Fig. 3 (compare curves A and B). This nonuniform reaction distribution will accelerate the failure due to pore plugging at the electrode surface. The zinc metal near the backing plate serves simply as an inert matrix and does not contribute to the cell capacity.

The loss of ZnO species into the counterelectrode compartment during discharge was very large for cells without a membrane (see Fig. 5), while for the cell with a membrane (Fig. 4), mass transfer of zincate ion into the counterelectrode compartment was restricted. However, KOH concentration was depleted significantly during discharge of a cell having one layer of RAI P2291 cation exchange membrane as was predicted in Fig. 2 (curve C). With two layers of RAI P2291 membrane, only 8% utilization resulted in the complete depletion of hydroxide ions inside the zinc electrode compartment (54).

Discharge failure mentioned above could be interpreted by a single process, i.e., the limited mass transfer of soluble species to and from the dissolving zinc surfaces. For the planar zinc electrode, discharge failure has been interpreted as a phenomenon called "passivation" which was described by a limited diffusion of product species, zincate ions, away from the dissolving surfaces (51-53). Discharge of the porous electrode involves more complicated and interrelated phenomena, and therefore it appears to be valuable to divide the limiting process into several sub-mechanisms having more precise meaning, i.e., passivation, pore plugging, and depletion of electrolyte. Each mechanism is defined as follows.

Consider a test electrode compartment which contains solution inside the porous electrode (designated as "pore solution"), and solution outside the pores but within that compartment ("reservoir solution"). Solution outside the test electrode compartment on the other side of the membrane separator which is usually contained in the counterelectrode compartment is denoted by "external solution." Discharge of the porous electrode may fail in three ways:

(i) If the reservoir solution is severely depleted of hydroxide ions due to the limited transfer of OH⁻ ions across the membrane, then the pore solution is also depleted of electrolyte KOH, as was predicted with a cell having one layer of RAI P2291 membrane (curve

C of Fig. 2). This causes passivation at the active zinc surfaces due to a decrease in solubility of ZnO and a rapid increase in the rate of ZnO precipitation, in addition to increased resistance losses. This phenomenon is defined as the electrolyte depletion. To reduce this effect, sufficient amount of electrolytes should be provided in the solution reservoir. Proper choice of the membrane, which leads to a maximal supply of OH⁻ ions from the counterelectrode compartment and also a minimal chance for zinc dendrite penetration, is also important.

(ii) The reservoir solution could retain the electrolyte concentration at a fairly constant level throughout the discharging process, provided that the reservoir has a large volume. But the pore solution still can be depleted of electrolyte due to the limited mass transfer across the reaction zone located near either side of the electrode surfaces, which has smaller pores. The consequences will be the depletion of electrolytes at discharging zinc surfaces, resulting in passivation. This is defined as pore plugging and can be eliminated by using high porosity electrodes. Discharge failure predicted with the solution boundary and type I membrane boundary are attributed to pore plugging (see Fig. 4 and 5).

(iii) Even if the KOH concentration of the pore solution as well as the reservoir solution remains appreciably high, passivation could occur by the physical blocking of the active zinc surface by a precipitated ZnO film, which forms due to the depleted hydroxide ion or due to the excess zincate at the zinc surface. This phenomenon is defined as passivation, having the same meaning as was used for planar electrodes. Passivation of this type could occur under very high current load. Electrodes with high active surface area and with uniform current distribution would reduce local transfer current density and thus the chance for passivation.

Failure during cycling.—Zinc electrode failure occurring after many cycles can be referred to as a phenomenon called "redistribution of solid zinc species (Zn and ZnO)." Inability of reforming the solid zinc species in their original position during cycling causes zinc dendrite penetration and shape change. High solubility of ZnO in KOH solution accentuates the redistribution of zinc species from one part of the electrode to the other.

Figure 5 shows that for the cell having no membrane only 55% of the discharge product (zincate ions) precipitates as ZnO and the remaining half diffuses into the counterelectrode compartment before precipitation occurs. On charge, once the zincate source in the zinc electrode compartment is depleted, zinc deposits will grow towards additional zincate which is transferring from the counterelectrode compartment. This type of mass transport leads to zinc dendrite formation which eventually causes short circuits to the counterelectrode. On the other hand, if a membrane is used as a separator, 95% of the discharge product precipitates as ZnO as shown in Fig. 4. Use of a membrane restricts zincate movement away from the test electrode. Charge of this electrode is less likely to cause dendrite growth through the separator because the source of zincate ions remains in the zinc test electrode. Comparison of these two examples shows the main reason why industrial cells having appropriate membranes successfully reduce dendrite formation and short circuits. These membranes could also prevent zinc metal dendrite nucleation within themselves.

Redistribution of solid zinc and zinc oxide from one part of the electrode to the other can occur through the movement of zincate ions. The process involving zincate movement, e.g., on discharging, include the charge transfer reaction which produces zincate ions, mass transfer of zincate, and chemical precipitation of ZnO which consumes zincate. Therefore, current distribution which characterizes the charge transfer re-

action, degree of super- (or un-) saturation which determines precipitation or dissolution of ZnO, and mass transfer modes (diffusion, migration, and convection) will govern the redistribution of solid zinc species.

Shape change is the redistribution process of the solid zinc species in the direction parallel to the electrode surface (y-direction). Choi *et al.* (12) have proposed that the shape change was caused by convective flows driven primarily by membrane electro-osmotic effects, while McBreen (7) has emphasized the effect of the difference in the y-direction current distribution during charge and discharge. Choi *et al.* (13) confirmed experimentally that sealing or tight packing of the cell, which was designed to prevent convective flow, successfully reduced the shape change. This observation favors the convection model over McBreen's model.

Discharge of a zinc electrode induces convective flow toward the counterelectrode, resulting in a decrease of the total volume of electrolytic solution in the zinc electrode compartment. If the electrode is vented, the solution in the top reservoir will flow downward. The solution picks up zincate ions along the flow path causing greater precipitation rates in the direction of flow. On the other hand, on charge the increase of total volume of electrolytic solution caused by electro-osmotic flow will push the unsaturated solution toward the reservoir. The reservoir solution now becomes unsaturated and greater dissolution is expected near the vent or reservoir. Repeated cycling causes movement of solid zinc species from near the reservoir portion of the electrode to positions remote from the reservoir. If the electrode is sealed, convective flow, and thus shape change, will be limited.

Similar treatment can be applied to the redistribution of solid zinc in the x-direction perpendicular to the electrode surface. The present work deals with a sealed electrode to minimize the convective flow driven by a membrane. Under this condition, the convective flow arising from the volume changes due to the overall electrode reaction is on the order of 10^{-7} cm/sec and is considered negligible.

The reaction or current distribution in the x-direction during discharge is highly nonuniform as shown in Fig. 3. On the other hand, current distribution on charging is more uniform compared to that on discharging, since precipitated ZnO reduces the effective zinc surface area near the electrode face and shifts the reaction toward the backing plate (see Fig. 6). On repeated cycling, this difference of anodic and cathodic current distributions together with differences in the degree of super- (or un-) saturation causes the redistribution of solid zinc species and thus significant distortion of the electrode structure. The distorted structure is shown in Fig. 7. This mechanism is similar to that described by McBreen. Similar structure was also observed experimentally by Sunu and Bennion (54). If convective flow due to membrane pumping is allowed, more serious redistribution is expected. Similarly, allowing free movement of zincate ion into the counterelectrode, by eliminating the membrane, showed a greater degree of redistribution (49). This movement of solid zinc species in the x-direction could contribute to the loss in the cell capacity on cycling service.

Other factors such as effects of gas generation and changes in morphologies and the active surface area with cycling were excluded from this work. The results of this work can be applied to the design of zinc electrodes to improve their utilization and cycle life. The results also point out areas where further research should be emphasized in order to gain further performance improvement.

Acknowledgments

The authors acknowledge the support of this work provided by the U.S. Air Force Systems Command

under Contract No. F 44620-76-C-0098 and the University of California, Los Angeles.

Manuscript submitted Nov. 26, 1979; revised manuscript received Feb. 15, 1980.

Any discussion of this paper will appear in a Discussion Section to be published in the June 1981 JOURNAL. All discussions for the June 1981 Discussion Section should be submitted by Feb. 1, 1981.

Publication costs of this article were assisted by the U.S. Government.

APPENDIX A

Parameters Used in the Numerical Calculations³

a_o	=	50 cm ² /cm ³
c_{3o}	=	0.008 moles/cm ³
c_{2o}	=	0.00066 moles/cm ³
D_{AA}	=	6.86 × 10 ⁻⁶ cm ² /sec
D_{BB}	=	see ³
D_{AB}	=	D_{BA} = 0.0
i_o^o	=	0.06 A/cm ²
k_{Ao}	=	0.001 cm/sec
k_{Bo}	=	0.003 cm/sec
k_{XTL}	=	0.005 cm/sec
L	=	0.1 cm
s_1	=	s_{1*} = 0.0
s_2	=	$-s_{2*}$ = -1.0
s_3	=	$-2s_{3*}$ = 4.0
s_o	=	0.0
s_{o*}	=	-1.0
t	=	t^* = 0.5
t_1	=	0.23
t_3	=	0.72 at 10M KOH
\bar{V}_A	=	67.0 cm ³ /mole
\bar{V}_B	=	17.8 cm ³ /mole
\bar{V}_o	=	18.07 cm ³ /mole
\bar{V}_{Zn}	=	9.15 cm ³ /mole
\bar{V}_{ZnO}	=	14.51 cm ³ /mole
V	=	0.0 cm ³ (definition in Eq. [24])
v_m	=	0.0 cm/sec
α_a	=	1.5
α_c	=	0.5
γ	=	0.75
ξ	=	0.0
ϵ_o	=	0.4
$(\epsilon_{Zn})_o$	=	0.5
$(\epsilon_{ZnO})_o$	=	0.1
$(\epsilon_i)_o$	=	0.0
K	=	see ³
λ	=	0.0
σ_{Zn}	=	2 × 10 ⁵ mho/cm
σ_{ZnO}	=	0.01 mho/cm
σ_I	=	100.0 mho/cm

APPENDIX B

Mass Transfer Coefficients (k_A , k_B , k_{s*}) and Active Surface Areas (a , a_m , a_s)

The mass transfer coefficients k_A , k_B , and k_{s*} defined in Eq. [8], [9], and [11] are approximated by the following equations [see Ref. (49) for derivation]

$$ak_i = \frac{D_{ii}}{\delta} \frac{a - a_m}{\ln\left(\frac{a}{a_m}\right)}; \quad i = A, B$$

$$\frac{1}{ak_{s*}} = \frac{1}{\left(\frac{D_{AA}}{\delta}\right) \frac{(a - a_s)}{\ln\left(\frac{a}{a_s}\right)}} + \frac{1}{a_s k_{XTL}}$$

where δ is the characteristic diffusion length between the active metal surface and the bulk within the pores, k_{XTL} is the chemical rate constant for precipitation or dissolution of ZnO, and D_{AA} and D_{BB} are the

³The conductivity of electrolytic solution, k , (55), solubility of ZnO in KOH solution (56), activity coefficients of KOH and potassium zincate (57, 58), and diffusion coefficients of potassium hydroxide, D_{BB} , (59) were expressed as a function of concentration based on the various reported data [see Ref. (49) for those equations and references].

diffusion coefficients of KOH and $K_2Zn(OH)_4$, respectively.

The area a_m and a_s represent the interfacial areas which are active for electrochemical reaction [A] and for chemical reaction [B], respectively. They were approximated as follows. It is assumed that the macroscopic averaged particles with uniform radius are arranged in face centered cubic closed packed positions. For a given reference porosity ϵ_o and radius R_o , the solid-solution interface area a_o per unit volume of the electrode can be estimated from the relation of $a_o = 3(1 - \epsilon_o)/R_o$. The specific surface area of the electrode at any state having porosity of ϵ can be related to the reference area a_o as $a/a_o = (1 - \epsilon)R_o/[1 - \epsilon_o]R$. Since the ratio R/R_o is equal to $(a/a_o)^{0.5}$, the specific area a can be represented as

$$a = a_o \left(\frac{1 - \epsilon}{1 - \epsilon_o} \right)^{2/3}$$

In the absence of the inert conducting material, the area a_m and a_s become a_{Zn} (zinc area) and a_{ZnO} (ZnO area), respectively. They are approximated by the following equation

$$a_{Zn} \text{ (or } a_m) = a - a_{ZnO} \text{ (or } a_s) = a \frac{(\epsilon_{Zn} - \epsilon_{Zn*})^p}{(\epsilon_{Zn} - \epsilon_{Zn*})^p + (\epsilon_{ZnO})^q}$$

where p and q are the constants relating volume to surface area ($p = q = 2/3$ was assumed for cubical or spherical crystals), and ϵ_{Zn*} represents the volume fractions of nonactive zinc which can be caused by pore plugging (blockage of the first kind) and by complete coverage on zinc surface by ZnO (usually called passivation or blockage of the second kind). The ϵ_{Zn*} is approximated by

$$\epsilon_{Zn*} = \epsilon_{Zn,plug} + \lambda(\epsilon_{Zn,max} - \epsilon_{Zn,plug})$$

The meaning of the various volume fractions is explained by using the following example.

Let us consider a local section of the electrode having porosity of 0.3, 60% Zn, and 10% ZnO by volume. The partial molar volumes of zinc and zinc oxide are 9.15 and 14.51 cm³/mole, respectively. Due to the difference in the partial molar volume, 85.3% conversion of Zn into ZnO results in pore plugging, i.e., $\epsilon = 0$, $\epsilon_{Zn} = 0.088$, and $\epsilon_{ZnO} = 0.912$. The remaining Zn cannot be converted into ZnO and is denoted by $\epsilon_{Zn,plug}$ (=0.088). On the other hand, if all ZnO is converted into Zn during a local deep charge, an electrode having $\epsilon_{Zn} = 0.663$, $\epsilon_{ZnO} = 0$, and $\epsilon = 0.337$ will result. This zinc content is the maximal amount of zinc available in the fully charged state and denoted by $\epsilon_{Zn,max}$ (=0.663). Then the quantity, $\epsilon_{Zn,max} - \epsilon_{Zn,plug} = 0.575$, can be interpreted by the maximal amount of active zinc which can be utilized. The fractional constant λ is defined based on this quantity to describe the nonactive zinc caused by passivation.

LIST OF SYMBOLS

a	specific surface area per unit volume of the electrode, cm ² /cm ³
a_m, a_s	specific active surface area for charge transfer reaction [A] and that for precipitation or dissolution of ZnO, cm ² /cm ³
c_i	concentration of species i , mole/cm ³
c_{io}	initial concentration of species i , mole/cm ³
c_{is}	concentration of species i at the active metal surface, mole/cm ³
D_{ii}	diffusion coefficients with respect to volume average velocity, cm ² /sec
$(D_{ii})_o$	diffusion coefficients with respect to solvent velocity, cm ² /sec
F	Faraday's constant, 96,487 C/equiv.
I	superficial applied current density, A/cm ²
i_1	superficial current density in the matrix phase, A/cm ²
i_2	superficial current density in the solution phase, A/cm ²
i_o^o	exchange current density, A/cm ²
j	local transfer current density per unit area of active zinc surface, A/cm ²
k_i	mass transfer coefficient of species i from active sites to bulk in the pores or vice versa, cm/sec

k_s	rate constant combining mass transfer of zincate, k_A , with the rate constant for precipitation or dissolution of ZnO, cm/sec
L	electrode thickness, cm
N_i	flux of species i in the x -direction, mole/cm ² -sec
RT	gas constant multiplied by absolute temperature, J/mole
R_i	production or consumption of species i in Eq. [11], mole/cm ³ -sec
R_e	defined in Eq. [21] as $a_{m_i}^0(\alpha_a + \alpha_c)F/RT$
s_i, s_i^*	stoichiometric numbers of species i defined by Eq. [6]
t, t^*	tortuosity factor
$t_i, (t_i)_0$	transference number of species i with respect to volume average velocity and that with respect to solvent velocity
\bar{V}_i	partial molar volume of species i , cm ³ /mole
v	superficial volume average velocity, cm/sec
x	distance from the backing plate, cm
z_i	charge number of species i

Greek Symbols

α_a	an anodic kinetic parameter
α_c	a cathodic kinetic parameter
γ	exponent in zincate concentration dependence of the exchange current density
ϵ	porosity of the electrode
ϵ_i	volume fraction of solid species i
ξ	exponent in OH ⁻ concentration dependence of the exchange current density
κ	conductivity of solution, mho/cm
ν_{ik}	number of ionic species i per molecule of electrolyte "k"
μ_i	chemical potential of ionic species i , J/mole
σ_i	conductivity of solid species i , mho/cm
ϕ_1	potential in the matrix phase, V
ϕ_2	potential in the solution phase, V

Subscripts

i	any arbitrary species i ; 1 for potassium ion, 2 for zincate ion, 3 for hydroxide ion, A for potassium zincate, and B for potassium hydroxide
0	solvent or initial values or values referred to the solvent velocity

REFERENCES

- H. G. Oswin and K. F. Blurton, in "Zinc-Silver Oxide Batteries," A. Fleischer and J. J. Lander, Editors, pp. 63-85, John Wiley & Sons, Inc., New York (1971).
- J. O'M. Bockris and G. A. Razumney, "Fundamental Aspects of Electrocrystallization," Chap. 6, Plenum Press, New York (1967).
- R. D. Naybour, *Electrochim. Acta*, **13**, 763 (1968).
- J. E. Oxley and C. W. Fleischmann, First Quarterly Report, contract NAS5-9591, N66-13568, 21 pp. (September 1965).
- S. Arouete, K. F. Blurton, and H. G. Oswin, *This Journal*, **116**, 166 (1969).
- H. K. Farmery and W. A. Smith, in "Batteries," D. H. Collins, Editor, p. 179, Pergamon Press, Inc., New York (1963).
- J. McBreen, *This Journal*, **119**, 1620 (1972).
- J. J. Lander, in "Zinc-Silver Oxide Batteries," A. Fleischer and J. J. Lander, Editors, pp. 457-469, John Wiley & Sons, Inc., New York (1971).
- G. A. Dalin, in "Zinc-Silver Oxide Batteries," A. Fleischer and J. J. Lander, Editors, pp. 87-95, John Wiley & Sons, Inc., New York (1971).
- D. P. Boden, V. J. Spera, and R. B. Wiley, Paper 13, presented at The Electrochemical Society Meeting, Detroit, Michigan, October 5-9, 1969.
- J. McBreen and G. A. Dalin, Paper 45 presented at The Electrochemical Society Meeting, Philadelphia, Pennsylvania, Oct. 9-14, 1966.
- K. W. Choi, D. N. Bennion, and J. Newman, *This Journal*, **123**, 1616 (1976).
- K. W. Choi, D. Hamby, D. N. Bennion, and J. Newman, *ibid.*, **123**, 1628 (1976).
- J. Newman and W. Tiedemann, *Am. Inst. Chem. Eng. J.*, **21**, 25 (1975).
- A. Winsel, *Z. Elektrochem.*, **66**, 287 (1962).
- J. Newman and C. W. Tobias, *This Journal*, **109**, 1183 (1962).
- R. C. Alkire, E. A. Grens II, and C. W. Tobias, *ibid.*, **116**, 1328 (1969).
- J. S. Dunning, D. N. Bennion, and J. Newman, *ibid.*, **120**, 906 (1973).
- H. Gu, D. N. Bennion, and J. Newman, *ibid.*, **123**, 1364 (1976).
- D. Simonsson, *ibid.*, **120**, 151 (1973).
- D. Simonsson, *J. Appl. Electrochem.*, **3**, 261 (1973).
- D. Gidaspow and B. S. Baker, *This Journal*, **120**, 1005 (1973).
- T. P. Dirkse, *ibid.*, **102**, 497 (1955).
- W. G. Sunu, D. N. Bennion, and J. Newman, To be published. Also see Ref. (49).
- T. P. Dirkse, in "Zinc-Silver Oxide Batteries," A. Fleischer and J. J. Lander, Editors, pp. 19-28, John Wiley & Sons, Inc., New York (1971).
- T. P. Dirkse, L. A. Vander Lugt, and N. A. Hampson, *This Journal*, **118**, 1606 (1971).
- D. D. Justice and R. M. Hurd, *ibid.*, **118**, 1417 (1971).
- H. Gerischer, *Z. Phys. Chem.*, **202**, 302 (1953).
- J. P. G. Farr and N. A. Hampson, *J. Electroanal. Chem. Interfacial Electrochem.*, **18**, 407 (1968).
- D. A. Payne and A. J. Bard, *This Journal*, **119**, 1665 (1972).
- J. P. G. Farr and N. A. Hampson, *J. Electroanal. Chem. Interfacial Electrochem.*, **13**, 433 (1967).
- J. P. G. Farr and N. A. Hampson, *Trans. Faraday Soc.*, **62**, 3493 (1966).
- R. D. Armstrong and G. M. Bullman, *J. Electroanal. Chem. Interfacial Electrochem.*, **25**, 121 (1970).
- J. O'M. Bockris, Z. Nagy, and A. Damjanovic, *This Journal*, **119**, 285 (1972).
- J. N. Butler, "Ionic Equilibrium—A Mathematical Approach," p. 285, Addison-Wesley Publ. Co. Inc., Reading, Mass. (1964).
- D. P. Boden, R. B. Wylie, and V. J. Spera, *This Journal*, **118**, 1298 (1971).
- T. P. Dirkse, C. Postmus, Jr., and R. Vandenbosch, *J. Am. Chem. Soc.*, **76**, 6022 (1954).
- A. O. Gubeli and J. Ste-Marie, *Can. J. Chem.*, **45**, 827 (1967).
- W. Van Doorne and T. P. Dirkse, *This Journal*, **112**, 1 (1975).
- J. S. Dunning, Ph. D. Dissertation, University of California, Los Angeles (1971).
- R. K. Schofield and C. Dakshinamurti, *Discuss. Faraday Soc.*, **3**, 56 (1948).
- R. E. Meredith and C. W. Tobias, *Adv. Electrochem. Electrochem. Eng.*, **2**, 15 (1962).
- E. G. Gagnon, *This Journal*, **120**, 1052 (1973).
- O. S. Ksenzhek, E. A. Kalinovskii, and E. L. Baskin, *Zh. Prikl. Khim.*, **37**, 1045 (1964).
- I. L. Romanova and I. A. Selitsky, *Elektrokhimiya*, **6**, 1776 (1970).
- T. P. Dirkse and N. A. Hampson, *Electrochim. Acta*, **17**, 383 (1972).
- J. Newman, *Ind. Eng. Chem., Fundam.*, **7**, 514 (1968).
- J. Crank and P. Nicolson, *Camb. Phil. Soc. Proc.*, **43**, 50 (1947).
- W. G. Sunu, Ph.D. Dissertation, University of California, Los Angeles (1978).
- M. Sinha and D. N. Bennion, *This Journal*, **125**, 556 (1978).
- N. A. Hampson and M. J. Tarbox, *ibid.*, **110**, 95 (1963).
- M. Eisenberg, H. F. Bauman, and D. M. Brettner, *ibid.*, **108**, 909 (1961).
- N. A. Hampson, P. E. Shaw, and R. Taylor, *Br. Corr. J.*, **4**, 207 (1969).
- W. G. Sunu and D. N. Bennion, *This Journal*, **127**, 2017 (1980).
- D. N. Bennion, Ph.D. Dissertation, University of California, Berkeley, Table A (1964).
- W. F. Linke, "Solubilities of Inorganic and Metal Organic Compound," Vol. II, 4th ed., pp. 1672-1676, Amer. Chem. Soc., Washington, D.C. (1965).
- R. A. Robinson and R. H. Stokes, "Electrolytic Solutions," 2nd ed., p. 501, Butterworths, London (1959).
- J. Newman, "Electrochemical Systems," pp. 91-95, Prentice-Hall Inc., Englewood Cliffs, N.J. (1973).
- J. Newman, D. N. Bennion, and C. W. Tobias, *Ber. Bunsenges.*, **69**, 608 (1965).

Transient and Failure Analyses of the Porous Zinc Electrode

II. Experimental

W. G. Sunu^{*1} and D. N. Bennion^{*2}

School of Engineering and Applied Sciences, University of California, Los Angeles, California 90024

ABSTRACT

Experiments were conducted to characterize behavior and failure mechanisms of porous zinc electrodes, prepared by pressing amalgamated zinc powder of particle size ranging from 250 to 325 mesh. The zinc test electrodes were disks with a cross-sectional area of 1 cm² and a thickness of 0.1 cm. Distribution of zinc and ZnO, and electrode overpotentials were measured during galvanostatic discharge in 40 w/o KOH solution saturated with ZnO. The observed reaction profiles were highly nonuniform and the reaction zone, located near the electrode surface, was very thin, typically 0.2 mm. The utilization of the present electrodes was very sensitive to the applied current density, initial porosity, amount of electrolyte, and the type of membrane. The measured reaction profiles and overpotentials were compared with the theoretical predictions of a recently developed mathematical model. The agreement between observations and predictions provides a good interpretation of the discharge failure modes of negative zinc electrodes.

A number of workers have extensively investigated the anodic zinc behavior in alkaline solution with the major efforts being concentrated on the studies of anodic passivation of the planar zinc electrode. It has been generally accepted that the applied current density can be fitted to a linear relationship with the inverse square root of the passivation time (1-4). The linear relationship which was derived from the Sand equation (5) implies that the diffusion of the zincate ion away from the electrode is the controlling process for passivation. Therefore, passivation is expected to occur when the layer of electrolytic solution adjacent to the zinc surface reaches a critical concentration of zincate (3, 4).

Porous electrodes involve much more complicated and interrelated phenomena than the planar electrodes. In addition to passivation, conversion of zinc into ZnO during discharge decreases the pore size and thus limits the transport of electrolyte into the interior of the porous electrode. Some workers (6, 7) have observed that the utilization of zinc depends strongly on the initial porosity of the zinc electrode. Membranes, which have been used to prevent zinc dendrite penetration, also limit the transport of electrolyte species to and from the counterelectrode as was discussed by Shaw and Remanick (8). Furthermore, porous electrodes have highly nonuniform current distribution, resulting in a thin reaction zone. The remaining part of the electrode acts as an inert matrix which does not contribute to the cell capacity. Highly localized current density can cause passivation under certain circumstances, e.g., under high current load. Nonuniform current distribution can also accelerate the decrease in pore size in the reaction zone.

Such processes and further failure mechanisms of porous zinc electrodes have been described in a mathematical model developed by Sunu and Bennion (9). The results of the mathematical predictions suggested that the zinc electrode could fail by one or any combination of the following mechanisms:

Failure during discharge—(i) blockage of the first kind (pore plugging), (ii) blockage of the second kind

* Electrochemical Society Active Member.

¹ Present address: Gold Incorporated, Gould Laboratories—Energy Research, Rolling Meadows, Illinois 60008.

² Present address: Chemical Engineering Department, Brigham Young University, Provo, Utah 84602.

Key words: porous zinc electrodes, failure mechanism, electrode overpotentials, current distribution.

(passivation or surface coverage on zinc surface by precipitated ZnO), and (iii) depletion of KOH electrolyte.

Failure during charge—(i) depletion of zincate, and (ii) zinc dendrite formation.

Failure after many cycles—(i) zinc dendrite formation and short circuit, (ii) shape change in the y-direction, parallel to the electrode surface, (iii) redistribution of zinc species in the x-direction, perpendicular to the electrode surface, and (iv) accumulated gas evolution.

The objective of this paper is to observe and verify experimentally the proposed failure mechanisms, particularly during discharge. To fulfill this, zinc electrode overpotentials and current distributions across the electrode thickness were measured during the galvanostatic discharge and the results were compared with mathematical predictions.

There are several procedures for fabricating zinc electrodes: pressing of ZnO powder mix (ZnO, HgO, and additives), which gives the zinc electrode in the discharged state (10); pressing of amalgamated zinc powder (7); metal spraying process, and electrodeposition process which results in the zinc electrode in the charged state. To observe and identify various discharge failure modes, initial porosities and the volume of electrolyte reservoir should be well controlled during preparation procedures. The pressing technique developed by Morrel and Smith (7) which satisfies most of our requirements was employed in the present study. Electrodes having two different porosities, 33 and 60%, were prepared in the charged state and used as zinc test electrodes.

Three approaches have been suggested for the experimental determination of current distribution. The first approach is the direct measurement of potential distribution by using numerous reference electrodes along the electrode thickness (11). The second approach is the direct measurement of the current distribution by using a sectioned electrode and measuring the current in each section (12, 13). The third approach is to measure the reaction distribution of the discharged electrode by electrode sectioning followed by the analysis of each section. The charge state of each section can be analyzed using chemical analysis as shown by Nagy and Bockris (14) for the zinc electrode, Bro and Kang (15) for the cadmium

electrode, and Alkire (16) for the copper electrode. The sectioning approach could be extended to determine the concentration distribution of electrolyte species as illustrated by Brenner (17) and Flatt *et al.* (18). By freezing the electrolytic solution followed by sectioning and chemical analysis, they have determined the concentration profiles of ionic species at dissolving anode surfaces and at a depositing cathode surface. In the present study, zinc and ZnO profiles were measured using the sectioning method with EDTA titration. Freezing was not tried.

Experiments

Preparation of the pressed zinc electrode.—The zinc powder with particle sizes between 250 and 325 mesh (60–44 microns) was amalgamated with mercury in a mercuric acetate solution containing an amount of mercury equivalent to 2.5 weight percent (w/o) of the zinc weight. The test zinc electrodes were prepared by pressing amalgamated zinc powder onto a backing plate. The backing plate consisted of a titanium foil (0.001 in. thick) upon which a silver screen (0.004 in. thick) had been spot welded.

Electrodes with two different porosities were tested. The low porosity electrodes were obtained by pressing the Zn(Hg) powder in a stainless steel mold using 13,000 psi. The resultant electrode contained about 0.5g of zinc amalgam and had a porosity of 0.33. The high porosity electrodes were prepared by the procedure given by Morrel and Smith (7). A mixture of NaCl powder and Zn(Hg) powder having the weight ratio of 40 NaCl–60 Zn(Hg) was pressed onto a backing plate using 20,000 psi. The NaCl powder used as a filler had a particle size of 250–325 mesh. The resultant electrode was soaked in distilled water for 24 hr. Complete dissolution of NaCl was confirmed during this period. This gave a highly porous structure having a porosity of 0.6. Each electrode contained about 0.3g of zinc.

The electrodes made by the above procedure were disks which had a cross-sectional area of 1 cm² and thickness of 0.1 ± 0.01 cm. A small cross-sectional area, 1 cm², was chosen to minimize the extent of nonuniform current distribution in the direction parallel to the electrode surface.

Potential measurements.—A schematic drawing of the test cell is shown in Fig. 1. The main body of the cell was made of Plexiglas. The zinc test electrode was completely sealed by two O-rings when the cell was assembled by tightening screws. A silver screen having a zinc deposit was used as a counterelectrode. Two layers of RAI P2291 (40/20) cation exchange membrane (0.001 in. thick) and one layer of dynel, used as separators, were placed on top of the test electrode. The RAI membrane is a beta radiation, cross-linked, low density polyethylene film which has been gamma-radiation grafted with methacrylic acid. The dynel is a porous, nonwoven acrylonitrile which is resistant to oxidation in the cell environment. The sealed test zinc electrode contained a limited amount of electrolytic solution (0.03–0.11 cm³), while the counter zinc electrode compartment contained a large amount of solution of 1.5 cm³.

After evacuation, filling the cell with solution, and assembling the cell, the test electrodes were discharged galvanostatically in a 40 w/o KOH solution saturated with ZnO. The potentials of the test zinc electrode were measured with respect to Hg/HgO reference electrodes at three different positions; one above the membrane, one on the electrode surface, and one on the backing plate. The Hg/HgO reference electrodes were made by the procedure given by Falk and Salkind (19). An external zinc-mercury cell was connected in series in the electrometer circuit to cancel out the equilibrium potential of the zinc electrode. This arrangement allowed zero potential at the open

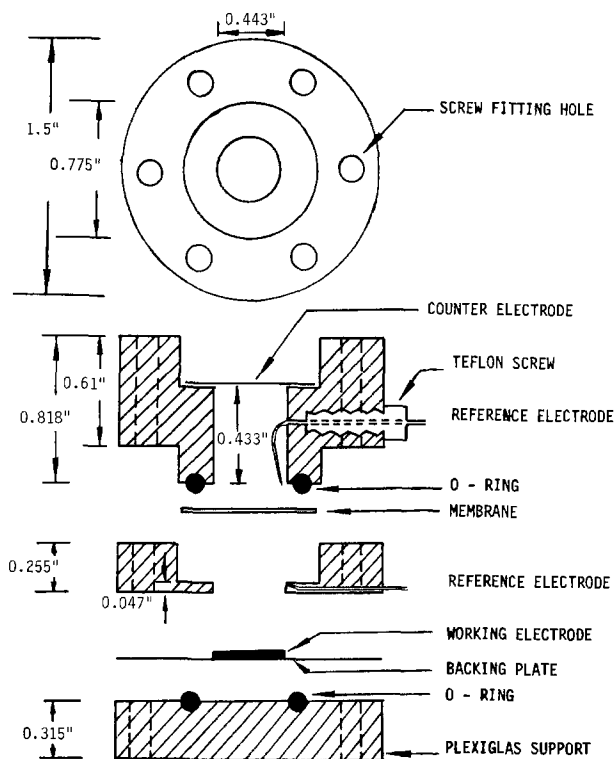


Fig. 1. Test cell assembly

circuit and the sensitivity of the potential data was improved. In retrospect, the net effect is using a Zn/ZnO (sat'd) reference electrode. Zinc electrode potentials at three locations and the potential difference between the zinc test and the zinc counter electrodes were recorded continuously using a Varian Associate 2000 recorder. The integrated current passed was counted by a coulometer, Model 541, Koslow Company.

Determination of reaction profiles.—Some electrodes were sectioned using the technique described by Bro and Kang (15). The discharged electrode was fitted into a fixture having a microadvancing screw which allowed the electrode to be advanced 0.025 in. per revolution. The electrodes having thickness of 0.1 ± 0.01 cm were then machined off by use of a milling machine in the direction parallel to the electrode surface. This sectioning operation usually resulted in 5–10 sections. The machined chips per each section were collected and analyzed to determine the amount of zinc and zinc oxide.

The standard technique for analyzing zinc and zinc oxide with EDTA titration has been described in detail by Welcher (20). The sectioned chips were dissolved in 1M NH₄Cl–NH₄OH buffer solution for 5 min. Previous studies (14, 21) have shown that this solution dissolves ZnO completely but attacks zinc negligibly during this period. The solution was vacuum filtered, adjusted to pH = 10 with 1M NH₄Cl–NH₄OH, and titrated with 0.1M (or 0.01M) disodium EDTA to determine the amount of ZnO. The weight of ZnO equivalent to 1 ml of 0.1M disodium EDTA was 8.14 mg. Following the analysis of the ZnO content, the filtered zinc powder was dissolved in a 10M HCl solution for several hours. The solution was adjusted to pH = 10 and then titrated with 0.1M (and 0.01M) disodium EDTA. The amount of zinc equivalent to 1 ml of 0.1M disodium EDTA was 6.538 mg.

In order to quantify the error caused by the dissolution of zinc, samples of amalgamated zinc powder were vigorously stirred in 1M NH₄Cl–NH₄OH solution for 5 min and vacuum filtered for 1 or 2 min. It was observed that the filtered solution contained

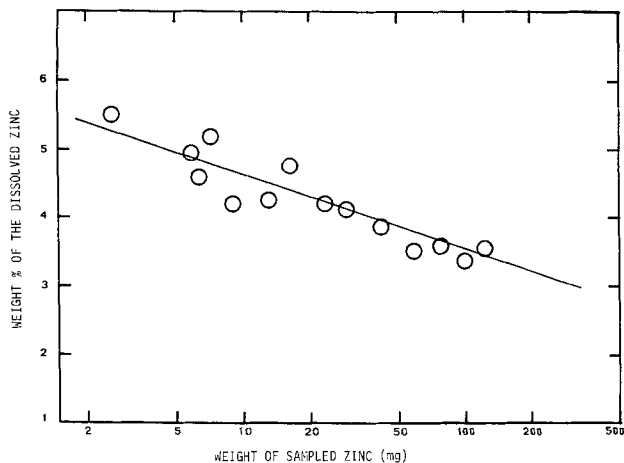


Fig. 2. Weight percent of the dissolved zinc in 1M $\text{NH}_4\text{Cl-NH}_4\text{OH}$ within 6 or 7 min contact time.

approximately 4 w/o of the initial zinc as shown in Fig. 2. When corrections for the amount of dissolved zinc during selective dissolution of ZnO from a Zn-ZnO mixture were accounted for, titration errors remained within 1%.

Result

The reaction distributions, observed with two different current densities of 50 and 20 mA/cm^2 and two different porosities of 0.33 and 0.6, are shown in Fig. 3 to 7 in terms of the volume fractions of zinc and ZnO. In these experiments, a dynel cloth was placed between the test electrode surface and the membrane. This arrangement is designated by "ZDM configuration." The total capacity of the low porosity electrode is 23.6 A-min corresponding to a discharge for 471 min with 50 mA/cm^2 and that of the high porosity electrode is 14.05 A-min. These capacities are referred to as "100% depth of discharge" or as "100% utilization" throughout this paper.

Some of the measured profiles were compared with the profiles predicted from the mathematical model of Sunu and Bennion (9). The data used for numerical calculations were as follows: the initial specific surface area, $a_0 = 300 \text{ cm}^2/\text{cm}^3$; initial KOH concentration, $c_{30} = 10\text{M}$; initial porosity, $\epsilon_0 = 0.33$ for the low porosity electrode and $\epsilon_0 = 0.6$ for the high porosity electrode; initial volume fractions of ZnO and inert conducting materials, $(\epsilon_{\text{ZnO}})_0 = 0$ and $(\epsilon_I)_0 = 0$; exchange current density, $i_0 = 0.1 \text{ A/cm}^2$ [taken from Ref. (22)]; tortuosity factor, $t = 0.5$; the transference number and the mass transfer coefficient of hydroxide ion across two layers of RAI P2291 membrane, $(t_3)_m = 0.5$ and $(L_{\text{BB}})_m = 1.5 \times 10^{-5} \text{ cm/sec}$ [from Ref. (23)]. See Ref. (9) for other parameters.

All the parameters used were taken either from the literature data or from theoretical considerations. One exception is the effective conductivity of the pore solution which was taken as 12-27% of the conductivity of the free electrolytic solution. This choice may not be unreasonable considering the observations of Simonsson (24) and Romanova and Selitsky (25). They observed an effective conductivity which was one-tenth of the conductivity of the free solution. They attributed this large reduction in conductivity to the gas contained in the pores.

Figure 3 shows the volume fractions of zinc and ZnO of a low porosity electrode (ZDM configuration) which has been discharged to 8% depth at 50 mA/cm^2 . The predicted profiles are shown as the smooth curves. The reaction profiles are highly nonuniform resulting in a very thin reaction zone. Discharge failure occurred at 8% depth in this experiment as well as in the theoretical calculation. The reaction profiles ob-

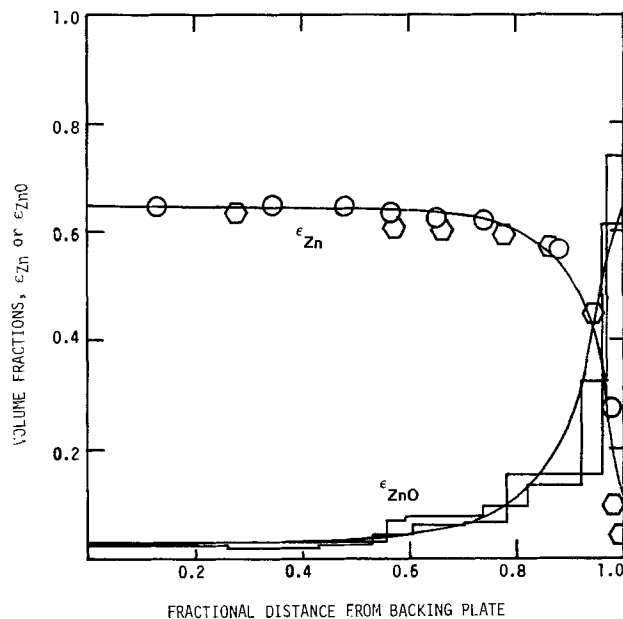


Fig. 3. Profiles of Zn and ZnO for the low porosity electrode discharged to 8% depth at 50 mA/cm^2 . \circ and \hexagon , measured profiles for Zn; histograms, measured profiles for ZnO; smooth curves, predicted profiles for Zn and ZnO.

tained with a low current density of 20 mA/cm^2 are shown in Fig. 4. Even for the 20 mA/cm^2 discharge, a thin reaction zone is still observed and only one-fifth of the electrode is effectively utilized prior to discharge failure. After 23% depth of discharge (271 min), all the zinc at the electrode face is used up and reaches the condition for pore plugging. Discharge failure occurred at 22% depth in the theoretical calculation but near 32% depth in our experiments. This deviation was due to the cracking or swelling of the real electrode which opened the pore structure and allowed further discharge to 32% depth of discharge. The original theoretical model did not allow for swelling and cracking. This effect will be described in detail with the discussion of Fig. 9.

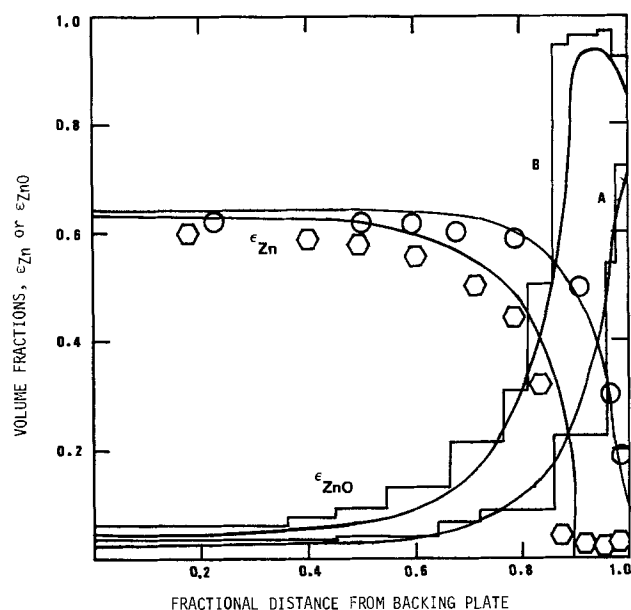


Fig. 4. Profiles of Zn (circles and hexagons) and ZnO (histograms) for the low porosity electrode discharged at 20 mA/cm^2 . \circ and histogram A, measured profiles after 10% depth; \hexagon and histogram B, measured profiles after 23% depth; smooth curves, predicted profiles after 10% and 23% depths of discharge.

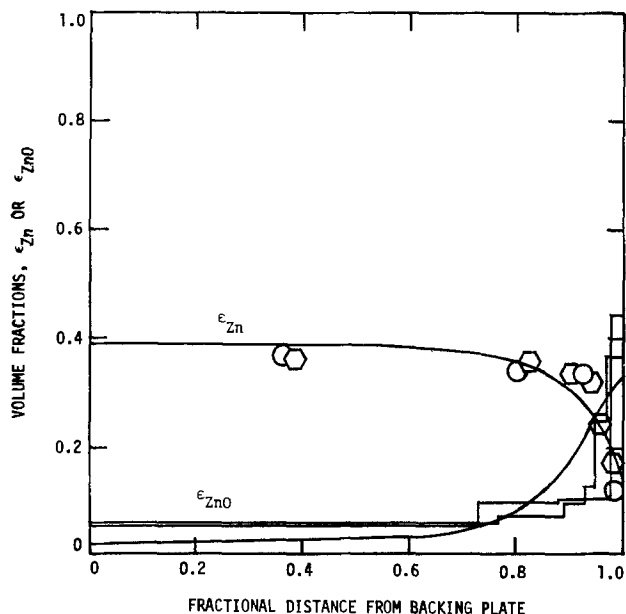


Fig. 5. Profiles of Zn and ZnO for the high porosity electrode discharged to 10% depth at 50 mA/cm². ○ and ◊, measured profiles for Zn; histograms, measured profiles for ZnO; smooth curves, predicted profiles for Zn and ZnO.

The zinc and ZnO profiles for the high porosity electrode discharged to 10% depth at 50 mA/cm² are shown in Fig. 5. Further discharge to 21% depth (1 hr discharge) resulted in the profiles of Fig. 6. Two sets of data as well as the predictions are presented. Generally, the observed profiles, in particular, of the zinc showed good agreement with the predictions. For the high porosity electrode, ohmic loss as well as concentration overpotentials through the solution are smaller than those for the low porosity electrode. This small solution resistance shifts the reaction profile toward the backing plate to produce a more uniform profile. Evidently the porosity of this electrode is large enough to eliminate the discharge failure due to pore plugging, at least in the short cycle range.

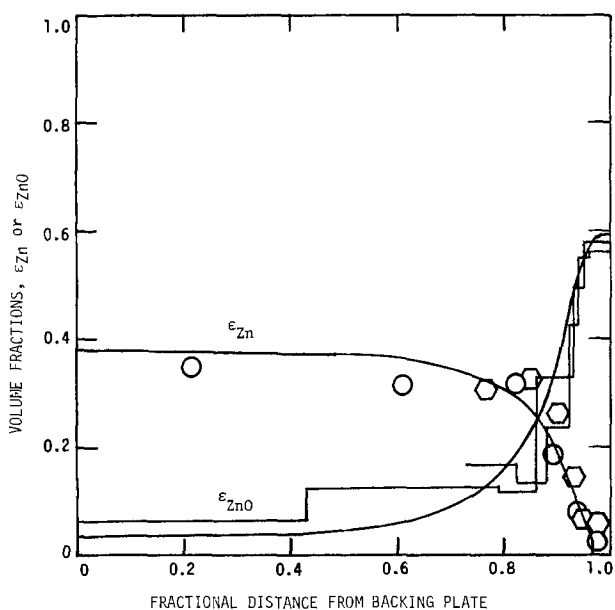


Fig. 6. Profiles of Zn and ZnO for high porosity electrode discharged to 21% depth at 50 mA/cm². ○ and ◊, measured profiles for Zn; histograms, measured profiles for ZnO; smooth curves, predicted profiles for Zn and ZnO.

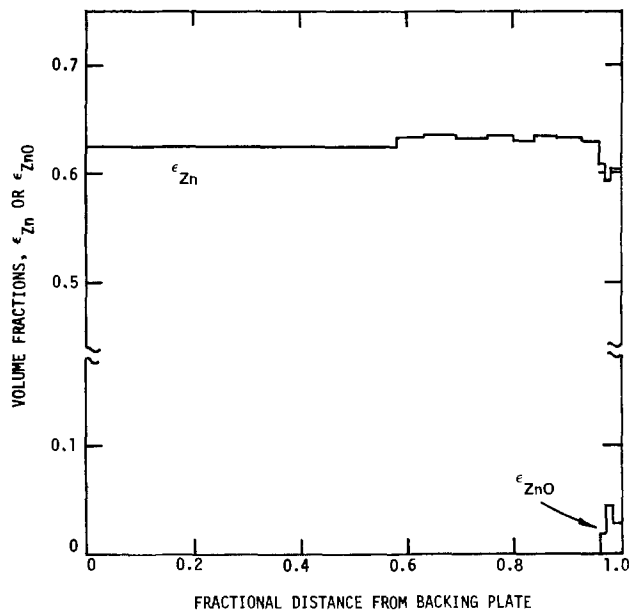


Fig. 7. Profiles of Zn (top line) and ZnO (bottom line) measured for the low porosity electrode after one cycle. At each half-cycle, 50 mA/cm² and 10% depth of initial zinc were applied.

Profiles shown in Fig. 7 were measured after one cycle of a low porosity electrode with an applied current density of 50 mA/cm². The total charge passed at each half cycle was equivalent to 10% conversion of initial zinc. Some of the ZnO precipitated on discharging was not dissolved completely on charging but remained near the face of the electrode. This type of Zn movement on cycling could cause electrode failure after many cycles.

The potential data taken during the preliminary test period were not reproducible. It was found that the reproducibility of the data was successfully improved when the amount of electrolytic solution accessible to the electrode was carefully controlled. Consequently, four different cell configurations having different amounts of electrolytic solution were used in the potential measurements. They include a low porosity electrode having dynel on top of the membrane (designated by L50-ZMD where numeric number represents the applied current density in mA/cm²), a low porosity electrode having dynel beneath the membrane (L50-ZDM), a high porosity electrode having dynel beneath the membrane (H50-ZDM), and a low porosity electrode having dynel but without a membrane (L50-ZD). For all the cases, dynel and membrane refer to the use of one layer of dynel cloth and two layers of RAI P2291 membrane, respectively. Placing dynel cloth below the membrane in ZDM configuration provides an additional solution reservoir of 0.03-0.04 cm³, but the dynel cloth used in the ZMD configuration simply serves as a supporting material to minimize the electrode swelling.

Figure 8 illustrates anodic overpotentials observed during discharge of low porosity electrodes at 50 mA/cm². The total capacity corresponding to a complete conversion of Zn into ZnO is 23.6 A-min (471 min at 50 mA/cm²) for the low porosity electrode and 14.05 A-min (281 min at 50 mA/cm²) for a high porosity electrode. The observed capacities were 1.65 A-min for L50-ZMD, 3.1 A-min for L50-ZDM, and 3.5 A-min for H50-ZDM. This observation indicates that the discharge failure is caused by KOH depletion since the capacity is approximately proportional to the electrolyte volume contained in the zinc electrode compartment. The theoretical result shown in Fig. 2 (curve c) of Ref. (9) is approximately comparable to this experimental result, the theory showing depletion of KOH concentration from an initial 8M to

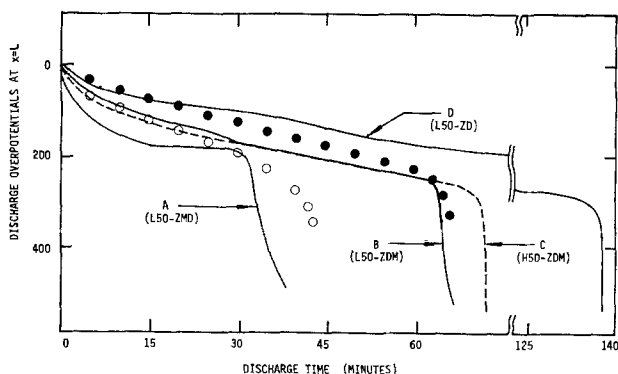


Fig. 8. Overpotentials at the face of the zinc electrode ($x = L$) on discharge at 50 mA/cm^2 . — and ---, measured overpotentials; ○, predicted overpotentials for L50-ZMD; ●, predicted overpotentials for L50-ZMD. L and H represent low porosity and high porosity electrodes, respectively, and Z, M, and D represent zinc electrode, membrane, and dynel, respectively (figure notation L50-ZMD represents a low porosity zinc electrode having a dynel beneath the membrane discharged at 50 mA/cm^2).

2M after 10% depth of discharge. The theoretical calculation was based on one layer of RAI/P2291 membrane while the experiment was with two layers of membrane. Thus, the experimental depletion of KOH was greater due to higher OH^- ion transport resistance and failure due to KOH depletion actually occurred in the experiment but failure did not quite occur in the theoretical calculation reported in Ref. (9). Although not specifically reported, theoretical calculations predict KOH depletion and failure for two layers of membrane under these operating conditions. Discharge of the L50-ZD cell which has no membrane continued to 6.85 A-min or 29% utilization of the initial zinc. Eliminating the membrane increases the supply of hydroxide ions from the counterelectrode compartment and thus the utilization. However, further discharge is expected to be limited due to pore plugging since discharge to 29% depth could lead to the reaction profile which is very similar to curve B of Fig. 4. The predicted overpotentials were plotted as white circles for L50-ZMD configuration and as black circles for L50-ZMD configuration. The predicted overpotentials agreed reasonably well with observations except for those near discharge cutoff.

Figure 9 shows the anodic overpotentials measured at the face of the zinc test electrode during discharge with 20 mA/cm^2 current density. Those for 50 mA/cm^2 discharge are shown for comparison. Curve C (L20-ZMD) and curves A and B (two sets of data for L20-ZMD) correspond to 7.2-8.4 A-min or 31-36% utilization. Discharge of the high porosity electrode (H20-ZMD) could continue further, beyond 9.6 A-min

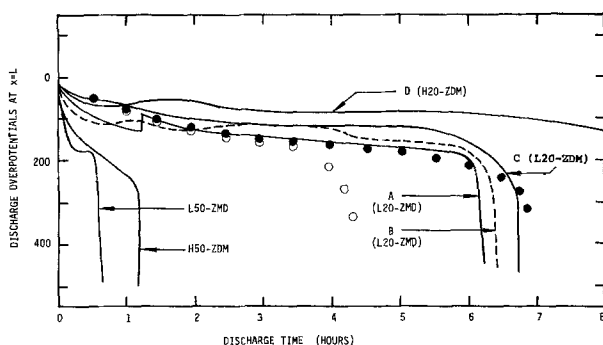


Fig. 9. Overpotentials at the face of the zinc electrode ($x = L$) on discharge at 20 mA/cm^2 . — and ---, measured overpotentials; ○ and ●, predicted overpotentials for L20-ZMD without and with correction for swelling, respectively. Explanation of figure notation is given in Fig. 8 caption.

or 68% utilization. The addition of a dynel cloth as a solution reservoir of $0.03\text{-}0.04 \text{ cm}^3$ (curve C) does not significantly increase the cell capacity compared to L20-ZMD cell (curves A and B). On the other hand, the use of a high porosity electrode which provides additional solution of 0.03 cm^3 and additional space for ZnO precipitation substantially increases the capacity. Irregular overpotential drops were frequently observed instead of continuous increase, as shown in curve A at 1.25 hr discharge and also in other curves as smooth humps. The swelling or cracking of the electrode is responsible for this irregular potential behavior. All these observations favor the pore plugging model, attributing the failure during a 20 mA/cm^2 in low porosity electrodes to pore plugging.

It was mentioned that the numerical discharge calculations used in Fig. 4 show failure at 22% of the total cell capacity. The predicted overpotentials are plotted as white circles. The predicted discharge failure occurs earlier than the observation. When numerical calculations were modified to include the effect of electrode swelling, the resulting overpotentials resemble the observed overpotentials as shown by black circles. The modified numerical procedure can be described as follows. The reaction zone of the low porosity electrode (initial porosity of 0.33) is assumed to retain a constant porosity of 0.3 due to swelling. The increase of solid volume during discharge is then regarded as the expansion of electrode thickness toward the reservoir of 0.01 cm^3 between the electrode surface and the dynel. When the porosity of this reservoir reaches 0.3, the porosity of the reaction zone is allowed to decrease further by the precipitation of ZnO. The result obtained with this numerical procedure agreed well with the observed overpotentials.

Figure 10 shows the overpotentials measured at three different positions and the potential difference between the zinc test (L50-ZMD) and the zinc counterelectrode. The potential difference of 80 mV between curves B and C, which is the potential drop across two layers of RAI P2291 membrane, is comparable to the ohmic loss of 90 mV calculated from the measured conductivities (23). The first discharge failed after 67.0 min. When the cell was allowed to rest for 8 min, it accepted an additional discharge for 12 min. Increase in the rest period leads to a longer time to failure for the second discharge. This result is further evidence that KOH depletion is the failure mechanism under this condition.

Figure 11 is the corresponding potential-time curves during continued charge with a current density of 50 mA/cm^2 . During continued charge, 3.9 A-min was

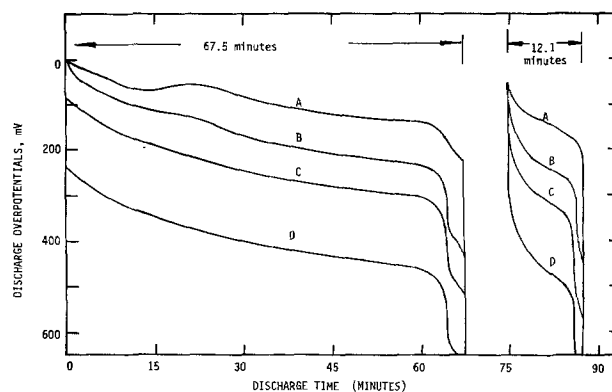


Fig. 10. Overpotentials measured at four different positions on discharge of L50-ZMD electrode at 50 mA/cm^2 . Curves A, B, and C represent the overpotentials measured at the backing plate, at the face of the test electrode, and above the membrane, respectively. Curve D is the potential difference between the zinc test and the zinc counterelectrodes.

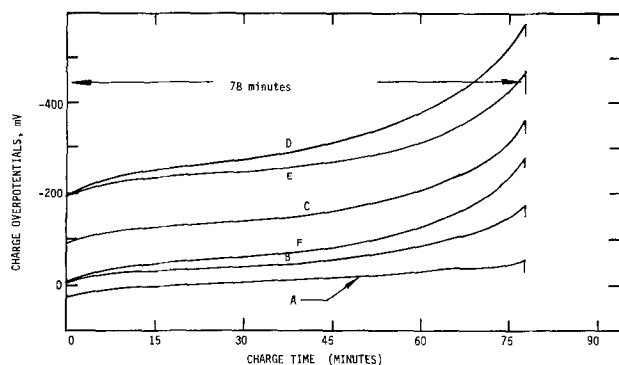


Fig. 11. Overpotentials measured at four different positions on charge of L50-ZDM electrode at 50 mA/cm². Explanation of curves A, B, C, and D is given in Fig. 10 caption. The gaps F-C and C-E are the overpotentials across the membrane and across the solution in the counterelectrode compartment, respectively.

recovered, prior to significant overpotential rise, out of 3.98 A-min applied during discharge. Curves A, B, and C are the overpotentials measured at the backing plate, at the electrode surface, and top of the membrane. Curve D is the potential difference between the zinc test and the zinc counterelectrodes. Curve E was drawn based on the solution ohmic loss in the counterelectrode compartment. The distance from the membrane to the counterelectrode surface (1.1 cm) and the conductivity of 10M KOH solution (0.51 mho/cm) (26) results in the ohmic loss of about 110 mV which is the gap C-E. The gap D-E represents anodic overpotentials of the counter zinc electrode.

Comparison of Fig. 10 with Fig. 11 provides useful information on the potential behavior. The test zinc electrode has 0.07 cm³ of electrolytic solution and porosity of 0.33, while the electrodeposited counter zinc electrode contains 1.5 cm³ of solution with porosity of 0.6-0.8. The anodic overpotential of the zinc test electrode (curve B of Fig. 10) is much larger than that of the zinc counterelectrode (gap D-E of Fig. 11). This indicates that the high anodic overpotential of the test zinc electrode is due to the use of a low porosity and a limited amount of electrolytic solution.

Another interesting point to note is the potential difference between the electrode surface and the top of the membrane, namely, line spacings B-C of Fig. 10 and 11. The gap B-C is the sum of the potential drops across the solution reservoir located between the electrode surface and the dynel, across the dynel, and across the membrane. The gap B-C of Fig. 11 rises with time and is much larger compared to the gap B-C of Fig. 10 which is nearly constant throughout the operation. The potential drop across the membrane of 80 mV, i.e., the gap B-C of Fig. 10 is used to produce the gap C-F of Fig. 11. The significant increase of the potential gap B-F, potential drops across the dynel and the solution reservoir, with time indicates that zinc deposition reaction takes place above the electrode surface and grows through the dynel toward the additional source for zincate ions.

The overpotentials during charge of zinc test electrodes following discharge of the electrodes shown in Fig. 8 are plotted in Fig. 12. The overpotentials were measured with an Hg/HgO reference electrode connected to the working zinc electrode surface by a capillary filled with 40% KOH in water. Observed failure times were 37, 78, and 112 min for the L50-ZMD, L50-ZDM, and H50-ZDM electrodes, respectively. Most of the charge withdrawn during discharging is replaced during charging prior to significant overpotential rise. For the cell without a membrane (curve D), very small cathodic overpotentials were observed. This result is further evidence that real cell overpotential losses can, to a considerable extent, be traced to mass transfer limiting processes across

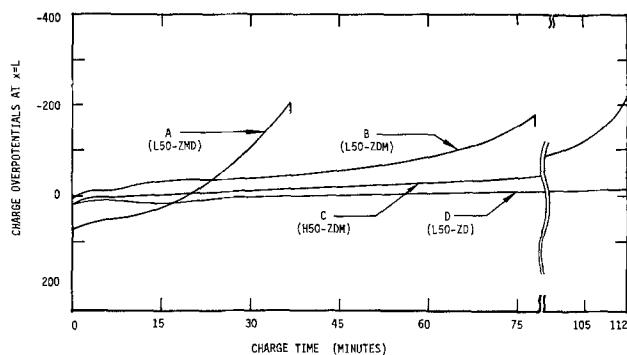


Fig. 12. Overpotentials measured at the face of the electrode (L50-ZDM) on charge at 50 mA/cm². Explanation of figure notation is given in Fig. 8 caption. The previous discharge time prior to onset of charge is 39.4 min for L50-ZMD, 69.6 min for L50-ZDM, 84.5 min for H50-ZDM, and 138.5 min for L50-ZD.

the membrane. Without the semipermeable membrane, zinc deposits penetrated the dynel cloth and continued to grow toward the counterelectrode. Because of the large electrode separation in the test cell, no failure was observed. However, dendritic growth of the type observed would have caused a short circuit in a practical battery cell. For test cells with a semipermeable membrane in the ZDM configuration, postoperation examination showed dendrite growth into the dynel stopping at the membrane surface.

Discussion

The present experimental data disclose three discharge failure modes: depletion of electrolyte, pore plugging, and passivation. The limiting process occurring during discharge, i.e., the depletion of OH⁻ ion at the dissolving zinc surfaces, is referred to as electrolyte depletion if it is caused by the insufficient electrolyte content provided from the zinc electrode compartment, or as pore plugging if diffusion across the outer layer of the electrode is the governing process, or as passivation if diffusion across the layer of the ZnO film precipitated over individual zinc crystals limits the discharge.

Depletion of electrolytes.—During discharge the zinc electrode consumes hydroxide ions and produces water. Depletion of hydroxide ions becomes serious for sealed or tight packed cells having membranes, which are designed to minimize failure due to zinc dendrite penetration and shape change. Tight packing decreases the volume of electrolytic solution reservoir and generally membranes used to prevent zinc dendrite formation also limit the mass transfer of hydroxide ions between two electrode compartments. A restricted amount of electrolytic solution and/or limited flux of hydroxide ions across the membrane can lead to a situation in which the zinc electrode fails on discharge earlier than if a large amount of electrolyte is available.

Failure observed during discharge of the zinc electrode having two layers of RAI P2291 membrane with a current density of 50 mA/cm² was attributed to the depletion of hydroxide ions (see curves A, B, and C in Fig. 8). Depletion of electrolyte strongly depends on the type of the membrane, volume of a solution reservoir, and the porosity of the electrode. If it is assumed that all the zincate ions produced by zinc dissolution are converted into ZnO and that OH⁻ concentration inside the electrode is completely mixed, then the variation of KOH concentration with time can be approximated by the following equation

$$\frac{V}{A} \frac{\partial c_3}{\partial t} = - \left[-(L_{BB})_m (c_3^0 - c_3) - \frac{t_{3m}}{F} I \right] - \frac{I}{F}$$

The solution is

$$\frac{c_3}{c_3^0} = 1 - \frac{I(1 - (t_3)_m)}{F(L_{BB})_m c_3^0} \left[1 - e^{-\frac{(L_{BB})_m A t}{V}} \right]$$

$$= 1 - \frac{1 - (t_3)_m}{M} \left[1 - e^{-\frac{M t}{\tau}} \right]$$

where V is the volume of the electrolytic solution contained in the zinc electrode compartment, A is the cross-sectional area of the electrode, I is the superficial current density, c_3 is the average (mixed) concentration of the hydroxide ion, c_3^0 is the initial hydroxide concentration, and $(L_{BB})_m$ and $(t_3)_m$ are the mass transfer coefficient of KOH and transference number of OH^- ions across the membrane, respectively. The characteristic time $\tau (= c_3^0 F V / I / A)$ is defined by the period required for complete consumption of hydroxide ions when the boundary is insulated with respect to OH^- flux. For the cell configuration L50-ZMD ($V = 0.033 \text{ cm}^3$, $c_3^0 = 0.01 \text{ mole/cm}^3$, and $I = 0.05 \text{ A/cm}^2$), the characteristic time τ is 637 sec and is equivalent to only 2.3% conversion of the initial zinc into ZnO . This number is surprisingly small. The dimensionless parameter $M (c_3^0 F (L_{BB})_m / I)$ corrects for the flux of hydroxide ions across the membrane.

If the above equation is applied to the present test cells using the transport parameters reported by Sinha and Bennion (23), i.e., $(L_{BB})_m = 1.5 \times 10^{-5} \text{ cm/sec}$ and $(t_3)_m = 0.5$, the ratio c_3/c_3^0 becomes zero after 31.7 min for the L50-ZMD electrode ($V = 0.033 \text{ cm}^3$) and after 65.4 min for the L50-ZDM electrode ($V = 0.068 \text{ cm}^3$), which are comparable to the experimental observations shown in Fig. 8 (curves A and B). The twofold increase in the amount of KOH contained in the zinc electrode doubles the electrolyte-limited discharge capacity. On the other hand, with 20 mA/cm², the calculated KOH concentration inside the low porosity electrode remains 3.1M at infinite time of operation. Discharge could continue until the decreased pore size near the electrode surface limit the diffusion of OH^- ions into the interior of the porous electrode. Consequently, the observed results of Fig. 8 and 9 lead to a conclusion that at high rate (50 mA/cm²), depletion of hydroxide ions causes the zinc electrode to fail prior to pore plugging, while discharge at a low rate of 20 mA/cm² continues until pore plugging causes a discharge failure.

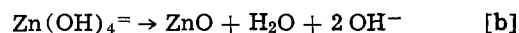
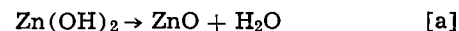
Pore plugging.—Discharge of most battery plates is accompanied by changes in the pore size because of the difference in the molar volumes of solid reactants and solid products. Since the molar volume of ZnO (14.51 cm³/mole) is larger than that of zinc (9.15 cm³/mole), the conversion of zinc into ZnO on discharge decreases the pore size near either side of the electrode surfaces. A nonuniform current distribution will accentuate this problem at the pore mouth. This phenomenon has been given some attention by Gidaspow and Baker (27) who emphasized porosity changes and pore plugging as a mechanism of discharge failure.

If all the zincate ions resulting from zinc dissolution precipitate as ZnO , the zinc electrode having a relatively low porosity of less than 0.4 can be easily blocked by the precipitation of ZnO . Failure due to pore plugging is expected to occur after 20% depth of discharge if penetration depth is assumed to be one-fifth of the electrode thickness. The pore plugging was confirmed both by experimental and theoretical reaction profiles shown in Fig. 4. The discrepancy between the observed and calculated overpotentials was interpreted by the effect of the electrode swelling or cracking. The test electrode used in our study was supported by Plexiglas except for the front surface, which had dynel cloth as a supporting material. Therefore, the stress arising either from the increase in

solid volume or from the gas evolution caused swelling and cracking of the frontal surface which could increase the time required for pore plugging. With a correction for the electrode swelling, numerical overpotentials agreed very well with the experimental overpotentials.

Complete pore plugging leading to zero porosity is not necessary to cause failure. The electrode face having pore size smaller than a certain critical value can limit significantly the supply of hydroxide ions into the interior of the porous electrode, resulting in depletion of hydroxide ions and then passivation. Simonsson (24, 28) has proposed this process, namely, blocking of the outer layer of the electrode by a discharge product followed by acid depletion in the inner part of the electrode, as a failure mechanism during high rate discharge of the porous PbO_2 positive electrode in a lead-acid battery.

Passivation.—A number of workers (1-4, 29-35) have studied passivation behavior of the planar zinc electrode in alkaline solution. It is generally agreed that two mechanisms exist for the formation of the passive film; (a) direct formation on the electrode surface through a solid state reaction, and (b) indirect formation from a supersaturated zincate solution through a precipitation reaction. The two reaction mechanisms can be written as [e.g., (35)]



Powers *et al.* (30, 33) and Hull *et al.* (34) have shown that a white porous film of ZnO (type I) forms by precipitation from a supersaturated solution before passivation occurs, while a coherent compact film of ZnO (type II) with color varying from light gray to black, which is responsible for passivation, appears directly on the surface beneath the type I film.

The passivation effect included in our mathematical model was the surface coverage of zinc surface by the precipitation of ZnO (blockage of the second kind) which corresponds to type I film. Our model did not include the passivation caused by type II film. Therefore, predicted overpotentials increased gradually until KOH solution in the pores decreased to zero (see circles in Fig. 8 and 9). These potential-time curves are similar in shape to those discussed by Elsdale *et al.* (36) and Coates *et al.* (37) who observed a gradual decrease in potentials in the vicinity of passivation. On the other hand, an abrupt increase in overpotentials was observed near the cutoff of discharge of the present cells which had limited amount of electrolytes (see Fig. 8 and 9). This is believed due to the formation of a type II passivating film which was confirmed visually by the gray color of the fully discharged, wet electrodes. The type II film of ZnO is expected to form if the zinc surface is severely depleted of hydroxide ion or if the ratio of zincate to OH^- ion concentration exceeds a certain critical value. Depletion of hydroxide ions at the active zinc surface would result in a decrease in solubility of ZnO , a rapid increase in the rate of ZnO precipitation or solid-state reaction, and eventually a rapid rise in overpotentials.

The exact details of how and when the dense, blocking type II film forms seem unknown. However, the following hypothesis is proposed to explain presently known behavior. Whenever the OH^- ion surface concentration drops below some critical value, Zn(OH)_2 precipitates and then converts to ZnO forming the dense type II deposit via mechanism [a]. Such an event would occur at high local transfer current rates or whenever OH^- ion depletion occurs generally in the electrode pores. When OH^- concentration is high, a light, porous ZnO precipitate forms from supersaturated zincate solutions via mechanism [b]. When the

porous type I film formed by mechanism [b] gets thick enough and/or local transfer current high enough, the OH^- ion surface concentrations at the bottom of the ZnO pores drops and type II film will form stopping further reaction. This type II film apparently redissolves much slower than type I films and can possibly be a cause of permanent failure of an electrode. It may be important to develop ways of preventing type II ZnO films.

Charge failure.—During charge, zincate becomes unsaturated and the limiting species is the zincate ion. Depletion of zincate ions could occur in two ways; slow dissolution of ZnO and the restricted diffusion of zincate. These two limiting factors were not observed in our experiments. Most of the coulombic charge applied during discharge was effectively recovered on charge without causing significant overpotential rise. This suggests that discharge products in any form of zincate, ZnO, or $\text{Zn}(\text{OH})_2$ can be converted into zinc without difficulty. The ZnO mentioned here does not include the reagent ZnO powder which has been used in the fabrication of commercial zinc electrodes. Previous studies (38, 39) have shown that the dissolution of ZnO is a slow process. Slow dissolution of ZnO and the depletion of zincate ions could play an important role in limiting the initial low charge acceptance during formation of the zinc electrodes made of ZnO powder.

During charge of the L50-ZD electrode which had no membrane separator, very small cathodic overpotentials were observed until no zincate ions were available from the counterelectrode compartment. Zinc deposits penetrated the dynel cloth and continued to grow toward the counterelectrode compartment at a fairly constant overpotential. In one experiment, charge was allowed to proceed until failure, but addition of drops of fresh electrolytic solution to the counterelectrode compartment restored the original performance. Dendrite growth of this type will short out an actual cell whenever the membrane is bridged during cycling.

Summary

Distribution of zinc and ZnO and electrode overpotentials were measured during galvanostatic discharge in a 40 w/o KOH solution saturated with ZnO and compared with the theoretical predictions. The zinc electrode behaviors observed on discharge were interpreted using proposed discharge failure modes: depletion of electrolyte, pore plugging, and passivation. Results with two current densities of 20 and 50 mA/cm² and two porosities of 0.33 and 0.60 were discussed.

Both observed and predicted reaction profiles were highly nonuniform, resulting in a very thin reaction zone located near the face of the electrode. The reaction zone which effectively participates in the discharge reaction prior to failure was equivalent to about 20% of the 1.0 mm electrode thickness. The remaining zinc metal served simply as an inert matrix and did not contribute to the cell capacity.

During discharge at 50 mA/cm² for both low porosity and high porosity electrodes, the utilization of zinc was severely limited by the depletion of electrolytes within the zinc electrode compartment. The utilization depends strongly on the applied current density, initial porosity, the amount of electrolytic solution, and the type of membrane. At a low current density of 20 mA/cm², the utilization of zinc was much higher than that observed with 50 mA/cm² and the discharge continued until the decrease in pore size in the reaction zone played an important role in limiting further discharge capacity. The highly nonuniform reaction distribution accentuates the phenomenon of pore plugging at the pore mouth. Low current discharge of the high porosity electrode, in which the possibility of pore plugging was eliminated, continued

to more than 50% utilization. Blockage of the zinc surface by the precipitated ZnO (or passivation) also could occur beyond this region.

The present cell showed much lower overpotentials during charge compared to those on discharge. Most of the coulombic charge applied during discharge was effectively recovered on charging. The reaction profile measured after one cycle shows that some of the zinc oxide which precipitated on discharge did not dissolve completely on charging but remained near the electrode surface. This accumulation after many cycles could decrease the pore size, at least locally, and deplete electrolytes in the interior of the electrode. It also could reduce the active zinc surface area, promoting high activation overpotential and the chance for an earlier passivation. Similar adverse effects are expected with the gas trapped in the pores. Further work is necessary to confirm this type of redistribution of zinc species on cycling.

The result of this work can be applied to the design of industrial zinc electrodes to improve their performance and cycle life. It also points out areas where further research should be emphasized to gain cycle life improvements.

Acknowledgments

The authors acknowledge financial support of this project by the U.S. Air Force Systems Command under Contract No. F44620-76-C-0098 and by the University of California, Los Angeles.

Manuscript submitted Nov. 26, 1979; revised manuscript received Feb. 15, 1980. This was Paper 45 presented at the Atlanta, Georgia, Meeting of the Society, Oct. 9-14, 1977.

Any discussion of this paper will appear in a Discussion Section to be published in the June 1981 JOURNAL. All discussions for the June 1981 Discussion Section should be submitted by Feb. 1, 1981.

Publication costs of this article were assisted by the U.S. Government.

REFERENCES

1. N. A. Hampson, M. J. Tarbox, J. T. Lilley, and J. P. G. Farr, *Electrochem. Technol.*, **2**, 309 (1964).
2. N. A. Hampson and M. J. Tarbox, *This Journal*, **110**, 95 (1963).
3. M. Eisenberg, H. F. Bauman, and D. M. Brettner, *ibid.*, **108**, 909 (1961).
4. N. A. Hampson, P. E. Shaw, and R. Taylor, *Br. Corr. J.*, **4**, 207 (1969).
5. H. J. S. Sand, *Philos. Mag.*, **1**, 45 (1901).
6. F. Pryzbyla and F. J. Kelley, in "Sixth International Power Source Symposium," p. 373, Brighton, Sussex, Pergamon Press, Elmsford, N.Y. (1969).
7. D. H. Morrel and D. W. Smith, in "Fifth International Power Source Symposium," p. 207, Brighton, Sussex, Pergamon Press, Elmsford, N.Y. (1967).
8. M. Shaw and A. H. Remanick, in "Zinc-Silver Oxide Batteries," A. Fleischer and J. J. Lander, Editors, p. 233, John Wiley & Sons, Inc., New York (1971).
9. W. G. Sunu and D. N. Bennion, *This Journal*, **127**, 2007 (1980).
10. J. A. Keralla, in "Zinc-Silver Oxide Batteries," A. Fleischer and J. J. Lander, Editors, p. 183, John Wiley & Sons, Inc., New York (1971).
11. R. J. Brodd, *Electrochim. Acta*, **11**, 1107 (1966).
12. J. J. Coleman, *This Journal*, **98**, 26 (1951).
13. E. C. Gagnon and L. G. Austin, *ibid.*, **118**, 497 (1971).
14. Z. Nagy and J. O'M. Bockris, *ibid.*, **119**, 1129 (1972).
15. P. Bro and H. Y. Kang, *ibid.*, **118**, 519 (1971).
16. R. C. Alkire, Ph.D. Dissertation, University of California, Berkeley (1968).
17. A. Brenner, "Electrodeposition of Alloys," Vol. 1, p. 295, Academic Press, London, (1963).
18. R. K. Flatt, R. W. Wood, and P. A. Brook, *J. Appl. Electrochem.*, **1**, 35 (1971).

19. S. U. Falk and A. J. Salkind, "Alkaline Storage Batteries," p. 532, John Wiley & Sons, Inc., New York (1969).
20. F. J. Welcher, "The Analytical Uses of EDTA," p. 149, Van Nostrand, Princeton, N.J. (1958).
21. N. Marincic and P. Bro, Paper 368 presented at The Electrochemical Society Meeting, Montreal, Canada, Oct. 6-11, 1968.
22. J. O'M. Bockris, Z. Nagy, and A. Damjanovic, *This Journal*, **119**, 285 (1972).
23. M. Sinha and D. N. Bennion, *ibid.*, **125**, 556 (1978).
24. D. Simonsson, *ibid.*, **120**, 151 (1973).
25. I. L. Romanova and I. A. Selitsky, *Elektrokhimiya*, **6**, 1776 (1970).
26. D. N. Bennion, Ph.D. Dissertation, University of California, Berkeley, Table A (1964).
27. D. Gidaspow and B. S. Baker, *This Journal*, **120**, 1005 (1973).
28. D. Simonsson, *J. Appl. Electrochem.*, **3**, 261 (1973).
29. F. Jolas, *Electrochim. Acta.*, **13**, 2207 (1968).
30. R. W. Powers and M. W. Breiter, *This Journal*, **116**, 719 (1969).
31. R. D. Armstrong and G. M. Bullman, *J. Electroanal. Chem. Interfacial Electrochem.*, **25**, 121 (1970).
32. M. W. Breiter, *Electrochim. Acta*, **16**, 1169 (1971).
33. R. W. Powers, *This Journal*, **117**, 192 (1970).
34. M. N. Hull, J. E. Ellison, and J. E. Toni, *ibid.*, **118**, 685 (1971).
35. N. A. Hampson, in "Zinc-Silver Oxide Batteries," A. Fleischer and J. J. Lander, Editors, p. 51, John Wiley & Sons, Inc., New York (1971).
36. R. N. Elsdale, N. A. Hampson, P. C. Jones, and N. A. Strachan, *J. Appl. Electrochem.*, **1**, 213 (1971).
37. G. Coates, N. A. Hampson, A. Marshal, and D. F. Porter, *ibid.*, **4**, 75 (1974).
38. T. P. Dirkse, L. A. Vander Lugt, and N. A. Hampson, *This Journal*, **118**, 1606 (1971).
39. D. D. Justice and R. M. Hurd, *ibid.*, **118**, 1417 (1971).

Technical Note



Hazard Investigations of LiClO₄/Dioxolane Electrolyte

G. H. Newman,* R. W. Francis, L. H. Gaines,* and B. M. L. Rao*

Exxon Research and Engineering Company, Linden, New Jersey 07036

During extensive multicycle testing of the rechargeable Li/TiS₂ system (1-3), using a LiClO₄/dioxolane electrolyte, a hazard problem was encountered. A cell which had been cycling overnight on automatic equipment, at constant current, between preset voltage limits, was found destroyed. The cell had been charred and the glass container was shattered. An explosion was presumed to have occurred. This event resulted in the immediate initiation of an investigation of the possibility of the existence of an inherent explosion hazard in the use of the LiClO₄/dioxolane electrolyte. This paper reports the results of the investigation.

Experimental

The electrolyte safety investigation was carried out in two parts: (i) an "in-house" electrochemical cell abuse test program, and (ii) a hazard evaluation program carried out, under contract, by Hazards Research Corporation, of Denville, New Jersey

Electrochemical cell-abuse tests.—The "in-house" program was restricted to cell-abuse tests. The abuse tolerance of cells during overcharge and overdischarge (cell reversal) conditions of the Li/TiS₂ cells containing 2.5M LiClO₄/dioxolane electrolyte were studied. A control test was also run with an electrolyte consisting of LiPF₆ dissolved in dioxolane.

The test cells were constructed with 1 × 1 in. lithium and TiS₂ electrodes in a parallel plate configuration (Li ≈ 600 mA-hr, TiS₂ ≈ 200 mA-hr, Celgard®, and 304 stainless steel grids), and placed in a polyethylene bag. The cell assembly was mounted in a hermetically sealable glass container with glass to metal electrical through-puts. All cells contained 2-3 ml of electrolyte and were assembled in a dry room with ~1.5% RH.

Hazards Research Corporation tests.—Two types of tests were performed on solutions of LiClO₄/dioxolane

and LiPF₆/dioxolane supplied by us and identical to the solutions tested by us in electrochemical cell-abuse tests. The tests were:

Impact tests.—A standard JANAF test was performed, wherein a known weight (2 kg) is dropped from various preset heights onto a carefully designed cup containing the electrolyte. A loud report (puncture of a retaining steel diaphragm), flame, or other evidence of

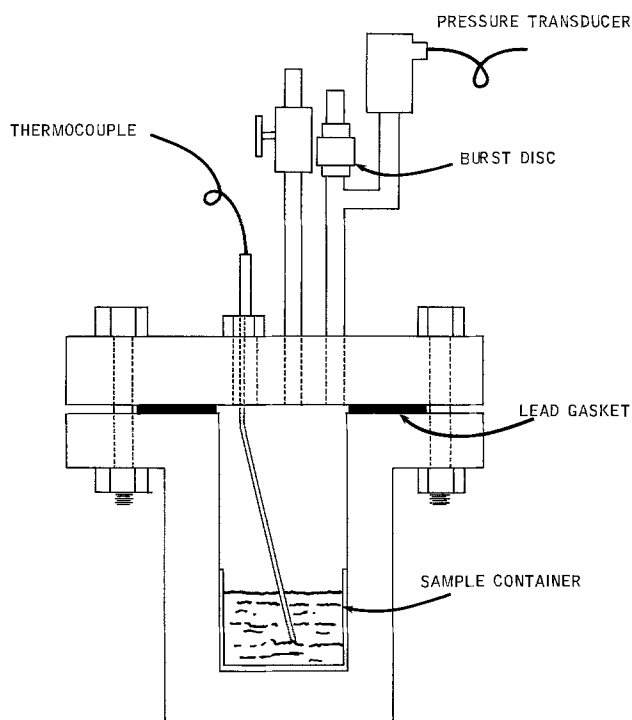


Fig. 1. Thermal stability apparatus

* Electrochemical Society Active Member.

Key words: electrolyte, organic, battery, energy storage.

Table I.

Cell No.	Salt	Mode	Current (mA/cm ²)	Time	Final voltage	Remarks
8	LiClO ₄	O.D.	150	~10 min	-9	Detonated
7	LiPF ₆	O.D.	150	~5 min	-40	No fire, peak temp. 135°C, electrolyte gelled
11	LiClO ₄	O.D.	150	~5 min	-4	Detonated
10	LiPF ₆	O.C.	150	15 min	+40	No fire
12	LiClO ₄	O.C.	150	10 min	+40	No fire
9	LiClO ₄	O.C.	150	30 min	+40	No fire
43	LiPF ₆	O.C.	150	30 min	+40	No fire, peak temp. 120°C
44	LiPF ₆	O.D.	150	—	≈0	Cell shorted; no fire
46	LiClO ₄	O.D.	15	6 hr	-24V	Detonated, overnight stand at 5¼ hr
48	LiClO ₄	O.D.	15	5½ hr	-1.5V	Detonated
32	LiClO ₄	O.D.	7.5	5½ hr	-9V	Detonated, triggered by 75 mA/cm ² pulse
33	LiClO ₄	O.D.	15	5 hr	-7V	Detonated
35	LiClO ₄	O.D.	7.5	9 hr	-35V	Detonated

combustion, are considered a positive test. Tests are performed up to 36 in., at which point hydrodynamic shock is sufficient to yield a positive test with water.

Isothermal decomposition temperature.—The constant temperature stability of a sample is determined in a stainless steel reactor vessel equipped with thermocouples and rapid response pressure transducers. The equipment is shown schematically in Fig. 1.

Results and Discussion

The Li/TiS₂ cell abuse tolerance test results during overcharge and overdischarge (cell reversal) for the 2.5M LiClO₄/dioxolane are shown in Table I.

Overcharging (O.C.) of the cells containing LiClO₄ and LiPF₆ solutes (cells 10, 12, and 43) showed an increase in IR (polarized to 40V) due to the polymerization of dioxolane. The resistive heating resulted in a cell temperature rise to 120°C. Independent experiments have shown that the anodic polarization of LiClO₄/dioxolane solutions on a platinum electrode resulted in the initiation of polymerization of dioxolane at 3.25V vs. a lithium reference electrode. No explosive hazard was noted for any cell with either solution under overcharge conditions.

Overdischarge or cell reversal resulted in a detonation and fire in the case of all LiClO₄/dioxolane electrolyte cells tested. Cells 8 and 9 containing this electrolyte, when discharged at high current density, 1A (~150 mA/cm²) detonated in 5-10 min. The onset of detonation was delayed up to 5 hr at lower current rates of 0.1A (15 mA/cm²), as seen in cells 33, 46, and

48. Further reduction in current to 0.05A (7.5 mA/cm²) extended the initiation time to ~9 hr. Although the measured overdischarge at all voltages varied in these experiments, the lowest voltage at detonation was noted to be -1.5V in cell 48.

Neither combustion nor detonation resulted under comparable conditions of discharge for cells with LiPF₆/dioxolane electrolyte, although peak temperatures of 130°C were measured (cells 7 and 44).

The results strongly suggested that the detonations on overdischarge are directly associated with the participation of the LiClO₄/dioxolane electrolyte.

Results of the impact testing are shown in Table II, along with the values for two known materials, NH₄ClO₄ and nitroglycerine. The expert opinion of Hazards Research Corporation is that the value of 25.5 in. obtained for the perchlorate solution is well within the range of "explosive materials." The value of 32.5 in. for the LiPF₆ solution signifies a solution which is "not very sensitive."

The isothermal decomposition test results are summarized in Table III. The conclusions of HRC were that "LiClO₄ solution is noticeably sensitive to impact, and detonates at elevated temperatures," and "LiClO₄ electrolyte and cell are obviously explosive materials and appropriate care should be observed in their handling and use."

Supplementary Data

1. We have found subsequent to the tests already described, that a cycled cell which "dead-shortened" internally from dendritic growth would also detonate.

2. During the course of our normal cell program, independent of the cell abuse tests described in this paper, several hundred cells were extensively cycled. Only six of these detonated. However, these detonations were quite violent, even though the cells contained only 3.5 ml of the solution.

Conclusions

Based on the results of the hazard investigation, it was concluded that LiClO₄/dioxolane electrolytes were unsafe for use in lithium secondary cells. All further development of secondary cells based on this electrolyte were terminated.

Table II. Impact test results (2 kg JANAF drop weight test)

Sample	Height, inches for 50% probability of "explosion"
Water	36.0
2.5M LiPF ₆ -dioxolane*	32.5
2.5M LiClO ₄ -dioxolane	25.5
NH ₄ ClO ₄ (dry solid)	18.9
Nitroglycerine	1.0

* No evidence of solvent polymerization at time of test.

Table III. Isothermal decomposition results (340 cm³ reactor)

Sample	Programmed temperature, etc.	T _{Max} , °C on exotherm	Pressure, PSIG after exotherm
50 cm ³ 2.5M LiPF ₆ in dioxolane	70 } Screen	135	8
	143 } 1°C/min rise	163	43
	185 }	360	500
50 cm ³	60 } Isothermal	72—4 hr (polymerization)	
	50 }	50—8 hr (stable)	
50 cm ³ 2.5M LiClO ₄ in dioxolane	130 } Screening	490	650 → >>6000
	253 }		
10 cm ³ 2.5M LiClO ₄ in dioxolane	90 } Screening	135	38
	195 }	250	140
	258 }	455 & 2300 °C/min	1490 & detonation
	200 } Isothermal	>500 (3.5 hr)	>270
	190 }	190—8 hr (stable)	

Acknowledgments

The authors wish to thank M. T. Vidnansky, R. J. Solarczyk, and J. Serrano for their invaluable assistance in the "in house" tests.

Manuscript submitted Feb. 8, 1980; revised manuscript received March 24, 1980.

Any discussion of this paper will appear in a Discussion Section to be published in the June 1981

JOURNAL. All discussions for the June 1981 Discussion Section should be submitted by Feb. 1, 1981.

Publication costs of this article were assisted by Exxon Research and Engineering Company.

REFERENCES

1. M. S. Whittingham, U.S. Pat. 4,009,052 (1977).
2. L. H. Gaines, R. W. Francis, G. H. Newman, and B. M. L. Rao, in "Proc. 11th IECEC" (1976).
3. G. H. Newman and L. H. Gaines, Ger. Pat. Applic. No. 2619-806 (1976).

Method of Selecting Expanded Metal Grids for Battery Electrodes

Richard M. Meighan*

Eltra Corporation, C&D Batteries Division, Plymouth Meeting, Pennsylvania 19462

Expanded metal grids, although in use today in battery electrodes of several types, are still being explored for new applications in batteries. Even in that oldest of the rechargeable systems, the lead-acid battery, its application to industrial and electric vehicle battery grids has only recently begun to be explored. Within the last five years, however, expanded grids have been making an impact in the maintenance-free SLI (starting, lighting, and ignition) type lead-acid battery (1, 2). This technical note provides a method for selecting the expanded metal grid pattern most effective for direct substitution for an existing cast (lead) grid in a pasted battery electrode. This analysis applies to expanded grids made by the progressive die expansion process and similar types. The principal basis for comparison is the relative paste (active material) volumes of the two types of electrode plates. It is assumed that the electrochemical capacity is directly proportional to paste volume. Thus, the relative paste volume (expanded to cast), P_R , should be equal to or greater than unity to achieve an advantageous substitution with regards to capacity. Structural, *i.e.*, stiffness, and other factors may impact on this goal.

It should be emphasized that the prime usefulness of this method is to analyze the feasibility of substituting one or more expanded grid patterns for a particular cast grid prior to a costly expenditure in equipment or contracted trials. Once samples are in hand, more direct experimental methods may be applied to determine relative paste volume.

Method

For the purpose of this analysis it is convenient to compare only the part of both grids (cast and expanded) that is below the top horizontal grid bar and lug. (If, as in the example at the end of this note, the bottom horizontal bars are nearly the same dimension, those bars can be excluded also.) Thus, we define the same rectangular volume for both types of plates having equal dimensions of height, H , width, W , and thickness, T , whose volume is

$$V = HWT \quad [1]$$

This plate volume can be divided into two components, the grid volume, G , and the active material volume, P , thus

$$V = P + G \quad [2]$$

P is composed of solids and voids and is characterized by its wet and dry densities. (It is assumed that

the densities of both grid and paste are respectively the same in both types of plates.)

The expanded grid (see Fig. 1) is considered here as a matrix of diamond-shaped holes each characterized by a long-way dimension, L , and a short-way dimension, S . S is measured parallel to the plane of the plate and from node corner to node corner whereas S' is measured parallel to the plane of expansion from node edge to node edge. (The nodes may have a length, n , but this does not enter into the following derivations.) The actual geometry of the holes is not important for the calculation of the grid metal volume as this quantity can be determined by considering the geometry of the metal prior to being expanded. (Some inaccuracy on the order of 1-6% will be incurred, *e.g.*, see later example.) The diamonds of length, L , are cut from sheet metal having a thickness, t_m , in strips w wide, the cutwidth. Therefore, the volume, v , of one strand of grid is

$$v = wt_m L \quad [3]$$

The total number of strands, N , in plate volume, V , is given by

$$N = 2N_s N_L \quad [4]$$

where N_s and N_L represent the number of diamonds in the short (S) and long (L) dimensional directions of the plate. The dimensions of the plate may be temporarily specified as D_s and D_L , which will be equal to either H and W or to W and H depending on the direction of expansion relative to the situation of the plate in the battery. Thus, N_s and N_L are defined by

$$N_s = D_s/S \quad \text{and} \quad N_L = D_L/L \quad [5]$$

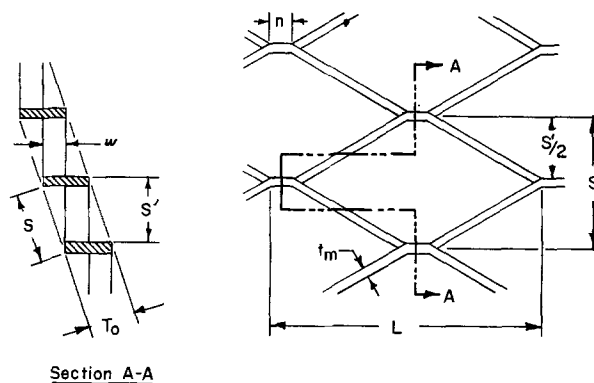


Fig. 1. Vertical and horizontal sectional views of a typical expanded metal grid showing various dimensions.

* Electrochemical Society Active Member.

Key words: batteries, capacities, expanded metal, grids, pasted plates.

The volume, G , of the grid metal in the plate is given by

$$G = Nv \tag{6}$$

If Eq. [3], [4], and [5] are substituted into [6] then

$$G = 2wt_mHW/S \tag{7}$$

Since the paste volumes of the expanded and cast grid plates are P_E and P_c and the relative paste volume, a figure of merit, is $P_R = P_E/P_c$ then by combining Eq. [1] and [7] into [2] and dividing by P_c one obtains

$$P_R = (HW/P_c) [T - 2wt_m/S] \tag{8}$$

P_c can be determined (for the cast grid) in a similar manner, but since the cast grid is usually complicated in shape it is often easier to determine the paste and grid volume experimentally. All of the variables in Eq. [8] except t_m , w , and S will be specified at the outset. Both w and S are principal characteristics of the expansion process, whereas t_m is usually selected in conjunction with w for optimal structural and corrosion characteristics. Usually, but not necessarily, w and t_m will be nearly equal, thereby providing nearly square strands. It is useful to derive an expression for the cutwidth, w , so as to be able to estimate the value of this dimension that is necessary to obtain a given pasted plate thickness (by the progressive die expansion process).

Referring to Fig. 2b, it can be seen that the thickness, T_o , of the expanded grid can be set equal to the sum of two dimensions normal to the plane of the grid

$$T_o = T' + t' \tag{9}$$

It is also apparent that

$$\cos \theta = T'/2w \text{ and } \sin \theta = t'/t_m$$

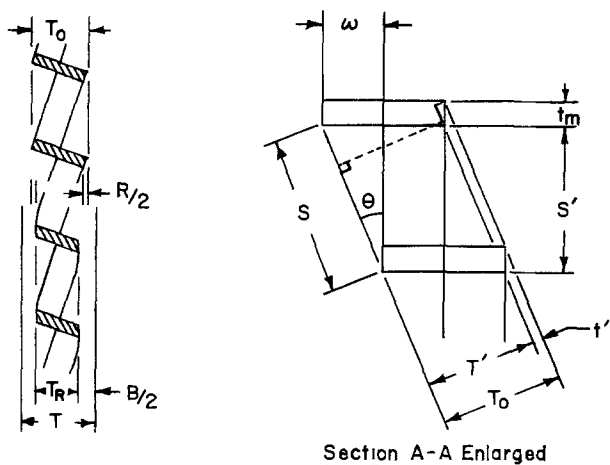
and therefore

$$T_o = 2w \cos \theta + t_m \sin \theta \tag{10}$$

Since the expanded grid will usually undergo a rolling operation to flatten it, to round off sharp node edges, and to perhaps size it, then a certain amount of reduction in grid thickness, expressed as a fraction, f_R , must be introduced. Also on pasting the grid a certain amount of overpasting, again expressed as a fraction, f_B , may occur, often intentionally. Both of these fractions are defined as follows

$$f_R = R/T_o \text{ and } f_B = B/T$$

where R and B are the linear dimensions of the grid reduction and overpasting (see Fig. 2a). The thickness,



a. b.

Fig. 2. More detailed views of Section A-A of Fig. 1

T_R , of the reduced (rolled) grid is therefore

$$T_R = T_o - R = T_o (1 - f_R)$$

The thickness of the pasted plate will then be

$$T = T_R + B = T_o (1 - f_R) + f_B T \tag{11}$$

Rearranging and combining [10] with [11] gives

$$T = F (2w \cos \theta + t_m \sin \theta) \tag{12}$$

where

$$F = (1 - f_R)/(1 - f_B) \tag{13}$$

As a first approximation we can assume $\theta \leq 10^\circ$ and then solve for w to obtain

$$w \cong 0.51[(T/F) - 0.174 t_m] \tag{14}$$

With this expression one can estimate w in terms of actual or expected values of f_R , f_B , and t_m .

In comparing the expanded grid to the cast grid one should also give consideration to the relative grid conductances. This factor will be most significant at the top of the plate in the set of strands leading into the top horizontal grid bar since all of the current derived from the rest of the plate must pass through this top set of strands to reach the plate lug for flow from the plate. As a minimal consideration the sum of the cross-sectional areas of the expanded grid strands ($2N_w w t_m$) should be comparable to a similar sum for the cast grid. Often, cast grids, especially industrial sizes, may be a bit oversized so that the expanded grid may not need to provide as much cross-sectional grid area to effectively carry the same current. A more detailed analysis is required to factor in the effect of grid path length from bottom to top in combination with strand area.

Example

As an example of the application of this method of analysis the cast and expanded grids and plates described in Tables I and II are compared. The relative paste volume, P_R , from Eq. [8] is plotted in Fig. 3 against the short diamond dimension, S , for four values of F , i.e., four combinations of f_R , f_B , and w . It can be seen that the expanded grid becomes more rapidly unfavorable ($P_R < 1$) to the left of $S = 1.0$ cm and that it becomes more favorable ($P_R > 1$) to the right. The point corresponding to the conditions stated in

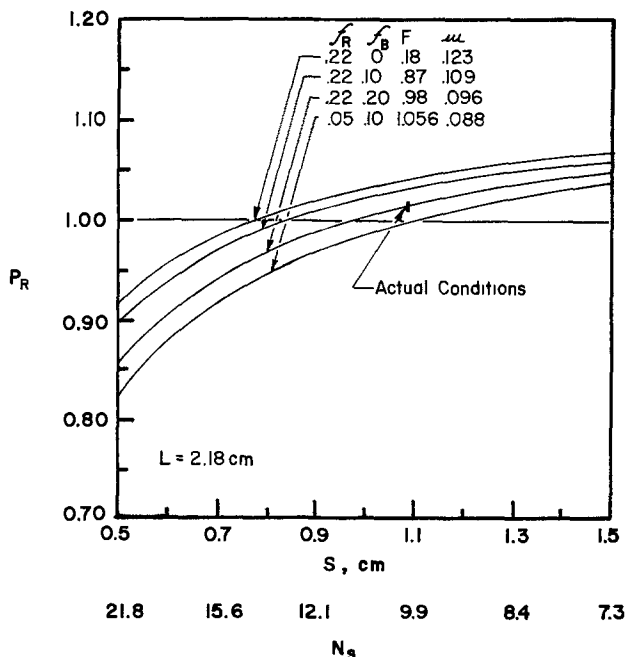


Fig. 3. Graph of P_R against S (and N_s) as it pertains to the example.

Table I. Comparison of plate specifications for cast and expanded SLI grids (dimensions in cm)

Grid	Height (no lug)	H	W	T	B	G (cm ³)	V (cm ³)	P (cm ³)	
								Est.	Meas.
Cast	11.43	10.99	15.24	0.2032	0.025	4.45	34.03	29.58	28.52*
Expanded	11.43	10.92	15.24	0.2032	—	3.79	33.82	30.03	28.29*

* Dry paste density (g/cm³): cast, 4.12; expanded, 4.04.

Table II. Expanded grid parameters

t_m (cm)	w (cm)	S (cm)	L (cm)	N_s	N_L	f_B (as- sumed)	f_R (re- sulting)
0.114	0.109	1.09	2.18	10	7	0.1	0.22

Tables I and II is shown at $P_R = 1.016$ and $S = 1.09$ cm as a vertical bar. It is apparent that other combinations of w , S , f_R , and f_B will provide many values of $P_R \geq 1.0$. The actual measured results, shown in Table III, indicate an initial advantage for the expanded plate relative to the cast grid plate in terms of discharge capacity (A-hr) per unit weight (kg) of plate. These values were observed after several initial conditioning cycles. It should be noted that although the cast grid volume (G) shown in Table I is 1.17 times that of the expanded grid volume, it is based only on the grid found between the top and bottom horizontal grid bars.¹ The actual grid weight ratio is 1.33 whereas the actual plate weight ratio is 1.12. Not unexpectedly the ratio of "A-hr per kg plate" values shown in Table III is also 1.12. This illustrates the heavy contribution that grid weight makes to energy density. Whereas the estimated paste volumes are in the ratio of 1.015 (expanded to cast), the ratio of the measured values is 0.99. This agrees well (to 2.5%) with the ratio of estimated values. Thus, if one had undertaken the goal of matching the capacity of the cast grid plate with the plate using the expanded grid of the configuration specified here, the goal would have been attained with the added advantage of increased energy density.

In conclusion, it can be seen that this analysis is useful for indicating the direction the grid designer should take when considering replacing a cast grid with an expanded grid in the same plate volume.

Acknowledgments

The author wishes to acknowledge the contributions of a refinement by R. Buchop, formerly of the Prestolite Division, and the experimental results by W. J. Schlotter of the C&D Batteries Division. Appreciation is also extended to C&D Batteries Division for the full support of this work.

¹ Note, that the G value of 3.79 cm³ for the expanded grid is a calculated value, whereas the measured value is 3.70 cm³, a difference of 2.4%.

Table III. Initial discharge results at the 3 hr rate

Grid	A-hr per plate	A-hr per kg plate	A-hr per kg PbO ₂
Cast	12.3	62.76	97.86
Expanded	12.3	70.15	100.54

Manuscript submitted Feb. 7, 1980; revised manuscript received March 28, 1980. This was Paper 101 presented at the Pittsburgh, Pennsylvania, Meeting of the Society, Oct. 15-20, 1978.

Any discussion of this paper will appear in a Discussion Section to be published in the June 1981 JOURNAL. All discussions for the June 1981 Discussion Section should be submitted by Feb. 1, 1981.

Publication costs of this article were assisted by Eltra Corporation.

LIST OF SYMBOLS

B	overpasting thickness
D_L	plate dimension parallel to L , equal to H or W
D_s	plate dimension parallel to S , equal to W or H
F	$= (1 - f_R)/(1 - f_B)$
f_B	fraction of plate thickness that is overpasted
f_R	fraction of initial expanded grid thickness reduced by rolling
G	volume of grid metal
H	grid height, appropriate for comparison to cast grid
L	long-way diamond length (expanded metal)
N	total number of grid strands
N_L	number of diamonds in L direction
N_s	number of diamonds in S direction
N_w	number of diamonds across plate width
n	node length
P	volume of active material in a plate
P_c	volume of active material in cast grid plate
P_E	volume of active material in expanded grid plate
P_R	relative paste volume, $= P_E/P_C$
R	reduction in initial grid thickness due to rolling
S	short-way diamond length parallel to plane of plate
S'	short-way diamond length parallel to plane of expansion
T	thickness of pasted plate
T_o	original thickness of expanded grid
T_R	thickness of expanded grid after rolling reduction
t_m	unexpanded sheet metal thickness
T'	partial grid thickness (used for derivation, see Fig. 2b)
t'	partial grid thickness (used for derivation, see Fig. 2b)
V	defined plate volume of interest
v	volume of one grid strand of length L
W	plate width
w	cutwidth defined by expanding process
θ	acute angle defined by S and S'

REFERENCES

- J. P. Badger, U.S. Pat. 4,102,024 (1978).
- D. P. Boden, C. W. Fleischmann, and J. P. Badger, ACS/CSJ Chemical Congress, Honolulu, April 1-6, 1979; Paper no. INDE 99.

Corrosion Behavior of Glassy Chromium-Containing Alloys Prepared by Sputtering

Ronald B. Diegle

Battelle, Columbus Laboratories, Columbus, Ohio 43201

and M. D. Merz

Battelle, Pacific Northwest Laboratories, Richland, Washington 99352

Glassy alloys containing Cr, P, and various other elements have been shown to possess excellent corrosion resistance by a number of workers (1-8), and were the subject of a recent review by Masumoto and Hashimoto (9). These alloys resist localized as well as general corrosion in electrolytes such as FeCl_3 and acidified NaCl. Furthermore, as little as 2 or 3 a/o of alloyed chromium are sufficient to confer this resistance (7). The interest in these alloys presently is of a rather fundamental nature, such as learning more about the influence of structure on corrosion and passivity. However, it is clear that glassy alloys have practical value as corrosion resistant coatings provided that a means can be developed for applying them as such.

An inherent feature of the fabrication of many corrosion resistant glassy alloys is the high quench rate, about 10^5 C/sec, necessary to attain the glassy structure upon solidification from the melt. Elaborate techniques, such as melt spinning (10) and melt extraction (11), typically are used to attain these high quench rates. A limitation of all liquid quenching techniques is that the dimension of the specimen is necessarily thin in the direction of heat extraction; typically, this dimension is about 50-75 μm , with about 125 μm a reasonable upper limit for this class of alloys. Although the filaments and narrow strips that result from liquid quenching are suitable for laboratory research studies, they cannot be utilized as coatings. Sputtering, on the other hand, is a vapor deposition technique used for coating large areas and complex geometries with thick deposits. Therefore, sputtering was investigated as a possible means for depositing extremely corrosion resistant Cr-containing alloys in the glassy state.

Experimental

The sputtering targets used during this research had the compositions $\text{Fe}_{45}\text{Ni}_{30}\text{Cr}_2\text{V}_2\text{P}_{15}\text{B}_6$ and $\text{Fe}_{31}\text{Ni}_{30}\text{Cr}_{16}\text{V}_2\text{P}_{15}\text{B}_6$. Vanadium was an impurity unintentionally added through use of a ferrophosphorus alloy. The primary variable was chromium, which was either 2 or 16 atomic percent (a/o). The alloys were prepared by melting together appropriate quantities of components in an induction furnace under an argon atmosphere, homogenizing for $\frac{1}{2}$ hr, and then pouring into cylindrical molds 13 cm in diam. Sputtering was performed at Battelle's Northwest Laboratories with triode sputtering equipment. It was performed in krypton at rates between 25 and 40 $\mu\text{m/hr}$. The substrate was copper, chilled either to -196°C or water cooled to about 15°C .¹ Three types of deposits were prepared, namely, 16 Cr sputtered onto copper at either 15° or -196°C , and 2 Cr sputtered onto copper at -196°C . The deposits were about 75 μm thick, non-porous, and extremely adherent to the substrates. For the purpose of comparison, liquid quenched specimens were prepared by melt spinning as previously described (7).

Key words: pitting, passivity, amorphous, melt-spinning.

¹For convenience the copper substrate temperatures are referred to either as -196° or 15°C . In actual fact the temperatures may have been somewhat higher because of the heat dissipated during the sputtering process.

The state of crystallinity of the deposits was examined by thin foil transmission electron microscopy (TEM), selected area electron diffraction (SAD), and differential scanning calorimetry (DSC). Surface topography was characterized by scanning electron microscopy (SEM), and composition by x-ray fluorescence (EDAX). Results were compared to those obtained from glassy alloys of nearly identical composition but prepared by melt spinning. Prior to structural characterization the deposits were removed from the copper substrates by dissolving the copper in concentrated nitric acid. The deposits were not noticeably affected by this treatment.

Corrosion was measured gravimetrically with coupons exposed in 10% FeCl_3 solution at ambient temperature, and by potentiodynamic anodic polarization in neutral and acidified 1M NaCl solutions. Sputtered deposits were subjected to gravimetric measurements after first removing them from the copper substrates as described above. For anodic polarization the specimens were left intact on the copper, which was masked with an acid resistant stop-off lacquer.

Results and Discussion

Structure.—Examination of the three sputtered deposits by TEM indicated the absence of resolvable structure, in particular, microcrystalline regions and associated grain boundaries. SAD verified the absence of detectable crystallinity, as denoted by broad diffuse ring patterns. Thus, the structures of the deposits were completely glassy within the limits of resolution of these two techniques.

DSC results from sputtered and melt spun alloys are summarized in Table I. The crystallization temperatures, T_c , of sputtered vs. melt spun alloys differed by 11°C for the 2 Cr alloys and by 4°C for the 16 Cr alloys. The heats of crystallization, ΔQ_c , varied by about 15% for the 2 Cr alloys and by about 12% for the 16 Cr specimens. There were no obvious trends in T_c and ΔQ_c relative to the method of specimen preparation, i.e., sputtering or melt spinning. Furthermore, the effect of substrate temperature on these parameters for the 16 Cr material does not appear to be significant. It is apparent from Table I that the crystallization behavior of the sputtered 2 Cr and 16 Cr deposits approximated that of melt spun alloys of the same compositions.

Compositions of the sputtering targets and corresponding deposits were compared to determine whether

Table I. Temperatures and heats of crystallization of sputtered and melt spun glassy alloys

Chromium content, a/o	Preparation technique	Substrate temperature, $^\circ\text{C}$	T_c , $^\circ\text{C}$	ΔQ_c , cal/g-atom
2	Sputtering	-196	428	1275
2	Melt spinning	~ 15	439	1095, 1115
16	Sputtering	-196	460	1070, 1110
16	Sputtering	~ 15	464	1230
16	Melt spinning	~ 15	461	1095, 1115

enrichment or depletion of any elements had occurred during sputtering. Variations in concentration between target and deposit were generally 1 a/o or less. An exception was the chromium content of the nominal 16 Cr alloy, which was 2.3 a/o higher in the deposit. An important observation is that phosphorus was not depleted in the deposit. Since phosphorus is needed to achieve the glassy state and to enhance corrosion resistance, it is significant that it can be sputtered at a concentration that is close to that in the target. No information could be obtained about the initial and final concentrations of boron, since quantification of boron by EDAX was not possible.

Surface topography.—The surfaces of sputtered specimens contained numerous hillock-shaped mounds. Figure 1 shows SEM photographs of the as-sputtered surfaces of several deposits. Figure 1(a) shows these hillocks, which were present to a greater or lesser degree on all sputtered specimens. Figure 1(b) is a higher magnification view of these features. Although still present, the hillocks were smaller and fewer on the 16 Cr specimen sputtered onto a water-cooled substrate, Fig. 1(c). This behavior agrees with prior sputtering experience with other alloys, *i.e.*, that warmer substrate temperatures favor less pronounced growth features. Chromium content in the alloy did not strongly affect their formation for, as shown in Fig. 1(d), they were also present on the deposit containing 2 Cr. (Several of the larger hillocks had been broken off during handling, hence their truncated appearance.) Hillocks such as those shown in Fig. 1 were not present on melt spun filaments, although shallower, less cone-shaped mounds could be found on the shiny surfaces of the filaments.

The source of the hillocks shown in Fig. 1 is not known, although they sometimes appear on other types of sputtered alloys including crystalline alloys of considerably different compositions than those reported in the present investigation. They are thought to result from growth instabilities that occur during deposition of atoms onto a substrate. Their significance to alloy properties is not known; however, it is shown in a later section that they were not preferred sites for localized corrosion, neither did they compromise the corrosion resistance of the deposits.

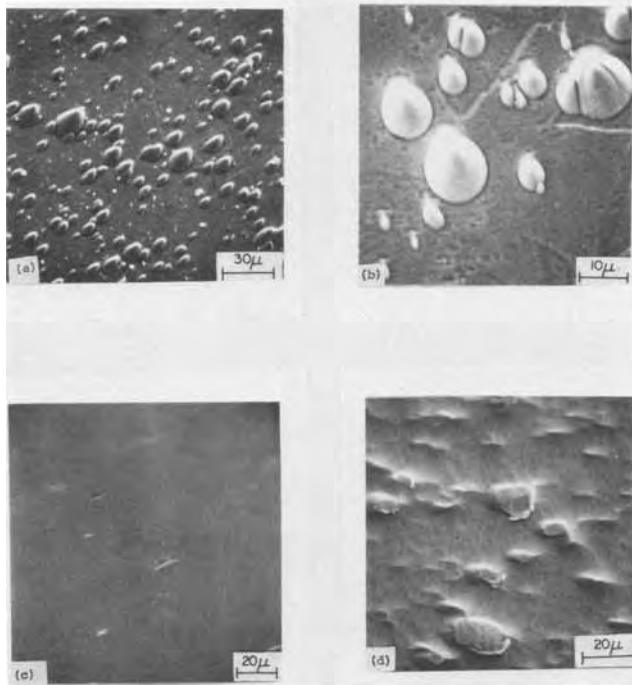


Fig. 1. SEM photographs of surfaces of sputtered deposits (a), (b) 16 Cr (LN_2 substrate); (c) 16 Cr (water-cooled substrate); (d) 2 Cr (LN_2 substrate).

Corrosion behavior.—The corrosion behavior of sputtered and melt spun specimens under freely corroding conditions was compared in 10% FeCl_3 solution. Data were obtained on duplicate specimens after 167 hr of exposure, and the corrosion rates were extrapolated to a $\mu\text{m}/\text{year}$ basis. The corrosion rates of the 2 Cr deposits averaged $1114 \mu\text{m}/\text{year}$, whereas those of the 2 Cr melt spun alloy averaged $427 \mu\text{m}/\text{year}$ or 38% of the former value. Analogously, the corrosion rates of the 16 Cr deposit averaged $1.8 \mu\text{m}/\text{year}$ and those of the 16 Cr melt spun alloy averaged $3.5 \mu\text{m}/\text{year}$, or 43% of the former value. Three features are particularly noteworthy regarding these data, as follows:

(i) The effect of increasing the chromium concentration in the sputtered deposits was to reduce greatly the corrosion rates, in parallel with the influence of chromium in melt spun specimens.

(ii) Corrosion rates of the 2 Cr deposits were about two to three times greater than those of the corresponding melt spun specimens.

(iii) Corrosion rates of both the melt spun specimens and the sputtered deposits containing 16 Cr were relatively low, indicating that the alloys were spontaneously passive in the FeCl_3 solution.

Anodic polarization was used to obtain more detailed information about corrosion behavior, as shown in Fig. 2 and 3. Figure 2 shows that the 2 Cr sputtered deposit underwent an active-passive transition in 1M NaCl, pH 3, whereas the 2 Cr melt spun filament was spontaneously passive. A reaction of unknown origin gave rise to a slight active-passive transition at about -0.45 to -0.50V (SCE). The critical current density for passivation for the sputtered alloys was about $10^{-3} \text{A}/\text{cm}^2$, and the minimum passive current density for all three specimens was about $9 \cdot 10^{-5}$ to $10^{-4} \text{A}/\text{cm}^2$.

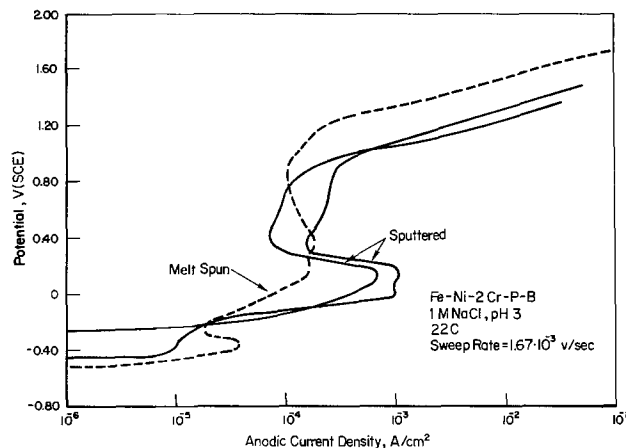


Fig. 2. Anodic potentiodynamic polarization curves of sputtered and melt spun 2 Cr alloys in 1M NaCl, pH 3, deaerated.

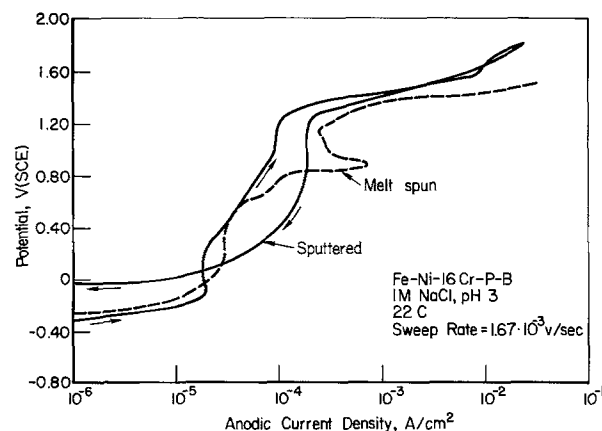


Fig. 3. Anodic potentiodynamic polarization curves of sputtered and melt spun 16 Cr alloys in 1M NaCl, pH 3, deaerated.

The steep increase in current at potentials above about 0.8V (SCE) was due to the selective oxidation of chromium as the hexavalent ion, Cr^{+6} .

As indicated in Fig. 3, the 16 Cr specimens were spontaneously passive in pH 3, 1M NaCl, with passive current densities in the approximate range of $2 \cdot 10^{-5}$ to $2 \cdot 10^{-4}$ A/cm². This spontaneous passivity extended even to pH 1 solutions (data not shown). The deposits exhibited passivity that was as complete, or nearly so, as that of corresponding melt spun alloys. Very significantly, the sputtered alloys resisted pitting corrosion to the same degree as those prepared by melt spinning. The positive hysteresis during the return sweep for the sputtered alloy was typical of polarization for all sputtered and melt spun specimens that were polarized to transpassive potentials. It may have been caused by temporary active dissolution in microscopic pits that formed at transpassive potentials, and then rapidly passivated at potentials in the passive region of polarization behavior.

Pitting could not be produced by polarization in the passive range of potentials, even for extended times. For example, the surface of a sputtered 2 Cr alloy that was potentiostatically polarized for 1 hr in 1M NaCl, pH 3, is shown in Fig. 4. The corrosion produced a scalloped appearance on the flat regions and no preferential attack of the hillock-shaped mounds. [The truncated tops evident in Fig. 4(b) were the result of surface damage prior to exposure to the electrolyte.] The corrosion that occurred in the passive potential range of behavior produced a sort of general attack, a surface roughening reminiscent of pits that were not able to propagate after initiating. Shallow pits were observed after potentiostatic polarization at potentials that were well into the oxygen evolution range, above about 1.3V (SCE). However, even at these very oxidizing potentials the pits that developed tended to propagate to depths of only several μm , after which they apparently passivated and new pits formed nearby. Shallow pit depths and high pit densities were a characteristic common to sputtered deposits polarized at transpassive potentials. Conversely, transpassive corrosion of melt spun filaments generally produced more through-pits and lower pit densities.

There was no substantial effect of substrate temperature on anodic polarization behavior. The polarization curves for the 16 Cr deposits sputtered at -196° and 15°C were similar. Both types of deposits were spontaneously passive in 1M NaCl at pH 7 and 3, with the passive current densities of the water-cooled deposits ranging to about twice those of the liquid nitrogen-cooled specimens. However, pitting susceptibilities were unaffected, with pitting occurring only at transpassive potentials (i.e., above about 1.20V (SCE) for the 16 Cr alloys). Examination of the specimens after polarization indicated that pits were shallower on the alloy sputtered at -196°C . The effect of substrate temperature on pitting and overall corrosion behavior needs further study to better define the role of this variable on corrosion.

Conclusions

Sputtering can be used to prepare alloys of the Fe-Ni-Cr-P-B variety with a completely glassy structure. Thermal characteristics, such as temperatures and heats of crystallization, of sputtered alloys are similar to those of alloys of the same nominal compositions but prepared by melt spinning. Because of these similarities it is inferred that the structures of the two classes of alloys are also similar. The corrosion and electrochemical behavior of the sputtered deposits resembled, but was not identical to that of melt spun alloys of the same composition. Specifically, open-circuit corrosion rates and oxidation rates during anodic polarization of the sputtered deposits exceeded those of melt spun specimens, sometimes by about an order of magnitude. However, the sputtered deposits exhibited the same resistance to pitting corrosion as

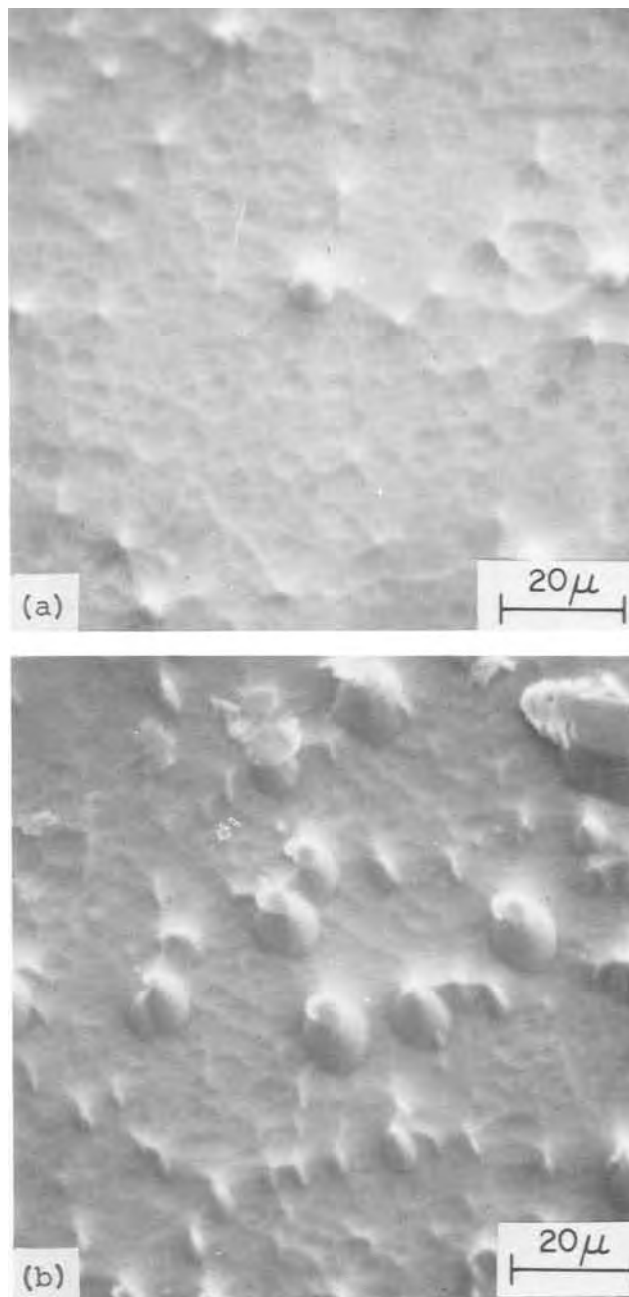


Fig. 4. SEM photographs of 2 Cr sputtered deposits polarized for 1 hr in 1M NaCl, pH 3, at the following potentials: (a) 0.60V (SCE); (b) 1.10V (SCE).

their melt spun counterparts, with pitting occurring to a large degree only at transpassive potentials in acidified chloride solutions. There is some evidence that a colder substrate temperature may favor improved corrosion resistance, but this tentative conclusion needs verification. Sputtering is a viable alternate technique for depositing extremely corrosion resistant glassy Fe-Ni-Cr-P-B alloys.

Acknowledgments

Thanks are due to D. M. Lineman and R. E. Maringer for, respectively, skillful technical assistance and preparation of the melt spun alloys. J. Brimhall of Battelle's Northwest Laboratories is credited with the TEM and selected area electron diffraction data. One of us (R.B.D.) is pleased to acknowledge financial support from the Office of Naval Research, Contract No. ONR-00014-77-C-0488.

Manuscript submitted Aug. 20, 1979; revised manuscript received March 26, 1980.

Any discussion of this paper will appear in a Discussion Section to be published in the June 1981 JOURNAL. All discussions for the June 1981 Discussion Section should be submitted by Feb. 1, 1981.

Publication costs of this article were assisted by Battelle.

REFERENCES

1. M. Naka, K. Hashimoto, and T. Masumoto, *Corrosion*, **32**, 146 (1976).
2. R. Diegle and J. Slater, *ibid.*, **32**, 155 (1976).
3. K. Hashimoto and T. Masumoto, in "Rapidly Quenched Metals," *Procs., Second Int. Conf. on Rapidly Quenched Metals*, N. J. Grant and B. C. Giessen, Editors, p. 285 (1975).
4. K. Hashimoto, K. Asami, T. Masumoto, and S. Shimodaira, *Corros. Sci.*, **16**, 71 (1976).
5. K. Asami, K. Hashimoto, T. Masumoto, and S. Shimodaira, *ibid.*, **16**, 909 (1976).
6. T. M. Devine, *This Journal*, **124**, 38 (1977).
7. R. B. Diegle, *Corrosion*, **35**, 250 (1979).
8. R. B. Diegle and D. M. Lineman, Technical Report No. ONR-00014-77-C-0488-2 to Office of Naval Research, May, 1979.
9. T. Masumoto and K. Hashimoto, *Ann. Rev. Mater. Sci.*, **8**, 215 (1978).
10. S. Kavesch, in "Metallic Glasses," pp. 55-70, American Society for Metals, Metals Park (1978).
11. R. E. Maringer and C. E. Mobley, in "Rapidly Quenched Metals III," pp. 49-56, The Metals Society (1978).

Electrochemical Studies on Amorphous Thin Film and on Sintered Polycrystalline CdS Electrodes

A. M. Redon* and J. Vigneron

Lab. Electrochimie Interfaciale, 1, Place A. Briand, 92190 Meudon, France

and R. Heindl*

Lab. de la Physico-Chimie des Matériaux par Techniques Avancées, 1, Place A. Briand, 92190 Meudon, France

The stability of semiconducting electrodes in photoelectrochemical cells is still the key problem to be resolved before these devices can be employed for solar energy conversion. Until now, only electrodes made of SrTiO₃ or TiO₂ or SnO₂ and similar materials have been found to be stable (1), but their bandgap (≈ 3 eV) is too high to utilize the solar spectrum efficiently. More recently, Tributsch (2) has demonstrated that electrodes made of single crystals of MoS₂ and TiS₂ are stable over a period of 9 months WSe₂ has also been used as a semiconductor electrode in photochemical cells (3).

For practical application, single crystals are too expensive, so we have investigated the stability of thin film amorphous CdS electrodes which can be obtained by a simple spray technique and of electrodes made of sintered polycrystalline CdS.

Recently, the thermodynamic stability of CdS electrodes in solutions of various pH (4), and on the charge transfer with Na₂S in the electrolyte have been investigated (5).

It has been also stated that electrodes made from crystalline CdS can be stabilized with the help of redox systems, such as Fe(CN)₆^{3-/4-} and S⁻²⁻ (6, 7). The use of thin film electrodes is especially interesting as cadmium is a metal which is found only in limited amounts on the earth. Thin film and polycrystalline CdS have the same bandgap (8).

Electrode Preparation

Amorphous thin film of CdS.—A spray of an aqueous solution of CdCl₂ and SC(NH₂)₂ is projected on a gold layer heated to 300°C. The gold, which has been previously deposited on a glass plate, provides the ohmic contact.

Polycrystalline sintered electrodes.—High purity CdS powder has been pressed practically at 50 kg bars and then sintered at 900°C under Ar for 4 hr. The light source is a 150W xenon lamp. Monochromatic illumination is performed with the help of a Jobin-Yvon monochromator (HRS₂). The dark current can be eliminated with the help of a chopper and a lock-in amplifier.

The stability of the electrodes has been investigated by the measurement of the photocurrents vs. the time in 0.1M solution, in the absence of any redox system, and then in the presence of 10⁻³M Fe(CN)₆^{3-/4-} and

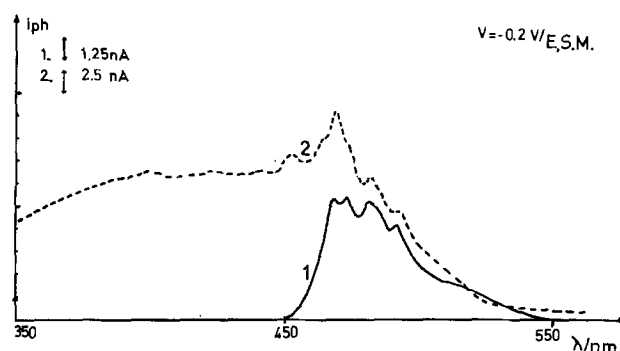


Fig. 1. Photocurrent vs. the wavelength of incident light (---) in 0.1M KOH electrolyte; (—) in 0.1M KOH + 1.5×10^{-3} M K₄Fe(CN)₆ + 1.5×10^{-3} M K₃Fe(CN)₆ in the dark.

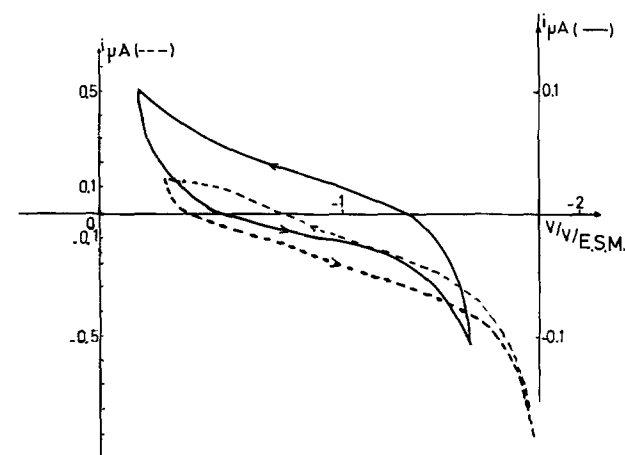


Fig. 2. Intensity potential curves in: (—) 0.1M KOH electrolyte; (---) in 0.1M KOH + 1.5×10^{-3} M K₄Fe(CN)₆ + 1.5×10^{-3} M K₃Fe(CN)₆ in the dark.

* Electrochemical Society Active Member.

10^{-3} M sodium polysulfide. The photocurrents decrease vs. the time, and the electrode is sensibly damaged after the experiment with the first redox couple, but stabilization is completely achieved with the second.

The bandgap can be obtained on Fig. 1. The differences in the curves at high energy are due to the absorption of the redox solution.

The intensity-potential curves in the dark are also recorded with and without the $\text{Fe}(\text{CN})_6^{3-/4-}$ (Fig. 2). The same kind of results has been obtained with electrodes made of polycrystalline CdS.

Conclusion

Electrodes made of amorphous film of CdS made by spray technique are not very expensive and so are very interesting. Appreciable photocurrents can be obtained with them. The stabilization is observed only with the sodium polysulfide and not with the $\text{Fe}(\text{CN})_6^{3-/4-}$ redox couple.

Manuscript submitted Feb. 19, 1980; revised manuscript received March 26, 1980.

Any discussion of this paper will appear in a Discussion Section to be published in the June 1981 JOURNAL. All discussions for the June 1981 Discussion Section should be submitted by Feb. 1, 1981.

REFERENCES

1. A. Fujishima, T. Inoue, and K. Honda, S.I.E.T. Budapest 1978, p. 62.
2. H. Tributsch, *Ber. Bunsenges. Phys. Chem.*, **82**, 169 (1978).
3. F. R. F. Fan *et al.*, *This Journal*, **127**, 518 (1980).
4. S. M. Park and M. E. Barber, *J. Electroanal. Chem. Interfacial Electrochem.*, **99**, 67 (1979).
5. R. H. Wilson, *This Journal*, **126**, 1187 (1979).
6. H. Gerischer, *J. Electroanal. Chem. Interfacial Electrochem.*, **82**, 133 (1977).
7. T. Inoue, T. Watanabe, A. Fujishima, and K. Honda, *This Journal*, **124**, 719 (1977).
8. B. Miller and A. Heller, *Nature*, **262**, 680 (1976).



The Interaction of Stress and Mechanical Property Effects during Oxidation of Tantalum Base Alloys

R. E. Pawel* and J. J. Campbell

Oak Ridge National Laboratory, Metals and Ceramics Division, Oak Ridge, Tennessee 37830

ABSTRACT

Specimens of the tantalum base alloys Ta-10 W and Ta-10 W-2.5 Hf (T-222) were observed to ignite after prolonged oxidation at elevated temperatures. The characteristics of this behavior were examined, and the time-temperature regime in which one might expect this catastrophic response to oxidation of thin specimens was defined. Ignition of specimens was found to be the final step in a sequence that involved oxygen penetration into the alloy in advance of the oxide-metal interface, a resulting embrittlement and stress buildup, and finally a relaxation of the strain energy of the system through a sudden disintegration of the specimen along grain boundaries that, if confined, led to a violent ignition.

The effects and interactions of stress generation and mechanical properties during the oxidation of metals and alloys have been the subject of numerous investigations (1). The existence of large mechanical stresses arising during isothermal oxidation as a result of the oxidation process itself has been demonstrated for many systems, and several mechanisms of stress generation have been examined. The response of the system to these stresses depends in large measure on mechanical behavior in both the substrate material and in the products of oxidation. Both dramatic and subtle responses have been observed.

The details of the kinetics of oxidation and stress generation in tantalum base alloys containing tungsten and hafnium have been discussed previously (2). Basically, over the temperature range 500°-850°C, in pure oxygen at atmospheric pressure, the alloys Ta-10 W and Ta-10 W-2.5 Hf (T-222) oxidize in the initial stages at a decreasing, approximately parabolic, rate, during which time a protective oxide scale (β -tantalum pentoxide) grows and oxygen is absorbed into the metal. These kinetics exhibit a classical temperature dependence, and the activation energy, about 234 kJ/mole, suggests that the rate is controlled by diffusion of oxygen in the growing oxide film. Conversely, the flexure characteristics of these alloys during oxidation on one side suggested that the stresses in the specimens were primarily a result of oxygen solution effects in the metal beneath the oxide film. The flexure behavior was qualitatively consistent with that observed for oxidation of pure tantalum (3).

Continued oxidation at temperatures in the lower end of the above range results eventually in a typical breakaway behavior in which a change from a decreasing oxidation rate to an increasing rate is observed. This process is generally sluggish, starting with localized breakdown of the protective film, followed by the formation and propagation of regions of porous, nonprotective oxide, leading to high oxidation rates.

For each alloy the time at which breakaway oxidation started decreased with increasing temperature up to some maximum temperature. Above this temperature, (about 650°C for the Ta-10 W alloy, and 700°C for the T-222 alloy), the breakaway was postponed, and compact and protective films grew for comparatively long periods of time. This behavior resulted in unusual comparisons of the extent of oxidation in different experiments. For example, after 2 hr in oxygen at 650°C, the average thickness of the oxide on a Ta-10 W specimen is many times greater than that for a 700°C exposure.

While the persistence of the parabolic kinetics, as opposed to breakaway kinetics, at high temperatures suggests a degree of improvement in the resistance to oxidation for these alloys, an unexpected complication may arise. In this paper, we shall present the details of a rather spectacular manifestation of stress and mechanical property effects during oxidation that may have a general applicability. This behavior involved a change in the mechanical properties of the specimens and the development of a tensile stress in the samples, both brought about by oxygen solution effects during the oxidation reaction.

Experimental Procedure

The materials investigated in this work were the refractory metal alloys Ta-10 W and Ta-10 W-2.5 Hf (T-222).¹ Specimens were prepared from 1 × 2 cm coupons cut from 0.05 and 0.13 cm thick sheet obtained from Teledyne-Wah Chang. The coupons were hand-ground on metallurgical papers to the desired thickness in the range 0.02-0.12 cm. They were then annealed in vacuum for 1 hr at 1650°C (except as noted), mechanically polished through 0.3 μ m alumina on a vibratory polisher, and then electropolished in a 90% H₂SO₄-10% HF solution.

The kinetic measurements were carried out in a quartz manometric oxidation rate apparatus in which

* Electrochemical Society Active Member.

Key words: alloy oxidation, kinetics, stress, embrittlement.

¹ Nominal analyses of these alloys were (i) Ta-10 W: 9.8 and 10.8 w/o W, <30 ppm C and N, <50 ppm O; and (ii) T-222: 10.5 w/o W, 2.5 w/o Hf, 140 ppm C, 22 ppm N, and 85 ppm O.

1565

the pressure change between a reaction volume and a reference volume was measured by either a capacitance or an oil manometer. Prior to oxidation, the specimens were heated to the reaction temperature in vacuum. The measurements of the ignition or disintegration times were made by allowing the oxidation to proceed in small quartz tubes designed either to confine the residue (ignition) or to allow the residue to fall into a cold region. In the former case the temperature recorder provided an accurate indicator for specimen ignition. All experiments were carried out in dry oxygen at atmospheric pressure.

Results and Discussion

The oxide formed on Ta-10 W and Ta-10 W-2.5 Hf alloys at temperatures above the transition from normal breakaway kinetics remained uniform, adherent, and protective for surprisingly long periods, although spallation and an increase in the oxidation rate eventually occurred in the later stages (2). However, for specimens in this regime of protective oxidation, many experiments came to a sudden and violent end, often signaled by the ignition of the specimen. This behavior is illustrated in Fig. 1, which shows oxidation rate curves for Ta-10 W specimens at 600°, 650°, and 700°C obtained in the manometric rate apparatus. At 600°C the kinetics are independent of specimen thickness and exhibit typical breakaway behavior beginning at about 120 min. At 650°C, breakaway begins at about 15 min and the rate increases sharply. At 700°C, the parabolic kinetics persist for longer times with a small amount of localized cracking and spalling moderately affecting the oxidation rate (for the thicker specimen) at about 200 min. However, the thinner specimen at this temperature showed an abrupt and calamitous increase in the rate at 198 min as the specimen ignited in the rate apparatus. It is of interest to note here that the recorder and controller thermocouples, located on the outside of the quartz reaction tube, signaled this event with a temperature spike of 500°C or more. Similar kinetic behavior was observed for the T-222 alloy; however, the onset of the regime of continued protective film formation is shifted upwards in temperature, from about 700°C to about 750°C.

The inconvenience occasioned by the first several observations of this phenomenon (ignition of a specimen in an apparatus employing an oil manometer becomes a doubly spectacular event, when the oil is sucked into the hot reaction zone), as well as the scientific aspects, prompted additional experiments to classify the behavior. We soon found that for oxidation in this range of temperatures, pure tantalum did not exhibit ignition, but that the alloys Ta-10 W and T-222 (as well as T-111, Ta-8 W-2 Hf) responded violently

for certain time-temperature exposures. On occasion, instead of ignition of the specimen at the appropriate time, the rate of oxygen consumption suddenly ceased. In these instances, it was observed that the residue of the specimen, essentially a collection of lightly oxidized grains, had managed to fall into a cold zone at the bottom of the apparatus rather than continuing to oxidize. Clearly, a disintegration of the specimen had taken place at the reaction temperature and this observation was a significant clue to the mechanism.

Such events are reminiscent of certain of the observations of Dooley and Stringer (4, 5) who studied the oxidation characteristics of Ta-4 weight percent (w/o) W and Ta-4 w/o Hf alloys. Although working predominantly at higher temperatures where linear oxidation kinetics dominated, these investigators reported grain boundary cracking and specimen fragmentation mainly during and after cooling for annealed specimens of Ta-4 w/o W oxidized at 950° and 1000°C. At 1050°C, these specimens ignited on admission of oxygen, as did similar specimens of Ta-4 w/o Hf. Ignition was not observed after extended periods of isothermal oxidation, although there were suggestions that some separation of the metal grains had taken place at temperature. It was postulated that the boundaries were "weakened by rapid oxygen diffusion along them" and that "stresses were increased by enhanced oxide strength and increased adherence between individual grains and the oxide." The "energetic event" that they report for oxidized specimens cooling from the reaction temperature appears to be comparable in kind to our observations of sudden and energetic fragmentation at the reaction temperature.

Several types of experiments were performed to describe this disintegration/ignition effect in a more quantitative fashion. First, we simply measured the time-to-ignition for specimens of these alloys by heating a specimen in vacuum in the bottom of a small quartz tube, admitting oxygen, and then noting the ignition time by the temperature spike on the temperature recorder. The ignition times proved to be different for the different alloys, and were a sensitive function of the specimen thickness as well as the temperature. Pure tantalum did not exhibit this behavior.

We also examined the microstructure of specimens oxidized very close to the point of disintegration or ignition. These specimens were obtained both by stopping the oxidation at an appropriate time, or by allowing the process to proceed so that the residue could quench itself by falling out of the hot zone of the furnace. It appeared that a fine grain size and at least some degree of confinement to the hot zone was necessary for complete ignition.

Finally, we did several experiments with a fine wire thermocouple attached directly to the specimen in order to see if any appreciable self-heating occurred prior to disintegration. We could detect no such temperature rise, thus indicating that the ignition is a result of—and not the cause of—the disintegration.

Plots of the ignition times as a function of specimen thickness at several temperatures are shown in Fig 2 for the Ta-10 W alloy. The open and filled symbols for data at each temperature represent results from two alloy heats containing nominally 9.8 and 10.8 w/o tungsten, respectively; the "#" points represent specimens of the indicated thickness that did not ignite, but rather oxidized to completion without a pyrotechnic response. Despite the scatter in the data, a series of straight lines on this log-log plot, constructed with a slope of 2, does describe the behavior with reasonable accuracy, and suggests that diffusion from the free surface, rather than wholly internal effects, is responsible for the events leading to ignition. Consistent with the fact that the specimen is clearly embrittled at the time of disintegration, oxygen is

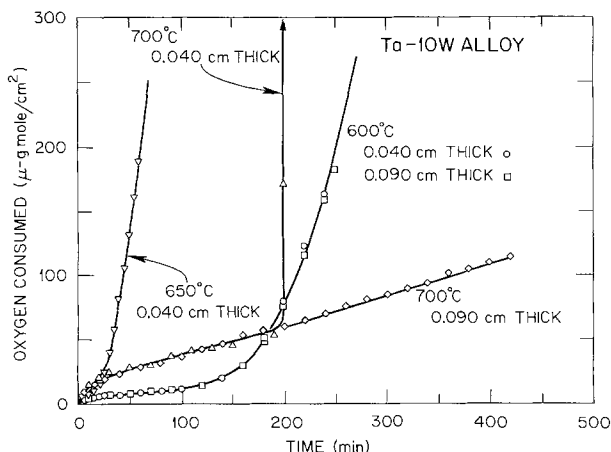


Fig. 1. Oxidation rate curves for Ta-10 W alloy in dry oxygen at atmospheric pressure. Specimens approximately 0.040 and 0.090 cm thick.

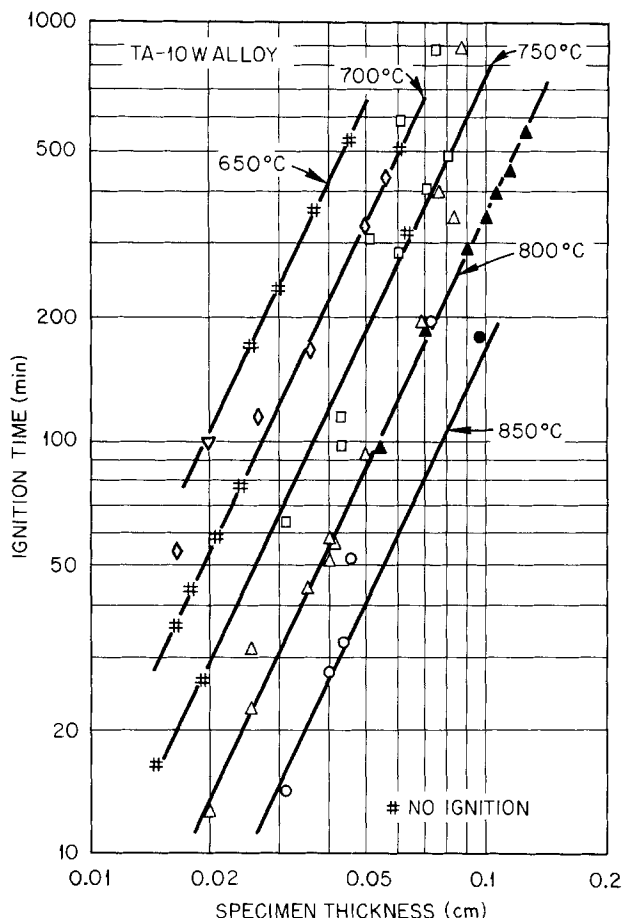


Fig. 2. Ignition times for the Ta-10 W alloy as a function of specimen thickness. ∇ : 650°C; \diamond : 700°C; \square : 750°C; \triangle : 800°C; \circ : 850°C. Open data points are for Ta-9.8 W specimens; filled data points are for Ta-10.8 W. "#" represents experiments for which ignition did not occur. Ignition is observed in this thickness range for $T \geq 700^\circ\text{C}$.

the logical agent and, if we use these data to determine an "activation energy for ignition" (from the slope of the log reciprocal ignition time vs. reciprocal temperature plot), the value of 125 ± 17 kJ/mole (30 ± 4 kcal/mole) is in qualitative agreement with that for interstitial oxygen diffusion in these materials. This is in accord with the concept that both the stress in the specimen and the extent of embrittlement are related to oxygen diffusion in the metal in advance of the oxide-metal interface.

It is also significant to point out that ignition was observed in this alloy only at temperatures where breakaway oxidation is not a predominant feature. While a line signifying ignition was placed on Fig. 2 for Ta-10 W at 650°C, it is based on a single observation out of twelve attempts and probably should not be included in the set. Similar behavior was observed for ignition of T-222 alloy specimens as indicated in Fig. 3. Breakaway behavior persists to a higher temperature in this alloy (2), and ignition was not observed here for oxidation temperatures lower than about 750°C. There was also a difference in the ignition time for a T-222 specimen of a given thickness, about twice the time being required compared to that for the Ta-10 W alloy. This figure again emphasizes the time perspective of the phenomenon: thicker specimens of this set oxidized in a protective mode for 10 hr or longer, then over a period of perhaps a few seconds they disintegrated completely.

Metallographic examinations of specimens oxidized for times close to the ignition point directed attention to the severity of the embrittlement. Extreme intergranular effects were generally observed, as shown

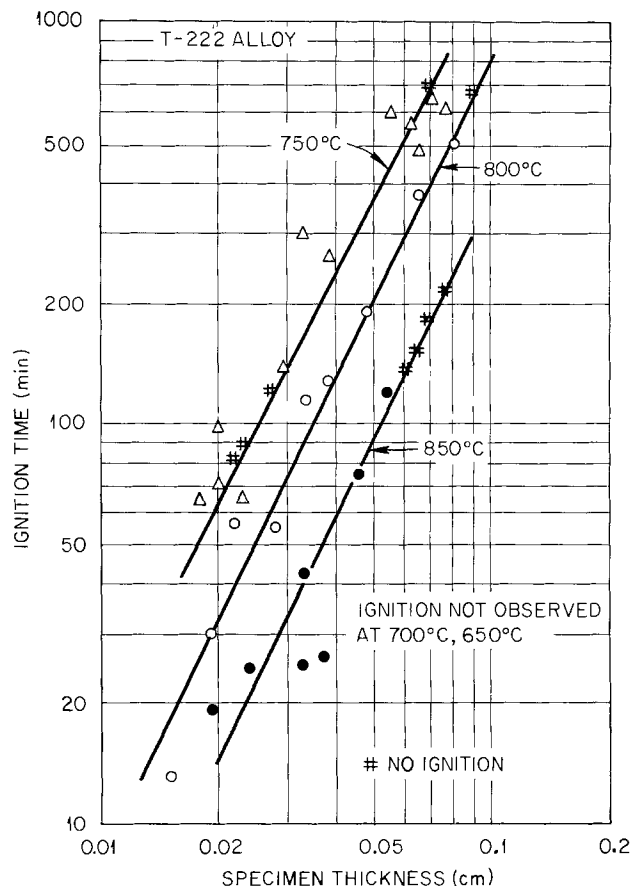


Fig. 3. Ignition times for the Ta-10 W-2.5 Hf (T-222) alloy as a function of specimen thickness. \triangle : 750°C; \circ : 800°C; \bullet : 850°C. "#" represents experiments for which ignition did not occur. Ignition was observed in this thickness range for $T \geq 750^\circ\text{C}$.

in Fig. 4, to the extent that the individual grains had a tendency to pop out during specimen preparation. Note that the thickness of the oxide film on this specimen is minimal compared to the oxygen embrittled zone suggested by the cracks. SEM examinations showed that the fracture surfaces of these specimens were essentially featureless at a resolution of a few tens of nm. A similar characterization of the structure and embrittlement in an oxygen-containing tantalum alloy (T-111) has been made by Liu, Inouye, and Carpenter (6), who suggested that the grain boundary cleavage was due to the formation of a thin, soft, precipitate-free-zone (PFZ) adjacent to the boundary.

A few specimens were prepared by vacuum annealing at 1800° and 2200°C to produce very large grains (up to about 1 mm diam) prior to oxidation. Appropriate isothermal exposures of these specimens led to disintegration at temperature but usually not to

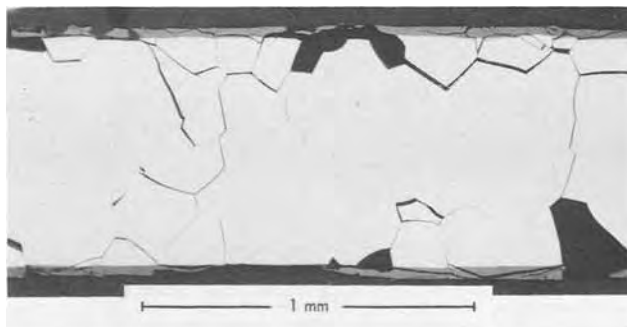


Fig. 4. T-222 specimen oxidized 120 min at 800°C. Note indication of extreme intergranular embrittlement. Specimen annealed in vacuum for 2 hr at 1800°C prior to oxidation.

ignition. The specimens came apart, with apparent force, at the grain boundaries but, as we shall propose in the next section, the surface-to-volume ratio in this case was insufficient to promote the catastrophic temperature increases from the rapid oxidation of fresh surfaces. The effect of grain size on the time required to disintegrate specimens was not large, but the few data available had a tendency to lie slightly above the standard time-to-ignition curve.

Conclusions

The phenomenon of embrittlement and ignition of these alloys undoubtedly arises as a consequence of oxygen solution into the alloy during the period of protective film growth. Speculation regarding the precise mode of the embrittlement is beyond the scope of this paper. However, it was affirmed here that comparable intergranular weaknesses were generated in both the hafnium-free and hafnium-containing alloys, and intergranular failure predominated in both without the observation of significant grain boundary precipitates in the SEM. Given this propensity for embrittlement, the period of protective oxidation is recognized to be of particular interest because, unlike breakaway oxidation where the oxide-metal interface moves more rapidly, the slower oxide growth results in a relatively high concentration of dissolved oxygen in the metal in advance of the interface.

We believe that the sudden and energetic disintegration of the embrittled specimen is brought about by the stress system built up by the oxidation process itself. During oxidation of these alloy specimens on one side, large mechanical bending strains have been observed (2). These strains were proposed to arise predominantly from oxygen solution effects, although the stress level in the oxide layers was also high. In any event, for a two-sided oxidation experiment, the gradient of compressive stress that exists concomitant with the oxygen concentration gradient requires that the central portion of the specimen cross section come under increasing tensile loads as oxidation proceeds. The strain energy is accumulated and then suddenly relieved by the mechanical failure of the specimen. Thus, the occurrence of this effect involves a critical interaction between stress generation, mechanical properties, and the relative rates of oxide formation and oxygen diffusion in the specimens. For example, a self-consistent explanation of the difference between the behavior of the Ta-10 W alloy and the T-222 alloy

presented here involves the fact that hafnium either decreases the effective oxygen diffusivity in the alloy or serves as an efficient saturable trap for diffusing oxygen atoms.

In summary, the catastrophic disintegration or ignition of thin tantalum alloy specimens is envisioned as being the final step in the following sequence: (i) oxygen penetration into the alloy in advance of the oxide-metal interface, resulting in (ii) grain boundary embrittlement and (iii) a stress gradient. The stress levels and extent of embrittlement increase with time leading to (iv) a sudden disintegration. If the grain size is sufficiently small and the residue is confined; (v) a violent ignition of the specimen may result.

Acknowledgments

The authors appreciate the helpful discussions with J. V. Cathcart, R. W. Carpenter, and C. T. Liu during this work and in the preparation of the manuscript. This research was sponsored by the Division of Materials Sciences, U.S. Department of Energy, under contract W-7405-eng-26 with the Union Carbide Corporation.

Manuscript submitted Dec. 3, 1979; revised manuscript received March 20, 1980.

Any discussion of this paper will appear in a Discussion Section to be published in the June 1981 JOURNAL. All discussions for the June 1981 Discussion Section should be submitted by Feb. 1, 1981.

Publication costs of this article were assisted by Oak Ridge National Laboratory.

REFERENCES

1. See, for example, J. Stringer, *Corros. Sci.*, **10**, 513 (1970); and J. Cathcart, in "Properties of High Temperature Alloys," Z. A. Foroulis and F. S. Petit, Editors, pp. 99-119, The Electrochemical Society Softbound Proceedings Series, Princeton, N.J. (1976).
2. R. E. Pawel and J. J. Campbell, in "Stress Effects and the Oxidation of Metals," J. V. Cathcart, Editor, pp. 330-351, The Metallurgical Society of AIME, New York (1975).
3. R. E. Pawel and J. J. Campbell, *This Journal*, **116**, 828 (1969).
4. R. B. Dooley and J. Stringer, *J. Less-Common Metals*, **25**, 15 (1971).
5. R. B. Dooley and J. Stringer, *ibid.*, **25**, 115 (1971).
6. C. T. Liu, H. Inouye, and R. W. Carpenter, *Metall. Trans.*, **4**, 1839 (1973).

Surface Irregularities Induced by Anodic Oxidation of n-Type GaAs

Tsutomu Tsuji

Nippon Electric Company, Limited, Central Research Laboratories, Takatsu-ku, Kawasaki 213, Japan

ABSTRACT

GaAs surface irregularities caused by anodic oxidation in the dark were studied by changing materials and oxidation conditions. Three different texture irregularities, pebbled appearance, lines, and a mottled color splotch, were found on the oxidized surface or the surface free of the oxide layer. For the vapor epitaxial GaAs with a $0.6 \sim 3.0 \times 10^{17} \text{ cm}^{-3}$ carrier concentration range, only the first irregularity was observed. None of these irregularities were observed on heavily doped epitaxial or bulk GaAs, whereas all of them were observed on n-type CZ material that had not been doped. Correlation to crystal defects is also discussed. It was found that pebbled texture and striations could be suppressed when anodization voltage was kept small or when electrolyte temperature was kept low.

GaAs microwave devices, such as GaAs FET's and optical devices, require very fine etching as well as occasionally passivation by an oxidized layer. Recently, it has been realized that anodic oxidation is a useful tool for very fine etching. For example, Rode *et al.* (1) demonstrated that anodic oxidation in the dark can be used for a self-controlled etching to get a uniform active layer for GaAs FET's. Müller *et al.* (2) used anodic oxidation for uniform and controlled fine etching of an ion-implanted GaAs layer. For these applications, surface smoothness of the oxidized layer and/or of the GaAs surface from which the oxide layer was removed is very important. Especially for the application to GaAs FET materials, a mirror-like smooth surface without any texture is needed to get a narrow gate ($\sim 0.5 \mu\text{m}$) which is essential for obtaining a higher power gain and lower noise figure for a GaAs FET.

After the anodic oxidation of GaAs, a gray or granular texture has been observed by Logan *et al.* (3) and Spitzer *et al.* (4) on n-type bulk GaAs, whose carrier concentration was $0.5 \sim 5 \times 10^{17} \text{ cm}^{-3}$, and on p-type bulk GaAs, whose hole concentration was $1 \sim 5 \times 10^{18} \text{ cm}^{-3}$, when they were oxidized in H_2O_2 . Hasegawa *et al.* (5) reported pits which spread from the fringe of the sample toward the inner area. There is no report of a systematic analysis of the surface after anodic oxidation. The purposes of this work are to study properties of irregularities, and to obtain a good smooth GaAs surface by anodic oxidation in the dark, which can be applied to the fabrication of GaAs FET's. Systematic study on the surface morphology for an oxidized surface has been accomplished by changing materials and conditions, such as anodization voltage or temperature.

This report lists three kinds of surface irregularities: pebbled appearance, lines, and a mottled color splotch on the oxide layer. All of these three irregularities were observed on undoped bulk GaAs, but none were observed on heavily doped vapor grown epitaxial or bulk GaAs. Only the first irregularity was observed on the vapor grown epitaxial GaAs with a low carrier concentration. Pebbled texture and striations (lines) were suppressed at a small oxidation voltage or at a low electrolyte temperature. The striations and the mottled color splotch were easily recognized by the naked eye. The lines and the pebbled texture had the same dependence on anodization conditions.

Experimental Procedure

The anodic oxidation studies were performed on Czochralski (CZ)-grown nondoped (not intentionally

Key words: defects, epitaxy, semiconductor, topography.

doped) n-type ($n \sim 4 \times 10^{16} \text{ cm}^{-3}$) boat-grown (BG) nondoped n-type ($n \sim 1.4 \times 10^{16} \text{ cm}^{-3}$), CZ-grown tin-doped ($n \sim 2 \times 10^{18} \text{ cm}^{-3}$), BG silicon-doped ($n \sim 2 \times 10^{18} \text{ cm}^{-3}$), and vapor-grown sulfur-doped ($n = 6 \times 10^{16} \sim 1 \times 10^{18} \text{ cm}^{-3}$) materials. The GaAs wafers were all (100) oriented. The bulk samples were chemomechanically polished with $0.1 \sim 0.3 \mu\text{m}$ ZrO_2 in an aqueous solution of NaOCl , then were cleaned in boiling trichloroethylene and acetone, followed by a rinse in water, and $11 \mu\text{m}$ was etched from the surface in a solution of $3 \text{ H}_2\text{SO}_4: 1 \text{ H}_2\text{O}_2: 1 \text{ H}_2\text{O}$ to remove the damaged layer.

Anodization was carried out in the so-called AGW electrolyte (5), which was a mixture of a 3% aqueous solution of tartaric acid and ethylene glycol in 1:2 proportions. The pH for the electrolyte was 2.60 and the temperature was held at $25^\circ \sim 27^\circ\text{C}$. In some cases, the electrolyte was heated with a water bath or was cooled down with ice or Dry Ice. The anodic oxidation was carried out with a constant voltage source which was connected to the cell in series with a current limiting resistor (5). The source voltage was set at 250V. Initial current densities were $1 \text{ mA}\cdot\text{cm}^{-2}$, controlled by the current limiting resistor. Oxide thickness was monitored by the rise in cell voltage, ΔV , during the oxidation. A conventional microscope lamp with a tungsten bulb was employed for the oxidation under illumination. Light intensity was 77,000 lx. The oxide and GaAs surfaces were observed by an optical or an interference color microscope. The oxide layer was removed in HCl solution when the GaAs surface was to be observed.

Results

Three surface irregularities.—A photograph of a typical oxide film surface after anodic oxidation in the dark is shown in Fig. 1(a). A sketch of Fig. 1(a) is shown in Fig. 1(b). The crystal is CZ-grown nondoped bulk with a carrier concentration of $4 \times 10^{16} \text{ cm}^{-3}$. Three surface irregularities are recognized as color differences on the oxide film: the first one is a pebbled texture observed all over the film. A specific sample of this irregularity is indicated by A in Fig. 1(a). The pebbled texture pits are roughly rounded in shape and about $0.5 \mu\text{m}$ in diam. The oxide inside of the pits is thinner than outside the pits. The second one, indicated by B, is striation with a line width of about $5 \mu\text{m}$. The last irregularity, indicated by C, is an example of a mottled color splotch on the oxide film, which can be recognized by the naked eye.

Irregularities A and B are also observed on the GaAs surface after the removal of the oxide. It is interesting that the pebbled appearance becomes faint around any pits on the surface and is diminished on one side

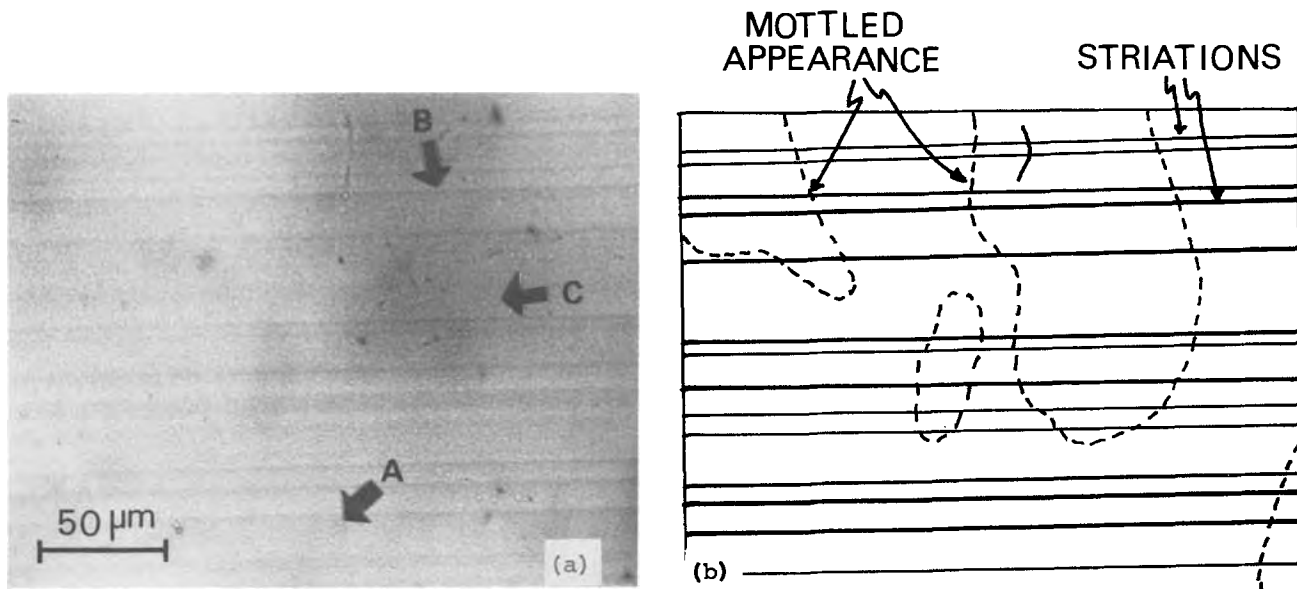


Fig. 1. Oxide surface irregularities produced by anodization in the dark. $\Delta V = 220V$. A: pebbled, B: lines, C: mottled color splotch

of the striations. Color differences for C irregularities correspond to $200 \sim 500\text{\AA}$ in oxide thickness. These three irregularities seem to not depend on current density.

Dependence on oxide voltage drop.—Interference colors appear locally on the GaAs surface just after starting the oxidation in the dark. Nonuniformity in color is shown in Fig. 2(a). When the voltage drop across the oxide, ΔV , becomes about 40V, color differences are recognized all over the wafer. At the same time, a stripe pattern is observed as represented by the arrow in Fig. 2(a) and striations start to appear on both edges of the stripe pattern. The striations are indicated by arrows in Fig. 2(b). In this photograph, a mottled color splotch with indeterminate form can be seen. The nonuniformity in the color is not changed during further oxidation. Striations are observed distinctly with an increase in ΔV , as shown in Fig. 2(b).

An interference color micrograph on oxide and GaAs surfaces after a 2° angle-lapping is shown in Fig. 3. The striations consist of ridged and recessed lines. The ridged (or recessed) line on the oxide is the ridged (or recessed) line on the GaAs surface. This correspondence between the oxide and the GaAs surface is possibly due to local (selective) dissolution of oxide at the lines.

The pebbled surface texture appears at high oxide voltage drop, or with large oxide thickness, in contrast with the mottled color splotch and striations which can be visible at low oxide voltage drop. No pebbled texture surface can be recognized on the oxide surface when the voltage drop is below 70V. When the voltage drop is increased to 110V, the pebbled texture surface starts to appear on a thicker oxide at the mottled color splotch, and then expands all over the wafer. The pebbled texture surface becomes more distinct with an increase in the oxide thickness, similarly to lines.

Standard deviations in oxide irregularities (both pebbled texture and striations), which were measured by a Talystep, were 32\AA at 140V and 89\AA at 260V. The degree of surface irregularities after anodization in the dark increased at a high rate with an increase in ΔV . It should be noted that threshold voltages exist in appearance of surface irregularities: about $70 \sim 100V$ to the pebbled appearance and about 40V to the striations.

Almost the same surface irregularities are left on the GaAs surface after removal of the oxide film. In order to see if these surface irregularities depend on the oxide thickness or amount of GaAs consumed during the anodic oxidation, two kinds of oxidations were

performed: (i) GaAs surface was oxidized until ΔV was $50 \sim 70V$, and then the oxide film was etched off. By repeating this procedure four times, a 3400\AA GaAs layer was etched off. (ii) GaAs was oxidized until ΔV was 177V, followed by removal of the oxide. In this way, a 2700\AA GaAs surface layer was etched off.

From a comparison of these two surfaces, it is found that the GaAs surface etched by the four oxidation-cycles, was almost completely flat and smooth, but the GaAs surface etched less deeply in a single oxidation exhibited a very irregular texture surface. This result means that the striations and the pebbled texture surface do not depend on the amount of GaAs consumed, but are affected by the voltage drop of the oxide, or oxide thickness.

Dependence on crystal and carrier concentration.—The surface irregularities appearance depends on the growth method of GaAs and on the carrier concentration. Striations were revealed on only nondoped CZ material. Mottled color splotch was observed on non-doped bulk (both CZ and BG) materials. The pebbled texture was observed on all the materials except heavily doped ones.

No surface irregularities have been observed on heavily doped CZ, BG, and epitaxial GaAs with a net donor concentration of $1 \sim 2 \times 10^{18} \text{ cm}^{-3}$, even if the anodization is carried out until ΔV increases up to 220V.

Dependence on temperature and pH of electrolyte.—Electrolyte temperature effects on surface irregularities are shown in Fig. 4. The electrolyte temperature was changed from -30° to 45°C , while the initial current density and voltage applied to the cell were kept the same at each temperature. The pebbled texture becomes fainter by lowering the temperature and almost disappears at -30°C . The striations also become fainter with decreasing temperature, but have not disappeared even at -70°C .

The appearance of surface irregularities did not depend on the pH of the tartaric acid solution, which was varied from 1.85 to 6.30.

Light illumination effect.—No irregularities were observed on surfaces anodized under a strong illumination, even on the surface of nondoped bulk GaAs oxidized with an applied voltage on the film or more than 200V.

A mottled color splotch, which had been revealed by the first anodization in the dark, disappeared upon successive oxidation under a strong illumination, but lines and pebbled irregularities were enhanced. In the case of the first anodization to $\Delta V = 140V$ in the dark,

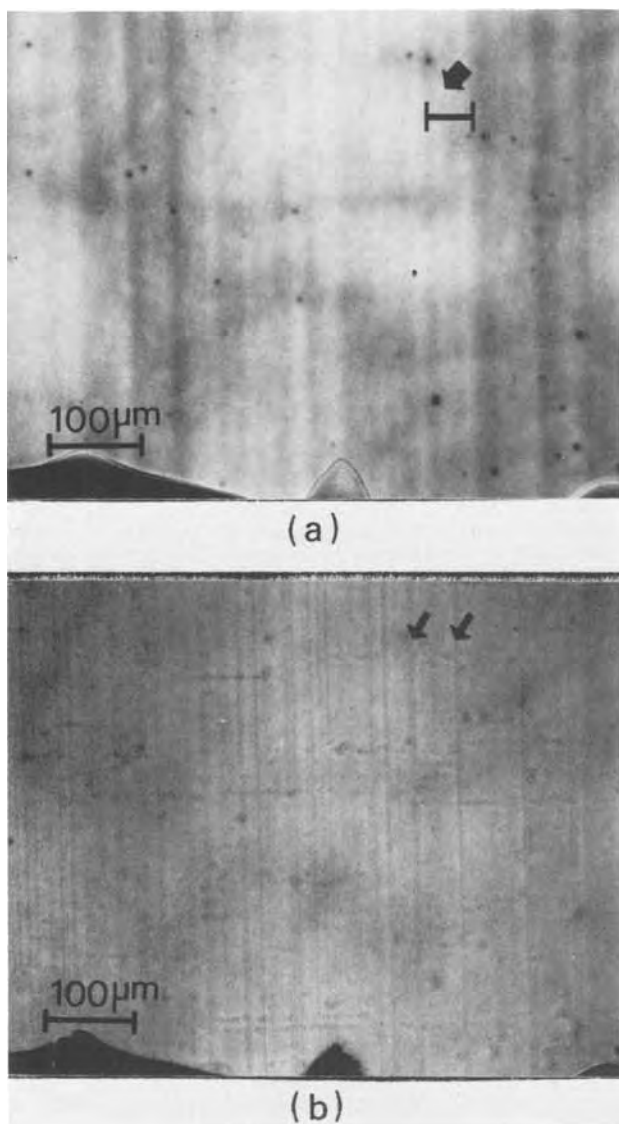


Fig. 2. Striations on the oxide surface with (a) voltage drop of the $\Delta V = 30V$, (b) $\Delta V = 200V$.

followed by the second anodization to $\Delta V = 140V$ under illumination, 280V total, the standard deviation of the surface irregularities after the additional oxidation under illumination was about 1.7 times larger than that after the first anodization in the dark. The three irregularities also appeared under the reverse sequence, namely when the first anodization was carried out under illumination and the successive anodization was in the dark. This fact means that, even when the GaAs surface is coated by a uniform smooth oxide film, surface irregularities will appear if oxida-

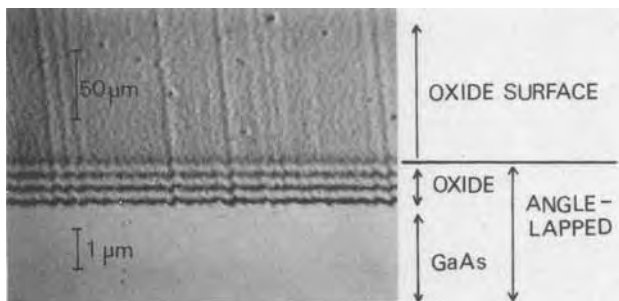


Fig. 3. Interference color micrograph showing 2° angle-lapped section.

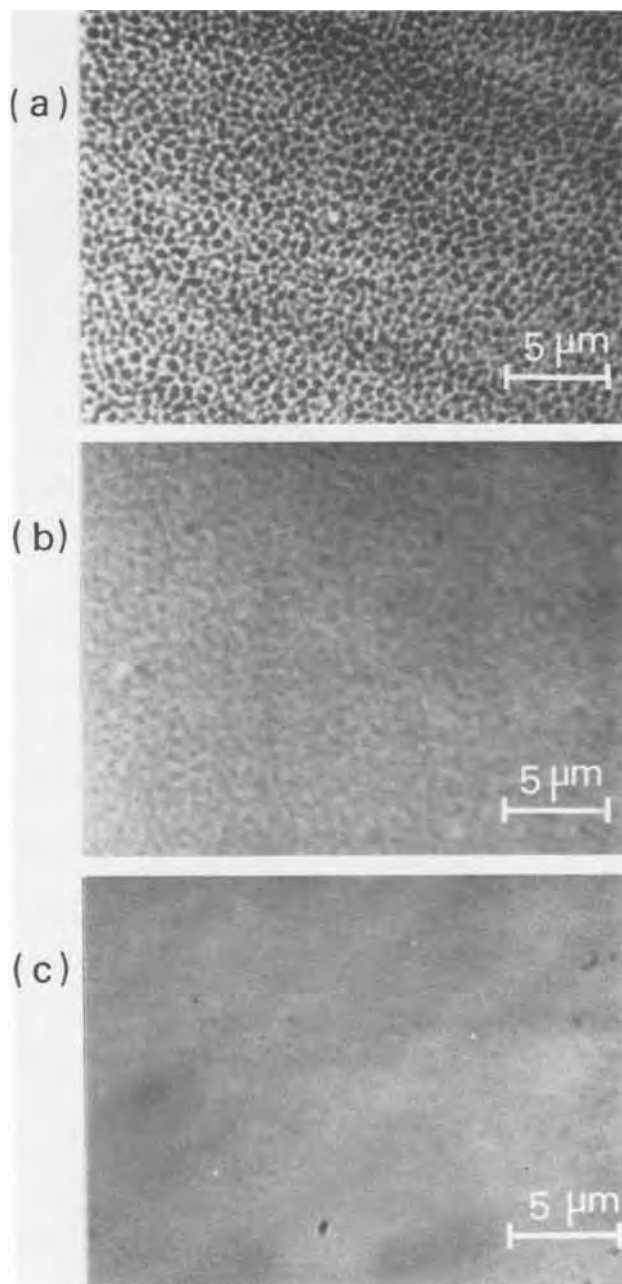


Fig. 4. Oxide surfaces after anodization at (a) $45^\circ C$, (b) $2^\circ C$, (c) $-30^\circ C$.

tion is carried out in the dark. From these results, it can be said that appearance of the surface irregularity is a specific phenomenon of an anodic oxidation in the dark.

Correlation to the striations revealed by the chemical etching.—It has been reported that an etchant consisting of HF, $AgNO_3$, CrO_3 , and H_2O reveals the GaAs crystal defects (6). Recessed patterns are obtained on crystal defects by etching in the dark.

One part of a GaAs wafer was etched in the dark using the etchant and the other part was anodized in the dark. The sample was CZ-grown nondoped bulk GaAs. The anodization was carried out in the dark until the cell voltage was 140V. Figure 5 shows the GaAs surface obtained by the chemical etching in the dark (bottom), and the anodic oxide surface (top). Many striations are observed on the chemically etched surface. There is a perfect correlation between the striations appearing on the anodic oxide layer and the striations revealed by the chemical etching. It was found by a Talystep that the striations revealed by

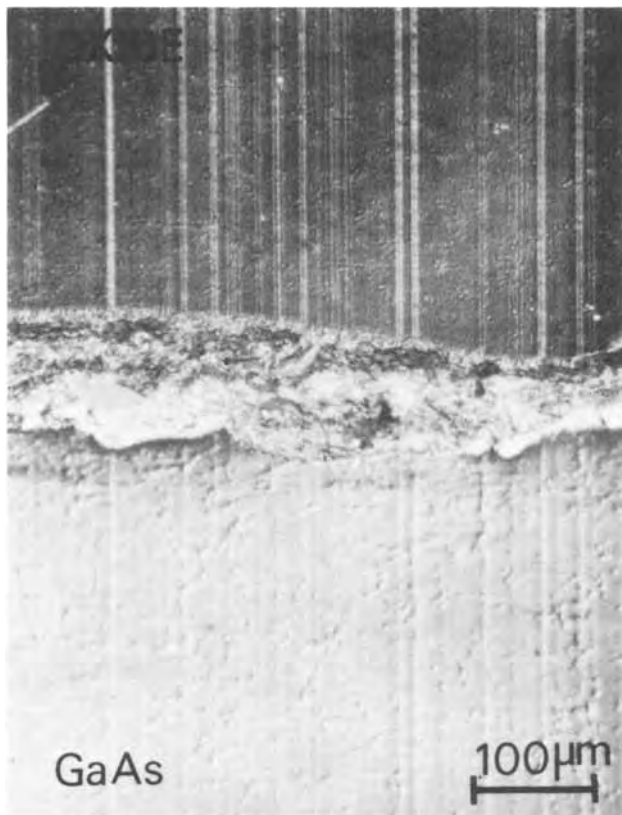


Fig. 5. Interference color micrograph of GaAs surface after chemical etching in the dark (bottom), and oxide surface produced by anodization in the dark at $\Delta V = 140V$ (top). The chemical etching depth is about $3.2 \mu\text{m}$.

this preferential etching in the dark were recessed, which means that the striation position is at the array of crystal defects.

The striations revealed by the chemical etching have been well known to be due to the periodic fluctuation of the impurity concentration along the pulling direction, which is caused by the thermal asymmetry in the crucible of the pulling installation. In the case of nondoped materials, silicon is the residual impurity.

Discussion

Cause of the surface irregularities.—Since mottled color splotch was eliminated by additional anodization under illumination, the mottled color splotch appearance can be explained very well as due to a doping inhomogeneity, as described by Colquhoun *et al.* (7). The doping inhomogeneity effect is eliminated by free carriers which are generated in a GaAs surface by illumination.

In aluminum anodization process, solvent action locally causes a pore on a point of the inhomogeneous oxide film, and a higher electrolyte temperature or a thicker film (*i.e.*, a longer pore) inclines to enhance the solvent action (8). For GaAs anodization, causes of striations and pebbled texture are possibly attributed to the solvent action, similarly to the aluminum anodization. From the present experiment, however, it should be difficult to discuss the detail of the generation mechanism of the striations and the pebbled texture.

Effect of depletion layer width on surface irregularities.—Striations due to the fluctuation of the impurity concentration exist in CZ crystals regardless of doped or nondoped materials. However, striations induced by the anodic oxidation process appeared on nondoped CZ materials, but did not appear on heavily doped CZ crystals. This is explained by differences of width of the depletion layer which is formed on the n-type

GaAs surface in contact with the electrolyte. Crystal imperfections within a depletion layer affect the anodization process and a smaller width of the depletion layer results in a weaker effect of crystal defects or doping inhomogeneity. The depletion layer width at the avalanche breakdown voltage becomes smaller with increasing carrier concentration, for example, 9000\AA for a carrier concentration of $4 \times 10^{16} \text{cm}^{-3}$ and 650\AA for $1 \times 10^{18} \text{cm}^{-3}$. Therefore, effect of crystal imperfections on the anodization process is weaker for heavily doped crystals as compared with nondoped ones.

Since no pebbled texture surface appeared on heavily doped (epitaxial or bulk) GaAs, the pebbled texture appearance is also affected by the depletion width. However, pebbled texture surface cannot be due to doping inhomogeneity because this irregularity cannot be eliminated out by illumination. Further detailed analysis will be needed.

Conditions for obtaining smooth surface.—A strong illumination is the most effective way to obtain a smooth surface in the anodization of any GaAs materials. However, for a self-controlled etching in a GaAs FET process, anodic oxidation must be carried out in the dark. Therefore, for this application of the anodization, a lower temperature and/or a smaller voltage drop across the oxide are useful conditions for suppressing the irregularities, such as pebbled texture and lines.

Conclusion

Surface irregularities induced by anodic oxidation in the dark for n-type GaAs were studied by changing materials and oxidation conditions. The results are as follows.

1. Three different surface irregularities were observed: pebbled texture, lines, and a mottled color splotch. All the irregularities are observed on undoped CZ material but none are observed on heavily doped (CZ, BG, and epitaxial) materials. In the case of vapor-grown epitaxial GaAs with a carrier concentration ranging from 0.6 to $3.0 \times 10^{17} \text{cm}^{-3}$, only the pebbled appearance is observed.

2. The lines correspond to the striations caused by the nonuniform distribution of the impurity in the CZ crystals. The mottled color splotch may be the result of doping inhomogeneity.

3. The pebbled texture and lines can be suppressed using a small oxidation voltage or a low electrolyte temperature.

Acknowledgments

The author wishes to thank Dr. F. Hasegawa, K. Katsukawa, and M. Kondo for their valuable discussions, and Drs. H. Watanabe and H. Terao for their valuable advice. The author is also grateful to Dr. K. Ayaki for his continuous support and encouragement during this work.

Manuscript submitted June 8, 1979; revised manuscript received April 10, 1980.

Any discussion of this paper will appear in a Discussion Section to be published in the June 1981 JOURNAL. All discussions for the June 1981 Discussion Section should be submitted by Feb. 1, 1981.

Publication costs of this article were assisted by Nippon Electric Company, Limited.

REFERENCES

1. D. L. Rode, B. Schwartz, and J. V. DiLorenzo, *Solid-State Electron.*, **17**, 1119 (1974).
2. H. Müller, F. H. Eisen, and J. W. Mayer, *This Journal*, **122**, 651 (1975).
3. R. A. Logan, B. Schwartz, and W. J. Sundburg, *ibid.*, **120**, 1385 (1973).
4. S. M. Spitzer, B. Schwartz, and G. D. Weigle, *ibid.*, **122**, 397 (1975).

5. H. Hasegawa and H. L. Hartnagel, *ibid.*, **123**, 713 (1976).
 6. T. Saitoh, S. Matsubara, and S. Minagawa, *ibid.*, **122**, 670 (1975).
 7. A. Colquhoun and H. L. Hartnagel, *Solid-State Electron.*, **19**, 819 (1976).
 8. F. Keller, M. S. Hunter, and D. L. Robinson, *This Journal*, **100**, 411 (1953).

Surface Segregation and Precipitation Phenomena in Ag-Al Alloys

A. G. Dirks and H. H. Brongersma

Philips Research Laboratories, Eindhoven, The Netherlands

ABSTRACT

A series of Ag-Al bulk alloys was made by argon arc melting, while thin films of these alloys were prepared by ultrahigh vacuum vapor deposition. By means of light microscopy, x-ray diffraction, transmission electron microscopy and low energy ion scattering under ultrahigh vacuum conditions, the precipitation events during low temperature annealing were investigated.

The Ag-Al system has been the subject of recent interest (1, 2); particularly much attention has been paid to the growth kinetics of the compound Ag_2Al . In this paper we report on our studies of Ag-rich Ag-Al alloys either in the bulk or as a thin film. With a variety of experimental techniques we have compared the precipitation phenomena in both types of Ag-Al alloys. In order to assess the role played by the surface of the samples, we studied the outermost atomic layers by low energy ion scattering (LEIS) in detail. Precipitation effects have been found to occur first at interfaces, such as grain boundaries or surfaces, as these generally are the most likely sites for segregation and precipitation events [see, for instance, Ref. (3)].

Experimental

$\text{Ag}_{1-x}\text{Al}_x$ alloys with $0 \leq x \leq 0.21$ were made by argon arc melting of the pure elements (Ag 99.9% and Al 99.99%) and homogenized in argon-filled sealed silica capsules for 160 hr at 600°C. Thin specimens of these alloys needed for the transmission electron microscope (TEM) investigations were obtained by means of ion milling.

Thin films up to 1 μm in thickness were made within the same composition range by ultrahigh vacuum vapor deposition ($\leq 10^{-10}$ Torr). In the vacuum chamber the alloys were prepared by simultaneous electron beam evaporation of the pure elements onto substrates at room temperature.

The compositions of the samples have been analyzed by LEIS. The diameter of the scattering ion beam was 1 mm, the ion current ~ 100 nA, and the scattering angle 142° . A detailed description of the ion-scattering equipment has been given elsewhere (4). Quantitative data for Ag and Al were obtained by calibration against the pure elements. The sensitivity of O relative to Al was determined by studying the oxidation of an Al surface. It was found that the atomic sensitivities are not influenced by chemical effects in the present case. This finding is similar to that for earlier LEIS measurements on other targets, such as Cu-Ni alloys (5).

Experimental Results

X-ray diffraction experiments with as-deposited $\text{Ag}_{1-x}\text{Al}_x$ films showed that the diffraction lines which are indicative of the presence of the $\mu\text{-Ag}_3\text{Al}$ equilibrium compound are visible for $x \geq 0.09$. With higher x values the intensity and the number of these diffrac-

tion lines increased. The microstructure of all films, as studied by TEM, revealed crystallites having dimensions smaller than 0.1 μm .

Rutherford backscattering experiments with 2.7 MeV He^+ ions were performed with films in the composition range $0 < x \leq 0.45$. Measurements of the as-deposited layers on SiO_2 substrates resulted in depth profiles having constant Al/Ag ratios.

As distinct from the thin films the x-ray diagrams for the bulk samples with $x \leq 0.15$ showed the Ag matrix reflections only. Neither x-ray analysis, nor TEM studies (at 100 keV and 1 MeV electrons) could reveal the presence of the second phase, even after annealing the alloy for 550 hr at 210°C. With light microscopy only a fine grain boundary precipitate was found, the grains having dimensions of about 0.1 μm . Figure 1 is a bright field image of part of a monocrystalline region in a thinned $\text{Ag}_{0.85}\text{Al}_{0.15}$ sample. The corresponding matrix diffraction spots are shown in the inset. The sharp diffraction ring reflects the presence of a circa 100 Å periodicity, which suggests the formation of a second phase ($\mu\text{-phase}$?).

In Fig. 2 the data for a bulk $\text{Ag}_{0.90}\text{Al}_{0.10}$ alloy analyzed by 2 keV He^+ ions are shown. The sample had first been sputter cleaned by prolonged He^+ and Ne^+ ion bombardment. Next, the target was heated for 15 hr to 500°C. Upon cooling to 270°C the surface concentrations remain close to that of the bulk. However, the surface concentrations change markedly

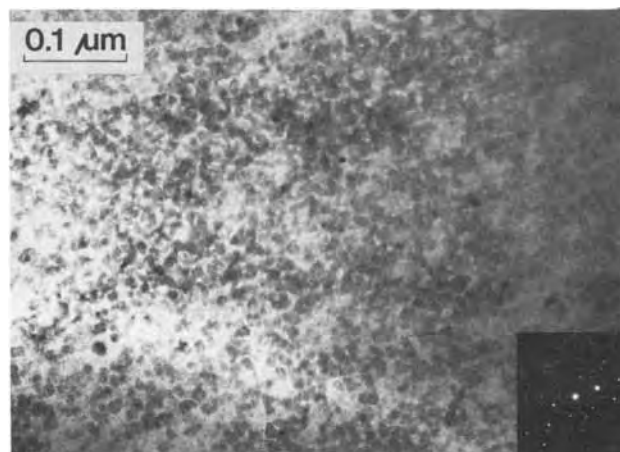


Fig. 1. 100 keV TEM micrograph of a thinned $\text{Ag}_{0.85}\text{Al}_{0.15}$ alloy. The inset shows the corresponding diffraction pattern.

Key words: surface segregation, precipitation, silver-aluminum alloys, low energy ion scattering, thin films.

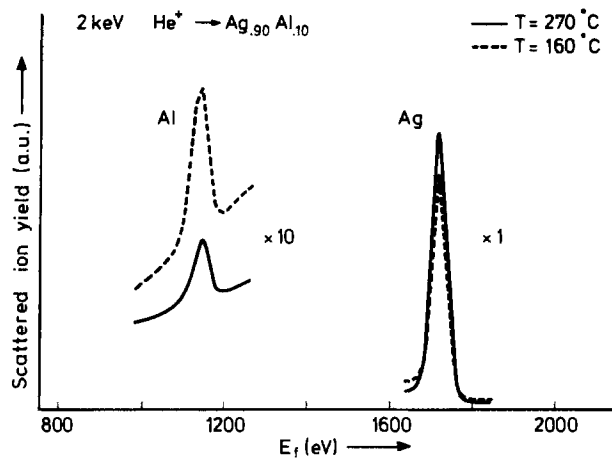


Fig. 2. Energy spectra for He^+ scattered from an $\text{Ag}_{0.90}\text{Al}_{0.10}$ alloy. The scattering angle is 142° .

when cooling further to 160°C . This effect is much more pronounced than expected from conventional surface segregation theories (see Discussion). When cooling the target to room temperature, the Al concentration in the surface decreases again since diffusion processes become slow as compared to the sputtering action of the analyzing beam. These results have prompted a detailed investigation of the surface composition as a function of temperature in other bulk Ag-Al alloys. Homogenized $\text{Ag}_{0.92}\text{Al}_{0.08}$ and $\text{Ag}_{0.89}\text{Al}_{0.11}$ were first sputter-cleaned by bombardment with 2 keV Ne^+ ions for 12 hr. During subsequent LEIS measurements in a vacuum in the 10^{-10} Torr range using 2 keV He^+ ions, we observed energy spectra showing three distinct peaks for O, Al, and Ag. Characteristic spectra for an $\text{Ag}_{0.92}\text{Al}_{0.08}$ alloy at 190°C are given in Fig. 3. Only after prolonged Ne^+ bombardment was it possible to reduce the oxygen coverage below 1 atomic percent (a/o). A summary of the LEIS measurements on a sample with $x = 0.11$ is shown in Table I. For the different temperatures of the alloy we calculated the net area of the three peaks within an energy range of about 100 eV, which is centered on the peak. The relative sensitivities are obtained as described above. This calibration resulted in the following relation $\text{O}:\text{Al}:\text{Ag} = 1:15:76$. Using

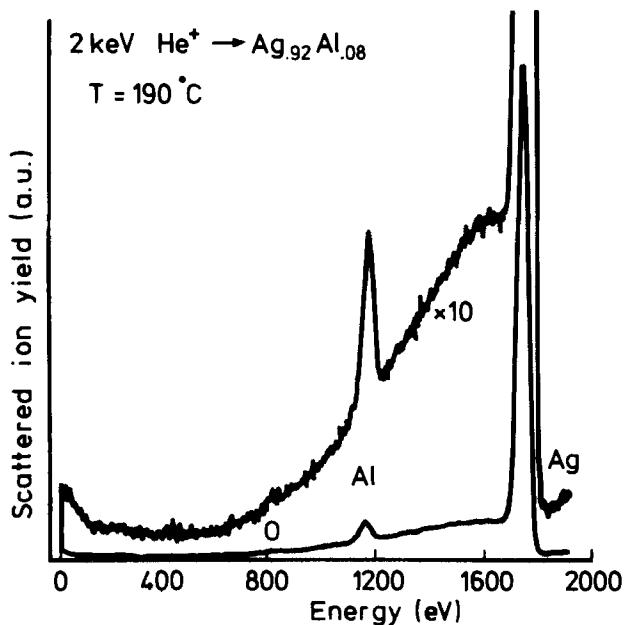


Fig. 3. Energy spectra for He^+ scattered from an $\text{Ag}_{0.92}\text{Al}_{0.08}$ alloy at 190°C .

Table I. LEIS results for 2 keV He^+ ions scattered from an $\text{Ag}_{0.89}\text{Al}_{0.11}$ alloy obtained on four successive runs on the same sample. The values are a measure for the net area of the O, Al, and Ag peaks at the temperatures indicated. This net area has been calculated from the energy spectra, within an energy range centered on the respective peak maxima. Calibration against the pure elements *cf.* oxidized Al yielded the following atomic sensitivities $\text{O}:\text{Al}:\text{Ag} = 1:15:76$. The atomic concentrations are shown in parentheses.

T ($^\circ\text{C}$)	O	Al	Ag
410	460 (1%)	70,379 (12%)	2,532,742 (87%)
300	0 (0%)	75,051 (12%)	2,698,458 (88%)
240	0 (0%)	85,904 (14%)	2,594,517 (86%)
210	0 (0%)	86,799 (14%)	2,661,394 (86%)
588	0 (0%)	80,789 (12%)	3,041,720 (88%)
240	455 (1%)	111,268 (16%)	2,988,087 (83%)
289	0 (0%)	104,827 (14%)	3,106,954 (86%)
507	0 (0%)	79,374 (11%)	3,108,687 (89%)
336	189 (1%)	97,786 (13%)	3,067,619 (86%)
242	0 (0%)	100,455 (14%)	3,039,318 (86%)
520	0 (0%)	80,498 (12%)	2,886,145 (88%)
266	0 (0%)	79,328 (12%)	2,833,099 (88%)
185	0 (0%)	108,980 (18%)	2,512,562 (82%)
103	0 (0%)	79,695 (14%)	2,481,320 (86%)
40	1459 (4%)	64,648 (11%)	2,500,216 (85%)

these relative sensitivities we calculated the atomic percentages present at the surface of the alloy: see Table I. The possible error in concentration is highest for oxygen. With the data in Fig. 3 we calculated an O concentration of 12 ± 8 a/o. This concentration is about the same as that found for Al, probably implying that Al_2O_3 is formed. Other results are presented in Table I. Here the calculated oxygen values at the surface of the $\text{Ag}_{0.89}\text{Al}_{0.11}$ alloy are rather low. In Fig. 4 the Al-surface concentrations have been given as a function of temperature. Upon cooling from $\sim 600^\circ\text{C}$ the Al content increases markedly between 300°C and 200°C . At lower temperatures this effect disappears due to the sputtering action of the ion beam.

Instead of measuring the whole energy spectrum at distinct temperatures, an impression of surface effects also can be obtained by continuous measurement of the peak height as a function of temperature. In Fig. 5 we have plotted the Al surface concentrations as calculated from the Al peak heights. Similarly as in the discontinuous heating experiments a rather sudden increase of the Al-surface content is found starting around 250°C .

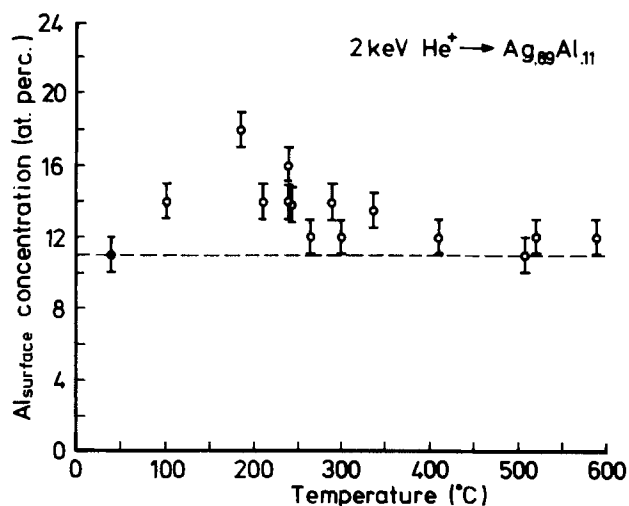


Fig. 4. Al surface concentration of an $\text{Ag}_{0.89}\text{Al}_{0.11}$ alloy as a function of temperature; data obtained by calculation of the peak area of energy spectra. The measurement at 40°C is less reliable, since the surface contained 4 a/o O.

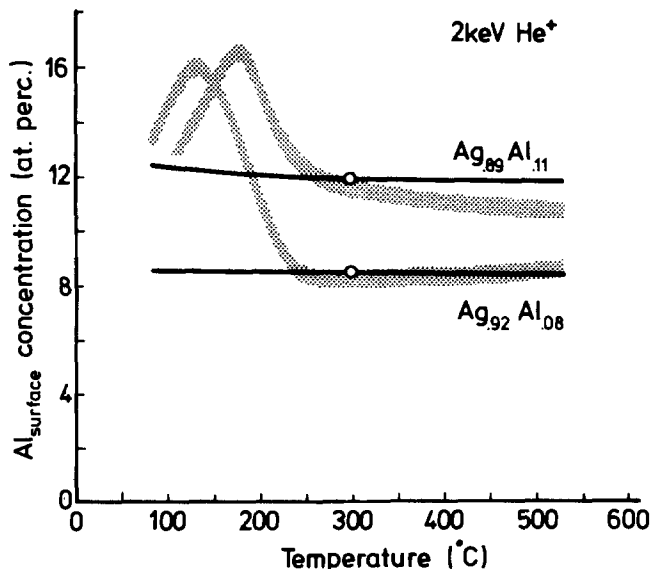


Fig. 5. Al surface concentration of $\text{Ag}_{0.89}\text{Al}_{0.11}$ and $\text{Ag}_{0.92}\text{Al}_{0.08}$ alloys as a function of temperature; data obtained by monitoring the Al-peak height (dotted regions) while cooling to 50°C in about 50 min. The drawn lines are calculated curves, normalized to the experimental curves at 300°C .

Discussion

When an Ag-rich Al alloy is cooled down from the α_{Ag} region of the Ag-Al phase diagram, the first precipitation phenomena, in equilibrium conditions, are observed at $T \sim 260^\circ\text{C}$ when $x = 0.11$ or $T \sim 185^\circ\text{C}$ when $x = 0.08$ (6). The LEIS data representing the surface concentrations (Fig. 4 and 5) revealed an increase of the Al content close to these temperatures.

From current surface segregation theories it is not immediately clear whether segregation will occur and if so, which element will be enriched at the surface. According to bondbreaking models (7) the element with the lowest heat of vaporization should segregate. This would be Ag ($\Delta H_{\text{vap.}} = 67.9$ kcal/mole at 298°K) and not Al ($\Delta H_{\text{vap.}} = 78.5$ kcal/mole at 298°K). However, heats of vaporization are not always a good measure of the strength of the cohesive bonds in a solid that are broken at a metal-vacuum interface (8). Therefore, a better approach is to consider the differences in surface energies rather than in heats of vaporization. The surface energies for Ag and Al at 0°K are 1250 and 1200 mJ/m^2 , respectively (9). This more accurate approach would thus predict hardly any segregation. Moreover, if segregation occurs, it would rather be Al than Ag segregation. When Al segregation occurs, the concentration of the Al and the Ag at the surface (y_{Al} resp. y_{Ag}) with respect to the concentrations in the bulk (x_{Al} resp. x_{Ag}) will be given by

$$\frac{y_{\text{Al}}}{y_{\text{Ag}}} = \frac{x_{\text{Al}}}{x_{\text{Ag}}} \cdot \exp\left(-\frac{\Delta E}{kT}\right)$$

where ΔE is an energy difference between atoms at the surface and in the bulk. Independent of the precise value of ΔE , which can be calculated using various surface segregation models, the $\ln(y_{\text{Al}}/y_{\text{Ag}})$ should always be directly proportional to $1/T$.

The results at higher temperatures are in agreement with these expectations, but significant differences are observed around 250°C . The Al surface concentration rises suddenly much faster with decreasing temperature. At still lower temperatures the Al concentration drops again. At these temperatures the diffusion processes are too slow to compete with the sputtering action of the scattering ion beam; the equilibrium surface precipitate will therefore be removed from the outermost atomic layers. This explains the drop in Al at lower temperatures (Fig. 5).

In order to illustrate the differences with the experimental theoretical curves for $x = 0.08$ and 0.11 are also shown in fig. 5. These curves have been normalized to the experimental curves at 300°C . It is clear that such a theoretical curve, which is in agreement with experiment at higher temperatures, cannot explain the results at lower temperatures. Since the deviations start close to temperatures, where it is known that phase separation (into Ag and an Ag_3Al μ -phase) occurs in the bulk (6), it is tempting to correlate the sudden increase of the Al surface concentration with this phase transition.

However, a phase transition in itself is only a re-ordering of atoms and does not affect the average surface composition. Apparently the phase transition is accompanied by another process that leads to an increase in the surface concentration of the Al. The origin for the Al-enrichment at the surface may be of a kinetic or a thermodynamic nature. Since a free surface is a well-known nucleation site it is quite possible that the growth of the Al-rich μ -phase will start preferentially at such an interface. One would expect, however, that the concentration of the μ -phase at the surface (and thus the concentration of the Al) would depend strongly on the details of the heat-treatment. This is not the case. Moreover, in-depth analysis of the samples show that the enriched layer has only a thickness of the order of a monoatomic layer.

A thermodynamic explanation seems, therefore, more likely. It could be that the surface energy of the μ -phase is lower than that of Ag, thus leading to segregation of the μ -phase to the surface. If the μ -phase would completely cover the surface this would lead to an Al-surface concentration of 25%. In view of the small differences between the surface energies and Ag and Al, it is doubtful that the differences between the μ -phase and Ag are large enough to explain the present results. Moreover, it would not explain that the enrichment is confined to the outermost atomic layer.

Another explanation is, that while the relative amounts of Ag and the μ -phase in bulk and surface are about the same, the Al is strongly enriched in the outermost layer of the μ -phase at the surface. Studies of van Santen and Sachtler (10) on Pt_3Sn alloys support this latter possibility. LEIS studies to try and further identify the origin of the strong low temperature segregation in Ag-Al alloys are underway.

Acknowledgment

The authors are grateful to Dr. Y. Tamminga for the Rutherford back-scattering experiments, to Mr. G. C. J. van der Ligt for his skillful performance of the LEIS measurements, and to Dr. G. E. Thomas for his constant interest in this work.

Manuscript submitted Nov. 15, 1979; revised manuscript received March 14, 1980. This was Paper 377 presented at the Los Angeles, California, Meeting of the Society, Oct. 14-19, 1979.

Any discussion of this paper will appear in a Discussion Section to be published in the June 1981 JOURNAL. All discussions for the June 1981 Discussion Section should be submitted by Feb. 1, 1981.

Publication costs of this article were assisted by Philips Research Laboratories.

REFERENCES

1. J. E. E. Baglin, F. M. d'Heurle, and W. N. Hammer, *J. Appl. Phys.*, **50**, 266 (1979).
2. R. D. Doherty, M. Ferrante, and Y. H. Chen, *Scr. Metall.*, **12**, 885 (1978).
3. L. E. Murr, "Interfacial Phenomena in Metals and Alloys," Addison-Wesley, Reading, Mass. (1975).
4. H. H. Brongersma, N. Hazewindus, J. M. van Nieuwland, A. M. M. Otten, and A. J. Smets,

- Rev. Sci. Instrum.*, **49**, 707 (1978).
 5. H. H. Brongersma, M. J. Sparnaay, and T. M. Buck, *Surf. Sci.*, **71**, 657 (1978).
 6. M. Hansen and K. Anderko, "Constitution of Binary Alloys," p. 2, McGraw-Hill Book Co., New York (1958).

7. F. L. Williams and D. Nason, *Surf. Sci.*, **45**, 377 (1974).
 8. A. R. Miedema, *Z. Metallkd.*, **69**, 455 (1978).
 9. A. R. Miedema, *ibid.*, **69**, 287 (1978).
 10. R. A. van Santen and W. M. H. Sachtler, *J. Catal.*, **33**, 202 (1974).

Avalanche-Induced Hot Electron Injection and Trapping in Gate Oxides on p-Si

A. K. Sinha,* W. S. Lindenberger, W. D. Powell, and E. I. Povelonis

Bell Laboratories, Murray Hill, New Jersey 07974

ABSTRACT

Hot electron trapping in gate oxides can lead to threshold drifts in short channel MOSFET's. Therefore, factors affecting the efficiency of hot electron trapping have been investigated by rf-bias aging of MOS capacitors followed by flatband voltage measurements. It was found that avalanche-injection electron current levels of $>5 \mu\text{A cm}^{-2}$ produce excessive amounts of hot electron trapping; currents of $<4 \mu\text{A cm}^{-2}$ were preferred for oxide characterization. A relatively small amount of hot electron trapping produced an enormous density of fast surface states. The observed flatband shifts would, therefore, contain significant contributions from surface states. The total flatband shift due to hot electron injection and trapping increased with higher p-Si substrate doping levels ($10^{16} \rightarrow 10^{17} \text{ cm}^{-3}$) and with increasing oxide thickness ($200 \rightarrow 1000 \text{ \AA}$). Electron beam irradiation ($5\text{--}30 \mu\text{C cm}^{-2}$) followed by a 450°C , H_2 anneal did not significantly change the hot electron trapping behavior of the gate oxide. Possible implications of these results on the generic reliability of VLSI devices are discussed.

An important generic reliability concern with NMOS-VLSI (n-channel metal oxide silicon—very large-scale integration) is possible threshold drifts due to hot electron trapping in the gate oxide (1). The use of saturating logic circuits with bootstrapping and shallow junctions creates large fields and avalanche multiplication near the drain edge, which increases the probability of hot electron injection and hence, of trapping. The extent of trapping is obviously dependent on device geometry and aging conditions. It is also a function of the oxide quality and its processing history. Thus, a wide range of trapping efficiencies for as-grown oxides has been reported in the literature (2). It has been also reported that exposure to E-beams can increase the tendency of gate oxides to trap electrons (3).

However, a quantitative comparison of various data is hampered by the fact, not generally appreciated in the literature, that the apparent trapping efficiency is a complicated function of the avalanche injection level, oxide thickness, and the substrate doping concentration. This paper documents such effects; it also presents independent data on the effect of E-beam irradiation on the neutral trap density of gate oxides.

Experimental

Measurements of the hot electron trapping efficiency were made by rf-bias aging of MOS capacitors, where, in each half-cycle, the p-Si goes into deep depletion and avalanche, hot electrons are accelerated across the potential barrier at the Si/SiO₂ interface, and a d-c electron current flows through the oxide to the gate (4). Any trapped electrons are manifested by a positive shift in the flatband voltage.

The apparatus for rf-bias aging followed that described by Nicollian and Berglund (5), and it is shown in Fig. 1. The rf-frequency was tuned in the range 400–600 kHz to obtain a series resonant circuit and maximize the displacement current through R_1 (10Ω) as displayed on the oscilloscope. The rf-generator voltage

was increased until the desired level of d-c current flowed through the electrometer. The latter was operated in the 30 mV (0.03X) full-scale range in order to avoid any appreciable d-c biasing of the MOS capacitor.

SCHEMATIC FOR HOT ELECTRON TRAPPING APPARATUS

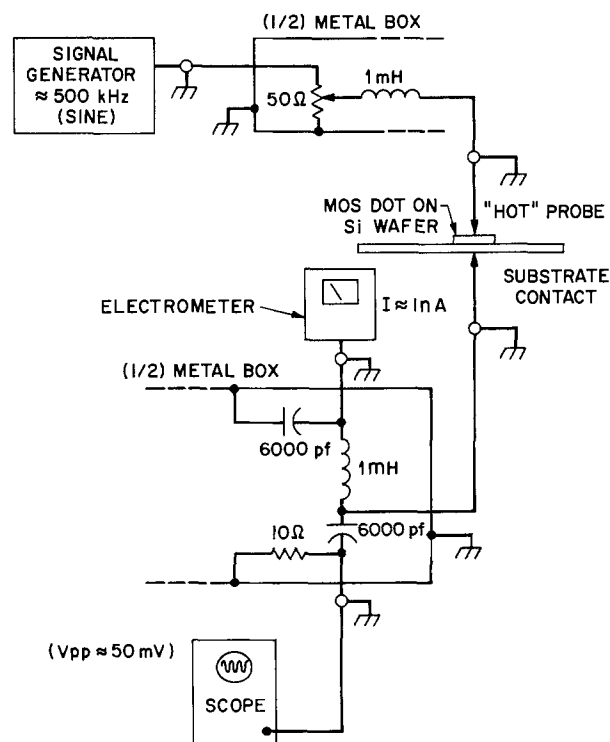


Fig. 1. Apparatus for rf-bias aging of MOS capacitors. [After Nicollian and Berglund, Ref. (5)].

* Electrochemical Society Active Member.

Key words: dielectrics, insulator, interfaces, reliability.

The samples were prepared by oxidizing p(100)Si wafers in dry $O_2 + 3\% HCl$ at $1000^\circ C$ followed by an *in situ* Ar anneal for 30 min. An Al 0.5% Cu alloy film $1 \mu m$ thick was (In-Source[®]) evaporated on the gate oxide using an inductively heated source, and then patterned into 10- or 20-mil diam dots using photolithography and wet chemical etching. The back side was stripped of any SiO_2 and a $1 \mu m$ thick film of Al back contact was deposited. The wafers were then given a $450^\circ C, H_2, \frac{1}{2}$ hr anneal to anneal out the surface states.

Prior to rf-bias aging, all wafers were subjected to capacitance-voltage (C-V) measurements at 1 MHz with \pm bias-temperature aging ($250^\circ C, 2 \times 10^6$ V/cm, 15 min) to ensure that they were free of Na^+ and excessive slow-trapping instability of the flatband voltage, V_{FB} ($\Delta V_{FB} < 0.2V$) (6). After rf-bias aging for specified periods of time with constant current through the electrometer, C-V measurements were made to determine the flatband voltage shift due to hot electron trapping. For a given sample, a period of 24 hr was usually sufficient to obtain adequate data.

Results

The above procedure gave the apparent density of neutral traps, N_{eff} , as a function of the total number Q_{in} , of injected electrons (3). The quantities N_{eff} and Q_{in} are defined as

$$N_{eff} = \frac{\Delta V_{FB}}{q} \frac{\epsilon_{ox}}{t_{ox}}$$

$$Q_{in} = \frac{1}{qA} \int Idt$$

where, ΔV_{FB} is the positive shift in the flatband voltage as a result of hot electron trapping, q is the electronic charge, ϵ_{ox} is the dielectric constant of SiO_2 , t_{ox} is the oxide thickness, A is the area of the capacitor, I is the average d-c component of the injected electron current, and t is the time. The hot electron trapping efficiency may be defined by dN_{eff}/dQ_{in} and it is generally a function of Q_{in} . The flatband voltage was read off the high frequency C-V curves using the depletion layer approximation; no corrections were made for surface states.

Effect of avalanche injection current level.—One of the unexpected results of this investigation was the observation that the density, N_{eff} , of electrons trapped at a given value of Q_{in} depends upon the magnitude of the average d-c component of the avalanche injection current. In order to eliminate any edge leakage effects due to fringing fields, these experiments were carried out on samples where the thin oxide area (450\AA , 10 mil diam) was surrounded by a thick oxide (5000\AA) guard ring, and the p-Si doping level was kept relatively high at $\sim 1 \times 10^{17} \text{ cm}^{-3}$. As shown in Fig. 2, the measured values of N_{eff} were found to be apparently independent of the current between 1 and 2 nA ($2\text{--}4 \mu A \text{ cm}^{-2}$) and between 40 and 80 nA ($0.08\text{--}0.16 \text{ mA cm}^{-2}$). However, there was a factor of 10 increase in the N_{eff} on going from 2 nA ($4 \times 10^{-6} \text{ A cm}^{-2}$) to 40 nA ($7.9 \times 10^{-5} \text{ A cm}^{-2}$). Moreover, at the higher currents (>10 nA) the observed trapping efficiencies were so dominated by the effect of injected current levels that it was difficult to evaluate other effects such as those due to substrate doping and thickness. Therefore, it was found practical to use an electron current of 1 nA for all the subsequent aging experiments; this level of current could be safely sustained by even the thinnest oxides (200\AA) on lighter doped material (10^{16} cm^{-3}) without catastrophic breakdown.

Effect of p-Si substrate doping.—MOS capacitors with N_A of $2 \times 10^{16} \text{ cm}^{-3}$ showed a negligible degree of hot electron trapping for $Q_{in} \leq 10^{17} \text{ cm}^{-2}$. This doping level is near the lower limit of that required for bulk avalanche and it may be associated with some field fringing in the Si-space charge region (4, 5).

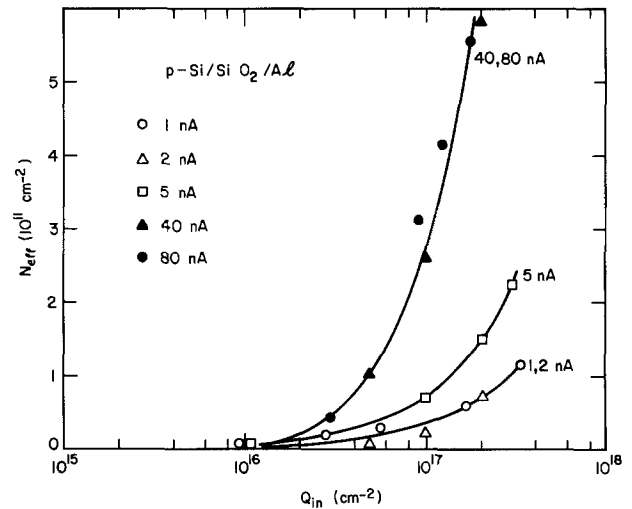


Fig. 2. Effective density of neutral traps vs. the total number per unit area of injected electrons for various levels of d-c electron currents.

Therefore, this observation of low trapping efficiency was reconfirmed by utilizing an MOS structure with a thick oxide guard ring. Upon going from an N_A of $2 \times 10^{16} \rightarrow 2.5 \times 10^{17} \rightarrow 6.8 \times 10^{17}$, the N_{eff} shows a rapid increase for $Q_{in} \sim 10^{17}$ (Fig. 3). The effect shown in Fig. 3 would become even greater if allowance is made for the fact that the 6.8×10^{17} Si had a thinner oxide and the 2×10^{16} Si had a thicker oxide than the 1.5×10^{17} material (see the next section). The observed increase in the hot electron trapping efficiency for higher substrate doping levels (N_A) appears to be over and above that simply attributable to edge effects, which dominate only at lower doping concentrations. Thus, the increase in the trapping efficiency with N_A continues to occur over the doping range ($10^{17} < N_A < 10^{18} \text{ cm}^{-3}$) where edge effects would be absent.

Effect of the oxide thickness.—As shown in Fig. 4, for a given doping level ($N_A \sim 2 \times 10^{17} \text{ cm}^{-3}$), the efficiency of hot electron trapping decreases on going from a gate oxide thickness of $970 \rightarrow 600 \rightarrow 150\text{\AA}$. This thickness effect can be reinforced by the doping effect, so that an MOS structure with 260\AA thick oxide on 3×10^{16} p-Si showed no measurable hot electron

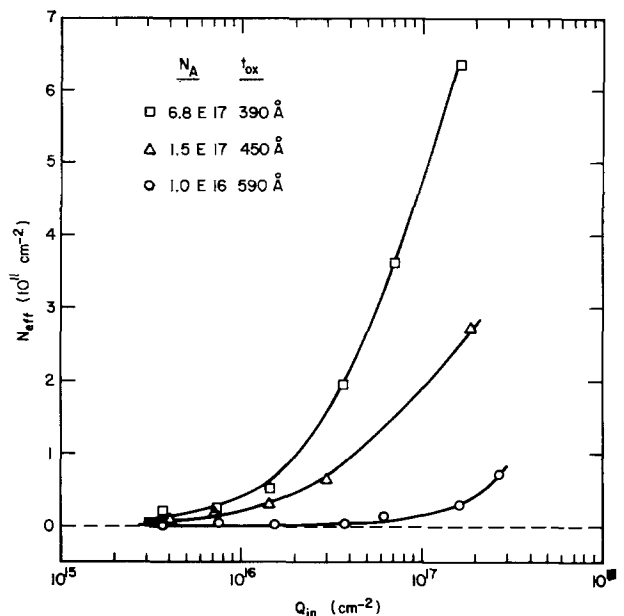


Fig. 3. The effect of p-Si substrate doping level on the hot electron trapping behavior of MOS capacitors on p-Si.

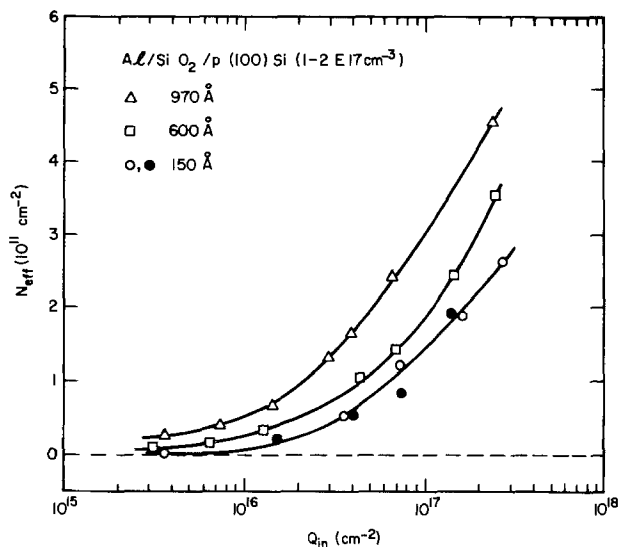


Fig. 4. The effect of gate oxide thickness on the hot electron trapping behavior of MOS capacitors on p-Si.

trapping induced flatband shift for Q_{in} as high as $2 \times 10^{17} \text{ cm}^{-2}$.

Effect of E-beam irradiation.—Aluminum-metallized MOS capacitors containing 810 \AA SiO_2 on p(100)Si ($N_A = 2.7 \times 10^{16} \text{ cm}^{-3}$) were E-beam irradiated with doses of 10, 20, and $30 \mu\text{C cm}^{-2}$ in three quadrants of a wafer whereas the fourth quadrant was left as a control. The irradiation produced a large number of surface states which were annealed out at 450°C , $\frac{1}{2}$ hr, H_2 . As shown in Fig. 5, no difference could be found in the hot electron trapping behavior of the nonirradiated control and the irradiated capacitors. In another experiment, various gate oxide areas were E-beam irradiated with 5, 15, and $20 \mu\text{C cm}^{-2}$ and then metallized with Al dots and annealed at 450°C , H_2 , $\frac{1}{2}$ hr. Again, no difference could be observed between the hot electron trapping behavior of irradiated and nonirradiated areas. These results indicate that for the presently used combination of Si-doping level, oxide thickness, and E-beam doses, hot electron trapping instability should not be abnormally high.

The present results cannot be directly compared with those of Aitken *et al.* (3) who observed a factor of 2 increase in the hot electron trapping on going from nonirradiated controls to samples irradiated with a high E-beam flux of $100 \mu\text{C cm}^{-2}$. Their samples had a higher doping level of $2 \times 10^{17} \text{ cm}^{-3}$, a smaller oxide thickness of 440 \AA , and were annealed at 400°C , 30 min in forming gas following E-beam exposure.

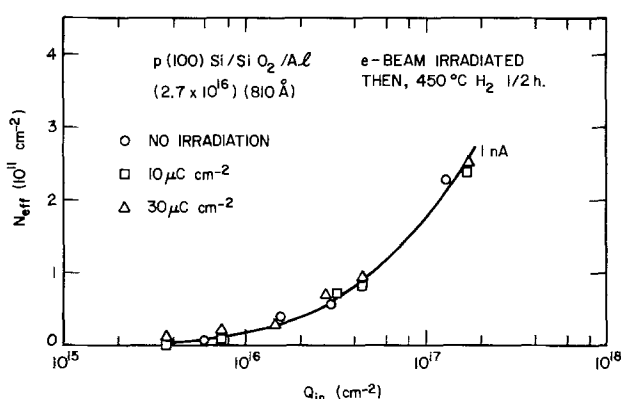


Fig. 5. Effect of E-beam irradiation of aluminumized MOS capacitors followed by 450°C H_2 anneal on the hot electron trapping behavior of the gate oxide.

Generation of surface states due to hot-electron injection.—Through quasi-static measurements in conjunction with high-frequency (1 MHz) C-V measurements (7), the density of surface states at midgap, N_{ss} , was determined for a limited number of samples subjected to avalanche injection and trapping. Figure 6 shows the results obtained for an MOS structure with a $0.5 \mu\text{m}$ thick oxide guard ring, 550 \AA gate oxide on p-Si with an acceptor concentration of $1.0 \times 10^{17} \text{ cm}^{-3}$. The electron injection current density was $6 \mu\text{A cm}^{-2}$ which is somewhat higher than the preferred levels. As may be seen from the right-hand ordinate of Fig. 6, an enormous density of surface states ($> 10^{12} \text{ cm}^{-2} \text{ eV}^{-1}$) is generated as a result of rf-aging. These surface states could not have been produced by any preferential conduction at the edges, since the acceptor concentration was relatively high and the edges were sealed with a thick oxide guard ring. The surface states also cause a stretchout of the high frequency C-V curves near the inversion point after extended aging, and this was found to be the case for all the samples studied. A detailed analysis of the surface states effect is being carried out and it will be published elsewhere.

Discussion

The present results on oxide thickness and Si-doping effects show that, through measurements of hot electron trapping efficiency, it is possible to distinguish between gate oxides which otherwise show the same (interface-dependent) MOS characteristics, *e.g.*, Q_{ss} and the slowtrapping instability. For this purpose, the choice of a low injection current at $\sim 1 \text{ nA}$ level ($\sim 2 \mu\text{A cm}^{-2}$) is important, because it enables one to best resolve the effect of materials and process parameters on the hot electron trapping efficiency. On the basis of the observed thickness dependence of hot electron trapping efficiency, it may be concluded that the neutral traps are distributed throughout the oxide as opposed to, *e.g.*, the slow traps or the fast states which predominantly reside at or near the interface.

This point is further illustrated by Fig. 7 where the hot electron trapping efficiency at a Q_{in} of 10^{17} cm^{-2} is plotted against the oxide thickness. A linear dependence through origin would indicate a t_{ox}^2 dependence of ΔV_{FB} , and hence, a uniform distribution of traps throughout the oxide thickness. This seems to be the case with the present samples except for the thinnest oxide (150 \AA), where there is a positive deviation from the line drawn through origin. It is probable that for the latter situation, additional traps related to the interface are present. Our conclusion on the overall thickness dependence of hot electron trapping at room temperature is very similar to that published recently

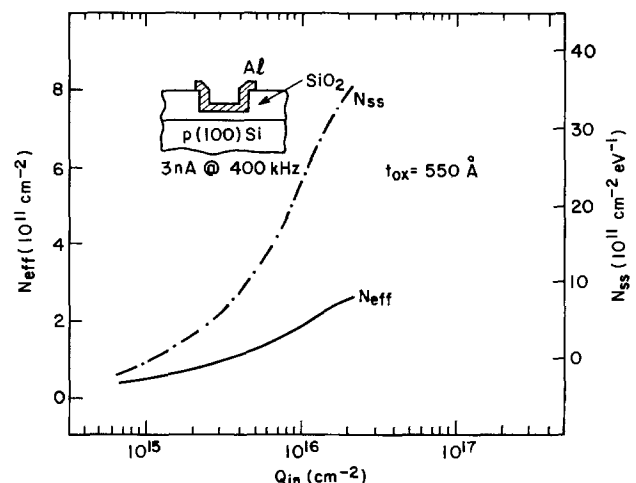


Fig. 6. The effect of gate oxide thickness on the hot electron trapping efficiency at Q_{in} of 10^{17} cm^{-2} .

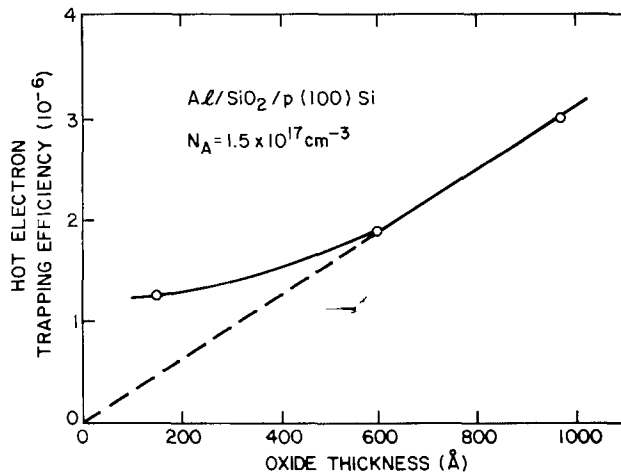


Fig. 7. Effective density of neutral traps and the density of surface states after rf-bias aging of an MOS capacitor with thick oxide guard ring.

(and after the present work was completed) by Young *et al.* (8).

In relating the present results to VLSI device technology, it may be concluded that the trend towards thinner gate oxides should be beneficial with regard to hot electron trapping instability. It should be emphasized, however, that even a small amount of hot electron trapping is always associated with an enormous increase in the surface states density. This factor alone may affect device performance, and also the estimate of the flatband voltage from C-V measurements after extended aging.

Conclusions

R-F-bias aging of MOS capacitors on p-Si was utilized to evaluate avalanche-induced hot electron trapping phenomena in gate oxides.

1. The hot electron trapping efficiency is a function of the avalanche injection current level: 1-2 nA (<4

$\mu\text{A cm}^{-2}$) are preferred values for controlled experiments, whereas with >10 nA (>5 $\mu\text{A cm}^{-2}$), an excessive degree of trapping is observed.

2. The flatband shift upon rf aging of capacitors increases with higher doping levels (10^{16} - 10^{17} cm^{-3}) in the p-Si substrate and with increased gate oxide thickness (200-1000Å).

3. Electron beam irradiation with a dose of 5-30 $\mu\text{C cm}^{-2}$ followed by a 450°C H_2 anneal did not appreciably degrade the hot electron trapping behavior of SiO_2 on p-Si ($N_A \approx 10^{16}$ cm^{-3}).

Acknowledgments

Thanks are due to C. Sarday for technical assistance, W. T. Lynch and L. R. Thibault for E-beam irradiation, and A. Kamgar, H. J. Levinstein, E. H. Nicollian, and H. A. Watson for helpful conversations.

Manuscript submitted Jan. 22, 1980; revised manuscript received March 31, 1980.

Any discussion of this paper will appear in a Discussion Section to be published in the June 1981 JOURNAL. All discussions for the June 1981 Discussion Section should be submitted by Feb. 1, 1981.

Publication costs of this article were assisted by Bell Laboratories.

REFERENCES

1. S. A. Abbas and R. C. Dockerty, *Appl. Phys. Lett.*, **27**, 147 (1975).
2. R. A. Gdula, *This Journal*, **123**, 42 (1976).
3. J. M. Aitken, D. R. Young, and K. Pan, *J. Appl. Phys.*, **49**, 3386 (1978).
4. A. Goetzberger and E. H. Nicollian, *ibid.*, **38**, 4582 (1967).
5. E. H. Nicollian and C. N. Berglund, *ibid.*, **41**, 3052 (1970).
6. A. K. Sinha and T. E. Smith, *This Journal*, **125**, 743 (1978).
7. M. Kuhn, *Solid-State Electron.*, **13**, 873 (1970).
8. D. R. Young, E. A. Irene, D. J. DiMaria, R. F. Dekeersmaecker, and H. Z. Massond, *J. Appl. Phys.*, **50**, 6366 (1979).

Optical Properties of $\text{Na}_3\text{La}_{1-x}\text{Nd}_x(\text{PO}_4)_2$ and $\text{Na}_3\text{La}_{1-x}\text{Nd}_x(\text{VO}_4)_2$

C. Parent, C. Fouassier, and G. Le Flem

Laboratoire de Chimie du Solide du C.N.R.S., Université de Bordeaux I, 33405, Talence Cedex, France

ABSTRACT

Diffuse reflectance and fluorescence spectra as well as lifetimes have been determined as a function of Nd^{3+} concentration in $\text{Na}_3\text{La}_{1-x}\text{Nd}_x(\text{PO}_4)_2$ ($0 < x \leq 1$) and $\text{Na}_3\text{La}_{1-x}\text{Nd}_x(\text{VO}_4)_2$ ($0 < x \leq 0.70$) phases. Due to the dissymmetry of the anionic environment and the higher covalency of the Nd-O bond, the vanadate has a strong luminescence intensity at low concentrations. Important self-quenching is likely due to electric dipole interactions between Nd^{3+} ions leading to cross-relaxation via the $^4\text{I}_{15/2}$ manifold.

The development of fiber optical communications is at the origin of many studies concerning neodymium microlasers. Due to their high neodymium content, these materials can be pumped by light emitting diodes (LED) and consequently constitute a potential light source for optical integrated systems.

The first neodymium lasers such as Nd:YAG (1) showed a very important concentration-quenching. The study of the optical properties of the neodymium ultraphosphate $\text{NdP}_5\text{O}_{14}$ (NdUP) gave rise to a second

Key words: inorganic, luminescence, lasers.

generation of materials with a high concentration in active ions, but reduced self-quenching. Most of them are borates and phosphates with a strongly covalent framework along two or three space directions isolating each rare-earth ion from one another. All these structures involve a large distance—about 5Å—between nearest neighbor Nd^{3+} ions.

An alternative way of obtaining large distances between active ions in crystals is to create cationic ordering within a given structure. This is the case for instance in the $\text{Na}_3\text{Ln}(\text{XO}_4)_2$ phases (Ln = rare-

earth; X = P, V, As) for which the Na-Ln ordering leads to large Ln-Ln distances (2-4).

Therefore, it was attractive to study the optical properties of the $\text{Na}_3\text{La}_{1-x}\text{Nd}_x(\text{PO}_4)_2$ and $\text{Na}_3\text{La}_{1-x}\text{Nd}_x(\text{VO}_4)_2$ phases, in order to estimate their possibilities as coherent light sources.

Experimental Procedure

Samples of the $\text{Na}_3\text{La}_{1-x}\text{Nd}_x(\text{PO}_4)_2$ and $\text{Na}_3\text{La}_{1-x}\text{Nd}_x(\text{VO}_4)_2$ phases have been prepared from stoichiometric mixtures of Na_2CO_3 (Merck 99.9%), $(\text{NH}_4)_2\text{HPO}_4$ (Merck min. 99%), V_2O_5 (99%), and Ln_2O_3 (Rhône-Poulenc 99.99%) (5).

The diffuse reflectance spectra have been recorded at 300°K with a Cary 17 spectrometer.

For the fluorescence study the excitation of Nd^{3+} ions has been carried out by the radiation of a xenon-lamp over the range 500-600 nm.

Measurements of fluorescence lifetimes have been made on samples excited by pulses of 500-600 nm wavelength radiation from a flash-tube, with a pulse duration of approximately 1 μsec . The decay curves were recorded on the screen of an oscilloscope.

Structures of the $\text{Na}_3\text{La}_{1-x}\text{Nd}_x(\text{PO}_4)_2$ and $\text{Na}_3\text{La}_{1-x}\text{Nd}_x(\text{VO}_4)_2$ Phases

The $\text{Na}_3\text{La}_{1-x}\text{Nd}_x(\text{PO}_4)_2$ and $\text{Na}_3\text{La}_{1-x}\text{Nd}_x(\text{VO}_4)_2$ solid solutions exist with different allotropic varieties. The stable room temperature forms investigated here derive from a glaserite surstructure with a sodium-rare-earth ordering. This type of ordering, which is the same over the whole composition range ($0 \leq x \leq 1$ for the phosphate and $0 \leq x \leq 0.70$ for the vanadate) induces a minimum Nd-Nd distance of 4.65 Å in $\text{Na}_3\text{Nd}(\text{PO}_4)_2$ (2) and a minimum La-La distance of 4.91 Å in $\text{Na}_3\text{La}(\text{VO}_4)_2$ (3).

The rare-earth ions are located, respectively, in six and two different crystallographic sites in the phosphates and in the vanadates. Their oxygen coordination is 8 or 9 in the phosphate and 8 in the vanadate, if we take only into account the Ln-O distances below or equal to 3 Å. Each LnO_y polyhedron ($y = 8$ or 9) is isolated from each other and its anionic configuration deviates notably from inversion symmetry.

Optical Properties

Diffuse reflectance.—The diffuse reflectance spectra of $\text{NdP}_5\text{O}_{14}$, $\text{Na}_3\text{La}_{0.80}\text{Nd}_{0.20}(\text{PO}_4)_2$, and $\text{Na}_3\text{La}_{1-x}\text{Nd}_x(\text{VO}_4)_2$ ($x = 0.05, 0.20, 0.65$) are shown in Fig. 1.

In the u.v. range the spectra of the vanadates consist of a charge transfer band typical of $(\text{VO}_4)^{3-}$ ions.

Although the optical densities can be affected by slight differences in the granulometry of the samples, we may conclude from the comparison of the spectra that the oscillator strengths in the vanadates are higher than in the phosphates.

A detailed investigation of the diffuse reflectance spectra of $\text{Na}_3\text{Nd}(\text{PO}_4)_2$ and $\text{Na}_3\text{La}_{0.35}\text{Nd}_{0.65}(\text{VO}_4)_2$ in the range of the $^4I_{9/2} \rightarrow ^2P_{1/2}$ transition has been made for determining the splitting of the $^4I_{9/2}$ level. In both structures, the rare-earth ions occupy several types of sites, so that an assignment of the various observed lines is impossible. The width of the group of lines gives an overestimation of the maximum splitting of the $^4I_{9/2}$ level and consequently of the local crystal-field around the Nd^{3+} ; these values are 611 cm^{-1} for the phosphate and 977 cm^{-1} for the vanadate.

The most intense $^4I_{9/2} \rightarrow ^2P_{1/2}$ lines which correspond to the lowest Stark level are located at 23,255 cm^{-1} for $\text{Na}_3\text{Nd}(\text{PO}_4)_2$ and 23,097 cm^{-1} for $\text{Na}_3\text{La}_{0.35}\text{Nd}_{0.65}(\text{VO}_4)_2$. These values are close to those observed for NdVO_4 (23,080 cm^{-1}) and $\text{Y}_3\text{Al}_5\text{O}_{12}:\text{Nd}$ (23,139 cm^{-1}) (6, 7), in which neodymium is in similar eightfold coordinated sites. Their difference may be explained by the nephelauxetic effect which is more pronounced in the vanadate: in so far as the P-O bonds are more covalent than V-O bonds, the com-

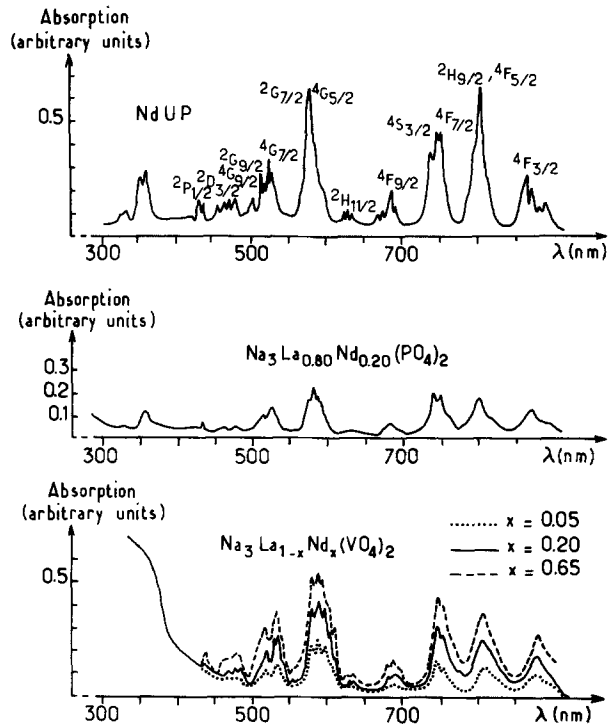


Fig. 1. Diffuse reflectance spectra of the $\text{NdP}_5\text{O}_{14}$, $\text{Na}_3\text{La}_{0.80}\text{Nd}_{0.20}(\text{PO}_4)_2$ and $\text{Na}_3\text{La}_{1-x}\text{Nd}_x(\text{VO}_4)_2$ phases ($T = 300^\circ\text{K}$).

petitive Ln-O bonds are more covalent in the case of the vanadate.

Study of the neodymium emission.—The $^4F_{3/2} \rightarrow ^4I_{11/2}$ emission spectra ($\lambda \approx 1060$ nm) recorded at 300°K are compared in Fig. 2 with the $\text{NdP}_5\text{O}_{14}$ spectrum obtained under similar conditions. The contribution to the emission of ions located in various different sites does not allow to distinguish the transitions between the various Stark levels, as previously for the diffuse reflectance spectra.

The neodymium concentration dependence of the fluorescence intensity is shown in Fig. 3: the emitted intensity of the vanadate is always higher than that of the homologous phosphate.

The variations of the $\text{Nd}^{3+} \ ^4F_{3/2}$ lifetime as a function of the neodymium content are plotted in Fig. 4. Over the whole composition range the lifetimes in the phosphate are longer, but the concentration dependence in both cases is very similar.

If we call τ_0 the observed decay constant at high dilution (which is assumed to represent the radiative lifetime) and $\tau_{(m)}$ the observed decay constant at a Nd^{3+} concentration $N = 4.10^{21}$ ions $\text{Nd}^{3+} \cdot \text{cm}^{-3}$, the quenching ratio $\tau_0/\tau_{(m)}$ for both materials is about 10.

For $\text{K}_3\text{La}_{1-x}\text{Nd}_x(\text{PO}_4)_2$, which has a related structure, Hong and Chinn had obtained $\tau_0/\tau_{(m)} = 16$ (8).

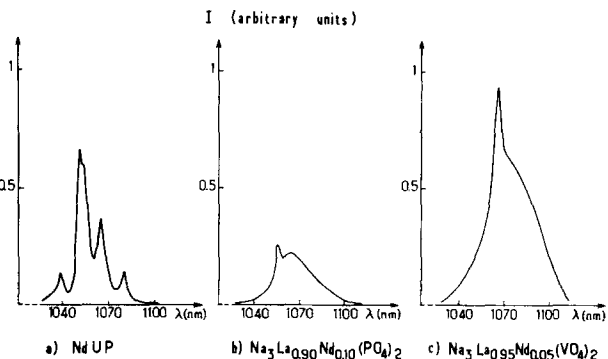


Fig. 2. $^4F_{3/2} \rightarrow ^4I_{11/2}$ emission in (a) $\text{NdP}_5\text{O}_{14}$ (b) $\text{Na}_3\text{La}_{0.90}\text{Nd}_{0.10}(\text{PO}_4)_2$, and (c) $\text{Na}_3\text{La}_{0.95}\text{Nd}_{0.05}(\text{VO}_4)_2$ ($T = 300^\circ\text{K}$).

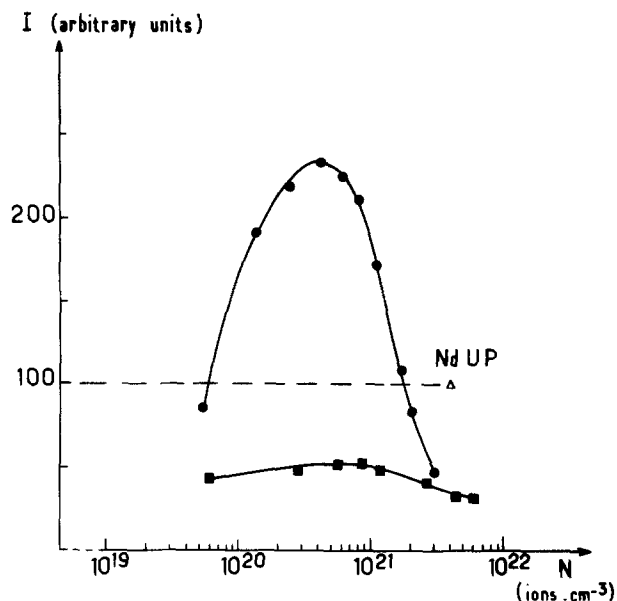


Fig. 3. Fluorescence intensity (${}^4F_{3/2} \rightarrow {}^4I_{11/2}$) as a function of Nd^{3+} concentration for: \blacksquare $\text{Na}_3\text{La}_{1-x}\text{Nd}_x(\text{PO}_4)_2$, \bullet $\text{Na}_3\text{La}_{1-x}\text{Nd}_x(\text{VO}_4)_2$.

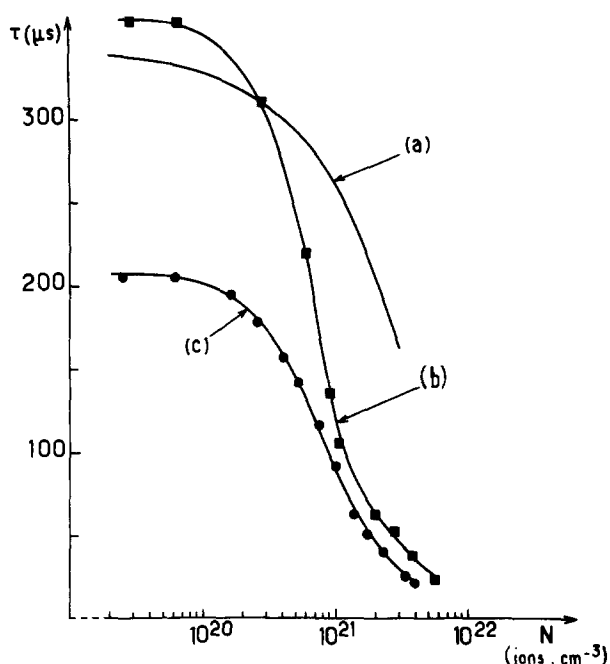


Fig. 4. ${}^4F_{3/2}$ lifetime as a function of Nd^{3+} concentration for: curve a, $\text{La}_{1-x}\text{Nd}_x\text{P}_5\text{O}_{14}$ [after (11)], curve b, $\text{Na}_3\text{La}_{1-x}\text{Nd}_x(\text{PO}_4)_2$, and curve c, $\text{Na}_3\text{La}_{1-x}\text{Nd}_x(\text{VO}_4)_2$.

Within the $4f^3$ configuration, the electric-dipole transitions are forbidden. However the lack of symmetry center at the Nd^{3+} sites creates an odd parity admixture of the $4f^3$ and $4f^25d^1$ configurations, allowing the transitions. With increasing deviation from inversion symmetry, the probability of electric-dipole radiative transitions increases and as a consequence the radiative lifetime shortens (9).

Whereas in $\text{K}_3\text{La}_{1-x}\text{Nd}_x(\text{PO}_4)_2$ ($\tau_0 = 460 \mu\text{sec}$) six among the seven oxygen atoms forming the neodymium site are close to inversion positions, in $\text{Na}_3\text{La}_{1-x}\text{Nd}_x(\text{PO}_4)_2$ ($\tau_0 = 360 \mu\text{sec}$), the six nearest neighbor oxygens around each neodymium atom form largely distorted octahedra: this less centrosymmetrical anionic configuration explains the shorter lifetime in our phosphate.

In the vanadate, as shown by the diffuse reflectance spectra, the Nd-O bonds are more covalent than in the phosphate: the probability of the radiative transitions increases and the lifetime of the ${}^4F_{3/2}$ level decreases.

Self-quenching analysis.—In strong self-quenching materials, deactivation is the result of electric-dipole interactions between Nd^{3+} ions and cross relaxation via the ${}^4I_{15/2}$ manifold (Fig. 5).

As showed previously by Auzel, such an energy transfer occurs only if the effect of the crystal field splitting compensates the energy difference between the transitions ${}^4F_{3/2} \rightarrow {}^4I_{15/2}$ and ${}^4I_{9/2} \rightarrow {}^4I_{15/2}$ of the free Nd^{3+} ion (10).

Figure 6, which gives schematically the energy levels of free Nd^{3+} ion and of Nd^{3+} in a crystal shows that self-quenching arises if $E_{2m} - E_{1m} > 0$. Following Auzel, this condition can be reduced to a single inequality (10)

$$\Delta E_1 \cong 470 \text{ cm}^{-1}$$

In the $\text{Na}_3\text{La}_{1-x}\text{Nd}_x(\text{XO}_4)_2$ ($\text{X} = \text{P}, \text{V}$) phases, the presence of Nd^{3+} ions in slightly different crystal field sites gives rise to an additional broadening of ΔE_1 . Thus the values obtained for our phosphate (611 cm^{-1}) and our vanadate (977 cm^{-1}) exceed largely 470 cm^{-1} and explain the observed strong self-quenching.

The self-quenching probability can be defined by $q_n = \tau_0 - \tau/\tau$ (where τ is the lifetime for a given neodymium concentration).

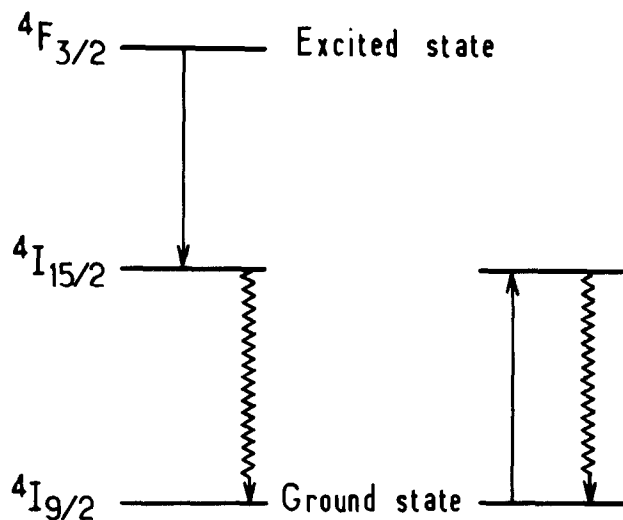


Fig. 5. Energy transfer and dissipation by cross-relaxation

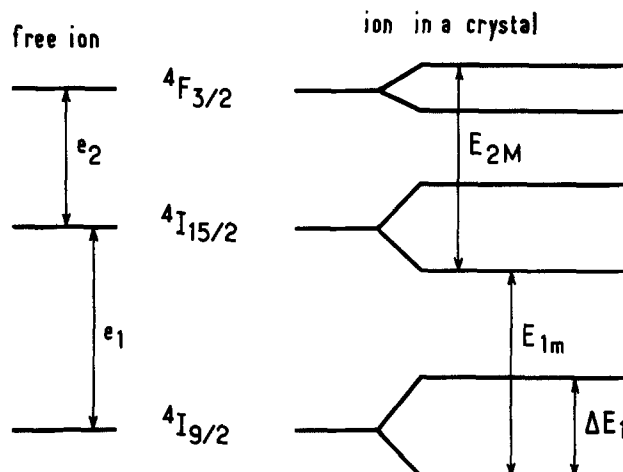


Fig. 6. Energy levels ${}^4F_{3/2}$, ${}^4I_{15/2}$, and ${}^4I_{9/2}$ of Nd^{3+} [following Auzel (10)].

Table I. Magnitude of the $^4I_{9/2}$ splitting and functional dependence of normalized concentration-quenching rate q_n on neodymium concentration N for several materials

Materials	ΔE_1 (cm $^{-1}$)	Functional dependence of $q_n = \frac{\tau_0 - \tau}{\tau}$ on concentration N
$La_{1-x}Nd_xP_5O_{14}$	320 (10)	$\sim N$ (13)
$LiLa_{1-x}Nd_xP_4O_{12}$	375 (10)	$\sim N$ (13)
$KLa_{1-x}Nd_xP_4O_{12}$	320 (10)	$\sim N$ (13)
$Na_3La_{1-x}Nd_x(VO_4)_2$	370 (10)	$\sim N$ (13)
$La_{1-x}Nd_xAl_3(BO_3)_4$	410 (10)	$\sim N$ (13)
$K_3La_{1-x}Nd_x(PO_4)_2$	465 (15)	$\sim N^{1.8}$
$La_{1-x}Nd_xF_3$	500 (10)	for $N \leq 0.4 \times 10^{21}$ (8) $\sim N^{1.8}$ for $N \geq 0.4 \times 10^{21}$ (8) $\sim N$
$Na_3La_{1-x}Nd_x(PO_4)_2$	611 (this work)	for $N \leq 2 \times 10^{21}$ (11) $\sim N^2$ for $N \geq 2 \times 10^{21}$ (11) $\sim N$
$Na_3La_{1-x}Nd_x(VO_4)_2$ ($La_{1-x}Nd_x$) $_2O_2S$	977 (this work) 410 (10)	for $N \leq 1 \times 10^{21}$ (This work) $\sim N^{1.8}$ for $N \geq 1 \times 10^{21}$ (This work) $\sim N^2$ (16)

Figure 7 shows the variation of q_n as a function of the neodymium concentration N for $Na_3La_{1-x}Nd_x(PO_4)_2$ and $Na_3La_{1-x}Nd_x(VO_4)_2$. In both cases the evolution is described in the logarithmic diagram by two intersecting straight lines with a slope of about 2 at low concentrations and 1 at high concentrations.

Similar behavior has been previously reported for $La_{1-x}Nd_xF_3$ (11) and $K_3La_{1-x}Nd_x(PO_4)_2$ (8).

Table I gives the magnitude ΔE_1 of the $^4I_{9/2}$ splitting and the functional dependence of q_n on neodymium concentration for several materials.

Self-quenching due to cross-relaxation is theoretically expected to occur with square dependence of q_n on N (1, 11-13). Such a variation is more or less observed in materials involving high values of ΔE_1 and for relatively low activator concentrations.

On the other hand, in weak self-quenching materials, q_n is found to increase linearly with N . Among the various processes assumed to be responsible for such a variation, it was stated recently that the most probable one is migration of energy between Nd^{3+} ions up to annihilation by defects (11-14).

In $Na_3La_{1-x}Nd_x(PO_4)_2$ and $Na_3La_{1-x}Nd_x(VO_4)_2$, the values of the splitting ΔE_1 are much larger than 470

cm $^{-1}$ and consequently lead to a great cross-relaxation probability.

In any way at low x values migration probability is likely weak and the observed fluorescence decay has to be ruled by cross-relaxation probability.

As x rises, energy migration probability increases strongly. The final exponential stage of the decay curve, which becomes the only one appearing, is ruled by self-quenching processes involving energy migration (11).

Finally, the particular behavior of the last material in Table I, ($La_{1-x}Nd_x$) $_2O_2S$, can be pointed out. In spite of a low ΔE_1 value, q_n increases as the square of Nd^{3+} concentration: strong self-quenching seems to be due to short Ln-Ln distances (4.19 Å).

In conclusion, two important criteria are simultaneously required for the development of efficient microlasers: a weak crystal field at the neodymium sites and a large distance between Nd-Nd nearest neighbors.

Acknowledgments

The authors express their thanks to B. Saubat and A. Garcia for their help in diffuse reflectance and fluorescence measurements and to B. Blanzat and J. P. Denis for providing them crystals of NdP_5O_{14} .

Manuscript submitted Feb. 25, 1980; revised manuscript received April 2, 1980.

Any discussion of this paper will appear in a Discussion Section to be published in the June 1981 JOURNAL. All discussions for the June 1981 Discussion Section should be submitted by Feb. 1, 1981.

Publication costs of this article were assisted by the Université de Bordeaux I.

REFERENCES

- H. G. Danielmeyer, M. Blätte, and P. Balmer, *Appl. Phys.*, **1**, 269 (1973).
- R. Salmon, C. Parent, M. Vlasse, and G. Le Flem, *Mater. Res. Bull.*, **13**, 439 (1978).
- M. Vlasse, R. Salmon, and C. Parent, *Inorg. Chem.*, **15**, 1440 (1976).
- C. Parent, J. Fava, R. Salmon, M. Vlasse, G. Le Flem, P. Hagenmuller, E. Antic Fidancev, M. Lemaitre-Blaise, and P. Caro, *Nouveau J. de Chimie*, **3**, 523 (1979).
- R. Salmon, C. Parent, A. Berrada, R. Brochu, A. Daoudi, M. Vlasse, and G. Le Flem, *C. R. Acad. Sci.*, **280**, 805 (1975).
- P. Caro and J. Derouet, *Bull. Soc. Chim. Fr.*, **1**, 46 (1972).
- P. Caro, O. Beaury, and E. Antic, *J. Phys.*, **37**, 671 (1976).
- H. Y-P. Hong and S. R. Chinn, *Mater. Res. Bull.*, **11**, 421 (1976).
- H. Y-P. Hong and S. R. Chinn, *ibid.*, **11**, 461 (1976).
- F. Auzel, *Mater. Res. Bull.*, **14**, 223 (1979).
- B. I. Denker, V. V. Osiko, A. M. Prokhorov, and I. A. Shcherbakov, *Sov. J. Quantum Electron.*, **8**, 485 (1978).
- A. Lempiki, *Opt. Commun.*, **23**, 376 (1977).

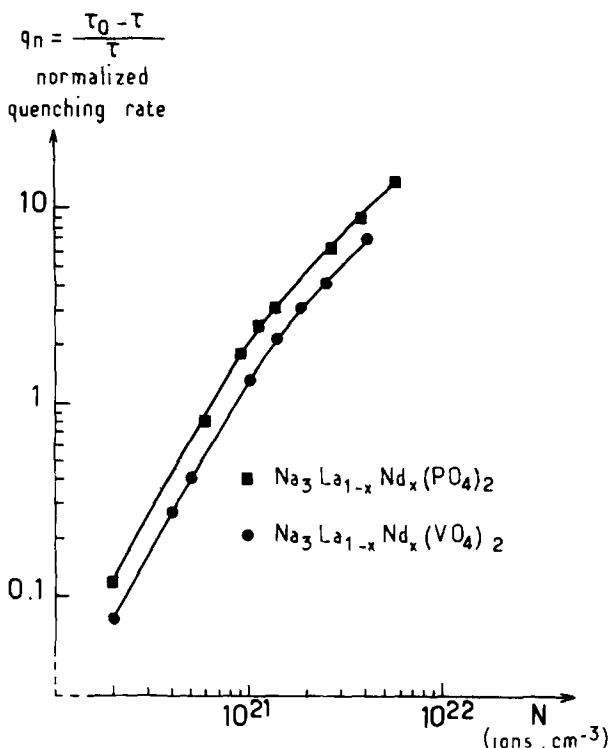


Fig. 7. Normalized concentration-quenching rate q_n as a function of neodymium concentration.

13. S. R. Chinn, H. Y-P. Hong, and J. W. Pierce, *Laser Focus*, **12**, 64 (1976).
14. H. G. Danielmeyer, in "Festkörperprobleme," (Advances in Solid State Physics), Vol. 15, H. J. Quieser, Editor, p. 253, Pergamon/Vieweg, Braunschweig, (1975).
15. V. B. Loshchenov, A. Ezhova, Yu. I. Krasilo, V. P. Orlovskii, N. T. Kuznetsov, and V. D. Vorob'ev, *Izv. Akad. Nauk. SSSR, Neorg. Mater.*, **15**, 1120 (1979).
16. R. V. Alves, R. A. Buchanan, K. A. Wickersheim, and E. A. C. Yates, *J. Appl. Phys.*, **42**, 3043 (1971).

Direct Thermal Nitridation of Silicon Dioxide Films in Anhydrous Ammonia Gas

Takashi Ito,* Takao Nozaki, and Hajime Ishikawa*

Fujitsu Laboratories Limited, Semiconductor Devices Laboratory,
1015 Kamikodanaka, Nakahara, Kawasaki, Japan

ABSTRACT

It has been found that SiO₂ can be converted directly to silicon nitride or oxynitride at the surface of SiO₂ films by heating oxidized silicon wafers in anhydrous ammonia gas. At temperatures above 900°C, nitrated SiO₂ films have graded composites with respect to their nitrogen fraction. This analysis was performed by AES, infrared transmittance spectroscopy, and etch-rate profiles. Nitrated surface regions on SiO₂ films, in which the nitride fraction ranged from 10% to 50%, showed remarkable masking effects against subsequent oxidation at high temperatures.

Silicon nitride is a technologically important material in the production of high performance integrated circuits because of its strong oxidation resistance, barrier against diffusion of impurities, and chemical stability (1-4). Nitride films deposited by chemical vapor are used as gate insulators for nonvolatile memory cells in the form of dual dielectrics (5-8). These metal-nitride-oxide-semiconductor structures were also examined for their properties as stable gate insulators for scaled short-channel devices where film thicknesses of less than 250Å are required (9). Thin Si₃N₄ and SiO₂ composites resulted in unsatisfactory threshold voltage stability which was due to the high trapping efficiency of the nitride and the nitride-oxide interface (10, 11).

During CVD processing of Si₃N₄, nitrogen atoms diffuse into SiO₂-Si interfaces (12, 13). Nitride which formed at SiO₂-Si interfaces in the local oxidation process was found to cause gate oxide thinning near the LOCOS edges and to result in low gate-breakdown voltages (14). Kooi *et al* (14) showed that exposure of oxidized silicon wafers in 3% ammonia gas lead to the formation of oxidation resistant layers. Annealing in nitrogen gas is frequently used to remove the oxide charge from thermally grown silicon dioxide films. Nitrogen atoms easily diffuse through SiO₂ and rarely react with the silicon at high temperatures (15, 16). This process was reported to degrade the electrical properties of MOS structures (17, 18). All these experiments showed only the reaction between nitrogen atoms and silicon substrates and never clearly mentioned any conversion of SiO₂ films.

This paper describes the direct conversion of SiO₂ to nitride or oxynitride. In anhydrous ammonia gas at high temperatures, thermal nitridation of SiO₂ on silicon substrates has been found to occur more predominantly than thermal nitridation of the silicon substrates, even if the SiO₂ film is less than 100Å thick. This fact was discovered in the course of the research on the direct thermal nitridation of silicon (19-21). The nitridation procedure and analysis of thermally nitrated SiO₂ films on silicon substrates are reported here. The electrical properties of the films and MOS

structures will be reported soon in another article (22).

Experimental Procedure

Sample preparation.—Silicon, p-type, (100) oriented, CZ wafers with resistivities ranging from 1 to 5 Ωcm were degreased, chemically cleaned in a hot aqueous solution of NH₄OH + H₂O₂, and rinsed in deionized water. Wafers were then oxidized at 1000°C in wet oxygen gas flowing through a water bubbler. The film thicknesses of the SiO₂ films ranged from 100 to 1600Å. The oxidized wafers were loaded on a quartz susceptor and inserted into a quartz tube which was heated to a temperature range of 900°-1200°C. Pure nitrogen gas was flowing through the tube when the wafers were set. No nitridation was observed on SiO₂ surfaces heated under these conditions. Just after the temperature of the oxidized wafers reached a specified point, highly purified anhydrous ammonia gas was substituted for the nitrogen gas. Heating in the ammonia gas ambient was for 1-5 hr or for 17 hr.

Measurement.—The film thicknesses and refractive indexes of films on silicon were measured by ellipsometry with a wavelength of 5461Å. To assign consistency to these values, it was assumed that nitrated films have uniform structures with respect to the depth and that optical constants of the silicon substrate did not change through the nitridation process. The etching rates of films in a solution of NH₄F:HF = 10:1 were also examined by step-by-step etching.

Auger electron spectroscopy (AES) with a cylindrical mirror analyzer and infrared transmittance spectroscopy were used for structural analyses. Dielectric constants were calculated from accumulation capacitances of MOS structures and ellipsometric film thicknesses. Aluminum films were evaporated on nitrated SiO₂ surfaces to a thickness of 5000Å. Further, the effects of nitrated SiO₂ films against oxidation in various conditions were examined.

Results

Process conditions.—The surfaces of the nitrated SiO₂ films were as smooth as those of clean SiO₂ films grown thermally on silicon. No morphologies were observed on any experimental wafers. Figure 1 shows changes in film thickness with respect to nitridation

* Electrochemical Society Active Member.

Key words: thin film, direct conversion, composite, silicon nitride, oxynitride.

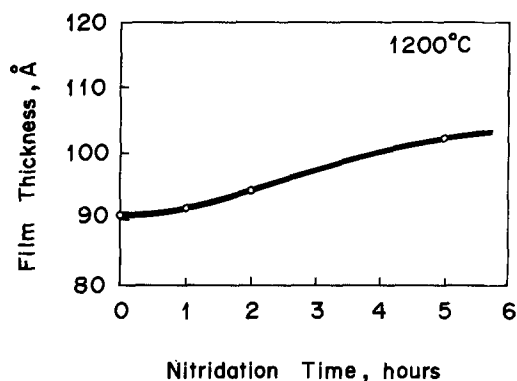


Fig. 1. Change in film thickness with respect to nitridation time at 1200°C.

time. The initial film thickness of 90Å increased slightly and then relatively rapidly in relation to nitridation time at a temperature of 1200°C. After 5 hr, the change in film thickness was about 10Å. Refractive indexes of the respective films are shown in Fig. 2. The initial value was 1.45, which is that of thermal SiO₂. The index rapidly increased to 1.65 after 1 hr of nitridation and little change was observed for films nitrided for longer periods. The rapid increase in refractive index was associated with the slight change in the film thickness shown in Fig. 1. Because nitrided SiO₂ films had nonuniform composites with respect to the depth, the refractive indexes depended on film thicknesses as shown in Fig. 2. Further data are shown in Table I.

Etching characteristics.—Etching rates in a solution of NH₄F:HF = 10:1 were measured for three samples. SiO₂ films were grown on all wafers to a thickness of 1600Å. Two wafers were heated in anhydrous ammonia gas at a temperature of 1200°C for 5 and 17 hr, respectively. One was used as a reference for SiO₂. Figure 3 shows change in film thickness with respect to etching time. The linear decrease in film thickness in the reference shows a general tendency of thermally grown SiO₂ films. On the other hand, the nitrided samples showed some retarding in changes of the film thickness. After 100 to 200 sec, both the films started to change in thickness at an etching rate of about one-third that of the reference. No significant difference was observed in the slope of the etching characteristics between the sample nitrided for 5 hr and that nitrided for 17 hr. This indicates that chemically passive layers, which have a very small etching rate in the solution, were formed on the surfaces.

Infrared transmittance spectroscopy.—Figure 4 shows the infrared absorption spectrum of a nitrided SiO₂ film with a thickness of about 100Å which was treated in anhydrous ammonia gas at 1200°C for 5 hr. A relatively thin film was chosen for the measurement

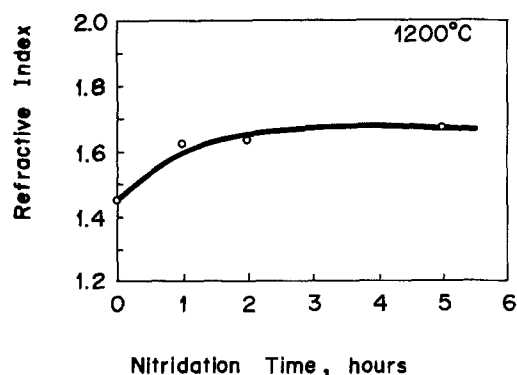


Fig. 2. Change in refractive index with respect to nitridation time at 1200°C. The saturated value shows a nitride fraction of about 50% in SiO₂ films.

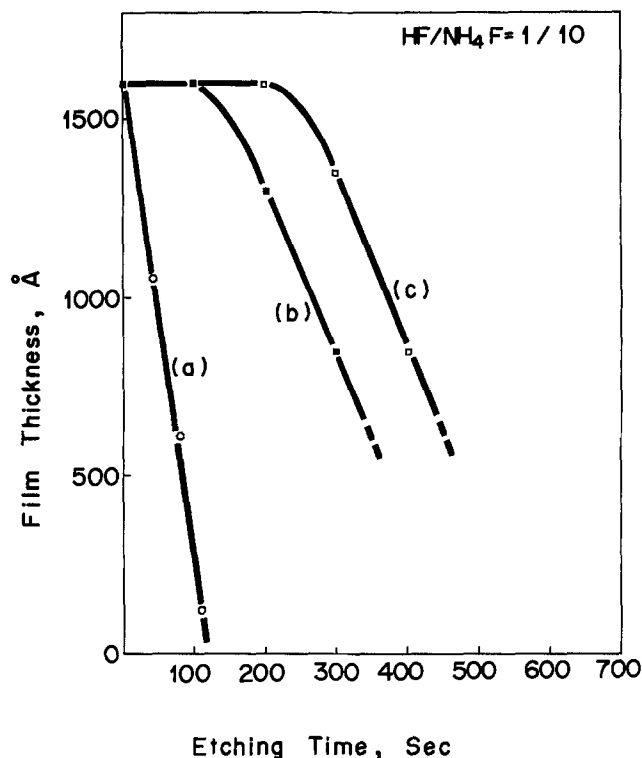


Fig. 3. Etching characteristics of films in a solution of NH₄F:HF = 10:1. SiO₂ film (a) is the reference. Films (b) and (c) were thermally nitrided at 1200°C for 5 and 17 hr, respectively.

because a large ratio of nitrided region to the remaining SiO₂ was expected if nitridation was limited to a region near the surface. Spectra (a) and (b) are for the wafers with no nitrided SiO₂ film and that with a nitrided SiO₂ film, respectively. Both were measured using a reference of an SiO₂ film which was grown under the same conditions as that in samples (a) and (b). The peak at 16.4 μm observed in (a) can be attributed to difference in thicknesses of the silicon wafers used for sample (a) and the reference. Due to the evenness in thicknesses of the SiO₂ films, the spectrum is almost flat over the range of 9-15 μm, all peaks being completely canceled.

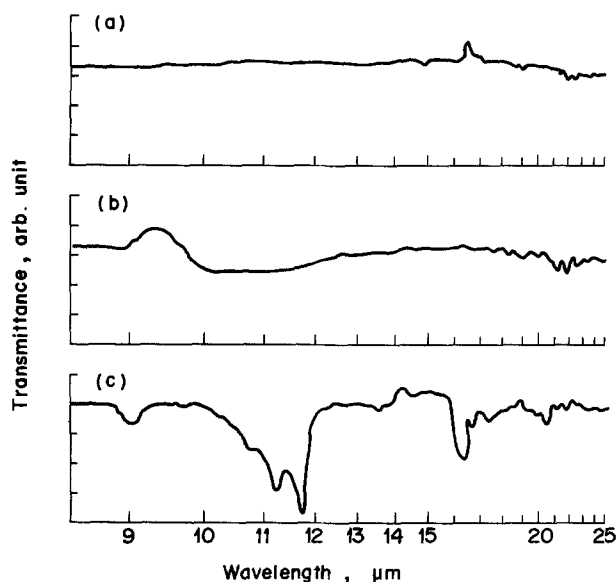


Fig. 4. Infrared transmittance spectra of a 100Å thick SiO₂ film (a), and of a film nitrided at 1200°C for 5 hr (b), where a 100Å thick SiO₂ film was used as a reference. (c) is for a thermally nitrided silicon film (19).

With the samples nitrided at 1200°C for 5 hr, transmittance increased at 9.4 μm and broad absorption appeared at wavelengths from 10 to 11.5 μm . The increase noted seems to be caused by dissociation of Si-O bonds. The phenomenon is believed to be associated with the subsequent formation of a nitrided layer on the SiO₂ films, which gives rise to the appearance of absorption peaks caused by stretching vibration of Si-N bonds. Absorption peaks of a direct thermal nitrided silicon film with a reference of air is shown in Fig. 4(c) (19). The 10.7, 11.2, and 11.8 μm peaks are most likely a result of Si-N bonds. The broad absorption peaks in Fig. 4(b) indicate that composition of the nitrided SiO₂ film was not uniform in depth, but rather changed gradually from SiO₂ to some nitride.

Auger electron spectroscopy.—A typical AES spectrum is shown in Fig. 5. The sample had a 500Å thick SiO₂ film nitrided at 1200°C for 1 hr. The sample surface was not bombarded with ions, and contamination by adsorptive carbon atoms were detected. Oxygen atoms were also adsorptive but identified with SiO₂ composites. Chemically shifted silicon peaks appeared mainly at 78 eV, indicating SiO₂ composites. Further, the very slight shoulder peak recognized at 87 eV is believed to indicate a chemically shifted silicon peak caused by the formation of silicon nitride (23). The intense peak at 375 eV is due to KLL transition in nitrogen atoms, something which was never observed with either as-grown SiO₂ films or nitrogen-annealed SiO₂ films.

Peak-to-peak depth profiles in AES spectra are shown in Fig. 6 and 7. In its initial state, the sample in Fig. 6 had the same structure as that shown in Fig. 5, but was bombarded step-by-step by argon ions with 2 keV of energy. The ion milling rate of both SiO₂ and Si₃N₄ was about 30 Å/min. The film surface was deficient in oxygen atoms. As measured by AES, the height of the oxygen peak rises with sputtering the nitrided SiO₂ film from the surface to the silicon interface. The nitrogen peak is the maximum at the film surface and gradually reduces with sputtering. Nitrogen atoms are localized mostly within a range of 30Å from the film surface. No pile-up was observed at the silicon interface. At the surface the nitrogen fraction was almost a third, demonstrating that escape probabilities of Auger electrons from nitrogen and oxygen are the same. Changes in the profiles of the chemically shifted silicon peaks appearing at 78-83 eV (a) and 62 eV (b), and the pure silicon peak at 92 eV (c) are associating with the observed nitrogen profile. Figure 7 shows a sample with a film thickness of 90Å. The

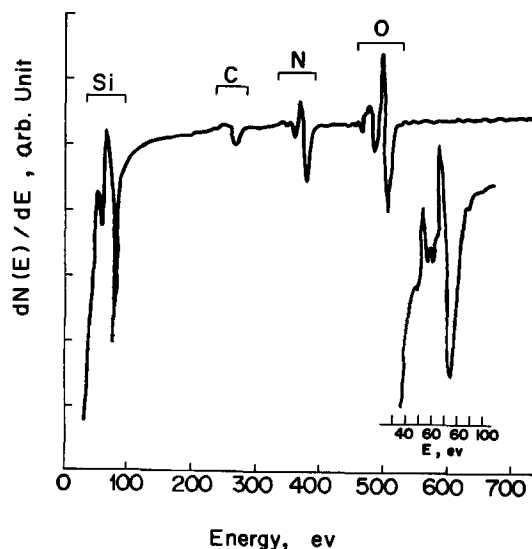


Fig. 5. AES spectrum of a nitrided SiO₂ film. A 500Å thick film was nitrided in anhydrous ammonia gas at 1200°C for 1 hr.

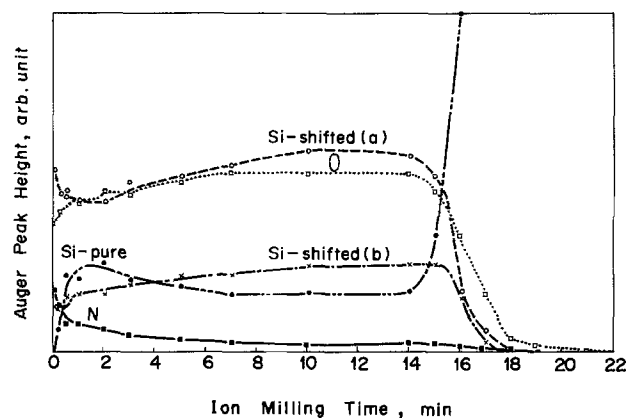


Fig. 6. Peak-to-peak depth profiles of various atoms in AES spectra of a 500Å thick SiO₂ film nitrided at 1200°C for 1 hr. Si-shifted (a) and (b) appeared at 78-83 and 62 eV, respectively.

conditions for nitridation were the same as those for the sample in Fig. 6. Gradual decrease of the nitrogen AES peaks shows that direct nitridation occurred predominantly on the SiO₂ surface rather than on the silicon interface, even when the SiO₂ film was thinner than 100Å. One consideration here is that silicon atoms may be provided through the SiO₂ film from the silicon interface. This, however, is excluded because the nitridation process does not depend on SiO₂ film thickness on silicon.

Dielectric constant.—Figures 8 and 9 show the dependence of relative dielectric constants on nitridation time. Film thicknesses of SiO₂ before nitridation were 100 and 500Å, respectively. Dielectric constants in both figures, measured at a frequency of 1 MHz using aluminum gate MOS structures, increased along with the nitridation time. After 5 hr, the value was 30% larger than that of the SiO₂ shown in Fig. 8. Referring to a relative dielectric constant of CVD Si₃N₄ films (24) (5.8 ± 0.1 at 1 MHz), the nitrided SiO₂ film seems to have dielectric properties similar to those of Si₃N₄. In

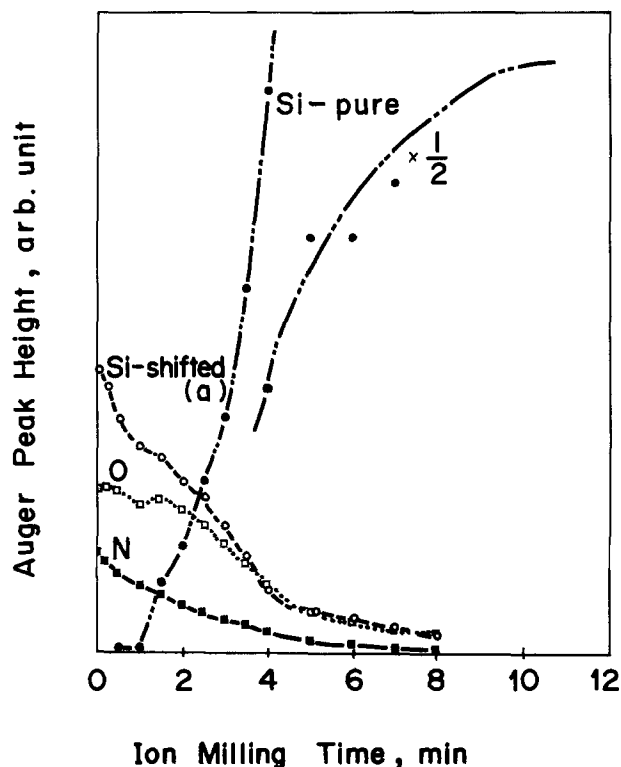


Fig. 7. Depth profiles of a 100Å thick SiO₂ film nitrided at 1200°C for 1 hr. Si-shifted (a) appeared at 78-83 eV.

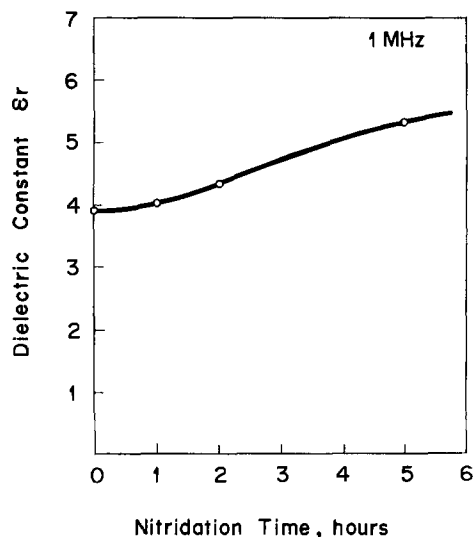


Fig. 8. Change in relative dielectric constant of a 100Å thick SiO₂ film nitrated at 1200°C, measured at a frequency of 1 MHz.

the case of the 500Å thick film shown in Fig. 9, the value was saturated after 1 hr of nitridation at both 1200°C (a) and 1000°C (b). This saturated value of 4.5, however, is 15% larger than that for the SiO₂ value. The difference between Fig. 8 and Fig. 9 is a result of the nitride fraction in SiO₂ films changing under those same nitridation conditions. The dependence on nitridation temperature is shown in Fig. 10, where 500Å thick SiO₂ films were employed. Nitridation of SiO₂ films apparently occurred at the relatively low temperature of 900°C which resulted in the 10% larger dielectric constant than for SiO₂.

Anti-oxidation masking.—Film thicknesses and refractive indexes of the samples after oxidation under various conditions are shown in Table I. All wafers were initially oxidized to produce an SiO₂ film thickness of 400Å having a refractive index of 1.45, sample A. Samples B and C were subjected to further oxidation in dry oxygen at 1150°C for 90 min and at 1200°C for 8 min, respectively. They yielded SiO₂ films which were 2200 and 850Å thick, respectively. When the wafer which was oxidized initially, sample D, was heated in anhydrous ammonia gas at 1200°C for 1 hr, the film thickness decreased by 10Å from the initial

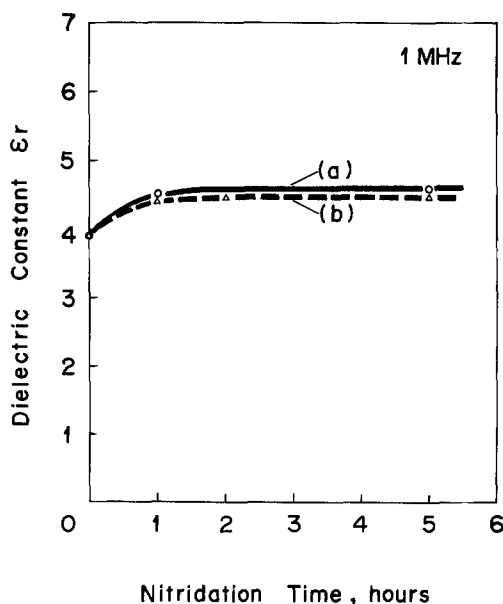


Fig. 9. Change in relative dielectric constant of 500Å thick SiO₂ films nitrated at 1200°C (a), and at 1000°C (b).

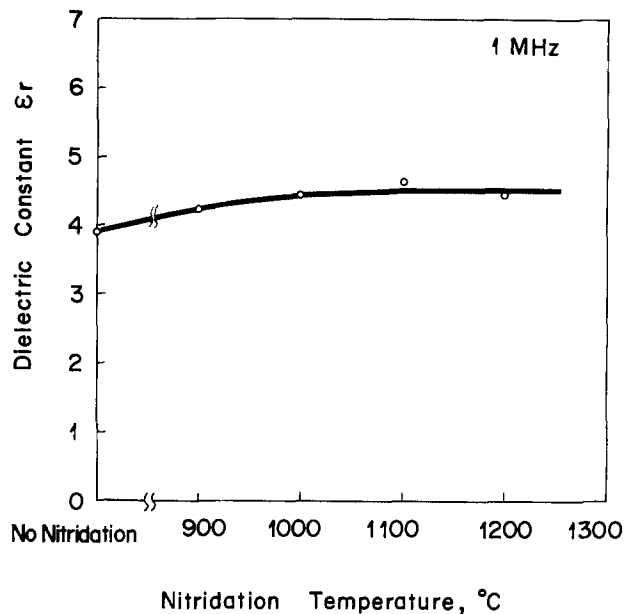
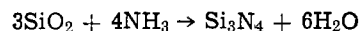


Fig. 10. Change in relative dielectric constant with respect to nitridation temperature of a 500Å thick SiO₂ film nitrated for 1 hr.

value and the refractive index increased to 1.57. This was due to direct conversion of SiO₂ to nitride which changed the film density. One nitrated SiO₂ film, sample E, was subjected to oxidation at 1150°C for 90 min, but the change was negligible. The composite of the nitrated surface region seems to approach that of SiO₂ in relation to the decrease in the refractive index. Further oxidation was performed on sample F at 1200°C for 8 min. The final thickness was not significantly changed from the initial value, and the film showed a masking effect against oxidation.

Discussion

The direct conversion of SiO₂ to nitride seems to obey the following reaction



Although the change in standard free energy is positive, it is small enough to allow the reaction to take place. It requires, for example, 54 kcal/mole at 1200°C. Direct reaction between SiO₂ and nitrogen is not practical because it requires a change in standard free energy of more than 400 kcal/mole even at 1200°C. Active hydrogen atoms generated at high temperatures from dissociative ammonia gas may play an important role in the above reaction; it is well known that hydrogen gas dissolves the Si-O bonds in SiO₂ at high temperatures. The active nitrogen atoms provided by ammonia gas surely react with free or unbonded silicon atoms while the dissociated oxygen atoms are eliminated from the surface as a volatile species. Anhydrous ammonia gas hardly provides any oxidant species to silicon substrates. Heating oxidized silicon wafers in ammonia gas, which generally contain some amount of water, is a wide-spread process in CVD of Si₃N₄ films. Some researchers have tried to heat

Table I. Effects of masking against oxidation with nitrated SiO₂ films

Sample	Wet oxidation, 1000°C, 27 min	Nitridation, 1200°C, 1 hr	Dry oxidation, 1150°C, 90 min	Dry oxidation, 1200°C, 8 min	d, Å	n
A	Yes	No	No	No	400	1.45
B	Yes	No	Yes	No	2200	1.45
C	Yes	No	No	Yes	850	1.45
D	Yes	Yes	No	No	390	1.57
E	Yes	Yes	Yes	No	427	1.50
F	Yes	Yes	Yes	Yes	439	1.49

oxidized silicon wafers in ammonia gas for other purposes (14, 25), but the direct conversion of SiO₂ to nitride was never pointed out in their reports. The chief reason for this difference would seem to be that the greater purity of ambient ammonia gas used here, anhydrous ammonia gas which was fully purified in a catalyzer, contributes to the conversion.

Silicon atoms are clearly provided by the dissociation of SiO₂ in relatively thick SiO₂ films. In SiO₂ films with a thickness of 100Å, for example, this is not the case. The lack of any decrease in oxygen atoms at a nitrated SiO₂ surface was shown in the AES profile in Fig. 7. Silicon atoms may be provided through the SiO₂ film from the silicon substrate. With SiO₂ films of any thickness of less than 100Å, it might become difficult to differentiate the direct thermal nitridation of SiO₂ films from that of silicon wafers. In any case, nitrated regions are formed predominantly at the surfaces of SiO₂ films. This process differs from nitride formation (15, 16) at Si-SiO₂ interfaces. As calculated with the refractive index of the nitrated sample shown in Fig. 2, the nitrogen fraction in a nitrated SiO₂ film with a thickness of about 100Å is about 50% on the average. The ratio was also deduced from the infrared spectrum shown in Fig. 4(b) and calibration data taken from CVD oxynitride films (26, 27). Reporting with ESCA data, Raider *et al.* asserted that homogeneous oxynitride films are composed of a range of species blended on a molecular scale and that they are not a mixture of silicon dioxide and silicon nitride (28). The composition of thermally nitrated regions on SiO₂ films is substantially oxynitride which surely cannot be a mixture.

Directly nitrated SiO₂ films exhibited strong masking effects against oxidation even at very high temperatures. They may be useful as diffusion masks against impurities, oxidation masks, and reaction barrier layers against unwanted material. A further advantage is that with nitrated SiO₂ films there is no interface region between the oxynitride and SiO₂ and there is a good interface with the silicon. This is because the films are chiefly thermally grown silicon dioxide. Although the microstructure of the films is not clear, stable thin insulator films with a higher density than SiO₂ might be formable. Nitrated surface regions might act as protective layers against contamination in device processes. Electrical characteristics of MOS structures with the nitrated SiO₂ films will be reported in the near future.

Conclusions

The direct thermal nitridation of SiO₂ films through heating oxidized silicon wafers in anhydrous ammonia gas has been found to be possible. The reaction is a direct conversion of SiO₂ to silicon nitride or oxynitride. At temperatures above 900°C, nitrated SiO₂ films have graded compositions with respect to their nitrogen fraction. A nitride fraction of about 50% was obtained at the SiO₂ surfaces. These surfaces exhibited remarkable masking effects against further oxidation at high temperatures. These films show great promise as thin protective layers against contamination and diffusion.

Acknowledgments

The authors wish to thank Drs. T. Misugi, Y. Fukukawa, and M. Shinoda for their encouragement through the course of this research.

Manuscript submitted Nov. 26, 1979; revised manuscript received ca. April 1, 1980.

Any discussion of this paper will appear in a Discussion Section to be published in the June 1981 JOURNAL. All discussions for the June 1981 Discussion Section should be submitted by Feb. 1, 1981.

Publication costs of this article were assisted by Fujitsu Laboratories Limited.

REFERENCES

1. V. Y. Doo, *IEEE Trans. Electron Devices*, **ed-13**, 561 (1966).
2. F. K. Heumann, D. M. Brown, and E. Mets, *This Journal*, **115**, 99 (1968).
3. N. C. Tombs and F. A. Sewell, *ibid.*, **115**, 101 (1968).
4. I. Franz and W. Langheinrich, *Solid State Electron.*, **14**, 499 (1971).
5. H. C. Pao and M. O'Connell, *Appl. Phys. Lett.*, **12**, 260 (1968).
6. D. Frohman-Bentchkowsky and M. Lenzlinger, *J. Appl. Phys.*, **40**, 3307 (1969).
7. J. R. Cricchi, J. E. Brewer, and D. W. Williams, *ISSCC Dig. Tech. Papers*, 204 (1974).
8. Y. Uchida, N. Endo, S. Sato, M. Konaka, I. Nojima, Y. Nishi, and K. Tamaru, *IEEE J. Solid-State Circuits*, **sc-10**, 288 (1975).
9. R. H. Dennard, F. H. Gaensslen, H. N. Yu, V. L. Rideout, E. Bassous, and A. R. LeBlanc, *IEEE J. Solid-State Circuits*, **sc-9**, 256 (1974).
10. L. A. Kasprzak, A. K. Gaid, and A. Hornung, *This Journal*, **124**, 1631 (1977).
11. P. K. Chaudhari, *ibid.*, **125**, 1657 (1978).
12. J. Liday, R. Harman, and M. Vesely, *Vacuum*, **27**, 129 (1978).
13. H. J. Stein, S. T. Picraux, and P. H. Holloway, *IEEE Trans. Electron Devices*, **ed-25**, 1008 (1978).
14. E. Kooi, J. G. vanLierop, and J. A. Appels, *This Journal*, **123**, 1117 (1976).
15. R. M. Barrer, *J. Chem. Soc.*, **136**, 378 (1934).
16. S. I. Raider, R. A. Gdula, and J. R. Petrak, *Appl. Phys. Lett.*, **27**, 150 (1975).
17. B. H. Vromen, *ibid.*, **27**, 152 (1975).
18. D. W. Hess and B. E. Deal, *ibid.*, **122**, 1123 (1975).
19. T. Ito, S. Hijiya, T. Nozaki, H. Arakawa, M. Shinoda, and Y. Fukukawa, *ibid.*, **125**, 448 (1978).
20. T. Ito, T. Nozaki, H. Arakawa, and M. Shinoda, *Appl. Phys. Lett.*, **32**, 330 (1978).
21. T. Ito, S. Hijiya, T. Nozaki, H. Arakawa, H. Ishikawa, and M. Shinoda, *IEEE Trans. Electron Devices*, **ed-26**, 906 (1979).
22. T. Ito, H. Arakawa, T. Nozaki, and H. Ishikawa, *This Journal*, To be published.
23. P. H. Holloway, *Surf. Sci.*, **54**, 506 (1976).
24. R. Hezel and E. W. Hean, *This Journal*, **125**, 1848 (1978).
25. S. P. Murarka, C. C. Chang, and A. C. Adams, *ibid.*, **126**, 996 (1979).
26. F. K. Heumann, D. M. Brown, and E. Mets, *ibid.*, **115**, 331 (1968).
27. E. A. Taft, *ibid.*, **118**, 1341 (1971).
28. S. I. Raider, R. Flitsch, J. A. Aboaf, and W. A. Pliskin, *ibid.*, **123**, 560 (1976).

The Effects of Abrasion Gettering on Silicon Material with Swirl Defects

C. L. Reed and K. M. Mar*

Motorola Incorporated, Semiconductor Research and Development Laboratories, Phoenix, Arizona 85008

ABSTRACT

The effects of back abrasion gettering on Si material with swirl defects were studied by the techniques of preferential etching and electrical characterization of p+n diodes. The damage layers were applied via lapping with particle slurries. Optical microscopy revealed the 0.5 μm lapping produces a polishing rather than an abrading effect. The etching results indicate that gettering with 2 and 15 μm abrasion reduces the etch pit density from 5×10^5 to $<5 \times 10^2/\text{cm}^2$. The electrical data shows a corresponding improvement: the I_R histograms of the gettered samples approach that of swirl-free material, and the wafer mapping of the diode reverse current I_R on the wafers indicates a definite positive effect of the gettering. Both the electrical and the etching results are interpreted with the current understanding of swirl defects, mass transport phenomena, and gettering action.

The first thermal process in the fabrication of Si devices is the growth of a masking oxide. With steam oxidation, swirl defects in the Si material can act as nucleation sites for the formation of oxidation-induced stacking faults, OISF (1, 2). It has been reported that these faults can cause a p-n junction's electrical characteristics to deviate considerably from the current-voltage curves of a defect-free diode (3). It is common practice to minimize a crystal defect's effect on device yield and performance by impurity gettering which aims to eliminate the species that act as nucleation centers for other defects, increase defect growth, and decorate existing defects. The trend of current thinking on gettering appears to emphasize the suppression of further nucleation rather than defect growth and/or decoration. Following this line of reasoning, an optimum time for a gettering step is before growth of the masking oxide, and this opinion is shared by the recent publications on the different preoxidation gettering techniques (4-10).

Pugh and Samuels (11) have studied in detail the defects that were produced by mechanical abrasion. During thermal annealing, dislocations will be generated in and propagated from the damage layer (12). These crystal defects are known to interact with impurities through the mechanisms of strain field interaction (13). Specific works on applying abrasion damage for impurity gettering to improve Si material quality have been reported (14-16). Mets (14) has observed that the combination of abrasion and thermal anneal can decrease the reverse current I_R of a p-n junction and that the generated dislocations were not annihilated after repetitive temperature cycles up to 1250°C. Pomerantz (15) and Rozgonyi *et al.* (16) have reported that preoxidation abrasion of the back-surface eliminated the epi faults that were nucleated by a defect in the substrate. This defect can be minimized by preoxidation gettering or abrasion of the back-surface of the wafer. In addition, Pomerantz indicated that effectiveness in reducing fault density depends somewhat on technique of damage layer application, viz., sandblasting, scribing, or lapping with Al_2O_3 grits of 1-50 μm particle size. However, the effect of abrasion gettering as indicated by the electrical characteristics of a p-n junction and preferential etching on material containing swirl type microdefects has not been reported.

For a gettering process in which the sinks, i.e., damage layer, is applied at room temperature, one ex-

pects an optimized process to include the following three steps: (i) applying the damage layer to the back of the wafer; (ii) annealing to generate and propagate dislocations which attract point defects through strain field interaction, then slow cool to allow precipitation at preferred sites in the damage layer; and (iii) removing the decorated damage layer to obviate the redistribution of the gettered species back into the active regions of the wafer. In this work, however, no specific anneal and damage layer removal steps were designed in the process because it was intended to serve as a base line. The results of this base line process as applied to material with a high density of swirl type microdefects are presented in this report.

Experimental

Starting material and damage application.—Small single ingots of silicon were chosen for this study to control the variation due to starting material. The selected crystals were grown from $\langle 111 \rangle$ oriented seeds and were phosphorus-doped to a nominal resistivity of 1-3 $\Omega\text{-cm}$. The growth technique for the swirled crystal was floated zone and that for the swirl-free material was Czochralski. Their crystal qualities were characterized by oxidizing polished wafers at 1150°C to activate the defects, subsequently Wright (17) etching to reveal the defects, and examining with an optical microscope to determine the defect density using the ASTM method (18).

Wafers were sliced from these ingots and shaped by the conventional processes to give specular, damage-free front surface and a chemically etched, strain-free back surface. The thickness of the wafers at this point was $305 \pm 13 \mu\text{m}$. Different degrees of back damage were applied by mechanically lapping the wafers with slurries that contained diamond particles with a mean size of 0.5 and 2.0 μm , and alumina particles of 15 μm . This lapping operation followed the established practice used in the wafer shaping operation. The topography of the damage layers were examined by optical microscopy.

Fabrication of test structure.—A square array of gated p+n diodes were fabricated by the ordinary processes for patterning and dopant deposition. A $4850 \pm 50\text{\AA}$ masking oxide was grown with pure steam at 1100°C. The wafers were pushed and pulled from the furnace at the rate of 12 in./min under O_2 . Boron diffusion was accomplished through a common two-step process using spin-on source containing B_2O_3 in a 2-methoxy-ethanol solution. The dopant deposition and redistribution temperatures were 960° and 1000°C, respectively. The resulting diffusion parameters in a

* Electrochemical Society Active Member.

Key words: back abrasion gettering, swirl defects, damage gettering, preoxidation gettering.

1-2 Ω -cm test wafer were 160 Ω /square and 0.4 μm . During this diffusion the back was also doped to a comparable sheet resistance. The ohmic contact pads consisted of 10 kÅ thick Al evaporated on unheated substrate.

Electrical testing data reduction.—All wafers were subjected to the same electrical testing procedures to obtain reverse bias characteristics of the diodes. In all measurements the gate was shunted to the base as shown in Fig. 1. To determine a suitable test voltage for measuring the reverse current, the mean avalanche voltage, \overline{BV}_R , was first established using the root mean square of the voltage readings at 10 mA. Then the diode distribution as a function of reverse current was determined for three test voltages of 0.1 \overline{BV}_R , 0.2 \overline{BV}_R , and 0.5 \overline{BV}_R . Initially these measurements were obtained manually on a 9 \times 9 matrix (every ninth column and row of devices) which represents about a 1% sampling. This data served to delineate the boundary conditions for automated testing and to provide a base for correlation with the values obtained from testing with a Fairchild Sentry VII. A graphic program was used to map the I_R data according to the device's position on the wafer and to group the I_R data into histograms.

Davies (19) test reveals the logarithmic nature of the I_R distribution; therefore, a geometric mean (20) of the reverse current for each group of wafers was calculated using the expression of

$$\bar{I}_R = \text{antilog} \sum_{i=1}^C \frac{n_i \log I_{Ri}}{N}$$

where n_i is the number of devices in leakage category i with leakage I_{Ri} , N is the total number of devices, and C is the number of categories in the histogram. This weighted mean was used as a figure of merit for each group, and detailed I - V curves were generated from devices whose I_R at 0.5 \overline{BV}_R were equal to the geometric mean.

Results and Discussion

Etch analyses of the substrate.—Figure 2 shows etched wafers with "swirl" that were nonabraded and with 2 and 15 μm abrasion. The nonabraded sample gave the characteristic milky appearance to the naked eye. The milky appearance is the result of light scattering by the many tiny etch figures. The wafer periphery displays the lowest density of etch figures and the core displays the highest density. This core pattern of swirl has a nearly uniform pit density. The pit sizes and the intensity of this milky appearance in the abraded samples are much smaller. The pit densities by the ASTM method are $5 \times 10^5/\text{cm}^2$ for the nonabraded wafers, $2 \times 10^2/\text{cm}^2$ for the 2 μm abraded, and $4 \times 10^2/\text{cm}^2$ for the 15 μm abraded sample. In comparison, the swirl-free ingot yields a pit density of $<50/\text{cm}^2$.

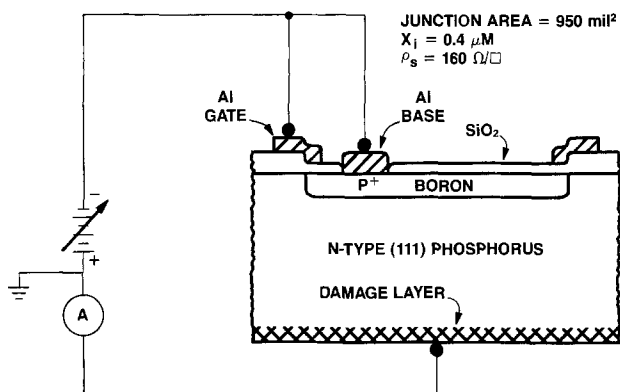


Fig. 1. Schematics of the measuring circuit and test structure

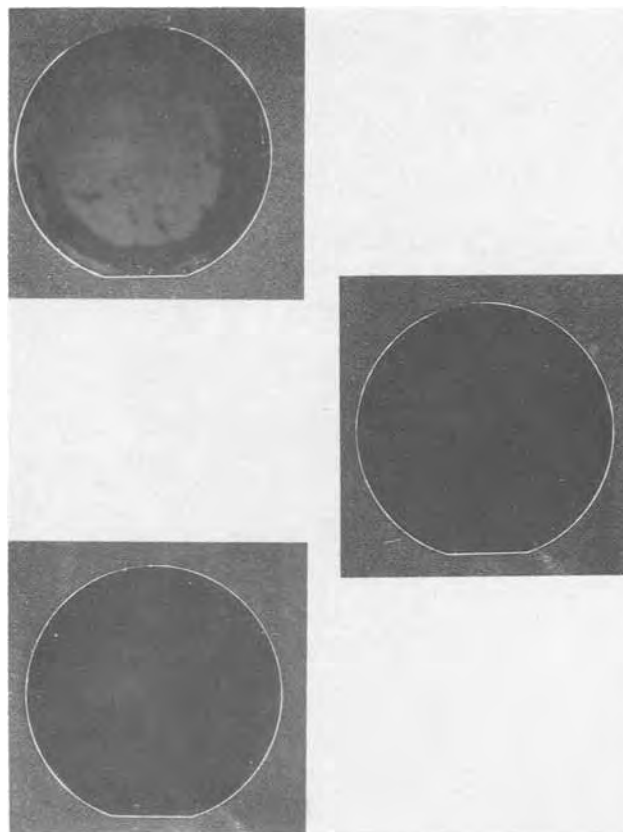


Fig. 2. Preferential etch decorated wafers that were gettered and ungettered. (a, top) is unabrased, (b, right) is 2 μm abraded, and (c, bottom) is 15 μm abraded.

A photomicrograph of the etch pits is shown in Fig. 3. This shallow etch pit morphology is the established characteristic for swirl defects (21). No characteristic etch figures for oxidation-induced stacking faults were observed after initial oxidation, or after diffusion in the region corresponding to the field oxide and the diffused regions of the device.

Damage layer characterization.—The topographies of the damage layers were examined optically before and after the growth of the masking oxide. The differences between the four groups are quite apparent to the naked eye and under a microscope. They are compared at 400 \times in Fig. 4. The nonabraded wafer shows an "orange peel" texture under Nomarski microscopy. In comparison, the 0.5 μm abraded wafer looks smoother to the naked eye and at 400 \times . This suggests that the 0.5 μm slurry served more to polish than to abrade the wafer. After the initial oxidation, optical microscopy revealed only slight remnants of the abrasion damage. Apparently, the growth of the masking oxide consumed most of the damage layer. Based on these observations and the preliminary electrical results showing marginal gettering effectiveness, this degree of abrasion damage was dropped from further consideration early in the study.

The topography of a 2 μm abrasion consists of scratches which are barely visible to the eye with oblique illumination, and the 15 μm abraded wafer exhibits a roughness which appears lusterless. Optical micrographs at 400 \times for the 2 μm scratches and the 15 μm roughness are shown in Fig. 4. The growth of 5 kÅ oxide produces no discernable difference in these topographies.

I_R histogram comparisons.—Figure 5 presents a comparison of the I_R histograms at $\frac{1}{2} \overline{BV}_R$ for the four groups of wafers. The vertical axis is the percent distribution of diodes in each I_R category and the horizontal axis represents the I_R categories in A/mil 2 .

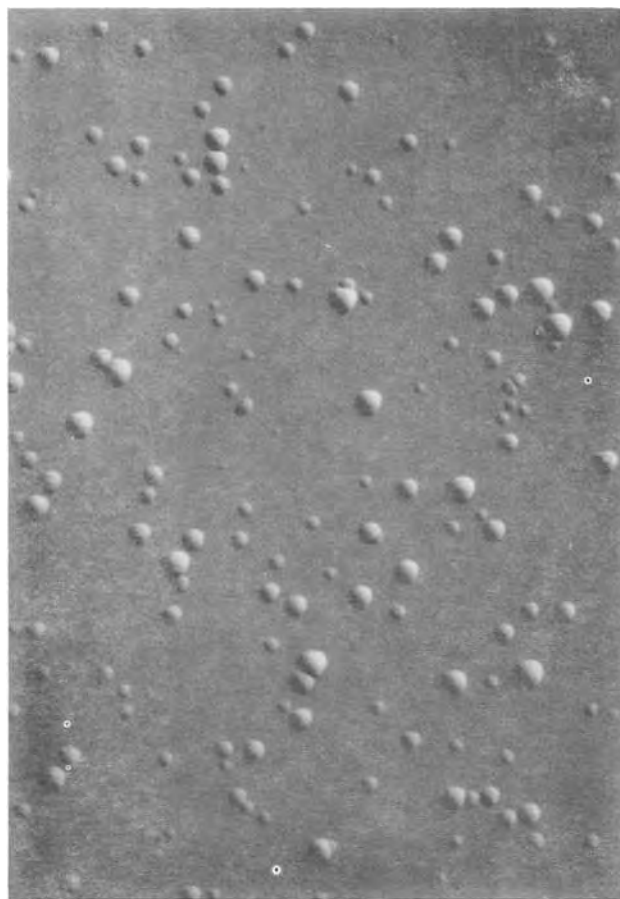


Fig. 3. Photomicrograph of the etch decorated surface of the ungettered wafer at $400\times$.

Each category is an order of magnitude wide except at the ends which include, respectively, all the diodes with $I_R \leq 10 \text{ pA/mil}^2$ and $> 10 \text{ } \mu\text{A/mil}^2$.

The top two patterns in Fig. 5 are typical cases for nonabraded swirl and swirl-free materials. This histogram for swirl-free material shows a strong skewing of the data into the lower I_R categories. In contrast, the pattern for swirl bearing material shows a broad or bimodal distribution. The bottom two histograms are for composite results of all wafers within each

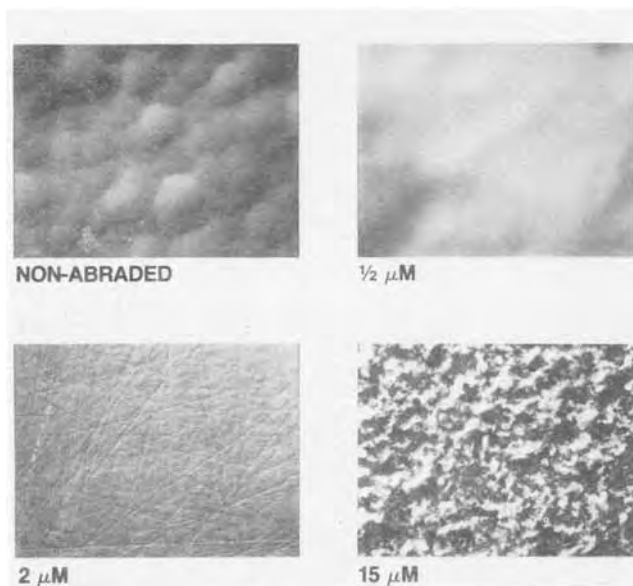


Fig. 4. Topographies of the nonabraded and abraded back surfaces at $400\times$.

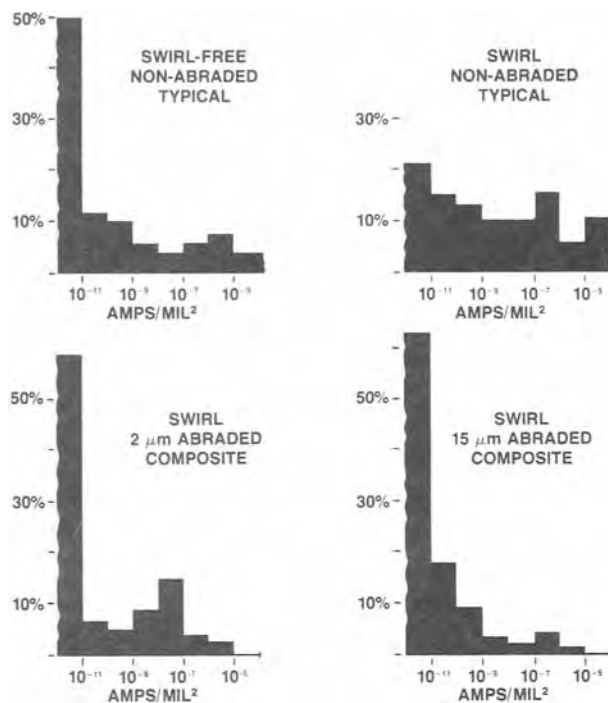


Fig. 5. I_R histograms at $V_R = 0.5 \overline{BV}_R$

abraded group. They also show skewing of the data into the lower I_R categories, and are comparable to the swirl-free case.

I_R mapping comparisons.—The mapping of I_R 's on their respective locations in a wafer provides a positional correlation between material and device qualities. Such a correlation is shown in Fig. 6 for the non-abraded and the abraded swirl groups. In each group the median quality wafer is presented. The cross hatched and the clear areas represent, respectively, the devices whose I_R 's are $\leq 10 \text{ pA/mil}^2$ and $> 10 \text{ pA/mil}^2$ at $\frac{1}{2} \overline{BV}_R$. The top left photograph shows the core pattern of swirl which represents $> 2/3$ of the wafer map diameter. The central region of the two abraded wafers show a higher density of low leakage devices than that of the nonabraded wafer. The densities of the two abraded wafers are too close to differentiate. These comparisons demonstrate the positive effect of abrasion gettering on the swirl defects.

I_R - V_R characterizations.— I_R histograms and wafer maps reflect the mean quality of the material, but

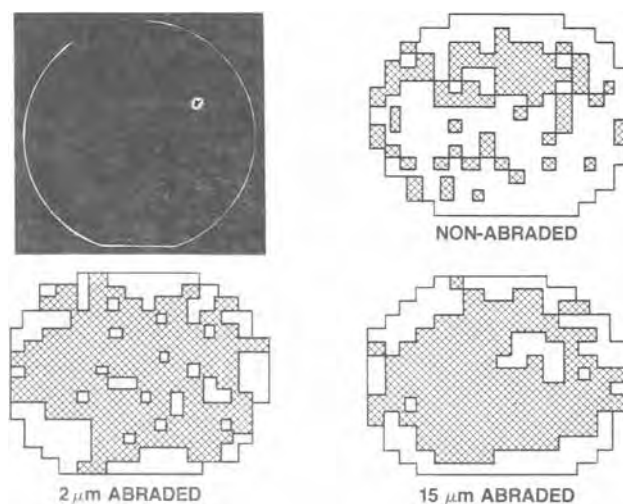


Fig. 6. I_R mappings of the gettered and ungettered swirl samples in comparison with the swirl pattern. The cross-hatched area contains devices whose I_R 's $\leq 10 \text{ pA/mil}^2$.

they do not offer information on how the gettering benefit was derived. A substantial portion of this information can be obtained from the analyses of I_R-V_R curves. In Fig. 7, schematic I_R-V_R curves of an ideal, defect-free, and a single dominating defect affected diode (3, 22-24) are compared. These curves are drawn to reflect only the general shape but not the actual magnitude of the current. A total of four linear regions between these curves are distinguishable through their associated slopes. The truly interesting differences between these curves lie in the voltage range of $> kt/q$ and $< BV_R$, where k is the Boltzmann's constant, T is temperature in degrees Kelvin, and q is the electronic charge. In this voltage range, the curve for ideal diode has a zero slope, for defect-free diode has a slope < 1 (0.33-0.5), and for defect affected diode has two linear regions whose slopes are < 1 (region II) and > 1 (region III).

Since the material and the fabrication processes of this work were controlled, I_R in region II can be assumed to reflect the concentration of the deep level traps in the depletion region of the junction (23). The possible candidates for these traps include point defects such as metallic impurities. The excess I_R in region III is caused by the precipitation of metallic impurities around a defect in the crystal lattice (3, 22-24).

The I_R-V_R curves of "typical" diodes for the four groups are given in Fig. 8, and a "typical" diode for this work is defined as the device whose I_R at $\frac{1}{2} BV_R$ is equal to the geometric mean of the I_R distribution. The actual measurements covered the voltage range from 10 mV to avalanche; however, only the regions of particular interest are shown in Fig. 8. The dashed line on the far right marks the avalanche voltage, and the other dashed line approximately designates the $\frac{1}{2} BV_R$ value.

Even though the curves in Fig. 8 are not clearly segmented, the drastic increase in slopes is apparent. It is reasonable to assume that 0.1V, which is $> kT/q$ (0.026V for 300°C), and 20V, which is $< BV_R$, are well into regions II and III, respectively. The correspond-

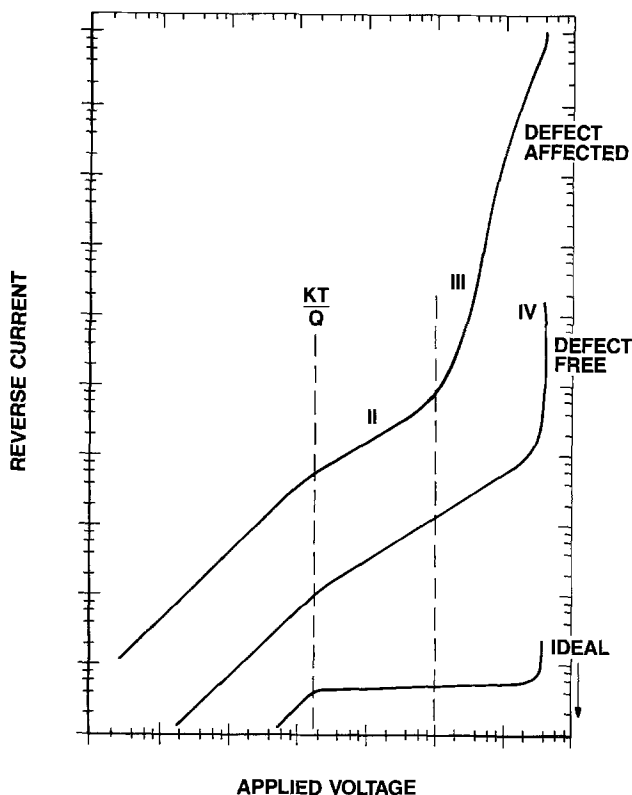


Fig. 7. Schematics of I_R-V_R curves for ideal, defect-free, and defect-affected diode.

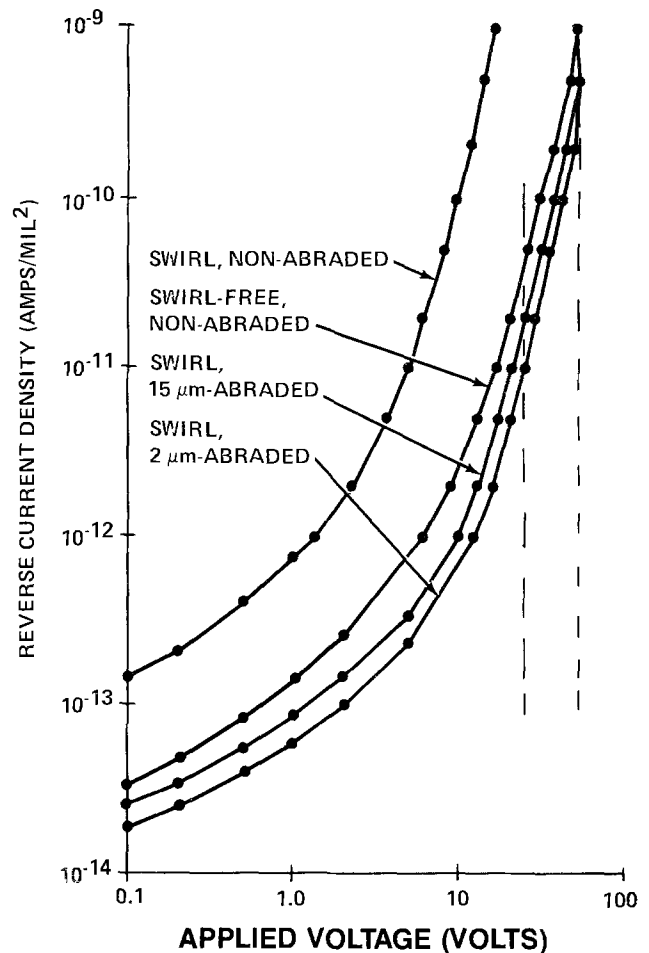


Fig. 8. I_R-V_R curves of "typical" diodes from the nonabraded and nonabraded swirl-free wafers.

ing differences in I_R 's for the gettered and ungettered swirl material are approximately one and two orders of magnitude for the two respective voltages. The differences between the two abraded groups and the nonabraded swirl-free group is too small to be definite. These trends are further confirmed by the \bar{I}_R-V_R curves in Fig. 9. As previously discussed, the I_R 's in

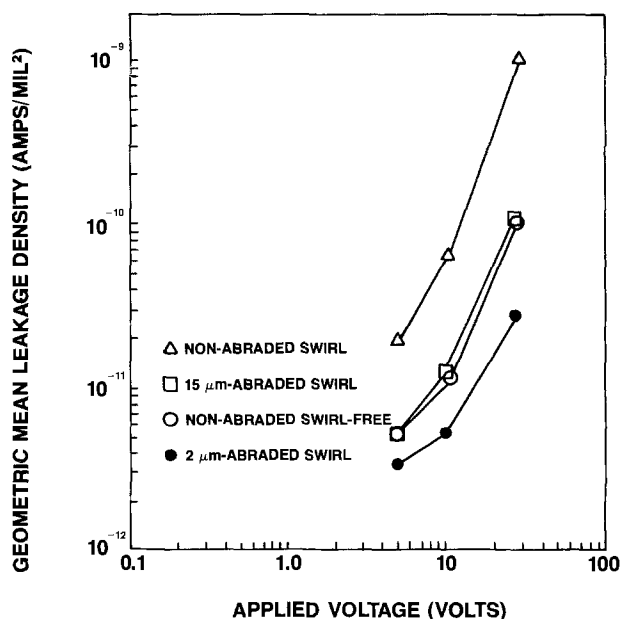


Fig. 9. $\bar{I}_R (V_R)$ plots of nonabraded and abraded swirl and non-abraded swirl-free wafers.

regions II and III are related to the metallic impurities. Therefore, a logical implication of these results is that a substantial portion of the gettering benefit was derived from the reduction of metallic impurities in the depletion region of the device.

Defect model interpretation of results.—The experimental data points toward two prominent results: the reduction of etch pit density and the decreasing magnitude of I_R which is interpreted as a reduction in metallic impurities. Preferential etching, as applied here, delineates strain field differential in the Si lattice, and its sensitivity is limited by the etchant's reactivity. The reduction of density and size of the etch pits is commonly interpreted as a reduction in density and size of the corresponding defects in Si.

The reported physical models of swirl defects are complexes of impurities (carbon and oxygen) and intrinsic point defects (25, 26) (Si interstitial and vacancy). Since Si is the host lattice, it is logical to assume that the size of the swirl defects is dominated by the component of the intrinsic point defect. The associated strain field of the defects would attract metallic impurities (extrinsic point defect), and consequently the swirl defects become impurity decorated.

In light of these defect models, the experimental results suggest that the damage layer and its thermally generated defects act as diffusion sinks for the fast diffusing point defects (27, 28). These enhanced solubilities (29) for the point defects in the damage region create concentration gradients in the nondamage region of the Si wafer. In turn, the concentration gradients act as the driving forces for the redistribution of these point defects.

After these gettering actions, the original defect nuclei of C-, O- intrinsic defect associates probably remain because, for the thermal temperature and time of this work, the diffusion lengths of C and O are insignificant in comparison to the fast diffusing species (30). However, the defect can become smaller in size and less decorated with impurities. This decrease in size explains the observed reductions of etch pit density and size in the preferential etching study.

Summary and Conclusions

The effects of back abrasion damage gettering on Si material with heavy swirl defect concentration were studied by the techniques of preferential etching and electrical characterization of p^+n diodes. The damage layers were applied via lapping the conventionally shaped wafer with slurries whose mean particle sizes were 0.5, 2, and 15 μm . Optical microscopy of the damage layers indicated that the 0.5 μm lapping produced a polishing rather than an abrasion effect. In addition, preliminary electrical results indicated that it produces no definite improvement in the diode distribution as a function of I_R .

The etching studies revealed that gettering with the 2 and 15 μm abrasion can reduce the etch pit density by 3 orders of magnitude from 5×10^5 to $<5 \times 10^2/\text{cm}^2$. This observation resulted more from a defect size than an actual defect density reduction. OISF's were not detected in any experimental or test wafers.

A corresponding improvement was observed in the statistical data of I_R histograms and maps of the p^+n diodes. This improvement, as inferred from I_R - V_R analysis of the "typical" devices, likely resulted from the reduction of metallic impurities within the active region of the device. Both of the electrical and etch results can be explained by the current understanding of swirl defects, mass transport phenomena, and gettering action.

In conclusion, this "base line" oriented back abrasion gettering process was able to improve the quality of material with a high swirl density to approach that of swirl-free.

Acknowledgments

The authors wish to express appreciation to Lee Campbell for application of different degrees of back

damage to the wafers, Vaughn Akins for use of his electrical test facility, Charles Varker for many helpful discussions, and Beth Gersitz for careful typing of the manuscript.

Manuscript submitted April 9, 1979; revised manuscript received Sept. 24, 1979. This was Paper 288 presented at the Seattle, Washington, Meeting of the Society, May 21-26, 1978.

Any discussion of this paper will appear in a Discussion Section to be published in the June 1981 JOURNAL. All discussions for the June 1981 Discussion Section should be submitted by Feb. 1, 1981.

Publication costs of this article were assisted by Motorola Incorporated.

REFERENCES

1. A. J. R. de Kock, *Philips Res. Rep. Suppl.* 1 (1973).
2. K. V. Ravi and C. J. Varker, *J. Appl. Phys.* **45**, 263 (1974).
3. C. J. Varker and K. V. Ravi, *ibid.*, **45**, 272 (1974).
4. G. A. Rozgonyi, Paper 59 presented at The Electrochemical Society Meeting, Washington, D.C., May 2-7, 1976.
5. G. A. Rozgonyi, P. M. Petroff, and M. H. Read, *This Journal*, **122**, 1725 (1975).
6. P. M. Petroff, G. A. Rozgonyi, and T. T. Sheng, *ibid.*, **123**, 565 (1976).
7. G. A. Rozgonyi and R. A. Kushner, *ibid.*, **123**, 570 (1976).
8. T. Y. Tan, E. E. Gardner, and W. K. Tice, *Appl. Phys. Lett.*, **33**, 175 (1977).
9. G. A. Rozgonyi and C. W. Pearce, Paper 335 presented at The Electrochemical Society Meeting, Atlanta, Georgia, Oct. 9-14, 1977.
10. G. H. Schwuttke and K. H. Yang, ARPA Contract No. DAHC 15-72-C-274, Technical Report No. 7, Part II (March 1976).
11. E. N. Pugh and L. E. Samuels *This Journal*, **111**, 1429 (1964).
12. R. Stickler and G. R. Booker, *ibid.*, **109**, 743 (1962).
13. R. Bullough and R. C. Newman, in "Progress in Semiconductors", Vol. 7, A. F. Gibson and R. E. Burgess, Editors, pp. 100-134, John Wiley & Sons Inc., New York (1963).
14. E. J. Mets, *The Journal*, **112**, 420 (1965).
15. D. Pomerantz, *J. Appl. Phys.*, **38**, 5020 (1967).
16. G. A. Rozgonyi, R. P. Deysher, and C. W. Pearce, *This Journal*, **123**, 1910 (1976).
17. M. W. Jenkins, *ibid.*, **124**, 757 (1977).
18. Annual Book of ASTM Standards, Part 8, Designation F47-70.
19. R. Langley, "Practical Statistics Simply Explained", pp. 71-88, Dover Publications, Inc., New York (1971).
20. P. T. Squire, *Am. J. Phys.*, **45** 1094 (1977).
21. K. V. Ravi and C. J. Varker, "Semiconductor Silicon 1973," H. R. Huff and R. R. Burgess, Editors, pp. 136, The Electrochemical Society Softbound Proceedings Series, Princeton, N.J. (1973).
22. A. S. Grove, "Phys. and Tech. of Semiconductor Devices," pp. 127-180, John Wiley and Sons, Inc., New York (1967).
23. A. Goetzberger and W. Shockley, *J. Appl. Phys.*, **31**, 1821 (1961).
24. H. H. Busta and H. A. Waggner, *The Journal*, **124**, 1424 (1977).
25. H. Foll, U. Gosele, and B. O. Koblesen, "Semiconductor Silicon 1977," H. R. Huff and E. Sirtl, Editors, pp. 366, The Electrochemical Society Softbound Proceedings Series, Princeton, N.J. (1977).
26. A. J. R. de Kock, *Appl. Phys. Lett.*, **16**, 100 (1970); *This Journal*, **118**, 1851 (1971).
27. S. M. Hu, "Atomic Diffusion in Semiconductors," D. Shaw, Editor, Chap. 5, Plenum Publishing Corp., London (1972).
28. G. J. Sprokel, *This Journal*, **112**, 807 (1965).
29. S. Kastner and J. Hesse, *Phys. Status Solidi A*, **25**, 261 (1974).
30. Research Triangle Institute, Technical Documentary Report No. ASD-TDR-63-316, Vol. IV (1964).

The Photocorrosion of N-Cadmium Telluride and Its Suppression

J. S. Curran¹

Commission of the European Communities, Joint Research Centre,
Ispira Establishment, 21020 Ispira (Varese), Italy

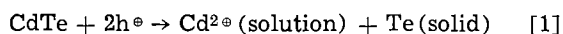
ABSTRACT

The photoelectrochemical properties of n-type cadmium telluride were studied in water and five other organic solvents, with a view to suppression of the photocorrosion reaction which prevents this and other n-type small bandgap semiconductors from being used in a practical semiconductor-electrolyte junction solar cell. Only the low donicity organic solvents propylene carbonate and methyl nitrate reduce the corrosion rate significantly. A stable photocurrent can be obtained using a solution of ferrocene in these two solvents but analysis of photoelectrolyzed solutions revealed a slow photocorrosion. The dependence of the flatband potential and of the photocorrosion kinetics on the solvent is discussed, and the practical significance with respect to solar cell applications considered.

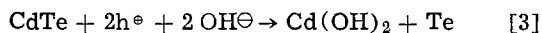
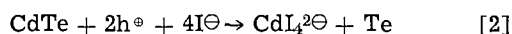
The current upsurge of interest in the behavior of the semiconductor-electrolyte interface reflects its possible application in the field of solar energy conversion, as recent review papers have stressed (1, 2). A major technical difficulty which must be overcome before any such application can be considered realistic is the persistent tendency for the small bandgap semiconductors (*i.e.*, those of interest for solar energy conversion) to undergo photocorrosion reactions, leading to the destruction of the electrode. This remains a fundamental obstacle whether the cell is regenerative or is designed to produce a fuel, and is exacerbated if the photoelectrode takes the form of a thin film. Any photocorrosion current flowing simultaneously with the current supporting the cell process must be extremely small if the cell is to operate over a period of years.

N-cadmium telluride typifies this problem; the only electrolyte which has so far been shown to stabilize this material contains toxic, colored, and air-sensitive polytelluride and telluride ions (3). Hence n-cadmium telluride was chosen as a basis for discussion of the general problem and as a model material to investigate experimentally the stabilizing ability of various organic solutions.

For n-type compound semiconductors the basic photocorrosion process in indifferent electrolyte is the dissolution of the more electropositive component; for n-cadmium telluride



If species are present in solution which are active towards cadmium (or tellurium) the reaction may be modified, *e.g.*,



The overall free energy change is more negative in reactions [2] and [3]. Furthermore, if the active species participates in the rate-determining step of the electrode kinetics then the corrosion will be accelerated.

For a stable regenerative cell there must be a successful competition with such corrosion reactions by a reversible redox reaction



Clearly reactions of type [2] and [3] should be avoided, but an anion which can promote reaction [2] may instead perform a redox reaction, as is reported to be the case for iodide ion in acetonitrile at illuminated cadmium sulfide (4).

Since the intermediates and the final product of the corrosion process are stabilized by partial or complete solvation, the solvent itself can influence the rate of this process. The influence of a change of solvent on the overall free energy change for process [1] is calculable from the free energy of transfer of the single metal ion. This, in turn, is calculable from electrochemical potential measurements under an extrathermodynamic assumption such as the TATB assumption (5).

Using such data it is not difficult to find a solvent which makes the overall thermodynamics of reaction [1] less favorable by up to 100 kJ/g ion (1 eV). There are, however, additional factors to consider, the first being that the solvent must dissolve sufficient inert salt to furnish a high conductivity. This requirement excludes very poor solvents of metal ions, restricting the choice to a very few organic solvents which have been used in electrochemical studies. Even a conductivity of $5 \times 10^{-3} \Omega^{-1} \text{cm}^{-1}$, regarded as "high" for an organic electrolyte, would lead to a substantial ohmic loss within a solar cell unless the electrolyte layer were very thin.

In this work the Gutmann Donicity Number was used as a guide to the choice of solvent. This empirical parameter correlates well with both thermodynamic and kinetic constants for solvent-related processes (6). A low donicity number indicates poor cation solvation. The five solvents used in this work were chosen to see if there is a correlation between corrosion rate and donicity number.

The redox system must be very soluble, stable chemically in both oxidation states, absorb little visible light, and possess a redox potential between the bandedges of the small bandgap semiconductors (1, 2), *i.e.*, not far from the potential of the standard calomel electrode. This makes for an extremely restricted choice once more. The only class of compounds which may be able to meet all these demands is that of the substituted ferrocenes, which have already been used successfully to prevent corrosion (7, 8).

In this investigation ferrocene ($E_0 = 0.37(\text{SCE})$, $k_0 = 0.7 \text{ cm sec}^{-1}$) (9) and iodide ion were used, the latter because of its reported ability to stabilize cadmium sulfide in acetonitrile (4).

¹ Present address: Laboratoire de Chimie, 69130 Ecully, France.
Key words: organic, electrolyte, semiconductor, stabilization, photoelectrochemistry.

Experimental

Single crystal slices of n-doped ($1.2 \times 10^{17} \text{ cm}^{-3}$) CdTe, already ohmically contacted on the back surface were obtained from Battelle Laboratory, Frankfurt. An additional thick gold layer was sputtered over the contacting film and a wire attached by silver epoxy. The whole was then sealed in a robust plexiglass or glass support with epoxy resin. This assembly was incorporated in a one-compartment sandwich cell, volume 2 ml, with a platinum grid counterelectrode behind a window.

Silicon rubber sealing rings were used. The reference electrode was always Ag/0.01M Ag⁺ and took the form of a Luggin capillary close to the photoelectrode. The reference electrode solution was normally made by *in situ* electrolysis of the silver wire in backing electrolyte.

Photoelectrochemical experiments with organic electrolytes were performed entirely inside a glove box flushed with dry nitrogen. Illumination was provided by a 500W high pressure xenon lamp in conjunction with filter solutions and a Spex monochromator.

Standard electrochemical apparatus supplied by Hi-Tek was employed in conjunction with a Hewlett-Packard 7045 A X-Y recorder. Because of the difficulty of making differential capacity measurements at high enough frequency to avoid the surface state capacity (10 kHz) in relatively poorly conducting organic electrolytes, Mott-Schottky plots were not used to measure the flatband potential (V_{FB}). Instead the method suggested by Butler was employed (10) which although it rests on some approximations is at least as reliable as the above alternative in this context.

The semiconductor electrode was polished with alumina down to 0.05 μm and then etched with a recommended solution (11) before each measurement. Chemicals used were all from commercial sources and were of reagent grade or better. Organic solvents and backing electrolytes were purified and dried according to procedures described in a comprehensive review (12).

For each solvent-solute combination the same procedure was followed. First an anodic potentiostatic scan was made, low intensity monochromatic light pulses being applied to obtain data for V_{FB} estimation. Thereby even in the presence of photocorrosion the total charge passed was low enough ($<10^{-3}\text{C}$) to obtain reproducible data. Then a higher photocurrent ($\approx 1 \text{ mA}_{\text{cm}^{-2}}$) was passed under potentiostatic conditions and its decay with time (if any) followed. Finally, the CdTe electrode was removed and examined microscopically.

A more sensitive technique was used to detect small amounts of photocorrosion, atomic absorption analysis of resulting solutions for cadmium (13). Having passed some coulombs of photocurrent under potentiostatic control the resulting solution was wet-ashed and analyzed by standard techniques using a Perkin Elmer 5000 atomic absorption spectrophotometer.

Results

A survey of solvent-redox combinations to determine V_{FB} and stability under illumination is summarized in Table I. Figure 1 illustrates a typical i - V plot, and a corresponding i_p^2 - V plot is given in Fig. 2. The intercept of this plot on the voltage axis gives an estimate of V_{FB} (10). Figure 3 illustrates the photocurrent-voltage behavior in the absence of any redox system, when only the pure photocorrosion process is occurring.

Ferrocene was found to have a strong stabilizing effect in both propylene carbonate (PC) and methyl nitrate (MN). This finding was further investigated in an experiment similar to Wrighton's (14). The solution undergoing controlled potential electrolysis was pumped through an optical cell and the absorp-

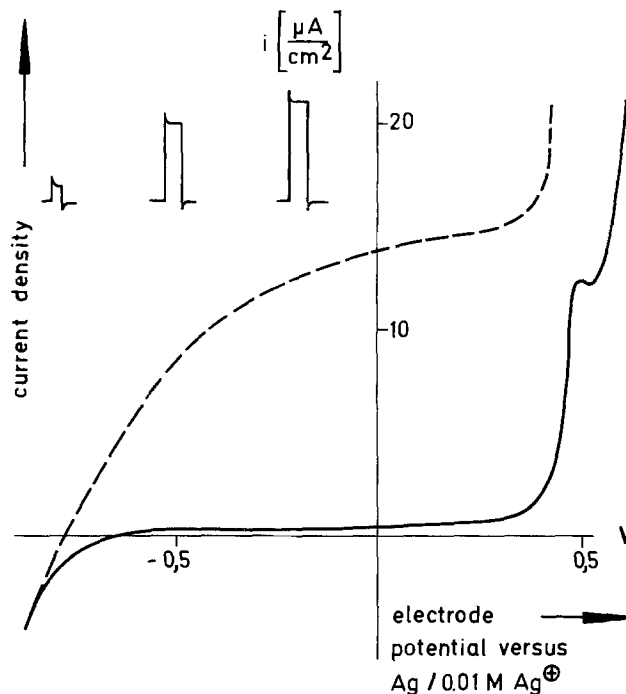


Fig. 1. Potentiostatic current-voltage plot for n-cadmium telluride in contact with methyl nitrate/0.1M $\text{Mg}(\text{ClO}_4)_2$ /0.1M ferrocene solution. Voltage scan rate 10 mV sec^{-1} . Solid curve in darkness, dashed curve under weak monochromatic illumination, 650-750 nm. Reference electrode Ag/0.01M AgClO₄. Insets illustrate transient behavior.

tion spectrum monitored. The optical density at 615 nm, a peak diagnostic of ferricinium ion (15) increased linearly with charge passed, confirming that the major product of photoelectrolysis was this ion.

The atomic absorption analysis technique was used to determine quantitatively the extent of corrosion suppression in MN and PC. The results are displayed in Table II. In these experiments the counterelectrode is able to remove some dissolved cadmium ion (it is very difficult to design a cell which avoids this) but a simple calculation shows the resulting underestimation of the photocorrosion is small. These measurements revealed that the qualitatively encouraging results of the earlier experiments in Table I were misleading and that considerable photocorrosion occurs. The corrosion rate appears to depend on the exact condition of the electrode surface, and is not reproducible.

The results for PC, in which ferrocene (saturated) has a low diffusion limited current (measured at a platinum electrode) show that as could be expected, the corrosion rate increases as the photocurrent approaches this value.

Some experiments were made with "as received" MN and PC/ferrocene solutions containing undried magnesium perchlorate, and also with electrolytes deliberately contaminated with a few percent water. Photocorrosion was increased in these solutions, but only slightly in the case of propylene carbonate.

In both MN and PC/ferrocene solutions with 1M tertiary butyl ammonium iodide as backing electrolyte photocorrosion occurs, though in PC the principal product of photoelectrolysis is evidently ferricinium ion, whose presence is easily observed because of its greenish color.

Discussion

An account of the photocorrosion process would be oversimplified if some attention were not paid to the kinetic complexity necessarily implied in a multi-electron process (16). Since a simultaneous two-electron process is unlikely because of the low density

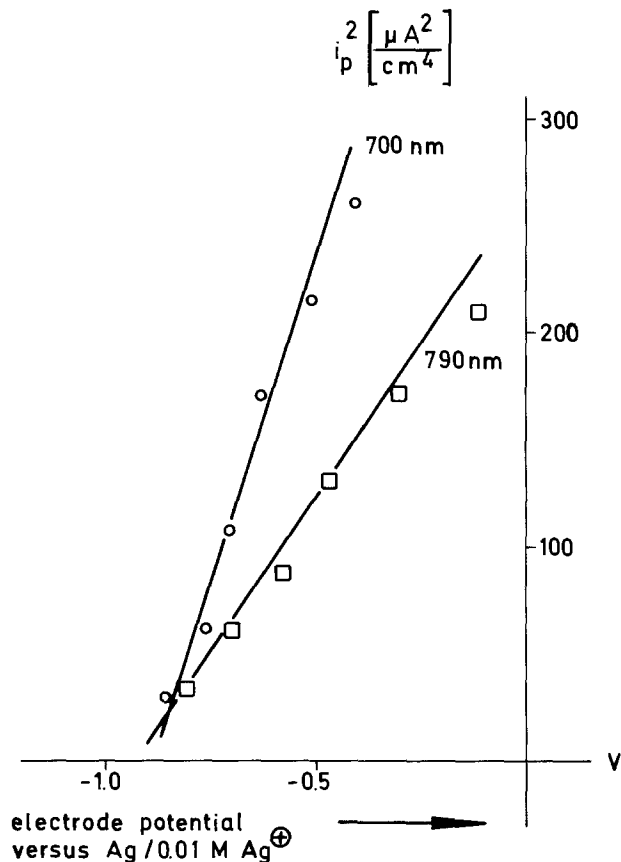


Fig. 2. Plot of photocurrent squared vs. voltage under potentiostatic conditions for n-cadmium telluride in contact with propylene carbonate/0.5M Mg(ClO₄)₂/0.05M ferrocene solution. Illumination 696-710 nm (○) and 780-800 nm (□). Reference electrode Ag/0.01M AgClO₄.

of states of holes at the surface under normal illumination at least one reaction intermediate is implied. The simplest representation is as follows

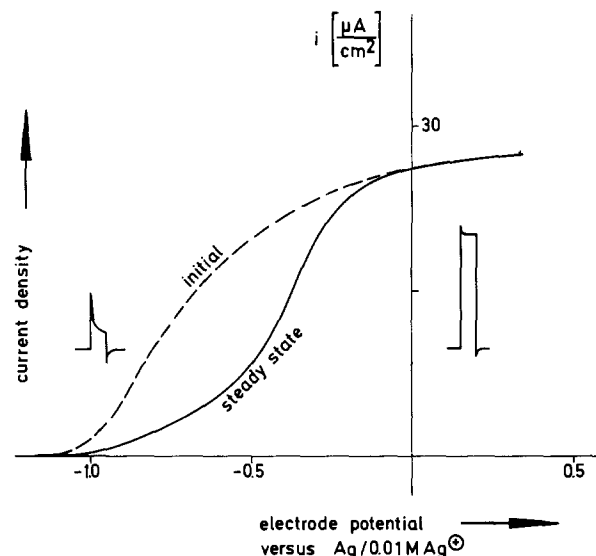
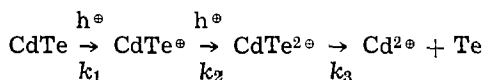


Fig. 3. Potentiostatic current-voltage plot for n-cadmium telluride in contact with propylene carbonate/0.1M Mg(ClO₄)₂ under weak pulsed illumination. Voltage scan rate 10 mV sec⁻¹, reference electrode Ag/0.01M AgClO₄.

The final step *k*₃ is only a rapid diffusional process if the bonding arrangement of the overall reaction is already complete; here it is assumed it may be a slow step.

If at potentials close to the flatband potential conduction band electrons can reach the surface and reduce the intermediates, then they act as recombination centers. Similarly at positive potentials it is possible for *k*₂ to be a conduction band (current doubling) process.

In the presence of a redox system the reduced species may be oxidized in principle by a hole at the valence bandedge or by any of the successive intermediates (17)

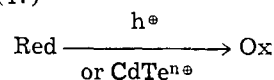


Table I. Flatband potentials and stabilities under illumination of n-cadmium telluride in various solutions

Solvent	PY	MeOH	H ₂ O	AN	PC	MN
Donicity No.	33	30	33	14.1	15.1	2.7
V _{FB} vs. NHE	0.0 (-0.70)	-0.10 (-0.10)	-0.50 (-1.30)	-0.25 (-0.85)	0.0 (-0.4)	0.10 (-0.50)
Redox stabilization						
Ferrocene	0	0	Insoluble	0	Stable	Stable
NaI	0	0	0	0	0	Insoluble
t _{Bu} ₄ N ⁺	0	0	0	0	Low	Low
Remarks	Ferrocene very soluble		Corrosion quite slow in 1M NaClO ₄ FE ^{II} soln		Low ferrocene solubility	Explosive dangerous vapor

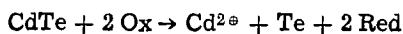
Py = pyridine/1M LiClO₄, MeOH = methanol/t_{Bu}₄ NClO₄, H₂O = aqueous/1M Na₂SO₄, AN = acetonitrile/1M LiClO₄, PC = propylene carbonate 0.5M Mg(ClO₄)₂, MN = methyl nitrate/0.1M Mg(ClO₄)₂. Tertiary butyl ammonium iodide also used as backing electrolyte. V_{FB} in brackets in the presence of approx. 1M iodide ion.

Solutions without iodide ion were saturated with ferrocene. Donicity numbers are from Ref. (6). A zero under the redox stabilization heading indicates that photocorrosion is the predominant process.

Table II. Photocorrosion current ratios in ferrocene solutions estimated by atomic absorption analysis. n-Cadmium telluride electrode maintained potentiostatically at -0.35V (0.01M Ag⁺/Ag)

Solvent	PC	PC	PC	PC	Wet PC	MN	MN
Average photocurrent (mA cm ⁻²)	0.1	0.5	0.5	2.0	0.3	1.1	0.8
<i>i</i> (corrosion)							
<i>i</i> (total)	0.015	0.03	0.007	0.08	0.03	0.003	0.0003
Remarks							
Diffusion-limited current			Polished electrode Approx. 1 mA cm ⁻²			Approx. 10 mA cm ⁻¹	

Then the species Ox may be capable of the overall chemical interfacial reaction



or only of performing one of the oxidation steps. Ferricium ion (made by electrolysis of ferrocene solution) and iodine solutions in PC and MN left in contact with CdTe do not discernibly chemically oxidize it on the time scale of these experiments. Thus the corrosion processes observed at the illuminated electrode are due to holes in the first instance; the possibility that Ox performs only one of the oxidation steps is not ruled out.

Noticeably different forms of photocurrent-voltage plots are obtained in blank PC and MN electrolytes (Fig. 3) and when either iodide ion or ferrocene are present (Fig. 1). In the latter case, despite the fact that iodide ion does not strongly stabilize the photoelectrode while ferrocene does, the plot takes the form indicated for a system in which minority carrier generation is the rate-determining step (10) and good i_p^2 -V plots can be obtained. In the former the steady-state quantum efficiency is decreased in the negative potential range, and a complex transient behavior appears. Nevertheless, the initial photocurrent (the peak of the photocurrent when a light pulse is applied) depends on the voltage in the same general way as above; $i_p^2(\text{peak})$ -V plots are good.

These facts are consistent with the explanation that the complex photocorrosion process leads to relatively slow charge transfer kinetics. The addition of iodide ion, which is probably adsorbed at the interface (see below) and which may form complexes with cadmium (18) accelerates the kinetics. The addition of ferrocene also accelerates the charge transfer kinetics, but this time by providing a rapid alternative route to the photocorrosion, hence suppressing the corrosion, but not completely. Recent calculations (19) show that slow charge transfer kinetics do indeed lead to the kind of curves illustrated in Fig. 3 under steady-state illumination. This analysis can in principle be extended to cases where some transient behavior is observed, as in Fig. 3, if it is assumed that the experimental system is able to accurately represent the initial photocurrent. When interfacial kinetic complications or recombination (or both) are important this initial current is partly nonfaradaic, but its value in the instant following the application of the light beam is nevertheless that of the hole flux initially reaching the surface. This in turn, under the appropriate conditions obeys the i_p^2 -V relation (10). The results for n-CdTe in the low donicity electrolytes MN and PC typified by Fig. 3 can be interpreted in this way.

The flatband potentials listed in Table I do not depend on such an extended argument, since the very marked transient behavior of Fig. 3 was not observed with the solutions used. However a conservative assessment of the errors implicit in such measurements should recognize that the values may be too positive, to a small and varying extent.

If a probable error of $\pm 0.15\text{V}$ is attributed to the estimated V_{FB} 's in Table I, the figures are consistent with the hypothesis that relatively small variations in V_{FB} occur upon changing the solvent, as would be expected if solvent dipole orientation is the only source of surface charging (20, 21).

The simplest explanation of the negative shifts in V_{FB} in the presence of iodide ion is the specific adsorption of the ion occurs. Once again, since the V_{FB} values are based on i_p^2 -V plots it is necessary to accept that this shift in principle may be due to more rapid charge-transfer kinetics at the interface, but it is unlikely that this effect can explain such large and consistent changes.

If it is accepted that the variations in both V_{FB} and the redox potential of ferrocene (22) upon a change of solvent are small and unimportant, it is

difficult to reconcile the sensitivity of the ferrocene stabilization effect upon solvent change with a mechanism involving a hole at the valence band edge. If ferrocene reduces one of the oxidized intermediates CdTe^{\bullet} or $\text{CdTe}^{2\bullet}$, which possess partial solvation shells then the solvent influence is easier to explain, especially if $\text{CdTe}^{2\bullet}$ is the intermediate involved.

In both PC and MN it is apparent by the yellow color of the solution after photoelectrolysis that tertiary butyl ammonium iodide has a small stabilizing effect (electrolysis at platinum electrodes gives a yellow solution at the anode and no color at the cathode at the same current density). Sodium iodide in PC has no such effect. This must be attributed to a subtle difference in the composition of the Helmholtz layer. Hence, once again, the direct oxidation of iodide ion by a hole at the valence band edge seems unlikely to display such sensitivity to the Helmholtz layer structure.

In terms of the kinetic scheme above and the subsequent assumptions the maximum possible corrosion suppression effect of low donicity solvent occurs when k_1 and $k_2 > k_3$ and the redox reaction is with $\text{CdTe}^{2\bullet}$. ΔG (transfer) for the Cd^{2+} ion from H_2O to a low donicity solvent can be estimated as 50 kJ/g ion (23). Since solvation can be partly developed for the $\text{CdTe}^{2\bullet}$ intermediate, the effect on the overall thermodynamics of the k_3 step will be somewhat less and that on the free energy of activation smaller still. This ultimately leads, in theory, to changes in the rate constant k_3 in the range of a factor of 10^{-3} , similar to those actually observed in electrochemical metal dissolution reactions (24). This figure is consistent with the extent of corrosion suppression effects found in this work and is of some practical significance for solar cells of this type. In order to function for some years at realistic current densities (10 mA cm^{-2}) the upper limit on i (corrosion)/ i (redox) is in the region of 10^{-8} . Should the photoelectrode material photocorrode in aqueous electrolytes then this limit will not be reached by changing the solvent.

Conclusions

The failure of the various attempts recounted above to stabilize n-cadmium telluride to the degree necessary for use in a solar cell (in the absence of telluride ion) reveals the dangers of assuming that any given semiconductor which shows some degree of photocorrosion in aqueous redox systems can be satisfactorily stabilized by a pure organic electrolyte system. Although the data relates only to cadmium telluride the conclusion can be extended to other n-type semiconductors by virtue of the large difference between attained and required corrosion rates.

Though low donicity solvents like MN and PC disfavor corrosion processes, even lower donicity solvents cannot be used because of their inability to give sufficiently conducting solutions. Thus, there is a distinct limit to the potential stabilizing ability of organic solvents. The theory and experiments herein point to a very approximate factor of 10^{-3} as the best available suppression. This figure makes sense when it is compared with the influence of the solvent on the thermodynamics of the overall process.

This conclusion is complemented by considering the associated difficulty of electrical conductivity. Taking $0.005 \Omega^{-1} \text{ cm}^{-1}$ as an average value for the conductivity of a low donicity electrolyte means the electrolyte layer must be only 0.1 mm thick to reduce internal series resistance to an acceptable $2 \Omega \text{ cm}^{-2}$. This in turn necessitates the use of a semitransparent counterelectrode acting also as a window, introducing further losses due to reflection, light absorption, sheet resistance, etc. Thin films of metal or metal oxide which can perform this latter function are not noted for their stability (25) and inevitably the cost and complexity of the cell is raised by their use.

There is some indication by analogy with the electrochemical dissolution of metals that mixed aqueous/organic electrolytes (26) and aqueous electrolytes containing surfactants (27) could suppress corrosion. Initial experiments in this laboratory were discouraging. In any case, the level of stabilization conceivable in such a system cannot again be expected to render an unstable photoelectrode useful in a solar cell.

Acknowledgments

The valuable contribution of Dr. W. Gissler towards this work is gratefully acknowledged, as is the technical assistance of Mr. A. Hoffmann and Mr. R. Schubert. The atomic absorption analysis was performed by Mr. P. Cavalli of the Joint Research Centre, Ispra. Dr. R. Memming gave some very constructive comments on the conduct of this work. The work described herein was entirely supported by a study contract with the Joint Research Centre, Ispra Establishment.

Manuscript submitted Oct. 15, 1979; revised manuscript received Feb. 20, 1980.

Any discussion of this paper will appear in a Discussion Section to be published in the June 1981 JOURNAL. All discussions for the June 1981 Discussion Section should be submitted by Feb. 1, 1981.

Publication costs of this article were assisted by the Commission of the European Communities.

REFERENCES

1. A. J. Nozik, *Ann. Rev. Phys. Chem.*, **29**, 189 (1978).
2. K. Rajeshwar, P. Singh, and J. duBow, *Electrochim. Acta*, **23**, 1117 (1978).
3. A. B. Ellis, S. W. Kaiser, and M. S. Wrighton, *J. Am. Chem. Soc.*, **99**, 2839 (1977).
4. K. Nakatani, S. Matsudaira, and H. Tsubomura, *This Journal*, **125**, 406 (1978).
5. B. G. Cox and A. J. Parker, *J. Am. Chem. Soc.*, **95**, 402 (1973).
6. V. Gutmann, *Electrochim. Acta.*, **21**, 661 (1976).
7. J. M. Bolts, A. B. Bocarsly, M. C. Palazzotto, E. G. Walton, N. S. Lewis, and M. S. Wrighton, *J. Am. Chem. Soc.*, **101**, 1378 (1979).
8. P. A. Kohl and A. J. Bard, *The Journal*, **126**, 603 (1979).
9. T. Saji, Y. Maruyana, and S. Aoyagui, *J. Electroanal. Chem. Interfacial Electrochem.*, **86**, 219 (1978).
10. M. A. Butler, *J. Appl. Phys.*, **48**, 1914 (1977).
11. A. Heller, K.-C. Chang, and B. Miller, *J. Am. Chem. Soc.*, **100**, 684 (1978).
12. C. K. Mann, *J. Electroanal. Chem. Interfacial Electrochem.*, **3**, 57 (1969).
13. H. Minoura and M. Tsuiki, *Electrochim. Acta*, **23**, 1377 (1978).
14. K. D. Legg, A. B. Ellis, J. M. Bolts, and M. S. Wrighton, *Proc. Natl. Acad. Sci. U.S.A.*, **74**, 4116 (1977).
15. Y. S. Sohn, D. N. Hendrickson, and H. B. Gray, *J. Am. Chem. Soc.*, **93**, 1559 (1971).
16. R. Memming, *Phil. Tech. Rev.*, **38**, 160 (1978).
17. R. Memming, *Electrochim. Acta.*, To be published.
18. Chemical Society Special Publication No. 17, "Stability Constant of Metal-Ion Complexes," pp. 340, Chemical Society, London (1964).
19. D. Laser, *The Journal*, **126**, 1011 (1979).
20. D. S. Ginley and M. A. Butler, *ibid.*, **125**, 1968 (1978).
21. R. Parsons, *Electrochim. Acta.*, **21**, 681 (1976).
22. H. M. Koepp, H. Wendt, and H. Strehlow, *Z. Elektrochem.*, **56**, 483 (1960).
23. A. J. Parker, *Electrochim. Acta*, **21**, 671 (1976).
24. T. Biegler, E. R. Gonzalez, and R. Parsons, *Coll. Czech. Chem. Commun.*, **36**, 414 (1971).
25. T. Osa and T. Kuwana, *J. Electroanal. Chem. Interfacial Electrochem.*, **22**, 289 (1969).
26. N. Tanaka, *Electrochim. Acta.*, **21**, 701 (1976).
27. J. W. Shultze and M. A. Habib, *J. Appl. Electrochem.*, **9**, 255 (1979).

Anomalous Behavior on I-V Characteristic Curves of n-TiO₂ and n-SrTiO₃ Electrodes in Aqueous Solution

J. F. Julião,*¹ Franco Decker,* R. Brenzikofer, and M. Abramovich**

UNICAMP, Instituto de Física, Campinas-SP, Brazil

ABSTRACT

Measurements of the I-V characteristics of n-TiO₂ and n-SrTiO₃ electrodes in aqueous KOH electrolyte in the dark show a deviation from the general behavior found in other semiconductor-electrolyte junctions, in the cathodic polarization region. The illumination of the semiconducting electrode with both u.v. and visible subbandgap light modifies these characteristics. We show that the observed phenomena are related to the reduction of oxygen dissolved in the electrolyte.

An interesting property of semiconductor-electrolyte (SE) junction devices is their ability to convert solar energy into either chemical (photoelectrolytic cell) or electrical energy (wet photovoltaic cell). This fact has drawn the attention of several researchers in the last few years (1-11). In particular, an understanding of the current flow mechanism should lend insight into chemical reactions occurring at the SE interface. In the present work we concentrate our study especially on the operation of these devices in the polarization

region where electrons are transferred from the n-type semiconductor to the electrolyte (cathodic current).

In previous studies of SE cells (12, 13) it has been found that for an external applied voltage, V_{bias} , greater than several kT ($T \approx 300^\circ\text{K}$), the cathodic current, i , is given by

$$i = i_0 \exp(bv_{\text{bias}}/kT) \quad [1]$$

where i_0 and b are empirically determined constants. This behavior is illustrated by the dashed curve of Fig. 1. Equation [1] shows that the current in SE junctions has a behavior similar to that of Schottky-barrier semiconductor-metal junctions (14), but with different values of the parameter b .

* Electrochemical Society Student Member.

** Electrochemical Society Active Member.

¹ Present address: Dept. de Física, Universidade Federal do Ceará, Brasil.

Key words: interfaces, cell, visible, reduction.

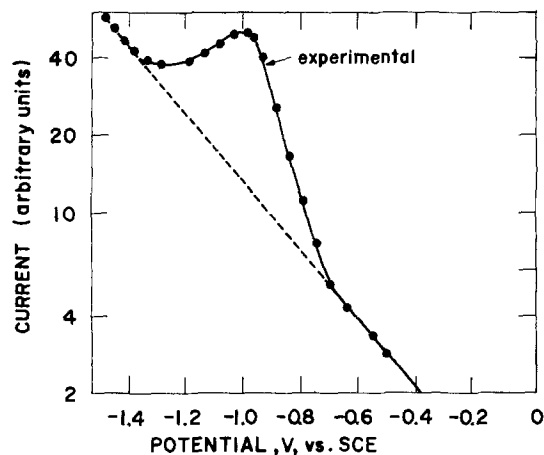


Fig. 1. Semilogarithmic plot of the current-modulus voltage characteristic of an $n\text{-TiO}_2/1\text{M KOH}_2/\text{Pt}$ cell. The solid curve shows the experimental results taken in the dark and the dashed curve represents the Schottky barrier behavior according to Eq. [1] in the text. The scan rate was 4 mV/sec.

Morisaki *et al.* (15) and Mavroides (16), working respectively with TiO_2 and SrTiO_3 electrodes, found I - V characteristics which deviate from the behavior suggested by Eq. [1]. Here we reexamine this anomalous behavior, previously reported. Our experiments, performed with $n\text{-TiO}_2/1\text{M KOH}/\text{Pt}$ and $n\text{-SrTiO}_3/1\text{M KOH}/\text{Pt}$ open to air-type cells, also showed for both materials, in the dark and under illumination, the anomalous I - V characteristics, namely, a cathodic current peak (Fig. 1). This peak occurs around -1.0V vs. SCE for TiO_2 and around -1.2V vs. SCE for SrTiO_3 ; its magnitude and position, in the dark and under illumination, are slightly different. Hardee and Bard (17) also have previously observed an increase in the cathodic current, comparing TiO_2 electrodes under illumination and in the dark. They suggested that the increase may be due to reduction of dissolved oxygen generated when a reverse scan into the negative potential region was made.

In order to investigate the origin of the observed peak we have performed further experiments varying the O_2 concentration in the electrolyte and the illumination condition of the semiconducting electrode.

In both materials we observed a sensitivity to sub-bandgap light when polarized in a potential region between ~ -1.2 and $\sim -1.4\text{V vs. SCE}$, which is dependent on the potential and O_2 concentration. From these observations and the results obtained with chronoamperometry we suggest a new explanation different from that given previously by Morisaki and Mavroides.

Experimental

The TiO_2 and SrTiO_3 monocrystals supplied by Materials Research Company and N. L. Industries Incorporated, respectively, were cut perpendicular to the (001) axis. The surface to be illuminated was polished with 0.2μ diamond powder. The samples were reduced in an H_2 atmosphere at temperatures near 1000°C , for periods varying from 30 to 60 min for TiO_2 and from 1 to 3 hr for SrTiO_3 , in order to produce n -type semiconductors. Subsequently, an ohmic contact was made at one sample surface by evaporation of a Cr and Au double layer, and a copper wire was attached to the contact by means of Ag paste. The samples were then encapsulated in polyester, leaving only the front surface free for contact with the electrolyte. We used a single compartment Teflon cell, open to air, containing an aqueous solution (1M KOH), a TiO_2 or SrTiO_3 working electrode, a Pt counterelectrode (about 10 cm^2 area), and an SCE reference electrode. As a light source, we used a 1000W ultrahigh pressure xenon lamp (infrared filtered by 10 cm of distilled water) focused on the entrance slit of a monochromator (Spex

14300). The visible light was obtained with the same lamp, crossing an Oriel LP-47 filter. Current-potential curves were obtained using a potentiostat circuit (18) with a sensitive current-to-voltage converter (10 nA) and a low phase shift for frequencies up to 100 kHz coupled to a triangular wave generator. The I - V curves were recorded on a Hewlett Packard Model 7004B X-Y recorder at a scan rate of 4 mV/sec in the sense of anodic to cathodic polarization. Figure 2 shows the scheme of this arrangement. The 1M KOH solutions were prepared from commercially available reagents, P.A. grade.

The I - V curves for each sample were recorded with the semiconducting electrode in the three following illumination conditions: in the dark, under visible radiation ($\lambda > 4700\text{\AA}$), and under u.v. radiation ($\lambda = 3250\text{\AA}$).

A first set of measurements was made with an electrolyte under standard conditions in contact with room atmosphere. Two other sets of measurements were performed by passing either N_2 or O_2 bubbles for several minutes before starting each voltage scan, in order to study the dependence on the degree of oxygenation. Before each experiment, the electrolyte was carefully stirred. We emphasize that in cells which remain open to air, such as the one described, it is not possible to obtain complete deoxygenation of the solution.

Experimental Results

Figures 3a and 3b show the I - V characteristics for typical samples of SrTiO_3 and of TiO_2 , respectively, under three different irradiation conditions: in the dark, visible ($\lambda > 4700\text{\AA}$), and u.v. ($\lambda = 3250\text{\AA}$) light, with the electrolyte in contact with air. In the interval of cathodic polarization on the current voltage curves shown in Fig. 3a and 3b, we distinguish three regions: (i) the low polarization region, when $V_{\text{on}} < V < 0$, V_{on} being the voltage in which the anodic photocurrent starts to increase ($V_{\text{on}} \approx -0.75\text{V}$ for TiO_2 and $\approx -0.90\text{V}$ for SrTiO_3); (ii) the middle polarization region, where $V_{\text{H}} < V < V_{\text{on}}$ ($V_{\text{H}} \approx -1.5\text{V}$ is the voltage at which significant H_2 evolution at the SE junction occurs and depends on the amount of O_2 dissolved in the solution); (iii) the high polarization region, when $V < V_{\text{H}}$. A common characteristics of the curves in these figures is that for $V < V_{\text{on}}$ the cathodic current presents a peak and a valley structure. The peak values are around -1.0V in TiO_2 and -1.2V in SrTiO_3 . This phenomenon is unexpected in the rectification characteristics of semiconductor-liquid junction cells described by Eq. [1], unless some electroactive species dissolved in the electrolyte or sticking to the electrode surface is being reduced at these potentials.

In addition, for $V_{\text{H}} < V < V_{\text{on}}$, Fig. 3a and 3b show that when the cell is under u.v. radiation the current peak is enhanced and slightly shifted in the direction

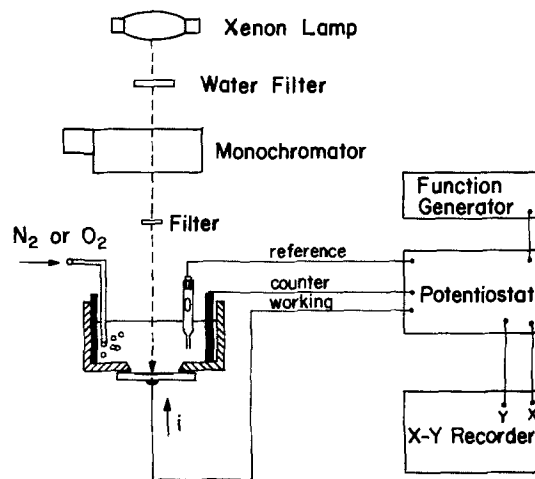


Fig. 2. Experimental setup for electrochemical measurements

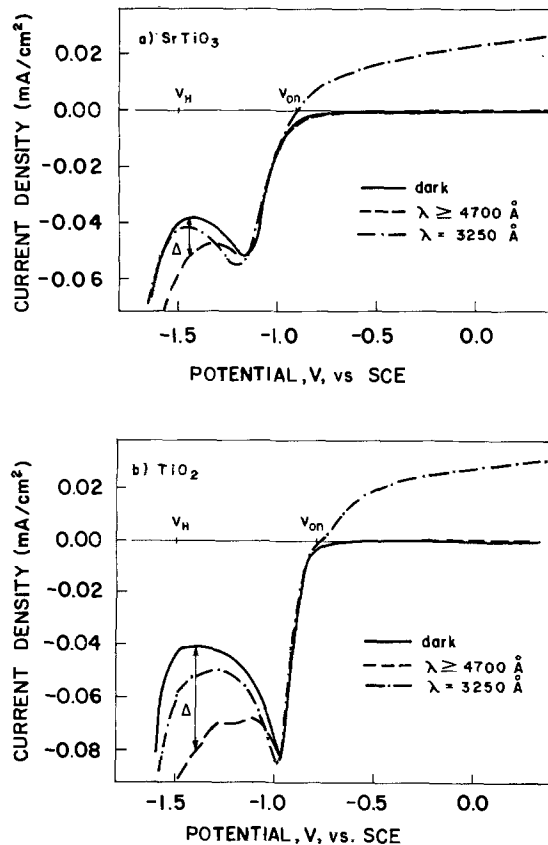


Fig. 3. Current-voltage characteristics of semiconductor-electrolyte junction under three different irradiation conditions. (a) SrTiO_3 electrode, (b) TiO_2 electrode. Δ is defined in the text. The scan rate was 4 mV/sec. Radiation intensity was $500 \mu\text{W}/\text{cm}^2$ for $\lambda = 3250\text{\AA}$ and $50 \text{ mW}/\text{cm}^2$ for $\lambda \geq 4700\text{\AA}$.

of more negative potentials and that an additional current stimulated by visible light appears. In these figures, the quantity Δ describes the variation I (dark) $- I$ (visible) for $V = -1.4\text{V}$. Morisaki *et al.* (15), working with TiO_2 cells, have called a similar behavior, observed with visible light, "anomalous photo-response," since it was produced with photons of lower energy than that of the semiconductor bandgap. The same phenomenon has been previously observed by Mavroides (16) with SrTiO_3 electrodes.

In order to understand how O_2 dissolved in the electrolyte affects the above results we have repeated the experiments with different O_2 concentrations in the solution. We have reduced the O_2 concentration by bubbling N_2 through the electrolyte and increased the O_2 concentration by either bubbling O_2 or by adding a small quantity of hydrogen peroxide, which becomes oxidized in basic solution (19). Our results show (Fig. 4) that the I - V characteristics are affected only for $V_{\text{H}} < V < V_{\text{on}}$. When the solution is submitted to a gradual deoxygenation, we observe a decrease in the absolute value of the cathodic current peak amplitude for the nonirradiated semiconductor electrodes, as shown in Fig. 4a. When increasing the concentration of O_2 in the electrolyte, the current peak increases and shifts in the direction of more negative potentials for the nonirradiated electrode as shown in Fig. 4b. At the same time the position of V_{H} also changes in the same direction. We have also examined the effect of several successive voltage scans in this region at a rate of 4 mV/sec, with the solution in air equilibrium or after bubbling N_2 for 30 min. In the first condition the peak amplitude diminished and reached a limit value of $\sim 40 \mu\text{A}/\text{cm}^2$. In the second condition the peak disappeared and the I - V curve reached a plateau with the current at a value of $\sim 10 \mu\text{A}/\text{cm}^2$.

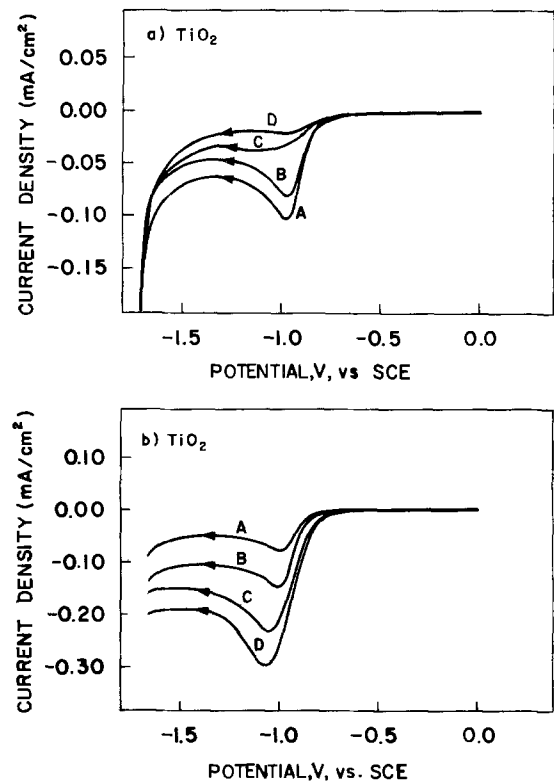


Fig. 4. Dark I - V characteristics of an $n\text{-TiO}_2/1\text{M KOH/Pt}$ cell. The scan rate was 4 mV/sec. (a) Effect of bubbling through the electrolyte: (A) first scan, no gas bubbling; (B) after N_2 bubbling for 2 min; (C) after N_2 bubbling for 7 min; (D) after N_2 bubbling for 12 min. (b) Effect of O_2 bubbling through the electrolyte: (A) first scan, no gas bubbling; (B) after O_2 bubbling for 2 min; (C) after O_2 bubbling for 4 min; (D) after O_2 bubbling for 6 min.

We have also observed a correlation between Δ and the O_2 concentration in the solution. After bubbling N_2 through the cell for enough time, in order to minimize the quantity of dissolved O_2 , Δ reaches a small limit value (Fig. 5, curve B). When the O_2 concentration in the solution is increased, Δ also increases (Fig. 5, curve A).

In order to investigate further the influence of visible irradiation on the O_2 reduction process, we have performed an experiment recording the current *vs.* time response of the cell when submitted to a -1.2V potential step (chronoamperometry). The results were recorded with the semiconductor in the dark and under visible light; in both cases the electrolyte was air saturated.

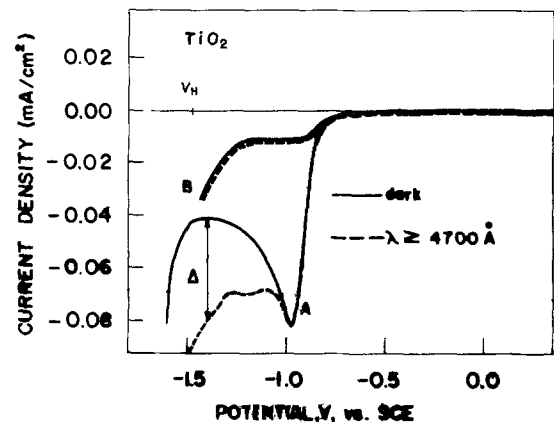


Fig. 5. Current-voltage characteristics of an $n\text{-TiO}_2/1\text{M KOH/Pt}$ cell: (A) with electrolyte in equilibrium with air; (B) after bubbling N_2 for 40 min. The solid curves were taken in the dark and the dashed curves with subbandgap radiation.

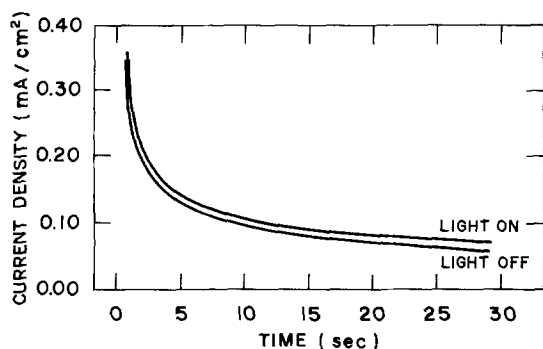


Fig. 6. Current vs. time response of the cell, submitted to a potential step of -1.2V vs. SCE.

In the last experiment the cell was allowed to reach thermal equilibrium with light on, before applying the potential step. The results are shown in Fig. 6.

Discussion

It is generally known that in the semiconductor, near the interface with the electrolyte, a potential barrier or band bending, V_B , appears as a consequence of the electric field which is intrinsic to the space charge region. This band bending prevents the conduction band electrons from reaching the semiconductor surface, and it can be reduced to zero when an adequate cathodic polarization of value equal to the flatband potential, V_{FB} , is applied to the semiconducting electrode. The flatband potential, V_{FB} , for TiO_2 and SrTiO_3 , according to most authors (8, 20, 21) is approximately -1.0 and -1.2V , respectively, in a 1M KOH electrolyte. A simple energy diagram (Fig. 7) shows the behavior of the TiO_2 -electrolyte junction, taken as an example, for three different values of the applied voltage. For an unbiased cell, no net charge transfer occurs through the junction except in the presence of light with energy greater than the semiconductor bandgap. For bias close to the flatband potential, V_{FB} , (Fig. 7B) the conduction electrons

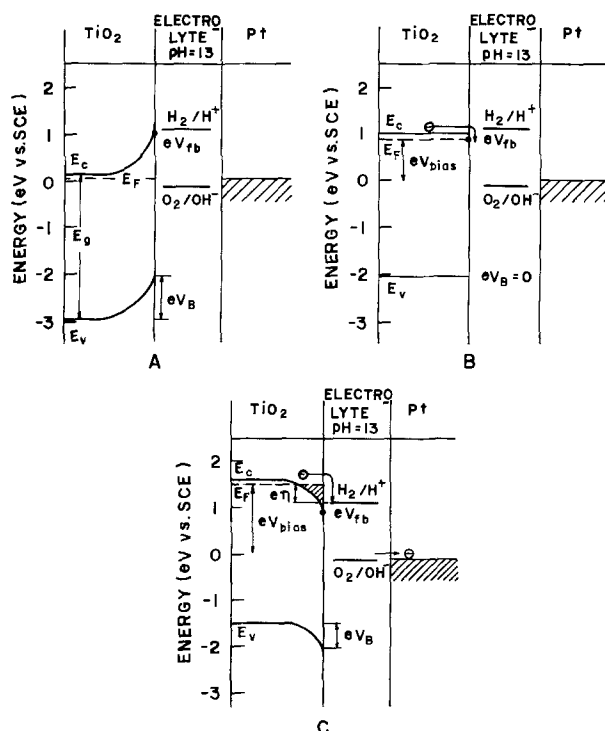
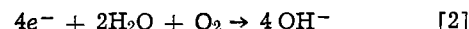


Fig. 7. Combined energy diagram for a $\text{TiO}_2/1\text{M}$ KOH/Pt cell: (A) without external bias, TiO_2 and Pt short circuited; (B) under cathodic polarization of TiO_2 , $V_{\text{bias}} = V_{\text{FB}}$; (C) under cathodic polarization of TiO_2 , $V_{\text{bias}} = -1.5\text{V}$.

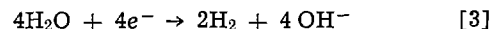
reach the semiconductor surface and can react with the electroactive species possibly present at the interface. As shown in Fig. 3a and 3b, the cathodic current reaches a peak at potentials near V_{FB} for TiO_2 as well as for SrTiO_3 . This peak shows a strong dependence on O_2 concentration (Fig. 4a and 4b), which suggests that it is associated with the reduction of dissolved O_2 . The results obtained when the electrolyte was submitted to several successive scans confirms this hypothesis. For an alkaline solution the reduction at the semiconductor cathode might be a four-electron reaction as given by Eq. [2] (16)



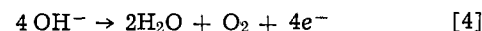
The energy level of the O_2/OH^- redox couple is about 1.2 eV below the conduction band edge (22). It would appear, therefore, that if we assume that the electron transfer from the TiO_2 to the O_2/OH^- couple has to be iso-energetic (23, 24), a surface state located at the same energy as the O_2/OH^- couple should exist to mediate it.

Wilson (25) also observed a peak in the I - V characteristics of TiO_2 in the same polarization region but he interpreted it as an evidence of a bound charge-transfer state which acts as an intermediate in the oxidation of the solvent.

For $V_{\text{bias}} < V_{\text{H}}$ (Fig. 7c) there is a current step which is due to the water reduction through the reaction



while at the Pt anode the reaction would be described by



accomplishing, therefore, the electrolysis of water.

The enhancement and the shift of the cathodic current peak, when the cell is under u.v. illumination (Fig. 3a and 3b) can be explained as an additional reduction of the oxygen produced at the semiconductor surface in the anodic region current. This agrees with the detected behavior of the cathodic current peak when the O_2 concentration in the electrolyte is increased (Fig. 4, curve A).

The correlation observed between Δ (additional current stimulated by subbandgap radiation) and the oxygen reduction reaction could be attributed to one of the following alternatives: (i) excitation of electrons from the valence band directly to surface states, possibly associated with adsorbed species, and then transferred to redox couples O_2/OH^- in the electrolyte. The time constant for this overall process was observed to be of the order of 1 min in Ref. (15, 16); (ii) additional reduction (by conduction band electrons) of the dissolved O_2 , because of the continuous renewal of the electrolyte near the interface by a convection process due to heating of the semiconductor surface under illumination.

The results of chronoamperometry were used to solve the ambiguity between the alternatives mentioned in the previous paragraph and to get more precise information about the O_2 reduction at the semiconductor interface. This experimental technique was applied to semiconductor electrodes on the basis of the following considerations. In most n-type semiconductors a potential barrier at a nonbiased SE interface prevents the bulk electrons from reaching the surface and reacting with electrochemical species at the expected potential. In our case, this implies that the O_2 reduction will occur at a potential slightly more negative than V_{FB} (Fig. 5 and 7A). Below this potential value, the electrode behavior becomes metal-like in respect to charge transfer to the electrolyte. In usual chronoamperometry, the potential of a metallic electrode is stepped to a region that is far removed from the equilibrium value. Therefore, this technique is particularly suitable for a semiconducting electrode if a potential step overcoming V_{FB} is applied.

The theoretical prediction for the decay current density, when the reaction is purely diffusion controlled, is described by the equation

$$I = nFAD^{1/2}Co\pi^{-1/2}t^{-1/2} \quad [5]$$

where F is Faraday's constant, D is the diffusion coefficient, Co is the concentration, and n is the number of electrons that are transferred at the electrode in the diffusion reaction.

In Fig. 8 we show the plot I vs. $t^{-1/2}$ for a potential step of $-1.2V$ vs. SCE, both in dark and with illumination. It can be seen that the experimental points in both cases are colinear as expected for diffusion-controlled processes (see Eq. [5]). Using the values of Co , D , and F given in Ref. (26), we have obtained 3.8 ± 0.3 for the slopes of the straight lines, which confirms the mechanism proposed for the O_2 reduction in Eq. [2] with the transfer of 4 electrons from the semiconductor to the solution.

The experimental points in Fig. 8 indicate that the diffusion-controlled mechanism for the decay current is valid for $t > 1$ sec. This is only compatible with the second alternative, mentioned before, that points out that the reduction rate is increased due to a convective flow stimulated by light heating. An electron transfer with time constant of the order of 1 min, associated with subbandgap light absorption, would not cause the straight line behavior observed in Fig. 8. We suggest that chronoamperometry could be used to study similar processes in semiconductor-electrolyte junctions.

In a separate publication (27) we show that the photocurrent Δ in Fig. 3 is a purely thermal effect and cannot be attributed to a subbandgap transition even if the photocurrent time constant is less than 1 sec.

Summary and Conclusions

The I-V characteristics of n-TiO₂/1M KOH/Pt and n-SrTiO₃/1M KOH/Pt cells were obtained in the cathodic polarization region in normal air equilibrium conditions or after N₂ or O₂ bubbling the electrolyte and under different illumination conditions. A deviation from the general behavior in SE junctions was observed and it is ascribed to a reduction at the semiconductor surface of the oxygen dissolved in the electrolyte.

The observed deviation in the I-V characteristics is sensitive to semiconducting electrode irradiation both with u.v. and with visible subbandgap light. Furthermore, we show that these photoeffects are entirely related to the electrolyte conduction rather than to a sensitivity of the semiconductor electrode when it is biased within the polarization region considered.

Acknowledgments

We are grateful to Dr. T. Rabockai, Prof. Carl H. Weis, Dr. A. Miguel, and Prof. George G. Kleiman for helpful advice and discussion with regard to this work. We also thank Dr. Ernesto Nagai and Dr. Reginaldo

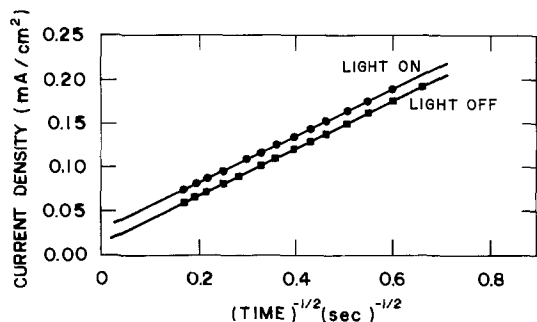


Fig. 8. Current vs. $(\text{time})^{-1/2}$ plot of the experimental curves shown in Fig. 6.

dos Santos for their support in the realization of the experiments. We would also like to thank Prof. R. C. C. Leite, Prof. George G. Kleiman, Dr. M. M. Collver, Dr. J. Busnardo, and Dr. M. A. Butler for several comments on the manuscript. This work was supported by FINEP-Financiadora de Estudos e Projetos S/A under contract Energia Solar/FINEP/UNICAMP No. IF/589, and FAPESP-Fundação de Amparo à Pesquisa do Estado de São Paulo.

Manuscript submitted Aug. 14, 1979; revised manuscript received Jan. 2, 1980.

Any discussion of this paper will appear in a Discussion Section to be published in the June 1981 JOURNAL. All discussions for the June 1981 Discussion Section should be submitted by Feb. 1, 1981.

Publication costs of this article were assisted by UNICAMP.

REFERENCES

1. A. Fujishima and K. Honda, *Bull. Chem. Soc. Jpn.*, **44**, 1148 (1971).
2. A. Fujishima and K. Honda, *Nature (London)*, **238** 37 (1972).
3. S. N. Paleocrassas, *Solar Energy*, **16**, 45 (1974).
4. A. Fujishima, K. Kohayakawa, and K. Honda, *This Journal*, **122**, 1487 (1975).
5. J. G. Mavroides, D. I. Tchernev, J. A. Kafalas, and D. F. Kolesar, *Mater. Res. Bull.*, **10**, 1023 (1975).
6. T. Watanabe, A. Fujishima, and K. Honda, *Bull. Chem. Soc. Jpn.*, **49**, 355 (1976).
7. J. G. Mavroides, J. A. Kafalas, and D. F. Kolesar, *Appl. Phys. Lett.*, **28**, 241 (1976).
8. J. M. Bolts and M. S. Wrighton, *J. Phys. Chem.*, **80**, 2641 (1976).
9. H. H. Kung, H. S. Jarret, A. W. Sleight, and A. Ferretti, *J. Appl. Phys.*, **48**, 2463 (1977).
10. A. K. Ghosh and H. P. Maruska, *This Journal*, **124**, 1516 (1977).
11. F. Williams and A. J. Nozik, *Nature (London)*, **271**, 137 (1978).
12. R. Williams, *This Journal*, **114**, 1173 (1967).
13. R. Williams, *J. Vac. Sci. Technol.*, **13**, 12 (1976).
14. S. M. Sze, "Physics of Semiconductor Devices," Chap. 8, p. 393, Wiley International ed., Wiley-Interscience, New York, London, Sydney, Toronto (1969).
15. H. Morisaki, M. Hariya, and K. Yazawa, *Appl. Phys. Lett.*, **30**, 7 (1977).
16. J. G. Mavroides, in "Semiconductor Liquid-Junction Solar Cells," A. Heller, Editor, p. 84, The Electrochemical Society Softbound Proceedings Series, Princeton, N.J. (1977); *J. Vac. Sci. Technol.*, **15**, 538 (1978).
17. K. L. Hardee and A. J. Bard, *This Journal*, **122**, 739 (1975).
18. R. Brenzikofer, Private communication.
19. F. A. Cotton and G. Wilkinson, "Advanced Inorganic Chemistry," p. 282, Wiley International ed., Wiley-Interscience, New York, London, Sydney, Toronto, (1962).
20. H. P. Maruska and A. K. Ghosh, *Solar Energy*, **20**, 443 (1978).
21. A. J. Nozik, in Proceedings of the 2nd World Hydrogen Energy Conference, Zurich, Switzerland, August 1978, p. 1217.
22. M. Tomkiewicz and H. Fay, *Appl. Phys.*, **18**, 1 (1979).
23. S. N. Frank and A. J. Bard, *J. Am. Chem. Soc.*, **97**, 7427 (1975).
24. (a) H. Gerischer, in "Physical Chemistry: An Advanced Treatise," Vol. 9A, H. Eyring, D. Henson, and W. Jost, Editors, Academic Press, New York (1970); (b) H. Gerischer, *Adv. Electrochem. Eng.*, **1**, 139 (1961).
25. R. H. Wilson, Abstract 415, p. 1038, The Electrochemical Society Extended Abstracts, Seattle, Washington, May 21-26, 1978.
26. I. M. Kolthoff and C. S. Miller, *J. Am. Chem. Soc.*, **63**, 1013 (1941).
27. F. Decker, J. F. Julião, and M. Abramovich, *Appl. Phys. Lett.*, In press.

On the Oxidation Kinetics of Silicon: The Role of Water

D. R. Wolters

Philips Research Laboratories, Eindhoven, The Netherlands

ABSTRACT

The theory of the kinetics of the thermal oxidation of silicon is extended after critical examination of the solubility and transport behavior of water in silica. From the solubility data for water in silica reported in the literature, the dissolution appears to be a two-stage process at temperatures up to 1200°C. In the first stage silanol groups are formed at a relatively slow rate. In the second stage these silanol groups react with water forming hydronium ions (H_3O^+) and silicate ions ($=\text{SiO}^-$) fixed to the silica network. The second stage is relatively fast compared to the first stage. Consistent with this the transport of water appears to occur by the ambipolar diffusion of hydronium (H_3O^+) and hydroxyl ions (OH^-). The dissolution and transport of water predict a linear-parabolic rate law, which differs slightly from the one obtained by Deal and Grove. The catalytic role of water in mixed ambients is explained by a simple interaction between O_2 and H_2 formed by the oxidation of Si by H_2O . An expression for oxide growth accounting for this interaction is derived and properly fits the experimental data reported in the literature. It predicts correctly the linear dependence of the parabolic rate constant and the square root dependence of the linear rate constant on water partial pressure. It predicts also the initial growth regime.

The well-known linear-parabolic law for growth of oxide layers on silicon from Deal and Grove (1) is expressed by the equation

$$x_o^2 + Ax_o = B(t + t_{in})$$

Sometimes it is formulated with inverse constants (2)

$$k_{par}^{-1}x_o^2 + k_{lin}^{-1}x_o = t + t_{in}$$

In these equations x_o is the oxide thickness, t is the oxidation time, t_{in} is a correction term for so-called initial growth, $k_{par} = B$ is the parabolic rate constant, $k_{lin} = B/A$ is the linear rate constant. The relationship is derived by equating the flux of diffusing species through the layer to the fluxes at the two interfaces of the silica layer under the condition of a steady-state growth. Hence

$$h(c^* - c_{out}) = D \frac{\partial c}{\partial x} = kc_{in}$$

where c^* , c_{out} , c , and c_{in} are the concentrations of the oxidant in the ambient, outer surface, in the silica layer, and at the Si/SiO₂ interface, respectively, h and k are reaction rate constants, and D is the diffusion coefficient. By solving the differential equation subject to the boundary conditions it follows that k_{par} (or B) = Dc and $k_{lin} = c(1/k + 1/h)^{-1}$.

The experimentally found parabolic rate constant k_{par} is proportional to the partial pressure of the oxidant. This proportionality would follow when $c \propto p$ (oxidant) which suggests that Henry's law is obeyed. The solubility of oxygen in silica has not been measured directly in terms of concentrations and pressures. From diffusion or permeation data it might be concluded that the solubility is proportional to oxygen pressure. As we shall see such a conclusion is possibly unjustified as long as the precise mechanism of transport is unknown.

The solubility of water in silica varies with the square root of water pressure (3) and this is contradictory to the assumption, made in the Deal-Grove theory, that Henry's law is obeyed. This was already noted by Revesz (4). Because the reaction at the Si/SiO₂ interface is supposed to be of first order the

linear rate constant $k_{lin} = B/A$ is assumed to vary proportionally with water pressure. For the oxidation of Si in pure water vapor this linear variation has indeed been reported (5). In mixed ambients, however, k_{lin} varies obviously with the square root of water partial pressure as will be demonstrated below. This cannot be accounted for by the theory of Deal and Grove. The anomalous variation of k_{par} and k_{lin} with water pressure demands a critical reexamination of the physicochemical model for dissolution and transport of oxidant in silica layers on silicon.

In the present paper a model for water incorporation is presented. The transport mechanism is derived from reported hydrogen profiles (6). An alternative linear-parabolic rate law is obtained by considering the diffusion process as time dependent. The interaction of water and oxygen flow through silica is deduced by considering the reaction of hydrogen, generated by the reaction of Si and water, and oxygen. The criteria to discriminate between the time-dependent diffusion and interface reaction-limited transport are given. The experimental evidence for the models are presented.

The Incorporation of Water in Silica

When water is incorporated in silica at very high temperatures (>1500°C) an Si-O-Si bond is broken to form two adjacent silanol groups (7). When water is incorporated at a lower temperature (e.g., 1000°C) by diffusion into the silica it is generally accepted that water dissolves by the formation of silanol groups in the same way (3, 8, 9). An indication of this would be the square root relationship of solubility¹ and water pressure. It is known from the extensive literature on water in silica (3) that the water content of a silica sample is not unambiguously determined by temperature and water partial pressure when the silica is treated in water containing ambients at temperatures below 1200°C. The thermal history of a sample is an important variable determining the water solubility (3). However, the thermal history or as it is called "the fictive temperature" is itself determined by water uptake as has been concluded by Brückner (10) and confirmed experimentally by Shackelford (11, 12).

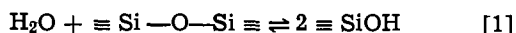
¹ Solubility is used in the sense of equilibrium concentration of species resulting from a particular reaction of silica with water.

Key words: silicon dioxide, oxidation kinetics, water transport, time-dependent diffusion, initial growth mechanism.

This dilemma is solved when two dissolution reactions are introduced with different reaction rates. One mechanism is assumed to dominate at high temperature; the other determines the dissolution at lower temperatures. At intermediate temperatures both reactions may proceed but in general with different reaction rates.

The two incorporation mechanisms which are proposed (13) are:

I. High-temperature incorporation



in which two adjacent silanol groups are formed (7).

II. Low-temperature incorporation



here the silanol groups resulting from reaction [1] are hydrolyzed.

The hydrolyzation can proceed only when silanol groups are present, hence, when they are being formed by reaction [1] (or have been formed by [1] in a preceding high temperature treatment). In this section only the case in which mechanism I is frozen in will be considered. When the silanol concentration is constant the solubility can be approximated by the concentration of H_3O^+ ions resulting from reaction [2].

Since the electroneutrality condition demands that $[\text{H}_3\text{O}^+] = [\equiv \text{SiO}^-]$ one obtains

$$[\text{H}_3\text{O}^+] = ([\text{H}_3\text{O}^+] \cdot [\equiv \text{SiO}^-])^{1/2} \propto [\equiv \text{SiOH}]^{1/2} \cdot p_{\text{H}_2\text{O}}^{1/2} \quad [3]$$

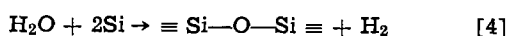
As long as the silanol concentration is constant the solubility of water in silica is proportional to the square root of water pressure. When the silanol concentration is changed (e.g., by thermal pretreatment) the low temperature solubility also changes.

This explains the variation of the solubility (3) at 750°C when samples were given thermal pretreatments at temperatures from 1000°-1300°C. Also the very slow changes of solubility when samples are kept at 1100°C for very long periods (3) can be explained by assuming two incorporation mechanisms of which one has a very slow reaction rate.

Transport of Water Through Silica

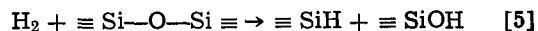
The nature of the diffusing species is investigated by inspection of the (H) profiles in oxide layers grown under steady-state conditions. In the first part the diffusion of single H_2O molecules is considered and the shape of the (H) profile is deduced. In the second part the diffusion of ionized water molecules (e.g., $\text{H}_3\text{O}^+ + \text{OH}^-$) is considered. Comparison of the theoretical and experimental profiles makes clear which species must be taken into account.

Diffusion of single water molecules.—Breed and Doremus (14) analyzed hydrogen profiles of Burkhardt (6) and explained the minima found in the profiles by taking into account the reactions of water and hydrogen with silica. Their method is adopted here in a slightly different version. When water diffuses in steady-state conditions through silica it reacts with the network to form $\equiv \text{SiOH}$ groups (or it reacts with a $\equiv \text{SiOH}$ group to form $\equiv \text{SiO}^- + \text{H}_3\text{O}^+$, as discussed above). The $\equiv \text{SiOH}$ groups are not mobile and the diffusion can proceed only when the reaction is reversed and water is formed from silanol groups. In such a situation the majority of water molecules can be present in the reacted form ($\equiv \text{SiOH}$) and only a minority in the mobile form (H_2O). Finally the water molecules react at the Si interface where they are converted into oxide and hydrogen. The reaction equation is



The hydrogen formed at the interface diffuses back

through the silica. Just as water the hydrogen reacts with the network to form $\equiv \text{SiOH}$ and $\equiv \text{SiH}$ groups. The reaction is given by



As has been shown by Van der Steen (9) reaction [5] proceeds rapidly at 1000°C.

Under steady-state conditions (15) the flux of oxidant J is constant or

$$J = -D \frac{\partial c}{\partial x} = \text{constant} \quad [6]$$

where $\partial c/\partial x$ is the concentration gradient of the diffusing oxidant.

By integration of Eq. [6] it follows that

$$c \propto \frac{x}{x_0} \quad [7]$$

where x_0 is the oxide layer thickness. When H_2O molecules constitute the diffusant a linear water profile is expected. Since the majority of water molecules is incorporated as $\equiv \text{SiOH}$ groups and two silanol groups are formed from one water molecule one finds

$$[\text{H}_2\text{O}] \propto [\equiv \text{SiOH}]^2 \propto \frac{x}{x_0} \quad [8]$$

Now, the contribution of $\equiv \text{SiH}$ groups to the H-profile will be derived. The H_2 flux is directed from the Si interface to the ambient. Because the net incorporated amount of hydrogen is small compared with the total amount to be transported it follows that under steady-state conditions

$$J_{\text{H}_2} = -J_{\text{H}_2\text{O}} = \text{constant} \quad [9]$$

The diffusant concentration varies proportionally with the distance from the Si interface

$$[\text{H}_2] \propto \frac{x_0 - x}{x} \quad [10]$$

From reaction [5] we see that at equilibrium

$$[\text{H}_2] \propto [\equiv \text{SiOH}] \cdot [\equiv \text{SiH}] \quad [11]$$

Substituting Eq. [8] and [10] in [11] the profile of the $[\equiv \text{SiH}]$ can be found, one obtains

$$[\equiv \text{SiH}] \propto \left(\frac{x_0 - x}{x_0} \right) \left(\frac{x}{x_0} \right)^{-1/2} \quad [12]$$

At the ambient side $x = x_0$ the expression in Eq. [12] equals zero and hence ($\equiv \text{SiH}$) is very small. The major part of the experimentally found hydrogen will consist of $\equiv \text{SiOH}$ groups and the profile will follow the expression of Eq. [8], i.e., $[\text{H}] \propto (x/x_0)^{1/2}$. At the Si interface $x = 0$ and the expression of Eq. [8] equals zero. The hydrogen profile will follow the expression in Eq. [12]. Because the first term on the right-hand side approaches unity we find that $[\text{H}] \propto (x/x_0)^{-1/2}$. The expressions of Eq. [8] and [12] are depicted schematically in Fig. 1 on a log-log plot. The slopes of the lines correspond to the powers $1/2$ and $-1/2$.

Diffusion of $\text{H}_3\text{O}^+ + \text{OH}^-$.—In this case the same method is used as above, but we must realize that from one diffusing particle ($\text{H}_3\text{O}^+ + \text{OH}^-$) four $\equiv \text{SiOH}$ groups can be formed. Instead of Eq. [8]

$$[\text{H}_3\text{O}^+ + \text{OH}^-] \propto [\equiv \text{SiOH}]^4 \propto \frac{x}{x_0} \quad [13]$$

is obtained. The [H] profile varies proportionally with the fourth root of x/x_0 , i.e., $[\text{H}] \propto (x/x_0)^{1/4}$.

The hydrogen flux is equal but in the opposite direction to the water flux. The hypothetical water concentration varies linearly with the square root of

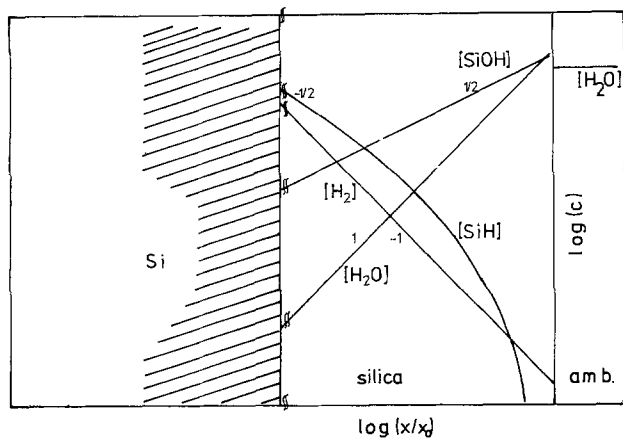


Fig. 1. Schematic representation of the expected concentration profiles of water, hydrogen, silane, and silanol groups when water molecules are the diffusing species in an oxide layer on oxidizing silicon. The concentrations of silane and silanol groups are assumed to exceed the concentrations of water and hydrogen.

$\text{H}_3\text{O}^+ + \text{OH}^-$ concentration, i.e., $[\text{H}_2\text{O}] \propto x/x_0)^{1/2}$. It is obvious that the $[\text{H}_2]$ profile is given by

$$[\text{H}_2] \propto \left(\frac{x_0 - x}{x} \right)^{1/2} \quad [14]$$

Substituting Eq. [11] and [13] in [14] the $[\equiv\text{SiH}]$ profile is obtained

$$[\equiv\text{SiH}] \propto \left(\frac{x_0 - x}{x} \right)^{1/2} \left(\frac{x}{x_0} \right)^{-1/4} \quad [15]$$

Contrary to the first case we obtain profiles with powers of $1/4$ and $-1/4$ (see Fig. 2).

The method outlined above can be generalized to all possible combinations of water-related species (see Table I). They all have their own characteristic number of H-atoms transported in one diffusional movement. The slopes on a log-log plot are equal to the reciprocal value of the number of H-atoms. Table I indicates that the slope of the H-profile on a log-log plot corresponds to the reciprocal of value of the number of H-atoms in the transported species.

The experimentally found profiles replotted from the data of Burkhardt (6) are given in Fig. 3, 4, and 5. The slopes at the ambient side are obviously $1/4$ for Fig. 3 and 4. The slopes at the Si-interface cannot be determined well for Fig. 3 and 4, but for the thinnest oxide layer in Fig. 5 there is a reasonable correspondence for calculated and measured profiles using the expression of Eq. [15]. It can be concluded that the probable mechanism is the simultaneous (or ambipolar) diffusion of H_3O^+ and OH^- , which

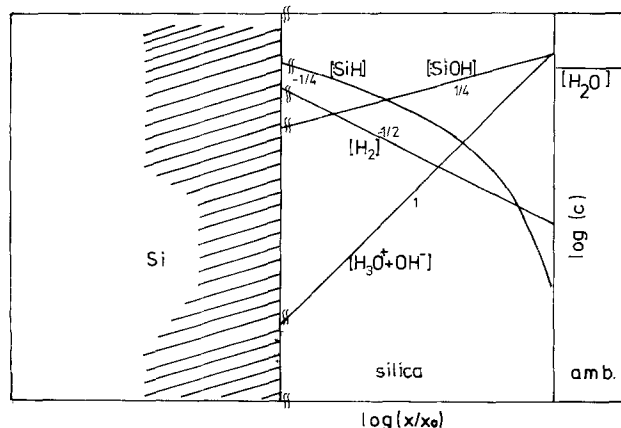
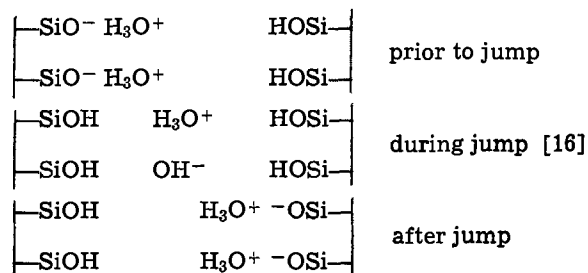


Fig. 2. The same as in Fig. 1 but here the diffusing species consist of $\text{H}_3\text{O}^+ + \text{OH}^- = (2\text{H}_2\text{O})$.

Table I.

Species	Number of H-atoms	Slope
$\text{OH}^- + \text{hole}$	1	1
$\text{H}_2\text{O}, \text{H}_2\text{O}^- + \text{hole}$	2	1/2
$\text{H}_3\text{O}^+ + \text{electron}$	3	1/3
$\text{H}_3\text{O} + \text{OH}^-$	4	1/4

is in accordance with the slopes of $1/4$. Now the question arises where is the hydroxyl ion (OH^-) generated? In the scheme below it is proposed that the two H_3O^+ ions bound electrostatically to the two $\equiv\text{SiO}^-$ groups at the left (see "prior to jump") can be liberated forming an $\text{H}_3\text{O}^+ + \text{OH}^-$ pair. They leave two silanol groups behind and jump simultaneously (see "during jump") to react with two adjacent silanol groups (see "after jump") forming two H_3O^+ ions and $\equiv\text{SiO}^-$ groups at the right. The mechanism is based on the consideration that the silanol groups are incorporated as adjacent pairs (7).



The Parabolic Oxidation

When the rate of growth is determined predominantly by the transport of diffusant through the layer it is given by

$$\frac{dx_0}{dt} = M_0^{-1} \left(D \frac{\partial c}{\partial x} \right)_{x=0} \quad [17]$$

where M_0 is the amount of diffusant needed to form a unity thickness of oxide. Under steady-state condition c varies linearly with x and hence we may replace $\partial c/\partial x$ by $(c_s - c_{in})/x_0$ where c_s is the surface concentration at the ambient side and c_{in} the interface concentration at the Si side (see Fig. 6).

After substitution of $\partial c/\partial x$ and subsequent integration Eq. [17] becomes

$$x_0^2 = 2M_0^{-1}D(c_s - c_{in})t \equiv k_{\text{par}}t \quad [18]$$

where $k_{\text{par}} = 2M_0^{-1}D(c_s - c_{in})$ is called the parabolic rate constant. At normal oxidant pressures $c_s \gg c_{in}$

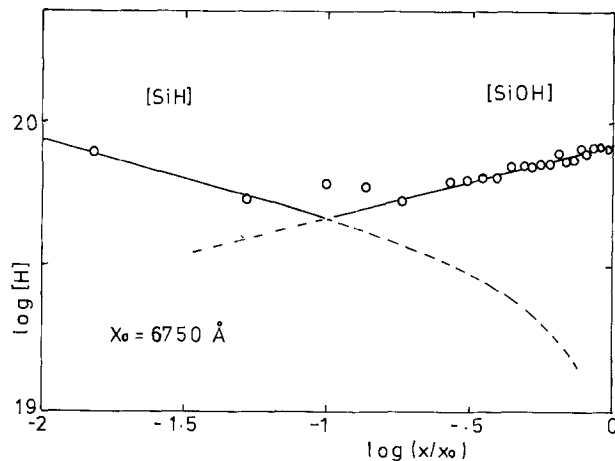


Fig. 3. Profiles measured by Burkhardt (6) in an oxide layer of 6750 \AA replotted on logarithmic scales showing the slope of $1/4$. From this it may be concluded that two water molecules are transported simultaneously ($\text{H}_3\text{O}^+ + \text{OH}^-$). Drawn curves are calculated.

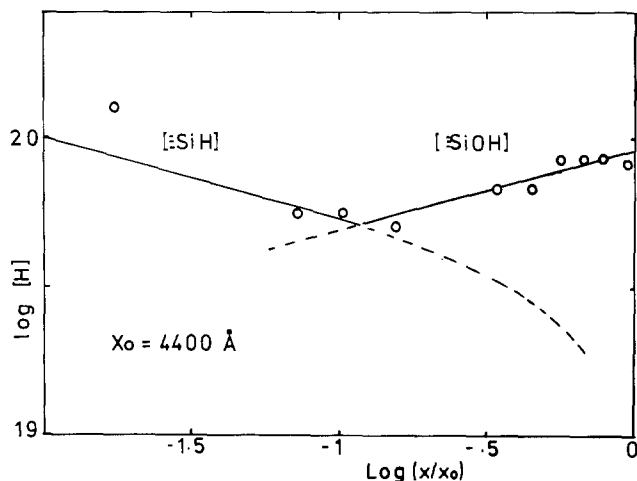


Fig. 4. The same as for Fig. 3 for an oxide-layer of 4400 Å.

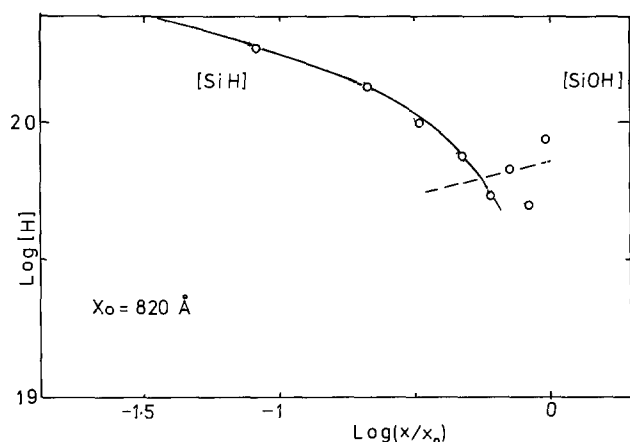


Fig. 5. The same as for Fig. 3 for an oxide-layer of 820 Å.

silicon silica Ambient

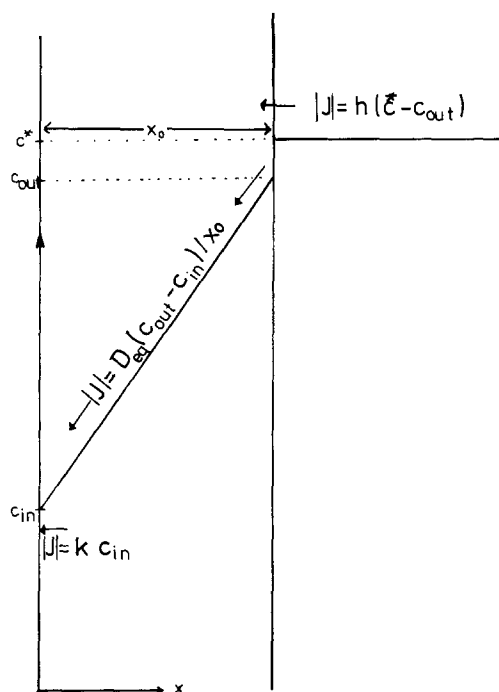


Fig. 6. Schematic profile of oxidant under steady-state condition

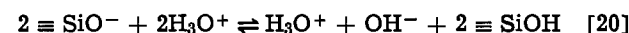
and hence

$$k_{par} \propto c_s \tag{19}$$

In the case that water vapor is used as oxidation agent c_s is equal to $[H_3O^+ + OH^-]$. It is convenient to relate c_s to the ambient pressure and for this purpose the exchange reaction or dissolution reaction of water in silica is needed. Earlier it was derived that

$$[H_3O^+] \propto p_{H_2O}^{1/2} \cdot [≡SiOH]^{1/2} \tag{3}$$

To generate an $H_3O^+ + OH^-$ couple it takes, however, two H_3O^+ ions as was depicted schematically above. Hence



or

$$[H_3O^+ + OH^-] \propto [H_3O^+]^2 \tag{21}$$

Substitution of Eq. [3] in Eq. [21] gives

$$[H_3O^+ + OH^-] \propto p_{H_2O} \cdot [≡SiOH] \tag{22}$$

From Eq. [22] and Eq. [19] it follows that

$$k_{par} \propto p_{H_2O} \cdot [≡SiOH] \tag{23}$$

It is evident that the linear relationship between k_{par} and p_{H_2O} results from the fact that two water molecules have to dissolve before diffusion is possible. The square root of the solubility relation is canceled by the power of two appearing in Eq. [21]. In other words, a linear absorption isotherm is found for the real diffusant ($H_3O^+ + OH^-$) and not for water which dissolves proportionally with the square root of water pressure.

The Linear Oxidation Regime

When, as is shown in the previous section in Eq. [23], the parabolic rate constant is dependent on the silanol concentration, it must also be dependent on thermal history and is expected to change slowly with time as discussed above. Thermal history-dependent changes of many physicochemical properties were reported by Brückner (10) and related to the silanol concentration.

In this section the time dependence of the diffusion coefficient is investigated and especially the influence of this time dependence on the growth curves of oxide layers on silicon. The approach is essentially based on the work of Crank (16) on slowly changing diffusion processes in history dependent systems [see Ref. (16), chap. 11.3.1]. Also the method of manipulation with the time dependence of the diffusion coefficient is taken from Crank [see Ref. (16) chap. 7].

The change of the diffusion coefficient is assumed to be a first-order change given by

$$\frac{\partial D}{\partial t} = (D_{eq} - D) \tau^{-1} \tag{24}$$

where D is assumed to increase with time until a final equilibrium value D_{eq} is obtained. τ is in general a concentration-dependent relaxation time. Crank introduces an instantaneous diffusion process which accounts for the flux immediately after increase of penetrant concentration and derives an overall expression for the rate of change of the diffusion coefficient on location x

$$\left(\frac{\partial D}{\partial t}\right)_x = \left(\frac{\partial D_1}{\partial c}\right) \left(\frac{\partial c}{\partial t}\right)_x + (D_{eq} - D) \tau^{-1} \tag{25}$$

where D_1 is the instantaneous diffusion coefficient. The number of adjustable parameters is so large, however, that comparison of theory and the experimental data cannot be very conclusive (16). In the following we shall make some assumptions which considerably restrict the number of parameters: (i) τ and D are assumed to be concentration independent, (ii) τ and D are assumed to be independent of x , and (iii) D_1 and $\partial D_1/\partial c$ are assumed to be negligibly small.

Now Eq. [25] reduces to Eq. [24] and after integration the diffusion coefficient is given by

$$D = D_{\text{eq}} \left[1 - \exp\left(-\frac{t}{\tau}\right) \right] \quad [26]$$

D is now only dependent on t and we shall use this property in the following derivation (16).² When D is only dependent on t , Ficks second law

$$\frac{\partial c}{\partial t} = \frac{\partial}{\partial x} \left[D(t) \frac{\partial c}{\partial x} \right] \quad [27]$$

may be rewritten as

$$\frac{\partial c}{\partial t} = D(t) \frac{\partial^2 c}{\partial x^2} \quad [28]$$

Now a new time variable T defined by

$$T \equiv D_{\text{eq}}^{-1} \int_0^t D(t) dt \quad \text{or} \quad dT = \frac{D(t)}{D_{\text{eq}}} dt \quad [29]$$

is introduced. With Eq. [29] we may convert Eq. [28] into

$$\frac{\partial c}{\partial T} = D_{\text{eq}} \frac{\partial^2 c}{\partial x^2} \quad [30]$$

By this manipulation the right-hand side of Eq. [30] has become time independent. In the steady state $\partial c/\partial t = 0$ and when t is a function $f(T)$ of T only then also

$$\frac{\partial c}{\partial T} \frac{\partial f(T)}{\partial t} = 0$$

which implies that $\partial c/\partial T = 0$ when

$$\frac{\partial f(T)}{\partial t} \neq 0$$

and then the right-hand side of Eq. [30] is equal to zero too.

We have defined now a steady-state situation but it must be kept in mind that we use another time variable T . In the steady-state condition $J(T) = D_{\text{eq}} \partial c/\partial x = \text{constant}$. This enables us to rewrite the growth rate, defined by Eq. [17]

$$\frac{dx_0}{dt} = M_0^{-1} \left[D(t) \frac{\partial c}{\partial x} \right]_{x=0} \quad [17]$$

into a form where the growth rate is (quasi) steady state

$$\frac{dx_0}{dT} = M_0^{-1} D_{\text{eq}} \left(\frac{\partial c}{\partial x} \right) \quad [31]$$

or

$$\frac{dx_0}{dT} = M_0^{-1} D_{\text{eq}} \frac{\Delta c}{x_0} \quad [32]$$

The concentration difference Δc has to be related to the ambient pressure p . Because D and Δc are effective quantities rather than a physically defined diffusion coefficient and concentration it is useful to ex-

² In the case of reaction of the diffusant with the lattice the loss of diffusant by immobilization must be taken into account [see Crank (16), chap. 14]. The continuity equation becomes, when $D \neq D(c, x)$

$$\frac{\partial c}{\partial t} = D \frac{\partial^2 c}{\partial x^2} - \frac{\partial s}{\partial t}$$

where the term $\partial s/\partial t$ accounts for the rate of change of absorbed or immobilized substance. In the case of a linear absorption isotherm (cf. Eq. [22]) the concentration of immobilized substances is given by

$$s = k \cdot c$$

where k is the absorption coefficient, $\partial s/\partial t$ can be substituted directly by $k \partial c/\partial t$, which gives

$$\frac{\partial c}{\partial t} = \frac{D}{k+1} \frac{\partial^2 c}{\partial x^2}$$

The continuity equation is reduced to the usual form without immobilization when an effective diffusion coefficient $D_{\text{eff}} = D/(k+1)$ is introduced [see also Ref. (17)].

press Eq. [32] in terms of permeation constant P and pressure difference Δp . In the case that D is constant and the absorption isotherm is linear (see preceding section) we may write

$$P_{\text{eq}} \frac{\Delta p}{x_0} = D_{\text{eq}} \frac{\Delta c}{x_0} \quad [33]$$

and substitute the corresponding terms in Eq. [32] to obtain

$$\frac{dx_0}{dT} = M_0^{-1} P_{\text{eq}} \frac{\Delta p}{x_0} \quad [34]$$

Integration of Eq. [34] gives

$$x_0^2 = 2M_0^{-1} \cdot P_{\text{eq}} \cdot \Delta p \cdot T \quad [35]$$

An expression for T can be found by substitution of $D(t)$ in Eq. [29] by the expression given in Eq. [26] and subsequent integration. By taking $T = 0$ when $t = 0$ one obtains

$$T = t + \tau \exp\left(-\frac{t}{\tau}\right) - \tau \quad [36]$$

Substitution of T in Eq. [35] gives the rate law for oxide growth as function of real time

$$x_0 = \sqrt{B} \cdot \sqrt{t + \tau \exp\left(-\frac{t}{\tau}\right) - \tau} \quad [37]$$

where

$$B = 2M_0^{-1} P_{\text{eq}} \Delta p \equiv k_{\text{par}}$$

This is a linear-parabolic oxidation law which may be compared with the expression given by Deal and Grove (1)

$$x_0 = \sqrt{B} \sqrt{t + \frac{A^2}{4B}} - \frac{A}{2} \quad [38]$$

where $A^2/4B$ is a characteristic time (to be compared with τ) and $A/2$ is the ratio of the effective diffusion coefficient D_{eff} and the reaction rates k and h for the exchange reactions at the interfaces given by

$$\frac{A}{2} = D_{\text{eff}} \left(\frac{1}{k} + \frac{1}{h} \right) \quad [39]$$

Equations [37] and [38] converge to the same parabolic rate law for relatively large times, i.e., $t \gg \tau$ and $t \gg A^2/4B$

$$x_0 \cong \sqrt{B} \cdot \sqrt{t} \quad [40]$$

For relatively small oxidation times, i.e., $t \ll \tau$ Eq. [37] becomes linear

$$x_0 \cong \sqrt{\frac{B}{2\tau}} \cdot t \quad [41]$$

and in the comparable situation, where $t \ll A^2/4B$, Eq. [38] reduces to the linear form

$$x_0 \cong \frac{B}{A} \cdot t \quad [42]$$

When the two linear-parabolic expressions are plotted, as may be seen in Fig. 7, the resemblance is considerable. The maximum difference between the oxide thicknesses at comparable t is only 22%. However, the experimental error is mostly small enough to enable the discrimination between the two growth curves.³ In order to discriminate between the two

³ Theoretically, it is possible that the exchange reaction at one of the interfaces and the time-dependent diffusion are equally rate determining, i.e., $\tau \cong A^2/4B$. In this case one may proceed with the derivation of the growth rate using the expression of Eq. [34] and equating the diffusion-controlled fluxes passing through the interfaces. The derivation is the same as that used by Deal and Grove substituting t with T . The full expression is a combination of Eq. [37] and Eq. [38] and is given by (13)

$$x_0 = \sqrt{B} \cdot \sqrt{t + \tau \exp\left(-\frac{t}{\tau}\right) - \tau} + \frac{A^2}{4B} - \frac{A}{2}$$

In the case that $\tau = A^2/4B$ and $t \ll \tau$ a square root law (i.e., $\sqrt{x_0} \propto t$) is obtained. The experimental evidence for the square root law was not found.

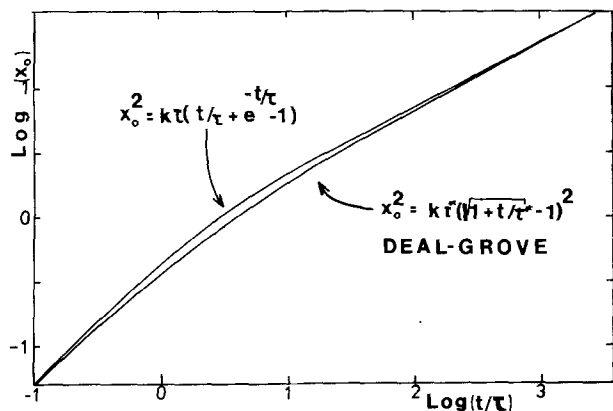


Fig. 7. Comparison of relationship given by Eq. [37] and [38]. $\tau^* \equiv A^2/4B$. The maximum difference between the two curves is only 22%.

linear-parabolic rates laws a curve-fitting procedure can be used. It is then advisable to take the derivative of the logarithmic form of the growth curves. This reduces the power n in the rate law $x_0 \propto t^n$ to a value, i.e., $d \log x_0 / d \log t = n$. The curves are now completely determined by x_0 , t , τ , and n (see Fig. 8). (For the experimental data see Discussion section.) A more sophisticated method is to investigate the dependence of the linear rate constants or the characteristic times on water partial pressure. In Table II the expected dependence for k_{lin} and k_{par} and $t_{\text{char}} = A^2/4B$ is given for the two alternative models.

Oxidation in O₂-H₂O Ambients

When silicon is oxidized in oxygen, trace amounts of water influence the oxidation rate. The parabolic rate constant increases significantly when, instead of ultra dry oxygen, normally dried oxygen with 25 ppm H₂O is used (19). Irene and Ghez (19) question the parallel and independent transport of water and oxygen. The influence of water is explained qualitatively by the assumption that traces of water loosen the silica network allowing the oxygen to move faster. There is one obvious argument which supports the assumption that the oxygen and water species do not move independently. Water reacts with silicon to form hydrogen (Eq. [4]). This hydrogen can diffuse back into an ambient of oxygen; it will then certainly react forming water again. It may also react with silica to form reduced species. These are reoxidized in a later step by diffusing oxygen.

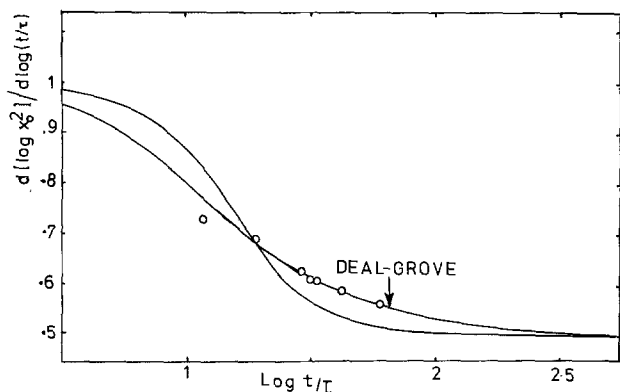


Fig. 8. The derivatives of the expressions in Eq. [37] and [38] in logarithmic form are plotted against the normalized time. The linear part of the growth curve corresponds to the value 1 on the vertical axis, the parabolic part corresponds to the value 1/2. The growth curves are totally defined by B , t , and τ (or $A^2/4B$). Drawn circles are representing the data of Pliskin (5) (see Discussion section).

It is assumed here that every hydrogen will encounter an oxygen, i.e., will be oxidized. It can only leave the silica in the oxidized state. The situation can be easily understood by inspection of a schematic plot of the concentration against distance in the oxide layer. In Fig. 9 the situation is drawn where the partial pressure of water is much smaller than the pressure of oxygen. Because the reaction rate is larger at high concentrations and smaller at low concentrations the silicon is oxidized by an excess of oxygen and water is hardly consumed. The concentration gradient for oxygen will be constant in a steady-state process. There is no concentration gradient for water.

When the water concentration is increased the horizontal waterline rises and will somewhere cross the oxygen gradient. Now water takes part in the oxidation of the silicon, hydrogen will be formed, diffuse back in the direction of the ambient, and will ultimately react forming water. When the reaction rate is fast enough the excess water will be formed left of the cross-over point and will diffuse back to the silicon again. In this region the hydrogen will consume part of the oxygen. The concentration of oxygen will be lowered. Relatively more water takes the place of oxygen in the reaction at the silicon interface. It is easily understood that the situation will end up as depicted in Fig. 10. Water will be the only diffusant, left of the point x_1 of equal concentration, and oxygen will be the only diffusant at the right-hand side. This means that the fluxes of diffusants must be equal in the two layers with thickness $0 - x_1$ and $x_1 - x_0$, hence

$$J_{(\text{H}_3\text{O}^+ + \text{OH}^-)} = J_{\text{O}_2} = J \quad [48]$$

From this flux J a fraction $(x_1/x_0)J$ increases the thickness of layer x_1 and a fraction $[(x_0 - x_1)/x_0]J$ is converted to increase the layer thickness $x_0 - x_1$.⁴ The increase of layer thickness dx_1 in the time dt is given by

$$dx_1 = \frac{x_1}{x_0} \cdot M_0^{-1} \cdot |J| \cdot dt \quad [49]$$

and for layer thickness $x_0 - x_1$

$$d(x_0 - x_1) = \frac{x_0 - x_1}{x_0} M_0^{-1} \cdot |J| \cdot dt \quad [50]$$

From Eq. [48] it is clear that

$$|J| = D_{(\text{H}_3\text{O}^+ + \text{OH}^-)}(t) \frac{c_1}{x_1} = D_{\text{O}_2}(t) \cdot \frac{c_0' - c_1'}{x_0 - x_1} \quad [51]$$

where c_1 is the water species concentration at x_1 and

⁴ It is a formal way of stating; in fact the layer thickness x_0 increases, and the layer thickness x_1 increases with a rate which is x_1/x_0 times the rate of the layer x_0 .

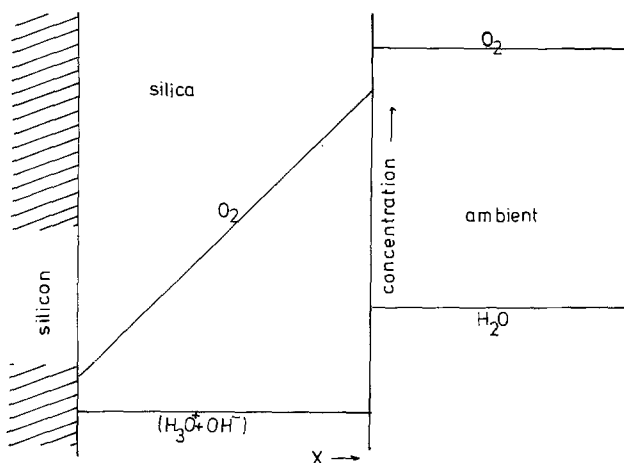


Fig. 9. Permeation of oxygen under steady-state conditions, when the pressure of water is extremely low. (The diffusion coefficient is assumed concentration independent.)

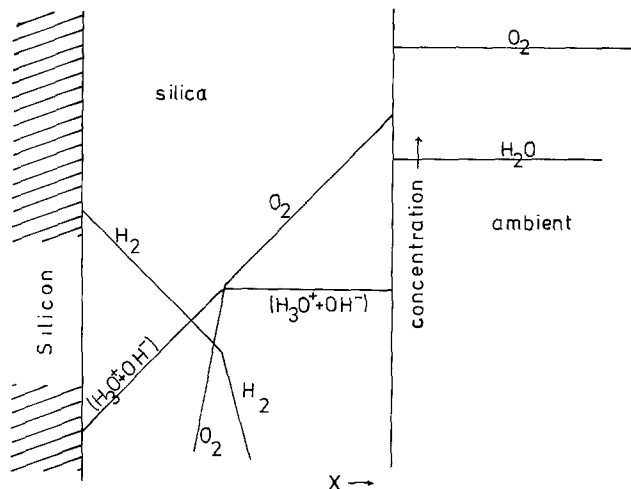


Fig. 10. The same as for Fig. 9 with a higher value for the partial pressure of water.

c_o' and c_i' the oxygen concentration at x_o and x_i , respectively. By substituting [31] and following the same method as in the previous section for Eq. [31]

$$\frac{dx_o}{dt} = M_o^{-1} \cdot |J| = \frac{k_{H_2O} \dot{T}_{H_2O}}{2x_i} = \frac{k_{O_2} \dot{T}_{O_2}}{2(x_o - x_i)} = \frac{k_t \dot{T}}{2x_o} \quad [52]$$

where $k_{H_2O}/2$, $k_{O_2}/2$, and $k_t/2$ are the parabolic rate constants for the water layer ($0 < x < x_i$), the "oxygen" layer ($x_i < x < x_o$), and the total oxide layer ($0 < x < x_o$), respectively, T_{H_2O} , T_{O_2} , and T are the various time functions dT/dt which are equal to the ratio of momentary and equilibrium diffusion coefficients, D/D_{eq} for the various layers. By substituting the corresponding expressions for $M_o^{-1}J$ in Eq. [49] and [50] the increase of the layer thickness becomes

$$dx_i = \frac{k_{H_2O}}{2x_o} T_{H_2O} dt \quad [53]$$

and

$$d(x_o - x_i) = \frac{k_{O_2}}{2x_o} T_{O_2} dt \quad [54]$$

By addition of Eq. [53] and [54] and subsequent integration, a general relationship for steady-state growth of a sandwich layer with two time-dependent diffusion coefficients is found

$$x_o^2 = k_{H_2O} T_{H_2O} + k_{O_2} T_{O_2} \quad [55]$$

in which the initial condition is used that $T_{H_2O} = T_{O_2} = 0$ when $x_o = 0$.

When we adopt the expression of Eq. [36] for T_{H_2O} and assume that oxygen diffusion is not retarded by absorption then $T_{O_2} = t$ and we can convert Eq. [55] to

$$x_o^2 = k_{O_2} t + k_{H_2O} \left[t + \tau \exp\left(-\frac{t}{\tau}\right) - \tau \right] \quad [56]$$

Equation [56] shows a three parameter expression and this may be compared to the expression used by Deal (18) which has three adjustable parameters too. One of the parameters in Deal's expression is an initial thickness x_{in} or initial time t_{in} correction term. This has to be introduced to correct for the so called "rapid initial oxidation phase." In the next section it will be shown that Eq. [56] predicts this nonlinear initial growth.

The "Initial Oxidation" Regime

The use of the Deal-Grove expression to describe the growth curves is consistent with the data only when a

correction term is introduced to account for what is called "the rapid initial oxidation phase." This super-linear initial growth is found only for mixed O_2 - H_2O ambients and for pure O_2 oxidation (1, 19). Deal and Grove (1) indicated that a field-assisted oxygen transport might be the explanation. The difference between oxygen and water vapor was explained from the difference in Debye length calculated from the number of charge carriers in the different oxides.

It was shown by Horiuchi *et al.* (20) that for extremely dry oxygen ambients an inverse logarithmic growth regime is found which is characteristic for the field-assisted growth (also called Mott-Cabrera mechanism). There is, however, a maximum thickness at which the Mott-Cabrera mechanism stops being effective. Horiuchi (20) shows that this thickness is about 60-70Å which is much less than the 200-800Å oxide thickness where the rapid initial growth is found (19).

After inspection of Eq. [56] it becomes clear that when

$$k_{O_2} \cdot t > k_{H_2O} \left[t + \tau \exp\left(-\frac{t}{\tau}\right) - \tau \right]$$

or

$$t < 2 \frac{k_{O_2}}{k_{H_2O}} \tau (\equiv t_{in}) \quad [57]$$

there must be a parabolic regime preceding the linear part of the growth curve. The physical meaning of this parabolic mechanism is the direct oxidation of Si by oxygen without the intervention of reacting hydrogen, at least the latter is not rate determining. t_{in} is defined as the time when the initial growth stops being effective.

Discussion

To check whether the time-dependent diffusional transport (model presented here) or the constant diffusional transport with limiting interface reactions (model of Deal and Grove) applies to the oxidation mechanism, the experimental data may be analyzed on three characteristics (cf. Table II): (i) dependence of characteristic time ($A^2/4B$) on water partial pressure, (ii) dependence of k_{lin} ($= B/A$) on water partial pressure, and (iii) fitting of Eq. [37] or [38] (or Eq. [56]) to experimental data.

In the case that there is a rapid initial growth we may also check if the relationship given in Eq. [57] is obeyed.

Oxidation in pure water vapor.—From the small number of pure water vapor oxidation data those of Pliskin (5) have been selected for analysis. The values of the characteristic time $k_{par}/4k_{lin}^2$ or $A^2/4B$ have been plotted against water partial pressure in Fig. 11. From this it can be concluded that there exists an inverse relationship indicating that we are dealing with an interface reaction-limited growth (Deal and Grove mechanism).

In Fig. 8 the data of Pliskin (5) have been replotted in a special way. The slope of the logarithmic growth curve is determined on each experimental point using the two adjacent points. The values of the slopes may be compared with the derivatives of Eq. [37] and [38]. From Fig. 8 it follows that the points coincide with the Deal and Grove curve which is consistent with the conclusion above. Finally also the values of B/A plotted against water partial pressure suggest a reciprocal relationship. This is obvious when $A^2/4B \propto p_{H_2O}^{-1}$ (and $B \propto p_{H_2O}$), but the power is not exact unity as can be seen in Fig. 11. The conclusion may be that the oxidation mechanism is probably of the Deal-Grove type. Whether the limiting reaction is at the inner or at the outer surface of the silica layer is not yet clear.

Mixed O_2 and H_2O ambients.—The analysis of mixed ambient oxidation was restricted to the data presented by Deal *et al.* (1, 18, 21) and Irene *et al.* (2, 19,

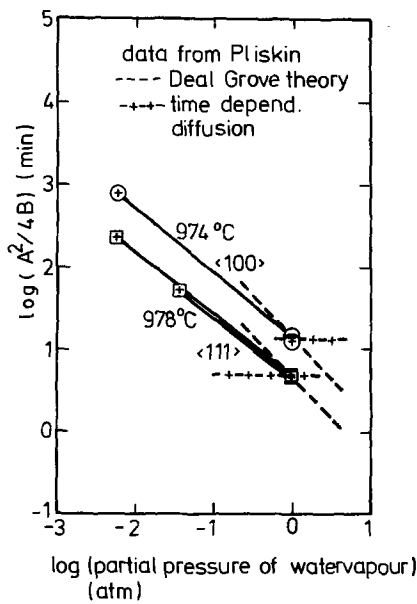


Fig. 11. Dependence of the characteristic time $A^2/4B$ on the water partial pressure in the ambient. Data taken from Pliskin (5).

22). The dependence of characteristic time $A^2/4B$ on water partial pressure can be seen in Fig. 12. The slightly inclined curves show that there is a very small variation of the characteristic time over several decades of water pressure. The slopes correspond to powers of less than 0.1. This suggests that the model of time-dependent diffusional transport may be applied.

The second criterion is to plot k_{lin} against water partial pressures. Deal (21) noticed a strong deviation of the experimental and theoretical dependence of k_{lin} on p_{H_2O} . As can be seen in Table II a linear dependence is expected in the Deal and Grove theory. It is shown in Fig. 13 that Deal's data for k_{lin} are consistent with the model presented here. Replotting k_{lin} against $p_{H_2O}^{1/2}$ a straight line is obtained with a remarkably small deviation. The difference between the <111> and <100> orientation is discussed later.

The third criterion is fitting the experimental data to Eq. [56]. This implies the sequential transport of oxygen by oxygen molecules and water species and excludes rate-determining exchange reactions. In addition, it assumes that the oxygen molecule diffusion coefficient is not time dependent. This assumption is based on results on tracer investigations by Rosencher *et al.* (23) which were reviewed by Mott (24). The experiments of Rosencher clearly prove that no oxygen is exchanged with the network oxygen during growth.

Deal's (21) and Irene's (22) data have been replotted in Fig. 14 and 15 together with the curves calculated by the expression given in Eq. [56]. The three parameters k_{O_2} , k_{H_2O} , and τ have been evaluated using a least squares technique. The deviation of the experimental data is almost everywhere within 3%, which is about the estimated error in the layer thickness determination Deal (21) and Irene (19) report a much larger

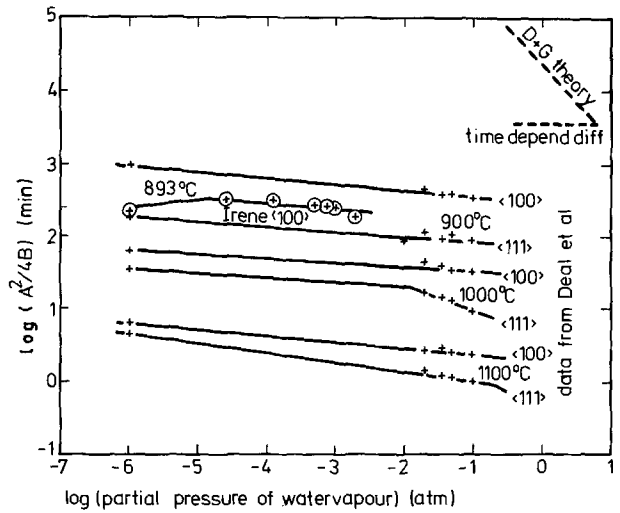


Fig. 12. The same as for Fig. 11 but now for mixed $O_2 + H_2O$ ambients. Data taken from Deal *et al.* (21) and Irene *et al.* (19).

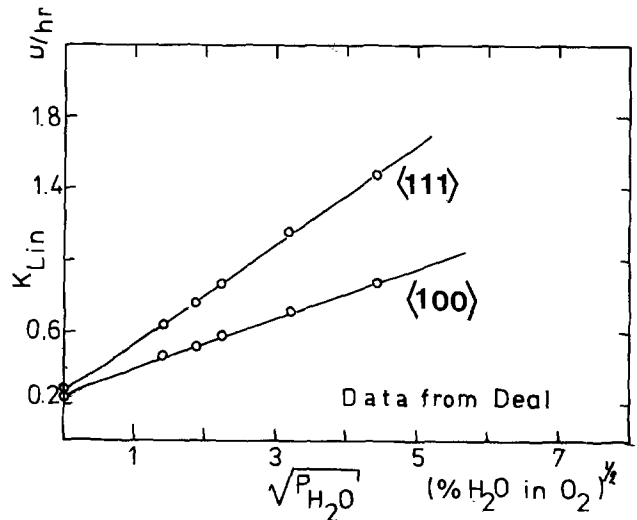


Fig. 13. The linear rate constant varies with the square root of water pressure as follows from Eq. [43] rather than being proportional to water pressure as would follow the Deal-Grove theory. Data taken from Deal *et al.* (21).

deviation of experimental and theoretical data when using independent O_2 and H_2O transport.

It follows from the model of sequential transport of O_2 and H_2O that, even at very small water concentrations in the ambient, water may play a role in the oxidation rate (2, 19). Because the effective diffusion coefficient of water is two orders of magnitude larger than that of oxygen (1), water plays an equal role in the oxidation process when the partial pressure is only 1% (i.e., $x_i = 1/2x_o$ when $p_{H_2O} = 0.01p_{O_2}$). In not thoroughly dehydrogenerated oxygen the partial pressure of water is expected to exceed 25 ppm (2). In a growing layer of about 1000Å, the region x_i , where

Table II. Dependence on water partial pressure of k_{lin} , k_{par} , and t_{char} for the two models

Model	Expression	k_{lin}	k_{par}	t_{char}
Totally diffusion determined $D = D(t)$	Eq. [37] $x_o = \sqrt{B} \cdot \sqrt{t + \tau} \exp\left(-\frac{t}{\tau}\right) - \tau$	Eq. [43] $\sqrt{\frac{B}{2\tau}} \propto \sqrt{p_{H_2O}}$	Eq. [45] $B \propto p_{H_2O}$	$\tau \neq f(p_{H_2O})$
Diffusion- and/or reaction rate at interface-determined. $D = \text{const.}$ (Deal + Grove model)	Eq. [38] $x_o = \sqrt{B} \cdot \sqrt{t + \frac{A^2}{4B}} - \frac{A}{2}$	Eq. [44] $\frac{B}{A} \propto p_{H_2O}$	Eq. [46] $B \propto p_{H_2O}$	Eq. [47] $\frac{A^2}{4B} \propto p_{H_2O}^{-1}$

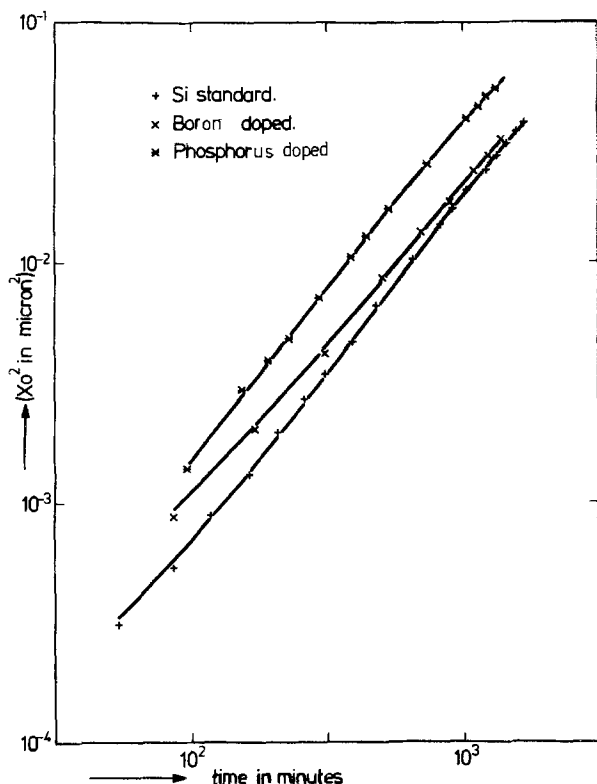


Fig. 14. Equation [56] fitted by a regression technique on the data of Irene *et al.* (22). The maximum deviation is within experimental error. It shows that the initial growth process is an implication of the model used here. P, B, and STD denote phosphorus, borium doped, and standard quality silicon, respectively.

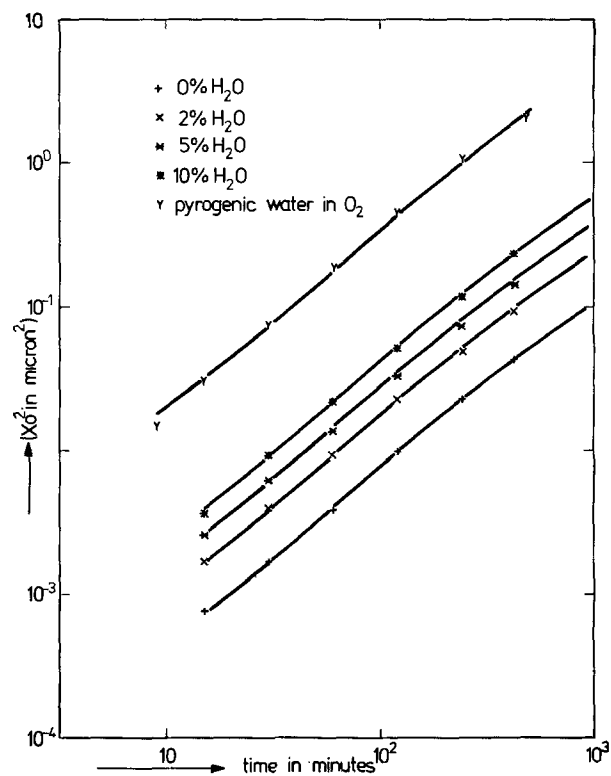


Fig. 15. The same as Fig. 14 fitted on the data of Deal *et al.* (21). Figures denote the volume percentage of H₂O in O₂. Pyr. denotes the use of H₂ + O₂ in a ratio corresponding to an H₂O/O₂ gas mixture from an oxygen gas stream bubbled through a water bath of 96°C. Using a model with independent fluxes of O₂ and H₂O through silica would give much larger deviations of experimental and theoretical curves (21).

water transport dominates, will extend to 25Å from the Si-interface.

The reversible increase and decrease of the oxidation rate by the variation of the water partial pressure from <1 ppm to 2000 ppm and back (19) can be explained in terms of the thickness variation of the region controlled by diffusion of H₃O⁺ + OH⁻.

Activation energies.—When for H₂O + O₂ ambients and for relatively dry O₂ ambients the values of τ are plotted against $1/T$, we expect to find a single activation energy for a model with a time-dependent diffusion. The values of τ [calculated from the data reported by Deal (5) and Irene *et al.* (19)] are plotted in such a manner for <100> and <111> Si orientation in Fig. 16 and 17, respectively. Below a certain value of $1/T$ an activation energy of 3.1–3.6 eV is found for all ambients and orientations. This indicates that it may be indeed a single activation energy which is thought to correspond to the incorporation reaction of water in the silica network. The strength of a Si–O–Si bond is expected to be in the order of 4 eV (8). This value is found for growth in pure water vapor (5). In mixed O₂ + H₂O ambients there is an effect of the two layer mechanism which can cause a lowering of the effective activation energy. In fact, the value x_1/x_0 in Eq. [49] and [50] is temperature dependent. In general, when we deal with a series-transport through two layers in steady-state conditions, then the layer with the highest resistance for transport will decrease in thickness and that with the lowest resistance will increase in thickness until the fluxes through the layers match. These layer thicknesses may be different for the same ratio of k_{H_2O} and k_{O_2} at different temperatures and therefore influence the apparent activation energies.

Above a certain value of $1/T$, *i.e.*, below 950°–1000°C, the activation energies scatter. These values of $1/T$, which are not easily determined from Fig. 16 and 17, correspond to the range of temperatures where the glass transition is expected. The glass transition range

is characterized by the time needed for a glass to accommodate to a strain by reorganizing the network (16). In this region we expect anomalous diffusion effects to occur (16). The question arises whether the simple transport models we have used in the previous sections are then allowed. In fact stress-induced transport is known to give moving boundary (*i.e.*, growth) curves which mostly follow linear-parabolic rate laws too (16). There is no doubt that these effects play a role in the oxidation of silicon. In fact Eernisse (25, 26) has shown that silica growing in wet ambients is subjected to compression. Pliskin (5) reported mea-

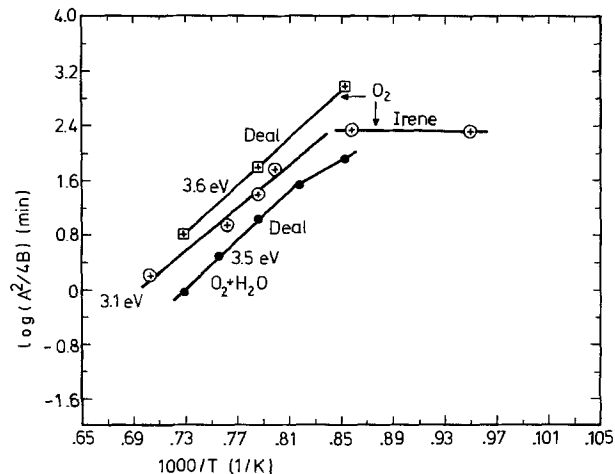


Fig. 16. Variation of the characteristic time $A^2/4B$ with reciprocal absolute temperature, typical is the sharp bending between 900° and 1000°C. Data for <100> Si. Data taken from Deal *et al.* (21) and Irene *et al.* (22).

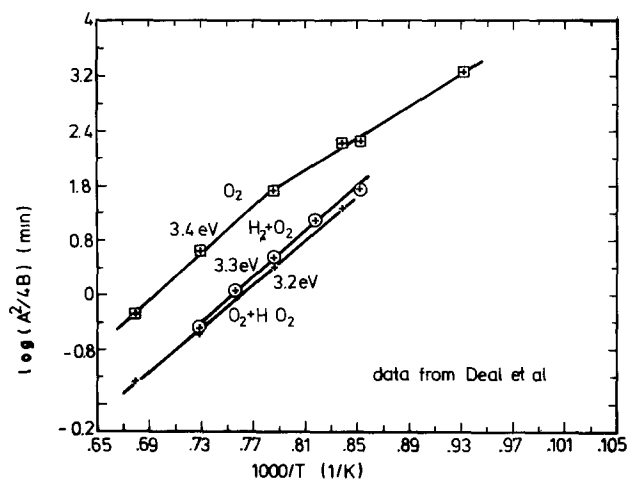


Fig. 17. The same as Fig. 16 but for $\langle 111 \rangle$ Si. Data from Deal et al. (1, 18, 21).

surable effects on the growth curves induced by stresses originating from locally stripped oxide films. There is one effect which may be explained qualitatively by the effect of the compression of silica during the growth. The compressive stress originates from the elastic deformation of the silicon substrate. It is expected to act especially on the first layers of silica adjacent to the Si/SiO₂ interface. In H₂O + O₂ ambients this is part of the layer where water transport is the prior mechanism. Because, as was stated above, the layer is thin when the resistance is large we expect especially a large effect of the compression in the region where the resistance to transport is large, i.e., the linear region of the growth curves. As was stated above, the compression originates from the elastic deformation and an effect is expected from the orientation of the Si-substrate.

Young's modulus for $\langle 111 \rangle$ oriented Si is about 1.5 times that for $\langle 100 \rangle$ oriented Si so it might have an appreciable effect. Indeed the k_{lin} for $\langle 111 \rangle$ oriented Si is found to be larger than k_{lin} for $\langle 100 \rangle$ oriented Si (see Fig. 13), in the same order of magnitude. The dependence of k_{lin} on Si-orientation was explained in terms of the Si-Si-bond breaking and the number of dangling bonds by Ligenza (27). In that case it ought to show up in an activation energy difference for $\langle 111 \rangle$ and $\langle 100 \rangle$ oriented Si. We can see from Fig. 16 and 17 that there is no significant difference in the activation energy for the characteristic time $k_{par}/4k_{lin}^2$. The parabolic rate constant is found to be independent of orientation and as a consequence k_{lin} must have the same activation energy for both orientations.

There is only a difference in the magnitude of k_{lin} which increases with water pressure. This increase is proportional to the square root of water pressure and originates probably from the total amount of water dissolved in the compressed layer.⁵ The swelling (11) of silica in water vapor is perhaps also the reason that the diffusion of water in silica is a process with a relatively small activation energy of about 0.7 eV (29). The activation energy was expected to correspond to the Si-O-Si bond breaking energy of about 4 eV [see Doremus (8)]. The swelling of silica may cause the bonds to break under mechanical strain.

The activation energy of 0.7 eV might equally well correspond to the activation energy for the formation of hydroxyl groups (OH⁻) (see the scheme in the section on Transport of Water Through Silica). The large effect of contamination on growth rate of oxide layers

⁵ The fact that Si oxidizes at low temperatures (28) of 400°C and even at room temperatures is difficult to explain when a surface reaction with a high activation energy of 1.9 eV controls the oxidation rate at 1000°C. The absence of the Arrhenius equation for k_{lin} and the change of the activation energy in the glass transition range indicate that another effect (e.g., stress effect) is involved.

might be because of the generation of (OH⁻) groups by reaction with water [e.g., Na⁺ accelerates the growth rate of oxide layers enormously (4)]. The experiments of Jorgensen and Norton (30) where the growth of oxide layers could be inhibited or accelerated by positive or negative fields can be explained also by assuming that the negative minority charge carriers OH⁻ are stopped or accelerated, respectively.

Conclusions

1. The solubility of water is proposed to proceed in two steps: (i) the formation of $\equiv\text{SiOH}$ groups. A relative slow process at temperatures up to 1100°C; and (ii) hydrolyzation of $\equiv\text{SiOH}$ under formation of $\text{H}_3\text{O}^+ + \equiv\text{SiOH}^-$. The process is relatively fast at temperatures even below 900°C.

2. It has been shown that water migrates through silica by species containing 4 H-atoms. The ambipolar diffusion of $\text{H}_3\text{O}^+ + \text{OH}^-$ has been proposed.

3. The linear variation of k_{par} or B with water pressure in growing silica layers follows directly from the proposed mechanisms in 1 and 2 above.

4. By adopting a time-dependent diffusion coefficient an expression can be obtained describing the oxide growth in terms of a parabolic rate constant and a relaxation time.

5. A model for the sequential diffusion of water and oxygen is proposed. An expression for the time dependence of x_0 (without surface reactions) has been obtained which includes the initial growth process also. Experimental growth curves can be represented accurately by the proposed expression.

6. The activation energy of the characteristic time $k_{par}/4k_{lin}^2$ has a value of 3.1-3.6 eV for dry and wet oxidations. The value is near to the Si-O-Si bond breaking energy.

7. It is argued that the difference in k_{lin} for various orientations may originate from stresses induced by the swelling of silica in water vapor.

Acknowledgments

The author wishes to thank Messrs. P. Hart, L. Heijne, J. Snel, J. Verwey, and H. Verwey for valuable discussions. He is indebted to Mr. C. van Oordorp for the suggestion of the use of the time-dependent diffusion coefficient which played an essential role in the achievement of the concept of the section on The Linear Oxidation Regime.

Manuscript submitted Feb. 5, 1980; revised manuscript received April 7, 1980.

Any discussion of this paper will appear in a Discussion Section to be published in the June 1981 JOURNAL. All discussions for the June 1981 Discussion Section should be submitted by Feb. 1, 1981.

Publication costs of this article were assisted by Philips Research Laboratories.

REFERENCES

- B. E. Deal and A. S. Grove, *J. Appl. Phys.*, **36**, 3770 (1965).
- E. A. Irene, *This Journal*, **121**, 1613 (1974).
- G. J. Roberts and J. P. Roberts, *Phys. Chem. Glasses*, **5**, 26 (1964); T. Drury and J. P. Roberts, *ibid.*, **4**, 79 (1963); I. Burns, and J. P. Roberts, *ibid.*, **11**, 106 (1970).
- A. G. Revesz, *This Journal*, **126**, 122 (1979), A. G. Revesz and R. J. Evans, *J. Phys. Chem. Solids*, **30** 551 (1969).
- W. A. Pliskin, *IBM J. Res. Dev.*, **10**, 198 (1966).
- P. J. Burkhardt, *This Journal*, **114**, 196 (1967).
- G. E. Walrafen, *J. Chem. Phys.*, **62**, 297 (1975).
- R. H. Doremus, "Glass Science," John Wiley & Sons, Inc., New York (1973).
- G. van der Steen and E. Papanikolaou, *Philips Res. Rept.*, **30** 103 (1975); **30**, 192 (1975); **30**, 309 (1975).
- R. Brückner, *J. Non-Cryst. Solids*, **5**, 123 (1970); **5**, 281 (1971).
- J. F. Shackelford, J. S. Masaryk, and R. M. Fulrath, *J. Am. Ceram. Soc.*, **53**, 417 (1970).

12. J. F. Shackelford, P. L. Studt, and R. M. Fulrath, *J. Appl. Phys.*, **43**, 1619 (1972).
13. D. R. Wolters, *Inst. Phys. Conf. Ser. No. 50*, chap. 1, pp. 18-27 (1980).
14. D. J. Breed and R. H. Doremus, *J. Phys. Chem.*, **80**, 2471 (1976).
15. F. Booth, *Trans. Faraday Soc.*, **44**, 796 (1948).
16. J. Crank, "The Mathematics of Diffusion," Clarendon Press, Oxford (1975).
17. R. H. Doremus, *J. Phys. Chem.* **80**, 1773 (1976).
18. B. E. Deal, *This Journal*, **125**, 576 (1978).
19. E. A. Irene and R. Ghez, *ibid.*, **124**, 1757 (1977).
20. M. Horiuchi, J. Kamigaki, and T. Hagiwara, *ibid.*, **125**, 766 (1978).
21. B. E. Deal, D. W. Hess, J. D. Plummer, and C. P. Ho, *ibid.*, **125**, 339 (1978).
22. E. A. Irene and D. W. Dong, *ibid.*, **125**, 1146 (1978).
23. E. Rosencher, A. Straboni, S. Rigo, and G. Amsel, *Appl. Phys. Lett.*, **34**, 254 (1979).
24. N. F. Mott, *Inst. Phys. Conf. Ser. No. 50*, chap. 1, pp. 12-17 (1980).
25. E. P. Eernisse, *Appl. Phys. Lett.*, **30**, 290 (1977).
26. E. P. Eernisse, *ibid.*, **35**, 8 (1979).
27. J. R. Ligenza, *J. Phys. Chem.*, **65**, 2011 (1961).
28. A. M. Goodman and J. M. Breece, *This Journal*, **117**, 982 (1970); F. Lukes, *Surf. Sci.*, **30**, 91 (1972); F. P. Fehler, *This Journal*, **119**, 1723 (1972).
29. G. H. Frishat, "Ionic Diffusion in Oxide Glasses," p. 34, Trans. Techn. Publications, Aedermannsdorf Sw. (1976).
30. P. J. Jorgensen and F. J. Norton, *Phys. Chem. Glasses*, **10**, 23 (1969); P. J. Jorgensen, *J. Chem. Phys.*, **37**, 874 (1962).



Reaction of Copper Oxide with H₂S

J. L. Sansregret

Exxon Research and Engineering Company, Advanced Energy Systems Laboratory, Linden, New Jersey 07036

The corrosion of copper by atmospheric pollutants is a problem of continuing interest to the electronics industry. A pollutant of particular concern is H₂S and its attack on copper has been a topic of some discussion in the literature. It has been shown that a thin oxide film on Cu protects the underlying metal from attack by H₂S in air at room temperature (1). It has also been reported that copper oxides grown in air (several hundred angstroms thick) provide good protection against H₂S at low relative humidities but little protection against H₂S at high relative humidities and that oxides grown in pure oxygen provide more protection than air grown oxides (2). Thus, it is speculated that in the attack of Cu₂O by H₂S an intermediate reaction path involving H₂O is required. We report here on conditions under which copper oxide films will suffer direct attack by H₂S and convert to Cu₂S without an intermediate reaction path involving H₂O. We propose that the crystallinity and porosity of a Cu₂O film are important parameters in determining its reactivity towards H₂S and comment briefly on the thermodynamics of this reaction.

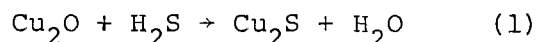
The attack of copper oxide by H₂S constitutes a gas-solid phase ion exchange reaction wherein the oxide ions in the anion sublattice are replaced by sulfide ions. We have recently developed a thin film ion exchange-chemical spray deposition (CSD) process (3) for

the growth of thin sulfide films that, in effect, models the attack of a copper oxide film by H₂S. In our process, thin sulfide films are grown through ion exchange of an oxide film to the sulfide by annealing in H₂S. We present here results relating to the problem of copper corrosion by H₂S and of protection by an overlaying copper oxide film.

Thin films of copper sulfide were grown by chemically spray depositing a copper oxide film and then annealing this film in H₂S to convert it to the sulfide. The copper oxide films were grown by spraying a water-methanol solution (25% H₂O by volume) of copper nitrate (0.01 M) onto a substrate to form the oxide. The films were then converted to the sulfide by annealing in flowing H₂S (5% in N₂) at 325°C for 30-45 minutes. Final film thicknesses were about 1.0 μ.

The resultant films were characterized by x-ray diffraction, ESCA and optical absorption measurements. The oxide films were found to consist of a bulk film of amorphous Cu₂O with crystalline particulates of CuO embedded in it. The sulfided films were found to contain three phases: Cu_{1.96}S, Cu_{1.8}S, and Cu_{1.75}S. There was no evidence of an oxide phase in the sulfided films.

The conversion of the oxide to the sulfide,



does occur despite the fact that the oxide is thermodynamically more stable than the sulfide (standard free energies of formation at 298°K for Cu₂O,

CuO, Cu₂S and CuS are, respectively, -34.98, -30.4, -20.6 and -11.7 kcal/mole (4). The driving force for the reaction of Equation 1 is the greater disparity in free energies of formation between H₂S and H₂O ($\Delta G^{\circ}_{298} = -46.74$ kcal/mole) than between Cu₂O and Cu₂S ($\Delta G^{\circ}_{298} = -14.38$ kcal/mole); the overall change in free energy for the reaction of Equation 1 is $\Delta G^{\circ}_{298} = -32.37$ kcal/mole, indicating spontaneity to the right as observed.

We propose that, in the direct conversion of copper oxide to copper sulfide by exposure to H₂S without an intermediate reaction path involving H₂O, the porosity and crystallinity of the oxide are controlling factors. Oxides that are amorphous and relatively porous will readily convert to the sulfide whereas those that are crystalline and structurally less porous (i.e., oxides grown by oxidation of Cu metal) will not. The fact that oxides grown in oxygen are structurally less porous and offer slightly greater protection against attack by H₂S (2) would appear to confirm this trend.

REFERENCES

1. W.H.J. Vernon, Trans. Faraday Soc., 23 113 (1927); 27 255 (1931).
2. S.P. Sharma, This Journal, 127 21 (1980).
3. J.L. Sansregret, patent pending, U.S. Serial No. 31421 (April 19, 1979).
4. "Handbook of Chemistry and Physics", Chemical Rubber Company, 54th Ed., p. D-64 (1973-74).

Manuscript received June 9, 1980.

Publication costs of this article were assisted by Exxon Research and Engineering Company.

Detection of Mobile Ion during the Anodic Oxidation of Silicon

G. Mende

Zentralinstitut für Kernforschung der Akademie der Wissenschaften der DDR,
Rossendorf, Bereich 2, DDR—8051 Dresden, Germany

INTRODUCTION

During anodic oxidation of silicon either the cation or the anion or both must move across the thickening oxide film(1). The mobile ion can be determined by labeling a thin surface layer with a completely immobile marker atom and detecting its position after anodizing the specimen (1).

Schmidt and Owen (2) labeled an oxide film on silicon by anodizing in tetrahydrofurfuryl alcohol containing ^{32}P as phosphate. When this film was anodized in the same electrolyte which contains nonradioactive phosphate, the radioactive ^{32}P was found in the inner layers. The authors concluded that the cation was the species that migrated.

However, by implanting a thin anodic oxide film on silicon with Kr and Xe and determining its position after anodizing by means of Rutherford backscattering analysis, Mackintosh and Plattner (1) found that the anion was responsible for anodic oxide growth in four different electrolytes. From their experiments the authors draw the conclusion that P moves inward during anodic oxidation.

Commenting on the paper of Mackintosh and Plattner (1), Schmidt (3) suggested identifying unambiguously the mobility of cations or anions by monitoring the sequence of cations before and after anodization with the help of epitaxial depositon of a very thin silicon layer isotopically enriched before anodizing in ^{30}Si on top of a normal silicon substrate.

In the present work an attempt is made to clarify this problem by comparing the depth distribution of ^{30}Si implanted into silicon with the depth distribution of ^{30}Si in anodic SiO_2 after anodization of silicon implanted with ^{30}Si . The amount of ^{30}Si can be identified as the radioactive isotope ^{31}Si after irradiation with thermal neutrons.

EXPERIMENTAL

Cleaned and polished $\langle 111 \rangle$ oriented samples of p-type silicon ($40\ \Omega\ \text{cm}$) were implanted nonaligned with ^{30}Si (dose = $3 \cdot 10^{16}$ atoms/ cm^2 , energy = 29 keV) and irradiated for $3.6 \cdot 10^3$ sec in the Rossendorf Research Reactor with a neutron flux of about

$4 \cdot 10^{13}\ \text{cm}^{-2}\text{sec}^{-1}$. After annealing treatment in a nitrogen atmosphere at 700°C for $1.8 \cdot 10^3$ sec the samples were anodized in a special galvanic cell (4). A 0.04N solution of KNO_3 ("purissimum per analysi") in ethylene glycol ("per synth.") served as an electrolyte. The current density was $7\ \text{mA}/\text{cm}^2$.

For determining the ^{30}Si implantation profile in silicon the implanted region (about 100 nm Si) was successively removed by anodizing of thin sheets (about 8 nm Si) under constant current and etching with HF (4). The radioactivity of the solution was detected with a Geiger-Muller-counter. The content of implanted ^{30}Si was calculated by means of a neutron-irradiated p-type silicon standard and by subtracting the natural content of ^{30}Si in silicon. The thickness of the removed layers was calibrated by anodic oxidation of neutron irradiated and annealed silicon which was implanted with ^{29}Si (dose = $3 \cdot 10^{16}$ atoms/ cm^2 , energy = 29 keV) to produce residual lattice damage similar to that in ^{30}Si implanted silicon after annealing treatment, and hence equal thickness/voltage increments during anodization.

For determining the ^{30}Si implantation profile in SiO_2 the implanted region (about 100 nm Si) was anodized in two steps (per step about 45 nm Si) under constant current density ($7\ \text{mA}/\text{cm}^2$) followed by a constant voltage period for $1.8 \cdot 10^3$ sec. The two films of anodized silicon were each successively removed (about 5 to 9 nm Si at a time) by etching for 60 sec with 1 ml of a 1:50 diluted solution containing 169 g NH_4F , 67.5 ml HF and 259 ml H_2O (5). The etch process was stopped by removing the buffered HF solution and by adding 1 ml of saturated boric acid solution in water. The radioactivity of the dissolved layers was determined in the above-mentioned way. The thickness (5-9 nm Si) of each removed layer (related to the Si content of SiO_2) was calibrated by anodic oxidation and by selective etching of neutron irradiated and annealed Si which was implanted with ^{29}Si (dose = $3 \cdot 10^{16}$ atoms/ cm^2 , energy = 29 keV).

Key words: silicon, anodic oxidation, mechanism of growing oxide film.

RESULTS AND DISCUSSIONS

The results of the experiments are summarized in Fig. 1. The theoretical depth

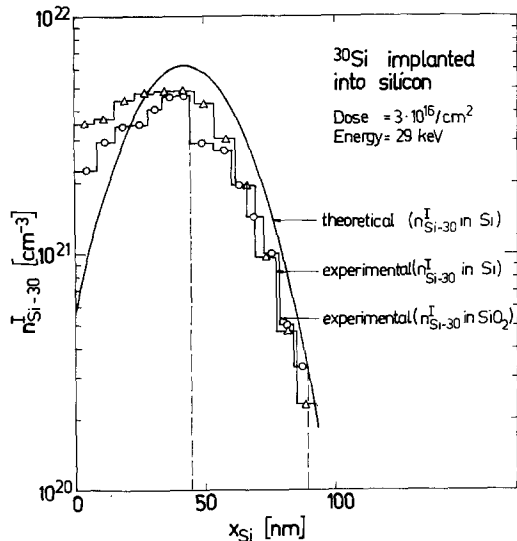


Fig. 1. The depth distribution of implanted ^{30}Si in silicon and in anodic SiO_2 (thickness related to the Si content of SiO_2). The standard deviation of thickness determination in SiO_2 is 15.5% and in Si is 9.5%. The standard deviation of determination of the implanted ^{30}Si content in SiO_2 is 15.7% and in Si is 10.7%.

distribution of ^{30}Si implanted into silicon was calculated with the help of the tables by Smith (6) according to the LSS-theory (7). The ^{30}Si profile in anodic SiO_2 (thickness related to the Si content of SiO_2) agrees well with the ^{30}Si profile in Si and with the theoretical profile. If the silicon ions are mobile during anodization and their order changes, a significant difference between the ^{30}Si profile in SiO_2 and the ^{30}Si profile in Si must be measured. But the results prove that the sequence of silicon ions does not change during anodization. This may be supportive evidence for the mobility of oxygen ions, but could equally be caused by silicon ions being mobile but maintaining their sequence during anodic oxide growth. It needs further investigations in order to identify the mobile species during anodic oxidation of silicon.

ACKNOWLEDGMENTS

The author wishes to thank Dr. P. F. Schmidt, Allentown, Pennsylvania, for his useful discussion and Mrs. Kuster, Mr. Muller, and Mr. Schneider for their technical assistance.

REFERENCES

1. W. D. Mackintosh and H. H. Plattner, *This Journal*, **124**, 396 (1977).
2. P. F. Schmidt and A. E. Owen, *This Journal*, **111**, 682 (1964).
3. P. F. Schmidt, *This Journal*, **124**, 1950 (1977).
4. G. Mende and G. Küster, *Thin Solid Films*, **35**, 215 (1976).
5. A. F. Bogenschütz, "Atzpraxis für den Halbleiter," München (1963).
6. G. Dearnaley, J. H. Freeman, R. S. Nelson, and J. Stephan, "Ion Implantation" Appendix 3, North Holland Company, Amsterdam (1973).
7. I. Lindhart, M. Scharff, and H. E. Schiott, *Kong. Danske Vid. Selsk., mat.-fys. Medd.*, **33**, No. 14 (1963).

Manuscript submitted Feb. 26, 1980;
revised manuscript received June 23, 1980.

A Chemical Method for Deposition of Thin Film of Bi_2S_3

P. Pramanik and R. N. Bhattacharya

Department of Chemistry, Indian Institute of Technology, Kharagpur 721302, India

Thin film formation of chalcogenides of Pb^{2+} by chemical deposition is a very well known process (1,2,3). But similar methods of deposition of thin films of Bismuth chalcogenides have not yet been reported. This brief communication describes a chemical method for the deposition of Bi_2S_3 thin films.

Thio-urea is used for slow release of S^{2-} ion and pH is maintained at 8. To keep Bi^{3+} ion in solution at pH 8, triethanolamine complex of Bi^{3+} is used.

One gm of bismuth nitrate ($\text{Bi}(\text{NO}_3)_3 \cdot 5\text{H}_2\text{O}$) is triturated with 10 ml triethanolamine and then 50 ml water is added to it. The resulting solution is continuously stirred till a nearly clear solution is obtained, which is then filtered.

A 20 ml of the Bi^{3+} solution is taken in a glass beaker. 30 ml of 1(M) thiourea solution and 1 ml of 17 (N) NH_4OH are added to it and the volume is made upto 100 ml with water. The substrate (glass or ceramic) is thoroughly cleaned and immersed in the solution. The container is placed into an oil bath at 100 - 110°C temperature for 40 minutes and then it is kept at room temperature for about 4 hours. Uniform films of Bi_2S_3 are obtained on the glass substrates. They are then taken out, washed with water and dried in air. The Bi_2S_3 films are about 0.05 - 0.1 microns thick.

NH_4OH is added to slow down the formation of Bi_2S_3 and to increase its adherence on the glass substrate.

X-ray diffraction data shows that films are amorphous in nature. Scanning electron micrograph shows that films contain random distribution of small crystallites, which is shown in figure (1). The films have high electrical resistance in comparison to single crystal. The resistivity lies in the range of

10-30 x 10^6 ohm-cm. The temperature variation of resistivity shows that activation energy of electrical conduction is 1.3 eV. The material has n-type conduction. The optical band gap of the film is found to be 1.47 eV shown in the figure (2) and it has feeble photo conductivity.

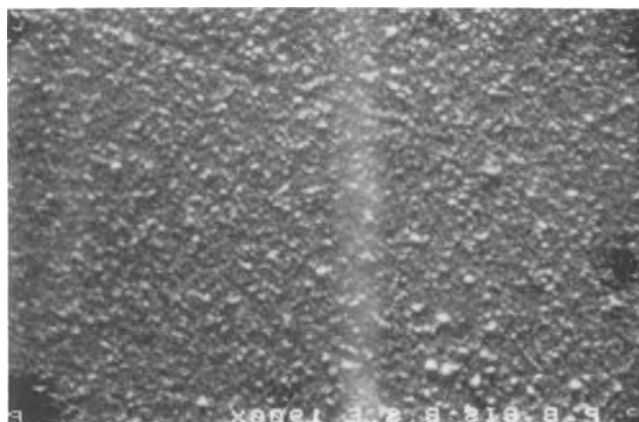


Fig. 1. Scanning Electron Micrograph of Bi_2S_3 thin film (B.S.E.; 1900X)

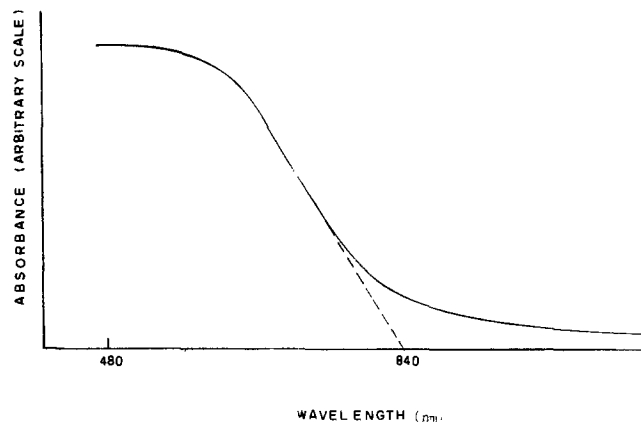


Fig. 2. Electronic spectra of Bi_2S_3

REFERENCES

1. J. Bloem, Appl. Sci. Res., **6B**, 92 (1956).
2. F. Kicinski, Chemistry and Industry, January (P. 24), 1948.
3. H.N. Acharya and H.N. Bose, Phys. Stat. Sol., (a) **6**, K43 (1971).

Key words - Bismuth sulfide, Thin film, Chemical deposition.

Manuscript submitted Feb. 29, 1980; revised manuscript received April 17, 1980.

Desalination by Photoelectrodialysis

George W. Murphy*

Solar Energy Research Institute, Golden, Colorado 80401

We report the experimental demonstration of photoelectrochemically powered electro dialysis--photoelectrodialysis--as a desalination process. The concept and nomenclature have been recorded previously (1). A photoelectrochemical cell n-GaAs/0.16 M Na₂Se-0.02 M Na₂Se₂-C-0.16 M Na₂Se-0.02 M Na₂Se₂/Pt (2,3) and the "driven" component of an electro dialysis cell -C-0.06 M NaCl-A-0.06 M NaCl-C- (4) are collapsed into a unit, the principle of which is illustrated in Fig. 1. Here C is a cation- and A an anion-selective membrane. P is an n-type semiconductor (n-GaAs) short circuited to electrode E (Pt), which is inert except for its electron-exchanging capability with solution redox species. The selenide-polyselenide couple (represented here as Na₂Se-Na₂Se₂) is known to stabilize the n-GaAs electrode against photo-corrosion. Compartments I and II contain this couple, and Compartments III and IV contain NaCl solution initially of the same concentration. Irradiation of the n-GaAs surface photooxidizes the selenide ion, thereby initiating the coupled chain of events illustrated: the reverse reaction occurs at the dark electrode, and the ion movements across the membranes result in demineralization of Compartment III and salt enrichment in IV.

This process will also be recognized as an application of a photochemical diode (5).

The experimental cell (not shown) was assembled from five machined ring discs of clear acrylic 2½ in. O.D. and 1 in. I.D. and two 2½ in. diameter end discs. An acrylic light tube was cemented to one end disc which served as a window. The light tube reduced the solution light path to approximately

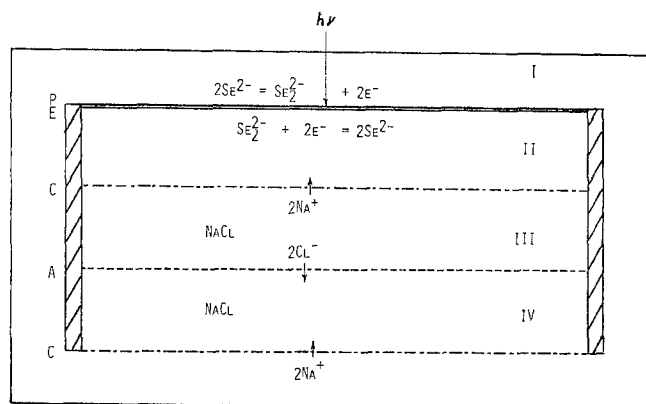


Fig. 1. Schematic Cross Section of Photoelectrodialysis Cell.

3 mm. The cell thus exposes 1-in. diameter circles of the electrode and three membranes, forming three internal compartments 1/4 in. thick. The 1-3/16 in. diameter disc electrode was sealed by O-rings in channels machined in two of the discs. Membranes were cut to the full O.D. disc diameter and served as their own gaskets. After the electrode, membranes, and end discs were in place, they were compressed between two stainless steel end plates with six screws running the cell length. In addition to screw holes, six additional holes had been cut in the acrylic rims and membranes so as to provide channels for the "external" compartment, i. e., Compartment I of Fig. 1. The cation-selective membranes were Nafion 427 (du Pont) and the anion-selective membrane Raipore 5025, both kindly furnished by the companies. A 1.5-mm thick silicon-doped 100-face gallium arsenide wafer, one side polished, was purchased from Laser Diode Laboratories, Inc. Carrier concentration (company-furnished) was $1.1 \times 10^{18} \text{ cm}^{-3}$. After making an ohmic contact to the unpolished side, a 1-mil platinum

disc of the same diameter was cemented to it with silver epoxy. The gallium arsenide was etched and dipped in 0.01 M RuCl_3 , after the procedure of Parkinson *et al* (3). With the electrode vs platinum in 0.8 M Na_2Se -0.1 M Na_2Se_2 -1 M NaOH, a voltammogram yielded 0.8 volt on open circuit and 7.25 mA cm^{-2} at short circuit under 1000 watt xenon lamp irradiation, intensity 1.5 W cm^{-2} .

Sodium selenide was 99.9% packed under argon obtained from Cerac Chemical Co. Selenium powder used to make polyselenide was obtained from Alfa Ventron. All operations with Na_2Se and solutions made therefrom were carried out in a nitrogen atmosphere glove box. A stock solution of 0.8 M Na_2Se -0.1 M Na_2Se_2 was prepared and diluted fivefold before use in the photoelectrodialysis cell. NaCl concentration was 0.06 M, which is typical for a brackish water. The Na_2Se - Na_2Se_2 solution was circulated through Compartments I and II at a rate of about 0.1 ml/min by gravity from a reservoir. NaCl was circulated similarly through Compartment IV. The electrode was illuminated by collimated light from a 300-watt quartz halogen projector lamp, intensity 0.33 W cm^{-2} . At intervals samples were withdrawn briefly by syringe from the demineralization compartment into a micro conductivity cell and the conductivity determined.

The progress of demineralization is indicated by the conductivity plot in Fig. 2. A steady state of approximately 79% demineralization was reached in about seven hours. The desalted solution contained a suspended solid, probably selenium, indicating that some leakage of anions had occurred across the cation-selective membrane. Since the photovoltage characteristic of the electrode itself is capable of carrying the demineralization substantially to completion with ideal membranes, the 21% of starting conductivity in the steady state is a measure of the membrane imperfection.

In summary, the technical feasibility of photoelectrodialysis has been demonstrated. Economic

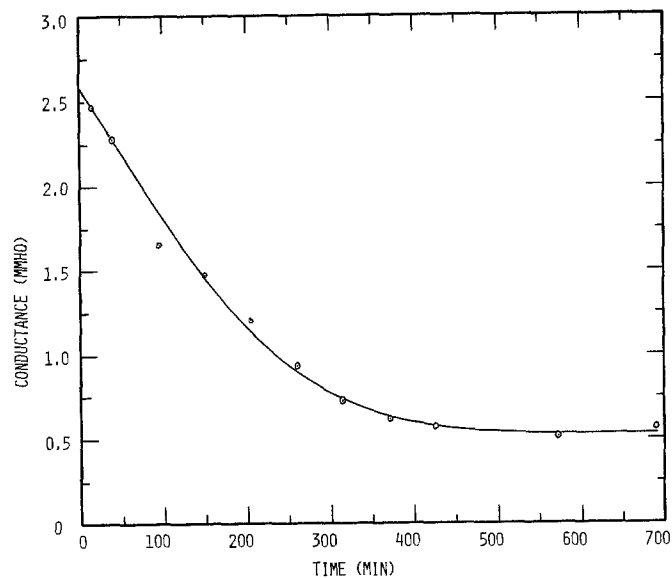


Fig. 2. Conductance of Compartment III vs Time During Desalination Experiment.

feasibility will depend in part on the development of inexpensive electrode and coupled redox materials, the same as for photoelectrochemical solar cells. Several research groups throughout the world have this as a primary objective. In addition, conditions must be found that result in negligible counterion leakage across the membrane. This might be accomplished with redox systems yielding good results at such low concentrations that the selectivity of available membranes is high, or improved membrane selectivity at the redox concentrations employed here.

Acknowledgment. I thank John Turner for the electrode voltammogram, Eric Mott for cell fabrication, and Arthur Nozik for helpful discussions.

*Electrochemical Society Active Member. Sabbatical leave 1979-80 academic year from the University of Oklahoma.

Key words: photoelectrochemistry, energy conversion.

Manuscript received March 3, 1980.

Publication costs of this article were assisted by the Solar Energy Research Institute.

REFERENCES

1. G. W. Murphy, *Solar Energy*, 21, 403 (1978).
2. K. C. Chang, A. Heller, B. Schwartz, S. Menezes, and B. Miller, *Science*, 196, 1097 (1977).
3. B. A. Parkinson, A. Heller, and B. Miller, *Appl. Phys. Lett.*, 33, 521 (1978).
4. L. H. Schaeffer and M. S. Mintz, "Principles of Desalination" (edited by K. S. Spiegler), p. 200. Academic Press, New York (1966).
5. A. J. Nozik, *Appl. Phys. Lett.*, 30, 567 (1977).



Some Chemistry in the Li/SOCl₂ Cell

K. M. Abraham* and R. M. Mank

EIC Corporation, Newton, Massachusetts 02158

ABSTRACT

Cyclic voltammetry and constant current electrolysis studies of SOCl₂/LiAlCl₄ solutions showed that SO₂Cl₂, SOCl⁺AlCl₄⁻, SCl₂, AlCl₃, and Cl₂ are produced as oxidation products. Mechanisms of oxidation reactions are proposed to explain the formation of these products. Forced overdischarge of cathode limited cells produces Li₂S which reacts with LiAlCl₄ present in the cell to form LiAlSCl₂. Materials formed in anode limited cells during forced overdischarge include SO₂Cl₂, SCl₂, Cl₂, SOCl⁺AlCl₄⁻, AlCl₃, and a substance with infrared absorption at 1070 cm⁻¹. "Charging" of Li/SOCl₂ cells involves regenerative processes so that only small amounts of products accumulate in the cell.

The Li/SOCl₂ primary cell has received considerable research and development interest (1-20) ever since the initial reports on its discovery appeared (1, 2). The cell consists of a Li anode, an inert carbon cathode comprising porous carbon with binder on an Ni screen, and SOCl₂/LiAlCl₄ solution serving both as the solvent and depolarizer. Cell discharge reactions which satisfactorily explain previous analytical data from this laboratory (14), the studies of Dey and co-workers (7), and the recent results of Schlaikjer and co-workers (13) are



Major areas of research during the past few years have included: design and optimization of cells for various applications (3-13), studies of the cell chemistry to fully characterize discharge reactions (13-16), investigations of the voltage delay problem (17, 18), and studies of safety aspects (7, 19, 20). While considerable progress has been made in most of these areas, the explosion hazard associated with several operational modes of the cell has served as a major deterrent to its widespread practical use.

Our recent studies (19, 20) on the behavior of Li/SOCl₂ cells during forced overdischarge indicated that anode limited cells are potentially hazardous. During such forced overdischarge, several anode limited cells showed burning type explosions. Individual electrode potential measurements revealed that explosions in all the cells occurred after the anode potential had risen to values greater than 4V for considerable length of time prior to the explosion. It appeared that the explosions were caused by sensitive chemicals, produced by oxidation of materials present in the cell.

On the other hand, cathode limited cells appeared to be safe during forced overdischarge. Forced overdischarge of cathode limited cells typically proceeded with small reverse cell voltages, remaining steady at about -100 mV. These cells could be overdischarged

for long periods of time during which the charge input considerably exceeded the amounts of both SOCl₂ and Li originally present in the cell. None of the cathode limited cells exploded during forced overdischarge. It appears that during forced overdischarge of cathode limited cells, Li dendrites form on the carbon electrode and lead to internal short circuits which readily accommodate the major part of the current. These short circuits provide the mechanism for the system to pass charges well in excess of stoichiometry. This situation has not appeared to constitute a specific hazard.

We have also found (21) that "charging"¹ of Li/SOCl₂ cells leads to regenerative cell processes so that there is no appreciable depletion of cell capacity even after an input of positive charge exceeding the amounts of SOCl₂ and Li originally present in the cell.

In this paper we present the results of analytical studies aimed at characterizing chemical and electrochemical reactions in Li/SOCl₂ cells during overdischarge and "charge." The various studies have been: (i) constant current electrolysis of SOCl₂/LiAlCl₄ solutions and analysis of products by infrared spectrometry; (ii) cyclic voltammetry of SOCl₂/LiAlCl₄ solutions; (iii) product analysis from Li/SOCl₂ cells after overdischarge and constant current "charge" using *in situ* cyclic voltammetry and infrared spectrometry.

Experimental

All experiments involving reagent handling and cell construction were carried out in the absence of air and moisture in the argon atmosphere of a dry box (Vacuum Atmospheres Corporation).

Electrolyte preparation.—The salt, LiAlCl₄, was prepared by melting at 190°C stoichiometric amounts of LiCl (Fisher Scientific Company, L-121, predried *in vacuo*, 10⁻³ Torr, at 400°C for 4 hr) and AlCl₃ (Fluka, puriss). The melt was purified by electrolysis between Al electrodes. The salt was dissolved in SOCl₂ (Eastman Kodak, Cat. No. 246) at room temperature. The solutions usually were 1.8M in LiAlCl₄.

¹ The term charging implies a positive current applied to the carbon electrode.

* Electrochemical Society Active Member.

Key words: Li/SOCl₂ cell, cyclic voltammetry, infrared spectrometry, overdischarge, charge.

Constant current electrolysis.—Constant current electrolysis of $\text{SOCl}_2/\text{LiAlCl}_4$ solutions was carried out in a two-compartment Pyrex glass cell having a $15\ \mu\text{m}$ glass-frit separator. The cathode was a Teflon-bonded carbon electrode of known area and the anode was an expanded nickel (5Ni5-5/o, Exmet Corporation) screen. The individual electrode potentials were measured vs. an Li reference electrode. The electrolysis products were analyzed by infrared spectrometry.

Infrared spectral measurements.—The infrared spectra were recorded on a Beckman Acculab-5 dual beam spectrometer covering the range from $4000\ \text{cm}^{-1}$ to $375\ \text{cm}^{-1}$. All spectra of liquid samples were obtained with Beckman TAC cells. These have AgCl windows and can be sealed permanently. The cells were of 0.025 or 0.1 mm path lengths. Spectra of gases were obtained with a Beckman Universal Gas Cell (10 cm path length) fitted with KBr or NaCl windows.

Cyclic voltammetry studies.—Cyclic voltammetry studies of $\text{SOCl}_2/\text{LiAlCl}_4$ (1.8M) solutions were carried out on both Ni and vitreous C electrodes. A three-electrode system with Li reference and counterelectrodes was used. The voltammetric scans were performed with an Amel Model 551 potentiostat in conjunction with their Model 566 function generator. The i - E curves were generally recorded using a Bascom-Turner Series 8000 Recorder equipped with microprocessor accessories.

Cyclic voltammetric studies of electrolyte from Li/ SOCl_2 cells after various tests were performed *in situ*. Small prismatic cells comprising multiple carbon cathode and Li anode plates were used. Each electrode plate measured $3 \times 2\ \text{cm}$ per side. The cells were designed and tested in both anode and cathode limited configurations. In cathode limited cells, the electrode arrangement was Li/C/Li/C/Li/C/Li and the cell contained 2 A-hr Li, $\sim 400\ \text{mg}$ carbon, and 4 ml of $\text{SOCl}_2/1.8\text{M LiAlCl}_4$ electrolyte. The electrode package in anode limited cells was in the sequence, C/Li/C/Li/C with the cells containing 0.70 A-hr Li, $\sim 400\ \text{mg}$ carbon, and 4 ml of $\text{SOCl}_2/1.8\text{M LiAlCl}_4$. The cells were slightly flooded with electrolyte, since the small excess of electrolyte was necessary for analytical studies. In order to make *in situ* cyclic voltammetry measurements, a vitreous carbon microelectrode of $0.07\ \text{cm}^2$ area was introduced into the cell through a side arm of the glass envelope as shown in Fig. 1. During galvanostatic test, the microcarbon electrode was pulled away from electrolyte contact to avoid possible surface passivation. Prior to recording the voltammogram after various stages of discharge, overdischarge, or "charge," the electrode was pushed down and contact with the electrolyte was established by tilting the cell. The cell electrodes served also as the reference

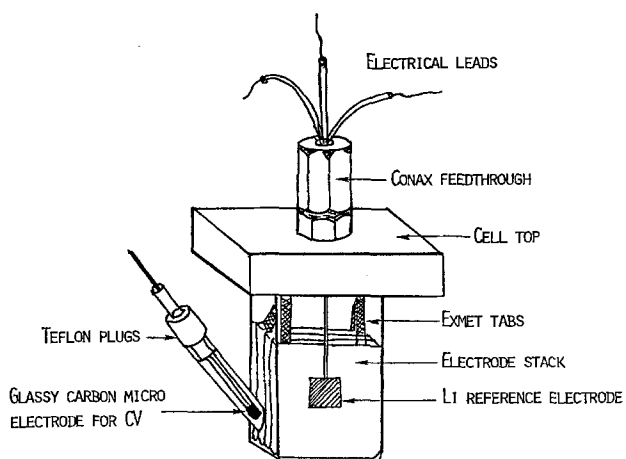


Fig. 1. Schematic view of the prismatic laboratory cell for *in situ* cyclic voltammetry.

and counterelectrodes for cyclic voltammetry. Subsequently, electrolytes from these cells were analyzed by infrared spectrometry.

Results and Discussion

Electrolysis of $\text{SOCl}_2/\text{LiAlCl}_4$ Solutions

Constant current electrolysis and product analysis.—Constant current electrolysis of $\text{SOCl}_2/1.8\text{M LiAlCl}_4$ solution on an Ni anode and carbon cathode proceeds with a constant anode potential of $\sim 4.6\text{V vs. Li}^+/\text{Li}$. The cell potential remains steady at $\sim -0.9\text{V}$. Infrared spectra of the catholyte and anolyte were recorded after electrolysis corresponding to $\sim 0.1e^-/\text{SOCl}_2$ and are shown in Fig. 2 and 3, respectively.

The only infrared identifiable product in the catholyte is SO_2 , with absorptions at 1335 and $1150\ \text{cm}^{-1}$ (22). The formation of SO_2 is consistent with the discharge reactions shown in Eq. [1] and [2]. The spectrum of the anolyte shows two new peaks at $1415\ \text{cm}^{-1}$ and at $1110\ \text{cm}^{-1}$. The peak at $1415\ \text{cm}^{-1}$ is due to SO_2Cl_2 . This was established by infrared spectral measurements after adding SO_2Cl_2 to the anolyte. Neat SO_2Cl_2 exhibits two strong absorptions at 1205 and $1420\ \text{cm}^{-1}$ (22). In the anolyte, the $1205\ \text{cm}^{-1}$ absorption is hidden inside the strongly absorbing SOCl_2 peak at $1230\ \text{cm}^{-1}$. The absorption at $1110\ \text{cm}^{-1}$ in the anolyte is most probably due to the S-O stretching vibration of the complex, $\text{SOCl}^+\text{AlCl}_4^-$ since a similar absorption was found in the infrared spectra of AlCl_3 solutions of SOCl_2 or $\text{SOCl}_2/\text{LiAlCl}_4$ electrolyte. The existence of the complex, $\text{SOCl}^+\text{AlCl}_4^-$,² in AlCl_3

² The ionic structure for the AlCl_3 complex of SOCl_2 is also consistent with the increasing conductivity of SOCl_2 with added AlCl_3 (24).

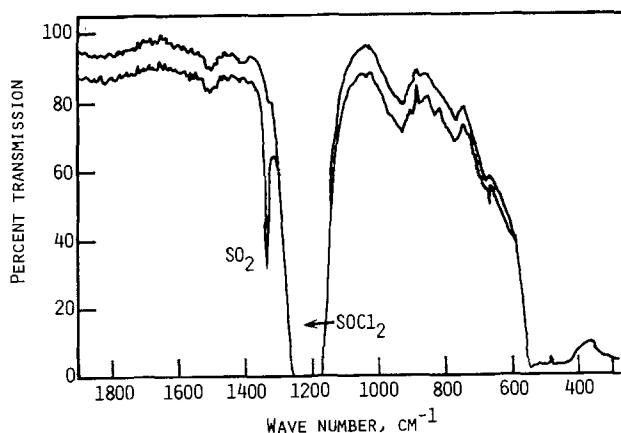


Fig. 2. Infrared spectrum of the catholyte (lower trace) after electrolysis of $\text{SOCl}_2/\text{LiAlCl}_4$ (1.8M) solution. The upper trace is the spectrum of the solution prior to electrolysis.

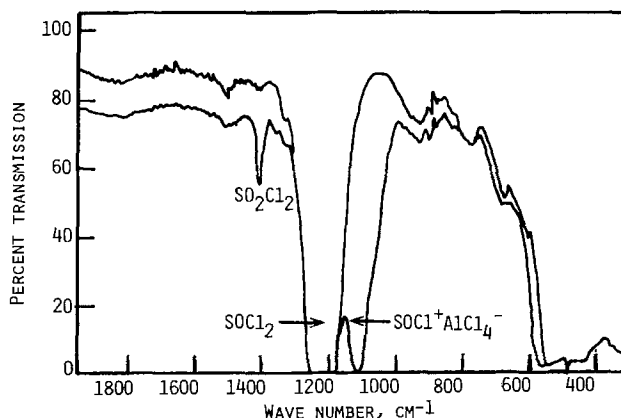


Fig. 3. Infrared spectrum of the anolyte (lower trace) after electrolysis of $\text{SOCl}_2/\text{LiAlCl}_4$ (1.8M) solution. The upper trace is the spectrum of the solution prior to electrolysis.

solutions of SOCl₂ has been previously established (23). The present work confirms its existence. The occurrence of the S-O symmetric stretching absorption in SOCl⁺AlCl₄⁻ at a lower frequency than in SOCl₂ is consistent with the ionic structure. Vapor phase infrared spectrometry showed SO₂Cl₂ also in the gas phase of the anode compartment. No other gaseous product could be identified by vapor phase infrared spectrometry. Reactions which would account for the oxidation products, SO₂Cl₂ and SOCl⁺AlCl₄⁻, are discussed in the next section.

Cyclic voltammetry studies and reaction mechanisms.—Prior cyclic voltammetry studies of SOCl₂/LiAlCl₄ solutions were primarily aimed at characterizing reduction reactions (15, 16). In the studies reported in this paper emphasis is on oxidation reactions in the SOCl₂/LiAlCl₄ solution.

A typical cyclic voltammogram on a glassy carbon electrode between 1.0 and 5.0V vs. Li⁺/Li in SOCl₂/1.8M LiAlCl₄ solution is shown in Fig. 4. A similar voltammogram was obtained also on a Ni disk electrode. Although the overall features of the voltammogram were identical on both of the electrodes, the peaks appeared sharper on the carbon electrode. Also the cathodic peaks on Ni were slightly shifted to lower potentials.

On scanning the electrode cathodically first from open circuit, only the high current peak, I, at 2.65V and the weak current peak, II, at 1.80V are found. These peaks may be assigned, respectively, to reductions of SOCl₂ and SO₂, in accordance with previous observations by others (15, 16). The assignments are in agreement with reactions [1] and [2].

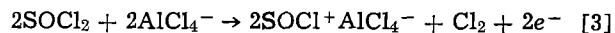
In the anodic region between 4.0 and 5.0V, the voltammogram shows two broad peaks, IV and V at 4.55V and 4.65V and a sharp, high current peak, VI, at 5.0V. In poorly resolved voltammograms, the two peaks IV and V merge together and appear as one peak. It was found that if the electrode was cycled several times between 4.0 and 1.0V, the height of the current peak around 4.6V became very large in a subsequent anodic sweep to 5.0V. In these cases current peaks IV and V generally appeared together as a single peak.

When the electrode is scanned cathodically below 4.0V after the anodic sweep to 5.0V, three reduction peaks, VII at 3.6V, VIII at 3.25V, and IX at 2.8V, appear in the voltammogram. These are evidently due to reductions of solution anodization products. The appearance of these peaks and their relative peak heights

were found to depend on the potential of scan reversal. None of these three peaks appear when the scan is reversed at potentials below 4.0V. When the scan is reversed at ~4.6V, the peak at 3.25V appears as the major one. On increasing the reversal potential to values greater than 4.6V, the height of the peak at 3.6V also increases along with the appearance of the shoulder at 2.8V. If the electrode is cycled several times between 4 and 5V before sweeping cathodically, all three peaks show increased peak heights.

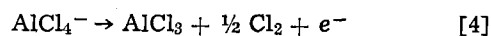
In a voltammogram obtained after addition of SCl₂ to SOCl₂/1.8M LiAlCl₄ solution and scanning the electrode cathodically first from open circuit, the onset of the cathodic current begins at ~3.8V with a peak at 3.65V. Similarly, the voltammogram obtained after adding Cl₂ to SOCl₂/1.8M LiAlCl₄ solution shows a reduction peak at 3.25V. When SO₂Cl₂ is added to SOCl₂/1.8M LiAlCl₄, a reduction peak is observed at ~2.9V as a shoulder to the SOCl₂ peak. It appears from these data that Cl₂, SCl₂, and SO₂Cl₂ are formed during the oxidation of SOCl₂/LiAlCl₄ solutions. We note that the reduction potentials of SCl₂, Cl₂, and SO₂Cl₂ observed here are in agreement with previous reports (15, 16).

Electrochemical oxidation of SOCl₂ was first studied by Spandau *et al.* (25). It was reported by these authors that electrolysis of 0.14M (C₂H₅)₃NHCl/SOCl₂ solution gave Cl₂ as the oxidation product. The primary cathodic product, according to the authors, was SOCl⁺, which decomposed subsequently to various substances, the nature of which depended on the temperature of the experiment. Using cyclic voltammetry Behl (14) also identified Cl₂ as an oxidation product of SOCl₂/LiAlCl₄ solutions. He suggested an oxidation reaction as shown in Eq. [3]

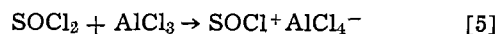


Our data, however, suggest more complex reactions.

The most probable reactions which correspond to current peaks, IV at 4.55V and V at 4.65V in the voltammogram would be oxidation of SOCl₂ as shown in Eq. [3] and oxidation of AlCl₄⁻ as depicted in Eq. [4]

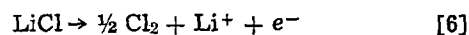


The AlCl₃ will immediately react with SOCl₂ to produce SOCl⁺AlCl₄⁻ (Eq. [5])



Because of the close proximity of the current peaks IV and V, it is difficult to assign them individually to the reactions [4] and [5]. However, we found the current peaks near 4.6V increased as a function of [LiAlCl₄] from 0.25M to 1.8M. This suggests that oxidation of AlCl₄⁻ occur in this region.

The following evidences suggest that oxidation of LiCl according to Eq. [6] also occurs at ~4.6V



Electrodes which become passivated with LiCl in an initial cathode sweep can be regenerated by anodizing at ~4.6V. A considerably enhanced current peak is observed at ~4.6V after a cathodic sweep to 1.0V such that LiCl has plated onto the electrode surface.

Between ~4.6 and ~5.0V oxidation of SOCl⁺AlCl₄⁻ may occur to produce SO₂Cl₂ and SCl₂. The assignment is based on the fact that the amounts of these materials increase with scan reversal potentials above 4.6V. It is possible to conceive of several reaction schemes by which these materials are produced. We may speculate on the scheme shown below in Eq. [7]-[10]

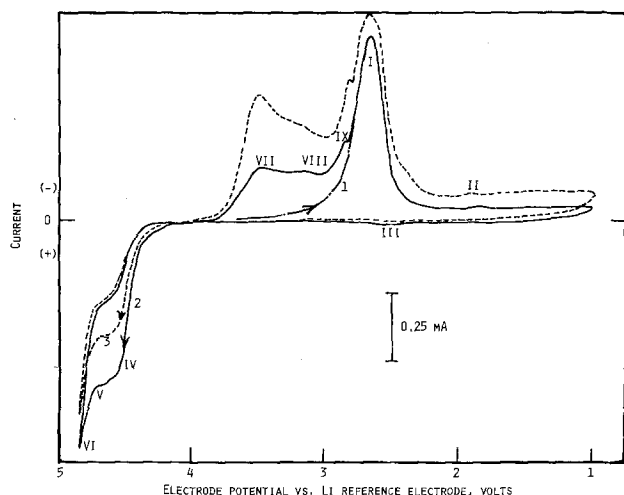
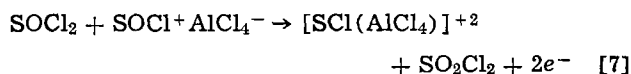
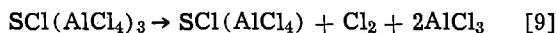
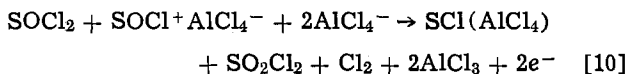


Fig. 4. Cyclic voltammograms of SOCl₂/1.8M LiAlCl₄ on a glassy carbon electrode. Scan rate = 100 mV/sec. Curve 1 was obtained by scanning the electrode cathodically first from 0CV, 3.65V. Curve 2 was obtained by scanning the electrode anodically first from 0CV. Curve 3 was obtained after twice cycling the electrode between 4.0 and 5.0V.



The overall reaction from Eq. [7]-[9] is



In reaction [7], the oxidation of the oxide moiety in $\text{SOCl}^+\text{AlCl}_4^-$ is considered in a manner similar to the oxidation of Cl^- , considered in the primary oxidation shown in Eq. [3]. The oxygen presumably oxidizes SOCl_2 to SO_2Cl_2 . The compounds $\text{SCl}(\text{AlCl}_4)_3$ and $\text{SCl}(\text{AlCl}_4)$ are AlCl_3 complexes, respectively, of SCl_4 and SCl_2 . The complex $\text{SCl}(\text{AlCl}_4)$ has been identified in the reaction of SCl_2 and AlCl_3 (26). The disproportionation reaction shown in Eq. [9] is justifiable on the ground that SCl_4 is unstable at room temperature and disproportionates to SCl_2 and Cl_2 (27).

Product Analysis from Li/SOCl₂ Cells

Cathode limited cells.—The typical behavior of a cathode limited cell during forced overdischarge is shown in Fig. 5. The potential profiles suggest that the major anodic process would be the electrostripping of Li. The stripped Li would be plated onto the cathode where it could remain in the elemental form, or could be intercalated into the carbon to form C_xLi_y . Intercalation of Li onto carbon has been shown to begin at potentials as high as 1.5V vs. Li^+/Li (28). The long periods of forced overdischarge possible in cathode limited cells, probably due to short circuit (19, 20) suggests the formation of Li dendrites on the cathode.

The infrared spectrum of the electrolyte from the cathode limited cell shown in Fig. 5 after the forced overdischarge is depicted in Fig. 6. The main features of the spectrum are the absorptions at 1340 and 1150 cm^{-1} due to SO_2 , the strong absorption centered at 1200 cm^{-1} due to SOCl_2 , and the absorptions of medium intensities at 790 and 660 cm^{-1} . We have found that it is possible to chemically produce species with infrared absorptions at 790 and 660 cm^{-1} by treating Li_2S with $\text{SOCl}_2/\text{LiAlCl}_4$ solutions. When Li_2S is added to SOCl_2 , no apparent reaction takes place, nor is there

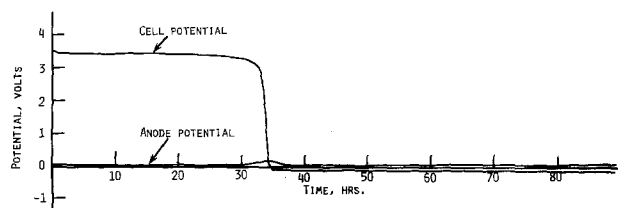


Fig. 5. Discharge and overdischarge of a cathode limited prismatic Li/SOCl₂ cell. Current = 36 mA; current density = 1 mA/cm².

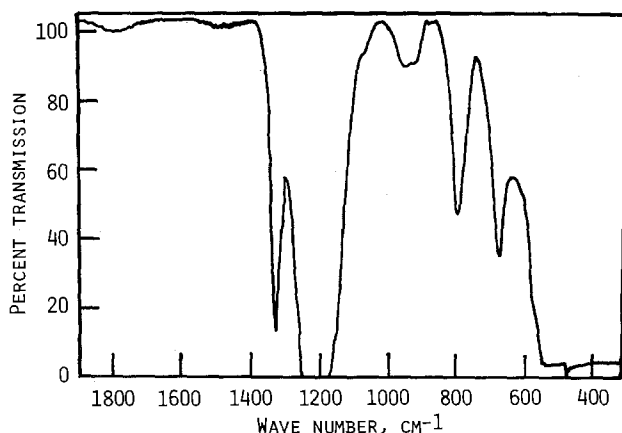


Fig. 6. Infrared spectrum of the electrolyte from cathode limited Li/SOCl₂ cell after forced overdischarge.

any apparent solubility of Li_2S . However, a reaction does take place when Li_2S is added to SOCl_2 containing LiAlCl_4 . The absorptions at 790 and 660 cm^{-1} are present in the infrared spectrum of the solution product of the reaction involving equimolar amounts of Li_2S and LiAlCl_4 in SOCl_2 . The reaction may be represented by Eq. [11]



The existence of AlSCl_2^- species has previously been identified (29) in solutions of Li_2S or Na_2S in $\text{NaCl}/\text{AlCl}_3$ molten salt electrolytes. The formation at room temperature of LiAlSCl_2 according to reaction [11] in a solvent such as SOCl_2 is not unreasonable. The infrared absorptions at 790 and 660 cm^{-1} may be associated with Al-S and Al-Cl bond vibrations, respectively, of LiAlSCl_2 . These may be compared to the infrared spectra of Al_2S_3 which shows a band near 800 cm^{-1} , and to that of Al_2Cl_6 , in which the terminal Al-Cl bond absorption is found at 630 cm^{-1} .

The above results suggest that during forced overdischarge of cathode limited cells, Li_2S is produced in the cell, Eq. [12], which reacts immediately with LiAlCl_4 to form LiAlSCl_2



It is probable that some LiAlS_2 is also present in these solutions.

Infrared spectral data showed the presence of LiAlSCl_2 also in the electrolyte from cathode limited cells which had been overdischarged on resistive load. It seems that in overdischarged cathode limited cells, which invariably contain S, the formation of Li_2S is a spontaneous process.

Anode limited cells.—Electrolytes from two types of anode limited cells were analyzed: (i) discharged cells in which the anode consisted of only an Ni grid with no Li on it. This type of cell represents an extreme case of anode limitation, (ii) complete cells which had been forced overdischarged.

The potential profile during discharge of a typical cell without Li on the anode is shown in Fig. 7. When discharged at a current density of 1 mA/cm², the anode polarized immediately to ~4.7V and remained steady at this value during the passage of 3.6 A-hr of charge. The cell potential remained steady at ~-1.0V. It has been found that these types of cells could be forced overdischarged almost indefinitely without any significant change in cell polarization from the above values. The data suggest that the reactions in these cells involve regenerative processes so that very little net chemical change takes place.

The infrared spectrum of the electrolyte from the cell shown in Fig. 7 exhibited absorptions due to SO_2Cl_2 (1420 cm^{-1}), SO_2 (1340 cm^{-1}), and $\text{SOCl}^+\text{AlCl}_4^-$ (1110 cm^{-1}). There was also an absorption band at 1070 cm^{-1} . The material exhibiting the latter band has not yet been identified, but it may be a sulfur-oxy compound since S-O stretching vibrations are often found as strong bands in this region of the spectrum. Since this material was absent either

³ We have synthesized LiAlSCl_2 from the reaction of LiCl and AlSCl_2 in SOCl_2 and its infrared spectrum in SOCl_2 has been verified. This will be the subject of a future paper.

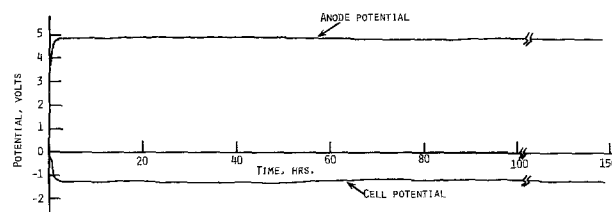
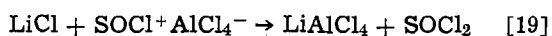
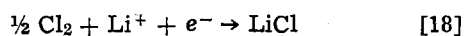
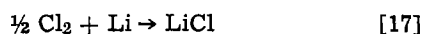
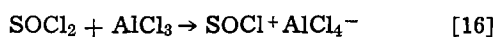
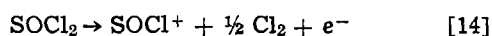
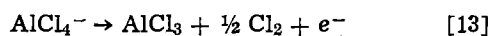


Fig. 7. Discharge curve for a prismatic Li/SOCl₂ cell without Li on the anode. Current = 24 mA.

in the catholyte or in the anolyte from the electrolysis cell, it must have been produced by chemical or electrochemical reaction(s) involving primary electrolysis products of SOCl₂/LiAlCl₄ solutions. Figure 8 shows the cyclic voltammograms at two different stages of discharge of the cell in Fig. 7. They show that SCl₂ (~3.6V) and Cl₂ (~3.2V) are also present in the cell.

Based on the analytical data as well as the oxidation reactions discussed in the previous section, the major regenerative processes in these cells may be explained by the following scheme



Note that the reaction shown in Eq. [19] regenerates the cell materials. As noted SO₂Cl₂ and SCl₂ are also produced in these cells and they would be formed according to reactions depicted in Eq. [7]-[9]. However, regenerative processes involving these materials may also occur so that they accumulate only in small amounts.

The potential profiles during forced overdischarge of an anode limited Li/SOCl₂ cell is shown in Fig. 9. The anode potentials exhibit considerable fluctuations, but they eventually arise to and stay at values con-

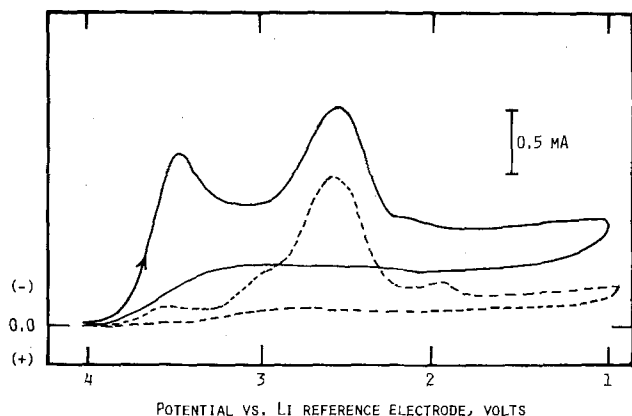


Fig. 8. Cyclic voltammograms of electrolyte from the cell in Fig. 7 on glassy carbon electrode. The solid curve represents the voltammogram obtained at the end of the test shown in Fig. 7. The voltammogram represented by broken lines was obtained after 0.10 A-hr discharge. The electrode was first scanned cathodically. Scan rate = 100 mV/sec.

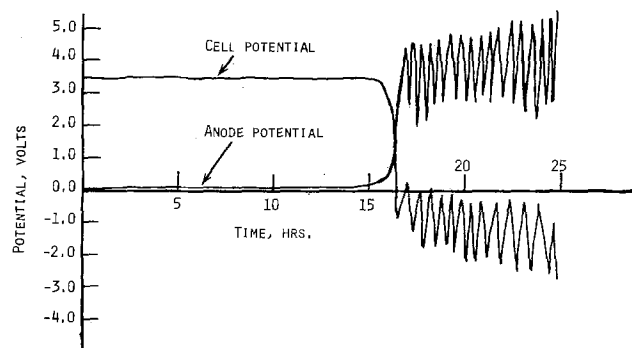


Fig. 9. Galvanostatic discharge and overdischarge of anode limited prismatic Li/SOCl₂ cell. Current = 24 mA; current density = 1.0 mA/cm².

siderably higher than 4.0V. Several C-size anode limited cells showing this type of behavior exploded (19, 20). The anode potential profiles suggest that oxidation of SOCl₂ or other materials present in the cell can occur during forced overdischarge. It is probable that explosions are caused by materials produced by the oxidation reactions.

The major feature of the infrared spectrum of the electrolyte from the cell shown in Fig. 9, which is typical of the many anode limited cells tested, was the absorption band at 1070 cm⁻¹ along with peaks due to SOCl₂ and SO₂. The cyclic voltammogram of the electrolyte was similar to that shown in Fig. 8 indicating the presence of SCl₂ and Cl₂.

The known chemical properties of SCl₂ and Cl₂ suggest that these materials may not cause the kind of explosions we have observed in anode limited cells. The material with the infrared absorption at 1070 cm⁻¹ could be a candidate, although no problems were encountered in the handling of the electrolyte containing the material. It is possible that other sensitive materials are produced in the cell which may have only transitory existence as intermediates but which may accumulate under special circumstances in the cell. As noted, the nature of the products or their eventual accumulation would depend on whether or not Li is present in the cell at the time it goes into the overdischarge mode, and on the degree of the regenerative processes in the cell. We have found (19, 20) that an Li/SOCl₂ cell may well be anode limited, even though it is not Li limited. The latter can result from poor electrical contact between Li and the anode current collector. These effects depend to a great extent on cell construction parameters and the amount of such products which accumulate during forced overdischarge would vary considerably from one cell to the other.

"Charged" Li/SOCl₂ cells.—The potential profiles during "charging" of a fresh Li/SOCl₂ cell is shown in Fig. 10. Upon applying a charging current of 1 mA/cm², the cell immediately polarized to 4.1V and showed no further change in polarization with continued "charging." The anode potential remained steady at -0.1V. In general, it was possible to subject the cells to "charging" currents utilizing charges considerably in excess of the amounts of SOCl₂ or Li originally present in the cell. Moreover, the cells could be discharged after the extended "charging" to yield capacities equivalent to those obtainable from fresh cells (21). The data suggest that the reactions associated with the charging of Li/SOCl₂ cells involve a sequence of regenerative cell processes. The behavior is similar to that found in the discharge of cells without Li on the anode.

The predominant reactions on a carbon electrode at potentials between 4.1 and 4.6V are the ones shown in Eq. [3] and [4]. The regenerative processes may then involve the same set of reactions shown in Eq. [13]-[18]. In this case the oxidation reactions take place on the C electrode and the reduction reactions take place on the Li electrode.

Cyclic voltammetry and infrared spectral data on electrolyte from cells after "charging" showed the net accumulation of several reaction products. The products identifiable from the infrared spectrum were

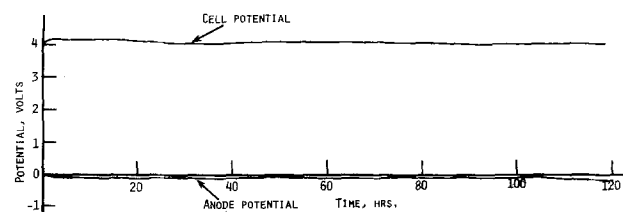


Fig. 10. Galvanostatic "charging" of prismatic Li/SOCl₂ cell. Current = 36 mA; current density = 1 mA/cm².

SO_2Cl_2 (1415 cm^{-1}) SO_2 (1335 cm^{-1} and 1150 cm^{-1}) and the material absorbing at 1070 cm^{-1} . The cyclic voltammogram is shown in Fig. 11. The compounds identifiable from the cyclic voltammogram are SCL_2 (reduction peak at $\sim 3.6\text{V}$) and Cl_2 (reduction peak at $\sim 3.2\text{V}$). All the materials except SO_2 are oxidation products of $\text{SOCl}_2/\text{LiAlCl}_4$ electrolyte. SO_2 is a reduction product of SOCl_2 .

There is a close similarity between the products accumulated in anode limited cells during forced overdischarge and those in cells during "charging." Thus, although none of the cells (both C-size and small prismatic cells) we have tested (21) exploded during "charging," it is advisable to employ caution when Li/SOCl_2 cells are subjected to a "charging" current. We note that explosions in anode limited cells during forced overdischarge occurred only under very special conditions (19, 20).

Conclusions

Oxidation processes in $\text{SOCl}_2/\text{LiAlCl}_4$ solutions have been shown to involve reactions more complex than previously suggested (15). The materials, SO_2Cl_2 , $\text{SOCl}^+\text{AlCl}_4^-$, AlCl_3 , SCL_2 , and Cl_2 have been identified as oxidation products. Reaction mechanisms have been proposed to account for the formation of these products.

Forced overdischarge of cathode limited Li/SOCl_2 cells leads to the formation of Li_2S . This reacts with LiAlCl_4 to form LiAlSCL_2 and probably LiAlS_2 .

Among the materials formed in anode limited cells during forced overdischarge are SCL_2 , Cl_2 , and a material with infrared absorption at 1070 cm^{-1} . The latter is probably a sulfur-oxy compound. Analytical data suggest that other materials such as SO_2Cl_2 and $\text{SOCl}^+\text{AlCl}_4^-$ may also form in these cells during overdischarge. The formation and/or accumulation of these and other materials may depend to a great extent on whether or not Li is present in the cell during forced overdischarge.

The "charging" of Li/SOCl_2 cells leads to regenerative cell processes so that after a long "charge" only small amounts of products accumulate in the cell. Similar products were identified from "charged" cells and from forced overdischarged anode limited cells. This suggests that "charging" of Li/SOCl_2 cells may be hazardous, although none of the cells we have "charged" exploded.

Acknowledgment

The experimental assistance of Mr. P. G. Gudrais during the early phases of the work is gratefully acknowledged. We also acknowledge fruitful discus-

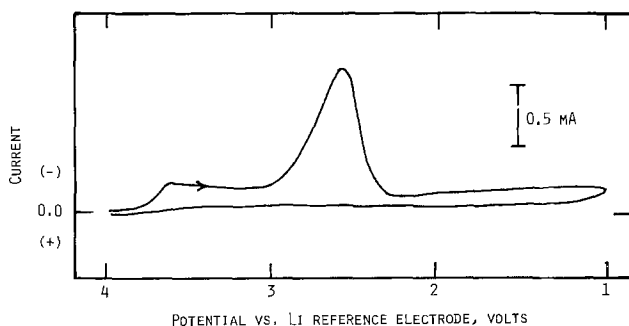


Fig. 11. Cyclic voltammogram of the electrolyte from the cell in Fig. 10 on glassy carbon electrode. The electrode was first scanned cathodically. Scan rate = $50\text{ mV}/\text{sec}$.

sions with Dr. G. L. Holleck and Dr. S. B. Brummer. This work was supported by U.S. Army Electronics Research and Development Command under Contract No. DAAB07-78-C-0564.

Manuscript submitted Jan. 24, 1980, revised manuscript received April 9, 1980.

Any discussion of this paper will appear in a Discussion Section to be published in the June 1981 JOURNAL. All discussions for the June 1981 Discussion Section should be submitted by Feb. 1, 1981.

REFERENCES

- J. J. Auborn, K. W. French, S. I. Lieberman, V. K. Shah, and A. Heller, *This Journal*, **120**, 1613 (1973).
- W. K. Behl, J. A. Christopoulos, M. Ramirez, and S. Gilman, *ibid.*, **120**, 1619 (1973); Report ECOM-4101 (April 1973).
- G. E. Blomgren and M. L. Kronenberg, German Pat. 2,262,256 (1972).
- A. N. Dey, *Electrochim. Acta*, **21**, 855 (1976).
- A. N. Dey, *This Journal*, **123**, 1262 (1976).
- N. Marincic and A. Lombardi, Contract No. DAAB07-74-C-0108, Final Report ECOM-74-0108F (April 1977).
- A. N. Dey, Contract No. DAAB07-74-C-0109, Final Report, ERADCOM-74-0109 (July 1978).
- N. Marincic, *J. Appl. Electrochem.*, **5**, 313 (1975).
- N. Marincic, *ibid.*, **6**, 51 (1976).
- N. Marincic and B. D. Hoffman, *ibid.*, **6**, 263 (1976).
- N. Marincic, *ibid.*, **6**, 463 (1976).
- H. Taylor, S. Simenas, and C. Ralto, in "Record of the 12th IECE Conference," p. 296 (1977).
- C. R. Schlaikjer, F. Goebel, and N. Marincic, *This Journal*, **126**, 513 (1979).
- J. R. Driscoll, G. L. Holleck, and D. E. Toland, in "27th Power Sources Conference," Atlantic City, N.J. (June 1976).
- W. K. Behl, in "Proceedings of the 27th Power Sources Conference," Atlantic City, N.J. (June 1976).
- G. E. Blomgren, V. Z. Leger, M. L. Kronenberg, T. Kalnoki-Kis, and R. J. Brodd, in "11th International Power Sources Conference," Brighton (1978).
- A. N. Dey, *Thin Solid Films*, **43**, 131 (1977).
- G. L. Holleck and M. J. Turchan, in "Record of the 10th IECE Conference," p. 449 (1975); Contract No. DAAB07-74-C-0030, Final Report, ECOM-74-0030 (March 1978).
- K. M. Abraham, P. G. Gudrais, G. L. Holleck, and S. B. Brummer, in "28th Power Sources Conference," Atlantic City, N.J. (June 1978).
- K. M. Abraham, G. L. Holleck, and S. B. Brummer, in "Battery Design and Optimization," S. Gross, Editor, p. 356, The Electrochemical Society Soft-bound Proceedings Series, Princeton, N.J. (1979).
- K. M. Abraham, R. Mank, and G. L. Holleck, Paper 38 presented at The Electrochemical Society Meeting, Los Angeles, California, Oct. 14-19, 1979.
- B. E. Martz and R. T. Lagemann, *J. Chem. Phys.*, **22**, 1193 (1954).
- V. Gutmann, in "Halogen Chemistry," V. Gutmann, Editor, Academic Press, New York (1967).
- J. P. Gabano, French Pat. 1,583,804 (1969).
- H. Spandau, A. Beyer, and F. Preugschat, *Z. Anorg. Allg. Chem.*, **306**, 13 (1960).
- S. Nabi and M. A. Khaleque, *J. Chem. Soc.*, 3626 (1965).
- F. A. Cotton and G. Wilkinson, "Advanced Inorganic Chemistry," 3rd ed. Interscience Publishers, New York (1972).
- J. O. Besenhard, *Carbon*, **14**, 111 (1976).
- J. Robinson, B. Gilbert, and R. A. Osteryoung, *Inorg. Chem.*, **16**, 3040 (1977).

Ambient Temperature Cycling of an Na-TiS₂ Cell

Gerald H. Newman* and Lawrence P. Klemann*

Exxon Research and Engineering Company, Corporate Research Laboratories, Linden, New Jersey 07036

ABSTRACT

Sodium-titanium disulfide cells have been cycled at ambient temperature in sodium triethyl(N-pyrrolyl)borate-dioxolane electrolyte. During primary discharge at 2.5 mA/cm² two voltage plateaus or steps are seen in plots of cell emf vs. sodium stoichiometry in Na_xTiS₂ and a limiting cathode composition is reached when x is 0.8. During repeated discharge and recharge cycling the capacity of the higher voltage step is lost while the capacity of the lower voltage step remains essentially constant. A simple prismatic design for sodium organic electrolyte cells is described and characteristic properties of the electrolyte are discussed.

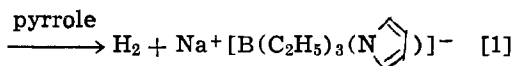
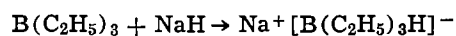
Considerable recent attention has been focused on lithium intercalation into the layered dichalcogenide, titanium disulfide. Detailed investigations into the structure (1-4) and physical properties (5) of lithium intercalates, and electrochemical intercalation studies (6-7) have contributed to the fundamental understanding of the chemical physics of the Li-TiS₂ system. Also, the results of early efforts to exploit the inherent reversibility of lithium intercalation for rechargeable batteries have been reported (6).

Pioneering investigations have extended the scope of intercalation reactions to include sodium as a guest element in the TiS₂ host lattice. Sodium intercalates of TiS₂ were prepared and characterized by Rouxel and co-workers (8) and by Silbernagel and Whittingham (9). Winn *et al.* (10) determined an equilibrium emf curve for Na_xTiS₂ as a function of sodium content. Their experimental procedure employed a sodium amalgam anode and a sodium vanadium bronze reference electrode in an electrolyte of NaI dissolved in propylene carbonate. More recently, Brummer *et al.* (11) cycled an Na-TiS₂ cell at 130°C. They used a cell configuration consisting of a molten sodium anode, a β-alumina separator, a TiS₂ cathode, and a 1,2-bis(methoxyethoxy)ethane solution of NaI as the electrolyte. The relatively elaborate experimental procedures employed in these previous electrochemical investigations of the Na-TiS₂ system were developed largely to circumvent the problem of sodium's reactivity toward organic electrolytes.

In our laboratories, investigations directed toward the systematic design of organic electrolytes for alkali metal batteries have led to the identification of a broad class of organoborate salts which are stable toward alkali metals. One of these electrolytes, a solution of sodium triethyl(N-pyrrolyl)borate in 1,3-dioxolane (12), has been used to cycle a simple prismatic Na-TiS₂ cell at ambient temperature as well as other solid-state cathodes (13).

Experimental

The steps involved in the preparation of Na[(C₂H₅)₃B(NC₄H₄)] in dioxolane are shown in Eq. [1]. The



intermediate, sodium triethylborohydride, was not isolated but was allowed to react with one equivalent of pyrrole to give a dioxolane solution of sodium triethyl(N-pyrrolyl)borate. The proton NMR spectrum of this solution showed peaks at 0.33 and 0.65δ (centers of multiplets, 15H, -C₂H₅ protons), 5.95 and

6.82δ (apparent triplets, 4H, -NC₄H₄ protons), and singlets for the dioxolane protons at 3.81 and 4.84δ (-CH₂CH₂- and O-CH₂-O, respectively).

Specific resistivities of electrolyte solutions were determined at room temperature with a Yellow Springs Instrument Company dip-type conductivity cell (cell constant 1/cm) and a Wayne Kerr conductivity bridge. Prismatic Na-TiS₂ electrochemical cells were constructed as shown schematically in Fig. 1. The electrode supports were tantalum Distex® screens, 6.5 cm² in area with about 8 cm long tabs. Thin slices of sodium metal from the center of an ingot of J. T. Baker reagent grade sodium were pressed into the Ta grid and served as the anode (and reference) electrodes. A dry mix of TiS₂ and 10% Teflon powder was pressed into a Ta grid and hot bonded at 300°C under He. Polypropylene mat and microporous polypropylene separators were placed between the layers of the anode-cathode-anode sandwich. The cells were inserted into polyethylene bags and electrode alignment was maintained by means of small clamps. The electrolyte (about 5 ml of ~1.5M solution) was added to the bag and the cell assembly was mounted upright in a glass test vessel which had a ground glass joint (for airtight sealing) and sealed glass to metal through-puts, terminated on the inside with alligator clips (for electrical contact with the cell electrodes). The assembly of the Na-TiS₂ cell was done under

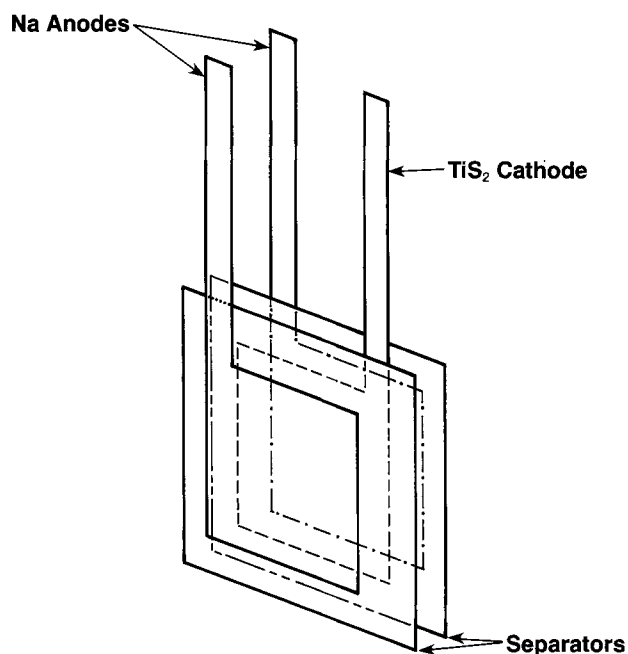


Fig. 1. Schematic construction design of prismatic Na-TiS₂ cells

* Electrochemical Society Active Member.

Key words: organic, battery, current density, diffusion.

an He atmosphere. The completed test units were removed from the dry box and clamped upright for cell testing which was accomplished using Propel automatic battery cycling equipment. Cycling was done at constant current to pre-set voltage limits.

Results and Discussion

The solubility of sodium triethyl(N-pyrrolyl)borate in 1,3-dioxolane is greater than 2.7m and its specific resistivity is concentration dependent. A minimum of 270 Ω -cm occurs at about 1.5m. The effect of solute concentration on specific resistivity is shown in Fig. 2, which also contains data for the analogous lithium and potassium boron complex anion salts for comparison. Proton NMR analysis of these salt adducts in dioxolane reveals significant changes in the chemical shifts of the aliphatic proton resonances associated with the $-\text{C}_2\text{H}_5$ groups bonded to boron, compared with their respective resonance positions seen in dioxolane solutions of free triethylboron. The changes seen in the NMR and the high conductivities observed for the final solutions are positive evidence for the formation of boron complex anion salts. We found no evidence to suggest that these anions undergo dissociation to free alkali metal pyrrole and triethylboron. Neither did we find evidence for rapid exchange between the $\text{B}(\text{C}_2\text{H}_5)_3$ complexed in the salt adduct and free triethylboron when both materials were intentionally mixed and examined by proton NMR. In this experiment resonances for both complexed and free $\text{B}(\text{C}_2\text{H}_5)_3$ were clearly distinguishable.

The alkali metal stability of the electrolyte coupled with its relatively low resistivity and high solubility enables the construction and ambient temperature high rate cycling of cells containing solid sodium anodes. We selected the Na-TiS₂ system for these investigations in order to compare our results with work previously reported and to study further the effects of multiple cycling.

The initial open-circuit voltages of the Na-TiS₂ cells were about 2.3V. Discharge of the cells was carried out at 2.5 mA/cm² resulting in a primary capacity equal to 80% of that theoretically possible for the amount of active TiS₂ present. Figure 3 contains the result of the primary discharge of one Na-TiS₂ cell and shows the dynamic cell emf (in volts)

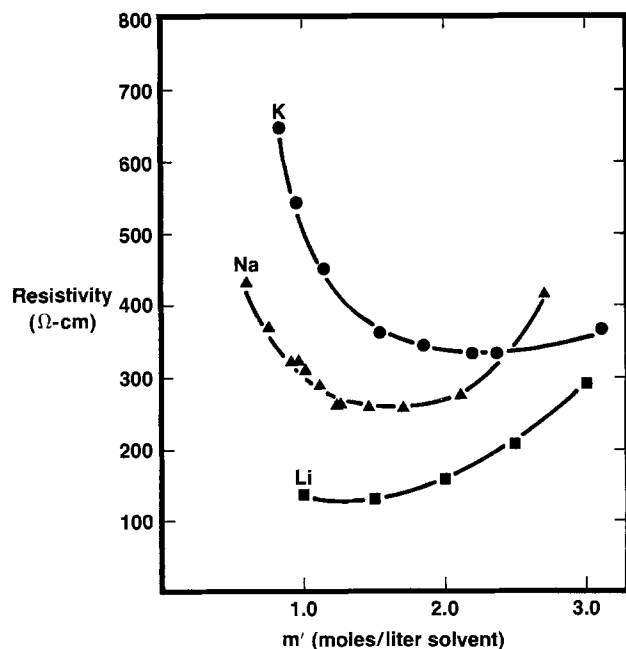


Fig. 2. Concentration dependence of $\text{M}^+ [\text{B}(\text{C}_2\text{H}_5)_3(\text{NC}_4\text{H}_4)]^-$ solution resistivity in 1,3-dioxolane.

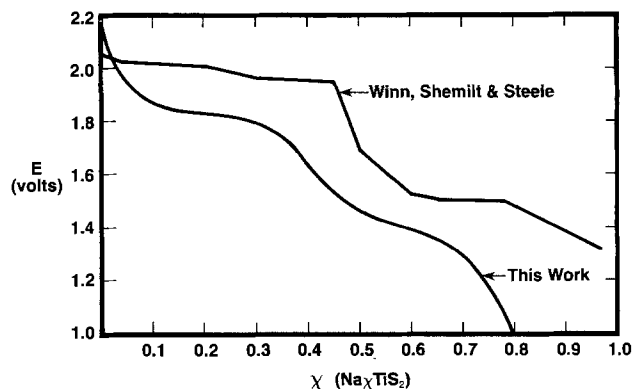


Fig. 3. Voltage vs. Na_xTiS_2 for the primary discharge of sodium-titanium disulfide cells.

as a function of the sodium stoichiometry, x , in Na_xTiS_2 . Two plateau regions or steps are clearly evident in Fig. 3. One step extends from TiS_2 to about $\text{Na}_{0.4}\text{TiS}_2$ and the second encompasses the composition range between $\text{Na}_{0.4}\text{TiS}_2$ and $\text{Na}_{0.8}\text{TiS}_2$, in qualitative agreement with previous reports (8-10).

Rouxel and co-workers (8) reported that ordering of the guest element during sodium intercalation produces three structurally distinct phases. These were described by Rouxel as being the 1st and 2nd stage trigonal prismatic coordination sites and the third phase being the trigonal antiprismatic coordination site. The data of Winn (10), included in Fig. 3 for comparison, was obtained at a maximum current rate of 40 $\mu\text{A}/\text{cm}^2$ and shows a third step (third phase) which contains additional sodium intercalation capacity for titanium disulfide above the $\text{Na}_{0.8}\text{TiS}_2$ composition. Silbernagel and Whittingham (9) did not obtain sodium contents above 0.8 using sodium naphthalenide as the sodium intercalation reagent for TiS_2 . They concluded that the small diffusion coefficient for Na^+ in the host's antiprismatic coordination sites probably limited the rate of sodium intercalation above $\text{Na}_{0.8}\text{TiS}_2$. Clearly then our 2.5 mA/cm² discharge rate is too high to allow significant sodium intercalation in the region above $\text{Na}_{0.8}\text{TiS}_2$.

After their primary discharge, the cells were cycled at constant current. The first recharge at 0.6 mA/cm² showed two voltage plateaus (analogous to those observed during primary discharge) as a function of sodium content in the TiS_2 lattice (Fig. 4). Cycling was continued for 16 complete cycles. The results are summarized in Table I. Worth noting in Table I is the fact that the discharge rate was reduced to 1.25 mA/cm² during cycles 3 through 7 and then to 0.3 mA/cm² during cycles 8 through 16. In order to return the cell to a "full" state of charge, the system was potentiostated prior to the final discharge.

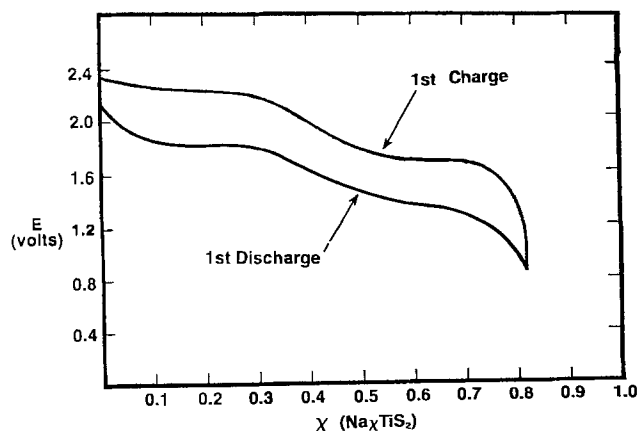


Fig. 4. Cell emf during primary discharge and first recharge

Table I. Cell cycling data for sodium/TiS₂ cell

Cycle No.	Discharge (mA/cm ²)	M.U. ^A -discharge Step 1	M.U. ^A -discharge Step 2
1	2.5	44	38
2	2.5	28	32
3	1.25	18	36
4	1.25	—	—
5	1.25	5.4	37
6	1.25	4.9	34
7	1.25	3.2	30
8	0.31	2.4	34
9	0.31	—	34
10	0.31	—	33
11	0.31	—	32
12	0.31	—	32
13	0.31	—	32
14	0.31	—	32
15	0.31	—	32
16 ^B	0.31	—	42

^A M.U. = (actual discharge capacity/cathode capacity) × 100.

^B Potentiostatically charged before this discharge.

Examination of the data contained in Table I shows that the capacity in the higher voltage plateau region (step 1 between TiS₂ and Na_{0.4}TiS₂) steadily and irreversibly decreases. Even when the discharge rate was lowered (between cycle No. 2 and 3 for example) there is no evidence for the recovery of lost capacity in this region.

On the other hand the cell cycling data demonstrates that very little capacity is lost in the lower voltage plateau (step 2 between Na_{0.4}TiS₂ and Na_{0.8}TiS₂) over 16 cycles. Even the minor loss in capacity that might be suggested by the data is essentially recovered completely when the rate of discharge is reduced (between cycle No. 2 and 3, and cycle No. 7 and 8). In fact, after the potentiostatic charge that followed cycle No. 15, the discharge capacity found (for step 2) in cycle No. 16 was 42% at 0.3 mA/cm². Comparison of this result with the 38% found in step 2 for the first discharge at 2.5 mA/cm² shows that there is no permanent loss of capacity in the lower voltage plateau (0.4 < x < 0.8 in Na_xTiS₂).

A composite of the voltage vs. composition curves for the 1st, 3rd, and 16th discharges is shown in Fig. 5. Here the loss of cycling capacity in the higher voltage plateau (0 < x < 0.4 in Na_xTiS₂) appears in sharp

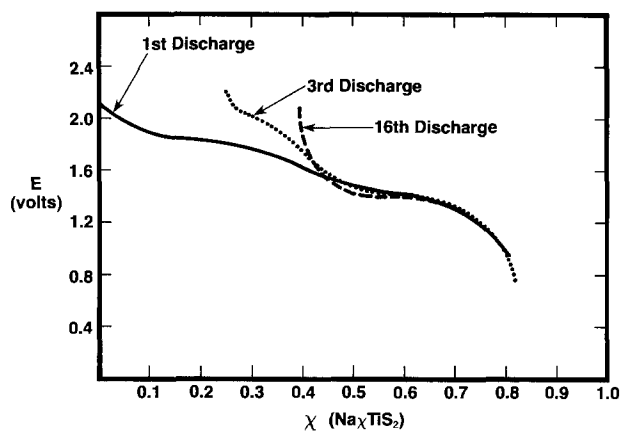


Fig. 5. Effect of cell cycling on voltage-Na_xTiS₂ curves

contrast to the essentially constant capacity observed in the lower voltage plateau (0.4 < x < 0.8 in Na_xTiS₂). These results strongly suggest that structural changes in the TiS₂ host lattice occur during sodium intercalation and deintercalation. Furthermore these structural changes appear to permanently affect the host's capacity to reversibly intercalate sodium ions. A more detailed interpretation of structural changes which are indicated must await the results of x-ray investigations of the sodium intercalates.

While we have demonstrated in this work the possibility of the reversible operation of an ambient temperature sodium anode cell we agree with an analysis (14) which shows the Na-TiS₂ system to be an impractical energy storage device. In fact, if the Na-TiS₂ couple were limited to the compositional range between Na_{0.4}TiS₂ and Na_{0.8}TiS₂, then the theoretical energy density would be only 144 W-hr/kg. This contrasts to the 480 W-hr/kg reported as the theoretical energy density for Li-TiS₂ (6).

Acknowledgments

The authors wish to acknowledge the skilled experimental assistance of Joan Serrano and John W. Swirczewski during the course of this work.

Manuscript submitted Feb. 28, 1980; revised manuscript received April 2, 1980. This was Paper 26 presented at the Los Angeles, California, Meeting of the Society, Oct. 14-19, 1979.

Any discussion of this paper will appear in a Discussion Section to be published in the June 1981 JOURNAL. All discussions for the June 1981 Discussion Section should be submitted by Feb. 1, 1981.

Publication costs of this article were assisted by Exxon Research and Engineering Company.

REFERENCES

1. M. S. Whittingham, *Prog. Solid State Chem.*, **12**, 41 (1978).
2. M. Danot, A. LeBlanc, and J. Rouxel, *Bull. Soc. Chim. Fr.*, 2670 (1969).
3. J. Rouxel, M. Danot, and J. Bichon, *ibid.*, 3930 (1971).
4. J. Bichon, M. Danot, and J. Rouxel, *C. R. Acad. Sci. Ser. C*, **276**, 1283 (1973).
5. B. G. Silbernagel and M. S. Whittingham, *J. Chem. Phys.*, **64**, 3670 (1976).
6. L. H. Gaines, R. W. Francis, G. H. Newman, and B. M. L. Rao, in "Proceedings of the 11th IECEC Meeting," Extended Abstracts pp. 418-423 (1976).
7. M. S. Whittingham, *This Journal*, **123**, 315 (1976).
8. A. LeBlanc-Soreau, M. Danot, L. Trichet, and J. Rouxel, *Mater. Res. Bull.*, **9**, 191 (1974).
9. B. G. Silbernagel and M. S. Whittingham, *ibid.*, **11**, 29 (1976).
10. D. A. Winn, J. M. Shemilt, and B. C. H. Steele, *ibid.*, **11**, 559 (1976).
11. K. M. Abraham, R. Schiff, and S. B. Brummer, Abstract 154, p. 399, The Electrochemical Society Extended Abstracts, Los Angeles, California, Oct. 14-19, 1979.
12. T. A. Whitney and L. P. Klemann, U.S. Pat. 4,104,450 (1978) and 4,117,213 (1978).
13. A. J. Jacobson, R. Chianelli, and M. S. Whittingham, U.S. Pat. 4,144,384 (1979).
14. B. M. L. Rao, in "Battery Design and Optimization," S. Gross, Editor, p. 457, The Electrochemical Society Softbound Proceedings Series, Princeton, N.J. (1979).

Behavior of Secondary Lithium and Aluminum-Lithium Electrodes in Propylene Carbonate

I. Epelboin,^{*1} M. Froment,* M. Garreau, J. Thevenin, and D. Warin

Groupe de Recherche No. 4 du CNRS, Physique des Liquides et Electrochimie,
Associé à l'Université Pierre et Marie Curie, 75230 Paris Cedex 05, France

ABSTRACT

The improvement of the lithium cycling efficiency obtained by substituting an aluminum substrate for a lithium substrate is explained by means of morphological and kinetic studies of the electrodes in the molar solution LiClO₄-propylene carbonate. SEM observations show that the insertion rate of the lithium deposit into aluminum can be sufficiently high so as to avoid dendritic growth; ESCA analysis reveals that propylene carbonate leads to a chemical formation of a polymeric membrane on the electrodes, which is less important on the aluminum than on the lithium substrate. Electrochemical impedance measurements associated with polarization curve data point out that most of the surface is active, giving rise to an exchange current density of about 17 mA/cm²; these studies also demonstrate that diffusion processes in the passivating layer and in the bulk of the electrode are responsible for the limited lithium cycling performances with the aluminum substrate.

The difficulties encountered in the development of high energy density lithium secondary batteries are mainly linked to the reactivity of lithium which leads to the formation of passivating layers on cathodically deposited lithium during both charge and storage periods. These layers are responsible for the failures observed during the experiments carried out to obtain a dissolution efficiency of the lithium deposit very close to 1, a condition required to make batteries which will work adequately for a great number of cycles.

Various attempts have been made to reduce the adverse effects of the chemical passivation either by a thorough purification of the electrolyte, or by introducing additives, or further, by altering the solvent reactivity by structural modifications (1-3). Nevertheless the improvements obtained by these different methods although appreciable are still limited.

Further attempts have been made using the property of lithium incorporation in metallic lattices, which is likely to lead to a reduction in the chemical activity of the electrode (4-6). As promising results have been obtained with an aluminum substrate (7), we have performed a systematic comparison of the electrochemical behavior of lithium deposited on this type of substrate and on a lithium substrate. In this study, we have used both electrochemical methods (polarization curves, electrode impedances), and surface study techniques: [scanning and transmission electron microscopy (SEM-TEM), x-ray photoelectron spectroscopy (ESCA XPS)].

Experimental

The experiments have been carried out with a molar lithium perchlorate (LiClO₄) solution in propylene carbonate (PC). LiClO₄ (Smith Chem. Company pure product) was dehydrated by heating under vacuum at a temperature close to its melting point. P.C. (Merck for synthesis) was dried over 3A activated molecular sieves (Merck). The residual water content in the solution thus obtained was below 10 ppm as determined by a coulometric titration based on the Karl-Fischer method (Aquavit Tacussel).

All experiments were conducted at 25° ± 1°C in a dry box (Jaram). The argon atmosphere was continuously recirculated through a column containing

molecular sieves and active carbon. The humidity was monitored by a hygrometer (Shaw) and reduced to about 5 ppm water vapor.

The surfaces of the working electrodes are disks ($A = 0.2 \text{ cm}^2$) formed by the cross sections of cylinders 5 mm high; they were fitted into glass tubes for the lithium (Alfa Ventron 99.9%) and into Teflon tubes for the aluminum (Johnson Matthey 99.99%).

The electrodes, washed successively in pure propylene carbonate and in anhydrous hexane were observed by scanning electron microscopy (Cambridge Stereoscan). The layers were analyzed by transmission electron microscopy (Jeol 100 B) and x-ray photon electron spectroscopy (AEI ES 200 B). Special apparatus were designed for the transfer of the lithium samples to the SEM (8) and ESCA (9) observation chambers to avoid any atmosphere contamination.

The cell polarization was controlled by a fast response potentiostat-galvanostat (10). The potential measured between the working electrode and the lithium reference electrode was determined after correction of the ohmic drop by an interrupted current technique. By using a rotating disk electrode, the measured potential is free of any term due to concentration gradients in the electrolyte. The impedance of the electrode was measured in the frequency range from 10⁺⁵ to 10⁻³ Hz using a function transfer analyzer (Schlumberger Solartron 1174) with an ohmic drop compensator device (11).

Results and Discussion

Cycling Operations

Lithium substrate.—We have shown elsewhere, with a motionless electrode preliminarily submitted to an anodic polarization (50 mV of overpotential and 10 C/cm² of charge density), that a quite reversible behavior of the lithium electrode was only obtained with limited overpotentials, current, and charge densities (12). Accordingly, more than 500 galvanostatic cycles have been performed with a current density of 1 mA/cm² and a charge density of 1 C/cm², with a very low evolution of the involved overpotentials ($15 < |\eta| < 25 \text{ mV}$).

Aluminum substrate.—The use of an aluminum substrate allowed a significant improvement in the cycling properties of lithium. With a motionless electrode submitted to an initial lithium incorporation ($Q = 50 \text{ C/cm}^2$ and $i = 5 \text{ mA/cm}^2$), we have obtained more than 1500 cycles with a current density of 2 mA/cm²

* Electrochemical Society Active Member.

¹ Deceased in February 1980.

Key words: Li cathodic insertion, kinetics of insertion, impedance measurements, cycling efficiency, film analysis, electrodeposition.

and a charge density of 1 C/cm^2 , corresponding to an average coulombic efficiency higher than 97%. It was still possible to obtain nearly 220 cycles (Fig. 1) with a current density of 2 mA/cm^2 and a cycling charge density of 2.5 C/cm^2 , with 94% coulombic efficiency. The above numbers of cycles have been determined by stopping cycling when the discharge potential of the electrode was increased to 100 mV with respect to its initial value.

Electrode Morphology

Lithium substrate.—The first morphological studies performed with a lithium substrate have shown that an anodic prepolarization was able to clean the electrode surface; the polycrystalline structure of the substrate was clearly revealed after a cleaning of the electrode surface by an anodic polarization of 50 mV overpotential and 10 C/cm^2 charge density (12). Alternatively, using larger overpotentials led to surface damaging.

During the cathodic step, the lithium began to grow, on a clean surface, mainly on the crystallographic defects of the metal, such as the grain boundaries. This deposit could be wholly dissolved during a subsequent anodic polarization at 50 mV overpotential, insofar as the cathodic and anodic charge densities remained lower than 1 C/cm^2 . With higher charge densities, or higher overpotentials, the electrode surface was spread with small islets of lithium deposit which could not later be dissolved under anodic polarization. With charge densities higher than 5 C/cm^2 , the lithium deposit underwent a dendritic growth.

Aluminum substrate.—The cathodic reduction of Li^+ ions in galvanostatic conditions, on an aluminum substrate, did not lead to a dendritic formation as long as the charge density was smaller than a threshold value Q_d . The value of Q_d depended on the current density used, e.g., $Q_d \sim 50 \text{ C/cm}^2$ for $i = 10 \text{ mA/cm}^2$, $Q_d \sim 100 \text{ C/cm}^2$ for $i = 1 \text{ mA/cm}^2$. The improvement corresponding to this slower formation of dendrites is linked to the formation of the intermetallic compound LiAl which was identified by x-ray diffraction analysis.

The way lithium was incorporated into aluminum depended on the type of preliminary treatment undergone by the aluminum substrate. For instance, the electropolishing of this metal in an anhydrous ethanol solution of lithium perchlorate induced the formation of a thick alumina layer leading to the dendritic growth of lithium for the lowest charge densities. The electrode surfaces used in this work had thus been prepared under strictly identical conditions consisting of a mechanical polishing inside the glove box.

The dissolution of the lithium incorporated in the aluminum could not be performed without a visible alteration of the substrate, unless this dissolution was limited to 30% of the initial lithium deposit. For higher percentages, the surface exhibited cracks which separated domains whose dimensions were similar to

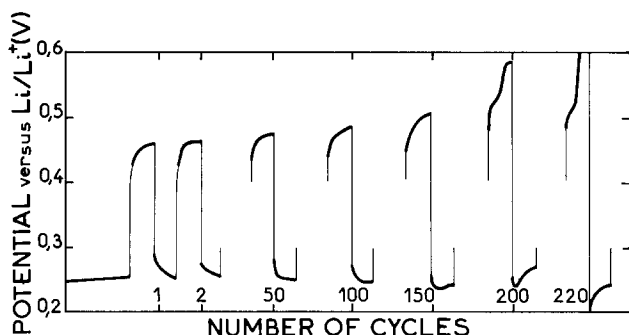


Fig. 1. Galvanostatic cycling with a motionless aluminum electrode. Initial lithium charge density of 30 C/cm^2 . Current density $i = 2 \text{ mA/cm}^2$. Charge density $Q = 2.5 \text{ C/cm}^2$.

those of the grain boundaries. This behavior might be due to an intergranular penetration of lithium into aluminum.

Analysis of the Passivating Layers

Thin films, stripped from surfaces of both lithium and aluminum substrates by means of copper grids, have been observed by TEM: the electrodes were covered with a layer always plastic and porous in appearance. Figure 2 shows a layer obtained from a lithium-aluminum electrode submitted to a cathodic charge density $Q_c = 30 \text{ C/cm}^2$ and a current density $i = 2 \text{ mA/cm}^2$. The microdiffraction patterns, corresponding to the area observed on Fig. 2, showed the existence, inside the pores, of tiny Li_2CO_3 and LiCl crystallites (Fig. 3). Let us recall that, in the case of the lithium substrate, the presence of LiClO_4 crystallites had also been detected (13). The analysis of the electrode surface by x-ray photoelectron spectroscopy (ESCA XPS) confirmed the presence of CO_3^{2-} , ClO_4^- , and Cl^- ions. The presence of lithium carbonate agreed with the decomposition of propylene carbonate, accompanied by formation of propylene, as proposed by Dey (14). However, in our opinion, the passivating properties of the layer were not due to a compact Li_2CO_3 layer, but rather to the plastic layer in which the crystallites have been observed, and which would be formed by polymerization of propylene as suggested by Bro in a discussion of Broadhead's paper (15). In the case of relatively thick layers formed on lithium substrate, it was possible to verify that the plastic part of the layer was

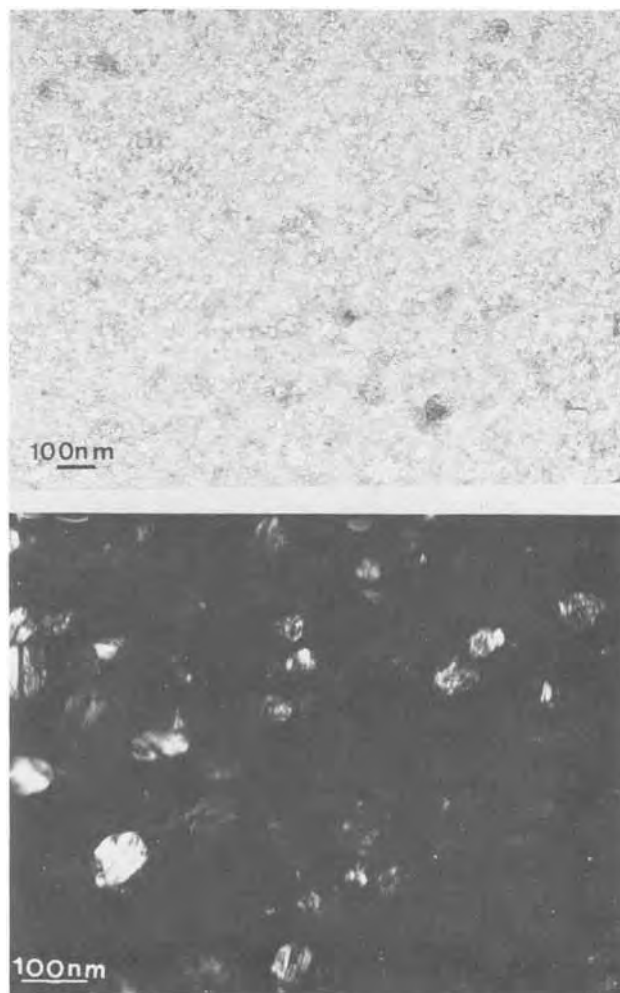


Fig. 2. Layer stripped from an aluminum-lithium electrode and observed in transmission electron microscopy: (a, top) bright field, (b, bottom) dark field.

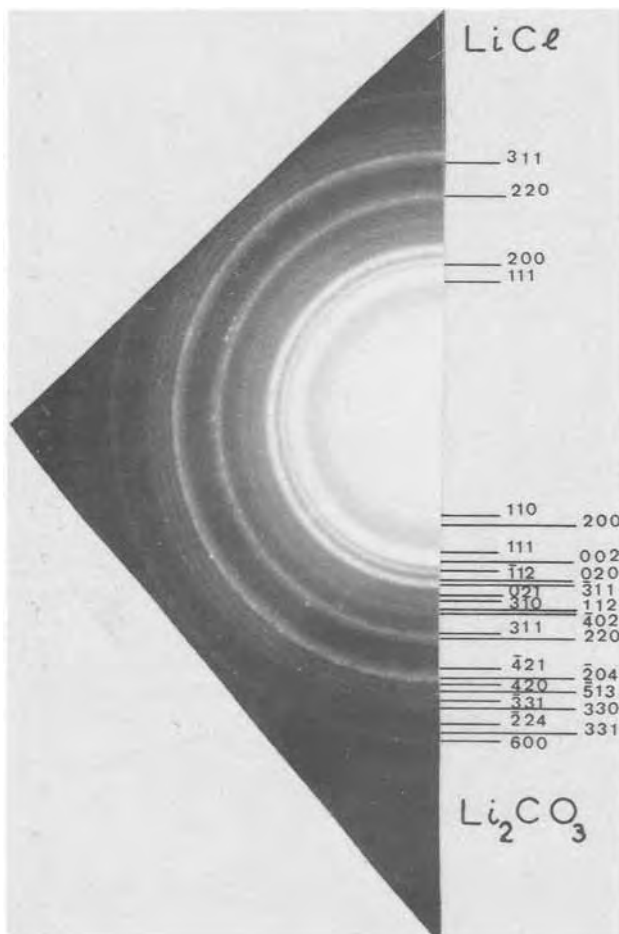


Fig. 3. Microdiffraction diagram of the area corresponding to the Fig. 2; electron beam 100 kV.

not soluble in any acid solution. Besides, mass spectroscopy analysis revealed the presence of organic compounds of molecular mass higher than the molecular mass of propylene, inside the layer submitted to a temperature of 150°C.

The decomposition of propylene carbonate has been observed whatever the treatment applied to the electrode: anodic dissolution, cathodic deposition, and standing time in the electrolyte. Therefore, the origin of these layers is certainly due to a chemical process of decomposition of propylene carbonate in the presence of lithium. On the other hand, the behavior of lithium during the aging of the solution (long periods of charge and discharge) remained the same so that completely removing the impurities did not avoid any formation of a passivating layer. This conclusion agreed with that of Koch about the electrolytes with tetrahydrofuran as the solvent (16). Thus, the formation of the plastic layer may be considered as unavoidable, and the more developed the more dendritic was the state of lithium deposit. The ionic erosion technique used during the ESCA study of the electrodes, allowed us to show, however, that the layer formed on aluminum was always thinner than the layer formed on massive lithium under similar conditions.

Electrode Kinetics

Polarization curves.—Lithium substrate.—We have shown elsewhere (12) that, for the clean electrode, the overpotential-current density curves $\eta = f(i)$ were symmetric and reversible when overpotentials were lower than 50 mV and when the cathodic polarizations were carried out fast enough to avoid any evolution of the area due to a dendritic growth. The analysis of these curves led to an exchange current density $i_0 = 3.3 \text{ mA/cm}^2$ and a transfer coefficient

$\alpha = 0.5$ for the charge transfer reaction $\text{Li} \rightleftharpoons \text{Li}^+ + e^-$, with a molar LiClO_4 solution in propylene carbonate and a residual water content lower than 10 ppm.

Aluminum substrate.—The curves (a) and (c) of Fig. 4 show the evolution of the current density vs. the potential of the aluminum electrode with respect to the lithium reference electrode, respectively, after and before correction for the ohmic drop. The analysis of these stationary curves obtained after a charge density of 20 C/cm^2 had shown, first, that the aluminum-lithium electrode tended to two different values of the open-circuit rest potential (OCP). Starting from a stationary polarization state obtained after a period of cathodic deposition, the electrodes reached an OCP $V_c \sim 335 \text{ mV}$. After an anodic dissolution amounting to about 1/10 of the initial charge, the electrode reached another OCP $V_a \sim 385 \text{ mV}$. This last value was corresponding to the free enthalpy for the formation of the intermetallic compound LiAl [$\Delta G \sim 8.9 \text{ kcal/mole}$ (5)]. The difference between V_a and V_c seemed thus to be attributed to the fact that there existed two equilibrium compositions of the aluminum-lithium electrode for anodic and cathodic polarizations.

The evolution of the free ohmic drop potential in the time $V = V(t)$ during a current interruption showed two distinct parts separated by a sharp discontinuity. The first part corresponds to the rapid discharge of the electrochemical double layer with a relaxation time τ of about $20 \mu\text{sec}$. The second part occurred with a relaxation time τ' between 10 and 100 sec. The relatively long times τ' could not be attributed to the vanishing of a gradient in the electrolyte since the polarization curve did not depend on the rotation speed of the electrode, at the high rotation speeds used in the experiments ($\Omega \cong 1000 \text{ rpm}$). They were due to a relatively slow solid-state diffusion process which modified the composition of the electrode, after the current interruption. The instantaneous OCP values V^* of the curve b (Fig. 4) correspond to the potentials of the discontinuities of the curve $V = V(t)$. As $\tau \ll \tau'$ these values V^* corresponded to OCP of electrodes whose superficial compositions did not appreciably differ from the solid-state compositions existing just before the current interruption.

The conventional treatment of the polarization curve $\eta = f(i)$ with $\eta = V - V^*$ led to an exchange current density i_0 higher than 15 mA/cm^2 with a transfer coefficient $\alpha = 0.5$. These values agreed with the variations of i_0 when using different values of concentration of Li^+ ions in the electrolyte.

Electrode impedances.—The previous approximate estimation of i_0 , for the aluminum substrate, has

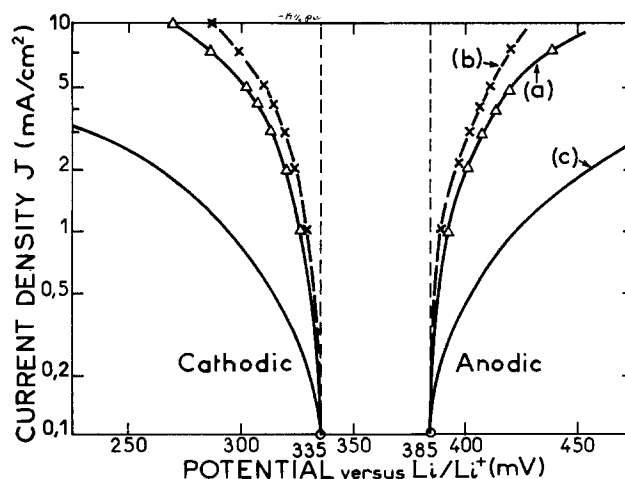


Fig. 4. Polarization curves with a disk aluminum electrode rotating at 2000 rpm. Curve (a) free ohmic drop potential, curve (b) instantaneous open-circuit potential, curve (c) potential vs. Li/Li^+ .

been made more precise with measurements of the electrode impedance (17). This technique allowed to get free from the difficulties linked to the variations in the composition of the electrode with the conditions of the electrolysis. Furthermore, it has been possible to confirm the phenomenon of solid-state diffusion mentioned above.

All the impedance diagrams obtained with a rotating disk electrode, under various stationary anodic and cathodic current densities between 0 and 10 mA/cm², comprised two distinct loops (Fig. 5), both independent from the rotation speed of the electrode ($\Omega \geq 1000$ rpm). The high frequency loop (between 10⁺⁵ and 2.5 Hz) was independent of the current density used. In contrast, the low frequency loops (between 2.5 to 10⁻³ Hz) had all the same shape with an initial straight line of slope 45°, but a size which was larger as the current density was lower.

These results can be explained if the previous results about the polarization curves are taken into account. In the case of the aluminum-lithium electrode, several kinds of electroactive lithium species are involved in the electrochemical reaction. The current density i is a function not only of the potential V and of the active part θ_a of the electrode area, but also of the concentrations c_i of the Li species on the surface of the metal, according to the relation

$$i = i(V, \theta_a, c_j) \quad [a]$$

The electrode impedance Z is then related to the derivative of Eq. [a] with respect to the voltage (18)

$$\frac{di}{dV} = \left(\frac{\partial i}{\partial V} \right)_{c_j, \theta_a} + \sum_j \left[\left(\frac{\partial i}{\partial c_j} \right)_{\theta_a} \times \frac{dc_j}{dV} + \left(\frac{\partial i}{\partial \theta_a} \right)_{c_j} \times \frac{d\theta_a}{dV} \right] \quad [b]$$

For a relatively high frequency, only the charge transfer process can follow the variations of the voltage imposed by the potentiostat (e.g., for frequencies such that $1/N \ll \tau$) the $(\partial i / \partial c_j)$ terms of Eq. [b] can be neglected. Under these conditions, the right side of Eq. [b] reduces to

$$\left(\frac{\partial i}{\partial V} \right)_{c_j, \theta_a} = \frac{1}{R_t} \quad [c]$$

where R_t is the transfer resistance corresponding to the charge transfer reaction $\text{Li} \rightleftharpoons \text{Li}^+ + e^-$. This transfer resistance equal to 1.5 $\Omega \cdot \text{cm}$, practically independent of the current density range of 0-10 mA/cm², showed that the electrode was in the micropolarization domain. From the conventional relation at zero current between

the exchange current density and the transfer resistance ($i_0 = RT/R_t F$ where R , T , and F had their usual meaning), an exchange current density of nearly 17 mA/cm² was calculated, corroborating the results deduced from the polarization curves. On the other hand, the high value of the double layer capacity ($C_d \sim 40 \mu\text{F}/\text{cm}^2$) measured with the aluminum-lithium electrode demonstrated that the active surface was larger than in the case of the lithium electrode ($C_d \sim 5 \mu\text{F}/\text{cm}^2$) (19).

Alternatively, for a relatively low frequency, the mass transfer processes can follow the variations of the voltage imposed by the potentiostat. Thus, the right hand of Eq. [b] tends to $di/dV = 1/R_p$ where R_p is the polarization resistance. In addition to R_t , this term R_p contains a contribution of a diffusion resistance R_d . The low frequency loops, with their initial straight line of slope 45°, confirmed that diffusion phenomena occurred in the bulk of the electrode. These phenomena might simultaneously occur in the porous layer covering the electrode and in the aluminum substrate. The diffusion of lithium could happen according to several processes, as those suggested by Nicholson (5) for a magnesium substrate: transport of lithium along the grain boundaries and penetration inside the grains.

Conclusion

Two essential facts have been demonstrated by comparison of the two kinds of electrodes made with a lithium and an aluminum substrate. First, the same chemical decomposition of propylene carbonate intervenes with both kinds of electrodes, yielding a plastic and porous layer. The lithium incorporation rate, though not fast enough to avoid the formation of a passivating layer onto aluminum, is however sufficiently high for cathodic charge densities 10-20 times larger than for a lithium substrate to be used without formation of dendrites; the development of a thick passivating layer, as in the case of lithium, is thus reduced. On the other hand, the incorporation of lithium into the aluminum substrate does not involve a prohibitive penalty voltage ($\Delta V < 0.4\text{V}$), and is homogeneous enough for obtaining a very large increase of the active part of the electrode surface intervening in the charge transfer process.

The results obtained with the aluminum substrate during the cycling operations, though more satisfactory than with lithium, are mainly limited by diffusion phenomena in the bulk of the electrode. The improvement of the performances of this kind of electrodes thus necessarily depends on an increase in the rate of these diffusion processes of lithium, through an adequate change of the structure of the substrate.

Acknowledgment

This research was sponsored by DRET Paris under Contract No. 78 34 265 00 480 75 01.

Manuscript submitted Dec. 4, 1979; revised manuscript received April 14, 1980. This was Paper 23 presented at the Los Angeles, California, Meeting of the Society, Oct. 14-19, 1979.

Any discussion of this paper will appear in a Discussion Section to be published in the June 1981 JOURNAL. All discussions for the June 1981 Discussion Section should be submitted by Feb. 1, 1981.

Publication costs of this article were assisted by Centre National de la Recherche Scientifique.

REFERENCES

1. R. D. Rauh and S. B. Brummer, *Electrochim. Acta*, **22**, 75 (1977).
2. V. R. Koch and S. B. Brummer, *ibid.*, **23**, 55 (1978).
3. V. R. Koch and J. H. Young, *Science*, **204**, 499 (1979).
4. A. N. Dey, *This Journal*, **118**, 1547 (1971).
5. M. M. Nicholson, *ibid.*, **121**, 736 (1974).

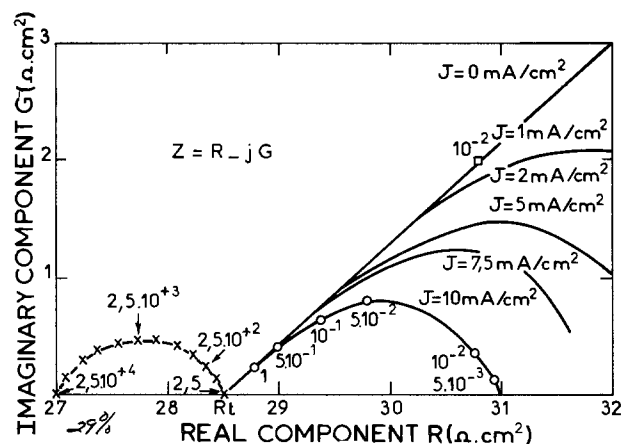


Fig. 5. Electrochemical impedance of the aluminum lithium electrode for various cathodic current densities. Experimental points correspond to frequencies in Hz.

6. B. M. L. Rao, R. W. Francis, and M. A. Christopher, *ibid.*, **124**, 1490 (1977).
7. J. R. Van Beek and P. J. Rommers, Paper 37 presented at the 11th International Power Sources Symposium, Brighton (1978).
8. M. Garreau and J. Thevenin, *J. Microsc. Spectrosc. Electron.*, **3**, 27 (1978).
9. J. P. Contour, A. Salesse, M. Froment, M. Garreau, J. Thevenin, and D. Warin, *ibid.*, **4**, 483 (1979).
10. C. Gabrielli and M. Keddum, *Electrochim. Acta*, **19**, 355 (1974).
11. C. Gabrielli, M. Ksouri, and R. Wiart, *ibid.*, **22**, 255 (1977).
12. M. Garreau, J. Thevenin, and D. Warin, *Prog. Batt. Solar Cells*, **2**, 54 (1979).
13. M. Froment, M. Garreau, J. Thevenin, and D. Warin, *J. Microsc. Spectrosc. Electron.*, **4**, 111 (1979).
14. A. N. Dey, *Thin Solid Films*, **43**, 131 (1977).
15. J. Broadhead and F. A. Trumbore, 10th International Power Sources Symposium, Brighton (England) **42** (1976).
16. V. R. Koch, *This Journal*, **126**, 181 (1979).
17. I. Epelboin and M. Keddum, *ibid.*, **117**, 1052 (1970).
18. I. Epelboin, *Metall. Oberfläche*, **27**, 113 (1973).
19. I. Epelboin, M. Garreau, and J. Thevenin, Paper 3 presented at The Electrochemical Society Meeting, Atlanta, Georgia, Oct. 9-14, 1977.

Zone Processes at the Formation of the Lead Acid Battery Positive Plate

D. Pavlov* and G. Papazov

Central Laboratory of Electrochemical Power Sources, Bulgarian Academy of Sciences, Sofia 1040, Bulgaria

ABSTRACT

The processes during formation at different current densities of the positive lead acid battery plates prepared with different phase compositions of the paste were studied. At the formation a PbO₂ zone is formed. The direction of its growth in the plate depends on the phase composition of the paste, the current density, the pH of the solution, the paste density, etc. It was found that at formation with a high current density of the plates with high sulfation pastes, the PbO₂ zone grows in the interior of the plate first and then to its surfaces. At formation with a low current density of the plates with low sulfation pastes this process is inverse. A diagram of chemical and electrochemical reactions which take place in a reaction layer is presented. The direction of the PbO₂ zone growth depends on the direction of H⁺ and SO₄²⁻ ion flows which keep electroneutrality of the solution in the reaction layer. When the H⁺ and SO₄²⁻ ion flows enter the reaction layer the PbO₂ zone grows in the surface layers of the plate and vice versa, when they go out of the reaction layer the PbO₂ zone grows first in the interior of the plate.

Formation is an essential process in the technology of the lead acid battery positive plate production. During formation lead oxide and basic lead sulfates of the cured paste turn into a lead dioxide active mass. Formation depends on the following conditions: (i) concentration of the formation H₂SO₄ electrolyte, (ii) phase composition of the cured paste, (iii) formation current density, (iv) paste density, and (v) temperature.

The overwhelming majority of previous studies were aimed at determining the influence of the above-mentioned conditions on the active mass performance (1-22). In a paper of ours (23) we elucidated the chemical and electrochemical reactions by establishing the change of the plate phase composition during formation in electrolytes with various H₂SO₄ concentrations. In another paper (24) we determined the influence of current density on formation. The present paper aims to define the influence of phase composition of the cured paste and formation current density on the rates of chemical and electrochemical reactions at the various regions of the cross section of the plate.

Experimental Methods

Formation was carried out on 14 A-hr plates of automotive batteries. The pastes were prepared at 30°C. The amount of H₂SO₄ with specific gravity of 1.4 g/cm³ was 0, 2, 4, 6, 8, 10, and 12% with respect to the 65% oxidized lead powder. Further in this paper we shall signify this amount by percent H₂SO₄ only.

* Electrochemical Society Active Member.

Key words: formation of PbO₂ battery plate, lead acid battery technology, processes in porous electrodes, movements of the electrochemical processes in space.

Through the variation of the quantity of added water all kind of pastes have been adjusted at a density of 4.2 g/cm³. Pb-6% Sb grids were pasted and the plates were cured for 72 hr at 35°C and 100% humidity. The experimental cells consisted of a tested positive plate combined with two negative plates. The formation electrolyte was H₂SO₄ with sp gr 1.05. Formation was carried out at 2 and 10 mA/cm² of the plate apparent area. During formation the potential of the positive plate under polarization was measured. Every hour the circuit was opened and the potential was measured for 5 min vs. the Hg/Hg₂SO₄/H₂SO₄ electrode. Periodically samples were cut out from the tested plate. After rinsing and drying part of the active mass was subjected to x-ray diffraction analysis and porosity measurements. To determine the distribution of the formed PbO₂ zones and unformed paste, a cross section of the other part of the sample was observed and photographed.

Experimental Results

Influence of the paste phase composition on the direction of growth of the PbO₂ zone during the first formation stage.—Lead oxide and basic lead sulfates are yellow to white in color. Lead dioxide is dark brown to black. Thus the formed and unformed zones in the plate can be clearly distinguished. By the change of the color in the plate cross section the formation process may be easily followed.

Figure 1 presents photographs of the cross section of partially formed plates with pastes of 0, 2%, 4%, 6%, 8%, 10%, and 12% H₂SO₄. The dark zones correspond to PbO₂ and the light ones to unformed paste. Formation was carried out at a current of 10 mA/cm².

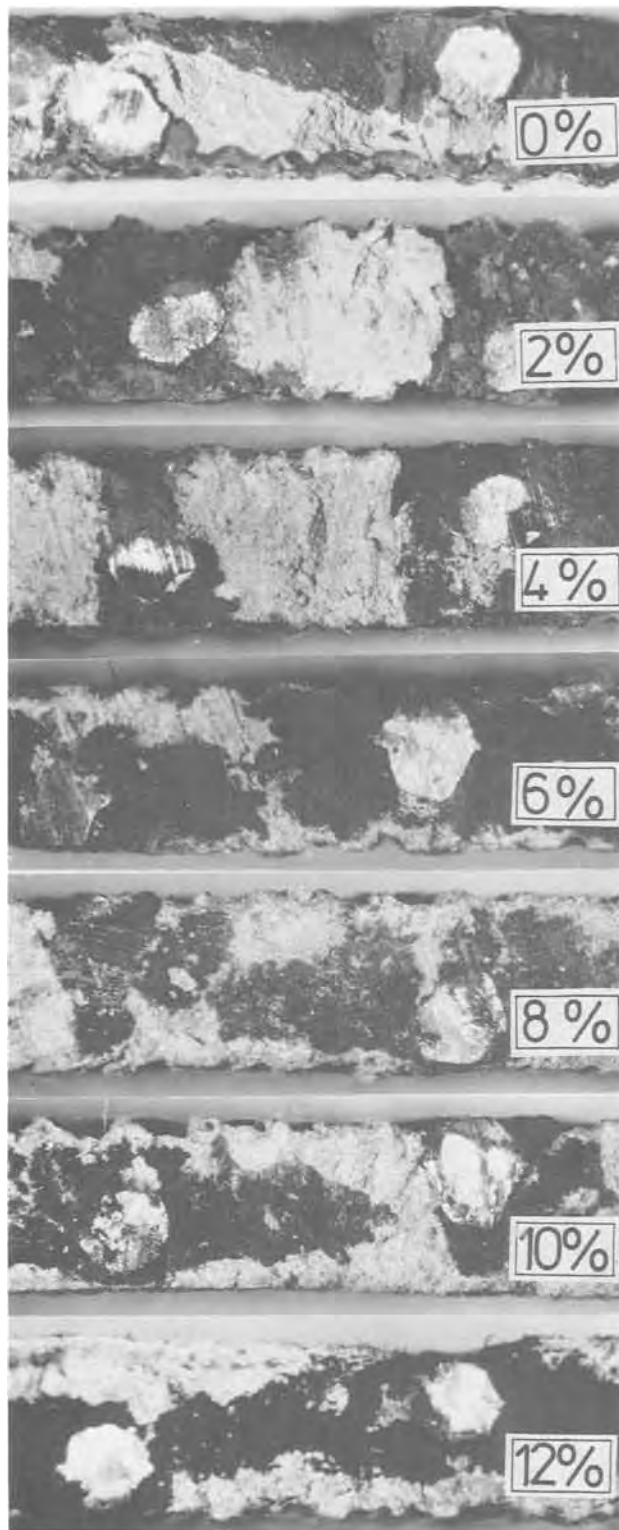


Fig. 1. Microphotograph of the cross section of segments between two grid bars of partially formed plates prepared with 0, 2%, 4%, 6%, 8%, 10%, and 12% H_2SO_4 pastes. The dark portions of the plates are PbO_2 zones while the light ones consist of unformed divalent lead compounds.

The photographs were made when 10 to 14 A-hr had passed through the plate.

Formation begins always from the grid bars but the direction of the PbO_2 zone growth depends on the percent H_2SO_4 used for paste preparation.

When 0% H_2SO_4 paste is under formation the PbO_2 zone grows initially in the surface layers of the plate. After covering the surfaces the PbO_2 zones advance into the interior of the plate. At paste with 2% H_2SO_4 ,

the rate of the PbO_2 zone growth in the surface layers slightly exceeds that into the interior. In the case of 6% and 8% H_2SO_4 pastes the direction of the PbO_2 zone growth is reversed in comparison with the low sulfation pastes. At 10% and 12% H_2SO_4 pastes the rate of growth of the PbO_2 zone into the interior exceeds many times the one in the surface layers.

Change of the plate phase composition during formation.—The relative intensity of the x-ray characteristic diffraction lines was adopted as a measure of the phase changes in the plate during formation (25). It is defined as a ratio of the “i” phase characteristic reflection intensity and the sum of the intensities of the characteristic diffraction lines of all phases. The reflections listed in Table I were adopted as characteristic. The values in brackets show intensities of the powder diffractograms. Since not all of them are equal to 10, the relative intensity values do not correspond to the absolute amounts of the phases in the plate. They can be used only as a measure for phase relative changes during formation.

The plates were prepared at 30°C using 0%, 4%, 8%, and 12% H_2SO_4 . Up to 8% H_2SO_4 the paste consists of tet-PbO and $3\text{PbO} \cdot \text{PbSO}_4 \cdot \text{H}_2\text{O}$ (26). The 12% H_2SO_4 paste contains $\text{PbO} \cdot \text{PbSO}_4$, $3\text{PbO} \cdot \text{PbSO}_4 \cdot \text{H}_2\text{O}$, and small amount of tet-PbO (26).

Figure 2 presents the changes of the relative intensity of the phases in the plate during formation with 10 mA/cm². It is seen that initially $\text{PbO} \cdot \text{PbSO}_4$, $3\text{PbO} \cdot \text{PbSO}_4 \cdot \text{H}_2\text{O}$, and tet-PbO react whereby α - PbO_2 , β - PbO_2 , and PbSO_4 are formed. This period determines the first stage of formation (23). The first stage is completed by the flow of less than 30 A-hr which is approximately equal to the theoretical capacity of the plate. At the end of this stage the plate consists of α - PbO_2 , β - PbO_2 , and PbSO_4 crystals which can be seen all over the cross section of the plate. During a second formation stage PbSO_4 is oxidized to β - PbO_2 .

The diffraction lines 0.312 and 0.350 nm chosen as characteristic of α - and β - PbO_2 are common with those of tet-PbO and PbSO_4 . However, at the end of the formation only negligible amounts of PbO and PbSO_4 remain in the plates. The above diffraction lines present the β/α PbO_2 ratio of the phases. Figure 3 shows the dependence of this ratio on the percent H_2SO_4 in the paste. At pastes prepared with less than 4% H_2SO_4 the amount of α - PbO_2 in the active mass exceeds that of β - PbO_2 . At more than 6% H_2SO_4 , β - PbO_2 predominates in the active mass. Practice has affirmed the use of 4-5% H_2SO_4 , which corresponds to a slightly larger amount of α - PbO_2 compared with that of β - PbO_2 .

Change of the electrode potential during formation.—Figure 4 presents the dependences of the potentials under polarization and at open circuit on the quantity of electricity passed during formation of the plates with 2%, 6%, and 12% H_2SO_4 pastes. The potentials were measured vs. $\text{Hg}/\text{Hg}_2\text{SO}_4/\text{H}_2\text{SO}_4$ electrode.

At the very beginning of formation only the plate grid is electroconductive. That is why the current density is high and the polarization is great. As PbO_2 zones are formed and begin to grow the current density decreases and the polarization decreases too.

During the first stage both potentials remain low. When the oxidation of PbSO_4 to PbO_2 begins potential under current increases and attains a constant value in

Table I.

Diffraction line (d/nm)	Phase
0.350	PbO_2 [9.1] + PbSO_4 [0.8]
0.333	$\text{PbO} \cdot \text{PbSO}_4$ [10] + PbSO_4 [10]
0.326	$3\text{PbO} \cdot \text{PbSO}_4 \cdot \text{H}_2\text{O}$ [10]
0.312	tet-PbO [10] + α - PbO_2 [10]
0.300	PbSO_4 [10]
0.279	tet-PbO [6.2] + β - PbO_2 [10]

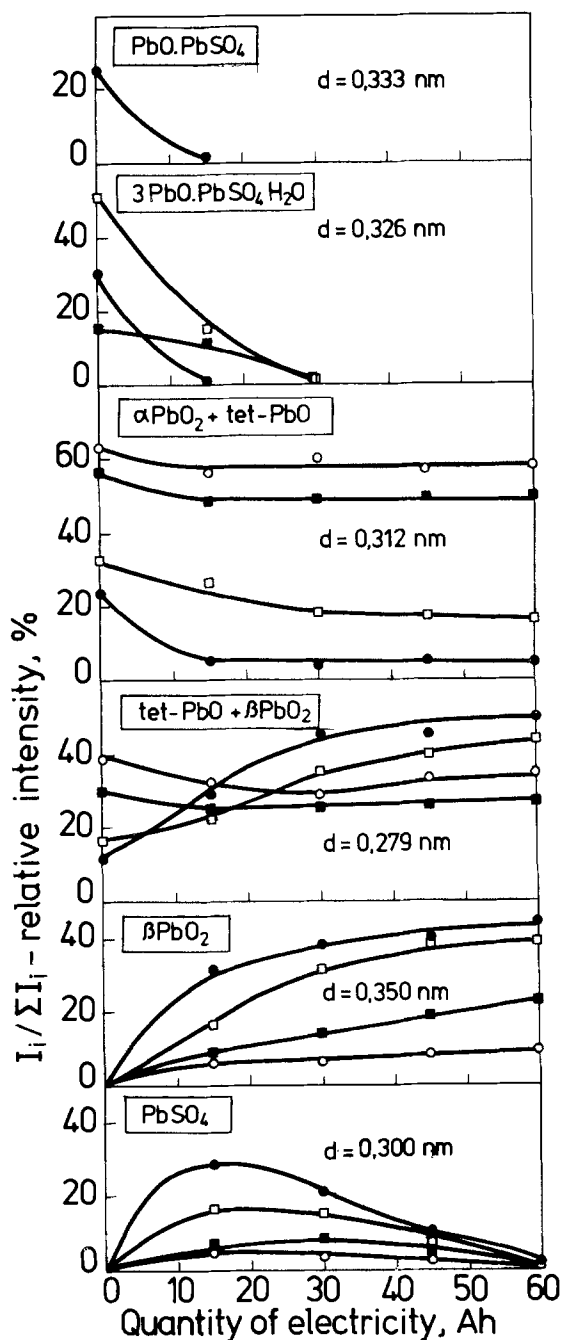


Fig. 2. Relative intensity changes of the phase characteristic diffraction lines during formation of plates with pastes prepared with: (○) 0% H_2SO_4 ; (■) 4% H_2SO_4 ; (□) 8% H_2SO_4 , and (●) 12% H_2SO_4 .

the second formation stage. In the first stage the potential under polarization is 150-200 mV more negative than that in the second one.

From Figure 4 it is also seen that plates with greater paste sulfation have higher electrode potentials under current and at open circuit than those plates the pastes of which are prepared with small amounts of H_2SO_4 . In the second formation stage the plates consist only of $\alpha\text{-PbO}_2$, $\beta\text{-PbO}_2$, and PbSO_4 , the open-circuit potential reaches a constant value which does not depend on the initial paste composition.

Table II presents the equilibrium potentials of $5\text{PbO}\cdot 2\text{H}_2\text{O}/\text{PbO}_2$, $\text{PbSO}_4/\text{PbO}_2$, and basic lead sulfates/ PbO_2 electrodes against the $\text{Hg}/\text{Hg}_2\text{SO}_4$ electrode. It can be supposed that the great difference between equilibrium potentials is the reason why formation takes place in two stages. The table shows also that the equilibrium potentials depend strongly on pH

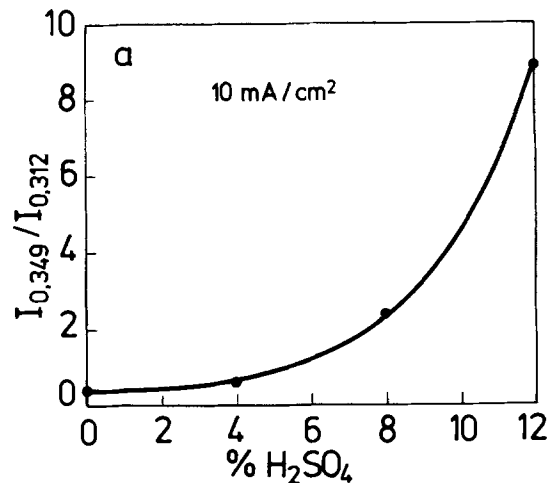


Fig. 3. Dependence of β/α PbO_2 ratio of the formed plates on the percent H_2SO_4 in the paste.

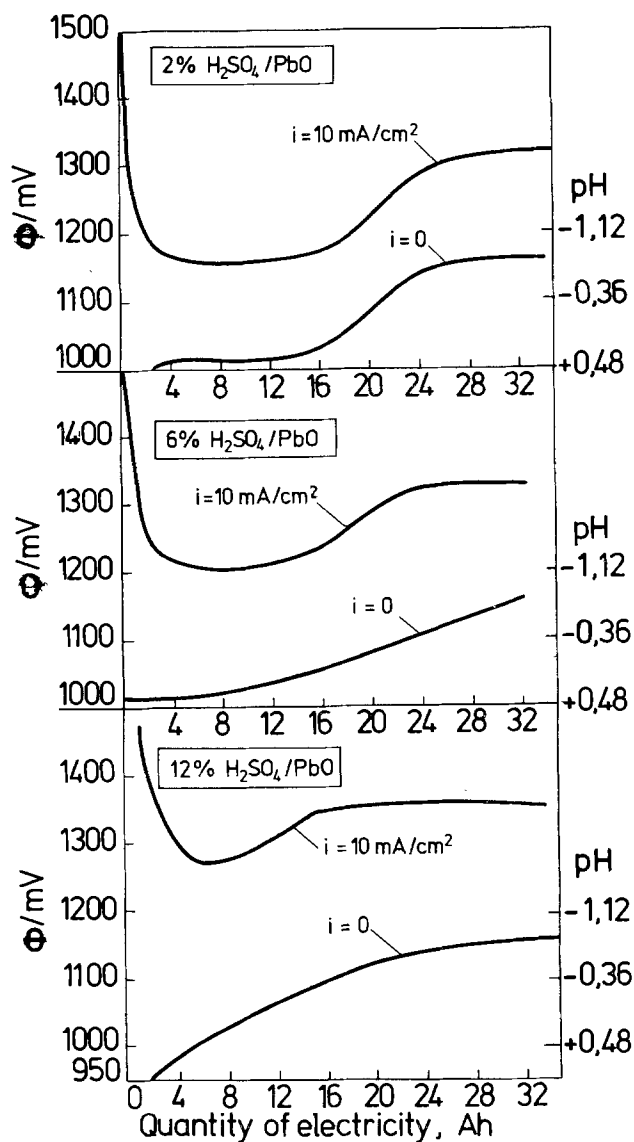
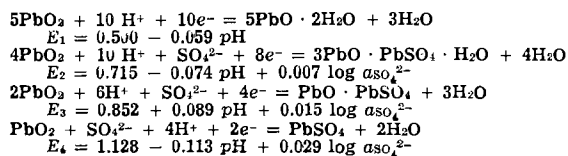


Fig. 4. Change of the plate potentials under polarization and at 5 min at open circuit $i = 0$ (vs. $\text{Hg}/\text{Hg}_2\text{SO}_4$ electrode) during formation.

and less on the SO_4^{2-} ion activity. When pH increases the potentials become more negative. If it is assumed that the open-circuit potential is determined by the equilibrium $\text{PbO}_2/\text{PbSO}_4$ electrode system, we can calculate pH of the solution in the plate using the equi-

Table II.



librium potential equation for this system. At $a_{\text{SO}_4^{2-}} = 10^{-2}$, from the open-circuit potential curve we obtain the pH values which are plotted on the right-hand ordinate in Fig. 4. It can be seen that the higher the paste sulfation is, the lower is the pH of the pore solution of the plate. Figure 4 also shows that during formation pH of the pore solution decreases.

Influence of the current density on the PbO₂ zone direction of growth during formation.—Investigation was carried out on paste, prepared with 6% H₂SO₄. This paste corresponds to the region in Fig. 1 where the growth rate of the PbO₂ zone in the plate interior slightly exceeds that in the surface layers.

Figure 5 presents the PbO₂ zone advance during formation with a current of 10 mA/cm². First, the PbO₂ zones grow in the plate interior (Fig. 5b, c, d) and

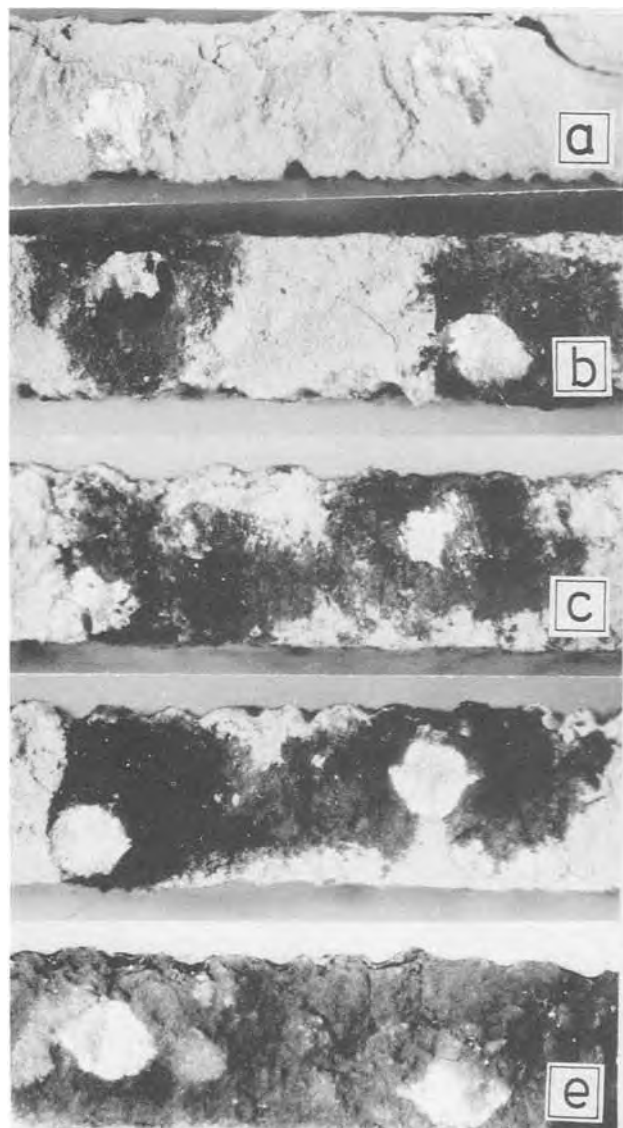


Fig. 5. Photomicrographs of the cross section of the plate prepared with 6% H₂SO₄ paste during formation with a current of 10 mA/cm². (a) Unformed plate, (b-d) during formation (the dark portions are PbO₂ zones), (e) completely formed plate.

then toward the surfaces. Sometimes a white layer is observed at the boundary between the PbO₂ zones and the unformed paste.

When the formation processes follow this way the unformed paste surface layers stay for a long time in contact with the H₂SO₄ solution. Chemical reactions of sulfation take place between the paste and the sulfuric acid. White PbSO₄ layers are formed on both surfaces. They are the last to be oxidized to PbO₂.

Figure 6 presents formation with a current density of 2 mA/cm². The PbO₂ zone rate of growth is a little higher in the surface layers than that into the interior of the plate. Therefore at lower current density the PbO₂ zone rate of growth in the plate interior decreases and formation processes in the surface layers are accelerated.

Influence of the current density on the change of the plate phase composition during formation.—Figure 7 shows the dependence of the diffraction line relative intensity of PbO and basic lead sulfates as well as that of α -PbO₂, β -PbO₂, and PbSO₄ on the quantity of electricity passed. The intensity curves are indicative

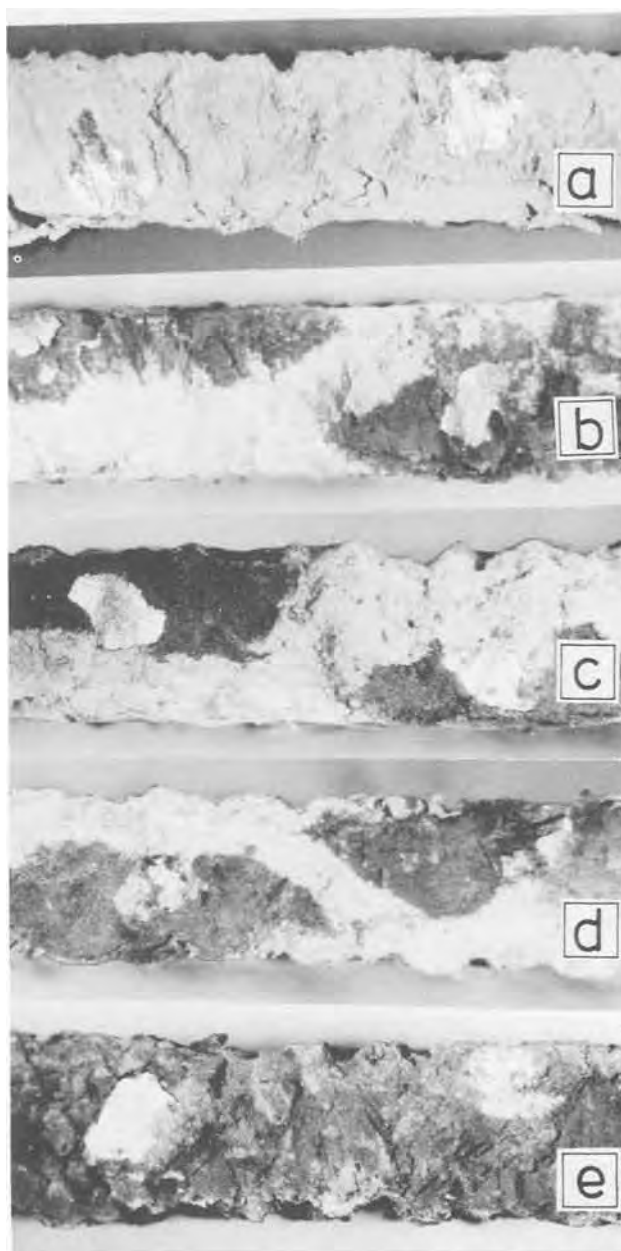


Fig. 6. Photomicrographs of the cross section of the plate prepared with 6% H₂SO₄ paste during formation with a current of 2 mA/cm². (a) Unformed plate, (b-d) plate during formation, (e) completely formed plate.

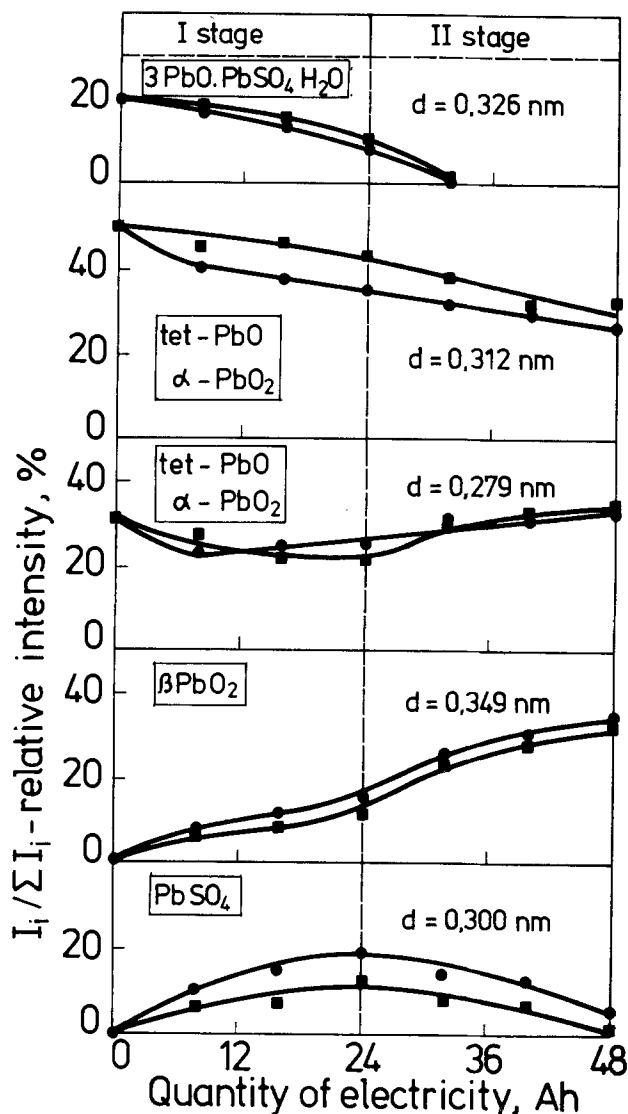


Fig. 7. Change of the phase composition of the plate during formation with a current of 10 mA/cm^2 . (●) At the surfaces of the plate; (■) in the interior of the plate.

of the phase composition changes in the surface layers and in the plate interior. Formation was performed at 10 mA/cm^2 . The plate was prepared with 6% H_2SO_4 paste. The amount of PbSO_4 in the plate reaches its maximum after passage of about 24 A-hr whereby the first stage is over.

Figure 8 presents formation of the above type of plates with current 2 mA/cm^2 . After the passage of about 20 A-hr, PbO and $3\text{PbO} \cdot \text{PbSO}_4 \cdot \text{H}_2\text{O}$ in the surface layers react completely. In the plate interior this process is over after about 28 A-hr. By this time the amount of PbSO_4 in the plate reaches its maximum and the first formation stage is over.

A comparison of Fig. 7 and Fig. 8 shows that in the first stage of formation at low current density the reactions are more advanced in the surface layers than in the plate interior. This coincides with the optical observations (Fig. 5 and 6).

Influence of the current density on the plate porosity during formation.—Table III presents the molar volume changes in the course of the chemical and electrochemical reactions. The table is based on data given by Burbank (8). The molar volume increases at the sulfation and oxidation of Pb and PbO to PbO_2 . At the oxidation of $3\text{PbO} \cdot \text{PbSO}_4 \cdot \text{H}_2\text{O}$ and PbSO_4 to PbO_2 it decreases.

The active mass porosity is characterized by two parameters: porosity and pore size distribution.

Table III.

Initial product	Final product	Change of volume with respect to the initial product for 1 g-atom Pb, % $\Delta V/V_{mi}$
tet-PbO	PbSO_4	+100
	$\beta\text{-PbO}_2$	+4.2
$3\text{PbO} \cdot \text{PbSO}_4 \cdot \text{H}_2\text{O}$	PbSO_4	+26.2
	PbO_2	-34.6
PbSO_4	PbO_2	-48.2
Pb	PbSO_4	+60.0
	PbO_2	+35.8

Figure 9 presents porograms of formation at 10 mA/cm^2 . The porograms of the surface layers and the interior of the plate are plotted and compared with those of an unformed plate. The average pore radius does not change practically during the first formation stage. Neither does the plate total porosity (Fig. 9a, b). Only the pore size distribution changes. The pore number with a radius from 0.01 to $0.2 \mu\text{m}$ increases whereas the number of pores with a radius from 0.3 to $1 \mu\text{m}$ slightly decreases. During this period the increase of the solid phase volume (caused by sulfation processes) is compensated by volume (caused by oxidation of $3\text{PbO} \cdot \text{PbSO}_4 \cdot \text{H}_2\text{O}$ to PbO_2). During the second formation stage, due to oxidation of PbSO_4 to PbO_2 the porosity rises and the average pore radius increases from 2 to about $4 \mu\text{m}$.

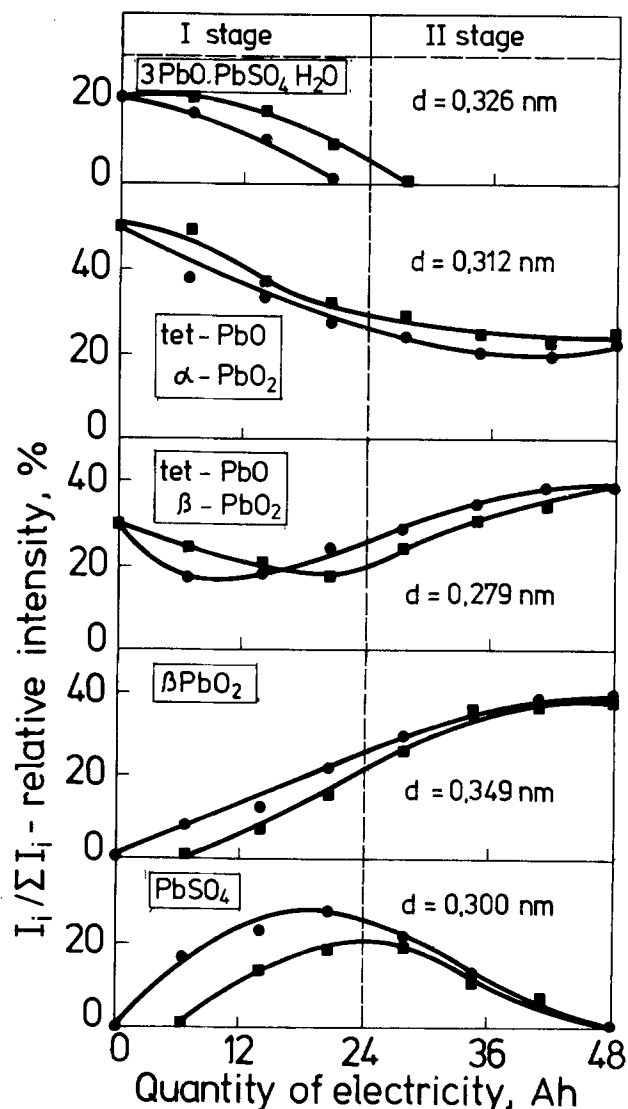


Fig. 8. Change of the phase composition of the plate during formation with 2 mA/cm^2 . (●) At the plate surface; (■) in the interior of the plate.

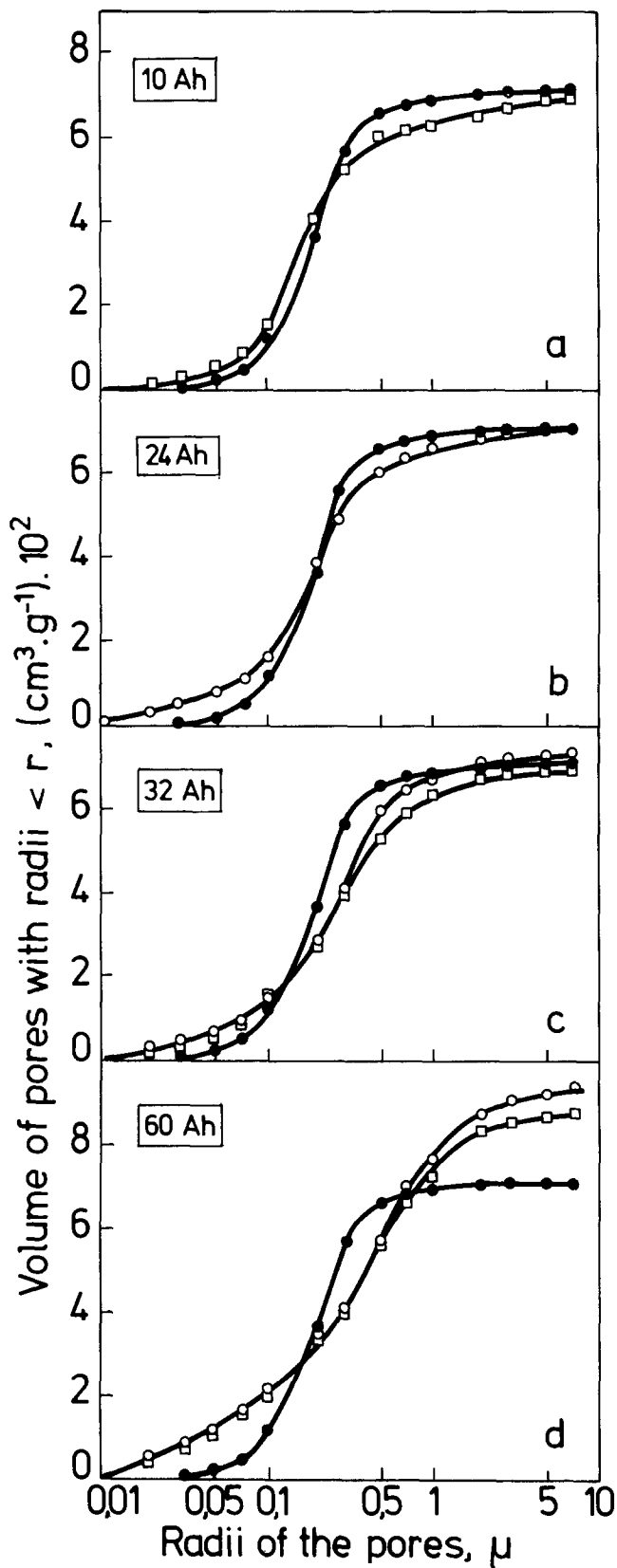


Fig. 9. Change in pore size distribution and volume porosity during formation with current 10 mA/cm. (●) Unformed plate, (○) at the surfaces of the plate, (■) in the plate interior.

Figure 10 presents porograms of formation at 2 mA/cm². The average pore radius remains almost unchanged after the passage of 12-17 A-hr (Fig. 10a, b). The number of the small pores increases and that of the large ones decreases. Total porosity decreases, which indicates that the processes of sulfation predominate over those of oxidation. In the second for-

mation stage due to oxidation of PbSO₄ to PbO₂ the average pore radius rises from 2-2.5 to 7-9 μm and the active mass total porosity increases.

A comparison of the porograms of Fig. 9d and 10d shows that current density influences the average pore

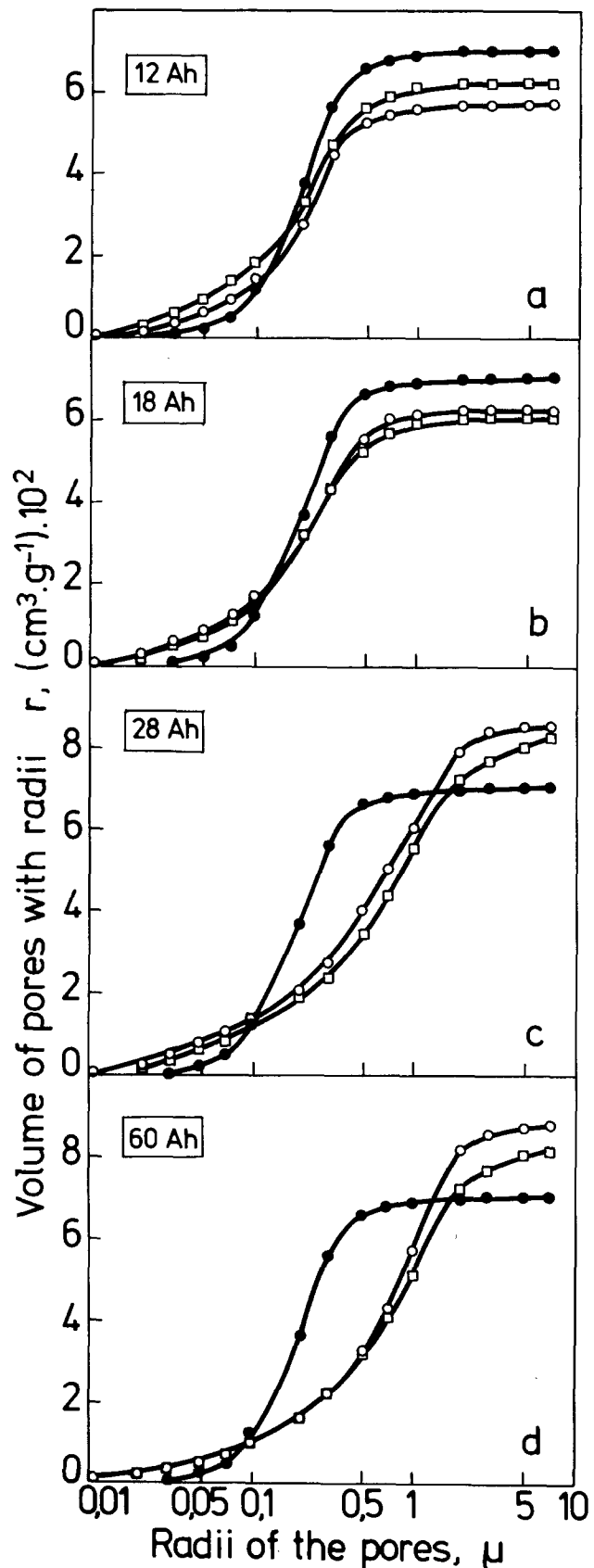


Fig. 10. Change in pore size distribution and volume porosity during formation with current 2 mA/cm². (●) Unformed plate, (○) at the surfaces of the plate, (■) in the plate interior.

size. When a larger amount of PbSO_4 crystals is formed in the first formation stage, the pores of the formed plate have a greater average radius. It is well known that porosity influences both the capacity and cycle life of the positive plate. Therefore, the formation current density determines to some extent the positive plate energy performances.

Discussion of the Results

The processes of formation should be studied in two scales (Fig. 11):

Elementary processes.—These are the physicochemical and electrochemical processes which take place at the crystal/solution interface and within the solid phases.

Zone processes.—They take place when the initial and the final products are solid porous phases which form zones permeable for the solution ions. Electrochemical reactions proceed in a reaction layer (Fig. 12). It is situated between the initial and final phases of the reactions (27). During the current flow the volume of the PbO_2 zone increases whereas the one of the reactant zone decreases. As a result of this process the reaction layer moves in space. This advance of the reaction layer in space represents the zone processes.

The zone processes during formation of lead acid battery plates pose to the theoretical electrochemistry an interesting problem for studying. It is necessary to establish the parameters which determine the growth direction of the product zone and the processes which control the reaction layer advance in space.

In this paper it was established that zone processes depend on the paste phase composition. When the paste sulfation is low, the PbO_2 zone grows at higher rate in the plate surface layers than in its interior. In paste with a high degree of sulfation the movement of the reaction layer in the plate is the reverse (Fig. 1).

The second parameter that zone processes depend on is current density. When pastes containing between 4% and 6% H_2SO_4 are subjected to formation at high current densities, the PbO_2 zone grows into the plate interior. The direction of the zone process is reverse that at formation with low current density.

In a previous paper (23) we established that the zone processes depend on the pH of the formation electrolyte. Thus in a strongly acidic electrolyte (H_2SO_4 with sp gr 1.15) the PbO_2 zone initially grows into the

plate interior and then advances toward the surfaces. When the same plates are formed in an Na_2SO_4 solution the zone process direction is reversed.

In order to establish which processes control the direction of the reaction layer movement in the plate it is necessary: (i) to establish the chemical and electrochemical reactions which take place in the reaction layer, (ii) to determine the conditions under which these reactions proceed at a maximum rate, and (iii) to define in which parts of the plate the conditions for maximum electrochemical reaction rate are present so that the product zone can grow in this direction.

The chemical and electrochemical reactions were established by x-ray diffraction analysis determinations of the phase composition changes in the plate during formation. In papers (23, 28) we presented a scheme of the stoichiometric reactions when the paste consists solely of $3\text{PbO}\cdot\text{PbSO}_4\cdot\text{H}_2\text{O}$. This scheme may be elaborated to become universal and to comprise all possible phases in the paste. By introduction of the necessary stoichiometric coefficients, this universal scheme may become a quantitative description of the system of reactions which proceed in the reaction layer during formation. This system is presented in Fig. 13. It gives the stoichiometry of the reactions only, and not the elementary processes.

The coefficient m takes an account of PbO "molecules" in the basic lead sulfate. When the paste consists solely of PbO , $m = \infty$. The corresponding values of the coefficients before PbO and PbSO_4 are 1 and 0. When the paste consists solely of PbSO_4 , $m = 0$ and the corresponding coefficients have values of 0 and 1. At $3\text{PbO}\cdot\text{PbSO}_4\cdot\text{H}_2\text{O}$, $m = 3$.

Figure 13 shows that the system of reactions requires an exchange of flows of H^+ and SO_4^{2-} ions and H_2O (signified by N_{H^+} , $N_{\text{SO}_4^{2-}}$, and $N_{\text{H}_2\text{O}}$) between the reaction layer and the bulk of the electrolyte. Let us assume that the exchange of H_2O is very rapid and does not control the processes in the reaction layer. The flows of H^+ and SO_4^{2-} ions may enter or leave the reaction layer depending on the paste phase composition, the current density, the electrolyte pH, etc. The scheme on Fig. 13 enables us to determine the direction of these flows. Let us express in terms of flow all ions which participate in the chemical and electrochemical reactions. This is possible if we consider the occurring processes in unit volume of the reaction layer per unit time.

We can determine the flow of H^+ ions, N_{H^+} , which enters or leaves the reaction layer, from the chemical reaction [5]. The OH^- and H^+ ions, formed as a result of reactions [1] and [3] should be expressed in terms of corresponding flows

$$N_{\text{H}^+} = n_{\text{OH}^-}[\text{1}] - n_{\text{H}^+}[\text{3}] \quad [6]$$

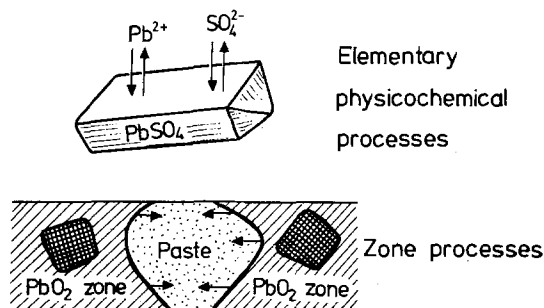


Fig. 11. Scheme of the elementary and zone processes

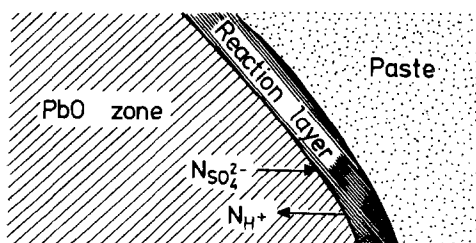


Fig. 12. Scheme of the reaction layer

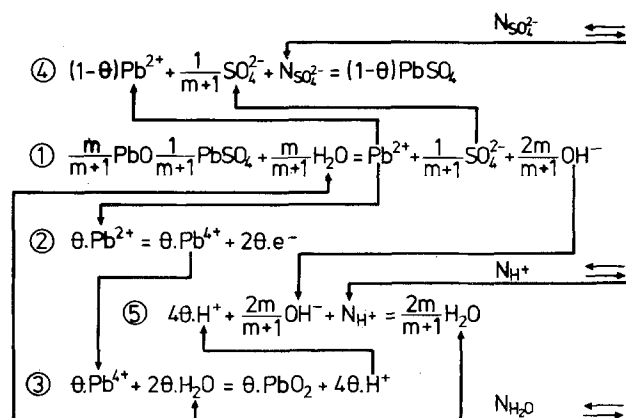


Fig. 13. Diagram of the chemical and electrochemical reactions occurring in the reaction layer during formation of the lead acid battery positive plate.

where $n_{OH-[1]}$ signifies the OH^- ions formed per unit time in reaction [1] and $n_{H+[3]}$ signifies the H^+ ions formed per unit time at reaction [3].

In the system of chemical and electrochemical equations in Fig. 13 the different "ion flows" are interconnected by their corresponding stoichiometric coefficients. Thus it becomes possible quantitatively to compare the "ion flows" with respect to one of them, for example that of the Pb^{2+} ions, formed in reaction [1]. The ratio of the flows is determined by the ratio of their stoichiometric coefficients in the corresponding chemical and electrochemical equations. For the OH^- [1] and Pb^{2+} [1] ions participating in reaction [1] (Fig. 13) this ratio is given by

$$\frac{n_{OH-[1]}}{n_{Pb^{2+}[1]}} = \frac{2m}{m+1} \quad [7]$$

The ratio of the H^+ [3] and Pb^{2+} [1] ions stoichiometric coefficients is

$$\frac{n_{H+[3]}}{n_{Pb^{2+}[1]}} = 4\theta \quad [8]$$

θ indicates what part of the Pb^{2+} [1] ion flow participates in the electrochemical reaction [2]

$$\theta = \frac{n_{Pb^{2+}[2]}}{n_{Pb^{2+}[2]} + n_{Pb^{2+}[4]}} = \frac{ki}{ki+v} \quad [9]$$

where $n_{Pb^{2+}[2]}$ is the part of Pb^{2+} ion flow which participates in the electrochemical reaction [2]. It is proportional to the current density i , and k is a coefficient of proportionality. $n_{Pb^{2+}[4]}$ is the part of Pb^{2+} ion flow which participates in the chemical reaction [4]. It is equal to the rate of the chemical reaction, yielding $PbSO_4$, which is expressed by V .

Combining Eq. [6], [7], [8], and [9] and transforming the expression one obtains for the N_{H^+} flow

$$N_{H^+} = \frac{2mV - 2(m+2)ki}{m+1} \quad [10]$$

In a similar way from chemical reaction [4] (Fig. 13) we can express the flow of SO_4^{2-} ions $N_{SO_4^{2-}}$, which the reaction layer exchanges with its surroundings

$$N_{SO_4^{2-}} = n_{Pb^{2+}[4]} - n_{SO_4^{2-}[1]} \quad [11]$$

where $n_{SO_4^{2-}[1]}$ is the SO_4^{2-} ion flow formed at reaction [1]. According to the scheme of Fig. 13, $n_{Pb^{2+}[4]}$ and $n_{SO_4^{2-}[1]}$ are correspondingly equal to

$$n_{Pb^{2+}[4]} = (1-\theta)n_{Pb^{2+}[1]} \quad [12]$$

$$n_{SO_4^{2-}[1]} = \frac{1}{m+1}n_{Pb^{2+}[1]} \quad [13]$$

Combining Eq. [11], [12], [13], and [9] we arrive at the following expression for the $N_{SO_4^{2-}}$ flow

$$N_{SO_4^{2-}} = \frac{mV - ki}{m+1} \quad [14]$$

Equations [10] and [14] show that the sign before N_{H^+} and $N_{SO_4^{2-}}$ depends on the paste phase composition through the coefficient m and depends on the current density through the value of i . When the term, comprising the rate of the chemical reaction in Eq. [10] and [14] is greater than the term comprising the rate the electrochemical reaction, the flows $N_{H^+} > 0$ and $N_{SO_4^{2-}} > 0$ so they will enter the reaction layer and vice versa. Table IV presents the coefficient values at the chemical and electrochemical reaction rates for several phases of the paste.

It is seen from the table that the H^+ and SO_4^{2-} ion flows mainly enter the reaction layer when the paste has a low degree of sulfation and the rate of chemical reaction [4] is high. On the contrary, when the paste has a high degree of sulfation and the forma-

Table IV.

Phase	m	N_{H^+}	$N_{SO_4^{2-}}$
PbO	∞	$2V-2ki$	V
$3PbO \cdot PbSO_4 \cdot H_2O$	3	$1.5V-2.5ki$	$0.75V-0.25ki$
$PbO \cdot PbSO_4$	1	$V-3ki$	$0.50V-0.50ki$
$PbSO_4$	0	$-4ki$	$-ki$

tion is carried out at high current density, H_2SO_4 is formed in the reaction layer and flows of H^+ and SO_4^{2-} ions come out of it.

The rate of the electrochemical reaction [2] (ki) determines the growth of the PbO_2 zone in the cross section of the plate. Positive charges are evolved in the electrochemical reaction [2] (Fig. 13). To preserve the electroneutrality of the reaction layer solution these charges must be transported into the bulk of the electrolyte. This occurs through exchange of N_{H^+} and $N_{SO_4^{2-}}$ flows between every unit volume of the reaction layer and the electrolyte. If in some part of the reaction layer this process is low, the solution in the pores there becomes positively charged. This decreases the electrochemical reaction rate and the growth of the PbO_2 zone in this direction is stopped or slowed down.

The velocity of N_{H^+} and $N_{SO_4^{2-}}$ flows is determined by the electric field intensity and by the H^+ and SO_4^{2-} ion diffusion gradients which in the case of an equal pore width depend on the distance between the considered unit volume of the reaction layer and the surface of the plate. The width of the pores is determined by the paste density.

The reaction layer electroneutrality is most easily maintained at the surface layers of the plate. The distance which the H^+ and SO_4^{2-} ions must overcome is the shortest there. It is to be expected that during the first formation stage the PbO_2 zone should grow in the plate surface layers only. However, optical observations of the formation process (Fig. 1 and 6) show that this is true on plates with low sulfation pastes (Fig. 1) and when formation is carried out at low current density (Fig. 6). Under the above conditions, according to Table IV the N_{H^+} and $N_{SO_4^{2-}}$ flows enter the reaction layer.

Figures 1 and 5 show, however, that this condition alone is not sufficient to determine the direction of the PbO_2 -zone growth. A second parameter controlling the advance of the product zone might be the potentials at which the electrochemical reactions take place in the reaction layer. The paste is built up by crystals of several phases (PbO , $3PbO \cdot PbSO_4 \cdot H_2O$, $PbO \cdot PbSO_4$, $PbSO_4$). Combined with PbO_2 phase each of them constitutes an electrode system. The potential of plate under current is defined by the equation

$$E = E^0 + \eta \quad [15]$$

where E^0 is the electrode system equilibrium potential and η is the electrode reaction overvoltage.

The reaction with the most negative equilibrium potential which has the lowest overvoltage will proceed at highest rate. According to Table II the equilibrium electrode potentials depend on the solution pH and in a lesser degree on the SO_4^{2-} ion activity in the reaction layer. pH of the reaction layer pore solution depends on reactions [1] and [3] (Fig. 13). The concentration of H^+ and SO_4^{2-} ions in the reaction layer increases when the formation is carried out with high current density on a paste with high degree of sulfation (Fig. 4). Since the reaction layer is surrounded by two different zones (PbO_2 zone and paste) the diffusion gradients of H^+ and SO_4^{2-} ions should be different at both boundaries of the layer. As H_2SO_4 reacts with PbO and basic lead sulfates, H^+ and SO_4^{2-} flows should be directed toward the paste. Hence, the highest pH would be maintained at those regions of the reaction layer where the paste has not yet reacted. Such is the interior of the plate.

Table IV shows that at high paste sulfation and high current density the N_{H^+} and $N_{SO_4^{2-}}$ flows leave the reaction layer. It can be seen in Fig. 1 and 6 that under these conditions the PbO_2 zone grows first into the interior of the plate.

As formation advances, the N_{H^+} and $N_{SO_4^{2-}}$ flows become hindered and the potential of the plate rises. It reaches values at which the oxidation of $PbSO_4$ crystals to PbO_2 becomes possible. This marks the transition from the first to the second formation stage.

Acknowledgments

The author would like to thank Mrs. M. Virbeva for her cooperation in preparing the photomicrographs.

Manuscript received May 1, 1980.

Any discussion of this paper will appear in a Discussion Section to be published in the June 1981 JOURNAL. All discussions for the June 1981 Discussion Section should be submitted by Feb. 1, 1981.

REFERENCES

1. V. H. Dotson, *This Journal*, **108**, 401 (1961).
2. A. C. Simon and E. L. Jones, *ibid.*, **109**, 760 (1962).
3. W. O. Butler, C. J. Venuto, and D. V. Wisler, *ibid.*, **117**, 1339 (1970).
4. J. R. Pierson, *Electrochem. Technol.*, **5**, 323 (1967).
5. J. Armstrong, I. Dugdale, and W. J. McCusker, "Power Sources 1966," p. 163, Pergamon Press, Oxford (1967).
6. G. Sterr, *Electrochim. Acta*, **15**, 1221 (1970).
7. A. I. Rusin, M. A. Dasojan, and N. N. Fedorova, *Electrotehnika*, **38**, 84 (1967).
8. J. Burbank, *This Journal*, **113**, 10 (1966).
9. J. E. Buskirk, P. D. Boyd, and V. V. Smith, Paper 19 presented at the Electrochemical Society Meeting, Houston, Texas, Oct. 9-13, 1960.
10. J. Burbank and E. J. Ritchie, *This Journal*, **116**, 125 (1969).
11. R. H. Greenburg and B. P. Caldwell, *Trans. Electrochem. Soc.*, **80**, 71 (1941).
12. J. E. Hatfield and O. W. Brown, *ibid.*, **72**, 361 (1937).
13. S. Ikari, S. Yoshizawa, and S. Okada, *J. Electrochem. Soc. Jpn.*, **27**, 426, 613 (1959).
14. P. Ruetschi and B. Cahan, *This Journal*, **105**, 376 (1958).
15. P. Ness, *Electrochim. Acta*, **12**, 161 (1967).
16. E. Skoluda, J. Kwasnik, K. Nowac, and J. Kranska, *ibid.*, **17**, 8, 1359 (1972).
17. S. Satoshi and J. Tensuo, *J. Electrochem. Soc. Jpn.*, **31**, 15 (1963).
18. E. F. Bordt, V. V. Novoderejkin, and Z. S. Kudzevich, *Sb. Rabot XIT*, **7**, 65, L. Energija (1972).
19. E. F. Bordt, G. A. Kalikova, V. V. Novoderejkin, and M. A. Dasojan, *ibid.*, **7**, 55 (1972).
20. E. F. Bordt, V. V. Novoderejkin, G. A. Kolikova, *ibid.*, **7**, 48 (1972).
21. E. F. Bordt, V. V. Novoderejkin, G. A. Kolikova, and M. A. Dasojan, *ibid.*, **8**, 10 (1973).
22. J. Armstrong, "Lead Acid Batteries," Oct. 1967, London.
23. D. Pavlov, G. Papazov, and V. Iliev, *This Journal*, **119**, 8 (1972).
24. G. Papazov and D. Pavlov, Extended Abstracts, 29th Meeting ISE, p. 830. Budapest, Hungary (1978).
25. D. Pavlov, V. Iliev, G. Papazov, and E. Bashtavelova, *This Journal*, **121**, 854 (1974).
26. D. Pavlov and G. Papazov, *J. Appl. Electrochem.*, **6**, 339 (1976).
27. D. Pavlov, *J. Electroanal. Chem. Interfacial Electrochem.*, **72**, 319 (1976).
28. D. Pavlov, Proceedings, Columbus Sympos. of Battery of Electrochem. Soc., p. 135 (1972).

The Corrosion of a Strontium-Lead Alloy in Sulfuric Acid

K. R. Bullock* and W. H. Tiedemann*

Johnson Controls, Incorporated, Corporate Applied Research Group, Milwaukee, Wisconsin 53201

ABSTRACT

A patented proprietary strontium-tin-aluminum-lead alloy, developed for use in lead-acid batteries, has electrochemical characteristics similar to cast calcium-lead alloys but casting characteristics similar to antimony-lead alloys. Corrosion tests on this strontium alloy are reported at constant potentials from 0.600 to 1.290V (vs. Hg/Hg₂SO₄/5.6 molal H₂SO₄), H₂SO₄ concentrations from 0.8 to 5.1 molal and temperatures from 27° to 82°C. The corrosion properties of the strontium-lead alloy are compared with those of pure lead and of antimony- and calcium-lead alloys.

The most widely used materials for lead-acid battery grids are antimony-lead and calcium-lead alloys. Pure lead is too soft to be easily handled in most manufacturing operations and is therefore used only in special battery designs (1).

Although alloys containing 3-12% antimony have good mechanical properties, antimony has several undesirable effects on the electrochemistry of the lead-acid battery. Antimonial alloys corrode faster than pure lead at potentials above open circuit. When the antimony in the positive grid oxidizes, it can dissolve in the electrolyte and deposit on the negative electrode, lowering the otherwise high overvoltage for hydrogen evolution on lead (2). This increases both the amount of gassing on overcharge and the rate of

self-discharge. The deposition of antimony on the lead electrode can also give rise to the evolution of toxic stibine gas on overcharge. (3).

Calcium-lead alloys were introduced (4) to overcome these problems and are now widely used to improve shelf life and to reduce the need for adding water to batteries. However, the calcium content of these alloys must be carefully controlled (5) to avoid formation of dross during casting and to minimize subsequent severe grid corrosion.

Recent development of lead-acid batteries for use in electric vehicles and load leveling has put even more stringent requirements on grid materials. The need to reduce the amount of lead in the grid requires the good casting characteristics of antimony-lead alloys while the need to improve efficiency and minimize maintenance requires the good electrochemical characteristics of calcium-lead alloys.

* Electrochemical Society Active Member.

† Globe-Union is now a division of Johnson Controls.

Key words: battery, cathode, potential, passivity.

A newly developed and patented strontium-tin-aluminum-lead alloy meets both these needs (6). It has electrochemical characteristics similar to those of calcium alloys but is easier to cast. Production costs are reduced because the strontium concentration is less critical than the calcium concentration and because the strontium alloy can be produced on equipment designed for manufacturing antimony alloys, eliminating the capital equipment expenditure required to cast calcium alloys. Production time is reduced because the strontium alloy age hardens faster than calcium alloys.

Since positive grid corrosion is a significant problem in lead-acid batteries, the corrosion behavior of lead and the common lead alloys has been studied in detail (7). If a new alloy is to find its proper place in the present multitude of lead-acid battery designs and applications, its corrosion behavior must be defined over a wide range of temperatures, potentials, and acid concentrations.

Two recently published papers contain some data on strontium-lead alloys. Bagshaw (8) studied the corrosion of strontium-lead alloys with additions of aluminum, cerium, and silver in H_2SO_4 (1.250 sp gr) by applying a 155 mA/cm² constant current for 1 day and by applying 8.5 mA/cm² under a 1.4 kg/mm² load. These conditions are much more severe than could be expected in typical battery operation. In addition, constant current corrosion does not allow separation of the possible corrosion mechanisms by their potential dependence. Weinlein, Pierson, and Marshall (7) studied the corrosion of a strontium-tin-aluminum alloy in 1.270 sp gr H_2SO_4 at constant potentials above the open-circuit voltage of the positive plate. They compared the corrosion behavior of typical antimony- and calcium-lead alloys oxidized under the same conditions.

In this paper, a more extensive series of constant potential corrosion tests on the strontium alloy is reported for potentials from 0.600 to 1.290V, acid concentrations from 0.8 to 5.1 molal (*M*) and temperatures from 27° to 82°C in order to provide working curves from which the corrosion behavior of the new alloy can be predicted for a specific application. The effects of acid concentration and temperature are carefully examined in regions where high corrosion rates can occur. Finally, the corrosion properties of the strontium alloy, of pure lead, and of typical antimony and calcium alloys are compared over a wide potential range.

Experimental Methods

Cast grids were corroded in electrolyte made from reagent grade sulfuric acid and distilled, deionized water. The temperature was controlled to $\pm 1^\circ C$ by a water bath and the potential was held constant to ± 1 mV with a three-electrode potentiostat. Two lead grids, placed on either side of the working electrode, were the counterelectrodes and $Hg/Hg_2SO_4/5.6M$ H_2SO_4 was the reference electrode. During the corrosion test, the current was repeatedly monitored.

After the grid had corroded for 4 days, the portion around the tab was cut out and allowed to self-discharge in the same solution at the same temperature. The open-circuit voltage of this grid sample was monitored as a function of time by a high impedance voltmeter.

The remaining portion of the grid was prepared for further analysis by rinsing it in distilled water and drying it at room temperature. The corrosion film of a 12g sample of the grid was stripped off with a solution containing sodium hydroxide, mannitol, and hydrazine dihydrochloride and the dissolved lead was analyzed by atomic absorption spectroscopy. Other portions of the grid were mounted in epoxy, cross sectioned, polished, and observed under cross-polarized light using a metallograph (American Optical Company Model 2400) with a 450W xenon lamp at 1000 \times magnification.

The strontium-lead alloy used to obtain the data shown in Fig. 2-6 and Fig. 9 contained 0.13% Sr, 0.04% Al, and 1.0% Sn. The strontium-lead alloy used in the temperature study shown in Fig. 7 and 8 contained 0.15% Sr, 0.02% Al, and 0.9% Sn. Average grid weights were 52.62g ($1\sigma = 1.06$) for the 0.13% Sr alloy and 53.61g ($1\sigma = 0.88$) for the 0.15% Sr alloy.

The pure lead grids (Fig. 2) were cast from corroding grade lead. Casting temperatures were 213°C for the upper mold, 227°C for the lower mold, and 460°C for the melt. The average grid weight was 72.4g ($1\sigma = 2.35$).

All grids used in this study were cast in the grid design shown in Fig. 1. They had a surface area of

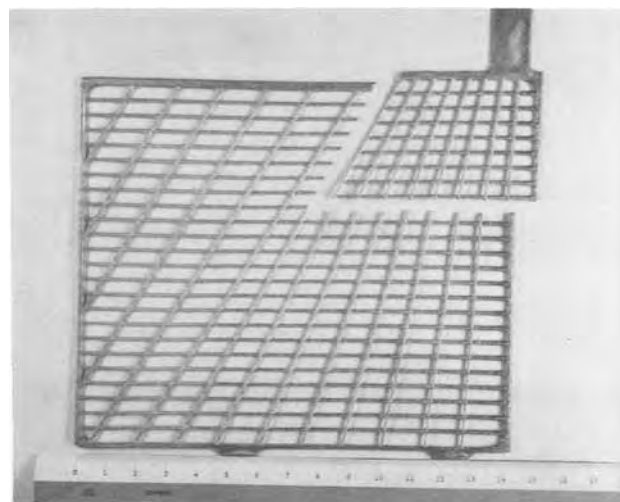


Fig. 1. Grid design used in all corrosion studies showing width in centimeters. Geometric surface area is approximately 170 cm².

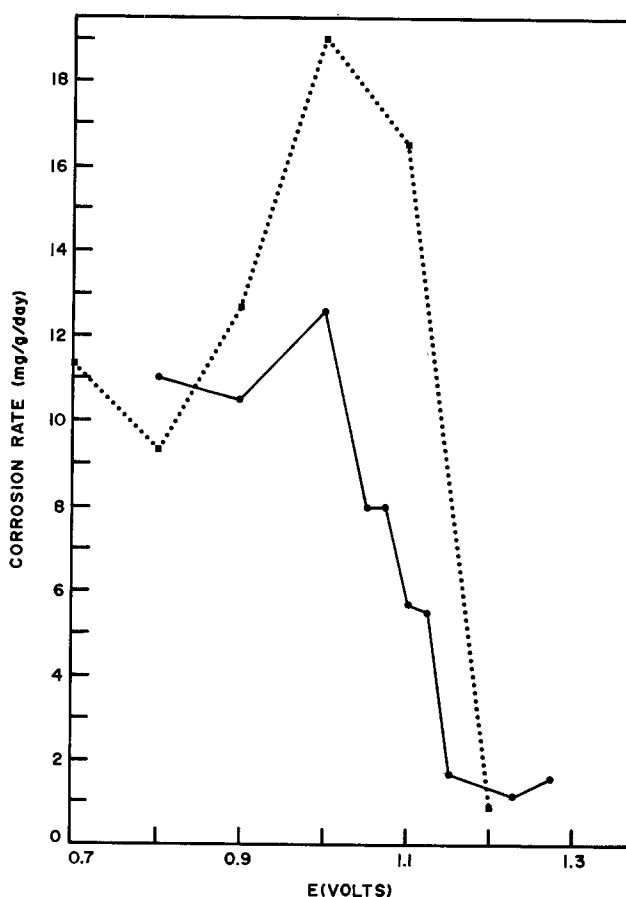


Fig. 2. The effect of potential on corrosion rate at 49°C in 5.1M H_2SO_4 . — Pure lead, ●●● strontium-lead alloy.

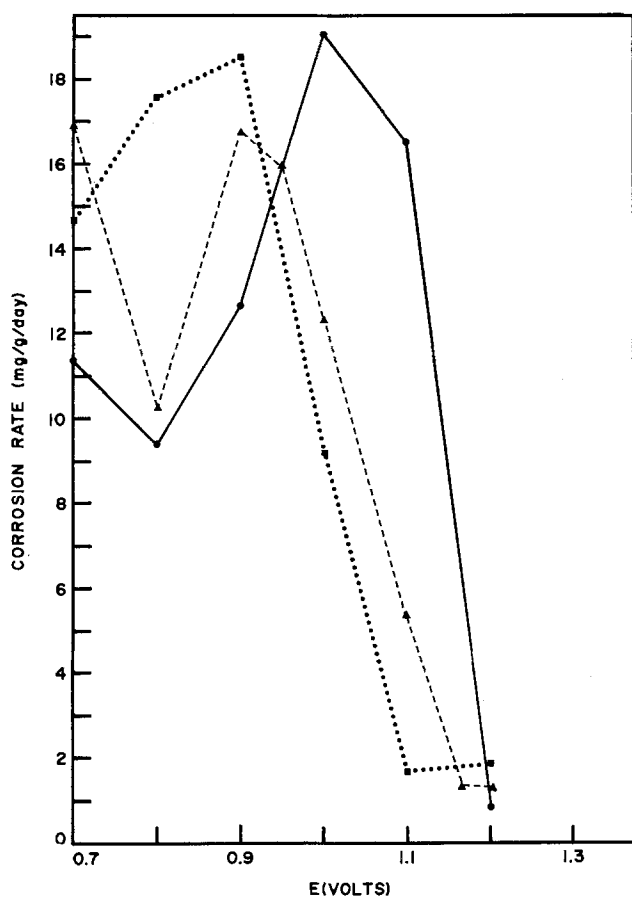


Fig. 3. The effects of acid concentration and potential on corrosion rate at 49°C. ●—● 5.1M H₂SO₄, ▲---▲ 2.7M H₂SO₄, ■—■ 0.8M H₂SO₄.

approximately 170 cm² and a thickness of approximately 1 mm. The tab portion of the grid used in the open-circuit voltage decay studies is shown in the figure slightly offset from the portion used for analysis.

Results and Discussion

Lander (9, 10) studied the constant potential corrosion of pure lead as a function of acid concentration, potential, and time. He observed a peak in the corrosion rate at 1.0V (*vs.* Hg/Hg₂SO₄/40.8% H₂SO₄) with a minimum from about 1.2 to 1.5V. According to Lander and to numerous authors of subsequent studies (6), this minimum corresponds to the passivation of lead by PbO₂ formation. At the corrosion peak, PbO₂, PbSO₄, and PbO all form simultaneously. At voltages below the peak, PbO forms in the interior of the corrosion film and PbSO₄ at the solution/film interface.

Our corrosion studies agree qualitatively with Lander's results, as Fig. 2 shows. The mg of lead in the corrosion film/g grid sample/day corroded is plotted as a function of the corrosion potential (*vs.* Hg/Hg₂SO₄/5.6M H₂SO₄). The corrosion peak occurs at 1.0V and the minimum begins at about 1.15V. (Our reference potential is within 20 mV of Lander's.) The results of electrochemical, metallographic, and analytical studies indicate that the corrosion products

follow the potential dependence outlined by Lander (10).

The strontium alloy curve in Fig. 2 is similar, with a minimum beginning at about 1.2V and a maximum at about 1.0V. Micrographs of strontium alloy corrosion films under cross-polarized light show brown PbO₂ in the minimum region, an outer white PbSO₄ film and inner red PbO film at potentials below the peak, and a heterogeneous layer at the peak which includes PbO, PbSO₄, and α- and β-PbO₂. The voltage plateaus in open-circuit voltage-time curves of these films agree with this visual interpretation. The main difference between the corrosion of pure lead and the strontium alloy is that the peak of the strontium curve is somewhat higher and broader.

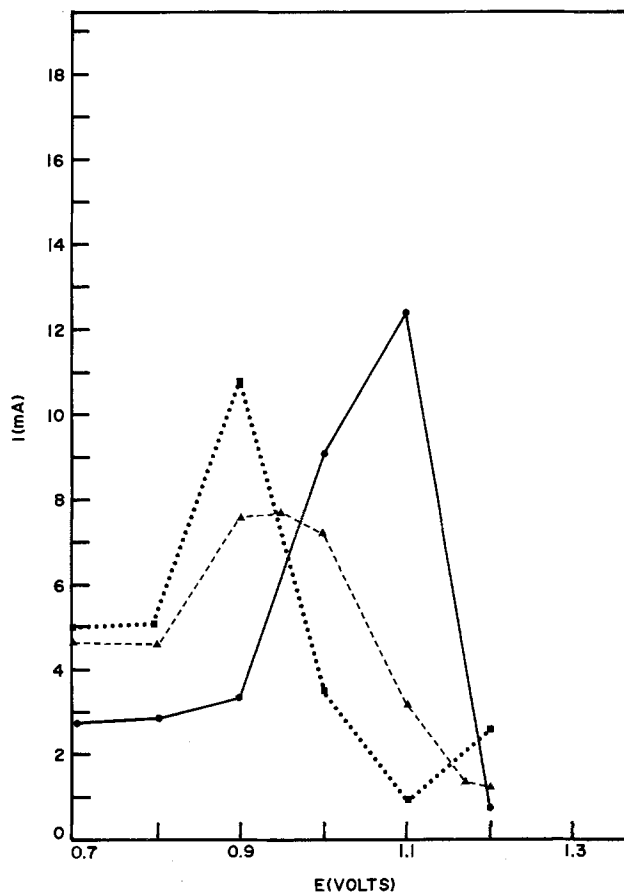


Fig. 4. The effects of acid concentration and potential on the steady-state current. ●—● 5.1M H₂SO₄, ▲---▲ 2.7M H₂SO₄, ■—■ 0.8M H₂SO₄.

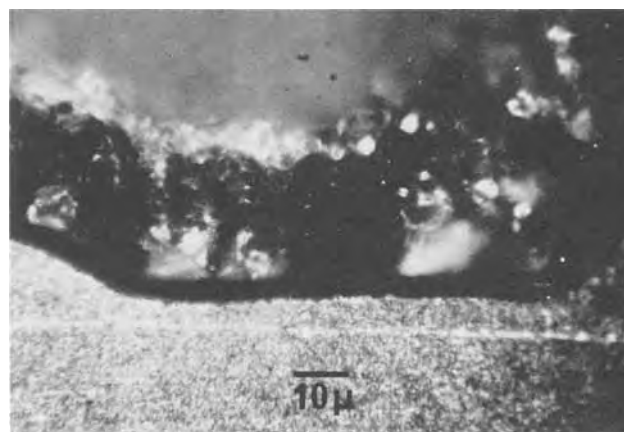


Fig. 5. Micrograph of cross section of grid corroded at 1.100V in 5.1M H₂SO₄ at 49°C. Magnification 1000×.

Table I. Potential of Hg/Hg₂SO₄/5.6M H₂SO₄/XM H₂SO₄/Hg₂SO₄/Hg

Molality (X)	ΔE (mV)
5.1	16
2.7	48
0.8	90

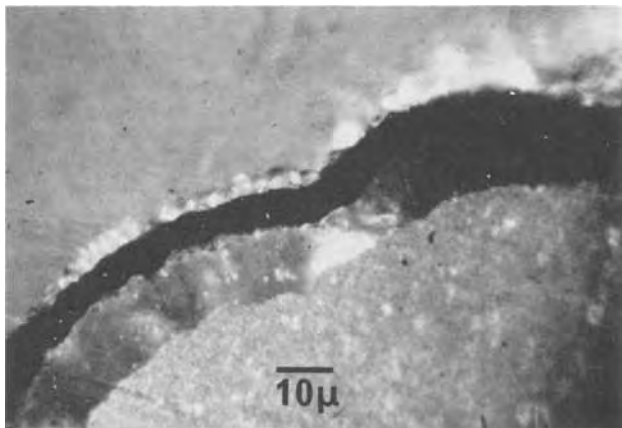


Fig. 6. Micrograph of cross section of grid corroded at 0.900V in 0.8M H₂SO₄ at 49°C. Magnification 1000X.

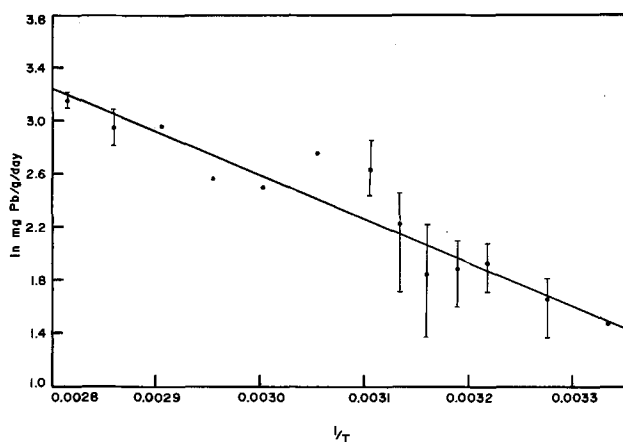


Fig. 7. The effect of temperature on the corrosion rates of strontium-lead alloy grids at 1.100V in 5.1M H₂SO₄.

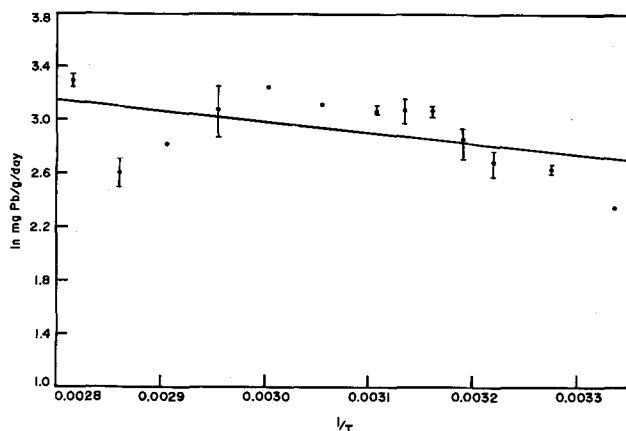


Fig. 8. The effect of temperature on the corrosion rates of strontium-lead alloy grids at 0.900V in 0.8M H₂SO₄.

The effect of the acid concentration on the corrosion of the strontium-lead alloy is shown in the three curves in Fig. 3 for 5.1, 2.7, and 0.8M H₂SO₄. In making a comparison of this type, the reference electrode must be considered. If a reference electrode with a fixed acid concentration is chosen, the junction potential between the acid in the corrosion cell and the acid in the reference electrode will vary, whereas if a reference electrode with the same acid concentration as the corrosion cell is chosen, the junction potential will be eliminated but the reference electrode potential will vary. We used an Hg/Hg₂SO₄/5.6M H₂SO₄ reference electrode in our experiments and measured the potential difference between this elec-

trode and Hg/Hg₂SO₄ electrodes containing 5.1, 2.7, and 0.8M H₂SO₄ to obtain the data shown in Table I. The curves in Fig. 3 may be shifted in the negative direction by these values to reference each curve to the Hg/Hg₂SO₄/H₂SO₄ electrode with the same acid concentration.

While measurement of the weight of lead in the corrosion layer for a fixed corrosion time (4 days) and a fixed grid weight (12g) gives an overall corrosion rate, measurement of the 4 day corrosion current gives a steady-state, instantaneous corrosion rate. Figure 4 shows the 4 day currents as a function of potential for the three acid concentrations: 5.1, 2.7, and 0.8M. Oxygen evolution may contribute to the current, especially at the higher potentials. However, both methods of measuring corrosion rate show a shift in the corrosion peak to lower potentials as the acid concentration decreases. The peak corrosion rate is lower in 2.7M than in 5.1 or 0.8M H₂SO₄. These trends apparently result from a change in the relative rates of the competing corrosion reactions as the acid concentration varies. Low concentrations favor formation of α-PbO₂ and tetragonal PbO, whereas higher concentrations favor formation of β-PbO₂ and PbSO₄ (11, 12).

Micrographs of cross sections of the corrosion films formed at the peaks in 0.8 and 5.1M H₂SO₄ show substantial differences. The corrosion film formed at 1.100V in 5.1M H₂SO₄, shown in Fig. 5, is quite heterogeneous. Under cross-polarized light, this film appears to have brown PbO₂ and white PbSO₄ crystals scattered throughout. A continuous black layer which is probably α-PbO₂ covers the grid at the base of the corrosion film and black boulders of α-PbO₂ grow out from this layer. Isolated areas of red underneath the PbO₂ and PbSO₄ particles suggest the presence of tetragonal PbO. The corrosion film formed at 1.000V in 5.1M H₂SO₄ looks nearly the same. On the other hand, in the film formed at 0.900V in 0.8M H₂SO₄, shown in Fig. 6, three separate layers appear. The outer surface is composed of white PbSO₄ crystals. Underneath this is a dense black layer of α-PbO₂ and next to the grid is a red layer of tetragonal PbO. X-ray diffraction powder patterns of particles picked from these films by the McCrone method (13) show predominantly PbSO₄ at 1.100V in 5.1M H₂SO₄ and tetragonal PbO at 0.900V in 0.8M H₂SO₄.

The effect of changing acid concentration at the two peak potentials is also different, as the data in

Table II. Number of experiments in corrosion temperature studies

Temperature (°C)	1.100V/5.1M H ₂ SO ₄	0.900V/0.8M H ₂ SO ₄
27	1	1
32	3	3
38	3	4
41	3	3
43	3	3
46	3	3
49	3	3
54	1	1
60	1	1
66	1	2
71	1	1
77	2	2
82	2	2

Table III. Results of corrosion temperature studies

	Corrosion conditions			
	1.100V/5.1M H ₂ SO ₄		0.900V/0.8M H ₂ SO ₄	
	mg Pb/g/day	Corrosion rate 4 day i	mg Pb/g/day	Corrosion rate 4 day i
Slope [(°K) ⁻¹]	-3319	-5386	-798	-1727
Index of determination	0.757	0.873	0.209	0.715
Activation energy [kcal/mole]	6.6	10.7	1.6	3.4

Fig. 3 and 4 show. At 0.900V, the corrosion rate decreases with increasing acid concentration, whereas at 1.100V, the corrosion rate increases with increasing acid concentration. These trends are consistent with the hypothesis that PbO formation is favored at the lower potential and PbSO₄ and β-PbO₂ formation at the higher potential (9, 10).

The effect of temperature on the peak corrosion rates of the strontium alloy in 5.1 and 0.8M H₂SO₄ is shown in the Arrhenius-type plots in Fig. 7 and 8, respectively. The number of experiments run at each temperature is shown in Table II. At the temperatures where the experiment was replicated, the error bars show the total spread in the data and the dot shows the ln of the average corrosion rate. Reproducibility is poor because several corrosion reactions are occurring simultaneously.

The straight lines shown in Fig. 7 and 8 were determined by linear regression analysis. Plots of the ln of the 4 day corrosion currents as a function of 1/T gave similar results. By using the equation

$$\ln \text{ corrosion rate} = -Ea/(RT)$$

where Ea is the activation energy of the corrosion process and R is the gas constant, approximate activation energies were calculated. Table III shows the slopes, indexes of determination, and activation energies for the two sets of corrosion conditions calculated using both measurements of corrosion rate.

The line shown in Fig. 8 has an index of determination of only 0.209. This shows that the uncertainty in the data is large compared to the effect of temperature, if the assumptions of the Arrhenius equation are upheld. Nevertheless, a Student's t test allows us to reject at a 99% confidence level the hypothesis that temperature has no effect. When the 4 day current is used as a measure of corrosion rate, the index of determination is 0.715. These data show that temperature has very little effect on the corrosion rate at 0.900V in 0.8M H₂SO₄. At 1.100V in 5.1M H₂SO₄,

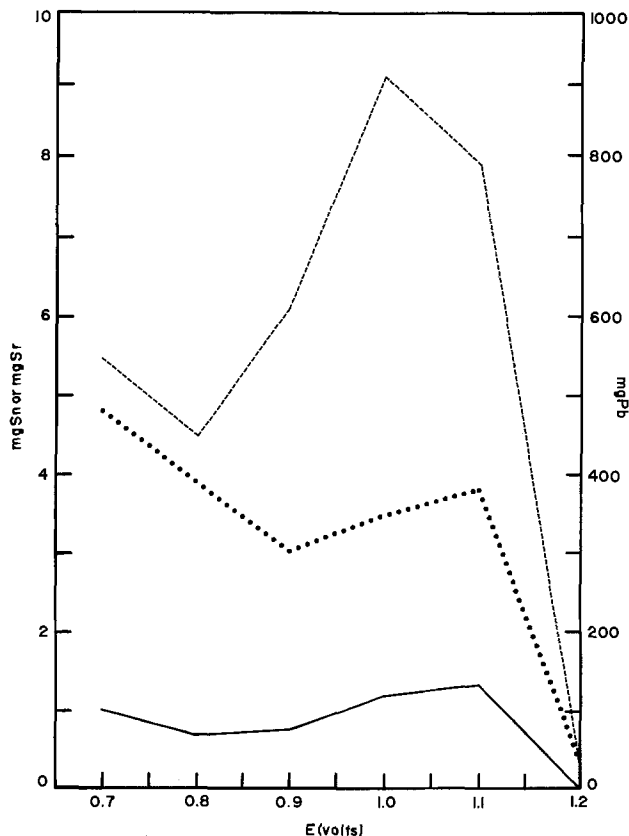


Fig. 9. Corrosion of alloying components as a function of potential. --- mg Pb, ··· mg Sn, — mg Sr.

the correlation is stronger and the activation energy is higher.

Since the corrosion experiments represented in Fig. 7 and 8 were replicated over a period of about 9 months on grids from the same production lot, the results could also be used to determine the effect of aging on corrosion rate. No correlation between grid age and corrosion rate was observed. This conclusion was further substantiated by corrosion tests at 1.100V in 4.4M H₂SO₄ on strontium-lead alloy grids aged at 100°C for 8.75–52.5 hr.

In Fig. 9, the total weights of oxidized tin and strontium in the 12g grid samples are compared with the total weight of oxidized lead as a function of the corrosion potential. The relative proportions of the oxidized components are about the same as in the metal throughout the active corrosion region.

In Fig. 10, the current-potential curve for a strontium-lead alloy at 82°C in 5.1M H₂SO₄ is compared with the curves for three lead alloys commonly used in lead-acid batteries: a 5.12% antimony-lead alloy, a 1.0% antimony-lead alloy, and a calcium-tin-lead alloy. The strontium and calcium alloys have lower corrosion rates at the peaks than the antimony alloys. The strontium peak occurs at a lower voltage than the peaks for the other alloys, giving it a broader passivation region. The poor reproducibility in the peak current measurements (due to the dramatic increase in corrosion rate) makes the exact peak location questionable, but these data as well as the data shown in Fig. 7 for 82°C indicate that the strontium alloy has at least as broad a passivation region as the calcium alloy and broader than the antimony alloys.

The antimony alloys have higher currents than the non-antimonial alloys at the higher potentials, both

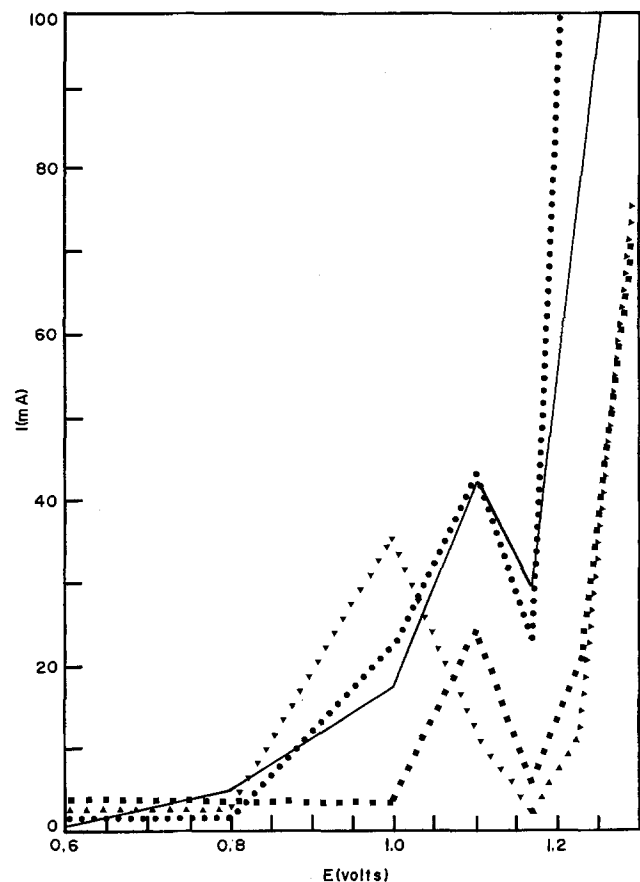


Fig. 10. Comparison of corrosion rates of typical lead alloys at 82°C in 5.1M H₂SO₄ as a function of potential. ▼▼▼ 0.13% Sr, 1.0% Sn, 0.02% Al; ■■■ 0.09% Ca, 0.5% Sn; — 5.12% Sb, 0.5% As, 0.23% Sn, 0.062% Cu, 0.002% S; ●●●● 1.0% Sb, 0.34% As, 0.15% Sn.

because the corrosion rates are higher and because the oxygen evolution rates are higher. Figure 11 shows cross sections of the corrosion films at 1.290V and Fig. 12 shows the microstructures of the 4 alloys. (The pictures in Fig. 12 were taken several years after the corrosion experiments were run.) The corrosion layers of the antimony alloys are much thicker and interdendritic corrosion is more significant, particularly for the 5.12% Sb alloy. The strontium alloy corrosion film is thin and looks very similar to the calcium alloy. Corrosion of the strontium alloy is apparently not influenced by the dendrite arm spacing, which is similar to that of the antimony alloys. There was no evidence of interdendritic penetration of the strontium alloy at any potential. The strontium alloy would be expected to withstand overcharge in a manner similar to the calcium alloy and better than the antimony alloys.

Conclusions

The corrosion behavior of the cast strontium-lead alloy is similar to cast pure lead and lead-calcium alloys. Two regions of high corrosion occur: (i) in high concentration acid (5.1M) near the open-circuit potential (1.0-1.1V vs. Hg/Hg₂SO₄/5.6M H₂SO₄) and (ii) in low concentration acid (0.8M) at low potentials (0.8-0.9V). Temperature greatly enhances the corrosion rate under the first set of conditions but not under the second. The strontium alloy corrodes less than antimony alloys at potentials above open circuit and has a broader passive region. These characteristics would be beneficial in float and cycling applications.

The corrosion behavior of the strontium-tin-aluminum-lead alloy thus appears to be acceptable for use in lead-acid batteries. This, coupled with its good electrochemical and metallurgical properties, makes

it a possible alloy candidate for use in many lead-acid battery applications.

Acknowledgments

The authors gratefully acknowledge the contributions of N. Quereshi and M. Mueller, who did the corrosion experiments and the metallographic work, D. Mongan and F. Graetz, who did the analyses of the corrosion films, and D. Marshall and R. Johnson, who contributed helpful discussions.

Manuscript submitted Nov. 15, 1979; revised manuscript received May 13, 1980. This was Paper 53 presented at the Los Angeles, California, Meeting of the Society, Oct. 14-19, 1979.

Any discussion of this paper will appear in a Discussion Section to be published in the June 1981 JOURNAL. All discussions for the June 1981 Discussion Section should be submitted by Feb. 1, 1981.

Publication costs of this article were assisted by Johnson Controls Incorporated.

REFERENCES

1. K. R. Bullock and D. H. McClelland, *This Journal*, **123**, 327 (1976).
2. J. T. Crennell and A. G. Milligan, *Trans. Faraday Soc.*, **27**, 103 (1931).
3. U. B. Thomas, *Bell Lab. Rec.*, **16**, 12 (1937).
4. H. E. Haring and U. B. Thomas, *Trans. Electrochem. Soc.*, **68**, 293 (1935).
5. M. V. Rose and J. A. Young, in "Lead 74," p. 37, edited Proceedings of the Fifth International Conference on Lead, Paris, Metal Bulletin Ltd. London (1976).
6. C. E. Weinlein, J. R. Pierson, and D. Marshall, in "Power Sources 7," J. Thompson, Editor, p. 67, Academic Press, New York (1979).

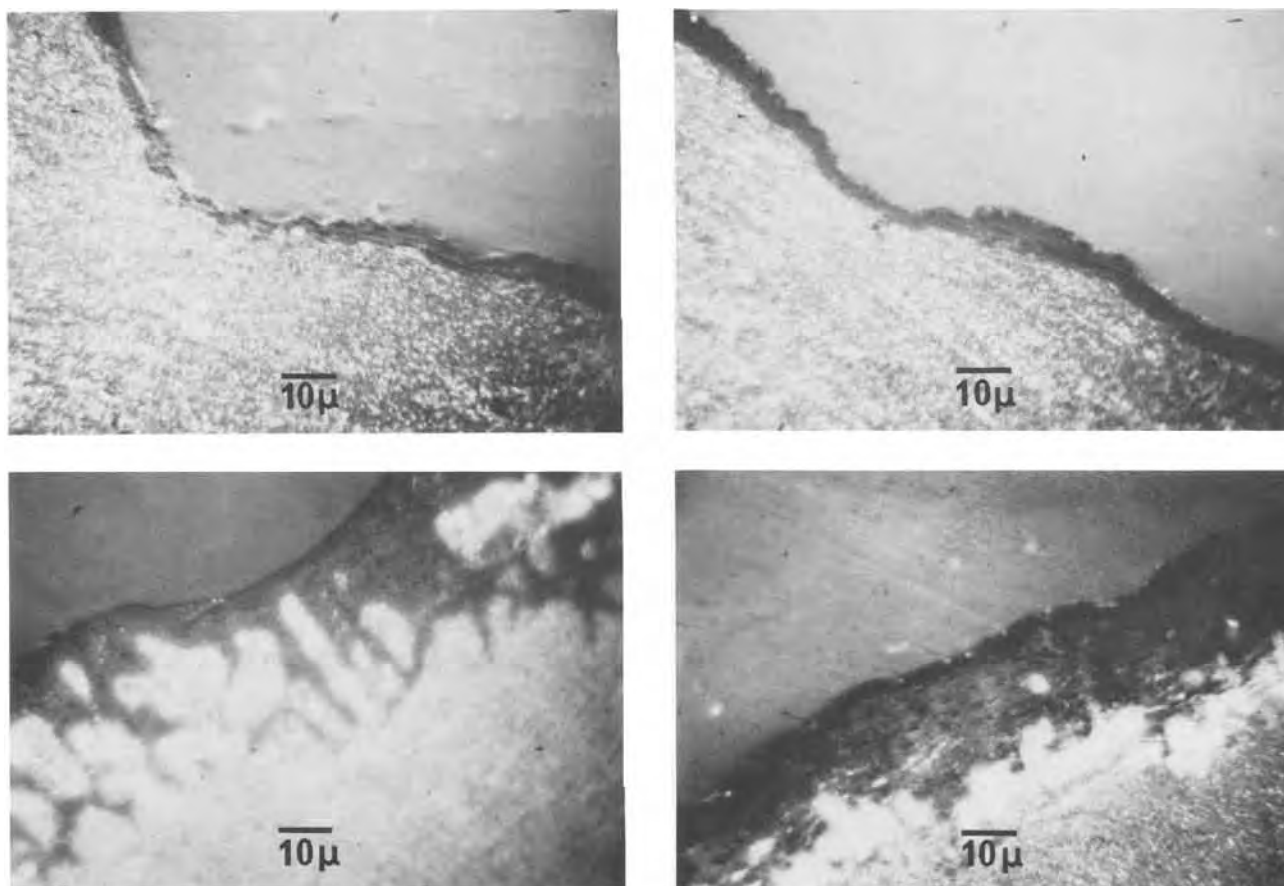


Fig. 11. Micrographs of cross sections of corrosion films of alloys shown in Fig. 9 at 1.290V. a (top left), Sr alloy; b (top right), Ca alloy; c (bottom left), 5.12% Sb alloy; d (bottom right), 1.0% Sb alloy.

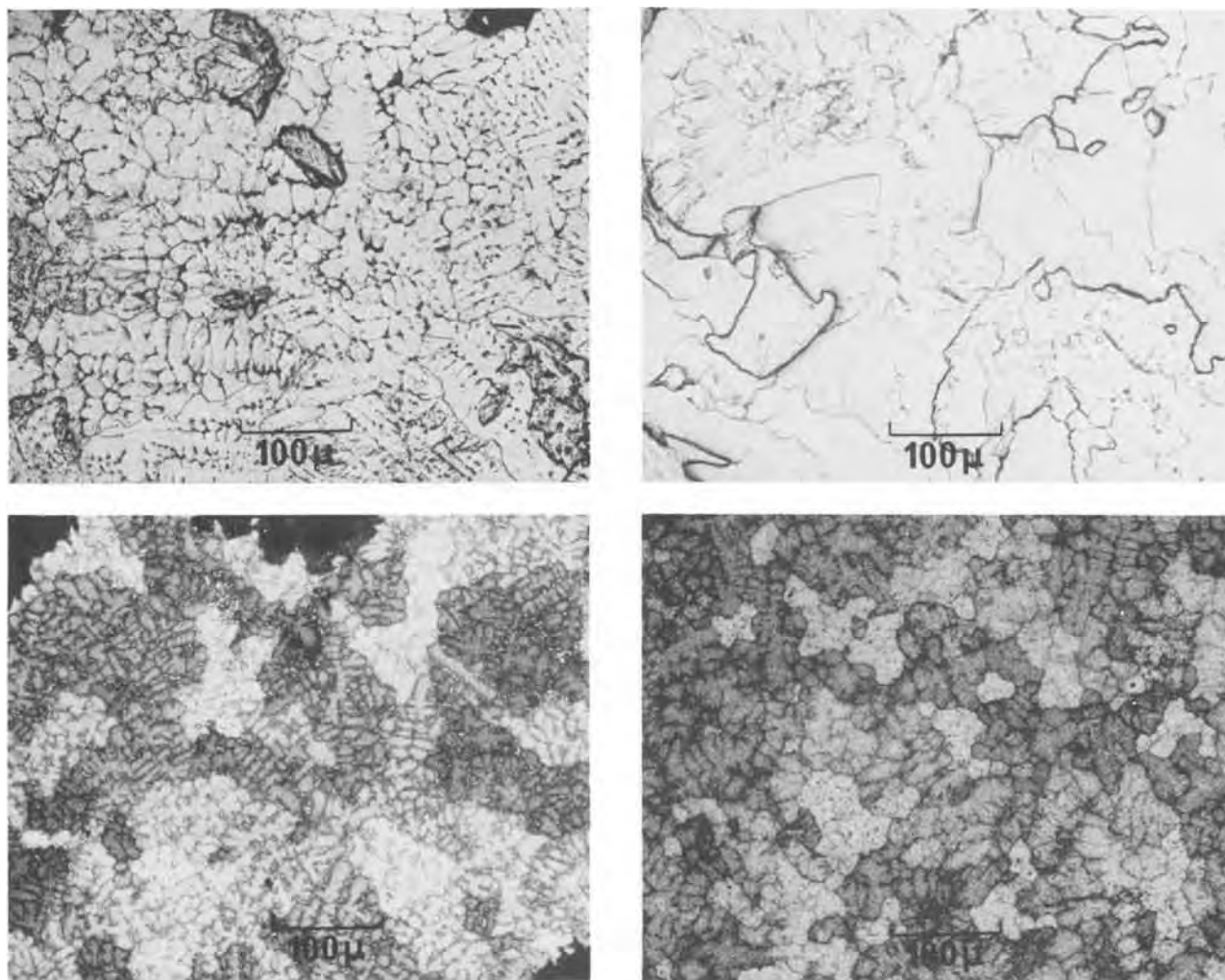


Fig. 12. Micrographs of etched samples of alloys shown in Fig. 9 and 10. a (top left), Sr alloy; b (top right), Ca alloy; c (bottom left), 5.12% Sb alloy; d (bottom right), 1.0% Sb alloy.

7. J. Burbank, A. C. Simon, and E. Willihnganz, in "Advances in Electrochemistry and Electrochemical Engineering," Vol. 8, P. Delahay and C. W. Tobias, Editors, p. 157, John Wiley and Sons, Inc., New York (1971).
8. N. E. Bagshaw, *J. Power Sources*, **2**, 351 (1978).
9. J. J. Lander, *This Journal*, **98**, 213 (1951).

10. J. J. Lander, *ibid.*, **103**, 1 (1956).
11. P. Ruetschi and R. T. Angstadt, *ibid.*, **111**, 1323 (1964).
12. K. R. Bullock, *ibid.*, **127**, 662 (1980).
13. W. C. McCrone and J. G. Delly, "The Particle Atlas," 2nd ed., Vol. I, pp. 119-129, Ann Arbor Science Publishers, Ann Arbor, Mich. (1973).

Side Reactions of Pyridine-Halogen Complexes

Arthur J. Coury* and Patrick T. Cahalan

Energy Technology, a Division of Medtronic, Incorporated, Minneapolis, Minnesota 55418

ABSTRACT

Halogen-pyridine charge transfer complexes have conductivities which make them useful as depolarizers in power cell cathodes. Pyridines and halogens undergo additional reactions of consequence to cell performance. Such side reactions include: alkyl group substitution, ring coupling, polymer molecular weight degradation, olefin addition, and ring substitution. Instrumental analysis of model systems and the commercial poly(2-vinyl-pyridine)/iodine (P2VP/I₂) system provided strong evidence for alkyl group substitution, coupling, and molecular weight degradation. The addition reaction was inferred from the presence of the needed reactants and their facile reactivity, but not confirmed analytically. Halogenation of the pyridine ring was not found, and, from literature sources, was assumed to be unlikely under conditions of cell use. The side reactions cited cause reduced cathode capacity. Hydrogen halides generated by such side reactions may cause corrosion, but may enhance conductivity properties. Deleterious pressure buildup or dimensional changes may result from side reactions occurring within sealed battery cans.

The combination of halogens (acceptors) with pyridine derivatives (donors) produces, initially, charge transfer complexes with conductivities useful as depolarizers in lithium-halogen power cell cathodes. The complex most often employed in pacemaker batteries is P2VP/I₂ (1).

Subsequently, several other reactions can occur depending on time, temperature, and stoichiometric ratio. The nature of these side reactions has recently been addressed by us as well as by other workers (2). Known reactions of pyridines which may be relevant to cell performance include: alkyl group substitution, ring coupling, polymer molecular weight degradation, olefin addition, and ring substitution. Insights into the reactions of halogens with pyridine and substituted pyridines were derived from literature sources and experimental studies of model complexes as well as from the commercial P2VP/I₂ system. The nature and magnitude of such reactions and some suggestions as to how they may affect the performance of power cells are discussed in this paper.

Experimental

Materials.—Pyridine (Aldrich, >99%, Gold Label), and ethylpyridine (Aldrich, 97%) were distilled before use. P2VP (Ionac Chemical Company, intrinsic viscosity range 0.8-1.0, 30C in pyridine) was oven dried before use. Iodine (Mallinckrodt, resublimed) and bromine (Mallinckrodt, purified grade) were used as received.

Apparatus and procedures.—Reactions studied at ambient or slightly elevated temperatures were performed by weighing the halogen and pyridine derivatives into glass containers sealed with glass or Teflon. For moderate heating <60°C, the glass containers were placed in forced-air ovens. High temperature studies (>100°C) were conducted in sealed glass ampules or Hastelloy C autoclaves, jacketed with heating mantles. Reagents were protected from moisture during weighing.

Analyses.—Infrared spectra were run on a Perkin-Elmer 457A grating infrared spectrophotometer (range 200-4000 cm⁻¹). Specimens were generally prepared as smears or solvent-cast films on potassium chloride plates. Nuclear magnetic resonance spectra were run on a Varian Anaspect EM360, using acetone D₆ as solvent. Mass spectra were determined using a du Pont

Model 21-492 instrument interfaced with a Honeywell 716 computer.

Results and Discussion

Complex formation.—From vapor pressure measurements, the P2VP:I₂ ratio in the charge transfer complex is 1:1 (3) when excess iodine is present. With equimolar ratios of halogen to pyridine or substituted pyridines, there is evidence for a mixture of 1:1 molecular complex and a 2:1 ionic structure, e.g., (C₅H₅N)₂I⁺I⁻ (4). Halogen molecules associate with pyridines at different strengths (Fig. 1) (5). Model reaction studies were performed on systems containing the halogens I₂ and Br₂, along with various monomeric and polymeric pyridines. Pyridine was chosen as one of the model compounds to eliminate alkyl group reactions.

Halogen-pyridine reactions.—Ambient mixing of equivalent amounts of Br₂ and pyridine resulted in an immediate exotherm and an orange solid followed by a slower reaction with transformation of the material to a tarry, black mass. The transformations assigned were complex formation followed by ring coupling to polypyridylene hydrobromide (Fig. 2). The reaction mechanism proposed by McElvain *et al.* (6) involves coupling of pyridines at activated ortho or

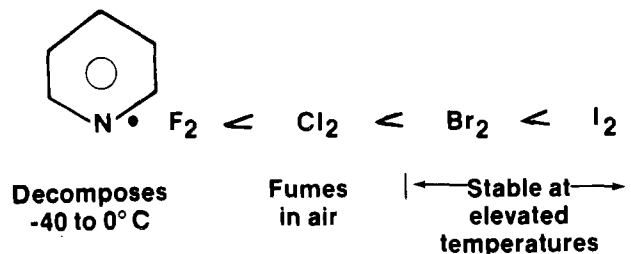


Fig. 1. Stability of halogen-pyridine complexes

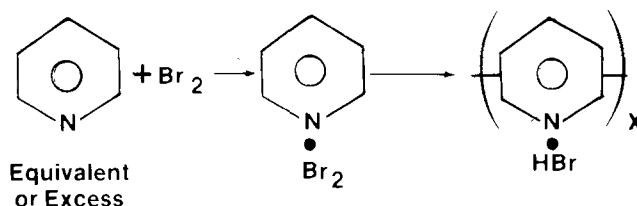


Fig. 2. Polypyridylene formation

* Electrochemical Society Active Member.

Key words: iodine cathode, organic reactions, halogenation.

para positions (Fig. 3). Crosslinking, hence the observed intractability, occurs when the pyridine coupling occurs at three ring sites. With Br_2 in excess pyridine, similar transformations were observed with a tarry precipitate forming which exhibited polypyridylene characteristics. These results are consistent with the equations in Fig. 3 which show that a stoichiometric excess of pyridine over Br_2 is necessary for polypyridylene formation to occur.

With pyridine in excess Br_2 , charge transfer complex formation was instantaneous and exothermic. The resulting liquid appeared to be stable indefinitely (Fig. 4). In agreement with literature sources (7, 8), no ambient temperature ring bromination was found at any Br_2 ratio. High temperatures are required for ring bromination (Fig. 5) (7). With unsubstituted pyridine in excess Br_2 , therefore, side reactions are suppressed at ambient conditions.

Halogen-alkyl pyridine reactions.—With alkyl-substituted pyridines, excess halogen induced another side reaction, halogenation at the carbon attached to the pyridine ring. It was slower than complex formation or ring coupling (when the latter occurred). For example, when 2-ethylpyridine was combined with excess Br_2 , conversion to α -bromo-2-ethylpyridinium bromide perbromide occurred, as determined by nuclear magnetic resonance spectroscopy (α -protons) and infrared spectroscopy (Table I) to the extent of 27 mole percent (m/o) in 4.5 months (Fig. 6), under ambient conditions of storage. Pyridine hydrohalide salts, it is noted, form stable complexes with Br_2 (8). Less alkyl bromination occurred with equivalent amounts of the reactants, but alkyl polypyridylene formation was suggested by the intractable nature and black color of the product.

Infrared results.—Qualitative indications of the chemical species previously described were observed in infrared spectra. Pyridine $\text{C}=\text{N}$ stretch frequencies, normally between 1585-1615 cm^{-1} , shifted upward

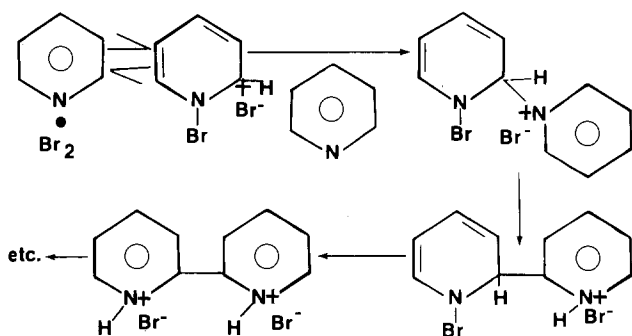


Fig. 3. Mechanism of polypyridylene formation

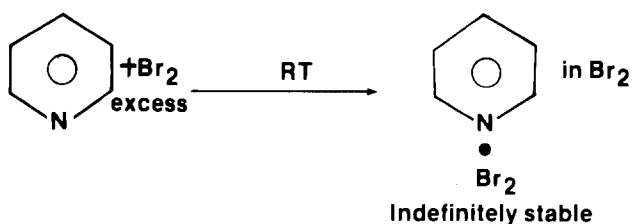


Fig. 4. Bromine-pyridine charge transfer complex

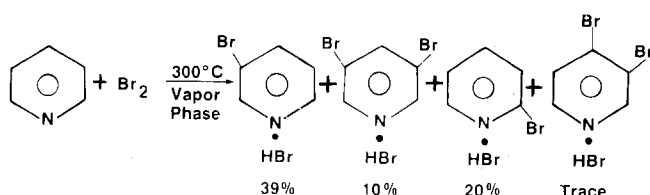


Fig. 5. High temperature, ring bromination of pyridine

Table I. Infrared group frequencies of pyridine/ Br_2 and alkyl pyridine/ Br_2 systems

Assignment	Frequency
Pyridine	
$\text{C}=\text{N}$	1585 cm^{-1}
Pyridine/ Br_2 (XS)	
$\text{C}=\text{N}\cdot\text{Br}_2$	1595 cm^{-1}
Pyridine (XS)/ Br_2	
$\text{C}=\text{N}\cdot\text{Br}_2$	1600 cm^{-1}
$\text{C}=\text{NH}\cdot\text{Br}^-$	1630 cm^{-1}
$(\text{N}-\text{H})\cdot\text{Br}^-$	2700-2800 cm^{-1} (broad)
2-ethylpyridine/ Br_2 (XS)	
$\text{C}=\text{N}\cdot\text{Br}_2$	1600 cm^{-1}
$\text{C}=\text{NH}\cdot\text{Br}^-$	1625 cm^{-1}
$(\text{N}-\text{H})\cdot\text{Br}^-$	2800 cm^{-1} (broad)
$\text{C}-\text{Br}$	595 cm^{-1}

$\sim 10 \text{ cm}^{-1}$ for charge transfer complexes and $\sim 15\text{-}40 \text{ cm}^{-1}$ for hydrohalide salts. A broad amine salt $(\text{N}-\text{H})^+$ absorption developed at 2700-2900 cm^{-1} as pyridine hydrohalides formed. A peak assigned to $\text{C}-\text{Br}$ stretching at 540-595 cm^{-1} appeared to be proportional to alkyl bromination. Examples of infrared group frequencies for model pyridine/ Br_2 systems are given in Table I.

Iodine acceptor systems.—When I_2 was substituted for Br_2 , complex formation was spontaneous but slower by virtue of being limited by diffusion of I_2 into the pyridine phase or dissolution of the I_2 by the pyridine phase. Side reactions were of the same chemical type, but considerably slower. For example, with equivalent amounts of 2-ethylpyridine/ I_2 , a dark liquid complex formed at room temperature which changed little by infrared analysis over seven days. Over 5.5 months, however, a massive amine salt vibration (centered at 2900 cm^{-1}) developed, possibly due to formation of the polypyridylene-type structure (Fig. 7). The analogous reactions occurred within hours with the use of Br_2 as acceptor.

P2VP-halogen systems.—With P2VP, reactions analogous to the model pyridine compounds were observed. Variations in the molecular weight and chemical structure of the P2VP were additional factors of concern for power cells.

Analytical results.—Infrared spectroscopy was used qualitatively to show development of side products in P2VP-halogen systems. Absorbances were analogous to those developed in the model reactions (Table II).

Nuclear magnetic resonance spectroscopy was valuable for quantitative estimates of alkyl chain halo-



Fig. 6. Alkyl bromination of ethyl pyridine

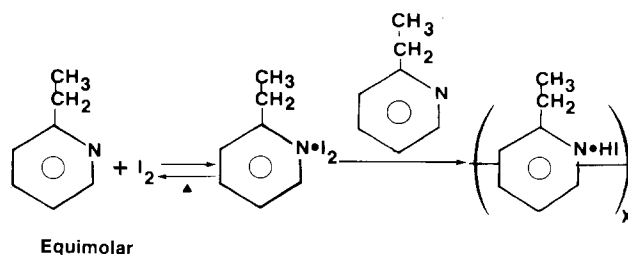


Fig. 7. Reactions of iodine/2-ethylpyridine

Table II. Infrared group frequencies of P2VP/halogen systems

Assignment	Frequency
P2VP/Br₂ (XS)	
C = N · Br ₂	1595 cm ⁻¹
C = NH ⁺ Br ⁻	1610 cm ⁻¹
(N - H) ⁺ Br ⁻	2800-2900 cm ⁻¹ (broad)
C - Br	540 cm ⁻¹
P2VP/I₂ (XS)	
C = N · I ₂	1595 cm ⁻¹
C = NH ⁺ I ⁻	1610-1620 cm ⁻¹
(N - H) ⁺ I ⁻	2800-2900 cm ⁻¹ (broad)
C - I	Ambiguous

generation by determining the ratio of integrated aliphatic (1.0-4.5 ppm, δ) to aromatic (7.0-10.0 ppm, δ) absorbances. Qualitative indications of pyridine salts (exchangeable protons) were detected near 15 δ and in an absorbance which varied between 6-12 δ dependent on temperature and concentration.

P2VP reactions in excess halogen.—In excess Br₂, at ambient temperatures, P2VP developed infrared absorbances indicative of alkyl chain halogenation within hours which increased over the length (seven days) of the study (Fig. 8).

At 120°/1.7 hr, a hard, insoluble product developed, indicating the possibility of polypyridylene formation. Any intermolecular coupling of P2VP would cause cross-linking and consequent intractability. The necessary free pyridine base is believed to be generated by thermal reversal of the charge transfer complex (Fig. 9).

With excess I₂, P2VP entered into side reactions more sluggishly. However, at 130°C/24 hr, significant salt and alkyl chain halogenation were detected. At 170°C/72 hr, nuclear magnetic resonance spectroscopy indicated the ratio of aliphatic to aromatic protons to be 2.4:4.0, i.e., ~60% of the tertiary hydrogens were substituted by iodine (Fig. 10).

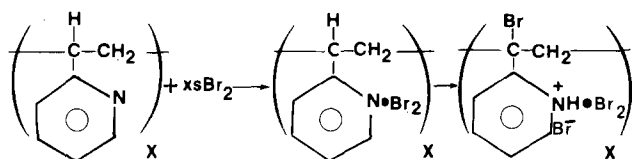


Fig. 8. Alkyl bromination of poly-2-vinylpyridine

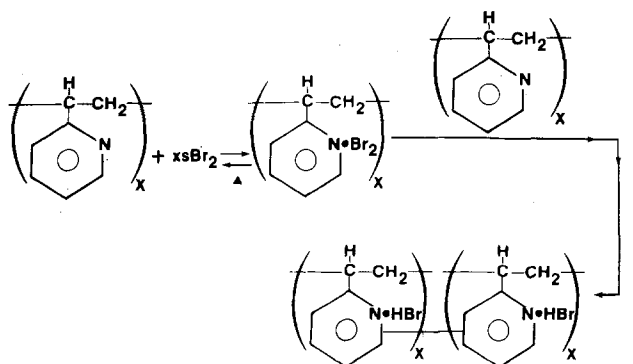


Fig. 9. Polypyridylene formation in poly-2-vinylpyridine

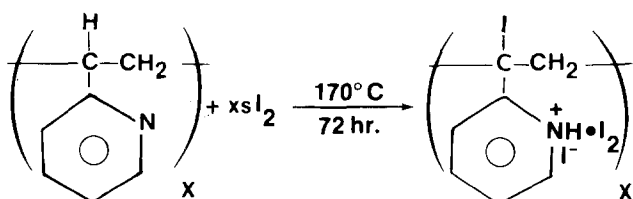


Fig. 10. Alkyl iodination of poly-2-vinylpyridine

Higher temperatures effected the conversion of P2VP/I₂ mixtures from paste to fluid form and caused the release of volatile fragments. Mass spectrometry of the volatile reaction gases indicated short-chain alkyl iodides (CH₃I, C₂H₄I₂), I₂, HI, pyridine, and vinylpyridine.

Data from the analyses employed did not give a definitive picture of the nature of the polymer backbone degradation resulting from treatment with halogens. The side products previously described were indicated to a large extent, however, in the degraded residues from the high temperature treated systems.

Unconfirmed reactions.—Other chemical transformations which may occur but are not yet confirmed analytically involve olefinic functionality in 2-vinylpyridine (2VP) monomer and P2VP backbone chain. The 2VP is inevitably present in P2VP starting material, and may form during thermal degradation of the polymer.

A facile combination of 2VP with pyridine hydrohalide groups has been reported (Fig. 11) (9). The pyridine hydrohalides are available as products of most of the side reactions already described.

Formation of halogenated alkyl products by the addition of halogens or hydrogen halides to olefinic moieties (in 2VP or the P2VP alkyl chain) are considered possible transformations (Fig. 12). This addition mechanism is difficult to isolate, however, because of the similarity of the products to those formed from substitution reactions.

Summary and Conclusions

Most of the side reactions cited cause reduced cell capacity by prematurely depleting halogen. The hydrogen halides generated may cause corrosion problems, but may enhance conductivity characteristics. Undesirable pressure buildup or dimensional changes may result from side reactions occurring within the sealed battery can. While useful indications of the nature and extent of side reactions were derived from these studies, our understanding of reaction mechanisms and products is still incomplete. Work continues on elucidating chemical transformations and relating them to cell performance.

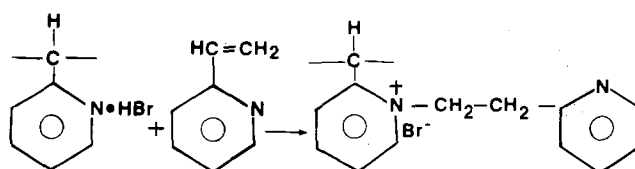


Fig. 11. Addition of pyridine hydrohalide to 2-vinylpyridine

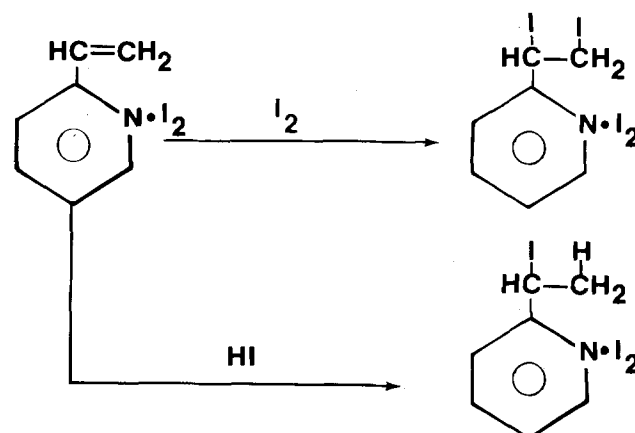


Fig. 12. Addition of iodine or hydrogen iodide to 2-vinylpyridine complex.

Manuscript submitted Nov. 12, 1979; revised manuscript received April 30, 1980. This was Paper 82 presented at the Los Angeles, California, Meeting of the Society, Oct. 14-19, 1979.

Any discussion of this paper will appear in a Discussion Section to be published in the June 1981 JOURNAL. All discussions for the June 1981 Discussion Section should be submitted by Feb. 1, 1981.

Publication costs of this article were assisted by Energy Technology, a Division of Medtronic, Incorporated.

REFERENCES

1. A. A. Schneider *et al.*, U.S. Pat. 3,660,163 (1972) and 3,674,562 (1972).

2. R. L. McLean and J. Blecher, Paper 81 presented at The Electrochemical Society Meeting, Los Angeles, California, Oct. 14-19, 1979.
3. K. R. Brennen and D. F. Untereker, Paper 60 presented at The Electrochemical Society Meeting, Pittsburgh, Pennsylvania Oct. 15-20, 1978.
4. O. Hassel *et al.*, *Acta Chem. Scand.*, **15**, 967 (1961).
5. M. Boudakian, in "Heterocyclic Compounds," pp. 407 ff, Interscience, New York (1974) and Vol. 14, Supplement, Part 2, Chap. VI, pp. 300 ff (1961).
6. S. McElvain and M. A. Goese, *J. Am. Chem. Soc.*, **65**, 2227 (1943).
7. Elderfield, in "Heterocyclic Compounds," pp. 397 ff, John Wiley, New York (1950).
8. S. McElvain, in "Heterocyclic Compounds," p. 2232, John Wiley, New York (1950).
9. Cislak, *et al.*, U.S. Pat. 2,512,789 (1950).

A New Membrane-Type pH Sensor for Use in High Temperature-High Pressure Water

Leonard W. Niedrach*

General Electric Company, Research and Development Center, Schenectady, New York 12301

ABSTRACT

The new sensor provides for the direct measurement of the pH of geothermal brines, water in nuclear reactors, and other high temperature solutions. The heart of the unit is an oxygen ion conducting ceramic that serves as the membrane in a structure somewhat akin to that of the conventional glass electrode. Yttria stabilized zirconias with both aqueous internal junctions and dry, metal-metal oxide internal junctions were employed in the present work. Test units were run continuously without failure for periods as long as 13 days at temperatures of 285°C and at pressures of 1200 psi. Under these conditions the response over the pH range 3-8 (at 285°) was linear with a slope up to 97% of theoretical. Unlike sensors involving electron transfer couples (*e.g.*, the hydrogen electrode, the palladium hydride electrode, metal-metal oxide couples) the membrane is insensitive to changes in the redox environment. In turn, the relatively inert membrane exerts no influence on the environment; this behavior contrasts markedly with that of the hydrogen electrode and many other candidates for use at high temperatures. Although primary emphasis was placed on high temperature performance, the ceramic membranes were also shown to function as pH sensors over the temperature range from 25° to 285°C. The conductivities of the yttria stabilized membranes, as measured in sensors, were found to be comparable in magnitude and activation energy with literature values for related materials measured at elevated temperatures in connection with their application in high temperature fuel cells and oxygen sensors.

Work leading to the concept of the new sensor was inspired by the recognized need for devices for the direct measurement of the pH at elevated temperatures of geothermal brines, of water in nuclear reactors, and in other high temperature applications including basic thermodynamic studies of aqueous systems. For such applications, membrane sensors are superior to those based on electron transfer couples (*e.g.*, the hydrogen electrode, the palladium hydride electrode, and metal-metal oxide couples) because unlike the latter, membrane electrodes are normally insensitive to changes in the redox environment and are resistant to poisoning by impurities such as sulfides. In turn, membrane materials can often be found that exert no significant influence on the environment. These considerations are paramount, of course, in accounting for the universal acceptance of the glass electrode for pH measurements at ambient temperature. In view of the difficulties that have been encountered in attempts to modify the classical glass electrode for high temperature-high pressure applica-

tions (1-3), alternative membranes were sought for the purpose.

In this connection the well-known lanthanum fluoride electrode for the determination of fluoride ion concentrations was selected as a useful model to establish criteria for the desired membrane material. This electrode functions because fluoride ions in the crystal and in the solution serve as the potential-determining species at the interface. At equilibrium the electrochemical potential of the fluoride ion, is defined in general form by

$$\bar{\mu}_{X-n} = \mu^\circ_{X-n} + RT \ln a_{X-n} + nF\phi \quad [1]$$

where $\bar{\mu}_{X-n}$ is the electrochemical potential, μ°_{X-n} is the standard chemical potential, a_{X-n} is the activity of the fluoride ion, ϕ is the inner or galvanic potential, n is the charge on the ion of interest, and the other terms have their usual meanings, is equal in both phases. The potential drop at the interface is therefore given by

$$\Delta\phi = \phi_m - \phi_a = \frac{1}{nF} ({}_m\mu^\circ_{X-n} - m\mu^\circ_{X-n} - RT \ln_m a_{X-n} + RT \ln_a a_{X-n}) \quad [2]$$

* Electrochemical Society Active Member.

Key words: oxygen ion conducting ceramics, stabilized zirconia, yttria stabilized zirconia, oxygen electrode.

where the subscripts a and m identify the aqueous and membrane phases, respectively. Since fluoride ion is the sole anion in the crystal, its activity in the solid phase remains constant and the only variable term involved in establishing the total potential drop across the interface is the fluoride ion activity in the aqueous phase.

It was reasoned that a parallel relation might exist between an oxygen ion conducting ceramic and the oxygen ion concentration (and hence indirectly the pH) in an adjacent aqueous phase. If so an oxygen ion conducting ceramic should function as a membrane-type pH sensor. This report shows that this sensitivity to pH is realized experimentally.

Stabilized zirconia tubes of the type employed in high temperature fuel cells and oxygen sensors were chosen as representative oxygen ion conducting membranes for initial tests. Zirconia is markedly less soluble than glass in water at elevated temperatures. Much work has also been done to characterize these ceramics and to develop fabrication techniques in connection with their earlier applications. Zirconia stabilized with yttria, calcia, and magnesia has been examined in the work to date, but the performance of the yttria containing materials has been far superior to the others, possibly because of their generally higher specific conductivities (4). The work to be reported will therefore be limited to yttria stabilized zirconia at two levels, 8.0 and 16.9 weight percent (w/o).

A variety of alternative oxygen ion conductors should be applicable as long as the transference number for the oxygen ion is close to 1.0 and that for electron and/or hole conduction is at least an order of magnitude, and preferably several orders of magnitude, less. An important criterion is the specific conductivity. While that of the yttria stabilized zirconia is adequate for practical applications at temperature above 95°C, it would be desirable to be able to cover the full temperature range from ambient upwards. Among the zirconias those stabilized with scandia have the highest reported conductivities (4, 5) and they may be adequate. Certain doped cerias also look promising from this point of view (5-7).

The purpose of this work was to demonstrate the performance of the new sensor in a preliminary way, establish some of its important operating characteristics, and obtain some indication of stability. Before it can become a practical device, an adequate system including reference electrode and calibration procedures will have to be developed, to which little attention was devoted. It will become clear, however, that the reference electrode may prove less stable and reproducible than the membrane sensor itself.

Most of the data were obtained at 285°C, but data obtained at lower temperatures indicate that with lower resistance ceramics the full range from ambient temperature to 285°C or higher can be encompassed with a practical device.

Experimental

Structure of the sensors.—Most of the sensors used in this work were somewhat akin to the conventional glass electrode in that a buffered saline solution in contact with a chlorided silver wire served as the internal element within the membrane sheath. For work in the temperature range 25°-95°C stabilized zirconia tubes closed at one end were employed. Initially a 0.1M NaCl or KCl solution containing one pH 7 pHydrion® buffer tablet per 100 ml was employed as the inner electrolyte, and contact was made by a chlorided silver wire immersed in this solution. In some cases the solution (including the buffer) was diluted by a factor of ten. For longer term experiments, particularly at 95°C, the open end of the tube was covered with a Teflon cap.

A few sensors for use at 25°-95°C were also prepared with "direct junction" internal connections. One such type was prepared by inserting a 30 mil, coiled copper

lead wire into the tube and packing it in place with a 50:50 mixture by weight of finely divided copper and cuprous oxide (Fisher Copper Metal-Electrolytic Dust, purified; Baker Cuprous Oxide Powder, Analyzed Reagent) to a depth of 3 in. This type of junction has been used in the past in the fabrication of the well-known stabilized zirconia high temperature oxygen sensors (8-10), and alternative metal-metal oxide or mixed oxide couples could also be used. A second direct junction contact was prepared by filling the tube with mercury to a depth of three inches and inserting a platinum lead wire. It was presumed that enough mercuric oxide was present as a contaminant that this too served as a metal-metal oxide type contact. Sensors of this type were also closed with Teflon caps.

To extend the work to higher temperatures, the sealed structure shown in Fig. 1 and 2 was employed. An important element is the compressible Teflon seal in the Conax pressure fitting. This maintains the pres-

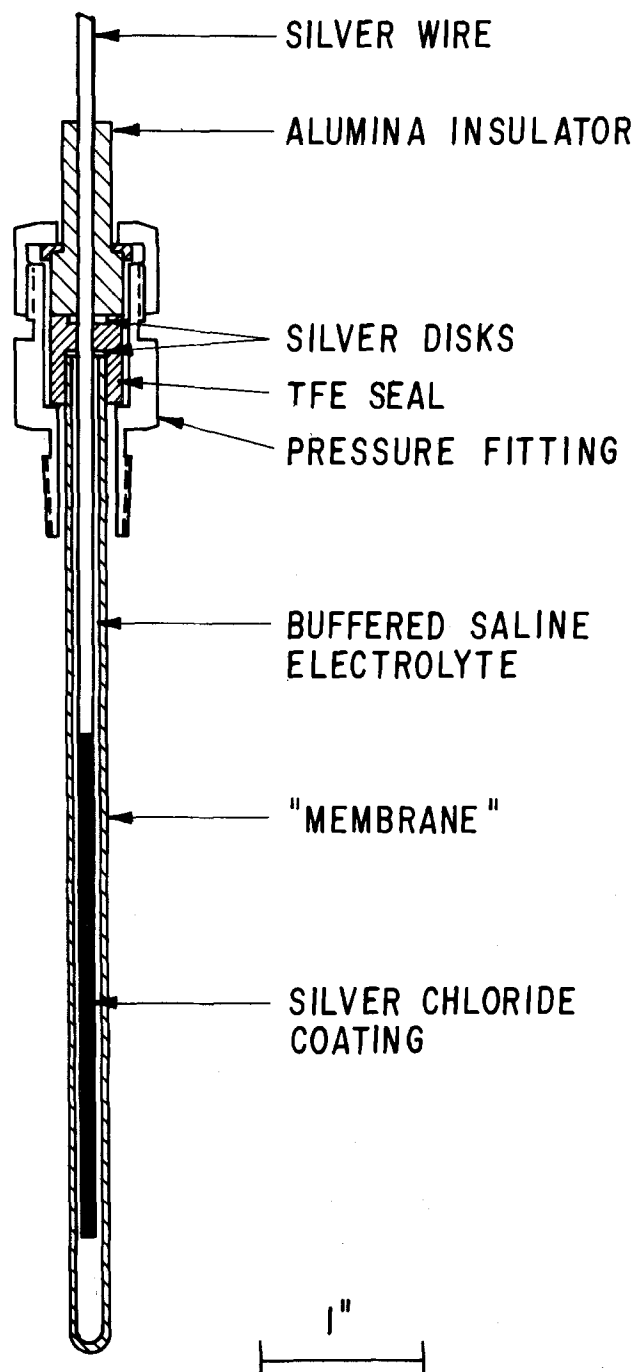


Fig. 1. Schematic diagram of sensor for use at elevated temperatures and pressures.

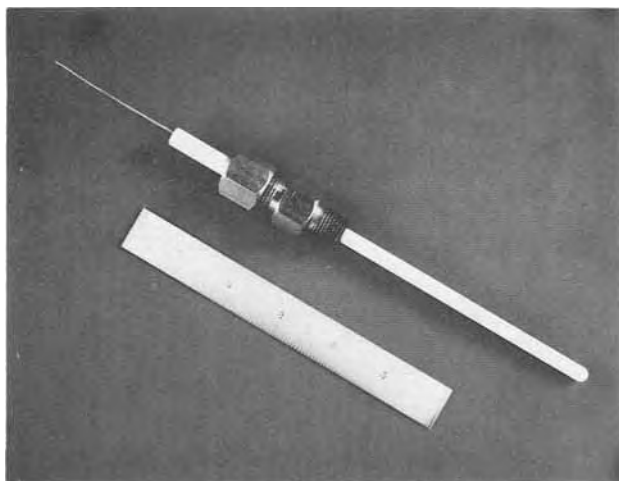


Fig. 2. Photograph of an assembled sensor

sure that builds up within the tube—the order of 1000 psi at 285°C—and serves to insulate the lead wire from the metallic parts of the fitting. The same internal electrolytes were employed as at lower temperatures, and in one case a solution containing 0.001m HCl and 0.009m KCl was used. Because of thermal expansion of such solutions, care was taken to allow sufficient free volume within the tube; normally they were filled to only 70% of capacity.

Some work was also done at the elevated temperature with the copper/cuprous oxide direct junction structure. This was sealed into the Conax fitting as above.

Test system and protocols.—Initial tests at ambient temperature were performed by immersing the sensor into appropriate solutions in an open beaker. An Ingold® combination electrode was used as a comparison standard, and its reference electrode also served the zirconia sensor. Because of the very high impedance of the ceramics at ambient temperature ($\sim 10^{11}\Omega$), it was necessary to make measurements in a faraday cage and to use a high input impedance electrometer (Keithley Model 602).

All other measurements were made with the test system shown schematically in Fig. 3. Here provision was made for pumping water, acid, or base into the heated and pressurized (if necessary) autoclave, which had a capacity of 1 liter. In this way the solution in the autoclave could be slowly “titrated” with acid or base, or aliquots of more concentrated reagent could be

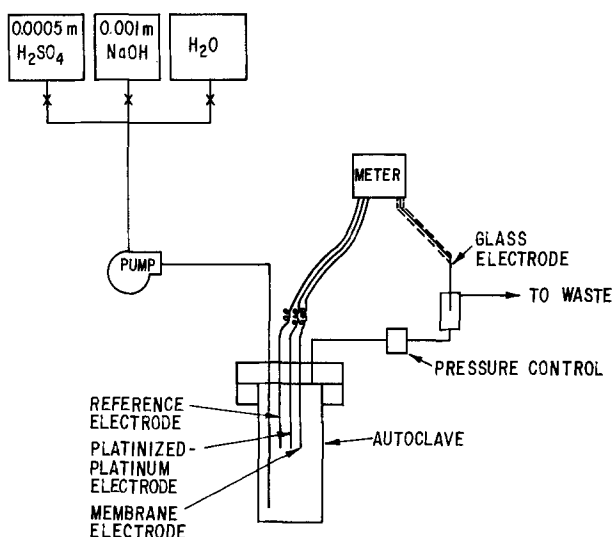


Fig. 3. System for evaluating sensors

introduced to cause more rapid changes in pH. Both 316 stainless steel and titanium autoclaves have been used.

The Conax fitting on the sensor permits direct mounting in the lid of the autoclave. Frequently two were tested concurrently. Also mounted to the lid through Conax fittings were an insulated platinumized platinum wire and a reference electrode which consisted of a chlorided silver rod immersed in a 0.01m KCl solution contained within an insulating tube (11); the latter communicated with the water in the autoclave through a porous asbestos or zirconia junction. For some of the measurements at 95°C an Ingold Series 514 Hi Temperature combination pH electrode was mounted through the lid in place of the special reference electrode. In such cases the system was not pressurized, but otherwise procedures were standard.

During a run the potentials of all electrodes as well as the autoclave were monitored against the reference. In addition the ambient temperature pH could be measured downstream of the pressure control with an Ingold combination pH electrode. Keithley electrometers (initially Model 602 and later Model 616) were used for all the potential measurements. Automatic switching among the electrodes was accomplished with an Orion Model 855 Automatic Electrode Switch. Output was recorded continuously on a Hewlett Packard Model 7100B Strip Chart Recorder.

The reagents were normally pumped through the system at a constant rate of 3 ml/min with a Lapp Pulsafeeder Pump Model LS-20 while the pressure was maintained at 1200 psi, a pressure of about 200 psi over the vapor pressure of water when the system is at the highest operating temperature of 285°C. When more rapid transients were under study, water was pumped at the same rate through the system and suitable aliquots of 0.1m NaOH or 0.05m H₂SO₄ were introduced into the stream. Thermal convection produced essentially ideal mixing within the autoclave particularly at the higher temperatures.

Temperatures were controlled with a Leeds and Northrup Electromax III controller. They were monitored continuously with a Chromel-Alumel thermocouple.

Resistance measurements.—Occasionally resistance measurements were desired on the sensors. These were accomplished with the electrometer by connecting the built-in shunts across the inputs from the sensor and the reference electrode. Under these conditions the resistance is given by

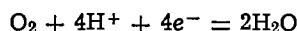
$$R = R_{sh}(E_{oc} - E_{sh})/E_{sh}$$

where R is the series resistance of the membrane, the solution in the autoclave, and the reference electrode, R_{sh} is the resistance of the shunt, E_{oc} is the voltage measured without the shunt, and E_{sh} is that with the shunt. At the lower temperatures, R approximates that of the membrane itself. At higher temperatures a correction was derived by measuring the resistance between the platinum electrode and the reference and/or between the autoclave and the reference. These measurements provided an estimate for the series resistance of the solution in the autoclave and the reference electrode. The resistance measurements were subsequently converted to specific conductivity on the basis of the physical dimensions of the tubes. In the calculations allowance was made for the expansion of the water within the tubes with increasing temperature. Measurements were made with the sensor immersed in acidic and basic solutions with no difference in results.

Comparison standards for pH sensors.—Ideally one would like to establish the performance of a new sensor on the basis of comparisons of experimental observations with values predicted from accepted thermodynamic data. Unfortunately, at the outset of this work it was not clear that the experimental system was

clearly enough defined for this purpose. Thus uncertain liquid junction potentials were anticipated at the reference electrode-solution interface, some consumption of acid through corrosion of the autoclave and connecting tubing as well as some ceramic parts could occur, and rigorous steps were not taken to exclude carbon dioxide from the basic solutions.

It was therefore elected to judge the performance of the sensors on the basis of comparisons with other acceptable standards. For measurements at ambient temperature and 95° this presented no problem because commercially available glass electrodes could be used unambiguously for the purpose. At higher temperatures, however, this is not the case, and an alternative comparison was sought. Although a hydrogen electrode would seem a natural choice, our system and experience had been geared for work with aerated solutions. We therefore elected to use the "oxygen electrode" formed at the platinized platinum wire in the autoclave as the comparison standard at 285°. This, in contact with the aqueous solutions, all of which were equilibrated with air at ambient temperature before entering the autoclave,¹ can, in principle, serve as a pH sensor because of the hydrogen ions involved in the potential determining reaction



Although not rigorously established as a pH sensor, the response of the oxygen electrode to pH has been demonstrated at ambient temperature (12), and during the course of the present work additional support was generated, particularly from direct comparisons with the glass electrode at 95°C. Comparison of its behavior at 285° with thermal data also proved reassuring, particularly during later experiments after the equipment had had time to age and passivate, cf. below.

Results and Discussion

pH Response

Performance at 25°.—Performance was first demonstrated in brief experiments at ambient temperature with yttria stabilized tubes. Data comparing the response of two membranes stabilized with 16.9 w/o yttria at 25° with that of a commercial glass electrode upon immersion in 0.1m sodium hydroxide, 2m hydrochloric acid, and a phosphate buffer (pHydrion at pH 7.0) are shown in Fig. 4. As can be seen the slopes of the two curves are very close to the ideal value of 1.000. While these results establish the response to pH, the high impedance of the yttria stabilized zirconia tubes at ambient temperature ($\sim 10^{11}\Omega$) makes them unacceptable for general application at this temperature. It is likely, however, that suitable membranes can be fabricated from alternative oxygen ion conducting ceramics, e.g., doped cerias, that will have lower resistivities and thereby permit practical measurements at ambient temperature. This is desirable, not with the aim of replacing the glass electrode, but in the interest of having a single sensor responsive to pH from ambient temperature to higher levels so that pH can be followed continuously over an entire heating or cooling transient. Low temperature capability would also permit ready calibration and testing with the minimal complications associated with ambient conditions.

Performance at 95°.—Data comparing the response of a membrane stabilized with 8.0 w/o yttria with that of the high temperature Ingold electrode at 95° are shown in Fig. 5. Also included in the figure are corresponding data for the oxygen electrode formed at the platinized platinum wire. Although the response of this membrane electrode is only 92% of the glass, it is still in an acceptable range. The response of the oxy-

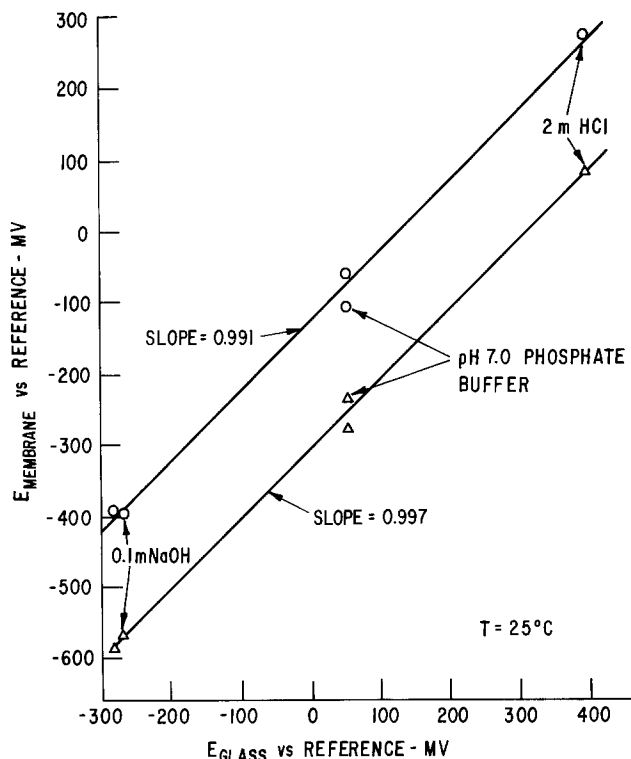


Fig. 4. Response of two sensors relative to that of a glass electrode at 25°C.

gen electrode at this temperature is 88% of the glass. Using the ratio of the two, it is found that in this case the membrane response is 104% of that of the platinum electrode. In two other runs the same membrane electrode (with fresh internal solution) was tested at 95° without the glass electrode in the system. In these cases comparison only with the oxygen electrode was possible and values of 106 and 107% were obtained for the sensor, in reasonable agreement with the above

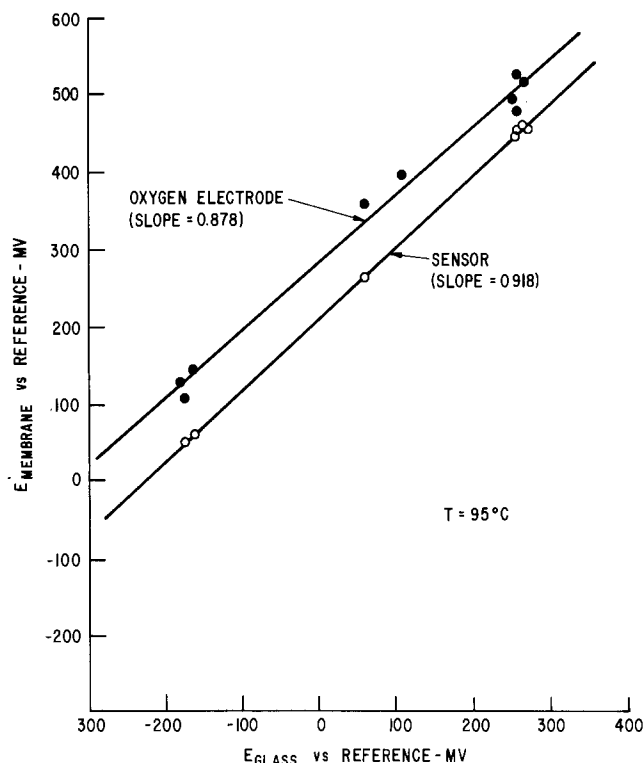


Fig. 5. Responses of a sensor and the oxygen electrode relative to that of a glass electrode at 95°C.

¹ Since the test system was operated about 200 psi above the saturation pressure of water at 285°C no gas phase was present in the autoclave and the concentration of dissolved oxygen in the water remained at the value established during the equilibration with air at ambient conditions.

Table I. Response of yttria stabilized zirconia membranes relative to that of the oxygen electrode at 285°C

Run No.	Sensor No.	Stabilizer conc. (w/o)	Internal solution	Data sets	Period of time (days)	Response (% of O ₂ electrode)
ZRO2-5	Y-7	8.0	0.1m NaCl, pH 7.0	5	2.8	95.1
ZRO2-6	Y-9	8.0	0.1m NaCl, pH 7.0	13	8.8	92.9
ZRO2-7	Y ₂ O ₃ -3	16.9	0.1m NaCl, pH 7.0	12	5.7	96.4
ZRO2-9	Y ₂ O ₃ -4	16.9	0.01m NaCl, pH 7.0	3	0.8	88.8
ZRO2-14	Y-15	8.0	0.01m NaCl, pH 7.0	2	0.2	87.8
ZRO2-16	Y ₂ O ₃ -5	16.9	0.01m NaCl, pH 7.0	8	4.0	96.2
ZRO2-16	Y-15	8.0	0.01m NaCl, pH 7.0	8	4.0	103.9
ZRO2-17	Y-17	8.0	0.01m NaCl, pH 7.0	10	3.7	95.2
ZRO2-18	Y-18	8.0	0.001m HCl/0.009m KCl	2	1st day	93.7
				3	2nd day	93.3
				5	12th day	98.2

Mean response for 8.0% stabilizer = 95.0; $\sigma = 4.6$.
 Mean response for 16.9% stabilizer = 93.8; $\sigma = 4.3$.
 Grand mean = 94.7; $\sigma = 4.4$.

value. (As will be discussed below, two additional sensors with direct junction internals were also examined at 95° and gave linear responses that were 101 and 103% of that of the Ingold glass electrode.) It is thus clear that quite reasonable, and close to theoretical responses can be obtained from the new electrodes at 95°.

Behavior at 285°.—Because primary interest in the new sensors is in their application at higher temperatures, most of the emphasis has been placed on tests at 285°. Data in Fig. 6 show that there is again an excellent linear correlation between the response of the membrane sensor and that of the oxygen electrode over a range of pH established at the extremes by 0.0005m H₂SO₄ and 0.001m NaOH. In this case 16.9 w/o yttria served as the stabilizer and the data in the figure were accumulated over a period of 5.7 days. The response is 96% of that of the oxygen electrode, which at this temperature probably performs close to theoretical; cf. below. For comparison purposes, similar data for eight independent sensors tested at 285° are summarized in Table I. Included is information about the stabilizing agent and internal filling solution as well as the number of data points used in making the comparison and the period over which the data were taken. The overall average response was 94.7% of that of the oxygen electrode with a standard deviation of 4.4%. No significant difference is seen between the sensors stabilized with 8.0 w/o yttria and those with 16.9 w/o.

Additional data showing the parallel dynamic responses of the new membrane type sensor and the oxygen electrode to pH changes are shown in Fig. 7. The first transition was accomplished by introducing a 15 ml aliquot of 0.1m NaOH when the solution in the autoclave was 0.0005m H₂SO₄. The second transition was brought about by back-titrating the base with 0.0005m H₂SO₄.

As further support for the performance of the new sensors, an attempt was made to compare their responses with that predicted from available thermodynamic data. For this purpose, the data of Marshall and Jones (13) for the second dissociation constant of sulfuric acid at elevated temperatures were employed along with those of Sweeton, Mesmer, and Baes (14) for the dissociation constant of water. Activity coefficients for the dilute solutions were estimated from the theoretical predictions of Helgeson and Kirkham (15).

Calculated values for the pH of the 0.0005m H₂SO₄ and 0.001m NaOH solutions at 285°C as well as the theoretical response from interchanging the two are summarized in Table II. It is to be noted that the relatively high pH for the acid (relative to 3.02 at 25°) results from the marked decrease in the second ionization constant of sulfuric acid with increasing temperature— 3.3×10^{-6} at 285° vs. 1.2×10^{-2} at 25°. For the 0.001m NaOH the pH is lower at 285° than at 25° because of the increased dissociation constant of water at the elevated temperature. Compared with these two effects, the influence of activity coefficient corrections

Table II. Theoretical potential change for 0.0005m H₂SO₄ \rightleftharpoons 0.001m NaOH at 285°C

pH of 0.0005m H ₂ SO ₄	3.32
pH of 0.001m NaOH	8.22
Δ pH	4.90
mV/pH unit	110.8
Δ mV	543

on the calculated pH values of these dilute solutions is minor—of the order of 0.03–0.05 units.

Response data for a number of sensors and the oxygen electrode based only on the full transition from acid to base or reverse are summarized in Table III. A definite trend is evident among the data in that the agreement with theory improves in the successive tests which are arranged in chronological order. This suggests in part, at least, that the discrepancies in the earlier runs reflect real variations in the pH of the solutions as a result of corrosion of the test system, most likely by the acidic solutions. During successive runs it would appear that a protective film developed on the walls and the rate of corrosion diminished,

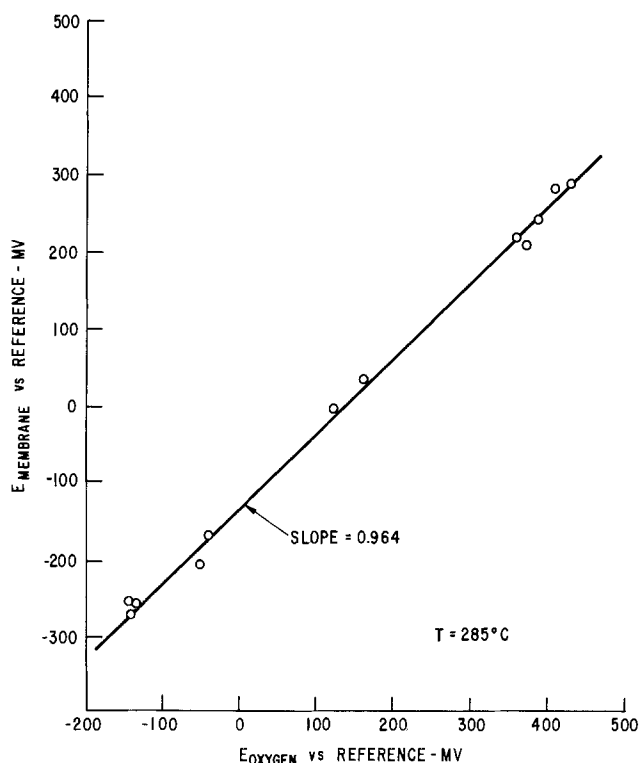


Fig. 6. Response of a sensor relative to that of the oxygen electrode at 285°C.

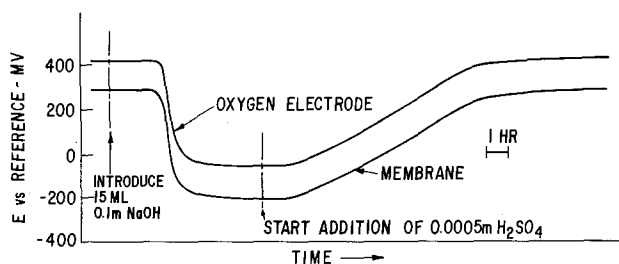


Fig. 7. Response of a sensor and the oxygen electrode to rapid and slow changes in pH at 285°C.

thereby introducing smaller discrepancies which by the time of run ZR02-17 were insignificant. The value for the oxygen electrode in Run ZR02-17 strongly supports the original assumption that the oxygen electrode at elevated temperatures functions well as a pH sensor and was a valid choice as a comparison standard. In comparing the sensors with the oxygen electrode in these tests a mean value of 95.3% was obtained, in good agreement with the data in Table I. The individual differences result from the fact that more data points were averaged for each run of Table I; only data obtained from the full transition between the acid and base were used for Table III.

Sensitivity to Redox Potential of the Environment

Because membrane-type sensors normally have the desirable feature of being insensitive to the redox potential of the solution being monitored, the behavior of the stabilized zirconia sensors was examined as the redox potential of the solution in the autoclave was changed. This was accomplished by changing from an air to a nitrogen purge of the 0.0005m H_2SO_4 solution being fed to the autoclave. The effect is illustrated by the data in Fig. 8 which includes plots of the potentials of the sensor, the oxygen electrode, and the autoclave against the reference electrode.

It is seen that after changing from an air to a nitrogen purge of the incoming 0.0005m H_2SO_4 a slow downward drift in potential was evident for the oxygen electrode and the autoclave. After several hours a more rapid drop occurred for both of these potentials. This is attributed to loss of the passive film on the autoclave with an associated increase in corrosion rate and liberation of hydrogen. The oxygen electrode then clearly showed its sensitivity to this change in the redox environment. The oxygen ion conducting ceramic membrane, however, retained an essentially constant potential throughout the transients. The small increase in potential at the time of the depassivation is believed to have been a response to a real transient change in pH.

It is useful to consider whether this behavior is consistent with the known properties of stabilized zirconia and whether it is likely to be a universal property of oxygen ion conducting ceramic membranes. A key factor to consider in this connection is the domain over which the ceramic functions "solely" as an oxygen ion conductor, i.e., $t_{O^2-} \cong 0.99$, where t_{O^2-} is the trans-

Table III. Measured potential changes for 0.0005m $H_2SO_4 \rightleftharpoons 0.001m NaOH$ at 285°C

Run	Oxygen electrode response		Membrane response		
	ΔmV	% of theor.	ΔmV	% of theor.	% of oxygen
ZR02-5	376	69.2	360	66.3	95.7
ZR02-6	436	80.3	392	72.2	89.9
ZR02-7	490	90.2	492	90.6	100.4
ZR02-9	526	96.9	494	91.0	93.9
ZR02-17	545	100.3	527	97.0	96.7
			Mean	95.3	
			σ	3.8	

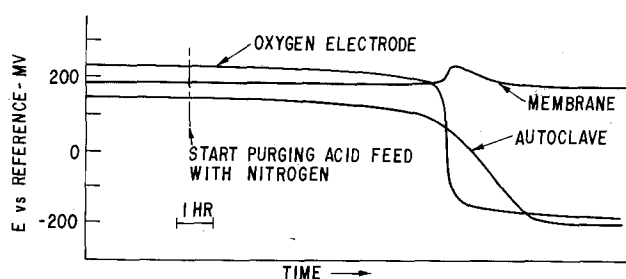


Fig. 8. Behavior of a sensor, the oxygen electrode, and the autoclave as the redox potential of the environment is changed at 285°C.

ference number for the oxygen ion. If electronic or positive hole conduction becomes significant, deleterious shunting can occur and the full signal cannot be developed across the membrane.

Since the same principle applies in the older applications of these ceramics in fuel cells and oxygen sensors, attention has been addressed to the influence of environmental redox conditions on the oxygen ion conductance, particularly by Patterson (16, 17), whose data for calcia stabilized zirconia (CSZ) and yttria-doped thoria (YDT) have been adapted to Fig. 9. In this figure the shaded areas to the right of the boundaries identify the oxygen ion conducting domains for the two ceramics as defined by $t_{O^2-} \cong 0.99$. At any given temperature, environments having oxygen partial pressures (or equivalent redox potentials) in excess of that of the upper boundary cause excessive positive hole conductivity while partial pressures below the lower boundary result in excessive electronic conductivity. Although less data are available for yttria stabilized zirconia, there is some indication (18) that the oxygen ion conducting domain is somewhat wider than that for CSZ.

Also shown on the figure is the domain of oxygen partial pressures and temperatures that is encompassed by the equilibrium established in an aqueous system in the presence of from 1 atm of oxygen to 1 atm of hydrogen. This was calculated from available thermal

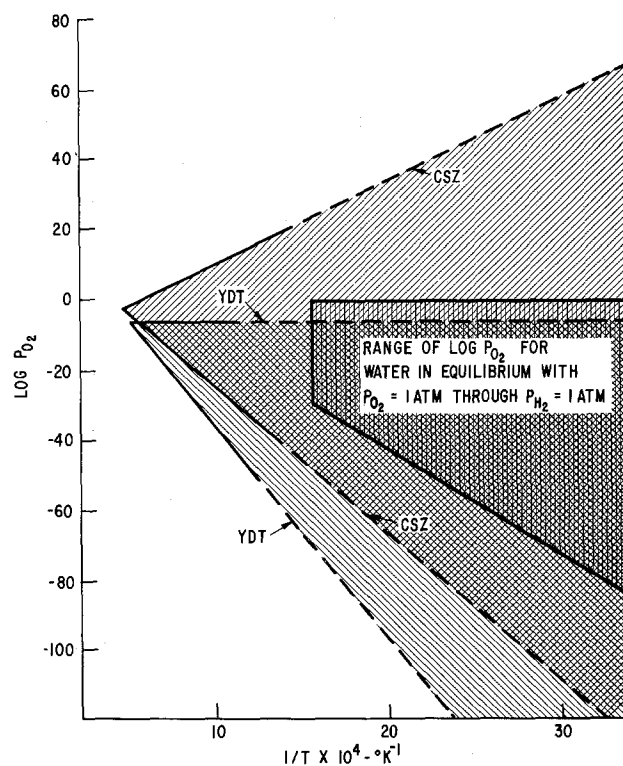


Fig. 9. Domains for oxygen ion conductivity in calcia stabilized zirconia and yttria-doped thoria.

data (19). It is evident that over this entire range of conditions CSZ is a satisfactory oxygen ion conductor. The data for YDT serve as an example of what can occur in other cases. Here it is seen that at oxygen levels greater than 10^{-6} atmosphere the positive hole conductivity exceeds 1% and less satisfactory performance than for CSZ is to be expected under such conditions. On the other hand, in reducing environments the YDT has a considerably larger margin of safety than the CSZ for the operating range postulated. [It has been reported, however, that under some situations YDT suffers further complications in that hydrogen can enter the lattice and introduce proton conduction (20) which would also influence performance.] Limited data for doped cerias (7) suggest that at 1 atm of hydrogen, their oxygen ion conductivity might be somewhat compromised, but that they should function satisfactorily at higher oxygen partial pressures.

The behavior of the cerias is of particular interest in that the oxygen ion conductivity is considerably higher than those of the zirconia or thoria systems and they should be attractive for use at temperatures closer to ambient. This factor has promoted interest in their use in fuel cells (6, 7) and recently their virtue in oxygen sensors operational at lower than usual temperatures has been demonstrated (21).

Drift

Drift arises from two principal sources: (i) changes in the electrolyte concentration within the reference electrodes, and (ii) changes in the internal electrolyte in the sensor especially when the poorly buffered 0.001M HCl-0.009M KCl electrolyte was used.

That a significant drift has been associated with the reference electrodes is illustrated by the data, all obtained with 0.0005M H_2SO_4 in the autoclave, in Fig. 10 from runs ZRO2-5, 7, and 18. The data from runs ZRO2-5 and 7 show the drifts of the oxygen electrode and the sensor to be essentially parallel. In both cases the more concentrated buffered electrolytes, which should have good stability, were used as the internals of the sensors. It is therefore felt that in these cases the drift was largely associated with the reference electrode. In run ZRO2-18 mixed results were obtained. The drift of the oxygen electrode over the first few days was similar to that from the other two runs, and it eventually reached a plateau. This is again believed to be associated with the reference electrode. The much larger drift of the sensor is clearly a result of changes in the very poorly buffered internal electrolyte, 0.001M HCl-0.009M KCl, most probably as a result of reaction of the small amount of acid with the zirconia or, more likely, with impurities in the zirconia. If so, pretreatments of the ceramic with acid or the use of a more concentrated acid as the filling solution, e.g., 0.01M HCl, should reduce the problem.

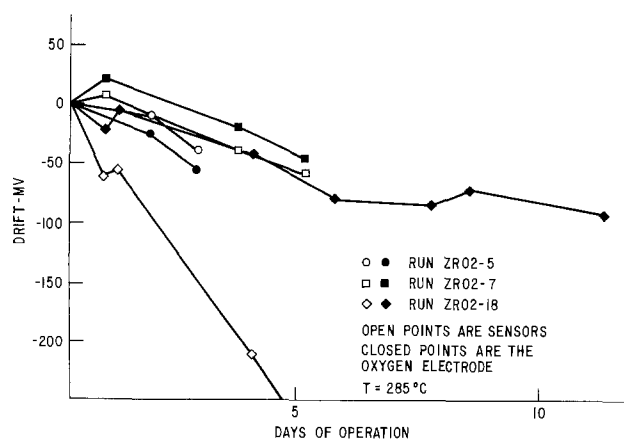
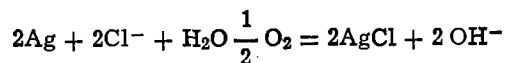


Fig. 10 Drift in potential of sensors and the oxygen electrode relative to 0.01M KCl/AgCl/Ag reference electrode at 285°C.

The drift in the reference electrode is larger than anticipated from previous experience (22). It may reflect differences in operating procedures. For example, we have normally been operating with solutions equilibrated with air (dissolved oxygen concentration about 8 ppm) while in earlier applications in simulated and actual nuclear reactor water (BWR type) the oxygen levels ran about 0.2 ppm. At the higher oxygen levels diffusion through the Teflon walls of the reference or through the diffusion junction itself could be higher and thereby promote chloride ion consumption from the solutions via the reaction



As chloride is removed from solution via such a mechanism the potential of the reference couple would increase thereby causing a decline in the potential of other electrodes measured against it. This type of behavior has been observed with neutral saline solutions in contact with silver/silver chloride electrodes in confined spaces in the past (23). The fact that the potential eventually leveled off in run ZRO2-18 is consistent with such behavior. At 285°C the solubility of silver chloride is much higher than at room temperature (24) and could be instrumental in establishing the plateau at a potential not too far removed from the initial value. It is likely too that some KCl is lost from the reference electrode by diffusion through the porous asbestos or zirconia plug. Detailed analysis of the solutions after use should be helpful in diagnosing the problem, but this has not yet been done.

This drift has not interfered with the work so far because responses to pH can be determined over relatively short periods of time when the influence from drift is minimized. It is clear however, that for the successful exploitation of the new pH sensors a better understanding of drift is required.

Conductivity of Membranes

In order to establish more firmly that the sensors are indeed functioning as true membranes, it was felt necessary to demonstrate that their conductivities are comparable with those normally associated with such ceramics from earlier measurements at high temperatures. This is necessary because under certain limited conditions porous media can give responses resembling those from an intact membrane. [Lev has discussed this type of behavior as encountered with "incompletely sealed" cation sensitive glass microelectrodes (25).] With relatively large pores the behavior is like a liquid junction and only a diffusion potential is established. However, with pores of dimensions small with respect to the thickness of a double layer, exclusion of cations or anions can occur and the theoretical response of a membrane can be achieved. Under such conditions, transport of current through the pores is by ionic migration in an aqueous medium and relatively low activation energies of the order of 5 kcal/mole, should be encountered.

Measurements of cell resistance were made at various temperatures with both 8.0 and 16.9 w/o yttria stabilized tubes using the electrometer and the parallel shunt method outlined above. Plots of the data in terms of the logarithm of the specific conductivity vs. reciprocal temperature are shown in Fig. 11. From a least squares fit of the data, the activation energies and conductivities at 1000°C were calculated. These are listed in Table IV along with data from the literature for zirconia stabilized with 10 mole per cent (16.9 w/o) yttria obtained at higher temperatures in connection with the application of these ceramics in fuel cells and oxygen sensors. [Fewer data are available for comparison with the 8.0 w/o material, but the activation energy has been observed to decrease slightly with decreasing yttria content (26, 27).] Our results are comparable with the earlier data and, in addition, the activation energies are high for conductivities in an

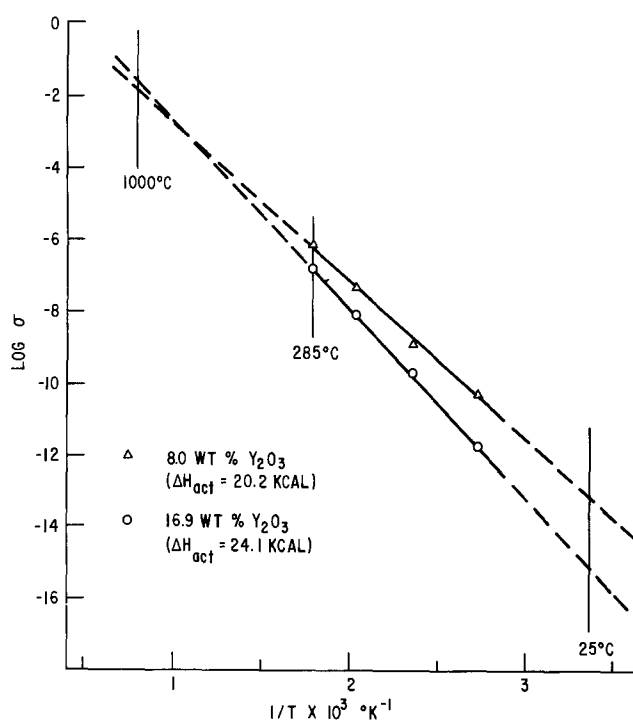


Fig. 11. Conductivities of yttria stabilized zirconias

aqueous phase. Both observations give assurance that the sensors are indeed functioning as true membranes. Helium leak tests also indicated that the sensors were impervious both before and after exposure in the autoclave, but it is difficult to translate this type of observation into behavior upon immersion in aqueous solutions.

One additional comment should be made about the behavior of porous media as sensors. It is improbable that they would show the pronounced specificity for hydrogen ion over the wide range actually observed. While it is possible that cation selectivity would prevail over the full range from 0.1m NaOH to 2m HCl at ambient temperature, it is likely that the response would shift from the hydrogen ion to the sodium ion as the solution became strongly basic. This would manifest itself by an inversion of the slope in the basic media when the sensor response is plotted against that of the glass electrode.

Alternative Internal Junctions

The behavior of the sensor was also examined briefly with dry internal junctions consisting of Cu/Cu₂O and Hg/HgO. The Cu/Cu₂O was employed in several sensors that were operated at both 95° and 285°C, while the single sensor prepared with the mercury couple was run only at 95°C.

Data obtained at 95°C with the Ingold glass electrode serving as the comparison standard are shown in Fig.

Table IV. Ionic conductivities and activation energies for zirconia stabilized with 16.9 w/o yttria*

Conductivity at 1000°C ($\Omega^{-1} \text{cm}^{-1} \times 10^2$)	Activation energy (kcal/mole)	
3.2	24.1	This work
1.5**	20.2**	This work
7.7	19.8	Ref. (4)
4.8	—	Ref. (4)
10.0	20.0	Ref. (4)
12.0	20.0	Ref. (4)
5.8	—	Ref. (4)
10.0	—	Ref. (4)
8.7	—	Ref. (4)
12.0	—	Ref. (4)

* This is equivalent to 10 m/o.

** 8.0 w/o yttria which is equivalent to 4.5 m/o.

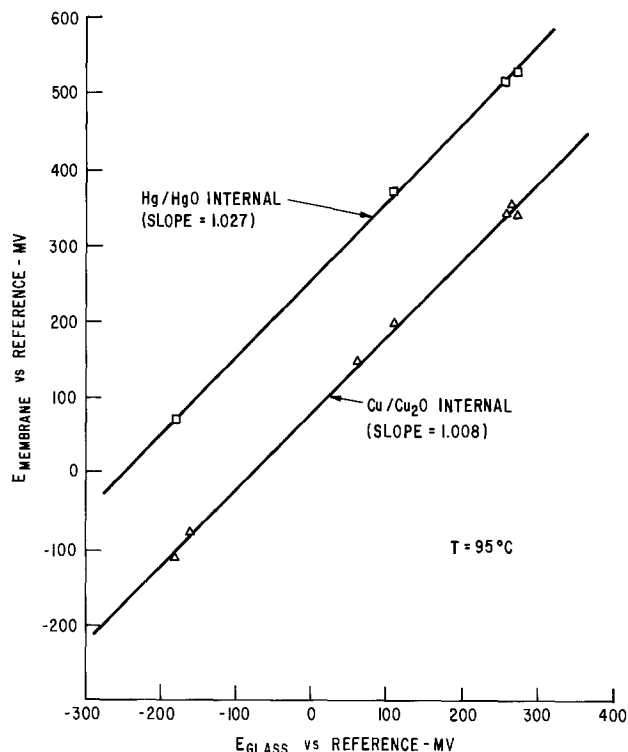


Fig. 12. Response of sensors with Cu/Cu₂O and Hg/HgO internal junctions relative to that of a glass electrode at 95°C.

12. Both internal junctions resulted in sensors having linear responses that were close to those of the glass electrode. An equivalent sensor prepared with an aqueous internal junction and tested in the same group was somewhat lower in response; c.f., Fig. 5.

At 285°C sensors with the Cu/Cu₂O internal junction again gave linear responses against the oxygen electrode as standard. In the two cases tested the responses were 89.8 and 96.1% of that of the oxygen electrode.

These results indicate that either the aqueous or nonaqueous type of internal should be satisfactory on the basis of pH response. A final choice may be dependent upon long term stability and/or the temperature coefficients of the two types of sensors.

Acknowledgments

I thank H. S. Spacil for providing zirconia tubes for use in this work, D. F. Taylor and M. E. Indig for furnishing reference electrodes, and W. H. Stoddard for assistance with the design of the Teflon seal and many of the measurements. I am also indebted to D. F. Taylor, O. H. LeBlanc, and J. N. Groves for helpful discussions. Figures 1 and 8 are reprinted with permission from *Science* (28) (Copyright 1980 by the American Association for the Advancement of Science).

Manuscript submitted Dec. 26, 1979; revised manuscript received April 9, 1980. This was Paper 276 presented at the Los Angeles, California, Meeting of the Society, Oct. 14-19, 1979.

Any discussion of this paper will appear in a Discussion Section to be published in the June 1981 JOURNAL. All discussions for the June 1981 Discussion Section should be submitted by Feb. 1, 1981.

Publication costs of this article were assisted by General Electric Company.

REFERENCES

- V. A. Dolidze, in "Ion Selective Electrodes," E. Pungor, Editor, p. 57, Elsevier Scientific Publishing Co., New York (1978).
- E. D. Linov and P. A. Kryukov, in "High Temperature, High Pressure Electrochemistry in Aqueous Solutions," R. W. Staehle *et al.*, Editors, p. 379, NACE (1976).
- M. LePeintre, *Bull. Soc. Fr. Electr.*, **1**, 584 (1960).
- T. H. Etsell and S. N. Flengas, *Chem. Rev.*, **70**, 339 (1970).

5. R. M. Dell and A. Hooper, in "Solid Electrolytes," P. Hagenmuller and W. Vangool, Editors, p. 291, Academic Press, New York (1978).
6. R. T. Dirstine, R. N. Blumenthal, and T. F. Kuech, *This Journal*, **126**, 264 (1979).
7. H. L. Tuller and A. S. Nowick, *ibid.*, **122**, 255 (1975).
8. J. Hladik, in "Physics of Electrolytes," Vol. 2, J. Hladik, Editor, p. 839, Academic Press, New York (1972).
9. W. L. Worrell, in "Solid Electrolytes," S. Geller, Editor, p. 143, Springer-Verlag, New York (1977).
10. F. E. Rizzo *et al.*, *Trans. Met. Soc. AIME*, **239**, 593 (1967).
11. M. E. Indig and A. R. McIlree, *Corrosion*, **35**, 288 (1979).
12. N. H. Furman, *J. Am. Chem. Soc.*, **44**, 2685 (1922).
13. W. L. Marshall and E. V. Jones, *J. Phys. Chem.*, **70**, 4028 (1966).
14. F. H. Sweeton, R. E. Mesmer, and C. F. Baes, Jr., *J. Solution Chem.*, **3**, 191 (1974).
15. H. C. Helgeson and D. H. Kirkham, *Am. J. Sci.*, **274**, 1199 (1974).
16. J. W. Patterson, in "Physics of Electronic Ceramics," L. L. Hench and D. B. Dove, Editors, p. 131, Marcel Dekker Inc., New York (1971).
17. J. W. Patterson, *This Journal*, **118**, 1033 (1971).
18. L. D. Burke, H. Rickert, and R. Steiner, *Z. Phys. Chem. N.F.*, **74**, 146 (1971).
19. JANEF Thermochemical Tables, NSRDS-NBS 37, Second Edition (1971).
20. D. A. Shores and R. A. Rapp, *This Journal*, **119**, 300 (1972).
21. R. T. Dirstine *et al.*, *Ceram. Bull.*, **58**, 778 (1979).
22. M. E. Indig, Private communication.
23. L. W. Niedrach, O. H. LeBlanc, and W. H. Stoddard, Jr., General Electric TIS Report 77CRD019, (May 1977).
24. W. F. Linke, "Solubilities of Inorganic and Metal Organic Compounds," Vol. 1, p. 60, 4th ed., D. Van Nostrand Co., Inc., New York (1958).
25. A. A. Lev, in "Glass Microelectrodes," M. Lavallée, O. F. Schanne, and N. C. Hebert, Editors, p. 76, John Wiley & Sons, Inc., New York (1969).
26. D. W. Strickler and W. G. Carlson, *J. Am. Ceram. Soc.*, **48**, 286 (1965).
27. J. M. Dixon *et al.*, *This Journal*, **110**, 276 (1963).
28. L. W. Niedrach, *Science*, **207**, 1200 (1980).

Effect of Molybdenum on the Anodic Behavior of Amorphous Fe-Cr-Mo-B Alloys in Hydrochloric Acid

K. Asami, M. Naka, K. Hashimoto, and T. Masumoto

The Research Institute for Iron, Steel, and Other Metals, Tohoku University, Sendai 980, Japan

ABSTRACT

The addition of a small amount of molybdenum to amorphous Fe-Cr-B alloys improves the corrosion resistance in hydrochloric acid. In particular, amorphous Fe-25Cr-20B-*x*Mo alloys containing 5 atomic percent or more molybdenum passivate spontaneously even in 6*N* HCl, showing no pitting by anodic polarization. However, an excess addition of molybdenum lowers the corrosion potential and raises the anodic current density in the passive region. This dual function of molybdenum was investigated with XPS and electrochemical methods. In the active region, an increase in the molybdenum content of the alloys decreases the anodic current density by the formation of a surface film containing large amounts of chromium and some molybdenum. The addition of molybdenum assists the formation of the passive hydrated chromium oxyhydroxide film. However, a passive film of molybdenum oxyhydroxide is unstable in comparison with the passive hydrated chromium oxyhydroxide film even at lower potentials in the passive region, and molybdenum suffers transpassive dissolution at higher potentials in the passive region. An excess of molybdenum results in a passive film whose content of molybdenum in an unstable valence state is high. Consequently, the addition of molybdenum is significantly effective in increasing the corrosion resistance, particularly in aggressive hydrochloric acid, but the lower the molybdenum content of the passive film the better is the protective quality of the film.

It is well known that addition of molybdenum to stainless steels increases their corrosion resistance toward pitting in chloride solutions, although the addition of molybdenum to iron or nickel is not effective in improving their corrosion resistance in hydrochloric acid (1). In particular, the combined addition of chromium and molybdenum to steels greatly improves their corrosion resistance in acidic chloride solutions, and hence molybdenum interacts synergistically with chromium (2).

It has been considered that molybdenum in the passive film reinforces its protective quality. Mahla and Nielsen (3) stripped a passive film from the surface of Type 317 stainless steel passivated in 5% HNO₃ + 0.5% K₂Cr₂O₇ at 60°C and found an enrichment of molybdenum in the passive film. Rhodin (4) confirmed the enrichment of both molybdenum and silicon in the passive film on molybdenum-bearing steels, which also contained a small amount of silicon.

Key words: corrosion resistance, passivity, passive film, XPS, surface analysis.

Nielsen and Rhodin (5) have assumed that the chemistry of a gel-like heteropoly acid complex controls both the mechanism of film formation and subsequent behavior of the steels on exposure to various corrosion environments.

Recent development of new techniques for surface analysis, such as AES and XPS, has enabled the determination of the constituents of a passive film without stripping it from the alloy substrate. Lumsden and Staehle (6), in reporting an AES study of a passive film formed on Type 316 stainless steel in a neutral chloride solution, stated that an enrichment of chromium occurs to some extent in the film, but that molybdenum and silicon are not concentrated in the film. Yaniv *et al.* (7) studied the composition of passive films formed on molybdenum-bearing ferritic stainless steels in acidic and alkaline solutions and found no enrichment of molybdenum.

XPS studies of passive films on ferritic stainless steels with and without molybdenum revealed that the passive films formed in 1*N* HCl consist mainly

of hydrated chromium oxyhydroxide $\text{CrO}_x(\text{OH})_{3-2x} \cdot n\text{H}_2\text{O}$ (8, 9) similar to the passive films formed on crystalline binary Fe-Cr alloys (10) and ferritic stainless steels (11) in 1N H_2SO_4 and on Types 304 and 316 stainless steels in 30% HNO_3 (12). Molybdenum has been found in the passive films formed on both austenitic (12) and ferritic (8, 9, 11) stainless steels, but its content is very low, and pitting does not lead to any substantial change in the average composition of the films (9).

On the other hand, it is known that rapidly quenched amorphous alloys containing a certain amount of chromium have extremely high corrosion resistance (13-15). Addition of molybdenum also increases the corrosion resistance of these chromium-bearing amorphous alloys (16, 17). Furthermore, recent studies revealed that the addition of molybdenum to amorphous Fe-P-C (18) and Fe-C (19) alloys without chromium also increases their corrosion resistance and leads to anodic passivation in 1N HCl in contrast to crystalline binary Fe-Mo alloys.

The amorphous alloys usually contain a large amount of metalloid elements such as boron, carbon, silicon, and phosphorus. These elements play an important role in the corrosion resistance of amorphous alloys (20). One of the most important factors for the extremely high corrosion resistance of rapidly quenched amorphous alloys is their chemically homogeneous single phase, which is free of defects formed by solid-state diffusion and associated with the crystalline state.

Passive films formed on chromium-bearing amorphous alloys are composed mostly of hydrated chromium oxyhydroxide, which is the major constituent of stable passive films on ordinary stainless steels. On the other hand, amorphous Fe-Mo-metalloid alloys passivate by the formation of hydrated iron oxyhydroxide (23, 24). In the active region, the latter alloys, however, form surface films in which molybdenum is highly enriched (23, 24). The significant enrichment of molybdenum in a surface film formed in the active region has also been found for crystalline ferritic stainless steels containing molybdenum (8).

These results suggest that the role of chromium and molybdenum in increasing the corrosion resistance of amorphous iron-metalloid alloys is not essentially different from that in crystalline stainless steels. It is, therefore, convenient to use the amorphous alloys for the study of the effect of molybdenum on the corrosion resistance of a single-phase solid solution containing iron and chromium.

Recently we (17) investigated the effect of chromium and molybdenum additions on the corrosion behavior of amorphous Fe-20B, Co-20B, and Ni-20B alloys in 1N HCl and found the dual function of molybdenum: The addition of small amounts of molybdenum to Fe-20Cr-20B and Co-20Cr-20B alloys led to spontaneous passivation, but excess addition of molybdenum raised the passive current density and lowered the open-circuit potential for spontaneous passivation.

The work reported herein aims to clarify the origin of the dual function of molybdenum in the corrosion behavior of amorphous Fe-Cr-Mo-B alloys in 1N and 6N HCl. XPS was used to determine the composition and thickness of the surface film formed on the alloys as a function of their molybdenum content.

Experimental

Alloy ingots were prepared by melting commercial metals under an argon atmosphere. Amorphous Fe-Cr-B alloys with and without molybdenum were prepared as a shape 1-2 mm in width and 10-40 μm in thickness by the rotating wheel method, which consists of impinging a jet of molten alloy onto the outer surface of a rapidly rotating wheel. The nominal compositions of the alloys are shown in Table I. Prior to

Table I. Nominal compositions of amorphous alloys

Alloy	Composition (a/o)			
	Fe	Cr	B	Mo
Fe-20 Cr-20 B-xMo	60	20	20	0
	57	20	20	3
	55	20	20	5
	50	20	20	10
Fe-25Cr-20 B-xMo	55	25	20	0
	52	25	20	3
	50	25	20	5
	45	25	20	10

electrochemical measurements, the alloys were polished mechanically in cyclohexane with silicon carbide paper up to No. 1500. Electrolytes used were 1N and 6N HCl, which were prepared from reagent grade chemical and deionized water. They were exposed to air. Polarization curves of Fe-25Cr-20B-xMo alloys ($x = 0, 3, 5,$ and 10) were measured potentiodynamically with a potential sweep rate of 2.37×10^{-3} V $\cdot\text{sec}^{-1}$ in 6N HCl. Potentiostatic polarization curves were also measured for the same alloys in 6N HCl after polarization for 3600 sec at various constant potentials. A new specimen was used for each potentiostatic measurement.

The stability of the surface film formed on the amorphous Fe-25Cr-20B-xMo alloys was evaluated by the measurement of potentiostatic current density-time curves in 6N HCl. The passivation behavior of the amorphous Fe-20Cr-20B-xMo alloys ($x = 0, 3, 5,$ and 10) was also examined by the measurement of the change in current density immediately after mechanical abrasion of the specimen surface during anodic polarization at various constant potentials in the passive region in 1N HCl. The abrasion of the alloy surface was carried out at a constant force with a bench drilling machine in which was installed an abrasive rod made of resin solidified with No. 2000 silicon carbide powder.

After polarization at various constant potentials, x-ray photoelectron spectra from the alloy surface were measured by means of AEI ES200 electron spectrometer with Mg $K\alpha$ excitation. Polarization was carried out for 3600 sec except for the Fe-25Cr-20B alloy in the active region. This alloy dissolved rapidly in the active region and hence this polarization was carried out for 1800 sec or less. The composition and thickness of the surface film were quantitatively determined from the integrated intensities of the spectral peaks. The detailed procedure of energy calibration and quantitative determination have been reported previously (25-27). The photoionization cross sections used have been summarized elsewhere (28). The measured spectrum of Mo 3d electrons was separated into spectra originating from Mo(VI), Mo(V); Mo(IV), and Mo(metallic) components in a manner similar to the separation method of the Fe 2p $_{3/2}$ spectrum into Fe(III), Fe(II), and Fe(metallic) components (29). The binding energies of the Mo 3d electrons in various states were taken as 235.54, 234.40, 229.30, and 228.05 eV for Mo(VI) 3d $_{3/2}$, Mo(V) 3d $_{3/2}$, Mo(IV) 3d $_{5/2}$, and Mo(metallic) 3d $_{5/2}$ electrons, respectively.

Results

Polarization curves.—Potentiodynamic polarization curves of amorphous Fe-25Cr-20B-xMo ($x = 0, 3, 5,$ and 10) alloys measured in 6N HCl are shown in Fig. 1. The most striking characteristic is that these alloys do not suffer pitting corrosion by anodic polarization even in 6N HCl. Spontaneous passivation occurs even in this high concentration of hydrochloric acid when the molybdenum content of the alloy is 5 atomic percent (a/o) or more. An increase in the molybdenum content up to 5 a/o ennobles the corrosion potential, but further increase is not effective. A significant increase in the current density in the passive region is

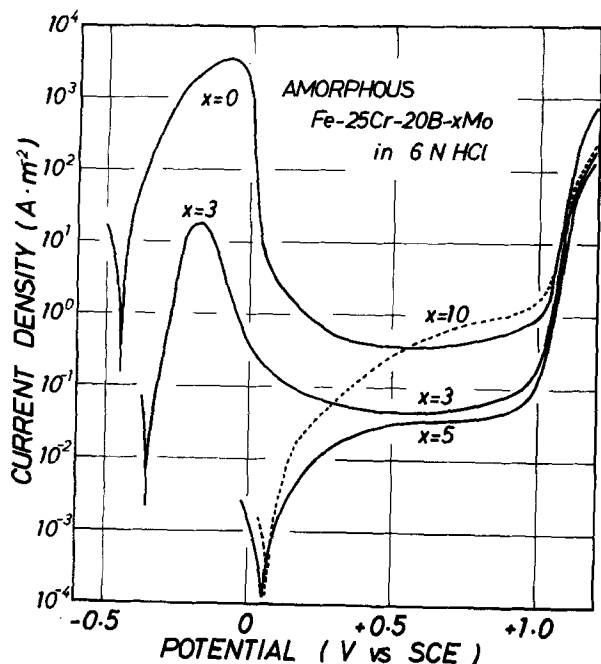


Fig. 1. Potentiodynamic polarization curves of amorphous Fe-25Cr-20B-xMo alloys in 6N HCl. The current density increase at negative potentials on each polarization curve corresponds to the cathodic current density.

observed by the addition of 10 a/o molybdenum, suggesting a detrimental function due to excess molybdenum. All the alloys show a transpassive region above 1.0V.

Potentiostatic polarization curves of the same alloys measured in 6N HCl are shown in Fig. 2. The potentiostatic polarization curve of the amorphous Fe-25Cr-20B alloy without molybdenum showed a high dissolution current similar to its potentiodynamic polarization curve and is not shown in the figure. The upper side of the figure corresponds to an anodic current and lower side to a cathodic current. Transpassive dissolution occurs above 1.0V for all the alloys.

The initial open-circuit potential of the 5Mo alloy in 6N HCl is between 0 and 0.5V. However, when the alloy is polarized at potentials lower than the initial open-circuit potential, an anodic current corresponding to the active state is observed as shown in Fig. 2. This is due to degradation of the air-formed film responsible for the initial spontaneous passivation. The current for this alloy is negative at potentials higher than about -0.2V and becomes positive at about 0.7V. In contrast, the 10 Mo alloy always shows a negative current by cathodic polarization, but a slight anodic polarization gives rise to a positive current at about 0.2V, which is quite low in the passive region, and further anodic polarization significantly raises the anodic current density.

The anodic current density in the passive region measured by potentiostatic polarization is generally lower than that obtained by potentiodynamic polarization. However, the potentiostatic anodic current density of the 3Mo alloy in the potential region between 0.5 and 1.0V is considerably higher than the potentiodynamic anodic current density. In addition, the current density of the 3Mo alloy measured at 0-0.5V was not reproducible, indicating a poor protective quality of the passive film on this alloy.

The stability of the surface film.—To compare the stability of the surface films on these amorphous alloys in 6N HCl, the change in current density with time was measured during potentiostatic polarization at various potentials. The results are shown in Fig. 3-5. Figure 3 shows the current density-time curves for the 3Mo alloy. In the active (-0.05, -0.15, and

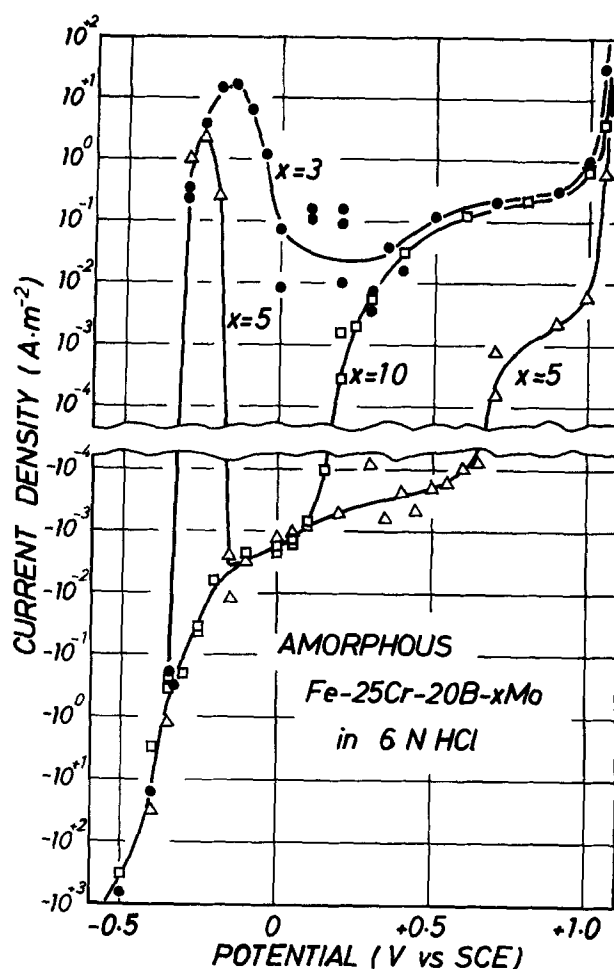


Fig. 2. Potentiostatic polarization curves of amorphous Fe-25Cr-20B-xMo alloys measured after polarization for 3600 sec at constant potentials in 6N HCl.

-0.30V) and transpassive (1.05V) regions, the current density is high and does not change appreciably with time. At a lower potential (0.3V) in the passive region, the current density decreases significantly and is often unstable, corresponding to the low reproducibility of the potentiostatic polarization curves for the 3Mo alloy in the vicinity of this potential as shown in Fig. 2.

The current density-time curves for the 5Mo alloy are shown in Fig. 4. The current density in the transpassive region (1.05V) does not decrease with time as in the case of the 3Mo alloy. In the passive region (0.4-0.9), prolonged polarization significantly lowers the current density. In particular, at lower potentials in the passive region (0.4, 0.55, and 0.65V) the current density sharply decreases with time and it finally becomes negative (cathodic). When the potential is lower in the passive region, the current turns negative in less time. The appearance of a negative current by potentiostatic polarization is attributable to the formation of a stable passive film. In contrast, the current in the potential region from -0.30 to -0.15V is initially negative but suddenly turns to a high positive value, suggesting breakdown of air-formed film in this potential region. This is responsible for the appearance of the active state in the potentiostatic polarization curve of the 5Mo alloy.

The change in the current density with time for the 10Mo alloy is shown in Fig. 5. The current density in the transpassive region (1.05V) is almost constant, similar to the 3Mo and 5Mo alloys. At lower potentials in the passive region, the current turns negative after a certain time, similar to the 5Mo alloy. At a higher potential in the passive region (0.8V), however, the initially high current density is maintained and is not

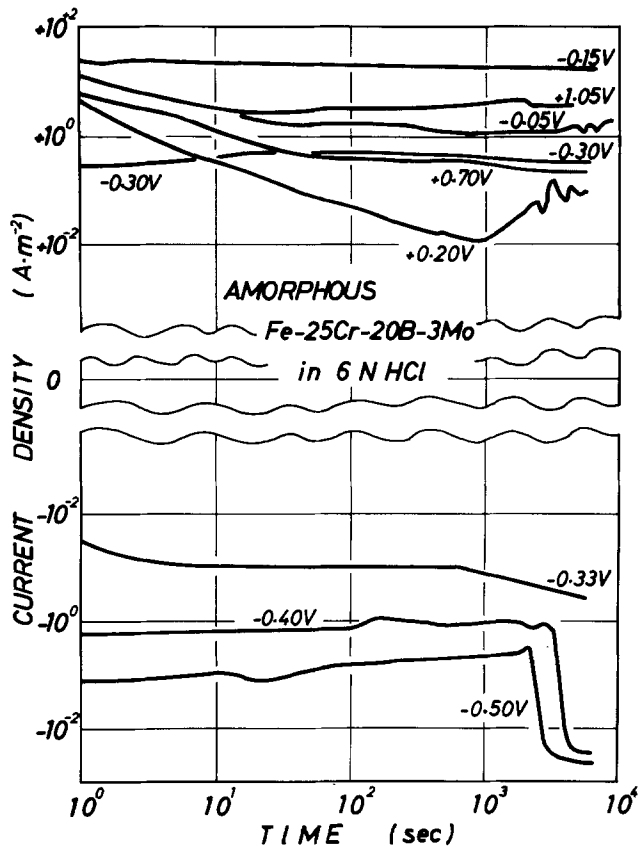


Fig. 3. Current density-time curves of amorphous Fe-25Cr-20B-3Mo alloy measured by potentiostatic polarization in 6N HCl. Polarization potentials are relative to the saturated calomel electrode.

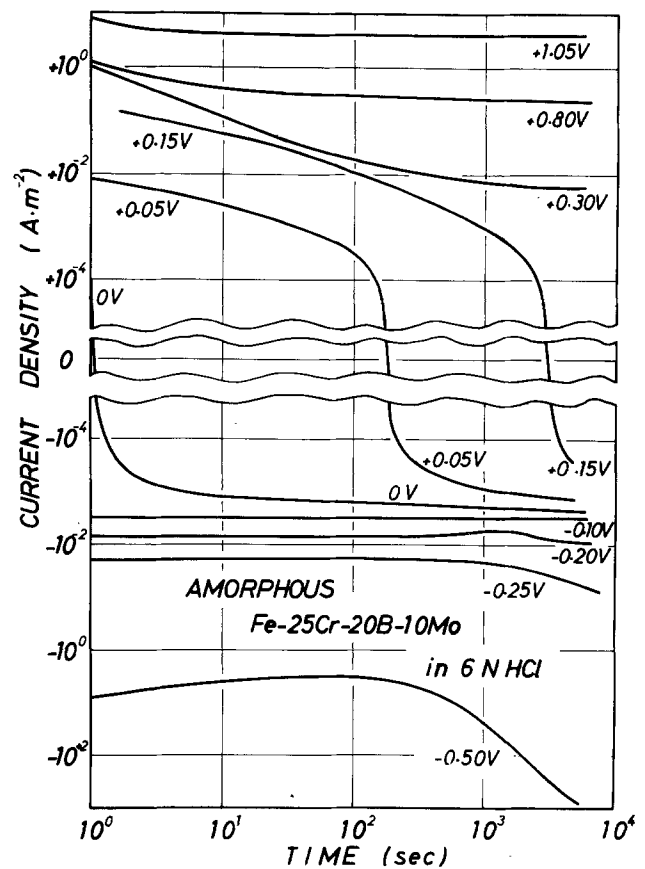


Fig. 5. Current density-time curves of amorphous Fe-25Cr-20B-10Mo alloy measured by potentiostatic polarization in 6N HCl. Polarization potentials are relative to the saturated calomel electrode.

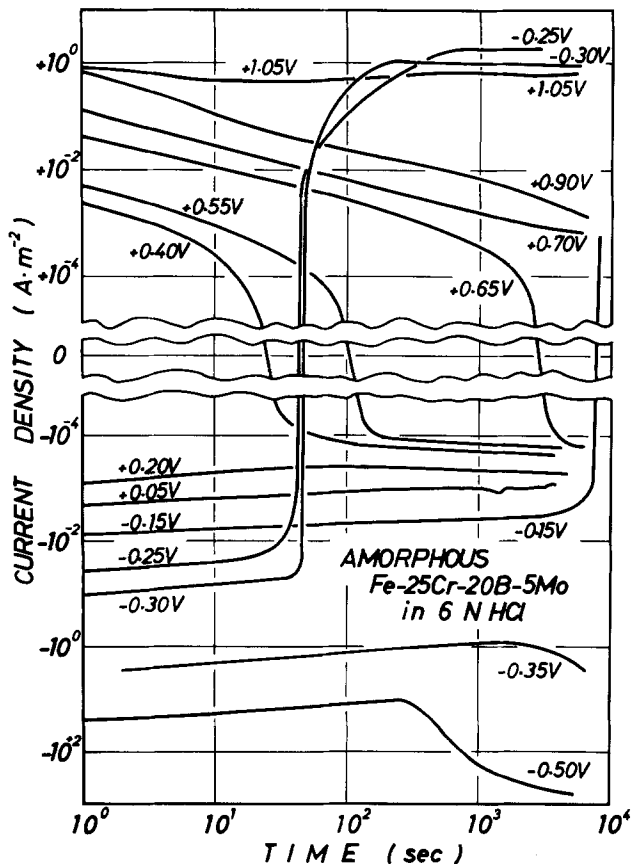


Fig. 4. Current density-time curves of amorphous Fe-25Cr-20B-5Mo alloy measured by potentiostatic polarization in 6N HCl. Polarization potentials are relative to the saturated calomel electrode.

lowered by prolonged polarization, in contrast to the 5Mo alloy. Another difference between these two alloys is that the active current is not observed in the potential region in which the 3Mo and 5Mo alloys exhibit the active state, suggesting a high stability of the surface film on the 10Mo alloy in this potential region.

Passivation behavior.—To compare the passivation behavior, the current decay curves were measured immediately after mechanical abrasion during potentiostatic polarization in 1N HCl. It was difficult to maintain a constant surface area for the 0Mo and 3Mo alloy specimens in 6N HCl due to rapid dissolution immediately after mechanical abrasion. Also, all the amorphous Fe-25Cr-20B- x Mo alloys passivate spontaneously in 1N HCl, and hence the difference in passivation behavior of some of the alloys was not clear in 1N HCl. Thus, current decay measurements were carried out in 1N HCl by using amorphous Fe-20Cr-20B- x Mo alloy specimens.

The current decay curves measured at 0.1 and 0.5V are shown in Fig. 6 and 7, respectively. After mechanical abrasion during polarization at 0.1V the Fe-20Cr-20B alloy without molybdenum did not passivate, showing a constant high current density, and its current-time curve is not shown. From the beginning, the difference between the alloys with and without molybdenum is clear; the current density of the alloys with molybdenum drops rapidly, while the 0Mo alloy shows a slow decay and high steady current density. An increase in the molybdenum content facilitates the current decay at the low potential in the passive region (Fig. 6) and results in a low steady-state passive current density.

At the high potential in the passive region (Fig. 7), the decrease in current density is fastest for the 10Mo alloy in the early stage (<0.5 sec). However, the current decay slows down and the 10Mo alloy exhibits a

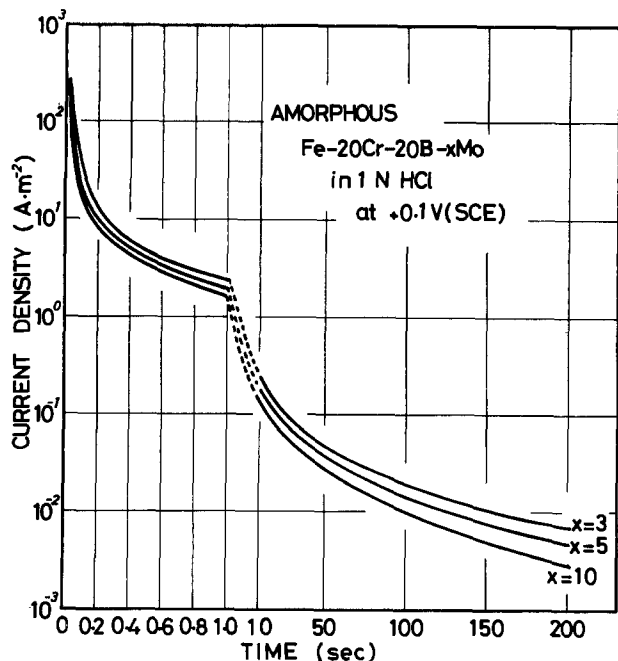


Fig. 6. Current decay curves of amorphous Fe-20Cr-20B-xMo alloys measured immediately after mechanical abrasion during potentiostatic polarization at 0.1V (SCE) in 1N HCl.

higher steady current density in comparison with the 3Mo and 5Mo alloys. This fact again indicates the dual function of molybdenum; the addition of molybdenum effectively suppresses active dissolution prior to passive film formation, but an excess of molybdenum decreases the protective quality of the passive film.

Analysis of film composition by XPS.—To determine a correlation between the surface film composition and the protective quality of the film, XPS analyses of the surface film were carried out for amorphous Fe-25Cr-20B-xMo alloys polarized at various constant potentials in 6N HCl. The Fe $2p_{3/2}$ and Cr $2p_{3/2}$ spectra consisted of two peaks corresponding to the oxidized state in the surface film and the metallic state in the underlying alloy. The Fe $2p_{3/2}$ spectrum for the oxidized state was further composed of spectra for ferrous and ferric

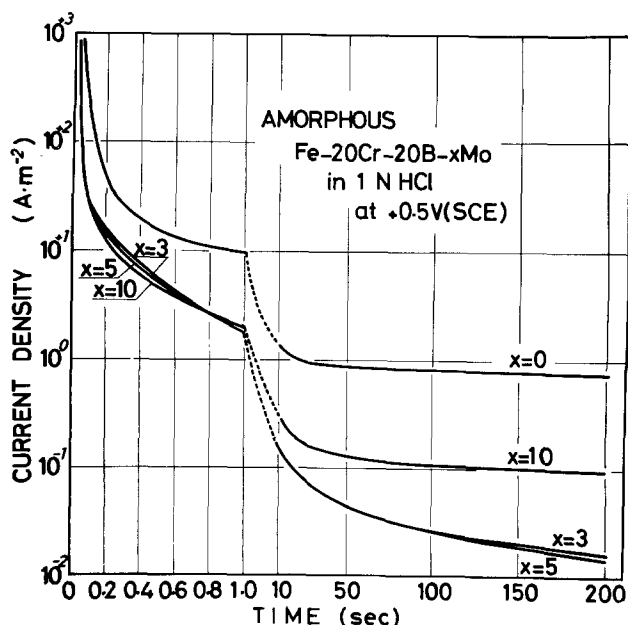


Fig. 7. Current decay curves of amorphous Fe-20Cr-20B-xMo alloys measured immediately after mechanical abrasion during potentiostatic polarization at 0.5V (SCE) in 1N HCl.

states (10, 26, 29). Chromium in the surface film was in the trivalent state (26). The Mo 3d spectrum showed the peaks corresponding to hexavalent, tetravalent, and metallic molybdenum (30). Oxidized molybdenum further contained pentavalent molybdenum (30), although it did not give clear peaks in the measured Mo 3d spectra. The B 1s spectrum showed two peaks which were assigned to boron in borate in the surface film (about 192 eV) and in the underlying alloy (about 187.7 eV) (20). The O 1s spectrum exhibited a broad peak in which the spectra for oxygen in borate and in metal-O-metal, metal-OH and metal-OH₂ bonds were superimposed (10, 20, 26). Chloride ion, which gave the Cl 2p signal at about 198.9 eV, was also found in small amounts in the surface film.

The change in the cationic fraction of chromium in the surface film with polarization potential is shown in Fig. 8. A remarkable enrichment of chromium is found in the surface films formed on the 5Mo and 10Mo alloys even at lower potentials in the active and cathodic current regions. The difference in the cationic fraction of chromium between the surface films on these two alloys is almost insignificant, despite the fact that the signs of the current are different in the active region. The 0Mo and 3Mo alloys show some chromium enrichment especially in the passive region. The chromium content of the passive film increases with an increase in the molybdenum content of the alloy in this aggressive hydrochloric acid; it is lowest for the 0Mo alloy and highest for the 10Mo alloy, though the difference between the 10Mo and 5Mo alloys is negligibly small.

Figure 9, whose ordinate is expressed on a logarithmic scale, shows the change in the fraction of iron ions in the surface film with the polarization potential. It is clear that the iron content of the surface film is remarkably low on the 5Mo and 10Mo alloys and decreases in the passive region with an increase in the molybdenum content of the alloy.

The change in the molybdenum content of the surface film is shown in Fig. 10. The ordinate is again on a logarithmic scale. The molybdenum content of the surface film on all the alloys shows a maximum in the active region even for the 10Mo alloy which exhibits only a negative current at potentials lower than 0.2V. This maximum is in the reverse order of the molybdenum content of the alloy. The present authors (8, 23, 24) have previously reported that the active dissolution of molybdenum-bearing alloys gives rise to the formation of molybdenum-enriched corrosion product films on the alloys, and the faster the active dissolution the higher is the concentration of molybdenum in the film. It can, therefore, be said that all the alloys dissolve actively in the active region, and hence the negative current observed for the 10Mo alloy just indicates that the anodic current is less than the cathodic

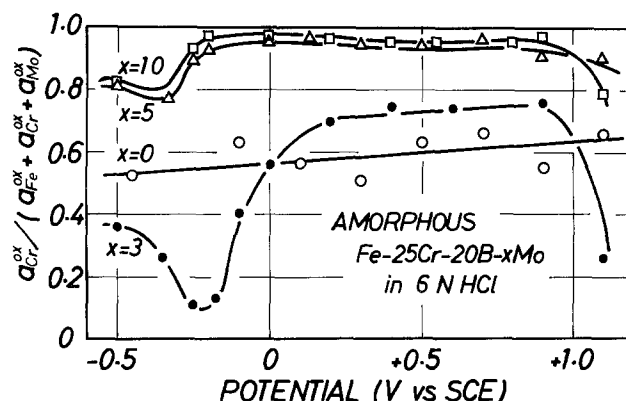


Fig. 8. Change in cationic fraction of chromium in the surface film formed on amorphous Fe-25Cr-20B-xMo alloys by potentiostatic polarization for 3600 sec in 6N HCl as a function of potential.

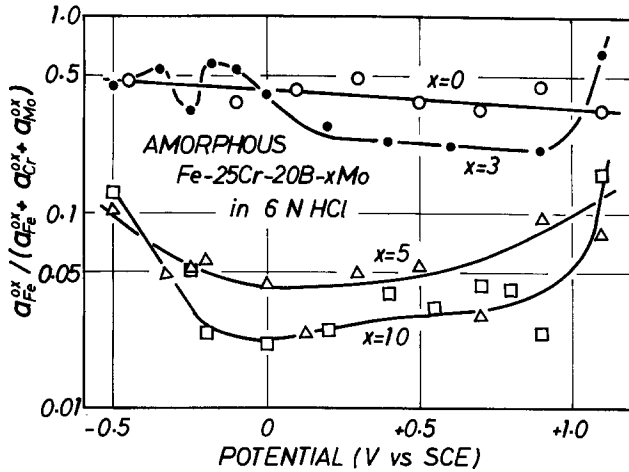


Fig. 9. Change in cationic fraction of iron in the surface film formed on amorphous Fe-25Cr-20B-xMo alloys by potentiostatic polarization for 3600 sec in 6N HCl as a function of potential.

current in this potential region. Similarly, a high molybdenum content in the surface film results from transpassive dissolution at 1.1V.

It can clearly be seen that molybdenum is deficient in the passive films formed on the 5Mo and 10Mo alloys. The molybdenum content shows a maximum at about 0.4V. Above this potential, the anodic current density of the molybdenum-bearing alloys tends to increase. The content and valence of chromium in the passive film are almost independent of the polarization potential showing no appreciable change in the vicinity of 0.4V. In contrast, the mean valence of molybdenum in the passive film clearly changes with the polarization potential as shown in Fig. 11, which gives the ratio of tetravalent or hexavalent molybdenum to total molybdenum in the film formed on the 3Mo alloy. Some pentavalent molybdenum species were also contained in the film but its ratio is not shown in the figure. The content of hexavalent molybdenum is higher than tetravalent molybdenum in the films formed in the active region and at potentials higher than 0.5V in the passive region. The formation of hexavalent molyb-

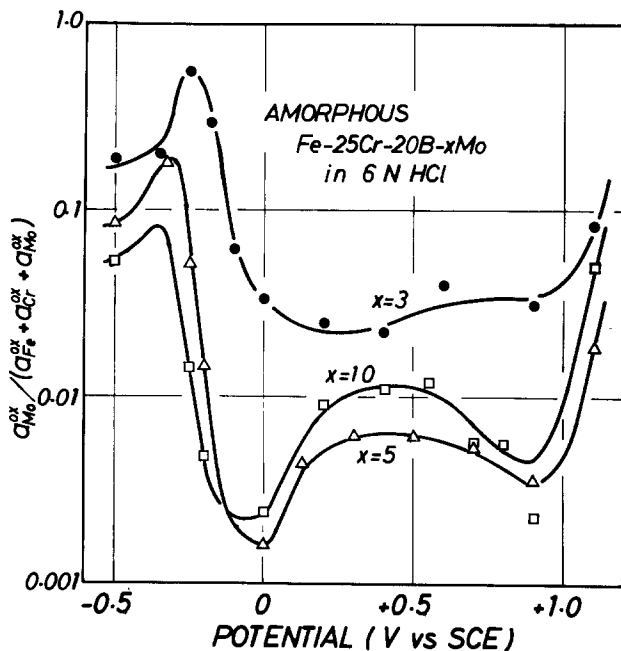


Fig. 10. Change in cationic fraction of molybdenum in the surface film formed on amorphous Fe-25Cr-20B-xMo alloys by potentiostatic polarization for 3600 sec in 6N HCl as a function of polarization potential.

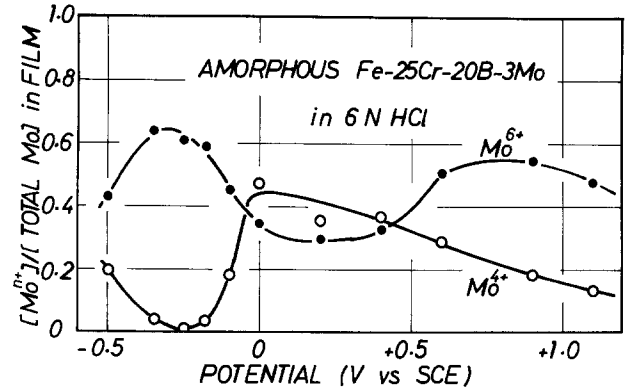


Fig. 11. Ratio of tetravalent or hexavalent molybdenum to total molybdenum in the surface film formed on amorphous Fe-25Cr-20B-3Mo alloy by potentiostatic polarization for 3600 sec in 6N HCl.

dium is thermodynamically impossible at potentials in the active region. Hence, the hexavalent molybdenum species found in the film formed in the active region appears to result from oxidation of tetravalent molybdenum during the transfer from the electrolyte to the XPS apparatus. This is a result of the poor protective quality of the film formed in the active region.

The change in the film thickness with polarization potential is shown in Fig. 12. All the molybdenum-bearing alloys form very thick surface films in the active region, including the 10Mo alloy which shows the negative current. In contrast, film thickening does not occur on the 0Mo alloy even at -0.1V where maximum anodic current density was observed. The passive film on the alloys with molybdenum tends to thicken with an increase in the molybdenum content. In particular, a thick passive film is formed on the 10Mo alloy at higher potentials in the passive region where hexavalent molybdenum species are accumulated in the surface film as shown in Fig. 11.

Discussion

It is most striking that, when amorphous Fe-25Cr-20B-xMo alloys contain 5 a/o or more molybdenum, spontaneous passivation occurs in 6N HCl with no pitting corrosion. This contrasts with the fact that any crystalline iron- or nickel-base alloy is not able to passivate spontaneously even in 1N HCl. The extremely high corrosion resistance of these amorphous

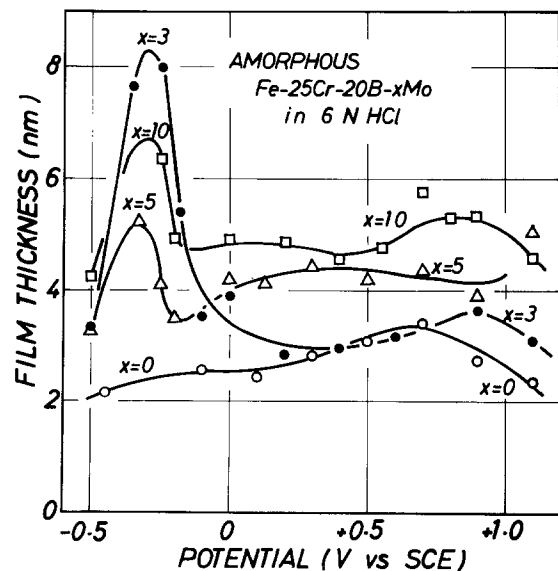


Fig. 12. Change in thickness of the surface film formed on amorphous Fe-25Cr-20B-xMo alloys by potentiostatic polarization for 3600 sec in 6N HCl as a function of polarization potential.

alloys is attributable to their chemically homogeneous defect-free, single-phase nature and the rapid passivation they exhibit (20, 31), as well as the beneficial effect of molybdenum. In this connection, these amorphous alloys contain boron but not phosphorus. The present authors (16, 20, 22, 32) have shown that phosphorus is the most effective metalloid in improving the corrosion resistance of amorphous alloys. Hence, it can be assumed that, if the boron in these amorphous alloys is substituted with phosphorus, spontaneous passivation in concentrated hydrochloric acid may occur at lower chromium and molybdenum contents.

Beneficial effect of molybdenum.—The anodic current density in the active region decreases with an increase in the alloy molybdenum content. In addition, a thick corrosion product film containing molybdenum ions is formed by polarization in the active region. The present authors (8, 23, 24) have reported that active dissolution of both amorphous and crystalline alloys containing molybdenum in 1N HCl gives rise to the formation of a molybdenum-enriched film, which suppresses active dissolution. Because molybdenum is passive in the active region of iron-base alloys, the faster the active dissolution the higher is the concentration of molybdenum in the film. This is reconfirmed in the present work.

In addition, it has been shown that a decrease in anodic current density in the active region in an aggressive concentrated hydrochloric acid is caused by the formation of surface films containing large amounts of chromium and some molybdenum. In the absence of molybdenum in the alloy, the maximum current density in the active region is of the order of $3000 \text{ A}\cdot\text{m}^{-2}$, even when some chromium enrichment occurs in the thin surface film. When the alloy contains 3 a/o molybdenum, a thick surface film whose molybdenum content is 60% of cations can grow; hence the maximum current density for active dissolution decreases to $15 \text{ A}\cdot\text{m}^{-2}$, although this current density is still high because the chromium content of the surface film is very low. When the molybdenum content of the alloy is raised to 5 a/o, the surface film, consisting of 80% chromium and 20% molybdenum as cations, suppresses the maximum current density for active dissolution to $2.5 \text{ A}\cdot\text{m}^{-2}$.

We have interpreted (8, 23, 24, 33) the role of molybdenum in the passivation of amorphous and crystalline iron-base alloys as follows: Active dissolution of alloy, which is necessary to accumulate beneficial metallic ions and/or OH^- ions at the alloy-solution interface prior to passive film formation in aggressive solutions, leads to the formation of a molybdenum-enriched corrosion product film which slows down the dissolution rate of passivating species through the film. This fact accelerates the accumulation of the passivating species under the film and hence facilitates the formation of a passive hydrated chromium or iron oxyhydroxide film between the corrosion product film and the underlying alloy. The corrosion product film is formed as a result of active dissolution and is not stable at high potentials in the passive region. Accordingly, when the condition for the rapid supply of molybdenum to form the corrosion product film fails by lowering the dissolution rate through passive film formation, the corrosion product film dissolves in the solution. Therefore, the passive film does not contain an appreciable amount of molybdenum. When a part of the passive film is chemically or mechanically broken, molybdenum in the alloy similarly assists repassivation.

It can be clearly seen from Fig. 6 and 7 that active dissolution of molybdenum-bearing alloys rapidly slows down. This fact results in the formation of a passive film with a higher protective quality. For instance, the 3Mo alloy shows a high passive current density, indicating a low protective quality of the passive film. The enrichment of beneficial chromium in the passive film is not high, but the content of unstable

molybdenum in the film is not low in comparison with the 5Mo and 10Mo alloys. When the molybdenum content of the alloy is low, it is not sufficient to suppress the dissolution of passivating species by the formation of molybdenum-enriched corrosion product film prior to the passive film formation in aggressive concentrated hydrochloric acids. As seen in the active region, the rapid dissolution of the alloy in the passive region appears to result in the formation of a passive film in which the iron and molybdenum contents are relatively high and chromium is relatively low. It can, therefore, be said that the addition of an insufficient amount of molybdenum to the alloy leads to insufficient suppression of active dissolution prior to the passive film formation and simultaneously to the formation of the passive film without a high protective quality due to insufficient chromium enrichment.

Detrimental effect of molybdenum.—It has been stated by many investigators (1-3, 34, 35) that incorporation of molybdenum into the passive film improves the protective quality of the film. When the dissolution rate of iron-base alloys is very high as in the active region, molybdenum selectively remains because the dissolution rate of molybdenum is slower than that of other constituents. Molybdenum, however, is not able to form its own passive film in the passive region of the alloys and dissolves even at the lower potentials in the passive region of the alloys, indicating a lower stability of the passive film of molybdenum in comparison with a passive hydrated chromium or iron oxyhydroxide film (8, 24).

The 5Mo and 10Mo alloys exhibit a negative current at lower potentials in the passive region, indicating the highly protective quality of the passive film. The passive film formed on those alloys at lower potentials in the passive region consists exclusively of chromium oxyhydroxide and chromium borate; the molybdenum content of the film is extremely low. In this connection, it has been known (20) that the formation of chromium borate is not effective in improving the protective quality of the passive hydrated chromium oxyhydroxide film. It can, therefore, be said that the protective quality of the film is provided by the formation of the hydrated chromium oxyhydroxide film without molybdenum. In particular, the passive film formed on the 10Mo alloy at the open-circuit potential has an especially high protective quality and can withstand polarization in the active region. Accordingly, the alloy shows a negative current in the active region, although the average composition of the passive film changes to some extent by polarization in the active region. When the molybdenum content of the alloy is low, for example 3 a/o, the chromium content of the passive film is not extremely high and the film contains a certain amount of molybdenum. Consequently, a high protective quality cannot be expected for a molybdenum-containing passive film.

On the other hand, polarization of the alloy containing an excess molybdenum, such as 10 a/o, at higher potentials in the passive region increases the content of unstable molybdenum in the passive film and hence results in an increase in the passive current density. In other words, molybdenum assists passive film formation and greatly improves the corrosion resistance, but the lower the molybdenum content of the passive film the higher is the protective quality of the film.

Relation between active dissolution and passivation.—The present authors (16), in reporting the effect of metalloid elements on the corrosion resistance of amorphous chromium-bearing alloys, have stated that phosphorus accelerates initial active dissolution of the alloys with a consequent enrichment of the beneficial chromic ions at the alloy-solution interface prior to passive film formation, which facilitates the rapid formation of the passive film in which these ions are highly concentrated. The beneficial effect of the high

anodic activity has also been found by comparison of amorphous iron- and nickel-base alloys (17). Amorphous Fe-Cr-20B alloys containing 30 a/o or more chromium passivate spontaneously in 1N HCl, while the amorphous Ni-30Cr-20B alloy shows a high active current density. Similarly, the amorphous Fe-20Cr-3Mo-20B alloy passivates spontaneously in 1N HCl, showing the corrosion potential at about 0.4 V(SCE). In contrast, even if the molybdenum content of amorphous Ni-20Cr-Mo-20B alloys is increased to 10 a/o, the active current is still clearly observed. In this manner, the higher anodic activity of iron-base alloys in comparison with nickel-base alloys is effective in accumulating the beneficial species at the alloy-solution interface and in facilitating spontaneous passivation.

Interesting results have been obtained by comparison of the passivation behavior of amorphous Fe-Mo-P-C alloys (24) and Fe-Mo-C alloys (23): the phosphorus-bearing alloys show a higher molybdenum content in the surface film formed in the active region and a lower active current density. The passive film formed on the alloys consists exclusively of hydrated iron oxyhydroxide, whereas the film formed on the Fe-Mo-C alloys contains a large amount of unstable molybdenum species. The passive current density of the phosphorus-bearing alloys is about one-tenth as high as that of the Fe-Mo-C alloys.

On the other hand, Fig. 7 and the investigation of ferritic stainless steels (8) clearly show that active dissolution of molybdenum-bearing alloys immediately after mechanical abrasion rapidly slows down in comparison with alloys without molybdenum, although molybdenum does not appreciably change the anodic activity of alloys.

These results lead to the following assumption: in the absence of phosphorus in the alloys, initial active dissolution is not sufficiently rapid to concentrate molybdenum in the corrosion product film prior to the passive film formation. This fact results in a corrosion product film which insufficiently suppresses dissolution of the passivating metallic ions through the film, and hence the relatively high dissolution rate leads to the formation of a passive film with a poor protective quality based on a high content of unstable molybdenum.

In this connection, the high anodic activity of the alloy is essentially different from the high aggressiveness of the solution with respect to passivation. Passivation is difficult in aggressive solutions (e.g., amorphous Fe-Cr-Mo-B in 6N HCl, Fe-Mo-metalloid in 1N HCl). The formation of the molybdenum-enriched corrosion product film is necessary to concentrate the passivating species under the film. Hence, the passivating species become concentrated in the passive film formed on the molybdenum-bearing alloys. In contrast, if the solution is not highly aggressive [e.g., ferritic 30Cr steels in 1N HCl (8)], passivation occurs even if molybdenum is not added. The addition of molybdenum assists passivation due to suppression of dissolution of the passivating species by the formation of the molybdenum-enriched corrosion product film prior to passive film formation. Therefore, the composition of the passive film is not appreciably different for the alloys with and without molybdenum. On the other hand, the high anodic activity of alloy leads to the formation of a corrosion product film in which molybdenum ions are highly concentrated. The effective suppression of dissolution of passivating species through the corrosion product film as well as the high anodic activity, facilitates the enrichment of the passivating species under the film and hence accelerates passive film formation.

We have proposed (8) that a passive film generally contains micropores which are repeatedly formed and repassivated. If the thickness and composition of the passive films formed on two alloys are apparently the

same [e.g., the films formed on ferritic 30Cr steels with and without molybdenum in 1N HCl (8)], the difference in the activity of micropores in these films is mainly responsible for the large difference in the passive current density. In other words, the repassivation process of micropores is the same as the passivation process mentioned above, and hence molybdenum assists the repassivation of micropores with a consequent decrease in the steady-state passive current density.

Film thickness.—Bond and Lizlovs (36) have pointed out the importance of film thickening in connection with an increase in the stability of the passive film with increasing time. Sugimoto and Sawada (1) have stated that the thickness of the passive film on 20Cr-25Ni-Mo stainless steels increases with molybdenum content of the steels in both sulfuric and hydrochloric acids. In the present work, among the molybdenum-bearing alloys, the thickness of the passive film increases with an increase in the molybdenum content of the alloy, but the change in the molybdenum content of the alloy is accompanied by a change in the composition of the passive film. In addition, the thickness of the passive film on the 3Mo alloy is almost the same as that of the film on the 0Mo alloy. Furthermore, we have shown that the addition of molybdenum to 19Cr (9) and 30Cr (8, 11) ferritic stainless steels does not lead to an appreciable change in both the thickness and composition of the passive film formed in 1N HCl and 1N H₂SO₄, despite the fact that the passive current density is greatly decreased by the addition of molybdenum. It is, therefore, difficult to correlate the high protective quality of the passive film with the film thickening that accompanies a change in the film composition.

Conclusions

1. Amorphous Fe-25Cr-20B- x Mo alloys ($x = 0, 3, 5,$ and 10) do not suffer pitting corrosion even by anodic polarization in 6N HCl, and the alloys containing 5 a/o or more molybdenum passivate spontaneously in the solution.
2. The anodic current density in the active region decreases with an increase in the molybdenum content of the alloy due to the formation of a thick surface film containing large amounts of chromium and small amounts of molybdenum.
3. Molybdenum does not form its own passive film and is unstable even at lower potentials in the passive region of the alloys, at which transpassive dissolution of molybdenum does not occur. Molybdenum assists the formation of a passive hydrated chromium oxyhydroxide film. At lower potentials in the passive region, spontaneous passivation for the 5Mo and 10Mo alloys occurs by the formation of highly protective passive film consisting exclusively of chromium as cations; the molybdenum content of the film is extremely low.
4. A low molybdenum alloy, such as the 3Mo alloy, shows a high passive current density in 6N HCl, indicating a low protective quality of the passive film. A decrease in the molybdenum content of the alloy leads to a decrease in the content of beneficial chromium in the passive film and to an increase in the content of unstable molybdenum in the film.
5. At higher potentials from 0.5 to 1.0V(SCE) in the passive region, molybdenum also suppresses active dissolution prior to passive film formation and hence assists the film formation. However, an excess of molybdenum deteriorates the protective quality of the passive film due to the formation of unstable molybdenum species which dissolve by a transpassive reaction.

Manuscript submitted March 10, 1980; revised manuscript received May 2, 1980. This was Paper 253 presented at the Los Angeles, California, Meeting of the Society, Oct. 14-19, 1979.

Any discussion of this paper will appear in a Discussion Section to be published in the June 1981

JOURNAL. All discussions for the June 1981 Discussion Section should be submitted by Feb. 1, 1981.

Publication costs of this article were assisted by the Tohoku University.

REFERENCES

1. K. Sugimoto and Y. Sawada, *Corros. Sci.*, **17**, 425 (1977).
2. M. A. Streicher, *Corrosion (Houston)*, **30**, 77 (1974).
3. E. M. Mahla and N. A. Nielsen, *Trans. Electrochem. Soc.*, **93**, 1 (1948).
4. T. N. Rhodin, *Corrosion (Houston)*, **12**, 123t, 465t (1956).
5. N. A. Nielsen and T. N. Rhodin, *Z. Electrochem.*, **62**, 707 (1958).
6. J. B. Lumsden and R. W. Staehle, *Scripta Metall.*, **6**, 1205 (1972).
7. A. E. Yaniv, J. B. Lumsden, and R. W. Staehle, *This Journal*, **124**, 490 (1977).
8. K. Hashimoto, K. Asami, and K. Teramoto, *Corros. Sci.*, **19**, 3 (1979).
9. K. Hashimoto and K. Asami, *ibid.*, **19**, 251 (1979).
10. K. Asami, K. Hashimoto, and S. Shimodaira, *ibid.*, **18**, 151 (1978).
11. K. Teramoto, K. Asami, and K. Hashimoto, *Corros. Engng. (Boshoku Gijutsu)*, **27**, 57 (1978).
12. K. Asami and K. Hashimoto, *Corros. Sci.*, **19**, 1007 (1979).
13. M. Naka, K. Hashimoto, and T. Masumoto, *J. Jpn. Inst. Metals*, **38**, 835 (1974); *Corrosion (Houston)*, **32**, 146 (1976).
14. K. Hashimoto, M. Kasaya, K. Asami, and T. Masumoto, *Corros. Engng. (Boshoku Gijutsu)*, **26**, 445 (1977).
15. M. Naka, K. Asami, K. Hashimoto, and T. Masumoto, *Proceedings of 3rd International Conference on Rapidly Quenched Metals (1978)*, The Metals Society, p. 449.
16. K. Hashimoto, M. Naka, J. Noguchi, K. Asami, and T. Masumoto, "Passivity of Metals." R. P. Frankenthal and J. Kruger, Editors, p. 156. The Electrochemical Society Monograph Series, Princeton, N.J. (1978).
17. M. Naka, K. Hashimoto, and T. Masumoto, *J. Non-Cryst. Solids*, **34**, 257 (1979).
18. M. Naka, K. Hashimoto, and T. Masumoto, *ibid.*, **29**, 61 (1978).
19. M. Naka, K. Hashimoto, A. Inoue, and T. Masumoto, *ibid.*, **31**, 347 (1979).
20. K. Hashimoto, M. Naka, K. Asami, and T. Masumoto, *Corros. Engng. (Boshoku Gijutsu)*, **27**, 279 (1978).
21. K. Asami, K. Hashimoto, T. Masumoto, and S. Shimodaira, *Corros. Sci.*, **16**, 909 (1976).
22. K. Hashimoto, K. Asami, M. Naka, and T. Masumoto, *Corros. Engng. (Boshoku Gijutsu)*, **28**, 271 (1979).
23. K. Hashimoto, K. Asami, M. Naka, and T. Masumoto, *Sci. Rep. Res. Inst. Tohoku University*, **A27**, 237 (1979).
24. K. Hashimoto, M. Naka, K. Asami, and T. Masumoto, *Corros. Sci.*, **19**, 165 (1979).
25. K. Asami, *J. Electron Spectrosc.*, **9**, 469 (1976).
26. K. Asami, K. Hashimoto, and S. Shimodaira, *Corros. Sci.*, **17**, 559 (1977).
27. K. Asami, K. Hashimoto, and S. Shimodaira, *ibid.*, **17**, 713 (1977).
28. K. Hashimoto and K. Asami, *Corros. Engng. (Boshoku Gijutsu)*, **26**, 375 (1977).
29. K. Asami, K. Hashimoto, and S. Shimodaira, *Corros. Sci.*, **16**, 387 (1976).
30. K. S. Kim, W. E. Baitinger, J. W. Amy, and N. W. Winograd, *J. Electron Spectrosc.*, **5**, 351 (1974).
31. K. Hashimoto, K. Osada, T. Masumoto, and S. Shimodaira, *Corros. Sci.*, **16**, 71 (1976).
32. M. Naka, K. Hashimoto, and T. Masumoto, *J. Non-Cryst. Solids*, **28**, 403 (1978).
33. K. Hashimoto, K. Asami, M. Naka, and T. Masumoto, *Corros. Sci.*, **19**, 857 (1979).
34. T. Kodama and J. R. Ambrose, *Corrosion (Houston)*, **33**, 155 (1977).
35. N. D. Tomashov, G. P. Chernova, and O. N. Marcova, *ibid.*, **26**, 166t (1964).
36. A. P. Bond and E. A. Lizlovs, *This Journal*, **115**, 1130 (1968).

The Dealloying of Copper-Manganese Alloys

D. S. Keir and M. J. Pryor*

Olin Corporation, Metals Research Laboratories, New Haven, Connecticut 06504

ABSTRACT

Binary copper alloys containing 25 and 50% manganese were corroded in sodium chloride solution at various fixed potentials spanning their corrosion potential. Both Cu-Mn alloys exhibited dealloying at a high rate. The Cu-25%Mn alloy exhibited dealloying behavior similar to that observed in the Cu-Zn and Cu-Ni systems. Selective loss of manganese was maximized at the most active potential at which the alloy was held. When the potential was raised some 0.25V above the corrosion potential, dealloying was largely prevented. The Cu-50%Mn alloy exhibited different behavior with very pronounced dealloying occurring over the whole potential range studied. The morphology and composition of the dealloyed residues was also investigated in detail. The mechanism of dealloying in the Cu-Mn system is discussed.

The dealloying of copper base alloys has been quite extensively studied over the years with the primary attention being directed to Cu-Zn alloys. In the early work of Bengough and May (1) later supported by Kenworthy (2), it was suggested that both copper and zinc dissolve anodically from brass but that the copper is subsequently redeposited on cathodic sites after reaching an appropriate concentration in solution. More recent work of Pickering (3) has offered an alternate explanation, i.e., that of the selective removal of zinc atoms from the alloy. Accordingly, in the de-

alloying of γ and ϵ brasses, Pickering was able to detect intermediate and more copper-rich phases in the alloy substrates after corrosion at controlled active potentials. Pickering and Byrne (4) also showed that the selective removal of zinc atoms predominated at potentials between the reversible potential for the anodic dissolution of zinc and that for copper; further as the latter potential was significantly exceeded proportionate alloy dissolution took place.

Studies similar to those of Pickering and Byrne were carried out by one of the authors on a range of copper-nickel alloys (5). Results essentially similar to those found by Pickering and Byrne on brasses were ob-

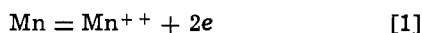
* Electrochemical Society Active Member.

Key words: aqueous corrosion, dealloying, copper, manganese.

tained. Dealloying was promoted by application of potentials more active than the corrosion potential of a Cu-Ni alloy and was inhibited by raising the potential to some 250 mV above the corrosion potential. Here, however, the extent of dealloying was very minor compared with that observed on the copper-zinc alloys. The cupro-nickels also grew quite protective thick films during the initial dealloying with the result that some 20% of the total cations leaving the alloy were found in the corrosion product film.

The present study was designed to clarify the dealloying behavior of binary Cu-Mn alloys. Manganese shows substantial solid solubility in copper and is an effective solid solution strengthening agent. Cu-Mn binary alloys have been reported to be relatively susceptible to stress corrosion cracking in ammonia (6,7). What little information exists on their general corrosion behavior (8) indicates that manganese decreases salt spray resistance with the weight loss increasing with manganese content up to 40 weight percent (w/o). However, no information was provided on whether dealloying occurred in the salt spray testing or in the stress corrosion process.

It would be expected that copper-manganese binary alloys should be quite susceptible to dealloying. The reversible potential (E_0) for the reaction



is -1.16V compared with only -0.763V for the half-cell reaction



Accordingly, on the basis of thermodynamic considerations alone, the Cu-Mn alloys could well be more susceptible to dealloying than the brasses.

In order to throw light on this point, the investigation described in this paper was conducted. Copper-manganese alloys nominally containing 25 and 50 w/o manganese were exposed to sodium chloride solution over a wide potential range which was designed to bracket the corrosion potential of each alloy. The copper to manganese ratios found both in the films formed during the corrosion process and also in the solution were analyzed. In addition, the morphology and composition of the dealloyed residues were studied.

Experimental and Results

Materials and procedure.—Cu-25%Mn (actual 25.30% Mn) and Cu-50%Mn (actual 49.55% Mn) alloys were chill cast as $2.5 \times 10 \times 20$ cm sections. Cu-25%Mn is a single phase (γ) alloy (10). It was hot-rolled at 800°C to a thickness of 0.63 cm, annealed at 700°C for 1 hr, milled, cold-rolled to 0.10 cm, annealed at 725°C for 1 hr, and water quenched. The Cu-50%Mn alloy may be single phase (γ) if quenched from above 650°C or two-phase ($\gamma + \alpha\text{-Mn}$) if heat-treated below 650°C . The Cu-50%Mn casting was homogenized at 750°C for 16 hr, hot-rolled at that temperature to a thickness of 0.63 cm, annealed at 750°C for 2 hr, water quenched, and milled. The alloy was then cold-rolled to 0.10 cm thickness. The alloy was then again annealed at 750°C for 2 hr followed by water quenching to yield the single phase (γ) condition. The two phase ($\gamma + \alpha\text{-Mn}$) condition was produced by further annealing selected specimens for 4 hr at 450°C .

Corrosion specimens measuring 1.5×5 cm were cut from the 0.10 cm thick sheet of the two above alloys. The surfaces were prepared by abrading on 400 and 600 grit fine metallurgical paper with a final polish. The specimens were degreased in benzene and methanol, dried in air, and then masked with electroplaters tape leaving an exposed circle with the total area of 1 cm^2 .

The sodium chloride used in this investigation had a concentration of 0.5M and was made up from reagent grade sodium chloride dissolved in distilled deionized water. All experiments were conducted with the sodium chloride solution freely exposed to air.

All corrosion experiments were carried out in duplicate at a temperature of $25^\circ \pm 0.05^\circ\text{C}$ with 150 ml of solution per specimen. The potential of the individual specimens was controlled by a Wenking Model 68-TS-3 potentiostat. A saturated calomel electrode was used as a reference electrode. It was contained in the same electrolyte in a separate vessel connected to the reaction vessel with a solution bridge. The Cu-25%Mn alloy was polarized at potentials varying from -0.25 to $+0.50\text{V}$ on the standard hydrogen scale.¹ The Cu-50%Mn alloy was polarized in both metallurgical conditions (γ or $\gamma + \alpha\text{-Mn}$) at potentials ranging from -0.60 to $+0.25\text{V}$.

After completion of an experiment, the solution was acidified and the copper and manganese determinations made by atomic absorption using a Techtron Model AA4 Spectrophotometer. The reaction product films were dissolved separately in deaerated 12% H_2SO_4 at 60°C with copper and manganese again being determined by atomic absorption. The blank correction described earlier (5) was used to correct for very minor acid attack on the unfiled alloys. A third specimen was always polarized in an identical fashion, carefully washed, and subjected to reflection electron diffraction at 100 kV. All specimens irrespective of alloy content or potential maintained showed surface films of Cu_2O only with the film being insufficiently thick to mask reflections from the underlying substrate.

The morphology and composition of the dealloyed residues were studied by SEM/microprobe analysis using an AMR Model 900 SEM with a PGT energy dispersive analyzer.

Results.—Table I shows the corrosion potential of copper and the two Cu-Mn alloys. Alloying with 25% Mn had only a minor effect on depressing the corrosion potential in the active direction. However, when copper was alloyed with 50% manganese irrespective of whether the alloy was single or two-phase, the corrosion potential dropped to close to -0.5V . In this respect, Mn at high concentration has an unusually strong influence in shifting the corrosion potential of the alloy in the active direction.

Analyses of the total reaction products (solid oxide film on the metal and copper and manganese ions in solution) were conducted as a function of time of polarization at $+0.25\text{V}$ for the Cu-25%Mn alloy. The reaction product composition became essentially constant with time after around 20 hr. Accordingly, this time was used as a standard for the remainder of the investigation.

Anodic polarization curves were determined for the Cu-25%Mn alloy at three different sweep rates (0.9, 1.5, and 3.0 V/hr) in the sodium chloride solution. The anodic polarization curves were only slightly sweep rate dependent and exhibited the same features as the anodic polarization curves of copper-nickel alloys in sodium chloride solution (9).

Figure 1 shows the weights of Cu + Mn in solution for the Cu-25%Mn alloy after 20 hr holding at various fixed potentials between -0.25 and $+0.50\text{V}$. Because the separately analyzed Cu + Mn in the surface oxide film was only around 1% of that found in solution, it is insignificant to mass balance considerations and so is not included in Fig. 1. The amount

¹ All potentials in this paper are expressed on the standard hydrogen scale.

Table I. Steady corrosion potentials of Cu, Cu-25%Mn, and Cu-50%Mn alloy in 0.5M NaCl at 25°C

Alloy	Steady corrosion potential (V)
Cu	0.00
Cu-25% Mn	-0.053
Cu-50% Mn	-0.470

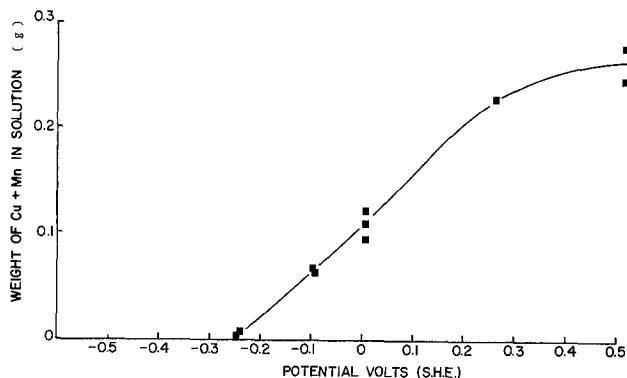


Fig. 1. Relationship between Cu plus Mn in solution from a Cu-25%Mn alloy held at five different potentials in 0.5M NaCl for 20 hr.

of copper and manganese dissolved from the alloy increased approximately linearly with increasing potential in the noble direction up to around +0.25V.

Figure 2 shows the effect of potential upon the percentage of manganese in solution. At -0.25V, the soluble corrosion product was almost 100% manganese. Between +0.25 and +0.50V, manganese left the alloy in a modestly greater weight percent than it was originally present. At the corrosion potential of the Cu-25%Mn alloy (-0.053V), the soluble corrosion product contained over 40% Mn. The form of the manganese content vs. potential curve is quite similar to that found earlier by Pickering and Byrne (4) for brasses and by one of the authors for copper-nickel alloys (5).

Figure 3 shows the weight of Cu + Mn in solution for the Cu-50%Mn alloy after 20 hr in 0.5M NaCl as a function of potential between -0.60 and +0.25V. Within the limits of experimental error, there was no difference in the results irrespective of whether the

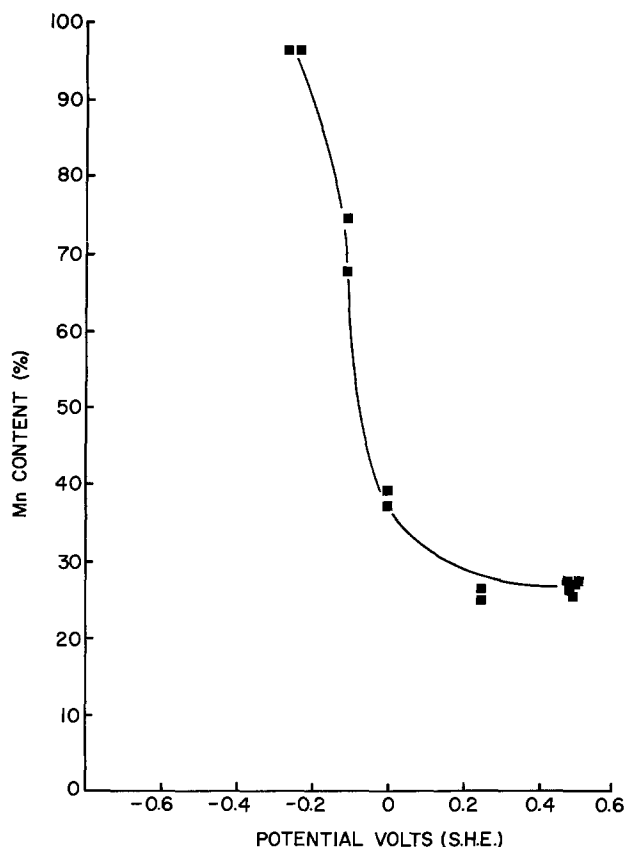


Fig. 2. Relationship between weight percent of Mn in solution from a Cu-25%Mn alloy held at five different potentials in 0.5M NaCl for 20 hr.

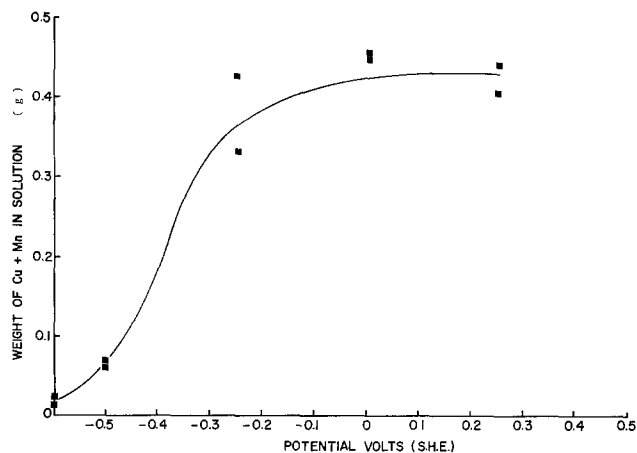


Fig. 3. Relationship between Cu plus Mn in solution from a Cu-50%Mn alloy held at five different potentials in 0.5M NaCl for 20 hr.

alloy was in the single phase (γ) or the two-phase ($\gamma + \alpha$ -Mn) condition. Figure 3 shows results for the single phase condition only. This curve is quite similar to that for the Cu-25%Mn alloy. Due to the much more active corrosion potential of the Cu-50%Mn alloy (Table I), most of Fig. 3 was determined under conditions of anodic polarization.

Figure 4 shows the percent of manganese in the soluble corrosion product for this alloy as a function of potential. Figure 4 illustrates dealloying behavior very different from that of the Cu-25%Mn alloy in Fig. 2. Even at potentials as high as +0.25V, the corrosion reaction still yielded in excess of 90 w/o Mn. This is a potential that is in excess of 0.7V more noble than the corrosion potential of this alloy. At the corrosion potential of the alloy, the manganese content of the soluble reaction product was around 99%. Further at 0.0V and above, the specimens were dealloyed throughout the whole cross section of the specimens. The Cu-50%Mn alloy exhibited extremely severe and rapid dealloying and it was not possible within the potential range studied to force the manganese to leave the alloy in the same proportion as it was present originally.

Figure 5 shows an SEM plan view of the dealloyed surface of a Cu-25%Mn alloy held at a potential of -0.10V for 20 hr. Magnification is $\times 1000$ and it is evident that the residue was very porous. The mass balance studies in Fig. 2 showed that Mn comprised some 70% of the Cu + Mn content of the solution. Energy dispersive x-ray spectra were then made of the

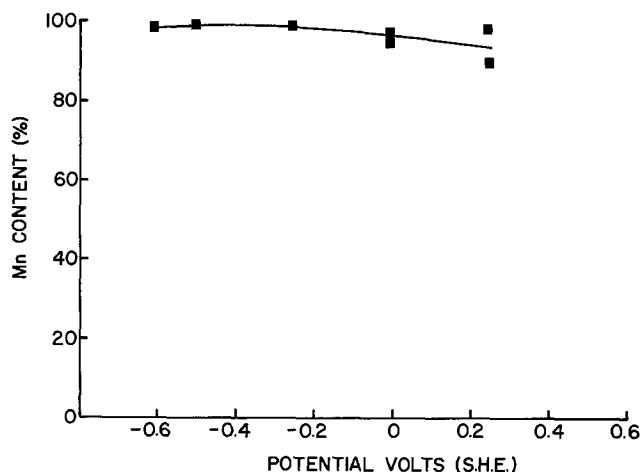


Fig. 4. Relationship between weight percent of Mn in solution from a Cu-50%Mn alloy held at five different potentials in 0.5M NaCl for 20 hr.

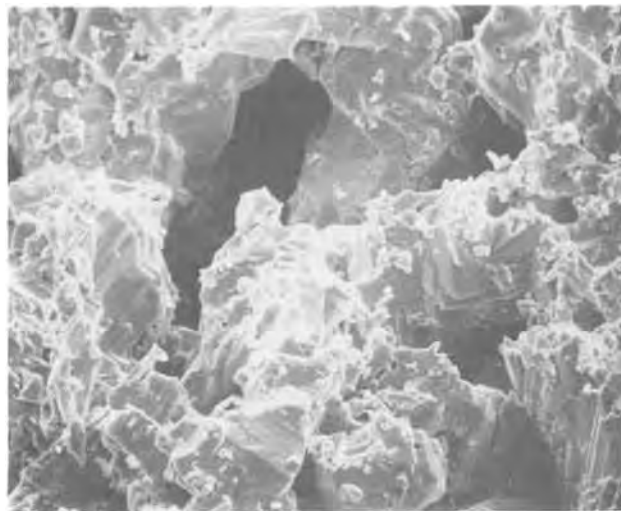


Fig. 5. Dealloyed surface of Cu-25%Mn alloy held at $-0.10V$ in $0.5M$ NaCl for 20 hr ($\times 1000$).

original alloy surface and of the dealloyed surface layer. The spectra for the original Cu-25%Mn alloy (upper spectrum) and for the dealloyed surface layer (lower spectrum) are shown in Fig. 6. The Mn peaks were completely absent after holding at $-0.1V$ for 20 hr thereby indicating that the dealloyed layer was substantially pure copper.

Figure 7 shows an SEM plan view ($\times 1000$) of the Cu-25%Mn alloy polarized for 20 hr at $+0.25V$. The dealloyed surface was much less porous as might be anticipated from Fig. 2 which shows that Mn comprised only slightly more than 30% of the Cu + Mn content of the solution. Energy dispersive x-ray spectra of the original alloy and of the dealloyed surface are shown in Fig. 8. From Fig. 8, it is evident that much manganese is lost from the surface layer² but that a small and infinite amount of the order of 2 w/o remains.

Figure 9 shows an SEM plan view ($\times 1000$) of the surface of the Cu-50%Mn alloy polarized for 20 hr at $0.00V$. This dealloyed surface was much more porous than that of the Cu-25%Mn alloy polarized for 20 hr at $+0.25V$ (Fig. 7). The dealloyed residue shown in Fig. 9 penetrated completely through the original alloy sheet. By careful manipulation, it was possible to fracture the quite brittle dealloyed residue and reveal two planes as shown in Fig. 10. The lower plane in Fig. 10 is the dealloyed surface shown in Fig. 9 but

² The effective analytical depth of penetration of the electron beam is around 0.8μ on a compact surface and as much as 4μ on very porous surfaces.

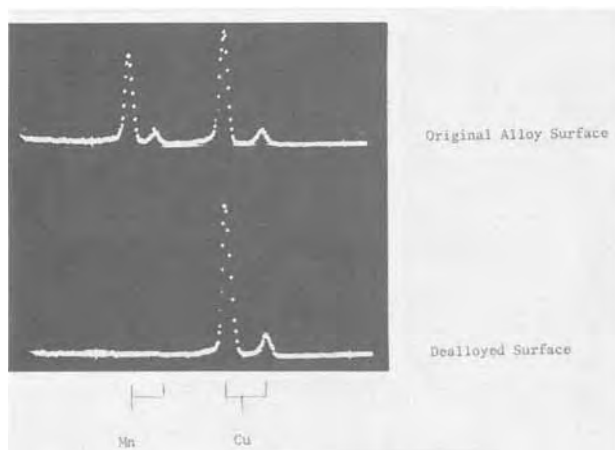


Fig. 6. Energy dispersive x-ray spectra from the surface of a Cu-25%Mn alloy. Upper, original alloy surface; lower, after holding at $-0.10V$ in $0.5M$ NaCl for 20 hr.

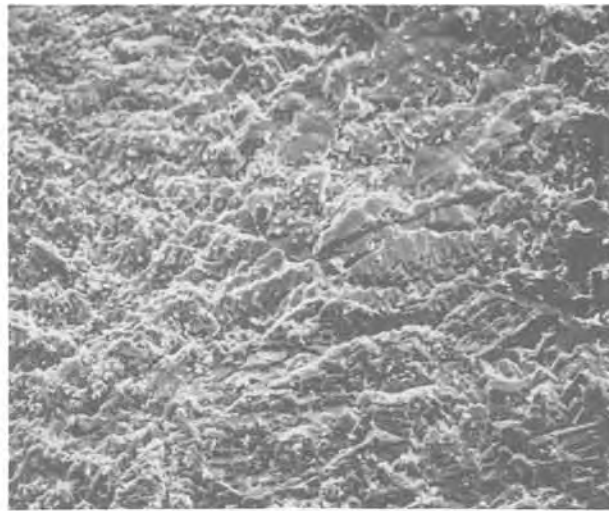


Fig. 7. Dealloyed surface of Cu-25%Mn alloy held at $+0.25V$ in $0.5M$ NaCl for 20 hr ($\times 1000$).

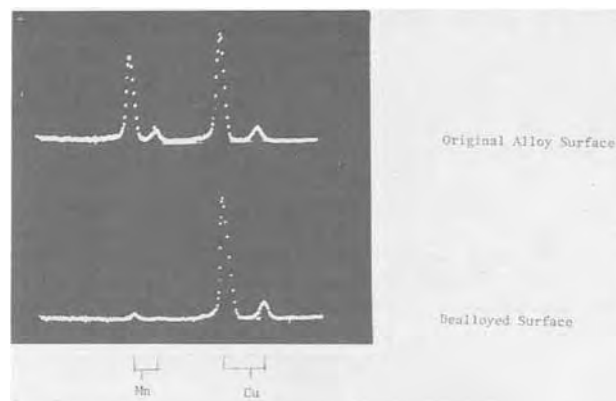


Fig. 8. Energy dispersive x-ray spectra from the surface of a Cu-25%Mn alloy. Upper spectrum, original alloy surface; lower spectrum, after holding at $+0.25V$ in $0.5M$ NaCl for 20 hr.

at a lower magnification ($\times 200$). The similarly appearing surface in the upper part of Fig. 10 is a parallel fracture plane located approximately midway through the thickness of the dealloyed residue. The intervening porous polyhedra in Fig. 10 are a transition zone between the two planes. Figure 11 contains a series of energy dispersive x-ray spectra of the dealloyed deposit shown in Fig. 10. The upper spectrum is that of

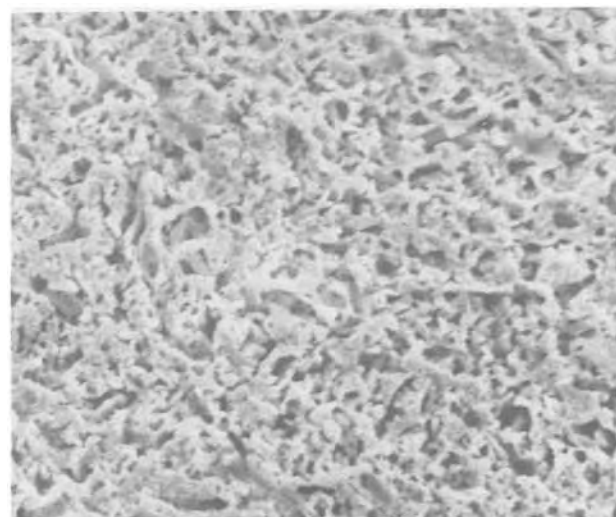


Fig. 9. Dealloyed surface of Cu-50%Mn held at $0.00V$ in $0.5M$ NaCl for 20 hr ($\times 1000$).

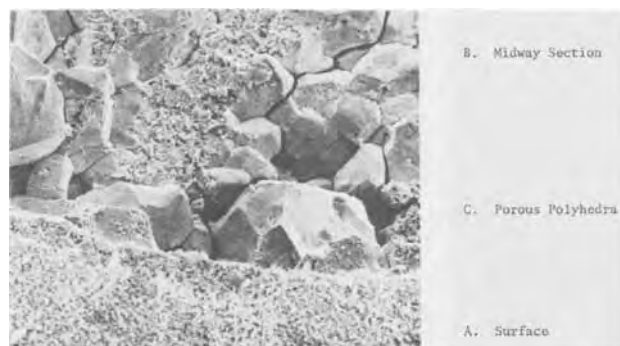


Fig. 10. Fractured sample of a dealloyed residue from Cu-50%Mn held at 0.00V in 0.5M NaCl for 20 hr—shows dealloyed surface (A), dealloyed plane midway through the section (B), porous polyhedra (C) ($\times 200$).

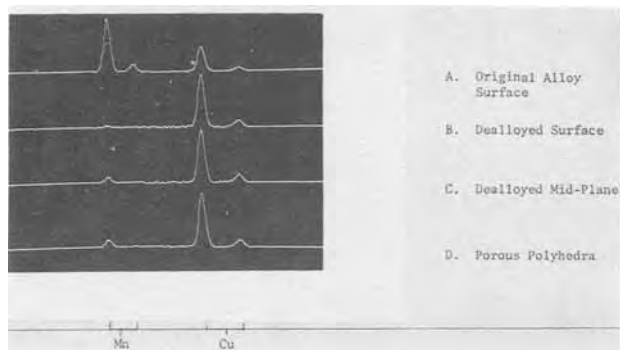


Fig. 11. Energy dispersive x-ray spectra from various features in Fig. 10. (A) original alloy surface; (B) dealloyed surface; (C) dealloyed mid-plane of residue; (D) porous polyhedra.

the original Cu-50%Mn alloy. The second (from the top) spectrum is from the dealloyed surface, Fig. 9. The manganese content is around 1.5 w/o. The third spectrum is from the fracture plane approximately midway through the dealloyed residue. This contains around 3.5 w/o Mn. The bottom spectrum is from the porous polyhedra in the transition zone between the two planes. These contain around 4.5 w/o Mn. Figure 12 shows the microstructure of the original Cu-50%Mn alloy at a magnification of 200 diam (similar to Fig. 10). There is no doubt that the porous polyhedra are original grains from the Cu-50%Mn alloy which have been almost completely dealloyed without changing size or contour. From Fig. 10, the individual dealloyed



Fig. 12. Microstructure of Cu-50%Mn alloy $\times 200$ etched in HCl-picric acid in isopropanol.

grains in the transition zone are also largely separate physically.

Discussion

For the Cu-25%Mn alloy (Fig. 2), the percentage of Mn found in solution (relative to the total Cu + Mn solution content) is influenced by potential in a similar manner to that found in α brass (4) and the cupro-nickels (5). At the corrosion potential of around -0.05 V for the Cu-25%Mn alloy, the solution contains around 40% Mn and the specimen exhibits moderate dealloying; as the potential is shifted to around -0.25 V, i.e., closer to the manganese potential and much further below the copper potential, the manganese content of the solution rises to around 95% and copper dissolution is almost completely prevented. When the potential is raised to $+0.25$ or to $+0.50$ V, i.e., some 300 mV or more above the corrosion potential, manganese is around 30% of the Cu + Mn passing into solution, i.e., only a modestly greater concentration than was present in the alloy. The resulting dealloying is relatively modest compared with that experienced at more active potentials. This potential dependent dealloying behavior is very similar to that reported previously for α brass (4) and for cupro-nickels (5).

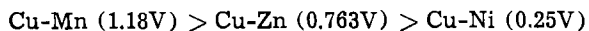
The Cu-50%Mn alloy shows different behavior and much more extreme dealloying. From -0.60 to -0.25 V, only manganese is found in solution with any copper being below the limits of the chemical analyses (< 0.1 ppm). The only copper leaving the alloy is found in minute amounts in the thin surface oxide film. Copper is found in solution in small quantities only at 0.0 and $+0.25$ V (Fig. 4). The corrosion potential of this alloy is -0.47 V and at this potential, 99.9% of the metal ions leaving the alloy are manganese. Even at the highest potential studied ($+0.25$ V), 92% of the cations leaving the alloy are manganese. Furthermore, the rate of dealloying at 0.0V and above was so high that the whole 0.1 cm cross section of the Cu-Mn alloy was penetrated from one side. It is evident that with the very highly alloyed Cu-50%Mn alloy, potential exhibits much less positive control over the dealloying phenomenon than at lower manganese contents of around 25%. Furthermore, even when the potential was raised some 0.7V above the corrosion potential, proportional alloy dissolution was not restored.

Based on past work and on the work reported in this paper, Cu-Ni alloys show the slowest kinetics of dealloying (5), α brass intermediate kinetics (4) and the Cu-Mn alloys by far the fastest kinetics, particularly the Cu-50%Mn alloy. If dealloying is regarded as being due to the selective removal of atoms of a more electrochemically active solute element, then some mechanism must be provided to explain the rapid propagation of dealloying into the alloy in real depth. Pickering (3) proposed a solid-state diffusion mechanism in Cu-Zn alloys with the diffusion rate being materially enhanced by the very large vacancy concentration occasioned by selective removal of the more electrochemically active zinc atoms. Diffusion data at room temperature and for this very selective metallurgical condition are not available in the literature. High temperature diffusion data for the three alloy systems within the temperature range of 750° - 800° C suggests that at around 30 w/o solute, the diffusion coefficients are around 3×10^{-12} cm²/sec for Ni in Cu-Ni (11), around 3×10^{-8} cm²/sec for Zn in Cu-Zn (12), and around 7×10^{-10} cm²/sec for Mn in Cu-Mn (13). Further, as the Mn content of Cu-Mn alloys is increased to around 50 w/o, D drops by around an order of magnitude. These high temperature diffusion data do not fit even qualitatively with dealloying kinetics falling in the order of

$$\text{Cu-Mn} > \text{Cu-Zn} > \text{Cu-Ni} \quad [3]$$

nor with the fact that Cu-50%Mn dealloys much more rapidly than Cu-25%Mn. Instead, dealloying kinetics seem to relate better to the difference between the po-

tential at which the alloy is maintained in solution and the half-cell potential of the solute element. If for instance the alloy potential is held at 0.00V, then the potential difference between the potential maintained in solution and the reversible potential of solute elements falls in the order of



[4]

which is in qualitative accord with the relative order of the kinetics of dealloying depicted in Eq. [3]. Such an analysis does not explain why dealloying kinetics increase with increasing solute content. This question will be addressed later in the Discussion.

The morphologies and compositions of the dealloyed structures provide convincing evidence favoring Pickering's view (3) that dealloying is the result of selective removal of solute atoms from the alloy as opposed to proportionate dissolution of the alloy followed by redeposition of copper (1, 2). Figures 5 and 7 show the surfaces of the Cu-25%Mn alloy at the same magnification (X1000) after dealloying for 20 hr at -0.10 and $+0.25$ V, respectively. Normally, it would be expected that if redeposition was involved, the crystal size of an electrodeposit would decrease as the deposition potential is moved progressively in the more active direction (14). However, the crystal size of the dealloyed residue at -0.10 V (Fig. 5) is much larger than that seen at $+0.25$ V (Fig. 7). Furthermore, the dealloyed surface residue shown in Fig. 7 contains around 2% Mn in the dealloyed matrix (Fig. 8). The manganese does not exist as a separate phase detectable in the electron diffraction study and must therefore be assumed to be in solid solution in the matrix. At a potential of $+0.25$ V, any redeposition of manganese from solution is quite impossible.

Even more convincing evidence supporting selective removal of manganese atoms from the lattice by application of appropriate electrochemical conditions is provided in Fig. 10 which shows a fractured sample of the residue from a Cu-50%Mn alloy dealloyed at 0.0V. Here, the original grain structure of the alloy may be clearly seen and the grain size is in the same 0.030-0.120 mm range as the original alloy (Fig. 12). There is further clear evidence of intergranular separation of many of the original alloy grains, presumably due to preferential attack of manganese-rich original grain boundaries. It is not believed that this intergranular separation is important in controlling the kinetics of the dealloying phenomenon. The original alloy grains, though maintaining their original size and morphology after dealloying, are in fact reduced to a porous network of dilute Cu-Mn solid solution. The morphology of the grain interiors may be seen from the dealloyed surface (Fig. 10) and from the similar center plane morphology in Fig. 10 which represents an area where one or more dealloyed grains were fractured during the specimen preparation. The surface plane, the center plane, and the unfractured dealloyed grains in Fig. 10 all contained a small amount of Mn presumed to be in solid solution at approximate levels of 1.5, 3.5, and 4.5 w/o, respectively (Fig. 11). The surface of the dealloyed grains is less porous than the grain interiors from Fig. 10. Assuming that the intergranular separation is due to a higher grain boundary manganese content, then the surface of the dealloyed grains should be more dense than their interior due to a manganese denuded layer being adjacent to the enriched grain boundaries.

The foregoing structural and compositional evidence clearly shows that the dealloying process in Cu-Mn alloys is the result of preferential electrochemical removal of Mn atoms from the alloys rather than a dissolution/redeposition mechanism. It is also more significant that dealloying only yields a pure copper residue only at the more electrochemically ac-

tive potentials studied. At other more noble potentials, the dealloying residue is a dilute Cu-Mn solid solution.

The final aspects requiring discussion are the mechanisms of propagation of dealloying through the specimens and the morphology of the dealloyed layers. One mechanism for propagation could involve the selective removal of Mn atoms from the surface and subsurface layers together with the resulting creation of a very high vacancy concentration. This high vacancy concentration might permit renewal of Mn diffusing from the alloy substrate into the surface and subsurface dealloyed zones so as to sustain the dealloying process. A relatively long-range thermally activated process of this nature hardly appears feasible at room temperature particularly at the high rate necessary to sustain the dealloying process. A diffusion mechanism based on extrapolation from available high temperature data does not fit qualitatively with the dealloying kinetics observed in the α solid solutions within the Cu-Mn, Cu-Zn, and Cu-Ni systems (Eq. [3]). Furthermore the high temperature diffusion coefficient for Mn in copper is substantially higher at 25 w/o Mn than at 50 w/o Mn (13) yet dealloying kinetics are much faster at 50% Mn than at 25% Mn (Fig. 1 and 3).

An alternate explanation, more nearly consistent with the overall dealloying characteristics of copper base alloys may be found by considering the short range reorientation of the dealloyed surface layers in Cu-Mn alloys. Assuming that Mn is substantially removed by electrochemical polarization from the alloy surface, then the remaining Cu atoms will find themselves at large and unacceptable interatomic distances. The copper atoms will rapidly seek their characteristic distance of closest approach leaving voids in the surface whose volume will increase with increasing atom percent of Mn removed, i.e., Fig. 10 for Cu-50%Mn vs. Fig. 7 for Cu-25%Mn. The atom rearrangement required to produce these skeletal Cu or Cu-rich structures is of an essentially much shorter range nature and does not require the diffusion of Mn over long distances. The rearrangement clearly results in the generation of new internal surfaces which should act as effective sinks for vacancies moving in the opposite direction to that in which the copper atoms collapse. The skeletal surface structure produced by the atomic contraction and vacancy annihilation permits access of the solution to the underlying alloy substrate and so the process may repeat itself without the necessity for anything other than short-range collapse of the copper atoms into an equilibrium crystal structure together with the attendant generation of new internal surfaces and vacancy annihilation. This model also explains why the dealloying kinetics of Cu-50%Mn are the same irrespective of whether the alloy was in the γ or in the $\gamma + \alpha$ -Mn conditions. In the latter condition, the α -Mn will be removed preferentially and will be followed by the Mn in the remaining γ solid solution. The void volume within the skeletal residue will be identical to that obtained from dealloying of the γ Cu-50%Mn solid solution when they are dealloyed to the same final composition. Only the morphology of the skeletal deposit will vary slightly with its internal volume and therefore solution access to the substrate being the same. This mechanism provides for the atomic rearrangement of the Cu atoms, together with vacancy annihilation at the new internal surfaces to occur on a short-range basis within the surface layers only. It does not require long-range manganese diffusion from the unattacked substrate. It permits propagation of dealloying by providing solution access to the unattacked substrate through the porous skeletal structures generated by the creation of new internal surfaces.

Using the foregoing model, dealloying kinetics should be hastened when the skeletal structure is most porous and permits easiest access of the solution, i.e., Cu-50%Mn at 0.00V (Fig. 10) and retarded when

the skeletal structure is denser and solution access is less favored, i.e., Cu-25%Mn at 0.25V in Fig. 7. An explanation of this nature can also account for the formation of intermediate more copper-rich phases during dealloying of applicable higher alloy phases as found by Pickering (3). Selective electrochemical conditions involving application of the more active potentials were required to dealloy to a pure Cu residue in this study. All other experiments at somewhat more noble potentials yielded dilute Cu-Mn solid solutions as the terminal residue. Throughout the course of the experiments, a complete range of α solid solutions must have existed transiently during the dealloying process. If the system was such that intermediate more copper-rich phases could exist, as for instance in the dealloying of ϵ or γ brasses (3), then the formation of the lower phases would clearly result at some point in time during dealloying.

In summary, the model proposed in this paper suggested that dealloying kinetics in solid solutions of Cu with Mn, Zn, and Ni are primarily controlled by the difference in potential between that at which the alloy is maintained in solution and the reversible potential of the solute element. Within the Cu-Mn system those electrochemical conditions which lead to the most open skeletal structures of Cu or dilute Cu-Mn γ solid solution correlate with the greatest rates of dealloying or the greatest selectivity of Mn removal.

Acknowledgment

The authors acknowledge the valuable discussions of Dr. J. Winter, Dr. J. F. Breedis, and Mr. J. C. Fister. They also acknowledge the help afforded by Mr. A. F. Beck in the morphological studies of the dealloyed residues. The authors also wish to thank the Brass Group of the Olin Corporation for their support of this work and their permission to publish the results.

Manuscript submitted Feb. 28, 1980; revised manuscript received May 19, 1980.

Any discussion of this paper will appear in a Discussion Section to be published in the June 1981 JOURNAL. All discussions for the June 1981 Discussion Section should be submitted by Feb. 1, 1981.

Publication costs of this article were assisted by the Olin Corporation.

REFERENCES

1. G. D. Bengough and R. May, *J. Inst. Met.*, **32**, 169 (1924).
2. L. Kenworthy and W. G. O. Driscoll, *Corros. Tech.*, **2**, 247 (1955).
3. H. W. Pickering, *This Journal*, **117**, 8 (1970).
4. H. W. Pickering and P. J. Byrne, *ibid.*, **116**, 1492 (1969).
5. R. G. Blundy and M. J. Pryor, *Corros. Sci.*, **12**, 65 (1972).
6. A. K. Lahiri and T. Banerjee, *ibid.*, **5**, 731 (1965).
7. U. K. Chatterjee, S. C. Sircar, and T. Banerjee, *ibid.*, **26**, 141 (1970).
8. A. K. Lahiri, K. P. Mukherjee, and T. Banerjee, *Trans. Indian Inst. Met.*, **81** (1964).
9. R. F. North and M. J. Pryor, *Corros. Sci.*, **10**, 297 (1970).
10. M. Hansen, "Constitution of Binary Alloys," p. 597, McGraw Hill Book Company, Inc., New York (1958).
11. G. Brunel, G. Azezon, and P. LaCombe, *C. R. Acad. Sci. Ser. C*, **269**, 895 (1965).
12. G. T. Horne and R. F. Mehl, *J. Metals*, **88**, January 1955.
13. Y. Iyima, K. I. Hirano, and K. Sato, *Trans. Jpn. Inst. Metals*, **12**, 18 (1977).
14. W. Blum and G. B. Hogaboom, "Principles of Electroplating and Electroforming," McGraw Hill, New York (1949).

Anodic Behavior of Cemented WC-6% Co Alloy in Phosphoric Acid Solutions

M. H. Ghandehari*¹

Fansteel Metals, Muskogee, Oklahoma 74401

ABSTRACT

The anodic behavior of WC-6% Co alloy in nitrogen saturated phosphoric acid solution was studied by means of potentiostatic dissolution, polarization curves, and micrographic studies. At anodic potentials between open circuit ($E = -300$ mV) and -100 mV (*vs.* SCE) the binder phase alloy (Co-W) dissolves actively to yield dissolved Co and W while the WC phase remains unattacked. At approximately -0.1 V the WC-Co alloy passivates resulting in an 80% decrease in current. Further anodic polarization causes the current to increase as active dissolution of the WC phase comes into play. Application of these results to Co/WC separation in alloy scrap recycling is discussed.

Cemented WC-Co alloys are dispersions of micron-size WC particles in a binder phase. These alloys are prepared by a liquid phase sintering process, during which some WC grains dissolve in Co producing a Co-W-C ternary binder alloy (1). The solubility of WC in Co is a function of physical and chemical properties of the constituents as well as the conditions of the sintering process (1). At room temperature, however, the amount of carbon remaining in the binder phase is small and hence difficult to measure. The thickness

of the binder phase has been reported to range from 20 to 100Å for cemented alloys containing less than 12% by weight cobalt (2).

Extensive use of these alloys under a variety of corrosive environments suggests the need for kinetic studies of the basic corrosion processes. Examples of some of these environments are geothermal brines in drilling applications, acid extracts from wood (3, 4) in cutting of lumber, and lubricants in metal finishing industries. While it is desirable to inhibit corrosion in the above circumstances, a totally opposite need arises in metal recycling industries in which corrosion and total disintegration of used and rejected alloys are desirable (5, 6). Published literature on corrosion of

* Electrochemical Society Active Member.

¹ Present address: Union Oil Company of California, Science and Technology Division, Brea, California 92621.

Key words: cemented carbides, binder phase, Co-W, corrosion, mixed potential.

cemented carbides is sparse and deals mostly with weight loss measurements (7, 9) as a means to compare corrosion resistances of these alloys under various conditions.

Because cemented carbide alloys are nonhomogeneous, the different components would be expected to dissolve at different rates and have different over-voltages for depolarizer reactions. Electrochemical measurements combined with mixed potential considerations (10) may provide a significant tool for investigating the corrosion behavior of these industrially important alloys.

In this study anodic polarization curves for WC-6% Co alloy have been determined in phosphoric acid solutions using the potentiostatic technique. Also, current vs. time behavior and current yields at several potentials have been measured. Finally, microstructural changes occurring during the corrosion have been examined. From these results a qualitative model is given describing the dissolution of WC-Co cemented alloys in dilute phosphoric acid solutions.

Experimental

A three electrode system was used to study anodic dissolution of WC-Co. WC, and Co electrodes. The cell consisted of a 600 ml Pyrex beaker which was filled approximately one-third with 1.2M H_3PO_4 . The test and counterelectrodes were suspended from the gas-tight lid and were separated by approximately 5 cm. Test electrodes were prepared as follows.

Sintered pieces of WC-6% Co were made according to standard powder metallurgical techniques (1). WC electrodes were prepared by hot-pressing powders of the elements in a graphite die at about 2200°C and 5000 psi of pressure for about 10 min. The cobalt electrode was prepared from a piece of high purity cobalt foil. The electrode surfaces of the WC-6% Co and Co were 1 × 1 cm and that of the WC electrode was 2 × 2 cm. The back sides of the test electrodes were coated with silicone rubber. Prior to each test, the surface of the carbide electrode was ground and polished to produce a new surface using a standard procedure (ASTM B276-54, 1954). The polished surface was rinsed with ethanol and distilled water prior to each test. Examination of the carbide electrode surfaces with a metallograph revealed that they were free from pores. The surface of the cobalt electrode was pretreated with a few drops of HF-HNO₃ solution followed by rinsing with deionized water.

A piece of Pt wire, 0.1 × 5 cm, was used as the counterelectrode. Electrode potentials were measured by means of a Keithley electrometer and with respect to a saturated calomel electrode (SCE) which was positioned outside the cell, contacting the test electrode through a salt bridge full of cell electrolyte and a Luggin capillary. The cell was equipped with a Teflon-coated magnetic stirring bar for agitation. Solutions were stirred at a moderate rate which was kept constant throughout the experiments. All tests were run at ambient temperature of 25° ± 1°C. Reagent grade chemicals and deionized water were used to prepare the solutions. Nitrogen of 99.99+ % purity, as specified by the manufacturer, was flushed through the solutions. Steady-state potentiostatic curves were obtained with either a Wenking or an Anotrol potentiostat by stepping the potential about 20 mV once each minute and recording the resultant pseudo steady-state current. The corresponding anodic and cathodic curves were constructed accordingly. For current-time measurement at a given electrode potential, the same potentiostat was used in conjunction with a Bristol X-Y recorder. Metallographic examinations were made using a Leitz Metallograph. Cobalt and tungsten dissolution was measured by analyzing the solutions for these elements using atomic absorption spectrometry (11). Relative standard deviations of 9% and 2.5% were found for the W and Co analyses, respectively. Standards were prepared in the same matrix to prevent

determinant errors. The current yields for tungsten and Co dissolution were obtained by comparing the recorded current to those obtained from solution analyses.

Four to five kg quantities of WC-6% Co were electrolyzed simultaneously in a particulate bed electrode system at constant potential. This system was essentially a barrel-tank electroplating unit, strengthened to meet the mechanical requirement and modified to facilitate monitoring of the average potential of the pieces during the electrolysis (5).

Results

Steady-state polarization curves.—Typical potentiostatic, steady-state polarization curves for anodic dissolution of WC-6% Co and WC and for H⁺-ion reduction on WC are shown in Fig. 1. The curve for Co dissolution is shown in Fig. 2. These polarization curves were repeatable upon successive cycling of the potential and gave essentially the same shape on the decreasing and increasing potential cycles except for some hysteresis. Changes in stirring did not influence the shapes of the curves. The open-circuit potential for WC-6% Co was typically about -300 mV which is between the open-circuit potential for Co (-500 mV) and WC (0-200 mV). The WC + 6% Co electrode shows three distinctive regions which are labeled A, B, and C in Fig. 1 for future reference. In region A the logarithm of the current density increases approximately linearly with the potential. At -0.1V the current drops abruptly by 70-80% and remains roughly constant while the potential increases some 0.7V. This

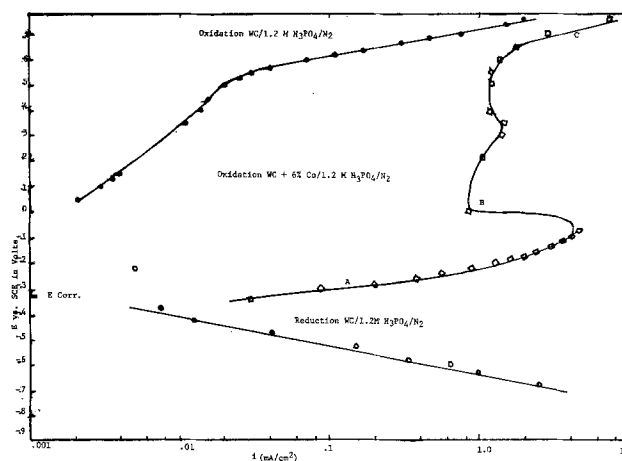


Fig. 1. Steady-state polarization curves for oxidation at WC-6% Co and the oxidation or reduction at the WC electrodes in 1.2M H_3PO_4 solution. Stirred solution, $T = 25^\circ C$.

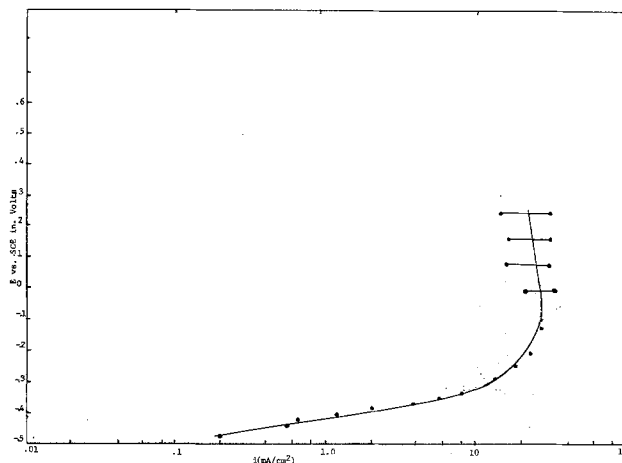


Fig. 2. Steady-state polarization curve for the oxidation at Co electrode in N_2 saturated solution of 1.2M H_3PO_4 . Stirred solution, $T = 25^\circ C$.

transition region is labeled "B." At $E \approx 0.6V$ the current again increases exponentially with an increase in potential.

Current-time behavior.—Pieces of WC-6% Co electrodes were potentiostated between -250 and -100 mV, i.e., potential region A of Fig. 1. At these potentials the current slowly decreased with time finally approaching a plateau in more than 10 hr. Figure 3 shows an $i-t$ curve at -200 mV which is typical of all plots obtained.

Metallographic examination.—Figure 4 shows a micrograph of a cross-sectional area of a piece of WC-6% Co which was anodized in $1.2M$ H_3PO_4 for 24 hr. A definite boundary is observed between the binder-free WC skeleton (Fig. 4I) and the WC-6% Co phase (Fig. 4-II). The anodization took place in the dynamic particulate bed system, potentiostated at -60 mV. Further metallographic examinations of selected pieces of anodized WC-6% Co revealed a uniform coating of porous WC phase which covered the entire surface of the cemented carbides.

Reaction products.—WC-6% Co electrodes were potentiostated for several hours at various potentials in regions A and C of the polarization curve of Fig. 1. The solutions were analyzed for Co and W after each

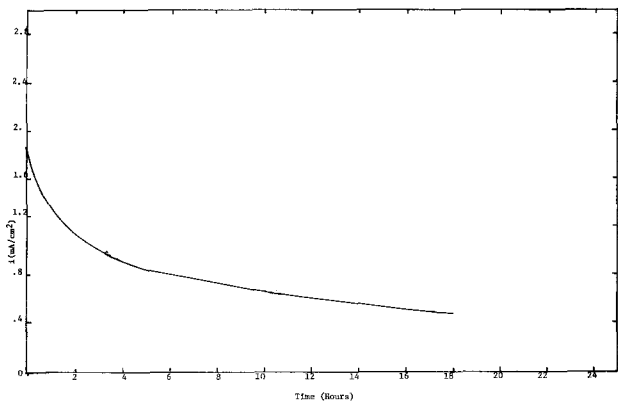


Fig. 3. Dissolution rate of the binder phase (Co-W) alloy from a WC-6% Co alloy as a function of time at -200 mV (vs. SCE) in N_2 saturated solution of $1.2M$ H_3PO_4 . Stirred solution, $T = 25^\circ C$.

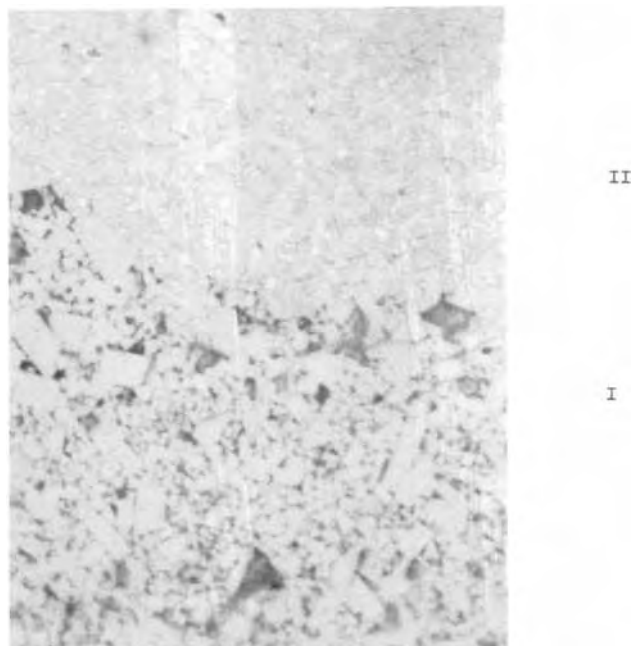


Fig. 4. Cross-sectional micrograph of a piece of WC-6% Co anodized in $1.2M$ H_3PO_4 solution for 24 hr in a particulate bed electrode system at -60 mV. $1200\times$. I—porous WC; II—WC-6% Co.

Table I. Cobalt and tungsten concentrations as a function of applied potential for a WC-6% Co cemented carbide
Solution: N_2 -saturated, stirred $1.2M$ H_3PO_4 at $25^\circ C$

E (mV vs. SCE)	Duration of expts., hr	Co dissolved (mg/cm ² -hr)	W dissolved (mg/cm ² -hr)	Weight fraction W Co + W
-315 to -305 (open circuit)	48	0.015	*	—
-335 to -305 (open circuit)	48	0.009	*	—
-250	17	0.30	*	—
-200	16	0.85	0.11	0.11
-100	8.75	2.30	0.39	0.14
+750	4.25	1.33	8.34	0.86

* Below detection limit using atomic absorption spectrometry for analysis of tungsten.

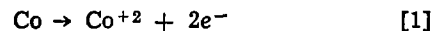
dissolution experiment, the results being shown in Table I. At potentials positive of $+600$ mV gas was observed evolving from the anode surface. A previous investigator (12) has identified the gaseous products as CO_2 which results from dissolution of WC in aqueous solution.

The weight fractions of W in the dissolved alloy were calculated from the experimental values and are shown in the right-hand column of Table I.

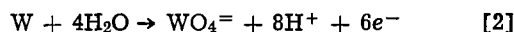
Discussion and Conclusions

Anodic Dissolution of WC-6% Co

Region A.—The solution analyses and micrographs (see Fig. 4) lead to the conclusion that the Co-W binder phase selectively dissolves in region A, leaving behind the WC grains. Binder dissolution thus may be represented by Eq. [1] and [2]. Although tungsten oxidation may be questioned



$$(E^\circ \approx -0.52V \text{ vs. SCE})$$



$$(E^\circ \approx -0.2V \text{ vs. SCE}) \quad (13)$$

at the negative end of region A, because $E < E^\circ$, the binder phase appears to dissolve in its entirety at the positive end of A. The tungsten in solution accounts for $\sim 11-14\%$ of the metal dissolved at -0.2 to $-0.1V$ (see Table I), which is in the same range as the fraction of tungsten expected in the binder phase based on the solubility of W in Co (14, 15). A charge balance based on Eq. [1] and [2] was tested by comparing the dissolution currents of Table I to the measured anodic current, i_a . Results are shown in Table II. The measured currents are explained within analytical precision. Inasmuch as insoluble tungsten oxides could not be detected, they were presumed to be insignificant compared to soluble tungsten, thus justifying Eq. [2].

Because most of the current is carried by cobalt dissolution, it is not surprising that the composite

Table II. Current yields for dissolution of Co-W alloy and WC from a WC-6% Co cemented carbide
Solution: N_2 -saturated, stirred $1.2M$ H_3PO_4 at $25^\circ C$

E (mV vs. SCE)	i_a (mA/cm ²)	i_1 (mA/cm ²)	i_2 (mA/cm ²)	i_3 (mA/cm ²)
-315 to -305 (open circuit)	0.0	0.014	*	0.0
-335 to -305 (open circuit)	0.0	0.008	*	0.0
-250	0.33	0.27	*	0.0
-200	0.81	0.79	0.34	0.0
-100	2.49	2.09	0.10	0.0
+750	13.25	1.21	0.16**	11.41

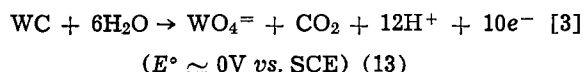
* Below detection limit (see Table I).

** Calculated (see the text).

polarization curve (Fig. 1) is similar to the cobalt polarization curve (Fig. 2), both in position and shape.

Region B.—Binder dissolution is accelerated with increasing potential but then undergoes an abrupt decrease by 80% at $\sim 0.05V$. This behavior is characteristic of an active-passive transition. (Figure 3 clearly shows that it is not caused by cobalt depletion.) The composition of the passive film was not identified from the present work, but could conceivably be caused by formation of either tungsten oxide or cobalt phosphate (Fig. 2 shows a somewhat similar curve for cobalt at $-0.1V$ as observed for WC-6% Co at the same potential). The current appears to be limited by dissolution of a film of one of these substances at the passivation points.

Region C.—As the potential is increased, after passivity occurs at B, the current increases slowly at first and then rapidly as E increases beyond $0.6V$. This is because reaction [3] becomes significant at potentials positive of its reversible potential. This reaction is characterized by electrode gassing and by complete consumption of the WC-Co alloy to



yield soluble products in the corresponding amounts. Also approximate charge balance is attained by considering Eq. [3] to produce all the soluble W except for a small amount produced by Eq. [2], this latter amount being calculated from the cobalt dissolution. The last entry of Table II shows the result of this comparison.

Application of Results to Corrosion of WC-Co Alloy

When an oxidant is present in solution, its rate of reduction coupled with alloy dissolution will define a corrosion potential and, from Fig. 1 a corrosion current (provided products of the reduction do not precipitate or otherwise complicate reactions [1] and [2]). In the absence of oxygen or other strong oxidants the reduction current will be H^+ -ion reduction, for which the polarization curve is shown in Fig. 1. Extrapolation of this curve to the corrosion potential, E_{CORR} , in Fig. 1 yields currents of the same order as those measured from cobalt dissolution at open circuit (see Table II). Thus binder phase dissolution proceeds selectively under these corrosion conditions. The corrosion rate of the binder phase in cemented carbides is also expected to depend on its thickness, which is determined by the amount of cobalt, grain size, and grain size distribution of the WC phase. Low cobalt concentration and small particle size WC decrease the thickness of the Co-W layer on WC. This is exemplified by tests in which decrease in dissolution rate of the binder phase was observed when pieces of $0.5\text{-}1\mu$ WC-5.5% Co were substituted for $1\text{-}2\mu$ WC-6% Co (16).

Selective dissolution of the binder phase can be and has been (5) used to advantage in the recycling indus-

try. In this case it is desirable to separate the cobalt from the tungsten carbide with as little energy expenditure as possible. Rather than dissolve the entire alloy with a strong oxidizing environment, it is possible to apply mild oxidizing conditions coupled with erosion to effect the separation with little expenditure of electrical energy. Thus particulate WC-6% Co was anodized in a rotating barrel-tank which contained the electrolyte. Anodic current dissolved the Co-containing binder phase, after which the WC phase (see Fig. 4-I) eroded by milling the partially anodized WC-6% Co to WC powder and fresh WC-Co surfaces.

Acknowledgment

This work was performed at Fansteel Research Center, Salt Lake City, Utah. The author wishes to thank T. N. Andersen for helpful discussions, J. K. Faulkner and D. C. Thorsen for their technical assistance, the Department of Chemistry, University of Utah, for use of the potentiostats and Fansteel Incorporated for permission to publish this article.

Manuscript submitted Aug. 3, 1979; revised manuscript received Feb. 21, 1980.

Any discussion of this paper will appear in a Discussion Section to be published in the June 1981 JOURNAL. All discussions for the June 1981 Discussion Section should be submitted by Feb. 1, 1981.

Publication costs of this article were assisted by Fansteel Metals.

REFERENCES

1. P. Schwarzkopf and R. Kieffer, "Cemented Carbides," Chap. 5, The Macmillan Company, New York (1960).
2. W. Dawihl and B. Irich, *Cobalt*, **22**, 22 (1964).
3. E. Kirbach and S. Chow, *For. Prod. J.*, **26**, 44 (1976).
4. L. F. Stepanova and E. M. Borovikov, *Izv. Vyssh. Uchebn. Zaved., Les. Zh.*, **17**, 78 (1974); (C.A., **81**, 67532r).
5. M. H. Ghandehari, M. Schussler, U. S. Patent Serial No. 33,037 (1979).
6. H. Yamamoto, *Nippon Tungsten Rev.*, **11**, 1 (1978).
7. K. Hijikata and K. Mirumachi, *Nippon Kinzoku Gakkai-Shi*, **32**, 7 (1968); (C.A., **68**, 107455h).
8. K. Mirumachi and K. Hijikata, *Nihon Daigaku Bunrigakubu Sheizenkagaku Kenkyusho Kenkyu Kiyo*, **8**, 1 (1973); (C.A., **79**, 132177d).
9. K. Mirumachi and K. Hijikata, *ibid.*, **9**, 1 (1974); (C.A. 110125Z).
10. K. J. Vetter, "Electrochemical Kinetics," Chap. 5, Academic Press, New York (1967).
11. M. H. Ghandehari, L. E. Pope, and F. D. Pierce, *Int. J. Powder Metall.*, **15**, 55 (1979).
12. J. D. Voorhies, *This Journal*, **119**, 219 (1972).
13. NBS Circular 500, "Selected Values of Chemical Thermodynamic Properties," Part I.
14. L. E. Pope, Unpublished results.
15. H. Suzuki and H. Kubota, *Planseeber. Pulvermetall.*, **14**, 96 (1966).
16. M. H. Ghandehari, Unpublished results.

Visible Light Response of Polycrystalline TiO₂ Electrodes

Y. Matsumoto, J. Kurimoto, Y. Amagasaki, and E. Sato

Department of Industrial Chemistry, Faculty of Engineering,

Utsunomiya University, Ishi-icho 2753, Utsunomiya, Japan

ABSTRACT

The photoelectrochemical properties of Co-doped polycrystalline TiO₂ electrodes (Ti/CoO_x) and undoped TiO₂ electrodes have been investigated. The undoped polycrystalline TiO₂ electrodes heated at temperatures over 700°C give the visible light response in addition to the original bandgap photoresponse. The Ti/CoO_x electrodes prepared at 400° ~ 550°C also give the apparent visible light response (550 ~ 420 nm), when the Co was highly doped in the TiO₂ layer from the TiO₂ surface to the interface of the Ti substrate/TiO₂ layer. The visible light response will be based on the newly formed d-band by the interaction of the interstitial Ti or Co ion in the TiO₂ lattice, which is below the π^* conduction band of the TiO₂ in energy position.

Many studies of TiO₂ electrodes which are used for the photoanode in the photoelectrolysis of water have been conducted (1-25). TiO₂ is suitable for the photoanode material in point of view of the stability in aqueous solution, but its large bandgap (3.0 eV) brings about only small efficiency in using the solar spectra: photons with shorter wavelengths than 400 nm responsible for hole production in TiO₂ is only about 3% in all solar photons (26). Therefore, some modifications of TiO₂ are necessary in using it as the photoanode material in order to increase the efficiency of solar energy conversion.

Recently, a few favorable results of the modified TiO₂ electrodes are reported. Maruska and Ghosh report that Al-doped and Cr-doped TiO₂ single crystals bring about the increases of the ultraviolet light (wavelengths shorter than about 420 nm) response and visible light (wavelengths longer than about 420 nm) response, respectively (16, 17). Augustynski *et al.* use polycrystalline TiO₂ electrodes doped with various elements, Al, Sr, Ga, Eu, B, and Be, as the photoanode (18, 19). Al and Be-doped TiO₂ electrodes show the interesting result that the quantum efficiencies to the ultraviolet light increase like Al-doped TiO₂ single crystal electrodes as stated above.

Polycrystalline TiO₂ electrode is more suitable for the photoanode than single crystal TiO₂ in preparation cost. Therefore, we use the polycrystalline TiO₂ electrodes doped with Co as the photoanode material in this paper, which is prepared with the thermal decomposition of aqueous solution of the Co salts. This electrode has also been investigated as the anode material in the chlorine and oxygen evolution reactions, and the high catalytic activity of Co₃O₄ formed on the electrode is demonstrated (27, 28). In this paper, as a result, Co₃O₄ layer does not influence the spectral dependence of the photocurrent but only the Co-doped TiO₂ layer shows interesting visible light response. Although the photocurrent of the polycrystalline TiO₂ due to the lights of the 500W xenon lamp fairly decreases by the Co coating, the extension of the spectral response by the Co-doping demonstrated in this paper suggests the possibility of raising the efficiency of solar energy conversion in spectra.

Experimental

The titanium plate (99.6%, 1.5 × 5 × 0.1 cm, Kobe Steel, Limited) was polished with emery papers and then washed with a cleanser (Marufuku, Limited). The sample was cleaned with the hypersonic technique, followed by washing with acetone. Coatings were applied by painting the Co(NO₃)₂ solution with a few drops of 30% H₂O₂ and then heating it in air

at 400°C for 10 min. Five separate coatings were applied. After the final coating, the specimen was finally heated in air at various temperatures over 400°C for 1 hr, unless otherwise stated. The geometric area exposed to the electrolyte was reduced to 1 cm² on one side by epoxy resin to mask off the remainder of the electrode. The above Co coating electrode is represented as Ti/CoO_x electrode for convenience in this paper.

Co₃O₄, rutile, and anatase were observed for the samples finally heated at the temperatures from 550° to 700°C by x-ray analysis. Similar oxides will exist on the samples finally heated at 400°C, although the clear diffraction peak was not observed.

The solution was pre-electrolyzed 0.5M H₂SO₄. Hg/Hg₂SO₄ electrode was used as the reference electrode and electrode potentials cited in this paper are referred to this electrode. The counterelectrode was a platinum plate. A quartz H-type cell was used as an electrolytic cell. The polarization curves were measured by using a potentiostat (Nichia Keiki Limited, NP-G1050) and a function generator (Nichia Keiki Limited), and recorded by an X-Y recorder (Yokogawa Electric Works Limited, Type-3036). The monochromatic light of various wavelengths was obtained by a prism monochromator. A 500W xenon lamp (1.1 W/cm²) was used as a light source. A sequence of measurements was done with the same experimental setup, so that the irradiation intensity is believed to have been kept constant during measurements. All measurements were done at room temperature.

Results

Figure 1 shows the current-potential curves under illumination with a 500W xenon lamp for the undoped TiO₂ and the Ti/CoO_x electrodes. For the Ti/CoO_x electrodes, two types are given in this figure. One is the nontreated Ti/CoO_x electrode and the other is the pre-electrolyzed Ti/CoO_x electrode at 2.5V for 2.5 hr under dark, at which oxygen evolution occurs. The potential for the onset of the photocurrent shifts to more positive potentials by the Co coating. This positive shift is undesirable for the photoelectrolysis with and without external voltage in a point of view of the energy conversion efficiency. However, the Ti/CoO_x electrodes were improved so that their photocurrent onset potentials come close to those of the TiO₂ electrodes by the pre-electrolyzed treatment, as the figure shows.

The Co₃O₄ layer on the Ti/CoO_x electrode probably causes positive shift in the flatband potential. This will be the main reason for the positive shift of the photocurrent onset potential by the Co coating. Oxygen evolution will strip off the Co₃O₄ layer from the

Key words: photoelectrolysis, photoanode, TiO₂.

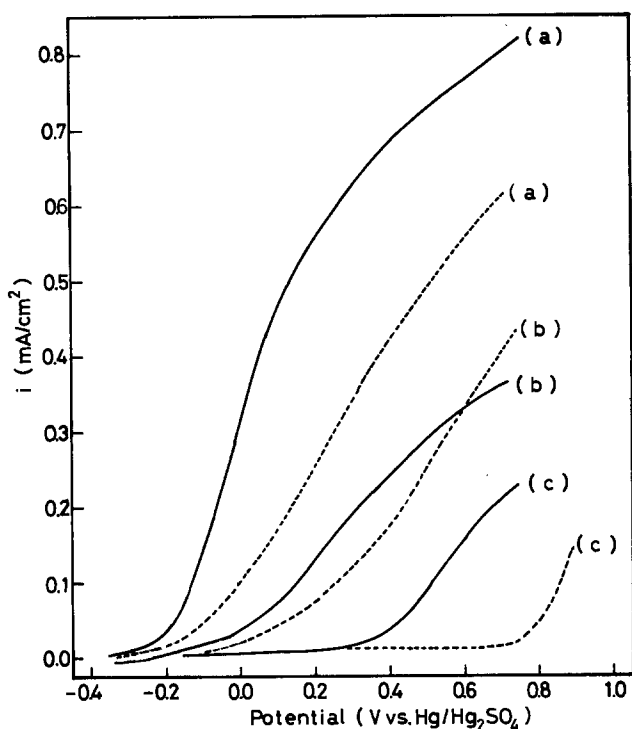


Fig. 1. Current-potential curves for TiO_2 and Ti/CoO_x electrodes heated for 1 hr under illumination with a 500W xenon lamp. (—) heated at 550°C , (---) heated at 400°C , curve (a) TiO_2 , curve (b) pre-electrolyzed Ti/CoO_x (2.4×10^{-7} mole Co/cm^2), curve (c) Ti/CoO_x (2.4×10^{-7} mole Co/cm^2).

electrode surface of the Ti/CoO_x electrode by its gas pressure, leading to the direct exposure of the TiO_2 layer of the electrode to the electrolyte. Therefore, the flatband potential of the pre-electrolyzed Ti/CoO_x electrode becomes to be near that of the TiO_2 electrode, so the photocurrent onset potential of the Ti/CoO_x electrode shifts to negative by the pre-electrolyzed treatment. In any case, the good characteristic of the visible light response of the Ti/CoO_x electrode is almost the same as that of the pre-electrolyzed Ti/CoO_x electrode as described in a later section, although the photocurrents of the Ti/CoO_x electrodes are smaller than that of the TiO_2 electrode under illumination of ultraviolet lights.

The typical photoresponses of the pre-electrolyzed Ti/CoO_x electrode, which was prepared at 550°C for 1 hr, to the monochromatic lights of 320 and 450 nm at a constant potential of 0.6V are shown in (a) and (b) of Fig. 2, respectively. Both of the photoresponses are fast, as the figure shows. Similar photoresponses are also observed to the other monochromatic lights. The real photocurrent is the difference between the dark current and the illumination current, and is determined by the difference between the constant dark current and the constant illumination current in this paper (represented as i_p in this figure).

The spectral dependences of the real photocurrents obtained by the above method are shown in Fig. 3, 4, 5, and 6. It should be noticed in Fig. 3 that the apparent photocurrents due to the lights with the longer wavelength than about 410 ~ 420 nm (LW lights) appear for the Ti/CoO_x electrodes in addition to the original bandgap photocurrent of TiO_2 due to the lights with the shorter wavelength than about 410 nm (SW lights). The quite similar spectral dependence to Fig. 3 for the Ti/CoO_x electrode is also observed in 1M NaOH. Therefore, the above photocurrents due to the LW lights are mainly based on the oxidation reaction of H_2O or OH^- due to the produced hole. Moreover, no difference between the Ti/CoO_x electrode prepared by using CoCl_2 solution

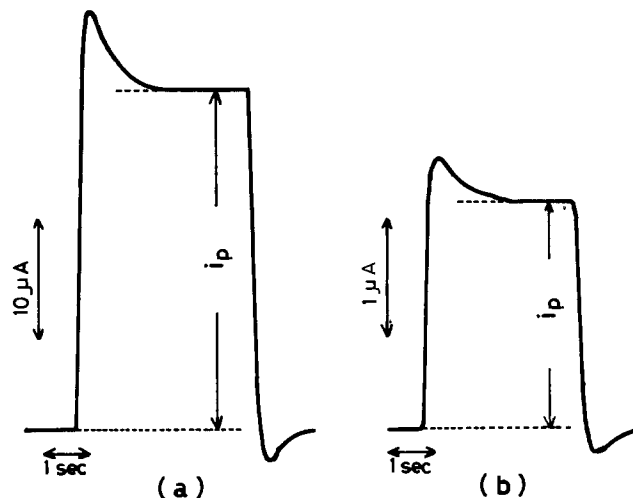


Fig. 2. Photoresponses of a pre-electrolyzed Ti/CoO_x (2.4×10^{-7} mole Co/cm^2) electrode. (a) for $\lambda = 320$ nm, (b) for $\lambda = 450$ nm.

and the above Ti/CoO_x electrodes which are prepared by using $\text{Co(NO}_3)_2$ solution as described in the Experimental section, was observed in the spectral dependence of the photocurrent. This result confirms that the photocurrents due to the LW lights are assigned to Co. The low photocurrents of the Ti/CoO_x electrodes due to the SW lights are mainly based on disturbing to light passing to the TiO_2 layer by Co_3O_4 layer formed on the surface, because the photocurrents due to the SW lights increase by the pre-electrolyzed treatment as the figure shows. The photoresponses of

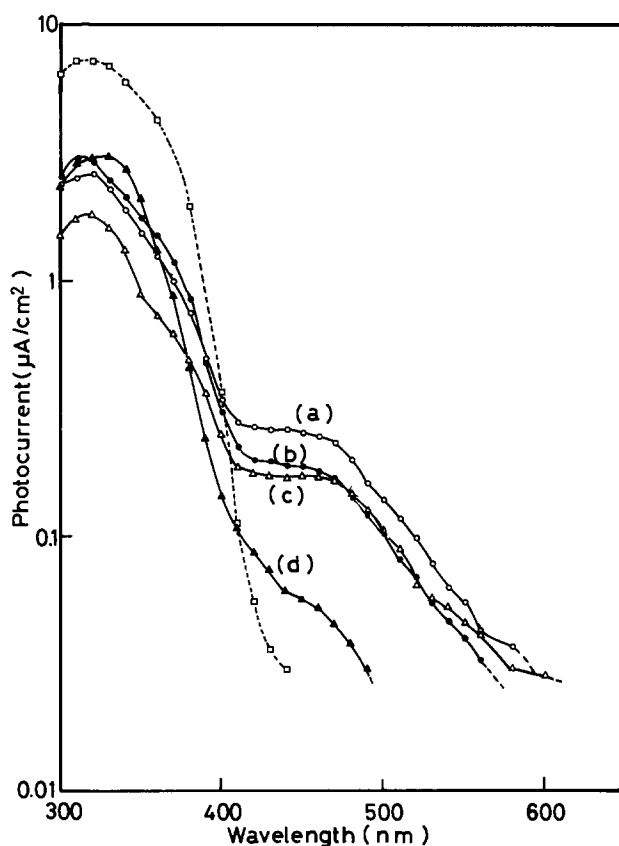


Fig. 3. Spectral dependences of the photocurrent (i_p) for the various electrodes heated for 1 hr (---) TiO_2 heated at 550°C , (a) Ti/CoO_x (2.4×10^{-8} mole Co/cm^2) heated at 550°C , (b) pre-electrolyzed Ti/CoO_x (2.4×10^{-7} mole Co/cm^2) heated at 550°C , (c) Ti/CoO_x (2.4×10^{-7} mole Co/cm^2) heated at 550°C , (d) pre-electrolyzed Ti/CoO_x (2.4×10^{-7} mole Co/cm^2) heated at 400°C .

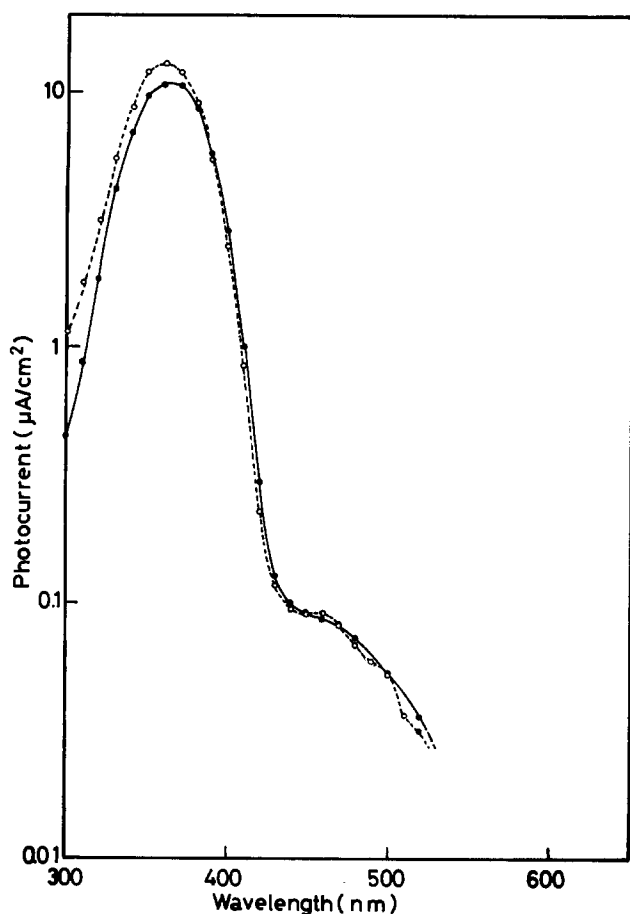


Fig. 4. Spectral dependences of the photocurrent (i_p) for TiO_2 and Ti/CoO_x (2.4×10^{-7} mole Co/cm^2) electrodes heated at 700°C for 1 hr (---○---) TiO_2 , (—●—) Ti/CoO_x .

the Ti/CoO_x electrodes to the LW lights are associated with the highly doped Co in the TiO_2 lattice as stated in a later section.

In the cases of the electrodes heated at 700°C , almost the same spectral dependences were obtained for both the TiO_2 and the Ti/CoO_x electrodes as shown in Fig. 4. As shown in Fig. 5, in which the spectral dependences of the photocurrents for the TiO_2 electrodes heated at various temperatures are shown, the photocurrents due to the LW lights were observed for the electrodes heated at temperatures over 700°C . The same spectral dependences as Fig. 5 are also obtained for the TiO_2 electrodes heated in gas mixture of 0.2 atm O_2 and 0.8 atm He. Therefore, the photocurrents due to the LW lights shown in Fig. 4 are not assigned to Co, but simply to the heat-treatment at high temperature. In other words, the effect of Co on the LW lights response disappears by the heat-treatment at temperature over 700°C .

Two remarkable features of the spectral dependences of the photocurrents for the TiO_2 electrodes are brought about by the heat-treatment at temperatures over 700°C as shown in Fig. 5. One is the appearance of the photoresponse to the LW lights at the TiO_2 electrode as described previously. This will be based on the newly formed narrow band in the bandgap of the TiO_2 . The other is of the photocurrents due to the SW lights. The peak of the photocurrent due to the SW lights becomes sharp and shifts to the long wavelength, showing that the conduction band and the valence band in the TiO_2 varied in energy. The TiO_2 electrodes which are prepared by using 99.9% Ti plate (High purity, Limited) also give quite similar spectral dependences to Fig. 5. Therefore, the above phenomena eventually will be given

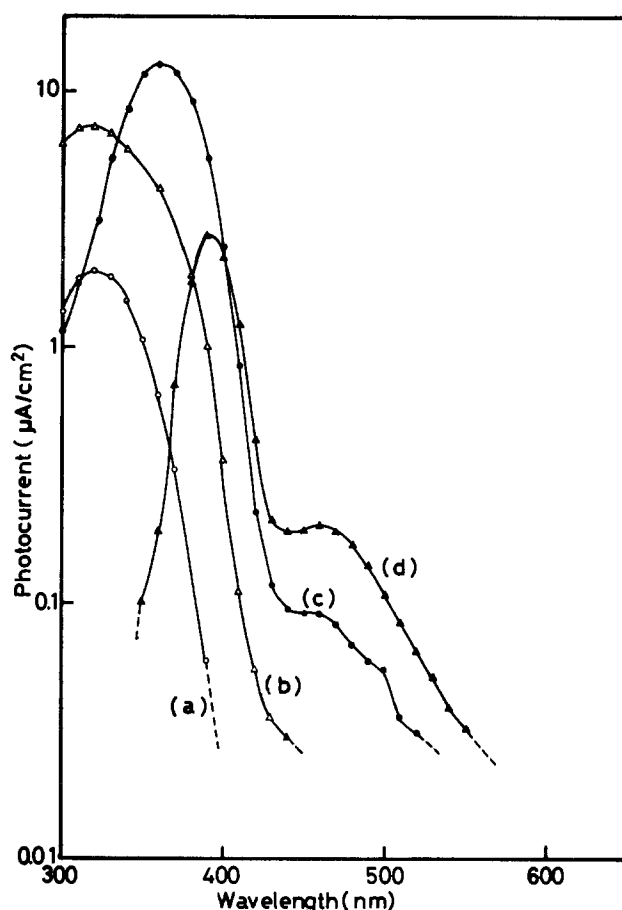


Fig. 5. Spectral dependences of the photocurrent (i_p) for TiO_2 electrodes heated for 1 hr. Curve (a) heated at 400°C , curve (b) at 550°C , curve (c) at 700°C , curve (d) at 800°C .

by some morphologic variations in the TiO_2 lattice due to the heat-treatment at high temperature.

Figure 6 shows the variation of the spectral dependences of the photocurrents of the Ti/CoO_x electrodes with the time of the final heat-treatment of 550°C . Although the appropriate time for the thermal diffusion of Co into the TiO_2 bulk will be desired, the photocurrents due to the LW lights decrease with the heat-treatment time. In this figure, the photoresponse of the $\text{Ti/TiO}_2/\text{CoO}_x$ electrode which is prepared as follows, is also shown. After the Ti plate coated by TiCl_4 solution (8.7×10^{-8} mole/ cm^2) was heated in air at 550°C for 1 hr, the $\text{Co(NO}_3)_2$ solution was coated on the surface so that the amount of Co is 2.4×10^{-7} mole/ cm^2 , and then decomposed at 400°C five times. Finally, the sample was heated at 550°C for 20 min. Therefore, the TiO_2 layer of the $\text{Ti/TiO}_2/\text{CoO}_x$ electrode is the thickest in the electrodes in Fig. 6, while the photocurrent due to the LW lights at this electrode is the smallest as the figure shows.

From the above results, it is concluded that the thick TiO_2 layer in the side of the Ti substrate of the Ti/CoO_x electrode is undesirable for the photoresponse to the LW lights. This is in line with the result that the photocurrents due to the LW lights decrease with the heat-treatment time, because the thickness of the TiO_2 layer increases with the heat-treatment time. Moreover, the above conclusion is confirmed by the result that no photoresponse to the LW lights is observed for the TiO_2 (single crystal)/ CoO_x electrodes which are prepared by coating the various amounts of Co on the single crystal TiO_2 and then heating at 550°C for 1 hr. Thus, it is required that the highly Co doped TiO_2 layer reaches to the Ti substrate interface for the purpose of obtaining the high LW lights photoresponse for the Ti/CoO_x electrode.

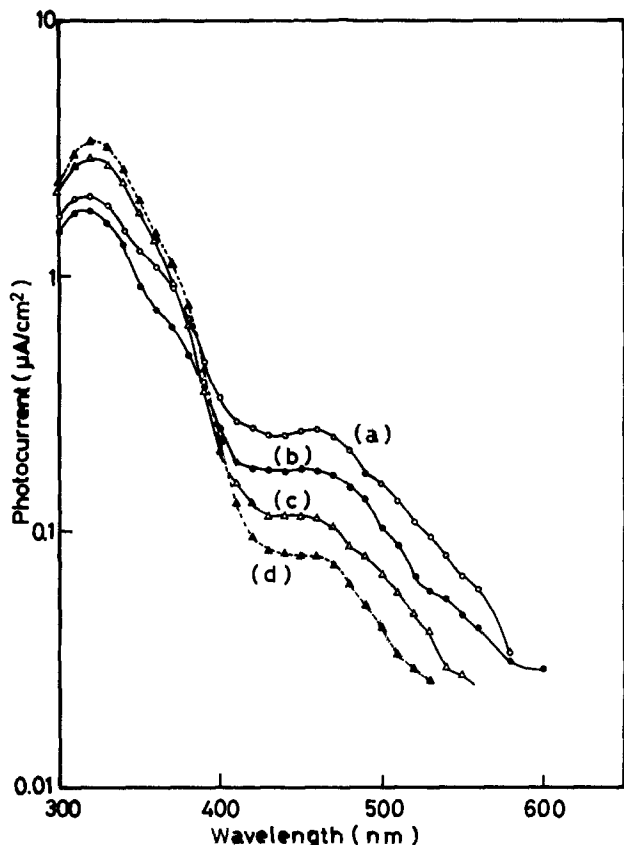


Fig. 6. Spectral dependences of the photocurrent (i_p) for Ti/CoO_x (2.4×10^{-7} mole Co/cm^2) electrodes heated at 550°C . Curve (a) for 20 min, curve (b) for 1 hr, curve (c) for 5 hr, curve (d) $\text{Ti/TiO}_2/\text{CoO}_x$.

Discussion

Spectral dependence of the thermally oxidized TiO_2 electrode.—The band structure of the TiO_2 rutile proposed by Goodenough (29) is shown in (a) of Fig. 7 (in other figures of band structures, $t_{||}$ -band is omitted). The valence band is the $\text{Ti-O } \pi$ band and the conduction band is the $\text{Ti-O } \pi^*$ band. The Ti cation is octahedrally surrounded by the oxygen ion in the lattice, therefore, the π and π^* bands are formed by the interaction between the t_{2g} orbital of the Ti cation and the p_π orbital of the oxygen ion (29). The anatase structure also has the same octahedral unit, but is

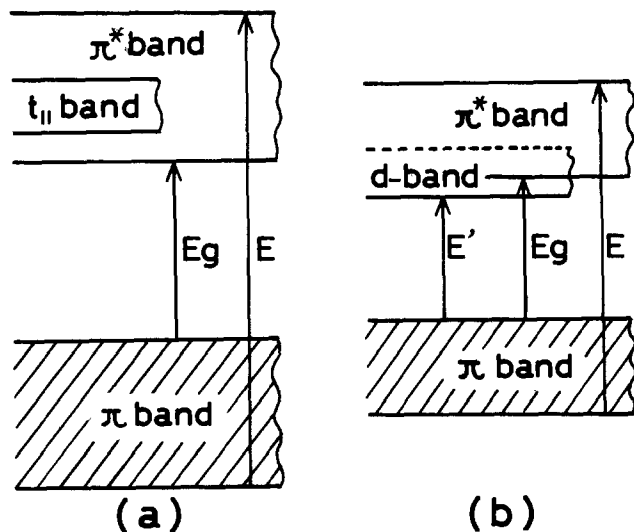


Fig. 7. Band structures of TiO_2 . (a) for TiO_2 rutile, (b) for TiO_2 heated at high temperature.

different only in the arrangement of this unit. This arrangement affects the π and π^* bands little, leading to the similar band structure to Fig. 8 for the anatase. Since the hole is formed in the π band by the π band \rightarrow the π^* band transition, the photocurrent appears only when the lights with the wavelengths corresponding to the energies from E_g (bandgap) to E are illuminated, as shown in Fig. 7. Therefore, the broadness and the position of the peak of the photocurrent due to the SW lights (see Fig. 5) will be mainly determined by the degree of the interaction between the t_{2g} orbital of Ti cation and the p_π orbital of the oxygen ion, which will depend on the distance between both ions. If the interaction becomes weak, the peak of the photocurrent becomes sharp and shifts to the long wavelength, i.e., the low energy transition. As shown in Fig. 5, the same variation of the photocurrent as stated above for the TiO_2 electrode heated at temperatures over 700°C , therefore, is based on the decrease of the degree of the $\text{Ti-O } \pi$ interaction. The interstitial Ti ions exist in the TiO_2 layer prepared by the thermal oxidation (29-32), especially in the Magnéli phase (33, 34). This is represented as $\text{Ti-(Ti)}_i\text{-Ti}$ in the lattice, and affects the Ti-O bond in the octahedral unit (29). The decrease of the degree of the $\text{Ti-O } \pi$ interaction for the electrode heated at high temperature will be brought about by a number of the interstitial Ti ions produced by the heat-treatment at high temperature. In addition, a number of the interstitial Ti ions will bring about the new band in the TiO_2 . This new band will be the d-band formed by the interaction between the d-orbitals of the Ti ion, $\text{Ti-(Ti)}_i\text{-Ti}$ in the lattice. Since the d-orbital of the Ti ion in the lattice is near or below the π^* band in energy position (29), the newly formed d-band will also be a little below the π^* band, and overlap the bottom of the π^* band. As a result, the photocurrent due to the LW lights, the low energy transition of the π band \rightarrow the d-band [E' in (b) of Fig. 7], appears for the electrode prepared at the heat-treatment at temperatures over 700°C . The band structure of this TiO_2 electrode is shown in (b) of Fig. 7, which also shows the energy variations of the π and π^* bands.

Spectral dependence of the Ti/CoO_x electrode.—The photoresponse to the LW lights does not appear on the Ti/CoO_x electrode when Co was highly doped only on the surface of the TiO_2 layer. If the Co impurity band or the surface state due to the Co is formed a little above the π valence band in energy position, the photoresponse to the LW lights should be observed at this type electrode because the hole is always produced in the Co impurity band or the surface state by the transition from this band or state to the π^* conduction band due to the LW lights. Therefore, this is not proper in energy position. The Co impurity band exists below the π^* conduction band in the Ti/CoO_x electrode. Figure 8 shows the two types

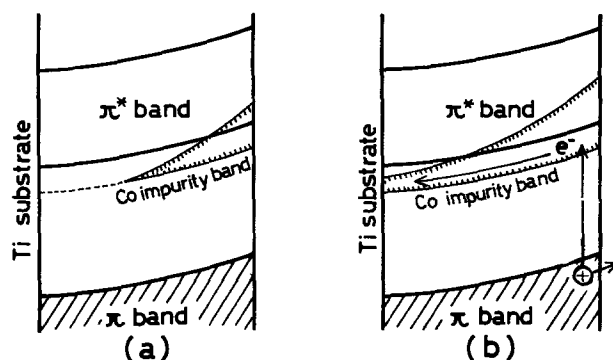


Fig. 8. Band structures of Co-doped TiO_2 layers of Ti/CoO_x electrodes. (a) Co impurity band is formed only in the surface region of the TiO_2 layer. (b) Co impurity band is formed throughout the TiO_2 layer.

of the band structures in this case. Figure 8(a) shows the case of the electrode doped only on the surface. As shown in (a) of this figure, the excited electron in the Co impurity band due to the LW lights cannot move to the bulk, leading to no photoresponse. On the other hand, in the case of the electrode in which Co was highly doped through the TiO₂ layer, from the surface to the interface of the TiO₂ and the Ti substrate, the excited electron in the Co impurity band can move into the Ti substrate through this band in the TiO₂ layer. This case leads to the appearance of the LW lights photoresponse, which is shown in (b) of Fig. 8.

The Co impurity band is formed only by the heat-treatment at the appropriate temperature (400° ~ 550°C). This implies that the Co is situated in the appropriate position in the TiO₂ lattice by the above temperature range so that the Co impurity band is formed. There will be two appropriate positions in the lattice. One is the Ti ion site in the TiO₂ lattice: the Ti ion is substituted by the Co ion. The other case is the interstitial site which is represented by Ti-(Co)_i-Ti as described in the previous section. In any case, the Co impurity band will be formed by the interaction between the d orbitals of the Co ions in the lattice.

In conclusion, the Ti/CoO_x electrode with small amounts of Co prepared at 550°C heat-treatment is superior in the visible light photoresponse. Therefore, this type of electrode is suitable for the photoanode for the photoelectrolysis of water with solar energy, but some improvements are further necessary in order to obtain the large photocurrent.

Manuscript submitted March 5, 1980; revised manuscript received May 16, 1980.

Any discussion of this paper will appear in a Discussion Section to be published in the June 1980 JOURNAL. All discussions for the June 1980 Discussion Section should be submitted by Feb. 1, 1980.

Publication costs of this article were assisted by Utsunomiya University.

REFERENCES

1. A. Fujishima and K. Honda, *Bull. Chem. Soc. Jpn.*, **44**, 1148 (1971).
2. A. Fujishima and K. Honda, *Nature*, **238**, 37 (1972).
3. A. Fujishima, K. Kohayakawa, and K. Honda, *Bull. Chem. Soc. Jpn.*, **48**, 1041 (1975).
4. M. S. Wrighton, D. S. Ginley, P. T. Wolczanski, A. B. Ellis, D. L. Morse, and A. Linz, *Proc. Natl. Acad. Sci. U.S.A.*, **72**, 1518 (1975).
5. T. Ohnishi, Y. Nakato, and H. Tsubomura, *Ber. Bunsenges. Phys. Chem.*, **89**, 579 (1975).
6. A. J. Nozik, *Nature*, **257**, 383 (1975).
7. J. G. Mavroides, D. I. Tchernev, J. A. Kafalas, and D. F. Kolesar, *Mater. Res. Bull.*, **10**, 1023 (1975).
8. K. L. Hardee and A. J. Bard, *This Journal*, **122**, 739 (1975).
9. W. Gissler, P. L. Lensi, and S. Pizzini, *J. Appl. Electrochem.*, **6**, 9 (1976).
10. J. Kenney, D. H. Weinstein, and G. M. Haas, *Nature*, **253**, 719 (1975).
11. A. Fujishima, K. Kohayakawa, and K. Honda, *This Journal*, **122**, 1487 (1975).
12. J. F. Houlihan, D. P. Madacsi, E. J. Walsh, and L. N. Mulary, *Mater. Res. Bull.*, **11**, 1191 (1976).
13. H. Tamura, H. Yoneyama, C. Iwakura, and T. Murai, *Bull. Chem. Soc. Jpn.*, **50**, 753 (1977).
14. J. H. Carey and B. G. Oliver, *Nature*, **259**, 554 (1976).
15. A. B. Bocarsly, J. M. Bolts, P. G. Cummins, and M. S. Wrighton, *Appl. Phys. Lett.*, **31**, 568 (1977).
16. A. K. Ghosh and H. P. Maruska, *This Journal*, **124**, 1516 (1977).
17. H. P. Maruska and A. K. Ghosh, *Sol. Energy Mater.*, **1**, 237 (1979).
18. J. Augustynski, J. Hinden, and C. Stadler, *This Journal*, **124**, 1063 (1977).
19. C. Stadler and J. Augustynski, *ibid.*, **126**, 2007 (1979).
20. L. A. Harris and R. H. Wilson, *ibid.*, **123**, 1010 (1976).
21. D. Laser and S. Gottesfeld, *ibid.*, **126**, 475 (1979).
22. R. Wang and C. H. Henager, Jr., *ibid.*, **126**, 83 (1979).
23. R. H. Wilson, L. A. Harris, and M. E. Gerstner, *ibid.*, **126**, 844 (1979).
24. M. A. Butler, *ibid.*, **126**, 338 (1979).
25. G. Blondeau, M. Froelicher, M. Froment, A. H. Goff, and J. Zerbino, *ibid.*, **126**, 1592 (1979).
26. M. D. Archer, *J. Appl. Electrochem.*, **5**, 17 (1975).
27. M. B. Kononov, V. I. Bystrov, and V. L. Kubasov, *Elektrokhimiya*, **12**, 1266 (1976).
28. Y. M. Kolotyarkin, *Denki Kagaku*, **47**, 390 (1979).
29. J. B. Goodenough, "Progress in Solid-State Chemistry," Vol. 5, pp. 145-399, Pergamon, Oxford (1971).
30. H. B. Huntington and G. A. Sullivan, *Phys. Rev. Lett.*, **14**, 177 (1965).
31. J. Yahia, *Phys. Rev.*, **130**, 1711 (1963).
32. R. D. Shannon, *J. Appl. Phys.*, **35**, 3414 (1964).
33. A. Magnéli, *Nature*, **115**, 356 (1950).
34. S. Anderson and L. Jahnberg, *Arkiv Kemi*, **21**, 413 (1963).

The Application of Linear Sweep Voltammetry to a Rotating Disk Electrode for the Reversible Deposition of an Insoluble Species

P. C. Andricacos* and H. Y. Cheh**

Department of Chemical Engineering and Applied Chemistry, Columbia University, New York, New York 10027

ABSTRACT

A Nernst diffusion model was employed to obtain an analytical expression for the transient current response of a reversible deposition reaction with insoluble product occurring on a rotating disk electrode under linear potential sweep conditions. The results indicated that for low sweep rates the current increases monotonically with time. However, at high sweep rates a maximum value for the current density at finite values of time is predicted. The peak current density normalized with respect to the diffusion limiting current density was found to be a linear function of the square root of a dimensionless sweep rate. Furthermore, in this region the response of a rotating disk electrode is the same as that in a stagnant system. An experimental investigation based on the reversible deposition of silver showed good agreement with the theoretical predictions.

Linear sweep voltammetry (LSV) in stagnant systems has developed into a useful analytical technique for the investigation of complex electrochemical mechanisms (1, 2). In a typical LSV experiment, the potential of a plane, cylindrical, or spherical electrode is increased linearly with time at a fixed rate and the current is measured. The electrolyte is stagnant and, therefore, the mathematical analysis is based on a semi-infinite diffusion model.

A complication often encountered in the application of LSV is the presence of natural convection. To reduce this effect, most investigations have been based on short time responses. An alternate approach would be to introduce well-defined forced convection. The rotating disk electrode (RDE) is a natural choice since the forced convection regime that it establishes has been described quantitatively in the literature (3). One can anticipate that the application of LSV to an RDE will lead to a powerful analytical tool.

An exact mathematical analysis of convective transport to an RDE with time-dependent electrode potential or current density is extremely complicated. Approximate methods have usually been employed in practice to perform this analysis. Let us describe two of these methods since both of them have been applied previously to the problem of LSV on the RDE.

Filinovskii and co-workers (4, 5) developed an analytical approximation in which the highest order term in the space coordinate was dropped from a transformed convective diffusion equation, using the argument that its effect would be small since the main region of concentration variation lies very near the electrode surface. The physical meaning of this approximation is dubious because the neglected term includes contributions from both convective and diffusive transport. For the problem of applying a step potential or current, Krylov and Babak (6) showed that the validity of this approximation deteriorates as time increases up to a maximum of approximately 7%. Similar conclusions were reached by Viswanathan and Cheh (7).

The other approximate method is based on the Nernst diffusion model. Convection is neglected in the governing diffusion equation. It is, however, included in the evaluation of the thickness of the diffusion layer. The Nernst diffusion model was first ap-

plied to the RDE by Siver (8, 9) for the application of galvanostatic and potentiostatic steps. Siver's results were compared by Hale (10) to numerical results which included convective effects. The maximum error by using the simple model was reported to be 4% for the case of the galvanostatic step. Other problems which have been based on the Nernst model include the investigations of Cheh (11, 12) on pulsed and periodically reversed currents, those of Buck and Keller (13) on step currents, and those of Tokuda and Matsuda (14-16) for a-c voltammetry. For the case of pulsed currents, Viswanathan *et al.* (17) have shown that the results based on the Nernst diffusion model agreed well with those based on a numerical calculation including convection for an RDE system.

Both Filinovskii's analytical approximation and the Nernst diffusion model have been applied to the problem of LSV on the RDE, the former by Girina *et al.* (18), the latter by Fried *et al.* (19-21). Both groups dealt with the problem of a reversible reaction with a soluble product. In the work by Fried and co-workers (19), the time dependence of the current density is given in terms of an integral which has to be evaluated numerically. As has been the case with LSV in stagnant systems, the quantities of interest are the dependence of the peak current density on the sweep rate and the value of the overpotential at which the current peak occurs. The current transient is of secondary importance. In this respect, the work of Fried and co-workers (19) fails to provide clear diagnostic criteria.

On the other hand, Girina *et al.* (18) reported that if the peak current density is normalized with respect to the diffusion limiting current density, and if the sweep rate is normalized with respect to the characteristic time of the RDE, then the resulting dimensionless current is a linear function of the square root of the dimensionless sweep rate, provided that diffusion is the rate-controlling process. Furthermore, these authors concluded that for short times, the response of the RDE is the same as that of a stagnant system. In other words, for short times the RDE is described by the classical Sevcik-Randles relation (22, 23). The same conclusion was reached by Fried *et al.* (21).

It is the purpose of the present paper to apply the Nernst diffusion model to the problem of LSV on an RDE for the simple case of a reversible reaction with an insoluble product. The theoretical results are then compared with experimental findings.

* Electrochemical Society Student Member.

** Electrochemical Society Active Member.

Key words: rotating disk, deposition, voltammetry.

Theoretical

Consider the reversible reaction



where O and R represent the chemical formula for the oxidized and reduced species, respectively, and n is the number of electrons transferred during the reaction. R is an insoluble species. The electrode potential, $E(t)$, is swept linearly with time at a rate v , i.e.

$$E(t) = E_i - vt \quad [2]$$

where E_i is the equilibrium potential based on the bulk concentration of O, c^b , and t is time. Since E_i is the equilibrium potential, no current flows initially through the system. Thus, the concentration of O on the electrode surface is initially equal to c^b . Let the RDE be situated at $x = 0$, and the edge of the Nernst diffusion layer at $x = \delta$. In terms of the following dimensionless variables

$$C(\xi, \tau) = 1 - c(\xi, \tau)/c^b \quad [3]$$

$$\xi = x/\delta \quad [4]$$

$$\tau = Dt/\delta^2 \quad [5]$$

the diffusion equation and the boundary conditions are

$$\frac{\partial C}{\partial \tau} = \frac{\partial^2 C}{\partial \xi^2} \quad [6]$$

$$C(\xi, 0) = 0 \quad [7]$$

$$C(1, \tau) = 0 \quad [8]$$

$$\frac{\partial C}{\partial \xi}(0, \tau) = -\frac{i(\tau)}{i_1} \quad [9]$$

where $C(\xi, \tau)$ is the dimensionless concentration defined by Eq. [3], ξ and τ are the dimensionless distance and time defined by Eq. [4] and [5], respectively, D is the diffusion coefficient of O, $i(\tau)$ is the current density passing through the system at time τ , and i_1 is the diffusion limiting current density defined by

$$i_1 = nFDc^b/\delta \quad [10]$$

Equation [6] subject to boundary conditions, Eq. [7]-[9], can be solved by the method of Laplace transform. Let $\bar{C}(\xi, p)$ be the Laplace transform of $C(\xi, \tau)$

$$\bar{C}(\xi, p) = L\{C(\xi, \tau)\} = \int_0^\infty e^{-p\tau} C(\xi, \tau) d\tau \quad [11]$$

where p is the Laplace parameter. The solution is straightforward, and we obtain the following equation for the transformed current

$$\frac{\bar{i}(p)}{i_1} = p\bar{C}(0, p) \times p^{-1/2} \coth(p^{1/2}) \quad [12]$$

$$= L\left\{\frac{\partial C}{\partial \tau}(0, \tau)\right\} \times L\{\theta_3(0, \pi i \tau)\} \quad [13]$$

where

$$\bar{i}(p) = L\{i(\tau)\} \quad [14]$$

and $\theta_3(0, \pi i \tau)$ is one of the theta functions (24) defined by

$$\theta_3(0, \pi i \tau) = 1 + 2 \sum_{j=1}^{j=\infty} \exp(-j^2 \pi^2 \tau) \quad [15]$$

By applying the convolution operation to Eq. [13], we obtain

$$\frac{i(\tau)}{i_1} = \int_0^\tau \frac{\partial C}{\partial \tau}(0, \tau - \lambda) \times \theta_3(0, \pi i \lambda) d\lambda \quad [16]$$

where λ is a dummy variable.

A comparison between Eq. [16] and the solution of the corresponding problem in a stagnant system reveals that the only difference between the response of the RDE and that of the stagnant system (25) is the kernel of the integral. Whereas the kernel in Eq. [16] is the function $\theta_3(0, \pi i \lambda)$, that of the stagnant system is $(\pi \lambda)^{-1/2}$. By using an alternate expression (24) for $\theta_3(0, \pi i \lambda)$

$$\theta_3(0, \pi i \lambda) = (\pi \lambda)^{-1/2} \left[1 + 2 \sum_{j=1}^{j=\infty} \exp(-j^2 \lambda^{-1}) \right] \quad [17]$$

one sees that either as $\delta \rightarrow \infty$ or as $t \rightarrow 0$, the two systems become identical.

An explicit expression for the current density can be obtained from Eq. [16], once the dependence of $C(0, \tau)$ on τ is known. By introducing the dimensionless sweep rate, σ

$$\sigma = nFv\delta^2/RTD \quad [18]$$

such a dependence can be obtained from the Nernst equation for the electrode potential and Eq. [2]. Assuming that reaction [1] proceeds under equilibrium conditions in an ideal solution

$$C(0, \tau) = 1 - \exp(-\sigma\tau) \quad [19]$$

from which

$$\frac{\partial C}{\partial \tau}(0, \tau - \lambda) = \sigma \exp(-\sigma\tau) \exp(\sigma\lambda) \quad [20]$$

By combining Eq. [20] and Eq. [16] an explicit expression can be obtained for the normalized current density as a function of dimensionless time

$$\frac{i(\tau)}{i_1} = 1 - \sigma^{1/2} \cot(\sigma^{1/2}) \exp(-\sigma\tau) + \sum_{j=1}^{j=\infty} \frac{2\sigma}{\sigma - j^2\pi^2} \exp(-j^2\pi^2\tau) \quad [21]^1$$

Equation [21] indicates that as $\tau \rightarrow \infty$, $i(\tau)/i_1 \rightarrow 1$. On the other hand, for $\tau = 0$, $i(\tau)/i_1 = 0$.¹ For intermediate times, the normalized current density is a continuous function of dimensionless time. Numerical illustration of Eq. [21] is presented in Fig. 1. It is seen that for small values of σ , $i(\tau)/i_1$ increases monotonically from 0 to 1 as τ increases from 0 to ∞ . For larger values of σ , a maximum value of the normalized

¹The identity

$$\cot(c\pi) = (\pi c)^{-1} - \pi^{-1} \sum_{j=1}^{j=\infty} \frac{2c}{j^2 - c^2}$$

has been used in this derivation (26).

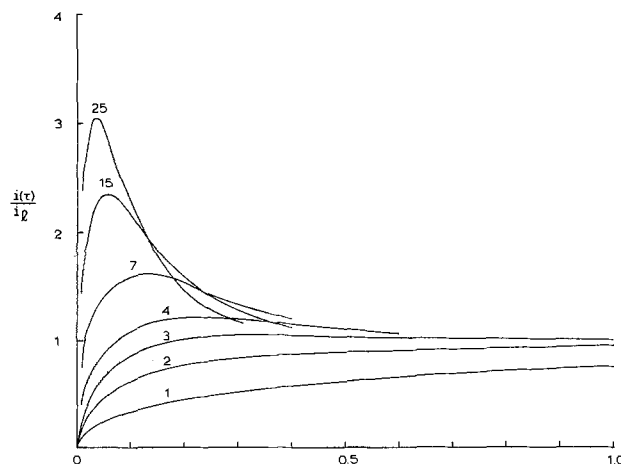


Fig. 1. Graphical representation of Eq. [21]. Numbers on curves indicate values of the dimensionless sweep rate.

current density occurs at finite values of τ . The condition at the maximum is

$$\frac{d}{d\tau} \left\{ \frac{i(\tau)}{i_1} \right\}_{\tau=\tau_m} = 0 \quad [22]$$

or

$$\sigma^{1/2} \cot(\sigma^{1/2}) \exp(-\sigma\tau_m) = \sum_{j=1}^{j=\infty} \frac{2j^2\pi^2}{\sigma - j^2\pi^2} \exp(-j^2\pi^2\tau_m) \quad [23]$$

A numerical analysis of Eq. [23] showed that τ_m is inversely proportional to σ for

$$\sigma > 4, \quad \sigma\tau_m = 0.854 \quad [24]$$

The maximum or peak current density, i_p , can be calculated by combining Eq. [23] and [21]

$$\frac{i_p}{i_1} = (\pi\tau_m)^{-1/2} \left[1 + 2 \sum_{j=1}^{j=\infty} \exp(-j^2\tau_m^{-1}) \right] \quad [25]$$

For $\sigma > 4$, the contribution of the series in Eq. [25] is negligible for all practical purposes. By neglecting the series and combining Eq. [25] and [24], one finds that

$$\frac{i_p}{i_1} = 0.611\sigma^{1/2} \quad [26]$$

This equation shows that the peak current density, i_p , normalized with respect to the limiting current density is a linear function of $\sigma^{1/2}$. The slope is a constant independent of any physical property of the system. Also, by substituting into Eq. [26] the value for δ as derived by Levich (3)

$$\delta = 1.61D^{1/3}\nu^{1/6}\omega^{-1/2} \quad [27]$$

we obtain

$$\frac{i_p}{i_1} = 0.98(nF\nu/RT\omega)^{1/2}(\nu/D)^{1/6} \quad [28]$$

where ν is the kinematic viscosity of the electrolyte and ω is the rotation speed of the RDE. Equation [28] indicates that i_p/i_1 has a weak dependence on the physical properties of the electrolyte.

Since for cases where there is no maximum for $i(\tau)/i_1$ its limiting value is 1, the minimum value of σ for which i_p/i_1 can occur at finite values of τ_m is governed by

$$0.611\sigma^{1/2} > 1 \quad [29]$$

or

$$\sigma > 2.68 \quad [30]$$

An important quantity associated with i_p is its corresponding electrode potential. By combining Eq. [2], [5], [18], and [24], we obtain

$$\eta_p = E_p - E_1 = -0.854RT/nF \quad [31]$$

$$= -22/n \text{ mV at } 25^\circ\text{C} \quad [32]$$

where η_p and E_p are the peak overpotential and the peak electrode potential, respectively. η_p is independent of the sweep rate, rotation speed, and physical properties of the system. Furthermore, in terms of dimensional quantities

$$i_p = 0.611n^{3/2}F^{3/2}R^{-1/2}T^{-1/2}D^{1/2}\nu^{1/2}c^b \quad [33]$$

$$= 367n^{3/2}D^{1/2}\nu^{1/2}c^b \text{ at } 25^\circ\text{C} \quad [34]$$

where i_p is in A/cm² and c^b is in moles/liter. Equation [33] implies that for $\sigma > 4$, i_p is independent of the rotation speed. Equations [31] and [33] are identical to the ones describing the LSV response of a reversible reaction with insoluble product in a stagnant system (27, 28). This result should not be surprising since the effects of convection are small at short times with high sweep rates.

Experimental

To experimentally verify the theory of LSV on an RDE for a reversible reaction with insoluble product, the deposition of Ag from AgNO₃ was chosen for the present study. This reaction has a very high exchange current density, which has been reported to be more than 1 A/cm² (29).

The experimental procedure involved two steps: (i) the determination of the limiting current density, and (ii) the determination of the peak current density upon linear sweeping of the potential. The cell employed had three compartments each for the reference, counter, and working electrodes. A Pt spiral and a saturated calomel electrode were used as counter and reference electrodes, respectively. The working electrode was a Pt rotating disk (Pine Instruments, DT6) mechanically polished to a mirror-like surface. It was rotated by a Pine Instruments Analytical Rotator modified by the addition of a low speed motor for use at low rotation speeds. A potentiostat/sweep generator (Pine Instruments, RDE3) and an X-Y recorder (Hewlett-Packard, 7044A) completed the electronic circuitry. The solution contained 2.057 mmoles AgNO₃, 1M KNO₃, and 0.01 g/liter gelatin. The latter was added to prevent the deposit from flaking off during the course of the experiment. The electrolyte was continuously deaerated with N₂. Prior to a run, Ag was deposited on the Pt RDE for 1/2 hr at approximately 50 μ A/cm². In this fashion, deposition during the runs occurred on Ag rather than on Pt. This procedure approximated the theoretical assumption that the deposit had unit activity. At rotation speeds higher than 200 rpm, it was found that limiting currents were irreproducible, probably due to a nonuniform deposition which increased the surface area. Hence, lower rotation speeds were used.

The Levich equation for the limiting current density (3) was obeyed well for all rotation speeds used in this study. This indicated that the effect of natural convection is negligible even at $\omega = 37$ rpm, corresponding to a Reynolds number of approximately 60. The effect of natural convection on limiting current densities at low values of the Reynolds number has been found negligible in several investigations (30-34). Regarding the peak current density, one should note that natural convection has even smaller effects, since the concentration gradient at the peak current is less pronounced than at the limiting current. This can be easily seen with the aid of Eq. [19] and [24] indicating that the surface concentration at the peak current is 43% of the bulk value, as opposed to 0 in the limiting current region.

Experimentally obtained currents transients for $\omega = 37$ rpm are shown in Fig. 2. The corresponding i_p/i_1 vs. $\sigma^{1/2}$ correlation is shown in Fig. 3. The value of 0.9×10^{-2} cm²/sec was used for the kinematic viscosity of the electrolyte (35). The corresponding value for the diffusion coefficient of Ag⁺ obtained from i_1 vs. $\omega^{1/2}$ lines was 1.2×10^{-5} cm²/sec. Peak overpotentials appeared at 30-55 mV to be compared with the theoretical value of 22 mV. Since peak overpotentials shift to more cathodic values as the sweep rate or peak current increases, their deviation from the theoretical value may be due to the uncompensated ohmic drop. Good agreement has been obtained between the theoretical predictions regarding the dependence of i_p/i_1 on $\sigma^{1/2}$ and the experimental findings.

It should be mentioned here that additional experiments were carried out for two other systems. These were the deposition of Cu from CuSO₄ and the evolution of H₂ on Pt from an HCl solution (36). Linear dependence of i_p/i_1 on $\sigma^{1/2}$ was observed in both cases. However, the slope of the lines and the peak overpotentials deviated considerably from the theoretical calculations. It is our postulate that the deviations from the theory are due primarily to the irreversibility of these reactions. Current work is being continued

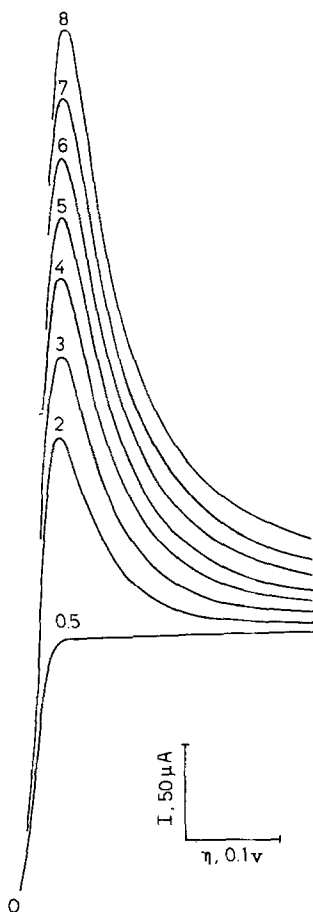


Fig. 2. Experimental current transients for the deposition of Ag. Numbers on curves indicate values of the sweep rate in volts/min. $\omega = 37$ rpm.

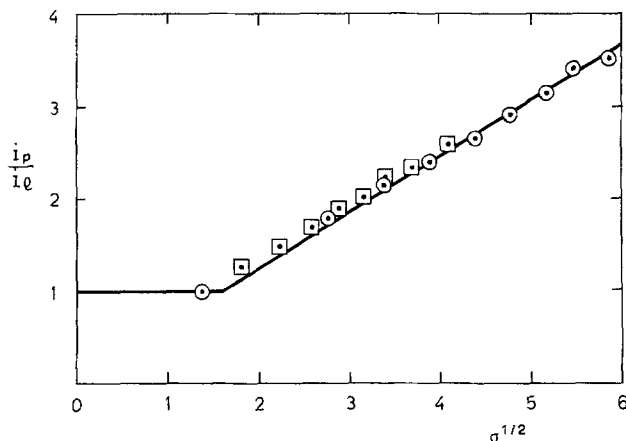


Fig. 3. i_p/i_l vs. $\sigma^{1/2}$ correlation for the deposition of Ag. (—, theoretical; experimental: \circ , $\omega = 37$ rpm; \square , $\omega = 85$ rpm).

to extend our theoretical investigation to include irreversible effects.

Conclusions

The problem of LSV on an RDE on which a reversible deposition reaction occurs was treated analytically by the use of a Nernst diffusion model. An explicit expression for the current transient was obtained. In terms of a dimensionless sweep rate and the peak current density normalized with respect to the limiting current density, the following conclusions were reached. For slow sweeps, no current maxima occur. For faster sweeps, the normalized peak current density is a linear function of the square root of the dimen-

sionless sweep rate. The slope is a constant independent of any physical property of the system. In addition, the normalized peak current density shows a weak dependence on the physical properties of the electrolyte. The overpotential at which the current peaks occur depends only on temperature and on the number of electrons transferred during the reaction. Furthermore, the RDE response is the same as that in a stagnant system.

Good agreement was observed between the theoretical predictions and experimental results obtained for the reversible deposition of Ag. Deviations from the theory occurred in reactions with irreversible kinetics, such as the deposition of Cu and the evolution of H_2 on Pt.

Acknowledgment

The authors wish to thank Dr. Samuel Ruben for his generous endowment of a Bergen Davis Fellowship at Columbia University. One of us (P. C. A.) was the recipient of the Fellowship during the course of this work.

Manuscript submitted Feb. 4, 1980; revised manuscript received May 6, 1980.

Any discussion of this paper will appear in a Discussion Section to be published in the June 1981 JOURNAL. All discussions for the June 1981 Discussion Section should be submitted by Feb. 1, 1981.

LIST OF SYMBOLS

c	concentration of species O
c^b	bulk concentration of species O
C	dimensionless concentration of species O, Eq. [3]
\bar{C}	Laplace transform of C , Eq. [11]
D	diffusion coefficient of species O
E_i	initial electrode potential
E_p	peak electrode potential
$E(t)$	electrode potential as a function of time
F	Faraday's constant
i	complex number, $\sqrt{-1}$
$i(\tau)$	current density as a function of τ
i_l	diffusion limiting current density, Eq. [10]
i_p	peak current density
$\bar{i}(p)$	Laplace transform of $i(\tau)$
j	summation index
L	Laplace operator
n	number of electrons transferred during reaction
O	chemical formula for oxidized species
p	Laplace parameter
R	chemical formula for reduced species
R	universal gas constant
t	time
T	absolute temperature
v	sweep rate
x	distance away from RDE
δ	thickness of the diffusion layer, Eq. [27]
η_p	peak overpotential
θ_3	a theta function, Eq. [15] and [17]
λ	dummy variable
ν	kinematic viscosity of the electrolyte
ξ	dimensionless distance, Eq. [4]
σ	dimensionless sweep rate, Eq. [18]
τ	dimensionless time, Eq. [5]
τ_m	value of τ at which i_p occurs
ω	rotation speed of the RDE

REFERENCES

- R. S. Nicholson and I. Shain, *Anal. Chem.*, **36**, 706 (1964).
- D. D. Macdonald, "Transient Techniques in Electrochemistry," Plenum Press, New York (1977).
- V. G. Levich, "Physicochemical Hydrodynamics," Prentice Hall, Englewood Cliffs, N.J. (1962).
- V. Yu. Filinovskii and V. A. Kiryanov, *Dokl. Akad. Nauk SSSR*, **156**, 1412 (1964).
- Yu. V. Pleskov and V. Yu. Filinovskii, "The Rotating Disc Electrode," Consultants Bureau, New York (1976).
- V. S. Krylov and V. N. Babak, *Soviet Electrochem.*, **7**, 626 (1971).
- K. Viswanathan and H. Y. Cheh, *J. Appl. Electrochem.*, **9**, 537 (1979).
- Yu. G. Siver, *Russ. J. Phys. Chem.*, **33**, 533 (1959).

9. Yu. G. Siver, *ibid.*, **34**, 273 (1960).
10. J. M. Hale, *J. Electroanal. Chem.*, **6**, 187 (1963).
11. H. Y. Cheh, *This Journal*, **118**, 551 (1971).
12. H. Y. Cheh, *ibid.*, **118**, 1132 (1971).
13. R. P. Buck and H. E. Keller, *Anal. Chem.*, **35**, 400 (1963).
14. K. Tokuda and H. Matsuda, *J. Electroanal. Chem. Interfacial Electrochem.*, **82**, 157 (1977).
15. K. Tokuda and H. Matsuda, *ibid.*, **90**, 149 (1978).
16. K. Tokuda and H. Matsuda, *ibid.*, **95**, 147 (1979).
17. K. Viswanathan, M. A. Farrell Epstein, and H. Y. Cheh, *This Journal*, **125**, 1772 (1978).
18. G. P. Girina, V. Yu. Filinovskii, and L. G. Feoktistov, *Soviet Electrochem.*, **3**, 831 (1967).
19. I. Fried and P. J. Elving, *Anal. Chem.*, **37**, 464 (1965).
20. I. Fried and P. J. Elving, *ibid.*, **37**, 803 (1965).
21. I. Fried and E. Shamir, *Electrochim. Acta*, **14**, 941 (1969).
22. A. Sevcik, *Coll. Czechoslov. Chem. Commun.*, **13**, 349 (1948).
23. J. E. B. Randles, *Trans. Faraday Soc.*, **44**, 327 (1948).
24. R. Bellman, "A Brief Introduction to Theta Functions," Holt, Reinhart, and Winston, New York (1961).
25. W. H. Reinmuth, *Anal. Chem.*, **34**, 1446 (1962).
26. K. Knopp, "Theorie und Anwendung der Unendlichen Reihen," Springer-Verlag, Berlin (1947).
27. T. Berzins and P. Delahay, *J. Am. Chem. Soc.*, **75**, 555 (1953).
28. N. White and F. Lawson, *J. Electroanal. Chem. Interfacial Electrochem.*, **25**, 409 (1970).
29. P. B. Price and D. A. Vermilyea, *J. Chem. Phys.*, **28**, 720 (1958).
30. E. A. Aikazyan and A. I. Fedorova, *Dokl. Akad. Nauk SSSR*, **86**, 1137 (1952).
31. J. D. Newson and A. C. Riddiford, *This Journal*, **108**, 695 (1961).
32. S. Azim and A. C. Riddiford, *Anal. Chem.*, **34**, 1023 (1962).
33. K. F. Blurton and A. C. Riddiford, *J. Electroanal. Chem.*, **10**, 457 (1965).
34. C. A. Emergy and H. E. Hintermann, *Electrochim. Acta*, **13**, 127 (1968).
35. "Handbook of Chemistry and Physics," R. C. Weast, Editor, 55th ed., CRC Press, Ohio (1974).
36. P. C. Andricacos, Unpublished results.

Concentration Dependence of Thermoelectric Powers in Aqueous Sulfamic Acid and Aqueous Perchloric Acid Using Hydrogen Electrodes

Arthur D. Payton,* Eric J. Amis,¹ Michael S. Showell,² Robert W. Smith,³
and Brent D. Koplitz⁴

Chemistry Department, Willamette University, Salem, Oregon 97301

ABSTRACT

The initial thermoelectric power (*TEP*) for hydrogen electrode thermocells has been determined for aqueous solutions of a weak acid, sulfamic acid at 29°C from 0.001 to 0.01 molal, and for aqueous solutions of a strong acid, perchloric acid at 25°C from 0.004 to 0.1 molal. For each acid the data have been fitted to a linear equation by least squares analysis and the linear coefficient for the *TEP* vs. a molality function has been compared with theoretical values. These values are calculated from a heat-of-transport theory, in which each theoretical linear coefficient consists of five terms. The theoretical and experimental values for each linear coefficient are in agreement to within 20% for NH₂SO₃H and 2.4% for HClO₄.

Investigation of the concentration dependence of initial thermoelectric powers (*TEP*) of hydrogen-electrode thermocells in this laboratory (1-3) led to application of our theory (2) to a weak electrolyte: aqueous sulfamic acid. This theory is an extension of other theories (4-7).

One difficulty in the analysis of experimental data for the *TEP* vs. κ (Debye-Hückel reciprocal length) in a weak electrolyte stems from the different equilibrium hydrogen-ion molalities in the hot and cold compartments of the thermocell due to the variation of the acid dissociation constant with temperature. In order to minimize this difficulty we chose to study the *TEP* as a function of concentration of aqueous sulfamic acid using a 10°C temperature difference centered at 29°C. At this temperature the acid dissociation constant has a maximum value of ca. 0.104

(8, 9). The equilibrium hydrogen-ion molalities at 24° and 34°C differ by less than 0.02% even at the highest acid molality studied (ca. 0.01 mole kg⁻¹). We also present results for aqueous perchloric acid for a 20°/30° temperature difference in order to show that the strong acid case is more easily analyzed.

The result for sulfamic acid at 29°C and the result for perchloric acid at 25°C are compared with each theoretical slope, which is calculated from the five terms that contribute to each slope (2).

These terms are: $(\hat{Q}_{HA}^+)^d$, $(\hat{Q}_{HA^-})^e$, $(\bar{S}_{H^+})^d$, $(\bar{S}_{H^+})^e$, and (t_{A^-}) . The first and second terms are from the concentration dependence of \hat{Q}_{HA} , the heat of transport of the acid. The third and fourth terms are from the concentration dependence of \bar{S}_{H^+} , the transported entropy of the hydrogen ion. The final term is from the concentration dependence of t_{A^-} , the transport number of the anion. In addition, the first and third terms arise from the "direct" effect (5-7, 10). The second and fourth terms arise from the "electrophoretic" effect. It was stated in an earlier paper (3) that the limiting value $\hat{Q}_{A^-}^0$ and $\hat{Q}_{H^+}^0$ are

* Electrochemical Society Active Member.

¹ Chemistry Department, University of Wisconsin, Madison, Wisconsin 53706.

² Chemistry Department, Purdue University, Lafayette, Indiana 47907.

³ Chemistry Department, University of Texas, Austin, Texas 78712.

⁴ Chemistry Department, Princeton University, Princeton, New Jersey 08540.

Key words: heat of transport, standard partial molar entropy, thermocell, transport number, transported entropy.

needed to calculate the $(\hat{Q}'_{HA})^e$ and $(\bar{S}'_{H+})^e$ terms. The limiting value \hat{Q}°_{HA} is also needed to calculate (t'_{A-}) .

Theoretical Calculations

In order to calculate values for the five contributing terms to the slope of the *TEP* vs. κ plot for perchloric and for sulfamic acids, we first consider the *TEP* of a hydrogen electrode thermocell containing an aqueous acid HA as given by Eq. [1] (4)

$$F(TEP) = (1/2)S^{\circ}_{H_2} - \bar{S}_e + t_{A-}(\hat{Q}'_{HA}/T) - \bar{S}'_{H+} \quad [1]$$

In Eq. [1] $S^{\circ}_{H_2} = 130.587$ or 130.974 J K⁻¹ mole⁻¹ (the standard entropy of hydrogen gas at 25° or 29°C (11, 3) and $\bar{S}_e = 0.430$ or 0.447 J K⁻¹ mole⁻¹ (the transported entropy of the electron in the nonisothermal part of the platinum at 25° or 29°) (12a). The transport number of the perchlorate or sulfamate ion is t_{A-} and \hat{Q}'_{HA} is the heat of transport of perchloric or sulfamic acid. It is convenient to define the function

$$Y = TEP - (R/F) \ln m \quad [2]$$

in which the *TEP* has been corrected by the mass-action term occurring in \bar{S}'_{H+} of Eq. [1]. As shown in Ref. (2), Eq. [4b]-[4d] express t_{A-} , \hat{Q}'_{HA} , and \bar{S}'_{H+} as an intercept plus a slope term. When these expressions of \sqrt{c} dependence are substituted into Eq. [1], the five contributing terms to the slope of the thermoelectric power (actually, *Y*) vs. $c^{1/2}$ are obtained, viz.

$$Y = Y^{\circ} + (1/F) [(t^{\circ}_{A-}/T)(\hat{Q}'_{HA})^d + (t^{\circ}_{A-}/T)(\hat{Q}'_{HA})^e - (\bar{S}'_{H+})^d - (\bar{S}'_{H+})^e + (\hat{Q}^{\circ}_{HA}/T)(t'_{A-})] \sqrt{c} \quad [3]$$

in which terms of higher order than $c^{1/2}$ have been neglected. In Eq. [3] the superscript zero denotes infinite-dilution limiting values of each function and the primes stand for the nonideal slope of each function vs. \sqrt{c} . The coefficients of the \sqrt{c} direct terms (5) (first and third terms of Eq. [3]) are given in Eq. [4] and [5]

$$\frac{t^{\circ}_{A-}}{T} (\hat{Q}'_{HA})^d \sqrt{c} = \frac{t^{\circ}_{A-}}{T} 4RT \varepsilon \left(\frac{1}{12} + \frac{3}{4} \frac{\partial \ln \varepsilon_r}{\partial \ln T} + \frac{1}{4} \alpha T \right) \sqrt{c} \quad [4]$$

$$(\bar{S}'_{H+})^d \sqrt{c} = -\frac{1}{3} R \varepsilon \sqrt{c} \quad [5]$$

where the term in parentheses will be denoted by ε' and the Debye-Hückel constant $\varepsilon = N^2 e^3 [\pi / (500 \varepsilon_r^3 R^3 T^3)]^{1/2}$. In Eq. [4] ε_r is the relative permittivity of the solvent, α is the isobaric expansivity of the solvent, e is the protonic charge in esu, T is the Kelvin temperature, N is the Avogadro number, and R is the universal gas constant.

The coefficients of the \sqrt{c} electrophoretic terms (2) (second and fourth of Eq. [3]) are given by Eq. [6] and [7]

$$(t^{\circ}_{A-}/T) (\hat{Q}'_{HA})^e \sqrt{c} = (t^{\circ}_{A-}/2T) (r_{H+} - r_{A-}) (\hat{Q}^{\circ}_{H+} - \hat{Q}^{\circ}_{A-}) B' \sqrt{c} \quad [6]$$

$$(\bar{S}'_{H+})^e \sqrt{c} = (r_{H+}/2T) (\hat{Q}^{\circ}_{H+} - \hat{Q}^{\circ}_{A-}) B' \sqrt{c} \quad [7]$$

in which r_i is the Stokes' radius of ionic species i . \hat{Q}°_i is the limiting value at infinite dilution of the individual ionic heats of transport, and the Debye-Hückel constant $B' = eN[\pi/(125\varepsilon_r RT)]^{1/2}$.

Although the factor $(\hat{Q}^{\circ}_{H+} - \hat{Q}^{\circ}_{A-})$ cannot be determined experimentally, we evaluated it using the method previously described (3). In this method \hat{Q}°_{HA} is first determined using Eq. [8]

$$FY^{\circ} = (1/2)S^{\circ}_{H_2} - \bar{S}_e + t^{\circ}_{A-}(\hat{Q}^{\circ}_{HA}/T) - \bar{S}^{\circ}_{H+} \quad [8]$$

in which the superscript zero denotes the limiting or standard value of each quantity. In order to obtain Eq. [8], we subtract the mass-action term $R \ln m$ from both sides of Eq. [1] and use standard-state values for the molality-dependent variables (*TEP*, t_{A-} , \hat{Q}'_{HA} , and \bar{S}'_{H+}). The values obtained were $\hat{Q}^{\circ}_{HClO_4} = 12.57 \pm 0.18$ kJ mole⁻¹ and $\hat{Q}^{\circ}_{NH_2SO_3H} = 14.17 \pm 0.24$ kJ mole⁻¹ using values at 25°C previously described (3) for $S^{\circ}_{H_2}$, t°_{A-} , \bar{S}°_{H+} , and $Y^{\circ}/\mu V K^{-1} = 507.60 \pm 0.54$ and 497.07 ± 0.83 for $HClO_4$ and NH_2SO_3H , respectively. We next calculated $\hat{Q}^{\circ}_{H+} = 12.60 \pm 0.04$ kJ mole⁻¹ on the absolute basis according to a suggestion of Ikeda (12b). Following Ikeda's interpretation of Wirtz's "Platzwechsel" theory (13a) for ion transport, we may write Eq. [9a] for the hydrogen ion

$$\hat{Q}^{\circ}_{H+} = RT(1 + \partial \ln \lambda^{\circ}_{H+} / \partial \ln T) \quad [9a]$$

where λ°_{H+} is the infinite-dilution limiting value of the ionic mobility of the hydrogen ion. In Eq. [9a] we have equated the individual ionic heat of transport

of the hydrogen ion \hat{Q}°_{H+} to the "Hemmungsenergie" (molar activation energy for detachment of a proton from its neighbors) only, since for a proton it is reasonable to neglect the "Lochbildungsenergie" (molar activation energy for creation of a hole into which the proton will enter).

The value for \hat{Q}°_{H+} determined from Eq. [9a] using $\partial \ln \lambda^{\circ}_{H+} / \partial T = 0.0137$ K⁻¹ from Owen and Sweeton (13b) differs from our earlier value of 13.127 kJ mole⁻¹ (3), which was determined from Eq. [9b] (5)

$$\bar{S}^{\circ}_{H+} = S^{\circ}_{H+} + (\hat{Q}^{\circ}_{H+}/T) \quad [9b]$$

with Ikeda's value (12b) ($S^{\circ}_{H+} = -5.1$ cal K⁻¹ mole⁻¹) for the absolute value of the partial molar standard entropy of the hydrogen ion in aqueous solution and with our value (1, 3) $\bar{S}^{\circ}_{H+} = 22.69 \pm 0.08$ J K⁻¹ mole⁻¹. For the hydrogen ion Eq. [9b] expresses the transported entropy (a measurable property of an individual ion that is not based on an arbitrary

convention) in terms of S°_{H+} and \hat{Q}°_{H+} , neither of which is experimentally accessible (5). References for ten values of S°_{H+} ranging between -1 and -7 cal K⁻¹ mole⁻¹ are given by Ikeda (12b). Furthermore, our value (3) for \bar{S}°_{H+} and the value for \hat{Q}°_{H+} calculated from Eq. [9a] may be combined according to Eq. [9b] in order to yield the absolute value $S^{\circ}_{H+} = -4.7 \pm 0.1$ cal K⁻¹ mole⁻¹.

We then determined \hat{Q}°_{A-} at 25°C for each acid by subtracting $\hat{Q}^{\circ}_{H+} = 12.60$ kJ mole⁻¹ from the values for \hat{Q}°_{HA} . This procedure yielded

$$(\hat{Q}^{\circ}_{H+} - \hat{Q}^{\circ}_{ClO_4-}) = 12.64 \pm 0.19 \text{ kJ mole}^{-1} \quad \text{and}$$

$$(\hat{Q}^{\circ}_{H+} - \hat{Q}^{\circ}_{NH_2SO_3-}) = 11.03 \pm 0.25 \text{ kJ mole}^{-1}$$

Finally, we made the assumption that the temperature coefficients of \hat{Q}°_i for all ions are the same.

The fifth term of Eq. [3] (2) is

$$\frac{\hat{Q}_{\text{HA}}^{\circ}}{T} (t_{\text{A}}^{\circ}) = \frac{\hat{Q}_{\text{HA}}^{\circ}}{T} \frac{B_2(t_{\text{A}}^{\circ} - 1/2)}{(\lambda_{\text{H}^+}^{\circ} + \lambda_{\text{A}}^{\circ})} \quad [10]$$

where $B_2 = Fe^2N/3$ (299.79) $(125 R_{\text{e}r}T)^{1/2}\eta_0$ with η_0 the viscosity of the solvent. The expression for (t_{A}°) appearing in Eq. [10] was derived by taking the infinite-dilution limit of the expression for the concentration variation of the transport number due to first-order electrophoretic terms according to Robinson and Stokes (9). Also appearing in Eq. [10] is the heat of transport of the acid at infinite dilution.

At 25°C for perchloric acid $\hat{Q}_{\text{HA}}^{\circ} = 12.57 \pm 0.18$ kJ mole⁻¹ and at 29°C for sulfamic acid $\hat{Q}_{\text{HA}}^{\circ} = 15.11 \pm 0.27$ kJ mole⁻¹.

Shown in Eq. [11] are the five terms from Eq. [4], [5], [6], [7], and [10] respectively

$$Y = Y^{\circ} + Y'\sqrt{c}$$

where

$$Y' = (1/F) [4t_{\text{A}}^{\circ} - R\varepsilon\varepsilon' - (-1/3R\varepsilon\varepsilon') + (B't_{\text{A}}^{\circ}/2T)(\tau_{\text{H}^+} - \tau_{\text{A}})(\hat{Q}_{\text{H}^+}^{\circ} - \hat{Q}_{\text{A}}^{\circ}) - (B'r_{\text{H}^+}/2T)(\hat{Q}_{\text{H}^+}^{\circ} - \hat{Q}_{\text{A}}^{\circ}) + \hat{Q}_{\text{HA}}^{\circ}B_2(t_{\text{A}}^{\circ} - 1/2)/T(\lambda_{\text{H}^+}^{\circ} + \lambda_{\text{A}}^{\circ})] \quad [11]$$

Displayed in Table I are the five contributions to the \sqrt{c} dependence of Y for sulfamic acid at 29°C and for perchloric acid at 25°C. Shown in Table II are the values of constants used in the calculation of these terms.

Experimental

The thermoelectric powers were measured using the method, electrodes, cell, and bubblers previously described (1), except for the following changes in experimental details. The previously used, W-shaped cell, which had been placed directly in the two thermostats, was replaced by a U-shaped external Pyrex cell with water jackets through which thermostated water circulated. The previously used electrode assemblies were replaced by electrodes in which each assembly consisted of a bubbler tube, two electrode tubes, and a thermocouple. A 3 mm OD, soft-glass tube, into which was sealed a No. 27 platinum wire,

was inserted into each Pyrex electrode tube and sealed with Apiezon W. Platinum black was deposited on the electrodes after every 15 runs by reducing a 2% platinum chloride solution that contained 0.02% lead acetate. The electrolysis was carried out for 15-30 sec at a current density of 100 mA cm⁻² until the deposit appeared uniformly black. No pre-soaking of the electrodes was necessary before a run.

Prepurified (99.995% pure, Airco) hydrogen was further purified by a "deoxo" cartridge (J. T. Baker Company) attached directly to the regulator. The hydrogen was then bubbled through deionized water to saturate it with water vapor before it entered the solution in the cell. Reagent grade sulfamic and perchloric acids were used to make stock solutions which were titrated with standardized NaOH solutions. The solutions for the TEP measurements were then prepared by dilution.

We determined the temperature difference with a one-junction iron-constantan thermocouple using values of 517 μV for 20°-30°C and 519 μV for 24°-34°C. These values were obtained by least squaring tabulated values (18) to a quadratic temperature equation. The temperature difference was known to within 0.01K, although the mean temperature varied up to 0.1K from the stated values. The thermocouples were immersed in paraffin oil and enclosed in a U-shaped, 3 mm OD, soft-glass tube and were suspended from each electrode assembly before being placed in each compartment of the thermocell.

After the solution had been deoxygenated by bubbling prepurified nitrogen through the saturators and the cell solution for 15 min, we switched to hydrogen and usually began taking readings after 20-30 min. The hydrogen bubbled at a rate of 10-20 sec⁻¹. Two readings were taken with each pair of electrodes, first with the current in the forward direction and then in the reverse direction. Any asymmetry in the electrodes was eliminated by interchanging the flow of the hot and cold water to the water jackets. Four more readings were again taken, making a total of eight in all. For all readings the thermocell was slightly tilted so that the hot compartment was elevated with respect to the cold, thus preventing the denser solution in the cold compartment from flowing into the hot compartment.

As in our work on HCl (1), all TEP's have been corrected so that the hydrogen pressure in both the

Table I. Contributions to the theoretical limiting slope $Y'/\mu\text{V } ^\circ\text{K}^{-1}$

Acid	$T/^\circ\text{K}$	Eq. [4]	Eq. [5]	Eq. [6]	Eq. [7]	Eq. [10]	Eq. [11]†
NH ₂ SO ₃ H	302.15	-47.92	-34.06	-12.76*	+17.03*	-30.54	-74.20
HClO ₄	298.15	-60.44	-33.80	-12.89	+19.03	-21.51	-80.07

* The factor $(\hat{Q}_{\text{H}^+}^{\circ} - \hat{Q}_{\text{NH}_2\text{SO}_3}^{\circ})$ used in Eq. [6] and [7] was determined from Eq. [8] and [9b] with $Y^{\circ} = 497.07 \pm 0.83 \mu\text{V } ^\circ\text{K}^{-1}$ at 25°C.

† This total contribution is obtained from Eq. [4] - Eq. [5] + Eq. [6] - Eq. [7] + Eq. [10].

Table II. Values of constants used in the calculations of the contributions to Y'

Acid	$T/^\circ\text{K}$	$\lambda_{\text{H}^+}^{\circ}$ (cm ² /Ω)	$\lambda_{\text{A}}^{\circ}$ (cm ² /Ω)	ε_r^b	ε (dm ^{3/2} / mole ^{1/2})	$-10^4 \frac{\partial \ln \varepsilon_r^b}{\partial \ln T}$	$10^{-8} B'$ (dm ^{3/2} / mole ^{3/2} cm)	$-10^8 \varepsilon'^d$	η_0^e (g m ⁻¹ sec ⁻¹)	B_2 (cm ² /Ω)	
NH ₂ SO ₃ H	302.15	368.90 ^f	52.99 ^g	76.93 <sub3< sub=""></sub3<>	1.18564 ^h	45.856	8894	0.32986 ^j	933.56	0.8147	66.413
HClO ₄	298.15	349.81 ^h	67.31 ^f	78.35 <sub8< sub=""></sub8<>	1.17675	45.878	7669	0.32903	923.42	0.8903	60.619

^a Stokes' radii may be calculated from $r_1 = Fe/6(299.79)\pi\eta_0\lambda^{\circ}$.

^b From Ref. (14a).

^c From Ref. (14b).

^d Calculated from the term in parentheses of Eq. [4].

^e From Ref. (15).

^f From Ref. (16).

^g Using Walden rule and data at 25°C from Ref. (17).

^h From Ref. (9), p. 463.

ⁱ At 24° and 34°C, $\varepsilon/\text{dm}^{3/2} \text{ mole}^{-1/2} = 1.1745$ and 1.1973.

^j At 24° and 34°C, $10^{-8} B'/\text{dm}^{3/2} \text{ mole}^{-3/2} \text{ cm}^{-1} = 0.32884$ and 0.33093.

Table III. Values for determination of TEP vs. \sqrt{m} in sulfamic acid at 29°C

Total molality ($10^4 m$ /mole kg^{-1})	$[10^2 \sqrt{m}/(1 + 1.5\sqrt{m})]$ (mole $^{1/2}$ $kg^{-1/2}$)	$-(R/F) \ln \sqrt{m_{34}m_{24}}$ ($\mu V K^{-1}$)	TEP ($\mu V K^{-1}$)	Y ($\mu V K^{-1}$) [*]
10.04	3.012	595.67	-93.72	501.95 (3)†
16.12	3.762	555.31	-54.94	500.37 (5)
20.14	4.171	536.40	-36.10	500.30 (3)
30.17	5.017	502.24	-3.30	498.94 (3)
32.20	5.167	496.76	3.02	499.78 (1)
40.35	5.715	477.84	20.39	498.23 (2)
50.11	6.287	459.76	36.88	496.64 (1)
56.39	6.619	449.96	49.11	499.07 (3)
80.50	7.703	420.63	76.48	497.11 (4)

* Using Eq. [12] and columns 3 and 4.

† Relative weighting factors in parentheses.

hot and cold compartments was 760 Torr (=101.325 kPa). Because of the extremely dilute solutions no correction was made for the lowering of the vapor pressure due to the presence of solute. Use of Antoine's equation (19) for the vapor pressure of water made it unnecessary to use four different sets of constants for linear interpolation within 0.1°C of the four thermostat temperatures.

Results

In all runs the polarity of the thermocell was such that the hot electrode was positive except for the 14 most dilute runs of sulfamic acid. Details of the calculation of Y as a function of $\sqrt{m}/(1 + 1.5\sqrt{m})$ are shown in Table III for sulfamic acid at a 24°/34° temperature difference. For convenience we used this function of the equilibrium hydrogen ion molality at 29°C rather than a function of c because densities are not required and equilibrium molalities can be readily calculated (Eq. [13] and [15]). Furthermore, this function was chosen because it is proportional to $\kappa/(1 + \kappa a)$ which occurs in the Debye-Hückel theory. By plotting Y against $\sqrt{m}/(1 + 1.5\sqrt{m})$ rather than \sqrt{c} or \sqrt{m} only, we extended the apparent range where a single linear term suffices to represent the concentration variation of the data (4).

For sulfamic acid, a weak acid, in which m (equilibrium hydrogen ion molality) is a function of temperature, the ordinate is given by Eq. [12]

$$Y = TEP - (R/F) \ln \sqrt{m_{34}m_{24}} - (R/F) (T/\Delta T) \ln (m_{34}/m_{24}) \quad [12]$$

This expression can be developed in analogous manner to the barometric pressure-correction factor (1, 20). We neglected the third term on the right-hand side of Eq. [12] because the maximum value at the highest molality is only 0.016 $\mu V K^{-1}$.

The equilibrium molalities at 24°, 29°, and 34°C were calculated from Eq. [13] for each of the nine runs of Table III

$$m = 1/2[-K_a + (K_a^2 + 4\gamma^2 K_a M)^{1/2}] \quad [13]$$

in which M is the total molality of sulfamic acid. The acid dissociation constant K_a was determined from Eq. [14] of King and King (8, 9)

$$-\log K_a = 3792.8/T - 24.122 + 0.04155T \quad [14]$$

and the activity coefficient from Eq. [15]

$$\ln \gamma = -z\sqrt{m}/[1 + (3.85 \times 10^{-8})B'\sqrt{m}] \quad [15]$$

The values used for the Debye-Hückel constants in Eq. [15] are shown in Table II. To calculate m in Eq. [13] we used an iterative technique in which γ was first set equal to unity. The value obtained for m was then used in Eq. [15] to obtain an improved value for γ , which was then used to obtain an improved value m . This iterative technique was con-

tinued until successive values of m agreed to within 1×10^{-11} mole kg^{-1} .

In the case of perchloric acid, a strong acid, the ordinate is $Y = TEP - (R/F) \ln m$ as in Eq. [2]. The abscissa is $\sqrt{m}/(1 + 1.5\sqrt{m})$ in which m is the molality of perchloric acid. Details of this calculation are shown in Table IV.

For each acid the data were fitted to a straight line by linear least squares by minimizing the squares of the vertical distances from the points to the line. In order to determine the limiting slopes, we used the points at concentrations shown in Tables III and IV. At concentrations greater than 0.01 mole kg^{-1} for sulfamic acid and 0.1 mole kg^{-1} for perchloric acid, the curve was apparently no longer linear and became concave upward.

Displayed in Table V are the limiting values for the slope and intercept of Y vs. $\sqrt{m}/(1 + 1.5\sqrt{m})$ for sulfamic acid and perchloric acid.

Discussion

A comparison may be made between our TEP with the work of Goyan (22). He measured the initial emf of a hydrogen-electrode thermocell containing 0.01M $HClO_4$ and obtained 1.25 ± 0.05 mV for $\Delta T = 9.9K$. For this result the mean temperature was 25°C and the hot electrode was positive. We corrected his value so that the hydrogen pressure in both hot and cold compartments was 760 Torr and obtained $TEP = 99.9 \pm 4 \mu V K^{-1}$ for Goyan's result. This value compares satisfactorily with our value of $104.24 \pm 0.63 \mu V K^{-1}$ at the same concentration of 0.01M. Our value of $\Delta G_{HClO_4}^\circ = 12.57 \pm 0.18$ kJ mole $^{-1}$ compares favorably with Haase's result (23) of 12.22 kJ mole $^{-1}$.

By multiplying the theoretical slopes of Table I by the square root of the density of water at 25° or 29° we were able to compare these values with the experimental slopes of Table V. This agreement is 19.9% and 2.4% for sulfamic acid and perchloric acid, respectively.

Table IV. Values for determination of TEP vs. \sqrt{m} in perchloric acid at 25°C

$10^2 m$ (mole kg^{-1})	$10^2 \sqrt{m}/$ ($1 + 1.5\sqrt{m}$) (mole $^{1/2}$ $kg^{-1/2}$)	$-(R/F) \ln m$ ($\mu V K^{-1}$)	TEP ($\mu V K^{-1}$)	Y ($\mu V K^{-1}$) [*]
0.388	5.697	478.41	24.75	503.16
0.662	7.251	432.38	69.07	501.45
0.970	8.581	399.45	101.75	501.20
1.324	9.813	372.62	127.69	500.31
1.854	11.307	343.61	155.68	499.29
2.65	13.084	312.85	183.76	496.61
4.26	15.756	272.01	223.99	496.00
6.63	18.575	233.83	258.29	492.12
9.65	21.192	201.47	290.28	491.75
9.72	21.244	200.84	289.99	490.83

* Using Eq. [2] and columns 3 and 4.

Table V. Values determined for intercept and slope of linear equation fitted to data of Tables III and IV

Acid	Mean temperature (°C)	Range of molality (m /mole kg^{-1})	n (No. of runs)	Standard error of estimate ^a ($\mu\text{V K}^{-1}$)	Y° ($\mu\text{V K}^{-1}$)	Y' ($\mu\text{V K}^{-1} \text{ dm}^{3/2} \text{ mole}^{-1/2}$)
$\text{NH}_2\text{SO}_3\text{H}$	29	0.001-0.008	9 ^b	1.19	$504.0_1 \pm 0.8_3$	$-90.0_3 \pm 15$
HClO_4	25	0.004-0.1	10	0.64	507.62 ± 0.54	-78.10 ± 3.76

^a (Standard error of estimate)² = $[Y(\text{obs}) - Y(\text{calc})]^2 / [n - 2]$, summed over the n data points.

^b The nine values reported in Table III are weighted averages of 25 experimental runs.

^c The errors indicated for each of the four constants are termed standard errors and were calculated by the method of Deming (21).

Use of a modified Walden rule ($\lambda\eta T = \text{constant}$) (24) led to no significant change in the theoretical value of Y' ($<0.05\%$). Use of conductivity data for sulfamic acid interpolated from the data of Mazzi and Alberti-Oggioni (25) at 25° and 50°C changed the theoretical Y' by less than 0.2%.

The comparison of values for perchloric acid is excellent although the comparison of values for sulfamic acid is not quite within the acceptable range of standard error (last column of Table V). Nevertheless, we are encouraged by our results and hope that improvements can be made in the theory for the electrophoretic terms for the heats of transport and the transported entropies in electrolytes.

Acknowledgment

We gratefully acknowledge that this work has been supported by an M. J. Murdock Charitable Trust grant of Research Corporation. We also wish to thank Texas Instruments Incorporated without whose TI-59 calculator and printer the calculations would have been much more difficult.

Manuscript submitted Aug. 20, 1979; revised manuscript received March 14, 1980.

Any discussion of this paper will appear in a Discussion Section to be published in the June 1981 JOURNAL. All discussions for the June 1981 Discussion Section should be submitted by Feb. 1, 1981.

Publication costs of this article were assisted by Willamette University.

LIST OF SYMBOLS

a	mean distance of approach for HA
B'	Debye-Hückel constant, first appearing in Eq. [6]
B_2	constant first appearing in Eq. [10]
c	molarity or equilibrium molarity, moles of solute per dm^3 of solution
e	protonic charge, 4.80325×10^{-10} esu
F	Faraday constant, 96,487 C/equiv ⁻¹
K_a	acid dissociation constant
m	molality or equilibrium molality, moles of solute per kg of solvent
N	Avogadro constant, 6.022169×10^{23} mole ⁻¹
\hat{Q}_1	heat of transport for an ion or acid, J K ⁻¹ mole ⁻¹
\hat{Q}_1°	limiting value at infinite dilution of \hat{Q}_1
R	universal gas constant, 8.31434 J K ⁻¹ mole ⁻¹ or 8.31434×10^7 erg K ⁻¹ mole ⁻¹
r_i	Stokes' radius of an ionic species, cm
S_i	partial molal entropy of an ion, J K ⁻¹ mole ⁻¹
S_i°	standard value of S_i
\bar{S}_i	transported entropy of an ion, J K ⁻¹ mole ⁻¹
\bar{S}_i°	transported entropy of an ion in the hypothetical standard state with $m = 1$ mole kg^{-1}
T	Kelvin temperature, K
TEP	initial thermoelectric power, $\mu\text{V K}^{-1}$
t_i	transport (transference) number of an ion
Y	thermoelectric power corrected for the mass-action term, defined by Eq. [2] and [12], $\mu\text{V K}^{-1}$
Y°	the value of Y at infinite dilution
α	isobaric expansivity, $= V^{-1} (\partial V / \partial T)_P$

ΔT	temperature difference between electrode compartments, K
ϵ_r	relative permittivity (dielectric constant)
γ	mean molal activity coefficient, $\text{NH}_2\text{SO}_3\text{H}$
κ	the Debye-Hückel reciprocal length = $B' \sqrt{c}$ for aqueous acid HA
λ_i°	limiting ionic mobility of an ion, $\text{cm}^2 \Omega^{-1}$
σ	Debye-Hückel constant, defined in Eq. [5]
σ'	constant in parentheses of Eq. [4]

REFERENCES

- A. D. Payton, B. H. Boyd, C. M. Houck, E. H. Temple, and A. H. Zimmerman, *This Journal*, **120**, 373 (1973).
- A. D. Payton, S. G. Angelos, E. L. Shuck, and A. H. Zimmerman, *J. Chem. Soc. Faraday Trans. I*, **71**, 2111 (1975).
- A. D. Payton and M. S. Showell, *J. Phys. Chem.*, **82**, 625 (1978).
- J. N. Agar, in "Advances in Electrochemistry and Electrochemical Engineering," Vol. 5, P. Delahay, Editor, Chap. 2, Interscience Publishers, New York (1963).
- E. Helfand and J. G. Kirkwood, *J. Chem. Phys.*, **32**, 857 (1960).
- E. Helfand, R. J. Bearman, and V. S. Vaidhyathan, *J. Math. Phys.*, **4**, 160 (1963).
- R. J. Bearman and V. S. Vaidhyathan, *J. Chem. Phys.*, **39**, 3411 (1963).
- E. J. King and G. W. King, *J. Am. Chem. Soc.*, **74**, 1212 (1952).
- R. A. Robinson and R. H. Stokes, "Electrolyte Solutions," 2nd ed., pp. 128, 172, 463, 531, Butterworth Scientific Publications, Ltd., London (1970).
- J. N. Agar, in "Annual Reviews of Physical Chemistry," Vol. 15, H. Eyring, Editor, pp. 469, 477, Annual Reviews, Palo Alto, Calif. (1964).
- H. M. Spencer and J. L. Justice, *J. Am. Chem. Soc.*, **56**, 2311 (1934).
- (a) M. I. Temkin and A. V. Khoroshin, *Zh. Fiz. Khim.*, **26**, 500 (1952); (b) T. Ikeda, *J. Chem. Phys.*, **43**, 3412 (1965).
- (a) K. Wirtz, *Z. Naturforsch.*, **3a**, 672 (1948); (b) B. B. Owen and F. H. Sweeton, *J. Am. Chem. Soc.*, **63**, 2811 (1941).
- (a) B. B. Owen, R. C. Miller, C. E. Milner, and H. L. Cogan, *J. Phys. Chem.*, **65**, 2065 (1961); (b) G. S. Kell, *J. Chem. Eng. Data*, **20**, 97 (1975).
- L. D. Eicher and B. J. Zwolinski, *J. Phys. Chem.*, **75**, 2016 (1971).
- R. Parsons, "Handbook of Electrochemical Constants," p. 85, Butterworths Scientific Publications, Ltd., London (1959).
- E. G. Taylor, R. P. Desch, and A. J. Catotti, *J. Am. Chem. Soc.*, **73**, 74 (1951).
- "Temperature Measurement Handbook," p. A-8, (supercedes *Nat. Bur. Std. Circ.* 561), Omega Engineering Inc., Stamford, Conn. (1978).
- N. A. Lange, Editor, "Handbook of Chemistry," 10th ed., p. 1438, McGraw-Hill Book Co., New York (1961).
- G. J. Hills and D. J. G. Ives, in "Reference Electrodes," D. J. G. Ives and G. J. Janz, Editors, Chap. 2, Academic Press, Inc., New York (1961).
- W. E. Deming, "Statistical Adjustment of Data," pp. 27, 226-230, Dover Publications, Inc., New York (1943).
- F. M. Goyan, Ph. D. Thesis, University of California, Berkeley (1937).
- R. Haase and K. Hoch, *Z. Phys. Chem. (Frankfurt)*, **46**, 63 (1965).

24. (a) J. O'M. Bockris and A. K. N. Reddy, "Modern Electrochemistry," Vol. 1, p. 386, Plenum Press, New York (1970); (b) R. L. Kay, in "Water—A Comprehensive Treatise," Vol. 3, F. Franks,

Editor, Chap. 4, p. 193, Plenum Press, New York (1973).

25. B. Mazzi and A. Alberti-Oggioni, *Ric. Sci., Rend., Sez. A8*, 1394 (1965).

Sinusoidal A-C Modulation of a Rotating Hemispherical Electrode

Der-Tau Chin*

Department of Chemical Engineering, Clarkson College of Technology, Potsdam, New York 13676

ABSTRACT

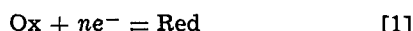
An analysis has been made for the concentration polarization and the Warburg impedance of a rotating hemispherical electrode when the electrode is superimposed with a sinusoidal alternating current (a.c.). Numerical results are presented for the changes in the concentration of the diffusing species and for the calculation of the concentration overpotential at the electrode. It is shown that for the values of a dimensionless a-c frequency greater than 10, the behavior of the hemispherical electrode becomes the same as that of a rotating disk electrode, and the location of the reference electrode in an experimental setup has no significant effect on the potential measurements.

Alternating current (a.c.) has an interesting effect on the electrode processes. It can reduce the electrode polarization, shift the rest potential, destroy the electrochemical passivity (1-3), and produce periodical changes in the concentration of the reacting species at the electrode surface (4). This paper is concerned with the a-c modulation of a rotating hemispherical electrode.

The rotating hemispherical electrode is a supplementary tool to the rotating disk electrode. It has the advantages that (i) its current distribution is uniform below the limiting current potentials (5), and (ii) it is more suitable for the study of corrosion and dissolution reactions because its geometry remains relatively unchanged during the experimental runs (6). In this work, an attempt has been made to provide a theoretical background for the use of the rotating hemispherical electrode in the study of a-c corrosions. The present paper discusses the concentration overpotentials when the electrode is modulated with a sinusoidal a.c.

Analysis

Consider the following redox reaction taking place at the surface of a rotating hemispherical electrode



The hemispherical electrode is mounted on a supporting rod of an equal radius r_0 , as shown in Fig. 1, and is rotating with an angular velocity Ω in a stationary, infinitely large, incompressible solution of constant properties. It is assumed that sufficient supporting electrolyte is present in the solution and the bulk concentration of Red species is much higher than Ox species such that the migration effect is negligible and the concentration polarization may be described by the convective diffusion of Ox species. When the electrode surface is subjected to the passage of a direct current (d.c.) superimposed with a sinusoidal alternating current density

$$\tilde{i} = i_p e^{j\omega t} \quad [2]$$

the concentration of Ox species may be expressed as a sum of a steady-state component \bar{c} and a fluctuat-

ing component \tilde{c}

$$c = \bar{c} + \tilde{c} \quad [3]$$

The problem for the steady-state component has been treated by Chin (6), and Nisancioglu and Newman (5). For the fluctuating component, the time-dependent convective diffusion equation in laminar flow may be given in the spherical polar coordinates (Fig. 1) as

$$\frac{\partial \tilde{c}}{\partial t} + v_r \frac{\partial \tilde{c}}{\partial r} + \frac{v_\theta}{r_0} \frac{\partial \tilde{c}}{\partial \theta} = D \frac{\partial^2 \tilde{c}}{\partial r^2} \quad [4]$$

with the boundary conditions

$$\left. \begin{aligned} \text{at } \theta = 0, \quad \frac{\partial \tilde{c}}{\partial \theta} &= 0 \\ r = \infty, \quad \tilde{c} &= 0 \\ r = r_0, \quad \frac{\partial \tilde{c}}{\partial r} &= -\frac{i_p}{nFD} e^{j\omega t} \end{aligned} \right\} \quad [5]$$

Here D represents the diffusivity of Ox species; v_r and v_θ are the radial and the meridional velocity components, respectively; i_p is the peak a-c density; ω is the a-c frequency; t is the time; and j is equal to $\sqrt{-1}$. One may normalize the above equations with the following dimensionless parameters and variables

$$\text{Schmidt number, } Sc = \nu/D \quad [6]$$

$$\text{Dimensionless a-c frequency, } K = \frac{\omega}{\Omega} Sc^{1/3} \quad [7]$$

$$\text{Dimensionless radial coordinate, } \eta = (r - r_0) \left(\frac{\Omega}{\nu} \right)^{1/2} \quad [8]$$

$$\text{Dimensionless time, } \tau = \Omega t \quad [9]$$

Dimensionless radial velocity,

$$H = \frac{v_r}{(\nu\Omega)^{1/2}} = H_1(\eta) + \theta^2 H_3(\eta) + \dots \quad [10]$$

* Electrochemical Society Active Member.
Key words: concentration overpotential, Warburg impedance, convection, diffusion.

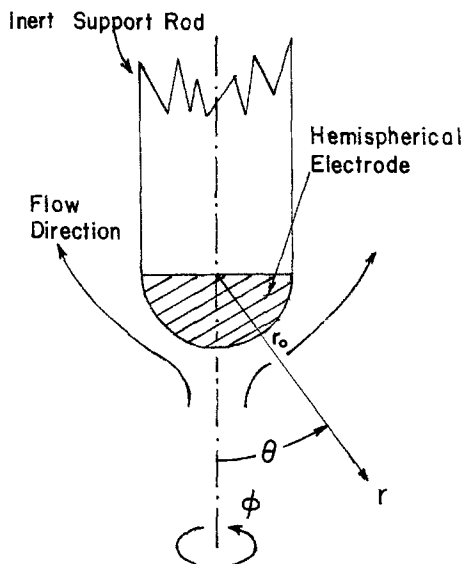


Fig. 1. Rotating hemispherical electrode and the spatial coordinates.

Dimensionless meridional velocity,

$$F = \frac{v_\theta}{r_0\Omega} = \theta F_1(\eta) + \theta^3 F_3(\eta) + \dots \quad [11]$$

Dimensionless concentration,

$$M = \frac{nFD}{i_p} \left(\frac{\Omega}{\nu}\right)^{1/2} \tilde{c} = [M_1(\eta) + \theta^2 M_3(\eta) + \dots] e^{jKSc^{-1/3}\tau} \quad [12]$$

Substituting Eq. [6]-[12] into Eq. [4]-[5] and equating the terms having the like power of θ on both sides of the resulting equations, one has

$$\frac{1}{Sc} \frac{d^2 M_1}{d\eta^2} - H_1 \frac{dM_1}{d\eta} - j \frac{K}{Sc^{1/3}} M_1 = 0 \quad [13]$$

$$\frac{1}{Sc} \frac{d^2 M_3}{d\eta^2} - H_1 \frac{dM_3}{d\eta} - \left(2F_1 + j \frac{K}{Sc^{1/3}}\right) M_3 = H_3 \frac{dM_1}{d\eta} \quad [14]$$

Boundary conditions

$$\left. \begin{aligned} \text{at } \eta = 0, \quad \frac{dM_1}{d\eta} = -1; \quad \frac{dM_3}{d\eta} = 0 \\ \eta = \infty, \quad M_1 = M_3 = 0 \end{aligned} \right\} \quad [15]$$

The dimensionless velocity components F_1 , H_1 , and H_3 can be expressed in terms of a power series of η ; they have been calculated by Cochran (7) and Banks (8). At high Schmidt numbers, the thickness of the concentration boundary layer is much smaller than the hydrodynamic boundary layer, and the first term in the power series can be used as a good approximation for the velocity components

$$F_1 = 0.51023\eta \quad [16]$$

$$H_1 = -0.51023\eta^2 \quad [17]$$

$$H_3 = 0.52762\eta^2 \quad [18]$$

Furthermore, for the analysis of concentration fluctuations at high Schmidt numbers, one may introduce a set of stretched variables and express the dimensionless concentrations in a complex form

$$z = \eta Sc^{1/3} \quad [19]$$

$$M_1 Sc^{1/3} = X(\eta) + jY(\eta) \quad [20]$$

$$M_3 Sc^{1/3} = U(\eta) + jV(\eta) \quad [21]$$

Substituting Eq. [16]-[21] into Eq. [13]-[15], and separating the real and the imaginary parts on both sides of the resulting equations, one has

$$\frac{d^2 X}{dz^2} + 0.51023z^2 \frac{dX}{dz} + KY = 0 \quad [22]$$

$$\frac{d^2 Y}{dz^2} + 0.51023z^2 \frac{dY}{dz} - KX = 0 \quad [23]$$

$$\begin{aligned} \frac{d^2 U}{dz^2} + 0.51023z^2 \frac{dU}{dz} - 1.02046zU + KV \\ = 0.52762z^2 \frac{dX}{dz} \quad [24] \end{aligned}$$

$$\begin{aligned} \frac{d^2 V}{dz^2} + 0.51023z^2 \frac{dV}{dz} - 1.02046zV - KU \\ = 0.52762z^2 \frac{dY}{dz} \quad [25] \end{aligned}$$

Boundary conditions

$$\left. \begin{aligned} \text{at } z = 0, \quad \frac{dX}{dz} = -1; \quad \frac{dY}{dz} = \frac{dU}{dz} = \frac{dV}{dz} = 0 \\ z = \infty, \quad X = Y = U = V = 0 \end{aligned} \right\} \quad [26]$$

Numerical Results and Discussion

Equations [22]-[26] have been solved numerically on a digital computer with a finite difference method (9). Results for the dimensionless concentration components, X , Y , U , and V are plotted in Fig. 2-5 as a function of z for various values of the dimensionless a-c frequency, K . It is seen that the profile of the concentration fluctuations is a strong function of the a-c frequency, K . The thickness of the concentration boundary layer does not appear to change with super-

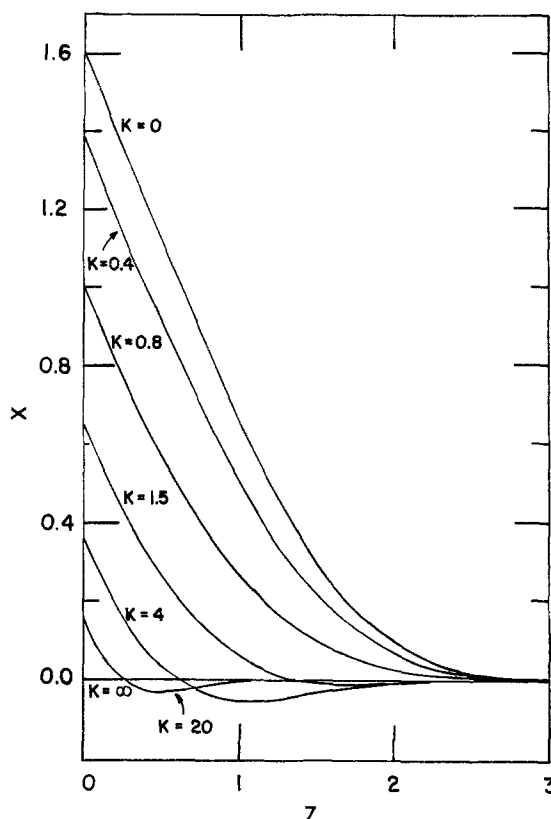


Fig. 2. Dimensionless concentration: X vs. z

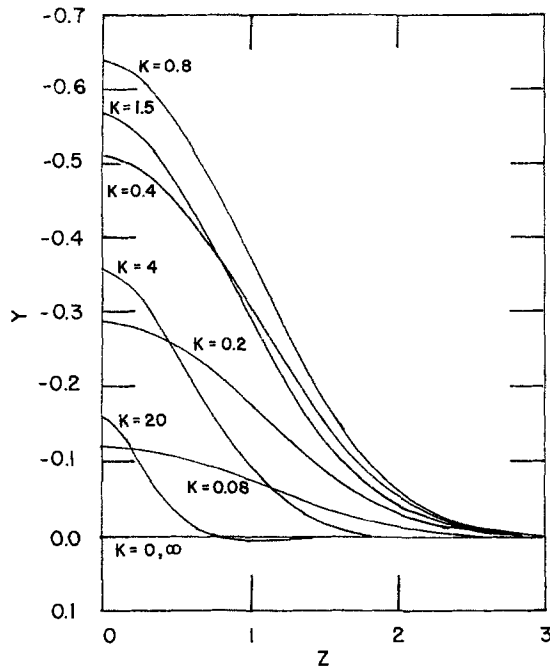


Fig. 3. Dimensionless concentration: Y vs. z

imposed a.c. for small values of K. The concentration changes occur within a region of $0 \leq z < 3.3$. However, at high a-c frequencies, the region diminishes rapidly with increasing values of K, and becomes zero at $K = \infty$.

The concentration overpotential caused by the convective diffusion of Ox species may be given as

$$\eta_{\text{conc}} = \frac{RT}{nF} \ln \frac{c_s}{c_\infty} \quad [27]$$

where c_s is the concentration of Ox species at the surface of the electrode. In the absence of a d-c component, the concentration at the surface may be expressed as $c_s = c_\infty + \tilde{c}_s$, and the concentration overpotential becomes

$$\eta_{\text{conc}} = \frac{RT}{nF} \ln \left(1 + \frac{\tilde{c}_s}{c_\infty} \right) \quad [28]$$

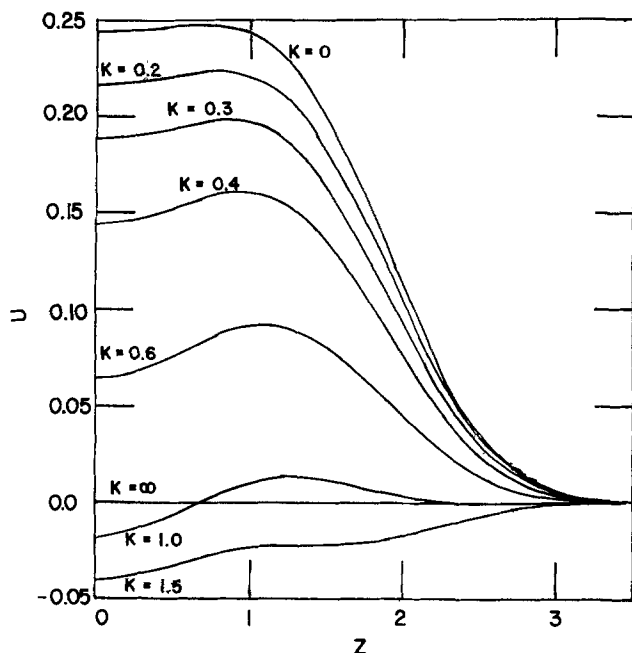


Fig. 4. Dimensionless concentration: U vs. z

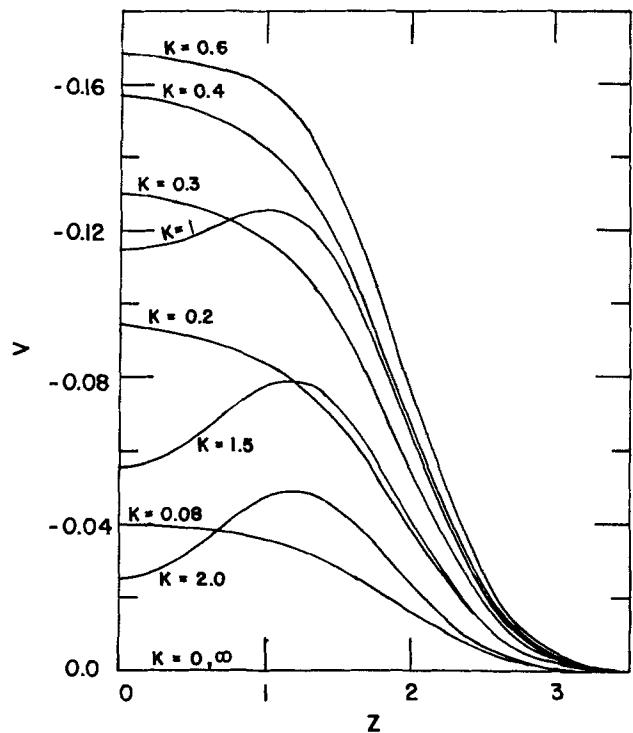


Fig. 5. Dimensionless concentration: V vs. z

where \tilde{c}_s is the concentration fluctuations at the electrode surface. Equation [28] may be rearranged to the following expression by making use of the dimensionless concentrations

$$\eta_{\text{conc}} = \frac{RT}{nF} \ln \{ 1 + N [(X_0 + \theta^2 U_0) + j(Y_0 + \theta^2 V_0)] e^{jKSc^{-1/2}\tau} \} \quad [29]$$

Here N is defined as

$$N = \frac{i_p}{nFc_\infty D^{2/3} \nu^{-1/6} \Omega^{1/2}} \quad [30]$$

and may be regarded as a dimensionless peak a-c density. The quantities $X_0, Y_0, U_0,$ and V_0 , are the values of the dimensionless concentration components, X, Y, U, and V, respectively, at z equal to zero; they are plotted in Fig. 6-7, and are tabulated in Table I for a range of K from 0 to 150. The corresponding plots for Y_0 vs. X_0 and V_0 vs. U_0 on the complex planes are given in Fig. 8 and 9 where the values of K are indicated on each curve as the parameters.

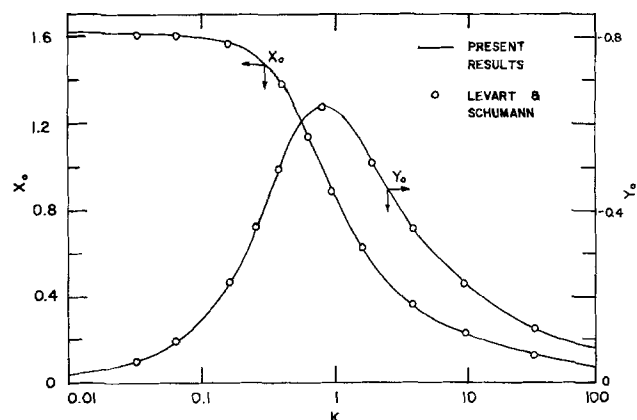


Fig. 6. Values of X and Y at z = 0 vs. the dimensionless a-c frequency, K. The present results are given as the solid lines. Levart and Schumann's results (10) for a rotating disk electrode are plotted as the open circles.

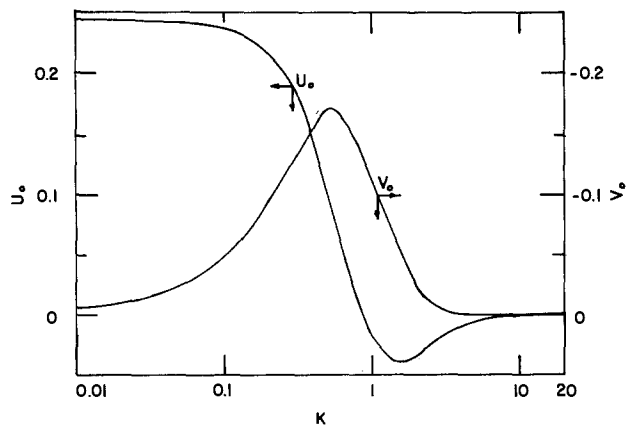


Fig. 7. Values of U and V at $z = 0$ vs. the dimensionless a-c frequency K .

For small dimensionless peak a-c densities, Eq. [29] may be simplified to

$$\eta_{\text{conc}} = \frac{RT}{nF} N [(X_0 + \theta^2 U_0)^2 + (Y_0 + \theta^2 V_0)^2]^{1/2} e^{j(KSc^{-1/2}\tau + \Psi)} \quad (\text{for } N \ll 1) \quad [31]$$

where

$$\Psi = -\cos^{-1} \frac{X_0 + \theta^2 U_0}{[(X_0 + \theta^2 U_0)^2 + (Y_0 + \theta^2 V_0)^2]^{1/2}} \quad [32]$$

The Warburg impedance is related to the concentration overpotential by

$$Z_w = \frac{\eta_{\text{conc}}}{i} \quad [33]$$

Substituting Eq. [2] and [31] into Eq. [33], one has

$$Z_w = \frac{RT}{n^2 F^2 c_x D^{2/3} \nu^{-1/6} \Omega^{1/2}} [(X_0 + \theta^2 U_0)^2 + (Y_0 + \theta^2 V_0)^2]^{1/2} e^{j\Psi}, \quad (\text{for } N \ll 1) \quad [34]$$

Equations [31] and [34] indicate that with a small superimposed sinusoidal a.c., the response in the concentration overpotential will also be a sinusoidal wave of the same frequency. However, the potential fluctuations will have a phase shift of Ψ whose magnitude depends upon the a-c frequency and the location

Table I. Values of the dimensionless concentration components at the electrode surface

K	X ₀	Y ₀	U ₀	V ₀
0	1.61173	0	0.24350	0
0.01	1.61057	-0.01618	0.24324	-0.00542
0.015	1.61038	-0.02270	0.24309	-0.00760
0.02	1.61006	-0.03025	0.24297	-0.01013
0.03	1.60912	-0.04539	0.24258	-0.01519
0.04	1.60788	-0.06040	0.24207	-0.02021
0.06	1.60457	-0.09043	0.24066	-0.03022
0.08	1.59999	-0.11997	0.23868	-0.04004
0.1	1.59416	-0.14914	0.23617	-0.04967
0.15	1.57463	-0.22055	0.22788	-0.07287
0.2	1.54844	-0.28737	0.21678	-0.09399
0.3	1.48025	-0.40820	0.18869	-0.12999
0.4	1.37645	-0.50951	0.14486	-0.15690
0.6	1.16799	-0.61970	0.06450	-0.16818
0.8	0.99974	-0.63914	0.01319	-0.14205
1.0	0.86454	-0.63441	-0.01842	-0.11493
1.5	0.65220	-0.56720	-0.04006	-0.05571
2.0	0.53800	-0.50058	-0.03414	-0.02530
3.0	0.42280	-0.40929	-0.01756	-0.00541
4.0	0.36118	-0.35415	-0.00950	-0.00153
6.0	0.29169	-0.28920	-0.00394	-0.00030
8.0	0.25138	-0.25061	-0.00216	-0.00011
10	0.22419	-0.22429	-0.00136	-0.00001
20	0.15744	-0.15909	-0.00033	0
30	0.12802	-0.13029	-0.00015	0
40	0.11046	-0.11317	-0.00008	0
60	0.08957	-0.09295	-0.00004	0
80	0.07703	-0.08096	-0.00002	0
100	0.06842	-0.07281	-0.000013	0
150	0.05486	-0.06024	-0.000006	0

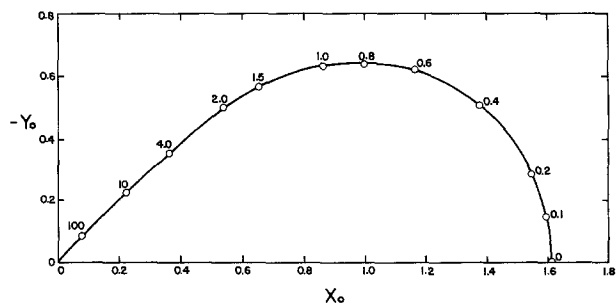


Fig. 8. Complex impedance plot of $-Y_0$ vs. X_0 . The values of K at the open circles are indicated on the curve.

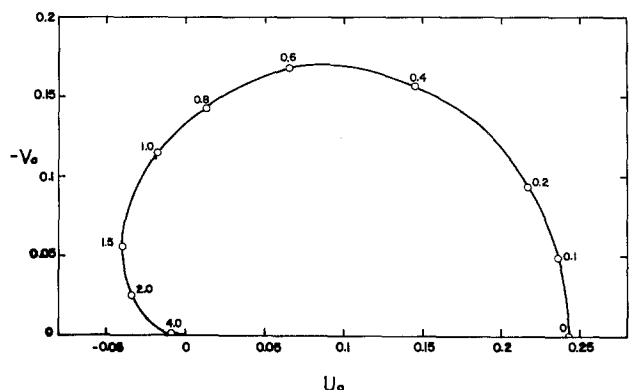


Fig. 9. Complex impedance plot of $-V_0$ vs. U_0 . The values of K at the open circles are indicated on the curve.

of the reference electrode relative to the axis of rotation of the hemispherical electrode. Figure 10 shows the phase shift as a function of the dimensionless a-c frequency, K , for two different values of θ . The lower curve ($\theta = 0$) corresponds to a reference electrode located near the pole of the hemispherical electrode. In this case, the phase shift of the concentration overpotential increases with a-c frequency, and becomes approximately equal to -45° at high frequencies. The upper curve ($\theta = \pi/2$) corresponds to a reference electrode located near the equator. In this case, the phase shift reaches a maximum of -52° at K equal to 1.6. Beyond this value, the phase shift decreases with increasing K and approaches to that of $\theta = 0$ at high a-c frequencies. This behavior could be explained by the fact that at large a-c frequencies the values of U_0 and V_0 become negligibly small as compared to the values of X_0 and Y_0 . At $K = 10$, for example, the neglect of the θ^2 terms in Eq. [29], [31], [32], and [34] would yield an error of less than

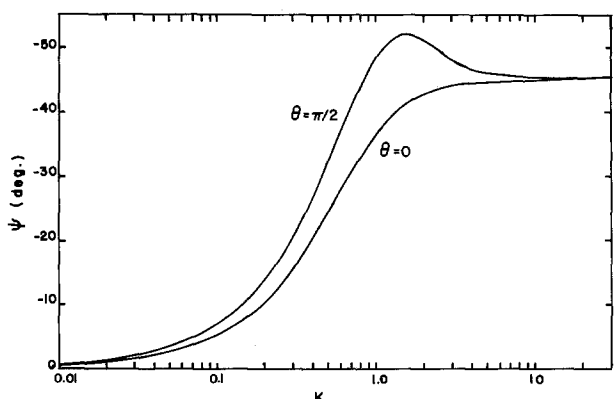


Fig. 10. Phase shift of the concentration overpotential, Ψ , vs. dimensionless a-c frequency, K , for the reference electrode located near the pole ($\theta = 0$) and the equator ($\theta = \pi/2$) of the hemispherical electrode.

1.5%. Thus, for K greater than 10, the position of the reference electrode in an experimental setup will have no significant effect on the potential measurements.

It should be noted that the present analysis is based on a series expansion for the concentration distribution at small values of θ . The rotating disk electrode can be treated as a special case by letting $\theta = 0$, and X_0 and Y_0 can be used to calculate the concentration overpotential and the Warburg impedance of the rotating disk electrode. For comparison, the values of X_0 and Y_0 calculated by Levart and Schumann (10) for a-c modulation at the rotating disk electrode are plotted in Fig. 6 as the open circles, \circ . The present results agree with their calculations to within 0.1%. This implies that the fluctuations in the concentration overpotential and the resulting Warburg impedance of the hemispherical electrode will be the same as those of the rotating disk electrode if the dimensionless frequency of superimposed a.c. is greater than 10.

Conclusions

A study has been made of the concentration overpotential and the Warburg impedance of a rotating hemispherical electrode when a sinusoidal a.c. is superimposed onto the electrode. It is shown that a.c. does not change the thickness of the concentration boundary layer, and the effect of a.c. decreases with increasing a-c frequency. For small superimposed a.c., the response in the concentration overpotential is also a sinusoidal wave of the same frequency with a phase shift depending on the magnitude of a-c frequency and the location of the reference electrode. At high a-c frequencies of $K \cong 10$, the behavior of the hemispherical electrode becomes the same as that of a rotating disk electrode, and the position of the reference electrode has no significant effect on the potential measurements.

Acknowledgment

Special thanks are due to Mr. K. L. Hsueh for his help in the computer calculations and to Mr. S. Venkatesh for his technical contributions. This work was supported in part by the National Science Foundation Grant ENG77-25153. Acknowledgment is also made to the Donors of the Petroleum Research Fund, administered by the American Chemical Society, for partial support of this research.

Manuscript submitted Oct. 1, 1979; revised manuscript received March 27, 1980.

Any discussion of this paper will appear in a Discussion Section to be published in the June 1981 JOURNAL. All discussions for the June 1981 Discussion Section should be submitted by Feb. 1, 1981.

Publication costs of this article were assisted by Clarkson College of Technology.

LIST OF SYMBOLS

c	concentration of the diffusing ion, g-mole/cm ³
c_s	bulk concentration, g-mole/cm ³
c_s	concentration at the electrode surface, g-mole/cm ³
\bar{c}	steady-state concentration component, g-mole/cm ³

\tilde{c}	fluctuating concentration component, g-mole/cm ³
c_s	concentration fluctuations at the electrode surface, g-mole/cm ³
D	diffusivity of the diffusing ion, cm ² /sec
F, F_1, F_3	dimensionless meridional velocity components defined in Eq. [11]
F	Faraday constant, 96,500 C/g-equiv., or 23,060 cal/(V) (g-equiv.)
H, H_1, H_3	dimensionless radial velocity components defined in Eq. [10]
i_p	peak a-c density A/cm ²
\tilde{i}	a-c density, A/cm ²
j	equal to $\sqrt{-1}$, dimensionless
K	dimensionless a-c frequency defined as $(\omega/\Omega)Sc^{1/3}$
M, M_1, M_3	dimensionless concentration components defined in Eq. [12]
N	dimensionless peak a-c density defined in Eq. [30]
n	number of electrons transferred in the electrode reaction, g-equiv./g-mole
R	universal gas constant, 8.314 J/(°K) (g-mole), or 1.987 cal/(°K) (g-mole)
r	radial coordinate, cm
r_0	radius of the hemispherical electrode, cm
Sc	Schmidt number defined as ν/D , dimensionless
T	temperature, °K
t	time, sec
U, V	dimensionless concentration components defined in Eq. [21]
U_0, V_0	values of U and V , respectively, at $z = 0$, dimensionless
v_θ	radial velocity component, cm/sec
v_r	meridional velocity component, cm/sec
X, Y	dimensionless concentration components defined in Eq. [20]
X_0, Y_0	values of X and Y , respectively, at $z = 0$, dimensionless
z	stretched dimensionless radial coordinate defined as $\eta Sc^{1/3}$
Z_w	Warburg impedance, Ω -cm ²
η	dimensionless radial coordinate defined as $(r - r_0)(\Omega/\nu)^{1/2}$
η_{conc}	concentration overpotential, V
θ	meridional coordinate, rad
ν	kinematic viscosity of the electrolyte, cm ² /sec
Ω	rotational speed of the hemispherical electrode, rad/sec
ω	a-c frequency, rad/sec

REFERENCES

- D-T. Chin and T-W. Fu, *Corrosion*, **35**, 514 (1979).
- D-T. Chin and S. Venkatesh, *This Journal*, **126**, 1908 (1979).
- S. Venkatesh and D-T. Chin, *Israel J. Chem.*, **18**, 56 (1979).
- E. Warburg, *Ann Phys.*, **67**, 493 (1899); **6**, 125 (1901).
- K. Nisancioglu and J. Newman, *This Journal*, **121**, 241 (1974).
- D-T. Chin, *ibid.*, **118**, 1434 (1971); **118**, 1764 (1971); **120**, 631 (1973).
- W. G. Cochran, *Proc. Cambridge Phil. Soc.*, **30**, 365 (1934).
- W. H. H. Banks, *ZAMP*, **16**, 780 (1965).
- V. G. Jenson and G. V. Jeffreys, "Mathematical Methods in Chemical Engineering," Academic Press, London (1977).
- E. Levart and D. Schuhmann, *J. Electroanal. Chem. Interfacial Electrochem.*, **28**, 45 (1970).

Electrochemical Reduction of Pyridinium Ions in Ionic Aluminum Chloride: Alkylpyridinium Halide Ambient Temperature Liquids

R. J. Gale¹ and R. A. Osteryoung^{*2}

Department of Chemistry, Colorado State University Fort Collins, Colorado 80523

ABSTRACT

Reduction of 1-alkylpyridinium cation in 0.8:1 molar ratio AlCl_3 :1-butylpyridinium chloride liquids at 40°C has been investigated by cyclic voltammetry and electrochemical pulse methods. A dimeric product of the primary pyridinyl radical coupling, 4,4'-tetrahydrobipyridine, forms in about 45% yield and undergoes fairly rapid chemical dissociation to the stable, electroactive, 1,1'-dibutyl-4,4'-bipyridinium monocation radical. This product may be reduced further by other dissociation fragments. The corresponding biquaternary bipyridyl base reduces in two steps, each with one-electron reversible behavior, at half-wave potentials of -0.56 and -0.96V vs. $\text{Al}(\text{O})$ in 2:1 solvent reference electrode. Tetrahydrobipyridine species with 1,2,4,6-substituted methyl groups were stable to dissociation under similar conditions. Molecular structural parameters that affect the reduction potentials of pyridinium ions and the stability of tetrahydrobipyridines are discussed briefly.

Mixtures of AlCl_3 :1-butylpyridinium chloride (1-BPC) form aprotic melts of variable Lewis acidity which are liquids at room temperature. In the course of investigating their acid-base properties, it was observed that the chloride ion-rich mixtures (*i.e.*, <1:1 molar ratio, respectively) reacted spontaneously with an aluminum wire electrode. This reaction arises from the reduction of the 1-alkylpyridinium cation and consequently this electrode process, rather than the reduction of an aluminum ion species to elemental aluminum, determines the negative potential limit of the electrochemical stability of the basic solvent. The present work has attempted to establish the mechanism of alkylpyridinium cation reduction in these solvents because a better understanding of how the pyridinium ion molecular structure relates to its reduction-oxidation might enable improvements to be made in the selection of discrete electrolyte properties.

A comprehensive review of dihydropyridine chemistry has been published encompassing reduction of pyridines and alkylpyridinium ions with specific metals and metallic ions (*e.g.*, Na, Zn, Mg, active Al, Cr^{2+} , V^{2+}), chemical reducing agents (*e.g.*, LiAlH_4 , $\text{Na}_2\text{S}_2\text{O}_4$, NaBH_4 , NaCNBH_3) and electrochemical methods (2). Also, the electrode reactions of diverse heterocyclic compounds have been reviewed by Lund (3). Many of these earlier reduction studies, particularly those of ring substituted 1-alkylpyridinium ions (4-7), resulted from attempts to understand the behavior of two key coenzymes, nicotinamide adenine dinucleotide (NAD^+) and nicotinamide adenine dinucleotide phosphate (NADP^+). Unsaturated double bonds contiguous to the hetero atom in heterocyclic compounds are more reactive than those in the benzene ring and they are usually the easiest to reduce, attack taking place at positions of low electron density, *i.e.*, the 2- or 4- positions in 6-membered rings. Pyridinyl radical production may occur by transferring one electron, from the appropriate metal for example, to the lowest unoccupied molecular orbital of the pyridinium ion species. Subsequent reactions of the radical intermediate, such as formation of a hydro-

genated monomer, dimerization, dissociation, or further reduction, depend both on the reductant and the solvent conditions, especially the availability of proton. Extensive ring cleavage has been proposed to occur in certain cases, for example through C = N bond rupture of AlCl_3 :pyridine Lewis acid-base adducts when pyridine solutions containing aluminum chloride are electrolyzed at mercury (8). Volke and Naarova (9, 10) have studied the electrochemical reduction of a series of 1-alkylpyridinium ions at a mercury electrode, in both aqueous and, because of adsorption complications, mixed aqueous/nonaqueous electrolytes. The half-wave potentials were found to vary only slightly (~ -50 mV maximum shift) with the 1-alkyl substituent (CH_3 to C_5H_{11}) but coulometric electrolysis values differed appreciably in the presence of a radical scavenger and it was suggested that the initial radical dimerization rates decreased as the 1-alkyl groups became increasingly bulky. Though not chemically identified, the main one-electron reduction products were postulated to be dihydropyridines. Nevertheless, a secondary dimeric alkyl viologen radical product was detected (<10% yield) and this could be easily characterized by electron paramagnetic resonance, ultraviolet spectroscopy, and its electrochemical behavior. More recently, Raghavan and Iwamoto (11, 12) have investigated the reduction of 1-alkylpyridinium ions in acetonitrile at platinum and mercury electrodes. As 1,1'-dialkyl-4,4'-bipyridinium monocation radical species were obtained by treatment of electrolyzed solutions with 1,4-benzoquinone, it was concluded that in this aprotic solvent the prime reduction product was a stable 1,1'-dialkyl-4,4'-tetrahydrobipyridine (alkyl = methyl, ethyl, or benzyl). In general, however, unequivocal characterization of the reduction product distribution has seldom been achieved and the experimental conditions and factors that can influence and determine mechanistic pathways are not fully understood. Further, scant electrochemical information is available for dihydropyridine and tetrahydrobipyridine compounds.

Results

The electron transfer characteristics of the alkylpyridinium ion reduction in melt may be readily studied by a Tafel plot of solvent electrolysis. Data illustrated in Fig. 1 were obtained from 10 msec potentiostatic pulses into the reduction background of

* Electrochemical Society Active Member.

¹ Present address: Engineering Research Center, Colorado State University, Fort Collins, Colorado 80523.

² Present address: Department of Chemistry, State University of New York at Buffalo, Buffalo, New York 14214.

Key words: chloroaluminate melts, butylpyridinium reduction, tetrahydrobipyridines, molten salts.

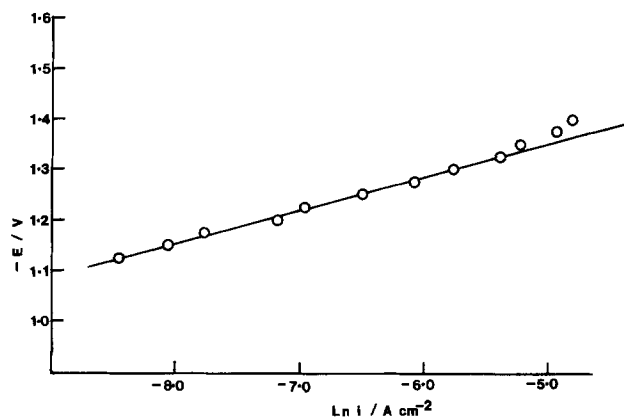
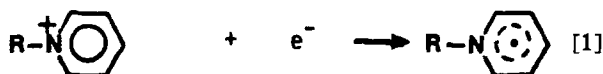


Fig. 1. Tafel plot of 0.8:1 melt reduction at a vitreous C electrode, 40°C.

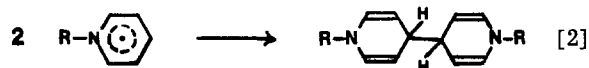
the 0.8:1 molar ratio AlCl_3 :1-BPC fused salt at 40°C, respectively. The short pulses were applied to minimize any complications from product formation and a Luggin probe reference electrode was used to minimize the IR drop. At constant values of the outer Helmholtz layer potential, the cathodic transfer coefficient α may be derived from the relation

$$\alpha = \frac{\alpha_c}{\nu} = - \left(\frac{RT}{nF} \right) \left(\frac{\partial \ln |I_c|}{\partial E} \right)_{T,P,c,1\dots}$$

where R is the gas constant, T the thermodynamic temperature, ν is the stoichiometric number, and I_c is the cathodic kinetic current. The value of the cathodic transfer coefficient, $\alpha = 0.408$, is consistent with the kinetic parameters for simple, rate-determining, one-electron processes and this may be taken as evidence that the primary reduction reaction is the formation of a pyridinyl radical species



followed by a rapid dimerization



DBTBP.—At potentials more negative than $\sim -1.40\text{V}$ vs. Al(O) reference, the overpotential $\eta/\ln i$ gradient increases, which may be an indication of either (i) commencement of product reduction or filming complications, (ii) a second electron charge transfer to the pyridinium ion [cf. electronic absorption behavior (13)], or (iii) coreduction from pyridinium ion and the tetrachloroaluminate ion species.

Figure 2 illustrates cyclic voltammograms obtained by scanning into the solvent background to -1.40V vs. Al(O) reference. Onset of 1-butyl-pyridinium ion reduction with vitreous carbon electrodes occurs at $\sim -1.1\text{V}$ vs. Al(O) reference. No reverse anodic currents could be detected at the negative background limit at scan rates as fast as 200Vsec^{-1} , or by scanning to -1.80V vs. Al(O) reference, which would be the case if the primary product from reduction undergoes an extremely rapid chemical reaction. At scan rates $dE/dt \lesssim 200\text{mVsec}^{-1}$, a predominant anodic current peak A appears at $-0.40 \pm 0.04\text{V}$ (C electrode). Because the peak potential of wave A coincides approximately to that assigned to the oxidation of dimeric 4,4'-tetrahydrobipyridine species in acetonitrile (11), it also can be assigned to the coupled product 1,1'-

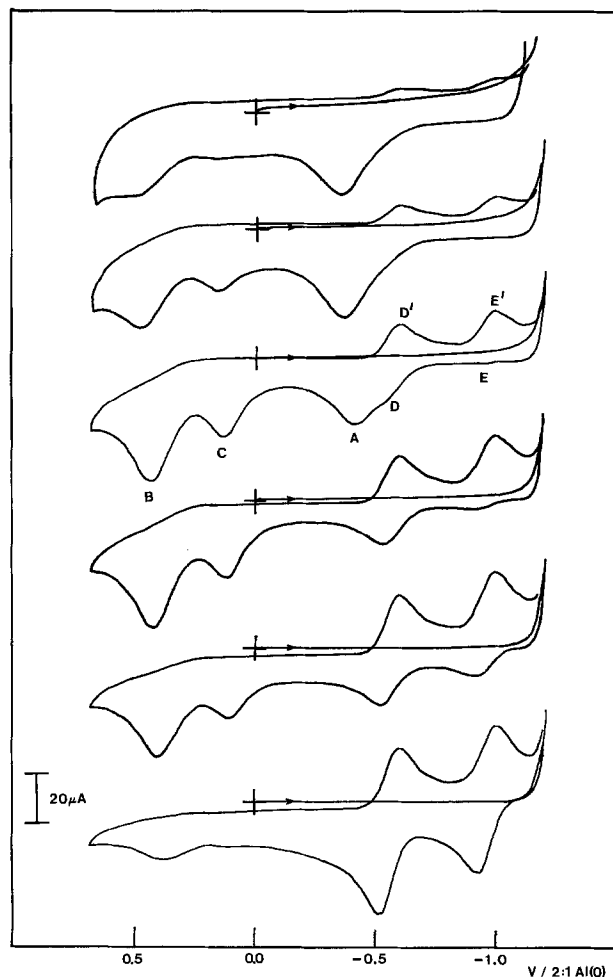


Fig. 2. Cyclic voltammetry of 0.8:1 melt reduction at 40°C, vitreous C electrode, 1Vsec^{-1} (top), 500mVsec^{-1} , 200mVsec^{-1} , 100mVsec^{-1} , 50mVsec^{-1} , 20mVsec^{-1} (bottom).

dibutyl-4,4'-tetrahydrobipyridine (DBTBP) in the melt. Unlike the behavior of 1,1'-dimethyl-4,4'-tetrahydrobipyridine in acetonitrile, at scan rates $dE/dt \lesssim 200\text{mVsec}^{-1}$, the peak current of A decreased markedly with decreasing scan rate and the wave is not defined at 50mVsec^{-1} (Fig. 2), indicating that DBTBP may be chemically unstable. In order to further characterize its electrochemistry in the basic melt, a sample of DBTBP was prepared by the reduction of 1-butylpyridinium chloride with sodium amalgam (14) (q.v. Experimental section). When 6.8×10^{-5} moles of DBTBP were micropipetted into $\sim 10\text{ml}$ of 0.8:1 melt at 40°C, the solution immediately became deep blue, the rest potential became -0.94V vs. Al(O) reference and approximately equal quantities of 1,1'-dibutyl-4,4'-bipyridinium monocation radical and the corresponding dihydrobipyridine were detected by cyclic voltammetry (Fig. 3) *vide infra*. After $\sim 30\text{min}$ and based on a diffusion coefficient of $7 \times 10^{-7}\text{cm}^2\text{sec}^{-1}$, the conversion yields were estimated to be about 25% for each product. Small anodic current peaks also were observed at $+0.18$ and $+0.55\text{V}$; however, the alkyl viologen radical and dihydrobipyridine comprised the major electroactive products. If a smaller quantity of DBTBP was added ($< 2 \times 10^{-5}$ moles), the rest potential was less negative at $\sim -0.60\text{V}$ and 1,1'-dibutyl-4,4'-bipyridinium monocation radical was the only major electroactive product detected. Although these experiments confirm the unstable nature of the 4,4'-tetrahydrobipyridine in the melt and support the premise that its decomposition produces 1,1'-dialkyl-4,4'-bipyridinium monocation radical, unfortunately they do not provide any insight to the mode of hydrogen loss or to the dissociation mechanism

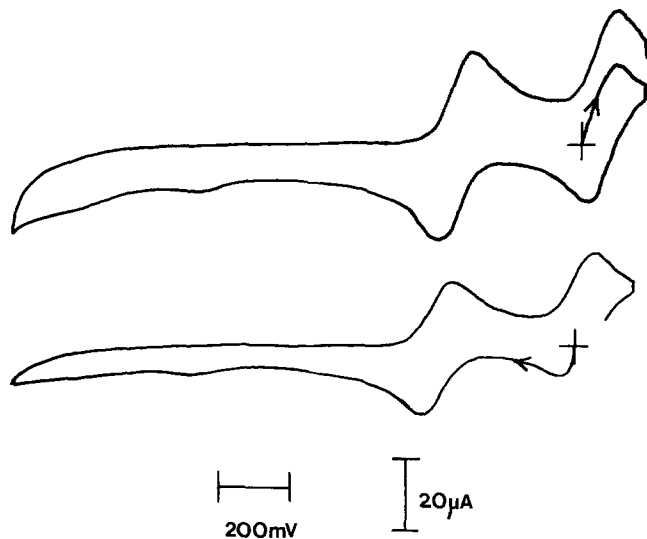
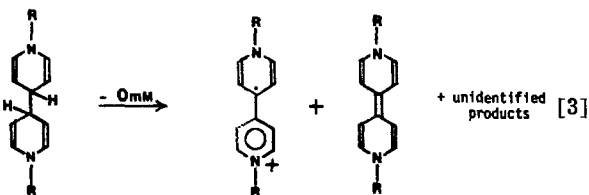
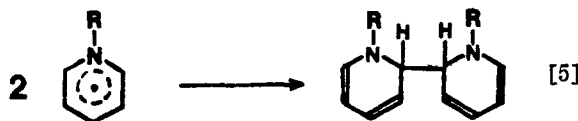
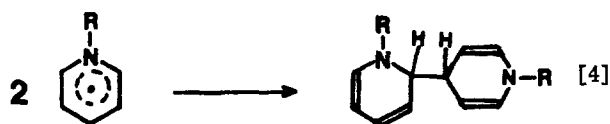


Fig. 3. Cyclic voltammograms after additions of 1,1'-dibutyl-4,4'-tetrahydrobipyridine to 0.8:1 AlCl_3 :1-BPC melts; upper 16 μl /~10 ml melt, rest potential -0.909V ; lower 20 μl /~10 ml melt, rest potential -0.940V ; $\nu = 200 \text{ mVsec}^{-1}$.



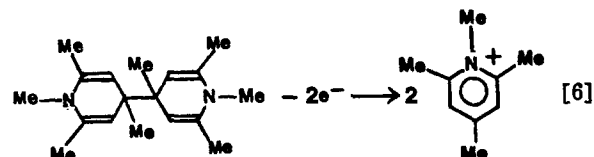
Coulometric experiments gave the ratio of the anodic charge (q_a) to cathodic charge (q_c) at a C electrode, $q_a/q_c = 45\%$ (50 msec double pulse, negative step 0.0 to -1.40V , positive -1.40 to 0.0V). These charge values were corrected for appropriate background double-layer charges to -1.00V negative limit. Raghavan has reported a corresponding figure of 70-95% coulometric ratio for 1-methylpyridinium ion in acetonitrile (11). In Fig. 2, the anodic current waves B and C exhibit time-dependent behavior at scan rates $dE/dt \lesssim 200 \text{ mVsec}^{-1}$, similar to wave A. They may be attributed to other chemically unstable byproducts of pyridinyl radical dimerization or hydrogen exchange products, such as the 2,4' or 2,2' coupled dimers, e.g.



Additionally, there is a possibility of electroactive products that arise from tetrahydrobipyridine decomposition or even cleavage of the pyridinyl ring. Some attempts were made to isolate the products obtained from melt electrolyses at -1.25V in a vitreous C crucible, but proved inconclusive. After the passage of $\sim 150\text{C}$, for example, the melt was poured into degassed water, neutralized, and extracted with cyclohexane. Evaporation of the cyclohexane left a viscous, brown, tar-like material which gave infrared absorption bands at 1672, 1259, 1195, 803, and 722 cm^{-1} . Amides absorb strongly in the $1600\text{-}1700 \text{ cm}^{-1}$ region

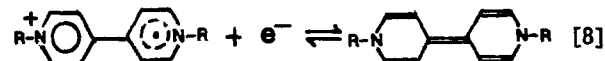
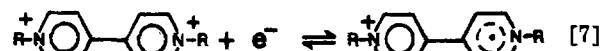
of the spectrum and the residue could contain amide fragments, similar to those believed to be found after alkaline hydrolyses of AlCl_3 :pyridine reduction products (8). In view of the likely air sensitivity and highly reactive nature of the primary products, this product analysis approach was considered to be unsatisfactory.

Figure 4 illustrates cyclic voltammograms of the background reduction of 0.8:1 molar ratio AlCl_3 :1-methyl-2,4,6-trimethylpyridinium iodide. An oxidation peak at $\sim -0.50\text{V}$ vs. Al(O) 2:1 AlCl_3 :1-BPC reference can be assigned to dimer product oxidation, e.g.



The primary radical could not be detected in cyclic voltammograms $\nu < 200 \text{ Vsec}^{-1}$ but the broad anodic wave is present at scan rates as low as 20 mVsec^{-1} and there is no evidence that this dimer can decompose to other electroactive products. The coulometric efficiency (q_a/q_c) was determined to be $67 \pm 11\%$. An anodic wave [-0.78V vs. Al(O) 2:1 AlCl_3 :1-BPC] is also obtained from reduction of 0.8:1 molar ratio AlCl_3 :1-butyl-4,tert.butylpyridinium chloride melt (60°C) and following the suggestion made by Raghavan (11), it is probable that 2,2' coupling ensues.

Melt electrochemistry of the biquaternary bipyridyl bases.—The two reversible couples D/D' and E/E' in Fig. 1 are indicative of the presence of the monocation radical and the dihydrobipyridine of 1,1'-dibutyl-4,4'-bipyridinium dication



The positive potential sweep reveals that at dE/dt

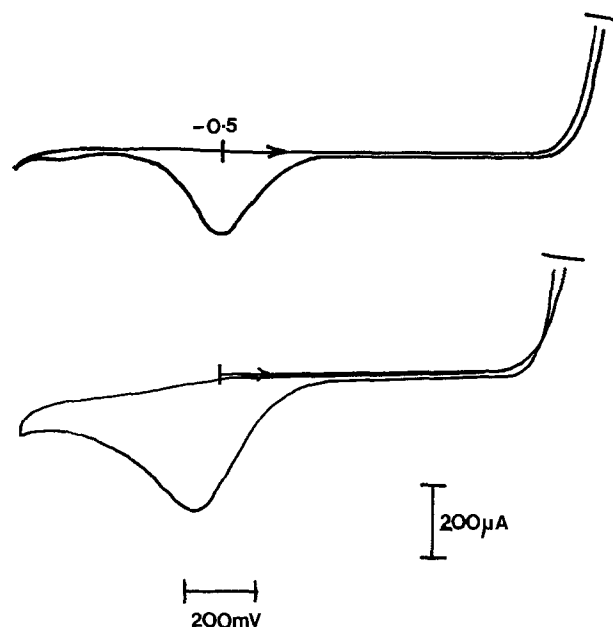


Fig. 4. Cyclic voltammetry of AlCl_3 :1,2,4,6-tetramethylpyridinium iodide reduction at vitreous carbon. Background sweep to -1.70V vs. Al(O) in 2L1 AlCl_3 :1-BPC reference, 60° . Upper $\nu = 20 \text{ mVsec}^{-1}$; lower $\nu = 1 \text{ Vsec}^{-1}$.

$> 100 \text{ mVsec}^{-1}$, the transient concentration of the dihydrobipyridine in the surface reaction zone is less than that of the monocation radical, suggesting that the latter is the initial decomposition product of 4,4'-tetrahydrobipyridine dimer. The iR uncompensated peak separations for both of the couples are $(E_p^c - E_p^a) \approx 70 \text{ mV}$, compared to the theoretical value of 62 mV for a one-electron process at 40°C . If a small quantity of aluminum metal is permitted to react with basic melt, the solution becomes deep blue and the u.v./visible spectrum of a diluted portion confirms that it contains the dialkyl viologen monocation radical [Fig. 5, cf. Fig. 2 (15)]. Acidification of the melt ($>1:1$) caused the disappearance of the blue radical in a chemically reversible manner because re-addition of 1-BPC restored the blue coloration. Presumably, the Al_2Cl_7^- anion is reduced by the mono-radical to elemental aluminum in a finely divided state, to a sub-valent aluminum species, or to a charge-transfer complex. Normal pulse voltammetric analyses of the viologen reduction waves (Fig. 6), which occur with half-wave potentials of -0.56 and -0.96 V vs. Al(O) reference, for reactions [7] and [8], respectively, have $\log(i_d - i)/i$ slopes of 67 mV in close agreement to the theoretical 62 mV slope for one-electron reversible behavior. Assuming that 2 electrons are required to form each molecule of the monocation radical through dissociation of a 4,4'-tetrahydrobipyridine intermediate, the yield from the normal pulse voltammetric limiting current based on aluminum oxidation ($3e^-$) is estimated to be $\sim 30\%$. The half-wave potentials for these two waves and their separation are reasonably consistent with values for dialkyl viologen reductions in nonaqueous solvents (e.g., Table I). The maximum on the second reduction wave is indicative of adsorption complications, which are well known to occur under aqueous conditions [e.g., (21-23)].

Discussion

From a comparison of the electrochemical potentials for the ferrocene/ferrocinium couple and the oxidation of 12 aromatic hydrocarbons in acetonitrile to those in the $\text{AlCl}_3:1\text{-BPC}$ molten salt (24), the Al(O) reference in the 2:1 melt lies approximately at $+0.15 \text{ V}$ vs. SCE and at -0.26 V vs. Ag/Ag^+ (0.1M). As Raghavan (11) has reported that the cyclic voltammetric peak potential for the reduction of 1-methylpyridinium ion occurs at -1.28 V vs. SCE in acetonitrile (ca. $5 \times 10^{-4} \text{ M}$; Hg electrode), it would seem that the electrode reduction potential for 1-butylpyridinium ion in melt ($\sim 4.4 \text{ M}$) is essentially unaffected by these changes in the solvent nature and electrode material. These studies

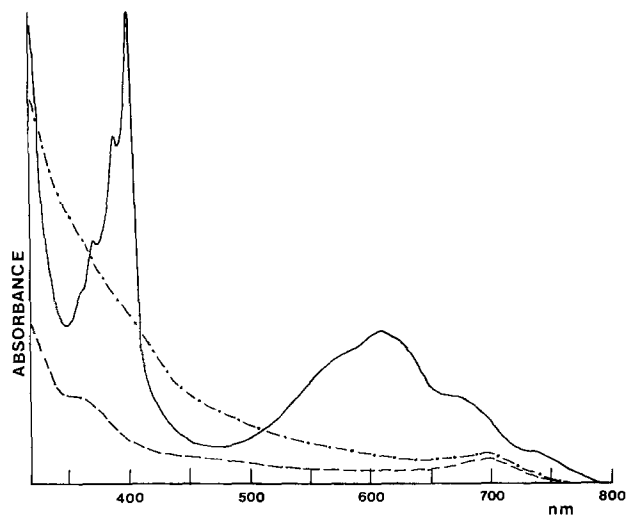


Fig. 5. U.V./visible spectrum of 0.8:1 melt reacted with aluminum (solid line), after AlCl_3 addition ($>1:1$) (dot-dash line), and background of 0.8:1 melt (dashed line).

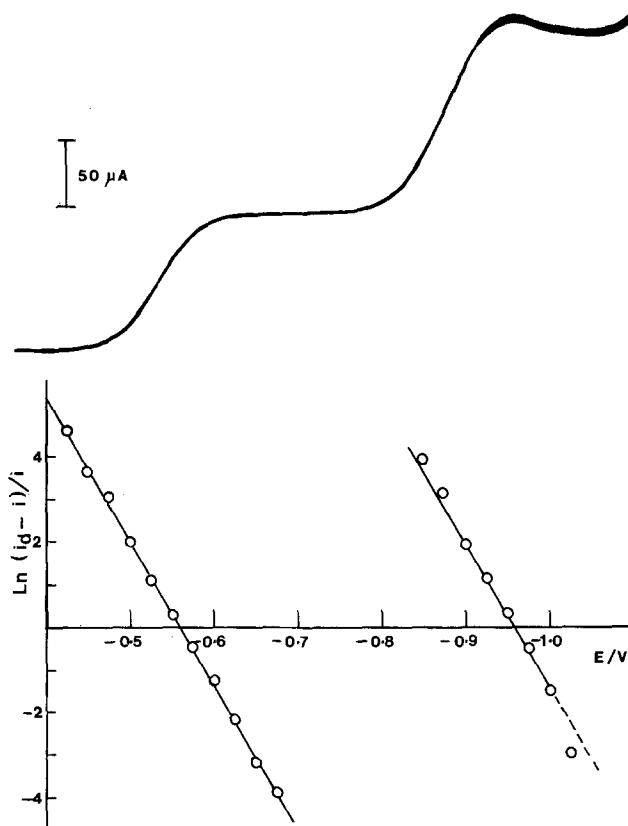


Fig. 6. Normal pulse voltammetry of 2.08×10^{-4} moles Al reacted with 8.7 ml 0.8:1 melt, 40°C , sweep rate 5 mVsec^{-1} , 100 mV pulse, C electrode.

affirm that the alkylpyridinium cation standard reduction potential in the basic $\text{AlCl}_3:1\text{-BPC}$ melt approximates to that found in aqueous or certain nonaqueous solvents. This is consistent with a simple ionic model for the solvent structure and seemingly no modification of the electron transfer reduction reaction by alkylpyridinium cation/aluminum species interactions. Electrophilic pyridinium ions generally are reduced at less negative potential than pyridines, although Lewis acid complexation may alter drastically the ease of electron transfer and ligand reduction of unquaternized heterocycles. For example, the AlCl_3 :pyridine adduct has an $E_{1/2}$ value of -1.00 V in distinction to the value of -2.20 V (vs. Hg pool reference) for the uncomplexed pyridine (8, 9).

There are two intrinsic factors that may be important to consider in the choice of an alkylpyridinium ion species for a particular molten solvent of this type, namely (i) the pyridinium ion reduction potential, and (ii) the relative stability of the primary pyridinyl radical. Each may be modified by the substituent groups that are present on the pyridinium ring and, as mentioned above, N-alkylation greatly facilitates reduction but changes in the chain length of N-alkyl

Table I. Comparison of literature data of dialkyl viologen half-wave potentials

Viologen salt	$E_{1/2}'/\text{V}$	$E_{1/2}''/\text{V}$	Solvent	Reference electrode	Ref.
Di-1-butyl	-0.56	-0.96	$\text{AlCl}_3:1\text{-BPC}$	Al(O)	This work
Di-methyl	-0.45	-0.86	CH_3CN	SCE	(11)
Di-1-butyl	-0.45	-0.98	CH_3CN	Ag/AgCl	(16)
Di-benzyl	-0.40	-0.82	CH_3CN	Ag/AgCl	(17)
Di-methyl	-0.68	-1.04	Aq. pH 5-13	SCE	(18)
Di-ethyl	-0.71	-1.09	Aq. KCl	SCE	(19)
Di-1-heptyl	-0.42	-0.73	Film	Perma probe	(20)

substituents have minimal effect on the reduction potential (10). C-alkylation modifies the reactivities of compounds by raising or lowering the reduction potential due to the electron-donating power of the alkyl groups (3). Despite the paucity of electrochemical data concerning substituted alkyipyridinium ion species, there has been a reasonably successful attempt to correlate the energies of the longest wavelength charge-transfer band of alkyipyridinium iodides and the appropriate half-wave reduction potentials (13, 7). A second (shorter wavelength) charge-transfer band, not unexpectedly, could not be related to the half-wave potentials, although Tafel slope analyses might be able to detect the occurrence of a closely spaced, second electronic transition (e.g., $\Delta E < 10$ kcal mole⁻¹). Kosower and Skorcz (25) have carefully measured the low energy, charge transfer bands of 20 different alkyipyridinium iodides and established that the transition energy is raised by either increasing the number of methyl groups attached to the ring or by changing the position of a single methyl group, 3-<2-<4-. Replacing a methyl by a t-butyl group in the 4-position had little net effect on the electron supply, suggesting that hyperconjugation does not contribute to the molecular ground state stabilization, unlike the effect found with the corresponding 2-constituents. Alkyl substitution is thought to afford greater stabilization to the ground state of the cation than to that of the radical (25). The commencement of reduction shifts negative, approximately -1.1, -1.3, and -1.4V for the cations 1-butylpyridinium, 1-butyl-4, tert. butyl-pyridinium and 1-methyl-2,4,6-trimethylpyridinium, respectively, thereby providing some increased accessibility to reduction processes. N-alkyl-pyridinium ions having electron withdrawing substituents, such as 2-, 3-, or 4-substituted cyano groups, reduce more readily than the unsubstituted compound. The effects of alkyl substitution on the chemical stability or the physical properties of the AlCl₃ melt mixtures, such as their liquidus characteristics, have not yet been investigated.

A second factor of interest is the stability of the primary pyridinyl radicals, whose reactivity is such that they cannot usually be detected by slow transient techniques. The product distribution arising from their subsequent reaction in AlCl₃:1-BPC solvents is more complex than that found from pyridinium ion reduction in acetonitrile (11) and it is complicated by the chemical instability of at least one of the dimers formed. The causes for this enhancement in the rate of the 4,4'-tetrahydrobipyridine dissociation are not understood but it could be related to the overall basicity of the media, i.e., the chloride ion nucleophile concentration, or to increased rates of electron transfer. Loss of the 4-hydrogen is evidently facile whereas the 4-methyl group forms a stable C-C bond. Apparently, little systematic work has been carried out on the ability of constituents to stabilize dihydro-pyridines, but polycyclic or highly substituted molecules seem to be less reactive, possibly because of steric effects (2). Effects due to other N- or ring substituents (e.g., OH⁻, -CN, -halides, etc.) have not been investigated to date, either from the standpoint of the reduction potentials of compounds, the reactivities of reduction products, or the fundamental physical characteristics of the chloroaluminate melts.

Experimental

Handling methods and preparation of melts have been described in previous publications from this laboratory. All electrochemical experiments were made in a Vacuum Atmospheres Company dry box under purified argon. The cyclic voltammetry and programmed pulse measurements were made with PAR Models 175 Universal Programmer and 173 Potentiostat/Galvanostat coupled to a Houston Instruments 2000 Omnigraphic X-Y recorder. Normal pulse voltammograms were made using the PAR Model 174

Polarographic Analyzer. The reference electrode comprised coiled Al wire immersed in 2:1 molar ratio AlCl₃:1-BPC melt, respectively, isolated in a glass fritted tube. Working electrodes were either vitreous carbon of geometrical area 0.0855 cm² sealed in Pyrex glass (G.C.20 grade, Tokai Electrode Manufacturing Company, Limited) or tungsten wire button electrodes sealed in uranium glass. U.V./visible spectra were recorded, using cells filled and sealed in the dry box, on a Cary 17 Spectrophotometer. Mass spectroscopy data were obtained with an A.E.I. MS 12 instrument with the source ~150°C and probe ~80°C. N.M.R. measurements were made with either the JEOLCO MH100 100MHZ Spectrometer, the Varian EM360A 60MHZ Spectrometer or the JEOLCO FX100 Fourier Transform Spectrometers, in 5 mm tubes.

Syntheses and characterization of 1,1'-dibutyl-4,4'-tetrahydrobipyridine.—Preparation.—0.0583 moles of 1-butylpyridinium chloride in 50 ml water was stirred for 20 min with 100 ml diethyl ether and 250g Hg (Na 0.6% wt.) in an argon atmosphere. The yellow ether layer was separated and the ether removed by vacuum, to leave a yellow/brown oily residue, which was used without further purification. Despite storage in a sealed glass container in the dry box the color deepened and the product slowly decomposed. C, H, N microanalyses were made by Galbraith Laboratories, Incorporated, Knoxville, Tennessee 37921, theory for C₁₈H₂₈N₂ C 79.37, H 10.36, N 10.28; found C 79.16, H 10.19, N 10.14; yield 90.5%; measured density, $\rho = 0.932$ (25°), M.wt. 272.4.

U.V. bands.—226 nm, 300 nm (sh)/solvent diethyl ether.

Mass spectrum.—Parent peak 272 (1.3%), loss of single N alkyl group 215 (1.4%), monomer radical formation 136 (100%) (bracketed figures are approx. relative intensities).

C.m.r. data.—131.6(d), 99.5(d), 53.2(t), 42.8(d), 32.9(t), 20.4(t), 14.1(q)ppm. The gated-mode off-resonance technique confirms the 4,4'-bridging between the two pyridine rings.

P.m.r. data.—5.87-5.80 (d, 4, J = 8 Hz, C-2, -2', -6, -6' vinyl), 4.29-4.17 (m, 4, C-3, -3, -3', -5, -5' vinyl), 3.00-2.84 (m, 2, C-4, -4' methine), 1.47-1.09 (m, butyl), 0.95-0.82 (t, CH₃)/solvent CD₃CN references to internal TMS.

Syntheses of 1-methyl-2,4,6-trimethylpyridinium iodide and 1-butyl-4, tert. butyl-pyridinium chloride.—Preparation.—Quaternizations are conveniently carried out in heavy-walled glass tubes (10 × 2 1/2 in. OD). ~100g of the pyridine was added to an equivalent molar quantity of the alkyl halide, the mixture frozen, the tube evacuated, sealed, and heated in an oven at 80°-100° for several days. Crude products were purified by 3 recrystallizations from acetonitrile/ethyl acetate mixtures.

Analyses.—C₉H₁₄NI, M.wt 263.1; theory C 41.08, H 5.36, N 5.32, I 48.23, found C 41.51, H 5.62, N 5.59, I 46.58 C₁₃H₂₂NCl, M.wt 227.8; theory C 68.55, H 9.74, N 6.15, Cl 15.56, found C 67.49, H 9.98, N 6.84, Cl 15.73.

Acknowledgment

This work was supported by the Office of Naval Research under contract NOO014-77-C-0004 and the Air Force Office of Scientific Research under Grant AFOSR-76-2978.

Manuscript submitted Oct. 18, 1979; revised manuscript received April 22, 1980.

Any discussion of this paper will appear in a Discussion Section to be published in the June 1981 JOURNAL. All discussions for the June 1981 Discussion Section should be submitted by Feb. 1, 1981.

Publication costs of this article were assisted by the State University of New York at Buffalo.

REFERENCES

- R. J. Gale and R. A. Osteryoung, *Inorg. Chem.*, **17**, 2728 (1978).
- U. Eisner and J. Kuthan, *Chem. Rev.*, **72**, 1 (1972).
- H. Lund, in "Advances in Heterocyclic Chemistry," Vol. 12, A. R. Katritzky and A. J. Boulton, Editors, pp. 213-316, Academic Press, New York (1970).
- D. Thevenot and R. Buvet, *J. Electroanal. Chem. Interfacial Electrochem.*, **39**, 429 (1972).
- A. L. Underwood and R. W. Burnett, "Electroanalytical Chemistry," Vol. 6, A. J. Bard, Editor, pp. 26-55, Marcel Dekker, New York (1972).
- P. J. Elving, C. O. Schmakel, and K. S. V. Santhanam, *C.R.C. Crit. Rev. Anal. Chem.*, **1976**, 1 (May 1976).
- E. M. Kosower, "Free Radicals in Molecular Biology and Pathology," Vol. II, W. A. Pryor, Editor, pp. 1-53, Academic Press, New York (1976).
- A. Cisak and P. J. Elving, *Electrochim. Acta*, **10**, 935 (1965).
- J. Volke and M. Naarova, *Coll. Czech. Chem. Comm.*, **37**, 3361 (1972).
- M. Naarova and J. Volke, *ibid.*, **38**, 2670 (1973).
- R. Raghavan, Ph.D. Thesis, Univ. of Kansas (1975).
- R. Raghavan and R. T. Iwamoto, *J. Electroanal. Chem. Interfacial Electrochem.*, **92**, 101 (1978).
- R. A. Mackay, J. R. Landolph, and E. J. Poziomek, *J. Am. Chem. Soc.*, **93**, 5026 (1971).
- E. J. Moriconi and R. E. Misner, *J. Org. Chem.*, **34**, 3672 (1969).
- E. M. Kosower and J. L. Cotter, *J. Am. Chem. Soc.*, **86**, 5524 (1964).
- H. T. van Dam and J. J. Ponjee, *This Journal*, **121**, 1555 (1974).
- S. Hunig, J. Gros, and W. Schenk, *Justus Liebigs Ann. Chem.*, **324** (1973).
- R. M. Eloffson and R. L. Edsberg, *Can. J. Chem.*, **35**, 646 (1957).
- W. M. Schwarz, E. M. Kosower, and I. Shain, *J. Am. Chem. Soc.*, **83**, 3164 (1961).
- R. J. Jasinski, *This Journal*, **124**, 637 (1977).
- S. G. Mairanovskii, *J. Electroanal. Chem. Interfacial Electrochem.*, **12**, 547 (1966).
- L. Pospisil, J. Kuta, and J. Volke, *ibid.*, **58**, 217 (1975).
- J. Kuta, L. Pospisil, I. Smoler, and G. P. Girina, *ibid.*, **65**, 661 (1975).
- J. Robinson and R. A. Osteryoung, *J. Am. Chem. Soc.*, **101**, 323 (1979).
- E. M. Kosower and J. A. Skorcz, *ibid.*, **82**, 2195 (1960).

Technical Notes



Development of a 7 kW H₂/O₂-Fuel Cell Assembly with Circulating Electrolyte in a Compact Modular Design

Karl Strasser

Siemens AG, Research Laboratories, D-8520 Erlangen, Germany

As a consequence of the energy crisis in the year 1973, the intensive discussion which followed, on the possibilities of a new orientation in the energy sector, has revived interest in fuel cells. The limited reserves of primary energy sources such as the fossile fuels and the resulting environmental strains due to their combustion have intensified the considerations of new energy systems in which hydrogen, among others, has received special importance.

In such energy converting systems, the application of the fuel cell is advantageous especially because of its favorable efficiency, noiseless conversion, low maintenance, and also due to the absence of polluting gases in the case of H₂.

In spite of these advantages the fuel cell could not find wide spread applications until now. The reasons lie not only in the relatively high costs of the fuel cell itself but also in the costs of reactants and their storage. The development of Siemens alkaline H₂/O₂-fuel cells was aimed at increasing the power density with simultaneous improvement in the reproducibility and in the engineering features of the unit (2).

Basic Principles

In an alkaline H₂/O₂-fuel cell system hydrogen is oxidized at the anode while oxygen is reduced at the cathode. A 30% potassium hydroxide solution is used as the electrolyte. Water and heat are the reaction products which dilute and heat up the electrolyte.

Figure 1 shows the schematic construction of the cell (3, 4). The free electrolyte between the gas-stop layers is typical of Siemens fuel cells. The electrodes consisting of Raney nickel (5-7) and doped silver (8) are gas diffusion electrodes which are compressed iso-

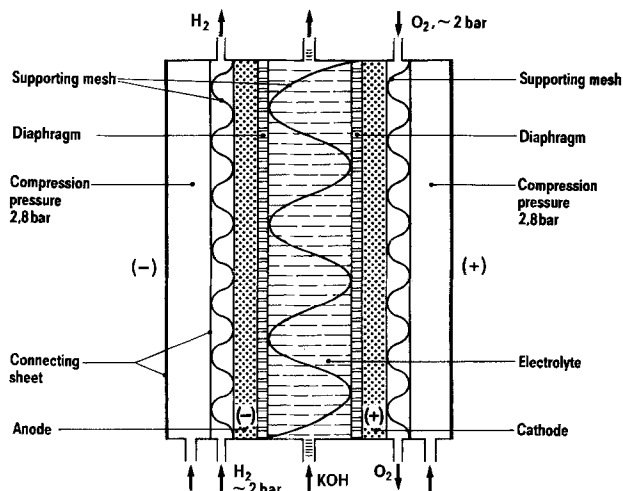


Fig. 1. Fuel cell with free electrolyte and supported gas diffusion electrodes.

statically over relatively flexible metallic contact sheets to improve the electrode contact on the electrolyte and current collecting sides (9). Due to the bipolar arrangement of electrodes, the cells of a stack are generally connected electrically in series. But it is also possible to connect groups of cells electrically in parallel.

The cells are operated with a hydrogen pressure of 2 bar, an oxygen pressure of 1.95 bar, and a compression pressure of 2.8 bar at 80°C approximately. Owing to the greater thickness of electrolyte layer through the "free electrolyte" the cell internal resistance and thus the voltage loss is larger than in comparable matrix systems.

Various auxiliaries are required in operating a fuel cell stack. They are shown in the functional schematic Fig. 2. Hydrogen and oxygen are supplied to the fuel cell stack via separate gas pressure regulators and gate valves which can be manipulated either by hand or over a potential-disconnected current circuit. The inert gas proportions are concentrated in the last step of a cascading system (10) and are removed by electrically regulated valves. Along with the in-streaming of the reacting gases inside the stack, the electrodes are simultaneously compressed isostatically over "pressure cushions" and pressure intensifiers or already "inflated" previously. During this course, a check valve prevents the "pressure gas" from escaping. Hydrogen also streams into the diffusion spaces of the evaporator through a pressure reducing valve. The resulting water and waste heat of reaction are initially removed from the fuel cell stack through the circulating electrolyte by means of a pump (11) and are again withdrawn from the electrolyte in the electrolyte regenerator. The waste heat is extracted from the electrolyte regenerator by a cooling water circulation in which the cooling water inflow is regulated by a valve depending on the temperature. According to the electrolyte level inside the tank the condensate emerging from the electrolyte regenerator is either led out or fed back to the electrolyte circulation.

The principle of electrolyte regeneration (12) through an evaporator is shown in Fig. 3. Due to the partial pressure gradients of vapor between the evaporating and condensing areas, water vapor is transported by diffusion from the electrolyte to the cooling water side where it condenses. In this manner, water and heat are simultaneously removed from the electrolyte.

Design of the 7 kW-Fuel Cell Unit

The construction assembly of the unit is represented in Fig. 4. The compact unit block having the dimensions of 245 × 240 × 1025 mm and the weight of 85 kg is composed of the functional groups of the fuel cell stack, the electrolyte regenerator, the electromechanical controlling unit, the supply system, and the electronic control device. It possesses electrical plugs on

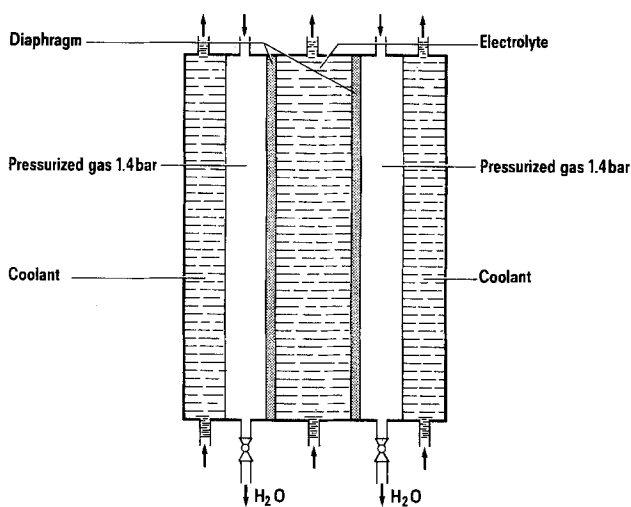


Fig. 3. Fuel cell unit: electrolyte evaporator cell

the fuel cell stack side for the consumer, and connections on the opposite side for hydrogen, oxygen, cooling water, condensate, and scavenging or leakage gas. All control elements are flange connected to a wall of the electrolyte tank that is created by the distribution block. The electronic control unit is bolted to the fuel cell stack on the service side and is joined to the control elements on the supply side through pilot connections.

The unit is designed as a module whose rated voltage can be varied by switching the cell groups in series and in parallel in four different steps (6-9; 12-18; 24.5-35 and 49-70V) and whose power can be set by altering the number of cells also in four steps. In a plant consisting of several modules, each unit is connected over a detachable plug-linkage with the supply system which forms a part of the module casing.

The most important functional group of the assembly is the fuel cell stack which, in general, consists of 70 cells switched electrically in series. Characteristic for the cells are the free electrolyte space, which is filled with textured plates for the reason of electrode supporting, the bonded gas diffusion electrodes, and the "pressure cushions" (Fig. 1). Due to the special structure of the textured plate the transport of gas bubbles is facilitated and, at the same time, a low flow resistance is ensured. By virtue of preparation, catalyst and binder are firmly bonded to a supporting texture which conducts the current further to a contacting sheet. This contacting sheet possesses imprinted flow channels for the reactants, and on its reverse side, pressure gas is admitted with the purpose of compressing the electrode isostatically.

Figure 5 shows an exploded view of the cell. The asbestos diaphragms (13) which prevent the mixing of

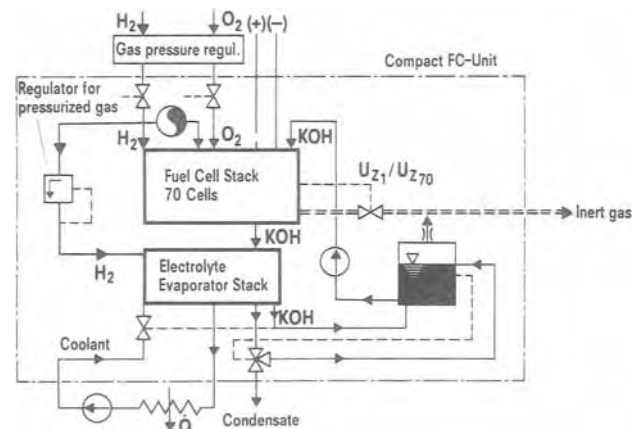


Fig. 2. Functional schematic of the fuel cell unit

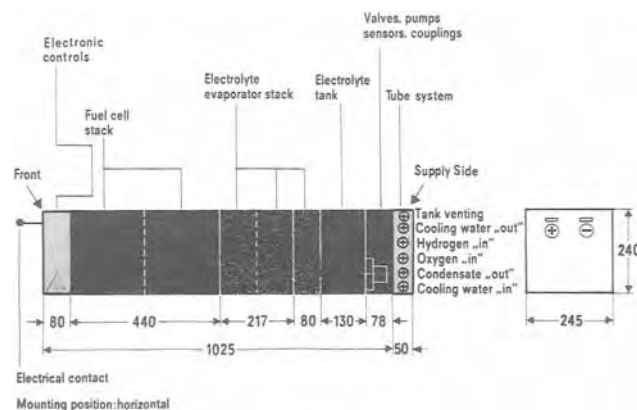


Fig. 4. Design and dimensions of the 7 kW compact fuel cell unit.

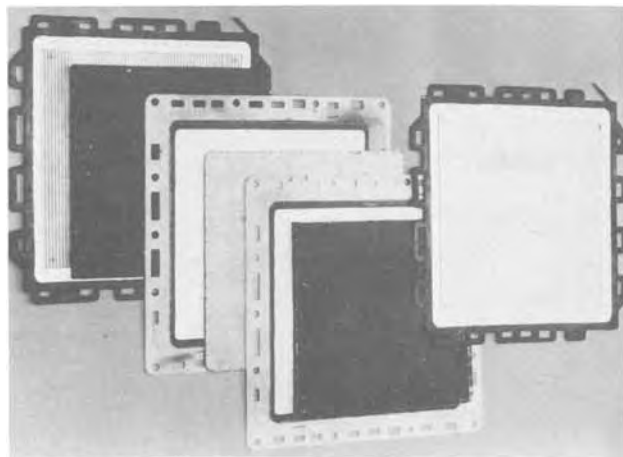


Fig. 5. Exploded view of the cell

gases and electrolyte are sealed tightly with polysulfone frames by means of an epoxy resin, and the contacting sheets of pure nickel are pressed around tightly with an elastomer frame. Owing to the grooves provided in the frames, the network of axial and radial channels for electrolyte, reactants, cooling water, and condensate is created while building the assembly. In preparing the electrodes a sedimentation process has proved useful. Raney nickel is used as catalyst for the anode. It is doped with small quantities of titanium for a better stability at 80°C and for a higher performance at lower temperatures. A silver catalyst precipitated from aqueous solution and containing stabilizing additives of the oxides of nickel, bismuth, and titanium is used for the cathode. The catalysts are powdery. The electrodes are obtained by whirling a mixture of catalyst powder, Teflon suspension, and a small amount of asbestos fibers in water and sedimenting it on a pure nickel texture. The electrodes thus obtained are mechanically stable, easy to handle, and their loading differences lie in the range of $\pm 5\%$. The catalyst loading density of anode is approximately 120 mg/cm² and that of cathode approximately 60 mg/cm². The electrode area is approximately 340 cm².

The assembly of the evaporator components is very similar to that of the fuel cell.

Developmental Problems

After initial difficulties concerning the reproducible properties of the anode catalyst, satisfactory results were achieved by using a titanium-doped catalyst.

The current-voltage characteristics which were measured with single cells could also be reproduced with fuel cell stacks by applying the isostatic compression method utilizing the so called "pressure cushions" in the fuel cell stacks.

Different potentials at the individual cells of a stack cause parasitic currents to flow through the electrolyte channel network, diminishing the efficiency. Moreover, an important requirement for a uniform removal of water and heat from the fuel cells is that the electrolyte volume is uniformly distributed over the cells which are streamed through in parallel. By dimensioning the electrolyte channels appropriately and by elaborate flow tests a deviation of less than $\pm 5\%$ was attained in the relative temperature distribution. In the permissible voltage range of 42-70V of the assembly, the parasitic losses amount to 15-35W, i.e., approximately 2% at the point of rated load and are thus negligible.

The diaphragms have caused considerable difficulties by gas leakages, owing to inhomogeneities of materials and the relatively low mechanical strength. Satisfactory results were achieved after improving the preparative method and altering constructive details.

Special conditions are not imposed on the insulation resistance because of the low voltage of the unit. How-

ever, it was found that even low currents can lead to operational inefficiency of the unit by electrochemical corrosion of the materials. This problem was solved by using materials having an electrical insulation resistance of more than $10^6 \Omega \text{cm}$.

Results of Measurements with 7 kW Types

After the successful test of trial stacks containing a small number of cells, the projected power was demonstrated with the first 7 kW assembly in June 1977. A 3.5 kW compact unit was put into operation in February 1978 after undergoing different improvements. The assembly differs from the standard model in its fuel cell stack which contains only half the number of cells (35 cells) and in its evaporator which is only half the standard size. The second 7 kW assembly was built in May 1978 and tested subsequently. The third 7 kW compact unit is under test successfully since February 1979. Figure 6 shows this unit mounted in a rack in order to investigate its performance under inclined positions.

The current-voltage characteristic of the unit is illustrated in Fig. 7. The curve is slightly bent due to the elevation of the mean electrolyte temperature from approximately 72°C at idling state to approximately 80°C at rated current. At a rated current density of 420 mA/cm², corresponding to a current of 142A, the mean cell voltage amounts to approximately 0.768V and the assembly voltage to 53.8V. The characteristic

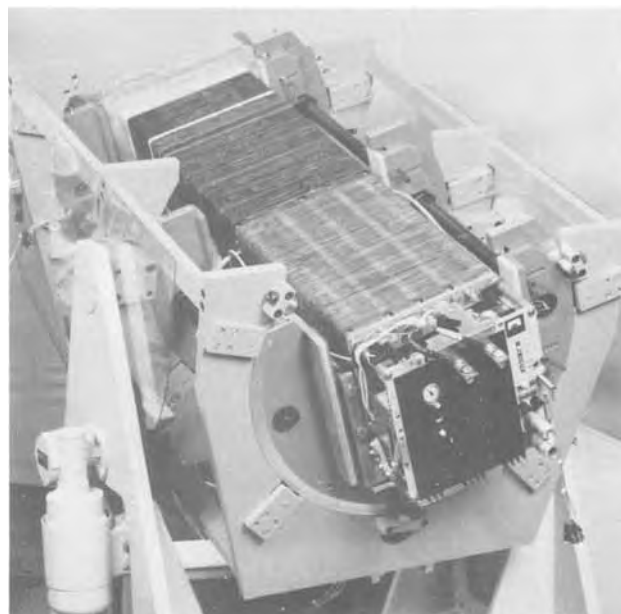


Fig. 6. 7 kW compact fuel cell unit

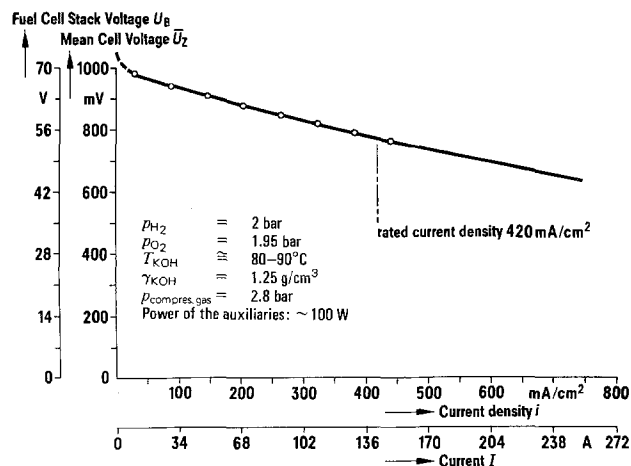


Fig. 7. Current-voltage characteristic of the 7 kW fuel cell unit

was measured at an H₂ pressure of 2 bar, at an O₂ pressure of 1.95 bar, and at a KOH concentration of 6-7M. The pressure of the enclosed compression gas system varies in a range of 2.4-3 bar along with the temperature.

Figure 8 shows the voltage of individual cells of the stack at the point of rated current. In spite of certain process-relevant deviations in the working conditions of individual cells of the stack, for example, the temperature, the inert gas concentration, the reactant pressures, or the loading due to parasitic currents, the scattering of the cell voltages in the stack is smaller than ±10 mV. The voltage of the cells 12, 13, 20, and 21 could not be measured due to difficulties in the electrical contacts. But a small deviation can be assumed even in these cells since the mean cell voltage value calculated from the total voltage is 0.768V. The voltage of cell 70, that of the reference cell which scavenges inert gas from O₂ side, is a function of the inert gas concentration. The cell voltage at rated current drops to about 200 mV between two cleanings in a period of about 30 sec.

The rated power of the assembly amounts to 7.55 kW; the internal consumption of 100W by the controls is already included. Figure 9 shows the power of the fuel cell stack as dependent on the current density. The point of rated load lies on the still ascending part of the curve. The permissible power is limited by the heat removal from the electrolyte circulation. However, 1.4 times the rated load is permissible for a short time. A further limitation in power is given by the anodic oxidation potential. The assembly is switched off by a voltage control at a mean cell voltage of 0.6V, before the anodic oxidation potential is reached.

However, owing to the deterioration in efficiency, these voltage ranges are generally not of importance. The efficiency at the point of rated load is about 51%. As shown in Fig. 10, it increases in the partial load

Measurement from: 29.5.78
First operation of the 7 kW-FC-Unit: 25.5.78

Operating conditions: $\gamma_{\text{KOH}} = 1.25 \text{ g/cm}^3$ $i = 420 \text{ mA/cm}^2$
 $T_{\text{KOH}} = 80-90^\circ\text{C}$ $p_{\text{H}_2} = 2 \text{ bar}$
 $U_B = 53.8 \text{ V}$ $p_{\text{O}_2} = 1.95 \text{ bar}$
 $I_B = 142.3 \text{ A}$ $p_{\text{compress gas}} = 2.8 \text{ bar}$

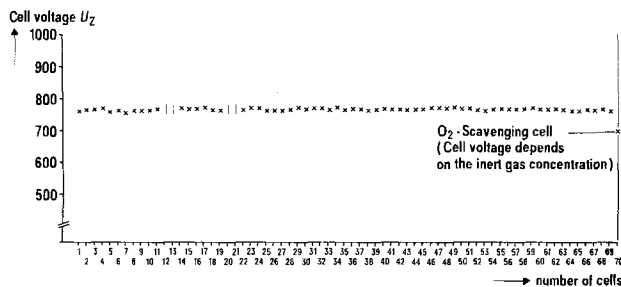


Fig. 8. Voltage of each cell in the fuel cell stack at rated load

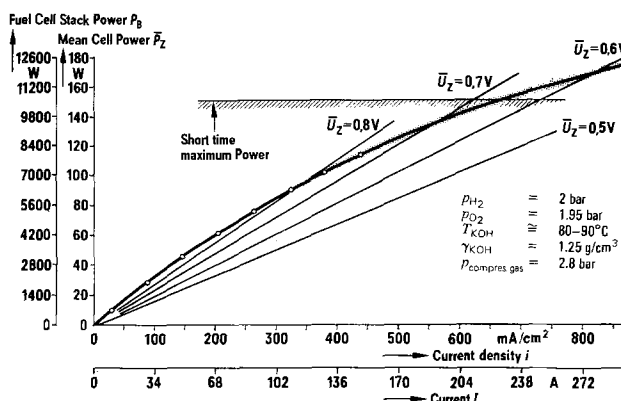


Fig. 9. Power of the fuel cell unit as a function of the current density.

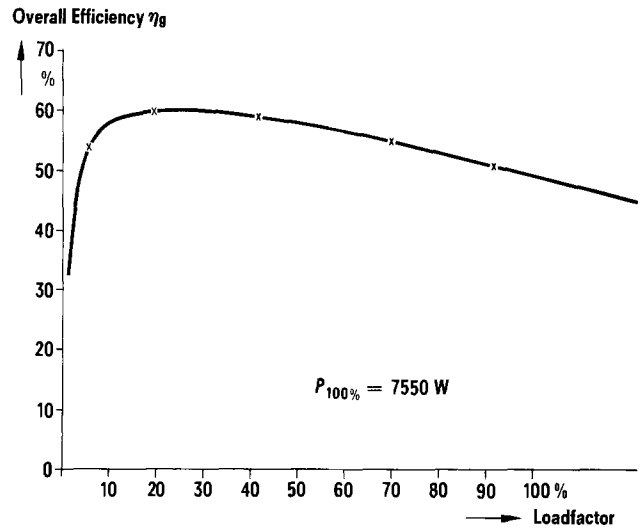


Fig. 10. Overall efficiency of the 7 kW fuel cell unit as a function of the load factor.

range and attains a maximum of over 60% at a load factor of 10-30%. In this particular behavior, the fuel cell is distinguished from all other known systems of energy conversion.

Under the switched off state, hydrogen is admitted to the fuel cells on anode and cathode sides. Upon re-switching, the assembly voltage increases slowly due to gas exchange on the O₂ side, and independent of loading, it attains after 4-5 sec, the final value corresponding to the current and the working conditions. Figure 11 shows the voltage rise in five different cases of loading on switching at normal operating conditions. Switching times of less than 1 sec were attained in tests with trial stacks. Switching times under 3 sec are attainable by dimensioning the gas channels appropriately, especially the channels of scavenging gas in the assembly.

Figure 12 shows the course of the stack voltage at changing the current from 0 to 140A. The voltage follows the current change with a time delay of roughly 200 msec. The voltage value is finally established after about 3 sec during loading as well as during idling. In this test only an ohmic resistance was connected and disconnected.

If the assembly is switched off the oxygen supply is cut out and oxygen present in the stack is let out at least partly by opening the O₂ scavenging valve. Gas exchange during switching is associated with a certain time lag. Since, it is also the case during switching off and moreover, since reacting gas is stored in the elec-

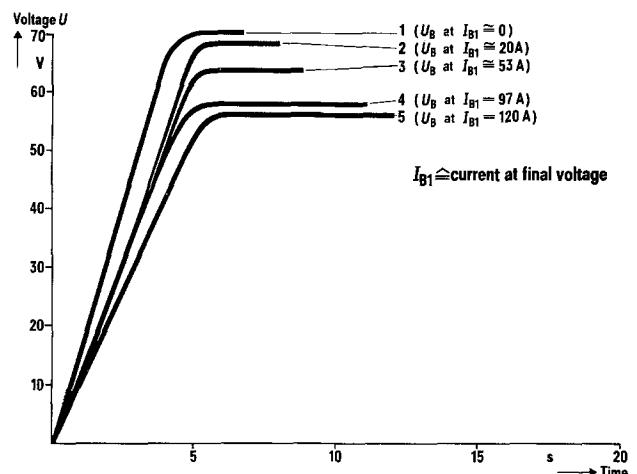


Fig. 11. Voltage of the fuel cell unit during switching on under normal operating conditions.

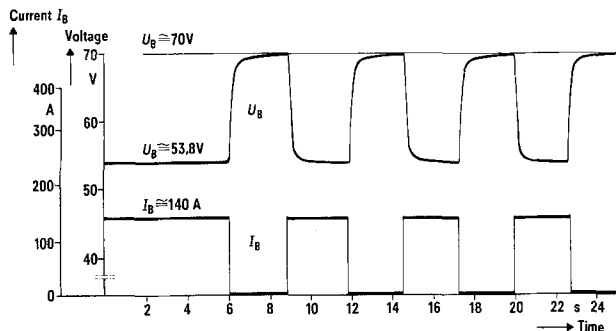


Fig. 12. Voltage of the fuel cell unit at changing load under normal operating conditions.

trodes, a longer period will be required for the voltage drop during switching off than required during switching on, as shown in Fig. 13. The figure shows the voltage behavior of the unit at four stages of switching off with different ohmic resistances as load. The wave-like shape of the curve is determined by the process and mode of control. The voltage drops to 20% of the rated value within 5 sec on switching off under rated power. According to investigations carried out with trial stacks, these times can still be reduced.

If the assembly is switched on at room temperature a certain time will be required until the working temperature is attained. The derivable power from the unit at room temperature at 49V is nearly 40% (Fig. 14). The rated power will be attained in 7-8 min if this voltage is kept constant by regulating the load during the warm-up phase. The assembly gets heated up by its own losses without additional internal heating. The lower the load the longer will be the start-up time.

Progress by Developmental Work

Figure 15 summarizes the progress made in the developmental work by comparing the current-voltage characteristics. The cells compared have almost the same dimensions. Section 1 represents the technical state available before beginning the project, a 2 kW unit with 33-celled stack, built 1970 and a 5 kW unit with 100-celled stack, built in 1973. Section 2 represents the technical stage reached by the first 7 kW unit, built in 1977. Section 3 represents the technical state of art, achieved with succeeding assemblies and other trial stacks.

Compared with the past technique which has been replaced now, the following progress could be made: an increase in current density by 100%, an increase in cell power by 300% at room temperature, an increase in cell power by 140% at working temperature, a reduction in start-up time by ~60%, and a reduction of power/weight ratio by ~70%.

A further increase of the power density of Siemens alkaline H₂/O₂ fuel cells containing free electrolyte and using non-noble metal catalysts is probable. The

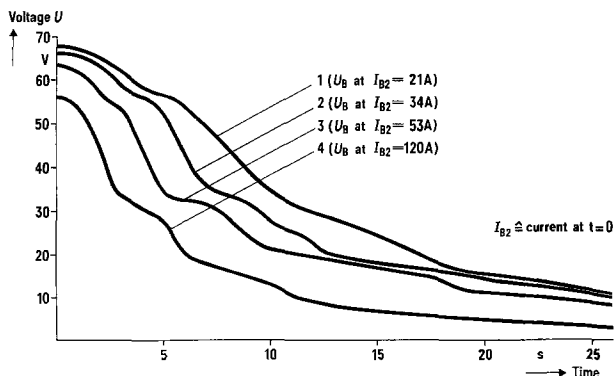


Fig. 13. Voltage of the fuel cell unit after switching off under normal operating conditions.

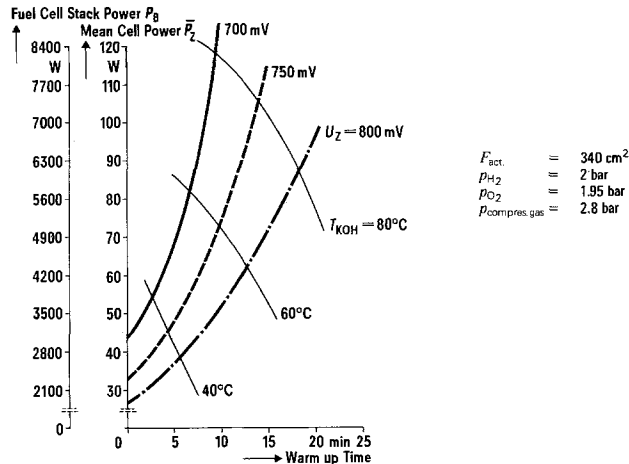


Fig. 14. Warm up behavior

practical use of such fuel cells, however, depends not only on technical characteristics such as the power density of the fuel cell unit, but just as much on the production costs of the units, the availability of storage capacity, and the costs of the reactants and the costs of the auxiliaries (H₂ tank, O₂ tank, cooling water condenser, etc.). The present overall situation limits the use of fuel cell units to special applications. However, if the importance of hydrogen as a fuel increases, and advances are made in its production, storage, and distribution, there would arise a number of possible applications including use in conjunction with a modified alkaline H₂/air fuel cell. The favorable part-load behavior of the fuel cell and its environmental acceptability, as well as the storage of energy in chemical form combined with the possibility of simple tanking, make it suitable for mobile and stationary power supplies (including standby power supplies) in that it will replace at least a proportion of conventional accumulators. In comparison with accumulators, the favorable weight of the entire system (power density inclusive of gas cylinders and cooling system is higher by a factor of 4) together with the aforementioned advantages, the possibility of rapid tanking, environmental acceptability, and favorable efficiency characteristic in the part-load range open up further application possibilities with respect to the electric propulsion of land and waterborne vehicles. The power density and the fact that operation is independent of the atmospheric air make fuel cells suitable for applications involving the propulsion of submarines, e.g., for research purposes or for the maintenance of technical equipment (submarine cables, drilling rigs, etc.). It is also quite conceivable that they could be used for producing electric energy locally with simul-

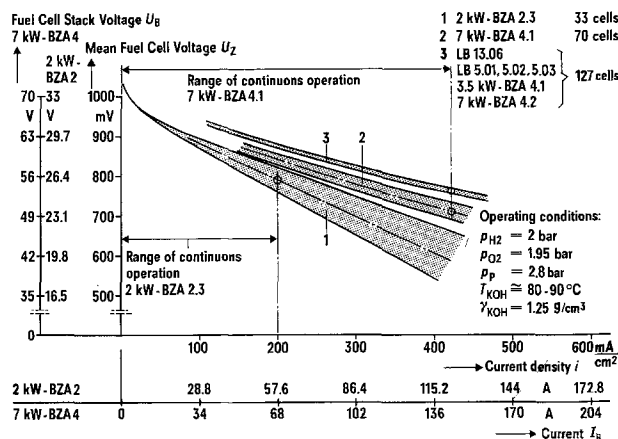


Fig. 15. Fuel cell units; comparison of the current voltage characteristics.

taneous utilization of the thermal losses for space heating. But we will first endeavor to collect experience with the operation of fuel cell pilot plants of small and medium ratings. Economic use of fuel cell units in the future will entail considerable effort to reduce costs and improve reactant production methods.

Acknowledgment

This work was supported by the Federal Minister of Research and Technology of the Federal Republic of Germany.

Manuscript submitted Sept. 4, 1979; revised manuscript received ca. May 8, 1980. This was Paper 16 presented at the Boston, Massachusetts, Meeting of the Society, May 6-11, 1979.

Any discussion of this paper will appear in a Discussion Section to be published in the June 1981 JOURNAL. All discussions for the June 1981 Discussion Section should be submitted by Feb. 1, 1981.

Publication costs of this article were assisted by Siemens AG.

REFERENCES

1. H. B. Gutbier, D. Hasenauer, and K. Strasser, Third International Conference of Space Technology, Rome (1971).
2. K. Strasser, H. Grüne, and H. B. Gutbier, 10th International Power Sources Symposium Brighton (1976).
3. G. Grüneberg, H. Spengler, and W. Vielstich, *Dt. Auslegeschrift*, 1086, 768 (1960).
4. F. v. Sturm, H. Nischik, and E. Weidlich, *Ingenieur-Digest*, 5, 52 (1966).
5. E. Justi and A. Winsel, "Kalte Verbrennung—Fuel Cells," Wiesbaden (1962).
6. G. Richter, Third International Symposium of Fuel Cells, Brussels, p. 8 (1969).
7. N. J. Schtscheglow and D. V. Sokolskii, *Prom. Kazakhstana Nauchn. Tekhn. Sbornik*, 3, 68 (1961).
8. K. Höhne, *Siemens-Forsch. Entwicklungsber.*, 1, 31 (1974).
9. K. Strasser, German Pat. 1,930,116.
10. H. Grüne, *Chem. Ing. Tech.*, 40, 185 (1968).
11. F. Kozdon, *Siemens Z.*, 6, 392 (1970).
12. H. B. Gutbier, *Chem. Ing. Tech.*, 40, 1209 (1968).
13. H. Fetzer, Fifth Internationale Dichtungstagung, Dresden (1974).

Electrical Conductivity of the LiI-H₂O-Al₂O₃ System

S. Pack

Center for Solid State Science, Arizona State University, Tempe, Arizona 85281

B. Owens*

Medtronics, Incorporated, Minneapolis, Minnesota 55418

and J. B. Wagner, Jr.*

Center for Solid State Science, Arizona State University, Tempe, Arizona 85281

A dispersion of insoluble particles in certain solid ionic conductors is known to increase their total electrical conductivity (1-3). This note reports data on the electrical conductivity of intermediate compositions within the LiI-H₂O-Al₂O₃ system.

Experimental

In view of the complex equilibria among various hydrates of LiI and anhydrous LiI (4), the following drying procedure was adopted. A commercially obtained anhydrous LiI (Foote Mineral Company) was heated under vacuum ($<1 \times 10^{-3}$ Torr) at 60°C for 5 hr followed by 100°C heating for another 5 hr. Finally, it was dried at 140°C under vacuum overnight. The kinetics of the drying process is not known but the x-ray powder diffraction of the samples prepared as above showed only the diffraction lines due to anhydrous LiI. Alumina powders (Adolf Meller Company) of 0.3 μ m nominal diameter¹ were dried under vacuum at $\sim 750^\circ\text{C}$ for 17 hr. Both dried materials were manipulated in a glove box in which air was dried by circulation through a column packed with P₂O₅ [0.04 ppm V H₂O (5)] to ensure that the water vapor pressure inside

was less than that required for the formation of the LiI monohydrate (0.5 ppm V at 25°C) (6, 7). Anhydrous LiI was observed to be stable even after extended exposure in the above-mentioned glove box. All salts (including the hydrates) were blended with the alumina in an agate mortar and pestle inside the glove box. A portion was loaded into a stainless steel die and pelletized at 120,000 psi at room temperature. At the same time another portion of the sample was sealed into a capillary for the x-ray diffraction measurements. The water content of the samples was qualitatively monitored by the x-ray powder diffraction method. Unusually long x-ray exposure times were required to record the weak diffractions of the minor component. The hydrates were prepared by exposing powdered anhydrous LiI to various humid environments. In the absence of any elaborate control of water vapor pressure, it was not possible to obtain pure mono-, di-, and tri-hydrates. Hence, for a given hydrate, a trace of a second equilibrium phase was always present. The sample pellets were sandwiched and spring loaded between various combinations of electrodes of stainless steel and/or Li metal. Generally, the measured values did not depend on the electrodes used. However, Li electrodes tended to deteriorate at elevated temperatures ($> \sim 50^\circ\text{C}$) when the H₂O content approached monohydrate level. The conductivity measurements (1.6 kHz a-c or d-c measurements at voltages below 0.5V) were carried out under a flow of dried argon using a Wayne-Kerr B221 Bridge, Keithley 616 Electrometer, and Keithley 260 Nanovolt source. No thermal pretreatment was carried out prior to the

* Electrochemical Society Active Member.

Key words: conductance, x-ray powder diffraction, hydrates.

¹ The reported size of Al₂O₃ is determined by two different methods. Using BET, Adolf Meller reports 30 m²/g while an independent laboratory reports to us ~ 23 m²/g. Using these numbers and assuming spherical particles one calculates ~ 0.05 μ m diam particle size. SEM observations show the particles to be platelet-like with the smallest dimension 0.2 μ m (undried) to 0.08 μ m (dried). There is a size distribution (unknown to us) and there is some agglomeration: 0.5-2 μ m (undried) and 1.5-4 μ m (dried).

measurements. Measurements were started at about 25°C and the temperature was monotonically increased.

Results and Discussion

The logarithm of a-c conductivity vs. $1/T$ for the LiI-H₂O system is shown in Fig. 1. The conductivity of anhydrous LiI is in good agreement with previously reported values (1, 8, 9) between 25° and 190°C. Because the di- and tri-hydrate are not stable above about 70°C, measurements were limited to lower temperatures. The x-ray powder pattern of the dihydrate is given in Table I. This pattern was identified as LiI · 2H₂O by interpolation of 100 plane d-spacings of LiI, LiI · H₂O, and LiI · 3H₂O.

When a trace amount of LiI · H₂O was present in LiI (denoted by Δ in Fig. 1), the Arrhenius plot was not linear and the conductivity increased sharply with temperature to ~130°C above which the conductivity values become erratic giving high values. Below ~130°C the curve was reproducible with respect to temperature cycles. Results using d.c. (Li electrodes) and a.c. (Li electrodes) on this sample were identical.

We cannot explain the curvature of this Arrhenius plot, however the maximum change in conductivity occurs at 130°C which corresponds to the reported eutectic of LiI · H₂O and LiI · 1/2H₂O. This result suggests that a highly conducting solid LiI · 1/2H₂O phase is formed or a fusion process occurs. Further study of the phase diagram is needed.

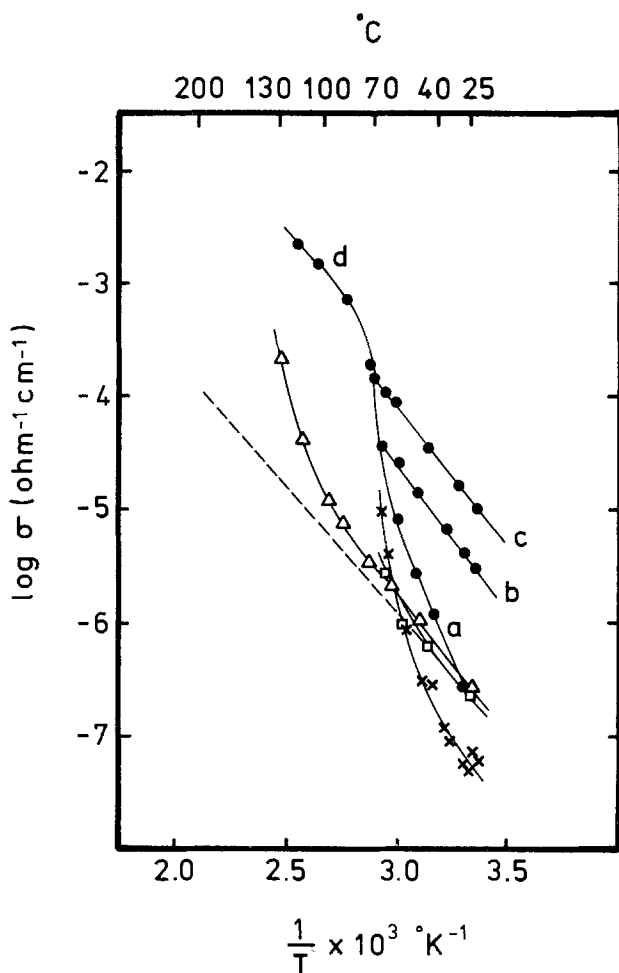


Fig. 1. Logarithm of the a-c conductivity of LiI-H₂O (no Al₂O₃ present) vs. $1/T$. --- LiI (this study); Δ LiI + trace LiI · H₂O; \bullet LiI · H₂O + trace LiI · 2H₂O (see text). Curve a: initial heat-up; curve b: annealed at 70°C and cycled; curve c: annealed above 100°C and cycled; curve d: annealed at 100°-130°C which on cooling follows curve c. \times LiI · 2H₂O + trace LiI · 3H₂O; \square LiI · 3H₂O.

Table I. X-ray powder pattern of LiI · 2H₂O (d-spacings, Å, and intensities)

5.60 S	3.22 S
4.69 S	3.14 M
4.50 S	3.08 S
3.98 S	2.85 S
3.81 S	2.65 M
3.41 M	2.33 M
	and 10 weak lines

Below ~70°C the conductivity of the monohydrate containing a trace amount of dihydrate depended on the annealing temperature of the conductivity pellet (~2 hr) as indicated by closed circles in Fig. 1. As the temperature of the sample was initially raised the conductivity followed the curve a. When it was annealed at 70°C and was cycled in temperature between 70°C and room temperature, curve b was followed. Heating the sample above ~100°C and temperature-cycling produced curve c. Heating between 100° and 130°C yielded curve d which on cooling followed curve c. The kink at ~78°C is believed to be due to the eutectic of LiI · H₂O and LiI · 2H₂O. The magnitude of the kink tends to become smaller with repeated temperature cycling and with higher annealing temperature (~120°C). The samples of lesser LiI · 2H₂O content behaved similar to curve c without complications shown in curves a and b. Above 130°C the system become unstable with slow sample deterioration. These data suggest that the conductivity of pure LiI · H₂O would extend below ~78°C (as an extension of curve d or parallel to d, because no eutectic would form), yielding a value of $\sim 2 \times 10^{-5} \Omega^{-1} \text{cm}^{-1}$ at 25°C, and would exhibit the same activation energy as LiI. It has been pointed out that this two orders of magnitude increase in conductivity, relative to that of pure LiI, is consistent with the reported structures (16).

The addition of 24 mole percent (m/o) dried Al₂O₃ to anhydrous LiI did not result in a conductivity enhancement (open circles in Fig. 2). However, the presence of Al₂O₃ extended the extrinsic region giving the knee temperature about 300°C compared with 250°C reported for pure LiI by Jackson and Young (8). There was no difference in conductivity between samples prepared by ground-mixing of LiI and Al₂O₃ and by ground-mixing followed by fusion. In the later case, the ground-mixed sample of dried LiI and Al₂O₃ was placed in a quartz boat inside a quartz reaction tube and the reaction tube was stopcock-sealed inside the dry box described earlier. The reaction tube, situated in a furnace, was evacuated and heated to 300°C while pumping. Finally the sample was fused in vacuum at 500°C for an hour. In contrast, when water was present along with Al₂O₃ there was an increased conductivity. This observed increase with the presence of water and Al₂O₃ is in accord with other observations (10, 2). The conductivity enhancing role of H₂O is also found in a similar electrolyte system, namely LiI · xAl₂(SO₄)₂ · nH₂O (11).

For two samples of LiI with a trace of LiI · H₂O denoted by Δ (case I) and by \times and \square (case II) in Fig. 2, the H₂O was introduced into the system of LiI Al₂O₃ through different paths. In case I, H₂O was carried in by undried Al₂O₃ while LiI carried water in the form of LiI · H₂O in case II. Invariably LiI · H₂O was indicated in both cases by x-ray diffraction. In case II, the magnitude of the conductivity varied qualitatively with H₂O content and the activation energy was 0.5-0.8 eV. The activation energy for case I was 0.76 eV and tended to decrease with Al₂O₃ and H₂O content. From the relative intensities of the powder diffraction lines, it was estimated that about 5 m/o of lithium iodide was present as the monohydrate phase with the balance being anhydrous lithium iodide for case II denoted by \square in Fig. 2. According to weight loss measurements on drying Al₂O₃ powder, the sample case I would contain 2 m/o LiI · H₂O. These

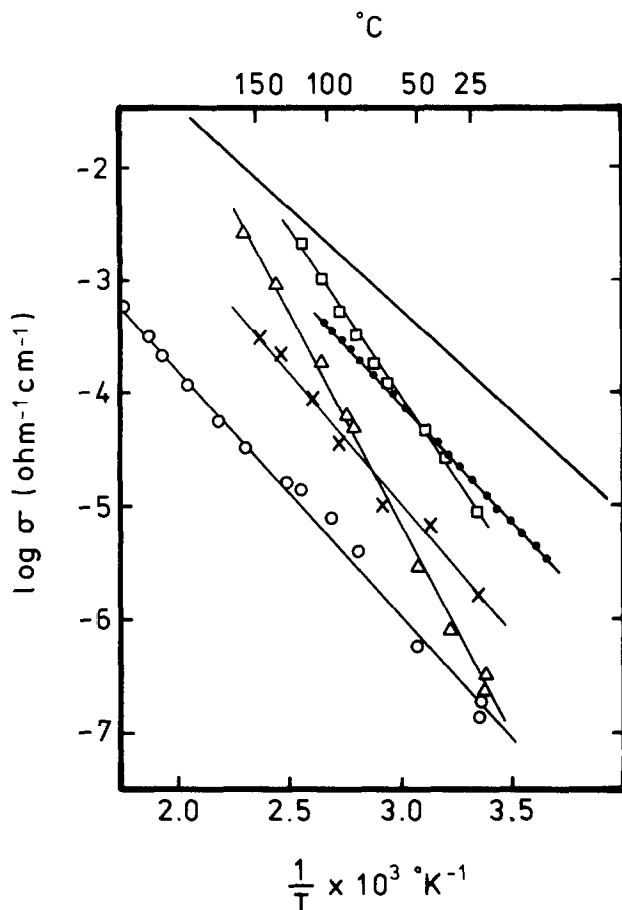


Fig. 2. Logarithm of a-c conductivity of $\text{LiI} \cdot \text{H}_2\text{O} \cdot \text{Al}_2\text{O}_3$ vs. $1/T$. \circ 24 m/o Al_2O_3 dried + LiI (prepared in glove box < 0.3 ppm V); \triangle 25 m/o Al_2O_3 as received + LiI + trace $\text{LiI} \cdot \text{H}_2\text{O}$; case I: moisture introduced by moist Al_2O_3 ; \times 35 m/o Al_2O_3 dried + LiI + trace $\text{LiI} \cdot \text{H}_2\text{O}$; case II: moisture introduced by hydrates; \square 35 m/o Al_2O_3 dried + $\text{LiI} \cdot \text{H}_2\text{O}$ + trace LiI ; case II: moisture introduced by hydrates and relatively more moist than sample denoted by \times (above). \bullet — \bullet — \bullet — \bullet — \bullet — 40 m/o Al_2O_3 + LiI [Ref. (1)]; — 50-60 m/o Al_2O_3 + LiI [Ref. (13)].

results suggest that the presence of a few mole percent of the hydrate phase in the $\text{LiI} \cdot \text{Al}_2\text{O}_3$ material increases the conductivity by one to two orders of magnitude.

X-ray powder diffraction showed both the dried and undried Al_2O_3 to be α -form.² Therefore one must infer the difference is due to the change in surface of Al_2O_3 resulting in the alteration of H_2O distribution. It is reasonable to assume that the undried Al_2O_3 localizes H_2O such that $\text{LiI} \cdot \text{H}_2\text{O}$ is under the influence of the surface since the dehydration efficiency of $\text{LiI} \cdot \text{H}_2\text{O}$ and Al_2O_3 are comparable being 0.5 ppm V and 1 ppm V (12) at room temperature, respectively. Either the increase in H_2O content or the deactivation of the Al_2O_3 surface by heating would result in more free $\text{LiI} \cdot \text{H}_2\text{O}$ and yield a lower activation energy approaching that of $\text{LiI} \cdot \text{H}_2\text{O}$ in case I.

It is noted that the conductivity of $\text{LiI} \cdot \text{H}_2\text{O} \cdot \text{Al}_2\text{O}_3$ with a trace of LiI is comparable to that of $\text{LiI} \cdot \text{H}_2\text{O}$ without Al_2O_3 . For comparison, the conductivity data of $\text{LiI} \cdot \text{Al}_2\text{O}_3$ in the literature (1, 13) are included in Fig. 2 (denoted by — and \bullet — \bullet — \bullet — \bullet — \bullet —). The authors did not specify the H_2O content in their samples. It is possible that some moisture in the samples (handled under <15 ppm V H_2O environment) affected their results. More recent reports (14) show that the degree of pre-

drying of the Al_2O_3 varied the resultant 25°C conductivity by one order of magnitude. Von Alpen and Bell (15) recently reported the conductivity of LiI and $\text{LiI}(\text{Al}_2\text{O}_3)$. Their conductivity data for anhydrous LiI agrees with previous values. Dried γ - Al_2O_3 (50 m/o) caused about an order of magnitude increase in σ but less than the two plus orders reported by Liang et al., for ~40-60 m/o Al_2O_3 of unspecified particle size.

Summary

The conductivity of LiI prepared under low $p\text{H}_2\text{O}$ (<0.05 ppm V) has been measured and results agree with earlier investigations. Additions of 24 m/o pre-dried Al_2O_3 particles, 0.3 μm nominal size mixed and pressed dry into pellets, did not enhance the conductivity. The conductivity of hydrates of LiI with and without Al_2O_3 particles has been measured and the enhanced conductivity was attributed to the presence of H_2O . The conductivity increase when Al_2O_3 particles were added is primarily due to the presence of H_2O .

The activation energy of the mixture depends on the thermal treatment of Al_2O_3 when the H_2O content is low. An understanding of the existence of the $\text{LiI} \cdot 1/2\text{H}_2\text{O}$ and the entire $\text{LiI} \cdot \text{H}_2\text{O}$ system requires further study.

Acknowledgment

This research was supported by a grant from the Center for Solid State Science at Arizona State University.

Manuscript submitted July 17, 1979; revised manuscript received May, 8, 1980. This was Paper 368 presented at the Boston, Massachusetts, Meeting of the Society, May 6-11, 1979.

Any discussion of this paper will appear in a Discussion Section to be published in the June 1981 JOURNAL. All discussions for the June 1981 Discussion Section should be submitted by Feb. 1, 1981.

Publication costs of this article were assisted by Energy Technology, a Division of Medtronic, Incorporated.

REFERENCES

1. C. C. Liang, *This Journal*, **120**, 1289 (1973).
2. B. B. Owens and H. J. Hanson, U.S. Pat. 4,007,122 (1977).
3. T. Jow and J. B. Wagner, Jr. *This Journal*, **126**, 1963 (1979).
4. G. F. Huttig and W. Stendemann, *Z. Phys. Chem.*, **126**, 105 (1927).
5. E. W. Morley, *J. Am. Chem. Soc.*, **26**, 1171 (1904).
6. C. Slonin and G. F. Huttig, *Z. Anorg. Chem.*, **181**, 57 (1929).
7. A. Lannung, *Z. Phys. Chem.*, **A170**, 134 (1934).
8. B. J. H. Jackson and D. A. Young, *J. Phys. Chem. Solids*, **30**, 1973 (1969).
9. C. R. Schlaikjer and C. C. Liang, *This Journal*, **118**, 1447 (1971).
10. K. Shahi and J. B. Wagner, Jr., Paper 369, presented at The Electrochemical Society Meeting, Boston, Massachusetts, May 6-11, 1979.
11. B. M. L. Rao and B. G. Silvernagel, U.S. Pat. 4,049,881 (1977).
12. J. H. Bower, *J. Res. Nat. Bur. Stand.*, **33**, 199 (1944).
13. C. C. Liang, A. V. Joshi, and N. E. Hamilton, *J. Appl. Electrochem.*, **8**, 445 (1978).
14. J. R. Rea, DOE Battery and Contractors Conference, Volume II, December 10-12, 1979.
15. U. von Alpen and M. F. Bell, in "Fast Ion Transport in Solids: Electrodes and Electrolytes," P. Vashita, J. N. Mundy, and G. K. Shenoy, Editors, pp. 463-469, North-Holland Publishing Co., Amsterdam, The Netherlands.
16. S. Lewkowitz, B. B. Owens, P. M. Skarstad, and D. F. Untereker, Paper 4, presented at The Electrochemical Society Meeting, Los Angeles, California, Oct. 13-19, 1979.

² Meller Company reports 0.3 μm Al_2O_3 to consist of 70% α - and 30% γ - Al_2O_3 .

Pyrolytic Deposition of MnO₂ Layers in Saturated Water Vapor Atmospheres

J. M. Albella, L. Fernández-Navarrete, and J. M. Martínez-Duart

Departamento de Física Aplicada and Inst. Física Estado Sólido,
C.S.I.C. Universidad Autónoma, Cantoblanco, Madrid, Spain

The pyrolytic decomposition of manganese nitrate to produce the MnO₂ layer in solid electrolyte tantalum capacitors results in a degradation of the electrical characteristics of the dielectric Ta₂O₅ and the contact resistance (1-4). The resulting harmful effects can be partially avoided by introducing moist air in the oven while performing the pyrolysis (5). In this case the resulting layers of MnO₂ present a higher degree of compaction and better contact with the rest of the cathode layers (6). In spite of its technical significance there is a lack of results in the literature on the characteristics of the MnO₂ pyrolytic deposition in saturated water vapor atmospheres and the influence of the MnO₂ layers in the electrical characteristics of capacitor structures using MnO₂ as electrolyte.

In this paper the pyrolysis of the manganese nitrate Mn(NO₃)₂ · 6H₂O was performed at 250°C in an oven saturated with water vapor. The pyrolytic decomposition of the nitrate usually took a minimum of 2 hr. The oven was provided with a small orifice to let the reaction gases escape and at the same time insure a relative humidity of practically 100% and a slight overpressure relative to atmospheric.

It has been found convenient in this work to follow the changes, during the decomposition of the manganese nitrate, of the products of the reaction. This provided a means of controlling step by step the pyrolytic reaction and gave direct information of the properties of the end product. For this purpose, the resistivity was measured by means of a cell provided with platinum electrodes and using a Hewlett Packard 4261-A LCR bridge at a frequency of 1 kHz. The platinum electrodes (size 5 × 5 mm², separated 2 mm) were fixed within the reaction cell and the temperature was measured with a sheathed thermocouple located close to the electrodes.

The cell in which the decomposition of the manganese nitrate was performed was generally introduced in the oven when the temperature was 100°C and subsequently the temperature of the oven was raised to 250°C. Figure 1 shows the variation of the resistivity and the temperature during the reaction in the saturated water vapor atmosphere. Three stages, indicated by the letters A, B, and C can be distinguished in the curve for resistivity. It is interesting to point out that these stages can be correlated to those found by Gallagher *et al.* using thermogravimetry and differential thermal analysis techniques (7-9).

The first stage in Fig. 1 of the pyrolytic decomposition is dominated by the loss of the water of crystallization and consequently the temperature increases very slowly. Similarly the resistivity rises slowly during this stage, probably as a consequence of a growing viscosity, but its variation with time becomes much steeper as the transformation of the nitrate in oxynitrate (MnONO₃) proceeds (stage AB). Next, the formation of the MnO₂ begins by the decomposition of the unstable MnONO₃ which cannot be isolated. Therefore, the section BC of the curve in Fig. 1 is characterized by a strong decrease in the resistivity due to the large electrical conductivity of the

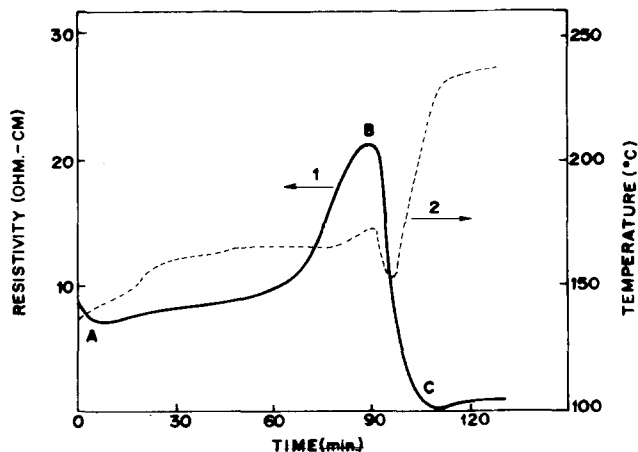


Fig. 1. Variation of the resistivity (solid line) and the temperature (broken line) during the manganese nitrate pyrolytic decomposition in a wet atmosphere.

MnO₂ which behaves as a nearly degenerate semiconductor.

Comparing the results of the pyrolytic decomposition in a saturated water vapor atmosphere with decomposition in a regular dry ambient, the former presents several technical advantages. The rate for the MnONO₃ → MnO₂ + NO₂ reaction is much faster in the moist atmosphere, as a consequence of the smaller activation energy for the reaction in this ambient (9). Also, the resistivity of the resulting MnO₂ is substantially lower when the pyrolysis is performed in the water vapor atmosphere, as will be seen below in more detail. Other differences are related to the porosity, density, and structure of the resulting MnO₂ product. Figure 2 shows a scanning electron micrograph of the MnO₂ layers deposited in the water vapor atmosphere. In this case, the layers present a higher degree of compaction, a better uniformity, and a smaller grain size (12 μm *vs.* 100 μm

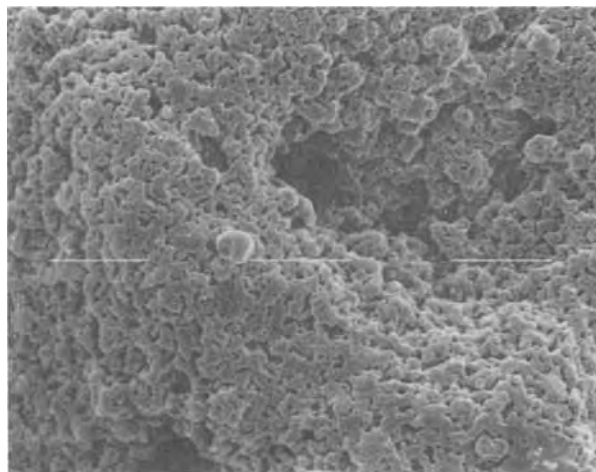


Fig. 2. SEM micrograph of the surface of the MnO₂ samples obtained in a wet atmosphere (reticule 100 μm).

Key words: solid electrolyte, semiconducting oxide, electrolytic capacitor.

for the dry atmosphere case). Furthermore, the apparent density¹ was 3.74 ± 0.10 g/cm³ for the samples formed in the wet atmosphere and 3.33 ± 0.10 g/cm³ for those obtained in dry air. X-ray determinations of structure were also performed showing that the interior of the MnO₂ layers essentially consisted of the β -MnO₂ phase. However, the surface region presented a high proportion of γ -MnO₂ (10) which could amount up to 52% of the total for the samples deposited in a dry atmosphere.

The resistivity of the MnO₂ samples was measured in d.c., under a polarization of 0.25V, and in low frequency a.c., yielding essentially the same results. The value of the resistivity and the slope of the log ρ vs. $1/T$ curve at 20°C is given in Table I. It can be observed from it that the samples pyrolyzed in the moist atmosphere show an electrical conductivity more than one order of magnitude higher than those pyrolyzed in the regular atmosphere. The electrical conduction in MnO₂ is supposed to be due to oxygen vacancies producing donor levels (n-type conduction). According to this, a value of 0.015 eV is obtained for the donor level in the MnO₂ samples deposited in the water vapor saturated atmosphere, value which is substantially lower than the corresponding value of the sample deposited in a dry atmosphere (Table I), and other values reported in the literature for samples pyrolyzed under this condition (10, 11).

Since an important technical application of the MnO₂ is as a solid electrolyte in the capacitor industry, the behavior of the MnO₂ layers pyrolyzed under different ambients were tested in capacitive structures of the TMM type (Ta-Ta₂O₅-MnO₂-metal) prepared on tantalum foil previously subjected to standard cleaning and chemical polishing procedures (12). For this purpose, the tantalum was anodized in a 0.01% H₃PO₄ aqueous solution at a constant current density of 1 mA · cm⁻² until a formation voltage of 100V was reached. After the pyrolytic deposition of the MnO₂ layer during a minimum of 2 hr the foil was reanodized at 55V in an HNO₃ electrolyte ($\rho = 800$ Ω -cm). The dielectric properties of the TMM structures were measured with a General Radio 1620 capacitance bridge in the 10²-10⁵ Hz frequency range and the contact resistance R_c was obtained from the dissipation factor (tan δ) following the series-circuit analysis of McLean (13). The values of R_c are also shown in Table I. The much better value of R_c obtained for the capacitive structures with the MnO₂ deposited in the saturated water vapor atmosphere might be attributed to the higher electrical conductivity and the smaller porosity of the corresponding MnO₂ layers.

The scintillation voltage V_s during the reanodization of the Ta-Ta₂O₅-MnO₂ structures was measured on samples formed at voltages V_f between 40 and 200V and reoxidized at a current density of 1 mA · cm⁻² until the scintillation or breakdown phenomenon first appeared. The results obtained for V_s as a function of V_f are shown in Table II, each value representing the average for three similar capacitive structures.

¹In order to determine the density, the volume considered is limited by the geometrical external surface of a given portion of mass in a container and therefore does incorporate the empty spaces due to the inherent porosity.

Table I. Electrical characteristics of the MnO₂ layers

Sample	Resistivity ($\Omega \cdot \text{cm}$)	Slope (eV)	Contact resistance (capacitive struct.) (Ω)
Wet pyrol.	0.42 + 0.01	0.015	0.50
Dry pyrol.	7.5 + 0.10	0.070	17.8

Table II. Scintillation voltage of the MnO₂ layers (V)

V_f	V_s (wet pyrol.)	V_s (dry pyrol.)
40	40	45
80	65	60
120	90	80
160	110	75
200	130	75

The largest uncertainty in the measurements of V_s was found in the higher formation voltage ranges (V_f between 160 and 200V) and was always less than 10%. It can be deduced from Table II that for low formation voltages ($V_f < 120$ V) V_s shows a close to linear variation for the capacitor structures with the MnO₂ deposited in both wet and dry atmospheres. However, when $V_f > 120$ V the former atmosphere causes a scintillation voltage approximately equal to $0.75 V_f$, whereas the latter shows a value of V_s always below 80V. This fact might be due to both a greater damage in the Ta₂O₅ dielectric caused by the pyrolytic deposition or a lesser degree of oxidation (14) of the MnO₂ layers deposited in the regular atmosphere as compared to the saturated water vapor one. In this respect, it can also be remarked that the leakage current density through these structures, measured after polarizing during 5 min at one-fourth the formation voltage ($V_f = 100$ V in this case), showed a value of about 10^{-7} A · cm⁻² for the structures in which the MnO₂ layers were deposited in the wet atmosphere, being approximately one order of magnitude larger for the case of the MnO₂ layers pyrolyzed in the standard ambient.

Acknowledgments

We would like to acknowledge the American-Spanish Committee for Scientific and Technological Cooperation and the Spanish Comisión Asesora de Investigación Científica y Técnica for partial support of this work.

Manuscript submitted Sept. 26, 1979; revised manuscript received April 18, 1980.

Any discussion of this paper will appear in a Discussion Section to be published in the June 1981 JOURNAL. All discussions for the June 1981 Discussion Section should be submitted by Feb. 1, 1981.

Publication costs of this article were assisted by the Universidad Autonoma de Madrid.

REFERENCES

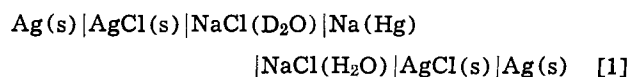
- D. M. Smyth, G. A. Shirn, and T. B. Tripp, *This Journal*, **110**, 1264 (1963).
- T. Takagi, F. Eguchi, H. Kihara-Morishita, and T. Takamura, *Denki Kagaku*, **44**, 713 (1976).
- T. Kudoh, M. Katoh, and M. Watase, *ibid.*, **40**, 70 (1972).
- See for example references cited in the paper of W. J. Bernard, *This Journal*, **124**, 403C (1977).
- F. F. Zind, U.S. Pat. 3,337,429.
- H. Bub, K. Gottschämmer, and H. Spiess, German Pat. 1,935,002.
- P. K. Gallagher, F. Scherey, and B. Prescott, *Thermochim. Acta*, **2**, 405 (1971).
- P. K. Gallagher and D. W. Johnson, *ibid.*, **2**, 413 (1971).
- P. K. Gallagher and D. W. Johnson, *This Journal*, **118**, 1530 (1971).
- S. S. Wiley and H. T. Knight, *ibid.*, **111**, 311 (1976).
- P. H. Klose, *ibid.*, **117**, 654 (1970).
- J. M. Albella, I. Montero, and J. M. Martinez-Duart, *Thin Solid Films*, **43**, 307 (1979).
- D. A. McLean, *This Journal*, **108**, 48 (1961).
- G. P. Klein and N. I. Jaeger, *Thin Solid Films*, **43**, 103 (1979).

Concentration Dependence of the Gibbs Energy of Transfer of NaCl from D₂O to H₂O

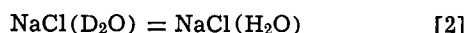
Mahmood Toofan and Peter A. Rock*

Department of Chemistry, University of California, Davis, California 95616

The thermodynamic properties of transfer of electrolytes from heavy to light water can provide useful data for the interpretation of the effect of electrolytes on the structure of water (1, 2). The most direct method for the determination of the molar Gibbs energy of transfer, $\Delta\bar{G}_{tr}$, of an electrolyte from one solvent to another solvent involves the use of electrochemical double cells without transference (3). An appropriate cell for the determination of $\Delta\bar{G}_{tr}$ of NaCl from heavy to light water is



where Na(Hg) represents a flowing sodium amalgam junction. The net cell reaction of cell [1], operating under reversible conditions, is



Voice (4) has used cells of type [1], and appropriate analogues, to determine $\Delta\bar{G}_{tr}$ from D₂O to H₂O for a variety of electrolytes; he has also summarized and critically evaluated the results of previous workers. All of the electrochemical investigations prior to the work reported herein were confined to concentrations below about 0.3M, and only a very slight effect, if any, of concentration on the $\Delta\bar{G}_{tr}$ values was observed.

The detailed structures of D₂O and H₂O are different owing to the greater strength of deuterium bonds relative to hydrogen bonds. Consequently, electrolytes that are water structure breakers (5) or water structure makers might be expected to exhibit concentration-dependent $\Delta\bar{G}_{tr}$ values. For this reason we decided to determine $\Delta\bar{G}_{tr}$ for reaction [2] over the range 0.3-4M in order to ascertain if the Gibbs energy of transfer of NaCl from heavy to light water exhibits a concentration dependence. We have found that $\Delta\bar{G}_{tr}$ for NaCl is concentration dependent and we have offered a qualitative explanation for this effect. The effect of different concentration scales on the values of $\Delta\bar{G}_{tr}$ is also discussed.

The Ag(s)|AgCl(s) electrodes were prepared by the thermal-electrolytic method (6); the bias potentials of the pairs of electrodes used were less than 0.03 mV. The mercury (Quicksilver Products, Incorporated, C.P. triple distilled) was covered with 0.001M HNO₃(aq) and agitated with a stream of air. The dried Hg was run out from the base of the cleaning vessel into a vessel containing a known quantity of clean Na(s) under an argon atmosphere. The Na(Hg) (ca. 0.003M) was agitated with a stream of argon gas for about 24 hr. The amalgam was stored under argon and agitated gently to allow any insoluble impurities to rise to the surface. A flowing amalgam junction was used in the cell. During measurements the amalgam was run continuously into the cell through capillaries at a flow rate of about 2-3 cm³ · min⁻¹. A doubling of the flow rate had no effect on the measured emf. The NaCl cell solutions were prepared from weighed quantities of dried primary standard NaCl(s) and oxygen-free H₂O(l) or D₂O(l) (99.7 atomic percent

D). The cell contents were continuously purged with argon gas delivered to the cell through presaturators. Continuous emf measurements were made using a Keithley 602 Solid-State Electrometer the output of which was fed to Mosley-Autograf Model 7101B chart recorder. The system was calibrated by feeding in known voltages from an NBS-certified L and N K-3 potentiometer. After a cell was set up it was allowed to equilibrate for about 2 hr before the amalgam flow was started. The Ag(s)|AgCl(s) electrodes were equilibrated with separate samples of respective cell solutions before insertion in the cell. The measured emf values were stable within ±0.05 mV. All measurements were made at 24° ± 1°C.

Two separate sets of experiments were run. In the first set of experiments the molalities (moles of solute/kilogram solvent) of NaCl in H₂O and D₂O were made equal in each experiment. In the second set of experiments the aquamolality (moles of solute per 55.508 moles of water) of NaCl in H₂O and D₂O were made equal in each experiment. The results are given in Table I, and the data are displayed graphically in Fig. 1.

As is evident from Fig. 1 the results for the equimolal and equiaquamolal cases are quite different. Up to 1M most of the difference $\mathcal{E} - \mathcal{E}_a$ can be accounted for solely on the basis of the difference in the two concentration scales because $\mathcal{E}^\circ - \mathcal{E}_a^\circ = (2RT/F)\ln(M_{D_2O}/M_{H_2O}) = 5.42$ mV, where the M_i values are the molecular weights. For example, at 1M, $\mathcal{E} - \mathcal{E}_a = 5.65$ mV. However above 1M the difference in $\mathcal{E} - \mathcal{E}_a$ increases and at 4M, $\mathcal{E} - \mathcal{E}_a = 8.85$ mV. The equimolal data are difficult to interpret in terms of the influence of NaCl on the structure of water because, although the moles of NaCl per kilogram of water is the same in the two solutions, the ratio of the moles of water to moles of salt is 55.51/M for NaCl(H₂O) and 49.93/M for NaCl(D₂O). In addition differences in ion-ion interactions arising from "dilution" of the NaCl on being transferred from D₂O to H₂O are superimposed on the effect of salt on the water structure. Over the range 1-4M, γ_{\pm} for NaCl increases with increasing m (7) and this effect will make $d\mathcal{E}/dm > 0$ [$-(2RT/F)\ln(\gamma_{\pm NaCl(H_2O)}/\gamma_{\pm NaCl(D_2O)}) > 0$]. These difficulties are essentially eliminated in the equiaquamolal case because the ratio of moles of isotopic water to moles of salt is the same in the two solutions, namely, 55.51/M.

Table I. Results of measurements on the cell (24° ± 1°C):
Ag(s)|AgCl(s)|NaCl(m,D₂O)|Na(Hg)|NaCl(m,H₂O)|AgCl(s)|Ag(s)

m	\mathcal{E}	\mathcal{E}_a
0.300	—	5.75
0.500	12.25	—
0.600	—	6.25
1.000	12.45	6.80
1.500	—	6.85
2.000	12.85	6.65
3.000	13.50	6.20
4.00	14.25	5.40

\mathcal{E} is the cell voltage for the equimolal solutions and \mathcal{E}_a is the cell voltage for equiaquamolal solutions. All voltages are ±0.05 mV except for the 0.5M cell which is ±0.15 mV.

* Electrochemical Society Active Member.

Key words: Gibbs energy, sodium chloride, heavy water, electrolyte transfer.

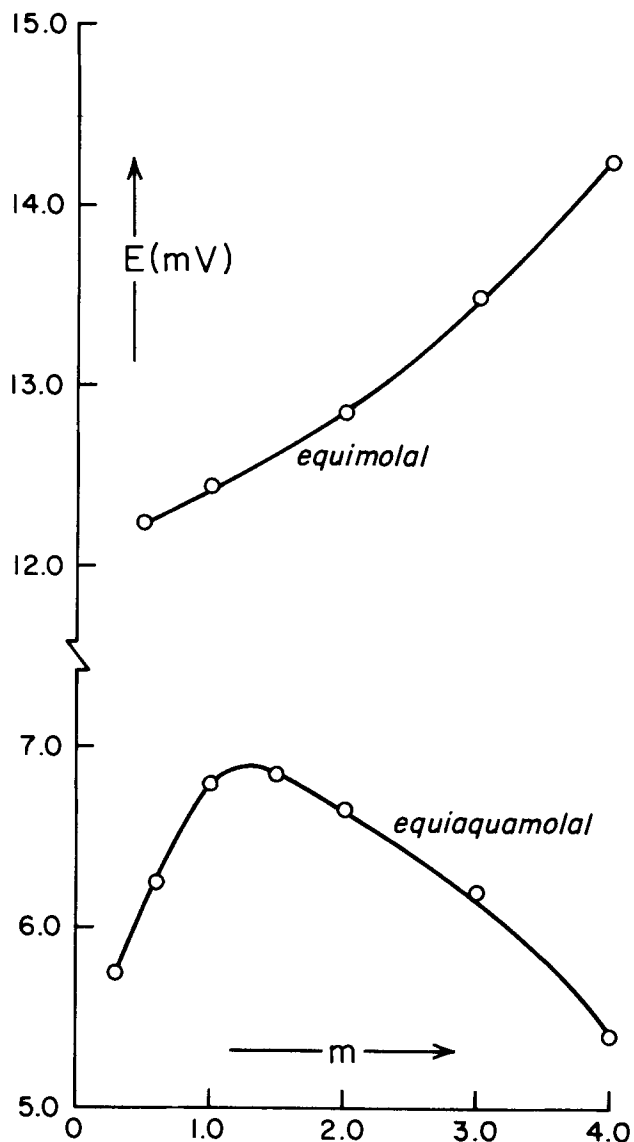
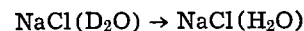
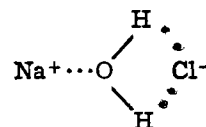


Fig. 1. Emf as a function of molality (24°C) of the cell: $\text{Ag(s)}|\text{AgCl(s)}|\text{NaCl}(m,\text{D}_2\text{O})|\text{Na(Hg)}|\text{NaCl}(m,\text{H}_2\text{O})|\text{AgCl(s)}|\text{Ag(s)}$.

We interpret the $\xi(m)$ data for the equiaquamolal transfer reaction as follows: because the $\text{O}-\text{D}\cdots\text{O}$ bonds (deuterium bonds) in D_2O are stronger (by about 0.5 kcal/mole) than the $\text{O}-\text{H}\cdots\text{O}$ bonds (hydrogen bonds) in H_2O , a water structure-breaking salt like NaCl (2, 1) will exhibit a negative $\Delta\bar{G}_{\text{tr}}$, and therefore a positive value of ξ_{tr} for the process



In other words more Gibbs energy is released on reforming the deuterium bonds on desolvation of the ions than is consumed on breaking the hydrogen bonds in resolvating the ions. This effect will increase with increasing aquamolality until the water structure is effectively completely broken down, *i.e.*, when all of the water molecules are involved in either primary or secondary coordination of the ions. This apparently occurs for NaCl in water at a ratio of moles of water to moles of ions of about 18 to 19, *i.e.*, at the maximum in the ξ vs. m curve, *ca.* 1.5M; with further increase in aquamolality solvent-separated ion pairs of the type



begin to appear, and because such ion pairs do not involve $\text{O}-\text{H}\cdots\text{O}$ (or $\text{O}-\text{D}\cdots\text{O}$) bonds, but rather the much weaker $\text{O}-\text{H}\cdots\text{Cl}^-$ (or $\text{O}-\text{D}\cdots\text{Cl}^-$) bonds, the isotope effect on $\Delta\bar{G}_{\text{tr}}$ decreases.

Acknowledgment

Acknowledgment is made to the Donors of the Petroleum Research Fund, administered by the American Chemical Society, for the partial support of this research.

Manuscript submitted Oct. 9, 1979; revised manuscript received May 5, 1980.

Any discussion of this paper will appear in a Discussion Section to be published in the June 1981 JOURNAL. All discussions for the June 1981 Discussion Section should be submitted by Feb. 1, 1981.

Publication costs of this article were assisted by the University of California.

REFERENCES

1. B. Conway, *Ann. Rev. Phys. Chem.*, **17**, 481 (1966).
2. E. M. Arnett and D. R. McKelvey, in "Solute-Solvent Interactions," pp. 344-395, Marcel Dekker, New York (1969).
3. H. S. Harned and B. B. Owen, "The Physical Chemistry of Electrolytic Solutions," 3rd ed., Reinhold Pub. Co., New York (1958).
4. P. J. Voice, *J. Chem. Soc. Faraday Trans.*, **1**, 498 (1974).
5. H. S. Frank and M. W. Evans, *J. Chem. Phys.*, **13**, 507 (1945).
6. D. J. G. Ives and G. J. Janz, Editors, "Reference Electrodes," p. 133, Academic Press, New York (1961).
7. G. N. Lewis, M. Randall, K. S. Pitzer, and L. Brewer, "Thermodynamics," pp. 643-645, McGraw-Hill, New York (1961).

The Multiplicity of Anodic Current Peaks Related to the Potentiodynamic Electro-oxidation of Carbon Monoxide on Polycrystalline Platinum

S. A. Bilmes, N. R. de Tacconi, and A. J. Arvía

*Instituto de Investigaciones Físicoquímicas Teóricas y Aplicadas,
División Electroquímica, Universidad Nacional de La Plata, 1900 La Plata, Argentina*

The adsorption of CO on platinum electrodes from acid aqueous solutions has been the subject of numerous publications over the last decades as shown in the recent review on the subject presented in Ref. (1). The reported results and their interpretations are still only partially understood and the advanced explanations open to discussion. Nevertheless it should be noticed that the difficulty in correlating some of the electrochemical data on the electro-oxidation of CO on platinum may arise from the fact that the results obtained by different authors using transient techniques are not strictly comparable. There is evidence, however, that the electro-oxidation of CO on platinum occurs as though two distinct and separable entities were involved (2).

On the other hand, the adsorption of CO on platinum from the gas phase has also been investigated over a long period of time (3). The pertaining literature is reviewed in Ref. (4). More recently the gas phase CO adsorption was studied on single crystal platinum surfaces and the chemisorption of CO on the Pt(111) surface, as deduced from the results using LEED techniques, thermal desorption, and work function measurements were also explained in terms of the existence of two different adsorption sites on the metal. Therefore, despite the differences of the above-mentioned interfaces and the difficulty for the straightforward comparison of the corresponding results, it seems reasonable to expect that the Pt-CO adsorption interaction in the presence of the electrolyte solution may also involve a relatively complex adsorption process which is reflected in a composite anodic potentiodynamic display.

In order to explain the existence of multiple current peaks associated with the potentiodynamic oxidation of CO species on platinum, potentiodynamic runs were performed with a systematic and stepwise increase and decrease of the cathodic switching potential, within the potential range where the oxygen-containing species formed on platinum to the order of the monolayer thickness are electroformed and electro-reduced (5). Within this potential range the adsorbed CO-species on platinum are also electro-oxidized. The potential/time program employed to perturb the electrochemical interface is chosen so that the maximal interaction between electroadsorbed oxygen and CO is achieved.

The experiments were carried out at 25°C on a polycrystalline spectroscopically pure smooth platinum wire electrode (0.24 cm² apparent area). The electrode was immersed in a purified 1N HClO₄ solution to minimize anion adsorption and interaction effects (6). The counterelectrode was also made from Pt. The potential of the working electrode was referred to the normal hydrogen electrode. The electrolyte was saturated at 1 atm pressure with CO prepared from AR chemicals and purified to satisfy the highest purity standards (7). The electrochemical cell as well as the CO generator and ducts were made of Pyrex glass, the stopcocks were lubricated with concentrated

AR sulfuric acid to avoid as far as possible the interference of any contaminants.

Figure 1 shows the conventional E/I profile recorded after holding the electrochemical interface at open circuit during 20 min in the CO saturated electrolyte at 1 atm pressure, and then running a symmetrical repetitive triangular potential sweep at 0.1 V/sec. For the sake of comparison the voltammogram obtained in the same conditions with the nitrogen saturated solution is also included in the figure. The E/I display exhibits the anodic and cathodic current peaks related to the hydrogen adatoms in the 0.04-0.35V range and the cathodic current peak related to the electroreduction of the oxygen-containing surface species on platinum in the 0.52-1.00V range. Within the 0.82-1.04V potential range, a large and relatively sharp anodic current peak is recorded. The latter is associated with the electro-oxidation of the CO species and it overlaps the first portion of the anodic current corresponding to the electroadsorption of the oxygen-containing species which extends up to 1.46V. This E/I display agrees, in principle, with those earlier reported by other authors (8-10). The comparison with the blank shows that the presence of CO produces a sharp decrease of the charge pertaining to the hydrogen adatoms while there is no significant influence as far as the charge corresponding to the oxygen-containing species is concerned.

Figure 2 shows the E/I profile obtained with stepwise increase of the cathodic switching potential. In order to have a clean metal surface free of adsorbed CO, the potential of the electrochemical interface was cycled between $E_{\lambda,c}$ and $E_{\lambda,a}$, during 2 min at a fast potential sweep (100 V/sec) before recording

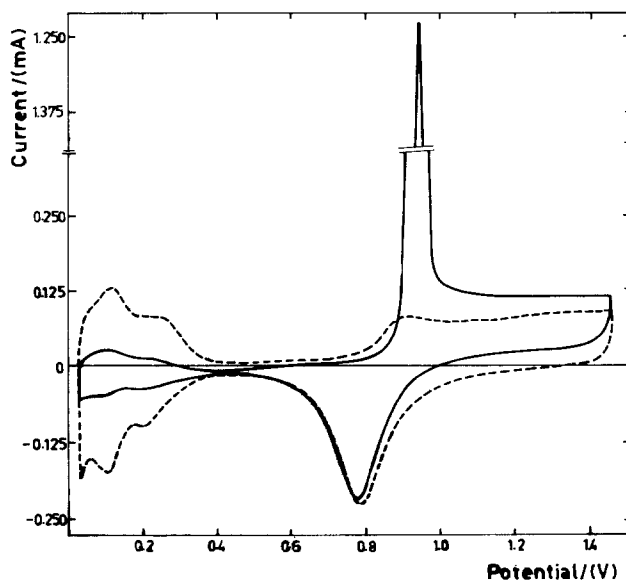


Fig. 1. Potentiodynamic E/I profiles of platinum in 1N HClO₄ run at 0.1 V/sec at 25°C. (—) CO (1 atm) saturated solution; (---) N₂ saturated solution.

* Electrochemical Society Active Member.
Key words: gas, electrode, adsorption.

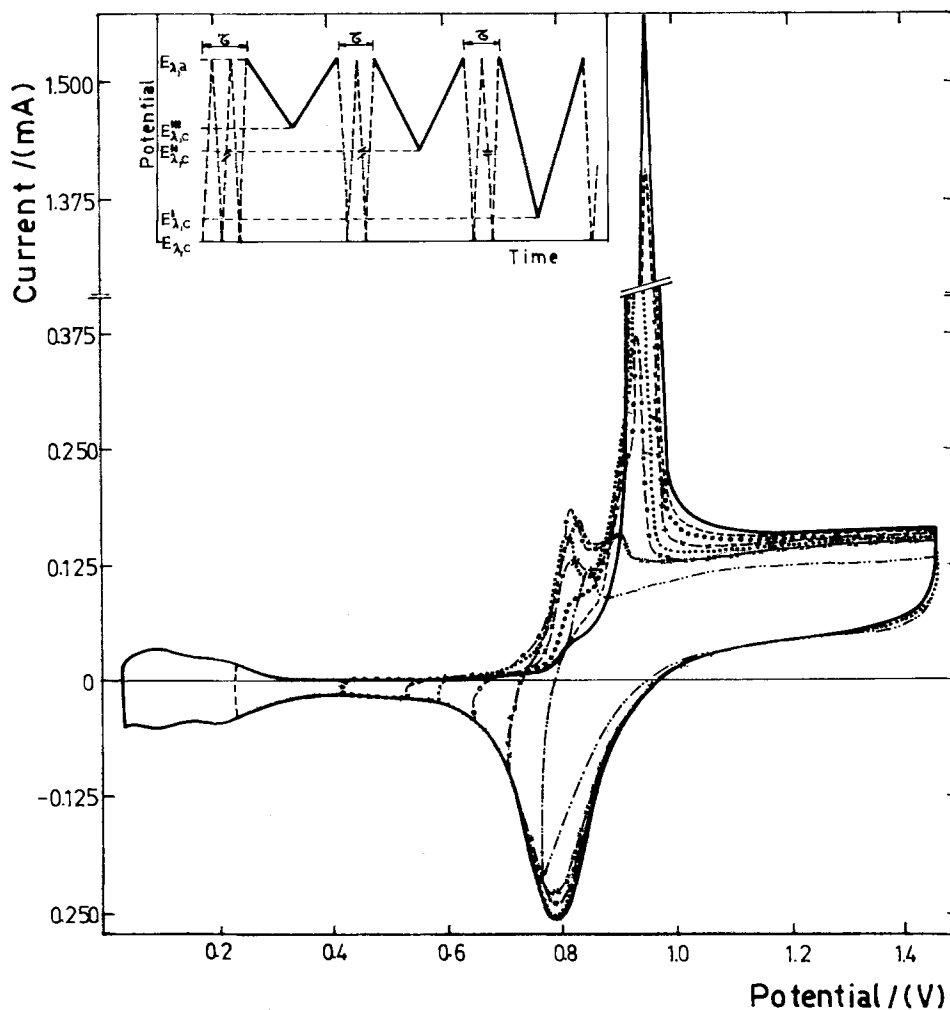


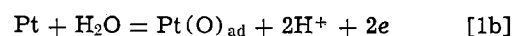
Fig. 2. Potentiodynamic E/I profiles in 1N HClO_4 run at 0.1 V/sec at 25°C. These profiles were obtained with different $E_{\lambda,c}'$ following the $E-t$ program depicted into the figure. (Before each profile the interface was cycled between $E_{\lambda,a}$ and $E_{\lambda,c}$ at 100 V/sec during $\tau = 2$ min).
 (— · — · —) $E_{\lambda,c}' = 0.77\text{V}$;
 (—XX—XX—) $E_{\lambda,c}' = 0.71\text{V}$;
 (—°—°—) $E_{\lambda,c}' = 0.65\text{V}$;
 (·····) $E_{\lambda,c}' = 0.59\text{V}$;
 (—x—x—x—) $E_{\lambda,c}' = 0.53\text{V}$;
 (°°°°) $E_{\lambda,c}' = 0.41\text{V}$; (— — —) $E_{\lambda,c}' = 0.23\text{V}$; (——) $E_{\lambda,c}' = 0.04\text{V}$.

the E/I profile at 0.1 V/sec between $E_{\lambda,c}'$ and $E_{\lambda,a}$. Figure 3 shows the E/I displays obtained under the same conditions as in Fig. 2 but the potential range of the sweep covers only the oxygen monolayer electrodesorption. From the E/I displays in the CO saturated electrolyte (Fig. 2 and 3) one concludes that at least three anodic current peaks can be assigned to the electro-oxidation of CO on platinum. The first peak is seen at 0.8V and starts to contribute only when the amount of oxygen remaining on the surface during the electroreduction process is slightly lower than 50% of the total electroreduction charge. The second, at 0.91V, is better defined when the fraction of clean metal is ca. 70% and finally, the third, at 0.95V, which coincides with the one found under conventional potentiodynamic experiments, requires that the oxygen-containing species has been practically completely electroreduced. The latter remains as the only anodic current contribution related to CO when the cathodic switching potential value falls within the potential range of the hydrogen adatoms. Under these circumstances no current contribution of the former current peaks is noticed. A comparison with the blank sweep (Fig. 1) shows that these current peaks can only be due to the presence of CO. For each E/I display (Fig. 3) which shows the multiplicity of peaks, a further potential cycling within the same potential range at 0.1 V/sec produces the progressive increase of the current peak at 0.91V at the expense of those current peaks located at 0.8V and at 0.95V. Unfortunately, as the CO readsorption effect has not been quantitatively determined, reliable charge ratios from the already described E/I displays cannot be evaluated. The presence of CO in the electrolyte only influences to a minor extent the characteristics of the

E/I profile in the oxygen electrodesorption potential range including the aging effects (11, 12).

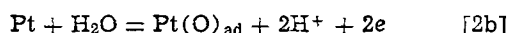
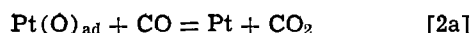
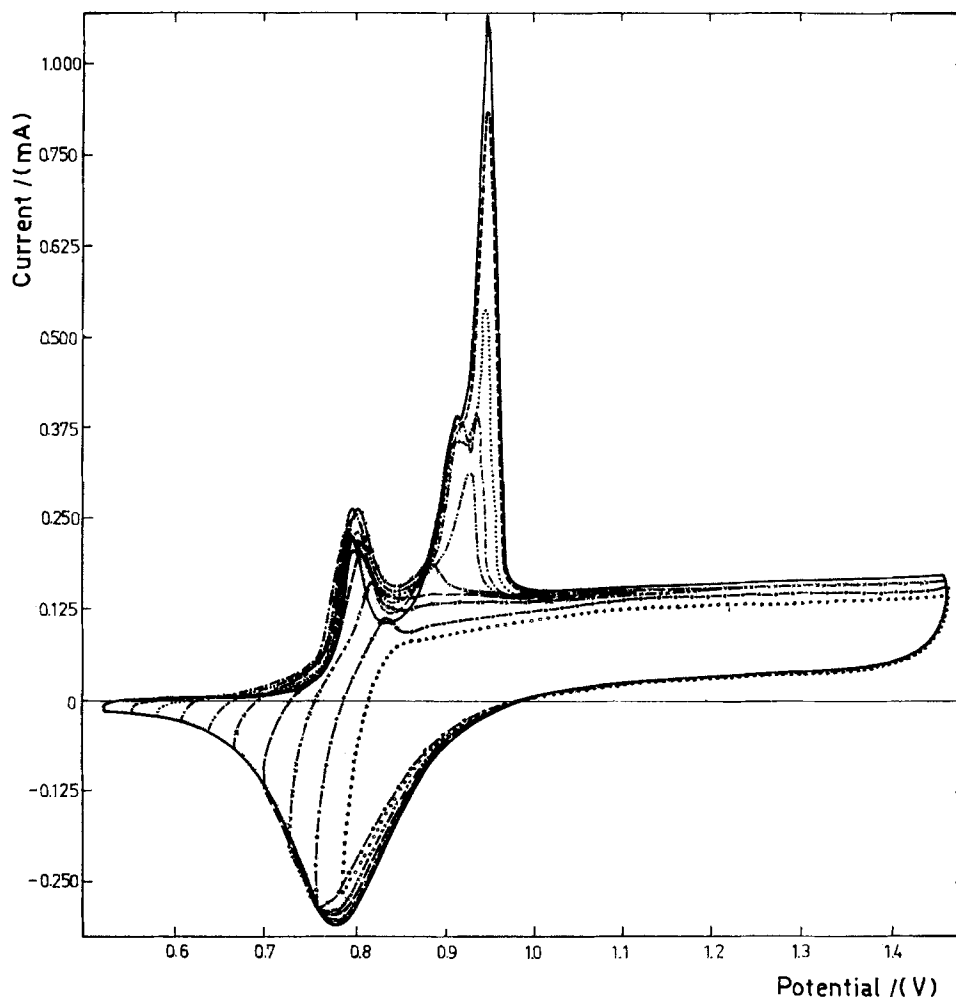
One is inclined to believe that the described effect on the anodic E/I display might be due to an impurity interference, but this apparently is not the case since the potential sweep comes from the positive potential side and it occurs when the fraction of free metal surface is still relatively small. Furthermore, the oxidation current peak indicates that the first adsorbed species is more easily electro-oxidized than that formed when CO adsorbs at more negative potentials. On the other hand, the multiplicity effect is more noticeable when the structure of the surface becomes more complex, *i.e.*, when free sites, PtOH, and various PtO species are simultaneously on the surface as one may conclude from the study of aging effects all along the potential range of the oxygen monolayer electroreduction on Pt (11, 12).

Therefore, the CO electro-oxidation reaction should comprise two different types of processes according to the adsorbed reactant entering the electrochemical oxidation. The two main type of adsorbed species are the $\text{Pt}(\text{CO})_{\text{ad}}$ species which originate through the Pt-CO chemical interaction and the various $\text{Pt}(\text{O})_{\text{ad}}$ species including Pt(OH) which result from the Pt- H_2O electrochemical interaction. The electro-oxidation of the different CO adsorbed species is represented by the overall reactions



and the direct electro-oxidation of CO through the electroadsorbed oxygen on platinum is given by the reactions

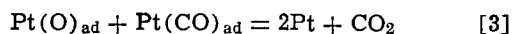
Fig. 3. Potentiodynamic E/I profiles in 1N HClO₄ run at 0.1 V/sec at 25°C obtained with the same conditions as Fig. 2. (°°°°) $E_{\lambda,c'}$ = 0.80V; (—°—°—) $E_{\lambda,c'}$ = 0.77V; (—XX—XX—) $E_{\lambda,c'}$ = 0.74V; (— — — —) $E_{\lambda,c'}$ = 0.71V; (—x—x—x) $E_{\lambda,c'}$ = 0.68V; (— · · · ·) $E_{\lambda,c'}$ = 0.65V; (— · — · —) $E_{\lambda,c'}$ = 0.62V; (· · · · ·) $E_{\lambda,c'}$ = 0.59V; (— · — · —) $E_{\lambda,c'}$ = 0.56V; (— — — —) $E_{\lambda,c'}$ = 0.53V.



where the parenthesis denote any of the possible either CO or O sorbed species on platinum. Reactions [1a] and [1b], which occur at lower potentials, involve a competition for metal sites by the CO and O species. Contrarily, reactions [2a] and [2b] are only related to the electrosorbed oxygen species on platinum.

The existence of a relatively large anodic background current in the potential range where the electrosorption of oxygen takes place suggests that the electro-oxidation of CO occurs also beyond the region of the corresponding main current peak. This effect could probably be associated with a chemical surface oxidation reaction involving CO according to reaction [2a] followed by the fast electrosorption of oxygen as indicated by reaction [2b].

On the other hand, a chemical surface reaction such as



is to be expected in lower potential range where free Pt sites are available. This conclusion is not surprising in view of recent results on the interaction between oxidized Pt and CO in the gas phase (13, 14).

Therefore, the present experiments furnish a clear evidence that CO can be oxidized in aqueous acid electrolytes on polycrystalline platinum electrodes in different reactions which are associated with the multiplicity of the corresponding electrochemical anodic spectrum. They also suggest the possible existence of different CO adsorbed species on Pt. This has just a resemblance to the results reported for the Pt/CO (gas) interface although it should be kept in mind

that at present a quantitative comparison between the behavior of the two interphases is impossible.

The present results are therefore, at least partially, relevant to the understanding of the contradictory interpretations of results presented in the literature on the electrochemistry of the Pt/aqueous acid solutions/CO (1 atm) interface.

Acknowledgment

This work is part of the research program of the Electrochemistry Division of INIFTA, sponsored by the Universidad Nacional de La Plata, the Consejo Nacional de Investigaciones Científicas y Técnicas, and the Comisión de Investigaciones Científicas de la Provincia de Buenos Aires.

Manuscript submitted April 25, 1979; revised manuscript received Feb. 27, 1980.

Any discussion of this paper will appear in a Discussion Section to be published in the June 1981 JOURNAL. All discussions for the June 1981 Discussion Section should be submitted by Feb. 1, 1981.

Publication costs of this article were assisted by the Instituto de Investigaciones Fisicoquímicas Teóricas y Aplicadas.

REFERENCES

1. A. Czerwinski and J. Sobkowski, *J. Electroanal. Chem. Interfacial Electrochem.*, **91**, 47 (1978).
2. S. Gilman, *J. Phys. Chem.*, **66**, 2657 (1962); P. Stonehart, *Electrochim. Acta*, **18**, 63 (1973).
3. I. Langmuir, *Trans. Faraday Soc.*, **17**, 621 (1922).
4. G. Ertl, M. Neumann, and K. M. Streit, *Surf. Sci.*, **64**, 393 (1977).
5. H. Angerstein-Kozłowska, B. E. Conway, and W. B. A. Sharp, *J. Electroanal. Chem. Interfacial Electrochem.*, **43**, 9 (1973); N. R. de Tacconi,

- A. J. Calandra, and A. J. Arvia, *ibid.*, **51**, 25 (1974).
6. P. Stonehart, *Electrochim. Acta*, **15**, 1853 (1970).
 7. H. Grubitsch, "Anorganisch-Präparative Chemie," p. 335, Wien, Springer-Verlag (1950).
 8. C. McCallum and D. Pletcher, *J. Electroanal. Chem. Interfacial Electrochem.*, **70**, 277 (1976).
 9. J. Bett, K. Kinoshita, K. Routsies, and P. Stonehart, *J. Catal.*, **29**, 160 (1973).
 10. A. B. Fasman and G. L. Padyukova, *Elektrokhimiya*, **10**, 39 (1974).
 11. N. R. de Tacconi, J. O. Zerbino, M. E. Folquer, and A. J. Arvia, *J. Electroanal. Chem. Interfacial Electrochem.*, **85**, 213 (1977).
 12. M. E. Folquer, J. O. Zerbino, N. R. de Tacconi, and A. J. Arvia, *This Journal*, **126**, 592 (1979).
 13. R. A. Shigeishi and D. A. King, *Surf. Sci.*, **75**, L. 397 (1978).
 14. W. H. Weinberg and R. P. Merrill, *J. Catal.*, **40**, 268 (1975).



The Observation of Effects of Finite Specimen Geometry on the Oxidation Kinetics of Zircaloy-4

R. E. Pawel and J. J. Campbell

Oak Ridge National Laboratory, Metals and Ceramics Division, Oak Ridge, Tennessee 37830

ABSTRACT

The oxidation of zirconium and zirconium-base alloys at temperatures above the alpha-beta transition involves the growth of layers of oxide and oxygen-stabilized alpha into the host beta phase. If the growth is governed by diffusion processes, the oxidation of thin specimens will exhibit significant variations in the kinetics of layer growth if the duration of the reaction is sufficient to promote large changes in the degree of saturation of the underlying metal with oxygen. We have examined this effect for the oxidation of Zircaloy-4 in steam by modeling analyses and by a series of extended-time oxidation experiments at 1300°C. These experiments confirmed the predicted increase in the kinetics of alpha layer growth as the beta phase becomes saturated. For example, at 1300°C, the rate constant increases by more than a factor of 2. While the appearance of "alpha incursions" leading to an irregular alpha-beta interface also seems to be initiated at this time, the experimental observations generally agreed well with those predicted on the basis of the modeling analysis. This behavior needs consideration in the interpretation and comparison of oxidation data, particularly where large differences in the specimen geometry or dimensions are involved.

The oxidation of Zircaloy-4 in steam at high temperatures has recently been examined from both kinetics (1) and diffusion modeling (2) standpoints. Despite the complex microstructure of the oxide phase, it has been shown that the isothermal growth of the product oxide and oxygen-stabilized alpha layers can be described accurately in the early stages by parabolic kinetics over the temperature range 1000°-1500°C. Furthermore, the modeling analysis produced sets of effective chemical diffusion coefficients for oxygen in both the oxide and alpha phases that compared favorably, where comparisons were possible, with data obtained by other means. The apparently ideal nature of the growth of the oxidation products, as well as the self-consistency of the treatments in terms of diffusion models, has increased our confidence in the applicability of a simplified modeling analysis to this system.

Previous modeling analyses for the oxidation of Zircaloy have been applied mainly to offer a foundation for the quantitative prediction of the extent of reaction during transient temperature exposures. While some of these treatments have been based simply on the parabolic rate constants for layer growth, at least two programs (3, 4) have been used that apply a more sophisticated finite-difference diffusion analysis to examine both layer growth and oxygen concentration gradient effects in all of the phases present. Programs of this sort, at least in principle, offer the ability to examine potential effects of a variety of boundary conditions on the oxidation characteristics, and they have provided a basis for comparison and evaluation for numerous oxidation experiments.

This paper presents calculations and experimental results describing the changes in layer growth kinetics

that occur as a consequence of finite geometry influences during extended isothermal reaction of a thin specimen. For the case of Zircaloy-4 oxidizing in steam, substantial effects are observed particularly for the growth rate of the alpha layer. The modeling and experimental results are compared and discussed in terms of their relevance to the design of experiments and their interpretation.

The Oxidation Model

In order to construct a useful mathematical model to describe the kinetic events during high temperature oxidation of Zircaloy, it is necessary to consider the reaction phenomenology with particular emphasis on the diffusion processes in the various phases. Numerous investigators have dealt with various aspects of this problem (5) and we will not detail them here. Our model has been discussed previously (2) and does not depart in substance from those of other workers. Basically, in the temperature range of interest to the present paper, we depict the oxidation of Zircaloy as the growth of uniform layers of oxide and oxygen-stabilized alpha into the host beta phase as shown in Fig. 1. We assume, with previous experimental justification, that the growth of these phases is diffusion controlled and that the diffusivity of the mobile reactant within each phase can be described by a single effective chemical diffusion coefficient. The rate of growth of the oxide layer is proportional to the velocity of the oxide-alpha boundary, which depends on diffusion and concentration parameters in the two product phases. Similarly, the rate of growth of the alpha layer is equal to the difference in the velocities of the alpha-beta and oxide-alpha boundaries.

Key words: zirconium, oxidation, diffusion, kinetics.

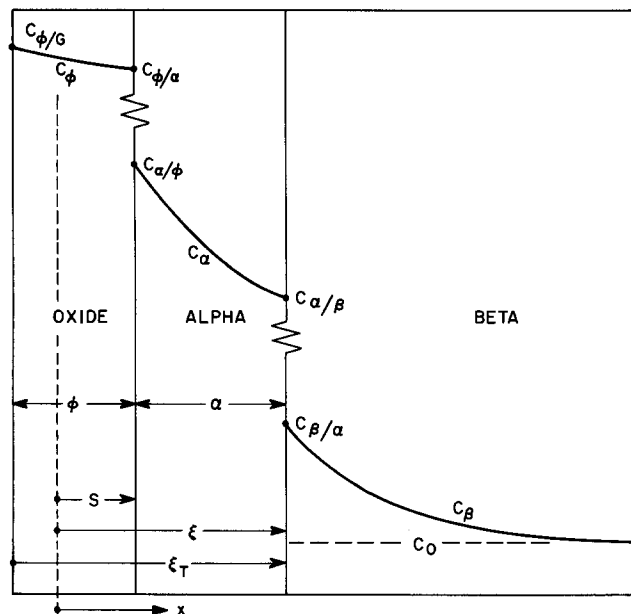


Fig. 1. Schematic diagram of the multiphase, moving boundary diffusion problem as beta Zircaloy reacts with oxygen to form layers of alpha and oxide. C_0 = initial oxygen concentration in Zircaloy; $C_{A/B}$ = concentration in the A phase at its interface with the B phase (G = gas; ϕ = oxide; α = alpha; β = beta); ϕ = oxide layer thickness; α = alpha layer thickness; S and ξ define the position of the oxide-alpha and alpha-beta boundaries with respect to the original specimen surface at $x = 0$.

In the oxide, growth is thought to take place by an anion diffusion mechanism, although for the temperature range under consideration here the particular modes of mass transport have not been clearly defined. Additionally, the oxide formed on Zircaloy-4, while uniform in thickness, has a complicated morphology (2, 6) that suggests the possibility of a similarly complicated influence on the diffusion behavior. However, no major influence or perturbation of the macroscopic growth characteristics has been observed, and we have considered the oxide to be structurally homogeneous for the purpose of our calculation. We view the value of D_ϕ (see Fig. 1) as an "average" or "effective" value of the chemical diffusion coefficient for oxygen in the oxide that, in conjunction with the concentration gradient, accurately describes the local mass transport.

The diffusion of oxygen in the metallic alpha and beta phases of Zircaloy-4 takes place by an interstitial mechanism, and again we have assumed concentration- (or position-) independent chemical diffusion coefficients for oxygen, D_α and D_β . To the extent that this assumption might not be valid, such an assignment implies that an "average" value is a useful entity in determining mass transport. Our earlier calculations of D_α from the kinetic data were made on this basis (2), and in support, arguments have been made that concentration effects are relatively small for oxygen diffusion in both alpha and beta Zircaloy at these temperatures (7, 8).

Thus, the model describes a classical multiphase, moving-boundary diffusion problem that, at least for the simpler boundary conditions, has analytical solutions relating layer growth to the concentration and diffusion parameters in each phase. A variety of approaches and solutions have been published, including several that have dealt specifically with the oxidation of zirconium and Zircaloy (2, 5a, 5d, 9-12). These treatments have been of value in interpreting and correlating oxidation results.

For the case of constant interface concentrations as indicated in Fig. 1, the ideal diffusion controlled growth of both oxide and alpha phases will remain parabolic (thickness squared proportional to time) so long as a semi-infinite geometry condition prevails for oxygen

diffusion in the beta phase. Parabolic kinetics will also be observed for the case where the original oxygen concentration in the beta phase is equal to the saturation concentration, $C_{\beta/\alpha}$, and no oxygen flux into the beta from the alpha-beta boundary exists. In this latter case, the absence of the oxygen flux into the beta leads to a comparatively faster movement of the alpha-beta boundary that results in a higher growth rate for the alpha layer. The alpha growth will still be parabolic, but the corresponding parabolic rate constant will be larger. Thus, it follows that for "thin" specimens in which the beta phase tends to fill up with oxygen during the period of reaction, the parabolic constants governing the rates of growth for both oxide and alpha layers must increase from their initial values to some final values. The effect will obviously be larger for growth of the alpha phase, although the influence will be felt in the oxide also. As we will point out later, an interesting result from this model requires that, despite increases in the rate constants for growth of both the oxide and alpha layers during oxidation of saturated specimens, the rate constant for oxygen consumption is slightly decreased.

The influence of geometrical effects has thus been recognized, and analytical descriptions dealing specifically with the finite geometry aspects of the diffusion problem have been discussed (10, 12). While these analytical expressions may furnish insight that is often overlooked in numerical solutions, they are cumbersome and the numerical solutions, which can easily handle a variety of complicated boundary conditions, have become more popular. Such a computer code, MULTRAN, was constructed in our laboratory by Malang (13). This program models idealized diffusion-controlled layer growth processes by solving the diffusion equations for mass flow in a one-dimensional, multiphase, moving boundary system with finite geometry. The program uses finite-difference calculations and can be applied to reactions with up to five separate product phases. It was used to model the reaction sequences and experiments reported in this paper for the oxidation of Zircaloy-4. The appropriate input to this program (diffusion coefficients, equilibrium concentrations, and densities for all phases) were obtained in part from the analysis (2) of our previous work (1) in this area. It should be pointed out that these data were obtained from sets of experimental measurements utilizing short reaction times at each temperature so that the observed kinetics were not influenced by geometrical effects.

Experimental Procedure

Oxidation tests were conducted for Zircaloy-4¹ in flowing steam at atmospheric pressure in a low thermal inertia oxidation apparatus that employed radiant heating. In this apparatus, described previously (1), a 3 cm length of 1.1 cm diam tubing was exposed to steam on its outer surface while being heated according to a programmed temperature cycle. Three Pt vs. Pt-10% Rh thermocouples were attached to the inner surface of the specimen tube at its midpoint and, in order to minimize temperature measurement errors, the interior of the tube was protected from oxidation by a slow flow of helium maintained at a slightly positive pressure relative to the external steam pressure. One thermocouple furnished the programmer/recorder signals, while the other two (180° apart) were attached to a computer-operated data-acquisition system, CODAS. The detailed record of the temperature history at these two points on the specimen served as the basis for calculation of the effective isothermal reaction time at the nominal oxidation temperature.

After oxidation, each specimen was sectioned at the elevation containing the thermocouple beads and prepared for metallographic examination by conventional

¹ Sandvik Special Metals Corporation. Reactor Grade Zircaloy-4 PWR Tubing. Nominal composition (weight percent): 1.60 Sn, 0.25 Fe, 0.12 Cr, 0.12 O, 0.009 C, 0.003 N, and 0.0025 H.

techniques (1). The specimens were lightly etched, anodized, and measurements of the oxide and alpha layer thicknesses were made at the two monitor thermocouple positions with a digital micrometer eyepiece. These measurements were reasonably straightforward except when the alpha-beta interface was heavily populated with "alpha incursions," i.e., irregular growths of alpha protruding into the beta region. In this latter case, two measurements of the alpha layer thickness were made: one measurement was that of the thickness of the "compact" (uniform thickness) portion only of the alpha layer; the other was of an "effective" alpha layer thickness that included a visual estimate of the average additional thickness attributable to the incursions. These "effective" thickness measurements were, of necessity, less accurate than the corresponding measurements of the compact layer thicknesses.

Results and Discussion

The experimental layer thickness measurements that define the growth of the oxide and alpha layers on Zircaloy-4 specimens in steam at 1300°C are presented in Table I. As noted above, we have also tabulated the "effective" alpha layer thickness that includes, where applicable, an estimate of the equivalent thickness due to the presence of the alpha incursions in the microstructure. In addition, based on the assumption of linear gradients in the oxide and alpha phases, a calculated value of the oxygen consumed for each specimen is included. The growth morphology is sampled in the progression of microstructures in Fig. 2 and 3. In order to assist the reader in visualizing the diffusion processes, included in each of these figures is a schematic drawing of the layer thicknesses and oxygen concentration gradients. The average oxygen concentration in the beta layer, expressed as a percentage of the saturation value, is also listed. These gradients and percentages were obtained from the modeling analysis using the MULTRAN program.

Morphology.—The series of micrographs confirms that the oxide and alpha layers grow uniformly in the early stages of the reaction. However, as the reaction proceeded, commensurate with the approach to oxygen saturation of the beta phase, the alpha beta boundary developed irregularities (Fig. 3) and, for longer times, extensive coarsening of the beta and incursions of the alpha in advance of the compact portion of the alpha layer were observed. In our isothermal experiments, the oxidation was terminated by switching off the power to the radiant heaters, allowing the specimen to cool mainly by radiation to the now-cold surround-

Table I. Layer thickness measurements for Zircaloy oxidized in flowing steam at 1300°C

Expt. No.	Time (sec)	Layer thickness			Oxygen consumed† (mg/cm ²)
		Oxide (μm)	Compact alpha* (μm)	Incursion compensated alpha** (μm)	
T-30/TC#2	96.4	47.7	55.2		9.71
T-30/TC#3	98.8	47.8	55.6		9.76
T-31/TC#2	201	65.8	79.0		13.6
T-31/TC#3	205	67.1	79.3		13.8
T-32/TC#2	379	88.8	106.6		18.3
T-32/TC#3	386	92.4	110.1		19.0
T-33/TC#2	607	109.9	137.7	156	23.0
T-33/TC#3	654	114.1	146.3	163	23.7
T-34/TC#2	754	122.2	157.2	186	25.5
T-34/TC#3	825	127.9	171.9	198	26.6
T-35/TC#2	934	136.6	185.1	220	28.3
T-35/TC#3	946	134.4	185.8	223	28.1
T-36/TC#2	1176	153.3	208.0	252	31.5
T-36/TC#3	1237	154.3	207.7	265	32.0

* Thickness of alpha layer that exhibits uniform growth; neglects presence of alpha incursions.
 ** Includes estimate of additional thickness created by presence of incursions.

† Computed on basis of linear oxygen gradients in both oxide and (compensated) alpha thicknesses.

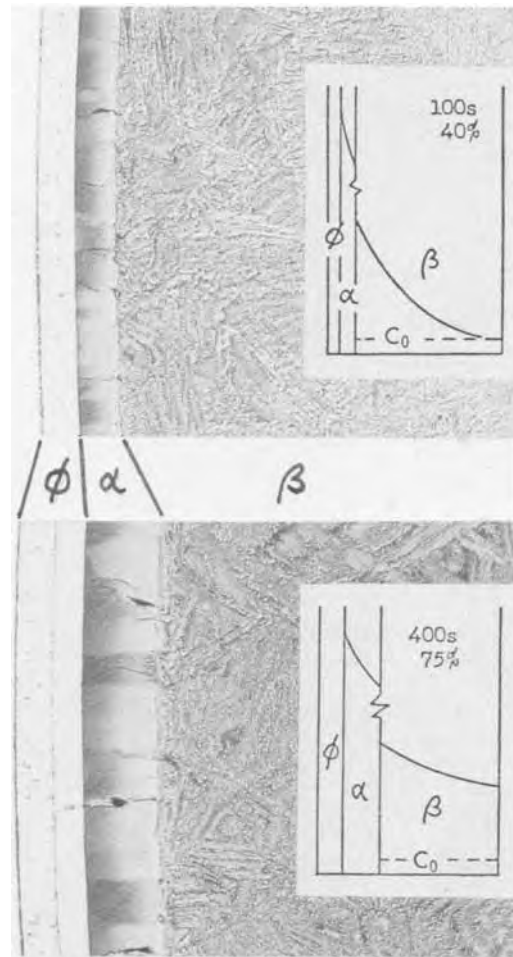


Fig. 2. Cross sections of Zircaloy-4 specimens oxidized in steam at 1300°C for 100 sec (above) and 380 sec (below). See Table I for details and experimental measurements. The inset schematics portray relative phase thicknesses and oxygen concentration gradients and indicate the average relative saturations of the (prior) beta phase. In both cases, the alpha/beta boundary has remained sharp with only a few minor asperities visible at higher magnification.

ings and by convection to the flowing steam. This resulted in initial cooling rates greater than 100°C/sec, and the temperature dropped below 1000°C within 5 sec, below 800°C in about 13 sec. Given this short cooling period, it is unlikely that the massive incursion structures form only on cooling as has been suggested (14), but they may form in large part during the isothermal oxidation, beginning at such a time as the oxygen concentration gradient in the beta phase in advance of the interface becomes relatively flat. The flat gradient implies a limited diffusion flux away from the alpha-beta interface as well as high oxygen concentrations all across the beta phase. These conditions favor departures from ideal, diffusion-controlled layer growth and tend to emphasize the influence of factors such as favored growth directions and other structural aspects of the process. In support of this argument, variations in the cooling rates after isothermal oxidation (see below) produced little change in the appearance of the interface. Thus, such departures from ideal layer growth imply that local growth rates become sensitive to some developing property or event in the system. While the identity of this event is not apparent, incursions have been observed only in the "late" stages of oxidation of a specimen of a given thickness, and they are observed much earlier for two-sided oxidation than for oxidation on one side only (11, 15, 16). Although the possibility of an altogether different correlation cannot be discarded, the consistent observa-

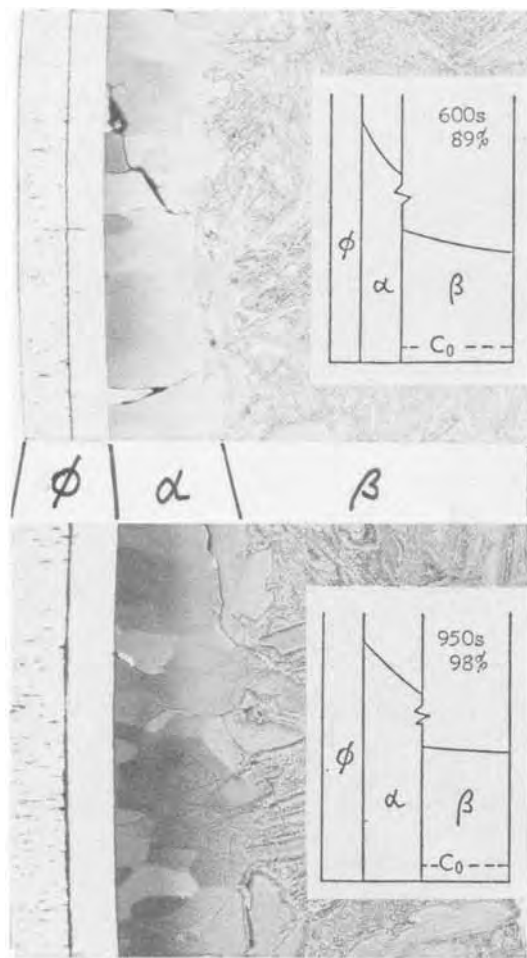


Fig. 3. Cross sections of Zircaloy-4 specimens after oxidation at 1300°C for 600 sec (above) and 950 sec (below). The alpha/beta interfaces now exhibit irregular growth shapes. While the thickness of the "compact" portion of the alpha layer is reasonably well defined in both instances, the observation of the alpha incursions signal the end of the period of ideal, diffusion-controlled growth.

tion of incursions at times that signal the filling-up of the beta phase with oxygen is potentially significant.

The present observations for oxidation at 1300°C suggest a correlation between the beginning of incursion formation and the attainment of oxygen concentration levels in the beta phase between 75% and 90% of the saturation value. In a similar sequence for oxidation at 1200°C (17), no incursions were found for a

600 sec exposure, although many incursions developed after 1200 sec, the two times corresponding to saturation values of about 70% and 90%. An earlier correlation (11, 15) indicated saturation levels of about 90-95% were required to produce alpha incursions during isothermal oxidation. However, this analysis was based on Mallett's (18) data for oxygen diffusion in beta Zircaloy rather than the recent measurements of Perkins (7). The latter diffusivity values are lower by almost a factor of 2, and a recalculation in terms of the newer data would suggest that the onset of incursions occurred at somewhat lower saturation values, viz., between about 80% and 90%.

It is reasonable to expect that slow cooling after isothermal oxidation would promote alpha incursion formation as well as alpha precipitation in advance of the interface for specimens containing sufficient oxygen in the remaining beta phase (11, 14). However, we have observed that cooling rates in the range of 2°-5° C/sec for specimens having lower oxygen levels in the beta phase do not stimulate extensive incursion growth. For example, Fig. 4 illustrates the microstructures for specimens cooled at 2°C/sec from 1300°C after 120 and 300 sec oxidation periods. At the start of the cooling cycle, the beta phases were about 45% and 66% saturated, respectively. The "prior" beta regions of these specimens exhibited coarser structures than those found in quenched specimens with similar amounts of oxidation (see Fig. 2 and 3). However, few incursions of the type found after extended isothermal exposures were observed. Similarly oxidized specimens cooled at 5°C/sec displayed comparable features with finer structures in the prior beta phase. While Sawatzky *et al.* (14) observed large incursions and very coarse prior beta structures for a similar cooling rate, their isothermal oxidation periods (at 1200°C) were long enough to saturate completely the beta phase prior to the start of cooling. Thus, it appears that cooling rates affect the incursion growth and microstructure to a greater extent when the beta phase is in a near-saturated condition.

Kinetics.—The kinetics of layer growth in the early stages of the reaction of Zircaloy-4 in steam have been examined in detail (1). Both oxide and alpha layers grow parabolically, and in our previous work the maximum time was purposely limited so that any geometrical effects would be minimized. For example, for these experiments at 1304°C, the longest oxidation time was about 150 sec. In the present work, we have extended the maximum experiment time to insure, for our particular specimen dimensions, that the shrinking beta phase eventually saturates with oxygen. The consequences of this effect on the kinetics were examined experimentally and through computer modeling.

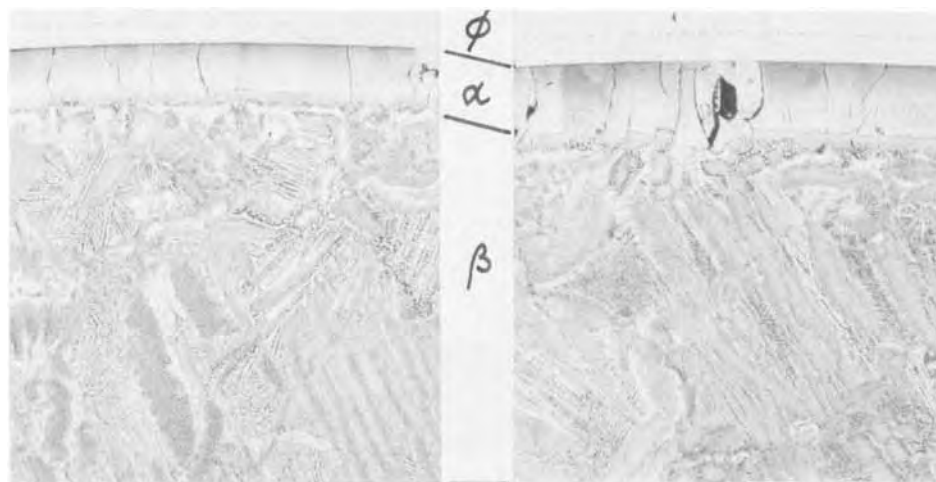


Fig. 4. Cross sections after oxidation for 120 sec (left) and 300 sec (right) at 1300°C followed by cooling at 2°C/sec to 800°C. At the start of cooling for these experiments, the beta phases were about 45% and 66% (average) oxygen saturated, respectively. While the structure in the (prior) beta phase of each specimen is coarse and shows evidence of precipitation in advance of the alpha-beta interface on cooling, few large alpha incursions are observed. Indeed, the decreased oxide/alpha thickness ratio for these specimens suggests that additional alpha growth during cooling was at least in part a uniform addition to the compact alpha layer.

The layer thickness data for oxidation at 1300°C listed in Table I are presented in the parabolic plot of Fig. 5. In this figure, we have also included curves based on (i) the rate constants for oxide and alpha growth for the short-time experiments (1), and (ii) those calculated by the MULTRAN computer program using the appropriate dimensions of our specimens (one-side reaction for 0.0635 cm wall thickness) and initial oxygen concentration [$C_0 = 0.12$ weight percent (w/o)].

Several significant points are immediately obvious from the figure. First of all, the short-time data are in excellent agreement with the previous parabolic growth correlations. However, for times greater than about 500 sec, the growth of both layers appears to deviate from the initial values. Finally, while the change in the kinetics of alpha growth is adequately predicted by the MULTRAN calculation, the smaller deviation exhibited by the oxide growth is not.

The good agreement of the two shortest experiments with the previous data for oxide growth supports the idea that this present data set should perhaps not be represented by a single parabolic growth constant but, rather, that after an initial period, the growth rate decreases at a slightly more rapid rate than would be expected for true parabolic behavior. As is evident from Fig. 5, the effect here is a small one, and the change in the apparent rate constant at longer times is only marginally different in the statistical sense. This is not an uncommon result when experimental data are examined in this sort of time regime. Structural effects in the oxide are usually involved (19).

On the other hand, longer oxidation times clearly promote positive deviations from the initial parabolic growth exhibited by the alpha layer. Such deviations are predicted by the modeling analysis based on our specimen geometry and ideal growth behavior. The fact that uniform alpha layer growth is not completely followed, because of the tendency toward incursion formation as growth proceeds or as the beta phase becomes saturated with oxygen, makes it difficult to assess completely the agreement between theory and experiment. The experimental data do show, however, increases in both the thickness of the compact portion of the alpha layer and, particularly, the incursion-compensated layer thickness that are consistent with the MULTRAN prediction of a factor of 2 increase in

the effective parabolic rate constant for alpha growth at this temperature as oxidation proceeds.

These experiments and calculations point out the importance of specimen geometry and initial oxygen concentration to the layer growth kinetics and to the kinetics of oxygen consumption. The initial layer growth kinetics on specimens of Zircaloy-4 containing (originally) little or no oxygen, and specimens saturated with oxygen at the reaction temperature, would be parabolic but be described by different rate constants. Thus, a specimen of "finite geometry" would exhibit changes in layer growth behavior as the oxygen concentration gradient in the beta phase became influenced by the fact that the beta was filling up with oxygen. On saturation of the beta phase, the layers would grow at the "new" parabolic rate. In Table II, the parabolic rate constants for oxide growth, $\delta_o^2/2$, alpha growth, $\delta_\alpha^2/2$, and oxygen consumption, $\delta_r^2/2$, are presented for Zircaloy-4 with a typical initial oxygen concentration ($C_0 = 0.12$ w/o) and for saturated samples at temperatures from 1000° to 1500°C. The two sets of rate constants were obtained from MULTRAN calculations using the inputs previously described (2). The table shows that for a saturated beta phase, the growth of both layers is faster while the rate of oxygen consumption is smaller (because no additional oxygen is being absorbed into the beta phase).

The effect of initial oxygen concentration on the rate of oxide growth should be comparatively small, the calculated ideal increase in the rate constants for saturated specimens ranging from about 3% to 17%, depending on the temperature, over that for a specimen containing little original oxygen. Very careful experiments would be required to detect differences of this magnitude. Our data actually show a small decrease in the rate constant for oxide growth at the longer times, as discussed above. On the other hand, the rate constants for alpha layer growth are increased from 45% to 135% for the same conditions, a change less apt to be overlooked in the spread of experimental data. Thus, the oxidation of a thin specimen should, and does, show geometrical effects on the alpha layer growth behavior. As noted above, despite the increased growth rates of the product layers for saturated specimens, the rate of oxygen consumption in this instance is actually reduced by a small amount. If the reaction is continued for a time sufficient to eliminate the beta phase from the system, then the alpha layer would itself become subject to saturation with oxygen. This occurrence would have more pronounced effects on the growth of the oxide phase and on the rate of oxygen uptake, calculated to be +74% and -41% changes, respectively, in the parabolic rate constants at 1300°C compared to that for an originally oxygen-free specimen. The experimental data of Pemsler (20) for pure zirconium reacting in oxygen exhibit at least qualitative agreement for the magnitude of these changes, showing about a factor of two increase at 1290°C for the rate constant for oxide growth.

The apparent sensitivity of the alpha growth to the degree of saturation of the underlying beta phase needs consideration when designing experiments and interpreting experimental results. For example, the experimental rate measurements from one-sided and from two-sided tests will be identical (other things being equal) so long as the conditions that define oxygen diffusion into the beta phase remain identical to the two cases. It is significant, however, to note that for a two-side test, the beta phase fills to a given degree of saturation in one-fourth the time required for the case of a one-side test. This situation is illustrated in Fig. 6 where computer-modeled alpha layer growth at 1300°C is plotted for saturated and unsaturated specimens and for one- and two-sided oxidation. The alpha growth for the two cases is identical only for about the first 100 sec, then the curves diverge, each

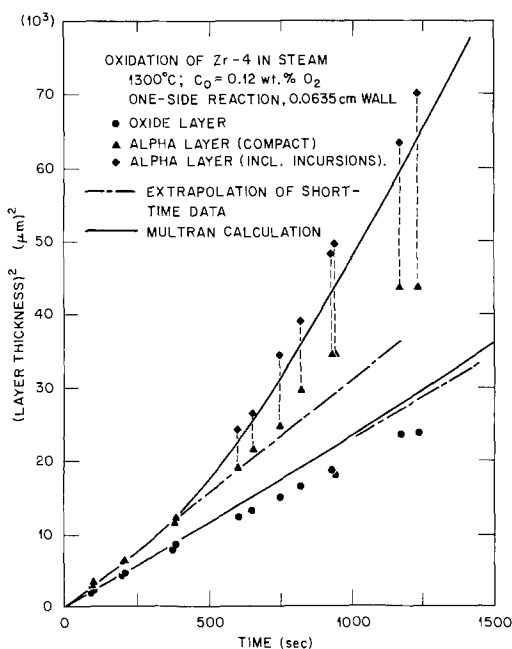


Fig. 5. Growth of oxide and alpha layers on Zircaloy-4 in steam at 1300°C. Data are compared with extrapolations of parabolic growth predicted from previous short-time experiments.

Table II. Parabolic rate constants for normal and for oxygen-saturated Zircaloy-4 computed by Multran program

Temperature (°C)	Parabolic rate constants*			Sat. conc., C_{Sat} (w/o)	Parabolic rate constants*					
	Normal oxygen, $C_0 = 0.12$ w/o				Saturated specs., $C_0 = C_{\text{Sat}}$					
	$\delta_0^2/2$ (cm ² /sec)	$\delta_\alpha^2/2$ (cm ² /sec)	$\delta_\tau^2/2$ [(g/cm ²) ² /sec]		$\delta_0^2/2$ (cm ² /sec)	Diff. (%)	$\delta_\alpha^2/2$ (cm ² /sec)	Diff. (%)	$\delta_\tau^2/2$ [(g/cm ²) ² /sec]	Diff. (%)
1000	7.929E-9	5.274E-9	2.338E-8	0.32	8.193E-9	+3.3	7.665E-9	+45.3	2.272E-8	-2.8
1100	2.186E-8	1.742E-8	7.226E-8	0.59	2.350E-8	+7.5	3.328E-8	+91.0	6.792E-8	-6.1
1200	5.314E-8	5.586E-8	1.918E-7	0.80	5.846E-8	+10.0	1.152E-7	+106.2	1.767E-7	-7.9
1300	1.157E-7	1.567E-7	4.526E-7	1.00	1.300E-7	+12.4	3.402E-7	+117.1	4.091E-7	-9.61
1400	2.305E-7	3.895E-7	9.672E-7	1.20	2.638E-7	+14.5	8.806E-7	+126.1	8.598E-7	-11.1
1500	4.260E-7	8.700E-7	1.906E-6	1.41	4.966E-7	+16.6	2.042E-6	+134.7	1.665E-6	-12.6

* $\delta x^2/2 = k dx/dt$.

eventually acquiring a slope approximately equal to that for the originally saturated specimen. Clearly, such experimental data must be interpreted with geometrical effects in mind. Additionally, because incursion formation begins when the oxygen concentration gradient in the beta phase becomes small, incursion formation should occur much earlier for a two-sided oxidation test. The figure also includes the percentage relative saturation of the beta phase for the one- and two-sided reactions for these specimens. As noted previously, incursions and serious deviations from semi-infinite geometry behavior are observed at saturation levels between about 75% and 90%.

The data of Leistikow, Schanz, and Berg (16) may be interpreted in terms of, and offer at least qualitative verification for, the above model. For two-sided oxidation at 1300°C under equivalent conditions, they observed alpha incursions after only 120 sec (their shortest experimental time). In addition, their parabolic rate constant for alpha growth, calculated on the basis of the compact alpha layer thickness, was measurably higher than ours (1) despite the fact that the rate constants for oxide growth agreed closely. This behavior is consistent with the analysis presented in Fig. 6 both as to the time at which incursion growth was initiated and to the apparent difference in the parabolic constants for alpha layer growth determined from the slope of the thickness squared vs. time plot.

Conclusions

1. The set of oxidation experiments for Zircaloy-4 in steam at 1300°C exhibited departures at longer times from the simple early stage parabolic growth of the product layers, oxide and oxygen-stabilized alpha Zircaloy. These changes in the kinetics were examined by modeling the system as a multiphase, moving-boundary diffusion problem. Within the accuracy of the experimental measurements, a reasonable conform-

ity of the observations and the model predictions was observed. It is thus important to consider the potential effects of specimen geometry when designing oxidation experiments or interpreting kinetic data.

2. Alpha incursions, irregular growths of alpha Zircaloy into the host beta phase, appeared to form during isothermal oxidation when the oxygen concentration gradient in the beta phase became small. Their presence was observed when the relative saturation in the beta phase was calculated to be between 75% and 90%. Slow cooling may promote incursion growth in specimens containing oxygen at or near this level.

3. Modeling the high temperature Zircaloy oxidation reaction in terms of an ideal diffusion-controlled layer growth process provided an explanation for certain of our observations of experimental behavior in terms of specimen geometry effects. Computer results yielding quantitative assessments of these effects for the Zircaloy-steam reaction as functions of temperature and specimen dimensions were presented.

Acknowledgments

The authors are grateful for the constructive ideas and support of J. V. Cathcart during this work and in the preparation of the manuscript. D. O. Hobson made numerous helpful comments. The assistance of Mrs. Kaye Russell with specimen metallography is appreciated. This research was sponsored by the Division of Materials Sciences, U.S. Department of Energy under Contract W-7405-eng-26 with the Union Carbide Corporation.

Manuscript submitted Dec. 5, 1979; revised manuscript received March 19, 1980. This was Paper 18 presented at the St. Louis, Missouri, Meeting of the Society, May 11-16, 1980.

Any discussion of this paper will appear in a Discussion Section to be published in the June 1981 JOURNAL. All discussions for the June 1981 Discussion Section should be submitted by Feb. 1, 1981.

Publication costs of this article were assisted by Oak Ridge National Laboratory.

REFERENCES

1. R. E. Pawel, J. V. Cathcart, and R. A. McKee, *This Journal*, **126**, 1105 (1979).
2. R. E. Pawel, *ibid.*, **126**, 1111 (1979).
3. S. Malang, SIMTRAN I—A Computer Code for the Simultaneous Calculation of Oxygen Distributions and Temperature Profiles in Zircaloy During Exposure to High-Temperature Oxidizing Environments, ORNL-5083 (November 1975).
4. W. G. Dobson and R. R. Biederman, ZORO 1—A Finite Difference Computer Model for Zircaloy-4 Oxidation in Steam, EPRI NP-347 (December 1976).
5. For example, reviews of the phenomenology and analytical descriptions may be found in: (a) C. J. Rosa, *J. Less Common Metals*, **16**, 173 (1968); (b) E. Cox, in "Advances in Corrosion Science and Technology," Vol. 5, M. G. Fontana and R. M. Staehle, Editors, Plenum Press, New York (1976); (c) P. Kofstad, "High Temperature Oxidation of Metals," John Wiley & Sons, Inc., New York (1966); (d) J. P. Pemsler, *This Journal*, **112**, 477 (1965).
6. G. J. Yurek, J. V. Cathcart, and R. E. Pawel, *Oxid. Met.*, **10**, 255 (1976).
7. R. A. Perkins, *J. Nucl. Mater.*, **68**, 148 (1977).

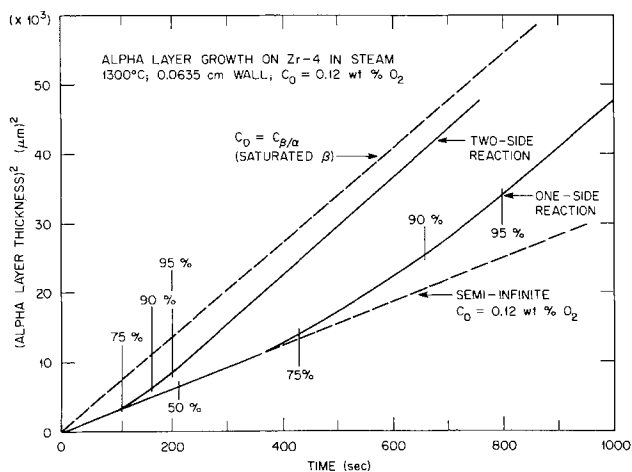


Fig. 6. Calculated alpha layer growth on 0.0635 cm thick Zircaloy-4 specimen in steam at 1300°C for one- and two-side reactions. Dashed curves depict semi-infinite geometry behavior for original oxygen concentrations in the beta phase of 0.12 and 1.00 w/o (saturation value at 1300°C). Ticks on curves represent percentage relative saturation of oxygen in the beta phase.

8. R. A. Perkins, *ibid.*, **73**, 20 (1978).
9. J. Debuigne, *Met. Corros.-Ind.*, **XLII**, 89 (1967).
10. R. E. Pawel, *J. Nucl. Mater.*, **49**, 281 (1974).
11. R. E. Pawel, *ibid.*, **50**, 247 (1974).
12. M. O. Tucker, A. F. Brown and T. Healey, *ibid.*, **74**, 41 (1978).
13. S. Malang, guest scientist from Gesellschaft für Kernforschung, Karlsruhe, FRG., unpublished research, ORNL, 1978. The MULTRAN code is an adaptation of the SIMTRAN code [Ref. (3), above].
14. A. Sawatzky, G. A. Ledoux, and S. Jones, in ASTM STP 633, A. L. Lowe and G. W. Parry, Editors, pp. 134-148, ASTM, Philadelphia (1977).
15. D. O. Hobson, in Proceedings, Topical Meeting on Water Reactor Safety, American Nuclear Society, Salt Lake City, Utah, March 26-28, 1973, CONF-730304.
16. S. Leistikow, G. Schanz, and H. V. Berg, "Kinetik und Morphologie der isothermen Dampf-Oxidation von Zircaloy-4 bei 700-1300°C" Kernforschungszentrum Karlsruhe, KfK 2587 (March 1978).
17. R. E. Pawel, R. A. McKee, and R. E. Druschel, Unpublished research.
18. M. W. Mallett, W. M. Albrecht, and P. R. Wilson, *This Journal*, **106**, 181 (1959).
19. For example, W. W. Smeltzer, R. R. Haering, and J. S. Kirkaldy, *Acta Metall.*, **9**, 880 (1961).
20. J. P. Pemsler, *This Journal*, **113**, 1241 (1966).

The Solubilities of NiO, Co₃O₄, and Ternary Oxides in Fused Na₂SO₄ at 1200°K

Dilip K. Gupta* and Robert A. Rapp**

Department of Metallurgical Engineering, The Ohio State University, Columbus, Ohio 43210

ABSTRACT

The solubilities of the oxides NiO and Co₃O₄ in molten Na₂SO₄ have been established as a function of Na₂O activity at 1200°K. A reference electrode of Ag/Na₂SO₄-10 m/o Ag₂SO₄ in a mullite tube was used as a sodium activity probe for the Na₂SO₄ melt. A second reference electrode of Pt, O₂ (air)/zirconia (3.5 w/o CaO) served as an oxygen activity probe for Na₂SO₄. The combination of measurements of the sodium probe and oxygen probe in the melt provided the Na₂O activity in Na₂SO₄ directly, and eliminated the necessity for any bare metal electrode. Saturated melts were analyzed by atomic absorption spectroscopy for the dissolved metal contents. The observed dependences of the solubilities of NiO and Co₃O₄ in Na₂SO₄ on the activities of sodium oxide are in agreement with those predicted from the Na-Ni-S-O and Na-Co-S-O phase stability diagrams, respectively. Activity coefficients were calculated for the solute species. Preliminary measurements were made of the aluminum contents in Na₂SO₄ melts saturated with NiO and Co₃O₄ in an alumina crucible. The unusual dependences of aluminum content on salt basicity suggested the existence of the ternary oxides NiAl₂O₄ and CoAl₂O₄. While the preliminary aluminum measurements were not considered reliable, a theoretical model was developed to predict the expected solubility behavior for a ternary oxide in Na₂SO₄.

Nickel- and cobalt-base alloys and coatings with excellent resistance to oxidation at high temperatures have been developed. These materials are designed to develop tightly adherent and slow growing Cr₂O₃ or Al₂O₃ scales when exposed to high temperature gases. But the oxidation of such alloys and coatings is sometimes accelerated considerably when an electrolytic deposit (a thin layer of fused salt) covers the surface of the metal at high temperatures. Although a number of fused salt films are known to cause serious hot corrosion attack of metals, sodium sulfate has received the greatest attention, and the phenomenology of the attack has been explored extensively.

A knowledge of the solubilities of pertinent oxides in the corrosion products as a function of the chemical state of Na₂SO₄ should assist in understanding the occurrence and importance of the fluxing (dissolution) of the protective oxides formed during hot corrosion.

Stroud and Rapp (1) reported the solubilities of α -Al₂O₃ and Cr₂O₃ in Na₂SO₄ at 1200°K as a function of P_{O₂} and a_{Na₂O} (or P_{S₂O₃}). Probably because of some reaction of Na₂SO₄ with the Pt wire electrode, some aspects of the Stroud and Rapp work are inconsistent with thermodynamic expectation. First, the minimum in the α -Al₂O₃ solubility dependence upon a_{Na₂O} did

not occur near the center of the Al₂O₃ stability regime. Secondly, counter to expectation, the basic solubility of Cr₂O₃ as CrO₄²⁻ ions was found to be higher at P_{O₂} = 10⁻⁴ atm than for P_{O₂} = 1 atm. A renewed study of Cr₂O₃ and Al₂O₃ solubilities using improved technique is underway. Liang and Elliott (2, 3) have also reported a few values for the equilibrium solubilities of Cr₂O₃, Al₂O₃, and NiO in Na₂SO₄ at 1200°K.

In the present work, the solubilities of the oxides NiO and Co₃O₄ have been established for P_{O₂} equal to 1 atm as a function of a_{Na₂O} at 1200°K. These solubilities have been related to the respective phase stability diagrams for NiO in Fig. 1 and for Co₃O₄ in Fig. 2. These phase stability diagrams are analogous to Pourbaix diagrams of E vs pH for aqueous solutions. The redox potential is plotted against the negative of salt basicity (defined as log a_{Na₂O}). The thermodynamic data needed for establishing these Pourbaix diagrams at 1200°K are listed in Table I. Other authors (4-6) have previously presented similar diagrams. In Fig. 1 and 2 dashed lines have been provided to indicate constant activities (10⁻², 10⁻⁴, 10⁻⁶) for the acid and basic salts in equilibrium with the metal oxide and liquid Na₂SO₄. These diagrams could provide quantitative values for the solubilities of metal oxides in the fused salts if the identity and the activity coefficients of the solute ions in Na₂SO₄

* Electrochemical Society Student Member.

** Electrochemical Society Active Member.

Key words: oxide solubilities, fused salt, sodium sulfate, hot corrosion.

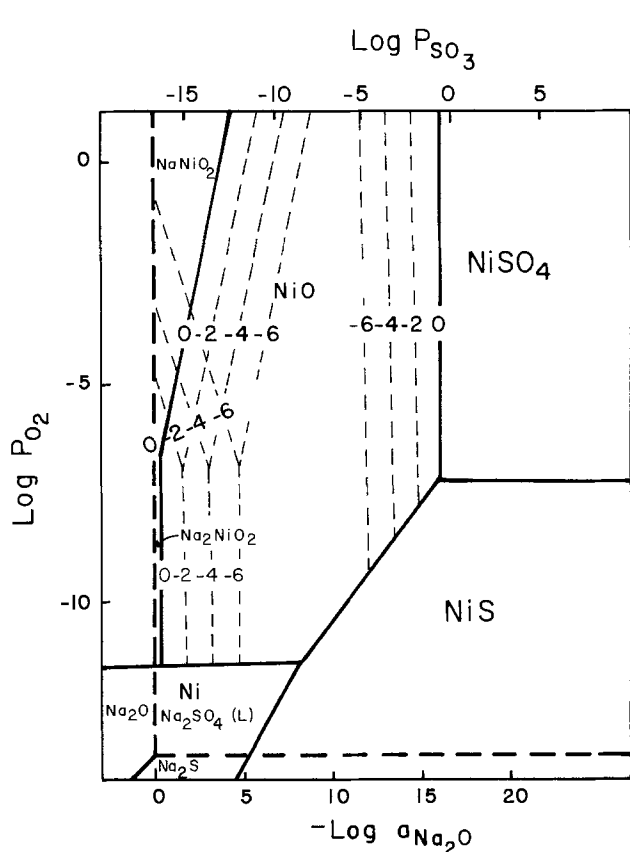


Fig. 1. Thermodynamic phase stability for Na-Ni-S-O system at 1200°K.

are known. Alternatively, if the solubility of the oxide in the fused salt is established experimentally as a function of $a_{\text{Na}_2\text{O}}$, both the identity and the activity coefficient of the solutes in dilute solutions can be obtained.

The reliability of the values thus obtained for the

(-) Au, O₂, SO₃, Na₂SO₄ | Mullite
Working electrode (WE) | (Na⁺)

activity coefficients depends on the accuracy of the Gibbs energy of formation data of the soluble metal salts, the metal oxides, Na₂SO₄, and the accuracy of the experimental results. Data are apparently not available for the Gibbs energy of formation of NaCoO₂. Hence the determination of the activity coefficient for the basic solute species of Co in sodium sulfate is not possible. However, for the sake of completeness of the Na-Co-S-O Pourbaix diagram, the Gibbs energy of formation of NaCoO₂ has been crudely estimated by assuming that the activity coefficient of NaCoO₂ in Na₂SO₄ is the same as that calculated for NaNiO₂ in Na₂SO₄ at 1200°K from this study.

Electrochemical Electrodes

Several studies (7-9) have demonstrated reversible electrochemical measurements of oxygen and SO₃ (or Na₂O) activities in liquid sulfates. Liang and Elliott (10) used a beta-Al₂O₃ electrolyte and a reversible W, WS₂, Na₂S reference electrode to determine the activity of sodium oxide (or P_{SO₃}) in sodium sulfate at 1200°K. The activity of sodium oxide in the Na₂SO₄ melt was fixed by an equilibrium with the prevailing pressures of SO₃, SO₂, and O₂. The limitation of this procedure is that the equilibration of the melt with P_{SO₃} of a gas phase limits the range of values of P_{SO₃} (or $a_{\text{Na}_2\text{O}}$) over which oxide solubilities can be studied.

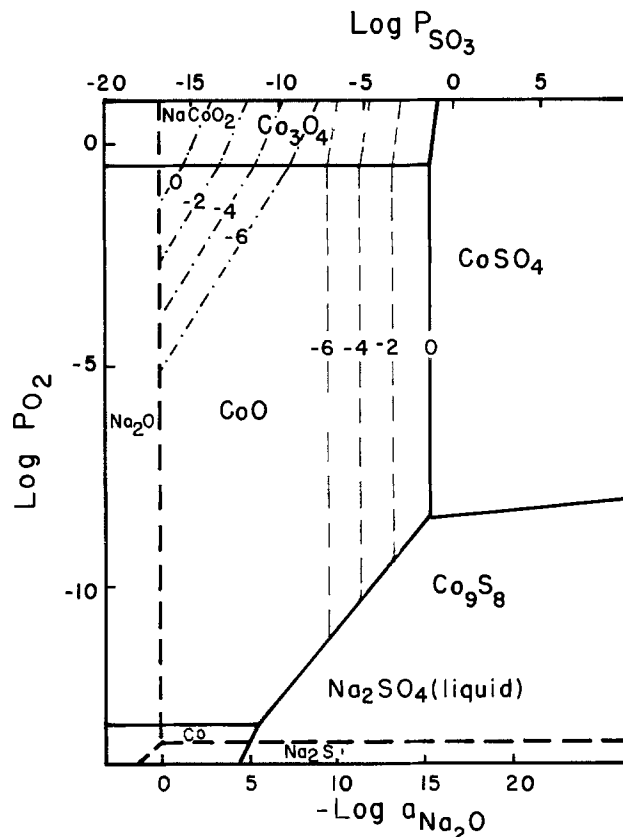


Fig. 2. Thermodynamic phase stability for Na-Co-S-O system at 1200°K.

Flood and Boye (11) utilized an SO₂, O₂ electrode to obtain thermodynamic information on the systems K₂SO₄-K₂S₂O₇-SO₃ and ZnO-ZnSO₄-SO₃. More recently, Stroud and Rapp (1) used a modification of this cell.

In the current study, the cell

Na₂SO₄-10 m/o Ag₂SO₃, Ag/Pt (+)
Reference electrode (RE) | [I]

was used to establish the activity of sodium oxide in the fused sodium sulfate melt at 1200°K. Because of its simplicity of construction and stability, many authors (12-17) have used the closed-end mullite (3Al₂O₃ · 2SiO₂) tube with the 90 Na₂SO₄/10 Ag₂SO₄ melt contacting an Ag wire as a reversible sodium ion

Table I. Pertinent thermodynamic data

Compound	ΔG°_f (1200°K) (kJ/mole)	Source
Ag ₂ SO ₄ (l)	-3.33×10^2	(27)
Al ₂ O ₃ (α)	-1.294×10^3	(23)
Al ₂ O ₃ (β)	-1.464×10^3	(25)
	-1.463×10^3	(24)
Al ₂ (SO ₄) ₃ (s)	-1.98×10^3	(23), (27)
CoO(s)	-1.496×10^2	(23)
Co ₃ O ₄ (s)	-4.509×10^2	(23)
Co ₂ O ₃ (s)	-4.5×10^2	(23)
Co ₉ S ₈ (l)	-5.26×10^2	(29)
NaAlO ₂ (s)	-8.65×10^2	(23)
NaCoO ₂ (s)	-2.913×10^2	This work
Na ₂ O(s)	-2.5×10^2	(23)
Na ₂ NiO ₂ (s)	-3.73×10^2	(22)
NaNiO ₂ (s)	-3.12×10^2	(22)
Na ₂ S(s)	-2.82×10^2	(23)
Na ₂ SO ₄ (l)	-8.93×10^2	(23)
NiO(s)	-1.32×10^3	(23)
NiS(l)	-59.92	(29)
NiSO ₄ (s)	-4.02×10^2	(27)
SO ₂ (g)	-2.737×10^2	(23)
SO ₃ (g)	-2.603×10^2	(23)
NiAl ₂ O ₄ (s)	-1.45×10^3	(26)
CoAl ₂ O ₄ (s)	-1.48×10^3	(26)

probe. A glassy grain boundary phase in the mullite provides exclusive sodium ion conduction.

As demonstrated by Watt, Andersen, and Rapp (12), among others, the voltage of cell [I] can be given as

$$E_I = E^{\circ}_I + \frac{2.3RT}{2F} \log \frac{a_{\text{Na}_2\text{O}}(\text{WE})}{P_{\text{O}_2}^{1/2}(\text{WE})} \quad [1]$$

where

$$E^{\circ}_I = E^{\circ}_{\text{I}} - \frac{2.3RT}{2F} \log \frac{a_{\text{Na}_2\text{SO}_4}(\text{RE})}{a_{\text{Ag}_2\text{SO}_4}(\text{RE})} \quad [2]$$

and

$$E^{\circ}_{\text{I}} = - \frac{1}{2F} \{ \Delta G^{\circ}_f(\text{Na}_2\text{SO}_4) - \Delta G^{\circ}_f(\text{Na}_2\text{O}) - \Delta G^{\circ}_f(\text{Ag}_2\text{SO}_4) \} \quad [3]$$

for the virtual cell reaction



To determine the value of E° , the ratio of the activity coefficients of Na_2SO_4 to Ag_2SO_4 in the 90 Na_2SO_4 :10 Ag_2SO_4 reference electrode was determined by Shores and John (18) at 900°C to equal 3.26. This corresponds to a value of 3.17 at 1200°K assuming regular solution behavior for the 90 Na_2SO_4 :10 Ag_2SO_4 melt. From the thermodynamic data in Table I and use of the ratio 3.17 for $\gamma_{\text{Na}_2\text{SO}_4}/\gamma_{\text{Ag}_2\text{SO}_4}$, the voltage of cell [I] at 1200°K is

$$E_I(\text{V}) = 1.454 + 0.119 \log \frac{a_{\text{Na}_2\text{O}}(\text{WE})}{P_{\text{O}_2}^{1/2}(\text{WE})} \quad [5]$$

The separate measurement of the oxygen activity in the Na_2SO_4 melt was established by the cell



where

$$E_{\text{II}} = \frac{RT}{4F} \ln \frac{P_{\text{O}_2}(\text{WE})}{0.21} \quad [6]$$

or

$$E_{\text{II}}(\text{V}) = 0.0403 + 0.0595 \log P_{\text{O}_2}(\text{atm})(\text{WE}) \quad [7]$$

Upon measuring the voltage between the individual reference electrodes of cells [I] and [II], equal to the algebraic sum of E_I and E_{II} , a voltage E_{III} is obtained which provides the measure of $a_{\text{Na}_2\text{O}}$ for the Na_2SO_4 melt without the influence of any corrosion reaction on the metallic wire contacting the melt

$$E_{\text{III}}(\text{V}) = 1.4943 + 0.119 \log a_{\text{Na}_2\text{O}}(\text{WE}) \quad [8]$$

Experimental Apparatus and Procedures

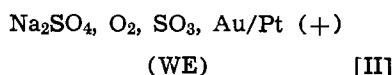
The experimental apparatus for the solubility studies is illustrated in Fig. 3. About 5-10g of reagent-grade oxide powders were charged with about 25g of reagent-grade sulfate powder (J. T. Baker Chemical Company) in an alumina crucible placed inside the external mullite tube. The mullite and zirconia electrodes were inserted into the melt through stainless steel adapters (Cajon) with o-rings epoxied into the water-cooled stainless steel flange.

The reference electrode of $\text{Ag}(\text{s})/\text{Na}_2\text{SO}_4$ -10 m/o Ag_2SO_4 was contained in a 1 cm OD mullite (MV30, McDanel) tube to serve as the sodium probe. A Pt-wire, spot-welded to the small piece of Ag wire served as the electronic lead wire for the sodium probe. The mullite tube was sealed at the top with a piece of Tygon tubing and a pinch clamp to minimize any drift caused by loss of SO_3 . However, some transport of Ag through the mullite tube occurred, as silver could be detected in the Na_2SO_4 in the crucible.

The 1 cm OD zirconia (3.5 w/o CaO) oxygen reference electrode was prepared by platinizing the in-

side bottom of the tube, and a stripe at 12 cm from the bottom. Two Pt-Pt/10% Rh thermocouples, each in alumina protection tubes, were placed inside the zirconia tube, such that one of the thermocouples touched the bottom while the other thermocouple touched the Pt stripe. The reference gas inside the zirconia tube was air. The zirconia tube was also platinized on its outside surface (contacting the chamber gas) at about 12 cm from the bottom. A Pt lead wire to this electrode served to measure the oxygen activity of the gas phase over the melt. A short gold electrode wire was immersed in the melt but was spot-welded to a Pt wire which served as the lead wire. Thus, no thermoelectric voltage contributions were introduced to cell readings. The temperature was controlled by a solid-state temperature controller (Barber-Colman) at $1200^\circ \pm 2^\circ\text{K}$.

All chemicals used were of reagent-grade quality without further purification. All gases were dried by passing them through silica gel. Gases were conducted to the surface of the melt through a quartz tube inserted through the stainless steel flange. Mixtures of SO_2 (Matheson) and O_2 (Liquid Carbonic) gases and Na_2O_2 additions were used to shift the melt basicity toward lower and higher activities of sodium oxide, respectively. Sodium peroxide was used rather than Na_2O because of the hygroscopic nature of Na_2O . The thermal decomposition of Na_2O_2 to Na_2O and O_2 was assumed to be rapid. The combination of the sodium and the oxygen probes enabled the monitoring of the $a_{\text{Na}_2\text{O}}$ of the melt at all times. Cell emf values showed a slight shift with time, presumably resulting from slight attack of the mullite, zirconia and alumina refractories. Such buffering behavior has been re-



ported elsewhere (3, 10).

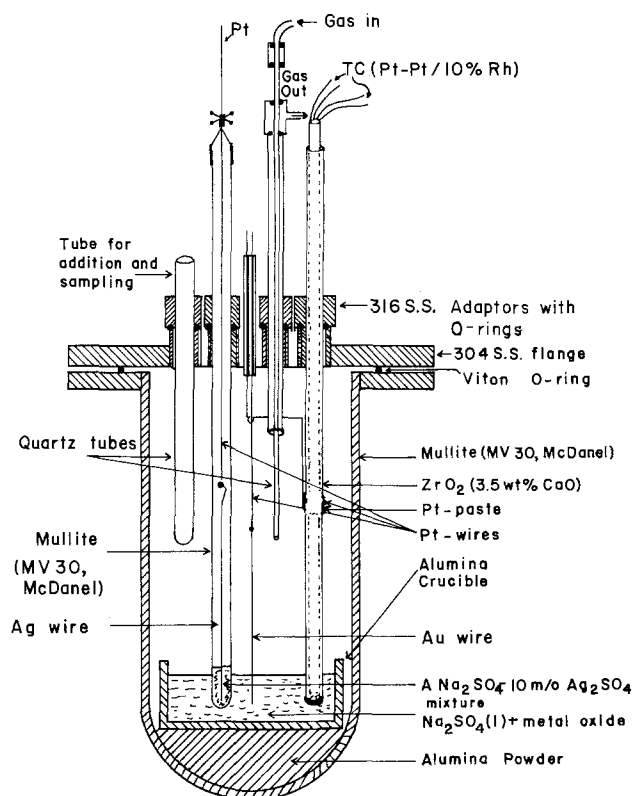


Fig. 3. Experimental setup for measuring the oxide solubility in fused sodium sulfate at 1200°K.

The $a_{\text{Na}_2\text{O}}$ values calculated from the emf readings of the sodium probe and oxygen probes using both the P_{O_2} above the melt and in the melt, respectively, became approximately equal after 2-3 days, which was inferred to indicate the equilibration of the melt with the gas phase.

The solubilities of the oxides NiO and Co_3O_4 in the molten Na_2SO_4 were determined after freezing saturated samples of the melt onto an alumina rod. The samples were weighed and dissolved in dilute acid (0.03N) having the same anions as that of their respective standard solutions for atomic absorption analysis. The amount of dissolved metal was determined in an atomic absorption spectrophotometer (Perkin Elmer; Series 360) using a graphite furnace. The amount of the dissolved compound was then calculated using known stoichiometries.

Results and Discussion

NiO solubility.—The experimental solubility data are shown in Fig. 4. Other values, reported by Liang and Elliott (3) for the solubility of NiO in Na_2SO_4 , after adjustment for the difference in their value for the Gibbs energy of formation of Na_2SO_4 to that in JANAF Tables (23), is also shown in this diagram.

After 24 hr from the attainment of the steady emf, the samples were taken at intervals of 12-24 hr. Under these conditions, no observable difference in the solubility as a function of time was noticed, implying that the measured solubilities are the saturation solubilities. In Fig. 4, the dependence of the acid solute concentration upon the basicity ($\log a_{\text{Na}_2\text{O}}$) agrees well with a line of slope 1 for the following reaction



and

$$\left\{ \frac{\partial(\log a_{\text{NiSO}_4})}{\partial(-\log a_{\text{Na}_2\text{O}})} \right\} = 1 \quad [10]$$

No dependence upon P_{O_2} for the acidic dissolution of NiO as Ni^{2+} is expected because the nickel valence is not changed upon dissolution (vertical line on Fig. 1). Excellent agreement with Liang and Elliott (3) is found for the solubility of NiO at $\log a_{\text{Na}_2\text{O}} = -11.79$

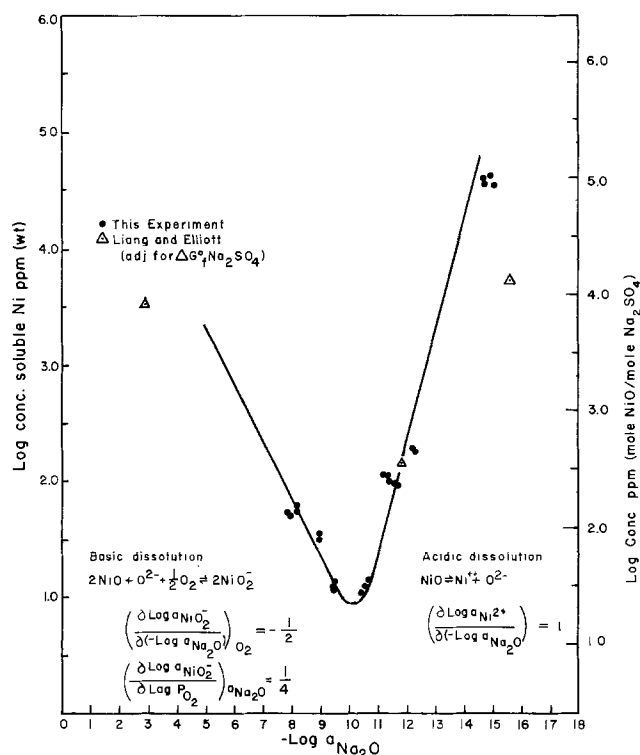
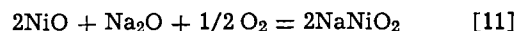


Fig. 4. Solubility of NiO in fused Na_2SO_4 at 1200°K

(corresponding to -12.69 of their study) of about 150 wt ppm. However, the solubility determined here for a very acid condition is about an order of magnitude higher than that reported by Liang and Elliott (3). The high solubility for NiO in acidic conditions is consistent with the observation of Wortman *et al.* (20), who have reported deposits of yellow NiSO_4 on blades from engines suffering hot corrosion at considerably lower temperatures.

For the basic dissolution of NiO in Na_2SO_4 , the measured solubility data of Fig. 4 agree well with the following reaction



where

$$\left\{ \frac{\partial(\log a_{\text{NaNiO}_2})}{\partial(-\log a_{\text{Na}_2\text{O}})} \right\}_{\text{O}_2} = -\frac{1}{2} \quad [12]$$

and

$$\left\{ \frac{\partial(\log a_{\text{NaNiO}_2})}{\partial(\log P_{\text{O}_2})} \right\}_{a_{\text{Na}_2\text{O}}} = \frac{1}{4} \quad [13]$$

Thus, in basic sodium sulfate melts at 1 atm oxygen, nickel oxide dissolves as nickelate ions, NiO_2^- , with trivalent nickel. Indeed, the correlation of Eq. [12] to Eq. [11] would also be valid for a multiple of NiO_2^- , such as $\text{Ni}_2\text{O}_4^{2-}$. Since the basic nickelate species has a valence (+3) different from that in its oxide (+2), an oxygen pressure dependence of Eq. [13] for NaNiO_2 solubility is expected. The data in Fig. 4 were corrected slightly from the measured P_{O_2} in the melt to 1 atm P_{O_2} , according to the theoretical oxygen dependence of Eq. [13]. Liang and Elliott (3) have reported the basic solubility of NiO as NaNiO_2 of 0.4 w/o at $\log a_{\text{Na}_2\text{O}} = -2.67$ (corresponding to -3.57 of their study). In the present experimental setup attainment of such high basicity was practically limited because of attack on the ceramics and metals by the highly reactive oxide ions.

The presence of NaNiO_2 in the quenched basic salt samples was confirmed by x-ray analysis. Goebel and Pettit (21) consider that the oxide ions in sodium sulfate react with NiO in forming a basic solute species to account for the accelerated hot corrosion of pure NiO in Na_2SO_4 in an oxygen environment.

The thermodynamic phase stability diagram for the Na-Ni-S-O system in Fig. 1 indicates NiO stability for 1 atm of P_{O_2} for $3.7 < -\log a_{\text{Na}_2\text{O}} < 16.2$. The Gibbs energy of formation for NiSO_4 was taken from the tabulation by Kellogg (27); an uncertainty of ± 2 kJ/mole is indicated. The Gibbs energy of formation of NaNiO_2 reported by Shaiu, Wu, and Chiotti (22) was used to establish the NiO/ NaNiO_2 boundary of Fig. 1; this value for $\Delta G^\circ_{\text{NaNiO}_2}$ is uncertain by ± 13 kJ/mole. The authors suggested that this value was not very reliable.

According to a Raoult's law choice of standard state, the activities of the condensed phases NaNiO_2 and NiSO_4 in equilibrium with molten Na_2SO_4 are considered to be unity at the NiO stability boundaries at $-\log a_{\text{Na}_2\text{O}}$ equal to 3.7 and 16.2, respectively.

The activity coefficients of the soluble NiSO_4 and NaNiO_2 species were calculated with respect to pure solid NiSO_4 and NaNiO_2 as the standard states

$$\{\gamma_{\text{NiSO}_4 \text{Na}_2\text{SO}_4}\}_{\text{dil. soln}} = \frac{a_{\text{NiSO}_4}}{N_{\text{NiSO}_4}}$$

$$\{\gamma_{\text{NaNiO}_2 \text{Na}_2\text{SO}_4}\}_{\text{dil. soln}} = \frac{a_{\text{NaNiO}_2}}{N_{\text{NaNiO}_2}} \quad [14]$$

The activity coefficient $\gamma_{\text{NiSO}_4 \text{Na}_2\text{SO}_4}$ was calculated to equal 0.12. But because of the uncertainty in the value for $\Delta G^\circ_{\text{NiSO}_4}$, the true value may lie between 0.09 and 0.20. The activity coefficient for NaNiO_2 in Na_2SO_4 , $\gamma_{\text{NaNiO}_2 \text{Na}_2\text{SO}_4}$, was calculated to equal 50. Again, because of uncertainties in the value for $\Delta G^\circ_{\text{NaNiO}_2}$, the true value may lie between 10 and 300.

The results in Fig. 4 show a minimum in the NiO solubility at $-\log a_{\text{Na}_2\text{O}} = 10.3$, which is consistent with that expected from the phase stability diagram for the Na-Ni-S-O system. The solubility minimum is expected to lie somewhere near the middle of the NiO stability range ($3.7 < -\log a_{\text{Na}_2\text{O}} < 16.2$), as decided by the actual values of Raoultian activity coefficients for the solutes.

Co₃O₄ solubility.—Experimental values for the solubility of the cobalt oxide Co₃O₄ in fused Na₂SO₄ at 1 atm O₂ are plotted in Fig. 5. Similar to nickel oxide, the saturated samples of Co₃O₄ dissolved in Na₂SO₄ were quenched for quantitative determination by atomic absorption spectrophotometry. No change in the solubility was observed after about 20 hr from the attainment of steady emf's for the melt probes.

Lines were drawn according to the theoretically predicted slope of 1 for acid dissolution according to the following equation



where

$$\left\{ \frac{\partial (\log a_{\text{CoSO}_4})}{\partial (-\log a_{\text{Na}_2\text{O}})} \right\}_{\text{O}_2} = 1 \quad [16]$$

and

$$\left\{ \frac{\partial (\log a_{\text{CoSO}_4})}{\partial (\log P_{\text{O}_2})} \right\}_{a_{\text{Na}_2\text{O}}} = -\frac{1}{6} \quad [17]$$

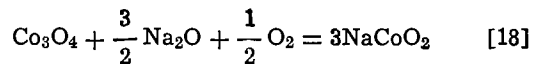
Because of the oxygen dependence of the solubility of Co₃O₄, the data points were corrected from the P_{O₂} values indicated by the zirconia probe in the melt to a common P_{O₂} of 1 atm. The corrected data of Fig. 5 agree with the expected dependence of acid solute concentration upon a_{Na₂O} according to Eq. [16].

The thermodynamic phase stability diagram for the Na-Co-S-O system at 1200°K was shown in Fig. 2. The line for unit activity of CoSO₄ at P_{O₂} = 1 atm, assuming pure liquid CoSO₄ as the standard state, lies at the value of $-\log a_{\text{Na}_2\text{O}} = 15.2$.

The Raoultian activity coefficient $\gamma_{\text{CoSO}_4}^{\text{Na}_2\text{SO}_4}$ was calculated by the same method just explained for NiO measurements. The calculated activity coeffi-

cient $\gamma_{\text{CoSO}_4}^{\text{Na}_2\text{SO}_4}$ equals 2.5. No previous data have been reported in the literature for comparison. From the uncertainty in $\Delta G^\circ_{\text{CoSO}_4}$, the true activity coefficient could have values between 1 and 5.

For the basic dissolution of Co₃O₄ in Na₂SO₄, the P_{O₂}-corrected data fitted well to a line of slope $-\frac{1}{2}$, according to reaction [18]



and

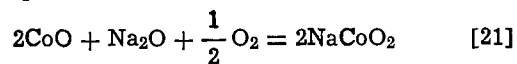
$$\left\{ \frac{\partial (\log a_{\text{NaCoO}_2})}{\partial (-\log a_{\text{Na}_2\text{O}})} \right\}_{\text{O}_2} = -\frac{1}{2} \quad [19]$$

also

$$\left\{ \frac{\partial (\log a_{\text{NaCoO}_2})}{\partial (\log P_{\text{O}_2})} \right\}_{a_{\text{Na}_2\text{O}}} = \frac{1}{6} \quad [20]$$

This implies that Co₃O₄ dissolves in Na₂SO₄ as a CoO₂⁻ solute species (or a multiple such as Co₂O₄²⁻) in a basic environment ($-\log a_{\text{Na}_2\text{O}} < 9.2$). There is no datum reported in the literature for $\Delta G^\circ_{\text{NaCoO}_2}$. Here, for the sake of completeness of the Na-Co-S-O phases stability diagram, a value for $\Delta G^\circ_{\text{NaCoO}_2}$ was estimated upon making the tenuous assumption that the activity coefficient $\gamma_{\text{NaCoO}_2}^{\text{Na}_2\text{SO}_4}$ equals 50, the same as $\gamma_{\text{NiO}}^{\text{Na}_2\text{SO}_4}$. Both cobalt and nickel dissolve as MO₂⁻ species for basic Na₂SO₄ melts, where M has the +3 valence state. The calculated boundary between Co₃O₄ and NaCoO₂ thus lies at about $-\log a_{\text{Na}_2\text{O}} = 1.3$. The calculated value for the Gibbs energy of formation for NaCoO₂ at 1200°K is $-291.3 \text{ kJ/mole} \pm 19 \text{ kJ}$. The measured Co₃O₄ solubility data exhibit a minimum at a value for $-\log a_{\text{Na}_2\text{O}} = 9.2$, which is consistent with that expected from the stability diagram.

The solubility of the higher oxide Co₃O₄ was determined in this study. However, the construction lines for constant solute activity of Fig. 2 point out the continuity in solute activity as cobaltous oxide CoO becomes stable at lower P_{O₂}. Thus the solubility curve for CoO at any lower P_{O₂} can be calculated upon using the same activity coefficients established in this study. Obviously, the acid solubility of CoO as CoSO₄ for a given value of log a_{Na₂O} will be slightly higher than that for Co₃O₄ at 1 atm. This acid solubility for CoO should not depend upon P_{O₂}. The basic solubility of CoO as NaCoO₂ for a given value of log a_{Na₂O} is significantly lower than that for Co₃O₄. According to the solubility equilibrium



$$\left\{ \frac{\partial (\log a_{\text{NaCoO}_2})}{\partial (-\log a_{\text{Na}_2\text{O}})} \right\}_{\text{O}_2} = -\frac{1}{2} \quad [22]$$

and

$$\left\{ \frac{\partial (\log a_{\text{NaCoO}_2})}{\partial (\log P_{\text{O}_2})} \right\}_{a_{\text{Na}_2\text{O}}} = \frac{1}{4} \quad [23]$$

The specific dependences of oxide solubility on a_{Na₂O} and P_{O₂} in the salt are important in testing certain proposed scale fluxing mechanisms and criteria for the hot corrosion of metals. For example, Rapp and Goto (28) have proposed that the existence of a negative solubility gradient for an oxide in the salt film would support a continuing scale dissolution and reprecipitation mechanism in hot corrosion.

Spinel solubility.—The same salt solutions saturated with NiO and Co₃O₄ were also analyzed by atomic absorption for soluble aluminum in Na₂SO₄ at 1200°K. The resulting data for an "apparent" solubility as a function of a_{Na₂O} are shown in Fig. 6. No solid alumina powder was charged into the Na₂SO₄ melts. Only the alumina crucible and the mullite tube (MV30, McDanel) were considered to be the sources

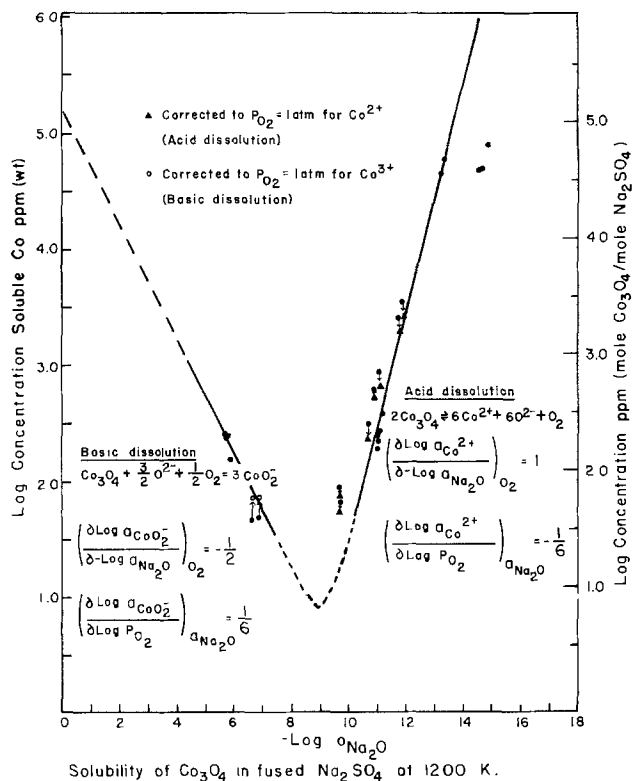


Fig. 5. Solubility of Co₃O₄ in fused Na₂SO₄ at 1200°K

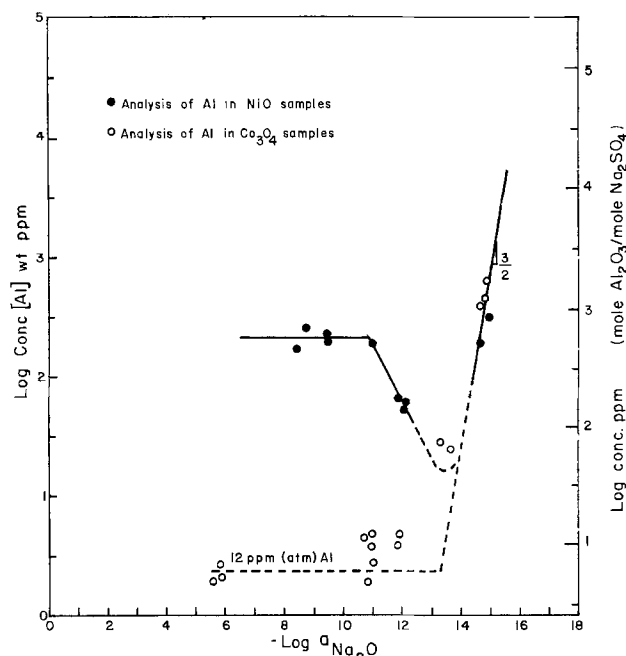


Fig. 6. Analysis for Al content in the quenched samples of NiO and Co_3O_4 .

of alumina. Gibbs energy data in Table I predict that over a large range of $a_{\text{Na}_2\text{O}}$, alumina should react to form spinels, NiAl_2O_4 or CoAl_2O_4 , in the presence of excess NiO and Co_3O_4 , except for very acid ($-\log a_{\text{Na}_2\text{O}} > 15.2$) conditions where these oxides (NiO and Co_3O_4) dissolve as their respective sulfates. The thermodynamic stability of NiAl_2O_4 is indicated on superimposed Na-Ni-S-O with Na-Al-S-O diagrams in Fig. 7, and CoAl_2O_4 stability is shown on the Na-Co-S-O and Na-Al-S-O systems in Fig. 8. The

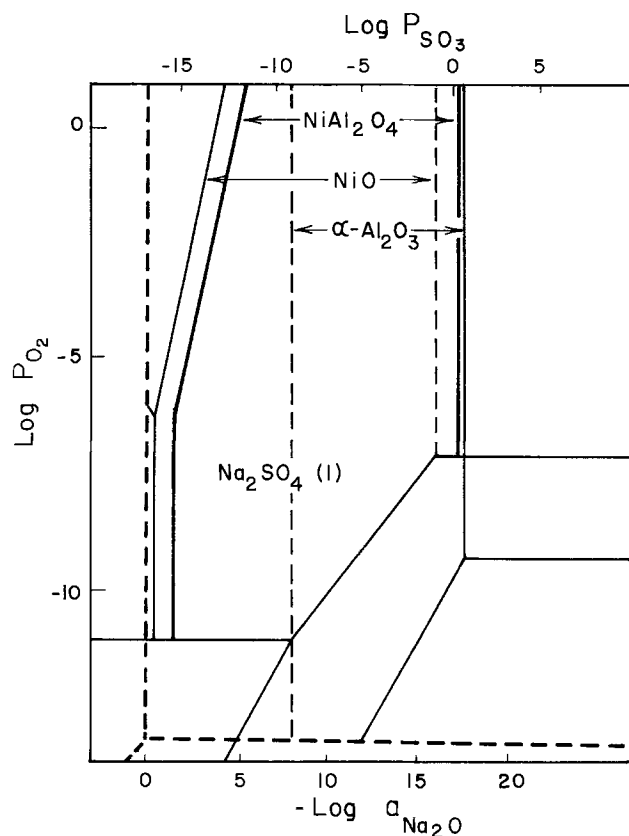
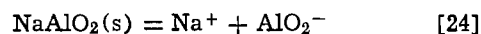


Fig. 7. Superimposed phase stability plots for the Na-Ni-S-O and Na-Al-S-O systems at 1200°K . The limits of stability for the phases NiAl_2O_4 , NiO, and $\alpha\text{-Al}_2\text{O}_3$ have been indicated.

NiAl_2O_4 stability extends from $4.7 < -\log a_{\text{Na}_2\text{O}} < 17.1$, and for CoAl_2O_4 , the boundary extends from $2.8 < -\log a_{\text{Na}_2\text{O}} < 16.8$. Unlike the dissolution of binary oxides in Na_2SO_4 at 1200°K , the solubility of a ternary oxide as a function of $a_{\text{Na}_2\text{O}}$ would be expected to exhibit a sequence of different regimes, depending on the predominant solute species present and the particular condensed phases which are stable and present. The following analysis is a novel treatment for the expected solubility for a ternary oxide:

Region I.—In a region of very basic melt, the stable condensed phase for aluminum is NaAlO_2 , and for metal M (M will be used for Ni or Co hereafter) is NaMO_2 . The solubilities of these condensed phases as AlO_2^- and MO_2^- solute species should not depend upon $\log a_{\text{Na}_2\text{O}}$ or P_{O_2} . Therefore, the dilute solution of the condensed phases NaAlO_2 and NaMO_2 in Na_2SO_4 should show no dependence of soluble Al on the Na_2O activity according to following reactions



where

$$\left\{ \frac{\partial (\log a_{\text{NaAlO}_2})}{\partial (-\log a_{\text{Na}_2\text{O}})} \right\}_{\text{O}_2} = 0 \quad [25]$$

Region II.—In a somewhat less basic melt, the binary oxide of metal M, MO (rather than NaMO_2), is the stable condensed phase, and is present in excess in Na_2SO_4 along with the stable NaAlO_2 phase. Again, the dissolution of Al as an AlO_2^- species (or multiple thereof) should exhibit no dependence of soluble Al concentration on $a_{\text{Na}_2\text{O}}$ because the preceding Eq. [24] and [25] would again apply.

Region III.—In this region of basic melt, both the spinel MAl_2O_4 and M-oxide are stable and present as condensed phases. The basic solute species AlO_2^- and MO_2^- are stable. The dissolution of MAl_2O_4 as AlO_2^- ions and MO_2^- is described by Eq. [26], and the basicity ($\log a_{\text{Na}_2\text{O}}$) dependence of soluble aluminum

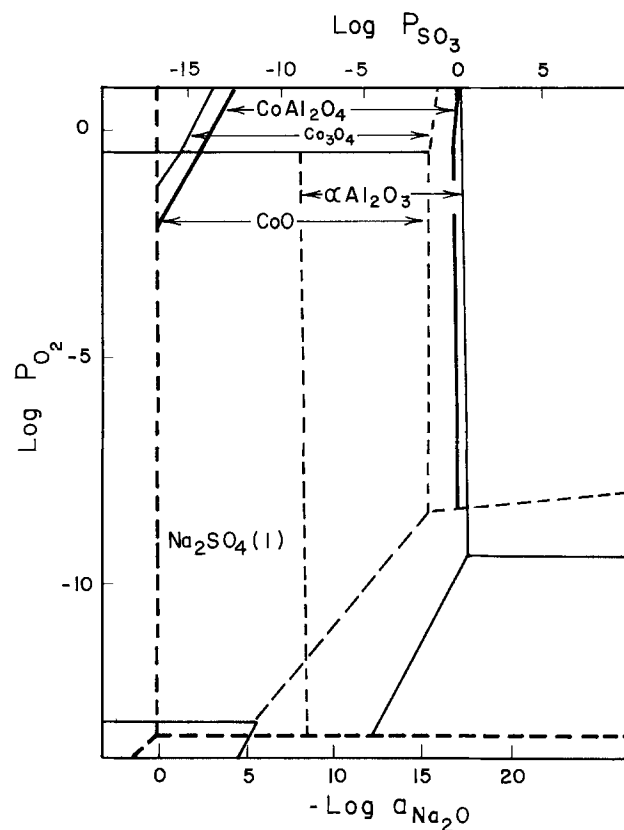
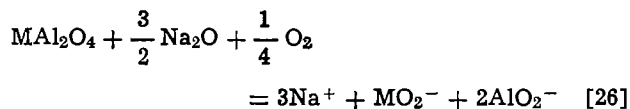


Fig. 8. Superimposed phase stability plots for the Na-Co-S-O and Na-Al-S-O systems at 1200°K . The limits of stability for the phases CoAl_2O_4 , Co_3O_4 , CoO, and $\alpha\text{-Al}_2\text{O}_3$ have been indicated.

concentration by Eq. [27]



and

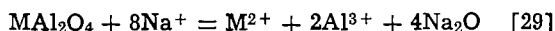
$$\left\{ \frac{\partial(\log [\text{Al}]_{\text{sol.}})}{\partial(-\log a_{\text{Na}_2\text{O}})} \right\}_{\text{O}_2} = \left\{ \frac{\partial(\log a_{\text{NaAlO}_2})}{\partial(-\log a_{\text{Na}_2\text{O}})} \right\}_{\text{O}_2} = -\frac{1}{2} \quad [27]$$

Region IV.—In this regime, the MAlO_2 spinel and MO are stable and present as the condensed phases and the soluble species are AlO_2^- and M^{2+} . Note that nickel oxide and cobalt oxide should dissolve as acid species (M^{2+} ions) at a basicity where aluminum dissolves as a basic species (AlO_2^- ions)



There is no expected dependence of soluble aluminum upon $a_{\text{Na}_2\text{O}}$.

Region V.—In this acid regime, MAlO_2 spinel and excess MO are stable and present as condensed phases, and Al^{3+} and M^{2+} are the soluble acidic species



Here, the dissolution of MAl_2O_4 as $\text{Al}_2(\text{SO}_4)_3$ depends also upon the dissolution behavior of NiO . Upon differentiation of the logarithm of the equilibrium constant for Eq. [29]

$$\left\{ \frac{\partial(\log [\text{Al}^{3+}]_{\text{sol.}})}{\partial(-\log a_{\text{Na}_2\text{O}})} \right\} = 2 - \frac{1}{2} \left\{ \frac{\partial(\log [\text{M}^{2+}]_{\text{sol.}})}{\partial(-\log a_{\text{Na}_2\text{O}})} \right\} \quad [30]$$

But according to the previous Eq. [9] and [10], the latter derivative equals unity, so that

$$\left\{ \frac{\partial(\log [\text{Al}^{3+}]_{\text{sol.}})}{\partial(-\log a_{\text{Na}_2\text{O}})} \right\}_{\text{O}_2} = \frac{1}{2} \left\{ \frac{\partial(\log a_{\text{Al}_2(\text{SO}_4)_3})}{\partial(-\log a_{\text{Na}_2\text{O}})} \right\}_{\text{O}_2} = \frac{3}{2} \quad [31]$$

Region VI.—In this very acid regime, the MAlO_2 spinel is stable and present as a condensed phase, but NiO or Co_3O_4 are no longer present at unit activity, because NiSO_4 or CoSO_4 are stable. Then the solubility of the Al^{3+} species is independent of the dissolution of NiO and Co_3O_4 as NiSO_4 and CoSO_4 , respectively. The MAl_2O_4 dissolution is again described by reaction [29], but the dependence of soluble Al concentration upon $a_{\text{Na}_2\text{O}}$ is given by the following equation

$$\left\{ \frac{\partial(\log [\text{Al}^{3+}]_{\text{sol.}})}{\partial(-\log a_{\text{Na}_2\text{O}})} \right\}_{\text{O}_2} = \frac{1}{2} \left\{ \frac{\partial(\log a_{\text{Al}_2(\text{SO}_4)_3})}{\partial(-\log a_{\text{Na}_2\text{O}})} \right\}_{\text{O}_2} = 2 \quad [32]$$

Region VII.—In this extremely acid regime, the spinels are not stable but alumina is the stable condensed phase. Alumina dissolves as the acid species Al^{3+} in a melt consisting of Na_2SO_4 and MSO_4



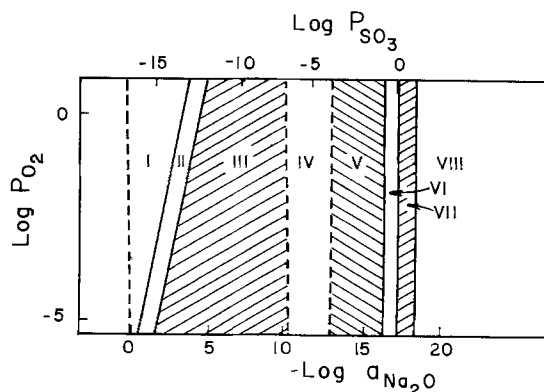
The dependence of the acid ion solubility on $a_{\text{Na}_2\text{O}}$ is given by

$$\left\{ \frac{\partial(\log [\text{Al}^{3+}]_{\text{sol.}})}{\partial(-\log a_{\text{Na}_2\text{O}})} \right\}_{\text{O}_2} = \frac{1}{2} \left\{ \frac{\partial(\log a_{\text{Al}_2(\text{SO}_4)_3})}{\partial(-\log a_{\text{Na}_2\text{O}})} \right\}_{\text{O}_2} = \frac{3}{2} \quad [34]$$

Region VIII.—In this most acid regime, the stable condensed phases are the sulfates of Al and Ni or Co. In this regime of total liquid miscibility, no dependence of soluble aluminum concentration on the $a_{\text{Na}_2\text{O}}$ would occur.

These different regimes are summarized for the Ni-Al-Na-S-O system in Fig. 9. The comparable boundaries for NiAl_2O_4 and CoAl_2O_4 differ only by about one order of magnitude (CoAl_2O_4 extending towards the more basic side). Obviously, a similar plot can be offered for the Co-Al-Na-S-O system. The theoretically predicted basicity dependences for the aluminum solute species are summarized in Fig. 10.

Because of practical experimental limitations (attack of the emf probes), the solubility measurements in very acid (right of region V) or very basic (left of



Condensed Phases	Solute Species
I NaNiO ₂ , NaAlO ₂	NiO ₂ ⁻ , AlO ₂ ⁻
II NiO, NaAlO ₂	NiO ₂ ⁻ , AlO ₂ ⁻
III NiO, NiAl ₂ O ₄	NiO ₂ ⁻ , AlO ₂ ⁻
IV NiO, NiAl ₂ O ₄	Ni ²⁺ , AlO ₂ ⁻
V NiO, NiAl ₂ O ₄	Ni ²⁺ , Al ³⁺
VI NiSO ₄ , NiA ₂ O ₄	Ni ²⁺ , Al ³⁺
VII NiSO ₄ , Al ₂ O ₃	Ni ²⁺ , Al ³⁺
VIII NiSO ₄ , Al ₂ (SO ₄) ₃	Ni ²⁺ , Al ³⁺

Fig. 9. A mapping of differing solubility regimes for the Ni-Al-Na-S-O system at 1200°K.

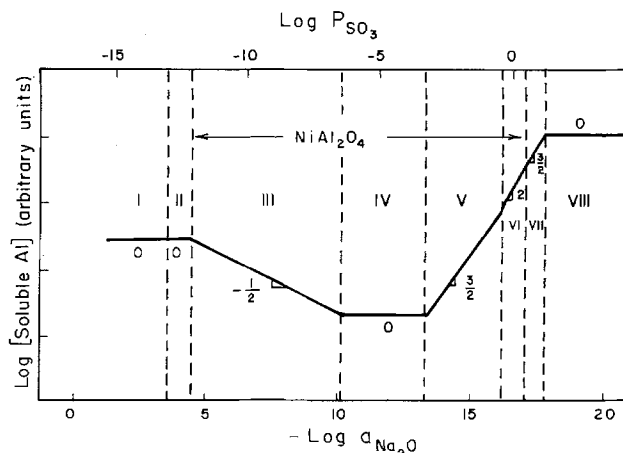


Fig. 10. Theoretical basicity dependences for the Al solute species in the Ni-Al-Na-S-O system at 1200°K.

region III) melts may not be possible. The steep rise in the experimentally measured aluminum contents in acid melts of Fig. 6 is not inconsistent with the slope of 3/2 expected for the regime V, but only little displacement is apparent in the data from the Co- and Ni-containing solutions. The existence of the broad plateau (Al solute concentration independent of $a_{\text{Na}_2\text{O}}$) in the Co_3O_4 -saturated solutions of Fig. 6 seems to correlate with behavior expected for regime IV, except that the plateau extends too far in the basic direction. The data from NiO-saturated melts of Fig. 6 seem to lack the expected plateau for regime IV, and the existing plateau for $-\log a_{\text{Na}_2\text{O}} < 11$ occurs in a melt insufficiently basic to correspond to regime II. Further, the difference by two orders of magnitude in the plateaus of Fig. 6 for the NiO- and the Co_3O_4 -saturated solutions is also not explainable. Then in general, the data of Fig. 6 do not fit the expected pattern of Fig. 10 for the solubility of aluminum in a system where ternary oxides are stable. But on the other hand, the observed pattern is also not consistent with that expected for a simple Al_2O_3 solubility, which should resemble Fig. 4 and 5 (but with different slopes) if only one acid and one basic species of aluminum were formed.

These seeming inconsistencies are explained by realizing that the experiments from which aluminum was analyzed were not designed or optimized to establish the spinel solubilities. Powdered Al_2O_3 or MAl_2O_4 were not available to the melt, and care was not taken to insure that equilibrium was reached with respect to saturation by the aluminum solute species. Then the data of Fig. 6 should not be considered as reliable equilibrium data, but rather they only suggest that inherently different results should be expected when a ternary oxide is present. The theory summarized in Fig. 9 and 10 is offered for comparison with future experiments which can be designed to establish the solubilities of ternary oxides.

Obviously, the theory should directly predict the solubilities of other ternary oxides in other oxyanion melts (nitrates, carbonates, borates, vanadates, silicates, etc.) The several assumptions made in this theory should be explained so that the theory can be extended or amended for other systems. The solute species for Ni, Co, and Al are assumed to be the same as those for the respective binary oxides. Thus, this treatment assumes that there are no Ni-Al-O or Co-Al-O soluble complex ions, e.g., NiAlO_4^{2-} or NiAlO_2^+ . Clearly, interactive soluble species may be possible in some systems. In principle, complex ionic species could be identified by the basicity and oxygen activity dependences of the solubilities.

Summary and Conclusions

The solubilities of NiO and Co_3O_4 in Na_2SO_4 in 1 atm O_2 at 1200°K, have been experimentally determined as a function of salt basicity ($\log a_{\text{Na}_2\text{O}}$).

Nickel oxide, which dissolves as nickel sulfate in acidic salts and as sodium nickelate (NiO_2^-) in basic salts, shows a well-defined minimum in solubility at $-\log a_{\text{Na}_2\text{O}} = 10.3$. The identification of these species is inferred upon comparing the dependence of NiO solubility upon the basicity ($\log a_{\text{Na}_2\text{O}}$) of Na_2SO_4 melts with models derived from the thermodynamic stability plot. The activity coefficients for nickel sulfate and sodium nickelate dilute solutions were established as 0.12 and 50, respectively, but a large uncertainty is inherent in the calculations.

The solubility of cobalt oxide, Co_3O_4 , is very similar in behavior to that of nickel oxide. Cobalt oxide is a slightly more basic oxide, and shows a minimum in the solubility plot at $-\log a_{\text{Na}_2\text{O}} = 9.2$. The Co_3O_4 dissolves as CoSO_4 (Co^{2+}) in acid dissolution and, as NaCoO_2 (CoO_2^-) in basic dissolution in Na_2SO_4 at 1200°K. The activity coefficient of 2.5 was established for a dilute solution of CoSO_4 in Na_2SO_4 .

The knowledge of the solubilities of NiO and Co_3O_4 should assist in understanding the occurrence of fluxing of protective oxides encountered during the hot corrosion of metals.

The Na_2SO_4 melts saturated with NiO and Co_3O_4 were also analyzed for soluble aluminum content, although the studies were not designed to establish the alumina or spinel solubility. The resulting data for soluble aluminum concentrations deviated from that expected for a simple binary oxide, and an influence of NiAl_2O_4 or CoAl_2O_4 formation was suspected. A novel theory was developed to interpret (predict) the solubility of a ternary oxide in Na_2SO_4 . The correlation of the theory to the measurement of soluble aluminum was not satisfactory, but an improved experiment would be expected to yield better results.

Acknowledgment

This research was supported by the National Science Foundation (Grant No. DMR75-17204 A 01). Helpful discussions with R. C. John are acknowledged.

Manuscript submitted Jan. 21, 1980; revised manuscript received April 11, 1980.

Any discussion of this paper will appear in a Discussion Section to be published in the June 1981 JOURNAL. All discussions for the June 1981 Discussion Section should be submitted by Feb. 1, 1981.

Publication costs of this article were assisted by The Ohio State University.

REFERENCES

1. W. P. Stroud and R. A. Rapp, in "High Temperature Metal-Halide Chemistry," D. L. Hildenbrand and D. D. Cubicciotti, Editors, p. 547, The Electrochemical Society Softbound Proceedings Series, Princeton, N.J. (1978).
2. W. W. Liang and J. F. Elliott, in "Properties of High Temperature Alloys," Z. A. Foroulis and F. S. Pettit, Editors, p. 557, The Electrochemical Society Softbound Proceedings Series, Princeton, N.J. (1976).
3. W. W. Liang and J. F. Elliott, MIT, Private communication.
4. G. J. Janz, A. Conte, and E. Neuenschwander, *Corrosion*, **8**, 292 (1963).
5. A. Rahmel, *Electrochim. Acta.*, **13**, 495 (1968).
6. J. S. Goebel and F. S. Pettit, *Metall. Trans.*, **7A**, 1943 (1970).
7. E. Erdoes and H. Altrofer, *Electrochim. Acta.*, **20**, 937 (1975).
8. C. H. Liu, *J. Phys. Chem.*, **66**, 164 (1962).
9. G. Danner and M. Rey, *Electrochim. Acta.*, **4**, 274 (1961).
10. W. W. Liang and J. F. Elliott, *This Journal*, **123**, 617 (1976).
11. H. Flood and N. Boye, *J. Electrochem.*, **66**, 184 (1962).
12. G. W. Watt, R. E. Andresen, and R. A. Rapp, Paper 343 presented at The Electrochemical Society Meeting, Pittsburgh, Pennsylvania, Oct. 15-20, 1978.
13. R. W. Laity, in "Reference Electrodes," C. J. Janz and D. J. G. Ives, Editors, p. 524, Academic Press, New York (1961).
14. B. W. Burrows and G. J. Hills, *Electrochim. Acta.*, **15**, 445 (1970).
15. C. A. C. Sequeira and M. G. Hocking, *J. Appl. Electrochem.*, **8**, 145 (1978).
16. D. A. Shores, *Corrosion*, **31**, 438 (1975).
17. A. Rahmel, *Electrochim. Acta.*, **15**, 1267 (1970).
18. D. A. Shores and R. C. John, *J. Appl. Electrochem.*, In print.
19. R. C. John and R. A. Rapp, Ohio State University, Unpublished Research.
20. D. J. Wortman, R. E. Fryxell, and I. I. Bessen, 3rd Conference on Gas Turbine Materials in a Marine Environment, U. of Bath (1976).
21. J. A. Goebel, F. S. Pettit, and G. W. Goward, *Metal. Trans.*, **4**, 261 (1973).
22. B. J. Shau, P. C. S. Wu, and P. Chiotti, *J. Nucl. Mater.*, **67**, 13 (1977).
23. JANAF Thermochemical Tables, 2nd. Ed., NBS **37**,

- U.S. Dept. of Commerce (1971).
24. J. T. Drummer, *Prog. Solid State Chem.*, **7**, 141 (1972).
25. N. S. Choudhury, *This Journal*, **120**, 1663 (1973).
26. J. D. Tretjakow and H. Schmalzried, *Ber. Bunsenges. Phys. Chem.*, **69**, 396 (1965).
27. H. H. Kellogg, *Trans. Metall. Soc. AIME*, **230**, 1663 (1973).
28. R. A. Rapp and K. Goto, Paper 350 presented at The Electrochemical Society Meeting, Pittsburgh, Pennsylvania, Oct. 15-20, 1978.
29. O. Kubaschewski, E. L. L. Evans, and C. B. Alcock, "Metallurgical Thermochemistry," 4th Ed., Pergamon Press, New York (1974).

Mechanism of Na_2SO_4 Induced Corrosion at $600^\circ\text{-}900^\circ\text{C}$

K. L. Luthra* and D. A. Shores*

General Electric Company, Corporate Research and Development, Schenectady, New York 12301

ABSTRACT

The kinetics of Na_2SO_4 -induced corrosion were measured by accelerated oxidation tests on Co-30Cr and Ni-30Cr as a function of temperature from $600^\circ\text{-}900^\circ\text{C}$, SO_3 in the environment and deposit composition. The alloys were rapidly attacked at temperatures between 650° and 750°C when a liquid sulfate phase was obtained from an initially pure solid Na_2SO_4 deposit. The rapid rate of attack resulted from sulfation of the transient surface nickel or cobalt oxides and the dissolution of these transition metal sulfates into Na_2SO_4 to yield a liquid phase. This retarded the formation of a protective Cr_2O_3 scale. The exposure conditions under which liquids could form from $\text{Na}_2\text{SO}_4\text{-CoSO}_4$ mixtures were calculated from thermodynamic considerations.

Many fossil-fueled devices for energy conversion are susceptible to rapid degradation of high temperature alloy components when subjected to molten salt deposits. Because of the nearly universal presence of sulfur and alkali metals in fossil fuels, the corrosive deposits usually contain alkali sulfates (Na_2SO_4 , K_2SO_4). The mechanism of Na_2SO_4 -induced corrosion at high temperatures, where Na_2SO_4 (mp = 884°C) is liquid, has been extensively studied. This form of attack, commonly known as hot corrosion, results in typical sulfidation with an aluminum and/or chromium depletion zone in the alloy.

Recently, a different, but related, form of hot corrosion has been identified in marine propulsion gas turbines under service conditions where the surface temperatures of the first stage blades and vanes were in the range of about $650^\circ\text{-}700^\circ\text{C}$ (1). The attack on Co-base coatings resulted in an unusual morphology: pitting, little or no depletion of Al or Cr in the alloy, and corrosion products which contained water soluble Co and Ni. Burner rig tests and other studies have been able to reproduce these characteristic features of intermediate temperature attack only when Na_2SO_4 -containing deposits are used in conjunction with sufficient SO_3 in an oxidizing environment (2, 3).

Only a few investigators have studied the mechanism of alkali sulfate induced corrosion at intermediate temperatures ($600^\circ\text{-}884^\circ\text{C}$) (4-6). Umland and Voigt (4) investigated the formation of soluble Ni, Co, and chromate ions in crucible-type corrosion tests. Several nickel-, cobalt-, and iron-base alloys were exposed to melts containing Na_2SO_4 , K_2SO_4 , or mixtures thereof in air or in air containing SO_3 over the temperature range $650^\circ\text{-}900^\circ\text{C}$. They found a maximum in corrosion rate at 750°C which coincided with the highest recovery of Ni and Co sulfates from the melt. This study was subsequently extended by Balajka and Danek (5), who observed enhanced corrosion of Ni in alkali sulfate melts containing CoSO_4 at intermediate temperatures. They interpreted their results in terms of Umland and Voigt's suggestion that cobalt

in the 2+ and 3+ valence states formed complex ions in sulfate melts. These ions were proposed as the basis of a redox system which enhanced the transport of oxidant through the melt. Recently, Jones and Gadomski (6) studied the behavior of four Co- or Ni-base alloys in corrosion tests at $538^\circ\text{-}871^\circ\text{C}$ with deposits of various eutectic composition sulfate mixtures. Those deposits which melted and liberated corrosive gas (probably SO_3), owing to the decomposition of the transition metal sulfate, produced rapid rates of attack. These included mixtures of Na_2SO_4 with the sulfates of Fe, Ni, Co, and Cu.

The present paper is concerned with the mechanism of Na_2SO_4 -induced corrosion at intermediate temperatures. Corrosion studies have been conducted on the model alloys Co-30Cr and Ni-30Cr as a function of P_{SO_3} in oxidizing environments from $600^\circ\text{-}900^\circ\text{C}$. The observed corrosion behavior has been correlated with the formation and stabilities of $\text{Na}_2\text{SO}_4\text{-CoSO}_4$ and $\text{Na}_2\text{SO}_4\text{-NiSO}_4$ liquids.

Experimental Procedure

The kinetics and mechanism of salt-induced attack at intermediate temperatures were studied by the accelerated oxidation test. In this test the alloy specimen was preliminarily coated with a thin film of salt and then exposed at the desired temperature in a slowly flowing, controlled gaseous environment. The kinetics of reaction were monitored by measuring weight changes as a function of time. The corrosion tests were carried out on two binary alloys, Ni-30Cr and Co-30Cr.¹ Specimens of Co-30Cr were machined from small, chill cast ingots, while those of Ni-30Cr were obtained from rolled sheets 1 mm thick. Materials used for the preparation of Ni-30Cr and Co-30Cr were 99.9% pure.

The alloy specimens ($6.3 \times 12.5 \times 1$ mm) were polished through 600 grit SiC abrasive paper and were degreased with alcohol and acetone. The salt deposit was applied to a warm ($\sim 150^\circ\text{C}$) specimen by spraying an aqueous solution of the desired salt with an

* Electrochemical Society Active Member.

Key words: kinetics, oxidation, corrosion, alloy, cobalt.

¹ Alloy compositions are listed as weight percent while the gas and salt compositions have been given as mole percent.

air brush. In most tests 2.5 ± 0.2 mg/cm² of salt was used. To start a test, specimens were brought to temperature in less than 10 min in the desired gas environment. Weight changes during the test were recorded with a Cahn microbalance with a precision of ± 0.01 mg. This was done at an interval of about 1 min during the first 10-15 min of test. The interval between the observations was increased as the reaction progressed, and the weight was monitored every 15-30 min after 3-4 hr. At the end of the experiments, which continued for 24-72 hr, specimens were cooled to room temperature in less than 10 min in the same environment in which the experiments were conducted.

After the corrosion tests, selected samples were rinsed with hot water for subsequent analysis of water soluble elements (Na, Ni, Co, Cr) in the corrosion products. These elements were determined by atomic absorption with an uncertainty of ± 5 μ g. On some specimens metallography, x-ray diffraction and electron microprobe analysis were used to characterize the reaction products.

Various O₂-SO₂ gas mixtures containing from 30 ppm to 10% SO₂ have been employed. Gas mixtures (analyzed grade) were prepared by Union Carbide Corporation (Linde Division) from gases of the following purity: oxygen 99.6% and anhydrous sulfur dioxide 99.9%. Many of the experiments were carried out in O₂-0.15% (SO₂ + SO₃). This mixture simulates the partial pressure of (SO₂ + SO₃) in combustion gases at 10 atm, such as would be derived from a fuel (CH_{1.7}) containing 1 weight percent (w/o) sulfur using an air/fuel ratio (by weight) of 60. The gases were passed over a platinum catalyst at the test temperature to ensure that the equilibrium partial pressure of SO₃ was attained. At temperatures from 600° to about 750°C a platinumized ceramic honeycomb catalyst was used, but this was replaced with several layers of platinum gauze for higher temperatures up to 900°C. In earlier experiments, the corrosion rates of IN-738 sprayed with Na₂SO₄ were observed to be erratic when the platinum catalyst was not used, and these rates were about 2-10 times lower than the rates obtained in equilibrated O₂-SO₂-SO₃ mixtures (7).

Results

A series of accelerated oxidation tests has been carried out on Co-30Cr and Ni-30Cr under a variety of exposure conditions in which the principal variables were temperature, concentration of SO₃ in the gas phase, and initial composition of the salt deposit. In many cases interactions involving the oxide scale, SO₃, and the salt led to substantial changes in the composition of the deposit. Because of the salt-gas-oxide interactions, the rate of attack under corrosive conditions was studied as a function of the amount of the salt deposit. Figure 1 shows for Co-30Cr that increasing the salt deposit from 2.5 to 5.7 mg/cm² of Na₂SO₄ yielded a substantially higher rate of attack after an initial period of 2-4 hr. Consequently, to establish a common basis for comparison, subsequent kinetic studies were carried out with 2.5 mg/cm² of Na₂SO₄ or in two special tests with mixtures of sulfates which contained 2.5 mg/cm² of Na₂SO₄.

The effect of temperature on the rate of attack of Co-30Cr coupons has been studied over the range of 600°-900°C in O₂-0.15% (SO₂ + SO₃) with an initial salt deposit of 2.5 mg/cm² of Na₂SO₄. Plots of weight gain as a function of time are shown in Fig. 2. The results were reproducible with an uncertainty of about $\pm 15\%$. As may be seen, the rate of attack varied with temperature, with the fastest rate occurring at an intermediate temperature. Since the corrosion rate also changed with time, two different criteria were chosen as a basis for comparing the behavior as a function of temperature: (i) the initial corrosion rate averaged over the first 4 hr, and (ii) the corrosion rate averaged over 24 hr. The average

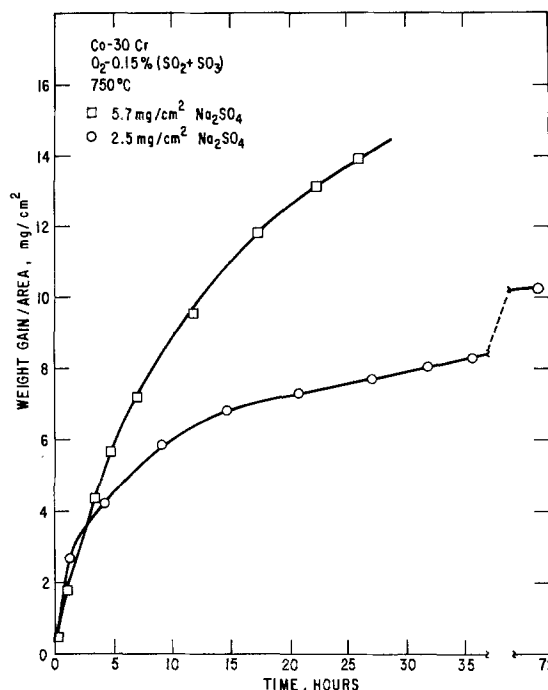


Fig. 1. Effect of the amount of salt on the Na₂SO₄ induced corrosion of Co-30Cr at 750°C in O₂-0.15% (SO₂ + SO₃).

corrosion rate was obtained by dividing weight gain/area over that period by time. By both criteria the corrosion rate is fastest at temperatures around 650°-700°C, as shown in Fig. 3. An identical series of tests was conducted with the Ni-30Cr specimens in O₂-1% (SO₂ + SO₃). The uncertainty in the initial corrosion rates averaged over the first 4 hr of reaction time was very high (up to about $\pm 25\%$). Therefore, only the corrosion rates averaged over 24 hr are shown in Fig. 4, which is a plot of the rate of attack vs. temperature. The corrosion rate is highest at about 650°-750°C.

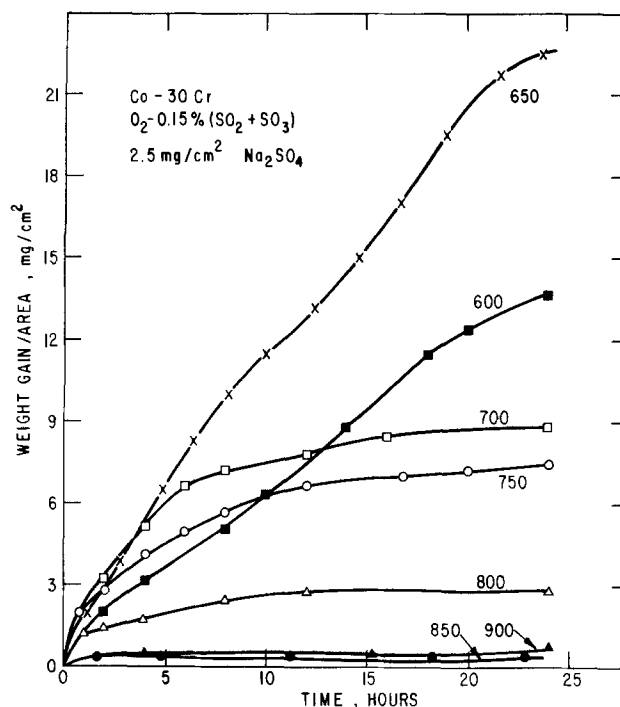


Fig. 2. Effect of temperature on the variation of weight gain/area with time for the corrosion of Co-30Cr, coated with 2.5 mg/cm² of Na₂SO₄, in O₂-0.15% (SO₂ + SO₃).

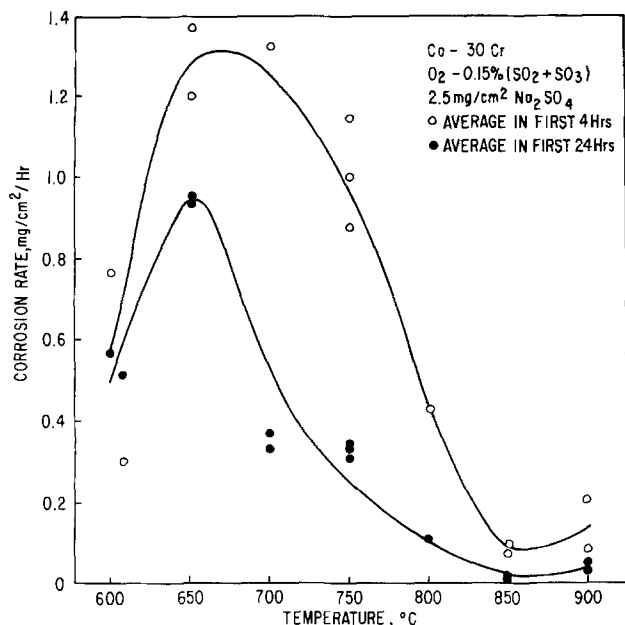


Fig. 3. Effect of temperature on the corrosion rate of Co-30Cr, coated with 2.5 mg/cm² of Na₂SO₄, in O₂-0.15% (SO₂ + SO₃).

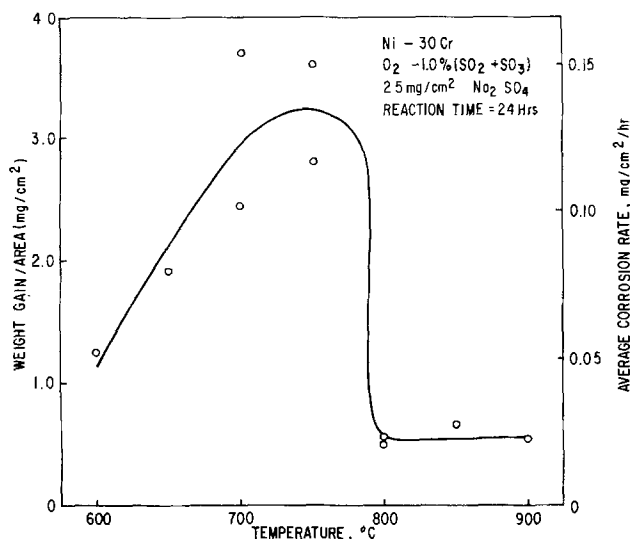


Fig. 4. Effect of temperature on the corrosion rate of Ni-30Cr, coated with 2.5 mg/cm² of Na₂SO₄, in O₂-1% (SO₂ + SO₃).

After the corrosion tests, selected specimens were rinsed in hot distilled water, and the solutions were analyzed for Na, Co, Ni, and Cr. The concentration of Cr was observed to be very small (<5 μg/cm² of sample surface). The water soluble nickel and cobalt were present as NiSO₄ and CoSO₄ in the corrosion products, as confirmed by x-ray diffraction. The results of the analysis for Co and Na in the salt deposits on the Co-30Cr specimens from the corrosion tests described in Fig. 2 are presented in Fig. 5. The ratio Co/(Co + Na₂) represents the degree to which the initially pure Na₂SO₄ deposit had become contaminated with CoSO₄. This ratio reaches a maximum at about 650°C. A similar analysis of the deposits on the Ni-30Cr specimens is summarized in Fig. 6. The cation ratio [Ni/(Ni + Na₂)] for these tests was highest at around 700°-750°C. In general, for both alloys rapid attack occurred in the temperature range where the deposit acquired substantial concentrations of transition metal sulfates.

The accelerated oxidation tests were also conducted as a function of gas and salt composition. In Fig. 7 is shown the effect of (P_{SO₂} + P_{SO₃}) for P_{O₂} ≅ 1 atm on the kinetics of attack of Co-30Cr with an Na₂SO₄

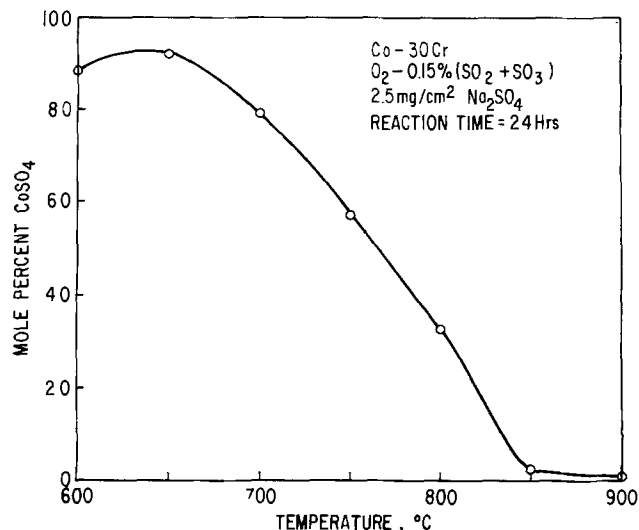


Fig. 5. Effect of temperature on the ratio of soluble corrosion products Co/(Co + Na₂) on Co-30Cr samples, coated with 2.5 mg/cm² of Na₂SO₄, in O₂-0.15% (SO₂ + SO₃). (Reaction time = 24 hr.)

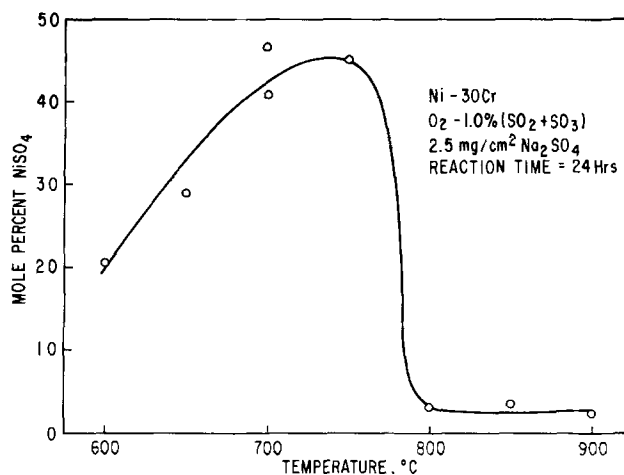


Fig. 6. Effect of temperature on the ratio of soluble corrosion products Ni/(Ni + Na₂) on Ni-30Cr samples, coated with 2.5 mg/cm² of Na₂SO₄, in O₂-1% (SO₂ + SO₃). (Reaction time = 24 hr.)

deposit. A very low corrosion rate was obtained in O₂ containing 30 ppm (SO₂ + SO₃), and it was found after the test that the salt had not melted. Under all other conditions, the salt had melted. Also, the corrosion rates increased with P_{SO₃} except for the rate in O₂-10% (SO₂ + SO₃), which was lower than in gas mixtures containing 1% or 2% (SO₂ + SO₃). Since the formation of a liquid phase at 750°C resulted from the formation of CoSO₄ (as will be discussed later), experiments were carried out in which the initial deposit was a mixture of sodium and cobalt sulfates. The results of these experiments are shown in Fig. 8. Although the salt was liquid in the case of Na₂SO₄-50% CoSO₄ from the beginning of the experiment, the extent of corrosion was much lower than that with pure Na₂SO₄. As discussed before, the corrosion rate tends to increase with an increase in salt amount (Fig. 1). To ensure that the above decrease in corrosion rate was not due to a decrease in the amount of Na₂SO₄, experiments were also carried out using salts which contained 2.5 mg/cm² of Na₂SO₄ instead of 2.5 mg/cm² of the total salt. Even under these conditions, the extent of corrosion was observed to be low for Na₂SO₄-60% CoSO₄. It should be noted that after a few hours, the rate

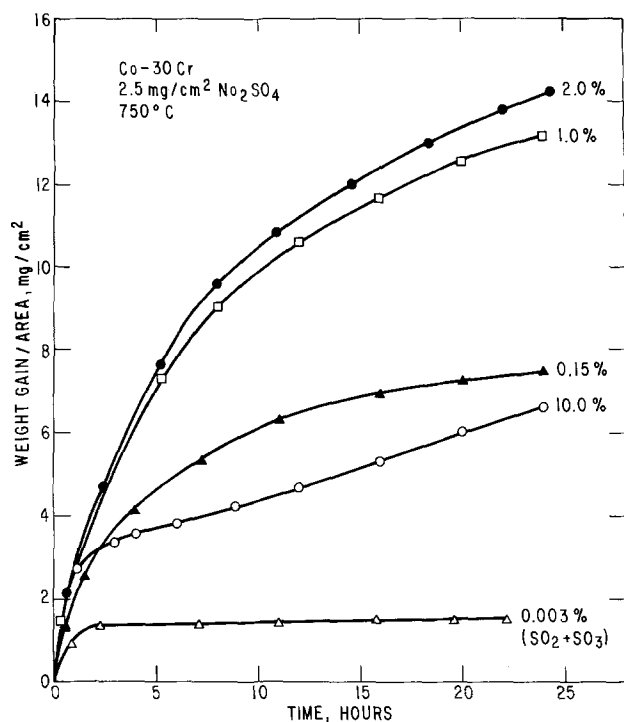


Fig. 7. Effect of ($\text{SO}_2 + \text{SO}_3$) on the corrosion of Co-30Cr at 750°C .

of attack with Na₂SO₄ was about the same as that with Na₂SO₄-CoSO₄ mixtures. The soluble salt analysis of the Co-30Cr sample reacted in Na₂SO₄ and Na₂SO₄-CoSO₄ mixtures showed that the melts reached a steady-state composition of Na₂SO₄-61 ± 8% CoSO₄.

A similar series of experiments was carried out with Ni-30Cr, and the results, shown in Fig. 9, were similar to those observed for Co-30Cr. The salt had melted on all the specimens except for the one exposed in

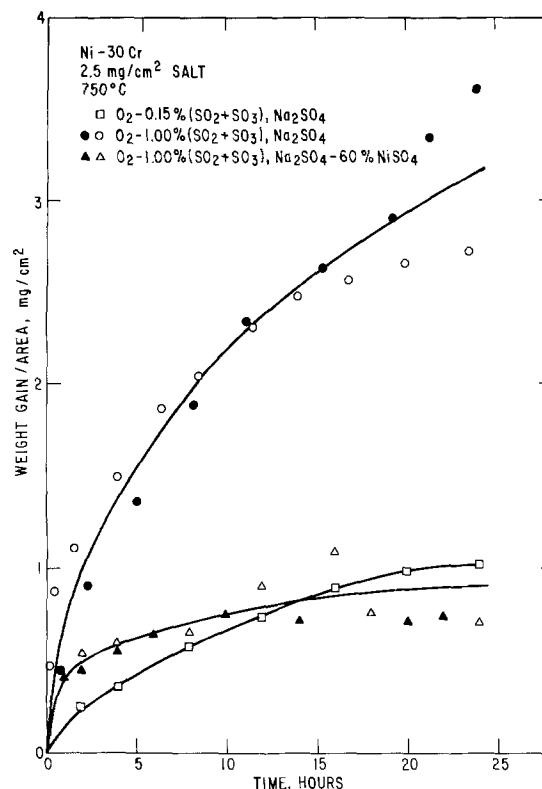


Fig. 9. Effect of salt composition and gas composition on the corrosion of Ni-30Cr at 750°C .

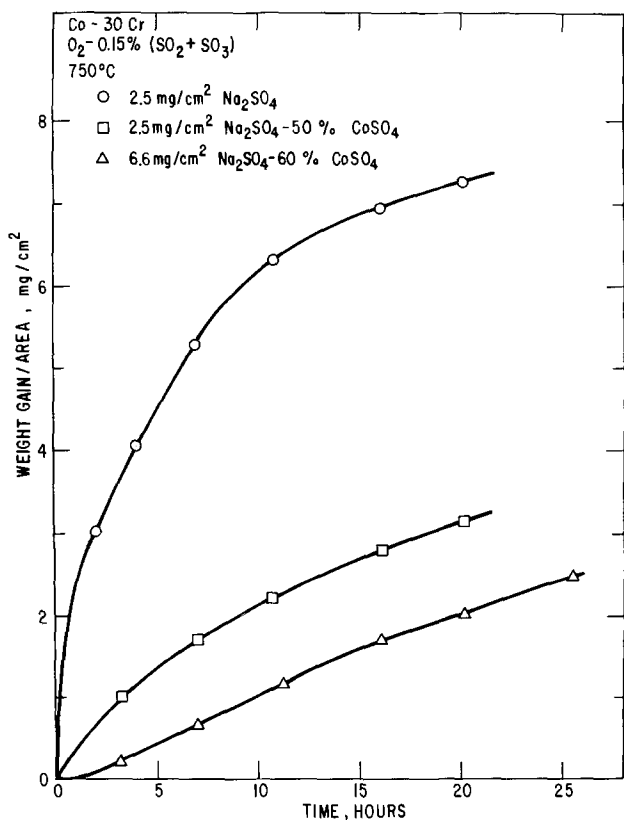


Fig. 8. Effect of salt composition on the corrosion of Co-30Cr at 750°C in O_2 -0.15% ($\text{SO}_2 + \text{SO}_3$).

O_2 -0.15% ($\text{SO}_2 + \text{SO}_3$). The reaction rates increased with the ($\text{SO}_2 + \text{SO}_3$) content of the gas. Also, the extent of corrosion as measured by weight change on specimens coated with Na₂SO₄-60% NiSO₄ was lower than that with pure Na₂SO₄.

Metallographic examination of the corroded specimens of Ni-30Cr and Co-30Cr showed sharp differences in the morphology of the reaction product. Corrosion occurred uniformly on the specimens of Ni-30Cr. However, the Co-30Cr specimens, exposed in an environment where a liquid phase could form on the surface, typically revealed pronounced nonuniform attack in the form of pits. To avoid dissolving and losing the water soluble sulfates of sodium and cobalt during metallographic preparation, the samples were polished using kerosene. The morphology of the pitting attack on a Co-30Cr sample in O_2 -0.15% ($\text{SO}_2 + \text{SO}_3$) is shown in Fig. 10. X-ray images for chromium and cobalt obtained by an energy dispersive analyzer on an SEM showed that chromium was concentrated in the area below the initial interface while cobalt was concentrated in the external areas. The white phase visible near the gas surface was identified as Co₃O₄. At the higher levels of P_{SO_3} in the gas, where Co₃O₄ was unstable [for example, in O_2 -2% ($\text{SO}_2 + \text{SO}_3$) at 750°C], pitting was still observed, but the outer section of the corrosion product consisted of CoSO₄ deposits instead of Co₃O₄.

Microprobe analysis of the internal regions of the pits (below the original salt/metal interface) showed the presence of sodium, chromium, cobalt, and sulfur, suggesting that the liquid Na₂SO₄-CoSO₄ had penetrated into the pit. Figure 11 shows a photomicrograph of the internal region of a pit on Co-30Cr under polarized light. Alternate bands, presumably of areas rich in Cr₂O₃ (bright) and the liquid CoSO₄-Na₂SO₄ (dark), can be clearly seen. That the liquid phase does indeed penetrate the pit was also confirmed by another test. One of the samples of Co-30Cr corroded in O_2 -0.15% ($\text{SO}_2 + \text{SO}_3$) was water washed and

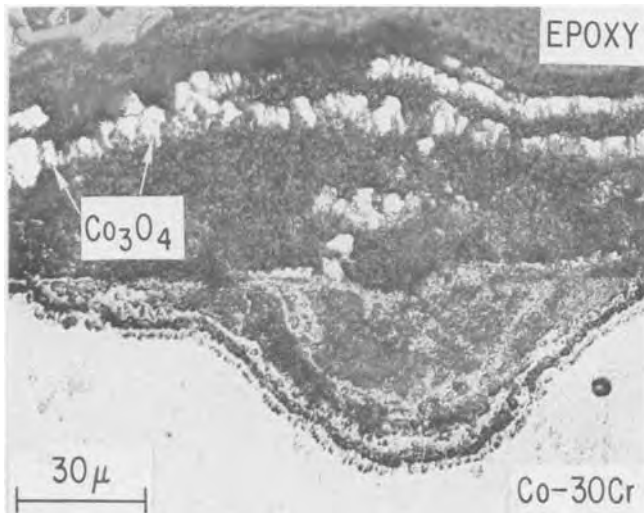


Fig. 10. Optical micrograph of a cross section of the corrosion product on Co-30Cr sprayed with 2.5 mg/cm^2 of Na_2SO_4 and reacted for 10.5 hr in O_2 -0.15% ($\text{SO}_2 + \text{SO}_3$) at 750°C . The penetration of the alloy occurs irregularly, normally in the form of pits. The large white particles near the gas interface are Co_3O_4 in an Na_2SO_4 - CoSO_4 liquid. $550\times$.

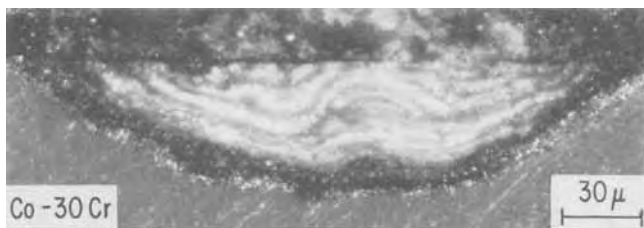


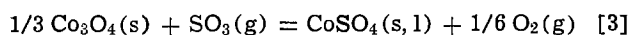
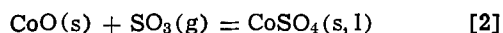
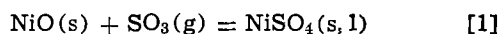
Fig. 11. Optical micrograph (under polarized reflected light) of a cross section of the internal region of a pit formed on Co-30Cr sprayed with 2.5 mg/cm^2 of Na_2SO_4 and reacted in O_2 -0.15% ($\text{SO}_2 + \text{SO}_3$) at 750°C . The bands seen in the pit are presumably the areas rich in Cr_2O_3 (white bands) and Na_2SO_4 - CoSO_4 liquid (dark bands). $350\times$.

a thick copper layer ($\sim 1 \text{ mm}$) was electroplated from a copper sulfate solution. Due to the high solubility of Na_2SO_4 and CoSO_4 in water, any salt present in the pits will be dissolved leaving pores to be filled with Cu. X-ray dispersive analysis of a cross-sectional area of a pit showed primarily Cu, Cr, and O; copper was observed to be rich in thin bands similar to the dark areas in Fig. 11.

Discussion

Thermodynamic considerations.—Pure sodium sulfate is not molten at the intermediate temperatures (650 – 750°C) where high corrosion rates have been observed in our experiments. However, the phase diagrams for Na_2SO_4 - CoSO_4 and Na_2SO_4 - NiSO_4 show eutectics that melt at 565°C for Na_2SO_4 -50% CoSO_4 and 671°C for Na_2SO_4 -38% NiSO_4 (8). Since a liquid phase is regarded as necessary for high corrosion rates, it is of interest to determine the conditions under which these eutectics can form on the alloy specimens containing nickel and/or cobalt.

The formation of NiSO_4 or CoSO_4 from their respective oxides can be expressed by



where the underline implies that the sulfate is present in solution at an activity less than one.

Solid Na_2SO_4 can dissolve NiSO_4 and/or CoSO_4 to a considerable extent (8). Figure 12 shows the Na_2SO_4 - CoSO_4 phase diagram with a schematic representation of the isoactivity lines for SO_3 in equilibrium with Co_3O_4 and the Na_2SO_4 - CoSO_4 liquid and/or solid. Liquid formation from an initially solid Na_2SO_4 will occur when the activity of CoSO_4 in Na_2SO_4 - CoSO_4 solid solution becomes equal to or greater than that corresponding to the liquidus line. The activity of CoSO_4 and the P_{SO_3} in equilibrium with oxide are constant across the two phase (solid and liquid) region. Similar considerations apply to the Na_2SO_4 - NiSO_4 system.

The minimum P_{SO_3} required to form an Na_2SO_4 - CoSO_4 liquid in equilibrium with Co_3O_4 has been estimated for temperatures between 650 and 900°C . The standard Gibbs energy data for $\text{SO}_2(\text{g})$, $\text{SO}_3(\text{g})$, CoO(s) , and $\text{Co}_3\text{O}_4(\text{s})$ were obtained from the JANAF Tables and supplements (9). At $P_{\text{O}_2} = 1 \text{ atm}$, Co_3O_4 is more stable than CoO at temperatures below 947°C . Thus, the P_{SO_3} required to form an Na_2SO_4 - CoSO_4 liquid can be obtained from the free energy data for reaction [3], taking the activity of Co_3O_4 as unity. The results are presented in Fig. 13 as curve A, which shows the estimated values of P_{SO_3} as a function of temperature for $P_{\text{O}_2} \cong 1 \text{ atm}$. The mole fraction of $\text{CoSO}_4(\text{s})$ needed to form the liquid was obtained from the phase diagram shown in Fig. 12. The activity coefficient of $\text{CoSO}_4(\text{s})$ in Na_2SO_4 - CoSO_4 solid solution was estimated from the phase diagram and the available thermodynamic properties of Na_2SO_4 . The procedure used for estimating $\gamma_{\text{CoSO}_4(\text{s})}$ is given in the Appendix. Also included in the Appendix are the results of experiments used to confirm curve A.

At any temperature, an increase in P_{SO_3} above that given by curve A will increase the activity of CoSO_4 in Na_2SO_4 - CoSO_4 liquid in contact with Co_3O_4 . The composition of the stable liquid phase will change progressively from that corresponding to the liquidus line at the Na_2SO_4 end of the phase diagram to that at the CoSO_4 end. Figure 12 shows that solid CoSO_4 does not dissolve any appreciable amount of Na_2SO_4 . The activity of $\text{CoSO}_4(\text{s})$ at the liquidus line on the CoSO_4 end should therefore be one. Curve B in Fig. 13 shows as a function of temperature the P_{SO_3} needed to form solid CoSO_4 . Thus, the equilibrium values of P_{SO_3} in contact with Co_3O_4 and Na_2SO_4 - CoSO_4 liquids corresponding to the two liquidus lines in Fig. 12 can be obtained from curves A and B in Fig. 13. At P_{SO_3} values higher than curve B Co_3O_4 is unstable, and the deposit should consist of $\text{CoSO}_4(\text{s})$ and a

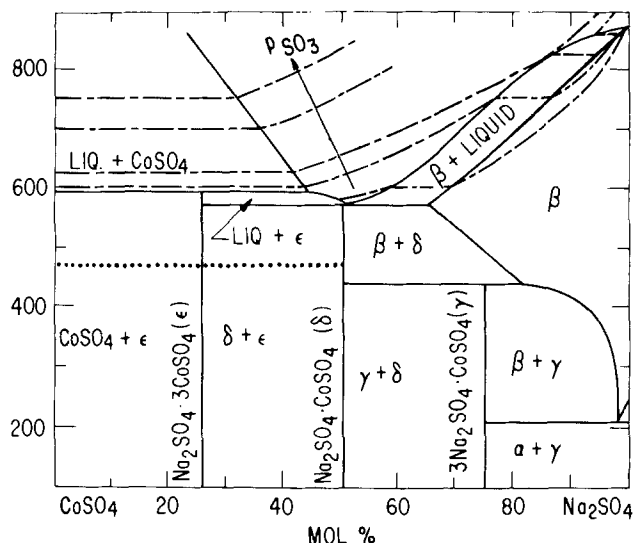


Fig. 12. Na_2SO_4 - CoSO_4 phase diagram with a schematic representation of the isoactivity lines for SO_3 in equilibrium with Co_3O_4 (8).

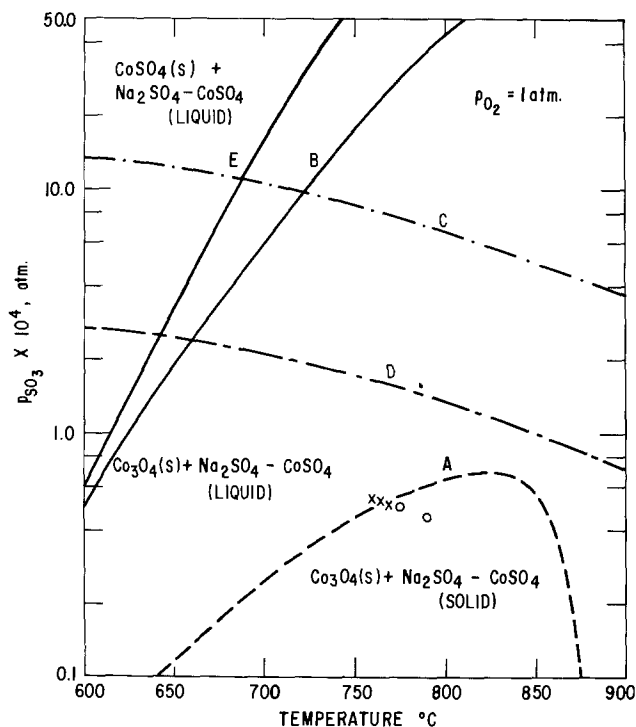


Fig. 13. Stability diagram for the $\text{Co}_3\text{O}_4\text{-CoSO}_4\text{-Na}_2\text{SO}_4$ system. A liquid phase is stable at P_{SO_3} values above curve A which shows the estimated values of P_{SO_3} in equilibrium with Co_3O_4 solid, an $\text{Na}_2\text{SO}_4\text{-CoSO}_4$ solid and an $\text{Na}_2\text{SO}_4\text{-CoSO}_4$ liquid. Curve B shows the P_{SO_3} in equilibrium with Co_3O_4 , $\text{CoSO}_4(\text{s})$ and liquid $\text{Na}_2\text{SO}_4\text{-CoSO}_4$. Curves C and D show the SO_3 content of $\text{O}_2\text{-}0.15\%$ ($\text{SO}_2 + \text{SO}_3$) and $\text{O}_2\text{-}0.03\%$ ($\text{SO}_2 + \text{SO}_3$) gas mixtures. For comparison with curve B for the $\text{Co}_3\text{O}_4\text{-CoSO}_4$ system, curve E shows the P_{SO_3} above which $\text{NiSO}_4(\text{s})$ is more stable than $\text{NiO}(\text{s})$. The symbols X (for liquid formation) and O (for no liquid formation) refer to experiments on Co_3O_4 to verify curve A.

liquid whose composition corresponds to the liquidus line on the CoSO_4 end of the phase diagram. The relative proportions of solid and liquid phases will be determined by the concentrations of Na_2SO_4 in the deposit.

Curves C and D in Fig. 13 show the equilibrium P_{SO_3} as a function of temperature for $\text{O}_2\text{-}0.15\%$ ($\text{SO}_2 + \text{SO}_3$) and $\text{O}_2\text{-}0.03\%$ ($\text{SO}_2 + \text{SO}_3$) gas mixtures, respectively. It can be seen that a far higher P_{SO_3} is available in these mixtures than is needed to stabilize liquid $\text{CoSO}_4\text{-Na}_2\text{SO}_4$ mixtures over the temperature range $600\text{-}850^\circ\text{C}$. Thus, on alloys and coatings whose oxidation products contain cobalt oxide, a liquid phase may be expected to form during the accelerated oxidation test at temperatures well below the melting point of Na_2SO_4 .

Reaction [3] shows that the activity of CoSO_4 in equilibrium with Co_3O_4 is inversely proportional to $P_{\text{O}_2}^{1/6}$. Thus, the P_{SO_3} needed to stabilize an $\text{Na}_2\text{SO}_4\text{-CoSO}_4$ liquid should decrease with a decrease in P_{O_2} . At low P_{O_2} values, where CoO is more stable than Co_3O_4 , P_{SO_3} values needed to stabilize $\text{Na}_2\text{SO}_4\text{-CoSO}_4$ liquids can be obtained from the free energy data for reaction [2]. For example, at 750°C , for $P_{\text{O}_2} \leq 5 \times 10^{-4}$ atm a liquid phase can form if $P_{\text{SO}_3} \geq 1.5 \times 10^{-5}$ atm. These P_{SO_3} values will be independent of P_{O_2} . Similarly, the P_{SO_3} needed to form solid CoSO_4 (curve B in Fig. 13) will decrease with P_{O_2} .

Similar calculations can be carried out for the $\text{NiSO}_4\text{-Na}_2\text{SO}_4$ system using the free energy data for reaction [1] from Ingraham (10). Curve E in Fig. 13 shows the equilibrium P_{SO_3} in contact with NiO and NiSO_4 at unit activities. Clearly, the P_{SO_3} needed to form solid NiSO_4 from NiO is higher than that needed to form solid CoSO_4 from Co_3O_4 . Similarly, higher SO_3 levels are needed to stabilize an $\text{Na}_2\text{SO}_4\text{-}$

NiSO_4 liquid than that needed to stabilize an $\text{Na}_2\text{SO}_4\text{-CoSO}_4$ liquid (curve A). Experiments described in the Appendix showed that the SO_3 level needed to form an $\text{Na}_2\text{SO}_4\text{-NiSO}_4$ liquid on NiO was $\sim 5 \times 10^{-4}$ atm at 750°C , which is about 10 times higher than the SO_3 level needed to form an $\text{Na}_2\text{SO}_4\text{-CoSO}_4$ liquid on Co_3O_4 at 750°C .

It should be noted that CoSO_4 and NiSO_4 have appreciable solid solubility in Na_2SO_4 (8, 11). Therefore, water soluble cobalt and nickel may be detected in the Na_2SO_4 deposits even for P_{SO_3} levels where a liquid phase is not obtained.

Reaction mechanism.—According to the current concepts of high temperature oxidation, when a resistant alloy is heated in an oxidizing environment, the surface will be oxidized through a series of stages (referred to as transient oxidation) before achieving a final, steady-state scale composition (12-14). Consider the oxidation of a cobalt-base alloy containing Cr. The rapid uptake of oxygen at the beginning of oxidation will be accompanied by the formation of nuclei of cobalt oxide and Cr_2O_3 on the surface. It is well known that the diffusion of cobalt through cobalt oxide is much faster than that of Cr through Cr_2O_3 . Therefore, cobalt oxide will soon cover the nuclei of Cr_2O_3 . Since Cr_2O_3 is more stable than cobalt oxide, alloys containing a sufficiently high concentration of Cr will eventually develop a continuous film of Cr_2O_3 underneath the cobalt oxide at the alloy/scale interface, and the oxidation rate will be reduced. At low or intermediate temperatures, the diffusion rates of Co and Cr in the alloy and oxides will be low, and the transient oxidation processes may persist for long times before a steady-state continuous scale of Cr_2O_3 is achieved. Oxidation of a nickel-base alloy containing chromium will occur in a similar fashion.

The presence of a porous, solid Na_2SO_4 deposit at the exposure temperature is unlikely to affect oxidation processes. During transient oxidation NiO or Co_3O_4 will come in contact with the deposit. With SO_3 present in the gas phase NiSO_4 and CoSO_4 will form via reactions [1] and [3]. If the partial pressure of SO_3 in the gas is lower than that necessary to form a liquid phase, the corrosion reaction will slow down in a short time owing to the formation of a protective film of Cr_2O_3 . At higher P_{SO_3} , however, a liquid phase may form. Under these conditions it is proposed that high corrosion rates are obtained as a result of the rapid dissolution of cobalt oxide or nickel oxide which prevents the formation of a protective Cr_2O_3 film. This may occur by undercutting and isolating particles of Cr_2O_3 before the film can become continuous, but the details of this process have not been established.

To help substantiate the role of transient oxidation processes three means of altering the initial kinetics were explored under conditions where liquid sulfate deposits were stable. The first test consisted of carrying out corrosion experiments with $\text{Na}_2\text{SO}_4\text{-CoSO}_4$ and $\text{Na}_2\text{SO}_4\text{-NiSO}_4$ mixtures to reduce or eliminate the driving force for sulfation of Co_3O_4 and NiO . This was expected to decrease the high initial rates of attack observed with Na_2SO_4 . In Fig. 8 the kinetics of attack of $\text{Co-}30\text{Cr}$ in $\text{O}_2\text{-}0.15\%$ ($\text{SO}_2 + \text{SO}_3$) with pure Na_2SO_4 are compared with those for Na_2SO_4 containing 50 and 60 mole percent (m/o) CoSO_4 . Clearly, the initial rate of attack is reduced with the mixed sulfate deposits. Similarly, the $\text{Ni-}30\text{Cr}$ alloy shows a lower rate of attack with an $\text{Na}_2\text{SO}_4\text{-}60\%$ NiSO_4 deposit than with an Na_2SO_4 deposit (Fig. 9).

As a second means of altering the corrosion rate, a $\text{Co-}30\text{Cr}$ sample was oxidized at 925°C in an $\text{H}_2/\text{H}_2\text{O}$ environment ($P_{\text{O}_2} \approx 10^{-19}$ atm) to establish a protective, steady-state scale of Cr_2O_3 with little or no cobalt and cobalt oxide on the surface. The sample was slowly cooled to room temperature in

1 hr and coated with Na_2SO_4 . The results of the accelerated oxidation test at 750°C in O_2 -0.15% ($\text{SO}_2 + \text{SO}_3$) are shown in Fig. 14. As expected, the initial rate of attack was reduced, but corrosion was not eliminated, presumably because of the presence of some cobalt on the surface, which allowed the formation of a liquid salt; indeed the reacted sample had an Na_2SO_4 - CoSO_4 liquid on the surface.

Third, by operating the accelerated oxidation test at high temperature (900°C) the transient oxidation stage can be appreciably shortened, and hence the protective Cr_2O_3 film may be obtained. Although the formation of a liquid phase was not a factor since Na_2SO_4 itself was molten, the potential for the sulfation reaction to yield an activity of CoSO_4 as high as at 750°C with O_2 -0.15% ($\text{SO}_2 + \text{SO}_3$) was ensured by raising the ($\text{SO}_2 + \text{SO}_3$) to 4%. As shown in Fig. 14, the initial corrosion rate at 900°C was lower than that at 750°C , and the rate decreased with time to very low values. Even with a somewhat higher potential for sulfation in O_2 -10% ($\text{SO}_2 + \text{SO}_3$), Fig. 14, the initial rate of attack was still less than that at 750°C , and as with the previous case corrosion essentially stopped after a few hours.

The above tests show that the initial high corrosion rates at intermediate temperatures result from the rapid sulfation of cobalt oxide or nickel oxide. The resulting liquid salt deposit prevents the formation of a protective Cr_2O_3 film. Appreciable rates of attack can be obtained beyond the time when the salt is apparently saturated with transition metal sulfates. The corrosion reaction can proceed by oxidation and sulfation at the scale/salt interface and/or dissolution at the scale/salt interface followed by the formation of Co_3O_4 or $\text{CoSO}_4(\text{s})$ at the gas interface. The reactions involved in these processes and differences from reaction models proposed in the literature will be described in a subsequent publication.

The corrosion rates of Ni-30Cr in O_2 -1% ($\text{SO}_2 + \text{SO}_3$) mixtures (Fig. 4) were observed to be much

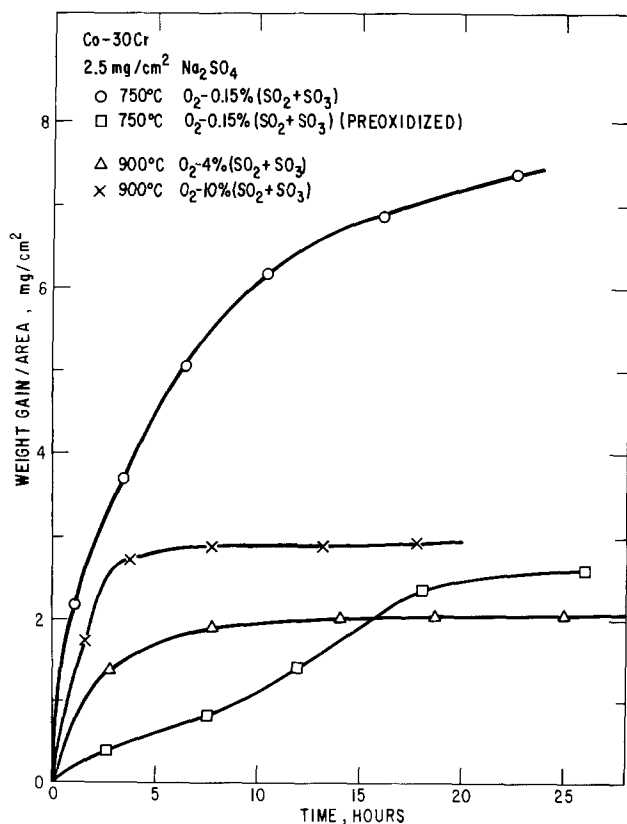


Fig. 14. Variation of weight gain/area with time for the corrosion of Co-30Cr samples, coated with 2.5 mg/cm^2 of Na_2SO_4 , exposed to different O_2 - SO_2 - SO_3 environments at 750° and 900°C .

lower than those of Co-30Cr in O_2 -0.15% ($\text{SO}_2 + \text{SO}_3$) (Fig. 3). This cannot be attributed to the lower stability of NiSO_4 in comparison to CoSO_4 because of the differences in P_{SO_3} . The higher P_{SO_3} level in the experiments with Ni-30Cr makes reaction [1] more favorable than reaction [3] in the experiments with Co-30Cr. For example, at 750°C , the activity of NiSO_4 in equilibrium with $\text{NiO}(\text{s})$ and O_2 -1% ($\text{SO}_2 + \text{SO}_3$) is 0.91 while that of CoSO_4 in equilibrium with Co_3O_4 and O_2 -0.15% ($\text{SO}_2 + \text{SO}_3$) is 0.50.

The higher corrosion rates for Co-30Cr can be correlated with the observed difference in the morphology of the corrosion product. It is observed that cobalt can dissolve at the bottom of the pit, migrate through the liquid salt, and form Co_3O_4 or $\text{CoSO}_4(\text{s})$ at the gas interface (see, for example, Fig. 11). Therefore, high corrosion rates can persist for long times on Co-30Cr. However, no such rapid migration of nickel was observed on Ni-30Cr. The transport processes involved in the migration of cobalt and oxidants (SO_3 , O_2) will be described in detail in a subsequent publication.

Effect of temperature and P_{SO_3} .—The effects of temperature and P_{SO_3} on the corrosion rates are interconnected because these variables influence the formation of a liquid from an Na_2SO_4 deposit. Accelerated oxidation tests on Co-30Cr in O_2 -0.15% ($\text{SO}_2 + \text{SO}_3$) and Ni-30Cr in O_2 -1% ($\text{SO}_2 + \text{SO}_3$) at 600° - 900°C yielded maxima in corrosion rate at 650°C for Co-30Cr and at 700° - 750°C for Ni-30Cr. Also, at 750°C the reaction rates increased with increasing P_{SO_3} (Fig. 7 and 9). As described before, the rapid sulfation of cobalt oxide or nickel oxide prevents the formation of a protective chromium oxide film during the early part of the corrosion reaction. On Co-30Cr the reaction can proceed rapidly for longer times because cobalt dissolves at the scale/salt interface and redeposits as CoSO_4 or Co_3O_4 close to the gas interface. The following discussion of the effect of P_{SO_3} and temperature pertains specifically to the initial stage, although some aspects of the argument can also be applied to the later reaction processes.

It is proposed that the rate of sulfation of cobalt and nickel oxides is influenced by diffusion of SO_3 through the liquid salt. The transport rate of SO_3 should increase with $(P_{\text{SO}_3} - P_{\text{SO}_3}^i)$, where $P_{\text{SO}_3}^i$ is the P_{SO_3} at the scale/salt interface. Thus, the reaction rate will tend to increase with P_{SO_3} . However, at very high P_{SO_3} the reaction rates may actually decrease, if the formation of solid sulfates impedes the transport of reactants in the reaction product layer. This is in agreement with our experimental results at 750°C on Co-30Cr which showed a higher corrosion rate in O_2 -1% ($\text{SO}_2 + \text{SO}_3$) than in O_2 -10% ($\text{SO}_2 + \text{SO}_3$).

The effect of temperature on the corrosion rate is influenced by many factors. Two important ones are: (i) the tendency to develop a protective oxide film, and (ii) the transport rate of SO_3 through the salt. Since the interdiffusion of Cr in the alloy and the diffusion of Cr through Cr_2O_3 will be faster at higher temperatures, the tendency to develop a protective Cr_2O_3 film will increase with temperature and will tend to decrease the corrosion rate. Also, as described before, the reaction rate is expected to increase with the transport rate of SO_3 through the liquid salt, which itself depends on two opposing factors: diffusion coefficient through the liquid salt and $(P_{\text{SO}_3} - P_{\text{SO}_3}^i)$. With increasing temperature the diffusion coefficient will increase, but P_{SO_3} will decrease. In addition, at lower temperature the transport rate of SO_3 may be inhibited by the formation of solid sulfates. Under these competing effects, the corrosion rate should exhibit a maximum at some intermediate temperature.

The concentration of water soluble cobalt and nickel in the corrosion products was observed to be a maximum at about 650° and 750°C , respectively. The de-

Table I. Effect of temperature on the composition of salt deposits

Temperature (°C)	Mole fraction of CoSO ₄ in liquid in equilibrium with CoSO ₄ solid*	Mole fraction of CoSO ₄ from samples of Co-30Cr exposed in O ₂ -0.15% (SO ₂ + SO ₃)**	% solid in salt deposits on Co-30Cr
600	0.56	0.88	74
650	0.60	0.92	81
700	0.64	0.79	32
750	0.68	0.57	0
800	0.72	0.33	0

* Obtained from the phase diagram in Fig. 12.

** Obtained from the data presented in Fig. 5.

crease in the concentration of nickel and cobalt at temperatures above 700°-750°C is due primarily to a decrease in the maximum activities of CoSO₄ and NiSO₄ in the melt. At lower temperatures, the salt chemistry may be modified by the formation of solid sulfates. For example, solid CoSO₄ is stable in O₂-0.15% (SO₂ + SO₃) at temperatures below about 725°C. That solid CoSO₄ does indeed form at lower temperatures was confirmed by comparing the mole fraction of Na₂SO₄ recovered from the salt deposits on corroded specimens of Co-30Cr (see Fig. 5) to the mole fraction of Na₂SO₄ in a liquid in equilibrium with solid CoSO₄ (Fig. 12). If solid CoSO₄ is present in the salt deposits, the experimental values of the mole fraction of Na₂SO₄ will be less than those obtained from the phase diagram. Table I shows that at temperatures below 725°C the salt deposits on corroded specimens of Co-30Cr consisted of solid CoSO₄ and an Na₂SO₄-CoSO₄ liquid.

Conclusions

High corrosion rates are obtained when Co-30Cr and Ni-30Cr alloys coated with Na₂SO₄ are exposed to O₂-SO₂-SO₃ environments containing sufficient SO₃ to form Na₂SO₄-CoSO₄ and Na₂SO₄-NiSO₄ liquids, respectively, on these alloys. Thermodynamic calculations show that these liquids can form at moderate SO₃ levels in the gas. For example, a liquid phase can be obtained on cobalt containing alloys at about 50 ppm SO₃ in the gas phase at 750°C and P_{O₂} = 1 atm. The rapid sulfation of cobalt and nickel oxides on the surface of the alloys prevents the formation of a protective Cr₂O₃ film, resulting in high corrosion rates. The corrosion rates on Co-30Cr were higher than on Ni-30Cr under equivalent sulfation conditions. On Co-30Cr the corrosion reactions can proceed rapidly for long times, because cobalt can dissolve at the scale/salt interface and precipitate as Co₃O₄ or CoSO₄ close to the gas interface. The combination of various factors involved in the sulfation reaction and the enhanced tendency to form a protective Cr₂O₃ film at high temperatures results in a maximum in the corrosion rates at about 650°-750°C.

Acknowledgment

The authors acknowledge the help of J. F. Fleischer in carrying out the corrosion studies. This work was partially supported by U.S. Navy Contracts N00024-77-C-4133 and N00024-78-C-4182.

Manuscript submitted Oct. 26, 1979; revised manuscript received ca. April 16, 1980.

Any discussion of this paper will appear in a Discussion Section to be published in the June 1981 JOURNAL. All discussions for the June 1981 Discussion Section should be submitted by Feb. 1, 1981.

Publication costs of this article were assisted by General Electric Company.

APPENDIX

Estimation of the P_{SO₃} Required to Form Na₂SO₄-CoSO₄ Liquid

The equilibrium P_{SO₃} required to stabilize an Na₂SO₄-CoSO₄ liquid on cobalt oxide can be determined at any temperature from the standard Gibbs

energy changes of reactions [2] and [3] and the Na₂SO₄-CoSO₄ phase diagram, provided the activity coefficient of CoSO₄ in the solid solution (γ_{CoSO₄(s)}) in equilibrium with the liquid phase is known. However, there are no measurements in the literature on the activity coefficient of CoSO₄ in liquid or solid solutions of Na₂SO₄ and CoSO₄. Therefore, values of the activity coefficient as a function of temperature were estimated from the phase diagram using the known thermodynamic properties of Na₂SO₄ and CoSO₄. The Gibbs energy data for CoSO₄(s), Na₂SO₄(s), and Na₂SO₄(l) were taken from the JANAF Tables and supplements (9), while that for CoSO₄(l) were obtained using the solid data, the melting point (15), and an estimated entropy of melting of 3.5 eu.

Because of the existence of compounds in the phase diagram of the CoSO₄-Na₂SO₄ system, liquid solutions are unlikely to be ideal. Activity coefficients calculated from the assumption of an ideal behavior of liquid Na₂SO₄-CoSO₄ resulted in activities of Na₂SO₄ greater than unity in Na₂SO₄-CoSO₄ solid solutions along the solidus line (for example, 1.25 at 650°C and 1.16 at 750°C). This is physically inconsistent and demonstrates that the Na₂SO₄-CoSO₄ liquid cannot be treated as an ideal solution.

As a first approximation, activity coefficients were obtained assuming both the solid and liquid solutions along the solidus and liquidus line to be regular. It should be noted that the models based on the regular solution approximation have been extensively used to calculate thermodynamic data in metal-slag systems, silicates and molten salts (16). Also, as shown below, these calculations yielded reasonable and consistent values of the activity coefficient over a small temperature range.

Let X₁ and X₂ be the mole fractions of CoSO₄ in solid and liquid solutions. Then

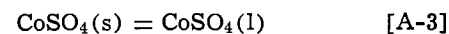
$$\frac{\ln \gamma_{\text{CoSO}_4(\text{s})}}{(1 - X_1)^2} = \alpha_s = \frac{\ln \gamma_{\text{Na}_2\text{SO}_4(\text{s})}}{X_1^2} \quad [\text{A-1}]$$

and

$$\frac{\ln \gamma_{\text{CoSO}_4(\text{l})}}{(1 - X_2)^2} = \alpha_l = \frac{\ln \gamma_{\text{Na}_2\text{SO}_4(\text{l})}}{X_2^2} \quad [\text{A-2}]$$

where γ denotes activity coefficients and α_s and α_l are the α-functions for the solid and liquid solutions, respectively.

For solid/liquid equilibrium



at temperature T

$$\Delta G^\circ_{\text{CoSO}_4(\text{l})} - \Delta G^\circ_{\text{CoSO}_4(\text{s})} = -RT \ln \frac{X_2 \gamma_{\text{CoSO}_4(\text{l})}}{X_1 \gamma_{\text{CoSO}_4(\text{s})}} \quad [\text{A-4}]$$

where ΔG° is the standard Gibbs energy of formation.

Combining Eq. [A-1], [A-2], and [A-4], one obtains

$$\frac{\Delta G^\circ_{\text{CoSO}_4(\text{l})} - \Delta G^\circ_{\text{CoSO}_4(\text{s})}}{RT} = -\ln \frac{X_2}{X_1} - (1 - X_2)^2 \alpha_l + (1 - X_1)^2 \alpha_s \quad [\text{A-5}]$$

The standard Gibbs energy of formation of CoSO₄ solid dissolved in Na₂SO₄ was approximated by the value for pure CoSO₄ solid owing to the lack of more relevant data. Similarly

$$\frac{\Delta G^\circ_{\text{Na}_2\text{SO}_4(\text{l})} - \Delta G^\circ_{\text{Na}_2\text{SO}_4(\text{s})}}{RT} = -\ln \frac{(1 - X_2)}{(1 - X_1)} - X_2^2 \alpha_l + X_1^2 \alpha_s \quad [\text{A-6}]$$

The simultaneous solution of Eq. [A-5] and [A-6] yields α_l and α_s, and hence the activity coefficients can be obtained from Eq. [A-1] and [A-2].

It was observed that in the range of 650°-750°C, the calculated values of α_s and α_l varied inversely with temperature. This suggests that in this temperature range the liquid and solidus composition vs. temperature data can be correlated with the assumption of a regular solution behavior. The resulting values of γ_{CoSO₄(s)} varied from 0.24 at 650°C to 0.20 at 750°C.

For determining the SO_3 levels required to form the liquid phase at temperatures above 750°C (curve A in Fig. 12), a constant $\gamma_{\text{CoSO}_4(\text{s})}$ value of 0.20 was used.

Owing to the high sensitivity of the calculated curve to small errors in the standard Gibbs energy values of reaction [3] and to the uncertainty associated with the calculated activity coefficient of CoSO_4 , curve A was experimentally verified in the temperature range of 750°C – 800°C . Cobalt and CoO coupons were oxidized in air or oxygen at 750°C to produce a thin film of Co_3O_4 (\approx a few microns) on the surface. These samples were sprayed with a thin film ($\approx 2.5 \text{ mg/cm}^2$) of Na_2SO_4 and exposed in O_2 – SO_2 – SO_3 environments for a few hours. The salt on the surface of the samples was then examined under a low power microscope at $\approx 20\times$ magnification for signs of melting. The results of these experiments are shown in Fig. 12. The symbols x and o denote the conditions of salt melting and not melting, respectively. These results are clearly in good agreement with curve A.

REFERENCES

1. D. J. Wortman, R. E. Fryxell, and I. I. Bessen, Paper 11 presented at Third Conference on Gas Turbine Materials in a Marine Environment, session V, University of Bath, England, September 1976.
2. D. J. Wortman, R. E. Fryxell, K. L. Luthra, and P. A. Bergman, *Thin Solid Films*, **64**, 281 (1979).
3. L. F. Aprigliano, Report No. MAT-77-78, David W. Taylor Naval Ship Research and Development Center, Bethesda, MD 20084, 1978.
4. F. Umland and H. P. Voigt, *Werk. Korrr.*, **21**, 254 (1970).
5. J. Balajka and V. Danek, *ibid.*, **25**, 513 (1974).
6. R. L. Jones and S. T. Gadowski, NRL letter report 6170-773, Nov. 1977.
7. D. A. Shores, K. L. Luthra, and D. W. McKee, in "High Temperature Metal Halide Chemistry," D. L. Hildebrand and D. D. Cubicciotti, Editors, p. 538, The Electrochemical Society Softbound Proceedings Series, Princeton, N.J. (1978).
8. K. A. Bol'shakov and P. I. Fedorov, *Zh. Obsch. Khim.*, **26**, 348 (1956).
9. JANAF Thermochemical Table and Supplements, The Dow Chemical Co., Midland, Michigan.
10. T. O. Ingraham, *Trans. TMS-AIME*, **236**, 1064 (1966).
11. K. A. Bol'shakov and P. I. Fedorov, *Zh. Neorg. Khim.*, **3**, 1896 (1958).
12. C. Wagner, *This Journal*, **103**, 627 (1956).
13. B. Chattopadhyay and G. C. Wood, *ibid.*, **117**, 1163 (1970).
14. B. H. Kear, F. S. Pettit, D. E. Fornwalt, and L. P. Lemaire, *Oxid. Met.*, **3**, 577 (1971).
15. I. Barin, O. Knacke, and O. Kubaschewski, "Thermochemical Properties of Inorganic Substances, Supplement," Springer-Verlag, Berlin (1977).
16. S. H. Risbud and J. A. Pask, *J. Am. Ceram. Soc.*, **60**, 418 (1977).

Nature of Atmospheric Rust on Iron

I. Suzuki and Y. Hisamatsu

Department of Metallurgy and Materials Science, Faculty of Engineering, University of Tokyo, Tokyo, Japan

and N. Masuko

Institute of Industrial Science, University of Tokyo, Tokyo, Japan

ABSTRACT

In order to elucidate the mechanism of self-protection of weathering steel, the action of atmospheric rust was studied through a discussion of physical, chemical, and electrochemical nature of rust, with special attention to the effect of copper addition. The aggregating state of rust layer is influenced by two factors: the time of exposure and beneficial elements added to steel. Copper addition inhibits the growth of primary colloidal particle. This action of copper has an effect on the properties of rust and serves to increase the protective ability of rust layer.

This paper is concerned with the self-protection mechanism of weathering steel.

The atmospheric rust on weathering steel protects the steel under it. The exposure time required to form a protective rust layer depends on atmospheric conditions (1-5). There is little difference between the corrosion rate of weathering steel and that of mild steel in the first months of exposure, but a difference in corrosion rates gradually becomes apparent after the first year of exposure. Even the corrosion rate of mild steel decreased with exposure time.

Such corrosion behavior of steel in the early stage of exposure means rust particles on steel form layers, the protectiveness of which is increased by aging process themselves and the alloy elements added to steel, such as copper, chromium, and phosphorous, etc.

The results of many exposure tests (2-5) comparing weathering steel and mild steel have repeatedly demonstrated the value of weathering steel for use in an industrial atmosphere. This fact indicates that weathering steel utilizes atmospheric pollutants, particularly SO_2 gas, to form protective layers.

Key words: weathering, self-protection, copper.

Interestingly, x-ray analysis has indicated that there is little difference in the crystalline substance between the rust on weathering steel and that found on mild steel. Therefore, it is suggested that the amorphous substances are very important.

On the other hand, many workers have indicated that the atmospheric corrosion of steel proceeds by an electrochemical mechanism. In 1965, Evans suggested that the atmospheric corrosion mechanism of rusted steel involved an electrochemical reduction of rusts formed on steel (6). Evans' mechanism has been supported experimentally, and the author supports this position, also. This mechanism suggests that some rusts accelerate the corrosion of steel.

These characteristics of atmospheric rust mean that the action of rust is quite complex. In this paper the action of atmospheric rust was studied through a discussion of physical, chemical, and electrochemical nature of iron rust, with special attention to the effect of copper addition.

Physical Properties of Rust

Appearance of rust.—The surface rusts of pure iron exposed for 4 months are yellow-orange and are apt

to flake off from the bulk rust. On the other hand, the surface rusts of iron copper alloy exposed for 4 months have red-brown color, which is converted to dark brown by further exposure. Small orange spots are observed on the surface rust after rain. The change of rusts on iron copper alloy in color is similar to that of rusts on weathering steel. The chemical compositions of pure iron and iron copper alloy are shown in Table I.

Figure 1 shows the scanning electron micrographs of the surface texture of pure iron and iron copper alloy exposed for 4 months.

The outer rust layer on pure iron is more loose and better crystallized than the inner layer. The rusts of iron copper alloy are quite different from those of pure iron. 0.2% copper addition improves the aggregating state of rust particles. The shape of an aggregate is like a mushroom, which is composed of many fine crystals.

Figure 2 shows the surface rust on weathering steel exposed for 4.5 years. The chemical composition of weathering steel is shown in Table I. These photographs explain the process of formation of outer layer very well.

A in Fig. 2 shows the area where the outer layer flaked off from the bulk rust, thus forming initial corrosion products. The shape of these corrosion products is similar to that of iron copper alloy as mentioned earlier. After an extended period of exposure, these corrosion products become interconnected (Fig. 2B) and are converted to a compact outer layer (Fig. 2C).

Artificial rust.—In order to make the effect of copper more clear, artificial rusts were studied.

Artificial rusts are prepared by an interfacial reaction between concentrated ferric-ferrous salt solution and sodium hypoxide solution. Figure 3 shows the process of producing artificial rust. Artificial rust is very useful because it is able to be produced in layers which are similar to atmospheric rust layers in their appearance and structure. In the case of artificial rust containing copper, the copper content is from 2 to 5 weight percent (w/o). Therefore, the effect of copper addition on artificial rust is magnified in comparison with that of atmospheric rusts.

In the research on artificial rust, two important effects of copper addition were found. One of them is the fact that copper addition increases the mechanical strength of rust layers. Namely, even if a shock were given to the test tube, the layers of artificial rust containing copper were not destroyed. It was concluded that copper addition improves the flocculent state of colloidal aggregate; that is, copper addition causes an increase in flocculent force of colloidal particles.

Another important effect of copper addition is to inhibit the formation of spinel-type oxide. Namely, β -FeOOH (Akaganeite) and Fe_3O_4 (Magnetite) are detected in the artificial rust without copper, while the artificial rust with copper does not contain magnetite. Therefore, copper addition inhibits the formation of spinel-type oxide and thus decreases the electric conductivity of the rust layer.

Physical quantities of rust.—Physical quantities of rust layer were calculated from nitrogen absorption isotherms measured in the relative pressure up to 0.93 by the method of Cranston and Inkley (7).

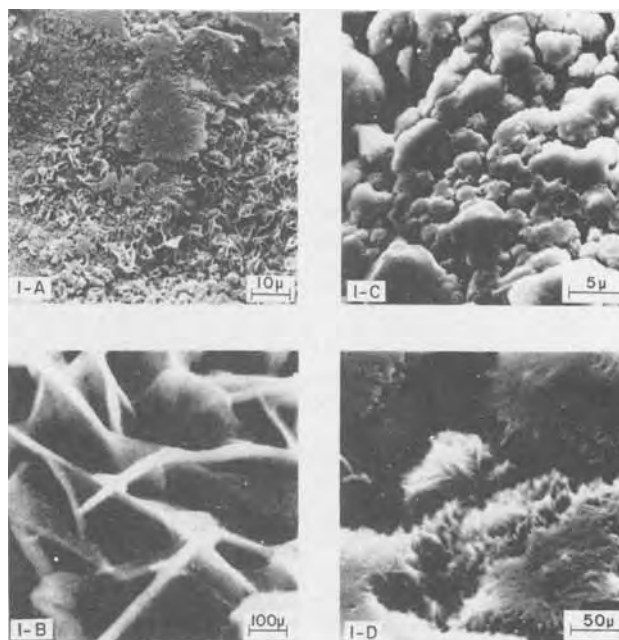


Fig. 1. Surface texture of rust layer on pure iron and iron copper alloy exposed for four months in urban atmosphere. (A,B) rust formed on pure iron, (C, D) rusts formed on Fe-0.2Cu alloy.

Figure 4 shows the pore-size distribution of the rust on pure iron exposed for 4 months and the rust on iron copper alloys exposed for one year. The pore sizes of atmospheric rusts are distributed in a range up to 15 nm, and the highest peak always appears in the diameter less than 5 nm.

Figure 5 shows the relationship between copper content and the total pore volume or the specific surface area of atmospheric rust. As the copper content increases, both factors tend to increase, but then decrease with extended exposure time.

These results show a same behavior of rust layer as shown in Fig. 1 and 2; that is, copper addition makes the rust layer more porous by inhibiting the growth of rust particles and, the longer the exposure time, the more compact is the layer formed by the aging process itself, in which the number of pores in the rust layer is decreased.

Chemical properties of rust.—Many results already reported show that the corrosion rate of steel depends on the nature of the atmospheric environment, in particular, there is a correlation between the corrosion rate, the concentration of SO_2 in the atmosphere, and that a weathering steel is less sensitive to SO_2 than a mild steel (2-5).

The relationship between the rust layer on steel and SO_2 in the atmosphere has been studied for about 20 years. The observation by Mayne (8) that iron sulfate in rust layers caused the breakdown of paint film led to the rusting mechanism of steel proposed by Schikorr (9) and Barton (10). The presence of SO_2 in the atmosphere results in the formation of H_2SO_4 in the rust layer, which attacks the steel under the rust layers. In regard to the relationship between SO_2 and the rusts on low alloy steel, Copson found that the greater the

Table I. Chemical composition of the materials exposed

Material	C	Si	Mn	P	S	Cu	Ni	Cr	Nb	Exposure site	Exposure time (yr)
Pure iron	0.002	0.005	—	0.003	0.005	—	—	—	—	Urban	1/3
Iron copper alloy	0.0031	0.005	—	0.003	0.005	0.20	—	—	—	Urban	1/3
Cu bearing steel	0.10	0.35	0.54	0.004	0.014	0.45	—	—	—	Urban	1
Plain steel	0.13	0.38	1.09	0.016	0.020	0.06	0.02	0.02	—	Rural	3
Weathering steel	0.08	0.35	0.40	0.090	0.008	0.32	0.32	0.59	0.04	Rural	3, 4.5

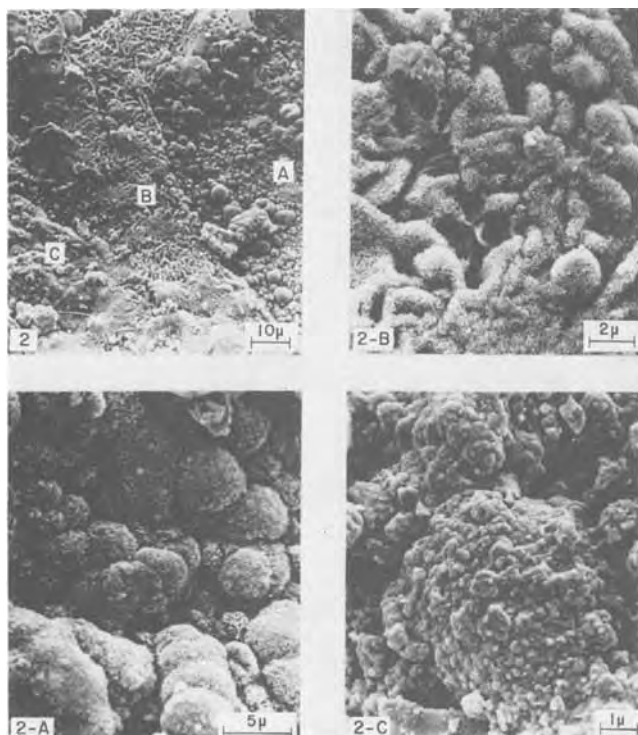


Fig. 2. Formation of outer rust layer on weathering steel. Top left, the area showing three growth steps of outer rust layer; (A) the area where outer rust layer flaked off and initial corrosion products were formed; (B) the area where corrosion products were interconnected; (C) the area where compact outer layer were formed.

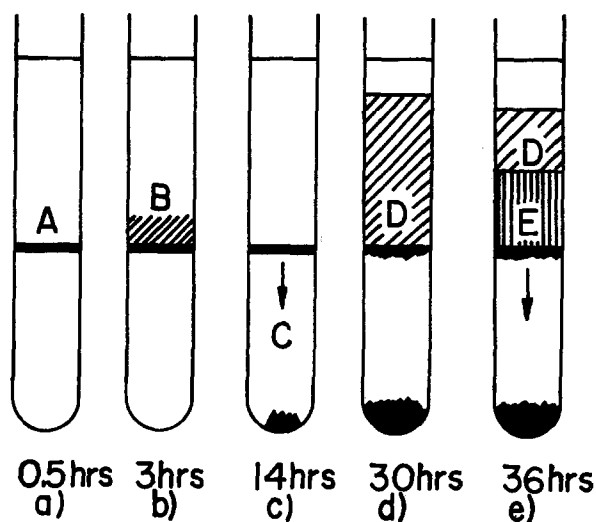


Fig. 3. Formation of artificial rust. (a) 5 ml of $\text{FeCl}_3\text{-FeCl}_2$ or $\text{FeCl}_3\text{-FeCl}_2\text{-CuCl}_2$ solution is gently added to 5 ml of 3M NaOH solution in a test tube with diameter 13 mm. A thin membrane is formed immediately at the interface (A). The total concentration of metallic salts is 0.75M. The notation of mixing ratio of them is indicated as (6-4-0), (6-3-1Cu) etc.; for example (6-3-1Cu) shows a solution of FeCl_3 , FeCl_2 , and CuCl_2 in the ratio of $0.6 \times 0.75:0.3 \times 0.75:0.1 \times 0.75\text{M}$. (b) After several hours it grows to a crust of hydrated oxide aggregate, over which yellow fine particles precipitate (B). (c) After 10 hr, some portions in contact with sodium hydroxide solution begin to fall down (C). (d) The floc of ferric hydroxide is formed over the crust facing metallic salt solution (D). (e) Black precipitated layer (E) by degrees is formed at the interface between a crust and D. After 24 hr, a crust is removed from the test tube and washed by deionized water. They are dried at room temperature after immersing in deionized water for 24 hr.

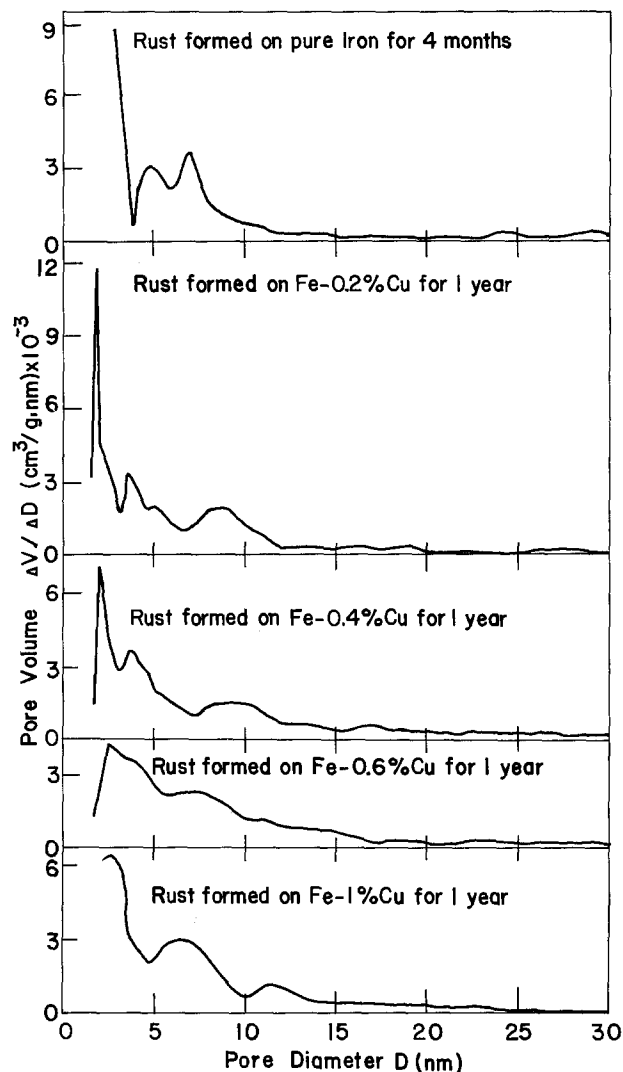


Fig. 4. Pore size distributions of rust layers on pure iron exposed for four months and iron copper alloys exposed for 1 year.

corrosion resistance of steel, the more sulfates existed in the loose layer (11). Copson (11) and Vernon (12) suggested that copper added to steel forms insoluble basic copper sulfate. However, basic copper sulfate has not been detected in the rust formed on copper-containing steel.

Since atmospheric rust layers have many pores as mentioned above, they are considered to have specific ability such as iron absorption.

In order to elucidate the chemical characteristics of the rust layer, the behavior of electrolytes in the rust layer, particularly the buffer ability of rust suggested by Barton (10), was investigated.

Buffer capacity of rust.—The buffer capacity, β , of a solution can be expressed in terms of the quantity of strong acid, C_A of the quantity of strong base, C_B , required to affect a unit change in pH of the solution, and may then be written

$$\beta = -\frac{dC_A}{dpH} = \frac{dC_B}{dpH}$$

It can be graphically represented by the slope of the titration curve. In this study the buffer capacity of rust, β , was determined from the titration curve of a suspension of 0.5g rust in 50 ml deionized water. The titration curve was obtained by using H_2SO_4 .

Therefore, the buffer capacity of rust may be written as

$$\beta = -\Delta(\text{H}_2\text{SO}_4)/\Delta pH$$

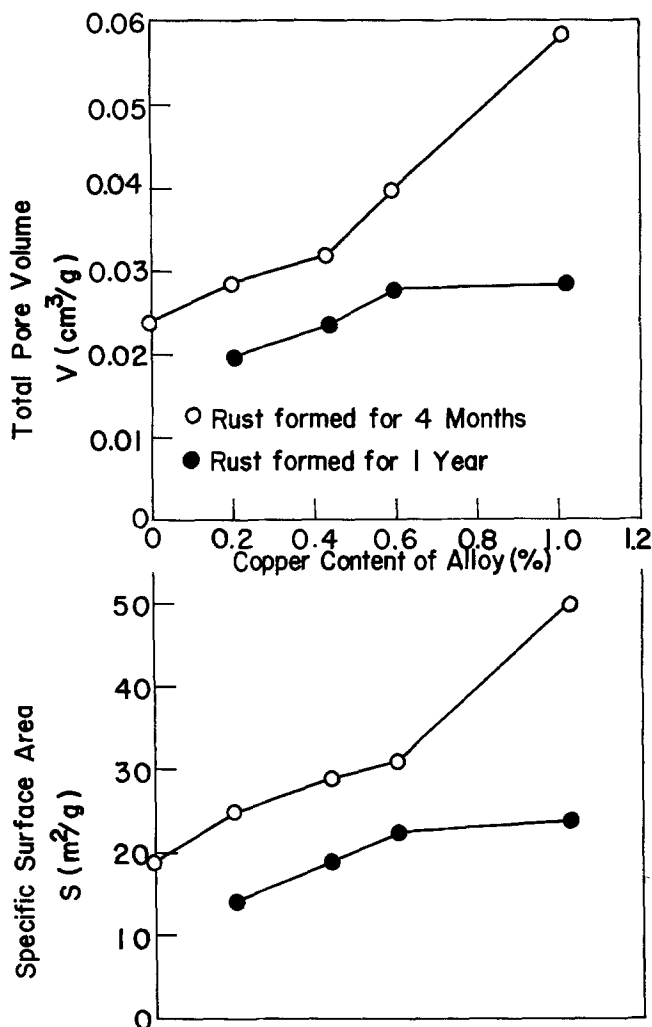


Fig. 5. Relationship between copper content of alloy and total pore volume or specific surface area of rust layer.

The dimension of buffer capacity of rust, β , is mole \cdot liter $^{-1} \cdot$ g $^{-1}$.

Figure 6 shows the buffer capacity of artificial and atmospheric rust. Atmospheric rusts were obtained from Cu bearing steel (in Table I) exposed for one year in an urban district. In the case of artificial rust, copper addition increased the buffer capacity in the whole pH range, and especially caused great buffer ability in the pH range from 4 to 6. On the other hand, the buffer capacity of atmospheric rust in pH range from 4 to 6 was not able to be determined since the pH of the suspension of atmospheric rust was less than 4. However, it is suggested from the buffer ability of artificial rust that atmospheric rusts with copper in the early stage of exposure have higher buffer capacity than those without copper in pH 4-6. In pH < 4, the same tendency was observed for atmospheric rust; that is, the rust on copper bearing steel had buffer capacity three times higher than that on pure iron. Therefore, copper added to steel increases the buffer capacity of the rust.

In the pH range from 3.5 to 7, the buffer ability results from the absorbing action of rust; in this instance, the rust layer keeps the concentrated H_2SO_4 in its pores (13). Consequently, the rust layers, in particular the outer layer, with great buffer capacity inhibit the attack of H_2SO_4 on steel. While in the rust layer, the H_2SO_4 which was absorbed accelerates the formation of a compact outer layer through the repeated dissolution and reprecipitation of rust particle in the presence of cupric ion. The formation of a compact outer layer promotes the growth of an inner layer.

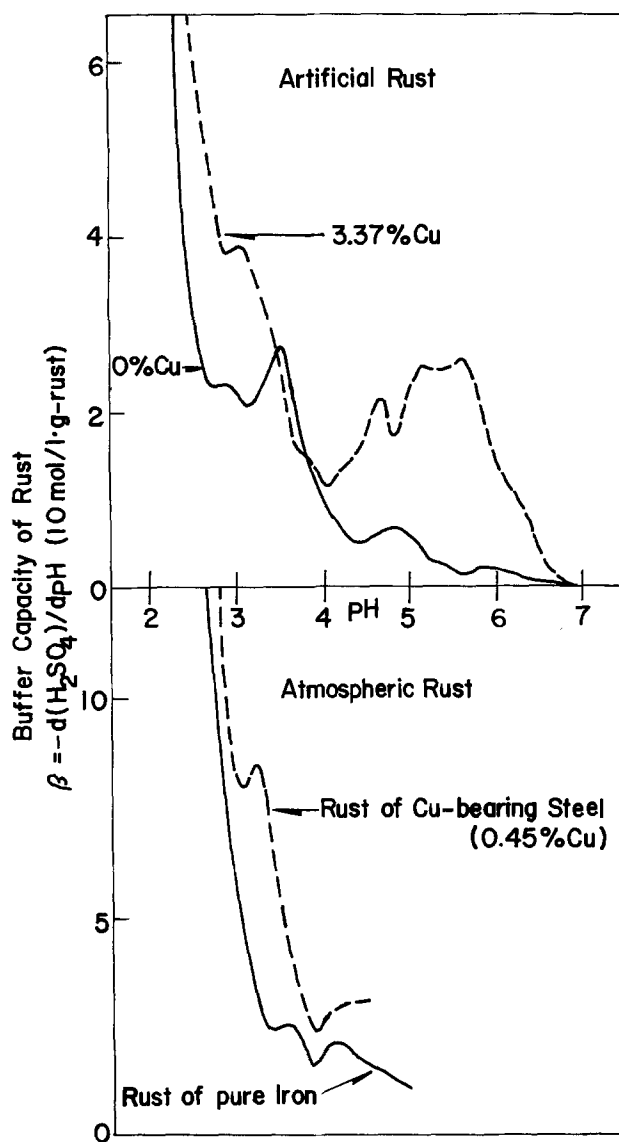


Fig. 6. Buffer capacity of artificial and atmospheric rust

Electrochemical properties of rust.—In order to elucidate the electrochemical properties of iron rust, the rust electrode was prepared from a rusty plate of pure iron. Pure iron specimens were exposed in an urban environment. The surface rust of pure iron exposed for 4 months was apt to flake off as a plate from the bulk rust. The thickness of rust plate was ca. 500 μ m.

Figure 7 shows two kinds of rust electrodes. The rust plate was fixed on an acrylic plate with a conductive adhesive. The rust electrode with a capillary (a) was prepared for studying cathodic polarization behavior of rust layers. The rust electrode (b) was prepared for examining the change in crystalline material in the rust layer during electrochemical reduction.

Figure 8 shows the internal polarization curves of various galvanic couples in 0.1M Na_2SO_4 . The internal polarization curve indicates the possibility that the rust layer acts as the cathode electrode in rusted iron. Internal polarization curves were determined in 0.1M Na_2SO_4 solution when exposed to air to be decreasing in steps the external resistance arranged in series in the short circuit of the galvanic couple of pure iron/electrode of rust [(a) in Fig. 7] or conductive adhesive. The apparent surface area of the electrode was 10 \times 10 mm. The distance between the electrodes was 20 mm. The rest potential of the rust electrode was Ca. 0.2V (SCE). The galvanic

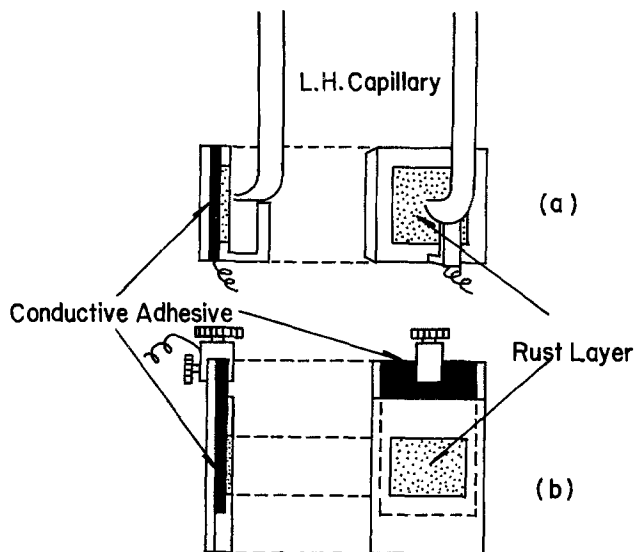


Fig. 7. Rust electrodes

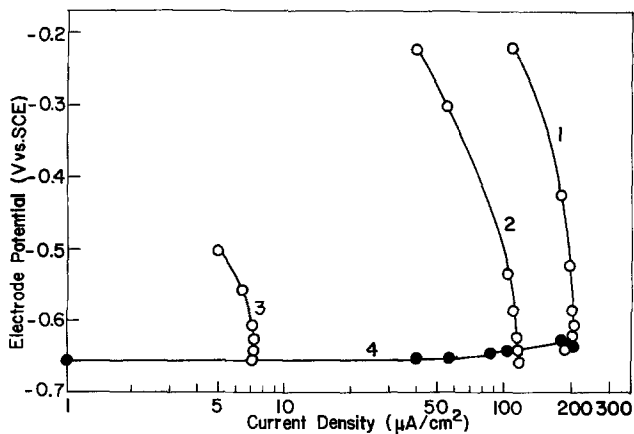


Fig. 8. Internal polarization curves of various couples. Curve 1: rust layer before reduction, curve 2: rust layer partially reduced, curve 3: conductive adhesive, curve 4: pure iron.

current of pure iron/electrode of conductive adhesive is $7 \mu\text{A}/\text{cm}^2$, which is very small in comparison with $200 \mu\text{A}/\text{cm}^2$ of pure iron/rust electrode and is the reduction current of dissolved oxygen on the surface of conductive adhesives. By comparison, the galvanic current density of pure iron, a partially reduced rust electrode is $100 \mu\text{A}/\text{cm}^2$. These results indicated that a part of the cathodic reaction of rusted steel is the reduction of the rust layer and that some rusts accelerate the corrosion rate beyond that of dissolved oxygen as Evans suggested (6).

Figure 9 shows the change of crystalline substance in rust layers by cathodic reduction. The sample was the rust electrode (b) in Fig. 7. The crystalline parts of pure iron rust plate were composed of $\gamma\text{-FeOOH}$ (Lepidocrocite), $\alpha\text{-FeOOH}$ (Goethite), and Fe_3O_4 (Magnetite). The crystalline materials in the surface layer were $\gamma\text{-FeOOH}$, $\alpha\text{-FeOOH}$, and Fe_3O_4 . The x-ray diffraction intensity of $\gamma\text{-FeOOH}$ was the strongest while that of $\alpha\text{-FeOOH}$ was very weak. The interior of the rust plate consisted mainly of Fe_3O_4 and a little $\alpha\text{-FeOOH}$. $\gamma\text{-FeOOH}$ was not detected. In the separating face from the bulk rust, the growth of crystalline material was inhibited and the intensity of $\alpha\text{-FeOOH}$ was stronger; that of Fe_3O_4 was weaker than those of the interior. $\gamma\text{-FeOOH}$ did not exist there. The reduction current density is $100 \mu\text{A}/\text{cm}^2$. Electrolyte solution is $0.1\text{M Na}_2\text{SO}_4$.

The x-ray identification of a crystalline substance was carried out by wetting the rust electrode with

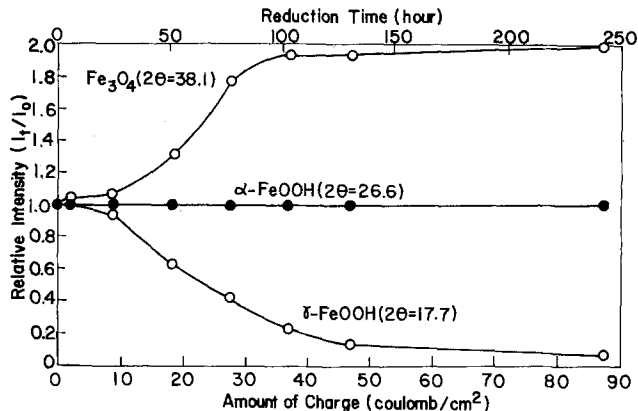


Fig. 9. Change in the intensity of crystalline substances in the rust layer with cathodic reduction. I_0 : The intensity of various crystalline substances before cathodic reduction; I_t : the intensity of various crystalline substances after t hr reduction.

deionized water to avoid drying of the rust. The relative intensity (I_t/I_0) in Fig. 9 is the ratio of the intensity of various crystalline substances before cathodic reaction to the intensity of various crystalline substances after t hr reduction. The pure Fe_3O_4 powder ($2\theta = 38.1$), which formed by a dry process, was used as a standard of crystalline substances. $\gamma\text{-FeOOH}$ is apt to be reduced cathodically, and $\alpha\text{-FeOOH}$ is not reduced. The effect of reduction on the x-ray intensity of $\gamma\text{-FeOOH}$ appears after 20 hr, 7Cm^{-2} being required.

From the fact that $\gamma\text{-FeOOH}$ was not identified in the inner layer, which occupied the major portion of the rust plate, and that $\gamma\text{-FeOOH}$ in the surface layer was not influenced in the initial reduction stage, it is concluded that the reduction of rust occurs in the inner layer and that the substance reduced electrochemically is not only $\gamma\text{-FeOOH}$; i.e., there are reducible amorphous substances in addition to $\gamma\text{-FeOOH}$ in the rust layer. $\gamma\text{-FeOOH}$ appears to be converted directly to Fe_3O_4 by cathodic reduction in Fig. 9. However, there may not be a direct relationship between $\gamma\text{-FeOOH}$ and Fe_3O_4 . Figure 9 shows that $\gamma\text{-FeOOH}$ changed into the other solid phase and that Fe_3O_4 was also formed from reducible amorphous substances. The reducible amorphous substances are hereafter referred to as intermediate substances.

Figure 10 shows the difference in electrochemical behavior between rusted plain steel and rusted weath-

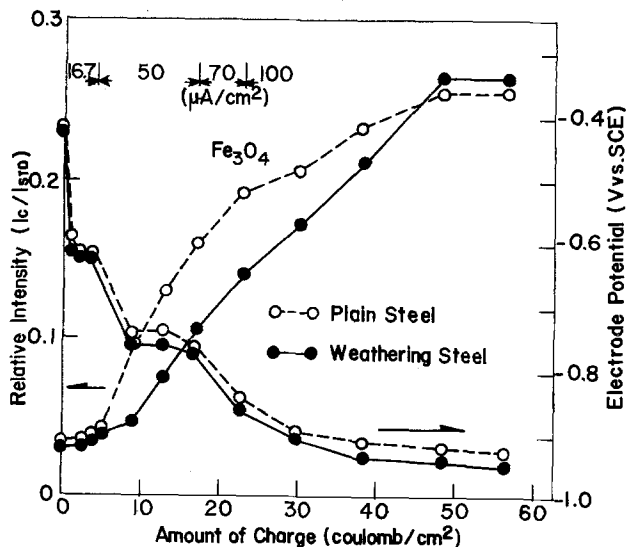


Fig. 10. Changes in the intensity of Fe_3O_4 and the potential of rusted steel with cathodic reduction.

ering steel. The chemical compositions of both steels are shown in Table I.

Specimens of both steels were exposed for three years in an urban atmosphere. The apparent surface area of the rusted steel electrode was 15×15 mm. The cathodic current density was increased from 16.7 to $100 \mu\text{A}/\text{cm}^2$ in steps. The x-ray diffraction intensity of Fe_3O_4 was slightly stronger in the rust on plain steel than that on the weathering one before cathodic reduction. Relative intensity (I_c/I_{std}) in Fig. 10 is the intensity ratio of Fe_3O_4 in the rust layer for that of pure Fe_3O_4 powder formed by a dry process. There is no difference in potential, but a great difference in the increase of Fe_3O_4 between them by cathodic reduction. The potential behavior of both rusted steels shows that the reduction of rust occurred in the rust layer on weathering steel as much as in that on plain steel. Therefore, the rust layers on weathering steel contain less intermediate substances, which are apt to be converted to crystalline magnetite by cathodic reduction, than those on plain steel. The cathodic reduction of rust at the initial stage occurs in the inner layer, which had been most affected by beneficial elements added during the exposure period. Therefore, the difference in the formation of crystalline magnetite at this initial stage between both rusted steels emphasized the electrochemical characteristics of the rust layer on weathering steel.

Generally rusts on steel are reduced electrochemically for a short time just after the rust layer is wetted by rain, etc. Even if the rust layer was wetted for a long time, the reduction of rusts does not contribute to the corrosion rate, except the initial time of rain, and the main cathodic reaction is the reduction of dissolved oxygen on steel or magnetite in the rust layer since magnetite is a good electric conductor, as Evans pointed out (6), and $\gamma\text{-FeOOH}$ and $\alpha\text{-FeOOH}$ are not electric conductors.

It is concluded that beneficial elements added to steel inhibit the formation of crystalline magnetite in the cathodic reaction process and thereby increase the electric resistance of the rust layer.

Conclusion

The atmospheric rust layers on steel are secondary aggregate of primary colloidal particles. The aggregating state of the rust layer is influenced by two factors: the time of exposure and beneficial elements added to steel. In particular, copper addition inhibits the growth of primary colloidal particles. This action of copper has an effect on the physical, chemical, and electrochemical properties of rust and serves to increase the protective ability of the rust layers.

The summary of results are shown as follows:

(i) Copper addition to iron inhibits the growth of iron oxide, in particular, spinel-type oxide in the

rust layer and accelerates the formation of amorphous substances. This effect induces an increase in flocculent force of colloidal aggregate and thereby develops mechanical strength of the rust layer and decreases the electric conductivity of the rust layer.

(ii) The pore size of atmospheric rust distributed in the range up to 15 nm, and the highest peak always appears below 5 nm.

The total pore volume in the rust layer formed for 1 year is $1.94\text{--}2.84 \times 10^{-2} (\text{cm}^3\text{g}^{-1})$.

The specific surface area of rust formed for 1 year is $14.2\text{--}23.9 (\text{m}^2\text{g}^{-1})$. Both factors increase with copper content and decrease with the time of exposure.

(iii) Atmospheric rusts on steel have buffer ability for H_2SO_4 . Copper added to steel increases the buffer capacity three times as much as those without copper at pH 3.3. This action of atmospheric rust inhibits the attack of H_2SO_4 on steel and accelerates the formation of the compact outer layer to protect the inner layer.

(iv) Beneficial elements added to steel decrease the formation of intermediate substances, which are converted to crystalline magnetite by cathodic reaction and thereby increase the electric resistance of the rust layer.

Manuscript submitted Aug. 31, 1979; revised manuscript received Jan. 18, 1980. This was Paper 111 presented at the Pittsburgh, Pennsylvania, Meeting of the Society, Oct. 15-20, 1978.

Any discussion of this paper will appear in a Discussion Section to be published in the June 1981 JOURNAL. All discussions for the June 1981 Discussion Section should be submitted by Feb. 1, 1981.

Publication costs of this article were assisted by Lehigh University.

REFERENCES

1. J. C. Hudson and J. F. Stanner, *J. Iron Steel Inst.*, **180**, 271 (1955).
2. C. P. Larrabee and S. K. Coburn, "1st Int. Cong. on Metallic Corrosion," p. 76, London (1961).
3. K. Horikawa *et al.*, *Boshoku Gijutsu*, **13**, 525 (1964).
4. K. Oma *et al.*, *ibid.*, **13**, 15 (1964).
5. R. Bruno, G. Agabio, and G. Bombara, *J. Br. Corros.*, **7**, 122 (1972).
6. U. R. Evans, *Nature*, **206**, 980 (1965).
7. R. W. Cranston and F. A. Inkley, *Adv. Catal.*, **9**, 143 (1957).
8. J. E. O. Mayne, *J. Appl. Chem.*, **9**, 673 (1959).
9. G. Schikorr, *Werkst. Korros.*, **14**, 69 (1963).
10. K. Barton and Z. Bartonova, *ibid.*, **20**, 216 (1969).
11. H. R. Copson, *Proc. Am. Soc. Test. Mater.*, **45**, 554 (1945); **52**, 1005 (1952).
12. W. H. J. Vernon, *J. Iron Steel Inst.*, **196**, 333 (1960).
13. I. Suzuki, N. Masuko, and Y. Hisamatsu, *Boshoku Gijutsu*, **21**, 417 (1972).
14. I. Matsushima and T. Ueno, *ibid.*, **17**, 458 (1968).

Properties of Thin Polyimide Films

L. B. Rothman*

IBM Data Systems Division, East Fishkill, Hopewell Junction, New York 12533

ABSTRACT

Polyimide is receiving increasing interest as a possible insulator on semiconductor devices, replacing SiO₂. Several commercially available polyimides have been characterized by testing films of them for electric breakdown strength, conductivity, adhesion, and other properties. The results of these tests are summarized, and the polyimides are compared to sputtered SiO₂.

Polyimide has excellent thermal stability and chemical resistance, along with good dielectric properties. This combination of characteristics makes it promising as a replacement for SiO₂ for insulating semiconductor devices. Several multilevel metal structures using polyimide as the insulator have been described in the literature (1-4).

To develop a base of understanding in support of this use of polyimide, several commercially available materials have been tested for a variety of functional properties. Film thickness ranged from 1 to 3 μm. Electrical and physical measurements were compared with measurements for sputtered SiO₂ films.

Sample Preparation

A description of the polyimide materials as received from the vendor is shown in Table I. There are considerable differences in these materials, including solvent system, solids content, and viscosity. Two of the materials were received in powder form, which is an advantage in terms of shelf-life. The materials received in solution, such as polyamic acid, had a shelf-life of approximately one year when stored at 4°C.

In order to cast films of 1-3 μm thickness by spin coating, the materials were diluted with additional solvent to the solids content shown in Table I. It is interesting that there is also a difference in the solids content of the solutions for coating the same film thickness. As received, all the materials had a great deal of particulates and, therefore, all the solutions had to be filtered prior to use. Filtering was done using silver membrane filters with a pore size of 0.45 μm. Thin films of 1-3 μm were prepared by spin coating at spin speeds of 4-6 krpm. Curing was done on hot plates. All of the testing was done on blanket polyimide films.

* Electrochemical Society Active Member.
Key words: electric breakdown strength, conductivity, adhesion, insulators.

Table I. Comparison of various polyimide resins as received and as used

Polyimide	As received			As used
	Solids content (w/o)	Viscosity (cps)	Solvent	Solids content (w/o)
A	16	6000	NMP	13
B	27	5600	NMP/acetone	18
C	38-42	250-350	DMF	32
D	63-67	3000-7000	NMP	47
E	55	4000	NMP/methanol	36
F	Powder		4:1	60
G	Powder			15

NMF: methylpyrrolidnone.
DMF: dimethylformamide.

Dielectric Properties

In order to use polyimide as a replacement for SiO₂ for insulating semiconductor devices, it must have good dielectric properties. Measurements of breakdown strength, conductivity, dielectric constant, and the dissipation factor have been made on fully cured polyimide films with comparisons made to sputtered SiO₂.

The cure cycle was determined by dissipation factor measurement, as suggested by Gregoritsch (5). An Al-polyimide-Al dot structure was used and the dissipation factor was measured at a frequency of 1 MHz, as a function of the final cure temperature. Some results are shown in Fig. 1a and b. The dissipa-

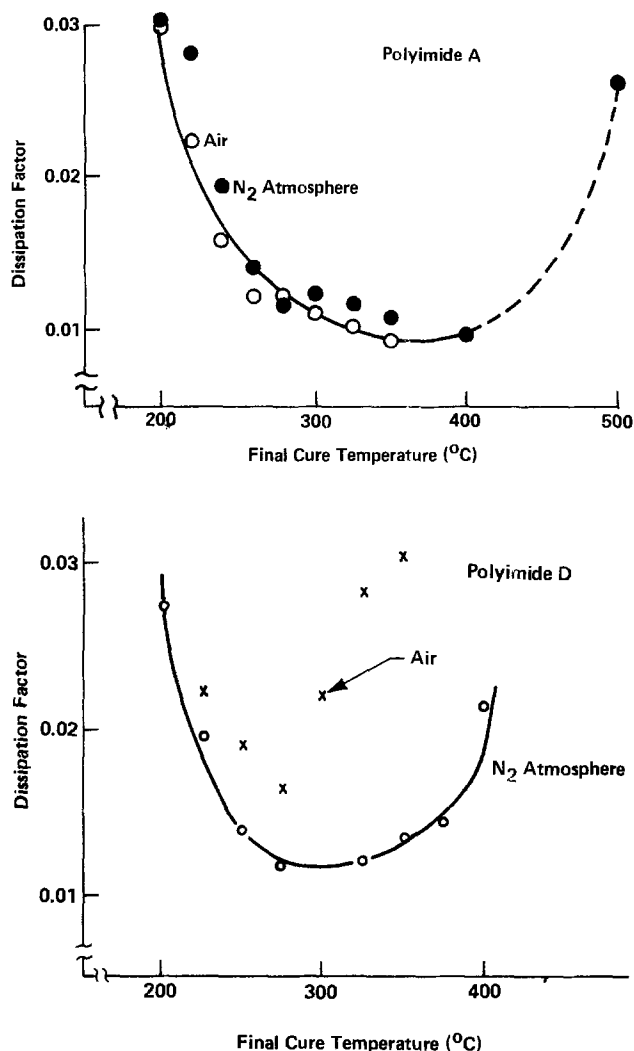


Fig. 1. Dissipation factor as a function of final cure temperature for (a) 1.5 μm film of Polyimide A, (b) 1.5 μm films of Polyimide D. Time at final cure temperature was 30 min.

tion factor decreases with increasing cure temperature until full cure is reached and then increases as decomposition starts to occur. Curing in nitrogen and air were investigated. Figure 1b shows that for Polyimide D there is a substantial difference in the dissipation factor between curing in air and nitrogen whereas Polyimide A does not exhibit this effect. For the data which follows, the curing of the polyimides was therefore done in a nitrogen atmosphere for the final cure. The dissipation factor of the fully cured 1.5 μm polyimide films was approximately 0.01 for all the materials tested.

The dielectric breakdown strength was measured using an Si-polyimide-Al dot structure. The polyimide film thickness used was 1.5 μm . Al dots of 1.5 mm diam were used. Fifty measurements were made on each wafer. The voltage was ramped at a rate of 1 V/sec until breakdown occurred. It can be seen in Table II that all of the polyimide films tested exhibited good dielectric breakdown strength, which is comparable to SiO_2 . The data reported in Table II are for polyimide films cast from carefully filtered solutions as described previously. Without filtering the raw materials the dielectric breakdown strength was in the low 10^5 V/cm range.

For measurements of conductivity, an Al-polyimide-Al dot structure was tested in electric fields ranging from 5×10^4 to 5×10^5 V/cm and temperatures up to 250°C. Figure 2 shows that the log of the resultant current varies linearly with the square root of the electric field for all of the materials tested. This exponential dependence of the current on the square root of the applied voltage has been reported previously for Kapton polyimide films (6). It is observed in Fig. 2 that the conductivities of individual polyimides differ widely, and all of them are considerably higher than that of sputtered SiO_2 . All of these materials, however, appear to be adequate insulators, since for typical semiconductor device use conditions (85°C, 10^5 V/cm) their resistivities are over 10^{12} $\Omega\text{-cm}$.

Data is not presented for Polyimide F due to problems of instability in the film, probably due to water absorption. The films of Polyimide F would appear quite conductive ($J > 10^{-3}$ A/cm²) as initially tested. After baking the test samples for an hour at 200°C and then immediately testing, the conductivity of the films was similar to the other polyimide films. If the test sample remained at ambient conditions for a few hours, it would become conductive once again. This phenomenon was not observed with any of the other materials.

The dielectric constant was measured at a frequency of 1 MHz and found to be approximately 3.5 for all of the polyimide films tested compared to 3.8 for sputtered SiO_2 . This lower dielectric constant of polyimide is an advantage over SiO_2 .

Planarization

For high density multilevel metal-insulator structures it is desirable to have a planar surface. It has been reported in the literature (1, 2) that polyimides can be used as the insulator to provide such a planar structure. During the cure cycle for the polyimide film there is a tendency for flow to occur. Also, during

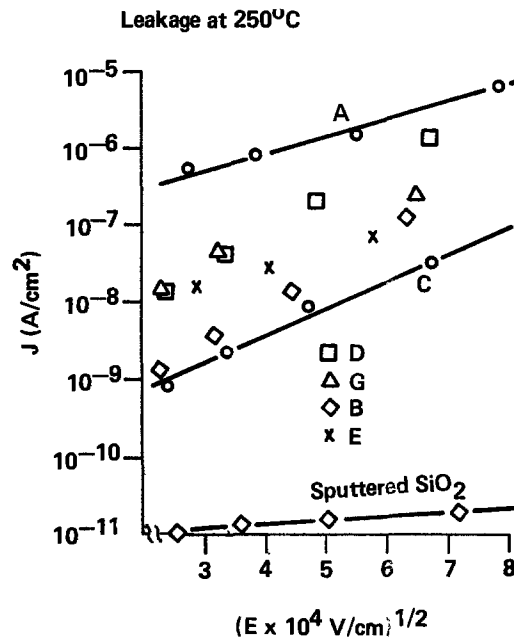


Fig. 2. Current density vs. applied field at 250°C for various polyimide films with a comparison to sputtered SiO_2 .

the cure cycle there is a great deal of shrinkage due to solvent loss. It was observed that some of the materials tested exhibited a combination of less shrinkage and more flow than others. It is the combination of shrinkage and flow during the three stages of the cure cycle which provides polyimide films with the ability to planarize or smooth out any topological structures on a substrate.

The degree of planarization is determined by the ratio of the step height resulting with the polyimide film to the initial step height of the metal pattern as shown in Fig. 3. Another factor in the degree of planarization is the slope of the resulting step.

The planarity measurements were made with a Taylor-Hobson Talystep and also SEM examination. Some general observations for all the polyimide films are that the degree of planarization is directly dependent on the thickness of the polyimide films. The slope of the polyimide over the metal land decreases with increasing polyimide thickness. It was also observed that the degree of planarization is dependent on both the width and spacings of the metal lines which the polyimide is covering as shown in Fig. 4. Thin lines with narrow spaces result in better planarization. Unfortunately, this geometry dependence of planarization becomes quite complicated since a group of closely spaced lines, separated by a large distance (≥ 12 μm) from other lines, act as one wide land. However, it seems that a group of narrow lines planarizes slightly better than a single line of the same overall width. The degree of planarization, therefore, is dependent on the geometry of the

Table II. Dielectric breakdown strength of 1.5 μm polyimide films

Polyimide	Average breakdown field ($\times 10^6$ V/cm)
B	4.74
D	5.62
A	5.94
G	6.28
E	6.63
C	7.06
F	7.50
SiO_2 (sputtered)	8.60

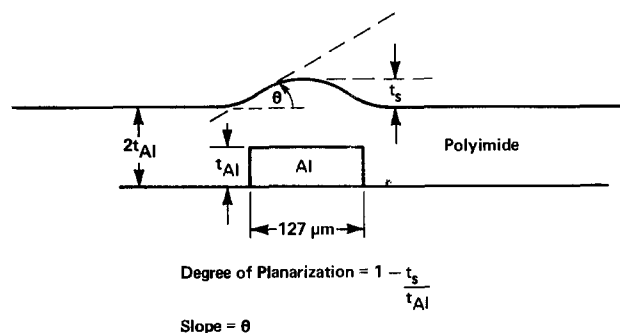


Fig. 3. Degree of planarization for polyimide over a metal step

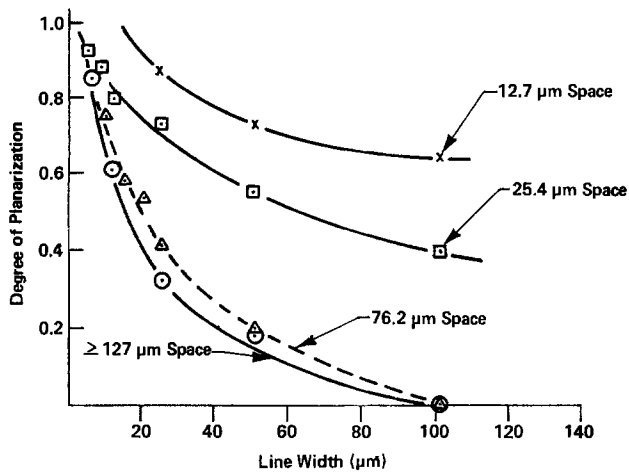


Fig. 4. Planarization as a function of line width and space for Polyimide C films.

metallization pattern (i.e., individual line widths, line spacings, and group dimensions).

A difference in the degree of planarization was observed for the various materials tested. Figure 5 shows Talystep measurements for two polyimides over a metal pattern of varying line widths. The trend toward more planarization as the line width decreases is seen for both materials; however, in general, Polyimide C planarizes more than Polyimide A. Figure 6 illustrates the difference in planarity of the two materials. In order to make an easy comparison of planarization, measurements were made over a single metal line of 12.7 μm in width. Table III shows the degree of planarization for the various polyimide films. Three of the materials seem to provide a conformal type coating, while the other four polyimides seem to planarize more. There appears to be a correlation between the solids content of the coating solution and the degree of planarization. Higher solids content material provides more planarization.

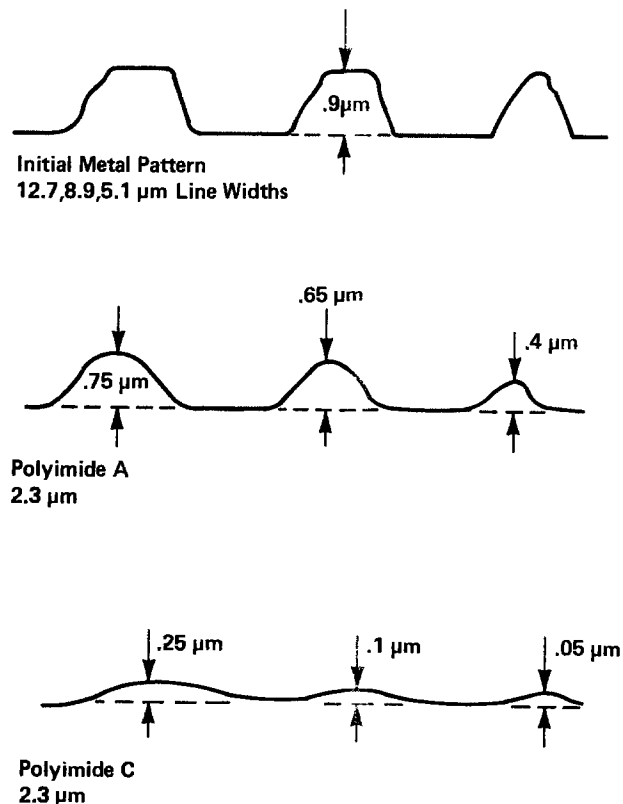


Fig. 5. Talystep measurements comparing degree of planarization achieved with Polyimide A and Polyimide C films.

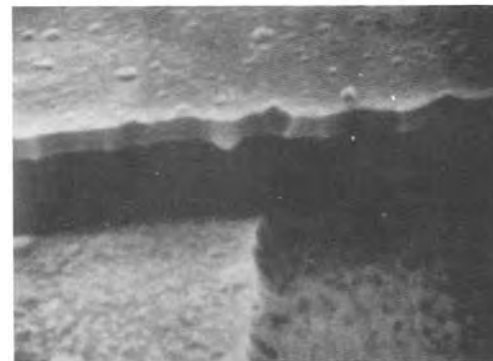
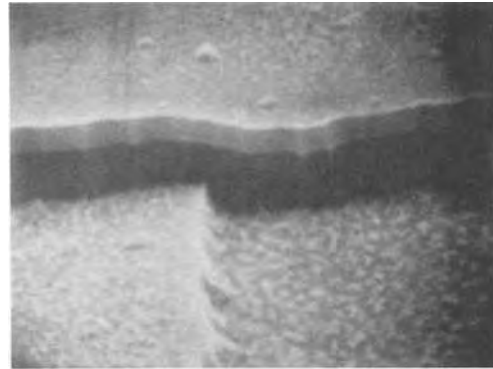


Fig. 6. SEM pictures compare the degree of planarization of Polyimides A (top) and C (bottom). Pictures show a cross section of a polyimide film (which is covered with Al) over a metal line. (The cross section was made by RIE and the Al over the polyimide was used as a mask). (6000 \times .)

Due to the many geometry effects, it does not seem possible to completely planarize a typical metal pattern with a polyimide film. Good edge coverage, however, is obtained with all of the various polyimide films even when planarization is not achieved. This good edge coverage of polyimide films is an advantage over standard sputtered SiO_2 films deposited with a re-emission coefficient of ~ 0.3 (7). Typically SiO_2 films are somewhat conformal but have a tendency to cusp at the edges of metal lines resulting in poor edge coverage.

Adhesion

One of the most important properties of a thin film, such as polyimide, is its adhesion to the semiconductor substrate and metallurgy, and the adhesion of other materials to the polyimide film. Of the numerous methods for the measurement of adhesion of thin films (8), the technique we found the most reliable was the peel force test.

A schematic of the peel force test apparatus is shown in Fig. 7. The force transducer is fixed on a sliding stage. It is connected by a long rod to the test sample. The test sample consists of a strip of wafer of known width attached by two sided tape to a glass slide. It is mounted such that approximately

Table III. Degree of planarization for 2 μm polyimide films over 1 μm Al lines

Polyimide	% of solids in solution used to coat 2 μm film	Degree of planarization (over 12.7 μm line)
A	13	0.17
B	18	0.30
G	15	0.32
C	32	0.72
D	47	0.78
E	36	0.78
F	60	0.82

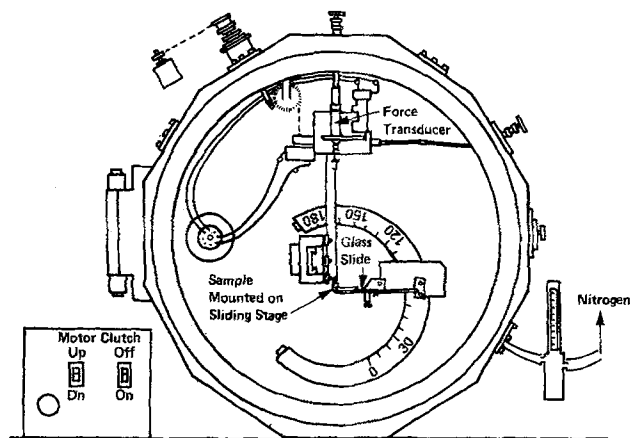


Fig. 7. Schematic of peel force test apparatus

a quarter inch of the wafer strip overhangs the edge of the glass slide. The wafer strip is carefully broken where it overhangs the glass slide, leaving the film intact. Then this part is bent up and attached to the flat end of the rod using glycolphalate. The stage was adjusted for a peel angle of 90° for consistency and ease of peeling. The peel rate is 0.15 mm/sec. The stage holding the test sample slides at the same rate as the stage holding the force transducer providing a constant peel angle. The output of the force transducer is recorded on a strip chart recorder. The peel test is performed in an enclosed chamber which is purged with dry nitrogen.

Strips of wafers of various widths were used to obtain a relative measure of adhesion. A graph of peel force vs. width as shown in Fig. 8 is plotted and the slope of this line (K) is used as the relative measure of adhesion. It is also observed that the intercept of this line is not always zero due to edge effects: damage inflicted to the interface at the edges while the wafers were scribed into strips.

Adhesion measurements were made after processing and again after temperature-humidity stress cycles.

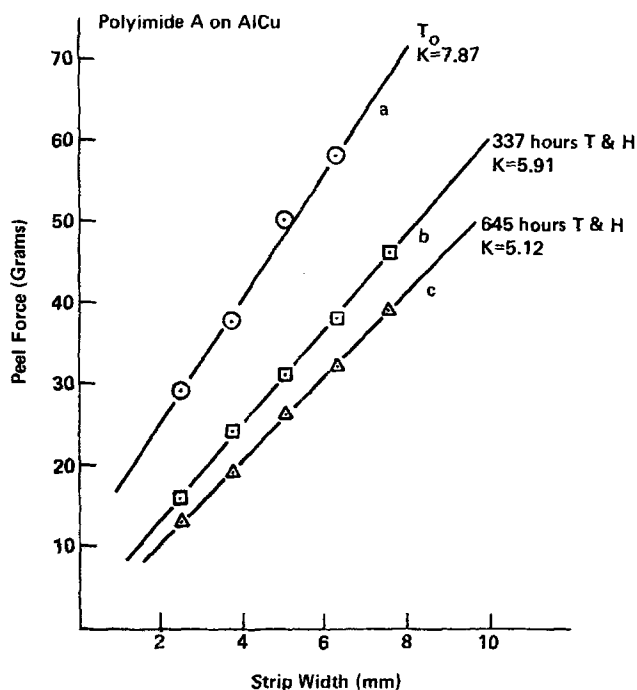


Fig. 8. Peel force vs. strip width for Polyimide A on AlCu, as a function of time in a temperature/humidity chamber. (a) initially $K = 7.87$ g/mm, (b) after 337 hr at 85°C , 80% relative humidity $K = 5.91$ g/mm, (c) after 645 hr $K = 5.12$ g/mm.

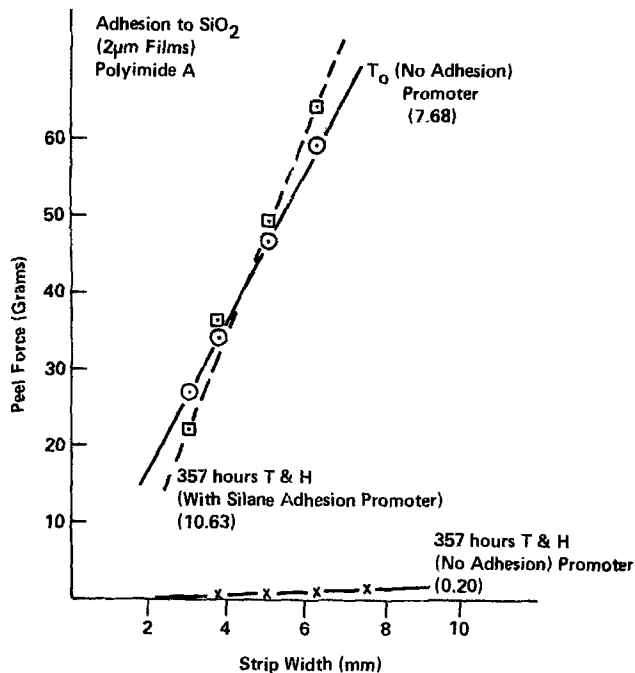


Fig. 9. Polyimide adhesion to SiO_2 . Using silane adhesion promoter: No peel at T_0 and $K = 10.63$ g/mm after 357 hr at 85°C , 80% relative humidity. Without any adhesion promoter: $K = 7.68$ at T_0 and $K = 0.20$ g/mm after 357 hr of T&H.

Figure 8 shows that the adhesion tends to degrade after exposure to temperature-humidity stressing.

The initial adhesion of polyimide to Si and SiO_2 surfaces was good; long exposure to stressing, however, tended to degrade the interface. It was found that silane adhesion promoters (9) improved the long-term stability of the bond. Figure 9 shows a comparison for Polyimide A on SiO_2 . Both at T_0 and after stressing the adhesion of the polyimide film to SiO_2 is improved when a silane-type adhesion promoter was used.

It is observed in Table IV and Fig. 8 that the major degradation in the adhesion appears after the initial exposure to T&H stressing.

The "no peel" condition shown in Table IV indicates excellent adhesion. It occurs when the peel starts and a full scale deflection is recorded on the chart recorder and the polyimide film tears, thereby implying a peel factor of 31.5 g/mm or greater. A partial peel condition is more difficult to interpret. This is when the polyimide film starts to tear unevenly as it is peeling, indicating that the adhesion of the film is not uniform across the surface, and that there are areas of very good adhesion where the polyimide film is not peeling.

For all the data presented a silane adhesion promoter was used on Si and SiO_2 surfaces. However, for Al surfaces no difference was found in the adhesion of polyimide with or without an adhesion promoter.

Table V illustrates that the adhesion at T_0 of polyimide to Si is good for all the materials tested. After T&H stressing, however, two of the materials show a degradation in their adhesion to Si surfaces.

Table IV. Polyimide adhesion to SiO_2 as a function of temperature and humidity stressing at 85°C , 80% relative humidity

Polyimide	Adhesion to SiO_2 : K (g/mm) hr T&H					
	T_0	357	762	1122	1770	2495
A	PP	11.03	9.06	10.24	6.70	8.27
B	NP	NP	NP	NP	NP	NP

NP: no peel, excellent adhesion. T&H: 85°C , 80% relative humidity. $2 \mu\text{m}$ polyimide films.

Table V. Polyimide adhesion to Si

Polyimide	Adhesion to Si: K (g/mm)	
	T ₀	After 563 hr T&H
F	NP	NP
D	NP	NP
C	NP	NP
G	PP	8.67
E	NP	NP
A	NP	18.52
B	NP	NP

3 μ m polyimide films on Si wafers.
 NP: no peel condition, excellent adhesion ≥ 31.52 g/mm.
 PP: partial peel, films start to peel unevenly then tear.
 T&H: 85°C, 80% relative humidity.

The adhesion of polyimide films over Al and Al alloys was excellent for almost all the materials tested as shown in Table VI. The adhesion of Al over polyimide was satisfactory before the T&H stress cycle, but severely degraded after it for all materials tested. Typically, values of K greater than 18 g/mm were measured at T₀; however, after 200 hr at 85°C, 80% relative humidity, the value of K went down below 3 g/mm. Annealing the metal at 350°C in nitrogen before test improves the Al to polyimide adhesion,

Table VI. Polyimide adhesion to Al

Polyimide	Adhesion to Al: K (g/mm)	
	T ₀	After 564 hr T&H
F	NP	NP
D	NP	NP
C	PP	PP
G	PP	PP
E	NP	NP
A	10.64	8.27
B	PP	PP

3 μ m polyimide films of Al surface without using any adhesion promoter.
 T&H: 85°C, 80% relative humidity.
 NP: no peel condition, excellent adhesion ≥ 31.52 g/mm.
 PP: partial peel, film starts to peel unevenly then tears.

resulting in a peel factor of approximately 10 g/mm after the stress cycle.

Conclusion

In summary, the polyimide films of various vendors exhibited differences in functional properties. The dielectric properties of polyimide films are not quite as good as sputtered SiO₂ with regard to breakdown strength and resistivity. The adhesion of polyimide to various materials is also not always as good as SiO₂ depending on the polyimide. Polyimide does provide an advantage in good edge coverage and some planarization of topography. Considering all of these properties, polyimide films seem to be more than satisfactory for application to semiconductor devices.

Manuscript submitted Dec. 6, 1979; revised manuscript received April 14, 1980.

Any discussion of this paper will appear in a Discussion Section to be published in the June 1981 JOURNAL. All discussions for the June 1981 Discussion Section should be submitted by Feb. 1, 1981.

Publication costs of this article were assisted by IBM Corporation.

REFERENCES

1. K. Sato, S. Harada, A. Saiki, T. Kimura, T. Okubo, and K. Mukai. *IEEE Trans. Parts, Hybrids, Packag.*, **ph-9** 176 (1973).
2. A. Saiki, S. Harada, T. Okubo, K. Mukai, and T. Kimura, *This Journal*, **124**, 1619 (1977).
3. J. C. Yen, Abstract 170, p. 444, The Electrochemical Society Extended Abstracts, Dallas, Texas, Oct. 5-9, 1975.
4. L. B. Zielinski, U. S. Pat. 3,985,597 (1975).
5. A. J. Gregoritsch in 14th Annual Reliability Physics Conference, Las Vegas, 1976.
6. J. R. Hanscomb and J. H. Calderwood, *J. Phys. D. Appl. Phys.*, **6**, 1093 (1973).
7. J. S. Logan, F. S. Maddocks, and P. D. Davidse, *IBM J. Res. Develop.*, **14**, 182 (1970).
8. K. L. Mittal, *Electrocomponent Sci. Technol.*, **3**, 21 (1976).
9. E. P. Plueddemann, in "Treatise on Coatings," Vol. 1, R. R. Meyers and J. S. Long, Editors, Part III, pp. 381-400, Marcel Dekker, Inc., New York (1972).

The Dependence of the Memory Effect in ZnS:Mn A-C Thin Film Electroluminescence on Mn Distribution

V. Marrello and A. Onton

IBM Research Laboratory, San Jose, California 95193

ABSTRACT

It is known that the width of the memory loop of the brightness-voltage characteristic in ZnS:Mn a-c thin film electroluminescence devices depends on the Mn doping concentration and on the ZnS:Mn film thickness. In this study we have varied the ZnS thickness fraction doped with Mn and its location. The results of this study show that the memory loop widens incrementally with the ZnS thickness fraction doped with Mn. We infer that the Mn doping is affecting the high-field bulk conductivity of the ZnS.

The "memory effect" in ZnS a-c thin film electroluminescence (EL) is related to the Mn doping of the ZnS (1). In addition, studies have shown that the width of the "memory loop," i.e., the width of the hysteresis in the brightness-voltage characteristic, is a function of the Mn doping concentration (2, 3)

Key words: electroluminescence, ZnS:Mn, thin film device.

and the ZnS:Mn film thickness (3, 4). The Mn doping can influence the memory effect by affecting the bulk conductive properties of the ZnS and or by introducing electronic trapping states near the ZnS-dielectric interface. The purpose of this study was to determine the relative importance of these effects on the "memory effect."

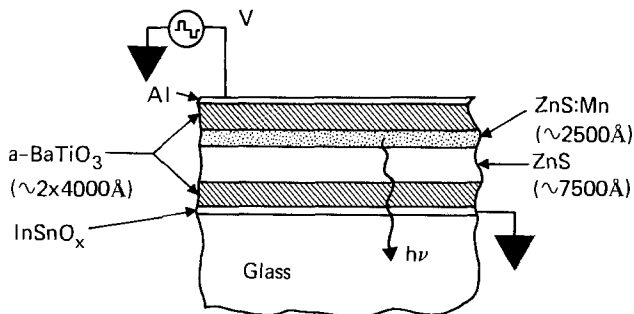


Fig. 1. A schematic cross section of a particular ZnS a-c thin film EL device used in this study having one-fourth of the ZnS film thickness doped with Mn and located at the "top" of the ZnS film.

This study was further stimulated by a recent result (5) that the Mn EL efficiency decreases strongly with distance from the cathodic to anodic region of the ZnS. In analogy with those measurements on EL efficiency (5), we measured the dependence of the "memory loop" width on the ZnS thickness fraction doped with Mn and its location.

For this purpose similar sets of three devices were fabricated by sequential depositions of sputtered a-BaTiO₃, evaporated ZnS, and sputtered a-BaTiO₃ with-

out breaking vacuum. During the ZnS deposition, the substrate temperature was ~175°C, resulting in a sticking coefficient of ~2/3. Within a set, devices having 1/4, 1/2, and 3/4 of the ZnS thickness doped with Mn were made. The ZnS was doped by co-evaporation of Mn. The Mn concentration in the doped region amounted to ~0.7 atomic percent. The device structure is shown schematically in Fig. 1 for a particular device which had the "top" one-fourth of the ZnS doped with Mn. Four such sets of devices were prepared with the Mn doping distributed as shown in the inserts to Fig. 2.

The brightness-voltage amplitude characteristics of such unaged devices were measured using 20 μsec wide, alternating polarity, voltage pulses at 2 kHz. The results are shown in Fig. 2 where we have plotted the "memory loop" width as a function of the ZnS thickness fraction that is Mn doped. Similar devices, with entirely undoped ZnS or with uniformly Mn doped ZnS had "memory loop" widths of 0 and 10% V_{th}, respectively. The results shown in Fig. 2 indicate that memory loop width increases with an increase in the fraction of the ZnS thickness doped with Mn for each set of devices. Also, for a given ZnS thickness fraction doped with Mn, the "memory loop" width depends on the location of the Mn doping. To facilitate comprehension of the data, they have been separated into four groups in Fig. 2: curve (a) Mn doping proceeding from the "top" down, curve (b) Mn doping proceeding from the "bottom" up, curve (c) outside in, and curve (d) inside out. We observe that:

1. The Mn doping of the first 1/4 thickness of the ZnS to deposit has negligible effect on the "memory

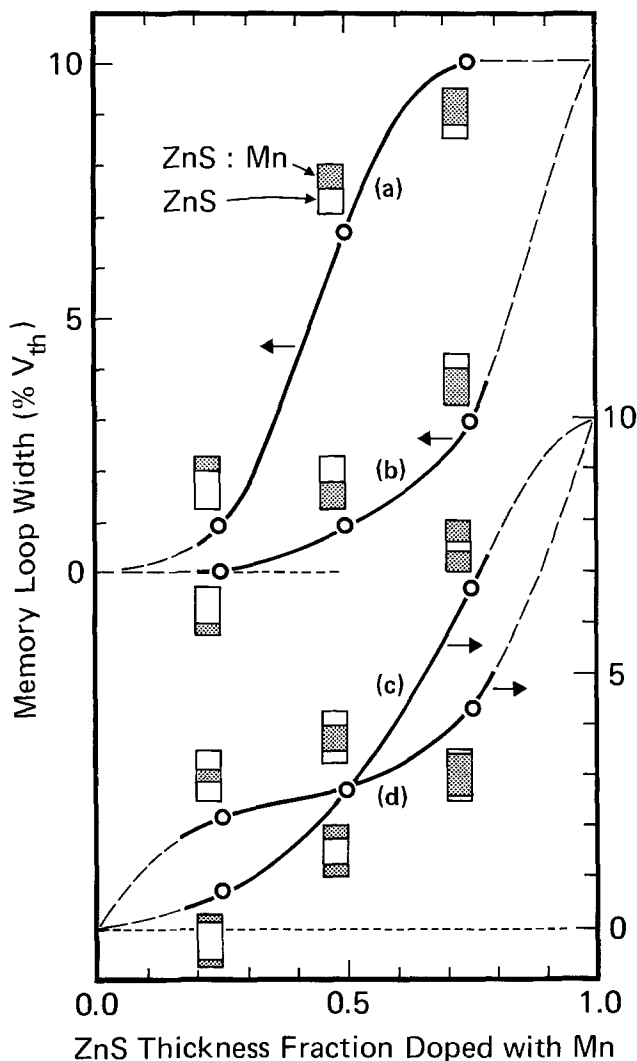
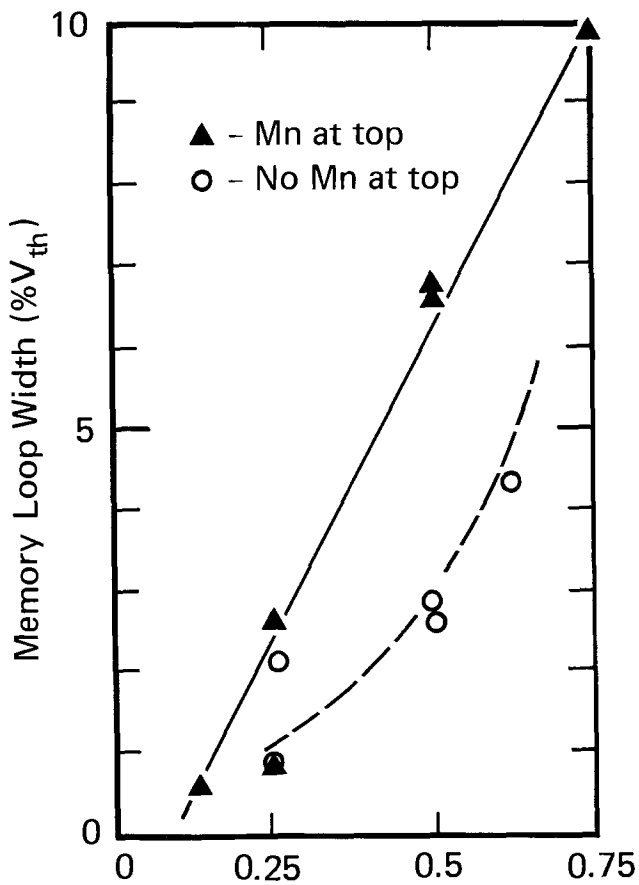


Fig. 2. The ZnS:Mn a-c thin film EL "memory loop" width in units of percent of the EL voltage threshold (~200V in these devices) as a function of the ZnS thickness fraction doped with Mn. The inserts show graphically the placement of the Mn doping in the ZnS layer. The bottom of the insert corresponds to the first to deposit ZnS.



ZnS Thickness Fraction Doped with Mn

Fig. 3. The data on the "memory loop" width as a function of the ZnS thickness fraction doped with Mn from Fig. 2 replotted omitting the effects of the "bottom" one-fourth of the ZnS and categorizing the data by whether the "top" layer was or was not doped with Mn.

loop" width when present, in curve (b), thickness fraction 1/4, (b, 1/4), or absent (a, 3/4). We speculate that this is related to poor morphology of the first to grow ZnS since it has been found that the EL efficiency in this region is also low (5).

2. Excluding the bottom 1/4 of the device from consideration, we find a satisfactory agreement of the "memory loop" width in devices (a, 1/4) = 0.9 and (c, 1/2) = 2.7, as well as in devices (b, 1/2) = 0.9 and (d, 1/4) = 2.2. These results are equivalent within the device fabrication reproducibility.

3. Although Mn doping near the top of the ZnS is not sufficient to produce a wide "memory loop" width alone, absence of Mn doping there has the most degrading effect on the "memory loop" width.

The last observation, 3 is illustrated in Fig. 3, where the "memory loop" width data presented in Fig. 2 has been replotted with the following modifications: (i) The bottom one-fourth of the device has been excluded, and (ii) the data have been categorized as to whether the Mn doped fraction did or did not include the top layer. The incremental "memory loop" width is related linearly to the ZnS film thickness fraction doped with Mn when the "top" interface is doped with Mn. Adding Mn to the "top" ZnS layer has a distinct (\sim factor of 2) effect on the incremental "memory loop" width. Presumably the same phenomena would occur at the "bottom" interface if the ZnS morphology were comparable to that at the "top" interface. We conclude that the "memory effect" phenomenon is related strongly to bulk conductivity characteristics produced by the Mn doping. The general behavior is consistent with the presence of bulk differential negative resistance in ZnS:Mn. The detailed analytical dependence is undoubtedly complicated by the nonuniformity of the ZnS in the thickness direction, filament formation (6), as well as the internal field enhancing polarization phenomenon (4)

which by themselves can lead to a hysteresis under suitable conditions such as have been studied for the case of the a-c plasma panel (7). This latter component, the internal field enhancement phenomenon, in the hysteresis is most likely what gives rise to the increase in the "memory loop" width as Mn doping is added to the "top" layer of the ZnS film. This is because the field enhancement phenomenon involves charge storage at the ZnS/dielectric interface which is also affected beneficially with respect to memory loop width by Mn doping of the ZnS.

Manuscript submitted Nov. 20, 1979; revised manuscript received April 23, 1980. This was Paper 305 presented at the Los Angeles, California, Meeting of the Society, Oct. 14-19, 1979.

Any discussion of this paper will appear in a Discussion Section to be published in the June 1981 JOURNAL. All discussions for the June 1981 Discussion Section should be submitted by Feb. 1, 1981.

Publication costs of this article were assisted by IBM Corporation.

REFERENCES

1. M. Takeda, Y. Kakihara, M. Yoshida, Y. Nakata, M. Kawaguchi, H. Kishishita, Y. Yamauchi, T. Inoguchi, and S. Mito, *Suppl. J. Jpn. Soc. Appl. Phys.*, **44**, 103 (1975).
2. J. M. Hurd and C. N. King, *J. Electron. Mater.*, **8**, 879 (1979).
3. V. Marrello and A. Onton, *IEEE Trans. Electron Devices*, To be published.
4. M. Yoshida, Y. Kakihara, T. Yamashita, K. Taniguchi, and T. Inoguchi, *Jpn. J. Appl. Phys.*, **17**, Suppl. 17-1, 127 (1978).
5. V. Marrello and A. Onton, *Appl. Phys. Lett.*, **34**, 525 (1979).
6. V. Marrello, W. Rühle, and A. Onton, *Appl. Phys. Lett.*, **31**, 452 (1977).
7. H. G. Slottow, *IEEE Trans. Electron Devices*, ed-24, 848 (1977).

Gas Phase Composition in the Low Pressure Chemical Vapor Deposition of Silicon Dioxide

P. J. Tobin,* J. B. Price,* and L. M. Campbell

Motorola Semiconductor Products Group, Integrated Circuits Division, Mesa, Arizona 85202

ABSTRACT

The gas phase composition during the low pressure chemical vapor deposition of silicon dioxide from silane and oxygen at 360°C has been studied as a function of oxygen to silane mole ratio. The total input flow was constant at 100 sccm. For each mole ratio, the system pressure, deposition rate, and exhaust gas composition were measured. Hydrogen was the major gaseous reaction product. A small amount of water was produced in a secondary reaction. Pressure variation with oxygen to silane ratio has been interpreted in terms of the variation of the exhaust gas viscosity with its composition. A theoretical calculation of the pressure in the system has shown good agreement with the experimental result. The dependence of total reaction efficiency and wafer reaction efficiency on O_2/SiH_4 was determined and used to deduce the efficiency of the reaction which occurs on other surfaces in the system or in the gas phase.

The chemical vapor deposition of thin films of SiO_2 using SiH_4 and O_2 at atmospheric pressure and low temperature (up to 450°C) is a process which has been well studied and widely used in the semiconductor industry (1).

Recently, the technology of low pressure chemical vapor deposition (LPCVD) has been extended to

this reaction (2-4). The introduction of commercial LPCVD systems with arsenic and phosphorus doping capability (5), along with the acknowledged economic advantages of this technology (6), ensures wider application in the future (7).

In this work, an LPCVD system designed for the deposition of SiO_2 , undoped or doped (8), was used to study some characteristics of the oxidation of silane to produce undoped SiO_2 on silicon wafers.¹ Specific-

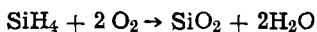
* Electrochemical Society Active Member.

Key words: silane oxidation, thin film deposition, gas composition.

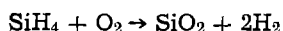
¹ Work on doped films is in progress.

ally, the deposition rate and the composition of the effluent gas were measured as a function of the composition of the input gas. An important aspect of the results to be described is the relationship between the effluent gas composition and the system pressure. Since pressure is easily measured and often used as a process control parameter, application of these results can be useful for the establishment or affirmation of the desired operating conditions.

Previous studies of this reaction at 15°-100°C showed that the oxidation of silane is a typical chain reaction, exhibiting the characteristic phenomena of an upper and lower critical explosion limit (9). In that work, water was the only gaseous product detected suggesting the overall reaction



More recently, the controlled oxidation of silane under conditions characteristic of 1 atm CVD has been reported (10, 11). In the work of Strater (10), nitrogen carrier gas with 0.4% SiH₄ and 0.8% O₂ flowed through a quartz chip filled gas reactor the temperature of which was varied from 240°-450°C. Use of a spectrophotometer to analyze the effluent gases led to the conclusion that H₂ rather than H₂O vapor is formed. A material balance of a partially complete SiH₄-O₂ reaction at 241°C suggested that any other gaseous reaction product, if present, would be below the 2% level for the conditions studied. These experiments therefore led to the conclusion that the best equation which would describe the SiH₄-O₂ reaction is the following one



It will be shown in this work that during low pressure CVD of SiO₂ on Si wafers at 360°C, the major gaseous product of SiH₄-O₂ reaction is H₂. A significant, but considerably smaller, amount of H₂O vapor is also produced.

These results are not necessarily inconsistent with the results of the work previously described. The absence of carrier gas and the low reaction pressure in the LPCVD case (~0.5 Torr) could significantly alter the kinetics of the oxidation, thereby affecting the effluent gas composition.

Experimental Techniques

The LPCVD system used for these experiments employs an enclosed, stainless steel, wafer boat (8). The enclosure was fabricated from perforated metal. Reactant gases are delivered to the center zone of a quartz diffusion tube using two metal tubes. A number of small holes in the wall of each tube distribute the gas along the length of the wafer boat. Oxygen is supplied by one manifold and SiH₄ by the other. A mechanical pump connected to the system through a tee evacuates the diffusion tube from both ends.

The pressure in the system was measured at the end cap (8) with a capacitance manometer.² The effluent gas was sampled at the same point for compositional analysis. This analysis was performed with a UTI Model SS-20 Gas Sampler in conjunction with a UTI Model 100C Precision Mass Analyzer.³ In order to sample gases at pressures greater than 50 mTorr (the specified maximum inlet pressure for the SS-20 Gas Sampler) a variable leak valve⁴ was installed between the LPCVD system and the sampler inlet. Use of this valve enabled the pressure in the mass analyzer to be maintained below 5×10^{-6} Torr, thus assuring linear detector response, even though the LPCVD system pressure was typically 0.3-0.5 Torr.

The possible influence of the sampling process on the measured composition must be considered. In general, such a technique may introduce some degree

of mass selectivity. However, for a properly designed system such as the one employed in this work, the relative partial pressures in the mass analyzer are the same as in the system being sampled as long as the gases do not have greatly differing adsorption coefficients (12).

The potential magnitude of errors introduced by differential adsorption are difficult to evaluate. In the present work other data which corroborate the results of mass analysis support the view that any errors introduced in the sampling process are insignificant.

The experimental procedure consisted of establishing O₂ and SiH₄ input flows corresponding to O₂ to SiH₄ mole ratios in the range of 0.4-10 with the total flow, O₂ plus SiH₄, maintained constant at 100 sccm.⁵ For each mole ratio, the deposition rate during a 1 hr run was measured using 10 test wafers which were distributed uniformly within a total boat load of 67 wafers (3 in.). Wafer spacing was 9.5 mm (3/8 in.). Film thickness was measured with a Nanometrics Film Thickness Analyzer.⁶

During the deposition, the effluent gas composition was measured by repeatedly scanning the mass range, 2-50 AMU and recording the output of the ion detector on a strip chart recorder. The pressure in the LPCVD system was simultaneously measured with a precision of approximately 0.3%.

Experimental Results and Discussion

Gas composition analysis.—A typical spectrum of the effluent gas is shown in Fig. 1. The current in the ion detector is shown plotted as a function of the mass to charge ratio (*m/e*) of the detected species. Due to cracking of the exhaust gas components in the quadrupole detector, each species is represented by a series of peaks. Occurrence of cracking fragments from two gas components of the same mass value⁷ can complicate interpretation of the spectra. For example, measurement of a pure O₂ spectrum shows that most of the O₂ is detected as O₂⁺ at 32 AMU. During deposition this ion detector current occurs at the same mass value as the current from SiH₄⁺. To avoid this problem, cracking fragments having mass values at which there was no overlap were used to monitor the parent gas concentration. A cracking pattern measured for the parent

⁵ Calibrated flow tubes were used for gas flow measurement.

⁶ Nanometrics Incorporated, Sunnyvale, California 94086.

⁷ Since all of the species detected were singly charged, identification can be made in terms of mass alone.

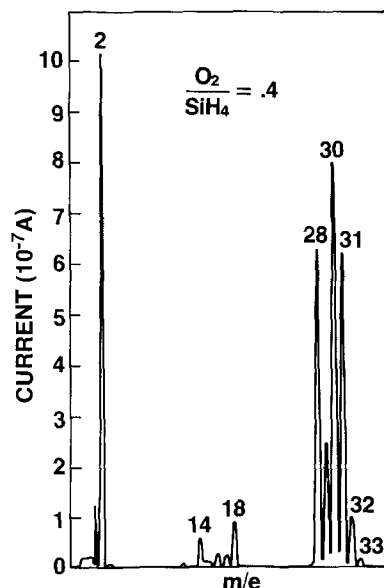


Fig. 1. Spectrum of the effluent gas for O₂/SiH₄ = 0.4. T = 360°C. Pressure = 380 mTorr. Total flow = 100 sccm.

² MKS Instrument Corporation, Burlington, Massachusetts 01803.

³ UTHE Technology International, Sunnyvale, California 94086.

⁴ Varian Vacuum Division, Palo Alto, California 94303.

gas alone was then used to infer the total detector current for the parent species.

The problem of overlap is shown in detail in Table I where the major cracking fragments of each effluent gas component are shown. Since SiH_2^+ has no interference and is a major component in the cracking pattern of SiH_4 , this peak was used to monitor the SiH_4 concentration.

The peak at 16 AMU was used to monitor O_2 concentration since the O^+ signal from H_2O is very small (2%). The amount of water vapor was determined from the H_2O^+ detector current at 18 AMU.

In order to determine the concentration of H_2 in the effluent gas using the H_2^+ ion current, it was necessary to first subtract out that portion of this current which arose from cracking of SiH_4 . This was accomplished by first measuring the ratio of the detector current at 2 AMU (H_2^+) to that at 30 AMU (SiH_2^+) for a pure SiH_4 spectrum. This ratio, together with the 30 AMU signal during the deposition run, was used to calculate that portion of the 2 AMU signal due to cracking of SiH_4 . The remainder of the signal amplitude at 2 AMU was identified with H_2 reaction product.

Calculation of the mole percent of each gas, M_i , was accomplished using the following approximate equation (13)

$$M_i = 100 \times \frac{\sum_{j=1}^N I_j}{\sum_{j=1}^M I_j} \quad [1]$$

The sum in the numerator extends over the ion currents arising from cracking fragments of species i while the sum in the denominator represents the total detector current for all cracking fragments of all four effluent gas species. Since no corrections were applied for mass dependent electron multiplier gain and quadrupole transmission (13, 14), the data to be presented may be only semiquantitatively correct, so far as relative concentrations at a particular O_2/SiH_4 are concerned. However, measurements of deposition rate and system pressure given below support the validity of the conclusions drawn from these data. The variation of composition with O_2/SiH_4 , on the other hand, is much less affected by the use of the approximate expression (Eq. [1]) since quadrupole transmission and multiplier gain are fixed instrumental constants.

The results of the compositional analysis are shown in Fig. 2. The silane concentration decreases and the O_2 concentration increases with increasing O_2/SiH_4 . Hydrogen is a major oxidation product whose concentration passes through a maximum at $\text{O}_2/\text{SiH}_4 = 1$. Water is detected as a secondary product with a maximum concentration (10%) occurring at $\text{O}_2/\text{SiH}_4 = 2$.

The average deposition rate, like the hydrogen concentration, has a maximum value (175 Å/min) at $\text{O}_2/\text{SiH}_4 = 1$ (Fig. 3). These results suggest that the following equation represents the primary reaction

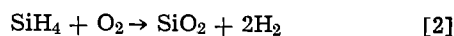


Table I.

m/e	Silane	Water	Oxygen	Hydrogen
32	SiH_4^+		O_2^+	
31	SiH_3^+			
30	SiH_2^+			
29	SiH^+			
28	Si^+			
18		H_2O^+		
17		OH^+		
16		O^+	O^+	
2	H_2^+	H_2^+		H_2^+

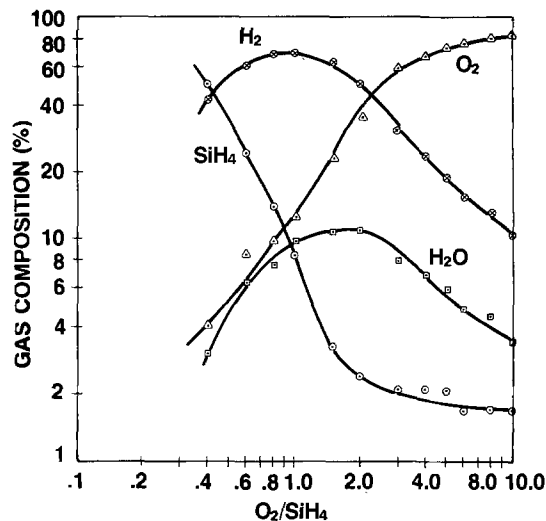


Fig. 2. Effluent gas composition as a function of O_2/SiH_4 . $T = 360^\circ\text{C}$. Total flow = 100 sccm.

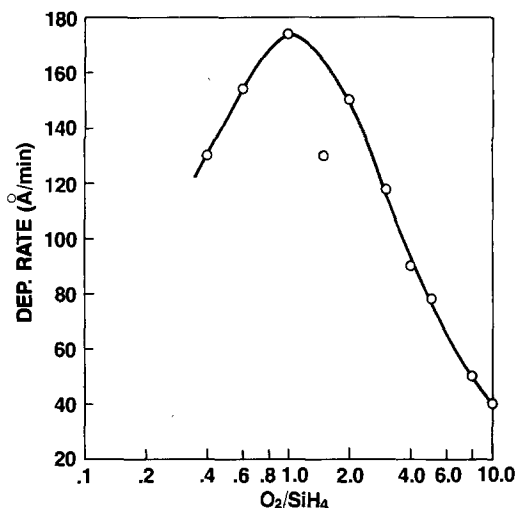
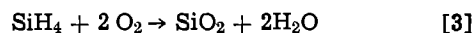


Fig. 3. Deposition rate as a function of O_2/SiH_4 . $T = 360^\circ\text{C}$. Total flow = 100 sccm.

while a secondary reaction represented by the following equation



occurs simultaneously. The stoichiometric ratios of O_2/SiH_4 for maximum H_2 and H_2O production, 1 and 2, respectively, coincide with the maxima shown in Fig. 2.

System pressure.—In this section, it will be shown that analysis of the variation of system pressure with O_2/SiH_4 lends further support to the identification of the hydrogen producing reaction (Eq. [2]) as the major one. The uppermost curve in Fig. 4 gives the dependence of system pressure on O_2/SiH_4 (top scale). A weak minimum is observed at $\text{O}_2/\text{SiH}_4 = 1$. This is shown in the following to be due to a minimum in the viscosity of the effluent gas which occurs at $\text{O}_2/\text{SiH}_4 = 1$.

The lower two curves in Fig. 4 show the pressure in the system when O_2 or SiH_4 alone is introduced into the system at the same flow value which it had under reaction conditions. The magnitude of the two flows may be read at the bottom of the figure. Even though the primary reaction (Eq. [2]) conserves volume, the sum of the pressures of O_2 and SiH_4 alone does not equal the pressure when both gases flow simultaneously (Fig. 4). This is due to variation in the viscosity of the effluent as is demonstrated below.

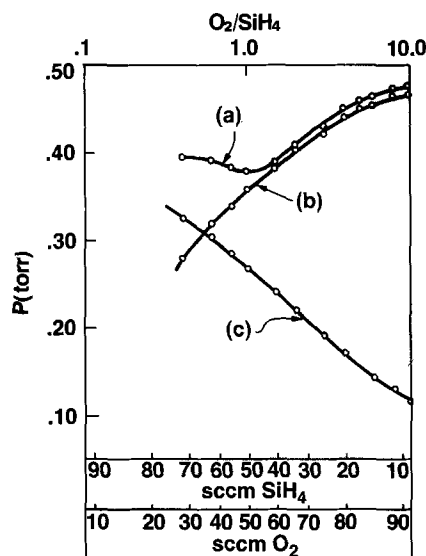


Fig. 4. (a). System pressure during reaction (O_2 and SiH_4) vs. O_2/SiH_4 (upper scale). (b) System pressure with O_2 only flowing vs. input O_2 flow (lower scale). (c) System pressure with SiH_4 only flowing vs. input SiH_4 flow (lower scale).

An analysis of the fluid flow in the system may be based on the Poiseuille equation for viscous flow in a straight tube as follows (15)

$$Q = \frac{\pi a^4}{8L} \frac{1}{\eta} P_{avg} (P_1 - P_0) \quad [4]$$

where Q = throughput (Torr-liter/min), a = tube radius (cm), L = tube length (cm), η = viscosity of the gas (centipoise), P_1 = inlet pressure (Torr), P_0 = outlet pressure (Torr), and $P_{avg} = \frac{1}{2}(P_1 + P_0)$ (Torr). It is now assumed that the above equation can be applied to the more complicated tube configuration (Fig. 5) which is employed in the LPCVD system (8), the geometrical constants in Eq. [4] being replaced by an experimentally determined constant, K . The inlet pressure is identified with the pressure in the process tube and P_0 with the pressure at the pump. By absorbing numerical factors into K , Eq. [5] can be applied to the present situation in the following form

$$Q = K \frac{1}{\eta} (P_1^2 - P_0^2) \quad [5]$$

The throughput, Q will therefore vary linearly with $P_1^2 - P_0^2$. The constant of proportionality, K/η along with a viscosity value for the gas may be used to deduce K . Pressure and flow data for SiH_4 and O_2 were analyzed in this manner using linear regression analysis. The coefficient of correlation in both cases was 0.999. The derived values for K/η and K are summarized in Table II. Viscosity values for SiH_4 and O_2 were taken from a tabulation by the flow tube manufacturer (15).⁸ As required by Eq. [5], the value of K is independent of the gas species (within 3%).

Using the experimentally determined value of K , Eq. [5] should be valid as the composition and, there-

⁸ Room temperature viscosity values (23°C) were used since the effluent gases quickly cool to ambient temperature as they enter the vacuum pumping line.

Table II.

	K/η (liter/ Torr-min)	η (cp)	K (cp-liter/ Torr-min)
O_2	400	0.02045	8.18
SiH_4	671	0.0115	7.71
			Avg. 7.94 ± 0.23

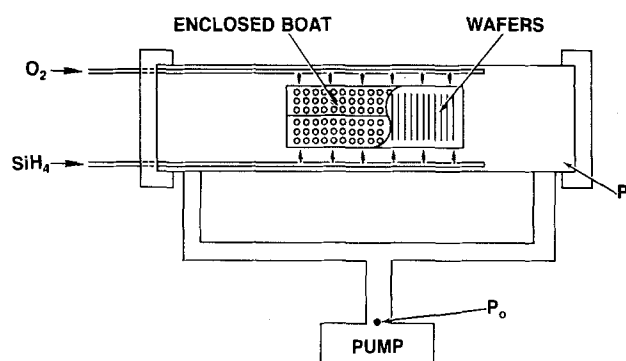


Fig. 5. Schematic of the LPCVD pumping system

fore, the viscosity of the effluent varies with O_2/SiH_4 under reaction conditions.

To test the validity of this expression in that case the kinetic theory model of Chapman and Enskog (17), as refined by Wilke (17), was used to calculate the viscosity of the effluent gas mixture as a function of O_2/SiH_4 . According to this theory, the viscosity of a mixture of O_2 , SiH_4 , H_2 , and H_2O can be calculated by means of the following expression

$$\eta = \sum_{i=1}^4 \frac{X_i \eta_i}{X_1 + \sum_{\substack{j=1 \\ j \neq i}}^4 \phi_{ij} X_j} \quad [6]$$

where η_i = viscosity of the i th component, X_i = mole fraction of the i th component, and ϕ_{ij} = interaction coefficient, i with j . Values of ϕ_{ij} were determined from the nomogram constructed by Brokaw (17). Viscosity values used for H_2 and H_2O are 0.0085 and 0.00926 cp, respectively (16). Viscosities for O_2 and SiH_4 are given in Table II. The results of the exhaust gas analysis shown in Fig. 2 were used for the mole fractions, X_i .

The results of the calculation were combined with Eq. [5] to derive a relation between the system pressure and the incoming O_2/SiH_4 . The input value of 76 Torr-liter/min was used for Q since the major reaction (Eq. [1]) conserves gas volume. That is, the throughput at the entrance to the pump-out line is almost equal to the throughput at the inlet to the process tube before any reaction takes place.

The results of the calculation are compared with a replot of the experimental data in Fig. 6. Clearly the agreement is quite good. Closer inspection of the theoretical expression for viscosity (Eq. [6]) shows that the minimum at $O_2/SiH_4 = 1$ is due to the large H_2 concentration in the system (Fig. 2). Hydrogen, being the least viscous component in the effluent gas, lowers the viscosity of the mixture to a minimum value which in turn leads to the pressure minimum at $O_2/SiH_4 = 1$ shown in Fig. 6.

Reaction efficiency.—The data shown in Fig. 2 may be used to calculate the overall percent SiH_4 reacted, herein referred to as total reaction efficiency. For example, at $O_2/SiH_4 = 2$, approximately 2.4% of the effluent gas is SiH_4 . From Fig. 4, the input SiH_4 concentration under these conditions is 33.3% (33.3 sccm out of a total of 100 sccm). Thus, the incoming SiH_4 is 93% reacted ($30.9/33.3 \times 100\%$). This figure for the efficiency of the reaction includes SiO_2 deposition on the walls of the diffusion tube and boat, gas phase reaction, and deposition on the wafer surfaces. The variation of total efficiency with O_2/SiH_4 is shown as curve (a) in Fig. 7. For $O_2/SiH_4 < 1$ the total efficiency is low simply because

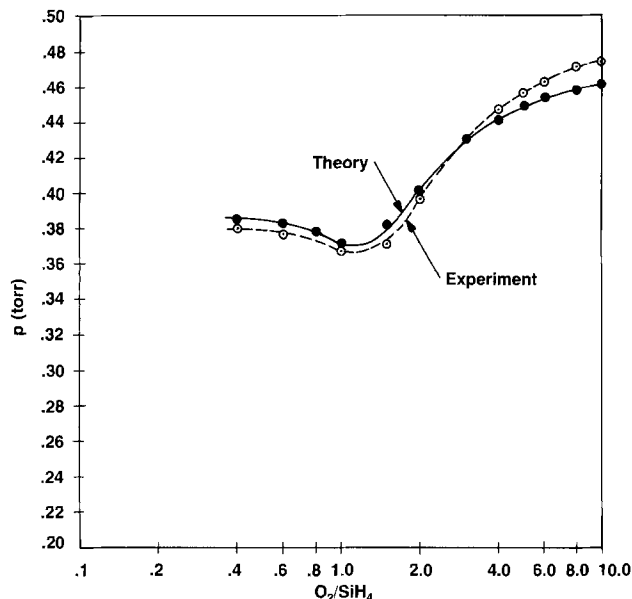


Fig. 6. System pressure vs. O_2/SiH_4 . Theory, solid curve; experiment, dashed curve.

there is less than a stoichiometric amount of O_2 available. The total efficiency reaches a maximum of 93% at $O_2/SiH_4 \approx 2.0$ and then drops slightly as O_2/SiH_4 increases further. This decrease may be due to inhibition by excess oxygen. That is, stoichiometric units of SiO_2 take longer to form because excess oxygen retards the incorporation of the necessary Si.

The efficiency of deposition on the wafers alone can be calculated from the data in Fig. 3 and 4. Using the total wafer surface area, the density of LPCVD SiO_2 (2.25 g/cm^3)⁹ and the stoichiometric relation that 1.25g SiO_2 form per 1 liter SiH_4 reacted, the following numerical relationship was derived

$$\text{reaction efficiency on wafers} = \frac{\text{dep. rate (Å/min)}}{\text{input } SiH_4 \text{ (sccm)}} \times 5.18$$

The results of this calculation are plotted as curve (b) in Fig. 7.

Although the wafer reaction efficiency shows the same general trend as the total efficiency [curve (a)], the rise to a maximum of 27% at $O_2/SiH_4 \approx 3$ occurs more gradually. Further, the decrease in efficiency at higher O_2/SiH_4 is smaller for curve (b) than for curve (a).

⁹ Determined gravimetrically.

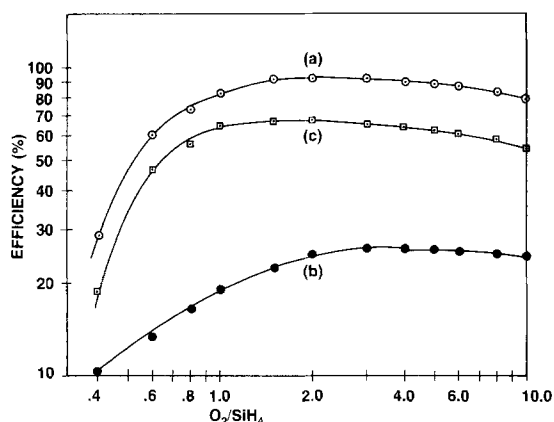


Fig. 7. Percent SiH_4 reacted vs. O_2/SiH_4 . Curve (a), Total reaction; curve (b), wafers only; curve (c), other surfaces plus gas phase reaction.

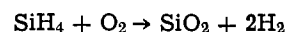
Subtraction of the wafer efficiency from the total efficiency yields curve (c) which corresponds to the reaction on all surfaces except the wafers plus any gas phase reaction. Comparison of (b) and (c) leads to the conclusion that unwanted deposition, which often leads to particulate contamination, is minimized by operation at $O_2/SiH_4 > 3$. Other considerations, however, such as high deposition rate, may require compromise in the choice of O_2/SiH_4 .

The exact relationship between the lower two curves in Fig. 7 may depend on system geometry, boat and tube design, as well as constructional material. The general trend, however, is probably characteristic of LPCVD SiO_2 systems.

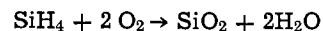
Summary and Conclusions

The LPCVD of SiO_2 from SiH_4 and O_2 at 360°C was studied as a function of O_2/SiH_4 with the total flow fixed at 100 sccm. A residual gas analyzer was used to measure the gas phase composition for each O_2/SiH_4 . Deposition rate and system pressure were also measured for each experimental run.

Analysis of the results of the gas phase composition measurements lead to the conclusion that the primary reaction produces H_2 as its gaseous by-product according to the following equation



A smaller amount of the SiH_4 ($\sim 10\%$ max) oxidizes by the following reaction which has H_2O as a gaseous by-product



The deposition rate showed a maximum at $O_2/SiH_4 = 1$ strongly supporting the identification of the hydrogen producing reaction as the primary one.

The pressure in the system passed through a weak minimum at $O_2/SiH_4 = 1$. Analysis showed that variation in the viscosity of the effluent gas with incoming O_2/SiH_4 produces the pressure minimum. A kinetic theory model for the viscosity of the four component gas effluent was used to derive a theoretical prediction for variation of pressure with O_2/SiH_4 . The theoretical result agrees quite well with the data, reproducing the pressure minimum observed at $O_2/SiH_4 = 1$.

Data on input flows and effluent gas composition were used to calculate the percent of the incoming SiH_4 reacted in the process tube (*i.e.*, the total efficiency) as a function of O_2/SiH_4 . This efficiency pertains to deposition on the wafers and all other surfaces (boat plus tube walls), as well as gas phase reaction. The efficiency has a maximum value of 93% at $O_2/SiH_4 = 2$ and drops slightly for higher O_2/SiH_4 . The reaction efficiency on the wafers alone was calculated from the deposition rate and the input flows. These results showed that a maximum of 27% of the incoming SiH_4 produces SiO_2 on the wafers. Comparison of the two efficiency curves suggested that $O_2/SiH_4 > 3$ minimizes unwanted reaction.

Acknowledgments

The authors are indebted to Wilma Sacramento for experimental assistance and to Fabio Pintchovski and T. C. Smith for several valuable suggestions.

Manuscript submitted Nov. 5, 1979; revised manuscript received Feb. 5, 1980.

Any discussion of this paper will appear in a Discussion Section to be published in the June 1981 JOURNAL. All discussions for the June 1981 Discussion Section should be submitted by Feb. 1, 1981.

Publication costs of this article were assisted by Motorola Incorporated.

REFERENCES

1. W. Kern, G. L. Schnable, and A. W. Fisher, *RCA Rev.*, **37**, 3 (1976).

2. R. E. Logar, M. T. Wauk, and R. S. Rosler, in "Proceedings of 6th International Conference on Chemical Vapor Deposition," L. F. Donaghey, P. Rai-Choudhury, and R. N. Tauber, Editors, pp. 195-202, The Electrochemical Society Softbound Proceedings Series, Princeton, N.J. (1977).
3. A. K. Hochberg and A. Dozier, Abstract 221, p. 592, The Electrochemical Society Extended Abstracts, Pittsburgh, Pa., Oct. 15-20, 1978.
4. H. Frima and J. Goldman, Abstract 282, p. 704, The Electrochemical Society Extended Abstracts, Seattle, Wash., May 21-26, 1978.
5. J. Hollahan, M. Wauk, and M. Hammond, in Proceedings of Applied Materials Seminar, 1978 Applied Materials Inc., Santa Clara, Calif.
6. M. L. Hammond and R. J. Gieske, Tech. Note 501, Tempres Micro-Electronics, Semicon, West, San Mateo, Calif. (1976).
7. W. Kern and G. L. Schnable, *Proc. IEEE Trans. Electron. Devices*, ed-26, 647 (1979).
8. R. A. Alberti and J. C. Goldman, U. S. Pat. 4,098,923 (1978).
9. H. J. Emeleus and K. Stewart, *J. Chem. Soc., (London)*, Part I, p. 1182 (1935); Part II, p. 677 (1936).
10. K. Strater, *RCA Rev.*, 29, 618 (1968).
11. L. L. Vasilyeva, V. N. Drozdov, S. M. Repinsky, and K. K. Svtashev, *Thin Solid Films*, 55, 221 (1978).
12. H. L. Brown, G. B. Bunyard, and K. C. Lin, *Solid State Technol.*, 21, 35 (1978).
13. UTI 100C Precision Mass Analyzer, Operating and Service Manual, UTI Technology International, Sunnyvale, Calif. 94086.
14. K. Lin and J. D. Burden, *J. Vac. Sci. Technol.*, 15, 373 (1978).
15. S. Dushman, in "Scientific Foundations of Vacuum Technique," 2nd ed., J. M. Lafferty, Editor, p. 82, John Wiley & Sons, Inc., New York (1962).
16. Data compilation by Brooks Instrument Div., Emerson Electric Co., Hatfield, Pa. 19440.
17. See for example, R. C. Reid and T. K. Sherwood, "The Properties of Gases and Liquids," 2nd ed., pp. 420-423, McGraw-Hill Book Co., New York (1958).

Segregation of Arsenic to the Grain Boundaries in Polycrystalline Silicon

B. Swaminathan,* E. Demoulin,¹ T. W. Sigmon,** R. W. Dutton, and R. Reif**²

Integrated Circuits Laboratory, Stanford University, Stanford, California 94305

ABSTRACT

The arsenic distribution in polycrystalline silicon films deposited on single crystal silicon and on oxide, was measured using 2.2 MeV, ⁴He⁺ ion backscattering, after various high temperature annealing steps. Pile up of arsenic was observed at the interfaces of the deposited films. This can be interpreted in terms of a model based on segregation of arsenic to the grain boundaries in the films.

There has been some controversy in the attempts to explain the higher resistivity observed for polycrystalline silicon when compared to monocrystalline silicon for similar doping concentrations. One model (1) proposes that the dopant atoms are trapped at the grain boundaries in the polycrystalline silicon where they are electrically inactive. The other model suggests (2) that the dopant atoms are distributed evenly throughout the polycrystalline silicon with the carriers trapped at the grain boundaries. In this paper we present evidence that there is some segregation of arsenic to the grain boundaries in polycrystalline silicon, contrary to what is reported for boron and phosphorus in a recent paper (3).

Most of the experiments involved 5000Å layers of polycrystalline silicon deposited at 620°C in a low pressure chemical vapor deposition reactor. Silicon wafers of <100> orientation doped with 10¹⁵ cm⁻³ of boron, both with and without 1000Å of thermal oxide were used as substrates for the deposition.

For the first set of experiments two identical quarter wafers of the polysilicon on single crystal silicon were used. One of these quarter wafers was annealed at 1200°C for 1 hr in a nitrogen ambient. Both wafers were then implanted with 10¹⁶ cm⁻² of arsenic at 40 keV. Following the implant 5000Å of oxide were deposited on both wafers which were then annealed at 1000°C for 5 hr in a nitrogen ambient. The oxide

was then removed from the wafers with hydrofluoric acid. The backscattering spectra, taken with 2.2 MeV ⁴He⁺, are shown in Fig. 1(a) and (b) for the two samples (4). The higher energy portion of the spectra (>1.5 MeV) represent ⁴He backscattered from the arsenic in the samples. Using the near surface approximation and a system energy calibration of 3.58 keV/channel, the depth scales shown on the figures can be obtained. It is seen that the arsenic distributions in both wafers are quite similar, the arsenic concentration in the polysilicon being approximately 1.4 × 10²⁰ cm⁻³ in both wafers. However, for the sample which did not receive the 1200°C preanneal there is a pile-up of arsenic at the polysilicon/single crystal silicon interface. The calculated number of arsenic atoms in the peak at the interface is 3 × 10¹⁴ cm⁻². By tilting the sample 60° with respect to the analyzing beam it was determined that this region is less than 100Å thick.

The observed pile-up can be explained in terms of segregation of arsenic to the grain boundaries. Consider the four sections shown in Figure 2. Sections 1 and 4 are planes which lie on an interface between the polysilicon grains and either oxide or single crystal silicon. The interface between the polysilicon grains and the single crystal substrate is analogous to the interface between grains in the polycrystalline material. Sections 2 and 3, through the middle of the deposited layer could pass through an occasional grain boundary, but are mainly through the bulk of the grains. The backscattering measurement averages over the 1 mm square area of the incident beam, and therefore if the arsenic segregates to the interfaces of the grains, a pile-up would be

* Electrochemical Society Student Member.

** Electrochemical Society Active Member.

¹ Present address: Universite Catholique de Louvain, Louvain-la-neuve, Belgium.

² Present address: Department of Electrical Engineering and Computer Science, Massachusetts Institute of Technology, Cambridge, Massachusetts 02140.

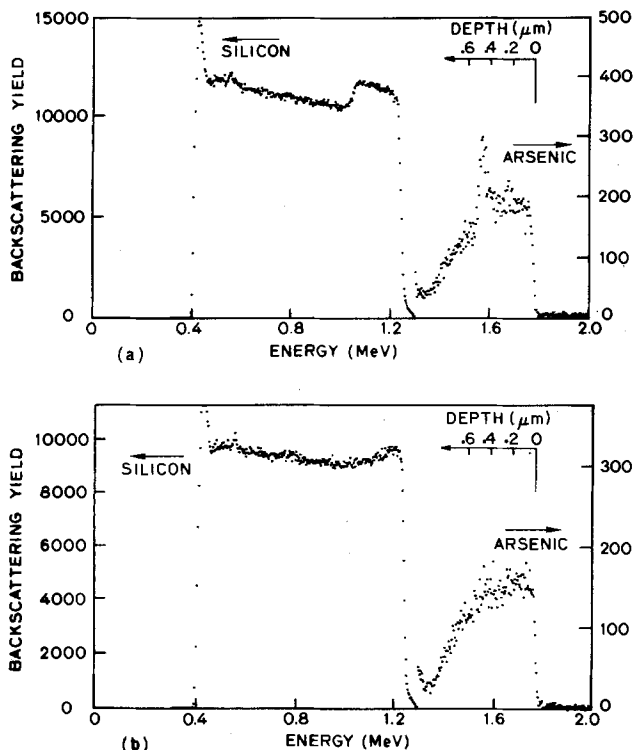


Fig. 1. (a) Energy spectrum of ^4He atoms backscattered from a 2.2 MeV $^4\text{He}^+$ beam incident on polycrystalline/single crystal silicon sample implanted with 10^{16} cm^{-2} of ^{75}As and annealed for 5 hr at 1000°C in nitrogen. (b) Backscattering spectrum from sample annealed at 1200°C for 1 hr before implantation and drive-in.

expected at both the top and bottom of the deposited layer.

There is no pile-up of arsenic for the sample pre-annealed at 1200°C , Fig. 1(b). This is because the 1200°C heat-treatment destroyed the grain structure of the deposited layer. Channeling measurements showed that the layer consists essentially of monocrystalline silicon oriented on the substrate, the residual defects being identified by TEM as a high density of twins and stacking faults.

The explanation of the arsenic pile-up in terms of segregation to the interfaces of the grains predicts a pile-up at both interfaces of the deposited layer. In Fig. 1(a), this pile-up is seen only at the bottom interface of the layer. This is believed to be caused by the removal of the arsenic at the polysilicon/oxide interface by the hydrofluoric acid used to etch away the oxide cap. To verify this an identical sample was measured with some of the oxide remaining. A pile-up was indeed observed at the polysilicon/oxide interface for this sample. Since the region in which the pile-up takes place is so easily removed by dilute hydrofluoric acid, further support is lent to the estimation of this region being less than 100Å thick. It is probably not more than a few monolayers thick.

The behavior of the polysilicon/oxide interface is somewhat different from that of polysilicon/single crystal silicon interface. To demonstrate this, a wafer with 5000Å of polysilicon deposited on oxide was

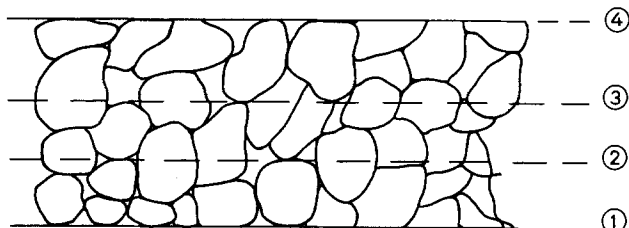


Fig. 2. Four sections through a polycrystalline layer

implanted with $2 \times 10^{15}\text{ cm}^{-2}$ of arsenic at 100 keV. An oxide cap was deposited and the sample annealed at 1000°C in nitrogen for 1 hr. Another similar wafer was prepared with an implant dose of 10^{16} cm^{-2} . For the sample with the lower concentration of arsenic a pile-up was again observed at the polysilicon/oxide interfaces at the top and bottom of the deposited layer, see Fig. 3(a). For the sample with the higher concentration of arsenic no pile-up was evident, see Fig. 3(b). We believe that this is due to the saturation of sites at the interface to which the arsenic atoms tend to segregate. In the case of the polysilicon/oxide interface these sites appear to be saturated when the arsenic concentration in the polysilicon is approximately $2 \times 10^{20}\text{ cm}^{-3}$. However for the polysilicon/single crystal silicon interface, pile-up was observed at arsenic concentration levels higher than $2 \times 10^{20}\text{ cm}^{-3}$.

A possible objection to the explanation of the pile-up as a manifestation of segregation of arsenic to the grain boundaries, is that the pile-up could be caused by interfacial impurities. In fact there is probably a thin native oxide layer at the interface for the low pressure chemical vapor deposited polysilicon on single crystal silicon samples. The effect of interfacial impurities was tested by the following experiment. An epitaxial layer was grown on a $\langle 100 \rangle$ silicon wafer using silane in an atmospheric pressure epitaxial reactor. The temperature was reduced to 600°C in the same run, with the hydrogen flowing, and then 5000Å of amorphous silicon was deposited. The interface between the epitaxial layer and the amorphous layer can therefore be assumed to be free of impurities. Arsenic was implanted into the amorphous silicon at a dose of 10^{16} cm^{-2} and the sample annealed at 900°C for 3 hr in nitrogen. During the anneal the amorphous layer becomes polycrystalline. Backscattering analysis again showed that there was indeed an arsenic pile-up at the polysilicon/single crystal silicon interface.

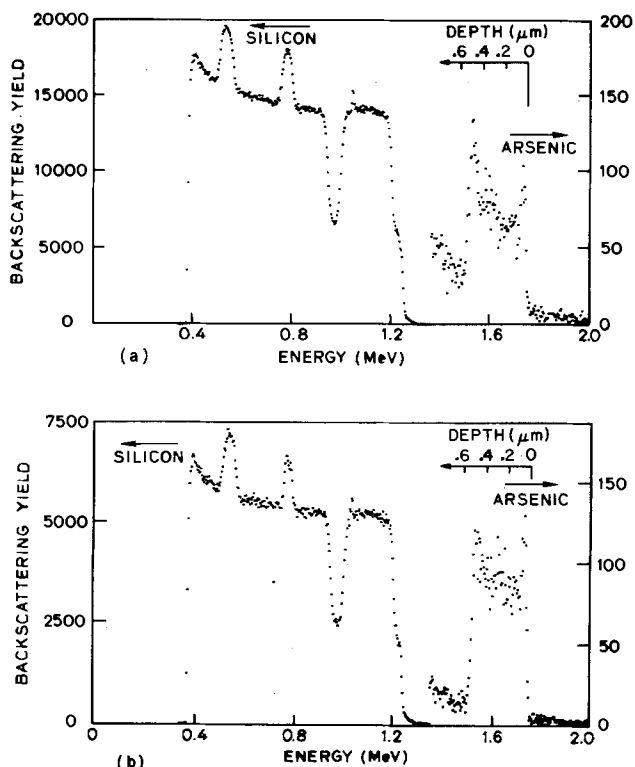


Fig. 3 (a) Backscattering spectrum using 2.2 MeV $^4\text{He}^+$ ions from sample of polysilicon deposited on oxide, implanted with $2 \times 10^{15}\text{ cm}^{-2}$ of ^{75}As and annealed at 1000°C in N_2 for 1 hr with a deposited oxide cap; spectrum taken with 1000Å of the oxide cap remaining. (b) Backscattering spectrum from similar sample with implantation dose of 10^{16} cm^{-2} ^{75}As .

Mandurah *et al.* (5) have recently made measurements of the resistivity of doped polycrystalline silicon films deposited on oxide, and from these measurements have deduced the existence of impurity trapping at grain boundaries. We measured the arsenic distribution in three of their samples. The samples were all 5000Å low pressure chemical vapor deposited polysilicon on oxide, and implanted with $2 \times 10^{15} \text{ cm}^{-2}$ of arsenic. One of the samples was annealed at 1000°C for 1 hr in nitrogen. The other two samples also received the 1000°C anneal and in addition were annealed in nitrogen at 900°C for 12 hr and at 850°C for 24 hr, respectively. The annealing times were chosen so that a steady-state value of resistivity was obtained for each annealing temperature. Pile-up of arsenic was observed in all three samples. Furthermore both the amount of the pile-up as well as the resistivity followed the same trend, being greatest for the sample annealed at 850°C and least for the sample annealed only at 1000°C.

Experiments were also performed in which polycrystalline silicon films deposited on single crystal silicon and implanted with arsenic, were oxidized in either dry or wet oxygen. The results for these samples were similar to those for the samples annealed in nitrogen. Pile-up of arsenic was again observed at the various interfaces.

Monkowski *et al.* (3) used a C-V technique to conclude that for boron and phosphorus, there is no segregation to the grain boundaries. The lowest temperatures at which their samples were annealed was 1225°C. Our experiments as well as those of Ref. (5) suggest that segregation to the grain boundaries is lower for polycrystalline samples annealed at higher temperatures. This could explain their negative results.

It is difficult to obtain quantitative information from the results presented here. However, an estimate of the percentage of arsenic present at the grains can be made for the sample annealed at 1000°C for 5 hr [Fig. 1(b)]. Let us assume that the grains are

cubes 2500Å on side. The 5000Å polycrystalline film will consist of two layers of such cubes. Taking into account the shared faces of the cubes, there will be an equivalent of 7 cube faces to which the arsenic can segregate in the polycrystalline film. It was observed that $3 \times 10^{14} \text{ cm}^{-2}$ atoms are present at the polysilicon/single crystal silicon interface. This figure multiplied by 7 or $2 \times 10^{15} \text{ cm}^{-2}$ is the approximate number of arsenic atoms at the grain boundaries. Thus approximately one-third of the arsenic in the polycrystalline layer appears at the grain boundaries.

Acknowledgment

Support through ARO Contract No. DAAG-29-77-C-006 is gratefully acknowledged.

Manuscript submitted Jan. 4, 1980; revised manuscript received April 25, 1980. This was Paper 381 presented at the Los Angeles, California, Meeting of the Society, Oct. 14-19, 1979.

Any discussion of this paper will appear in a Discussion Section to be published in the June 1981 JOURNAL. All discussions for the June 1981 Discussion Section should be submitted by Feb. 1, 1981.

Publication costs of this article were assisted by Stanford University.

REFERENCES

1. M. E. Cowher and T. O. Sedgwick, *This Journal*, **119**, 1565 (1972).
2. T. I. Kamins, *J. Appl. Phys.*, **42**, 4357 (1971).
3. J. R. Monkowski, J. Bloem, L. J. Giling, and M. W. M. Graef, *Appl. Phys. Lett.*, **35**, 410 (1979).
4. W. K. Chu, J. W. Mayer, and M. A. Nicolet, "Backscattering Spectrometry," Academic Press, New York (1978).
5. M. M. Mandurah, K. C. Saraswat, and T. I. Kamins, Paper 571 presented at The Electrochemical Society Meeting, Los Angeles, California, Oct. 14-19, 1979.

Ion Migration Study in a Sodium Borate Glass: Proposal of a New Oxide Transport

F. G. K. Baucke

Jenaer Glaswerk Schott u. Gen., Mainz, West Germany

and J. A. Duffy

Chemistry Department, University of Aberdeen, Old Aberdeen, AB9 2UE, Scotland

ABSTRACT

Electrolysis of the cell

(+) Pb/35 m/o Na₂O sodium borate glass/Hg (—)

was investigated at 50°C, using a modified moving boundary method (in the anode region) based upon sodium and lead concentration profiles (obtained by ion beam ablation) and ultraviolet spectroscopy of the Pb²⁺ ion. It was found that Na⁺ ions left the anode region for the cathode but, contrary to related experiments with silicate glasses, there was not an equivalent replacement by the Pb²⁺ ions generated at the anode. Instead, O²⁻ ions migrated to the anode and most of the Pb²⁺ ions formed PbO. It is suggested that a "structure-switching ion transport" mechanism operates, migration of the O²⁻ ions involving an interchange between threefold and fourfold coordination by the boron atoms as the oxygens are handed on from one borate group to the next. The ultraviolet spectrum of the small concentration of Pb²⁺ ions in the Na₂O-depleted anode region registered a lower basicity than the original glass (optical basicity values 0.49 and 0.60, respectively) but the sites were more basic than for a corresponding borate glass obtained from the melt.

Oxide glasses, such as silicate, borate, and phosphate glasses, usually are ionic conductors. Although most glasses are fairly good conductors when hot, at lower temperatures, *e.g.*, ambient temperature, the conductivity is very low, and for measuring any changes arising from the electrolysis (assuming a reasonable period of time) it is necessary to employ sensitive analytical techniques. For example, the combination of coulometry, subsurface cation concentration profiling [by the ion beam ablation method (1)] and absorption spectroscopy has recently been used for carrying out modified moving boundary experiments in alkali silicate glasses (2-4). The results of these experiments have shown that conductivity is due to the migration solely of metal ions. There appears to be no migration of O²⁻ ions, and presumably this is on account of the stability of the silicon-oxygen network.

The question arises as to what factors might allow O²⁻ ions to migrate when an oxide glass is electrolyzed. Perhaps the most obvious factor is the ability of the glass-forming cation to switch readily from one coordination number to another. In the case of silicate glasses, the silicon(IV) species is reluctant to be anything but four-coordinate. On the other hand, borate glasses are well known to contain boron in threefold and fourfold coordination, preference for one or the other depending directly on the proportion of O²⁻ ions originally used in making the glass (*i.e.*, the NaO₂:B₂O₃ ratio in the case of a sodium borate glass, for example). Thus, whereas electrolysis of a silicate glass results in the metal anode being converted to its cation with subsequent migration into the glass, it is possible, in the case of a borate glass, that the process of oxide ion migration to the anode will occur as an additional or even an alternative process.

If migration of both oxide ions and metal ions of the glass proceeds, this will result in a lowering of the basicity of the glass, since, for example in a sodium borate glass, there would be a loss of Na₂O. It would be useful therefore if the glass basicity could be

monitored during the electrolysis. The basicity of glass has been probed very successfully by measuring the shifts in the ultraviolet spectra of s² metal ions such as Pb²⁺ (5,6). The use of lead as anode material therefore suggests itself for experiments designed to investigate ion migration in glasses. The intense and characteristic u.v. absorption of the Pb²⁺ ion should indicate whether the lead anode has formed Pb²⁺ ions which have entered the glass, and furthermore if this did occur, the position of the u.v. absorption maximum should reveal the basicity of the sites occupied by the Pb²⁺ ions.

These principles are exploited in the present study of ion migration in sodium borate glass.

Experimental

Thin plates (20 × 30 × 0.5 mm³) of a sodium borate glass containing 35 mole percent (m/o) Na₂O were vacuum-coated with a 50 nm thin layer of metallic lead covering an area of 10 × 20 mm². The particular glass composition was chosen since it represented an optimum compromise of conductivity ($\sigma = 6 \times 10^{-10} \Omega^{-1} \text{ cm}^{-1}$ at 50°C), ultraviolet transparency, and durability. The lead layer was contacted with a thin platinum wire and was made the anode of an electrolytic cell whose cathode was a pool of mercury on which the glass floated

(+) Pb/glass/Hg (—) [1]

The cell was operated in argon atmosphere, and the total applied voltage of 800V generated a current density of 5-10 $\mu\text{A cm}^{-2}$ so that an electric charge of 0.01-0.05C was transported through the 0.5 mm thickness of glass during 15-90 min of electrolysis. Sparking between the edges of the lead layer and the mercury pool was eliminated by placing the glass plate in a PTFE box with open top and a 10 × 20 mm² rectangular opening in the flat bottom through which the lower (uncoated) surface of the plate contacted the mercury cathode. This distorted the electric field through the gas space thus decreasing the field strength between the two metals.

Key words: migration, anode, spectroscopy.

After electrolysis the glass plate was removed from the mercury pool and the unreacted lead on the coated surface was dissolved in clean mercury. The resulting, optically transparent, glass was then subjected to a combined (ultraviolet) spectroscopic/ion ablation study in order to investigate sodium and lead ion concentration profiles below the anodic surface.

The ion sputtering method for measuring concentration profiles (1), its application to moving boundary experiments in solids (2-4), and the principles of obtaining optical basicities from ultraviolet spectra (5, 6) have been detailed previously.

Contact between the lead layer and the platinum wire was made by a narrow stripe of platinum paint applied to the glass prior to vacuum deposition of the lead layer. It should be noted that such plates could be used only within a limited time (several weeks) after preparation. After longer periods, the electrical contact deteriorated and also the lead area covering the platinum became nonconducting. Presumably storage results in some of the lead being converted into PbO, the lead having behaved as the electrode of an electrically shorted cell involving the glass as electrolyte (with perhaps traces of water) and the platinum as the other electrode.

Results and Discussion

Figure 1a shows the sodium concentration profile from the surface inwards (to a depth of approximately 200 nm) for a sample of the 35 m/o Na₂O sodium borate glass. The concentration profile of another sample of the same glass, which had been coated with a thin film of metallic lead subsequently removed with mercury, was found to be identical to that in Fig. 1a, indicating that the lead coating treatment had no effect on the sodium ions in the glass. It is apparent from Fig. 1a that the sodium concentration of the bulk glass extends up to a few nm below the glass surface; the slight change within this region was caused by ion exchange involving adsorbed water molecules of the atmosphere during storage, which leads to the formation of protonated glass and of a layer consisting of sodium oxide, hydroxide, or carbonate, according to the conditions of storage, on the glass surface. This corrosion has been studied in detail previously (1, 7).

Figure 1b presents sodium and lead concentration profiles near the anodic glass surface after an electrolysis during which a charge of 0.049C was trans-

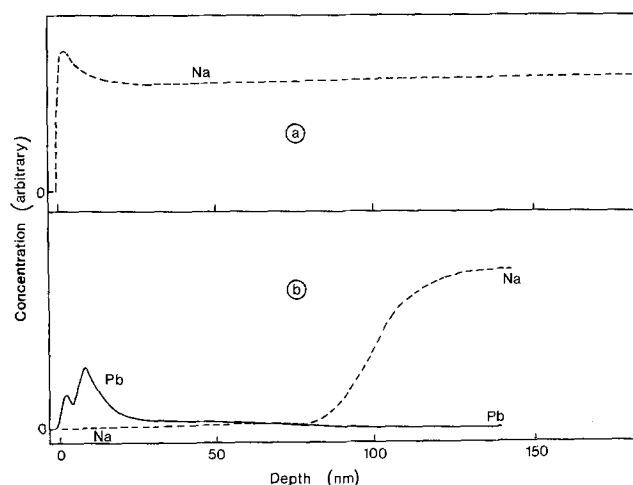


Fig. 1. (a) Sodium concentration profile below the surface of untreated sodium borate glass (35 m/o Na₂O). The same profile is obtained after vacuum deposition of thin lead layer (50 nm) and subsequent dissolution in mercury. (b) Sodium and lead concentration profiles near the anodic surface of a sodium borate glass covered with a 50 nm thick lead layer after electrolysis and subsequent removal of lead (see text for details). Total charge transported: 0.049C; current density: 8 μ A cm⁻²; 50°C.

ported through the glass plate with subsequent removal of the metallic lead with mercury. It is apparent from the low sodium ion concentration in the anode region that there has been almost complete migration of the sodium ions towards the cathode. The ultraviolet absorption spectrum of the glass prior to subjecting the former anode surface to ion ablation (that is, just after dissolving away the unreacted lead with mercury) is shown in Fig. 2a. This is quite different from the spectrum of Pb²⁺ in sodium borate glass (which usually has a distinct peak in the range 42,000 cm⁻¹ to 47,000 cm⁻¹) and strongly suggests that a process other than substitution of an equivalent quantity of Pb²⁺ ions for Na⁺ ions has occurred during electrolysis of the glass. The lead profile, obtained by ion ablation, (Fig. 1b) reveals a high lead concentration to a very short depth (about 20 nm) and then a very low concentration of lead to much greater depth. From previous experience of ion ablation experiments with PbO films on glass, carried out in these laboratories, it seems likely that the initially high lead concentration in Fig. 1b is due to the formation of PbO. Furthermore, the ultraviolet spectrum in Fig. 2a is very similar to that obtained for PbO vacuum deposited as a thin film, see Fig. 2b (the absorption of Pb²⁺ ions that have entered the glass does not significantly affect the spectral comparison). Thus, it appears that during the electrolysis, most of the lead which is anodically oxidized is converted into PbO.

In order to detect the remaining Pb²⁺ ions which had entered the glass, further samples of electrolyzed glass were subjected to sufficient ion ablation to remove the PbO and were scanned in the ultraviolet region. An example of the resulting spectra is shown in Fig. 3. It is typical of a solution of Pb²⁺ in sodium borate glass (5). Further experiments indicated that

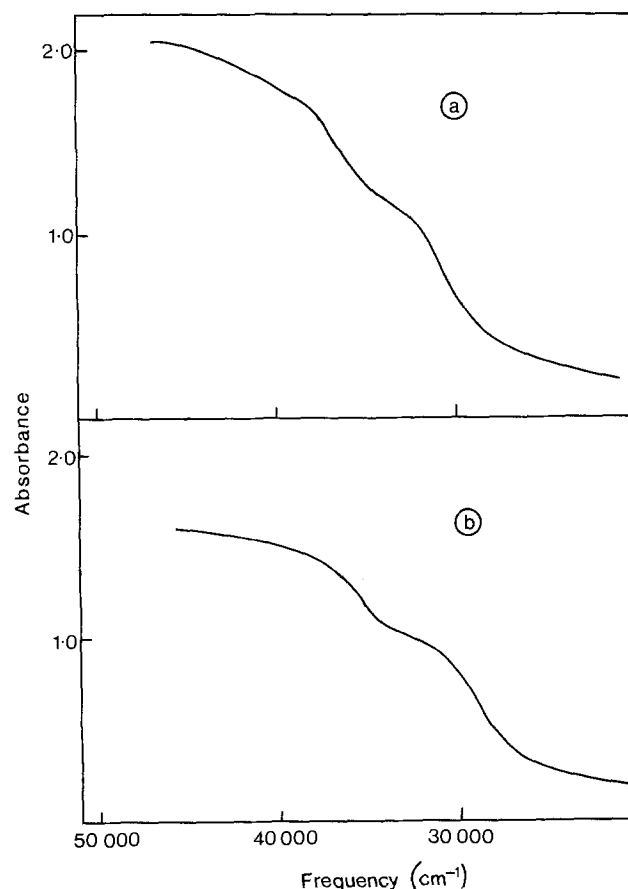


Fig. 2. (a) U.V. spectrum of a sodium borate glass after electrolysis and removal of lead anode [see Fig. 1(b) and text for details]. (b) U.V. spectrum of PbO film (40 nm) vacuum deposited onto vitreous silica substrate.

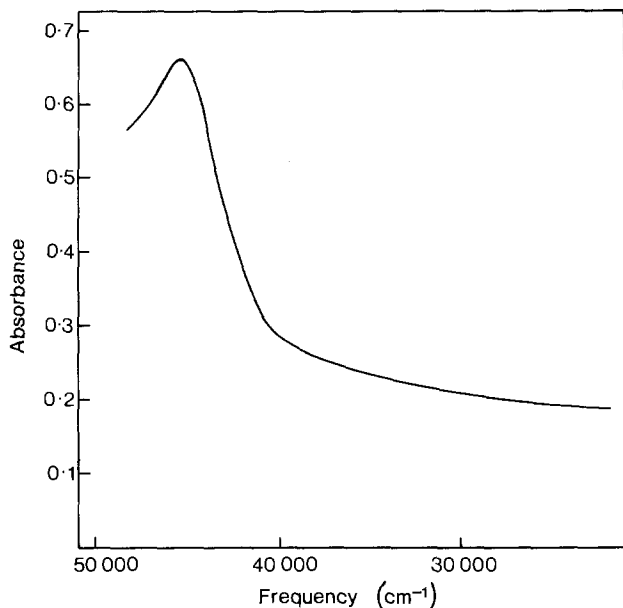
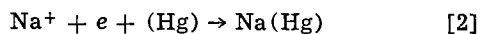


Fig. 3. U.V. spectrum of the sodium borate glass plate [of Fig. 2(a)], after removal of PbO layer.

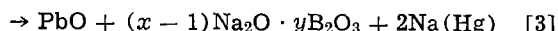
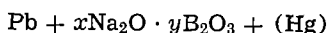
at depths beyond the Na^+ concentration change, no Pb^{2+} was detectable.

Thus, the processes occurring in the anode region appear to be (i) migration of Na^+ ions towards the cathode, (ii) migration and formation of O^{2-} ions at the anode, (iii) oxidation of lead to Pb^{2+} ions, and (iv) combination of Pb^{2+} and O^{2-} ions to form PbO . This process is in contrast to those typically occurring in silicate glasses if truly nonblocking electrodes, i.e., electrolyte solutions, are employed. For example, in the field-driven protonation of alkali silicate glass, all of the alkali ions are replaced by protons (2-4). It has been recently suggested, however, that small amounts of O^{2-} ions may be displaced towards the anode even in an $\text{Li}_2\text{O}\cdot 2\text{SiO}_2$ glass if completely blocking electrodes are applied (8).

Since the cell operates with only mercury as the cathode, it is reasonable to assume that the cathode reaction consists of Na^+ ion drift to the surface, their discharge, and dissolution of the sodium thus formed in mercury



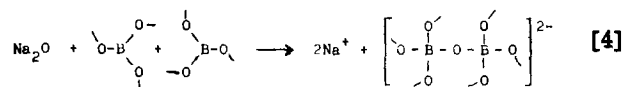
Combination of anode and cathode reactions yields the cell reaction



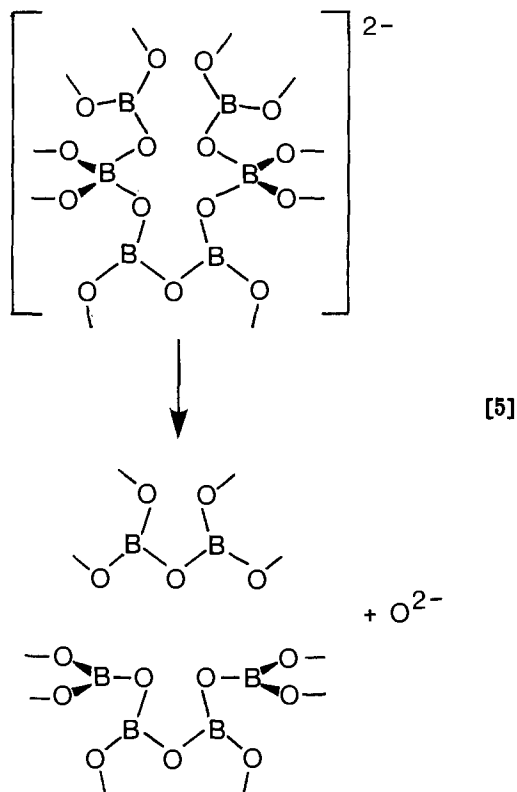
In effect, this reaction is reversible, since after the electrolysis an emf of several hundred mV was observed which had the same sign as the electrolyzing voltage applied. Moreover, it was found that the electrolysis could be reversed to regenerate approximately the original glass composition, corresponding to Fig. 1a. Equation [3] therefore might represent a reversible battery process.

It was suggested earlier in this paper that the property of boron to switch its coordination between threefold and fourfold could assist the migration of O^{2-} ions. Since the results of the experiments indicate that O^{2-} ions have indeed arrived at the anode, it is worthwhile considering the possible transport mechanism. Of course, O^{2-} ions as such do not exist in the glass; the addition of ionic oxides, such as Na_2O , to a borate glass involves boron atoms increasing their coordination from three to four, rather than the introduction of O^{2-} ions. The stoichiometry of this process (but not the structural details since BO_4

units are seldom found linked directly to each other) may be represented by



This is in contrast to the addition of a basic oxide to a silicate glass where instead bridging oxygens are converted to terminal. It is essentially the reverse of this reaction (Eq. [4]) which is invoked for the migration and formation of O^{2-} ions at the anode

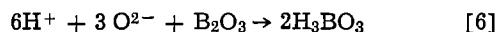


The above mechanism would represent the generation of O^{2-} at the anode, ready for combination with Pb^{2+} ions to form PbO . However, if the mechanism were extended so that instead of an O^{2-} ion being generated it was "handed over" by one of the four-coordinate boron atoms to a nearby three-coordinate boron atom (which then became four-coordinate), it can be appreciated how an apparent movement of oxide ions through the medium could be achieved. All that is required is a continuous interchange between threefold and fourfold coordination on the part of the boron atoms with an appropriate rotation or other slight oscillation of the borate groups. The conduction of the borate glass might therefore be described as a "structure-switching ionic transport."

Migration of O^{2-} ions rather than Pb^{2+} ions is obviously the favored process during the electrolysis (Fig. 1b). It is possible that Pb^{2+} migration is hindered owing to the larger size of Pb^{2+} compared with Na^+ (ionic radii are 1.20 and 0.96Å, respectively). The primary reason, however, is perhaps the dipositive charge of the Pb^{2+} ion which would have to enter the glass where cationic sites were originally occupied by unipositive ions. The Pb^{2+} ion would occupy only one site (to which it would be relatively tightly bound) while, because of electroneutrality, one cationic site for each Pb^{2+} entered would have to remain without countercharge. This reasoning is supported by the observation (9) that silver ions do enter the borate glass when a silver rather than lead metal layer is made the anode in cell (Eq.

[1]), although the ionic radii of Ag^+ (1.26Å) and Pb^{2+} (1.20Å) are comparable. Silver oxide was not detected at the surface during these experiments. From the drastic increase observed for the resistance during the electrolysis of the silver-covered glass it must also be concluded that Ag^+ ions have a much lower mobility than Na^+ ions in the borate glass. Further, it appears that the presence of Ag^+ ions, once in the network (in the anode region), prevents the structure-switching mechanism of the borate groups, and thus it is possible that this mechanism only operates when a large proportion of metal ions (Na^+ , Ag^+ , etc.) have withdrawn from the network.

Because of the O^{2-} ion migration towards the anode during the electrolysis, a platinum anode is not expected to behave as a blocking electrode but to evolve oxygen. This expectation is supported experimentally by the observation that electrolysis with such an electrode results in only a minor increase in resistance, whereas for a silicate glass typical blocking behavior is observed. Furthermore, it is found that a proton-injecting electrode, consisting of a thin Pt layer on the glass in a dry hydrogen atmosphere, causes crystallization in the anode region (9). Obviously hydrogen ions produced at the Pt, H_2 anode combine with the O^{2-} ions to give water which reacts with the boric oxide glass to give boric acid, i.e.



This is not a good glass former and thus crystallizes.

With effective removal of Na_2O from the anode region, a marked decrease should be observed in the basicity compared with the original glass (see beginning of paper). Glass basicity is expressed conveniently on the optical basicity scale (5,6) and most glasses have optical basicities, Λ , in the range 0.4-0.7. The 35 m/o Na_2O sodium borate glass has $\Lambda = 0.60$ (5,6). It is possible to calculate the optical basicity registered by the Pb^{2+} ions that have entered the Na_2O -depleted anode region from the frequency maximum, $45,700\text{ cm}^{-1}$, observed for the absorption band (Fig. 3) (5,6)

$$\Lambda = \frac{61,000 - 45,700}{31,000} = 0.49$$

Thus, as anticipated, there is a decrease in optical basicity. This decrease, however, is less than ex-

pected, since the sodium concentration profile (Fig. 1b) suggests that the Na_2O content of the anode region is no more than approximately 3%, corresponding to an optical basicity of around 0.44. The observed value corresponds to a sodium borate glass of 18 m/o Na_2O . The reason for this apparent discrepancy may be due to the sites available to the Pb^{2+} ions, that enter the glass, being markedly different from those adopted by Pb^{2+} when a glass is formed from the melt. This result is worth further study, especially using other anode materials which give rise to s^2 basicity probe ions, e.g., thallium or bismuth.

Acknowledgment

The authors thank Dr. H. Bach, Jenaer Glaswerk Schott u. Gen., for useful discussions and advice, especially concerning the application of the ion beam ablation technique, and Miss Lautenbach, Jenaer Glaswerk, for careful experimental work. J.A.D. also acknowledges support from the Royal Society under their European Science Exchange Programme.

Manuscript submitted Dec. 26, 1979; revised manuscript received April 31, 1980.

Any discussion of this paper will appear in a Discussion Section to be published in the June 1981 JOURNAL. All discussions for the June 1981 Discussion Section should be submitted by Feb. 1, 1981.

Publication costs of this article were assisted by the Jenaer Glaswerk Schott u. Gen.

REFERENCES

1. H. Bach and F. G. K. Baucke, *Phys. Chem. Glasses*, **15**, 123 (1974).
2. F. G. K. Baucke, in "Mass Transport Phenomena in Ceramics," A. R. Cooper and A. H. Hener, editors, pp. 337-354, Plenum, New York (1975).
3. F. G. K. Baucke in "Proc. XIth International Congress on Glass," pp. 347-356, C V T S - Dům techniky Praha, Prague (1977).
4. F. G. K. Baucke, *J. Non-Cryst. Solids*, in press.
5. J. A. Duffy and M. D. Ingram, *J. Am. Chem. Soc.*, **93**, 6448 (1971).
6. J. A. Duffy and M. D. Ingram, *J. Non-Cryst. Solids*, **21**, 373 (1976).
7. F. G. K. Baucke, *ibid.*, **14**, 13 (1974); **19**, 75 (1975).
8. K. Takizawa, *J. Am. Ceram. Soc.*, **61**, 475 (1978).
9. F. G. K. Baucke, Unpublished results.

New Complex Fluorides EuMgF_4 , SmMgF_4 , SrMgF_4 , and Their Solid Solutions: Photoluminescence and Energy Transfer

E. Banks,* S. Nakajima, and M. Shone¹

Department of Chemistry, Polytechnic Institute of New York, Brooklyn, New York 11201

ABSTRACT

Three previously unknown compounds, EuMgF_4 , SmMgF_4 , and SrMgF_4 , and solid solutions, have been prepared by a method involving the use of Mg metal as a reducing agent for the Eu and Sm. Both EuMgF_4 and SmMgF_4 appear to be excited via a $4f \rightarrow 5d$ transition (broad band). EuMgF_4 emits a bright blue under 356 nm peak excitation, the emission peak being at 437 nm. SmMgF_4 has sharp line emission assigned to ${}^5D_0 \rightarrow {}^7F_{0-6}$ transitions. In solid solutions $\text{Sr}_{1-x}\text{Eu}_x\text{MgF}_4$, maximum efficiency is found at $x = 0.75$ and the efficiency of EuMgF_4 is only about 5% less, adding EuMgF_4 to the small group of known "stoichiometric phosphors." This is correlated with magnetic measurements which show little or no exchange interaction between neighboring rare earth ions. The magnetic behavior of the Sm^{2+} ion in SmMgF_4 suggests the possibility of mixing of the $J = 0$ and $J = 1$ states of the ground state manifold, owing to strong acentric crystal fields. In solid solutions $\text{Eu}_{1-x}\text{Sm}_x\text{MgF}_4$, there is remarkable energy transfer from Eu^{2+} to Sm^{2+} , the Eu^{2+} emission being barely detected at $x = 0.01$ and completely absent at higher Sm concentrations. Evidence for both radiative and nonradiative transfer was found, but the nonradiative mechanism appears to predominate.

Compounds of the type BaMF_4 ($M = \text{Mg, Mn, Fe, Co, Ni, Cu, or Zn}$) crystallize in the orthorhombic space group $A2_1am$ (1-3). Over the past few years, several technologically useful properties have come to light. Among the most important properties are piezoelectric behavior in $M = \text{Mg, Co, Ni, Mn, and Zn}$ (2), magnetoelectric effect in BaCoF_4 (4), greater piezoelectric coupling in BaMnF_4 than quartz, and excellent microwave ultrasonic transmission characteristics in this same compound (5).

Bergman *et al.* (6) reported BaMnF_4 and BaMgF_4 to be noncritically phase matchable at room temperature for a $1.06 \mu\text{m}$ pump laser and resistant to optical damage at powers of up to 10^9 W/cm^2 .

All of the known materials of this class have magnetically inert Ba^{2+} in planes between puckered sheets of corner sharing MF_6 octahedra (7). It was the intention of this study to substitute magnetically and optically active Eu^{2+} and Sm^{2+} for Ba^{2+} . In addition we prepared what was hoped to be the Sr^{2+} analogue of BaMgF_4 .

In the first parts of this paper a qualitative outline of the structure, preparative methods, and experimental findings concerning EuMgF_4 , SmMgF_4 , and SrMgF_4 is presented. The spectroscopic and magnetic properties are then discussed in detail.

Crystal Structure of $(\text{Eu,Sm,Sr})\text{MgF}_4$

As yet, no definitive crystal structure has been determined for SrMgF_4 , EuMgF_4 , or SmMgF_4 . Table I presents a summary of the lattice parameters taken from high angle x-ray diffraction patterns, along with x-ray and measured densities.

While the cell parameters show clearly that these compounds are orthorhombic, tests for second harmonic generation were negative. Therefore, it is tentatively concluded that none of the new compounds have the space group $A2_1am$. The space group Amm then suggests itself from preliminary examination of a Patterson function map (8).

* Electrochemical Society Active Member.

¹ Present address: Airtron, Incorporated, Morris Plains, New Jersey 07950.

Key words: complex fluorides, rare earth luminescence, energy transfer, stoichiometric phosphors.

Table I. Summary of lattice parameters and density

Compound and lattice parameters	Density (x-ray) (g/cm ³)	Density $\pm 5\%$ (measured) (g/cm ³)
1. EuMgF_4		
$a_0 = 3.933 \pm 0.003\text{A}$		
$b_0 = 14.43 \pm 0.011$		
$c_0 = 5.608 \pm 0.004$		
Cell vol. = 320.41A^3	5.23	5.34
2. SmMgF_4		
$a_0 = 3.915 \pm 0.002\text{A}$		
$b_0 = 14.440 \pm 0.009$		
$c_0 = 5.661 \pm 0.003$		
Cell vol. = 324.41A^3	5.13	4.91
3. SrMgF_4		
$a_0 = 3.917 \pm 0.004\text{A}$		
$b_0 = 14.459 \pm 0.013$		
$c_0 = 5.637 \pm 0.005$		
Cell vol. = 319.64A^3	3.90	3.89

Nevertheless, the point symmetry around Eu, Sm, and Sr should be almost equivalent to that of BaMnF_4 , that is, an eight-fold coordination of F^- ions all of whose Ba-F bond lengths are unequal. The possibility of such low point symmetry is supported by the appearance of an intense 5D_0 - 7F_0 optical transition seen in SmMgF_4 . The point symmetry around (Eu, Sm, Sr) is now thought to be C_s similar to that of Ba in BaMnF_4 .

Experimental

All preparations and purifications were carried out in graphite (Ultra Carbon, F purity) crucibles in an argon (Matheson, prepurified) flow system. A two-zone Cu work coil connected to an rf generator supplied heat to the sample while a Leeds and Northrup optical pyrometer was used to measure temperature.

Purification of the starting materials [EuF_3 (ROC/RIC, 99.9%), SmF_3 (Lindsay Division of American Potash, 99.9%), SrF_2 (ROC/RIC, 99.9%, optical grade), and MgF_2 (British Drug House, 99.9%)] was accomplished by drying to constant weight at 250°C and subjecting these materials to treatment with dried NH_4F (Fisher, 99%) in a flow system. Water was scrubbed from the argon by flowing the gas over Drierite and through an acetone-Dry Ice trap.

In some experiments EuF_2 and SmF_2 were used. These were prepared by hydrogen reduction (Mathe-

son Gas Products) of the trifluoride at 850°C for 4 hr, with regrinding and reheating. All purified materials were stored in a vacuum desiccator over MgClO_4 .

SrMgF_4 was prepared by combining stoichiometric amounts of SrF_2 and MgF_2 in a capped graphite crucible and heating for three 5 hr runs at 875°C. After each run the product was checked for starting materials.

EuMgF_4 was most easily prepared by reduction of mixtures of EuF_3 and MgF_2 in the ratio of 2:1 within the graphite crucible. A five-fold excess over stoichiometry of fresh Mg turnings (Fisher Reagent Grade) was added above the mixture. The position of the crucible in the work coil is shown in Fig. 1. Heat was applied so that the temperature in the hot zone was 850°C while that of the cool zone was 750°C. The initial heating period of 2 hr was followed by three 3 hr heating cycles. After each heating period the sample was ground, checked by x-rays for excess EuF_2 or MgF_2 , and returned for further heating after adjusting the composition.

The second method of EuMgF_4 production involved combination of EuF_2 and MgF_2 with only one piece of Mg added. The same procedure of extra heating, grinding, and adjusting of starting materials is performed as for the method above.

SmMgF_4 could only be prepared from SmF_3 and MgF_2 with an excess of Mg. The two heating zones were measured at 830° and 730°C, respectively, for successful preparation. No secondary heating periods were found to be helpful.

All excitation and emission spectra were recorded using an Hitachi-Perkin Elmer Model MPF2A spectrofluorimeter. Liquid nitrogen spectra were obtained with the aid of a cryostatic Dewar provided for this instrument.

Quantum efficiencies were measured against the fluorescent output of sodium salicylate which had been calibrated against a known halophosphate lamp phosphor. Fluorescence was recorded under 365 nm Hg excitation using a Jarrell-Ash spectrometer and the area under the emission curve was then integrated. Corrections were made for scattering from nonfluorescent MgO at 365 nm.

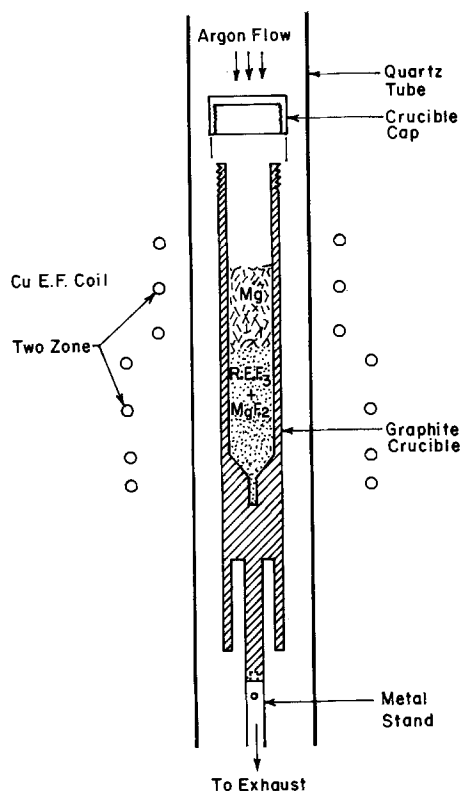


Fig. 1. Crucible and heater assembly

The lifetimes of the 437 nm emission of EuMgF_4 , $\text{Eu}_{0.995}\text{Sm}_{0.005}\text{MgF}_4$ and $\text{Eu}_{0.99}\text{Sm}_{0.01}\text{MgF}_4$ were measured on an SLM series 4000 spectrofluorometer. A demodulation technique was used to record the lifetimes.

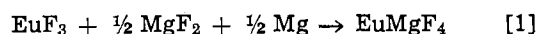
Magnetic measurements were made with a Princeton Applied Research vibrating sample magnetometer (VSM) to liquid helium temperature.

Densities of EuMgF_4 , SrMgF_4 , and SmMgF_4 were determined by the pycnometer method of Reilly and Rae (9). A 2 milliliter pycnometer bottle was used. Carbon tetrachloride was chosen as the pycnometric liquid because of its lack of reactivity and high density.

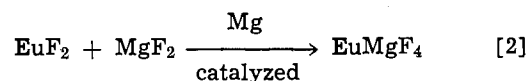
Results and Discussion

With the preparative methods that were used, it was found to be difficult to prepare EuMgF_4 directly from EuF_2 and MgF_2 . Such experiments yielded only 20% conversion even after 3 days of heating. Longer experiments gave products which were already decomposed. This is thought to be due to small amounts of water vapor accumulating during grinding and, in general, during the long run periods.

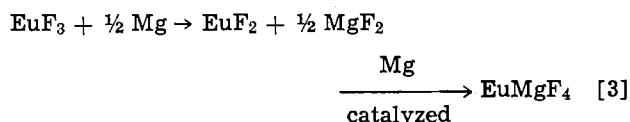
Two possible equations for the formation of EuMgF_4 are then



and



Mg, present as vapor at reaction temperature, is believed to have four functions. First, it acted as an oxygen and water scavenger. Second, it appeared to catalyze the reaction. Third, it acted as a strong reducing agent. Fourth, it was used to make up Mg deficiencies in the compounds. To test this, EuF_3 and Mg alone were reacted. The outcome was partial conversion to EuMgF_4 . A possible course for the reaction is

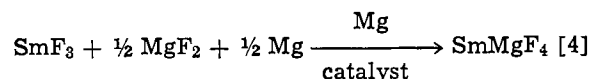


Indeed, the appropriate amount of EuF_2 is observed in the x-ray diffraction pattern. During the course of the preparations only one complex phase (EuMgF_4) was evident utilizing x-ray diffraction analysis.

EuMgF_4 was found to be a white powder, stable in moist air, when prepared in a pure state.

In distinction to EuMgF_4 , SrMgF_4 was preparable by using the two binary fluorides directly. This leads one to believe that SrMgF_4 is somewhat more stable in the presence of hydroxyl than its lanthanide counterparts. SrMgF_4 was also found to be a white, air stable compound.

The reactive nature of Sm^{2+} precluded the use of multiple grinding and heating operations because of the deleterious effect of moisture. Formation of SmMgF_4 is thought to proceed by the pathway



SmMgF_4 is a red compound which appears to be stable in moist air even when exposed for periods in excess of one week.

All three new compounds appear to melt incongruently at about 900°C. Samples heated above that temperature were found to have melted. X-ray patterns showed only mixtures of the binary fluorides (e.g., EuF_2 and MgF_2).

For EuMgF_4 , both the excitation and emission spectra (Fig. 2 and 3) show the f-d band transition typical of Eu^{2+} compounds. The room temperature excitation spectrum shows a peak at 356 nm while

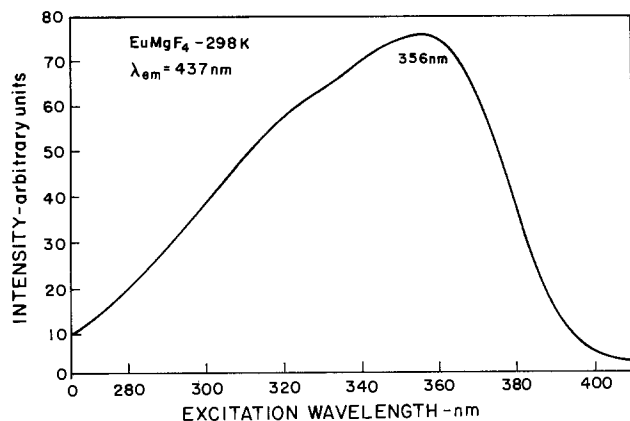


Fig. 2. Excitation spectrum of EuMgF_4 , 298°K

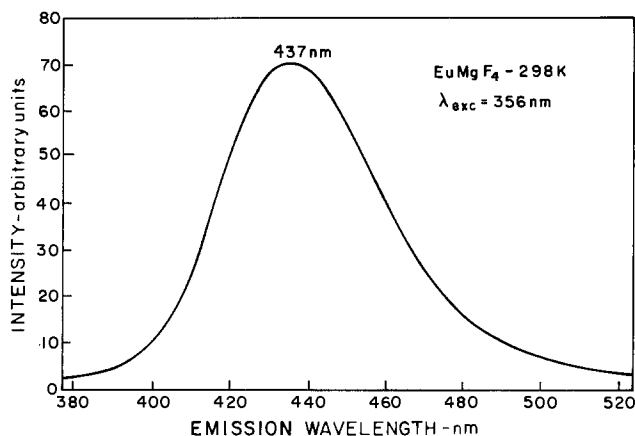


Fig. 3. Emission spectrum of EuMgF_4 , 298°K

the emission spectrum shows a maximum at 437 nm. No f-f transitions were observed, in accord with the findings of Fouassier (10) for eight coordinate Eu^{2+} .

At room temperature, the emission and excitation bands have meaningful spectral overlap only in the region of 380-400 nm. The 33% quantum efficiency measured for EuMgF_4 is remarkable considering the rather poor quality of the product. This is only 5% less than the maximum found in $\text{Eu}_{0.75}\text{Sr}_{0.25}\text{MgF}_4$. At 77°K the bands narrow because of lower molecular vibrational amplitude and there is no overlap at all. This implies, by the theories of Forster (11) and Dexter (12), that there will be neither coulombic interactions between distant bivalent europium ions nor significant exchange interactions among neighboring Eu^{2+} ions. The lack of coulombic interaction is attributed to the symmetrical nature of the $^8\text{S}_{7/2}$ ground state (13).

Measurements of magnetic susceptibility were made on EuMgF_4 and SmMgF_4 to determine the magnitude of any exchange interactions that might be present which could mediate energy transfer and concentration quenching behavior. Paramagnetic susceptibilities were measured from 4.2°K to room temperature on EuMgF_4 , SmMgF_4 , and the solid solution $\text{Eu}_{0.5}\text{Sm}_{0.5}\text{MgF}_4$, which behaved as expected for a random distribution of Eu^{2+} and Sm^{2+} in the structure. EuMgF_4 was found to obey a Curie-Weiss law, remaining paramagnetic down to 4.2°K, with a Weiss constant, $\theta = -3^\circ\text{K}$. This indicates very weak exchange coupling. The effective moment for Eu^{2+} calculated from the high temperature magnetic data was $\mu_{\text{eff}} = 7.8 \text{ BM}$, which agrees well with the literature value of 7.9 BM (14), so there is little doubt that all the Eu is in the bivalent state. The magnetic data on SmMgF_4 are discussed below, after the discussion of its fluorescence.

A firm explanation of the exchange interactions in EuMgF_4 cannot be given at this time because the

structure is not known with certainty. However, the following line of thought seems most sensible at this stage. By linearizing the ratio of unit cell volumes of EuMgF_4 to BaMnF_4 it is found that the average europium-europium distance would be approximately 4.4Å. In EuF_2 , a cubic antiferromagnet, the europium-europium distance is 4.1Å and there are eight antiferromagnetic pathways through coordinate fluoride ions (15). However, assuming the BaMnF_4 structure, some of the europium-fluorine pathways may not lead to other europium atoms directly, therefore limiting the amount of antiferromagnetic interaction compared to EuF_2 . McGuire and Shafer (15) also show that direct exchange falls off sharply at distances of 4.4Å or greater in europium chalcogenides while antiferromagnetic superexchange was weak in all cases regardless of distance. Fluorides would show weaker antiferromagnetic superexchange than chalcogenides because of the greater ionicity of fluorides.

The fluorescence of various solid solutions of EuMgF_4 in SrMgF_4 show that there is very little concentration quenching as the amount of europium is increased. (Fig. 4).

The wavelength required to promote the electron into the d band decreases from $\lambda_{\text{ex}} = 356 \text{ nm}$ in EuMgF_4 to $\lambda_{\text{ex}} = 316 \text{ nm}$ in $\text{Sr}_{0.99}\text{Eu}_{0.01}\text{MgF}_4$. In the latter compound, the lattice becomes more rigid and resistant to electron cloud expansion due to the higher charge to size ratio of strontium as compared with europium.

At 77°K the excitation and emission spectra of $\text{Sr}_{0.99}\text{Eu}_{0.01}\text{MgF}_4$ (Fig. 5) show considerable fine structure which is unresolved in the same spectra of EuMgF_4 . This fine structure could possibly arise from excitations from the f level to various vibrational d band levels, although the possibility of f-f transitions cannot now be ruled out.

In Fig. 6, the excitation spectrum of SmMgF_4 at 298°K shows a broad band excitation extending from below 340 nm to above 620 nm. At 77°K the same spectrum extends from below 340 nm but shows a sharp drop-off above 560 nm. This is directly attributable to depopulation of the $J > 0$ levels in the $^7\text{F}_{0-6}$ ground state known to exist in bivalent samarium. All of the spurious weak lines on the excitation band are due to xenon lamp lines or diffraction effects.

The room temperature emission spectrum of SmMgF_4 (Fig. 7) consists of a number of lines superimposed on a broad band continuum. Transitions from the $^5\text{D}_0$ to the $^7\text{F}_{0-6}$ are responsible for the lines while transitions from the $4f^5-5d$ band to the $^7\text{F}_0$ produce the continuum. At 77°K the continuum disappears and there is an increase in the number and intensity of the lines in the spectrum (Fig. 8).

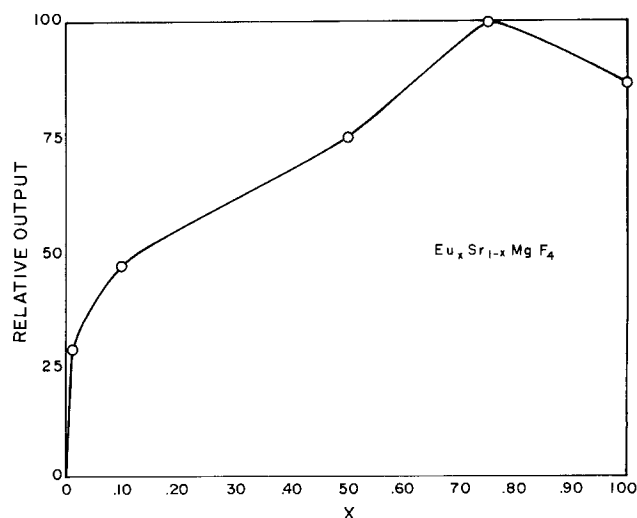
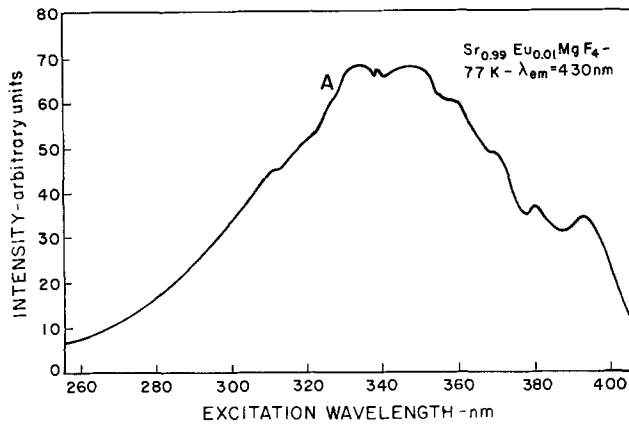
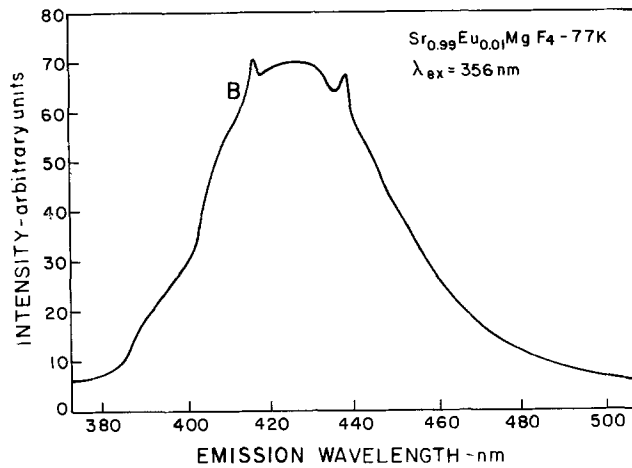
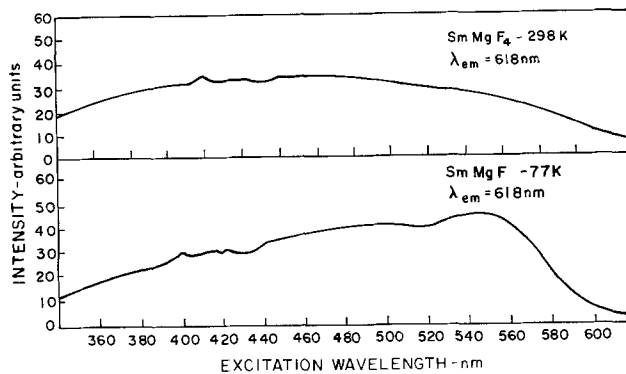
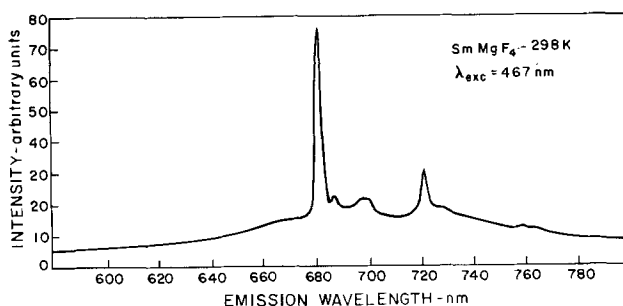
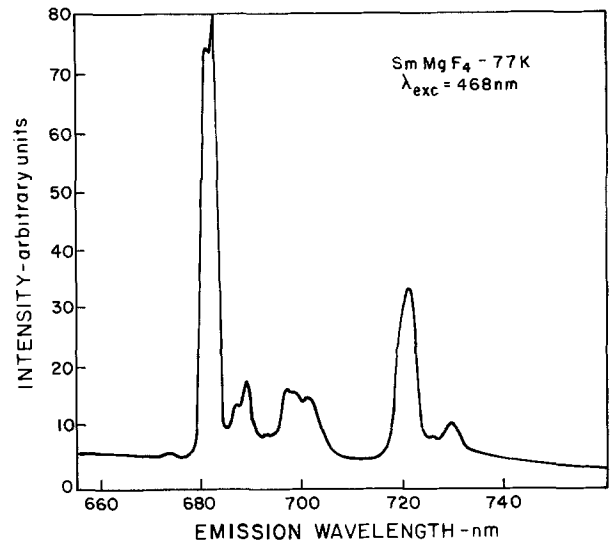
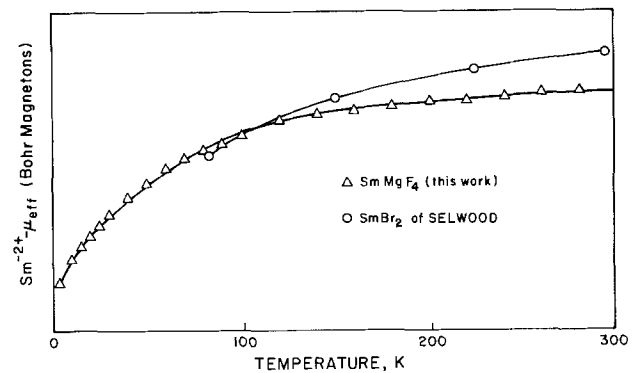


Fig. 4. Concentration dependence of Eu^{2+} emission peak intensity (298°K) in $\text{Sr}_{1-x}\text{Eu}_x\text{MgF}_4$.

Fig. 5a. Excitation spectrum of $\text{Sr}_{0.99}\text{Eu}_{0.01}\text{MgF}_4$ at 77°K Fig. 5b. Emission spectrum of $\text{Sr}_{0.99}\text{Eu}_{0.01}\text{MgF}_4$ at 77°K Fig. 6. SmMgF_4 excitation spectra, 77° and 298°K Fig. 7. SmMgF_4 emission spectrum, 298°K

Since temperature quenching of the $^5\text{D}_1$ and $^5\text{D}_0$ levels occurs through an intervening $4f^5-5d$ band (16), the appearance of considerable sharp line emission at room temperature is an indication of substantial asymmetry at the samarium site. Such emission fol-

Fig. 8. SmMgF_4 emission spectrum, 77°K Fig. 9. Effective magnetic moment of Sm^{2+} in SmMgF_4 and SmBr_2 , temperature dependence.

lows only from severe breakdown in the selection rules.

Assignments of the peaks were made on the basis of comparisons with the work of Dieke (17) on Sm^{2+} and Blasse (18) on Eu^{3+} . Room temperature peak assignments are listed in Table II. The designation of the first peak at 681 nm as $^5\text{D}_0-^7\text{F}_0$ is consistent with the postulated low symmetry around bivalent samarium, which is supported by the observation of an intense line spectrum at room temperature. The positions and sizes of the other peaks then fit easily into a general scheme when the first peak is assigned to $^5\text{D}_0-^7\text{F}_0$.

Bivalent samarium becomes nonmagnetic at 0°K because at that temperature only the $J = 0$ state of the $^7\text{F}_{0-6}$ ground manifold is populated. The result of depopulation of the upper states with decreasing temperature is a nonlinear decrease in the effective Bohr magneton number. This phenomenon was first observed by Selwood (19) for SmBr_2 . SmMgF_4 follows approximately the same pattern. Susceptibility measurements were made down to 4.2°K where $\mu_{\text{eff}} = 0.62 \text{ BM}$ (Fig. 9). No attempt is made to evaluate the Weiss con-

Table II. Positions and designations of transitions in SmMgF_4 at room temperature

Position (nm)	cm^{-1}	Designation	Intensity
---------------	------------------	-------------	-----------

681	14,684	$^5\text{D}_0-^7\text{F}_0$	vs
687	14,556	$^5\text{D}_1-^7\text{F}_3$	w
697	14,358	$^5\text{D}_0-^7\text{F}_1$	m
701	14,266	$^5\text{D}_0-^7\text{F}_2$	m
721	13,870	$^5\text{D}_1-^7\text{F}_4$	s
729	13,717	$^5\text{D}_1-^7\text{F}_4$	vw
762	13,123	$^5\text{D}_0-^7\text{F}_3$	vw

stant as the anomalous temperature coefficient renders this parameter meaningless. The magnetic data show that at 300°K $\mu_{\text{eff}} = 3.13$ BM while Selwood (19) give 3.6 BM for SmBr_2 . At 83°K Selwood measured $\mu_{\text{eff}} = 2.29$ BM while SmMgF_4 gave a value of 2.35 BM. Following a van Vleck theoretical curve down to about 12°K, the divergence between the curve and the measured value for SmMgF_4 becomes roughly 0.3 BM with the measured value being the greater. It should be remarked that Selwood's measurements closely follow van Vleck's theory for bivalent samarium (19).

These observations may be indicating a slight mixing of the 7F_0 and 7F_1 states. Although this type of mixing has not been seen in the past, it is possible if the crystal field strength is very high at the bivalent samarium site, with very low site symmetry. Such mixing is easier in bivalent samarium than in trivalent europium because the ${}^7F_{0-6}$ levels are considerably closer together in the former ion.

The series $\text{Sr}_{1-x}\text{Sm}_x\text{MgF}_4$ shows considerable concentration quenching at $x = 0.1$. Since temperature independent concentration quenching in bivalent samarium originates only from exchange interaction and not from a multipolar resonance mechanism (width of the ${}^7F_{0-6}$ manifold is much smaller than the distance from this manifold to the 3D level), a moderately strong antiferromagnetic exchange interaction may be present. Direct exchange is precluded because of the estimated large $\text{Sm}^{+2}\text{-Sm}^{+2}$ distances and the small μ_{eff} . The low symmetry of the F state would be especially effective in strengthening antiferromagnetic interactions.

All of the solid solutions in the series $\text{Eu}_x\text{Sm}_{1-x}\text{MgF}_4$ show the excitation spectra for both bivalent europium and bivalent samarium (Fig. 10). However, the bivalent europium emission is not seen in any of the solid solutions except $\text{Eu}_{0.99}\text{Sm}_{0.01}\text{MgF}_4$ (Fig. 11).

Since the emission band of bivalent europium overlaps the absorption band of bivalent samarium, it was suspected that the observed energy transfer could well be the trivial case of radiative transfer, the Eu emission exciting the Sm ions. Comparison of mechanically mixed samples of EuMgF_4 and SrMgF_4 with EuMgF_4 and SmMgF_4 showed that the bivalent europium emission was attenuated to a greater extent by SmMgF_4 than in the SrMgF_4 mixture. This leads to the conclu-

sion that there is emission and reabsorption. However, lifetime measurement of the 437 nm Eu^{2+} emission band ranged from 1.08×10^{-6} sec in EuMgF_4 to 9.73×10^{-8} sec in $\text{Eu}_{0.99}\text{Sm}_{0.01}\text{MgF}_4$, indicating the presence of nonradiative transfer. Both mechanisms may be operative in the solid solutions, but radiative transfer cannot be very significant, judging from the complete quenching of the Eu^{2+} emission.

The actual energy transfer may well take place by coulombic (dipole-induced dipole) interactions which should be greater between Eu^{2+} and Sm^{2+} than between Eu^{2+} and Eu^{2+} . This is because of the differences in the symmetry of the ground state ions.

Acknowledgments

The authors thank Dr. William Thornton of the Westinghouse Corporation for quantum efficiency measurements and Prof. William Boo of the University of Mississippi for the magnetic measurements. This research was supported by Grants DAAG-29-75-G-0096 and DAAG-29-78-G-0105 from the Army Research Office, Durham, North Carolina and Contract No. F44620-74-C-0056, Joint Services Electronics Program. This paper is part of a dissertation submitted by one of the authors (M.S.) to the Polytechnic Institute of New York in partial fulfillment of the requirements for the degree of Doctor of Philosophy (Chemistry).

Manuscript submitted Jan. 31, 1980; revised manuscript received April 21, 1980.

Any discussion of this paper will appear in a Discussion Section to be published in the June 1981 JOURNAL. All discussions for the June 1981 Discussion Section should be submitted by Feb. 1, 1981.

Publication costs of this article were assisted by the Polytechnic Institute of New York.

REFERENCES

1. M. Eibschutz and H. J. Guggenheim, *Solid State Commun.*, **6**, 737 (1968).
2. M. Eibschutz, *Phys. Lett. A*, **29**, 409 (1969).
3. M. Samouel, *Rev. Chim. Miner.*, **8**, 537 (1971).
4. B. I. Al'Shin, *Soviet Phys.-JETP Lett.*, **12**, 142 (1970).
5. E. G. Spencer, *Appl. Phys. Lett.*, **17**, 300 (1970).
6. J. G. Bergman, *J. Appl. Phys.*, **46**, 4645 (1975).
7. E. T. Keve, *J. Chem. Phys.*, **51**, 4928 (1969).

Fig. 10. $\text{Eu}_{0.99}\text{Sm}_{0.01}\text{MgF}_4$ excitation spectrum, 298°K.

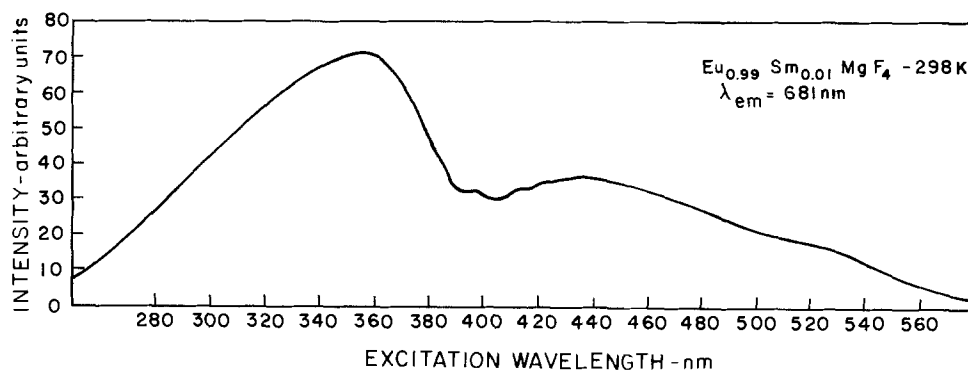
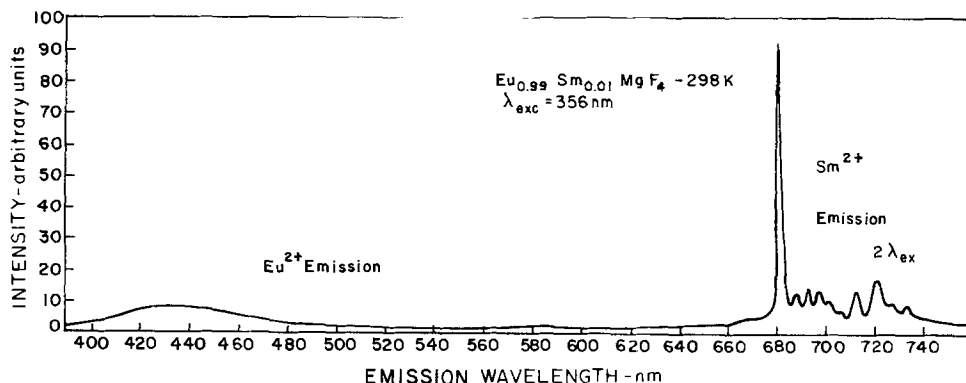


Fig. 11. Sm^{2+} and Eu^{2+} emission (350 nm excitation) in $\text{Eu}_{0.99}\text{Sm}_{0.01}\text{MgF}_4$, 298°K.



8. R. Jenkins, Ph.D. Thesis, Polytechnic Institute of New York, Brooklyn, N.Y., To be published
9. J. Reilly and W. N. Rae, "Physico-Chemical Methods," 5th ed., p. 586, Van Nostrand, New York (1954).
10. C. Fouassier, B. Latourette, J. Derouet, and P. Hagenmuller, in "Spectroscopie des Elements de Transition et des Elements Lourds dans les Solides," Editions du Centre National de la Recherche Scientific, p. 83, Paris (1977).
11. Th. Forster, *Ann. Phys.*, **6**, 55 (1948).
12. D. L. Dexter, *J. Chem. Phys.*, **21**, 836 (1953).
13. P. W. Selwood, *J. Am. Chem. Soc.*, **55**, 4869 (1933).
14. W. Klemm, *Z. Anorg. Allg. Chem.* **190**, 123 (1936).
15. T. R. McGuire and M. W. Shafer, *J. Appl. Phys.*, **35**, 984 (1964).
16. H. V. Lauer and F. K. Fong, in "Spectroscopie des Elements de Transition et des Elements Lourds dans les Solides," Editions du Centre National de la Recherche Scientific, p. 155, Paris (1977).
17. G. H. Dieke and R. Sarup, *J. Chem. Phys.*, **36**, 371 (1962).
18. G. Blasse and A. Bril, *Philips Tech. Rev.*, **31**, 304 (1970).
19. P. W. Selwood, *J. Am. Chem. Soc.*, **56**, 2392 (1934).

Stoichiometry and Masking Ability of LPCVD Silicon Nitride Against Arsenic Diffusion

Anant Dixit,* C. S. Chen,¹ and C. E. Volk*

Burroughs Corporation, San Diego, California 92127

ABSTRACT

Masking failure of LPCVD silicon nitride films during high temperature arsenic diffusion is observed, when these films are deposited with ammonia to dichlorosilane ratio <7:1 at the deposition temperature of <760°C. This masking failure is noticed after diffusion when the silicon nitride film is stripped in HF: a number of unetchable areas are left on the silicon wafer. The unetchable areas are not visible on as-deposited films. Helium back-scattering data indicate that this masking failure occurs in nonstoichiometric silicon-rich films.

Chemically vapor deposited silicon nitride films are widely used in semiconductor processing for masking against diffusion into silicon. Correct stoichiometry of the silicon nitride film plays an important role in this masking ability of the film.

Before the advent of low pressure CVD systems, silicon nitride was deposited at atmospheric pressures around 900°C, using a large ammonia to silicon compound ratio of approximately 1000:1 (1). The larger ratio was required to suppress the rate of silicon deposition in comparison to the silicon nitride deposition. In low pressure CVD systems it is desirable to keep the operating pressure during deposition below 1 Torr for better uniformity (2). For LPCVD silicon nitride systems where dichlorosilane is the preferred source for simpler and better reactor operation, the low pressure condition requires smaller ammonia to dichlorosilane ratio. At the lower pressures reactant gases mix more completely, allowing these much smaller ammonia to dichlorosilane ratios during deposition. However, as the smaller gas flow ratio approaches the theoretical limit of 1.33 (ratio of stoichiometric Si_3N_4), the resulting silicon nitride film may deviate from correct stoichiometry due to the silicon deposition process competing with the silicon nitride deposition process.

In this paper, we report the observation of localized fluctuations in the stoichiometry of the LPCVD silicon nitride films and consequent masking failure against arsenic diffusion, when these films are deposited under certain conditions.

Procedure

LPCVD silicon nitride films were prepared under different deposition conditions on thermally oxidized silicon substrates. The wafers were then processed through a standard arsenic buried layer diffusion

process, after which the film was stripped in conc HF or hot phosphoric acid, and inspected for diffusion damage.

Results

Depending on the process condition, a number of unetchable or slowly etching nitride spots were visible on the wafer, often with an unaided eye. Two such illustrations are shown in Fig. 1. The size of these spots was in the range of a few microns to several centimeters, sometimes extending over large portions of the wafer.

The standard diffusion cycle consists of coating the wafers with spin-on arsenic glass followed by a drive-in cycle at 1200°C for several hours. A few wafers were processed through an arsenic implant/drive cycle. The implanted wafers also had unetchable spots, although at a much reduced scale as compared with the wafers processed through the standard diffusion cycle.

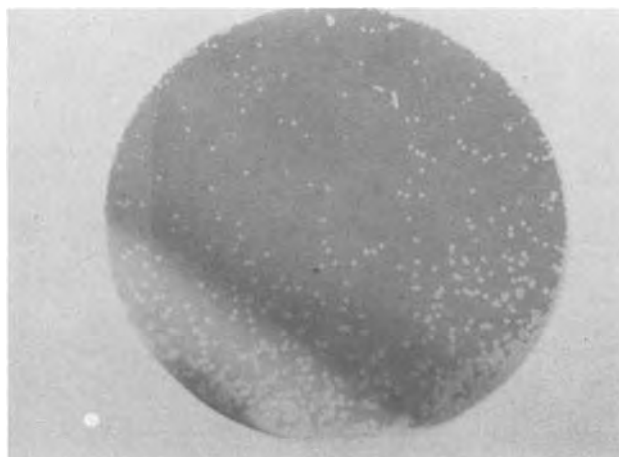


Fig. 1a. Nitride spots on 3 in. silicon wafer

* Electrochemical Society Active Member.

¹ Present address: Hughes Aircraft, Newport Beach, California 92663.

Key words: LPCVD silicon nitride, arsenic diffusion, stoichiometry.

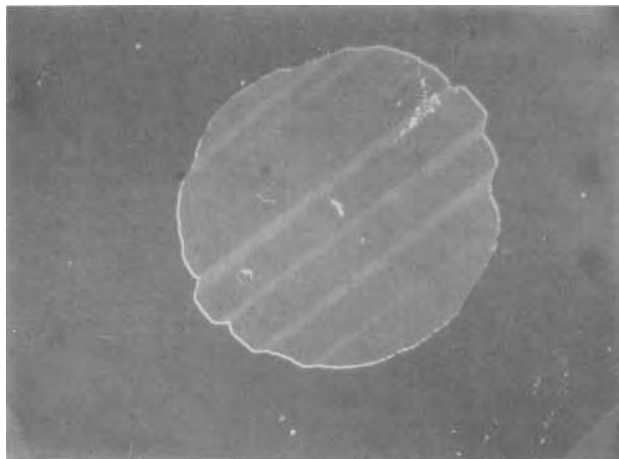


Fig. 1b. Microscopic picture of one of the nitride spots shown in Fig. 1a. (300X).

It must be noted that these defects are not visible on the as-deposited silicon nitride films or films heat-treated in a diffusion furnace without an arsenic source, and subsequent nitride etch did not reveal any unetchable nitride spots. The defects are revealed on the arsenic diffusion treated wafers only after the nitride etching step. The effect is more enhanced when etched in hot phosphoric acid. The nitride films were essentially free of cracks, and free of pinholes as evaluated by a Navonics bubble tester.

The final wafer quality depended on a number of process conditions: (i) oxide thickness under the nitride film, (ii) nitride deposition temperature, (iii) ammonia to dichlorosilane ratio during deposition, (iv) lower diffusion temperature, and (v) wafer handling.

Increasing the thickness of the oxide films, in general, reduced the density of unetchable spots, but did not eliminate them completely, as illustrated in Table I.

Reduced diffusion temperature reduced the density of spots significantly. An extensive study also revealed that poorly handled wafers enhanced the density of the unetchable nitride spots. However, an arsenic diffusion was essential to produce these unetchable nitride spots.

High deposition temperature and higher ammonia/dichlorosilane ratio during deposition eliminated the etchable nitride spots as can be seen from the data in Table II. Thus, at the deposition temperature of 760°C, a defect-free wafer could be obtained if the ammonia to dichlorosilane ratio during deposition was greater than 7:1. However, if the deposition temperature was raised to 790°C, a lower ammonia/dichlorosilane ratio of 4:1 could be used to obtain a defect free wafer.

In order to understand the effect of deposition conditions on the properties of silicon nitride films the refractive index and the etch rate of the films were monitored. The refractive index was measured by the Gaertner ellipsometer and calculated using the NBS ellipsometer program. The etch rate of the films in conc HF was measured at the constant room tem-

Table I. Effect of oxide thickness

Oxide thickness (Å)	Defect count in 200 fields of view
10,000	1-3
5,000	3-7
3,000	10-15
1,000	Often all across the wafer

Silicon nitride—1500Å, NH₃/DCS—4:1, Dep. temp—760°C.

Table II. Arsenic diffusion effect on silicon nitride, underlying oxide thickness 3000Å

Ammonia/DCS	Dep. temp (°C)	Wafer condition after arsenic diffusion and nitride strip
2:1	760	Large nitride spots
4:1	760	Small nitride spots
7:1	760	Clean wafer
2:1	790	Small nitride spots
4:1	790	Clean wafer
7:1	790	Clean wafer

perature of 22°C. Four wafers from each test condition were used to collect data on refractive index and etch rate. Measurement were made on the center of the wafer and the average values are recorded. The results are summarized below.

Refractive index.—At 790°C, an increase in dichlorosilane flow by more than 200% increased the refractive index by only 0.04 as can be seen in Fig. 2a. This suggests an increased silicon content or higher density of the films. However, it may be noted that no such trend is seen for films deposited at 760°C. No trends are noticed with respect to changes in ammonia flow and deposition temperature as can be seen from Fig. 3a and 4a.

Etch rate in conc HF.—Etch rate seemed to be invariant with respect to changes in dichlorosilane flow at either deposition temperature of 760° or 790°C as seen in Fig. 2b. However, etch rate increased significantly with increasing deposition temperature, as seen in Fig. 3b and 4b. This variation again suggests an increased silicon content or higher density of the films resulting in lower etch rates.

AMMONIA FLOW SET AT 100 cc/min

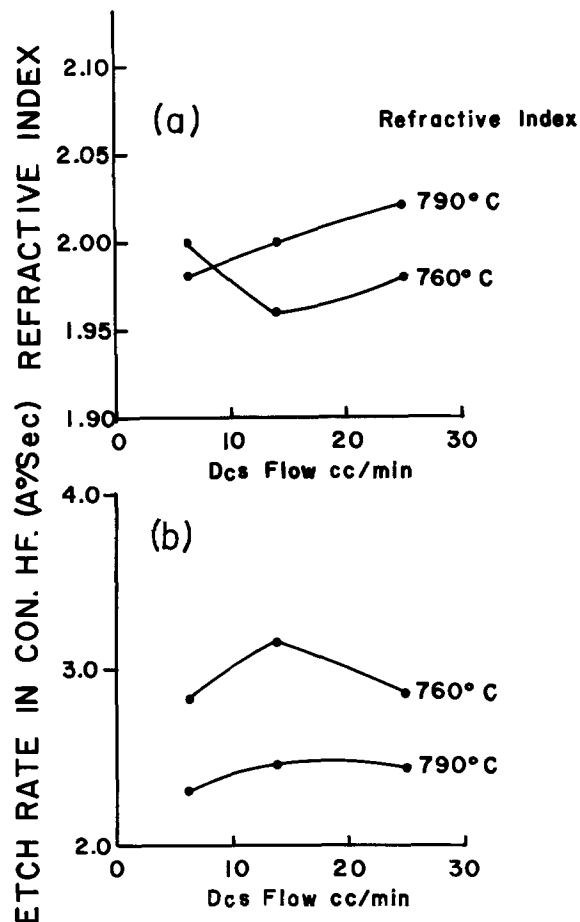


Fig. 2. Effect of dichlorosilane flow on nitride parameters. (a) Refractive index, (b) etch rate.

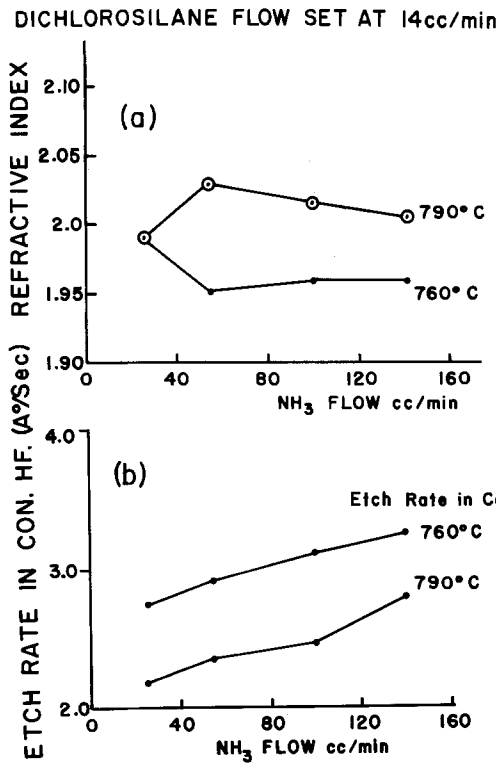


Fig. 3. Effect of ammonia flow on nitride parameters. (a) Refractive index, (b) etch rate.

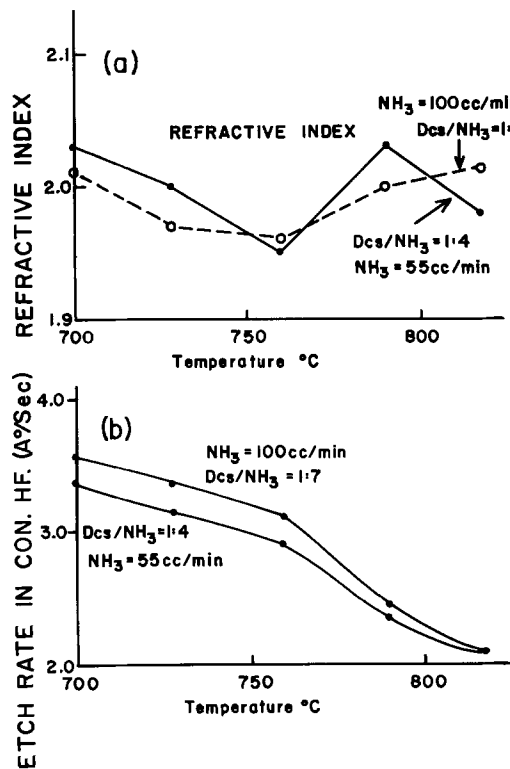


Fig. 4. Effect of temperature on nitride parameters. (a) Refractive index, (b) etch rate.

The study of refractive index and etch rate variation of the films, however, did not provide any indication about the origin of the unetchable nitride spots. To resolve this problem, a few samples of silicon nitride, deposited at 760°C on 1000Å thermally oxidized substrates were produced under various deposition conditions. Half of these wafers were processed through the arsenic diffusion cycle. The other half of these

wafers were analyzed by helium backscattering to obtain film compositions (3).

In Fig. 5 a typical backscattering yield is plotted as a function of energy for an as-deposited silicon nitride film. The compositions are calculated from the areas under the peaks of nitrogen, oxygen, and silicon, and their corresponding energy losses and capture cross sections. The composition was averaged over four different areas of the samples. Chlorine as a trace impurity of 0.25% of the nitride is also seen.

A typical backscattering yield distribution for the unetchable nitride spots is shown in Fig. 6. It was not possible to calculate the composition of these films due to the nonuniformity of the interface. A clear arsenic peak is seen in this film.

The alternate method of Auger analysis to estimate the composition of the film was inconclusive. All films deposited appeared to have correct stoichiometry although some of the films exhibited a high density of unetchable nitride spots. This is possibly because the sputter etch, required during the Auger analysis, changes the composition of the atomic layers that are being analyzed (4).

The nitride/silicon ratio for the as-deposited films, from the backscattering analysis and the corresponding gas flow ratios are entered in Table III. Defect density on the corresponding wafers which were processed through the arsenic diffusion is also sum-

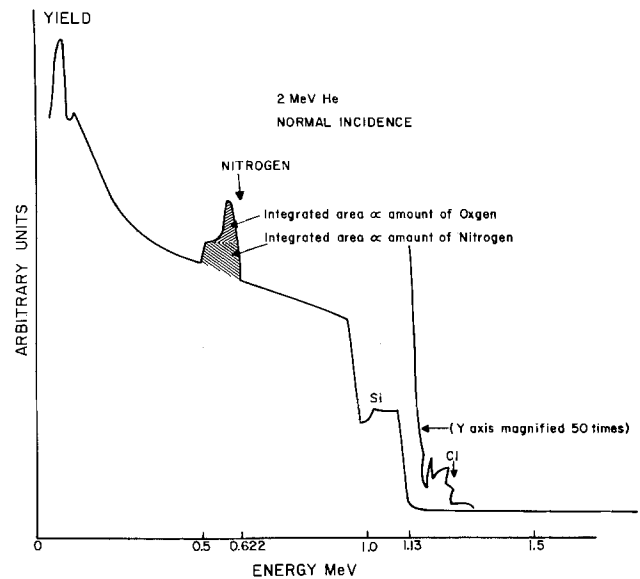


Fig. 5. He backscattering on as-deposited silicon nitride

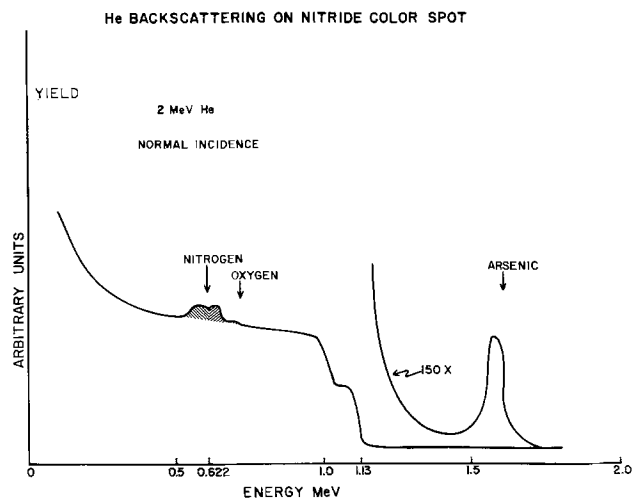


Fig. 6. He backscattering on unetchable silicon nitride spots

Table III. Dependence of unetchable nitride spots on process conditions. Deposition temp 760°C; arsenic diffn 1200°C

Defect count in 200 fields of view at 100x	Visible spots without optical aid	Ammonia/DCS ratio	Nitrogen/silicon ratio from He backscattering
2	Few spots on edges	4:1	1.31
89	All over the wafer	4:1	1.15
1.0	No	5:1	1.28
1.0	No	8:1	1.31
0	No	13:1	1.34
0	No	16:1	1.34

marized in Table III. It can be seen from these data that as the ammonia/dichlorosilane ratio increased the films had more correct stoichiometry. Films produced with smaller ammonia/dichlorosilane ratios have higher silicon content and correspond to those which failed during arsenic diffusion and therefore had a high density of unetchable nitride spots.

Conclusions

Unetchable nitride spots remain on silicon wafers when the wafers are processed through an arsenic diffusion cycle using LPCVD silicon nitride as a diffusion mask. The diffusion damage under these spots indicate failure of the impurity masking property of the nitride film in the region of the nitride spot. The random occurrence of these spots suggests that there are fluctuations in the masking property of the film. It is seen that the density of these spots is reduced significantly as the silicon nitride films become less silicon rich, approaching the proper stoichiometry, as evaluated by He backscattering. Since these spots occur randomly across the wafer, it indicates random fluctuations in the stoichiometry of the nitride film across the wafer. These spatial fluctuations could not be identified with the refractive index and etch rate measurements.

We believe that arsenic atoms diffuse through these silicon-rich regions forming a complex compound with the underlying silicon dioxide film and the silicon substrate; these silicon-rich regions etch very slowly in conc HF. Increased underlying oxide thickness

reduces this occurrence, since oxide is a diffusion mask which reduces the total number of arsenic atoms reaching the silicon substrate, thereby diminishing the role of the silicon substrate in the formation of this complex compound. Similarly a reduced diffusion temperature decreases the defect density because of the reduced Dt product of arsenic in oxide. The exact mechanism of formation of these unetchable nitride spots as well as the structure of these spots could not be determined in the present work. The nitride spots occur when either arsenic spin on glass source or arsenic ion implant source is used during the arsenic diffusion cycle, indicating that the nitride spots occur primarily due to the failure in the masking ability of the nitride films and secondarily related to the type of arsenic source.

Proper stoichiometry and hence proper masking ability of the nitride films are obtained when higher ammonia/dichlorosilane ratio and higher temperature during deposition are selected in producing these films.

Acknowledgments

The authors would like to thank Dr. Tseng for providing the backscattering analysis and Dr. Simon Thomas for the helpful discussion on the film composition analysis. Additionally they are grateful to the bipolar technical staff for their assistance in this work.

Manuscript submitted Aug. 27, 1979; revised manuscript received March 5, 1980. This was Paper 100 presented at the Boston, Massachusetts, Meeting of the Society, May 6-11, 1979.

Any discussion of this paper will appear in a Discussion Section to be published in the June 1981 JOURNAL. All discussions for the June 1981 Discussion Section should be submitted by Feb. 1, 1981.

Publication costs of this article were assisted by Burroughs Corporation.

REFERENCES

1. M. T. Duffy and W. Kern, *RCA Rev.*, **31**, 742 (1970).
2. R. S. Rosler, *Solid State Tech.*, **20**, 63 (1977).
3. He Backscattering Analysis from Dr. Tseng, California Institute of Technology.
4. S. Thomas and R. J. Mattox, *This Journal*, **124**, 1942 (1977).

Oxidation Enhanced Diffusion of Boron and Phosphorus in (100) Silicon

K. Taniguchi,* K. Kurosawa, and M. Kashiwagi*

NEC-Toshiba Information Systems, Incorporated, Kawasaki City, Kanagawa 210, Japan

ABSTRACT

Diffusion of boron and phosphorus in dry O₂, wet Ar, and wet O₂ ambients was investigated to obtain a formula describing the oxidation enhanced diffusion. At low impurity concentration, the diffusion coefficient is expressed as a function of oxide growth rate, depth, and temperature

$$D = D_0 \exp\left(-\frac{\Delta E_1}{kT}\right) + F \cdot \left(\frac{dX_o}{dt}\right)^{0.3} \exp\left(-\frac{X}{25}\right) \exp\left(-\frac{2.07}{kT}\right)$$

where dX_o/dt is in $\mu\text{m/hr}$ and X is in μm . F value is $6.0 \times 10^{-2} \text{ cm}^2/\text{hr}$ for boron and $5.2 \times 10^{-2} \text{ cm}^2/\text{hr}$ for phosphorus. This equation can be explained by a dual mechanism involving both vacancy and interstitial silicon atoms. A depth dependence of the diffusion coefficient is explained by a model that excess interstitial silicon atoms are captured by vacancies migration into bulk silicon. At high impurity concentration, less enhanced diffusion was observed.

Since characteristics of semiconductor devices depend strongly on the final impurity profiles in the electrically active region, detailed understanding of impurity diffusion is generally required to reproducibly control the impurity profiles. The current state of the art for optimization of diffusion processes in the fabrication of integrated circuits, however, relies on an empirical approach based on the trial and error method. Recently, there has been an intensive effort in the industry in the development of the computer-aided process simulation for integrated circuits (1). Though a large number of reports (2-10) have been published on oxidation enhanced diffusion, any generally acceptable model has not been available yet. The simultaneous presence of both oxidation enhanced diffusion and anomalous diffusion due to high impurity concentration makes it difficult to interpret the experimental results precisely and accounts for the remarkable spread among the values of the diffusion coefficient found in the literature. The main purpose of this study is to distinguish the oxidation enhanced diffusion from the anomalies due to high impurity concentration and to present a useful model for process simulation at low impurity concentration.

Experimental

The starting material was p- and n-type, (100) oriented Czochralski silicon wafers with resistivity of 6-8 $\Omega\text{-cm}$. All the wafers were chemically mirror finished on one side. Boron and phosphorus were deposited on the surfaces as diffusion sources, the concentration of which were in the range of 2×10^{14} - 4×10^{16} atoms/cm² by using BN and POCl₃ sources, respectively. The wafers were then thermally oxidized at 900°C for 5 min in wet O₂. To avoid out-diffusion of deposited impurities and to protect the silicon surface from oxidation, the silicon surface was initially covered with a 0.1 micron thick Si₃N₄ layer.

The drive-in of impurities was carried out at 1100° and 1200°C in a nitrogen ambient to obtain a wide variety of junction depths ranging from 1-5 microns. The oxide and nitride were photolithographically engraved into parallel stripes to define oxidizing and nonoxidizing surfaces on the wafer. Then, oxidation was carried out at temperatures in the range of 950°-1150°C in dry oxygen, wet Ar (H₂O partial pressure in Ar gas varying from 0.05 to 1 atm), or

wet oxygen. The sample structures before and after oxidation are illustrated in Fig. 1. X_{jf} and X_{jfo} show the junction depths under the masked and unmasked surface, respectively. Note that X_{jfo} is measured from the original silicon surface. The thicknesses of the oxide film grown on the silicon surface during oxidation have been determined by ellipsometry and interferometry. The sheet resistivity and the junction depth were also determined by four point probe and grooving staining, respectively. The junction depth was measured at four position on each piece, and the

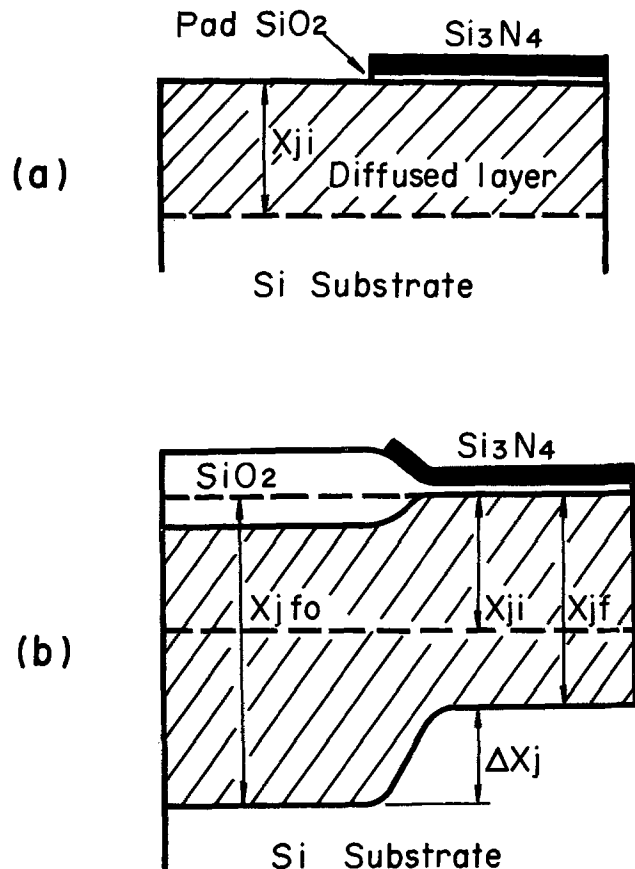


Fig. 1. Schematic diagram illustrating the sample structures, (a) before and (b) after oxidation.

* Electrochemical Society Active Member.

Key words: oxidation, diffusion, boron, phosphorus.

average and standard errors were estimated from these measurements. The standard errors for junction depth were about 0.02 micron in this study.

Analysis

In this study, diffusion length ($2\sqrt{Dt}$) for drive-in is much larger than that for predeposition. Thus, the extent of penetration in the predeposition profile can be regarded as negligibly small in comparison to that for the final profile resulting from the drive-in diffusion. Accordingly, the predeposition profile can be mathematically represented by a delta function. The impurities distribution after drive-in diffusion subjected to this approximation then will be given by the well-known Gaussian distribution

$$C(x) = \frac{Q}{\sqrt{\pi B}} \exp(-X^2/4B) \quad [1]$$

where Q is the total number of impurity atoms in a 1 cm² section of silicon and $2\sqrt{B}$ is the effective diffusion length of impurity atoms.

The values of Q and B can be calculated from the initial junction depth, X_{ji} , and sheet resistivity, ρ_s , before oxidation using the following equations

$$\rho_s^{-1} = q \int_0^{x_{ji}} \mu_{(c)} \cdot C(x) dx \quad [2]$$

$$X_{ji} = \sqrt{-4B \ln \frac{\sqrt{\pi B} N_B}{Q}} \quad [3]$$

According to Caughey and Thomas (11), the mobility, $\mu_{(c)}$ can be expressed by the following equation

$$\mu_{(c)} = \mu_{\min} + \frac{(\mu_{\max} - \mu_{\min})}{1 + (C/C_{\text{ref}})^\beta} \quad [4]$$

where μ_{\max} and μ_{\min} are the minimum and maximum mobility values, C_{ref} a reference concentration value, and β an exponential factor that controls the slope around $C = C_{\text{ref}}$. From the work of Antoniadis (7), the following values are chosen for this work

Impurity	μ_{\min}	μ_{\max}	C_{ref}	β
Boron	49.70	467.7	1.6×10^{17}	0.70
Phosphorus	55.24	1388.2	1.1×10^{17}	0.73

when μ_{\min} and μ_{\max} are in cm²/Vsec and C_{ref} is in atoms/cm³. If the drive-in profile is given by Eq. [1], then the profile under the masked surface after oxidation can be represented by the equation

$$C(x) = \frac{Q}{\sqrt{\pi(B + D_N t)}} \exp[-X^2/4(B + D_N t)] \quad [5]$$

Equation [5] can be applied directly to evaluate the diffusion coefficient, D_N , under the masked surface which was computed by matching the corresponding measured junction depth to the calculated one.

The diffusion coefficient, D , under the oxidized surface was also calculated by assuming Gaussian distribution for simplicity

$$C(x) = \frac{Q}{\sqrt{\pi(B + Dt)}} \exp[-X^2/4(B + Dt)] \quad [6]$$

where X is measured from the original silicon surface. The coefficient, D , is separated into two terms; $D = D_N + \Delta D_o$. One is the diffusion coefficient in the nonoxidizing ambient, D_N . The other is the increment of diffusion coefficient due to oxidation, ΔD_o . This Gaussian assumption is somewhat questionable since it neglects the impurity redistribution at the moving oxide-silicon interface.

In the following, we will verify this assumption under the oxidized surface. Figure 2 shows impurity profiles for two typical segregation coefficients which were calculated by using the Kato and Nishi theoretical model (12). Though changes in the segregation coefficient alter the profile near the silicon surface, they influence sheet resistivity while producing little effect on junction depth. The two cases can be considered as follows: in one case $k = 0.1$, the oxide has a tendency to take up impurity, in the other case, $k = 10$, the oxide has a tendency to reject impurity. Therefore, the Gaussian profile which takes no account of the impurity redistribution is expected to be between the two curves as shown in Fig. 2. For convenience, the difference between these two junction depths of $k = 0.1$ and $k = 10$ is defined as δx_j . The theoretical calculation using the possible maximum diffusion coefficient of 1.5×10^{-9} cm²/hr proves that the δx_j values fall inside the experimental error (0.02 micron) for large initial junction depths of more than 1.1 micron in this study. Since the diffusion coefficients obtained in this work are smaller than 1.5×10^{-9} cm²/hr as shown in the later section, the diffusion coefficients calculated by this simple Gaussian model are proved to be accurate within experimental accuracy.

In this connection, we check the errors in diffusion coefficients ascribed to the experimental measurement error of junction depth. For example, in the case of $D = 10 \times 10^{-10}$ cm²/hr and $Q = 10^{14}$ cm⁻², the errors in diffusion coefficient are evaluated as ± 3.5 , ± 4.5 , and $\pm 7.0 \times 10^{-11}$ cm²/hr for 1.0, 2.5, and 4.5 microns of junction depth, respectively, by using the simple Gaussian model and the 0.02 micron of measurement error. The error-calculations for various Q values ($Q = 10^{13} \sim 10^{15}$ cm⁻²) give nearly the same result. Therefore, the errors in diffusion coefficients are estimated as less than 7% in this work. It should be noted that the diffusion coefficient thus obtained

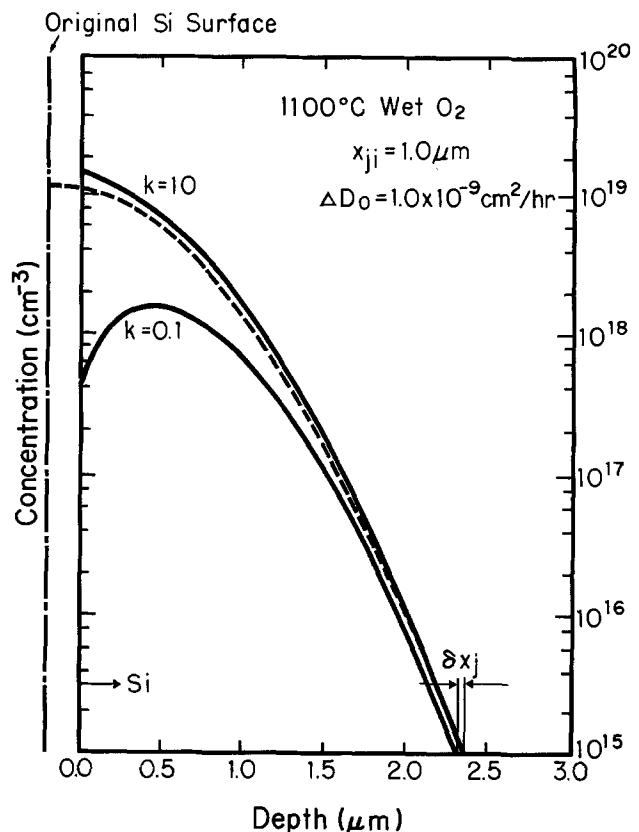


Fig. 2. Calculated impurity profile after oxidation for two typical segregation constants; $k = 10$ and 0.1. The dashed line shows the Gaussian profile which takes no account of impurity redistribution as Si/SiO₂ interface.

is an effective value near the junction depth because the changes in the segregation coefficient as well as diffusion coefficient near the silicon surface have little influence on the junction depth.

Dependence of impurity concentration.—Figure 3 shows the relationship between the diffusion coefficient and total amount of impurities. The initial junction depths for these samples are 3.2 microns and oxidation was carried out at 1100°C in the wet O₂ ambient. It can be seen from this figure that the diffusion coefficients do not show concentration dependence when the total amount of impurity is less than 3×10^{15} atoms/cm². A remarkable feature of the data presented here is that the diffusion coefficients of boron and phosphorus in a nonoxidizing ambient increase with impurity concentration while ΔD_0 decreases with impurity concentration. These results indicate that boron and phosphorus diffuse via a dual mechanism in oxidizing ambient.

Dependence on junction depth.—Figure 4 shows the relationship between ΔD_0 and initial junction depth

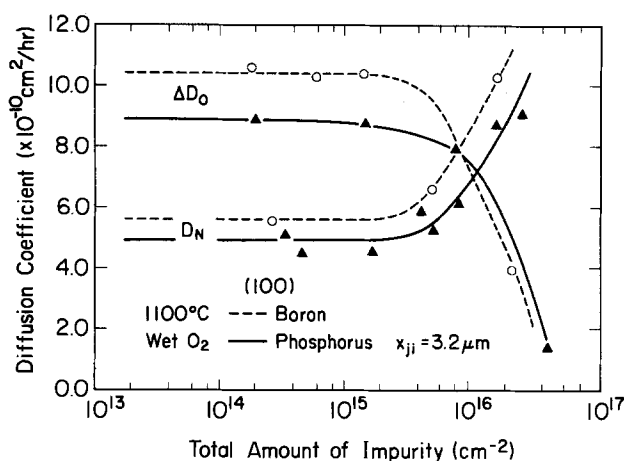


Fig. 3. Diffusion coefficient vs. total amount of impurity for boron and phosphorus diffusion at 1100°C in wet O₂ ambient.

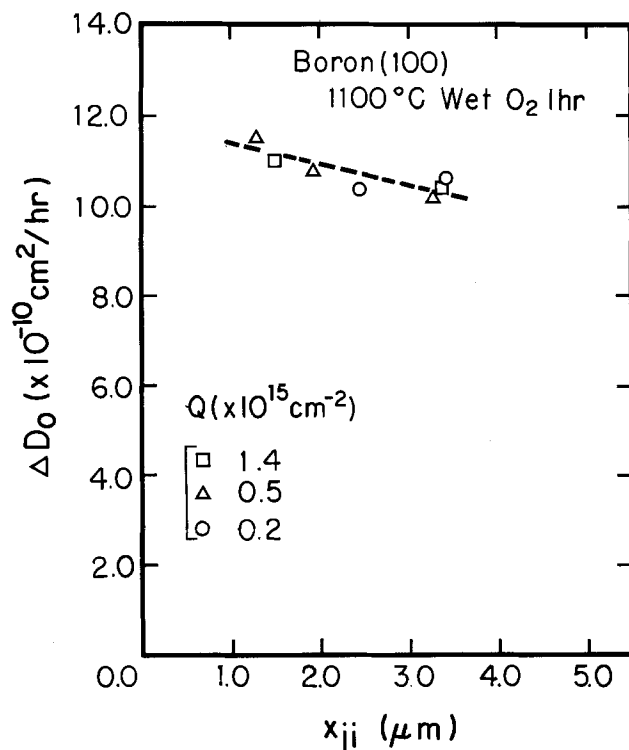


Fig. 4. Depth dependence of ΔD_0 for boron at 1100°C in wet O₂ ambient for (100) Si surface.

for various amounts of boron atoms. It is clear that ΔD_0 depends on the distance from the silicon surface. This approximately linear dependence suggests that some mobile species formed on the silicon surface during oxidation, which are responsible for the enhanced diffusion, must penetrate into the silicon bulk crystal and be captured during migration into bulk silicon. The diffusion length of the species is estimated at about 25 microns from the extrapolated line on the abscissa. If the amount of impurity is less than 3×10^{15} atoms/cm², this value is independent of kind of impurity. Figure 5 shows the ΔD_0 vs. initial junction depth for various amounts of phosphorus atoms. Depth dependence and diffusion length of mobile species are similar to those of boron.

Dependence on oxidation rate.—Figure 6(a) and (b) show log plots of ΔD_0 as a function of the time-averaged oxide growth rate for boron and phosphorus, respectively. Straight lines have been drawn through the experimental open circle points which are obtained in wet Ar ambient. Although the enhancement of the diffusion constant, ΔD_0 , is believed to be proportional to the averaged oxide growth rate (6), Fig. 6(a) and (b) show $\Delta D_0 \propto (X_o/t)^{0.3}$. Note that ΔD_0 is the measured time-averaged diffusion coefficient. Masetti (6) reported that phosphorus diffusion coefficient is strongly influenced by the nature of the ambient and that there is different ambient dependence between dry O₂ and wet O₂. In the present study, however, there is no difference in ΔD_0 between dry O₂ and wet Ar at the same oxide growth rate, as shown in Fig. 6(a) and (b) by the solid circles. It was found that the diffusion coefficients obtained from the profiles under the masked surface were independent of the oxidation rate.

Dependence on oxidation temperature.—Figure 7 shows the relationship between the oxidation temperature and ΔD_0 for boron and phosphorus. In this experiment, the oxidation time when diffusion occurred simultaneously was chosen for each temperature to obtain the same oxide thickness, that is, 0.8 microns. The points in Fig. 7 follow quite accurately Arrhenius law with activation energy of 2.55 eV for both impurities. The same activation energy for boron and phosphorus diffusion suggests that these two impurities diffuse by the same mechanism. About the same activation energy is also obtained from the experiments (14) on stacking fault growth which could result from the flow of interstitial silicon atoms

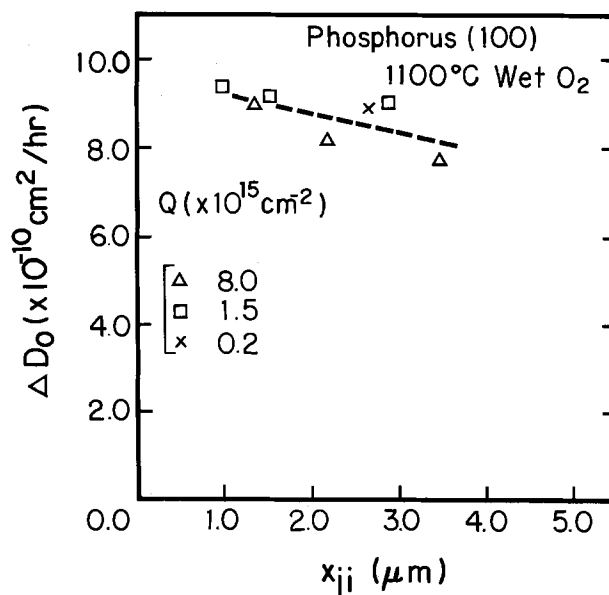


Fig. 5. Depth dependence of ΔD_0 for phosphorus at 1100°C in wet O₂ ambient for (100) Si surface.

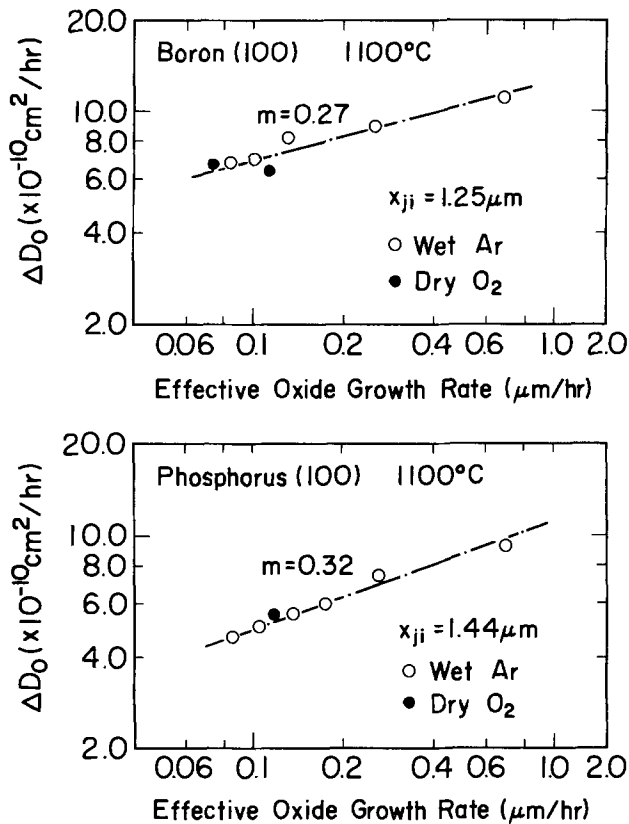


Fig. 6. Oxide growth rate dependence of ΔD_0 for (100) surface (a, top) boron and (b, bottom) phosphorus.

from the interface into the silicon bulk. For comparison with these experimental data, the diffusion coefficients obtained by Fair (15) and Antoniadis (7) under nonoxidized ambient are also plotted in Fig. 7 by dotted lines. A remarkable feature of the data presented here is the multifold increase in boron and phosphorus diffusion coefficient at lower temperature.

Discussion

Since the diffusion coefficient in the oxidizing ambient is shown by the sum of ΔD_0 and D_N which have different activation energies, and different concentration dependence, the oxidation associated diffusion is assumed to take place via a dual mechanism. One of them, D_N , the diffusion coefficient in an inert atmosphere, is described by the vacancy mechanism as widely accepted. On the other hand, the oxidation enhanced diffusion term, ΔD_0 , can be considered to take place via an interstitial mechanism.

Oxidation induced stacking fault growth behaves almost the same as oxidation enhanced diffusion, as far as activation energy value (18) and orientation dependence (17) are concerned. These facts strongly support the idea that the two phenomena can be ascribed to a common origin. Moreover, the growth of stacking faults is due to an enhanced interstitial silicon concentration in the vicinity of the oxide-silicon interface relative to the thermal equilibrium value as pointed out by Sanders and Dobson (19).

Now, we propose a diffusion model to explain the depth dependence of the oxidation enhanced diffusion by analogy with the behavior of stacking fault growth, in which excess interstitial silicon atoms generated at the silicon surface will be captured by vacancies during migration into bulk silicon. Following Hu (13), motion of the interstitial silicon atoms will be described by the following equation

$$\frac{\partial c_i}{\partial t} = D_i \frac{\partial^2 c_i}{\partial x^2} - kC_v(C_i - C_i^*) - R_{ppt} \quad [7]$$

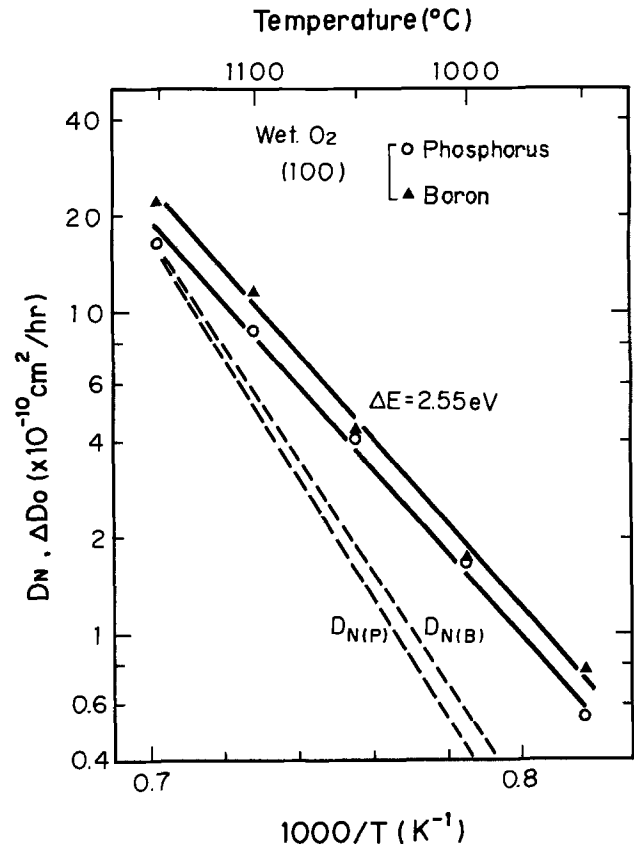


Fig. 7. Temperature dependence of ΔD_0 and D_N for boron and phosphorus. Dashed lines show diffusion coefficient in nonoxidizing ambient [after Antoniadis (7) and Fair (15)].

where D_i is the diffusion coefficient of interstitial silicon atoms and C_i^* , C_v , and R_{ppt} are the thermal equilibrium concentration of interstitial silicon, the concentration of vacancy, and the rate of precipitation, respectively. Hence, $kC_v(C_i - C_i^*)$ shows the recombination rate of vacancy and interstitial silicon. For an approximate solution, $\partial c_i / \partial t = 0$ is assumed because of the extremely fast diffusion of silicon self-interstitials.

Though excess interstitial silicon atoms reduce the concentration of vacancies near Si/SiO₂ interface by recombination, we make the assumption that the number of interstitial silicon atoms generated at the interface is very small compared to that of vacancy near surface. Therefore, C_v/C_v^* nearly equals unity regardless of the distance from the silicon surface. (C_v^* is the thermal equilibrium concentration of vacancy in bulk.)

For low impurity concentration, when R_{ppt} in Eq. [7] is negligible, the distribution of interstitial silicon is given by

$$C_{i(x)} = C_i^* + [C_{i(0)} - C_i^*] \exp(-X/L_D) \quad [8]$$

where L_D is the effective diffusion length of interstitial silicon atoms. Since the enhanced diffusion coefficient of impurity is directly proportional to the concentration of the interstitial silicon, ΔD_0 also follows the exponential law

$$\Delta D_0 = K[C_{i(0)} - C_i^*] \exp(-X/L_D) \quad [9]$$

In the case of $X \ll L_D$, the oxidation enhanced diffusion coefficient can be expanded into a simple formula which shows linear depth dependence

$$\Delta D_0 = K_0[1 - X/L_D] \quad [10]$$

Thus, there is a good qualitative agreement between theory and experimental results shown in Fig. 4 and Fig. 5.

Since this equation does not have a concentration term, oxidation enhanced diffusion should be concentration independent in the case of low impurity concentration. This is justified in comparison with the results as shown in Fig. 3. On the other hand, for $Q > 3 \times 10^{15} \text{ cm}^{-2}$, the oxidation enhanced diffusion coefficients, ΔD_0 , decrease drastically. This behavior is qualitatively explained as follows. The vacancy concentration in this case is proportional to the doped impurity concentration. If the vacancy concentration is high enough to reduce the concentration of the excess interstitial silicon to very low by recombination of vacancy and interstitial silicon atoms, there will be no oxidation enhanced diffusion, which coincides with the annihilation of oxidation induced stacking fault at high substrate impurity concentration (16).

To obtain the model utilized in process simulation, we will derive the relationship between an instantaneous diffusion coefficient ΔD_0^i and the measured time averaged diffusion coefficient ΔD_0 , in the following way.

We suppose that ΔD_0^i is proportional to instantaneous oxidation rate, dX_0/dt , with an exponent, n , to be determined

$$\Delta D_0^i = K \left(\frac{dX_0}{dt} \right)^n \quad [11]$$

As expected, the oxide growth is observed to follow accurately the usual parabolic law

$$X_0^2 = Bt \quad [12]$$

where B is the parabolic rate constant. Therefore, the time averaged diffusion coefficient ΔD_0 can be derived by using Eq. [11] and [12]

$$\begin{aligned} \Delta D_0 &= \frac{1}{t} \int_0^t \Delta D_0^i dt = \frac{KB}{X_0} \int_0^{X_0} \left(\frac{dX}{dt} \right)^n \frac{2X}{B} dX \\ &= \frac{2K}{2-n} \left(\frac{1}{2} \right)^n \left(\frac{X_0}{t} \right)^n \quad [13] \end{aligned}$$

To be consistent with the experimental data in Fig. 6(a) and (b), one can choose $n = 0.3$. Then, Eq. [13] becomes

$$\Delta D_0 = 0.95K \left(\frac{X_0}{t} \right)^{0.3} \quad [14]$$

By comparison with Eq. [11], one sees that the pre-power value, K , in Eq. [11] is enhanced by a factor of 1.05 compared with that of the time averaged diffusion coefficient, ΔD_0 .

In the following, we discuss only ΔD_0^i instead of ΔD_0 and neglect the subscript, i , for simplicity.

From the aforementioned results and Eq. [9], in the case of low impurity concentration, the following formula is obtained describing ΔD_0 as a function of oxide growth rate ($= dX_0/dt$), depth, and temperature for wet oxidation

$$\Delta D_0(x) = F^{\circ} \left(\frac{dX_0}{dt} \right)^n \exp(-X/L_D) \exp(-\Delta E_2/kT) \quad [15]$$

where $F = 6.0 \pm 0.4 \times 10^{-2} \text{ cm}^2/\text{hr}$ for boron, and $5.2 \pm 0.4 \times 10^{-2} \text{ cm}^2/\text{hr}$ for phosphorus, and $\Delta E_2 = 2.07 \pm 0.04 \text{ eV}$. The uncertainties which affect the activation energy and F values come primarily from the uncertainty associated with the junction depth measurements. It should be noted that activation energy in the last term is a converted value at 1 micron/hr oxidation rate. The exponent, n , and the diffusion length of interstitial silicon, L_D , decrease very slightly with temperature; $n = 0.33$ at 1000°C and $n = 0.30$ at 1100°C , $L_D = 30$ microns at 1000°C and $L_D = 25$ microns at 1100°C . Therefore, in case of relatively shallow diffusion, the temperature dependence of these values is neglected. Consequently, the diffusion coefficient in an oxidizing ambient can be

described by the following formula at low impurity concentration

$$D = D_0 \exp(-\Delta E_1/kT) + F \cdot \left(\frac{dX_0}{dt} \right)^n \exp(-X/L_D) \exp(-\Delta E_2/kT) \quad [16]$$

where $D_0 \exp(-\Delta E_1/kT)$ is the diffusion coefficient in an inert atmosphere.

Finally, to check the accuracy of our oxidation enhanced diffusion model, comparisons between computed and measured ΔX_j and oxidation time have been made. Figure 8 shows the relationship between ΔX_j and oxidation time, together with the corresponding theoretical curves computed by using the Kato and Nishi model (12) and the diffusion coefficient values given in Eq. [15]. The dashed line calculated by using the linear oxidation rate dependence of diffusion coefficient, however, does not follow the experimental points. On the other hand, the solid lines calculated by using the present model is in very good agreement with experimental results.

Conclusions

The diffusion coefficient of chemically deposited boron and phosphorus in (100) silicon has been obtained experimentally under various oxidizing ambients. The diffusion coefficients were calculated from the values of X_j and ρ_s by using a simple Gaussian distribution after oxidation. From the experimental results, the following behavior of impurity diffusion can be observed.

1. The oxidation enhanced diffusion coefficient can be described by the following formula for low impurity concentration

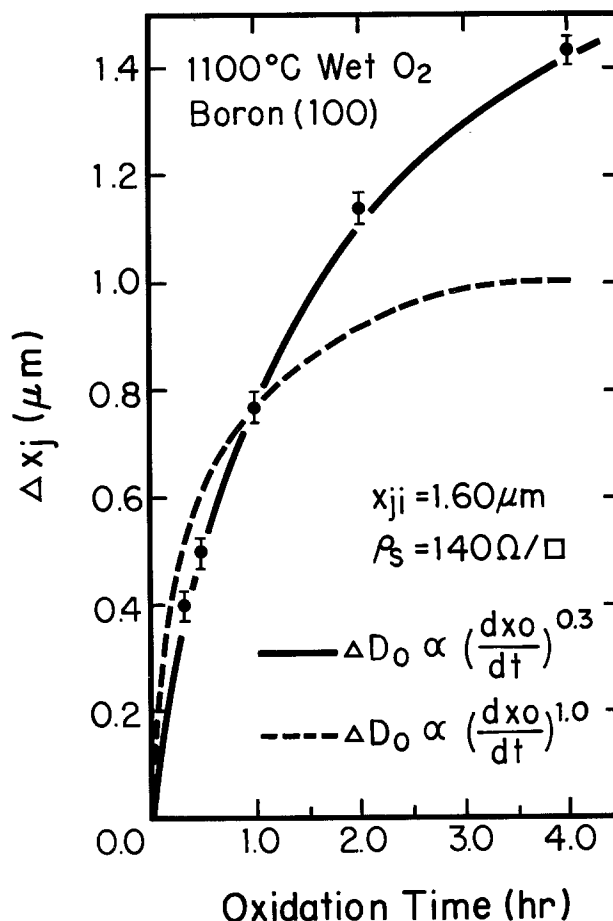


Fig. 8. Oxidation time vs. ΔX_j . The solid curve is calculated by using the present model.

$$D = D_0 \exp\left(-\frac{\Delta E_1}{kT}\right) + F \cdot \left(\frac{dX_0}{dt}\right)^n \exp\left(-\frac{X}{L_D}\right) \exp\left(-\frac{\Delta E_2}{kT}\right)$$

The depth dependence of ΔD_0 is explained by assuming that excess interstitial silicon atoms are captured by vacancies during migration into bulk silicon.

2. The oxidation enhanced diffusion expressed by the above formula can be explained by a dual mechanism, i.e., the vacancy and interstitialcy mechanism.

Acknowledgments

The authors are grateful to A. M. Lin of Stanford University for useful discussions. In addition, they would like to thank Dr. Y. Nishi for reviewing the manuscript and suggesting improvements.

Manuscript submitted Sept. 27, 1979; revised manuscript received April 10, 1980.

Any discussion of this paper will appear in a Discussion Section to be published in the June 1981 JOURNAL. All discussions for the June 1981 Discussion Section should be submitted by Feb. 1, 1981.

Publication costs of this article were assisted by NEC-Toshiba Information Systems, Incorporated.

REFERENCES

1. D. A. Antoniadis, S. E. Hansen, and R. W. Dutton, SEL 78-020, Stanford Electronics Labs, June 1978.
2. W. G. Allen and K. V. Anand, *Solid-State Electron.*, **14**, 397 (1971).
3. W. G. Allen, *ibid.*, **16**, 709 (1973).
4. G. Masetti, S. Solmi, and G. Soncini, *ibid.*, **16**, 1419 (1973).
5. G. Masetti, S. Solmi, and G. Soncini, *ibid.*, **19**, 545 (1976).
6. G. Masetti, S. Solmi, and G. Soncini, *Philos. Mag.*, **33**, 613 (1976).
7. D. A. Antoniadis, A. G. Gonzales, and R. W. Dutton, *This Journal*, **125**, 813 (1978).
8. D. A. Antoniadis, A. M. Lin, and R. W. Dutton, *Appl. Phys. Lett.*, **33**, 1030 (1978).
9. R. Francis and P. S. Dobson, *J. Appl. Phys.*, **50**, 280 (1979).
10. A. M. Lin, R. W. Dutton, and D. A. Antoniadis, Abstract 133, p. 356, The Electrochemical Society Extended Abstract, Boston, Massachusetts, May 6-11, 1979.
11. D. M. Gaughey and R. E. Thomas, *Proc. IEEE*, **55**, 2192 (1967).
12. T. Kato and Y. Nishi, *Jpn. J. Appl. Phys.*, **3**, 377 (1964).
13. S. M. Hu, *J. Appl. Phys.*, **45**, 1567 (1974).
14. S. P. Murarka and G. Quintana, *ibid.*, **48**, 46 (1977).
15. R. B. Fair, and T. C. C. Tsai, *This Journal*, **124**, 1107 (1977).
16. J. E. Lawrence, *J. Appl. Phys.*, **40**, 360 (1969).
17. W. A. Fisher and J. A. Amick, *This Journal*, **113**, 1054 (1966).
18. S. P. Murarka, *ibid.*, **48**, 5020 (1977).
19. I. R. Sanders and P. S. Dobson, *Philos. Mag.*, **20**, 881 (1969).

Retardation of Destructive Breakdown of SiO₂ Films Annealed in Ammonia Gas

Takashi Ito, Hideki Arakawa, Takao Nozaki, and Hajime Ishikawa*

Fujitsu Laboratories Limited, Semiconductor Devices Laboratory, Nakahara, Kawasaki, Japan

ABSTRACT

It has been found that a remarkable improvement in dielectric breakdown characteristics of MOS structures can be achieved by annealing SiO₂ films in purified NH₃ gas at 900°-1200°C even if sodium-contaminated Al electrodes are used. This effect is due to the surface nitrated region of SiO₂ which acts as a barrier against ion migration.

A thinner reproducible and reliable gate insulator is needed for very large scale integration in metal-oxide-semiconductor structures (1). The practical problems faced in this are instability due to hot carrier trapping (2) and nonuniformity of breakdown characteristics of such insulators (3). Oxide films thinner than those now used widely are so fragile that they must be protected from destruction throughout their production and use. Si₃N₄ deposited on thermally grown SiO₂ (4) and phosphorus-doped oxide (5) were studied as methods of protection against contamination. Further, direct thermal nitridation of Si was proposed as a method for producing uniform and dense gate insulators (6).

The breakdown characteristics of thermally grown SiO₂ on Si were found to be markedly influenced by processing and materials (7). SiO₂ films grown under carefully controlled conditions, for which breakdown phenomenon relates to the nature of the material, are destroyed as current concentrates into the relatively low energy-barrier points on the film.

This paper demonstrates that the breakdown characteristics of thin SiO₂ films are greatly improved by annealing them in purified ammonia gas. Importantly, high field current instability does not occur until the current increases to about two orders greater than that allowed with conventional SiO₂ films. This effect is attributed to a surface region of nitrated SiO₂ (8).

Experimental MOS diodes were fabricated using boron-doped, p-type, 0.8-1.2 Ωcm, (100) oriented silicon wafers which were 2 in. in diameter.

After cleaning, SiO₂ films were thermally grown in wet oxygen ambient at a temperature of 1000°C. The film thickness was from 500 to 700 Å. Relatively thick oxide films were chosen here because the onset of current instability comes sooner as the oxide becomes thicker (9). The wafers were then annealed in fully purified ammonia gas at temperatures ranging from 900° to 1200°C. The annealing time was from 1 to 5 hr. Aluminum electrodes with a thickness of 5000 Å were evaporated from a tantalum boat. A tungsten boat was partly used in an experiment involving intentional sodium contamination. Al dot electrodes with diameters from 100 to 1200 μm were patterned photolithographically. The Al electrode was

* Electrochemical Society Active Member.

Key words: MOS, silicon nitride, current distribution equilibrium, contamination barrier.

thick enough to preclude so-called self-healing breakdown and to allow the lowest breakdown voltages to be measured. The back sides of the wafers were lapped and evaporated with 5000Å thick aluminum films. The diodes were sintered in pure nitrogen at 450°C for 15 min.

The typical breakdown characteristics of both unannealed and NH₃ annealed SiO₂ films are shown in Fig. 1. The polarity of the applied voltage was a negligible factor. The following experiments were done by applying negative voltage to Al dot electrodes; hole accumulation in p-type Si. A conventional MOS diode with an unannealed 700Å thick SiO₂ film and a dot electrode 400 μm in diameter showed fast transition from an initial high resistive state (a) to a conductive state (b) as soon as the maximum internal field exceeded the breakdown field. Current instability occurred at values below 50 μA. The breakdown was destructive. A 64 kΩ current-limiting resistor was used to take the photograph of the transition.

The maximum field strength was about 8.5 MV/cm. In the case of a diode with an SiO₂ film annealed in NH₃ at 1100°C for 2 hr this transition was not observed until the current increased to a few hundred microamperes. This equilibrium current shown in Fig. 1(c) did not lead to any destructive breakdown. This photograph was taken without using an external current-limiting resistor. Because of the film's nondestructive characteristics, its breakdown voltage increased a little.

The relation of breakdown current, *i.e.*, the maximum equilibrium current just prior to final breakdown, on NH₃ annealing conditions is shown in Fig. 2 and 3. Diodes measured were those with an SiO₂ thickness of 500Å and an Al dot diameter of 400 μm. All measurements of breakdown voltages were done on a curve tracer. Time-dependence of breakdown characteristics was not measured. As the series resistance was less than 10Ω and the ramp rate of the applied voltage was about 3 MV/cm·sec, the initial and final breakdown voltages were identical. The distribution of breakdown current through more than 50 diodes within a wafer is also indicated in both figures. The unannealed oxide film allowed an equilibrium current of only 20-30 μA. The breakdown current increased as the annealing temperature increased and saturated at about 10³ μA. This was 2 times larger than that of the unannealed film. Because the breakdown current was found to be nearly proportional to the peripheral length of the electrode and not to its area, current density, which is derived from average current per unit area, was meaningless. Increases in the breakdown current appeared clearly at temperatures above about 900°C. The breakdown current gradually increased over time until 2 hr

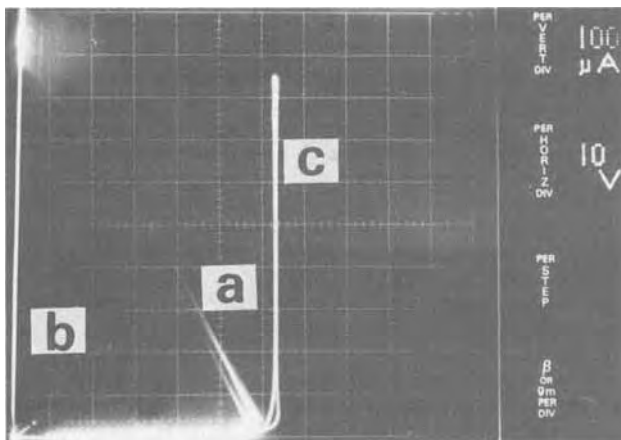


Fig. 1. Typical breakdown characteristics of a conventional 700Å thick SiO₂ film (a) and (b), and of an NH₃ annealed film (c). Negative voltages were applied to 400 μm diam Al dot electrodes.

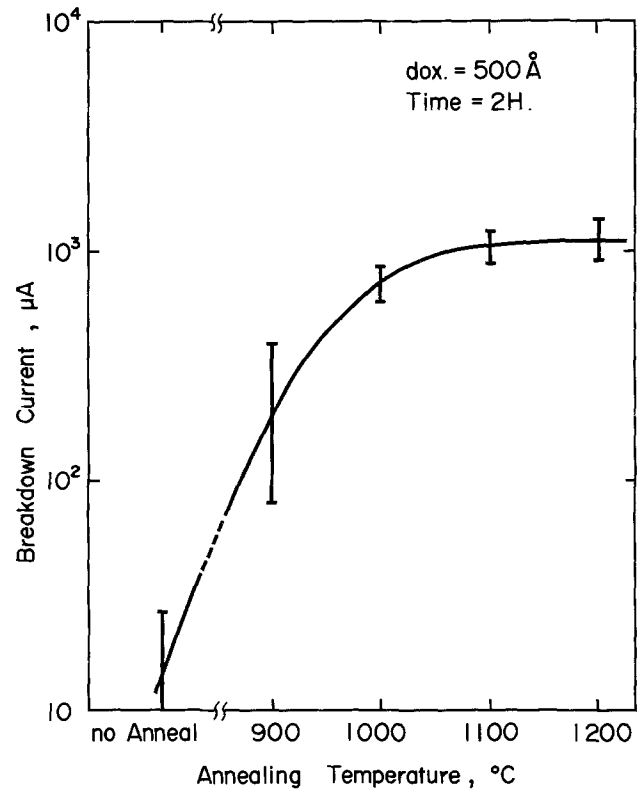


Fig. 2. Breakdown current, defined as the maximum equilibrium current just prior to breakdown, vs. NH₃ annealing temperature. Diameter of Al dots was 400 μm.

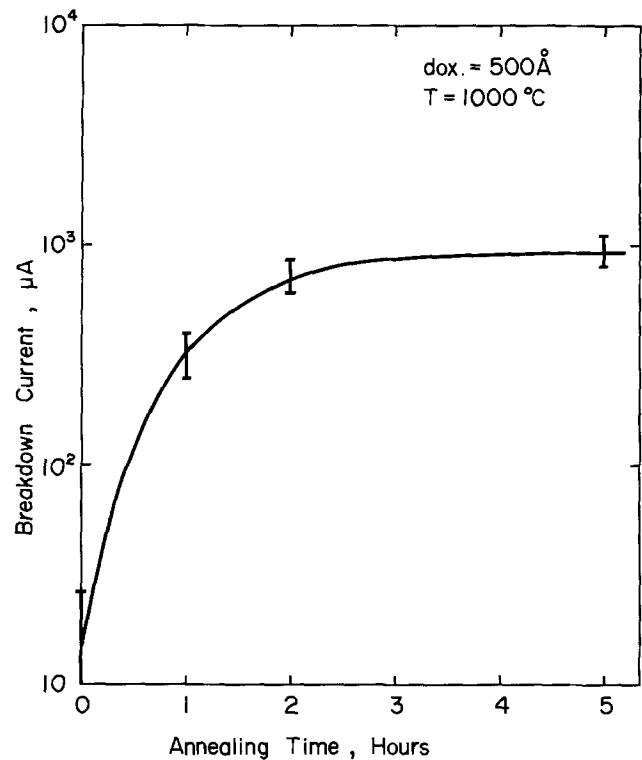


Fig. 3. Breakdown current vs. NH₃ annealing time

passed at 1000°C as shown in Fig. 3. Higher temperatures are expected to reduce the saturation time. It is projected to be only 1 hr at 1200°C. As shown in Fig. 1, breakdown voltage was also improved through NH₃ annealing. Figure 4 shows the increase of breakdown field along annealing time at 1200°C. The value of the NH₃ annealed oxide film was 10% higher than that of the unannealed film.

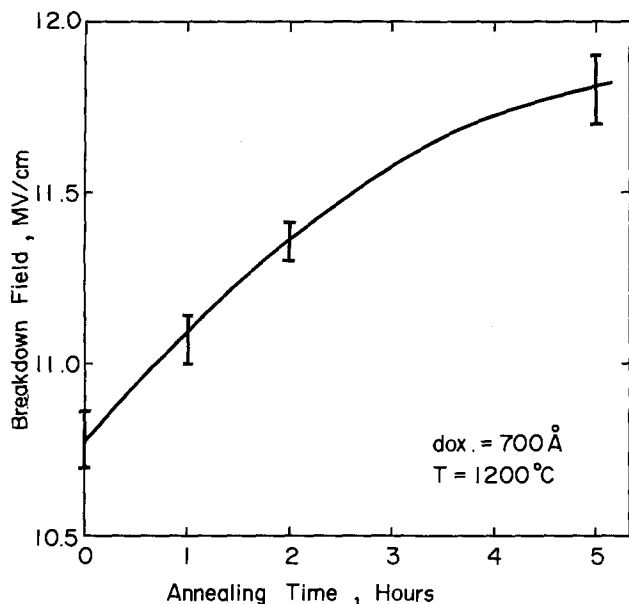


Fig. 4. Maximum field strength of NH_3 annealed SiO_2 films

Observation of the Al dot electrode surfaces after oxide breakdown revealed partly removed regions where material had evaporated. Figure 6(a) shows the surface of a diode with an NH_3 annealed SiO_2 film. Although there are some small pits evident on the plane surface, it is clear that the breakdown occurred mainly at the electrode's periphery. This phenomenon was identical with unannealed and NH_3 annealed SiO_2 films. This means that NH_3 annealing brings about no change in the breakdown energy of SiO_2 films because of almost the same areas of the removed regions.

The present experimental results may be explained by using the oxide breakdown mechanism model proposed by Ridley (10). This model is based on Fowler-Nordheim tunnel injection of carriers from a cathodic protuberance, filamentary joule heating, and activation of mobile ions which enhance the injection field. The current flow just prior to breakdown, which is increased about 2 times after NH_3 annealing, is distributed nearly uniformly on the dot electrodes. This may be a result of the uniform surface structure of NH_3 annealed SiO_2 films. Because localized heating is avoided, high current is allowable.

The current distribution just prior to breakdown shown schematically in Fig. 5(a) is for an MOS diode with conventional SiO_2 . Current concentrations occur at low energy-barrier points as demonstrated by DiStefano (11) with internal photoemission scanning.

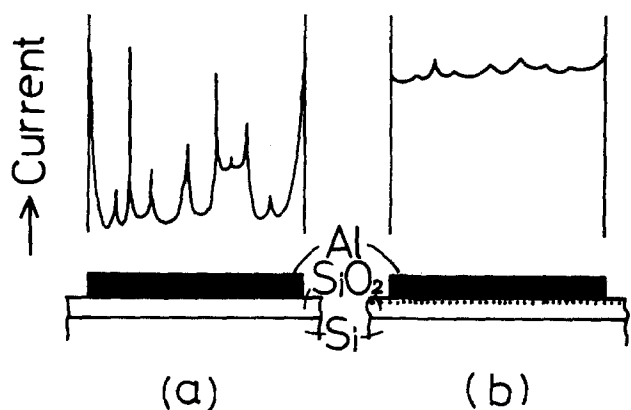


Fig. 5. Schematic diagrams of current distribution on Al dot electrodes of MOS diodes for conventional (a) and NH_3 annealed (b) SiO_2 films.

NH_3 annealed SiO_2 (b) allows far higher current flow as a result of greater uniformity of its surface.

To make this effect clear, Al electrodes which were evaporated from a sodium-contaminated W boat were used. The effect of NH_3 annealing was as remarkable as in the case of contamination-free samples. The surfaces of Al electrodes after breakdown are shown in Fig. 6(b) and (c). The results are far different from those shown in (a). The SiO_2 films in (b) and (c) are unannealed and NH_3 annealed, respectively. Many self-healing breakdown pits which will eventually lead to final breakdown, can be recognized in Fig. 6(b). They are thought to be associated with the fluctuation of potential on the SiO_2 surface which is caused by sodium-ion contamination. After NH_3 annealing, these lower energy-barrier points were removed. Current flowed almost uniformly on the Al electrode until it led to final breakdown. In this case, final breakdown occurred at the weakest point, as shown in Fig. 6(c). The breakdown current was a little lower than that for sodium-free samples. This notable occurrence in the sodium-contaminated samples is believed to be caused by the formation of a protective surface layer on the SiO_2 film which acts as a barrier against sodium contamination or as a gettering region for mobile ions.

The NH_3 annealed SiO_2 was subjected to analysis by Auger electron spectroscopy. A nitrogen peak was detected in the AES spectra of all SiO_2 films annealed in NH_3 gas at temperature above 900°C . Further chemical etching in hydrofluoric acid showed a nitrated surface layer on the SiO_2 (8). Argon sputter etching revealed the thickness of the nitrated layer to be a few tens of angstroms.

Because of the existence of the nitrated layer, a nondestructive breakdown model might possibly be applied to the explanation of the breakdown data for deposited Si_3N_4 films (12). The current-voltage characteristics of the NH_3 annealed SiO_2 were, however, due to the Fowler-Nordheim tunnel model and not to the Poole-Frenkel model. Therefore, that model (12) cannot be used.

A distribution histogram breakdown of voltages of the NH_3 annealed SiO_2 film was exceptionally sharp. Vromen (13) reported degradation of the breakdown field for SiO_2 films annealed in nitrogen. This is caused by defects generated on the interface between SiO_2 and Si. Although some reaction between NH_3 and Si at the Si- SiO_2 interfaces may be possible, the total uniformity in the breakdown-voltage histogram indicates that none occurred. Nitrated surface layers should prevent nonuniform localized reaction.

In summary, it has been found that a remarkable improvement in the breakdown characteristics of MOS structures can be achieved by annealing SiO_2 films in fully purified NH_3 gas at 900°C - 1200°C , even if sodium-contaminated Al electrodes are used. This effect is due to the surface nitrated region of SiO_2 which acts as a barrier against contamination. Interfacial properties of MOS structures with surface nitrated SiO_2 films will be reported soon in other articles.

Acknowledgments

The authors wish to thank T. Misugi, Y. Fukukawa, M. Shinoda, and S. Hijiya for many stimulating discussions and steady encouragement.

Manuscript submitted Nov. 26, 1979; revised manuscript received April 1, 1980.

Any discussion of this paper will appear in a Discussion Section to be published in the June 1981 JOURNAL. All discussions for the June 1981 Discussion Section should be submitted by Feb. 1, 1981.

Publication costs of this article were assisted by Fujitsu Laboratories, Limited.

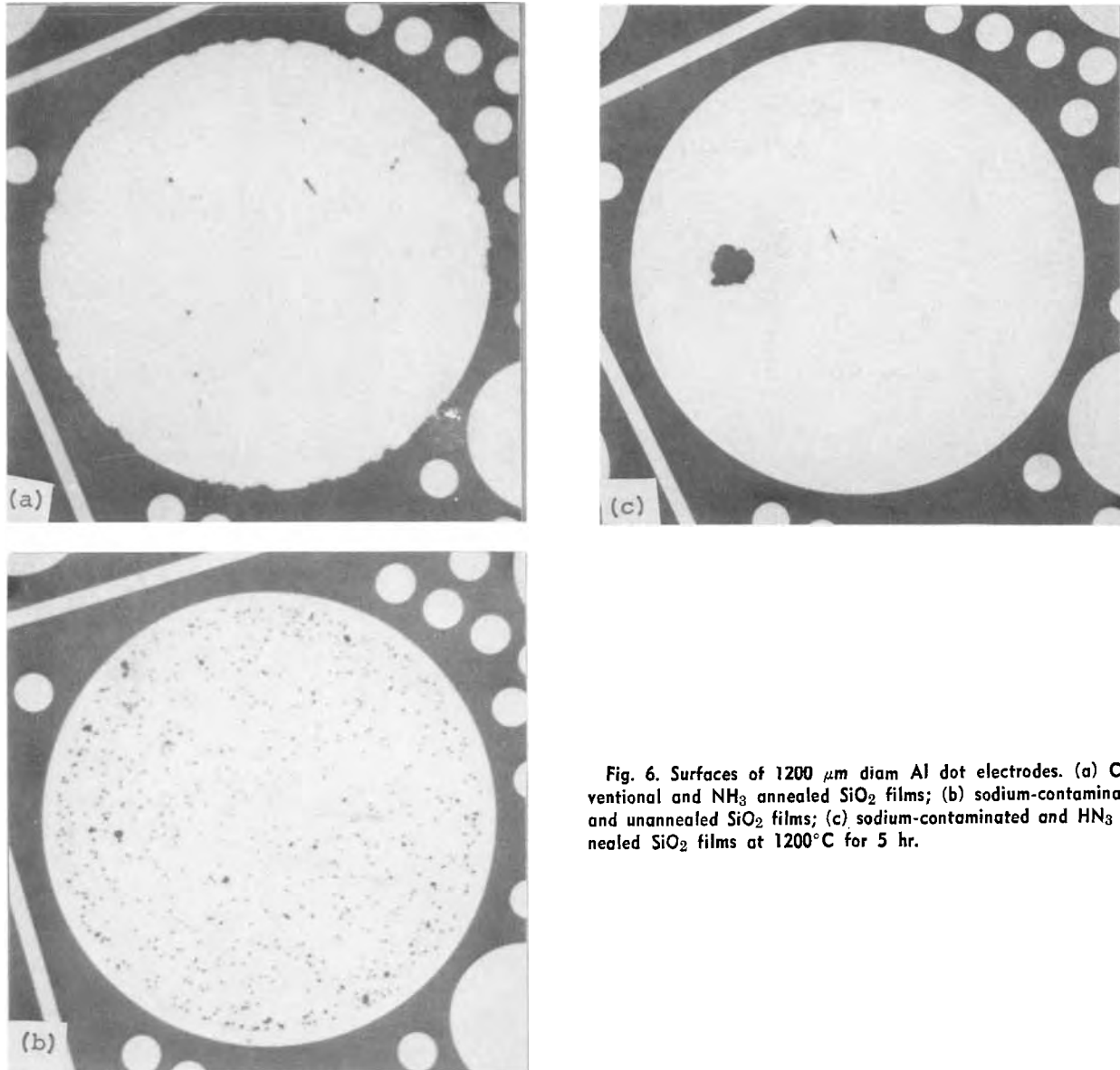


Fig. 6. Surfaces of 1200 μm diam Al dot electrodes. (a) Conventional and NH_3 annealed SiO_2 films; (b) sodium-contaminated and unannealed SiO_2 films; (c) sodium-contaminated and NH_3 annealed SiO_2 films at 1200°C for 5 hr.

REFERENCES

1. R. H. Dennard, F. H. Gaensslen, H. N. Yu, V. L. Rideout, E. Bassous, and A. R. LeBlanc, *IEEE J. Solid-State Circuits*, **sc-9**, 256 (1974).
2. T. H. Ning, P. W. Cook, R. H. Dennard, C. M. Osburn, S. E. Schuster, and H. N. Yu, *IDEM Dig. Tech. Papers*, 472 (1978).
3. E. Harari, *J. Appl. Phys.*, **49**, 2478 (1978).
4. P. K. Chaudhari, *This Journal*, **125**, 1657 (1978).
5. P. K. Chaudhari, R. A. Michaud, and R. M. Quinn, *ibid.*, **124**, 1897 (1977).
6. T. Ito, T. Nozaki, H. Arakawa, and M. Shinoda, *Appl. Phys. Lett.*, **32**, 330 (1978).
7. C. M. Osborn and D. W. Ormond, *This Journal*, **119**, 597 (1972).
8. T. Ito, T. Nozaki, and H. Ishikawa, *ibid.*, To be published.
9. C. M. Osburn and E. J. Weitzman, *ibid.*, **119**, 603 (1972).
10. B. K. Ridley, *J. Appl. Phys.*, **44**, 527 (1973).
11. T. H. DiStefano, *ibid.*, **44**, 527 (1973).
12. N. Klein and C. M. Osburn, *IEEE Trans. Electron. Devices*, **ed-24**, 559 (1977).
13. B. H. Vromen, *Appl. Phys. Lett.*, **27**, 152 (1975).

Painted, Polycrystalline Thin Film Photoelectrodes for Photoelectrochemical Solar Cells

Gary Hodes,* David Cahen, Joost Manassen, and Monica David

The Weizmann Institute of Science, Rehovot, Israel

ABSTRACT

A simple, versatile method for fabricating semiconductor layers for use as photoelectrodes in photoelectrochemical cells is described. This method, in which a slurry of the semiconductor is painted onto a substrate, is demonstrated particularly for Cd (and Zn) chalcogenides, but is shown to be applicable to other materials of photovoltaic interest, such as CuInS_2 . Also, the method allows for simple fabrication of layers of solid solutions, such as cadmium mixed chalcogenides.

The future of photovoltaic devices for terrestrial use depends, to a large extent, on the ability to pro-

duce thin film semiconductor layers at a competitive price (1). Devices using a semiconductor/liquid junction (photoelectrochemical cell: PEC) instead of a semiconductor/semiconductor or a semiconductor/metal one, are receiving a great deal of attention,

* Electrochemical Society Active Member.

Key words: photoelectrochemistry, semiconductor layers, sintering.

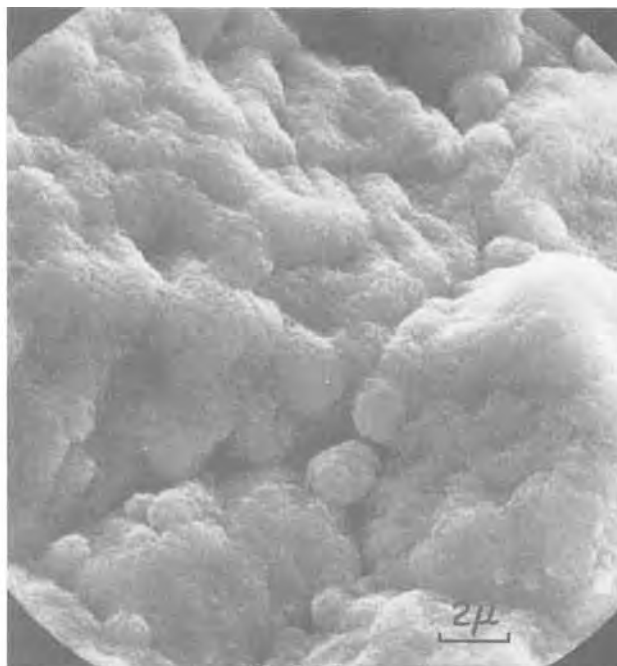
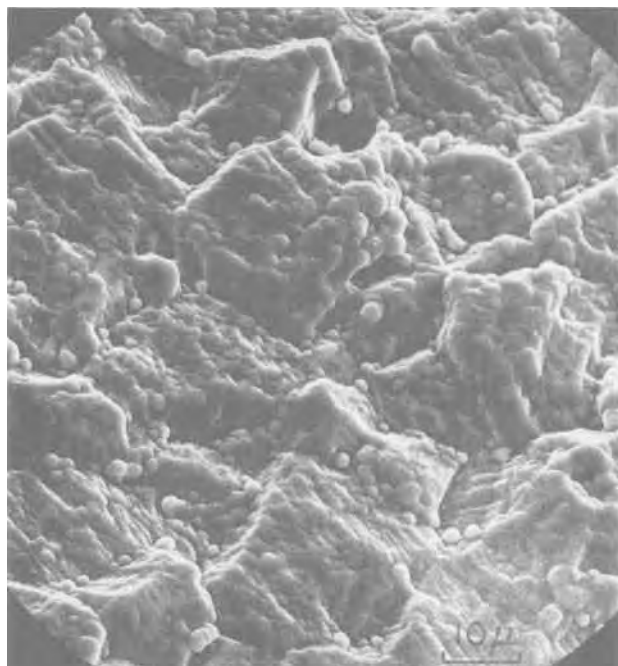


Fig. 1. SEM pictures at two magnifications of a painted CdSe layer on Ti. ZnCl_2 flux; after etching in 3% HNO_3 in HCl

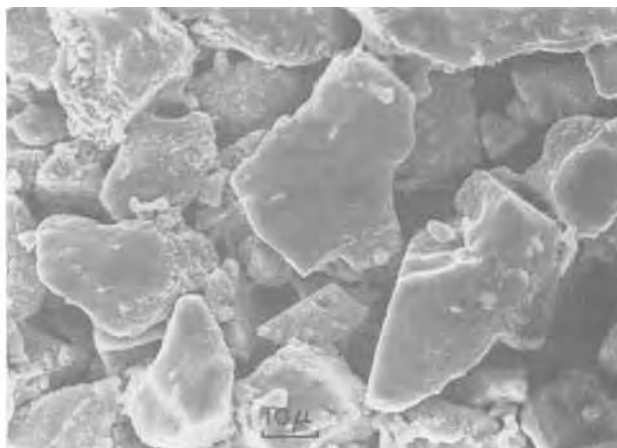
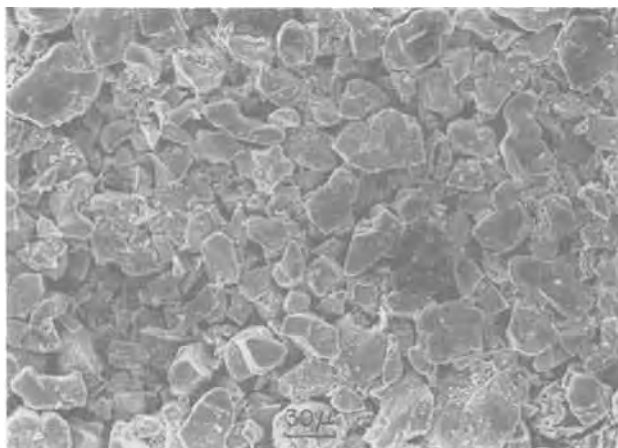


Fig. 2. SEM pictures at two magnifications of a painted $\text{CdSe}_{0.65}\text{Te}_{0.35}$ on Ti. CdCl_2 flux; after etching in 3% HNO_3 in HCl. Starting material prepared by presintering CdSe and CdTe with CdCl_2 .

inter alia because here conversion efficiency suffers less when the semiconductor single crystal is replaced by a polycrystalline layer (2).

We report here on a new simple method for preparation of thin film, polycrystalline semiconductor layers on a conducting substrate. Such layers are suitable for use as photoelectrodes in a PEC. The method is related to silk screen printing but is considerably less complicated for laboratory use.

Many of the uses of thin film polycrystalline semiconductors in solid-state photovoltaics have been limited to the use of a single crystal substrate, onto which the polycrystalline layer is applied (often by vacuum evaporation) to form the active junction (3). Some notable exceptions, using silk-screen printing, are the preparation of CdS-Cu₂S cells (4) and the fabrication of CdS/CdTe solar cells (5). In the latter case 8% conversion efficiency was achieved, while in the former case the cell had too high a series resistance to be able to compete with the various other methods of fabricating thin film CdS-Cu₂S cells [see (6) for a review of other methods].

Previously we reported on electroplating techniques for the preparation of thin film photoelectrodes, such as CdSe (2, 7). The present method yields photoelectrodes with similar conversion efficiencies, and has the advantage of greater versatility and can be adopted for, and applied to, preparation of layers of a wide range of materials.

Photoelectrodes with conversion efficiencies comparable to those of electroplated ones (in the case of CdSe) can be prepared in the following general way: a powder of the material of choice is used as such, or prepared by cosintering its components, in an inert atmosphere. This powder is mixed with a suitable fluxing material (e.g., ZnCl₂), and dispersed in liquid to obtain a slurry. The slurry is painted on a conducting substrate and dried. Subsequently it is annealed at elevated temperature and, after cooling a well-adhering polycrystalline layer is obtained.

Table I gives some examples of binary and ternary chalcogenide photoelectrodes prepared in this manner. Preparative conditions have been optimized for Cd-chalcogenides only. It should be noted, however, that even without attempts to adjust conditions the method yields photoactive layers of such other materials as CuInS₂, GaAs, and MoS₂.

All electrodes are given a standard etch of 10 sec in 3% HNO₃ in HCl at room temperature. Some electrodes are given an additional "ion treatment" which results in an increase of open-circuit voltage of the electrodes. For the ZnCl₂ treatment, the electrode is immersed in a 1M aqueous solution of ZnCl₂ (or any soluble Zn salt) then rinsed very lightly with water, and dried. For the K₂CrO₄ treatment, a similar dipping in an aqueous K₂CrO₄ solution is carried out, but rinsing is not necessary.

An important advantage of this painting method is the case with which the composition of the semiconductor can be varied in a controlled way. An example of this versatility is the solid solution system, Cd (Se, Te), preparation of which is described later. This enabled us to study the effect of changes in alloy composition on conversion efficiency and output stability.

Figures 1 and 2 show SEM pictures of electrodes prepared using commercially available CdSe (Fig. 1) and using a cosintered mixture of CdSe and CdTe (65:35 atomic percent; Fig. 2). From these pictures we see that the average final particle size is larger in the mixture as a result of the annealing cosintering step.

Although all entries in Table I refer to layers on Ti substrates it is possible to use other substrate materials as well, notably Cr or Mo.

The fluxing agent has a dual role in formation of the layers. Primarily, by dissolving the outer layers of the semiconductor grains, and subsequently vaporizing off, it binds the grains together and thus imparts structural coherence to the layer. It also promotes re-

Table I.

Compound	Flux ⁽¹⁾ (for mixed powder)	Flux ⁽²⁾ (for paint)	Post ⁽³⁾ annealing treatment	Ion treatment	Electrolyte OH ⁻ /S ²⁻ /S	Light intensity (%AMI)	OCV (mV)	SCC (mA/cm ²)	η (%)
CdSe	—	ZnCl ₂ /CdSO ₄ (8:1)	—	ZnCl ₂ (1M)	1/1/1 + mM Se	1	660	10.5	3.6
CdSe _{0.57} Te _{0.43} (cubic)	CdTe	CdCl ₂ /CdSO ₄ (8:1)	—	—	1/1/1 + mM Se	0.8	520	14.0	2.9
CdSe _{0.5} Te _{0.5} (cubic)	CdCl ₂ · (2.5)H ₂ O	CdCl ₂ /CdSO ₄ (8:1)	—	K ₂ CrO ₄ (2M)	1/1/1	0.79	642	13.3	5.0
CdSe _{0.35} Te _{0.65} (hex)	CdCl ₂ · (2.5)H ₂ O	CdCl ₂ /CdSO ₄ (8:1)	—	—	1/1/1	0.82	610	12.0	4.4
CdTe ((cubic) (0.3% InS ₂))	CdCl ₂ · (2.5)H ₂ O	InCl ₃ /CdCl ₂ (1:1)	1 min, 300°C air	—	1/1/1 3/0.1/0.1 (OH ⁻ /Te ²⁻ /Te)	0.83	441	7.0	1.6 (n-type)
CdTe (cubic)	—	CdCl ₂	5 min, 240°C	—	1/2/1	0.9	30	0.7	~0.01 (p-type)
CuInS ₂ (n) (Cd annealed)	—	InCl ₃ ZnBr ₂ /CdSO ₄ (5:1)	1:2 H ₂ :Ar	—	—	0.83	130	1.1	~0.06
ZnSe	—	—	—	ZnCl ₂ (1M)	1/2/0.1	High pressure Hg lamp	650	2.0	—

⁽¹⁾ 25% by weight, mixtures heated for 30-50 min at 630°C in Ar, subsequently washed with water.

⁽²⁾ 5:10% by weight.

⁽³⁾ Annealing procedure: 8-12 min in Ar containing 20 ppm O₂ at 625°-650°C.

All electrodes 1 cm². Starting powders Alfa 4N, $\leq 10 \mu\text{m}$ for CdTe, 5N, 3 μm for CdSe, analytical grade for others. Slurry prepared from 50 mg powder and 0.05 ml liquid or multiples thereof. Liquid composition: 5% nonionic detergent in water (v/v) or a 1:5 mixture of a saturated solution of ethylcellulose in toluene with ethylene glycol monobutyl ether (8).

crystallization and growth of larger grains. In addition, it can act as a dopant for the semiconductor. The halide component of most fluxes can act as an n-type dopant for most of the II-VI semiconductors. An even greater degree of n-type doping occurs if a group III halide is used instead of, or together with, another flux (see, e.g., CdTe in Table I prepared with, and without, an InCl_3 -containing flux).

For the preparation of the mixed semiconductor layers, the desired solid solution is prepared by heating the individual components in powder form together with a flux, which is usually CdCl_2 . For example, to prepare $\text{CdSe}_{0.65}\text{Te}_{0.35}$, CdSe and CdTe (in a molar ratio of 6.5/3.5) are mixed with ~25% (w/w) CdCl_2 , and sintered in argon at 650°-670°C for 40 min. X-ray diffraction shows the powders have the expected compositions (assuming the validity of Vegard's law for the lattice dimensions). The product is ground up, washed with water (to remove any excess CdCl_2), and used to prepare a layer as described above. In this case, the flux serves mainly to facilitate formation of a true solid solution, in this respect, it is not absolutely essential, because a solid solution could be prepared also by sintering a pressed pellet of the components without flux (9). The flux method, however, is generally the more convenient one.

The liquid to be used for preparing the slurry has to wet the powder thoroughly (thus, if water is used, some detergent is added), and enable the preparation of a smooth slurry for equal distribution of the powder over the substrate. Also its boiling point should not be so low that excessive evaporation occurs during drying. With these conditions in mind we do not find the nature of the liquid to be critical, and water suffices in most cases.

As in the case of electroplated layers, the annealing process determines the final (photo-) electrical properties of the layer, and the exact conditions for it, as well as the optimal fluxing agent will depend on the material used. As shown here, though, once such conditions are determined they can be applied, with minor changes only, to a series of similar materials.

Finally, we comment on the performance of painted photoelectrodes. Table I shows that their efficiencies are comparable to those of electroplated thin layer photoelectrodes (10). Output stability, too, is comparable, and $>10,000 \text{ C/cm}^2$ at $\sim 35 \text{ mA/cm}^2$ can be passed through CdSe or $\text{CdSe}_{0.65}\text{Te}_{0.35}$ electrodes with less than 10% decrease in output. CdSe electrodes of 4 cm^2 area with 3% conversion efficiency can be prepared routinely by this method.

Acknowledgment

Partial support of the U.S.-Israel Binational Science Foundation, Jerusalem, Israel, is gratefully acknowledged.

Manuscript submitted March 21, 1980; revised manuscript received May 8, 1980.

Any discussion of this paper will appear in a Discussion Section to be published in the June 1981 JOURNAL. All discussions for the June 1981 Discussion Section should be submitted by Feb. 1, 1981.

Publication costs of this article were assisted by The Weizmann Institute of Science.

REFERENCES

1. R. M. Moore, *Solar Energy*, **18**, 225 (1976).
2. "Semiconductor-Liquid Junction Solar Cells," A Heller, Editor, The Electrochemical Society Soft-bound Proceedings Series, Princeton, N.J. (1977).
3. See, for example, F. Buch, A. L. Fahrenbruch, and R. H. Bube, *J. Appl. Phys.*, **48**, 1596 (1977).
4. S. Vojdoni, A. Sharifnaji, and M. Doroudian, *Electron. Lett.*, **9**, 128 (1973).
5. S. Ikegami and T. Yamashita, *J. Electron. Mater.*, **8**, 705 (1979), *Nat. Techn. Report (Jpn.)* **24**, 361 (1978).
6. A. G. Stanley, *Appl. Solid State Sci.*, **5**, 251 (1975).
7. J. Manassen, G. Hodes, and D. Cahen, U.S. Pat. 4,064,326 (1977).
8. Y. T. Sihvonen, S. G. Parker, and D. R. Boyd, *This Journal*, **114**, 96 (1967).
9. R. N. Noufi, P. A. Kohl, and A. J. Bard, *ibid.*, **125**, 375 (1978).
10. D. Cahen, G. Hodes, and J. Manassen, *ibid.*, **125**, 1623 (1978).

A Model of SIPOS Deposition Based on Infrared Spectroscopic Analysis

W. R. Knolle* and H. R. Maxwell, Jr.*

Bell Laboratories, Reading, Pennsylvania 19604

ABSTRACT

SIPOS deposited rapidly at atmospheric pressure (AP) is different from SIPOS deposited more slowly at low pressure (LP). The transmission infrared spectra of the AP and LP SIPOS films can be different for the same oxygen content. We interpret our infrared data for AP SIPOS in terms of a statistical model for the bonding of silicon and oxygen that predicts less than 1% SiO_2 character [$\text{Si}(\text{O}_4)$ tetrahedra] for the AP SIPOS. The LP SIPOS films have more SiO_2 character than the AP SIPOS. We believe this arises from the slower deposition rate for LP SIPOS where oxygen can preferentially bond to an already oxygen-bonded Si. Stress measurements and reactivity to HF for LP SIPOS films correlate with the infrared data and are consistent with our interpretation of the infrared data.

SIPOS (semi-insulating polycrystalline silicon) is an oxygen-doped silicon film that can be used as part of a passivation scheme on high voltage semiconductor devices (1). The SIPOS is deposited by the reactive decomposition of silane (SiH_4) and nitrous

oxide (N_2O) either at atmospheric pressure (AP) or at a lower pressure (LP). The oxygen content of the film can be controlled by the ratio of the N_2O to SiH_4 gas flows in the deposition reactor (1).

We have used transmission infrared spectroscopy to investigate the SIPOS films deposited at AP and LP. The differences between the infrared spectra

* Electrochemical Society Active Member.

Key words: semiconductor, passivation, thin films.

are explained in terms of silicon-oxygen bonding differences between the two films. A statistical model of film deposition we believe explains the AP deposition while the LP SIPOS has more SiO₂ character than would be predicted by this model. The physical properties of the SIPOS not only depend on oxygen content but rate of deposition as well.

We describe the deposition of the AP and LP SIPOS and present the infrared spectra and our analysis of these data. Stress measurements and reactivity of the SIPOS to conc HF corroborate our interpretation of the infrared data. The SIPOS films that we believe have some SiO₂ character are in compression (SiO₂ is in compression on Si) and react with conc HF (SiO₂ etches rapidly in HF). Finally we describe how this physical difference between the films might arise.

It should be noted that the results reported here apply to as-deposited SIPOS films that have received no postdeposition anneal. Annealed SIPOS films have quite different physical properties from the as-deposited films (2).

Experimental Details

SIPOS deposition.—AP SIPOS films were deposited on 2 in. diam Si wafers in a radiantly heated cold wall reactor at 650°C. The wafers were laid flat on a susceptor in the reactor and SIPOS was deposited on one side of the wafer. For oxygen determination by the gravimetric technique (3) SIPOS should be on both sides of the silicon-nitride-covered wafer. Therefore, two consecutive runs were made with the same N₂O to SiH₄ ratio. Five different ratios were used to obtain SIPOS films with oxygen contents between 18 and 37 atomic percent (a/o) oxygen. The data for these runs are presented in Table I. The thickness of the SIPOS film was determined by angle lapping the wafer and counting the interference fringes under sodium light ($\lambda = 5890\text{\AA}$) (4). The average thickness and average deposition rate are presented for the two depositions at each oxygen content. As can be seen in Table I the deposition rate depends inversely on the oxygen content of the film (1).

The LP SIPOS films were deposited in a hot wall reactor at 644°C. The Si wafers were loaded on a boat and held vertically in the furnace, perpendicular to the gas stream so that deposition occurred on both sides of the wafer. The SIPOS was deposited over a range of conditions in order to vary the deposition rate and oxygen content of the LP SIPOS. Deposition rates ranged from 143 to 23 Å/min. For example, a 37 a/o O LP SIPOS film was deposited at 0.16 Torr at a deposition rate of 29 Å/min. Another LP SIPOS film with 22.7 a/o O was deposited at 0.35 Torr at a deposition rate of 63 Å/min. The N₂O/SiH₄ ratio was greater for the higher oxygen content LP SIPOS film. Detailed analysis of these LP SIPOS films deposited under various conditions will be presented in a forthcoming paper (5).

Infrared measurements.—The transmission infrared spectra were recorded on a Perkin-Elmer Model 621 Grating Infrared Spectrophotometer. An Si substrate without any SIPOS was placed in the reference beam to eliminate interference from the substrate in the sample beam. A wafer adjacent to the silicon-nitride-covered wafer was used for the infrared measure-

ment. The absorbance, A , of an infrared peak was measured by the base line technique (6) and the area of an absorption was approximated by $A \cdot W$ where W is the full width at half of the maximum absorbance (7). The transmission infrared technique is not as sensitive to the condition of the SIPOS surface as are other techniques that have been used to investigate SIPOS (8, 9) and so the infrared spectra should be representative of the bulk of the as-deposited SIPOS films. There was no physical or chemical treatment of the SIPOS film prior to recording the infrared spectrum.

Stress and HF reactivity.—The stress of the SIPOS film was measured with an optically levered laser technique (10). The difference between the radius of curvature of the Si wafer measured before and after deposition can be related to the stress in the deposited SIPOS film. The precision of the stress measurement is $\pm 1 \times 10^9$ dynes/cm².

SIPOS films can be etched in a solution of buffered HF and hydrogen peroxide (1). The peroxide presumably oxidizes the SIPOS film and the buffered HF etches the newly formed oxide. HF is not believed to etch suboxides of Si, so as an indication of SiO₂ content, the reactivity of the SIPOS film to conc HF was measured by immersing the wafer in HF and noting the time when a reaction began. Times up to 15 min in HF were measured.

Results

Table II lists the infrared results for the AP SIPOS films. The oxygen content x of a SIPOS film SiO _{x} is listed in column 1. The average of the infrared data for the two runs at each N₂O to SiH₄ ratio is listed. Since the absorbance of a peak is proportional to the thickness and oxygen content of the SIPOS the infrared absorbances in Table II have been divided by the SIPOS thickness. Figure 1 shows the infrared spectra of the $x = 0.33$ (25 a/o O) and $x = 0.58$ (37 a/o O) AP SIPOS films. There are two infrared peaks in this range: a strong absorption at 1025 cm⁻¹ believed due to an Si-O-Si stretching vibration and a weak absorption at 865 cm⁻¹. For the AP SIPOS films the strong and weak absorptions increase in intensity with increasing oxygen content. Furthermore, as is apparent from column 4 of Table II as well as Fig. 1, the width of the strong absorption increases with increasing oxygen content. Also, the strong absorption remains at 1025 cm⁻¹ \pm 5 cm⁻¹ over the range of oxygen contents investigated.

Figure 2 shows the infrared spectra of AP and LP SIPOS with the same oxygen content. The LP SIPOS was deposited at 0.16 Torr with a deposition rate of 29 Å/min while the AP SIPOS was deposited at a rate of 370 Å/min. For the infrared spectrum of LP SIPOS the same two peaks appear, however, the strong absorption shifts to higher frequency with increasing oxygen content while the 865 cm⁻¹ peak actually decreases in intensity. Plotted in Fig. 3 is the ratio of the 865 cm⁻¹ peak intensity to the strong absorption intensity as a function of oxygen content for the AP and LP SIPOS films. For the AP SIPOS the ratio increases monotonically while for the LP SIPOS the ratio rises to a maximum at about 25 a/o O ($x = 0.33$) and then decreases.

Table I. AP SIPOS deposition data

Oxygen content		Deposition time (min)	N ₂ O		Thickness (μm)	Deposition rate (Å/min)
a/o O	x		SiH ₄	SiH ₄		
19	0.23	8	0.4	0.41	510	
25	0.33	9	0.6	0.45	500	
29	0.41	10	1.0	0.46	460	
35	0.54	10	1.7	0.34	340	
37	0.58	10	2.0	0.37	370	

Table II. Infrared data for AP SIPOS films

Oxygen content x	Absorbance + thickness		Width (cm ⁻¹)	$A(865) \div A(1025)$	$AW + \text{thickness}$ ($\mu\text{m}^{-1} \text{cm}^{-1}$)
	1025 cm ⁻¹ (μm^{-1})	865 cm ⁻¹ (μm^{-1})			
0.23	0.359	0.011	149	0.031	54
0.33	0.395	0.022	155	0.056	61
0.41	0.495	0.038	161	0.077	80
0.54	0.616	0.064	159	0.10	98
0.58	0.614	0.069	166	0.11	102

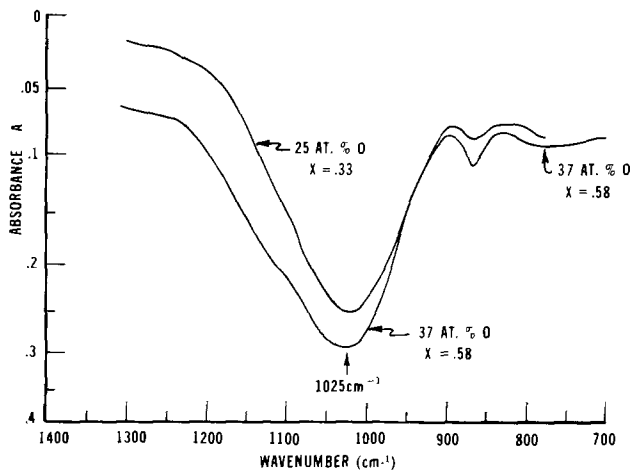


Fig. 1. Infrared spectra of AP SIPOS films, SiO_x , with oxygen content $x = 0.33$ and $x = 0.58$.

Figure 4 summarizes the infrared, stress, and HF reactivity data for various LP SIPOS films. In Fig. 4 a P beside a point means the SIPOS film lasted at least 15 min in HF without showing any physical reaction to the HF. An F means the film lifted off the substrate or that lifting of the film had begun within 15 min. The ordinate in Fig. 4 is the measured stress in units of 10^9 dynes/cm² with the convention that positive stress is tensile and negative stress is compressive. The abscissa is the infrared peak position in cm⁻¹ for the strong absorption. Since the strong absorption remains at 1025 cm⁻¹ for the AP SIPOS we did not plot the data for the AP SIPOS films. These films were all in tension and did not lift off in HF.

The data in the upper left-hand quadrant of Fig. 4 are either for low oxygen content (less than 30 a/o O) or rapidly deposited (greater than 45 Å/min) LP SIPOS or both. These films are all in tension and do not react to HF. The four data points in the lower right-hand quadrant are for higher oxygen content LP SIPOS or LP SIPOS films deposited at a slower rate or both. These films are in compression and react to HF in less than 15 min.

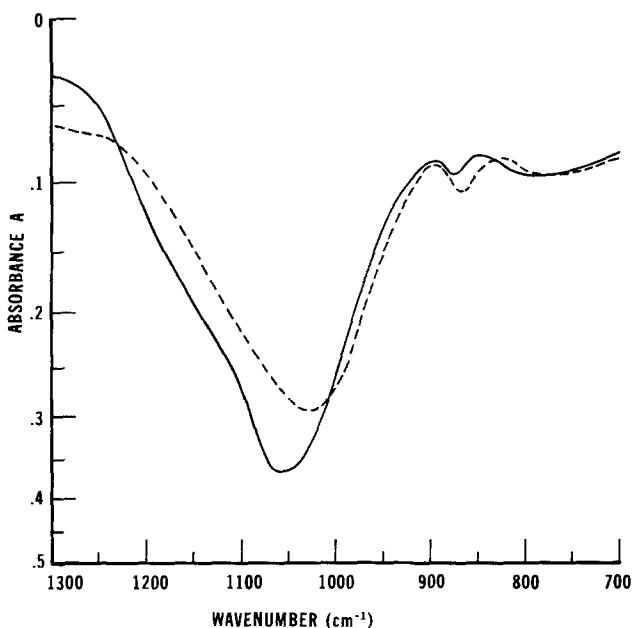


Fig. 2. Infrared spectra of AP and LP SIPOS films with identical oxygen content of 37 a/o O. The strong absorption is shifted to higher frequency and the intensity ratio of the 865 cm⁻¹ peak to the strong absorption is less for the LP SIPOS. Solid line is LP SIPOS and dashed line is AP SIPOS.

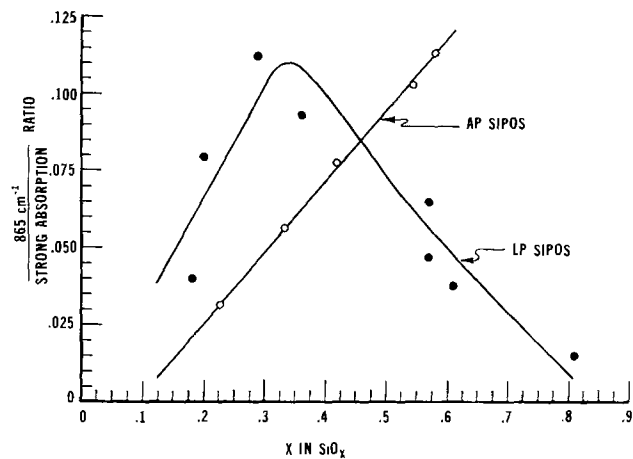


Fig. 3. Ratio of the 865 cm⁻¹ peak to the strong absorption intensity as a function of oxygen content. The ratio increases for AP SIPOS while it increases and then decreases for LP SIPOS.

Discussion

Statistical model for AP SIPOS.—Philipp (11) concluded from an analysis of optical data that SiO_x films with $1 \leq x \leq 2$ have a structure made up of a statistical distribution of Si tetrahedra of the type $\text{Si}(\text{Si}_y\text{O}_{4-y})$. We have calculated these statistical distributions for the five different oxygen content AP SIPOS films that were deposited. The results are presented in Table III. Briefly, the table is generated in the following way. For a SIPOS film deposited with SiO stoichiometry, the probability of an O atom bonding to an Si atom in the film is 0.5. And so, for SiO_x stoichiometry, the probability of an O atom bonding to an Si atom is $0.5x$. When an O atom does not bond to an Si atom, it is assumed that an Si atom does. The probability of an Si atom bonding to an Si atom for SiO_x stoichiometry is just $1-0.5x$. The probability of obtaining an $\text{Si}(\text{SiO}_3)$ tetrahedron is $4(1-0.5x)(0.5x)^3$ for an SIPOS stoichiometry of SiO_x . The 4 arises because there are 4 possible ways of arranging the atoms about the central Si atom in

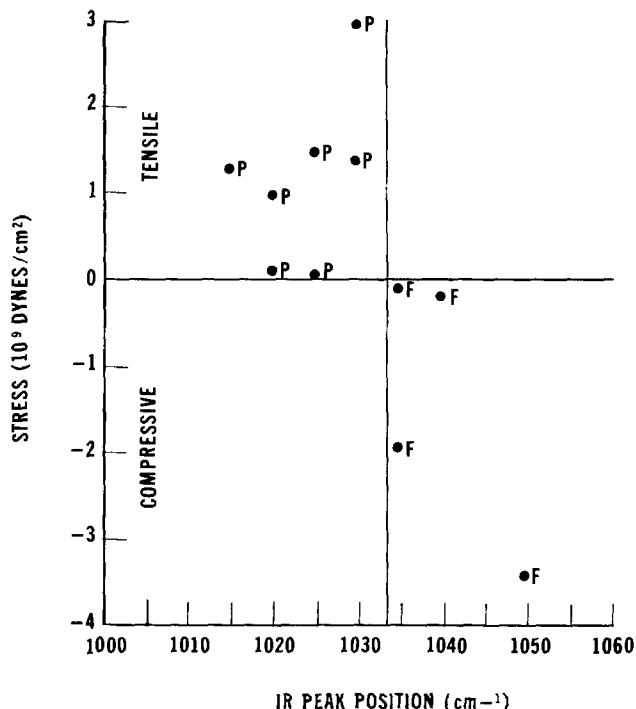


Fig. 4. Correlation of stress and HF reactivity with position of the strong infrared absorption for various LP SIPOS films. P means SIPOS did not react with HF in 15 min. F means film lifted or began to lift within 15 min.

Table III. Probability of an Si tetrahedral structure for various oxygen content SIPOS films

Silicon tetrahedra	SIPOS				
	SiO _{0.28}	SiO _{0.38}	SiO _{0.41}	SiO _{0.54}	SiO _{0.58}
Si(O ₄)	0.000 (0.000)	0.001 (0.001)	0.002 (0.003)	0.005 (0.007)	0.007 (0.009)
Si(SiO ₃)	0.005 (0.014)	0.015 (0.029)	0.027 (0.046)	0.058 (0.080)	0.069 (0.093)
Si(Si ₂ O ₂)	0.063 (0.161)	0.114 (0.222)	0.159 (0.265)	0.233 (0.326)	0.255 (0.341)
Si(Si ₃ O)	0.319 (0.825)	0.384 (0.748)	0.412 (0.686)	0.420 (0.587)	0.415 (0.557)
Si(Si ₄)	0.613 —	0.486 —	0.400 —	0.284 —	0.254 —

The numbers in parentheses are the renormalized probabilities excluding the Si(Si₄) tetrahedron.

the SIPOS film. The probabilities for the other tetrahedra are calculated in a similar way. The numbers in parentheses in Table III are the renormalized probabilities of the Si/O tetrahedra excluding Si(Si₄) since it does not contribute to the infrared absorption. Note that the sum of each column in Table III is 1.0, that is, all of the Si atoms are bonded tetrahedrally to either Si or O.

To explain the infrared results for the AP SIPOS films we consider the probabilities of the various Si tetrahedra listed in Table III. At higher oxygen content there is less likelihood for Si(Si₄) tetrahedra and there will be more of the four different Si/O tetrahedra. For example, SiO_{0.23} should have a Si-O-Si stretching vibration primarily defined by the Si(Si₃O) tetrahedra (82.5% of the possible Si/O tetrahedra). For SiO_{0.58}, the Si(Si₃O) tetrahedra contribute only 55.7% of the possible Si/O tetrahedra while Si(Si₂O₂) and Si(SiO₃) now make substantial contributions. Therefore the Si-O-Si stretching vibration for SiO_{0.58} arises from a less well-defined state and the infrared absorption at 1025 cm⁻¹ should be broader. This broadening of the infrared absorption with increasing oxygen content is observed for the AP SIPOS.

The amount of Si(O₄) tetrahedra, that is, SiO₂, calculated for any of the SIPOS films is small, being less than 1% for the highest oxygen content AP SIPOS film investigated. If we assume that only the SiO₂ component will shift the strong absorption to higher frequency then no shift for these films would be expected and in fact no shift for the AP SIPOS is observed.

Addition of SiO₂ to SIPOS.—We do not believe that the infrared results for the LP SIPOS films can be explained by the statistical model since the statistical model predicts very little SiO₂ component in the SIPOS films. With very little SiO₂ component (less than 1%) then no shift in the peak position of the strong infrared absorption would be expected. However, the shift to higher frequency with greater oxygen content of the strong absorption in the infrared spectrum of LP SIPOS can be simulated by adding the measured infrared spectrum of a 900°C thermally grown SiO₂ film to the infrared spectrum of an SIPOS film. Figure 5 shows the results for the addition of small amounts of the SiO₂ infrared spectrum to the measured infrared spectrum of a 22.7 a/o O ($x = 0.294$) LP SIPOS film. The SIPOS and SiO₂ spectra were digitized and added as $a\text{SiO}_2 + b\text{SiO}_{0.294}$ with $a + b = 1$. From Fig. 5 it can be seen that the infrared absorption occurs at 1025 cm⁻¹ for this LP SIPOS film. Furthermore this film did not lift off in conc HF and therefore presumably this LP SIPOS film had very little SiO₂ character. Figure 6 is a plot of the calculated shift of the strong absorption as a function of percent SiO₂ added. The top abscissa of Fig. 6 shows the stoichiometry of the film resulting from the addition of SiO₂ and SiO_{0.294}. No difference in the position of the strong absorption could be measured for less than about 4% SiO₂ character. The shift to higher frequency of the Si-O-Si absorption with increasing oxygen content had been reported for films with stoichiometry between SiO and SiO₂ (12).

We believe it is the difference in the amount of SiO₂ that accounts for the difference in the amount of infrared spectra of SIPOS films shown in Fig. 2. Two SIPOS films with the same oxygen content but different calculated infrared spectra can be generated by the addition of different amounts of SiO₂ to different initial SIPOS films. For example, if 6% of the SiO₂ strong absorption is added to 59.2% of the SiO_{0.294} LP SIPOS (22.7 a/o O) strong absorption then an infrared spectrum is generated for an SIPOS film with a stoichiometry of SiO_{0.45} (31 a/o O). This film has 9.2% SiO₂ character and a calculated strong absorption in the infrared at 1050 cm⁻¹. The same 31 a/o O film can be obtained by adding 2% of the SiO₂ absorption to 98% of the strong absorption of an AP SIPOS film with stoichiometry of SiO_{0.414} (29.3 a/o O). For this AP SIPOS film the strong infrared absorption occurred at 1025 cm⁻¹ and the film did not lift off in conc HF and so should have had little SiO₂ character. The resulting film is calculated to have a strong infrared peak at 1030 cm⁻¹. In Fig. 2 the measured strong absorption occurs at 1050 cm⁻¹ for the LP SIPOS film which is a shift of 25 cm⁻¹ in the position of the strong absorption. In Fig. 6 we would conclude from the infrared shift that the LP SIPOS film has about 10% SiO₂ character whereas the random bonding model (see Table III) predicts less than 1% SiO₂ character [Si(SiO₄) tetrahedra].

We believe the data summarized in Fig. 4 are consistent with more SiO₂ character in LP SIPOS films that have the strong infrared absorption shifted to higher frequency. In Fig. 4, the LP SIPOS films that reacted to HF and were in compression had the strong infrared absorption at higher frequency. If this shift is due to more SiO₂ then the reactivity of these films to conc HF is understandable since HF etches SiO₂ rapidly whereas it is believed not to attack suboxides rapidly. Furthermore SiO₂ on Si is in compression. The SIPOS films with the higher frequency infrared

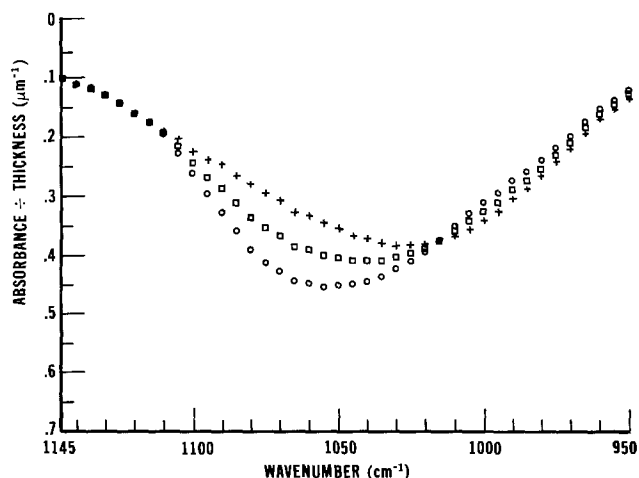


Fig. 5. Synthesized SIPOS spectra from the addition of the SiO₂ infrared absorption to the strong infrared absorption of an LP SIPOS film, SiO_{0.294} (22.7 a/o O). +, no addition of SiO₂; □, 5.2% SiO₂; ○, 10.4% SiO₂.

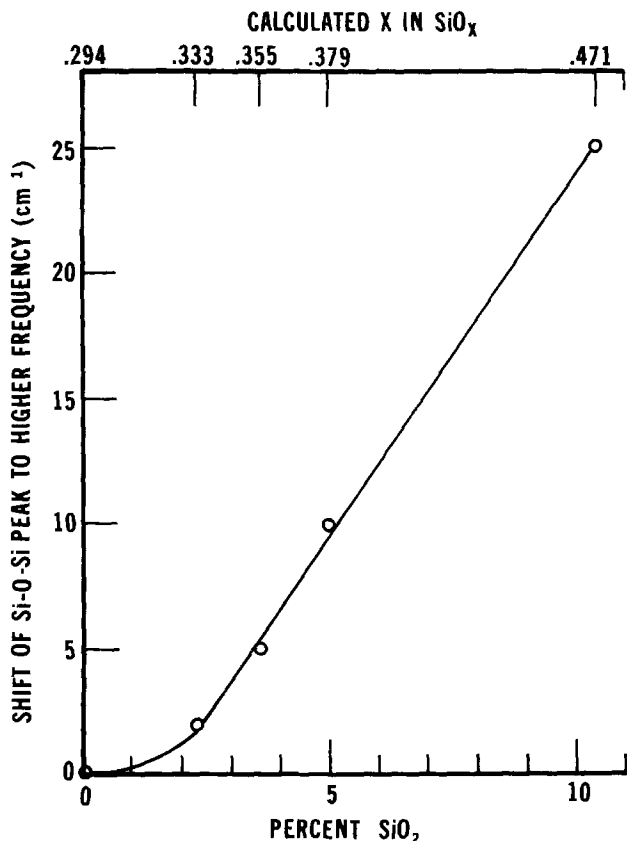


Fig. 6. Calculated shift of the position of the strong absorption as a function of added SiO₂ to the infrared spectrum of LP SIPOS with 22.7 a/o O ($x = 0.294$). The top abscissa is the resultant SIPOS stoichiometry.

absorption and presumably more SiO₂ character are in compression rather than tension.

Deposition rate.—During the deposition of SIPOS we would expect the Si-O bond in SIPOS to be polarized, that is, have some ionic character represented as Si^{δ+}-O^{δ-}, where δ+ represents a small amount of positive charge on the Si atom due to the greater electronegativity of the oxygen atom. Another incoming oxygen atom would be attracted preferentially to the Si^{δ+} rather than to an Si atom that is not bonded to anything but other Si atoms. In the case of Si bonded to other Si atoms, there is no reason to suppose that the Si-Si bond is polarized and therefore the oxygen atom would not be preferentially attracted to it. For the low oxygen content AP SIPOS films, the growth rate is so rapid that there is evidently not enough time for the O atom from N₂O to seek out the Si^{δ+} atom that already is bonded to an O atom. And so, the random bonding model governs the deposition of rapidly deposited AP SIPOS. For example, a SIPOS deposition rate of 410 Å/min (typical for the AP SIPOS) corresponds to a deposition rate of 2.5 monolayers/sec taking the density of SIPOS to be the same as Si. In contrast, a deposition rate of 27 Å/min (typical for higher oxygen content LP SIPOS) corresponds to only one monolayer deposited every 6 sec. Therefore these films have more SiO₂ character than would be predicted by the statistical model. This SiO₂ character is evident in the infrared spectrum as well as the film stress and reactivity toward HF.

Model of SIPOS.—For the rapidly deposited AP SIPOS the statistical or random bonding model predicts a large fraction of Si(Si₄) tetrahedra—0.613 for SiO_{0.23} to 0.254 for SiO_{0.58} (see Table III). Within this network of amorphous Si¹³ are the remaining Si/O tetrahedra with less than 1% Si(O₄), that is, SiO₂. For the more slowly deposited LP SIPOS we

believe there is more SiO₂ character, that is, more Si(O₄) tetrahedra, and so for the same oxygen content the LP SIPOS should have more Si(Si₄) tetrahedra than the corresponding AP SIPOS film. The Si(Si₄) tetrahedra are expected to form a connected network (14) and, therefore, the random bonding model would predict for SIPOS a phase of Si and a phase of Si/O tetrahedra. Our results support the model of SIPOS deduced from ESCA (8) and electron diffraction (9).

Conclusions

AP and LP SIPOS films are different. The differences between the films depend on the rate of deposition: rapid for the AP and slow for the LP SIPOS.

An analysis of the transmission infrared spectra of AP and LP SIPOS leads us to conclude that LP SIPOS has more SiO₂ character than an AP SIPOS film with the same oxygen content under the deposition conditions described herein. The infrared data for AP SIPOS films can be explained by a statistical model of Si-O bonding. For these SIPOS films the incoming O atom does not have time to find an Si atom already bonded to an O atom and so statistics govern the deposition and the distribution of Si-O bonds. For the slowly deposited SIPOS there is enough time for some of the incoming O atoms to find the already oxygen-bonded Si atom and so there is more SiO₂ character to the slowly deposited SIPOS than would be predicted by the statistical model.

Stress measurements and reactivity of SIPOS films to HF are consistent with the interpretation of the shift to higher frequency for the strong infrared absorption of LP SIPOS films.

Manuscript submitted Jan. 21, 1980; revised manuscript received May 5, 1980. This was Paper 572 presented at the Los Angeles, California Meeting of the Society, Oct. 14-19, 1979.

Any discussion of this paper will appear in a Discussion Section to be published in the June 1981 JOURNAL. All discussions for the June 1981 Discussion Section should be submitted by Feb. 1, 1981.

Publication costs of this article were assisted by Bell Laboratories.

REFERENCES

- H. Mochizuki, T. Aoki, H. Yamoto, M. Okayama, M. Abe, and T. Ando, *Suppl. Jpn. J. Appl. Phys.*, **15**, 35 (1976); also, T. Matsushita, T. Aoki, T. Otsu, H. Yamoto, H. Hayashi, M. Okayama, and Y. Kawana, *ibid.*, **15**, 41 (1976).
- H. R. Maxwell, Jr. and W. R. Knolle, Paper 166 presented at The Electrochemical Society Meeting, Boston, Massachusetts, May 6-11, 1979.
- H. R. Maxwell, Jr. and W. R. Knolle in "Semiconductor Characterization Techniques," P. A. Barnes and G. A. Rozgony, Editors, p. 180, The Electrochemical Society Softbound Proceedings Series, Princeton, N.J. (1978).
- W. A. Pliskin and S. J. Zanin in "Handbook of Thin Film Technology," L. I. Maissel and R. Glang, Editors, McGraw-Hill Book Co., New York (1970).
- H. R. Maxwell, Jr. and W. R. Knolle, Paper 296 presented at The Electrochemical Society Meeting, Hollywood, Florida, Oct. 5-10, 1980.
- W. Bruegel, "An Introduction to Infrared Spectroscopy," p. 301, John Wiley and Sons, New York (1962).
- W. Bruegel, "An Introduction to Infrared Spectroscopy," p. 292, John Wiley and Sons, New York (1962).
- M. Hamasaki, T. Adachi, S. Wayakama, and M. Kikuchi, *J. Appl. Phys.*, **49**, 3987 (1978).
- J. T. McGinn and A. M. Goodman, *Appl. Phys. Lett.*, **34**, 601 (1979).
- A. K. Sinha, H. J. Levinstein, and T. E. Smith, *J.*

- Appl. Phys.*, **49**, 2423 (1978).
 11. H. R. Philipp, *J. Phys. Chem. Solids*, **32**, 1935 (1971).
 12. G. V. Jorgenson and G. K. Wehner, *J. Appl. Phys.*, **36**, 2672 (1965).
 13. H. R. Maxwell, Jr., A. R. Hartman, Jr., and T. T. Sheng, *This Journal*, **125**, 257C (1978).
 14. J. W. Cahn, *J. Chem. Phys.*, **42**, 93 (1965).

Continuum Formulation of Spreading Resistance Correction Factors

John Albers

National Bureau of Standards, Electron Devices Division, Washington, DC 20234

ABSTRACT

A continuum formulation of spreading resistance correction factors is derived from the Choo *et al.* recursion relation for the kernel of the spreading resistance correction factor integral. Specifically, a differential equation for the kernel of the correction factor integral is derived in the limit as the layer thickness approaches zero. The resulting differential equation is nonlinear and inhomogeneous but can be transformed into a linear second order equation which can be solved analytically in several cases. The continuum form of the correction factor is compared with the correction factor generated from the finite-layer thickness version of the Laplace equation description for the case of an exponentially varying resistivity. Depending upon the number of layers used, the exponential constant, and the total thickness of the structure, the continuum and discrete forms of the correction factor differ by factors as large as 2.75 thus indicating a limitation in the accuracy of finite layer algorithms for spreading resistance data interpretation.

The multilayer Laplace equation description of spreading resistance described by Schumann and Gardner (1, 2) is based upon the assumption that the resistivity of each of the layers used in the model is constant over the entire thickness of the layer. The resistivity is then assumed to change abruptly at the interface between the layers. However, the probes of a spreading resistance apparatus view the material as a continuum. This distinction leads to a possibility of error in the analysis depending upon such variables as material thickness and the actual rate of change of the resistivity over distances comparable to the thickness of the layers used in the multilayer analyses. Both Schumann and Gardner and Choo *et al.* (3) observed that the calculated correction factor depends upon the number of layers used in the calculation. This observation is, of course, due to the failure of the basic assumption of constant resistivity over the thickness of the layer. Both sets of authors found that up to 50 layers are required to ensure convergence of the resulting calculated correction factor to within 5%. However, the dependence of the relation between the calculated correction factor and the number of layers upon such variables as the rate of change of the resistivity with depth, the substrate resistivity, and the total thickness of the structure is not evident.

The purpose of this paper is to present an exact solution to this problem by allowing the layer thickness to approach zero. The limiting process gives rise to a differential equation for the kernel of the correction factor integral in terms of the derivative of the natural logarithm of the resistivity. The differential equation so derived is nonlinear and inhomogeneous, but because it is of the Riccati type (4) it can be transformed into a linear second order differential equation which can be solved analytically for several forms of the resistivity. This analysis provides the basis for the investigation of the error incurred in the use of the finite-layer thickness algorithms in the analysis of spreading resistance data.

Key words: resistivity, interface, Laplace equation.

Derivation of the Continuum Differential Equation

The multilayer solution of Laplace's equation relates the spreading resistance of an n -layer structure to the resistivities of the n layers through the relation (1, 2)

$$R_n = \frac{\rho_n}{2a} CF_n \quad [1]$$

where ρ_n is the resistivity of the layer contacted by the probes, a is the effective electrical contact radius of the probes, and CF_n is the n -layer correction factor which depends upon the resistivities of the n layers. Specifically, the correction factor for the two-probe configuration may be expressed as (1, 2)

$$CF_n = \frac{4}{\pi} \int_0^\infty A_n(\lambda) \left\{ \frac{J_1(\lambda a)}{\lambda a} - \frac{J_0(\lambda S)}{2} \right\} \sin(\lambda a) \frac{d\lambda}{\lambda} \quad [2]$$

where S is the separation between the probes, $J_0(X)$ and $J_1(X)$ are Bessel functions of zero and first order, respectively, and λ is the integration variable. The explicit dependence of the kernel of the correction factor integral, $A_n(\lambda)$, on the resistivities of the n layers and the layer thickness, t , has been suppressed for simplicity. As noted by Choo *et al.* (3), the dependence of the kernel of the correction factor integral upon the resistivities of the n layers may be obtained from the original formulation of the problem by Schumann and Gardner; but it is more convenient to introduce the functions $T_m(\lambda)$, defined as

$$T_m(\lambda) = \rho_m A_m(\lambda) \quad [3]$$

where $m = 1, \dots, n$. The utility of these functions is that they are related to each other by means of the recursion relations

$$T_m(\lambda) = \frac{W(\lambda t)\rho_m + T_{m-1}(\lambda)}{1 + W(\lambda t)T_{m-1}(\lambda)/\rho_m} \quad (m = 2, \dots, n) \quad [4]$$

where all layers are chosen to have the same thickness, t

$$T_1(\lambda) = \rho_1 \quad [5]$$

and

$$W(\lambda t) = \frac{1 - \exp(-2\lambda t)}{1 + \exp(-2\lambda t)} \quad [6]$$

The layer indexes are chosen such that ρ_1 is the resistivity of the deepest layer and ρ_n is that of the surface layer.

Before considering the limit as t approaches zero, it is important to note from Eq. [4]-[6] that

$$T_m(0) = T_{m-1}(0) = \dots = T_1(0) \quad [7]$$

and hence from Eq. [3]

$$A_m(0) = \rho_1/\rho_m \quad [8]$$

i.e., the value of the kernel of the correction factor at $\lambda = 0$ is uniquely determined by the ratio of the substrate resistivity and the resistivity of the layer being considered. Also, it can be shown from Eq. [3], [4], and [6] that

$$\lim_{\lambda \rightarrow \infty} A_m(\lambda) = 1 \quad [9]$$

Equations [8] and [9] in conjunction with the condition

$$A_1(\lambda) = 1 \quad [10]$$

which follows from Eq. [3] and [5], provide constraints and the initial condition for the solution of the continuum model differential equation.

The basis for calculating the continuum limit of the multilayer equations is founded in the observation that if the position of the first layer is chosen as the origin of a coordinate system and the positions of the m th and $(m-1)$ st layers are taken as x and $x-t$, respectively, then the recursion relation (Eq. [4]) takes on the form

$$T(x, \lambda) = \frac{W(\lambda t)\rho(x) + T(x-t, \lambda)}{1 + W(\lambda t)T(x-t, \lambda)/\rho(x)} \quad [11]$$

This recursion relation defines a function $[T(x, \lambda)]$ at the position x in terms of another function $[\rho(x)]$ evaluated at the same position and the function being defined $[T(x-t)]$, evaluated at the position $x-t$. It is important to emphasize that Eq. [11] is really Eq. [4] cast in a version suitable for calculating the continuum (zero layer thickness) limit. The values of x allowed in Eq. [11] are $x = nt$ where $n = 1, 2, \dots$. The functions $\rho(x)$, $A(x, \lambda)$, and $T(x, \lambda)$ as used in the above are evaluated at a discrete set of points. Once the continuum limit has been taken, $\rho(x)$, $A(x, \lambda)$, and $T(x, \lambda)$ will be functions of the continuous variable x . After some rearrangement, Eq. [11] may be written in the form

$$\frac{T(x, \lambda) - T(x-t, \lambda)}{W(\lambda t)} = \rho(x) - \frac{T(x, \lambda)T(x-t, \lambda)}{\rho(x)} \quad [12]$$

From Eq. [6], it can be shown that $W(\lambda t)$ approaches zero as λt . Hence, for sufficiently small t , $W(\lambda t)$ may be replaced by λt . Further, the derivative $dT(x, \lambda)/dx$ is defined as $\lim_{t \rightarrow 0} \frac{T(x, \lambda) - T(x-t, \lambda)}{t}$. Then in the

limit as t approaches zero, Eq. [12] becomes

$$\frac{dT(x, \lambda)}{dx} = \lambda \left\{ \rho(x) - \frac{T^2(x, \lambda)}{\rho(x)} \right\} \quad [13]$$

which is a differential equation for the function $T(x, \lambda)$ which is to be solved subject to the initial condition

$$T(0, \lambda) = \rho(0) \quad [14]$$

However, the principal concern of the present paper is in a differential equation for the kernel of the correction factor integral. Hence, making use of the continuum form of Eq. [3], i.e.

$$T(x, \lambda) = \rho(x)A(x, \lambda) \quad [15]$$

Eq. [13] may be written in the form

$$\frac{dA(x, \lambda)}{dx} + F(x)A(x, \lambda) + \lambda A^2(x, \lambda) - \lambda = 0 \quad [16]$$

where the function, $F(x)$, is defined as

$$F(x) = \frac{1}{\rho(x)} \frac{d\rho(x)}{dx} = \frac{d \ln \rho(x)}{dx} \quad [17]$$

Equation [16] is nonlinear and inhomogeneous, but is of the Riccati type (4). Hence, under the transformation

$$A(x, \lambda) = \frac{1}{\lambda U(x, \lambda)} \frac{dU(x, \lambda)}{dx} \quad [18]$$

Eq. [16] may be written in the form

$$\frac{d^2U(x, \lambda)}{dx^2} + F(x) \frac{dU(x, \lambda)}{dx} - \lambda^2 U(x, \lambda) = 0 \quad [19]$$

Equations [17]-[19] form the central result of the analysis.

The above formulation may be used to calculate the continuum form of the kernel of the correction factor integral and, by numerical integration of Eq. [2], the correction factor and, hence, spreading resistance. For a specific choice of the resistivity function, $\rho(x)$, and the function $F(x)$ is calculated according to Eq. [17] and is used in Eq. [19] to obtain the function $U(x, \lambda)$. As Eq. [19] is a second order linear equation, two constants of integration appear in the solution. Calculation of $A(x, \lambda)$ from $U(x, \lambda)$ by means of Eq. [18] and imposing the initial condition on $A(x, \lambda)$, i.e., $A(0, \lambda) = 1$, eliminates the need for an explicit form for the two constants of integration. The solution, $A(x, \lambda)$, is required to satisfy the constraints that: (i) $A(x, 0) = \rho(0)/\rho(x)$, and (ii) $\lim_{\lambda \rightarrow \infty} A(x, \lambda) = 1$ which have been previously discussed.

It is of interest to note that the resistivity enters Eq. [19] as $d \ln \rho(x)/dx$. Because the resistivity vs. depth for most semiconductor device applications is approximately of the form of an exponential or a Gaussian, the function, $F(x)$, in Eq. [19] has a simple form. It must be emphasized that the substrate point is used as the origin of the coordinate system in the above development and hence all functions and their derivatives are defined relative to that point.

Calculation of Kernel for Uniform Resistivity Material

As an example of the continuum form of the kernel of the correction factor integral as presented in Eq. [17]-[19], consider the case of a material of uniform resistivity $\rho(x) = \text{const}$. In this case, $F(x) = 0$ and Eq. [19] takes on the form

$$\frac{d^2U(x, \lambda)}{dx^2} - \lambda^2 U(x, \lambda) = 0 \quad [20]$$

which has the general solution

$$U(x, \lambda) = C_1 \exp(-\lambda x) + C_2 \exp(\lambda x) \quad [21]$$

Using Eq. [18] and [21] to calculate $A(x, \lambda)$ and imposing the initial condition on $A(x, \lambda)$, i.e., $A(0, \lambda) = 1$, leads to the conclusion that $C_1 = 0$. Hence, for a material of uniform resistivity, the kernel of the correction factor integral is unity for all x and λ . The same conclusion may be obtained from the finite layer thickness formulation (see Eq. [3]-[5]).

Calculation of the Kernel for a Material Having Exponential Resistivity

Consider a material having a resistivity defined relative to that of the substrate ($x = 0$) by

$$\rho(x) = \rho(0) \exp(Cx) \quad [22]$$

where the exponential constant, C , can have either positive or negative values. In this case, the function $F(x)$ takes on the form, $F(x) = C$ and equation for the continuum form of the kernel of the correction factor integral becomes

$$\frac{d^2U(x, \lambda)}{dx^2} + C \frac{dU(x, \lambda)}{dx} - \lambda^2 U(x, \lambda) = 0 \quad [23]$$

which, being a second order linear equation with constant coefficients, has the general solution

$$U(x, \lambda) = C_1 \exp(m^+x) + C_2 \exp(m^-x) \quad [24]$$

where

$$m^\pm = \frac{-C \pm (C^2 + 4\lambda^2)^{1/2}}{2} \quad [25]$$

Substituting Eq. [24] into Eq. [18] and imposing the boundary condition, $A(0, \lambda) = 1$, yields the following relation for the constants

$$C_1 = C_2 \Gamma(\lambda) \quad [26]$$

where $\Gamma(\lambda)$ is defined as

$$\Gamma(\lambda) = \frac{(\lambda - m^-)}{(m^+ - \lambda)} \quad [27]$$

Hence, the kernel of the correction factor integral for an exponentially varying resistivity may be written in the form

$$A(x, \lambda) = \frac{\Gamma(\lambda) m^+ \exp(m^+x) + m^- \exp(m^-x)}{\Gamma(\lambda) \lambda \exp(m^+x) + \lambda \exp(m^-x)} \quad [28]$$

From Eq. [25] it is straightforward to obtain

$$m^+ m^- = -\lambda^2 \quad [29]$$

Dividing the numerator and denominator of Eq. [28] by $\exp(m^+x)$ and making use of Eq. [29] yields the following equation for the kernel of the correction factor for an exponentially varying resistivity

$$A(x, \lambda) = \frac{(m^+ + \lambda) - (m^- + \lambda) \exp(-\gamma x)}{(\lambda - m^-) + (m^+ - \lambda) \exp(-\gamma x)} \quad [30]$$

where

$$\gamma = (C^2 + 4\lambda^2)^{1/2} \quad [31]$$

One of the important conclusions to be drawn from Eq. [30] is that the kernel depends only upon the variables C , x , and λ and does not depend upon the value of the resistivity *per se*. From Eq. [30], it is relatively straightforward to show that: (i) $A(0, \lambda) = 1$, (ii) $A(x, 0) = \exp(-Cx)$, and (iii) $\lim_{\lambda \rightarrow \infty} A(x, \lambda) = 1$. Further, in the limit as C approaches zero, the kernel of the correction factor for an exponentially varying resistivity as given by Eq. [30] reduces to the uniform layer result.

Comparison of Continuum and Discrete Correction Factors for an Exponentially Varying Resistivity

In order to gain insight into the difference between the correction factor as calculated from the continuum formulation and as calculated from the finite layer thickness formulation, several exponentially varying resistivities were used to calculate the correction factor according to the continuum form for the kernel, Eq. [30], and according to the finite-layer thickness form, for the kernel, Eq. [2]-[6]. In all cases, a probe radius of 2 μm and a probe separation of 50 μm were used in the calculations.

Specifically, a resistivity having a value of $10^{-3} \Omega \cdot \text{cm}$ at the surface and a value of $10^8 \Omega \cdot \text{cm}$ at the substrate was used to simulate a junction-like structure. For the simulations of a high resistivity layer over a low resistivity layer, two situations were used. The first has a surface resistivity of $10^8 \Omega \cdot \text{cm}$ and a substrate resistivity of $10^{-3} \Omega \cdot \text{cm}$. The second was less strongly graded, having a surface resistivity of $10^1 \Omega \cdot \text{cm}$ and a substrate resistivity of $10^{-3} \Omega \cdot \text{cm}$. In all of the above cases, calculations were performed for total layer thicknesses of 1, 5, 10, 50, and 100 μm . The continuum form of the correction factor was evaluated at 51 points, and the finite-layer thickness approximation to the correction factor was evaluated for the 51 layer case. In addition, the various 1 μm structures were investigated with varying number of layers in order to determine the effect of the number of layers used in the finite-layer thickness formulation.

In all cases considered, the calculated correction factor is found to be approximately constant over most of the structure. The results of the calculation and comparison of the continuum and finite-layer thickness form the correction factor for a resistivity which is meant to mimic junction structure are presented in Table I. The surface values of the continuum and finite-layer thickness correction factor are presented and the ratio is also given. It is important to notice that the ratio is approximately constant over the range of layer thicknesses considered.

The results of the equivalent calculation for the cases of a surface resistivity of $10^8 \Omega \cdot \text{cm}$ and $10^1 \Omega \cdot \text{cm}$ and a substrate resistivity of $10^{-3} \Omega \cdot \text{cm}$ are presented in Tables II and III, respectively.

The results of the calculation of the dependence of the calculated correction factor upon the number of layers used in the calculation of the finite-layer

Table I. Comparison of continuum and finite-layer thickness surface correction factors for exponential resistivity (surface resistivity = $10^{-3} \Omega \cdot \text{cm}$, substrate resistivity = $10^8 \Omega \cdot \text{cm}$)

Thickness (μm)	Step (μm)	Exponential constant	CF(cont)	CF(disc)	CF(cont)/CF(disc)
1	0.02	25.32844	109.2	85.67	1.275
5	0.1	5.065687	21.936	17.216	1.274
10	0.2	2.532844	11.102	8.720	1.273
50	1.0	0.5065687	2.698	2.157	1.251
100	2.0	0.2532844	1.753	1.441	1.216

Table II. Comparison of continuum and finite-layer thickness surface correction factors for exponential resistivity (surface resistivity = $10^8 \Omega \cdot \text{cm}$, substrate resistivity = $10^{-3} \Omega \cdot \text{cm}$)

Thickness (μm)	Step (μm)	Exponential constant	CF(cont)	CF(disc)	CF(cont)/CF(disc)
1	0.02	-25.32844	2.17E-2	2.77E-2	1.274
5	0.1	-5.065687	0.101	0.128	1.269
10	0.2	-2.532844	0.184	0.232	1.262
50	1.0	-0.5065687	0.515	0.628	1.219
100	2.0	-0.2532844	0.661	0.781	1.181

Table III. Comparison of continuum and finite-layer thickness surface correction factors for exponential resistivity (surface resistivity = $10^1 \Omega \cdot \text{cm}$, substrate resistivity = $10^{-3} \Omega \cdot \text{cm}$)

Thickness (μm)	Step (μm)	Exponential constant	CF(cont)	CF(disc)	CF(cont)/CF(disc)
1	0.02	-9.21034	5.81E-2	6.36E-2	1.095
5	0.1	-1.842068	0.237	0.259	1.093
10	0.2	-0.921034	0.378	0.413	1.091
50	1.0	-0.1842068	0.719	0.775	1.08
100	2.0	-0.0921034	0.820	0.872	1.06

thickness description are presented in Fig. 1-3. Figure 1 depicts the results for the calculation of the correction factor for a surface resistivity of $10^{-3} \Omega \cdot \text{cm}$ and a substrate resistivity of $10^8 \Omega \cdot \text{cm}$. This, as mentioned previously, is meant to be an approximation to a junction isolated structure. Figure 2 presents the results for the case of a surface resistivity of $10^8 \Omega \cdot \text{cm}$ and a substrate resistivity of $10^{-3} \Omega \cdot \text{cm}$ while the results of the calculation for a surface resistivity of $10^1 \Omega \cdot \text{cm}$ and a substrate resistivity of $10^{-3} \Omega \cdot \text{cm}$ are presented in Fig. 3. Both are meant to represent a high resistivity layer over a low resistivity layer. It is seen that for each case significant errors arise in the finite layer approximation formulation and that the magnitude of the error is almost exactly equal to the normalized change of the resistivity over a distance of one-half the step size, *i.e.*, $(\rho(x) - \rho(x - t/2))/\rho(x) = 1 - \exp(-Ct/2)$. For strongly graded structures, at least 200 points are required to obtain a 6% accuracy level for the finite layer approximation. For less strongly graded structures, at least 50-100 points are needed to assure 6% accuracy.

It is possible that errors in the finite-layer approximation might be reconciled by shifting the x-axis one-half interval or by redefining the probe location (again by one-half interval).

Discussion

It is important to note one of the limitations of the Schumann and Gardner formulation of the Laplace equation description of spreading resistance. In the original formulation (1,2), the coefficients of the expansion of the potential in each of the layers in terms of the solution of Laplace's equation for a uniform, laterally semi-infinite material are obtained by means of assumed continuity of the potential and

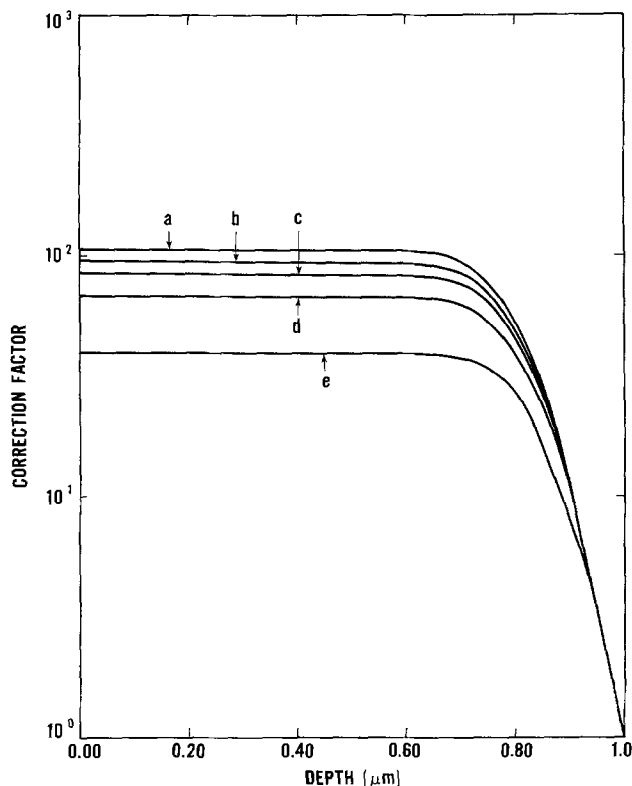


Fig. 1. Correction factor calculated from continuum formulation and correction factors calculated from finite-layer thickness model for variable number of layers for a $1 \mu\text{m}$ structure with a surface resistivity of $10^{-3} \Omega \cdot \text{cm}$ and a substrate resistivity of $10^8 \Omega \cdot \text{cm}$. Continuum calculated correction factor (a), finite-layer thickness correction factors calculated with 101 layers (b), 51 layers (c), 26 layers (d), and 11 layers (e).

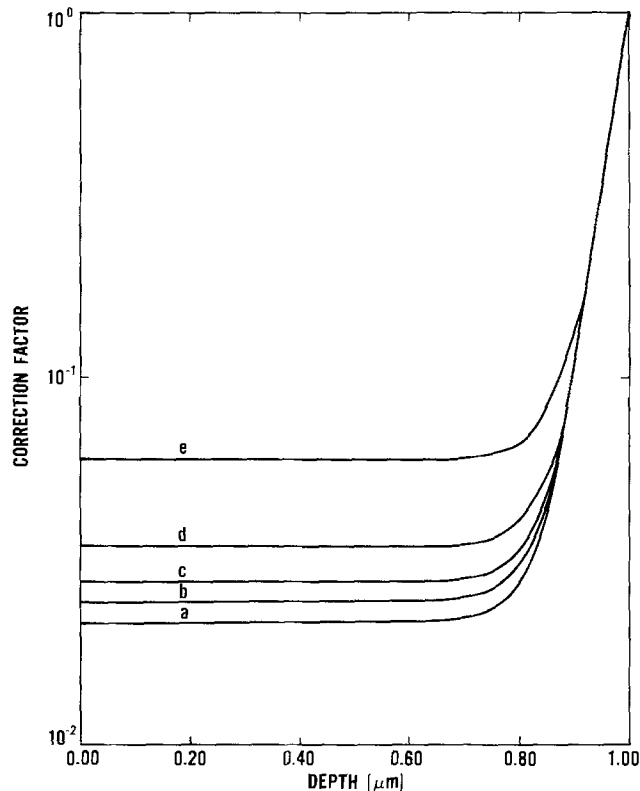


Fig. 2. Correction factor calculated from continuum formulation and correction factors calculated from finite-layer thickness model for variable number of layers for a $1 \mu\text{m}$ structure with a surface resistivity of $10^8 \Omega \cdot \text{cm}$ and a substrate resistivity of $10^{-3} \Omega \cdot \text{cm}$. Continuum calculated correction factor (a), finite-layer thickness correction factors calculated with 101 layers (b), 51 layers (c), 26 layers (d), and 11 layers (e).

the current density across the interface between the layers.

For the case of an insulating but nonjunction type substrate, the correction factor for the substrate point is approximately unity, independent of the value of the substrate resistivity. This is inherent in the use of Eq. [5] for the finite-layer calculation or the use of Eq. [10] for the continuum calculation. For the case of an insulating junction structure, the same conclusion as above also holds. Again, this may be directly traced to the use of Eq. [5] or [10]. The resistivity in the region of the insulating interface may be made as large as possible; however, the correction factor as calculated by means of the Schumann and Gardner equations will always give a correction factor which is approximately unity. Spreading resistance measurements made on junction-isolated structures indicate that the correction factor becomes very large in the vicinity of the junction. This is, of course, due to the restriction of the current path between the probes owing to the presence of the junction. This current restriction is not contained in the Laplace equation description of Ref. (1) and (2).

There is another point which further hinders the use of the Laplace equation description both in the generation of model data and in the analysis of experimental data for junction structures. This point focuses upon the depletion region present in the region of the junction. The accompanying charge accumulation would indicate that the approximation of the Poisson equation by the Laplace equation, which is far easier to solve, is not justifiable. Away from the depletion region local charge neutrality is certainly maintained, thus, justifying the use of Laplace's equation. Consequently, the use of a very high resistivity to model a junction region is not correct in the junction region itself but is useful in the region

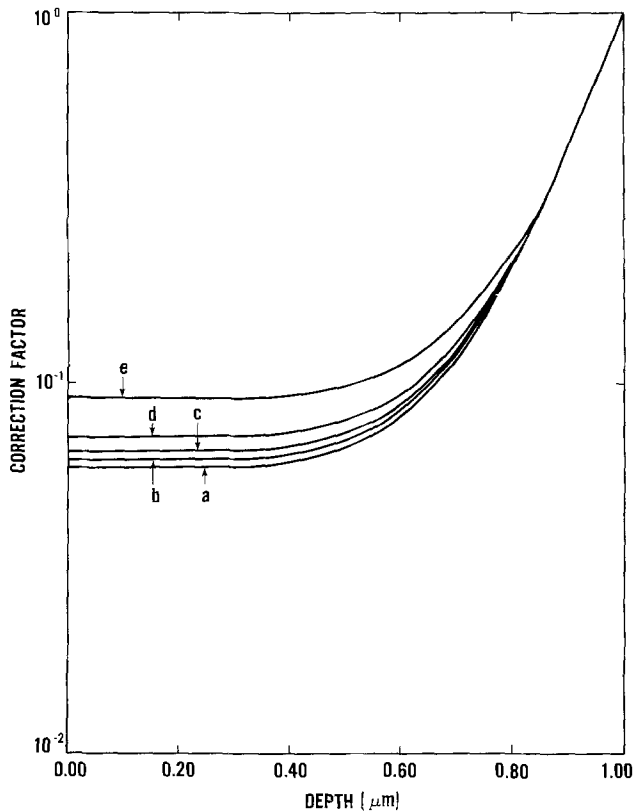


Fig. 3. Correction factor calculated from continuum formulation and correction factors calculated from finite-layer thickness model for variable number of layers for a $1 \mu\text{m}$ structure with a surface resistivity of $10^1 \Omega \cdot \text{cm}$ and a substrate resistivity of $10^{-3} \Omega \cdot \text{cm}$. Continuum calculated correction factor (a), finite-layer thickness correction factors calculated with 101 layers (b), 51 layers (c), 26 layers (d), and 11 layers (e).

away from the junction. Consequently, the correction factor which is calculated from a resistivity which is meant to mimic an insulating junction structure will be greater than unity away from the high resistivity end point.

It should be noted that closed form analytic solutions of Eq. [17]-[19] can be obtained only for a constant resistivity or an exponentially varying resistivity. For resistivities of the Gaussian form, a power series solution can be obtained. These, however, cannot be summed to obtain a closed form solution.

Conclusions

A differential equation has been derived for the kernel of the correction factor integral in the limit of zero layer thickness. The equation has been solved analytically for the case of an exponentially varying resistivity and the corresponding calculated correction factors have been compared with the correction factors calculated from the finite-layer thickness formulation of the Laplace equation description of spreading resistance. For a 51 layer approximation, the differences fall in the range of approximately 6-27% for the cases considered. When fewer layers are used in the approximation, the differences are larger. This implies that the use of finite-layer thickness algorithms on a limited data base is subject to inherent errors. This is especially important in the

analysis of spreading resistance data on very shallow implants (typically in the $0.1 \mu\text{m}$ range) where state-of-the-art bevelling techniques provide for 10-20 data points at most to be obtained in the shallow layer (5). The results of the calculations presented in Table I indicate that the finite-layer algorithms predict correction factors which are too small. This, in turn, would lead to dopant profiles which are lower in concentration relative to the actual profile. The same conclusion would be obtained for deep diffusions ($50\text{-}100 \mu\text{m}$) typical of power device structures where the total thickness of the structure and the need for a reasonable size data set would necessitate a depth spacing in the $1\text{-}2 \mu\text{m}$ range. For these deep structures, the above calculations indicate that increased accuracy of profile determination can be achieved by increasing the number of points in the data set.

The above conclusions would further lead to the prediction that the sheet resistance obtained from finite-layer thickness algorithm analysis of spreading resistance data on junction-type structures are large when compared with four-probe sheet resistance measurements. This follows from the observation that the continuum correction factor is typically larger than that obtained from the layered description.

For a buried layer structure, the results of the calculations presented in Tables II and III and Fig. 2 and 3 indicate that finite-layer algorithms predict correction factors which are too large. Hence, the dopant densities in profiles obtained from finite-layer algorithms are larger than those in the actual profile. Further, the sheet resistance obtained from finite-layer thickness algorithm analysis of structures of this type are small compared to four-probe sheet resistance measurements.

Acknowledgments

The author wishes to acknowledge discussions with James R. Ehrstein and David R. Myers concerning the discrete and continuum formulations of spreading resistance. This research was conducted as part of the NBS Semiconductor Technology Program and was supported by the Defense Advanced Research Projects Agency (Order 2397) and the NBS.

Manuscript submitted Oct. 1, 1979; revised manuscript received May 12, 1980.

Any discussion of this paper will appear in a Discussion Section to be published in the June 1981 JOURNAL. All discussions for the June 1981 Discussion Section should be submitted by Feb. 1, 1981.

Publication costs of this article were assisted by the National Bureau of Standards.

REFERENCES

1. P. A. Schumann and E. E. Gardner, *This Journal*, **116**, 87 (1969).
2. E. E. Gardner and P. A. Schumann, *Solid-State Electron.* **12**, 371 (1969).
3. S. C. Choo, M. S. Leong, and K. L. Kuan, *ibid.*, **19**, 561 (1976).
4. H. T. Davis, "Introduction to Nonlinear Differential and Integral Equations," pp. 57-78, Dover, New York (1962).
5. J. R. Ehrstein, in "Measurement Techniques for High Power Semiconductor Materials and Devices: Annual Report, October 1, 1977 to September 30, 1978," F. F. Oettinger, Editor, NBSIR 79-1756 (July 1979).

Photoelectrolysis of Water with Natural Mineral TiO₂ Rutile Electrodes

J. F. Julião,^{*1} Franco Decker,^{*} and M. Abramovich^{**}

UNICAMP, Instituto de Física, Campinas, S.P., Brazil

ABSTRACT

Natural mineral rutile (TiO₂) was studied as anode for photoelectrolysis of water. Both its photoelectrochemical behavior and semiconducting properties are examined in comparison with those of Fe-doped synthetic single crystal TiO₂, the latter independently studied to simulate the high impurity content existent in the mineral. The natural and synthetic Fe-doped TiO₂ electrodes showed a performance comparable to that of arc-plasma sprayed raw rutile, including a low breakdown potential. Flatband potentials and donor densities were determined from Mott-Schottky plots and evidence for deep and shallow donors is discussed. Photoresponse measurements allowed us to verify the influence of the iron impurities on the performance of such electrodes.

The photoelectrolysis of water has been investigated by several authors (1-7) in the last few years. Electrodes of polycrystalline TiO₂ made by hot-pressing powdered rutile (2), by oxidation of metal foils (2-4), and by chemical vapor deposition (CVD) (5, 6) show a behavior similar to that of single crystal TiO₂ (7) and have the advantage of being easier to prepare. Until now, little attention has been paid to the semiconductor properties of natural TiO₂ rutile crystals, perhaps because these minerals are usually impure (8). However, it has been recently shown that impure polycrystalline TiO₂ electrodes, prepared by arc-plasma sprayed raw rutile powder (9), behave similarly to other polycrystalline ones with respect to photoelectrolysis. In the present paper we report the photoelectrochemical behavior of electrodes made either of single crystal or polycrystalline natural TiO₂, obtained from mines located in different regions of Brazil. These electrodes showed a performance comparable to that of synthetic single crystal or other polycrystalline TiO₂ electrodes. The results demonstrate the possibility of using low cost raw materials in primitive form for photoelectrolysis of water.

Since large amounts of iron impurities were detected by x-ray analysis in the mineral samples, their effect on the performance of the photoelectrolytic cell is discussed by comparing the behavior of the natural rutile electrodes with that of two intentionally Fe-doped TiO₂ synthetic single crystal electrodes.

Experimental Procedure

Sample characterization and heat-treatments.—Samples of titanium oxide were obtained from three Brazilian states: Bahia, Ceará, and Minas Gerais. X-ray diffractometry and powder diffraction analysis showed that the samples from Ceará and Minas Gerais were TiO₂ with rutile structure, while the sample from Bahia was closer to (Fe, Fe, Ti)_{1.71}O₃ (crichtonite). Figure 1 shows the diffraction data for the sample from Ceará

The rutile sample from Ceará was a dark stone and contained impurities of Fe, Cu, Pb, Mn, Ni, Cr, and Nb, with high predominance of iron, according to x-ray spectroscopic analysis. It was shown to be polycrystalline, from Laue diffraction analysis and from now on it will be labeled NPC TiO₂ (natural polycrystalline TiO₂). The rutile sample from Minas Gerais was a small, slightly violet, semitransparent

crystal and contained diverse impurities other than the Fe, which is, however, the predominant one. It was shown to be a single crystal, so that from now on it will be labeled NSC TiO₂ (natural single crystal TiO₂). Comparing the x-ray spectrograms we found that the NPC TiO₂ sample had a concentration of iron higher than the NSC TiO₂ sample.

Heat-treatment in a reducing atmosphere was used to obtain n-type semiconducting samples in the conditions described in the Table I. The high resistivity of the samples from Bahia did not decrease even after a prolonged treatment; therefore, its use as an electrode in the cell was not attempted. For the other natural rutile samples, the treatment decreased their resistivities and changed the relative intensity between the diffraction peaks, but not their relative positions. Therefore, we can conclude that the samples maintained their crystal structure, even though several defects were introduced in the lattice (8, 10, 11).

The synthetic TiO₂ single crystal was supplied by Materials Research Company and contained Si, Fe, Al, and Nb as its major impurities, according to data from the manufacturer.

To allow a comparison between natural and synthetic electrodes, and since Fe is the main impurity in natural rutile, we raised the Fe concentration in two synthetic single crystal samples by doping. Iron impurities were introduced by diffusing a thin film of Fe metal previously deposited on the sample surface by vacuum evaporation, following the method used by Andersson (12). The final iron concentrations were 290 and 410 ppm and these doped samples will be labeled, respectively, SSC-Fe(A) TiO₂ and SSC-Fe(B) TiO₂. Another synthetic single crystal TiO₂ sample

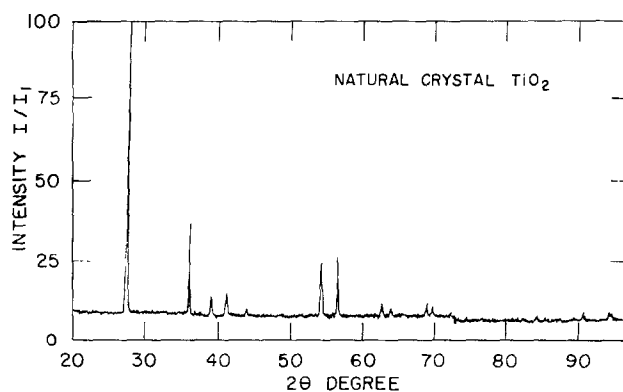


Fig. 1. X-ray diffraction data indicating the rutile structure for the natural polycrystal (NPC) TiO₂.

* Electrochemical Society Student Member.

** Electrochemical Society Active Member.

¹ Permanent address: Departamento de Física, Universidade Federal do Ceará, Caixa Postal 1262, 60 000 Fortaleza, CE, Brazil.

Key words: natural, polycrystalline, semiconductor, doping, electrode, photoelectrolysis.

Table I. Reduction conditions used for the various samples studied. The reduction atmosphere was 90% N₂ + 10% H₂ at 1 atm. T_r is the reduction temperature and t_r the reduction time. The table also shows the Fe-impurity contents and the final resistivity, ρ, for each sample.

TiO ₂ electrodes	Reduction T _r (°C)	Parameters t _r (min)	Resistivity (Ω-cm)	Fe-impurities (ppm)
NPC	800	60	3.8	Unknown
NSC	800	20	4.0 × 10 ²	Unknown
SSC	700	20	1.1 × 10 ²	60*
SSC-Fe(A)	700	20	1.0 × 10 ²	290
SSC-Fe(B)	700	20	1.7 × 10 ²	410

* Residual impurity, according to manufacturer analysis.

(SSC-TiO₂) was also used as a "standard" anode. In the Table I we give the reduction conditions, final resistivity, and Fe-impurities for each samples used here.

Electrode preparation.—The electrodes were prepared by cutting 1 mm thick slices from both the natural and the synthetic crystals with a diamond saw. The samples NSC, SSC, SSC-Fe(A), and SSC-Fe(B) samples had the (001) surface exposed. The NPC sample was cut so that its surface was visually free of cracks. The samples were then mechanically polished flat to optical grade, using diamond paste. Then, each crystal was washed with the following sequence: trichloroethylene, isopropanol, acetone, methanol, deionized water, concentrated HCl, and deionized water. After reduction treatments, ohmic contacts (checked with a curve tracer) were provided by rubbing In-Ga paste on the back crystal surface. A copper wire was then attached to the samples by means of Ag cement. Finally, the contact was coated with epoxy and the electrode was imbedded in a polyester capsule leaving an ~0.15 cm² active area exposed to the solution. Finally, each crystal was cleaned again following the procedure described above.

Electrochemical measurements.—The electrochemical measurements were performed in 1M NaOH electrolyte under potentiostatic conditions, using a three compartment cell, provided with a flat quartz window and a saturated calomel electrode (SCE) as the reference electrode. The counterelectrode was a Pt bright foil with 10 cm² area. The space charge capacitances were determined from measurements of impedance and phase angle between a-c current and a-c potential with a lock-in amplifier (PAR-124 A). For this purpose a small a-c voltage of 3 mV at 1 kHz was superimposed on the externally applied d-c voltage; other frequencies have also been used in the interval 10-10,000 Hz.

The photocurrent measurements with high intensity u.v. light (~80 mW/cm²) were performed using a 100W high pressure mercury lamp with the beam focused on the semiconductor electrode through a bandpass filter (WBS-320: 4000Å ≧ λ ≧ 2000Å). For spectral photoresponse measurements the light source used was a xenon arc lamp run through a monochromator giving ~1 mW/cm² intensity over the spectral region of interest. The intensity of light was measured by an IL 700 Research Radiometer with an SE-400 W detector. A digital electrometer (Keithley 616) was used to measure the potential vs. SCE of the counterelectrode.

The electrolyte in the cathode compartment was purged with high purity nitrogen. The solutions were prepared with commercially available reagents without further purification. Before each experiment the samples were rinsed with methanol (CH₃OH) and deionized water.

Results and Discussion

Flatband potential.—An easy method to obtain the flatband potential, V_{FB} (the particular value of the Fermi level for which the energy bands of the semiconductor are not bent), is to measure the space charge capacitance, C_{sc}, in function of the interface potential, V. In the case of highly doped semiconductors (16) the total capacitance C of the TiO₂/electrolyte interface is determined by C_{sc}, and described by the well-known Mott-Schottky equation

$$1/C_{sc}^2 = \frac{2}{q\epsilon\epsilon_0 N_D} \left(V - V_{FB} - \frac{kT}{q} \right) \approx \frac{1}{C^2} \quad [1]$$

where ε and ε₀ are the dielectric constants of TiO₂ and vacuum, respectively, N_D is the concentration of donors, V - V_{FB} gives the potential drop across the space charge layer and q and kT have the usual value.

Figures 2a and b show the Mott-Schottky plots for all samples, constructed from capacitance vs. electrode potential measurements at 1 kHz. Flatband potentials were obtained from the intercepts of 1/C² vs. V, and subtracting kT/q = 0.025V. Donor densities, N_D, were calculated from the slope of these curves. For the corresponding calculation a dielectric constant ε = 173 was used for single crystal (17), while for the polycrystalline sample we used an average value of ε = 120 (18). The slope and the intersection with the V axis depend on the frequency. Therefore, the values of V_{FB} and N_D, presented in Table II, are only approximate.

The 1/C² vs. V curves for the NPC and SSC-Fe(B) show a striking feature. They are not single straight lines but bent curves. This result may be interpreted by assuming two linear slopes for each 1/C² vs. V plot, with a steep slope at lower potentials and a much lower slope at higher anodic potentials. A break in the capacitance curve may occur if nonionized deep donor levels are present within the bulk (19). With increasing the band bending, however, the occupation of these levels may change within the space charge

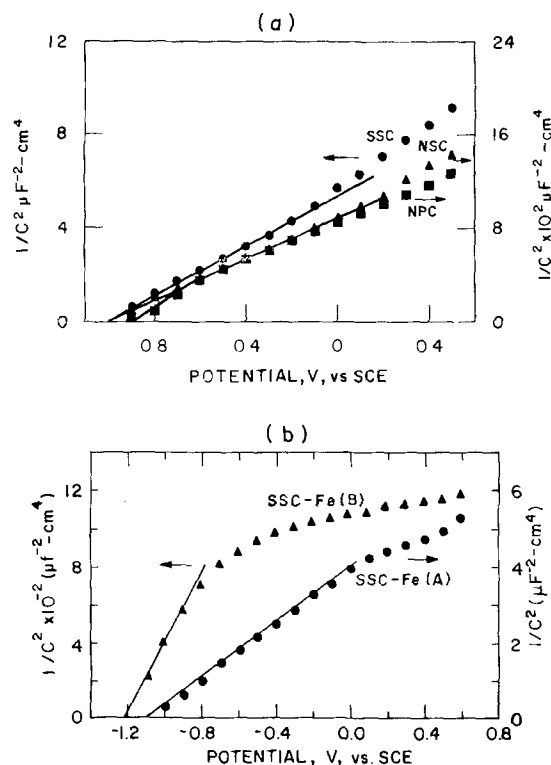


Fig. 2. Mott-Schottky plots for: (a) natural (NPC and NSC) and synthetic (SSC) TiO₂; (b) Fe-doped synthetic single crystal [SSC-Fe(A) and SSC-Fe(B)] TiO₂. The electrodes were in dark at T = 25°C in a solution 1M NaOH.

Table II. Onset potential for anodic photocurrent (V_o); flatband potential (V_{FB}), donor density (N_D), shallow (N_1), and deep (N_2) donor densities obtained from Mott-Schottky plots for various samples of TiO_2 in 1M NaOH, $pH = 13$. W_o is the space charge region thickness.

TiO ₂ electrodes	V_o (V vs. SCE)	V_{FB} (V vs. SCE)	V_C (V vs. SCE)	N_D (cm ⁻³)	N_1 (cm ⁻³)	N_2 (cm ⁻³)	$N_1 + N_2$ (cm ⁻³)	$W_o N_D$ (Å)	$W_o(N_1 + N_2)$ (Å)
NPC	-0.92	-0.88	~-0.6	—	9.2×10^{18}	5.8×10^{18}	1.5×10^{19}	—	$\sim 0.05 \times 10^4$
SSC-Fe(B)	-1.09	-1.19	~-0.9	—	4.4×10^{14}	4.3×10^{15}	4.7×10^{15}	—	2.0×10^4
SSC-Fe(A)	-1.03	-1.07	—	2.2×10^{14}	—	—	—	0.92×10^4	—
SSC	-1.00	-0.98	—	1.7×10^{17}	—	—	—	0.34×10^4	—
NSC	-0.96	-0.98	—	9.4×10^{14}	—	—	—	0.05×10^4	—

region. Assuming only one discrete energy level for such an additional donor of a density N , two Mott-Schottky slopes can be derived from Eq. [1], representing the existence of two kind of donor levels. The first slope, measured at small band bendings, is only determined by the ionized shallow donors with density N_1 , and the second by the sum of both the shallow and the deep donor levels with density $N = N_1 + N_2$: here, N_2 is the density of the deep donor levels. The critical potentials (V_C), where the slope changes value, represent the ionization potential for the deep donor and are given in Table II.

From considerations about the Fermi-Dirac distribution function governing the number of ionized donors, Kennedy and Frese (20) studying the change in slope for polycrystalline α -Fe₂O₃ showed that the relation below is valid

$$q(V_C - V_{FB}) \cong E_F - E_{D_2} \quad [2]$$

where E_F is the Fermi level and E_{D_2} is the deep donor level. Using this relation we can estimate from our data that the deep donor level is located in the energy gap ~ 0.3 eV below the Fermi level. Although we have not measured the position of the Fermi level relative to the bottom of the conduction band, it is known (10) that for highly reduced TiO₂ with an oxygen vacancy density of the order of 10^{17} cm⁻³, the Fermi level is located ~ 0.2 eV below the conduction band. The position of the deep donor level is then ~ 0.5 eV below the conduction band.

From EPR studies on Fe-doped single crystal TiO₂, Andersson (12) showed that strong reduction, made in vacuum, probably causes a transformation of Fe³⁺ into Fe²⁺ ions. These Fe²⁺ ions, will preferentially occupy the Fe²⁺ level near the conduction band that is vacant before the reduction treatment. This level is located ~ 0.5 eV below the conduction band, according to Mizushima (21). The evidence presented supports our proposition that the deep donor level is Fe²⁺, assuming that the reduction of the TiO₂ in an H₂ + N₂ atmosphere causes the same transformation between the Fe ions. It is interesting to note that a similar behavior for the Mott-Schottky plots was observed for polycrystalline α -Fe₂O₃ (20) in which the deep donor level is assigned also as being Fe²⁺.

Current-potential characteristics.—Figures 3a and b show the current-potential (I - V) characteristics of the different electrodes in 1M NaOH with $pH = 13$. In the dark and beyond a certain potential, V_{BR} , a significant increase in the anodic current was observed for the natural TiO₂ as well as for the synthetic Fe-doped TiO₂ electrodes. These breakdown potentials, V_{BR} , are in the range of 0.5-0.7 vs. SCE, close, therefore, to the values observed for some polycrystalline TiO₂ electrodes, made by arc-plasma sprayed raw rutile (0.4V) and by CVD or oxidation of metal foils (0.6-2.0V). For the SSC TiO₂ electrodes, we did not observe appreciable anodic currents for potentials up to 10V.

For TiO₂ the high anodic currents in the dark have been attributed to tunneling of electrons from the solution through the narrow space charge region into the conduction band (6); this tunneling process could occur via grain boundaries containing impurity atoms in polycrystalline samples (9). In our samples, how-

ever, the thickness of the space charge region is not the most important factor for occurrence of this current. In fact, with synthetic crystals a breakdown was observed associated with Fe doping and independently on the donor density N_D . Therefore, we conclude that in our samples the iron impurities play the most important role in the breakdown phenomenon, facilitating the tunneling of electrons from solution and into the conduction band. This tunneling of electrons is likely to occur via iron precipitates that are known to form on lattice defects in TiO₂ (12, 13). In fact, in our Fe-doped single crystal samples, reddish-brown iron precipitates were visually observed. This fact and the estimated thickness of the space charge region, W_o , listed in Table II support our hypothesis. In the NPC sample W_o is narrow and the formation of precipitates may be more accentuated because of the grain boundaries. This might explain the lower breakdown potential (0.5V) observed for such electrodes.

Under u.v. illumination (~ 80 mW/cm²) the electrodes show different values for the onset of anodic photocurrent, V_o . The measurements of V_o were performed by using a chopped light beam. Values of V_o close to V_{FB} were observed for all samples (see Table

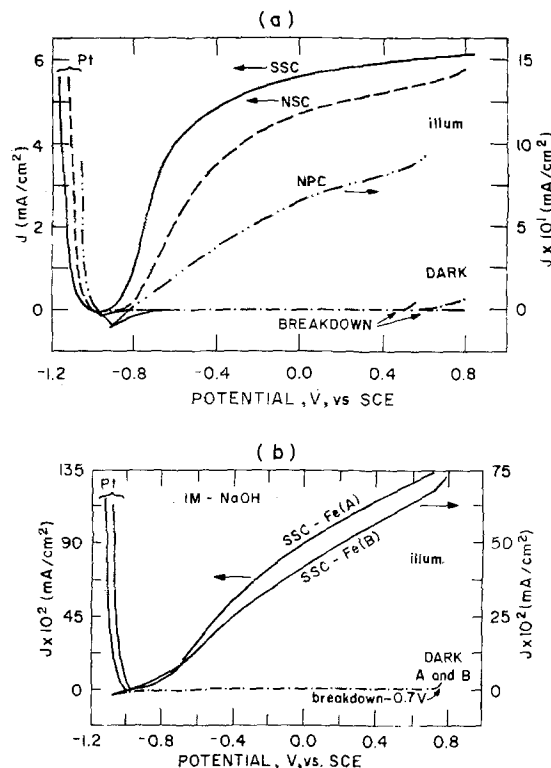


Fig. 3. Typical current-potential characteristics for n-TiO₂ electrodes in 1M NaOH, $pH = 13$, both in dark and under polychromatic u.v. illumination (~ 80 mW/cm²). (a) Synthetic single crystal (SSC), natural polycrystalline sample (NPC), and natural single crystal (NSC); (b) Fe-doped synthetic single crystal: SSC-Fe(A) and SSC-Fe(B). The electrolyte in the Pt compartment was deoxygenated with high purity nitrogen.

II). In electrolytes of lower pH, V_0 is shifted by 58 mV/pH in the direction of more positive potentials. The shape of the photocurrents *vs.* potential curves are different too; at 0V *vs.* SCE, the photocurrent density, J_0 , for the SSC and NSC electrodes is about four times larger than J_0 for the NPC and SSC-Fe(A) and about ten times larger than J_0 of the SSC-Fe(B) electrode. These results show that the photocurrent density is limited by the amount of Fe impurities in the material. A similar decrease in the value of the photocurrent density with the increase of Fe impurity contents in single crystals TiO_2 was also observed by Butler (14) and by Ghosh and Maruska (15). This behavior may be explained considering that the Fe ions act as traps for the photogenerated carriers, thus diminishing the current observed in the external circuit.

Quantum efficiency.—Figures 4a and b show the quantum efficiency η , (defined as the number of electrons flowing/incident photons), as a function of wavelength for the different electrodes used in this work. They were calculated from their spectral photoresponse, corrected for the spectral distribution of the light source and for the reflection at the quartz window. The electrodes were polarized at 0V *vs.* SCE

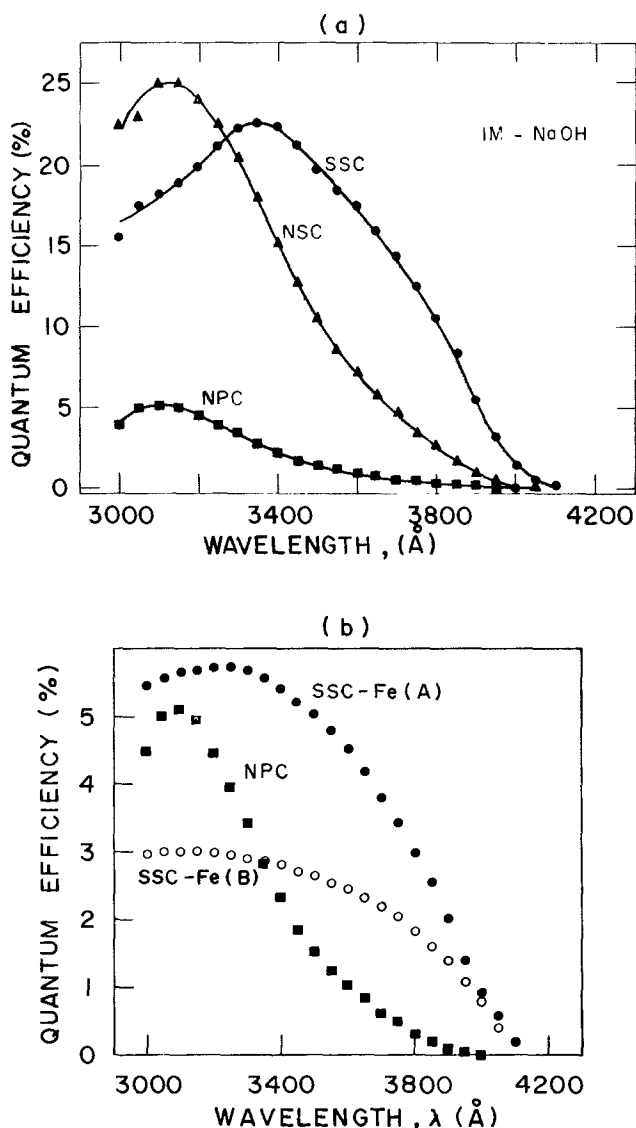


Fig. 4. Quantum efficiency in percent as a function of λ (Å): (a) natural (NPC and NSC) and synthetic (SSC) TiO_2 ; (b) Fe-doped synthetic single crystal [SSC-Fe(A) and SSC-Fe(B)] TiO_2 and NPC TiO_2 . The electrodes were polarized at 0V *vs.* SCE. The solution was 1M NaOH and was deoxygenated in the Pt compartment. $T = 25^\circ\text{C}$.

in a solution of 1M NaOH ($\text{pH} = 13$), and scanning was toward longer wavelength.

The quantum efficiency drops to zero in all samples for $\lambda \sim 4100\text{Å}$. This indicates that the NPC TiO_2 electrode has a well-defined band structure in the same way as the natural and synthetic single crystal TiO_2 electrodes. The bandgap, E_g , for the NPC electrode obtained from the plot of $(\eta h\nu)^{1/2}$ *vs.* $h\nu$, as shown in Fig. 5a, was ~ 3.1 eV, typical for TiO_2 . The plots in that figure are based on the relation

$$\eta h\nu = |L_p + W_0(V - V_{\text{FB}})^{1/2}| A (h\nu - E_g)^{n/2} \quad [3]$$

given by Butler (22), assuming the validity of the Schottky barrier theory for these semiconductor-electrolyte junctions, and that near the bandedge the optical absorption coefficient is proportional to $(h\nu - E_g)^{n/2}/h\nu$, with $n = 4$ or an indirect bandgap. The value of n was calculated from the slope of the straight line in the plot of $\ln(\eta h\nu)$ *vs.* $(h\nu - E_g)$, as shown in Fig. 6. The bandgap for the other samples, SSC and NSC, had approximately the same value, but for the two Fe-doped TiO_2 $E_g \sim 2.9$ eV (Fig. 5b). This value shows that the iron impurities present in the synthetic single crystal TiO_2 , even when their concentration exceeds the saturation limit (presence of precipitates), do not introduce an absorption band that significantly shifts the bandgap of these crystals toward longer wavelength.

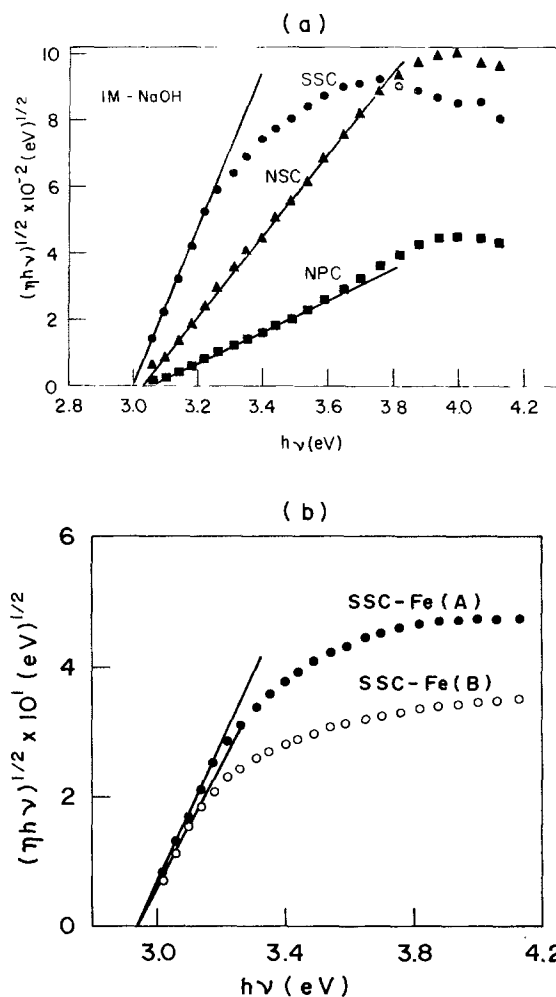


Fig. 5. The variation of quantum efficiency with photon energy for determination of the bandgap of the semiconductor electrodes, according to Eq. [3]. (a) Natural TiO_2 rutile (NPC and NSC) and synthetic single crystal TiO_2 (SSC); (b) Fe-doped samples of synthetic single crystal TiO_2 . The corresponding bandgap are: ~ 3.1 eV for the NPC; ~ 3.0 eV for NSC and SSC; and ~ 2.9 eV for SSC-Fe(A) and SSC-Fe(B).

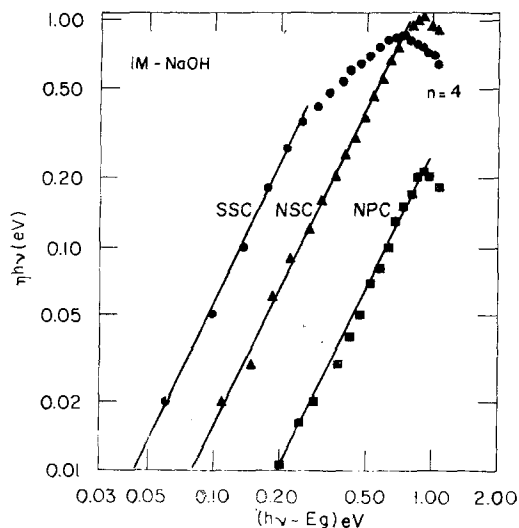


Fig. 6. The behavior of the quantum efficiency with photon energy for the NPC, NSC, and SSC TiO_2 electrodes as described by Eq. [3]. The solid lines present a slope indicating an indirect bandgap for the natural and synthetic TiO_2 .

The overall quantum efficiency of the NPC electrode has a lower value than that of the NSC and SSC electrodes (Fig. 4a) and is comparable with the overall quantum efficiency of the SSC-Fe(A) and SSC-Fe(B) electrodes (Fig. 4b). This result agrees with that mentioned for the I - V characteristics of the electrodes, where it was seen that the presence of iron impurities reduces the photocurrent and where it shows that the impurity sensitization with Fe ions is a rather inefficient way of enhancing the solar energy conversion of the TiO_2 electrodes.

Conclusions

The photoelectrochemical behavior of natural TiO_2 rutile was shown to be similar to that of synthetic single crystal TiO_2 , except for a lower breakdown potential, that is comparable with that reported for arc-plasma sprayed raw rutile. Flatband potentials and donor densities were determined from Mott-Schottky plots, and evidence for deep and shallow donors in the NPC TiO_2 is discussed. The deep donor level was proposed to be Fe^{2+} . By comparison with the behavior of synthetic Fe-doped TiO_2 we were able to show that the Fe impurities existent in the natural TiO_2 rutile are the most important factor in the occurrence of the low breakdown potential. We showed also that in TiO_2 the quantum efficiency diminishes with the concentration of Fe impurities. In addition to these general results we also found that for each sample the flatband potential calculated from the Mott-Schottky plots is in good agreement with the potential for onset of anodic photocurrent. From the wavelength dependence of photocurrent we were able to determine the nature of the gap as being indirect and to estimate the size of the gap, which was ~ 3.1 eV both for the poly and single crystalline natural TiO_2 samples.

Finally our results demonstrate the possibility of using natural TiO_2 rutile, a very abundant mineral in Brazil, as semiconducting anode for photoelectrolysis of water. The results show also that the impurity

sensitization with Fe ions is a rather inefficient way of enhancing the solar energy conversion of the TiO_2 electrodes.

Acknowledgments

We are grateful to Professor Mauro Villar de Queirós and Dr. F. E. A. Melo, of the Universidade Federal do Ceará, and to Dr. Carlos do Prado Barbosa, of the Brazilian Minerals Office, who generously donated the natural rutile samples from Ceará and Minas Gerais. We also thank Dr. Iris Torriani for her collaboration in the x-ray analyses, Dr. Reginaldo dos Santos, of the Centro Técnico Aeroespacial (CTA), for his support in the realization of these experiments, and Dr. René Brenzikoffer for his participation in the early part of this work. Finally we would also like to thank Dr. J. Busnardo and Dr. John Rogers for their comments on the manuscript. This work was partially supported by FINEP, FAPESP, UFC, and PICD.

Manuscript submitted Nov. 5, 1979; revised manuscript received May 7, 1980.

Any discussion of this paper will appear in a Discussion Section to be published in the June 1981 JOURNAL. All discussions for the June 1981 Discussion Section should be submitted by Feb. 1, 1981.

Publication costs of this article were assisted by UNICAMP.

REFERENCES

1. A. Fujishima and K. Honda, *Nature*, **238**, 37 (1972).
2. A. Fujishima, K. Kohayatawa, and K. Honda, *This Journal*, **122**, 1487 (1975).
3. J. G. Mavroides, D. I. Tchernev, J. A. Kafalas, and D. F. Kolesar, *Mater. Res. Bull.*, **10**, 1023 (1975).
4. J. F. Houlihan and D. P. Madacs, *ibid.*, **11**, 1191 (1976).
5. K. L. Hardee and A. J. Bard, *This Journal*, **122**, 739 (1975).
6. K. L. Hardee and A. J. Bard, *ibid.*, **124**, 215 (1977).
7. J. M. Bolts and M. S. Wrighton, *J. Phys. Chem.*, **80**, 2641 (1976).
8. D. C. Cronmeyer, *Phys. Rev.*, **87**, 876 (1952).
9. R. Wang and C. H. Henager, *This Journal*, **126**, 56 (1979).
10. R. G. Breckenridge and W. R. Hosler, *Phys. Rev.*, **91**, 793 (1953).
11. V. I. Bartanel', V. N. Bogomolov, S. A. Borodin, and S. I. Budarino, *Soviet Phys.,-Solid State*, **11**, 431 (1969).
12. P. O. Andersson, E. L. Kolberg, and A. Jelenski, *J. Phys. C: Solid State Phys.*, **7**, 1868 (1974).
13. O. W. Johnson, W. D. Ohlsen, and P. I. Kingsbury, *Phys. Rev.*, **175**, 1102 (1968).
14. M. A. Butler, Private communication.
15. A. K. Ghosh and H.P. Maruska, Private communication.
16. M. Tomkiewicz and H. Fay, *Appl. Phys.*, **18**, 1 (1979).
17. F. A. Grant, *Rev. Mod. Phys.*, **31**, 646 (1959).
18. F. Möllers, H. J. Tolle, and R. Memming, *This Journal*, **121**, 1160 (1974).
19. V. A. Myamlin and Y. V. Pleskov, "Electrochemistry of Semiconductors," Plenum Press, New York (1967).
20. J. H. Kennedy and K. W. Freese, *This Journal*, **125**, 723 (1978).
21. K. Mizushima and S. Iida, *J. Phys. Soc. Jpn.*, **32**, 1519 (1972).
22. M. A. Butler, *J. Appl. Phys.*, **48**, 1914 (1977).

Interfacial Reactions in Plasma-Grown Native Oxide-GaAs Structures

G. P. Schwartz,* B. Schwartz,* and J. E. Griffiths

Bell Laboratories, Murray Hill, New Jersey 07974

and T. Sugano

Department of Electronic Engineering, University of Tokyo, Tokyo, Japan

ABSTRACT

The presence and growth of elemental arsenic in as-grown and thermally annealed plasma oxidized films have been studied using Raman scattering and x-ray photoemission. The origin of arsenic growth observed in the annealed samples is fully consistent with the presence of a thermodynamically driven interfacial reaction involving As_2O_3 in the film and the substrate. The products of this reaction are Ga_2O_3 and As.

Current interests in native oxides on GaAs have tended to focus on determinations of the bulk and interfacial oxide compositions resulting from various growth procedures. The presence of elemental arsenic in the region of the oxide-substrate interface has been of particular interest due to its possible influence on electrical characteristics in device related applications. Two recent developments suggest that certain aspects of the current understanding of the interfacial composition problem may need to be re-examined when thermal processing or long-term compositional stability become important considerations.

The first development involves a recent estimate of the condensed phase portion of the Ga-As-O ternary diagram (1) which indicates that the interfacial phases which can exist in thermodynamic equilibrium with GaAs during its oxidation are Ga_2O_3 and As. The second development concerns the observation of thermally induced interfacial reactions between As_2O_3 and GaAs in electrochemically anodized films (2, 3). Similar reactions should occur in any type of native oxide film which contains As_2O_3 whenever there is sufficient energy available to overcome diffusion and reaction barriers.

The purpose of the present work was to examine the compositional properties of dc and rf plasma oxides with particular emphasis being placed on the detection of elemental arsenic in as-grown and thermally annealed films. Both x-ray photoelectron spectroscopy (XPS) and Raman scattering were employed for these purposes.

Experimental

n-Type Si-doped ($1.0-1.1 \times 10^{18} \text{ cm}^{-3}$) GaAs wafers were used in the preparation of the dc and rf plasma-grown native oxides. The samples were mechanically and chemically polished and then

* Electrochemical Society Active Member.

Key words: films, x-ray, thermodynamics.

etched in $H_2SO_4:H_2O_2:H_2O$ (4:1:1) for 2 min at 50°C followed by a 2 min room temperature etch in $NH_4OH:H_2O_2:H_2O$ (1:1:40). Oxidation conditions for the rf and dc plasma samples are presented in Table I. The samples labeled RF5 through RF8 received a postoxidation anneal at 300°C for 1 hr under argon.

The bare substrate and electrochemically anodized reference wafers were Sn-doped ($\sim 2 \times 10^{18} \text{ cm}^{-3}$) samples which had been alumina-lapped ($0.2 \mu\text{m}$) and bromine-methanol polished. The electrochemical oxidation was carried to 75V ($\sim 1500\text{\AA}$) under constant current (0.2 mA/cm^2) conditions utilizing a 3% phosphoric acid/ethylene glycol electrolyte (1:2 by volume) adjusted to $\text{pH} = 6.2$ with NH_4OH .

The apparatus involved in the dc and rf plasma oxidations has been described in detail in Ref. (4) and (5). XPS and Raman spectra were acquired using a Physical Electronics Industries (Model 548) electron spectrometer and an Instruments SA (Model HG-2S) Raman spectrometer. For Raman spectra the impinging laser excitation (5145\AA) was polarized in the plane of incidence (H) and the polarization of the light scattered normal to the incident beam was either unanalyzed (U) or analyzed perpendicular to the scattering plane (V). These two polarization configurations are denoted by HU and HV, respectively.

Results and Discussion

Bulk oxides.—The primary oxide species comprising the bulk films were examined using x-ray photoemission. Normal Raman cross sections associated with transparent materials are insufficient in the present case involving 1000-2000Å films to permit similar information to be obtained by that technique. The detection of arsenic by Raman scattering, however, is quite sensitive due to resonance enhancement of its scattering cross section which occurs in mate-

Table I

Sample No.	Oxidation method	Substrate orientation	Oxygen pressure (Torr)	Current density (mA/cm^2)	Oxidation time (min)	Substrate temperature ($^\circ\text{C}$)	Oxide color
DC1	dc plasma	(100)	1	5.3	10	103	Light blue
DC2		(100)	1	5.3	30	64	Yellow
DC3		(111)A	1	5.3	20	100	Yellow
DC4		(100)	1	5.3	40	28	Blue
DC5		(100)	1	5.3	40	200	Pink
DC6		(100)	1	12.0	20	25	Blue
DC7		(100)	1	2.6	90	25	Light blue
RF (1-8)	rf plasma	(100)	0.2	1.0	10	80	Blue
EC1	Electrochemical	(100)		1.0	10	25	Yellow

rials possessing electronic absorption bands that overlap the excitation frequency.

Photoemission spectra of the arsenic and gallium 3d core states in dc plasma films are presented in Fig. 1 for purposes of identifying the oxide species in the surface, bulk, and interfacial regions. No significant differences were observed between the XPS spectra of dc and rf plasma oxidized samples. The relevant 3d core level binding energy separations necessary for the chemical identification of the film components are provided in Table II.

The 3d core state intensities representative of an as-grown surface (sample DC-1) are shown in Fig. 1A. Ga_2O_3 and As_2O_3 are the anticipated products; one notes however, that the As 3d-Ga 3d binding energy difference (24.6 eV) on this surface is larger than expected (24.0 eV) for those species. In addition the As 3d linewidth is exceptionally large (3.1 eV) compared to spectra from pure As_2O_3 (6-8). The broad As 3d linewidth and its shift to higher binding energies indicate the presence of an admixture of +3 and +5 arsenic in the detected surface depth (40-60Å). Although it is not possible at present to identify the pentavalent species, GaAsO_4 and As_2O_5 would be the most likely candidates.

Evaluation of the surface As/Ga ratio observed on the dc and rf samples ranged from 0.7 to 0.8. These estimates were based on atomic cross sections derived from cleaved (110) GaAs, and are somewhat lower than the bulk value of 0.93 obtained by Kauffman *et al.* (9) using ion-induced x-ray analysis on rf plasma films.

Figure 1B shows the 3d photoemission intensities on an argon ion sputtered film (2 kV, 2×10^{-5} Torr Ar). The reduction in the As/Ga 3d area ratio and the growth of a low binding energy shoulder on the As 3d peak are indicative of selective sputtering and argon beam reduction artifacts. The observed binding energy shift between the main As 3d peak and its shoulder (2.7 eV) is consistent with the reduction of As_2O_3 down to elemental arsenic (8). To demonstrate that the shoulder on the main arsenic peak was a sputtering artifact rather than intrinsic deposits of unoxidized arsenic in the bulk film, we dissolved ~100Å of the argon-bombarded sample with a 1/5 (volume) mixture of H_3PO_4 /methanol. This chemically etched sample (Fig. 1C) shows no evidence of the former shoulder, only Ga_2O_3 and As_2O_3 are evident. Resputtering the chemically etched sample regenerated the lower binding energy arsenic peak. The bulk As/Ga ratios in the films cannot be accurately determined unless a careful measurement of selective sputtering in As_2O_3 and Ga_2O_3 mixtures is performed. Similarly, chemical etching can also result in selective dissolution. We did not pursue this aspect of the compositional analysis.

Several of the samples were chemically stripped of their oxides using either H_3PO_4 /methanol (1:5) or $\text{HCl}/\text{H}_2\text{O}$ (1:2) etching solutions. Oxide removal by the H_3PO_4 /methanol solution was relatively slow and proceeded somewhat nonuniformly as judged by the pattern of interference colors observed after etching.

Table II

Compounds	Components	Binding energy separation (eV)	Ref.
GaAs	Ga-As	22.0	(8)
		22.0	(6)
$\text{Ga}_2\text{O}_3/\text{GaAs}$	Ga-Ga	1.2-1.4	(8)
		1.4	(6)
$\text{As}_2\text{O}_3/\text{GaAs}$	As-As	3.4-3.6	(8)
		3.4	(6)
$\text{As}_2\text{O}_3/\text{Ga}_2\text{O}_3$	As-Ga	24.2	(8)
		24.0	(6)
As/GaAs	As-As	0.4-0.6	(8)
$\text{As}_2\text{O}_3/\text{GaAs}$	As-As	4.5-4.7	(8)
		4.7	(6)
$\text{GaAsO}_4/\text{GaAs}$	As-As	4.7	(6)

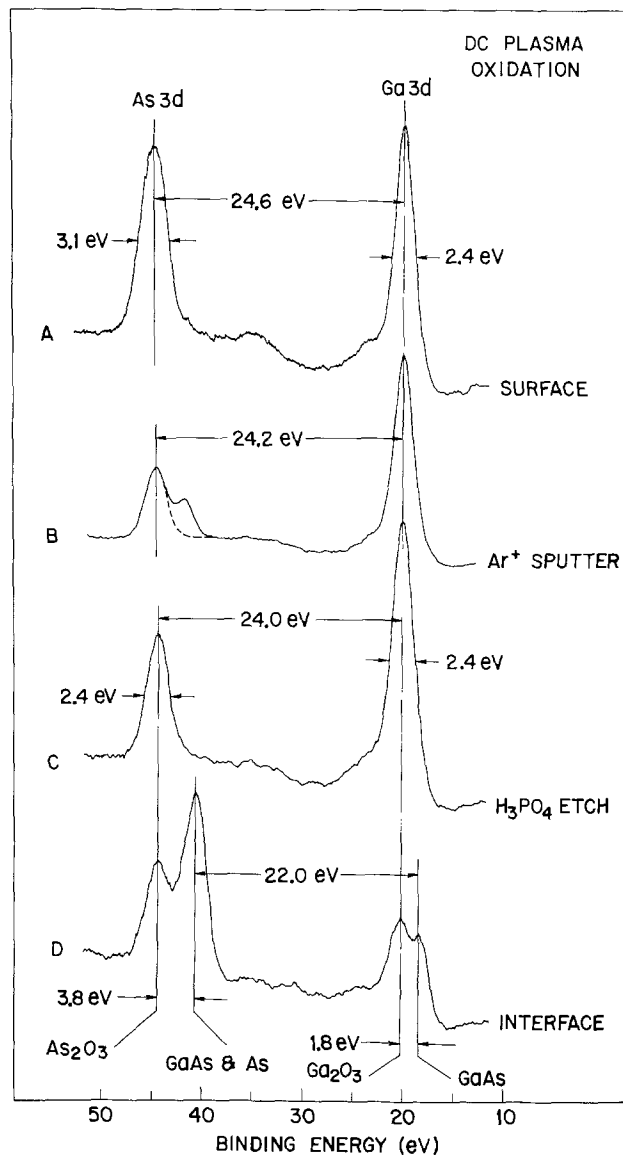


Fig. 1. As and Ga 3d core level photoemission stimulated by $\text{AlK}\alpha$ radiation. The binding energy positions of oxide and substrate components are marked by vertical lines. The maximum Ga peak height corresponds to approximately 800 counts/sec.

The interfacial region on a chemically stripped (H_3PO_4 /methanol) film is shown in Fig. 1D. Both substrate and residual oxide components are apparent in both sets of 3d core states. Even without a rigorous deconvolution of the As and Ga 3d peaks into separate oxide and substrate components, it is readily apparent that the As/Ga area ratio associated with the substrate signals at 40.8 and 18.8 eV exceeds the value of 1.31 observed on cleaved (110) GaAs. The presence of elemental arsenic in the interfacial region is consistent with this observation since the chemical shift between the arsenic 3d core levels in GaAs and As is sufficiently small [0.4 eV, Ref. (8)] relative to typical measured substrate linewidths (~1.9 eV) that these two signals would effectively add and thus increase the expected As/Ga area ratio. Raman scattering data in the following section further supports this assignment.

Binding energy reference levels were established in the following manner. The Ga 3d photopeak of Ga_2O_3 was used to establish the relative alignment of the spectra. The overall binding energy scale was then fixed by assigning the Ga 3d core level in GaAs to a value at 18.8 eV. Oxide charging due to secondary electron emission is apparent in Fig. 1D where one has the substrate signal with which to reference the

oxide binding energy positions. Both the Ga and As 3d signals associated with their oxides are shifted to 0.4 eV higher binding energy relative to the substrate than anticipated from Table II; this charging phenomena is commonly observed in photoemission on insulators.

Even though Raman scattering performed prior to any chemical etching indicated comparable amounts of elemental arsenic were present in these samples, no evidence for interfacial arsenic was obtained on samples chemically stripped in HCl/H₂O solutions. We surmise that the HCl solution dissolved whatever arsenic was originally present along with the oxide. Similar results were obtained on one sample using NH₄OH/H₂O (1:1) for an etchant.

Arsenic detection in as-grown and thermally annealed films.—The optical transparency of the oxide components of these films at the laser excitation wavelength (514.5 nm) allows *in situ* surface reflection Raman scattering to be performed. In general, only materials with Raman allowed, resonance enhanced cross sections will be detected. In the present case, both arsenic and GaAs will be detected with high sensitivity. The identification and structural form of the detected species are obtained by examination of the position of the Stokes shifted Raman peaks and their lineshape. The incident excitation impinges on the sample at Brewster's angle and the Raman scattered light is collected normal to the direction of the incident beam.

Raman scattering in the HU polarization configuration is shown in Fig. 2 for bare and oxidized GaAs. All wafers were (100) oriented with nominal 1000Å as-grown films on the oxidized samples. Scattering from the bare substrate in the region of primary interest (150-300 cm⁻¹) consists of the zone center longitudinal and transverse optic modes (LO, TO) at 291 and 268 cm⁻¹, respectively, along with two-phonon scattering of transverse acoustic modes between 150-240 cm⁻¹ (10). Coupled LO-plasmon features (11) and additional two-phonon scattering are also present above 300 cm⁻¹.

Two primary features are apparent in Fig. 2 in the region between 150-300 cm⁻¹. The first is the variation in intensity nominally associated with the TO phonon of GaAs at 268 cm⁻¹. The second feature is the observation of a new peak around 205 cm⁻¹ superimposed on the two-phonon scattering from the substrate. An accurate analysis of the intensity around 268 cm⁻¹ is complicated because of the multiplicity of scattering processes which can contribute to the Raman intensity in this spectral region. There will be a contribution from allowed TO substrate scattering because the propagation of light into the substrate is not parallel to the (100) direction in a surface reflection configuration. In addition, there will be strain-induced (12) enhancement of this TO scattering due to roughening of the substrate during the oxidation process. This TO enhancement is particularly apparent from a comparison of the bare substrate and electrochemically anodized sample. For carrier concentrations around 10¹⁸/cm³, the L- mode of the coupled LO-plasmon interaction will occur in this vicinity (11). Any amorphous GaAs present in the interfacial region would also contribute a broad peak centered at roughly 260 cm⁻¹ (13). Finally, both orthorhombic and rhombohedral structures of crystalline arsenic display sharp A_g type modes in the region between 265-257 cm⁻¹ (14-16). We will not treat the scattering around 268 cm⁻¹ in any further detail.

A variety of evidence suggests that the additional scattering observed around 205 cm⁻¹ on the two-phonon background should be assigned to elemental arsenic. Raman spectra for amorphous arsenic (17, 18) typically display a broad band (180-160 cm⁻¹) in the HU configuration which contains a weak peak

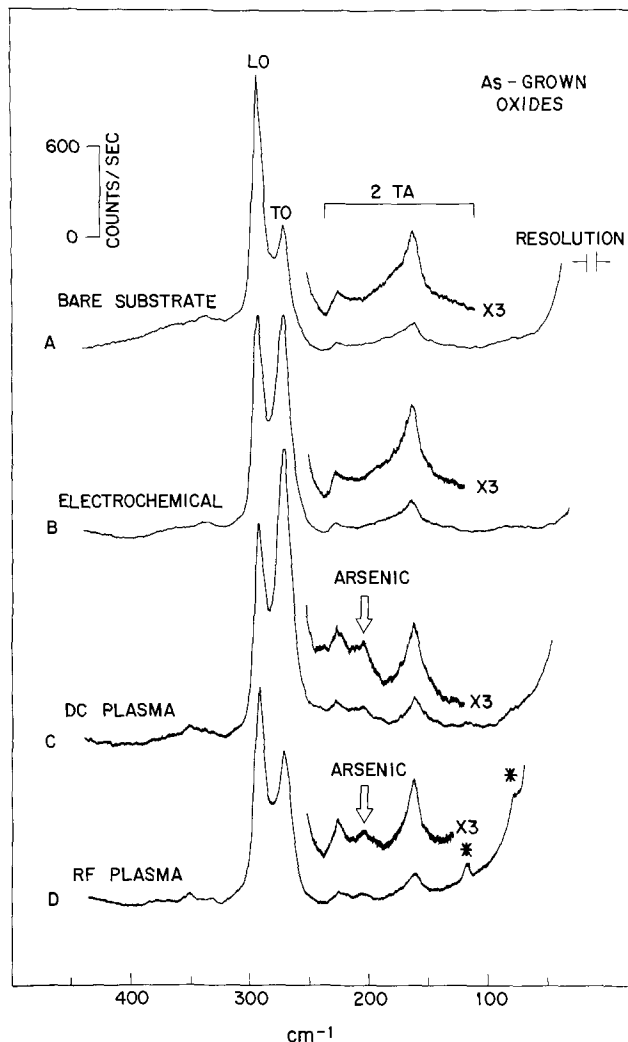
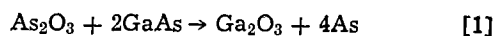


Fig. 2. Raman scattering (HU) from as-grown films of native oxides on GaAs. Asterisks denote the position of laser plasma lines.

at ~200 cm⁻¹. Crystalline arsenic modes of E_g character would also contribute between 195-200 cm⁻¹ (14-16). Crossed polarization spectra (HV) effectively suppress the two-phonon contribution from the substrate. Such spectra showed a broad, structureless band of low intensity extending from 180-260 cm⁻¹ consistent with reported crossed polarization spectra of amorphous arsenic (17, 18). The Raman data thus supplement and are fully consistent with the suggestion of elemental interfacial arsenic obtained from the photoemission spectrum of Fig. 1D. In addition, recent reports utilizing the nondestructive optical technique of spectroscopic ellipsometry have observed optically absorbing components in rf plasma oxidized (19) and electrochemically anodized (20) films. The identity of the absorbing species is somewhat difficult to assess in this technique however. Photoemission intensity from elemental Ga would be observed some 1.1 eV (8) to lower binding energies than the Ga 3d signal in GaAs. The lack of asymmetry on the low binding energy side of the Ga 3d in Fig. 1D in conjunction with the As/Ga ratio being greater than one rather than less than one suggests that elemental Ga is not present as the absorbing species. Small particles of GaAs embedded in the oxide during oxidation are also highly unlikely and would not explain the observed Raman scattering peak around 200 cm⁻¹. The bulk of the existing evidence favors elemental arsenic as the absorbing species in these films.

Comparison of Fig. 2B-D in the vicinity of 200 cm^{-1} demonstrates that the electrochemically anodized film contains less elemental arsenic than either the rf or dc oxides in the as-grown state. A qualitative estimate of the detection sensitivity of the Raman technique for crystalline arsenic (3) suggests that 10-20Å of As should be observable. A comparable figure for amorphous As may be 2-3 times larger. The recent ellipsometric studies support the observed differences between electrochemically anodized and plasma oxidized films. In those studies, electrochemically anodized films grown at 0.1 mA/cm^2 were observed to contain less than 6Å of total arsenic and to display interface widths less than 25Å (20). In addition, the interface widths were observed to be current density dependent. Our efforts to establish the arsenic detection sensitivity of Raman scattering (3) suggest that a total of 6Å would not be detected in our measurements. In the rf films analyzed, high current density growth resulted in the sharpest interface ($\sim 84\text{Å}$) which contained $\sim 20\text{Å}$ of arsenic (19). In addition, the bulk films contained between 1-2 volume percent of a-As (assumed), which would contribute another 9-18Å of As in 900Å of a bulk film. Detection of 30-40Å of a-As is consistent with the additional scattering intensity observed around 200 cm^{-1} in Fig. 2C and D. All of the rf samples including those annealed at 300°C for 1 hr (RF-5-8) showed comparable Raman intensity in this region. Somewhat more variation was exhibited by the dc plasma oxides. In particular, samples DC3 and DC5 showed weaker though discernible scattering peaks around 200 cm^{-1} .

The ternary Ga-As-O phase diagram (1) mentioned in the introduction specifies that Ga_2O_3 and As are the phases which can coexist in thermodynamic equilibrium with GaAs. Diffusion of As_2O_3 from any region of the film to the oxide-substrate interface should result in a reaction according to



whenever there is sufficient energy available to overcome the reaction barrier. The existence of this reaction has already been verified using Raman scattering in electrochemically anodized films which were thermally annealed (2, 3). TEM (21) and ellipsometric studies (22) of annealed rf plasma oxides have also observed the presence of crystalline arsenic deposits in the interfacial region. The connection between these observations and the reaction scheme presented in Eq. [1] was not made in Ref. (21) and (22) however.

The thermodynamic origin of Eq. [1] implies that interfacial reactions involving native oxides on GaAs should occur at sufficiently high temperatures independent of the growth technique provided that As_2O_3 is one of the film constituents. Rutherford backscattering and ion-induced x-ray data support the contention that the $\text{As}_2\text{O}_3/\text{Ga}_2\text{O}_3$ ratio of As/Ga is close to 1:1 in bulk films of both rf plasma oxidized (9) and electrochemically anodized (23) samples. In order to verify the reaction on plasma films and to compare the reaction rates, the three samples of Fig. 2B-D were encapsulated together in an evacuated quartz tube (5×10^{-7} Torr) and inserted in a tube furnace at $400 \pm 10^\circ\text{C}$ for 1 hr. Figure 3 shows the results of Raman scattering from these thermally annealed samples.

Intense crystalline modes of metallic arsenic are now observed around 200 and 260 cm^{-1} . The variation observed in the different lineshapes suggests that a mixture of crystalline and amorphous arsenic is present. The crystallization rate appears to differ among the samples and may be sensitive to certain details of the film composition such as water inclusion during electrochemical anodization. The spatial location of these deposits at the oxide-substrate interface has previously been demonstrated in annealed anodic (3) and rf plasma (21, 22) films.

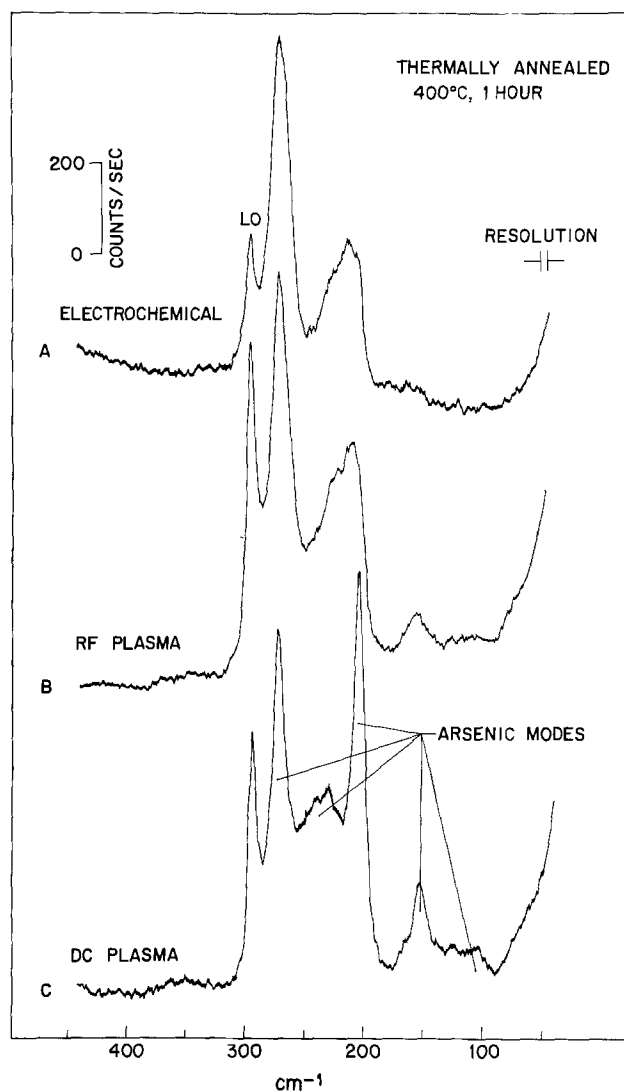


Fig. 3. Raman scattering (HU) from thermally annealed films. Crystalline and amorphous arsenic modes as well as the substrate LO are shown.

From a comparison of the Raman intensities observed in Fig. 2 and 3, it is readily apparent that the total As content of these films has increased substantially during the annealing. This feature is consistent with arsenic generation implicit in Eq. [1] but is inconsistent with a model of the plasma oxide-GaAs interface proposed by Chang (24). In that model, the primary effect of thermal annealing ($T < 450^\circ\text{C}$) supposedly is to convert amorphous arsenic present in the as-grown state to one of its crystalline allotropes. Such a model clearly cannot account for the considerable increase in the arsenic intensity observed after annealing.

In summary, photoemission and Raman scattering have been employed to study the nature of plasma oxide films grown on GaAs. The bulk films consist of As_2O_3 and Ga_2O_3 with evidence for some form of pentavalent arsenic in the surface layers. As-grown electrochemically anodized films were observed to contain less elemental arsenic than their dc and rf plasma counterparts over the limited range of plasma oxidation conditions employed in this study. Thermal annealing results in an interfacial reaction between As_2O_3 and the substrate independent of the growth procedure for the oxide film. Substantial deposits of elemental arsenic are generated and subsequently incorporated in the oxide during this reaction.

Acknowledgments

We wish to thank Drs. F. Koshiga and K. Yamasaki for the preparation of the plasma oxidized films and C. D. Thurmond for informative discussions concerning the Ga-As-O phase diagram. G. J. Gualtieri's assistance in the electrochemical anodizations is gratefully acknowledged.

Manuscript submitted Feb. 6, 1980; revised manuscript received April 28, 1980.

Any discussion of this paper will appear in a Discussion Section to be published in the June 1981 JOURNAL. All discussions for the June 1981 Discussion Section should be submitted by Feb. 1, 1981.

Publication costs of this article were assisted by Bell Laboratories.

REFERENCES

1. C. D. Thurmond, G. P. Schwartz, G. W. Kammlott, and B. Schwartz, *This Journal*, **127**, 1366 (1980).
2. G. P. Schwartz, B. Schwartz, D. DiStefano, G. J. Gualtieri, and J. E. Griffiths, *Appl. Phys. Lett.*, **34**, 205 (1979).
3. G. P. Schwartz, J. E. Griffiths, and B. Schwartz, *J. Vac. Sci. Technol.*, **16**, 1383 (1979).
4. F. Koshiga and T. Sugano, *Thin Solid Films*, **56**, 39 (1979).
5. K. Yamasaki and T. Sugano, *Jpn. J. Appl. Phys.*, **17**, Suppl. 17-1, 321 (1978).
6. G. P. Schwartz, G. J. Gualtieri, G. W. Kammlott, and B. Schwartz, *This Journal*, **126**, 1734 (1979).
7. Y. Mizokawa, H. Iwasaki, R. Nishitani, and S. Nakamura, *J. Electron Spectrosc. Relat. Phenom.*, **14**, 129 (1978).
8. Y. Mizokawa, H. Iwasaki, R. Nishitani, and S. Nakamura, *ibid.*, **14**, 129 (1978).
9. R. L. Kauffman, L. C. Feldman, J. M. Poate, and R. P. H. Chang, *Appl. Phys. Lett.*, **30**, 319 (1977).
10. T. Sekine, K. Uchinokura, and E. Matura, *J. Phys. Chem. Solids*, **38**, 1091 (1977).
11. A. Pinczuk, G. Abstreiter, R. Trommer, and M. Cardona, *Solid State Commun.*, **21**, 959 (1977).
12. D. J. Evans and S. Ushioda, *Phys. Rev. B*, **9**, 1638 (1974).
13. J. E. Smith, M. H. Brodsky, B. L. Crowder, and M. I. Nathan, in "Proceedings of the Second International Conference on Light Scattering in Solids," M. Balkanski, Editor, p. 330, Flammarion Press (1971).
14. R. N. Zitter, in "The Physics of Semi-metals and Narrow Gap Semiconductors," D. L. Carter and R. T. Bate, Editors, p. 285, Pergamon, New York (1971).
15. J. S. Lannin, J. M. Calleja, and M. Cardona, *Phys. Rev. B*, **12**, 585 (1975).
16. J. S. Lannin and B. V. Shanabrook, in "Vibrational Spectra and Bonding in the Black Phosphorous Structures of As and P," presented at the 14th Intern. Conf. Phys. Semicond., Edinburgh, 1978.
17. J. S. Lannin, *Phys. Rev. B*, **15**, 3863 (1977).
18. R. J. Nemanich, G. Lucovsky, W. Pollard, and J. D. Joannopoulos, *Solid State Commun.*, **26**, 137 (1978).
19. D. E. Aspnes, J. B. Theeten, and R. P. H. Chang, *J. Vac. Sci. Technol.*, In press.
20. D. E. Aspnes, G. P. Schwartz, G. J. Gualtieri, and B. Schwartz, "Analysis of the Layer Structure of Anodic Oxides on GaAs by Spectroscopic Ellipsometry," Materials Research Society Conference, Cambridge, 1979.
21. R. P. H. Chang, T. T. Sheng, C. C. Chang, and J. J. Coleman, *Appl. Phys. Lett.*, **33**, 341 (1978).
22. J. B. Theeten, D. E. Aspnes, and R. P. H. Chang, *J. Appl. Phys.*, **49**, 6097 (1978).
23. L. C. Feldman, J. M. Poate, F. Ermanis, and B. Schwartz, *Thin Solid Films*, **19**, 81 (1973).
24. R. P. H. Chang, *ibid.*, **56**, 89 (1979).

Etching Characteristics of Defects in the InGaAsP-InP LPE Layers

Tsuyoshi Kotani, Satoshi Komiya, Saburo Nakai, and Yutaka Yamaoka

Fujitsu Laboratories Limited, Nakahara-ku, Kawasaki, Japan

ABSTRACT

Defects in the InGaAsP-InP multiepitaxial layers on the InP (111)P substrate were investigated using chemical etching techniques. Threading dislocations, stacking faults, dislocation rosettes, and dislocation crowds were revealed on InP epitaxial layers by the AB etch at 60°C. They were identified from their etch features and it was suggested that dislocation rosettes and crowds were caused by localized mismatch stress.

There is considerable interest in the quaternary InGaAsP for injection laser (1, 2), LED (3, 4), and photodiode (5, 6) applications in fiber optic communication systems (7, 8) developed for the 1.0-1.5 μm wavelength range, since in this quaternary alloy layers bandgap can be varied while maintaining lattice match to the InP substrate (9, 10). It is known that the first degradations of GaAlAs-GaAs DH lasers or LEDs are caused by some defects in the active layer (11-13). Ettenberg and Nuese reported that the degradation rate depends on the energy gap of the active layer (14). Therefore, it is important to investigate defects in the InGaAsP-InP LPE multilayers matched to the InP substrate. This paper describes the etching characteristics of defects in the InGaAsP-InP LPE layers on the InP (111)B substrate.

Key words: etch pit, dislocation, liquid phase epitaxy, InGaAsP.

Experimental Procedure

The LPE growth method utilized in this work was the well-known slider boat technique. An InP (111)B substrate was chemically polished and its damage layer was removed. The solutions for LPE growth were saturated at 670°C for an hour and cooled at the rate of 0.5°C/min over a temperature interval of 40°C. After the InP buffer layer was grown, the growth of the quaternary layer was started from 648°C at the matching condition (15). A super cool of 2°C was employed for the growth of the 2nd and 4th InGaAsP layers. The energy gaps of the second active layer and the 4th layer for p-contact are 1.00 and 1.06 eV, respectively. The characteristics of wafer 1 with a typical double heterostructure are shown in Table I.

The lattice match between the epitaxial layers and substrate was evaluated using a double crystal x-ray

Table I. Characteristics of wafer 1

	Substrate and epitaxial layers	Dopant	Carrier conc. (cm ⁻³)	Thickness (μm)
Sub.	InP (111)B	Sn	$n = 5 \times 10^{17}$	
1st	InP	Sn	$n = 5 \times 10^{17}$	5
2nd	In _{0.75} Ga _{0.25} As _{0.52} P _{0.48}	—	—	1.0
3rd	InP	Zn	$p = 1 \times 10^{18}$	1.0
4th	In _{0.75} Ga _{0.25} As _{0.58} P _{0.42}	Zn	$p = 5 \times 10^{18}$	0.8

diffractometer with parallel setting of the (333) plane. The half angles of rocking curves from the (333) reflection of the (111)B InP substrates were about 8-10 sec. Figure 1 shows the diffraction profile of wafer 1 shown in Table I. While the sharp main peak 1 is due to the InP layers and substrate, the much broader diffraction peak 2 is due to InGaAsP layers and may suggest large distribution of the lattice constants. The lattice mismatch between peaks 1 and 2 is $\Delta a/a = 9.1 \times 10^{-4}$. Other DH wafers have similar diffraction profiles, when the same compositions of melts are employed.

There are a few reports on the etchants revealing defects in the InP substrate (16, 17),¹ but they are inadequate to evaluate thin epitaxial layers as shown in Table I. It is well known that the AB etch, which consists of a mixture of 2 ml H₂O, 8 mg AgNO₃, 1g CrO₃, and 1 ml HF, reveals defects in the GaAs substrate (18). Stirland has also reappraised the etching properties of the AB etch for the GaAs substrate (19). InGaAsP-InP epitaxial wafers were also studied by the AB etch (20-22). The etch features of the InP (111)B and (100) substrates by the AB etch maintained at 60°C are shown in Fig. 2(a) and (b), respectively, and two specimens were etched simultaneously. These etch features are very similar to those observed on the Si-doped GaAs substrate (19), i.e., most of dislocations are mainly delineated as the dot- and dash-like features in Fig. 2(a) and (b). These features represent a two-dimensional projection onto the surface produced by the etch of the dislocations con-

¹Since the etchant (1HBr:5HF) has no memory effect and revealed no striations on any substrates, these samples were etched by (1HBr:5HF) without being polished by any etchants after the AB etchant. Therefore, the striation image on Fig. 2(c) and (d) is the afterimage of that revealed by the AB etch, while deep etch pits correspond to dislocations through etched surfaces.

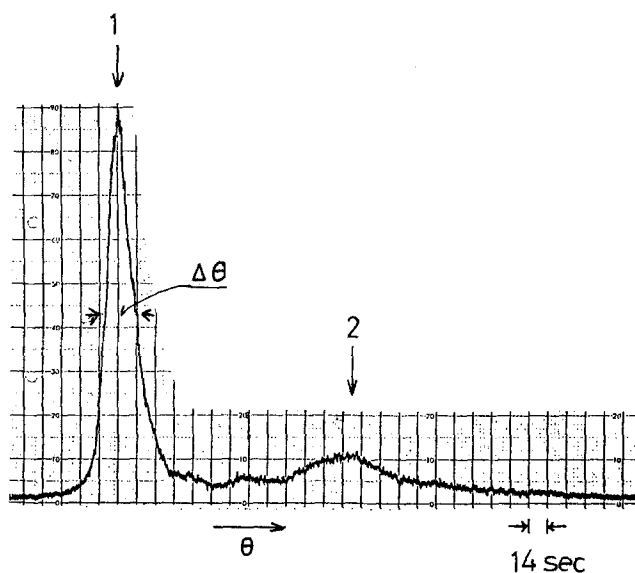


Fig. 1. Rocking curve of the (333) reflection of wafer 1 by using a double crystal x-ray diffractometer. The (333) reflection plane of the similar InP (111)B substrate was employed as an x-ray monochromator and they were set in parallel. Cu-K_{α1} radiation was employed and confined to 0.5 mm on the wafer surface by point slits. The half-angle of peak 1 is of $\Delta\theta = 24$ sec and the mismatch of the peak 2 is of $\Delta a/a = -9.1 \times 10^{-4}$.

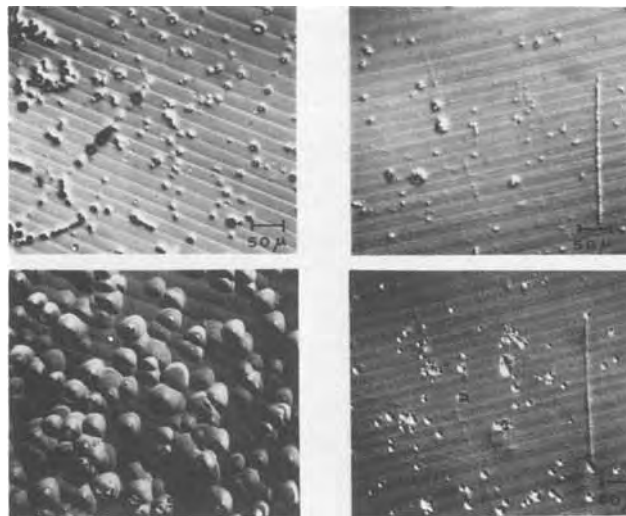


Fig. 2. The interference contrast micrographs of the etched surfaces of the InP (111)B and (100) substrates by the AB etch and (1HBr:5HF). Figures (a, top left) and (b, top right) show the (111)B and (100) surfaces of the InP substrates, respectively, after 15 min AB etch at 60°C. Figures (c, bottom left) and (d, bottom right) show the (111)B and (100) surfaces of the InP substrate after 2 min (1HBr:5HF) etch at room temperature, respectively.

tained within the volume of InP removed by the etch. However, some of dislocations are revealed as conical etch pits on the InP (111)B substrate. The straight lines or band-like features are associated with striations and were frequently observed on the InP substrates, but not observed on the epitaxial layers. Figures 2(c) and (d) show the etch pit patterns of the same areas on the two InP substrates with (111)B and (100), respectively, when subsequently etched by the dislocation etchant of (1HBr:5HF) (17). The etch features at emergent dislocations are different owing to the etchants, however, the etched pattern in Fig. 2(b) compares well with the etch pit pattern in Fig. 2(d).

Wafer 1 has been examined using these etchants as follows. When the wafer was etched for 2.5 min by the AB etch, the 4th InGaAsP layer was preferentially etched off because of more rapid etch rate and then the etch feature of the third InP layer was examined by interference contrast. After the remaining third layer was selectively polished by the (1HBr:10HF) etchant (17), it was also etched by the AB etch and the etch features of the first InP layer were examined too.

Results and Discussion

Dislocation etch pits.—Figures 3(a) and (b) show the etch features of the same area on the third and first InP layers of wafer 1 by the AB etch at 60°C, respectively. As shown in Fig. 3(a) and (b), conical etch pits were revealed on the epitaxial InP layers by the AB etch, although only part of the etch feature was observed as conical etch pits on the InP (111)B substrate. The multiplication of threading dislocation in the epitaxial layers was observed in Fig. 3(a) in comparison with that shown in Fig. 3(b). For example, each of the etch features "p," "q," and "r" consists of several etch pits on the third InP layer in Fig. 3(a) but is observed as only a single etch pit on the first InP layer in Fig. 3(b). Most of dislocation etch pits on the third InP layer of other DH wafers by the AB etch were observed as a cluster of several triangular etch pits, as shown in Fig. 3(a). This multiplication of threading dislocation is caused by the generation of dislocations due to plastic deformation and its details were discussed in another paper (23).²

²As shown in Fig. 4 of this reference (23) etch pits were revealed on as-grown homoepitaxial InP layer by the AB etch, so etch pits on the first InP layer in Fig. 3(c) are not due to the memory effect of the AB etch.

Stacking faults.—Stacking faults having three different configurations, *i.e.*, the single line “i,” triangle “a,”

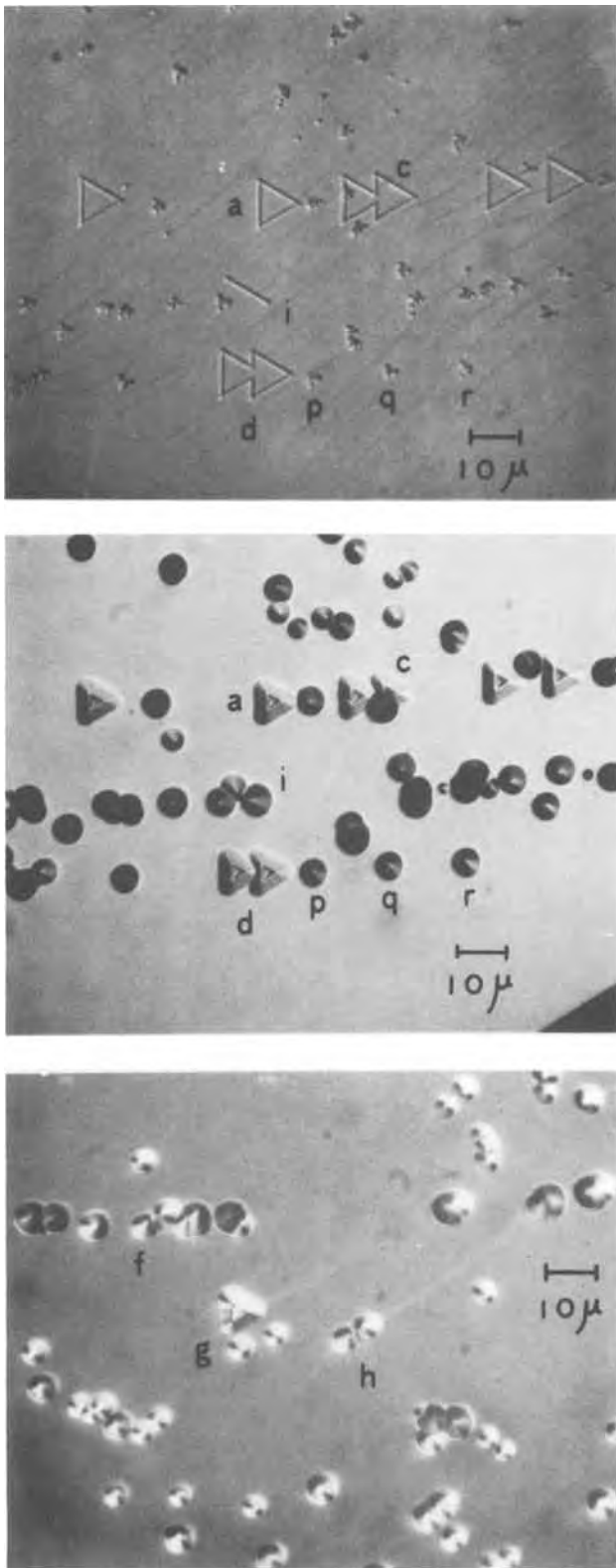


Fig. 3. The micrographs of the etched surface of the third and first InP layers of wafer 1 by the AB etch. Figure (a, top) is the etch pit pattern on the third InP surface after 2.5 min AB etch at 60°C. After the third InP layer of wafer 1 was preferentially removed by the etchant (1HBr:10HF), it was etched by the AB etch at 60°C for 3 min. Figures (b, middle) and (c, bottom) show the etch pit patterns on the first InP layer surface. An etch pit or triangle defects are denoted with the same letters in Fig (a) and (b).

and their combination “c” were observed in Fig. 3(a). Considering the etched shape of the triangle “a” in Fig. 3(b), these stacking faults have also a three-dimensional structure consisting of (111) surfaces for the (001) growth plane (24, 25). Their original position can be known from their size on the surface, though it is present clearly behind the second layer. It is evident that all the stacking faults in Fig. 3(a) occur at the interface between the first epitaxial layer and the substrate. Comparing Fig. 3(a) with 3(b), they pierce through the three epitaxial layers without any perturbation at two heterointerfaces between the InP and InGaAsP layers (26), and probably through the 4th InGaAsP layer, too. However, the stacking faults were not observed on the as-grown surface of the 4th InGaAsP epitaxial layer by optical microscope. They were frequently observed as surface imperfections on the epitaxial surface of VPE Si (27) or GaAs (28). The structure of the surface imperfections, the so-called “shadow,” are formed as a result of the blocking or perturbation of lateral growth. These surface imperfections were also observed on the surface of liquid phase epitaxial wafer with similar double heterostructure of GaAlAs-GaAs (29). In the case of LPE growth, it is probable that the surface imperfection due to stacking fault is also caused by the perturbation of dominant lateral growth such as terrace steps. However, such typical terrace steps were rarely observed on the InGaAsP LPE layer doped by various dopants, Sn, Te, Zn, and Cd, even when it had sufficiently the lattice constant matched to the InP substrate ($\Delta a/a \lesssim 1 \times 10^{-4}$). Furthermore, such surface imperfections with the regular square shape were sometimes observed on the lattice matched ternary InGaAs layer grown on the InP(001) substrate. This implies that two-dimensional epitaxial growth such as nucleation, step growth, and bunching mechanisms may be blurred, because this quaternary alloy consists of four elements with very different ionic radii as opposed to the ternary GaAlAs. Anyhow, it seems that some growth mechanism of the quaternary layer affects formation of the surface imperfections associated with stacking faults.

There were several reports on etching characteristics of stacking faults on VPE Si layer (24, 25). The partial dislocations terminating line defect with Burgers vector of $+a/6 \langle 211 \rangle$ were revealed as deep etch pits at the ends of etched groove, whereas terminating triangle defect with Burgers vector of $+a/6 \langle 110 \rangle$ were not revealed as etch pits at the corners of etched triangular grooves. As shown in Fig. 3(b) and (c), the conical deep etch pits are observed at both ends of line defects “h” and “i” but the etch pits at the apexes of triangle such as “a” are not so clear. This result suggests that the partial dislocations terminating this line defect have Burgers vector of $+a/6 \langle 211 \rangle$, and agree with the results of Mahajan *et al.* (30) on stacking faults in the LPE homoepitaxial InP layer. The stacking fault combination “c” or “d” resulted from the interaction of two triangle defects and partially annihilated on the third InP etched surface. Therefore, it seems that the two triangles of the combining stacking fault are of similar types.

Dislocation rosette and crowd.—Figure 4 shows the etch pit pattern on the first InP layer of wafer 1. In addition to randomly distributed etch pits, two types of etch pit clusters “D” and “E” were observed in Fig. 4 and they were sometimes revealed on each epitaxial layer of the similar DH wafers by the AB etch. Figures 5 and 6 show the typical patterns of their etch pit clusters. The cluster in Fig. 5 is usually called the dislocation rosette though it is produced by intentional indentation experiment (31) or bonding process (32). The cluster in Fig. 6 consists of randomly distributed etch pits from its center region of high density and we call it the dislocation crowd in order to distinguish the dislocation rosette.

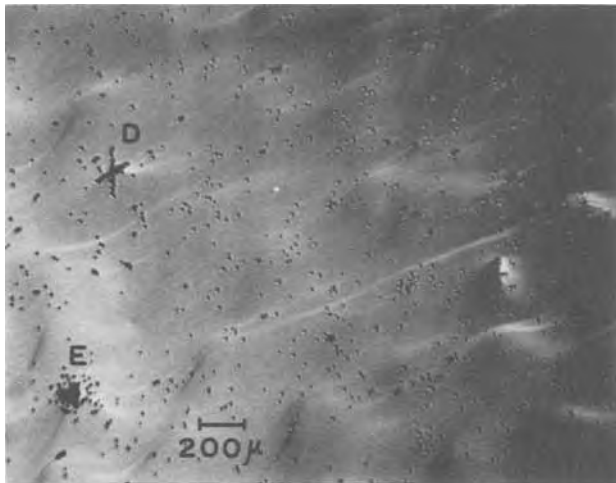


Fig. 4. Etch pit pattern on the first InP layer

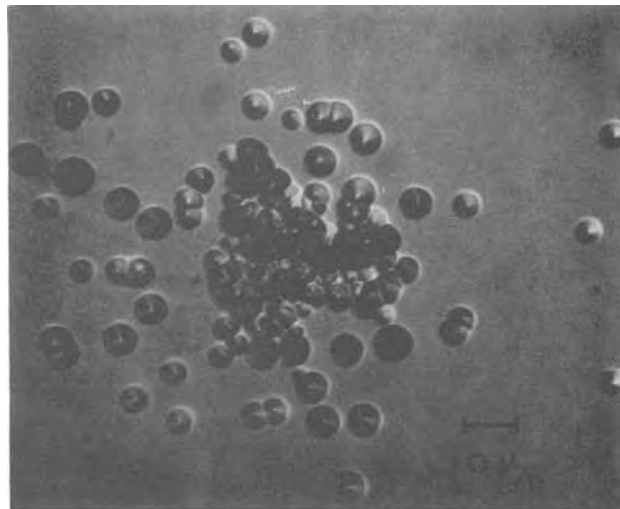


Fig. 6. A typical dislocation crowd pattern revealed on the first InP epitaxial layer of wafer 1 by the AB etch.

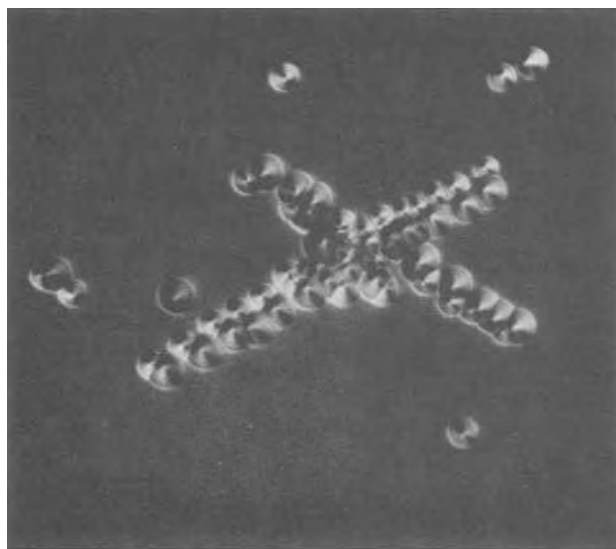


Fig. 5. A typical dislocation rosette pattern revealed on the first InP epitaxial layer of wafer 1 by the AB etch.

The dislocation rosette consists of two etch pit arrays along only two $\langle 110 \rangle$ directions among the equivalent three in the (111) plane and each array consists of pairs of large and small etch pits. The one side of the double lines of etch pits in a $\langle 110 \rangle$ array consists of the small etch pits and the other consists of the large etch pits. Maeda *et al.* reported on the three slip modes of a dislocation rosette on the indented (111)B GaP surface (31). Considering the rosette pattern of Fig. 6, it seems that a pair of etch pits in a $\langle 110 \rangle$ array is associated with the dislocation half-loop along a prismatic glide cylinder and the Burgers vector is of equivalent six modes of $+a/2 \langle 110 \rangle$ in the (111) growth plane.

Figure 7 (a) shows many dislocation rosettes on the thicker InGaAsP layer of $4.3 \mu\text{m}$ with the close composition to one of the second quaternary layer of wafer 1, and the lattice mismatch is of $\Delta a/a = -10 \sim +6 \times 10^{-4}$ as a result of the compositional gradient along the growth direction (33, 34). Figure 7 (b) shows the growth pattern on the first InP layer after the quaternary layer was etched by the etchant ($\text{H}_2\text{SO}_4:\text{H}_2\text{O}_2:\text{H}_2\text{O} = 90:5:5$). The notable wavy patterns and many parallel lines to three $\langle 110 \rangle$ directions due to misfit dislocations are observed in Fig. 7(b). As shown by "A"-"F" in both figures, the dislocation rosettes correspond to the fronts of the wavy patterns, respectively. Furthermore, all of them consist of only two $\langle 110 \rangle$ arrays of etch pits. Generation of these dislo-

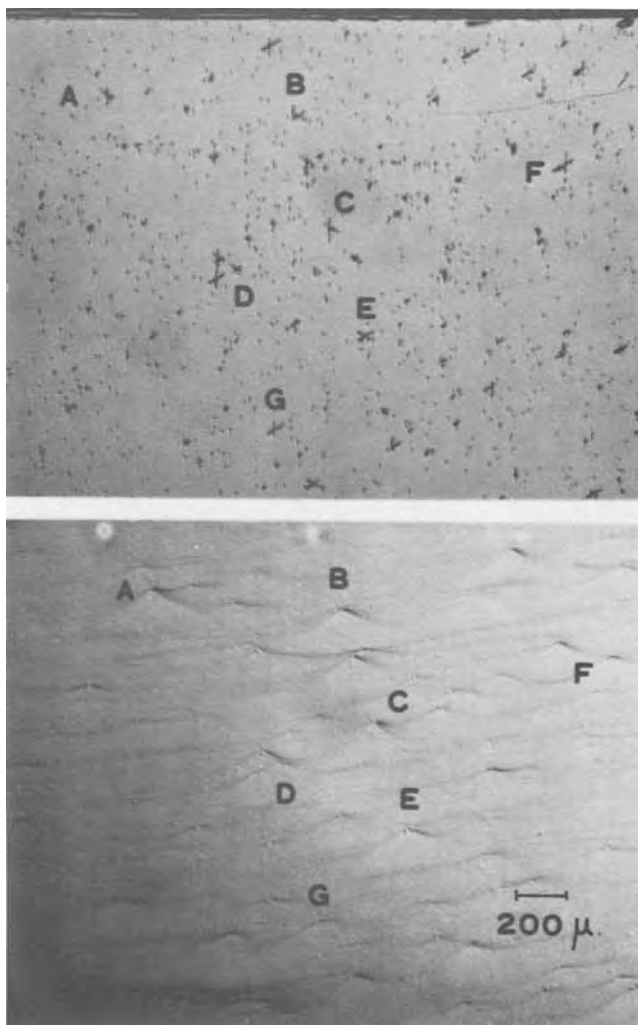


Fig. 7. (a, top) A distribution of the dislocation rosettes on the etched InGaAsP quaternary layer. (b, bottom) The wavy pattern on the first InP layer.

to that of the InP (35), the inner stress σ in the (001) plane due to the lattice mismatch is derived from a formula $\sigma = E/(1 - \nu)\alpha\Delta a/a$ (34, 36). When the stress σ is approximately estimated from the values of $E/(1 - \nu) = 1.2 \times 10^{12}$ dyne/cm² for GaAs [37], the value σ equals to 1.1×10^9 dyne/cm² at room temperature. Though the lattice match at high temperatures is probably more important (38, 39), this mismatch stress had never induced in wafer 1 any misfit dislocations. Nevertheless, this misfit stress is not sufficiently small, and it may be sufficient to induce local plastic deformation when it was localized at the smaller area. Then, it is probable that this notable wavy pattern on the first InP layer has caused such localization. While the dislocation rosette with three or six etch pit arrays is usually induced by symmetric stress around a point in such a case of indentation experiment (31), this localized stress should be asymmetric because of geometry of the wavy pattern and it induced the dislocation rosette with only two etch pit arrays. Furthermore, dislocation crowd may also be caused by such localized stress at a similar wavy pattern, although it rarely was observed.

Mahajan *et al.* (40) has recently reported that dislocation clusters in optically degraded regions in InGaAsP layer were developed from threading and inclusion-generated dislocation by the glide process. Inclusion in the epitaxial layer can probably cause localization of the mismatch stress, but it is not apparent whether this rosette is the same defect.

In summary, the defects in the InGaAsP-InP DH wafer grown on the InP (111)B substrate were investigated by the observations of chemical etching features. The threading dislocations, stacking faults, dislocation rosettes, and dislocation crowds were observed and it was suggested that the dislocation rosettes and crowds were caused by localization of mismatch stress.

Acknowledgments

The authors wish to thank Drs. Y. Furukawa and M. Fujimoto of ECL for their encouragement. We thank Dr. O. Ryuzan and K. Akita for continuous encouragement.

Manuscript submitted Oct. 1, 1979; revised manuscript received April 30, 1980.

Any discussion of this paper will appear in a Discussion Section to be published in the June 1981 JOURNAL. All discussions for the June 1981 Discussion Section should be submitted by Feb. 1, 1981.

Publication costs of this article were assisted by Fujitsu Laboratories, Limited.

REFERENCES

- J. J. Coleman, W. R. Hitchens, N. Holonyak, Jr., and M. J. Ludomise, *Appl. Phys. Lett.*, **25**, 725 (1974).
- J. J. Hsieh, J. A. Rossi, and J. P. Donnelly, *ibid.*, **28**, 709 (1976).
- G. A. Antypas and L. Y. L. Shen, *Inst. Conf. Ser.*, **33b**, 96 (1976).
- T. P. Pearsall, B. I. Miller, and R. J. Capike, *Appl. Phys. Lett.*, **28**, 499 (1976).
- H. H. Wieder, A. R. Clawson, and G. E. Mcwilliams, *ibid.*, **31**, 468 (1977).
- M. Feng, T. H. Windhorn, M. M. Tashima, and G. E. Stillman, *ibid.*, **32**, 758 (1978).
- D. N. Payne and W. A. Lanibling, *Electron. Lett.*, **11**, 176 (1975).
- M. Horiguchi, *ibid.*, **12**, 310 (1976).
- G. A. Antypas, R. L. Moon, L. W. James, J. Edgecumbe, and R. L. Bell, in "Gallium Arsenide and Related Compounds, 1972," Conference Series No. 17, p. 48, Institute of Physics and Physical Society, London (1973).
- J. J. Hsieh, M. C. Finn, and J. A. Sossi, in "Gallium Arsenide and Compounds, 1976."
- P. W. Hutchinson and P. S. Dobson, *Philos. Mag.*, **32**, 745 (1975).
- P. Petroff and L. C. Kimerling, *Appl. Phys. Lett.*, **29**, 461 (1976).
- O. Ueda, S. Isozumi, T. Kotani, and T. Yamaoka, *J. Appl. Phys.*, **48**, 3950 (1977).
- M. Ettenberg and C. J. Nuese, *ibid.*, **46**, 2137 (1975).
- K. Nakajima, T. Kusunoki, K. Akita, and T. Kotani, *This Journal*, **125**, 123 (1978).
- R. C. Clarke, D. S. Robertson, and A. W. Veke, *J. Mater. Sci.*, **8**, 1349 (1973).
- K. Akita, T. Kusunoki, S. Komiya, and T. Kotani, *J. Cryst. Growth*, **46**, 783 (1979).
- M. S. Abrahams and C. J. Buiochi, *J. Appl. Phys.*, **36**, 2855 (1965).
- D. J. Stirland, *Inst. Phys. Conf. Ser.*, **33a**, 150 (1977).
- P. D. Wright, E. A. Rozek, and N. Holonyak, Jr., *J. Cryst. Growth*, **41**, 254 (1977).
- Y. Takada, A. Sasaki, Y. Imamura, and T. Takagi, *This Journal*, **126**, 130 (1978).
- F. A. Thiel and R. L. Barns, *ibid.*, **127**, 1272 (1979).
- S. Komiya and K. Nakajima, *J. Cryst. Growth*, **48**, 403 (1980).
- T. L. Chu and J. R. Gavaler, *This Journal*, **110**, 388 (1963).
- S. Mendelson, *J. Appl. Phys.*, **35**, 1570 (1964).
- T. Kotani, O. Ueda, K. Akita, Y. Nishitani, T. Kusunoki, and O. Ryuzan, *J. Cryst. Growth*, **38**, 85 (1977).
- H. Sunami, T. Terasaki, N. Miyamoto, and J. Nishizawa, *J. Appl. Phys.*, **40**, 4670 (1969).
- Y. Nonomiya, Y. Okuno, and J. Nishizawa, *J. Cryst. Growth*, **46**, 795 (1979).
- K. K. Shih, G. R. Woolhous, A. E. Blakeslee, and J. H. Blum, *Inst. Phys. Conf. Ser.*, **24**, 165 (1975).
- S. Mahajan, K. J. Bachmann, D. Brasen, and E. Buehler, *J. Appl. Phys.*, **49**, 245 (1978).
- K. Maeda, O. Ueda, Y. Murayama, and K. Sakamoto, *J. Phys. Chem. Solids*, **38**, 1173 (1977).
- W. A. Brantley and D. A. Harrison, *This Journal*, **120**, 1281 (1973).
- M. Feng, L. W. Cook, M. Tashima, T. H. Windhorn, and G. E. Stillman, *Appl. Phys. Lett.*, **34**, 292 (1979).
- J. Matsui, K. Onabe, T. Kamejima, and I. Hayashi, *This Journal*, **126**, 664 (1979).
- K. Oe, Y. Shinoda, and K. Sugiyama, *Appl. Phys. Lett.*, **33**, 962 (1978).
- K. Ishida, J. Matsui, T. Kamajima, and I. Sakuma, *Phys. Status Solidi A*, **31**, 255 (1975).
- W. A. Brantley, *J. Appl. Phys.*, **44**, 534 (1973).
- S. G. Simashko, N. P. Bezhan, and V. D. Martynko, *Sov. Phys.-Solid State*, **19**, 146 (1977).
- K. Nakajima, S. Komiya, K. Akita, T. Yamaoka, and O. Ryuzan, Paper 593 presented at The Electrochemical Society Meeting, Los Angeles, California, Oct. 14-19, 1979.
- S. Mahajan, W. D. Johnston, Jr., M. A. Pollack, and R. E. Nahory, *Appl. Phys. Lett.*, **34**, 717 (1979).

Control of Zn Doping for Growth of InP pn Junction by Liquid Phase Epitaxy

O. Wada,¹ A. Majerfeld,² and P. N. Robson

Department of Electronic and Electrical Engineering, University of Sheffield, Sheffield S1 3JD, England

ABSTRACT

The method of Zn doping for the liquid phase epitaxial growth of a high quality InP pn junction has been investigated. The evaporation of Zn from the growth melt was found appreciable at the growth temperature as low as 640°C and therefore causing the unwanted Zn diffusion into the substrate from the vapor. The diffusion of Zn from the growth melt was also observed and its effective diffusion coefficient in undoped InP was estimated to be $1.0 \pm 0.3 \times 10^{-10} \text{ cm}^2 \text{ sec}^{-1}$ at 620°-640°C. The characterization of grown layers was carried out over a wide range of the Zn doping density. The distribution coefficient of Zn was determined from Hall measurement to be 0.84 below the Zn fraction in the melt of 10^{-2} atomic percent. Above this fraction, it was speculated that a strong carrier compensation limits the N_A-N_D value below $2-3 \times 10^{18} \text{ cm}^{-3}$ and also results in the energy decrease and the half-width increase of the photoluminescence. In order to eliminate these disadvantages of Zn doping, an improved growth method was developed by an optimized use of *in situ* etch. The etching of the substrate by pure In solution was found to be characterized by the apparent diffusion coefficient of P in In, $6 \times 10^{-4} \text{ cm}^2 \text{ sec}^{-1}$ at 640°C, and the structure grown by this method was found free from the misplacement of pn junction and also exhibiting the current-voltage characteristics of a nearly abrupt junction.

Recently InP has been receiving considerable interest because of its promising application to microwave devices as well as optical devices. One of the important technologies in processing InP devices is the formation of high quality pn junctions, which are widely required for various devices like InP IMPATT diodes and light emitting diodes. Several investigators have studied the liquid phase epitaxial (LPE) method to realize InP pn junctions consisting of Zn- or Cd-doped p⁺-type layer and Sn-doped n-type layer (1, 2).

Since it has been shown that both Ge and Si, which behave as amphoteric dopants in GaAs, cannot produce a p-type conduction in InP grown by the LPE method (1, 3), Zn is considered to be one of the most convenient dopants to prepare p-type InP layers. When Zn is chosen as p-type dopant in the LPE growth, however, one should pay attention to its high vapor pressure as well as to the relatively high diffusion coefficient in the semiconductor bulk at the growth temperature. The evaporation of Zn in the Ga melt during GaP growth has resulted in the carrier density profile decreasing toward the epitaxial layer surface (4). The misplacement of the pn junction observed in the GaAs (5) and the InP (2) homojunctions and the InP-In_{1-x}Ga_x-As_{1-y}P_y heterojunction (6) is considered to be attributable to either the Zn diffusion during the p⁺-type layer deposition or to the cross-contamination of melts caused by the Zn evaporation. However, the understanding of this kind of problem in the LPE method has been left vague since no systematic studies have been carried out. Concerning the electrical characteristics of a Zn-doped layer, the net acceptor concentration has been reported to saturate at $3-4 \times 10^{18} \text{ cm}^{-3}$ for higher Zn fractions in the growth melt (1). The effect of high doping has not been fully investigated so far, regardless of its importance in the p⁺n junction structure.

The purpose of the present paper is to investigate the properties of Zn as a dopant for p-type InP layers, in order to develop the LPE growth technique to fabricate a high quality p⁺n junction. In the course of our

experiment, we have found that anomalous layers are formed in the n-type substrates during the growth of a Zn-doped p-type layer. The mechanism of this anomaly is analyzed in conjunction with the evaporation of Zn from the melt as well as the diffusion of Zn into the substrate. The effect of the Zn doping density is investigated in terms of the electrical property determined by the Hall measurement and the optical property obtained by the photoluminescence measurement. Finally, a growth method which can eliminate the formation of such anomalous layers is demonstrated and the suitable growth procedures for the fabrication of high quality pn junctions are discussed.

Growth Techniques

The growth system consisted of a horizontal furnace with a transparent gold-plated reflector and a sliding boat made of high purity graphite. The spacing of the Kanthal winding and the thickness of the gold film were optimized and a flat temperature profile within $\pm 0.5^\circ\text{C}$ deviation was obtained over the length of the boat. The furnace temperature was controlled by a Eurotherm Model 120 controller monitoring the temperature near the bottom of the graphite boat. The hydrogen was introduced into the reactor tube having the inner diameter of 43 mm through a Pd-diffused purifier at the rate of approximately 0.3 liter/min.

Two different sliding boats were used in our experiment. Boat 1 had a single 4 mm thick slider which had two melt bins with the cross section of $4 \times 4 \text{ mm}^2$. An additional $8 \times 8 \text{ mm}^2$ window was prepared in the slider. An InP plate set in this window protected the substrate during the pregrowth heating; this technique was useful to eliminate the thermal erosion of the substrate surface (7). Boat 2 had two sliders on the framework. Three $6 \times 8 \text{ mm}^2$ melt bins as well as a $14 \times 11 \text{ mm}^2$ window for the substrate cover were provided in the lower slider, the thickness of which was 3 mm. The top slider also had melt bins with same sizes as lower ones. A part of the melt stored together with the source InP in the upper bin can be introduced into the lower bin and made out of contact with the source InP by sliding the top slider on the lower one. The growth melt can be thus completely isolated in this system so that the losses of P and Zn are mini-

¹ Present address: Fujitsu Laboratories Limited, Nakahara, Kawasaki 211, Japan.

² Present address: Department of Electrical Engineering, University of Colorado, Boulder, Colorado 80309.

Key words: Zn evaporation, diffusion coefficient, distribution coefficient, photoluminescence.

mized. The surfaces of the framework and the lower and the top sliders were finished to give intimate contacts, and the upper melts were protected by graphite covers over the bins.

The growth melt was saturated with InP mostly at 650°C for more than 30 min. It was once cooled down and then Zn of an appropriate amount was added to it and also the substrate was charged before the growth run. The substrate rested in the downstream of H₂ flow during the pregrowth period, and the minimum separation between the substrate and the growth melt was ~3 cm in both boat systems. The growth was carried out by contacting the melt, supercooled to 6°–13°C below the saturation temperature, to the substrate during either the isothermal growth or the ramp growth. The cooling rate used was 0.6°–2.6°C/min and the growth time was varied from 1 to 45 min.

Undoped bulk crystals with the carrier concentration around $4 \times 10^{15} \text{ cm}^{-3}$ and the mobility of about 5000 cm²/V · sec were used as both phosphorus sources and growth substrates. Fe- and Cr-doped semi-insulating substrates with the resistivity ranging in 10⁵–10⁶ Ωcm were also used. The substrate and the source InP were etched in 0.5% Br · CH₄O solution and then stored in isopropylalcohol until they were charged into the furnace. High purity In (99.9999%, Johnson Matthey, Grade A1) and Zn (99.9998%, Metals Research) were weighed and etched by dilute HNO₃ just prior to the charging.

Results and Discussion

Junction cross section.—The cross section of the grown layer was stained with a solution of KOH + K₃[Fe(CN)₆] (8) at room temperature: this etchant has been found more sensitive to the effect of our interest than the AB etchant (9). Most of the samples grown without any special precaution showed either two or three lines after staining regardless of a single deposition of the p⁺-layer on the substrate. Figure 1 demonstrates an example of a microphotograph showing the formation of anomalous layers below the Zn-doped layer. In this case, a layer having two regions with different thicknesses has been grown by means of the shift of the melt bin using boat 1. The substrate with ~3.5° off <111> plane has been used and the growth times have been 15 and 30 min for the two regions, respectively. The straight line M shows the metallurgical interface. It is noticed that the additional lines, L and V, are deeper for longer growth duration. The depths of these two lines measured from the metallurgical interface are plotted vs. the growth time in Fig. 2. In this measurement, the growth has been carried out by boat 1 at ~640°C from a supercooled

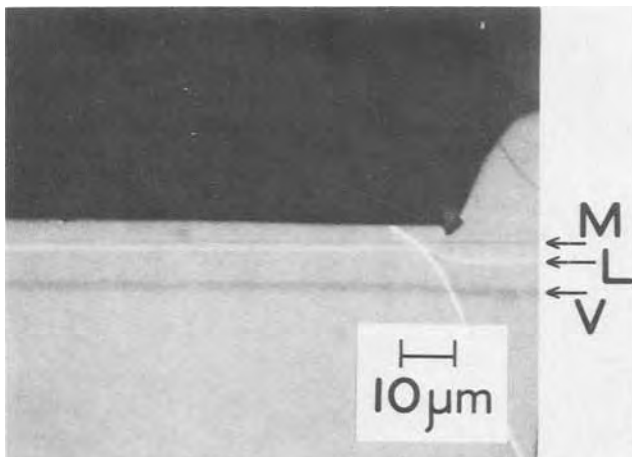


Fig. 1. Microphotograph showing the stained cross section of a p⁺ layer grown on an undoped substrate. The growth time is 36 min on the right end and 16 min for the rest. The stained line M corresponds to the metallurgical interface, below which two extra lines L and V are revealed.

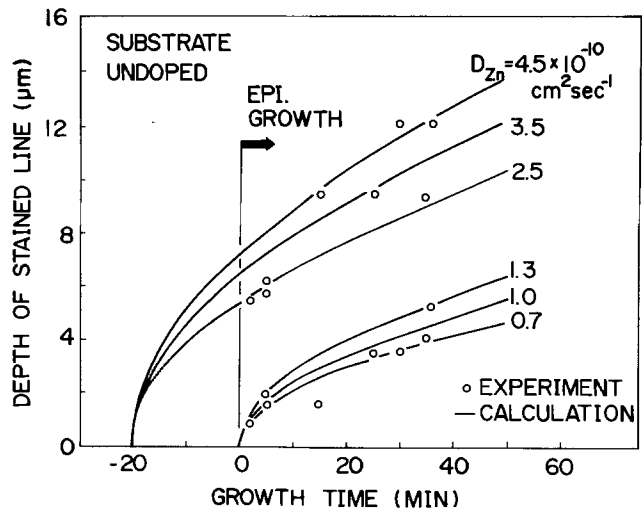


Fig. 2. Relationship of the depth of the stained line measured from the metallurgical interface vs. the growth time. The lines have been calculated with the assumption of a simple Zn diffusion for various values of the diffusion coefficient. The preheat duration of 20 min has been assumed.

melt with the Zn atomic fraction in the range of 0.06–0.02%. As seen in Fig. 2, line V is already several micrometers deep even on the early stage of the growth, whereas line L appears after the growth initiates.

The following possible origins can be considered to account for this anomaly: (i) the thermal conversion of the surface of the undoped substrate, (ii) the in- or out-diffusion of impurity, and (iii) the diffusion of Zn into the substrate. Our ancillary experiment showed that an anomalous layer is formed when the melt includes Zn even if it is located away from the substrate during heating. On the contrary, neither the growth of an undoped layer nor the heat-treatment of the substrate without Zn in the reactor exhibited any trace of anomaly. These facts suggest that possibility (iii) is working in our case, and the following mechanism is considered to operate. First, a fraction of Zn in the melt evaporates out and the Zn atoms in the vapor diffuse into the substrate even before actual contact of the melt with the substrate. After the contact the Zn atoms remaining in the melt diffuse into the substrate. These two processes are generating, primarily, the layer far below the interface and the one next to the interface, respectively. If the diffusion profile is assumed to obey a complementary error function, the diffusion depth d is expected to be given by

$$d \simeq (D_{Zn}t_d)^{1/2} \quad [1]$$

where D_{Zn} is the diffusion coefficient of Zn in InP and t_d stands for the diffusion time. The lines shown in Fig. 2 have been calculated by this equation with assumed values of D_{Zn} . Although the pregrowth duration in which ramp cooling took place ranged from 10 to 30 min, we have used 20 min as the median value in the calculation. The values of D_{Zn} are obtained to be $3.5 \pm 1.0 \times 10^{-10} \text{ cm}^2 \text{ sec}^{-1}$ for the diffusion from the vapor in the temperature range of 620°–650°C and $1.0 \pm 0.3 \times 10^{-10} \text{ cm}^2 \text{ sec}^{-1}$ for the diffusion from the liquid in the temperature range of 620°–640°C. Taking into account the Zn evaporation continuously occurring during the growth and also the appreciable variation of the initial Zn fraction in the melt, these values are considered to be in a reasonable agreement with earlier works (10, 11).

In order to know the loss of Zn in the melt during the growth, a sequence of weight measurement of the melt was carried out after each heat-treatment period. The melt consisted of 330 mg In with or without InP saturated at the heating temperature. First, the melt saturated with InP was heated at 650°C in boat 1 in

order to know the loss rate of P, and it was found very small, $9.5 \times 10^{-3} \text{ hr}^{-1}$; this is in a good agreement with Hsieh's data (12). Next, the melts having different Zn weights were charged in boat 1 and were heated at 650°C . As for the set of melts unsaturated, the one with higher Zn fraction was located at the upper-stream of the H_2 flow and the other one at 2.7 cm downstream from it. As shown in Fig. 3, the melt rapidly loses weight because of the Zn evaporation. The error bars indicated in the figure are for inaccuracies in determining small weight differences by a microbalance. A point worthwhile mentioning is that the melt with a lower Zn fraction initially gains its Zn weight until it reaches the same Zn weight fraction as the other one has. Essentially same effect is observed on InP-saturated melts. In this measurement, the melt with lower Zn weight was located 1.2 cm upstream with respect to the higher Zn melt. These features indicate that the Zn atoms in the higher Zn melt are transported to the lower Zn melt via the vapor phase. Judging from a relatively small Zn weight difference found between two InP-saturated melts after 30 min heating, the Zn transportation is considered to be nearly independent of the gas flow direction at least at the flow rate used (~ 0.3 liter/min). The slightly slow Zn loss in the InP-saturated melt may be attributable to the formation of solid phase Zn_3P_2 which is stable at this temperature (13). It is remarked that, when the melt is protected by the top slider in boat 2, the Zn loss is well prohibited. If the Zn loss is fully controlled by the evaporation into the free atmosphere, the time dependent weight of Zn ($W(t_e)$, W_0 at $t_e = 0$) at a fixed temperature is considered in an analogy of vacuum pumping (14) and is expressed in a form of

$$W(t_e) = W_0 \exp(-t_e/\tau) \quad [2]$$

where τ is the time constant being proportional to the reciprocal of the melt surface area. Our data are well approximated by this equation and τ is estimated to be 12 and 200 min for the unprotected and the protected melts, respectively, indicating that the effective surface area is decreased by 18 times by the protection regardless of the three times larger bin cross section of boat 2 than that of boat 1.

The effect of Zn evaporation from the melt has been reported in LPE growth of GaAs (5) and GaP (4), and Solomon and Defever (15) proposed a technique of sealing the melt by means of a floating plug. The

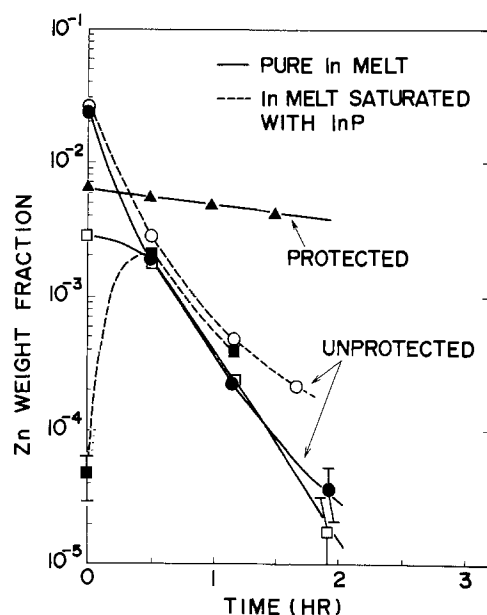


Fig. 3. Results of the weight measurement of the Zn included in the melt at 650°C for unprotected melt and at 640°C for protected melt. The unprotected melt shows rapid gain and loss of Zn weight, whereas the protected melt exhibits a slow weight loss.

growth temperatures for those materials are much higher than ours. However, the present results indicate that even at $640^\circ\text{--}650^\circ\text{C}$ the Zn evaporation can affect the melt composition. The absorption of Zn observed here is supporting the possibility of the cross contamination of the multiple melt as has been suggested by Coleman (6). Moreover, as shown in the present case, the direct diffusion of Zn evaporated from the melt into the substrate prior to the actual growth can contribute to the misplacement of the pn junction, especially when the carrier concentration of the substrate is relatively low.

Electrical characteristics of p^+ layer.—Successive light etching followed by Van der Pauw Hall measurement was applied to determining the spatial distributions of the net carrier concentration $N_A - N_D$ and the hole mobility up in a p^+ -type layer grown on a Cr-doped substrate. The data were analyzed by the method reported by Darwish (16) so that the values of $N_A - N_D$ and μ_p , averaged over the thickness of the etched segment of epitaxial layer, were deduced. An example of the result measured on the layer grown by an unprotected melt with boat 1 is shown in Fig. 4. The etched thickness has been shown as error bar length in this figure. The arrows show the positions of the stained lines. The arrow at $X = 1.8 \mu\text{m}$ shows the metallurgical interface and the one at $X = 5.1 \mu\text{m}$ indicates the diffusion front of Zn in vapor, though the stained line corresponding to the diffusion front of Zn in liquid is missing in this example. $N_A - N_D$ exhibits a long tail into the substrate, confirming the formation of a p-type layer due to the Zn diffusion. Although the width of this layer ($3.3 \mu\text{m}$) is much smaller than that estimated from Fig. 2 for the growth time of 20 min, this has been a common experience in our measurement on Cr- and Fe-doped substrates and the mechanism of the carrier generation due to the Zn diffused in a semi-insulating InP is suspected to be more complicated than in an undoped InP. A sharp peak of $N_A - N_D$ observed at the interface is considered to be caused by a high surface concentration of Zn associated with the diffusion (17). $N_A - N_D$ is found to

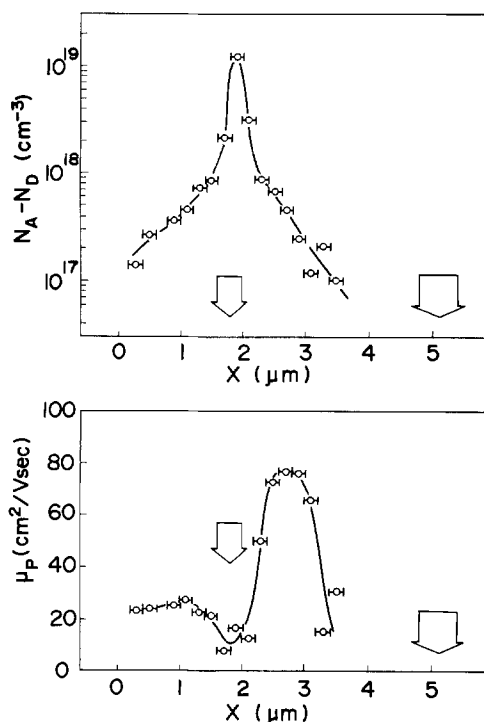


Fig. 4. Profiles of the net carrier concentration and the hole mobility in the depth direction of the layer. The epitaxial layer surface is at $X = 0$, and the arrows at 1.8 and $5.1 \mu\text{m}$ show the positions of the stained lines.

be much smaller inside the epitaxial layer than at the interface. The value of μ_p is also very small inside the epitaxial layer compared to that in the diffused layer. Since the value of μ_p in the diffused layer is in an agreement with the result of Hooper and Tuck (18), small N_A-N_D together with correspondingly small μ_p in the epitaxial layer is considered to imply that the net carrier concentration is less than the concentration of Zn atoms actually introduced in the crystal.

The net carrier concentrations were measured on samples with different Zn doping densities. The effect of Zn diffusion was minimized by adopting a quick growth procedure with a protected melt, and the Hall measurement data were analyzed in accordance with the thickness calibrated for the Zn diffusion depth. The plot of N_A-N_D vs. Zn atomic fraction in the melt is shown in Fig. 5 together with the data reported by Astles *et al.* (1). In the smaller range of Zn fraction, a linear relationship is obtained and the distribution coefficient of Zn, k_{Zn} , is estimated to be 0.84, which is smaller than $k_{Zn} = 1.4$ determined by Astles *et al.* (1). At the Zn fraction above 0.01 atom percent (a/o), N_A-N_D saturates at $2-3 \times 10^{18} \text{ cm}^{-3}$ and even decreases as indicated by a single experimental data included in Fig. 5. Although the behavior of N_A-N_D above the Zn fraction of 0.1 a/o would need more work to be explained, the saturation effect observed here is considered to indicate that a high Zn doping causes a lowering of the ratio of the electrically active Zn atom concentration to the total concentration of Zn atoms introduced, being consistent to our hypothesis made in regard to Fig. 4. This is also consistent with the result of Kundukhov *et al.* (19). As for the result in Fig. 4, the fraction of Zn remaining in the melt during the growth has been estimated to be more than 0.01 a/o; this fraction is large enough for the lowering of the carrier to atom concentration ratio to occur. Mahajan *et al.* (20) recently found by the transmission electron microscopic analysis on the crystal with the carrier concentration of $2-5 \times 10^{18} \text{ cm}^{-3}$ that some of Zn atoms introduced in the crystal can form precipitate. Such precipitate could contribute to reduce the numbers of free carriers. However, the observed decrease of the carrier concentration exceeds $1 \times 10^{19} \text{ cm}^{-3}$ at the Zn fraction of 0.1 a/o (see Fig. 5) and this is considered to be too high to be explained by the precipitate density, equivalently below 10^{13} cm^{-3} as determined by Mahajan *et al.* Instead, the most likely model to interpret the lowering of the carrier to atom concentration ratio would be the occurrence of the carrier compensation as suggested by Hooper and Tuck (18), in which the Zn atoms are incorporated in the interstitial sites to create donors due to the formation of some kind of complex.

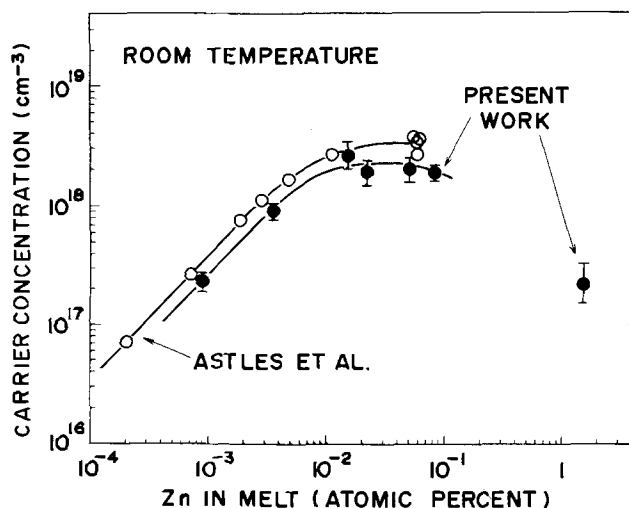


Fig. 5. A plot of the net carrier concentration vs. the Zn atomic fraction in the melt.

Photoluminescence properties of p^+ layers.—Photoluminescence (PL) measurement was carried out at RSRE, Malvern, England, on a number of Zn-doped layers at 6°K by a setup similar to that reported earlier (21), in which a high pressure mercury arc was used as the excitation source. A few samples were made of undoped substrates heat-treated in the furnace with the presence of a melt containing Zn, so that we could examine PL on Zn-diffused layers. Zn is a common residual impurity in In and has been found to exhibit a PL peak due to band-acceptor recombination at 1.37-1.38 eV (3, 22, 23). The PL peak of the Zn-diffused layer was found in our experiment at 1.374 eV, which exhibited the typical Zn peak, and this peak maintained its energy at low Zn fractions. However, above the Zn fraction of 0.003 a/o, the peak shifted to lower energy and simultaneously broadened. The changes of peak energy and the full half-width are plotted in Fig. 6 and 7, respectively, where the results reported by Williams *et al.* (22) and Röder *et al.* (23) are also plotted on the basis of the linear relationship shown by Astles *et al.* (1) between the net acceptor concentration and the Zn fraction in the melt. Although our data involve inaccuracies in estimating the Zn fraction, the peak shift and the increase of the half-width are obvious above the Zn fraction of 10^{-3} - 10^{-2} a/o and their variations qualitatively agreed with the reported results shown. It is interesting to note a coincidence of the behavior between the carrier concentration and the PL data. As has been shown in Fig. 5, N_A-N_D begins to saturate at the Zn fraction of 10^{-2} a/o, above which the PL peak shifts and broadens. Such PL characteristics are considered

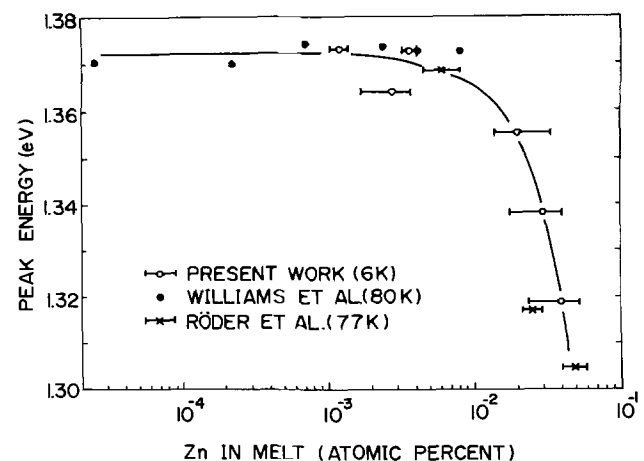


Fig. 6. Dependence of the photoluminescence peak energy on the Zn fraction in the melt.

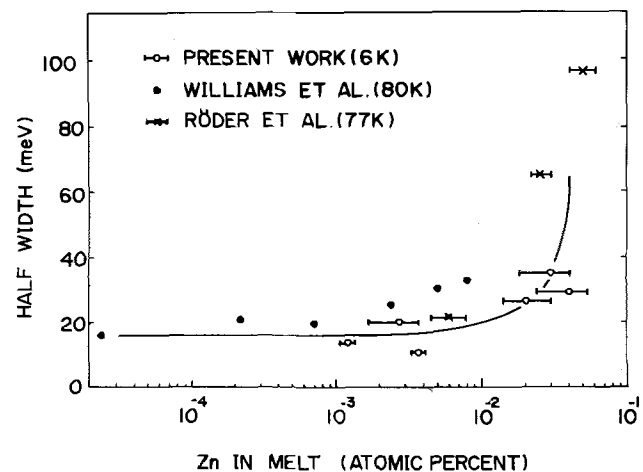


Fig. 7. Dependence of the half-width of the photoluminescence peak on the Zn fraction in the melt.

to be partly due to the development of the acceptor band in this range of Zn concentration. The acceptors are considered to form an impurity band above a net concentration of $1 \times 10^{18} \text{ cm}^{-3}$ and the PL transition is dominated by the band acceptor recombination near the top of the acceptor band. Since the top of the acceptor band moves deeper into the forbidden gap with the increase of the concentration, the PL peak energy is reduced; similar effect has been found in Zn-doped GaAs (24). However, more characteristically in higher doping range, the effect of carrier compensation, which has been pointed out previously, may also play an important role in the reduction of PL peak energy through the shift of the Fermi energy inside the impurity band, as has been reported on Zn-doped GaAs by Tuck (25). This model is likely able to explain the coincidence between the behavior of the carrier concentration and the PL in the high doping range, although a clear understanding of the compensation mechanism is subject to more detailed investigations.

Improved method of growing pn junctions.—As has been pointed out in previous sections, the evaporation of Zn from the melt before the growth, followed by its diffusion into the substrate during the growth is one of the unwanted effects associated with the Zn doping. The melt protection has been proposed for the minimization of this effect. The protection, however, may not be satisfactory to completely eliminate the unwanted Zn vapor around the substrate. Therefore, we examined a method to get rid of the Zn-diffused layer after its formation by extensively applying the *in situ* etch technique (26). When this technique is incorporated in our growth procedure, it is important to optimize the etching duration since the Zn diffusion is able to occur even from the Zn-contaminated etching solution if the etching velocity is not larger than the Zn diffusion velocity.

We measured, therefore, the etching characteristic using a pure In solution. In the measurement, the substrate was made in contact with the etching solution for a certain time at a constant temperature. The weight loss of the substrate was then measured and converted into the etched depth using the solution-substrate contact area. Boat 2 was most suitable for this experiment because a constant solution thickness could be realized all over the substrate surface. The etched depth of a substrate with 3.5° off (100) plane at 640°C is plotted vs. the etching time in Fig. 8. When the effect of solution convection can be neglected, the etching process is considered to be limited by the diffusion of P in In and the total weight $M(t)$ of the substrate etched in time t for unit substrate area is expressed (27) by

$$\frac{M(t)}{M(\infty)} = 1 - \sum_{n=0}^{\infty} \frac{8}{(2n+1)^2\pi^2} \exp[-D_P(2n+1)^2\pi^2t/4l^2] \quad [3]$$

where D_P and l stand for the diffusion coefficient of P in In and the solution thickness measured perpendicular to the substrate surface. The data calculated from $l = 3 \text{ mm}$ (boat 2) for different values of D_P are also shown in Fig. 8. The saturation level of the etched thickness has been estimated to correspond to a weight fraction of InP in In solution of 8.5×10^{-3} which is in a good agreement with the solubility of P in In at this temperature (13). It is found in the figure that our experimental data are well explained when $D_P = 6.0 \times 10^{-4} \text{ cm}^2 \text{ sec}^{-1}$ is assumed. Hsieh (12) used a theory of the diffusion-limited LPE growth to derive a value of D_P of $6.1 \times 10^{-5} \text{ cm}^2 \text{ sec}^{-1}$ at 640°C . Recently Srnanek and Hobovcik (28) carried out the desolution experiment similar to ours to obtain the D_P value close to Hsieh's. Although the origin of the discrepancy between our and other's D_P values is not known yet, it is particularly useful for the present purpose that

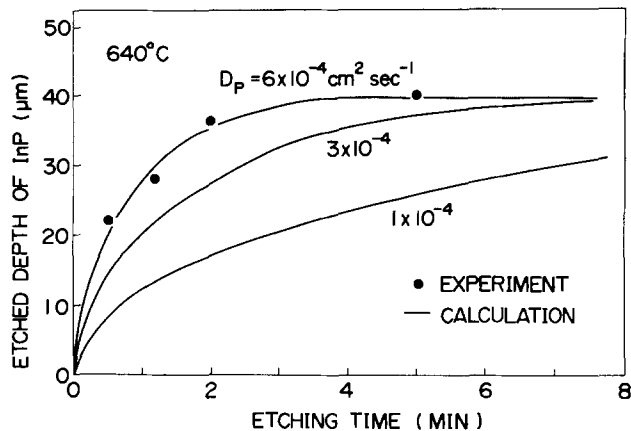


Fig. 8. A plot of the depth of InP substrate etched by a pure In solution with a fixed volume vs. the etching time. The calculations with three different values of the diffusion coefficient of P have been shown.

the etching is appreciably quick and also characterized by a single value of D_P equal to $6.0 \times 10^{-4} \text{ cm}^2 \text{ sec}^{-1}$ at 640°C .

The layer Zn-contaminated prior to the etching, the thickness of which would be several microns, can be completely removed within the etching duration only less than 10 sec, as known from Fig. 8. The exact velocities of the InP etching and the Zn diffusion from the solution can be determined, respectively, from the derivatives of Eq. [3] and [2] together with the values of D_P and D_{Zn} determined in our experiment. From this consideration, it is shown that the etching velocity is ten times greater than the Zn diffusion velocity up to 2.7 min after the solution-substrate contact. On the basis of the present data, we grew a p^+ -layer using the *in situ* etch technique. Typical examples of photomicrographs of stained cross sections are demonstrated in Fig. 9. The layer shown in Fig. 9(a) has been grown with the etching time of 10 min and the growth time of 2 min, and the appearance of line L indicates that the Zn diffusion occurred during the etching process because of a too long etching time. On the other hand, Fig. 9(b) shows a single layer without any effect of Zn diffusion both from the vapor and from the liquid. The times of the etching and the growth in this case were, respectively, 40 sec and 1 min, and the Zn fraction in the melt was restricted below 10^{-2} a/o. This result shows the effectiveness of the *in situ* etch with an optimized duration as well as the control of the Zn fraction in the melt.

As described so far, (i) the use of the *in situ* etch by a pure In melt in addition to the protection of the melts, (ii) the minimization of the growth period, and (iii) the control of the Zn fraction in the melt give a solution to diminish the major problems associated with the Zn doping. In order to confirm our findings, we measured the current-voltage (I - V) characteristics of pn junctions made by various methods in the course of the present study. Figure 10 shows the forward I - V characteristics of junctions prepared with and without the *in situ* etch. The diodes used in these measurements consisted of mesa etched junctions with the area of approximately $2 \times 10^{-3} \text{ cm}^2$ having the p- and the n-contacts of alloyed Au-Zn and Au-Ge/Ni films, respectively. For both junctions, the forward current density, J , can be approximated by $J = J_s \exp(-V/nkT)$, where J_s , V , and n represent the saturation current density, the applied voltage, and the ideality factor. As seen in Fig. 10, the junction which is contaminated by Zn shows poor and unreproducible characteristics; the ideality factor is much larger than 2, and, in particular, a strong current saturation is observed at fairly low voltages, indicative of the existence of a high resistivity layer in the transition region between the Zn-diffused layer and the n-type bulk. The capaci-

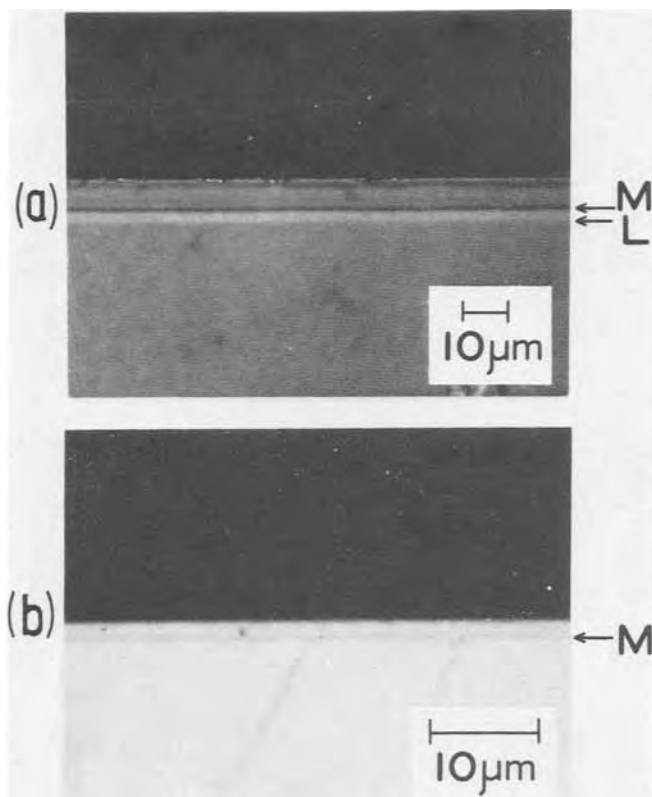


Fig. 9. Photomicrographs showing the stained cross sections of the p^+ -layers grown after the *in situ* etch; the etching time and the growth time are, respectively, (a) 10 min and 2 min and (b) 40 sec and 1 min.

tance-voltage (C-V) measurement on the same junction has indicated the graded nature of the carrier concentration profile in the n-type substrate, and this is consistent with the high resistivity in the transition region. On the other hand, the junction fabricated by the improved method with the *in situ* etch exhibits a reasonable characteristic with the ideality factor as small as 2.0 and an excellent linearity of the $\ln I$ -V is found over a range of the current exceeding 10^6 times difference. The current saturation observed above 0.9V is caused by the series resistance of the n-type substrate. The C-V analysis carried out on the same junction has confirmed a fairly constant distribution of the carrier concentration and also has given the built-in potential of 1.14 eV which is close to the value, 1.21 eV, predicted for a p^+n abrupt junction.

Summary

The formation of anomalous layers below the metallurgical junction between the Zn-doped p^+ -layer and the n-type substrate was interpreted in terms of the evaporation of Zn from the melt followed by its diffusion from the vapor phase into the substrate and also the diffusion of Zn remaining in the melt into the substrate. The evaporation of Zn was confirmed by the separate measurement of the weight loss of the melt, and the diffusion of Zn in InP was found to exhibit a value of diffusion coefficient, $1-4 \times 10^{-10} \text{ cm}^2 \text{ sec}^{-1}$, at a temperature around 630°C . The depth profiles of the net carrier concentration and the hole mobility were analyzed and found to agree with the above model. A low net carrier concentration found in the epitaxial layer was presumed to be caused by the effect of compensation of the carriers. The carrier reduction was revealed above the Zn fraction of 10^{-2} a/o in the melt by the Hall measurement. PL measurements showed the energy decrease and the broadening of PL peak in higher range of Zn doping. By considering these features, we developed an improved method to prepare a pn junction free from the Zn contamination. The ap-

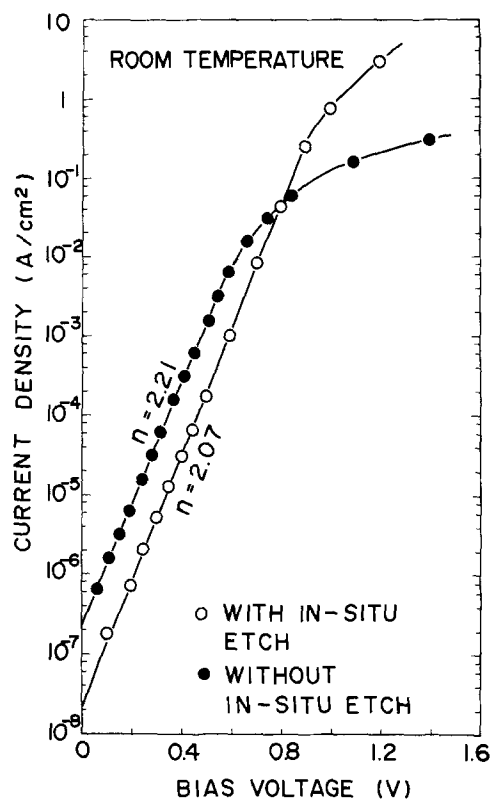


Fig. 10. Forward current-voltage characteristics of pn junctions fabricated by the growth methods with and without the *in situ* etch technique.

plication of *in situ* etch technique as well as the use of a melt protector were found effective to eliminate the Zn diffusion. The *in situ* etch was characterized by the apparent diffusion coefficient of P in In, $6 \times 10^{-4} \text{ cm}^2 \text{ sec}^{-1}$ at 640°C . Also quick growth process with the Zn amount suppressed was found preferable. This knowledge enabled us to optimize the growth sequence and the resulted junction was free from anomaly. This method was confirmed, by the measurement of the I-V and C-V characteristics of p^+n junctions, to greatly improve the quality of the devices.

Acknowledgments

The authors are grateful to R. L. Messham and N. Moyes of this laboratory, P. D. Greene of STL, England, A. M. White of RSRE, England, and K. Akita and H. Nishi of Fujitsu Laboratories Ltd., Japan, for their stimulating discussions. This work has been supported by S.R.C., U.K. Thanks are also due to T. Misugi, Y. Fukukawa, H. Takanashi, and Y. Toyama of Fujitsu Laboratories Limited, Japan, for their encouragement and supporting publication of this work.

Manuscript submitted June 11, 1979; revised manuscript received March 28, 1980.

Any discussion of this paper will appear in a Discussion Section to be published in the June 1981 JOURNAL. All discussions for the June 1981 Discussion Section should be submitted by Feb. 1, 1981.

Publication costs of this article were assisted by Fujitsu Laboratories Limited.

REFERENCES

1. M. G. Astles, F. G. H. Smith, and E. W. Williams, *This Journal*, **120**, 1750 (1973).
2. G. M. Blom and J. M. Woodall, *Appl. Phys. Lett.*, **17**, 373 (1970).
3. G. G. Baumann, K. W. Benz, and M. H. Pilkuhn, *This Journal*, **123**, 1232 (1976).
4. P. D. Sudlow, A. Mottram, and A. R. Peaker, *J. Mater. Sci.*, **7**, 168 (1972).

5. M. Ettenberg and C. J. Nuese, *J. Appl. Phys.*, **46**, 3500 (1975).
6. J. J. Coleman and F. R. Nash, *Electron. Lett.*, **14**, 599 (1978).
7. S. Guha, A. Majerfeld, N. Moyes, and P. N. Robson, *ibid.*, **14**, 303 (1975).
8. M. C. Hales, J. R. Knight, and C. W. Wilkins, in Proceedings of International Symposium on GaAs and Related Compounds, Aachen, 1970, *Inst. Phys. Conf. Ser. 9*, p. 51 (1971).
9. M. S. Abrahams and C. J. Buiochi, *J. Appl. Phys.*, **36**, 2855 (1965).
10. B. Tuck and A. Hooper, *J. Phys. D*, **8**, 1806 (1975).
11. E. A. Rezek, P. D. Wright, and N. Holonyak, *Solid State Electron.*, **21**, 325 (1978).
12. J. T. Hsieh, in Proceedings of International Symposium on GaAs and Related Compounds, St. Louis, 1976, *Inst. Phys. Conf. Ser. 33b*, p. 74 (1977).
13. J. C. Bailar, Jr., H. J. Emeleus, R. Nyholm, and A. F. Trotman-Dickenson, Editors, "Comprehensive Inorganic Chemistry," Vol. 3, p. 231, Pergamon Press, Oxford (1973).
14. A. Roth, "Vacuum Technology," chap. 2 and 3, North-Holland, Amsterdam (1976).
15. R. Solomon and D. DeFevere, *J. Electron. Mater.*, **1**, 26 (1972).
16. M. Y. Darwish, *IEEE Trans. Electron Devices*, **ed-21**, 397 (1974).
17. B. Tuck and M. D. Zahari, in Proceedings of International Symposium on GaAs and Related Compounds, *Inst. Phys. Conf. Ser. 33a*, Edinburgh, 1976, p. 177 (1977).
18. A. Hooper and B. Tuck, *Solid State Electron.*, **19**, 513 (1976).
19. R. M. Kundukhov, S. G. Metreveli, and N. V. Siukaev, *Sov. Phys. Semicond.*, **1**, 765 (1976).
20. S. Mahajan, W. A. Bonner, A. K. Chin, and D. C. Miller, *Appl. Phys. Lett.*, **35**, 165 (1979).
21. E. W. Williams and R. A. Chapman, *J. Appl. Phys.*, **38**, 2547 (1967).
22. W. W. Williams, W. Elder, M. G. Astles, M. Webb, J. B. Mullin, B. Straughan, and P. J. Tufton, *This Journal*, **120**, 1741 (1973).
23. O. Röder, U. Heim, and M. H. Pilkuhn, *J. Phys. Chem. Solids*, **31**, 2625 (1970).
24. R. K. Willardson and A. C. Beer, Editors, "Semiconductors and Semimetals," Vol. 8, p. 321, Academic Press, New York (1972).
25. B. Tuck, *J. Phys. Chem. Solids*, **28**, 2161 (1967).
26. V. L. Wrick, G. J. Scilla, and L. F. Eastman, *Electron. Lett.*, **12**, 395 (1976).
27. J. Crank, "The Mathematics of Diffusion," p. 45, Oxford University Press, London (1957).
28. R. Srnanek and P. Habovcik, *J. Cryst. Growth*, **46**, 55 (1979).

The Use of Electrical Test Structure Arrays for Integrated Circuit Process Evaluation

Martin G. Buehler*

National Bureau of Standards, Electron Devices Division, Washington, DC 20234

ABSTRACT

Four different classes of electrical test structure arrays for the analysis of integrated circuit manufacturing processes are described. They include test structures that evaluate the density of random faults, the variation of parameters within a chip, the alignment between photomasks, and the carrier generation lifetime of small diodes. All of the structures allow for the rapid collection of large amounts of data through the use of electrical test methods. Thus, a statistically significant amount of data can be collected that allows a detailed study of processing steps.

The successful fabrication of a large scale integrated circuit chip requires that process and device parameters be confined to tight design windows and that random fault densities be uniformly low (1). Because many of these parameters vary unpredictably across a wafer, they cannot be effectively evaluated by the measurement of a few elements on a wafer. Electrical test structure arrays fabricated across a wafer allow a detailed evaluation through the rapid acquisition of a statistically significant number of data points.

The variations in process and device parameters across a wafer may be divided into three categories. First, some parameter variations are identical from wafer to wafer but are unrelated to the periodicity of the chip dimension. These are introduced by such processing steps (2) as diffusion, ion implantation, epitaxial layer growth and plasma etching. Second, other parameter variations are repeated periodically across a wafer with a periodicity corresponding to the chip dimension. These variations are introduced by optical pattern generation and step and repeat processes. Finally parameter variations may be random in nature. These are caused by such effects as crys-

talline imperfections in the semiconductor material, faults in the patterning of the various layers, or distortions introduced by the many fabrication steps.

Spatial variations in parameters directly impact chip yield. In addition, they affect the circuit designer who uses the mean value of the parameters for his circuit model and assumes that the circuit has enough margin in performance to function in spite of parameter variations.

This paper describes four classes of test structure arrays used to diagnose integrated-circuit manufacturing processes. They include test structures that evaluate the density of random faults, the variation of parameters within a chip, the alignment between photomasks, and the carrier-generation lifetime of small diodes. It is hoped that this paper will encourage the use and further development of this class of characterization techniques.

Random Fault Density

In this paper, the term random fault refers to such faults as breaks in metal lines or metal-to-silicon-contacts. The density of random faults is determined from a random fault test structure which is a collection of elements such as metal-to-silicon contacts or metal crossovers that are tested for electrical continuity or isolation. The elements are usu-

* Electrochemical Society Active Member.

Key words: integrated circuit; linewidth; photomask alignment; process control; random faults, test patterns; test structures.

ally connected in series as is the case for the metal-to-silicon contact test structure. If enough elements are used, the structure is useful for process control, design rule optimization, and new process and equipment evaluation (3). In many test patterns observed by the author, the random fault test structures have an insufficient number of elements. Such structures are useful only for the identification of catastrophic fabrication problems.

A comprehensive metal-to-silicon contact test structure (3) is illustrated by the metal mask shown in Fig. 1. The test pattern is a square 200 mil (5.08 mm) on a side and contains a large number (38,400) of contacts subdivided into the eight arrays shown in the figure. The test pattern which is repeated periodically across the photomask is replicated across a wafer. The yield of a particular array with the same number of contacts is calculated from the fraction of good arrays found on the wafer. In the testing of an array, it is assumed that when a fault is encountered only one fault has occurred and that the fault is the intended fault (in this case a metal-to-silicon contact fault). The yield calculation assumes that faults occur randomly across the wafer. When such assumptions obtain, then the expected yield of an array containing N contacts follows the exponential relation (4)

$$Y = \exp(-DN) \quad [1]$$

where D is the characteristic number of faults per contact.

The pattern shown in Fig. 1 was fabricated periodically across various silicon-on-sapphire wafers. Within each wafer, one of four possible contact dimensions was used. The result are indicated in Fig. 2. An analysis of the yield curves shown in Fig. 2 leads

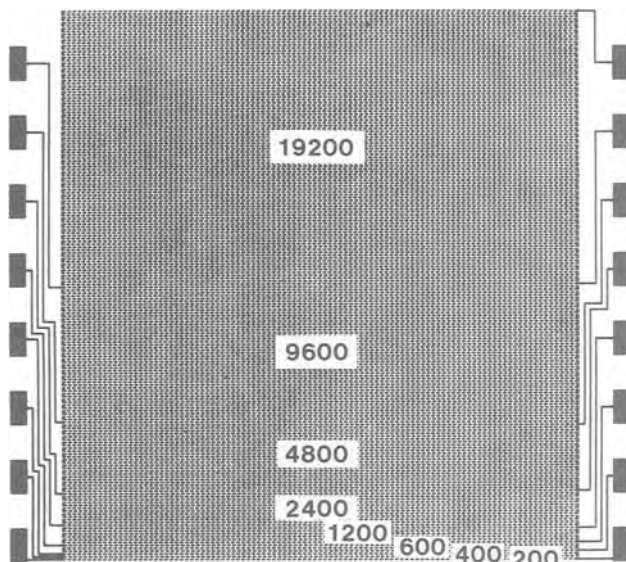


Fig. 1. Metal mask used in the fabrication of various metal-to-silicon contact arrays. The number of contacts in each array is indicated by the numerical value (3).

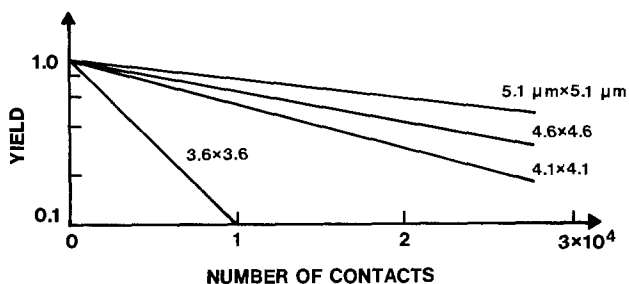


Fig. 2. The integrity of various metal-to-silicon contacts with different dimensions (3).

Table I. Fault densities for contacts shown in Fig. 2

Contact dimension (μm)	D (faults/contact)	D^{-1} (contacts/fault)
3.6	2.3×10^{-4}	4,300
4.1	6.0×10^{-5}	17,000
4.6	4.3×10^{-5}	23,000
5.1	2.6×10^{-5}	38,000

to a fault density, D , for each curve. These values are listed in Table I along with the reciprocal fault density, D^{-1} , which indicates the number of elements found in an array with a yield of 37%. For example, for the 3.6 μm contact, 37 out of 100 arrays, each composed of 4300 contacts, can be expected to be good. In the design of a circuit with a particular number of contacts, the appropriate contact dimension to be used for a high yield circuit can be estimated from the D^{-1} values listed in Table I. As seen in the table, a modest change in the contact dimension from 3.6 to 5.1 μm results in almost a tenfold change in D^{-1} from 4,300 to 38,000 contacts/fault.

An effective yield analysis requires a well-designed random fault test chip that has a collection of arrays where the number of elements in each array progresses from a few to many contacts. Such a progression allows the construction of a yield curve and the evaluation of the fault density. For a successful analysis, the number of elements in each array must be chosen *a priori* when the photomask is designed so that the yield in some of the arrays lies between zero and 100%.

As explained earlier, the application of Eq. [1] to a yield analysis of random fault test structures assumes one fault per array, that the fault is the intended fault, and that the faults do not cluster. Faults can cluster in certain regions of a wafer due to the introduction of crystalline defects (4, 5), wafer handling, or poor mask alignment. For example, rotational misalignment between certain photomasks can appear as a spurious radial component in the fault density. A well-designed random fault test structure will have liberal design rules where possible so that the effect of photomask misalignment is minimized.

Random fault test structures tend to be complex structures so that the faults encountered may not be those which the structures are intended to detect (6). For example, in a contact array, a fault could occur at a step in the metallization, or an entire metal connection could be missing. Other unintended faults can occur due to mechanical probing problems. To avoid probing errors, structures were designed with extra large probe pads as shown in Fig. 3. The probes touch down at the X points and electrical continuity between probes on the same pad determines that both probes are down. Such an arrangement avoids unintended faults due to probing errors.

Once a fault has been identified electrically, the array must be examined optically to verify that the fault is the intended fault. This requires a careful microscopic inspection of the array which can be time consuming. In addition, some faults, like a poor metal-to-silicon contact, may not be amenable to visual inspection. Because of the complex nature of these arrays, some workers (6) recommend against using these structures for predicting circuit yield.

Despite the shortcomings mentioned above, the structures are useful when used with caution for process control, design rule optimization, and equipment evaluation (3). Because a comprehensive random fault test structure requires a large amount of area, it should be fabricated on a special test wafer, such as a process validation wafer (1), which is processed along with production wafers.

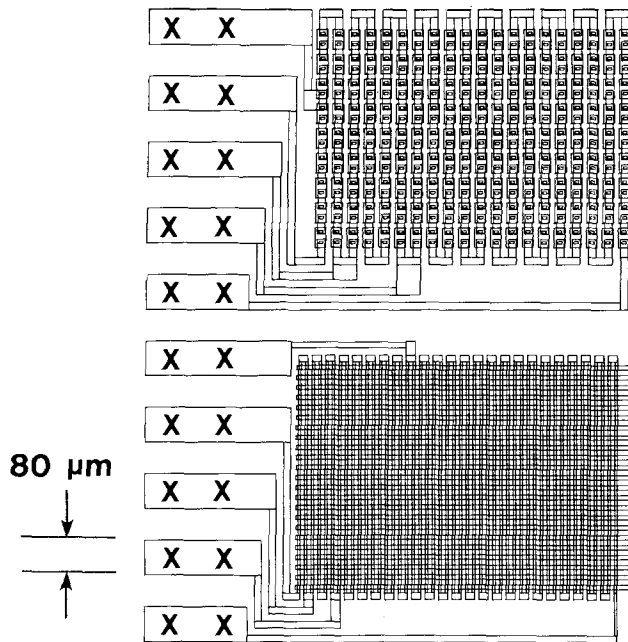


Fig. 3. Metal-to-silicon contact array (upper) and metal-step coverage array (lower) probeable with a 2 by 10 probe.

Intrachip Parameter Variation

The importance of the variation in parameters within a test chip was stressed by Ham (7) in pointing out that the local variations within a chip can easily exceed the chip-to-chip variation across a wafer. Ham's observations of intrachip threshold variations and our observations of intrachip linewidth variations serve to illustrate the effect.

Intrachip MOSFET parameters were studied with the use of a comprehensive test pattern (or chip) (6) designed for silicon-on-sapphire. Each chip, which is 259 mil (6.55 mm) on a side, contains 43 individually probeable MOSFET's arranged across the pattern. The transistors are self-aligned silicon gate devices with a channel length of 0.3 mil (7.6 μm) and a channel width of 0.6 mil (15.2 μm). Each photomask level was prepared from a master reticle by a step and repeat procedure.

The gate voltage required to produce 0.1, 1.0, or 10 μA current through each channel transistor in the intrachip array is shown in Fig. 4. In this figure, data were purposely omitted near the chip boundaries for ease of viewing.

For the 0.1 μA current, the gate voltage varies periodically with the chip dimension. A possible explanation for this intrachip variation at low currents is that the device current is predominantly an edge current which is more sensitive to gate dimensions than the main channel current which dominates at higher current level (8). If this explanation is correct, the shape of the 0.1 μA curve in Fig. 4 indicates that the gate length is varying periodically with the chip dimension.

The second example of intrachip parameter variations concerns the variation in linewidth within a test pattern (9). This was studied by fabricating a test pattern consisting of 120 cross-bridge sheet resistors (10) arranged in 8 rows across a pattern (or chip) 200 mil (5.08 mm) on a side. The linewidth was determined by first evaluating the sheet resistance, R_s , at the intersection of the cross and then evaluating the bridge portion of the structure. The linewidth, W , was calculated from

$$W = LR_s I / V_{12} \quad [2]$$

where L is the distance between the voltage taps, I is the current through the current carrying channel,

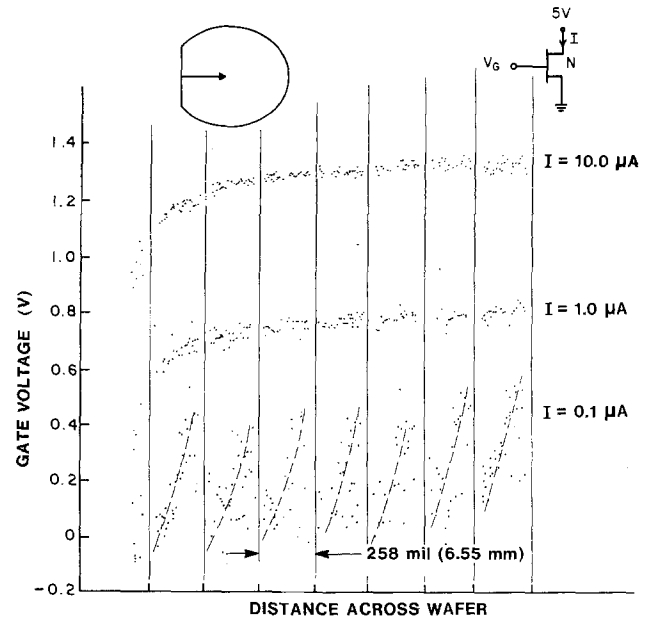


Fig. 4. The gate voltage at various source/drain current levels as a function of position across a wafer where a large intrachip variation is apparent at low currents (7).

and V_{12} is the voltage difference between the voltage taps of the bridge.

As with the MOSFET example, the photomask was prepared from the same master reticle by a step and repeat procedure. The pattern was exposed with the use of a contact printing alignment system and etched in an 800 nm thick, 0.044 Ω/\square e-gun evaporated aluminum layer deposited on an oxide film thermally grown on a 2 in. (5.08 mm) diam silicon wafer.

The chip-to-chip linewidth variation for the cross bridge located in the lower left-hand corner of the chip is shown by the wafer map in Fig. 5 for each of the 53 chips tested. In the wafer map, every fourth symbol represents a measured value; all other points are interpolated. The photomask linewidth was 0.60 mil (15.2 μm) and, as seen from the key in the figure, the final average linewidth is about 11.4 μm . The key shows the number of values that lie in each linewidth increment. The variability in the linewidth across the wafer as shown in Fig. 5 is attributed to those factors which affect the contact between the photomask and the photoresist-covered wafer, such as the flatness of the silicon wafer, the flatness of the photomask, the pressure applied between the wafer

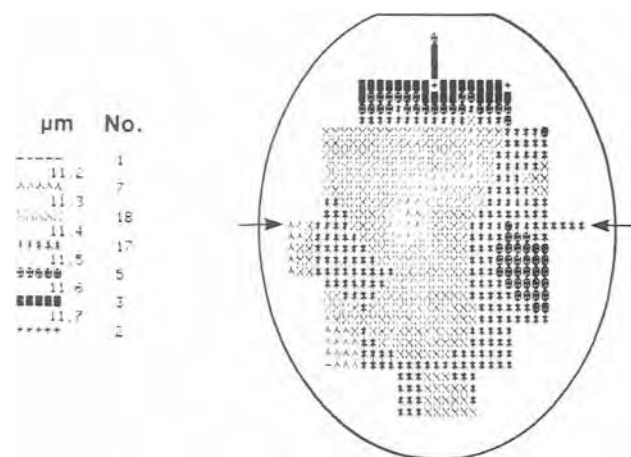


Fig. 5. Intrachip linewidth variations across a 2 in. (50.8 mm) diameter silicon wafer due primarily to the variability in the contact between the photomask and the photoresist-covered wafer.

and photomask, dust particles located between the wafer and photomask, and nonuniform etching across the wafer (11).

The intrachip linewidth variation is plotted in Fig. 6 as a function of position across the wafer. These data were taken from the bottom row of each chip. The row chosen for this plot is indicated by the arrows in Fig. 5. The plot, shown in Fig. 6, indicates that the linewidth varies periodically with the chip dimension across the wafer. This periodic variation is superimposed on the nonperiodic chip-to-chip linewidth variation. At this time, the periodic linewidth variation is assumed to be due to aberrations in the optics of the image repeater used to step and repeat the $10\times$ reticle. The periodic linewidth variations observed in Fig. 6 are comparable with the linewidth distortion of $0.1\ \mu\text{m}$ expected for the wafer imaging system used in this study.

Care must be exercised in interpreting linewidth data. In addition to the effects mentioned above, such as wafer flatness and optical aberrations, the sheet resistance variations must also be considered. As seen from Eq. [2], the sheet resistance directly influences the linewidth. For the linewidth data shown in Fig. 6, the sheet resistance varies very smoothly; it has a slope of $0.0005\ \Omega/\square/\text{cm}$ in the middle of the wafer and a relative standard deviation less than 0.05%. The influence of the sheet resistance variation on the linewidth shown in Fig. 6 is less than the size of the symbols used to represent the data.

The periodic variations shown in Fig. 6 are relatively small, being about 1.5% of the mean linewidth of $11.4\ \mu\text{m}$, but it is expected that the variation of $0.17\ \mu\text{m}$ will be independent of the linewidth. For example, for a linewidth of $1\ \mu\text{m}$, the variation is expected to be a significant 17%. Such variations can be a limitation in a manufacturing process and indicate that improved techniques, such as electron beam lithography, will be needed for the fabrication of submicrometer lines.

The linewidth information obtained from the cross-bridge array is potentially useful in developing control of the very small dimensions needed in future circuits. Studies of linewidth variations within a chip can assist in the evaluation of pattern generators, image repeater systems, and mask alignment machines. In addition, the linewidth array is useful in establishing design rules and margins for circuit design parameters.

Photomask Alignment

Three test structures for measuring alignment electrically are shown schematically in Fig. 7 as the tap-shift (12), contact-shift (13), and production-compatible (14) test structures.¹ The structures described in Ref. (12-14) differ in design detail but not in principle from those shown in Fig. 7. As shown in the figure, current is forced along the channel from point I_1 to I_2 . The voltage differences, V_{12} and V_{23} , are used to evaluate the alignment. If $V_{12} = V_{23}$, then the alignment is perfect.

The three structures, shown in Fig. 7, differ in the manner in which the channel is tapped at point V_2 . In the tap-shift and contact-shift structures, the tap rectangle and contact square both appear on the photomask used to define the conducting channel. This photomask is used twice. The first time, it is used to define the conducting channel. The second time, it is shifted by an appropriate amount and used to form the shift feature. In the production-compatible test structure, the contact feature appears on a separate photomask.

In the shift-type structures, photomask step-and-repeat error and photomask runout are eliminated.

¹ Another structure was reported recently (15). With this structure, the alignment is determined from the width of a current-carrying channel formed by a shift-type sequence explained in the text.

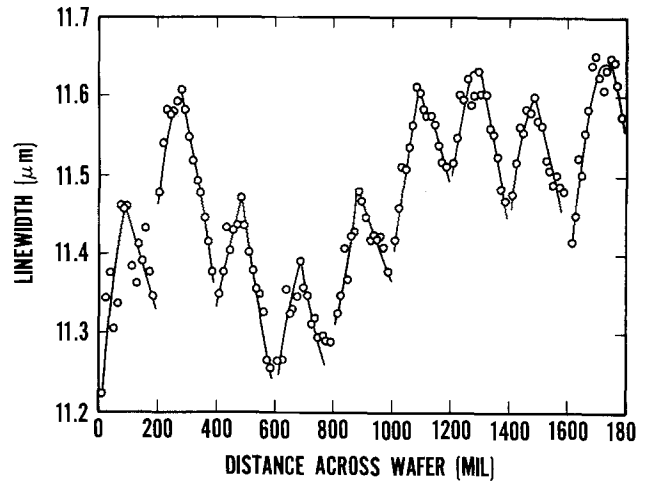


Fig. 6. Intrachip linewidth variations across the wafer shown in Fig. 5. The period of the linewidth variations corresponds to the width of the chip, 200 mil (5.08 mm). The periodic linewidth variation is assumed to be due to aberrations in the optics of the image repeater used to step and repeat the $10\times$ reticle.

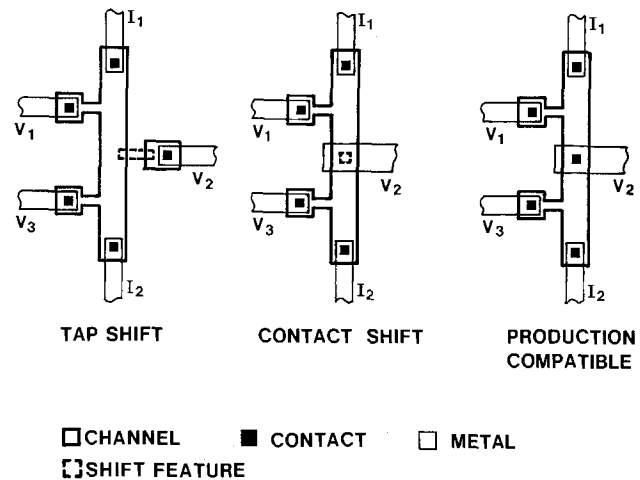


Fig. 7. Three different electrical alignment test structures

In the tap-shift structure, the results are not complicated by irregularities introduced by the contacting step. Unfortunately, these structures are not production-compatible.

A complete production-compatible test structure (16) is shown in Fig. 8. The vertical or y-alignment is determined by forcing a current between points I_1 and I_2 and measuring the voltage differences, V_{12} , V_{23} , and V_{34} . The displacement of the contact window at point V_3 from the midpoint between taps V_2 and V_4 is given by

$$L_y = L_{12}(V_{34} - V_{23}) / (2V_{12}) \quad [3]$$

where L_{12} is the distance between taps V_1 and V_2 . The horizontal or x-alignment is determined in a similar manner by forcing the same current as used above between points I_2 and I_3 and measuring V_{56} and V_{67} . The x-alignment is given by

$$L_x = L_{12}(V_{67} - V_{56}) / (2V_{12}) \quad [4]$$

The x- and y-alignments are then combined to form a vector representing the local displacement in the vicinity of the test structure.

The test structure shown in Fig. 8 was used to evaluate the alignment between the contact and channel photomask steps. This structure is part of the NBS-15 test pattern (17) which is a rectangle $1.7 \times 2.4\ \text{mm}$. The pattern was repeated on 100 mil (2.54 mm) centers across a wafer 2 in. (50.8 mm) in

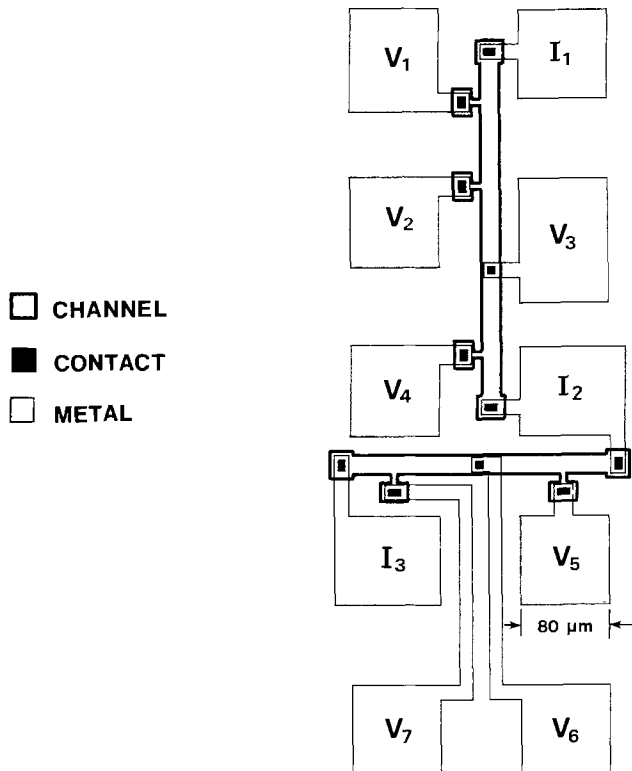


Fig. 8. Production-compatible electrical alignment test structure for evaluating the contact-to-channel alignment (16).

diameter. The conducting channel was formed by a high temperature diffusion step. An array of 62 test structures located on 200 mil (5.08 mm) centers was measured. The displacement vectors for each of the 62 test structures are shown in the wafer map displayed as the original data in Fig. 9.

The mean rotation and translation components, introduced by the operator in aligning the contact photomask relative to the channel photomask, were determined by performing a least squares fit to the vectors from the 62 test structures. These mean components were then removed from the original data, and the difference vectors were plotted in the other wafer map shown in Fig. 9. This wafer map is indicative of alignment distortions that occurred between the channel and contact photomask steps. Such distortions are introduced by a variety of factors, such as deformation of the wafer or photomasks due to small temperature gradients during mask alignment, wafer warpage due to the high temperature diffusion step used to form the conducting channel, photomask step-and-repeat errors, or photomask runout.

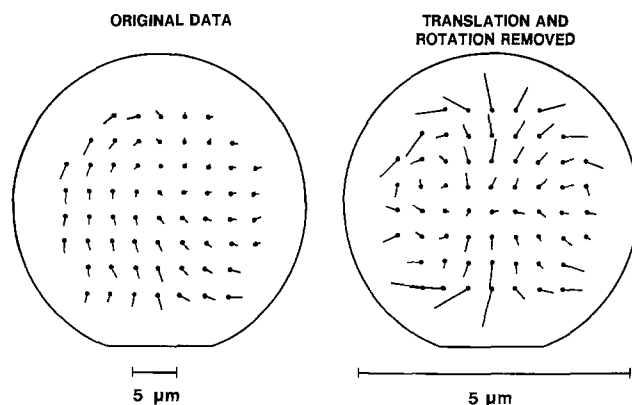


Fig. 9. Wafer maps of the contact-to-channel alignment as determined from the production-compatible test structure shown in Fig. 8.

Vector maps derived from a van der Pauw-type tap-shift test structure (12) are shown in Fig. 10. These data were obtained from an array of 118 test structures fabricated on a 3 in. (75 mm) diam silicon wafer and located on 222 mil (5.64 mm) centers. The mean rotation and translation components were again evaluated by a least squares fit technique. Removal of these components leads to the results shown in Fig. 10 which indicates a net expansion behavior. Because this is a tap-shift test structure, this behavior is not influenced by photomask step-and-repeat error or photomask runout. In addition, wafer warpage is not a factor because the conducting channel and tap features were defined at room temperature prior to the formation (ion implantation) of the channel. The expansion behavior might be explained by the wafer bowing that occurs in an oxidized silicon wafer when some of the oxide is removed, especially from the back side of the wafer. Alternatively, this behavior might be due to a net thermal expansion of the photomask between its first and second image.

The vector maps shown in Fig. 9 and 10 were both obtained using contact-printing mask alignment systems. The magnitude of the largest misalignment vectors, after removal of the operator-induced translation and rotation components, is about $1 \mu\text{m}$. This residual misalignment is characteristic of the various processing steps used to fabricate the wafer. It represents the best alignment an operator can hope to achieve. In order to reduce the residual misalignment, more advanced processes must be used. Such misalignments are expected to be a limitation on the ability to fabricate integrated circuits with submicrometer dimensions. The alignment test structures have proved useful in evaluating the performance of mask aligners (12), alignment markers (13), and operators (13).

Carrier Lifetime

Gated diodes have been used for a number of years to evaluate the surface and bulk leakage currents of p-n junctions (18). Such measurements are slow, requiring many minutes, and they generally require test structures that are large compared to circuit elements. Because of the very small currents involved, these measurements are not compatible with production-oriented test equipment.

The integrated gated-diode electrometer is a production-compatible test structure (19) shown in Fig. 11 and consists of three on-chip circuit elements: a gated diode, MOSFET switch, and output MOSFET. The output MOSFET is connected in a source-follower configuration with its drain connected to the supply voltage, V_B , and its source connected to an external resistor, R_L , that is returned to the substrate potential, V_S . In operation, the MOSFET switch is closed momentarily by applying an appropriate switch bias, ϕ_R . This connects the reverse-bias voltage, V_R , to the gated diode. The voltage, V , of the gated diode is sensed through the output MOSFET at the

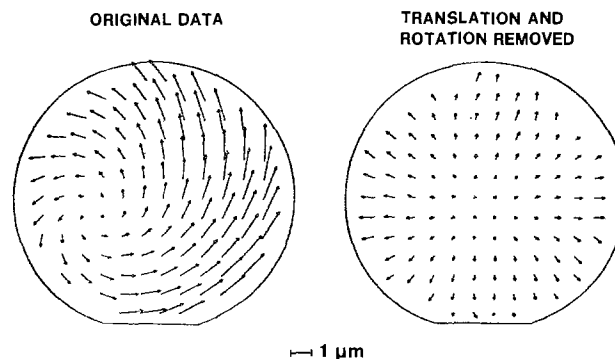


Fig. 10. Wafer maps of the tap-to-channel alignment as determined from a tap-shift test structure (10).

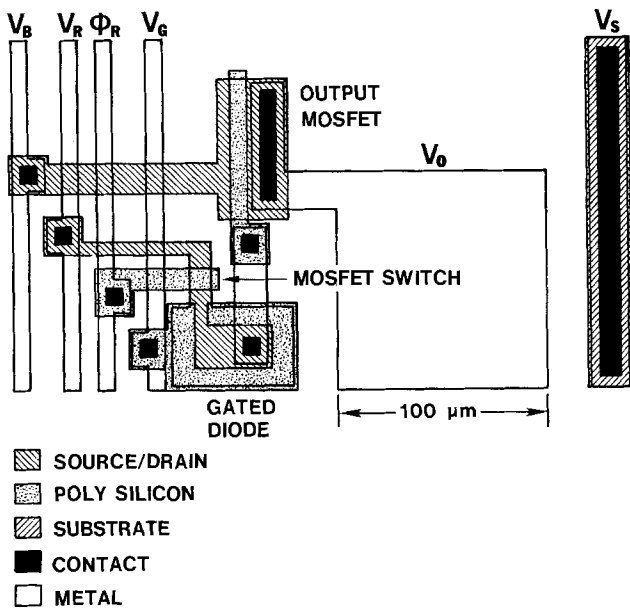


Fig. 11. Integrated gated-diode electrometer fabricated with a self-aligned polysilicon gate process (18).

point, V_0 . The rate of decay of the voltage on the gated diode is indicative of the leakage currents in the diode. By measuring the voltage decay at various gate biases, V_G , the bulk lifetime and the surface recombination velocity can be determined.

The carrier-generation lifetime, τ , characteristic of the gated diode is given by the following expression

$$\tau = \beta(n_i/N) (V_R + V_b - \sqrt{V_b \sqrt{V_R + V_b}}) / (dV_0/dt) \quad [5]$$

where β is the d-c voltage gain, V_b is the built-in voltage, n_i is the intrinsic carrier concentration, and N is the dopant density on the lightly doped side of the diode. The parameter V_b is determined from $V_b = (kT/q) \ln(N/n_i)$ where k is the Boltzmann constant, T is the temperature, and q is the electronic charge. The d-c voltage gain is given by $\beta = g_m / (g_m + R_L^{-1})$ where g_m is the MOSFET mutual transconductance; for the devices studied here $\beta \approx 0.8$.

The lifetime derived from the above expression is the bulk lifetime beneath the metallurgical junction when the gate of the diode accumulates the silicon beneath the gate. When the gate inverts the silicon beneath the gate, the lifetime derived from Eq. [5] is an effective lifetime composed of a weighted sum of the lifetimes beneath the junction and the gate. When the gate depletes the silicon beneath the gate, the V vs. time plot can be analyzed to reveal the surface recombination velocity.

The circuit shown in Fig. 11 was connected with other circuits to form the array seen in Fig. 12. This array is repeated in a test pattern that is 197 mil (5.00 mm) by 217 mil (5.51 mm). Such an array allows a detailed examination of the local variation in lifetime and surface recombination velocity using diodes that are the same size as circuit elements.

The use of the array shown in Fig. 12 is illustrated by the wafer map shown in Fig. 13. In the wafer map, every fourth symbol represents an average lifetime; all other points are interpolated. The average lifetimes were determined from the six integrated gated-diode electrometers labeled V_{01} to V_{06} in Fig. 12. A detailed profile across the wafer is included in Fig. 13 where the six lifetime values are shown individually. The total number of lifetime values represented by the wafer map is 324.

The lifetimes shown in Fig. 13 were obtained with the gate of the gated diode biased so as to invert the surface beneath the gate. Thus, an effective bulk

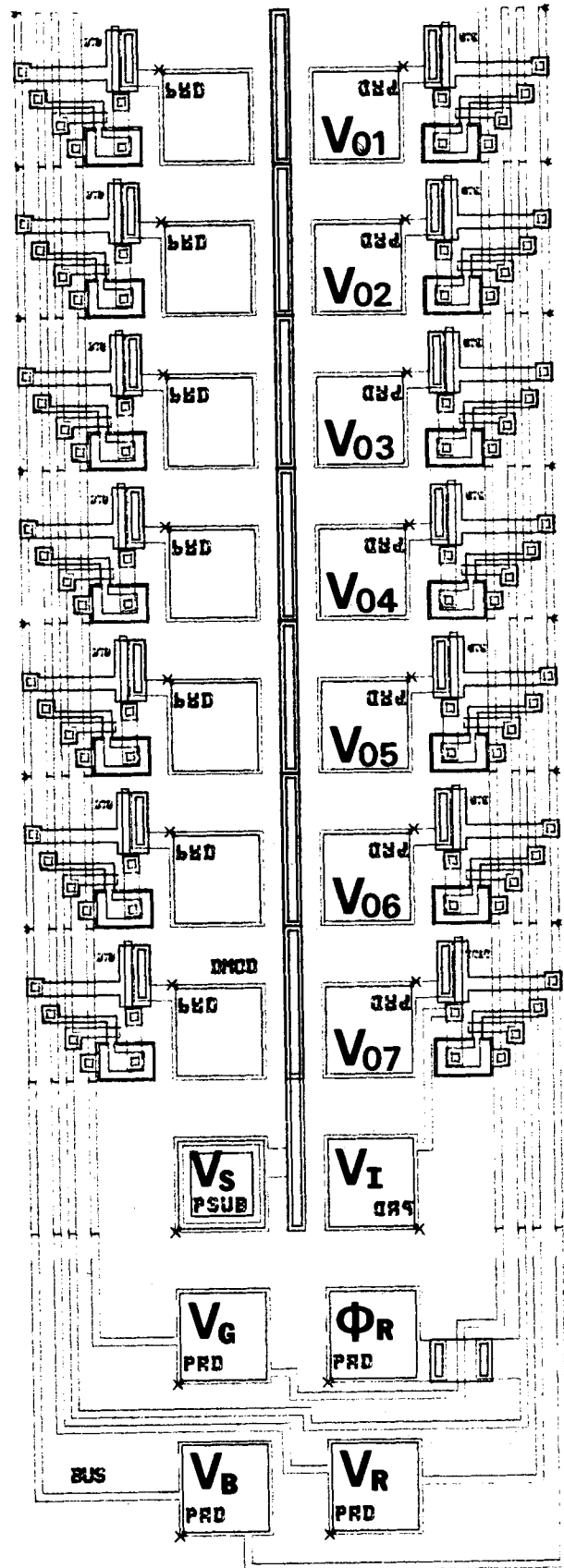


Fig. 12. Integrated gated-diode electrometer array composed of the circuit shown in Fig. 11 (18).

lifetime was determined. The lifetime values as seen in Fig. 13 were obtained on a wafer that was gettered by implanting phosphorus on the back surface of the wafer. This procedure improved the lifetime around the periphery of the wafer, but the values in the center remained close to the values observed on un-

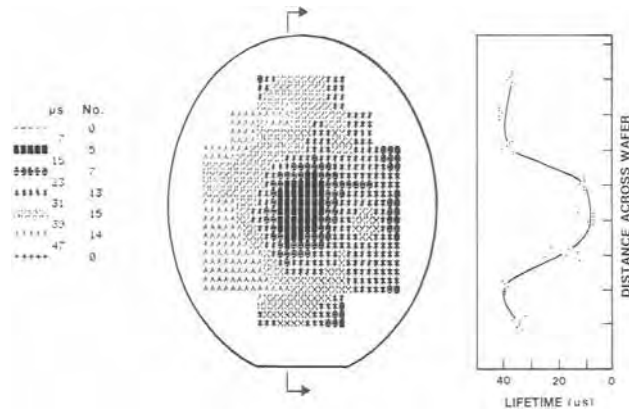


Fig. 13. Bulk lifetime wafer map and profile determined with the use of the integrated gated-diode electrometer array. The wafer map represents the average of six lifetime values measured in one array.

gettered wafers. Notice that the detailed lifetime profile shown in Fig. 13 does not show an intrachip dependence.

The importance of this test structure is found in the amount of detailed information that can be obtained concerning fundamental material parameters. As such, this array is useful in developing processes that produce long bulk lifetimes. In addition, this array is useful to the circuit designers who must allow for distributions in parameters such as memory retention time.

Conclusions

As presented here, the test structure arrays provided detailed information about integrated circuit manufacturing processes that cannot be obtained by conventional test pattern approaches. As the circuit elements become smaller and the wafers larger, the information derived from such arrays is needed to optimize processes and design rules, to evaluate machine and operator performance, and to provide circuit designers with proper design values and distributions.

The arrays discussed in this paper allow for the rapid collection of a statistically significant amount of data. Results from several test structures (MOSFET and cross bridge) illustrated that establishing the "average" value for a parameter from the measurement of only one structure in a test pattern is not sufficient when the parameter has a strong intrachip variation. Because some of the arrays (random fault) require a large amount of area for an effective analysis, they are best implemented on a separate process validation wafer.

Acknowledgment

The author wishes to thank L. W. Linholm and M. R. Doggett, NBS, for the data appearing in Fig. 5 and 6 and D. McCarthy and J. Acevedo, Westinghouse, for the data shown in Fig. 13. In addition the detailed review and suggestions of D. S. Perloff, Signetics, are much appreciated. Portions of this work

were supported by the Defense Advanced Research Projects Agency (Order No. 2397, Program Code 7D10), the Defense Nuclear Agency (IACRO 77-809), and the Air Force Avionics Laboratories (FY117579N2100).

Manuscript submitted May 31, 1979; revised manuscript received April 29, 1980. This was Paper 182 presented at the Pittsburgh, Pennsylvania, Meeting of the Society, Oct. 15-20, 1978.

Any discussion of this paper will appear in a Discussion Section to be published in the June 1981 JOURNAL. All discussions for the June 1981 Discussion Section should be submitted by Feb. 1, 1981.

Publication costs of this article were assisted by the National Bureau of Standards.

REFERENCES

1. M. G. Buehler and D. E. Sawyer, *Circuits Manufacturing*, **17**, 46 (February 1977).
2. D. S. Perloff, F. E. Wahl, and J. D. Reimer, *Solid State Technol.*, **20**, 31 (February 1977).
3. A. C. Ipri and J. C. Sarace, *RCA Rev.*, **38**, 323 (1977).
4. O. Paz and T. R. Lawson, *IEEE J. Solid-State Circuits*, **sc-12**, 540 (1977).
5. A. Gupta, W. A. Porter, and J. W. Lathrop, *ibid.*, **sc-9**, 96 (1974).
6. W. E. Ham, NBS Special Publication 400-56 (January 1980), p. 243.
7. W. E. Ham, International Electron Devices Meeting, Tech. Digest, p. 406 (December 1977).
8. D. W. Flatley and W. E. Ham, Abstract 100, p. 478, The Electrochemical Society Extended Abstracts, 74-2, New York, Oct. 13-17, 1974.
9. L. W. Linholm and M. G. Buehler, Abstract 191, p. 502, The Electrochemical Society Extended Abstracts, 79-1, Boston, Massachusetts, May 6-11, 1979.
10. M. G. Buehler and W. R. Thurber, *This Journal*, **125**, 655 (1978).
11. T. F. Hasan and D. S. Perloff, Abstract 605, p. 1515, The Electrochemical Society Extended Abstract 79-2, Los Angeles, California, Oct. 14-19, 1979.
12. D. S. Perloff, *IEEE J. Solid-State Circuits*, **sc-13**, 436 (1978).
13. D. H. Leebrick and D. W. Kisker, in Proceedings of Kodak Microelectronics Seminar, p. 66 (October 1977).
14. D. R. Thomas and R. D. Presson, in Govt. Microelectronics Applications Conference, Digest of Papers, p. 196 (November 1974).
15. I. J. Stemp, K. J. Nicholas, and H. E. Brockman, Abstract 184, p. 491, The Electrochemical Society Extended Abstract, 78-2, Pittsburgh, Pennsylvania, Oct. 15-29, 1978.
16. T. J. Russell, T. F. Leedy, and R. L. Mattis, in International Electron Devices Meeting, Technical Digest, p. 7A (December 1977).
17. T. J. Russell and D. A. Maxwell, NBS Special Publication 400-51 (April 1979).
18. A. S. Grove, "Physics and Technology of Semiconductor Devices," pp. 298 ff., John Wiley & Sons, Inc., New York (1967).
19. D. McCarthy, M. G. Buehler, J. Acevedo, B. Stamps, and M. Lonky, Abstract 183, p. 488, The Electrochemical Society Extended Abstract, 78-2, Pittsburgh, Pennsylvania, Oct. 15-20, 1978.
20. G. P. Carver and M. G. Buehler, *IEEE Trans. Electron Devices*, To be published.

Resistivity-Dopant Density Relationship for Boron-Doped Silicon

W. R. Thurber, R. L. Mattis, and Y. M. Liu*¹

National Bureau of Standards, Electron Devices Division, Washington, DC 20234

and J. J. Filliben

National Bureau of Standards, Statistical Engineering Division, Washington, DC 20234

ABSTRACT

New data for the resistivity-dopant density relationship for boron-doped silicon have been obtained for boron densities between 10^{14} and 10^{20} cm^{-3} and temperatures of 296°K (23°C) and 300°K. For dopant densities less than 10^{18} cm^{-3} , results were calculated from resistivity and junction capacitance-voltage measurements on processed wafers. For more heavily doped material, boron densities were obtained from the nuclear track technique and from Hall effect measurements on specimens cut from bulk silicon slices. The Hall factor was assumed to be 0.8 in the calculation of hole density. The results differ significantly from the commonly used Irvin curve for boron densities greater than 10^{16} cm^{-3} with a maximum deviation of 45% at 5×10^{17} cm^{-3} . The data are in better agreement with the Wagner curve, but for boron densities less than 10^{17} cm^{-3} , the measured resistivities were always higher than those predicted by the Wagner expression. Least squares fits to analytical expressions were determined for the resistivity-dopant density product as a function of resistivity and of dopant density for temperatures of 23°C and 300°K. Similar fits were obtained for the calculated hole mobility as a function of resistivity and of hole density.

The conversion between resistivity and dopant density of silicon is widely used in the semiconductor industry. During the past decade, the most frequently used conversion curves for both n- and p-type silicon were those formulated by Caughey and Thomas (1) based on the curves of Irvin (2). Irvin's curve for p-type material included results of measurements on silicon doped with aluminum, gallium, and boron. More recently, Wagner (3) published a conversion for boron-doped silicon based on ion implantation results which differed from that of Irvin by up to 50% for boron densities in the range 10^{16} - 10^{18} cm^{-3} . Because of the magnitude of this discrepancy, a comprehensive redetermination of the relationship was undertaken. This paper gives the results of measurements on boron-doped silicon with dopant densities in the range 10^{14} - 10^{20} cm^{-3} .

Experimental

The test structures and experimental procedures for the electrical measurements were essentially the same as those used in a similar study on phosphorus-doped silicon (4). For dopant densities of 10^{18} cm^{-3} or less, data were obtained from test structures fabricated on silicon slices. The resistivity was measured directly on planar four-probe square array structures (5). The dopant density was determined from capacitance-voltage (C-V) measurements on n⁺p junction diodes. These test structures and other diagnostic structures were assembled on microelectronic test patterns NBS-3 (6) and NBS-4 (7). The starting material, in both ingot and slice form, was obtained from several different suppliers and was selected for minimum resistivity gradients by mechanical four-probe measurements prior to fabrication of the test patterns by bipolar processing (8). Spreading resistance measurements were made on a number of the wafers and no fine structure was seen. The maximum resistivity

gradient over the size of a test structure was judged to be less than 1% and the gradient over the distance separating resistivity and C-V structures was less than 2%. The resistivity data obtained from the square array structures after processing agreed to within a few percent with the mechanical four-probe measurements prior to fabrication. Various measurements were made on the wafers to verify the fabrication and to assure that leakage currents were low enough for proper operation of the test structures.

For dopant densities greater than about 10^{19} cm^{-3} , Hall effect and resistivity measurements were made on van der Pauw specimens ultrasonically cut from bulk silicon slices. The measurements were made at controlled temperatures of 296°K (23°C) and 300°K for a magnetic flux density of 0.6T (6 kG) following standard procedures (9). The hole density, p , was calculated from the expression $p = r/qR_H$ where q is the electronic charge, R_H is the Hall coefficient, and r is the Hall factor. The factor r was set equal to 0.8 as the majority of experimental results (10-13) and recent calculations (14) on moderately doped p-type material suggest a value in this range. No measurements of r for dopant densities greater than 2×10^{18} cm^{-3} appear to be available. The complex nature of the valence band in silicon is the reason why r is less than unity, even for degenerate material. In a preliminary account (15) of this work, r was taken as unity, but the probability of a different value was mentioned.

The nuclear track technique (NTT) was used to determine boron densities in the range 10^{15} - 10^{20} cm^{-3} ; the procedure and results have been published previously (16). The NTT determines the total boron density in contrast to the C-V and Hall effect techniques which measure the electrically active p-type dopant density less any compensation by n-type dopants. Considering the similar results from ingots and wafers from different suppliers covering a wide range of boron density, as well as the agreement between NTT and C-V/Hall effect measurements, compensation and electrically inactive boron do not appear to be significant in the material used for this work.

* Electrochemical Society Active Member.

¹ Present address: Westinghouse Advanced Technology Laboratory, Baltimore, Maryland 21203.

Key words: capacitance-voltage technique, Hall effect, hole mobility, Irvin curves, semiconductor.

Results

Figure 1 is a graph of resistivity as a function of effective dopant density. Experimental points are from the junction C-V, Hall effect, and NTT measurements. The curves are those of Irvin (2) and Wagner (3). It is apparent even on the log-log scale that the data between 10^{16} - 10^{19} cm^{-3} depart considerably from the Irvin curve.

Figure 2 is a graph of the product of resistivity and dopant density as a function of resistivity at 300°K. Since to the first approximation resistivity is inversely proportional to dopant density, a plot of the product allows deviations from this relationship to be seen, particularly for low resistivities where the product is large. To obtain the data points shown for the Hall effect, the factor r was taken as 0.8 in computing the hole density from the Hall measurements of Chapman *et al.* (17), Crowder (18), and this work as discussed in the previous section. The NTT results are seen to be in good agreement with both the Hall effect and the junction C-V data. The curves shown are the Irvin relationship for p-type silicon, the Wagner relationship for boron-implanted silicon, and an analytical fit to selected data. The fitting procedure is discussed in the next section.

Figure 3 is a plot of calculated hole mobility as a function of hole density at 300°K. The data from this work as well as the other plotted points were converted to hole density for calculations of the mobility using the results of Li (19) for percent ionization. The fairly recent data of Tsao and Sah (20) are significantly lower than the data of this work. This may result from the fact that back-surface contact resistance can strongly affect resistivity values obtained from the spreading resistance structure used by Tsao and Sah. The Caughey and Thomas (1) curve is a fit to the Irvin relationship with the assumption that the hole density equals the dopant density. The same assumption was used to obtain the Wagner curve; however, it was not a point-by-point determination but simply a change in one parameter of the Caughey and Thomas expression as required to fit data on boron-implanted silicon. Just as the Irvin curve is a poor fit to the resistivity-dopant density data of this work the Caughey and Thomas expression is a poor fit to the mobility data. The Wagner expression is considerably better, but there are still noticeable deviations with respect to the experimental data.

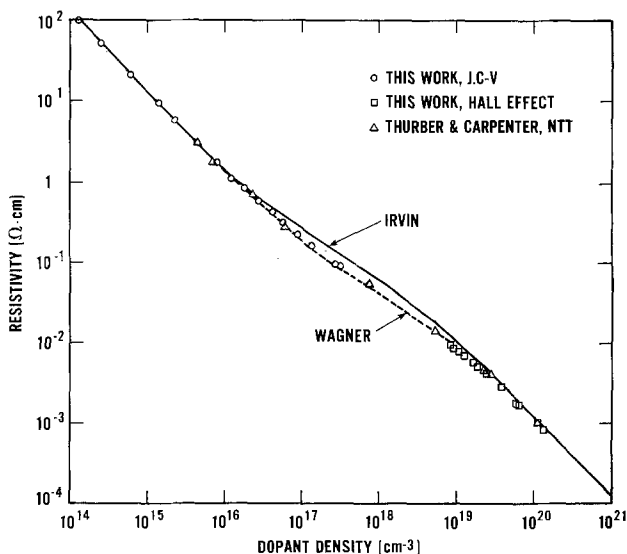


Fig. 1. Resistivity as a function of effective dopant density for p-type silicon at 300°K. Data points are from junction capacitance-voltage, Hall effect, and nuclear track technique measurements. Curves shown are the Irvin (2) relationship for p-type silicon and the Wagner (3) expression for boron-implanted silicon.

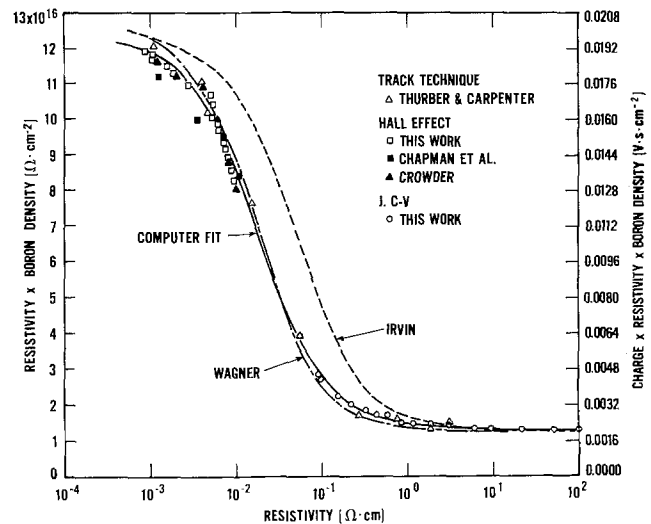


Fig. 2. Resistivity-dopant density product as a function of resistivity at 300°K for boron-doped silicon. The junction capacitance voltage and Hall effect measurements are compared with the published work of Thurber and Carpenter (16), Chapman *et al.* (17), Crowder (18), Irvin (2), and Wagner (3). The solid curve is an analytical fit to portions of this data as discussed in the text. Values of the product $q\rho N$ are on the right ordinate.

The theoretical calculation of Li (19) in Fig. 3, valid for densities less than 3×10^{18} cm^{-3} , is in excellent agreement with the C-V data of this work.

Computer Curve Fits

The curve fits of the data were done using the DATAPLOT language (21) for nonlinear least squares fitting. The expressions for the earlier fits to phosphorus-doped silicon (4) were in the form of quotients of two third-degree polynomials in order to fit the shape of the product and mobility curves at high phosphorus densities. However, for boron-doped silicon, the product is well behaved at very high densities such that "min-max" relationships similar to those proposed by Caughey and Thomas (1) give satisfactory fits. Modifications are necessary for the fits of mobility as will be discussed later. These relationships have the advantage that two of the parameters,

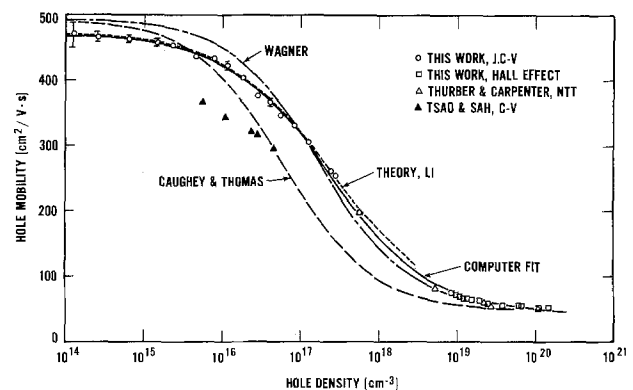


Fig. 3. Hole mobility as a function of calculated hole density for boron-doped silicon at 300°K. All data points, except those in the heavily doped range, have been corrected for incomplete ionization using the work of Li (19). The curves are from Caughey and Thomas (1), Wagner (3), Li (19), and an analytical fit to the data shown on the graph with the exception of the points of Tsao and Sah (20). The Caughey-Thomas and Wagner expressions were obtained without consideration of deionization and are plotted assuming equivalence of hole and dopant densities. This gives lower mobility in the range 10^{17} - 10^{19} cm^{-3} . The error bars on the C-V data of this work show the standard deviation calculated from the individual mobility values for that wafer. When not shown, the error bars lie within the plotted symbol.

$(q\rho N)_{\min}$ and $(q\rho N)_{\max}$, have a readily identified physical significance in that they approximately equal the true value of these quantities.

The expression for the product $q\rho N$ as a function of ρ was taken as

$$q\rho N = (q\rho N)_{\min} + \frac{(q\rho N)_{\max} - (q\rho N)_{\min}}{1 + \left(\frac{\rho}{\rho_{\text{ref}}}\right)^\alpha} \quad [1]$$

where q is the electronic charge, N is the boron density, ρ is the resistivity, $(q\rho N)_{\min}$ and $(q\rho N)_{\max}$ are the asymptotic minimum and maximum values of the product, ρ_{ref} is a reference value corresponding to the resistivity for which the derivative of the product is a maximum, and α is a measure of the slope of the curve near the reference value. The data used for the fit were the junction C-V and Hall effect results of this work, and the NTT results for boron densities greater than $5 \times 10^{17} \text{ cm}^{-3}$. The NTT results are omitted for lower values of dopant density because the NTT data, while in general agreement with the C-V results, show somewhat more scatter. For high boron densities, the NTT results may be better than those from the Hall effect because of the need to assume a value for the Hall factor. This same set of 300°K data, and its counterpart at 23°C, was used for all of the curve fits. The resistivity values of the 39 fitted data points spanned the range 0.00085–100 $\Omega\text{-cm}$ with corresponding dopant densities between 1.4×10^{20} and $1.3 \times 10^{14} \text{ cm}^{-3}$. The least squares curve at 300°K is shown in Fig. 2 for comparison with experimental data and other curves. All four parameters as determined by the fit are given in Table I for 23°C and 300°K. The approximate standard deviation is given for each parameter in its own units, and the residual standard deviation (RSD) for the fit is listed in units of $q\rho N$. The RSD is the square root of the quotient of the sum of the squared residuals divided by the number of degrees of freedom.

The expression for the product $q\rho N$ as a function of dopant density has the same form as Eq. [1] except for a negative value of the exponent because of the inverse relationship between ρ and N

$$q\rho N = (q\rho N)_{\min} + \frac{(q\rho N)_{\max} - (q\rho N)_{\min}}{1 + \left(\frac{N}{N_{\text{ref}}}\right)^\alpha} \quad [2]$$

The fit was made to the same set of data. The four parameters are listed in Table II for 23°C and 300°K. The curve for 300°K and the experimental data used to obtain it are shown in Fig. 4.

Hole mobilities were calculated from resistivity and hole density values. Except in the heavily doped range,

Table I. Parameters and residual standard deviation (RSD) for the fit of $q\rho N$ vs. ρ using Eq. [1]

Temperature	23°C	300°K
$(q\rho N)_{\min}$ (V sec/cm ²)	0.00213 ± 0.00069	0.00220 ± 0.00009
$(q\rho N)_{\max}$ (V sec/cm ²)	0.01947 ± 0.00018	0.01973 ± 0.00017
ρ_{ref} ($\Omega \cdot \text{cm}$)	0.01833 ± 0.00067	0.01782 ± 0.00060
α	1.105 ± 0.035	1.086 ± 0.032
RSD (V sec/cm ²)	0.000292	0.000266

Table II. Parameters and residual standard deviation (RSD) for the fit of $q\rho N$ vs. N using Eq. [2]

Temperature	23°C	300°K
$(q\rho N)_{\min}$ (V sec/cm ²)	0.00209 ± 0.00009	0.00215 ± 0.00008
$(q\rho N)_{\max}$ (V sec/cm ²)	0.02024 ± 0.00024	0.02053 ± 0.00022
N_{ref} (cm ⁻³)	$3.88 \times 10^{18} \pm 0.21$	$4.09 \times 10^{18} \pm 0.20$
α	-0.737 ± 0.024	-0.727 ± 0.021
RSD (V sec/cm ²)	0.000268	0.000240

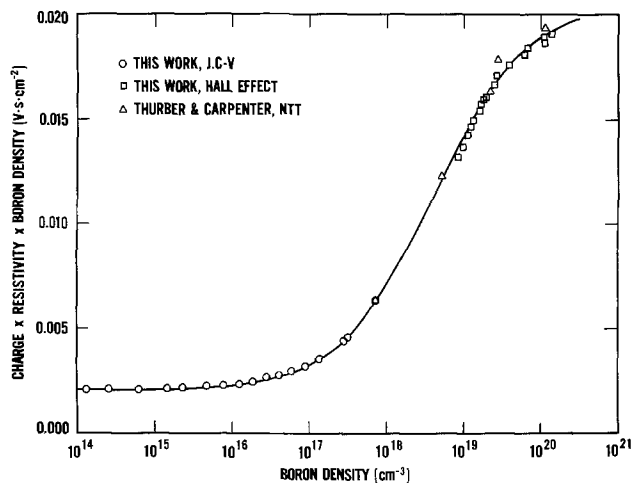


Fig. 4. Graph of the $q\rho N$ product as a function of N for 300°K. The curve is an analytical fit to the data points shown.

where hole density is assumed to equal dopant density, hole densities were obtained from dopant densities using the percent ionization calculations of Li (19). A suitable expression for the hole mobility, μ_h , as a function of hole density, p , was found to be

$$\mu_h = A \exp(-p_c/p) + \frac{\mu_{\max}}{1 + \left(\frac{p}{p_{\text{ref}}}\right)^\alpha} \quad [3]$$

This form gave a significantly better fit than the simpler form of the type used for fitting the product curves. The effect of the exponential factor in the first term is to increase the mobility in the region of the curve where the dopant and hole densities deviate significantly from each other. The hole mobility approaches the constant value A for very large hole densities. The five parameters, determined by the fit to the same 39 data points, are listed in Table III for 23°C and 300°K. The curve for 300°K is shown in Fig. 3 for comparison with experimental data and other curves.

The form for the hole mobility as a function of resistivity was taken as

$$\mu_h = A \exp(-\rho/\rho_c) + \frac{\mu_{\max}}{1 + \left(\frac{\rho}{\rho_{\text{ref}}}\right)^\alpha} \quad [4]$$

It was also found that the simple "min-max" form did not fit the mobility vs. resistivity data well, particularly in the low resistivity range. The inclusion of the exponential in the first term improved the fit considerably and its effect is similar to that of the exponential in Eq. [3]. In this expression, the mobility is dominated by the first term at low resistivities and by the second term at high resistivities. Again, the fit was made to the same set of data, and the parameters are listed in Table IV for 23°C and 300°K. The curve for 300°K and the experimental data used for the fit are shown in Fig. 5. The curve fits the shape of the experimental data very well at low resistivities so that extrapolation of Eq. [4] at the low

Table III. Parameters and residual standard deviation (RSD) for the fit of μ_h vs. p using Eq. [3]

Temperature	23°C	300°K
A (cm ² /V sec)	45.2 ± 1.3	44.9 ± 1.2
p_c (cm ⁻³)	$9.00 \times 10^{16} \pm 2.3$	$9.23 \times 10^{16} \pm 2.3$
μ_{\max} (cm ² /V sec)	486.1 ± 1.9	470.5 ± 1.8
p_{ref} (cm ⁻³)	$2.11 \times 10^{17} \pm 0.09$	$2.23 \times 10^{17} \pm 0.10$
α	1.105 ± 0.035	1.086 ± 0.032
RSD (cm ² /V sec)	3.18	3.07

Table IV. Parameters and residual standard deviation (RSD) for the fit of μ_{h} vs. ρ using Eq. [4]

Temperature	23°C	300°K
A (cm ² /V sec)	52.4 ± 3.8	51.6 ± 3.7
ρ_c (Ω · cm)	0.00409 ± 0.00077	0.00406 ± 0.00077
μ_{max} (cm ² /V sec)	482.8 ± 2.4	467.3 ± 2.4
ρ_{ref} (Ω · cm)	0.0825 ± 0.0020	0.0794 ± 0.0019
α	-0.811 ± 0.018	-0.808 ± 0.019
RSD (cm ² /V sec)	4.89	4.78

resistivity end should give reasonable values. Thus, A can be considered to be approximately equal to the minimum value of the mobility. The mobility vs. hole density fit is not as good at the low mobility end, as it is slightly below the data at $p = 10^{20}$ cm⁻³ and goes to a lower asymptotic value than is the case for Eq. [4]. Consequently, an extrapolation of Eq. [3] at the low mobility end is less likely to be correct.

In comparing the product fits as a function of resistivity with those as a function of dopant density, it is evident that minimum and maximum values which should be correspondingly equal are somewhat different. This is, of course, a consequence of the independent fits where no parameters are fixed. The $(q\rho N)_{\text{min}}$ values differ by 2% and the fits differ by this same percentage at $N = 10^{14}$ cm⁻³. The $(q\rho N)_{\text{max}}$ values differ by 4%; however, these are asymptotic values, and at the upper limit of the experimental data ($N \approx 10^{20}$ cm⁻³) there is still considerable curvature. The difference between the fits in this region is less than 1%. The product fits are self-consistent within 3% for all dopant densities (and corresponding resistivities) in the range 10^{14} - 10^{20} cm⁻³. That is, when the product $q\rho N$ is calculated for a given dopant density with Eq. [2], a resistivity is derived which can be used in the $q\rho N$ vs. ρ expression (Eq. [1]) to again calculate the product. The latter product will be within 3% of the former.

The μ_{max} values for the mobility fits as a function of hole density differ by about 0.7% from the μ_{max} values for the fits as a function of resistivity. The mobility fits are self-consistent within 2% for all hole densities (and corresponding resistivities) in the range 10^{14} - 5×10^{17} cm⁻³. In the 10^{18} cm⁻³ range, there are differences of up to 8%. The self-consistency improves in the low 10^{19} cm⁻³ range but increases again to 6% at 10^{20} cm⁻³ as the fits depart for very heavy doping.

Conclusions

The resistivity-dopant density results obtained from this work differ significantly from the commonly used Irvin curve for boron densities greater than 10^{16} cm⁻³ with a maximum deviation of 45% at 5×10^{17} cm⁻³. Hole mobility values, calculated from this work with

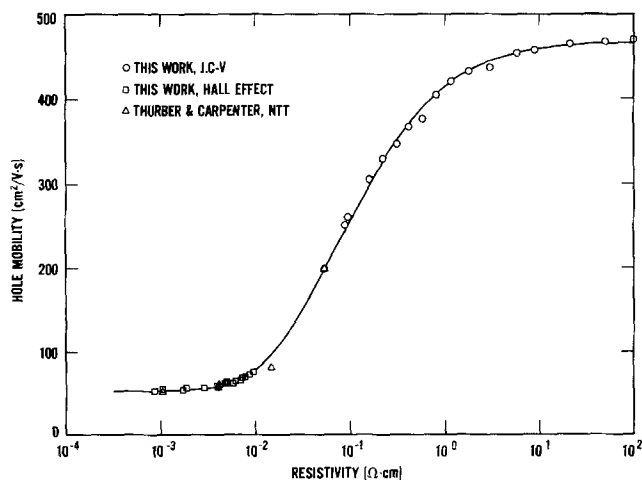


Fig. 5. Graph of hole mobility as a function of resistivity for 300°K. The curve is an analytical fit to the data points shown.

correction for percent ionization of the dopant atoms, are much larger than similar experimental data of Tsao and Sah, but are in good agreement with the theoretical calculations of Li. Analytical expressions, convenient for engineering calculations, were fitted to the resistivity-dopant density data as a function of resistivity and dopant density for temperatures of 23°C and 300°K. Similar analytical expressions were fitted to the calculated hole mobility as a function of resistivity and hole density. The expression for hole mobility vs. hole density is in reasonable agreement with Wagner's result. The maximum discrepancy occurs in the low 10^{18} cm⁻³ range where the Wagner mobility is 10% lower because deionization effects were not included. In the lightly doped range, the mobility from this work is 5% lower than that of Wagner.

Acknowledgments

The authors are indebted to D. R. Ricks for the mechanical four-probe resistivity measurements, to F. H. Brewer for the Hall effect measurements, and to J. Krawczyk and L. A. Robinson for specimen preparation. Special thanks are due Dr. M. G. Buehler for designing the test structures used in this work. This work was conducted as part of the Semiconductor Technology Program at NBS. Portions of this work were supported by the Defense Advanced Research Projects Agency (order No. 2397).

Manuscript submitted Feb. 11, 1980; revised manuscript received April 28, 1980.

Any discussion of this paper will appear in a Discussion Section to be published in the June 1981 JOURNAL. All discussions for the June 1981 Discussion Section should be submitted by Feb. 1, 1981.

Publication costs of this article were assisted by the National Bureau of Standards.

REFERENCES

- D. M. Caughey and R. E. Thomas, *Proc. IEEE*, **55**, 2192 (1967).
- J. C. Irvin, *Bell Syst. Tech. J.*, **41**, 387 (1962).
- S. Wagner, *This Journal*, **119**, 1570 (1972).
- W. R. Thurber, R. L. Mattis, Y. M. Liu, and J. J. Filliben, *ibid.*, **127**, 1807 (1980).
- M. G. Buehler and W. R. Thurber, *IEEE Trans. Electron Devices*, **ed-23**, 968 (1976).
- M. G. Buehler, *Nat. Bur. Stand. Spec. Publ.*, 400-22 (June 1976).
- W. R. Thurber and M. G. Buehler, *ibid.*, 400-32 (April 1978).
- T. F. Leedy and Y. M. Liu, *ibid.*, 400-53 (December 1978).
- ASTM Method F 76, "Annual Book of ASTM Standards," Part 43 (November 1979).
- F. J. Morin and J. P. Maita, *Phys. Rev.*, **96**, 28 (1954).
- K. B. Wolfstirn, *J. Phys. Chem. Solids*, **16**, 279 (1960).
- D. K. Schroder, T. T. Braggins, and H. M. Hobgood, *J. Appl. Phys.*, **49**, 5256 (1978).
- L. C. Linares, Ph.D. Dissertation, University of Florida (1979).
- H. Nakagawa and S. Zukotynski, *Can. J. Phys.*, **56**, 364 (1978).
- W. R. Thurber, R. L. Mattis, and Y. M. Liu, in "Semiconductor Characterization Techniques," P. A. Barnes and G. A. Rozgonyi, Editors, pp. 81-92, The Electrochemical Society Softbound Proceedings Series, Princeton, N.J. (1978).
- W. R. Thurber and B. S. Carpenter, *This Journal*, **125**, 654 (1978).
- P. W. Chapman, O. N. Tufte, J. D. Zook, and D. Long, *J. Appl. Phys.*, **34**, 3291 (1963).
- B. L. Crowder, *This Journal*, **118**, 943 (1971).
- S. S. Li, *Solid-State Electron.*, **21**, 1109 (1978).
- K. Y. Tsao and C. T. Sah, *ibid.*, **19**, 949 (1976). See also T. J. Woodley and C. T. Sah, *ibid.*, **20**, 385 (1977).
- J. J. Filliben, in "Proc. Statistical Computing Section of American Statistical Association," pp. 343-353, 1978 Annual Meeting, San Diego, California.

Vapor Phase Epitaxial Growth of ZnSe Films Using Metallic Zn and Metallic Se

Tetsuo Muranoi and Mitsuo Furukoshi

Department of Electronics, Faculty of Engineering, Ibaraki University, Hitachi City, 316 Japan

ABSTRACT

Single crystal layers of ZnSe have been epitaxially grown on GaAs and sapphire substrates using metallic Zn and Se. A nozzle for the Se flow was placed at about 1 cm in front of the substrate, and this arrangement resulted in much less Se consumption than in the case when the nozzle was further separated from the substrate. The epitaxial conditions were investigated as a function of the source and substrate temperatures. When the substrate temperature and one of the source temperatures were fixed, the growth rate increased with the other source temperature and then saturated. Below the saturation point, the growth rate is proportional to the flow rate and the vapor pressure of each source material. Dependence on substrate temperature of growth rate is shown to be surface-controlled phenomenon below 770°C and is one of mass transfer controlled phenomena above 770°C. The epitaxial growth on GaAs substrates occurred in the substrate temperature range of 650°-880°C with a growth rate ranging from 1 to 30 $\mu\text{m/hr}$. The resistivity of the as-grown layer was too high ($10^6 \Omega \cdot \text{cm}$) to be useful for LED application.

ZnSe is a promising material for various optoelectronic devices, such as light emitting diodes in the blue region of the spectrum. Several methods for the vapor phase epitaxy of ZnSe film have been reported. As the source material in an open tube method, ZnSe powder (1-3), Zn-H₂Se (4), and organometallic zinc-H₂Se (5) have been used previously. When ZnSe powder is used, HCl is sometimes added to the reaction system in order to transport material (1, 2), but etching of the substrate can be a problem. Without the use of HCl (3), however, the growth rate is relatively low. Organometallic zinc-H₂Se system (5) requires only one hot temperature zone and allows a good controllability of the source material flow. But these materials are very toxic or are difficult to handle. Yim *et al.* (4) has reported on Zn-H₂Se that the single crystal epitaxy of ZnSe has been achieved with 10^{-5} mole/min Zn and 2×10^{-6} mole/min H₂Se.

This paper describes the vapor phase epitaxial condition of ZnSe film using metallic Zn and Se as the source materials. This method has an advantage that one could investigate the growth conditions of ZnSe epitaxial films by applying a simple reaction mechanism between elemental Zn and Se, without toxic and difficult materials to handle, under various ratios of the source materials by varying only the source temperature and carrier gas flow rates.

Experimental

Film deposition was investigated mainly by the growth rate with 5° angle lapping and the deposition time, which was 30 min in most cases. The film thickness was proportional to the time within the experimental error.

The nominal purity of Zn was six-nine (supplied by High Purity Chemical Laboratory) and that of Se was five-nine (supplied by Mitsui Mining and Smelting Company, Limited). (100)GaAs was mainly used as the substrates. (111)B-GaAs and (1 $\bar{1}02$)-sapphire were also used. Mirror-smooth etched wafers of GaAs and sapphire were supplied by Hitachi Electric Cable Company, Limited and Kyoto Ceramic Company, Limited, respectively.

A reflection electron microscope was used to determine single crystallinity. Specimens were cleaved and

chemically etched to investigate the interface between ZnSe and the substrate.

Figure 1 is a schematic diagram of the experimental apparatus and typical temperature profiles used. A quartz reaction tube, 150 cm long and 27 mm ID, was used. Several substrates were placed horizontally on a quartz boat in the reaction tube and the temperature was maintained by an electric furnace 72 cm long having five zones. The reaction was completed by pulling the furnace followed by air-cooling with a blower. Zn and Se were held in quartz vessels as shown in Fig. 1. The end of the Zn and Se vessels and the top of the substrate boat were set at the desired temperatures. A nozzle of 6 mm ID quartz tube for the Se flow was placed at about 1 cm in front of the substrates. With this arrangement, the Se vapor was kept from reacting with Zn until it reached the close proximity of the substrate, and therefore the amount of Se consumed for any given run was only one-tenth or one-twentieth of the amount required for the case of 10 cm separation between the nozzle and the substrate. Zn and Se flow rates were obtained from the source consumption, which was measured by weighing the source vessels before and after the deposition, and was determined with a cross-sectional area at the Se nozzle. The carrier gas over molten Zn was a mixture of Ar (300 cm³/min) and H₂ (100 cm³/min), and the carrier gas over molten Se was also Ar (100 cm³/min) and H₂ (10 cm³/min). It is important to mention that H₂ was used as a carrier gas since without H₂ a white deposit (presumably ZnO) formed near the Zn boat even though Ar used was a 6-nine purity and that it was passed over DEOXO and zeolite gas dryer.

Results and Discussion

Figure 2 shows some examples of the microstructure and the reflection electron diffraction patterns of the films. It can be seen from the net patterns that (100), (111), and (110) oriented ZnSe grew on (100) GaAs, (111) B-GaAs, and (1 $\bar{1}02$) sapphire, respectively.

Figure 3 shows the growth rate at $T_{\text{sub}} = 800^\circ\text{C}$ as a function of Zn temperature, Zn flow rate, and published equilibrium vapor pressure (6). Figure 4 gives similar properties in the case of Se (7). Epitaxial growth was achieved below the deposition rate of 30 $\mu\text{m/hr}$. For any given T_{se} in Fig. 3, the deposition

Key words: heteroepitaxy, open tube method, growth rate, nozzle for Se.

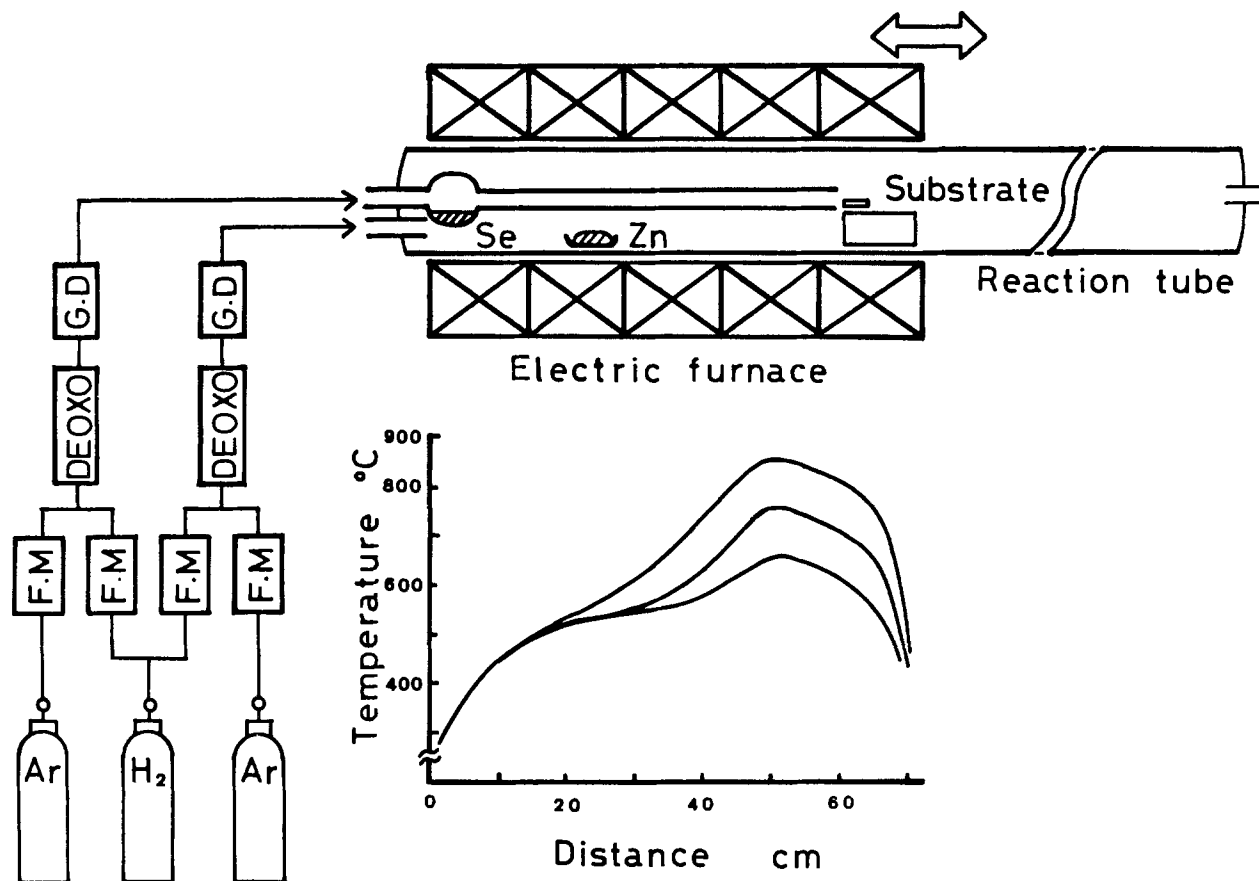


Fig. 1. Experimental apparatus for the film deposition and typical temperature profiles. The flow meters and zeolite gas dryers are denoted by F.M. and G.D.

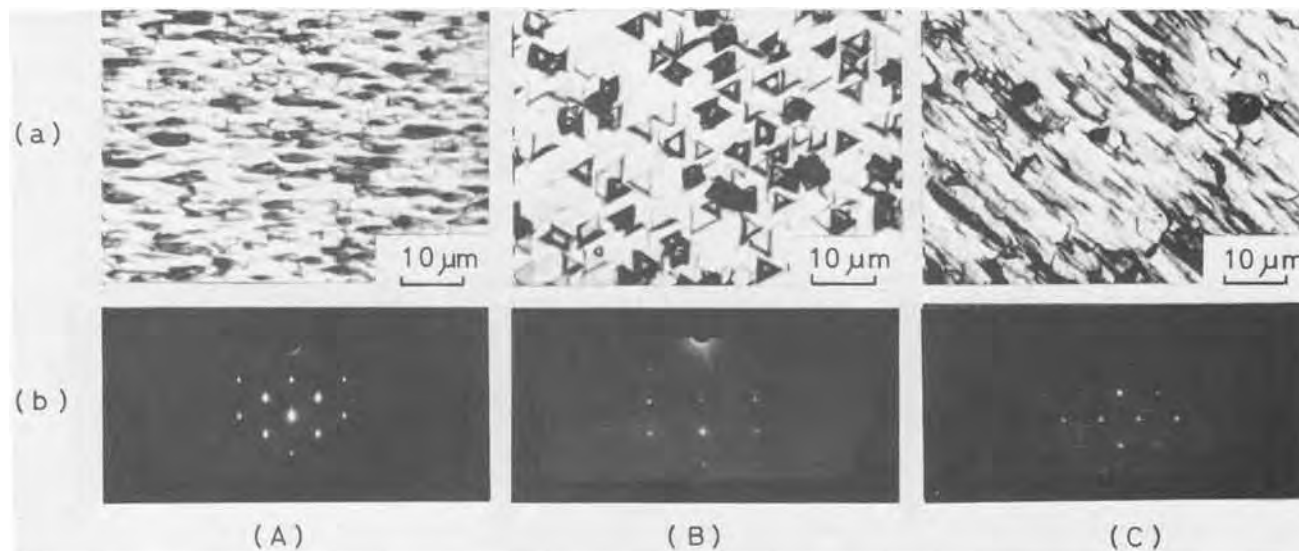


Fig. 2 (a) Photomicrographs and (b) reflection electron diffraction patterns of ZnSe layers on (A) (100) GaAs, (B) (111) B-GaAs, and (C) (1102) sapphire. (T_{sub} , T_{Zn} , T_{Se}) = (700°C, 558°C, 342°C) for (100) GaAs, (800°C, 593°C, 342°C) for (111) B-GaAs, and (800°C, 558°C, 380°C) for sapphire.

rate increased with T_{Zn} and then saturated. The saturation temperature became higher with higher T_{Se} . The film grew in an excess Zn in the saturation region and grew in an excess Se below the saturation point since the flow rates of both source materials were nearly the same at the saturation point. For a given T_{Zn} , $T_{\text{Zn}} = 593^\circ\text{C}$ shown in Fig. 4, the deposition rate showed a similar tendency to saturate. The equilibrium vapor pressure, the source material flow rate, and the deposition rate below saturation had the same temperature dependence. This showed that the deposition rate below saturation is proportional

to the source material flow rate and the vapor pressure.

Epitaxial growth commenced within 5 cm of the Se nozzle. However, for properly adjusted flow rates, epitaxial growth could be achieved for substrates 10 cm from the nozzle. For the 10 cm separation, T_{Se} had to be increased to compensate for material deposited on the reaction tube prior to the substrate. For example, when a growth condition was set at (T_{sub} , T_{Se}) = (800°C, 416°C), the epitaxial growth was realized at T_{Zn} in the range 540°–630°C as shown in Fig. 3.

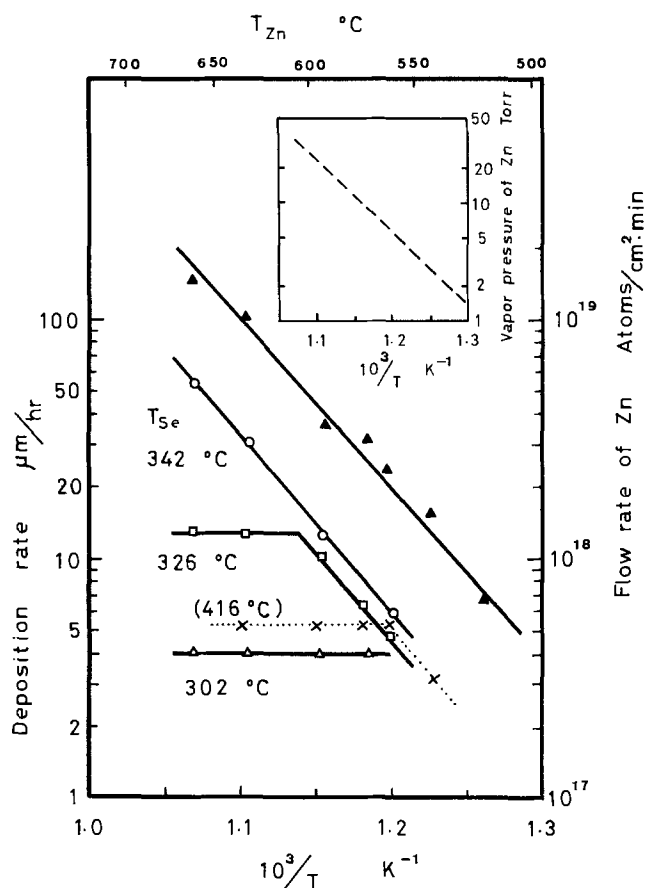


Fig. 3. Deposition rate at $T_{\text{sub}} = 800^\circ\text{C}$ (open symbols and crosses), flow rate of Zn (closed symbols), and equilibrium vapor pressure of Zn (broken line) as a function of Zn temperature. Cross symbols (\times) denote deposition rates at $T_{\text{Se}} = 416^\circ\text{C}$ when the substrate and the nozzle were placed 10 cm apart.

The epitaxy on GaAs took place in a relatively wide range of T_{sub} : 650°C – 880°C , T_{Zn} : 540°C – 660°C , and T_{Se} : 300°C – 380°C , while on sapphire it was only one case at $(T_{\text{sub}}, T_{\text{Zn}}, T_{\text{Se}}) = (800^\circ\text{C}, 558^\circ\text{C}, 380^\circ\text{C})$ that epitaxy occurred over the entire substrate surface although the epitaxy itself was partly observed above $T_{\text{sub}} = 650^\circ\text{C}$. This can be understood because of the difference in the crystal structure and the lattice parameter between ZnSe and sapphire.

Figure 5 shows the growth rate as a function of T_{sub} for $(T_{\text{Zn}}, T_{\text{Se}}) = (558^\circ\text{C}, 342^\circ\text{C})$ and $(558^\circ\text{C}, 300^\circ\text{C})$. For T_{sub} below 770°C , the growth rate increased with T_{sub} and was the same for $T_{\text{Se}} = 342^\circ\text{C}$ and 300°C . Above 770°C , the growth rate was constant for $T_{\text{Se}} = 342^\circ\text{C}$ but decreased for $T_{\text{Se}} = 300^\circ\text{C}$ due to reevaporation. For $T_{\text{sub}} = 940^\circ\text{C}$, film growth was not observed for $T_{\text{Se}} = 342^\circ\text{C}$. Such temperature dependences of deposition rates are observed for heterogeneous reactions (8). Such surface-controlled phenomena are expected to be temperature dependent and flow rate independent. The region below 770°C is seen to be temperature dependent but flow rate independent. Above 770°C , the growth rate is seen to be mass transfer controlled.

The data of Yim *et al.* (4) are plotted with the present results in Fig. 5. These slopes are almost the same although the experimental conditions were different. This indicates the same reaction mechanism in both cases. The roles of H_2Se and Se molecules in the reaction are unclear. H_2Se was produced by a reaction between Se molecules and H_2 . This is shown in Fig. 6 which shows the Se consumption in 30 min at $T_{\text{Se}} = 342^\circ\text{C}$ vs. H_2 content when the total gas flow rate over the molten Se was fixed at $110 \text{ cm}^3/\text{min}$. H_2Se was formed because the Se consumption increased with H_2 content.

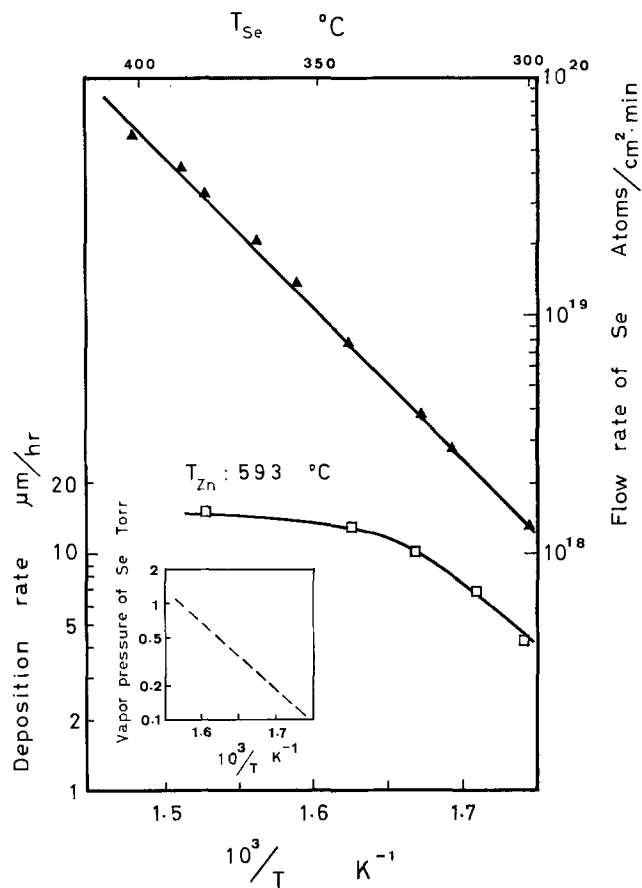


Fig. 4. Deposition rate at $T_{\text{sub}} = 800^\circ\text{C}$ (open symbols), flow rate of Se (closed symbols), and equilibrium vapor pressure of Se (broken line) as a function of Se temperature.

Yim *et al.* reported (4) that Ga_2Se_3 resulted from excess H_2Se (10^{-5} mole/min) on GaAs and that the Zn vapor concentration had little effect on film formation for the Zn concentration studied (10^{-6} – 10^{-5} mole/min). Here epitaxial growth of ZnSe could be obtained with excess Se even at 4×10^{-5} mole/min Se flow rate. The limitation here on epitaxial growth

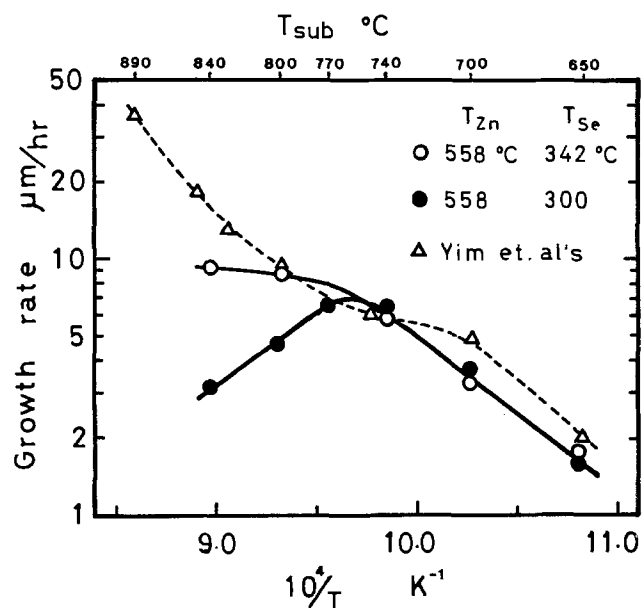


Fig. 5. Growth rate of ZnSe film on (100) GaAs vs. reciprocal of substrate temperature. Open circles (○) and closed circles (●) denote $(T_{\text{Zn}}, T_{\text{Se}}) = (558^\circ\text{C}, 342^\circ\text{C})$ and $(558^\circ\text{C}, 300^\circ\text{C})$, respectively. The data of Yim *et al.* on Zn- H_2Se (4) are plotted with triangles (Δ).

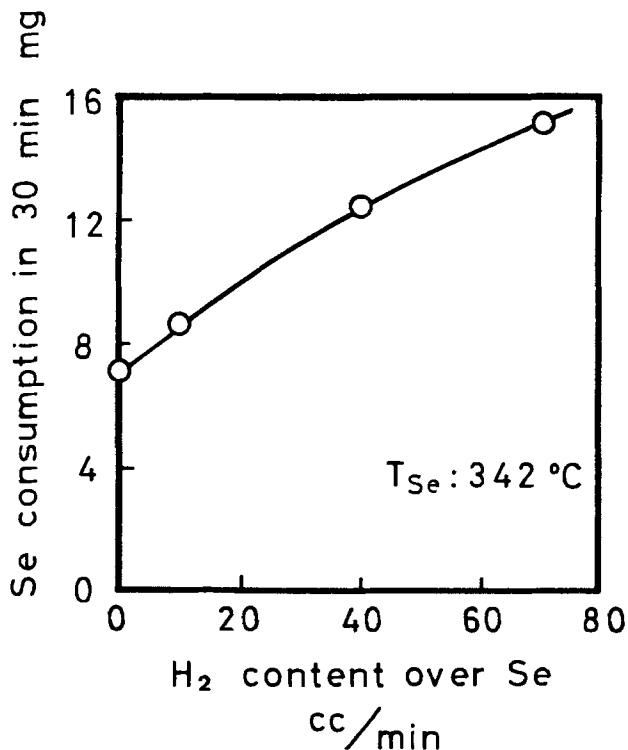


Fig. 6. Se consumption in 30 min for $T_{Se} = 342^\circ\text{C}$ vs. the H_2 content of the selenium Ar + H_2 carrier gas. The total Ar + H_2 flow was $110\text{ cm}^3/\text{min}$.

was the deposition rate itself. It is difficult generally to grow epitaxially at high deposition rates.

Specimens grown on (100) GaAs and (111) B-GaAs were cleaved and chemically etched in 40% NaOH aqueous solution at $75^\circ\text{--}80^\circ\text{C}$ for a few minutes to investigate the ZnSe-GaAs interfaces. The dark gray part is ZnSe, the white GaAs. The as-cleaved surface shows a clear and smooth interface. The etched surface shows that the region within 1 or 2 μm of the interface was strongly etched. This indicates that stacking faults occurred. The epitaxy interface of either (100) GaAs or (111) B-GaAs showed much the same etched appearance. However, the as-deposited film surfaces were different. Films grown on (111) GaAs were almost flat. Films grown on (100) GaAs sometimes had a hill-and-valley structure, especially for film thickness greater than 10 μm ; also, the (111) and (331) planes appeared on bevels judging from the angles (55° and 46°) between the bevel and the interface as shown in Fig. 7(a)-(A') since a cubic structure makes angles of 54.7° between (100)- and (111)-planes and 46.5° between (100)- and (331)-planes.

The film resistivity measured with a sandwich structure on p-type GaAs was about $10^8\ \Omega \cdot \text{cm}$, a value too high to be useful for a light emitting diode. Impurity doping must be investigated to lower the resistivity.

Conclusions

Single crystal layers of ZnSe have been epitaxially grown on GaAs and sapphire substrates using metallic Zn and metallic Se. The nozzle for the Se flow was about 1 cm from the substrate. The Se consumption was only one-tenth or one-twentieth of the case when the separation between the nozzle and the substrate was 10 cm. Epitaxial conditions were investigated as

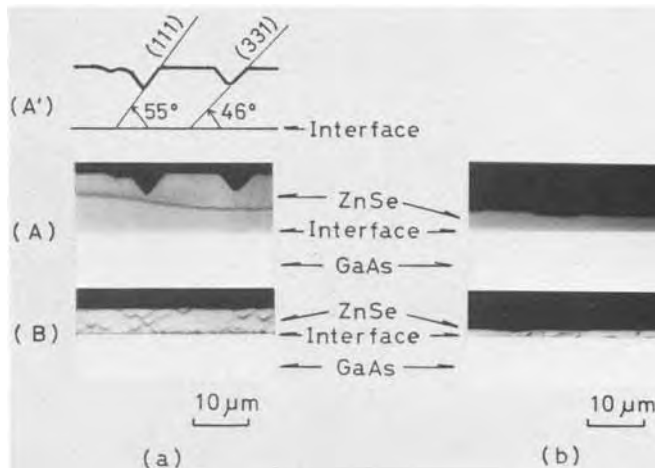


Fig. 7. Interface of ZnSe layer and GaAs substrate. (A) As-cleaved and (B) chemically etched surfaces; (a) (100) GaAs and (b) (111) B-GaAs.

a function of the source and substrate temperatures. (100), (111), and (110) oriented ZnSe grew on (100) GaAs, (111) B-GaAs, and (110) sapphire, respectively. When T_{sub} and one of the source temperatures were fixed, the growth rate increased with the other source temperature and then saturated. Below the saturation point, the growth rate is proportional to the flow rate and the vapor pressure of each source material. For GaAs, epitaxial growth occurred for T_{sub} in the range $650^\circ\text{--}880^\circ\text{C}$ ($1\text{--}30\ \mu\text{m}/\text{hr}$ in Fig. 3 and 5). Temperature dependence of the growth rate is a surface-controlled phenomenon below 770°C and is mass transfer controlled above 770°C . The interface region within 1 or 2 μm was strongly etched, indicating that stacking faults occurred at the interface. The resistivity was too high ($10^8\ \Omega \cdot \text{cm}$) for LED application.

Acknowledgments

The authors are grateful to their former student Mr. H. Yoshida for assistance with the experimental work, and to Mr. M. Kobiyama for his kindness in teaching them how to operate the electron microscope.

Manuscript submitted Feb. 11, 1980; revised manuscript received April 21, 1980.

Any discussion of this paper will appear in a Discussion Section to be published in the June 1981 JOURNAL. All discussions for the June 1981 Discussion Section should be submitted by Feb. 1, 1981.

Publication costs of this article were assisted by the authors.

REFERENCES

1. A. Baczewski, *This Journal*, **112**, 577 (1965).
2. H. J. Hovel and A. G. Milnes, *ibid.*, **116**, 843 (1969).
3. N. Matsukura and Y. Machi, *Jpn. J. Appl. Phys.*, **18**, 233 (1979).
4. W. M. Yim and E. J. Stofko, *This Journal*, **119**, 381 (1972).
5. H. M. Manasevit and W. I. Simpson, *ibid.*, **118**, 644 (1971).
6. J. H. Perry, "Chemical Engineers' Handbook," 4th ed. pp. 3-46, McGraw-Hill Book Co., New York (1963).
7. L. I. Maissel and R. Gland, "Handbook of Thin Film Technology," pp. 1-16, McGraw-Hill Book Co., New York (1970).
8. E. G. Bylander, *This Journal*, **109**, 1171 (1962).

Chemical Vapor Deposition of Tin on Iron or Carburized Iron

S. Audisio

Laboratoire de Physicochimie Industrielle,
Institut National des Sciences Appliquées de Lyon, 69621 Villeurbanne Cedex, France

ABSTRACT

An experimental investigation of the chemical vapor deposition of tin on iron and carburized iron substrates is presented, using stannous chloride vapor as the source of tin, in an inert or reducing atmosphere. At temperatures between 450° and 750°C, the mechanism of vapor coating is the displacement reaction in an inert or reducing atmosphere, but in a reducing atmosphere, reduction reactions also occur. The coating consists of iron-tin compounds or iron-tin carbides, the structure of which is obtained by diffusion and thus influenced by the time and temperature of deposition. The relations between nuclei formed at the beginning of the deposition and the substrate show that these nuclei may have an epitaxial growth. Epitaxial relationships between the FeSn nuclei and the iron substrate are given.

The surface of many materials must be protected from hostile environments of their applications. For many situations protective coatings are applied by hot dipping, electrodeposition, metal spraying, evaporation, sputtering or chemical vapor deposition (CVD) to minimize effects such as wear, erosion, corrosion, or high temperature oxidation. CVD coatings are widely used in the technologies of aeronautics, nuclear engineering, solid-state electronics, and refractory protective coatings.

Various aspects of CVD of tin (stannizing) have been clarified by previous investigators (1, 2) on copper, brass, and bronze, but a complete analysis has not yet been carried out for a study of tin deposits on iron and carburized iron.

The first purpose of this study is to develop a fuller understanding of the CVD of tin on such materials. This includes study of the chemical reactions which occur, and correlation of the rates of coating formation and the coating structures with the factors controlling the kinetics (temperature, duration). The second purpose is to establish the crystallographic relations between the tin-iron compounds and the substrates.

Chemical Reactions-Kinetics, Coating Composition, and Morphology

CVD apparatus and process.—The CVD of tin was obtained by the pack cementation method. Pack stannizing was carried out in cylindrical iron retorts closed with a slip-fitted iron cap and thus was not tightly sealed. The pack consisted of powder mixtures of 99.93% pure tin, various activators (NH₄Cl, FeCl₂, or SnCl₂), and MgO as inert filler. Prior to use, the filled retort was evacuated to less than 0.01 Torr (1.334 Pa). It was then backfilled by argon and placed quickly in the heated reactor chamber. During the coating operation a flow of hydrogen or argon was maintained. Coating temperatures ranged from 450°-750°C and duration from 1-10 hr. Substrates used in this study included pure iron (iron decarburized under moist hydrogen for 150 hr at 1050°C) or carburized iron (CH₄/H₂ gas mixture at 1050°C for 4 hr).

The iron or carburized iron samples were either small plates (20 × 10 × 2 mm) or wires (diameter 0.4 mm, length 30 mm). Surface preparation consisted of light abrasion followed by chemical polishing. Three or four specimens were placed in the center of the pack. After holding at the temperature for the desired time interval, the retort was swiftly removed

from the furnace and allowed to cool to room temperature in a hydrogen atmosphere. After cooling, the weight gains (Δm) of the samples were measured. Some samples were prepared for metallographic examination, hardness test, chemical and x-ray analysis. The samples were covered by electrodeposited nickel and then were cross-sectioned and polished with diamond paste using standard metallographic techniques. When the thickness of the coating is very small, particularly on the carburized iron, a special microscope technique was used to facilitate the investigation. Every sample was ground at an angle of 5° to the surface. In this way the surface layer was effectively enlarged by a factor of about 10. Microhardness tests were conducted on the coating using a Vickers indenter with a 10g load. X-ray diffraction data were obtained from the wire samples (Debye-Scherrer method) or from the flat samples (diffractometer method) with x-ray apparatus using Fe-filtered CoK α radiation.

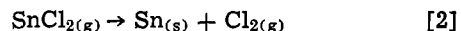
Results and discussion.—The chemical reactions were studied in argon-SnCl₂-FeCl₂ and hydrogen-SnCl₂-FeCl₂ systems. In both cases the same temperature (600°C) and the duration of treatment (4 hr) were chosen. The quantity of deposited tin (m_d) was chemically analyzed after the complete dissolution of the sample (iodometric method). From the weight increase, Δm , and the quantity m_d , it was possible to evaluate the ratio $n_{\text{Sn}}/n_{\text{Fe}}$ where n_{Sn} and n_{Fe} are the number of atoms of deposited tin and the number of atoms of iron which left the sample

$$m_d = n_{\text{Sn}} \cdot M_{\text{Sn}} \quad M_{\text{Sn}} = \text{relative atomic mass of tin}$$
$$\Delta m = m_d - n_{\text{Fe}} \cdot M_{\text{Fe}} \quad M_{\text{Fe}} = \text{relative atomic mass of iron}$$

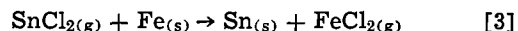
$$\frac{n_{\text{Sn}}}{n_{\text{Fe}}} = \frac{m_d}{m_d - \Delta m} \cdot \frac{M_{\text{Fe}}}{M_{\text{Sn}}} \quad [1]$$

The following reactions were believed to occur when SnCl₂ was used:

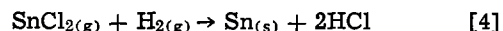
a. Thermal decomposition reaction



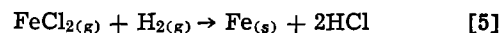
b. Displacement or exchange reaction



c. Reduction reaction



In a reducing atmosphere, the following reaction can occur



Key words: mechanism, coating, epitaxial growth, intermetallic.

In the temperature range 450°-750°C, reaction *a* is strongly endothermic, so it is not considered likely.

When the displacement reaction occurs, the weight increase of the sample should be somewhat less than the weight of the tin deposited and the $n_{\text{Sn}}/n_{\text{Fe}}$ ratio ought to be equal to 1. Then, from Eq. [1] we can calculate Δm

$$\Delta m = m_d \left(1 - \frac{M_{\text{Fe}}}{M_{\text{Sn}}} \right) = 0.53m_d$$

In the case of a reduction reaction, the weight increase of the sample should be equal to the weight of deposited tin. There is no departure of iron ($n_{\text{Fe}} = 0$)

$$\Delta m = m_d$$

Table I shows the weight increase of samples, the amount of tin deposited, and the $n_{\text{Sn}}/n_{\text{Fe}}$ ratio, in inert (argon) and reducing (hydrogen) atmospheres. In argon-SnCl₂-FeCl₂ system the $n_{\text{Sn}}/n_{\text{Fe}}$ ratio is equal to 1, and the chemical reaction is mainly the displacement reaction. In hydrogen-SnCl₂-FeCl₂, the $n_{\text{Sn}}/n_{\text{Fe}}$ ratio is greater than 2. The displacement and the reduction reactions occur simultaneously.

Kinetics, coating composition, and morphology.—The kinetics and coating composition of stannized iron or stannized carburized iron were studied in a hydrogen-SnCl₂-FeCl₂ system. The high temperature treatment (>450°C) allows diffusion of the deposited atoms to take place. Consequently, the coating consists of different tin-iron compounds or tin-iron carbides depending on the operating parameters, i.e., temperature duration.

Tables II and III list the compounds formed when stannizing temperature is in the range 450°-650°C. The metallographic cross sections of the coated iron are shown in Fig. 1 and 2. The coating appears to be uniform in thickness and free of cracks. Over this range of temperature, it consists of one layer, although the x-ray patterns show the presence of several compounds corresponding to the phase diagram of the tin-iron system, Fig. 3. In the accompanying micrographs of stannized iron coatings, electrolytic nickel deposited on the coating is shown at the top of each picture and the base metal is shown at the bottom.

Table I. Weight increase of samples, amount of tin deposited, and $n_{\text{Sn}}/n_{\text{Fe}}$ ratio for inert or reducing atmospheres

Atmosphere	Δm (mg)	m_d (mg)	$n_{\text{Sn}}/n_{\text{Fe}}$
Reducing (H ₂)	16.9	22.03	2.04
Inert (argon)	12.1	19.41	1.23

Table II. Variation of composition and microhardness for tin-iron compounds with temperature

Temperature (°C)	Compounds found by x-ray diffraction	Hardness values of a stannized layer (Hv)
<500	FeSn (very little), FeSn ₂	370
500 < θ < 650	FeSn	436
650	FeSn, Fe ₃ Sn ₂ (very little)	440
650 < θ < 750	FeSn, Fe ₃ Sn ₂	442

Table III. Variation of composition of tin-iron compounds and tin-iron carbides with temperature

Temperature (°C)	Compounds found by x-ray diffraction
<500	FeSn, FeSn ₂ , Fe ₃ Sn ₂ C _x
500 < θ < 650	FeSn, Fe ₃ Sn ₂ C _x , Fe ₃ SnC _x
650 < θ < 750	FeSn, Fe ₃ Sn ₂ , Fe ₃ Sn ₂ C _x , Fe ₃ SnC _x
$\theta = 750$	Fe ₃ Sn ₂ , Fe ₃ Sn ₂ C _x , Fe ₃ SnC _x

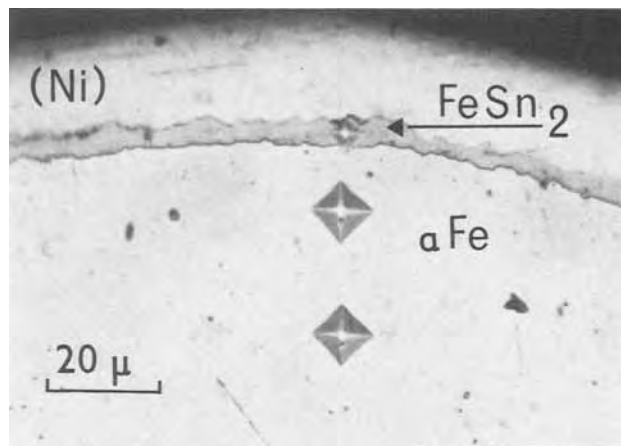


Fig. 1. Metallographic cross section of stannized iron. Treatment 6 hr at 495°C.

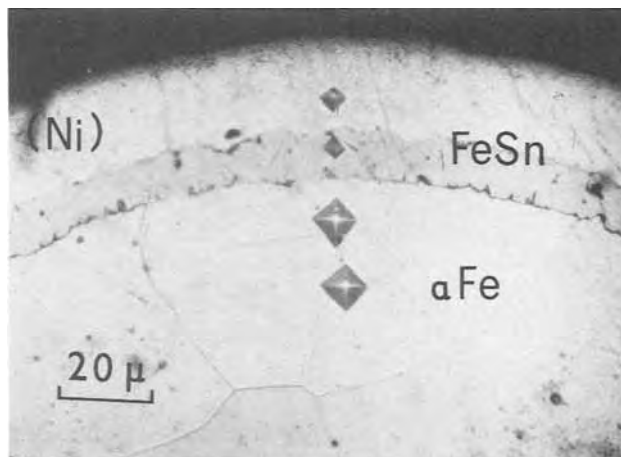


Fig. 2. Metallographic cross section of stannized iron. Treatment 8 hr at 580°C.

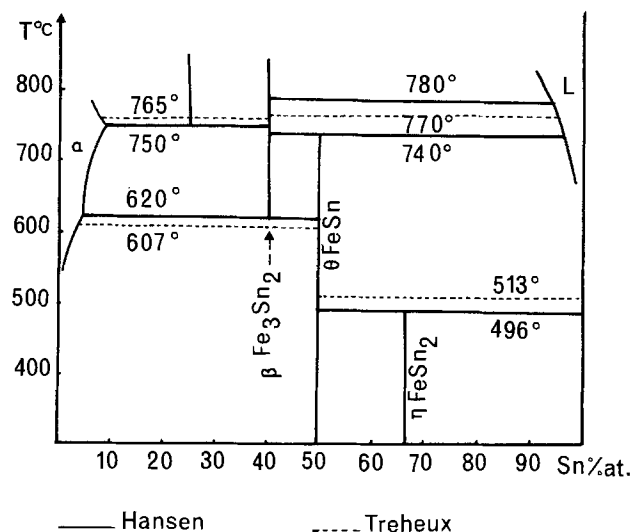


Fig. 3. Phase diagram of the iron-tin system

For carburized iron, the coating consisted mainly of two layers due to the tin-iron compounds and to the tin-iron carbides. These layers are shown in the metallographic section of Fig. 4. The coating formed at 580°C for 10 hr consists of the FeSn compound at the surface and the tin-iron carbide Fe₃Sn₂C_x next to the carburized iron base.

Figure 5 shows the influence of temperature and duration of treatment on the thickness of tin-iron deposits. The thickness (e) of the FeSn₂ compound

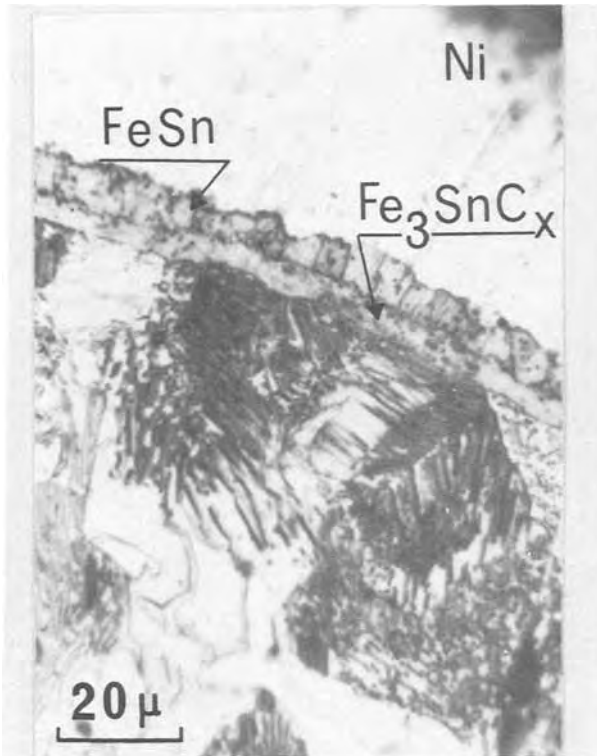


Fig. 4. Metallic cross section of stannized carburized iron. Treatment 10 hr at 580°C.

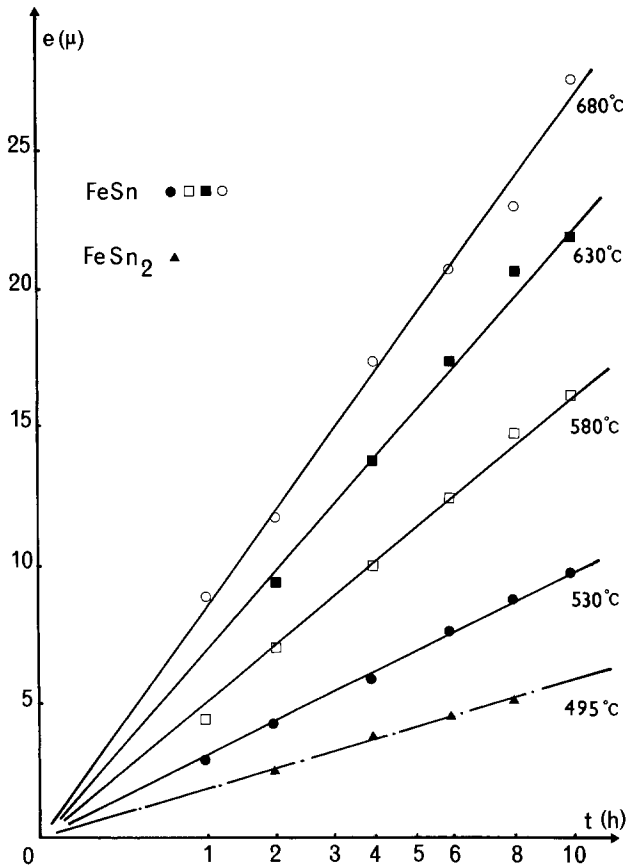


Fig. 5. Effect of temperature and duration of treatment on deposit thickness.

at 495°C and of the FeSn compound between 530°C and 680°C vs. the coating time (*t*) follows the general law $e = A\sqrt{t}$. When varying only the temperature (treatment time 4 hr), the growth of the FeSn compound followed an Arrhenius law

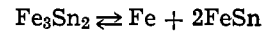
$$e_{\text{FeSn}} = A'e - \frac{Q_{\text{FeSn}}}{RT}$$

The apparent activation energies determined from the slope of the FeSn line in Fig. 6 are about

$$Q_{\text{FeSn}}: 14 \text{ kcal/mole for } \theta < 610^\circ\text{C}$$

$$Q_{\text{FeSn}}: 7 \text{ kcal/mole for } \theta > 610^\circ\text{C}$$

The parabolic behavior of the FeSn₂ and FeSn compound growth indicates that the rate-limiting factor is the intermetallic diffusion. Thermodynamic equilibrium at the gas-metal interface is probably realized. The appearance of even a new submicroscopic phase must have an influence on the growth kinetic of the coating according to the Kidson theory (3). Thus, the slope discontinuity observed for 610°C on the curve $e = f(1/T)$ (Fig. 6) corresponds to the appearance of submicroscopic nuclei of the Fe₃Sn₂ compound as expected from the phase diagram (Fig. 3)



Treheux (4), during a study on the diffusion of tin in iron dipped in molten tin, also observed a slope discontinuity in a similar curve at $T = 607^\circ\text{C}$. These submicroscopic nuclei are not visible by microscopy, though the x-ray data show their existence (cf. Table II).

On carburized iron, the coating thickness vs. temperature does not follow an Arrhenius law. Above 600°C, the thickness does not increase further, Fig. 6. The Fe₃Sn₂ carbide formed impedes diffusion of the iron atoms at the surface and stops growth of the coating.

Epitaxial Growth of FeSn Compound on Iron Substrate

Samples coated by pack cementation showed a coating morphology which was relatively smooth and fine-grained in the range 450°-750°C. However, when the substrate had coarse grains, the deposit had a different aspect in relation with these grains. Several publications have dealt with crystallographic de-

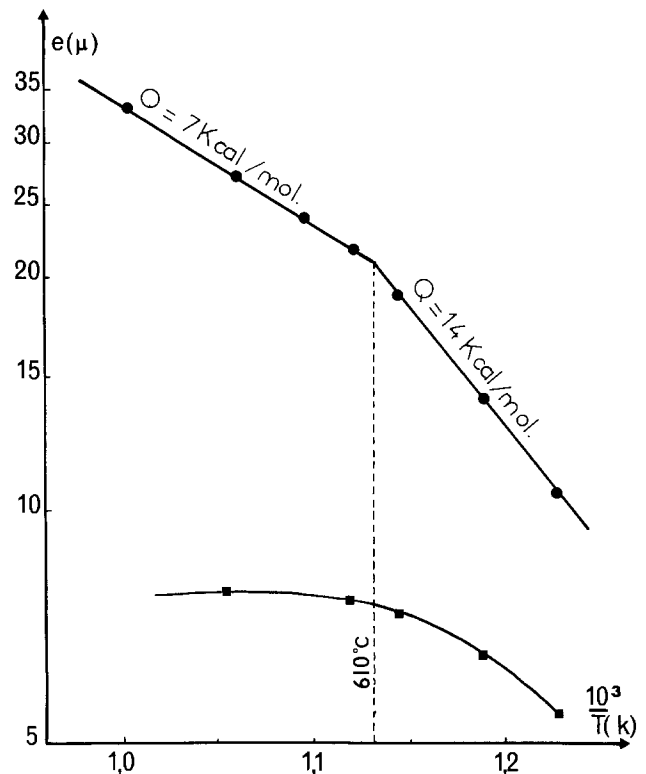


Fig. 6. Arrhenius plot of the FeSn compound (●) and of the tin-iron carbide (■) deposition.

pendence of the nuclei formed on the substrate during CVD process (5-8). The observations related above, and previous studies of epitaxial growth of the Fe_3Si compound during siliconizing and chromizing (9, 10, 11), suggest a relation between the tin-iron compound and the substrate if particular conditions of treatment are realized. Thus, we studied these relations for the FeSn compound at 600°C on iron substrate.

Experimental equipment and procedure.—For this study, we used a conventional CVD process with the silica coating tube extending through two sections of a furnace. The coating reagent (anhydrous stannous chloride) was placed in an alundum boat in the first heating zone of the furnace at 450°C . The sample to be coated [Armco iron plate, $60 \times 10 \times 0.5$ mm, with fine grains or large grains (single crystals)] obtained by the critical strain-hardening method (12) was placed in the second zone at 600°C . The samples were chemically polished and cleaned of any residual contamination. They could be introduced or removed quickly from this zone. Hydrogen completely purged of oxygen was allowed to flow through the system. The coating mixture was 95% hydrogen, 5% SnCl_2 . After holding at temperature for the desired time interval (5-40 min), the sample was quickly removed under a hydrogen flow to a cold zone. A combination of optical microscopy and x-ray diffraction techniques was used to study the sample surface.

Results and discussion.—**Optical microscopy.**—In short treatments of 5-10 min, the nucleation of the deposit appears in some particular points. Some grains have few or no nuclei (e.g., grains A and B, Fig. 7). Others are almost completely covered (grains C and D, Fig. 7; A' and B', Fig. 8). In one grain, the size and the shape of the nuclei are generally the same. Surface defects such as polishing scratches (r), grain-boundaries, and impurities (p), affect the nucleation as shown in Fig. 7-10. At the boundary grains, the nuclei are larger and shaped differently from those in the adjacent grains.

Film growth proceeds by enlargement of islands around these nuclei, or by generation of fresh nuclei. At later stages (after 20 min of treatment) the remaining interstices in the layer are filled, and a completely continuous structure results without special orientation.

X-ray analysis.—X-ray diffraction patterns of the nuclei were not similar to those obtained with a powder of the FeSn compound. Some lines of the

pattern are missing, others are stronger than those of the powder pattern, which suggests an orientation phenomena. On a stannized iron, single crystal which

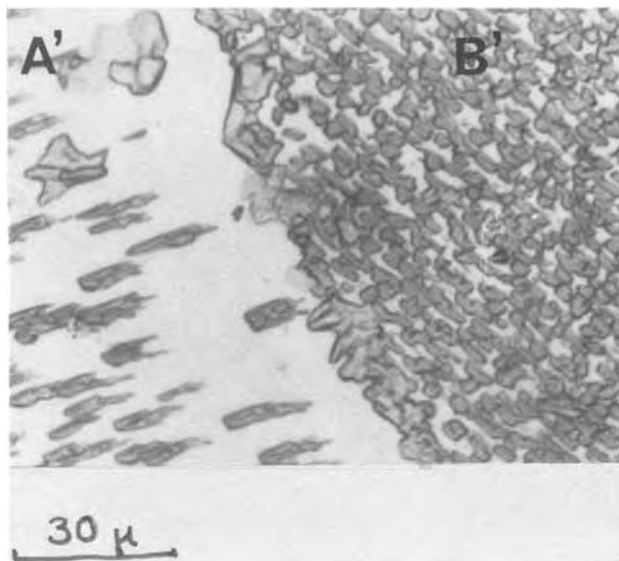


Fig. 8. Influence on the FeSn nucleation of the crystalline orientation of the iron substrate.

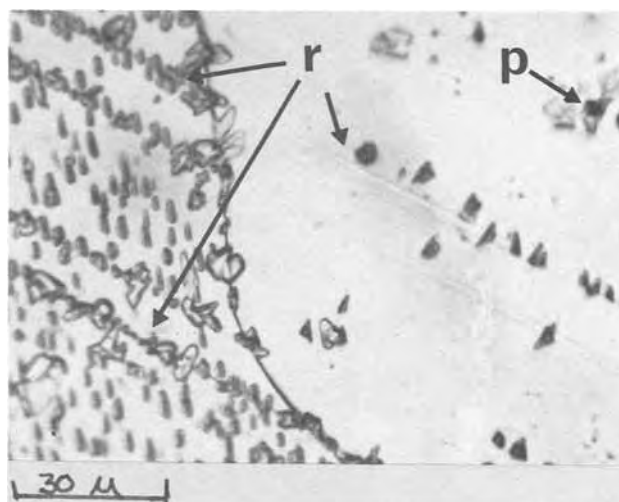


Fig. 9. Influence on the FeSn nucleation of the surface defects, (r) polishing scratches and (p) impurities.

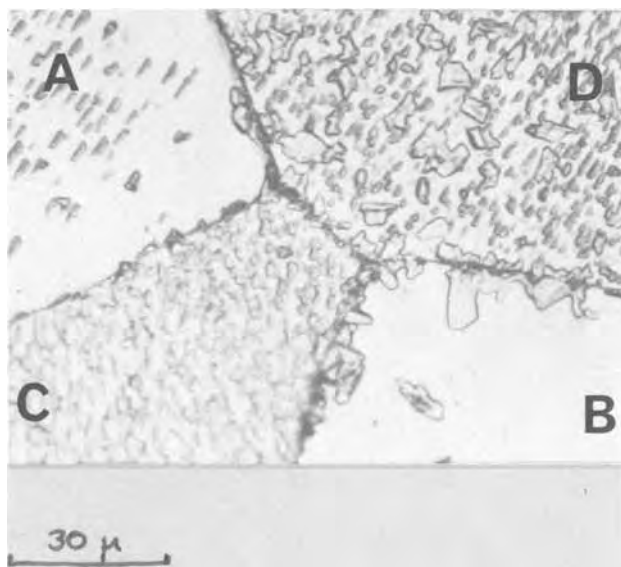


Fig. 7. Influence on the FeSn nucleation of the crystalline orientation of the iron substrate.

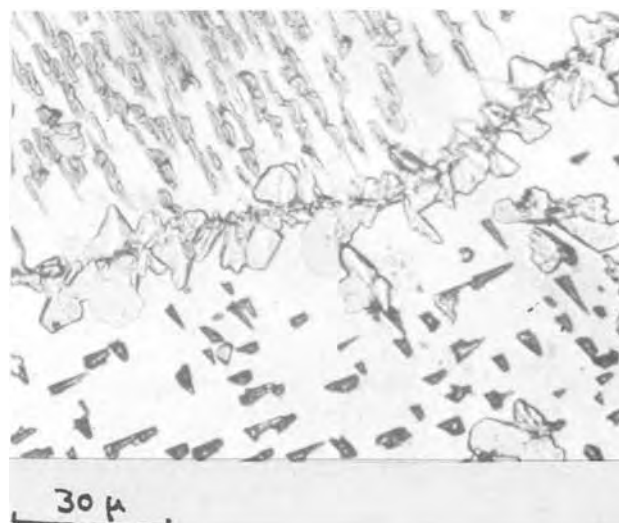


Fig. 10. Influence on the FeSn nucleation of the grain boundaries

has the (211) orientation, the diffraction curve shows only two peaks: those corresponding to the (211) iron planes and those corresponding to the (20 $\bar{2}$ 0) planes of the FeSn compound, Fig. 11. Laue back-diffraction patterns on iron single crystals before and after stannizing show diffraction rings instead of diffraction spots for treatment times longer than 20 min.

FeSn compound has a hexagonal structure, with P 6/mmm as Hermann-Mauguin space group and $a = 5.29\text{\AA}$, $c = 4.44\text{\AA}$ as parameters. There is a set of 6 atoms (3 Sn, 3 Fe) per lattice point. The coordinates of the tin atoms (000) (1/2 3/2 1/2) (2/3 1/3 1/2) and those of iron atoms are (1/2 00) (0 1/2 0) (1/2 1/2 0). The iron atoms are all in the (0001) planes, Fig. 12. The (0001) and (20 $\bar{2}$ 0) planes are those with highest planar density in iron atoms. In these planes, there are unit cells which have lattices almost similar to cells in the (110) and (211) iron planes, Fig. 13. The misfits in both cases are respectively 7.7% and 6.8% for a and a' , and 13.3% and 9.9% for b and b' . A relationship can exist between the closest packed directions of FeSn and iron. For instance, when the FeSn nuclei have their (20 $\bar{2}$ 0) planes parallel to the (211) iron planes, the $|\bar{1}2\bar{1}0|$ direction of the FeSn compound is parallel to the $[\bar{1}11]$ direction of iron. Therefore, conditions are favorable for epitaxial growth (13). We think that nuclei on the surface of an iron substrate are oriented by the underlying grains, followed by epitaxial growth. For polycrystalline substrates, the planes parallel to the surface are randomly orientated and the closest packed directions form various angles with these planes. Epitaxial growth is favored when these angles are smallest (13). When plane orientation is not favorable for epitaxial growths the FeSn nuclei appear preferentially as macrographic defects such as polishing scratches or grain boundaries. Later ($t > 10$ min) they appear inside the grains at crystallographic defects or areas of chemical contamination, cf. micrographs Fig. 7-9. As treatment time increases, nonoriented nuclei increase. The iron base eventually loses its influence on the epitaxial nuclei, and the deposit degenerates completely into a polycrystalline deposit. Some preferential orientations can still remain for a short time and then disappear.

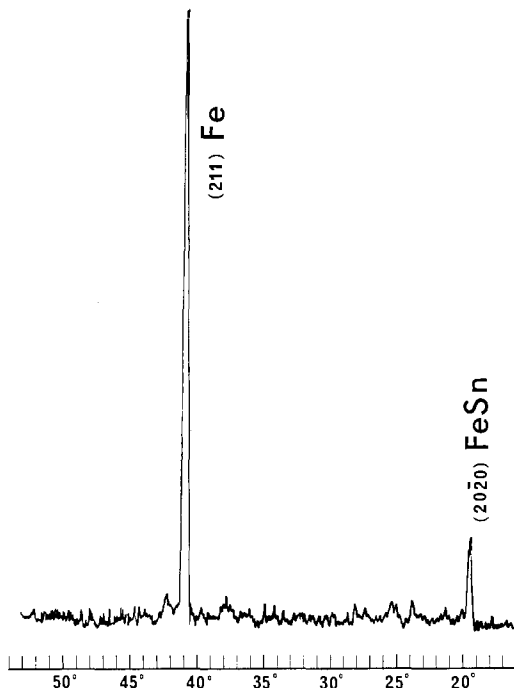


Fig. 11. X-ray curve of a stannized (211) iron single crystal made with the K_{α} Co radiation.

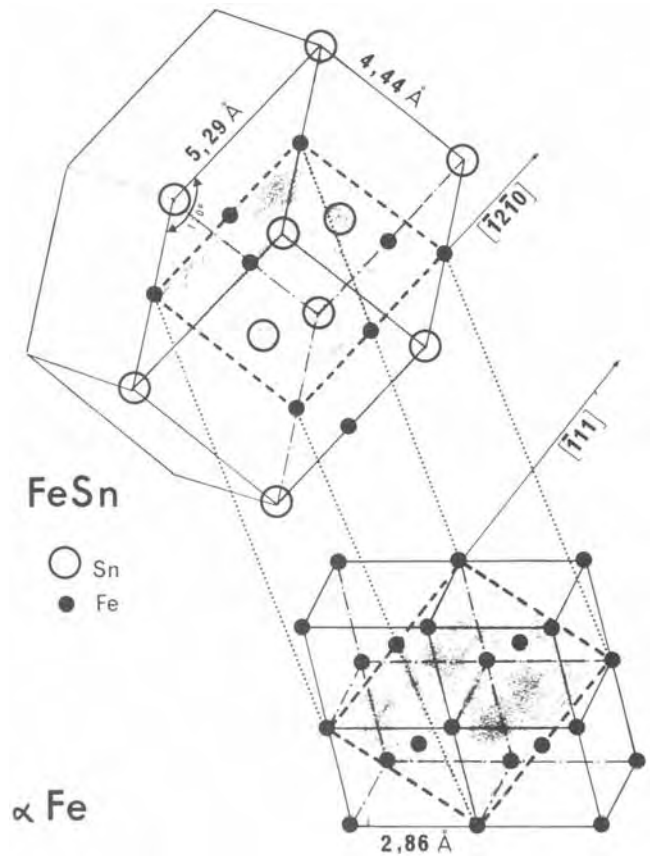


Fig. 12. Relationships of the FeSn compound to the underlying iron substrate.

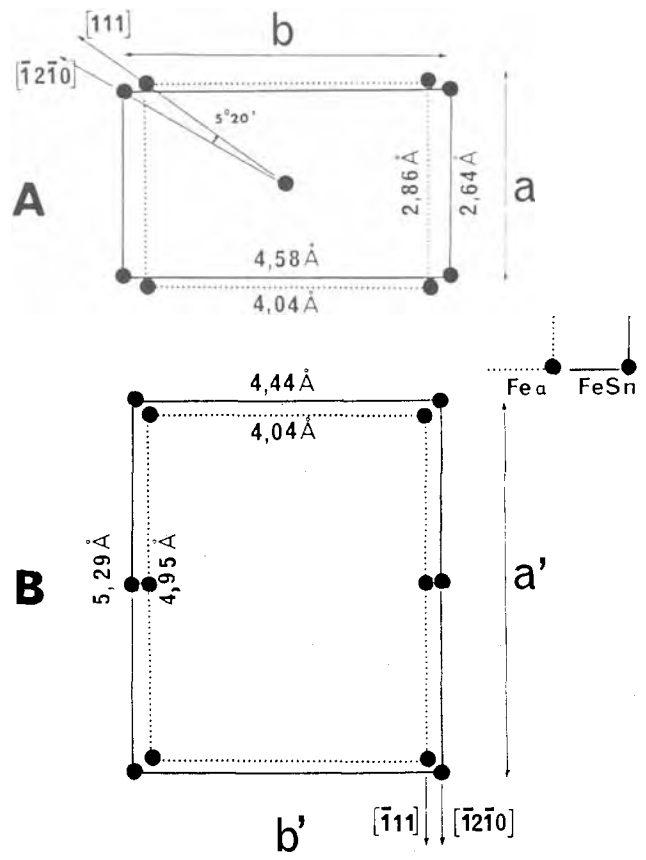
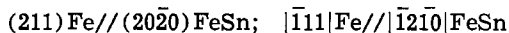


Fig. 13. Relation of the FeSn compound to the underlying iron substrate when crystal planes in the FeSn nuclei and substrate lie parallel to their common interface. A, Common interface (110)Fe and (0001) FeSn; B, common interface (211) Fe and (20 $\bar{2}$ 0) FeSn.

The results thus demonstrate that at the beginning of CVD deposit of tin on iron, the FeSn nuclei formed can be oriented by the substrate and have epitaxial relationships with the underlying iron substrate. The parallel epitaxy of FeSn on iron is given in terms of Miller indices as



Manuscript submitted Sept. 24, 1979; revised manuscript received March 12, 1980. This was Paper 443 presented at the Los Angeles, California, Meeting of the Society, Oct. 14-19, 1979.

Any discussion of this paper will appear in a Discussion Section to be published in the June 1981 JOURNAL. All discussions for the June 1981 Discussion Section should be submitted by Feb. 1, 1981.

Publication costs of this article were assisted by the Institut National des Sciences Appliquées de Lyon.

REFERENCES

1. B. W. Gonser and E. E. Slowter, Tech. Pub. Int. Tin Res. and Dev. Council, Serie A, No. 76 (1938).
2. E. A. G. Croom, Thesis, Cambridge (1950).
3. G. V. Kidson, *J. Mater. Nucl.*, **3**, 21 (1961).
4. D. Treheux, Thesis, Lyon (1973).
5. C. A. Neugebauer, J. B. Newkirk, and D. A. Vermilyea, Editors, "Structure and Properties of Thin Films," John Wiley & Sons, Inc., New York (1959).
6. J. W. Matthews, Editor, "Epitaxial Growth," Academic Press, New York (1975).
7. B. E. Barry, *Thin Solid Films*, **39**, 35 (1976).
8. J. C. Anderson, Editor, "The Use of Thin Films in Physical Investigations," Academic Press, New York (1966).
9. S. Audisio, R. Riviere, and G. Monnier, *C.R. Acad. Sci., Ser. C*, **266**, 211 (1968).
10. G. Monnier, S. Audisio, and E. Rakotomaria, *C.R. Acad. Sci.*, **268**, 929 (1969).
11. M. Papapietro, Thesis, Lyon (1967).
12. J. Talbot, Thesis, Paris (1956).
13. J. Benard, "L'Oxydation des Métaux," Gauthier-Villard, Paris (1962).



A Flow Model for Autodoping in VLSI Substrates

G. R. Srinivasan*

IBM Data Systems Division, East Fishkill, Hopewell Junction, New York 12533

Substrates used in VLSI technology have a high density of buried layer device elements that cause enhanced autodoping during the epitaxial growth. Since autodoping affects many of the device characteristics, it is important to know the level of autodoping, and its variation between devices, in substrates with different device densities. A model was proposed recently that relates autodoping to the buried layer density (1). In this communication we provide experimental support for the model, based on the analysis of autodoping from VLSI substrates with varying areas of arsenic buried layers.

The model is based on the solution to the transport equation that describes the dopant redistribution in a flow system of uniform velocity. We can write for this case

$$D_g \nabla^2 C_g - V \frac{\partial C_g}{\partial x} = 0 \quad [1]$$

where C_g and D_g are the concentration and diffusivity of the dopant in the carrier gas, and V is the flow velocity along X . If we assume that the autodoping concentration, C_a , (i.e., maximum concentration in the lateral autodoping peak) is proportional to C_g , we can obtain an expression for autodoping due to a point source by solving Eq. [1]. This is given by (See Ref. 1 for details)

$$C_a = (A/r) \exp \{(-V/2D_g) (r - x)\} \quad [2]$$

where A is the proportionality constant, r is the lateral distance from the point autodoping source, and x is the projection or r along the flow direction.

For autodoping contribution from a rectangular array of point sources that represent

the buried layer pattern in a typical LSI wafer, we sum the contribution from each point source, and define an average autodoping concentration, \bar{c} , as (1)

$$\bar{c} = \langle \sum_i \sum_j C_a \rangle \quad [3]$$

where i and j are the indices of the point in the rectangular array, and the angular brackets indicate a spatial average of C_a in the unit grid element in the array.

Figure 1 shows the result of this calculation using Eq. [3] where \bar{c} is plotted as a function of n , the number of point sources in the array for several grid sizes. We see from this figure that $\bar{c} \propto n^{1/2}$ for grid size $\lesssim 100 \mu\text{m}$, which is typical of the LSI substrates. We also calculate the autodoping uniformity by defining the maximum variation, Δc , in \bar{c} within a unit grid element. Figure 2 shows the variation of Δc with n for $1 \mu\text{m}$ and $1000 \mu\text{m}$ grid spacings. We note that for both these cases $\Delta c < 5\%$ for $n > 1000$. By associating an infinitesimal area around each point we now define an areal fraction, f , occupied by the buried layers in the substrate as

$$f = \lim_{N \rightarrow \infty} n/N, \quad [4]$$

where N is the total number of points in the wafer. Thus, we can write

$$\bar{c} \sim Kf^{1/2}. \quad [5]$$

where K is a constant of proportionality.

Figure 3 shows the experimental data (2) for the variation of arsenic autodoping (reciprocal epitaxial sheet resistance, R_s) with

*Electrochemical Society Active Member.

Key words: epitaxy, impurity, integrated circuits, semiconductor.

the buried layer subcollector density in VLSI substrates that are used in bipolar circuitry. These data are obtained by measuring epitaxial sheet resistance, R_s on device wafers which had various buried layer densities. The epitaxial depositions were made in a Laminar flow reactor system with identical deposition conditions. $1/R_s$ is a measure of total autodoping in the epitaxial layer. We see that the data can be represented by the equation $10^4/R_s = 2.25 f^{1/2}$ in agreement with Eq. [5]. Thus, the theory is successful in predicting the autodoping enhancements in VLSI substrates.

The model is also capable of explaining the autodoping increases due to increases in the wafer load in the epitaxial reactor by summing up contributions from each wafer using a procedure similar to that indicated here. Finally, the model can also be extended to buried layers of finite size and special geometries, upon which we will report elsewhere (3) and discuss the flow effects in some detail.

ACKNOWLEDGMENTS

I thank J. F. Cholley of IBM (France) for the data used in Fig. 3.

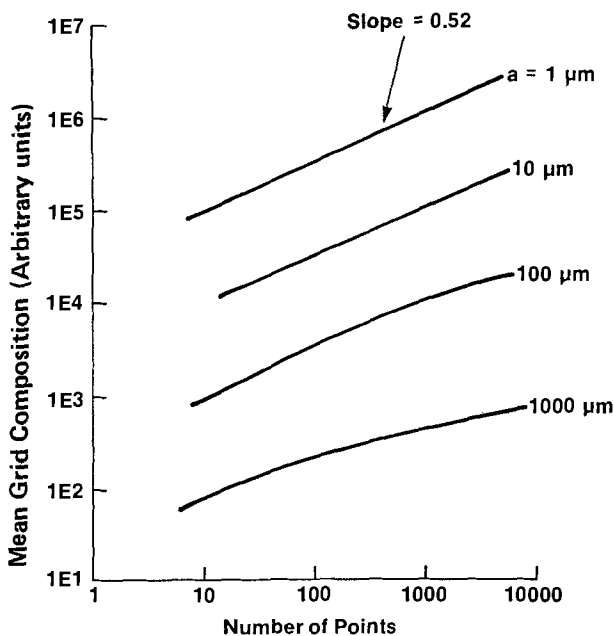


Fig. 1. Variation of mean grid composition with number of point sources in the array for various grid spacings.

Manuscript received April 24, 1980.

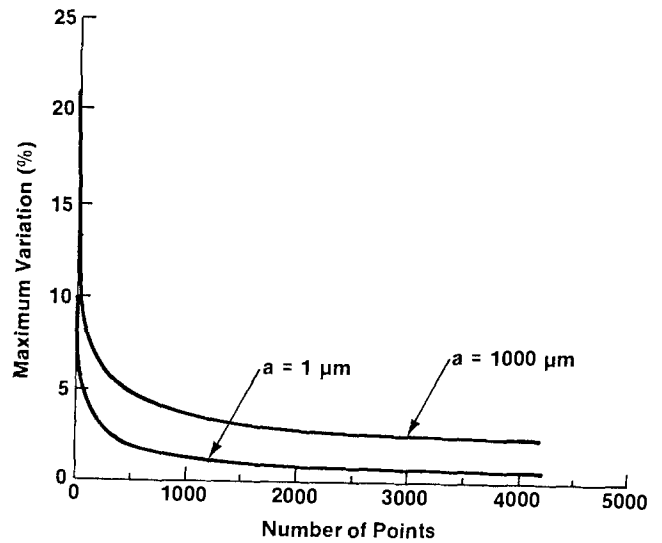


Fig. 2. Maximum compositional variation in the grid as a function of number of point sources in the array for two grid spacings.

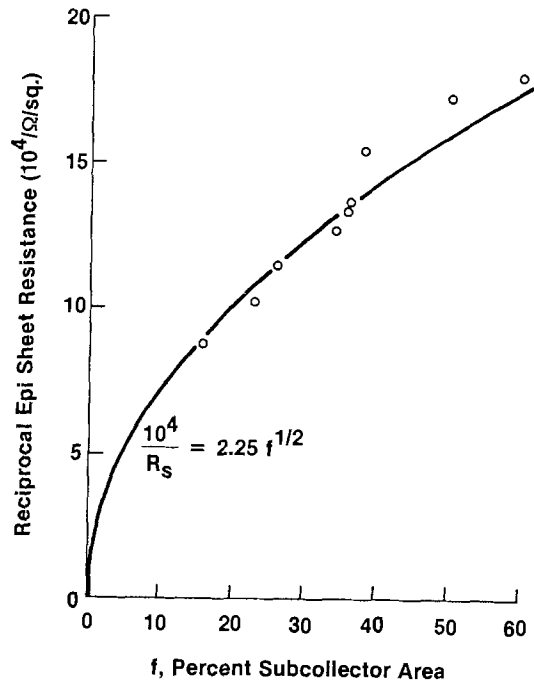


Fig. 3. Variation of epitaxial sheet resistance with percent arsenic subcollector area for LSI substrates.

REFERENCES

1. G.R. Srinivasan, Second Joint VLSI Issue of IEEE Trans. Electron Devices and IEEE J. Solid State Circuits, August 1980.
2. J.F. Cholley, Private Communication.
3. G.R. Srinivasan, to be published in J. Appl. Phys., Sept. 1980 issue.

Publication costs of this article were assisted by IBM Corporation.

α -Fe₂O₃ Photoanodes Doped with Silicon

John H. Kennedy,* Ruth Shinar, and John P. Ziegler

Department of Chemistry, University of California, Santa Barbara, California 93106

INTRODUCTION

Previous papers reported on the photoelectrochemical properties of α -Fe₂O₃ (1,2) in which undoped high purity and titanium-doped polycrystalline materials were used. Undoped material exhibited high photocurrents even at 0 V vs. SCE and, in general, were superior to Ti-doped α -Fe₂O₃. More recent purchases of high purity α -Fe₂O₃ (99.999%) showed that the sintered pellets were highly resistive and exhibited no photocurrent. Varying the sintering conditions had little effect although the sintering in the presence of a reducing atmosphere (90% N₂ - 10% H₂) yielded electrodes with some photoactivity. However, they also showed large dark currents.

Analysis of the original α -Fe₂O₃ by emission spectroscopy showed it to contain a silicon impurity of ca. 0.1 a/o whereas the later batches only contained several ppm Si. Experiments were conducted in which the new high purity α -Fe₂O₃ was doped with varying amounts of SiO₂ and the results are reported here.

EXPERIMENTAL

Si-doped electrodes were prepared from α -Fe₂O₃ (99.999%, Apache Chemical Co. and Alfa Products) by mixing with reagent grade SiO₂ powder, pressing and sintering. Sintering was carried out in air at 1250°-1350°C for from 4 to 24 hr followed by quenching to room temperature. The silicon doping level was varied from 0.001-2 a/o. Electrodes containing 1 a/o TiO₂ were also prepared for comparison. Old, nominally pure α -Fe₂O₃ (Apache Chemical Co.) which contained ca. 0.1 a/o Si by emission spectroscopy analysis was used without additional doping. Pressed pellets of this material were sintered in air at 1300°C for 14 hr. Densities were from 85 to 100% of the theoretical value.

Electrical connections were made using silver epoxy as previously described (1). Typical resistances measured at 1 KHz with a conductivity bridge were from 1 to 2 k Ω .

The cell arrangement consisted of the

α -Fe₂O₃ working electrode, Pt counterelectrode and a SCE reference electrode. Current-potential curves were obtained with a PAR Model 174 polarographic analyzer at a scan rate of from 2 to 10 mV/sec. Electrodes were illuminated with a 150 W Xenon lamp. For spectral response a Bausch and Lomb visible grating monochromator was employed.

RESULTS

Photocurrent vs. applied potential for the nominally "pure", 0.1 a/o Si-doped, and 1 a/o Ti-doped α -Fe₂O₃ in 1M NaOH is shown in Fig. 1. The match in characteristics was quite close for the undoped old material and the new high purity material doped with 0.1 a/o Si. The match was even closer in an electrolyte containing 0.05M borax buffer at pH 9. As can be seen from Fig. 1 the Ti-doped material exhibited the same plateau value of photocurrent but only at considerably higher applied potentials. Only Si-doped materials gave high photocurrents at 0 V vs. SCE. Measurements shown in Fig. 1 were taken with polychromatic light with only an infra-red filter in the light path.

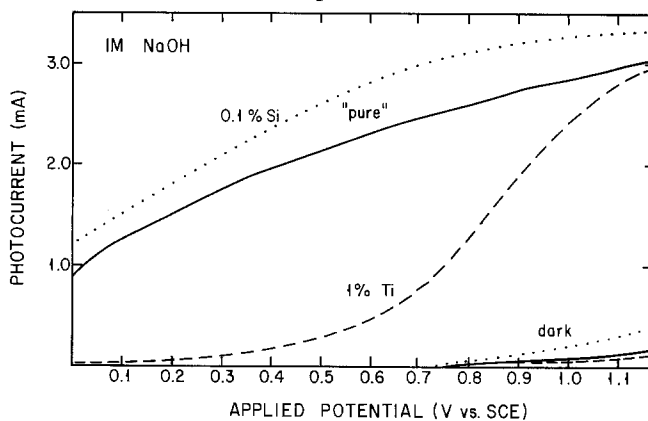


Fig. 1. Photocurrent vs. applied potential observed for undoped, 0.1 a/o Si-, and 1 a/o Ti-doped α -Fe₂O₃ electrodes in 1M NaOH. Polychromatic light from 150 W Xenon source.

Photocurrents were somewhat higher with 2 a/o Si doping and considerably less with

0.01 a/o Si as shown in Fig. 2. High doping levels (>1 a/o) have not been studied in depth yet because it was found that dark currents were significantly higher at applied potentials >0.4 V vs. SCE and frequently increased with age of the electrode.

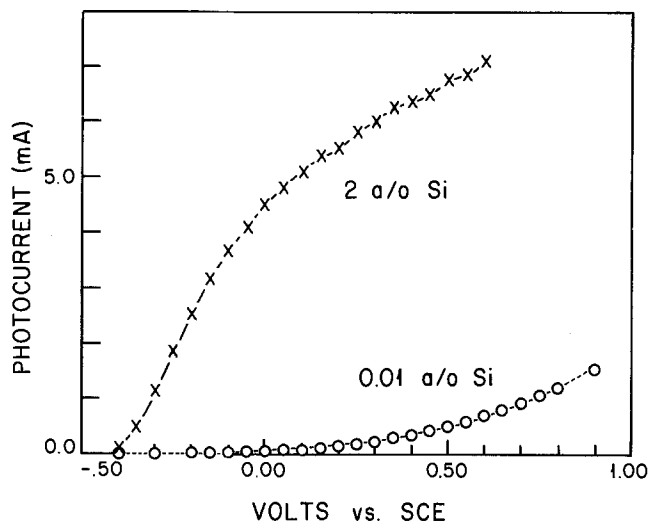


Fig. 2. Photocurrent vs. applied potential observed for 0.01 a/o and 2 a/o Si-doped α - Fe_2O_3 in 1M NaOH. Dark current started to rise above +0.6 V vs. SCE for 2 a/o Si-doped electrode. Polychromatic light from 150 W Xenon source.

Spectral response for the old "pure" material and Si-doped α - Fe_2O_3 was identical and, aside from the maximum photocurrents obtained, was the same as Ti-doped electrodes as shown in Fig. 3.

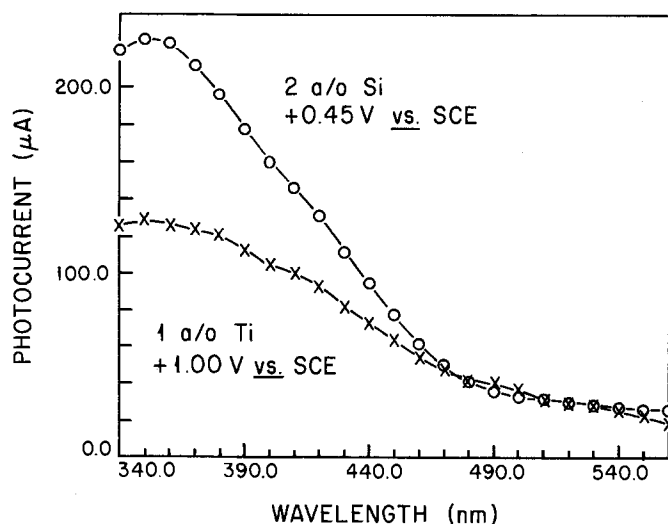


Fig. 3. Spectral response for 2 a/o Si-doped electrode compared to 1 a/o Ti-doped electrode.

Photocurrent vs. applied potential for electrodes illuminated at 400 nm is shown in Fig. 4. The characteristics are similar to

those seen in Fig. 1. It should be noted that dark current for the 2 a/o Si-doped electrode started to rise when the applied potential was >0.4 V vs. SCE while dark currents for lower doping levels (<1 a/o) were quite low until the applied potential was >0.8 V vs. SCE.

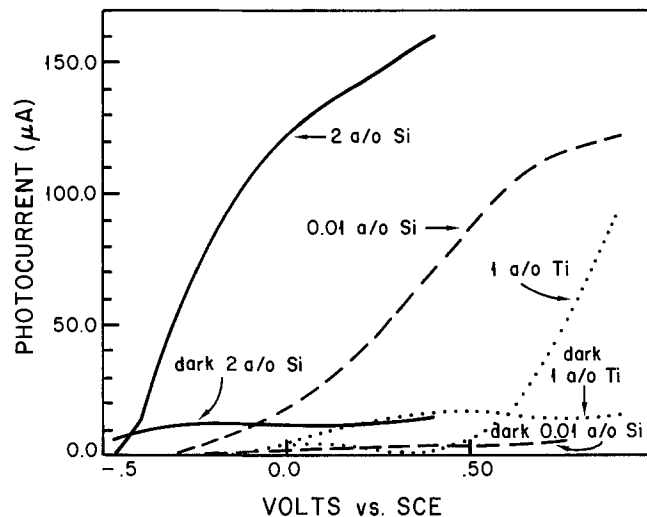


Fig. 4. Photocurrent vs. applied potential for Si and Ti-doped α - Fe_2O_3 illuminated with 400 nm light.

Surface effects for these electrodes were also found to play an important role in determining photoresponse. Dipping an electrode that showed a fairly low photocurrent in 1M KI solution at pH 9 improved the electrode's response to light when illuminated in 1M NaOH. Photocurrents were observed to increase by a factor of 3 after 3 weeks of soaking in 1M KI at pH 9. This is shown in Fig. 5 for a 0.1 a/o Si-doped electrode. The high photocurrent remained stable for more than two months and disappeared only after heating the electrode to 130°C . Electrodes which showed the highest photocurrents could be improved a small amount by the KI treatment but it was apparent that the treatment primarily improved the surface of poorer electrodes to the point where they would match the performance of the best electrodes. Treatment with iodide in 1M NaOH did not improve the electrodes. This was attributed to strong adsorption by OH^- in 1M NaOH preventing iodide from reacting with the surface.

CONCLUSIONS

The earlier results obtained with undoped α - Fe_2O_3 were actually a consequence of an incidental silicon impurity. Silicon, a group IV A element, is a better dopant for

α -Fe₂O₃ than titanium, a group IV B element. This conclusion is presently being pursued with other group IV elements as dopants.

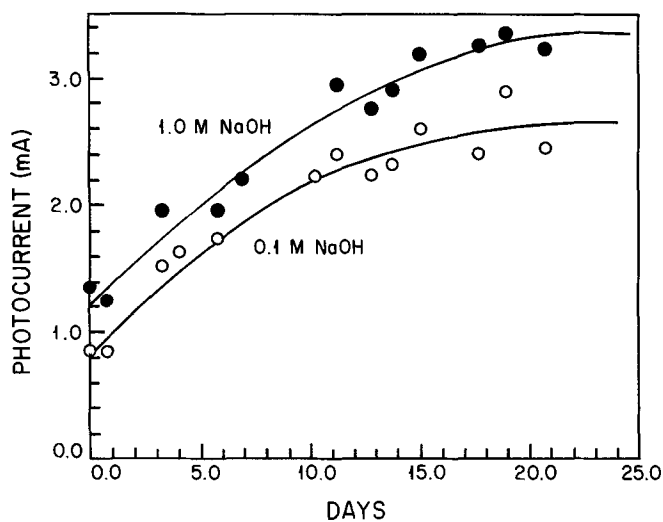


Fig. 5. Photocurrent observed at +0.9 V vs. SCE in 0.1 M and 1 M NaOH as a function of time immersed in 1 M KI at pH 9.

Photocurrent at 0 V vs. SCE increases with increasing silicon content but dark current also increases, especially above 1 a/o.

Surface effects caused by solutes in the electrolyte may play a significant role in modifying the photoresponse exhibited by the α -Fe₂O₃ electrodes. Competition reactions between OH⁻ and other solutes such as halide ions will be reported at a later date.

ACKNOWLEDGEMENT

This work is supported by the Division of Chemical Sciences, Office of Basic Energy Sciences, U.S. Department of Energy.

REFERENCES

1. J. H. Kennedy and K. W. Frese, Jr., J. Electrochem. Soc. 125, 723 (1978).
2. J. H. Kennedy and K. W. Frese, Jr., J. Electrochem. Soc. 125, 709 (1978).

*Electrochemical Society Active Member.

Manuscript received July 24, 1980.

Publication costs of this article were assisted by the University of California.

Protection of n-GaAs Photoanodes with Photoelectrochemically Generated Polypyrrole Films

Rommel Noufi,* Dennis Tench,* and Leslie F. Warren

Rockwell International Electronics Research Center, Thousand Oaks, California 91360

It is generally recognized that the key obstacle to the development of electrochemical solar cells is photodegradation of the semiconductor electrodes. In principle, this problem could be overcome by the use of an electrically conducting polymer film on the electrode. By acting as a barrier to ion/solvent transport, such an insoluble film would prevent photodegradation while permitting electron exchange with the electrolyte. Good adhesion, uniformity and interfacial charge transport properties are expected for electrochemically generated films since deposition is initiated at the interface by electrochemical oxidation/reduction. Electrodeposition of polypyrrole films, having conductivities in the 10 to $100 \Omega^{-1} \text{ cm}^{-1}$ range, on Au and Pt electrodes has recently been reported (1-3). In this communication, we describe the photoelectrochemical generation of polypyrrole films on n-GaAs and the characteristics of the resulting photoanodes.

Electrodeposition of polypyrrole on n-GaAs was performed with tungsten-halogen illumination (50 mW/cm^2) at a constant electrode potential of 0.45 V vs SCE (saturated calomel electrode) from mechanically stirred acetonitrile solution containing 0.1 M pyrrole and 0.1 M Et_4NBF_4 (supporting electrolyte). The semiconductor electrodes were single crystals (3×10^{16} carriers/ cm^3) and were etched in $1:1 \text{ H}_2\text{SO}_4/\text{H}_2\text{O}_2$ solution before use. Deposition on illuminated n-GaAs begins at a less anodic potential (0.2 V) than on Pt (0.8 V), as might be expected for a photo-assisted process. During deposition, the current remained practically constant at $100 \mu\text{A/cm}^2$. Based on the charge passed, the film thickness was usually in the 100 monolayer range (assuming $50 \mu\text{C/cm}^2$ per

monolayer). Details of the electrode mounting and measurement techniques have been described previously (4). In all experiments reported here, electrode illumination was provided by a tungsten-halogen lamp. The counter electrode was generally Pt ($\sim 25 \text{ cm}^2$).

Figure 1 shows linear sweep cyclic voltammograms at various sweep rates for a polypyrrole-coated n-GaAs electrode under illumination in an acetonitrile solution containing only supporting electrolyte. As indicated by the corresponding anodic and cathodic current peaks, the film itself is reversibly oxidized and reduced. This film redox reaction is also observed with Pt substrates and apparently involves anion exchange with the solution (1). The onset of film oxidation corresponds with the flatband potential on n-GaAs (-1.0 V), although it occurs at more anodic potentials on Pt (-0.4 V). Likewise, the voltammetry peaks for the film-covered semiconductor occur at more cathodic potentials (about -0.5 V compared to -0.1 V vs SCE). As expected, the film redox reaction does not occur on n-GaAs in the dark. It is remarkable, however, that the cathodic peak still occurs when illumination is interrupted after the anodic portion of the cycle. This indicates that electron exchange between the film and the semiconductor valence band occurs in both the anodic and cathodic directions.

Cyclic voltammetric studies were also performed for film-covered and bare n-GaAs electrodes, with and without illumination, in aqueous solutions containing redox couples covering a range of redox potentials (V_R), i.e., $\text{Fe}^{3+/2+}$ (0.53 V vs SCE), $\text{Fe}(\text{CN})_6^{3-74-}$ (0.12 V) and $\text{Fe}(\text{III})\text{EDTA}/\text{Fe}(\text{II})\text{EDTA}$ (-0.13 V). The pH was varied from 0 to 14 to vary the flatband potential (V_{fb}), measured by ac impedance, from -0.4 to -1.4 V . V_{fb} values were equivalent for the film-covered and bare electrodes and open circuit photovoltages were always close to the predicted values ($V_R - V_{fb}$). These results

*Electrochemical Society Active Member

Key Words: electrochemical solar cells, photoelectrode stabilization, polymer films

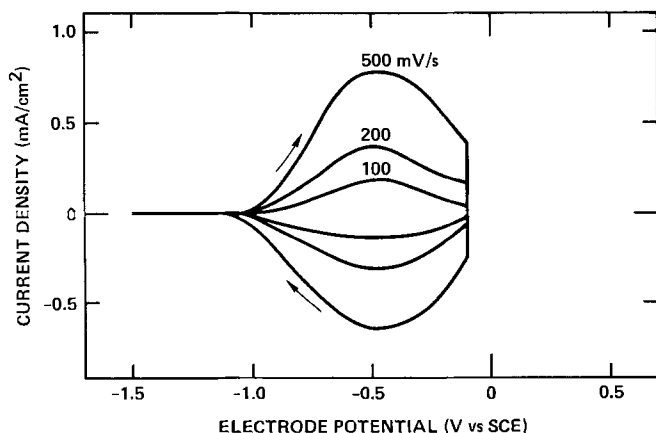


Fig. 1 Cyclic voltammograms for a polypyrrole-coated GaAs photoanode illuminated at 60 mW/cm^2 in acetonitrile solution containing $0.1 \text{ M Et}_4\text{NBF}_4$.

indicate that Fermi level pinning does not occur for n-GaAs in these aqueous systems.

Figure 2 shows a current-voltage curve for a polypyrrole-coated GaAs photoanode under illumination at 170 mW/cm^2 in an aqueous $0.2 \text{ M Fe(CN)}_6^{3-/4-}/0.1 \text{ M NaCN}/0.1 \text{ M NaOH}$ solution. Although unprotected GaAs photodissolves in this system, the film-covered electrode is stable, i.e., the curve in Fig. 2 was not perceptively changed after 50 cycles at 100 mV/s . The output characteristics are comparable with the protective film compared to the bare electrode except that the short circuit photocurrent is reduced 39% (from 31 mA/cm^2 to about 19 mA/cm^2). This photocurrent reduction presumably results from suppression of the photodissolution process, light absorption in the relatively thick films used here, or both. The open circuit voltage (1.37 V) is noteworthy since it is practically equivalent to the bandgap of GaAs (1.4 eV). In aqueous systems, film peeling is presently a problem, usually occurring within 10 to 20 minutes under illumination and apparently originating at the edges of the film (which are exposed to the electrolyte). However, polypyrrole-coated GaAs photoanodes have operated at 5.5 mA/cm^2 (90 mW/cm^2) in methanol/ 0.2 M each tetraethylammonium $\text{Fe(CN)}_6^{3-/4-}/0.1 \text{ M Et}_4\text{NBF}_4$ solutions for 100 h without detectable weight loss or deterioration of the electrode surface, whereas the photocurrent for unprotected GaAs decays to a negligible value in less than one minute in this system.

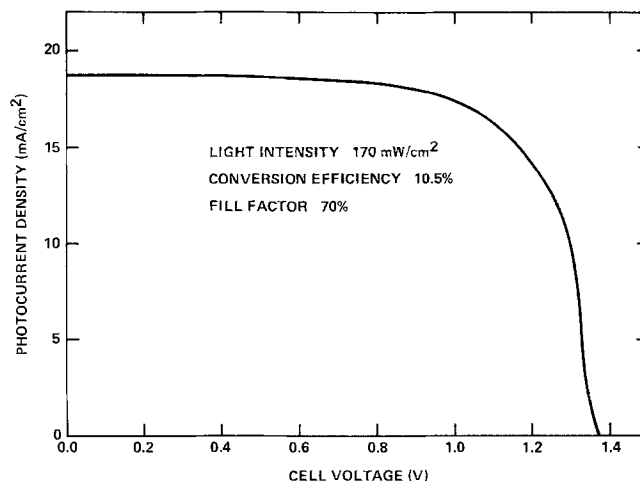


Fig. 2 Photocurrent-voltage curve for the cell polypyrrole-coated GaAs/aqueous $0.2 \text{ M Fe(CN)}_6^{3-/4-} + 0.1 \text{ M NaCN} + 0.1 \text{ M NaOH/Pt}$ under illumination at 170 mW/cm^2 .

These results show that electro-deposited polypyrrole films protect n-GaAs photoanodes from dissolution while permitting electron exchange with the electrolyte. With further work, such films could provide the photoelectrode stability and performance characteristics required for a practical electrochemical solar cell.

ACKNOWLEDGEMENT

The authors gratefully acknowledge support of a portion of this work by the Solar Energy Research Institute under subcontract No. XP-9-8002-1.

REFERENCES

1. A. F. Diaz, K. K. Kanazawa and, G. P. Gardini, J.C.S. Chem. Comm., 635 (1979).
2. K. K. Kanazawa, A. F. Diaz, R. H. Geiss, W. D. Gill, J. F. Kwak, J. A. Logan, J. F. Rabolt, and G. B. Street, J.C.S. Chem. Comm., 854 (1979).
3. A. F. Diaz and J. I. Castillo, J.C.S. Chem. Comm., 397 (1980).
4. R. Noufi and D. Tench, This Journal, 127, 188 (1980).

Manuscript received July 28, 1980.

Publication costs of this article were assisted by Rockwell International.

Resistance Rise in Sodium-Sulphur Cells

D. S. Demott

British Rail, Research and Development Division, Derby, England

Resistance increases in sodium-sulphur cells during extended periods of cycling have been reported by various groups of workers (1-4). These increases have usually been ascribed to corrosion of metallic components in the sulphur electrode compartment or to impurities in either the sodium or sulphur electrodes. Recently, however, we have experienced very severe rates of resistance increase which, as we show here, are attributable to the sodium/ β'' -alumina interface.

The rate of resistance rise which we have observed in our cells has been very variable. Formerly the average rate of rise was 0.4 ohm cm² per 100 cycles but the problem has gradually become so severe that the resistance can now double within ten cycles (equivalent to a rate of rise of 20 ohm cm² per 100 cycles) or even less. This resistance rise has been most pronounced during cell discharge, the charge resistance usually remaining relatively constant. This type of asymmetric resistance behaviour of β'' -alumina has been observed previously in both sodium-sulphur cells and sodium/ β'' -alumina/sodium tests (5-8). We have also frequently found two further effects to be associated with the rapid rise in discharge resistance. Firstly, an even higher transient resistance occurs at the start of discharge; this high transient discharge resistance also appears after the cell has been left on open circuit at any state of discharge, the effect even being detectable after a current interruption of only a few seconds. Secondly, the minimum discharge resistance decreases with increasing current.

All these effects are illustrated in Fig. 1 which shows discharge and charge curves for a typical high resistance cell. The time dependent and non-ohmic effects are also very apparent in polarisation curves which were plotted for the same cell (Fig. 2). These curves were obtained by allowing the cell to stand on open circuit until a steady voltage was obtained (approximately 5 minutes)

Key Words: sodium-sulfur cells, beta alumina, resistance.

before applying each constant discharge or charge current; the cell voltage was then measured after 1, 30 and 120 seconds.

No correlation could be found between the variation in magnitude of these effects and any known differences in cell construction (e.g. types of sulphur electrode, current collector and sodium electrode and minor variations in the β'' -alumina tubes - nominal composition 8.9% Na₂O, 0.7% Li₂O, <10% β -phase). This, and the observation that similar effects can occur in sodium/ β'' -alumina/sodium tests, was strong evidence that the problem was associated with the sodium/ β'' -alumina interface. Consequently, it was decided to investigate whether renewal of the sodium led to any improvement in cell resistance.

With our central sulphur cell design (1) renewal of the sodium electrode is a straightforward matter. This is done by cooling the cell in the fully charged state and cutting away the mild steel cell case. Sodium is removed from the outside of the β'' -alumina tube by scraping and by reaction with ethanol; the complete β'' -alumina tube and sulphur electrode assembly can then be reassembled into a new cell case with fresh sodium. When applied to cells which have shown a rapid resistance increase this procedure invariably results in a reduced cell resistance; a typical example is shown in Fig 3. Not only is the subsequent discharge resistance usually lower than the previous minimum value but it normally remains constant over a large number of cycles and the time dependent and non-ohmic effects are eliminated. However, we have found that cells which are subjected to sodium renewal after only a few cycles can again rise in resistance; 20-30 cycles appear necessary before renewal in order to achieve a stable resistance. It has, furthermore, been found that cells which have shown a relatively modest rate of resistance rise (e.g. a 50% rise over 600 cycles), without showing the pronounced

non-ohmic and time dependent effects described above, can also be restored to their original resistance by renewal of the sodium electrode.

Various experiments have been performed to elucidate the cause of these improvements following sodium electrode renewal.

Briefly, these have shown that:-

- i) the improvement is not simply due to the thermal cycle experienced by the cell.
- ii) improvement cannot be achieved by washing of new β -alumina tubes in the same solutions used for sodium removal.
- iii) no correlation can be found between the resistance of cells and any impurities in the sodium removed from them; the fact that the resistance problems can be eliminated by sodium renewal further indicates that if impurities are responsible they do not arise from the sodium or any other components of the sodium electrode since these are invariant.
- iv) heating of a high resistance cell to 500°C (with the sulphur electrode in the single phase region), with and without current flowing, in order to improve the wetting of the β -alumina surface by the sodium (7), led to no improvement when the cell was returned to 350°C.
- v) renewal of the bulk of the sodium in a cell without disturbing the sodium in contact with the β -alumina surface does not have the observed beneficial effect. This was done by cutting off the bottom of the cell case, melting the sodium out of the pressure can, replacing it with fresh sodium and re-welding the bottom of the cell. Unlike cells in which the β -alumina was cleaned free of sodium this cell continued to exhibit the high resistance effects.

Although, at present, we have not been able to establish the mechanism of resistance increase, it is evident that the cause of the observed effects is removed during the sodium renewal procedure. Clearly, for practical reasons, renewal of the sodium electrode cannot provide the ultimate solution to this problem and further experimentation is necessary in order to locate the source of

the resistance rise and means of preventing it. However, since we have found the effect to occur to varying degrees over a range of β -alumina compositions, it is possible that it is a contributory factor to the resistance increases frequently observed in sodium-sulphur cells of different design.

Acknowledgement

The author is grateful to colleagues at British Rail for their help and particularly to D.R. Swift for dismantling the cells. Thanks are also due to British Railways Board for permission to publish this paper.

REFERENCES

1. M.D. Hames, D.G. Hartley, and N.M. Hudson, "Power Sources 7" (J. Thompson, ed.), p.743, Academic Press Inc., London (1979).
2. Y. Lazennec, C. Lasne, P. Margotin, and J. Fally, This Journal, 122, 734 (1975).
3. I. Yasui and R.H. Doremus, *ibid*, 125, 1007 (1978).
4. National Science Foundation Ann. Rep., Contract No. NSF-C805 (1978).
5. D.S. Demott and P. Hancock, Proc. Br. Ceram. Soc 19, 193 (1969).
6. J.L. Sudworth, A.R. Tilley, and K.D. South, "Fast ion transport in solids" (W. van Gool, ed.), p.581, North-Holland (1973).
7. A. Gibson, "Power Sources 6" (D.H. Collins, ed.), p.673, Academic Press Inc., London (1977).
8. M.W. Breiter, B. Dunn, and R.W. Powers, Extended Abstracts of the Los Angeles, California, Meeting. The Electrochemical Society, Princeton, N.J. (1979).

Manuscript submitted May 29, 1980.

Publication costs of this article were assisted by the British Rail.

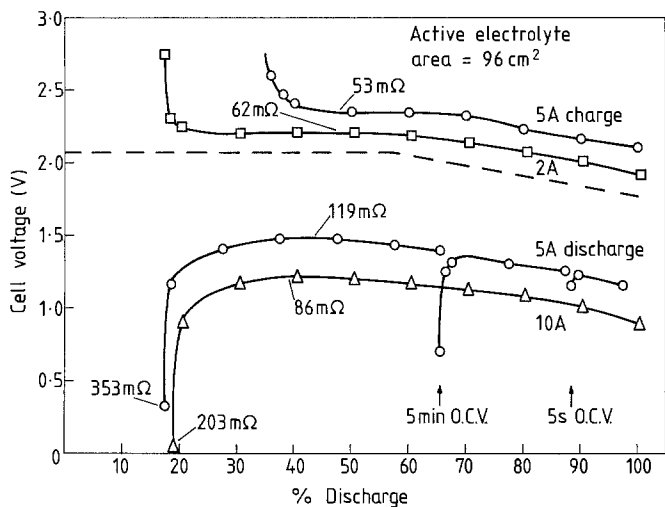


Fig. 1. Charge/discharge behaviour of a typical high resistance cell.

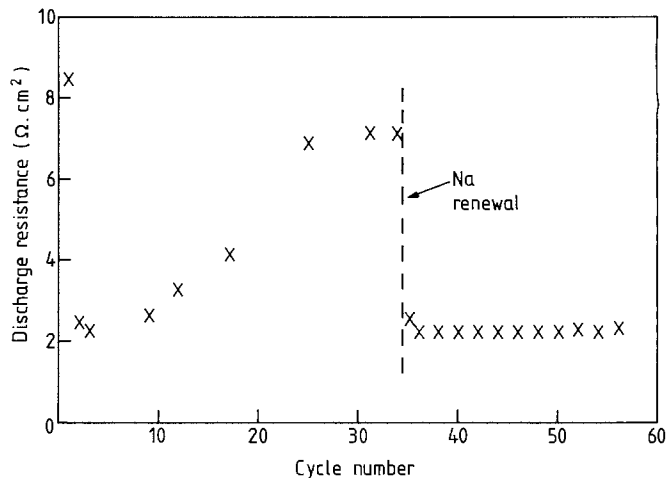


Fig. 3. Resistance behaviour of a typical cell before and after sodium renewal.

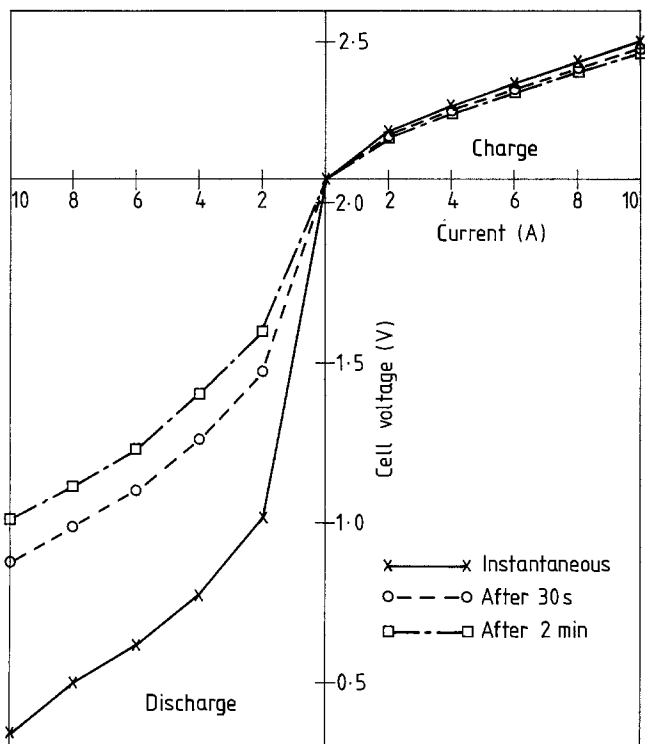


Fig. 2. Two-phase region polarisation data for the same cell shown in Fig. 1.



Molybdenum Oxide Cathodes in Secondary Lithium Cells

P. A. Christian,¹ J. N. Carides, F. J. DiSalvo, and J. V. Waszczak

Bell Laboratories, Murray Hill, New Jersey 07974

ABSTRACT

The electrochemical behavior of molybdenum oxide cathode materials with stoichiometries between MoO_2 and MoO_3 in nonaqueous lithium secondary cells are examined. Of the oxides Mo_4O_{11} , $\text{Mo}_{17}\text{O}_{47}$, $(\text{Mo}_{0.92}\text{V}_{0.08})_5\text{O}_{14}$, Mo_8O_{23} , and Mo_9O_{26} the greatest reversible capacity (>1 Li/Mo) after several deep discharge/charge cycles was exhibited by $\text{Mo}_{17}\text{O}_{47}$ in cells with a LiClO_4 /propylene carbonate electrolyte. Excepting Mo_4O_{11} , which gives a reversible capacity of >0.75 Li/Mo after 20 deep discharge/charge cycles, the reversible capacities of the other molybdenum oxides are considerably less than that of $\text{Mo}_{17}\text{O}_{47}$. The limiting reversible lithium capacity of 1.5 Li/Mo for $\text{Mo}_{17}\text{O}_{47}$ was determined by treating $\text{Mo}_{17}\text{O}_{47}$ with an n-butyllithium solution and the lithium bronze formed with an I_2 solution. For an average cell voltage of 1.85V and a capacity of 1.5 Li/Mo, the theoretical energy density of $\text{Mo}_{17}\text{O}_{47}$ (~ 490 W-hr/kg) is comparable to that reported for TiS_2 and stoichiometric V_6O_{13} . The magnetic properties of both $\text{Mo}_{17}\text{O}_{47}$ ($\text{MoO}_{2.765}$) and the lithium bronze $\text{Li}_{1.41}\text{MoO}_{2.765}$ were also investigated and are discussed.

Various transition metal chalcogenides with two-dimensional layered or one-dimensional chain structures have been reported to topochemically incorporate lithium reversibly (1). However, there are relatively few reports of reversible lithium incorporation by compounds with three-dimensional framework structures (1-10). Recently, we reported that several vanadium oxides, VO_y ($2 < y < 2.5$), with structures shear-related to that of ReO_3 reversibly incorporate lithium at room temperature both in model chemical reactions and in electrochemical cells (11, 12). Of these vanadium oxides, V_6O_{13} ($\text{VO}_{2.167}$) affords cathodes with high capacity and excellent rechargeability in secondary (rechargeable) lithium cells (11). The empty perovskite-like cavities and interconnecting channels in the structures of these vanadium oxides can serve as sites and routes, respectively, for lithium incorporation as do the expandable van der Waal's gaps of chalcogenides with layered or chain structures. A variety of other transition metal oxides have structures which are shear-related to that of ReO_3 , including the molybdenum oxides Mo_9O_{26} , Mo_8O_{23} , and Mo_4O_{11} (13). In a study of the electrochemistry of MoO_3 Besenhard and Schöllhorn also reported (3) that cathodes containing Mo_8O_{23} can be galvanostatically reduced resulting in the uptake of more than 1.0 Li per Mo. However, the reversibility of the reduction and lithium incorporation were not determined in that study. More recently, Pistoia and co-workers (7, 8) have examined the use of Mo_9O_{26} , Mo_8O_{23} , and Mo_4O_{11} as cathodes in secondary lithium cells. They have reported that cathodes containing Mo_8O_{23} exhibited a capacity of up to 0.8 Li/Mo and maintained good recharge efficiencies for over 15 cycles (9). However, no detailed results were presented for cells with Mo_9O_{26} or Mo_4O_{11} cathodes.

In the present paper, reversible lithium incorporation by the known molybdenum oxides with stoichiometries between MoO_2 and MoO_3 is reported. In addition to those molybdenum oxides structurally related to ReO_3 , we have evaluated $\text{Mo}_{17}\text{O}_{47}$ and Mo_5O_{14} for use as possible cathode materials. Both of these oxides have complex three-dimensional structures based on mixed networks of polyhedra and are permeated by large, open channels (13, 14) similar to those present in the tetragonal and hexagonal tungsten bronzes (15, 16). Although Mo_5O_{14} is apparently metastable (17), the structure can be stabilized by a partial substitution of vanadium for molybdenum (18). A ternary phase with the composition $(\text{Mo}_{0.92}\text{V}_{0.08})_5\text{O}_{14}$ was used in our study. This material was prepared from the appropriate amounts of V_2O_5 , MoO_3 , and MoO_2 as described by Ekström and Nygren (18). The other molybdenum oxides were prepared from mixtures of the appropriate amounts of MoO_3 and Mo powders pressed into pellets and heated in evacuated, sealed quartz tubes (13, 19). The identities of the phases formed were verified by x-ray powder diffraction using $\text{CuK}\alpha$ radiation (17). All attempts to grow single crystals of $\text{Mo}_{17}\text{O}_{47}$ and $(\text{Mo}_{0.92}\text{V}_{0.08})_5\text{O}_{14}$ by vapor transport with I_2 or TeCl_4 afforded only mixtures of Mo_4O_{11} and MoO_3 .

The results of our electrochemical cell studies of Mo_9O_{26} , Mo_8O_{23} , and Mo_4O_{11} cathode materials are essentially in agreement with those of Pistoia and co-workers (6-8) (Table I). However, they reported detailed cycling data only for the Mo_8O_{23} cathodes (6, 8). For the other two oxides, the capacities of the first cycle discharges were given. In our experience, the performance of a cell on the first cycle discharge is not a reliable indicator of subsequent cell performance. For example, cells containing NbSe_3 (20) or TiS_3 (21) cathodes exhibit dramatic differences between the shapes of the first and subsequent discharge curves.

¹ Present address: Western Electric Company, Engineering Research Center, Princeton, New Jersey 08540.

Key words: stoichiometry, discharge, electrolyte.

Table I. The extent of reaction of molybdenum oxides with n-butyllithium and the reversible cell capacities after one, five, and twenty cycles are shown. Ideally, for a given compound the lithium content would be independent of the method of determination or cycle number. The cell capacities are in Li/Mo, while the upper and lower voltage limits are 2.8 and 1.5V, respectively. See text for further discussion.

Mo ₂ O ₇	MoO _{3-n}	Equiv. n-BuLi/Mo	Cell capacities		
			Cycle 1	Cycle 5	Cycle 20
MoO ₃	MoO ₃	1.62 ± 0.03	1.3	—	—
Mo ₉ O ₂₆	MoO _{2.889}	1.55 (9)	1.5 (3, 30)	—	—
Mo ₁₈ O ₅₃	MoO _{2.889}	1.08 ± 0.03	0.67	0.42	0.35
Mo ₈ O ₂₃	MoO _{2.875}	—	0.50 (8)	—	—
(Mo _{0.92} V _{0.08}) ₂ O ₁₄	Mo _{0.92} V _{0.08} O _{2.80}	1.26 ± 0.14	1.5 (3)	—	—
Mo ₄ O ₁₁	MoO _{2.705}	—	0.90	0.55	0.29
Mo ₉ O ₂₆	MoO _{2.875}	1.71 ± 0.05	0.92 (8)	0.73	0.64
Mo ₈ O ₂₃	MoO _{2.705}	1.78 ± 0.05	1.0 (3)	—	—
Mo ₄ O ₁₁	MoO _{2.75}	1.62 ± 0.05	1.22	0.54	0.37
MoO ₃	MoO ₃	1.00 (26)	1.23	1.08	1.02
			1.35	0.82	0.77
			0.63 (8)	—	—
			1.00 (26)	0.65	0.56

Furthermore, we typically find for the vanadium oxides (22), at least, that the decrease in capacity between the first cycle discharge and the second is greater than that between any two subsequent consecutive discharge cycles. The "extra" irreversible capacity of the first discharge may be attributed tentatively to reactions of lithium with trace impurities in the electrolyte, passivation of surfaces of the cathode particles, irreversible incorporation of lithium by some sites, and possibly other extrinsic causes such as loss of mechanical and electrical integrity of the cathode due to volume changes on charge and discharge.

The electrochemical test cells used in our studies have been described in detail elsewhere (23). The electrolyte used in these cells was 1.0M LiClO₄ in dried, vacuum distilled propylene carbonate. Approximately 10-20 mg of active cathode material were used in a 1 cm diam cathode. Discharge currents were typically in the range 0.2-0.5 mA. Cells were cycled automatically between appropriate upper and lower voltage limits.

Pistoia and co-workers have estimated the maximum amount of lithium which can be incorporated by

Mo₄O₁₁, Mo₈O₂₃, and Mo₉O₂₆ as 2.1, 2.3, and 2.3 Li/Mo, respectively, by extrapolating to zero current a plot of cell capacity vs. discharge current (2). The values of cell capacity used were themselves based on an extrapolation of the voltage vs. capacity plots to 0.0V because of electrolyte decomposition below 0.8V. Consequently, the values calculated for the specific energies of these three oxides approach 1000 W-hr/kg! We have estimated the limiting values of lithium incorporation for Mo₄O₁₁, Mo₈O₂₃, and Mo₉O₂₆ as 1.62, 1.26, and 1.08 Li/Mo (Table I), respectively, by treating them with excess n-butyllithium in hexane (24, 25). The reduction potential of n-butyllithium under these reaction conditions has been estimated as ~ 1.1V vs. Li/Li⁺ (12). The theoretical energy densities calculated using our n-butyllithium values for these oxides are on the order of 400-500 W-hr/kg.

Cycling data for cells containing Mo₄O₁₁, Mo₈O₂₃, and Mo₉O₂₆ cathode materials are shown in Fig. 1. The cell capacities observed for the first, fifth, and twentieth cycles are given in Table I. For Mo₈O₂₃ our values closely correspond to those of Pistoia and co-workers

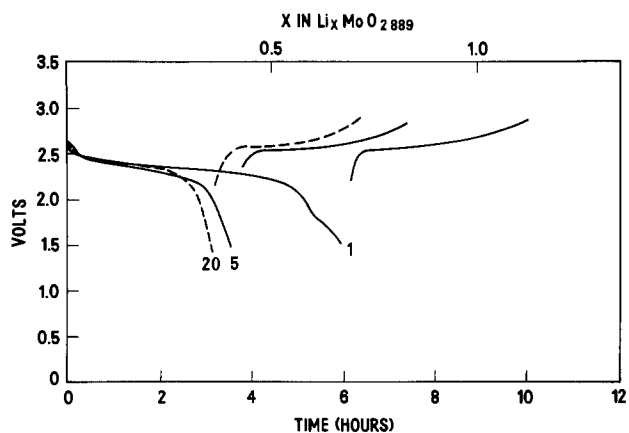
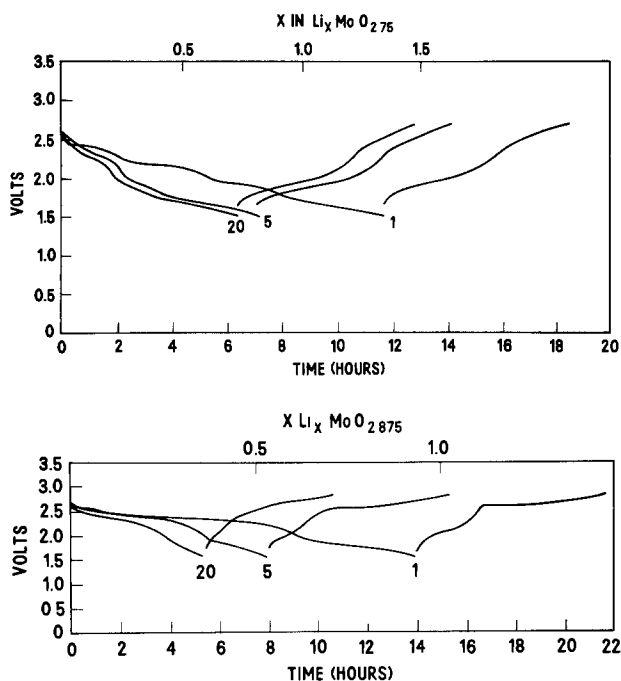


Fig. 1. Cycle data for cells containing (a, top left) Mo₄O₁₁, (b, top right) Mo₈O₂₃, and (c, bottom left) Mo₉O₂₆ cathodes. Cycle numbers are indicated as are specific capacities.

(8). Although Mo_5O_{23} exhibits good rechargeability (9), $\text{Mo}_{17}\text{O}_{47}$ has greater reversible capacity after several cycles resulting in better overall cell performance.

Our previous studies of lithium incorporation by rutile-related metal dioxides (20) and ReO_3 -related vanadium oxides (11, 22), as well as the present study of lithium incorporation by molybdenum oxides all support our earlier suggestion (26) that both channel/site size and electronic conductivity are the predominant factors influencing the extent of reversible lithium incorporation by metal oxides with framework structures. Kihlberg (17) has measured the specific electrical resistivities of compressed powder samples of Mo_9O_{26} , Mo_8O_{23} , Mo_4O_{11} , and $\text{Mo}_{17}\text{O}_{47}$. Like V_6O_{13} , $\text{Mo}_{17}\text{O}_{47}$ is also metallic at room temperature ($\rho < 0.05 \Omega \cdot \text{cm}$), whereas the other oxides are semiconductors with specific resistivities of about $1 \Omega \cdot \text{cm}$ or greater (17). The electrical resistivity of $(\text{Mo}_{0.92}\text{V}_{0.08})_5\text{O}_{14}$ has not been reported.

Treatment of samples of $\text{Mo}_{17}\text{O}_{47}$ and $(\text{Mo}_{0.92}\text{V}_{0.08})_5\text{O}_{14}$ with excess n-butyllithium in hexane at room temperature for several days, leads to apparent limiting compositions of $1.78 \pm 0.05 \text{ Li/Mo}$ and $1.71 \pm 0.05 \text{ Li/Mo}$ respectively. The x-ray powder diffraction patterns of these bronzes have been measured and are tabulated in Tables II and III. A preliminary indexing of the pattern of lithiated $\text{Mo}_{17}\text{O}_{47}(\text{Li}_{1.78}\text{MoO}_{2.765})$ suggests that the unit cell expands in the b direction and contracts in both the a and c directions upon incorporation of lithium. The unit cell volume, however, increases by less than 4%. The corresponding values for $\text{Li}_6\text{V}_6\text{O}_{13}$ and $\text{Li}_3\text{V}_6\text{O}_{13.2}$ are 6% and 15%, respectively (22). The unit cell volume of $(\text{Mo}_{0.92}\text{V}_{0.08})_5\text{O}_{14}$ increases by about 10% upon lithium incorporation. In this case, the unit cell appears to expand in all three directions. Chemical oxidation of $\text{Li}_{1.78}\text{MoO}_{2.765}$ with a solution of I_2 in acetonitrile removed about 80% of the lithium from the bronze. This implies that either the potential of the bronze $\text{Li}_x\text{MoO}_{2.765}$ is greater than that of I_2 ($\sim 2.85\text{V}$ vs. Li/Li^+) at low lithium contents or that at high lithium contents some irreversible reduction occurs. Direct measurement of the potential of the bronze as a function of the lithium content in electrochemical cells revealed very little capacity above 2.85V. This suggests that some structural degradation occurs at high lithium contents, as has been observed for framework compounds such as $\text{Li}_x\text{V}_2\text{O}_5$ for $x > 1.0$ (27), and also for layered oxides such as Li_xMoO_3 for $x > 1.5$ (1). We have assumed that the products of any irreversible part of the reaction are poorly crystalline or amorphous, so that they do not contribute to the observed x-ray diffraction pattern. This is usually the case, for example, as observed for V_2O_5 , MoO_3 , and MoS_2 (1). Using the results of the butyllithium and I_2 reactions, we estimate the maximum reversible lithium incorporation to be 1.5 Li/Mo in $\text{Mo}_{17}\text{O}_{47}$. $\text{Mo}_{17}\text{O}_{47}$ can be assigned the following Mo valence distribution: $\text{Mo}_{13}^{6+}\text{Mo}_4^{4+}$. If reversible lithium incorporation produced all Mo^{4+} , the expected lithium uptake would be 26/17 (1.53) Li/Mo—a value close to that estimated from the butyllithium and I_2 reactions.

Electrochemical cells containing $\text{Mo}_{17}\text{O}_{47}$ and $(\text{Mo}_{0.92}\text{V}_{0.08})_5\text{O}_{14}$ cathode materials were tested for 30 or more charge/discharge cycles (Fig. 2). The capacity of the $(\text{Mo}_{0.92}\text{V}_{0.08})_5\text{O}_{14}$ cathode appear to decrease much more rapidly than that of $\text{Mo}_{17}\text{O}_{47}$ cathodes (Fig. 3). Voltage limits have been optimized to ensure good cyclability of the $\text{Mo}_{17}\text{O}_{47}$ cathodes. These empirically determined limits are 2.9V for the upper charging limit and 1.4V for the lower discharging limit. Increasing the upper voltage limit or decreasing the lower voltage limit leads to lower cell capacity after several cycles, suggesting that irreversible changes occur when the cathode potential is greater than 2.9V or less than 1.4V vs. Li. This in turn suggests that some irreversible reaction will always occur when using n-butyllithium as a lithiating agent, since its equivalent

Table II. A preliminary indexing of the x-ray power diffraction pattern of a lithiated $\text{Mo}_{17}\text{O}_{47}$ sample of nominal stoichiometry $\text{Li}_{1.78}\text{MoO}_{2.765}$ resulting from the reaction with excess n-butyllithium.

$\text{Li}_{1.78}\text{MoO}_{2.765}$					
$a = 21.583\text{Å}$					
$b = 20.300\text{Å}$					
$c = 3.962\text{Å}$					
$V = 1736\text{Å}^3$					
hkl	d (Å)	I	hkl	d (Å)	I
240	4.639	VW	550	2.959	M
430, 340	4.169	W	511	2.885	VW
001	3.962	VS	800	2.698	VVW
440	3.694	VW	541; 080	2.539	VVW
610, 600	3.581	VVW	910; 840	2.380	VW
231	3.268	VW	860; 281	2.103	VVW
041	3.101	VVW	590; 2, 10, 0	1.998	M
710	3.027	VVW	712; 13, 0, 0; 13, 1, 0	1.659	W

Table III. The x-ray powder diffraction pattern of $(\text{Mo}_{0.92}\text{V}_{0.08})_5\text{O}_{14}$ and its lithiated product $\text{Li}_{1.28}\text{Mo}_{0.92}\text{V}_{0.08}\text{O}_{2.80}$.

$(\text{Mo}_{0.92}\text{V}_{0.08})_5\text{O}_{14}$			$\text{Li}_{1.28}\text{Mo}_{0.92}\text{V}_{0.08}\text{O}_{2.80}$		
$a = 22.837\text{Å}$ (22.837) (18)			$a = 23.354\text{Å}$		
$c = 3.966\text{Å}$ (3.990) (18)			$c = 4.166\text{Å}$		
$V = 2068\text{Å}^3$			$V = 2272\text{Å}^3$		
hkl	d_{obs} (Å)	I_{obs}	d_{obs} (Å)	I_{obs}	
310	7.237	VW	7.369	W	
400	5.702	VW	5.836	VVW	
330	5.392	W	5.478	W	
420			5.218	VVW	
510			4.599	VW	
520	4.242	VW	4.332	VW	
440	4.082	S	4.154	VVW	
600	3.809	M	3.929	S	
610	3.751	W			
620	3.613	VW	3.672	VS	
540	3.569	VS			
630	3.405	W	3.482	VVW	
550, 331	3.228	M	3.317	W	
640	3.167	M	3.242	M	
431, 730	2.997	VW			
441, 800, 740	2.834	S	2.925	S	
621			2.778	VW	
820	2.761	W			
660	2.688	W			
750	2.656	M	2.685	VW	
631	2.589	VVW			
760	2.501	VVW	2.516	VW	
641	2.473	VVW			
770	2.308	W	2.349	W	
10, 1, 0	2.276	VVW			
841	2.145	VVW			
10, 4, 0	2.120	VVW			
10, 5, 0	2.043	VW			
970	2.001	W	2.049	W	
302			2.012	VW	
12, 0, 0	1.903	VW			
402	1.872	W	1.974	VW	
422	1.853	VW	1.940	VW	
442			1.859	VW	
			1.804	VW	
990	1.793	W	1.765	M	
11, 7, 0, 612	1.752	VW			
622	1.738	VW			
991	1.702	M			
12, 6, 0	1.635	VW			
10, 10, 0	1.616	VVW			
11, 7, 1; 11, 9, 0	1.605	VVW	1.642	VVW	
832	1.593	VW			
762	1.547	W	1.610	VVW	
842	1.566	VVW			
11, 10, 0	1.536	VVW			

potential is about 1.1V. Ideally the maximum lithium uptake of any material would be independent of its method of determination (e.g., reaction with n-butyllithium or a particular cycle of an electrochemical cell). However, in reactions with n-butyllithium some irreversible changes may occur (such as producing Li_2O or other decomposition products) resulting in artificially high estimates of the maximum reversible lithium incorporation. In electrochemical cells not only can irreversible reactions occur but also poor mechanical and electrical integrity of the cathode can occur especially after cycling. In the latter case artificially low estimates of the maximum reversible lithium content are obtained. Based on the limiting capacity estimated from the n-butyllithium reaction, the subsequent reversible I_2 reduction (1.5 Li/Mo), and the

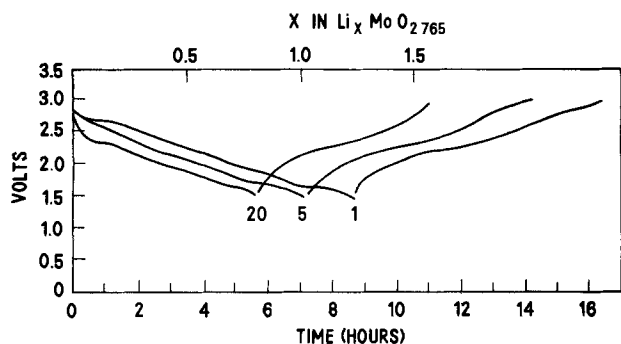


Fig. 2. Cycle data for a cell containing a $\text{Mo}_{17}\text{O}_{47}$ cathode. Beyond the 20th cycle the cell had a 98% recharge efficiency (to at least the 35th cycle, at which point data collection stopped).

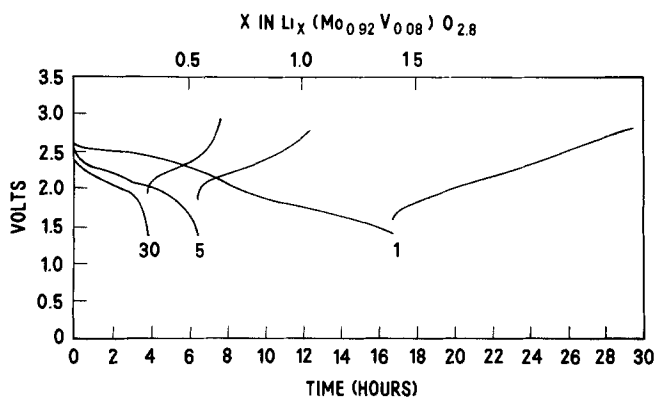


Fig. 3. Cycle data for a cell containing a $(\text{Mo}_{0.92}\text{V}_{0.08})_5\text{O}_{14}$ cathode. Cycle numbers and capacities are as indicated.

average cell potential of 1.85V (Fig. 2) a theoretical energy density of 490 W-hr/kg is calculated for $\text{Mo}_{17}\text{O}_{47}$. This is comparable to the 480 W-hr/kg reported (28) for TiS_2 .

In addition to investigating the electrochemical properties of $\text{Mo}_{17}\text{O}_{47}$ we have also investigated the magnetic properties of both $\text{Mo}_{17}\text{O}_{47}$ and the bronze $\text{Li}_{1.41}\text{MoO}_{2.765}$. In order to determine if there is any change of the Pauli paramagnetism of $\text{Mo}_{17}\text{O}_{47}$ to local moment behavior at high lithium contents, the magnetic susceptibilities of both $\text{Mo}_{17}\text{O}_{47}$ and $\text{Li}_{1.41}\text{MoO}_{2.765}$ were measured from 4.2° to 300°K (Fig. 4). A weak local magnetic moment appears to be present when the sample is lithiated. This is in marked contrast to the magnetic susceptibility of V_6O_{13} which is effected at very low levels of lithium incorporation (22). The magnitude of the susceptibility of $\text{Mo}_{17}\text{O}_{47}$ at 300°K is $\chi_g = 3.08 \times 10^{-7}$ emu/g compared to the previously reported value of 0.85×10^{-6} emu/g (29). However, it might be expected that the magnetic susceptibility is anisotropic, and random orientation of the powder crystallites is not assured in this or the previous work. The susceptibility decreases slightly with decreasing temperature to $\chi_g = 2.60 \times 10^{-7}$ emu/g at 4.2°K. This weakly temperature dependent, positive value of the susceptibility is due to the Pauli paramagnetism of the conduction electrons in the metallic compound. The susceptibility of the bronze $\text{Li}_{1.41}\text{MoO}_{2.765}$ can be fit by a simple Curie-Weiss expression above 15°K: $\chi_g = 0.85 \times 10^{-6} + 72.2 \times 10^{-6}/(T + 7.0)$ (emu/g). The magnetic moment per molybdenum calculated from the Curie constant is only 0.29 Bohr magnetons. However, this temperature dependent term may arise from a small fraction of the sample irreversibly reduced by butyllithium. Consequently, it is not certain that this part of the susceptibility is intrinsic. The positive temperature independent contribution to the susceptibility suggests that the lithium bronze is also a metallic conductor.

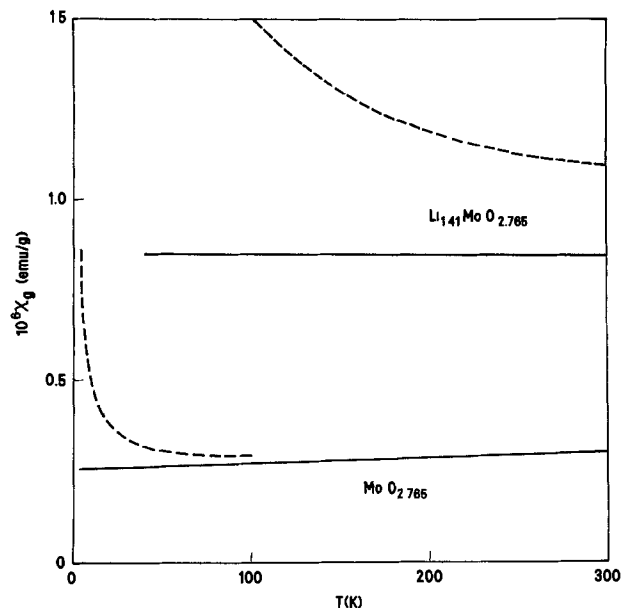


Fig. 4. Magnetic susceptibilities of $\text{Mo}_{17}\text{O}_{47}$ and $\text{Li}_{24}\text{Mo}_{17}\text{O}_{47}$ bronzes. The dashed lines show the Curie part of the susceptibility. In $\text{Mo}_{17}\text{O}_{47}$ the Curie part most likely arises from paramagnetic impurities, while in the lithiated product the much larger Curie contribution may arise from a small irreversibly lithiated fraction of the sample.

From this and previous work (26, 30) it is clear that all molybdenum oxides with compositions MoO_x for $2 \leq x \leq 3$ reversibly incorporate Li. In our cells $\text{Mo}_{17}\text{O}_{47}$ has the highest capacity after several cycles. However the voltage drop for $\text{Mo}_{17}\text{O}_{47}$ on full discharge ($\sim 1.9\text{V}$) is greater than that for both TiS_2 ($\sim 0.6\text{V}$) and off-stoichiometric $\text{V}_6\text{O}_{13.2}$ ($\sim 0.8\text{V}$). Also, the average cell voltage of the $\text{Mo}_{17}\text{O}_{47}$ (1.85V) is somewhat below that of V_6O_{13} (2.2V). Thus, the theoretical energy density of $\text{Mo}_{17}\text{O}_{47}$ cathodes (490 W-hr/kg) is considerably less than that calculated for off-stoichiometric $\text{V}_6\text{O}_{13.2}$ (~ 800 W-hr/kg) cathodes (11). Consequently, $\text{Mo}_{17}\text{O}_{47}$ is not as promising a candidate for use as the active cathode in secondary lithium batteries as off-stoichiometric V_6O_{13} .

Manuscript submitted April 7, 1980; revised manuscript received June 10, 1980.

Any discussion of this paper will appear in a Discussion Section to be published in the June 1981 JOURNAL. All discussions for the June 1981 Discussion Section should be submitted by Feb. 1, 1981.

Publication costs of this article were assisted by Bell Laboratories.

REFERENCES

1. M. S. Wittingham, *This Journal*, **123**, 315 (1976); *Prog. Solid State Chem.*, **12**, 41 (1978).
2. B. C. H. Steele, in "Superionic Conductors," G. D. Mahan and W. L. Roth, Editors, pp. 47-64, Plenum Press, New York (1976).
3. J. O. Besenhard and R. Schöllhorn, *J. Power Sources*, **1**, 267 (1976/77).
4. J. O. Besenhard and R. Schöllhorn, *This Journal*, **124**, 968 (1977).
5. H. Ikeda, T. Saito, and H. Tamura, *Manganese Dioxide Symp. Proc.*, **1**, 384 (1975).
6. B. DiPietro, V. Filippeschi, M. Lazzari, G. Pistoia, and B. Scrosati, Paper No. 34, 10th International Power Sources Symp., Brighton (1976).
7. P. Cignini, M. Icovi, S. Panero, G. Pistoia, and C. Temperoni, *J. Electroanal. Chem. Interfacial Electrochem.*, **102**, 333 (1979).
8. M. Icovi, S. Panero, A. D'Agate, G. Pistoia, and C. Temperoni, *ibid.*, **102**, 343 (1979).
9. M. S. Wittingham and M. B. Dines, *This Journal*, **124**, 1387 (1977).

10. C. R. Walk and J. S. Gore, Paper 27 presented at the Electrochemical Society Meeting, Toronto, Canada, May 11-16, 1975.
11. D. W. Murphy, P. A. Christian, F. J. DiSalvo, and J. N. Carides, *This Journal*, **126**, 498 (1979).
12. D. W. Murphy and P. A. Christian, *Science*, **205**, 651 (1979).
13. L. Kihlberg, *Arkiv Kemi*, **21**, 471 (1963).
14. L. Kihlberg, *Acta Chem. Scand.*, **14**, 1612 (1960).
15. A. Magneli, *Arkiv Kemi*, **1**, 213 (1949).
16. A. Magneli, *Acta Chem. Scand.*, **7**, 315 (1953).
17. L. Kihlberg, *ibid.*, **13**, 954 (1959).
18. T. Ekström and M. Nygren, *ibid.*, **26**, 1827 (1972).
19. Z. M. Hanafi, M. A. Khilla, and A. Abu-El saud, *Rev. Chim. Miner.*, **12**, 546 (1975).
20. F. A. Trumbore, *J. Pure Appl. Chem.*, In press.
21. D. W. Murphy and F. A. Trumbore, *J. Crystal Growth*, **39**, 185 (1977).
22. D. W. Murphy, P. A. Christian, J. N. Carides, F. J. DiSalvo, and J. V. Waszczak, Submitted to *This Journal*.
23. D. W. Murphy, J. N. Carides, F. J. DiSalvo, C. Cros, and J. V. Waszczak, *Mater. Res. Bull.*, **12**, 825 (1977).
24. M. B. Dines, *ibid.*, **10**, 287 (1975).
25. D. W. Murphy, F. J. DiSalvo, G. W. Hull, and J. V. Waszczak, *Inorg. Chem.*, **15**, 17 (1976).
26. D. W. Murphy, F. J. DiSalvo, J. N. Carides, and J. V. Waszczak, *Mater. Res. Bull.*, **13**, 1395 (1978).
27. D. W. Murphy, P. A. Christian, F. J. DiSalvo, and J. N. Carides, *Inorg. Chem.*, **18**, 2800 (1979).
28. M. S. Wittingham, *Science*, **192**, 1126 (1976).
29. T. Ekström, *Acta Chem. Scand.*, **26**, 3381 (1972).
30. N. Margalit, *This Journal*, **121**, 1460 (1974).

The Use of Tetravalent Sulfur in Molten Chloroaluminate Secondary Batteries

G. Mamantov,* R. Marassi, M. Matsunaga, Y. Ogata, J. P. Wiaux, and E. J. Frazer*

Department of Chemistry, University of Tennessee, Knoxville, Tennessee 37916

ABSTRACT

A new rechargeable cell Na/Na⁺ ion conductor/SCL₃⁺ in molten AlCl₃-NaCl is described. This cell operates at temperatures in the range of 180°-250°C and has an open-circuit voltage of 4.2V. The discharge process involves the reduction of tetravalent sulfur to the elemental state; sulfur can be further reduced to sulfide. The preferred sodium ion conductor is β"-alumina. High energy density values, large percent utilization of the active material, and good energy efficiency have been demonstrated. The performance of cells prepared in the discharged and charged states were found to be the same. The number of deep charge/discharge cycles has exceeded 400.

High energy density batteries for load leveling and electric vehicle applications have received considerable attention in recent years. Aqueous, organic, molten salt, and solid electrolytes have been extensively studied; different systems have been tested as possible electrodes (1-6). During the last few years we have examined several possible positive electrodes for batteries using molten chloroaluminates (mainly AlCl₃-NaCl mixtures) as solvents and aluminum or sodium as anodes (7-12). Molten chloroaluminates offer many advantages, such as low liquidus temperatures and high conductivity (13, 14), for molten salt battery applications. The acid-base properties of AlCl₃-NaCl mixtures and the factors affecting the stability of different oxidation states as a function of both temperature and melt composition are well characterized (15-19). The use of aluminum as the negative electrode is potentially attractive since this metal is quite electropositive, relatively inexpensive, and has a low equivalent weight. In addition, with aluminum electrodes it is possible to obtain high currents without appreciable polarization (20-22). Potential problems caused by dendrite formation during charging and by passivation phenomena (formation of a poorly conducting Al₂Cl₆ layer at high current densities) during the dissolution of aluminum can be minimized by adding selected additives (23) and by using proper melt compositions (24). The compatibility of the sodium electrode separated by β- (or β"-) alumina with chloroaluminate melts has also been demonstrated (25-27).

Molten chloroaluminates have been used as solvents in the Al/Cl₂ (28, 29), Na/Cl₂ (25), Al/S (30, 31), Al/MCl_x (32), and Na/MCl_x (25-27, 33, 34) batteries. Al/Cl₂ batteries have an open-circuit voltage (OCV)

of about 2.2V and a high theoretical energy density (~ 1400 W-hr/kg) (28); an OCV of ~ 3.5V has been reported for Na/Cl₂ batteries (25). The problems associated with the use of chlorine, normally adsorbed on carbon powder, make, however, the above batteries somewhat less desirable. Low OCV's (about 1.2V at 200°C) and a relatively poor performance or discharge are reported for Al/S batteries (30, 31). The most developed battery using chloroaluminates is based on the Na/SbCl₃ system for which an OCV of 2.83V and a theoretical energy density of 825 W-hr/kg have been reported (25, 34).

This paper describes investigations on the use of positive oxidation states of sulfur, mainly S(IV), as positive electrode materials in AlCl₃-NaCl melts in laboratory cells using either aluminum or sodium negative electrodes (7-12). The electrochemistry of sulfur in these melts has been the subject of several studies by our group (35-37) as well as by others (38, 39) and will be recalled here only to the extent which is necessary for a better understanding of the experimental results.

Experimental

Melt preparation and other experimental procedures have been reported elsewhere (40, 41). Sulfur was purified by repeated sublimations under vacuum. S(IV) was introduced into the melt either by electrochemical oxidation of elemental sulfur or as SCl₃AlCl₄. Sulfur tetrachloride could not be used because it is not stable at room temperature. On the other hand, SCl₃AlCl₄ may be prepared rather easily by reacting sulfur with the stoichiometric amount of AlCl₃ and a 10% excess chlorine in sealed Pyrex tubes. Details of the preparation and characterization of this salt are reported elsewhere (42). The adduct is stable if handled in a dry

* Electrochemical Society Active Member.
Key words: battery, fused salts, cell.

atmosphere and may be dissolved in molten chloroaluminates [stable solutions up to $\sim 1M$ in S(IV) have been prepared provided the mole fraction of $AlCl_3$ is greater than 0.5 (see below)].

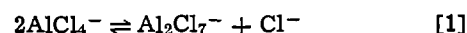
Different types of cells and separators have been used for single cell experiments. A typical cell consisted of a Pyrex compartment filled with the positive mix which was separated from the negative electrode by means of a β'' -alumina tube containing sodium. In some experiments the negative electrode was an aluminum coil immersed in the melt and separated from the positive electrode compartment by means of glass or ceramic frits or coarse α -alumina crucibles. Beta-alumina (or β'' -alumina) tubes were obtained from Ceramtec, Incorporated, Ford Motor Company, or the General Electric Company. A typical cell arrangement for an Na/S(IV) cell is shown in Fig. 1. The cells were normally equipped with an Al(III)/Al reference electrode separated from the other compartments by a thin Pyrex membrane. Additional information on laboratory cells is given below.

Commercially available electrochemical instrumentation, such as a Wenking potentiostat Model 66TS3 and Princeton Applied Research potentiostats and digital coulometer Models 173/179, 371, and 379 were used.

Brief review of solvent properties and of sulfur electrochemistry in molten chloroaluminates.—The acid-base properties of molten chloroaluminates and sulfur electrochemistry in these melts are crucial to the understanding of the cells utilizing positive oxidation states of sulfur and are reviewed briefly below.

In the molten chloroaluminate systems the terms "acid" and "base" denote a chloride ion acceptor and a chloride ion donor, respectively (15-18, 43). The acidity of the medium is usually described in terms of pCl ($\equiv -\log [Cl^-]$). For a given ratio of $AlCl_3$ to NaCl the pCl is determined by several equilibria, the predominant equilibrium near the 1:1 $AlCl_3/NaCl$ ratio

being



The pCl may be measured with either an aluminum or a chlorine electrode immersed in the melt. The lowest pCl corresponds to a melt saturated with NaCl; at $175^\circ C$ $pCl = 1.1$ for an $AlCl_3$ - $NaCl_{sat.}$ melt (43). The maximum variation in pCl occurs near the 1:1 $AlCl_3$ - $NaCl$ ratio. As a result of this variation, concentration cells using aluminum electrodes in melts of different composition have been reported (32); voltages of $\sim 0.6V$ may be obtained when one of the Al electrodes is in an $NaCl_{sat.}$ melt and the other electrode is in an $AlCl_3$ - $NaCl$ [63-37 mole percent (m/o)] melt (\equiv 63/37 melt) (16).

Elemental sulfur, present in the melt predominantly as S_8 (44), can be either oxidized or reduced in both basic (excess of NaCl) and acidic (excess of $AlCl_3$) melts (35-38). The reduction of sulfur results in sulfide, probably present as either $AlSCl$ or AlS_2Cl (39). The cyclic voltammograms at low temperatures ($\sim 175^\circ C$) indicate the presence of a large overpotential for the sulfur/sulfide couple; this couple becomes more reversible at higher temperatures ($\sim 250^\circ C$).

The oxidation of sulfur in basic melts leads to S(I) (36, 38); some evidence for the formation of S(II) at high temperatures ($\sim 270^\circ C$) has also been obtained (36).

In acidic melts (52-63 m/o $AlCl_3$) the electrochemical oxidation of sulfur is quite complex (37, 45). The final oxidation product is S(IV), present as SCl_3^+ as indicated by Raman and potentiometric measurements (46, 47). The intermediate electrochemical oxidation products include S_{16}^{2+} (or S_8^+), S_8^{2+} , and S_2^{2+} . Evidence for S_4^{2+} and S(II) in acidic melts, in addition to the species mentioned above, has been obtained by spectrophotometric measurements (46, 48).

Formal potentials estimated from voltammetric data for various sulfur redox couples in both acidic (63/37) and basic ($NaCl_{sat.}$) melts at $250^\circ C$ vs. three reference electrodes are given in Table I. The potential values in Table I also represent approximate open-circuit voltages (OCV) for cells consisting of the respective sulfur redox couple as the positive electrode and either sodium or aluminum electrode as the negative electrode. Thus, the highest OCV should result for a cell consisting of tetravalent sulfur dissolved in an acidic melt and a sodium electrode. The need for an acidic melt throughout the discharge process, in which S(IV) is reduced to elemental sulfur, stems from the instability of S(IV) in basic melts (36, 47).

Sodium electrode.—Since sodium reacts with molten chloroaluminates to produce aluminum, the sodium electrode must be separated from the melt by means of an Na^+ -ion conductor such as β - (or the better conducting β'' -) alumina (49, 50). The use of the Na/ β -alumina electrode with acidic chloroaluminate melts has been reported previously (26, 27, 34). We have

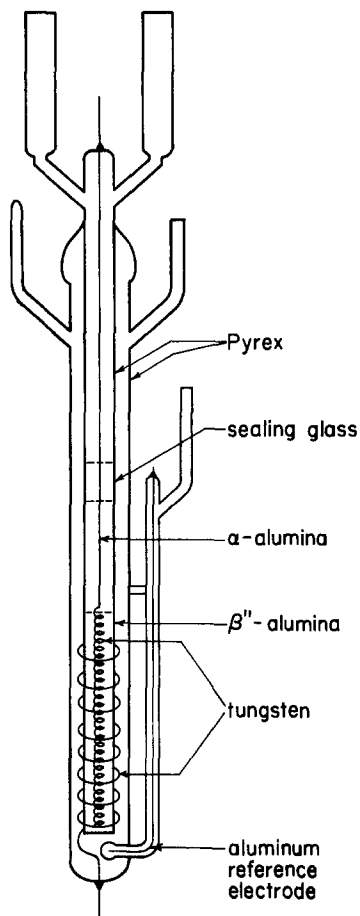


Fig. 1. Typical laboratory cell (not to scale)

Table I. Formal potentials of various sulfur redox couples at $250^\circ C$

Redox couple	Melt composition	Potentials		
		E° vs. Al(III)/Al in $NaCl_{sat}$ melt (V)	E° vs. Al(III)/Al in 63/37 melt (V)	E° vs. Na \ddagger (V)
S(IV)/ S_2^{2+}	63/37	2.57*	1.95*	4.17
S_2^{2+}/S_8^{2+}	63/37	2.52*	1.90*	4.12
$S_8^{2+}(S_{16}^{2+})/S_8$	63/37	2.14*	1.52*	3.74
S_8/S_2^{2+}	63/37	1.77**	1.15**	3.37
S_8/S_2^{2+}	$NaCl_{sat}$	1.92**	—	3.52
S_8/S_2^{2+}	$NaCl_{sat}$	1.15**	—	2.75

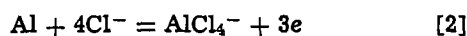
* Values obtained from the plots E_p (differential pulse voltammograms) vs. $\log C_{S_8}$ for $\log C_{S_8} = 0$.

** Values estimated from cyclic voltammetric peak potentials and differential pulse peak potentials.

† Values obtained by adding 1.60V (see text) to the values in the third column.

measured the potential of the Na/ β "-alumina electrode immersed in the 63/37 melt vs. the Al(III)/Al reference electrode in the NaCl saturated melt as $-1.60 \pm 0.02V$ at 250°C. The behavior of the Na/ β "-alumina electrode under discharge (or charge) conditions is largely dependent on the pretreatment of the β "-alumina tube before and after the addition of sodium and on the temperature of the operation. Additional information is presented below.

Cell chemistry and capacity and energy densities.—Based on the above results several possible cells may be devised using either an aluminum or a sodium negative electrode separated from the positive electrode compartment by a suitable separator. The possible negative electrode reactions are

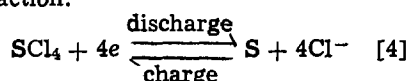


In the case of the Al electrode the availability of Cl^- ions is ensured by saturating the melt in the negative electrode compartment with NaCl.

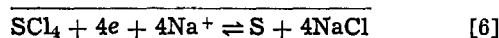
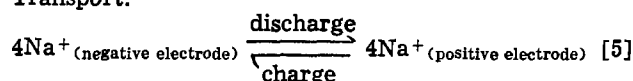
In discussing the chemistry of the positive electrode, the following assumptions are made: (i) S(IV) is assumed to be present as SCL_4 in order to simplify the pertinent stoichiometry. (ii) S^{2-} is assumed to be solvated by the solvent ions to give AlSCL and AlSCL_2^- in acidic and basic melts, respectively. The reactions describing the discharge and charge of the positive electrode may be written as follows

First step

Electrochemical reaction:

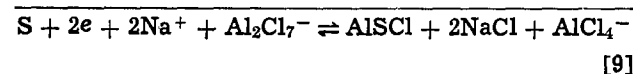
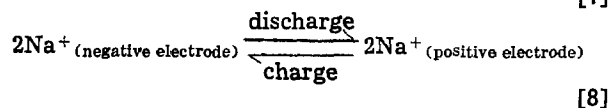
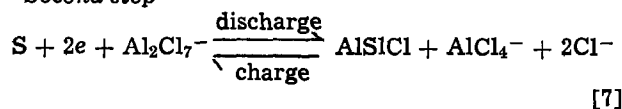


Transport:



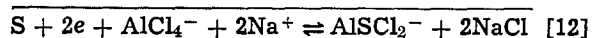
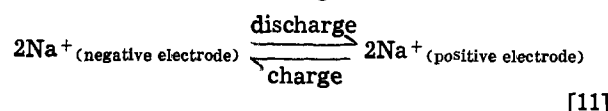
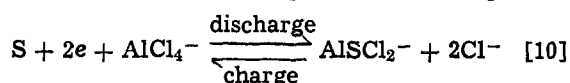
where reactions [4] and [6] occur only in acidic melts because of the stability of S(IV).

Second step

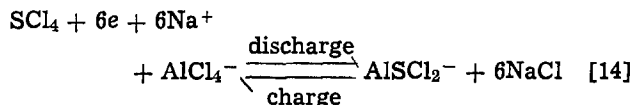
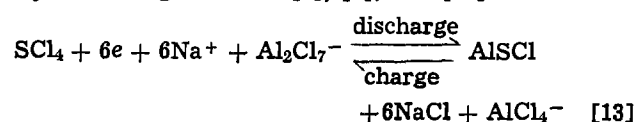


where reactions [7] and [9] occur in acidic melts. The Cl^- ions produced in [6] and [9] react with Al_2Cl_7^- ions to produce AlCl_4^- ions.

In basic melts the following reactions take place



By combining reactions [6], [9], and [12] one obtains



where reaction [13] represents the overall electrode reaction for a 6 electron process occurring in two steps in acidic melts, and reaction [14] represents the same 6 electron process in which the first step occurs in acidic and the second in basic melts. In both cases the net result of the electrochemical reaction is a gain of 6 moles of NaCl per mole of S(IV) reduced in the positive electrode compartment. Thus, the melt $p\text{Cl}^-$ continues to decrease during the discharge process until the melt becomes saturated with NaCl.

The maximum capacity and energy densities (ED) which may be obtained in the case of reactions [13] and [14], respectively, for two selected initial compositions of the solvent are shown in Table II. The energy densities have been computed on the basis of the reactions listed in the first column of Table II which are equivalent to reactions [13] and [14] if the solvation of S^{2-} by the solvent ions is not taken into account. This does not introduce errors because the aluminum content in the positive electrode compartment does not change during the charge or discharge; the weight of the solvent has been included in the energy calculations. The same OCV values have been used in the ED calculations for both initial solvent compositions although the measured OCV's in the 70/30 melt are slightly higher than those in the 63/37 melt. In the case of Al/S(IV) cells the ED's are not listed because their evaluation requires the weight of the solvent in the negative electrode compartment which would be required to keep the compartment basic. It is clear, however, that the additional weight of the solvent, together with the lower OCV's, decreases the specific energy of Al cells compared with Na cells.

Laboratory cells.—We have examined cells using both sodium and aluminum electrodes and S(IV) as the active positive electrode material. The results obtained confirm the feasibility of rechargeable cells of this type. With aluminum electrodes the main problem involves dendrite formation during the charging process. The dendrites can penetrate the separator (such as a coarse $\alpha\text{-Al}_2\text{O}_3$ crucible) causing short circuit of the cell. Additional studies of aluminum deposition in the presence of additives to minimize dendrite formation (23) are required in order to demonstrate a practical rechargeable aluminum electrode in these melts. Another problem associated with Al/S(IV) cells is the considerable difference in vapor pressure between the positive and the negative electrode compartments which operate with acidic and basic melts,

Table II. Calculated capacity and energy densities for several cell reactions

Overall cell reaction	OCV (V)	A-hr/g (10^{-2})		ED (W-hr/kg)	
Case A: The discharge stops when the solvent composition in the cathode compartment reaches the Al(III)/Na(I) mole ratio of 1:1.					
$\text{SCL}_4 + 4\text{Na} = \text{S} + 4\text{NaCl}$	4.17	63/37*	70/30*	63/37*	70/30*
$\text{SCL}_4 + 6\text{Na} = \text{Na}_2\text{S} + 4\text{NaCl}$	4.17**	5.67	7.80	236.4	325.2
$\text{SCL}_4 + 2\text{Al} + 2\text{NaAlCl}_4 = \text{Na}_2\text{S} + 4\text{AlCl}_3$	3.37†	5.85	8.14	228.3	317.9
	2.57**	7.19	9.35	—	—
	1.77‡				
Case B: The four electron process occurs until the solvent composition becomes equimolar; the two electron process occurs in NaCl _{sat.} melts.					
$\text{SCL}_4 + 6\text{Na} = \text{Na}_2\text{S} + 4\text{NaCl}$	4.17**	8.30	11.32	306.8	418.5
	2.75‡				

* Initial mole ratio of total Al(III) to Na(I).

** First step.

‡ Second step.

respectively, in order to obtain the maximum operating voltage (Table II).

Na/S(IV) cells have given much more satisfactory results. The feasibility of this system has been demonstrated with 4.5 A-hr and smaller capacity cells. The cell size was determined by the dimensions of the ceramic tube. Size A cells used 10 cm long, 10 mm OD β'' -alumina tubes which were sealed to an α - Al_2O_3 tube which in turn was sealed to glass; the coulombic capacity of these cells was in the range of 1.5 A-hr. The larger capacity (~ 4.5 A-hr) size B cells utilized ~ 20 cm long, 15 mm OD β'' -alumina tubes which were either sealed in the same manner as size A cells or to Corning 7052 glass (51). The cells were kept under vacuum at 300°-450°C for several days before adding sodium to the ceramic tube; the baking was continued for a few days to improve wetting of the β'' -alumina by sodium before adding the positive mix to the external compartment. The performance of the cells depends greatly on the quality and pretreatment of β'' - (or β -) alumina, since most of the polarization is related to the separator (see below). The positive mix was prepared by either mixing the acidic melt (typical composition 63/37) with an appropriate amount of $\text{SCl}_3\text{AlCl}_4$ in the dry box or by oxidizing elemental sulfur added to a neutral or slightly acidic melt (typical composition 50/50). In some experiments carbon (Shawinigan Black or vitreous carbon foam from Chemotronics International) was also added to the cathode compartment in an attempt to increase the effective surface area of the current collector. However, best results to date have been obtained in the absence of carbon using only a tungsten spiral as the current collector. Tungsten was also used as the current collector in the negative electrode compartment.

Typical galvanostatic charge-discharge curves for a size B cell and the potentials of each electrode vs. an

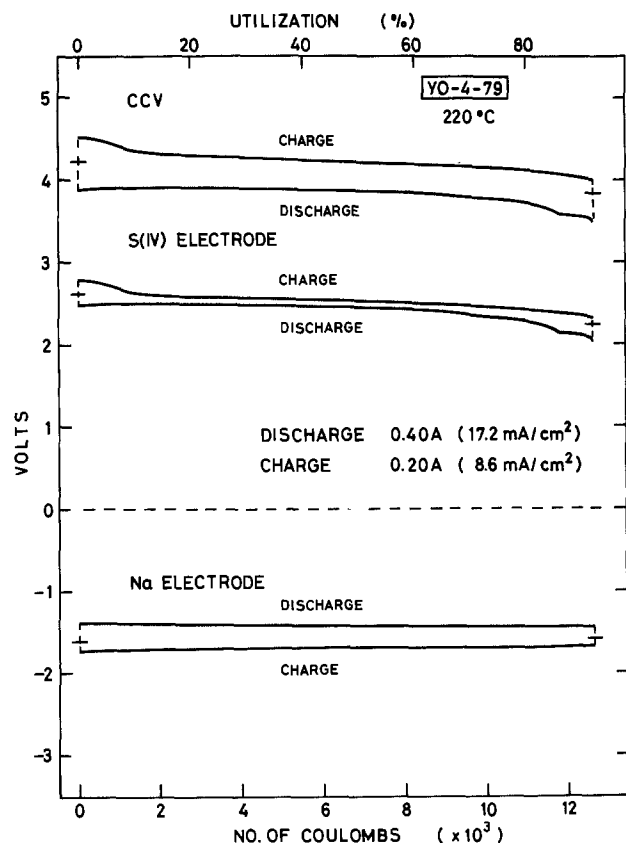


Fig. 2. Galvanostatic charge-discharge curves and potentials of S(IV) and Na electrodes vs. Al(III)/Al (in NaCl_{sat} -melt) reference electrode at 220°C. Current density 17.2 mA/cm² for discharge and 8.6 mA/cm² for charge. Discharge time 8.8 hr. Percent utilization is calculated for the $4e^-$ process.

aluminum reference electrode are shown in Fig. 2. The discharge corresponds to the formation of elemental sulfur; it was terminated at the beginning of a sharp drop in the potential of the positive electrode. In some cells the reduction of sulfur to sulfide was also investigated; such discharge curves exhibit a second plateau with a closed-circuit voltage (CCV) of ~ 1 V less than that of the first plateau. Only a cursory study of the second plateau has been performed to date. In one size A cell 20 charge/discharge (to sulfide) cycles were attained before failure occurred (see below).

Most of the studies have involved only the first plateau. It may be seen from Fig. 2 that the potential of the sodium electrode is quite constant for both charge and discharge. It is apparent that the processes responsible for the polarization of the Na electrode (more likely, polarization occurring at the β'' -alumina interfaces) are the major causes of polarization for the whole cell. The increase in the potential of the S(IV) electrode at the end of the charge process is accompanied by some chlorine evolution. However, the chlorine reacts rapidly with any sulfur species that have not been electrochemically oxidized to the +4 state. This conclusion is supported by the results of vapor pressure measurements during charge and discharge processes (52). The pressures measured differed little from those obtained for pure chloroaluminate melts thus indicating that no significant amounts of gaseous products are formed during normal cell operation. No deleterious effects on the separator by chlorine produced by some overcharge have been observed.

A decrease in the utilization of the active positive electrode material and an increase in polarization were observed with increasing current density (Fig. 3). With the present configuration the maximum current densities applied were 70 mA/cm² for discharge and 35 mA/cm² for charge (current densities were based on the inner area of the β'' -alumina). At high current densities the mass transfer of sulfur species probably could not keep up with the electrochemical steps. A different cell configuration will be required to solve this problem. The variation of CCV with current density at three different temperatures is shown in Fig. 4. Ohmic polarization is indicated by the linearity of the plots; approximately equal slopes are observed for both charge and discharge processes. The effective "resistance" of the β'' -alumina separator that may be estimated from Fig. 4 ($\sim 80 \Omega \text{ cm}$ at 220°C) is considerably higher than the value reported for pure β'' -alumina (6.5 $\Omega \text{ cm}$ at 220°C) (53). Further studies of the causes of polarization at the separator interfaces are currently in progress (54).

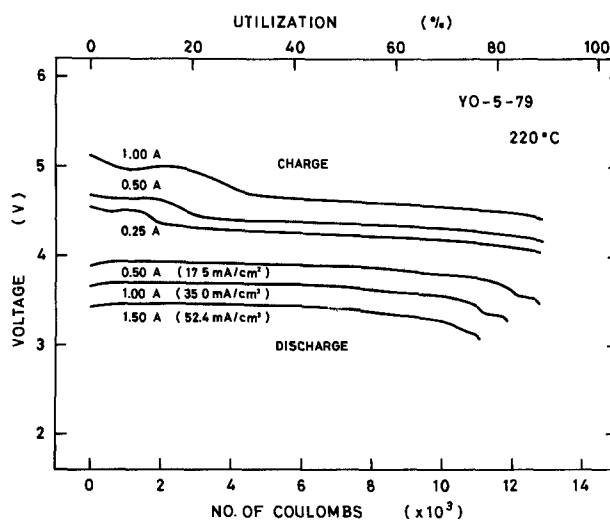


Fig. 3. Galvanostatic charge-discharge curves at several current densities at 220°C.

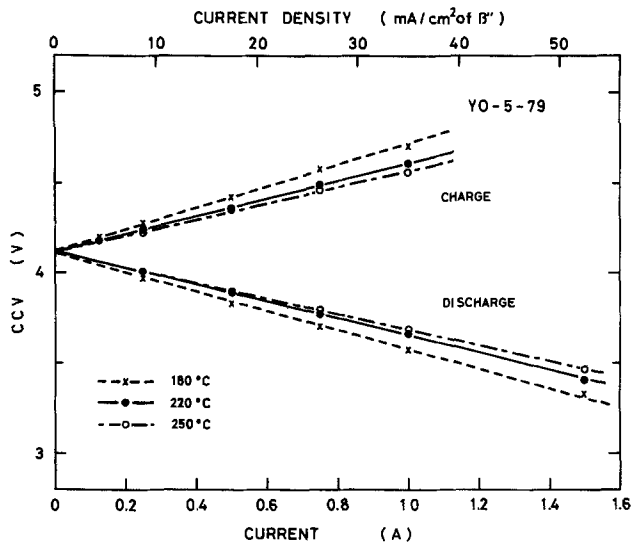


Fig. 4. Current dependence of the CCV measured at the midpoint of discharge at three temperatures.

The cell performance was studied in the temperature range 180°-255°C. As expected, the polarization decreased with increasing temperature (Fig. 4, 5). However, some loss in the percent utilization of S(IV) and in the energy density (this parameter does not include the weight of the separator or that of the cell) with temperature was observed (Fig. 6). Further studies in this area are in progress. Typical cell parameters are given in Table III.

The variation of the percent utilization of S(IV) and average discharge and charge voltage with the number of cycles is shown in Fig. 7. It may be seen that the voltages and percent utilization are reasonably constant. One cell has been in continuous operation for more than 9 months; the number of deep discharge/charge cycles has exceeded 400.

Most of the early cell failures were caused by the formation of cracks in the β'' -alumina or in the β'' - α alumina seal. These problems have been minimized by lengthening the pretreatment of the separator (currently 2 weeks at 350°C). The performance of the cells is independent of which species, elemental sulfur or $\text{SCL}_3\text{AlCl}_4$, is chosen as the starting material.

Only β'' -alumina has been found satisfactory as the separator material. The cells prepared with β -alumina tubes exhibited excessive polarization. The NASICON is gradually attacked by the solvent.

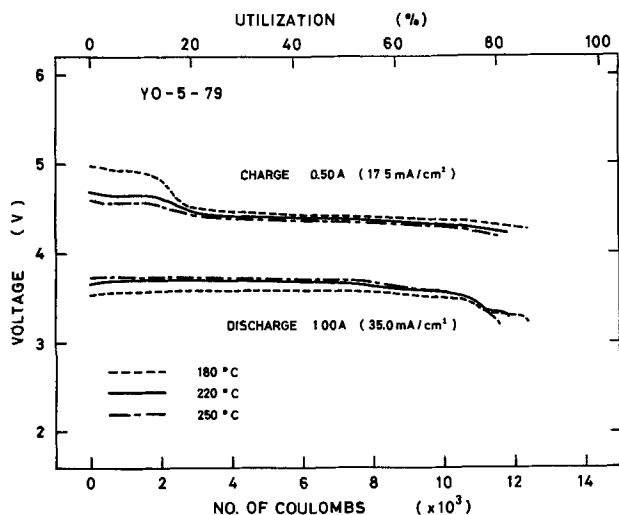


Fig. 5. Galvanostatic charge-discharge curves at three temperatures.

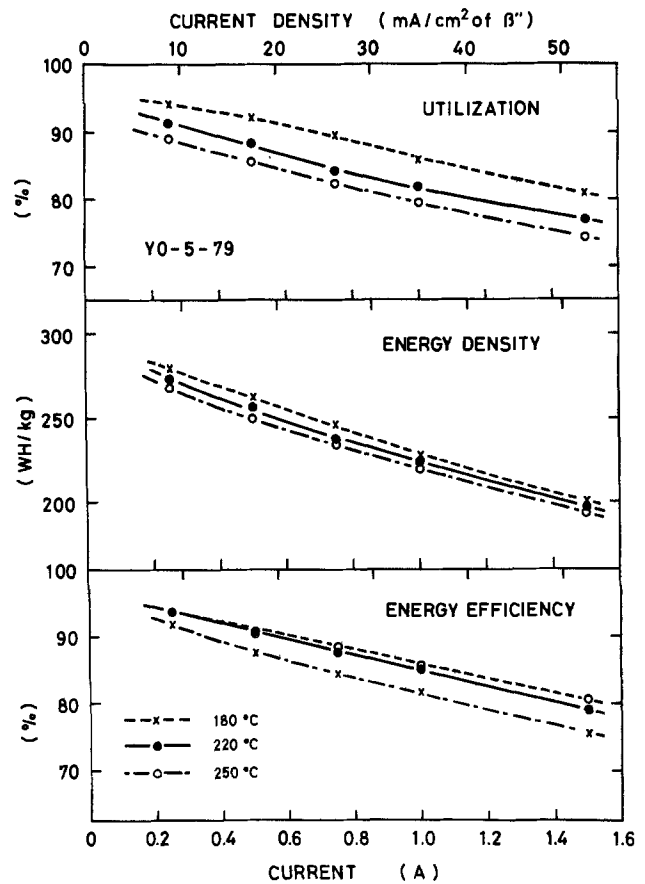


Fig. 6. The dependence of the percent utilization and energy efficiency and of the energy density on the current density at three temperatures.

In summary, our experimental results obtained with laboratory cells demonstrate the feasibility of the rechargeable Na/S(IV) chloroaluminate battery. Such a battery possesses several advantages, such as (i) very high voltage, (ii) high energy densities, (iii) low operating temperature compared to the lithium (aluminum)-iron sulfide and the sodium-sulfur batteries, (iv) effective utilization of sulfur (4 or 6 electrons exchanged per sulfur atom), and (v) inexpensive active electrode materials (sulfur and sodium).

Good energy efficiency values have been obtained with relatively simple cell designs.

Based on considerations presented above we believe that the development of the Na/S(IV) chloroaluminate

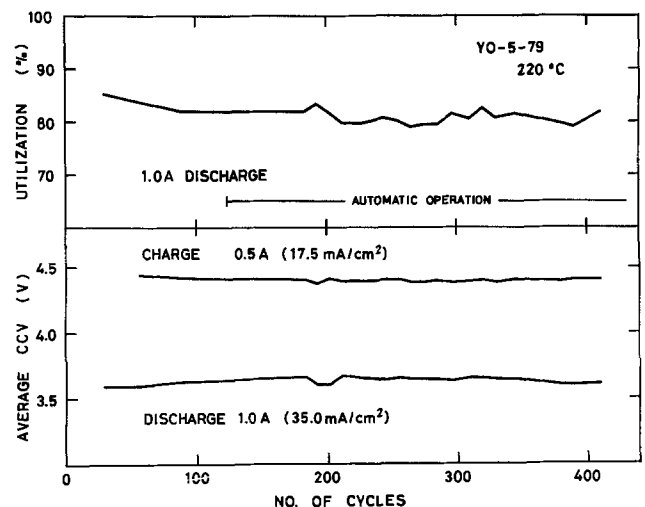


Fig. 7. Average charge and discharge voltage and percent utilization of S(IV) vs. number of cycles.

Table III. Typical parameters for size B (capacity 4.0 A-hr) Na/S(IV) cell*

Cycle No.	Current** density [mA/cm ²]	Average cell voltage		Energy† density [W-hr/kg]	Energy‡ efficiency [%]	Utilization of S(IV) [% theor.]
		Discharge [V]	Charge [V]			
180°C						
105	8.7	3.94	4.32	280	92	94
103	17.5	3.78	4.51	263	88	92
102	35.0	3.52	4.84	229	82	86
118	52.4	3.28	—	200	76	81
220°C						
93	8.7	3.97	4.26	274	94	91
86	17.5	3.85	4.40	257	90	89
88	35.0	3.63	4.70	225	85	82
89	52.4	3.39	—	197	79	77
58	69.9	3.11	—	171	72	73
250°C						
76	8.7	3.98	4.24	268	94	89
77	17.5	3.86	4.38	250	91	86
73	35.0	3.66	4.62	220	86	80
72	52.4	3.44	—	193	81	74

* Initial cathode mix composition: 11.5g SCl₂AlCl₃ in 38-1g 66/34 melt. OCV = 4.25V.

** Current density based on the inner surface area of β'-alumina.

† Maximum energy density 309 W-hr/kg [the required weight of Na is included].

‡‡ Charge current density 8.7 mA/cm².

battery should be intensively pursued because of its high promise, particularly in load leveling applications.

Acknowledgment

This work has been supported by the Department of Energy, Contract EY-76-S-05-5053, and University of California, Subcontract 4502810.

Manuscript submitted March 4, 1980; revised manuscript received May 12, 1980.

Any discussion of this paper will appear in a Discussion Section to be published in the June 1981 JOURNAL. All discussions for the June 1981 Discussion Section should be submitted by Feb. 1, 1981.

Publication costs of this article were assisted by the University of Tennessee.

REFERENCES

- D. A. J. Swinkels, in "Advances in Molten Salt Chemistry," Vol. 1, J. Braunstein, G. Mamantov, and G. P. Smith, Editors, pp. 165-223, Plenum Press, New York (1971).
- E. J. Cairns and R. K. Steunenberg, in "Progress in High Temperature Physics and Chemistry," Vol. 5, C. A. Rouse, Editor, pp. 63-124, Pergamon Press, New York (1973).
- K. V. Kordes, in "Modern Aspects of Electrochemistry," No. 10, J. O'M. Bockris and B. E. Conway, Editors, pp. 339-443, Plenum Press, New York (1975).
- J. R. Birk and N. P. Yao, in "Proceedings of the Symposium on Load Leveling," N. P. Yao and J. R. Selman, Editors, pp. 229-250, The Electrochemical Society Softbound Proceedings Series, Princeton, N.J., (1977).
- R. J. Brodd and A. Kozawa, in "Techniques of Electrochemistry," Vol. 3, E. Yeager and A. J. Salkind, Editors, pp. 200-290, J. Wiley and Sons, New York (1978).
- G. Halpert, in "Techniques of Electrochemistry," Vol. 3, E. Yeager and A. J. Salkind, Editors, pp. 291-368, J. Wiley and Sons, New York (1978).
- G. Mamantov, R. Marassi, and J. Q. Chambers, "High Energy Cathodes for Fused Salt Batteries," Technical Report ECOM-0060-F, April 1974.
- G. Mamantov, R. Marassi, and J. Q. Chambers, Abstract 8, p. 24, The Electrochemical Society Extended Abstracts, New York, N.Y., October 13-17, 1974.
- G. Mamantov, R. Marassi, and J. Q. Chambers, U.S. Pat. 3,966,491 (1976).
- G. Mamantov, R. Marassi, J. P. Wiaux, S. E. Springer, and E. J. Frazer, Abstract 89, p. 243, The Electrochemical Society Extended Abstracts, Atlanta, Georgia, October 9-14, 1977.
- G. Mamantov and R. Marassi, U.S. Pat. 4,063,005 (1977).
- G. Mamantov, R. Marassi, J. P. Wiaux, S. E. Springer, and E. J. Frazer, in "Proceedings of the Symposium on Load Leveling," N. P. Yao and J. R. Selman, Editors, pp. 379-383, The Electrochemical Society Softbound Proceedings Series, Princeton, N.J., (1977).
- P. V. Clark, "Fused Salt Mixtures—Specific Conductivity Tables," Report SC-R-69-1386, National Bureau of Standards, U.S. Department of Commerce, October 1969, p. 58.
- R. C. Howie and D. W. MacMillan, *J. Inorg. Nucl. Chem.*, **33**, 3681 (1971).
- B. Tremillon and G. Letisse, *J. Electroanal. Chem. Interfacial Electrochem.*, **17**, 371 (1968).
- G. Torsi and G. Mamantov, *Inorg. Chem.*, **10**, 1900 (1971).
- A. A. Fannin, L. A. King, and D. W. Seegmiller, *This Journal*, **119**, 801 (1972).
- L. G. Boxall, H. L. Jones, and R. A. Osteryoung, *ibid.*, **120**, 223 (1971).
- J. D. Corbett, in "Preparative Inorganic Reactions," Vol. 3, W. L. Jolly, Editor, pp. 1-33, Interscience, New York (1966).
- G. L. Holleck and J. Giner, *This Journal*, **119**, 1161 (1972).
- B. S. Del Duca, *ibid.*, **118**, 405 (1971).
- R. J. Gale and R. A. Osteryoung, *ibid.*, **121**, 983 (1974).
- R. C. Howie and D. W. MacMillan, *J. Appl. Electrochem.*, **2**, 217 (1972).
- B. Gilbert, D. L. Brotherton, and G. Mamantov, *This Journal*, **121**, 773 (1974).
- J. J. Werth, U.S. Pat. 3,847,667 (1974); U.S. Pat. 3,877,984 (1975).
- J. J. Werth, EPRI Report EM-230, December 1975.
- A. M. Chreitzberg, EPRI Report EM-751, April 1978.
- J. Giner and G. L. Holleck, NASA Report CR 1541, March 1970.
- G. D. Brabson, A. A. Fannin, Jr., L. A. King, and D. W. Seegmiller, Abstract 26, p. 61, The Electrochemical Society Extended Abstracts, Chicago, Illinois, May 13-18, 1973.
- L. Redey, I. Porubszky, and I. Molner, 9th International Power Sources Symposium, Brighton, England, September 17-19, 1974.
- J. Greenberg, U.S. Pat. 3,573,986 (1971); 3,635,765 (1972).
- G. D. Brabson, J. K. Erbacher, L. A. King, and D. W. Seegmiller, FJSRL Technical Report 76-0002, January 1976.
- R. O. Miller, NASA Tech. Memo. TMS-3245 (1975).
- W. P. Sholette, I. S. Klein, and J. Werth, in "Proceedings of the Symposium on Load Leveling," N. P. Yao and J. R. Selman, Editors, pp. 306-317, The Electrochemical Society Softbound Proceedings Series, Princeton, N.J., (1977).
- R. Marassi, G. Mamantov, and J. Q. Chambers, *Inorg. Nucl. Chem. Lett.*, **11**, 245 (1975).
- R. Marassi, G. Mamantov, and J. Q. Chambers, *This Journal*, **123**, 1128 (1976).
- R. Marassi, G. Mamantov, M. Matsunaga, S. E. Springer, and J. P. Wiaux, *ibid.*, **126**, 231 (1979).

38. K. A. Paulsen and R. A. Osteryoung, *J. Am. Chem. Soc.*, **98**, 6866 (1976).
39. J. Robinson, B. Gilbert, and R. A. Osteryoung, *Inorg. Chem.*, **16**, 3040 (1977).
40. G. Torsi, K. W. Fung, G. M. Begun, and G. Mamantov, *ibid.*, **10**, 2285 (1971).
41. R. Marassi, J. Q. Chambers, and G. Mamantov, *J. Electroanal. Chem. Interfacial Electrochem.*, **69**, 345 (1976).
42. G. Mamantov, R. Marassi, F. W. Poulsen, S. E. Springer, J. P. Wiaux, R. Huglen, and N. R. Smyrl, *J. Inorg. Nucl. Chem.*, **41**, 260 (1979).
43. G. Mamantov and R. A. Osteryoung, in "Characterization of Solutes in Non-Aqueous Solvents," G. Mamantov, Editor, pp. 223-249, Plenum Press, New York (1978).
44. R. Huglen, F. W. Poulsen, G. Mamantov, R. Marassi, and G. M. Begun, *Inorg. Nucl. Chem. Lett.*, **14**, 167 (1978).
45. G. Mamantov, V. E. Norvell, and L. Klatt, **127**, 1768 (1980).
46. N. J. Bjerrum in "Characterization of Solutes in Non-Aqueous Solvents," G. Mamantov, Editor, pp. 251-271, Plenum Press, New York (1978).
47. K. Tanemoto, R. Huglen, and G. Mamantov, Unpublished work.
48. R. Fehrmann, N. J. Bjerrum, and F. W. Poulsen, *Inorg. Chem.*, **17**, 1195 (1978).
49. J. T. Kummer, in "Progress in Solid State Chemistry," Vol. 7, H. Reiss and J. O. McCaldin, Editors, pp. 141-175, Pergamon Press, New York (1972).
50. J. H. Kennedy, in "Solid Electrolytes," S. Geller, Editor, pp. 105-141, Springer Verlag, New York (1977).
51. A. Pelton, Private communication.
52. E. J. Frazer and G. Mamantov, Unpublished work.
53. Ceramatec, Incorporated, Private communication.
54. Y. Ogata, G. Mamantov, C. E. Vallet, and J. Braunstein, Unpublished work.

Defect Structure, Ionic Conductivity, and Diffusion in Calcia-Stabilized Zirconia

Akio Nakamura* and J. Bruce Wagner, Jr.*

Center for Solid State Science, Arizona State University, Tempe, Arizona 85281

ABSTRACT

A quantitative theoretical model which accounts for the variations of ionic conductivity of calcia-stabilized zirconia, $\text{Ca}_{2x}\text{Zr}_{1-2x}\text{O}_{2-2x}$, with oxygen vacancy concentration, x , and temperature, T , has been developed based on the consideration of effective anion-site coordination of effectively negatively charged calcium ion, Ca^{2-} . The theory extends the conventional concept of dopant-defect complexes (or associates) and demonstrates that ionic conduction in this system proceeds by a multimode mechanism through and between different degrees of dopant-defect associates. The primary mechanism is oxygen transport through the channel of onefold effectively Ca^{2-} coordinated anion sublattice, that is, oxygen vacancy V_{O}^{2-} transport inside the onefold bonded ($\text{Ca}^{2-}\text{-V}_{\text{O}}^{2-}$) defect complex. The theory subsequently predicts the occurrence of a rather sharp maximum of ionic conductivity at oxygen vacancy concentration $x = 0.0625$ and reproduces the experimental isothermal $\log \sigma$ vs. x curves reported by various investigators quite satisfactorily. Accordingly, numbers of parameters which characterize the defect structure, the ionic conduction, and the diffusion process in this system are derived from the curve-fitting procedure of the theoretical expression for ionic conductivity with experimental ones.

It is now well recognized that zirconia stabilized in the cubic fluorite structure by substitution of aliovalent oxides, such as CaO , Y_2O_3 , and rare earth oxides, is essentially an oxide ion conductor with its high ionic conductivity due to high oxygen vacancy concentration introduced into the anion sublattice by these substitutions (1). Numerous experimental works on electrical conductivity on these systems have shown that ionic conductivity of these systems exhibits a maximum value around the minimum dopant level required to stabilize the cubic fluorite phase at constant temperature. For example, in CaO -stabilized zirconia, $\text{Ca}_{2x}\text{Zr}_{1-2x}\text{O}_{2-2x}$, the maximum occurs around 12-13 mole percent (m/o) CaO content (2-5) ($x = 0.060$ - 0.065) and in the Y_2O_3 -stabilized zirconia, $\text{Y}_{4x}\text{Zr}_{1-4x}\text{O}_{2-2x}$, around 8-9 m/o Y_2O_3 content (2, 4, 6) ($x = 0.037$ - 0.041). At higher concentrations within the cubic fluorite phase regions, the ionic conductivity decreases with increasing dopant content. The activation energy for ionic conduction is also reported to increase with increasing dopant content (4, 5). Similar behavior is also reported in the other fluorite oxide systems, i.e., ThO_2 (7) and CeO_2 (8) based solid electrolytes, where,

since pure thoria and ceria have cubic fluorite structure, dopants such as CaO and Y_2O_3 are used only to introduce the extrinsic oxygen vacancies into the anion sublattice. This decrease in ionic conductivity with increasing vacancy concentration has been qualitatively regarded as the result of vacancy ordering (5) vacancy clustering (9), or dopant-vacancy association (10) in the higher oxygen vacancy concentration range.

Recently, several attempts to explain this behavior have been undertaken: O'Keeffe (11) and Barker and Knop (12) have shown that when vacancy-vacancy repulsive interaction is so strong that the numbers of the first and the second nearest neighbor vacancy-vacancy configurations are prohibited, the maximum in ionic conductivity shifts to the lower vacancy concentration ranges than that expected from the usual hopping model in which $\sigma \propto x(1-x)$, so that σ_{max} is expected at $x = 0.5$. Casselton (6) for the Y_2O_3 - ZrO_2 system and Hammou (13) for the Y_2O_3 - ThO_2 system, respectively, proposed models to explain this behavior using the extended Lidiard model (14) which is based on the presence of dopant-vacancy complexes and Debye-Hückel type interactions. Hammou also tested Barker's model mentioned above. None of these models resulted in quantitative agreement with experimental data.

* Electrochemical Society Active Member.

Key words: electrolyte, conductance, transport.

Most recently, Schmalzried (15) interpreted these phenomena under the assumptions of (i) Debye-Hückel type electrostatic interaction for low defect concentration range and (ii) ordering of oppositely charged defects for high defect concentration range, neglecting the formation of defect associates. Schmalzried showed that these assumptions lead to a decrease of the correlation factor of defects with increasing defect concentration and also to an increase in the activation energy for defect motion in a qualitative manner. Judging from the preceding brief literature survey, there seems to exist no theoretical model which accounts for the phenomena in these systems in a quantitative manner. Accordingly, the aim of the present paper is to propose an alternative theoretical model to serve this purpose by choosing calcia-stabilized zirconia as a representative system.

In the next section, a brief survey of the ionic conductivity data of calcia-stabilized zirconia reported in literature is given, and in the subsequent section the theoretical model is described.

Ionic Conductivity Data of Calcia-Stabilized Zirconia, $\text{Ca}_{2x}\text{Zr}_{1-2x}\text{O}_{2-2x}$ System

Figure 1 shows the isothermal $\log \sigma$ vs. oxygen vacancy concentration x plots at $T = 600^\circ, 800^\circ, 1000^\circ, 1200^\circ,$ and 1400°C reported in literature. Included are data only by the authors who studied σ as a function of dopant content in a systematic manner.

The data of Stricker and Carlson (2), Tien (3), Dixon *et al.* (4), and Tien and Subbarao (5) all agree that the stability region of the cubic fluorite phase extends from around 12-13 m/o CaO to around 20-22 m/o CaO at temperatures between approximately 600° and 1400°C . Furthermore, the conductivity maximum exists inside the cubic fluorite phase near the monoclinic-cubic solid solution phase boundary, *i.e.*, at 12-13 m/o CaO content ($x = 0.060-0.065$). In contrast, Carter and Roth (16) report that the stability region extends from about 10 to 19 m/o CaO at 1400°C and their data seem to show the tendency that the conductivity maximum shifts from around 13 m/o CaO at 1000°C to 15 m/o CaO at 1400°C .

As is apparent from Fig. 1, the ionic conductivity of calcia-stabilized zirconia initially increases with oxygen vacancy concentration x , and reaches a maximum around 12-13 m/o CaO content ($x = 0.060-0.065$). The conductivity then decreases, initially rather sharply and then more slowly, with oxygen vacancy concentration x within the cubic fluorite phase region. The rate of decrease of ionic conductivity with x increases with decreasing temperature and the conductivity decreases by a factor of $\sim 1/20$ at 600°C when x increases from 0.065 to 0.100. This means that the activation energy for ionic conduction increases with x . Typical values are 26.2 kcal/mole for 13 m/o CaO and 31.1 kcal/mole for 20 m/o CaO (5).

Another interesting feature is the order-disorder transition. Subbarao *et al.* (5, 17) observed this phenomenon below 1000°C in samples with higher CaO content (18 and 20 m/o CaO). Some of these data, designated as "ordered," are also included in Fig. 1. "Ordered" samples at these compositions have a lower but finite conductivity which is converted to that of the "disordered" phase after heat-treatments at 1400°C . Carter and Roth (16) also examined this order-disorder phenomenon rather extensively. Their data indicate that below 1100°C , even in samples with low CaO content (13.2 and 14.2 m/o CaO), in some cases the resistivity changes by a factor of over 10, showing no tendency to saturate with time. The reason for this discrepancy between Subbarao *et al.* (5, 17) and Carter and Roth (16) is not clear at present, although it seems reasonable to assume from these observations that in samples with higher CaO content and at lower temperatures calcium ions Ca^{2+} and oxygen vacancies V_O^{2-} would order in some fashion which causes the

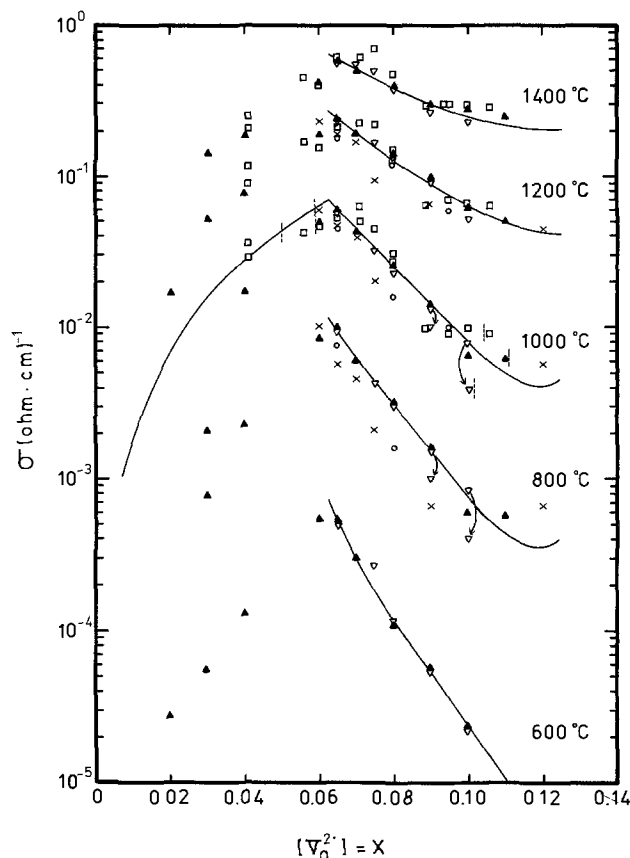


Fig. 1. Isothermal $\log \sigma$ vs. oxygen vacancy concentration x plots at $600^\circ, 800^\circ, 1000^\circ, 1200^\circ,$ and 1400°C

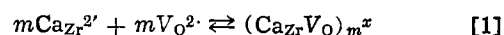
Experimental points	Reference number
○ Stricker and Carlson	(2)
▲ Tien	(3)
× Dixon, LaGrange, Merten, Miller and Porter	(4)
▽ Tien and Subbarao	(5)
□ Carter and Roth	(16)
— Theoretical curves according to Eq. [13] at $0.0625 \leq x \leq 0.125$ and Eq. [13] at $0 \leq x \leq 0.0625, T = 1000^\circ\text{C}$	
↓ The phase boundary of the cubic fluorite phase according to the above authors.	
▽ Lower values indicated by arrow. σ at ordered state according to Ref. (5) and (17).	

substantial decrease in ionic conductivity after prolonged heat-treatments.

Theoretical

The main aim of the theoretical model is to reproduce the experimental $\log \sigma$ vs. x curves shown in Fig. 1 over the entire temperature ranges in a quantitative manner consistent with the physical reality of the system. This includes the increase in activation energy for ionic conduction with x .

As far as the authors are aware, Kröger (10) was the first to suggest that ionic conduction and oxygen diffusion in calcia-stabilized zirconia (CSZ) probably occurs via migration of oxygen vacancies V_O^{2-} in $(\text{Ca}_z\text{rV}_\text{O})_m^x$. Kröger described this association process by a usual defect equilibrium equation



Applying the mass action law to the above equation and assuming electrostatic binding energy of the defect complex, Kröger concluded that most of the calcium (and therefore V_O^{2-}) is present as neutral calcium ion-oxygen vacancy pairs or clusters. This description corresponds in general form with the theory of Lidiard

for aliovalent impurity diffusion in alkali-halide systems (14). But when the impurity (dopant) concentration and therefore also the defect concentration becomes as high as in CSZ, these treatments do not appear to be valid. First, let us assume that oxygen and therefore $V_{O^{2-}}$ diffusion proceeds via defect complexes $(Ca_{2x}V_O)_x$ ($m = 1$ in Eq. [1]). In the fluorite structure, since every cation has 8-first, 24-second, 24-third . . . nearest neighbor anion sites, all the anion sites will be just effectively onefold coordinated by dopant cations Ca^{2+} when the dopant concentration reaches $2x = 2/Z'$ for $Ca_{2x}Zr_{1-2x}O_{2-2x}$, i.e., in this case $Z' \cdot 2x = 2$, where Z' is the effective anion site coordination number of Ca^{2+} in this system. This means that at the composition $x = 1/Z'$, every $V_{O^{2-}}$ jump occurs inside $(Ca^{2+}-V_{O^{2-}})$ onefold effectively associated defect complexes. Therefore, conductivity should be a maximum. Beyond this composition the average effective Ca^{2+} coordination number to the anion sublattice becomes greater than 1, i.e., the number of density of 2-fold Ca^{2+} coordinated anion sites becomes an appreciable fraction of the total available jump sites; so the ionic conductivity should decrease, because the effective path for $V_{O^{2-}}$ migration through $(Ca^{2+}-V_{O^{2-}})$: 1-fold effectively Ca^{2+} associated defect complexes decreases. This is indeed the case for CSZ if we assume an effective anion site coordination number of Ca^{2+} : $Z' = 16$: the experimental observed ionic conductivity maximum occurs around $x = 0.060-0.065$, whereas the theoretically derived conductivity maximum is expected at $x = 1/Z' = 1/16 = 0.0625$. If only the first nearest neighbor $Ca^{2+}-V_{O^{2-}}$ configuration is taken into account, Z' becomes equal to 8, and the conductivity maximum is expected at $x = 1/8 = 0.125$, which is almost twice the observed oxygen vacancy concentration at the maximum. This means that the second and the higher order nearest neighbor $Ca^{2+}-V_{O^{2-}}$ configurations also contribute to the effective anion site coordination number of Ca^{2+} , Z' , with a contribution that is equal to that from the first nearest neighbor $Ca^{2+}-V_{O^{2-}}$ configuration ($Z' = 8$). This fact seems to be quite reasonable in the light of the rather long-range character of electrostatic interaction between charged defects $Ca^{2+}-V_{O^{2-}}$ (18). We might regard the first nearest neighbor Ca^{2+} and $V_{O^{2-}}$ configuration as the ground state of the $(Ca^{2+}-V_{O^{2-}})$ defect complex, and the second (and the higher order) nearest neighbor $Ca^{2+}-V_{O^{2-}}$ configuration as the first excited state (and the higher order excited states) of the $(Ca^{2+}-V_{O^{2-}})$ defect complex.

But actually the greater the distance between Ca^{2+} and $V_{O^{2-}}$, the more the electrostatic interaction between them would be increasingly screened and weakened. Consequently we include here only the first nearest neighbor and the second nearest neighbor $Ca^{2+}-V_{O^{2-}}$ configurations, assuming further that Ca^{2+} coordination number to each 24-second nearest neighbor anion sites is $\sim 1/3$. At this level of approximation, the total effective coordination number of Ca^{2+} to anion sites Z' becomes equal to $(8 \times 1) + (24 \times 1/3) = 16$, which yields the conductivity maximum at $x = 0.0625$ in accordance with experimental observations.

When the CaO content becomes 25 m/o, i.e., $x = 0.125$, the effective anion site coordination number of Ca^{2+} becomes 2, i.e., $Z' \cdot 2x/2 = 2$. This situation is shown in Fig. 2a. Figure 2a shows the unit cell of $Ca_{0.25}Zr_{0.75}O_{1.75}V_{0.25}$ ($x = 0.125$). The unit cell of the fluorite structure contains 4 cations and 8 anions. So at the composition $2x = 1/4$, one out of four cations is Ca^{2+} . In Fig. 3 these Ca^{2+} are situated at the eight corner cation sites of the unit cell. The remaining three cations are Zr^{2+} , which are situated at the face center position of six face planes. One out of 8 anions in the unit cell is $V_{O^{2-}}$ ($x = 1/8$). As is apparent from this figure, 1/4 of the four (=1) first nearest neighbor cations around $V_{O^{2-}}$ is Ca^{2+} , which yields onefold Ca^{2+} coordination to $V_{O^{2-}}$, and 1/4 of the twelve (=3) second nearest neighbor cations around $V_{O^{2-}}$ are Ca^{2+} ,

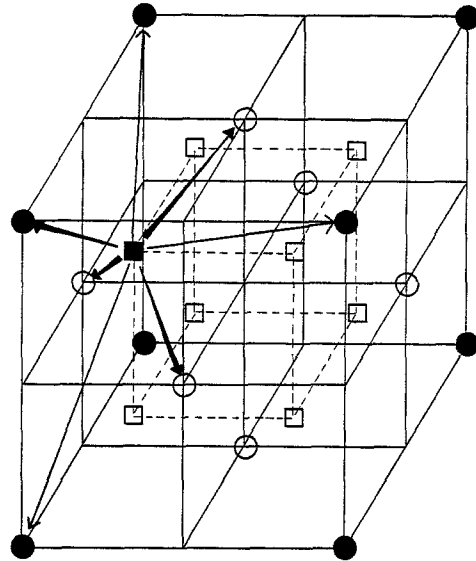


Fig. 2a. Unit cell of the fluorite lattice of $(CaO)_{0.25}(ZrO_2)_{0.75}$ ($2x = 1/4$, $x = 0.125$).

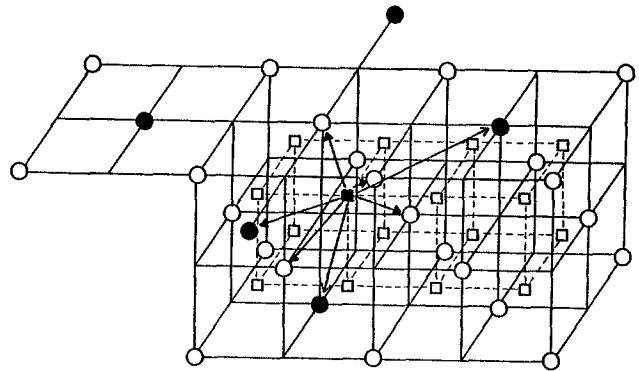


Fig. 2b. $Ca^{2+}-V_{O^{2-}}$ configuration in $(CaO)_{0.125}(ZrO_2)_{0.875}$ ($2x = 1/8$, $x = 0.0625$). ● Ca^{2+} , ○ Zr^{2+} , □ O^{2-} , ■ $V_{O^{2-}}$, → 4 first nearest neighbor cations around $V_{O^{2-}}$, → 3 (out of 12) second nearest neighbor Ca^{2+} around $V_{O^{2-}}$.

which yields another onefold coordination to $V_{O^{2-}}$. So, at this composition every $V_{O^{2-}}$ (and anion site) is on an average twofold coordinated and every $V_{O^{2-}}$ jump occurs inside effectively twofold associated $(Ca^{2+}-V_{O^{2-}}-Ca^{2+})$ defect complexes. Similarly, Fig. 2b shows the $Ca^{2+}-V_{O^{2-}}$ configuration in $Ca_{0.125}Zr_{0.875}O_{1.875}V_{0.125}$ ($x = 0.0625$) where every two unit cells contain one Ca^{2+} ($2x = 1/8$) and one $V_{O^{2-}}$ ($x = 1/16$). In Fig. 2b, Ca^{2+} are situated at face centered positions of the top plane or bottom plane in an alternative array. Every $V_{O^{2-}}$ (and anion site) is just onefold coordinated by Ca^{2+} , either by one first nearest neighbor Ca^{2+} (= 1) or by three second nearest neighbor Ca^{2+} ($1/3 \times 3 = 1$). So at this composition every $V_{O^{2-}}$ jump occurs inside effectively onefold associated $(Ca^{2+}-V_{O^{2-}})$ defect complexes.

Note that the stabilized cubic fluorite phase appears just when onefold associated $(Ca^{2+}-V_{O^{2-}})$ defect complexes extend throughout the anion sublattice, giving rise to a conductivity maximum ($x = 0.0625$); and disappears with the disappearance of this defect complex ($x = 0.125$). In these defect concentration ranges, conventional defect equilibria treatments such as Eq. [1] are not applicable, for there exist no more free dissociated anion sites on which $V_{O^{2-}}$ can reside.

Description of the Theoretical Model

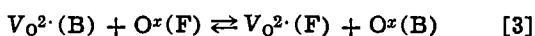
Let us designate at a given composition x , the relatively free state, and the relatively bound state of the

anion sublattice for $V_{O^{2-}}$ as F and B, respectively. In the case of CSZ within the vacancy concentration range $0.0625 \leq x \leq 0.125$ over which the cubic fluorite phase extends, we can assume that the F-state and the B-state correspond to the 1-fold Ca^{2+} coordinated and 2-fold Ca^{2+} coordinated anion sublattice, respectively. This follows because the Ca^{2+} -average coordination number to the anion sublattice is $1 \leq \frac{Z' \cdot 2x}{2}$

$= 16x \leq 2$. For each concentration of F-state and B-state, the site fractions N_F and N_B will be given by the following equation

$$\begin{aligned} 1 \times N_F + 2 \times N_B &= Z' \cdot 2x/2 = 16x, & N_F + N_B &= 1, \\ N_F &= 2 - 16x, & N_B &= 16x - 1 \\ 0.0625 &\leq x \leq 0.125 \end{aligned} \quad [2]$$

Equation [2] neglects the statistical fluctuations of the system. The distribution of oxygen vacancies $V_{O^{2-}}$ and oxide ions O^x between these states is assumed to be given by the following quasi-chemical equilibria



Applying the mass action law to Eq. [3] yields

$$\begin{aligned} K &= \exp\left(-\frac{\Delta G^\circ}{RT}\right) = \exp\left(\frac{\Delta S^\circ}{R}\right) \cdot \exp\left(-\frac{\Delta H^\circ}{RT}\right) \\ &= \frac{[V_{O^{2-}}(F)][O^x(B)]}{[V_{O^{2-}}(B)][O^x(F)]} \end{aligned} \quad [4]$$

where K , ΔG° , ΔH° , and ΔS° denote the equilibrium constant, standard Gibbs free energy change, standard enthalpy change, and standard entropy change for Eq. [3], respectively, and $[]$ designates the concentration of each chemical species in site fractions.

From the site and mass conservation, the following equations hold

$$\begin{aligned} [V_{O^{2-}}(\text{total})] &= [V_{O^{2-}}(F)] + [V_{O^{2-}}(B)] = x \\ N_F + N_B &= 1 \\ [V_{O^{2-}}(F)] + [O^x(F)] &= N_F \\ [V_{O^{2-}}(B)] + [O^x(B)] &= N_B \end{aligned} \quad [5]$$

Rearranging Eq. [5] yields

$$\begin{aligned} [V_{O^{2-}}(B)] &= x - [V_{O^{2-}}(F)] \\ [O^x(F)] &= N_F - [V_{O^{2-}}(F)] \\ [O^x(B)] &= 1 - N_F - x + [V_{O^{2-}}(F)] \end{aligned} \quad [6]$$

Inserting Eq. [6] into [4], the following quadratic equation for $[V_{O^{2-}}(F)]$ is obtained

$$\begin{aligned} (1 - K)[V_{O^{2-}}(F)]^2 + \{K(x + N_F) \\ + (1 - N_F - x)\}[V_{O^{2-}}(F)] - K \cdot N_F \cdot x &= 0 \end{aligned} \quad [7]$$

Solving Eq. [7] for $[V_{O^{2-}}(F)] (> 0)$ yields

$$[V_{O^{2-}}(F)] = \frac{-\{K(x + N_F) + (1 - N_F - x)\} + \sqrt{\{K(x + N_F) + (1 - N_F - x)\}^2 + 4xK(1 - K)N_F}}{2(1 - K)} \quad [8]$$

Then, from Eq. [8] and [6], all the concentrations of each chemical species can be obtained given K and x .

The total ionic conductivity of the system σ_{total} will be given by the sums of partial ionic conductivity $\sigma_{i,j}$ ($i, j = F, B$)

$$\sigma_{\text{total}} = \sum_{i,j=F,B} \sigma_{i,j} = \sum_{i,j=1,2} \sigma_{i,j} \quad [9]$$

For simplicity, the indexes F and B were designated by 1 and 2 respectively, where σ_{1-1} and σ_{2-2} designate the partial ionic conductivity due to $V_{O^{2-}}$ transport through

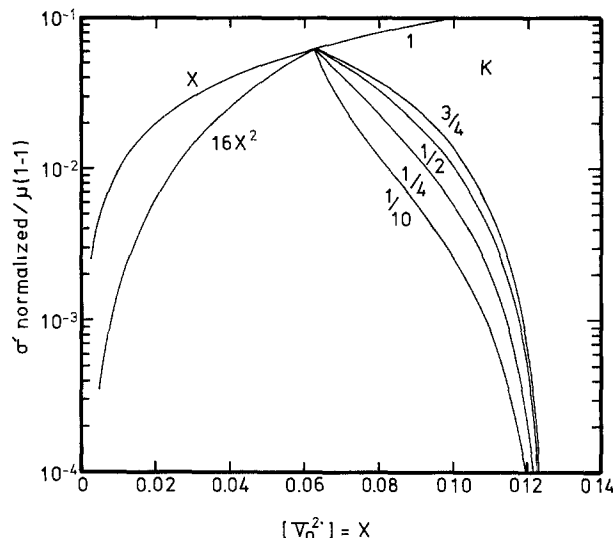


Fig. 3. Schematic variation of σ with oxygen vacancy concentration x when $V_{O^{2-}}$ transport only through Ca^{2+} -1-fold coordinated anion sublattice is assumed. Numbers beside each curve at $0.0625 \leq x \leq 0.125$ designate K values of Eq. [16].

the channels of the 1-fold Ca^{2+} coordinated and 2-fold Ca^{2+} coordinated anion sublattice, respectively, and $\sigma_{1 \rightarrow 2}$ and $\sigma_{2 \rightarrow 1}$ designate those due to $V_{O^{2-}}$ transport from 1- to 2- (or reverse) fold Ca^{2+} -coordinated anion sublattice.

Each partial ionic conductivity will be given by the following expression utilizing the usual form for hopping ionic conduction

$$\begin{aligned} \sigma'_{i,j} &= \frac{\sigma_{i,j}}{N \cdot Z \cdot e} \\ &= [V_{O^{2-}}(i)] \cdot \frac{N_j}{N_i + N_j} \cdot \left(1 - \frac{[V_{O^{2-}}(j)]}{N_j}\right) \cdot \mu_{(i,j)} \\ &= \frac{[V_{O^{2-}}(i)][O^x(j)]}{N_i + N_j} \cdot \mu_{(i,j)} \end{aligned} \quad [10]$$

where $\mu_{(i,j)}$ denotes the mobility of $V_{O^{2-}}$ for the i - j jump process. Each partial ionic conductivity $\sigma'_{i,j}$ is normalized by the numerical factor, $(N \cdot Z \cdot e)^{-1}$ from the actual ionic conductivity $\sigma_{i,j}$. In this expression N is numbers of anion sites per unit volume (cm^3), Z is valence number of $V_{O^{2-}}$, and e is the electronic charge.

From dynamic equilibria between 1- and 2-states

$$\sigma'_{1 \rightarrow 2} = \sigma'_{2 \rightarrow 1} \quad [11]$$

Combination of Eq. [4], [10], and [11] yields

$$K = \frac{\mu_{(2 \rightarrow 1)}}{\mu_{(1 \rightarrow 2)}} = \exp\left(-\frac{\Delta G^\circ}{RT}\right) \quad [12]$$

Equation [12] is the well-known relationship for chemical equilibria resulting from opposing elementary reaction processes.

Inserting Eq. [10] into Eq. [9], the final expression for the normalized total ionic conductivity of the system is obtained

$$\begin{aligned} \sigma'_{\text{normalized}} &= \frac{\sigma_{\text{total}}}{N \cdot Z \cdot e} = \sigma'_{1-1} + \sigma'_{2-2} + 2\sigma'_{2 \rightarrow 1} \\ &= [V_{O^{2-}}(1)][O^x(1)]\mu_{(1-1)} + [V_{O^{2-}}(2)][O^x(2)]\mu_{(2-2)} \\ &\quad + 2[V_{O^{2-}}(2)][O^x(1)]\mu_{(2 \rightarrow 1)} \quad (N_1 + N_2 = 1) \end{aligned} \quad [13]$$

where $[V_{O^{2-}}(i)]$ and $[O^x(i)]$ ($i = 1, 2$) are given by Eq. [6] and [8] for a given K and x .

Basic Character of Theoretical Model

We will first examine the theoretical model in more qualitative but illustrative manner. For this purpose, for mathematical simplicity, we will adopt the following approximation in this section: $[V_{O^{2-}}(i)] \ll [O^x(i)] \cong N_i$ ($i = F, B$), (which corresponds to neglecting the $(1-x)$ term in the conventional $\sigma \propto x(1-x)$ form by assuming $(1-x) \sim 1$). At this level of approximation, Eq. [3] can be easily solved to give

$$[V_{O^{2-}}(F)] = \frac{x \cdot N_F \cdot \exp(-\Delta G^\circ/RT)}{N_B + N_F \cdot \exp(-\Delta G^\circ/RT)}$$

$$= \frac{x \cdot N_F \cdot K}{N_B + N_F \cdot K}$$

$$[V_{O^{2-}}(B)] = x - [V_{O^{2-}}(F)]$$

$$= \frac{x \cdot N_B}{N_B + N_F \cdot \exp(-\Delta G^\circ/RT)} = \frac{x \cdot N_B}{N_B + N_F \cdot K} \quad [8']$$

Using Eq. [2] for N_F and N_B , and also Eq. [13] for $\sigma'_{\text{normalized}}$ the following expression for $\sigma'_{\text{normalized}}$ is obtained, valid for $0.0625 \leq x \leq 0.125$

$$\sigma'_{\text{normalized}} = \frac{\sigma_{\text{total}}}{N \cdot Z \cdot e} = \frac{x}{(16x-1) + (2-16x) \cdot K}$$

$$\times \{(2-16x)^2 \cdot K \cdot \mu_{(1-1)} + 2(2-16x)(16x-1) \cdot \mu_{(2 \rightarrow 1)} + (16x-1)^2 \mu_{(2-2)}\} \quad [14]$$

Following the same procedure, for the composition range $0 \leq x \leq 0.0625$

$$N_F = N_0 = (1-16x): (\text{Ca}^{2+}\text{-0-fold state})$$

$$N_B = N_1 = 16x: (\text{Ca}^{2+}\text{-1-fold state})$$

and

$$\sigma'_{\text{normalized}} = \frac{x}{16x + (1-16x) \cdot K'} \times \{(1-16x)^2 \cdot K' \cdot \mu_{(0-0)} + 2 \cdot (1-16x) \cdot 16x \cdot \mu_{(1 \rightarrow 0)} + (16x)^2 \cdot \mu_{(1-1)}\} \quad [15]$$

where $K' = \exp(-\Delta G^\circ/RT)$ and ΔG° designates the Gibbs free energy difference between Ca^{2+} -0-fold and 1-fold states.

When $\Delta G^\circ = \Delta G^\circ = 0$ ($K' = K = 1$), all the sites become energetically equivalent, so all the $\mu_{(i-j)}$ become equal and $\sigma'_{\text{normalized}} \propto x$ from Eq. [14] and [15].

Another interesting limiting case is the one in which ionic conduction occurs exclusively inside the channel of the Ca^{2+} -1-fold coordinated anion sublattice, (i.e., $K' \ll 1$, $\mu_{(1-1)} \gg \mu_{(0-0)}$, $\mu_{(1 \rightarrow 0)}$, $K < 1$, $\mu_{(1-1)} \gg \mu_{(2-2)}$, $\mu_{(2 \rightarrow 1)}$). In this case from Eq. [14] and [15]

$$\sigma'_{\text{normalized}} = x \cdot 16x \cdot \mu_{(1-1)}; \quad 0 \leq x \leq 0.0625$$

$$= \frac{x(2-16x)^2 \cdot \mu_{(1-1)} \cdot K}{(16x-1) + (2-16x) \cdot K}$$

$$0.0625 \leq x \leq 0.125 \quad [16]$$

Figure 3 shows $\sigma'_{\text{normalized}}/\mu_{(1-1)}$ vs. x curves using $K = \exp(-\Delta G^\circ/RT)$ as parameter. Included also is the usual curve, $\sigma \propto x$. It is apparent from this figure that if ionic conduction proceeds only via Ca^{2+} -1-fold associated ($\text{Ca}^{2+}\text{-}V_{O^{2-}}$) defect complexes, there appears a rather sharp conductivity maximum at $x = 0.0625$, and then σ decreases more rapidly, the smaller the value of K .

These features are qualitatively in fair agreement with experimental observations as shown in Fig. 1.

From Eq. [16] the maximum conductivity σ'_{max} at $x = 0.0625$ is given by

$$\sigma'_{\text{normalized(max)}} = \sigma'_{1-1}(x = 0.0625) = 0.0625\mu_{(1-1)} \quad [17]$$

However, in this approximation, according to Eq. [16] ionic conductivity becomes equal to zero at $x = 0.125$ where the Ca^{2+} -1-fold coordinated anion sublattice disappears. At this composition, only the Ca^{2+} -2-fold coordinated anion sublattice exists (see Fig. 2a), so from Eq. [14] we obtain

$$\sigma'_{\text{normalized}}(x = 0.125) = \sigma'_{2-2}(x = 0.125)$$

$$= 0.125 \cdot \mu_{(2-2)} \quad [18]$$

Equations [17] and [18] indicate that from the conductivity data at $x = 0.0625$ and 0.125 , we can obtain the mobility $\mu_{(1-1)}$ and $\mu_{(2-2)}$ inside the separate channels. Using these values of $\mu_{(1-1)}$, $\mu_{(2-2)}$, we can draw the theoretical $\log \sigma$ vs. x curves over the whole range of $0.0625 \leq x \leq 0.125$, choosing appropriate values of K and $\mu_{(2 \rightarrow 1)}$.

Numerical Evaluation of the Theoretical Model

In order to obtain mobilities $\mu_{(1-1)}$ and $\mu_{(2-2)}$, approximate values of $\sigma_{\text{total(max)}} = \sigma_{1-1}(x = 0.0625)$, and $\sigma_{\text{total}}(x = 0.125) = \sigma_{2-2}(x = 0.125)$ were read from experimental $\log \sigma$ vs. x plots shown in Fig. 1. For $x = 0.125$ which is well beyond the cubic fluorite phase so that experimental points for σ_{total} are not available, extrapolations from the data points around $x \sim 0.100$ composition were made. Moreover, the values of σ_{max} at $x = 0.0625$ and σ_{total} at $x = 0.125$, were also adjusted to get the best fit between theoretical and experimental curves in the subsequent calculations. At a given pair of such σ 's, $\mu_{(1-1)}$ and $\mu_{(2-2)}$ were calculated from Eq. [17'] and [18']

$$\sigma'_{\text{max}} = \sigma'_{1-1}(x = 0.0625) = x(1-x) \cdot \mu_{(1-1)}$$

$$= \frac{15}{16^2} \cdot \mu_{(1-1)} \quad [17']$$

$$\sigma'_{\text{total}}(x = 0.125) = \sigma'_{2-2}(x = 0.125)$$

$$= x(1-x) \cdot \mu_{(2-2)} = \frac{7}{8^2} \cdot \mu_{(2-2)} \quad [18']$$

Using these values of $\mu_{(1-1)}$ and $\mu_{(2-2)}$, and assuming approximate values of K and $\mu_{(2 \rightarrow 1)}$, the theoretical $\log \sigma$ vs. x curves were constructed at each temperature in intervals of $\Delta x = 0.005$ for $0.0625 \leq x \leq 0.125$ until the best fit to the experimental curves was obtained.

At $T = 600^\circ$ and 800°C , the best fits are already obtained without introducing $\sigma_{2 \rightarrow 1}$ terms, i.e., assuming

$\mu_{(2 \rightarrow 1)} \sim 0$, $\sigma_{2 \rightarrow 1} \sim 0$. At higher temperatures $T = 1000^\circ$, 1200° , and 1400°C , the relative contribution from the partial ionic conductivity $\sigma_{2 \rightarrow 1}$ becomes appreciable, and to obtain the best fit these contributions cannot be neglected.

Results and Discussion

The best fit theoretical curves obtained using the rigorous formula for σ_{total} (Eq. [13]) and for concentrations of the respective chemical species as given by Eq. [6] and [8] are shown in Fig. 1 as solid lines at each temperature within the composition range $0.0625 \leq x \leq 0.125$. Numbers of characteristic parameters used to construct these curves are tabulated in Tables I and II. Also included is the theoretical curve for σ_{total} for $0 \leq x \leq 0.0625$ at 1000°C when it is assumed that only σ_{1-1} contributes to the ionic conductivity: i.e.

$$\sigma'_{\text{normalized}} = \frac{\sigma_{1-1}}{N \cdot Z \cdot e} = x(16x-x) \cdot \mu_{(1-1)}$$

$$= x \cdot 15x \cdot \mu_{(1-1)}, \quad 0 \leq x \leq 0.0625 \quad [13']$$

Agreement between the theoretical curves and the experimental ones is quite satisfactory over the entire

Table I. K , σ_{\max} ($x = 0.0625$), and σ ($x = 0.125$) used to construct the theoretical curves in Fig. 1

T ($^{\circ}\text{C}$)	$\sigma_{\max} = \sigma_{1-1}$ ($x = 0.0625$) ($\Omega \cdot \text{cm}$) $^{-1}$	$\sigma_{2-2} = \sigma$ ($x = 0.125$) ($\Omega \cdot \text{cm}$) $^{-1}$	K
600	7.341×10^{-4}	5.203×10^{-6}	0.060
800	1.165×10^{-2}	4.0×10^{-4}	0.12
1000	7.013×10^{-2}	4.5×10^{-3}	0.20
1200	2.70×10^{-1}	4.2×10^{-2}	0.28
1400	6.40×10^{-1}	2.0×10^{-1}	0.37

Table II. Mobility of oxygen vacancy V_{O}^{2-} , $\mu_{V_{\text{O}}^{2-}}$ ($i - j$) ($i = 1, 2$) through and between Ca^{2+} -1-fold and Ca^{2+} -2-fold coordinated anion sublattice

T ($^{\circ}\text{C}$)	$\mu_{(1-1)}$ ($\text{cm}^2/\text{sec V}$)	$\mu_{(2-2)}$ ($\text{cm}^2/\text{sec V}$)	$\mu_{(2-1)}$ ($\text{cm}^2/\text{sec V}$)	$\mu_{(1-2)}$ ($\text{cm}^2/\text{sec V}$)
600	6.684×10^{-7}	2.507×10^{-9}	—	—
800	1.048×10^{-5}	1.927×10^{-7}	—	—
1000	6.306×10^{-5}	2.168×10^{-6}	6.500×10^{-5}	3.25×10^{-7}
1200	2.428×10^{-4}	2.024×10^{-5}	1.500×10^{-5}	5.357×10^{-5}
1400	5.756×10^{-4}	9.640×10^{-5}	7.500×10^{-5}	2.027×10^{-4}

temperature range: $600^{\circ}\text{C} \leq T \leq 1400^{\circ}\text{C}$ and the stability range of the cubic fluorite phase: $0.0625 \leq x \leq 0.10$.

Figure 4 shows Arrhenius plots of $\sigma_{i-1}(x)$ ($i = 1, 2$; $x = 0.0625, 0.125$) and $\sigma_{i-1}(x) \cdot T$ ($i = 1, 2$; $x = 0.0625, 0.125$). From this figure, we can obtain the Arrhenius equations for σ_{i-1} and $\sigma_{i-1} \cdot T$, respectively

$$\sigma_{1-1}(x = 0.0625) = \sigma_{\max} = 1.138 \cdot 10^3$$

$$\exp\left(-\frac{25.022 \text{ kcal/mole}}{RT}\right) (\Omega \cdot \text{cm})^{-1}$$

$$\sigma_{2-2}(x = 0.125) = 2.317 \cdot 10^4$$

$$\cdot \exp\left(-\frac{38.835 \text{ kcal/mole}}{RT}\right) (\Omega \cdot \text{cm})^{-1} \quad [19]$$

and

$$\sigma_{1-1}(x = 0.0625) \cdot T = \sigma_{\max} \cdot T = 4.57 \cdot 10^6$$

$$\cdot \exp\left(-\frac{27.474 \text{ kcal/mole}}{RT}\right) (\Omega \cdot \text{cm})^{-1} \cdot ^{\circ}\text{K}$$

$$\sigma_{2-2}(x = 0.125) \cdot T = 7.18 \cdot 10^7$$

$$\cdot \exp\left(-\frac{40.936 \text{ kcal/mole}}{RT}\right) (\Omega \cdot \text{cm})^{-1} \cdot ^{\circ}\text{K} \quad [20]$$

To obtain the actual value of ionic conductivity the number of charge carriers per cubic centimeter is necessary. To this end, the average lattice constant: $a_0 = 5.131 \text{ \AA}$ (1) for the nominal composition $\text{Ca}_{0.15}\text{Zr}_{0.85}\text{O}_{1.85}$ was adopted, neglecting the relatively small variation of a_0 with composition. Then

$$\sigma_{i-1}(x) \quad (i = 1, 2; x = 0.0625, 0.125)$$

$$= N \cdot Z \cdot e \cdot x(1-x) \cdot \mu_{(i-1)}$$

$$= N \cdot x(1-x) \cdot \frac{Z^2 \cdot e^2 \cdot D_{(i-1)}}{kT} \quad [21]$$

where N is the number of anion sites per cm^3 and given $N = 5.922 \times 10^{22}/\text{cm}^3$ using the above a_0 value. In the latter part of Eq. [21] the Nernst-Einstein relation was used

$$\mu_{(i-1)} = \frac{Z \cdot e \cdot D_{(i-1)}}{kT} \quad [22]$$

Combining Eq. [19], [20], and [21] leads to the Arrhenius equations for $\mu_{(i-1)}$ and $D_{(i-1)}$

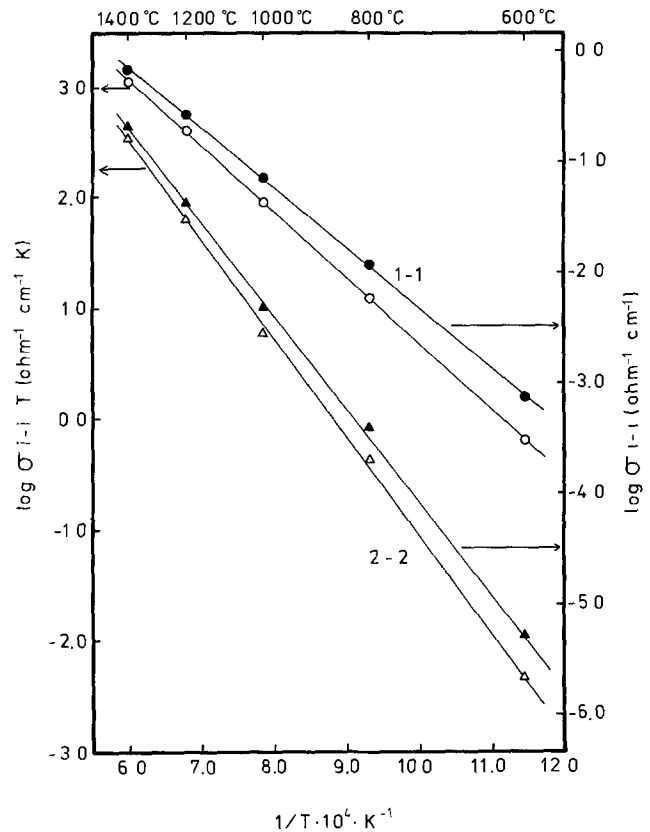


Fig. 4. $\log \sigma_{i-1}(x)$ and $\log \sigma_{i-1}(x) \cdot T$ ($x = 0.0625, 0.125, i = 1, 2$) vs. $1/T$ plots.

$$\mu_{(1-1)} = 1.19 \cdot \exp\left(-\frac{25.022 \text{ kcal/mole}}{RT}\right) \text{cm}^2 \cdot \text{sec}^{-1} \cdot \text{V}^{-1}$$

$$\mu_{(2-2)} = 1.16 \cdot 10^{11} \cdot \exp\left(-\frac{38.835 \text{ kcal/mole}}{RT}\right) \text{cm}^2 \cdot \text{sec}^{-1} \cdot \text{V}^{-1} \quad [23]$$

$$D_{(1-1)} = 1.77 \cdot 10^{-1} \cdot \exp\left(-\frac{27.474 \text{ kcal/mole}}{RT}\right) \text{cm}^2 \cdot \text{sec}^{-1}$$

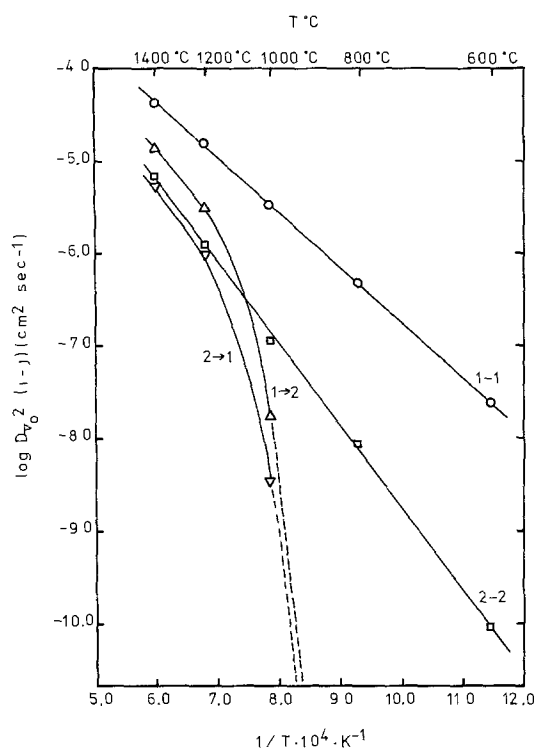
$$D_{(2-2)} = 1.49 \cdot 10^0 \cdot \exp\left(-\frac{40.936 \text{ kcal/mole}}{RT}\right) \text{cm}^2 \cdot \text{sec}^{-1} \quad [24]$$

Values of $\mu_{(i-1)}$ and $D_{(i-1)}$ are tabulated in Tables II and III, respectively, together with $\mu_{(i-j)}$ ($i \neq j = 1, 2$) and $D_{(i-j)}$, which were also used to derive the theoretical curves. To obtain $\mu_{(1-2)}$ from $\mu_{(2-1)}$ Eq. [12] and K values in Table I were used.

Figure 5 shows Arrhenius plots of the various diffusion coefficients of the oxygen vacancy $D_{(i-j)}$. From this figure it is apparent that $D_{(1-1)} \gg D_{(2-2)} \sim D_{(1-2)}$

Table III. Diffusion coefficients of oxygen vacancy V_{O}^{2-} , $D_{(i-j)}$ through and between Ca^{2+} -1-fold and Ca^{2+} -2-fold coordinated anion sublattice

T ($^{\circ}\text{C}$)	$D_{(1-1)}$ (cm^2/sec)	$D_{(2-2)}$ (cm^2/sec)	$D_{(2-1)}$ (cm^2/sec)	$D_{(1-2)}$ (cm^2/sec)
600	2.514×10^{-8}	9.429×10^{-11}	—	—
800	4.844×10^{-7}	8.910×10^{-9}	—	—
1000	3.459×10^{-6}	1.189×10^{-7}	3.565×10^{-9}	1.783×10^{-8}
1200	1.541×10^{-5}	1.284×10^{-6}	9.521×10^{-7}	3.400×10^{-6}
1400	4.149×10^{-5}	6.946×10^{-6}	5.407×10^{-6}	1.461×10^{-5}

Fig. 5. $\log D_{V_O^{2+}}(i-j)$, $(i, j = 1, 2)$ vs. $1/T$ plots

$> D_{(2 \rightarrow 1)}$ as expected. This means that diffusion of V_O^{2+} through the relatively free state (1-1) proceeds much more easily with a lower activation energy and with a higher absolute value than that through the relatively more bound state (2-2).

An interesting feature of $D_{(2 \rightarrow 1)}$ and $D_{(1 \rightarrow 2)}$ is the fact that there exists a rather sharp kink in the Arrhenius plots for $D_{(2 \rightarrow 1)}$ and $D_{(1 \rightarrow 2)}$ around and below 1000°C. Indeed, as was mentioned in the previous section, the theoretical curves at $T = 600^\circ$ and 800°C were constructed without any contribution from $\sigma_{(2 \rightarrow 1)}$, and yet shows good agreement with the experimental ones. At 1000°C, their contributions are still small but at higher temperatures $T = 1200^\circ$ and 1400°C , they become considerable. It seems premature to draw any definite conclusion concerning the origin of this phenomenon. However, it is interesting to note that even in "disordered" samples, it is often reported that there seems to exist a slight hump in the Arrhenius plots of $\log \sigma$ vs. $1/T$ above 1000°C, which becomes more apparent in the samples with higher CaO content (1, 5). Figure 6 shows the $\log K$ vs. $1/T$ plot for the chemical equilibria given by Eq. [3] and tabulated in Table I. A good straight line relationship holds for $600^\circ\text{C} \leq T \leq 1400^\circ\text{C}$. From this figure we obtain for the equilibrium constant K

$$K = \exp\left(\frac{\Delta S^\circ}{R}\right) \cdot \exp\left(-\frac{\Delta H^\circ}{RT}\right) = \exp\left(-\frac{\Delta G^\circ}{RT}\right)$$

$$= 2.7 \cdot \exp\left(-\frac{6.606 \text{ kcal/mole}}{RT}\right) \quad [4]$$

Accordingly

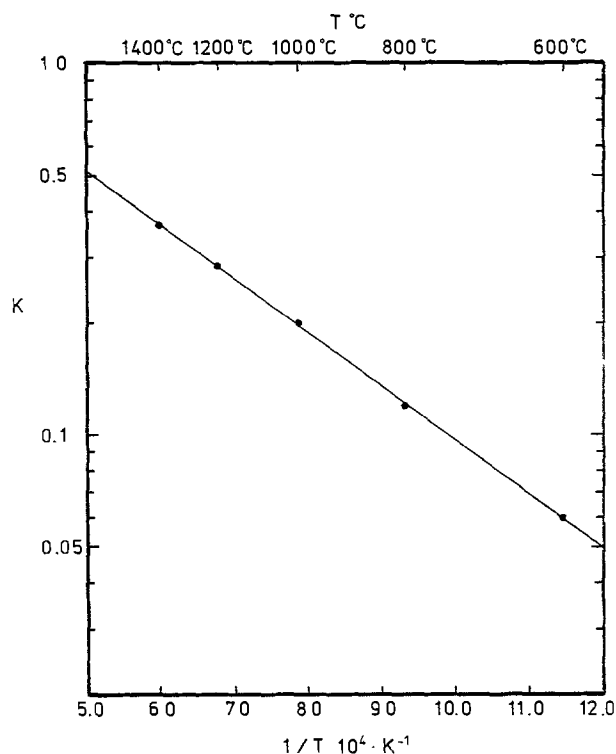
$$\Delta S^\circ = 0.993 \text{ eu} = 1.974 \text{ cal/mole } ^\circ\text{K} \sim R$$

$$\Delta H^\circ = 6.606 \text{ kcal/mole}$$

$$\Delta G^\circ = \Delta H^\circ - T\Delta S^\circ = 6.606 \times 10^3 - 1.974 \cdot T \text{ cal/mole}$$

[25]

Figure 7 shows the variations of oxygen vacancy concentrations on the Ca^{2+} -1-fold coordinated and

Fig. 6. $\log K$ vs. $1/T$ plot

Ca^{2+} -2-fold coordinated anion sublattices; V_O^{2+} (1) and V_O^{2+} (2), with total oxygen vacancy concentration $[V_O^{2+}]_{\text{total}} = x$ at 600°, 1000°, and 1400°C calculated according to Eq. [6] and [8]. Also included in Fig. 7 are the site fractions of 1- and 2-state; N_1 and N_2 . It is interesting to note that the variations of $[V_O^{2+} \cdot 1]$ and $[V_O^{2+} \cdot 2]$ with x is steepest at $x = 0.0625$ and become more gradual with increasing x . The equiconcentration point $[V_O^{2+} \cdot 1] = [V_O^{2+} \cdot 2]$ shifts to the higher x value position as temperature increases, but remains in the low x region in these temperature ranges.

Experiment shows that the activation energy for ionic conduction increases with increasing x and decreases with increasing temperature at constant x . Both features are accounted for by the present model. These follow because with increasing x , the relative contributions from $\sigma_{1 \rightarrow 2}$ and $\sigma_{2 \rightarrow 2}$ which have activation energies higher than σ_{1-1} increase, and, as shown in Fig. 7 at constant x , the higher the temperature, the higher the relative contribution from $[V_O^{2+} \cdot 1]$ and hence the contribution from σ_{1-1} , which has the lower activation energy, increases.

Oxygen diffusion measurements on this system reported so far are those by Kingery *et al.* (19), Simpson and Carter (20), and Hagel (21). References (19) and (20) report agreement of the measured oxygen diffusion coefficient $D_{O_{18}^*}$ with that calculated from ionic conductivity assuming an oxygen transport number of 1 and the correlation factor of 0.65 for the fluorite structure. In contrast, Hagel (21) obtained an oxygen diffusion coefficient $D_{O_{18}^*}$ appreciably lower than that calculated from his own conductivity data. If the ionic conduction and therefore the oxygen diffusion in this system are multimode processes as described by the present model, the penetration profile of O_{18}^* from the gas phase would not yield a curve characterized by one error function complement. Such experiments are quite difficult to carry out and, depending on the relative contributions of each mode, the result may appear to fit a single error function complement as was shown for the diffusion of sulfur in NiO by Howng and Wagner (22).

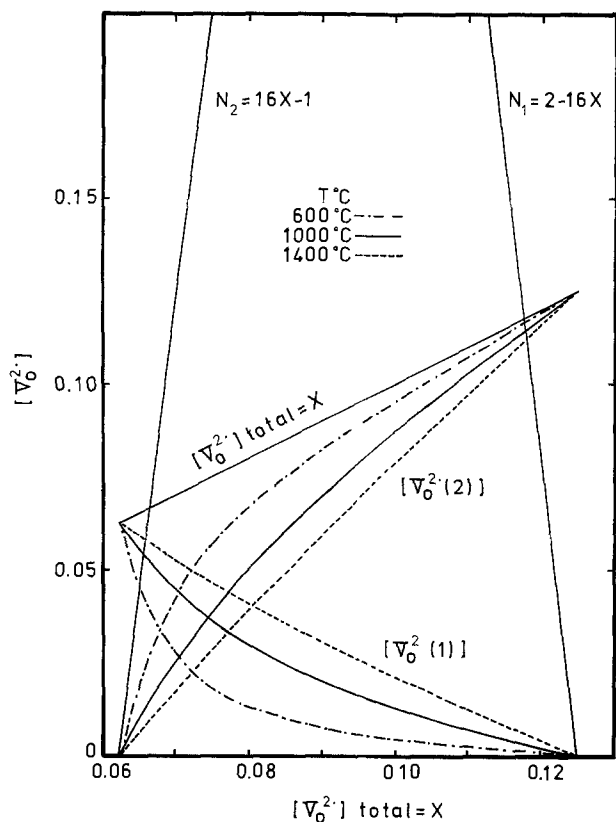


Fig. 7. Oxygen vacancy distribution between Ca^{2+} -1-fold and Ca^{2+} -2-fold coordinated anion sublattices as a function of total oxygen vacancy concentration $[\text{V}_{\text{O}^{2-}}]_{\text{total}} = x$. $T = 600^\circ, 1000^\circ, 1400^\circ\text{C}$. $[\text{V}_{\text{O}^{2-}} 1]$: oxygen vacancy concentration on Ca^{2+} -1-fold coordinated anion sublattice. $[\text{V}_{\text{O}^{2-}} 2]$: oxygen vacancy concentration of Ca^{2+} -2-fold coordinated anion sublattice. N_1 : site fraction of Ca^{2+} -1-fold coordinated anion sublattice. N_2 : site fraction of Ca^{2+} -2-fold coordinated anion sublattice.

Internal friction measurements on this system conducted by Wachtman and Corwin (23) seem to support the above speculation on the oxygen diffusion coefficient and partially substantiate our proposed theoretical model. Wachtman and Corwin observed the symmetrical peaks associated with $\text{V}_{\text{O}^{2-}}$ motion in the cubic fluorite phase region, but the peaks were too broad to result from a relaxation process with a single relaxation time. They thought that the concentrations of $\text{V}_{\text{O}^{2-}}$ and Ca^{2+} are so high that many complex groupings and/or various arrangements of Ca^{2+} and $\text{V}_{\text{O}^{2-}}$ occur which cause the various types of local $\text{V}_{\text{O}^{2-}}$ jumps and therefore a distribution of relaxation times. Their interpretation is similar to that of Kröger (10) mentioned previously.

As was shown in the foregoing, the proposed theoretical model seems to succeed to some extent in giving a quantitative character to these qualitative interpretations. The basic feature of the theoretical model is that it extends the conventional concept of dopant (impurity)-defect complex or associate for highly defective systems and shows in a straightforward way the occurrence of a maximum of the ionic conductivity and a multimode transport mechanism for these systems. However, in formulating the theoretical model, crude assumption for the effective anion site coordination number of Ca^{2+} to the second nearest neighbor (Ca^{2+} - $\text{V}_{\text{O}^{2-}}$) configuration was made. So far, our knowledge about defect interaction at the second (and the higher order) nearest neighbor configuration is quite lacking. Moreover, the statistical fluctuations of the system were also neglected. (See Eq. [2]. Even in the composition range $0.0625 \leq x \leq 0.125$, there exist also small numbers of Ca^{2+} -0-fold, 3-fold, 4-fold anion sites, which were all neglected. Also, the existence of

nonintegrally Ca^{2+} coordinated sites such as Ca^{2+} -1/3-fold, Ca^{2+} -5/3-fold anion sites were neglected.) These fluctuations would be dependent on the Ca^{2+} distribution and should be important in dealing with the order-disorder transition in this system.

Summary

A quantitative theoretical model to explain the variations of ionic conductivity of calcia-stabilized zirconia with oxygen vacancy concentration and temperature has been presented. The theory extends the conventional concept of the impurity (dopant)-defect complex or associate for highly defective systems and shows that ionic conduction in this system proceeds by a multimode mechanism: Eq. [13]. The theory predicts the occurrence of a rather sharp maximum of ionic conductivity at oxygen vacancy concentration $x \sim 0.0625$ (12.5 m/o CaO), at which the entire anion sublattice is just covered by onefold associated (Ca^{2+} - $\text{V}_{\text{O}^{2-}}$) complexes, in accordance with experimental observations.

Values of characteristic parameters such as the diffusion coefficients and mobilities of oxygen vacancies $\text{V}_{\text{O}^{2-}}$ through and between 1-fold and 2-fold Ca^{2+} coordinated anion sublattice; $D_{(i-j)}$, $\mu_{(i-j)}$, and the equilibrium constant K for the distribution of oxide ions and oxygen vacancies between 1-fold and 2-fold Ca^{2+} coordinated anion sublattice were obtained by a curve-fitting procedure of the theoretical expression for ionic conductivity to experimental $\sigma(x, T)$ data reported in the literature. Resultant theoretical curves of isothermal $\log \sigma$ vs. oxygen vacancy concentration x , inside the stability region of the cubic fluorite phase $0.0625 \leq x \leq 0.10$ and $600^\circ\text{C} \leq T^\circ\text{C} \leq 1400^\circ\text{C}$ were shown to reproduce satisfactorily the experimental curves reported by various investigators.

Acknowledgment

This research was sponsored by the United States Army Research Office under Contract DAAG 29-78-G-0032.

Manuscript submitted Dec. 14, 1979; revised manuscript received April 30, 1980. This was Paper 53 presented at the St. Louis, Missouri, Meeting of the Society, May 11-16, 1980.

Any discussion of this paper will appear in a Discussion Section to be published in the June 1981 JOURNAL. All discussions for the June 1981 Discussion Section should be submitted by Feb. 1, 1981.

Publication costs of this article were assisted by Arizona State University.

REFERENCES

1. See comprehensive review by T. H. Etsell and S. N. Flengas on these subjects; i.e., T. H. Etsell and S. N. Flengas, *Chem. Rev.*, **70**, 339 (1970).
2. D. W. Strickler and W. G. Carlson, *J. Am. Ceram. Soc.*, **47**, 122 (1964).
3. T. Y. Tien, *ibid.*, **47**, 430 (1964).
4. J. M. Dixon, L. D. LaGrange, U. Merten, C. F. Miller, and J. T. Porter, II, *This Journal*, **110**, 276 (1963).
5. T. Y. Tien and E. C. Subbarao, *J. Chem. Phys.*, **39**, 1041 (1963).
6. R. E. W. Casselton, *Phys. Status Solidi A*, **2**, 571 (1970).
7. M. F. Lasker and R. A. Rapp, *Z. Phys. Chem. N.F.*, **49**, 198 (1966).
8. R. N. Blumenthal, F. S. Brugner, and J. E. Garnier, *This Journal*, **120**, 1230 (1973).
9. D. W. Strickler and W. G. Carlson, *J. Am. Ceram. Soc.*, **48**, 286 (1965).
10. F. A. Kröger, *ibid.*, **49**, 215 (1966).
11. M. O'Keefe, in "Chemistry of the Extended Defects in Non-Metallic Solids," L. Eyring and M. O'Keefe, Editors, p. 609, North Holland Publishing Co., Amsterdam (1970).
12. W. W. Barker and O. Knop, *Proc. Br. Ceram. Soc.*, **19**, 15 (1971).
13. A. Hammou, *J. Chim. Phys.*, **72**, 439 (1975).

14. A. B. Lidiard, *Phys. Rev.*, **94**, 29 (1954).
15. H. Schmalzried, *Z. Phys. Chem., N.F.*, **105**, 47 (1977).
16. R. E. Carter and W. L. Roth, in "Electromotive Force Measurements in High Temperature Systems," C. B. Alcock, Editor, p. 125, I.M.M., London (1968).
17. E. C. Subbarao and P. H. Sutter, *J. Phys. Chem. Solids*, **25**, 148 (1964).
18. J. S. Anderson, in "Problems of Nonstoichiometry," A. Rabenau, Editor, p. 1, American Elsevier Publishing Co., New York (1970).
19. W. D. Kingery, J. Pappis, M. E. Doty, and D. C. Hill, *J. Am. Ceram. Soc.*, **42**, 393 (1959).
20. L. A. Simpson and R. E. Carter, *ibid.*, **49**, 139 (1966).
21. W. C. Hagel, *This Journal*, **110**, 63C (1963), quoted in Ref. (20).
22. W. Y. Hwang and J. B. Wagner, Jr., *J. Phys. Chem. Solids*, **39**, 1019 (1978).
23. J. B. Wachtman, Jr. and W. G. Corwin, *J. Res. Natl. Bur. Stand.*, **A69**, 457 (1965).

Thermal Decomposition of LiSCN-Containing Lithium Battery Electrolyte

B. M. L. Rao* and G. E. Milliman

Advanced Energy Systems Laboratory, Exxon Research and Engineering Company, Linden, New Jersey 07036

ABSTRACT

Thermal decomposition of LiSCN in 1:3-dioxolane was investigated to understand the safety aspects in its usage as an electrolyte for ambient temperature, high energy density organic electrolyte cells. TGA and direct combustion techniques were used in the studies. Attention was given to assess the volatile hydrogen cyanide content in the decomposition products, because of a possible toxic hazard. The results indicated that the thermal decomposition of LiSCN at 650°C in air formed 0.01 weight percent (w/o) volatile cyanide, presumably due to impurities. However, the presence of moisture and/or the solvent (1:3-dioxolane) enhanced the extent of cyanide generation to 0.5-1.5 w/o. Based on the results, caution is recommended in dealing with thermal runaway conditions.

In electrolyte development efforts for ambient temperature, high energy density lithium batteries, many lithium salts and organic solvents combinations have been explored. This area of electrochemical research has been recently reviewed by Basenhard and Eichinger (1). Compatibility of the electrolyte components with the electrode materials on stand and under operating conditions, electrolyte conductivity, and cost considerations have played an important role in this venture. Recently, increased attention is being given to safety and environmental impact aspects, as required. This paper deals with a safety-related investigation on the thermal decomposition of LiSCN·1.3-dioxolane electrolyte developed for use in ambient temperature rechargeable lithium cells (2, 3). It was carried out to assess the possible release of toxic cyanide fumes during thermal runaway conditions that may be encountered in the manufacture (e.g., welding operations), in storage (cell shorting, warehouse fire, etc.), in service (i.e., high current or high voltage conditions), and during disposal (i.e., incineration) of the batteries.

LiSCN is a pseudohalide. It is reported (4) to undergo decomposition in a solid state near its melting point of 237°C. Lee (5) indicates <1 weight percent (w/o) decomposition in air at 400°C, from thermogravimetric analysis. Although decomposition products are not obvious from these experiments alkali thiocyanates are known to release cyanide and hydrogen cyanide, among other products, during reactions with hydrogen or metals in fused salt media.

Lithium thiocyanate is highly soluble (>4.5 moles/liter) in 1:3-dioxolane. An electrolyte composition with 2.0-3.0 moles/liter LiSCN in 1:3-dioxolane with $2-3 \times 10^{-3} (\Omega \cdot \text{cm})^{-1}$ specific conductivity (23°C) was investigated in Li/TiS₂ cells (3) and, as such, has been the subject of safety interest of this work. The present

study was carried out because of the low flash point of the cyclic ether solvent (13°C) and the associated combustion possibilities.

Experimental and Results

Thermogravimetric analysis.—Anhydrous LiSCN forms a monosolvate upon recrystallization from 1:3-dioxolane. As solvent loss from leaky cells, or thermal conditions, prior to electrolyte combustion are likely to result in this compound, initial experiments were performed using thermogravimetric analysis (TGA) on monosolvate prior to detailed studies on thermal decomposition. TGA data for the anhydrous LiSCN 1:3-dioxolane monosolvate carried out in air and dry nitrogen are given in Fig. 1.

Procedures for the thermal decomposition.—Thermal decomposition experiments were performed in a tube furnace setup, shown in Fig. 2. Test samples were weighed into combustion boats, placed in the tube furnace (shown in Fig. 2), heated to 600°-650°C in the course of an hour, held at the maximum temperature for 2 hr, and then gradually cooled to room temperature in 3-5 hr. During this procedure, dry or moist air was passed to ensure combustion and to flush the gaseous effluents into absorber traps of 100 ml, 1M NaOH, provided for cyanide analysis.

Procedure for cyanide analysis.—The measurement of cyanide in aqueous sodium hydroxide solutions was accomplished in two ways. If the cyanide content of the absorber solutions was sufficiently high, >25 μg CN⁻/ml, the solutions could be potentiometrically titrated with 0.005M Ag⁺, using a Metrohm Model E-536 automatic recording titrator equipped with Metrohm EA-107 glass and EA-275 silver electrodes to the equivalence point corresponding to Ag⁺ + 2CN⁻ → Ag(CN)₂⁻. If the cyanide content of the absorber solutions was <25 μg CN⁻/ml, the cyanide was measured using an Orion Model 94-06 cyanide-ion selective

* Electrochemical Society Active Member.

Key words: organic electrolyte, safety, HCN formation, LiSCN dioxolane, cyanide analysis.

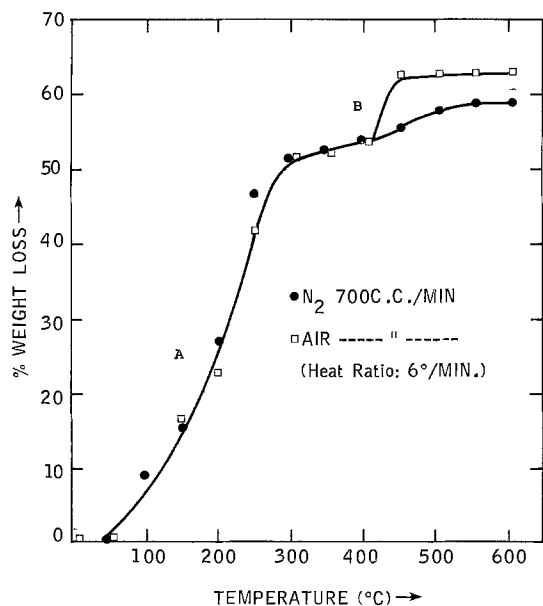


Fig. 1. Thermogravimetric analysis of LiSCN-dioxolane monosolvate.

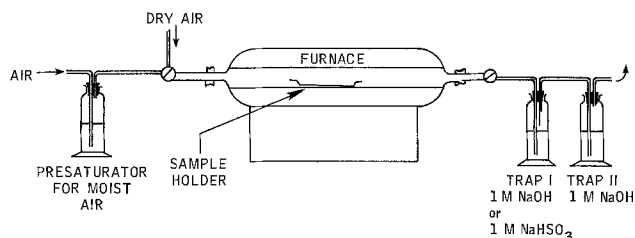


Fig. 2. Schematic of combustion arrangement

electrode, an Orion Model 90-01 single-junction reference electrode, and an Orion Model 801-A Digital Ion-analyzer. The Ionalyzer was calibrated using solutions containing between 0.05 and 5 $\mu\text{g CN}^-/\text{ml}$, obtained by dilutions of a 1000 $\mu\text{g CN}^-/\text{ml}$ solution, prepared from potassium cyanide in 0.5M NaOH, with 0.5M NaOH. The cyanide content of the absorber traps was adjusted to calibration range by dilution with water or NaOH solution, so that the solution which was used for measurement was 0.5M in NaOH. Since sulfide could possibly arise from the degradation of LiSCN and traces of sulfide interfere with the measurement of cyanide using the cyanide electrode, the absorber solutions were treated to ensure the absence of sulfide prior to cyanide measurements. This was accomplished by the addition of a small amount of cadmium carbonate to the solutions and the subsequent removal of cadmium sulfide and excess cadmium carbonate and/or cadmium hydroxide by filtration.

Thermal decomposition of anhydrous LiSCN.—Results of cyanide determination in the scrubbing solution obtained from thermal decomposition in anhydrous

LiSCN, using the above procedure, is provided in Table I.

Thermal decomposition of 3M LiSCN in 1:3-dioxolane.—During potentiometric determination of cyanide in the scrubbing solutions from thermal decomposition of 3M LiSCN in 1:3-dioxolane, an erratic behavior of potential between the ion-selective electrode and the reference electrode was encountered. The establishment of steady rest potential took an inordinately long time, and there was a memory effect when electrodes were placed in subsequent solutions. This behavior had not previously been encountered during measurement of cyanide in NaOH solutions. It was hypothesized that this behavior was caused by formaldehyde, formed by the decomposition of dioxolane (6), reacting directly with the silver bromide sensing element of the cyanide electrode, or complicating the system via formation of a formaldehyde-cyanide complex. The removal of the formaldehyde was accomplished by the addition of an NaHSO_3 scrubber to the absorption train in front of the NaOH scrubber. Both the ion selective electrode and the potentiometric titration procedures were used for cyanide analysis in some of the NaOH absorption traps. The results obtained by the two independent procedures, given in Table I, are in excellent agreement.

Discussion

TGA data for LiSCN:1:3-dioxolane monosolvate, given in Fig. 1, indicate weight loss in regions A and B. These regions correspond to loss of solvent from the monosolvate and the thermal decomposition of LiSCN, respectively. This is based on the estimate which indicates a 53% weight loss due to solvent from LiSCN 1:3-dioxolane monosolvate, which appears to be complete in region A (Fig. 1) independent of carrier gas. Thermal decomposition of anhydrous LiSCN ensues in region B, with increased weight loss in air compared to nitrogen. Lee (5) indicates <1% decomposition for LiSCN below 400°C.

Data in Table I indicate that the quantity of volatile cyanide, *i.e.*, HCN, generated by the anhydrous LiSCN in dry air, is low (<0.01 w/o), as expected. However, the decomposition of anhydrous salt in moist air enhances the amount of volatile cyanide released to 0.4 w/o, a fortyfold increase over the amount of cyanide released in dry air. The electrolyte, *i.e.*, 3M LiSCN, 1:3-dioxolane solution, yields volatile cyanide, both in the absence and presence of moisture, with the latter yielding 1.5 w/o decomposition of LiSCN to cyanide.

It is seen, from the data in Table I, and the amount of cyanide in the solid residue, that the quantity of cyanide generated from 10 ml of 3M LiSCN 1:3-dioxolane solution, under the experimental conditions, is low (< $5 \times 10^{-3}\text{g}$). Although HCN is a combustible gas, its escape to the environment presents a potential hazard, because of its toxicity. It is to be noted that relatively large amounts of HCN may be produced by incomplete combustion of certain nitrogen-containing materials, such as wool, silk, urethane, polyamide, and acrylics. Established safety procedures, as in these cases, may be applicable to handling of combustion incidents involving the LiSCN-1:3-dioxolane electrolyte.

Table I. Thermal decomposition of LiSCN electrolyte and cyanide analysis

Material	Quantity of LiSCN combusted (g)	Combustion condition	CN ⁻ determined (g) by		% LiSCN decomposition to CN ⁻
			Sp. ion	Ag ⁺ titration	
10 ml 3M LiSCN in dioxolane	1.95	Dry air 650°C, ~2 hr	3.7×10^{-3}	3.5×10^{-3}	0.45-0.47
		Moist air 650°C, ~2 hr	11.2×10^{-3}	11.1×10^{-3}	1.42-1.43
LiSCN anhydrous	1.95	Dry air 650°C, ~2 hr	2.4×10^{-6}	—	3×10^{-6}
		Moist air 650°C, ~2 hr	3.1×10^{-3}	—	0.4

The degree of sophistication of precautions would depend on the quantity of electrolyte involved. Appropriate safety experts need to be consulted in this regard.

Acknowledgment

The authors wish to acknowledge the participation of Mr. M. T. Vidnansky in carrying out the combustion experiments.

Manuscript submitted March 28, 1980; revised manuscript received May 5, 1980.

Any discussion of this paper will appear in a Discussion Section to be published in the June 1981 JOURNAL. All discussions for the June 1981 Discussion Section should be submitted by Feb. 1, 1981.

Publication costs of this article were assisted by Exxon Research and Engineering Company.

REFERENCES

1. G. Eichinger and J. O. Besenhard, *J. Electroanal. Chem. Interfacial Electrochem.*, **72**, 1 (1976).
2. B. M. L. Rao, U.S. Pat. 4,192,912 (1980).
3. B. M. L. Rao, D. J. Eustace, and J. A. Shropshire, Submitted to *J. Appl. Electrochem.*
4. "Analytical Chemistry of Sulfur and Its Compounds," J. H. Karchner, Editor, Wiley-Interscience, New York (1970).
5. D. A. Lee, *Inorg. Chem.*, **3**, 289 (1966).
6. W. B. Guenther and W. D. Walters, *J. Am. Chem. Soc.*, **73**, 2127 (1951).

Hydrogen Evolution and Zinc Nodular Growth in the Zinc Chloride Battery

Dennis Kralik*¹ and Jacob Jorne*

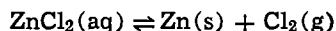
Department of Chemical Engineering, Wayne State University, Detroit, Michigan 48202

ABSTRACT

The problem of hydrogen evolution in the zinc chloride battery is investigated experimentally with special respect to the magnitude of the phenomenon under various ZnCl_2 and supporting electrolyte concentrations, pH, current density, and electrolyte purity. Metallic impurities of low hydrogen overvoltage can be responsible for accelerated hydrogen evolution during charge and discharge. In addition, the morphology and porosity of the zinc deposit and the presence of dendrites affect the magnitude of hydrogen evolution. Low hydrogen evolution rates are observed on rough and dendritic deposits and vice versa. Two methods of decreasing hydrogen evolution are presented: (i) pretreatment of the ZnCl_2 electrolyte with zinc particles, and (ii) potentiostatic deposition of metallic impurities in flow-through porous-graphite electrode above the zinc deposition potential.

Hydrogen evolution in the zinc chloride battery results in two disadvantages: (i) the hydrogen formed may react explosively with chlorine (1), and (ii) hydrogen evolution represents a coulombic inefficiency during both the charge and discharge processes.

In our experiments a single zinc chloride cell was used. The cell, shown in Fig. 1, consists of a dense graphite electrode on which zinc is deposited, and a porous flow-through graphite electrode on which chlorine is evolved. In the actual battery, the chlorine is then stored as chlorine hydrate. The overall reactions of the battery are



$$x \sim 5.9$$

Hydrogen evolution on electrodeposited zinc can be caused by two mechanisms: (i) corrosion of zinc, i.e., anodic dissolution of zinc accompanied by simultaneous hydrogen evolution, the so-called local cell action, and (ii) cathodic hydrogen evolution (electrochemically) during zinc deposition. The net result of these two mechanisms is identical. Hydrogen evolution on pure zinc is very low (the exchange current density is in the range of 10^{-10} A/cm²). However, the presence of metallic impurities such as iron, copper, chromium, vanadium, arsenic, and germanium, even at the ppm level, in the solution and consequently in the zinc de-

posit can cause a dramatic increase in hydrogen evolution by creating local cells (2). It is assumed in the present work that the increased hydrogen evolution is caused by the presence of impurity ions in the solution and, consequently, in the zinc deposit. Attempts to determine the origin of the impurities identify the degradation of the graphite chlorine electrode as the source of contamination leading to hydrogen evolution (3). Several metallic impurities are found capable of causing considerable hydrogen evolution. Antimony is probably the most detrimental impurity tested. At the

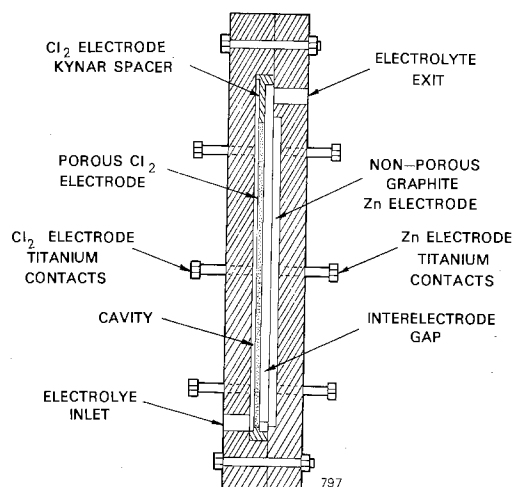


Fig. 1. Schematic cross section of the zinc chloride single cell

* Electrochemical Society Active Member.

¹ Present address: Diamond Shamrock Corp., Painesville, Ohio.
Key words: zinc, chlorine, impurities, zinc chloride, dendrite, roughness.

1 mg/liter level, cobalt, germanium, nickel, and tin also cause considerable hydrogen evolution (3). Surprisingly, arsenic is not observed to be a catalyst for hydrogen evolution on zinc (3), as indicated by others (2).

Experimental

Hydrogen evolution was measured volumetrically in acidic zinc chloride solutions, as shown in Fig. 2. The evolved hydrogen was collected in inverted burettes which were placed above the zinc cathode, zinc anode, and reference zinc. All the zinc plates were obtained in the single cell by electrodeposition from various $ZnCl_2$ solutions which were prepared by direct reaction of chlorine gas and pure zinc in aqueous solution. The zinc deposits were peeled gently off the graphite substrate, washed thoroughly, dried, and weighed. The single cell was made of Kynar by Energy Development Associates, Madison Heights, Michigan.

The apparent active area of the electrode was 68 cm^2 , the total current was 3A, and the charging process lasted for 1-2 hr. The experimental setup is shown in Fig. 3. A 2.5 liter $ZnCl_2$ (2m) solution was circulated through a flowmeter and the cell using a Kynar pump with a Teflon gear. The evolved chlorine was stripped during the charging by nitrogen bubbling throughout the experiment. Prior to each experiment, the pH was adjusted by adding HCl and nitrogen was bubbled to remove oxygen and remaining dissolved chlorine. The charging time was adjusted so that the amount of electricity was always the same: 0.080 Ahr/ cm^2 . No additives or leveling agents have been used.

Hydrogen evolution was investigated in acidified zinc chloride solutions, with and without sodium chloride or potassium chloride supporting electrolytes. The magnitude of the hydrogen evolution was measured under various conditions, such as zinc chloride concentration, electrolyte purity, supporting electrolyte, current density, and pH.

Two methods for the removal of metallic impurities were used: the first method consisted of suspension of

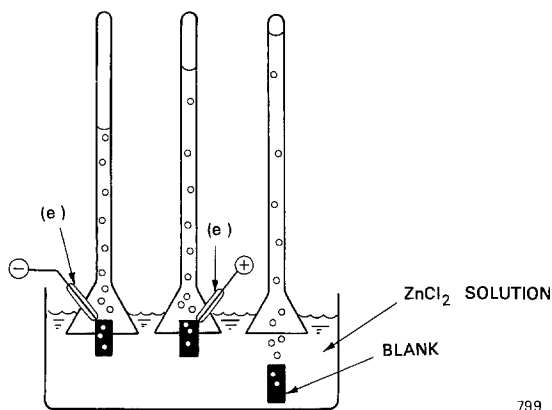


Fig. 2. Apparatus for measuring the volume of hydrogen evolved. (e.) = Epoxy coating.

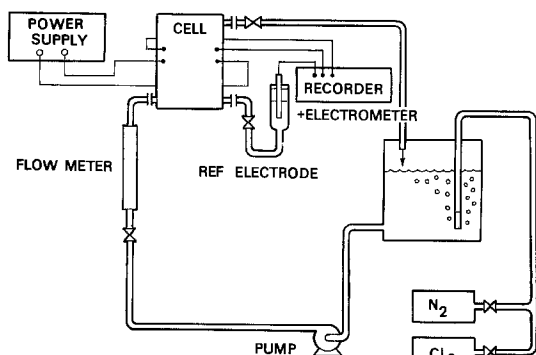


Fig. 3. The experimental apparatus of the zinc chloride single cell.

zinc pieces in zinc chloride solution. Since impurities are ions of more noble metals than zinc, they should deposit on the zinc particles suspended in the electrolyte. This method is referred to as zinc pretreatment. The second method consisted of a potentiostatic removal of impurities in a flow-through porous graphite electrode held above the zinc deposition potential ($-0.76V$). The impurity ions were cathodically electrodeposited on the porous graphite cathode and removed from the solution. Because of the low concentration of impurities, it is believed that their removal was mass transfer limited. The counterelectrode consisted of zinc deposit on a nonporous graphite substrate and was prepared by charging the zinc chloride single cell. Under this arrangement chlorine was absent and could not react with the deposited impurities.

Results and Discussion

Hydrogen evolution from potentiostatically treated zinc chloride solution was much lower than from untreated solution as can be seen in Fig. 4. Figure 5 shows the rates of hydrogen evolution for zinc anode, zinc cathode, and reference zinc in zinc-treated and untreated 2m $ZnCl_2$ + 4m KCl solution. Pretreatment with zinc pieces resulted in a decrease of hydrogen evolution for all cases. The hydrogen evolution rate increased with time on the cathode as can be seen from the slope of the curve, while it decreased with time on the anode. This is due to the fact that the surface of the cathode became increasingly rougher due to zinc deposition, while the surface of the anode became smoother during the electrodisolution. The cathodic area increased with time, and consequently the rate of hydrogen evolution is increased on the zinc cathode while decreased on the zinc anode. The rate of hydrogen evolution on the reference zinc is lower than the rate on the zinc anode, although it is expected that the zinc anode is becoming progressively smoother through electrodisolution. This apparent contradiction probably is due to the fact that the deposition rate of the impurities is mass transfer limited and is enhanced by the natural convection at the anode.

The effects of the current density on the hydrogen evolution, on the apparent density of the deposit, and on the coulombic efficiency are shown in Fig. 6. The nodular growth increased as the current density was increased, in accord with the prediction that a higher

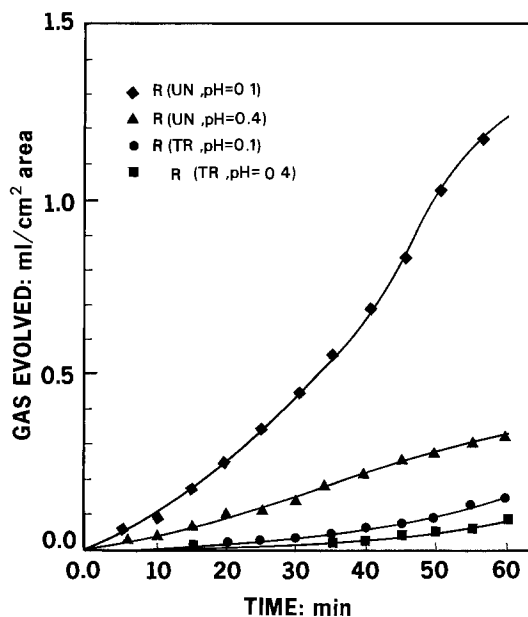


Fig. 4. Hydrogen evolution in potentiostatically treated solution containing 2m $ZnCl_2$. Only the reference zinc is presented. Current density $i = 40 mA/cm^2$. R = reference zinc, UN = untreated solution, TR = treated solution.

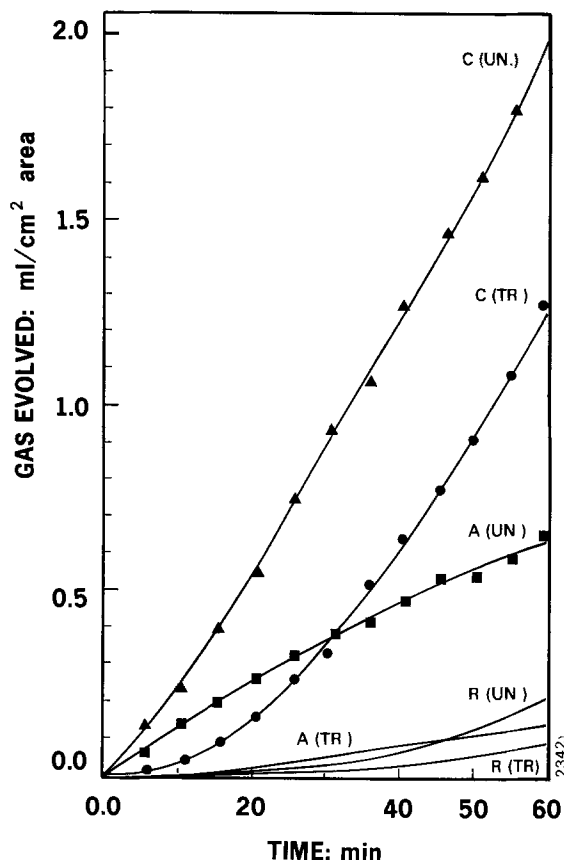


Fig. 5. Hydrogen evolution from zinc pretreated solution containing 2m $ZnCl_2$ + 4m KCl . pH = 0.4; current density: $i = 40$ mA/cm². C = cathode zinc, A = anode zinc, R = reference zinc, UN = untreated solution, TR = treated solution.

current density at the nodular tips promotes their growth. As a result, the apparent densities (weight per apparent unit volume) of the deposits decreased with increasing the current density.

On the other hand, the hydrogen evolution rate increased with increasing current density since the higher the current density, the larger the actual surface area of the deposit available for hydrogen evolution. By increasing the current density the deposition

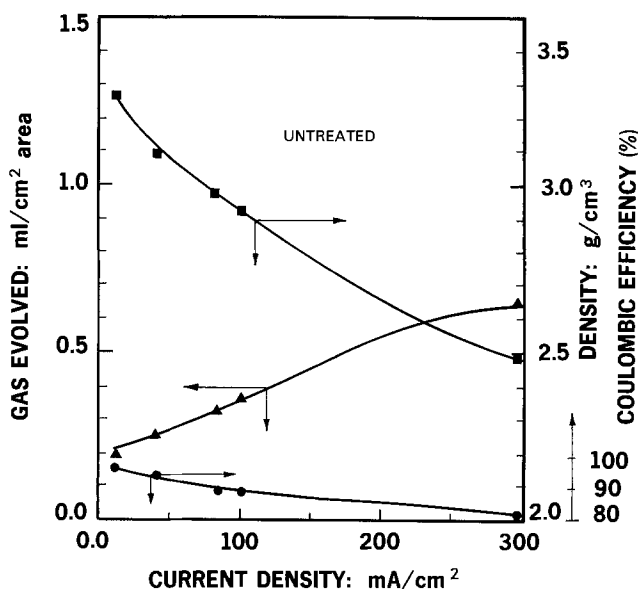


Fig. 6. Effect of current density on hydrogen evolution and on the apparent density of zinc deposits. Gas evolution is presented for the reference zinc after 40 min. Electrolyte: 0.6m $ZnCl_2$ + 2.0m $NaCl$ + 2.0m KCl . pH = 0.1, untreated.

rate of the zinc ions increases, while the deposition rate of the impurities remains constant because it is mass transfer limited. Since the impurity ion concentration is several orders of magnitude smaller than the zinc ion concentration, it is very probable that the surface of the rapidly growing zinc nodules is kept clean because adsorbed impurity atoms are buried as fast as they reach the surface. So the only reason for increased hydrogen evolution rate is the increased surface area of the zinc deposit.

Figure 7 shows the dependence of hydrogen evolution on the pH of the solution. All the zinc deposits were prepared in untreated 2m $ZnCl_2$ solution, pH = 0.1. However, the hydrogen evolution tests were repeated in 2m $ZnCl_2$ solutions of pH = 0.1 and 0.4. Higher hydrogen evolution rates can be observed on the cathode, anode, and reference zinc at pH = 0.1, as expected. The rates of hydrogen evolution are lower on the reference zinc in comparison to the zinc anode. This behavior is probably due to the smoothing of the anode through electrodisolution. An opposite trend is shown in Fig. 5 and is believed to be due to natural convection at the anode. However, the data of Fig. 8 were obtained in treated solution and in the absence of impurities in the solution. In all the experiments the rate of hydrogen evolution decreased with time on the anode and increased with time on the cathode, again, probably due to the smoothing of the anode and the roughening of the cathode.

The presence of sodium chloride and potassium chloride as supporting electrolytes generally decreased the rate of hydrogen evolution as shown in Fig. 8. A qualitative correlation was found between the rate of hydrogen evolution and the morphology of the zinc deposit. Nodular zinc was obtained at high zinc chloride concentration. When the zinc chloride concentration was reduced from 2.0 to 0.2m, the nodular growth was eliminated and the rate of hydrogen evolution increased substantially.

Figure 9 summarizes the results on reference zinc and shows that as the zinc chloride concentration decreases, the apparent density of the deposit increases (nodules are eliminated), and hydrogen evolution is increased. In addition, the coulombic efficiency of zinc deposition starts to decrease as the zinc chloride con-

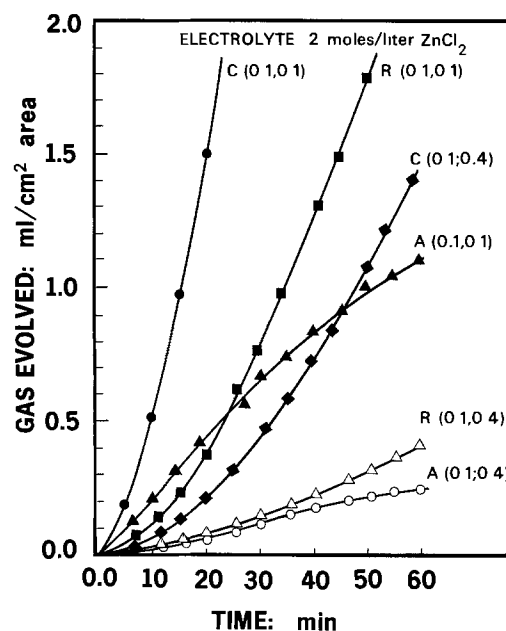


Fig. 7. Effect of pH on hydrogen evolution. First index refers to pH of deposition, second index to pH of hydrogen evolution test. Deposits were obtained from untreated 2m $ZnCl_2$ solution, and hydrogen evolution tests were performed in zinc-treated solution. Current density: $i = 40$ mA/cm². C = cathode zinc; A = anode zinc; R = reference zinc.

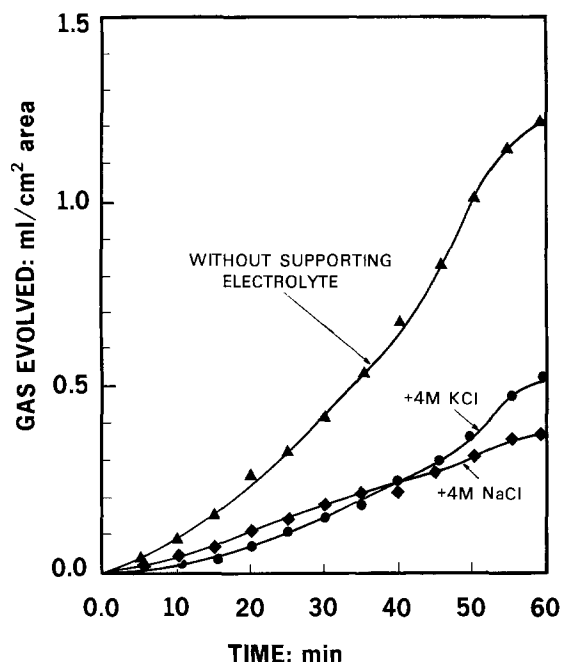


Fig. 8. Effect of supporting electrolytes on hydrogen evolution. Electrolyte: 2m $ZnCl_2$; pH = 0.1; current density: $i = 40$ mA/cm². Electrode: reference zinc prepared in untreated solution.

centration drops below 0.6m; the current density is 40 mA/cm² and zinc deposition becomes partially mass transfer limited. Since it is believed that the source of impurities is the slow degradation of the graphite chlorine electrode (3), the concentration of the impurities is not proportional to the zinc chloride concentration.

The critical current density (I_c) and the minimum concentration of zinc ions (C_m) required for nodular growth can be estimated according to the theory of Price, Vermilyea, and Webb (4). According to this

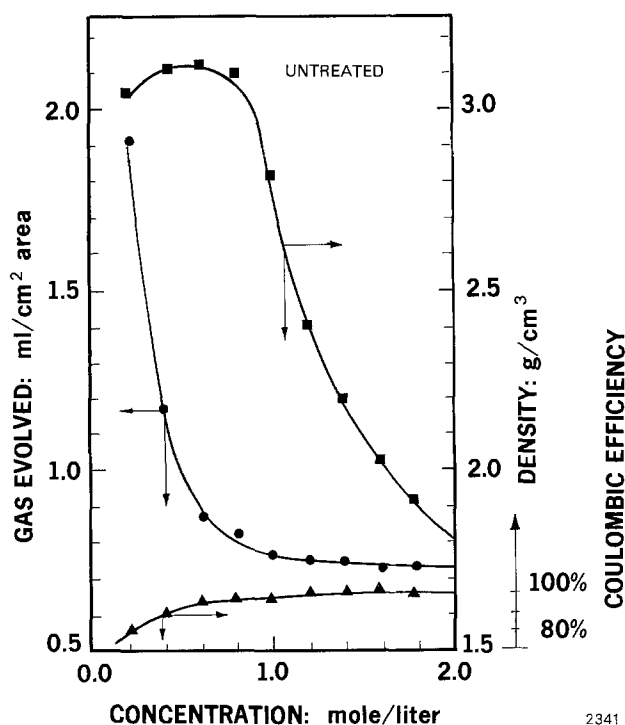


Fig. 9. Effect of zinc chloride concentration on hydrogen evolution and on the apparent density of the deposit. Zinc chloride solutions without supporting electrolyte. pH = 0.1; current density: $i = 40$ mA/cm². Hydrogen evolution is presented on reference zinc after 40 min.

theory impurity atoms adsorb on the surface of a growing crystal and interfere with the motion of lattice steps over the surface. When the concentration of impurity atoms adsorbed on the surface is above a critical value depending on the overvoltage, step motion is completely blocked and no further growth of the crystal occurs. A critical radius for the curvatures of the steps can be estimated, given by the following equation

$$\rho_c = \frac{\delta}{\Delta G_v} \quad [1]$$

where δ is the edge energy of the step per unit area and ΔG_v is the free energy decrease per unit volume (ΔG_v is proportional to the supersaturation or overvoltage). It is assumed that a strongly adsorbed particle can prevent the part of the step with which it is in contact from moving. When a section of a step encounters two adsorbed particles which are closer together than $2\rho_c$ it cannot advance past the particles because in so doing the radius of curvature of a portion of the step would become less than ρ_c . Hence, if the average distance between particles adsorbed on the surface is greater than $2\rho_c$ the steps will be able to advance freely, while at greater coverages the growth of the crystal may be entirely prevented (4). In other words, if the impurity ion concentration is high in the solution and consequently on the surface of the growing zinc crystals, two adsorbed neighboring impurity atoms will be closer to each other than $2\rho_c$, thus the zinc crystals will not be able to grow, and the nodular growth will be prevented. This case results in a smooth zinc deposit possessing a high surface concentration of impurity atoms, thus yielding a high hydrogen evolution rate.

On the other hand, when the impurity concentration is low, two adsorbed impurity atoms will be further apart on the zinc surface than $2\rho_c$, thus the steps of the nodular growth can advance freely. In this case the impurity atoms adsorbed on the rapidly growing surface will be incorporated into the crystal as lattice steps move around and past them. Finally, the result is a rough, nodular zinc deposit with a low surface concentration of impurity atoms yielding a low hydrogen evolution rate.

A significant prediction of the theory of Price, Vermilyea, and Webb (4) is that there is a critical current density for the continued growth of a metal crystal in a solution containing impurity ions. At the critical current density there is a balance between the rate of diffusion of impurity ions to the zinc surface and the rate of their incorporation into the crystal. The equation for the critical current density for a spherical crystal of a given metal and for a given metal ion concentration and temperature is (4)

$$I_c = \text{const.} \left(\frac{C_1}{r} \right)^{1/3} \quad [2]$$

where C_1 is the concentration of impurity ions in the $ZnCl_2$ solution and r is the radius of the growing zinc crystal. The above equation is valid for crystals with radii less than about 10 μm .

The minimum concentration of zinc ions for nodular growth is given by (4)

$$C_m = \frac{I_c r}{ZFD_{Zn}} \quad [3]$$

where Z is the valency of zinc ion, and D_{Zn} is the diffusivity of zinc ion, $D_{Zn} \sim 10^{-5}$ cm²/sec.

According to these equations, a zinc ion concentration below approximately 0.06m $ZnCl_2$ and a current density below approximately 240 mA/cm² are needed to prevent nodular growth. Below this concentration the diffusion of zinc ions to the nodular tips is too slow, the nodular growth ceases, and a denser zinc deposit is obtained.

When the zinc chloride concentration was reduced from 2.0 to 0.2M the nodular growth became mass transfer limited. When zinc was deposited from 0.2M $ZnCl_2$ solution the impurities, in spite of their reduced concentration, reached the surface faster than they could be buried, thus the smooth surface possessed relatively high surface concentration of impurity atoms and yielded a high hydrogen evolution rate.

Figure 10 shows the zinc nodules developed during cathodic deposition from 1.85M zinc chloride $pH = 0.5$ untreated solution. The crystalline structure of the nodules and the layers formed by the steps during crystal growth are clearly visible. One can even roughly estimate the radii of the nodular tips at approximately $10 \mu m$.

Figures 11 and 12 show zinc surfaces deposited from the same 1.23M zinc chloride $pH = 0.7$ untreated solution. The surface, exposed to anodic dissolution, reveals the fine structures of the nodules. At the greater enlargement, the sizes of the steps and the radius of the nodular tip can be estimated with acceptable accuracy. Figure 11 shows an almost perfect zinc crystal not yet destroyed by anodic dissolution. In Fig. 12, the single nodule and its crystals are partially exposed by anodic dissolution, thus revealing the steps, in reversed chronological succession, by which the impurity ions were embedded in the crystals of the nodules.

In conclusion, relatively low hydrogen evolution is observed on rough and nodular zinc deposits. Higher hydrogen evolution is observed on smooth and dense deposits which are obtained from $ZnCl_2$ solutions of low concentration. Both zinc pretreatment and potentiostatic removal of impurities are effective methods in reducing the rate of hydrogen evolution on zinc in acidic $ZnCl_2$ solutions. Both methods were successful in reducing the hydrogen evolution rate to a low level below 1 mA/cm^2 which corresponds to less than 2.5% current inefficiency.

The source of impurities is believed to be the graphite of the flow-through porous electrode (3). The nature of the impurities is not verified, however, traces of antimony, cobalt, germanium, nickel, and tin can cause considerable hydrogen evolution even at the ppm range. In order to achieve a smooth zinc deposit, free of dendrites, and low hydrogen evolution, a search should be made for a cationic leveling agent which

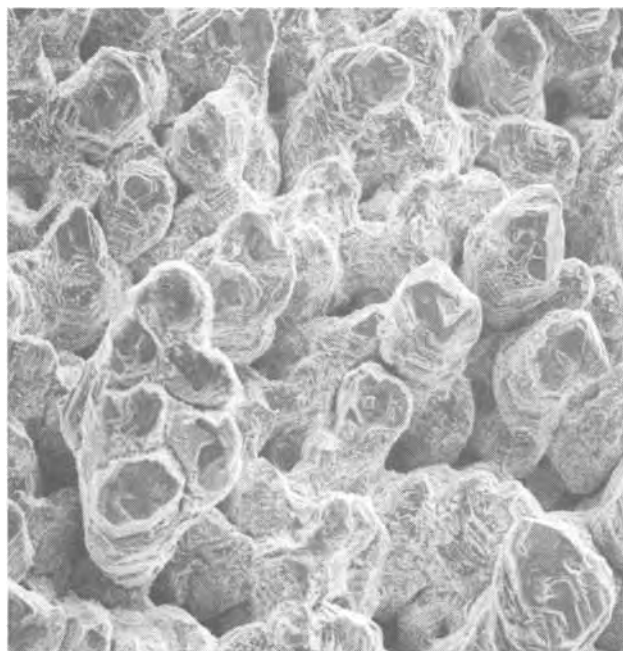


Fig. 10. Scanning electron micrograph of zinc surface. Deposited from 1.85M $ZnCl_2$; $pH = 0.5$, untreated solution, with no supporting electrolyte. Surface was formed by cathodic deposition. $i = 40 \text{ mA/cm}^2$. $200\times$.

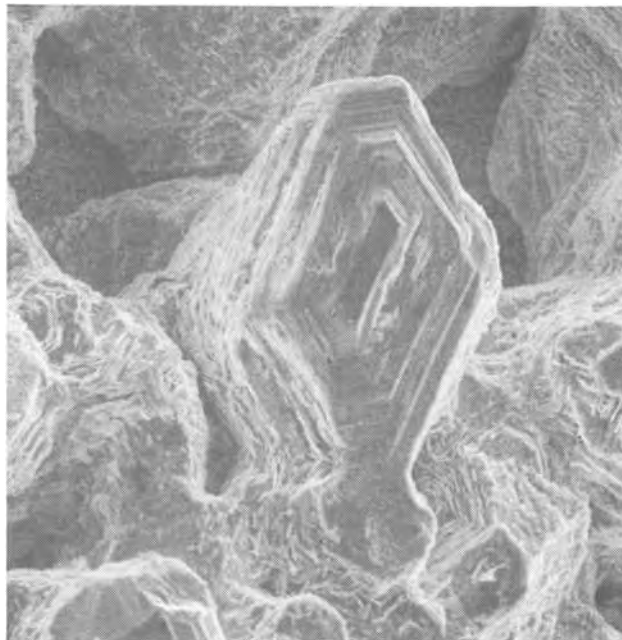


Fig. 11. Scanning electron micrograph of a zinc crystal. Deposited from 1.23M $ZnCl_2$, $pH = 0.7$, untreated solution, with no supporting electrolyte. Surface was exposed by anodic dissolution. $i = 40 \text{ mA/cm}^2$. $400\times$.

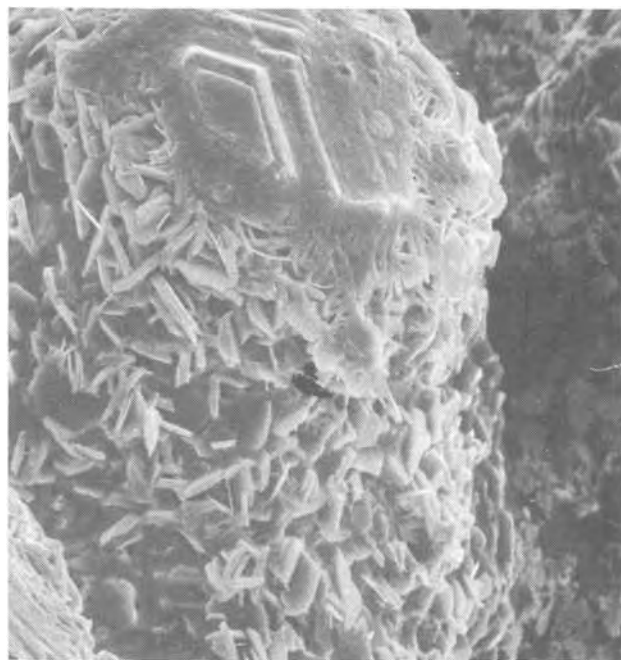


Fig. 12. Scanning electron micrograph of a dissolving zinc nodule. Deposited from 1.23M $ZnCl_2$ solution. Surface was exposed by anodic dissolution. $i = 40 \text{ mA/cm}^2$. $1000\times$.

exhibits high overvoltage for hydrogen evolution. In addition, the $ZnCl_2$ solutions should be purified by zinc pretreatment or potentiostatic pretreatment in order to remove metallic impurities.

Acknowledgments

This work was partially supported by Energy Development Associates, a Gulf+Western Company, and the Electric Power Research Institute. The work was carried out in partial fulfillment of the requirements for the M.S. degree in Chemical Engineering, Wayne State University, Detroit, Michigan, 1978.

Manuscript submitted Feb. 29, 1980; revised manuscript received May 23, 1980.

Any discussion of this paper will appear in a Discussion Section to be published in the June 1981 JOURNAL. All discussions for the June 1981 Discussion Section should be submitted by Feb. 1, 1981.

Publication costs of this article were assisted by Wayne State University.

REFERENCES

1. W. C. Eichelberger and W. M. Hartford, *Electro-*

chem. Technol., 5, 104 (1967).

2. R. C. Kerby and T. R. Ingraham, *Can. Mines Br., Res. Rep. R. 243*, 35 pp. (1971).

3. "Development of the Zinc-Chlorine Battery for Utility Applications," Palo Alto, Calif.: Electric Power Research Institute, April 1979. EM-1051, pp. 37-8-16.

4. P. B. Price, D. A. Vermilyea, and M. B. Webb, *Acta Metall.*, 6, 524 (1958).

Kinetics of Electroless Copper Plating

IV. Empirical Rate Law for H₂CO-EDTA Baths

Francis M. Donahue, K. L. M. Wong,¹ and R. Bhalla

Department of Chemical Engineering, The University of Michigan, Ann Arbor, Michigan 48109

ABSTRACT

Data for H₂CO-EDTA electroless copper plating baths were correlated by

$$\tau_p = 2.81 \frac{[\text{Cu}^{2+}]^{0.43} [\text{HCHO}]^{0.16}}{[\text{OH}^-]^{0.70} [\text{EDTA}]^{0.04}} \exp \left[11.5 \frac{(T - 313)}{T} \right]$$

This rate law was compared with published data for EDTA and Rochelle salt baths. Mass transport effects and/or substrate catalytic activity were shown to explain some of the differences among the various authors.

In recent years the kinetics of electroless copper plating have been well studied. Shippey and Donahue (1) and El-Raghy and Abo-Salama (2), examining solutions with Rochelle salt as the ligand, and Molenaar, Holdrinet, and van Beek (3), with EDTA, determined complete rate laws for their plating baths. Dumesic, Koutsky, and Chapman (4) and Saranov, Bulatov, and Mokrushin (5) obtained reaction orders for some or all of the solution species, but did not determine the rate constant. Although Goldie (6) did not determine any of the components of the rate law, sufficient data were reported for the partial evaluation of a rate law. Schoenberg demonstrated the effects of pH (7) and organic additives (8), but determined no components of the rate law.

Dumesic and co-workers (4), using a rotating cylinder in order to achieve a well-defined forced convection condition, have shown that variations in the mass transfer coefficient affect the value of the apparent reaction order for cupric ion. Donahue (9), noting that most studies of electroless plating have been performed in the absence of traditional forced convection conditions, has shown that a well-defined (if nonuniform) mass transport condition exists due to the hydrogen gas evolved during the plating reaction. He ascribed differences in the apparent reaction orders for cupric ion in the literature to the effects of mass transport.

This paper will present data for EDTA baths and determine an empirical rate law from these data. Further, since this work represents the seventh published study leading to, at least, partial rate laws, it is now possible to compare the results obtained by the various authors and to evaluate the common and unique properties of the empirical rate laws which have been reported.

Experimental

The principal features of the experimental arrangement and procedure have been given elsewhere (1, 10). Ethylenedinitroacetate anion (EDTA) was the ligand.

¹ Present address: BASF Wyandotte Corporation, Pigments Division, Holland, Michigan 49423.

Key words: catalytic properties, electroless copper plating, kinetics, mass transport, rate laws.

The bath was not agitated and had a volume of 200 ml (this assured that less than 0.5% of the copper in solution would be consumed in the normal plating process). Plate thickness measurements were taken at 5 min intervals (the 1/2 in. plastic tubing was replaced by 6 mm glass tubing with a substantial decrease of the mass of the resistance probe; this permitted relatively fast thermal equilibrium of the reference leg with the solution).

Plating rates were determined from linear regressions of plate thickness-time data when the measured mixed potentials were essentially constant. Reaction orders were determined from linear regressions of the appropriate log plating rate-log concentration data (1). The specific rate constant was determined by solving

$$k = \frac{\tau_p}{[\text{Cu}^{2+}]^a [\text{OH}^-]^b [\text{HCHO}]^c [\text{EDTA}]^d} \quad [1]$$

for each of the data sets rather than the "intercept" method proposed previously (1).²

Results

The data for the plating baths are given in Table I. The rate law parameters computed from the data are summarized in Table II. The low correlation coefficients for the reaction orders of HCHO and EDTA reflect the uncertainties associated with the reported values.

The empirical rate law is

$$\tau_p = 2.81 \frac{[\text{Cu}^{2+}]^{0.43} [\text{HCHO}]^{0.16}}{[\text{OH}^-]^{0.70} [\text{EDTA}]^{0.04}} \exp \left(11.5 \frac{(T - 313)}{T} \right) \quad [2]$$

Approximately 90% of the measured plating rates were within 20% of the predicted values.

² The method employed here gives equal weighting to all experiments while the intercept method can create a bias depending upon the number of experiments used to compute the respective reaction orders.

Table I. Data for electroless plating baths

System No.	[Cu ²⁺] (M)	[OH ⁻] (M)	[H ₂ CO] (M)	[EDTA] (M)	t (°C)	$\frac{-\psi_0}{\text{mV vs. SCE}}$	r _p (μm/hr)
1	0.05	0.25	0.33	0.14	30	725	1.46
						725	1.17
2	0.01	0.25	0.33	0.14	40	857	0.68
						860	1.04
						855	0.91
3	0.025	0.25	0.33	0.14	40	774	1.58
						797	1.66
4	0.05	0.25	0.33	0.14	40	782	1.69
						730	1.80
						725	2.18
						727	1.72
						736	2.11
5	0.10	0.25	0.33	0.14	40	663	2.36
						666	2.36
						681	3.00
						661	2.11
6	0.05	0.125	0.33	0.14	40	694	2.49
						697	3.68
						684	3.48
7	0.05	0.375	0.33	0.14	40	748	1.19
						744	1.79
						742	1.52
8	0.05	0.25	0.16	0.14	40	734	1.75
						733	1.25
						732	1.28
9	0.05	0.25	0.65	0.14	40	728	1.72
						714	1.33
						710	2.38
10	0.05	0.25	0.33	0.07	40	712	2.02
						728	1.98
						718	1.54
11	0.05	0.25	0.33	0.28	40	729	1.63
						730	1.71
						727	1.84
12	0.05	0.25	0.33	0.14	50	738	2.64
						721	2.28
						709	2.71
13	0.05	0.25	0.33	0.14	60	729	4.24

Table II. Rate law parameters

Specific rate constant at 40°C:	$2.81 \frac{\mu\text{m M}^{0.15}}{\text{hr}}$	(0.48)*
Reaction orders		
Cu ²⁺ :	0.43	(0.93)**
OH ⁻ :	-0.70	(-0.90)**
HCHO:	0.16	(0.41)**
EDTA:	-0.04	(-0.22)**
Activation energy:	7.2 kcal/mole	(0.95)**

* Standard deviation.

** Correlation coefficient.

Discussion

It is evident that sufficient kinetics studies of electroless copper plating have been performed to permit some generalizations to be made concerning the empirical rate law. The reaction orders for bath components from published works are summarized in Table III. These data represent two different ligands, *i.e.*, Rochelle salt (1, 2, 5, 6) and EDTA (3, 4), with copper sulfate, formaldehyde, and sodium hydroxide as the other bath components.

The role of mass transport in the apparent reaction orders of cupric ion has been discussed elsewhere (9). It is sufficient to note that, if the computed interfacial concentrations are used to evaluate the reaction order,

Table III. Summary of reaction orders for electroless copper plating

Reference No.	Cu ²⁺	OH ⁻	H ₂ CO	Ligand
(1)	0.47	0.18	0.07	—
(2)	0.37	0.08	0.25	0.19
(5)	0.6	—	0.2	—
(6)*	0.36	0.74	0.04	0.09
(3)	0.78	<0.02	0.13	<0.02
(4)**	1.0	0.37	0.0	—
This work	0.43	-0.70	0.16	-0.04

* Partial analysis of "strong" solutions.

** "Final deposition rate" of 0 rpm.

the differences among the various reactions for cupric ion are substantially diminished, and the reaction order has a value of approximately 0.3. Further, the higher the reaction order (based on bulk concentrations), the greater is the effect of mass transport. It has also been shown that the other bath components are generally insensitive to mass transport effects.

Schoenberg (7) has shown that an optimum pH exists for electroless copper plating. This observation is supported if the summary for EDTA baths is taken as a unit. Dumesic and co-workers (4) obtained a positive reaction order for hydroxide while the results of this work showed a negative reaction order. Molenaar and co-workers (3), with the highest plating rates of the set, obtained a reaction order of approximately zero. Therefore, this summary reflects the transition from a rate increase with increasing hydroxide concentration through a maximum to a region where the rate decreases with increasing hydroxide concentration. However, since the pH's of these solutions were all similar, it is evident that the substrate plays some role in this "optimum pH" phenomenon. The data for Rochelle salt baths are also consistent with an optimum pH, but are less convincing since no negative reaction orders have been reported.

The reaction order of the ligand, where evaluated, is seen to be very small and more or less independent of its chemical nature. Similarly, the reaction order of formaldehyde is also low.

These generalizations concerning the reaction orders of the bath components, while demonstrating a degree of unity among published rate studies, have underlined essential differences among them which, in all likelihood, cannot be resolved. These points are (i) the catalytic properties of the surface on which the deposition occurs, and (ii) the effects of mass transport on the apparent specific rate constant and the apparent reaction order for cupric ion.

Because each of the authors used a particular method of measuring the plating rate (five different methods were used by the authors cited), the substrates on which plating was performed (two different classes of substrates were used, *i.e.*, metal and sensitized non-conductors) probably possessed different initial morphologies and, depending on the plating rates, which could have changed during the plating process [*e.g.*, note the "initial" and "final" rates of Dumesic and co-workers (4)]. Therefore, one intuitively that all of the authors studied the plating rate of the electroless copper process on surfaces with different catalytic (or electrocatalytic) properties. This could explain the fact that large differences in plating rates have been reported for similar baths, *e.g.*, compare Shippey (1) with El-Raghy (2) and Goldie (6). Since no method of defining the catalytic properties of the surface is available and the suggestion that differences exist *a posteriori*, the question cannot be resolved.

The effects of mass transport are also intimately associated with the previous question of catalytic properties of the surface. If an interfacial reaction is slow (*i.e.*, the surface has a low catalytic activity), mass transport effects are usually small.³ The previous remarks about the apparent low reactivity of the surfaces in the studies of El-Raghy (2) and Goldie (6) and the comment of Donahue (9) that "... Goldie and El-Raghy evidently were operating in a region where mass transfer effects were minimal..." would tend to support this argument. Molenaar (3) and Dumesic (4), where mass transfer effects were large (9), were probably operating with highly catalytic surfaces. The role of mass transport of cupric ion and its effect on the apparent reaction order have been adequately treated elsewhere (9), but, from these comments, it is evident that these effects cannot be assayed adequately until the experiments have been completed. Simi-

³ This assumes, of course, that the concentration of reactant is not particularly low.

larly, the apparent specific rate constant is strongly influenced (see Eq. [1]) by both the concentration (interfacial or bulk) and the apparent reaction order ("interfacial" or "bulk") of cupric ion used in the computation.

The remarks given to this point in this "Discussion" have been aimed at understanding the unity among published rate studies and attempting to resolve the differences which exist. In conclusion, it seems appropriate to focus on the reasons for the diverse results and on the nature and purpose of empirical rate laws. An empirical rate law is a mathematical description of data obtained for a collection of plating baths. To the extent that the rate computations and concentration measurements are correct and the procedure (1) is followed, the empirical rate law is a valuable descriptor of the process under consideration. Thus, if one wants to ascertain the optimum plating bath composition,⁴ the rate law can be used (11) provided the mass transport conditions are not changed in the transition from laboratory to plant, the sample preparation procedure is not changed and concentrations of bath components are interpolated (not extrapolated) in the computations. Therefore, given our present knowledge of the nature of the electroless plating process and the uncertainties associated with the substrate-mass transport interactions, it is to be expected that different sample preparation procedures will lead to different rate laws.

Conclusions

Kinetics studies of Cu^{2+} -HCHO-EDTA baths have resulted in an empirical rate law. This rate law has been compared with those for other EDTA baths, and the resulting analysis has shown that mass transport of cupric ion plays some role in all baths, an apparent optimum hydroxide ion concentration exists (which, however, depends on the nature of the substrate) and formaldehyde and EDTA have low reaction orders. Similar conclusions were drawn for Rochelle salt baths.

The interaction between substrate catalytic activity and mass transport were discussed, but no resolution of these effects for published rate studies seems feasible at this time.

⁴This optimization is based on kinetic considerations only. A complete optimization would have to consider "extra-kinetic" properties of the deposit such as morphology, ductility, adhesion, etc.

The utility and limitations of empirical rate laws were discussed.

Acknowledgment

This material is based upon work supported by the National Science Foundation under Grant No. ENG 7511869.

Manuscript submitted July 20, 1979; revised manuscript received May 30, 1980.

Any discussion of this paper will appear in a Discussion Section to be published in the June 1981 JOURNAL. All discussions for the June 1981 Discussion Section should be submitted by Feb. 1, 1981.

Publication costs of this article were assisted by the National Science Foundation.

LIST OF SYMBOLS

a	reaction order for cupric ion
b	reaction order for hydroxide ion
c	reaction order for formaldehyde
d	reaction order for EDTA
k	specific rate constant, $\mu\text{m M}^{0.15}/\text{hr}$
r_p	plating rate, $\mu\text{m}/\text{hr}$
T	temperature, $^{\circ}\text{K}$
[]	concentration, M

REFERENCES

1. F. L. Shippey and F. M. Donahue, *Plating*, **60**, 43 (1973).
2. S. M. El-Raghy and A. A. Abo-Salama, *This Journal*, **126**, 1/1 (1979).
3. A. Molenaar, M. F. E. Holdrinet, and L. K. H. van Beek, *Plating*, **61**, 238 (1974).
4. J. Dumesic, J. A. Koutsky, and T. W. Chapman, *This Journal*, **121**, 1405 (1974).
5. E. I. Saranov, N. K. Bulatov, and S. G. Mokrushin, *Protection of Metals* (English translation of *Zashchita Metallov*), **4**, 142 (1968).
6. W. Goldie, *Plating*, **51**, 1069 (1964).
7. L. N. Schoenberg, *This Journal*, **118**, 1571 (1971).
8. L. N. Schoenberg, *ibid.*, **119**, 1491 (1972).
9. F. M. Donahue, *ibid.*, **127**, 51 (1980).
10. F. L. Shippey, C. U. Yu, and F. M. Donahue, *Plating*, **59**, 762 (1972).
11. F. M. Donahue, Paper 167 presented at The Electrochemical Society Meeting, Pittsburgh, Pa., Oct. 15-20, 1978.

An Electron Diffraction Study on Mixed PdCl₂/SnCl₂ Catalysts for Electroless Plating

Tetsuya Osaka* and Hideaki Nagasaka

Department of Applied Chemistry, Waseda University, Okubo, Shinjuku-ku, Tokyo 160, Japan

and Fumio Goto

Nippon Electric Company, Limited, Memory Research Laboratory,
Basic Technology Research Laboratories, Miyazaki, Takatsu-ku, Kawasaki 213, Japan

ABSTRACT

The activated or catalyzed surface conditions for initiating electroless metal deposition were studied by means of transmission electron microscopy and electron diffraction analysis. Four mixed PdCl₂/SnCl₂ catalysts, including two commercial samples, and five accelerators (NaOH, HCl, H₂SO₄, NH₄OH, and NH₄BF₄) were used in this study. The acceleration with NaOH gave the finest remaining particles which were almost bare active nuclei, while the acceleration with ammonate group (NH₄OH and NH₄BF₄) coagulated small particles to produce high density particles. The electron diffraction patterns after activation, for the catalysts prepared in our laboratory, showed amorphous broad diffraction rings which were explained as fcc structure, while for the commercial catalysts, they showed relatively sharp and netlike profiles which could be attributed to orthorhombic structure. The electron diffraction patterns after acceleration with NaOH became the sharper profiles of fcc structure, however in the case of ammonate group, they showed the complicated profiles of non-fcc structure. Finally the catalytically active sites or nuclei are discussed.

There have been two groups of investigations of the PdCl₂/SnCl₂ catalyst solution initiating electroless plating onto nonmetallic substrates, namely, to focus on whether the catalytic activity is due to Pd-Sn solute complexes or to the presence of colloidal particles in the catalyst solution. Matijević *et al.* (1) concluded that colloidal particles in solution exhibit catalytic activity on the basis of colloid science measurements. The present authors (2) also showed the colloidal states to be active by photospectroscopy (u.v. and vl) and electron microscopy. The final active sites initiating metal deposition have been discussed with some results of electron diffraction (3, 4), Mössbauer (5), and Rutherford scattering spectroscopies (6). By electron diffraction analysis Feldstein *et al.* (3) showed the fcc diffraction patterns which were due to Pd₃Sn. Cohen *et al.* (5) using Mössbauer spectroscopy constructed a model in which the colloidal particles consist of Pd-Sn alloy core with a stabilizing layer of adsorbed Sn(II) ions. Meek (6) indicated from Rutherford scattering measurement that the Pd/Sn ratio becomes (\lesssim) 1 after activation and ≈ 3 after acceleration and finally ≈ 6 at the initial stage of copper plating. The present authors (2) derived the conclusion from x-ray photoelectron spectroscopy that the Pd/Sn ratio after acceleration depends on the catalyst activity and that it is less than unity. In this communication, we will discuss the surface conditions of Pd-Sn particles on the substrate revealed by electron diffraction study and also investigate the acceleration effect on surface conditions.

Experimental

Three samples of PdCl₂/SnCl₂ catalysts which were employed in the previous study (2) and the commercial sample "F" were used and the detailed preparations and compositions were previously shown in Ref. (2). The sample "A" (low catalytic activity) and "D" (high catalytic activity) were prepared in our laboratory with reference to some patents and

Matijević's experiments (1). Sample "E" (Hitachi Kasei Company HS-101B) and "F" (Shipley Company Cataposit No. 44) were used as typical commercial samples (cf. Table I). Sample "F" is one of the salty catalysts using NaCl instead of HCl. Five accelerators (1M NaOH, 6M HCl, 1.12M H₂SO₄, 1M NH₄OH, and 1M NH₄BF₄) were used for the test of acceleration effect. The catalyst activity and the acceleration effect were tested with mixed potential measurements in an electroless nickel plating bath (composition and conditions: NiCl₂·6H₂O 29.4 g/l, malonic acid 20 g/liter, L-aspartic acid 21.0 g/liter, demethylamine borane 3.54 g/liter, pH 9.5 adjusted with NH₄OH, bath temperature 70°C). All solutions were prepared with reagent grade chemicals and doubly distilled water. The immersion time was 3 min for activation and acceleration processes, respectively. A water rinse step was added between each step of pretreatment for electroless plating. Copper wire and collodion film were adopted as substrates for mixed potential measurements and transmission electron microscopy. Electron microscopy measurements were made using a JEOL JEM-7A instrument with a 100 kV electron source. Electron diffraction patterns were analyzed with reference to the instrumental factor determined by a standard sample of evaporated gold.

Results and Discussion

Acceleration effect on catalyst functionality.—The mixed potential measurement in the plating bath was proposed to investigate the functionality of catalysts in the previous paper (2), and it was shown that the catalyst activity order corresponds to the reverse order of the induction time (i.e., initiation time of electroless plating after immersion of copper wire). The induction time can be easily determined from the drastic change of the mixed potential of copper wire. Table II shows the induction time measured in the Ni-B electroless plating bath. The activity order of catalyst solutions, previously shown in Ref. (2), is A < D < E, and the salty catalyst "F" is situated in position between "A" and "D". The reason that the commercial sample "F" has lower activity can be attributed to the increase

* Electrochemical Society Active Member.

Key words: electroless plating, mixed PdCl₂/SnCl₂ catalyst.

Table I. Compositions of mixed PdCl₂/SnCl₂ Catalyst solutions

Sample name	A	D	E	F
PdCl ₂ (g)	1	1	HS101B 60 ml	Cataposit No. 44 30 ml
SnCl ₂ ·2H ₂ O (g)	22	50	—	Cataprep No. 404 270g
Conc. HCl (ml)	60	300	320	—
Water (ml)	to 1000	600	620	840

of charged metal atoms which is caused by the usage of salt instead of HCl (cf. the later discussion). The accelerators NaOH and HCl are more active than the others. Although the differences are not so clear, the order of catalyst activity after acceleration is NaOH \approx HCl > NH₄BF₄ > NH₄OH > H₂SO₄. Rantell and Holtzman (4a) found a similar order of NaOH > NH₄HF₄ > H₂SO₄, while the deterioration of catalytic activity through prolonged treatment in the case of acid group accelerators, which was pointed out by Rantell and Holtzman, was not so clearly noticed in our experiments.

Transmission electron microscopy.—The activated surface conditions were investigated by transmission electron microscopy using collodion film. The colloidal particle sizes of catalysts "A", "D", and "E" adsorbed on collodion films, which were previously discussed in Ref. (2), were uneven particles of several tens Å or less, more uniformly patches of 400 ~ 700 Å particles, and uniformly high density particles 300 ~ 600 Å in diameter. The salty catalyst "F" gives uniform distribution with colloid sizes 300 ~ 400 Å in diameter similar to that of "E." Typical examples after the acceleration process using "D" with several accelerators are demonstrated in Fig. 1. The appearance after acceleration can be classified into three groups (NaOH, H₂SO₄; HCl; NH₄OH, NH₄BF₄). Sodium hydroxide strips the surface layers most effectively,

Table II. Effect of acceleration on induction time in electroless Ni-B plating bath (sec)

Acti- vator	Accel- erator				
	NaOH	HCl	H ₂ SO ₄	NH ₄ OH	NH ₄ BF ₄
A	2.4	2.6	3.6	3.3	2.9
D	0.7	1.0	1.3	1.3	1.5
E	1.0	1.1	1.5	1.4	1.0
F	2.0	1.9	3.7	2.2	3.6

and the finest remaining particles seem to be almost bare active nuclei after removing stannous and stannic oxides or hydroxides. Sulfuric acid also strips the surface particles but it is clear from the larger remaining particle sizes that the acceleration action of H₂SO₄ is lower than that of NaOH. With HCl accelerator the remaining particles become smaller and uniform particle contribution of several tens Å particles. In the case of NH₄OH or NH₄BF₄, it is shown that the acceleration process coagulates the small particles to produce high density particles. Since it is confirmed by the electrochemical potential sweep technique as shown in Ref. (2) that the acceleration with NH₄BF₄ clearly removes adsorbed Sn, leaving Pd nuclei on gold, it may be concluded that the coagulating particles whose diameters become larger than those after activation do not consist of Sn oxides or hydroxides but ammonate compounds such as Pd-ammonia complexes which are produced by chemical reactions. Rantell and Holtzman (4b) reported phenomena similar to those with ammonate accelerators, that the catalyst particle sizes become larger after acceleration with NH₄HF₄ on ABS surfaces, and they discussed the formation of Pd(NH₃)₄²⁺ complex in the case of ammonium hydroxide. Thus, it is concluded from the electron microscopy observation that the catalyst activity after acceleration is affected not only by the catalytic grain density and size but also by

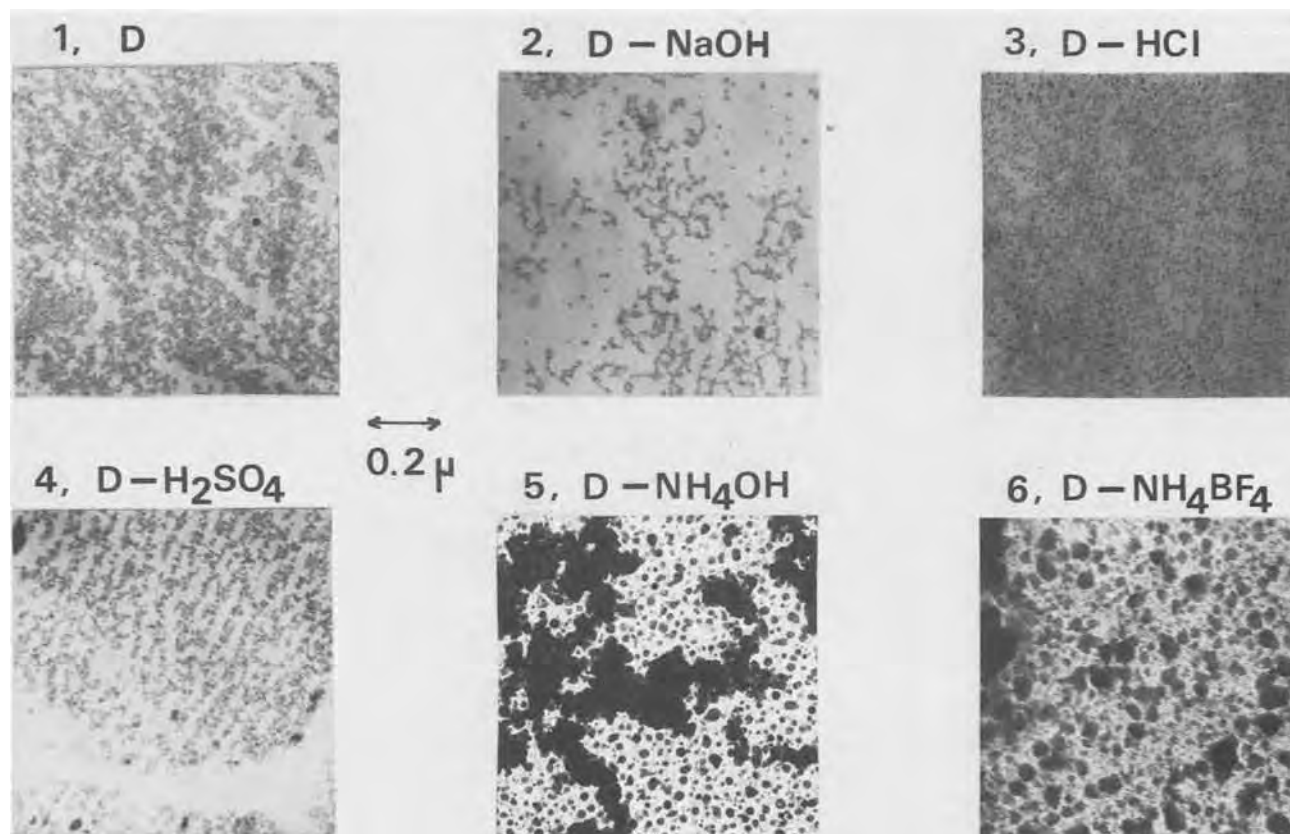


Fig. 1. Electron micrographs of various samples on collodion film after activation or acceleration. 1: after activation with catalyst "D," 2, 3, 4, 5, 6: after activation with catalyst "D" and acceleration with each solution.

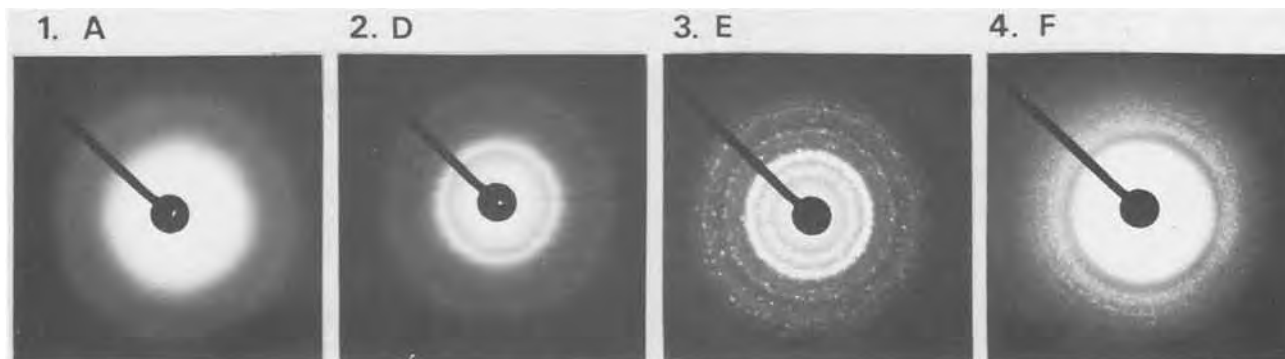


Fig. 2. Electron diffraction patterns of various samples on collodion film after activation. 1: catalyst "A," 2: catalyst "D," 3: catalyst "E," 4: catalyst "F."

the other factors as seen in the case of NH_4OH or NH_4BF_4 accelerators.

Electron diffraction patterns after activation process.—An electron diffraction analysis was applied to the activated surfaces in order to obtain further insight into the catalyst particle conditions after activation and/or acceleration. Figure 2 shows the electron diffraction patterns after activation with four catalyst samples. Both catalysts "A" and "D" which were prepared in our laboratory according to some patents give amorphous broad fcc (face-centered cubic) profiles with lattice parameters $a = 3.719$ and 3.986 , respectively. Whereas, the commercial samples "E" and "F" do not show simple fcc profiles, but relatively highly crystallized and unlike patterns which can be attributed to orthorhombic structure. Feldstein *et al.* (3) and Rantell *et al.* (4b) reported from electron diffraction studies that the product after acceleration has fcc structure, though it is amorphous after activation only. The results of "A" and "D" in Fig. 2 are obviously amorphous conditions with broad diffraction rings, but they can be interpreted as fcc structure similar to those after acceleration with NaOH accelerator (cf. Table IV). The composition for Pd-Sn alloys was reported as follows (7, 8): the solid solubility of Sn in Pd is approximately 17 atomic percent (a/o) and the fcc solid solution transforms into Pd_3Sn (27 a/o Sn) which also has the fcc structure. The lattice parameters for pure Pd and for Pd_3Sn are $a = 3.89$ and 3.97 , respectively. Above ca. 30 a/o the orthorhombic compounds such as Pd_2Sn , PdSn_2 (or pseudotetragonal), and PdSn_4 are reported except for the composition range around 40 a/o in which the compound of Pd_3Sn_2 has the hexagonal structure. Therefore, the samples "A" and "D", although their diffraction rings are broadened by some stannic compounds in the surface layer on active sites, may consist of fcc Pd-Sn alloys having less than 27 a/o Sn. In contrast to "A" and "D" the commercial samples "E" and "F" may have the surface layer of Sn-rich compounds on active sites, which might be produced by aging process which would increase the size of the colloidal particles in catalyst solution. The aging effect will be discussed later.

Electron diffraction patterns after the acceleration process.—The typical results of sample "D" after acceleration with various kinds of accelerators are demonstrated in Table III, corresponding to the electron micrographs in Fig. 1, respectively. Electron diffraction patterns can be explained as fcc only in the cases of

NaOH and H_2SO_4 accelerators. The accelerators NaOH and H_2SO_4 remove the surface layers on the active nuclei effectively and the sodium hydroxide which gives the finest remaining particles can show the bare conditions of catalytic nuclei which consists of Pd-Sn alloy of fcc structure. The electron diffraction pattern with HCl accelerator (D-HCl) whose electron micrograph shows rearranged uniform and small particle contribution can be apparently explained as tetragonal structure and it might be attributed to some products of chloride or changes of the lattice from fcc Pd-Sn alloy. The electron diffraction patterns with ammonates (D- NH_4OH and D- NH_4BF_4) which can be seemingly explained as orthorhombic structure might be due to some Pd-ammonia complexes, and it seems to be supported by the results of the coagulation of the particles shown in Fig. 1. Therefore, the electron diffraction patterns of the most characteristic two accelerators (i.e., NaOH and NH_4BF_4) are shown in Fig. 3. In the case of NaOH accelerator [Fig. 3(a)] all catalysts give the electron diffraction patterns of fcc structure, while in the case of NH_4BF_4 [Fig. 3(b)], all patterns show the non-fcc structure which can be apparently explained as orthorhombic. Therefore, the results after NaOH acceleration are considered to show the bare active nuclei and the results after NH_4BF_4 acceleration are considered to be produced by the different surface conditions from the usual active sites, which may result from some ammonate compounds such as Pd-ammonia complexes. Since it can be concluded that the electron diffraction patterns after NaOH acceleration process give the information of bare catalytically active nuclei, the discussion about the active sites or nuclei is considered to be advanced with the results after the NaOH acceleration process. In the cases of "A" and "D" the diffraction rings change from broad to sharp rings, and the change may be caused by the removal of Sn-rich surface layer of particles. The change from non-fcc to fcc in the case of the commercial samples seems to correspond to the fact that the catalytic active sites of fcc structure appear after removing the surface layer consisting of Pd-Sn alloy of orthorhombic structure whose Sn content is much higher than that of fcc structure. Cohen and Meek (6b) pointed out that the lattice constant for Pd-Sn alloy of Pd-rich region of fcc structure can be changed from $a = 3.89$ (pure Pd) to 3.97 (Pd_3Sn) with the increase in Sn concentration. Only in the two cases of sample "A" activation and F-NaOH acceleration in Table IV does the lattice constant not fall in this range, namely, it is smaller than that of pure Pd ($a = 3.89$) (see Table IV). Though a lattice constant smaller than that of pure Pd is not usually expected, it might be caused by the facts that the surface particles contain many defects and/or charged metal atoms, and that the surface energy in minute particles is lower than that of the bulk conditions. The amorphous conditions of the surface particles suggest that they contain many defects. The XPS results previously shown (2) derived the conclusion

Table III. Dependence of acceleration on the crystal structure of Pd-Sn core

D	D-NaOH	D-HCl	D- H_2SO_4	D- NH_4OH	D- NH_4BF_4
fcc $a = 3.986$	fcc $a = 3.949$	non-fcc	fcc $a = 3.937$	non-fcc	non-fcc

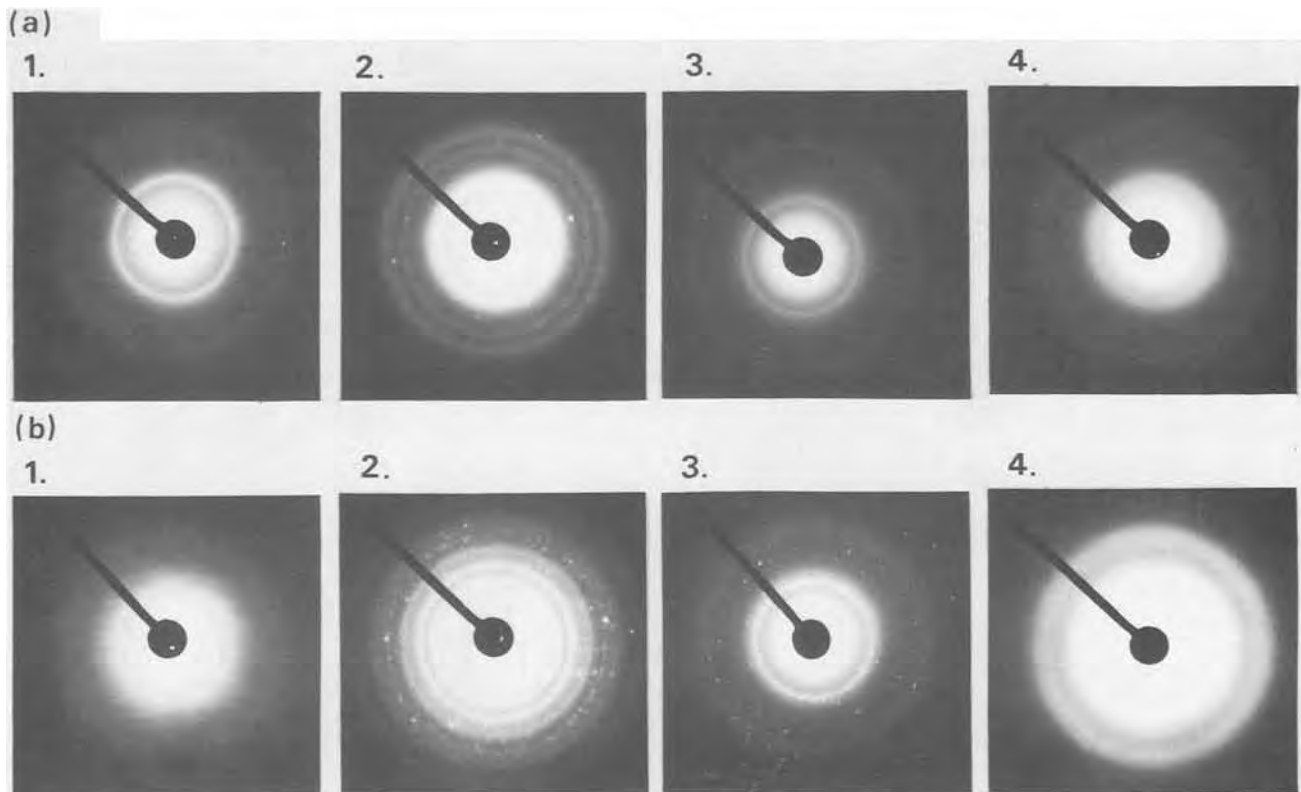


Fig. 3. Electron diffraction patterns of various samples on collodion film after acceleration. (a): accelerator 1M NaOH, (b): accelerator 1M NH_4BF_4 . Each number is the same as in Fig. 2.

that the high activity catalyst shows shifts in binding energies of Pd and Sn toward the metals and that the acceleration process causes the chemical shifts for Pd and Sn to occur toward the metals with lower binding energies. The possibility of lower activity catalysts of "A" and "F" containing many charged metal atoms can be inferred from the XPS conclusion. The change of lattice parameter from 3.986 to 3.949 in the case of sample "D" is considered to be caused by the removal of an Sn-rich surface layer of Pd-Sn alloy, while in the case of sample "A," the change from 3.719 to 3.878 may be due to the removal of a surface layer which contains many charged metal atoms.

The effect of aging on the catalyst solution was observed in our experiments, for example, catalyst "D" gave the major change of lattice parameter from $a = 3.766$ to 3.986 with aging approximately for 3 ~ 4 weeks. The aging effect was also reported by Feldstein *et al.* (3) and it was confirmed that the aging effect on the copper deposit is to render the product similar to that employing an improved conventional sensitizer. It seems to be concluded that the aging effect changes the charged metal atom to the metallic state and that it produces the distribution of well-formed colloidal particles in solution.

Finally, the activated surface conditions can be regarded as that the catalytically active sites consisting of Pd-Sn alloy have the fcc structure with various concentrations of Sn in the Pd-rich region, and that the active cores are usually covered with Sn-rich surface layers which stabilize the colloidal particles in solution. The accelerator usually removes the sur-

face layer to give the active core with fcc structure, however, the accelerator of the ammonate group renders the activity lower by producing some Pd-ammonia complexes which give the catalytically low activity.

Acknowledgments

The authors would like to thank Professor Dr. Tadashi Yoshida, Waseda University, Dr. Takashi Furuoya, and Mr. Yoji Sugauma, Basic Technology Research Laboratories, Nippon Electric Company, for their encouragement of this research and Dr. Masaki Miyahara, Waseda University, for his useful discussion. They are also greatly indebted to the Kurata Research Grant from the Kurata Foundation and the Research Fund of Waseda University for financial support.

Manuscript submitted March 24, 1980; revised manuscript received May 23, 1980.

Any discussion of this paper will appear in a Discussion Section to be published in the June 1981 JOURNAL. All discussions for the June 1981 Discussion Section should be submitted by Feb. 1, 1981.

Publication costs of this article were assisted by Nippon Electric Company, Limited.

REFERENCES

1. E. Matijević, A. M. Poskanzer, and P. Zuman, *Plating*, **62**, 958 (1975).
2. T. Osaka, H. Takematsu, and K. Nihei, *This Journal*, **127**, 1021 (1980).
3. N. Feldstein, M. Schlesinger, N. E. Hedgecock, and S. L. Chow, *ibid.*, **121**, 738 (1974).
4. a) A. Rantell and A. Holtzman, *Plating*, **61**, 326 (1974); b) *Trans. Inst. Metal Finishing*, **51**, 62 (1973); *ibid.*, **52**, 31 (1974).
5. R. L. Cohen and K. W. West, *This Journal*, **120**, 502 (1973).
6. a) R. Meek, *ibid.*, **122**, 1177 (1975); b) R. L. Cohen and R. L. Meek, *J. Colloid Interface Sci.*, **55**, 156 (1976).
7. J. R. Knight and D. W. Rhys, *J. Less Common Metals*, **1**, 292 (1959).
8. M. Hansen, "Constitution of Binary Alloys," p. 1126, McGraw-Hill Book Co., New York (1958).

Table IV. Dependence of activation and/or acceleration on the crystal structure of Pd-Sn core

Acc \ Act	A	D	E	F
Activation only	fcc $a = 3.719$	fcc $a = 3.986$	non-fcc	non-fcc
NaOH	fcc $a = 3.878$	fcc $a = 3.949$	fcc $a = 3.917$	fcc $a = 3.796$
NH_4BF_4	non-fcc	non-fcc	non-fcc	non-fcc

Ga_xIn_{1-x}P (n) (0 ≤ x ≤ 1) Semiconducting Alloys Studies in Photoelectrochemical Cells

A. M. Redon* and J. Vigneron

Laboratoire d'Electrochimie Interfaciale du C.N.R.S., 92190 Meudon-Bellevue, France

ABSTRACT

The Ga_xIn_{1-x}P (n) (0 ≤ x ≤ 1) alloys are very interesting semiconducting compounds for solar energy conversion purposes as their bandgaps vary from 1.30 to 2.25 eV. The studies are performed in acidic pH (pH ~ 1) (0.5M KCl + 0.1M HCl), as the photocurrents observed are only stable in this medium. The photodecomposition gives rise to the formation of In(OH)₃ and Ga(OH)₃ which are soluble products at low pH, but insoluble at higher pH. A maximum efficiency is obtained with the reducing agent Fe²⁺. This result was interpreted as depending on the relative positions of the bands. A maximum efficiency was also observed for the composition x = 0.36 in all the media investigated. This was interpreted as a change in the different parameters of the alloys.

Recently, there has been much interest in utilizing semiconducting electrodes for solar energy conversion purposes by the photoassisted electrolysis of water, or for chemical storage by means of electrochemical reactions with redox systems.

In fact, by illuminating an n-type electrode with photon energy of incident light greater than the bandgap, holes are produced in the valence band, and then, as a result of the electric field at the semiconductor electrolyte interface, they migrate to the surface where they can react with species in solution (1-3). Thus, it should be easy, with suitable semiconductor electrodes, to oxidize water to oxygen by means of solar energy.

For this purpose, many semiconducting electrodes have been investigated. But photocorrosion remains an important problem. Generally more stable materials in aqueous solutions have a large bandgap energy. In fact, compounds with small bandgaps have little cohesion energy, so that the photodecomposition potential is often lower than the potential associated with oxygen evolution. So photodecomposition generally occurs preferentially (4-5).

In this work, semiconducting alloys (n) (Ga_xIn_{1-x}P) (0 ≤ x ≤ 1) are considered. These compounds are very interesting because their bandgaps, which vary from 1.30 eV (InP) to 2.25 eV (GaP), cover the whole visible solar spectrum.

Some previous studies were made with these materials. First, they were investigated with physical methods, such as electroreflectance, cathodoluminescence, and optical transmission (6-9). Then, the flat-band potential and the concentration of majority carriers were determined by means of electrochemical impedance measurements and compared with the results obtained in the absence of any electrolyte (10-11).

In previous work, these compounds were used as electrodes in photoelectrochemical cells, in the absence of any redox system (12-13), and some fundamental physical properties, such as the bandgap energy, the transition mode, and the diffusion length of minority carriers, were deduced and compared with those found in literature (6-9).

While GaP compounds have been studied a great deal by photoelectrochemistry (14-19), studies on InP electrodes are more recent and not so extensive (20-23). But to our knowledge, there are no papers up to now on Ga_xIn_{1-x}P compounds on photoelectrochemical studies, except those realized in this laboratory.

The results obtained with various redox systems in the same aqueous electrolyte (0.5M KCl + 0.1M HCl, pH = 1), are given here.

The main purpose of this work is to determine the reducing agents and the composition associated with a maximum efficiency for the conversion of solar energy into electricity.

Experimental

Apparatus.—The apparatus consisted of a 150W xenon lamp and a Jobin Yvon HRS 2 monochromator. The light is chopped with a PAR 121 in order to eliminate the dark current.

Cyclic voltammetry curves are performed with the aid of a Fabelle potentiostat controlled by a voltage scan generator Wenking VSG 72.

Electrodes.—The photoanodes used are n-type Ga_xIn_{1-x}P polycrystalline alloys (0 ≤ x ≤ 1). They are doped with sulfur at a concentration ~ 10¹⁷/cm³, at 300°K, for all the compositions (9, 11, 12). The percentage in Ga and In was determined with an electron microprobe.

The ohmic nature contact to the semiconductor is insured by diffusion of tin. Before the experiment, the surfaces of the electrodes exposed to the light, and in contact with the electrolyte, are mechanically polished with diamond paste (1 μm < grain size < 25 μm), and then etched with a 2% bromine-methanol solution. But, after this treatment, dark currents and photocurrents slowly decrease, probably due to some modification of the surface. So, this etching with bromine-methanol was not done before each experiment, but only before the first one; an electrochemical polishing of the electrodes was performed with many cyclic voltammetric sweeps.

Electrode areas were determined by numerical integration on a photograph.

Electrolyte.—All the experiments in this work were performed at pH = 1, in 0.5M KCl + 0.1M HCl. In basic, and neutral pH, photocurrents are not stable, due to electrode decomposition. Interpretation of these results is discussed in the following.

The reducing agents Ti³⁺, Ce³⁺, Fe²⁺, and the hydroquinone were then introduced into the cell. In these different media, the cyclic voltammograms are recorded in the dark and under a monochromatic light in order to compare the efficiencies of the different compounds in electrolyte alone and with reducing agents. These efficiencies are determined by the ratio between photocurrents by unit area, and the diode current obtained at the same place as the photoelectrode, after the electrolyte. So the absorption of the electrolyte is taken into account.

* Electrochemical Society Active Member.

Key words: semiconductors, photoelectrochemistry, stabilization, solar energy, solar cell.

The sweep rate chosen for all the recording is $v = 10$ mV/sec.

Samples were always positioned very carefully in the same place to achieve a maximum photocurrent. This was realized, by fixing the cell into a plate which can be rotated around three axes and displaced following these three directions.

Results

Current potential curves under a monochromatic light.—Without a redox system.—With n-type semiconductors, in the absence of any redox system, it is easy to observe an anodic photocurrent at more positive potentials due to oxygen evolution or decomposition of the electrode.

The shapes of the curves on Fig. 1, can be explained very well by the relative differences between the parameters of the compounds (absorption coefficient α , diffusion length L_p of the minority carriers) (12). In fact, following Gärtner's theory (24), and with relative values of αL_p and the width of the depletion layer, the saturation voltage in the intensity-potential curves goes to lower values of the anodic potential. ($\alpha_{GaP} \sim 10^3$ cm $^{-1}$, $\alpha_{InP} \simeq 10^4$ cm $^{-1}$, $\bar{L}_{pGaP} \sim 2.7$ cm, $\bar{L}_{pInP} \sim 0.9$ cm).

On Fig. 2, we can see the different efficiencies obtained as a function of the wavelength of the incident light, and for the same polarization of the electrodes ($V = 1$ V/SCE) in the electrolyte alone. All the results refer to the unit area of the electrode. Photocurrent values are corrected from the intensity of the xenon lamp spectrum and for the response of the photodiode. For this, a P.D.P. 11 computer was utilized.

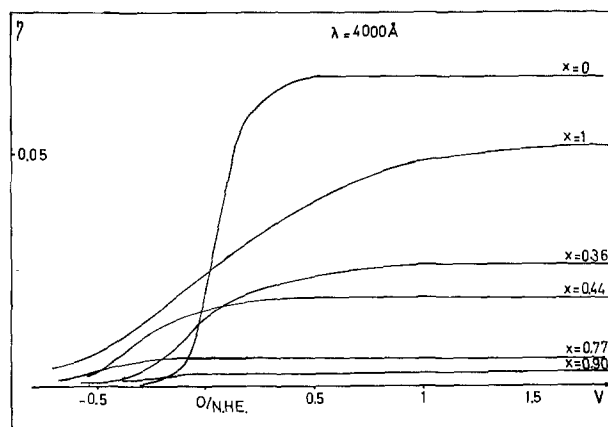


Fig. 1. Efficiencies for different compositions x of the alloys, in 0.5M KCl + 0.1M HCl ($pH = 1.2$) vs. the applied electrode potential values are corrected from the area of the electrodes. Wavelength of the incident light is $\lambda = 4000\text{\AA}$.

The photoaction spectra does not vary with sample history, or with different portions of the same sample. They only depend on the composition of each sample.

With reducing agents.—The different efficiencies are then observed in the presence of several reducing agents under monochromatic illumination.

On Fig. 3 the efficiencies are given vs. applied potential, and with the reducing agents, at the same concentration ($10^{-3}M$) and with the same base electrolyte ($pH = 1.2$). The composition investigated here is $x = 0.77$, and the wavelength chosen $\lambda = 500$ nm.

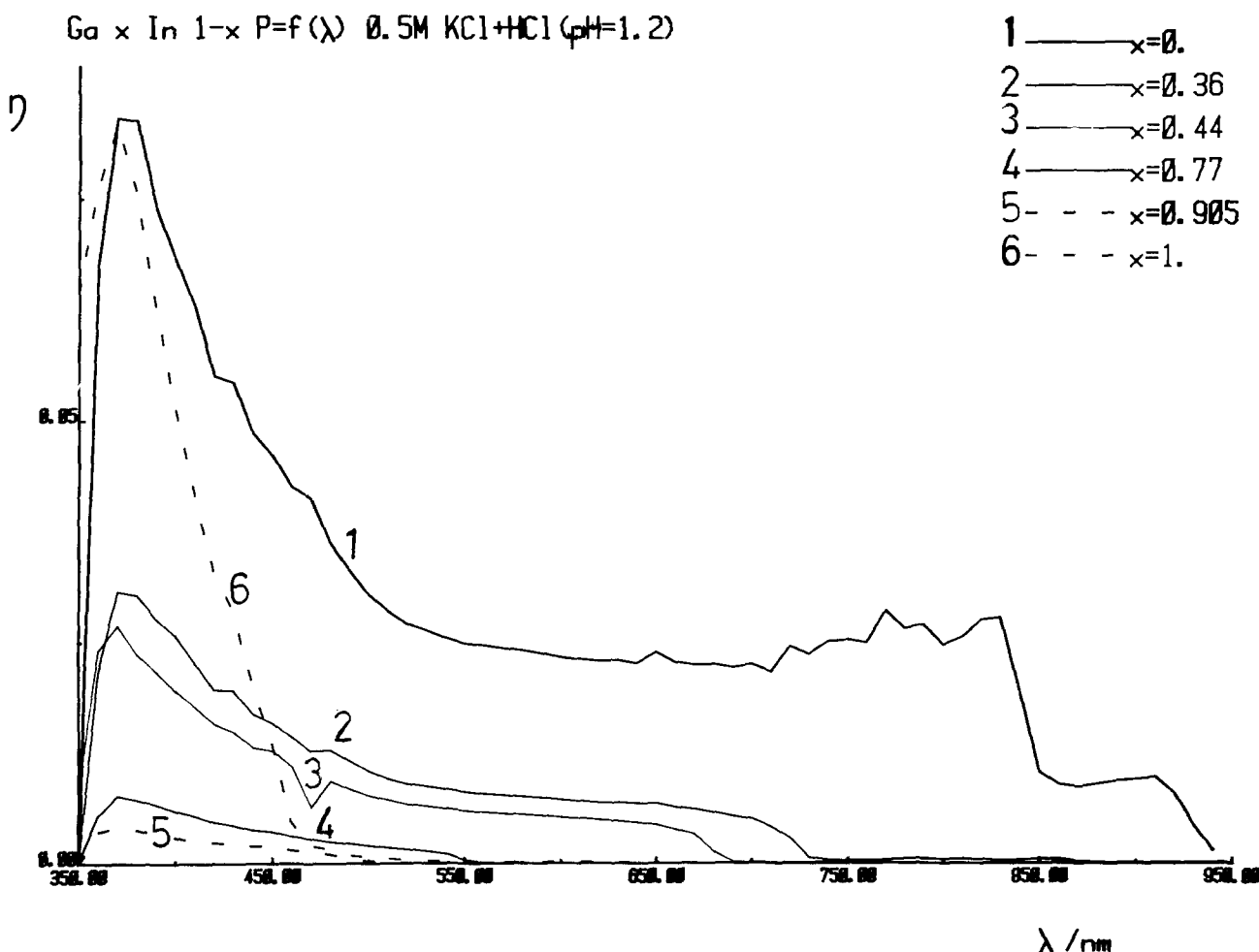


Fig. 2. Efficiencies for the different compositions x vs. the wavelength of the incident light. Electrode potential $V = +1$ V/NHE. All the values are corrected for the area of the electrodes.

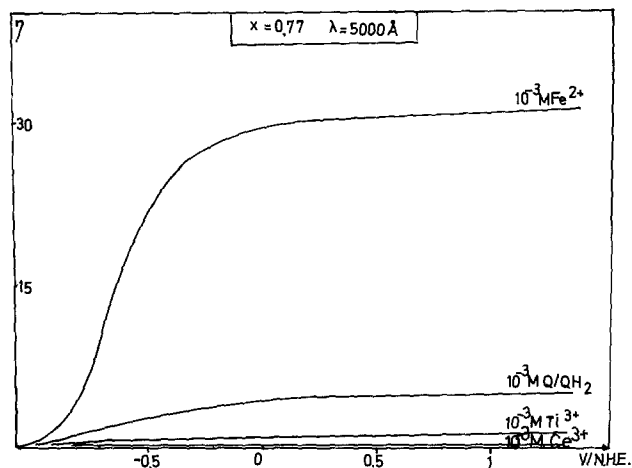


Fig. 3. Efficiencies vs. applied potential at $\lambda = 5000\text{\AA}$ for $\text{Ga}_{0.77}\text{In}_{0.23}\text{P}$ in the presence of: 10^{-3}M Fe_2SO_4 , 10^{-3}M hydroquinone, 10^{-3}M TiCl_3 , 10^{-3}M CeCl_3 and base electrolyte.

If the intensity varies with the composition, and the redox system, the shapes of the curves remain the same and so they are not drawn here, consequently a comparison between the different alloy compositions are given in the base electrolyte (Fig. 4a). On Fig. 4b, we can see that the photocurrent depends on the composition of the electrode, the normalization to the maximum photocurrent being realized. On Fig. 5a and b, the magnitude of the photocurrents is given vs. the

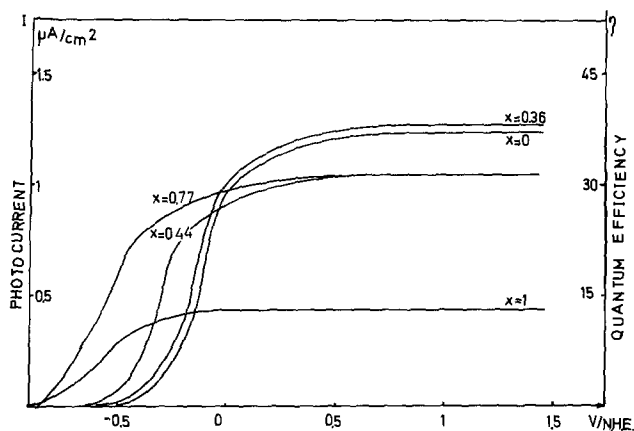


Fig. 4a. Efficiencies for $\lambda = 4000\text{\AA}$, in the base electrolyte, for the different compositions x vs. the applied potential.

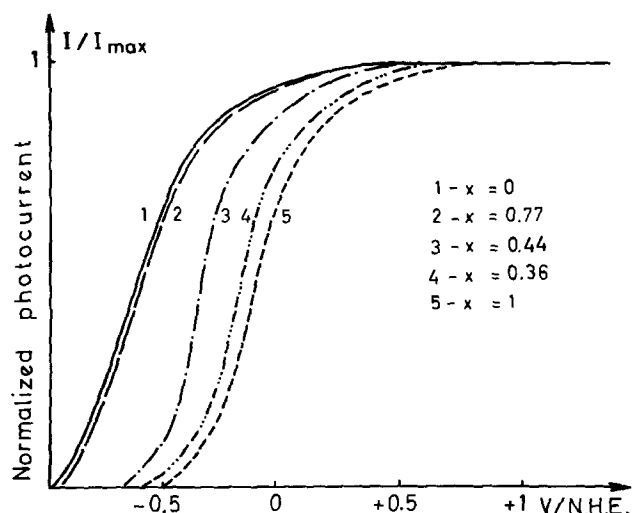


Fig. 4b. Normalized intensities relative to the maximum photocurrent of each curve.

composition of the electrodes, with different reducing agents investigated and with the hydroquinone.

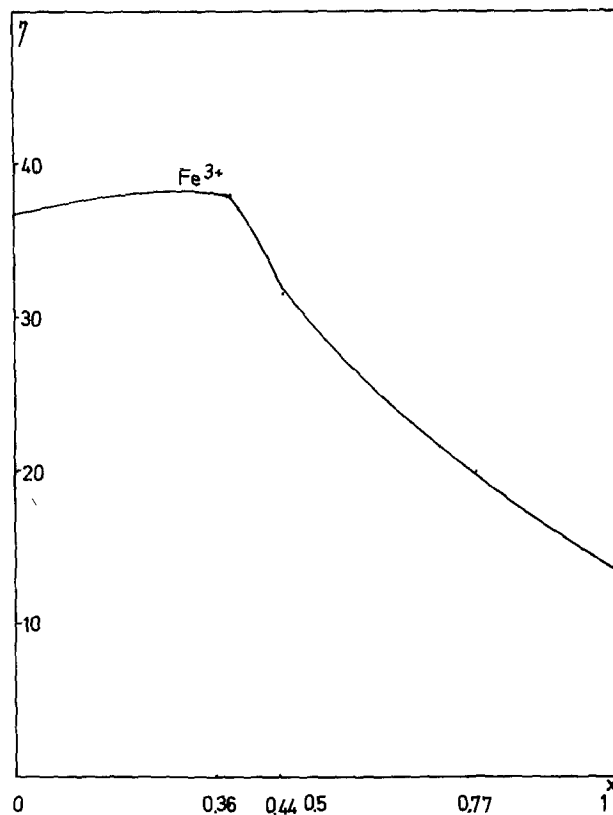


Fig. 5a. Efficiencies obtained vs. the composition x of the alloys in 10^{-3}M Fe^{2+} . Wavelength of the incident light is $\lambda = 5000\text{\AA}$ and the applied potential $V = 1.7$ V/NHE.

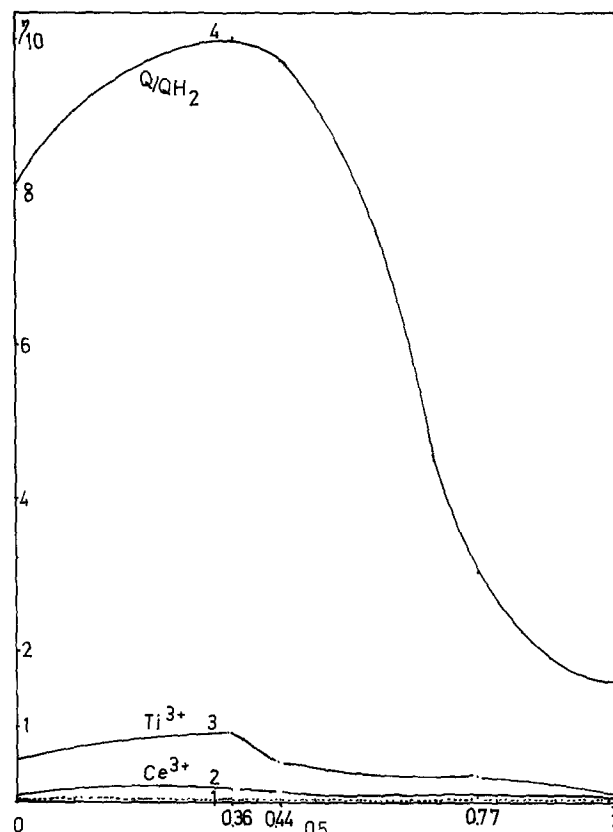


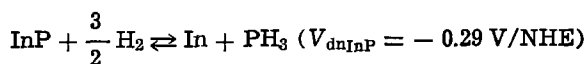
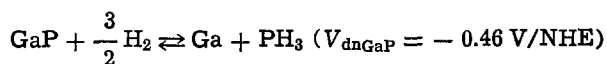
Fig. 5b. Efficiencies obtained vs. the composition x of the alloys in different media: curve 1, electrolyte alone; curve 2, 10^{-3}M Ce^{3+} ; curve 3, 10^{-3}M Ti^{3+} ; curve 4, 10^{-3}M Q/QH_2 . Wavelength of the incident light $\lambda = 5000\text{\AA}$. Applied polarization $V = 1.7$ V/NHE.

Results obtained show that maximum efficiency is always obtained in all media for the same composition $x = 0.36$ (bandgap 1.72 eV).

Discussion

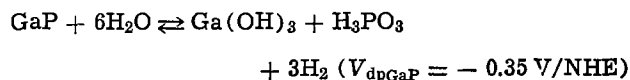
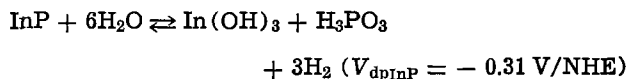
In order to discuss results obtained in the base electrolyte it is necessary to know the position of the bands of the compounds studied, relative to the Gibbs energy of the decomposition reactions, Fermi levels associated with the electrolysis of the water (Fig. 6), and redox reactions (Fig. 7).

At negative potentials, cathodic currents correspond not only to the protons reduction, but also to the cathodic decomposition of the electrodes. Reactions involved are the following (12)



V_{dn} is the potential associated with the cathodic decomposition at $\text{pH} = 1$.

The reactions of anodic decomposition of the electrodes, giving rise to anodic currents, are the following (12, 25, 26)



V_{dp} is the potential associated with the anodic decomposition at $\text{pH} = 1$. These values show that anodic, as well as cathodic, decomposition occurs at negative potentials relative to the 0 V/NHE and that InP decomposes more easily than GaP, as values of decomposition potentials are lower.

After holding a $\text{Ga}_x\text{In}_{1-x}\text{P}$ alloy several hours at anodic potentials in the electrolyte alone ($\text{pH} = 1$), under a maximum light intensity, the solution was analyzed by colorimetry (27) in order to detect indium and gallium. Both elements were detected. Moreover, the surface of the electrodes was covered with

Fig. 6. Position of the anodic decomposition potentials of the crystals, and Fermi levels associated with the electrolysis of the water, relatively to the bands of the $\text{Ga}_x\text{In}_{1-x}\text{P}$ compounds ($0 \leq x \leq 1$, n-type).

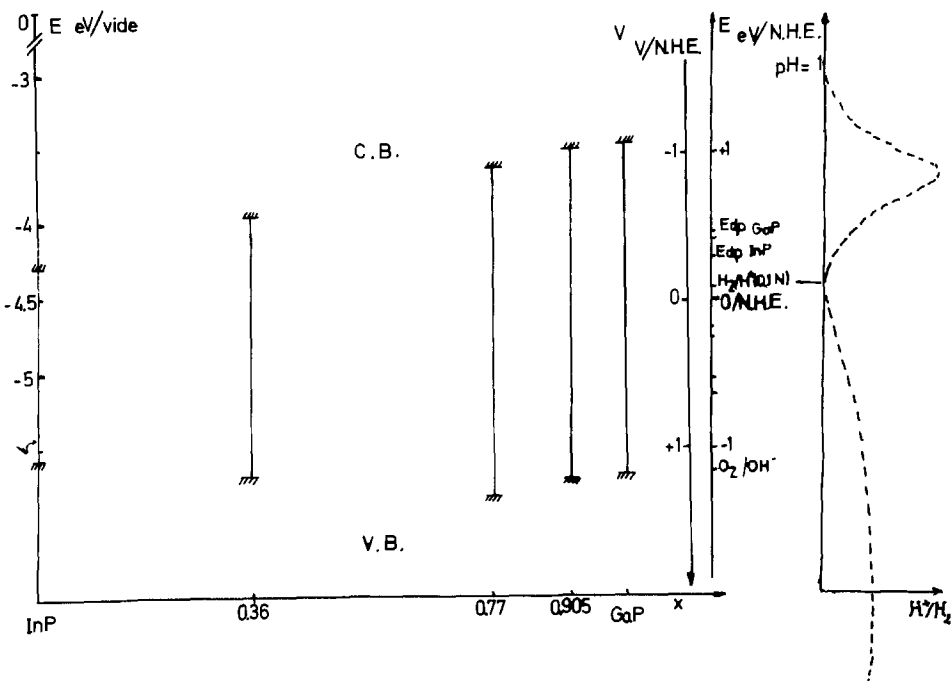
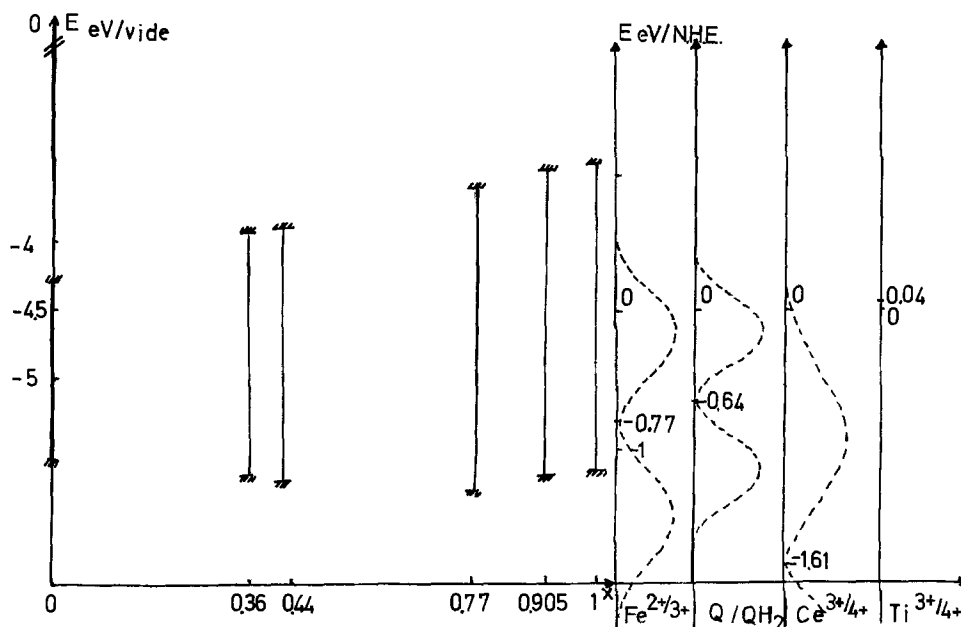


Fig. 7. Band diagram of the $\text{Ga}_x\text{In}_{1-x}\text{P}$ compounds and distribution of the different redox couples used.



a gray substance which probably was due to the formation of $\text{In}(\text{OH})_3$ and $\text{Ga}(\text{OH})_3$.

So, photocurrent obtained at anodic potentials is probably due to both oxygen evolution and anodic decomposition.

Then, if the Fermi levels of the redox reactions are considered, relative to the bandedges at the surface, Fig. 7 can explain our experimental results.

As we can see by comparison of Fig. 3 and 7, reducing agents having a Fermi level near the valence band must give rise to higher photocurrents. This is in accordance with experimental results: quantum efficiencies are greater with Fe^{2+} than with Q/QH_2 or Ti^{3+} . Moreover, since the Fermi level of Ce^{3+} is below the valence band, the anodic photocurrent is very small.

But, the widths of the different redox couples used can also be taken into account to interpret this result, Table I (28).

A diagram of the bands of our semiconductors may be arranged relative to the electronic distribution of redox reactions (Fig. 6-7).

The redox system with highest overlap of its filled levels with the edge of the valence band are expected to give larger photocurrents if the different efficiencies obtained in this work are compared to position and distribution of the different redox couples investigated.

A maximum efficiency is obtained for the composition $x = 0.36$ ($E_g = 1.72$ eV). This result can be associated with a change in the behavior of the compound. In fact, with the composition there is change in the optical transition mode (12), and the absorption coefficient is very different ($\alpha = 10^4$ cm^{-1} for InP and $\alpha = 10^{+2}$ cm^{-1} for GaP). As we can see, this result is obtained for all the reducing agents used.

Conclusion

In this paper, we explore the efficiencies of photocells realized with $\text{Ga}_x\text{In}_{1-x}\text{P}$ alloys ($0 < x \leq 1$), n-type, at $\text{pH} = 1$, with and without Ce^{3+} , Ti^{3+} , Fe^{2+} , and Q/QH_2 at the same concentration, 10^{-3}M . In the electrolyte alone, there is a substantial decomposition of the electrode, as well in the dark as under the light.

With the different reducing agents investigated, it appears a maximum efficiency with Fe^{2+} . This result agrees with the relative positions of the bands of the alloys and the Fermi levels of the redox couples investigated.

Another important result is that a maximum efficiency is obtained with all the reducing agents used for the composition $x = 0.36$ of the alloys. This probably is due to the evolution of the different parameters of the compounds: diffusion length of minority carriers, width of the depletion layer, absorption coefficient, and transition mode.

Acknowledgments

The authors wish to thank Dr. J. Bourneix for the fabrication of the $\text{Ga}_x\text{In}_{1-x}\text{P}$ compounds, and Mme. De Mende for the mounting of the electrodes. We

would also like to acknowledge helpful discussions with Dr. Parsons and Dr. H. Tributch. This work was performed with support from D.G.R.S.T. Contract No. 6501617.

Manuscript submitted Feb. 21, 1980; revised manuscript received May 21, 1980. This was Paper 358 presented at the Boston, Massachusetts, Meeting of the Society, May 6-11, 1979.

Any discussion of this paper will appear in a Discussion Section to be published in the June 1981 JOURNAL. All discussions for the June 1981 Discussion Section should be submitted by Feb. 1, 1981.

REFERENCES

1. R. Memming, in Proceedings of Permanent School on Solar Energy Processes, V. Silvestrini Sogesta, Editor, Urbino, Italy (November 1978).
2. R. Memming, *Phil. Tech. Rev.* (1978).
3. M. Tomkivich and H. Fay, *Appl. Phys.*, **18**, 28 (1979).
4. H. Gerischer, in "Semiconductor Liquid Junction Solar Cells," A. Heller, Editor, pp. 1-9, The Electrochemical Society Softbound Proceedings Series, Princeton, N.J. (1977).
5. H. Gerischer, *J. Electroanal. Chem.*, **82**, 133 (1977).
6. P. Alibert, G. Bordure, A. Laugier, and J. Chevallier, *Phys. Rev. B.*, **6**, 1301 (1972).
7. H. Rodot, J. Horak, G. Rouy, and J. Bourneix, *C. R. Acad. Sci., Ser. B*, **269**, 381 (1969).
8. P. Merle, D. Auvergne, H. Mathieu, and J. Chevallier, *Phys. Rev.*, **15**, 2032 (1977).
9. J. Chevallier, Thesis of Doctorat d'Etat, Paris (1975).
10. J. L. Sculfort and A. M. Baticle, S.I.E. Budapest (1978), Extended Abstract p. 465.
11. J. L. Sculfort and A. M. Baticle, *Surf. Sci.*, **85**, 137 (1979).
12. A. M. Redon, J. Vigneron, and J. Chevallier, *This Journal*, **127**, 605 (1980).
13. A. M. Redon, J. Vigneron, J. L. Sculfort, and A. M. Baticle, *C. R. Acad. Sci., Ser. C*, **289**, 279 (1979).
14. M. J. Madou, F. Cardon, and W. P. Gomes, *Ber. Bunsenges. Phys. Chem.*, **82**, 819, 823 (1978).
15. M. J. Madou, W. P. Gomes, and F. Cardon, in Proceedings of the International Photovoltaic Solar Energy Conference, Luxembourg, Sept. 27-30, 1977, pp. 417-424. D. Riedel, Publ. Comp. Dordrecht-Holland-Boston USA.
16. Eletsii, V. V. Kulyavik, and Yu Pleskov, Yu. V. Trad. Elektrokhem, Vol. 3, 197, p. 753.
17. A. B. Ellis, J. M. Bolts, and M. S. Wrighton, *This Journal*, **124**, 1603 (1977).
18. R. Memming and G. Schwandt, *Electrochim. Acta*, **13**, 1299 (1968).
19. J. L. Sculfort, A. M. Baticle, and J. Gautron, *C. R. Acad. Sci., Ser. C*, **287**, 317 (1978).
20. A. M. Van Wezemael, W. H. Laflere, and F. Cardon, *J. Electroanal. Chem.*, **87**, 105 (1978).
21. A. A. K. Vervaet and W. P. Gomes, *ibid.*, **91**, 133 (1978).
22. P. A. Kohl and A. J. Bard, *This Journal*, **126**, 598 (1979).
23. A. B. Ellis, J. M. Bolts, and M. S. Wrighton, *ibid.*, **124**, 1603 (1977).
24. W. W. Gartner, *Phys. Rev.*, **116**, 84 (1959).
25. M. J. Madou, F. Cardon, and W. P. Gomes, *Ber. Bunsenges. Phys. Chem.*, **82**, 819, 823 (1978).
26. R. Memming, in "Semiconductor Liquid Junction Solar Cells," A. Heller, Editor, The Electrochemical Society Softbound Proceedings Series, Princeton, N.J. (1977).
27. G. Charlot and D. Bezier, "Analyse quantitative minérale," Masson et Cie Editeurs (1955).
28. R. Memming, *Ber. Bunsenges.*, **76**, 475 (1972).

Table I.

	$\text{Fe}^{2+}/\text{Fe}^{3+}$ (eV)	$\text{Ce}^{3+}/\text{Ce}^{4+}$ (eV)	Q/QH_2 (eV)	H^+/H_2 (eV)
λ	1.25	1.75	0.5	1.5 (H^+) 3 (H_2)

Lattice-Gas Treatment of Supercritical Phase Behavior in Fluid Mixtures

L. A. Kleintjens and R. Koningsveld

Central Laboratory DSM, 6160 MD Geleen, The Netherlands

ABSTRACT

Recently, Trappeniers *et al.* have shown that gas-gas demixing phenomena can be described qualitatively with the lattice-gas model in its simplest form. We have tried to develop this treatment into a quantitative theory with the least possible number of parameters. The extended model has proven to permit a fairly accurate description and prediction of supercritical fluid phase behavior in a number of systems. The applicability of the model is illustrated with experimental data on the system methane/water which shows gas-gas demixing of the second kind.

Lattice models have frequently been used in the description of phase behavior of liquid mixtures. One of the assumptions underlying such treatments is the equality of the partial specific volumes of the components in all liquid phases at constant pressure and temperature. In gas-liquid and supercritical fluid equilibria the densities of the phases may differ a great deal and the conventional rigid-lattice model is less suited for describing such phenomena.

This problem is circumvented in the lattice-gas model which introduces randomly distributed vacancies in the lattice. The density of a system or phase can be reproduced easily by adjustment of the concentration of vacancies. The model was developed by Mermin (1) and by Mulholland and Rehr (2) for one-component systems on the basis of the hole theory of liquids devised by Altar (5), Cernuschi and Eyring (4), Frenkel (3), and others.

Trappeniers *et al.* (6, 7) extended the theory combining Guggenheim's (8) two-component lattice model with the lattice-gas treatment and were able to give a qualitatively correct description of the various forms in which gas-gas demixing occurs. The more-component lattice-gas model has also been used by a number of authors for other purposes (9-12). Quantitative descriptions allowing predictions of phase behavior, however, have so far been very rare. In this paper we analyze how Trappeniers' treatment can be extended into a quantitative predictive description of fluid phase behavior, retaining the simplicity of the model and introducing the smallest possible number of adjustable parameters.

Pure Substances

In the lattice-gas model a pure substance is conceived as a binary mixture composed of occupied and vacant lattice sites in which the vacancies contribute to the entropy but not to the internal energy. Temperature and pressure changes cause variations in the concentration of vacancies (holes) but v_0 , the volume per lattice site (also hole size), is constant. We further assume only nearest neighbor interactions to contribute significantly to the interaction energy.

Since we want to describe phase behavior of supercritical systems the model should be valid for liquids and gases alike. Gas-liquid equilibrium in a pure substance is considered as a fluid 1-fluid 2 equilibrium where the two fluid phases differ in hole concentration only. A change in hole concentration alters the number of contacts between occupied sites and thereby the total internal (nearest-neighbor interaction) energy.

Key words: equation of state, supercritical fluids, hole theory, lattice-gas description.

Following the recipe of Trappeniers and co-workers (6, 7) we extend the treatment applying a suggestion of Staverman (13). We drop the rigid-lattice condition that each site will have the same number of nearest neighbors (lattice coordination number) and assign an interacting-surface area σ_1 to the molecules. Likewise a surface area σ_0 can be assigned to the vacancies, which serves as a unit to relate σ_1 -values also. The adjustable parameter thus arising is the surface-area ratio $\rho_1 (= \sigma_1/\sigma_0)$ which, however, must have a value within a range imposed by the tolerances of the model. Such a relaxation of the rigid-lattice model has also been introduced by other authors (9, 11, 14, 15) and has proven to be very useful when dealing with various thermodynamic properties. Recently we noticed the same in the description of liquid-liquid phase behavior of linear and branched polyethylene solutions (16, 17).

A further extension we found useful consists of allowing the molecules to occupy more than one lattice site and even permitting broken numbers for the occupancy. By now the lattice has become an abstraction serving merely as a framework for convenient derivation of usable thermodynamic relations. Such a procedure has already been suggested in general terms by Rowlinson (18). All this leads to the following expression for ΔF , the Helmholtz free energy of mixing N_0 holes and N_1 molecules of substance 1, occupying m_1 sites each (19)

$$\Delta F/N\phi kT = \phi_0 \ln \phi_0 + \phi_1 m_1^{-1} \ln \phi_1 + \phi_0 \phi_1 [\alpha_1 + g_{11} (1 - \gamma_1) (1 - \gamma_1 \phi_1)^{-1}] \quad [1]$$

where ϕ_0 , ϕ_1 = volume fractions of vacancies and occupied sites, $g_{11} = -\frac{1}{2} w_{11} \sigma_0/kT$; $\phi_0 = N_0/N_\phi$; $\phi_1 = N_1 m_1/N_\phi$; $N_\phi = N_0 + N_1 m_1$, w_{11} = interaction energy of adjacent molecules 1 per unit surface area, σ_0 , σ_1 = surface areas of holes and molecules; $\sigma_1/\sigma_0 = \rho_1$, $\gamma_1 = 1 - \rho_1$, and kT has its usual meaning.

In the application of Eq. [1] to vapor-liquid equilibrium data we found that a purely empirical entropy correction parameter α_1 must be included. The other parameters, though adjustable, have a clear physical meaning which allows their magnitude to be estimated. The number of sites m_1 occupied by a molecule 1 is related to v_0 by

$$d_1 = \phi_1 M_1 / v_0 m_1 \quad [2]$$

where d_1 and M_1 stand for density and molar mass of substance 1.

Expressions for experimentally accessible quantities can be derived from Eq. [1] by standard procedures. For instance, the pressure is obtained by applying

$$p = (\partial \Delta F / \partial V)_{T, N_1}$$

which leads to

$$-pv_0/kT = \ln \phi_0 + (1 - m_1^{-1})\phi_1 + \phi_1^2[\alpha_1 + g_{11}(1 - \gamma_1)^2(1 - \gamma_1\phi_1)^{-2}] \quad [3]$$

Within the model the total volume V is given by $V = N_0v_0$. Introduction into Eq. [3] and series development of the logarithmic term shows Eq. [3] to reduce to Boyle's law at low gas density ($\phi_1 \ll 1$) and to a virial series in reciprocal volume at higher densities.

Vapor-liquid equilibrium conditions are the equality of pressure (defined by Eq. [3] and of the chemical potential of component 1 in the two phases (denoted by ' and "). The chemical potential follows from

$$\mu_1 = (\partial\Delta F/\partial N_1)_{T,V}$$

and the equilibrium condition

$$\mu_1' = \mu_1''$$

yields a relation between the concentrations of occupied and empty lattice sites in the two phases

$$m_1^{-1} \ln(\phi_1'/\phi_1'') = \phi_0'^2[\alpha_1 + g_{11}(1 - \gamma_1)(1 - \gamma_1\phi_1'')^{-2}] - \phi_0''^2[\alpha_1 + g_{11}(1 - \gamma_1)(1 - \gamma_1\phi_1')^{-2}] + (1 - m_1^{-1})(\phi_1'' - \phi_1') \quad [4]$$

This equation, together with Eq. [3] in $p' = p''$, allows calculation of ϕ_1' and ϕ_1'' and, by Eq. [2], of the densities d_1' and d_1'' of the phases.

Expressions for the spinodal (limit of thermodynamic stability) and the gas-liquid critical point are derived from $(\partial^2\Delta F/\partial\phi_1^2)_{T,V} = 0$ and $(\partial^3\Delta F/\partial\phi_1^3)_{T,V} = 0$, respectively (7, 19). We obtain

$$(1/\phi_0) + (1/m_1\phi_1) = 2g_{11}(1 - \gamma_1)^2(1 - \gamma_1\phi_1)^{-3} + 2\alpha_1 \quad (\text{spinodal}) \quad [5]$$

and

$$(1/\phi_0^2) - (1/m_1\phi_1^2) = 6g_{11}\gamma_1(1 - \gamma_1)^2(1 - \gamma_1\phi_1)^{-4} \quad (\text{critical point}) \quad [6]$$

The parameters in Eq. [1]-[6] can be calculated from the gas-liquid critical point (p_c , T_c , d_c) of the substance by a suitable combination of Eq. [2], [3],

[5], and [6]. Since the interaction energy term g_{11} usually showed a temperature-dependence departing slightly from that indicated in Eq. [1] additional data are needed, e.g., from vapor-liquid equilibrium at another temperature, to establish this dependence which can be described with

$$g_{11} = g_{110} + g_{111}/T \quad [7]$$

We have done so with a number of pure substances and found the present treatment to lead to good reasonable descriptions of gas-liquid densities in a wide range of pressure and temperature. Examples, referring to CH_4 and H_2O , are shown in Fig. 1. Close to the critical point more or less serious deviations between data and calculated curves can be seen. This may either indicate a need for further refinement of the model [see, e.g., Ref. (11) or (20)] or point to nonclassical critical behavior that is clearly not covered by the present procedure. We leave this question open because the aim here is to describe fluid phase behavior in a general way which proves well possible with the outlined simple model.

Binary Mixtures

The Helmholtz free-energy expression for a binary mixture—vacancies and two kinds of sites (1 and 2)—can be derived along analogous lines; it reads

$$\Delta F/N_0kT = \phi_0 \ln \phi_0 + \phi_1 m_1^{-1} \ln \phi_1 + \phi_2 m_2^{-1} \ln \phi_2 + \phi_0 \phi_1 [\alpha_1 + g_{11}(1 - \gamma_1)q^{-1}] + \phi_0 \phi_2 [\alpha_2 + g_{22}(1 - \gamma_2)q^{-1}] + \phi_1 \phi_2 [\alpha_m + g_m(1 - \gamma_2)q^{-1}] \quad [5]$$

where $q = 1 - \gamma_1\phi_1 - \gamma_2\phi_2$; $\gamma_1 = 1 - \rho_1$; $\gamma_2 = 1 - \rho_2$.

The sets of parameters (α_1 , g_{11} , ρ_1 , m_1) and (α_2 , g_{22} , ρ_2 , m_2) can be deduced from pure-component data as indicated above, and the binary mixture then calls for two more parameters, viz. α_m and g_m . These can be derived from vapor-liquid or fluid-fluid critical data on the mixture. To avoid the need of designing mixing rules for v_0 , and the consequent uncertainties introduced when derivatives with respect to concentration are taken, we postulate that all constituents in a mixture shall have the same v_0 , independent of the composition of the system. There will be as many values of ρ as there are components and these values

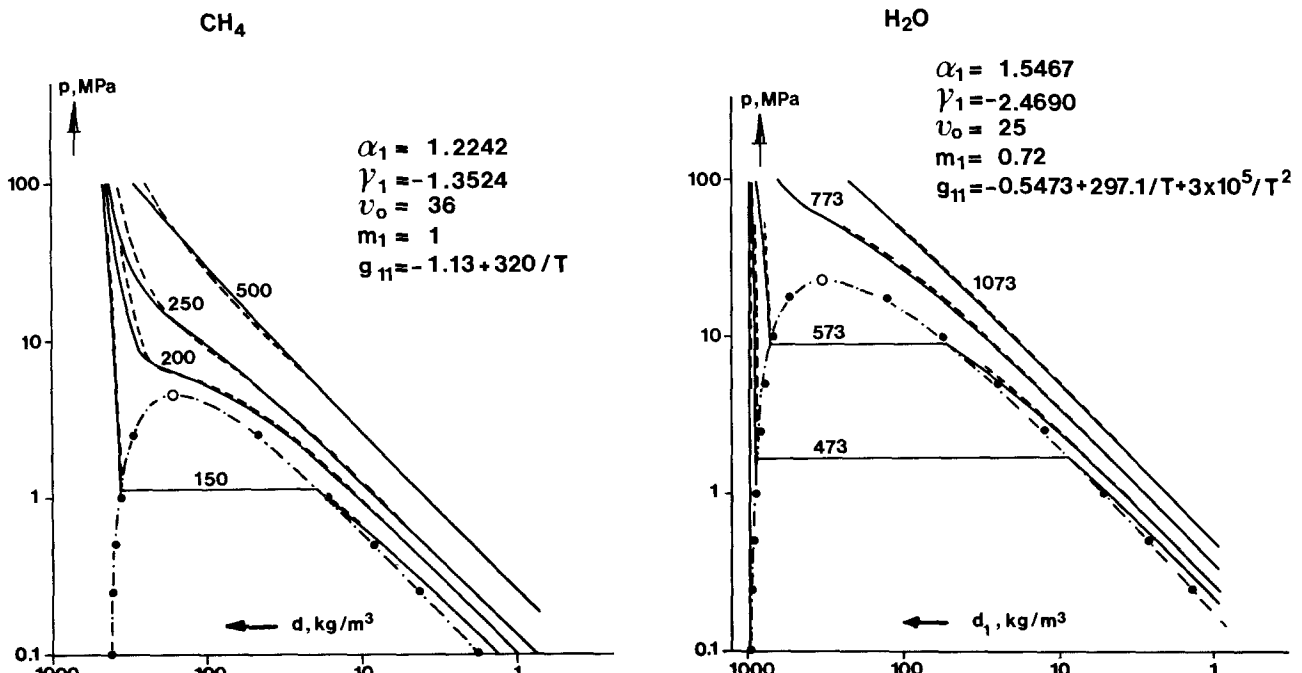


Fig. 1. pVT diagrams for indicated temperatures in $^{\circ}\text{K}$. Calculated; one phase densities (—) and gas-liquid coexistence densities. Experimental (literature) data; smoothed isotherms (---), gas-liquid coexistence (●) and critical point (○).

may differ, in accordance with the shapes of the various molecules.

Expressions for chemical potentials, spinodal, and critical point can be derived straightforwardly from Eq. [5]. The resulting equations being complex we only state the binary analogue of Eq. [3] here, Ref. (19) contains a full report. The equation for the pressure now reads

$$-pv_0/kT = \ln \phi_0 + (1 - m_1^{-1})\phi_1 + (1 - m_2^{-1})\phi_2 + (\alpha_1\phi_1 + \alpha_2\phi_2)(\phi_1 + \phi_2) - [\alpha_m + g_m(1 - \gamma_2)q^{-2}]\phi_1\phi_2 + [g_{11}(1 - \gamma_1)\phi_1 + g_{22}(1 - \gamma_2)\phi_2](q - \phi_0)q^{-2} \quad [6]$$

A set of binary critical data ($T_c, p_c, x_{2,c}$) can be used for the calculation of α_m and g_m , after which the complete phase diagram of the fluid 1-2 mixture can be computed and compared with experimental data. The mole fraction of the second component x_2 is given by

$$x_2 = [1 + (\phi_1 m_2 / \phi_2 m_1)]^{-1} \quad [7]$$

The calculated curves can be represented as isotherms on a ternary diagram; Fig. 2 shows an example referring to the system CO₂/CH₄. The pressure varies along the curves but is obviously equal at both ends of a tie line which represent coexisting phase compositions in terms of $\phi_1, \phi_2,$ and ϕ_0 . Equation [7] then serves to convert the lattice-site fractions ϕ into mole fraction numbers and isothermal $p(x_2)$ plots can thus be constructed from the calculated curves in Fig. 2 and compared with the actual situation. For one of the isotherms in Fig. 2 this comparison is made in Fig. 3. The agreement between experiment and prediction can be considered satisfactory particularly in view of the fact that the only information used on the mixture was the critical point. The situation is comparable to that encountered with pure substances where the critical point supplies the essential information for reasonable to good descriptions of liquid/vapor densities.

The system CH₄/H₂O exhibits gas-gas demixing of the second kind (21-23). This involves the occurrence of two miscibility gaps in $p(x_2)$ isotherms at temperatures just under the critical temperature of water. One of these is of the upper-critical-miscibility type with a maximum critical pressure, the other, located at higher pressures, is a lower critical miscibility gap with a minimum critical pressure. Determination, as above, of α_m and g_m from some upper critical data proved to suffice for an essentially correct

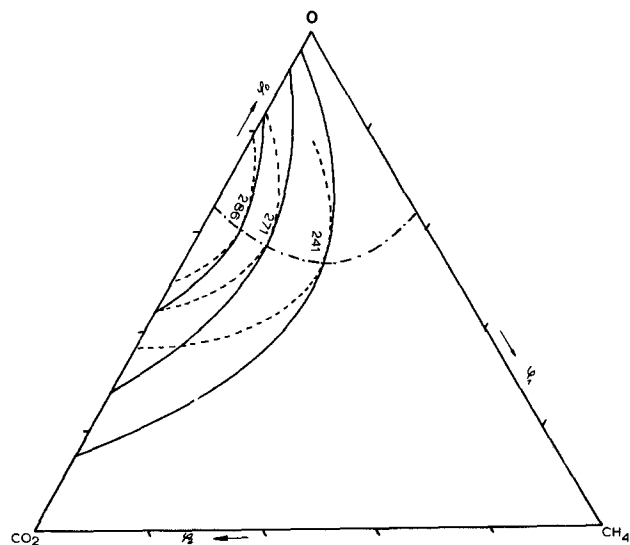


Fig. 2. Calculated "ternary" phase diagram of the system CO₂-CH₄ for indicated temperatures in °K. — coexistence curves, - - - spinodals - · · · critical line.

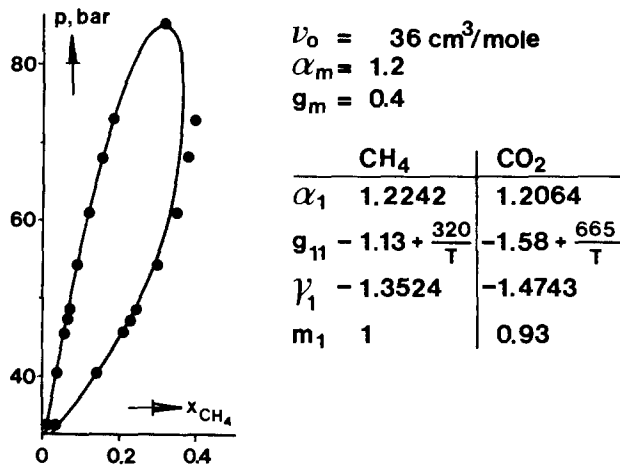


Fig. 3. Gas-liquid coexistence at 271.4°K in the system CO₂-CH₄. Calculated with indicated values of the parameters from Fig. 2 (—); experimental data (●).

description of the full phase diagram, including the gas-gas lower-critical miscibility gap. "Ternary" isotherms calculated for this system are illustrated in Fig. 4 and compared with experimental $p(x_2)$ sections in Fig. 5. The calculated curves are spinodals and comprise a narrower $p(x_2)$ region than the corresponding coexistence curves, as they should do. The location of the calculated spinodals is in good agreement with that of the experimental coexistence curves.

Discussion

The aim of the present study was the development of adequate equations describing fluid-fluid phase be-

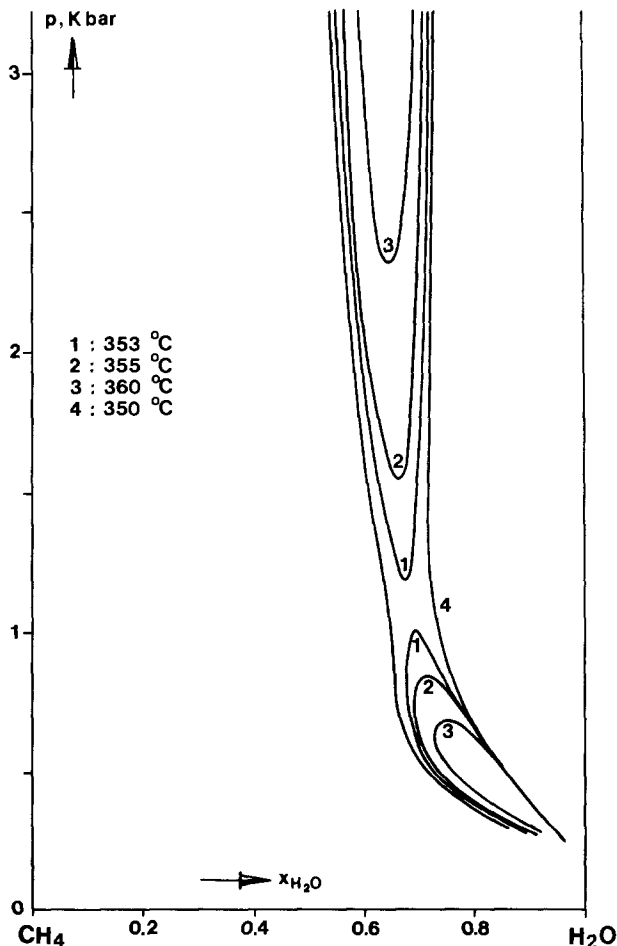


Fig. 4. Spinodals calculated with $v_0 = 25, m_{CH_4} = 1.35,$ and $m_{H_2O} = 0.72$ at indicated temperatures in °K.

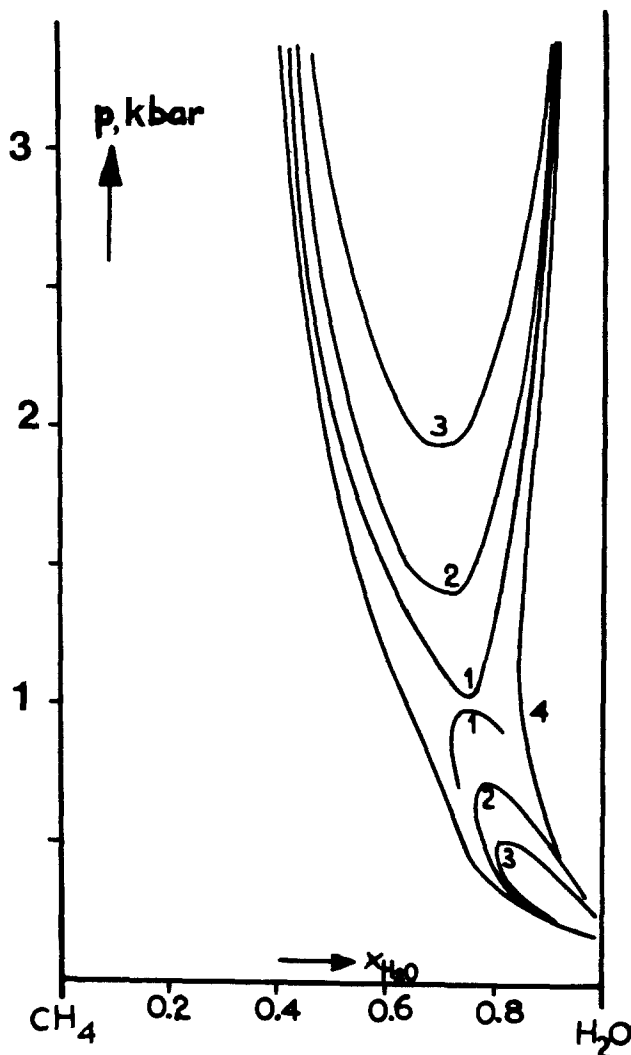


Fig. 5. Experimental coexistence curves, in the system $\text{CH}_4\text{-H}_2\text{O}$. For temperatures see caption of Fig. 4.

havior and involving a minimum number of adaptable parameters. Using the two-component lattice-gas model as a starting point we found the introduction of interacting-surface-area ratios to relax the lattice model sufficiently without undue increase in number of adjustable parameters. As yet we did not ascertain whether this favorable situation is either brought about or limited by an important assumption underlying all our calculations, *viz.* the independence of the lattice cell volume v_0 of concentration, temperature, and pressure. This assumption was made to avoid the need to draw up arbitrary mixing rules for v_0 , and thus to reduce the number of purely empirical parameters. It should be noted, however, that the choice of the number of lattice sites m , occupied by molecules, fixes the value of v_0 for a substance. Intuitively one would object to values of m deviating considerably from unity when small molecules like CO_2 are concerned. The values we used for v_0 on a number of substances and systems (about $20 \text{ cm}^3/\text{mole}$) agree fairly well with the equilibrium value estimated by Frenkel (3).

The surface-area ratios ρ , number of occupied lattice sites m , and cell volume v_0 are parameters open to appraisal on physical grounds. This is also true for

the parameter g which is related to the interaction energy between adjacent molecules. It proved necessary, however, to correct the entropy of mixing terms in the Helmholtz free energy expressions (logarithmic terms in Eq. [1] and [5]) with merely empirical parameters (α and g_{110}) which have to be accepted at face value. Yet, the fact that the ΔF expressions developed here can be fitted so well to experimental data gives some credence to the mathematical form of the equations. It is probably the interacting surface-area ratio which mainly provides for the versatility of the present treatment.

In this study we derived values for the various parameters from a minimum number of experimental data, in order to be able to test the predictive value of the procedure. Alternatively, one might optimize the parameters using all experimental data available and thus possibly obtain better descriptions. Apart from phase-equilibrium data, the present objective, one could also use compressibilities and thermal expansion coefficients. This is a subject of current study.

Manuscript submitted April 16, 1980; revised manuscript received June 10, 1980. This was Paper 548 presented at the St. Louis, Missouri, Meeting of the Society, May 11-16, 1980.

Any discussion of this paper will appear in a Discussion Section to be published in the June 1981 JOURNAL. All discussions for the June 1981 Discussion Section should be submitted by Feb. 1, 1981.

Publication costs of this article were assisted by the Central Laboratory DSM.

REFERENCES

1. N. D. Mermin, *Phys. Rev. Lett.*, **26**, 957 (1971).
2. G. W. Mulholland and J. J. Rehr, *J. Chem. Phys.*, **60**, 1297 (1974).
3. J. Frenkel, "Kinetic Theory of Liquids," Dover Publ., New York (1947).
4. F. Cernuschi and H. Eyring, *J. Chem. Phys.*, **7**, 547 (1939).
5. J. Altar, *ibid.*, **5**, 577 (1937).
6. N. J. Trappeniers, J. A. Schouten, and C. A. ten Seldam, *Chem. Phys. Lett.*, **5**, 541 (1970).
7. J. A. Schouten, C. A. ten Seldam, and N. J. Trappeniers, *Physica*, **73**, 556 (1974).
8. E. A. Guggenheim, "Mixtures," Clarendon Press, Oxford (1952).
9. G. Kanig, *Kolloid Z. Z. Polym.*, **190**, 1 (1963); **233**, 829 (1969).
10. J. T. Bartis and C. K. Hall, *Physica*, **78**, 1 (1974).
11. I. C. Sanchez and R. H. Lacombe, *J. Phys. Chem.*, **80**, 2352, 2568 (1976).
12. Y. Arai and S. Saito, *J. Chem. Eng. Jpn.*, **5**, 9 (1972).
13. A. J. Staverman, *Rec. Trav. Chim.*, **56**, 885 (1937).
14. P. J. Flory, *J. Am. Chem. Soc.*, **87**, 1833 (1965).
15. M. L. Huggins, *J. Phys. Chem.*, **74**, 371 (1970); **75**, 1255 (1971).
16. L. A. Kleintjens, H. M. Schoffeleers, and R. Koningsveld, *Ber. Bunsenges.*, **81**, 980 (1977).
17. L. A. Kleintjens, R. Koningsveld, and M. Gordon, *Macromolecules*, **13**, 303 (1980).
18. J. S. Rowlinson, "Liquids and Liquid Mixtures," Butterworth, London (1959).
19. L. A. Kleintjens, Ph.D. Thesis, Essex U.K. (1979).
20. H. E. Stanley, "Introduction to Phase Transitions and Critical Phenomena," Clarendon Press, Oxford (1971).
21. See, e.g., G. M. Schneider, *Pure Appl. Chem.*, **47**, 277 (1976).
22. H. Welsch, Ph.D. Thesis, Karlsruhe (1973).
23. R. G. Sultanov, V. G. Skriřka, and A. Yu. Namiot, *Russ. J. Phys. Chem.*, **46**, 1238 (1972).

Pressure Dependence of the Oxygen Electrode

Eddie Morild¹ and Jan E. Ølmheim

Department of Chemistry, University of Bergen, N-5014 Bg-U, Bergen, Norway

ABSTRACT

A commercial oxygen electrode (YSI 5750) has been calibrated from 1 to 1500 bar. The theory of the pressure dependence of the electrode processes, the oxygen fugacity, and the membrane permeability is presented. A short treatment of the use of the electrode in measuring kinetic processes under pressure is also given. The activation volume for the diffusion through the membrane has been found to be $58 \pm 2 \text{ cm}^3 \text{ mole}^{-1}$. The diffusion is always the rate-determining step. When the increase in oxygen fugacity with pressure is not taken into consideration, the observed activation volume is $25 \pm 2 \text{ cm}^3 \text{ mole}^{-1}$.

It is of general interest to learn how oxygen is produced and consumed in different environments and under different circumstances. By means of the Clark oxygen electrode, *in situ* measurements can be continuously performed all over the earth, and also down to depths of 10⁴m in the oceans. In principle, all kinds of oxygen exchange in chemical and biological systems can be studied with this electrode at high pressures. But the electrode itself is influenced by pressure to such an extent that a thorough calibration is necessary before use. Nevertheless, some earlier workers have made detailed investigations both of the oxygen content of old bottom seawater and of the respiration of biological organisms without this calibration. It is a drawback that the processes taking place at the electrode are complex and not properly known as functions of pressure. A calibration is therefore necessary and suffices when supplied with data on the high pressure oxygen partial pressure. The instruction note states: "The membrane passes oxygen at a rate proportional to the pressure difference across it. Since oxygen is rapidly consumed at the cathode, it can be assumed that the oxygen concentration under the membrane is zero. Hence, the force causing the oxygen to diffuse through the membrane is proportional to the absolute pressure of oxygen outside the membrane. If the oxygen pressure increases, more oxygen will diffuse through the membrane and more current flows through the sensor. A lower pressure results in less current." This is all perfectly true at ordinary pressures, say, to a few atmospheres. But we shall see that it is no longer true at high pressure. We seek here to develop the theory of this electrode at high pressure as far as possible and present the calibration curve up to more than 10³ bar.

Experimental

The oxygen electrode (cathode) used is a Yellow Springs Instrument Company (YSI) 5750 nonstirring B.O.D. bottle probe, a complete voltammetric system. The oxygen cathode (Fig. 1) is a thin circular gold foil covered with a 0.001 in. FEP Teflon permeable membrane stretched over the sensor system. This isolates the sensor elements from the environment, but allows gases to enter. The reference electrode in lower middle is a silver/silver chloride electrode with half-saturated KCl as electrolyte and also functions as anode. When a polarizing voltage of 0.8V is applied across this sensor system, oxygen that has passed through the membrane reacts at the cathode, causing a current to flow. The probe current with air as medium at 30°C is 19 μ , according to specifications. A small problem was caused by the pressure difference over the membrane due to the compression of the inner electrolyte volume. Some irregularities followed, and the membrane was often damaged. Usually, this was

avoided by not fastening the membrane too tight. Another type of dissolved oxygen probe (YSI 5739) has a pressure compensating system with an electrolyte bypass through a vent on the side of the probe to the inside of the membrane. In this way there is no build-up of pressure across the membrane.

For proper functioning of the electrode, stirring is required. This was achieved magnetically, by enclosing the small beaker above an electromotor equipped with a bar magnet within a Teflon tube as shown in Fig. 2. The oxygen probe was brought into the beaker through a rubber stopper, ensuring that no air bubbles were trapped between the solution and the stopper.

The pressure chamber was made of steel, with an inside diameter of 3.5 cm and 30 cm depth. The whole chamber was filled with hydraulic oil and surrounded by a thermostatted oil bath. The electrode system was immersed in the oil with electrical connections through the lid. Control of the stirring rate at high pressure was obtained by measuring the rotation frequency with an oscilloscope coupled in parallel with the electromotor. The rate was reduced to about one-fifth at 1000 bar, due to viscosity increase of the oil, and this had to be compensated by an increased voltage. The temperature of the thermostatted chamber was maintained at $25.0^\circ \pm 0.1^\circ \text{C}$.

The pressure was generated by an Enerpac hand-pump system, and was known to ± 10 bar at the highest pressures.

Oxygen content was determined by the Winkler method, using analytical reagent chemicals. As a check on the linearity of the response of the electrode system, it was standardized every day with three solutions: (i) distilled water, boiled with $\text{Na}_2\text{S}_2\text{O}_5$ to remove traces of oxygen (this fixed the zeropoint reading on the recorder), (ii) distilled water saturated with air at 5°C and allowed to stand for equilibration with air at 25°C, (iii) distilled water saturated with pure oxygen at 5°C and allowed to stand for equilibration

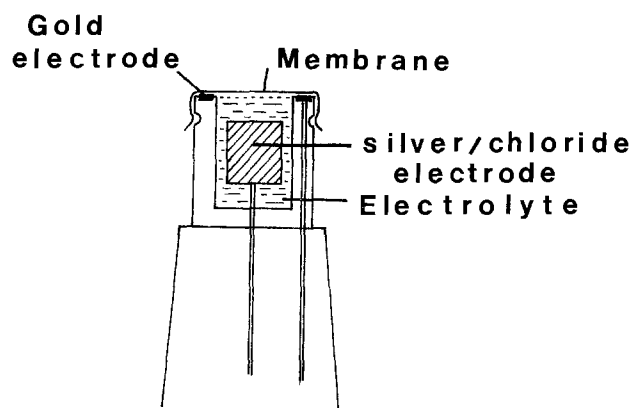


Fig. 1. The oxygen electrode (cathode)

¹Also at The Norwegian Underwater Institute N-5034 Gravdal, Bergen, Norway.

Key words: membrane, kinetics, diffusion.

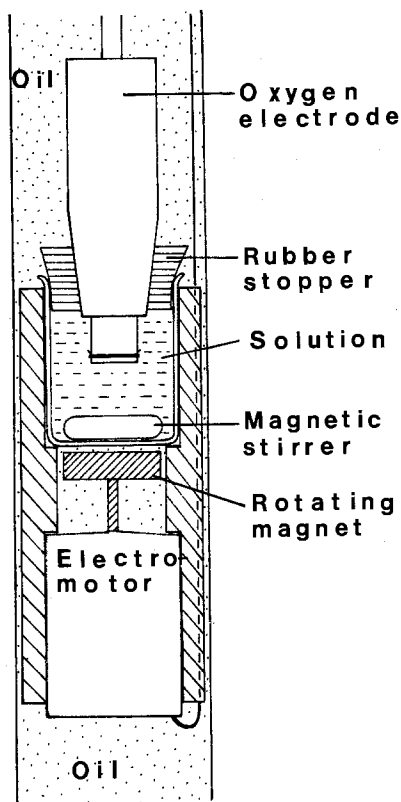


Fig. 2. Experimental setup during the high pressure calibration measurements. The electrode, beaker, and electromotor were immersed in the oil-filled pressure chamber.

with oxygen at 25°C. In both cases saturation was obtained by bubbling gas through the solution for 15 min.

Partial molal volume measurements of H_2O_2 were performed with a Paar DMA O2C digital densimeter. The accuracy was of the order 10^{-6}g cm^{-3} . All densities were measured with pure water and expressed relative to the density of water, 0.997075g cm^{-3} at 25.00°C. The temperature control was automatic, with a Hewlett-Packard quartz thermometer, and had an accuracy of $\pm 4^\circ \times 10^{-3}\text{C}$. The partial molal volume was determined from the equation

$$V = 1000(d_o - d_s)/md_o d_s + M_s/d_s$$

where d_o is the density of water, d_s the density of the solution, m the molarity of the solution, and M_s the molecular weight of the solute. $V^\circ(\text{H}_2\text{O}_2)$ at infinite dilution was obtained by extrapolation along the m -axis. The H_2O_2 used was Merck 30% hydrogen peroxide "Medizinisch Rein."

Membrane permeability of the Teflon membrane at high pressure was studied with the apparatus shown in Fig. 3. An oxygenated solution was brought into one compartment, and boiled, nearly oxygen-free solution was brought into the other compartment, separated by the membrane. Stirring was effected by an electro-motor in each end. Diffusion was allowed for an hour at various pressures, and oxygen content was checked by means of the electrode before and after diffusion. Corrections were applied for the time of mounting and dismounting the pressure chamber system.

Theory

There are at least five different factors influencing the measured current when high pressure is applied. These will be treated in order, but first it must be emphasized that the analysis of charge-transfer reactions under pressure is difficult due to the indeterminacy of single electrode potentials. In principle, every rate process may be described in terms of the transition-state theory, assuming formation of an activated complex. Strictly, the volume of activation

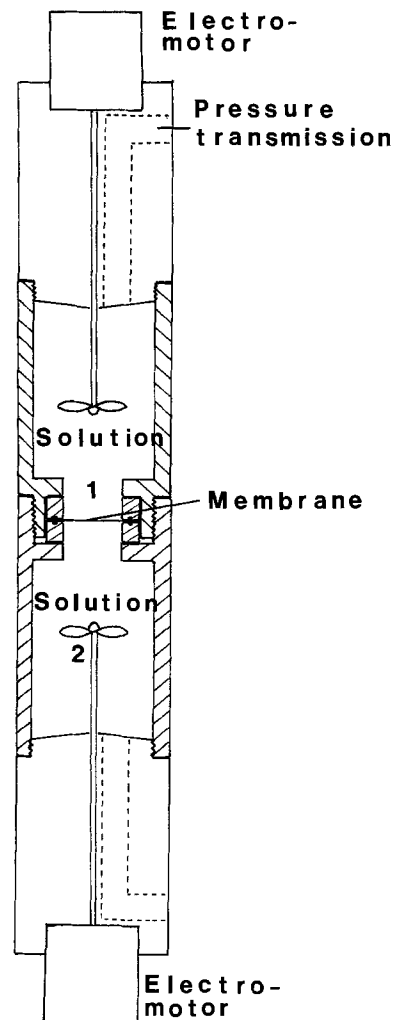
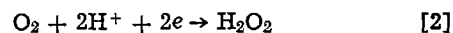


Fig. 3. Experimental setup for measurement of membrane permeability at high pressure. This compartment system was made of PVC and was completely filled with the two solutions, one oxygenated and one deoxygenated. The system was immersed in the oil-filled pressure chamber, and the pressure was transmitted through holes in the top and the bottom block.

$$\Delta V^\ddagger = RT \left(\frac{\partial \ln i}{\partial p} \right)_{T, \mu, \phi} \quad [1]$$

is here indeterminate due to the inconstancy of the inner (Galvani) potential of the electrode participating in the charge-transfer process with current i (1). Nevertheless, we will use the quantity ΔV^\ddagger in search of a qualitative indication on the rate-determining process at high pressure.

Activation at the Au electrode.—The electrode reaction for the reduction of oxygen occurs via hydrogen peroxide which is a more or less stable intermediate (2)



This reaction is followed by a certain activation volume characteristic of the transition step in the electrode process. If this activation volume was large enough, this electrode process could in principle be rate determining at high pressure.

Activation at the Ag/AgCl electrode.—Because the current density at this electrode is small and the electrode surface relatively large, its influence on the overall process is probably negligible. Even if there were a large activation volume associated with the AgCl formation, it is very unlikely that this electrode process should be rate determining at high pressure.

Oxygen partial pressure change.—If we denote by k some effective rate-determining parameter at any pres-

sure, and the fugacity (partial pressure) of oxygen is f_{O_2} , then the current i flowing through the system is given by the simple proportionality

$$i = kf_{O_2} \quad [3]$$

This strict linearity is specified by YSI and has also been verified by us by means of Winkler titration of oxygen. The solubility of oxygen in terms of mole fraction x_{O_2} is related to the fugacity through Henry's law

$$f_{O_2} = Hx_{O_2} \quad [4]$$

H is Henry's constant, ($H = 43,800$ bar). Now, the mole fraction is pressure independent, but the fugacity increases with total pressure because Henry's constant is pressure dependent. (Or can be chosen to be pressure dependent, otherwise the pressure dependence must be projected into the activity coefficient, which for our purpose amounts to the same.) Taking the standard state of oxygen to be pressure independent and at 1 bar, the variation of Henry's constant with pressure follows the relation (3)

$$\left(\frac{\partial \ln H}{\partial p} \right)_T = \left(\frac{\partial \ln (f_{O_2}/x_{O_2})}{\partial p} \right)_T = \frac{V(O_2)}{RT} \quad [5]$$

with $V(O_2)$ as the partial molar volume of dissolved oxygen. This leads to the integrated form

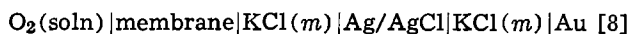
$$\ln (f_{O_2}/x_{O_2}) = \ln H^\circ + pV(O_2)/RT \quad [6]$$

where H° is Henry's constant at the standard state. The fugacities $f_{O_2}(p)$ and $f_{O_2}(0)$ at the pressure p and at atmospheric pressure are then related by

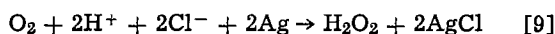
$$\ln f_{O_2}(p) = \ln f_{O_2}(0) + pV(O_2)/RT \quad [7]$$

The partial molar volume $V(O_2)$ has been determined by Enns *et al.* (4) to 32.1 ± 0.2 cm³ mole, and is practically constant in the actual pressure interval.

Pressure dependence of cell potential.—The oxygen electrode can be represented by the electrochemical cell



The overall reaction determined by this cell is



with the Nernst expression

$$\Delta\epsilon = \Delta\epsilon^\circ + \frac{RT}{2F} \ln \frac{[H^+]^2 [Cl^-]^2 f_{O_2}}{[H_2O_2]} \quad [10]$$

In the unbuffered solution, H^+ ions will be produced from water by increased ionization with pressure

$$\left(\frac{\partial \ln K_w}{\partial p} \right)_T = - \frac{\Delta V_w}{RT} \quad [11]$$

$$\begin{aligned} \left(\frac{\partial \Delta\epsilon}{\partial p} \right)_T &= \left(\frac{\partial \Delta\epsilon^\circ}{\partial p} \right)_T + \frac{RT}{F} \left(\frac{\partial \ln K_w^{1/2}}{\partial p} \right)_T \\ &\quad - \frac{RT}{2F} \left(\frac{\partial \ln V}{\partial p} \right)_T + \frac{RT}{2F} \left(\frac{\partial \ln f_{O_2}}{\partial p} \right)_T \end{aligned} \quad [12]$$

Now using the relations

$$-nF \left(\frac{\partial \Delta\epsilon}{\partial p} \right)_T = \left(\frac{\partial \Delta G}{\partial p} \right)_T = \Delta V \quad [13]$$

and

$$\kappa_T = - \left(\frac{\partial \ln V}{\partial p} \right)_T \quad [14]$$

Eq. [12] turns into

$$\begin{aligned} \Delta V &= \Delta V^\circ + RT \left(\frac{\partial \ln K_w}{\partial p} \right)_T \\ &\quad - RT \left(\frac{\partial \ln f_{O_2}}{\partial p} \right)_T - RT\kappa_T \end{aligned} \quad [15]$$

which by means of Eq. [5] and [11] results in

$$\Delta V = \Delta V^\circ + \Delta V_w - V(O_2) - RT\kappa_T \quad [16]$$

The standard volume of reaction ΔV° can be obtained from knowledge of all partial molar volumes in Eq. [8]

$$\begin{aligned} \Delta V^\circ &= 2\rho_{AgCl}^{-1} + \frac{1}{2} V(H_2O_2) \\ &\quad - 2\rho_{Ag}^{-1} - 2V(HCl) - V(O_2) \end{aligned} \quad [17]$$

The pressure dependence of the cell potential can then be calculated.

Change of diffusion rate with pressure.—There is a diffusion of oxygen molecules through the Teflon membrane, and the measured current may be described by the oxygen gradient over the membrane

$$i = -D_c \frac{dc}{dx} = D_f \frac{f_{O_2}}{\delta} \quad [18]$$

where D_c and D_f are diffusion coefficients on concentration and fugacity scales, respectively. δ is the diffusion distance, the thickness of the membrane. The last term in Eq. [18] holds when the diffusion process is rate determining. In the case of homogeneous diffusion in solution we could have written

$$\left(\frac{\partial \ln i}{\partial p} \right)_T = - \frac{\Delta V_{D^\ddagger}}{RT} \quad [19]$$

where ΔV_{D^\ddagger} would have been the usual volume of activation due to the pressure dependence of the diffusion coefficient. Then, ΔV_{D^\ddagger} would be of the order of $+(10-20)$ cm³ mole⁻¹, so that diffusion rate would be reduced with pressure. Considering the diffusion problem with the dropping mercury electrode, Hills (5) argues that the product $cD^{1/2}$ is not appreciably pressure independent. So in the present problem we have to consider the change in membrane permeability, with unknown ΔV^\ddagger , along with changes in f_{O_2} and δ

$$\left(\frac{\partial \ln i}{\partial p} \right)_T = \left(\frac{\partial \ln D_f}{\partial p} \right)_T + \left(\frac{\partial \ln f_{O_2}}{\partial p} \right)_T - \left(\frac{\partial \ln \delta}{\partial p} \right)_T \quad [20]$$

From the diffusion measurements under pressure we are only able to measure the combined effect of the first and last term of the rhs of Eq. [20]

$$\left(\frac{\partial \ln k}{\partial p} \right)_T = \left(\frac{\partial \ln D_f/\delta}{\partial p} \right)_T = - \frac{\Delta V_{k^\ddagger}}{RT} \quad [21]$$

If the diffusion is rate determining, the measured current change with pressure should be described by the relation

$$\left(\frac{\partial \ln i}{\partial p} \right)_T = - \frac{\Delta V_{i^\ddagger}}{RT} = - \frac{\Delta V_{k^\ddagger}}{RT} + \frac{V(O_2)}{RT} \quad [22]$$

corresponding to Eq. [3].

If the measured values of ΔV_{i^\ddagger} and ΔV_{k^\ddagger} does not satisfy Eq. [22], it is probable that one of the electrode reactions is rate determining. In this case, ΔV_{k^\ddagger} can be reinterpreted and calculated from

$$\Delta V_{k^\ddagger} = \Delta V_{i^\ddagger} + V(O_2) \quad [23]$$

Calibration and Use

In any case, a measurement of i vs. p yields a sufficient calibration of the electrode. Integration of Eq. [22] results in

$$\ln i(p) = \ln i(0) - \frac{p\Delta V_{i^\ddagger}}{RT} \quad [24]$$

and by using [3], we obtain

$$f_{O_2}(0) = (i(p)/k(0)) \exp(p\Delta V_{i^\ddagger}/RT) \quad [25]$$

Here $f_{O_2}(0)$ is the fugacity of oxygen measured at the pressure p , reduced to atmospheric pressure. The measured current at p is $i(p)$ and the proportionality constant in Eq. [3] is $k(0)$ at atmospheric pressure.

An interesting application of the oxygen electrode is its use as a probe of oxygen in kinetic process under pressure. Differentiating Eq. [3] with respect to time, we get

$$v_c = \frac{di}{dt} = k \frac{df_{O_2}}{dt} = kv_{O_2} \quad [26]$$

where v_c is the rate of current change and v_{O_2} is the rate of fugacity change. The oxygen-producing (consuming) process is characterized by a certain activation volume $\Delta V_{O_2^\ddagger}$, which is the interesting quantity. Then

$$\left(\frac{\partial \ln v_{O_2}}{\partial p} \right)_T = - \frac{\Delta V_{O_2^\ddagger}}{RT} \quad [27]$$

The logarithm of Eq. [26] is

$$\ln v_c = \ln k + \ln v_{O_2} \quad [28]$$

which by differentiation with respect to pressure yields

$$\left(\frac{\partial \ln v_c}{\partial p} \right)_T = \left(\frac{\partial \ln k}{\partial p} \right)_T + \left(\frac{\partial \ln v_{O_2}}{\partial p} \right)_T \quad [29]$$

The first term is characterized by an activation volume ΔV_{c^\ddagger} , and then

$$\Delta V_{O_2^\ddagger} = \Delta V_{c^\ddagger} - \Delta V_{k^\ddagger} = \Delta V_{c^\ddagger} - \Delta V_{i^\ddagger} - V(O_2) \quad [30]$$

It is rather probable that the $\ln v_c$ vs. p curve is not a straight line, but of the general form

$$\ln v_c = a_0 + a_1 p + a_2 p^2 + a_3 p^3 + \dots \quad [31]$$

so that

$$\left(\frac{\partial \ln v_c}{\partial p} \right)_T = a_1 + 2a_2 p + 3a_3 p^2 + \dots \quad [32]$$

The correction necessary to find the curve of $\ln v_{O_2}$ vs. pressure is then

$$\left(\frac{\partial \ln v_c}{\partial p} \right)_T - \left(\frac{\partial \ln k}{\partial p} \right)_T = a_1 + \frac{\Delta V_{i^\ddagger}}{RT} + \frac{V(O_2)}{RT} + 2a_2 p + 3a_3 p^2 + \dots \quad [33]$$

and at last

$$\ln v_{O_2}(p) = \ln v_{O_2}(0) + \left[a_1 + \frac{\Delta V_{i^\ddagger}}{RT} + \frac{V(O_2)}{RT} \right] p + a_2 p^2 + a_3 p^3 + \dots \quad [34]$$

Results

To calculate the standard volume of reaction, ΔV° in Eq. [17] we need the molar volume of H_2O_2 , which has not been found in the literature. From density measurements on a dilution series of aqueous H_2O_2 , $V(H_2O_2)$ was determined by extrapolation to infinite dilution, Fig. 4. The volume was found to be $V(H_2O_2) = 22.8 \pm 0.4 \text{ cm}^3 \text{ mole}^{-1}$.

From known values of the density of solid Ag and AgCl (6), the partial molar volumes of HCl (7) and O_2 (4), we found

$$\Delta V^\circ = 2 \cdot 25.8 + 22.8 - 2 \cdot 10.3 - 2 \cdot 17.9 - 32.1 = -18.1 \text{ cm}^3 \text{ mole}^{-1}$$

Then the pressure dependence of the standard potential is

$$\left(\frac{\delta \Delta \epsilon^\circ}{\delta p} \right)_T = \frac{\Delta V^\circ}{2F} = 9.3 \cdot 10^{-6} \text{ V bar}^{-1}$$

which means that the potential increases 9.3 mV with a pressure increase of 10^3 bar.

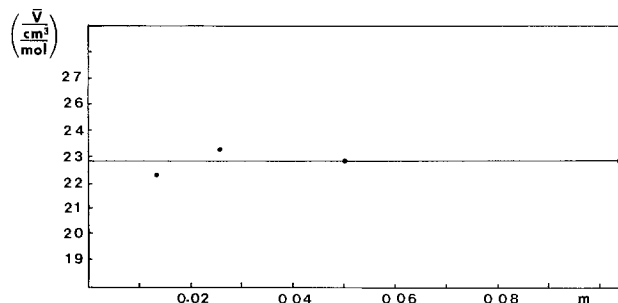


Fig. 4. Concentration (molality) dependence of the partial molar volume of H_2O_2 .

The overall volume change, considering dissociation and compression, is given by Eq. [15]

$$\Delta V = -18.1 - 22.1 - 32.1 - 1.1 = -73.4 \text{ cm}^3 \text{ mole}^{-1}$$

where ΔV_w° is taken from Ref. (8). This represents a pressure dependence of the equilibrium potential

$$\left(\frac{\delta \Delta \epsilon}{\delta p} \right)_T = 38.5 \cdot 10^{-6} \text{ V bar}^{-1}$$

This means an increase of 38.5 mV at 1000 bar. Now, the polarographic process is a nonequilibrium situation and the calculated values cannot be directly applied here. However, a polarographic study of this system (9) has shown that potential changes of less than 100 mV result in negligible changes in current, because the current-voltage curve has a plateau centered at the applied voltage. It is therefore reasonable to believe that the change in current due to indirect effects of pressure on the polarization voltage can be neglected. Figure 5 is a plot of $\ln i$ vs. p for different oxygen fugacities. The lower curve, No. 1, represents the oxygen fugacity in air-saturated water and No. 3 represents about half oxygen-saturated water. No. 2 represents an intermediate between these and No. 4 represents water saturated with oxygen from enzymatic degradation of H_2O_2 to O_2 under a pressure of 33 bar. With the possible exception of curve No. 1, they are all linear with pressure and have a slope

$$\left(\frac{\delta \ln i}{\delta p} \right)_T = - \frac{\Delta V_{i^\ddagger}}{RT} = -1.013 \cdot 10^{-3} \text{ bar}^{-1}$$

which yields a volume of activation, $\Delta V_{i^\ddagger} = 25.1 \text{ cm}^3 \text{ mole}^{-1}$. Now the volume change of the rate-determining process, deduced from Eq. [23] can be calculated

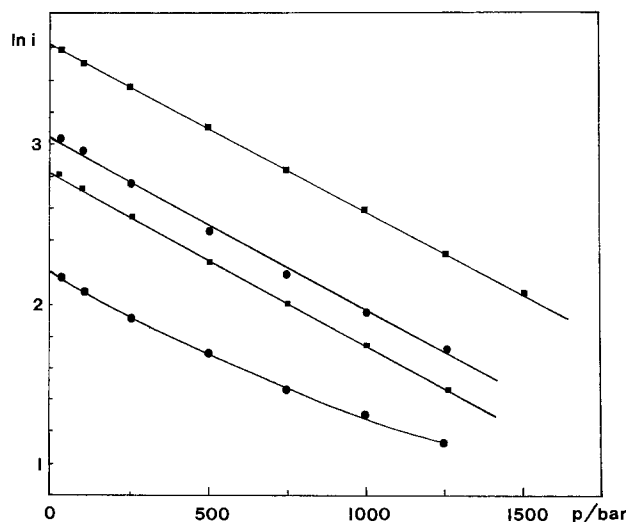


Fig. 5. Plot of the logarithm of the measured current i , as a function of total hydrostatic pressure p . See text.

$$\Delta V_{k\ddagger} = 25.1 + 32.1 = 57.2 \text{ cm}^3 \text{ mole}^{-1}$$

This is the volume change that results when it is taken into account that the oxygen fugacity increases with pressure. All other factors being constant, the current should increase when the oxygen fugacity is increased. When this is not so, it must be because the other processes going on have a total pressure dependence that more than compensates for the effect of the fugacity increase. The result from the studies of the membrane permeability as a function of pressure is shown in Fig. 6. The ordinate is the logarithm of a relative measure of the amount of oxygen that has permeated the membrane during 1 hr. The initial slope of the curve corresponds to a volume change which can be interpreted as the activation volume for the diffusion process in the membrane. The oxygen flux j through the membrane has a pressure dependence given by

$$\left(\frac{\partial \ln j}{\partial p} \right)_T = \left(\frac{\partial \ln D_f/\delta}{\partial p} \right)_T + \left(\frac{\partial \ln f_{O_2}}{\partial p} \right)_T$$

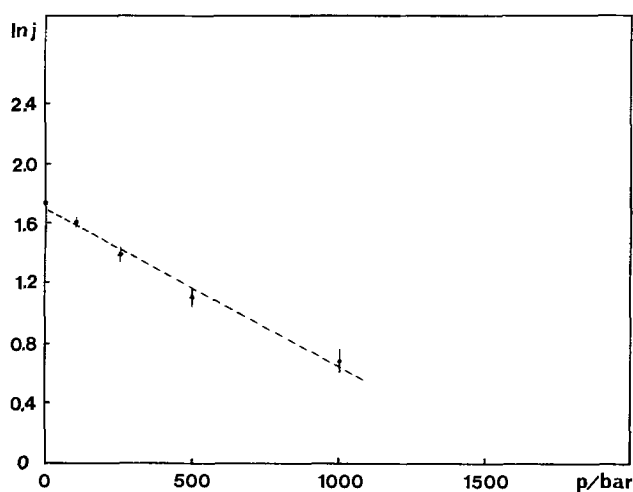


Fig. 6. Plot of the logarithm of the oxygen flux j through the Teflon membrane, as a function of total hydrostatic pressure p .

associated with the volume changes

$$\Delta V_{j\ddagger} = \Delta V_{k\ddagger} - V(O_2)$$

The average value of the slope was found to be $\Delta V_{j\ddagger} = 26 \text{ cm}^3 \text{ mole}^{-1}$ and this leads to the value $\Delta V_{k\ddagger} = 58 \text{ cm}^3 \text{ mole}^{-1}$. This is an appreciable pressure dependence, and it is clear that the membrane diffusion is rate determining. The experimental uncertainty here is about $\pm 2 \text{ cm}^3 \text{ mole}^{-1}$, so this value is in good agreement with the value $57.2 \text{ cm}^3 \text{ mole}^{-1}$. Then, as could be expected, the whole electrode is operating under total mass transfer control also at high pressure. The pressure effects on the Au and the Ag/AgCl electrodes are screened by the effect on the membrane and cannot be observed.

Acknowledgment

We are grateful to Prof. J. G. Hills for reading part of the manuscript.

Manuscript submitted Jan 29, 1980; revised manuscript received approximately May 26, 1980.

Any discussion of this paper will appear in a Discussion Section to be published in the June 1981 JOURNAL. All discussions for the June 1981 Discussion Section should be submitted by Feb. 1, 1981.

REFERENCES

1. G. Hills, in "Second Austr. Conf. on Electrochem.," p. 39, Melbourne, Butterworths & Co., Sydney (1968).
2. I. Koryta, J. Dvorak, and V. Bohackova, "Electrochemistry," p. 311, Methuen & Co., London (1970).
3. M. G. Gonikberg, "Chemical Equilibria and Reaction Rates at High Pressures," Ch. IV., Israel Prog. Sci. Trans., Jerusalem (1963).
4. T. Enns, P. F. Scholander, and E. D. Bradstreet, *J. Phys. Chem.*, **69**, 389 (1965).
5. G. Hills, *Talanta*, **12**, 1317 (1965).
6. "Handbook of Chemistry and Physics," **57**, CRC (1976).
7. F. J. Millero, *Chem. Rev.*, **71**, 147 (1971).
8. G. Olofsson and L. G. Hepler, *J. Solut. Chem.*, **4**, 127 (1975).
9. D. E. Carritt and J. W. Kanwisher, *Anal. Chem.*, **31**, 5 (1959).

Oxygen Evolution on $\text{La}_{1-x}\text{Sr}_x\text{Fe}_{1-y}\text{Co}_y\text{O}_3$ Series Oxides

Y. Matsumoto, S. Yamada, T. Nishida, and E. Sato*

Department of Industrial Chemistry, Faculty of Engineering,
Utsunomiya University, Ishi-icho 2753, Utsunomiya, Japan

ABSTRACT

$\text{La}_{1-x}\text{Sr}_x\text{Fe}_{1-y}\text{Co}_y\text{O}_3$ series oxides with perovskite-type structure were synthesized and were examined as the electrode for the oxygen evolution reaction in alkaline solution. The oxides except for $\text{SrCoO}_{2.5}$, LaFeO_3 , and their neighbors were suitable for the electrode with respect to high conductivity. The catalytic activity for the oxygen evolution reaction increases along the direction from LaFeO_3 to SrCoO_3 in composition. It is concluded that the following two conditions are desirable for the perovskite-type oxide with high catalytic activity for the oxygen evolution reaction: (i) the oxide has a broad σ^* band and (ii) the transition metal cation in the oxide exists as the higher oxidation state. In addition, it was found that the catalytic activity of $\text{La}_{0.2}\text{Sr}_{0.8}\text{Fe}_{0.2}\text{Co}_{0.8}\text{O}_3$ is the highest in the oxides prepared in this study.

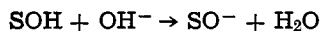
Some of the perovskite-type oxides with high electronic conductivity show good catalytic activity for the oxygen evolution reaction (1-3) and the oxygen reduction (4-7). In particular, the perovskite-type oxides containing Co, Fe, and Ni ions in the lattice

are excellent in catalytic activity for the oxygen evolution reaction in alkaline solution (1-3). For example, the overvoltages of the partly substituted SrFeO_3 with Ni and Co ions are very low for the oxygen evolution reaction (3). The catalytic activity will be mainly determined by the σ^* band formation of the M-O-M in the lattice which enhances electron transfer from the chemical species, OH^- , into the electrode surface

* Electrochemical Society Active Member.

Key words: oxygen evolution, perovskite-type oxide, electrocatalysis.

(1). In addition to the electron transfer step, chemical reaction steps are also in the process of the oxygen evolution reaction. For the chemical reaction step such as



the higher oxidation state of the transition metal ion in the perovskite-type oxide is preferable to the lower oxidation state as shown in the previous paper (2), where S stands for the transition metal ion on the surface.

Therefore, as for the oxygen evolution reaction on the perovskite-type oxide electrode with high conductivity, (i) the σ^* band formation and (ii) the higher oxidation state of the metal ion in the oxide will be desirable for high catalytic activity. In this paper, the catalytic properties of $\text{La}_{1-x}\text{Sr}_x\text{Fe}_{1-y}\text{Co}_y\text{O}_3$ series oxides with perovskite-type structure for the oxygen evolution reaction in alkaline solution are studied and the above two conclusions for the catalytic property are deduced from the variation of the catalytic activity with x and y . The oxide electrocatalyst with the highest catalytic activity in this series of oxides is $\text{La}_{0.2}\text{Sr}_{0.8}\text{Fe}_{0.2}\text{Co}_{0.8}\text{O}_3$.

Experimental

$\text{La}_{1-x}\text{Sr}_x\text{Fe}_{1-y}\text{Co}_y\text{O}_3$ series oxides were synthesized by using La_2O_3 , SrCO_3 , CoO , and Fe_2O_3 as the starting materials. These materials were stoichiometrically mixed with an agate mortar and then heated at 1000°C for 2 hr in air. The mixtures were reground and heated at $1250^\circ\text{--}1300^\circ\text{C}$ for 6 hr in air. The materials were shown to be synthesized perovskite-type oxides by x-ray analysis with the scanning rate $2\theta/\text{min} = 0.5^\circ/\text{min}$. The powders were pressed into tablet form with $100 \text{ kg}/\text{cm}^2$, followed by sintering at 1350°C for 1 hr. The compositions of the perovskite-type oxides are represented as ABO_3 in this paper, although the prepared oxides have some oxygen ion vacancies in the lattice, especially for the oxides having a large amount of Sr. The specific resistivities at room temperature were measured by the four-probe method. The type of the conductivity of each sample at room temperature was determined by the temperature dependence of the resistivity. The types of the semi-conductivity, n or p, were judged from the signs of the measured thermoelectric power. The thermoelectric power was measured by a digital voltmeter. In this measurement, the sintered rod samples ($10 \times 2 \times 2 \text{ mm}$) were used and the one tip was heated ($\sim 100^\circ\text{C}$). The electrodes were prepared in the same manner as described in previous papers (1-3). The current densities shown in this paper are indicated by the apparent ones based on geometrical area.

The solution was pre-electrolyzed 1M KOH. An Hg/HgO electrode was used as the reference electrode and electrode potentials cited in this paper are referred to this electrode. The main electrochemical test was made by the potential sweep method with the sweep rate of $500 \text{ sec}/\text{V}$ at 25°C . The Tafel slopes were obtained from the polarization curve under steady state in the same manner as described in previous papers (1-3).

Results

The synthesized oxides, except for SrCoO_3 , consisted of a single phase of the perovskite-type structure. The oxides synthesized in the present study are denoted by the symbol of a circle in Fig. 1, which shows the phase diagram giving the composition region of the cubic crystal system in $\text{La}_{1-x}\text{Sr}_x\text{Fe}_{1-y}\text{Co}_y\text{O}_3$. In this figure, SrCoO_3 is not of the perovskite-type structure and exists as $\text{SrCoO}_{2.5}$ in composition (8). The shaded parts indicate the cubic system and the other region was the tetragonal or the rhombohedral system except for $\text{SrCoO}_{2.5}$. The phase diagram for the resistivity is shown in Fig. 2. The oxides with $y \geq 0.2$ and $x = 1$ could not be so tightly sintered and the sintering was impossible in the region of $0.6 \leq y < 1$

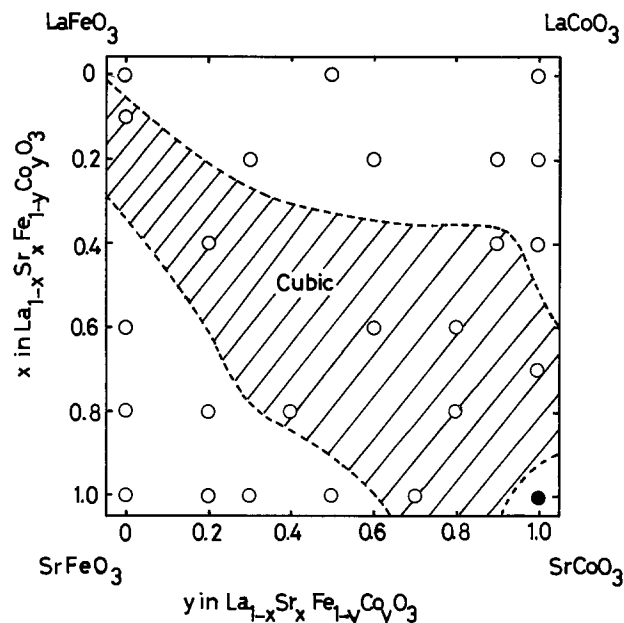


Fig. 1. Composition region of cubic crystal system in the phase diagram of $\text{La}_{1-x}\text{Sr}_x\text{Fe}_{1-y}\text{Co}_y\text{O}_3$ oxides. The shaded parts indicate the cubic crystal system. The circles denote the compositions of the oxides prepared in this study. ● denotes other structure.

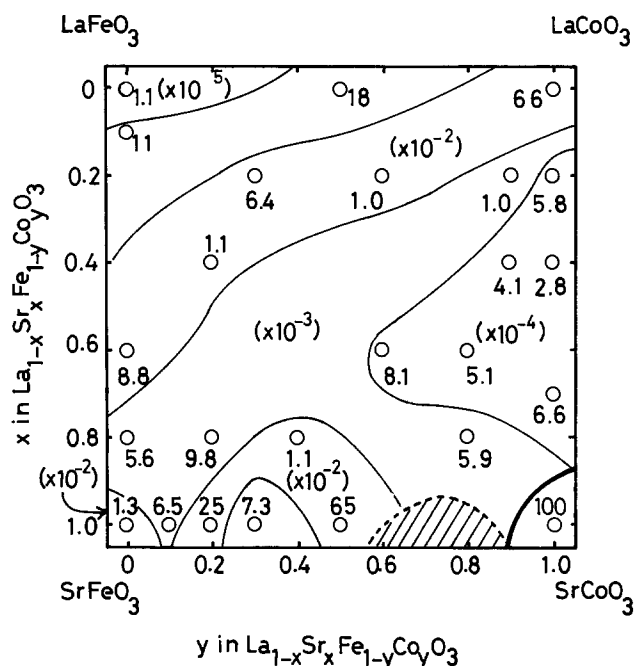


Fig. 2. Distribution of resistivity at room temperature. The unit for each value in the figure is $\Omega \cdot \text{cm}$. The shaded parts indicate the composition region of the oxides impossible for sintering.

for the case of $\text{SrFe}_{1-y}\text{Co}_y\text{O}_3$ series oxides. The shaded parts in this figure indicate the composition region where sintering is impossible. The resistivities of $\text{La}_{1-x}\text{Sr}_x\text{CoO}_3$ (8) and $\text{La}_{1-x}\text{Sr}_x\text{FeO}_3$ decrease with an increase of x , since the partially filled π^* or σ^* band comes to be formed, with an increase of M^{4+} ion to bring a large interaction with the O^{2-} ion in the lattice (9). The d orbitals of the Co ion overlap more largely with the s, p orbitals of O^{2-} ion than those of the Fe ion in the lattice of the perovskite-type oxide, leading to a large contribution to the formation of the σ^* and π^* bands. Therefore, in the case of $\text{LaFe}_{1-y}\text{Co}_y\text{O}_3$, the resistivity decreases with an increase of y (10). It follows from the above results and the theories that the resistivity is expected to decrease with the increases of x and y , i.e., along

the direction from LaFeO_3 to SrCoO_3 , in composition. In the region surrounded by LaCoO_3 , $\text{La}_{0.2}\text{Sr}_{0.8}\text{Fe}_{0.2}\text{Co}_{0.8}\text{O}_3$, and LaFeO_3 , the above expected result was qualitatively obtained as the figure shows, but not in the other region. The unexpected result in the latter region is based on the oxygen ion vacancies formed in the lattice. The oxygen ion vacancies lead to a decrease of the conductivity because of the vanishing of the interaction between the transition metal ion and the oxygen ion, M-O-M, in the lattice. There exists a large number of oxygen ion vacancies in the lattice for the oxides in the composition region having large x values. The amount of oxygen ion vacancies is qualitatively determined by the electrochemical technique described in the following section. The high resistivity of $\text{SrCoO}_{2.5}$ is assigned to the other structure in which the perfect oxygen octahedra around Co ions do not exist. After all, $\text{La}_{1-x}\text{Sr}_x\text{Fe}_{1-y}\text{Co}_y\text{O}_3$ series oxides are suitable for electrode materials of low resistivity except for $\text{SrCoO}_{2.5}$, LaFeO_3 , and their neighbors.

Figure 3 shows the type of the conductivity of the $\text{La}_{1-x}\text{Sr}_x\text{Fe}_{1-y}\text{Co}_y\text{O}_3$ series oxides, which was determined by the thermoelectric power. Strictly speaking, $\text{La}_{0.4}\text{Sr}_{0.6}\text{Fe}_{0.2}\text{Co}_{0.8}\text{O}_3$ only showed metallic conductivity and the other oxides showed semiconductivity. However, the thermoelectric powers of the oxides in the shaded parts are small, in line with the low resistivity of the oxides in this part as shown in Fig. 2. Therefore, these oxides are denoted as "semi-metal" in this figure. The semiconducting type converts at about $x = 0.5$ from p type (in the region of $x < 0.5$) to n type (in the region of $x > 0.5$), except for $\text{SrFe}_{0.7}\text{Co}_{0.3}\text{O}_3$ and $\text{SrCoO}_{2.5}$. The ratio of La to Sr ion may be responsible for the type of semiconduction in the $\text{La}_{1-x}\text{Sr}_x\text{Fe}_{1-y}\text{Co}_y\text{O}_3$ series oxides, but the type of semiconduction has no effect on the catalytic properties for the oxygen evolution reaction described in the following section. In any case, the semiconducting property, especially rectification, was not observed in the electrochemical tests, because of the degeneration of the surface due to a large number of surface states formed on the sintered disk samples.

Electrochemical properties.—Figure 4 shows the voltammogram of $\text{La}_{0.2}\text{Sr}_{0.8}\text{Fe}_{0.2}\text{Co}_{0.8}\text{O}_3$ electrode in 1M KOH at 25°C. The other oxide electrodes, except for

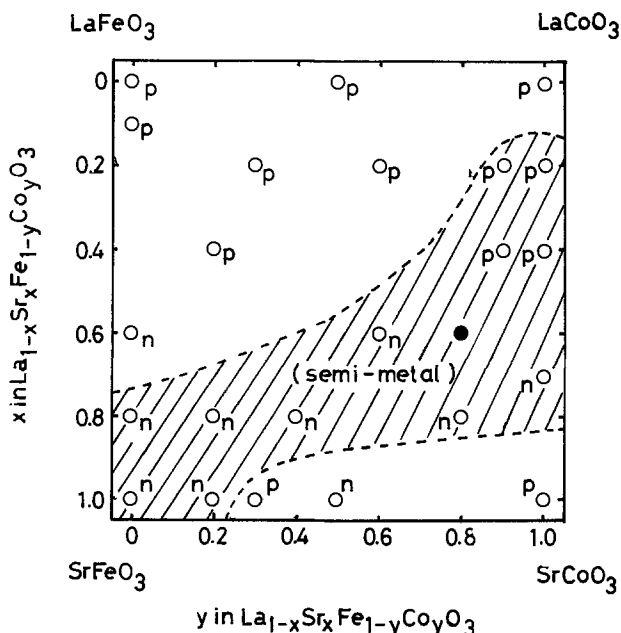


Fig. 3. Type of the conductivity. ● denotes the metallic conductivity. The shaded parts indicate "semi-metal" with small thermoelectric power.

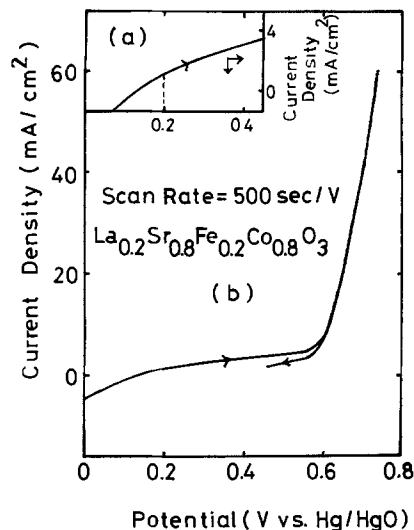


Fig. 4. Potential sweep voltammogram of $\text{La}_{0.2}\text{Sr}_{0.8}\text{Fe}_{0.2}\text{Co}_{0.8}\text{O}_3$ electrode in 1M KOH at 25°C: (a) is the figure magnifying (b) in the potential range between 0 and 0.45V.

LaFeO_3 , also showed voltammograms similar to Fig. 4. The voltammogram was taken in a restricted potential region between 0V and the potential at which the oxygen evolution current density exceeds about 65 mA/cm^2 . The plateau oxidation current observed prior to the oxygen evolution current [see (a) in Fig. 4] is assigned to the following oxidation reaction of the electrode



The oxygen ion vacancies formed in the oxide surface region are filled with oxygen ion in the OH^- by the above electrochemical reaction. The phase diagram for the current densities at 0.2V [see (a) in Fig. 4] produced by the above electrochemical oxidation reaction of the oxide is shown in Fig. 5. In the composition region with large x value in $\text{La}_{1-x}\text{Sr}_x\text{Fe}_{1-y}\text{Co}_y\text{O}_3$ series oxides, a high current density was observed, showing that the oxides in this composition region have a large amount of oxygen ion vacancies in the lattice. This is in line with the resistivity as described in the previous section.

Figures 6 and 7 show the phase diagrams for the overvoltages (η) of the oxygen evolution reaction at 40 and 60 mA/cm^2 , respectively, which were determined from the voltammograms measured under the same conditions as Fig. 4. From the contour line of the overvoltages, in general, the catalytic activity increases with increases of x and y , i.e., along the direction from LaFeO_3 to SrCoO_3 in composition. The catalytic activity of the $\text{La}_{0.2}\text{Sr}_{0.8}\text{Fe}_{0.2}\text{Co}_{0.8}\text{O}_3$ electrode was the highest in the oxide electrodes studied in the present paper as the figures show. However, the possibility will exist from the tendency of the contour lines that the catalytic activity of SrCoO_3 with perovskite-type structure is the highest in this series of oxides, if preparation is possible. The variations of the potentials with time during anodic polarization at 100 mA/cm^2 for the $\text{La}_{0.2}\text{Sr}_{0.8}\text{Fe}_{0.2}\text{Co}_{0.8}\text{O}_3$ electrode is shown in Fig. 8. The electrode potential slowly rises during 35 hr, but becomes almost invariant after 40 hr. $\text{La}_{0.2}\text{Sr}_{0.8}\text{Fe}_{0.2}\text{Co}_{0.8}\text{O}_3$ electrode, therefore, is good for use over long periods. Since there is little dissolution of this electrode, this oxide and its neighbors are suitable as anode materials in alkaline solution.

Discussion

The mechanism for the oxygen evolution reaction on the perovskite-type oxides in alkaline solution is proposed as follows (1-3, 11)

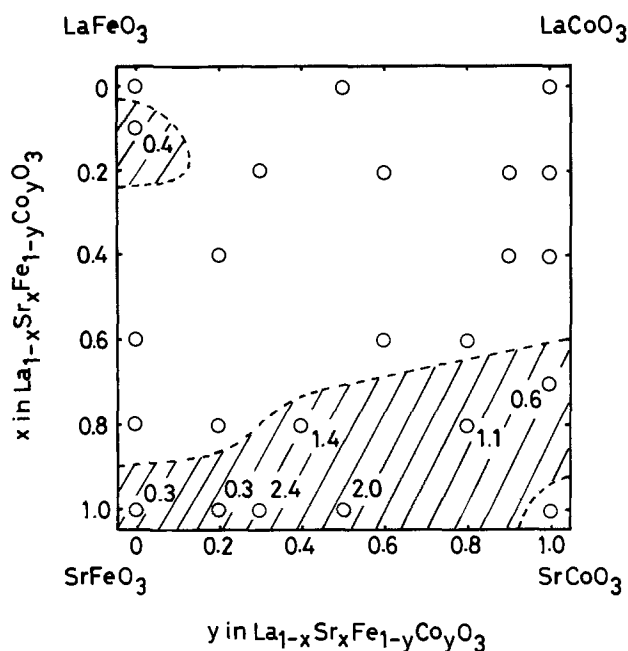


Fig. 5. Distribution of oxidation current density of electrodes at 0.2V (vs. Hg/HgO). The unit is mA/cm². The shaded parts indicate the composition region of the oxides giving the oxidation currents.

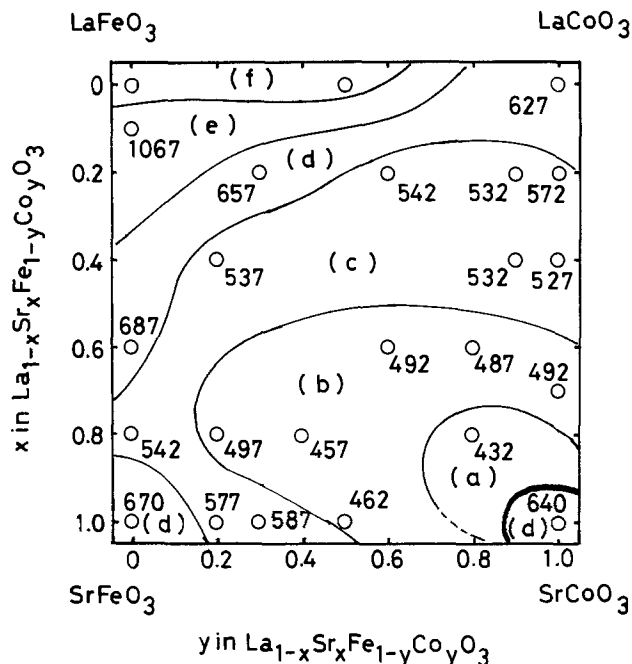


Fig. 7. Distribution of overvoltage (η) at 60 mA/cm². The unit is mV. (a) $\eta \leq 450$ mV; (b) $450 \text{ mV} < \eta \leq 500$ mV; (c) $500 \text{ mV} < \eta \leq 600$ mV; (d) $600 \text{ mV} < \eta \leq 700$ mV; (e) $700 \text{ mV} < \eta \leq 1100$ mV; (f) $\eta > 1100$ mV.

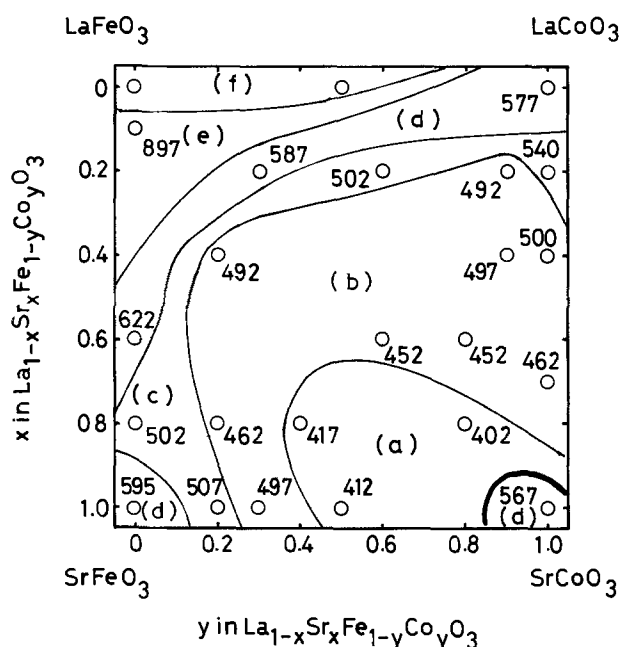
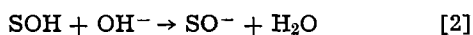
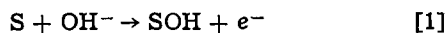


Fig. 6. Distribution of overvoltage (η) at 40 mA/cm². The unit is mV. (a) $\eta \leq 450$ mV; (b) $450 \text{ mV} < \eta \leq 500$ mV; (c) $500 \text{ mV} < \eta \leq 550$ mV; (d) $550 \text{ mV} < \eta \leq 650$ mV; (e) $650 \text{ mV} < \eta \leq 900$ mV; (f) $\eta > 900$ mV.



where S stands for the transition metal ion on the surface as described already. The rate-controlling step is the second step in the above process for the SrFeO₃ and La_{1-x}Sr_xCoO₃ electrodes (1, 2). The third step is rate controlling for the SrFe_{0.9}Co_{0.1}O₃, SrFe_{0.9}Ni_{0.1}O₃, and SrFe_{0.9}Ti_{0.1}O₃ electrodes (3), and the first step is rate controlling for the La_{1-x}Sr_xMnO₃

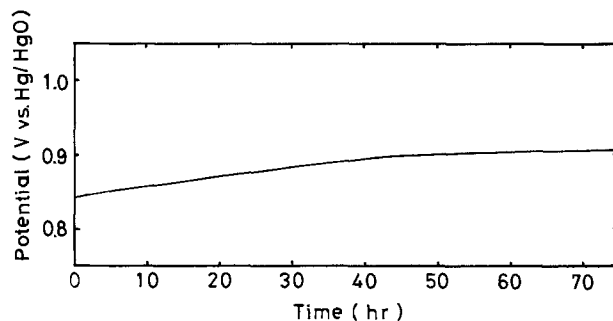


Fig. 8. Potential-time curve under anodic polarization of La_{0.2}Sr_{0.8}Fe_{0.2}Co_{0.8}O₃ electrode in 1M KOH at 100 mA/cm² at 25°C.

and SrFe_{0.9}Mn_{0.1}O₃ electrodes (3, 11) as described in the previous papers. The values of the Tafel slopes of La_{1-x}Sr_xFe_{1-y}Co_yO₃ series oxides for the oxygen evolution reaction are in the range of about 45-80 mV/decade except for SrFe_{0.7}Co_{0.3}O₃ and its neighbors as shown in Fig. 9. Under the assumption of Langmuirian adsorption conditions, this result suggests that the rate-controlling step is the second or third step for the La_{1-x}Sr_xFe_{1-y}Co_yO₃ electrodes (12). The resistivities of SrFe_{0.7}Co_{0.3}O₃ and its neighbors are relatively high, as Fig. 2 shows, and a large amount of oxygen ion vacancies exist in these oxides. Although the oxygen ion vacancy is electrochemically filled with oxygen ion, the bond strength between the newly filled oxygen ion and the transition metal ion in the lattice will be weak. Therefore, a relatively large barrier, such as a depletion layer, will be formed in the surface region of these oxides, leading to the large Tafel value.

The rates of the first and the third steps are mainly determined by the σ^* band width, that is, the rate of electron transfer increases with the increase of the σ^* band width. The d-electron configurations of LaFeO₃, SrFeO₃, LaCoO₃, and SrCoO₃ are shown in Fig. 10. In the case of SrCoO₃, the d-electron configuration is given for the ideal stoichiometrical SrCoO₃ with perovskite-type structure. The σ^* band width increases with increase of x for the

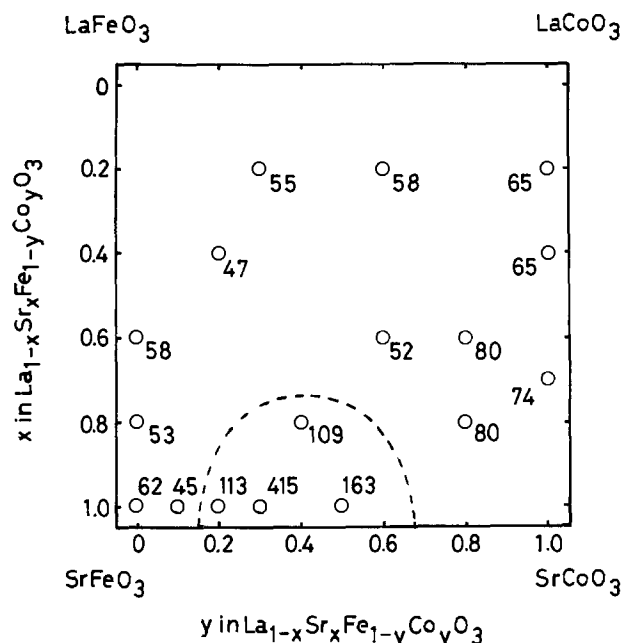


Fig. 9. Distribution of Tafel value for the oxygen evolution reaction. The unit is mV/decade.

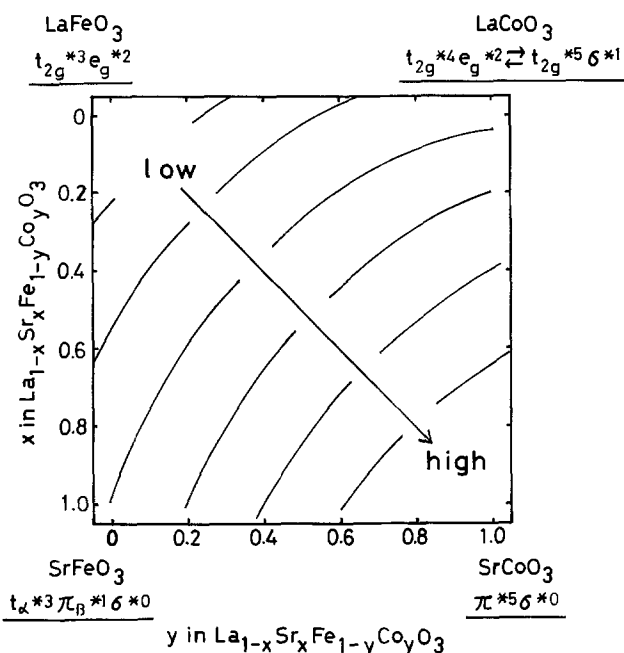


Fig. 10. Model of tendency of catalytic activity and d-electron configurations. The contour line for the activity is arbitrary.

La_{1-x}Sr_xFeO₃ and La_{1-x}Sr_xCoO₃ series oxides and increases with increase of y for the LaFe_{1-y}Co_yO₃ series oxides. This leads to the conclusion, as a matter of course, that the σ* band width of the La_{1-x}Sr_xFe_{1-y}Co_yO₃ series oxides also will increase with the increases of x and y, i.e., along the direction from LaFeO₃ to SrCoO₃ in composition. As a result, the rates of the first and third steps increase with

increases of x and y. On the other hand, for the second step, the rate is determined by the positive charge density of the transition metal cation, that is, the rate increases with the increase of the amount of Sr, leading to the increase of quadrivalent cation in the lattice, as proposed in the previous paper (2).

Consequently, the rate of the oxygen evolution reaction will increase with the increases of x and y for La_{1-x}Sr_xFe_{1-y}Co_yO₃ series oxides, since the rate-controlling step will be either the second or the third step as the Tafel slopes suggest. Therefore, if the σ* band width of SrFeO₃ is almost the same as that of LaCoO₃, the contour line of the catalytic activity in Fig. 10 is qualitatively suggested. In this figure, the contour line is arbitrary, and the activity increases along the direction from LaFeO₃ to SrCoO₃ as shown by the arrow. This phase diagram is consistent with the experimental results of Fig. 6 and 7 in the qualitative tendency of the catalytic activity except for SrCoO_{2.5}, SrFeO₃, and their neighbors. The high resistivity and the low activity of SrCoO_{2.5} are based on the nonperovskite-type structure, in which the d-electron configuration will not be suitable for these properties. In the cases of SrFeO₃ and its neighbors, the σ* band width may be different from expectation.

If SrCoO₃ with perovskite-type structure could be prepared in some way, the catalytic activity would be the highest of this series of oxides. Considering that the dissolution of SrCoO₃ would be small according to the mechanism described in the previous paper (2), sintered SrCoO₃ with perovskite-type structure must be a superior catalyst for the oxygen evolution reaction in alkaline solution. At the present stage, La_{0.2}Sr_{0.8}Fe_{0.2}Co_{0.8}O₃ is the best electrocatalyst of the oxides investigated in this study.

Manuscript submitted Jan. 8, 1980; revised manuscript received May 9, 1980.

Any discussion of this paper will appear in a Discussion Section to be published in the June 1981 JOURNAL. All discussions for the June 1981 Discussion Section should be submitted by Feb. 1, 1981.

Publication costs of this article were assisted by Utsunomiya University.

REFERENCES

1. Y. Matsumoto, J. Kurimoto, and E. Sato, *J. Electroanal. Chem. Interfacial Electrochem.*, **102**, 77 (1979).
2. Y. Matsumoto, H. Manabe, and E. Sato, *This Journal*, **127**, 811 (1980).
3. Y. Matsumoto, J. Kurimoto, and E. Sato, *Electrochim. Acta.*, **25**, 539 (1980).
4. T. Kudo, H. Obayashi, and M. Yoshida, *This Journal*, **124**, 321 (1977).
5. A. C. C. Tseung and H. L. Bevan, *J. Electroanal. Chem. Interfacial Electrochem.*, **45**, 429 (1973).
6. Y. Matsumoto, H. Yoneyama, and H. Tamura, *ibid.*, **79**, 319 (1977).
7. Y. Matsumoto, H. Yoneyama, and H. Tamura, *ibid.*, **83**, 237 (1977).
8. H. Ohbayashi, T. Kudo, and T. Gejo, *Jpn. J. Appl. Phys.*, **13**, 1 (1974).
9. J. B. Goodenough, *J. Appl. Phys.*, **37**, 1415 (1966).
10. C. N. R. Rao, O. M. Parkash, and P. Ganguly, *J. Solid State Chem.*, **15**, 186 (1975).
11. Y. Matsumoto and E. Sato, *Electrochim. Acta*, **24**, 421 (1979).
12. J. O'M. Bockris, *J. Chem. Phys.*, **24**, 817 (1956).

An Electrochemical Instrumentation System for Agriculture and the Plant Sciences

W. Gensler

Department of Electrical Engineering, University of Arizona, Tucson, Arizona 85721

ABSTRACT

The basic technique in this system is the placement of a noble metal probe invasively in the stems, petioles, or peduncles of higher plants. A reference electrode is placed in the soil. The time history of the potential arising between these two electrodes, termed an electrophytogram, can be related to the physiological status of the plant. The potentials arising in this circuit vary from 200 to 500 mV relative to a silver chloride electrode. The variations in the potential are coherent and highly reproducible. There are six broad categories of potential-time variation. The system has been tested under laboratory and field conditions wherein the potential data is stored locally or is transmitted via an rf telemetry link to a central site for analysis. The system is capable of long term, remote monitoring at low labor intensity under laboratory or field conditions.

The basic objective of this system is the determination of the physiological status of plants by a continuous, direct, *in vivo*, electrical measurement. In essence, the technique consists of placing a noble metal electrode invasively in the plant tissue. A second electrode is placed in the root environment. The bioelectrochemical electropotential arising from this circuit is monitored, plotted, and interpreted in terms of the status of the plant, the plant-soil continuum, and environmental conditions. Figure 1 illustrates the technique in schematic form.

There are several aspects of the measurement circuit that must be stressed. First of all, the measurement is made under normal conditions, that is, there is almost no disturbance of the crop canopy, nor the structure of the individual plant. The measurement is as passive as possible. An absolute minimum amount of energy is extracted from the plant by the measuring circuitry. The galvanic circuit path giving rise to the electropotential consists of the measuring probe-tissue interface, the stem and/or main trunk, the roots, the root-soil interface, the soil, and the soil-reference electrode interface. The measured potential at the output of the two electrodes arises from the electrode interfaces, plus any series galvanic potentials in the circuit path. The measurement is usually made every 15 min, 24 hr a day for almost the entire life of the plant.

Typical d-c levels range from 200 to 500 mV relative to a silver chloride electrode in the soil. A-C variations of 100 mV are common, variations as high as 250 mV have been observed. The potential is plotted to yield a time history of the potential variation. This time history has been termed an electrophytogram, or EPG (1). The ultimate objective of the system is the derivation of numerical indexes of plant water and growth status based on the electrophytogram information.

General Methods and Materials

The noble metal probe consists of a palladium rod, 250 microns in diameter and approximately 8 to 10 mm long. The electrode is inserted tangentially or at an angle to the tissue surface to a depth of 1.5-2.5 mm. Penetration depth normally carries the probe well into the secondary xylem. The electropotential between the measuring probe in the tissue and the reference electrode in the soil is monitored with a high impedance amplifier. The amplifier output is

converted to digital form for further processing, transfer, and storage. The following discussion is principally addressed to the transduction aspects of the measurement technique since the electrical data processing is relatively conventional.

The probe-wire connection and the wire leading from the probe is of first-order importance and must be handled with great care. Many connection methods have been attempted under both laboratory and field conditions. The optimum technique up to the present time consists of stripping away 3-4 cm of insulation from a No. 30 (7 × 38) stranded wire; cutting away all but two of the strands, twisting these strands, and wrapping them mechanically around the probe at a 90° angle to the long axis of the probe and 1 mm below the end of the probe. The wires are then soldered to the probe. The probes can be cleaned and taken to the field in plastic bags for connection to the buried wires and ultimate connection to the plant.

The reason for this care is necessitated by two problems encountered principally under field conditions. Tests have shown that solar radiation impinging on the insulated wire results in a rise in temperature of the metal wire of as much as 6°C. This leads to

The reason for this care is necessitated by two problems encountered principally under field conditions. Tests have shown that solar radiation impinging on the insulated wire results in a rise in temperature of the metal wire of as much as 6°C. This leads to

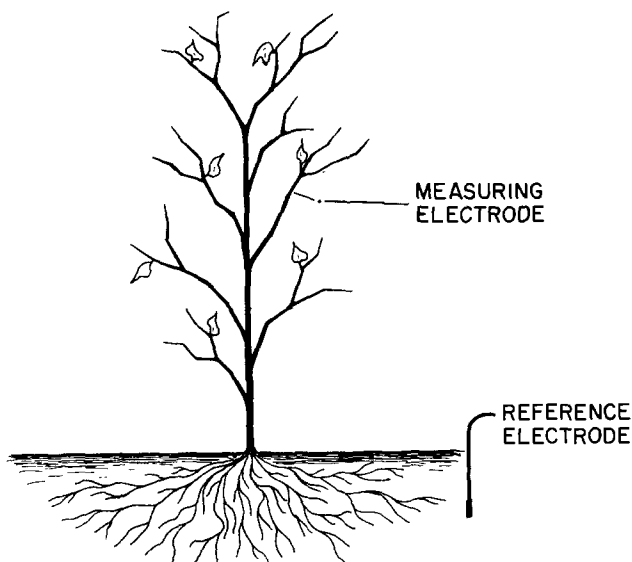


Fig. 1. Basic electrode arrangement of the electrophytogram technique.

an abnormal influx of heat energy into the probe-tissue interface. Further testing has indicated that a 3 cm length of uninsulated wire between the insulation and the probe permits heat transfer from the wire to the environment and a very considerable decrease in the elevated temperature of the probe. The decrease in thermal mass as well as the increase in thermal resistance as a result of using two strands further lessens this abnormal heat transfer. The second reason for this procedure arises from the need for mechanical isolation of the probe from the wire to insure proper healing and normal information transfer. Wind loading and mechanical movement of the plant requires mechanical isolation of the probe. The use of only two strands of No. 38 wire and the presence of substantial slack between the probe and main wire produces the required electrical connection at a minimum mechanical connection. The angle of approach of the wire to the probe decreases any "cantilever effect" of the probe by the wire. The main wire itself is attached to the plant with strips of self-adhesive nylon mesh. With proper care in the handling of the lead wire, the plant will form a callous around the probe entry point firmly bonded to the metal surface. This will yield a probe-tissue interface below the surface that appears normal and gives no evidence of necrosis over long intervals of time. Microscopic examination has indicated the tissue ultimately will grow in an invaginated manner around the probe.

The success in achieving a stable probe-tissue interface depends on the age and type of tissue. *Lycopersicon esculentum* (tomato), *Kalonchoë blossfeldiana*, and *Gossypium hirsutum* (cotton) readily accept the probe at all ages. *Carya pecan* (pecan) appears to accept the probe only before the tissue becomes woody. It is very difficult to penetrate the woody secondary xylem since palladium is a soft metal.

The amount of energy and power which can be sustained by the plant during the measurement is difficult to assess since the electropotential source has no simple Thevenin equivalent circuit. A crude model of the measuring circuit would consist of a current dependent voltage source in series with a relatively low output resistance. Under field conditions, the energy required to charge the wires has been estimated to exceed the energy required to drive the amplifier. For this reason, No. 30 and No. 32 wire have been used to carry the electropotential signal. Further reduction in energy drain has been achieved by carrying the leads in buried conduit. This further reduces the wire to soil capacitance and at the same time protects the leads from mechanical damage under field conditions. The maximum distance between the probe and the amplifier tested up to the present time has been 40m. The input impedance of the amplifier must remain above $10^9\Omega$ (2). The published values of amplifier input impedance have little meaning because of surface resistivities of wire insulation, amplifier packages, and mounting boards under the extreme humidity variations encountered under field conditions. Teflon mounts, sealed enclosures, and dessicant within the enclosures have been employed to reduce surface leakage. These precautions have been found to be necessary when the electronic equipment operates in the middle of a "lake" during flood irrigation.

Acquisition time to determine the electropotential has been limited to approximately 2 sec/measurement. During this interval, the electropotential is measured three times. The use of triple redundancy has been found to be a very valuable means of determining system and/or probe malfunction. Resolution of 1 mV has been routinely obtained under field conditions.

The kinetics of the electropotential variations are such that a sampling rate of 12-15 min is sufficient to obtain an indication of the timing of most of the

variations. This means the upper bound on the bandwidth of electropotential variations is approximately 2.0 radians/min (3).

Since the subject of reference electrodes is such an extensive one, the detailed discussion of its characteristics is given in the Appendix.

It is interesting to note that the d-c electropotential levels measured with a hydroponic root environment do not differ from those encountered with several soil types under field conditions. This would indicate the magnitude of the potential contribution of the circuit path from the reference electrode to the roots is relatively unaffected by both the root-soil interface and the soil.

Several generations of electronic techniques have been employed. The present acquisition sites have between 32 and 64 channels. In addition to the electropotential data, the temperature, humidity, photosynthetically active radiation level, reference electrode, and electronic equipment status are monitored. The equipment operating at the remote sites is entirely solar powered.

Signal processing circuitry is conventional. However, extreme care must be taken to electrically isolate the transduction circuit from line driven equipment. Optoisolators, magnetic amplifiers, fiber optic links, relays, and battery driven amplifiers have all been employed to achieve electrical isolation of the transduction circuit in growth chambers as well as in the field.

Field measurements were initiated in the spring of 1977. During the 1978 and 1979 growing seasons, electropotentials and associated environmental readings were obtained via a 120 km rf telemetry net wherein the data was transmitted directly to the University of Arizona Campus for computer processing. Figure 2 shows one of the field test sites. The methods of probe placement and data acquisition were tested with cotton and pecans. They have been found operable within the scope of normal commercial agronomic operations

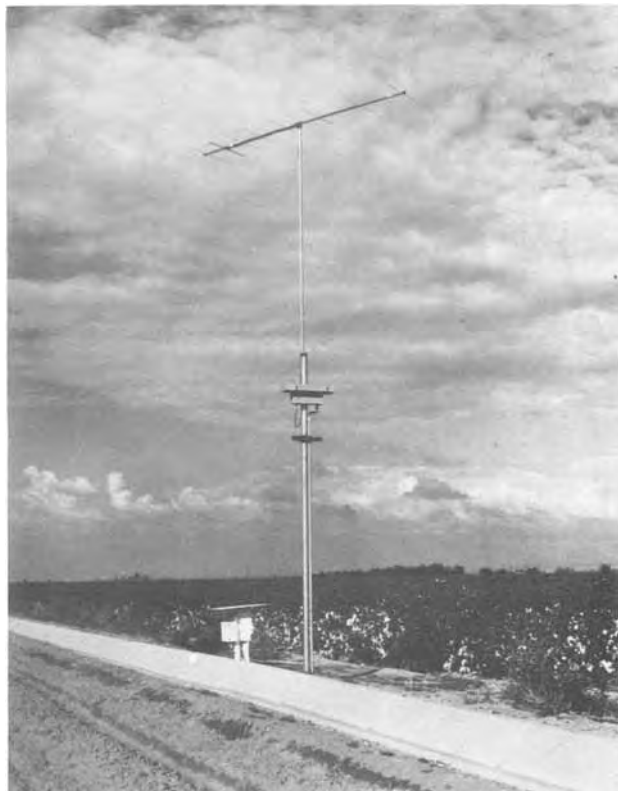


Fig. 2. Commercial cotton field test site showing data acquisition equipment and radio frequency telemetry equipment. Avra Valley, Southern Arizona.

such as ripping, plowing, cultivation, and irrigation. The system is capable of remote, long term, multiplexed measurements of electropotential and associated environmental data at low labor intensity.

Categories of Potential Variation

The potentials measured are coherent and highly reproducible. An examination of the phytograms yields a variety of potential pulses and long duration time shifts in potential level. There are six relatively distinct categories of potential variations. Each of these is briefly described.

Healing potentials are observed immediately after the penetration of the probe into the tissue (4, 5). The potential drops precipitously. The potential then rises in a roughly exponential manner during the healing process and levels off at a stable equilibrium value. The magnitude of the rise is 200-300 mV. Under growth chamber conditions at low light intensities and moderate temperature conditions, the 90% rise point is attained in about 3 days. In the field, the rate of rise is in the order of 8 hr at similar magnitudes. The healing response is extremely consistent. A rewounding response of the same basic form, but of faster duration, is observed when an impulsive mechanical stress is applied to the probe lead wire.

A hypothesis of healing has been developed based on the drop in potential with wounding and then the monotonic rise in potential during the healing process. The basic electrochemical principle invoked is the correlation of more negative oxidation-reduction potentials with the presence of more highly reduced reactants. The initial decrease in potential is caused by a sudden increase of electron availability at the wound site as a result of a mixing of hitherto separated reactants. This enhanced electron availability or reducing power is then consumed in an ordered manner as manifest by the monotonic rise in potential during the subsequent healing reaction.

Transition potentials arise at dawn and dusk. These potentials occur for approximately 1 hr following the light transition. They have been studied almost exclusively under laboratory conditions wherein it is possible to expose the plants to a definitive, short duration light transition. Under field conditions, the change in light intensity is very slow at dawn and dusk and it is difficult to separate out a potential variation which can be attributed exclusively to a light disturbance. The transition potentials do not appear to be related to short term growth, but there is a correlation of the magnitude of the transition potential with the 24 hr growth rate (1).

Diurnal potentials are potentials which occur with the normal 24 hr time cycle. Figure 3 illustrates a typical diurnal potential which has been observed in *Kalanchoë blossfeldiana*. The cyclic waveshape shows the sharp transition potential notches at light transition points and the subsequent shift in d-c potential several hours after the light transition. The potential is a manifestation of an endogenous rhythm as seen by the fact that the rhythm continues for approximately 2 cycles after the onset of continuous darkness. The potential variation has been correlated

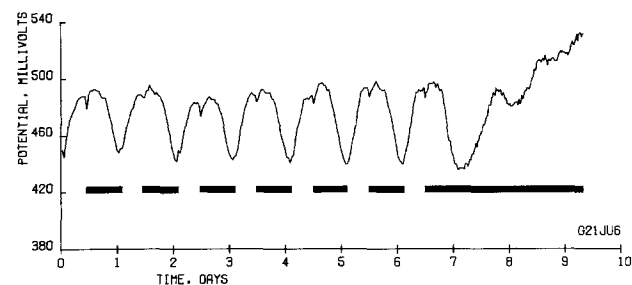


Fig. 3. Diurnal potential variations in *Kalanchoë blossfeldiana*. Black bars indicate dark conditions (night) in the growth chamber.

with pH changes in the leaves, the variations can be induced by shifting the plant from long (12/12 hr) days to short (8/16 hr) days (unpublished results). This has led to the hypothesis that this potential variation is a measure of the shift from C3 to crassulacean acid metabolism in *Kalanchoë blossfeldiana*.

Water-related potentials have been observed in two forms (6). In the first, there is an immediate drop in d-c level by the addition of water in the root zone. This potential is believed to be due to a change in the potential of the root-soil interface. The second form of water-related potential has been observed in the field following irrigation. The potential shows no response in the short term, but a very dramatic burst of electropotential activity after a period of at least one day.

The fifth category of observed potential variations are high frequency oscillations. These oscillations have a frequency of 1-6 radians/hr and a peak to peak magnitude of a few millivolts to as high as 20-30 mV. They come in bursts lasting from a few hours to as long as several days.

Nocturnal potentials have been observed under field conditions only. Figure 4 shows a typical nocturnal potential observed in the peduncle of *Carya Pecan*. These occur in the absence of any observable external environmental disturbance. They are believed to be related to water status.

The separation of potential variations into these relatively distinct categories does not imply that the origin of the potentials are mutually exclusive. The distinctions have grown out of observations of the electrophytograms under externally induced environmental disturbances such as light or water. Internal regulatory or developmental mechanisms can and do give rise to potential disturbances as seen in the diurnal potential waveshape in Fig. 3 and the nocturnal potential waveshape in Fig. 4. Sharp changes in potential level occurred under constant light conditions and constant or nearly constant temperature conditions.

With the exception of the healing potential, the entire range of potential variations follows a definite pattern insofar as the potential variations are characterized by an upper bound. Variations are normally a drop and return to an upper bound. Figure 3 shows an example of this relatively general observation. The diurnal potentials and nocturnal potentials also illustrate this phenomenon.

Electropotential measurements have been made extensively under growth chamber and field conditions. The magnitude of the potential variations observed in field conditions are substantially greater than those encountered in growth chambers. It is very difficult to attribute an origin to this difference since the environmental conditions, age, and type of plant studied all vary. The d-c electropotential levels encountered in the lab and the field are the same. The magnitudes of healing potentials are also the same. One encounters the same d-c levels if the root environment is a hydroponic nutrient solution or soil.

The previous discussion has concerned individual potential variations arising from a single probe. Be-

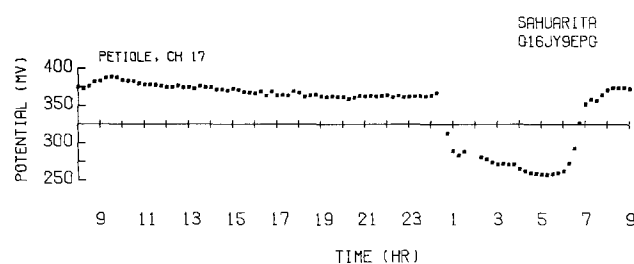


Fig. 4. Nocturnal electropotential variation in *Carya pecan* under field conditions. Sahuarita, Southern Arizona.

cause the electrophytogram technique is a macroscopic measurement, it is possible to implant probes at many locations in the same plant. Figure 5 shows the locations of multiple probes in the fruiting branch of cotton during the 1978 growing season. An example of the comparative phytograms from the peduncle of the apical boll and the petiole of its companion leaf is shown in Fig. 6. There is a striking similarity in the potential variation even though the probes are approximately 3-5 cm apart on opposite sides of a fruiting branch.

Discussion

The use of the noble metal probe results in a measurement of the electropotential status of the extracellular electrolyte at the probe-tissue interface. Assuming no algebraic cancellation of potentials along the circuit path, the d-c levels encountered are reasonable since the plant is very likely not going to

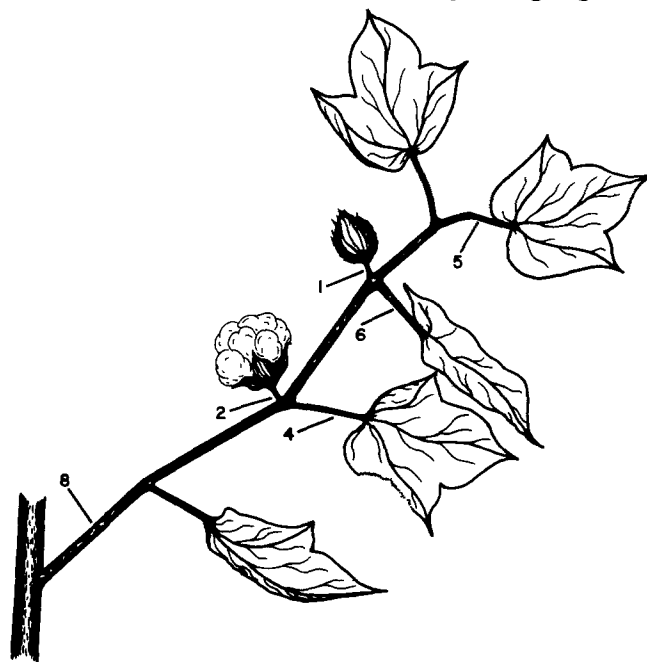


Fig. 5. Multiple probe technique applied to the fruiting branch of *Gossypium hirsutum*. Probes are placed in the stem, peduncles, and petioles for simultaneous recording.

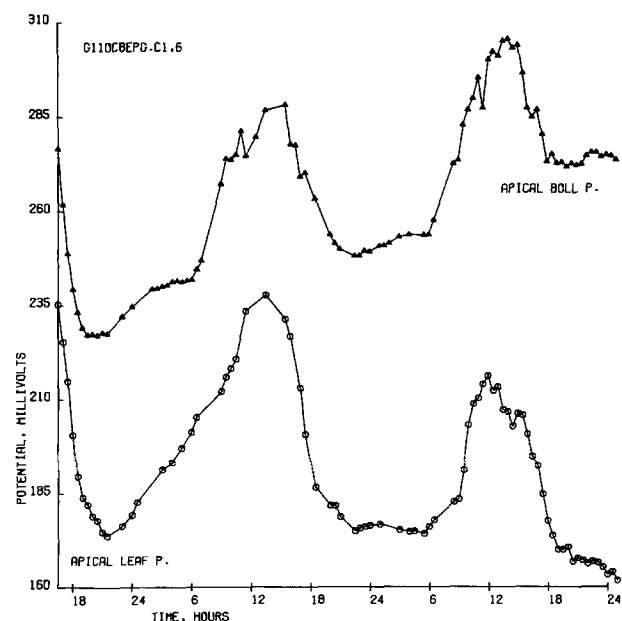


Fig. 6. Simultaneous electrophytogram of the apical boll peduncle and companion leaf petiole in a fruiting branch of *Gossypium hirsutum*.

maintain its extracellular fluid at a high energy level. By using multiple probes one can establish a partial common circuit path between the reference electrode and the measuring probes. Variations in potential along this common path are easily observable when examining the simultaneous phytograms of each probe. For example, a malfunction in the reference electrode will show up as a change in potential of all the probes at the same time and of the same magnitude. This has led to the conclusion that the electropotential variations in most cases are believed to be due to the conditions at the measuring probe-tissue interface (2).

There are a number of problems with the technique that must be recognized. First, of all, the physiological origin or origins of the potential variations have not been determined. Second, the spatial origin of the potential is not well defined. The probe surface is an equipotential surface bathed in a heterogeneous electrolyte. The d-c potential and potential variation can arise from a variety of sources: a change in reactants, a change in reactant concentration, pH level, or possible electrostatic influence. In addition, some of the observed changes may be due to conditions along the circuit path other than at the measuring probe-tissue interface.

While the variations in potential are coherent, consistent, and reproducible, the d-c values exhibit a wide range of values. This range is present even under stringent probe cleaning techniques and similar placement methods.

The simplicity of the probe renders the interpretation difficult. It is possible to assert that the probe measures the potential status of the fluid adjacent to its interface. Furthermore, the measurement is extracellular. But the transition from a measured galvanic potential to a biochemical or biophysical origin is a difficult one.

Another serious problem associated with the technique is the need for long-term data acquisition to remove or lessen the influence of multiple uncontrollable environmental disturbances.

The number of probes required to assess physiological status is presently unknown. The answer to the question of probe numbers is dependent on a more fundamental question: where in the plant should the probes be placed to obtain the maximum information? The probe locations shown in Fig. 5 are directed to answering the question of obtaining the maximum information with the minimum number of probes.

Given these problems, if the potential variations can be related to specific physiological activity, then the potential can be used as an easily acquired, non-destructive measure of such activity. Furthermore, each plant has definite electropotential characteristics. The electropotential activity may be used as a means of genetic selection. The electropotential can be monitored from juvenility to senescence.

With regard to field usage of the electrophytogram system, the most labor intensive operation in monitoring field crops is the need to bury the lead wires in the fall and raise them again in the spring. This procedure is required to prevent the destruction of the wires during mechanical harvesting in the fall and soil preparation in the spring. All electrical equipment in the field must be buried at least 60 cm below the surface to clear the ripping operation. The raising of the cables must be delayed until after mechanical seeding because of the equipment involved. Portable equipment would obviate this problem but requires more electrical complexity and also introduces a security problem.

It has been found necessary to run the lead wires directly along the line of plant main stems. The tractor tolerances are such that only about 5-10 cm of undisturbed soil exists on each side of the stem line. The wires cannot be seen by the tractor operator.

Furthermore, it is not feasible to require special care on the part of the tractor operator in the region of the probes.

The telemetry antennas have been found to present no problem to airborne crop dusters.

The ultimate hardware and software configuration of the system is dependent on the crop type, irrigation practice, and the size of the agricultural unit. For example, in a section (259 hectares) of cotton planted in smaller subunits to stagger the water demand, the system would consist of semiportable acquisition pods capable of acquiring the primary data and transmitting it a maximum of 1.5 km to an intermediate transfer center. The data would be stored and subsequently transferred via a long distance rf link to a central processing site for evaluation and formulation of numerical indexes. In discussions with growers it is apparent that the mass of electropotential data must be presented in very quickly assimilated form. Numerical indexes derived from the electropotential data is the most logical form of presentation.

In summary, the electrophytogram system is a technique for remotely monitoring the physiological status of plants under laboratory or field conditions for long intervals of time at low labor intensity. Coherent, reproducible electropotential variations can be observed at various locations in the individual plant. The major problem at the present time is the determination of the physiological origin of these variations. Once this origin is established, the EPG should provide insight into the fundamental physiology of the plant in laboratory studies and provide a quantitative backup to agricultural decision making under field conditions.

Acknowledgments

This project was supported in part by the Department of Interior, Office of Water Research and Technology, Grant B-061-ARIZ. The data for Fig. 3 was obtained while the author was on Summer Appointment at the Argonne National Laboratory, Argonne, Illinois.

Manuscript submitted April 1, 1980; revised manuscript received approx. May 15, 1980. This was Paper 528 presented at the Seattle, Washington, Meeting of the Society, May 21-26, 1978.

Any discussion of this paper will appear in a Discussion Section to be published in the June 1981 JOURNAL. All discussions for the June 1981 Discussion Section should be submitted by Feb. 1, 1981.

Publication costs of this paper were assisted by the University of Arizona.

APPENDIX

The Reference Electrode

The interpretation of the electrophytogram is heavily dependent on the assumption of a constant galvanic potential between the return wire to the amplifier and the bulk soil. Furthermore, the comparison of phenomena which occur days and even months apart requires long term stability in the reference electrode potential. The electrode assembly described below is employed to maintain a constant interfacial potential and at the same time permit a continuous assay of the potential.

Figure A-1 illustrates the basic technique in schematic form. In essence, the assembly consists of an AgCl concentration cell in which the soil functions as part of the galvanic current path. Electrode assembly A is an AgCl electrode employing a 0.5M potassium chloride electrolyte. The electrolyte wets a KCl-saturated polyacrilamide salt bridge. The acrilamide salt bridge in turn wets a porous ceramic plug, the outer surface of which is in contact with the soil.

Electrode assembly B is a duplicate of electrode assembly A except a 1.0M KCl electrolyte is employed. Either electrode may be employed as the reference

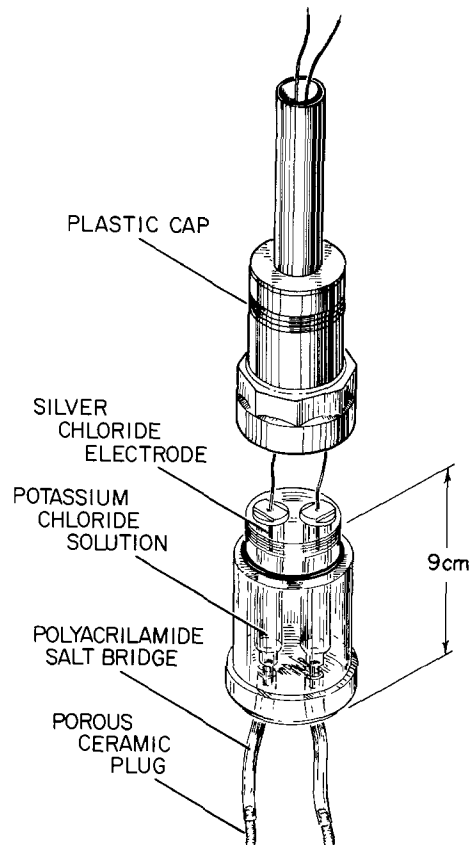


Fig. A-1. Reference electrode assembly

electrode although it is customary to use electrode assembly B as the reference electrode in the electrophytogram transduction circuit because of the resultant electronic simplicity (single rail amplifiers can be employed).

If electrode assembly B functions as the reference electrode, then electrode assembly A becomes an electrode used to monitor the stability of the main reference electrode. The manner in which it does this can be seen by an examination of the circuit path. The concentration cell circuit path begins at the copper wire of assembly B, passes through the chloridized silver electrode into the 1.0M electrolyte, through the acrilamide gel and porous plug, across the ceramic-soil interface, through the soil, and then into electrode assembly A in a reverse manner. There are two ceramic-soil interfaces which in practice have been separated by at least 15 cm of soil. The assumption is made that changes in the interfacial potential at these interfaces will not "track" or produce algebraically similar potential variations. If this is the case, and it is highly probable, then any change of galvanic potential at any interface or series element will show up as a potential change in the two copper wires.

Employing these principles, electrodes of the type shown in Fig. A-1 have been built and tested. A potential of between 12-18 mV results when the electrodes are buried 1m below the surface. The overall variation in potential for a given electrode is approximately 4 mV and it is felt that some of this variation is due to the soil temperature difference in Southern Arizona between summer and winter. Electrodes of this type have been in continuous service for as long as fifteen months at the time of this writing.

Soil type does not appear to influence the potential. The units have been tested only in normal farmland as opposed to drier desert soils. It is assumed that wetting of the ceramic comes from soil moisture since the polyacrilamide gel passes almost no fluid.

The location of the reference electrode is not significant in measuring plant potentials. The maximum distance between the plant and the reference electrode that has been employed up to the present time is 20m. The insensitivity of this distance to the potential reading is reasonable since the impedance level of soil

is not more than 100's of ohms while the impedance level of the electronic amplifier is at least $10^{10}\Omega$.

It is also interesting to observe that the soil itself, a very rich mixture of redox reactants, yields a highly stable circuit path between the two ceramic plugs.

REFERENCES

1. W. Gensler, in 4th Int. Sym. on Bioelectrochemistry, Woods Hole, Mass., October 1977; *Bioelectrochem.*

Biogenergetics, 5, 152 (1978).

2. W. Gensler, *Ann. N.Y. Acad. Sci.*, 238, 280 (1974).

3. P. Delrusso, R. Roy, and C. Close, "State Variables for Engineers," John Wiley & Sons, Inc., New York (1965).

4. W. Gensler, *Am. J. Bot.*, 65 (2), 152 (1978).

5. W. Gensler, *Biophys. J.*, 27, 461 (1979).

6. W. Gensler, U.S. Pat. 3,967,198 (1976).

The Suppression of GaAs Photocorrosion in Aqueous Solutions by Sulfonated Anthraquinones

F. Decker¹ and B. A. Parkinson*

Ames Laboratory, USDOE, Iowa State University, Ames, Iowa 50011

ABSTRACT

The water soluble organic redox couples 1, 5-anthraquinone disulfonate (1, 5 AQD) and 2, 6-anthraquinone disulfonate (2, 6 AQD) were investigated as possible redox reagents for use in the stabilization of GaAs electrodes in semiconductor liquid junction solar cells. The redox potentials and electron transfer kinetics of these anthraquinones measured at various pH's on a rotating glassy carbon electrode indicated that the reduced form of the couple could effectively compete with photocorrosion reactions for photogenerated holes on a GaAs surface in basic electrolytes. A rotating GaAs disk-glassy carbon ring electrode was constructed and the collection at the ring electrode of the photo-oxidized product from the illuminated semiconductor was measured. Competition between light flux, mass transport of the reducing agent, and photocorrosion reactions, as well as redox couple adsorption, were measured at the rotating electrode. The long term stability of illuminated cells containing these redox species was investigated and photocurrent spectra were measured. The importance of redox couple adsorption in the stabilization of semiconductor surfaces in liquid junction cells is assessed.

The n-GaAs/1M KOH, 0.8M K₂Se 0.1M K₂Se₂/C semiconductor liquid junction solar cell is presently the most efficient cell of this type for both single crystal (1) and polycrystalline (2) gallium arsenide. There is considerable room for improvement of both long term stability and energy conversion efficiency, however. The selenide solutions used in these cells are colored, air sensitive, and highly toxic, properties which would make a suitable substitute attractive. Bard (3) and others (4, 5) are attempting to use nonaqueous solvents to avoid the photocorrosion reactions which involve water and to make available a wider range of organic and organometallic redox couples for use in these cells, however the limited solubility of many of these couples has precluded their use at light intensities near or above solar levels (3). The difficulty of permanently removing water from the organic solvents and the additional expense they would add to cell construction are other problems associated with the use of these solvents. Our approach was to take anthraquinone, which Bard (3) has shown stabilizes the GaAs surface at low light intensities in acetonitrile, with sulfonate groups attached to the molecule to make it more water soluble. In some solutions the requirement of fast electron transfer kinetics to the solution redox species is satisfied by anthraquinones. Rapid kinetics are necessary to avoid overpotential losses in the cell and to effectively compete with photocorrosion reactions for photogenerated holes at the semiconductor surface.

Rotating electrode techniques are particularly suited for the investigation of the interactions between dark reactions, photocorrosion, mass transport of redox couples, and light flux at semiconductor electrodes (6,

10). We have employed rotating disk and ring disk electrodes of glassy carbon and gallium arsenide to elucidate the interaction of photochemical and electrochemical processes in gallium arsenide photoelectrochemical cells containing disulfonated anthraquinones. The wavelength response and long term stability of the photocurrent in these systems were investigated. An experiment which demonstrates the adsorption of these redox couples on GaAs is also presented.

Experimental

Electrodes.—GaAs crystals obtained from Laser Diode Laboratories were silicon-doped with a carrier density of $2 \times 10^{17} \text{ cm}^{-3}$ and a resistivity of 0.01 Ω -cm. The (100) face with a back ohmic contact was attached by means of silver epoxy to a copper wire (stationary electrodes) or to a steel shaft (rotating electrodes). Both types of electrodes were then insulated with epoxy and, in the case of the rotating electrodes, machined to a cylindrical form. (The geometric parameters of the rotating GaAs disk/glassy carbon ring in cm are $r_1 = 0.195$, $r_2 = 0.325$, and $r_3 = 0.595$.) The GaAs electrodes were etched in 1:1 H₂SO₄-30% H₂O₂ before each test. The reference electrode was Ag/AgCl and the counterelectrode was a carbon rod or platinum gauze.

Materials and Techniques.—Anthraquinone-1, 5 and -2, 6 disulfonic acids as the disodium salt (Aldrich Chemical Company) were purified by repeated recrystallization from water. Stock solutions of the purified reagent were prepared at concentrations close to saturation, around 40 and 30 mM for the 1, 5 and 2, 6, respectively, at ambient temperature. Solutions of the anthraquinones in different supporting electrolytes were electrolyzed at Pt gauze (in base) or a large area carbon electrode (in acid). Since these solutions

* Electrochemical Society Active Member.

¹ Permanent address: University of Campinas, SP, Brazil.

Key words: semiconductor, mass transport, energy conversion.

are air sensitive the photoelectrochemical cell experiments were run in the electrolysis cell which was being flushed with nitrogen or, alternatively, the electrolyzed solution was transferred to a second cell under anaerobic conditions. The light sources were a 10 mW He-Ne laser, beam-expanded to cover the electrode for the efficiency measurements, and a 100W quartz-halogen lamp, for the RRDE experiment. For the long term runs and the photocurrent spectrum measurements the illumination was through an optical flat on the bottom of the cell. The laser power was measured with a Metrologic radiometer.

Results

The electrochemical behavior of a 50% reduced solution of 1,5-AQD and 2,6-AQD on a rotating glassy carbon electrode as a function of the electrolyte pH is shown in Fig. 1. The inset of the figure shows that the potential of the couple shifts negative as the pH is made more basic at very close to the theoretical rate of 59 mV/pH unit for the reaction written in Eq. [1]

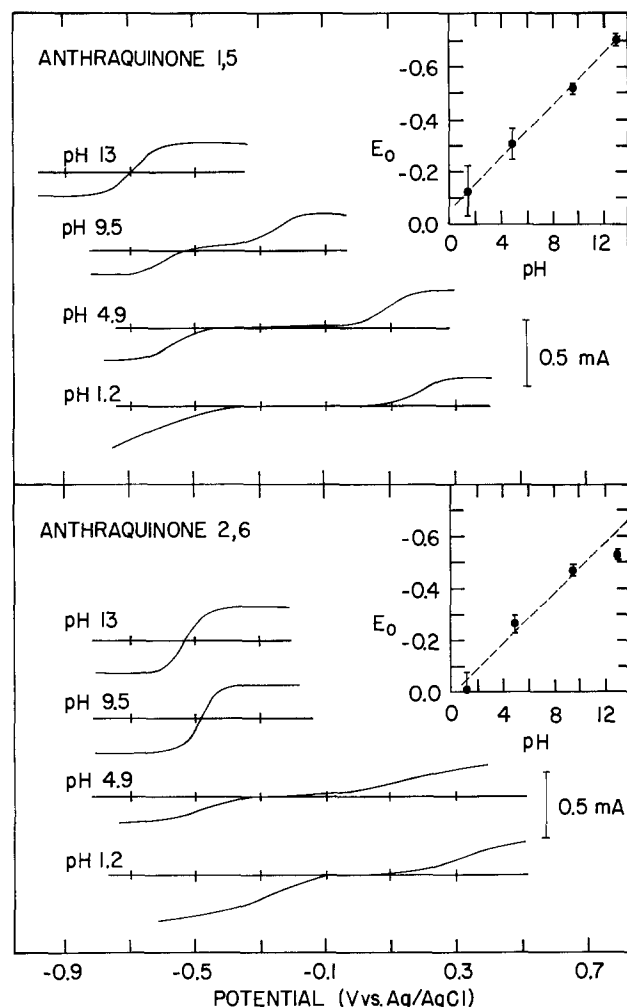
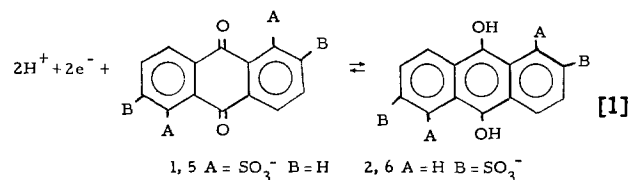


Fig. 1. Electrochemical behavior of a 50% electrolyzed solution of the anthraquinones used in this study at a rotating glassy carbon disk electrode (1000 rpm) in aqueous electrolytes: pH 13 0.1M NaOH; pH 9.5 0.2M ammonia buffer; pH 4.9 0.2M acetate buffer; pH 1.2 0.2M HClO₄. The insets show the equilibrium redox potential as a function of pH.

The potentials shown in Fig. 1 are in good agreement with values reported by Furman and Stone (7) at a dropping mercury electrode in 10% ethanol solutions.

The coalescence of the oxidation and reduction waves in basic solutions indicates that the electron transfer rate is faster than in acid. The potential of the 2, 6 AQD in highly basic electrolytes falls below the line extrapolated from more acid pH's which indicates that no protonation step occurs upon reduction of this molecule in very basic solution.

Table I shows the results with 1, 5-AQD and 2, 6-AQD in an n-GaAs liquid junction cell at two monochromatic illumination intensities and different pH. The data in Table I was taken with the GaAs surface in the "shiny" etch (8) condition due to the greater ease of reproducing this surface. A good "matte" etch would increase the short-circuit current and efficiency by up to 50% (8). The table shows that the best cells made from either couple are at pH ~ 9 even though the redox potential and electron transfer rate constant would appear to be more favorable in more basic solutions. This is because at pH 12 the predominant form of the reduced quinone in solution is the highly colored dianion which absorbs an appreciable fraction of incident radiation. An intriguing aspect of Table I is that the open-circuit voltage (OCV) of a cell is dependent on the solution pH for 2, 6-AQD and independent of pH for the 1, 5-AQD couple. In Fig. 2 the cell voltage at constant monochromatic intensity at the semiconductor is plotted vs. the redox potential of the anthraquinone solution.

A slope of zero, as drawn for 1, 5 AQD in Fig. 2, might be expected if the flatband potential of the electrode and the redox potential of the solution were shifting in the same direction at the same rate as the pH of the solution is changed. Gomes and Cardon have measured flatband potential shifts of about 56 mV/pH unit for n-GaAs in various buffers (9). However this shift has been attributed to protonation of surface oxides, a process which may be influenced by redox couple adsorption which will be discussed later in this paper.

The data in Table I does not yield any information about the stability against photocorrosion of the cells and rotating electrodes were used for this purpose. Figure 3 shows the interaction of corrosion and redox couple mass transport at a rotating glassy carbon ring-gallium arsenide disk electrode under constant white light illumination from a tungsten halogen lamp. The dotted lines show the photocorrosion current for the gallium arsenide electrode with no redox couple in the solution and the ring current at -0.9V shows no

Table I. Open-circuit potential (V_{oc}), short-circuit current (I_{sc}), fill factor (ff), and monochromatic (632.8 nm) power efficiency (η) of different n-GaAs/10 mM anthraquinone in 0.2M aqueous electrolyte/carbon cells.

Anthraquinone 1, 5 Disulfonate					
pH	V_{oc} (V)	I_{sc} (μ A)	ff	η (%)	Intensity (mW)
13.2	0.35	21	0.67	3.8	0.13
9.6	0.30	32	0.69	5.5	0.12
4.9	0.39	30	0.44	3.7	0.14
13.2	0.44	140	0.56	3.8	0.90
9.6	0.40	190	0.43	4.1	0.81
4.9	0.45	32	0.33	0.51	0.95
Anthraquinone 2, 6 Disulfonate					
pH	V_{oc} (V)	I_{sc} (μ A)	ff	η (%)	Intensity (mW)
13.1	0.54	8	0.62	2.2	0.12
9.6	0.37	19	0.66	4.7	0.10
4.9	0.29	12	0.57	1.5	0.13
13.1	0.60	56	0.60	2.2	0.90
9.6	0.44	127	0.60	5.0	0.67
4.9	0.31	13	0.54	0.22	0.96

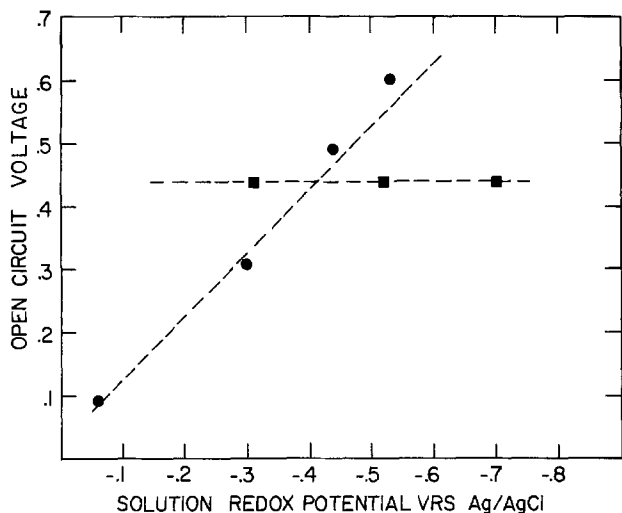


Fig. 2. The open-circuit voltage generated plotted with respect to the solution redox potential at a constant illumination intensity (1 mW 632.8 nm) for an n-GaAs electrode in a 10 mM solution of 2,6 anthraquinone disulfonate (●) and 1,5 anthraquinone disulfonate (■).

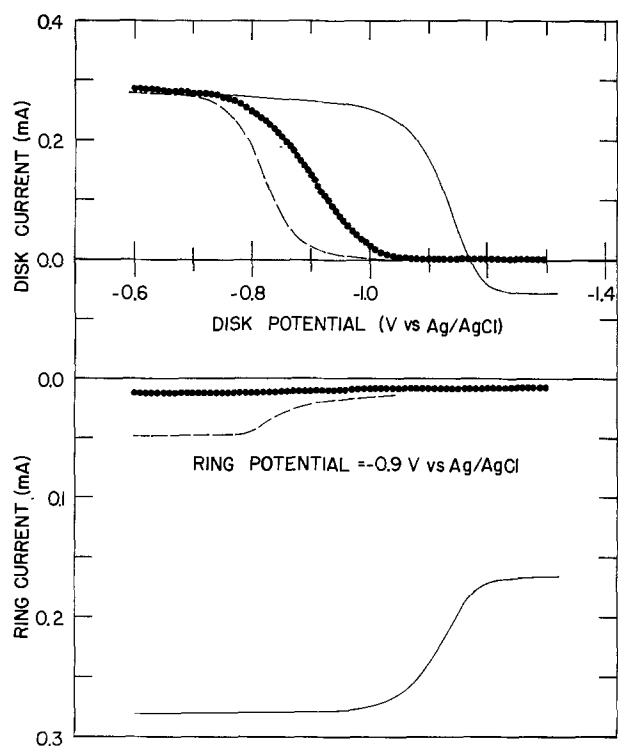


Fig. 3. Current-voltage behavior of a rotating glassy carbon ring-illuminated n-GaAs disk electrode in various electrolytes. Dotted lines—0.2M ammonia buffer; dashed lines—0.2M ammonia buffer + 4 mM hydroquinone; solid lines—0.2M ammonia buffer + 4 mM 2,6-AQD. Illumination was from a 150W tungsten lamp. Rotation speed 1500 rpm. scan rate 5 mV/sec.

collection of photocorrosion products at this potential. When hydroquinone is added to the solution (the dashed lines) the photocorrosion reaction is shifted in a positive direction by about 0.1V and the photo-oxidized product can be reduced at the ring electrode. The percentage of stabilization can be calculated from the limiting current and the collection efficiency of the electrode to be about 25% which is consistent with a number reported by Memming (10). The solid lines show the disk and ring currents for an 80% reduced solution of 4 mM 2,6 AQD. The photocurrent onset is now about 200 mV more negative than the photocorrosion reaction and the ring current (which is superimposed on a background of

unreduced bulk 2,6 AQD) shows an increase in current which is within experimental error equal to the disk current multiplied by the collection efficiency, indicating that virtually all the photogenerated holes are reacting with the redox couple.

The rotation speed dependence of the currents shown in Fig. 4 demonstrates the separation of the 2,6 AQD wave from the corrosion wave when the mass transport of 2,6 AQD is less than the hole flux. The stable plateau of the ring current at the lower rotation speeds demonstrates that the photo-oxidation of 2,6 AQD is continuing at a mass transport limit even at potentials where the gallium arsenide disk is undergoing a simultaneous photocorrosion. The greater than 200 mV separation of the 2,6 AQD wave from the photocorrosion indicates the effectiveness of this redox couple for suppression of gallium arsenide photocorrosion. Similar results are obtained with 1,5 AQD, however the potential difference between anthraquinone photo-oxidation and the photocorrosion reaction is about 150 mV. Miller has observed similar behavior on rotating GaAs electrodes with photo-oxidation of selenide; however, in this case, the photocorrosion products (As^{3+} and Ga^{+3}) interfere with the polyselenide before it can be reduced at the ring electrode (6).

The photocurrent spectra of cells containing the hydroquinone form of 2,6 AQD and 1,5 AQD in pH 9.5 ammonia buffer and selenide/polyselenide in 1M KOH are compared in Fig. 5. The predominate form of the anthraquinone in this pH range is the monoprotonated anion (AQDH^-) which is lightly colored but absorbs strongly in the blue region of the spectra. A photoresponse spectrum for the selenide/polyselenide couple at its usual concentration is also shown and indicates that the anthraquinone couples transmit a larger fraction of the incident light, albeit at these lower concentrations.

The long term stability under illumination of cells containing 1,5 AQD and 2,6 AQD was investigated in pH 9.5 solutions. The GaAs electrode was rapidly corroded when illuminated at solar irradiation inten-

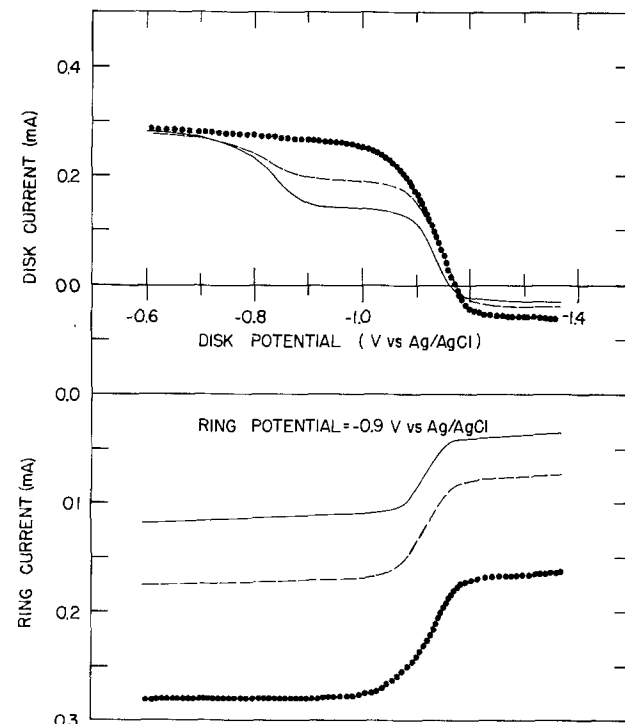


Fig. 4. Competition between redox couple mass transport and photocorrosion at a rotating glassy carbon ring-illuminated n-GaAs disk electrode in 0.2M ammonia buffer + 4 mM 2,6-AQD. Solid line—250 rpm; dashed line—500 rpm; dotted line 1500 rpm. Illumination from a 150W tungsten lamp. Scan rate was 5 mV/sec.

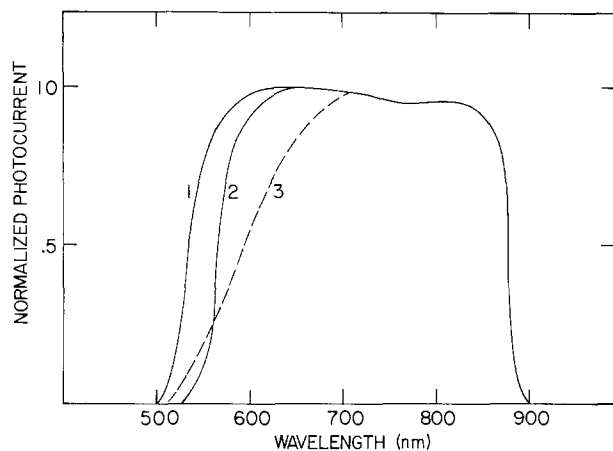


Fig. 5. Photocurrent spectra for n-GaAs liquid junction cells with various electrolytes. Curve 1, 10 mM solution of reduced 1, 5-AQD in 0.2M ammonia buffer; Curve 2, 10 mM solution of reduced 2, 6-AQD in 0.2M ammonia buffer; Curve 3, 1M KOH, 0.8M K_2Se , 0.1M K_2Se_2 .

sities in stirred solutions containing 20-40 mM of the reduced anthraquinone. Apparently the mass transport of the redox couple at these concentrations is not large enough to compete with corrosion reactions at air mass one intensities. This is not surprising in light of the fact that GaAs cells at these intensities require an excess of 0.3M selenide ion to reduce the ratio of corrosion current to the total current to below 0.01 (11). Also the results of a simple diffusion calculation based on the Sand equation predicts that currents of ~ 20 mA/cm² cannot be sustained with the concentration of the redox couple below 0.05M.

Upon extended illumination of the GaAs at lower intensities, two different types of behavior are shown by -1, 5 AQD or 2, 6 AQD. In some cells the power output at 100 μ A/cm² was stable over a period of days while other cells had an immediate but gradual loss of output without apparent corrosion. Once the cell output had decayed significantly the original output could not be restored even upon repeated etching in the sulfuric acid-hydrogen peroxide etchant or by treatments with methanol. The formation of a blocking surface film by the anthraquinones (12), impurities, or photochemical products (13) is probably responsible for this behavior. The formation of robust insulating surface films on platinum electrodes by the oxidation of phenolic compounds is well established (12). Subtle surface structure differences which influence the film nucleation could be an explanation for the fact that some electrodes passivate and others do not.

Chronocoulometric measurements by Anson and Epstein of the adsorption at mercury electrodes from solutions of 10^{-5} - 10^{-3} M in 2-anthraquinone monosulfonate have established the existence of approximately monolayer coverages on the surface (14). They reported only a small electrode charge and potential dependence of the adsorption, except at very negative potentials. This indicates that the adsorption is driven mainly by the hydrophobicity of the large organic molecule. Considering these results the adsorption on GaAs electrodes of the molecules in this study (2, 6-AQD and 1, 5-AQD) can certainly be expected especially in solutions of more than millimolar concentration.

The adsorption of the reduced form of 1, 5-AQD on gallium arsenide can be demonstrated by an experiment the results of which are shown in Fig. 6. The gallium arsenide disk electrode is potentiostatted in the absence of light at various potentials in a solution containing the reduced form of 1, 5 AQD. Unlike a metal electrode at these potentials, the absorbed or bulk anthraquinone cannot be oxidized in the dark at the semiconductor surface. At time T_1 the

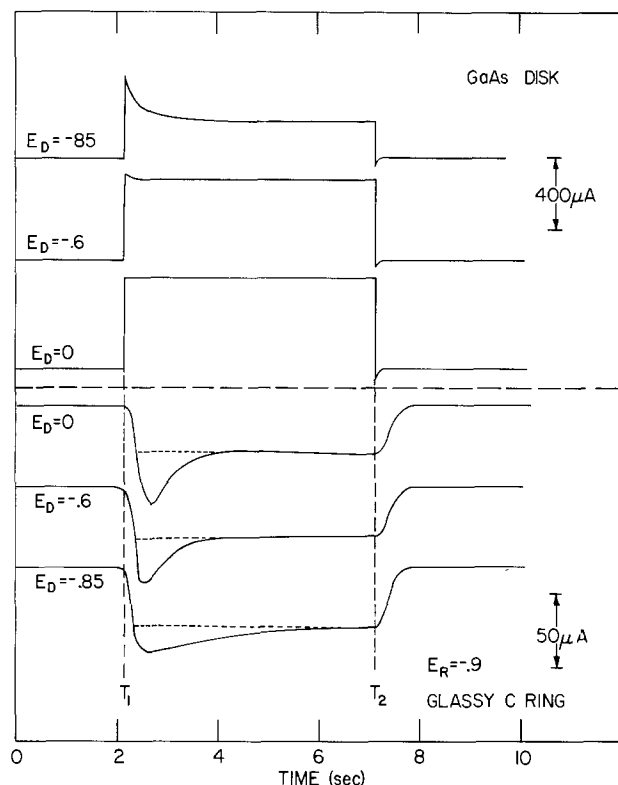


Fig. 6. Current response at a rotating n-GaAs disk-glassy carbon ring electrode to a pulse of ~ 50 mW/cm² white light (T_1 to T_2) at various disk potentials with a rotation speed of 540 rpm in a solution of 0.2M ammonia buffer with 6 mM of reduced 1, 5-AQD.

disk is illuminated and quickly reaches a steady-state current, while a peak of current is seen at the ring electrode which is held at a potential where the photo-oxidized anthraquinone can be reduced (-0.9 V). The light induced hole flux in these experiments is higher than the reductant mass transfer which results in corrosion however an initial stabilization of the surface results due to the surface excess of the anthraquinone. The steady-state ring current, which decays after the light is turned off at T_2 , represents the fraction of stabilization of the GaAs surface by this redox couple under steady-state conditions ($\sim 25\%$). Photocorrosion products from the disk do not influence the ring current at this ring potential (see Fig. 1).

Integration over time of the excess current (above the dotted lines in Fig. 6), and correcting for the collection efficiency of the electrode, yields a charge which corresponds to a surface coverage of about 30×10^{-10} moles/cm².

A monolayer of sulfonated anthraquinone, as determined experimentally or by geometric considerations, is about 1.5×10^{-10} moles/cm² (14) so the coverage of the adsorbed reduced 1, 5 AQD in the collection experiment corresponds to about 20 monolayers at all the potentials where measurements were made. This coverage resulted from an accumulation for about 30 sec before the light pulse.

Discussion

Although the cells examined in this study are not stable at solar illumination levels we feel that they are still interesting from several viewpoints. The use of organic redox couples allows fine tuning of the redox potential of a molecule by purposeful substitution on an existing carbon framework or by altering the framework of the redox center(s) in the molecule. The contrasting behavior of the open-circuit voltage for very similar molecules shown in Fig. 2 is a good example of how subtle changes in a molecule can produce dramatically different behavior in a photo-

electrochemical cell. Also organic redox couples also have the potential to be synthesized very cheaply.

Photodegradation of organic redox couples by the ultraviolet component of sunlight (13) may be a disadvantage for their use in practical cells, however the use of antireflection coatings, which are usually composed of wide bandgap semiconducting materials absorbing much of the ultraviolet light on the cell windows, may solve this problem. The long term thermal stability of organic redox couples may also be a problem with many compounds.

The other problems associated with the redox couples (1, 5 AQD and 2, 6 AQD) used in this study are lack of solubility, absorbance of blue light (Fig. 5), and blocking film formation. The first problem might be overcome by the use of a more soluble sulfonic acid salt or by the addition of additional sulfonic acid groups to the molecule (1, 2, 5, 6 anthraquinone tetrasulfonic acid). The solution absorbance would become unimportant if a blackwall illumination of the cell is adopted. In this configuration a layer of semiconductor on the order of the space charge layer thickness is deposited on a transparent substrate and illuminated through the substrate rather than the solution. In such a cell the very negative redox potential and fast electron transfer kinetics of the highly colored anthraquinone dianions may be exploited. Recent advances on blackwall illumination of thin film CdSe cells (15) are encouraging in this regard.

Adsorption of the redox couple at the semiconductor-electrolyte interface is very important for stabilizing the semiconductor against photocorrosion. Preventing polymerization of quinones on the GaAs surface will probably be difficult. Recent studies concerning the electroanalytical detection of phenols which have demonstrated techniques for the *in situ* removal of similar films from platinum electrodes are encouraging (16). The photo-oxidation and desorption of the reduced 1, 5 AQD as shown in Fig. 6 is a good example of how a surface excess of the redox couple initially stabilizes the electrode against photocorrosion. If the adsorption kinetics of the redox couple are fast and the bulk concentration is high enough, this stabilization could be expected to continue even at high light intensities. The importance of adsorption is also demonstrated by the difficulty experimenters have encountered in preparing a stable regenerative liquid junction cell using redox couples such as $\text{Fe}^{+2}/\text{Fe}^{+3}$ (10) and $\text{Fe}(\text{CN})_6^{-4}/\text{Fe}(\text{CN})_6^{-3}$ (17) which are not expected to be strongly chemisorbed at surfaces. Ginley and Butler have demonstrated the importance and extent of sulfide adsorption on the cadmium chalcogenides (18). Using capacity measurements Tyagai (19) has also shown sulfide strongly interacts with the CdS surface and also reported an apparent lack of $\text{Fe}(\text{CN})_6^{-4}$ adsorption on this semiconductor. Indeed the most successful cells reported at this writing have used the highly surface active polysulfide (20, 21), polyselenide (1, 2), or triiodide (22) ions. The stabilization of a silicon surface against oxide passivation in aqueous solutions by chemically bonded ferrocenes (23) is another example of the importance of an expeditious reaction of highly energetic holes to form a stable surface species and thus protect the surface from undesirable reactions. However an extreme can be reached if the adsorbed layer gets too thick and becomes insulating as in some of the long term experiments in this study.

The photoelectrochemical desorption with collection experiment (Fig. 6) has potential of being a useful technique for measuring redox couple adsorption at semiconductors. The current transients resulting from the illumination of a semiconductor disk electrode are very difficult to quantitatively interpret because they are a combination of currents due to space charge layer charging, faradaic reactions of adsorbed and transported redox couple, and corrosion. The ring

potential is held constant at a potential where corrosion products do not react so the current transient measured is due only to the photoreacted redox couple. Peaks of current above the steady-state current can then be interpreted as arising from the photoreaction of the redox couple adsorbed on the disk electrode. Further studies of the extent, kinetics, and potential dependence of redox couple adsorption on semiconductor surfaces, using this and other techniques, are underway in this laboratory.

Acknowledgments

Ames Laboratory is operated for the U.S. Department of Energy by Iowa State University under Contract No. W-7405-Eng-82. This research was supported by the Assistant Secretary for Energy Research, Office of Basic Engineering Sciences, WPAS-KC-02-03.

Manuscript submitted April 10, 1980; revised manuscript received June 10, 1980.

Any discussion of this paper will appear in a Discussion Section to be published in the June 1981 JOURNAL. All discussions for the June 1981 Discussion Section should be submitted by Feb. 1, 1981.

Publication costs of this article were assisted by Iowa State University.

REFERENCES

1. B. A. Parkinson, A. Heller, and B. Miller, *Appl. Phys. Lett.*, **33**, 521 (1978).
2. A. Heller, B. Miller, S. Chu, and Y. T. Lee, *J. Am. Chem. Soc.*, **101**, 7633 (1979).
3. P. A. Kohl and A. J. Bard, *This Journal*, **126**, 603 (1979).
4. K. D. Legg, A. B. Ellis, J. M. Bolts, and M. S. Wrighton, *Proc. Natl. Acad. Sci. U.S.A.*, **74**, 4116 (1977).
5. R. D. Rauh, M. E. Langmeier, J. P. Goldman, and E. McGinley, Quarterly Progress Reports No. 1 & 2 SERI subcontract XP-9-8002-7 (1979).
6. B. Miller, S. Menezes, and A. Heller, *This Journal*, **126**, 1483 (1979).
7. N. Howell Furman and K. G. Stone, *J. Am. Chem. Soc.*, **70**, 3055 (1948).
8. B. A. Parkinson, A. Heller, and B. Miller, *This Journal*, **126**, 954 (1979).
9. W. P. Gomes and F. Cardon in "Semiconductor Liquid Junction Solar Cells," A. Heller, Editor, p. 120, The Electrochemical Society Softbound Proceedings Series, Princeton, N.J. (1977).
10. R. Memming in "Semiconductor Liquid Junction Solar Cells," A. Heller, Editor, p. 38, The Electrochemical Society Softbound Proceedings Series, Princeton, N.J. (1977).
11. K. C. Chang, A. Heller, B. Schwartz, S. Menezes, and B. Miller, *Science*, **196**, 1097 (1977).
12. J. F. Hedenberg and H. Freiser, *Anal. Chem.*, **25**, 1355 (1953).
13. J. Malcolm Bruce, in "The Chemistry of the Quinones," S. Patai, Editor, Chap. 9, Interscience, New York (1979).
14. F. C. Anson, and B. Epstein, *This Journal*, **115**, 1155 (1968).
15. M. A. Russak, J. Reichman, H. Witzke, S. K. Deb, and S. N. Chen, *This Journal*, **127**, 725 (1980).
16. R. C. Koile and D. C. Johnson, *Anal. Chem.*, **51**, 741 (1979).
17. T. Inoue, T. Watanabe, A. Fujishima, and K. Honda, in "Semiconductor Liquid Junction Solar Cells," A. Heller, Editor, p. 210, The Electrochemical Society Softbound Proceedings Series, Princeton, N.J. (1977).
18. D. S. Ginley and M. A. Butler, *This Journal*, **125**, 1968 (1978).
19. V. A. Tyagai, *Electrokhimiya*, **1**, 387 (1965).
20. G. Hodes, J. Manassen, and D. Cahen, *Nature (London)*, **261**, 403 (1976).
21. A. B. Ellis, S. W. Kaiser, and M. S. Wrighton, *J. Am. Chem. Soc.*, **98**, 6418 (1976).
22. J. Gobrecht, H. Tributsch, and H. Gerischer, *This Journal*, **125**, 2085 (1978).
23. M. S. Wrighton, R. G. Austin, A. B. Bocarsly, J. M. Bolts, O. Haas, K. D. Legg, L. Nadjjo, and M. C. Palazzotto, *J. Am. Chem. Soc.*, **100**, 1603 (1978).

Oxide Ion Titrations in Molten NaCl with the Zirconia Electrode

Kurt H. Stern*

Chemistry Division, Naval Research Laboratory, Washington, D.C. 20375

ABSTRACT

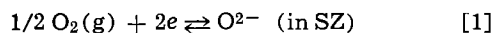
Stabilized zirconia electrolytes can be used to titrate O^{2-} into and out of molten NaCl. Relations between the oxide activity in the melt and the charge passed through the ceramic have been derived and verified. The technique is applicable to the purification of melts and the determination of oxide solubility products.

Zirconia stabilized with several percent CaO, MgO, or Y_2O_3 is finding increasing use in a variety of applications at high temperatures. All of these depend on the fact that charge transport through this material occurs by migration of oxide (O^{2-}) ions (1). Electrochemical applications may be divided into equilibrium methods in which the stabilized ZrO_2 (SZ) is used as part of an indicator electrode, and nonequilibrium methods in which a sensible amount of charge is passed through the material.

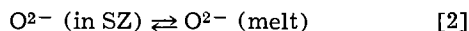
Indicator electrodes made of SZ have been used to: (i) measure O_2 partial pressure in gases (2), (ii) measure solubility of O_2 in metals (2), (iii) measure the dissociation pressures of solid oxides (2), (iv) measure the oxide activity in molten salts (3-5) and glasses (6).

The transport of O^{2-} through SZ under an applied potential has been used to: (i) operate an oxygen fuel cell (2), (ii) change the O_2 content of gases (7, 8), (iii) measure the diffusivity of O_2 in metals (9), (iv) titrate oxygen into metals (9).

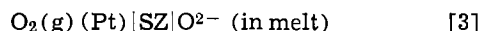
Most of the applications depend on two properties of SZ: (i) at an interface of the type $O_2(M)|SZ$, the potential-determining process is



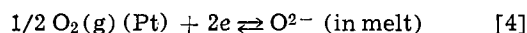
where M is an inert metal such as platinum. Studies of such interfaces have shown that the process is readily reversible, at least at temperatures above 500° (2); (ii) applications involving the measurement of O^{2-} activities in molten salts depend on the equilibrium



The reversibility of these processes under potentiometric conditions (very small currents) can be regarded as established. In this case the "zirconia electrode," which can be described as



functions as an O^{2-} -specific electrode for which the half-cell reaction is given by the sum of reactions [1] and [2]



Thus, the zirconia electrode functions operationally as does the glass electrode for H^+ , although the mechanisms responsible for the potential-determining reactions are not entirely analogous.

Reaction [4] has so far been applied only potentiometrically (3-5, 10, 11). Although the oxygen gas electrode ($O_2(Pt)|O^{2-}$ (in melt)) has also been used in oxide-containing melts, the advantages of the zirconia electrode are (i) specificity to the O^{2-} ion (no response to O_2^{2-} and O_2^-), and (ii) the oxygen

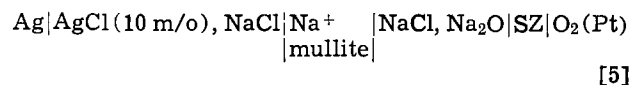
gas pressure over the melt can be varied independently of the operating O_2 pressure of the electrode. Construction of the electrode and its potentiometric applications in molten salts have been described elsewhere (3-5, 10, 11).

The purpose of the present paper is to report on the exploration of the "kinetic" properties of the zirconia electrode. If the electrode behaves reversibly, as indicated by reaction [4], and if the temperature is sufficiently high for the conductivity of the ceramic to be appreciable, it should be possible to titrate O^{2-} ions into and out of melts by the application of an applied potential between the $O_2|Pt$ electrode attached to one side of the zirconia and a suitable counterelectrode. The resulting change in the O^{2-} activity of the melt is measured by a cell which has been described in detail elsewhere (5, 11). NaCl was used as the molten salt medium since the chemistry of oxides dissolved in it had been studied previously (5).

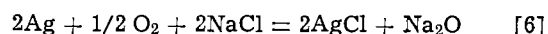
Experimental Procedure

All experiments were carried out in a controlled atmosphere glove box (Vacuum Atmospheres Corporation) with moisture and CO_2 content in the ppm range with the O_2 content set (O_2 -He mixtures) for each experiment. NaCl was vacuum-dried at 500° for several days. Melts were contained in high purity (99.8%) Al_2O_3 crucibles. These crucibles are subject to slight corrosion by alkaline melts, but only when the Na_2O concentration approaches 1 mole percent (m/o). Since the Na_2O concentrations in this work are less than that by one to two orders of magnitude, corrosion is not significant.

For experiments in which changes in the Na_2O activity of the melt were to be detected, the measuring cell can be written as



for which the cell reaction is

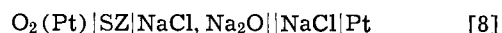


and

$$E_{\text{cell}} = E^\circ - (RT/2F) \ln \left[\frac{a_{AgCl}^2 a_{Na_2O}}{P_{O_2} a_{NaCl}^2} \right] \\ = E^{\circ'} - (RT/2F) \ln a_{Na_2O} \quad [7]$$

where all the constant terms in the brackets have been absorbed into E° .

The cell used for the electrolysis experiments can be written as



The platinum counterelectrode was not studied in detail and may not behave reversibly. This was not considered significant since the pinhole liquid junc-

* Electrochemical Society Active Member.
Key words: ceramics, molten salts, coulometry.

tion prevents mass transport of reaction products into and out of the counterelectrode compartment and since substitution of the liquid junction by an Na^+ -conducting mullite membrane gave exactly the same results, and in this case reaction products are confined inside the membrane. Therefore, all composition changes in the $\text{NaCl-Na}_2\text{O}$ melt must be produced by charge transport through the zirconia.

Potentials were measured with high impedance potentiometers (Orion 801 and PAR 136). Most coulometric titrations were carried out at constant current (Keithley 225 current source), usually at 10 mA, in series with an electronic coulometer (Koslow Model 541). Since most experiments turned out to be rather long, charge passed and emf's measured were recorded automatically at intervals on a Digitem recorder.

Results

Some information on the current-voltage characteristics of electrode [3] was obtained by measuring the current as a function of voltage applied to cell [8]. As can be seen in Fig. 1, the behavior is slightly nonohmic above 0.1V. 0.13V is the OCV against the Pt counterelectrode. The points represent the current 1 min after each change of voltage. The curve is independent of the direction of the current. One matter of interest is the current flow which the electrode can sustain (by reaction [4]) without undergoing irreversible processes, such as the reductions of the ZrO_2 itself. Examination of the electrode after electrolysis showed no such deleterious effects of the voltage and current span used.

In order to explore the coulometric applications of the zirconia electrode, cell [8] was put in series with a voltage or current source and a coulometer. The following observations were made:

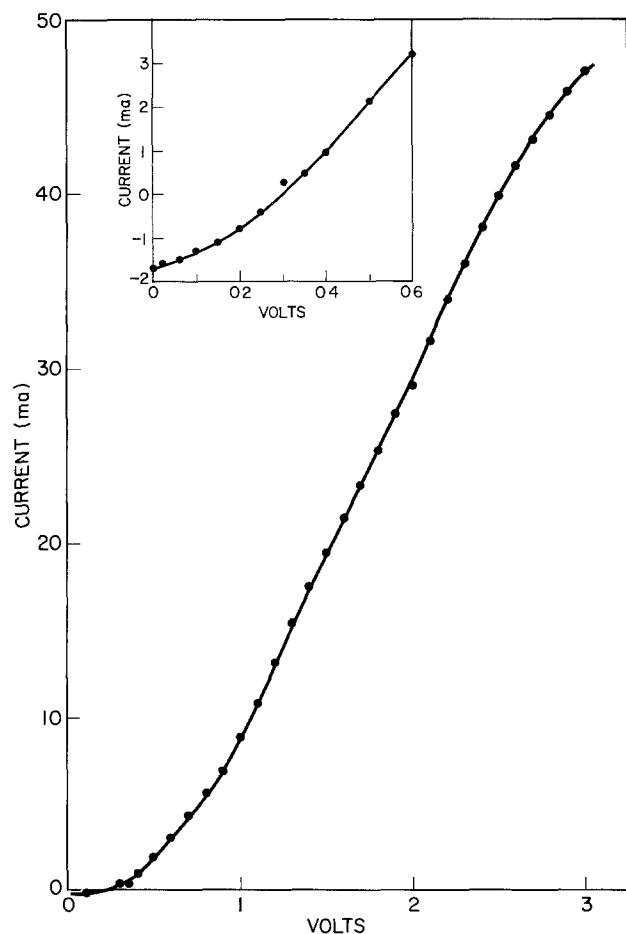


Fig. 1. Current-voltage characteristics of electrode [3], measured with cell [8]. P_{O_2} (zirconia reference) = 1 atm. Helium atmosphere above melt.

(i) When the zirconia electrode is made the anode, current flows only in a direction consistent with reaction [4] from right to left (oxidation); when the electrode is made the cathode, reaction [4] goes from left to right (reduction).

(ii) For current passage in either direction, the current decreases with time at constant voltage, but eventually comes to a constant value.

(iii) The electrode is highly "polarized" by the passage of current in either direction, i.e., after the applied voltage is removed, the OCV decays for several hours toward the value which would have been observed with an electrode through which no current had been passed. Therefore, the same electrode cannot be used for both electrolysis and as an indicator electrode.

This last observation necessitated use of a dual electrolysis and measurement system in order to study the relation between the charge passed through the zirconia and the resulting oxide activity changes in the melt. As described previously, cell [5] was used for the measurement of oxide activity, and cell [8] for the electrolysis. By interfacing the potentiometer measuring the emf of cell [5] and the coulometer measuring the charge Q passing through cell [8] with a data logger, both quantities could be measured and recorded simultaneously.

Figure 2 illustrates an experiment in which O^{2-} was electrolyzed out of a melt containing some added Na_2O . The measured emf changes very little until ~ 100 μequ had been passed through the zirconia. The curve then steepened progressively until a limiting slope was reached. The duration of this experiment was ~ 20 hr. Current reversal resulted in an increase of O^{2-} in the melt, as indicated by the emf.

In this case the emf at first changes very little with increasing Q , and then approaches a limiting slope of $RT/2F$. Both observations are consistent with the equations derived in the Appendix. A more detailed analysis is being published elsewhere (12).

Since the above-described experiments showed that O^{2-} ions could be coulometrically titrated into a melt through zirconia, it seemed reasonable to see if this technique could be applied to determining the solubility product of a metal oxide. The procedure consisted of dissolving 2×10^{-3} μequ CuCl in $\sim 100\text{g}$ NaCl and adding O^{2-} through the zirconia, as described above. After the addition of CuCl the emf of cell [5] changed from ~ 200 to 560 mV, showing that the addition of Cu^+ decreased the oxide activity in the melt by ~ 3 orders of magnitude, presumably

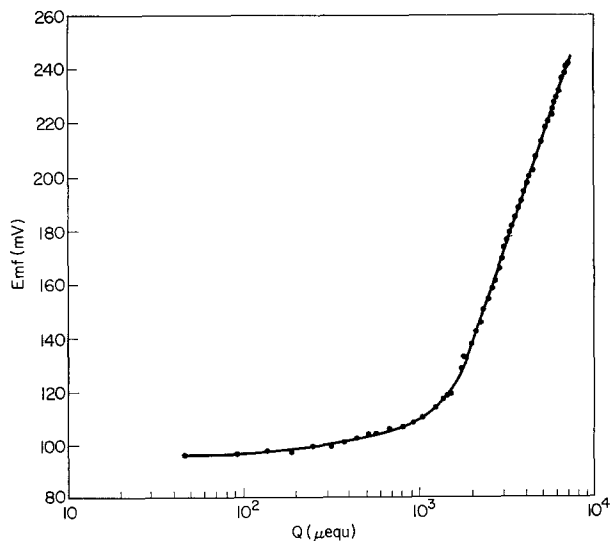


Fig. 2. Electrolysis of O^{2-} out of an $\text{Na}_2\text{O-NaCl}$ melt at 830°C . Current = 10 mA, 20% O_2 above melt.

because some Cu_2O was being precipitated. The relation between E and Q during the titration is shown in Fig. 3. The curve is typical of potentiometric titrations resulting in the precipitation of an insoluble compound, Cu_2O in this case. The steepest portion of the curve is close to the endpoint expected on the basis of the precipitation of Cu(I) as Cu_2O . The method is thus applicable to the determination of solubility products of slightly soluble oxides in molten salts. A more detailed exploration of this application will be described elsewhere (13).

Discussion

The purpose of this paper is to report a new application of stabilized zirconia: the coulometric titration of O^{2-} ions into and out of molten salts. The experiments described show how such titrations can be carried out. The E vs. $\ln Q$ curves obtained are consistent with the equations derived in the Appendix.

Electrolyzing O^{2-} out of a melt can be used to purify it of a dissolved oxide. The lower limit of attainable oxide concentration is expected to be the solubility of the zirconia itself, although lower concentrations could be obtained if (i) the electrolyzing cell is withdrawn from the melt immediately after cessation of the electrolysis, and (ii) a nonoxide crucible, e.g., platinum, is used.

It should also be emphasized that the measuring zirconia electrode responds to changes in the O^{2-} activity, whereas the coulometric zirconia passes equivalents. In dilute melts, the activity coefficients are most likely constant and thus activities are proportional to equivalents; but the situation is more complicated for solubility products. The solubility product of an oxide Mo is defined as

$$K_{sp} = a_{\text{M}^{2+}} \cdot a_{\text{O}^{2-}}$$

but $a_{\text{M}^{2+}}$ is set by the thermodynamics of the MCl_2 - NaCl system, whereas $a_{\text{O}^{2-}}$ is related to that of the Na_2O - NaCl system. Thus, equality of activities does not necessarily imply equality of concentrations.

Manuscript submitted Feb. 25, 1980; revised manuscript received May 23, 1980. This was Paper 348 presented at the Pittsburgh, Pennsylvania, Meeting of the Society, Oct. 15-20, 1978.

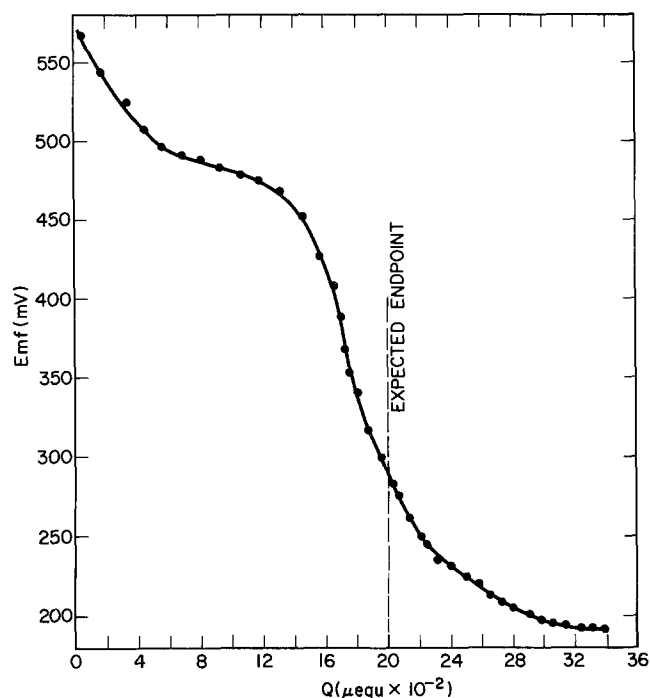


Fig. 3. Coulometric titration of Cu(I) in a CuCl-NaCl melt with O^{2-} .

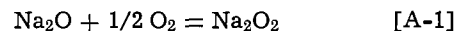
Any discussion of this paper will appear in a Discussion Section to be published in the June 1981 JOURNAL. All discussions for the June 1981 Discussion Section should be submitted by Feb. 1, 1981.

Publication costs of this article were assisted by the Naval Research Laboratory.

APPENDIX

The relation between charge passed and the measured emf can be derived as follows:

It is known (5) that in molten NaCl , oxide and peroxide ions are in equilibrium. The equilibrium constant for the reaction



is 3.1 at 1100°K (5). At constant P_{O_2} , the ratio

$$[\text{Na}_2\text{O}_2]/[\text{Na}_2\text{O}] = K_e P_{\text{O}_2}^{1/2} = K_e' \quad [\text{A-2}]$$

where the brackets denote mole fractions. Since the electrolysis is slow, it is reasonable to assume that this equilibrium is maintained.

Case I. *Electrolysis of Na_2O into the melt.*—Let $[\text{Na}_2\text{O}]_0$ and $[\text{Na}_2\text{O}_2]_0$ equal the initial Na_2O and Na_2O_2 concentrations, respectively, at equilibrium. These concentrations may be impurities or result from prior addition of Na_2O . They can be calculated from the emf of cell [5], i.e., Eq. [7], if E° and the activity coefficients are known.

For Q equivalents electrolyzed into the melt, $Q/2$ moles O^{2-} will initially form. The initial O^{2-} concentration is then $Q/2n$, where n = number of moles of solvent, and it is assumed that the melt is very dilute. Some fraction X of this O^{2-} concentration is converted to O_2^{2-} when the melt comes to equilibrium. The new equilibrium concentrations of Na_2O and Na_2O_2 then are

$$[\text{Na}_2\text{O}]_e = [\text{Na}_2\text{O}]_0 + Q/2n - X \quad [\text{A-3}]$$

$$[\text{Na}_2\text{O}_2]_e = [\text{Na}_2\text{O}_2]_0 + X \quad [\text{A-4}]$$

Substitution of [A-3] and [A-4] into [A-2] gives

$$X = \frac{K_e' Q}{2n(K_e' + 1)} \quad [\text{A-5}]$$

Therefore

$$[\text{Na}_2\text{O}]_e = [\text{Na}_2\text{O}]_0 + \frac{Q}{2n(K_e' + 1)} \quad [\text{A-6}]$$

Substituting [A-6] into [7] gives the relationship between E and the charge passed

$$E = E^\circ - (RT/2F) \ln \left\{ [\text{Na}_2\text{O}]_0 + \frac{Q}{2n(K_e' + 1)} \right\} \quad [\text{A-7}]$$

where the activity coefficient of Na_2O has been absorbed into E° . One sees from the form of [A-7] that $dE/d \ln Q$ will be small for small Q , since then $[\text{Na}_2\text{O}]_0$ will exceed the term in Q . When the second term in the bracket becomes much larger than the first, the limiting slope $dE/d \ln Q = -RT/2F$ will be reached, in agreement with experimental observation.

Case II. *Electrolysis of Na_2O out of the melt.*—The same assumptions are made as for Case I. As Na_2O is electrolyzed out of the melt the equilibrium [9] is maintained and therefore

$$[\text{Na}_2\text{O}]_e = ([\text{Na}_2\text{O}]_0 - Q/2n)/K_e' + 1 \quad [\text{A-8}]$$

Therefore

$$E = E^\circ - (RT/2F) \ln \left[([\text{Na}_2\text{O}]_0 - Q/2n)/K_e' + 1 \right]$$

In this case the measured emf remains nearly constant in the beginning of the electrolysis and asymptotically approaches infinity at $Q/2n$ approaches $[\text{Na}_2\text{O}]_0$. Although the curve in Fig. 2 shows the expected flat portion, followed by a steeper section, the latter appears linear, rather than steepening as expected. The reasons are not clear.

REFERENCES

1. T. H. Etsel and S. N. Flengas, *Chem. Rev.*, **70**, 339 (1970).
2. For a list of many references, see (1).
3. R. Combes, J. Vedel, and B. Tremillon, *Anal. Lett.*, **3**, 523 (1970).
4. D. R. Flinn and K. H. Stern, *J. Electroanal. Chem. Interfacial Electrochem.*, **63**, 39 (1975).
5. K. H. Stern, R. Panayappan, and D. R. Flinn, *This Journal*, **124**, 641 (1977).
6. G. C. Charette and S. N. Flengas, *Can. Metall. Quart.*, **7**, 191 (1969).
7. C. Deportes, P. Donneaud, and G. Robert, *Bull. Soc. Chim. Fr.*, 2221 (1964).
8. D. Yuan and F. A. Kroger, *This Journal*, **116**, 594 (1969).
9. R. L. Pastorek and R. A. Rapp, *Trans. Met. Soc. AIME*, **25**, 1711 (1969).
10. K. H. Stern, *Electrochim. Acta*, **24**, 509 (1979).
11. K. H. Stern, M. L. Deanhardt, and R. Panayappan, *J. Phys. Chem.*, **83**, 2848 (1979).
12. M. L. Deanhardt and K. H. Stern, *J. Phys. Chem.*, In press.
13. M. L. Deanhardt and K. H. Stern, Paper 656 presented at The Electrochemical Society Meeting, Hollywood, Florida, Oct. 5-11, 1980.

Electrodeposition of CdSe Films from Selenosulfite Solution

M. Skyllas Kazacos* and B. Miller*

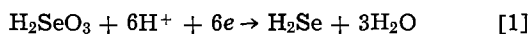
Bell Laboratories, Murray Hill, New Jersey 07974

ABSTRACT

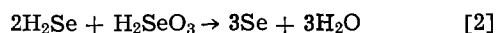
A route to CdSe film formation by reduction of selenosulfite ion in the presence of cadmium-EDTA complex has been devised. The as-deposited product is free from the selenium contamination characteristic of prior methods and also shows better n-type photoactivity in sulfide-polysulfide cells. The interfacial reactions have been clarified by rotating ring-disk electrode and related techniques. Electrochemical control of the process is shown to be simple.

Photoactive CdSe films have been electrodeposited both cathodically and anodically, the former with selenious acid-cadmium ion solutions (1) and the latter with Cd anodes in selenide media (2). Such methods would be attractive for the production of low cost, large area photoelectrochemical cells. Anodic n-CdSe layers have the advantage of fairly good as-formed photoresponse but are restricted in growth by the transport of cadmium ions through the film. Cathodic deposition of CdSe is not limited in thickness as only electron transport to the solution interface is required, but post-thermal treatment is necessary to develop respectable photoactivity (1). In the cathodic method, millimolar solutions of SeO₂ (H₂SeO₃) are reduced in the presence of relatively high concentrations of CdSO₄ to yield a film of CdSe at the cathode surface. Layers up to several microns have been achieved with good adherence on a Ti substrate after a 600°C anneal (1). Higher SeO₂ concentrations result in electrode passivation due to the formation of a red insulating layer of Se.

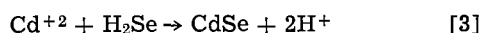
A recent study of the reduction of selenious acid and CdSe formation (3) in H₂SO₄ solution has shown that the initial cathodic reaction involves an overall transfer of six electrons



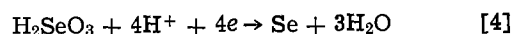
The H₂Se formed may react by



yielding elemental selenium. This step competes with the desired deposition of CdSe



The rate of the chemical reaction [2] is dependent on the concentration of H₂SeO₃ and is sufficiently rapid at high H₂SeO₃ concentrations so that the net process taking place at the surface of the electrode is



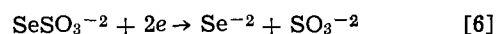
Plating of CdSe from dilute H₂SeO₃ solutions minimizes the level of selenium codeposited in the cathodically generated films (3). However, even at low H₂SeO₃ concentrations, contamination of the CdSe films with excess selenium cannot be eliminated. This results usually in mixed n- and p-type behavior in photocurrent spectra, and even dominant p-type response in white light, for the as-formed film (3). In addition, this poor photoresponse makes a postannealing process at elevated temperature essential, both for the improvement of poor crystallinity and for the vaporization of excess Se from the films (1).

A process for cathodic generation of CdSe not subject to codeposition of Se would allow either elimination or modification of the presently essential annealing stage. Ideally, the room temperature cathodic product would have the n-type response of the anodic films without meeting the passivity which limits the latter to crystallite sizes and thicknesses less than visible light absorption depths. Since the main problem in the reduction method (1) arises from the interaction between the starting material H₂SeO₃ and the electron transfer product, H₂Se, we have sought a route to cathodic selenide generation avoiding higher valent selenium species or other active oxidant capable of reacting with selenide.

We find the reduction of selenosulfite, SeSO₃⁻², suited to this purpose. Selenosulfite is readily prepared *in situ* by the dissolution of elemental selenium in excess sulfite by



Selenide can be generated from this ion by the reaction (4)



The photoelectrochemical behavior of CdSe electrodes prepared by carrying out reaction [6] in the presence of cadmium species was examined. Rotating disk and ring-disk electrode methodology was applied to ascertain the nature of the reactions taking place.

* Electrochemical Society Active Member.

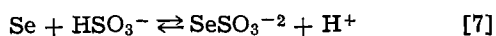
Key words: energy conversion, semiconductor, voltammetry.

Experimental

Voltammetric study of the reduction of selenosulfite in 1M $\text{NH}_3/\text{NH}_4^+$ buffer was carried out using gold and cadmium rotating disk and silver-cadmium rotating ring-disk electrodes, the construction and electronics of which have already been described (5). Sinusoidal hydrodynamic modulation (SHM) experiments were also performed with the apparatus previously reported (6).

A silver ring-cadmium disk electrode with disk, inner ring, and outer ring radii of 0.238, 0.253, and 0.320 cm, respectively, was used. The theoretical geometric collection efficiency, N (7), was 0.383.

Approximately 5 mM Na_2SeSO_3 solutions were prepared by shaking 0.1M Na_2SO_3 and weighed powdered selenium in 1M $\text{NH}_3/\text{NH}_4^+$ buffer until the selenium dissolved. The high concentration of Na_2SO_3 and the use of ammonium buffer were necessary to achieve 5 mM, as the equilibrium constant of reaction [5] is around unity (8). Thus a pH 10 medium assists dissolution from



The SeSO_3^{2-} and SO_3^{2-} ions (or their protonated forms) do not oxidize Se^{2-} (or its protonated form), as happens for H_2SeO_3 in reaction [2]. Thus selenium contamination of CdSe is not expected, both because there is no obvious mechanism of its generation and, further, it is soluble in excess sulfite. An ammonia buffer was initially chosen as this ligand allows the necessary cadmium ion solubility in base to attempt deposition of CdSe films.

All solutions were prepared with triply distilled water and reagent grades of Na_2SO_3 , NH_4OH , NH_4Cl , CdSO_4 , and EDTA (ethylenediaminetetraacetic acid). The rotating disk electrodes were examined in a standard three-compartment cell. All potentials are referred to a saturated calomel electrode unless otherwise specified.

CdSe films were prepared on stationary vertical $\frac{3}{4}$ in. titanium disks in magnetically stirred solutions as well as on gold and cadmium rotating disk electrodes. The Ti surfaces were degreased with acetone and etched in 5% HF, prior to use (9). The metal disk edges were protected by epoxy mounting after film deposition and any annealing step, before observing photoresponse characteristics under 100W tungsten-halogen lamp illumination at white light levels producing the equivalent of about AM1 solar short-circuit current with single crystal n-CdSe cells.

Results and Discussion

Reduction of SeSO_3^{2-} in $\text{NH}_3/\text{NH}_4^+$ buffer.—The cathodic behavior of selenosulfite in 0.3M NaNO_3 at a dropping mercury electrode has been ascribed to Se^{2-} formation in a single two-electron step at a half-wave potential of -1.06V vs. SCE (4). Figure 1 presents the typical behavior of a gold disk electrode in 2 mM SeSO_3^{2-} -0.1M Na_2SO_3 in 1M $\text{NH}_3/\text{NH}_4^+$ buffer solution. A single reduction wave can be observed starting near -1.0V vs. SCE. Curve 2 of Fig. 1 shows the corresponding SHM response which was obtained by superimposing a 1 Hz sinusoidal variation of $\Delta\omega^{1/2}$ on the rotation speed $\omega^{1/2}$ and extracting the corresponding Δi_ω value. The near superposition of the $\Delta i_\omega \times \omega^{1/2}/\Delta\omega^{1/2}$ and i curves indicates that the process obeys the Levich equation and that the SeSO_3^{2-} reduction reaction is convective diffusion controlled. The SHM response plateau is also seen to continue unchanged into the H_2 evolution region, indicating no further stage of reduction for SeSO_3^{2-} can be detected. (Hydrogen evolution at gold is irreversible and, since it is not limited here by convective diffusion of an electroactive species to the electrode surface, it is insensitive to ω variation.)

In order to verify that the species Se^{2-} was being generated during the reduction of SeSO_3^{2-} , a cadmium

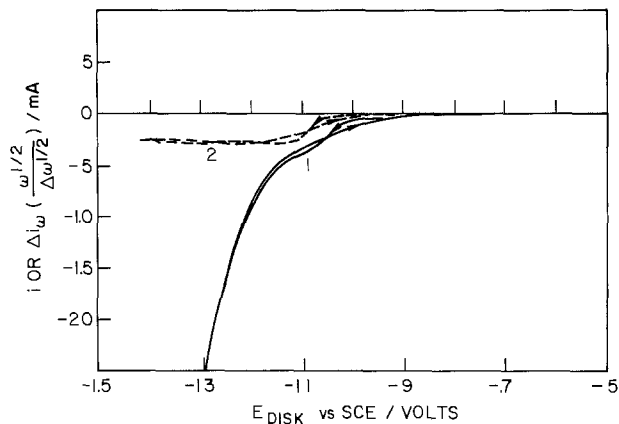
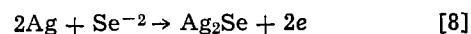


Fig. 1. Curve 1: Controlled potential sweep cycle of 0.175 cm^2 gold disk in 2 mM Na_2SeSO_3 -0.1M Na_2SO_3 -1M $\text{NH}_3/\text{NH}_4^+$ at 10 mV sec^{-1} scan rate. Curve 2: Modulated component of disk current for potential scan of Curve 1. Central rotation speed $\omega = 1600\text{ rpm}$; modulation amplitude, $\Delta\omega^{1/2} = 2\text{ rpm}^{1/2}$, modulation frequency, $f = 1\text{ Hz}$.

disk-silver ring electrode experiment was performed (the substitution of Cd for Au in the disk does not alter the reduction process here). The silver ring was potentiostatted at -0.4V vs. SCE while the cadmium disk was scanned negatively from approximately -0.8V . Under this ring condition a mass transfer limited film formation reaction



can be used to detect Se^{2-} generation at the disk in the manner applied to S^{2-} (10). An anodic ring current corresponding to the cathodic disk reaction was observed as in Fig. 2. Visual examination of the ring electrode after cycling the disk between -0.8 and -1.5V showed the presence of a black deposit of Ag_2Se on the silver surface. If the species Se^{2-} (HSe^-) is being generated at the disk electrode from SeSO_3^{2-} by reaction [6], then the ratio of ring to disk current, i_R/i_D , should be given by N since $2e$ are involved per Se^{2-} in both disk and ring reactions. Figure 3 shows the i_R vs. i_D trace during the disk reduction wave of Fig. 2(b). The initial slope of 0.309 is in adequate agreement with the calculated N , considering that the disk current contains an increasing component of electrolyte reduction with negative potential scan, producing curvature in the trace.

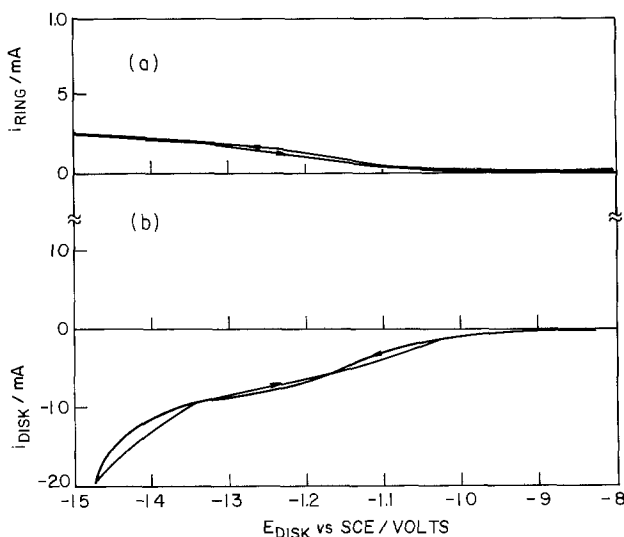


Fig. 2. (a) Ring current response to cadmium disk behavior of Fig. 2(b). $E_R = -0.4\text{V}$ vs. SCE. (b) Controlled potential sweep cycle of 0.178 cm^2 cadmium disk in 5 mM Na_2SeSO_3 -0.1M Na_2SO_3 -1M $\text{NH}_3/\text{NH}_4^+$ at 10 mV sec^{-1} scan rate, and $\omega = 1600\text{ rpm}$.

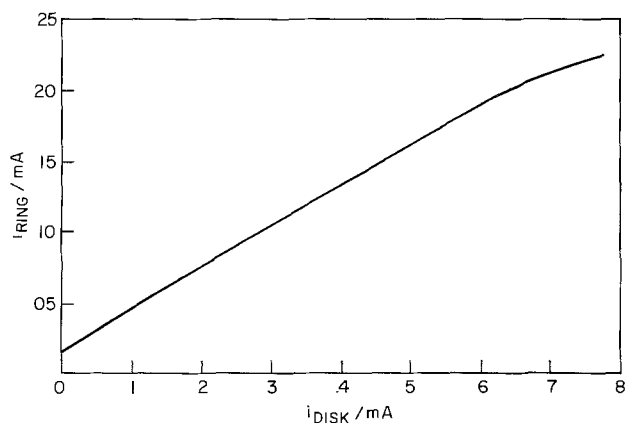


Fig. 3. Ring current vs. disk current trace corresponding to data of Fig. 2.

CdSe film deposition.—The above evidence establishes Se^{-2} as the product of SeSO_3^{-2} reduction in $\text{NH}_3/\text{NH}_4^+$ buffer at a gold or cadmium electrode. Importantly, this reaction does not appear to be complicated by subsequent redox reactions as was the case in the $\text{H}_2\text{SeO}_3/\text{Se}^{-2}$ system (3). Thus, carrying out the reduction in the presence of cadmium ions should permit forming a CdSe film at the surface of the electrode without the problem of selenium contamination found with H_2SeO_3 as selenide source. The situation is complicated, however, by the reduction potential of Cd^{2+} in $\text{NH}_3/\text{NH}_4^+$, which is positive with respect to the potential of the SeSO_3^{-2} reduction, as seen in the curves of Fig. 4(a) and 5(a). The deposition of Cd metal under these circumstances is evidenced by its oxidative redissolution, essentially unaffected by SeSO_3^{-2} being absent [Fig. 4(a)] or present [Fig. 5(a)]. The corresponding SHM traces in these figures show the convective-diffusion controlled Cd(II) reduction and the partially kinetically controlled anodic response (11) on positive-potential going scan. In order to generate Se^{-2} in the presence of Cd(II), an additional complexing agent for Cd^{2+} , stronger than NH_3 , is necessary to shift the potential for Cd(II) reduction to more negative values, while at the same time not interfering with the selenosulfite reduction. The success of EDTA addition for this purpose is illustrated in Fig. 4(b) and 5(b) for Cd^{2+} in $\text{NH}_3/\text{NH}_4^+$ and $\text{Cd}^{2+} + \text{SeSO}_3^{-2}$ in $\text{NH}_3/\text{NH}_4^+$, respectively.

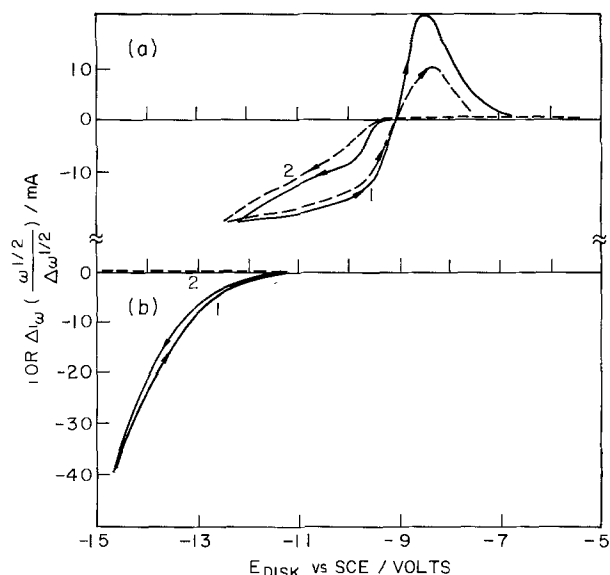


Fig. 4. (a) Curves 1 and 2: As for Fig. 1, except solution is 2 mM CdSO_4 -1M $\text{NH}_3/\text{NH}_4^+$. (b) Curves 1 and 2: As for (a), except 0.01M EDTA added.

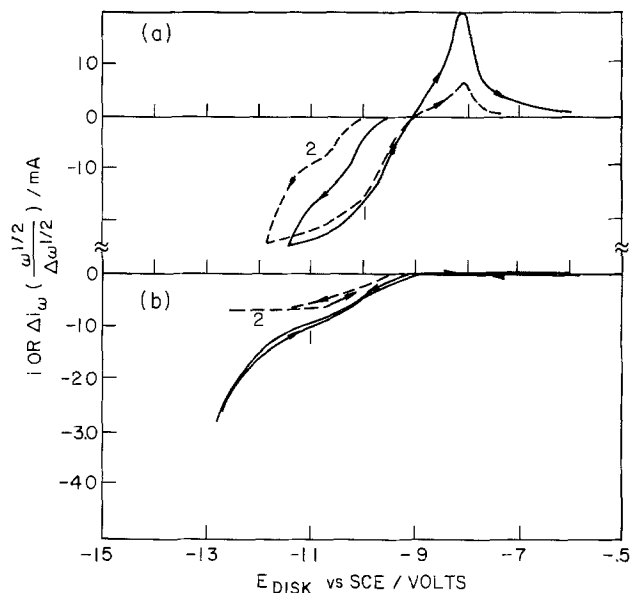


Fig. 5. (a) Curves 1 and 2: As for Fig. 1, except solution is 2 mM Na_2SeSO_3 -2 mM CdSO_4 -0.1M Na_2SO_3 -1M $\text{NH}_3/\text{NH}_4^+$. (b) Curves 1 and 2: As for (a), except 0.01M EDTA added.

In Fig. 4(b), the EDTA complex of Cd(II) is no longer reducible over the potential range up to supporting electrolyte reduction, evidenced both by no SHM response and no anodic dissolution on positive scan. The curves in Fig. 5(b) are virtually identical to those of Fig. 1 and 2, for a solution containing no cadmium. Under the conditions of Fig. 5(b) then, the desired situation of Se^{-2} generation in the presence of Cd(II) species is achieved. The stability of the Cd-EDTA complex is insufficient to prevent the formation of the very insoluble CdSe, qualitatively shown by the black film on the electrode in a Fig. 5(b)-type experiment.

A number of CdSe films were prepared on gold, cadmium, and titanium substrates from solutions consisting of 5 mM Na_2SeSO_3 + 0.1M Na_2SO_3 + 0.2M CdSO_4 + 0.2M EDTA in 1M $\text{NH}_3/\text{NH}_4^+$ [EDTA always kept just in excess of Cd(II)]. The relatively high Cd-EDTA complex concentrations were found necessary to precipitate the film at the electrode surface in an adherent form. The metal electrodes were held at -1.1 to -1.2V vs. SCE, during which time the current ranged from 0.5 to 1.0 mA/cm^2 . For vertically mounted disks the solution was magnetically stirred; the other electrodes were rotated. Deposition times of 1-4 hr were employed to achieve calculated film thicknesses of 1.5-12 microns. The solution was replaced after the current dropped below 0.5 mA/cm^2 .

The electrodes obtained as above were examined for photoresponse in a cell with a 1M Na_2S_2 + 1M NaOH -0.07M Se solution (12) and a carbon counter-electrode. The values of short-circuit photocurrents (I_{sc}) and open-circuit photopotentials (V_{oc}) under white light ranged from 0.25 to 3.1 mA/cm^2 and 0.1 to 0.55V, respectively. A selection of these data appear in Table IA. There were no distinct differences in the behavior of films deposited on gold, cadmium, or titanium disks. The thickness of the CdSe film, however, does have an effect on both the I_{sc} and V_{oc} , as shown in the curves of Fig. 6, which appears significant beyond the scatter evidenced in Table IA. However, the range of results does not presently allow evaluating this relation more quantitatively. The dark current levels probably vary with residual porosity in the film as deposited and after transfer from the forming to testing solution.

To place these electrodeposited film results in the perspective of the behavior of an aqua regia etched (12) single crystal n-CdSe electrode, cell curves as

Table I. Characteristics of 6 μm electrodeposited CdSe films

A. As deposited Substrate									
Electrode	Ti			Cd			Au		
	1	2	3	4	5	6	7	8	9
V_{oc} , V	0.41	0.39	0.38	0.38	0.31	0.55	0.13	0.35	0.41
I_{sc} , mA cm^{-2}	0.6	3.1	0.8	0.4	0.3	0.2 _s	1.0	3.1	0.7

B. Following 10 min at 600°C in N ₂ * Substrate—Ti				
Electrode	10	11	12	13
V_{oc} , V	0.49	0.33	0.45	0.33
I_{sc} , mA cm^{-2}	2.0	1.1	2.0	2.0

* Four additional specimens in this sequence lost film adherence and were not measured.

those in Fig. 6 were obtained for both types under the same illumination. These results indicate film short-circuit currents typically 1/5 of that of single crystals and equivalence to 1% AM2 solar conversion efficiency, given the 7% (12) found for the crystals in this cell.

The effect of heat-treatment on the performance of the films was briefly investigated. Some of the electrodes deposited on Ti were annealed at 600°C for 10 min under an argon atmosphere (9). These were then epoxy mounted and current-voltage plots obtained. The electrodes subjected to the heat-treatment exhibited ranges in photocurrent and photovoltage similar to those of untreated disks and no consistent improvement in performance could be related to this step (Table IB). In fact, a slight deterioration in the appearance of the films was usually apparent, in particular shrinkage, flakiness, and poorer adherence, leading to total failure of perhaps half the specimens before cell testing.

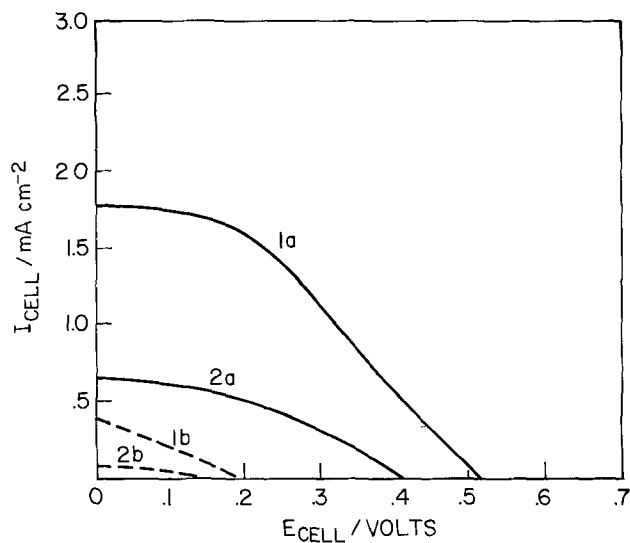


Fig. 6. Curve 1(a): Output power characteristic for 6 micron CdSe film on Ti substrate in 1M Na₂S-1M S-1M NaOH-0.07M Se under illumination. Curve 1(b): As for 1(a) but no illumination. Curve 2(a): As for 1(a) but for 1.5 micron CdSe film. Curve 2(b): As for 2(a) but no illumination.

Another direction requiring further investigation is the effect of etching on the electrodeposited films. Preliminary etching experiments with 1 HNO₃-4 HCl-5 H₂O solutions at room temperature suggest that cell currents could be initially improved by as much as a factor of two, but concurrent overall degradation of the thin films makes the results inconclusive. A milder surface treatment would be needed.

Summary

The reduction of SeSO₃⁻² ion to Se⁻² has been demonstrated by a variety of rotating disk electrode techniques. In a solution in which the SeSO₃⁻² is stable to dissociation into Se⁰ and cadmium ion is complexed strongly enough to be reduced at more negative potentials than SeSO₃⁻², CdSe films may be generated by a surface precipitation process. The film is clearly n-type and photoactive, and, in our experience (3), a better photoanode in the as-deposited condition for the S⁻²/S_x⁻²|C cell than that produced from H₂SeO₃ reduction where Se⁰ contamination appears an intrinsic problem.

Conditions of concentration and mass transfer are not nearly so critical in the SeSO₃⁻² process as they are in H₂SeO₃ reduction because of the intermediacy of Se⁰ in the latter. The electrochemical control of the SeSO₃⁻² route to CdSe is relatively simple. The reactions and precautions as understood for CdSe film formation could be applied to doping such photoelectrodes or producing other selenides. Surface treatment for optimizing the photoanodic behavior of the film and an annealing procedure to improve its crystallinity remain to be established.

Manuscript submitted April 3, 1980; revised manuscript received June 12, 1980.

Any discussion of this paper will appear in a Discussion Section to be published in the June 1981 JOURNAL. All discussions for the June 1981 Discussion Section should be submitted by Feb. 1, 1981.

Publication costs of this article were assisted by Bell Laboratories.

REFERENCES

- G. Hodes, J. Manassen, and D. Cahen, *Nature*, **261**, 403 (1976).
- B. Miller and A. Heller, *ibid.*, **262**, 680 (1976).
- M. Skyllas Kazacos and B. Miller, *This Journal*, **127**, 869 (1980).
- V. F. Toropova, L. N. Medvedeva, and Yu N. Polyakov, "Issledovaniya po Elektrokhemii, Magnetokhemii i Elektrokhemicheskim Metodam Analiza," Vol. 3, Kazanskiy, Universitet, p. 12 (1970).
- B. Miller, *This Journal*, **116**, 1117 (1969).
- B. Miller and S. Bruckenstein, *Anal. Chem.*, **46**, 2026 (1974).
- W. J. Albery and S. Bruckenstein, *Trans. Faraday Soc.*, **62**, 1920 (1966).
- S. M. Golyand, *Khim. Prom.*, 45 (1947).
- G. Hodes, Private communication.
- B. Miller, S. Menezes, and A. Heller, *J. Electroanal. Chem. Interfacial Electrochem.*, **94**, 85 (1978).
- B. Miller, M. I. Bellavance, and S. Bruckenstein, Paper 97 presented at The Electrochemical Society Meeting, Boston, Mass., Oct. 7-11, 1973.
- A. Heller, G. P. Schwartz, R. G. Vadimsky, S. Menezes, and B. Miller, *This Journal*, **125**, 1156 (1978).



The Sulfospinel-Lithium Battery System: Initial Study of Three Sulfospinels

M. Eisenberg*

Electrochimica Corporation, Mt. View, California 94040

The discovery that chalcospinels (*e.g.*, sulfospinels) of certain transition metals can make useful reversible cathode materials in an aprotic electrolyte battery system was recently reported (1, 2). These face-centered cubic materials represent sulfur equivalents of the well-known oxospinels of a general formula $M_1^{II}M_2^{III}S_4$, where M_1 and M_2 denote divalent and trivalent metal ions. This communication describes additional tests on $CuCo_2S_4$ -Li cells as well as several new sulfospinels, in the preparation of which nickel and iron were used in place of cobalt as the trivalent transition metal ion.

Experimental Studies and Results

All sulfospinel materials discussed in this paper have been synthesized from metal powders or simple sulfides in quartz furnaces by a method described previously (1). Experimental studies were carried out on partial "C" cells employing cathodes 1.3×5 in. long supported on nickel grids and coiled with a 6 in. lithium anode. Polypropylene separators were used in between. A crimped seal was produced on the cylindrical cells in an argon dry box. Subsequently cell tests could be carried out in a normal laboratory atmosphere. A typical discharge of a cell with a $CuCo_2S_4$ cathode is illustrated in Fig. 1 for an 8 hr rate of discharge (0.63 mA/cm^2).

Figure 1 shows the initial discharge of a freshly assembled cell and its subsequent charge. The horizontal scale also indicates delivered capacity in terms of electrons per mole. As can be seen, there is a relatively prompt drop during the first hour to a voltage level of 1.55V after which the cells discharge remarkably linearly. Linearity is preserved at least over the range of two electrons per mole. The same is also true during the charge as shown from the upper curve of Fig. 1.

The experimental slope of the discharge curve is $0.165 \text{ V}/\bar{e}/\text{mole}$. It should be noted that this slope is under discharge conditions for a complete cell including polarized potentials of both cathode and anode. (It is not a plot of the open-circuit cathode potential *vs.* lithium take-up for which the slope should be $0.059 \text{ V}/\bar{e}/\text{mole}$ in accordance with the Nernst equation for the emf of a pure concentration cell.) A greater slope should be expected even for the cathode alone, since its polarization can be expected to increase as discharge proceeds and the take-up of lithium causes a decrease in the intrinsic conductivity of the sulfospinel.

This initial study included the first preparations of the sulfospinels of nickel and iron (in addition to copper). These were the first synthetic efforts and optimum conditions for their preparation still remain to be determined. However, some encouraging results in comparison to $CuCo_2S_4$ have been obtained

as illustrated in Table I which summarizes the initial cycling results (8 cycles) for 8 groups of partial C-cells consisting of 3 cells each.

All cells were connected in series and operated on the same cycling circuit. In this manner the same amount of charge was passed through all of them and they all experienced the same cycling history. Since the amount of active cathode material varied slightly from group to group, the number of moles per cell varied somewhat and, consequently it was more useful to express the depths of discharge in terms of electrons per mole. For the discharges this ranged from 1.87 to $2.73 \bar{e}/\text{mole}$. Since electrochemical reversibility has clearly been established and n-butyl lithium titrations indicate the preservation of the face-centered cubic structure of the sulfospinel (and possibly even up to 3 electrons per mole) (1), it was considered conservative to designate a 2 electron per mole discharge to correspond to a 100% depth of discharge (DOD) corresponding to 167 mA-hr/g in case of $CuCo_2S_4$.

The following observations can be made on the basis of the results given in Table I:

1. The $CuCo_2S_4$ cell (group No. 2) showed typical satisfactory behavior. An initial scan to 3.12 mA/cm^2 (equivalent to a 1.6 hr rate) cell voltage was 1.0V and a $2\bar{e}/\text{mole}$ 10 hr rate discharge yielded an end-voltage of 1.45V (average value). The recharge of $2\bar{e}/\text{mole}$ required an end-voltage of 2.70V.

2. The two $CuNi_2S_4$ groups (No. 6 and 7) showed (for slightly greater depth of discharge and charge) desirable higher discharge end-voltages and particularly lower charge end-voltages of 2.34V.

3. Substituting one of the Ni by Fe in the sulfospinel appears to increase the starting discharge voltage, lowering its end-voltage. It substantially increases the charging end-voltage which is undesirable.

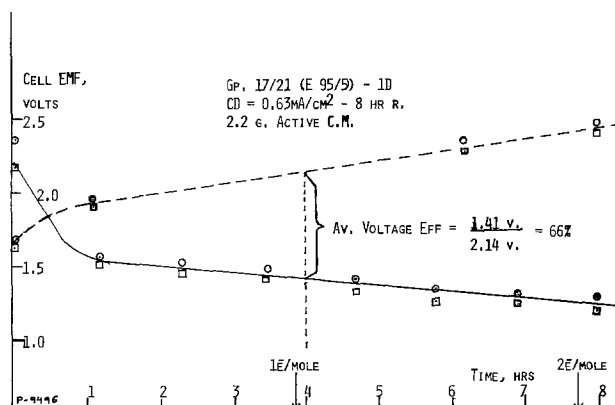


Fig. 1. Typical discharge and charge of $CuCo_2S_4$ -Li cells within the reversible range.

* Electrochemical Society Active Member.
Key words: battery, cathode, sulfospinel.

Table I. Cell cycling performance of new sulfospinel cathode materials

Sub. gp. No.	Cathode	Batch	Mole/cell $\times 10^3$	Groups 17-28—10 hr rate (0.5 mA/cm ²) charge and discharge					
				1D Scan Volts at		Disch 7D		Charge 8C	
				1.25	3.12 (mA/cm ²)	V-range	e/mole	V-range	e/mole
-2	CuCo ₂ S ₄	13B	7.5	1.88	1.40	2.20-1.45	2.03	1.82-2.70	2.0
-6	CuNi ₂ S ₄	3A	5.6	1.85	1.38	2.16-1.57	2.73	1.80-2.39	2.96
-7	CuNi ₂ S ₄	3B	7.4	1.88	1.52	2.18-1.48	2.07	1.92-2.34	2.15
-5	CuNiFeS ₄	1	6.5	1.51	1.10	2.60-1.28	2.35	1.75-3.60	2.32
-3	CuFe ₂ S ₄	4A	4.6	1.42	1.08	2.10-1.12	2.40	1.60-3.10	2.01
-4	CuFe ₂ S ₄	4B	7.3	1.46	1.09	2.45-1.33	2.10	1.70-3.60	2.07
-8	CuFe ₂ S ₄	5	8.2	1.51	1.12	2.55-1.36	1.87	1.75-3.46	1.84
-9	CuFe ₂ S ₄	6	7.8	1.75	1.34	2.52-1.38	1.96	1.76-3.42	1.93

4. The CuFe₂S₄ groups (No. 3, 4, 8 and 9) show similarly lower end-voltages on discharge and particularly higher end-voltage on charge (3.1-3.6V) which is symptomatic of greater kinetic irreversibility for charge acceptance.

Conclusions

The sulfospinels are a new promising group of cathode materials for high energy ambient temperature cells. Their utility in high temperature lithium cells has also been established (3), but so far for an initial discharge only. Since they are good electrical conductors, they provide the basis for a high rate capability.

Their reversible cycling behavior appears due to an interstitial migration of lithium into the face-centered cubic structure. This is based on the x-ray confirmation (1) that the face-centered cubic structure is retained when up to 3 lithium equivalents are introduced per mole of sulfospinel by the n-butyl lithium titration.

Of the compounds presented in this paper, CuCo₂S₄ and CuNi₂S₄ appear most promising. The somewhat poorer results obtained for CuFe₂S₄ may be due to a poor preparation. Further studies of these compounds, especially of the x-ray structure before and after discharge or charge, are now indicated for future optimization of the preparation methods.

Manuscript submitted Oct. 16, 1979; revised manuscript received May 30, 1980. This was Paper 27 presented at the Los Angeles, California, Meeting of the Society, Oct. 14-19, 1979.

Any discussion of this paper will appear in a Discussion Section to be published in the June 1981 JOURNAL. All discussions for the June 1981 Discussion Section should be submitted by Feb. 1, 1981.

REFERENCES

1. M. Eisenberg, in "Proc. 28th Power Sources Conf.," p. 155, The Electrochemical Society, (1978).
2. M. Eisenberg, U.S. Pat. 4,136,223 (1979).
3. R. Steunenberg, Private communications.

Simultaneous Discharge of Two Reacting Species under Pulsed Current Conditions

K. Viswanathan,*¹ M. A. Farrell Epstein, and H. Y. Cheh*

Department of Chemical Engineering and Applied Chemistry, Columbia University, New York, New York 10027

In recent years there has been considerable interest in the application of pulsed current to electrodeposition processes. One of the questions addressed is whether or not higher mass transfer rates are possible under pulsed conditions. Viswanathan *et al.* (1-4) examined the mass transport behavior under various periodic currents and potentials and concluded that for a single reaction occurring at the electrode surface, it is impossible to exceed the d-c electrolysis rate by any non-d-c methods. However, in a number of alloy as well as single metal deposition processes, two or more reactions can occur simultaneously (5). It is therefore interesting to examine the effects of applying non-d-c electrolysis to a system where two reactions occur. Recently, Haynes (6) has discussed current efficiencies under pulsed condition. Unfortunately, several assumptions made by Haynes are of doubtful validity (7).

This study involves the use of a simple model to demonstrate the point that pulsed current can be bene-

ficial in certain instances. Consider two irreversible reactions occurring simultaneously at an electrode surface. Reaction [1] produces an unwanted by-product while reaction [2] produces the desired substance. Assume also that reaction [1] is kinetically favored over reaction [2]. In other words, reaction [2] will not proceed until the applied current density exceeds the limiting current density of reaction [1]. To simplify the analysis, the reacting species are assumed to have equal diffusivities and bulk concentration. These assumptions can be relaxed to suit specific situations under consideration. Because of the irreversible nature of these assumed reactions, the current density is zero for each reaction during the off-period of the pulse.

Under d-c conditions, the current density for reaction [2] is zero when the applied current density is equal to or less than the limiting current density for reaction [1]. Based on the assumptions stated previously, both reactions have equal limiting current densities and the limiting current density for reaction [2] is reached when the applied current density is twice the d-c limiting current density for reaction [1]. The d-c current efficiency for reaction [2], $(\eta_2)_{d-c}$, is given by

* Electrochemical Society Active Member.

¹ Present address: Hooker Development Center, Niagara Falls, New York 14302.

Key words: pulsed electrolysis, current efficiency, mass transfer.

$(\eta_2)_{d-c} =$

$$\frac{\left(\begin{array}{l} \text{Applied d-c} \\ \text{current density} \end{array} \right) - \left(\begin{array}{l} \text{d-c limiting current density} \\ \text{for reaction [1]} \end{array} \right)}{\left(\text{Applied d-c current density} \right)} \times 100 = \frac{i_{d-c} - (i_{d-c})_{1,1}}{i_{d-c}} \times 100 \quad [1]$$

where i_{d-c} is the applied d-c current density and $(i_{d-c})_{1,1}$ is the d-c limiting current density for reaction [1]. Obviously, the maximum value for the current efficiency for reaction [2] is 50% when i_{d-c} is equal to $2(i_{d-c})_{1,1}$. It is therefore apparent that in order to approach the 50% current efficiency for reaction [2], one

plied pulsed current density be $2(i_p)_{1,1}$ during the on-period of a pulse. The equivalent d-c current density is

$$i_{d-c} = i_p t_1 / t_c = 2(i_p)_{1,1} t_1 / t_c \quad [2]$$

where i_p is the applied pulsed current density, t_1 is the duration of the on-period, and t_c is the cycle time. The d-c current efficiency for reaction [2] can be calculated by substituting Eq. [2] into Eq. [1]

$$(\eta_2)_{d-c} = \frac{(2i_p)_{1,1} t_1 / t_c - (i_{d-c})_{1,1}}{2(i_p)_{1,1} t_1 / t_c} \times 100 \quad [3]$$

If we assume that reaction [1] proceeds at a current density $(i_{int})_{1,1}$, the current efficiency for reaction [2] by pulsed current is given by

$$\begin{aligned} (\eta_2)_p &= \frac{\left(\begin{array}{l} \text{Time-averaged applied} \\ \text{pulsed current density} \end{array} \right) - \left(\begin{array}{l} \text{Time-averaged intermittent} \\ \text{limiting current density} \\ \text{for reaction [1]} \end{array} \right)}{\left(\text{Time-averaged applied pulsed current density} \right)} \times 100 \\ &= \frac{2(i_p)_{1,1} t_1 / t_c - (i_{int})_{1,1} t_1 / t_c}{2(i_p)_{1,1} t_1 / t_c} \times 100 \\ &= \frac{2(i_p)_{1,1} - (i_{int})_{1,1}}{2(i_p)_{1,1}} \times 100 \quad [4] \end{aligned}$$

must apply a current density whose magnitude should be close to $2(i_{d-c})_{1,1}$. On the other hand, one realizes that as the limiting current density of reaction [2] is being approached, the quality of the electrodeposit generally deteriorates rapidly (8). To better utilize the applied current density, it would be beneficial to reduce the fraction of current density which is consumed by reaction [1]. A possible way to accomplish this task is by the application of a pulsed rather than a d-c current. This advantage can be explained by the following consideration.

In order to enhance the current efficiency of reaction [2], one should apply a current which is considerably higher than the limiting current density for reaction [1]. Under pulsed current conditions, the pulsed limiting current density, $(i_p)_{1,1}$, can be calculated by the method described by Cheh (9). The pulsed limiting current density has been defined to be the applied current density which causes the concentration of the reacting species to drop to zero at the end of the on-period during a pulse cycle. In contrast to d-c conditions, if a pulsed current with a magnitude of $2(i_p)_{1,1}$ is applied, reaction [2] will proceed under conditions not completely controlled by mass transfer. This is because reaction [1], being kinetically favored, will proceed at a current higher than $(i_p)_{1,1}$. The concentration of the reacting species for reaction [1] will drop to zero during the pulse instead of at the end of the pulse. The highest current that reaction [1] can achieve is given by the intermittent potential case (4), which corresponds to the situation where the concentration of the reacting species drops to zero instantaneously at the onset of a pulse. This is a limiting case. For the concentration of a reacting species to drop to zero instantaneously, one must apply an infinite current density initially. In reality, a high current density is needed for a short period of time at the onset of the on-period. The overall current density for reaction [1] during the on-period is nevertheless close to the limiting current density of reaction [1] for the intermittent potential case, $(i_{int})_{1,1}$. The calculation of $(i_{int})_{1,1}$ has been presented recently by Viswanathan *et al.* (4).

Let us now proceed to calculate the current efficiency for reaction [2] under d-c conditions and compare it with the time-averaged current efficiency under pulsed conditions for the same number of coulombs passed in a given time period. Let the ap-

plied pulsed current density be $2(i_p)_{1,1}$ during the on-period of a pulse. The equivalent d-c current density is

Since $(i_p)_{1,1}$ and $(i_{int})_{1,1}$ are functions of pulse characteristics and stirring (4, 9), a numerical comparison of $(\eta_2)_{d-c}$ and $(\eta_2)_p$ has to be carried out according to the following procedure. For various values of the dimensionless on- and off-periods defined by $\tau_1 = Dt_1/\delta^2$ and $\tau_2 = Dt_2/\delta^2$ where τ_1 and τ_2 are the dimensionless on- and off-periods, D is the diffusivity of the reacting species, and δ is the thickness of the Nernst diffusion layer, $(i_p)_{1,1}$ and $(i_{int})_{1,1}$ can be calculated by methods outlined by Cheh (9) and by Viswanathan *et al.* (4), respectively. These values are then used to calculate $(\eta_2)_{d-c}$ and $(\eta_2)_p$ by using Eq. [2] and [3]. Results from similar calculations are summarized in Table I.

For example, when $\tau_1 = 0.04$ and $\tau_c = 0.10$, $(i_p)_{1,1}/(i_{d-c})_{1,1} = 1.9825$ (9) and $(i_{int})_{1,1}/(i_{d-c})_{1,1} = 2.17$ (4). Therefore, according to Eq. [3], $(\eta_2)_{d-c} = [(2 \times 1.9825 \times 0.4 - 1)/(2 \times 1.9825 \times 0.4)] \times 100\% = 36.94\%$, and according to Eq. [4], $(\eta_2)_p = [(2 \times 1.9825 - 2.17)/2 \times 1.9825] \times 100\% = 45.25\%$.

These results clearly indicate that the maximum current efficiency for reaction [2] is 50% for a system with equal diffusivities, valency, and bulk concentration for both reacting species. This value is reached when one applies a d-c current density which is the sum of the d-c limiting current densities for both species. On the other hand, when the applied current is lower than the sum of the d-c limiting current densities, the current efficiency for reaction [2] under pulsed conditions is generally higher than that under d-c conditions. The faster the pulse, the higher is the current efficiency for reaction [2]. This is expected

Table I. Current efficiencies for reaction [2] by d-c and by pulsed electrolysis

τ_1	τ_2	$(\eta_2)_{d-c}$	$(\eta_2)_p$
1.000	0.000	50.00	50.00
0.800	0.200	40.50	44.50
0.600	0.400	27.20	40.98
0.400	0.600	6.87	38.87
0.100	0.000	50.00	50.00
0.080	0.020	47.05	48.20
0.060	0.040	43.07	46.84
0.040	0.060	36.94	45.25
0.020	0.080	24.24	43.94
0.010	0.000	50.00	50.00
0.008	0.002	49.07	49.42
0.006	0.004	47.81	48.84
0.004	0.006	45.87	48.43
0.002	0.008	41.86	47.64

because $(i_p)_{1,1}$ approaches $(i_{int})_{1,1}$ as the duty cycle approaches zero (4). It is also important to note that since $(i_{int})_{1,1}$ is the highest limiting current density among all non-d-c electrolysis, $(n_2)_p$ calculated by Eq. [3] provides the lower bound for the current efficiency for reaction [2] by pulsed electrolysis. The actual current efficiency for reaction [2] by pulsed electrolysis will be between the value calculated by Eq. [3] and 50%. Meanwhile, Viswanathan *et al.* (4) has shown that $(i_{int})_{1,1} \times t_1/t_2$ is always lower than $(i_{d-c})_{1,1}$. Thus, by applying a pulsed current, the time-averaged rate of pulsed electrolysis for reaction [1] is lower than that by d.c., thereby increasing the time-averaged rate of electrolysis and the current efficiency for reaction [2].

Acknowledgment

The authors wish to thank Dr. Samuel Ruben for his generous endowment of a Bergen Davis Fellowship at Columbia University and one of us (K.V.) was the recipient of the Fellowship during the course of this work.

Manuscript submitted Jan. 14, 1980; revised manuscript received May 23, 1980.

Any discussion of this paper will appear in a Discussion Section to be published in the June 1981 JOURNAL. All discussions for the June 1981 Discussion Section should be submitted by Feb. 1, 1981.

REFERENCES

1. K. Viswanathan, M. A. Farrell Epstein, and H. Y. Cheh, *This Journal*, **125**, 1772 (1978).
2. K. Viswanathan and H. Y. Cheh, *ibid.*, **125**, 1616 (1978).
3. K. Viswanathan and H. Y. Cheh, *J. Appl. Electrochem.*, **9**, 537 (1979).
4. K. Viswanathan, H. Y. Cheh, and G. L. Standart, *J. Appl. Electrochem.*, **10**, 37 (1980).
5. F. A. Lowenheim, "Modern Electropolating," 3rd Ed., Wiley, New York (1974).
6. R. Haynes, *This Journal*, **126**, 881 (1979).
7. P. Radhakrishnamurty, *ibid.*, **127**, 1320 (1980).
8. N. Ibl, *Adv. Electrochem. Electrochem. Eng.*, **2**, 49 (1962).
9. H. Y. Cheh, *This Journal*, **118**, 551 (1971).

The Application of Linear Sweep Voltammetry to a Rotating Disk Electrode for a Reversible Reaction with Soluble Product

P. C. Andricacos* and H. Y. Cheh**

Department of Chemical Engineering and Applied Chemistry, Columbia University, New York, New York 10027

The theory of linear sweep voltammetry (LSV) in a stagnant system for a reversible reaction with soluble product was first worked out independently by Sevcik (1) and Randles (2). Subsequently, several authors (3-6) contributed to its further development. Reviews on the subject can be found in the classical paper by Nicholson and Shain (7) and in the monograph by Macdonald (8).

One of the advantages in performing LSV experiments in systems with controlled forced convection, such as that established by a rotating disk electrode (RDE), is that the effect of natural convection is suppressed even at low values of the Reynolds number. However, the application of LSV on an RDE has not been used extensively. One probable cause is the insufficient development of its theory.

In a recent paper (9), we applied the Nernst model of transient diffusion to an RDE, to obtain an analytical expression for the current transient associated with a reversible deposition (insoluble product) reaction. We have found that for slow dimensionless sweep rates, no current peaks are obtained. Instead, the current density increases monotonically with time to an asymptotic value equal to the diffusion limiting current density. However, as the dimensionless sweep rate is increased and after a relatively short transition region, peaks are obtained the behavior of which is the same for all practical purposes as those obtained in a stagnant system. As a result, the linear dependence of the peak current density on the square root of the sweep rate originally derived by Berzins and Delahay (10), is retained. In addition, the peak current density normalized with respect to the limiting current density has been shown to depend linearly on the square root of the dimensionless sweep rate.

A particular advantage of this conclusion is that the correlation exhibits a weak dependence on the physical properties of the electrolyte.

In the present note, the LSV response of an RDE on which a reversible reaction with soluble product occurs, is analyzed. The same problem has been dealt with by Girina *et al.* (11) and by Fried and Elving (12), but to an insufficient detail. A review of the work of these authors has been provided elsewhere (9).

Consider the reaction



where both reduced and oxidized species are soluble. Assuming that the diffusion coefficients of O and R are equal to a common value D , a unique diffusion layer thickness, δ , has been derived by Levich (13)

$$\delta = 1.61D^{1/3}\nu^{1/6}\omega^{-1/2} \quad [2]$$

where ν is the kinematic viscosity of the electrolyte and ω is the rotation speed of the RDE. If c_O^b and c_R^b are the bulk concentrations of O and R, respectively, the following dimensionless quantities can be introduced

$$C_O(\xi, \tau) = 1 - c_O(\xi, \tau)/c_O^b \quad [3]$$

$$C_R(\xi, \tau) = 1 - c_R(\xi, \tau)/c_R^b \quad [4]$$

$$\xi = x/\delta \quad [5]$$

$$\tau = Dt/\delta^2 \quad [6]$$

where C_O and C_R are dimensionless concentrations, and ξ and τ are dimensionless distance and time, respectively. Under the assumptions of the Nernst diffusion model discussed elsewhere (9), the diffusion of O towards the RDE surface is described by the following equations

* Electrochemical Society Student Member.

** Electrochemical Society Active Member.

Key words: rotating disk, deposition, voltammetry.

$$\frac{\partial C_O}{\partial \tau} = \frac{\partial^2 C_O}{\partial \xi^2} \quad [7]$$

$$C_O(\xi, 0) = 0 \quad [8]$$

$$C_O(1, \tau) = 0 \quad [9]$$

$$\frac{\partial C_O}{\partial \xi}(0, \tau) = -\frac{i(\tau)}{i_{O,1}} \quad [10]$$

where $i(\tau)$ is the unknown current density and $i_{O,1}$ is the diffusion limiting current density defined as follows

$$i_{O,1} = nFDc_0^b/\delta \quad [11]$$

A similar set of equations describes the diffusion of R. The only difference is in Eq. [10], which reads

$$\frac{\partial C_R}{\partial \xi}(0, \tau) = \frac{i(\tau)}{i_{R,1}} \quad [12]$$

The resulting boundary value problems can be solved by the Laplace transform method. A simple computation in the Laplace domain followed by convolution yields the following relations

$$C_O(0, \tau) = \int_0^\tau \frac{i(\lambda)}{i_{O,1}} \times \theta_2(0, \pi i(\tau - \lambda)) d\lambda \quad [13]$$

$$C_R(0, \tau) = -\int_0^\tau \frac{i(\lambda)}{i_{R,1}} \times \theta_2(0, \pi i(\tau - \lambda)) d\lambda \quad [14]$$

$$\frac{i(\tau)}{i_{O,1}} = \int_0^\tau \frac{\partial C_O}{\partial \tau}(0, \lambda) \times \theta_3(0, \pi i(\tau - \lambda)) d\lambda \quad [15]$$

$$i_{O,1}C_O(0, \tau) + i_{R,1}C_R(0, \tau) = 0 \quad [16]$$

where λ is a dummy variable of integration, and θ_2 and θ_3 are theta functions originally used for the solution of electrochemical diffusion problems by Tokuda and Matsuda (14-16). They are defined as follows (17)

$$\theta_2(0, \pi i(\tau - \lambda)) = 2 \sum_{j=0}^{j=\infty} \exp(-(j + 1/2)^2 \pi^2 (\tau - \lambda)) \quad [17]$$

$$\theta_3(0, \pi i(\tau - \lambda)) = 1 + 2 \sum_{j=1}^{j=\infty} \exp(-j^2 \pi^2 (\tau - \lambda)) \quad [18]$$

Equation [15] is important in that it provides an expression for the current density $i(\tau)$, once $\partial C_O/\partial \tau(0, \lambda)$ is known. Furthermore, Eq. [16] is a relation between the dimensionless concentrations of O and R, derived by the elimination of the common integral between Eq. [13] and [14]. An expression for $\partial C_O/\partial \tau(0, \lambda)$ can be obtained from the assumptions concerning the mechanism of reaction [1].

In an LSV experiment, the electrode potential, $E(t)$, is given by

$$E(t) = E_i - vt \quad [19]$$

where E_i is the initial potential and v is the sweep rate. For no current to flow initially through the system, E_i is taken to be the equilibrium potential of the electrode, computed from the Nernst equation and c_0^b , c_R^b . Since the reaction is reversible and assuming that it occurs in an ideal solution, we obtain

$$\frac{c_O(0, t)}{c_R(0, t)} = \frac{c_0^b}{c_R^b} \exp\left(-\frac{nF}{RT} vt\right) \quad [20]$$

Introducing the dimensionless sweep rate, σ

$$\sigma = nFv\delta^2/RTD \quad [21]$$

and the concentration ratio

$$\mu = c_0^b/c_R^b = i_{O,1}/i_{R,1} \quad [22]$$

Eq. [20] can be written in dimensionless variables as follows

$$\frac{1 - C_O(0, \tau)}{1 + \mu C_O(0, \tau)} = \exp(-\sigma\tau) \quad [23]$$

Combining Eq. [15] and [23] an expression for the normalized current density is obtained

$$\frac{i(\tau)}{i_{O,1}} = \frac{\sigma}{4} \left(1 + \frac{1}{\mu}\right) \int_0^\tau \frac{1 + 2 \sum_{j=1}^{j=\infty} \exp(-j^2 \pi^2 (\tau - \lambda))}{\cosh^2((\ln \mu - \sigma\lambda)/2)} d\lambda \quad [24]$$

where the singularity at the upper limit can be removed by integration by parts.

Equation [24] can be used in principle for the computation of the current transient. However, further substitutions originally introduced by Matsuda and Ayabe (3) for the corresponding problem in a stagnant system can considerably simplify the calculations. Let

$$a = \ln \mu \quad [25]$$

$$\xi = \sigma\lambda - a \quad [26]$$

$$\psi = \sigma\tau - a \quad [27]$$

Eq. [24] then acquires the following form

$$\frac{i(\psi)}{i_{O,1}} = (1 + e^{-a}) \times \frac{1}{4} \int_{-a}^\psi \frac{1 + 2 \sum_{j=1}^{j=\infty} \exp(-j^2 \pi^2 (\psi - \xi)/\sigma)}{\cosh^2(\xi/2)} d\xi \quad [28]$$

By using a transformation formula for θ_3 (17, 9) and defining a new variable, ρ , by

$$\rho = (\psi - \xi)^{1/2} \quad [29]$$

Eq. [28] acquires its final form

$$\frac{i(\psi)}{i_{O,1}} = \sigma^{1/2} \Phi_{rde}(\psi, \sigma, a) \quad [30]$$

where Φ_{rde} is the current function defined as follows

$$\Phi_{rde}(\psi, \sigma, a) = (1 + e^{-a}) \times \frac{1}{2\pi^{1/2}} \int_0^{(\psi+a)^{1/2}} \frac{1 + 2 \sum_{j=1}^{j=\infty} \exp(-j^2 \sigma/\rho^2)}{\cosh^2((\psi - \rho^2)/2)} d\rho \quad [31]$$

The integral in Eq. [31] is well defined everywhere.

It would be interesting at this point to compare $\Phi_{rde}(\psi, \sigma, a)$ to the current function $\Phi_{st}(\psi, a)$ obtained by Matsuda and Ayabe (3) for the solution of the corresponding problem in a stagnant system. The expression derived by these authors in the present nomenclature is as follows

$$\Phi_{st}(\psi, a) = (1 + e^{-a}) \times \frac{1}{2\pi^{1/2}} \int_0^{(\psi+a)^{1/2}} \frac{1}{\cosh^2((\psi - \rho^2)/2)} d\rho \quad [32]$$

The most important difference between Eq. [31] and [32] is that the latter is not a function of the sweep rate. Indeed, given a value of a , Φ_{st} is only a function of ψ , whereas Φ_{rde} is still parametrized with respect to σ . One can also note that for small values of ρ or high values of σ , Eq. [31] and [32] tend to become identical.

The integral in Eq. [31] has been computed numerically by the use of Simpson's rule. Figure 1 shows a graphical representation of Eq. [31] for $a = 12.0$.

For small values of the dimensionless sweep rate, the current function increases monotonically from 0 to a steady-state value

$$\Phi_{rde} \rightarrow \sigma^{-1/2} \text{ as } \psi \rightarrow \infty \quad [33]$$

For larger values of σ , a maximum is obtained, while the subsequent steady-state value is again described by Eq. [33]. Combining Eq. [30] and [33] we find that as $\tau \rightarrow \infty$, $i(\tau)/i_{0,1} \rightarrow 1$. For $\sigma > 20$

$$\Phi_{rde,max} = 0.446 \text{ at } \psi = 1.1 \quad [34]$$

Combining Eq. [30] and [34] we obtain

$$\frac{i_p}{i_{0,1}} = 0.446 \sigma^{1/2}, \quad \sigma > 20 \quad [35]$$

Maxima appear for $\sigma > 3$. Thus, the region $3 < \sigma < 20$ is the transition region. Figure 2 summarizes the dependence of $i_p/i_{0,1}$ on $\sigma^{1/2}$. In the region $10 < \sigma < 20$, deviation from Eq. [35] is less than 2%.

Equation [35] indicates that the peak current density, i_p , normalized with respect to the diffusion limiting current density, $i_{0,1}$, is a linear function of the square root of the dimensionless sweep rate, σ , provided that σ is large enough. The slope is a constant, independent of any physical property of the system.

In terms of dimensional quantities, Eq. [35] can be written as

$$i_p = 0.446 n^{3/2} F^{3/2} R^{-1/2} T^{-1/2} D^{1/2} c_0 b \nu^{1/2} \quad [36]$$

Equation [36] is the same as the one describing the response in a stagnant system (3). However, the use of the RDE allows both Eq. [35] and [36] to be used for correlating results. As previously (9), Eq. [36] offers the advantage of the weak dependence on the physical properties of the electrolyte

$$\frac{i_p}{i_{0,1}} = 0.718 (nFv/RT\omega)^{1/2} (\nu/D)^{1/6} \quad [37]$$

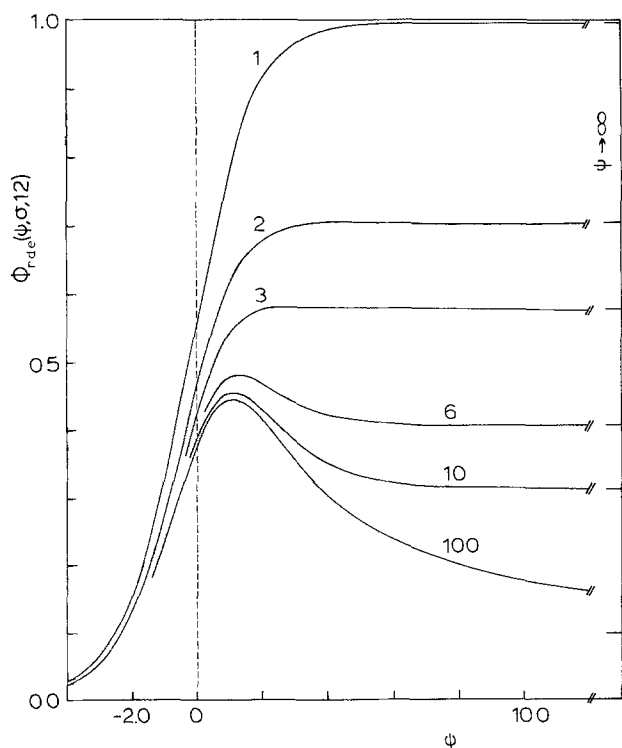


Fig. 1. RDE current function for a reversible reaction with soluble product, Eq. [31]. Numbers on lines indicate values of the dimensionless sweep rate.

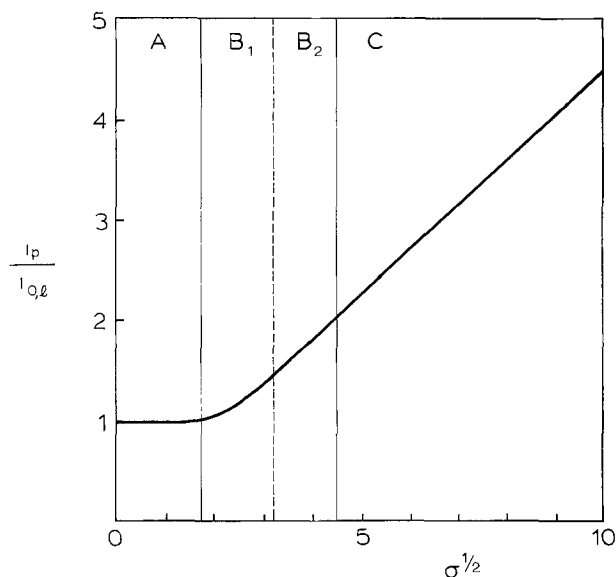


Fig. 2. $i_p/i_{0,1}$ vs. $\sigma^{1/2}$ correlation for a reversible reaction with soluble product occurring on an RDE under LSV conditions. A: region of no maxima; B₁ and B₂: transition region (B₂: less than 2% deviation from linearity); C: region of validity of Eq. [35].

The value of the overpotential at which the current peak appears, η_p , can be easily found to be

$$\eta_p = -\frac{RT}{nF} (1.1 + \ln \mu) \quad [38]$$

The behavior of the current function is not affected by the value of a when the latter is greater than approximately 4. For instance, when $a = 4$ and within the region of validity of Eq. [35], the value of the peak overpotential is unaltered; however, the slope of the $i_p/i_{0,1}$ vs. $\sigma^{1/2}$ correlation is about 1% lower than the one predicted by Eq. [35].

Experimental investigations to verify the $i_p/i_{0,1}$ vs. $\sigma^{1/2}$ correlation have been conducted by Girina *et al.* (11) for the $Tl^+/Tl(Hg)$ reaction. In this case, the reaction product is soluble in the electrode. These authors also discuss the results of Fried and Elving (18) obtained for the oxidation of $Fe(CN)_6^{4-}$. It should be noted that Girina *et al.* have erroneously assumed that the current peaks appear at $\sigma \tau \sim 1$. By assuming so, the dependence on μ has been eliminated erroneously.

Acknowledgment

The authors wish to thank Dr. Samuel Ruben for his generous endowment of a Bergen Davis Fellowship at Columbia University. One of us (P.C.A.) was the recipient of the Fellowship during the course of this work.

Manuscript received May 5, 1980.

Any discussion of this paper will appear in a Discussion Section to be published in the June 1981 JOURNAL. All discussions for the June 1981 Discussion Section should be submitted by Feb. 1, 1981.

REFERENCES

1. A. Sevcik, *Coll. Czechoslov. Chem. Commun.*, **13**, 349 (1948).
2. J. E. B. Randles, *Trans. Faraday Soc.*, **44**, 327 (1948).
3. H. Matsuda and Y. Ayabe, *Z. Elektrochem.*, **59**, 494 (1955).
4. W. H. Reinmuth, *Anal. Chem.*, **34**, 1446 (1962).
5. W. H. Reinmuth, *J. Am. Chem. Soc.*, **79**, 6358 (1957).
6. K. B. Oldham, *J. Electroanal. Chem. Interfacial Electrochem.*, **105**, 373 (1979).
7. R. S. Nicholson and I. Shain, *Anal. Chem.*, **36**, 706 (1964).

8. D. D. Macdonald, "Transient Techniques in Electrochemistry," Plenum Press, New York (1977).
9. P. C. Andricacos and H. Y. Cheh, *J. Electrochem. Soc.*, **127**, 2153 (1980).
10. T. Berzins and P. Delahay, *J. Am. Chem. Soc.*, **75**, 555 (1953).
11. G. P. Girina, V. Yu. Filinovskii, and L. G. Feoktistov, *Sov. Electrochem.*, **3**, 831 (1967).
12. I. Fried and P. J. Elving, *Anal. Chem.*, **37**, 464 (1965).
13. V. G. Levich, "Physicochemical Hydrodynamics," Prentice-Hall, Englewood Cliffs, New Jersey (1962).
14. K. Tokuda and H. Matsuda, *J. Electroanal. Chem. Interfacial Electrochem.*, **82**, 157 (1977).
15. K. Tokuda and H. Matsuda, *ibid.*, **90**, 149 (1978).
16. K. Tokuda and H. Matsuda, *ibid.*, **95**, 147 (1979).
17. R. Bellman, "A Brief Introduction to Theta Functions," Holt, Reinhart, and Winston, New York (1961).
18. I. Fried and P. J. Elving, *Anal. Chem.*, **37**, 803 (1965).

Meso- and Dl- Diethyl 2,3-Diphenylsuccinate from the Electrochemical Reduction of Ethyl α -Bromophenylacetate

L. Rampazzo and A. Inesi

Institute of Chemistry, Faculty of Engineering, University of Rome, Rome, Italy

A variety of chemical methods for the preparation of the stereoisomeric *meso*- and *dl*-diethyl 2,3-diphenylsuccinates (I, II) have been developed (1-9). Other routes to $(\text{PhCHCOOEt})_2$ are the electrochemical oxidation of the enolate of ethyl phenylacetate $\text{PhCH}_2\text{COOEt}$ (III) (10, 11) and the photolysis of ethyl α -chlorophenylacetate (12). The purpose of this paper is to summarize some experimental observations related to the electrochemical reduction of ethyl α -bromophenylacetate (IV) on Hg in $\text{DMF-Et}_4\text{NClO}_4$ 0.1M solutions, providing a synthetically useful preparation of *meso*- and *dl*- 2,3-diphenylsuccinates.

Additional experimental results on the electrochemical reduction of ethyl- α -bromophenylacetate on platinum and glassy carbon electrodes are also reported.

Experimental

Chemicals.—N,N-dimethylformamide (DMF) (RIEDEL-DE HAEN spectranal.) was treated with neutral Al_2O_3 for chromatography, which was previously heated for 3 hr at 600°C. The solvent was then passed through molecular sieves 4A (BDH) and distilled under nitrogen flux at 5 mm Hg. The product of the first distillation was collected over P_2O_5 and stored at 0°C in the dark. The water content of the purified DMF was not greater than 0.01% as measured by the Karl-Fischer titration. Polarographic grade Et_4NClO_4 (Carlo Erba) was vacuum dried at 60°C and used as the supporting electrolyte without additional purification. Bu_4NBr was Carlo Erba RS grade for polarography. Commercially available ethyl α -bromophenylacetate (K&K, 99.5%) was used as received. TLC on silica gel (eluent benzene) showed that it contained a trace of a product moving slower than IV. 3,4-xylene and trifluoroacetic acid used in some experiments were reagent grade chemicals, BDH and K&K, respectively. Ethyl phenylacetate (K&K) was used for comparative purposes. All other chemicals used were commercially available and of the best purity.

Apparatus.—Conventional polarographic data were obtained with a three-electrode AMEL MOD 471 instrument. The reference electrode was a calomel-type as described by Fujinaga (13). Its potential, -0.059V vs. SCE, remained constant during several months; all potentials are quoted with respect to this reference electrode. The counterelectrode was a mercury pool. The dropping mercury electrode operated with a head

of 70 cm. Two capillaries, 1 and 2, were used, giving values of $tg(1) = 4.01$ sec, $tg(2) = 5.01$ sec at open circuit, $tg(1) = 3.40$ sec, $tg(2) = 4.40$ sec at $E = -1.00\text{V}$; the Hg flux was $m(1) = 1.10$ mg \times sec $^{-1}$ and $m(2) = 1.36$ mg \times sec $^{-1}$. An AMEL MOD 552 potentiostat equipped with an AMEL MOD 721 integrator were used in controlled potential electrolyses (c.p.e.) and coulometric experiments. A stirred mercury pool served at the cathode; the counterelectrode was a cylindrical platinum gauze immersed in the 0.1M Et_4NClO_4 -DMF solution. A porous plug filled with methylcellulose and $\text{DMF-Et}_4\text{NClO}_4$ 0.1M separated the counterelectrode from the test solution. Before each electrolysis, all solutions were deoxygenated with N_2 (PP), and nitrogen was passed over the solution during c.p.e.

A Bruker spectrospin operating at 90 MHz was employed to record NMR spectra, and all chemical shifts are reported in ppm downfield from TMS as internal standard. The solvent was CDCl_3 . Mass spectrometric data for $(\text{PhCHCOOEt})_2$ were obtained by direct insertion with an Hitachi-Perkin Elmer RMU-6 spectrometer at 70 eV. Infrared spectra were recorded on a Perkin-Elmer MOD 177 grating spectrophotometer using CCl_4 as solvent. Melting points were determined in glass capillaries with a BUCHI mp apparatus and are uncorrected. All electrochemical experiments were performed on freshly prepared solutions of IV. Preliminary experiments on the polarographic behavior revealed that ethyl- α -bromophenylacetate, when dissolved in DMF, can be slowly hydrolyzed by traces of water still present in the solvent. In fact, test polarograms were recorded on solutions which were from just prepared to five days old; the waves slowly changed in height on standing, and the Br^- ions determined the appearance of a characteristic anodic wave.

Voltammetric measurements on solid electrodes were performed using a pulsed electrode (14), which was assembled either with a platinum electrode of about 1 mm diam (PPE), or with a glassy carbon electrode of 3 mm diam (GCPE). Both electrodes were polished by conventional methods.

Controlled potential electrolysis.—C.p.e. of 2.78 g of $\text{PhCH}_2\text{BrCOOEt}$ (IV) in 300 ml of $\text{DMF-0.1M Et}_4\text{NClO}_4$ using a mercury pool cathode at -1.500V was accomplished by adding the bromo-ester in small portions at a time, so that during electrolysis the concentration of IV to be reduced was never greater than $3 \times 10^{-3}\text{M}$.

Key words: d-c polarography, ethyl α -bromophenylacetate, diethyl 2,3-diphenylsuccinate, controlled-potential electrolysis, reductive coupling.

The maximum value of current intensity was about 0.6A; when the current value dropped to ca. 0.003A, electrolysis was interrupted and 810C were measured. At this time, no starting product or other substances reducible in the interval 0.00 to $-2.700V$ were present in the solution, as ascertained by recording the polarogram. The electrolyzed solution was dried under vacuum ($t = 40^\circ C$) to remove DMF; the product was extracted with ether, the ethereal solution was concentrated to a volume of about 20 ml. On cooling, a yellow-brown precipitate was formed; recrystallization from ethanol afforded 0.300g of colorless crystals melting at $139^\circ-40^\circ C$ [lit. (2, 8) for *meso* I: mp = $140^\circ-1^\circ C$]. Infrared (I): ν_{max} (CCl_4): 1725, 1153, 700 cm^{-1} (all strong); the other medium-weak peaks at 3080, 3050, 3020, 2980, 1490, 1450, 1365, 1300, 1285, 1250, 1230, 1200, 1095, 1070, 1030, and 850 cm^{-1} matched the literature data (12). NMR (I): δ ($CDCl_3$)/ppm: 7.36 (multiplet, Ph); 4.37 (singlet, CH); 3.83 (quartet, $J = 7.0$ Hz, CH_2); 0.89 (triplet, $J = 7.0$ Hz, CH_3), according to literature data (5, 8) for *meso*-diethyl 2,3-diphenylsuccinate.

Mass spectrum of I ($t = 120^\circ C$), m/e : 326 (M^+), 325 ($M-H$), 324 ($M-2H$), 281 ($M-OEt$), 280 ($M-EtOH$), metastable peak for the transition $326 \rightarrow 280$ at $m^* = 240.5$, 253 ($M-COOEt$), 252 ($M-EtOH-CO$, metastable peak for $280 \rightarrow 252$ at $m^* = 226.8$), 248 ($M-H-PH$), 235 ($M-H-2 OEt$), 224, 223, 207, 206, 195, and appropriate peaks at lower m/e .

The remaining ethereal solution was filtered, the solvent removed under vacuum, obtaining a yellow-brown substance which was crystallized from petroleum ether to white crystals (0.200g) melting at $74^\circ-77^\circ C$ [lit. (2, 8) for *dl* (II): $79^\circ C$]. The infrared spectrum was identical peak by peak to the spectrum of *meso* (I). NMR showed all peaks of *dl* (II) at δ /ppm ($CDCl_3$): 7.36 (Ph), 4.22 (singlet, CH), 4.14 (quartet, $J = 7$ Hz, CH_2), 1.17 [triplet, $J = 7$ Hz, CH_3 , according to Ref. (8)], together with the peaks of I in minor amount, i.e. 75% *dl* and 25% *meso*.

The mother liquors of the two preceding crystallizations were collected, dried and recrystallized from petroleum ether to afford 0.25g of white crystals, mp $70^\circ-110^\circ C$, of a mixture of 33.5% *meso*- and 66.5% *dl*-diethyl 2,3-diphenylsuccinate (NMR), as determined by the integrated peaks of the well-separated methyl triplets at $\delta = 0.89$ and $\delta = 1.17$ for I and II, respectively. No peaks between the signals of methine and phenyl- protons were apparent, indicating that no α -para dimers were present in detectable amounts.

Results and Discussion

Figure 1 (a, b, c) shows the polarograms for ethyl α -bromophenylacetate on a dropping mercury electrode in dimethylformamide containing 0.1M Et_4NClO_4 , when the concentrations of IV are of the order of $10^{-4}M$. If the concentration is raised over $10^{-3}M$, a sharp maximum appears, followed by the normal diffusion current plateau. The presence of this maximum hides all

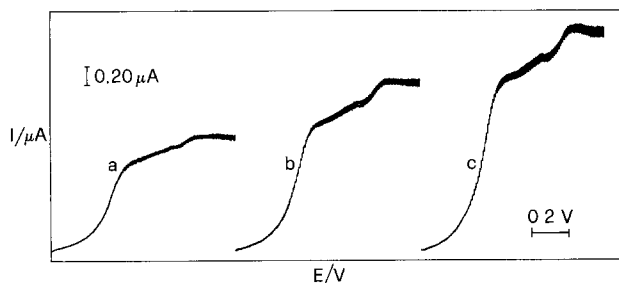


Fig. 1. Polarographic reduction waves of PhCHBrCOOEt (IV) in DMF- Et_4NClO_4 0.1M; curve a, C(IV) = $3.0 \times 10^{-4}M$; curve b, C(IV) = $5.0 \times 10^{-4}M$; curve c, C(IV) = $7.0 \times 10^{-4}M$. Each curve starts from $E = 0.200V$; E/V vs. the SCE as indicated in the experimental section; capillary 2.

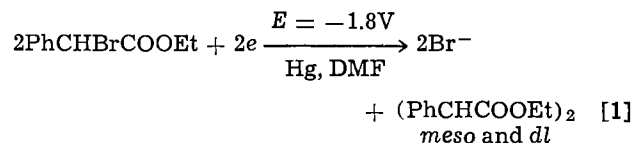
the features between the ascending part of the first wave and the diffusion current. No significant deviation from diffusion control was observed on the polarographic waves; the limiting currents were proportional to the concentration of IV in the range 10^{-4} - $10^{-3}M$, and to the square root of the height of the mercury reservoir. The two waves observed, with $E_{1/2} = -0.13V$ and $-0.48V$, respectively, show limiting currents in the ratio of about 2/1 for the same concentration range.

Coulometric reduction of $2 \times 10^{-3}M$ IV with a mercury pool cathode at $E = -1.8V$ gave $n_{app} = 0.75-0.80$ in repeated experiments; other polarographic and coulometric data are reported in Table I.

The effect of addition of 3,4 xylenol and trifluoroacetic acid (TFA) on the polarograms is shown in Fig. 2. The first reduction wave remains unaffected when 3,4 xylenol is added, whereas the second wave increases with increasing concentration of 3,4 xylenol, until a saturation value is obtained. Addition of TFA affects the height of the first wave, without shifting its half-wave potential, until about the same saturation value is obtained when excess TFA is added. It should be remembered that 3,4 xylenol is a weak acid in DMF; TFA is a strong acid in this solvent; the reduction wave of the latter, due to hydrogen discharge, is at $E_{1/2} = -1.48V$ (15). Polarographic and coulometric data for reduction of CHPhBrCOOEt in the presence of proton donors are collected in Table II.

As described in the experimental section, the isolated nonvolatile products of controlled-potential electrolysis of IV at a mercury pool cathode at $-1.8V$ are *meso*- and *dl*-diethyl 2,3-diphenylsuccinate I and II, the overall relative ratio being 57.3% *meso*- and 42.7% *dl*. The overall current yield was about 60% after the working up of the electrolyzed solution. No effort was made to improve this procedure to optimize the yield, so it is likely that absolute yield would be better; moreover, commercially available PhCHBrCOOEt was used without further purification, so that nonreducible hydrolysis products could be present at the beginning of the electrolysis.

The products formation is clearly a consequence of the overall main electrode process



The presence of dimers in the products of electrochemical reduction of monosubstituted halides has been

Table I. Polarographic and coulometric data for reduction of CHPhBrCOOEt in DMF containing 0.1M Et_4NClO_4

C, mM $\times 10^{-1}$	I^b	n_{app}^c
6×10^{-2}	3.40	
8×10^{-2}	3.19	
1×10^{-1}	2.87	
2×10^{-1}	2.42	
3×10^{-1}	2.08	0.97
3×10^{-1}	2.12	0.93
3×10^{-1}	2.12	1.04
5×10^{-1}	2.03	
7×10^{-1}	1.95	
3.0	1.72	0.93
5 ^a	1.56	0.85
38.4	max	0.75 ^d

^a Result obtained with capillary 1; all other data were obtained using capillary 2.

^b Diffusion current constant, $I = \frac{i_{lim}}{m^{2/3}t^{1/3}} \mu A \times mM^{-1} \times 1 \times mg^{-2/3} \times sec^{1/2}$.

^c Number of F/mole obtained by coulometry at $E = -1.8V$.
^d Low values of $n_{app} < 1$ at $C > 1$ mM/l were obtained by others in the one-electron reduction of carbon-halogen bond in DMF, cf. for example, C. M. McNamee, B. C. Willet, D. M. La Perriere, and D. G. Peters, *J. Am. Chem. Soc.*, 99, 183 (1977); a similar explanation may hold for the present case.

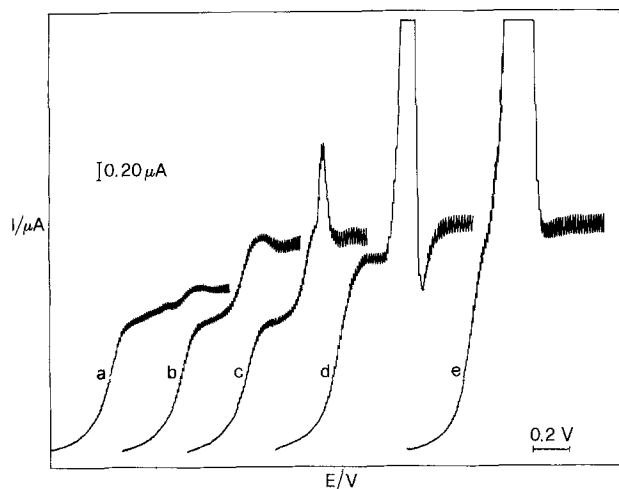


Fig. 2. Effect of 3,4-xyleneol (HA) and trifluoroacetic acid (TFA) on the polarographic reduction waves of PhCHBrCOOEt (IV) in DMF-Et₄NClO₄ 0.1M; curve a, C(acid) = 0.0; curve b, C(HA) = 2.5 × 10⁻⁴M; curve c, C(HA) = 5.0 × 10⁻⁴M; curve d, C(TFA) = 2.5 × 10⁻⁴M; curve e, C(TFA) = 5 × 10⁻⁴M. Each curve starts from E = 0.200V; capillary 2.

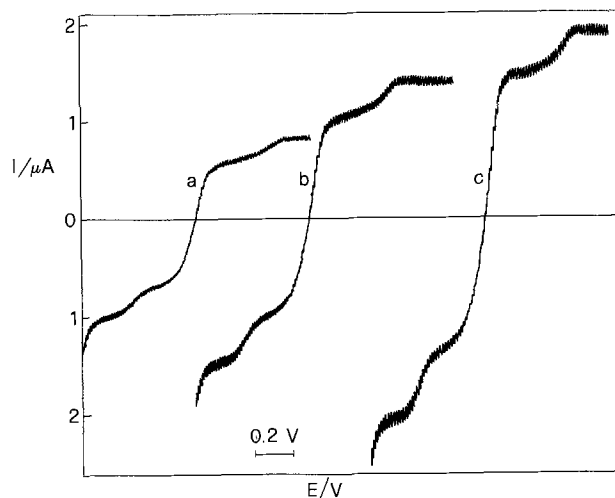


Fig. 3. Polarographic reduction waves of PhCHBrCOOEt (IV) in DMF-Et₄NClO₄ 0.1M containing Bu₄NBr: curve a, C(IV) = 3 × 10⁻⁴M; C(Bu₄NBr) = 3 × 10⁻⁴M; curve b, C(IV) = 5 × 10⁻⁴M; C(Bu₄NBr) = 5 × 10⁻⁴M; curve c, C(IV) = 7 × 10⁻⁴M; C(Bu₄NBr) = 7 × 10⁻⁴M. Each curve starts from E = 0.450V vs. SCE; capillary 2.

reported (16) or suggested (17). Figure 3 shows the polarographic behavior of RBr in the presence of Bu₄NBr, C(RBr)/C(Bu₄NBr) = 1/1, at various concentrations of RBr. The same behavior is obtained with Et₄NBr instead of Bu₄NBr. If c.p.e. is performed at the potential of ~ -0.350V, i.e., before the second wave, on a 3 × 10⁻³M solution of RBr in aprotic DMF-0.1M Et₄NClO₄, the first wave disappears after about 0.6 F/mole RBr are passed. The second wave remains unchanged (Fig. 4), showing that it represents the reduction of a compound which is stable in the conditions of the experiments. The half-wave potential $E_{1/2}^{(2)}$, τ is consistent with that found for HgR₂ in various solvents (18). A subsequent c.p.e. on this solution, at -1.8V, showed $n_{app} \approx 0.6$. Direct reduction of RBr, C = 3 × 10⁻³M, at -1.8V showed $n_{app} \approx 0.9$. During the preparative c.p.e. performed at E = -1.8V < $E_{1/2}^{(2)}$, in aprotic DMF, the red color of carbanion R⁻ was observed.

The simplest mechanism which can explain the data on Hg is probably the following (19)

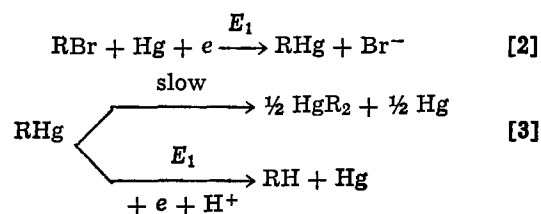


Table II. Polarographic and coulometric data for reduction of PhCHBrCOOEt in the presence of proton donors HA in DMF - 0.1M Et₄NClO₄

C, mM/l	C _{HA} , mM/l	I	n_{app}	D_{calc} , cm ² × sec ⁻¹
3	(X) 3	2.55	0.95; ^a 1.15 ^c	
5 × 10 ⁻¹	(X) 5 × 10 ⁻¹	2.86	1.11; ^a 1.33 ^c	
3 × 10 ⁻¹	(X) 3 × 10 ⁻¹	3.14		
5 × 10 ⁻¹	(FA) 5 × 10 ⁻¹	3.15		
5 × 10 ⁻¹	(TFA) 5 × 10 ⁻¹	3.19		
3 × 10 ⁻¹	(P) 3 × 10 ⁻¹	3.20	1.4 ^b	1.04 × 10 ⁻⁵ d

(X) = 3,4 xyleneol; (FA) = CH₂FCOOH; (TFA) = CF₃COOH; (P) = HClO₄.

n_{app} = number of F/mole obtained by coulometry ^a at E = -1.8V ^b at E = -0.350V ^c in two consecutive coulometric reductions at E = -0.350V and E = -1.8V.

^d Calculated from the corresponding I and n_{app} values. For D values of similar organic substances in DMF see, for example, A. J. Fry "Synthetic Organic Electrochemistry," Harper and Row, p. 72, New York (1972). All data were obtained using capillary 2.

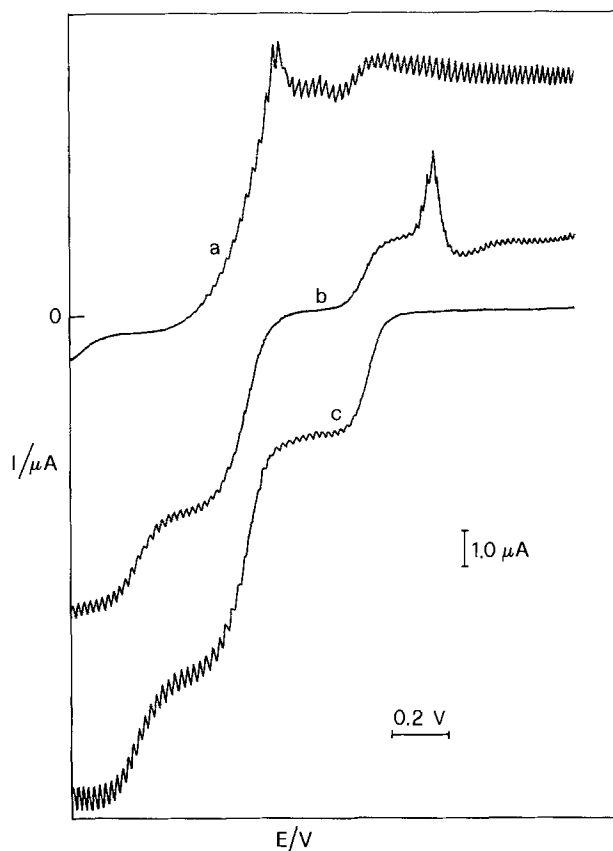
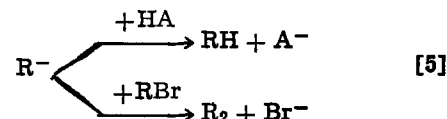
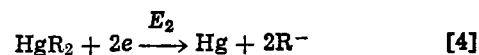


Fig. 4. Polarographic reduction waves of PhCHBrCOOEt (IV) in DMF-Et₄NClO₄ 0.1M; C(IV) = 3 × 10⁻³M; curve a, before c.p.e.; curve b, after c.p.e. at E = -0.350V; curve c, after c.p.e. at -1.80V of the solution obtained in the first electrolysis. Each curve starts from E = 0.450V vs. SCE; capillary 2.



The general pattern shown suggests that the electrochemical reduction of PhCHBrCOOEt should be

dependent on electrode nature. Typical d-c voltammetric curves for reduction of PhChBrCOOEt in DMF using glassy carbon and platinum electrodes are reported in Fig. 5 and 6. Voltammograms show one well-defined wave with $E_{1/2} = -1.04V$ for the vitreous carbon electrode. The height of the wave remains constant in the subsequent voltammograms. If excess 3,4-xyleneol is added, the wave increases in height. At the platinum electrode, a wave with $E_{1/2} = -0.75V$ is observed, followed by a second wave with $E_{1/2} = -1.14V$. No further experiments with solid electrodes were performed, as we were interested mainly in determining the $E_{1/2}$ values of IV in DMF at electrodes different from mercury. Thus the PhChBrCOOEt electrochemical characteristics are strongly dependent on electrode nature. Our results come into line with the conclusions made by Lambert *et al.* in their investigation of the carbon tetrachloride reduction at the glassy carbon electrode (20) as compared with the reduction of the same compound at the dropping mercury electrode.

After this work had been submitted, Bard and Merz (21) reported studies on the electrochemical reduction of some allyl halides in CH_3CN at mercury, platinum, and vitreous carbon electrodes. The special mode of electrochemical behavior of allyl bromide and

iodide on mercury is interpreted in terms of a specific surface reaction of the halide with the mercury electrode (6), $RBr + Hg \rightleftharpoons RHgBr$. It appears that in the case of the allyl halides concerned and in the solvent employed, the equilibrium (6) lies far to the left, allowing direct transfer of electrons to allyl-HgX to occur at the potential of the first wave.

Acknowledgments

We are greatly indebted to Dr. A. M. Giuliani for the NMR measurements, to Dr. S. Daolio for determining the mass spectra, and to CNR (Rome) for support.

Manuscript submitted May 22, 1979; revised manuscript received May 28, 1980.

Any discussion of this paper will appear in a Discussion Section to be published in the June 1981 JOURNAL. All discussions for the June 1981 Discussion Section should be submitted by Feb. 1, 1981.

Publication costs of this article were assisted by CNR, Rome.

REFERENCES

1. C. Hell and S. Weinzweig, *Ber.*, **28**, 2445 (1895).
2. H. Wren and C. J. Still, *J. Chem. Soc.*, **107**, 444 (1925).
3. C. B. V. Tronov and V. M. Aksenenko, *Zhur. Obshchei Khim.*, **26**, 1393 (1956).
4. H. H. Morris, R. H. Young, Jr., C. Hess, and T. Sottery, *J. Am. Chem. Soc.*, **79**, 411 (1957).
5. A. Giumanini, *Chim. Ind. (Rome)*, **49**, 1340 (1967).
6. W. G. Kofron and C. R. Hauser, *J. Org. Chem.*, **35**, 2085 (1970).
7. M. W. Rathke and A. Lindert, *J. Am. Chem. Soc.*, **93**, 4605 (1971).
8. L. Gortler, K. Brandspiegel, E. Harman, S. Hecht, and R. Leavitt, *J. Org. Chem.*, **38**, 4048 (1973).
9. J. K. Stille and K. S. Y. Lau, *J. Am. Chem. Soc.*, **98**, 5841 (1976).
10. T. Okubo and S. Tsusumi, *Bull. Chem. Soc. Jpn.*, **31**, 1794 (1964).
11. M. Tokuda, T. Shigei, and M. Itoh, *Chem. Lett.*, **621** (1975).
12. B. Matuszewski, *J. Photochem.*, **7**, 1 (1977).
13. T. Fujinaga, K. Izutsu, and K. Takaota, *J. Electroanal. Chem. Interfacial Electrochem.*, **12**, 203 (1966).
14. R. Andruzzi and A. Trazza, *ibid.*, **77**, 10 (1977).
15. A. Inesi and L. Rampazzo, *ibid.*, **49**, 85 (1974).
16. L. W. Marple, L. E. Hummelstedt, and L. B. Rogers, *This Journal*, **107**, 437 (1960); G. Klopman, *Helv. Chim. Acta*, **44**, 1908 (1961); J. Grimshaw and J. S. Ramsey, *J. Chem. Soc. B*, **60** (1968); P. J. Elving, I. Rosenthal, J. R. Hayes, and A. J. Martin, *Anal. Chem.*, **33**, 330 (1961); Y. Matsui, T. Soga, and Y. Dake, *Bull. Chem. Soc. Jpn.*, **44**, 513 (1971); J. G. Lawless, D. E. Bartak, and M. D. Hawley, *J. Am. Chem. Soc.*, **91**, 7121 (1969); S. Wawzonek and S. M. Heilmann, *This Journal*, **121**, 516 (1974); J. H. Wagenknecht, *J. Electroanal. Chem. Interfacial Electrochem.*, **52**, 489 (1974); See also F. Beck, *Angew. Chem. Internat. Ed.*, **11**, 760 (1972) for earlier references and patents.
17. L. G. Feotkistov and S. I. Zhdanov, *Electrochim. Acta*, **10**, 657 (1965).
18. K. P. Butin, I. P. Beletskaya, and O. A. Reutov, *Sov. Electrochem.*, **2**, 587 (1966); K. P. Butin, I. P. Beletskaya, A. N. Kashin, and O. A. Reutov, *J. Organometal. Chem.*, **10**, 197 (1967).
19. See for example the following representative papers: C. K. Mann, J. L. Webb, and H. M. Walborsky, *Tetrahedron Lett.*, 2249 (1966); J. L. Webb, C. K. Mann, and H. M. Walborsky, *J. Am. Chem. Soc.*, **92**, 2042 (1970); R. E. Dessy, W. Kitching, T. Psarras, R. Salinger, A. Chen, and T. Chivers, *J. Am. Chem. Soc.*, **88**, 460 (1966).
20. F. L. Lambert, B. L. Hasslinger, and R. N. Franz II, *This Journal*, **122**, 737 (1975).
21. A. J. Bard and A. Merz, *J. Am. Chem. Soc.*, **101**, 295 (1979).

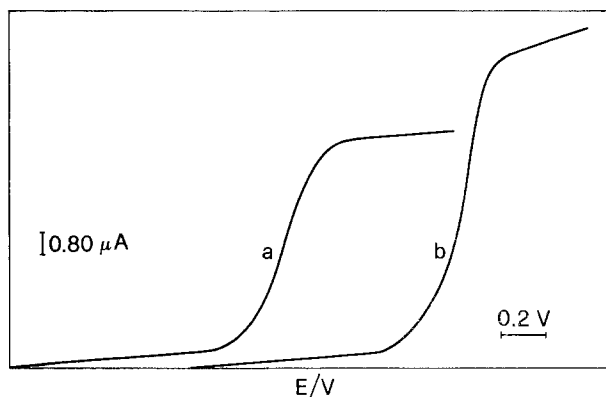


Fig. 5. Voltammograms of PhChBrCOOEt reduction in DMF- Et_4NClO_4 0.1M at the glassy carbon electrode (GCPE); $t(\text{pulse}) = 2$ sec. Curve a, $C(IV) = 1.0 \times 10^{-3}M$; curve b, $C(IV) = 1.0 \times 10^{-3}M + 3,4\text{-xyleneol (excess)}$. Starting potential $E = 0.200V$; conditions as described in the experimental section.

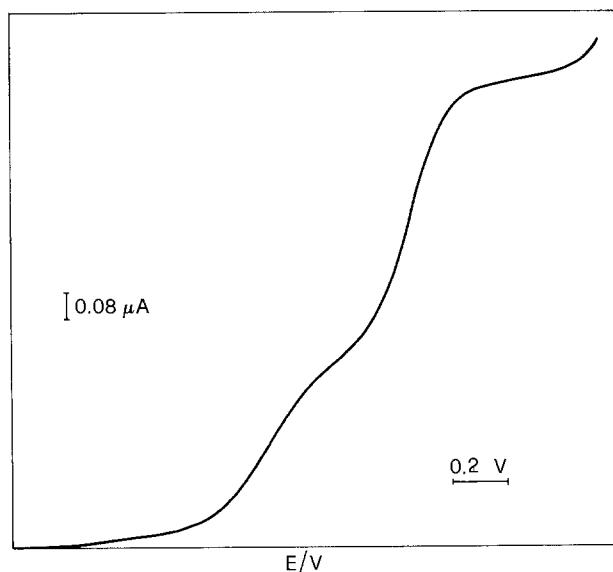


Fig. 6. Voltammograms of PhChBrCOOEt (IV) reduction at the platinum electrode (PPE); $C(IV) = 1.0 \times 10^{-3}$. Starting potential $E = 0.200V$; $t(\text{pulse}) = 2$ sec. Conditions as described in the experimental section.



Control of Volume Resistivity in Inorganic-Organic Separators

Dean W. Sheibley* and Michelle A. Manzo

National Aeronautics and Space Administration, Lewis Research Center, Cleveland, Ohio 44135

ABSTRACT

Control of resistivity in NASA inorganic-organic separators is achieved by incorporating small percentages of high surface area, fine-particle silica with other ingredients in the separator coating. The volume resistivity appears to be predictable from coating composition, that is, from the surface area of filler particles in the coating. The approach has been applied to two polymer-"plasticizer"-filler coating systems, where the filler content of each is below the generally acknowledged critical pigment volume concentration of the coating. Application of these coating systems to 0.0254 cm thick (10 mil) fuel-cell grade asbestos sheet produces inexpensive, flexible, microporous separators that perform at least as well as the original inorganic-organic concept, the Astropower separator.

The usefulness of the inorganic-organic separators developed at the Lewis Research Center for alkaline batteries (*i.e.*, Ag-Zn, Ni-Zn, and Ni-Cd batteries) depends on an optimum balance of resistivity and microporous-structure uniformity. Over the past few years separators have been developed with longer cycle life, more uniform current density, greater flexibility, and lower cost than the original Astropower inorganic-organic separator.

The Astropower separator [Ref. (1)] and several other microporous separators contain relatively high filler volumes such that the amount of binder is insufficient to completely coat the filler particles and fill the interstices. That is, their filler volume is above the critical pigment volume concentration (CPVC) of 40-45 volume percent (v/o). These separators derive their ionic conductivity through the pathway created by the particle-to-particle contact of the fillers. Bozek (2) described the structure and function of the Astropower separator. Philipp and May (3) studied the reaction of the plasticizer with the electrolyte, the ionic resistivity of simulated inorganic-organic separators, and the zincate diffusion through various separators. Sheibley (4) discussed factors that influence the flexibility, resistivity, and zinc dendrite penetration rate of the Astropower separator and NASA improved inorganic-organic separators. A significant conclusion of that work was that the volume resistivity of the improved separators could be maintained in an acceptable range (10-25 Ω -cm) while keeping the volume percentage of fillers in the polymer below the CPVC (5). This also ensured good coating flexibility. Another significant conclusion of Ref. (4) was that the zinc dendrite penetration rate is controlled principally by the tortuosity produced by the presence of inert fillers in the coating. The acceptable range of resistivity was achieved by judicious selection of fillers that combined inertness and reactivity with the potassium hydroxide (KOH) electrolyte while pro-

viding a multiplicity of tortuous conduction paths. These paths were created by filling the spaces between larger particles with smaller particles (a filler packing effect).

Ion permeability of coatings rises very rapidly by several orders of magnitude at the CPVC (5). The key to film permeability below the CPVC in these improved inorganic-organic separators was the use of a proper polyester plasticizer. Philipp and May (3) pointed out that the plasticizer must be a polar compound that preferentially adsorbs on the filler particles, which are also polar compounds. Sheibley (4) showed that one of the products of the plasticizer reaction with the electrolyte must be a short-chain (two or three carbons) glycol. It was also shown that resistivity could be further improved by using an electrolyte-reactive filler in the coating.

This paper discusses the development of resistivity control in NASA microporous separators that contain filler volumes significantly less than the CPVC. First, the effect of filler volume on volume resistivity is shown for a typical inert filler. Then the effect of an electrolyte-reactive filler on volume resistivity is illustrated. Next, the effect on volume resistivity of combinations of fillers plus a selected organic additive (plasticizer) in the polymer is demonstrated. Finally, the incorporation of high surface area, fine-particle fillers is shown to be a predictable means of controlling resistivity.

Experimental Procedure

Preparation of coating mixture.—The coatings used for the separator materials were prepared by weighing an amount of polymer [either polyphenylene oxide¹ (PPO) or Kraton G² resin] into a ball mill, adding chloroform or another solvent, and then adding the weight of filler or filler plus organic additive (plasticizer) needed to provide the desired total volume percentage of filler in the resin. Before ballmilling, the Kraton G must be cut into solution with the

* Electrochemical Society Active Member.

Key words: separators, alkaline batteries, resistivity control, inorganic-organic coating, filler volume content, filler surface area.

¹ General Electric Company, Schenectady, New York 12301.

² Shell Chemical Company, Houston, Texas 77001.

solvent in a high-shear mixer. After the materials were milled for 20 hr, chloroform was added to reduce the viscosity of the mixture to 15 to 16 sec as measured with a number 3 Zahn cup at $\sim 22^\circ\text{C}$.

The fillers used in these studies were magnesium silicate (Microtalc), aluminum silicate (kaolinite), synthetic magnesium aluminosilicate (NAS-100), magnesium titanate (Mg_2TiO_4), natural calcium silicate (wollastonite), lead titanate, reprecipitated calcium silicate (Silene EF), and fumed silicon dioxide (Cab-O-Sil). The organic additives (plasticizers) were a polymeric polyester (P-9750), used with the PPO, and an epoxidized soya bean oil (Paraplex G-62), used with the Kraton G resin. The trade names and manufacturers of these fillers and additives are given in Table I. Coating compositions are given in Table II and discussed later.

Coating the asbestos substrate.—Fuel-cell-grade asbestos sheet 0.0254 cm thick (10 mils) and impregnated with 2 weight percent (w/o) PPO was the substrate for all experimental materials. The coating mixtures were applied to the asbestos with an adjustable knife-blade applicator with the blade height set typically 0.0254 cm above the substrate. Two layers were applied at a wet thickness of 0.0254 cm for each coating. The second layer was applied after the first had dried. In the laboratory coating method the substrate was held flat by means of a vacuum plate while the knife blade was pulled over the fixed substrate. On factory production equipment the knife blade was fixed and the substrate moved beneath it. The final dry coating thickness was 0.00762–0.01016 cm (3–4 mils) which gave a total separator thickness, including substrate, of 0.0330–0.0355 cm (13–14 mils).

Determination of volume resistivity.—Volume resistivities were measured with a test apparatus and procedure based on those described by Lander and Weaver in Ref. (6). In most cases, resistivities were measured on at least two samples to establish precision, which ranged from ± 3 to $\pm 6\%$. Measurements were made in ~ 45 w/o KOH at room temperature. The two samples (3.8 by 3.8 cm) of each material were pretreated by soaking them in 45 w/o KOH overnight at 90° – 100°C . The test area in the conductivity cell was 0.95 cm^2 . The dry thickness of the separator was used in calculating volume resistivity because it was difficult to measure the wet thickness

of the separator once it was positioned in the resistivity cell and the cell halves were tightened together. The wet thickness of some separators is 25% greater than their dry thickness in an uncompressed state.

Determination of plasticizer associated with fillers.—The amount of plasticizer associated with the fillers was estimated from the ratio of plasticizer to PPO in the liquid phase. It is known (3) that the plasticizer (polar compound) is preferentially adsorbed on the fillers (also polar compounds), but the PPO is not. Any selective adsorption on the balls of the ball mill used to prepare the coatings should not affect the result because the surface of a ball is about $5 \times 10^{-6}\text{ m}^2$ and the surface contribution from fillers was always at least 1 m^2 .

Samples of various coating mixtures were allowed to stand until all the filler particles had settled out and a relatively clear supernatant was left. The ratio of plasticizer to PPO in the supernatant was determined by infrared spectroscopy. A calibration curve was obtained from a series of solutions of known ratios; and a straight line was fit to the data by regression analysis.

The spectrometer used was a Beckman Model IR 18A. The samples were diluted 6:1 with chloroform and run against a chloroform blank in sodium chloride cells. The peak at 1595 cm^{-1} (distinctive for aromatic substituted compounds and easily measured) was used to determine the PPO content. The peak at 1725 cm^{-1} (carbonyl stretching) was used to determine the plasticizer content. A typical infrared spectrum is shown in Fig. 1. Table II contains information on the composition of formula X39NF. The precision of this method was estimated to be from 3 to 5%.

Measurement of filler surface area.—The specific surface area of the dry fillers was determined by the standard multipoint Braunauer-Emmett-Teller (BET) technique (7) with krypton and nitrogen gas adsorption. This work was performed by a contractor,³ who used an Orr Model 2100 surface-area pore-volume analyzer.

Results and Discussion

The effect of filler volume content on volume resistivity was studied initially with various fillers in

³ Micromeritics Instrument Corporation, Norcross, Georgia 30091.

Table I. Fillers and organic additives used in coatings

Filler	Trade name	Manufacturer
Magnesium silicate	Microtalc MP-12-50	Pfizer Minerals, Pigments and Metals Division, New York, New York 10017
Aluminum silicate	Kaolinite (Hydrite UF)	Georgia Kaolin Company, Elizabeth, New Jersey 07207
Synthetic magnesium aluminosilicate	Barasym NAS-100	NL Industries, Baroid Division, Houston, Texas 77001
Magnesium titanate	TICON Mt (C)	NL Industries, TAM Division, Hightstown, New Jersey 08520
Natural calcium silicate	Wollastonite P-15	Interpace Corporation, Willsboro, New York 12996
Lead titanate	TICON PT	NL Industries, TAM Division, Hightstown, New Jersey 08520
Reprecipitated calcium silicate	Silene EF	PPG Industries, Pittsburgh, Pennsylvania 15219
Fumed silicon dioxide	Cab-O-Sil, grade M-5	Cabot Corporation, Boston, Massachusetts 02110
Polymeric polyester	P-9750	Emery Industries, Cincinnati, Ohio 45202
Epoxidized soya bean oil	Paraplex G-62	Rohm and Haas Company, Philadelphia, Pennsylvania 19105

Table II. PPO coating compositions

	Formula									
	X47NF	X47	X37NF	X37	X39NF	X39	X31	X47W	X47W1	X47W2
Weight, g:										
PPO	47	47	47	47	47	47	47	47	47	47
P-9750	47	47	47	47	47	47	47	47	47	47
Magnesium titanate	36	36	71	71	142	142	36	36	36	36
Wollastonite P-15	0	0	0	0	0	0	0	26.2	26.2	26.2
Cab-O-Sil	0	0	0	4.8	0	4.8	4.8	0	2	4
Silene EF	0	19	0	0	0	0	0	0	0	0
Volume resistivity, $\Omega\text{-cm}$	243	54.6	141	17.7	28.5	17.8	19	445	46	21
Total filler surface area, m^2/g (47g of PPO)	125	1207	247	1258	494	1505	1137	183	604	1025
Ratio of P-9750 to PPO (peak heights, Fig. 4)	1.73	1.69	1.63	1.40	1.77	1.70	—	1.93	—	—

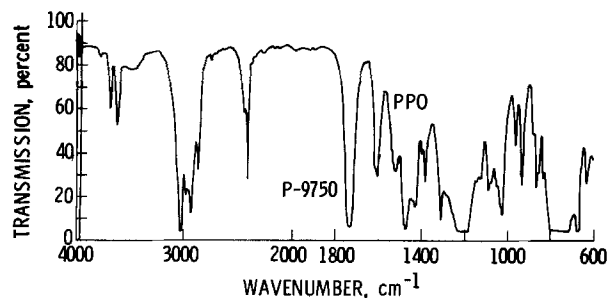


Fig. 1. Infrared spectrum of supernatant from formula X39NF (Table II).

PPO. Some fillers were reactive with the electrolyte; some were unreactive (inert). The fillers comprised a large range of particle sizes as well as different chemical compounds, both synthetic and natural. The effect was studied with and without a saponifiable organic additive (plasticizer) in the filler-PPO mixture. Table II presents information on PPO coatings discussed in this section. Table III presents data on particle sizes and surface areas of all fillers used in the PPO coatings (Table II) and in the Kraton G resin-base coatings (Table IV). Similar, but limited, studies on the volume content of fillers in Kraton G were also performed to establish that the resistivity results were not unique to PPO but were a more general result and usable with other resin-filler-plasticizer systems.

Effect of volume content of fillers in PPO on volume resistivity.—The volume resistivities of separators made with the fillers used in this evaluation are shown in Fig. 2. These fillers were milled into PPO-chloroform solutions without an organic additive. The curve for Microtalc in PPO shows a decreasing volume resistivity with increasing volume percent. This material has a surface area of ~ 3 m²/g (Table III). The curve for synthetic magnesium aluminosilicate (NAS-100) in PPO is similar to that for Microtalc except that the larger surface area of NAS-100 (280 m²/g, ~ 100 times greater than that of Microtalc) produces a correspondingly greater reduction in volume resistivity as filler volume content increases. The curve for P-9750 shows the effect of just a polyester plasticizer in PPO without any fillers. Since P-9750 is only slightly soluble in a dry PPO film [$<10\%$ by weight, (3)], it was assumed that when it was dispersed in the dry PPO film, it would segregate into discrete globules similar to filler particles. The plasticizer

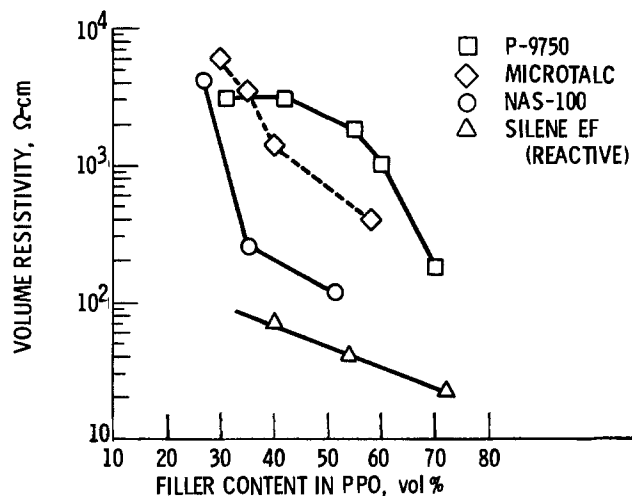


Fig. 2. Effect of filler volume content on volume resistivity, no plasticizer.

volume content without fillers had little effect on the volume resistivity until its volume percent was greater than 50% (greater than the CPVC). Reprecipitated (synthetic) calcium silicate filler (Silene EF), with a surface area of ~ 57 m²/g (Table III), reacts with the electrolyte and leaves voids filled with gelatinous, hydrated calcium oxide. This curve is described in Ref. (4) and is shown here for comparison as typical of reactive filler formulations.

Effect of volume content of filler with organic additive (plasticizer) in PPO on volume resistivity.—The data in Fig. 3 provide an insight into the interaction that results from combining the proper (4) organic additive (P-9750) with an inert filler. Magnesium titanate (Mg_2TiO_4) has a surface area of approximately 3.5 m²/g and a mean particle diameter of 1.7 μ m, about the same as Microtalc (Fig. 2). However, the Mg_2TiO_4 with plasticizer results in a volume resistivity an order of magnitude lower than that for Microtalc without plasticizer (data from Table II for formulas X47NF, X37NF, and X39NF). As the filler surface area increases the resistivity decreases. When the filler volume percent exceeds the CPVC ($\sim 40-45\%$), the resistivity is lower than would be expected from a linear extrapolation of the other two points.

Figure 3 also shows the effect of a fixed amount of fine-particle fumed silicon dioxide (Cab-O-Sil) com-

Table III. Particle sizes and surface areas of reactive and inert fillers

	Particle size, μ m	Surface area, m ² /g
Reactive fillers:		
Reprecipitated calcium silicate (Silene EF)	0.03	57
Fumed silicon dioxide (Cab-O-Sil)	0.015	210
Inert fillers:		
Lead titanate (TICON PT)	1.14	1.88
Natural calcium silicate (wollastonite P-15)	4.6	2.21
Magnesium titanate (TICON MT(C))	1.7	3.48
Magnesium aluminosilicate (NAS-100)	—	281
Magnesium silicate (Microtalc)	—	3

Table IV. Effect of reactive fillers in KRATON G (no plasticizer)

Reactive filler	Content, v/o	Surface area, m ² /40g of Kraton G	Volume resistivity, Ω -cm
Silene EF	10	524	6717
	29.9	2278	182
	39.1	3417	63
	50	5308	18
Cab-O-Sil	2.2	463	4071
	6.3	1361	3473
	10.1	2317	61

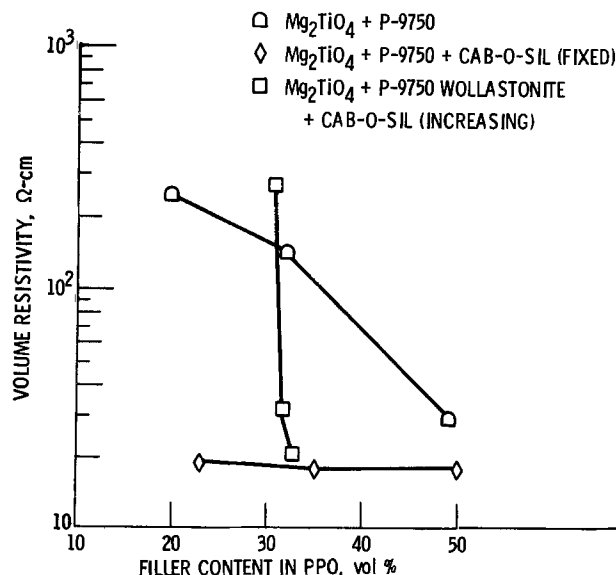


Fig. 3. Effect of volume content of filler plus organic additive (plasticizer) on volume resistivity.

bined with a larger amount of magnesium titanate with plasticizer. The curve represents the total for both fillers. The addition of electrolyte-reactive Cab-O-Sil, which has a mean particle size of $0.015 \mu\text{m}$ and a surface area of $\sim 210 \text{ m}^2/\text{g}$ (Table III), decreased the volume resistivity of Mg_2TiO_4 plus P-9750 by an order of magnitude. The data for formulas X31, X37, and X39 from Table II show that adding Cab-O-Sil increased the surface area significantly so that doubling the Mg_2TiO_4 content had little effect (20%) on surface area. Volume resistivity did not decrease significantly over the range investigated, even when the CPVC was exceeded (X39).

Figure 3 also shows the effect of an inert filler combination of magnesium titanate, natural calcium silicate (wollastonite P-15), and an increasing content of electrolyte-reactive Cab-O-Sil (0-3 v/o) with the plasticizer present. Data from Table II (formulas X47W, X47W1, and X47W2) show a pronounced drop in volume resistivity ($445 \Omega\text{-cm}$ to $21 \Omega\text{-cm}$) and at the same time a sharp increase in surface area ($183 \text{ m}^2/\text{g}$ to $1025 \text{ m}^2/\text{g}$) as the Cab-O-Sil content increased. The actual relationship of volume resistivity to filler surface area is described in detail later.

Effect of organic-additive (plasticizer) content on volume resistivity.—To more fully understand the role of the plasticizer and to estimate the thickness of the adsorbed layer on the filler particles, we attempted to measure the amount of P-9750 associated with the filler by using the ratio of P-9750 to PPO determined as described in the section Experimental Procedure. The calibration data, the regression line, and the results for the various formulas are shown in Fig. 4. The formulas are shown in Table II. Except for two points (X37 and X47W in Fig. 4), the data indicate that from 28 to 32 cm^3 of P-9750 remained in solution. The remaining $12\text{--}16 \text{ cm}^3$ are assumed to be associated with the settled filler particles.

From the surface areas given for the fillers in Table III, the total filler surface areas of the coating materials shown in Fig. 3 range from 1.8×10^6 to $1.5 \times 10^7 \text{ cm}^2$. Since an average 14 cm^3 of P-9750 is assumed to be associated with the fillers, the organic-additive film deposited on the particles is $8\text{--}23 \text{ nm}$ (80 to 230 \AA) thick. This is in the same range as the average pore size ($5\text{--}15 \text{ nm}$)⁴ for PPO-based separators as determined by water permeability (6) on KOH-soaked separators treated as described in the section Determination of Volume Resistivity.

The X47W point in Fig. 4, even though it is outside the range of the other points, is apparently consistent. The material (Table II) has a small calculated surface area ($183 \text{ m}^2/\text{g}$) and would therefore be associated with less plasticizer. The calculated plasticizer layer is 3.2 nm thick, which could account for the high resistivity ($445 \Omega\text{-cm}$) that was measured. The other outside point (X37) indicates a greater adsorption of plasticizer on the particles than for the other cases. There is no obvious or plausible explanation for it at this time.

⁴ M. Reid of Lewis, Unpublished data (1977).

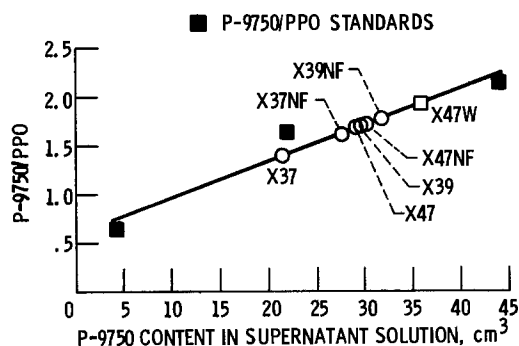


Fig. 4. Ratio of P-9750 to PPO as related to amount of P-9750 in supernatant solution.

BET measurements of separator pore size show a fairly sharp peak in the 2.5 nm region and a less well-defined region from 5 to 25 nm , the limit of the method. The smaller, 2.5 nm pores presumably are due to the pathway left by the evaporating solvent. Hence, it appears that ionic conduction through the separator depends primarily on the thickness of the ionic conduction pathway through and around the filler particles. This pathway is created by reaction of KOH with the adsorbed organic additive. A model of this pathway concept is shown in Fig. 5. Ion conduction is improved because pores are created by the reaction of fine-particle fillers with the KOH electrolyte. The pathways created by solvent evaporation probably also contribute. The reaction of the polymeric polyester (organic additive) with the KOH produces 1,2 propanediol and the potassium salt of azelaic acid. The diol, soluble in KOH, tends to improve volume resistivity while the salt presumably remains in the pathway as insoluble potassium azelate and further restricts the average diameter of the pathway.

Effect of filler surface area on volume resistivity.—The volume resistivity data in Fig. 3 show a marked dependence on the amount of fine-particle silica added to the coating formula. Figure 6 shows volume resistivity as a function of total filler surface area, in $\text{m}^2/47\text{g}$ of PPO (with 47g of P-9750). The symbols are identical to those in Fig. 3 and represent the same materials as well as X47 (circle) from Table II.

The two triangular points determine the line passing through the data points. This line was predicted from coefficients derived from a linear regression analysis of $\log(\Omega\text{-cm})$ as a function of total filler surface area in 47g of PPO (with 47g of P-9750). The correlation coefficient is -0.88 . The fit is good considering that the data were taken from coating formulas containing from 1 to 3 fillers with varying surface areas. The two data points in Fig. 6 labeled X47W2 and X37 (Table II) demonstrate the proportional relationship of volume resistivity to the surface area of the fillers. The volume of Cab-O-Sil in X47W2 (1.9 cm^3) is 84% of that in X37 (2.28 cm^3). The surface area of X47W2 ($1025 \text{ m}^2/\text{g}$) is 81% of that of X37 ($1258 \text{ m}^2/\text{g}$), and the reciprocal volume resistivity of X47W2 ($1/21 \Omega\text{-cm}$) is 84% of that of X37 ($1/17.7 \Omega\text{-cm}$).

Effect of volume percentage of fillers in Kraton G on volume resistivity.—A more flexible separator system than could be obtained with PPO was desired for Ni-Zn cells. Based on results of 500 hr of immersion in 45% KOH at $105^\circ\text{--}110^\circ\text{C}$, a Kraton G block copolymer was selected as the coating resin for this application.

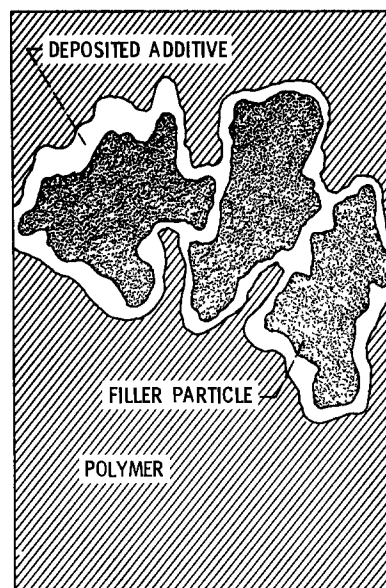


Fig. 5. Simplified ionic conduction model

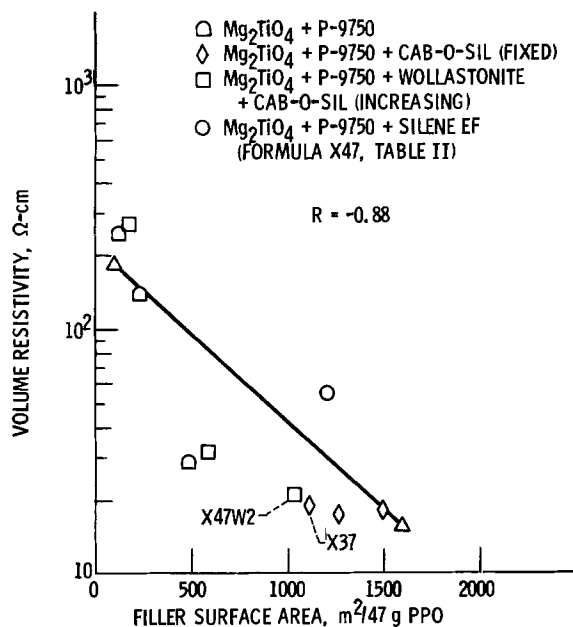


Fig. 6. Effect of total filler surface area on volume resistivity of PPO coatings.

Tests were performed to determine if the control of volume resistivity in PPO was more generally applicable to other polymer systems. An epoxidized soya bean oil plasticizer, Paraplex G-62 (a polar compound), was used with the Kraton G. One of its reaction products with KOH was ethylene glycol [Ref. (4), Table IV].

The effect on volume resistivity of the volume percentage of fillers in Kraton G (with no plasticizer) was studied. Table IV shows the effect of Silene EF and Cab-O-Sil on volume resistivity. These data indicate that 10.1 v/o of Cab-O-Sil is equivalent to 39.1 v/o of Silene EF. The effect is presumably due to the greater surface area of Cab-O-Sil. Table V shows the effect of adding the plasticizer to the polymer along with fillers; compare formulas K52, K53, and K51. The addition of a small volume percentage of Cab-O-Sil (formula K53, Table V) to the Silene EF mixture (formula K51) produced a substantial drop in volume resistivity.

This effect was then tested in actual separator coatings that applied the principle demonstrated in Fig. 3, that of increasing the amount of the fine-particle reactive silica in a coating mixture containing the Kraton G polymer, a plasticizer, and two unreactive fillers—lead titanate and natural calcium silicate (wollastonite).

These results are shown in Table V and Fig. 7. Formula K19W contains no Cab-O-Sil. Formula K19W2 contains twice as much as K19W1. The K19W/2 is a mixture of equal volumes of Silene EF and wollastonite, the total volume of which is equal to the volume percentage of wollastonite in the other formulas. The square points in Fig. 7 used to draw the curve represent two points predicted by the linear

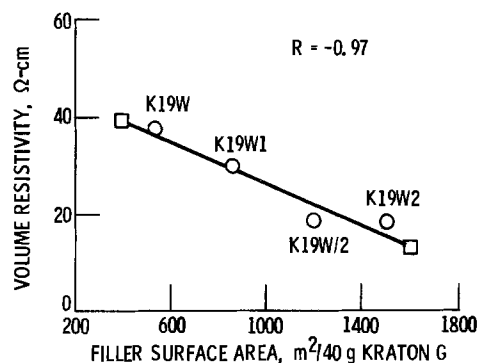


Fig. 7. Effect of total filler surface area on volume resistivity of Kraton G coatings.

regression analysis of volume resistivity as a function of the surface area of fillers in 40g of Kraton G. The linear correlation coefficient for the regression analysis is -0.97 .

These data show an effect similar to that observed with fillers and an organic additive to PPO. This method of resistivity control is therefore also useful and predictable in at least one other resin-plasticizer system and may be generally applicable.

Concluding Remarks

Small percentages of high surface area, fine-particle silica incorporated in coating systems where the filler content is below the critical pigment volume concentration have been shown to be a predictable means of controlling the volume resistivity of the coated substrate. Many of the formulas described in this paper have also been evaluated as separators in nickel-zinc and silver-zinc cells. Some of these cells have shown acceptable performance (9).

Manuscript submitted Dec. 4, 1979; revised manuscript received April 18, 1980. This was Paper 45 presented at the Pittsburgh, Pennsylvania, Meeting of the Society, Oct. 15-20, 1978.

Any discussion of this paper will appear in a Discussion Section to be published in the June 1981 JOURNAL. All discussions for the June 1981 Discussion Section should be submitted by Feb. 1, 1981.

Publication costs of this article were assisted by NASA.

REFERENCES

1. F. C. Arrance and A. G. Rosa, U.S. Pat. 3,625,770 (1971).
2. J. M. Bozek, Structure and Function of an Inorganic-Organic Separator for Electrochemical Cells—Preliminary Study," NASA TM X-3080 (1974).
3. W. H. Philipp and C. E. May, "Functioning of Inorganic/Organic Battery Separators in Silver-Zinc Cells," NASA TM X-3357 (1976).
4. D. W. Sheibley, "Factors Influencing Flexibility, Resistivity, and Zinc Dendrite Penetration Rate of Inorganic Separators for Alkaline Batteries," NASA TM X-3199, (1975).
5. P. Nylen and E. Sunderland, "Modern Surface Coat-

Table V. KRATON G coating compositions

	Formula						
	K52	K53	K51	K19W	K19W1	K19W/2	K19W2
Weight, g:							
Kraton G	40	40	40	40	40	40	40
Paraplex G-62	16	16	16	16	16	16	16
Wollastonite P-15	0	0	0	55.2	55.2	27.6	55.2
Lead titanate	0	0	0	20	20	20	20
Cab-O-Sil	0	1.6	0	1.6	3.2	1.6	6.4
Silene EF	0	40	40	0	0	20	0
Volume resistivity, Ω -cm	8175	15.3	35.7	37.6	30	18.2	17.4
Total filler surface area, $m^2/40g$ of Kraton G	0	2606	2278	535	833	1802	1507

- ings; A Textbook of the Chemistry and Technology of Paints, Varnishes, and Lacquers," pp. 384-386, Interscience Publ., Inc., New York (1965).
6. J. E. Cooper and A. Fleischer, Editors, "Characteristics of Separators for Alkaline Silver Oxide Zinc Secondary Batteries. Screening Methods." Air Force Systems Command, Air Force Aero Propulsion Laboratory, Wright-Patterson AFB, Ohio (1964).
 7. S. Braunauer, P. H. Emmett, and E. Teller, *J. Am. Chem. Soc.*, **60**, 309 (1938).
 8. P. H. Emmett, "Advances in Colloid Science," Vol. I, p. 139, Interscience Publ., Inc., New York (1942).
 9. D. W. Sheibley, "Improved Low Cost Inorganic-Organic Separators for Rechargeable Silver-Zinc Batteries," NASA Technical Paper 1476 (1979).

On High Temperature Oxidation of Chromium

I. Oxidation of Annealed, Thermally Etched Chromium at 800°-1100°C

K. P. Lillerud and P. Kofstad

Department of Chemistry, University of Oslo, Blindern, Oslo 3, Norway

ABSTRACT

Oxidation of annealed, thermally-etched chromium has been studied at different oxygen pressures ranging from 10^5 to $7 \cdot 10^{-2}$ Pa in the temperature range 800°-1100°C. A varied oxidation behavior is observed: at 10^5 Pa O_2 and 800°C the oxidation is approximately logarithmic, while above 900°C it is parabolic followed by repeated breakdowns and protective stages. At reduced oxygen pressures the oxidation behavior changes and becomes linear at the lower oxygen pressures. The different kinetics are correlated with properties of the Cr_2O_3 scales which may crack, wrinkle, or balloon depending upon the reaction conditions. Large compressive stresses are built up in the scales during oxidation and the ability of the scale to deform increases dramatically with decreasing partial pressure of oxygen. Under most conditions the oxide scales become detached from the metal substrate. It is concluded that volume diffusion and transport along cracks and grain boundaries contribute to the growth of Cr_2O_3 scales.

Chromium-bearing alloys owe their high temperature corrosion resistance to formation of protective layers of Cr_2O_3 (1-3). In spite of the importance in innumerable practical applications, the growth mechanism of Cr_2O_3 scales under various conditions is still in need of further clarification. This also applies to the defect structure and transport properties of Cr_2O_3 (4).

Although unalloyed chromium is not used as a constructional material, the reaction of chromium with oxygen at high temperatures has been extensively studied in order to characterize the reaction behavior and unravel the growth mechanism of Cr_2O_3 (5-18). This work extends such studies. This and the subsequent paper (19) deal with the oxidation behavior of annealed, thermally etched chromium at different oxygen pressures in the temperature range 800°-1100°C, properties of Cr_2O_3 scales, and the oxidation mechanism of chromium.

Literature Survey

The chromium-oxygen system.— Cr_2O_3 is the only solid chromium oxide that is thermodynamically stable at high temperatures. Cr_2O_3 has the corundum structure and can be grouped with oxides such as $\alpha-Al_2O_3$, Fe_2O_3 a.o. This structure can be considered to consist of hexagonally close-packed oxygen atoms (ions) where the chromium atoms (ions) occupy two-thirds of the octahedral sites (4).

Solid CrO is a metastable oxide, but it can, for instance, be produced by partial decomposition of chromium oxalate (20). The oxide has been identified in chromium oxide layers on oxidized chromium by means of secondary ion mass spectrometry (21). Hagel (9) also reports in connection with studies of oxidation of chromium that in one exposure at 1100°C five lines for an unknown fcc compound of $a_0 = 4.02\text{Å}$ were found. This may reflect CrO. The

pattern could not be repeated on other samples treated in the same manner (9).

Higher oxides of chromium, e.g., CrO_2 , CrO_3 , are only stable in solid form at low temperatures (22), and have as solids not been shown to be of importance in high temperature oxidation of chromium. However, volatile chromium oxide species may be important (23). CrO_3 is the important specie to consider in oxidizing atmospheres (15, 24-26). It evaporates from Cr_2O_3 in oxygen atmospheres: $1/2 Cr_2O_3 + 3/4 O_2 = CrO_3(g)$. Accordingly the evaporation rate is proportional to $p_{O_2}^{3/4}$ (24-26). Thus CrO_3 evaporation is important at "high" partial pressures of oxygen, i.e., at atmospheric or near-atmospheric oxygen pressures, at high temperatures.

Oxidation of chromium in oxygen.—The high temperature reaction behavior of chromium in oxygen has been investigated at temperatures up to 1400°C (5-18). A number of publications report results of kinetic studies. Chromium exhibits protective oxidation behavior, i.e., the reaction rate decreases with time.

The kinetics above 700°C are generally interpreted as parabolic. Reported values of corresponding parabolic rate constants are summarized in Fig. 1. A striking feature is that the k_p values vary by more than four orders of magnitude in the temperature range 1000°-1200°C. It may be noted that some investigators, and apparently depending on the pretreatment of specimens and reaction conditions, find periodic increases in the reaction rate and where the overall kinetics can be considered as a sequence of stages with protective behavior.

Below 700°C the reaction behavior changes. Young and Cohen (17) report that the oxidation in the temperature range 300°-600°C involved an initial logarithmic stage, which duration decreased with increasing temperature, followed by parabolic oxidation. The logarithmic rate constant exhibited a posi-

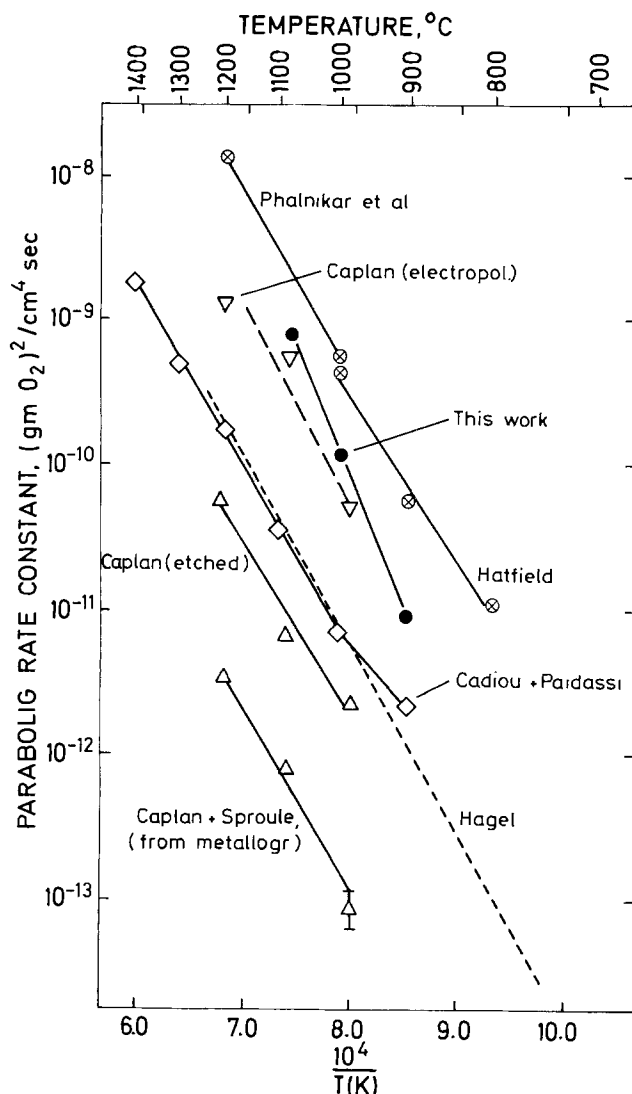


Fig. 1. Summary of reported parabolic rate constants for oxidation of chromium in oxygen in the temperature range 700°–1400°C. Results of this study on annealed, thermally etched chromium are also included. Studies by Hatfield (5), Phalnikar, Evans, and Baldwin (7), Hagel (9), Cadiou and Paidassi (10), and Caplan and Cohen (11, 14). Values of Gulbransen, and Andrew (6, 8), which are not included in the graph, are similar to those of Hagel.

tive pressure dependence, while the parabolic rate constant had a negative pressure dependence, *i.e.*, this rate constant increased with decreasing oxygen pressure. Such a pressure dependence cannot be explained in terms of a reaction governed by homogeneous diffusion through the scale (*e.g.*, Wagner mechanism), and a model is advanced where it is assumed that the concentration of adsorbed oxygen species is determined by an adsorption equilibrium on thin compact areas of the oxide scale, while the rate-determining growth occurred at areas with thicker porous oxide.

Much effort has been expended to explain the large discrepancies in oxidation rates at high temperatures. Various factors have been demonstrated or suggested as reasons for the differences.

An important factor is specimen preparation. This has particularly been demonstrated by Caplan *et al.* (11–14). The surfaces were prepared in different ways: abrading, electropolishing in various electrolytes, etching, and combinations of these. A general feature of these results is that electropolished specimens oxidized rapidly; for etched chromium some orientations oxidized rapidly, while others oxidize much slower. Non-uniform oxide layers exhibiting nodule growth, blistering, wrinkling, and multilayered ballooning are

formed during the more rapid oxidation. Caplan *et al.* conclude that the growing Cr_2O_3 scales develop compressive stresses. The slower oxidation, which takes place on some etched orientations, involves formation of plane-parallel layers of Cr_2O_3 consisting of monocrystalline (and apparently stress-free) oxide. It may be noted that the smallest k_p values in Fig. 1 are evaluated from metallographic cross sections by measuring the oxide thickness on areas with such monocrystalline oxide-layers (14). All other k_p values represent overall k_p 's determined from thermogravimetric measurements.

Caplan and Sproule (14) deduced that the monocrystalline oxide grows by cation lattice diffusion. Nonuniform growth in the form of nodules, blisters, and multilayered balloons are concluded to take place by a two-way transport: metal ion (lattice) diffusion outward and oxygen ion diffusion inward along grain boundaries. The periodic sequences in protective reaction kinetics reflect breakdown of the scale and formation of new protective oxide underneath. They have further shown that the oxide formed on "rapidly" oxidizing, electropolished chromium is fine-grained, and that this in turn facilitates a rapid transport (grain boundary diffusion) through the scale. During blistering and ballooning the oxide is separated locally from the metal. However, this does not affect the oxidation rate, as the vapor pressure and evaporation rate of chromium (at sufficiently high temperature) is high enough to sustain the supply of chromium at the underside of the separated oxide layer(s). Gulbransen and Andrew (8) have also pointed out that the high vapor pressure of chromium is an important factor in oxidation of chromium at high temperatures ($> \sim 1000^\circ\text{C}$).

Evaporation of CrO_3 is particularly important at high temperatures ($> \sim 1000^\circ\text{C}$) and high oxygen pressures (15, 24, 26). In thermogravimetric studies of chromium oxidation one measures the net difference between oxygen uptake and oxide evaporation. Depending upon the reaction conditions, CrO_3 may accumulate in the gas space surrounding the specimen, and the surrounding gas may serve as a barrier to the CrO_3 evaporation (24, 25). Thus the measured net weight change of oxidizing specimens will be different for static gas conditions and various degrees of gas flow, size of the reaction chamber, the temperature gradient in furnace, etc.

It has been suggested that differences in the impurity levels of the chromium metal used in different studies may be responsible for differences in reaction rates. However, it is difficult to find any clear-cut correlations between impurity contents and reaction rates. This should not necessarily be taken to mean that impurities are without any effects. Caplan and Sproule (14) have, for instance, demonstrated differences in the growth mechanism of Cr_2O_3 on chromium metal and Fe-25% Cr.

The observed reaction behavior may be affected by the experimental procedure. In various studies the specimen may as part of each run be rapidly heated in the reacting gas from room temperature to the reaction temperature, or alternatively be heated in high vacuum to the reaction temperature before admitting oxygen. With these procedures thin oxide films are formed either in air prior to introducing the specimen in the apparatus, or through the heating to the reaction temperature either in the reacting gas or "vacuum." The oxide films thus formed may have different thickness, grain size, and morphology, and as such represent different "pretreatments" of the specimen surfaces prior to the recorded experiments. A type of pretreatment which has not been emphasized in previous studies is whether the chromium specimens are annealed, used in hot-rolled condition without annealing, as electrolytically prepared metal, etc.

Despite the large discrepancies in the values of k_p , there are surprisingly small differences in the values of the corresponding activation energies above about 700°C. The activation energy is approximately 250 kJ/mole (60 kcal/mole). However, at lower temperatures (<700°C) the observed activation energies are smaller, about 145-165 kJ/mole (16, 17).

Hagel (9) measured oxidation of chromium at 750° and 1100°C at oxygen pressures ranging from 10² to 1 Pa O₂. He observed no or but a small decrease in k_p with increasing p_{O_2} . Within the reproducibility of the results the smallest value of the exponent n in the relationship $k_p \propto p_{O_2}^{1/n}$ was estimated to be about 40.

Walters and Grace (18) studied the reaction rate at 700°-990°C in H₂/H₂O mixtures with partial pressures close to those of the decomposition pressure of Cr₂O₃. The parabolic rate constant was interpreted in terms of the relationship $k_p \propto p_{O_2}^{3/16}$, which is the expected relationship if the oxidation is governed by lattice diffusion of triply charged chromium vacancies as the predominant defect. It should be noted, however, that diffusion-controlled parabolic oxidation at oxygen pressures close to the decomposition pressure of the oxide will always yield a positive pressure dependence. In this case the measurements were not sufficiently accurate and reproducible to discriminate between different defect structure models [see, for instance, Ref. (4)].

Materials and Methods

Materials

Chromium metal.—The chromium metal was prepared electrolytically. The supplier (Koch-Light Laboratories) reported the metal to have a purity of 99.99+%. Spectrographic analysis gave the following results: Al-not detected (<0.005%), Fe-150 ppm, Mg-n.d. (<0.001%), Ca-10 ppm, Cu-16 ppm, Ti-n.d. (<0.01%), Si-n.d. (<0.005%). Vacuum fusion gas analysis gave: H-200 ppm and 0-4150 ppm.

The as-received metal was brittle and could not be mechanically worked. The specimens, measuring approximately 1 · 10 · 15 mm, were therefore prepared by spark induction. The brittleness was to a large extent caused by the hydrogen content. The hydrogen escaped by heating the specimen in high vacuum up to 560°C. After this treatment the metal was considerably less brittle.

Specimen preparation.—The many methods of surface preparation often suffer from some disadvantage (11-14). Mechanical polishing deforms a thin, outer layer of the metal, and this part of the metal may exhibit a different reactivity than the "bulk" layers (17). Electropolishing and etching give surfaces with relatively large topography, and furthermore the etchant and electrolyte may not be completely removed from the surface. By electropolishing the oxide film may possibly have unusual oxidation states as it is formed in applied electric field. In this work a new method of specimen preparation was used: thermal etching in high vacuum.

Prior to the thermal etching the specimens were mechanically polished with emery paper of grade 220. After extended polishing with the same polishing paper, removed chromium filled the pores and the surface roughness of the paper, and during the latter polishing stage chromium was polished against chromium. This gave a surface with no visible polishing stripes at 500×. The as-received metal was examined by the Guinier method. This gave broad, diffuse lines indicating that the electrolytically prepared chromium was highly microcrystalline.

The thermal etching was done by heat-treating the polished specimens in the reaction chamber in high vacuum (<10⁻³ Pa) at 1075°C for 20 hr. During this treatment the vapor pressure and the corresponding

evaporation rate of chromium was so high that the thin, room temperature oxide film was removed and no new oxide was formed on the surface. The specimens lost weight at a linear rate, which at 1075°C mounted to 0.44 mg/cm² hr. During this 20 hr high vacuum annealing the outer 12 microns of the chromium specimen were removed. The annealing produced well-developed crystallites and sharp diffraction lines by the Guinier method.

Chromium vapor pressures were calculated from the linear rates of weight loss during chromium evaporation in high vacuum by means of the Hertz-Langmuir equation. Values obtained at different temperatures are in excellent agreement with previously reported vapor pressure values (6, 27).

The oxidation runs were made by adjusting the temperature in the furnace to the desired reaction temperature while maintaining high vacuum. During the temperature change the specimens continued to lose weight corresponding to the vapor pressure of chromium. After the new temperature equilibration, the reaction was started by introducing oxygen in the system.

By this treatment the deformed outer layer of the specimen was removed, and it is believed that the surface was essentially free from any oxide at the start of the reaction.

Oxygen gas.—The oxygen gas was dried over silica gel before being introduced into the reaction chamber, but no further attempts were made to purify the gas.

Methods

Balance, thermogravimetric measurements.—The thermogravimetric measurements were made with a magnetic levitation balance of Sartorius Type 4201. The apparatus was evacuated with a pair of diffusion and rotary pumps giving a high vacuum of <10⁻³ Pa as measured with an ion gauge located above the reaction chamber.

The reaction chamber consisted of a mullite tube, which was directly melted on to the borosilicate glass in the rest of the high vacuum system. The temperature was continuously monitored with Pt/Pt 10% Rh thermocouple located next to the suspended specimen in the constant temperature zone of the reaction chamber. The specimen was suspended with a 0.2 mm Pt thread. Oxygen was continuously pumped through the reaction chamber from the top to the bottom during the oxidation run.

The reacted specimens were characterized by means of optical metallography, scanning electron microscopy, and x-ray diffraction.

Experimental Results

Thermogravimetric Measurements

Results at 10⁵ Pa O₂.—The results of the thermogravimetric measurements of oxidation of annealed, thermally etched chromium at 10⁵ Pa (1 atm) O₂ and at 800°, 900°, 1000°, and 1075°C are summarized in a double logarithmic plot of weight gain *vs.* time in Fig. 2. The fully drawn lines represent the directly measured, net weight gain during oxidation. The reproducibility of parallel runs were within 2%.

Figure 2 illustrates some salient features of the oxidation behavior of thermally etched chromium: (i) the reaction rate at 800°C decreases much faster with time than for a parabolic behavior. As illustrated in the semilogarithmic plot [weight gain *vs.* log (time)] in Fig. 3, the reaction kinetics can be described as approximately logarithmic. (ii) Up to approximately 10 hr of oxidation the amount of oxidation is approximately the same at 800° and 900°C. This feature, and a distinct change in the reaction kinetics from 800° to 900°C, points to a marked change in the oxidation mechanism between 800° and 900°C. (iii) The reaction kinetics at 900°, 1000°, and 1075°C

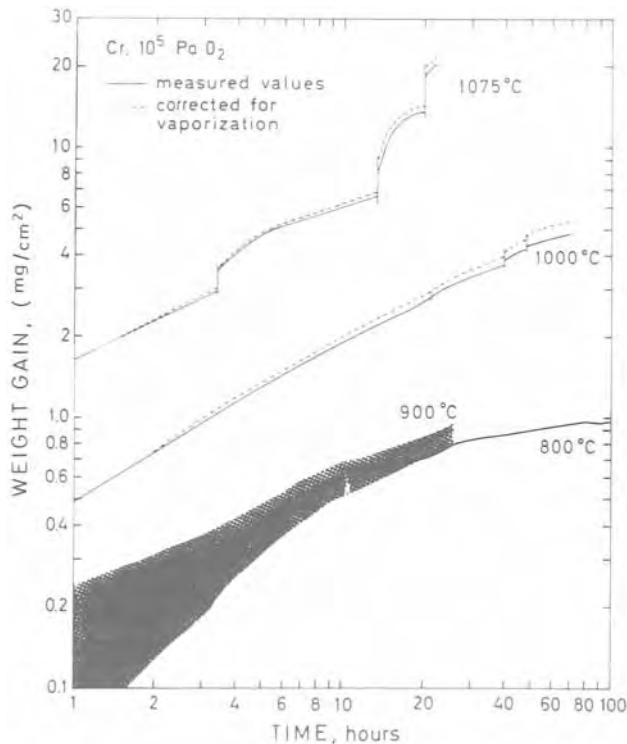


Fig. 2. Double-logarithmic plot (weight gain vs. time) of oxidation of thermally etched chromium at 800°, 900°, 1000°, and 1075°C and 10^5 Pa O_2 . The fully drawn line shows the measured net weight gain during oxidation, while the stippled lines illustrate the total reaction by adding the weight loss due to CrO_3 evaporation to the net weight gain. The hatched regions indicate the uncertainties in the measurements (± 0.1 mg) at low weight gains.

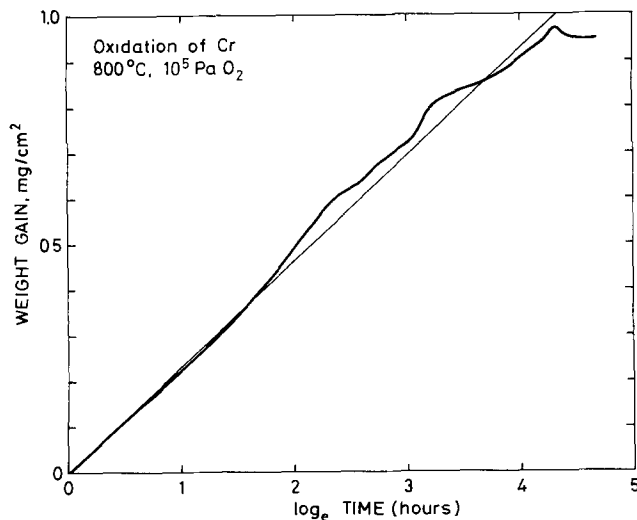


Fig. 3. Semilogarithmic plot [weight gain vs. \log (time)] of oxidation of thermally etched chromium at 800°C and 10^5 Pa O_2 .

can be described as approximately parabolic. This is further illustrated in Fig. 4 where the square of the weight gain is plotted as a function of time. But it may also be noted that the kinetics do not conform with an ideal parabolic rate. (iv) After extended oxidation (a weight gain of 2-3 mg/cm²) at 1000°C and 1075°C sudden increases take place in the oxidation rates, and the overall kinetics may be described as a sequence of stages with protective oxidation. This effect is much larger at 1075° than at 1000°C.

The parabolic rate constants during the initial oxidation at 900°, 1000°, and 1075°C corrected for oxide evaporation (see below) are included in Fig. 1. The values lie in the upper region of the previously re-

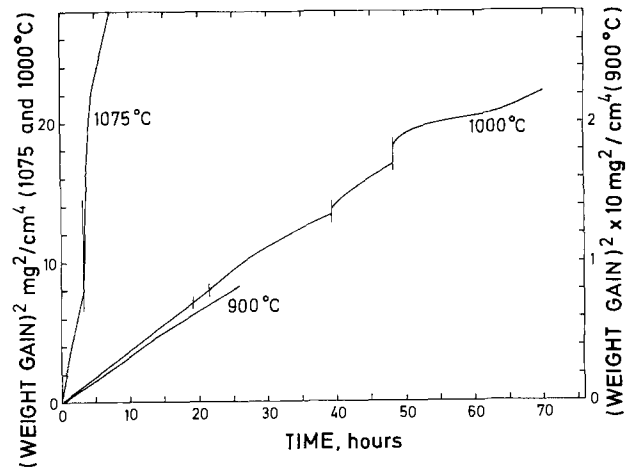


Fig. 4. Parabolic plot [(weight gain)² vs. time] of oxidation at 900°, 1000°, and 1075°C.

ported results. The activation energy as determined from these three points is 330 kJ/mole (78 kcal/mole), which is 30% higher than the average value from other studies. It should be noted that if values of k_p were evaluated from later stages of the reaction, as has been done in other studies (9, 10) somewhat lower values would have been obtained.

Oxidative vaporization of Cr_2O_3 during oxidation.—Oxidative vaporization of Cr_2O_3 as CrO_3 is significant during oxidation of chromium at high oxygen pressures and high temperatures. In order to correct the measured oxidation rates for this evaporative loss, the weight loss of a completely oxidized chromium specimen was measured at different temperatures and 1 atm O_2 . The evaporation was followed for 24 hr at each temperature, and during each run a gas flow equal to that in the oxidation runs was maintained. The linear rates of weight loss at 1 atm O_2 were found to be $2.2 \cdot 10^{-2}$ mg/cm² hr at 1100°C, $6.7 \cdot 10^{-3}$ at 990°C, $2.1 \cdot 10^{-3}$ at 900°C. These results gave a straight-line relationship in an Arrhenius plot with an activation energy of 155 kJ/mole (37 kcal/mole). Extrapolation of these values gave a loss rate of $5 \cdot 10^{-4}$ mg/cm² hr at 800°C. These results have been used to correct the oxidation results to show the total rate of reaction at different temperatures. This is illustrated by the stippled lines in Fig. 2.

It is emphasized that these evaporation rates give no information about the thermochemistry of the reaction-controlled oxidation vaporization, but only provide information about the weight loss during the oxidation under the particular experimental conditions used. In the present study the oxygen atmosphere surrounding the specimens serves as a barrier to the free evaporation of CrO_3 . The measured evaporation rates are much lower than calculated values for reaction-controlled vaporization at 1 atm O_2 as estimated from the data of Stearns *et al.* (6).

Results at reduced oxygen pressures.—800°C.—The results of thermogravimetric measurements at 800°C and oxygen pressures of 10^5 (760), $1.1 \cdot 10^3$ (8), 8 ($6 \cdot 10^{-2}$), and $6.7 \cdot 10^{-2}$ Pa O_2 ($5 \cdot 10^{-4}$ Torr) are shown in Fig. 5. The reaction kinetics at 10^5 Pa O_2 can be described as approximately logarithmic (Fig. 3). When the pressure is reduced to $1.1 \cdot 10^3$ and 8 Pa O_2 , the initial period of rapid oxidation becomes shorter. This is followed by a period of slowly decreasing oxidation rate until the oxidation reaches the stage with essentially no oxidation.

With further reduction in oxygen pressure the oxidation kinetics are changed and can, within the sensitivity of the balance, be described as linear at $7 \cdot 10^{-2}$ Pa. It may be noted that the gas pressure is measured with gauges outside the furnace zone, and as molecular flow prevails in the reaction cham-

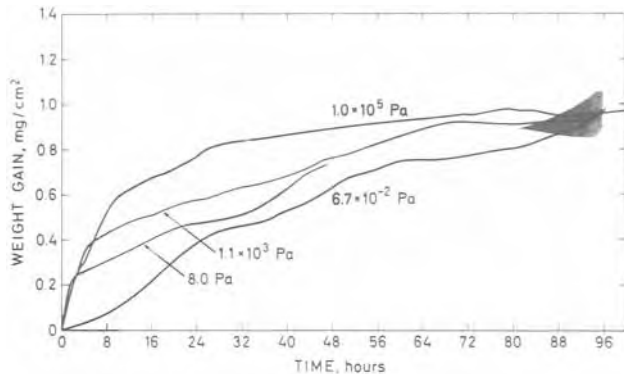


Fig. 5. Oxidation of thermally etched chromium at 800°C and oxygen pressures ranging from 10^5 Pa (760 Torr) to $6.7 \cdot 10^{-2}$ Pa ($\sim 4.5 \cdot 10^{-4}$ Torr). Weight gain of specimens (mg/cm^2) during oxidation as a function of time (hr). The hatched regions indicate the uncertainties in the weight gain measurements (± 0.1 mg).

ber at this pressure, the real pressure at the specimen is slightly higher than indicated (28).

900°-1100°C.—When the temperature was increased to 900°C and further on to 1000° and 1075°C the studies revealed an unexpected change in the reaction behavior at different oxygen pressures.

At 900°-950°C the oxidation decreases slowly with decreasing partial pressure of oxygen in a manner similar to that at 800°C. At the lowest oxygen pressure, $7 \cdot 10^{-2}$ Pa O_2 , the oxidation is again approximately linear. However, as the temperature is increased to 1000° and 1075°C the oxidation is faster at oxygen pressures of 10^3 - 10^2 Pa than at 10^5 Pa. Furthermore, the kinetics are changed and can under these conditions be considered to be approximately linear within the time periods studied (up to 25 hr at 1075°C). On further reduction of oxygen pressure the oxidation rate again decreases with decreasing oxygen pressure and at the lowest pressure, $7 \cdot 10^{-2}$ Pa O_2 , the reaction is again linear. These features are illustrated in Fig. 6 and 7, which summarize results at 1000° and 1075°C, respectively.

Characterization of Specimens

In most cases the most descriptive information on topography, morphology, and microstructure of Cr_2O_3 scales is obtained by examining fractured scales directly in the scanning electron microscope. Optical metallography and plane-polished cross sections often fail to uncover important details.

Oxide scales never spall at temperature. But specimens oxidized at atmospheric pressure at 800° and 900°C may exhibit violent spallation on cooling to room temperature. This is in all probability due to poor adherence of the scale to the metal substrate, growth stresses in the oxide, and the smaller thermal expansion coefficient of Cr_2O_3 compared to chromium metal.

Specimens reacted at 800°C.—Exposure at 1 atm O_2 .—After oxide spallation only a few local areas are still covered with oxide scale. Figures 8 and 9 show examples of such fractured scales after oxidation at 800°C. Figure 8 refers to a specimen oxidized for 50 hr. The weight gain at this point was about 0.9 mg/cm^2 , and the thickness of this layer is about 2 microns. At this stage, part of the scale is fine-grained, but also some larger grains are formed. These do not exhibit any crystal facets and also appear to consist of smaller crystallites. All in all, the morphology of the scale has similarities to that described by Young and Cohen (17) for chromium specimens (mechanically polished with subsequent electropolishing) oxidized for extended periods in oxygen at 300°-600°C.

These features may be compared with the morphology and microstructure of oxide scales after more

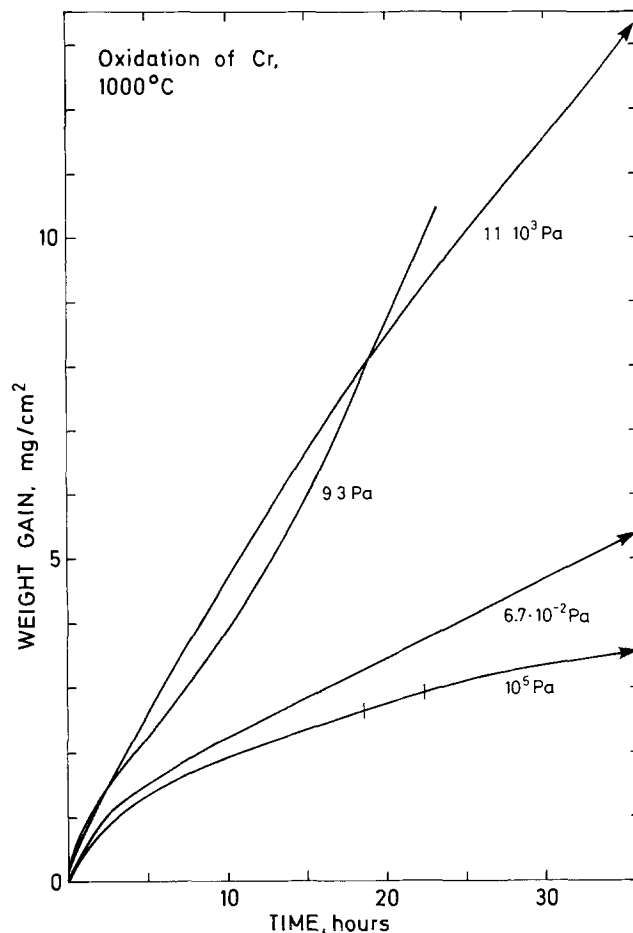


Fig. 6. Oxidation of thermally etched chromium at 1000°C and oxygen pressures ranging from 10^5 Pa to $7 \cdot 10^{-2}$ Pa. Weight gain of specimens during oxidation as a function of time.

extended oxidation as illustrated in Fig. 9a and b. These illustrations refer to a specimen oxidized for 127 hr, at which point the weight gain was about 1 mg/cm^2 and the oxidation rate was almost nil (Fig. 2). The scale is under these conditions highly protective. The larger grains have at this stage grown in number and size and the crystals have developed facets. Thus during the "logarithmic" oxidation the scales undergo recrystallization and crystal growth, and each oxide crystal tends to become more perfect. From these observations it can be concluded that the protective ability of the oxide is less dependent on the thickness of the scale than its morphology and microstructure and how well the crystals are developed.

Further examinations of Fig. 8 and 9 show that the scale is, at least partially, separated from the metal. No oxide can be detected on the metal after 127 hr of oxidation, and particularly Fig. 9 shows that the metal surface exhibits facets. From this it is concluded that there is a gap between the scale and the metal over most of the surface after prolonged oxidation. This is also probably a reason for the ease of spallation of the oxide on cooling.

Marker experiments were made at 800°C. A porous layer of gold (1-1.5 μm thick) was sputtered on one side of a few specimens. Such gold-sputtered specimens oxidized at the same rate as the ones without a gold layer. After oxidation for 24 hr the gold was located on the metal surface or at the inner layer of the oxide. However, there were indications that the gold influenced the morphology and microstructure of the scale in that plane-polished metallographic cross sections revealed more porosity on the unsputtered side than on the sputtered one.

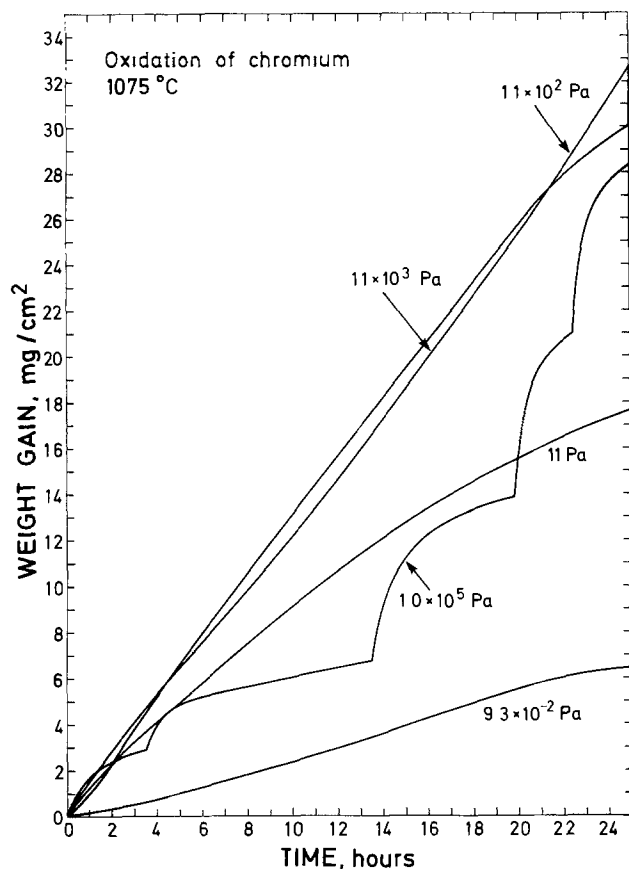


Fig. 7. Oxidation of thermally etched chromium at 1075°C and oxygen pressures ranging from 10^5 Pa to $7 \cdot 10^{-2}$ Pa. Weight gain of specimens during oxidation as a function of time.



Fig. 8. Scanning electron micrograph of chromium specimen oxidized for 50 hr at 800°C and 10^5 Pa O_2 . The picture shows a fractured edge of the scale with the chromium metal beneath.

Exposure at reduced oxygen pressures.—The morphology and microstructure of the scale changes markedly with oxygen pressure. On reducing the oxygen pressure to $1.1 \cdot 10^3$ Pa, marked changes in the scale are evident. This is illustrated in Fig. 10. On cooling to room temperature the scale has separated into 2-3 layers. The outer and middle layer of the scale exhibit large topography and adhere to each other in many places. The inner layer is flat and is separated from the other two layers. The crystallite size in the scale decreases inward through the layers of the scale, and for the inner layer the crystallite size is small and crystal facets can no longer be discerned.

On further reduction of the oxygen pressure to less than 10 Pa O_2 the scale is again single-layered and its microstructure resembles the inner layer in Fig. 10 (10^3 Pa O_2).

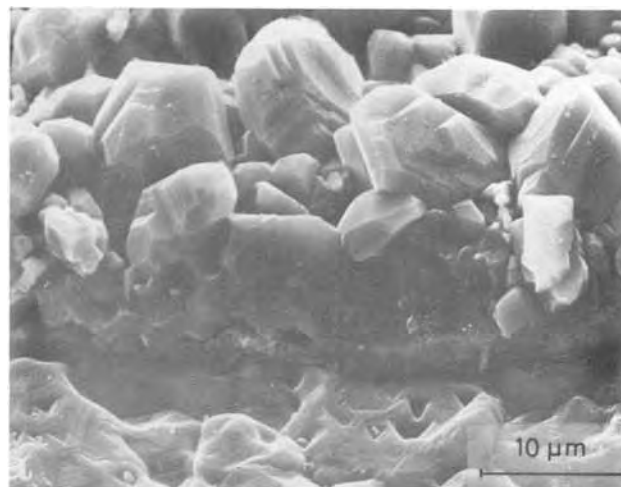


Fig. 9. Scanning electron micrograph of chromium specimen oxidized for 127 hr at 800°C and 10^5 Pa O_2 . a shows a fractured edge of the oxide scale with the metal beneath, and b a detail of a at larger magnification showing the inner surface of the scale and the surface of the metal.

At $7 \cdot 10^{-2}$ Pa O_2 the morphology and microstructure of the scale is again markedly changed. Under these conditions the oxide grows as a single layer and is completely separated from the metal on the plane surfaces of the specimens. The scale neither cracks nor spalls on cooling to room temperature. Various features of the scale may be noted: the scale wrinkles and buckles. This feature is illustrated in Fig. 11a which shows the underside of the scale (facing the metal). By comparing with the surface appearance of the thermally etched metal before oxidation (Fig. 11b), it appears that the oxide scale has particularly deformed in areas where the oxide originally grew on the metal grain boundaries.

Figure 12a shows the fractured cross section of the scale. The oxide thickness is about $2 \mu\text{m}$. An additional feature under these conditions is that whiskers are formed on the outer surface. This is illustrated in Fig. 12b. Crystal growth also takes place at the inner surface of the scale (facing the metal). This is further illustrated at a larger magnifications in Fig. 12c and d.

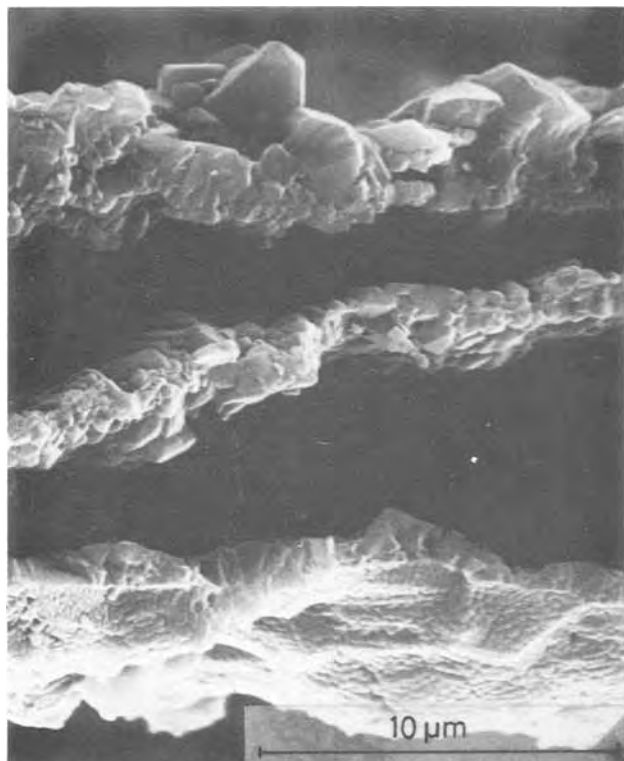


Fig. 10. Scanning electron micrographs of fractured scale of Cr_2O_3 after oxidation for 94 hr at 800°C and 10^3 Pa. The scale consists of three distinct layers.

All in all, the changes in topography, morphology, and microstructure of the scale with oxygen pressure points are important aspects of the properties of the oxide and the reaction mechanism. The results show that considerable growth stresses build up in the scale during its growth. These are partially alleviated by plastic deformation of the scale, and the oxide plasticity increases markedly with decreasing partial pressure of oxygen. The buckling and wrinkling of the scale and the large concurrent increase of the scale surface clearly suggests that the oxide not only grows in thickness, but also sideways (along the metal surface). This, in turn, suggests that the oxide, at least partially, grows within the scale probably as a result of countercurrent transport of the reactants.

Specimens reacted at $900^\circ\text{--}1100^\circ\text{C}$.—Exposure at 10^5 Pa O_2 .—At $900^\circ\text{--}1075^\circ\text{C}$ the initial oxidation is approximately parabolic. After extended oxidation at 1000° and 1075°C the kinetics involve a sequence of protective stages. It is reasonable to assume that this behavior reflects a periodic breakdown of the scale and formation of a new protective layer.

When the oxidation is stopped before the kinetics suggest any scale breakdown, the scales appear to be compact. But after more extended oxidation, and after one or more sequences of protective stages, fractured edges reveal some porosity in the scale. This is illustrated in Fig. 13a, which shows the fractured edge of the oxide scale on a specimen oxidized for 22 hr in 10^5 Pa at 1075°C . There is no clearly delineated layered structure which reflects each individual change in the kinetics; rather relatively large pores are distributed throughout the outer layer of the scale.

Figure 13b shows a detail of the surface of the metal and the inner surface of the scale. The metal surface is partly covered with oxide. But also here it is suggested that there has been a gap at temperature between the metal and the oxide scale over most of the surface. There is also considerable porosity in the oxide at the metal/scale interface.

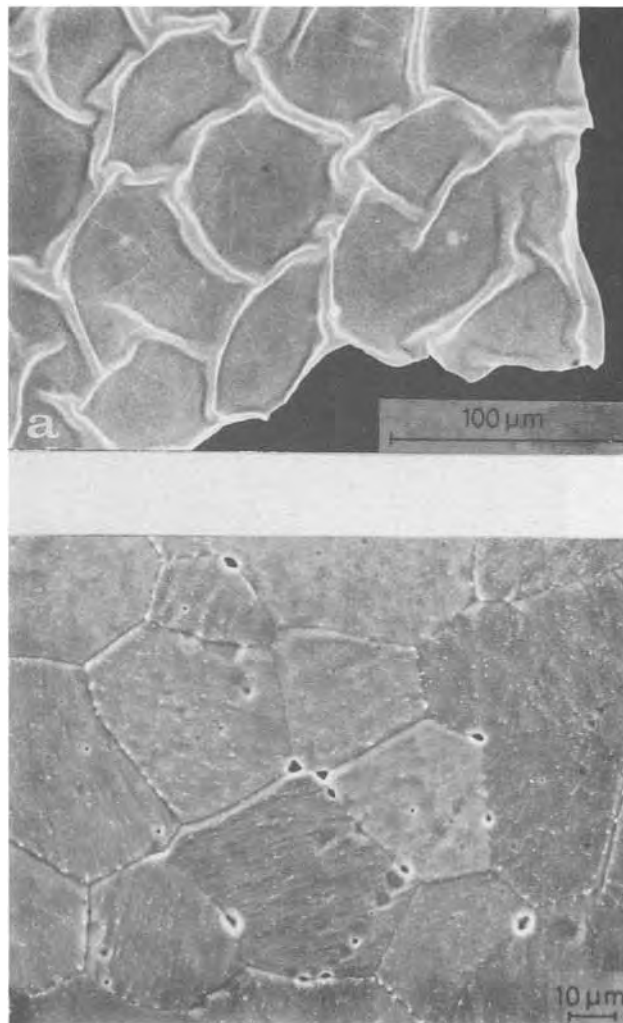


Fig. 11. (a) Scanning electron micrograph of fractured edge of Cr_2O_3 after oxidation for 3 hr at 800°C and $7 \cdot 10^{-2}$ Pa O_2 ; (b) scanning electron micrograph of surface of thermally etched and annealed chromium prior to oxidation.

After more extended oxidation at 10^5 Pa O_2 at and above 1000°C the individual oxide grains appear to be single crystals. This is illustrated in Fig. 14a, where oxide crystals from an area within the scale close to the inner surface are shown. The micrograph is taken from the specimen shown in Fig. 13. The individual crystals have a shape consistent with hexagonal structure. But it is also interesting to note that the shape of the crystals at the inner surface of the scale appear to reflect a cubic symmetry (Fig. 14b). This probably reflects the presence of a crystal layer different from Cr_2O_3 . It is tentatively concluded that these crystals consist of CrO, as one of its modifications has the NaCl structure. X-ray diffraction studies were made directly on the inner surface of the scale, but these failed to reveal any diffraction lines other than those of Cr_2O_3 . This may reflect that CrO is only present in small amounts or that CrO disproportionates or has been oxidized to Cr_2O_3 on exposure to the atmosphere.

It is also important to note that the Cr_2O_3 scales formed during extended oxidation at and above 1000°C , and involving one or more breakdowns of the scale, do not spall during cooling to room temperature. Although there is a loss of contact between the scale and the metal during cooling, the scales are retained on the specimens. This feature suggests that the breakdown of the scale alleviates growth stresses in the scale. Increased creep and plastic flow of the oxide

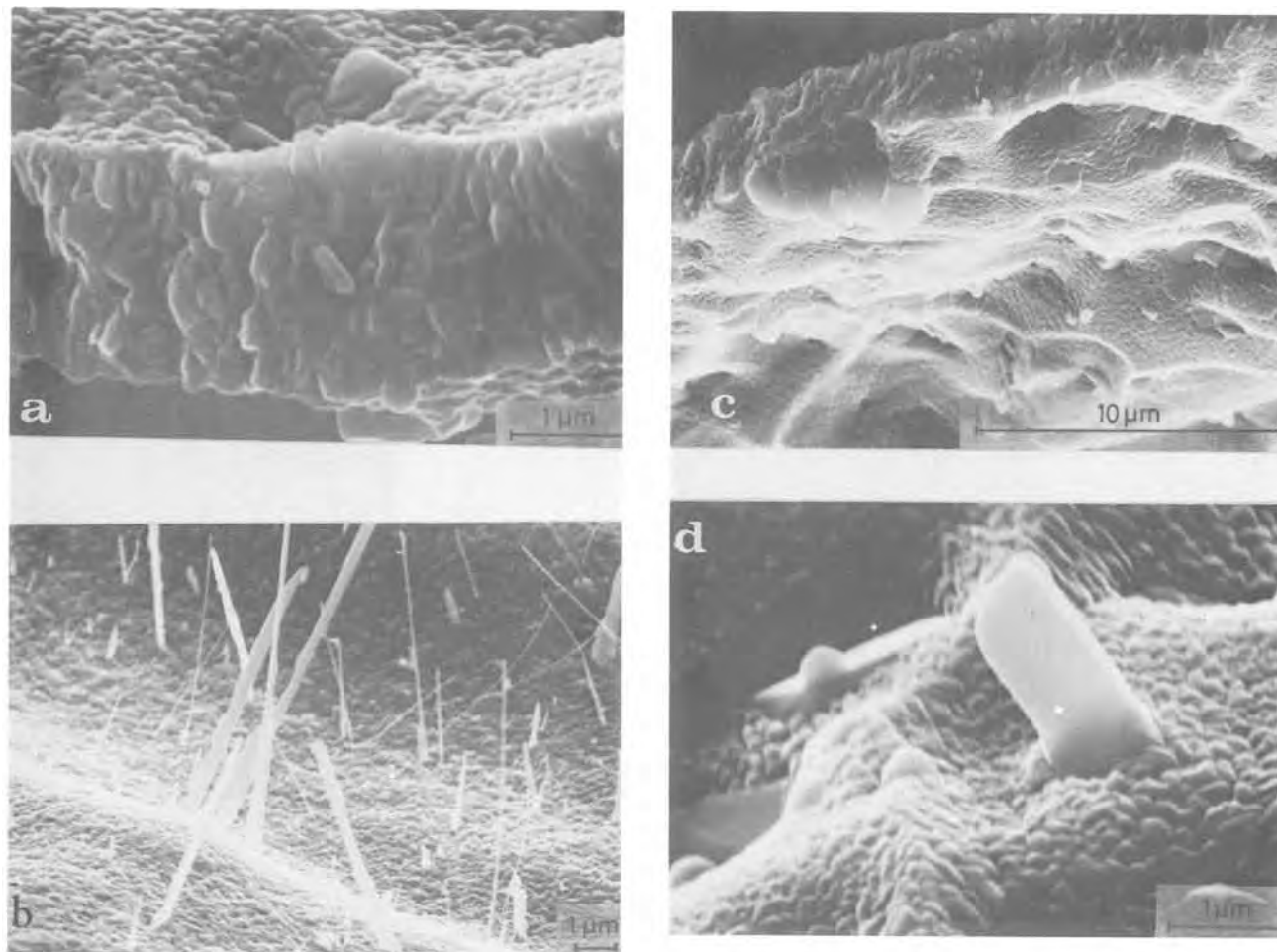


Fig. 12. (a) Scanning electron micrograph of fractured edge (cross section) of Cr_2O_3 scale after oxidation for 96 hr at 800°C and $7 \cdot 10^{-2}$ Pa O_2 (Fig. 11); (b) part of the outer surface of the scale shown in (a) showing examples of whisker growth; (c) part of the inner surface of the scale in (a); (d) Figure (c) at higher magnification.

with higher temperature will probably also be a contributing factor (19).

Exposure at reduced oxygen pressures.—The changes in the kinetics and oxidation rates when chromium is exposed to different oxygen pressures are directly associated with changes in the mode of oxide growth. Different aspects are illustrated by the scanning electron micrographs given in Fig. 15-22. In general the same features are observed at both 1000° and 1075°C .

There are marked differences in the surface appearance of specimens oxidized at different oxygen pressures. This is illustrated in Fig. 15a-c, which show scanning electron micrographs at low magnification of specimens reacted at 1075°C at 10^5 , 130 , and $7 \cdot 10^{-2}$ Pa O_2 , respectively.

After oxidation at about 100 Pa O_2 the surface has an uneven appearance. It is best described and illustrated by a view at higher magnification. This is given in Fig. 16, which shows the fractured edge of the oxide on a specimen oxidized for 23 hr at 1000°C and 100 Pa O_2 . The oxide is heavily buckled and deformed. This indicates that large growth stresses are produced during the scale growth. Compared to 10^5 Pa O_2 , the oxide formed at this lower oxygen pressure is considerably more deformed and the stresses are partially alleviated by this process.

But closer examination also shows that the oxide cracks in numerous sites during oxidation. This is illustrated in Fig. 17a and b. Figure 17a shows a detail where cracking has occurred just before the oxidation was stopped. The cracking always occurs on the inside of the layer; when viewed from the outside there is no evidence of cracks. Figure 17b

shows another detail where a crack has been healed by further deformation and secondary oxide growth.

The approximately linear kinetics observed under these conditions are concluded to reflect that a large number of cracks are being formed during the course of oxidation. The higher oxidation rate at this pressure range than at 10^5 Pa O_2 is probably due to penetration of oxygen gas at the cracks before these are healed. This is further corroborated by the fact that oxide crystals are being formed also on the metal surface under these reaction conditions. This may be seen in Fig. 16 and at a higher magnification in Fig. 18. It may be noted that the oxide crystals on the chromium metal surface have an external geometry characteristic of compounds with a cubic metal structure. The same cubic crystals were observed at 10^5 Pa, and are tentatively concluded to consist of CrO . These cubic oxide crystals are found in varying amounts at the chromium metal surface on all specimens examined in this work. But they are particularly observed in the pressure range with the relatively high oxidation rates caused by cracking of the scales (Fig. 16-18).

When the oxidation is carried out at even lower oxygen pressures (< 100 Pa), the oxide scales grow detached from the larger, plane surfaces of the specimens. The scales bulge away from the metal surface; an example of this is shown in Fig. 16c. The scales exhibit a high degree of plasticity. A particularly remarkable example of this is shown in Fig. 19 which refers to a specimen oxidized at 1075°C and $7 \cdot 10^{-2}$ Pa O_2 . In this case the scale has sagged giving the specimen a pear-shaped appearance.

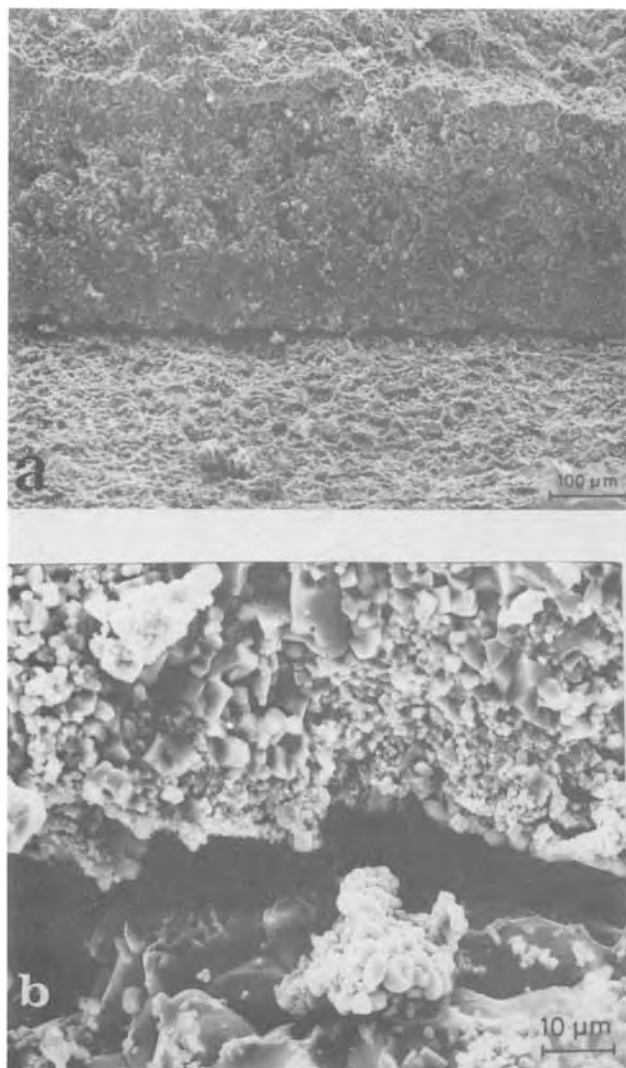


Fig. 13. Scanning electron micrograph of chromium specimen oxidized for 22 hr at 1075°C and 10^5 Pa O_2 , (a) fractured edge of the oxide scale on the metal surface. The outer part of the scale contains appreciable porosity in the form of voids; (b) detail of (a) showing the inner surface of the scale and the surface of the metal.

Figure 20a shows the cross section (fractured edge) of the scale from a specimen oxidized for 23 hr at 1075°C and $7 \cdot 10^{-2}$ Pa O_2 . Such scales showed no evidence of cracking. The crystallite size changes gradually through the scale from relatively fine-grained at the outer surface (Fig. 20b) to more coarse-grained in the inner part of the scale (Fig. 20c). The fine-grained microstructure and smooth surface gave the specimens a shiny appearance.

For specimens oxidized at 1000° and 1075°C and at $7 \cdot 10^{-2}$ Pa O_2 single crystals of chromium metal were observed on the inner surface of the oxide scale. This feature is illustrated in Fig. 21a and b. This clearly illustrates the importance of chromium vapor transport across the gap between the metal and the bulging oxide scale. It may be noted that the chromium crystals are located at one end (the lower end) of the specimen. This feature, and the relatively large amount of chromium crystals, suggests that there has been a vapor transport of chromium as a result of a temperature gradient along the specimen. The amount of chromium crystals is too large to be explained by the condensation and crystallization of the chromium metal vapor present in the cavity between the metal and the oxide scale during cooling of the specimen to room temperature when the oxidation run was discontinued.

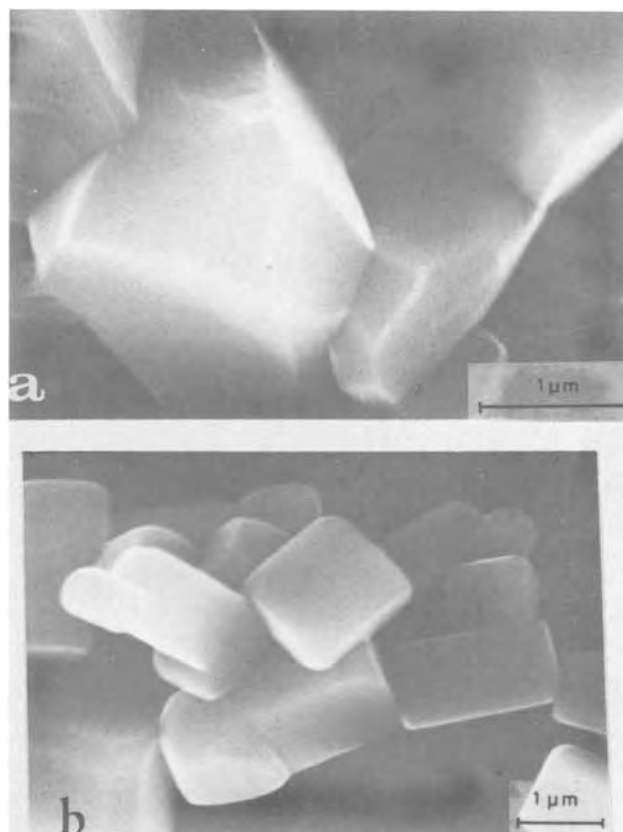


Fig. 14. Scanning electron micrograph of chromium specimen shown in Fig. 13; (a) detail of crystal morphology a few crystal layers away from the inner surface; (b) detail of crystal morphology of crystals at inner scale surface.

It was furthermore found that threadlike oxide crystals or whiskers were formed on some areas of the inner surface of the scale. This is illustrated on Fig. 22a. At these areas the inner crystal layer had poorly developed crystals. In other areas, however, this type of oxide growth was almost absent, and here the crystal facets were better developed. This feature is illustrated in Fig. 22b.

Discussion

In this work the oxidation of annealed, thermally etched chromium has been studied in the temperature range 800°-1100°C at different oxygen pressures ranging from 10^5 to $7 \cdot 10^{-2}$ Pa. During the thermal etching the specimens are stress-relieved, and approximately 12 μ m of the outer layer of the specimens were removed through chromium evaporation prior to the start of the oxidation. This pretreatment gives remarkably reproducible results. It is different from previously reported studies where a number of other pretreatments have been used: mechanical polishing, electropolishing, etching, etc. Such pretreatments have been demonstrated to have large effects on subsequent oxidation behavior (11-15).

This study shows that chromium exhibits remarkable changes in the oxidation behavior when exposed to different oxygen pressures, particularly at and above 1000°C. Important general features are that large stresses develop in the scale during the oxide growth and that the ability of the scale to deform plastically increases dramatically with decreasing partial pressure of oxygen. The Cr_2O_3 scales may crack, wrinkle, or balloon depending upon the reaction conditions. On prolonged oxidation oxide scales become detached from the metal substrate.

A major change in the kinetics takes place between 800° and 900°C. At 10^5 Pa O_2 and 800°C the kinetics may be described as approximately logarithmic. At

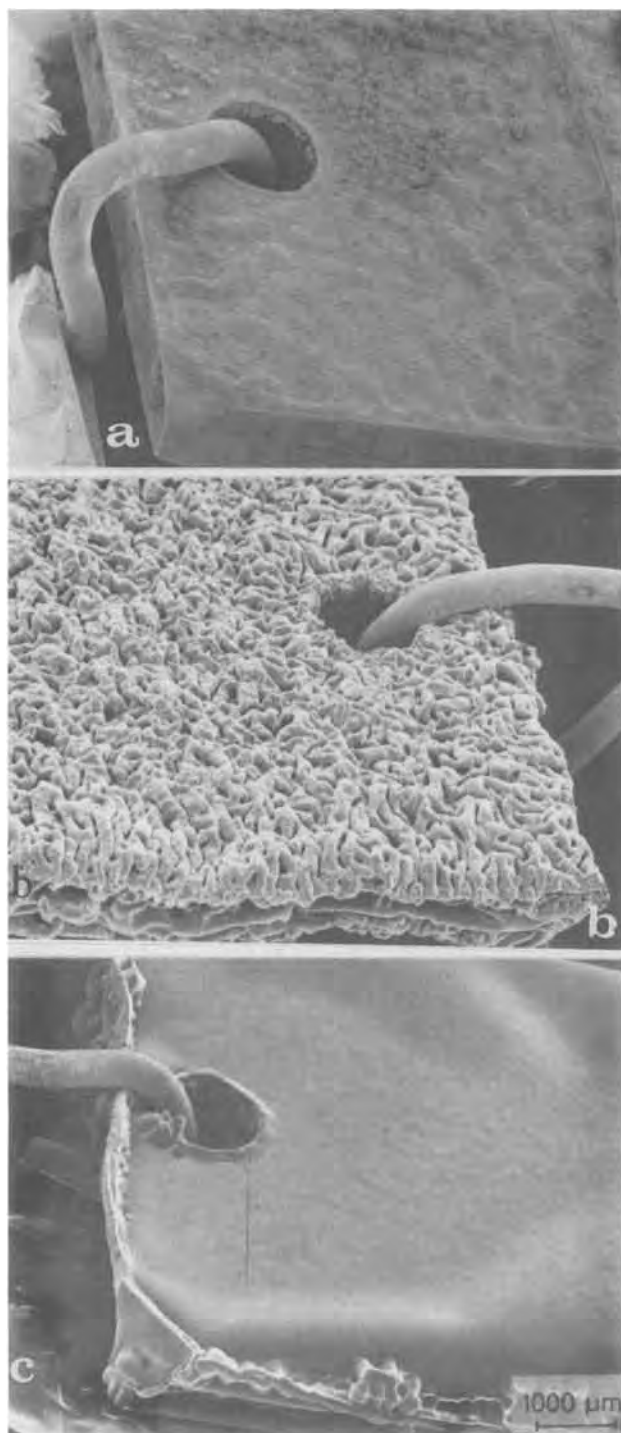


Fig. 15. Scanning electron micrographs ($15\times$) of chromium specimens oxidized at 1075°C : (a) 10^5 Pa O_2 for 25 hr, (b) 130 Pa O_2 for 43 hr, (c) $7 \cdot 10^{-2}$ Pa O_2 for 72 hr.

900°C the oxidation is approximately parabolic within the time periods studied. This also applies to the initial oxidation at 1000° and 1075°C , but with increasing oxide thickness the oxidation exhibits abrupt changes which reflect cracking and breakdown of the scale. New protective oxide is formed, and the overall oxidation takes the form of a sequence of protective oxidation stages. The oxide scale formed under these conditions exhibits but small ability to deform plastically. It may also be noted that the oxidation at 800°C is much faster than would be expected if the oxidation behavior at the higher temperatures were extrapolated to 800°C .

When the oxidation at 800°C is carried out at decreasingly lower oxygen pressures, the period of

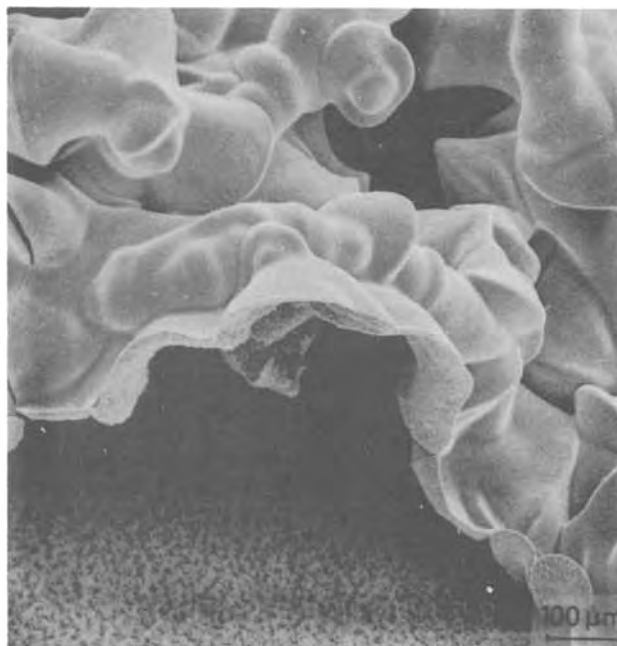


Fig. 16. Scanning electron micrograph of Cr_2O_3 scale after oxidation for 23 hr at 1075°C and 100 Pa O_2 . The picture shows the buckled, heavily deformed outer scale and a fine-grained oxide on the metal surface.

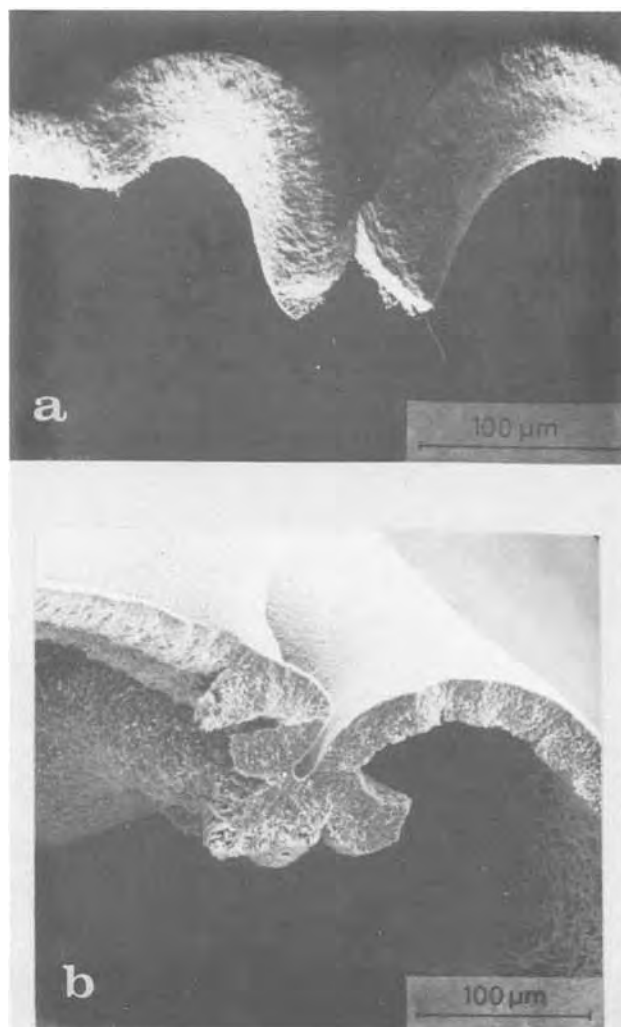


Fig. 17. Details of Fig. 16: (a) region where cracking has occurred just before oxidation was discontinued, (b) region where crack has been healed by further deformation and secondary oxide growth.

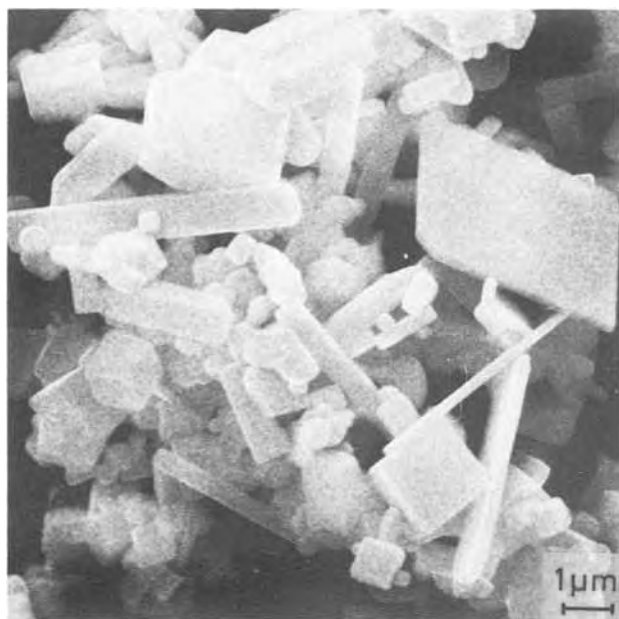


Fig. 18. Scanning electron micrograph of oxide crystals on metal surface of specimen shown in Fig. 7. Note external geometry characteristic of cubic crystal structure.

initial rapid oxidation becomes shorter. At pressures down to about 10 Pa the oxidation rate becomes slow and almost nil after extended oxidation. However, as the oxygen pressure is decreased to $7 \cdot 10^{-2}$ Pa the oxidation is approximately linear, and after extended oxidation may become faster than at the higher oxygen pressures. The oxide scale shows increasing ability to deform plastically with decreasing partial pressure of oxygen.

At and above 1000°C the oxidation increases as the oxygen pressure is reduced from 10^5 Pa to the pressure of about 100 Pa O_2 . Under the latter conditions the oxidation rate is approximately linear. This is associated with the formation of a large number of cracks that are continuously and statistically formed and subsequently healed during the oxide growth. To some extent this allows oxygen penetration through the detached oxide scale and formation of new oxide at the metal surface.

As the oxygen pressure is further decreased the ability of the oxide to deform plastically becomes sufficiently large that the scale no longer cracks or breaks down. Rather, due to the large growth stresses, the oxide deforms and bulges away from the metal surface. The scale is single-layered and continuous. The oxidation is slower than at pressures of about 100 Pa O_2 . At $7 \cdot 10^{-2}$ Pa O_2 the oxidation can be described as approximately linear. It is also to be noted that the oxide scale under these conditions is more fine-grained than at higher oxygen pressures.

In order to interpret the reaction behavior under various conditions it is necessary to consider various features and questions: (i) what are the mechanisms of transport of the reactants through continuous Cr_2O_3 scales? Where does the oxide formation take place? (ii) Why does the deformability of the Cr_2O_3 scales increase with decreasing partial pressure of oxygen? (iii) Does chromium transport across the gap between the metal and the scale limit the rate of reaction? An overall interpretation clearly must be based on a thorough knowledge of the defect structure and defect-dependent properties of Cr_2O_3 . In this respect it is considered useful to review the properties of Cr_2O_3 . This will be presented in Part II of this work (19).

At this stage it will be provisionally concluded from the results that transport of both chromium and

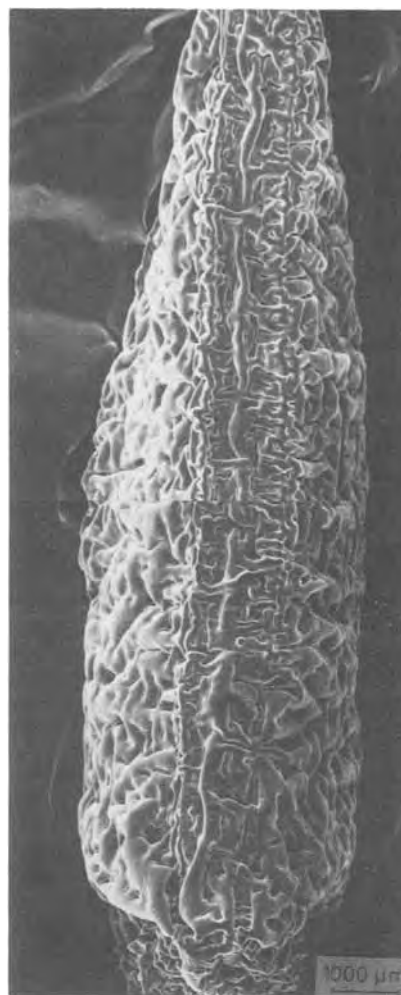


Fig. 19. Appearance of chromium specimen oxidized for 26 hr at 1075°C and $7 \cdot 10^{-2}$. The detached scale has deformed and given the specimen a pear-shaped appearance.

oxygen through the scale is important during growth of continuous Cr_2O_3 scales. Furthermore, the transport may take place by lattice diffusion and along microcracks and grain boundaries in the scale. This conclusion is based on the observations that large growth stresses develop in the scale and that the oxide not only grows normal to, but also horizontally along the metal surface—i.e., oxide formation also takes place within the oxide scale. The extensive deformations of the scales also suggest that both chromium and oxygen atoms are mobile species in the lattice. In previous studies of growth of Cr_2O_3 scales it has also been concluded that transport of the reactants may take place by various paths. Caplan *et al.* (6-10) have for instance suggested that Cr_2O_3 grows by both lattice and grain boundary diffusion and specifically propose that chromium diffuses outwards by lattice diffusion and that oxygen moves inwards along grain boundaries (9).

Without going into further details as to the defect-dependent properties of Cr_2O_3 , two features of the oxidation behavior may be discussed at this point: (i) the mechanism of the logarithmic oxidation at 800°C and 10^5 Pa O_2 , and (ii) Cr transport across the gap between the scale and the metal substrate.

Logarithmic oxidation at 800°C and 10^5 Pa O_2 .—Logarithmic oxidation of chromium has been previously reported, but always for thin film formation of Cr_2O_3 at considerably lower temperatures (17). The unusual feature of the present results is that a logarithmic type behavior is observed at such a high temperature and for relatively thick scales ($>1 \mu m$

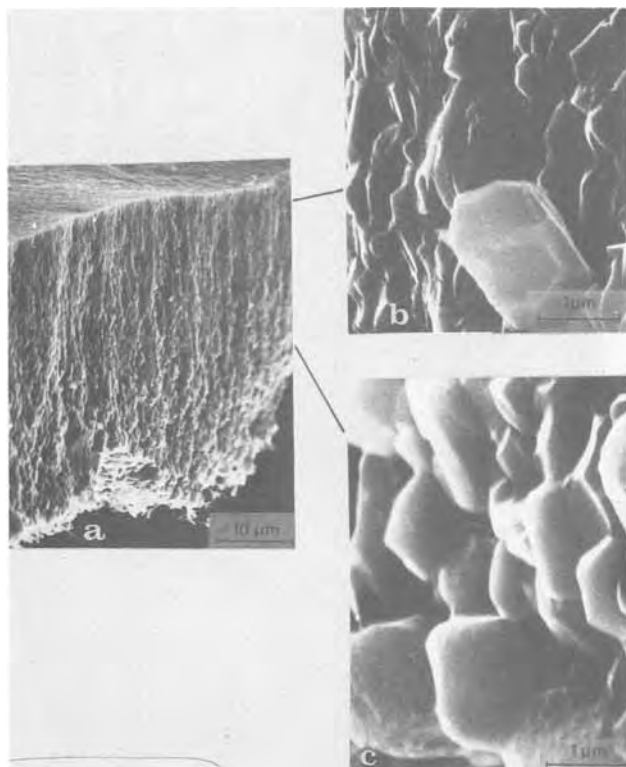


Fig. 20. Scanning electron micrograph of fractured edge of Cr_2O_3 scale after oxidation for 23 hr at 1075°C and $7 \cdot 10^{-2}$ Pa O_2 ; (b) detail of the outer part of the cross section in (a), (c) detail of the inner part of the cross section in (a).

thickness). This suggests that the thin film models, e.g., the Mott-Cabrera theory (17), cannot be applied in the present case. Furthermore, important changes take place in the scale during its growth.

Various mechanisms have been advanced to explain logarithmic-type kinetics or behavior where the reaction rate decreases faster with time than for

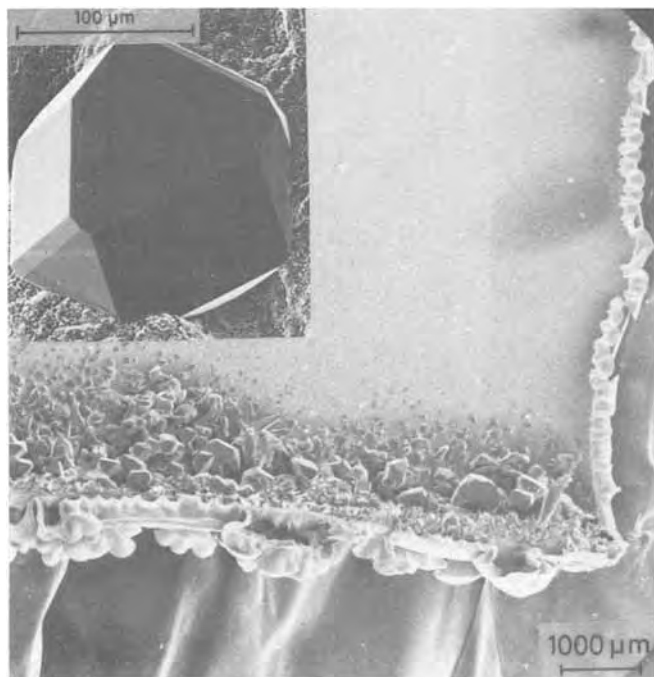


Fig. 21. Scanning electron micrograph of single crystals of chromium on the inner surface of detached Cr_2O_3 scale after oxidation for 72 hr at 1000°C and $7 \cdot 10^{-2}$ Pa ($15\times$). The insert shows a single crystal at higher magnification ($600\times$).

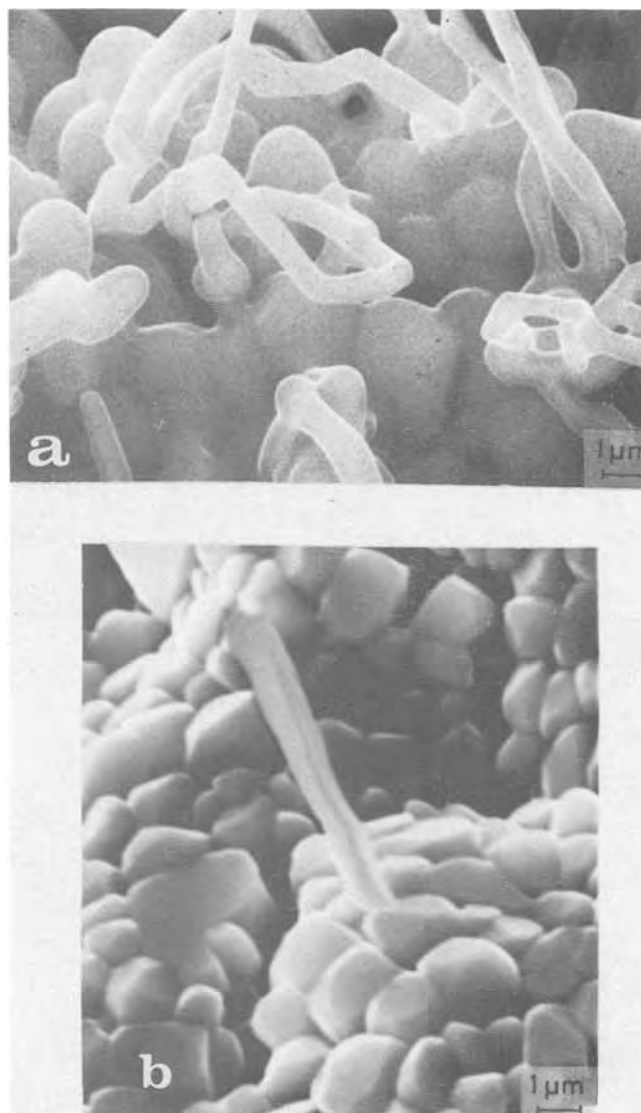


Fig. 22a. Scanning electron micrograph of threadlike oxide crystals on the inner surface of detached Cr_2O_3 scale after oxidation for 24 hr at 1075°C and $7 \cdot 10^{-2}$ Pa O_2 ; (b) different area of specimen shown in (a) with better developed crystal facets and whiskers.

parabolic oxidation. These models often involve transport of reacting atoms or ions along grain boundaries, dislocations, or lines of disarrayed atoms and that these diffusion paths gradually become blocked, deactivated, or annealed out with time (2, 29, 30). An alternative model by Evans (29) assumes that only part of the film thickens, as may occur, for instance, if cavities, voids, or obstructions develop during oxide growths and thereby continuously shrinks the area of the scale through which solid-state transport may take place. An example in case is development of cavities at the metal/oxide interface due to outward migration of cations through the scale.

The logarithmic type behavior in this study is associated with two main features as regards the scale growth: (i) a gradual detachment of the scale from the metal substrate, and (ii) an increased grain growth and developments of crystal facets on the grains during the oxidation. Both features may give rise to a rapidly decreasing reaction rate with time.

If the gradual detachment is the important factor that determines the kinetics, it is implied that the supply of gaseous chromium across the gap eventually becomes the rate-limiting factor. However, such an interpretation does not conform with the results at

the lower oxygen pressure ($7.2 \cdot 10^{-2}$ Pa) at 800°C. In this case the scale detachment is even more pronounced than at 10^5 Pa O_2 ; the oxidation rate is essentially linear and eventually becomes faster than at 10^5 Pa O_2 . The results at the lower oxygen pressure thus suggest that a limited chromium supply is not the reason for the logarithmic type behavior.

An alternative interpretation is that the logarithmic type behavior is related to the grain growth in the scale during oxidation. This implies that transport via easy diffusion paths is particularly important during initial oxidation, and that their concentration gradually decrease with time through the grain growth. Such an interpretation is also qualitatively in accord with the fact that the initial oxidation is relatively high at 800°C compared to what would be expected if the oxidation rates at the higher temperatures are extrapolated to 800°C. Qualitatively one expects that the size of oxide nuclei and crystallites increase with increasing temperature.

Cr transport across the gap between the scale and the metal substrate.—The results at the lower oxygen pressure at 800°C and the latter interpretation of the logarithmic type behavior implies that there is sufficient chromium at the inner surface of the detached scale. In this respect it is of interest to estimate the rate of supply of gaseous chromium by chromium evaporation from the metal substrate.

At the highest temperatures (1000° and 1075°C) and reduced oxygen pressures single crystals of chromium are found on the inner surface of the oxide scale. Under these conditions the vapor pressure of chromium is sufficiently high to explain the oxidation rates. Thus at 1075°C the linear rate of oxidation at $7 \cdot 10^{-2}$ Pa O_2 is approximately 0.2 mg O/cm^2 hr. This corresponds to a consumption of 0.43 mg Cr/ cm^2 hr. By use of the Herz-Langmuir equation an estimate of the rate of evaporation of chromium yields 0.47 mg/ cm^2 hr. If the chromium metal surface is faceted, the rate of evaporation may be higher by at least a factor of 2. Thus the supply of chromium vapor is sufficiently large under these conditions.

At 800°C the situation is different. At $7 \cdot 10^{-2}$ Pa O_2 the linear oxidation rate is approximately $1 \cdot 10^{-2}$ mg O/cm^2 hr, while the estimated rate of evaporation of chromium by means of the Herz-Langmuir equation is only $8.7 \cdot 10^{-5}$ mg Cr/ cm^2 hr. Thus even for a highly faceted chromium metal surface, the rate of supply of chromium metal vapor would not be sufficiently high to sustain the oxidation.

This discrepancy cannot be satisfactorily explained at present. One may speculate if an enhanced rate of evaporation from the chromium metal substrate in the form of a Cr-O molecule may take place at the low partial pressures of oxygen existing in the gap between the scale and metal. Is the presence of cubic oxide crystals (tentatively suggested to consist of CrO) at the inner oxide surface related to such an enhanced evaporation? According to available thermodynamic data for the vapor species of various chromium oxides in equilibrium with Cr and Cr_2O_3 such an enhanced evaporation would not be expected (23, 31, 32). However, when the scale is detached from the chromium metal over most of the surface, Cr and Cr_2O_3 are not necessarily in equilibrium, and conditions for enhanced evaporation could possibly exist. It may be noted that Fryburg *et al.* (25) observed enhanced oxidative vaporization of chromium at temperatures below 800°C in 15 Pa O_2 containing 2.5% oxygen atoms. The atomic oxygen is the "reactive" component, and these results cannot be directly translated to the conditions existing in the gap between the metal and the scale. But the study may indicate that an easily evaporated Cr-O specie can be formed at reduced pressures at temperatures below 800°C.

As regards the results of the present study it would be of interest to obtain further information on the conditions favoring the formation of the cubic oxide crystals, e.g., by studies of oxidation of chromium at very reduced oxygen pressures.

Acknowledgment

Part of this study has been carried out under a project supported by the Royal Norwegian Council for Scientific and Technical Research.

Manuscript submitted Dec. 26, 1979; revised manuscript received July 9, 1980.

Any discussion of this paper will appear in a Discussion Section to be published in the June 1981 JOURNAL. All discussions for the June 1981 Discussion Section should be submitted by Feb. 1, 1981.

REFERENCES

- O. Kubaschewski and B. E. Hopkins, "Oxidation of Metals and Alloys," Butterworths, London (1962).
- P. Kofstad, "High-Temperature Oxidation of Metals," Wiley, New York (1966).
- S. Mrowec and T. Werber, "Gas Corrosion of Metals," publ. for National Bureau of Standards and the National Science Foundation by the Foreign Scientific Publications, Department of the National Center for Scientific, Technical and Economic Information, Warsaw, Poland (1978).
- P. Kofstad, "Nonstoichiometry, Diffusion, and Electrical Conductivity in Binary Metal Oxides," Wiley-Interscience, New York (1972).
- W. H. Hatfield, *J. Iron Steel Inst.*, **115**, 483 (1927).
- E. A. Gulbransen and K. F. Andrew, *This Journal*, **99**, 402 (1952).
- C. A. Phalnikar, E. B. Evans, and W. M. Baldwin, Jr., *ibid.*, **103**, 429 (1956).
- E. A. Gulbransen and K. F. Andrew, *ibid.*, **104**, 334 (1957).
- W. C. Hagel, *Trans. Am. Soc. Met.*, **56**, 583 (1963).
- L. Cadiou and J. Paidassi, *Mem. Sci. Rev. Metall.*, **66**, 217 (1969).
- D. Caplan and M. Cohen, *This Journal*, **112**, 5 (1964).
- D. Caplan, A. Harvey, and M. Cohen, *ibid.*, **108**, 134 (1961).
- D. Caplan, A. Harvey, and M. Cohen, *Corros. Sci.*, **3**, 161 (1963).
- D. Caplan and G. I. Sproule, *Oxid. Met.*, **9**, 5 (1975).
- D. Caplan and M. Cohen, *This Journal*, **108**, 438 (1961).
- E. I. Alessandrini, *J. Vac. Sci. Technol.*, **9**, 83 (1972).
- D. J. Young and M. Cohen, *This Journal*, **124**, 775 (1977).
- T. F. Kassner, L. C. Walters, and R. E. Grace, in "Proc. of Symposium on Thermodynamics with Emphasis on Nuclear Materials and Atomic Transport in Solids," IAEA, Vienna (1966).
- P. Kofstad and K. P. Lillerud, *This Journal*, **127**, 2410 (1980).
- T. Rakke, Private communications.
- H. W. Werner, H. A. M. de Grefte, and J. van den Berg, *Adv. Mass. Spectrom.*, **6**, 673 (1974).
- M. Hansen and K. Anderko, "Constitution of Binary Alloys," McGraw-Hill, New York (1958).
- C. A. Stearns, F. J. Kohl, and G. C. Fryburg, *This Journal*, **121**, 945 (1974).
- H. C. Graham and H. H. Davis, *J. Am. Ceram. Soc.*, **54**, 89 (1971).
- C. A. Stearns, F. J. Kohl, and G. C. Fryburg, *This Journal*, **121**, 952 (1974).
- R. A. Rapp, AGARD Conference Proceedings No. 120 on "High Temperature Corrosion of Aerospace Alloys, 1972."
- H. Speiser, H. I. Johnston, and P. Blackburn, *J. Am. Chem. Soc.*, **72**, 4142 (1950).
- P. Kofstad and S. Espevik, *J. Less-Common Metals*, **12**, 382 (1967).
- U. R. Evans, "The Corrosion and Oxidation of Metals," Edward Arnold, Ltd., London (1960).
- W. W. Smeltzer, R. R. Haering, and J. S. Kirkaldy, *Acta Metall.*, **9**, 880 (1961).

31. S. A. Jansson and E. A. Gulbransen, 4th International Congress on Metallic Corrosion, Amsterdam, September 1969.

32. E. A. Gulbransen and S. A. Jansson, in "Oxidation of Metals and Alloys," American Society for Metals (1971).

On High Temperature Oxidation of Chromium

II. Properties of Cr_2O_3 and the Oxidation Mechanism of Chromium

P. Kofstad and K. P. Lillerud

Department of Chemistry, University of Oslo, Blindern, Oslo 3, Norway

ABSTRACT

Chromium specimens oxidized at 1000°-1100°C and at different oxygen pressures (10^5 - $7 \cdot 10^{-2}$ Pa O_2) have been treated in high vacuum at temperature as a direct continuation of the oxidation runs. All specimens lost weight during the high vacuum treatment. During an initial period the rate of weight loss slowly decreased, but after longer time the loss rate became essentially linear. It is concluded that the weight loss is due to chromium evaporation due to chromium transport through the scales by lattice diffusion and transport along paths of easy diffusion and microcracks. On the basis of the properties of Cr_2O_3 scales and available literature data on defect-dependent properties of Cr_2O_3 , a defect structure model has been proposed for the oxide. It is proposed that interstitial chromium ions are the predominating point defects at partial pressures of oxygen near the Cr/ Cr_2O_3 phase boundary. At near-atmospheric pressures the oxide is an intrinsic electronic conductor. Parabolic rate constants calculated from the diffusion data and the proposed defect structure model are compared with experimental values. The oxidation mechanism of chromium is discussed. Important factors are lattice diffusion, transport along paths of easy diffusion and microcracks through the scale, growth stresses in the scale, the ability of the scale to deform, and vapor transport from the metal substrate to detached scales.

Part I of this work describes studies of oxidation of annealed, thermally-etched chromium in the temperature range 800°-1100°C at different oxygen pressures ranging from 10^5 to $7 \cdot 10^{-2}$ Pa (1). This paper, Part II, presents results on high vacuum treatment of oxidized chromium specimens and discusses the properties and defect structure of Cr_2O_3 as a basis for an overall consideration of the high temperature oxidation mechanism of chromium.

A literature survey of oxidation of chromium and a description of materials and methods have been given in Part I (1).

High Vacuum Treatment of Oxidized Specimens

Thermogravimetric measurements.—If the oxidation runs at and above 1000°C (1) were discontinued by pumping high vacuum on the system while keeping the specimens at temperature, it was found that the oxidized specimens began to lose weight. A few specimens were therefore treated in high vacuum after oxidation and their weight losses were recorded for extended periods. During this treatment the vacuum, as measured with an ionization or Penning gauge located just outside the furnace region, was $<10^{-3}$ Pa.

Figure 1 shows an example of the weight loss as a function of time for specimens oxidized at 1100°C. During an initial period of the high vacuum treatment the rate of weight loss slowly decreased, but after longer time the loss rate became essentially linear with time. Provided sufficiently good vacuum was maintained, all specimens continued to lose weight within the time periods studied. The vacuum treatments were in some cases continued for several hundred hours.

All specimens lost weight irrespective of prior oxidation conditions. But differences in weight loss were observed. For instance, for specimens oxidized at 10^5 Pa and 1100°C the rate of weight loss was smaller if the

high vacuum treatment was started before the first major breakdown of the scale [as noted by sudden weight gain in the oxidation curves (1)], than for specimens oxidized past the first "breakdown" stage.

If the temperature was increased (e.g., from 1100° to 1200°C) during the high vacuum treatment, the rate of weight loss increased. But on return to the starting temperature (1100°C), the rate of weight loss was smaller than the original rate.

During the high vacuum treatment the cooler zones just outside the furnace were covered with a black-gray deposit, presumably consisting of chromium metal.

The rates of weight loss became too small to be detected accurately at temperatures below 1000°C.

Characterization of specimens.—Specimens which were oxidized in 10^5 Pa O_2 and subsequently high vacuum treated, exhibited no major change in surface

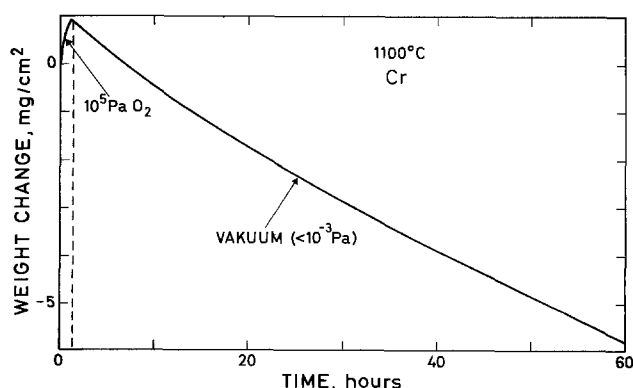


Fig. 1. Weight change of thermally etched Cr specimen during oxidation at 10^5 Pa O_2 at 1100°C and subsequent treatment in high vacuum.

and cross-sectional appearance as a result of the high vacuum treatment. But the specimens oxidized in $7 \cdot 10^{-2}$ Pa O_2 underwent marked changes in appearance. This is illustrated in Fig. 2a and b, which show specimens at the end of the oxidation and of the high vacuum treatment, respectively. During oxidation at $7 \cdot 10^{-2}$ Pa O_2 the oxide scale deforms and bulges away from the metal (1). During the high vacuum treatment this process continues. The oxide scale balloons out as shown in Fig. 2b. At the end of the oxidation the oxide at the scale/gas interface is extremely fine-grained (Fig. 3a), but after the subsequent high vacuum treatment the oxide grains have grown and have developed crystal facets (Fig. 3b). The same features are ob-

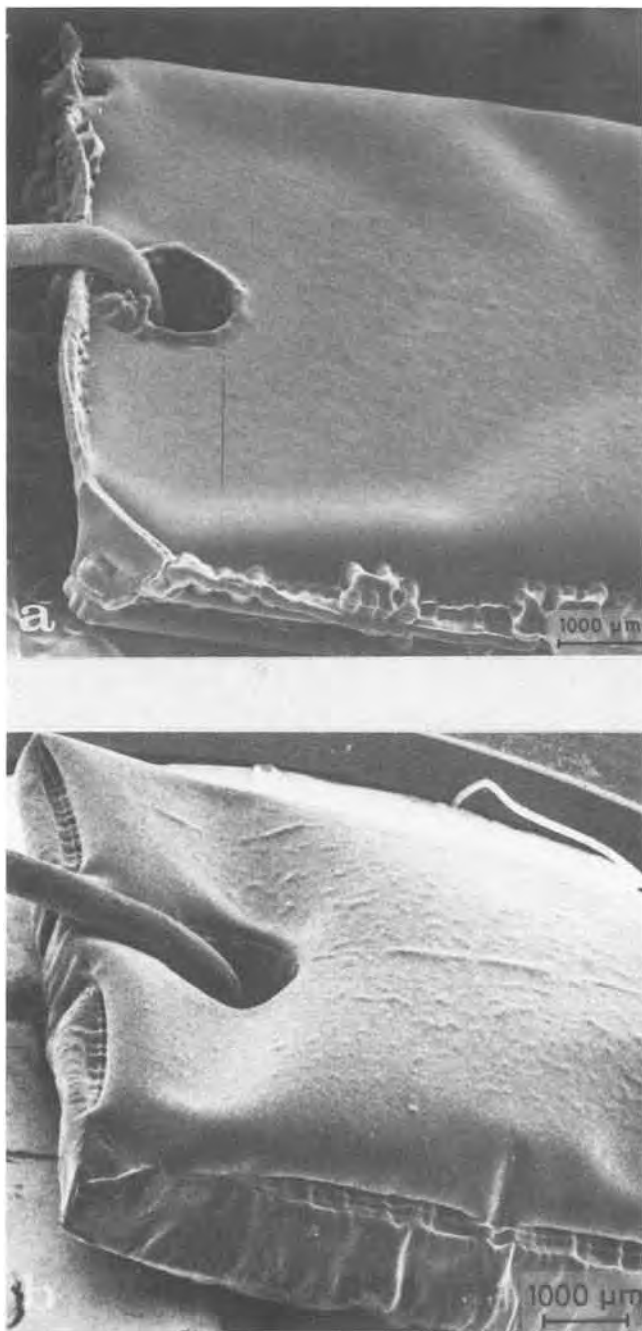


Fig. 2. Change in appearance of oxidized specimens after high vacuum treatment at temperature $15\times$. (a) Specimen appearance after oxidation at 1000°C and $7 \cdot 10^{-2}$ Pa O_2 for 72 hr; (b) appearance of a specimen after oxidation for 71 hr at 1000°C and $7 \cdot 10^{-2}$ Pa O_2 and subsequent treatment in high vacuum for 84 hr at the same temperature.

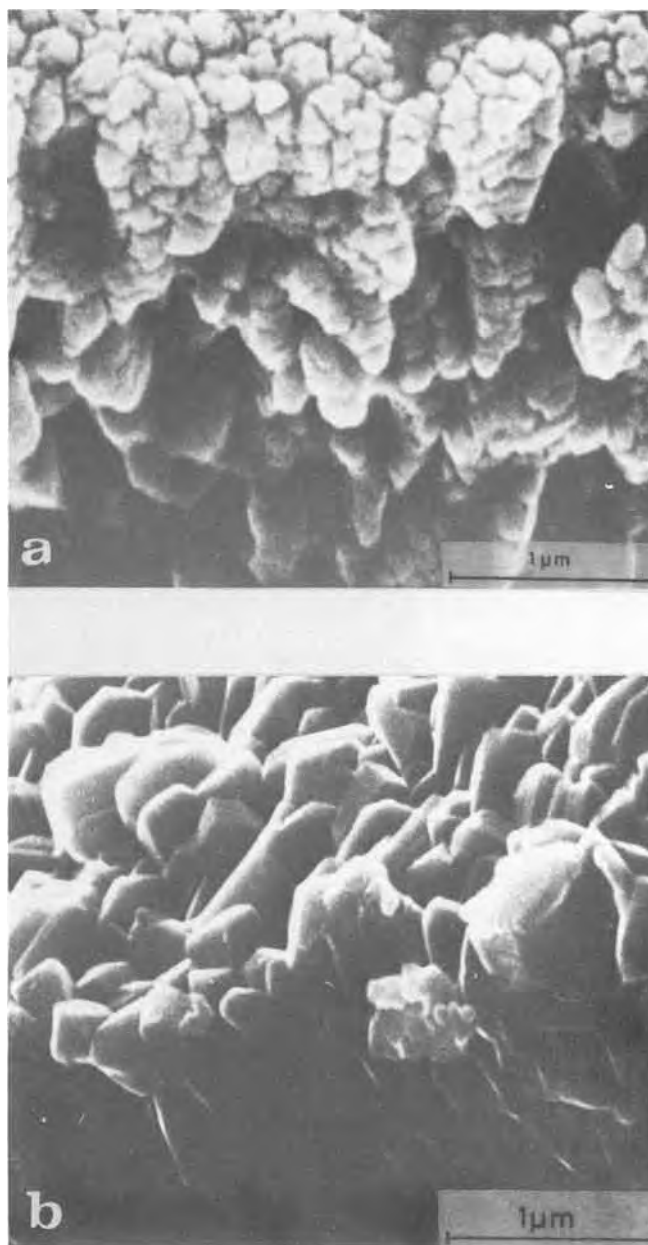


Fig. 3. SEM micrographs of the structure of the oxide scales at the gas/oxide interface after (a) oxidation for 25 hr at $7 \cdot 10^{-2}$ Pa O_2 at 1075°C ; (b) subsequent high vacuum treatment at 1075°C for 47 hr.

served at the inner surface of the scale. This is illustrated in Fig. 4a and b.

Discussion.—The deformation of the scale reflects further alleviation of growth stresses in the scale. During the high vacuum treatment the whole scale can be considered to be equilibrated with chromium metal, and the effective partial pressure of oxygen throughout the scale essentially becomes equal to the decomposition pressure of Cr_2O_3 in equilibrium with chromium metal. The results suggest that the ability of Cr_2O_3 to deform is even higher at this low partial pressure of oxygen than at higher ones.

The weight loss in all probability reflects loss of chromium metal. Chromium may penetrate the scale by lattice diffusion and by transport along grain boundaries, easy diffusion paths, and microcracks. The latter transport processes are concluded to be significant as evidenced by the gradual decrease in rate of weight loss during an initial period of the high vacuum

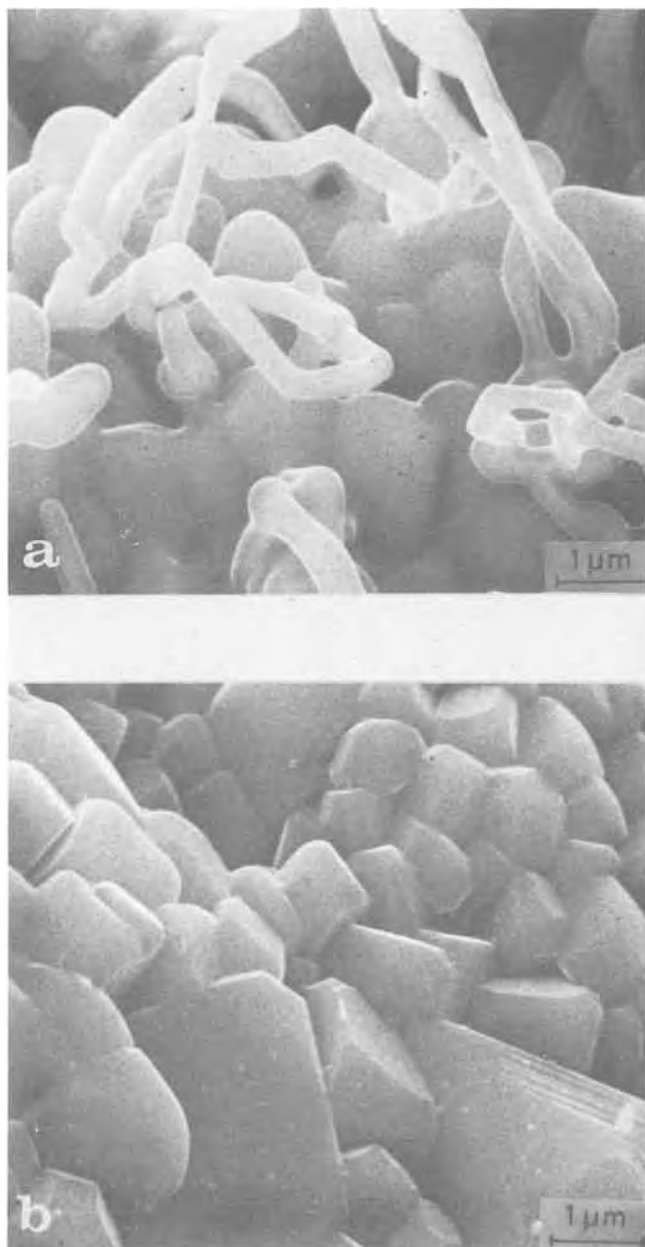


Fig. 4. SEM micrographs of the structure of the inner scale surface after (a) oxidation for 25 hr at $7 \cdot 10^{-2}$ Pa O_2 at 1075°C ; (b) subsequent high vacuum treatment at 1075°C for 47 hr.

treatment and the simultaneous increase in crystal perfection in the scale.

Defect-Dependent Properties of Cr_2O_3

An overall interpretation of the oxidation mechanism of chromium must be based on a thorough understanding of the defect structure and defect-dependent properties of Cr_2O_3 . It is appropriate therefore briefly to survey available data on Cr_2O_3 , and to attempt to interpret these in terms of a consistent model. A number of studies have been reported on electrical conductivity, diffusion, sintering, etc. (2).

Nonstoichiometry.—Variations in the deviation from stoichiometry in Cr_2O_3 at high temperatures and different partial pressures of oxygen are apparently small. So far it has proved difficult to determine experimentally (2). An added difficulty is that measurements at high oxygen pressures, where the largest weight changes are expected if chromium vacancies are the predominating defects, are also significantly influenced by evaporation of CrO_3 .

Hay (3,4) has attempted to measure variations in the deviation from stoichiometry at $950^\circ\text{--}1200^\circ\text{C}$ and near-atmospheric pressures by measuring the weight change of Cr_2O_3 specimens when changing the ambient oxygen pressure from one value to another. Small weight losses were observed when the oxygen pressure was decreased. The results were not sufficiently accurate to determine the exact oxygen pressure dependence of the weight loss, and accordingly no definite conclusion could be drawn as to the predominating defects. But by assuming that these are chromium vacancies, Hay estimated the extent of nonstoichiometry to be of the order of 10^{-4} vacancies per chromium site. It may be noted however, that regardless of whether the predominating defects are chromium or oxygen vacancies or interstitials, Cr_2O_3 specimens will lose weight when the partial pressure of oxygen is reduced. It appears that the only conclusion that can be drawn at this time is that the deviation from stoichiometry in Cr_2O_3 is "small" at near-atmospheric oxygen pressures.

Cojocar (5) has reported that Cr_2O_3 produced by heating CrO_3 for 4 hr at $673^\circ\text{--}1273^\circ\text{K}$ exhibited nonstoichiometry up to $x = 0.12$ in $\text{Cr}_{2-x}\text{O}_3$. The "nonstoichiometry" increased with decreasing temperature. These results probably do not represent equilibrium values for Cr_2O_3 .

Electrical conductivity (2,5-14).— Cr_2O_3 is an electronic semiconductor. When the electrical conductivity is measured as a function of temperature at near-atmospheric oxygen pressures, the behavior may be divided into two main regions: (i) a high temperature region above about $1000^\circ\text{--}1200^\circ\text{C}$ with activation energies reported to range from 155 to 175 kJ/mole (1.6-1.8 eV) and (ii) a low temperature region where the activation energy is much smaller. While the different results for the high temperature region are in reasonably good agreement, the results for the low temperature show large discrepancies.

It is generally concluded that the high temperature region reflects the intrinsic electronic equilibrium in the oxide (2,10-13). [Fe_2O_3 , which has the same crystal structure as Cr_2O_3 , is also probably an intrinsic electronic conductor (2).] The electrical conductivity is independent of the partial pressure of oxygen at near-atmospheric oxygen pressures. If one as a first approximation neglects the activation energy associated with the mobility of electrons/electron holes, the measured activation energy should be expected to be one-half of the value of the bandgap. This is reported to be 330 kJ/mole (3.4 eV), in satisfactory agreement with the conductivity measurements.

Hay *et al.* (4) have from measurements of thermoelectric power on Cr_2O_3 estimated that the concentration of electron holes is $2 \cdot 10^{17} \text{ mm}^{-3}$ at 1500°C . They conclude from their studies that the high temperature electrical conductivity cannot be intrinsic electronic conductivity. However, the concentration of electron holes may also be estimated from the equation

$$p \cdot n = K_i = 4 \left(\frac{2\pi kT}{h^2} \right)^3 (m_e \cdot m_h)^{3/2} \exp \left(- \frac{E_g}{kT} \right) \quad [1]$$

where k is the Boltzmann constant, h is the Planck constant, m_e and m_h the effective masses of electrons and electron holes, respectively, and E_g is the bandgap. If m_e and m_h are set equal to the rest mass of the electron, Eq. [1] gives a value of $p = 9 \cdot 10^{16} \text{ mm}^{-3}$, which is in reasonable agreement with the measured value.

The reason for the transition to the low temperature region is not clear. For sufficiently low temperatures a possible explanation is that the concentration of electronic defects produced by the intrinsic electronic equilibrium becomes so small that their concentration is determined by unavoidable impurities. When specimens are exposed to high temperatures in ceramic

tubes or chambers (2, 11), the majority of such impurities are lower valent, *e.g.*, Na, Ca, etc., and their presence may determine the concentration of electron holes, *e.g.*

$$[\text{Ca}'_{\text{Cr}}] = p \quad \text{or} \quad 2[\text{Na}'_{\text{Cr}}] = p \quad [2]$$

This may explain that "pure" Cr_2O_3 is found to be a p-type semiconductor in the low temperature region and that the measured electrical conductivities in this region may differ by several orders of magnitude from one study to another (2). It may also be noted that Cr_2O_3 becomes an n-conductor when doped with higher valent cations, *e.g.*, TiO_2 (11). This is the expected behavior if Ti is dissolved substitutionally, *e.g.*, $n = [\text{Ti}_{\text{Cr}}]$.

In the low temperature region the electrical conductivity may be dependent on the oxygen pressure if the lattice solubility of impurities or dopants vary with the oxygen pressure. It has alternatively been suggested that the electrical conductivity at the lower temperatures reflects a defect structure which is "frozen in" at the low temperatures (12).

Regardless of a detailed interpretation of the electrical conductivity, it appears that such results do not provide any clear-cut information as to the predominating point defects in Cr_2O_3 .

Self-diffusion.—Both ^{51}Cr - and ^{18}O -tracer diffusion studies have been made on Cr_2O_3 (12, 15-18). The reported values are summarized in Fig. 5.

Hagel and Seybolt (12) made their studies on hot-pressed and sintered specimens, respectively. The hot-pressing was performed in graphite dies. Owing to the strongly reducing conditions during the process, the

hot-pressed specimens contained some chromium metal. This was chemically determined to be in amounts of 0.1-0.2 weight percent (w/o) (12). The hot-pressed compacts had a density of 99.5% of the theoretical limit.

The sintered specimens were prepared by sintering in argon (with reported partial pressure of oxygen of about 10^{-1} Pa O_2) at 1700°C and had a density approaching 93.7%. The diffusion anneals were made in high purity nitrogen atmospheres with a reported partial pressure of oxygen of about 10^{-2} Pa O_2 . Thus the sintering and diffusion anneal were made at partial pressures of oxygen of 10^{-1} - 10^{-2} Pa O_2 .

As shown in Fig. 5 the self-diffusion coefficients of chromium were higher for the hot-pressed than for the sintered specimens. The activation energies were also different and amounted to 255 and 415 kJ/mole (61 and 100 kcal/mole), respectively. The tracer diffusion coefficients can be expressed as (12-15)

$$\text{sintered: } D = 4.3 \cdot 10^3 \exp(-415,000/RT) \quad [3]$$

$$\text{hot-pressed: } D^* = 0.167 \exp(-255,000/RT) \quad [4]$$

Lindner and Åkerström (15) have also studied self-diffusion of Cr in sintered Cr_2O_3 . As shown in Fig. 5 their results are in reasonable agreement with those of Hagel and Seybolt on the same type of specimens.

Hagel and Seybolt (12) believe that the results on the hot-pressed and more compact specimens represent the more correct value for the self-diffusion coefficient of chromium in Cr_2O_3 . However, this conclusion is surprising considering that the self-diffusion in the hot-pressed specimens are considerably higher than in the sintered specimens. If grain boundary diffusion were important in the less compact, sintered specimens, it would be expected that diffusion in the sintered specimens were higher. Contribution from grain boundary diffusion should also have been noted in the tracer penetration curves.

We would like to suggest a possible alternative explanation for the difference between the two types of specimens. Hagel and Seybolt report that the hot-pressed specimens contained some chromium metal. This suggests that the hot-pressed specimens had a nonstoichiometry approximately corresponding to that of Cr_2O_3 at the Cr/ Cr_2O_3 phase boundary, *i.e.*, the effective partial pressure of oxygen within the specimens was close to the decomposition pressure of Cr_2O_3 in equilibrium with chromium metal. The sintered specimens, on the other hand, were prepared and diffusion-annealed at partial pressures of oxygen of 10^{-1} - 10^{-2} Pa O_2 . If these are the important differences between the two types of specimens, one can conclude from these studies that the self-diffusion coefficient of Cr in Cr_2O_3 in this pressure range increases with decreasing partial pressure of oxygen. This cannot be explained by assuming that chromium vacancies are the predominating chromium point defects in Cr_2O_3 . Rather, it is reasonable to assume that the important cation defects are chromium interstitials at partial pressures of oxygen close to the decomposition pressure of Cr_2O_3 .

Walters and Grace (16) measured the self-diffusion in Cr_2O_3 single crystals at 1300°C in $\text{H}_2 + \text{H}_2\text{O}$ mixtures. The partial pressures of oxygen ranged from $1 \cdot 10^{-11}$ to $5 \cdot 10^{-11}$ Pa O_2 , which is close to the decomposition pressure of Cr_2O_3 at this temperature, $p_{\text{O}_2}^* = 5 \cdot 10^{-12}$ Pa. As shown in Fig. 5 their values agree with those of Hagel and Seybolt for the hot-pressed specimens. This is consistent with the above interpretation. It may be added that Walters and Grace interpreted their data on the basis of a Cr-vacancy model. This was based on measurements of the self-diffusion coefficients in the narrow pressure range from $1 \cdot 10^{-11}$ to $5 \cdot 10^{-11}$ atm O_2 . However, the scatter in their results is appreciable, and other interpretations seem possible (2).

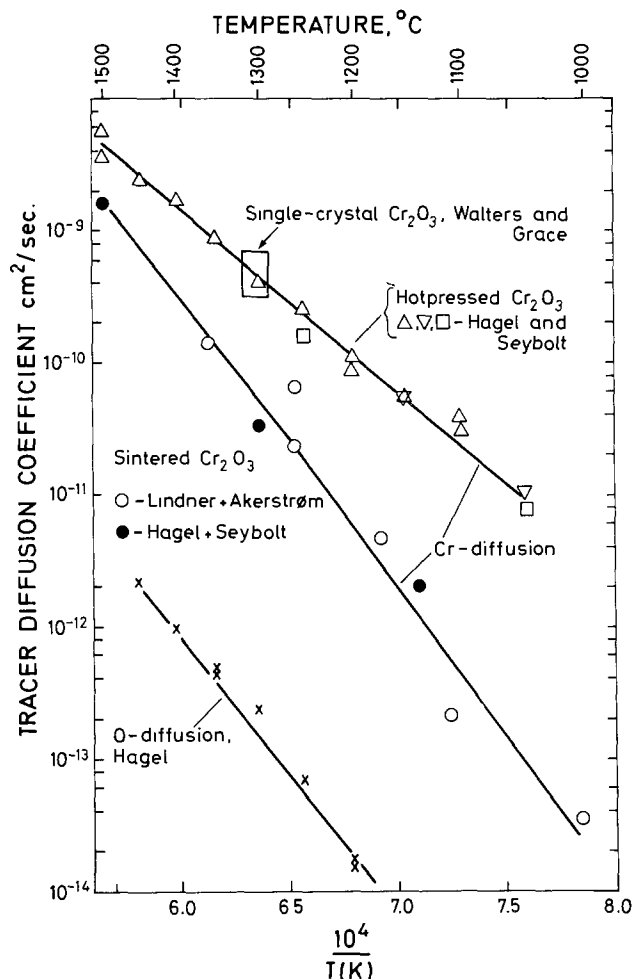


Fig. 5. Literature values of tracer self-diffusion of ^{51}Cr and ^{18}O in Cr_2O_3 . Values of Hagel and Seybolt (12) (hot-pressed and sintered specimens), Lindner and Åkerström (15) (sintered specimens), Walters and Grace (16), and Hagel (17) (O-diffusion).

Self-diffusion of oxygen in Cr_2O_3 at $p_{\text{O}_2} = 1.6 \cdot 10^4$ Pa O_2 have been studied by Hagel (18) by means of ^{18}O -exchange in the temperature range $1100^\circ\text{--}1450^\circ\text{C}$. The data are included in Fig. 5. The oxygen tracer self-diffusion coefficient under these conditions can be expressed by

$$D_{\text{O}^T} = 15.9 \exp(-422,000/RT) \text{ (act. energy in J/mole)}$$

[5]

The oxygen self-diffusion coefficient at $p_{\text{O}_2} = 1.6 \cdot 10^4$ Pa is smaller than the chromium self-diffusion coefficient for sintered specimens (at $p_{\text{O}_2} 10^{-1}\text{--}10^{-2}$ Pa) by about three orders of magnitude.

High temperature oxidation.—In discussions of the growth mechanism of Cr_2O_3 scales it is commonly assumed in the literature that the important lattice defects are chromium vacancies. If this were so, parabolic oxidation of chromium governed by lattice diffusion should exhibit a significant oxygen pressure dependence, i.e., $k_p \propto p_{\text{O}_2}^{1/n}$ where n is determined by the defect structure. Such a pressure dependence has never been observed. Rather, available data suggest that the parabolic rate constant is approximately independent of oxygen pressure (1). This is the expected relationship if chromium interstitials are the predominating point defects.

Sintering (2, 19-24).—Sintering of Cr_2O_3 at atmospheric or near-atmospheric pressures of oxygen yields fine-grained, highly porous and partially sintered, structures with poor densification (20). However, when the partial pressure of oxygen is reduced, sintering rates are markedly increased (19-22). Thus Halloran and Anderson (21) found that the initial sintering, i.e., the fractional shrinkage rate at 3% linear shrinkage at 1100°C , only was observed at partial pressures of oxygen < 1 Pa O_2 . The shrinkage rate increased with further decrease in oxygen partial pressure and reached a maximum at the decomposition pressure of Cr_2O_3 . Ownby and Jungquist (20) studied final sintering of Cr_2O_3 at 1600°C . After a sintering time of 1 hr the theoretical density only reached 63% at 10^5 Pa O_2 , while essentially 100% density was reached at partial pressures of oxygen close to the decomposition pressure of Cr_2O_3 . A particularly rapid increase in densification took place at oxygen pressures close to the decomposition pressure were approached.

Without going into the details of sintering mechanisms, these results clearly demonstrate a markedly increased rate of transport (i.e., increased concentration) of point defects with decreasing partial pressure of oxygen. Diffusion-controlled sintering is governed by the transport of the slower diffusion species, i.e., the oxygen atoms. It is tentatively concluded that oxygen vacancies constitute the oxygen point defects, and that these are the minority defects in Cr_2O_3 , at least at partial pressures of oxygen near the decomposition pressure of Cr_2O_3 .

Discussion of defect structure and transport properties of Cr_2O_3 .—Available data on electrical conductivity, self-diffusion, and sintering of Cr_2O_3 suggest that this oxide has a complex defect structure. But a few major conclusions may be drawn:

(i) Chromium point defects are the majority point defects in Cr_2O_3 , at least at reduced oxygen pressures.

(ii) Chromium diffusion increases from specimens prepared and equilibrated in partial pressures of oxygen of 10^{-2} to 10^{-2} Pa O_2 (sintered specimens) to specimens containing small amounts of chromium metal (hot-pressed specimens) for which the effective partial pressure of oxygen is close to the decomposition pressure of Cr_2O_3 in equilibrium with chromium metal. This is inconsistent with Cr vacancies being the predominating chromium defects in this range of partial pressures of oxygen. Rather it is concluded that Cr interstitials are the predominating chromium point

defects under these conditions. [The predominating iron defects in Fe_2O_3 have also been shown to be iron interstitials (25)].

(iii) Cr_2O_3 is an intrinsic electronic conductor at high temperatures ($>1000^\circ\text{--}1200^\circ\text{C}$) and at oxygen pressures from 1 atm O_2 down to partial pressures of oxygen existing in argon atmospheres ($<10\text{--}10^{-1}$ Pa O_2 depending upon the purity of argon). The electrical conductivity has not been studied at partial pressures close to the decomposition pressure of Cr_2O_3 . Cr_2O_3 is a p-conductor at atmospheric and near-atmospheric oxygen pressures. This suggests a higher mobility for electron holes than for electrons.

(iv) At lower temperatures ($<1000^\circ\text{--}1200^\circ\text{C}$) the factors affecting the electrical conductivity are more difficult to evaluate. The behavior may be caused by the presence of unavoidable impurities or that defect equilibria are "frozen in" and slow to be established.

As electronic defects predominate at near-atmospheric oxygen pressures, details of the point defect equilibria in this oxygen pressure range are as yet difficult to ascertain.

Defect structure model.—All in all it appears reasonable to divide the stability range of Cr_2O_3 into two main regions:

(i) At near-atmospheric oxygen pressures Cr_2O_3 is an intrinsic electronic semiconductor.

(ii) At oxygen pressures near the decomposition pressure of Cr_2O_3 the oxide has excess metal; the predominating point defects are chromium interstitials. The minority defects are probably oxygen vacancies.

This model is illustrated schematically in Fig. 6. Let us first consider the low pressure region. Following the conclusions drawn above, the self-diffusion coefficient measured for the hot-pressed specimens represents diffusion in Cr_2O_3 in equilibrium chromium metal. This means that these results do not represent values of the self-diffusion coefficient at a constant partial pressure of oxygen, but at the decomposition pressure of Cr_2O_3 in equilibrium with chromium metal. The decomposition pressure of Cr_2O_3 changes with temperature according to

$$p_{\text{O}_2}^* = \exp\left(-\frac{2\Delta G^\circ(\text{Cr}_2\text{O}_3)}{3RT}\right) \\ = \exp\frac{2\Delta S^\circ(\text{Cr}_2\text{O}_3)}{3R} \exp\left(-\frac{2\Delta H^\circ(\text{Cr}_2\text{O}_3)}{3RT}\right) \quad [6]$$

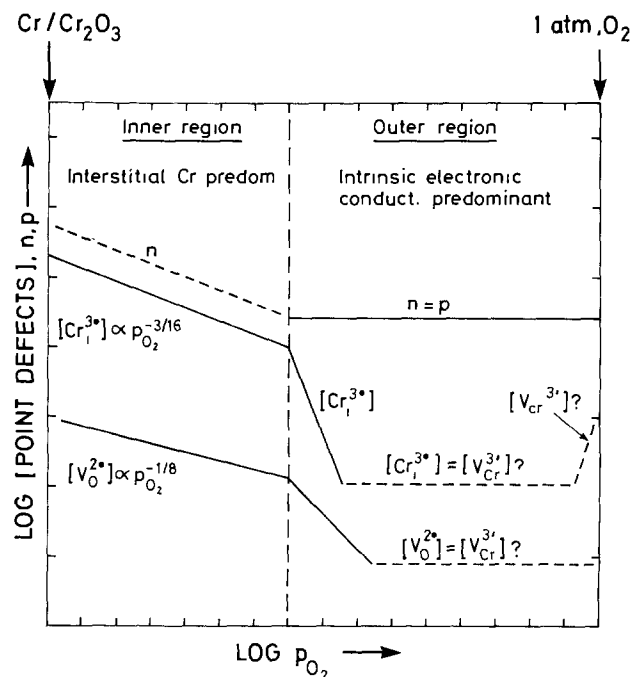
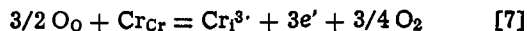


Fig. 6. Defect structure model for Cr_2O_3

where $\Delta G^\circ(\text{Cr}_2\text{O}_3)$, $\Delta H^\circ(\text{Cr}_2\text{O}_3)$, and $\Delta S^\circ(\text{Cr}_2\text{O}_3)$ represent, respectively, the standard free energy, enthalpy, and entropy of formation of Cr_2O_3 at temperature T . The value of $\Delta G^\circ(\text{Cr}_2\text{O}_3)$ is given by $\Delta G^\circ(\text{Cr}_2\text{O}_3) = \Delta H^\circ(\text{Cr}_2\text{O}_3) - T\Delta S^\circ(\text{Cr}_2\text{O}_3) = 111,300 + 250 T$ J/mole (26). The decomposition pressures range from $p_{\text{O}_2} = 10^{-16.8}$ atm at 1000°C to $p_{\text{O}_2} = 10^{-8.2}$ at 1500°C .

If the diffusion coefficient of Cr at constant partial pressures of oxygen is to be estimated from the diffusion coefficient for the hot-pressed specimens, the defect structure of Cr_2O_3 near the decomposition pressure of Cr_2O_3 must be known. Let us for the sake of illustration assume that the predominating point defects under these conditions are chromium interstitials with three positive effective charges. Their formation may be written (2)



If the electroneutrality condition is given by $n = 3[\text{Cr}_i^{3+}]$, the equilibrium concentration of chromium interstitials is given by (2)

$$[\text{Cr}_i^{3+}] = \left(\frac{K_1}{27}\right)^{1/4} \cdot p_{\text{O}_2}^{-3/16} \quad [8]$$

where K_1 is the equilibrium constant for Eq. [7].

The self-diffusion coefficient in Cr_2O_3 at the phase boundary $\text{Cr}_2\text{O}_3/\text{Cr}$ (in hot-pressed specimens), D_{Cr}^* , is then related to the self-diffusion of chromium at constant partial pressure of oxygen, $D_{\text{Cr}} = D_{\text{Cr}}^* p_{\text{O}_2}^{-3/16}$, by the equation

$$D_{\text{Cr}}^* = D_{\text{Cr}} (p_{\text{O}_2})^{-3/16} \quad [9]$$

Experimentally D_{Cr}^* (hot-pressed specimens) is given by $D^* = 0.167 \exp(-255,000/RT)$.

The temperature dependence of D_{Cr} can be expressed by

$$D_{\text{Cr}} = D_{\text{Cr}}^* \exp(-\Delta H_{\text{Cr}}/RT) \quad [10]$$

where ΔH_{Cr} is the activation energy for chromium self-diffusion at constant partial pressure of oxygen.

It may be shown that ΔH_{Cr} is given by (3)

$$\begin{aligned} \Delta H_{\text{Cr}} &= 255 + \frac{2}{3} \frac{3}{16} \Delta H^\circ(\text{Cr}_2\text{O}_3) \\ &= 255 + 140 = 395 \text{ kJ/mole} \quad [11] \end{aligned}$$

This may be compared with the activation energy for the sintered specimens ($p_{\text{O}_2} \sim 10^{-1}$ - 10^{-2} Pa O_2) of about 415 kJ/mole. If it were assumed that the chromium interstitials were doubly charged, Cr_i^{2+} , then the oxygen pressure dependence of $D_{\text{Cr}} \propto p_{\text{O}_2}^{-1/4}$ and the activation energy $\Delta H_{\text{Cr}} = 440$ kJ/mole. The approximate agreement in activation is consistent with this type of model.

The results of the model assuming that Cr_i^{3+} predominates may be illustrated in Fig. 7. The figure includes the experimental values for the hot-pressed and sintered specimens, and estimated diffusion coefficients of chromium at different partial pressures of oxygen in the low pressure region.

The model must also explain the markedly increased sintering rates in the low pressure region. This is assumed to be governed by transport of oxygen vacancies. Their formation may be written



For the electroneutrality condition $n = 3[\text{Cr}_i^{3+}]$, it follows that the oxygen pressure dependence of the oxygen vacancies is given by $[\text{V}_0^{2+}] \propto p_{\text{O}_2}^{-1/8}$. This would qualitatively explain the increased sintering rate with decreasing partial pressure of oxygen.

A Kröger-Vink diagram giving a qualitative picture of the variations of these point defects as function of the partial pressure of oxygen is shown in Fig. 6.

For the high pressure region with predominant intrinsic electronic equilibrium one may only speculate as to the important point defects. The electroneutral-

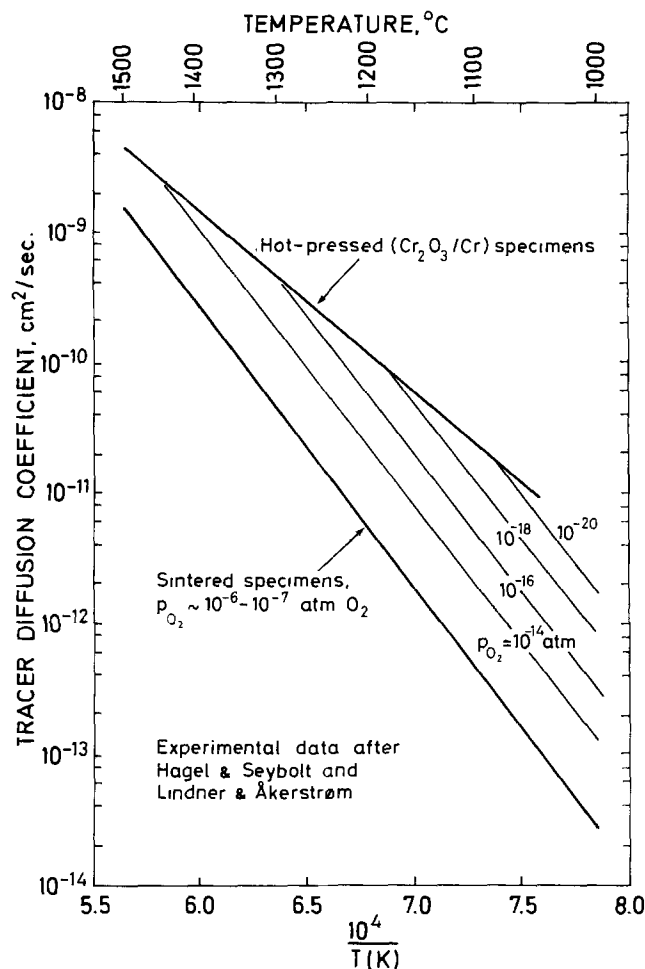


Fig. 7. Estimated values of the chromium self-diffusion in Cr_2O_3 at different partial pressures of oxygen. Fully drawn lines represent the experimental values for hot-pressed and sintered specimens (12, 15) (cpr. Fig. 5).

ity condition is given by $n = p = K_1^{1/2}$, and this in turn means that the concentration of the chromium interstitials and oxygen vacancies vary as $[\text{Cr}_i^{3+}] \propto p_{\text{O}_2}^{-3/4}$ and $[\text{V}_0^{2+}] \propto p_{\text{O}_2}^{-1/2}$. Thus the concentration of both defect species decrease rapidly with increasing partial pressure of oxygen. But at sufficiently high oxygen pressure, other point defect structure situations may begin to predominate. Thus chromium vacancies may become important or a Frenkel or Schottky defect structure situation may predominate. In this latter case the concentration of chromium point defects will be independent of the partial pressure of oxygen. The same would then also apply to the concentration of oxygen vacancies.

Such a defect structure situation is also illustrated in the Kröger-Vink diagram in Fig. 6.

The relative concentrations of the chromium point defects and oxygen vacancies cannot be ascertained and depend on the values of the equilibrium constants for the Frenkel and Schottky defect equilibrium. It is not obvious that the concentration of oxygen vacancies are much smaller than that of the chromium defects in this region.

As regards creep and stress-induced deformation of Cr_2O_3 at high temperatures it is expected that this will qualitatively follow the same oxygen pressure dependence as for sintering: creep rates are relatively small at near-atmospheric oxygen pressures and will increase rapidly in the region near the decomposition pressure of Cr_2O_3 .

The authors would like to emphasize that the proposed model is not pretended to constitute a "final"

defect structure model for Cr_2O_3 . It is, of course, realized that details of the interpretations may vary. It would, for instance, be valuable to confirm by electrical conductivity measurements whether the oxide is an excess metal semiconductor in the stability region near the $\text{Cr}_2\text{O}_3/\text{Cr}$ phase boundary. The importance of the model lies in the major trends that are suggested for the defect structure as a function of partial pressure of oxygen and the implications on the properties of the oxide.

Mechanism of High Temperature Oxidation of Chromium

Chromium exhibits an extremely complex reaction behavior at high temperatures. A number of factors must be considered in order to make an overall description of the oxidation mechanism: transport of the reactants through the Cr_2O_3 scale in the form of volume diffusion and along grain boundaries, easy diffusion paths, and microcracks, the build-up of compressive stresses in the growing oxide scale, cracking and deformation of the scale, detachment of the scale from the metal surface and a possible rate-limiting supply of chromium vapor across the gap between the metal and the scale, evaporation of CrO_3 from the outer oxide surface at the higher oxygen pressures, etc. It is not surprising that the reaction kinetics may vary considerably with experimental conditions.

Oxidation at 900-1100°C.—Let us first consider oxidation at atmospheric pressure at and above about 900°C. Under these conditions the initial oxidation decreases with time; as the scale builds up, cracking occurs, and the overall kinetics can be considered to consist of a sequence of protective stages where new protective oxide is formed after cracking.

Volume diffusion. Comparison of experimental k_p 's with values calculated from diffusion data.—The initial, protective oxidation conforms approximately with parabolic kinetics, and parabolic rate constants can be evaluated for this stage (1). It is reasonable to assume that the oxidation during this initial stage is governed by transport of the reactants through a thin scale, which initially grows as an approximately plane-parallel layer on the surface. In view of the discussion of the defect structure and transport properties of Cr_2O_3 , it is of interest to compare experimentally observed rate constants with values calculated from the reported diffusion data by means of the Wagner theory. Such a comparison should only be considered an order of magnitude exercise to test the overall consistency of the diffusion and oxidation data. It is emphasized that the Wagner theory represents an ideal model that presupposes the growth of dense scales governed by lattice diffusion. For previously reported studies the k_p 's have usually been evaluated for extended periods of oxidation where CrO_3 -evaporation, a rate-limiting Cr-evaporation across the gap between the detached scale and the metal, grain boundary transport, etc. will affect the measured values.

For an oxide scale growing by volume diffusion the partial pressure of oxygen will change from the ambient oxygen pressure at the oxide/gas interface, p_{O_2} , to the decomposition pressure of the oxide in equilibrium with the metal at the inner surface of the scale, $p_{\text{O}_2}^*$. Following the proposed defect structure model the growing Cr_2O_3 scale can be considered to consist of two regions: an inner region where interstitial chromium ions predominate the lattice diffusion process and an outer region where intrinsic electronic equilibrium predominates. The lattice diffusion of chromium in the inner region will be much faster than the transport processes in the outer region. Accordingly the inner region will be assumed to be considerably thicker than the outer region. For the outer region it is not known whether chromium predominates or whether oxygen transport is also a contributing factor. As a first

approximation an evaluation of k_p may be made assuming that the inner region comprises essentially the complete scale.

Let us consider the parabolic rate constant k_p in $\Delta X^2 = k_p t$, expressed in terms of cm^2/sec . For Cr_2O_3 growing by lattice diffusion of interstitial chromium ions with an effective charge α (electroneutrality condition $\alpha[\text{Cr}_i^{\alpha}] = n$, k_p is related to the self-diffusion coefficient of chromium in Cr_2O_3 through the relation (2, 27)

$$k_p (\text{cm}^2/\text{sec}) = 2(\alpha + 1) D_{\text{Cr}} \{ (p_{\text{O}_2}^*)^{-3/4(\alpha+1)} - p_{\text{O}_2}^{-3/4(\alpha+1)} \} \quad [13]$$

where $p_{\text{O}_2}^*$ is the decomposition pressure of Cr_2O_3 in equilibrium with Cr and $p_{\text{O}_2}^a$ is the partial pressure of oxygen at the outer border of the oxide layer under consideration. When $p_{\text{O}_2}^* \ll p_{\text{O}_2}^a$, Eq. [13] reduces to

$$k_p = 2(\alpha + 1) D_{\text{Cr}} (p_{\text{O}_2}^*)^{-3/4(\alpha+1)} = 2(\alpha + 1) D_{\text{Cr}}^* \quad [14]$$

The self-diffusion coefficient of chromium at constant partial pressure of oxygen is given by $D_{\text{Cr}} = D_{\text{Cr}}^* p_{\text{O}_2}^{-3/4(\alpha+1)}$ and D_{Cr}^* is the value of D_{Cr} at the $\text{Cr}_2\text{O}_3/\text{Cr}$ phase boundary. As seen, k_p is determined by D_{Cr}^* .

Values of k_p [expressed in $(\text{weight gain of O})^2/\text{cm}^4 \text{ sec}$] have been calculated for $\alpha = 3$ and assuming that the diffusion data for the hot-pressed specimens are equal to D_{Cr}^* . As the details of the diffusion mechanism are not known, the correlation coefficient is neglected. The values are plotted in Fig. 8 and are compared with the experimental values of Hagel (28), Cadiou and Paidassi (29), and of this work (1). The calculated and experimental values are of the same order of magnitude. The calculated values are somewhat higher than those of Hagel and of Cadiou and Paidassi, but lower than the results of this study. In this connection it should be noted that the k_p 's of this study have been evaluated from the initial oxidation, while those of the other studies after extended reaction. With regard to the calculated values of k_p it should be recalled that the values of D_{Cr}^* involve considerable experimental error (12) and that k_p will be lower for lower values of α .

The approximate agreement between calculated and measured k_p 's and that D_{Cr}^* and essentially all measured k_p 's have the same activation energies is consistent with the conclusion that lattice diffusion in general constitutes an important mode of transport in growth of Cr_2O_3 scales. Growth of Cr_2O_3 by interstitial chromium diffusion should also be independent of the ambient oxygen pressure.

A note should be added regarding the extremely low values of k_p estimated from metallographic cross sections by Caplan and Sproule (30). These values are lower than those of Hagel by almost two orders of magnitude. The values are estimated from small, local areas with special orientations where the oxide layer is proposed to be monocrystalline. The values are not corrected for oxide evaporation. From similar studies by other investigators this correction would be expected to be much larger than the oxidation involved in forming the thin monocrystalline layers. If the monocrystalline layers do reflect the total oxidation in these local areas, one may speculate if diffusion in Cr_2O_3 single crystals is highly dependent on crystal orientation.

Diffusion and oxide growth along grain boundaries.—In addition to volume diffusion, a number of other factors affect or significantly influence the oxidation behavior. An important factor is the development of compressive stresses in the growing Cr_2O_3 scales. This feature has earlier been emphasized by Caplan *et al.* (30-34). This behavior shows that oxide formation also

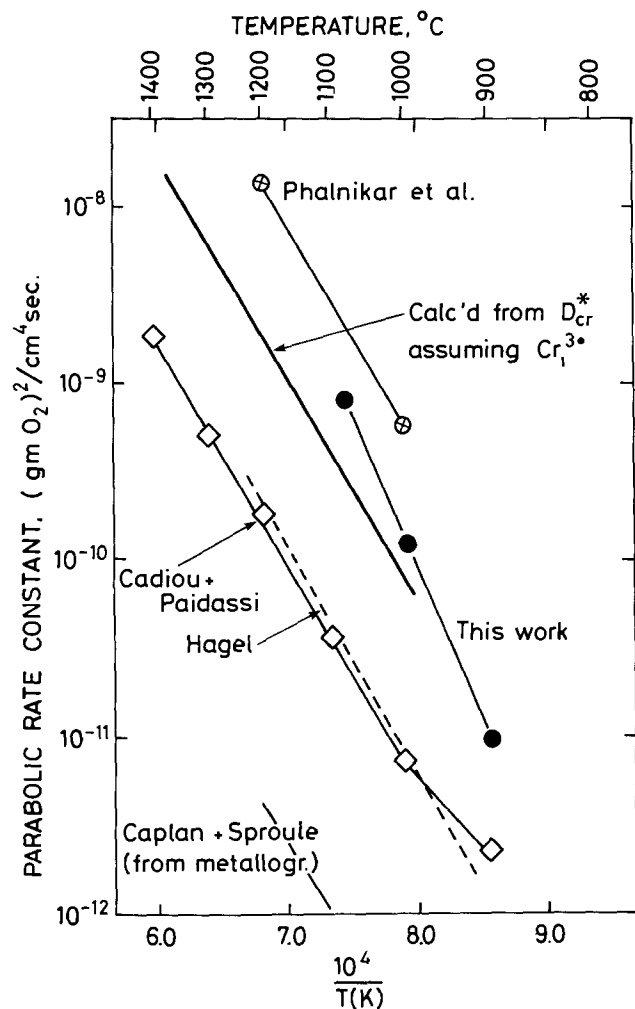


Fig. 8. Values of the parabolic rate constant for oxidation of chromium calculated from the self-diffusion coefficient of chromium compared with experimental values of Hagel (28), Cadiou and Paidassi (29), and of this work (1).

takes place within the scales. In addition to the increase in oxide thicknesses during oxidation, the oxide also grows along the metal surface. This in turn strongly suggests that the oxide scales grow by countercurrent chromium and oxygen diffusion. This may take place through volume diffusion processes in the oxide scale. But the important effect is concluded to be countercurrent grain boundary diffusion of both chromium and oxygen and the consequent oxide formation along grain boundaries. This would account for the development of large compressive stresses in the growing scales and also the very fine-grained oxide structure and the imperfect crystals observed in parts of the scales.

Due to the changing orientations and the disarray of atoms along grain boundaries, small and imperfect oxide crystallites are probably formed along grain boundaries. If sintering of these small oxide crystallites is slow, small amounts of porosity probably exist at such areas with newly formed oxide. These regions may as far as transport is concerned possibly be considered as microcracks or "channels." The rapid loss of chromium during high vacuum treatment after oxidation at $7 \cdot 10^{-2}$ Pa O_2 , where the oxide is particularly fine grained, is proposed to reflect such a situation.

The relative importance of transport of chromium and oxygen along grain boundaries and microcracks is difficult to assess. It is believed, however, that such oxygen transport is most important at atmospheric oxygen pressure; this would account for the fact that the oxide crystals in an outer layer have relatively large, well-developed crystals, while the oxide crystals

at the inner surface are small and imperfect under these conditions. But as the ambient oxygen pressure is lowered, the relative importance of oxygen grain boundary transport is also reduced. As a first approximation, it may be postulated that the oxygen grain boundary transport is proportional to $p_{O_2}^{1/2}$ or p_{O_2} if the oxygen diffuses as atoms or molecules, respectively. At the very lowest oxygen pressure used in this study chromium diffusion along grain boundaries and microcracks is believed to predominate (see also further discussion below).

Formation of cavities and gap between the metal and the scale.—In addition to the development of compressive stresses, pores and cavities are formed, and these finally grow to form a gap between the metal and the scale. It is concluded that this is a result of the outward diffusion of chromium both along grain boundaries and by volume diffusion in the inner region of the scale. In all previously published discussions of chromium oxidation, this is assumed to reflect vacancy condensation. However, such cavity formation may also in general result from outward interstitial metal diffusion. Under conditions where the oxide is easily deformed (at the lower oxygen pressures), the gap may be dramatically increased after extended oxidation.

Scale deformation.—Another important factor, particularly as regards the oxygen pressure dependence of the oxidation behavior, is the ability of the oxide to deform. This is believed to take place by creep processes induced by the growth stresses in the scale. The rate-limiting factor in creep is the diffusion of the minority defects, i.e., oxygen vacancies. Following the proposed defect structure model for Cr_2O_3 , the creep rate is concluded to increase with decreasing partial pressure of oxygen, the increase being particularly large at the lower oxygen pressures.

For a continuous oxide scale the partial pressure of oxygen decreases from that of the ambient gas pressure at oxide/gas interface to the decomposition pressure of the oxide at the metal/oxide interface. Accordingly the creep properties of the scale vary significantly through the scale. For Cr_2O_3 scales the ability to deform will be smallest at the oxide/gas interface.

Cr_2O_3 scales formed at 1 atm O_2 show little or no tendency to deform. This is concluded to reflect that the creep in an outer region of the scale (the region with intrinsic electrons predominant) is small. In this region the ability to deform is small, and the oxide cracks abruptly giving kinetics with abrupt increases in oxidation rates. The resulting porosity of the scale is found in the outer layer of the scale. The scale easily spalls off by cooling to room temperature.

As the oxygen pressure is reduced to about 100 Pa O_2 , the ability of the scale to deform increases. The oxide buckles and, as viewed from the surface, has wavy appearance. But the oxide cannot deform sufficiently rapidly in an outer layer; the oxide continuously cracks and heals in a large number of sites statistically distributed over the scale. During this cracking process oxygen penetrates the scale, and the metal beneath the scale becomes oxidized. The reaction is accordingly approximately linear, and the overall oxidation is faster than at 1 atm O_2 . After extended oxidation, and as new oxide is formed in the metal, the surface oxide may essentially build up to form two or more layers. The oxidation rate may as a result of this slow down with time after extended oxidation.

With further decrease in oxygen pressure, the deformation of the scale increases. At the low oxygen pressure of $7 \cdot 10^{-2}$ Pa O_2 the deformation of the oxide is sufficiently high that no cracking occurs. Rather the oxide balloons away from the oxide surface. The stresses in the scale are sufficiently alleviated that there is no oxide spallation during cooling to room temperature.

As high vacuum is pumped on such oxidizing specimens, the ballooning continues further. Under these conditions the supply of oxygen at the surface becomes very small, and as chromium metal vapor is continuously supplied, the partial pressure throughout the entire scale becomes equal to that for Cr_2O_3 in equilibrium with chromium metal. Under these conditions the ability of the scale to deform is concluded to be at its maximum.

Temperature dependence of the oxidation at different oxygen pressures.—As discussed above, most studies of oxidation of chromium at atmospheric pressure yield parabolic rate constants with an activation energy of about 255 kJ/mole. In this work, the oxidation rates are higher than in most other studies and the activation energy determined from the k_p 's at three temperatures amounts to 315 kJ/mole (1). The reason for this difference is not clear. But it appears to be related to a higher amount of easy diffusion paths and microcracks in the Cr_2O_3 scales when specimens are pretreated through thermal etching. The presence of such paths or cracks in the scales is clearly indicated by the results of the high vacuum treatments after oxidation.

Figure 9 shows the temperature dependence of the oxidation at 130 Pa O_2 . The kinetics are different from that at 10^5 Pa O_2 (1). The amount of oxidation at 1000° and 1075°C is also larger at this pressure than at atmospheric pressure.

The results at $7 \cdot 10^{-2} \text{ Pa O}_2$ are presented in Fig. 10. In going from 1000° to 1075°C one observes an unexpected crossover in the weight gain curves, and after more than about 30 hr of oxidation the net weight gain at 1000°C becomes larger than at 1075°C . A possible explanation is that at such a low ambient oxygen pressure there is not sufficient oxygen absorbed on the Cr_2O_3 surface to react with all the chromium that is transported outwards through easy diffusion paths and microcracks, and that part of the chromium is lost as

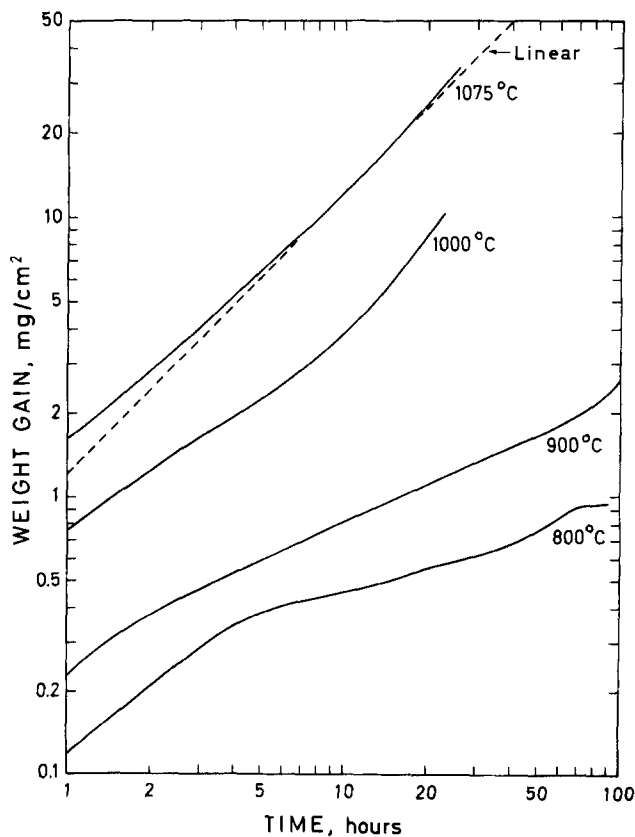


Fig. 9. Oxidation of chromium at 130 Pa O_2 at temperatures from 800° to 1075°C .

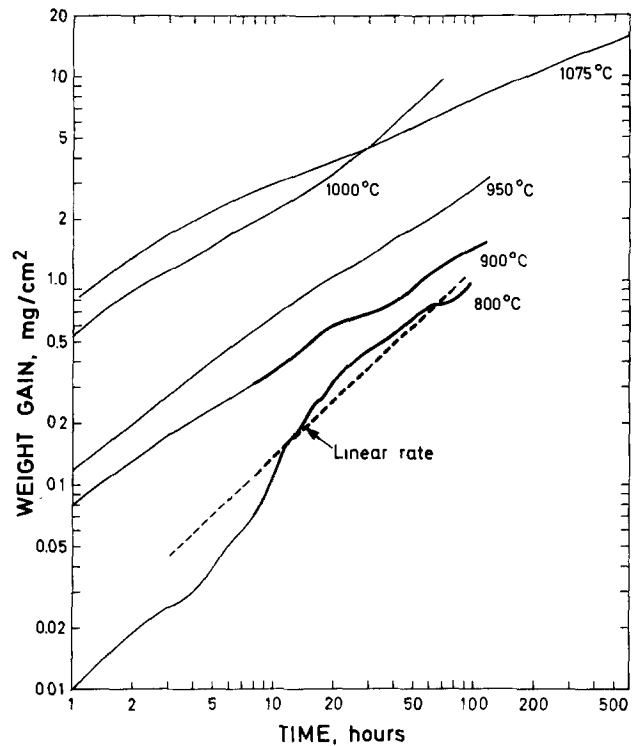


Fig. 10. Oxidation of chromium at $7 \cdot 10^{-2} \text{ Pa O}_2$ at temperatures from 800° to 1075°C .

vapor. If this is the case the "oxidation" is higher than that indicated by the net weight gain. Furthermore, the loss of chromium will be higher at 1075° than at 1000°C as judged from the weight losses observed in high vacuum after evaporation. If approximate (but too high) corrections are made by adding the rates of weight loss observed in high vacuum after oxidation, a more "regular" increase in oxidation from 1000° to 1075°C is found. However, such an interpretation should be confirmed by other direct measurements, e.g., mass spectrometric studies on oxidizing specimens.

Oxidation at 800°C . Chromium transport across the gap between the scale and the metal substrate.—These aspects have been discussed in Part I (1). By way of summary it is concluded that the logarithmic type behavior observed at 800°C and 10^5 Pa O_2 involves rapid transport along easy diffusion paths during initial oxidation, but that these are gradually eliminated through grain growth as the oxidation proceeds. It is difficult to explain the observed results at lower oxygen pressures at 800°C without assuming an enhanced oxidative evaporation of chromium across the gap between the scale and the metal substrate (1).

Acknowledgment

Part of this study has been carried out under a project supported by the Royal Norwegian Council for Scientific and Technical Research.

Manuscript submitted Dec. 26, 1980; revised manuscript received July 8, 1980.

Any discussion of this paper will appear in a Discussion Section to be published in the June 1981 JOURNAL. All discussions for the June 1981 Discussion Section should be submitted by Feb. 1, 1981.

REFERENCES

1. K. P. Lillerud and P. Kofstad, *This Journal*, **127**, 2397 (1980).
2. P. Kofstad, "Nonstoichiometry, Diffusion, and Electrical Conductivity in Binary Metal Oxides," Wiley-Interscience, New York (1972).
3. K. A. Hay, Central Electricity Research Laboratories, Laboratory Report No. RD/L/R 1673 (1970).

4. K. A. Hay, F. G. Hicks, and D. R. Holmes, *Werkst. Korros.*, **21**, 917 (1970).
5. L. N. Cojocaru, *Z. Phys. Chem. N.F.*, **64**, 255 (1969).
6. L. N. Cojocaru, T. Costea, and I. Negoescu, *ibid.*, **60**, 152 (1968).
7. D. J. M. Bevan, J. P. Shelton, and J. S. Andersson, *J. Chem. Soc., (London)*, 1729 (1948).
8. K. Hauffe and J. Block, *Z. Phys. Chem.*, **198**, 232 (1961).
9. S. W. Weller and S. E. Voltz, *Z. Phys. Chem., N.F.*, **5**, 100 (1955).
10. W. A. Fischer and G. Lorenz, *Arch. Eisenhuettenwes.*, **28**, 497 (1957).
11. W. A. Fischer and G. Lorenz, *Z. Phys. Chem., N.F.*, **18**, 265, 308 (1958).
12. W. C. Hagel and A. U. Seybolt, *This Journal*, **108**, 1146 (1961).
13. J. A. Crawford and R. E. West, *J. Appl. Phys.*, **35**, 2413 (1964).
14. J. B. Goodenough, "Metallic Oxides, Progress in Solid State Chemistry," Vol. 5, Pergamon Press, London (1972).
15. R. Lindner and A. Akerström, *Z. Phys. Chem., N.F.*, **6**, 162 (1956).
16. L. C. Walters and R. E. Grace, *J. Appl. Phys.*, **8**, 2331 (1965).
17. T. F. Kassner, L. C. Walters, and R. E. Grace, in "Proceedings of Symposium on Thermodynamics with Emphasis on Nuclear Materials and Atomic Transport in Solids," IAEA, Vienna (1966).
18. W. C. Hagel, *J. Am. Ceram. Soc.*, **48**, 70 (1965).
19. W. C. Hagel, P. J. Jorgensen, and D. S. Tomalin, *ibid.*, **49**, 23 (1966).
20. P. D. Ownby and G. E. Jungquist, *ibid.*, **55**, 433 (1972).
21. J. W. Halloran and H. U. Anderson, *ibid.*, **57**, 150 (1973).
22. J. M. Neve and R. L. Coble, *ibid.*, **57**, 274 (1974).
23. W. D. Kingery, *ibid.*, **2**, 42 (1954).
24. D. L. Johnson, *J. Appl. Phys.*, **40**, 192 (1969).
25. R. H. Chang and J. B. Wagner, Jr., *J. Am. Ceram. Soc.*, **55**, 211 (1972).
26. F. N. Mazandarany and R. D. Pehlke, *This Journal*, **121**, 711 (1974).
27. P. Kofstad, "High-Temperature Oxidation of Metals," Wiley, New York (1966).
28. W. C. Hagel, *Trans. Am. Soc. Met.*, **56**, 583 (1956).
29. L. Cadiou and J. Paidassi, *Mem. Sci. Rev. Metall.*, **66**, 217 (1969).
30. D. Caplan and G. I. Sproule, *Oxid. Met.*, **9**, 5 (1975).
31. D. Caplan and M. Cohen, *This Journal*, **112**, 5 (1964).
32. D. Caplan, A. Harvey, and M. Cohen, *ibid.*, **108**, 134 (1961).
33. D. Caplan, A. Harvey, and M. Cohen, *Corros. Sci.*, **3**, 134 (1963).
34. D. Caplan and M. Cohen, *This Journal*, **108**, 438 (1961).

Electrochemical Methods for Measuring Diffusivities of Hydrogen in Palladium and Palladium Alloys

Reiner Kirchheim¹ and Rex B. McLellan

*Department of Mechanical Engineering and Materials Science,
William Marsh Rice University, Houston, Texas 77001*

ABSTRACT

A palladium bielectrode has been used in a viscous electrolyte consisting of glycerin and phosphoric acid. The transport of molecular hydrogen from and to the electrode is remarkably diminished in this electrolyte in comparison with aqueous electrolytes. Therefore, changes of the electrode potential are unambiguously related to concentration changes caused by diffusion within the electrode. A single current pulse and a potentiostatic technique were applied to determine the diffusion coefficients of H in Pd over a wide range of concentration and at different temperatures. New evaluation methods for current-time and potential-time curves also yield values of the initial concentration, which are in excellent agreement with the values calculated from previous coulometric titrations. A special arrangement of two bielectrodes also allows the measurement of small differences in the diffusivities of hydrogen in the two electrodes. Results for hydrogen diffusion in pure palladium are in excellent agreement with Gorsky effect measurements.

Because of the importance of hydrogen metal systems, a large variety of experimental methods are available to determine their thermodynamic and transport properties. The activity of dissolved hydrogen in metals is usually obtained from a direct measurement of the equilibrium pressure (1). The diffusivity of hydrogen has been measured by permeation, electrochemical, and anelastic measurements (2). Among these, the Gorsky effect, where the transport of hydrogen is caused by an elastic strain field, is an especially reliable method at room temperature because it is independent of surface properties.

Electrochemical methods are mostly used for the Pd-H system since the noble metal palladium is less vulnerable to surface contaminations and, although different surface preparation techniques are used (3-5) the results agree rather well with data from

Gorsky-effect measurements (6). Electrochemical studies done before 1965 yield substantially lower diffusivities (2), which may be due to a less careful sample preparation (annealing, purity, and surface cleaning) or to making measurements at lower concentrations where an exchange of molecular hydrogen between electrode and electrolyte changes the boundary conditions of the diffusion experiment (1). The magnitude and the direction of this flux of molecular hydrogen in the electrolyte depends on the hydrogen activity and mobility in the electrolyte. This process is similar to an absorption or desorption of hydrogen for palladium exposed to a gas phase containing molecular hydrogen. Especially at low hydrogen contents in the electrode, the flux causes higher relative changes of the hydrogen concentration and reliable results are only expected for diffusion fluxes in the sample which are large in comparison with the flux of molecular hydrogen in the electrolyte. Another drawback of electrochemical studies is the limited

¹ Permanent address: Max-Planck-Institut für Metallforschung, Institut für Werkstoffwissenschaften, Stuttgart, Germany.
Key words: electrolyte, palladium, electrode.

temperature range over which they may be carried out.

In the present study, a viscous electrolyte was used in order to decrease the mobility of molecular hydrogen in the electrolyte. The reliability of this electrolyte was checked by the coulometric titration of hydrogen into high purity palladium and subsequent emf measurements. A single current pulse and a potentiostatic technique were applied to measure hydrogen diffusivities in palladium. Special evaluation procedures also enabled the determination of the initial hydrogen concentration before the diffusivity measurement and its comparison with the value obtained from coulometric titration.

Recently, a difference method has been developed to measure directly the difference in oxygen diffusivities between a pure metal and an alloy (7). A similar experimental setup and evaluation procedure for hydrogen diffusion is described in this study. The method is especially appropriate for measuring directly the influence of a metallurgical treatment (plastic deformation, alloying, etc.) on hydrogen activity and diffusivity. An example of this technique is presented showing the change of the diffusion coefficient effected by small concentrations of niobium in the palladium.

Experimental Procedure

Electrode.—The electrodes were prepared from high purity palladium of different stock (one was MARZ grade Pd from MRC and one was 5N Pd from Alfa Company). After rolling down to a final thickness of about 0.25 mm, the samples were annealed under high vacuum conditions for 30 min at 500°C. In some cases the surface was etched with nitric acid or covered with palladium black (3). However, no essential difference has been found in comparison with vacuum annealed surfaces. The area exposed to the electrolyte was 1 cm².

Electrolyte.—A highly viscous electrolyte was prepared by mixing two volume parts of glycerin with one volume part of phosphoric acid (85%). This electrolyte is hygroscopic and has, therefore, to be renewed after several measurements.

Cell.—Two bielectrodes (1) were mounted in a Plexiglas container, consisting of four electrolytic compartments as shown schematically in Fig. 1. The potentials at both sides of the samples (s_0, s_1) were measured against saturated calomel electrodes via Haber-Luggin capillaries (R_1, r_1, R_0, r_0). Auxiliary electrodes (a_1, a_0, A_1, A_0) were made with platinum wires. Although the cell is symmetric, only the compartments d_1 and d_0 were used for carrying a hydrogen current to or from the one side of the working electrodes (w_0, w_1) which were connected to potentiostats or constant current sources in order to dope or deplete the samples with hydrogen. Open-circuit potential measurements were made in the compartments m_1 and m_0 using the reference electrodes R_1 and R_0 . The auxiliary electrodes were used from time to time in order to check the symmetry of the arrangement, i.e., to show if a surface contamination was present at the other side of the bielectrode. Temperature was measured with precise thermometers in

the electrolyte and was kept constant by immersing the whole cell in a temperature bath. Independent measurements with the samples s_0 and s_1 , as well as difference measurements, can be made using the double cell depicted in Fig. 1.

Voltage and current supply, meters.—The potentiostat and constant current source were combined in the "Electroscan 30" (Beckman Instruments, Incorporated), which could be run in a potentiostatic and galvanostatic mode. Digital voltmeters with infinite input impedance (potentiostatic technique) were used to measure voltages between W and R. Their analog output was connected to a chart recorder.

Evaluation

For an infinitely dilute solution of hydrogen in palladium, the relation between the hydrogen concentration c and the emf E is given by the following well-known equation

$$E = E_0 + \frac{RT}{F} \ln c \quad [1]$$

where E_0 is constant with respect to c and c is the concentration of hydrogen in the electrode at the electrolyte/electrode interface. Changes of c caused by diffusion are described by Fick's Second law

$$\frac{\partial c}{\partial t} = D \frac{\partial^2 c}{\partial x^2} \quad [2]$$

Concomitant with different initial and boundary conditions, various solutions of Eq. [2] are known (8) and may be inserted into Eq. [1] to calculate the expected emf changes. Sometimes overpotentials restrict the validity of Eq. [1] and it becomes more convenient to measure the current, which is related to the concentration gradient at the electrode/electrolyte interface using the following relation

$$i = FD \frac{\partial c}{\partial x} \quad [3]$$

We are looking for solutions of Eq. [2] for two different sets of boundary and initial conditions which are fulfilled during a single current pulse or a potentiostatic procedure. The two boundaries of the bielectrode, of thickness s , are denoted by $x = 0$ and $x = s$ describing the surfaces of the electrode facing the doping and measuring compartments of the cell respectively (see Fig. 1).

Single Current Pulse Technique

A single current pulse of height i_0 and duration t_0 is sent through the doping compartment of the cell. After switching off the current the following boundary conditions are fulfilled

$$\frac{\partial c}{\partial x} = 0 \quad \text{for } x = 0 \text{ and } x = s \text{ and } t \geq t_0$$

With a homogeneous concentration distribution in the beginning, $c(x, 0) = c_0$, and a sufficiently short pulse duration, Züchner (3) has obtained a solution of Eq. [2]. He defined a time t_d , which describes a time lag for the onset of emf changes (between w and R in Fig. 1) and which is caused by the diffusion of hydrogen through the bielectrode. This evaluation procedure was used in this study, together with a new one, which described the emf changes using a semi-infinite solution of Eq. [2]. Similar to Züchner, the hydrogen concentration distribution at $t = 0$ to $t = t_0$ which is caused by the current pulse, will be described by a Dirac-Delta function

$$c(x) = Q\delta(x)$$

where Q is the amount of hydrogen doped by the current pulse

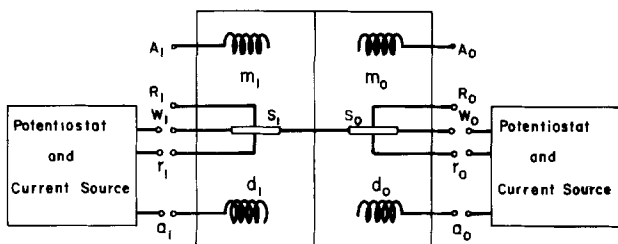


Fig. 1. Schematic outlay of apparatus

$$Q = \frac{i_0 t_0}{F}$$

The solutions of Fick's Second law for semi-infinite samples (planar source solution) is known (8)

$$c(x, t) = c_0 + \frac{Q}{(\pi Dt)^{1/2}} \exp\left(-\frac{x^2}{4Dt}\right) \quad [4]$$

This function is shown in Fig. 2 as the solid line. According to Seith (9), the solution for a finite sample of thickness s is obtained by reflecting the concentration profile at $x = s$ (dashed curve 1' in Fig. 2) and superposing it on the original profile (line 1 + 1' in Fig. 2). Thus the concentration at $x = s$ can be written

$$c(s, t) = c_0 + \frac{2Q}{(\pi Dt)^{1/2}} \exp\left(-\frac{s^2}{4Dt}\right)$$

which is valid for $t < s^2/\pi^2 D$ (dashed line 1' does not reach the other boundary $x = 0$). Corresponding emf changes are given by Eq. [1] in the form

$$\Delta E = \frac{RT}{F} \ln \left[1 + \frac{2i_0 t_0}{F c_0 (\pi Dt)^{1/2}} \exp\left(-\frac{s^2}{4Dt}\right) \right]$$

For small emf changes (less than 3 mV), the second term in the argument of the logarithm is small in comparison with [1], and we have

$$\Delta E = \frac{2RTi_0 t_0}{F^2 c_0 (\pi Dt)^{1/2}} \exp\left(-\frac{s^2}{4Dt}\right) \quad [5]$$

Straight lines are obtained by plotting $\ln(\Delta E t^{1/2})$ vs. reciprocal time, and these intersect the ordinate at $\ln(2RTi_0 t_0 / F^2 c_0 (\pi D)^{1/2})$ and have a slope of $-s^2/4D$. The diffusivity and the initial concentration can be evaluated from these quantities. Compared to the procedure used by Züchner, more information is obtained (initial concentration) and the diffusion coefficient is not only evaluated from one quantity (time lag) but from a set of data points. However, in order to utilize these advantages it is necessary

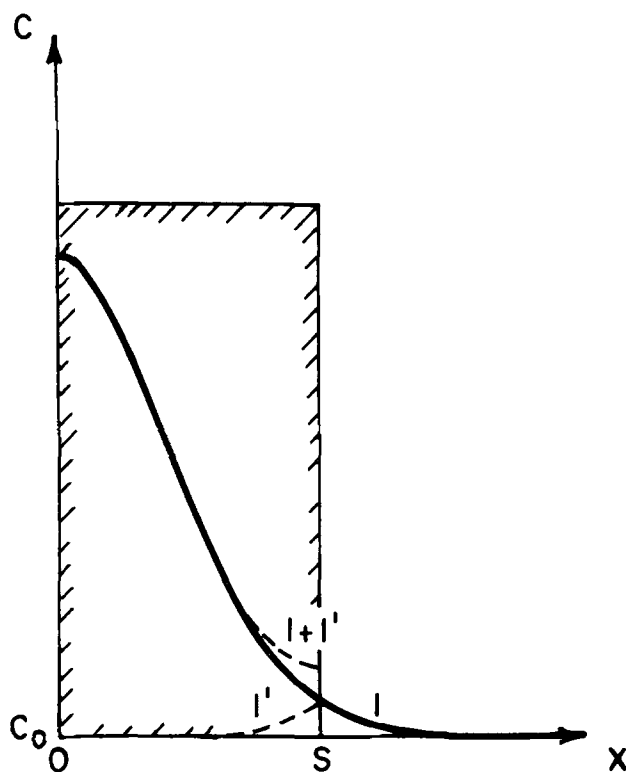


Fig. 2. Illustration of solution of Fick's Second law for samples of finite thickness.

to measure small emf changes and obviate emf drifts caused by absorption and desorption of molecular hydrogen.

Potentiostatic Technique

A constant potential is applied at the doping side of the bielectrode (wr in Fig. 1), which should be high enough to maintain a hydrogen concentration at $x = 0$ close to zero. Or strictly speaking, $c(0, t)$ should always be very small compared with the mean hydrogen concentration in the sample. Assuming again a homogeneous concentration distribution before experiment, we have the following boundary conditions

$$\begin{aligned} c(x, 0) &= c_0 \\ c(0, t) &= 0 \\ \left(\frac{\partial c}{\partial x}\right)_{x=s} &= 0 \end{aligned}$$

The corresponding solution of Eq. [2] is a series of exponential time functions with different time constants (8, 10). For $t > 4s^2/\pi^2 D$, all of them except the one with the highest constant can be neglected and we have

$$c(x, t) = \frac{4}{\pi} c_0 \exp\left(-\frac{\pi^2 Dt}{4s^2}\right) \sin \frac{\pi x}{2s} \quad [6]$$

and the emf changes are $x = s$ are

$$\Delta E = \frac{RT}{F} \ln \frac{4}{\pi} - \frac{RT\pi^2 Dt}{4Fs^2} \quad [7]$$

Plotting E directly with a strip chart recorder gives a straight line. The diffusion coefficient D is calculated from the slope of the straight line in accord with Eq. [7]. An obvious advantage of the potentiostatic technique is a lack of any intermediate evaluation and plotting procedure. Another advantage is the possibility of changing the temperature during the experiment. Thus values of D can be obtained from plots of the emf vs. time at a series of temperatures (10).

The emf changes described in Eq. [7] are caused by the current flowing from w to a in Fig. 1 and the corresponding depletion of the sample with respect to hydrogen. This current can be obtained from Eq. [3] and [6] in the form

$$i = \frac{2FD}{s} c_0 \exp\left(-\frac{\pi^2 Dt}{4s^2}\right) \quad [8]$$

Plotting $\ln i$ vs. t gives straight lines with the slope $-\pi^2 D/4s^2$. Diffusivities evaluated from this slope should agree with values obtained from the emf change at the other side of the bielectrode. The validity of Eq. [8] as well as Eq. [6] is restricted to $t > 4s^2/\pi^2 D$. For smaller times the sample can be treated as a semi-infinite sample (8) giving the following relations between current and time

$$i = Fc_0 \left(\frac{D}{\pi t}\right)^{1/2} \quad [9]$$

which may be used to calculate either c_0 or D , if one of these values is given from Eq. [8]. Thus the potentiostatic technique gives several values for D and c_0 during one diffusion run and, therefore, enables systematic errors to be revealed, i.e., those caused by surface contamination.

Difference Technique

For samples of the same thickness s and the same initial concentration c_0 , but slightly different diffusivities D_1 and D_2 , a direct measurement of the difference $\Delta D = D_1 - D_2$ is achieved by applying potentiostatic conditions to both electrodes at the same time (7). The emf changes $w_1 R_1$ and $w_0 R_0$ in the

measuring compartments of the double cell (Fig. 1) are given by Eq. [7] again, where the voltage difference from R_0 to R_1 is described by

$$\Delta(\Delta E) = \frac{RT\pi^2\Delta Dt}{4F_s^2} \quad [10]$$

There might be also a constant contribution resulting from slightly different potentials of the saturated calomel electrodes or diffusion potentials in salt bridges. If floating potentiostats are not used, w_0 and w_1 are both grounded.

Results

The high viscosity of the electrolyte used diminishes the influence of a flux of molecular hydrogen into or from the electrolyte, as the mobility of molecular hydrogen decreases with increasing viscosity according to the Stokes-Einstein relation. Stable emf values were obtained especially for hydrogen concentrations in the samples of less than 100 at ppm. In dilute sulfuric acid (1N) an emf drift towards positive values was observed, and usually a doped sample was totally depleted of hydrogen after some hours, depending on the initial concentration. The depletion is due to a flux of hydrogen atoms dissolved in palladium toward the surface subsequent to the formation of H_2 molecules and a flux of these molecules into the electrolyte. The last step is sensitive to the viscosity of the electrolyte. Doping of the samples with hydrogen was achieved by coulometric titration. For the viscous electrolyte, the emf of a pure palladium electrode measured against the SCE is shown in Fig. 3 for various concentrations at $T = 295^\circ\text{K}$. As can be seen, Nernst's law, (Eq. [1]), is obeyed over a wide concentration range because the slope of the straight line in Fig. 3 has the theoretical slope RT/F . Deviations of the data points from the straight line behavior are expected at lower and higher concentrations and will be explained in the next section. It is a special feature of the viscous electrolyte and, therefore, of this study that the relationship between emf and hydrogen concentration in Pd is shown to obey Nernst's law. Because the electrolyte is hygroscopic it loses its viscosity and changes its pH and the values shown in Fig. 3 cannot be reproduced after a prolonged use of the same electrolyte.

Diffusivity measurements were made by using the current pulse and the potentiostatic technique as described above. For a single current pulse, a typical plot of $\ln \Delta E t^{1/2}$ vs. t^{-1} is shown in Fig. 4. According to Eq. [5], the data points can be represented by a straight line. Diffusion coefficients calculated from the slope of this line agreed excellently with values

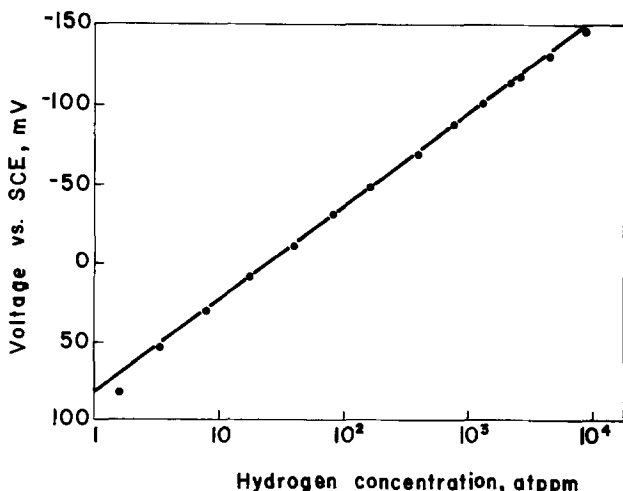


Fig. 3. EMF of pure Pd electrode at 295°K measured against SCE plotted against hydrogen concentration in the sample.

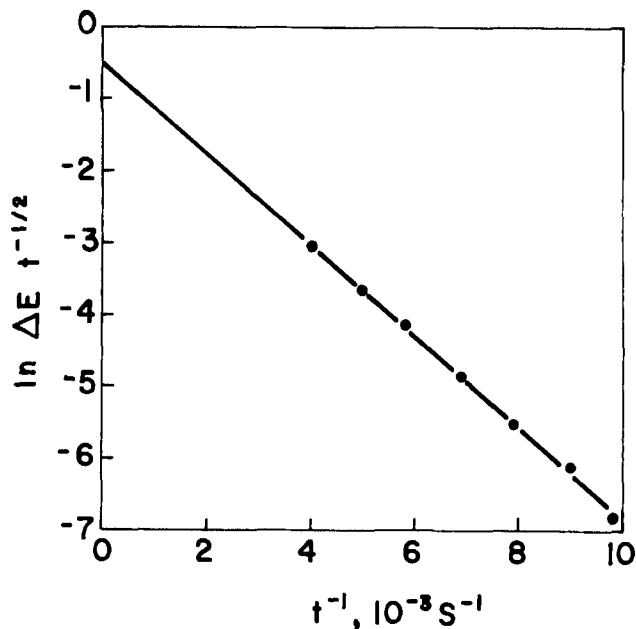


Fig. 4. Plot of $\ln \Delta E t^{1/2}$ vs. reciprocal time

obtained by the time lag method (3). The initial concentrations evaluated from the ordinate intercept usually differ less than 10% from the values of the previous coulometric titration.

The current pulse technique is not very sensitive to the interaction with molecular hydrogen, if the change of hydrogen concentration is high enough and the time lag is short. Thus sulfuric acid may also be used as an electrolyte, although the mutual agreement between the differently-evaluated results is not as good.

The use of a viscous electrolyte is however essential to the potentiostatic technique. Sulfuric acid never gave reliable results. Figure 5 shows that for the viscous electrolyte, a straight line is obtained for the emf vs. time curve as predicted by Eq. [7]. The D value from the slope is in agreement with the value from a current pulse experiment. Deviations were usually smaller than 5%. The chart recorder plot as depicted in Fig. 5 was made at 295°K and Eq. [7] gives a value of 6.2 mV for the difference between the extrapolated straight line and the actual emf at $t = 0$, which is in good agreement with the experimental value of 5.5 mV. This agreement was often even better. During the same diffusion run, the current delivered by the potentiostat was recorded. Figure 6 shows the logarithm of this current plotted vs. time. Deviations from the straight line (cf. Eq. [8]) at smaller times originate due to the neglect of exponential terms with smaller time constants in the exact solution. For small times, Eq. [9] is an appropriate description of the current, which decreases with the reciprocal square root of time, as can be seen in Fig. 7. Using D values calculated from the slopes of the straight lines in Fig. 5 and 6, the initial concentration c_0 is obtained either from the slope in Fig. 7 or from the current i_0 , at which, in Fig. 6, the extrapolated straight line intersects the ordinate. A comparison of different D and c_0 values for one experimental run is given in Table I. The agreement of the c_0 values shows that the current yield was 100% for the coulometric titration ($i < 100 \text{ mA/cm}^2$).

A surface contamination of the electrodes was observed after the samples were exposed for more than two days to the electrolyte. Nonlinearities were seen in plots like those of Fig. 4-6 and the overpotential during a coulometric titration was increased remarkably. These effects vanished after cleaning the samples with xylol and carbon tetrachloride. The voltage applied to wr (Fig. 1) for a potentiostatic measurement

Table I. Comparison of diffusivities and initial hydrogen concentration as determined by the different techniques discussed. The values refer to both pure Pd and alloys at different temperatures

Quantity	Eq.*												
D (10^{-7} cm ² /sec)	[7]	1.65	1.46	2.29	7.7	3.40	2.7	7.6	10.4	6.4	3.6	1.59	
D (10^{-7} cm ² /sec)	[8]	1.65	1.42	2.24	7.5	3.40	2.7	8.3	9.5	6.7	3.7	1.90	
c_0 (at ppm)	[8]	2090	1840	1130		1790	1680	5450	3930	3470	1800	1924	
c_0 (at ppm)	[9]	1900	1630	1100		1950	1820	5500	4300	3460	1810	1880	
c_0 (at ppm) coulom. titration		1950	1860	1090		1850	1520			3500	2000	1970	

* Equation used for evaluation.

was 0.5V. At lower voltages, the results were more dependent on surface contaminations and at higher values of dissolution of the Pd-electrode was observed, increasing the current and changing the color of the electrolyte.

In order to study the influence of foreign solute atoms on the diffusivity of hydrogen in palladium, the methods described have been used for palladium alloys (11). The precision of these methods is high enough to reveal changes of the diffusivity of more than 20%. For smaller differences between pure and alloyed palladium, the difference technique should be used. An example is shown in Fig. 8, where pure palladium was used as the working electrode w_0 and Pd-0.1 at %Nb as w_1 . Both samples had the same thickness and about the same initial concentration. From the recorder trace of R_0w_0 , the diffusivity of H in pure Pd is obtained, while the simultaneously recorded voltage R_1R_0 gives the diffusivity difference. The diffusivity of hydrogen is decreased by the niobium atoms concomitant to the voltage R_1R_0 , increasing with time. The ratio of the slopes in Fig. 8 is $2.5 \cdot 10^{-2}$ which is equal to the relative decrease of the diffusivity (cf. Eq. [7] and [10]).

The diffusion coefficient of hydrogen in high purity palladium was measured at different temperatures using the current pulse and the potentiostatic tech-

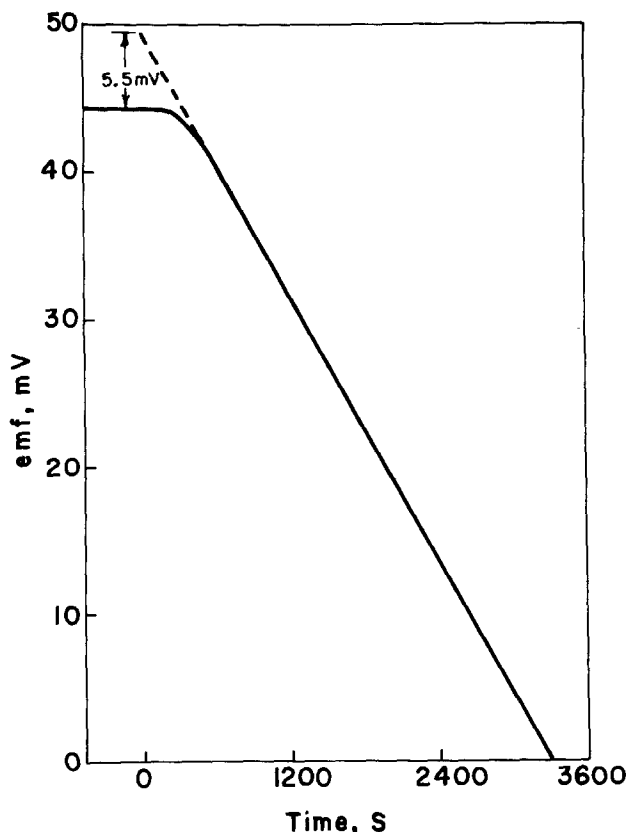


Fig. 5. Plot of EMF vs. time in seconds. The viscous electrolyte was used and $T = 295^\circ\text{K}$. The diagram was drawn directly from a chart recorder trace.

Table II. Measured diffusivities of hydrogen in palladium

T ($^\circ\text{K}$)	D (10^{-7} cm ² /sec)	T ($^\circ\text{K}$)	D (10^{-7} cm ² /sec)
334	9.4	298	3.8
322.5	7.3	296.5	3.55
321.5	7.1	295.5	3.4
317	6.05	294.5	3.3
310	5.25	293	3.1
308	4.9	287.5	2.7
305.5	4.6	281	2.15
302	4.15	273	1.6

Table III. Diffusivity values measured at differing initial concentrations. The temperature was 295°K

C_0 (at ppm)	0.5	4	8	20	100	500	1000
D (10^{-7} cm ² /sec)	2.2	3.2	3.2	3.1	3.1	3.05	3.1

niques. The results are compiled in Table II, where the D values are mean values of 2-5 measurements. Table III contains D values measured with the current pulse technique at different initial concentrations.

Deviations from the straight line in Fig. 3 at lower and higher concentrations are explained by attractive interaction of hydrogen atoms with lattice defects (grain boundaries and dislocations), or with other hydrogen atoms. In both cases hydrogen activity is lowered compared with the ideal dilute behavior. Their influence on hydrogen mobility, however, could not be detected (cf. Table III).

Discussion and Conclusions

The results in Table II are shown in Fig. 9 in an Arrhenius plot, where the solid line is the best representation of different measurements proposed by Völkl and Alefeld (2). The frequency factor is $D_0 = 2.90 \cdot 10^{-3}$ cm²/sec and the activation energy is $Q = 22.2$ kJ/mole. Because of the excellent agreement with the data of the present study, no effort was

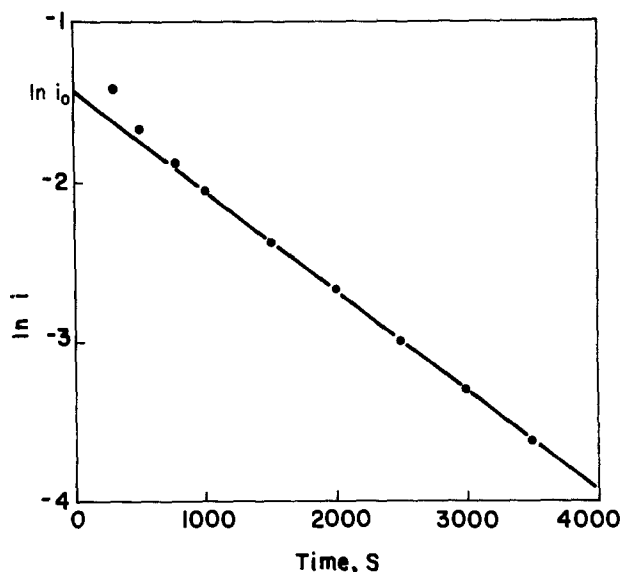


Fig. 6. Plot of $\ln i$ vs. time in seconds

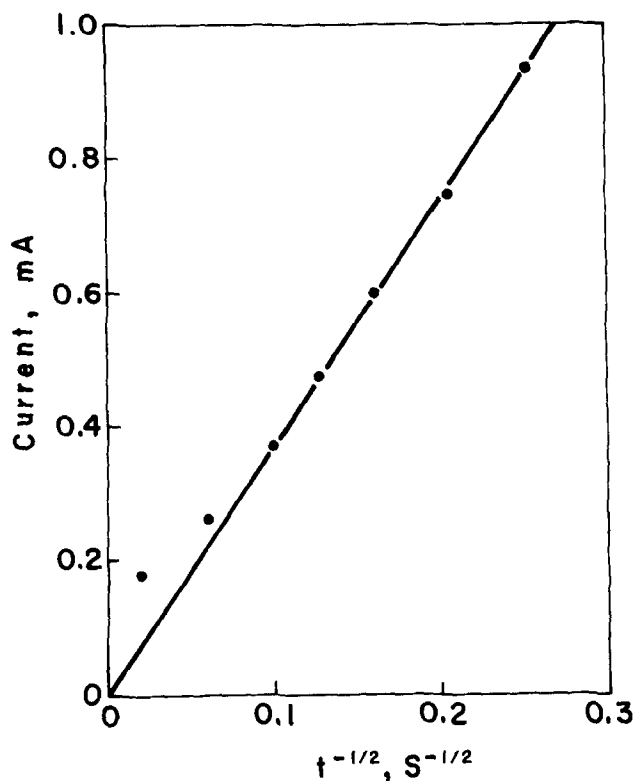


Fig. 7. Plot of current (mA) vs. $t^{1/2}$ in $\text{sec}^{-1/2}$

made to fit the current values to an Arrhenius equation. The current measurements, when extrapolated

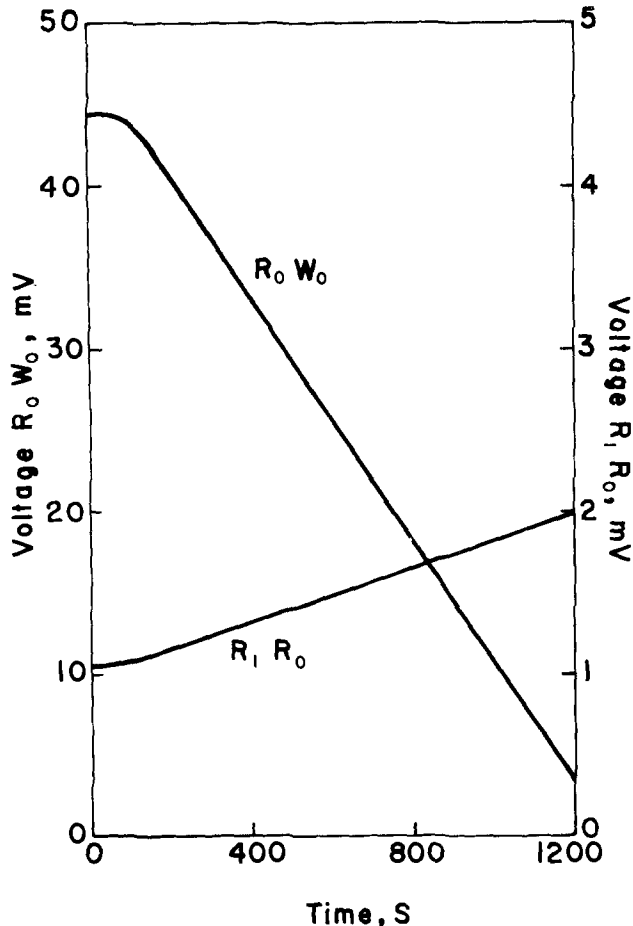


Fig. 8. Illustration of determination of the diffusivity difference ΔE . The working electrode W_0 was pure Pd, and the electrode W_1 was Pd containing 0.1 at% Nb in solid solution.

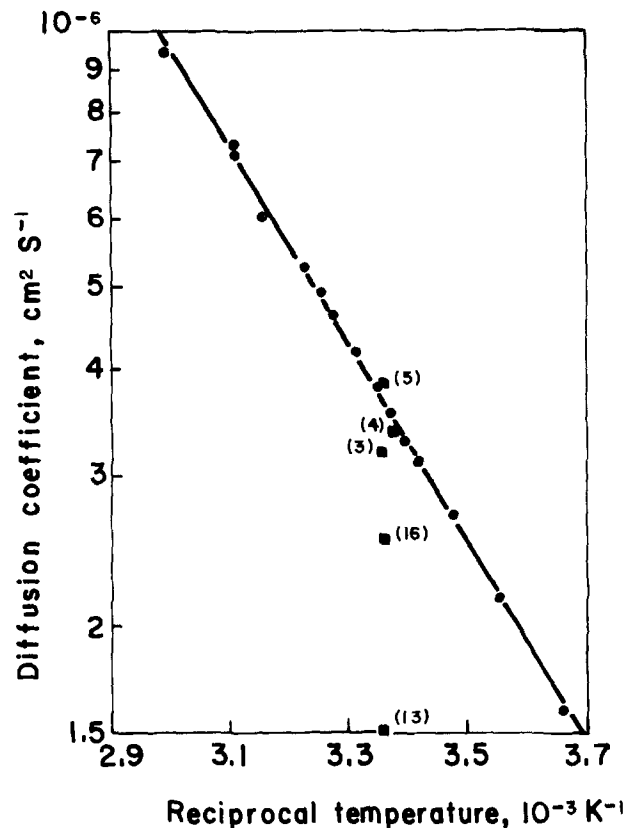


Fig. 9. Arrhenius plot of the diffusivities measured for hydrogen in palladium. The solid line is taken from the "best representation" of Völkl and Alefeld. The solid squares indicate previous data.

to high temperatures, are in excellent agreement with permeability measurements of the diffusivity of H in palladium (14).

It has not been the aim of this study to add another set of diffusivity data to the already existing huge volume in the literature, but rather to demonstrate that electrochemical methods are precise and reliable. The improvement of electrochemical data becomes obvious in Fig. 9, where some results at room temperature are shown in filled squares. The scatter of these data may be explained by the interaction of molecular hydrogen between electrode and electrolyte, which, depending on the boundary conditions of the diffusion experiment, leads to more or less large systematic errors.

With the introduction of a new viscous electrolyte, this source of systematic errors was obviated in this study and it has been shown that reliable diffusivity measurements can be made over a wide concentration range. At concentrations of only a few at ppm H, the current pulse technique is still applicable and in conjunction with the difference technique, it may be used to study the influence of lattice defects on hydrogen diffusion. In regard to the extensive measurements which have to be made to study diffusion of hydrogen in alloys of different composition (11) the electrochemical methods offer another advantage: simple experimental setup and quick measurement and evaluation procedures.

Acknowledgments

The authors are grateful for the financial support provided by the Robert A. Welch Foundation and the U.S. Army Research Office.

Manuscript submitted Feb. 11, 1980; revised manuscript received May 2, 1980.

Any discussion of this paper will appear in a Discussion Section to be published in the June 1981 JOURNAL. All discussions for the June 1981 Discussion Section should be submitted by Feb. 1, 1981.

Publication costs of this article were assisted by Rice University.

REFERENCES

1. F. A. Lewis, "The Palladium Hydrogen System," Academic Press, London (1967).
2. J. Völkl and G. Alefeld, in "Diffusion in Solids, Recent Developments," A. S. Nowick and J. J. Burton, Editors, p. 141, Academic Press, New York (1975).
3. H. Züchner, *Z. Naturforsch.*, **25a**, 1490 (1970).
4. J. G. Early, *Acta Metall.*, **26**, 1215 (1978).
5. K. Sekine, *J. Res. Inst. Catal., Hokkaido Univ.*, **25**, 73 (1977).
6. J. Völkl *et al.*, *Z. Naturforsch.*, **26a**, 922 (1971).
7. R. Kirchheim *et al.*, *Acta Metall.*, To be published.
8. J. Crank, "The Mathematics of Diffusion," Oxford University Press (1956).
9. W. Seith, "Diffusion in Metallen," p. 17, Springer-Verlag, Berlin (1955).
10. R. Kirchheim *et al.*, *Scripta Metall.*, **11**, 651 (1977).
11. R. Kirchheim and R. B. McLellan, *Acta Metall.*, To be published.
12. J. W. Simons and R. B. Flanagan, *J. Phys. Chem.*, **69**, 3581 (1965).
13. M. v. Stackelberg and P. Ludwig, *Z. Naturforsch.*, **19a**, 93 (1965).
14. H. Katsuta and R. B. McLellan, *Acta Metall.*, **27**, 1111 (1979).

Thermodynamic Stabilization of the Solid Electrolyte RbAg₄I₅

Nilo Valverde¹

Forschungsinstitut Berghof GmbH, D-74, Tübingen, Germany

ABSTRACT

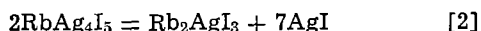
Partial substitution (up to about 6 mole percent) of iodine in RbAg₄I₅ by S, Se, or Te leads to solid solutions with the crystal structure of RbAg₄I₅ and with ionic/electronic conductivities much the same as the unsubstituted compound. While RbAg₄I₅ is thermodynamically unstable and decomposes rapidly when kept at low temperatures, the substituted compounds RbAg_{4+y}I_{5-y}S_y, RbAg_{4+y}I_{5-y}Se_y, and RbAg_{4+y}I_{5-y}Te_y show no tendency to such decomposition under the same conditions. The partial substitution of iodine by S, Se, or Te, however, does not prevent the resulting compounds from very rapid decomposition in the presence of moisture. The final decomposition products in air saturated with water vapor are not in accord with the decomposition mechanism proposed by Owens (5).

Solid phases of the general composition MAg₄I₅ (M = K, Rb, NH₄, etc.) show the highest ionic conductivity at room temperature among all known solid electrolytes (1-3). The exceptionally high ionic conductivity of these compounds can be explained by the singular constitution of the elementary cell. According to Geller (4) there are 56 available sites for the 16 Ag⁺ ions per unit cell, therefore, there is a large number of unoccupied silver sites in the elementary cell. This arrangement makes possible a great mobility of the silver ions.

The compounds KAg₄I₅ and RbAg₄I₅ are, however, thermodynamically unstable below 36° and 27°C and decompose according to the equations (1, 5)



and



respectively.

It has been found experimentally (1) that the above-mentioned decomposition takes place very slowly at moderately low temperatures, especially in absence of water vapor in the air (6). It has not yet been studied, however, what happens when the mentioned compounds are kept for long periods of time at very low temperatures in dry atmosphere. For practical purposes it is desirable to extend the range of existence of these solid phases to lower temperatures so that the galvanic cells with RbAg₄I₅ as solid electrolyte could be operative at temperatures much below 0°C during long periods of time (several years).

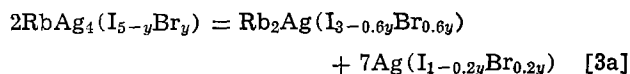
The purpose of this work is, therefore, to find a method for extending the range of existence of RbAg₄I₅ at temperatures well below the decomposition point

(< + 27°C). Simultaneously the influence of water vapor on the decomposition of RbAg₄I₅ at temperatures below its existence range has been investigated.

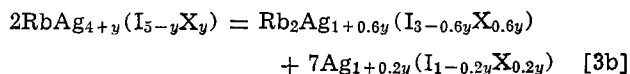
Theoretical Considerations

It is a well known fact that the range of existence of a molten phase can be extended to lower temperatures, if new components are added which show very little tendency to form solid solutions with the first segregated solid phase. The same principle can be applied to extend the stability range of RbAg₄I₅ to lower temperatures.

A partial substitution of I in the compound RbAg₄I₅ by Br or the chalcogenides S, Se, or Te should lead accordingly to solid solutions of the general composition RbAg₄(I, Br)₅ or RbAg_{4+y}(I_{5-y}X_y) with greater thermodynamic stability, where X denotes S, Se, or Te. The decomposition Eq. [2] would consequently take the form



or, respectively



The magnitude of the elastic energy in the solid solutions Rb₂Ag(I, Br)₃ and Ag(I, Br) or Rb₂Ag_{1+y}(I, X)₃ and Ag_{1+y}(I, X) with higher order of lattice and more dense packing of the anions in the crystal is presumably greater than in solid solutions of the type RbAg₄(I, Br)₅ or RbAg_{4+y}(I, X)₅, which have more cation defects and probably not such dense packing of the ions. This is schematically represented in Fig. 1.

¹ Present address: Instituto de Química-Física "Rocasolano," Consejo Superior de Investigaciones Científicas, Serrano 119, E-Madrid 6, Spain.

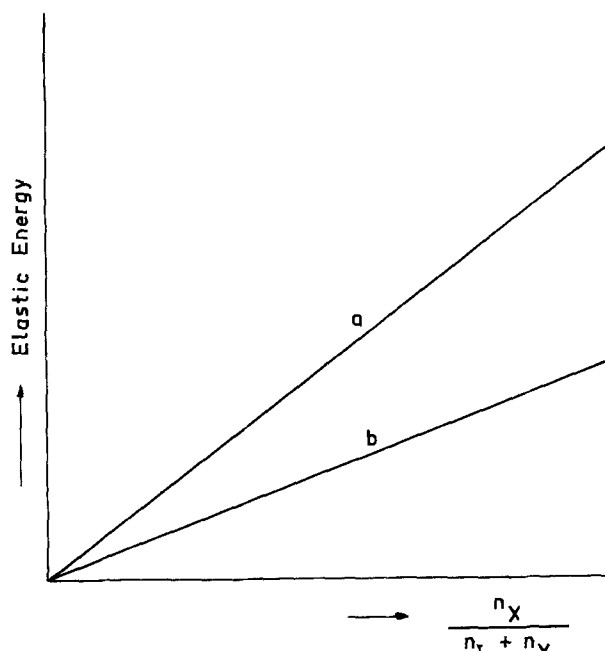


Fig. 1. Schematic representation of the variation of the elastic energy in solid solutions, with some of their ions partially substituted, as a function of the substitution mole fraction. Curve a, elastic energy for $\text{RbAg}_{4+y}(\text{I}, \text{X})_3 + 7\text{Ag}_{1+y}(\text{I}, \text{X})$; curve b, elastic energy for $2\text{RbAg}_{4+y}(\text{I}, \text{X})_5$.

According to the above suppositions, the variation of the Gibbs energy of reactions [3a] and [3b] will be enhanced through the partial substitution of I by Br or X and consequently the range of existence of the phase with higher conductivity of the silver ions will be extended to the region of lower temperatures.

It is unlikely that iodine ions can be substituted in all proportions by Br, S, Se, or Te in the compound RbAg_4I_5 , since phases of general composition RbAg_4Br_5 or $\text{RbAg}_4\text{X}_{2.5}$ do not exist. Moreover in the decomposition Eq. [3a] and [3b], the assumption has been made that the ratio Br/I or X/I in each of the resulting new phases is the same as in the primary compounds. This supposition is based on the very low exchange frequency of the anions at room temperature. The new resulting phases are probably in metastable equilibrium. It is expected that a redistribution of the ions with the time could take place gradually, and accordingly a decomposition of the new resulting products $\text{Ag}(\text{I}, \text{Br})$ or $\text{Ag}_{1+y}(\text{I}_{1-y}, \text{X}_y)$ into the secondary products AgI , AgBr , or Ag_2X , respectively, is likely to happen. The products resulting from the secondary reaction imply a diminution of the Gibbs energy and they are consequently thermodynamically more stable than the products resulting from the reaction [3a] or [3b]. It follows that the extension of the range of existence of the resulting phases $\text{RbAg}_4(\text{I}, \text{Br})_5$ and $\text{RbAg}_{4+y}(\text{I}_{5-y}\text{X}_y)$ to lower temperatures is supposedly not quite so wide as it could be expected to be.

Preparation of Samples

The solid electrolyte RbAg_4I_5 and the corresponding solid solutions $\text{RbAg}_{4+y}(\text{I}_{5-y}\text{S}_y)$, $\text{RbAg}_{4+y}(\text{I}_{5-y}\text{Se}_y)$, and $\text{RbAg}_{4+y}(\text{I}_{5-y}\text{Te}_y)$ resulting from the partial sub-

stitution of I, respectively, by S, Se, or Te, were prepared according to the procedure described by Owens and Argue (3). The identification of the resulting products was carried out by means of x-ray diffraction.

Partial substitutions of I by S, Se, or Te (up to 6%) lead to solid solutions with the crystal structure of the compound RbAg_4I_5 . When the substitution is beyond that amount, other compounds besides $\text{RbAg}_{4+y}(\text{I}_{5-y}\text{X}_y)$, such as AgI , Rb_2AgI_3 , and Ag_2X , are originated. On the contrary, as long as the substituted compounds $\text{RbAg}_{4+y}(\text{I}_{5-y}\text{X}_y)$ with values of y between 0.05 and 0.3 were kept in inert dry atmosphere and protected from exposure to light, no evidence of decomposition was observed for periods of time longer than three years.

The Role of Water Moisture in the Decomposition of RbAg_4I_5 and Its Substituted Compounds

In order to study the influence of moisture on the decomposition of RbAg_4I_5 and its substituted compounds, samples of RbAg_4I_5 and of $\text{RbAg}_{4+y}(\text{I}_{5-y}\text{X}_y)$ were placed in a refrigerator at temperatures of 3° and -25°C , respectively. At appropriate time intervals the samples were removed from the refrigerator and analyzed with the help of x-ray diffraction. According to Eq. [2] the decomposition products Rb_2AgI_3 and AgI after a thorough decomposition of RbAg_4I_5 should be present in a ratio of about 28.4 weight percent (w/o) Rb_2AgI_3 to 71.6 w/o AgI .

In a first run of experiments samples of RbAg_4I_5 and of $\text{RbAg}_{4.1}(\text{I}_{4.9}\text{S}_{0.1})$ were investigated. After 15 days of exposure to the moist air of the refrigerator the decomposition was not completed (Table I).

In a second run of experiments, 7 samples of $\text{RbAg}_{4+y}\text{I}_{5-y}\text{S}_y$, with values of y between 0.1 and 0.7 were placed in a refrigerator at 3°C for 73 days. Similarly 7 samples of the same composition were placed in a refrigerator at -25°C for the same time. After that time the decomposition of the original compounds was completed. The results of the experiments conducted at 3°C confirmed the decomposition proposed in Eq. [2]. On the contrary, the mechanism of decomposition at -25°C seems to be somewhat different from that proposed in Eq. [2]. While the decomposition products $\beta\text{-AgI}$ appear in much the same proportion in both series of experiments, corresponding approximately to the proportion of that compound in Eq. [2], no presence of Rb_2AgI_3 has been observed at all among the decomposition products. Instead, it appears as a new compound which has not been identified.

The two preceding experiments have been performed without considering the relative humidity of the air. In a third run of experiments the water vapor pressure in the air at one determined temperature was adequately fixed. Six samples of each of RbAg_4I_5 and $\text{RbAg}_{4.2}(\text{I}_{4.8}\text{S}_{0.2})$ were placed in a desiccator containing a saturated aqueous solution of NaCl on the bottom. The desiccator was closed and put in a refrigerator at 3°C . After periods of time one sample of each substance was taken out and analyzed with the help of x-ray diffraction. The results of these experiments have been summarized in Table II.

The presence of a nonidentifiable phase among the decomposition products at 3°C , with its diffraction lines identical to the unknown phase by the decomposition at -25°C in slightly wet air, excludes the possibility of a low temperature modification of Rb_2AgI_3 .

Table I. Decomposition products (in weight percent) resulting after 15 days exposure of RbAg_4I_5 and $\text{RbAg}_{4.1}(\text{I}_{4.9}\text{S}_{0.1})$ to moist air at 3° and -25°C

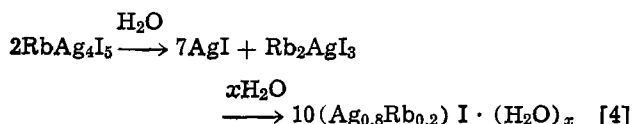
Original compound	Exposure at 3°C				Exposure at -25°C			
	RbAg_4I_5	Rb_2AgI_3	$\beta\text{-AgI}$	$\gamma\text{-AgI}$	RbAg_4I_5	Rb_2AgI_3	$\beta\text{-AgI}$	$\gamma\text{-AgI}$
RbAg_4I_5	25	35	15	25	15	45	15	25
$\text{RbAg}_{4.1}(\text{I}_{4.9}\text{S}_{0.1})$	20	30	15	35	70	10	15	5

Table II. Decomposition products (in weight percent) of RbAg_4I_5 and $\text{RbAg}_{4.2}(\text{I}_{4.8}\text{S}_{0.2})$ in air containing well-defined water vapor pressure at 3°C

Time of exposure (days)	Experiments with RbAg_4I_5				Experiments with $\text{RbAg}_{4.2}(\text{I}_{4.8}\text{S}_{0.2})$			
	RbAg_4I_5	Rb_2AgI_3	$\beta\text{-AgI}$	No identified phase	RbAg_4I_5	Rb_2AgI_3	$\beta\text{-AgI}$	No identified phase
0	100	0	0	0	100	0	0	0
0.5	25	22	50	0-10	25	25	50	0
1	0	0	60-70	30	0	0	60	40
3	12	0	80	0-10	Above this time of exposure it was completely impossible to analyze the samples, since the intensities and position of the Debye-Scherrer lines were changing continuously during the determination.			
8	0	0	65-80	20-30				
15	0	0	80	20				
30	0	0	90	5-15				

The unknown phase is therefore most probably a hydrate of Rb_2AgI_3 .

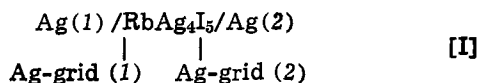
It seems that some of the primary decomposition products, especially the Rb_2AgI_3 hydrate, are not stable and a second decomposition reaction takes place simultaneously, the overall reaction being



Equation [4] is based on the fact that no lines of the Debye-Scherrer spectrum corresponding to RbI have been observed.

The Ionic Conductivity σ_i of RbAg_4I_5 and Its Substituted Compounds

The method used for the measurements of the electrical conductivity of the samples has been used previously by Miyatani (7), Rickert (8), and Valverde (9) and it has been called after Wagner the "IR drop method." With the help of the cell



is measured the IR-drop = ΔE -drop (potential drop) between the silver-grids (1) and (2), originated by the passage of a direct current (d.c.) across the specimen placed between the two silver-disk electrodes (1) and (2). The samples were pressed cylindrical pellets of 8 mm diam and about 15 mm length.

Considering that the electronic conductivity of RbAg_4I_5 and its substituted compounds is almost negligible (see next section), the measured conductivity σ coincides practically with the ionic conductivity σ_i of the compounds. Two series of measurements have been performed. First of all the variation of the ionic conductivity σ_i as a function of temperature for RbAg_4I_5 as well as the substituted compounds was investigated. In the second series of experiments the variation of the ionic conductivity with the composition y of the sample has been studied. The temperature for the first series of experiments could be gradually regulated from about 150°C to -50°C . The measurements have always been performed first with decreasing temperature and afterward with increasing temperature. Some of the results of these measurements have been represented in the Fig. 2-4.

The conductivity-temperature plots for all tested RbAg_4I_5 samples always show an inflection point between about 15° and 27°C . Moreover the two curves obtained with decreasing and increasing temperature do not fall together (see Fig. 2). It seems that below the inflection point an irreversible decomposition process sets in. After one complete round the final conductivity of the sample (curve b) is much lower than the initial one (curve a) which may be attributed to the fact that low temperatures notably accelerate the decomposition of the compound RbAg_4I_5 even in absence of moist air.

An inflection point can likewise be observed in the electrical conductivity-temperature plots of the first series members of the substituted compounds $\text{RbAg}_{4+y}\text{I}_{5-y}\text{S}_y$ and $\text{RbAg}_{4+y}\text{I}_{5-y}\text{Se}_y$ (Fig. 3), but this inflection point is less pronounced and will be displaced toward lower temperatures with increasing amounts of I substituted by S or Se. Moreover the two curves observed with decreasing and increasing temperature fall together. By the substituted compounds of the series $\text{RbAg}_{4+y}\text{I}_{5-y}\text{Te}_y$ no inflection points in

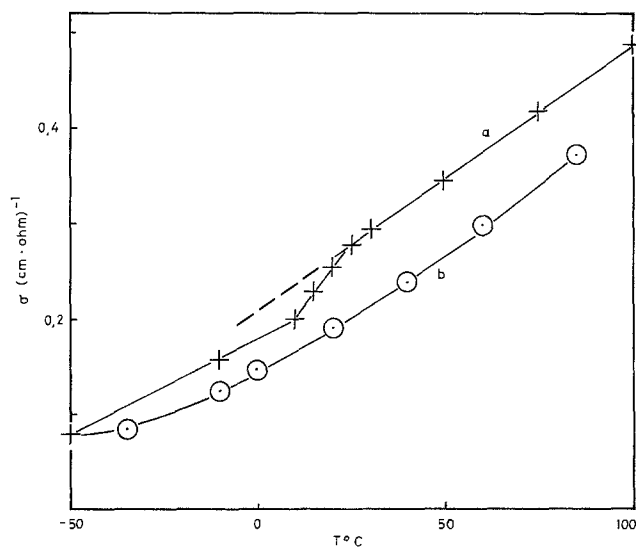


Fig. 2. Ionic conductivity σ_i of RbAg_4I_5 as a function of temperature. Curve a, measurements conducted with decreasing temperature; curve b, measurements conducted with increasing temperature.

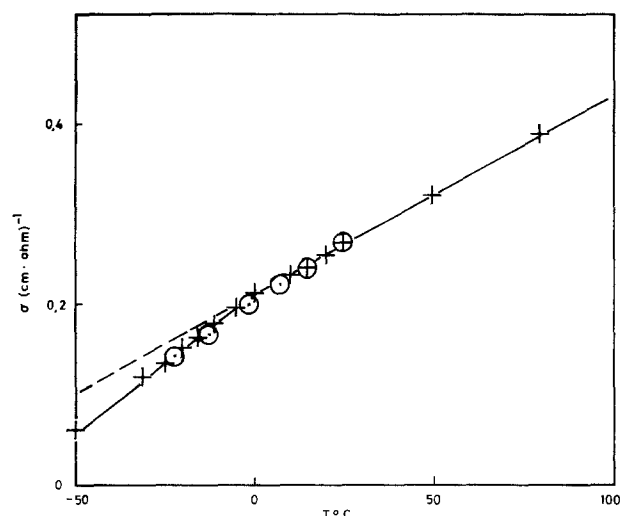


Fig. 3. Ionic conductivity σ_i of $\text{RbAg}_{4.2}\text{I}_{4.8}\text{Se}_{0.2}$ as a function of temperature. $+ - +$, Measurements conducted with decreasing temperature; $\odot - \odot$, measurements conducted with increasing temperature.

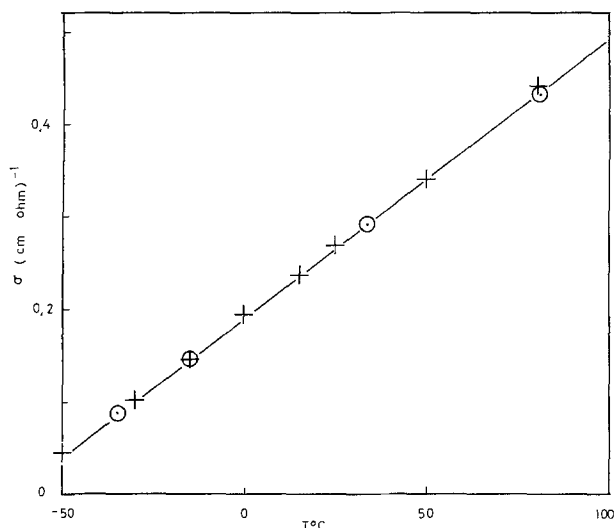


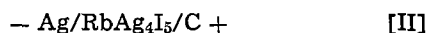
Fig. 4. Ionic conductivity σ_i of $\text{RbAg}_{4.1}\text{I}_{4.9}\text{Te}_{0.1}$ as a function of temperature. $+ - +$, Measurements conducted with decreasing temperature; $\circ - \circ$, measurements conducted with increasing temperature.

the electrical conductivity-temperature curves have been observed (see Fig. 4). The variation of the ionic conductivity σ_i with the composition y of the sample have been studied at 27°C in much the same way as the previous series of measurements. The results of these measurements for the compounds of the series $\text{RbAg}_{4+y}\text{I}_{5-y}\text{S}_y$ are shown in Fig. 5. The conductivity curves of the other two series $\text{RbAg}_{4+y}\text{I}_{5-y}\text{Se}_y$ and $\text{RbAg}_{4+y}\text{I}_{5-y}\text{Te}_y$ are very similar both qualitatively as well as quantitatively. Substitutions as large as 14% of the I by S, Se, or Te in the compound RbAg_4I_5 result in a decay in the electrical conductivity of only about 30% with respect to the value for pure RbAg_4I_5 .

The Electronic Conductivity σ_e of RbAg_4I_5 and Its Substitution Compounds

The values reported for the electronic conductivity of RbAg_4I_5 vary between 10^{-8} ($\Omega \cdot \text{cm}$) $^{-1}$ (10, 11) and 10^{-11} ($\Omega \cdot \text{cm}$) $^{-1}$ (12, 13). The method used for this measurement has been the one first used by Hebb (14) and Wagner (15, 16) and has been called by the last author the polarization method.

Using the cell



with the positive pole on the right side and applying a voltage below the decomposition potential of RbAg_4I_5 , silver ions migrate at first from the $\text{RbAg}_4\text{I}_5/\text{C}$ interface toward the silver electrode and electrons in the opposite direction. At the $\text{RbAg}_4\text{I}_5/\text{C}$ interface a metal deficit originates since the first migrated silver ions

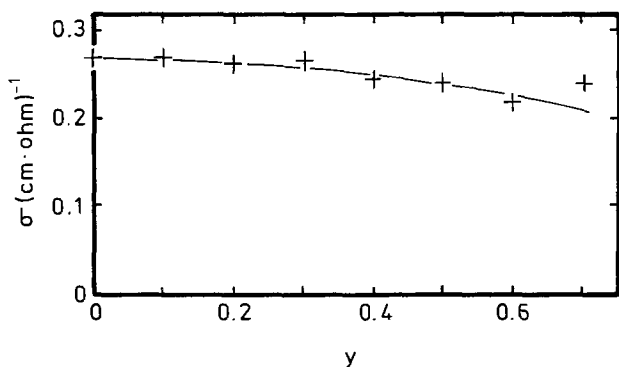


Fig. 5. Ionic conductivity σ_i at 27°C of the compound $\text{RbAg}_{4+y}\text{I}_{5-y}\text{S}_y$ as a function of the substituted mole fraction y .

are not replaced. That creates therefore a concentration gradient of silver ions across the sample of RbAg_4I_5 . Due to the concentration gradient formed, silver ions migrate in the opposite direction. Finally, under steady-state conditions the two flows in opposite directions are balanced and the current is carried only by excess electrons or electron holes.

The intensity I of the current in cell (II) according to Wagner and Wagner (17) is

$$I = \frac{RT}{F} \cdot \frac{A}{L} [\sigma_n^0(1 - e^x) + \sigma_p^0(e^x - 1)] \quad \text{[5]}$$

where A is the cross-section area and L the thickness of the sample, σ_n^0 and σ_p^0 are the conductivities due to excess electrons and electron holes, respectively, (for $a_{\text{Ag}} = 1$) and finally x denotes EF/RT .

Plotting the obtained values of I against the applied potentials E (V) one obtains curves like that in Fig. 6. Every obtained curve shows undoubtedly a plateau region, at which the value of the current I corresponds to a conductivity caused exclusively by excess electrons. Under these conditions the component of the electronic conductivity due to electron holes is negligible and Eq. [5] takes the form

$$\sigma_n^0 = \frac{I(\text{plateau})}{RT/F} \cdot \frac{L}{A} \quad \text{[6]}$$

For values of $I \gg I(\text{plateau})$ the electronic conductivity is essentially due to electron holes. One obtains likewise from Eq. [5]

$$\sigma_p^0 = \frac{I}{RT/F} \cdot \frac{L}{A} \cdot \frac{I}{e^x - 1} - \sigma_n^0 \quad \text{[7]}$$

the partial conductivity of the electron holes σ_p^0 . The point where the prolonged two branches of the curve meet together gives approximately the decomposition potential of the compound (see Table III). The value found for the decomposition potential of RbAg_4I_5 ($\sim 0.65\text{V}$) at 27°C is in good agreement with the value (0.67V) found by other authors (18). The de-

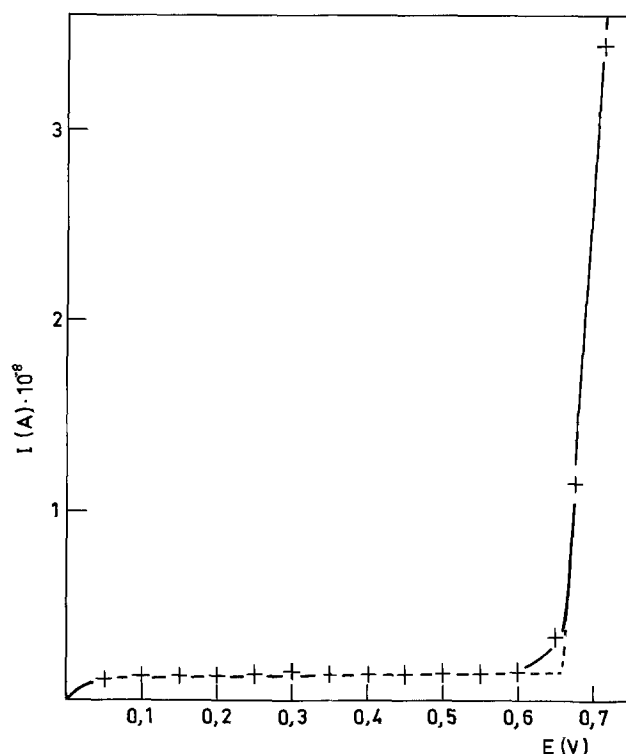


Fig. 6. Intensity-potential curve obtained by the determination of σ_e in RbAg_4I_5 at 27°C, using cell (II) and Wagner's polarization method.

Table III. Electronic conductivity and decomposition potential of RbAg_4I_5 and of several of its substitution compounds

Compound	Melting point ($^{\circ}\text{C}$)	Electronic conductivity at 27°C ($\Omega \cdot \text{cm}$) $^{-1}$	Decomposition potential at 27°C (mV)
RbAg_4I_5	228	$6 \cdot 10^{-8}$	650
$\text{RbAg}_{4-x}\text{I}_{4-x}\text{S}_{0.1}$	225	$8.5 \cdot 10^{-8}$	575
$\text{RbAg}_{4-x}\text{I}_{4-x}\text{S}_{0.1}$	230	$3.2 \cdot 10^{-8}$	650
$\text{RbAg}_{4-x}\text{I}_{4-x}\text{Te}_{0.2}$	235	$3.6 \cdot 10^{-8}$	600

composition potentials of the other studied compounds are about the same as, or only slightly smaller than, that of RbAg_4I_5 .

Concluding Remarks

The partial substitutions of iodine in RbAg_4I_5 by S, Se, or Te do not deteriorate the remarkably good ionic conductivity of this compound when the substituted amounts are $\leq 14\%$. These substitutions do not prevent the decomposition caused in RbAg_4I_5 by small amounts of water vapor in the air. The decomposition is very rapid in air saturated with water vapor. The final decomposition products under these conditions are not the ones corresponding to Eq. [2], as it can be seen by the results of Table II. Most probably the first originated compound Rb_2AgI_3 is not stable either under these conditions and the decomposition reaction proceeds further according to Eq. [4].

The ionic conductivity of RbAg_4I_5 is considerably deteriorated when samples of this compound are placed in inert dry atmospheres to low temperatures (up to -50°C) for prolonged periods of time. On the other hand, the substituted compounds behave quite differently under the same experimental conditions. No irreversible reaction has been observed. The curves are either straight lines over the whole range of temperature (Fig. 4) or, in a few cases, show a bending below the room temperature (Fig. 3). The position of the bend point is displaced toward lower temperatures with increasing amounts of substituted iodine. But even in those cases the samples recover their original conductivity when the temperature is increased again. These results are interpreted as sufficient evidence for a thermodynamic stabilization of the solid electrolyte RbAg_4I_5 by partial substitution of I by S, Se, or Te.

Acknowledgments

The financial support of this work by the Firm Robert Bosch GmbH in Stuttgart, Germany Federal

Republic, is gratefully acknowledged. I am very much indebted to the late Prof. Carl Wagner for his suggestions and helpful discussions. I also thank Dr. Reuter from Robert Bosch GmbH for the x-ray structural analysis of the samples.

Manuscript submitted July 19, 1979; revised manuscript May 2, 1980.

Any discussion of this paper will appear in a Discussion Section to be published in the June 1981 JOURNAL. All discussions for the June 1981 Discussion Section should be submitted by Feb. 1, 1981.

Publication costs of this article were assisted by Instituto de Quimica-Fisica "Rocasolano."

REFERENCES

1. J. N. Bradley and P. D. Greene, *Trans. Faraday Soc.*, **62**, 2069 (1966).
2. J. N. Bradley and P. D. Greene, *ibid.*, **63**, 424 (1967).
3. B. B. Owens and G. R. Argue, *Science N.Y.*, **157**, 308 (1967).
4. S. Geller, *ibid.*, **157**, 310 (1967).
5. L. E. Topol and B. B. Owens, *J. Phys. Chem.*, **72**, 2106 (1968).
6. S. Chandra and V. K. Mohabey, *J. Phys. D*, **8**, 576 (1975).
7. S. Miyatani, *J. Phys. Soc. Jpn.*, **10**, 786; **13**, 317, 341 (1958).
8. H. Rickert, *Z. Physik. Chem.*, **23**, 355 (1960).
9. N. Valverde, *ibid.*, **70**, 128 (1970).
10. M. DeRossi and B. Scrosati, *Elettrotecnica*, **52**, 1 (1970).
11. G. R. Argue, G. R. Hills, and B. B. Owens, U.S. Pat. 3,443,997.
12. J. E. Oxley and J. R. Humphrey, *Atomics Int. Final Rep.*, July 22-Oct. 22, 1968.
13. G. R. Argue, I. J. Groce, and B. B. Owens in *Proceedings of International Power Sources Symposium*, Brighton, p. 241 (1968).
14. M. Hebb, *J. Chem. Phys.*, **20**, 185 (1952).
15. C. Wagner, in *Int. Com. Electrochem. Thermodyn. and Kinet.*, Proc. 7th Meeting, Lindau, 1955, Butterworth Scientific Publications, London (1957).
16. C. Wagner, *Z. Electrochem.*, **60**, 4 (1956).
17. J. B. Wagner and C. Wagner, *J. Chem. Phys.*, **26**, 1597 (1957).
18. M. DeRossi, G. Pistola, and B. Scrosati, *This Journal*, **116**, 1642 (1969).

Crystallization of Amorphous Alloys of Rare Earths and 3d Transition Metals

K. H. J. Buschow and A. G. Dirks

Philips Research Laboratories, Eindhoven, The Netherlands

ABSTRACT

Amorphous rare earth rich alloys of 3d transition metals were prepared by melt spinning. Their crystallization behavior was studied by means of differential scanning calorimetry, x-ray diffraction, and transmission electron microscopy. In order to obtain an estimate of the relative importance of the rare earth component the thermal stability of various amorphous alloys of the type $R_{69}Ni_{31}$ has been studied. The role played by the transition-metal component was assessed by investigating the crystallization behavior of various $Gd_{1-x}M_x$ alloys. Finally, a series of amorphous $Tb_{1-x}Fe_x$ and $Er_{1-x}Fe_x$ alloys has been made in search of the influence of the R/M ratio upon the crystallization characteristics.

The low thermal stability of amorphous Gd-Fe alloys (1) contrasts sharply with the relatively high thermal stability ($T \sim 400^\circ\text{C}$) of Zr-Fe or Th-Fe alloys (2) in which Fe is combined with metals having metallic radius and electronegativity similar to those of Gd. Furthermore the tendency to glass formation generally is highest near deep eutectics (3). The Gd-Fe system seems to be an exception (1) to this rule. This apparent anomalous behavior of the Gd-Fe alloys has prompted a more detailed investigation of the crystallization behavior of amorphous rare earth transition metal alloys.

In order to obtain an estimate of the relative importance of the rare earth component (R) some results obtained on alloys of the series $R_{69}Ni_{31}$ ($R = \text{La, Nd, Gd, Tb, Dy, Er}$) will be presented first. Various $Gd_{1-x}M_x$ alloys ($M = \text{Fe, Mn, Co, Ni}$) were also investigated making it possible to assess the role played by the transition metal component. In these alloys the 3d atom concentration was chosen to be equal to $x = 0.40$. In some cases also slightly lower and higher 3d atom concentrations were applied. Finally, the results obtained on the R-Fe systems ($R = \text{Tb, Er}$) will be discussed.

Experimental

Amorphous alloys were prepared by arc melting followed by melt spinning in a purified argon gas atmosphere. Small parts of each ribbon were investigated by means of x-ray diffraction. CuK_α radiation was applied in combination with an x-ray monochromator. The thermal stability of the alloys was studied by means of a differential scanning calorimeter (DSC) du Pont 910, again using an atmosphere of purified argon gas, we used a heating rate of $50^\circ\text{C}/\text{min}$. The origin of the observed heat effects has been studied by heating the ribbons to the distinct stages in the crystallization process followed by cooling and x-ray diffraction. Thin specimens of the samples, needed for transmission electron microscopy (TEM) were obtained by means of ion milling.

Results

DSC and x-ray diffraction.—The crystallization temperatures (corresponding to the first peak maximum in the DSC tracings) of various amorphous rare earth nickel alloys of the composition $R_{69}Ni_{31}$ are compared in Fig. 1. It is seen that T_{cr} increases steadily in going from La to the heavier rare earth elements. The change in thermal stability upon variation of the transition-metal species was investigated by DSC measurements of series of $Gd_{1-x}M_x$ ribbons. It was found

Key words: crystallization, alloy, TEM.

that this stability increases in the sequence $M = \text{Fe, Mn, Co, Ni}$ ($x = 0.4$) when x was kept constant.

Typical results of DSC tracings are shown in Fig. 2. The behavior of $Gd_{69}Ni_{31}$ is an example where the crystallization involves two stable crystalline phases (Gd_3Ni : $T_{cr} = 285^\circ\text{C}$ and $GdNi$: $T_{cr} = 345^\circ\text{C}$). Crystallization in amorphous $Gd_{65}Co_{35}$ first involves the phase Gd_3Co_3 and at slightly higher temperatures also the phase Gd_3Co . In amorphous $Gd_{55}Co_{45}$ crystallization entails the phase Gd_4Co_3 . The amorphous alloy $Gd_{60}Co_{40}$ (not shown in Fig. 2) crystallizes at 310°C . The behavior of $Gd_{60}Mn_{40}$ is an example where the crystallization proceeds already slightly above room temperature and involves a metastable Gd-Mn compound. The broad peak centered around 300°C in the DSC diagram presumably reflects the increase with temperature of the amount of the material that has crystallized. This crystallization is not accompanied by a sharp thermal effect. The peak shown at 460°C in the DSC tracing (Fig. 2) is due to crystallization of the stable C15 compound $GdMn_2$. In the case of amorphous Gd-Fe alloys the first crystallizing phases are α -Gd and α -Fe. Crystallization of the cubic C15 phase $GdFe_2$ takes place again at much higher temperatures.

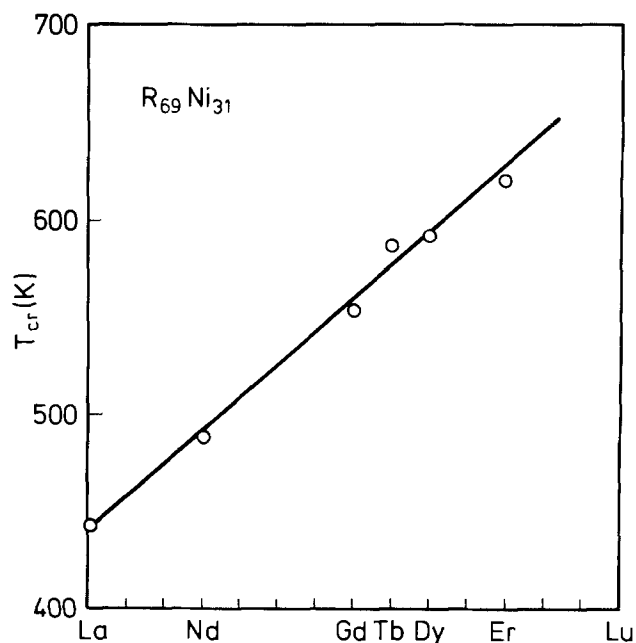


Fig. 1. Crystallization temperature in various amorphous rare earth nickel alloys.

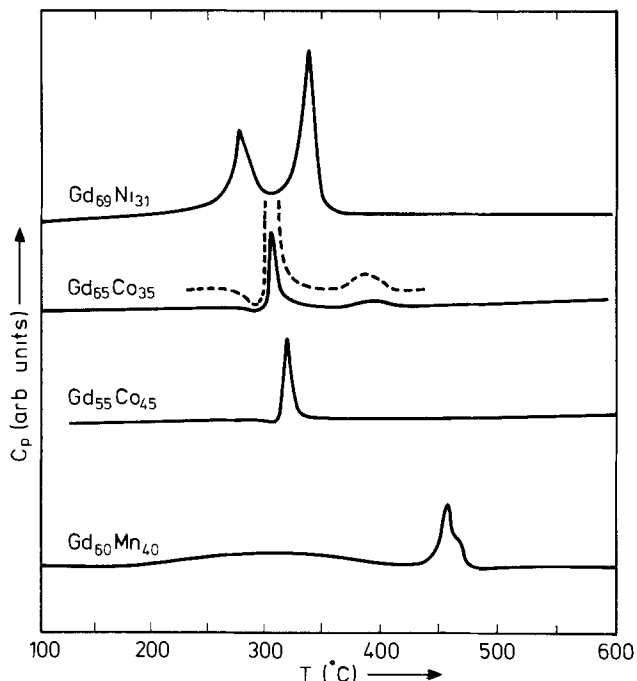


Fig. 2. DSC tracings of various amorphous alloys of Gd with 3d transition metals. The broken line in the case of $Gd_{65}Co_{35}$ was obtained by using a ten times higher sensitivity.

DSC data on series of Tb-Fe and Er-Fe ribbons are shown in Fig. 3. All Tb-containing alloys show up a similar behavior: at temperatures between 100° and 400°C the smeared-out thermal effect is due to the crystallization of α -Tb. The broadened x-ray diffraction lines of the α -Tb phase formed at low temperatures (circa 100°C) indicate the presence of rather small crystallites. According to the x-ray diagrams it can be concluded that the $Tb_{1-x}Fe_x$ ribbons heated to temperatures above 400°C are composed of a mixture of

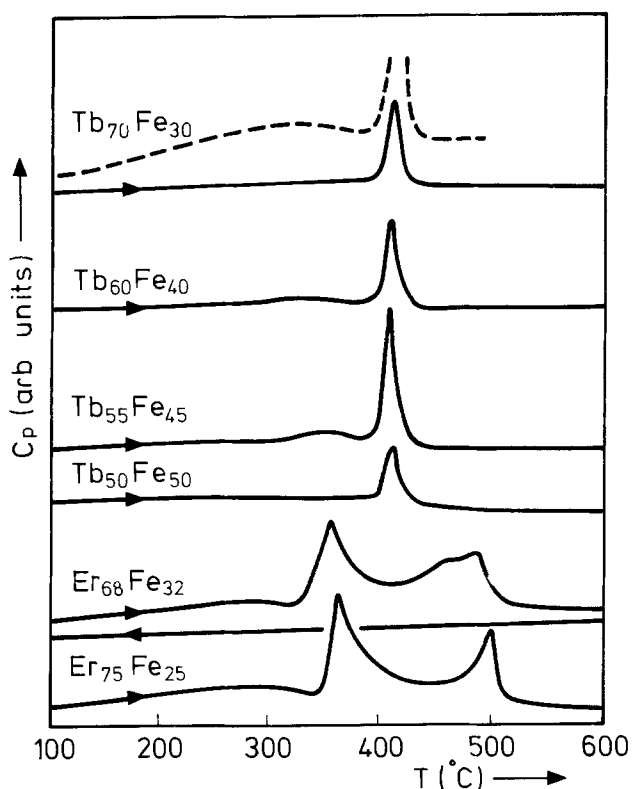


Fig. 3. DSC tracings of various amorphous terbium-iron and erbium-iron alloys. The broken line in the case of $Tb_{70}Fe_{30}$ was obtained with a ten times higher sensitivity.

the crystalline phases $TbFe_2$ and α -Tb. This is in agreement with the expectations based on published data on R-Fe equilibrium diagrams (4, 5). The DSC data in Fig. 3 for the $Er_{1-x}Fe_x$ ribbons make it clear that in the Er alloys, too, crystallization sets in considerably below the temperature where the sharp crystallization peak is found in the DSC tracings. However, the first crystallizing phase is not the rare earth metal, as in Gd-Fe (1) and Tb-Fe alloys, but some metastable Er-Fe intermetallic compound. The smeared-out thermal effect is correlated with the formation of a metastable compound with unknown structure: only one diffraction peak corresponding to a spacing $d = 2846\text{\AA}$ is observed. Heating to temperatures over 300°C initiates the crystallization of another metastable compound ($d = 2.919\text{\AA}$) and of α -Er. Diffraction lines due to the compound $ErFe_2$ (cubic Laves phase) occur together with those of α -Er in samples heated to temperatures higher than 500°C. These results can be summarized as follows. The two peaks in the DSC tracings near 350°C and 500°C are heat effects due to the formation of crystalline α -Er and $ErFe_2$, respectively. Minor precipitation of α -Er occurs already at temperatures somewhat below 350°C, but at much lower temperatures crystallization involves two metastable Er-Fe phases.

TEM results.—The TEM investigations were restricted to a few representative examples. In all amorphous Gd-Co and R-Ni ribbons mentioned above primary crystallization involves a crystalline phase, present in the corresponding phase diagram, that has a composition not much different from that of the amorphous alloy. This crystallization is accompanied by a sharp peak in the DSC tracing (T_{cr}). Below T_{cr} , x-ray diffraction revealed no crystalline phases. Examination of a $Gd_{65}Co_{35}$ sample by TEM revealed the presence of still intact amorphous regions together with regions in which crystallization had taken place. The nature of the crystalline material was inferred from the corresponding SAD patterns. These patterns were quite complex and pointed to the presence of a low symmetry Gd-Co intermetallic compound rather than to α -Gd or α -Co.

A quite different picture emerges from the TEM investigation of R-Fe ribbons, represented by $Gd_{60}Fe_{40}$ and $Tb_{70}Fe_{30}$ heated to 250° and 100°C, respectively. The microstructure of these alloys consists of crystalline regions embedded in an amorphous matrix (see, for example, Fig. 4). Electron diffraction data made it clear that part of the crystalline material is α -Gd resp. α -Tb. In the Gd-alloy a second phase was

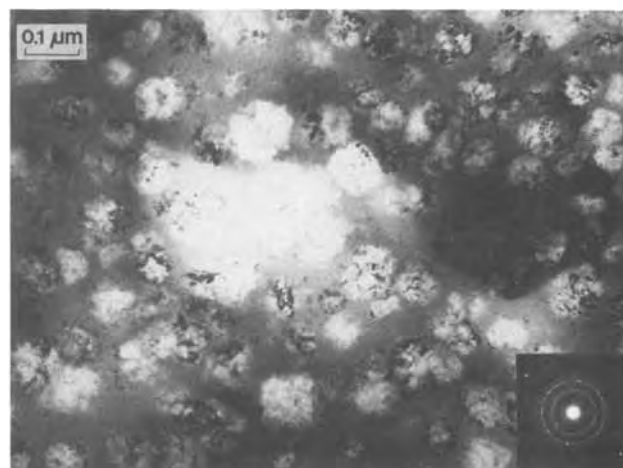


Fig. 4. Transmission electron micrograph of an ion-milled $Tb_{70}Fe_{30}$ ribbon after heating to 100°C. The bright field image shows primary crystallites in an amorphous matrix. The electron diffraction pattern in the inset shows both patchy rings (α -Tb crystals) and diffuse halos.

found to consist of α -Fe in the form of crystallites of rather small dimensions (diameter $\leq 100 \mu\text{m}$); this might explain the absence of α -Fe peaks in the x-ray diagrams. In the Tb-alloy no evidence was found of the presence of α -Fe crystallites with electron diffraction techniques. These results seem to indicate that with increasing temperature part of the Tb can precipitate in amorphous $\text{Tb}_{70}\text{Fe}_{30}$, leaving an amorphous matrix of slightly higher Fe content.

Discussion

The above results can be reasonably well understood in terms of the cluster model of liquid structures (6,7). The occurrence of clusters can be considered as resulting from compositional fluctuations. The tendency to cluster formation between unlike atoms increases as the heat of mixing ΔH_m of the two composing elements becomes more negative (cluster formation between like atoms decreases in the same sense). The reason for this is the gain in free energy that is obtained if the coordination of a given atom with unlike atoms becomes higher than that associated with the random distribution of atoms in the amorphous state. It can be shown (8,9) that for rare earth 3d alloys $\text{Gd}_{1-x}\text{M}_x$ (with $x < 0.5$) ΔH_m becomes more negative in the sequence $M = \text{Fe, Mn, Co, Ni}$. It is about -1 kJ/mole alloy in the case of Fe but larger than -30 kJ/mole alloy in the case of Ni. Clustering in the liquid state between unlike atoms will therefore be low in the case of Fe but will increase towards Ni. In the amorphous alloys such clusters can be regarded as embryos that facilitate nucleation. It is understandable therefore that nucleation of intermetallic compounds proceeds less easily in the case of the amorphous Gd-Fe alloys. On the other hand it was shown by Zielinski and Matyja (10) that large negative ΔH_m values lead to low interdiffusion constants and hence to low growth rates. As a result glass formation will be easier in alloys with large negative ΔH_m values.

Once an amorphous alloy has been obtained by means of rapid quenching from the melt, its thermal stability will be largely determined by the temperature dependence of the viscosity (11,12). Crystallization will set in whenever the temperature is high enough to match ΔE . In previous investigations ΔE has been taken equal to the energy ΔH_{1v} needed to create a hole of the size of the smallest type of atom in the solid alloy (2). Using the results of an analysis of the enthalpies of formation of monovacancies in pure metals given by Miedema (13) it can be shown that the enthalpy of formation of a hole of the size of a 3d atom (ΔH_{3d}) in rare earth rich R_{1-x}M_x alloys is considerably less than ΔH_{3d} in the pure 3d metals. Furthermore, in alloys of fixed composition x and fixed element M, the values of ΔH_{3d} increase if one proceeds through the rare earth series from La to Lu. This means that T_{cr} is expected to increase in the same sense. Inspection of the results in Fig. 1 shows that, qualitatively, good agreement exists with experimental findings.

The discussion of ΔH_{3d} given above refers to a situation where no account has yet been taken of a posi-

tive or negative interaction between the R atoms and the 3d atoms. One may expect that it will be more difficult to create a hole in the alloy if there exists a strongly attracting interaction between the R and 3d atoms. In other words, ΔH_{3d} will increase as ΔH_m becomes more negative in going from $R = \text{La}$ to $R = \text{Lu}$ and also in the sequence $M = \text{Fe, Mn, Co, Ni}$ as already mentioned above. In the first sequence the effect of an increasingly negative ΔH_m is to reinforce somewhat the R dependence of T_{cr} mentioned above in connection with the results of Fig. 1. With regard to the second sequence we note that ΔH_m of Fe and Mn alloys is almost negligible whereas it is strongly negative in Co and Ni alloys.

Conclusions

It has been shown that there are appreciable differences in the crystallization behavior of amorphous rare earth transition metal alloys R_{1-x}M_x . The thermal stability is lowest in alloys of light rare earth elements but increases if one proceeds through the lanthanide series. It also increases in the sequence $M = \text{Fe, Mn, Co, Ni}$. It is proposed that the observed differences in the type of the crystallization originate primarily from differences in the heats of alloying, leading to nucleation difficulties in the case of small heats of alloying. In order to explain differences in the temperature of crystallization other heat effects also have to be taken into consideration.

Manuscript submitted Nov. 15, 1979; revised manuscript received May 16, 1980. This was Paper 396 presented at the Los Angeles, California, Meeting of the Society, Oct. 14-19, 1979.

Any discussion of this paper will appear in a Discussion Section to be published in the June 1981 JOURNAL. All discussions for the June 1981 Discussion Section should be submitted by Feb. 1, 1981.

Publication costs of this article were assisted by Philips Research Laboratories.

REFERENCES

1. K. H. J. Buschow, *J. Less-Common Met.*, **66**, 89 (1979).
2. K. H. J. Buschow and N. M. Beekmans, *Phys. Rev. B* **19**, 3843 (1979); *Phys. Status Solidi A*, **56**, 505 (1979).
3. P. Duwez and S. C. H. Lin, *J. Appl. Phys.*, **38**, 4096 (1967).
4. K. H. J. Buschow, *J. Less-Common Met.*, **16**, 45 (1968).
5. K. H. J. Buschow and A. S. van der Goot, *Phys. Status Solidi*, **35**, 515 (1969).
6. R. J. Hodgkinson, *Philos. Mag.*, **23**, 673 (1971).
7. J. Sak and M. H. Cohen, *J. Non-Cryst. Solids*, **8-10**, 696 (1972).
8. A. R. Miedema, *J. Less-Common Met.*, **32**, 117 (1973) and **46**, 67 (1976).
9. A. R. Miedema, F. R. de Boer, R. Boom, and J. W. F. Dorleijn, *Calphad*, **1**, 341 (1977).
10. P. G. Zielinski and H. Matyja, in "Rapidly Quenched Metals," N. J. Grant and B. C. Giessen, Editors, p. 237, MIT Press, Cambridge, Mass.
11. D. R. Uhlmann, *J. Non-Cryst. Solids*, **7**, 337 (1972).
12. H. A. Davies, *Phys. Chem. Glasses*, **17**, 159 (1976).
13. A. R. Miedema, *Z. Metallkd.*, **70**, 345 (1979).

Pattern Etching of CVD $\text{Si}_3\text{N}_4/\text{SiO}_2$ Composites in HF/Glycerol Mixtures

Cheryl A. Deckert*¹

RCA Laboratories, Princeton, New Jersey 08540

ABSTRACT

Solutions of concentrated (49%) aqueous HF in glycerol have been found to etch CVD Si_3N_4 films faster than thermally grown SiO_2 over a wide temperature range. Since silicon dioxide films are etched much faster than silicon nitride films in aqueous HF media, this result is quite surprising, and the mechanism for the etch rate reversal is not understood at present. HF/glycerol mixtures have been used to pattern a variety of $\text{Si}_3\text{N}_4/\text{SiO}_2/\text{Si}$ composite structures using either photoresist or metal masks.

Several types of integrated circuit devices are fabricated using multiple dielectric coatings. Structures bearing films of silicon nitride over silicon dioxide are useful in such applications as high reliability devices, localized nitride-masked oxidation processes, MNOS memory devices, etc.

In many cases, the composite structures consist of a high temperature, chemically vapor-deposited (CVD) Si_3N_4 film over either thermally grown SiO_2 or a densified CVD SiO_2 film on silicon (Fig. 1a). Depending on the particular application, an overlying film of undensified CVD SiO_2 may also be included (Fig. 2a). In order to pattern these composites, openings must be etched through the nitride and oxide films using a masking layer.

Dry etching techniques, such as plasma etching (1), have greatly increased in popularity over the past few years, and $\text{Si}_3\text{N}_4/\text{SiO}_2$ composites can be patterned in this manner, using, for instance, a CF_4 plasma. Plasma etching offers the advantage that only minimal mask-to-substrate adhesion is required, since the tendency for etchant undercutting is negligible; hence plasma etching is quite suitable for complex, high resolution pattern delineation.

The steep edge profiles characteristic of many dry etching processes do facilitate fabrication of high density microstructures, but patterning of multiple dielectric layers typically involves only the opening

of contact holes. Ideally, for this step, the etching process should produce slightly tapered walls in the dielectric films (Fig. 1b and 2b), so that subsequently deposited metal films will cover the edges uniformly and completely. The usefulness of sloped dielectric layers in achieving metallization of high yield and reliability is well known, since thinning of the metal layer can occur over sharp corners in the dielectric (1, 2). Ideally a 45° taper should be used; however, lower angles are acceptable if resolution of the top surface of the delineated film, of course, will maintain the same dimension as the masking material unless either significant undercutting or overetching takes place. Thus use of tapering procedures does not typically require lithographic biases. Although it is possible, in some cases, to achieve tapered edges using plasma-assisted etching techniques (1), plasma etching processes generally involve poor selectivity and, hence, involve some etching of the layer beneath the one(s) being etched. Thus we centered our efforts toward achieving the desired type of edge profile on wet chemical procedures. Both for the sake of simplicity and to avoid formation of an undesirable film "lip," (3-5) it would be advantageous if the etching process could be carried out in a single step, using an etchant that would dissolve all the various layers sequentially.

In order to etch a multiple layer film so as to obtain a sloped edge, it is necessary that the etch rates of the various films decrease in the order $r_1 \geq r_2 \geq \dots \geq r_n$, where r_1 is the etch rate of the uppermost layer and r_n is the etch rate of the bottommost layer.

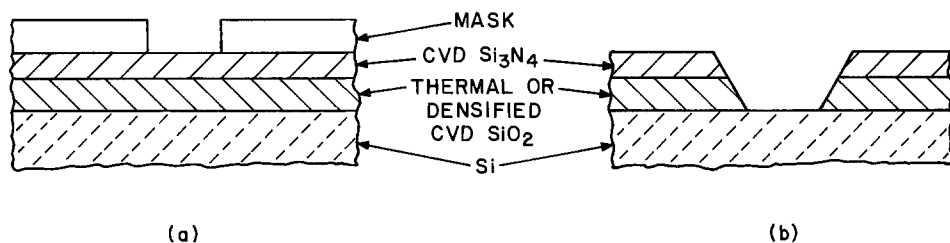


Fig. 1. (a) $\text{Si}_3\text{N}_4/\text{SiO}_2/\text{Si}$ composite structure bearing delineated mask film; (b) etched composite structure having desired sloped edges (vertical dimension exaggerated).

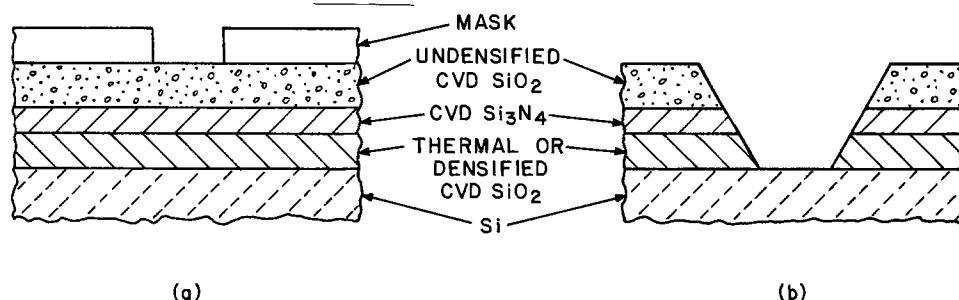


Fig. 2. (a) $\text{SiO}_2/\text{Si}_3\text{N}_4/\text{SiO}_2/\text{Si}$ composite structure bearing delineated mask film; (b) etched composite structure having desired sloped edges (vertical dimension exaggerated).

* Electrochemical Society Active Member.

¹ Present address: Shipley Company, Newton, Massachusetts 02162.

Key words: dielectric films, taper, fluoride, integrated circuit processing.

Thus, for the silicon nitride-silicon dioxide composite structures, a suitable wet chemical process should have r (undensified CVD SiO_2) $\cong r$ (CVD Si_3N_4) $\cong r$ (thermal or densified CVD SiO_2) $\gg r$ (Si).

In general, CVD Si_3N_4 is a rather difficult material to etch at an appreciable rate. The use of hot (160°–180°C) orthophosphoric acid (85% H_3PO_4) (6) or phosphoric-sulfuric acid (4) mixtures are well-known methods, but decomposition of the etchants (loss of water and conversion into higher phosphates) occurs with prolonged heating. Thus, even if an appropriate reagent were added to promote simultaneous etching of SiO_2 , control of the relative etch rates of the films would be very difficult to achieve.

Other systems have been proposed for simultaneous etching of Si_3N_4 and SiO_2 films (3, 5, 7). All these systems suffer from a combination of disadvantages, including the necessity of maintaining high temperatures (>90°C) in aqueous systems or the difficulty of achieving the desired etch rate ratio. In particular it is often difficult to etch the nitride film at a sufficiently fast rate because Si_3N_4 etching characteristics may vary considerably depending on the exact film deposition conditions used, specifically the deposition temperature and the ammonia/silane ratio in the reactant mixture.

The use of H_3PO_4 - HBF_4 mixtures at 100°–110°C has been reported (7) to give r (CVD Si_3N_4) $\cong r$ (thermal SiO_2), but in practice we have found that some typical nitride compositions etch more slowly than SiO_2 under these conditions. The system HF/ H_2O at 90°–100°C gives (3, 5) the desired etch rate ratio at very low HF concentrations only ($\leq 0.1\text{M}$); under these conditions evaporation of H_2O and HF tends to alter the relative and absolute etch rates (8). Another reported (9) etchant system for $\text{Si}_3\text{N}_4/\text{SiO}_2$ composites is high temperature water (>100°C), this requires use of a high pressure reactor, which is undesirable for a factory process.

From several recent studies (3, 5, 10), it is known that aqueous fluoride etchants can be made to etch CVD Si_3N_4 faster relative to thermal SiO_2 by increasing temperature. For this reason it was attempted to utilize, as a preferential Si_3N_4 etchant, moderately high temperature (100°–140°C) HF solutions in a relatively nonvolatile solvent resembling water in its ionization and solvation behavior. Glycerol ($\text{CH}_2\text{OHCHOHCH}_2\text{OH}$) [$K_a = 7 \times 10^{-15}$ (25°C, aqueous solution), bp = 290°C] was chosen as a suitable solvent for these studies, and this paper deals with the interesting etching characteristics of the HF/glycerol system.

Experimental

The substrates used in both the etch rate tests and the composite layer patterning tests were polished, single crystal silicon wafers.

For the etch rate tests, a single dielectric was produced on the wafers by one of the following methods: (a) Approximately 6000Å of thermally grown SiO_2 was produced at 1000°C in steam at atmospheric pressure. (b) Approximately 1 μm of undensified CVD SiO_2 was deposited from a silane-oxygen-nitrogen gas mixture at 450°C. (c) Densified CVD SiO_2 was prepared by baking undensified CVD SiO_2 at 800°C in dry nitrogen for 15 min.

Three different formulations of CVD Si_3N_4 were used as described below. In order to avoid excessive stress buildup, nitride film thicknesses were limited to about 2100Å. (d) The flow rates of SiH_4 , NH_3 , and N_2 were 0.55, 3.14, and 40 liters/min; the NH_3/Si molar ratio was therefore ≈ 6 . A 750°C reactor temperature was employed. (e) The flow rate of N_2 carrier gas through SiCl_4 at 25°C was 110 cm^3/min , resulting in transport of 0.21 g/min SiCl_4 . The flow rate of NH_3 was 600 cm^3/min . These conditions give $\text{NH}_3/\text{Si} = 20$. The nitrogen main flow was 225 liters/min and the

reactor temperature was 875°C. (f) Using the same reactor as (e), the SiCl_4 supplied to the reactor = 0.22 g/min; NH_3 flow = 450 cm^3/min ; N_2 main flow = 224 liters/min. Thus $\text{NH}_3/\text{Si} \approx 14$.

The initial thicknesses of the SiO_2 films were measured by the interference fringe method utilizing a Beckman DB-G spectrophotometer. Initial thicknesses of the Si_3N_4 films were measured by a technique based on relative reflectivity of a monochromatic beam of light (11). Two different wavelengths of light were employed. All oxide and nitride samples were etched nearly to completion, and the final thicknesses were determined based on the interference color of the residual films. The order number was verified by masking off an area of each etched sample and stripping the remaining film. The estimated error in the etch rates was ± 5 –8%; this accuracy was thought to be sufficient for our purposes.

HF/glycerol solutions were prepared by mixing a specified volume (33, 67, or 100 ml) of concentrated (49%) aqueous HF with reagent grade glycerol (assay <0.4% water) to give 1, 2, or 3M solutions.

Other materials used in formulating etchants, as is described in the text, were also of reagent grade quality. Etchant temperatures were controlled to within $\pm 0.5^\circ\text{C}$.

For the composite layer patterning tests, various types of Si_3N_4 /thermal SiO_2 or undensified CVD $\text{SiO}_2/\text{Si}_3\text{N}_4$ /thermal SiO_2 samples were prepared, masked as described below and etched in an HF/glycerol solution.

Etch Rates Studies

As discussed earlier, the original motivation for studying the HF/glycerol system was that relatively high (>100°C) etching temperatures were thought necessary to achieve r (CVD Si_3N_4) $\cong r$ (thermal SiO_2). Initial experiments conducted at 110°C using moderately concentrated HF/glycerol solutions did, in fact, produce the desired etch rate ratios, (r (Si_3N_4)/ r (SiO_2) > 1). However, the observed etch rates are anomalous in two respects, based on the rates in aqueous HF (3, 8). First, the nitride is etched much more rapidly, relative to the oxide, than would be expected at this temperature; and second, the absolute values of the etch rates for both nitride and oxide are considerably smaller than would be expected. Based on the first of these observations, it appeared that acceptable etch rate ratios could be achieved at even lower temperatures (<100°C), and indeed this was found to be the case. Etch rates were determined for undensified and densified CVD SiO_2 films, thermal SiO_2 , and three different formulations of CVD Si_3N_4 (NH_3/Si molar ratio in gas mixture varying from 6 to 20) in 1, 2, and 3M HF/glycerol solutions at 25°, 70°, 80°, and 90°C. These etch rate data are summarized in Fig. 3–6. The following observations can be made: (i) In all cases, undensified CVD SiO_2 is etched faster than CVD Si_3N_4 , which is etched faster than thermal SiO_2 . (ii) All three types of CVD Si_3N_4 are etched at very similar rates. This fact is especially useful for utilization of the etchant in different manufacturing areas. (iii) Densified CVD SiO_2 is etched slightly faster than nitride at 25°C, but slightly slower at the elevated temperatures.

Based on these etch rates, it is seen that a wide range of temperatures and HF concentrations can be used to produce sloped edges in the two- or three-layer dielectric film composites of Fig. 1 and 2. The desired etch rates and edge contours will determine the exact parameters used. In practice, HF concentrations lower than $\sim 1\text{M}$ lead to prohibitively long etching times for dielectric films of typical thicknesses, and concentrations greater than $\sim 3\text{M}$ lead to handling problems. Similarly, the temperature range from 60° to 90°C is thought to be optimum.

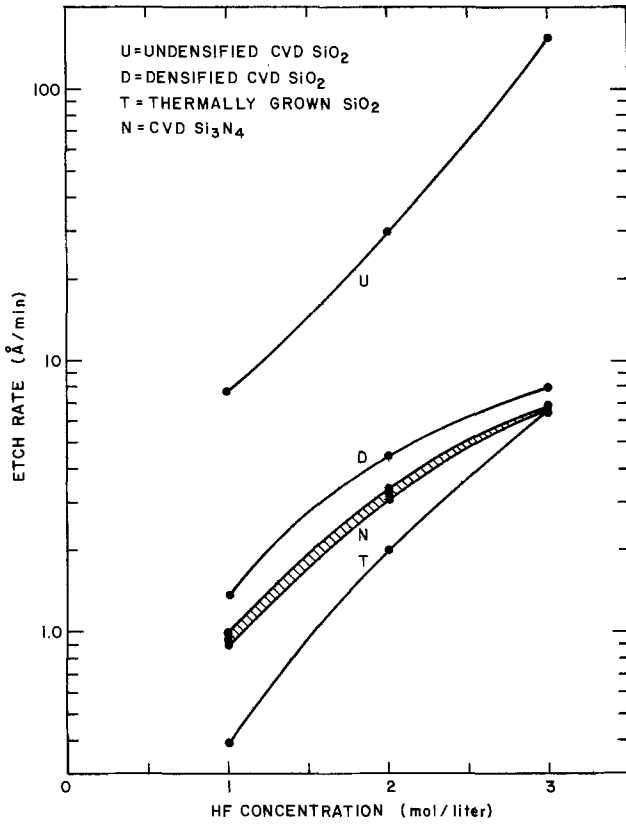


Fig. 3. Etch rates of Si₃N₄ and SiO₂ films in HF/glycerol solutions at 25°C.

Reversal of Nitride/Oxide Etch Rate Ratio

As mentioned above, both the absolute and relative etch rates of Si₃N₄ and thermally grown SiO₂ in HF/glycerol were unexpected, based on previous etch rate studies conducted using aqueous HF systems (3, 8). For ease of comparison, the etch rates for these two

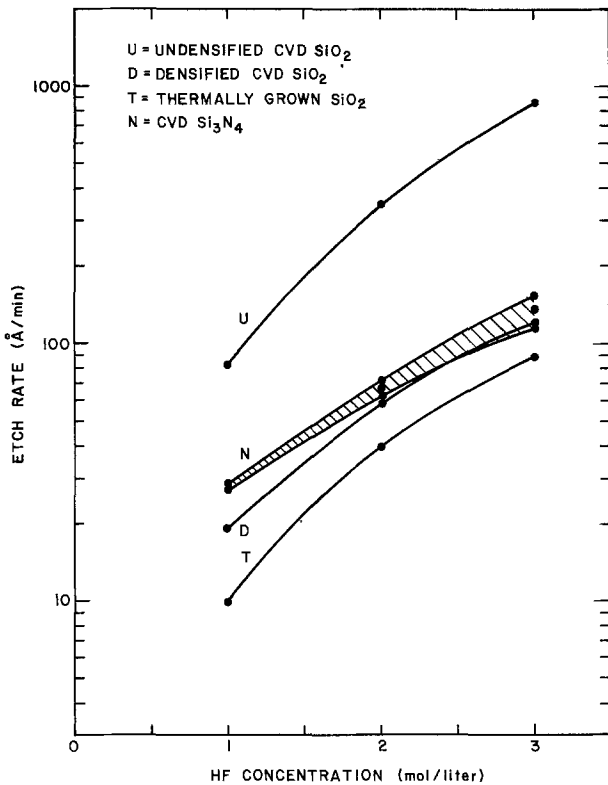


Fig. 4. Etch rates of Si₃N₄ and SiO₂ films in HF/glycerol solutions at 70°C.

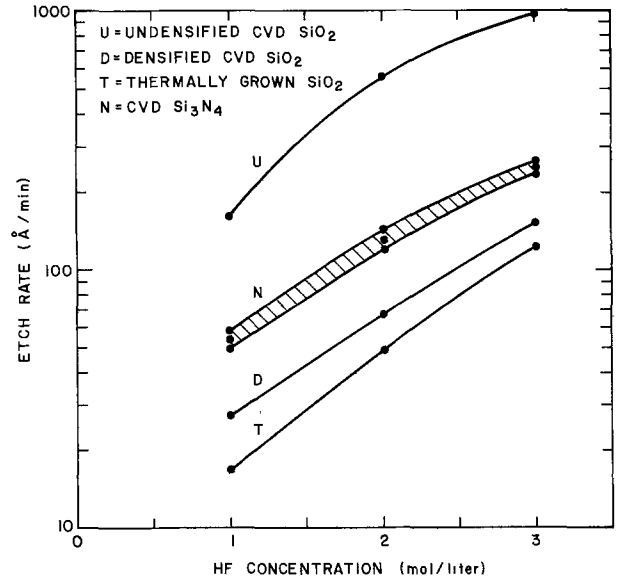


Fig. 5. Etch rates of Si₃N₄ and SiO₂ films in HF/glycerol solutions at 80°C.

materials in HF/glycerol are summarized in Fig. 7, and etch rates in HF/water are shown in Fig. 8. The nitride etch rates shown in Fig. 7 and 8 were obtained using the deposition conditions listed as (e) in the Experimental section. Clearly, in the glycerol system, it is much easier to choose conditions giving r (CVD Si₃N₄) > r (thermal SiO₂).

The mechanism for the unexpected reversal in the etch rate ratio and the decrease in absolute magnitudes of the etch rates is not clear. To elucidate the situation somewhat, HF solutions of several other high boiling solvents were tested. The results of etch rate tests, conducted at 80°C using 2M HF solutions, are summarized in Table I. It is seen that in aqueous solution, large absolute etch rates and a small etch rate ratio [r (Si₃N₄)/ r (SiO₂)] are obtained, while in hydroxylated organic solvents the absolute etch rates are greatly reduced, but the SiO₂ etch rate is reduced more than the Si₃N₄ etch rate, leading to a relatively

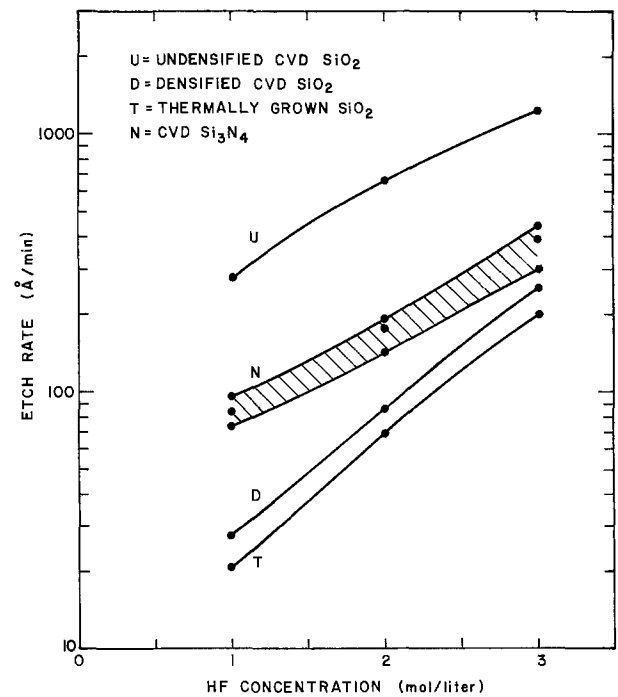


Fig. 6. Etch rates of Si₃N₄ and SiO₂ films in HF/glycerol solutions at 90°C.

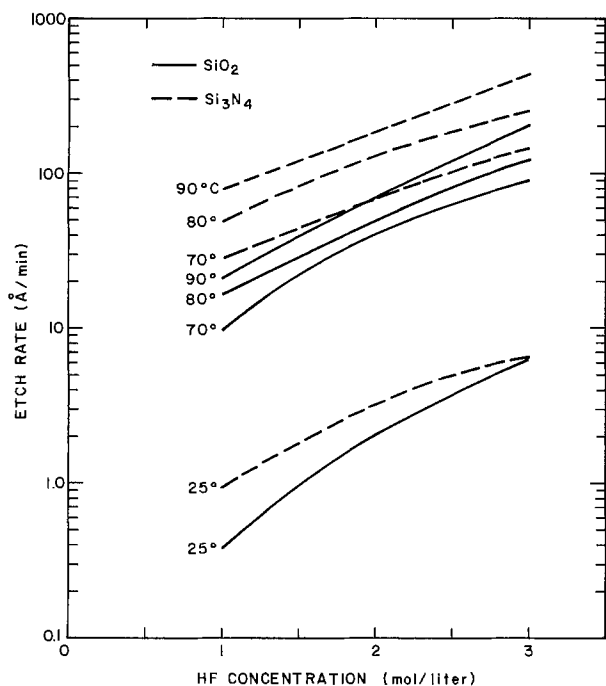


Fig. 7. Summary of etch rates of thermally grown SiO_2 and CVD Si_3N_4 in HF/glycerol solutions.

large etch rate ratio. Finally, in DMF, the nitride etch rate is reduced even further, the SiO_2 etch rate is slightly larger, and a small ratio is obtained. (It should be mentioned that although these solvents were of reagent quality, no special attempts were made to remove residual water.)

These differences in etch rates and ratios of etch rates depending on solvent indicate that the dependence of SiO_2 and Si_3N_4 etch rates on the various equilibrium solution species is more complicated than had

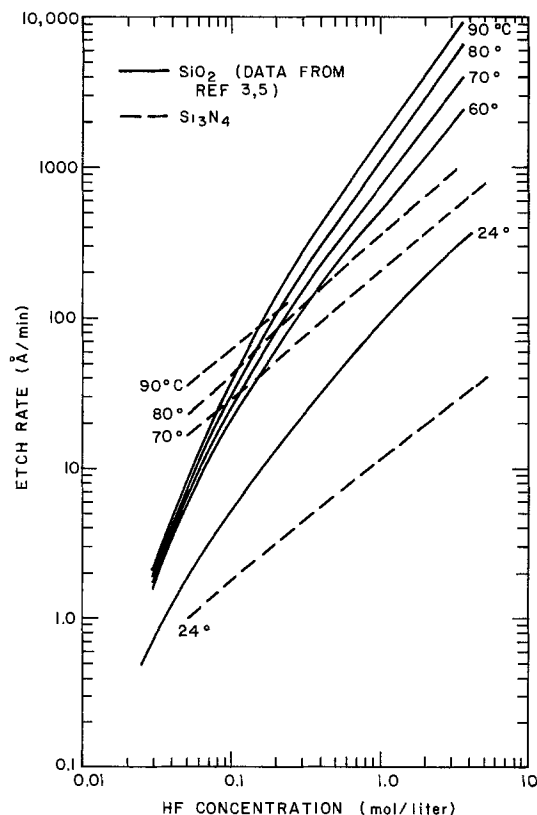


Fig. 8. Summary of etch rates of thermally grown SiO_2 and CVD Si_3N_4 in HF/water solutions.

Table I. Etch rates ($\text{\AA}/\text{min}$) of CVD Si_3N_4 and thermal SiO_2 in 2M HF solutions* at 80°C

Solvent	$r(\text{Si}_3\text{N}_4)$	$r(\text{SiO}_2)$	$r(\text{Si}_3\text{N}_4)/r(\text{SiO}_2)$
Water	650	2900	0.22
Glycerol	125	49	2.6
Ethylene glycol	120	49	2.4
Dimethyl formamide	32	76	0.42
Ethylene glycol monoethyl ether	112	40	2.8

* Prepared using conc hydrofluoric acid (49% HF).

previously been thought. It has been demonstrated (10, 12) that in dilute aqueous solution (i.e., 1M ionic strength), etch rates of SiO_2 and Si_3N_4 depend on $[\text{HF}]$ and $[\text{HF}_2^-]$ only. Since the ionic strengths of the solutions used in the present study are well below those at which higher polymeric species have been observed in aqueous media, it seems likely that only monomeric species are involved in the etching mechanism. It does appear that large etch rate ratios, as required for patterning CVD Si_3N_4 /thermal SiO_2 composites, can be achieved in HF solutions of numerous high boiling, hydroxylated solvents.

Although a relatively limited HF concentration range was used in this study (1-3M HF \approx 2-6% HF by weight), it seems useful to use the observed temperature dependence of etch rates on HF concentration to calculate apparent activation energies. Over the 1-3M HF concentration range and the 70°C - 90°C temperature range, $\Delta E_A = 8.7$ kcal/mole for thermally grown SiO_2 and 12.5 kcal/mole for CVD Si_3N_4 . These results can be compared with about 7.8 and 13.6 kcal/mole for SiO_2 and Si_3N_4 , respectively, determined over a similar concentration and temperature range in previous etching studies (3) carried out in dilute aqueous HF solutions. Thus, the activation energies support our observation that the Si_3N_4 etching process is facilitated, relative to that of SiO_2 , when HF/glycerol etchants are used rather than HF/water.

A quantitative analysis of the solution equilibria involved in the fluoride-water-glycerol system was not attempted because of the complexity of the required calculations. Qualitatively, it may be concluded that the presence of water enhances SiO_2 etch rate more than Si_3N_4 etch rate. Since previous mechanistic studies (10, 12) of SiO_2 and Si_3N_4 etching processes in fluoride media involved only aqueous systems, the effect of the solvent on etch rate was not demonstrated. Clearly, the complete rate law for etching of SiO_2 and Si_3N_4 must contain one or more terms involving solvent species, since the observed effects, in particular the etch rate ratio reversal, cannot be explained on the basis of solvent-induced concentration shifts.

Results of a few more experiments, which further highlight the complexity of the etching process, are listed in Table II. In these experiments it is seen that addition of NH_4F , either as a solid or as an aqueous solution greatly enhances the SiO_2 etch rate relative to the Si_3N_4 etch rate. Addition of NH_4F to aqueous HF would tend to raise the pH and shift the fluoride equilibrium towards HF_2^- , the species which predominates in SiO_2 etching processes in solutions of 1M ionic strength (12). However, the observed SiO_2 etch rate enhancement exceeds (by at least a factor of 10) that predicted simply on the basis of a moderate increase in solution fluoride content and a shift to the HF_2^- species. This enhancement is yet another feature which must be explained if the mechanism of SiO_2 and Si_3N_4 dissolution in fluoride media is to be eventually understood.

Patterning Studies

It was desired to demonstrate that $\text{Si}_3\text{N}_4/\text{SiO}_2/\text{Si}$ composites similar to those shown in Fig. 1a and 2a

Table II. Etch rates ($\text{\AA}/\text{min}$) of CVD Si_3N_4 and thermal SiO_2 in selected HF/glycerol systems

Temp ($^{\circ}\text{C}$)	Fluoride content	r (Si_3N_4)	r (SiO_2)	r (Si_3N_4)/ r (SiO_2)
70	1M HF	28	10	2.8
70	1M HF, satd. with solid NH_4F ($\sim 1.3\text{M}$ total fluoride)	77	918	0.08
70	2M HF	66	40	1.6
80	1M HF	54	16	3.4
80	2M HF	125	49	2.6
80	1M HF, 1.5M BHF* (2.5M total fluoride)	100	>350	<0.3
80	3M HF	250	120	2.1

* BHF: Buffered HF, Transene Company.

can be patterned in HF/glycerol solutions to produce the desired tapered side walls. Since composite structures of this type are typically used as dielectrics under metallization patterns in integrated circuit devices, contact openings are the usual pattern structure. Thus our test pattern consisted of various size holes (4–25 μm) on a planar background.

Several types of masking materials were tested, as were several types of dielectric composites. Naturally, a primary mask (photoresist) would be preferable to a secondary masking material (such as a metal or dielectric unaffected by HF), which would itself require patterning by photolithographic techniques. The patterning experiments described below are divided into these two categories. All the nitride layers used in the patterning experiments were prepared as in procedure (d) described earlier.

Photoresist masks.—Both positive- (Shipley AZ 1350 B or J) and negative-working (Kodak 747, Waycoat IC, HR200) photoresists were tested. In general it was found that the negative resists could not withstand the heated etchants long enough for the pattern etching to take place. Thus most of the work employing photoresist masks centered on AZ 1350 B or J. (When AZ 1350B was employed, a double coating of resist was spun on to improve pinhole resistance.) In each case described, the dielectric sandwich structure was treated with the adhesion promoter hexamethyldisilazane by an immersion technique prior to photoresist application.

A composite film consisting of 500 \AA CVD Si_3N_4 over 500 \AA of thermally grown SiO_2 on Si was patterned using AZ 1350B, in a 1M HF/glycerol solution at 80 $^{\circ}\text{C}$. The etch time employed was about 40 min. After resist removal, a scanning electron micrograph was obtained. This is shown in Fig. 9. The average angle of taper is about 35 $^{\circ}$ in this case.

A composite film consisting of 7000 \AA undensified CVD SiO_2 /500 \AA Si_3N_4 /500 \AA thermal SiO_2 on Si was etched, using an AZ 1350B mask, in 1M HF/glycerol at 80 $^{\circ}\text{C}$ for 85 min. The SEM-graph is shown in Fig. 10. A slope averaging about 25 $^{\circ}$ was obtained. For this type of film, an alternate procedure is to etch through the upper SiO_2 in BHF, then use the glycerol etch.

In neither of these photographs can the interface between the Si_3N_4 and thermal SiO_2 be distinguished, but the gradual slope of the edge indicates that the desired etch rate ratio (r (Si_3N_4) $\geq r$ (SiO_2)) has been achieved. In the latter example, the interface between the CVD oxide and Si_3N_4 is clearly distinguishable. Particles remaining in the etched areas are apparently due to the difficulty of wetting the surfaces in glycerol solution and can probably be eliminated by employing a prepip in a surfactant solution, or by using a surfactant in the etchant itself, as is often done when SiO_2 is patterned.

Since the etching time required in 1M HF/glycerol can be excessive, a similar composite, consisting of

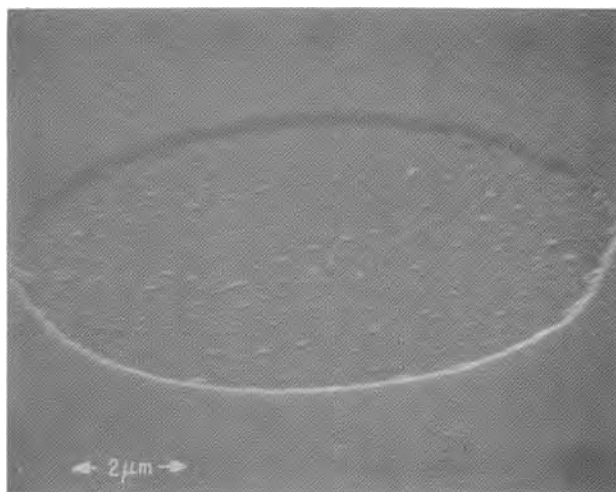


Fig. 9. Composite structure consisting of 500 \AA CVD Si_3N_4 over 500 \AA thermally grown SiO_2 on Si, patterned using AZ 1350B photoresist, and etched in 1M HF/glycerol at 80 $^{\circ}\text{C}$ for 40 min.

7000 \AA undensified CVD SiO_2 /1000 \AA Si_3N_4 /500 \AA SiO_2 on Si was patterned using AZ 1350B in 3M HF/glycerol at 80 $^{\circ}\text{C}$. In this case, only 17 min etch time was required. A satisfactory sloped edge was also observed in this case.

As a final example, a composite consisting of 1000 \AA CVD Si_3N_4 /500 \AA thermal SiO_2 on Si was patterned with AZ 1350J and etched in 1M HF/glycerol at 60 $^{\circ}\text{C}$ for 160 min. A satisfactory pattern was again achieved.

Naturally it is desirable to utilize the highest temperatures and concentrations possible in these patterning processes in order to achieve as short as possible etch times. However, when photoresist is used as a mask, adhesion to the underlying substrate is always of concern, and thus somewhat lower than desirable HF concentrations and temperatures must be tolerated. In particular, when the uppermost dielectric film is Si_3N_4 , and when the dielectric films are fairly thick, photoresist adhesion can be problematic; we found, for instance, that use of 3M HF/glycerol at 60 $^{\circ}\text{C}$ or of 1 or 2M HF/glycerol at 70 $^{\circ}\text{C}$ or higher caused adhesion failure of AZ 1350J when a composite comprised of 2000 \AA Si_3N_4 /2000 \AA SiO_2 on Si was etched.

Metal masks.—A sputtered molybdenum mask was found to give very good results. A dielectric composite consisting of 2000 \AA Si_3N_4 /2000 \AA SiO_2 on Si was coated with a (nominally) 1000 \AA film of sputtered molyb-

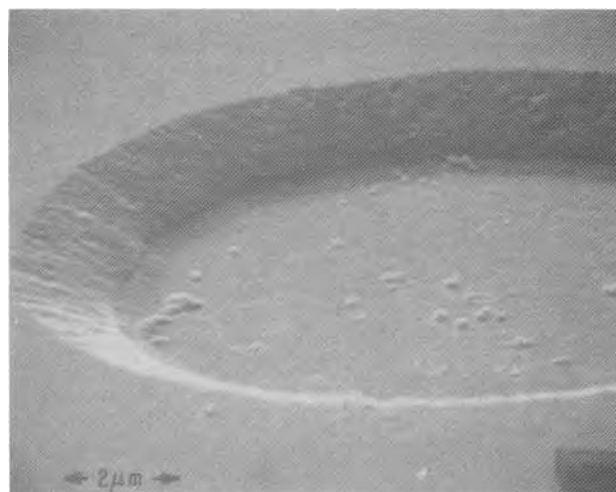


Fig. 10. Composite structure consisting of 7000 \AA undensified CVD SiO_2 /500 \AA CVD Si_3N_4 /500 \AA thermally grown SiO_2 on Si, patterned using AZ 1350B photoresist, and etched in 1M HF/glycerol at 80 $^{\circ}\text{C}$ for 85 min.

denum. The Mo was patterned at room temperature using Kodak 747 photoresist, and employing an etchant of 1 part concentrated H_2SO_4 , 1 part concentrated HNO_3 , and 2 parts water. Only a few seconds immersion were required to etch the Mo film. After stripping the resist, the dielectric composite was etched at 80°C in 2M HF/glycerol for 60 min. The metal mask was then stripped. It was found that patterns of sloped edges were produced in the dielectric composite.

Another type of mask which has been tested is a lead fluoride/gold composite. This material reportedly (13) adheres very well to glass substrates; but unfortunately it did not adhere well to Si_3N_4 during our attempts at pattern etching.

Alternatively, secondary masks of dielectric materials which are unaffected by HF etchants (2) might be used. Some such materials are crystalline Al_2O_3 or sapphire, crystalline Ta_2O_5 (>500°C heat-treatment required), or spinel ($MgAl_2O_4$).

Conclusions

Mixtures of concentrated aqueous hydrofluoric acid in various high boiling, hydroxylated organic solvents such as glycerol appear to be suitable for chemical etching of CVD Si_3N_4 /thermally grown SiO_2 on Si composite structures. Since the nitride etch rate is somewhat higher than the oxide etch rate over a wide temperature and HF concentration range, gradually sloped pattern edges are easily achieved. Undensified CVD SiO_2 films are etched even faster than Si_3N_4 films; thus similar composites bearing such a layer uppermost can also be pattern-etched using this method.

The exact mechanism for the etch rate ratio reversal, relative to that observed in aqueous media, is not understood at present.

If the etch times required for patterning a composite are not excessive, a positive photoresist such as AZ 1350J may be used as a masking material. A sputtered molybdenum film, patterned using a negative photoresist process, may also be used as a mask. If the Si_3N_4 and thermal SiO_2 layers are fairly thin, a thick film of a CVD SiO_2 film can be employed as a mask, with some of this uppermost oxide material being "sacrificed" during the nitride etching process.

Acknowledgments

The author wishes to thank G. L. Schnable, who has actively supported this work and critically reviewed the manuscript. The assistance of W. Hobson, R. Dawson, and R. Vibronek is also acknowledged.

Manuscript submitted Nov. 19, 1979; revised manuscript received May 19, 1980.

Any discussion of this paper will appear in a Discussion Section to be published in the June 1981 JOURNAL. All discussions for the June 1981 Discussion Section should be submitted by Feb. 1, 1981.

Publication costs of this article were assisted by RCA Laboratories.

REFERENCES

1. C. M. Melliar-Smith and C. J. Mogab, in "Thin Film Processes," J. L. Vossen and W. Kern, Editors, pp. 497-556, Academic Press, New York (1978).
2. W. Kern and C. A. Deckert, *ibid.*, pp. 401-481.
3. V. Harrap, in "Semiconductor Silicon 1973," H. R. Huff and R. R. Burgess, Editors, p. 354, The Electrochemical Society Softbound Proceedings Series, Princeton, N.J. (1973); Abstract 124, p. 313, The Electrochemical Society Extended Abstracts, Chicago, Illinois, May 13-18, 1973.
4. V. D. Wohlheiter, *This Journal*, **122**, 1736 (1975).
5. V. Harrap, U.S. Pat. 3,607,480 (1971).
6. W. Van Gelder and V. E. Hauser, *This Journal*, **114**, 869 (1967).
7. A. S. Squillace, A. E. Martin, and J. J. Rudmann, U.S. Pat. 3,811,974 (1974).
8. C. A. Deckert, Unpublished results.
9. J. Sato and T. Tanabe, U.S. Pat. 3,709,749 (1973).
10. C. A. Deckert, *This Journal*, **125**, 320 (1978).
11. (a) I. Franz and W. Langheinrich, *Solid State Electron.*, **11**, 59 (1968); (b) I. Franz and W. Langheinrich, *ibid.*, **11**, 987 (1968); (c) M. J. Rand, *J. Appl. Phys.*, **41**, 787 (1970).
12. (a) J. S. Judge, *This Journal*, **118**, 1772 (1971); (b) J. S. Judge, Abstract 42, p. 122, The Electrochemical Society Extended Abstract, Washington, D.C., May 2-7, 1976.
13. G. J. Zyzdik, L. G. Van Uitert, S. Singh, and T. R. Kyle, *Appl. Phys. Lett.*, **31**, 697 (1977).

AES Measurements on P-Doped Silicon Dioxide: Electron and Ion Beam Irradiation Artifacts

G. Queirolo* and G. U. Pignatelli

SGS/ATES Componenti Elettronici S.p.A., Physics Department, Castelletto di Settimo Milanese, Milano, Italy

ABSTRACT

The phosphorus content of P-doped silicon dioxide films of various compositions was measured with Auger electron spectrometry. Electron and ion beam irradiation were found to severely affect both the energy and the shape of the PL_{VV} peak: for very low primary electron current densities a PL_{VV} peak, attributed to the phosphorus bonded to oxygen, was found at 110 eV; for higher current densities the 110 eV peak disappeared, and the well-known PL_{VV} peak of elemental phosphorus was found at 120 eV. A reduction effect was also noticed after an ion beam irradiation with 1 keV Ar^+ ions; in this case a reconstruction of the broken P-O bonds was found to take place after irradiation.

Phosphorus-doped silicon dioxide films are widely used in semiconductor device fabrication. The desired phosphorus content of these films, usually deposited by a chemical vapor deposition method, depends on the

particular application and is typically between 2 and 12 mole percent (m/o). Several methods can be used to measure the phosphorus content in a P-doped silica glass (1,2): dissolution rate in a suitable etchant, sheet resistance of the layer obtained in silicon when the film is used as a diffusion source, infrared absorption, x-ray microanalysis, neutron activation analysis,

* Electrochemical Society Active Member.

Key words: phosphosilicate glass (PSG), Auger electron spectrometry, phosphorus concentration measurement.

etc. In this paper we discuss the measurement of the phosphorus concentration in P-doped silica glass with Auger electron spectrometry and describe the effects of the electron and ion beam irradiation on both the P_{LVV} peak energy and shape.

Experimental

Sample preparation.—All the P-doped silicon dioxide films studied in this work were 1 μm thick and were CVD deposited on silicon slices within an AMT 2000, continuous silox reactor. The flows of the reactant gases (SiH_4 , O_2 , PH_3) and of the N_2 carrier were adjusted for every phosphorus concentration to obtain good thickness and doping uniformity along the boat. Czochralsky grown, 7.62 cm diam single crystal silicon wafers, (100) oriented, boron-doped ($N_A \approx 10^{15} \text{ cm}^{-3}$) were used throughout. The polished wafers (SMIEL and Wacker Chemitronic) were cleaned in $\text{H}_2\text{SO}_4 + \text{H}_2\text{O}_2$ and $\text{HCl} + \text{H}_2\text{O}_2$ solutions prior to the deposition; after the film growth the wafers were cut in half in a clean hood and stored in dry nitrogen for neutron activation and Auger electron spectrometry analyses.

Neutron activation analysis.—The neutron activation analysis of the bulk phosphorus content of the P-doped silicon dioxide films were performed on the CESNEF reactor (Politecnico di Milano). The samples were irradiated for 10–15 min at a thermal neutron flux of $4 \times 10^{11} \text{ cm}^{-2} \text{ sec}^{-1}$; after the irradiation the P^{32} decay was followed, in order to eliminate the interference from other β^- decaying nuclides. Identical samples gave a 3% reproducibility, whereas a total absolute error of $\pm 8\%$ was estimated, a majority of which ($\pm 5\%$) came from uncertainties in the nuclear data used for computation of the phosphorus content. These samples were used as standards for the AES measurements.

Auger electron spectrometry.—AES measurements were performed with a Varian scanning Auger spectrometer equipped with a single pass CMA analyzer.

To obtain meaningful results, it was necessary to lower the electron current density on the sample by rastering the defocused primary beam over the acceptance area of the spectrometer. When the cylindrical mirror analyzer (CMA) was operated with the wider slits (energy resolution $\Delta E/E = 1.2\%$ and 2.4%) it was possible to keep the current density in the range of 10^{-4} A/cm^2 , while maintaining a relatively high total current (1 μA). At these $\Delta E/E$ settings the resolution of the low energy Si and P_{LVV} peaks was still good and, at the same time, the electron beam artifacts described above were avoided. A low energy electron gun (Varian Model 981-2781) was used to neutralize the positive charging of the samples when they were ion etched.

Chemical shift in AES measurements.—It is well known that the low energy Auger peaks involving electrons in the valence band are very sensitive for a number of elements to the chemical environment. This occurs, for instance, for boron, aluminum, and silicon in the respective oxides; the low energy LVV peaks are very similar [see Fig. 1 of Ref. (3) for B and Si], both in their shape, energy shift from the elemental peak, and separation of the satellite peak at the low energy side. For phosphorus the P_{LVV} peak, both for phosphorus implanted or diffused in silicon and for phosphorus in P-glass, is reported in the literature at 120 eV. Only recently a chemical shift has been observed in P-doped thermal oxide films grown on heavily doped polysilicon (4).

In the present work it is found that the P_{LVV} peak in the phosphosilicate glass (PSG) exhibits a 10 eV chemical shift from the elemental P_{LVV} peak at 120 eV and that the shape of this peak is very similar to that of the LVV peaks of oxidized B, Al, and Si.

Results

Auger electron spectrometry.—*Measurements at low current density.*—The results of the Auger measurements on the PSG system depend on the previous history of the sample and on the primary current density used during the analysis. A preliminary investigation was therefore necessary to establish the experimental conditions at which no electron beam artifacts could be observed for an irradiation time of several minutes, required for obtaining Auger spectra.

The following conditions were found to fulfill the requirement: primary energy, 1.5–2.0 keV; primary current, 1 μA ; CMA modulation voltage, 2 eV. In addition the primary beam was fully defocused and rastered over an area of $640 \times 640 \mu\text{m}^2$; this area is comparable with the acceptance area of the spectrometer when operated at 1.2% energy resolution and well within it for the 2.4% setting. Measurements were performed either in high vacuum ($p \sim 1 \times 10^{-9}$ Torr), or in argon at a static pressure of 5×10^{-5} Torr.

The low energy region of the Auger spectrum obtained on sample 14, not previously ion etched, is shown in Fig. 1. This spectrum displays the usual Si_{LVV} peak of silicon bonded to oxygen at 76 eV, while the P_{LVV} peak is displayed at 110 eV, with a minor satellite peak at 94 eV.

The magnitude of the chemical shift of the P_{LVV} peak (10 eV) is very similar to that of B, Al, and Si in their oxides (respectively 11, 12, and 14 eV). Moreover, both the shape and the separation between the main and the satellite peaks are very similar for these four elements. We therefore assign the peak at 110 eV to the phosphorus bonded to oxygen.

The P (110 eV)/Si (76 eV) peak-to-peak height ratio is plotted in Fig. 2 as a function of the phosphorus content, as determined from activation analysis. A straight line passing through the origin is obtained, showing very good correlation between the two measurements. In this calibration curve several points are reported for sample 14; the measurements were taken at different times after the end of an ion etch. We will discuss this point in more detail later. A good reproducibility of the AES measurements was also found, as shown by the error bars in Fig. 2, provided no ion etching was performed. It was assumed that the P/Si

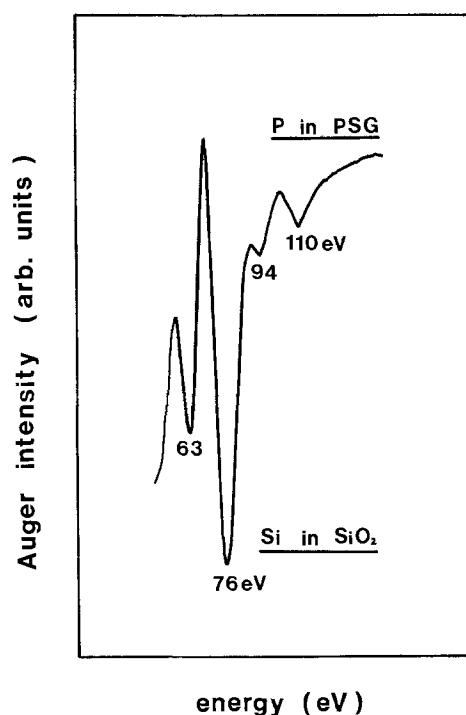


Fig. 1. LVV silicon and phosphorus peaks in P-doped CVD silicon dioxide.

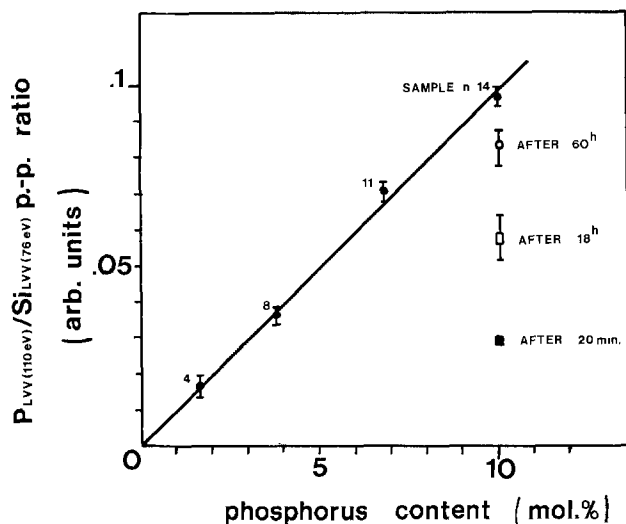


Fig. 2. Calibration curve of the $P_{LVV}(110\text{ eV})/Si_{LVV}(76\text{ eV})$ peak-to-peak ratio vs. the phosphorus content (m/o) in P-doped silicon glass. The experimental points at the right-hand side represent the surface restoration with time after the ion beam irradiation.

ratio was relatively unaffected by the presence of the slight carbon contamination present on the samples, because both peaks will likely to be attenuated by the same amount.

Measurements at high current density: effect of the electron beam irradiation.—If the primary electron current density is increased, for instance by focusing the beam and decreasing the scan width, the P_{LVV} shifted peak disappears, while the unshifted, elemental phosphorus peak starts to increase after some "delay time." In Fig. 3 the p-p height of the $P_{LVV}(120\text{ eV})$ peak is reported as a function of the irradiation time. After the delay time the apparent surface concentration first increases linearly with the irradiation time, reaches a steady state, and then decreases to a very low value; finally the onset of charging occurs, which suggests that a variation in secondary emission coefficient has taken place. A similar variation of the P signal vs. irradiation time was also found by Chang in P-glass (5) and in silicon dioxide grown on heavily P-doped polysilicon (6).

The delay time, the steady-state value, and the onset of the final decrease of the P (120 eV) signal are functions of the current density. For a high enough current, the decrease can occur before the steady state is reached, or even shortly after the beam is turned on.

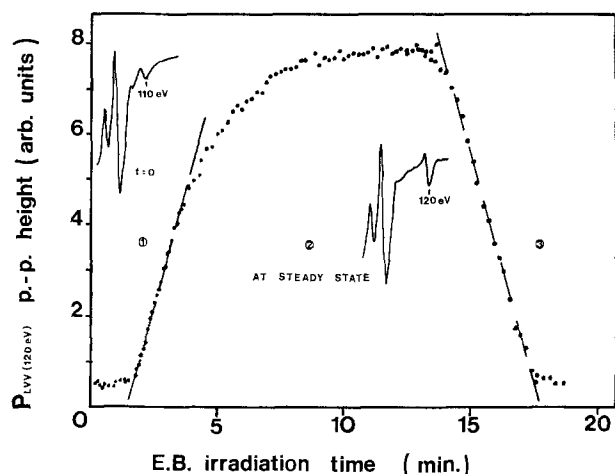


Fig. 3. Elemental phosphorus (120 eV) peak-to-peak height vs. electron beam irradiation time: region 1, surface accumulation; region 2, steady-state; region 3, desorption.

These facts explain the measurement difficulties encountered in the early attempts in obtaining AES spectra of P-doped silicon dioxide.

Effect of the ion beam irradiation.—The bombardment with 1 keV Ar^+ ions causes a reduction effect in the PSG system. As shown in Fig. 4, the amplitude of the elemental phosphorus peak increases quickly with the irradiation time, reaching a steady state in a very short time; in the meanwhile the shifted phosphorus peak disappears. In contrast with the reduction effect caused by the electron beam irradiation, no delay time was found between the time the ion beam was turned on and the increase of the elemental peak amplitude.

When the ion beam is switched off, the elemental phosphorus peak decreases, while the shifted peak increases, as also shown in Fig. 4. The difference in the p-p height of the elemental peak before and after the ion beam was switched off is likely due to a charging effect or to an interference between the ion and electron beams. After the ion beam irradiation, the p-p amplitude of the shifted P_{LVV} peak does not immediately return to its original value but reaches a level which is only about 30% of the pre-irradiation value, showing that a partial phosphorus desorption is also induced by the ion irradiation. Nevertheless a nearly complete surface restoration was observed if the samples are left in the vacuum ambient for a long enough time. This is shown in the right-hand side of Fig. 2 where the P (110 eV)/Si (76 eV) peak amplitude ratio is reported, for sample 14, for different times after the irradiation experiment.

Discussion

Evaluation of the phosphorus content.—The AES measurements reported in this work show that the phosphorus in the PSG gives a P_{LVV} peak at 110 eV, which is chemically shifted from the elemental P peak at 120 eV. A direct evaluation of the phosphorus content from this peak and from the Si and O peaks was not possible, *a priori*, because no elemental sensitivity factors were available. In fact, the data obtained from activation analysis were used to generate the calibration curve of Fig. 2, which correlates the phosphorus content to the ratio between the shifted LVV peaks of phosphorus and silicon. This curve can now be used to obtain the phosphorus concentration in an unknown sample, provided that the electron and ion beam artifacts described above are avoided; moreover, from our data, we were able to obtain, *a posteriori*, an elemental sensitivity factor for the $P_{LVV}(110\text{ eV})$ relative to silicon in $SiO_2(76\text{ eV})$ of 0.3.

A small carbon contamination does not hinder the phosphorus content evaluations because a similar at-

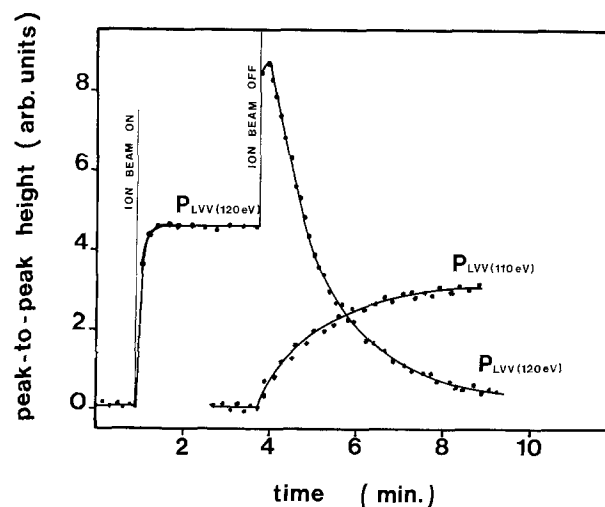


Fig. 4. Effects of ion beam irradiation (1 keV Ar^+) on the elemental (120 eV) and the oxidized (110 eV) phosphorus peaks.

tenuation of both Si and P peaks is expected. On the other hand, meaningful data can be also obtained after the removal of a heavy carbon contamination with ion beam etching if the sample is left in the vacuum ambient for a sufficiently long time.

Electron beam artifacts.—The effects produced by the electron beam irradiation are: a reduction of the phosphorus oxide, a P enrichment in the irradiated area, and a P desorption. At present the mechanism responsible for the phosphorus pileup in the electron irradiated zone is not well understood. A local thermal activation does not seem to justify the high mobility of P in PSG, since the temperature increase in the sample due to the energy dissipation of the electron beam was estimated to be a few degrees centigrade. Also not clear is the role of the “delay-time” which elapses between the electron beam switching on and the onset of the surface phosphorus enrichment.

Otherwise, in our experimental conditions the secondary electron yield is expected to be greater than unity (7). This means that a positive charge builds up in the oxide and a negative space charge, composed of low energy electrons, forms in front of the insulator. This space charge may be responsible for the surface phosphorus pileup found in region I of our irradiation experiment. The occurrence of a flat region after the surface accumulation denotes the onset of a steady-state condition in which the number of phosphorus ions reaching the sample surface is equal to the number of atoms leaving it. When no more P is available within a “diffusion length” from the irradiated volume, only the desorption mechanism is effective, as shown by the decrease of the P signal in region III of Fig. 3.

The phosphorus desorption is confirmed by the depth profile of Fig. 5, in which the p-p amplitude of the P_{LVV} peak at 120 eV is reported as a function of the sputtering time. To obtain this profile, it was necessary to take into proper account the effects of both the ion and electron beam irradiation. After the desorption step the primary current density was lowered by decreasing the beam current. The sputter etch rate during the sputtering was sufficiently high to avoid the P enrichment effect. The scanning width and the focus condition of the electron beam were left unchanged to avoid the collection of Auger electrons from areas not previously irradiated.

Another experimental evidence of the e-beam induced P desorption was obtained by etching the irradiated sample with a P-etch solution (1) which is known to be sensitive to the P concentration. The monochromatic light microphotograph of Fig. 6 shows a silicon-dioxide (nearly) phosphorus-free island of about 100 μm in diameter left on the silicon slice after the chemical etch. The etch rate of the irradiated zone was found to be very close to that of undoped CVD SiO_2 (~ 10

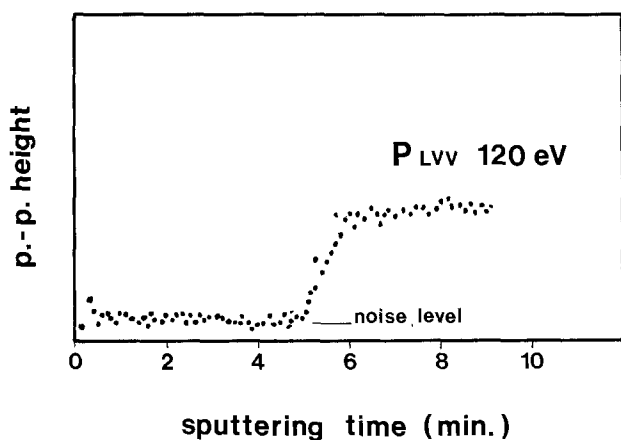


Fig. 5. P_{LVV} (120 eV) peak-to-peak amplitude from an irradiated area as a function of the sputtering time.

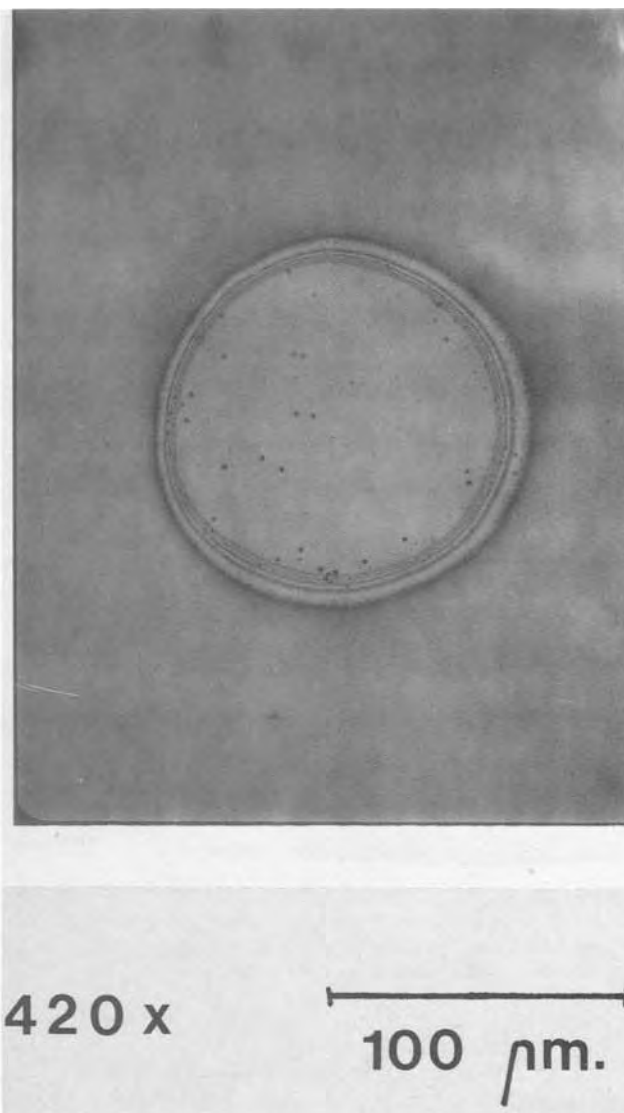


Fig. 6. Microphotograph showing a slow etching silicon dioxide island left after chemical etch of an electron beam irradiated sample.

$\text{\AA}/\text{sec}$) in contrast with a fast etch rate ($\sim 150 \text{\AA}/\text{sec}$) for the PSG. With additional chemical etch after removal of the PSG around the island, there was evidence of an increase of the chemical etch rate after a few seconds of overetch. This means that the P depleted zone is only near the surface, and likely equal to the energy dispersion volume of the primary e-beam in the oxide.

It has to be mentioned that a glass sintering, which can occur during the e-beam irradiation, cannot explain the observed variation in etch rate. In fact, as already mentioned, only a very limited heating is expected with the primary current density used in the experiments; in addition we found that only a limited decrease in the etch rate was observed in the bulk of a P-doped CVD silicon dioxide film (about 10% phosphorus concentration) after a 2.25 hr annealing in dry nitrogen at temperatures ranging from 940° to 1050°C (8). In these annealing experiments, a noticeable variation in the etch rate was observed at the film/vacuum and film/silicon interfaces, which was attributed to a phosphorus depletion due to the P out-diffusion into the ambient and, respectively, the P diffusion into the silicon; these results also support the hypothesis that the electron beam induced variations in the etch rate are in fact due to the phosphorus desorption.

A numerical value for an "effective" diffusion coefficient of P^+ in PSG under electron irradiation can be obtained directly taking the conventional diffusion length $\lambda = 2\sqrt{Dt}$ equal to the range Rg of the primary electrons in the oxide, ignoring effects due to bulk or lateral boundary diffusion. From Ref. (9) and from Fig. 3 we have $Rg = 360\text{\AA}$, $t = 10^3$ sec, and then $D = 3.24 \times 10^{-15} \text{ cm}^2 \text{ sec}^{-1}$. For comparison, this value is nearly equal to the diffusion coefficient of P in SiO_2 at 700°C (10). Moreover our AES measurements show that in the PSG system, the P-O bonds are weaker than the Si-O bonds; in fact, while in our experimental conditions the silicon peak is practically unaffected by the e-beam, a complete reduction of the shifted P_{LVV} peak is noticed. So we can assume that in the PSG network the Si-O groups are the immobile constituents, while the P ions can move, for instance, under the influence of an electrostatic field. The fact that these ions, after the emission of an Auger electron, are double ionized can probably account for their very high mobility in the PSG system.

Ion beam effects.—In the ion beam irradiation experiments the increase of the peak-to-peak height of the elemental P_{LVV} peak and the occurrence of a steady state have a quite different meaning from the electron beam irradiation experiment. In fact, in this case the phenomenon is probably not connected with the P diffusion to the surface, but with a dynamical equilibrium between breaking of P-O bonds and their reconstruction. This is demonstrated by the disappearance of the elemental phosphorus peak at 120 eV and the concomitant appearance of the oxidized phosphorus peak at 110 eV after the ion beam is switched off. A similar effect has been recently reported by Chuang (11) for cobalt, iron, and nickel oxides.

Now let N_A be the number of the P-O broken bonds in the steady state and suppose that the P-O recombination follows a first-order kinetics law. After the ion beam is switched off we can write

$$\frac{dN}{dt} = -KN$$

and on integration, with the initial conditions $t = 0$, $N = N_A$, we obtain

$$N = N_A \exp(-Kt)$$

Provided that the peak-to-peak height in the Auger spectrum is proportional to the number of the emitting atoms, a plot in semilog coordinates of the peak-to-peak height of the elemental P_{LVV} peak (120 eV) vs. time should give a straight line. This was actually found experimentally as reported in Fig. 7 supporting the hypothesis of a first-order reaction kinetics.

Conclusions

The following results were obtained in the present work.

1. The P_{LVV} peak in the PSG system has an energy of 110 eV. Its shape is very similar to that of LVV peak in oxidized B, Al, Si.

2. The ratio of the p-p amplitude of Si in SiO_2 and P in PSG peaks can be used to evaluate the phosphorus content of P-doped silicon dioxide.

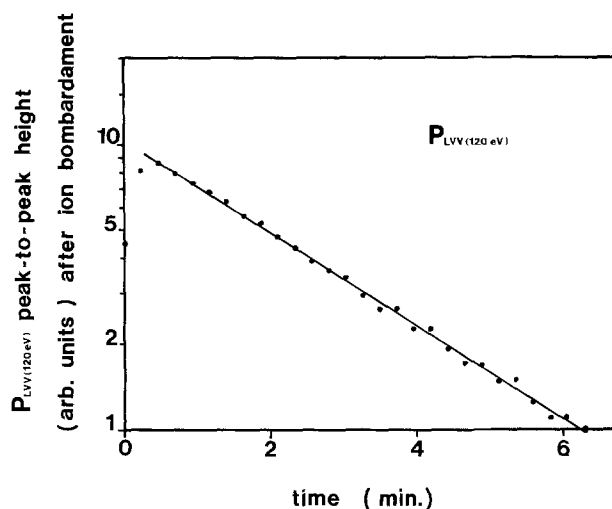


Fig. 7. Log-lin plot of the elemental phosphorus decay after the ion beam was switched off.

3. The electron beam was found to induce, at high current density, a reduction effect, a diffusion-controlled phosphorus pileup, and finally a phosphorus desorption, which completely alters the oxide composition in the irradiated volume.

4. The ion beam was found to induce a reversible reduction effect, which recovers nearly completely if the sample is left in the vacuum ambient for long enough time.

All these artifacts demonstrate that great care must be taken when performing or interpreting depth profile experiments in P-doped silicon dioxide.

Manuscript submitted Dec. 9, 1979; revised manuscript received May 23, 1980. This was Paper 343 presented at the Los Angeles, California, Meeting of the Society, Oct. 14-19, 1979.

Any discussion of this paper will appear in a Discussion Section to be published in the June 1981 JOURNAL. All discussions for the June 1981 Discussion Section should be submitted by Feb. 1, 1981.

Publication costs of this article were assisted by SCS/ATES Componenti Elettronici S.p.A.

REFERENCES

1. W. Kern, *RCA Rev.*, **37**, 78 (1976).
2. A. C. Adams and S. P. Murarka, *This Journal*, **126**, 334 (1979).
3. G. U. Pignatelli and G. Queirolo, *ibid.*, **126**, 1805 (1979).
4. A. N. Saxena and R. A. Powell, in "The Physics of SiO_2 and Its Interferences," Proceedings of the International Topic Conference, Yorktown Heights, March 22-24, 1978, S. Pantelides, Editor, Pergamon, New York.
5. C. C. Chang, A. C. Adams, G. Quintana, and T. T. Sheng, *J. Appl. Phys.*, **45**, 252 (1974).
6. C. C. Chang, Private communication.
7. D. M. Taylor, *J. Phys. D.*, **11**, 2443 (1978).
8. G. Cerofolini, Personal communication.
9. S. Ichimura and R. Shimizu, *J. Appl. Phys.*, **50**, 6020 (1979).
10. H. F. Wolf, "Silicon Semiconductor Data," Pergamon Press, Oxford (1969).
11. T. J. Chuang, C. R. Brundle, and K. Wandelt, *J. Vac. Sci. Technol.*, **16**, 797 (1979).

Effects of Conductor Stress on Bubble Propagation in Contiguous Disk Devices

I. L. Sanders and S. M. Kane

IBM Research Laboratory, San Jose, California 95193

and K. Y. Ahn

IBM Thomas J. Watson Research Center, Yorktown Heights, New York 10598

ABSTRACT

Stress gradients associated with overlay conductors significantly degrade the propagation margins in ion-implanted contiguous-disk bubble devices. A study has been made of the influence of various conductor metallurgies, including Au, AlCu, and Cr deposited by vacuum evaporation and electroplating, on the bias margins of 1 μm bubble propagation along tracks with 5 μm circuit period. The conductors were 2.5 μm wide by 0.5 μm thick and were spaced 0.2 μm from the garnet surface. Annealing the devices at 250° and 350°C for 30 min in a helium atmosphere generally resulted in an increase in conductor stress and a further reduction in propagation margin. The bias margin loss due to the presence of the overlays depended upon track orientation, but for the so-called "good" tracks was typically 20% for evaporated Au and 27% for AlCu after the final anneal. A correlation between margin loss and the stress level in sheet films of the conductor metals was established and reveals a monotonic loss of margin with increasing stress. The results imply that for a margin reduction of no more than 10%, the conductor stress should not exceed $\sim 10^8$ dynes/cm².

It is known that metal stress effects can seriously impair the operation of magnetic bubble devices (1). Contiguous disk devices in particular are likely to be more sensitive to stress gradients at the edges of control conductors overlaying the propagation patterns than conventional permalloy devices. This is a consequence of the device structure which utilizes ion implantation to create a garnet drive layer with stress-induced planar anisotropy. The effect of the ion-implantation process is to place the garnet in a state of compression, so that providing the magnetostriction coefficient is negative (and sufficiently large), the stress-induced anisotropy predominates over the original perpendicular growth anisotropy. Charged domain walls in the garnet drive layer are responsible for bubble propagation. (2).

Stress interactions are of particular concern in the region of the transfer switches where a conductor may overlap the minor and major loops. If the conductor stress is too high, bubbles are frequently trapped preventing reliable minor loop propagation in addition to hindering the transfer function itself. Indeed, stress effects have been regarded so serious that considerable ingenuity has been exercised by device designers to produce novel chip layouts which do not require conductors that cross the propagation paths—these are the so-called self-aligned chips in which the control conductors and ion-implantation pattern are combined (3). Although it is too early at this stage in device development to be certain which approach, conventional or self-aligned, will find favor, it is clear that in either case a very low stress metallurgy must be sought in order to optimize contiguous disk technology.

In this paper, data are presented comparing the influence on bubble propagation of overlaid conductors of different metals deposited by vacuum evaporation and electroplating. The effect of annealing is considered and the dependence of bias margin degradation on stress level in the overlay is discussed.

Device Fabrication and Materials

The composition and characteristics of the double layer garnet composites used in this study are given

Key words: metals, magnetism, stress-strain.

in Table I. In order to enhance domain contrast during visual testing, a thin reflective coating of chromium (500Å) was deposited by vacuum evaporation over a 200Å film of SiO₂ which served as a diffusion barrier between the garnet surface and the reflective layer, preventing interfacial diffusion during annealing (4). An additional 2000Å of SiO₂ was then sputtered onto the chromium as a spacer, simulating an actual device structure. The 5 μm period ion-implanted propagation patterns were defined with a 1.2 μm layer of Shipley AZ1350J photoresist. Prior to ion implantation, the photoresist was hardened by baking for 2 hr at 80°C; hardening of the resist image preserves the original pattern by preventing flow of the photoresist during the implantation process. The wafers were implanted with 3.5×10^{15} He⁺/cm² at 135 keV, after which the resist mask was removed by ashing in an oxygen plasma.

Metallic stripes of chromium, aluminum-copper, and gold (2.5 and 5.0 μm wide and nominally 0.5 μm thick) running perpendicular to the direction of the propagation patterns, as shown in Fig. 1, were deposited by electron-beam evaporation using a lift-off technique. A 100Å film of niobium was evaporated beneath the gold to ensure adhesion to the SiO₂ layer. In addition, stripes of plated gold [BDT 510 and Pura 401¹] were electrodeposited through a photoresist mask. Sheet films of the conductor metals were simultaneously deposited onto optically flat substrates to enable stress measurements to be made. The force due to the stress in these films produced bending of the

¹ Commercial baths available from the Sel-Rex Company, Nutley, New Jersey.

Table I. Material characteristics

	Storage layer Eu _{0.8} Tm _{0.2} Y _{1.5} Ga _{0.5} Fe _{1.5} O ₁₂				Drive layer Gd _{0.8} Tm _{0.2} Y _{1.0} Ga _{0.4} Fe _{1.0} O ₁₂		
	Thick- ness (μm)	4 π M _s (G)	w _s (μm)	Q	Thick- ness (μm)	4 π M _s (G)	Q
Wafer 1	0.97	730	1.01	2.6	0.40	650	1.2
Wafer 2	0.98	700	0.97	2.6	0.40	650	1.2

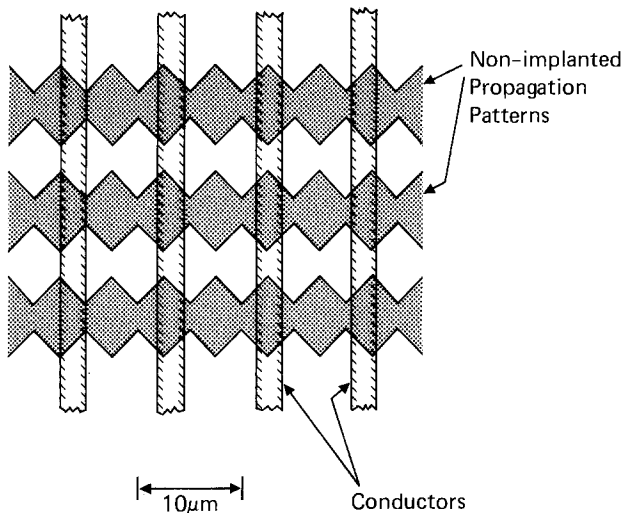


Fig. 1. Schematic showing placement of conductor overlay with respect to propagation tracks.

thin optical flats which was measured by the optical interference technique for observing Newton's rings (5).

Propagation margins were determined in the as-deposited state and after annealing for 30 min at 250° and 350°C in a helium atmosphere. The stress monitors were subjected to identical annealing conditions for the determination of stress levels.

Results and Discussion

Comparison of the effects of high stress Cr and low stress AlCu overlay conductors on quasistatic bias margins is made in Fig. 2, as a function of track orientation. Margins are also shown for similar propagation patterns over which there was no conductor. The data shown were taken after the sample had been annealed at 250°C. The dependence of propagation margins on track orientation with respect to the crystallographic axes of the drive layer has been discussed at length by Lin *et al.* (6) and will not be reiterated. It is sufficient here to note that good tracks are those in which the propagation axis is parallel to one of the bubble stripeout directions (that is, the $[11\bar{2}]$, $[\bar{1}2\bar{1}]$, or $[2\bar{1}\bar{1}]$ crystal directions), and that the super (bad) tracks are those having a stripeout direction pointing into (away from) the cusps. The variations in margins with track type shown in Fig. 2 are quite typical and are consistent with previously reported results.

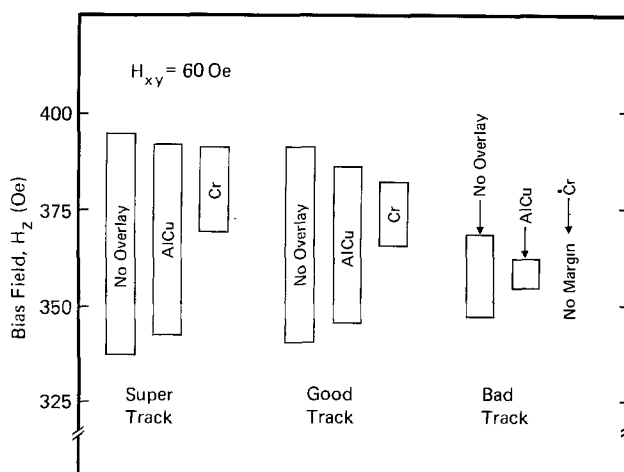


Fig. 2. Effect of high stress (Cr) and low stress (AlCu) overlay on margins for the three principal track orientations. Data taken after annealing device at 250°C for 30 min.

Although the data given in this section apply to conductors of 2.5 μm width, little difference could be detected with the wider (5.0 μm) overlays and suggests that conductor width is not critical in this range. The measured stress in sheet films of the Cr and AlCu was 92×10^8 and 17×10^8 dynes/cm², respectively, after annealing at 250°C. It is apparent that at 60 oe in-plane drive the highly stressed Cr significantly reduced the propagation margins on all tracks and actually prohibited any reliable bubble propagation on the bad track. As expected the effect of the AlCu conductors was much less severe, but was also most noticeable on the bad track where a 62% (13 oe) reduction in margin occurred. In contrast, a margin loss of only 12% (7 oe) was found for the super track, whilst the good tracks suffered a degradation of 29% (11 oe).

The failure mechanism at the lower limit of the margin due to the overlay was usually bubble hang-up at the point where the edge of the conductor crossed the propagation pattern. More rarely the bubble was observed to stripeout along the conductor edge to an adjacent propagation loop. At high bias the failure mode was invariably bubble collapse at the edge of the conductor. A roughly equal loss of upper and lower margin on the good track was typical.

A systematic study of the effect of varying the placement of the conductor with respect to the propagation patterns was not made. However, the overlay mask was designed such that the spacing between conductors was not an integral number of propagation periods. In this way the conductor edges did not coincide with any one particular point on the propagation track, but rather allowed a worst-case assessment of the margins to be made. On the good tracks it was found that, at low bias, the bubbles were most susceptible to hang-up when the conductor edge was slightly displaced from the center of the cusp, toward the direction of propagation. Under these conditions a bubble encounters the stress gradient just as it attempts to leave the cusp, where, it should be noted, the inherent edge affinity can sometimes cause hang-up (7) even in the absence of any external stress effects. This position of the conductor also seemed to be least favorable at the higher margin limit and resulted in early bubble collapse.

Isochronal annealing of the devices at 250° and 350°C for 30 min generally caused an increase in the conductor stress level and a consequent degradation of propagation margins. Propagation along tracks on which there was no overlay also suffered some reduction of margin; the data for the good tracks is summarized in Table II. For consistency, therefore, the relative margin loss due to conductor stress effects is referred to propagation margins determined on chips subjected to identical anneals. Figure 3 shows the dependence of this margin loss on annealing conditions for overlay conductors of evaporated AlCu, and evaporated and electroplated Au. In each case the margins steadily deteriorate with increased annealing temperature. Although wafer 1 was not tested in the as-deposited state, the close correlation with the data from wafer 2 for the AlCu overlay after annealing at 250° and 350°C is very encouraging. The BDT 510 plated Au and the evaporated Nb/Au metallurgies were found to be superior to AlCu from the point of view of stress effects and resulted in a margin loss of 20% after the final anneal, compared to ~26% for the AlCu. Pura 401 plated Au produced

Table II. Bias margins at 60 oe drive, before and after annealing for 30 min periods

	As-deposited	250°C anneal	350°C anneal
Wafer 1	—	340-391 oe	342-390 oe
Wafer 2	344-399 oe	356-407 oe	367-407 oe

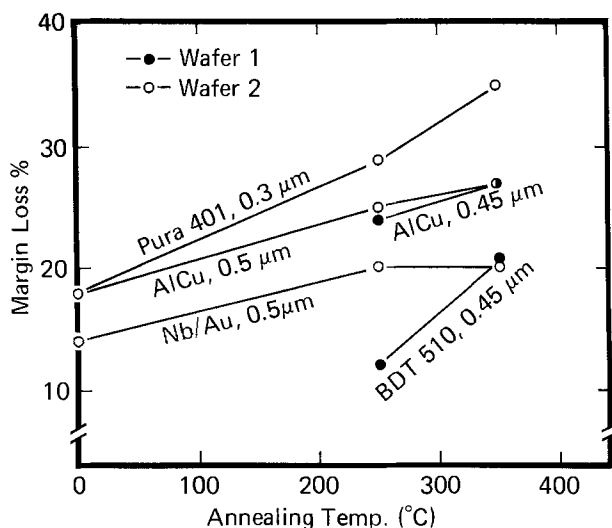


Fig. 3. Dependence of margin loss on annealing conditions for good tracks at 60 oe in-plane drive. Data for 0°C corresponds to as-prepared sample.

the greatest margin loss at each stage of the annealing process.

The measured stress levels in sheet films of the metals considered above can be deduced from the numbered data points of Fig. 4 where margin loss is plotted vs. tensile stress. The figure reveals a monotonic loss of bias margin with increasing conductor stress in the range 1×10^8 - 90×10^8 dynes/cm², regardless of metal type or annealing condition. Although there is considerable scatter in the data, the correlation between margin degradation and stress

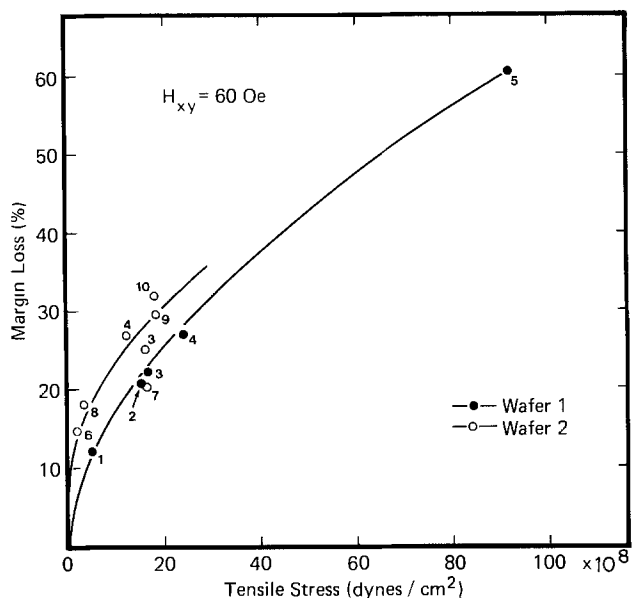


Fig. 4. Relationship between margin loss and tensile stress in sheet films. 1, Au, BDT 510-annealed 250°C; 2, Au, BDT 510-annealed 350°C; 3, AlCu-annealed 250°C; 4, AlCu-annealed 350°C; 5, Cr-annealed 250°C; 6, Nb/Au-as deposited; 7, Nb/Au-annealed 250°C/350°C; 8, Au, Pura 401-as deposited; 9, Au, Pura 401-annealed 250°C; 10, Au, Pura 401-annealed 350°C.

is nevertheless felt to be remarkable in view of the variables involved in an experiment of this nature. Wafer 1 appears to show a somewhat smaller margin loss than wafer 2 for comparable conductor stress levels; the reason for this difference is not obvious. However, for the type of device structure described here, the results imply that if a margin loss of greater than ~10% cannot be tolerated, conductor metallurgies with stress not exceeding 10^8 dynes/cm² are required.

Conclusions

The interaction between overlay conductors and bubble propagation in 5 μm period ion-implanted structures has been studied. The results which have focused on good track behavior, show that the presence of conductor stress is manifest as a bias margin loss at the upper and lower extremes. At high bias the conductor caused premature bubble collapse while at low bias bubble stripeout or hang-up was observed along the conductor edge. The loss of margin invariably became more significant after annealing samples at 250° and 350°C. Evaporated gold was found to produce less deterioration of bias margin than evaporated AlCu of the same thickness (~0.5 μm), both before and after annealing. A correlation between margin degradation and stress level in sheet films of the conductor metal has been established and indicates that a conductor stress of less than 10^8 dynes/cm² is necessary for a margin loss on the order of 10%. Clearly, low-stress metallurgies for contiguous disk device applications must be developed; there would seem to be a considerable amount of work still to be done in this area.

Acknowledgments

The authors are grateful to A. Gangulee and J. A. Morrow who supplied the garnet films and to W. E. Bogholtz for the device pattern generation. We also thank M. H. Kryder and T. J. Gallagher for their contributions in an early phase of this study.

Manuscript submitted Feb. 4, 1980; revised manuscript received May 9, 1980. This was Paper 76 presented at the St. Louis, Missouri, Meeting of the Society, May 11-16, 1980.

Any discussion of this paper will appear in a Discussion Section to be published in the June 1981 JOURNAL. All discussions for the June 1981 Discussion Section should be submitted by Feb. 1, 1981.

Publication costs of this article were assisted by IBM Corporation.

REFERENCES

1. J. M. Dishman, R. D. Pierce, and B. J. Roman, *J. Appl. Phys.*, **45**, 4076 (1974).
2. Y. S. Lin, D. B. Dove, S. Schwarzl, and C. C. Shir, *IEEE Trans. Magn.*, **mag-14**, 494 (1978), Sept. 1978.
3. Y. S. Lin, G. S. Almasi, G. E. Keefe and E. W. Pugh, *IEEE Trans. Magn.*, To be published.
4. K. Y. Ahn and G. E. Keefe, Paper 5B-5 presented at Joint Intermag-MMM Conf., New York, July 1979.
5. J. D. Finigan and R. W. Hoffman, in "Trans. 8th National Vacuum Symposium," pp. 935-942, Pergamon Press, New York (1961).
6. Y. S. Lin, G. S. Almasi, D. B. Dove, G. E. Keefe, and C. C. Shir, *J. Appl. Phys.*, **50**, 2258 (1979).
7. G. S. Almasi, Private communication.

Stability of LPCVD Polysilicon Gates on Thin Oxides

S. P. Murarka,* A. K. Sinha,* and H. J. Levinstein

Bell Laboratories, Murray Hill, New Jersey 07974

ABSTRACT

Polysilicon films of thicknesses in the range of 1000-4700Å were characterized as regards (i) pinhole density and (ii) electrical properties of the fabricated MOS capacitors on 1000Å gate oxide. The effect of processing treatments were examined. It was found that (i) the phosphorus diffusion led to pinholes and higher freak population, the density of these being higher in thinner films, and (ii) the phosphorus glass flow caused lower median breakdown fields and higher freak population. On the other hand thermal oxidation and the exposure to window plasma etch did not have any effect on the breakdown field or freak population. High temperature anneal after aluminum deposition led to lower Q_{ss} and breakdown field in all films. It is concluded that polysilicon films thicker than 2000Å can be safely used as the MOS gate for VLSI devices.

The evolution towards higher levels of MOS-IC integration has led to the use of thinner polysilicon films and this raises concern about its integrity during processing. Degradation of the polysilicon films and consequently of the underlying gate oxide could result from pinholes formed either during the deposition of the film or during such processing steps which consume polysilicon, namely, phosphorus doping in an oxidizing ambient (1), oxidation (2, 3.), and aluminum silicon interactions (4-7) during low temperature hydrogen anneal. To the best of the authors' knowledge no similar studies have been reported except that Kamins *et al.* (8) have reported the results of their study of the structure of LPCVD [low pressure chemical vapor deposition (9)] polysilicon films and their stability during further heat-treatment.

The object of the present work was to characterize polysilicon films of various thicknesses as regards to (i) the pinhole density in such films and (ii) the electrical properties of the fabricated MOS gates. The effect of various processing treatments on these properties was evaluated. Polysilicon films of thicknesses from 1000 to 4700Å deposited on 1000Å gate oxide were used. It was found that polysilicon films more than 2000Å thick are stable under all individual processing conditions and are stable under most sequential processings required to produce MOS capacitors. Although the results are given for a 1000Å thick gate oxide, most of the results should be applicable to thinner oxides.

Experimental

Only (100) p-type 7.5 cm diam and nominally 8-12 Ω -cm Si wafers were used. After cleaning thermal dry oxide was grown at 1100°C to form 1000Å gate oxide which was annealed *in situ* for 30 min in argon at the same temperature. Low pressure CVD polysilicon films were then deposited at 630°C. Doping was carried out in PBr_3 at 1000°C for 30 min. The resulting phosphorus glass was approximately 300-400Å thick. The glass was removed in dilute HF solution. In some cases a second doping of the polysilicon films was carried out in a similar manner. The sheet resistance of doped films was measured using a four-point probe. Aluminum metal films (~7000Å thick) were evaporated through a shadow mask on the front surface giving 500 μ m dots. The polysilicon films were then plasma-etched using the aluminum dots as mask. A back-aluminum contact was applied and the structure was annealed at 450°C in hydrogen for 30 min prior to electrical measurements.

Oxide breakdown measurements were made with negative applied fields (4), so as to keep the capacitor under accumulation. At least 100 breakdown measure-

ments were made on each wafer using a General Automation minicomputer controlled test system (10) with increasing voltage ramp. The current was set at 2 μ A. Figure 1 shows a typical log-normal distribution plot of the breakdown voltage (BV). From this, the median dielectric strength, $\epsilon_{50\%}$, the standard deviation, σ [$= \ln \epsilon_{50}/\epsilon_{16}$] and the percent of freaks, f were obtained, freaks being defined as capacitors with a breakdown field of < 6 MV cm^{-1} (11). In many cases, the usual MOS characteristics (such as C-V plots, bias temperature effect etc.) were also measured to qualify the oxide.

Several kinds of treatments were given to the polysilicon films prior to metallization with Al. Tables I, II and IV describe these experimental procedures.

Results

Pinholes in Undoped and Doped Polysilicon Films

Experiment 1.—In employing the technique described in Table I, it was assumed that if there were pinholes in the polysilicon films, by immersing such wafers in buffered hydrofluoric acid (BHF) solution for a reasonably long time, the etching of the gate oxide underneath would reproduce the pinholes in oxide. KOH solution would then etch the substrate and thus reproduce the pinholes in oxide as etch pits. The etch pits have crystallographic features depending on the substrate orientation and thus are easily distinguished from any other pits or contaminants on surface.

No etch pits were observed on the undoped polysilicon films with thickness in the range of 1000-4700Å. On the other hand, etch pits were observed in thinner polysilicon films prior to metallization with Al. Tables Figure 2 shows the SEM micrographs of the pinholes in 1000 and 2000Å polysilicon films doped once in

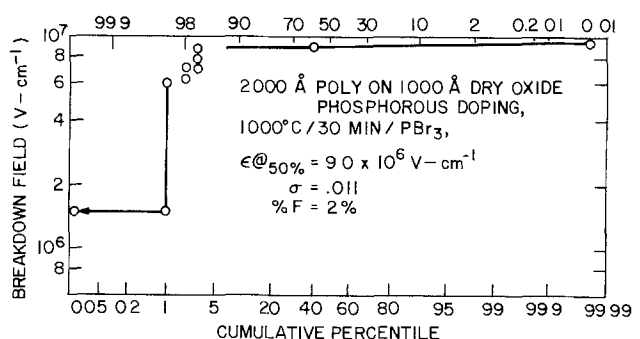


Fig. 1. A typical log-normal distribution plot of the breakdown field. The sample had 1000Å gate oxide and polysilicon film doped once at 1000°C with PBr_3 for 30 min and was annealed at 450°C in hydrogen for 30 min after aluminum.

* Electrochemical Society Active Member.

Key words: films, electrical properties, MOS capacitors.

Table I. Experiment 1: direct observation of pinholes in polysilicon films

1. Various thicknesses of the film (1000, 2000, 3000, 4000, and 4700Å) were used in this experiment. All were deposited on a 1000Å thermal oxide on silicon substrates.
2. Samples were divided in various groups.
 - a. Undoped films
 - b. Single doping at 1000°C/30 min in PBr₃, P-glass removed in 50:1 HF
 - c. Double doping, i.e., a second 1000°C/30 min in PBr₃ (after the first and P-glass removal), P-glass removed in 50:1 HF
3. All exposed to 20 min in (10:1) BHF.
4. Polysilicon etched in all cases, in KOH solution, Exposure to KOH solution was always a minute or two longer than that required for etching polysilicon only.
5. Examine all oxides for holes.

PBr₃. The density of pinholes in 1000Å film was high and variable across the wafer surface as shown in Fig. 2A (high density) and in Fig. 2B (low density). Figure 2C shows the density of etch pits caused by pinholes in 2000Å polysilicon film. The halo around the dark pits is due to undercutting of the silicon under the oxide.

The pinhole density, represented by the etch pit density such as those shown in Fig. 2, decreased in going from 1000 to 2000Å polysilicon films. For 3000Å film, only a few pinholes were found near the edge of the wafer. For all practical purposes there were no pinholes in films with thicknesses of 3000, 4000, and 4700Å. Also the density of pinholes in thinner films was higher in those cases where two phosphorus diffusions were carried out as compared to films where only one phosphorus diffusion was carried out. This is due to conversion of a few hundred angstroms of polysilicon into SiO₂ during each diffusion step.

Electrical Measurements—Effect of Doping and BHF Exposure

Experiment 2.—If there are pinholes in polysilicon, which lead to holes in oxide during a BHF exposure, aluminum metallization of the polysilicon will cause substrate to metal shorts. Thus electrical measurements of the oxide breakdown characteristics provide a means to substantiate the findings of the previous section. As a result of the wafer processing described in Table II, we had 4 sets of wafers for measurements.

Figure 3 shows a plot of the sheet resistance as a function of the nominal polysilicon thickness for as-deposited films. Points for both singly and doubly doped films have been shown. The sheet resistance increased considerably for thinner films, and after the second doping the 1000Å film is no longer conducting. As suggested above, this was due to consumption of polysilicon during the two diffusions. For thicker films

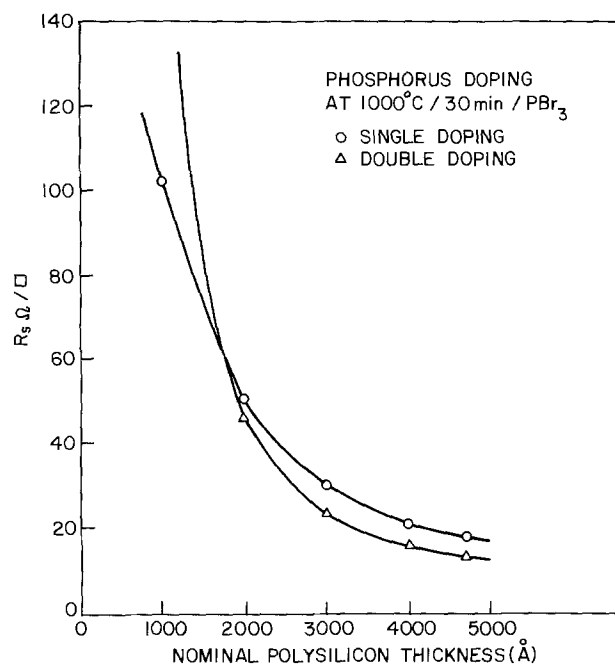


Fig. 3. Sheet resistance of various polysilicon films as a function of the thickness for one or two diffusions.

sheet resistance decreased as a result of the second phosphorus diffusion.

Table IIA summarizes the results of the breakdown measurements on the four sets of samples processed according to Table II. All devices, irrespective of the polysilicon film thickness, show excellent breakdown voltages. The freak population f is high for capacitors made on singly doped 1000Å film and there were no working capacitors on 1000Å polysilicon films in sets B, C, and D. Similarly the freak population increased after the second doping and after BHF exposure indicating an increase in the number of capacitors with premature breakdowns after these treatments. None of the thicker polysilicon devices showed these trends. These results clearly confirm the pinhole density results of the previous sections.

Effect of Phosphorus Glass Deposition and Flow

Experiment 3.—Samples for this experiment were processed as described in Table II, steps 1-4. This was then followed by a -10,000Å P-glass deposition, glass

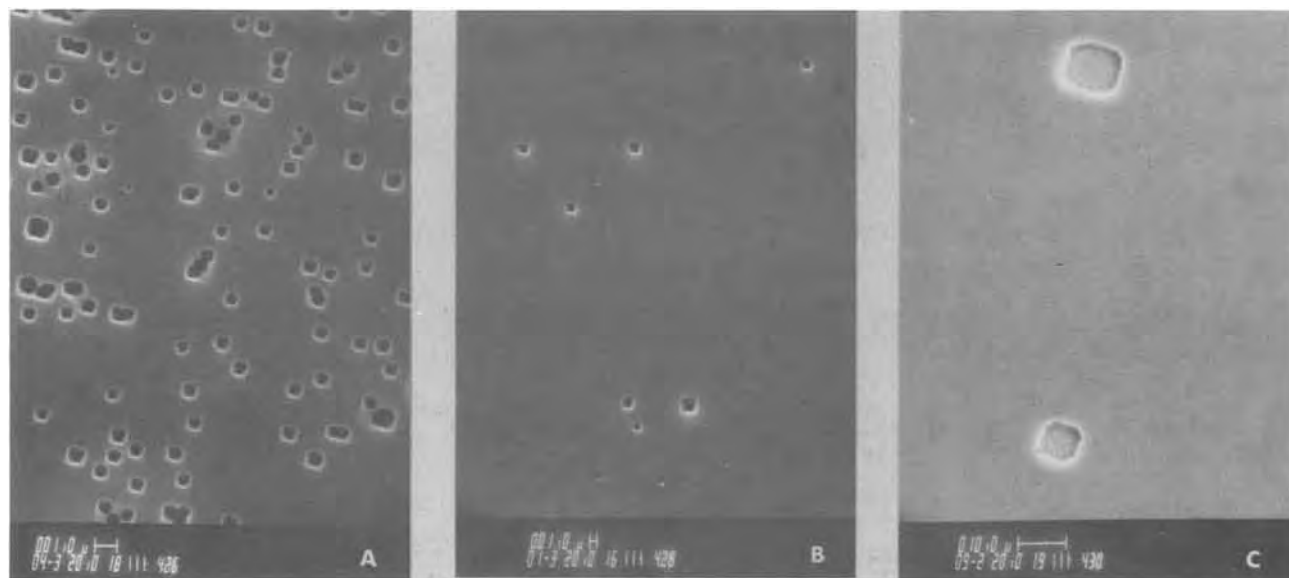


Fig. 2. SEM photographs of the holes in substrate silicon (and oxide). A and B show varying pinhole density across the surface of the wafer with 1000Å polysilicon film and C shows the pinhole density, in case of 2000Å polysilicon film (see Table I).

Table II. Experiment 2: effect of doping and BHF exposure on the electrical characteristics

1. All wafers, 1000°C/PBR₃/30 min. Remove p-glass in 50:1 HF. Measure sheet resistance. Remove controls (Set A) and those for second doping.
2. Expose wafers to 20 min in (10:1) BHF. Measure sheet resistance (set B).
3. Wafers from (1), for second doping, all these wafers, 1000°C/PBR₃/30 min. Remove p-glass in 50:1 HF. Measure sheet resistance. Remove controls (set C).
4. Expose these second group of wafers to 20 min in 10:1 BHF. Measure sheet resistance (set D).
5. All 4 sets of wafers: evaporate aluminum 7000Å through a mask to form 500 μm dots. Evaporate Al on back for back contact. Etch polysilicon using Al dots as mask, clean, and anneal 450°C/30 min/H₂.
6. Electrical measurements.

reflow, removal of all P glass in (10:1) BHF, aluminum metallization (step 5, Table II), and electrical measurements. Table III presents the results. The effect of phosphorus glass deposition and flow is noticeable in the median breakdown voltage as is shown in Fig. 4. Only the results of singly doped films are shown. Results are similar (and worse) for doubly doped films. It is clear from these results that the use of phosphorus glass leads to lowering of the breakdown voltage in all the films.

A summary of all the data on freak population is shown in Fig. 5. In this figure A, B, C, and D on abscissa define the samples described by set A, B, C, and D, respectively, for each thickness of the polysilicon films. For thin films ($\leq 2000\text{\AA}$), the freak population increases with any additional processing following the first doping of the films. For thicker

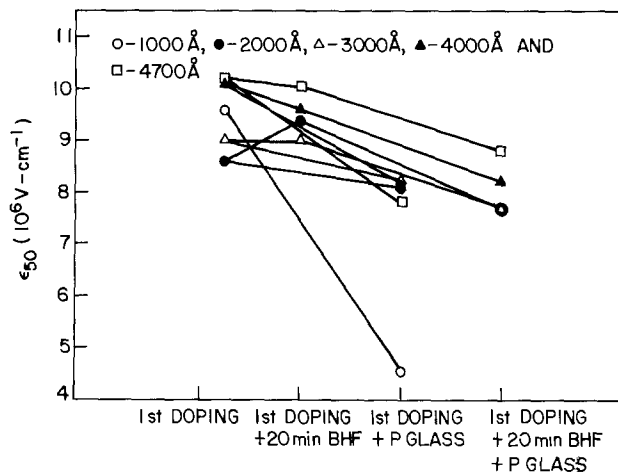


Fig. 4. Shows a plot of the median breakdown field as a function of various treatments given to polysilicon films of various thicknesses. A line between two points indicate direct jump from one process to another represented by those points.

films, the freak population is invariant for all additional processings except for the phosphorus glass deposition and flow. In all cases the use of phosphorus glass led to a higher freak population.

Effect of Oxidation and Window Plasma Etch

Experiment 4.—During device processing polysilicon films go through oxidation, oxide removal, and are

Table II.A. Summary of breakdown measurements of sets A, B, C, and D—Experiment 2

Measurement at step	Polysilicon thickness				
	1000Å	2000Å	3000Å	4000Å	4700Å
Set A: After first phos. diffusion ε at 50% (10 ⁶ V-cm ⁻¹)	9.6 × 10 ⁶ 0.021 10	8.6 × 10 ⁶ 0.012 1	9 × 10 ⁶ 0.017 10	10.1 × 10 ⁶ 0.088 5	10.2 × 10 ⁶ 0.017 0
Set B: After 20 min in BHF following first diffusion ε at 50% (10 ⁶ V-cm ⁻¹)	†	9.4 × 10 ⁶ 0.032 8	9 × 10 ⁶ 0.069 1	9.6 × 10 ⁶ 0.122 0	10.05 × 10 ⁶ 0.046 0
Set C: After second phos. diffusion following first diffusion ε at 50% (10 ⁶ V-cm ⁻¹)	†	9 × 10 ⁶ 0.011 2	9.1 × 10 ⁶ 0.045 1	10.1 × 10 ⁶ 0.072 1	>10 ⁷ •
Set D: After 20 min in BHF following second diffusion ε at 50% (10 ⁶ V-cm ⁻¹)	†	9.3 × 10 ⁶ 0.033 15	9.2 × 10 ⁶ 0.033 1	9.9 × 10 ⁶ 0.052 0	>10 ⁷ •

†Could not be measured.

• Could not be accurately determined since only 4 (of 100) dots broken down by test.

Table III. After P-glass deposition and flow following these steps and prior to Al deposition

Measurement at step	Polysilicon thickness				
	1000Å	2000Å	3000Å	4000Å	5000Å
Set A: After first phos. diffusion ε at 50% (10 ⁶ V-cm ⁻¹)	5.05 × 10 ⁶ 0.040 13	8.1 × 10 ⁶ 0.012 3	8.25 × 10 ⁶ 0.006 5	8.2 × 10 ⁶ 0.018 2	7.8 × 10 ⁶ 0.013 5
Set B: After 20 min in BHF following first diffusion ε at 50% (10 ⁶ V-cm ⁻¹)	X	7.7 × 10 ⁶ 0.026 4	8.2 × 10 ⁶ 0.012 1	8.2 × 10 ⁶ 0.006 4	8.8 × 10 ⁶ 0.042 8
Set C: After second phos. diffusion following first diffusion ε at 50% (10 ⁶ V-cm ⁻¹)	X	3.35 × 10 ⁶ 0.062 9	8.5 × 10 ⁶ 0.012 5	8.2 × 10 ⁶ 0.012 5	8.25 × 10 ⁶ 0.007 8
Set D: After 20 min in BHF following second diffusion ε at 50% (10 ⁶ V-cm ⁻¹)	X	X	8.1 × 10 ⁶ 0.012 2	8.0 × 10 ⁶ 0.019 7	8.4 × 10 ⁶ 0.024 60

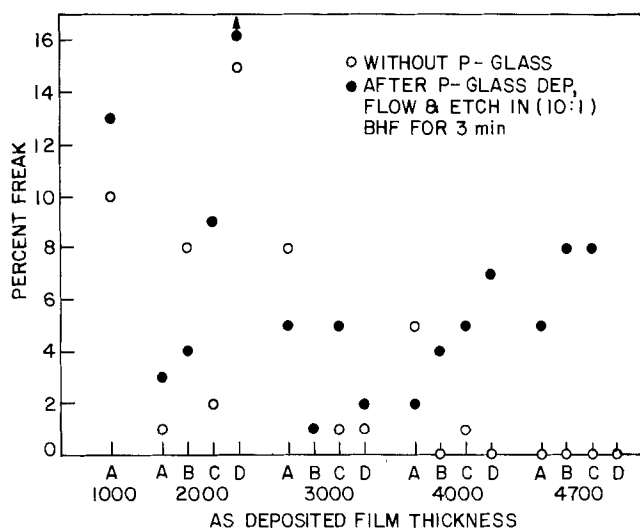


Fig. 5. Shows a plot of the freak population (f) as a function of the various processing and the polysilicon film thickness. Results for samples with and without phosphorus glass deposition and flow are shown. For 1000Å polysilicon films, no working capacitors were left after treatments B, C, and D.

exposed to window plasma etch. Experiment 4 was carried out (using 4700Å thick polysilicon films) to determine the stability of the gate oxide MOS capacitors exposed to these conditions.

The results of this experiment (Table IV) are presented in Table IVA. It is clear from these data that dry oxidation and exposure to phosphorus glass removal etch did not have any damaging effect on the breakdown characteristics of the gate oxide under the 4700Å polysilicon film.

Effect of 450°C vs. 550°C Hydrogen Anneal on the Stability of MOS Capacitors

Experiment 5.—Some of the samples, which were annealed at 450°C in hydrogen for 20 min, were re-annealed (after electrical measurements) at 550°C in hydrogen for 30 min. This second anneal was carried out to evaluate the effect of aluminum-polysilicon interaction on the breakdown and MOS characteristics of the gate-oxide capacitors. Table V presents these results for polysilicon films of various thicknesses. Al-

Table IV. Experiment 4: effect of oxidation and P-glass plasma etch on the electrical characteristics of the 4700Å polysilicon films on gate oxide

- All six wafers, 1000°C/PBr₃/30 min. Remove P-glass in 50:1 HF. Hold control wafer (No.1).
- One wafer (No. 2) only—immerse in 20 min BHF.
- Three wafers (No. 3, 4, 5) only. 1000°C/40 min/dry oxide. Oxide removed in BHF (10:1) 2 min. Remove control (No. 3).
- One wafer (No. 4) only—immerse in 20 min BHF.
- Two wafers (No. 5 and 6), expose to P-glass—removal (plasma) etch for 4 min.
- All six wafers, clean (12), evaporate 500 μm aluminum dots through mask and contact aluminum on back. Etch polysilicon using Al as mask to define dots, clean, 450°C/30 min/H₂ anneal.
- Electrical measurements.

Table IVA. Effect of oxidation and windows plasma etch on the gate oxide breakdown characteristics

Wafer No.	ϵ_{50} (10 ⁶ V-cm ⁻¹)	σ	f (%)
1	9.95	0.025	0
2	9.3	0.011	1
3	9.6	0.021	1
4	8.6	0.072	1
5	9.4	0.022	0
6	9.65	0.016	0

* See Table IV for processing details.

Table V. 450°C vs. 550°C hydrogen anneal

Polysilicon ^a film thickness (Å)	Anneal temperature (°C)	Q_{ss} (10 ¹⁰ cm ⁻²)	ϵ_{50} (10 ⁶ V-cm ⁻¹)	σ	f (%)
1000	450	1.7	9.6	0.021	10
	550	0.24	7.8	0.026	30
2000	450	9.0	8.6	0.012	1
	550	5.6	8.5	0.023	5
3000	450	7.1	9.0	0.017	10
	550	5.4	9.3	0.021	3
4000	450	14	10.1	0.088	5
	550	10	8.4	0.036	2
4700	450	7.4	10.2	0.017	0
	550	6.5	8.7	0.012	0

* All polysilicon films doped once at 1000°C in PBr₃ for 30 min.

though Q_{ss} (the fixed surface state charge, given in units electron charge) is highly variable for samples with different polysilicon film thicknesses, the important thing is that Q_{ss} and the breakdown field (ϵ_{50}) are lowered as a result of 550°C anneal. Freak population appears to increase in thin polysilicon capacitors and decrease in thicker (>2000Å) polysilicon capacitors. Similar results were obtained for MOS devices made from 4000Å thick polysilicon films subjected to 20 min BHF immersion and to second phosphorus diffusion with or without 20 min BHF immersion. Breakdown field was always lowered due to 550°C anneal.

Effect of Aluminum-Silicon Interactions on the Integrity of the Polysilicon Films

Aluminum and silicon interact at the device annealing temperatures, leading to a voluminous movement of silicon into the aluminum (4-7). As a result of this movement, holes are left in the silicon and precipitates of silicon are formed in aluminum. The surface of the polysilicon films on our samples of Experiment 3 was examined after the aluminum was etched off in hot (60°-70°C) phosphoric acid diluted with acetic acid, nitric acid, and water



SEM was used to examine the surface. Pinholes were found in all polysilicon films irrespective of thickness or the treatment prior to aluminum deposition and anneal. Figure 6 (A and C) shows the SEM micrographs of some of the samples which were all doped with phosphorus once (1000°C, 30 min, PBr₃). The density of holes is high for the thinner (2000Å) films. For thicker films the density appears to be lower. Prior to aluminum deposition, there were no pinholes in polysilicon films of 3000, 4000, and 4700Å films (Experiment 1). The hot aluminum etch, used for less than a minute, does not attack polysilicon films. Therefore, the holes in these films are solely due to the aluminum-silicon interaction.

In contrast to the results of Fig. 6 (A and C), we saw both holes and precipitates on polysilicon films which were doped twice at 1000°C in PBr₃. Figure 6 (B and D) shows the surface of the various polysilicon films after aluminum had been etched off. Once again hole density is larger in 2000Å films than in thicker films. The density of the precipitated particles appears to be more or less the same in all cases. Also as in case of Fig. 6 (A and C), we saw only holes near the edge of the capacitors. The density of the holes in the area near the edge was much larger than that in the rest of the capacitor surface.

The holes in the polysilicon never have a simple defined geometrical shape. It appears that holes always form at the grain boundaries in the polysilicon. We are not certain if they run through the whole thickness of the film to the oxide surface or through only a small part of the polysilicon. In the latter case, exposure to BHF will not lead to pinholes in oxide and consequently to aluminum substrate shorts.

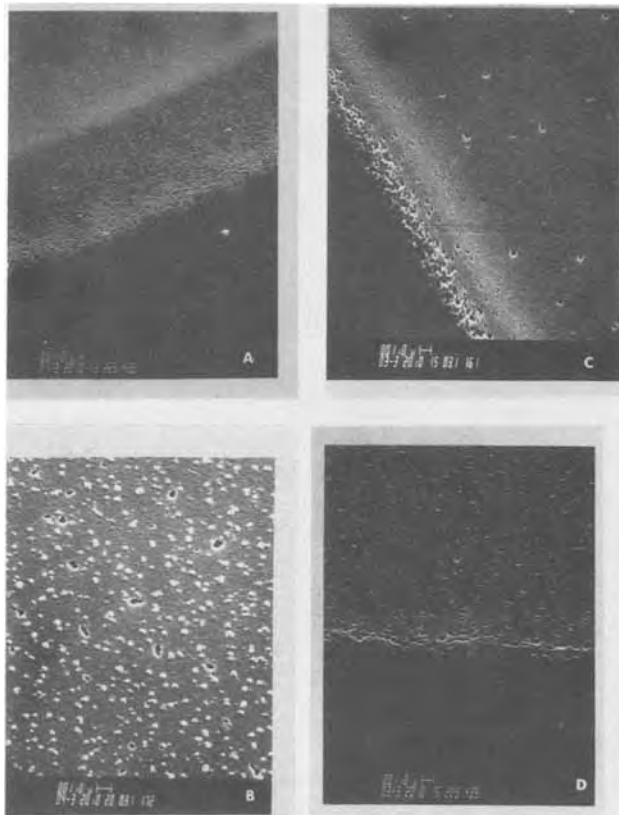


Fig. 6. Defects in polysilicon films formed as a result of the 450°C/30 min/hydrogen anneal after aluminum deposition. Aluminum was etched off prior to examination. A and C: Polysilicon was doped with phosphorus once at 1000°C for 30 min in PBr_3 . B and D: Polysilicon in these samples was doped twice with phosphorus, each time at 1000°C for 30 min in PBr_3 .

Discussion

Depending on the thickness, the polysilicon films may have pinholes (i) in as-deposited films, (ii) due to phosphorus diffusion which is known to cause preferential grain growth (13, 14) perpendicular to the substrate surface and consumption of silicon, (iii) during oxidation, which may oxidize the grain boundaries followed by BHF exposure which then etches out oxide from grain boundaries, (iv) during phosphorus glass deposition and reflow, the effect being similar to that during phosphorus diffusion; this treatment may also lead to diffusion of unwanted impurities into the active areas of the devices, (v) during plasma etching, which may preferentially etch along grain boundaries and also drive the impurities in the gate region, and (vi) during the hydrogen anneal with aluminum metal on, due to the ensuing Al-Si interactions.

The undoped polysilicon films even as thin as 1000Å thick, did not have pinholes through which BHF could etch the oxide underneath. On phosphorus doping, pinholes did form. The density of these holes decreased very rapidly with increasing film thickness (Experiment 1). This density increased due to second doping as is evidenced by the high resistivity (Fig. 2) of 1000Å film after second doping and higher failure rate of the capacitors in 1000 and 2000Å films. The second phosphorus doping did not affect the median breakdown field of the working capacitors. Similarly dry oxidation and/or exposure of polysilicon to phosphorus glass plasma etch (no phosphorus glass deposition or flow) did not affect the breakdown characteristics of the capacitors (Table IIA). Thus in the

absence of pinholes, phosphorus diffusion or BHF exposure or P-glass plasma etch does not affect gate oxide breakdown characteristics.

Deposition of the phosphorus glass and the subsequent reflow seem to affect the breakdown characteristics. The median breakdown field was lowered and the freak population increased (Fig. 3 and 4). These results indicate that the phosphorus glass deposition and reflow, which is a high temperature process, cause damage to the gate oxide. Phosphorus glass could trap impurities which then diffuse to Al-gate-oxide polysilicon interface and which also get into the oxide grown on polysilicon. This leads to lower median breakdown fields. The increase in the freak population could both be due to the pinholes due to phosphorus diffusion as discussed earlier and due to entrapment of excessive impurities in some areas of the wafer.

The device degradation, as evidenced by the lowering of the median breakdown field due to 550°C anneal (Table V), could also occur due to the migration of aluminum to gate oxide-polysilicon interface and due to silicon dissolution into aluminum. In an independent study with aluminum alone as the gate metal, it was found that the 550°C anneal indeed decreased the median breakdown field. In view of the above our recommendations for the LPCVD polysilicon film, as gate material, would be to: (i) use films of thickness greater than 2000Å; (ii) dope the films with phosphorus preferably at lower temperatures and for lower time periods; (iii) avoid direct contact with phosphorus glass (which usually flows at 1100°C), a thermal oxide between polysilicon and phosphorus glass may act as a barrier to the diffusants which lower breakdown fields and cause higher failure rates; and (iv) use lower aluminum annealing temperatures, to avoid Al-Si interactions.

Acknowledgments

The authors would like to thank C. Sarday for all the electrical measurement, W. S. Lindenberger for the SEM work, M. Grieco for polysilicon deposition, E. I. Povilonis for the processing help, and E. Kinsbron for discussions concerning grain growth in polysilicon.

Manuscript submitted Jan. 25, 1980; revised manuscript received April 15, 1980.

Any discussion of this paper will appear in a Discussion Section to be published in the June 1981 JOURNAL. All discussions for the June 1981 Discussion Section should be submitted by Feb. 1, 1981.

Publication costs of this article were assisted by Bell Laboratories.

REFERENCES

1. T. I. Kamins, *This Journal*, **126**, 833 (1979).
2. H. Sunami, *ibid.*, **125**, 1892 (1978).
3. T. I. Kamins, *ibid.*, **126**, 838 (1979).
4. R. J. Anstead and S. R. Floyd, *IEEE Trans. Electron Devices*, **ed-16**, 381 (1969).
5. K. Nakamura, M.-A. Nicolet, J. W. Mayer, R. G. Blattner, and C. A. Evans, Jr., *J. Appl. Phys.*, **46**, 4678 (1975).
6. A. J. Learn, *This Journal*, **123**, 894 (1976).
7. H. M. Nag and L. H. Hobbs, *ibid.*, **124**, 573 (1977).
8. T. I. Kamins, M. M. Mandurah, and K. C. Saraswat, *ibid.*, **125**, 927 (1978).
9. R. S. Rosler, *Solid State Technol.*, **20**, 63 (1977).
10. W. S. Lindenberger, Unpublished work.
11. D. L. Crook, *I EDM Tech. Digest*, p. 44 (1978).
12. For cleaning procedure see S. P. Murarka, H. J. Levinstein, R. B. Marcus, and R. S. Wagner, *J. Appl. Phys.*, **48**, 4001 (1977).
13. C. D. Ouwens and H. Heylingers, *Appl. Phys. Lett.*, **26**, 569 (1975).
14. Y. Wada and S. Nishimatshu, *This Journal*, **125**, 1499 (1978).

Electrochromism in Solid Phosphotungstic Acid

B. Tell

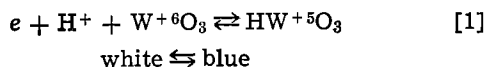
Bell Laboratories, Holmdel, New Jersey 07733

ABSTRACT

The performance of electrochromic cells containing solid phosphotungstic acid including voltammograms, degradation, field-assisted bleaching, and open-circuit memory is presented.

We have previously discussed various aspects of the operation of electrochromic cells containing the heteropoly acids, such as phosphotungstic acid (PWA) (1, 2). These materials are hydrates forming a cubic structure (3) with representative formula $H_3PO_4(WO_3)_{12} \cdot 29H_2O$. PWA is a proton superionic conductor [$\sigma = 1 (\Omega\text{cm})^{-1}$ near room temperature] (4, 5) and an electronic insulator, which makes possible a self-contained electrochromic cell without the necessity of an additional electronic blocking layer. Our previous reports discussed various aspects of the electrochromic performance. In the present report, we present additional data of these effects, as well as voltammograms and a discussion of the open-circuit memory.

The basic arrangement is shown in Fig. 1. A powder of PWA containing a few percent of an opacifier such as TiO_2 is compressed to a thickness of 1-2 mm at $\sim 150 \text{ kg/cm}^2$ in a ceramic tube against the working electrode, a transparent SnO_2 coated glass slide (2). The coloration mechanism is assumed similar to that of the WO_3 electrochromic cells and results from the reduction of W^{+6} under injection of electrons at the SnO_2 contact with simultaneous space charge neutralization by protons from the medium. The reaction, associated with the tungsten cage, is then



The back or counterelectrode was usually a carbon powder with a carbon rod for contact to the external world. For comparison purposes, as will be discussed later, the PWA was also contacted directly with metal electrodes such as copper and stainless steel. While the SnO_2 working electrode is capable of electron injection only, the counterelectrode must provide charge neutrality by proton or other ion injection, or readily exist in several oxidation states.

Shelf-life degradation of these cells due to loss of water has been a major problem. This degradation is manifested by an increase in cell resistance along with nonuniform coloration at the viewing electrode. However, with more careful cleaning and encapsulation procedures, including encapsulating the carbon rod, adequate cell performance has been achieved after a shelf-life of two to three months. If a degraded cell is opened and placed for several days in a humidifier, approximately the original performance is regained. This indicates that the shelf-life degradation is still due to inadequate hermetical sealing permitting a slow loss of water from the cells.

Electrochromic Performance

Important factors concerning electrochromic cells include the achievable optical density change, the coloration and bleaching speeds, the efficiency, and the lifetime. In the present cells, which are compressed powders, the change in diffuse reflectivity at the viewing electrode is the quantity of interest. Optical density (OD) changes of -0.1 where $OD = \log_{10} (R/R_0)$

Key words: voltammograms, degradation, field-assisted bleaching, open-circuit memory.

are observable in PWA in ordinary room light. OD changes ~ -0.3 are readily obtained at $0.6 \mu\text{m}$ in 25 msec with voltages of $\sim 1\text{V}$.

The optical coloration efficiency is defined as $\text{Eff} = OD/(Q/A)$ which is the optical density change divided by the injected charge per unit area in units of cm^2/C . At the peak of the efficiency wavelength curve, the efficiency is typically in the range of 100-150 cm^2/C . These values are comparable to or larger than those observed in WO_3 (6,7). A typical wavelength dependence is shown in Fig. 2 for a 1V, 25 msec pulse yielding an injected charge density of 2.7 mC/cm^2 (obtained from the average current times the time). In Fig. 3 is shown the OD change as a function of injected charge. It is seen that the efficiency is constant for OD changes below ~ -0.3 , but decreases at higher injected charge. This decrease could be due to the coloration depth becoming greater than the optical penetration depth.

Although we have not been able to quantitatively fit the bleaching profiles, we wish to show that the

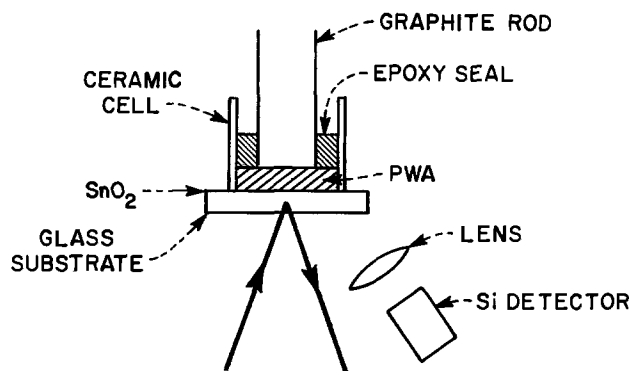


Fig. 1. The diagram of the experimental setup. The direct scattered light is blocked, while the diffuse scattered light is focused by a large diameter lens into an Si detector.

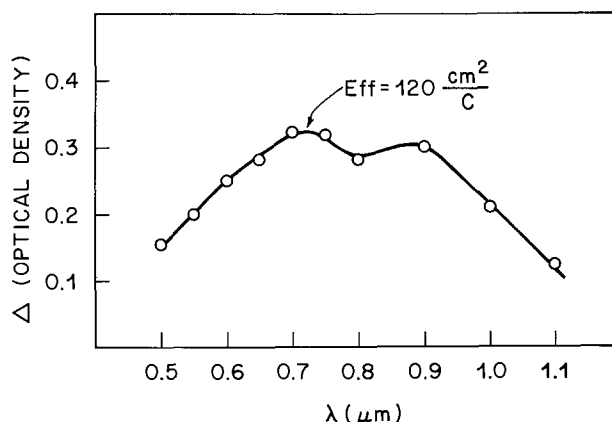


Fig. 2. Typical optical density change as a function of wavelength for a 1V, 25 msec coloring pulse and 1.3V bleaching pulse. The peak efficiency is indicated.

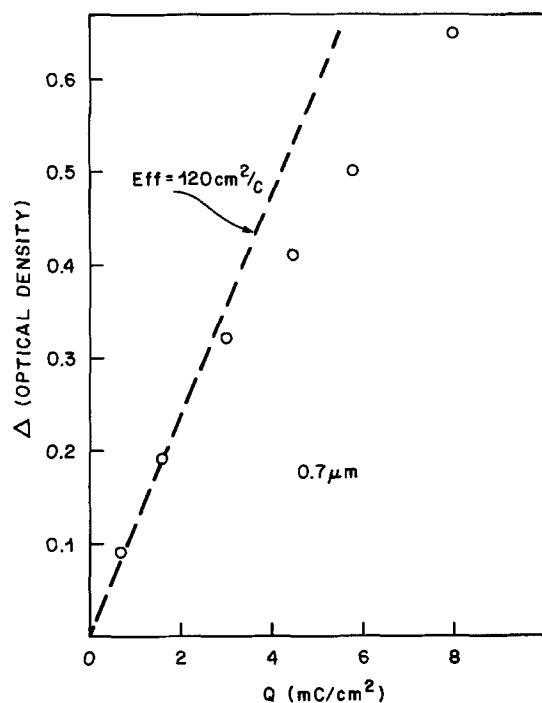


Fig. 3. The optical density change as a function of injected charge illustrating the deviation of the efficiency from linearity at higher optical density changes.

field-assisted bleaching is a diffusion-type phenomena. The bleaching time is insensitive to the magnitude of the bleaching voltage, at least for voltages above ~ 0.5 V. However, the field-assisted bleaching time varies with the OD change, presumably due to an increase in coloration depth. This effect is illustrated in Fig. 4, where a PWA sample was colored in 25 msec to an OD of -0.26 (triangles) and -0.6 (circles), respectively, and bleached with a positive voltage of 1.2V applied between the SnO_2 viewing electrode with respect to a carbon counterelectrode. For purposes of comparison, the initial OD change has for both cases been normalized to unity.

The actual distribution of colored centers (*i.e.*, W^{+5}) due to electron injection at the SnO_2 contact is not known. However, it appears that for large initial OD changes, the coloration depth is larger than the optical absorption length. Then, a fit to the shape of the bleaching curve can be obtained by assuming diffusion in a semi-infinite medium with the SnO_2 boundary acting as a perfect sink. The distribution of reduced centers $N_R(x, t)$ is given by

$$N_R(x, t) = N_R(0) \operatorname{erf} \frac{x}{\sqrt{4Dt}} \quad [2]$$

where x is the distance from the SnO_2 contact, and $N_R(0)$ is the initial distribution of reduced centers which is assumed to be constant. The optical density change is proportional to the total number of reduced centers within an optical absorption length l . That is

$$OD \sim \int_0^l N_R(x, t) dx \quad [3]$$

The OD as a function of time can be obtained in terms of the parameter $l^2/4D$, and a fit to the bleaching profile can be obtained, as shown by the dashed line in Fig. 4. The shape is fit for times less than 700 msec, after which the experimental OD values become less than the calculated profile. This deviation results from the assumption of a constant density semi-infinite depth distribution, whereas the actual profile must peak near the origin and drop off in a finite distance. It is also seen in Fig. 4 that when colored to a relatively low OD (given by the triangles) the OD decreases significantly faster. For coloration depths shorter or comparable to the absorption length, the detailed distribution of reduced centers is important, and a fit of the bleaching curve has not been obtained.

Another illustration of an increase in bleaching time is given in Fig. 5. Here, a PWA cell is colored to an OD change of -0.4 (*i.e.*, diffuse reflectivity 40% of its bleached value), and in one case immediately bleached (bleaching potential ~ 1.2 V) and in the other case maintaining open-circuit conditions for 100 msec. The open-circuit condition produces a slower decay of the optical density, which can again be attributed to diffusion of the colored centers (*i.e.*, electrons) away from the SnO_2 contact during the open-circuit condition. The removal of the electrons from a greater coloration depth results in a longer bleaching characteristic.

As far as operating stability, we have obtained OD changes of -0.3 with 25 msec coloration time run at 2 Hz for more than 10^5 cycles, without noticeable degradation. We have found that provided the cell is not overdriven (so that large optical density changes followed by incomplete bleaching are not produced), the operating life does not appear limited. Even in the above, if high operating voltages (> 2 V) have not produced noticeable damage at the SnO_2 interface, cells with C electrodes can be revitalized by sustained bleaching. On the other hand, cells with metal electrodes can become irreversibly colored.

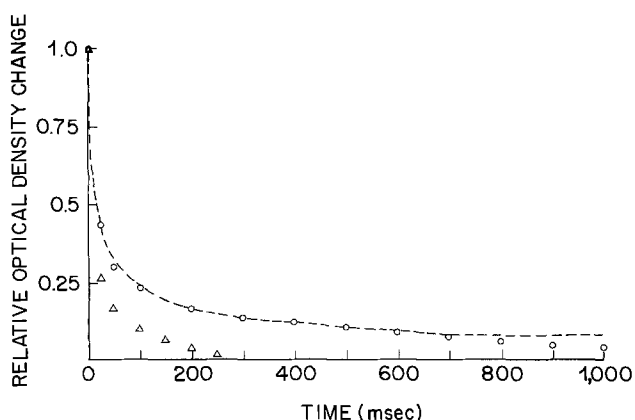


Fig. 4. Illustration of the increase in bleaching time for a cell colored to an initial OD of -0.6 (circles) compared to a cell colored to -0.26 (triangles), with the initial coloration normalized to unity.

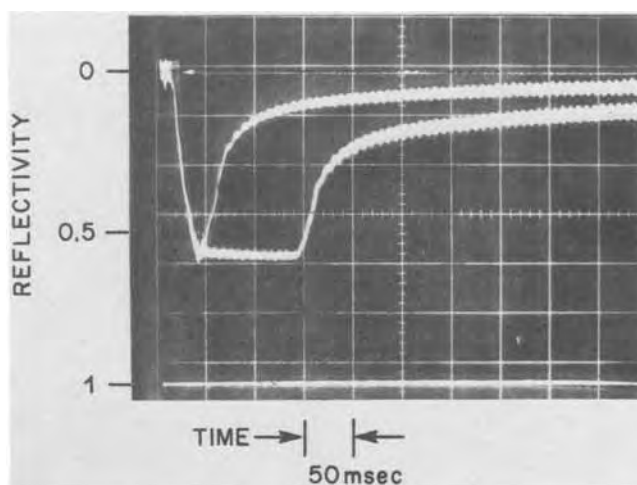


Fig. 5. Illustration of the increase in bleaching time for a cell maintained open circuit for 100 msec compared to a cell immediately bleached.

Voltammograms

The voltammograms for PWA were obtained with respect to an Ag reference electrode inserted in a hole drilled in the ceramic tube. The Ag had been previously anodized in H_3PO_4 . Voltammograms are given for the SnO_2 working electrode and for carbon, copper, and stainless steel counterelectrodes as shown in Fig. 6a, b, and c, respectively. The purpose was to compare carbon electrodes with electrodes capable of injecting mobile foreign ions such as Cu^+ , and noninjecting electrodes containing readily oxidizable elements such as Fe and Ni. The possibility of the carbon-containing surface groups to absorb the redox charge requirements while releasing H^+ has been previously discussed (2). It is seen that the carbon electrode is slightly anodic and maintains a nearly constant potential over the oxidation-reduction cycle. The Cu electrode is slightly cathodic and also exhibits only a small potential change over the entire cycle. The stainless steel electrode remains cathodic over the entire cycle, but exhibits a large potential variation. This electrode

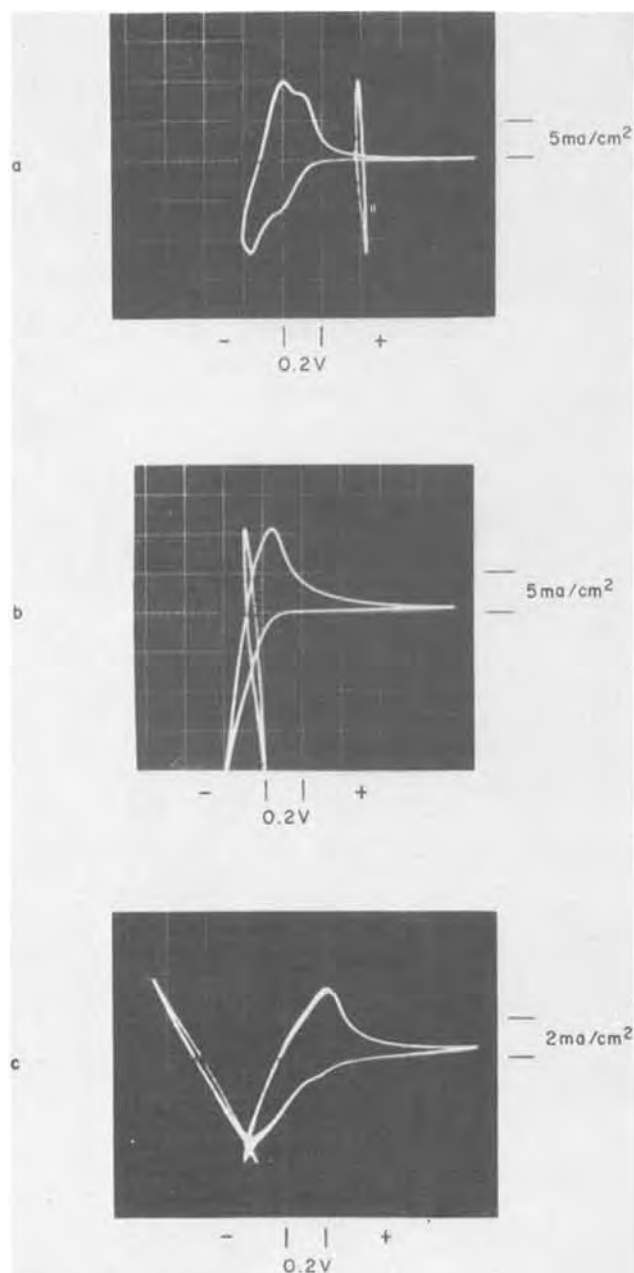


Fig. 6. Voltammograms of the SnO_2 working electrode and the counterelectrode (a, carbon; b, copper; c, stainless steel) with respect to the reference electrode for a sweep rate of 1 V/sec. The polarity with respect to the reference electrode is indicated.

becomes highly cathodic under reducing conditions, i.e., it must be brought to a large negative potential to be reduced, but readily oxidizes. It is also seen from these voltammograms that in the two electrode configuration (i.e., working electrode and counterelectrode), the Cu and stainless steel cells will color under short-circuit conditions whereas the carbon cell will bleach, and that in the latter case, coloration requires application of a small negative potential to the SnO_2 electrode, i.e., a slight coloration threshold. In addition to this short-circuit coloration, cells containing metal electrodes become significantly colored in about one week under open-circuit conditions. This is presumably due to the spontaneous reduction of tungsten by various metals, followed by a slow diffusion of the colored species to the viewing electrode. The coloration can be removed by application of a bleaching voltage, but returns when open-circuit conditions are reestablished. Both from the voltammograms and the discussions above, carbon electrodes are superior to the other electrodes discussed.

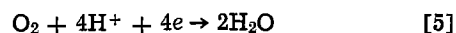
Memory

The existence of open-circuit memory is a potentially attractive feature of electrochromic cells. Here, we wish to discuss the long-term memory in distinction from the short (~ 100 msec) memory discussed previously. Once a pattern has been impressed by means of an electric field, it may be retained without further expenditure of power for various times. The memory decay reported here does not appear to be an intrinsic property of the PWA, but is more likely due to the presence of residual oxygen. In WO_3 cells, the memory can be appreciably shortened as well as the efficiency being reduced by the presence of oxygen (8, 9). A possible reaction describing the loss of memory due to oxygen is



blue \rightarrow white

In addition, the loss of efficiency during coloration could be due to a reaction such as



This means that a percentage of the injected electrons and the accompanying protons are not available for reduction of tungsten as given by Eq. [1], but are instead expended in a parasitic reaction such as given above. When an oxidizing agent such as H_2O_2 or HNO_3 is intentionally added, we have found both a large reduction in the efficiency (factors of 2 or 3) and especially the open-circuit memory (\sim orders of magnitude). However, simple techniques for reducing the residual oxygen, such as bubbling argon through the PWA during preparation have not given significant improvement.

In addition to the memory decay due to residual oxygen, a possible diffusion loss could occur since the colored depth is only a fraction of the sample length. Since the residual oxygen decay appears faster, we have not yet observed evidence for a diffusion mechanism.

The OD decrease has been various combinations of linear and exponential with time. An exponential decay indicates a simple loss mechanism, when the oxidizing agent is within the same geometrical region. A linear decay can indicate a loss mechanism in a porous medium when the oxidizing agent comes from outside the colored region (10). The loss of the reduced species N_R can be described by

$$\frac{dN_R}{dt} = -\frac{N_R}{\tau} - a \quad [6]$$

where τ is the loss time constant, which if due to tungsten oxidation by oxygen would be equal to a rate

constant per oxygen atom divided by the oxygen concentration, while a is the flux of oxygen entering the colored region from the PWA bulk. The solution is

$$N_R = N_R(0) e^{-t/\tau} - a\tau(1 - e^{-t/\tau}) \quad [7]$$

where $N_R(0)$ is the reduced density at $t = 0$. When the oxygen density in the colored region is high compared to $N_R(0)$, the first term dominates and exponential decay occurs. If $N_R(0)$ is large compared to the immediate oxygen density, τ is long and the second term dominates, and the decay becomes linear. Also, as suggested above, the time constant τ is only constant if the oxygen density is large compared to the reduced tungsten density. If, during coloration, a significant fraction of the oxygen is depleted, as suggested by Eq. [5], the time constant will be different for successive colorations if the oxygen level has not returned to its original value. For a given cell, we expect the memory decay to be slower the higher the original optical density, and to be slower for successive cycles provided the residual oxygen has not been regenerated. An example of such memory behavior is shown in Fig. 7. The curve marked first cycle was bleached ($\sim 1.5V$ bias) prior to coloration and fits an exponential decay (solid curve) with a time constant of ~ 100 sec. After the initial OD change had decayed to near zero, the cell was maintained in open-circuit condition, and then colored a second time (second cycle). It is seen that the OD has increased compared to the first cycle, but more noticeable, the loss of memory is now characterized by a time constant or perhaps linear decay closer to 1000 sec. Finally, if the cell is now bleached,

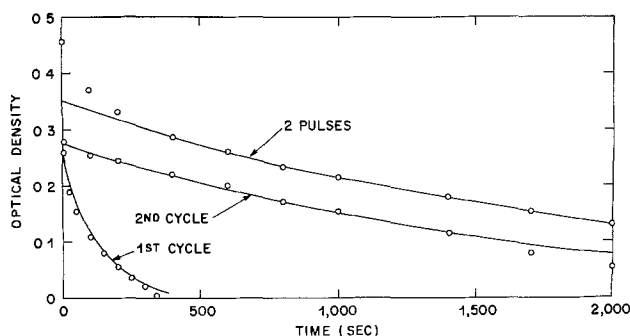


Fig. 7. Typical open-circuit memory for PWA as discussed in text.

and then colored by two successive pulses spaced approximately a second apart, an initial fast memory decay occurs, followed by a slow decay which appears linear. Although there are cell-to-cell variations in the times involved, the general features of the memory are such as described above.

Conclusions

In this paper, we have presented a fuller discussion of our results on PWA-type electrochromic cells. It is shown that these cells are simple to fabricate and are capable of reasonably efficient and fast electrochromic performance. However, the shelf-life is still unsatisfactory, while the open-circuit memory is complex and variable. Any further work on these cells should be concerned with increasing the shelf-life and removing all traces of residual oxygen.

Manuscript submitted Feb. 27, 1980; revised manuscript received ca. April 28, 1980. This was Paper 300 presented at the Los Angeles, California, Meeting of the Society, Oct. 14-19, 1979.

Any discussion of this paper will appear in a Discussion Section to be published in the June 1981 JOURNAL. All discussions for the June 1981 Discussion Section should be submitted by Feb. 1, 1981.

Publication costs of this article were assisted by Bell Laboratories.

REFERENCES

1. B. Tell and S. Wagner, *Appl. Phys. Lett.*, **33**, 837 (1978).
2. B. Tell and F. Wudl, *J. Appl. Phys.*, **50**, 5944 (1979).
3. A. J. Bradley and J. W. Illingworth, *Proc. R. Soc., London, Ser. A*, **157**, 113 (1936).
4. O. Nakamura, T. Kodama, I. Ogino, and Y. Miyake, *Chem. Lett.*, **17** (1979).
5. S. K. Mohapatra, G. D. Boyd, F. G. Storz, S. Wagner, and F. Wudl, *This Journal*, **126**, 805 (1979).
6. B. W. Faughman, R. S. Crandall, and P. M. Heyman, *RCA Rev.*, **36**, 177 (1975).
7. I. F. Chang, in "Nonemissive Electro-optic Displays," A. R. Knetz and F. K. vonWillisen, Editors, p. 155, Plenum, New York (1976).
8. I. F. Chang and W. E. Howard, *IEEE Trans. Electron Devices*, **ed-22**, 749 (1975).
9. S. K. Mohapatra, *This Journal*, **125**, 284 (1978).
10. W. W. Webb, J. T. Norton, and C. Wagner, *ibid.*, **103**, 107 (1956).

A Novel Method for Measuring the Thermal Conductivity of Electrodeposited Gold Films

Peter G. Borden

Varian Associates, Incorporated, Corporate Solid State Laboratory, Palo Alto, California 94303

ABSTRACT

A simple method for determining the thermal conductivity, K , of electrodeposited gold films is described. Specifically, it is shown how a comparison of the resistance-temperature and resistance-current characteristics of a ribbon of the film leads to a unique determination of K . When applied to a film typical of those used in semiconductor device heat sink structures, the technique yields a value of $K = 2.50 \pm 0.13$ W/cm $^{\circ}$ K, as compared to the value for bulk gold of 3.15 W/cm $^{\circ}$ K.

Thick electrodeposited gold films are frequently used to heat sink power semiconductor devices such as FET's (1) and microwave diodes (2). The observed

Key words: gold plating, thick gold films.

performance of such devices often indicates that the thermal conductivity of such films is well below that of bulk gold (3). It is quite surprising, then, that a thorough literature search, including computer searches

of NTIS and journal publications, has found no reported study of the thermal conductivity of electrodeposited gold since 1949 (4). Furthermore, the 1949 value of 2.96 W/cm²°K is incorrectly referenced, making confirmation impossible.

The present investigation considers the thermal conductivity of gold platings with respect to semiconductor device applications. Specifically, a simple, straightforward technique for the measurement of the thermal conductivity of such films is described. This is then applied to a film formed by methods typical of modern device fabrication, yielding a value about 20% below that of bulk gold.

Theory

The technique employs a comparison of the resistance-temperature and resistance-current characteristics of a self-supporting ribbon of the film to uniquely determine the thermal conductivity. A ribbon of the gold film, of length L and cross-sectional area A , is mounted between two supports of constant temperature T_0 , as shown in Fig. 1. As a current I causes ohmic heating, the ribbon's resistance will rise due to its temperature coefficient of resistivity. Knowledge of this coefficient, the current, and the sample resistance at T_0 allows determination of the thermal conductivity, K .

The conduction of heat generated by an electrical current in a wire has previously been considered (5). Here we follow similar procedures to find the resistance-current relation required to determine the thermal conductivity. Typically, the sample is long and of small cross section, so that the one-dimensional heat flow equation describes the temperature distribution; that is

$$KA \frac{\partial^2 T(x)}{\partial x^2} = -P \quad [1]$$

Here, P is the dissipated power per unit length. The thermal conductivity is assumed constant in temperature and thermal expansion is ignored. For a sample resistivity ρ of the form

$$\rho(T) = \rho_0 + \rho_1 T \quad [2]$$

Equation [1] takes the form

$$\frac{\partial^2 T}{\partial x^2} + \frac{I^2 \rho_1}{A^2 K} T + \frac{I^2 \rho_0}{A^2 K} = 0 \quad [3]$$

It should be noted that the linear form of Eq. [2] is usually accurate for bulk metals, and, as will be seen, appears to hold for the electrodeposited gold considered here. This assumption allows a straightforward solution of Eq. [3] under the assumption of constant temperature at the ends ($T(x = -L/2) = T(x = L/2) = T_0$), yielding a temperature distribution in the ribbon of

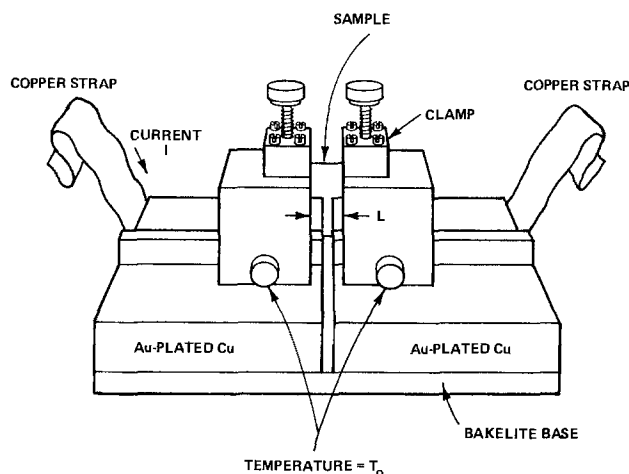


Fig. 1. The sample jig

$$T(x) = \left(T_0 + \frac{\rho_0}{\rho_1} \right) \sec \frac{\alpha L}{2} \cos \alpha x - \frac{\rho_0}{\rho_1} \quad [4]$$

where

$$\alpha = \frac{I}{A} \sqrt{\frac{\rho_1}{K}} \quad [5]$$

Finally, the sample resistance is found from Eq. [2] and [4]

$$R(I) = \frac{1}{A} \int_{-L/2}^{L/2} \rho(x) dx = R_0 \frac{\tan \left(\frac{\alpha L}{2} \right)}{\left(\frac{\alpha L}{2} \right)} \quad [6]$$

with R_0 the resistance at temperature T_0

$$R_0 = (\rho_0 + \rho_1 T_0) L/A \quad [7]$$

Thus, a measurement of $R(I)$ allows α to be found through Eq. [6]. An independent measurement of the temperature coefficient of resistance, ρ_1 , gives the thermal conductivity K through Eq. [5].

As an example, a 1 cm long, $100 \times 12.5 \mu\text{m}$ gold ribbon with $\rho_0 = -1.77 \times 10^{-7} \Omega\text{-cm}$ and $\rho_1 = 8.05 \times 10^{-9} \Omega\text{-cm}/^\circ\text{K}$ (these values are obtained from a fit of published resistivity data (6)) has a resistance of $R_0 = 0.179 \Omega$ at $T_0 = 300^\circ\text{K}$. With a current of $I = 0.2\text{A}$ and a thermal conductivity of $K = 3.15 \text{ W/cm}^\circ\text{K}$ (7), $\alpha = 0.809 \text{ cm}^{-1}$ and the fractional change in resistance is 5.8%. The temperature rise at the center is 25°K .

The principal loss mechanisms are convection and blackbody radiation. Convective loss is difficult to estimate; for this reason, the experiment is conducted in a vacuum. Empirical results indicate that for pressures under 10^{-3} Torr, the resistance of a typical sample is independent of pressure. Blackbody losses are considered in the Appendix, where it is shown that a prudent choice of sample dimensions will minimize this effect.

Sample Preparation

The sample is prepared with techniques similar to those used in plating a heat sink structure to the back of a semiconductor device. A standard ohmic contact metallization of 40 nm Au-Ge, 7.5 nm Ni, and 60 nm Au is laid down on a GaAs wafer doped to $1 \times 10^{18}/\text{cm}^3$ with Te. The wafer is then held in a bath of Selrex 125, a pH-5 critic acid-based solution designed for fast plating of thick, high purity matte-finish films. The bath was held in a beaker at 60°C and kept under circulation with a magnetic stirrer. About $10 \mu\text{m}$ of gold were plated out at a current density of 0.3 mA/cm^2 .

Ribbons are formed by photolithographic definition and etching in a KI-I₂ etch. After stripping the photoresist, the ribbons are separated from the substrate by etching the GaAs with a 5H₂SO₄:1H₂O₂:1H₂O etch.

Figure 2 shows top and side SEM views of a typical ribbon. The cross section, as determined by both weighing (assuming the density of bulk gold) and photography, is $60.0 \times 9.7 \mu\text{m}$. Figure 3 shows an SEM picture of the grain structure; the average size is 550 nm. Figure 4 is a Laue backscatter picture of the gold on the GaAs wafer, indicating that its crystallographic orientation is essentially random. This isotropy is significant, as it implies the thermal conductivity should be independent of direction. Thus, a longitudinal measurement is equivalent to a measurement through the thickness of the film.

Experimental Setup

The sample jig is made of gold-plated copper to ensure both good thermal conductivity and corrosion-free mechanical and electrical connections. Heavy copper straps are used as leads in order to minimize series resistance.

Initially, the jig with a mounted sample is placed in a vacuum oven. The resistance vs. temperature charac-

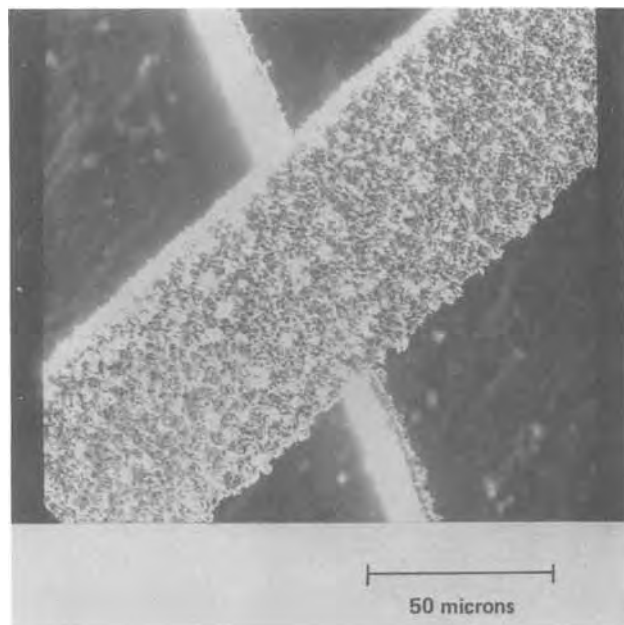


Fig. 2. Top and side views of a typical ribbon of electrodeposited gold.

teristic is measured. The jig is next removed from the vacuum oven and placed in a high vacuum system, where the resistance *vs.* current characteristic is determined. Analysis of the data, as already outlined, yields the thermal conductivity.

In the vacuum oven, temperature was monitored with a mercury thermometer. The wire resistance was found with a 5½ digit multimeter. Shorting the sample with a strap allowed measurement of the stray resistance. The current-resistance measurement used a PAR 172 precision current source, a 3½ digit DVM to monitor the current, and the 5½ digit multimeter to find the voltage drop at the sample. Samples are measured twice, once from low to high current and once from high to low. The resistance is found to be stable and reproducible for each value of current.

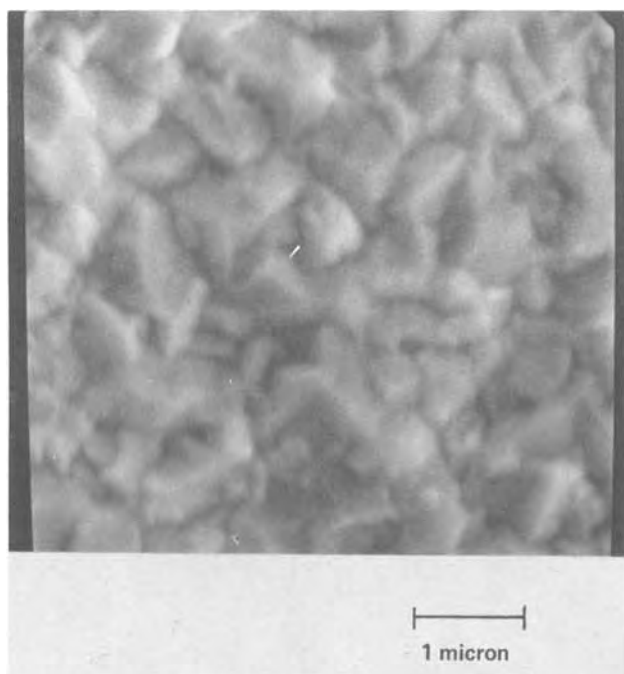


Fig. 3. An SEM view of the grain structure of a ribbon of electrodeposited gold. The average size is 550 nm.

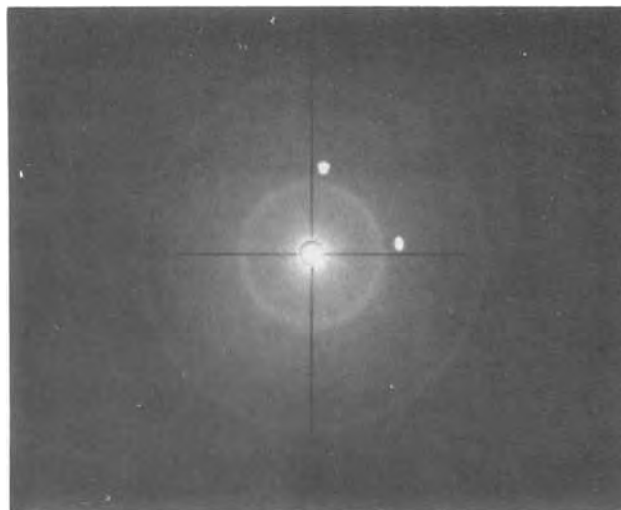


Fig. 4. A Laue backscatter picture of the electrodeposited film on the GaAs substrate. The concentric rings indicate isotropy of the film. The dots are due to the substrate.

Results

Measurements have been performed on both cold-rolled $11 \times 100 \mu\text{m}$ bonding ribbons and ribbons of electrodeposited gold formed by the technique already described. Figure 5a shows a plot of the resistivity-temperature characteristic for a 1.07 cm length of the bonding ribbon. The thermal coefficient of resistivity $\rho_1 = 8.14 \times 10^{-9} \Omega\text{-cm}/^\circ\text{K}$ compares well to the tabulated value of $8.05 \times 10^{-9} \Omega\text{-cm}/^\circ\text{K}$ (7). Differences in the value of ρ_0 from tabulated values are largely due to series resistance and do not have an effect on the thermal conductivity measurement.

Figure 6a shows the current-resistance characteristic for this ribbon. Analysis of these data yields a thermal conductivity of $K = 2.9 \text{ W/cm}^\circ\text{K}$, in reasonable agreement with the bulk value of $3.15 \text{ W/cm}^\circ\text{K}$ (6). Note also the excellent fit of the data to Eq. [6].

The resistivity-temperature characteristic of the electrodeposited gold ribbon is shown in Fig. 5b. The sample was 0.884-cm long with a cross-sectional area of $5.8 \times 10^{-6} \text{ cm}^2$. The thermal coefficient of resistance is $9.93 \times 10^{-9} \Omega\text{-cm}/^\circ\text{K}$, 22% higher than for the bonding ribbon. The current-resistance characteristic is shown in Fig. 6b. The thermal conductivity of $2.50 \pm 0.13 \text{ W/cm}^\circ\text{K}$ is 20% below the bulk value. This is consistent with estimates obtained from the performance of microwave devices employing similar gold films in their heat sink structures.

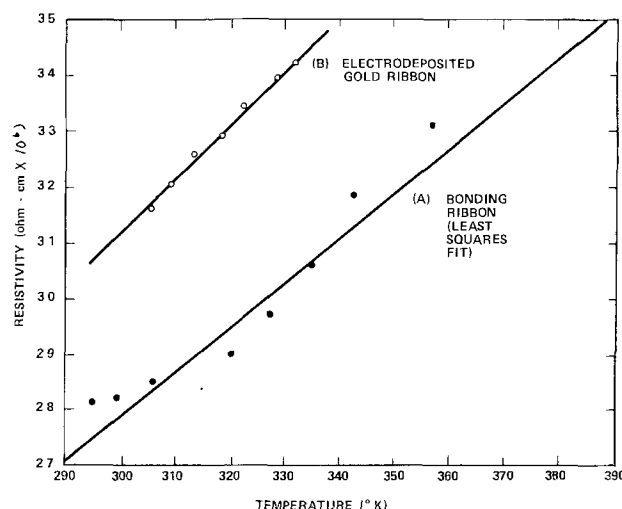


Fig. 5. Resistivity-temperature characteristics for (a) a gold bonding ribbon and (b) a ribbon made from electrodeposited gold.

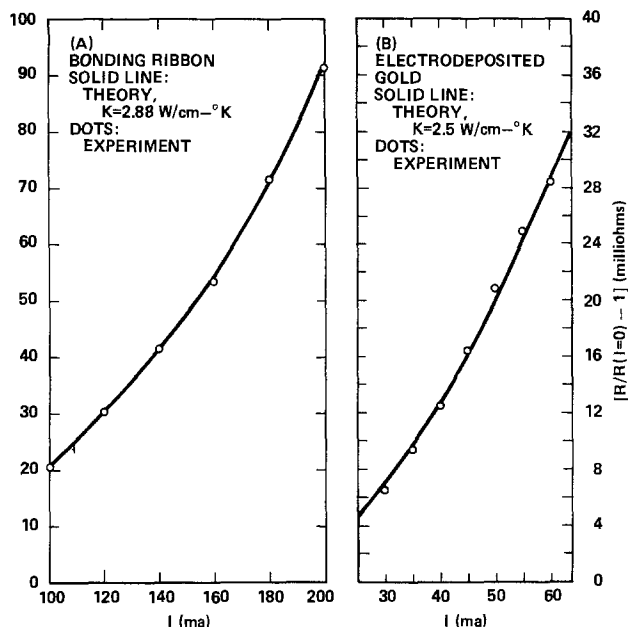


Fig. 6. The current-resistance characteristic of (a) the 1.07 cm long, $11 \times 100 \mu\text{m}$ bonding ribbon and (b) the 0.884 cm long, $60.0 \times 9.7 \mu\text{m}$ ribbon of electrodeposited gold. The theoretical characteristic, as determined by Eq. [6], is also plotted for both cases.

Conclusions

The great diversity in plating solutions and conditions in common use make the thermal conductivity of electrodeposited gold films quite variable. Nevertheless, because this property significantly affects the performance of devices employing plated gold in heat sinks, it is important to have available a technique for measuring the thermal conductivity of these films. This study has addressed this situation in two ways. First, a simple and straightforward measurement technique has been described. Second, a value has been found for a film typical of those used in semiconductor device plated heat sinks, showing that the thermal conductivity can indeed be significantly below the bulk value. This might be expected, both because of the large number of grain boundaries in the electrodeposited film and the possibility of the inclusion of impurities during formation.

It must be re-emphasized that the technique's simplicity to a large degree stems from assuming isotropy of the thermal conductivity. This appears to be valid on the basis of Laue backscatter photographs of the plated film, which show an essentially random crystal orientation.

Finally, it is noted that the technique may be applicable to other materials that are electrically conducting and can be formed as self-supporting ribbons, such as silver, nickel, and copper.

Acknowledgments

The author gratefully acknowledges the assistance and advice of Ramona Walsh and Joe Dully during sample preparation, James Andrews for aid in taking data and setting up the apparatus, Jack Bash for taking the Laue backscatter pictures, and Nancy Anderson for manuscript preparation.

Manuscript submitted Feb. 19, 1980; revised manuscript received May 13, 1980.

Any discussion of this paper will appear in a Discussion Section to be published in the June 1981 JOURNAL. All discussions for the June 1981 Discussion Section should be submitted by Feb. 1, 1981.

Publication costs of this article were assisted by Varian Associates, Incorporated.

APPENDIX

Blackbody Losses

The blackbody loss per unit length for a ribbon with an arbitrary shaped cross section of perimeter p is

$$L_{BB} = \sigma e p (T^4 - T_o^4) \quad [\text{A-1}]$$

with e the emissivity and σ the Stefan-Boltzmann constant. Writing the temperature $T = T_o - \Delta$. With $\Delta \ll T_o$, and using Eq. [4] to find the temperature change $\Delta = T - T_o$, the blackbody loss is

$$L_{BB} = 4\sigma e p T_o^3 \left(\frac{\rho_o}{\rho_1} + T_o \right) \left(\sec \frac{\alpha L}{2} \cos \alpha x - 1 \right) \quad [\text{A-2}]$$

The blackbody heat flux, F_{BB} , must be small compared to the heat flux through the ends of the ribbon, F_E . The former is given by

$$F_{BB} = \int_{-L/2}^{L/2} L_{BB} dX = 4L\sigma e p T_o^3 \left(\frac{\rho_o}{\rho_1} + T_o \right) \left[\frac{2}{\alpha L} \tan \frac{\alpha L}{2} - 1 \right] \quad [\text{A-3}]$$

and the latter by

$$F_E = KA \left[\frac{\partial T}{\partial x} \Big|_{x=L/2} - \frac{\partial T}{\partial x} \Big|_{x=-L/2} \right] = \frac{8KA}{L} \left(T_o + \frac{\rho_o}{\rho_1} \right) \frac{\tan \frac{\alpha L}{2}}{\frac{\alpha L}{2}} \quad [\text{A-4}]$$

For the case considered in the example below Eq. [7], assuming a worst case emissivity of $e = 1$

$$\frac{F_{BB}}{F_E} = 0.015$$

so that a prudent choice of the sample dimensions makes the blackbody loss small. It is also important to use currents small enough to avoid excessive heating of the sample.

REFERENCES

1. D. R. Decker and M. Omori, U.S. Pat. 3,986,196 (1976).
2. J. V. DiLorenzo, W. C. Niehaus, J. E. Velebir, and D. E. Islesias, *IEEE Trans. Electron Devices*, ed-22, 509 (1975).
3. Harry F. Cooke, Private communication.
4. J. S. Anderson, *Electroplating*, 84 (November 1949).
5. H. S. Carslaw and J. C. Jaeger, "Conduction of Heat in Solids," chap. 4, Oxford University Press, London (1959).
6. American Institute of Physics Handbook, D. E. Gray, Editor, p. 4-154, McGraw Hill, New York (1972).
7. *Ibid.*, p. 9-41.

Investigation of Energy Traps and Phosphorescence in Zinc Silicate Phosphors by Photostimulated Emission

I. F. Chang* and G. A. Sai-Halasz

IBM Thomas J. Watson Research Center, Yorktown Heights, New York 10598

ABSTRACT

The manganese activated zinc silicates doped with or without arsenic are investigated using photostimulated luminescence technique in addition to conventional photoluminescence and phosphorescence measurements. The experimental results provide information about the energy levels of the Mn^{++} and the traps and how they interact during the luminescence process. Based on conclusions deduced from experimental data, a physical model is proposed for interpreting the zinc silicate luminescence and phosphorescence with some clues on the role of the arsenic doping and its effect on phosphorescence.

Manganese-doped zinc silicate is a useful phosphor in CRT applications due to its high efficiency and relatively long persistence. The green color emission is attributed to the spin flip transition of the d-orbital electron associated with the Mn^{++} ion (1). The Mn^{++} ion has been identified to be located on the two non-equivalent zinc sites in the rhombohedral crystal with a tetrahedral site symmetry (2). Thus, the luminescence transition is ascribed as $4T_{1g}-6A_{1g}$ transition, a forbidden one according to the selection rules (3). The intrinsic decay of the emission after u.v. excitation is exponential having a decay time constant (to 1/e point) on the order of 10 msec.

In addition to the intrinsic phosphorescence decay, one often observes in zinc silicate phosphors a long persistent phosphorescence with a much greater time constant(s). Often, this long persistence phosphorescence is too weak in intensity to be of any practical use. However, a properly tailored long persistent light decay can be utilized to reduce flicker (4) in a refreshed CRT display or in a illuminating light source.

There have been some empirical phosphor synthesis techniques reported in the literature (5, 6) for the purpose of enhancing or controlling this long persistence. One of the accepted and successful methods is to dope the manganese-activated silicate phosphor with a minute amount of arsenic (6). However, this technique has never been precisely described and the role of arsenic in the material has never been quite understood. Suggestions have been made that the long decay is mainly due to the fact that the excited electrons spend some appreciable time in traps before reaching the luminescent centers. Besides this type of qualitative description, we find surprisingly few facts or answers to the following questions: where are the electron-trap states and the Mn^{++} energy states located in relation to the energy bands of zinc silicate? How do they interact? What is the state of arsenic, where is it and its energy level and how does it prolong persistence?

We report here our early effort to find answers to the above questions. Taking a new approach we have carried out some photostimulated luminescence (PSL) experiments in addition to ordinary photoluminescence (PL) and phosphorescence (PP) measurements. The PSL is the luminescence stimulated by photons having energy lower than the emitted photons. This is possible if there were traps; then, the low energy photons can stimulate the trapped electrons (or holes) which have been previously excited and captured at the traps. The released electrons can then be captured by manganese ions. Such a process is expected to be a function

of excitation energy. Thus, we expect that the PSL data can provide information about traps and how they interact with the luminescence process. In the following, we report the results of these experiments and other PL and PP measurements for manganese doped zinc silicates both with and without arsenic doping. We correlate these data with chemical analysis made on the materials and with other experimental data. Furthermore, based on these findings, we propose a physical model for interpreting the zinc silicate luminescence and phosphorescence.

Experimental Work

Phosphor materials investigated.—Numerous samples of commercial and laboratory synthesized zinc silicate phosphors have been investigated. The commercial phosphors are known as P1 (without As doping) and P39 (with As doping). The laboratory samples were synthesized (7) by solid reaction of $MnCO_3$, $ZnCO_3$, SiO_2 , and/or As_2O_5 at temperatures between 1200° to $1450^\circ C$.

The laboratory samples give essentially the same luminescent properties as the commercial phosphors do. In Table I we list the chemical compositions of the materials that received detailed investigation in this work. The first three samples (A, B, and C) are P1-like materials which have no As doping. The remaining samples (D, E, and F) are P39-like materials which contain small amounts of arsenic doping and considerable less manganese than the P1 samples. Since the arsenic ions were more effectively introduced from As_2O_5 in the oxidizing atmosphere during synthesis, we assume that they remain as As^{+5} ions. All samples were identified by x-ray diffraction as zinc silicates and by chemical analysis as having slight excess of silica. Some high concentration manganese (>1%) zinc silicates have also been synthesized which exhibit a PSL intensity inversely proportional to the manganese concentration. This result will be reported elsewhere (8). The present work is mainly concerned with manganese concentration less than 1% which covers the doping range of commercial zinc silicate phosphors.

Table I. Chemical analysis of phosphor samples

Sample ID	C_{Mn} (w%)	C_{As} (ppm)	C_{Zn} (w%)	C_{Si} (w%)
A (P1)	0.523		51.8	16.1
B (P1)	0.605		52.2	16.3
C (P1)	0.431		55.4	14.7
D (P39)	0.048	330	52.8	15.8
E (P39)	0.033	76	51.5	17.2
F (P39)	0.063	88	52.6	15.9

* Electrochemical Society Active Member.

Key words: inorganic, photoluminescence, ultraviolet, visible.

Experimental procedure.—An experimental setup capable of making PL, PP, and PSL measurements is schematically shown in Fig. 1. The PL excitation sources used were a u.v. lamp with monochromator and an Argon laser tuned at 488 nm. The emission was measured with a Spex monochromator equipped with a GaAs detector and photon counter. For the PP decay curve and PSL measurements, the monochromator was set near the peak emission wavelength of the Mn^{++} green emission (~ 525 nm). Two laser sources (YAG- 1.06μ and He-Ne-633 nm) were used to stimulate the green emission. The samples, all in powder form, were pressed into a sample holder which could be mounted on a heater stage capable of being heated up to $400^\circ C$. A fast electromechanical shutter with 1 msec response time was used to control the exposure of the laser lights on the phosphor samples. For PP spectral decay, an OMA (optical multichannel analyzer) was used in lieu of the monochromator.

Results and Discussion

In order to examine the excitation and emission processes involving the Mn^{++} ion and electron traps, we have selected two excitation energies, one being 488 nm which can directly excite the Mn^{++} ion and the other one being 254 nm which may excite the electrons from the Mn^{++} into the conduction band and cause filling of the traps. These above assumptions are consistent with the absorption (9) and excitation (10) data in zinc silicate which show only a set of characteristic absorption bands between 3000 to 5000Å corresponding to Mn^{++} ions and are also consistent with the photoconductivity data in willemite (11) which show strong excitation bands near 2800Å and below. However, one should point out an alternative possibility, i.e., the 254 nm excitations may also excite the valence electron directly into the trap levels.

The spectra of photoluminescence and phosphorescence, decay curve, and photostimulated luminescence results are discussed below.

Photoluminescence spectra.—The PL spectra produced by these two excitations in zinc silicate are shown in Fig. 2. One notes that the two spectra have similar shape and identical peak wavelength, 525 nm (2.36 eV). This suggests that the final emitting state is the same for both excitations. It is also important to know at which excitation power density does the PL saturate so that we only use excitation power below

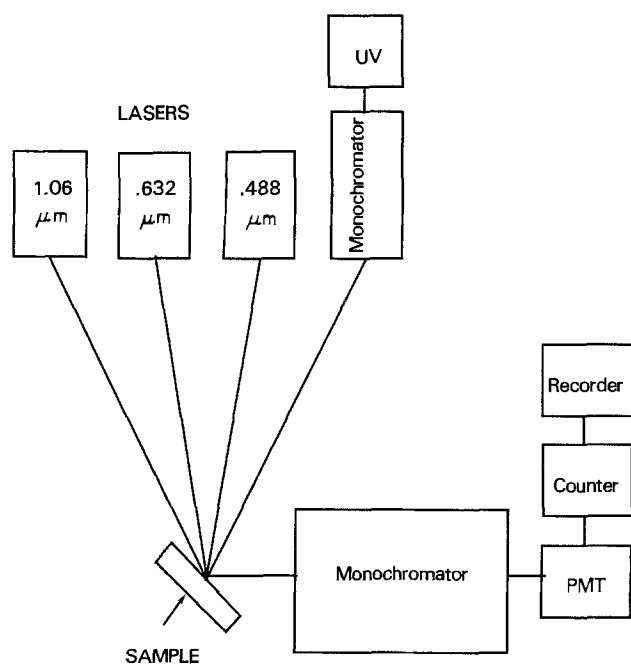


Fig. 1. Experimental arrangement for PL and PSL measurements

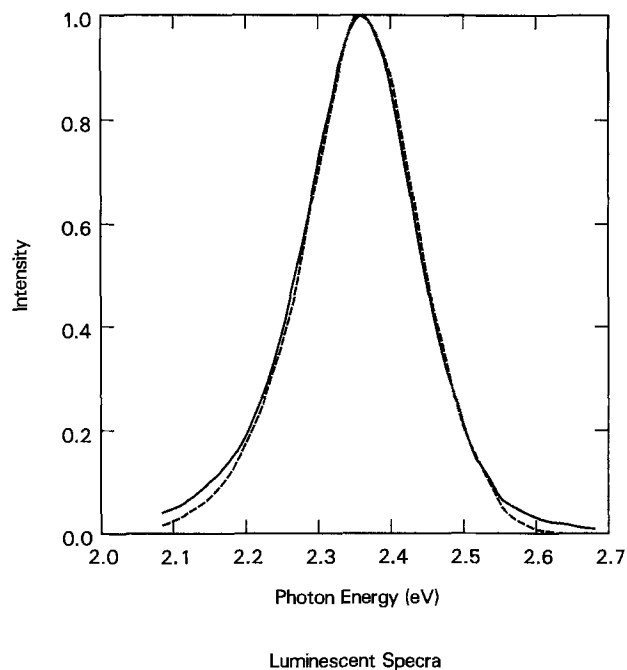


Fig. 2. Emission spectra of Mn^{++} in zinc silicate by 254 nm (solid line) and 488 nm (dash line) excitation.

the saturation level. Figure 3 shows the PL as a function of the 488 nm power density. One notes that the PL is approximately proportional to the power density up to 3 W/cm^2 . Since the u.v. light source used in our experiments has much less power than the Argon laser, one can safely assume that both excitations used in our experiments are not causing any PL saturation effect.

Phosphorescence spectra.—The time resolved PP spectra was measured using an Optical Multichannel Analyzer (OMA) system. Only electron beam excitation can produce sufficient emission intensity to allow an unambiguous PP spectra measurement. Figure 4 shows the phosphorescence spectra taken at 1, 2, 3, 5, 10, and 30 msec with time integration interval of 200 μsec for a P1 sample. Again, the spectra exhibit identical shape and peak position. Thus it is reasonable to conclude that the final emitting state is also identical with the PL during PP decay. Similar conclusion can be made for the P39-like silicates.

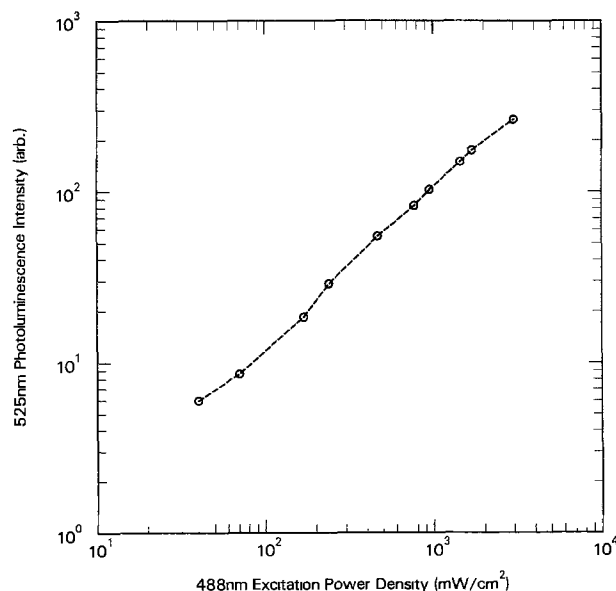


Fig. 3. Dependence of PL on excitation power density of 488 nm

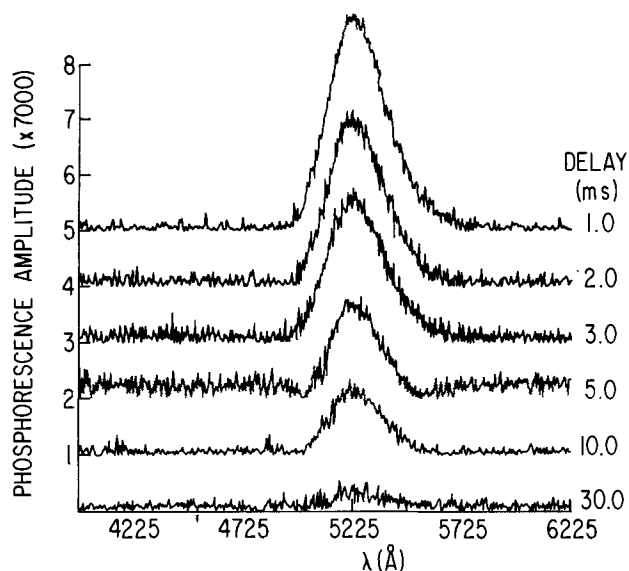


Fig. 4. Phosphorescence spectra for a P1 phosphor at the time of 1, 2, 3, 5, 10, and 30 msec after excitation removal. Spectra were recorded with a OMA having 200 μ sec integration time.

Decay curve.—Although the PP spectra do not change with time for both P1 and P39-like samples, the PP decay curves are quite significantly different. The decay curves for the samples listed in Table I are shown in Fig. 5 for both 488 and 254 nm excitations. One notes that the P1-like samples (A, B, C) under 488 nm excitation show an exponential decay (left upper three curves of Fig. 5) with time constant, τ_e , being ~ 10 msec, a characteristic decay time of Mn^{++} emission in silicate. The same samples under 254 nm excitation also exhibit (right upper three curves of

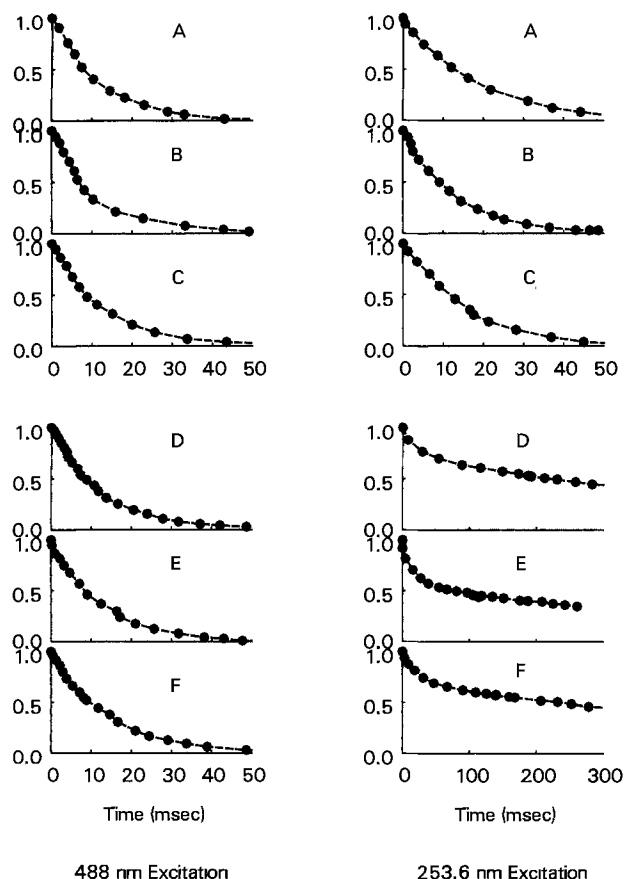


Fig. 5. Decay characteristics of sample A, B, and C (P1-like) and samples D, E, and F (P39-like) by 488 and 254 nm excitations.

Fig. 5) similar decay time constant, however, with slightly more light output at longer decay time (much beyond 10 msec).

The decay curves of the arsenic-doped samples (D, E, F in Table I) by 488 nm excitation are shown in the left lower three curves of Fig. 5. One notes that the characteristic exponential decay is again observed. However, as shown in the right lower three curves of Fig. 5, a much slower decay is observed when excited by 254 nm. The decay curves do not show any 10 msec like decay time constant; instead they exhibit time constant on the order of a second. It is also noted that the initial decay time constant seems to be longer for higher arsenic content sample (sample D vs. E and F).

To probe where the arsenic level is, one should use excitation energies greater than 2.54 eV to find the threshold excitation energy for which the characteristic decay behavior changes to the long decay time constant attributed to arsenic trapping. This threshold excitation energy is found to be 3.96 eV (~ 313 nm) in P39-like material. This fact suggests that the arsenic level may be 3.96 eV above the manganese ground state or the valence band depending on where the electron is emitted from.

Photostimulated luminescence (PSL).—The PSL is a technique to probe the trap states in the zinc silicate material. The photostimulated green emission is obtained by exciting the zinc silicate phosphor with u.v. and then stimulating it with lower energy photon such as red or infrared. This effect is shown in Fig. 6 for a P1-like material. The samples are typically excited with 254 nm for 1 or 2 min and then exposed to a He-Ne laser (633 nm) light during or after the u.v. excitation. The sharp spike is the stimulated green emission. The PSL decays to equilibrium with fairly slow time constants (i.e., not with the characteristic Mn^{++} decay time constant) as shown in Fig. 7. The area under the PSL spike represents the stored energy in the traps being released. The traps are apparently

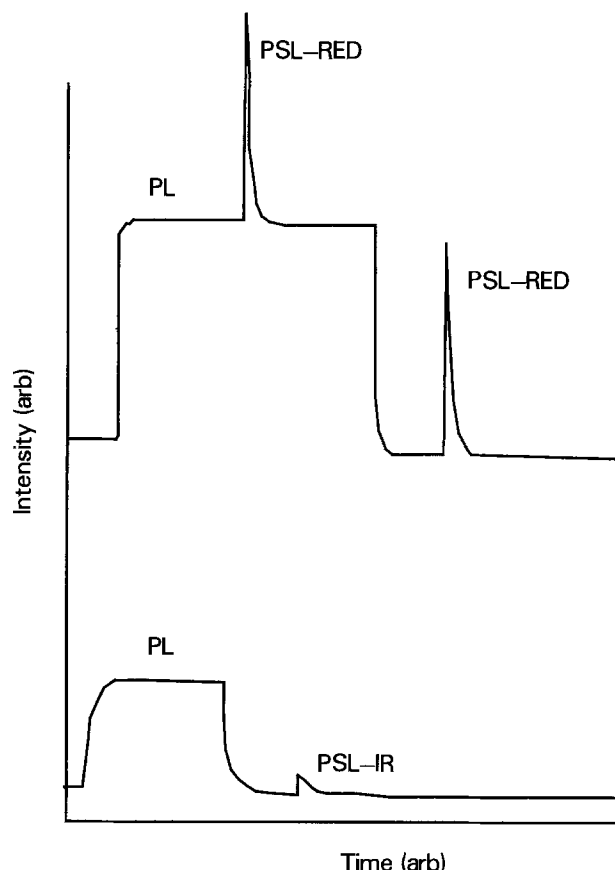


Fig. 6. The photostimulated luminescence effect by red (633 nm) and infrared (1.06μ) stimulation.

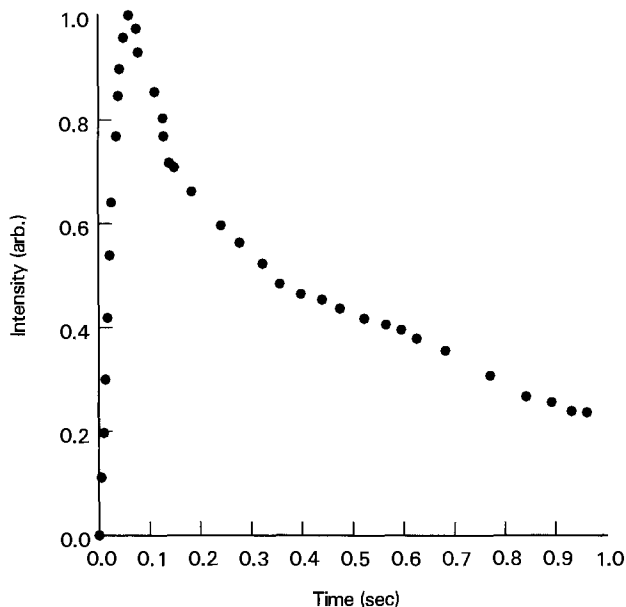


Fig. 7. Decay characteristics of the PSL-red

very stable at room temperature since the PSL can be observed hours later after the u.v. excitation is removed. The intensity of PSL depends on the u.v. excitation strength and duration and the stimulating power density. In general, more u.v. excitation and more intense stimulation produces greater PSL effect (8). One other important observation with PSL experiments is the threshold excitation energy for the PSL effect. The PSL-red is sufficiently intense to allow such an observation. Table II lists the PSL intensities measured at 2 min of continuous excitation (PSL-red-2) and after 30 sec excitation removal (PSL-red-2-30) for various excitation wavelengths. The PL intensities are also included for comparison. These results suggest that only the excitation energy greater than 3.65 eV is able to fill the intrinsic traps for red stimulation.

The PSL observed in P39 is generally much weaker in intensity. When stimulated with an infrared light source (1.06μ) (PSL-IR), the effect is even smaller. The PSL-IR is generally too weak to be observed during u.v. excitation. After u.v. removal (during PP decay), one can stimulate the PSL as shown in Fig. 8a and b for infrared stimulation in a P39 material. One notes that the PP decay shows its slow decay. As the infrared stimulation is applied, a slow buildup much slower than the buildup in red stimulation (Fig. 7) is observed. As the infrared stimulation is interrupted intermittently, one notes clearly that there are two time constants involved in the buildup and decay of PSL-IR.

The various PSL effects are summarized in Table III where the first column contains the PL intensity excited by 254 nm as a reference for the PSL effects. The different decay times to 10% point serve to qualitatively illustrate the time dependences of the decay

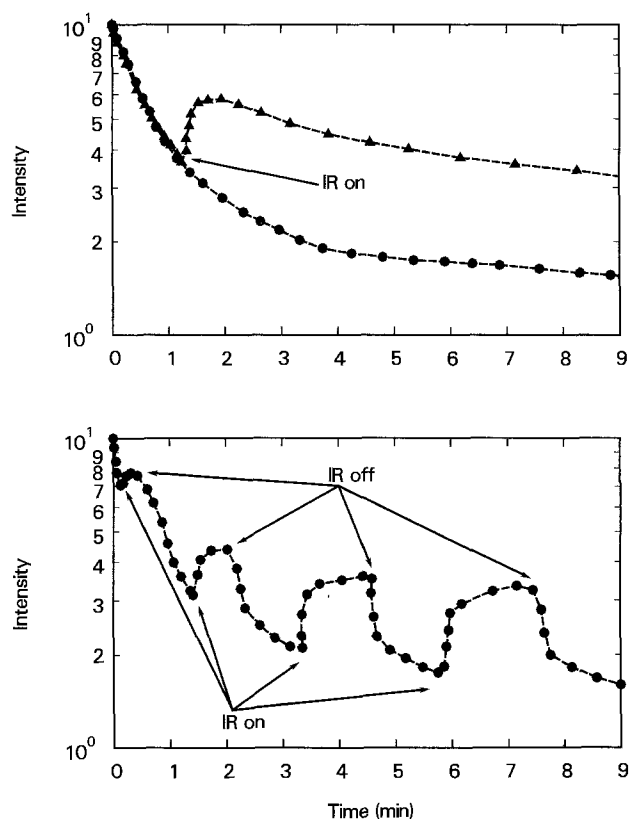
Table II. Dependence of PSL on excitation wavelength

Wavelength (nm)	254	280	300	320	340	366	420	440	480
PL ^a	10 ⁵	10 ³	10 ⁴	10 ⁴	10 ³	10 ³	10 ³	10 ³	10 ⁴
PSL-2 ^b	10 ⁵	10 ³	10 ⁴	10 ³	10 ³	0	0	0	0
PSL-2-30 ^c	10 ⁴	10 ³	10 ⁴	10 ³	10 ³	1	10	5	5

^a The intensities are given by order of magnitude only since light source, monochromator and filters are not calibrated precisely.

^b PSL-2 means luminescence stimulated by 633 nm at 2 minutes of 254 nm excitation.

^c PSL-2-30 means luminescence stimulated by 633 nm after 2 minutes of 254 nm excitation and 30 seconds of excitation removal.



Decay with 1060 nm excitation

Fig. 8 (a, top) Decay characteristics of a P39 sample with and without 1.06μ light stimulation; (b, bottom) decay characteristic of a P39 sample with periodic stimulation of 1.06μ light.

processes involved. The PL of sample A (P1) and D (P39) reaches to 10% point at 25 msec and 1600 msec, respectively. The PSL-red decays to 10% point at 1.5 sec for sample A and 30 sec for sample D.

Discussions.—From Fig. 2 we can conclude that the final emitting state is the same for both the 254 and the 488 nm excitations. It is also evident from Fig. 4 that the final emitting state is also identical with the PL and PP decay. Similar conclusions can be made for both P1 and P39-like silicates. In the decay curves shown in Fig. 5, the slow component suggests that there are possibly some trapping states in the P1-like materials which can trap the excited electrons and have a very small probability of releasing them to the Mn^{++} emission. These traps may be intrinsic to the zinc silicates or may be induced by the half percent or so manganese doping. They should be distinguished from the traps induced by the arsenic doping as having different decay characteristics.

Since the 254 nm (4.88 eV) excitation produces no component of the characteristic decay in the arsenic-doped materials, it may be suggested that the luminescence decay is a cascading process of an electron being captured first in an As level, then transferred to one of the excited state of Mn^{++} , and finally reached the emitting state. Since in P39-like materials, the man-

Table III. PL and PSL in zinc silicate phosphors by 254 nm

Sample	I_{PL}^\dagger	$T_{10\%}/oPL$ (msec)	$I_{PSL-Red}^*$	$T_{10\%}/oPSL-Red$ (sec)	I_{PSL-IR}^*	$T_{10\%}/oPSL-IR$ (sec)
A (P1)	100	25	57	1.5	0.09	180
D (P39)	30	1600	2.3	30	0.015	>3000

* Instantaneous peak intensity.

† Normalized with respect to P1 of sample A.

ganese content is, comparable to that of the arsenic, on the order of several hundred parts per million (by weight), it is possible that the arsenic and manganese in the silicate may be paired in such a way that the arsenic energy states are coupled somewhat efficiently with the Mn^{++} excited states. If one assumes that the Mn^{++} and As^{+5} were randomly distributed in the lattice with respect to each other, then the probability would be so small (based on their concentrations) for an As^{+5} ion to transfer an electron to the Mn^{++} ion that one should observe the intrinsic decay of the Mn^{++} emission instead of the slow decay as shown in the right lower three curves of Fig. 5. Comparing PL efficiencies of P1 and P39-like materials, it is noted that the P39-like materials generally have efficiency about one-third of that of the P1 efficiency and yet have a manganese content reduction about one-tenth. This suggests that the introduction of arsenic actually increases PL efficiency on a per manganese ion basis probably because the arsenic has much greater capture cross section than the other intrinsic traps in the manganese doped zinc silicates. However, one cannot arbitrarily increase the arsenic content because it will reduce PL efficiency if exceeded 1000 ppm. One also cannot arbitrarily increase the Mn content since it will cause domination of the 10 msec manganese intrinsic decay if exceeded 1%. It appears that the optimal synthesis requires a comparable manganese and arsenic doping with a pair-like (efficient) coupling in the zinc silicate.

Referring to the PSL results presented above, it is interesting to point out that the threshold excitation energy (3.65 eV) and the red stimulation energy (1.95 eV) happen to be added up to be greater than the bandgap energy (9) (5.5 eV) of zinc silicate. This may suggest that it is the valence electrons that are excited into the traps. The holes left behind are then trapped somewhere else, perhaps in the Mn^{++} ground state. If this is true, one would expect a higher excitation threshold energy for the PSL-IR. Unfortunately, such experiments have not been conclusive due to difficulties in measuring very-weak PSL-IR effect.

On the other hand, if one assumes that the intrinsic traps are filled via conduction band electrons which are excited from the Mn^{++} ground state, then one could definitively assign the Mn^{++} ground state to be located at 3.65 eV below the conduction band. In this case, the threshold excitation energy will be constant for different stimulation energies.

Experimentally we have confirmed that the PSL-red can occur even after the PSL-IR is first exhausted (but not vice versa). Because of this result and the fact that the PSL-red is greater for higher energy u.v. excitation, one may suggest that the electron traps may not be a discrete level, rather that they have a distribution in energy which may undergo retrapping during stimulation (redistribution). Since the PSL-red decay rates are different for the samples with and without arsenic doping as explained in Table III, one may also suggest that the traps are not necessarily coupled with Mn^{++} excited states directly.

The PSL-IR in P39-like materials deserves more discussion. The PSL buildup shown in Fig. 8a is similar to the PL buildup in P39-like materials. This suggests that the buildup in both cases is due to filling up the arsenic traps. In the PL case, the 254 nm may excite electrons from the manganese ground states and fills them in the arsenic traps via conduction band, whereas in the PSL case, the infrared may stimulate the electrons from the intrinsic traps into the arsenic traps. As one notes in Fig. 8a, after reaching saturation (*i.e.*, the redistribution of trapped electrons reaches quasi-equilibrium), the decay resumes its initial decay which is attributed to the cascading decay process of transferring an electron from an intrinsic trap to an arsenic trap and then to the Mn^{++} causing emission. This interpretation is demonstrated by interrupting the

infrared stimulation intermittently as shown in Fig. 8b. Clearly there are two time constants involved in the buildup and decay of PSL-IR. The first buildup is thought to be due to the filling of the arsenic states and the second buildup with slower rate (minutes) is thought to be due to the retrapping and redistribution of the intrinsic states with trapped electrons shifting to shallower states. The decay time constant associated with the arsenic state is smaller than that of the intrinsic states. Therefore, the PSL-IR first exhibits the refilling of the arsenic states, the first buildup curve, as shown in Fig. 8b. As time progresses, the arsenic states are filled to near saturation and then the redistribution of electrons in the intrinsic states also take effect, thus the PSL-IR exhibits the second buildup as seen in Fig. 8b.

As summarized in Table III, longer decay time of both PL and PSL are observed in the arsenic-doped sample. This is consistent with the cascade decay process discussed above. Similarly it is also true for the PSL-IR decay. The infrared stimulated luminescence have much longer decay time which may be attributed to the slower trap redistribution process under infrared stimulation.

One also notes that there are factors of 25 and 6 in intensity difference, respectively, for PSL-red and PSL-IR in samples A and D. This is likely due to the fact that the arsenic doping creates more trapping states which can shunt out the intrinsic traps in the capturing process in zinc silicates. This is supported by the thermoglow measurements made in P1 and P39-like materials (12). The glow peak near $T = 295^{\circ}K$ in P39-like material is about 50 times larger than the corresponding peak in P1-like material. As suggested earlier, the arsenic states may be coupled with the Mn^{++} excited states. The arsenic state may be a discrete energy level and may not be stimulated efficiently by the red and infrared laser light, which may be responsible for the PSL intensity difference observed in samples with and without arsenic doping.

One further notes, in Table III, that the PSL-IR intensities are smaller by a factor of several hundred than the PSL-red intensities in both types of samples. This observation may be due to the reason that the 254 nm (4.88 eV) does not fill all the shallow traps (assuming valence electron excitation scheme) that the infrared can stimulate.

Physical Model and Conclusions

As stated earlier, the main questions are that we do not know where the Mn^{++} energy states and the electron-trap states, especially the arsenic states, are located in relation to the energy bands of zinc silicate. In the following, we list several conclusions deduced from the above described results which leads to a proposal of a physical model:

1. The ground state of Mn^{++} is located in the energy bandgap of zinc silicate—this is supported by the fact that the Mn^{++} ground state can stay empty for hours and allow long persistence PL, PP and long storage time of PSL.

2. The Mn^{++} emitting state is identical for PL (both directly excited by blue light or indirectly excited by higher energy photons) and for PP—this is borne out by the identical emission spectra of PL and PP.

3. There are intrinsic traps probably having an energy distribution which can be stimulated by the red and infrared photons—this is supported by the fact that the PSL intensity is greater for higher energy excitation and the fact that the PSL-red can occur even after the PSL-IR is exhausted.

4. The As^{+5} doping introduces an energy state which seems to be coupled with the Mn^{++} excited state and lies at least 2.54 eV above the Mn^{++} ground state perhaps about 3.96 eV—this is suggested by the fact that the blue excitation (2.54 eV) does not cause long persistence in an arsenic-doped sample and the change-

over of decay behavior occurs for excitation of 3.96 eV.

5. The As^{+5} ions probably form pairs with the Mn^{++} ions during material synthesis—this is because we have found that, in the samples having low Mn^{++} concentration (0.05%) the PL efficiency on a per ion basis is enhanced by the presence of comparable arsenic doping.

6. In the As^{+5} doped samples the energy transfer seems to proceed from the intrinsic traps through the As^{+5} to the Mn^{++} emitting state—this is suggested by the rise and decay behavior in the PSL-IR experiment (Fig. 8).

7. There is an uncertainty of reference point for the threshold energies determined—there exists a threshold excitation energy, 3.65 eV, for the PSL-red effect in all samples and a threshold excitation energy, 3.96 eV, for change over from short to long persistence decay in arsenic-doped zinc silicates, but whether they are measured from the valence band or the Mn^{++} ground state is not determined.

In considering a physical model, the uncertainty stated in 7 (above) leads to several possibilities. If the 3.65 threshold is measured from the Mn^{++} ground state to the conduction band, then the traps would be filled by the conduction band electrons which are excited from the Mn^{++} ground state by energy greater than 3.65 eV. The As^{+5} states could be filled the same way except they are coupled with the Mn^{++} excited states to exhibit long persistent decay. However, this picture is not consistent with the 3.96 eV threshold for decay behavior change. One cannot assign the As^{+5} states 3.96 eV above the Mn^{++} ground state (they would be in the conduction band) nor 3.96 eV above the valence band by assuming their excitation by the valence band electrons (they would be below the Mn^{++} emitting state). Therefore, one would prefer suggesting that the 3.65 eV threshold is measured from the valence band to the intrinsic traps and they would be filled by valence electrons during excitation [since $3.65 \text{ eV} + 1.95 \text{ eV} > 5.5 \text{ eV}$ (bandgap)]. In this picture, the Mn^{++} ground level cannot be assigned precisely in relation to the conduction band. The Mn^{++} ground state is believed to be still above the valence band because they can stay empty for hours after excitation as exhibited by the PSL effect. The 3.96 eV threshold for decay behavior change can add some restrictions to the location of Mn^{++} ground state. This is shown schematically in Fig. 9 where (A) is based on the assignment of 3.96 eV being above the valence band and (B) is corresponding to the assignment of 3.96 eV being above the Mn^{++} ground state. Case (A) restricts the Mn^{++} ground state to be less than 1.6 eV above the valence band ($<3.96 - 2.36 = 1.6$) whereas case (B) does not limit the energy level of Mn^{++} ground state at all. Since the blue light excitation (2.54 eV) does not cause long decay in As-doped samples, the As^{+5} level must couple with one or more higher level excited state of the Mn^{++} ion. Both cases are consistent with our experimental results presented above.

In summary, using PSL experiments in addition to conventional PL, PP, and decay curve measurements, we have obtained some clues on the physical picture of the PL and PP mechanisms in zinc silicate phosphors. The long persistence on arsenic-doped zinc silicate phosphors seems to be attributable to a pair-like (perhaps Mn-O-As) coupling of the Mn^{++} and As^{+5} ions. Experimental findings suggest that in order to obtain long persistence one should incorporate comparable amounts of Mn^{++} and As^{+5} in the zinc silicate and the Mn^{++} concentration should be limited so that pairing or cluster of Mn^{++} will not dominate over the manganese-arsenic pairs. A preliminary physical model is proposed for the phosphorescence behavior of $\text{Zn}_2\text{SiO}_4:\text{Mn},\text{As}$. Further work on the luminescence and excitation energy threshold for PSL effect and

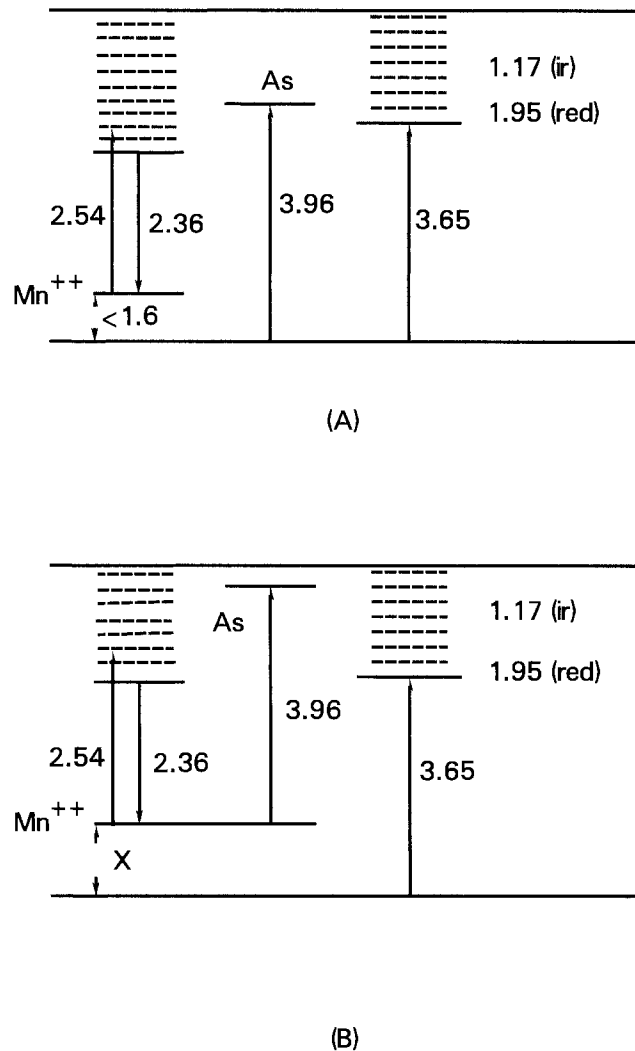


Fig. 9. Schematic energy band diagram for manganese doped zinc silicate with and without As doping.

correlation with thermoglow peaks may provide a more precise picture of the luminescence processes and a quantitative account of the kinetics of the emission and decay processes.

Acknowledgment

The authors would like to express their appreciation for the technical assistance of J. Wilson and many useful discussions with T. Morgan, M. Shafer, and D. Dove. The chemical analysis of the samples investigated were carried out by B. Olson.

Manuscript submitted Feb. 11, 1980; revised manuscript received May 7, 1980.

Any discussion of this paper will appear in a Discussion Section to be published in the June 1981 JOURNAL. All discussions for the June 1981 Discussion Section should be submitted by Feb. 1, 1981.

Publication costs of this article were assisted by IBM Corporation.

REFERENCES

1. R. J. R. S. B. Bhalla and E. W. White, *This Journal*, **119**, 740 (1972).
2. H. K. Perkins and M. J. Sienko, *J. Chem. Phys.*, **46**, 2398 (1967).
3. L. E. Orgel, *ibid.*, **23**, 1004 (1955).
4. D. C. Krupka and H. Fukui, *Proc. SID*, **14**, 89 (1973).
5. H. C. Froelich, U.S. Pat. 2,206,280 (1940).
6. H. C. Froelich and G. R. Fonda, *J. Phys. Chem.*, **46**, 878 (1942).
7. I. F. Chang and M. W. Shafer, *J. Appl. Phys. Lett.*,

- 35, 229 (1979). Some samples were also prepared by J. Brownlow and M. W. Shafer using different methods.
8. I. F. Chang, G. Sai-Haslasz, and M. W. Shafer, *J. Lumin.*, **21**, 323 (1980).
9. F. A. Kroger, "Some Aspects of the Luminescence of Solids," Elsevier, Amsterdam (1948).
10. D. T. Palumbo and J. J. Brown, Jr., *This Journal*, **117**, 1184 (1970).
11. R. C. Herman and R. Hofstadter, *Phys. Rev.*, **59**, 79 (1941).
12. Unpublished results.

LPE Growth of (Nd,Y)P₅O₁₄ Layers from Tin Melt

Hiroyuki Kasano and Yoshio Furuhashi

Hitachi Limited, Central Research Laboratory, Kokubunji, Tokyo 185, Japan

ABSTRACT

Metal fluxes such as Ga, In, and Sn are developed for liquid phase epitaxial growth of rare earth ultraphosphates in place of phosphoric acid flux. Solubility curves of NdP₅O₁₄ for these fluxes are obtained. Using a tin flux, (Nd,Y)P₅O₁₄ layers having a few to twenty microns thickness are successfully grown both on the (100)-oriented NdP₅O₁₄ and (001)-oriented Gd_{0.33}Y_{0.67}P₅O₁₄ substrates. A preliminary growth mechanism is also reported.

To date single crystals of rare earth ultraphosphates, which are favorable for miniature solid-state laser materials, have been grown only by the phosphoric acid flux method (1). This method is suitable for bulk crystal growth, through undesirable for thin film crystal growth with controlled micron-order thickness. This is because (i) crystal growth occurs and proceeds under the nonequilibrium state of dehydration of polyphosphoric acid, (ii) due to the high viscosity of the flux it takes a long time, i.e., about 3 days to increase the degree of supersaturation to a level capable of sustaining crystal growth, and (iii) the very corrosive nature of the fluid and vapor of the flux makes it difficult to employ crucible materials suitable for multiple liquid phase epitaxy (LPE). To achieve a solid-state device system, it is desirable that a planer-type laser be formed on a common crystalline base together with both its exciting source, i.e., an LD or LED array, and an electro-optical modulator (2). In this system, the optically pumped laser and waveguide are constructed from the same thin film. The top and back surfaces of this film are coated with a film having a smaller refractive index. These sandwich structures are preferable because propagation loss is reduced. These multilayer structures of rare earth ultraphosphates can be obtained by using the sliding boat technique (3) if a proper flux can be developed. This flux must produce low vapor pressure, be noncorrosive for the boat at growth temperatures, and have sufficiently large solubility for ultraphosphates (in practical use, more than 10⁻³ mole fraction at elevated temperatures).

This study presents pure metal fluxes having low melting points. One of these fluxes, i.e., tin, was successfully employed in growing rare earth ultraphosphate films.

Experimental

Seed crystals as well as source crystals of rare earth ultraphosphates were prepared by using the phosphoric-acid flux method; 4 nines purified rare earth oxide powder (Nd₂O₃, Y₂O₃, Gd₂O₃, or CeO₂), manufactured by shin-Etsu Kagaku, was charged in a glassy carbon crucible with commercial orthophosphoric acid (85% H₃PO₄ + 15% H₂O). The ratio of oxide powder to orthophosphoric acid was 2.0-2.3% in weight. A crucible containing these starting materials was loosely sealed with a glassy carbon lid and was loaded in a quartz reaction tube set in an electric furnace. Wet argon was passed over the con-

tainer at a rate 300 ml/min during the entire run. Before growth, the water component (~15%) in commercial orthophosphoric acid was removed by heating at 200°C for 2 days. Then, oxide powders were completely dissolved in dehydrated orthophosphoric acid at 300°C during the next 2 days. Ultimately, rare earth ultraphosphates were grown at 560°C for 12 days. Growth temperature was controlled to an accuracy of 0.1°C.

Crystal dissolution for measuring solubility and liquid phase epitaxy (LPE) using the metal fluxes were carried out in a dry argon atmosphere using a graphite boat as is shown in Fig. 1(a). For the metal fluxes, In, Ga, and Sn were chosen because both their melting points and vapor pressures below 1000°C were relatively low. In this study, a graphite block weight was used to sink the source crystals into the molten flux at elevated temperatures. To promote crystal dissolution, the molten metal was intermittently vibrated during heating. To measure solubility, the source crystals (~1.0g in weight) were held for 7 hr in the molten flux (~4 ml). This period was determined from experimental data at 650°C, where solubility was found to be independent of the heating time beyond 7 hr. After the 7 hr run, the flux was rapidly cooled. During cooling, the dissolved source recrystallized as slag and covered the flux surface as well as the residual source surface. The residual source weight was measured after the solidified flux was first removed with a hot HCl solution, and then the recrystallized slag was taken off in ethyl alcohol by utilizing ultrasonic vibration.

For LPE, only tin flux was used because solubility of NdP₅O₁₄ in a relatively low temperature range was highest while the flux incorporation into NdP₅O₁₄ was lowest among these fluxes. The LPE processes are as shown in Fig. 1. The system was purged with argon gas prior to increasing the temperature. At this stage, the surface of (100)-oriented NdP₅O₁₄ and/or (001)-oriented Gd_{0.33}Y_{0.67}P₅O₁₄ substrates were exposed to the argon flow. Then, the temperature was increased. When the substrate temperature T₂ reached 400°C, the substrate surfaces were covered by the graphite boat upper wall by sliding the substrate-loaded graphite plate. The substrate was kept at 400°C until the growth conditions were fulfilled. The source temperature T₁ was further increased to 800°C where the NdP₅O₁₄ or Nd_{0.15}Y_{0.85}P₅O₁₄ source crystals were dissolved. Five hours later, T₁ was decreased to the desired growth temperature at which substrates were put in contact with the tin melt by sliding the graphite

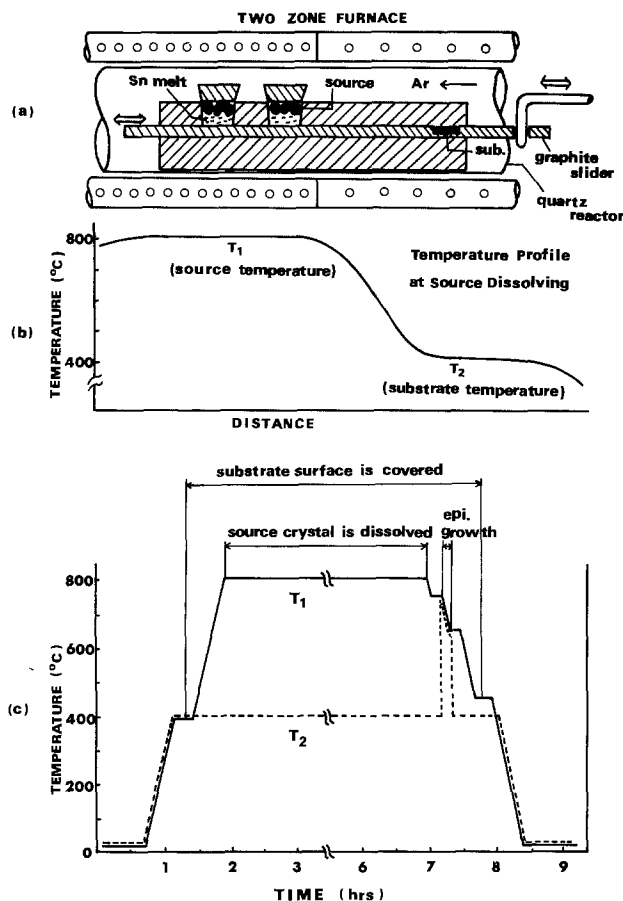


Fig. 1. Schematic diagrams for LPE growth of rare earth ultraphosphates. (a) Equipment used for LPE growth. (b) Temperature profile at source dissolving. (c) T - t diagram showing LPE growth program.

plate. At this stage, T_2 became nearly equal to T_1 . Rare earth ultraphosphate was epitaxially grown in the course of the additional temperature decrease. At a temperature a hundred degrees lower than the one at contact, the substrates were removed from the tin melt while still covered by the graphite boat wall. When T_1 was decreased to 450°C , the substrates kept at 400°C were reexposed in an argon ambient and cooled to room temperature. Samples were then boiled in HCl solution. To measure epitaxial layer thickness, a cleaved face of the sample was etched for 10 min in phosphoric acid heated at 300°C . XMA and x-ray powder diffraction analyses were also carried out to obtain information on the compositions of the growth crystals.

To deduce a preliminary phase diagram of the system $\text{Sn}:\text{NdP}_5\text{O}_{14}$, differential temperature analysis (DTA) was performed at several Sn-rich compositions where the liquidus was clearly below the decomposing temperature ($\sim 1090^\circ\text{C}$) of $\text{NdP}_5\text{O}_{14}$, i.e., in the compositional range where $\text{NdP}_5\text{O}_{14}$ was less than 5 mole percent (m/o). For DTA apparatus a Rigaku Denki Model YGHD system was used. Starting materials, Sn and $\text{NdP}_5\text{O}_{14}$, were crushed and intimately mixed prior to being charged in an alumina cell. For a reference sample, $\alpha\text{-Al}_2\text{O}_3$ powder (No. 2000 mesh) was used. The measurement (DTA) was carried out in N_2 ambient in a temperature range $20^\circ\text{--}1250^\circ\text{C}$. Heating-cooling rate was 10 deg/min and a sensitivity was $\pm 100 \mu\text{V}$ (full scale). Liquidus temperatures were determined from the heating curves, because the heating curves did not indicate significant overheating effects, while the cooling curves often indicated large supercooling effects.

Since Sn does not completely wet Nd_5O_{14} at elevated temperatures, a compositional error results. The mag-

nitude of the error was estimated on a basis of the scanning XMA data of the differential temperature analyzed samples to be at most ± 0.25 m/o; unreacted $\text{NdP}_5\text{O}_{14}$ crystals had a diameter above 0.1 mm whereas that of recrystallized $\text{NdP}_5\text{O}_{14}$ was less than $30 \mu\text{m}$.

Results

Solubility curves of $\text{NdP}_5\text{O}_{14}$ in the metal fluxes.—Solubility curves of $\text{NdP}_5\text{O}_{14}$ for Ga, In, and Sn in a temperature range $620^\circ\text{--}950^\circ\text{C}$ are shown in Fig. 2. For comparison, $\text{Nd}_{0.15}\text{Y}_{0.85}\text{P}_5\text{O}_{14}$ was used as the source crystals in the tin flux case. A few data points in Fig. 2 indicate that solubility of $\text{Nd}_{0.15}\text{Y}_{0.85}\text{P}_5\text{O}_{14}$ is comparable to that of $\text{NdP}_5\text{O}_{14}$ for the tin flux. This is similar to the phosphoric-acid flux case (4). The solubility curves for column III metals become steep at the higher end of the dissolution temperature, i.e., 950°C for Ga and 800°C for In, while the solubility increase was still gradual for tin flux. Flux temperatures at which solubility reaches 1 [atomic percent (a/o)] are estimated from this curve to be nearly 990° , 780° , and 810°C for Ga, In, and Sn, respectively. From the gradient of the straight part of the solubility curves, the enthalpy of a dissolution reaction is estimated to be $1.35 \times 10^5 \text{ J/mole}$ (32.2 kcal/mole). This value is common for gallium, indium, and tin fluxes. Apparently, the fluxes are chemically free from the dissolving reaction of $\text{NdP}_5\text{O}_{14}$. Data scattering observed in the indium flux case may be due to the poorer wetting of indium and the source crystals as compared with the other two cases.

The body color of the undissolved core of the $\text{NdP}_5\text{O}_{14}$ source crystals changed to reddish in the column III flux case, while it remained only slightly darkened in the tin flux case. The color of precipitates deposited on the undissolved cores was the same. The data of the x-ray diffraction analysis suggested that a few mole percent of the flux were incorporated in the recrystallized $\text{NdP}_5\text{O}_{14}$ crystals in the gallium and indium flux cases. The incorporated Ga concentration is coincident with the reported value by Kruehler *et al.* [less than 2.2 a/o (5)]. However, no detectable amount (less than 1%) of the flux was observed in the tin flux case. Laser spectroscopic analysis results

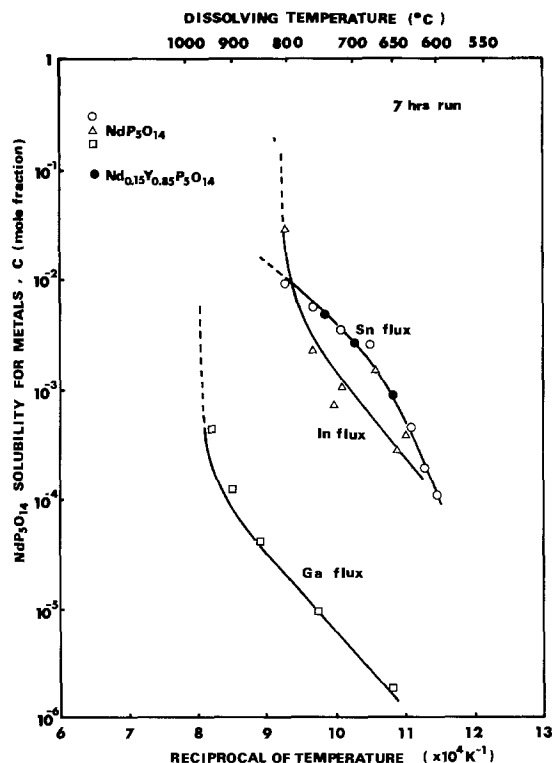


Fig. 2. Solubility curves of $\text{NdP}_5\text{O}_{14}$ for metal fluxes

indicated the presence of only 100-500 ppm tin. Therefore, tin is judged to be the most suitable of these metals as a flux for LPE of ultraphosphates.

Liquid-phase epitaxy using tin flux.—Neodymium-yttrium pentaphosphates were epitaxially grown from the tin flux both on (001)-oriented $\text{Gd}_{0.33}\text{Y}_{0.67}\text{P}_5\text{O}_{14}$ and (100)-oriented $\text{NdP}_5\text{O}_{14}$ substrates which were simultaneously charged in the same run. In this experiment, $\text{Nd}_{0.15}\text{Y}_{0.85}\text{P}_5\text{O}_{14}$ crystals were used as the source. Though $\text{Gd}_{0.33}\text{Y}_{0.67}\text{P}_5\text{O}_{14}$ and $\text{NdP}_5\text{O}_{14}$ belong to different crystalline phases at growth temperature, i.e., the space group $C2/c$ of the monoclinic system for the former and the space group $Pcmm$ of the orthorhombic system for the latter, the $\text{Nd}_{0.15}\text{Y}_{0.85}\text{P}_5\text{O}_{14}$ source can crystallize in both phases provided it is first dissolved or vaporized (6). As a result, LPE growth of $\text{Nd}_{0.15}\text{Y}_{0.85}\text{P}_5\text{O}_{14}$ can be achieved on these substrates. A combination of a $\text{Nd}_{0.15}\text{Y}_{0.85}\text{P}_5\text{O}_{14}$ epitaxial layer and a $\text{Gd}_{0.33}\text{Y}_{0.67}\text{P}_5\text{O}_{14}$ substrate is preferable because (i) the lattice parameter of the layer is well suited to that of the substrate (2), (ii) the optical refractive index of the layer is larger than that of the substrate (2), and (iii) the layer composition is out of the range of the ferroelastic species (7).

The surface of an epitaxial layer was slightly wrinkled and partly covered with a white precipitate. The origin of the precipitate was deduced to be SnHPO_4 on the basis of the x-ray diffraction analysis data. The hydrogen source may be water vapor which back diffused from a water vessel used as a gas trap. After removing the precipitate by lapping, the grown layers were confirmed to be epitaxial by an x-ray back Laue technique. Hence, these precipitates were probably formed during the cooling process from the residual tin flux stuck on the sample surface. A typical grown layer is shown in Fig. 3. The Nd/Y ratio of the epitaxial layer was examined by XMA and was found to shift slightly to the Y-rich side compared with the source crystals. The shift was 2-3% for the growth at 800°C. Grown layers were epitaxial at temperatures above 650°C. Layer thickness was measured as a function of the growth temperatures. The results obtained are shown in Fig. 4. The growth period in each run was limited to 100°C. The cooling rate in this period was controlled to 10 deg/min. The magnitude of the solubility difference caused by this cooling is calculated for $\text{NdP}_5\text{O}_{14}$ and $\text{Nd}_{0.15}\text{Y}_{0.85}\text{P}_5\text{O}_{14}$ in the tin flux based on Fig. 2 data. This is also shown in Fig. 4 for comparison.

Discussion

Dissolving mechanism of $\text{NdP}_5\text{O}_{14}$ in metal fluxes.—Solubility data of $\text{NdP}_5\text{O}_{14}$ in the metals are presented for the first time in Fig. 2. However, the dissolving mechanism in the metal fluxes is still unknown. Based on the DTA data, a preliminary phase diagram for the system Sn- $\text{NdP}_5\text{O}_{14}$ is proposed in a compositional range $x < 5$ (m/o), i.e., in a very tin-rich region. During the temperature increasing process in DTA, only three peaks or knees were detected below 1200°C for each composition. These peaks or knees correspond in turn to a point on the solidus (the tin mp 232°C), a point on the liquidus, and the $\text{NdP}_5\text{O}_{14}$ decomposing point ($\sim 1090^\circ\text{C}$), as is shown in Fig. 5. Though the data in the $\text{NdP}_5\text{O}_{14}$ -rich side could not be obtained because liquidus temperatures exceed the decomposition temperature of $\text{NdP}_5\text{O}_{14}$, we believe that this diagram is reasonable. This is because (i) the $\text{NdP}_5\text{O}_{14}$ layers recrystallized on the substrate along the liquidus curve during cooling (Fig. 4), and (ii) a point on the solidus was experimentally confirmed to be $\sim 232^\circ\text{C}$ even at very $\text{NdP}_5\text{O}_{14}$ -rich compositions. That is, it is believed that any stable compound other than $\text{NdP}_5\text{O}_{14}$ was not formed during heating. The x-ray diffraction analysis of the slag by which the surface of the metal flux was covered showed that

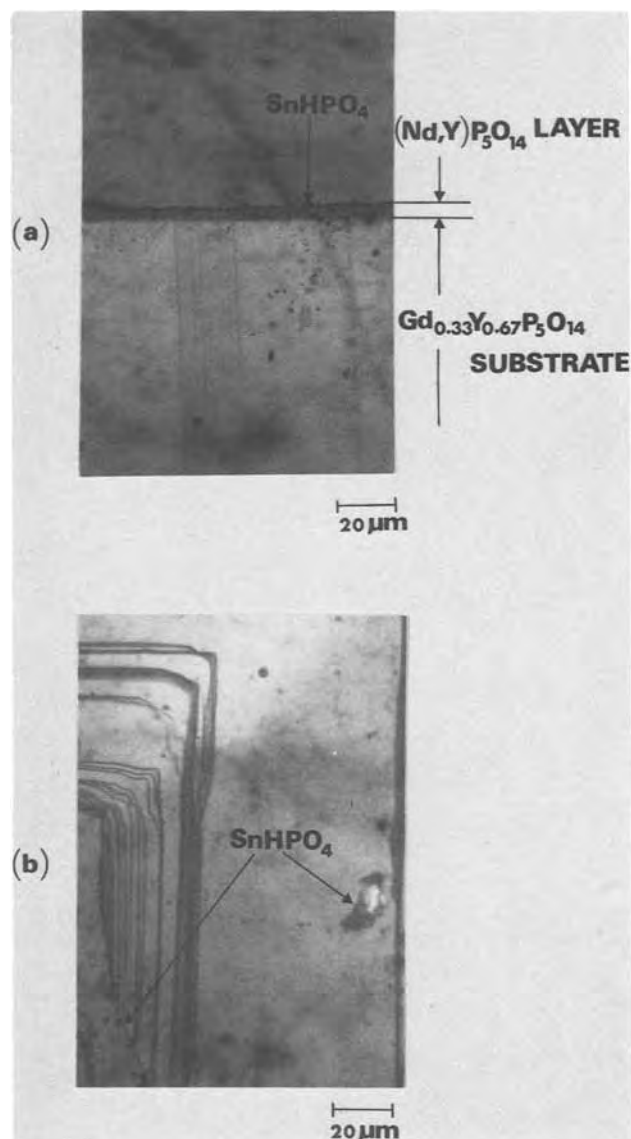


Fig. 3. Photographs of $(\text{Nd,Y})\text{P}_5\text{O}_{14}$ epitaxial layer grown on (001)-oriented $\text{Gd}_{0.33}\text{Y}_{0.67}\text{P}_5\text{O}_{14}$ substrate. $\times 500$. (a) Cleaved face after etching with heated (300°C) phosphoric acid for 10 min. (b) As-grown surface of epitaxial layer.

the greater part was $\text{NdP}_5\text{O}_{14}$. The residual was metal oxide along with a slight amount of metal phosphate. As indicated above, metal phosphate was also found on the epitaxial layer. We consider that these residues were formed during cooling only at the surface of the melt as a result of chemical reactions among Sn, $\text{NdP}_5\text{O}_{14}$, and H_2O which came from the exhaust. The most probable mechanism is a simple diffusion such as $\text{NdP}_5\text{O}_{14}(\text{s}) \rightarrow \text{NdP}_5\text{O}_{14}(\text{l})$. The case where a metastable compound is first formed in the molten flux heated at high temperatures and then decomposes to Sn and $\text{NdP}_5\text{O}_{14}$ during the cooling stage is also conceivable.

Epitaxial growth process from tin melt.—The LPE growth mechanism from the tin melt is expected to be an ordinary spiral growth. From the grown-layer thickness data and the solubility difference curve shown in Fig. 4, the relationship between the growth rate V and the degree of supersaturation σ is readily obtained as is shown in Fig. 6. Though the data for the solubility decrease occurring during a hundred degree period were for the system Sn- $\text{NdP}_5\text{O}_{14}$, we consider that those for the system Sn- $(\text{Nd,Y})\text{P}_5\text{O}_{14}$ are consistent with the former on the basis of the data in Fig. 2. The quadratic dependence of V on σ is

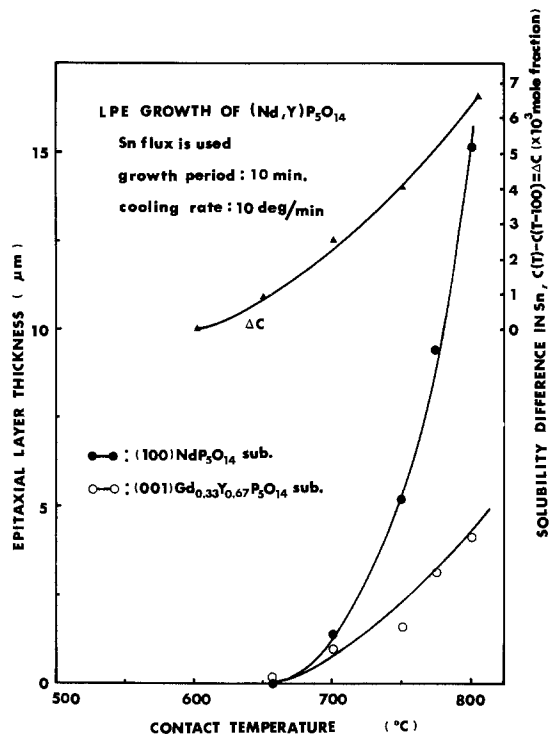


Fig. 4. Epitaxial layer thickness of (Nd,Y)P₅O₁₄ grown on (100)-oriented NdP₅O₁₄ and (001)-oriented Gd_{0.33}Y_{0.67}P₅O₁₄ as a function of dipping temperature. Growth time was held to 10 min. In this period, flux temperature was linearly decreased by a hundred degrees. Magnitude of NdP₅O₁₄ solubility decrease corresponding to this 100°C cooling is calculated from Fig. 2.

indicated both in the NdP₅O₁₄ and Gd_{0.33}Y_{0.67}P₅O₁₄ substrate cases.

According to Elwell and Dawson (8), spiral growth from the flux is qualitatively explained using the Burton-Cabrera-Frank model modified by the diffusion effect. This gives

$$V = (A\sigma^2/\sigma_1) \tanh(\sigma_1/\sigma) \text{ (Bennema's modification)}$$

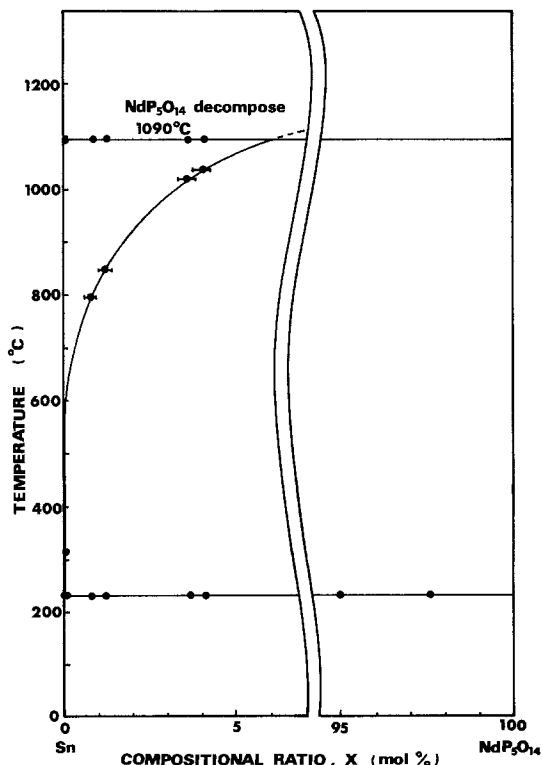


Fig. 5. Proposed phase diagram for Sn-NdP₅O₁₄ system

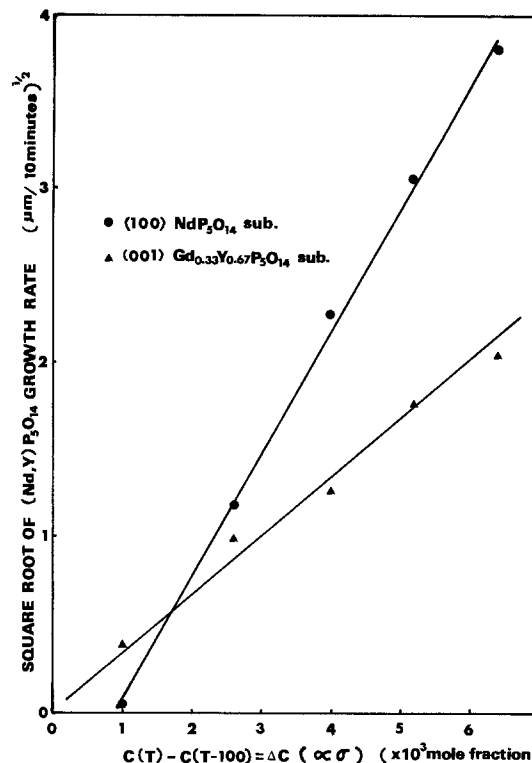


Fig. 6. Growth rate V of (Nd,Y)P₅O₁₄ as a function of the degree of supersaturation σ . $V \propto \sigma^2$ is indicated.

where σ_1 is the threshold of σ and A is a constant. Corresponding to the magnitude of the relative degree of supersaturation, this equation can be approximated in two cases

$$V \simeq A\sigma^2/\sigma_1$$

when $\sigma < \sigma_1$ (relatively low supersaturation) and

$$V \simeq A\sigma$$

when $\sigma \geq \sigma_1$ (relatively high supersaturation). The fact that LPE growth of (Nd, Y)P₅O₁₄ took place under a relatively low degree of supersaturation in this study is suggested in Fig. 6.

Conclusions

Bearing thin film integrated optics in mind, metal fluxes adaptable to LPE growth of rare earth ultraphosphates have been developed. Metals with low melting points, e.g., Ga, In, and Sn, were tested. It was found that ultraphosphates were soluble in these metals at relatively low temperatures (600°-800°C) and that the ultraphosphates were recrystallized during the cooling stage. The solubility curves of NdP₅O₁₄ for these fluxes were experimentally obtained. Then, LPE growth of (Nd, Y)P₅O₁₄ was successfully carried out using the tin flux.

It is noteworthy that for multilayer growth with submicron order thickness control these metal fluxes are more suitable than phosphoric acid flux from the viewpoint of handling and stability.

Manuscript submitted Nov. 19, 1979; revised manuscript received May 1, 1980.

Any discussion of this paper will appear in a Discussion Section to be published in the June 1981 JOURNAL. All discussions for the June 1981 Discussion Section should be submitted by Feb. 1, 1981.

Publication costs of this article were assisted by Hitachi Limited.

REFERENCES

1. M. Beucher, *Les Elements des Terres Rares*, Coll. No. 180, 1, 261 (1970).
2. G. Winzer, L. Vité, W. Kruehler, R. Plaettner, P.

- Moeckel, and H. Pink, *Siemens Forsch. Entwicklungsber.*, **5**, 287 (1976).
- M. Panish, S. Sumski, and I. Hayashi, *Metall. Trans.*, **2**, 795 (1971).
 - H. Kasano and Y. Furuhashi, *This Journal*, **126**, 1567 (1979).
 - W. W. Kruehler, J. P. Jeser, and H. G. Daniel-

- meyer, *Appl. Phys.*, **2**, 329 (1973).
- H. Y. P. Hong and J. W. Pierce, *Mater. Res. Bull.*, **9**, 179 (1974).
 - W. W. Kruehler, G. Huber, and H. G. Danielmeyer, *Appl. Phys.*, **8**, 261 (1975).
 - D. Elwell and R. D. Dawson, *J. Cryst. Growth*, **13/14**, 555 (1972).

A Method for Area Saving Planar Isolation Oxides Using Oxidation Protected Sidewalls

D. Kahng, T. A. Shankoff, T. T. Sheng, and S. E. Haszko

Bell Laboratories, Murray Hill, New Jersey 07974

ABSTRACT

A process has been developed to fabricate buried isolation oxide structures with a near-perfect topography. The method uses the combination of preoxidation silicon etching to the required depth with the added feature of sidewall oxidation protection used to control the profile at feature edges. The latter is achieved by the deposition of a second silicon nitride layer and a processing sequence of simple steps which are shown to be quite reproducible.

We have succeeded in fabricating buried isolation oxide structures with almost perfectly planar topography. The method borrows from the full-ROX (1, 2) technique in that the substrate is etched to a depth approximately 50% of the final, desired oxide thickness after silicon nitride patterning and prior to oxidation. It deviates from that technique in that sidewall oxidation protection is used to control the profile at feature edges and to eliminate the well-known form "bird's head and beak" and its abrupt, sharp and dimension robbing characteristics. The processing sequence itself involves the proper combination of simple steps and is quite reproducible.

Our concept of sidewall protection involves chemical vapor deposition of a second nitride layer after silicon substrate etching using the first nitride (or oxidation mask) as the etch mask; if the second nitride is etched after it is deposited using a straight-line method, then the sidewall will still contain the second nitride layer on the silicon quarter circles under the first nitride overhang after etching. The bulk of the to-be thick oxide device regions (isolation oxide) will be open to oxidation, but there will be masking at the sidewalls during oxidation. Thus for example, our initial experiments involved a straight-line process, ion implantation, which resulted in both etching and chemical conversion of nitride in the to-be oxidized regions. We implanted oxygen as O atoms into 300-500Å of the second nitride to a depth of 200-250Å (15 keV) so that whatever nitride that did not sputter off in the O atom implant would be converted to oxidizable oxynitride. Coupled with this set of experiments was the use of varying second nitride thicknesses arranged so that slight oxidation at the sidewalls would occur toward the end of the isolation oxidation in order to "smooth or round-out" the topography. The transmission electron micrographs in Fig. 1a and 1b respectively detail the full-ROX profile and the typical O atom implant result when the second nitride was thick enough so that no oxidation took place at the sidewalls. Experimentally we found that about 400Å of second silicon nitride is consumed during 10,000Å of wet isolation oxidation. Figure 2 shows the case where less than 400Å of nitride was used to allow some sidewall oxidation. In practice, we found that deposition control of silicon nitride composition and to a lesser extent thickness and uniformity control over a wafer

essentially precludes consideration of the partial oxidation method on a practical basis.

Although the results using O atom implantation were encouraging, the process was fraught with variability. We always found some residual oxidation resistance in the presumed to be "opened" thick oxide silicon.

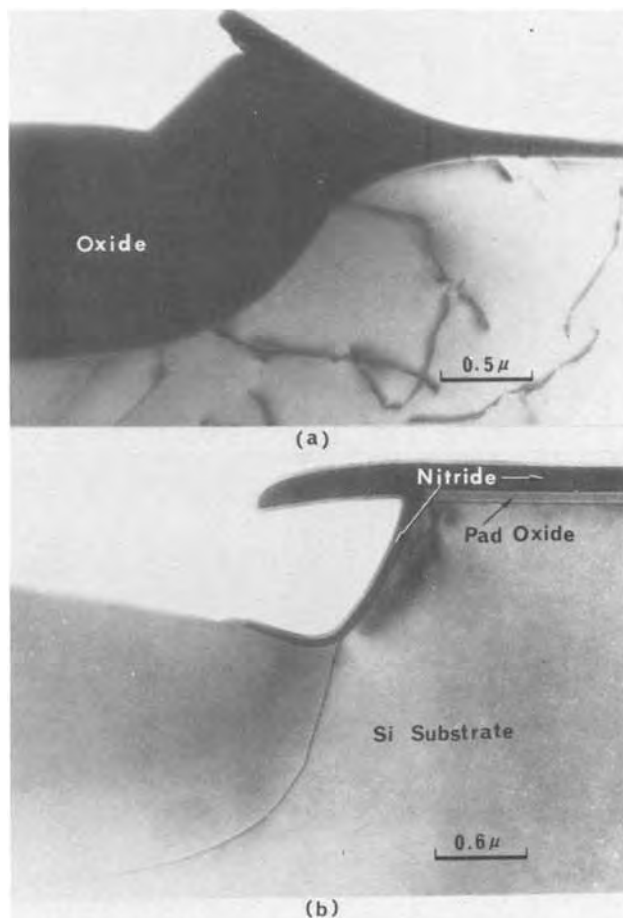


Fig. 1. (a) TEM profile of standard full-ROX structure. (b) TEM profile of O atom implant, 500Å second nitride method.

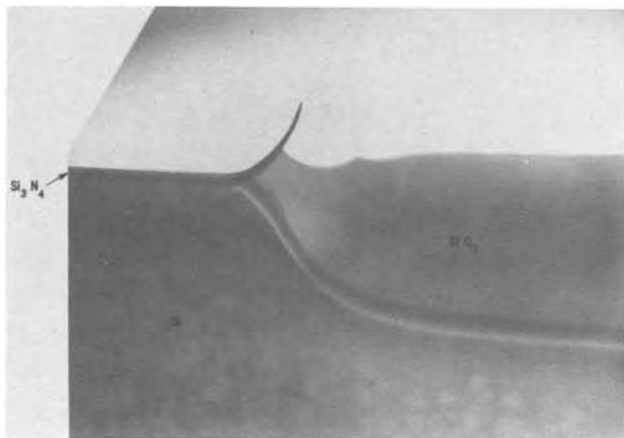


Fig. 2. TEM profile of O atom implant, less than 400Å second nitride method.

For example, in one case 7000Å of SiO₂ grew when 10,000Å was expected, while a 14,000Å oxidation time furnished the requisite 10,000Å. The important point was that we were on the proper track to achieving the desired end result. Processing details for the technique are set out in Table I using step 10a.

Our best results were achieved using reactive ion etching of the second nitride layer which is, if properly applied, a straight-line etching procedure. It was also decided to eliminate any attempts to use "thin" second nitride so that partial oxidation would be relied on to smooth-out the topology. Thus, for 10,000Å isolation oxidation, 500Å of second silicon nitride has been used and is reactive ion etched in anisotropic etching conditions so as to leave the entire feature-edge region coated with the full 500Å thickness at the isolation oxidation step. Silicon nitride in these thickness ranges is believed not to introduce stress during the oxidation (2). The processing sequence for this modification is included in Table I as step 10b. Typical results can be seen in Fig. 3. It is clear that too much sidewall protection is obtained with this method resulting in the sharp unoxidized notches at the feature edges. It became evident that the best situation would be achieved if oxidation is allowed to proceed up the sidewall, but in a controllable fashion in limited degree. A simple way to achieve the result is to use a pad oxide beneath the second nitride layer in much the same way that a pad oxide is employed beneath the first masking nitride film; the H₂O oxidant diffuses in the pad and allows some penetration of growing oxide further up the sidewall. Experiments were done with "second" pad oxide thicknesses of 100 and 300Å; the results can be seen in Fig. 4a and 4b. Clearly the 100Å case gives the best result. Use of a thin 100Å pad oxide beneath the 500Å nitride layer (which is too thick to be consumed during isolation oxidation) presents no control problem whatsoever since dry oxide thicknesses are relatively easy to control even at 100Å.

The only negative aspect of the pad oxide technique proves to be slight "spill-over" of the isolation oxide into the future thin oxide portions of the structure as evidenced by the thin, tapered edges in Fig. 4a and 4b

Table I.

1. Grow pad oxide (100-500Å).
2. Deposit CVD nitride (1200-2500Å).
3. Pattern isolation oxide features.
4. Plasma etch nitride, stop in pad oxide.
5. Resist strip.
6. Etch pad oxide in BHF.
7. Etch Si substrate in CrO-HF-H₂O.
8. Grow pad oxide (100Å).
9. Deposit second CVD nitride (300-500Å).
10. a. Implant O atoms at 15 keV (10¹⁶-10¹⁷/cm²).
- b. Reactive ion etch second nitride.
11. Grow isolation oxide.
12. Nitride strip.
13. Grow gate oxide.

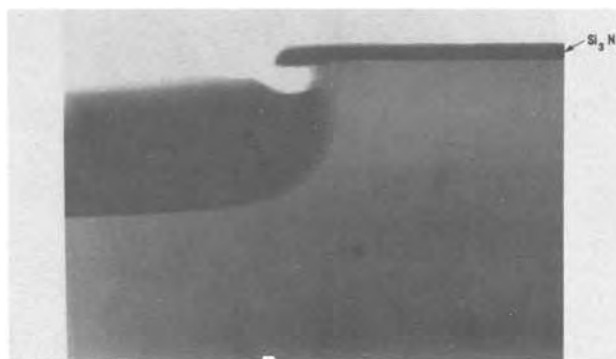


Fig. 3. TEM profile of reactive ion etch of second nitride with no second pad oxide.

and Fig. 5a and 5b. A simple 30 sec oxide etchback in BHF to remove 500Å thermal oxide (30 sec removes more oxide than has spilled over by about a factor of 2, although this may be the only real variable connected with the process) easily solves this problem. After this BHF treatment, the structure which is finally achieved is essentially planar and contains no trace of "spilled-over" isolation oxide. Even more important, the intrusion of thick oxide into the thin oxide regions of a device chip stops at the edge of the original isotropically etched quarter circle formed in the silicon. Since this will typically be about 50% of the isolation oxide thickness in dimension at each feature edge, a significant saving of device real estate can be realized (note the intrusions of typically 15,000Å are found for selective-oxidation structures such as the semi-ROX structure owing to the "bird's beak"

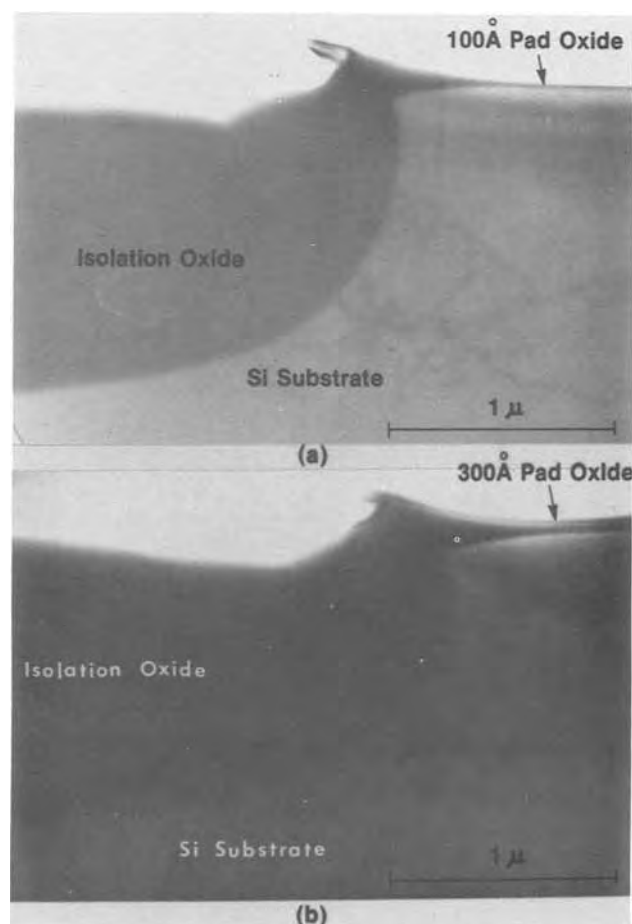


Fig. 4. (a) TEM profile of reactive ion etch of second nitride with 100Å second pad oxide. (b) TEM profile of reactive ion etch of second nitride with 300Å second pad oxide.

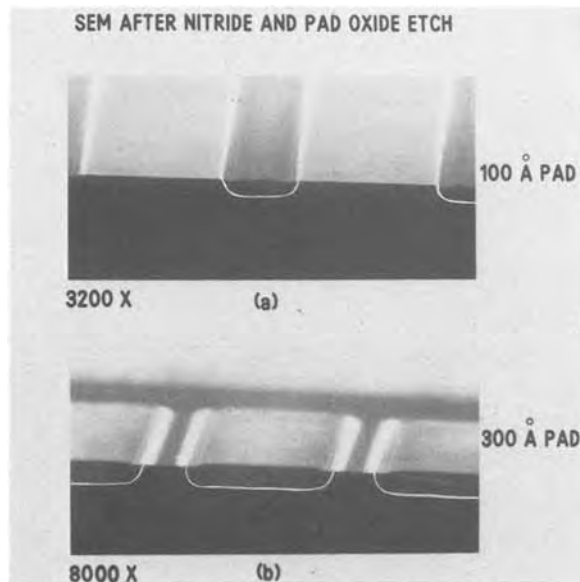


Fig. 5. (a) SEM profile of reactive ion etch of second nitride with 100Å second pad oxide. (b) SEM profile of reactive ion etch of second nitride with 300Å second pad oxide.

and close to 10,000Å for the full-ROX structure because of the bird's head).

A secondary, but important aspect of this work is the etchant used to achieve the desired isotropic quarter circle features used in this technique. It was found that the CrO_3 -HF- H_2O etching system provides completely isotropic etching in the composition and etching thickness range studied during this program. The silicon substrate "floor" on which the isolation oxidation will be done is as defect-free and smooth as noted with any etching technique either dry or wet-chemical. The etching rate is sensitive to substrate doping, however, and calibration etching curves must be obtained for each new substrate doping used. Obviously, devices which have previously defined and doped structures will be difficult to process using this etchant, although a suitable etching alternative should not be difficult to find. The only parameter which will affect etching rate of the silicon for routine work, temperature, is readily controlled and inconsequential. Etch rate data for the CrO_3 -HF- H_2O system in the applicable ranges are presented in Fig. 6.

In practice, it is important to use sufficient first nitride (perhaps 1200-1500Å) so that RIE of the second 500Å nitride with 25% overetch will not affect the oxidation masking by the first layer. Allowance also must be made for some loss of nitride in the CrO_3 -HF- H_2O etchant (about 100Å per minute), perhaps increasing the original first nitride thickness to 1500-1800Å. Excellent etching results of the substrate are obtained when the CrO_3 concentration is in the 1 weight percent range (about 25Å/sec silicon etching rate for lightly boron-doped substrate and 1-2Å-sec for silicon nitride). The silicon etch depth can be controlled to within 100Å if desired and should be computed from the following considerations: 56% of thermal oxide growth is above the substrate, removal of the first nitride in 160°-180°C H_3PO_4 loses 5Å of thermal oxide per minute of etch time (30 min for 1500Å first nitride), removal of the first pad oxide (typically 300-400Å) with overetching in BHF for 30 sec costs 500Å of isolation oxide, and finally trimming the spilled-over oxide costs an added 500Å if BHF is used for 30 sec. Thus for 10,000Å final isolation oxide, an etching depth of 5100Å would be used and 11,150Å oxide grown, for a planar topography.

It came to our attention after much of this work was completed that the patent literature describes two attempts at sidewall oxidation protection to achieve

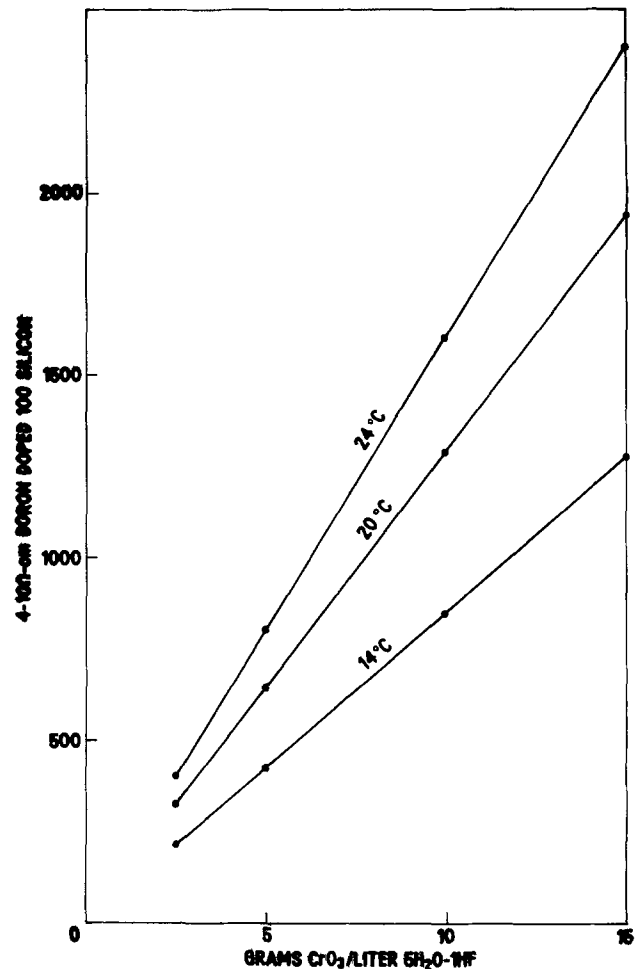


Fig. 6. Silicon etch rate curve for CrO_3 -HF- H_2O system Å/min

the planar topography. In one method (3), "spin-on" oxide is used to preferentially fill the feature edges at the quarter circle; subsequent isolation oxidation is impeded at the feature edges because of this blocking oxide, giving the essentially planar structure. In the other technique (4), a second nitride layer is used, but instead of using a straight-line etching technique, photoresist is used to clog the feature-edge nitride overhang/quarter circles (spinning resist on forces resist into these crevices preferentially). Exposure and development should leave some thickness of resist in the quarter circles because of the thickness differential; subsequent nitride etching should leave nitride within the quarter circles to mask the sidewalls against the isolation oxidation. It was not possible to assess the degree of success with these approaches from the literature. However, it appears that the photolithographic exposure is difficult to control because of light diffraction at the quarter circles with the second method; the first method will have "spin-on" oxide within the device structure, seemingly undesirable from a contamination and quality control standpoint.

Conclusions

We have demonstrated a method for achieving a planar isolation oxide structure based on a significant modification of the full-ROX technique for buried oxide. Sidewall masking with a second layer of silicon nitride prevents intrusion of the isolation oxide into the thin oxide regions to save real estate and to prevent formation of the bird's head. Use of a thin second pad oxide beneath the second nitride is a key step in achieving the planar structure. The CrO_3 -HF- H_2O etching system provides a good means of isotropically etching the silicon substrate during processing.

Acknowledgments

The authors wish to thank E. I. Povilonis for his help in processing our experiments and D. N. K. Wang for reactive ion etching our samples.

Manuscript submitted March 21, 1980; revised manuscript received ca. April 29, 1980.

Any discussion of this paper will appear in a Discussion Section to be published in the June 1981 JOURNAL. All discussions for the June 1981 Discussion Section should be submitted by Feb. 1, 1981.

Publication costs of this article were assisted by Bell Laboratories.

REFERENCES

1. E. Kooi and J. A. Appels, "Semiconductor Silicon 1973," H. R. Huff and R. R. Burgess, Editors, p. 860, The Electrochemical Society Softbound Proceedings Series, Princeton, N.J. (1973).
2. E. Bassous, H. N. Yu, and V. Maniscalco, *This Journal*, **123**, 1729 (1976).
3. H. Kondo, T. Nitta, and Y. Moriguchi, U.S. Pat. 4,088,516 (1978).
4. P. W. D. Webb, U.S. Pat. 3,958,040 (1976).

The Role of Carrier Diffusion and Indirect Optical Transitions in the Photoelectrochemical Behavior of Layer Type d-Band Semiconductors

W. Kautek, H. Gerischer,* and H. Tributsch¹

Fritz-Haber-Institut der Max-Planck-Gesellschaft, D-1000 Berlin 33, Germany

ABSTRACT

Photocurrents at n-type single crystals of MoS₂, MoSe₂, and WSe₂, with the van der Waals surfaces exposed to the electrolyte, have been studied by varying the voltage applied and the wavelength of the light. The experiments have been performed under conditions where a depletion layer is formed beneath the semiconductor surface and in the presence of I⁻ ions in the electrolyte which act as scavengers for the photogenerated holes and prevent corrosion of the electrodes. An evaluation of the quantum yield in relation to the absorption coefficient and the extension of the space charge layer shows that generation of minority carriers outside the space charge layer contributes to a large extent to the photocurrents. A mean diffusion length for holes of 1.4×10^{-4} cm (MoS₂) and 5×10^{-4} cm (MoSe₂) is derived from the experiments. The wavelength dependence of the photocurrent yield is analyzed in terms of light absorption for indirect transitions. This gives a measure of the bandgaps in these materials which turn out as 1.17 eV (MoS₂), 1.06 eV (MoSe₂), and 1.16 eV (WSe₂) in good accordance with optical measurements.

The theory of photovoltaic power conversion devices based on semiconducting materials like, e.g., Si, Ge, GaAs, TiO₂, etc., shows that the efficiency is mainly determined by the diffusion process of the photogenerated minority charge carriers (1-3). The contribution of carriers generated in the space charge layer can be neglected because its extension in moderately doped samples mostly is several orders of magnitude smaller ($\sim 10^{-6}$ - 10^{-5} cm) than the minority carrier diffusion length which can reach the order of 10^{-4} cm [TiO₂, Ref. (2)], 10^{-3} cm (GaAs), or 1 cm (Ge, Si), respectively (4). We studied whether the situation is different or similar in layer type molybdenum and tungsten dichalcogenides which have also been shown to be interesting semiconductors for electrochemical (5-7) and solid-state (8) solar cells.

It was the aim of this investigation to distinguish between the extent of charge separation in the Schottky barrier and in the diffusion zone and to correlate the efficiency of energy conversion with the peculiar band structure of these systems. An electrochemical Schottky barrier is the easiest to fabricate and therefore has been employed for this study.

Transmission spectra with the incident light normal to the plane of the layers (electric field vector *E* normal to the c-crystal axis) have been known for a long time (9). Two peaks at the absorption edge, called A and B, have generally been accepted to be the result

of ground state excitons with the separation A-B being a measure of the spin-orbit interaction.

There has been the idea that excitons exist in layer-type materials (GaSe₂, MoSe₂, etc.) in the hydrogen-like Wannier-Mott form (10) though these compounds exhibit very anisotropic physical properties. This has been confirmed for 2H-crystals in numerous experimental papers (11-17). The optical dissociation energy of these excitons lies between 0.04 and 0.06 eV which obviously is in the range of the lattice vibrational energy at room temperature (11, 12, 15, 17). It has been stated that the originally excited excitons dissociate inside the crystal to give free electrons and holes (18, 11, 19). An exciton-phonon ionization model was consequently proposed (20). The lifetime of excitons will therefore be extremely short at normal temperatures.

Intrinsic conduction measurements above 700°K of n-type MoS₂ and MoSe₂ yielded a thermal bandgap of the order of 1.1 eV (14, 21), which agrees well with the indirect bandgap suggested by band structure calculations (26), and is supported by photoemission measurements (27-34) and optical absorption measurements (35). On the other hand, there is still a valid discussion going on regarding the symmetry of the valence band involved in the direct and indirect optical transition. There has been a long tradition based on tight binding band structure calculations (36), optical absorption measurements (35), and consideration on EPR data (37, 38) to situate the direct A-exciton transition between the mainly p-like chalcogen valence

* Electrochemical Society Active Member.

Key words: solar, semiconductor, photoeffects.

¹ Present address: Centre National de la Recherche Scientifique Laboratoires de Bellevue, F-92190 Meudon, France.

band and the d-like metal conduction band (25, 23). The fundamental indirect absorption edge however was associated with a d-d transition. In contrast to this picture, there is strong evidence from various band structure calculations (39, 22-26) and photoemission results (40, 33, 34) that both direct and indirect transitions are associated with the valence d- and conduction d-band of the transition metal.

Experimental and Materials

Materials.—All semiconducting materials used were n-type. Synthetic MoS₂ single crystals were obtained from Dr. F. Lévy (Laboratoire de Physique Appliquée, Ecole Polytechnique Fédérale de Lausanne, Switzerland) (41). The MoSe₂ and WSe₂ single crystals were prepared by J. Gobrecht (Fritz-Haber-Institut) by bromine transport from the gas phase (42). Molybdenum dichalcogenides crystallize in sandwich layers which are held together only by relatively weak van der Waals forces. The sandwiches are arranged in such a way that the molybdenum atom layer is placed between two layers of chalcogen atoms. The solid-state and crystal-chemical properties of transition metal dichalcogenides have been extensively reviewed (9, 43-48).

Electrode preparation.—The electrode preparation and the surface classification techniques have been described previously (49).

Electrolytes.—Electrolytes were prepared using reagent grade chemicals (Merck) and triply distilled water. A solution of 1M KCl served as supporting electrolyte. It was found that photocurrent spectra in electrolytes with and without 0.05M hydroquinone did not differ from the same experiment in 0.05M KI solution if the I₂- or I₃⁻-concentration was kept low enough. Therefore all the results presented here have been achieved with 0.05M KI electrolytes. The pH value was adjusted to 1 by addition of HCl and continuously monitored with a glass-electrode pH meter.

Experimental procedures.—Electrochemical quasi-stationary current-potential (*j*-*U*) characteristics and photocurrent spectra were determined in a Duran cell with an optical glass bottom. The platinum foil counterelectrode was located in a compartment separated by a glass diaphragm. In all cases a commercial-type saturated calomel electrode served as reference electrode, but all data have been transformed to the normal hydrogen electrode as the reference (*U*_H). All measurements have been performed at room temperature under controlled potential conditions. A monochromatic light source was used as described previously (49). It could be confirmed by means of a rotating electrode device that diffusion in the electrolyte never was determining the current.

The quotient of the charge carrier flux (anodic limiting photocurrent density) and the incident photon flux was taken as the apparent quantum efficiency Φ_a (value with no correction for light reflection).

Results

Figure 1 shows the characteristic *j*-*U* dependence which is practically identical for all absorption coefficients although α differs by four orders of magnitude. An anodic saturation current is reached within a band bending range of 0.2-0.4V independent of the wavelength of the light. The penetration depth of light increases proportionally to 1/ α . One should therefore expect that the slope of the *j*-*U* dependence would gradually decrease with increasing wavelength if the main contribution to the photocurrent should come from light absorbed in the space charge layer, since a higher potential would have to be applied to collect the same number of photogenerated holes. Such a dependence cannot be observed with molybdenum and tungsten dichalcogenides. Figure 1c has been derived from measurements with a WSe₂ electrode showing an appreciable amount of surface not normal to the *c*-lattice vector. The consequences are discussed elsewhere (49, 60). The onset and slope of the anodic

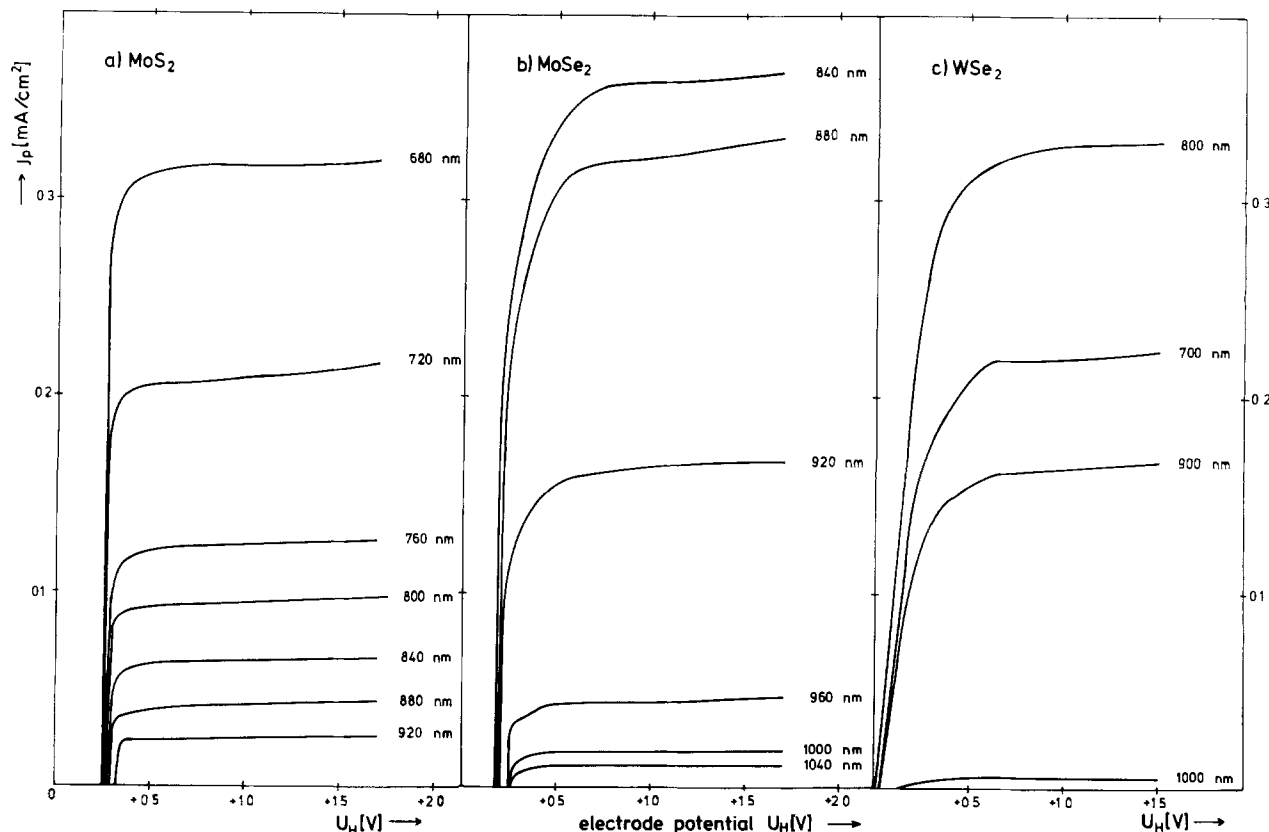


Fig. 1. Photocurrent-voltage curves of n-type transition-metal dichalcogenide semiconductor electrodes in contact with a redox electrolyte (0.05M KI, 1.0M KCl, pH = 1) at various wavelengths. Illumination intensity 1-2 mW/cm².

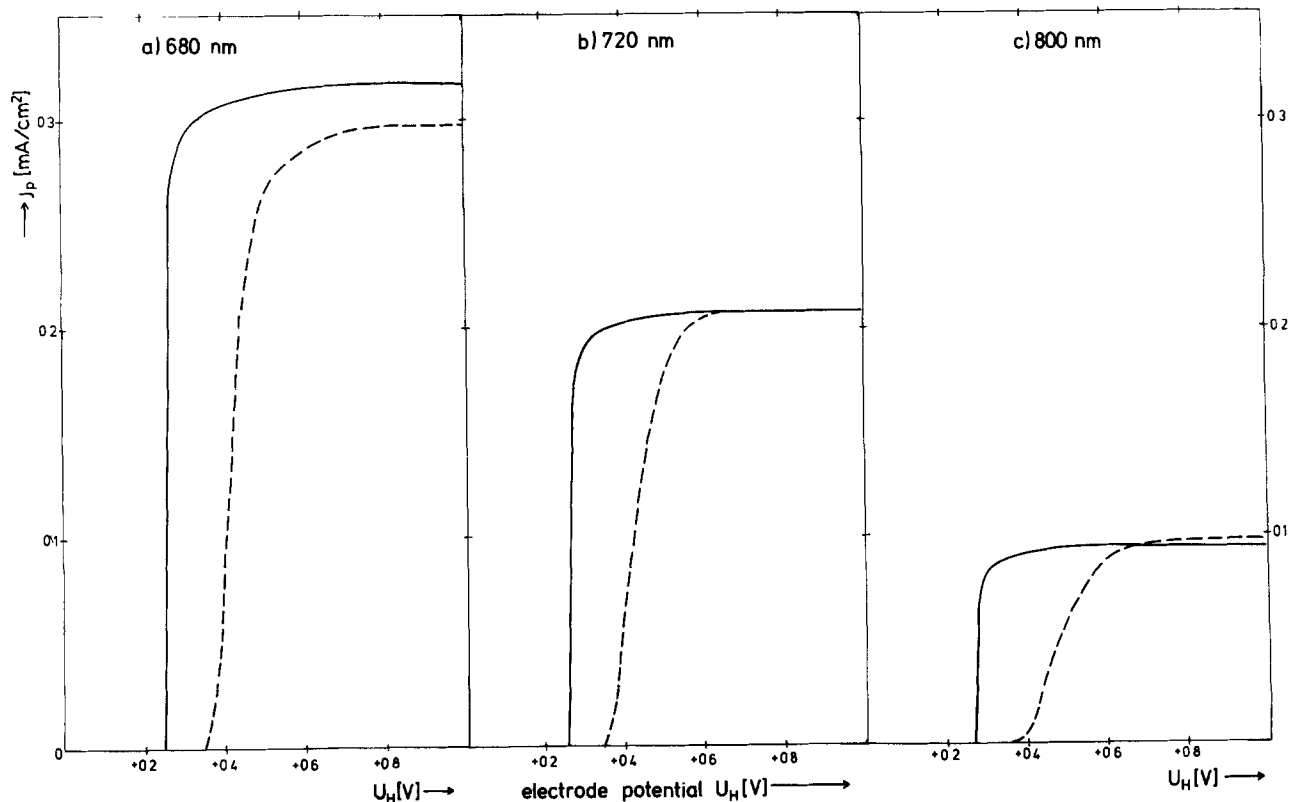


Fig. 2. Photocurrent-voltage curves of a n-type MoS_2 electrode in contact with a redox electrolyte (0.05M KI, 1.0M KCl, pH = 1) at three wavelengths corresponding to absorption coefficient values of (a) 10^5 cm^{-1} , (b) 10^4 cm^{-1} , (c) 10^3 cm^{-1} . Solid lines: practical ideal van der Waals surface; dashed lines: some surface fraction not normal to the c-lattice vector produced by anodic photoelectrochemical corrosion.

photocurrents depends to some extent on the quality of the electrode surface which is determined by the percentage of surfaces not normal to the c-lattice vector. The saturation current, however, is not greatly affected. Figure 2 shows the difference between a smooth and a corroded surface.

The photocurrent across a semiconductor-liquid interface does not necessarily reflect the absorption spectrum of the material. It is well known that there are intermediate processes, such as diffusion, migration, trapping and recombination of charge carriers, or transfer of excitation energy, which determine how many charge carriers can reach the electrode surface and undergo electrochemical reactions. A comparison of absorption spectra and photocurrent spectra in the saturation range is therefore a helpful means to identify intermediate processes. Figure 3 shows such a comparison for the layer-type semiconductors MoS_2 , MoSe_2 , and WSe_2 where the absorption coefficients plotted in a logarithmic scale are taken from data in the literature (35). A remarkable detail which can immediately be recognized is that the apparent quantum efficiency (ϕ_a) still stays above 10% at wavelengths corresponding to light penetration depths two orders of magnitude deeper ($1/\alpha = 10^{-3} \text{ cm}$) than that of the wavelengths exciting the direct A-exciton (λ_A , $1/\alpha = 10^{-5} \text{ cm}$). With negligible diffusion the efficiency should decay abruptly at wavelengths beyond λ_A due to the difficulty of collecting the majority of holes generated outside the space charge layer. That means that field-independent diffusion of free charge carriers must play an important role.

Discussion

Photocurrent-potential relationships.—The prominent result is that the photocurrents are practically independent of the electrode potential in a wide polarization range (Fig. 1) even at wavelengths where the light penetrates deeply into the bulk. The meaning of this result can be derived from the traditional

model for photocurrent-potential relationships of illuminated semiconductor electrodes (51). The n-type semiconductor-electrolyte half-cell is divided into four regions (Fig. 4): (i) a neutral electrolyte with redox couples present, (ii) the Helmholtz double layer between electrolyte and electrode surface, (iii) the space charge depletion region of width W across which charge carriers can migrate in the electric field of a potential drop V_{sc} , and (iv) a neutral region in the bulk of the semiconductor in which the hole lifetime is τ and where the holes can diffuse with mobility μ_p . Light penetrates through the practically transparent electrolyte (very low concentration of I_2 and I_3^-) into the space charge region and the neutral bulk region to a depth given by the reciprocal value of the absorption coefficient, α , of the semiconducting material at a given wavelength.

We make the following assumptions in our model: (a) Absorption of the light quantum generates one electron hole pair. (b) The potential drop across the Helmholtz-layer is constant. (c) The doping level N_D is uniform. (d) The photoexcitation does not disturb the electric field in the space charge layer. (e) All holes in the depletion region can reach the surface, and the barrier height V_{sc} is large enough to prevent all surface recombination as well as the reverse electron transfer reactions. (f) The charge transfer rate across the Helmholtz layer is fast and not rate determining.

In the depletion approximation the depletion width (defined as distance x from the interface up to the plane where $dV/dx = 0$) is

$$W = \left(\frac{2\epsilon\epsilon_0 V_{sc}}{eN_D} \right)^{1/2} \quad [1]$$

with

$$V_{sc} = U - U_{fb} \quad [2]$$

where ϵ_0 is the permittivity of the free space, ϵ the relative dielectric constant, e the electric elementary

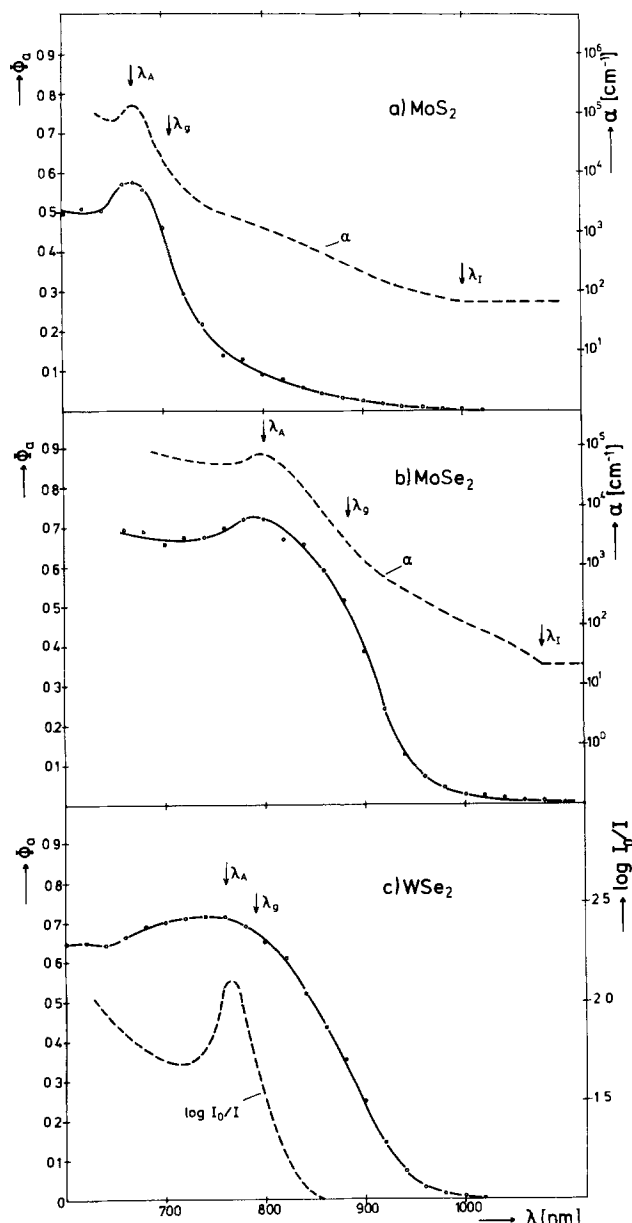


Fig. 3. Spectral dependence of the photoelectrochemical apparent quantum efficiency Φ_a depicted together with corresponding absorption spectra [α -values of MoS_2 and MoSe_2 from Ref. (35), $\log I_0/I$ values from Ref. (50)]. λ_g , assumed bandgaps in (a) Ref. (5), (b) Ref. (6), (c) Ref. (7) on the basis of energy conversion efficiency measurements. λ_A , wavelengths of the direct excitonic A-transition. λ_L , threshold wavelength of the indirect transition [Ref. (35)].

charge, N_D the donor concentration, and U_{fb} the flat-band potential of the semiconductor. The diffusion length of the holes L_p is given by (4)

$$L_p = (D\tau_p)^{1/2} \quad [3]$$

where D_p , the diffusion coefficient of the holes, is related to the mobility μ_p by the Einstein relation

$$D_p = \frac{\mu_p kT}{e} \quad [4]$$

L_p therefore becomes

$$L_p = \left(\frac{\mu_p kT}{e} \right)^{1/2} \quad [5]$$

With the above assumptions one obtains for the theoretical photocurrent j_p (51)

$$j_p = j_{sc} + j_D \quad [6a]$$

$$j_p = eI [1 - \exp(-\alpha W)] + eI \frac{\alpha L_p}{1 + \alpha L_p} \exp(-\alpha W)$$

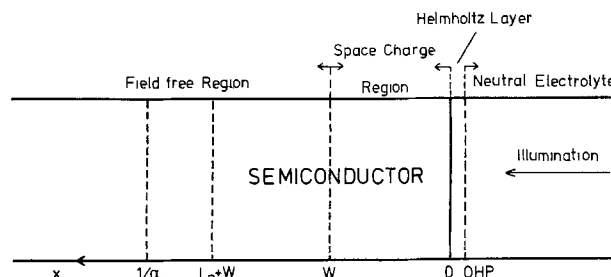


Fig. 4. Model of the illuminated semiconductor-electrolyte interphase region. $1/\alpha$, depth of light penetration; W , width of space charge layer; L_p , mean diffusion length of minority carriers; OHP, outer Helmholtz plane.

$$j_p = eI \left[\left(1 - \frac{1}{1 + \alpha L_p} \right) \exp(-\alpha W) \right] \quad [6b]$$

j_p is the sum of the currents of holes generated in the space charge region (j_{sc}) and the diffusion current of the holes generated in the adjacent bulk of the electrode (j_D), I designates the photon flux. Equation [6] expresses that minority charge carriers generated outside the depletion region (W) can only contribute to the photocurrent if they can reach the space charge domain by diffusion, i.e., if they are generated within a distance of L_p behind the space charge layer. The rest of the photogenerated carriers recombine in the bulk.

We can calculate the depletion layer width W in the dependence of V_{sc} with Eq. [1] for our MoS_2 sample with $N_D = 2 \times 10^{17} \text{ cm}^{-3}$ (52) and the dielectric constant for the electric field vector parallel to the c-lattice vector of the layer lattice $\epsilon = 4.9$ (16, 53). With $V_{sc} > 0.3 \text{ V}$, W is in the order of 10^{-5} cm for N_D above 10^{16} cm^{-3} . If L_p would be small compared with $1/\alpha$, that $\alpha L_p \ll 1$, we would get $j_p \approx j_{sc}$, and, therefore, a considerable potential dependence of j_p . This theoretical case is plotted in Fig. 5a and b as dashed lines. In Fig. 5c this case would give a negligible current. The graph does not show such a dependence and indicates that the observed photocurrents are mainly due to diffusive transport, particularly if $\alpha < 10^4 \text{ cm}^{-1}$. This conclusion does not depend on the absolute values of α as long as $1/\alpha$ is not in the order of magnitude of W , which is certainly not the case for the range of the indicated bandgap.

The diffusion length of holes.—In such cases, the photocurrent can be used to calculate the diffusion length L_p at long wavelengths where space charge layer effects can be neglected ($\alpha W \ll 1$). Equation [6b] can be transformed using the quantum efficiency Φ

$$\Phi = \frac{j_p}{eI} \quad [7]$$

$$\frac{1}{\Phi} = \frac{1}{\alpha L_p} + 1 \quad [8]$$

According to this relation a plot of $1/\Phi$ vs. $1/\alpha$ should give a straight line the slopes of which should be the reciprocal diffusion length. This method gives relative deviations $< 20\%$ from the exact L_p value as long as $L_p < 0.5d$ (d : electrode thickness) (3). This relation was satisfied by our samples. In order to compare this theory with the experiment we have to correct our data for photon flux losses by reflection. The real efficiency will be given by

$$\Phi_r(\lambda) = \frac{\Phi_a(\lambda)}{T(\lambda)} \quad [9]$$

$\Phi_r(\lambda)$ is the real quantum efficiency at wavelength λ , $\Phi_a(\lambda)$ is the experimental apparent efficiency neglecting reflection losses, $T(\lambda)$ is the transmittivity. With assumption (a) that absorption of one light quantum

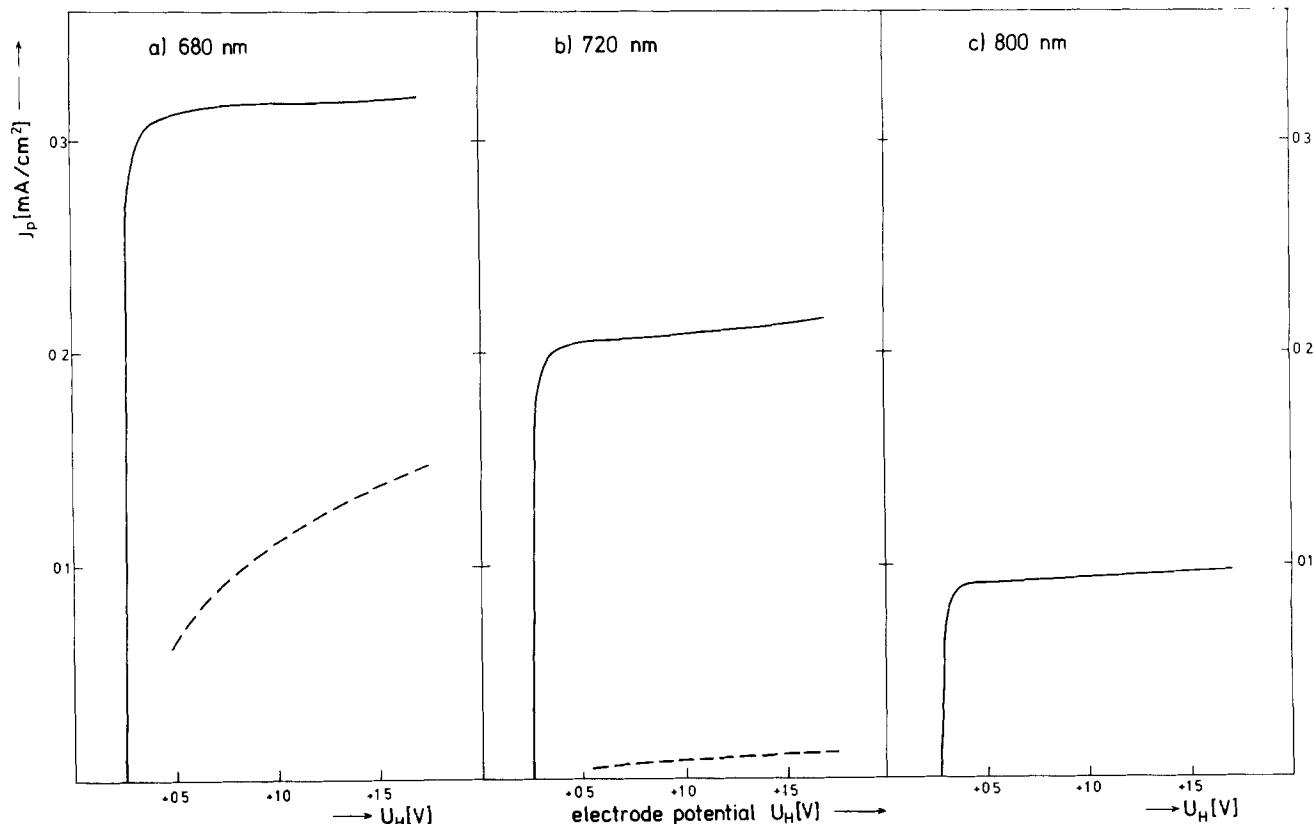


Fig. 5. Photocurrent-voltage relationship at a liquid junction of an n-type MoS_2 electrode (solid lines) compared with theoretical j_p - U curves according to Eq. [6b] neglecting diffusion of minority carriers (dashed lines).

generates one electron-hole pair we can set the real efficiency at the A-exciton wavelength, $\Phi_r(\lambda_A)$, equal to unity

$$\Phi_r(\lambda_A) \equiv 1 = \frac{\Phi_a(\lambda_A)}{T(\lambda_A)} \quad [10]$$

The relative wavelength dependence of the transmittivity can be taken from reflectivity measurements (54) and will be expressed by the factor $f(\lambda)$

$$f(\lambda) = \frac{T(\lambda)}{T(\lambda_A)} \quad [11]$$

Introducing Eq. [10] and [11] into [9] yields for the real quantum efficiency

$$\Phi_r(\lambda) = \frac{\Phi_a(\lambda)}{\Phi_a(\lambda_A)f(\lambda)} \quad [12]$$

One can see in Fig. 6 that the theory describes the experiment fairly well if one bears in mind that the accuracy of the available α -values is moderate and may vary from sample to sample in the range of low α -values. The slopes of the straight lines increase somewhat after considering the correction factor $f(\lambda)$. The corrected slopes for photon penetration depth ranges between 10^{-4} and 10^{-2} cm give mean diffusion length values for MoS_2 , $L_p = 1.4 (\pm 0.2) \times 10^{-4}$ cm and for MoSe_2 , $L_p = 5 (\pm 3) \times 10^{-4}$ cm.

The correctness of these figures depends on the accuracy of the α -values used in this treatment. Since we could not measure these data independently there remains a considerable uncertainty, which however, will not affect the order of magnitude.

With the knowledge of the hole mobility (μ_p) and the hole diffusion length (L_p) we can estimate the lifetime τ_p . Hole mobilities normal to c ($\mu_{p\perp}$) have been derived for p-type MoS_2 specimen with $N_D \approx 2 \times 10^{17}$ cm^{-3} around $200 \text{ cm}^2/\text{V sec}$ (55). With an anisotropy of $\mu_{p\perp}/\mu_{p\parallel} \approx 2200$ (56), the hole mobility along c ($\mu_{p\parallel}$) would be around $0.1 \text{ cm}^2/\text{V sec}$. After Eq. [5] the mean hole lifetime would result in $\tau_p \approx 10^{-4}$ sec

(MoSe_2) and $\tau_p \approx 10^{-5}$ sec (MoS_2). With a less pronounced anisotropy of about 10 due to lattice defects, we would obtain 10^{-6} sec (MoSe_2) or 10^{-7} sec (MoS_2). These results will be checked by direct lifetime measurements.

The indirect bandgap.—It is generally accepted that transition metal dichalcogenides are indirect bandgap semiconductors, as has been stated above, which should have serious consequences for the applicability of these compounds as energy converting electrodes. The photocurrent spectra in Fig. 3 show apparent quantum efficiencies up to 10% even at wavelengths corresponding to absorption coefficients almost three orders of magnitude smaller than that of the direct A-transition. If one assumes a sufficiently high density of states at the indirect conduction band minimum, ($N(E_c)$), the Fermi level will be located somewhat below in the n-type semiconductors of high enough doping levels as used here (Fig. 7). The decisive parameter for electrochemical regenerative and electrolysis cells is the distance between the Fermi energy at flatband condition and the valence band maximum, which determines the limit of the free enthalpy of the photogenerated holes which can be reached at high illumination intensities and can be used for electrochemical work.

A promising method for determining the size of this energy gap is based on the wavelength dependence of light absorption for indirect transitions, which is reflected in the photoresponse of the semiconducting electrode if the photocurrent is fully diffusion controlled. This condition is met for the present compounds at wavelengths near the onset of the indirect absorption (λ_I) (Fig. 3). There, αW and αL will be much less than unity so that Eq. [6b] and [7] simplify to

$$\Phi = \alpha L_p \quad [13]$$

The frequency dependence of the absorption coefficient α for an indirect transition is given by the relation (57, 58)

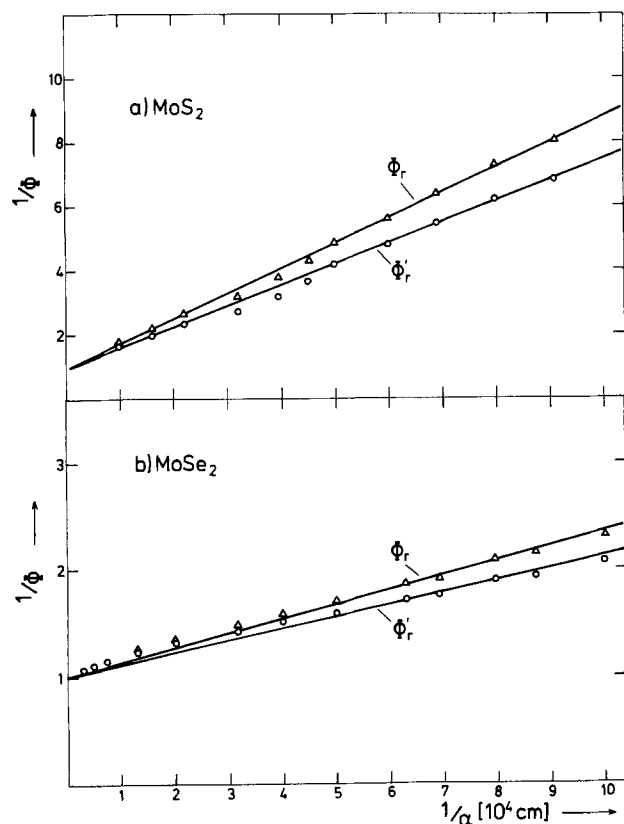


Fig. 6. The reciprocal of the quantum efficiency Φ is a linear function of the light penetration depth, $1/\alpha$ [α = absorption coefficient from Ref. (35)]. Φ_r' , real quantum efficiency assuming constant transmittivity $T(\lambda) = T(\lambda_A)$; Φ_r , real quantum efficiency corrected for varying transmittivity, $T(\lambda)$, from Ref. (54).

$$\alpha = \frac{A(h\nu - E_g)^2}{h\nu} \quad [14]$$

where A is a constant, E_g is the energy gap. Inserting [14] into [13] yields

$$(\Phi h\nu)^{1/2} = (LA)^{1/2}(h\nu - E_g) \quad [15]$$

If this equation can be applied, a plot of $(\Phi h\nu)^{1/2}$ vs.

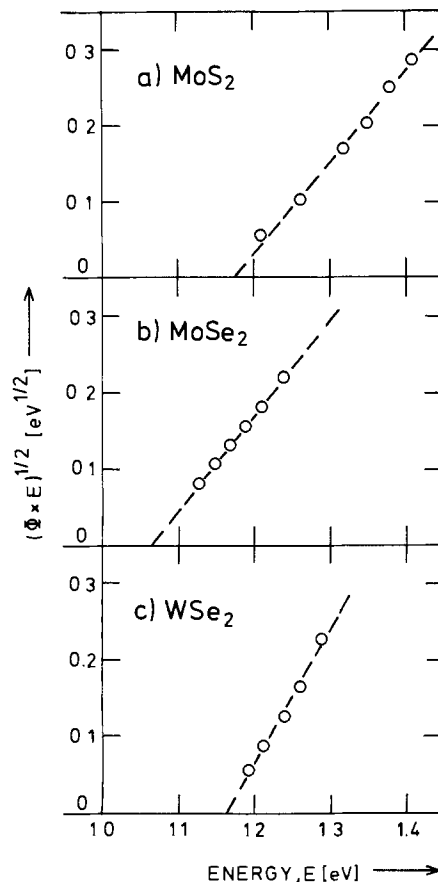


Fig. 8. Photoyield spectra near the energy threshold for electron injection from an iodide-containing electrolyte into the semiconductor valence band. The intercepts with the energy axis are taken as the fundamental energy gaps (see Table I).

$h\nu$ should be linear with the intercept of the photon energy axis being the bandgap edge.

This theory can describe our experimental finding well, as is depicted in Fig. 8. The real quantum efficiencies were used here after correction for reflection losses. The bandgap values derived from this figure are listed in Table I. The comparison with other data in this table shows that this method gives results in

Fig. 7. Schematic representation of the d-band structure close to the optical gap of 2H-MoS₂ [after (26)] and density of states [after (25)]. Hybrid band designations from Ref. (49). Possible direct and indirect electronic transitions are indicated. E_c , conduction band minimum; E_v , valence band maximum.

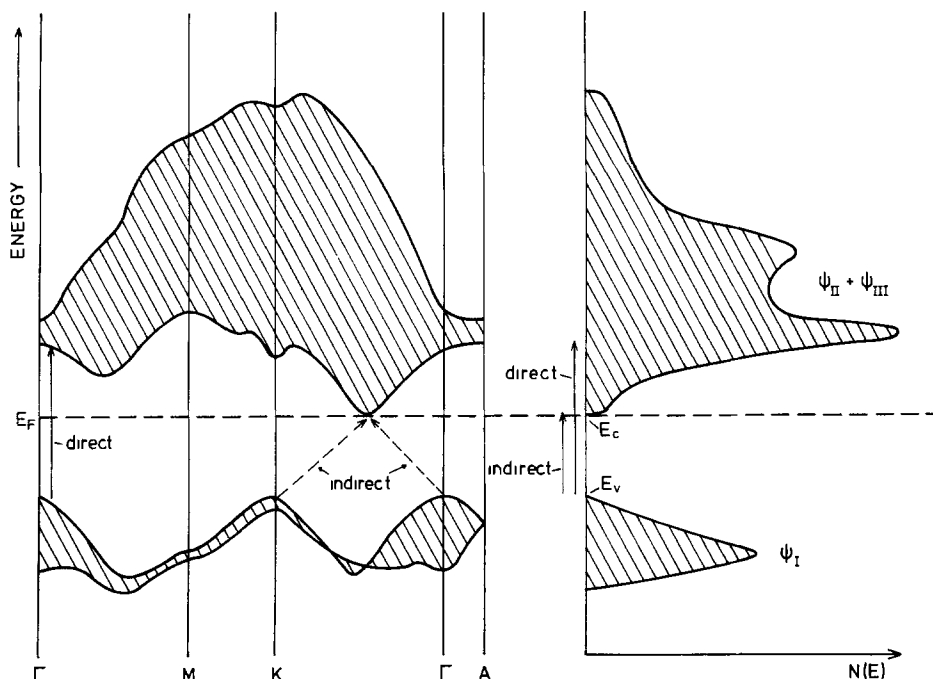


Table I. Fundamental indirect bandgap (eV)

	Photoelectrochemical	Optical absorption (35)	Photo-emission (33)	"APW" calculation (25)
MoS ₂	1.17 ± 0.03	1.13 ± 0.01	1.0 ± 0.2	1.16
MoSe ₂	1.06 ± 0.03	1.09 ± 0.01	—	—
WSe ₂	1.16 ± 0.03	—	—	—

good agreement with findings of other authors and methods. It should be mentioned that numerous photo-emission experiments (29-34) indicated that the valence band maximum lies about 1 eV under the Fermi level on the energy scale in n-type semiconductors. This supports our conclusion that the electrochemically effective bandgaps are substantially smaller (Table I) than has been assumed up to now on the basis of energy conversion efficiency measurements (λ_g 's in Fig. 3: MoS₂ 1.75 eV (5), MoSe₂ 1.4 eV (6), WSe₂ 1.57 eV (7). Consequently, these photoelectrode materials can only catalyze redox processes with reaction enthalpies less than 1 eV. The photoelectrochemical splitting of water which needs 1.23 eV will be impossible without additional applied voltage. Solar cells on the basis of these layer-type materials will be very similar in their behavior to silicon and their efficiency will depend largely on the lifetime of the minority carriers.

We now also understand why photopotentials greater than 0.7V could never be measured. At electronic equilibrium, the maximum band bending is limited by the gap size. The loss in free energy of electron hole pairs generated by light absorption due to charge separation, electrochemical overpotentials, etc. (59) has been estimated to amount to ~ 0.5V. Subtracting this value from the indirect bandgap (~ 1.2V) yields a maximum effective photovoltage of 0.7V in accordance with the experimental findings.

Acknowledgments

We acknowledge the support of the Deutsche Forschungsgemeinschaft and thank Dr. F. Lévy (Lausanne) for providing MoS₂ single crystals and Dr. W. Eckardt (Fritz-Haber-Institut) for valuable discussion.

Manuscript submitted Feb. 11, 1980; revised manuscript received May 14, 1980.

Any discussion of this paper will appear in a Discussion Section to be published in the June 1981 JOURNAL. All discussions for the June 1981 Discussion Section should be submitted by Feb. 1, 1981.

REFERENCES

- S. M. Sze, "Physics of Semiconductor Devices," p. 640 ff, John Wiley & Sons, Inc., New York, London, Sidney, Toronto (1969).
- a. A. K. Gosh and H. P. Maruska, *This Journal*, **124**, 1516 (1977).
b. H. P. Maruska and A. K. Gosh, *Solar Energy Materials*, **1**, 237 (1979).
- K. Graff and H. Fischer, *Top. Appl. Phys.*, **31**, 173 (1979).
- S. M. Sze, "Physics of Semiconductors Devices," p. 50 ff., John Wiley & Sons, Inc., New York, London, Sidney, Toronto (1969).
- H. Tributsch, *Z. Naturforsch., Teil A*, **32**, 972 (1977).
- H. Tributsch, *Ber. Bunsenges. Phys. Chem.*, **82**, 169 (1978).
- J. Gobrecht, H. Gerischer, and H. Tributsch, *ibid.*, **82**, 1331 (1978).
- C. Clemen, X. I. Saldana, P. Munz, and E. Bucher, *Phys. Status Solidi A*, **49**, 437 (1978).
- J. A. Wilson and A. D. Yoffe, *Adv. Phys.*, **18**, 193 (1969).
- P. G. Harper and J. A. Hilder, *Phys. Status Solidi*, **25**, 69 (1968).
- B. L. Evans and P. A. Young, *Proc. R. Soc. London, Ser. A*, **284**, 402 (1965).
- B. L. Evans and P. A. Young, *Proc. R. Soc. London, Ser. A*, **298**, 74 (1967).
- B. L. Evans and P. A. Young, *Phys. Status Solidi*, **25**, 417 (1968).
- B. L. Evans and R. A. Hazelwood, *Phys. Status Solidi A*, **4**, 181 (1971).
- A. R. Beal, J. C. Knights and W. Y. Liang, *J. Phys. C*, **5**, 3540 (1972).
- R. A. Neville and B. L. Evans, *Phys. Status Solidi B*, **73**, 597 (1976).
- A. R. Beal and W. Y. Liang, *J. Phys. C*, **9**, 2459 (1976).
- R. F. Frindt and A. D. Yoffe, *Proc. R. Soc. London, Ser. A*, **273**, 69 (1963).
- B. L. Evans and K. T. Thompson, *Br. J. Appl. Phys., Ser. 2*, **1**, 1619 (1968).
- T. J. Wieting and A. D. Yoffe, *Phys. Status Solidi*, **37**, 353 (1970).
- V. L. Kalikhman and L. L. Praverova, *Inorg. Mater.*, **10**, 1021 (1974).
- K. Wood and J. P. Pendry, *Phys. Rev. Lett.*, **31**, 1400 (1973).
- R. V. Kasowski, *ibid.*, **30**, 1175 (1973).
- L. F. Mattheiss, *ibid.*, **30**, 784 (1973).
- L. F. Mattheiss, *Phys. Rev. B*, **8**, 3719 (1973).
- N. J. Doran, *Physica B*, **99**, 227 (1980).
- J. C. McMennan and W. E. Spicer, *Phys. Rev. Lett.*, **29**, 1501 (1972).
- P. M. Williams and F. R. Shepherd, *J. Phys. C*, **6**, L36 (1973).
- R. H. Williams, *ibid.*, **6**, L32 (1973).
- G. K. Wertheim, F. J. DiSalvo, and D. N. E. Buchanan, *Solid State Commun.*, **13**, 1225 (1973).
- R. B. Murray and R. H. Williams, *Philos. Mag.*, **29**, 473 (1974).
- F. R. Shepherd and P. M. Williams, *J. Phys. C*, **7**, 4427 (1974).
- J. C. McMennan and W. E. Spicer, *Phys. Rev. B*, **16**, 5474 (1977).
- I. T. McGovern, R. H. Williams, and A. W. Parke, *J. Phys. C*, **12**, 2689 (1979).
- A. M. Goldberg, A. R. Beal, F. A. Levy, and E. A. Davis, *Philos. Mag.*, **32**, 367 (1975).
- R. A. Bromley, R. B. Murray, and A. D. Yoffe, *J. Phys. C*, **5**, 759 (1972).
- F. Mehran, R. S. Title, and M. W. Shafer, *Solid State Commun.*, **20**, 369 (1976).
- S. A. Komolov and L. T. Chadderton, *Philos. Mag. B*, **39**, 13 (1979).
- R. Huisman, R. De Jonge, C. Haas, and F. Jellinek, *J. Solid State Chem.*, **3**, 56 (1971).
- J. A. Wilson, F. J. DiSalvo, and S. Mahajan, *Adv. Phys.*, **24**, 117 (1975).
- F. Lévy, Ph. Schmid, and H. Berger, *Philos. Mag.*, **34**, 1129 (1976).
- J. Gobrecht, Doctoral thesis at the Technical University, Berlin (1979).
- A. D. Yoffe, *Festkörperprobleme*, **8**, 1 (1973).
- A. D. Yoffe, *Ann. Rev. Mater. Sci.*, **3**, 147 (1973).
- A. D. Yoffe, *Chem. Soc. Rev.*, **5**, 51 (1976).
- J.-L. Calais, *Adv. Phys.*, **26**, 847 (1977).
- G. A. Tsigdinos, "Topics in Current Chemistry," Vol. 76, p. 65, Springer Verlag, Berlin, Heidelberg, New York (1978).
- E. Mooser (Managing Editor), "Physics and Chemistry of Materials with Layered Structures," Vol. 1-5, D. Reidel Publishing Co., Boston, Mass. (1978).
- W. Kautek, H. Gerischer, and H. Tributsch, *Ber. Bunsenges. Phys. Chem.*, **83**, 1000 (1979).
- R. F. Frindt, *J. Phys. Chem. Solids*, **24**, 1107 (1963).
- W. W. Gärtner, *Phys. Rev.*, **116**, 84 (1959).
- W. Kautek, Doctoral thesis at the Technical University, Berlin (1980).
- R. Bailley, *Am. Mineral.*, **33**, 519 (1948).
- A. R. Beal and H. P. Hughes, *J. Phys. C*, **12**, 881 (1979).
- R. Mansfield and S. A. Saloam, *Proc. Phys. Soc. B*, **66**, 377 (1953).
- S. R. G. Thakurta, *Indian J. Phys.*, **43**, 169 (1969).
- F. Stern, *Solid State Phys.*, **15**, 299 (1963).

58. E. S. Johnson, "Semiconductors and Semimetals," Vol. 3, R. K. Williardson and A. C. Beer, Editors, p. 153, Academic Press, New York (1967).
 59. H. Gerischer, "Topics in Applied Physics," Vol.

- 31, B. O. Seraphin, Editor, p. 115, Springer Verlag, Berlin, Heidelberg, New York (1979).
 60. H. J. Lewerenz, A. Heller, and F. S. DiSalvo, *J. Am. Chem. Soc.*, **102**, 1877 (1980).

Diffusion of Dopants from Optical Coatings and Single Step Formation of Antireflective Coating and P-N Junction in Photovoltaic Cells

Bulent E. Yoldas

Westinghouse Research and Development Center, Ceramic and Glasses Department, Pittsburgh, Pennsylvania 15235

ABSTRACT

The p-n junction in a silicon chip and an antireflective (AR) oxide coating on the surface of the chip are formed simultaneously from a clear polymerized solution derived from alkoxides of titanium and a p or n dopant. The partially hydrolyzed and polymerized solution is applied to the surface of the silicon by liquid application methods. The silicon cell is then heated to convert the solution to a solid oxide coating which meets the antireflective optical film requirements and induces the migration of the dopants into the chip, forming a p-n junction in the chip. Other expected advantages of this method are: attainment of very uniform dopant diffusion on unusually large samples and polycrystalline substrates; deep diffusion while avoiding excessive surface carrier concentration; and multi-dopant diffusion in differential areas of a sample by a single heat-treatment.

In the conventional preparation of a photovoltaic solar cell, a p-n junction is formed by diffusion of either boron or phosphorus into a silicon base material. The diffusions are generally made from the vapor phase, in an oxidizing atmosphere at 850°-1000°C.

A separate step is required for the application of a quarter-wave optical thickness antireflective film to the surface of the cell. The antireflective coating may increase the efficiency of the cell by as much as 50% (1-5). Such optical coatings are applied by vacuum deposition, sputtering, or other techniques. Recently, it was discovered that polymerized titanium dioxide solutions could be made which would deposit optical coatings of the desired thickness and index of refraction by dipping, spinning, or spraying (1). A cost analysis of this new method suggests that in volume production the cost of applying the AR coating can be reduced to less than \$0.01 W-package (1980\$) (6).

When the above titanium-oxide based solution is doped with a p-type dopant compound such as boron, the dopant will diffuse into the n-type silicon and form a p-n junction during the baking of the antireflective coating. Thus the antireflective coating and the p-n junction are formed simultaneously. This eliminates several steps which are required for the present method of diffusion and junction formation. Tests using this method (where the boron diffusion source is the doped antireflective coating) have resulted in surface concentrations (C_0) of boron in silicon of $10^{19}/\text{cm}^3$ (as measured by the spreading resistance). Other boron diffusion techniques generally lead to C_0 's of 10^{21} to $10^{22}/\text{cm}^3$. In photovoltaic devices, a lower C_0 in the back-surface region is preferable, because of decreased carrier combination at the back-surface.

At high surface carrier concentrations, the junction depth is restricted due to the increasing number of recombinations. In this process, where the carrier concentration appears to be self-limiting at an ideal

value, coupled with the passivated surface, the formation of deeper junctions with less shunting becomes feasible, and requirement for shallower junctions, e.g., 0.3 μm , becomes less critical.

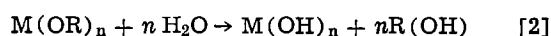
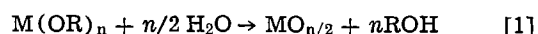
Another advantage of this new process is that very uniform dopant diffusion and junction depth can be obtained on large devices, photovoltaic or otherwise. This is due to the fact that the dopant diffuses from an optical film which is homogeneous in composition at the molecule level and uniform in thickness below the wavelength of light, no matter how large the substrate. This fact coupled with the fact that the amount of dopant available for diffusion over a given substrate area is finite and well defined might make the method attractive for doping polycrystalline materials evenly.

It should also be obvious that diffusion on well-defined areas of a substrate may be accomplished without masking the rest of the sample, simply by coating only those areas where diffusion is desired. Multi-doping of a sample can be done in a single heat-treatment by applying solutions containing different dopants to those areas where the particular doping is desired.

Approach and Experiments

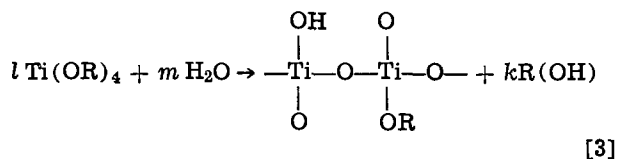
A clear titanium-oxide based solution, derived from the partial hydrolysis and polymerization of titanium alkoxides, is applied to obtain an antireflective optical coating on a silicon base material. Other alkoxides useful in preparing the solutions have the general formula $M(\text{OR})_n$ where M represents a metal ion (for example, Ti), O is oxygen, R is an alkyl group, and n is the valence of M.

Metal alkoxides, in general, hydrolyze vigorously when brought into contact with water. They form oxides and hydroxides as represented by the following reactions

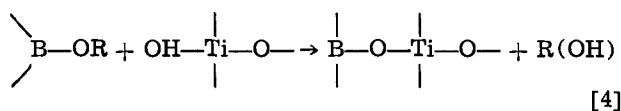


Key words: coatings, optics, doping.

Whether the oxide or the hydroxide forms during the hydrolysis depends on the nature of the alkoxide. In either case, the resultant material is particulate and precipitates out; it is therefore not useful for optical coating. The alkoxides of titanium and tantalum show a particular tendency to form precipitates, even under insufficient water hydrolysis; under normal conditions, the formation of precipitates cannot be prevented. However, we have developed a method of preparing a soluble polymerized species, capable of forming a continuous oxide network, from these alkoxides (7, 8)



These polymerized solutions are somewhat different than those available commercially for dopant sources and passivation purposes. Precipitate formation and self-condensation (which would normally occur during the hydrolysis) are prevented by careful control of the molecular interaction during the hydrolysis, so that certain amounts of OR groups are left in the molecular structure. When applied to substrates, these solutions leave a film which, upon heat-treatment at temperatures as low as 325°C, converts to a glass-like oxide film. The dopants (such as boron) may be introduced into the coating solution either from soluble compounds or by chemical polymerization of dopant into the precursor solution, for example



The coating is applied by spinning and by dipping. Spin application is used for Czochralski-type round silicon wafers. For ribbon-like dendritic-web silicon, the spin method is not suitable; rather, the samples are coated by dipping. Extremely uniform AR coatings may be readily obtained by either method.

The antireflective coating on silicon solar cells in an air environment must have a refractive index of 2 and a thickness of about 750Å, as calculated from Fresnel's equations. An undoped TiO₂ coating baked in air gives an index slightly over 2.1; the same coating baked in vacuum has an index around 2.4 (1). The refractive index of the coating is controlled by the composition of the solution. For example, the index of refraction in the TiO₂-SiO₂ binary can vary from 1.4 to 2.4. The thickness of the coating is controlled by the properties of the solution (such as its concentration and viscosity) and also by the application rate (1).

The p- and n-type dopant compound may be added directly to these alkoxide-derived solutions. The most common n and p dopants are phosphorus and boron, but other dopants such as aluminum, arsenic, antimony, or gallium may be used. To prepare a boron-doped solution, a boron compound is added to the Ti solution; such compounds include boron trimethoxide, boron triethoxide, boron triisopropoxide, phosphorus pentabutoxide, phosphorus pentaethoxide, phosphoric acids, etc. Whichever dopant compound is used, it must be compatible with the alkoxide solution: that is, it may go into the precursor solution either by reaction with the metal alkoxide (as shown in Eq. [4]) or by dissolution, but it must not form a precipitate. When the deposited coating is baked, the boron or phosphorus dopant in the coating acts as a diffusion source. If the dopant is added from an alkoxide, it may be partially hydrolyzed with 1.0-1.5 moles of water per mole of alkoxide to prevent its vaporization or precipitation. However, this may not

be necessary if the base solution contains enough hydroxyl groups.

The silicon substrate materials which are generally available and suitable for this method come in two forms: as wafers about 2-12 cm in diameter, and as strips (that is, dendritic web silicon) up to 4 cm wide. The nominal thickness is 125-250 μm. For the purposes discussed here, the silicon should have some base dopant, either p-type or n-type. Most of the work discussed here was carried out on n-type silicon, using the doped antireflective coating as a boron diffusion source.

The temperature range for boron dopant diffusion is about 850°-1100°C; below 850°C very little boron diffuses into the silicon, and above 1100°C the silicon properties deteriorate. A temperature of 900°C appears to be optimal. The oxide film (after heat-treatment) is continuous, has a uniform thickness to within several angstroms, and is tenaciously bonded onto the substrate.

The heat-treatment provides for boron diffusion into the substrate. After the heat-treatment, however, the coating must be able to meet the optical requirements for antireflectivity, as defined by the Fresnel equations, for photovoltaic devices. Since the coating is affected by the diffusion process, the initial composition and thickness of the coating must be tailored to give (using silicon as an example) an index of refraction equal to 2 and a thickness of about 750Å after the heat-treatment. Boron can be added to alter the index of refraction of the coating as well as be the source of substrate dopant.

Results and Discussion

At 850°C, very little boron diffused into the silicon. At 900°C, however, the diffusion was significant and controlled; therefore most of the diffusion investigation was conducted at this temperature. A striking feature of the boron diffusion from the TiO₂ coating is that it results in very uniform, sharp, well-defined, and predictable diffusion depths. Figure 1 shows the spreading resistance diffusion profile from a 10% B₂O₃-90% TiO₂ coating, for various diffusion times,

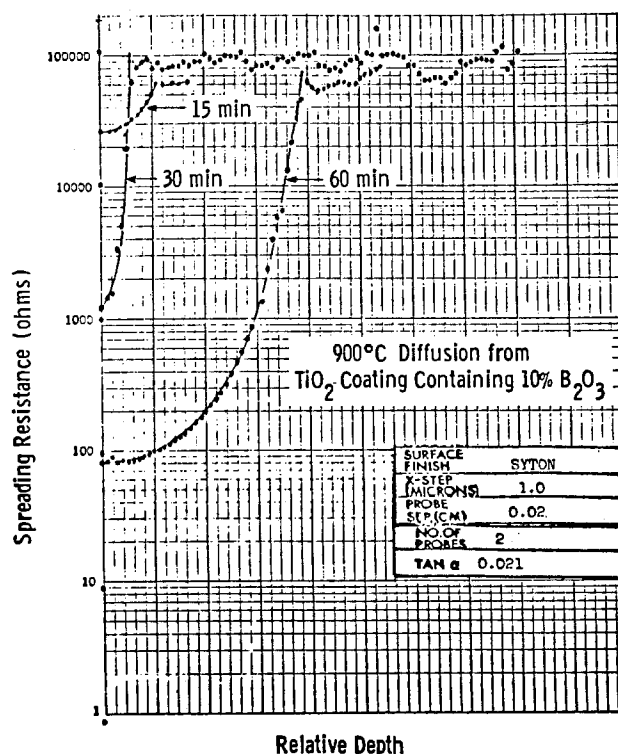


Fig. 1. Spreading resistance profiles as a function of time, at 900°C, for a 90% TiO₂-10% B₂O₃ optical coating on silicon.

baked at 900°C. The junction depths and surface concentrations reported here were obtained by simple spreading resistance profiles. Even though these measurements are not precise for a single sample, they provide comparison within a given set of samples, and established general trends. In these respects, the measurements were consistent to a degree that enabled us to predict these parameters, for a given condition, within a small error (usually less than 10%).

The concentration of boron in the coating affects the surface concentration and the junction depth in an n-type silicon substrate (10 Ω -cm resistivity). These effects are shown, for diffusion at 900°C for 1 hr, in Table I and Fig. 2 and 3. These figures are significant in that boron concentrations above 20 weight percent do not seem to affect either the carrier concentration or the junction depth. In this way boron diffusion from a TiO₂ coating differs from boron diffusion from conventional glass coatings. If this type of boron diffusion were used to produce a back-surface field in a p-type silicon, the stable C_0 value of $\sim 10^{19}$ would approach the optimum value required for minimum recombination of the back-surface.

In order for the coating to meet the antireflective requirements, its index of refraction after the diffusion heat-treatment must be 2. Figure 4 shows the index of refraction of the coating, following heat-treatment for 1 hr at 900°C, as a function of B₂O₃ concentration in the TiO₂. It can be seen from the figure that over 50% B₂O₃ is needed to produce a coating with an index close to 2. This is acceptable, although for B₂O₃ concentrations greater than 40% the coating tends to become cloudy, and its chemical and environmental resistance may also drop.

A preferred method for adjusting the index of the coating to 2 is by limiting the boron addition to less than 30% (which is more in line with the diffusion requirement), and lowering the index by introducing another constituent with a low index—SiO₂, for example. The SiO₂ component may be added from alkoxides or partially hydrolyzed alkoxides by a process similar to the dopant introduction. Figure 5 shows the amount of equivalent SiO₂ required to lower the index of refraction to about 2, as a function of the amount of B₂O₃ dopant present in a titania-based AR coating subjected to 900°C vacuum treatment for 45 min. As an example, a precursor solution which would deposit a coating composed of 70% TiO₂, 20% B₂O₃, and 10% SiO₂ satisfies the index requirement for antireflectivity.

The spectral reflectivity curve in Fig. 6 shows zero reflection at 580 nm; this indicates the formation of an ideal single layer antireflective film on silicon, which meets the index of refraction and thickness requirements. When the boron diffusion measurements were done, it was found that this sample had a surface concentration of about 3×10^{19} and a junction depth of about 0.5 μ m. Junction depth and carrier concentration on the entire sample were very uniform. The silicon samples, comprising an n-type dopant with 10-12 Ω -cm resistivity and a 10 cm silicon wafer, were spin-coated at 1000 rpm. The samples were baked at 900°C for 45 min and were divided into 1 cm² photovoltaic cells. The results of these unoptimized cells are shown in Table II.

Table I. Effect of boron concentration in coating on carrier concentration and junction depth (as determined by spreading resistance)

Weight percent B ₂ O ₃ in AR coating (%)	Apparent surface concentration (C ₀) (per cm ²)	Junction depth (μ m)
10	1×10^{19}	0.40
20	3×10^{19}	0.70
30	3×10^{19}	0.75
40	3×10^{19}	0.75
50	3×10^{19}	0.75

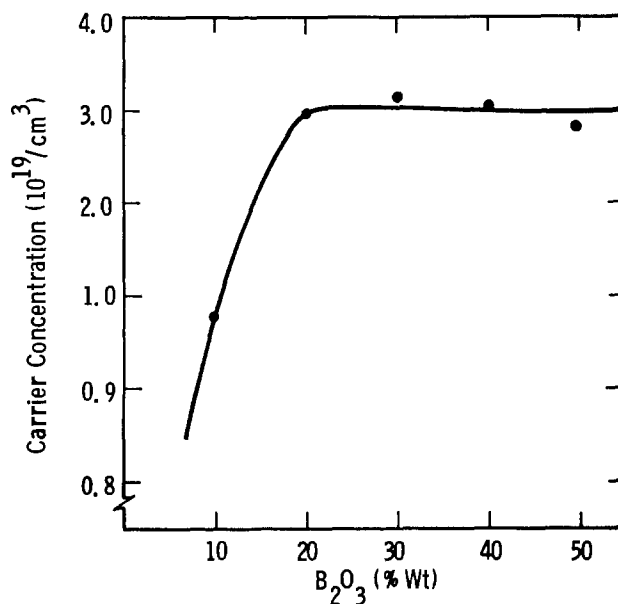


Fig. 2. Surface carrier concentration on a silicon chip as a function of boron presence in TiO₂ coating (as measured by spreading resistance).

These cells did not have a back-surface field. With the exception of sample 4, an OCD lifetime of 4-6 μ sec is reasonable for the 10 Ω -cm n-type silicon used as a substrate. The low current density (J_{sc}) and fill factor (FF) are due to process related factors which, at the time of these experiments, were not optimized. When the process and structure design optimization is completed after the basic studies, back-surface field cells yielding current densities around 30 mA/cm² and efficiencies of $\sim 15\%$ are expected.

The experiments with phosphorus diffusion from the TiO₂ coating were less successful. There was no difficulty in obtaining antireflective coatings with phosphorus-containing TiO₂ coatings, however, diffusion into the silicon substrate required high temperatures. Understanding of the detailed diffusion mechanism from these coatings requires further studies including diffusion of dopants other than boron, use of optical coatings other than TiO₂, and use of polycrystalline substrates.

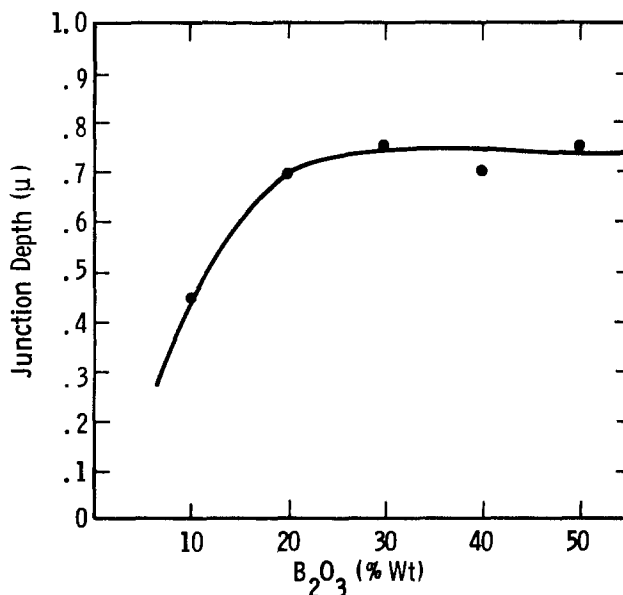


Fig. 3. Junction depth as a function of B₂O₃ concentration in the TiO₂ coating at 900°C for 1 hr.

Table II. Initial test results showing efficiencies of silicon solar cells whose p-n junctions were produced from the AR coating in a single step

Sample	J_{sc} (mA/cm ²)	V_{oc} (V)	FF	Eff. (%)	OCD (μsec)
1	24.60	0.515	0.734	9.83	5.60
2	24.60	0.515	0.738	9.89	5.60
3	24.60	0.515	0.729	9.77	5.20
4	22.20	0.511	0.503	6.03	5.10
5	22.80	0.516	0.735	9.15	4.55

Acknowledgment

The author thanks R. B. Campbell, P. Rai-Choudhury, and A. Rohatgi for the assistance they have provided in the investigation and preparation of this manuscript.

Manuscript submitted Jan. 31, 1980; revised manuscript received May 2, 1980.

Any discussion of this paper will appear in a Discussion Section to be published in the June 1981 JOURNAL. All discussions for the June 1981 Discussion Section should be submitted by Feb. 1, 1981.

Publication costs of this article were assisted by Westinghouse Electric Corporation.

REFERENCES

1. B. E. Yoldas and T. W. O'Keefe, *Appl. Opt.*, **18**, 3133 (1979).
2. D. L. Reynold and A. Andrew, *ibid.*, **5**, 23 (1966).
3. G. Seibert, in "European Space Research & Technology, Increased Solar Cell Output by Improved

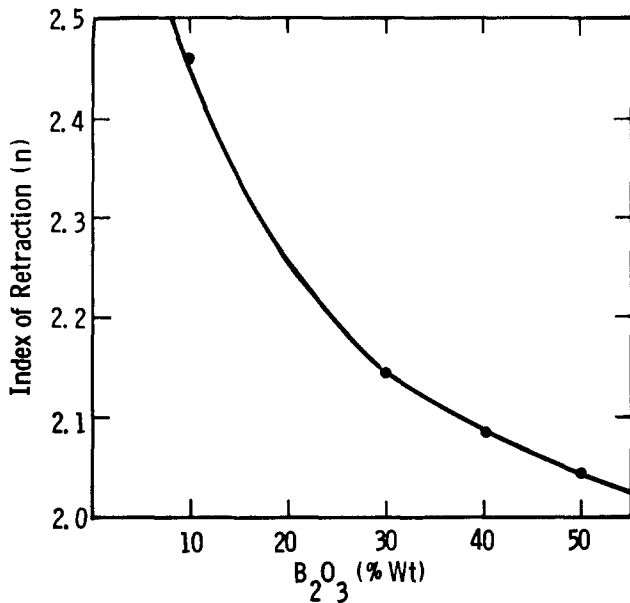


Fig. 4. Index of refraction of the optical coating, after diffusion heat-treatment at 900°C for 1 hr, as a function of B₂O₃ content in TiO₂.

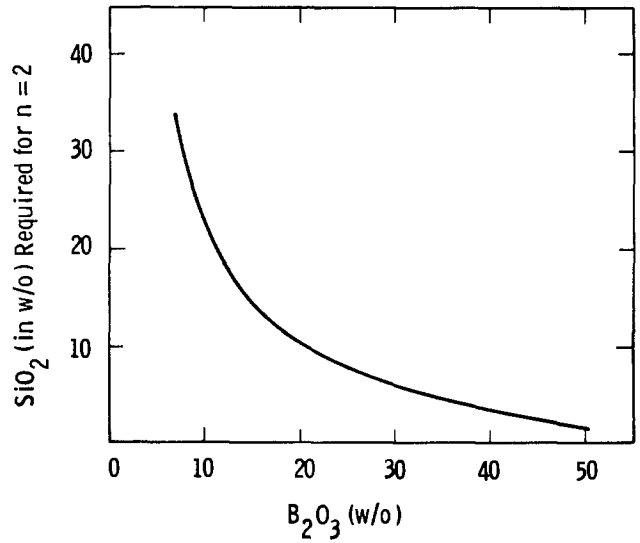


Fig. 5. Amount of SiO₂ required to produce an optical coating with an index of refraction of 2, after diffusion heat-treatment, as a function of B₂O₃ content.

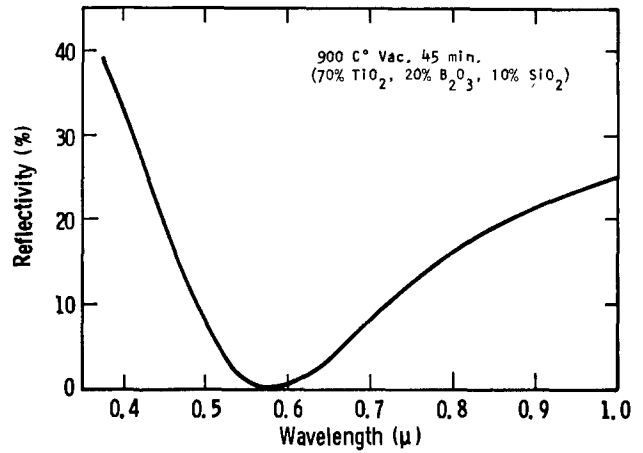


Fig. 6. Spectral reflectivity curve of an AR coating which also produced a suitable p-n junction on a silicon solar cell.

4. A. G. Revesz, in "Conference Record of the Tenth IEEE Photovoltaic Specialists Conference, Vitreous Oxide Antireflection Films in High-Efficiency Solar Cells," Palo Alto, Calif. (1974).
5. W. Y. Wang, in "Conference Record of the Tenth IEEE Photovoltaic Specialists Conference, Optimum Design of Antireflection Coating for Silicon Solar Cells," Palo Alto, Calif. (1974).
6. R. B. Campbell, in "First Annual Report on Phase 2 of the Array Automated Assembly Task for the Low Cost Solar Array Project," JPL Contract 954873 (1978).
7. B. E. Yoldas, *J. Mater. Sci.*, **12**, 1203 (1977).
8. B. E. Yoldas, *ibid.*, **14**, 1843 (1979).

Experimental Observations on Conduction Through Polysilicon Oxide

H. R. Huff,^{*1} R. D. Halvorson, T. L. Chiu,² and D. Guterma³

Texas Instruments Incorporated, Houston, Texas 77001

ABSTRACT

The current-time characteristics of a polysilicon-polysilicon oxide-polysilicon structure were determined as a function of several MOS IC process parameters. We found a strong dependence of the current with the polysilicon oxidation temperature (900°-1100°C) in the case of an oxygen ambient. The data were empirically analyzed by an equation of the form $J = At^{-n}$ where "A" and "n" are constants; the current and "n" factor dependencies with measurement temperature (23°-135°C) and MOS bias (reference) electric field ($1-3 \times 10^8$ V/cm) will be discussed. Interpretation of the data within the framework of surface asperities at the polysilicon-polysilicon oxide interface and a Fowler-Nordheim injection model will be discussed.

The understanding and control of defects in both semiconductor and dielectric materials are becoming more important for improved semiconductor device performance. Such device systems often involve wide bandgap amorphous and/or polycrystalline materials in conjunction with hot electron injection. In the double level poly floating gate Electrically Alterable Read Only Memory (abbreviated as EAROM henceforth), for example, programming is accomplished by the transport of hot electrons from the high electric field surface channel region adjacent to the drain through the gate oxide to the first level polysilicon floating gate. This procedure is identical to the programming of the Electrically Programmable Read Only Memory (EPROM) in that a high positive voltage is applied to both the drain and the second polysilicon control gate. Erase, however, is achieved by electron transport from the first level polysilicon floating gate through the thermally grown inter-level oxide on the floating gate to the second level polysilicon control gate. This is made possible by applying a higher positive voltage on the control gate while maintaining the source and drain at ground potential.

A desirable characteristic of the polysilicon oxide grown on the floating gate is a large gradient of current with respect to electric field. In this manner, the current through the polysilicon oxide is negligible at the relatively low electric field present during programming and reading (to minimize polysilicon oxide wear-out as well as read-disturb) and yet is high enough at the relatively high electric field present in the polysilicon oxide during the erase cycle. In all cases, it is desired that the current exhibit a minimum decay with time under constant voltage applied across the polysilicon oxide.

We shall present below several results of our investigation of the oxide thermally grown on the polysilicon floating gate. The impact of the oxidation temperature on the current conduction through the polysilicon oxide will be emphasized. Interpretation of the data within the framework of surface asperities at the polysilicon-polysilicon oxide interface (1-3) and a Fowler-Nordheim injection model will be discussed.

Experimental Procedures

Slice preparation.—Three in. diam, (100) oriented, 11-15 Ω -cm boron and 6-9 Ω -cm phosphorus-doped dislocation-free Czochralski crystals grown in resistance-heated pullers were used throughout the investi-

gation. The final polished slice was 18 ± 1 mil thick; saw damage was removed by chemically etching one and a half mils off the slice prior to a single-sided free-floating polish by silica slurry in an alkaline medium.

Device fabrication.—Slice clean-up was performed via a sequence of dipping in organic and inorganic solutions prior to gate oxidation at 1100°C in an OHCl ambient utilizing 8 volume percent (v/o) HCl in these experimental tests.⁴ Oxidation was followed by an *in situ* 10 min nitrogen anneal at temperature, prior to a 15 min cool down in nitrogen. Push/pull rates for these tests were between 7-10 in./min; the slices were loaded perpendicular to the gas stream (120 mil spacing). After photolithographic patterning and selective etching of the gate oxide, a 5000Å LPCVD polysilicon film was deposited at 622°C by the thermal decomposition of SiH₄. The polysilicon contacted the silicon substrate in selected areas thus permitting study of the transport process between poly I and poly II through the polysilicon oxide (see Fig. 1). The polysilicon was ion-implanted with either singly charged boron (35 keV) or phosphorus (50 keV) ions at a dose of $1 \times 10^{14}/\text{cm}^2$ in the case of a p- or n-type substrate, respectively.

Polysilicon oxidation was performed at either 900°, 1000°, or 1100°C with an oxygen ambient containing less than 1 ppm water (in the same furnace); similar preoxidation clean-up and furnace procedures were performed as for the gate oxidation case. A second polysilicon film was deposited as above, prior to doping with phosphorus at 1000°C via POCl₃ in a standard silicon IC procedure and subsequent electron beam aluminum evaporation. Several variously shaped and sized capacitor structures were fabricated by standard photolithographic techniques; the structure mainly utilized in this study was 1500 mils². The slices were then annealed in hydrogen at 450°C for 30 min prior to removal of the back-surface polysilicon and oxide layers.

⁴ Before insertion of the slices into the furnace, the boat sat at the furnace end for approximately 1 min, enabling both warm-up of the slices and volatilization of residual water, etc. The gate oxide was 950 ± 50 Å.

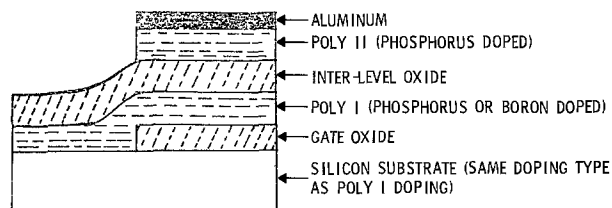


Fig. 1. Schematic of test structure

* Electrochemical Society Active Member.

¹ Present address: Signetics Corporation, Sunnyvale, California 94086.

² Present address: Universal Semiconductor, San Jose, California 95113.

³ Present address: Bostek Corporation, Carrollton, Texas 75006.

Key words: polysilicon, oxidation, conduction.

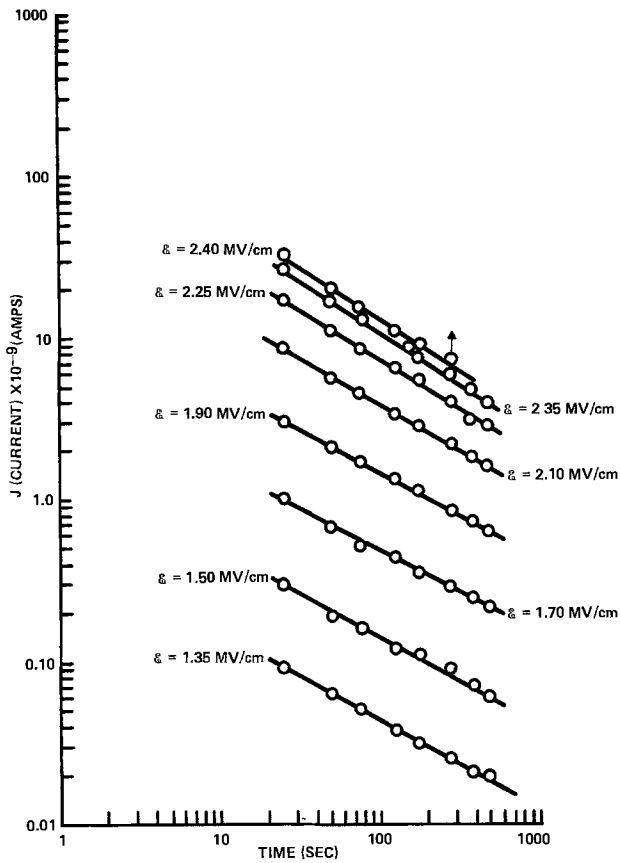


Fig. 2. Log current-log time graph for 1000°C polysilicon oxidation temperature. Poly I doping-phosphorus, $1 \times 10^{14}/\text{cm}^2$, 50 keV. Lot A, slice No. 7.

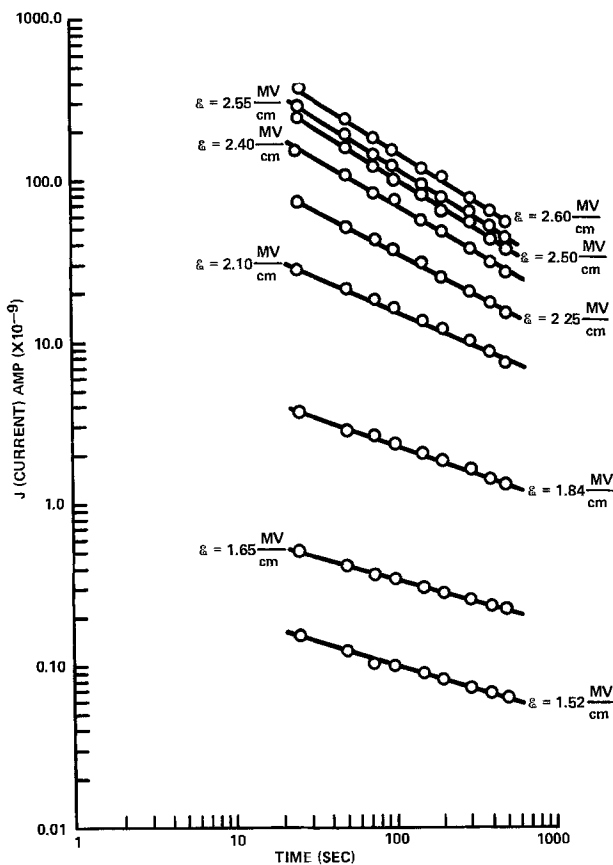


Fig. 3. Log current-log time graph for 1000°C polysilicon oxidation temperature. Poly I doping-boron, $1 \times 10^{14}/\text{cm}^2$, 35 keV. Lot B, slice No. 9.

Device measurement/analysis procedure.—A negative voltage was applied to the back-surface of the slice (aluminum contact on the front-surface was ground) to reduce spurious noise pickup. The voltage range was chosen to obtain a reference electric field of $1-3 \times 10^6$ V/cm across the polysilicon oxide. The current through the oxide was monitored as a function of time using a Keithley instrument logarithmic picoammeter and a chart recorder. A large displacement current flowed at $t = 0^+$, the transient typically expiring within 10 sec. Log current (J)-log time (t) curves were graphed from which the linearly extrapolated current at 1 sec, J_1 , and the slope n , degradation constant, were derived.

A total of 172 measurement runs from 60 slices processed through 4 split lots constituted the basis of the room temperature experimental data. In addition, a number of experiments were performed at various measurement temperatures to obtain some estimates of the energy levels of the traps. A number of other experiments addressing the polysilicon surface condition and multiple ion implantations of the first polysilicon film were performed but shall not be discussed in this communication.

Experimental Results and Analysis

Figure 2 illustrates the log J -log t plot for a 1000°C polysilicon oxidation temperature in the case of a phosphorus implantation of poly I. It is observed that the current decreases and does not saturate with time and may be fitted by an equation of the form $J = At^{-n}$, where "A" and "n" are constants. Both the current level and the degradation exponent "n" increase as the reference electric field increases. The current level was asymmetric under polarity inversion of the aluminum contact. That is, the current is lower by a

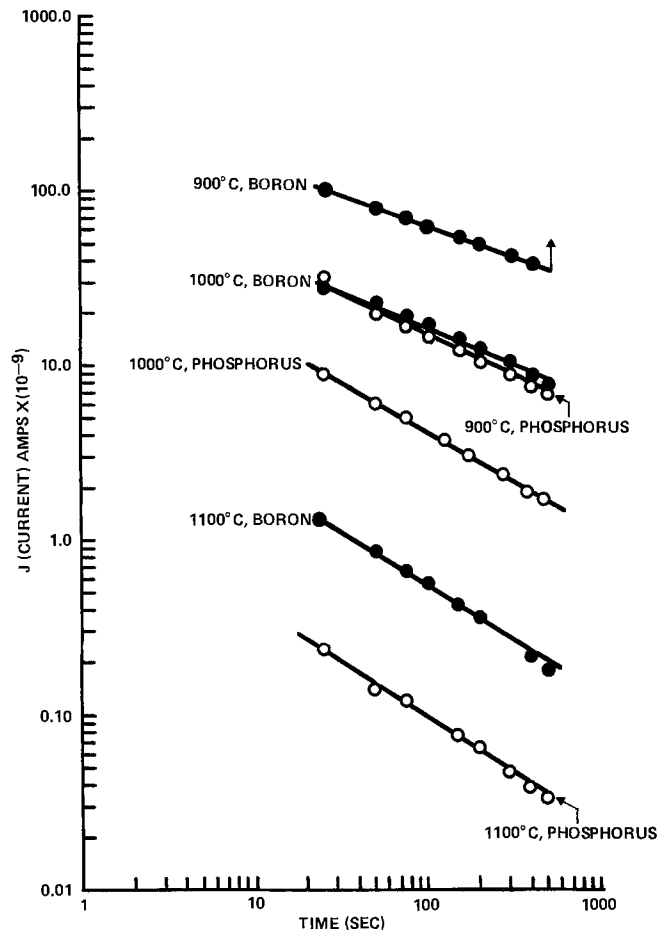


Fig. 4. Log current-log time representative summary graph for 900°, 1000°, 1100°C polysilicon oxidation temperatures. Poly I doping-boron (●)—lot B. Poly I doping-phosphorus (○)—lot A. Reference electric field equals 2.1 MV/cm.

factor of approximately 10^{+3} when the aluminum contact was made negative. Similar data are presented in Fig. 3 for boron doping of poly I, except that the current level, for a given reference electric field, was higher.

Figure 4 summarizes the influence of the polysilicon oxidation temperature for samples from the same split lots noted in Fig. 2 and Fig. 3. The current J_1 through the polysilicon oxide increases and the degradation exponent n decreases with decreasing inter-level oxidation temperature for a given polysilicon I doping (in the case of a reference electric field of 2.1×10^6 V/cm). Figures 5 and 6 summarize the influence of the polysilicon oxidation temperature on the current J_1 and degradation exponent "n", respectively.

The degradation exponent is a relatively weak function of reference electric field at room temperature for phosphorus-doped poly I and a 1000°C polysilicon oxidation temperature. In the case of boron doped poly I, however, the degradation exponent significantly decreases as the reference electric field decreases (see Fig. 7). Similar phenomena as above for both phosphorus and boron-doped poly I were also observed for 900° and 1100°C polysilicon oxidation temperatures.

A series of experiments were performed to monitor the current with time as a function of measuring temperature (23°-135°C) and reference electric field ($1-3 \times 10^6$ V/cm) in order to clarify the conduction mechanism responsible for the emission/transport of current through the polysilicon oxide. Figure 8 illustrates the Fowler-Nordheim characteristic⁵ for phosphorus-doped poly I and polysilicon oxidation temperatures of 1000° and 1100°C (4). One notes the

⁵ An electron effective mass of $0.4 m_0$ was used for these calculations.

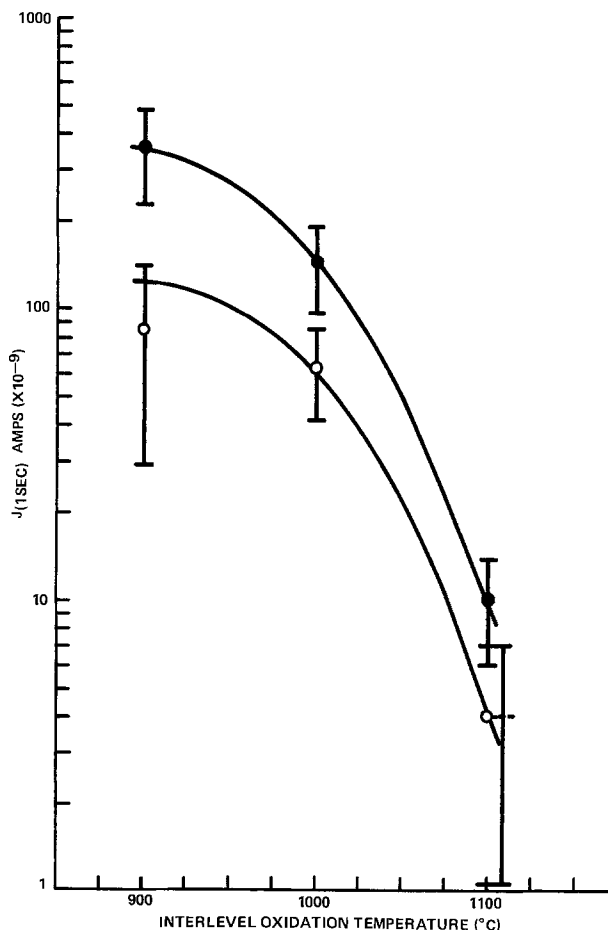


Fig. 5. Correlation of log current (1 sec) with polysilicon oxidation temperature. Poly I doping-boron (●)—lot B. Poly I doping-phosphorus (○)—lot A. Reference electric field equals 2.1 MV/cm.

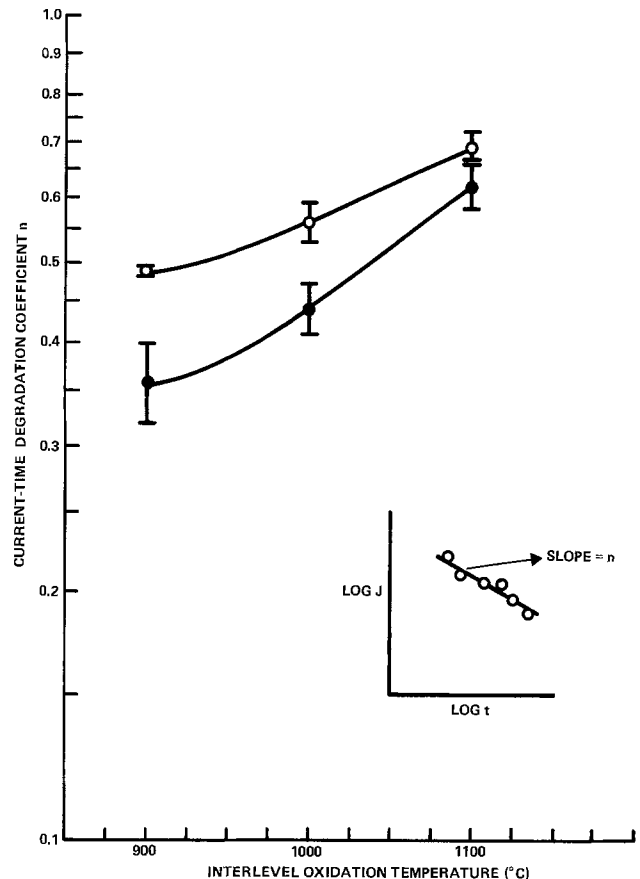


Fig. 6. Correlation of degradation exponent "n" with polysilicon oxidation temperature. Poly I doping-boron (●)—lot B. Poly I doping-phosphorus (○)—lot A. Reference electric field equals 2.1 MV/cm.

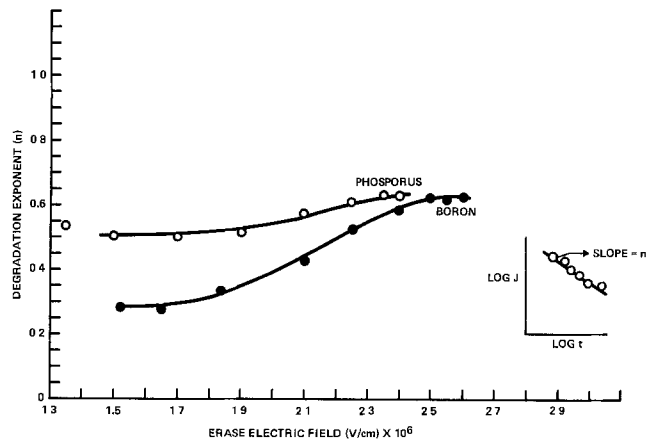


Fig. 7. Correlation of degradation exponent "n" with reference electric field for polysilicon oxidation temperature of 1000°C. Poly I doping-boron (●)—lot B, slice No. 9. Poly I doping-phosphorus (○)—lot A, slice No. 7.

tight packing of characteristics—slight increase of current as measuring temperature increases from 23° to 135°C—for the 1000°C case and the significant reduction in current level (for a given electric field) in the case of the 1100°C polysilicon oxidation. Nevertheless, the barrier height deduced from the Fowler-Nordheim curves was essentially constant at 0.48-0.52 eV, in good agreement with the 900°C oxidation data for the same lot and with that of another independent run (see Table I).⁶

⁶ The barrier heights quoted are to be regarded as merely parameters (see Discussion).

Table I. Summary of Fowler-Nordheim and Frenkel-Poole analysis for phosphorus-doped poly I

Fowler-Nordheim analysis							
Lot No.	Slice No.	Inter-level oxidation temperature (°C)	Measurement temperature (°C)	Barrier height (eV)			
A	1	900	23	0.46			
	7	1000	23	0.50			
	7	1000	41	0.52			
	7	1000	72	0.49			
	7	1000	101	0.49			
	7	1000	135	0.50			
	15	1100	39	0.48			
C	7	1000	23	0.39			
	12*	1000	23	0.46			
	17*	1000	23	0.45			
	23*	1000	23	0.43			
Frenkel-Poole analysis							
Lot No.	Slice No.	Inter-level oxidation temp. (°C)	Measurement temperature (°C)	Dielectric constant		Electric field (MV/cm)	Barrier height (eV)
				Experimental	Optical value		
A	1	900	23	4.0	2.2	—	—
	7	1000	23	4.3	2.2	1.6	0.80
	7	1000	41	4.3	2.2	1.9	0.88
	7	1000	72	4.2	2.2	2.1	0.85
	7	1000	101	4.4	2.2	2.35	0.89
	7	1000	135	3.5	2.2	—	—

* Poly I doped with phosphorus, followed by additional (undoped) polysilicon layer: Slice 12 (1000Å); Slice 17 (1500Å); Slice 23 (2000Å)—Total poly thickness = 4500Å.

A Frenkel-Poole analysis of the same data was also performed, although this interpretation does not appear as clear as that of the Fowler-Nordheim analysis. Figure 9 illustrates the $\log J/\mathcal{E}$ vs. T^{-1} characteristic, for which a barrier height of 0.80-0.89 eV is derived for reference electric fields in the range of $1.6-2.35 \times 10^6$ V/cm (see Table I). In a similar fashion, a $\log J/\mathcal{E}$ vs. $\mathcal{E}^{1/2}$ characteristic (Fig. 10) yields a dielectric constant of approximately 4, in poor agreement with the optical value of 2.2 (see Table I).

Similar analyses were performed for the boron-doped poly I samples. The Fowler/Nordheim characteristics increase slightly with measuring temperature for the 900°C polysilicon oxidation; the current significantly decreases (for a given electric field) in the case of the 1100°C oxidation. The barrier height was essentially constant at 0.57-0.69 eV (see Fig. 11 and Table II). The 1000°C data from another lot yielded

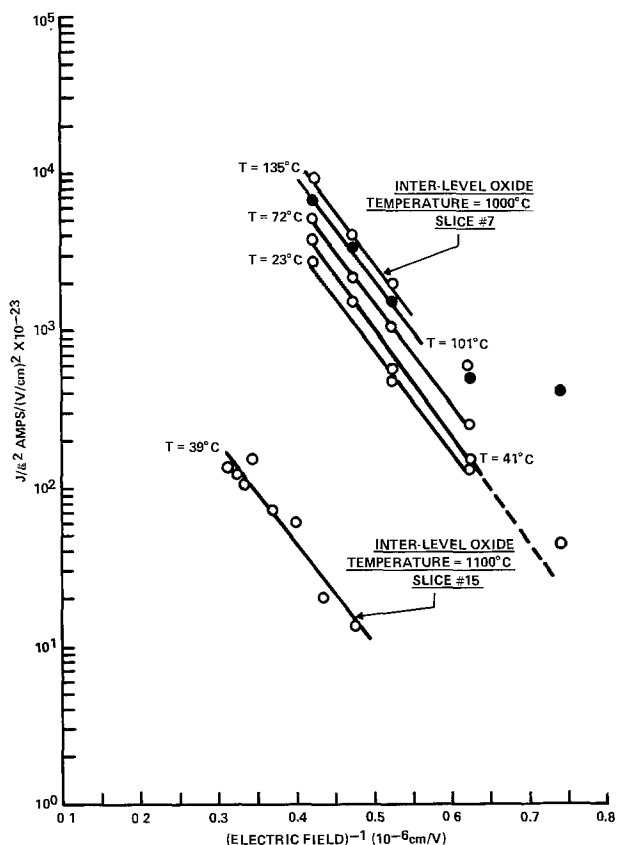


Fig. 8. Fowler-Nordheim characteristic for phosphorus-doped poly I. Lot A.

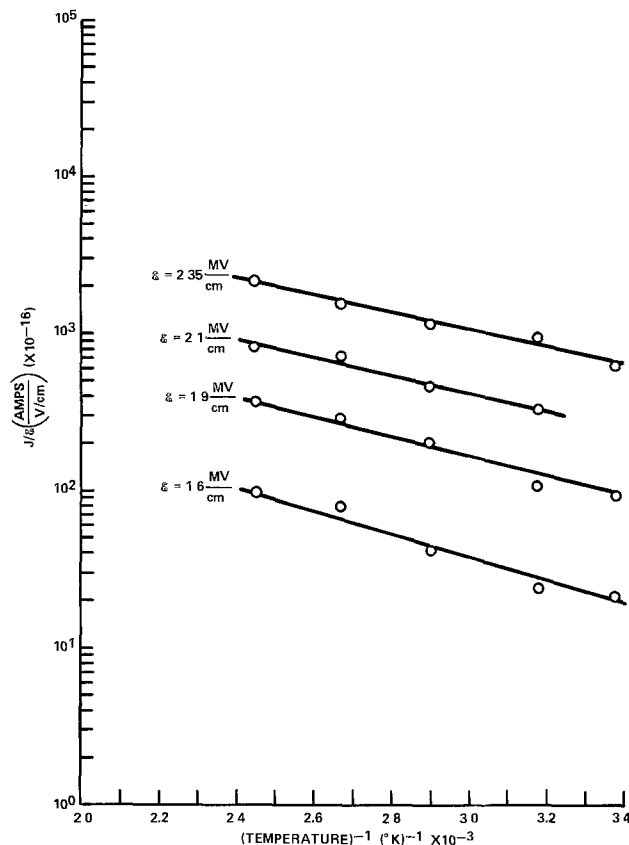


Fig. 9. Frenkel-Poole characteristic for phosphorus-doped poly I, polysilicon oxidation temperature of 1000°C. ($\log J/\mathcal{E}$ vs. T^{-1}). Lot A, slice No. 7.

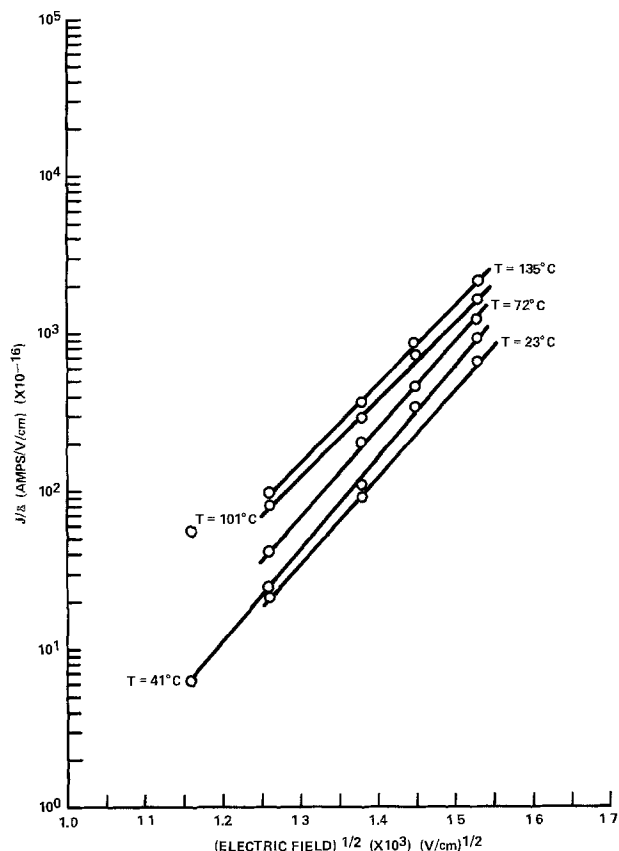


Fig. 10. Frenkel-Poole characteristic for phosphorus-doped poly I, polysilicon oxidation temperature of 1000°C. (log J/G vs. $G^{1/2}$). Lot A, slice No. 7.

similar barrier height (see Table II). A Frenkel-Poole analysis yielded a dielectric constant of 1.2-4.5, in poor agreement with the optical value of 2.2 (see Fig. 12 and Table III). The barrier height derived by a log J/G vs. T^{-1} analysis exhibited a rather complicated temperature dependence and will require further experimental analysis (see Table III).

Discussion

The experimental observation of the decrease of current through the polysilicon oxide with respect to time, under the condition of a fixed voltage across the polysilicon oxide, implies a trap-related loss mechanism. Unfortunately, our understanding of traps in electrically stressed silicon dioxide films remains far from clear (5-10). Differentiation between models emphasizing the continuous generation of electron traps during large current flow in silicon dioxide subjected to high electric fields or the filling of previously existing traps, however, is not straightforward. Further complications as to the trap characteristics—shallow, large cross section and/or deep, small cross section—surely complicate the situation. Our discussion below is essentially an empirical interpretation of the experimental data within the framework of surface asperities at the polysilicon-polysilicon oxide interface and a Fowler-Nordheim injection mechanism.

The current transported through the polysilicon oxide increased strongly with decreased oxidation temperature in oxygen ambient (<1 ppm H_2O), consistent with recent observations (2, 11, 12). Scanning electron micrograph (SEM) analysis revealed pronounced surface asperities, similar to those data previously published in the literature (1-3), on the poly I surface after oxygen oxidation at 900°C while a rather smooth poly I surface was observed after an 1100°C oxygen oxidation.⁷ It may be that at higher oxidation temperatures, the transport of the oxidizing

⁷ These oxidations were performed in the same furnace tube.

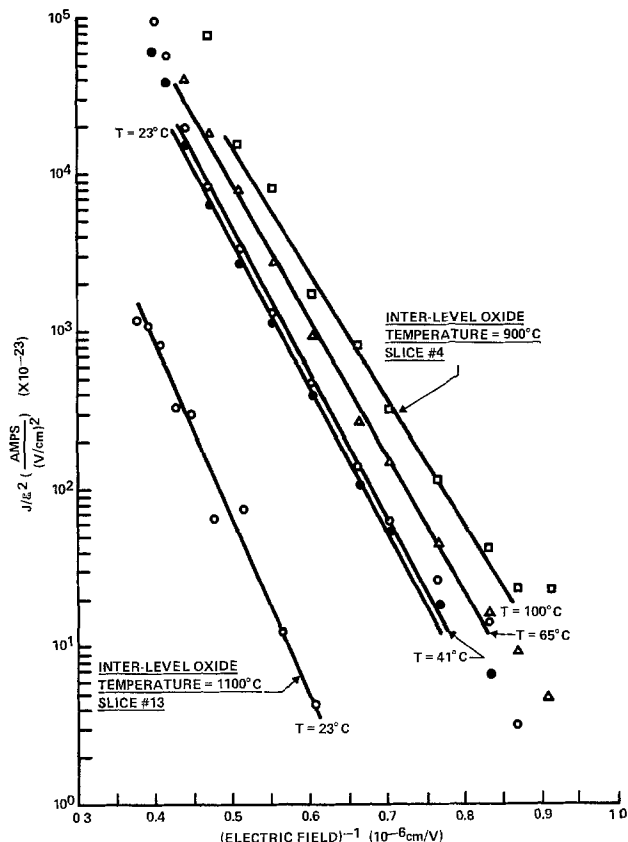


Fig. 11. Fowler-Nordheim characteristic for boron-doped poly I lot B.

species through the oxide may be the limiting factor and the poly I surface irregularities may be effectively obliterated. On the other hand, the lower temperature (900°C for example) may accentuate the surface dominated reaction, i.e., the (110) dendrites in the poly I surface (13) exhibit higher oxide growth rate, resulting in fingers of poly grains of other orientations protruding into the oxide. The enhanced electric field around the tips of these fingers shrinks the potential barrier width and thereby increases the carrier injection locally at the interface.

For all polysilicon oxidation temperatures, the current was observed to decrease with time for a constant voltage applied across the oxide similar to previously published data (11, 12, 14). A reference electric field was defined, for convenience, as the applied voltage divided by the polysilicon oxide thickness.⁸ The degradation exponent "n", i.e., the slope of the current-time curve on a log-log graph, was observed to increase considerably with the reference electric field for the boron-doped poly I, while it

⁸ The polysilicon oxide thickness was estimated by measuring the oxide thickness of several single-crystal silicon slices which were phosphorus-implanted and oxidized concurrent with the test slices.

Table II. Summary of Fowler-Nordheim analysis for boron-doped poly I

Lot No.	Slice No.	Inter-level oxidation temperature (°C)	Measurement temperature (°C)	Barrier height (eV)
B	4	900	23	0.61
	4	900	41	0.63
	4	900	65	0.60
	4	900	100	0.57
	13	1100	23	0.69
D	7	1000	23	0.64
	7	1000	40	0.73
	7	1000	70	0.66
	7	1000	100	0.69
			135	0.59

Table III. Summary of Frenkel-Poole analysis for boron-doped poly I

Lot No.	Slice No.	Inter-level oxidation temperature (°C)	Measurement temperature (°C)	Dielectric constant		Electric field (MV/cm)	Barrier height (eV)		
				Experimental	Optical value		Low temp	High temp	
B	4	900	23	2.4	2.2				
	4	900	41	1.9	2.2				
	4	900	65	1.7	2.2				
	4	900	100	1.2	2.2				
	9	1000	23	1.6	2.2	1.5	0.90	1.12	
	9	1000	41	1.6	2.2	1.7	0.94	1.00	
	9	1000	72	1.5	2.2	1.9	1.07	0.82	
	9	1000	101	2.0	2.2	2.1	1.00	0.82	
	9	1000	135	2.2	2.2	2.3	0.85	0.85	
	13	1100	23	4.5	2.2				
	D	7	1000	23	3.4	2.2			
		7	1000	41	2.1	2.2			
		7	1000	65	2.0	2.2			
7		1000	100	1.4	2.2				

increased only slightly for the phosphorus-doped poly I. It was observed that the current always returns to the previous end point if one resumes the current-time measurement after an interruption of the measurement. It was also observed on separately processed device structures on circuit slices that although a transient recovery in the current level was achieved by a u.v. erase, the current rapidly decayed to the previous pre-u.v. level. This phenomenon suggests that some detrapping of electrons without annihilation of the traps occurs during the u.v. erase (14). On the other hand, a 450°C H₂ anneal was observed to recover the current to its virgin characteristic. One interpretation of this may be that the 450°C H₂ anneal annihilates those traps previously present.

It was observed that upon voltage polarity reversal, the current decreases significantly, suggesting that the dominant mechanism governing current flow is electrode-limited injection from the interfaces, rather than bulk-limited transport (1, 2, 11). The emission of

current from single crystal silicon into thermally-grown silicon dioxide has previously been shown to occur by a Fowler-Nordheim process (15). The present polysilicon-polysilicon oxide data appear to be consistent with such a model, although we have not quantitatively corrected for the electric field enhancement at the polysilicon-polysilicon oxide interface due to the effects of the asperities and the space-charge at the interface. Therefore, the barrier heights deduced by the present Fowler-Nordheim analysis are to be regarded as merely parameters. Although these barrier heights do not represent "true" interface energy levels—such as observed by optical probing or deduced by utilization of the effective interface electric field—they may nevertheless be useful for comparison to similar data in the literature.

Shatzkes (16) has recently noted that the distribution of trapped electrons in the insulator can play an important role in the interpretation of the experimental data. Not only does trapped charge partially terminate the applied reference electric field, thereby reducing the effective electric field magnitude at the polysilicon-polysilicon oxide interface, but the barrier shape itself becomes distorted. Therefore, corrections to the barrier width for tunneling should be included to account for the field dependence and current decay observed. The negative charge trapped within the barrier provides an alternate explanation for the interpretation of reduced barriers derived from a Fowler-Nordheim analysis (16).

Probably a combination of both enhanced electric field at asperities and electron trapping within the barrier region apply in our case. Unfortunately, we are still unable to provide clear differentiation between electron traps previously present and "activated" by the electron transport through the oxide—such as perhaps the case for steam grown oxides (17, 18)—and continuously generated traps during at least a portion of the current transport. Clearly, further experimentation will be required for elucidation of the interfacial trap characteristics of the polysilicon-polysilicon oxide system.

Manuscript submitted June 5, 1979; revised manuscript received May 27, 1980. This was RNP 392 presented at the Pittsburgh, Pennsylvania, Meeting of the Society, Oct. 15-20, 1978.

Any discussion of this paper will appear in a Discussion Section to be published in the June 1981 JOURNAL. All discussions for the June 1981 Discussion Section should be submitted by Feb. 1, 1981.

Publication costs of this article were assisted by Texas Instruments Incorporated.

REFERENCES

1. D. J. DiMaria and D. R. Kerr, *Appl. Phys. Lett.*, 27, 505 (1975).
2. D. R. Kerr, Abstract 326, p. 839, The Electrochemical Society Extended Abstracts, Las Vegas,

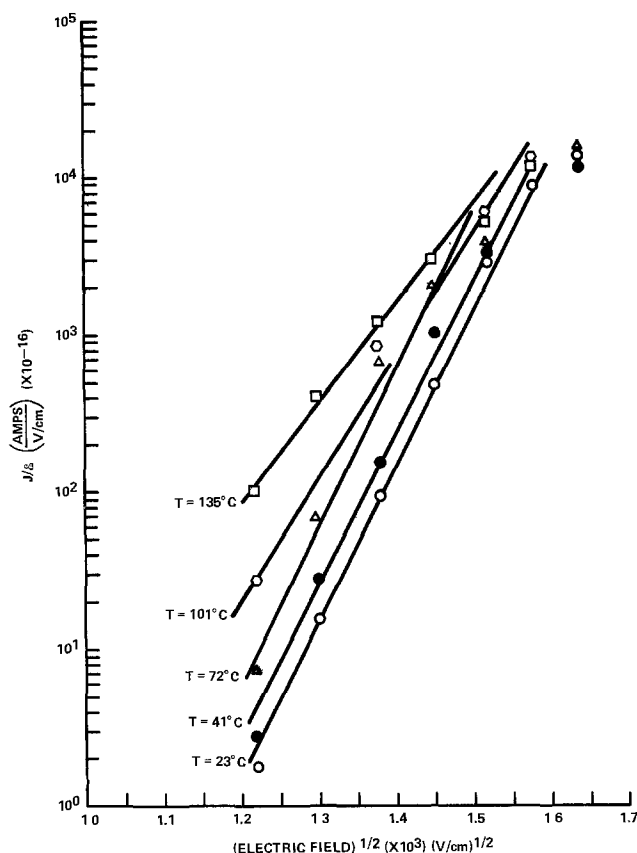


Fig. 12. Frenkel-Poole characteristic for boron-doped poly I. Polysilicon oxidation temperature of 1000°C. (Log J/E vs. $E^{1/2}$). Lot B, slice No. 9.

- Nevada, Oct. 17-22, 1976.
3. R. M. Anderson and D. R. Kerr, *J. Appl. Phys.*, **48**, 4834 (1977).
 4. S. M. Sze, "Physics of Semiconductor Devices," p. 496, Wiley-Interscience, New York (1969).
 5. C. M. Osburn and E. J. Weitzman, *This Journal*, **119**, 603 (1972).
 6. P. Solomon, *J. Appl. Phys.*, **48**, 3843 (1977).
 7. E. Harari, *Appl. Phys. Lett.*, **30**, 601 (1977).
 8. E. Harari, *J. Appl. Phys.*, **49**, 2478 (1978).
 9. H. Iizuka *et al.*, *IEEE Trans. Electron Devices*, **ed-23**, 379 (1976).
 10. D. J. DiMaria, in "The Physics of SiO₂ and Its Interfaces," S. T. Pantelides, Editor, pp. 160-178, Pergamon Press Inc., Elmsford, New York (1978).
 11. S. A. Abbas, C. A. Barile, and R. C. Dockerty, Abstract 327, p. 842, The Electrochemical Society Extended Abstracts, Las Vegas, Nevada, Oct. 17-22, 1976.
 12. P. L. Garbarino, *This Journal*, **125**, 470C (1978).
 13. T. I. Kamins and E. L. MacKenna, *Metall. Trans.*, **2**, 2292 (1971).
 14. S. A. Abbas and C. A. Barile, in "13th Annual Proceedings, Reliability Physics Symposium, 1975," pp. 1-5.
 15. M. Lenzlinger and E. H. Snow, *J. Appl. Phys.*, **40**, 278 (1969).
 16. M. Shatzkes, *J. Appl. Phys.*, **49**, 4868 (1978).
 17. E. H. Nicollian, A. Goetzberger, and C. N. Berglund, *Appl. Phys. Lett.*, **15**, 174 (1969).
 18. E. H. Nicollian, C. N. Berglund, P. F. Schmidt, and J. M. Andrews, *J. Appl. Phys.*, **42**, 5654 (1971).

Oxide-Substrate and Oxide-Oxide Chemical Reactions in Thermally Annealed Anodic Films on GaSb, GaAs, and GaP

G. P. Schwartz,* G. J. Gualtieri, J. E. Griffiths, C. D. Thurmond, and B. Schwartz*

Bell Laboratories, Murray Hill, New Jersey 07974

ABSTRACT

A fundamental pattern of oxide-substrate reactions has been identified in thermally annealed anodic films on GaSb and GaAs through the use of Raman scattering and ternary phase diagrams. The relevant reactions on GaAs and GaSb yield interfacial deposits of As and Sb via $\text{As}_2\text{O}_3 + 2\text{GaAs} \rightarrow \text{Ga}_2\text{O}_3 + 4\text{As}$ and $\text{Sb}_2\text{O}_3 + 2\text{GaSb} \rightarrow \text{Ga}_2\text{O}_3 + 4\text{Sb}$. The failure to observe elemental P generation in annealed anodic films on GaP in conjunction with an estimate of the Ga-P-O phase diagram suggests that oxide-oxide reactions occur in the film instead. Formation of either ortho or metaphosphate will depend on the $\text{Ga}_2\text{O}_3/\text{P}_2\text{O}_5$ ratio in the film according to $\text{P}_2\text{O}_5 + \text{Ga}_2\text{O}_3 \rightarrow 2\text{GaPO}_4$ and $3\text{P}_2\text{O}_5 + \text{Ga}_2\text{O}_3 \rightarrow 2\text{Ga}(\text{PO}_3)_3$.

The current and future utilization of III-V compounds in the semiconductor industry reemphasizes the need for a more definitive understanding of the chemical and physical phenomena that occur at oxide-semiconductor interfaces. The factors affecting the initiation and propagation of chemical reactions at such interfaces, the nature and spatial distribution of the products formed, and their effect on the electronic properties of such structures are inadequately characterized. Moreover, little is known about the effects of such processes on the long term stability of these interfaces. Of special interest is the presence or absence of elemental constituents of the semiconductor in the oxide-semiconductor interfacial region, largely because it has often been assumed that their presence may have a deleterious effect on the electronic properties of III-V solid-state devices.

In the present work, anodic oxide films that were electrochemically grown in aqueous solutions at room temperature on GaAs, GaSb, and GaP were examined by reflection Raman scattering for evidence of elemental deposits of As, Sb, or P in the as-anodized state and for evidence of interfacial oxide/substrate reactions induced by thermal annealing. Estimates of the ternary phase diagrams for the Ga-As-O, Ga-Sb-O, and Ga-P-O systems were derived from binary phase stability experiments, thermodynamic calculations, and Raman scattering. The resulting phase diagrams indicate that the interfacial chemical constituents which can exist in thermodynamic equilib-

rium with GaSb and GaAs are $\text{Ga}_2\text{O}_3/\text{Sb}$ and $\text{Ga}_2\text{O}_3/\text{As}$, respectively. Neither Sb_2O_3 nor As_2O_3 or their higher oxides are thermodynamically stable in the interfacial region. Oxidation processes which produce sharply delineated oxide-substrate interfaces containing these latter products are indicative of oxide growth under conditions far from thermodynamic equilibrium. Thermal annealing provides the necessary energy to overcome the reaction barriers associated with the reactions $2\text{GaSb} + \text{Sb}_2\text{O}_3 \rightarrow \text{Ga}_2\text{O}_3 + 4\text{Sb}$ and $2\text{GaAs} + \text{As}_2\text{O}_3 \rightarrow \text{Ga}_2\text{O}_3 + 4\text{As}$, thus depleting the group Vb oxides in the interfacial region with subsequent generation of elemental deposits of antimony or arsenic.

Similar work involving Raman scattering from anodic oxides on GaP coupled with thermodynamic estimates of the Ga-P-O system revealed a quite different pattern. No evidence was found for the generation of elemental phosphorus in the anodic films in either the as-grown or annealed conditions. The oxide-oxide reaction $\text{Ga}_2\text{O}_3 + \text{P}_2\text{O}_5 \rightarrow 2\text{GaPO}_4$ was verified in bulk mixtures. Some doubt as to the proper Ga-P-O phase diagram still remains.

Experimental

Sample preparation.—N-type substrates of GaP ($4-8 \times 10^{17} \text{ cm}^{-3}$, (111) oriented), GaAs ($2-5 \times 10^{18} \text{ cm}^{-3}$, (100) oriented), and GaSb ($1-3 \times 10^{17} \text{ cm}^{-3}$, (111) oriented) were prepared first by an alumina lapping ($0.2 \mu\text{m}$) and then by bromine-methanol polishing to a mirror finish. The electrochemical anodizations were carried out at room temperature

* Electrochemical Society Active Member.

Key words: Raman scattering, ternary phase diagrams.

under white light illumination in an AGW (1) electrolyte. This electrolyte consists of 3% H_3PO_4 , adjusted to a pH of 6.2 with NH_4OH , which is then diluted in a 1:2 volume ratio with ethylene glycol. Post-anodization treatment involved rinsing the wafers in methanol followed by drying under a stream of nitrogen gas. The wafers were anodized at constant current (1 mA/cm²) up to 50V. Film growth factors of approximately 10, 20, and 30 Å/V result under these conditions on GaP, GaAs, and GaSb, respectively. Thermal annealing of anodized wafers at 250° and 300°C took place in a nitrogen-purged oven. For temperatures exceeding 300°C, the samples were routinely sealed into evacuated (5×10^{-7} Torr) quartz tubes before treating at the appropriate temperature. Encapsulation served merely to avoid the dissemination of potentially toxic materials; the Raman scattering results are not affected by the choice of annealing under an inert atmosphere or under vacuum.

Samples of Ga_2O_3 , $GaOOH$, Sb_2O_3 , As_2O_3 , and P_2O_5 were purchased in the form of finely divided powders. The latter three products were individually encapsulated in quartz, taken to their boiling points, and then cooled slowly in order to obtain samples of vitreous Sb_2O_3 , As_2O_3 , and P_2O_5 . An amorphous gallia gel was prepared by the addition of dilute ammonium hydroxide to an aqueous gallium nitrate solution (2).

Raman scattering.—Surface reflection Raman spectra were obtained by coupling the incident laser light (5145Å, argon ion) into the films at Brewster's angle and detecting the light scattered normal to the sample surface. The optical constants given by Aspnes *et al.* (3) for anodized films on the respective substrates were used in the calculation of Brewster's angle. An Instrument S. A. Ramanor monochromator (Model HG-2S) equipped with holographic gratings and $f/1.8$ collection optics was used to analyze the scattered light. The analyzed light was detected with a cooled Hamamatsu R-928P photomultiplier coupled to conventional photon counting electronics.

A polarization rotator was inserted into the excitation beam path so that the electric vector of the incident light could be adjusted to be either in the scattering plane (H) or perpendicular to it (V). The polarization properties of the Raman scattered light emitted normal to the surface could be analyzed by inserting a polarization filter before the entrance slit. For most of the reported work this filter was omitted, and the scattered light is designated as unanalyzed (U). A polarization scrambler in the pre-slit optical path was present during the acquisition of all spectra to insure that the grating response did not distort the relative intensities of the polarized spectra.

Phase diagrams.—A series of binary mixture phase stability experiments were performed in order to check critical sections of the ternary phase diagrams for the Ga-Sb-O, Ga-As-O, and Ga-P-O systems. Powdered mixtures of the III-V substrates and their respective group V oxides (Sb_2O_3 , As_2O_3 , or P_2O_5) were sealed in evacuated quartz tubes and heated to elevated temperatures. The P_2O_5 was sublimed at 10^{-5} Torr prior to use to remove contaminant traces of P_2O_3 and H_2O and was subsequently handled under dry conditions.

The reaction products were analyzed by x-ray powder diffraction and Raman scattering. The latter technique is particularly useful for identifying vitreous phases (Sb_2O_3 , As_2O_3 , and P_2O_5) which would otherwise go undetected. Raman scattering can also supplement x-ray diffraction results for the positive identification of crystalline phases. In Fig. 1, for example, the reaction products for an initial mixture of 2:1 $Sb_2O_3/GaSb$ display Raman peaks associated with $\beta-Ga_2O_3$ (labeled G_n) and unreacted Sb_2O_3 (senarmonite, labeled S_n) which was originally present in excess. Crystalline Sb is not particularly obvi-

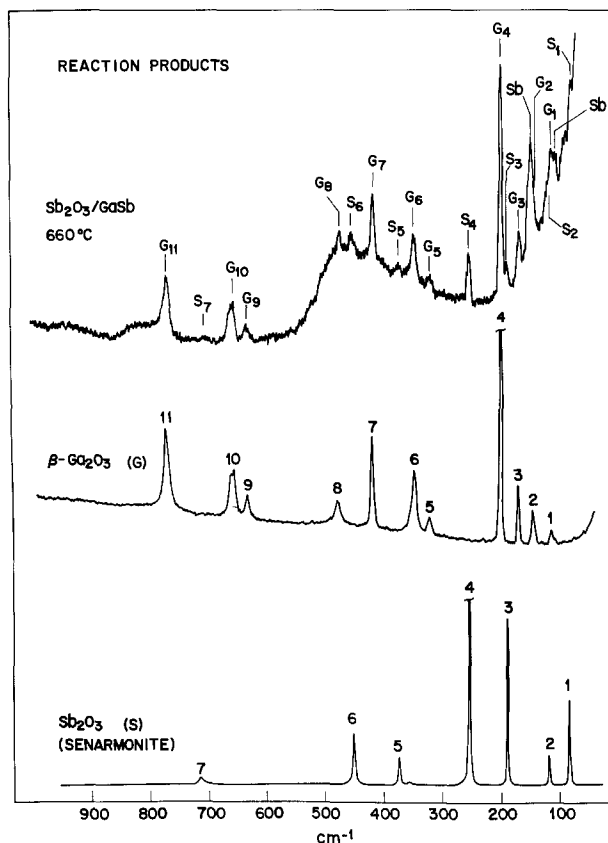


Fig. 1. Raman scattering analysis of a reaction product mixture containing crystalline Ga_2O_3 , Sb_2O_3 , and Sb along with vitreous Sb_2O_3 . The latter species contributes the broad band between 300-500 cm^{-1} .

ous due to interferences from Ga_2O_3 (G_1 , G_2), but pellets of that material could be picked out of the mixture and easily identified by x-ray techniques. The broad Raman band between 300-500 cm^{-1} indicates that the reaction conditions have left vitreous as well as crystalline Sb_2O_3 . Better spectra of the vitreous form were obtained from material adhering to the walls of the quartz tube in places where there were no other reaction products.

Detailed results for the Ga-As-O phase diagram have been reported previously (4). Tables I and II summarize the data for the pseudobinary $GaSb/Sb_2O_3$ and GaP/P_2O_5 , Ga_2O_3/P_2O_5 systems. Reaction temperatures above 680°C exceed the congruent evaporation temperature of GaP (5). Nevertheless, we did not observe thermal decomposition of the GaP which leads us to suspect that a thin oxide layer has formed in insufficient quantity to be detected but in sufficient quantity to prevent thermal decomposition of the GaP. The application of the data in Tables I and II to the

Table I. Phase stability of $GaSb-Sb_2O_3$ mixtures

Reaction conditions	$Sb_2O_3/GaSb$ mole ratio	Detected phases	Method	Comments
660°C/2 days	2:1	$\beta-Ga_2O_3$ Sb_2O_3 (senarmonite + glass) Sb	Raman Raman	No GaSb detected
660°C/2 days	1:1	$\beta-Ga_2O_3$ Sb_2O_3 (senarmonite + glass) Sb	x-ray dif- fraction Raman Raman	No GaSb detected
660°C/2 days	1:3	$\beta-Ga_2O_3$ GaSb (zinblende) Sb	x-ray dif- fraction Raman Raman	No Sb_2O_3 detected

Table II. Phase stability of GaP-P₂O₅, Ga₂O₃-P₂O₅ mixtures

A:	Reaction conditions	P ₂ O ₅ /GaP mole ratio	Detected phases	Method	Comments
	550°C/1 day	4:5	GaP P ₂ O ₅	Raman Raman	No evidence for reaction
	750°C/1 day	4:5	GaP P ₂ O ₅	Raman Raman	No evidence for reaction
	850°C/1 day	4:5	GaP P ₂ O ₅	Raman Raman	Three extra faint lines in the x-ray diffraction pattern which could not be assigned to GaP. Possible trace of GaPO ₄ , β-Ga ₂ O ₃ .
B:	Reaction conditions	P ₂ O ₅ /Ga ₂ O ₃ mole ratio	Detected phases	Method	Comments
	750°C/1 day	1:1	GaPO ₄	Raman	Reaction goes to completion

determination of the Ga-Sb-O and Ga-P-O phase diagrams are discussed in the next section.

Results

General

Since the reflection Raman spectra should, in principle, contain contributions from the bulk oxide as well as from the interfacial layer and substrate, some preliminary comments are in order concerning the detection of the relevant chemical species. Anodic oxide films on GaP, GaAs, and GaSb are currently believed to consist of mixtures of Ga₂O₃ and either P₂O₅, As₂O₃, or Sb₂O₃, respectively. These films are both amorphous and optically transparent (3) in the region between 1.5 and 4 eV. It is this optical transparency at the excitation wavelength (~2.4 eV) and the limited number of molecules in these thin (500 ≤ d ≤ 1500 Å) films that allow effective penetration of the laser beam to the oxide/semiconductor interface. It is thus possible to observe resonance enhanced Raman signals from minute amounts of arsenic and antimony that may be present in the interfacial region.

The group V oxides P₂O₅, As₂O₃, and Sb₂O₃ are well-known glass formers whose vitreous spectra are shown in Fig. 2. Amorphous Ga₂O₃ is not a well-characterized material; we have prepared a gallium oxide gel in order to obtain some idea of where the bands might be expected to occur. The Raman spectrum of this gel along with crystalline β-Ga₂O₃ and GaOOH are shown in Fig. 3. Crystalline spectra for P₂O₅, As₂O₃, and Sb₂O₃ have also been reported in the literature (6). Neither the crystalline nor vitreous Raman peaks associated with any of these oxide species is observed in surface reflection scattering from films ranging from 500 to 1500 Å thickness. The normal Raman cross sections for inelastic light scattering from these films are apparently too low to allow their detection in such thin layers. Similarly, the conversion of amorphous Ga₂O₃ (gallia gel) to either GaOOH or β-Ga₂O₃ cannot be detected following the 250°C thermal anneal which is typically employed to remove loosely bound water. Analysis of Raman scattering from 8000 Å anodic oxides on GaAs further indicates that there is insufficient cross section for oxide component identification even at this thickness. High temperature annealing (T = 600°C) of the 8000 Å structures did not result in observable Raman peaks for β-Ga₂O₃.

In contrast to the anodic film components, the group V metalloids P, As, and Sb all possess electronic absorption bands which overlap the excitation frequency (7-9). Resonance enhancement of the Raman cross sections occur under such conditions with a concomitant increase in the detection sensitivity for these chemical species. A review of resonance enhanced Raman scattering in III-V semiconductors and the group V semimetals has recently been presented by Richter (10).

The relative resonance enhanced Raman cross sections for the A_{1g} and E_g modes of As and Sb have been measured by Renucci *et al.* (9) in the range from 1.6 to 2.7 eV. Examination of the data at ~2.4 eV (5145 Å)

provides a measure of the relative detection sensitivity between Sb and As, *i.e.*, σ_{Sb}/σ_{As} = 5.6. Comparable data for elemental phosphorus do not appear to be available. Estimates of the minimum detection level for crystalline arsenic have recently been obtained from a comparison of internal standards and correlations with ellipsometric determinations of the absorptive component of these anodic films (11). The available data currently indicate a detection level of approximately 10-20 Å of crystalline arsenic in the present experimental configuration. The detection of antimony should be 5-6 times more sensitive. Although the detection sensitivity for phosphorus is probably less favorable than for As and Sb, we are currently unable to provide a reasonably firm estimate of the detection limit for this material.

Raman Scattering and Ternary Phase Diagrams

GaSb.—Raman.—For <111> oriented substrates crystallizing with a zincblende structure, both longitudinal and transverse optic modes (LO, TO) are

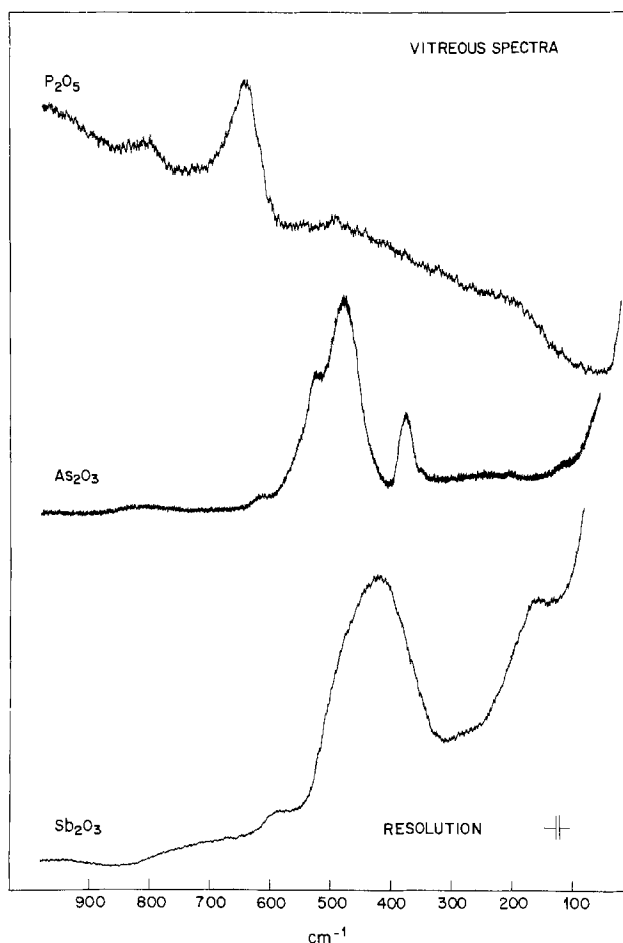


Fig. 2. Raman spectra of the vitreous glasses P₂O₅, As₂O₃, and Sb₂O₃ between 100-1000 cm⁻¹.

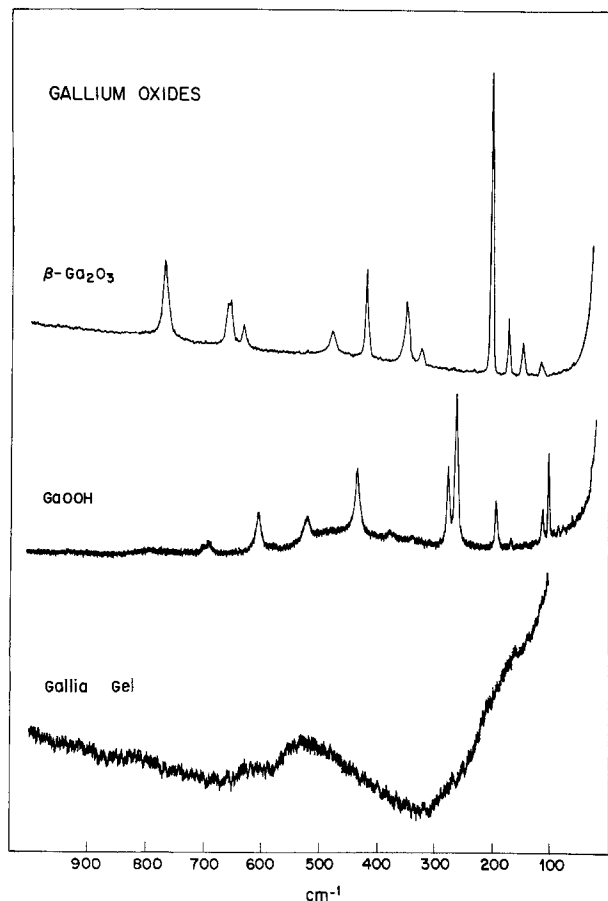


Fig. 3. Raman spectra of amorphous (gel) and crystalline forms of gallium oxide which would be anticipated in thermally annealed anodic films.

Raman allowed by the selection rules (12). Combination and overtone bands derived primarily from two-phonon processes will also be active. The two-phonon continuum shows sharp structure in its phonon frequency distribution at certain critical points in the Brillouin zone. In the case of the zincblende structure the relevant critical points allowed by the selection rules occur at the zone center Γ (0, 0, 0), the face center L (1/2, 1/2, 1/2), and X (1, 0, 0), the coordinate peak W (1, 1/2, 0), and the zone edge K (3/4, 3/4, 0).

The surface reflection Raman spectra for anodized samples (oxide thickness $\sim 1500\text{\AA}$) in the as-anodized (A) and thermal annealed (B, $450^\circ\text{C}/1\text{ hr}$) states are shown in Fig. 4. The positions of the crystalline antimony bands (13, 14) for the trigonally distorted cubic A7 structure are denoted by S_1 and S_2 . S_1 (150 cm^{-1}) corresponds to the symmetric A_{1g} mode of this structure, whereas S_2 (115 cm^{-1}) is the doubly degenerate E_g mode. Amorphous antimony (15) displays a broad, featureless band between $\sim 120\text{--}170\text{ cm}^{-1}$. The numbered peaks ($n = 1, 16$) in Fig. 4A can be rigorously assigned (16, 17) to one and two-phonon scattering from the substrate (Table III). Part of the two-phonon GaSb spectrum ($n = 1\text{--}3$) overlaps the region in which elemental Sb (crystalline or amorphous) would be found if it were present in the as-anodized film. Within the peak-to-peak noise ($\sim 30\text{ c/sec}$) in the vicinity of 150 cm^{-1} , no differences were detected between the bare substrate (not shown) and the anodized GaSb wafer (Fig. 4A). The estimated detection limit for crystalline Sb is an equivalent thickness of $\sim 5\text{\AA}$; detection of the amorphous allotrope will be somewhat less sensitive.

Annealing the anodized sample of Fig. 4A *in vacuo* (5×10^{-7} Torr) at 450°C for 1 hr leads to dramatic changes in the spectrum. The presence of crystalline antimony now dominates the spectral features. The LO

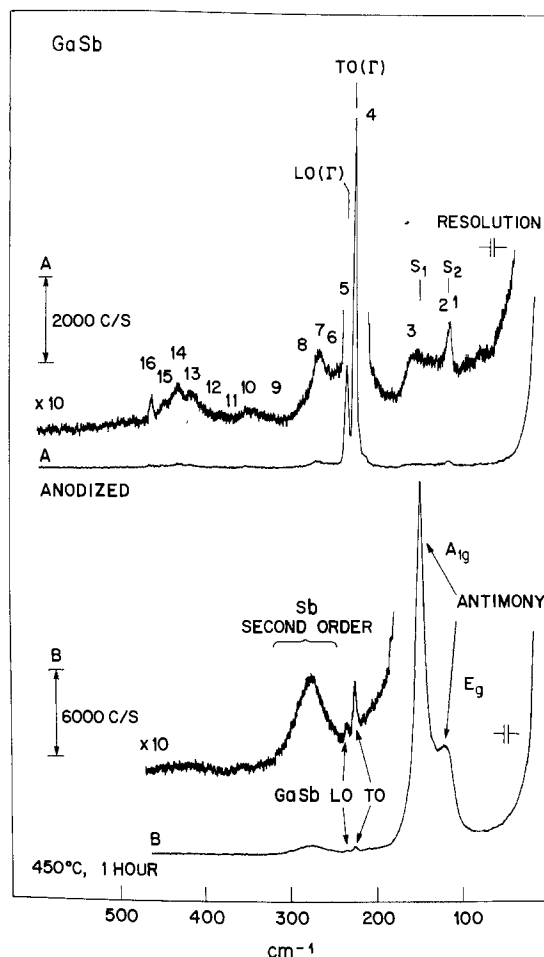


Fig. 4. Raman scattering intensity from as-anodized (A) and thermally annealed (B) films on GaSb. S_1 and S_2 denote the positions of crystalline Sb modes, the numbered features 1-16 correspond to substrate scattering. The scattered light polarization is unanalyzed.

and TO modes of the GaSb substrate are now nearly totally attenuated by optical absorption of the excitation beam by the thermally generated Sb. Farrow *et al.* (18) have previously observed similar spectra for the case of thermally oxidized samples of GaSb. Cross polarized spectra (VH) attenuated the 150 cm^{-1} band by a factor of ~ 200 , which is consistent with their assignment of this band as the A_{1g} mode of crystalline antimony.

Table III. GaSb

n	Frequency (cm^{-1})	Assignment*
1	111	2TA (X)
2	117	2TA (Z)
3	160	2TA (W)
4	227	TO (Γ)
5	237	LO (Γ)
6	256	TA + TO (L)
7	272	TA + TO, LO (X)
8	286	2LA (Q)
9	320	2LA (X)
10	356	LA + LO (X)
11	373	LA + TO (X) LA + LO (X) LA + TO (L)
12	393	2TO (Σ)
13	425	2TO (X) 2LO (X)
14	438	2TO (L)
15	455	2TO (Γ)
16	472	2LO (Γ)
S_1	150	A_{1g}
S_2	115	E_g

* References (16, 17) assigned $n = 1$ to 16. References (13, 14) assigned S_1, S_2 .

The thermally induced formation of elemental Sb in electrochemically anodized films on GaSb is consistent with the pseudobinary phase stability experiments involving $\text{Sb}_2\text{O}_3/\text{GaSb}$ mixtures insofar as Eq. [1] was observed to occur



Figure 5 provides some idea of just how readily this reaction occurs in anodic films (typically $\sim 2000\text{\AA}$) as a function of temperature. Elemental Sb is not readily detected after a 250°C bake for 2 hr (Fig. 5A). The spectral feature at $\sim 117\text{ cm}^{-1}$ is a superposition of a laser plasma line and part of the two-phonon structure of the substrate. The E_g mode of crystalline Sb appears at a slightly lower wavenumber position and is typically broader. After a thermal treatment of 300°C for 1 hr (Fig. 5B), an antimony signal can be detected in the form of an amorphous deposit. After heating at 350°C for 1 hr, well-defined crystalline A_{1g} and E_g modes of Sb become clearly visible (Fig. 5C).

In order to verify that the reaction proposed in Eq. [1] is actually occurring in these films at the oxide/GaSb interface, a series of chemical etching experiments were performed in which the oxide film was successively dissolved in a dilute methanol/ H_3PO_4 solution and the remaining film thickness was monitored by interference colors. The results are shown in Fig. 6, in which one observes no decrease in the signal associated with Sb down to a film thickness of $\sim 300\text{\AA}$, at which point interference colors are no longer visible. The strong increase in the Rayleigh wing which causes marked changes in the shifting background scattering appears to be due to surface roughening effects occurring during etching. The Sb formed during annealing at 350°C for 1 hr is thus found to be local-

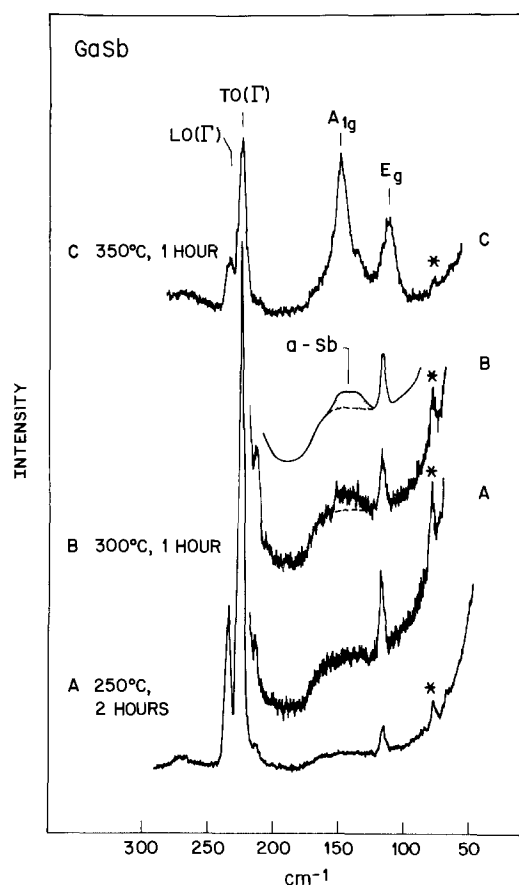


Fig. 5. Thermal evolution of the interfacial reaction which generates elemental Sb as detected by Raman scattering. Plasma lines are denoted by an asterisk. In frames A and B, the peak at $\sim 117\text{ cm}^{-1}$ is a superposition of a plasma line and a two-phonon substrate peak.

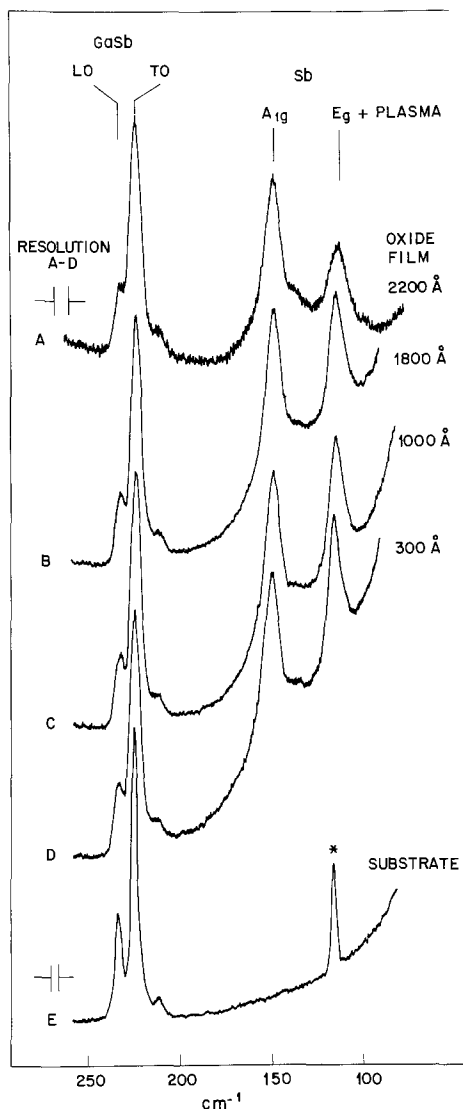


Fig. 6. Chemical etching and Raman scattering of a thermally annealed anodized GaSb wafer. The thermally generated Sb is seen to be localized within 300\AA of the substrate. Plasma lines denoted by an asterisk.

ized within an interfacial layer whose position lies no more than 300\AA from the actual oxide-semiconductor interface.

The Raman scattering experiments on as-anodized GaSb thus show that there is no evidence for either amorphous or crystalline Sb anywhere in these films down to the detection limits of this technique. Thermal annealing results in the generation of strong antimony Raman signals (primarily as a crystalline phase), and chemical etching experiments show that antimony deposits are within 300\AA of the oxide/GaSb interface.

Phase diagram.—An estimate of the lower section of the Ga-Sb-O phase diagram was generated from a combination of binary mixture experiments and thermodynamic calculations. Many aspects of this diagram were guided by prior results on the Ga-As-O system (4), which is shown for comparison in Fig. 7. All equilibria are assumed to be pseudobinary, i.e., the phase fields are composed of mixtures of pure components in which mutual solid solubility is ignored.

The constituents in phase field I (Fig. 7) at equilibrium were obtained from the binary mixture results in Table I for initial $\text{Sb}_2\text{O}_3/\text{GaSb}$ mole ratios greater than 1:2. The observed products were Ga_2O_3 , Sb, and Sb_2O_3 . The latter component was initially present in quantities sufficient to consume all the initial GaSb

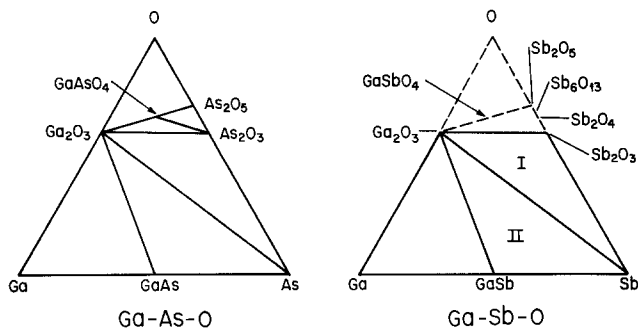


Fig. 7. Ternary phase diagrams for the Ga-As-O and Ga-Sb-O systems. The upper regions of the latter diagram have not been fully determined (dashed lines).

and still be present in excess. The absence of GaSb in the final product mixture indicates that the reaction has gone to completion, i.e., the minor component (GaSb) has been totally consumed. In addition, no evidence could be found for the formation of GaSbO₄, which would have indicated the existence of a tie line between GaSbO₄ and Sb. The tie line instead connects Ga₂O₃ and Sb₂O₃ as shown in the phase diagram.

For reaction mixtures which initially contain excess GaSb ($Sb_2O_3/GaSb < 1/2$), the materials at the apexes of phase field II should be observed. Table I indicates that the products are Ga₂O₃, Sb, GaSb, as would be anticipated from Fig. 7. The total consumption of the Sb₂O₃ from the initial mixture again shows that the reaction has gone to completion. The crossing point between the Ga₂O₃-Sb tie line and an imaginary line connecting GaSb and Sb₂O₃ is represented by the reaction in Eq. [1].

The only part of the upper diagram which has been determined is the reaction between Ga₂O₃ and Sb₂O₃ to yield the intermediate product GaSbO₄ (2). Only the lower section of the diagram need concern us, however, since current evidence suggests that anodic oxides consist of Ga₂O₃/Sb₂O₃ mixtures.

A thermodynamic check on the correctness of the lower section of the phase diagram is made possible by calculating the relative stability of the various possible tie lines. The principle of the method is illustrated in Fig. 8.

An equation involving mass balance is written at any point at which two tie lines can intersect. Only one of these tie lines can be stable, its determination is made by calculating the Gibbs free energy for reaction for the balanced equation at the intersection point. Table IV presents the balanced equations which occur at intersection points 1, 2, and 3 on Fig. 8 along with the calculated free energy of reaction. The standard states

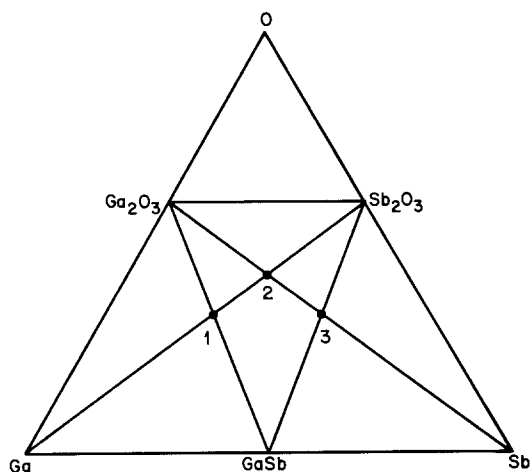


Fig. 8. Location of the crossing point equations which connect pseudobinary pairs of phases.

Table IV.

Crossing point	Equation	ΔG°_{298} (kcal)	Error sum (kcal)
1	$4Ga + Sb_2O_3 \rightarrow 2GaSb + Ga_2O_3$	-105.7	± 14
2	$2Ga + Sb_2O_3 \rightarrow 2Sb + Ga_2O_3$	-87.1	± 10
3	$2GaSb + Sb_2O_3 \rightarrow 4Sb + Ga_2O_3$	-68.5	± 14

* Reference data.

Compound	Gibbs energy of formation (kcal/mole)	Assigned error (kcal/mole)
β -Ga ₂ O ₃ (c)	-238.6	± 6.0
GaSb (c)	-9.3	± 2.0
Sb ₂ O ₃ (cubic)	-151.5	± 4.0

Reference states: Ga (s), Sb (s), O₂ (g).

were obtained from Ref. (19). Our estimates of probable errors in these free energies are also included. Considerations of such factors as the spread in ΔG values encountered in crystalline modifications of the substances guided the error assignments. The quantity listed under "error sum" in Table IV is a summation of the assigned errors in the individual products for the reactions as listed and should thus represent an upper limit in the uncertainty in ΔG for the reaction.

Crossing point Eq. [1], (see Table IV and Fig. 8) for instance, indicates that the tie line which connects Ga₂O₃-GaSb is more stable than the Ga-Sb₂O₃ tie line by -105.7 ± 22 kcal. The negative sign of ΔG for the reactions shows that the tie lines associated with the binary couples on the right-hand sides of Eq. [1]-[3] (Table IV) are stable. These thermodynamic calculations thus predict tie lines connecting Ga₂O₃-GaSb and Ga₂O₃-Sb, a result consistent with the observed phases generated in the binary mixture experiments (Fig. 7).

GaAs.—Raman.—Raman scattering results from as-anodized and thermally annealed samples have been previously reported (11, 20) so that only a brief synopsis of the results are given here. A polished <100> oriented substrate was anodized to 50V (~1000Å anodic film) in an AGW electrolyte. Figure 9 shows the Raman spectra for the as-anodized (Fig. 9A) and annealed (Fig. 9B, 450°C/1 hr) samples. As before, the numbered peaks ($n = 1$ to 11) are associated with one and two-phonon scattering from the substrate. A detailed comparison of bare and anodized substrates is available in Ref. (20). Table V contains a compilation of the observed peaks and the assignments given by Sekine *et al.* (21). The positions of the totally symmetric A_{1g} (257 cm⁻¹) and doubly degenerate E_g (195 cm⁻¹) modes of crystalline arsenic (13, 14, 20) in its A7 structure are denoted by A₁ and A₂. Amorphous arsenic (15, 20) also has a characteristic spectrum in

Table V. GaAs

n	Frequency (cm ⁻¹)	Assignment*
1	133	2TA(L)
2	157	2TA(X)
3	163	2TA(Z)
4	217	2TA(W)
		2TA(Q)
5	269	TO(Γ)
6	291	LO(Γ)
7	335	TA(L) + TO(L)
		TA(X) + TO(X)
8	371	2LA(Q)
9	510	2TO(L)
10	537	2TO(Γ)
11	588	2LO(Γ)
A ₁	257	A _{1g}
A ₂	195	E _g

* $n = 1$ to 11 assigned from Ref. (21). A₁, A₂ assigned from Ref. (13, 14).

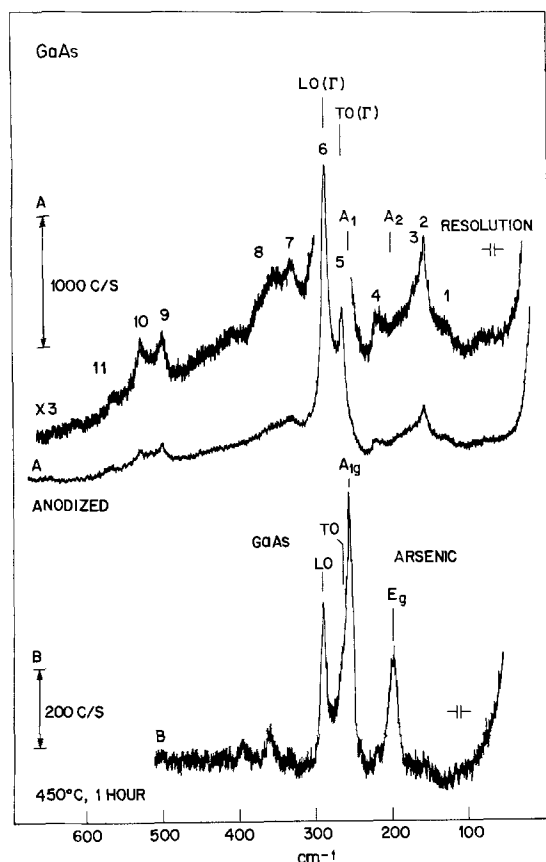


Fig. 9. Raman scattering from as-anodized (A) and thermally annealed (B) anodic films on GaAs. The crystalline modes of elemental arsenic are positioned at A_1 and A_2 , the numbered peaks 1-11 in A arise from substrate scattering. The scattered light polarization is unanalyzed.

this region in the form of a broad band between 200-250 cm^{-1} .

Whereas the as-anodized spectrum of Fig. 9A does not indicate the presence of arsenic within the present limits of detectability, annealing at 450°C for 1 hr (Fig. 9B) results in a spectrum dominated by crystalline arsenic. The origin of this signal has been related to the interfacial reaction given in Eq. [2]



and the localization of the thermally induced arsenic deposits at the oxide/GaAs interface has been verified by chemical etching experiments (11).

Phase diagram.—The ternary phase diagram for the Ga-As-O system has already been developed (4) and was presented earlier in Fig. 7. The important point which should be reiterated is that the phases which are thermodynamically stable in the interfacial region are Ga_2O_3 , As, and GaAs, not Ga_2O_3 , As_2O_3 , and GaAs. The thermally induced interfacial reaction given by Eq. [2] and observed in Raman scattering provides the pathway for the transition from an unstable to a thermodynamically stable interfacial mixture. This is discussed in the Discussion section.

GaP.—Raman.—N-type $\langle 111 \rangle$ GaP wafers were anodized at 50V ($\sim 500\text{A}$ of oxide) in an AGW electrolyte at constant current density. The one- and two-phonon assignments of Sushchinsky *et al.* (22) were used to identify and tabulate (Table VI) individual spectral features $n = 1-16$ in Fig. 10A. The first order LO mode at $\sim 403 \text{ cm}^{-1}$ is not sharply defined on any of our wafers; we believe this to be due to LO-plasmon coupling which broadens and shifts this mode in the strong coupling regime.

Table VI. GaP

n	Frequency (cm^{-1})	Assignment*
1	31	LO(X) - TO(X)
2	48	LO(L) - TO(L)
3	179.5	LO(L) - LA(L)
	181	2TA(L)
4	209	2TA(X)
5	256	TO(X) - TA(X)
6	287	LO(X) - TA(X)
7	366.3	TO(Σ)
8	403	LO(Σ)
9	426	2LA(L)
	465	TO(X) + TA(X)
	483	LO(L) + TA(L)
	496	LO(X) + TA(X)
	508	2LA(X)
10	605.5	LO(L) + LA(L)
11	689	2TO(L)
12	721	2TO(X)
13	737	LO(L) + TO(L)
14	752	LO(X) + TO(X)
15	784	2LO(X)
16	805.6	2LO(Σ)
P_1	467	—
P_2	349	—

* $n = 1$ to 16 assigned from Ref. (22). P_1 and P_2 from Ref. (25).

Phosphorus is known to exist in white, red, black, and amorphous allotropic forms. Raman spectra from black phosphorus and amorphous phosphorus (23) have been reported by Lannin and Shanabrook. White phosphorus is a molecular crystal consisting of P_4 tetrahedra whose spectrum we have observed to be similar to data reported for P_4 gas phase species (6). Neither white nor black phosphorus allotropes are anticipated however; the former converts rapidly to red phosphorus above 260°C and the latter occurs only at very high temperatures or pressures or when its lattice is stabilized by small additions of Hg or other heavy metal impurities. Quite recent Raman experiments aimed at detecting phosphorus in thermally oxidized films in InP (24) corroborate that

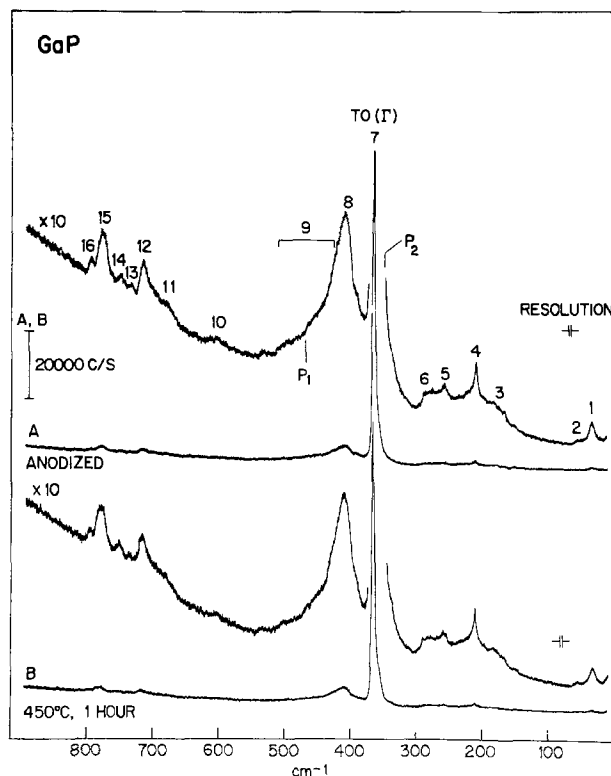


Fig. 10. Raman scattering from as-anodized (A) and thermally annealed (B) anodic films on GaP. The dominant crystalline red phosphorus peaks would occur at P_1 - P_2 , the numbered peaks 1-16 in A arise from substrate scattering. The scattered light polarization is unanalyzed.

either crystalline or amorphous red P will be the stable allotropes. For the annealing temperatures employed in these studies ($T \geq 450^\circ\text{C}$), only crystalline red P is anticipated.

Data (24) on red phosphorus crystallized at $\sim 500^\circ\text{C}$ indicate that there are no fewer than 35 observable Raman lines lying between 20 and 500 cm^{-1} . Their intensities are somewhat dependent on thermal treatment, but the two strongest modes consistently occur at ~ 467 and 349 cm^{-1} . The two dominant modes are denoted as P_1 and P_2 in Fig. 10A.

Comparison of the bare substrate (not shown) and anodized spectra (Fig. 10A) showed the two to be virtually superimposable. No evidence could be found for the presence of either crystalline or amorphous phosphorus in the as-anodized films, although it should be noted that the broad line shape (23) anticipated for amorphous P could be masked by the two-phonon and coupled plasmon features of the substrate. Annealing the anodized sample at 450°C for 1 hr leads to no observable changes in the Raman spectrum (Fig. 10B). These experiments were extended to 650°C for 1 hr (not shown), but in no case was any structure observed which could not be associated with the GaP substrate.

Crossed polarization (VH) spectra were also analyzed in order to reduce the background interference from the two-phonon and coupled-plasmon scattering of the substrate. The results for as-anodized and thermally annealed (450° and 650°C) anodic films are presented in Fig. 11. Except for a gradual reduction in the overall intensity as one employs more severe annealing conditions, there is no evidence for any changes in the spectra consistent with the formation of any allotropic form of phosphorus. Consequently neither the detectable presence of elemental P in the as-anodized state nor its thermally induced growth were observed.

Phase diagram.—Thermodynamic calculation of the condensed phase portion of the Ga-P-O diagram is subject to considerable uncertainty. The upper limit for the temperature of an isothermal section representative of solid condensed phases is set by the melting point of P_2O_5 , i.e., 23.8°C . The latter product disproportionates above its boiling point (173°C) to form

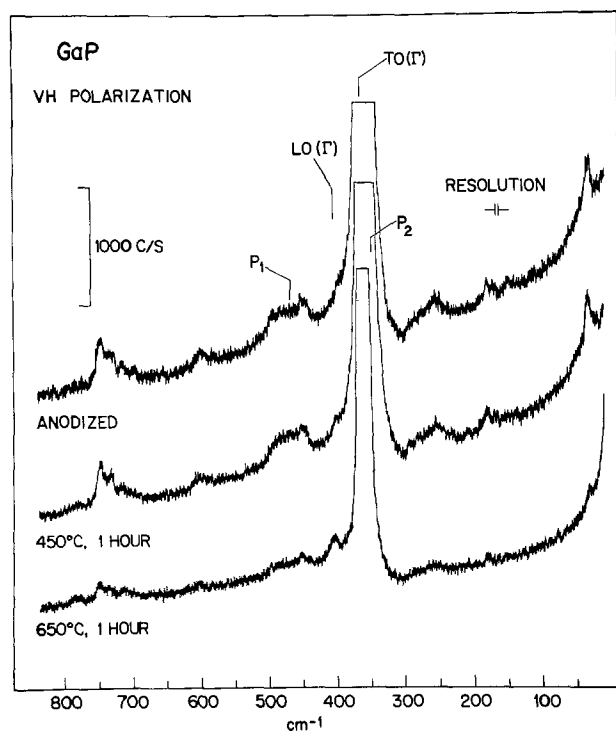


Fig. 11. Raman scattering in a crossed polarization configuration for anodized and thermally annealed films on GaP. The selected Raman scattered light is polarized in the plane of incidence.

red phosphorus and a range of polymeric phosphorus oxides of variable composition (25). There is currently insufficient data appropriate to a binary P-O phase diagram to determine with certainty whether such chemical species as P_4O_8 , P_4O_7 , or P_4O_9 exist as thermodynamically stable compounds. Without definitive evidence in favor of such a proposition, we will assume that the condensed phases comprising the Ga-P-O diagram consist of Ga, GaP, P, Ga_2O_3 , P_2O_5 , GaPO_4 , and $\text{Ga}(\text{PO}_3)_3$. There are 24 possible phase diagrams associated with these 8 condensed phases.

Crossing point stability equations were examined for all relevant binary combinations of the condensed phases for which thermodynamic data are available. There are no data for $\text{Ga}(\text{PO}_3)_3$ to the best of our knowledge, and the data for GaPO_4 are relatively uncertain. The appropriate equations, reference states, and estimated errors are presented in Table VII. For P_2O_5 , the ΔG value was calculated using the tabulated (19) ΔH value and by observing the trends between ΔH and ΔG for the series Sb_2O_3 , As_2O_3 , and P_2O_3 . The large estimated uncertainty in the ΔG value for GaPO_4 is associated with a $\pm 9\%$ deviation present in the original solubility product data which formed the basis for the calculation of this free energy in Ref. (19). The error assigned to P_2O_5 primarily reflects the known variation between crystalline and amorphous structures. As in Table IV, the column designated as "error sum" is a worst case value assuming all errors to be additive and to scale with the appropriate number of moles of each product involved in the reaction.

Figure 12 shows the manner in which the stable tie lines were calculated. The condensed phase portion of all 24 diagrams lies below the tie line which connects Ga_2O_3 to P_2O_5 . Gas phase equilibria bounded by the Ga_2O_3 - P_2O_5 -O triangle were not studied and are an excluded part of the phase diagram. Crossing point Eq. [1] through [3] occur as shown in Fig. 12 (top) and indicate the relative stability of the Ga_2O_3 -GaP couple to crossing originating at the Ga apex of the diagram. No connections to $\text{Ga}(\text{PO}_3)_3$ are shown in Fig. 12 due to lack of thermodynamic data. It should be noted, however, that, if the Ga-GaPO₄, Ga-P₂O₅, and Ga-P₂O₃ couples cannot intersect the Ga_2O_3 -GaP tie line, then neither can the Ga-Ga(PO_3)₃ couple. Unlike the calculations encountered in the Ga-As-O and Ga-Sb-O systems, the large values of the error sums relative to the calculated reaction Gibbs free energies for many of the crossing point equations reflect the uncertainty present in the form of the Ga-P-O diagram.

In our estimation, the most critical tie line of the phase diagram involves the GaPO_4 -GaP couple. Ac-

Table VII.

Crossing point	Equation	$\Delta G^{\circ}_{\text{rxn}}$ (kcal)	Error sum (kcal)
1	$8\text{Ga} + 3\text{GaPO}_4 \rightarrow 4\text{Ga}_2\text{O}_3 + 3\text{GaP}$	-95.5	± 114
2	$16\text{Ga} + 3\text{P}_2\text{O}_5 \rightarrow 5\text{Ga}_2\text{O}_3 + 6\text{GaP}$	-368.6	± 66
3	$4\text{Ga} + \text{P}_2\text{O}_5 \rightarrow \text{Ga}_2\text{O}_3 + 2\text{GaP}$	-100.2	± 20
4	$2\text{Ga}_2\text{O}_3 + 2\text{P}_2\text{O}_5 \rightarrow 3\text{GaPO}_4 + \text{GaP}$	-124.9	± 118
5	$4\text{Ga}_2\text{O}_3 + 8\text{P} \rightarrow 3\text{GaPO}_4 + \text{GaP}$	-94.9	± 118
6	$4\text{P}_2\text{O}_5 + 5\text{GaP} \rightarrow 5\text{GaPO}_4 + 8\text{P}$	-141.9	± 182
7	$4\text{P}_2\text{O}_5 + 3\text{GaP} \rightarrow 3\text{GaPO}_4 + 8\text{P}$	-154.9	± 110

* Reference data.

Compound	Gibbs energy of formation (kcal/mole)	Assigned error (kcal/mole)
GaP (c)	-23.8	± 2.0
P_2O_5 (c)	-176.0	± 10.0
P_2O_5 (c)	-322.4	± 8.0
GaPO_4 (c)	-310.1	± 28.0
β - Ga_2O_3 (c)	-238.6	± 6.0

Reference states: Ga(s), P(white), O₂(g).

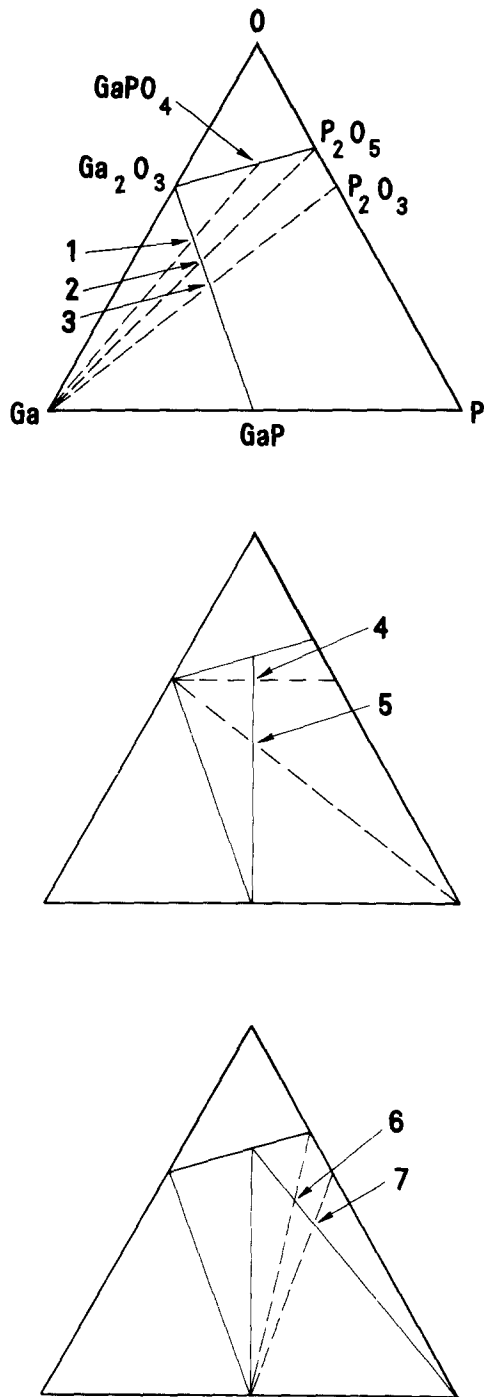


Fig. 12. Crossing point positions used in the calculation of the stable tie lines for the Ga-P-O system.

According to Table VII and crossing point Eq. [4] and [5] of Table VII (see Fig. 12, center), the GaPO_4 -GaP tie line is stable to crossing by the couples Ga_2O_3 -P and Ga_2O_3 - P_2O_3 , although the uncertainty is large. Crossing by the Ga- P_2O_5 and Ga- P_2O_3 couples is excluded by the presence of the proposed Ga_2O_3 -GaP tie line. In any case, the stability to crossing from these latter lines was calculated to be -323.3 ± 118 and -345.3 ± 111 kcal, respectively. The stability of the GaPO_4 -GaP tie line implies that O_2 oxidation should yield a single phase oxide composed of GaPO_4 . This expectation is consistent with the high temperature thermal oxidation studies of Rubenstein (26), in which GaPO_4 was identified as the primary reaction product (95%) by x-ray diffraction. GaPO_4 has also been identified as the oxide formed at lower temperatures (600° - 950°C) in photoemission experiments (27).

Establishing the Ga_2O_3 -GaP and GaPO_4 -GaP tie lines serves to eliminate 18 of the 24 possible phase diagrams. The remaining 6 are shown in Fig. 13. At this point the calculations are severely hampered by the lack of thermodynamic data for $\text{Ga}(\text{PO}_3)_3$ and the uncertainty in the GaPO_4 data. One notes that only one of the 6 diagrams (Fig. 13, top, center) contains a tie line which connects P_2O_5 and GaP. The presence of this tie line is consistent with the binary mixture experiments involving the absence of reaction between P_2O_5 and GaP (Table II). The failure to observe phosphorus in the Raman experiments on annealed wafers also suggests the elimination of the bottom 3 diagrams. Equations [6] and [7] (Table VII), however, are at variance with the stability of the P_2O_5 -GaP and P_2O_3 -GaP couples relative to the GaPO_4 -P tie line. A GaPO_4 -P tie line, however, requires that the 4:5 molar mixture of P_2O_5 and GaP should have reacted to yield phase products which include GaPO_4 and P. Neither product was observed in the binary mixture experiments even after reaction at 850°C for 1 day.

There are a number of possible explanations which might account for this discrepancy. The simplest of these is kinetic in origin, i.e., the solid-state reaction between P_2O_5 and GaP is sufficiently slow even at 850°C that the thermodynamically stable phases do not form. Alternatively, one might argue that the uncertainty in the available thermodynamic data (especially in GaPO_4) precludes an accurate description of the system. The failure to observe elemental phosphorus in thermally annealed films using Raman scattering may have still another explanation since there is a competing reaction channel involving P_2O_5 and Ga_2O_3 to yield GaPO_4 or $\text{Ga}(\text{PO}_3)_3$. If the kin-

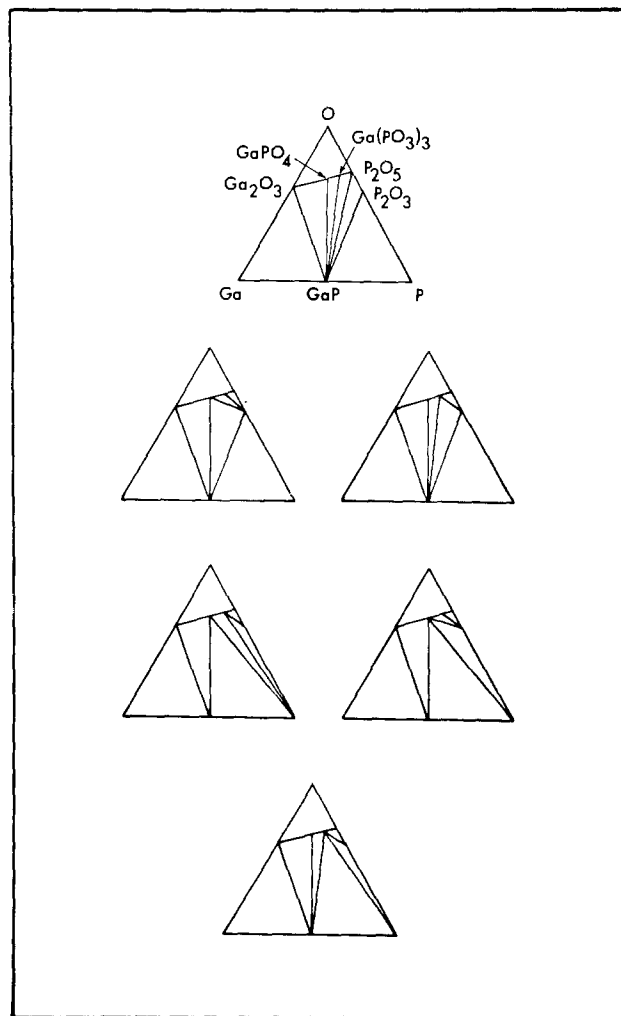


Fig. 13. Six possible choices for the Ga-P-O phase diagram

etics of those reactions were fast compared to reaction between P_2O_5 and GaP, the P_2O_5 would be removed from the film before it could react to generate phosphorus. In addition, direct volatilization of P_2O_5 will also deplete that component from the film, in view of the uncertainties involved in both the calculations and experiments, it is difficult to assess the relative merit of the final choices for the Ga-P-O condensed phase diagram ($T < 23.8^\circ\text{C}$) shown in Fig. 13.

Discussion

The ternary phase diagrams can be used to specify the oxide phase composition if film growth has occurred under near equilibrium conditions. A comparison of the thermodynamically anticipated phases with those observed in anodic oxides provides the basis for understanding the interfacial reactions observed in thermally annealed anodic films.

The thermodynamic predictions for the oxide phase compositions utilizing O_2 as the oxidant are shown in Fig. 14 for GaSb, GaAs, and GaP. This figure was constructed from the phase diagrams in the following manner. A line connecting oxygen to the appropriate substrate is constructed, and the oxide components present in the film are read from the apexes of the various phase field triangles cut by the oxygen-substrate line. Movement along the oxygen-substrate line toward oxygen is equivalent to movement in the direction of increased oxygen chemical potential, *i.e.*, for the isothermal section represented by the diagram this would mean increasing the O_2 partial pressure in the gas phase. The progression from weak (W) to intermediate (I) to strong (S) oxidizing conditions qualitatively describes movement along the oxygen-substrate line toward oxygen. The molar ratios of the oxide film components can be determined by examining the intersection of the oxygen-substrate line with the phase field boundary. The molar ratios

of oxide products are presented in Fig. 14 at the left of the various oxide regions found under different oxidizing conditions. The thickness of each layer is only a schematic representation of that region; kinetic parameters generally control these features in real oxide growth.

The stable interfacial phase products are of primary interest. On GaSb and GaAs the stable phases which grow in equilibrium with those substrates are Ga_2O_3/Sb_2O_3 and Ga_2O_3/As_2O_3 , respectively. From a strictly thermodynamic point of view, one anticipates interfacial deposits of the elemental group V component to be present. On GaP, the tie line which connects $GaPO_4$ to GaP admits to only one oxidation product ($GaPO_4$) under all oxidizing conditions using O_2 as the oxidant. Since all the phase diagrams in Fig. 13 contain this tie line, it is not possible to distinguish among them from experimental oxidation studies using O_2 or air.

The experimental determination of composition profiles on anodic films is summarized in Table VIII and Fig. 15 and in Ref. (28-40). Although the available data are somewhat sketchy for GaSb and GaP, a number of essential features emerge from the literature. The ellipsometric and Raman scattering results indicate that the bulk films are essentially nonabsorbing in a spectral region in which elemental Sb, As, or P would be detected if present at a level of 1-2 volume percent or greater. This result is in contrast to the phase diagram predictions for the Ga-Sb-O and Ga-As-O systems. Thermally oxidized films on GaSb and GaAs have in fact already been shown to contain substantial deposits of elemental Sb and As, respectively (18, 30, 31).

The variability with electrolyte composition and pH of the Ga/P ratio in bulk anodic films on GaP (34, 39-40) demonstrates that $GaPO_4$ is not the unique product evolved during anodic oxidation. These films

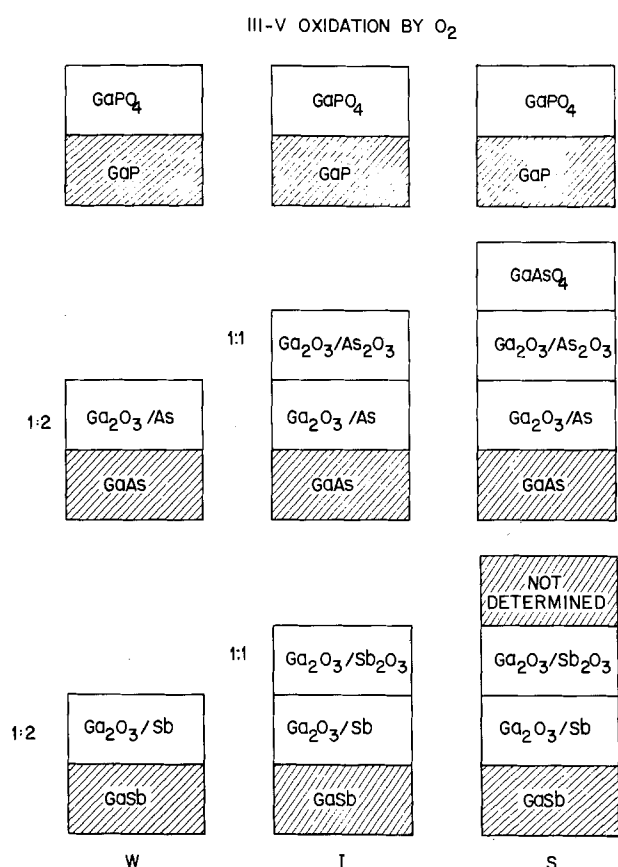


Fig. 14. Predicted oxide phase compositions for O_2 oxidation of GaSb, GaAs, and GaP under weak (W), intermediate (I), and strong (S) oxidizing conditions.

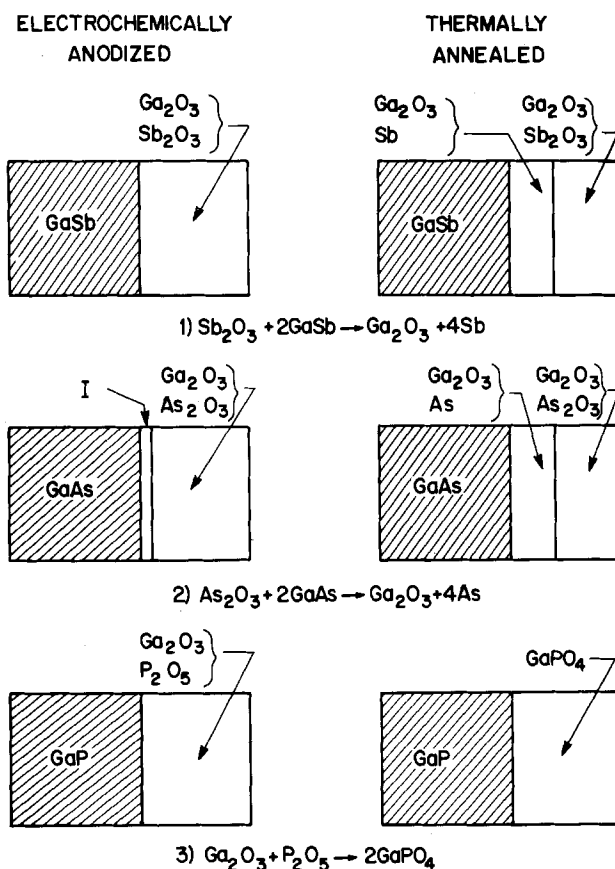


Fig. 15. Comparison of experimentally observed film compositions for as-anodized and thermally annealed samples. $GaPO_4$ is the presumed product of annealed anodic films on GaP; its presence was not directly verified by Raman scattering.

Table VIII. Electrochemical anodization

Substrate	Analysis Technique*	Observations	Reference
1. GaSb	XPS	Oxide composed of Ga ₂ O ₃ and Sb ₂ O ₃	Unpublished data
	Raman Ellipsometry	Elemental antimony not detected in films ε ₁ data consistent with trivalent antimony in the oxide; films non-absorbing between 1.4 and 4 eV	This work (3, 28)
2. GaAs	XPS Coulometry	Bulk films composed of Ga ₂ O ₃ and As ₂ O ₃ Passive film formation entails passage of 6.0 Faradays/g mole of GaAs consumed	(30, 31)
	IXE RT	Ga:As ratio ≈ 1 in bulk films Evidence for electrolyte dependent selective dissolution of film components during growth	(29) (32, 33)
	ISS	Homogeneous oxides observed for low current density growth; interface width and composition varies with current density	(34)
	Raman	Elemental arsenic below detection limits in bulk films	(35) (11, 20)
	Ellipsometry	Bulk films free of optical absorption between 1.5 and 4.5 eV; narrow interfaces possible which depend on current density	This work (3, 36, 37)
3. GaP	XPS RBS	Trivalent Ga and pentavalent P observed in bulk films Ga:P ratio varies in bulk films as a function of electrolyte composition and pH; oxide constituents assumed to be Ga ₂ O ₃ and P ₂ O ₅	(38)
	RT Raman	Bulk film observed with P:Ga = 1.6 in glycol based electrolyte Elemental phosphorus not detected	(39, 40) (34)
	Ellipsometry	Films nonabsorptive between 1.5 and 6 eV; evidence for compositional inhomogeneities noted; ε ₁ consistent with pentavalent phosphorus	This work (3)

* XPS = x-ray photoelectron spectroscopy.
 IXE = ion-induced x-ray emission.
 RT = radioactive tracer.
 ISS = ion scattering spectroscopy.

are believed instead to consist of an amorphous mixture of Ga₂O₃ and P₂O₅ whose ratio in the film is sensitive to selective dissolution of these components in the electrolyte.

A comparison of the film compositions appropriate to thermodynamic equilibrium (Fig. 14) and those found experimentally (Fig. 15) in electrochemically anodized films suggests that in the latter case oxide growth has not occurred under near equilibrium conditions. Some support for this point of view is available from observations that the oxide-GaAs interfacial composition and width are both dependent on the current density (growth rate) (35, 41). This interface can be quite narrow when grown under optimal conditions (41). Thermal annealing provides the necessary energy to overcome diffusion and reaction barriers. At sufficiently high temperatures the appropriate group V oxide component can react with the substrate on GaSb and GaAs according to Eq. [1] and [2] (Fig. 15). The products of this reaction yield an interfacial region composed of Ga₂O₃ and either Sb or As. For anodized GaP, the failure to observe P in thermally annealed films suggests either that the P₂O₅-GaP tie line is stable or that the P₂O₅ is either volatilized or reacted with Ga₂O₃ to form the phosphate or metaphosphate. The latter product is anticipated only if the P₂O₅/Ga₂O₃ ratio of the film is greater than one.

Summary

Interfacial oxide-substrate reactions have been observed on thermally annealed samples of electrochemically anodized GaSb and GaAs. This phenomenon involves diffusion of the group V oxide component of the film to the substrate followed by subsequent reaction to yield the thermodynamically stable interfacial phases. Estimates of the Ga-Sb-O and Ga-As-O ternary phase diagrams indicate that the phase constituents in thermodynamic equilibrium with GaSb and GaAs will be Ga₂O₃/Sb and Ga₂O₃/As, respectively. The interfacial reactions thus generate deposits of elemental Sb or As whose slow growth with time may prove deleterious in device applications involving native oxides on those substrates. Since the driving force for the interfacial reaction is thermodynamic in origin, native oxides produced via plasma oxidation techniques will also be subject to their occurrence whenever there is sufficient energy available to overcome the diffusion and reaction barriers. The reaction

rate at a fixed temperature was observed to be much faster on GaSb than on GaAs.

An analogous reaction between P₂O₅ and GaP was not observed either in anodic films or powdered mixtures. Both GaPO₄ and Ga(PO₃)₃ can form, however, as a consequence of the reaction between P₂O₅ and Ga₂O₃. The actual product will depend on the P₂O₅/Ga₂O₃ ratio present in the film, this latter parameter being sensitive to the details of the anodization.

Manuscript submitted Jan. 29, 1980; revised manuscript received May 2, 1980.

Any discussion of this paper will appear in a Discussion Section to be published in the June 1981 JOURNAL. All discussions for the June 1981 Discussion Section should be submitted by Feb. 1, 1981.

Publication costs of this article were assisted by Bell Laboratories.

REFERENCES

- H. Hasegawa and H. L. Hartnagel, *This Journal*, **123**, 713 (1976).
- R. Roy, V. G. Hill, and E. F. Osborn, *J. Am. Ceram. Soc.*, **74**, 719 (1952).
- D. E. Aspnes, B. Schwartz, A. A. Studna, L. Derick, and L. A. Koszi, *J. Appl. Phys.*, **48**, 3510 (1977).
- C. D. Thurmond, G. P. Schwartz, G. W. Kammlott, and B. Schwartz, *This Journal*, **127**, 1366 (1980).
- C. D. Thurmond, *J. Phys. Chem. Solids*, **26**, 785 (1965).
- I. R. Beattie, K. M. S. Livingston, G. A. Ozin, and D. J. Reynolds, *J. Chem. Soc. (A)*, 449 (1970).
- T. S. Moss, "Photoconductivity in the Elements," pp. 141-178, Academic Press, New York (1952).
- M. Cardona and D. L. Greenaway, *Phys. Rev. A*, **133**, 1685 (1964).
- J. B. Renucci, W. Richter, M. Cardona, and E. Schönherr, *Phys. Status Solidi B*, **60**, 299 (1973).
- W. Richter, "Springer Tracts in Modern Physics," Vol. 78, pp. 121 ff., Springer Verlag (1976).
- G. P. Schwartz, J. E. Griffiths, and B. Schwartz, *J. Vac. Sci. Technol.*, **16**, 1383 (1979).
- R. Loudon, *Adv. Phys.*, **13**, 432 (1964).
- R. N. Zitter, in "The Physics of Semimetals and Narrow Gap Semiconductors," D. L. Carter and R. T. Bate, Editors, p. 285, Pergamon, New York (1971).
- J. S. Lannin, J. M. Calleja, and M. Cardona, *Phys. Rev. B*, **12**, 585 (1975).
- J. S. Lannin, *ibid.*, **15**, 3863 (1977).
- P. B. Klein and R. K. Chang, *ibid.*, **14**, 2498 (1976).
- T. Sekine, U. Uchinokura, and E. Matsuura, *Solid*

- State Commun.*, **18**, 1337 (1976).
18. R. L. Farrow, R. K. Chang, S. Mroczkowski, and F. H. Pollak, *Appl. Phys. Lett.*, **31**, 768 (1977).
 19. D. D. Wagman, W. H. Evans, V. B. Parker, I. Halow, S. M. Bailey, and R. H. Schumm, NBS Tech. Note 270-3, Government Printing Office, Washington, D.C. (1969).
 20. G. P. Schwartz, B. Schwartz, D. DiStefano, G. J. Gualtieri, and J. E. Griffiths, *Appl. Phys. Lett.*, **34**, 205 (1979).
 21. T. Sekine, K. Uchinokura, and E. Matsuura, *J. Phys. Chem. Solids*, **38**, 1091 (1977).
 22. M. M. Sushchinsky, V. S. Gorelik, and O. P. Maximov, *J. Raman Spectrosc.*, **7**, 26 (1978).
 23. J. S. Lannin and B. V. Shanabrook, 14th International Conference on the Physics of Semiconductors, Edinburgh (1978); *Solid State Commun.*, **28**, 497 (1978).
 24. G. P. Schwartz, W. A. Sunder and J. E. Griffiths, Unpublished results.
 25. A. D. F. Toy, "Comprehensive Inorganic Chemistry," Vol. 2, pp. 389 ff., Pergamon Press, Oxford (1973).
 26. M. Rubenstein, *This Journal*, **113**, 540 (1966).
 27. R. Nishitani, H. Iwasaki, Y. Mizokawa, and S. Nakamura, *Jpn. J. Appl. Phys.*, **17**, 321 (1978).
 28. C. W. Fisher, N. Leslie, and A. Etchells, *J. Vac. Sci. Technol.*, **13**, 59 (1976).
 29. W. W. Harvey and J. Kruger, *Electrochim. Acta*, **16**, 2017 (1971).
 30. G. P. Schwartz, G. J. Gualtieri, G. W. Kammlott, and B. Schwartz, *This Journal*, **126**, 1737 (1979).
 31. Y. Mizokawa, H. Iwasaki, R. Nishitani, and S. Nakamura, *Jpn. J. Appl. Phys.*, **17**, 327 (1978).
 32. L. C. Feldman, J. M. Poate, F. Ermanis, and B. Schwartz, *Thin Solid Films*, **19**, 81 (1973).
 33. T. Ishii and B. Jeppson, *This Journal*, **124**, 1784 (1977).
 34. J. C. Verplanke and R. P. Tijburg, *ibid.*, **124**, 802 (1977).
 35. M. Croset, J. Diaz, D. Dieumegard, and L. M. Mercandalli, *ibid.*, **126**, 1543 (1979).
 36. K. Lösckke and G. Kühn, *Krist. Tech.*, **11**, 645 (1976).
 37. H. W. Dinges, *Thin Solid Films*, **50**, L17 (1978).
 38. We have observed that anodic films on GaP are subject to strong selective sputtering artifacts and reduction of the phosphorus oxide component during argon ion milling. Electron beam reduction of the phosphorus oxide occurred even more rapidly than ion beam reduction. Heating the anodic film at 250°C/2 hr did not change the surface Ga/P ratio, which is a further indication that the films do not contain P₂O₃ (bp 173°C) as a major constituent.
 39. J. M. Poate, T. M. Buck, and B. Schwartz, *J. Phys. Chem. Solids*, **34**, 779 (1973).
 40. J. M. Poate, P. J. Silverman, and J. Yahalom, *ibid.*, **34**, 1847 (1973).
 41. D. E. Aspnes, G. P. Schwartz, G. J. Gualtieri, and B. Schwartz, Materials Research Society Meeting, Cambridge (1979).

Intermediate Oxide Formation in Double-Polysilicon Gate MOS Structure

Hideo Sunami, Mitsumasa Koyanagi, and Norikazu Hashimoto

Hitachi Limited, Central Research Laboratory, Kokubunji, Tokyo 185, Japan

ABSTRACT

An intermediate insulator formation technique is realized using the concentration-dependent oxidation (CDO) of the phosphorus-doped first polysilicon gate. Utilizing the CDO effect, that is, heavily doped Si is oxidized faster than lightly doped Si, a thick intermediate oxide is formed to cover the first gate with its own oxide and a substrate surface to form the second gate oxide with simultaneous wet oxidation at 700°-900°C. Electrical properties of the intermediate insulator are discussed in terms of the formation conditions and topographical structures of the overlapped region. It is found that oxidation temperatures of around 900°C and moderate oxide thicknesses produce superior electrical properties and preferable geometries. In response to these requirements a dry-wet-dry oxidation (D-W-D) technique is successfully developed. A 5-17-5 min D-W-D oxidation at 900°C causes a 50 nm oxide to be formed on single crystal (100) silicon and a 210 nm oxide on the phosphorus-doped polysilicon. The autodoping effect of phosphorus atoms incorporated in the polysilicon gate is also discussed. It gives rise to harmful threshold voltage lowerings for the second gate n-channel transistors.

Following the application of the double-polysilicon gate MOS structure to CCD's (1), it is currently being extensively applied to large scale integration of MOS memories (2). These structures require an intermediate insulator between the two gates, which are electrically isolated at small capacitance to maximize circuit speed. Conventional techniques to realize the structure consist of CVD oxide formation on the first polysilicon gate, patterning of the double layer of the CVD oxide and the polysilicon gate, thermal oxidation of the gate edge, and subsequent second gate deposition. This structure has the disadvantages of possible shorts between adjacent second gates due to residual polysilicon under overhangs of the CVD

Key words: concentration-dependent oxidation, double polysilicon, dielectric breakdown, autodoping effect.

oxide (3) and of lowering of the dielectric breakdown between the two gates by the thin oxide at the second gate edge.

SELOCS (selective oxide coating of silicon-gate) technology (4-6) has been introduced to reduce these drawbacks in the conventional CVD technology. Differences in processing sequences and the topographical structures of these two technologies are shown in Fig. 1. This SELOCS technology utilizes concentration-dependent oxidation (7-10), in which heavily doped silicon is oxidized faster than lightly doped silicon, thus producing simultaneous formation of the intermediate thick oxide and the second gate thin oxide at low temperature wet oxidation. Instead of the wet oxidation, a low temperature dry oxidation technique called differential oxidation, developed by Barnes,

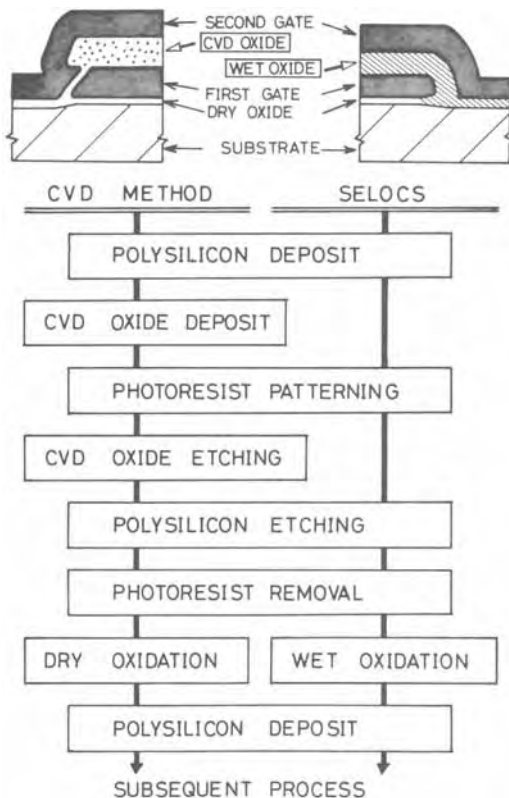


Fig. 1. Process sequences and resulting topographical structures for a conventional CVD oxide method and for SELOCS. A polysilicon film of the first gate is doped by phosphorus predeposition with a POCl_3 source.

DeBlasi, and Deal (11), also gives the identical structure, particularly concerned with the shallow junctions and thin oxide.

Even though SELOCS features a reduction in the number of processing steps, as previously shown in Fig. 1, and less probability of electrical shorts from the CVD oxide overhang, dielectric breakdown of the intermediate oxide between the two gates is still possible unless the processing conditions are appropriately chosen. Besides the dielectric breakdown SELOCS technology may have other limitations such as difficulties in formation of intermediate oxide of thicker than around 300 nm, inferior oxide integrity of the polysilicon oxide itself compared with that of single silicon oxide due to surface asperity of the polysilicon (12, 13), and increased sheet resistance due to the reduced thickness of the polysilicon gate.

The purpose of this study was to characterize parameters affecting oxide integrity and to choose better formation conditions for the coming VLSI double or triple level polysilicon devices. This paper presents the results of an empirical study on oxide formation and electrical properties affecting MOS transistors.

Experimental

A 400 nm thick polysilicon film was deposited by thermal decomposition of SiH_4 at 625°C onto a p-type (100) wafer with a resistivity of around 10 $\Omega\text{-cm}$, on which a 50 nm oxide had been grown at 1000°C in a dry oxygen ambient. Then the film was doped with P using either a gaseous predeposition at 1000°C for 5-60 min using a POCl_3 source or P-ion implantation. Resultant sheet resistivity of the film was 15-60 Ω/square , depending on the P concentration. Initial grain size of the film of around 50 nm was increased to around 1 μm by P predeposition just as in the case of ion implantation with subsequent annealing (14). There was no significant structural or electrical differences between predeposition and ion implantation. A PSG film grown on the polysilicon film during the predeposition

in an oxidizing ambient was removed by HF-buffered solution prior to subsequent processing. Then, the polysilicon film with patterned AZ1350 photoresist was etched by a conventional plasma etching technique using $\text{CF}_4 + 4\%\text{O}_2$ gas at 0.1 Torr in a barrel-type etching machine. The etching was automatically shut off by a plasma probe monitor (15) so as to obtain better reproducibility of the edge shape of the film. An etch rate of around 100 nm/min was obtained with 100W input rf power. In most cases, the 50 nm thick first gate oxide was etched off with HF-buffered solution to expose the substrate surface.

After the wafer was spin-dried, SELOCS oxidation was performed in a hydrogen-burning type furnace. A three-zone, resistance-heated furnace with a high purity alumina liner was used in this study. The oxidation chamber was a single wall, fused silica tube. Flow rates of oxygen and hydrogen for wet oxidation were 1.0 and 1.8 liters/min, respectively. The oxygen flow rate was 3.0 liters/min for the dry oxidation in the same furnace. Oxide thicknesses were determined by an ellipsometer for oxides on single crystal silicon and by a Talystep meter or a scanning electron microscope (SEM) for those on polysilicon films.

Currents flowing through the oxides were measured with a Model 26000 Keithley logarithmic picoammeter by the I - V method. A 3 V/sec ramp voltage was applied to the samples to characterize the oxide quality. All I - V measurements were made at room temperature while the samples were being blown with dry nitrogen in an electrostatic shield box used to block out the light.

Cross-sectional configurations of the samples were observed by field emission type SEM. Polysilicon gates were lightly etched after cleaving the samples to obtain clear images for SEM observation. The etching also removed small amounts of the high P content oxide film.

Results

Concentration-dependent oxidation.—Arrhenius plots of oxide thickness *vs.* the inverse of oxidation temperature are shown in Fig. 2 for polysilicon film which was doped with P ($C_B = 3 \times 10^{20} \text{ cm}^{-3}$) by the gaseous predeposition and 10 $\Omega\text{-cm}$ (100) single crystal silicon with wet oxidation (10). The P concentration was evaluated by a chemical method. The ratio of the thickness of the oxide on the polysilicon to that of the oxide on the single crystal shows a remarkable increase in the lower oxidation temperature region. Extrapolation of the experimental data in Fig. 2 gives 1050°C as the temperature at which the two oxides would be equally thick. To maximize circuit speed, larger values of the ratio are preferable when the second gate oxide thickness is kept constant. However, relatively low oxidation temperatures and thicker polysilicon oxides often give rise to dielectric breakdown between the two gates. This failure phenomenon is discussed in a later section.

Double-polysilicon gate structure.—The typical double-polysilicon gate structure shown in Fig. 3 was obtained by dry oxidation at 1000°C for 45 min subsequent to wet oxidation at 750°C for 90 min in two different furnaces. Of the 50 nm thickness of the second gate oxide, 30 nm was produced by the wet oxidation and 20 nm by the subsequent dry oxidation. The cross-sectional structure was mostly determined by the initial wet oxidation. The purpose of adding the dry oxidation was not primarily to improve the edge shape, but to improve the wet oxide of the second gate MOS transistors, since the wet oxide was relatively leaky compared to the dry oxide in this study.

As shown in Fig. 3, the second gate oxide became thinner in the vicinity of the gate edge. This phenomenon may well be the same as the "gate oxide thinning at the isolation wall" described by Sheng and Marcus (16).

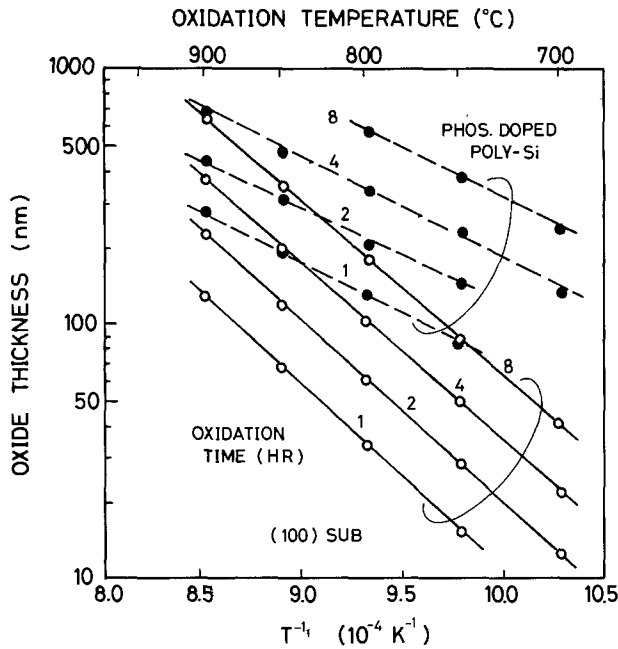


Fig. 2. Arrhenius plots of wet oxidation for 10 Ω -cm (100) silicon substrates and polysilicon films phosphorus doped (C_B) = 3×10^{20} cm^{-3}) by POCl_3 gaseous predeposition.

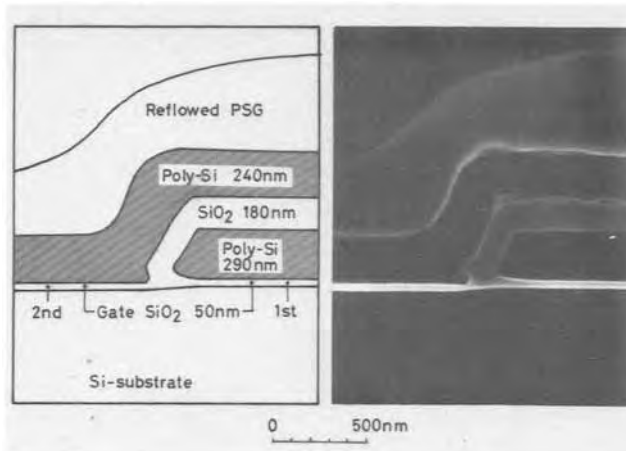


Fig. 3. Typical double-polysilicon gate structure realized by dry oxidation at 1000°C for 45 min subsequent to wet oxidation at 750°C for 90 min. The phosphorus concentration of the first gate measured 4.5×10^{20} cm^{-3} . The role of the dry oxidation was to electrically cure the oxide; the structure was mainly determined by the wet oxidation.

Leakage current.—Results of the leakage current measurements for an intermediate oxide and a second gate oxide are shown in Fig. 4 and 5, respectively. Structures measured were striped first polysilicon gates covered with their own oxide on which a plane second gate was overlaid and were designed to be 455 μm in edge length and 1680 μm^2 in plane area. Cross sections of the obtained structures were previously shown in Fig. 1. To pick up effects caused by topographical features independent of the oxide quality second gate oxides in both structures were produced by the same dry oxidation in the same furnace. Process sequences were as follows:

1. CVD structure: The sample to be oxidized had patterned double layers of polysilicon gates and 400 nm thick CVD oxides. The first gates were delineated by the automatically shutoff plasma etcher using the patterned CVD oxides as etching masks. Substrate surfaces were made bare and exposed to the ambient by etching off the oxide except in the regions where the first gates were deposited. Then a 50 min dry oxidation was done at 1000°C to produce a 50 nm thick second

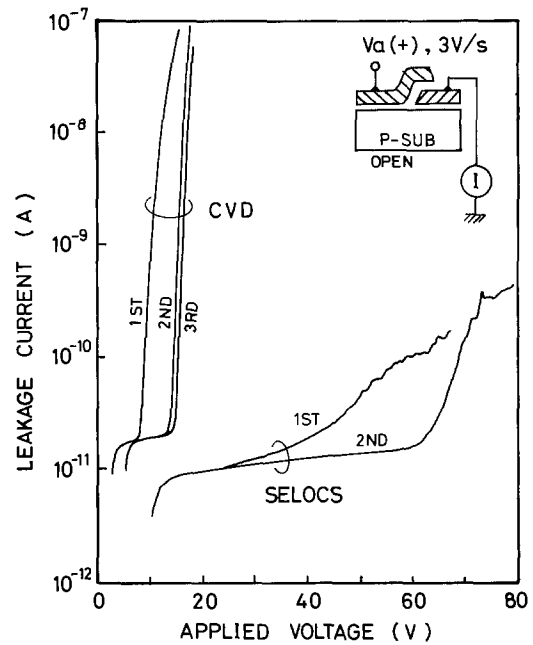


Fig. 4. Leakage currents through intermediate oxides obtained by a conventional CVD method and by SELOCS. The ramp rate of the applied voltage was 3 V/sec. Constant levels of the leakage currents in low voltage area are displacement currents. The area between the first and the second sweeps correspond to the amount of traps filled by electrons composing the leakage currents.

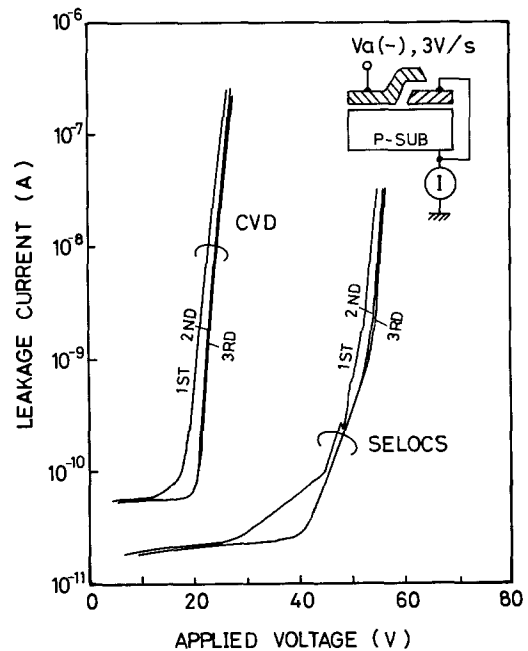


Fig. 5. Leakage currents for 50 nm thick second gate oxides and the intermediate oxides obtained by conventional CVD method and SELOCS.

gate oxide on the bare substrate surface and slightly thicker oxide on the edges of the first gates.

2. SELOCS structure: The samples to be oxidized had patterned first polysilicon gates. Substrate surfaces were bare just as in the CVD structure formation. Then a 4 hr wet oxidation at 800°C was made on the sample to produce a 120 nm thick oxide on the bare substrate surface and a 300 nm thick oxide on the first gates. Then an HF-buffered solution was used to etch off the 120 nm thick oxides. Consequently, the initial 300 nm thickness of the polysilicon oxides was reduced to around 200 nm. Then the same dry oxidation as in the CVD structure was done, resulting in a 50 nm thick second gate oxide on the substrate surface.

The constant levels of the leakage currents in the low applied voltage region, clearly shown in Fig. 4 and 5, are displacement currents defined by the equation: $I = dQ/dt = C(dV/dt)$. As the ramp rate was 3 V/sec, capacitances are evaluated from the curves shown in Fig. 4 to be about 6 and 3 pF for the CVD and the SELOCS structures, respectively.

The areas between the first and the second curves, also shown in Fig. 4 and 5, correspond to the amounts of traps filled by electrons composing the leakage currents. Thus the trap density can be evaluated by the I - V measurements. The trap density was evaluated to be on the order of 10^{12} cm^{-2} from these results.

For good circuit performance, thicker intermediate oxides are required. However, it was clear that the SELOCS method was markedly superior to the CVD method from the electrical point of view. Furthermore, breakdown voltages of the oxide in the CVD structure were lower than the expected value of 40V for 50 nm thick SiO_2 (calculated from the electric field of the dielectric breakdown of dry $\text{SiO}_2: 8 \times 10^6 \text{ V/cm}$). The electrical inferiority of the CVD structure may originate from an electric weakness of the polysilicon oxide itself. The breakdown voltage obtained for the polysilicon oxide is about half that of single silicon oxide of the same thickness. It is fairly consistent with expectations, since the dielectric breakdown between the second gate and the substrate electrically connected to the first gate occurred at about 20V, as shown in Fig. 5, and the voltage was limited mostly by the polysilicon oxide at the first gate edge for the CVD structure.

Failure of overhang formations.—Extreme oxidations in the SELOCS structure gave rise to an overhang of the intermediate oxide at the first gate edge. A cross section of a typical overhang is shown in Fig. 6. This structure resulted from 4 hr wet oxidation at 750°C . The overhang was caused by oxide forming beneath the first gate edge as if it were penetrating under it, raising the edge. A speculated sequence for the overhang formation is schematically shown in Fig. 7.

Since the thickness of an SiO_2 formed from polysilicon is nearly twice that of the original polysilicon, the front edges of the polysilicon oxide expand by approximately the same thickness of the polysilicon converted to SiO_2 . Thus the polysilicon oxide edge begins to expand out over the substrate oxide surface as shown in (2) in Fig. 7. Furthermore, the oxide growing on the heavily P-doped polysilicon is thicker than that growing on the lightly doped silicon substrate. This expansion and lifting of the polysilicon oxide edge produces the overhang shown in (3) in Fig. 7. The overhang resulted in a very thin intermediate oxide at the gate edge, much like a previously reported process (16), giving rise to low dielectric breakdown voltages and shorts. In this study, it was found that thicker oxides and lower oxidation temperatures caused these failures. We found an empirical relationship between elec-

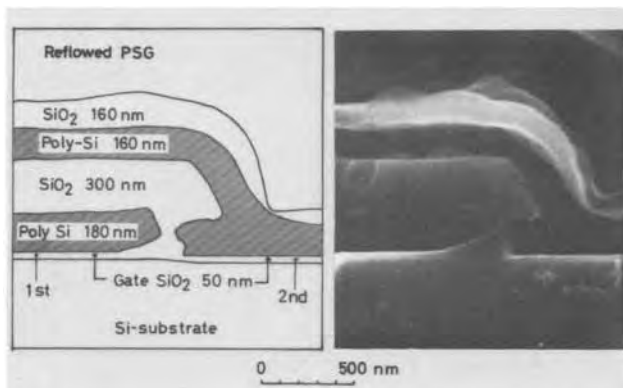


Fig. 6. An extreme case obtained by 4 hr wet oxidation at 750°C . An overhang of a 300 nm thick intermediate oxide was formed at the first gate edge.

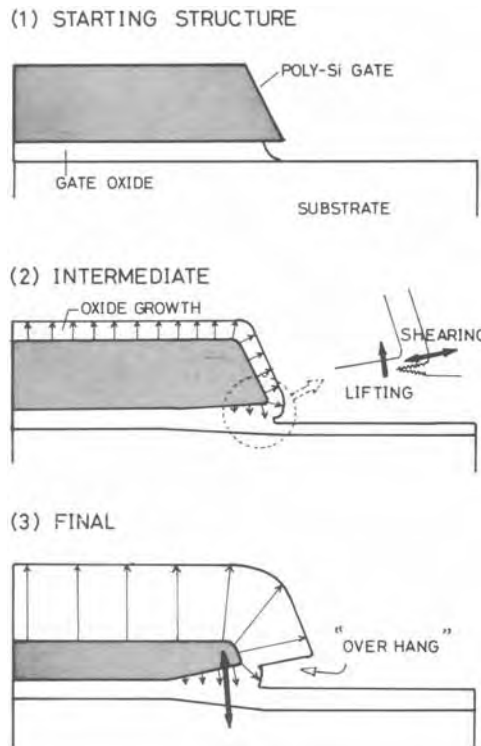


Fig. 7. Speculated sequence for overhang formation during oxidation of the first polysilicon gate.

trical properties and structures, on the one hand, and oxide thickness and oxidation temperature, on the other, as shown in Fig. 8. Preferable electrical performances, which mean sufficiently high and reproducible dielectric breakdown voltage, less time-dependent degradation of oxide integrity, and overhangless structures, are marked by o, failures by x, and intermediate by Δ . Thus the shaded region should give desirable performances for double polysilicon structures.

Discussion

Mechanism of overhang formation.—To characterize overhang formation the overhang wedge model shown in Fig. 9 was introduced. Parameters which seem to affect the formation were polysilicon gate thickness T_g , impurity concentration in the gate C_g , pad oxide thickness T_p , length of the pad oxide undercut L_p , intermediate oxide thickness $T_i \cdot \alpha$, and second gate

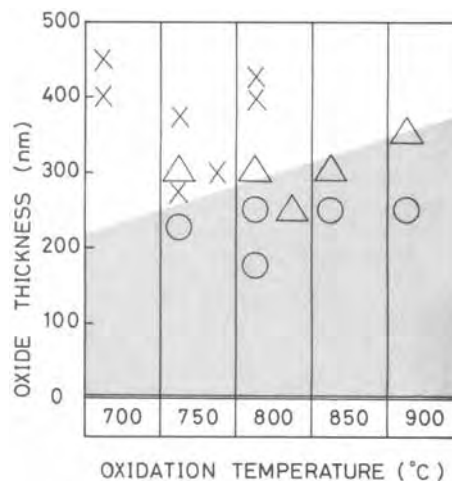


Fig. 8. Empirical relationship between electrical and structural integrity and both oxide thickness and oxidation temperature. Open circles denote preferable electrical and structural properties, \times marks unpreferable, and triangles intermediate. Processing conditions in the shaded region give preferable performances.

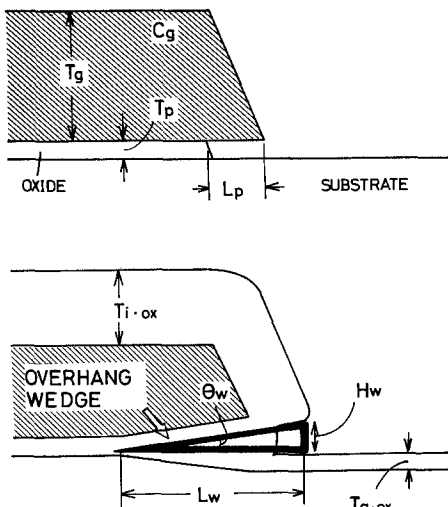


Fig. 9. Proposed model to explain the overhang formation. T is thickness, C impurity concentration, H height, L length, and θ angle, respectively.

thickness $Tg \cdot ox$. Wedge height Hw was defined as a figure of merit for the intermediate oxide formation. It was found that smaller Hw led to better dielectric performances. Large values of Hw led to formation of relatively thin intermediate insulator and electrical shorts between adjacent second gates because of a residual polysilicon underneath the overhang. To shorten Hw , wedge length Lw and/or wedge angle θ_w must be small according to the equation, $Hw = Lw \tan \theta_w$ (Lw and θ_w were not absolutely independent but had mutual influence).

Parameters influencing Hw were thus qualitatively analyzed as follows.

Oxidation temperatures.—According to the general relationship (17) for thermal oxidation, relatively low temperatures lead to surface reaction controlled oxidation. In fact, this oxidation theory also fits that of P-doped polysilicon (10). Surface reaction controlled oxidation gives a linear increase in oxide thickness x with respect to the oxidation time t : $x = (B/A)t$. A parabolic increase is obtained in the diffusion-controlled regime: $x = (Bt)^{0.5}$. Here, A and B are the oxidation rate constants (17). Since oxidant transportation is thus not the rate-limiting process in surface reaction controlled oxidation, i.e., at lower temperatures, oxidants can penetrate deeper than at higher temperatures, resulting in greater Lw .

Besides the effect of increasing Lw , surface reaction limited oxidation also has the effect that once a thin oxide layer at the first polysilicon gate edge is produced by the overhang formation and so forth, the thin place remains thin even after subsequent oxidation. This is because oxide thickness increasing rates are equal in spite of differing oxide thicknesses of the starting materials when oxidation is assumed to be absolutely surface reaction controlled. Unlike the surface reaction, in diffusion-controlled oxidation the thickness of the thin oxide formed at the first gate edge increases faster than that of thick oxide, resulting finally in equal oxide thicknesses for the entire area. To summarize the above, low oxidation temperatures lead to possible dielectric breakdowns between the two gates.

Oxide thickness.—Fundamentally the same as the above, an increase in oxide thickness $Ti \cdot ox$ also causes an increase in Hw when the thickness exceeds some optimum value which seems to depend strongly on the oxidation temperature. While increases in the gate oxide thickness $Tg \cdot ox$ decrease Hw , the ratio of $Ti \cdot ox$ to $Tg \cdot ox$ is a substantial parameter affecting breakdown. In this sense, higher temperatures also cause preferable small values of the thickness ratio.

The effect of pad oxide thickness Tp on Hw was somewhat complicated. It was found that increases in Tp did not necessarily result in an increase in Hw , but in small decreases in Hw . It seemed that since lifting of the first gate edge region occurred deeper from the edge due to increased oxidant supply, the bending angle of the gate edge became smaller, resulting in smaller Hw . In fact, breakdown voltages were higher for the structures on thick field oxides than for those on thin gate oxide.

Impurity concentration of doped polysilicon.—Since the oxidation is closer to the ideal diffusion-limited oxidation with increases in P concentration (10), heavy doping is expected to decrease Hw . However, the oxide thickness increases with the increase of impurity concentration and Hw tends to increase. These two effects on dielectric breakdown oppose each other, and substantial resultant effects on dielectric performance have not yet been found.

Undercut of pad oxide.—The undercut of the pad oxide Lp had a considerable influence on Hw . Increasing Lp caused an increase in Lw . In this sense it might be preferable not to remove the pad oxide prior to a subsequent second gate oxidation if the second gate oxide was allowed to be thicker than the pad oxide and was sufficiently cleaned prior to the subsequent oxidation.

To summarize these considerations, the empirical tendency in the relation between oxidation temperature and oxide thickness shown in Fig. 8 can be qualitatively explained with respect to oxidation temperature, oxide thickness, and the impurity concentration. Since the thick intermediate oxide resulted in the formation of thin oxide at the first gate edge, oxide thickness of the intermediate oxide among these factors seemed to have the strongest influence on the topographical configuration in connection with electrical performance.

Enlarged grain effect.—Heavy doping of the polysilicon gate caused grain growth up to several microns in diameter even for 0.5 μm thick polysilicon film (14). Enlarged grains were found to have a great influence on patterning of the gate by plasma etching with CH_4 gas. Gate edge shapes are shown in Fig. 10 for both undoped and P-doped ($1 \times 10^{21} \text{ cm}^{-3}$) polysilicon films. Fjord-like edges were obtained for the P-doped gate which seemed to reveal the grain boundaries of the gate. Maximum depth of the Fjord measured about 0.3 μm , as shown in the photograph. Since plasma etching using 0.1 Torr CH_4 gas provided an essentially isotropic chemical reaction, grain boundaries having more active silicon bonds, defined by dangling bonds, were likely to be attacked much more strongly than nearly single crystalline grains.

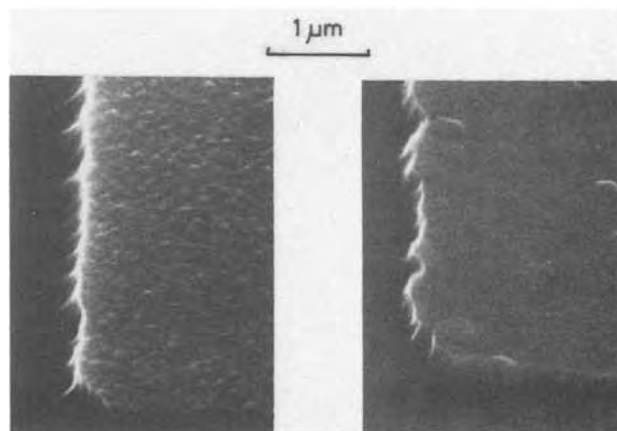


Fig. 10. Edge shapes delineated by plasma etching using CH_4 gas for undoped polysilicon and phosphorus-doped ($C_B = 1 \times 10^{20} \text{ cm}^{-3}$) films. (a, left), as deposited; (b, right), phosphorus doped.

It is considered that these Fjord-like edges cause the electric field concentration resulting in the lowering of dielectric breakdown. In addition, these edges made definition of gate length more difficult for scaled down MOS transistors. These points make strongly directional dry etching, such as reactive ion etching (18) or microwave plasma etching (19), preferable to isotropic plasma etching. These grains also gave rise to chipping and/or rising of the grains themselves similar to earthquake faults at the gate edges. This also degraded the electrical performance of the double-polysilicon devices.

Autodoping of phosphorus atoms.—Phosphorus concentrations greater than $1 \times 10^{21} \text{ cm}^{-3}$ caused very rapid oxidation resulting in "initial oxide." It was previously speculated that the initial oxide consisted of P-rich SiO_2 , or possibly phosphosilicate glass (10). In fact, SIMS depth profiles (Fig. 11), obtained in this study, clearly indicate the existence of a P-rich SiO_2 surface (20). The total amount of phosphorus in the polysilicon films was evaluated by chemical methods. The matrix effect between P and Si both in the oxide and in Si was found to be about 2 for evaluation of concentrations from the SIMS signals. These profiles were obtained for oxidized polysilicon films of which initial concentration of P were 2×10^{21} and $1 \times 10^{21} \text{ cm}^{-3}$ for (a) and (b), respectively. The oxidation was carried out in wet oxygen at 900°C for 5 min. This phenomenon that P concentration increases toward the oxide surface is highly reproducible. At present it is speculated that P atoms which exceed a solid solubility at the oxidation temperature came out from the polysilicon at the very early stage of the oxidation.

One polysilicon film of P concentration $2 \times 10^{21} \text{ cm}^{-3}$, (a) in Fig. 11, caused a concentration of about $1 \times 10^{21} \text{ cm}^{-3}$ at the oxide surface, while another P concentration $9 \times 10^{20} \text{ cm}^{-3}$ caused a concentration of $2 \times 10^{20} \text{ cm}^{-3}$ at the surface. Thus the P concentration ratio at the oxide surface was 4.5 ($= 9 \times 10^{20} / 2 \times 10^{20}$), while that of polysilicon films was 2 ($= 2 \times 10^{21} / 1 \times 10^{21}$). Furthermore, the P profile in the oxide for (a) was clearly distinguished by the higher P concentration near the surface, though effective segregation coefficients (ratio of impurity concentration in silicon to that in oxide at oxide-silicon interface) under nonequilibrium conditions did not differ as much as the surface concentrations in the profile. The effective segregation coefficients were evaluated to be around 10 for both (a) and (b) from the curves

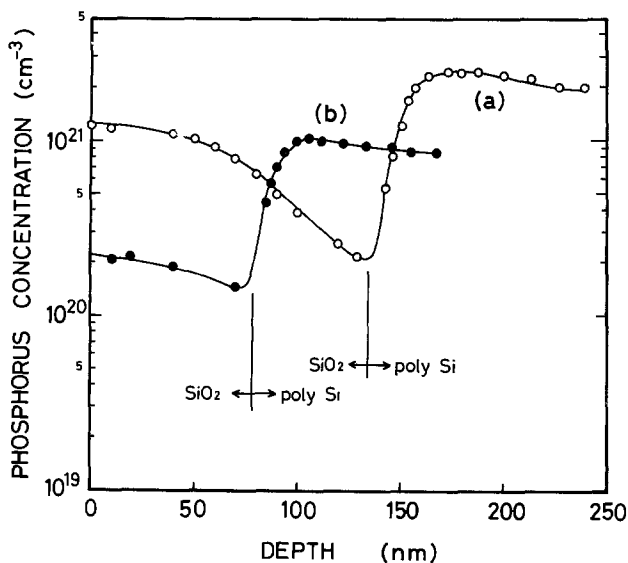


Fig. 11. SIMS depth profiles of phosphorus atoms in polysilicon films which were doped with P by implantation and their oxides obtained by 5 min wet oxidation at 900°C . Initial concentrations of implanted P were $2 \times 10^{21} \text{ cm}^{-3}$ for (a) and $1 \times 10^{21} \text{ cm}^{-3}$ for (b) prior to the wet oxidation.

shown in Fig. 11. The ratio of P surface concentration C_S to bulk concentration C_B had been reported to be 4 at 900°C wet oxidation for single silicon (21). The ratio of 1.5 was obtained for (a) in this experiment. The difference between these two values may be validly attributed to strongly enhanced diffusion of P in polysilicon (22).

Higher P concentration toward the oxide surface implies that P atoms can be vaporized into the oxidation ambient, causing harmful autodoping into bare silicon surfaces where second gate transistors will be subsequently formed. Threshold voltage lowerings of 0.1-0.5V were observed for n-channel transistors with phosphorus-doping concentrations greater than $2 \times 10^{21} \text{ cm}^{-3}$. It was also found that the lowering depended on various conditions such as relative wafer locations in an oxidation furnace, gas flow rates, distance between adjacent wafers, and oxidation temperatures. Thus autodoping effects depend on detailed oxidation conditions and sample preparations may be extremely complex, quantitative analysis has not yet been done.

Dry-wet-dry (D-W-D) oxidation.—Among the various oxidation conditions tried in this study, the best results regarding oxide breakdown characteristics were obtained with dry-wet-dry (D-W-D) oxidation at 900°C . The results are shown in Fig. 12 compared to the next best results obtained from 750°C wet + 1000°C dry oxidations. The effective influence of high temperature oxidation was obviously observed in 900°C D-W-D oxidation in the same furnace, particularly for double polysilicon structures (B) on a 50 nm thick gate oxide. The initial 5 min dry oxidation improved oxide thickness uniformity due to uneven temperature rising within wafer surfaces and among different wafers to be simultaneously oxidized. The last 5 min dry oxidation was intended not to eliminate the overhang formation but to improve the wet oxide produced by the intermediate wet oxidation. In fact, a much longer 40 min, 1000°C dry oxidation in wet-dry

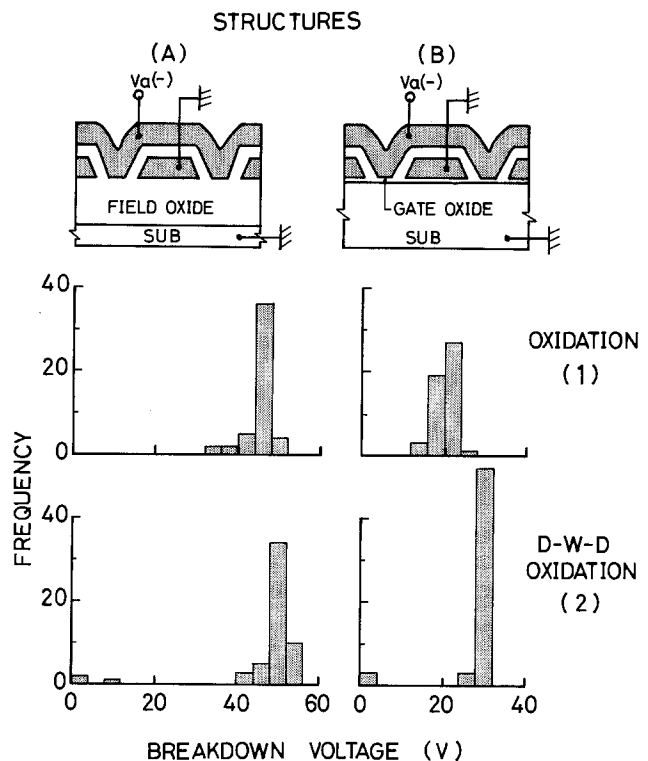


Fig. 12. Measured breakdown voltages of structures (A) and (B) for oxidations 1 and 2. Oxidation 1 = 750°C wet 90 min + 1000°C dry 40 min. Oxidation 2 = 900°C (D-W-D), 5-17-5 min. Around 50 samples were measured for $5 \mu\text{m}$ wide, 10 mm long striped gates. The cumulative total area and edge length were 25 mm^2 and 5m, respectively.

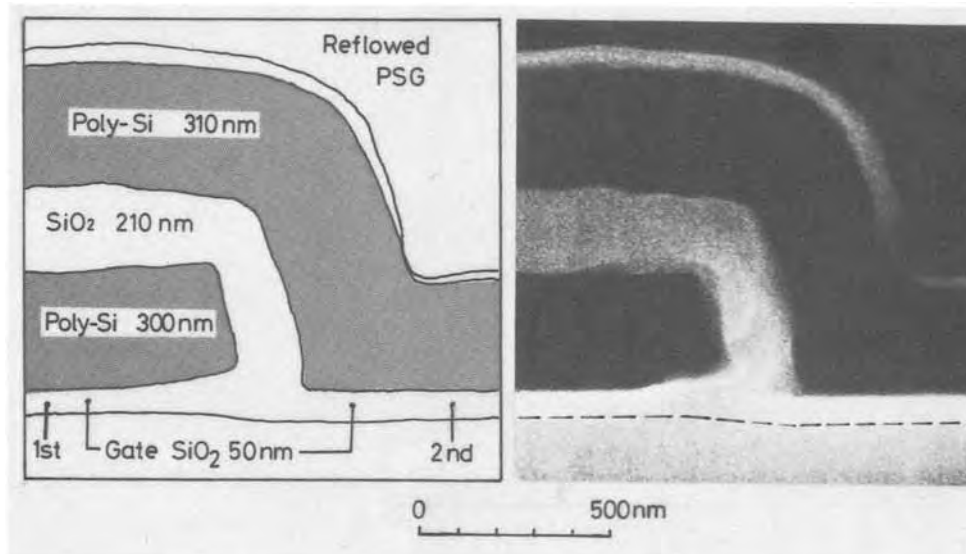


Fig. 13. Nearly perfect structure obtained by the D-W-D oxidation previously shown in Fig. 12 as Oxidation 2. The broken line has been added to the photograph to indicate the oxide-substrate interface.

oxidation (Fig. 12, (oxidation 1)) improved the breakdown field strength, but not to the level of the D-W-D oxidation.

A cross section of a double polysilicon structure realized by the D-W-D oxidation is shown in Fig. 13. Both a 50 nm gate oxide and a 210 nm intermediate oxide were formed by the D-W-D oxidation (Fig. 12, 2). A very smooth edge shape was obtained with no resulting overhang due to moderate intermediate oxide thickness of 210 nm and relatively higher temperature of 900°C. Oxidation temperatures higher than 900°C are expected to be more preferable, however, an oxidation temperature of around 900°C is a maximum one in a case that an intermediate oxide of thicker than 200 nm and a second gate oxide of thinner than 50 nm are needed.

Summary

An intermediate oxide formation technique has been realized using the concentration-dependent wet oxidation of phosphorus-doped first polysilicon gates at 700°-900°C for application to multilevel polysilicon devices. This technique, named SELOCS, gave significantly improved breakdown field strength and easier delineation of the overlaid second gate polysilicon. In particular, topographical effects regarding the overhang formation of the intermediate oxide were considered.

In this study, it was found that higher oxidation temperatures and moderate intermediate oxide thicknesses gave desirable electrical performances and topographical structures. According to this guiding principle, D-W-D oxidation was introduced to significantly improve performances. For a 5-17-5 min sequence at 900°C D-W-D oxidation, a 50 nm gate oxide and 210 nm intermediate oxide were formed on single crystal 10 Ω -cm (100) silicon and on P-doped ($C_B = 1 \times 10^{21}$ cm $^{-3}$) polysilicon, respectively. Anomalously thin intermediate oxide due to overhang is eliminated from relatively higher temperatures of around 900°C and the second gate oxide integrity is improved by the additional 5 min dry oxidation. In device structures realized by the D-W-D technique, a breakdown voltage of more than 25V between the first and the second gates on the gate oxide was obtained. In addition, the fact that autodoping of P atoms incorporated in the first polysilicon gate was pronounced when P concentration exceeded about 1×10^{21} cm $^{-3}$ in the gate was discussed.

Acknowledgments

The authors wish to thank Dr. Y. Wada for his valuable discussions regarding grain growth, M. Ozawa, Y. Kawamoto, H. Usui, and S. Iijima for their technical assistance in LSI fabrication, plasma etching and SEM

observation, ion implantation, and oxidation, respectively.

Manuscript submitted Feb. 13, 1980; revised manuscript received ca. May 8, 1980.

Any discussion of this paper will appear in a Discussion Section to be published in the June 1981 JOURNAL. All discussions for the June 1981 Discussion Section should be submitted by Feb. 1, 1981.

Publication costs of this article were assisted by Hitachi Limited.

REFERENCES

- C. H. Sequin, D. A. Sealer, W. J. Bertram, Jr., and R. R. Buckley, in "International Solid State Circuits Conference, Digest of Technical Papers," pp. 24-25, February 1974.
- S. Matsue, H. Yamamoto, K. Kobayashi, T. Wada, M. Maeda, T. Okuda, and Y. Inagaki, in *ibid.*, pp. 232-233, February 1980.
- A. K. Sinha, T. T. Sheng, T. A. Shankoff, W. S. Liderberger, E. N. Fuls, and C. C. Chang, in "Reliability Physics Symposium, Technical Digest," pp. 35-38, San Francisco, April 24-26, 1979.
- M. Koyanagi, H. Sunami, N. Hashimoto, and M. Ashikawa, in "International Electron Devices Meeting, Digest of Technical Papers," pp. 348-351 (December 1978).
- M. Koyanagi, T. Kamiyama, H. Sunami, and N. Hashimoto, Abstract 87, p. 225, The Electrochemical Society Extended Abstract, Boston, Mass., May 6-11, 1979.
- H. Sunami and M. Koyanagi, Supplement to *Jpn. J. Appl. Phys.*, **18-1**, 255 (1979).
- B. E. Deal and M. Sklar, *This Journal*, **112**, 430 (1965).
- R. M. Burger and R. P. Donovan, "Fundamentals of Silicon Integrated Device Technology," Vol. 1, Prentice-Hall, Inc., Englewood Cliffs, N.J.
- C. P. Ho, J. D. Plummer, J. D. Meindl, and B. E. Deal, *This Journal*, **125**, 665 (1978).
- H. Sunami, *ibid.*, **125**, 892 (1978).
- J. J. Barnes, J. M. DeBlasi, and B. E. Deal, *ibid.*, **126**, 1779 (1979).
- H. Iizuka, T. Sato, F. Masuoka, K. Ohuchi, H. Hara, H. Tango, M. Ishikawa, and Y. Takeishi, Supplement to *Jpn. J. Appl. Phys.*, **42**, 158 (1973).
- R. M. Anderson and D. R. Kerr, *J. Appl. Phys.*, **48**, 4834 (1977).
- Y. Wada and S. Nishimatsu, *This Journal*, **125**, 1501 (1978).
- Y. Kawamoto and N. Hashimoto, Supplement to *Jpn. J. Appl. Phys.*, **18-1**, 277 (1979).
- T. T. Sheng and R. B. Marcus, *This Journal*, **125**, 432 (1978).
- B. E. Deal and A. S. Grove, *J. Appl. Phys.*, **36**, 3770 (1965).
- J. A. Bondur, *J. Vac. Sci. Technol.*, **13**, 1023 (1976).

19. K. Suzuki, S. Okudaira, and I. Kanomata, *This Journal*, **126**, 1024 (1979).
 20. N. Hashimoto and H. Tsuyama, *Shitsuryo Bunseki* (in Japanese), **25**, 363 (1978).
 21. A. S. Grove, O. Leistiko, and C. T. Sah, *J. Appl. Phys.*, **35**, 2695 (1964).
 22. T. I. Kamins, J. Manoliu, and R. N. Tucker, *J. Appl. Phys.*, **43**, 83 (1972).

A Simple Model for the Deposition of Boron in Silicon by Using a BN Diffusion Source

S. F. Guo*

Institute of Electronics, National Chiao Tung University, Hsinchu, Taiwan, China

ABSTRACT

A physical model based on the multiple charge state vacancy statistics is proposed to express the boron diffusivity in silicon during the deposition step using the BN disk as a diffusion source in an inert ambient. The diffusion equation with concentration dependent diffusivity is solved numerically. A universal shape of the normalized profiles is observed. The surface concentration of the deposited layer has been determined experimentally. The calculated sheet resistance as a function of deposited time and temperature is in good agreement with the measured data. With a slight modification, this simple vacancy statistics model can also be applied to other deposition sources.

One of the most important advantages of the boron nitride (BN) source deposition process is its high reproducibility. It is also possible to describe the deposition sheet resistance in mathematical terms (1). High surface concentrations are generated by the BN diffusion system and anomalous effects have been observed under different diffusion conditions (2). To explain concentration-dependent diffusion in an inert atmosphere, Fair (3) proposed a donor-type mono-vacancy diffusion model and showed that the boron profiles fit a normalized universal curve which is a polynomial approximation to the solution of the diffusion equation with linear concentration-dependent diffusivity.

Recently, it was reported that vacancies in silicon can exist in V^+ , V^- , and $V^=$ charge states, each having a definite energy level in the forbidden bandgap (4). Based on the multiple charge state vacancy statistics, Ho and Plummer (5) have successfully explained the commonly observed enhanced oxidation rates of heavily doped silicon. The purpose of this paper is to illustrate that the same statistics can also be applied to the behavior of high concentration boron deposition in a dry nitrogen ambient.

Although Fair (6) has examined the contribution of each charge state to the total diffusivity, it will be a good approximation that the diffusion coefficient of boron in silicon under an inert atmosphere is directly proportional to the total vacancy concentration. Furthermore, the enhanced diffusions in oxidized ambients can be explained by a surface space charge effect. The electric field factor generally encountered in the diffusivity expression will be omitted, since its variation is very small (from 1.45 to 2) and the localized Fermi level involved in the vacancy statistics might include the localized electric field effect.

As found by Armigliato *et al.* (7), although dopant concentration is much higher than the solubility value at deposition temperature, precipitation is hard to occur. It is reasonable to assume that each boron atom in silicon provides a free hole in the diffusion coefficient and sheet resistance calculations. The hole mobility deduced by Antoniadis *et al.* (8) will be used in the surface concentration and sheet resistance calculations.

Experimental

The diffusion source employed in this work was Carborundum BN-975 boron nitride disks. The silicon materials used were 2 in. diam (111) oriented, one-side polished, high resistivity ($>20 \Omega\text{-cm}$) n-type wafers. The source and silicon wafers are edge-stacked in the deposition carrier face to face with a spacing of approximately 1 mm. The diffusion furnace used was Thermco-Ranger Type-3000. The furnace ambient was dry nitrogen at a flow rate of 1 liter/min.

The sheet resistance of deposited layers was measured using a Veeco Model FPP-100 four-point probe. In order to obtain information on the dopant profile, the surface concentration was determined from a differential sheet resistance measurement. The thickness of anodic oxides was measured using a Rudolph Auto EL-II ellipsometer. The volumetric ratio of 0.4 for silicon converted to silicon dioxide and the concentration-dependent hole mobility value of Antoniadis *et al.* (8) were used in the concentration calculation. The measured results of surface concentrations as a function of temperature is shown in Fig. 1 along with other reported data for both BN solid source (2) and BB-liquid source (7).

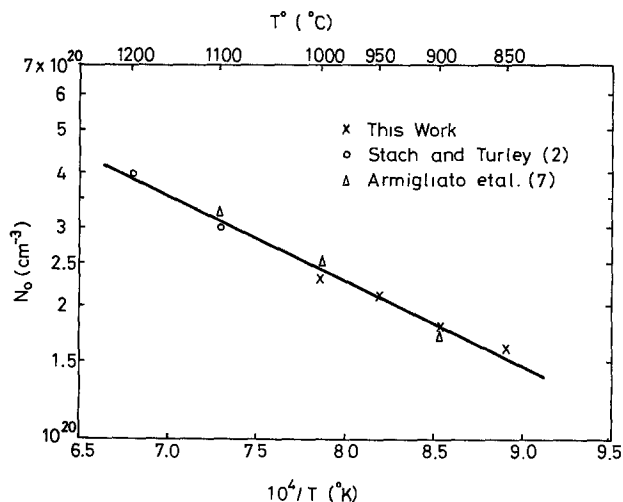


Fig. 1. Surface concentration of boron in silicon as a function of temperature.

* Electrochemical Society Active Member.

Key words: diffusion model, boron deposition, BN source, vacancy statistics.

Diffusion Model

The atomic theory of diffusion for substitutional impurities in silicon is based on the lattice vacancy diffusion mechanism. The effect of equilibrium vacancy concentration variation on the impurity diffusivity was first considered by Hu and Schmidt (9), and an expression of concentration-dependent diffusivity based on single charged state had been derived.

At the present time, it is known that silicon vacancies exist in neutral V^0 and multiple charged states V^+ , V^- , and $V^{=}$. The charged vacancy states have definite energy levels in the bandgap (4). The donor level E tracks the valence bandedge E_v

$$E^+ = E_v + 0.37 \text{ eV} \quad [1]$$

while the acceptor levels E^- and $E^{=}$ track the conduction bandedge E_c

$$E^- = E_c - 0.57 \text{ eV} \quad [2]$$

$$E^{=} = E_c - 0.11 \text{ eV} \quad [3]$$

as the bandgap narrows with increasing temperature

$$E_G = E_c - E_v = 1.17 - 4.73 \times 10^{-4} \left(\frac{T^2}{T + 636} \right) \quad [4]$$

From the Shockley-Last theory (10), the thermal equilibrium concentrations of vacancies at various charged states C^r ($r: +, -, =$) are related to the Fermi level E_F by

$$C^+ : C^- : C^{=} = \exp \frac{E^+ - E_F}{kT} : 1 : \exp \frac{E_F - E^-}{kT} : \exp \frac{2E_F - E^- - E^{=}}{kT} \quad [5]$$

where the degeneracy effects have been neglected. It has been argued by Shockley and Moll (11) that the equilibrium concentration of neutral vacancies is a function of temperature only while the concentration of charged vacancies is a function of the Fermi level as well. The total vacancy concentration normalized to the neutral vacancy concentration is thus given by

$$C^T = 1 + \exp \frac{E^+ - E_F}{kT} + \exp \frac{E_F - E^-}{kT} + \exp \frac{2E_F - E^- - E^{=}}{kT} \quad [6]$$

By the use of Boltzmann approximation

$$\exp \frac{E_i - E_F}{kT} = \frac{p}{n_i} \quad [7]$$

where E_i is the intrinsic Fermi level

$$E_i = \frac{F_G}{2} - \frac{kT}{4} \quad [8]$$

and n_i is the intrinsic carrier concentration approximately given (12) by

$$n_i = 3.87 \times 10^{16} T^{3/2} \exp \left(- \frac{0.605}{kT} \right) \quad [9]$$

Equation [6] can be expressed as

$$C^T = 1 + \beta^+ \left(\frac{p}{n_i} \right) + \beta^- \left(\frac{n_i}{p} \right) + \beta^{=} \left(\frac{n_i}{p} \right)^2 \quad [10]$$

where

$$\beta^+ = \exp \frac{E^+ - E_i}{kT}$$

$$\beta^- = \exp \frac{E_i - E^-}{kT} \quad [11]$$

and

$$\beta^{=} = \exp \frac{2E_i - E^- - E^{=}}{kT}$$

On the assumption that the effective diffusivity is directly proportional to the total vacancy concentration (9), one gets

$$\frac{D}{D_i} = \frac{1 + \beta^+ \left(\frac{p}{n_i} \right) + \beta^- \left(\frac{n_i}{p} \right) + \beta^{=} \left(\frac{n_i}{p} \right)^2}{1 + \beta^+ + \beta^- + \beta^{=}} \quad [12]$$

where D_i is the intrinsic diffusivity. The value of D_i for boron in silicon has recently been determined by Antoniadis *et al.* (8) as

$$D_i = 0.55 \exp \left(- \frac{3.42 \text{ eV}}{kT} \right) \text{ cm}^2/\text{sec} \quad [13]$$

under nonoxidized atmosphere.

Numerical Analysis

The classical solution of diffusion equation with constant diffusivity and constant surface concentration is a well-known complementary error function. However, for a high-concentration deposition, the diffusion coefficient is concentration-dependent and no analytic solution is available. Most recently a great deal of attention has been given to the use of computer simulation to determine dopant profiles (13).

For a concentration-dependent diffusivity, the diffusion equation is

$$\frac{\partial N}{\partial y} = \frac{\partial}{\partial y} \left(D \frac{\partial N}{\partial t} \right) \quad [14]$$

This problem should be solved numerically by discretizing the space y and time t coordinates

$$y = y_j = j\Delta y \quad j = \dots, -2, -1, 0, 1, 2, \dots$$

$$t = t_i = i\Delta t \quad i = 0, 1, 2, \dots$$

and writing the differential Eq. [14] as a set of difference equation (14)

$$N(y_j, t_{i+1}) = M [D(y_{j+1}, t_i) N(y_{j+1}, t_i) + D(y_{j-1}, t_i) N(y_{j-1}, t_i)] + [1 - 2MD(y_j, t_i)] N(y_j, t_i) \quad [15]$$

where $M = \Delta t / (\Delta y)^2$ is called the mesh ratio and $D(y_j, t_i)$ is evaluated from Eq. [12] by letting $p = N(y_j, t_i)$ for $N(y_j, t_i) > n_i$ and $p = n_i$ for $N(y_j, t_i) \leq n_i$. The boundary condition for a constant surface concentration deposition is $N(y_0, t_i) = N_0$ and the corresponding diffusivity is D_0 . The numerical calculation can be performed on a TI 59 programmable calculator. It would take about 2 hr to generate a profile, if a mesh ratio M of $1/4 D_0$, a space interval Δy of $\sqrt{4D_0 t} / 10$, and a time interval Δt of $t / 100$ are chosen.

The calculated profiles of N/N_0 vs. $y/\sqrt{4D_0 t}$ for several deposition temperatures are shown in Fig. 2. These normalized curves show a universal shape in the high concentration region ($N > n_i$) and a complementary error function tail in the low concentration region ($N < n_i$). It is interesting to note that the universal curve can be expressed as

$$\frac{N}{N_0} = 1 - 0.631 \left(\frac{y}{\sqrt{4D_0 t}} \right) - 0.214 \left(\frac{y}{\sqrt{4D_0 t}} \right)^2 \quad [16]$$

which is in good agreement with the approximate solution for arsenic diffusion in terms of Chebyshev polynomials (15). As a matter of fact, Fair's normalized boron profile [Fig. 3 of Ref. (3)] can also be approximated by Eq. [16] if the space coordinate is normalized to the surface diffusion length $\sqrt{4D_0 t}$.

Results and Discussion

The experimental result of sheet resistance as a function of deposition time at various temperatures are

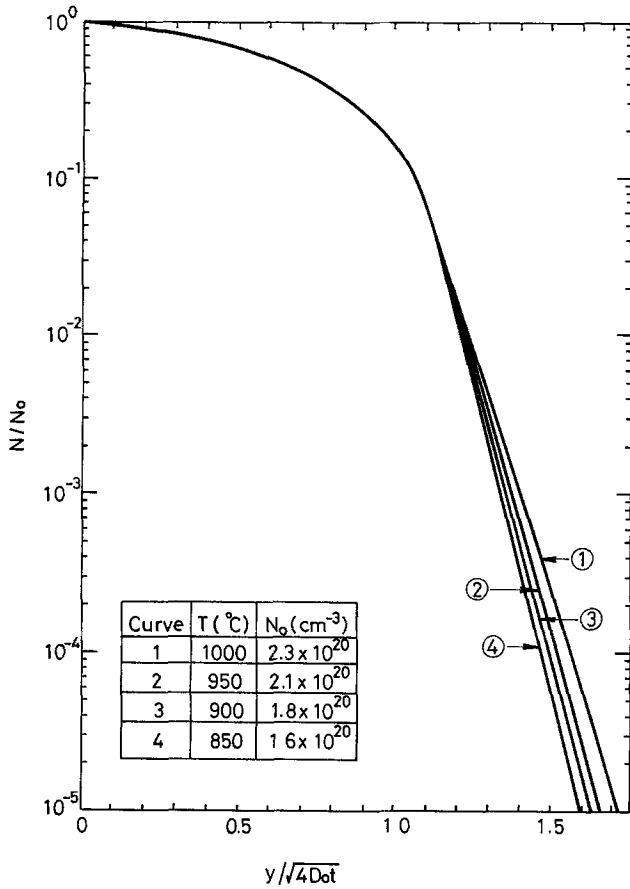


Fig. 2. Normalized profiles of N/N_0 vs. $y/\sqrt{4D_0t}$ for various temperatures.

shown in Fig. 3 along with data reported by Rupprecht and Stach (16). Assuming that boron atoms in the diffused layer are fully ionized, the deposited sheet resistance R_s can be calculated from

$$R_s^{-1} = \int q\mu_p N dy \quad [17]$$

where μ_p is the concentration-dependent hole mobility given (8) by

$$\mu_p = 49.7 + \frac{418}{1 + (N/1.6 \times 10^{17})^{0.7}} \quad [18]$$

As shown in Fig. 3, the numerically calculated results of sheet resistance are in good agreement with measured values.

Alternatively, Eq. [17] can be expressed as

$$R_s^{-1} = q\bar{\mu}_p Q \quad [19]$$

where $\bar{\mu}_p$ is the average hole mobility and Q is the deposited quantity of boron atoms per unit area. From numerical calculations it has been found that $\bar{\mu}_p \approx 54 \text{ cm}^2/\text{Vsec}$ for $N_0 \approx 2 \times 10^{20} \text{ cm}^{-3}$ and $Q \approx 0.628 N_0 \sqrt{4D_0t}$ for all deposited temperatures used in this work. Therefore, the sheet resistance expression [19] becomes

$$R_s = 9.2 \times 10^{16}/N_0 \sqrt{D_0t} \Omega/\text{sq} \quad [20]$$

where N_0 and D_0 are temperature dependent.

If the junction depth was defined as the distance from the surface at which N/N_0 had fallen to 10^{-2} in Fig. 2, then

$$y_j \approx 2.4 \sqrt{D_0t} \quad [21]$$

This is in approximate agreement with Fair's approximation [Eq. [12] of Ref. (3)].

It is suggested from Eq. [20] and [21] that the surface diffusivity D_0 can be determined experimentally by profile fitting or sheet resistance and surface concentration measurements. Some experimentally determined values of D_0/D_1 and theoretically calculated curves of D/D_1 vs. N/n_1 are shown in Fig. 4. The multiple charge state vacancy model proposed in this work gives a result for the low temperature deposition using BN disks as diffusion source in a dry nitrogen ambient. For comparison, the D_0/D_1 values for BBr_3 sources (7) as deduced from profile fitting are also shown in Fig. 4. Enhanced diffusion is observed. This phenomenon may be explained as follows.

The BBr_3 liquid source deposition is generally carried out in an oxidized ambient. This may result in some negative ions in the oxide layer. This surface charge causes the energy band of silicon to bend upward at the surface and the hole concentration p is then enhanced by a Boltzmann factor

$$\frac{p}{N} = e^{\Delta} \quad [22]$$

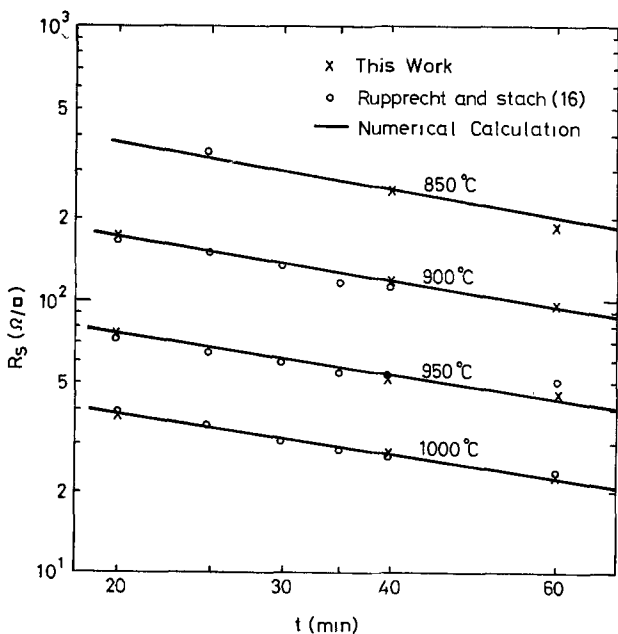


Fig. 3. Sheet resistance vs. deposition time for several temperatures.

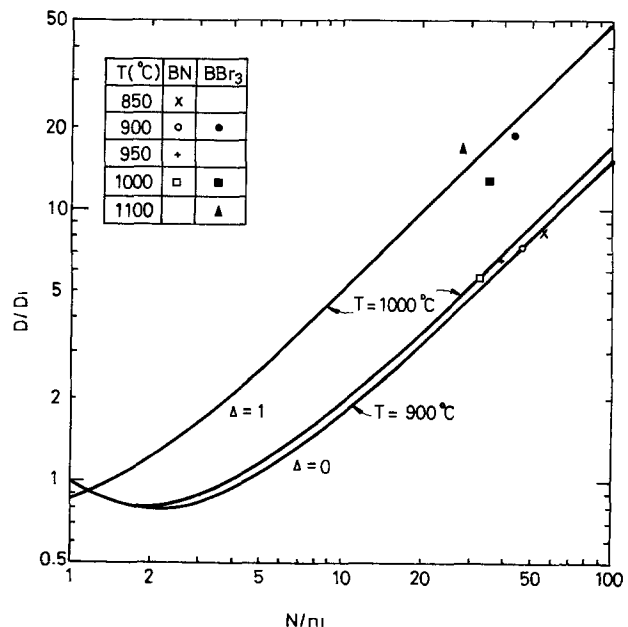


Fig. 4. Normalized diffusivity vs. normalized boron concentration under different conditions.

where Δ is the amount of energy band bending upward normalized to the thermal energy kT and N is the boron concentration. Taking this into account, the effective diffusivity, Eq. [12], is modified to

$$\frac{D}{D_i(0)} = \frac{1 + \beta^+ e^{\Delta} \left(\frac{N}{n_i}\right) + \beta^- e^{-\Delta} \left(\frac{N}{n_i}\right)^{-1} + \beta^= e^{-2\Delta} \left(\frac{N}{n_i}\right)^{-2}}{1 + \beta^+ + \beta^- + \beta^=} \quad [23]$$

where $D_i(0)$ is the intrinsic diffusivity without energy band bending given by Eq. [13]. In Fig. 4, a band bending of $1 kT$ shows a good fit for the surface diffusivity of the BBr_3 source deposition.

In addition to the neutral vacancy concentration, the intrinsic diffusivity at the surface also depends on the band condition

$$\frac{D_i(\Delta)}{D_i(0)} = \frac{1 + \beta^+ e^{\Delta} + \beta^- e^{-\Delta} + \beta^= e^{-2\Delta}}{1 + \beta^+ + \beta^- + \beta^=} \quad [24]$$

The effect of band bending on the intrinsic diffusivity is shown in Fig. 5. Due to negatively charged vacancies, the intrinsic diffusivity decreases slightly with a small upward band bending. The values used in this work and the data reported by Fair (6) are also shown in Fig. 5. It is interesting to note that the increase of the enhancement of intrinsic diffusivity in oxidizing ambient with decreasing temperature (8) can be ex-

plained by the band bending effect. It is well known (17) that the positive oxide charge near the silicon dioxide-silicon interface increases with decreasing temperature. This positive surface charge will cause a downward band bending and the magnitude of band bending will increase with decreasing temperature. Therefore, Eq. [24] gives a good explanation for the diffusivity enhancement.

Conclusion

A simple diffusion model based on the vacancy statistics gives a satisfactory prediction of the behavior of BN source deposition. Although the charged state of lattice vacancies might have a different contribution to the diffusion coefficient, the different behaviors for different diffusion conditions can be explained by a band-bending effect.

Acknowledgment

The author is indebted to Mr. T. Y. Chu and Tatung Institute of Technology for carrying out most of the experimental works.

Manuscript submitted March 11, 1980; revised manuscript received May 19, 1980.

Any discussion of this paper will appear in a Discussion Section to be published in the June 1981 JOURNAL. All discussions for the June 1981 Discussion Section should be submitted by Feb. 1, 1981.

Publication costs of this article were assisted by National Chiao Tung University.

REFERENCES

1. M. Crooke and A. G. K. Lutsch, *This Journal*, **124**, 457 (1977).
2. J. Stach and A. Turley, *ibid.*, **121**, 722 (1974).
3. R. B. Fair, *ibid.*, **122**, 800 (1975).
4. J. A. Van Vechten and C. M. Thurmond, *Phys. Rev. B*, **14**, 3539 (1976).
5. C. P. Ho and J. D. Plummer, *This Journal*, **126**, 1516 (1979).
6. R. B. Fair, in "Semiconductor Silicon 1977," H. R. Huff and E. Sirtl, Editors, p. 968, The Electrochemical Society Softbound Proceedings Series, Princeton, N.J. (1977).
7. A. Armigliato, D. Nobili, P. Ostojka, M. Servidori, and S. Solmi, in "Semiconductor Silicon 1977," H. R. Huff and E. Sirtl, Editors, p. 638, The Electrochemical Society Softbound Proceedings Series, Princeton, N.J. (1977).
8. D. A. Antoniadis, A. G. Gonzalez, and R. W. Dutton, *This Journal*, **125**, 813 (1978).
9. S. M. Hu and S. Schmidt, *J. Appl. Phys.*, **39**, 4272 (1968).
10. W. Shockley and J. T. Last, *Phys. Rev.*, **107**, 392 (1957).
11. W. Shockley and J. L. Moll, *ibid.*, **119**, 1480 (1960).
12. F. J. Morin and J. P. Maita, *ibid.*, **96**, 28 (1954).
13. D. A. Antoniadis, S. E. Hansen, and R. W. Dutton, "SUPREM II-A Program for IC Process Modeling and Simulation," SEL 78-020, Stanford University, June 1978.
14. H. W. Carlsaw and J. C. Jaeger, "Conduction of Heat in Solids," 2nd ed., Chap. 18, Oxford University Press, (1960).
15. R. B. Fair, *J. Appl. Phys.*, **43**, 1278 (1972).
16. D. Rupprecht and J. Stach, *This Journal*, **120**, 1266 (1973).
17. R. R. Razouk and B. E. Deal, *ibid.*, **126**, 1573 (1979).

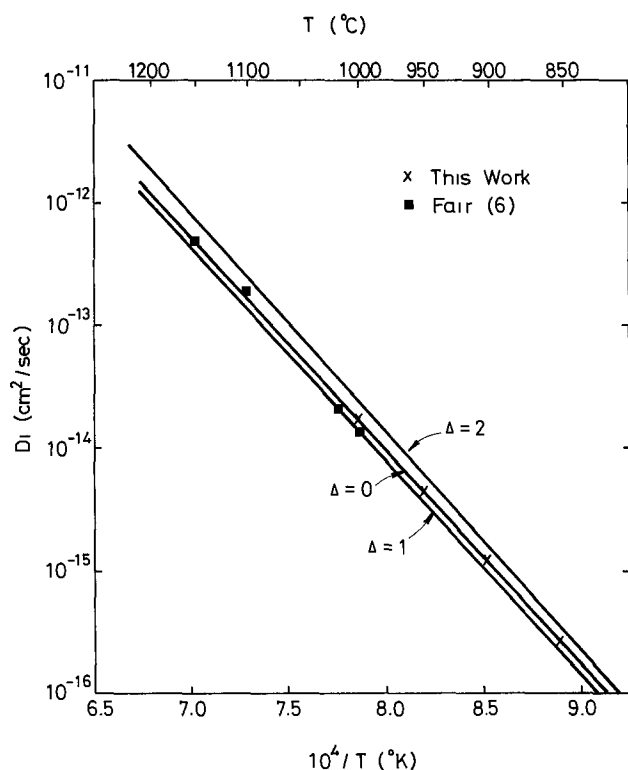


Fig. 5. Intrinsic diffusivity of boron in silicon with and without band bending.

Preliminary Evaluation of Copolymers of Methyl Methacrylate and Acyloximino Methacrylate as Deep U.V. Resists

C. W. Wilkins, Jr., E. Reichmanis, and E. A. Chandross

Bell Laboratories, Murray Hill, New Jersey 07974

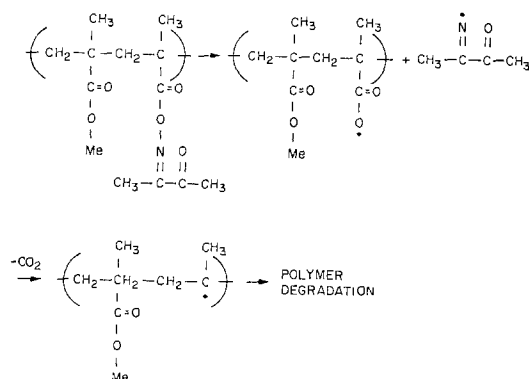
ABSTRACT

Copolymers of methyl methacrylate and acyloximino methacrylate esters have been evaluated as deep u.v. (200-250 nm) resists. Poly (methyl methacrylate-co-3-methacryloyl-oximino-2-butanone) has been found to be ~ 5 times faster than PMMA at $\lambda > 240$ nm and capable of submicron resolution. It has been found that the acetyl group of the 3-oximino-2-butanone substituent is more effective than the related species containing t-butyl, phenyl, or benzoyl groups in promoting polymer degradation. The copolymers have also been exposed to 20 kV electron beam radiation and have been found to be about as sensitive as PMMA (5×10^{-5} C/cm²).

Deep (200-250 nm) u.v. photolithography is gaining a great deal of interest as a method of achieving small feature size ($\sim 1 \mu\text{m}$) with high aspect ratios (1-7). The reduction in exposure wavelength from 400 to 250 nm should reduce diffraction effects and improve resolution (1). However, the technique requires the development of new resist materials. The ideal resist for deep u.v. lithography should possess good photosensitivity in the 200-250 nm region with little or no absorption at longer wavelengths to eliminate the need for the difficult task of removing the long wavelength light from a conventional mercury source. Additionally, the resist should be capable of high resolution, and be compatible with conventional microstructure fabrication.

Delzenne (8) has reported that copolymers of poly(methyl methacrylate) (PMMA) and acyloximino methacrylate esters undergo grafting in the presence of the other monomers, but that they degrade rapidly in monomer-free benzene solution upon irradiation with light of $\lambda = 365$ nm. We decided to investigate the solid-state photodegradation of similar copolymers and their possible utility as deep u.v. photoresists, and also as electron beam resists. The acyloximino ester chromophore has a strong absorption at ~ 225 nm ($\epsilon \sim 10^4 \text{ M}^{-1} \text{ cm}^{-1}$, Fig. 1) and the tail of this band is strong enough to give useful sensitivity at ~ 240 nm. These copolymers undergo a rapid photolytic decomposition involving cleavage of the N—O bond (scheme 1), yet they are sufficiently thermally stable to be compatible with conventional IC processing. Additionally, they should retain the high resolution properties of PMMA provided that the oxime methacrylate ester mole fraction is low.

Scheme 1



Key words: ultraviolet, copolymers, degradation.

Experimental

Polymer preparation.—Polymers were prepared in toluene solutions at 60°C using azobisisobutyronitrile as initiator. They were isolated by two precipitations from methyl ethyl ketone solution into methanol, and dried under vacuum. Molecular parameters for the polymers evaluated are listed in Table I.

Preparation of 3-oximino-2-butanone methacrylate.—To a cold (0°) stirred solution of butane dione

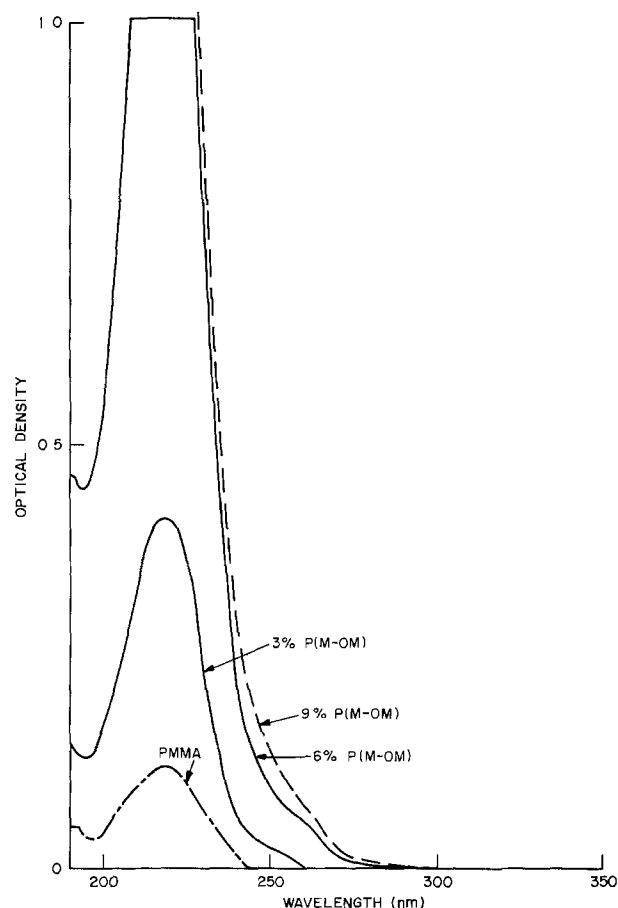


Fig. 1. Absorption spectra of copolymers of methyl methacrylate and 3-oximino-2-butanone methacrylate. The films are obviously not the same thickness, but the spectra are shown to illustrate the concentration dependence of the long wavelength tail.

Table I.

Polymer	Mole percent 3-oximino-2-butanone methacrylate	$M_w (\times 10^5)$	M_w/M_n	Absolute at 240 nm (Jcm^{-2})	T_g ($^{\circ}C$)	Sensitivity relative from 200-400 nm	Electron beam ($\times 10^{-5} C/cm^2$)
PMMA	0	^a	—	3.4	—	1	—
P(M-OM)	3	1.39	2.06	—	—	0.5	—
P(M-OM)	3	5.35	3.00	0.9	103	0.4	3.1
P(M-OM)	6	2.87	1.86	—	103	0.25	4.0
P(M-OM)	6	10.1	2.35	1.3	—	0.25	5.0
P(M-OM)	9	—	—	0.7	—	0.25	4.0

^a Elvacite 2010 (du Pont) "high molecular weight."

monoxime (54.5g, 0.54 mole) and triethylamine (120 ml, 1.1 mole) in ether (100 ml) under N_2 was added methacryloyl chloride (56.2 ml, 0.54 mole) in ether (250 ml) during the course of 1 hr. Stirring was continued at 0° under N_2 for 3 hr, after which the mixture was filtered, the filtrate washed with water (300 ml), dried, concentrated, and recrystallized from cyclohexane to afford 45g (50%) of product. (mp 38.5° - $39^{\circ}C$).

Other monomers were prepared by the same general procedure as for the preparation of 3-oximino-2-butanone methacrylate.

Resolution.—The resolution capability of the materials was determined by proximity printing with a Kasper Model 2001 printer modified for deep u.v. exposure. The materials were exposed to the full output of a 200W xenon cadmium lamp.

Materials.—Poly(methyl methacrylate) (Elvacite 2010), a high molecular weight polymer available from du Pont, was used as the standard for measuring sensitivities.

Sensitivity.—Polymers were dissolved in methyl cellosolve acetate (10% solution) and were coated onto silicon substrates with a Headway Research spinner. Films were prebaked for 60 min at $100^{\circ}C$.

Photon sensitivities are reported relative to PMMA and were obtained by imaging a slit for varying exposure times across substrates coated with resist. Exposure times were recorded as the time necessary to completely remove the resist in the irradiated area, using methyl isobutyl ketone as the developer under conditions where there was essentially no thinning of the unirradiated areas. A 1000W high pressure mercury lamp was used as the exposure source. Absolute sensitivities were determined by using a monochromator and a thermopile to measure light flux.

Electron sensitivities were obtained by writing rectangular bars at different doses. The bar patterns were developed and the thickness remaining at each

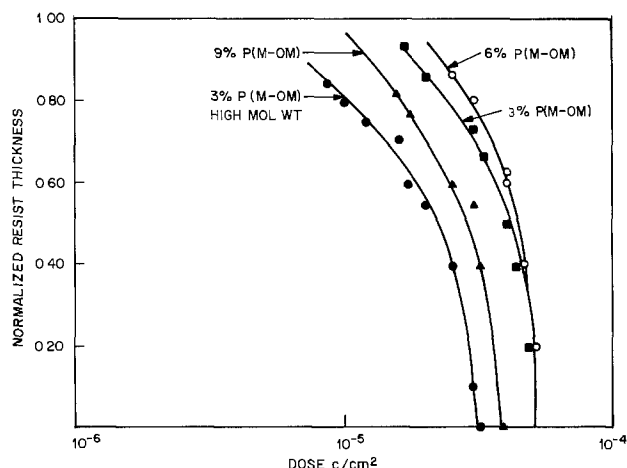


Fig. 2. Plots of normalized resist thickness vs. electron-beam dose for copolymers of methyl methacrylate and 3-oximino-2-butanone methacrylate.

dose was measured. Figures 2 and 3 show plots of normalized resist thickness vs. dose for the polymers exposed at 20 kV.

Results and Discussion

Sensitivity.—We have found that incorporation of small (3-9 mole percent) amounts of 3-oximino-2-butanone methacrylate into PMMA renders the copolymers approximately 5 times more sensitive than PMMA, the standard material for deep u.v. lithography. In this section, we report the effect of both photosensitizer concentration and copolymer molecular weight on sensitivity.

Figure 1 reveals that the 3% 3-oximino-2-butanone copolymer has an optical density of 0.1 at 240 nm. This weak absorption allows light to be absorbed uniformly through the polymer film and results in patterns with high aspect ratios, but the materials are only marginally sensitive. Figure 1 shows the absorption spectrum of the copolymer as a function of acyl-oxime chromophore fraction. The OD of the 3% copolymer at 240 is 0.1, while that of the 9% copolymer is 0.3, but this approach is only marginally effective in improving sensitivity. Inspection of Table

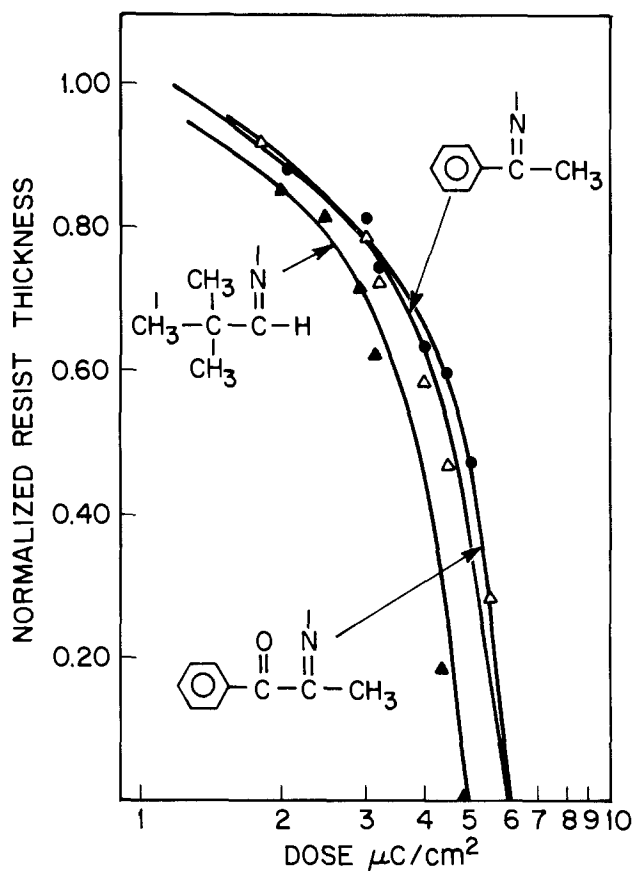


Fig. 3. Plots of normalized resist thickness vs. electron-beam dose for copolymers of methyl methacrylate and acyl-oxime methacrylate esters.

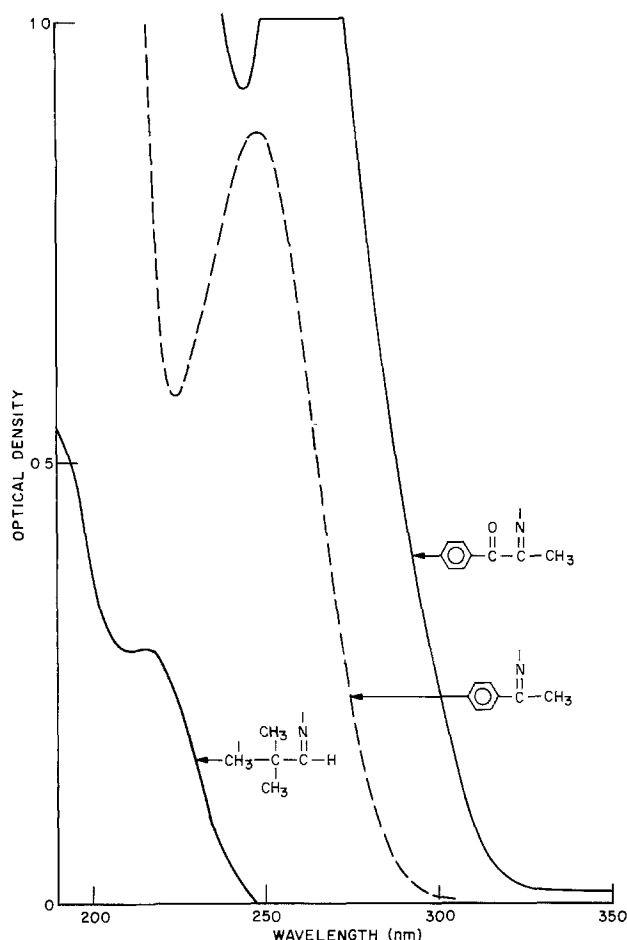


Fig. 4. Absorption spectra of copolymers of methyl methacrylate and oxime methacrylate esters.

I reveals that upon exposure to the full output of the mercury lamp the 6% acyl-oxime copolymer is more sensitive than the 9% copolymer. However, the 6% material has a monochromatic sensitivity at 240 nm of 1.3 J/cm^2 while the 9% copolymer has a sensitivity of 0.7 J/cm^2 , compared to 3.4 J/cm^2 for PMMA. The effect of increasing the acyl-oxime content still further is under study and will be reported in the future.

Inspection of Table I reveals that only a minor improvement in sensitivity of the 3% copolymer was realized by increasing the polymer molecular weight, and that this effect was not realized with the 6% acyl-oxime copolymers.

Oxime structure.—We have also examined the effect of changing the structure of the oxime or acyl-oxime chromophore. We incorporated pivalaldehyde oxime methacrylate as well as species in which the acetyl group of 3-oximino-2-butanone has been replaced by phenyl or benzoyl substituents. The latter two groups push the absorption spectrum to longer wavelengths (Fig. 4), thus enabling a closer match with the

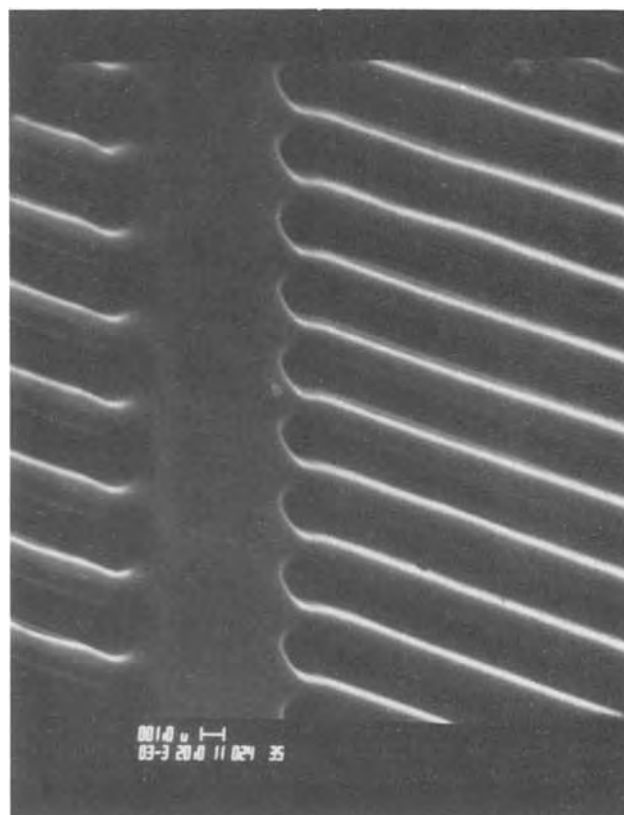


Fig. 5. Lines and spaces ($1.25 \mu\text{m}$) obtained in poly (methyl methacrylate-co-3-oximino-2-butanone methacrylate).

emission spectrum of the high pressure mercury lamp for exposure at longer wavelengths.

Figure 4 shows the absorption spectra of the polymers investigated. Table II shows that these substituents were not as effective as the 3-oximino-2-butanone chromophore in promoting PMMA degradation.

Resolution.—PMMA is known to be an extremely high resolution material. We found that by keeping the co-monomer concentration low we were able to improve the polymer's sensitivity at $\lambda > 230 \text{ nm}$ without any concurrent loss in resolution. Figure 5 shows $1.25 \mu\text{m}$ lines and spaces obtained routinely in poly (methyl-methacrylate-co-3-oximino-2-butanone methacrylate) (P(M-OM)). Electron beam exposure experiments (Fig. 6) reveal that the material is inherently capable of still higher ($0.5 \mu\text{m}$) resolution.

Electron beam irradiation.—Several workers have attempted to improve the sensitivity of PMMA to electron beams by copolymerization with other types of monomers, and we have also evaluated our polymers for their e-beam response. Figure 2 shows the effect of incorporating 3-9% 3-oximino-2-butanone methacrylate into PMMA. The most sensitive material is the 3% copolymer which requires a dose of $3.1 \times 10^{-5} \text{ C/cm}^2$. This result is not understood, for

Table II.

Polymer	Mole percent acyl-oxime (%)	$M_w (\times 10^5)$	M_w/M_n	Relative sensitivities ^a		T_g ($^{\circ}\text{C}$)	Electron sensitivities ($\times 10^{-5} \text{ C/cm}^2$)
				Air	N_2		
P(M-OM)	3			<0.25	0.25		3.1
P(M-t-BO)	3	4.13	1.88	<1.5	2	100	5.0
P(M-AO)	2	4.10	1.86	<2	1.5	102	6.1
P(M-BO)	5	6.41	2.17	<1.5	1	102	6.0

^a Sensitivities are reported relative to PMMA.

P(M-t-BO)—poly (methyl methacrylate-co-1-oximino-2, 2-dimethyl-propyl methacrylate).

P(M-AO)—poly (methyl methacrylate-co-acetophenone oxime methacrylate).

P(M-BO)—poly (methyl methacrylate-co-1-phenyl-1, 2-propanedione-2-oxime methacrylate).

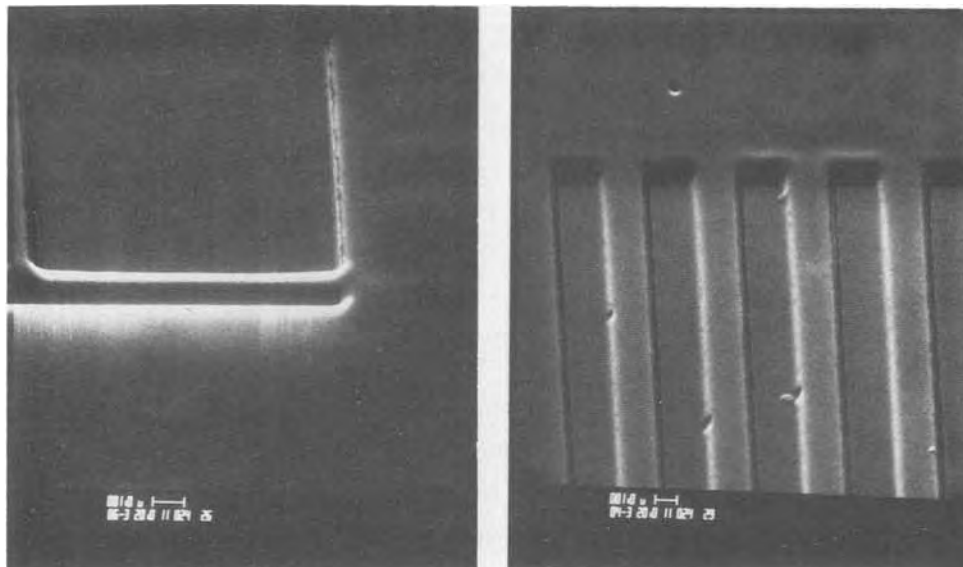


Fig. 6. Electron beam exposure patterns of poly(methyl-methacrylate-co-3-oximino-2-butanone methacrylate).

the higher acyl-oxime concentration copolymers of comparable molecular weight are not as sensitive. Additionally, the materials cannot be made appreciably faster than PMMA (5×10^{-5} C/cm²) by changing the structure of the acyl-oxime monomer. Figure 3 shows that the acetophenone and 1-phenyl-1,2-propanedione oxime polymers are slower than PMMA.

Conclusion

Copolymers of methyl methacrylate and acyl-oxime methacrylate esters have been evaluated as deep u.v. photoresists.

1. Poly(methyl methacrylate-co-3-oximino-2-butanone methacrylate) (94:6) is approximately 5 times faster than the base resin.

2. Sensitivity can only be marginally improved by increasing the polymer molecular weight.

3. The acetyl group of the acyl-oxime chromophore is more effective than t-butyl, phenyl or benzoyl groups in promoting polymer degradation.

4. Copolymers of methyl methacrylate and acyl-oxime methacrylate have about the same sensitivity as PMMA to 20 kV electron beams.

Acknowledgments

The authors thank L. V. Dodd for scanning electron microscopy, W. Q. McKnight for proximity printing, and L. E. Stillwagon for gel permeation chromatographic analyses. The authors acknowledge helpful

conversations held with E. D. Feit and S. R. Fahrenholtz.

Manuscript submitted Dec. 26, 1979; revised manuscript received May 27, 1980.

Any discussion of this paper will appear in a Discussion Section to be published in the June 1981 JOURNAL. All discussions for the June 1981 Discussion Section should be submitted by Feb. 1, 1981.

Publication costs of this article were assisted by Bell Laboratories.

REFERENCES

1. M. J. Bowden and L. F. Thompson, *Solid State Technol.*, 72 (May 1979).
2. J. Appelbaum, M. J. Bowden, E. A. Chandross, M. Feldman, and D. L. White, in "Proceedings of the Kodak Microelectronics Seminar Interface 75," Oct. 19-21, 1975.
3. B. J. Lin, *J. Vac. Sci. Technol.*, 12, 1317 (1975).
4. B. J. Lin, *IBM J. Res. Dev.*, 20, 213 (1976).
5. Y. Nakane, T. Tsumori, and T. Mifune, "Semiconductor International," No. 45 (1979).
6. Y. Yamashita, K. Ogura, M. Kunishi, R. Kawazu, S. Ohno, and T. Mizokami, 15th Symposium on Electron, Ion and Photon Beam Technology, Boston, Mass., May 1979.
7. C. W. Wilkins, Jr. and L. E. Stillwagon, Unpublished results.
8. G. A. Delzenne, U. Laridon, and H. Peeters, *Eur. Polym. J.*, 6, 933 (1970).

The Effect of Sensitizers on the Photodegradation of Poly (Methyl Methacrylate-co-3-Oximino-2-Butanone Methacrylate)

E. Reichmanis, C. W. Wilkins, Jr., and E. A. Chandross

Bell Laboratories, Murray Hill, New Jersey 07974

ABSTRACT

With the prospect of shorter wavelength photolithography, the need has arisen for new resist materials that will work efficiently at wavelengths where conventional resists are optically opaque. Poly(methyl methacrylate-co-3-oximino-2-butanone methacrylate) (P(M-OM) (94:6)), a resist that absorbs in the 220-250 nm range, has been sensitized for both this and the 280-320 nm range (an area where the new Perkin Elmer Printer is capable of making exposures). Its inherent sensitivity can also be improved by the incorporation of methacrylonitrile. Sensitized P(M-OM-CN) has a sensitivity of 75 mJ/cm² and is capable of better than 1 μ m resolution.

The use of conventional photolithography becomes severely limited with the current trends towards increased device complexity. By the use of shorter wavelength (200-300 nm) u.v. light, diffraction effects will be reduced, and thus higher resolution should be obtainable (1). However, new resist materials that will work efficiently in the "deep u.v." need to be developed.

We have previously reported our efforts to improve the photosensitivity of poly(methyl methacrylate) (PMMA) in the 200-250 nm region (2) by the incorporation of oxime and α -keto-oxime methacrylate esters as co-monomers. These units contain a moderately labile N—O bond which, when cleaved, could lead to a carboxylate radical and subsequent polymer degradation. Of the materials examined, the 3-oximino-2-butanone group had the greatest positive effect on the overall photosensitivity of the polymer. Poly(methyl methacrylate-co-3-oximino-2-butanone-methacrylate) (P(M-OM)) (94:6) was found to be five times more sensitive than PMMA at $\lambda = 220$ -250 nm.

We have extended the above work through the addition of external sensitizers and the incorporation of other monomer units into the polymer in an effort to increase its photosensitivity still further.

Experimental

Monomers and polymers were prepared as described previously (2).

Materials.—Poly(methyl methacrylate) ((PMMA); Elvacite) is a high molecular weight polymer available from du Pont which was used as a standard for measuring sensitivities.

The benzoic acid sensitizers, triphenylamine, and dibenzothiophene were purchased from Aldrich Chemical Company, while the acylcarbazoles were synthesized by known procedures (3).

Sensitivity.—Poly(methyl methacrylate-co-3-oximino-2-butanone methacrylate) (P(M-OM)) copolymer solutions were prepared as described previously, Poly(methyl methacrylate-co-3-oximino-2-butanone methacrylate-co-methacrylonitrile) (P(M-OM-CN)) terpolymers were dissolved in chlorobenzene or cyclohexanone (10% solution). Where appropriate, the specified amount of sensitizer was added to the solutions before coating onto a silicon substrate with a Headway Research spinner. Films were prebaked for 60 min at 110°C.

Key words: deep u.v. resists, photoresists, photodegradation.

Photon sensitivities are reported relative to PMMA and were obtained by imaging a 1 mm wide slit, illuminated by a 1000W Hg arc lamp focused through quartz condenser optics, for varying times across the substrate coated with resist, or by isolating either the 313 or 240 nm line from a 1000W Hg-Xe lamp with a monochromator (Jarrell Ash Model 82-410) and using a 1 mm diam circular contact mask. Exposure times were recorded as the time necessary to allow complete removal of the resist in the irradiated areas. The irradiated films were developed with methyl isobutyl ketone (MIBK) in the case of the copolymers, and with MIBK/isopropanol (8:2 v/v) in the case of the terpolymers.

Resolution.—Resolution was determined by proximity printing on a substrate coated with 1 μ m of resist using a Kasper Model 2001 Proximity Printer fitted with a Xe-Cd lamp (output from 200-500 nm).

Results and Discussion

As discussed earlier (2), photochemically induced cleavage of the N—O bond in P(M-OM) can lead to decarboxylation followed by chain cleavage, the "usual" mechanism for PMMA chain scission. The absorption tail of the keto-oxime chromophore is sufficiently strong that addition of the 3-oximino-2-butanone group as the methacrylate ester confers added photosensitivity to the polymer in the range of 230-260 nm. Generally, it was found that the sensitivity of the copolymer increased with oxime ester concentration up to ~6 mole percent (m/o) OM. The effect of molecular weight on the system appeared minimal.

An additional, potential advantage of the keto-oxime chromophore is that it possesses a low-lying excited state ($\lambda \approx 350$ nm) which could be sensitized. We proposed to test this by "externally" sensitizing P(M-OM) to promote degradation at longer wavelengths (300-330 nm, a region which would match the output of a Model III Perkin Elmer Printer with modified optics). The sensitizer must satisfy a number of criteria: (i) its excited state energy must match (or be greater than) that of the keto-oxime chromophore; (ii) it must transfer energy efficiently; (iii) it must not absorb at longer wavelengths than the range desired; (iv) it must be sufficiently nonvolatile to remain in the polymer film during the initial baking; and (v) it must be compatible with the polymer. The materials which were tested and satisfied the above criteria, were triphenylamine, N-acetyl and N-benzoylcarbazole, and dibenzothiophene. The absorption spectra of P(M-OM) (94:6) films containing 10

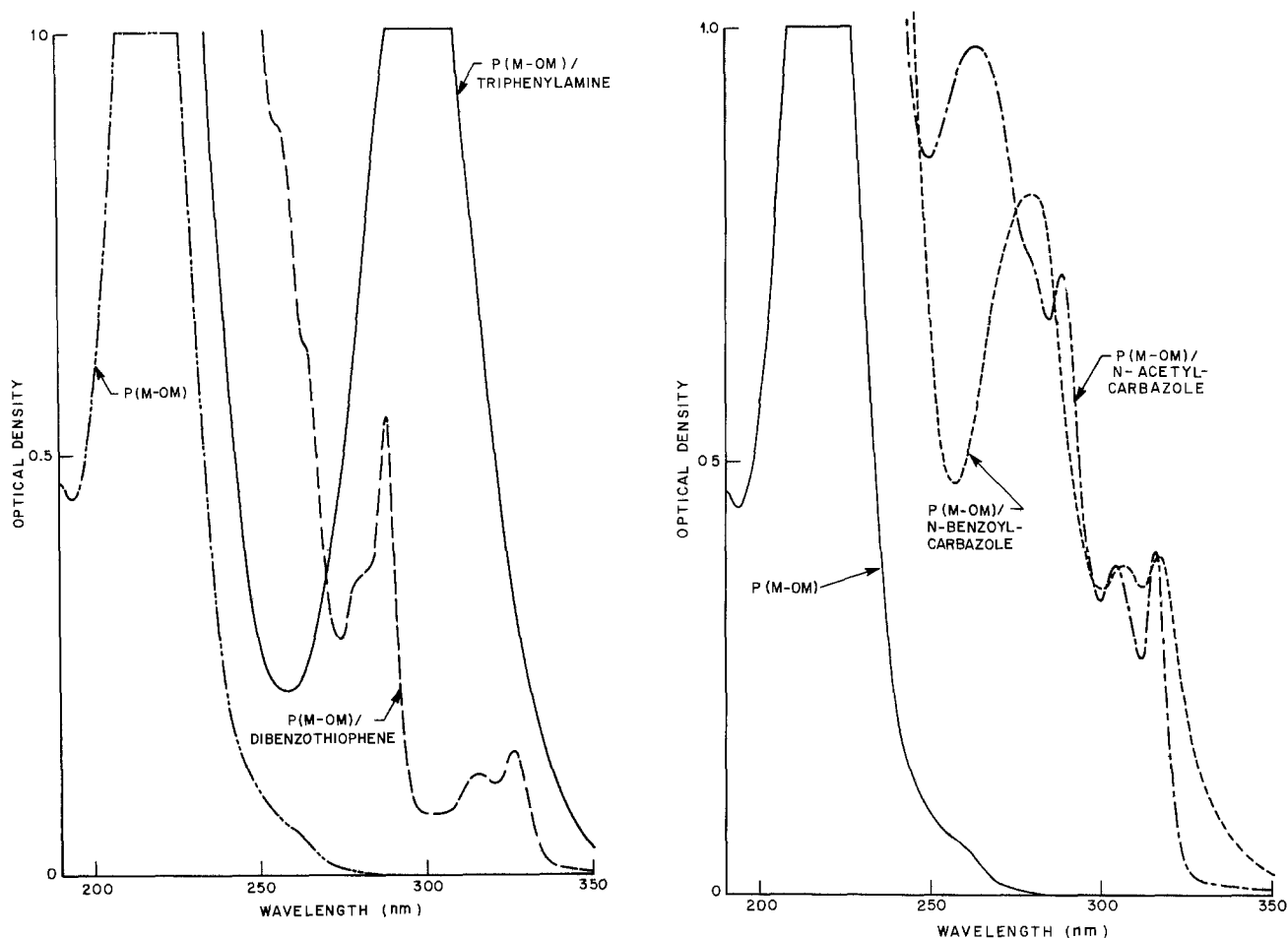


Fig. 1. Ultraviolet absorption spectra of 1 μm films of P(M-OM) and P(M-OM) containing (a, left) 10 w/o of triphenylamine or dibenzothiophene, (b, right) 10 w/o N-acetylcarbazole or N-benzoyl carbazole.

weight percent (w/o) of each of the above materials are shown in Fig. 1 and the results are given in Table I.

Clearly, addition of a sensitizer enhanced the sensitivity of the copolymer at longer wavelengths. Note that at 313 nm, where the copolymer has no significant absorption (see Fig. 1) and is quite insensitive to irradiation, a dramatic improvement in monochromatic sensitivity is observed upon the addition of sensitizer (see Table I). The most efficient sensitizer at 313 nm is N-acetylcarbazole. Upon irradiation with the full output of the Hg lamp, all of the materials examined become 4-5 times faster than the unsensitized copolymer under the same conditions (Table I). That the film containing triphenylamine is insensitive to 313 nm light but does degrade more rapidly when exposed to the full output of the Hg lamp may be explained by the observation that while it is opaque at 313 nm, longer wavelength light, up to $\lambda \approx 360$ nm, does penetrate the bulk of the film and may effect sensitization. The absorptions of the carbazole containing films are relatively flat across the region of 280-320 nm.

Table I.

Polymer	Sensitizer (w/o)	Sensitivity	
		Absolute at $\lambda 313$ nm (J/cm^2)	Relative from $\lambda 200$ to 400 nm
P(MMA)	—	—	1.00
P(M-OM) ^a	—	4.6	0.25
P(M-OM)	triphenylamine (5)	—	0.25
P(M-OM)	triphenylamine (10)	>9	0.05
P(M-OM)	N-acetylcarbazole (10)	1.8	0.06
P(M-OM)	N-acetylcarbazole (15)	1.8	0.06
P(M-OM)	N-benzoylcarbazole (10)	3.6	0.06
P(M-OM)	dibenzothiophene (10)	—	0.10

^a P(M-OM) (94:6), M_w : 2.87×10^5 , $M_w/M_n = 1.86$.

The optimum sensitizer concentration is about 10 w/o. A lower percentage has no effect on polymer sensitivity, while larger amounts provide no additional effect.

While these materials do sensitize P(M-OM) to longer wavelengths (300-350 nm), they are not usable at shorter wavelengths due to too large an absorption coefficient which, at the concentrations required, results in too high an optical density. Substituted benzoic acids which were found to sensitize poly(methylisopropenyl ketone) (PMIPK) (4), should have both singlet and triplet energy levels sufficiently high that either could effect sensitization of the keto-oxime chromophore. Also, their extinction coefficients would afford usable absorbances at ~ 250 nm in polymer films containing 10% of the acid. Three materials were tested. The absorption spectra of P(M-OM) films containing each of the sensitizers are shown in Fig. 2 and the results are tabulated in Table II. The film containing p-t-butylbenzoic acid proved to be most sensitive. Sensitivity was enhanced by a factor

Table II.

Polymer	Sensitizer (w/o)	Sensitivity	
		Absolute at $\lambda 240$ nm (mJ/cm^2)	Relative from $\lambda 200$ to 400 nm
P(MMA)	—	3400	1.00
P(M-OM) ^a	—	1300	0.25
P(M-OM)	p-t-butylbenzoic acid (10)	150	0.10
P(M-OM)	p-t-butylbenzoic acid (20)	—	0.10
P(M-OM)	p-methoxybenzoic acid (10)	—	0.20
P(M-OM)	3,4-dihydroxybenzoic acid (10)	—	0.25

^a P(M-OM) (94:6), M_w : 2.87×10^5 , $M_w/M_n = 1.86$.

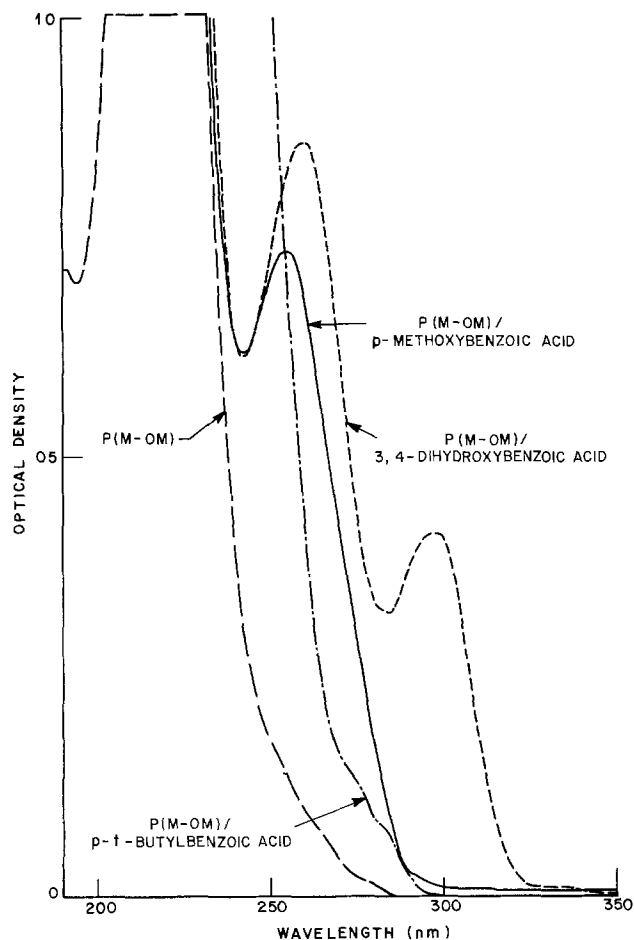


Fig. 2. Ultraviolet absorption spectra of $1 \mu\text{m}$ films of P(M-OM) and P(M-OM) containing 10 w/o p-t-butylbenzoic acid, p-methoxybenzoic acid, and 3,4-dihydroxybenzoic acid.

of 2.5 over the unsensitized sample, employing the full output of the Hg lamp. Monochromatic sensitivity at 240 nm increased by a factor of ~ 9 . The two other species studied have little or no effect on the sensitivity of the polymer.

An additional means of improving sensitivity is to incorporate methacrylonitrile (CN) into the copolymer. It is generally accepted that conjugation with a nitrile group stabilizes a radical. One might then expect the polymer backbone to break more easily at a point adjacent to a nitrile substituent, thus improving the sensitivity. Since incorporation of CN into PMMA affords an increase in sensitivity to electron beam exposure (5), we were prompted to examine its effect on the u.v. sensitivity of P(M-OM).

Examination of the data in Table III shows that the incorporation of 14 m/o MACN into P(M-OM) containing 6 m/o OM affords a fourfold increase in sensitivity. Somewhat anomalously, the polymer containing 28 m/o CN is slower, *i.e.*, its sensitivity over P(M-OM) is only doubled. This effect is not readily rationalized. [It may, however, be noted that a similar effect was observed for poly(methyl methacrylate-co-methacrylonitrile) (P(M-CN)) copolymers on electron beam exposure (5).] In addition to being more sensitive, the resolution remains excellent. As may be seen in Fig. 3a, $1.5 \mu\text{m}$ lines and spaces obtained by proximity printing are clearly resolved.

Further enhancement of sensitivity is obtained by addition of p-t-butylbenzoic acid. The absorption spectra of the unsensitized and sensitized terpolymer are depicted in Fig. 4, and the sensitivity data are given in Table III. Employing the full output of the mercury lamp, P(M-OM-CN)/10% p-t-butylbenzoic acid is 30 times as fast as PMMA. At 240 nm, the material requires an exposure of 75 mJ/cm^2 . As may be seen in Fig. 3b, addition of a sensitizer does not alter the high resolution characteristics of the polymer. A resolution of $1 \mu\text{m}$ is readily obtained by proximity printing.

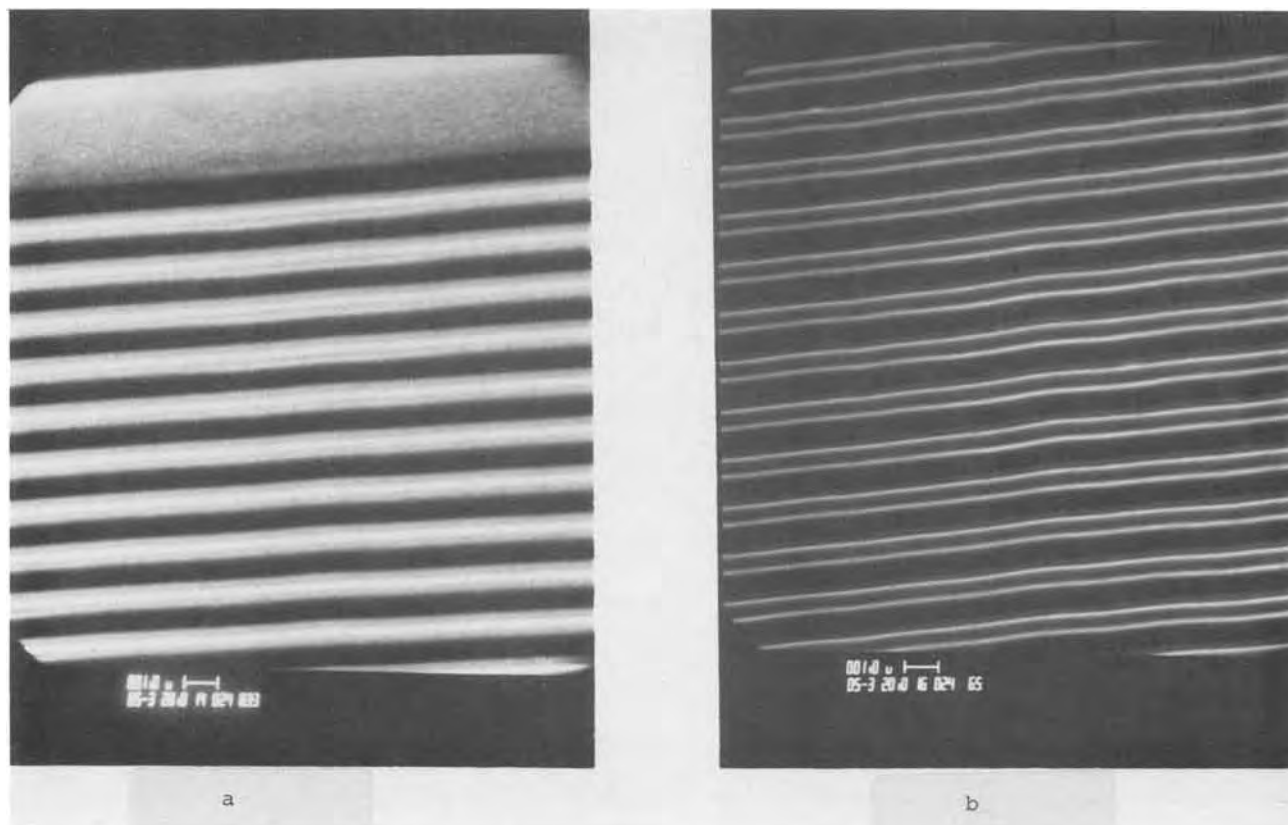


Fig. 3. SEM micrograph illustrating (a) $1.5 \mu\text{m}$ lines and spaces delineated in $1 \mu\text{m}$ P(M-OM-CN) (8:0.6:1.4) and (b) $1 \mu\text{m}$ lines and spaces delineated in $1 \mu\text{m}$ P(M-OM-CN) (8:0.6:1.4)/10% p-t-butylbenzoic acid.

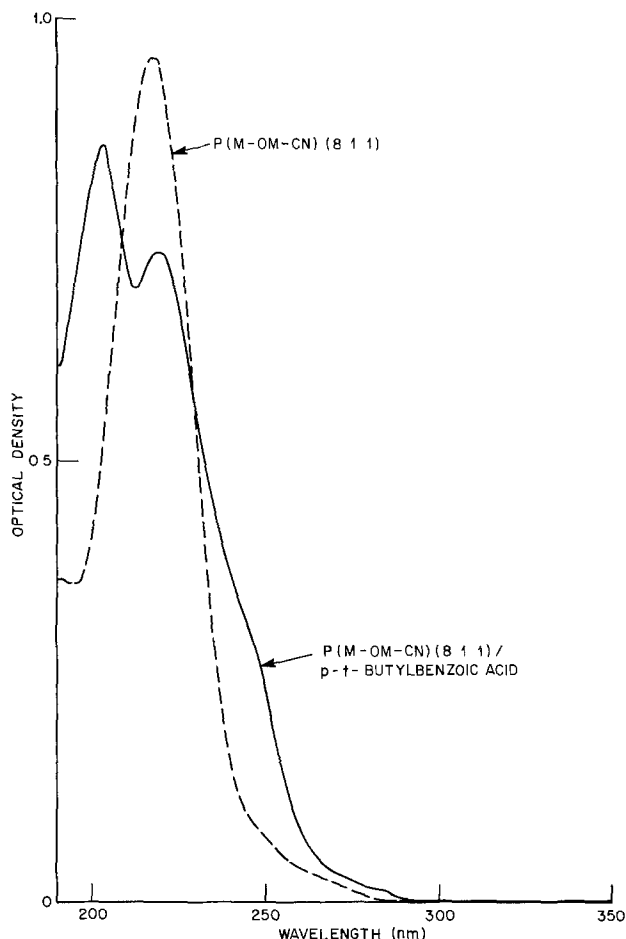


Fig. 4. Ultraviolet absorption spectra of P(M-OM-CN) (8:0.6:1.4) and P(M-OM-CN) (8:0.6:1.4)/10% p-t-butylbenzoic acid. (The films are obviously not of the same thickness but are shown to illustrate the effect of the addition of sensitizer on the absorption spectrum of the material.)

Conclusion

Incorporation of small percentages of 3-oximino-2-butanone methacrylate into PMMA affords added photosensitivity to the polymer. An additional four-fold increase in sensitivity is obtained by incorporating methacrylonitrile into the copolymer. Further addition of external sensitizers more than doubles the rate of polymer degradation. At 240 nm, the exposure required for (P(M-OM-CN)) (8:0.6:1.4) containing 10 w/o p-t-butylbenzoic acid is 75 mJ/cm², compared to 3400 mJ/cm² for PMMA. In addition,

Table III.

Polymer	m/o MACN	w/o Sens. ^a	M_w/M_n ($\times 10^6$)	Sensitivity	
				Absolute at λ_{240} nm (mJ/cm ²)	Relative from λ_{200} to 400 nm
P(MMA)	0	—	—	3400	1.00
P(M-OM) ^b	0	—	2.87	1300	0.25
P(M-OM-CN) ^b	14	—	0.93	330	0.06
P(M-OM-CN) ^b	28	—	0.91	660	0.12
P(M-OM-CN) ^b	14	10	0.93	75	0.03
P(M-CN)	12	—	8.2	—	1.00
P(M-CN)	12	10	8.2	—	0.68

^a p-t-butylbenzoic acid.

^b P(M-OM-CN) (8:0.6:1.4).

the high resolution characteristics of PMMA have been retained.

Acknowledgments

The authors wish to thank W. J. Tomlinson for the use of his Hg-Xe lamp and monochromator for determining absolute sensitivities, L. V. Dodd for obtaining the SEM micrographs, and W. Q. McKnight for the Kasper exposures. We also thank E. D. Feit for many helpful discussions.

Manuscript submitted Dec. 26, 1979; revised manuscript received May 27, 1980.

Any discussion of this paper will appear in a Discussion Section to be published in the June 1981 JOURNAL. All discussions for the June 1981 Discussion Section should be submitted by Feb. 1, 1981.

Publication costs of this article were assisted by Bell Laboratories.

REFERENCES

- (a) M. Feldman, D. L. White, E. A. Chandross, M. J. Bowden, and J. Appelbaum, "Proceedings of the Kodak Microelectronics Seminar," *Interface* 75, p. 40, October 19-21, 1975; (b) M. J. Bowden and E. A. Chandross, *This Journal*, 122, 1370 (1975); (c) B. J. Lin, *J. Vac. Sci. Technol.*, 12, 1317 (1975); (d) B. J. Lin, *IBM J. Res. Dev.*, 20, 213 (1975); (e) C. W. Wilkins, Jr. and L. E. Stillwagon, Private communication.
- C. W. Wilkins, Jr., E. Reichmanis, and E. A. Chandross, *This Journal*, 127, 2510 (1980).
- M. Zander, *Ber. Bunsenges.*, 72, 1161 (1968).
- (a) Y. Nakane, T. Tsumori, and T. Mifune, *Semicond. Internat.*, 45 (1979), (b) M. Tsuda, S. Oikawa, Y. Nakamura, H. Nakane, et al., *Photogr. Sci. Eng.*, 23, 290 (1979).
- L. E. Stillwagon, E. M. Doerries, L. F. Thompson, and M. J. Bowden, "ACS Division of Organic Coatings and Plastics Preprints," Vol. 37, No. 2, p. 38, Chicago (1977).



On the Nature of CVD Si-Rich SiO_2 and Si_3N_4 Films

E. A. Irene,* N. J. Chou,* D. W. Dong,* and E. Tierney

IBM Thomas J. Watson Research Center, Yorktown Heights, New York 10958

There are several published studies on the preparation of Si-rich SiO_2 (1-7) and Si_3N_4 (6-11) films. An early report (5) on chemically vapor deposited (CVD) Si-rich SiO_2 films described the material as "semi-insulating," because the material displayed an electrical conductivity intermediate between SiO_2 and Si. The implication is that the bandgap of the material is also intermediate and therefore that a homogeneity range exists in this system. Work at our laboratory (6) showed evidence that both Si-rich SiO_2 and Si_3N_4 are composed of two phases: silicon and either oxide or nitride. Later studies (7, 12) on Si-rich SiO_2 supported the multi-phase proposition but also suggested that the oxide phase is something other than normal CVD SiO_2 . In the present study, our transmission electron microscopy (TEM), and x-ray photoelectron spectroscopy (XPS) observations are presented as a comparison of stoichiometric and Si-rich SiO_2 and Si_3N_4 films. From this comparison of CVD films, we conclude that the Si-rich films are indeed two phase materials: one phase Si and the other either normal CVD oxide or nitride. The nature of the so-called normal CVD oxide and nitride is not addressed in this study.

Experimental Procedures

CVD was used to prepare 100 nm films for this study. The films were deposited at 700°C onto cleaned

* Electrochemical Society Active Member.
Key words: films, CVD, electrical conductivity.

single crystal Si substrates via the reaction SiH_4 with N_2O for the Si-rich SiO_2 and with NH_3 for Si-rich Si_3N_4 . The gas phase ratios $\text{N}_2\text{O}/\text{SiH}_4$, R_o , and NH_3/SiH_4 , R_N , were used to control the solid phase compositions. The details of this CVD procedure and preparations for TEM were previously discussed (6). The stoichiometric films were prepared using a large excess of N_2O for SiO_2 ($R_o = 25$) and NH_3 for Si_3N_4 ($R_N = 100$).

X-ray photoelectron spectra (XPS) of the nitride and oxide films were obtained using a UHV system with an Mg K_{α} source and PHI Model 255 double pass analyzer. The surfaces of both as-deposited and annealed specimens were chemically cleaned in lieu of the conventional ion etching technique which is known to have preferential sputtering effects. The annealed specimens were found to be surface oxidized, and a 200Å thick top layer was chemically removed to obtain a truly representative spectrum. The surface charging effect was minimized by an electron flood gun, and the work function of the spiraltron detector was corrected with the Au $4f_{7/2}$ line at 84.0 eV. A Gaussian curve fitting computer program¹ was used to resolve the measured spectra.

Results and Discussion

Transmission electron microscopy (TEM).—Figure 1 shows that the as-deposited Si-rich SiO_2 is nearly

¹ The computer program was kindly provided by R. H. Lacombe, IBM, East Fishkill Facility.

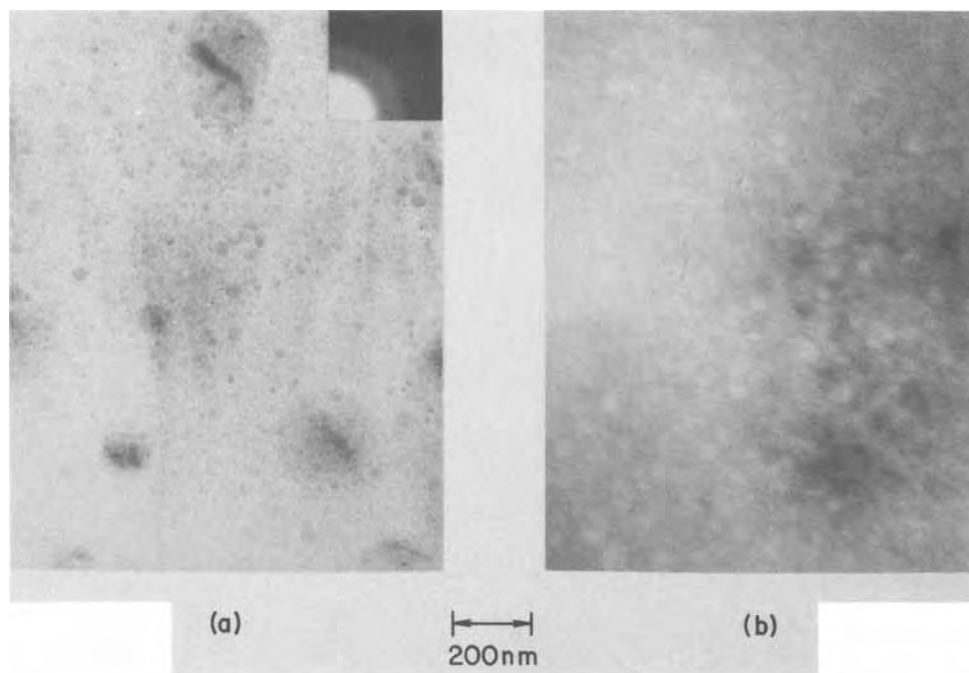


Fig. 1. Si-rich SiO_2 , with $R_o = 3$ or about 10% excess Si, unannealed (a) bright field with diffraction, (b) dark field.

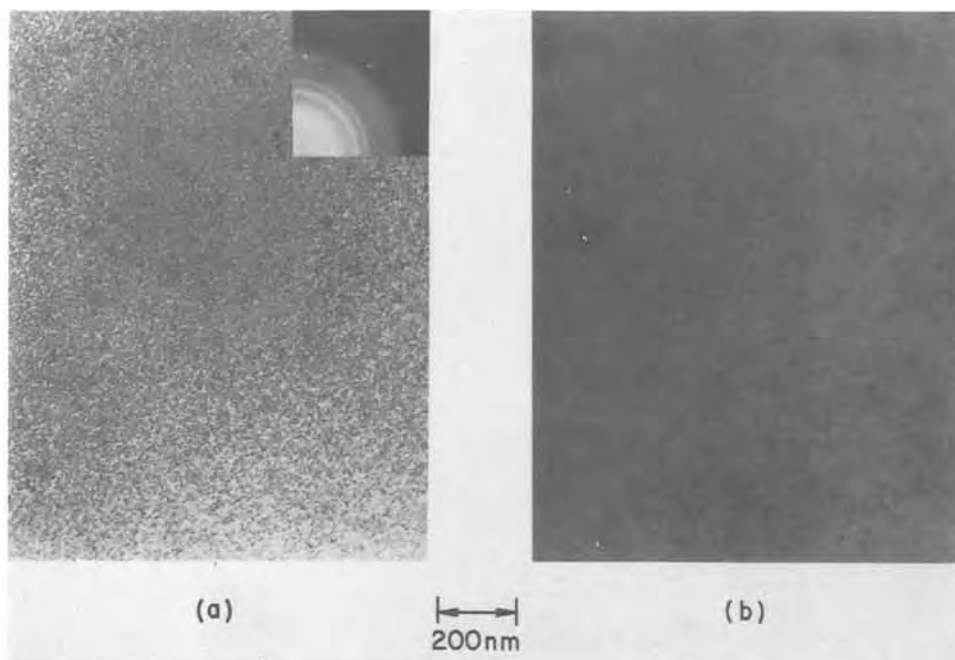


Fig. 2. Si-rich SiO_2 with $R_o = 3$ or about 10% excess Si, annealed 1000°C in N_2 , 15 min (a) bright field with diffraction, (b) dark field.

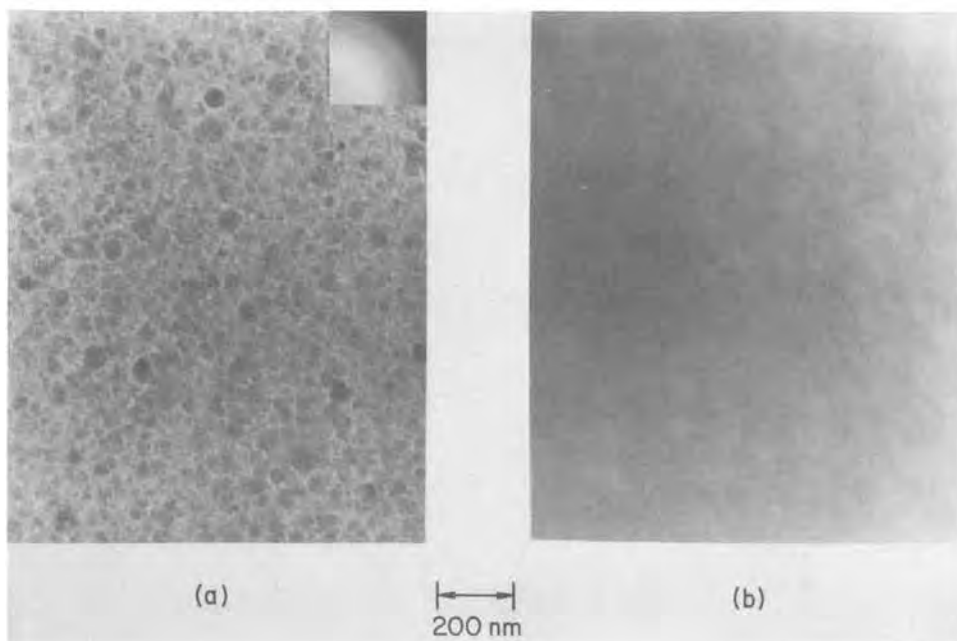


Fig. 3. Si-rich Si_3N_4 , with $R_N = 0.5$ or about 8% excess Si, unannealed (a) bright field with diffraction, (b) dark field.

entirely amorphous. A careful look at the dark field micrograph reveals small (2 nm) and widely separated crystallites. Figure 2 shows that upon annealing, the excess Si crystallizes to form 10 nm randomly oriented grains. Both bright and dark field TEM show [as was previously reported (6)] that these films have a rough texture presumably due to differential attack by the etchant used to prepare these compositionally inhomogeneous films for TEM. Figures 3 and 4 show similar results for Si-rich Si_3N_4 except that there are more and larger (5 nm) Si crystallites in the as-deposited material, which grow to more than 10 nm after the 1000°C anneal.

ESCA.—The XPS of our stoichiometric CVD oxide films shown in Fig. 5 exhibited a single peak at 102.5 eV, which shifted to 103.5 eV upon annealing, and therefore these peaks may be identified with Si(2P) electrons associated with possibly incomplete or disordered Si—O bonds for the as prepared samples that are converted into tetrahedral Si—O bonds when annealed (7). As shown in Fig. 6(a), the unannealed Si-rich SiO_2 shows broad peaks which can be decomposed into three Gaussian peaks at 97, 99, and 102 eV.

Figure 6(b) shows that upon annealing, the two peaks at 98.6 and 102.5 dominate the spectrum. Figure 7(a) shows that Si-rich Si_3N_4 contains a broad peak decomposed into two Gaussians at 97.5 and 102 for as-deposited samples and Fig. 7(b) shows that after annealing there is little change in the spectrum.

The TEM and ESCA results are understood by considering that both Si-rich oxide and nitride are composed of two phases: Si and either CVD SiO_2 or Si_3N_4 . Since the overall stoichiometry does not change after annealing, the shifts in the Si and oxide and nitride peak is likely due to ordering of the as-deposited phases. This is illustrated best by the (TEM) observation of predominantly amorphous Si in the as-deposited Si-rich oxide presumably with the 97 eV ESCA peak. Upon annealing, this peak shifts to higher energy which yields the reported 99 eV for crystalline Si (7). The insulator peaks in the Si-rich films correspond to the normal stoichiometric CVD SiO_2 and Si_3N_4 films whatever is the details of the bonding in these films. For the Si-rich Si_3N_4 films, the as-deposited film already contains considerable crystalline

Fig. 4. Si-rich Si_3N_4 , with $R_N = 0.5$ or about 8% excess Si, annealed 1000°C in N_2 , 15 min (a) bright field with diffraction, (b) dark field.

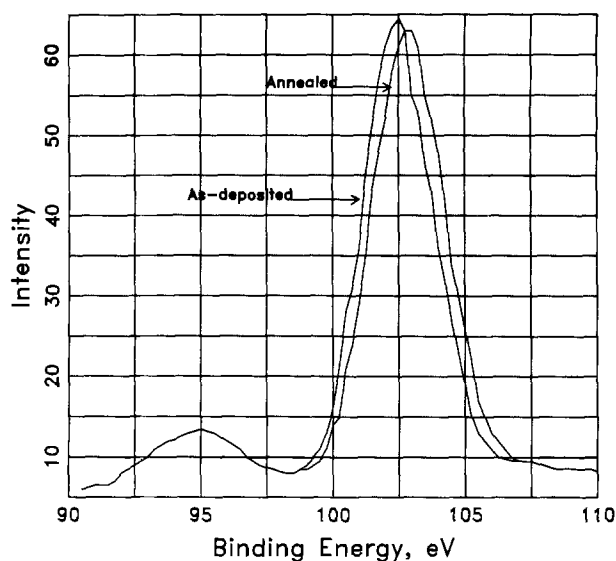
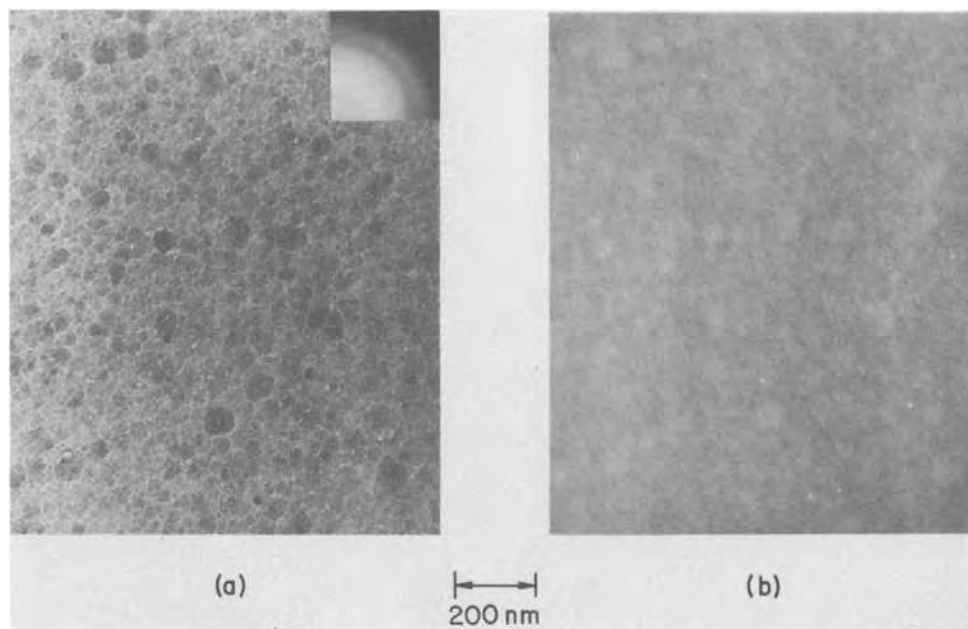


Fig. 5. ESCA spectrum of normal stoichiometric CVD SiO_2 as-deposited and annealed.

Si, thus, the spectrum does not change substantially upon annealing.

The higher conductivities for these materials (5-7) is probably attributable to localized field enhancement effects caused by the inhomogeneous material rather than a smaller bandgap (7) or filamentary conduction (6).

Acknowledgment

This research was partially supported by the Defense Advanced Research Projects Agency and monitored by the Deputy for Electronic Technology, RADC, under Contract F19628-76-C-0249.

Manuscript submitted Feb. 5, 1980; revised manuscript received May 1, 1980.

Any discussion of this paper will appear in a Discussion Section to be published in the June 1981 JOURNAL. All discussions for the June 1981 Discussion Section should be submitted by Feb. 1, 1981.

Publication costs of this article were assisted by IBM Corporation.

REFERENCES

1. H. R. Philipp, *J. Phys. Chem. Solids*, **32**, 1935 (1971).
2. M. V. Coleman and D. J. D. Thomas, *Phys. Status Solidi.*, **22**, 593 (1967).
3. B. J. Joyce, H. F. Sterling, and J. H. Alexander, *Thin Solid Films*, **1**, 481 (1967/1968).
4. J. S. Johannessen and W. E. Spicer, *J. Appl. Phys. Lett.*, **27** (1975).
5. T. Aoki, T. Matsushita, H. Yamoto, H. Hayashi, M. Okayama, and Y. Kawara, Paper 148 presented at the Toronto, Canada, Meeting of the Society, May 11-16, 1975.
6. D. W. Dong, E. A. Irene, and D. R. Young, in "Chemical Vapor Deposition 1977," L. F. Donaghey, P. Rai-Choudhury, and R. N. Tauber, Editors, p. 483, The Electrochemical Society Soft-bound Proceedings Series, Princeton, N.J. (1977);

Fig. 6. ESCA spectrum of unannealed (a) and annealed (b) Si-rich SiO_2 . The solid lines are for the Gaussian curves.

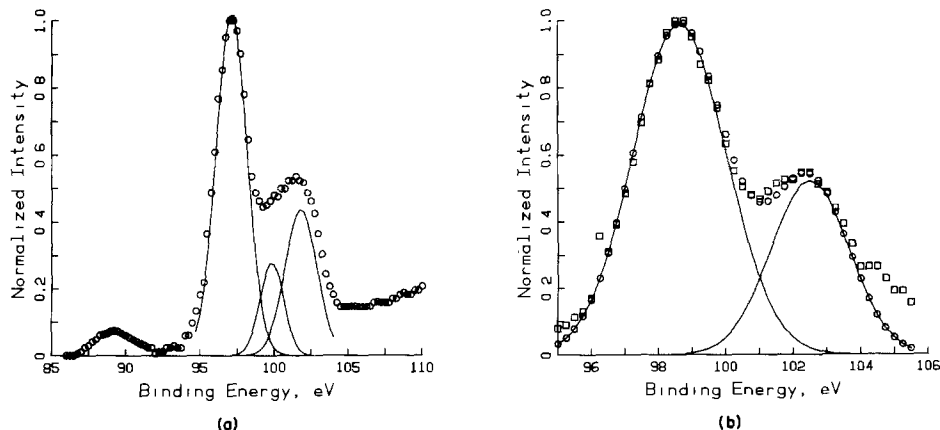
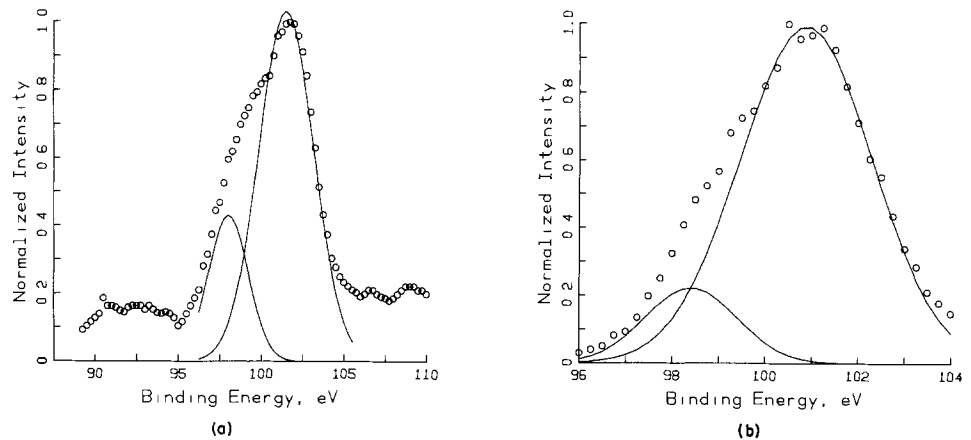


Fig. 7. ESCA spectrum of un-annealed (a) and annealed (b) Si-rich Si₃N₄. The solid lines are for the Gaussian curves.



- This Journal*, 125, 819 (1978).
 7. M. Hamasaki, T. Adachi, S. Wakayama, and M. Kikuchi, *J. Appl. Phys.*, 49, 3987 (1978).
 8. W. A. Kohler, *Metall. Trans.*, 1, 735 (1970).
 9. J. R. Yeagan and H. L. Taylor, *This Journal*, 115, 273 (1978).

10. V. Y. Doo, D. R. Kerr, and D. R. Nichols, *ibid.*, 115, 61 (1968).
 11. K. Tanabashi and K. Kobayashi, *Jpn. J. Appl. Phys.*, 12, 641 (1973).
 12. J. H. Thomas and A. M. Goodman, *This Journal*, 126, 1766 (1979).

Surface Roughness Studies of Native Oxides of GaAs

N. Bottka and J. H. Dancy

Naval Weapons Center, Physics Division, Michelson Laboratories, China Lake, California 93555

The native oxide of GaAs is of significant technological importance to warrant a detailed study of its physical properties. A significant amount of work has already been done in developing the various techniques to grow these oxides on GaAs surfaces (1-3). Their optical and electrical properties have been determined and the interface of the GaAs/oxide region well characterized by various surface probe techniques (4-7).

Although much is known about the surface and the GaAs/oxide interface chemistry, little information is available about the surface roughness and morphology of these oxides and their GaAs interfaces. The objective of this work was to obtain such surface-related information of thick native oxides of GaAs by means of surface roughness measurements, reflection electron diffraction, and transmission electron microscopy (TEM), using single-stage Pt/C surface replicas. Emphasis has been placed on oxides grown anodically from an aqueous solution. The surface properties were studied both as a function of substrate preparation and growth conditions (such as the current density for anodization and the thickness of the grown oxide).

Experimental

The samples under investigation were n-type GaAs both Te- and Sn-doped to $N_D \sim 10^{18} \text{ cm}^{-3}$. The surface orientation of all the samples was {100}.

Care was taken in preparing the surface of the GaAs substrates prior to oxidation. With the exception of a few samples, most of the GaAs substrates in this study were mechanically polished to a 1/4 μm finish and then polished chemically in a 0.4% bromine-methanol solution on a Buehler Microcloth. After proper rinsing in methanol and deionized water, they were cleaved into 1 cm^2 working units. The individual samples were then anodically oxidized in an aqueous solution (pH 2.7) (3) under various constant current density conditions. The anodization constant for the

growth of the native oxide of GaAs was about 20 $\text{\AA}/\text{V}$ (3).

Table I summarizes the surface preparation and oxidation conditions for the various wafers used in the experiment. The last three entries in this table refer to wafers that have been repeatedly oxidized and stripped with a solution of 1:1 $\text{NH}_4\text{OH}:\text{H}_2\text{O}$. This was done to determine the effect of repeated oxidation on the surface roughness both for thick and thin oxides.

Surface roughness measurements on the polished GaAs substrate, the grown oxide, and the GaAs/oxide interface after oxide stripping were made with a Talystep profilometer utilizing a special conical diamond stylus with a radius of 1 μm (8).¹ The stylus loading is continuously adjustable from about 50 mg to less than 1 mg. A loading of 2 mg is generally used with the standard stylus. This is adequate to make good contact and does not permanently mark surfaces. When using the sharper styluses the loading is generally reduced to about 0.5 mg. The total possible stylus travel across the sample is 2 mm, but 1-mm-long scans are generally used for the surface statistics. Three stylus traverse speeds are available; the slowest one, 3 $\mu\text{m}/\text{sec}$, is used for the surface statistics. When the data are sampled every 20 msec, the spacing between adjacent points on the surface is 0.061 μm .

The output of the amplifier of the Talystep is fed into a Hewlett-Packard Model 5480B signal averager which digitizes the signal and stores it in a block of 1000 data points. These data can be transferred to a Hewlett-Packard Model 2100A minicomputer with 32K memory for computation of the autocovariance function, height and slope distribution functions, and other surface statistics. The output from the minicomputer can be plotted on 10 \times 15 in. graph paper using a Hewlett-Packard Model 7210A digital plotter, punched

¹ Talystep Step Height Measuring Instrument (Metric) Model No. 75-1001 112/1037m obtained from Rank Precision Industries, Incorporated, Des Plaines, Illinois 60018; stylus manufactured by Ernst F. Weinz WEKA-OHG, 658 Idar, Oberstein-2, Germany.

Table I. The GaAs wafers used in this experiment, their surface preparation, and oxidation

Sample No.	Surface preparation	Conditions for anodic oxidation		Comments
		Current density J (mA/cm ²)	Thickness \AA	
BH-2E/Te	Wafer polished by manufacturer	12.5	1600	
BH-7F/Te	Bromine-methanol polish	10.0	1000	
BH-6D/Te		10.0	800	
BH-6E/Te		2.0	800	
BH-6B/Te	Bromine-methanol polish	0.1	800	Oxide stripped with 1:1 NH ₄ OH:H ₂ O
BH-6C/Te		0.1	800	
EM-1/Te	Pitch-lapped and polished by manufacturer	3.2	2000	The wafer was reoxidized after stripping with 1:1 NH ₄ OH:H ₂ O
		3.2	2000	
		5.0	800	
		1.0	200	
		0.5	200	
		0.1	200	
		0.1	200	
		3.2	2000	
CS-30/Sn	Bromine-methanol polish	1.0	800	The wafer was reoxidized after stripping with 1:1 NH ₄ OH:H ₂ O
		2.1	2000	
		2.1	2000	
		0.1	200	
		0.1	200	
CS-4/Sn	1 μm mechanical polish followed by bromine-methanol polish	2.0	2000	Oxide stripped with 1:1 NH ₄ OH:H ₂ O and surface reoxidized
		0.1	200	
		0.1	200	

on paper tape, or printed on a teletype. Depending on the roughness of the surface being measured, different gains can be used on the Talystep amplifier and signal averager input. Using the maximum gain on the Talystep, the instrument has a noise equivalent to an rms roughness of 1 \AA . To obtain this type of sensitivity, the instrument is mounted on a vibration isolation table which in turn rests on a granite slab. An acrylic plastic box encloses the entire instrument (excluding the amplifier, control unit, and recorder). Measurements are generally made after the sample has become temperature stabilized, and noise generated by the rest of the equipment in the laboratory is at a minimum. The instrument is microphonic on the most sensitive scale and will pick up frequencies in the audio range. Thermal drifts are generally linear and can be eliminated from the surface statistics by putting a least squares straight line through the measured data. During stable periods, instrumental drifts are about 10 $\text{\AA}/\text{min}$ or less, and drift rates as low as 3 $\text{\AA}/\text{min}$ have been obtained. Depending on the settings on the signal averager, sampling distances can be varied from 1.5 μm to less than 0.06 μm . The lateral resolution achievable with a stylus profiling instrument depends on the radius of the stylus and the slope of the surface. With a small surface slope, lateral resolution much less than the stylus radius is possible. The rms slopes of most surfaces we have studied are under 1°, so that the lateral resolution is of the order of 0.1 μm when using the sharper styluses. Thus, a sampling distance of 0.06 μm is adequate to show all the surface detail the instrument is capable of detecting.

All roughness measurements were made on center areas away from edges. An effort was made to measure surface areas that were representative of the sample studies. On both the oxide and GaAs areas of each sample, a 15 μm and a separate 610 μm scan were made. On most of the samples an additional set of 3 μm scans (10 scans encompassing an area of about $5 \times 0.1 \text{ mm}^2$) were made. These scans allowed us to observe any variation across the surface. Generally speaking, the 610 μm scans represent the figure of merit of our polished surface; whereas, the 15 and 3 μm scans represent the actual surface roughness.

Results and Discussion

After measuring the surface roughness of the first six wafers (the first six entries in Table I), it became evident that the thickness of the grown oxide and not necessarily the current density, J , of anodization controlled the resulting surface roughness of the oxide and the underlying GaAs surface at the GaAs/oxide

interface. No noticeable change in surface roughness was observed between the initial GaAs surface and the oxide surface grown on it when the oxide thickness was 1000 \AA or less. This was true even for the oxides grown at relatively large current densities (10 mA/cm² or larger).

There was a systematic degradation of the surface (the surface becoming rougher on the 3 μm and 15 μm scale) observed both on the oxide surface and the underlying GaAs/oxide interface when the oxide was grown thicker than 1000 \AA , even for moderate current densities (3 mA/cm² or less). This condition of surface deterioration continued even after the oxide was stripped with an ammonia solution and a new thick oxide grown on it. The reverse of this process was observed when the grown oxide was thin (less than 1000 \AA), i.e., thin oxides produced smoother oxide surfaces and GaAs/oxide interfaces. Moreover, this smoothing process continued after the oxide was stripped, and a new thin oxide was grown on it. The stripping of the oxide with the 1:1 NH₄OH:H₂O solution did not deteriorate the underlying GaAs surface.

An interesting application of this smoothing action of anodic oxidation of GaAs surfaces is indicated by the experiment performed on wafer EM 1/Te, results of which are summarized in Fig. 1. This wafer was polished by the manufacturer to a very fine finish. It had a good figure of merit (9 \AA rms surface on the 610 μm scale) and a very smooth short-range surface roughness rms (2.1 \AA on the 3 μm scale). Electron diffraction studies showed this GaAs surface to be polycrystalline, thus indicating that the layers underlying the surface were damaged by the polish. This damage was revealed after the first oxide growth. Both the oxide surface and the underlying GaAs/oxide interface (after oxide stripping) showed a substantial surface deterioration both in the short- and long-range scale roughness measurements (point A in Fig. 1). Successive oxide growth and stripping removed the crystal damage. Continued thin oxide growth followed by stripping smoothed the surface by a factor of three. A final thick oxide reversed this process and deteriorated the surface almost by a factor of four (point B in Fig. 1). Aside from the absence of crystal damage, similar results were observed on the chemically polished samples, C5-30/Sn and CS-4/Sn.

The surface roughness deterioration process observed in thick anodically-grown native oxides of GaAs may have its origin in the chemical nature of the GaAs/oxide interface. It is known from Auger electron spectroscopy (7) that this interface is not abrupt but has a graded composition extending as much as 700 \AA in a 2000 \AA thick oxide (7). Most likely,

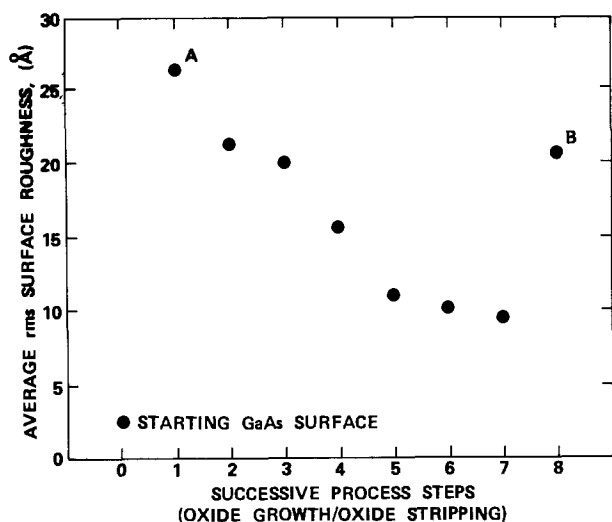


Fig. 1. Average rms surface roughness of GaAs sample EM-1/Te on the 15 μm scan after successive thin (1000Å or less) oxide growth and oxide stripping with 1:1 $\text{NH}_4\text{OH}:\text{H}_2\text{O}$. Points A and B indicate the surface roughness after stripping the thick (>1000Å) native oxide layers.

the width of this interface is proportional to the thickness of the grown oxide. We would expect, therefore, that during NH_4OH stripping of the oxide the etch rate of this interface is highly nonuniform, causing additional roughness to occur on the newly exposed GaAs surface. Subsequent growth of a thick oxide on this new surface would replicate the surface roughness. Further stripping would continue this process of surface degradation. For thin oxides (and more abrupt GaAs/oxide interfaces), the action of this nonuniform etching rate would be less severe and might even reverse the process of surface degradation.

The electron diffraction studies on these native oxides indicate that, with the exception of sample BH-2E/Te, all oxide films were amorphous even for the high current densities (10 mA/cm^2 and higher). No polycrystalline $\beta\text{-Ga}_2\text{O}_3$ phase was observed as reported by other workers (5). The oxide on sample BH-2E/Te was polycrystalline. Its surface was polished by the manufacturer of the wafer, and had an initial average rms roughness of 11Å on the 15 μm scale. No attempt was made by us to improve the quality of this surface prior to oxide growth. After oxide growth, surface roughness measurements and transmission electron micrograph on BH-2E/Te showed that this sample had a much rougher surface

than any of the other samples measured. This seems to indicate that the formation of the polycrystalline phase (at least for GaAs, having a net carrier concentration of 10^{18} cm^{-3} or larger) during the oxide growth is determined primarily by the initial surface roughness of the substrate rather than the oxide thickness or current density of anodization.

In summary, surface roughness measurements, TEM, and reflection electron microscopy were made on thick native oxides of GaAs and correlated with oxide growth conditions and substrate surface preparation. Results indicate that the growth of polycrystalline Ga_2O_3 is more a result of surface roughness than anodic growth conditions. The polycrystalline oxide surface is rougher than the initial substrate surface. Substrate surfaces polished to an rms finish of 5Å or better and anodically oxidized in an aqueous solution give rise to an amorphous oxide film even for large current densities. The short-range rms roughness both for the oxide surface and the underlying GaAs/oxide interface depends more on the thickness of the oxide than the current density of anodization. Successive thick oxides (1000Å or thicker) grown on polished or oxide-stripped GaAs surfaces show successive deterioration in the short-range surface roughness. Successive thin oxides (1000Å or thinner) reverse this process and act to smooth the oxide surface and the underlying GaAs/oxide interface.

Manuscript submitted Dec. 26, 1979; revised manuscript received April 15, 1980.

Any discussion of this paper will appear in a Discussion Section to be published in the June 1981 JOURNAL. All discussions for the June 1981 Discussion Section should be submitted by Feb. 1, 1981.

Publication costs of this article were assisted by the Naval Weapons Center.

REFERENCES

1. B. Schwartz, *Crit. Rev. Solid State Sci.*, **5**, 609 (1975).
2. C. W. Wilmsen, and S. Szpak, *Thin Solid Films*, **46**, 17 (1977).
3. B. Schwartz, F. Ermanis, and M. H. Brastad, *This Journal*, **123**, 1089 (1976).
4. C. C. Chang, P. H. Citrin, and B. Schwartz, *J. Vac. Sci. Technol.*, **14**, 943 (1977).
5. B. Weiss, E. Kohn, B. Bayraktaroglu, and H. L. Hartnagel, in "Gallium Arsenide and Related Compounds," Inst. Phys. Conf. Ser. No. 33a, p. 168, Edinburgh (1976).
6. S. Szpak, J. L. Tomlinson, and G. H. Narayanan, *This Journal*, **124**, 466 (1977).
7. C. C. Chang, B. Schwartz, and S. P. Murarka, *ibid.*, **124**, 922 (1977).
8. J. M. Elson and J. M. Bennett, *J. Opt. Soc. Am.*, **69**, 31 (1979).

Room Temperature CVD Process for Preparing Boron Diffusion Sources

Károly Dobos

Budapest Technical University, 1521 Budapest, Hungary

A room temperature CVD method has been developed for forming homogeneous layers of boron oxide, silicon dioxide, borosilicate, and phosphosilicate glass diffusion sources. A procedure suitable for industrial applications is proposed which is based on a reactor developed for this purpose. In recent work the prop-

erties of B_2O_3 x n H_2O diffusion source layers have been investigated.

Boron nitride disks are often used to attain maximum solid solubility in the silicon diffusion process (1). To satisfy special requirements, such as the preparation of precisely controlled surface concentrations, the use of silane plus gas phase dopants has been used widely, (2-4). Alternatively, the simpler

liquid dopant sources can be used; these are normally applied to the substrate by centrifuging methods. The method developed by us combines the advantages of both of these techniques, the deposition is going on from the gas phase, but at room temperature and during a very short time, with the same simplicity as obtained by the liquid source method.

The halide compounds BBr_3 and POCl_3 , frequently used in semiconductor technology, are known to be readily decomposed in the presence of water, and the hydrolytic reaction goes on spontaneously, owing to the negative charge of free energy. The reaction velocity coefficient is generally very high, particularly in the hydrolysis of BBr_3 . The final product of reaction is the corresponding acid to be used as diffusion source. The present paper describes the method developed by us which is based on these reactions.

Experimental Equipment

For carrying out controlled gas phase hydrolysis the following equipment, shown in Fig. 1, has been developed.

BBr_3 saturator (Fig. 1A).—In this unit nitrogen carrier gas containing BBr_3 is produced. The nitrogen has to be desiccated to avoid premature hydrolysis in the saturator. The nitrogen gas generated from liquid nitrogen is adequate for this purpose. The gas is streaming through the glass saturator over the BBr_3 surface while it is entraining BBr_3 vapor. The quantity of the carried BBr_3 can be controlled by the temperature and the geometry of the saturator, and by the carrier gas flow rate.

Water saturator (Fig. 1B).—The nitrogen gas flowing through this part of the system is saturated with water vapor at a rate controlled by the temperature in the saturator.

Gas mixing head (Fig. 1C).—The gas mixing head is placed in a small enclosure flushed with nitrogen. The substrate slices are placed into this closed space through a lock by a simple moving mechanism. The

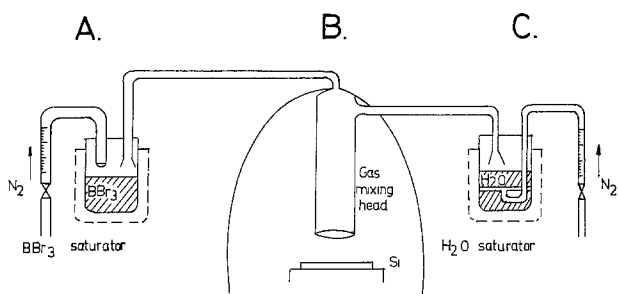


Fig. 1. Schematic drawing of CVD reactor

Deposition
rate, Å/min

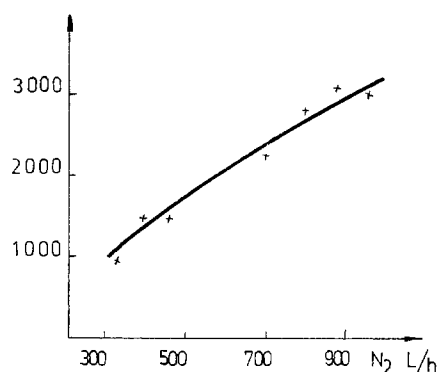


Fig. 2. Deposition rate vs. nitrogen carrier flow rate

whole system can be made of Plexiglas as well, since the reaction does not require an elevated temperature.

Deposition
rate, Å/mm

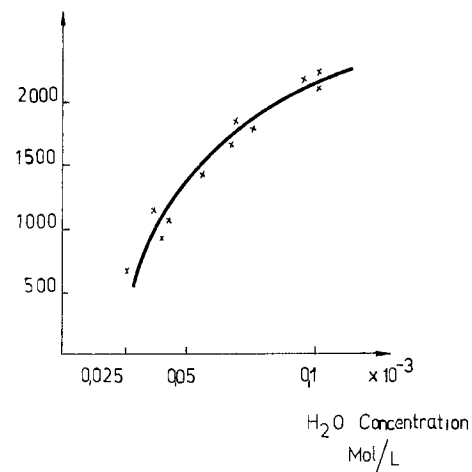


Fig. 3. Deposition rate vs. water concentration

Deposition
rate Å/min

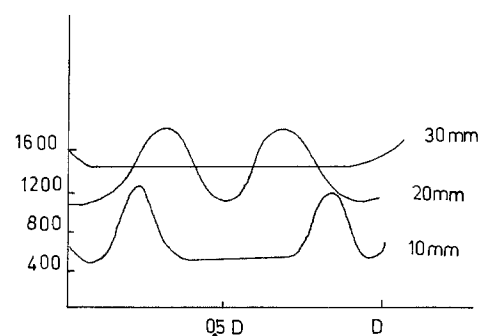


Fig. 4. Deposition rate variation along the 5 cm diameter of a silicon slice with the gas mixing head to substrate distance as parameter.

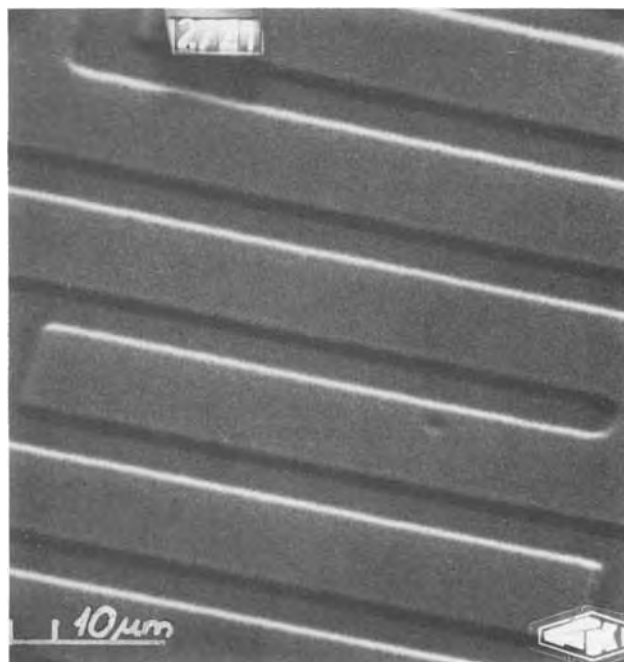


Fig. 5. Scanning electron micrograph of a deposited and heat-treated layer.

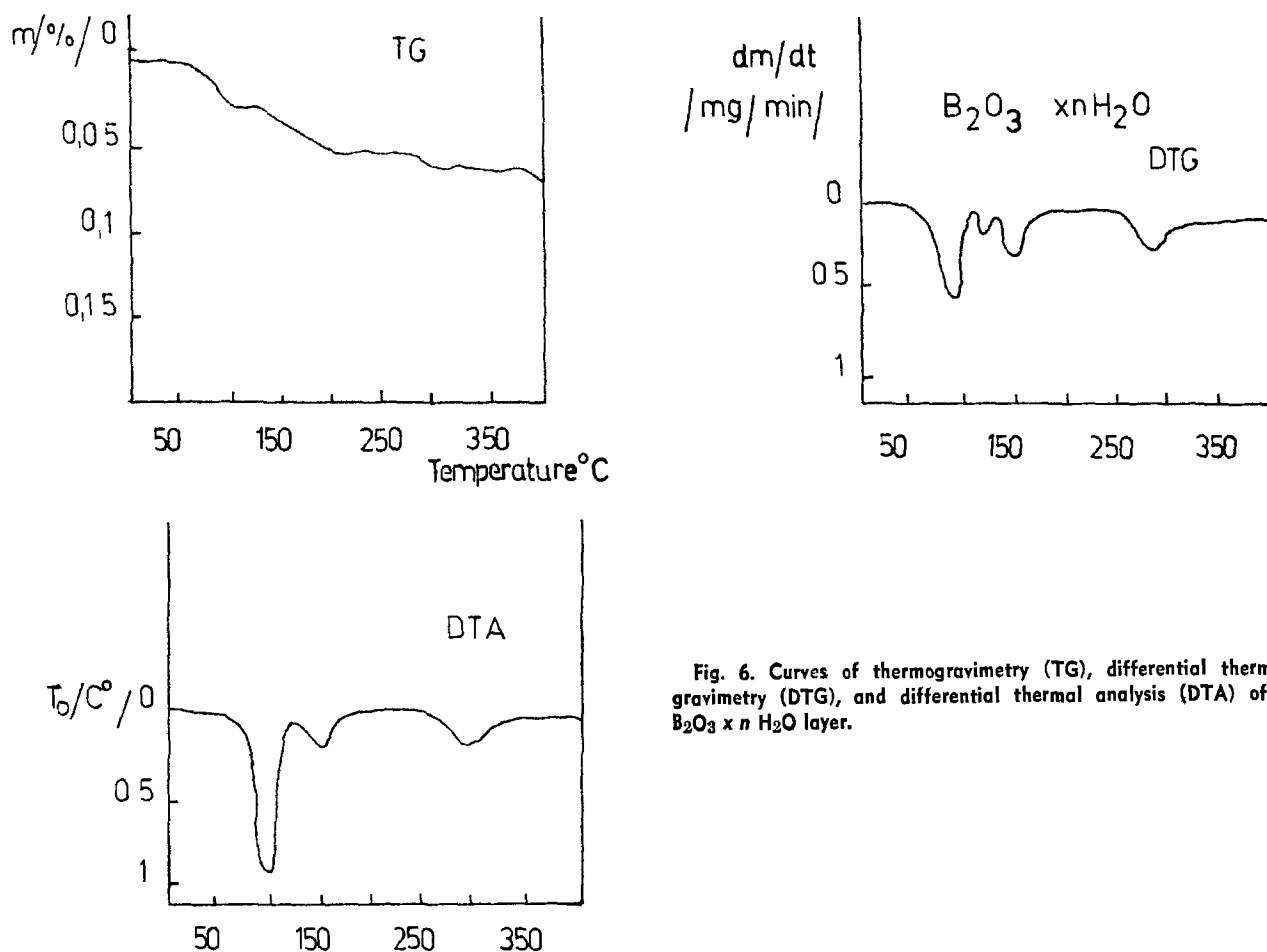
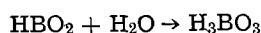
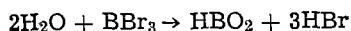


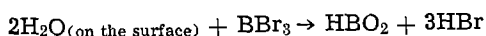
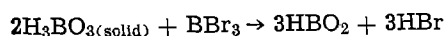
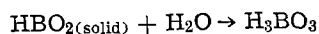
Fig. 6. Curves of thermogravimetry (TG), differential thermogravimetry (DTG), and differential thermal analysis (DTA) of a $B_2O_3 \times n H_2O$ layer.

Kinetics of Deposition

During the deposition process the following chemical reactions take place in the gas phase



In addition, some other reactions are possible on the surface of a silicon slice in the reactor



Accordingly, on the silicon surface a film of HBO_2 and H_3BO_3 mixture will be deposited. The composition of this film depends on the concentration of the materials taking part in the reaction and the geometry of the reactor. The adhesion, the optical, and morphological properties of this mixture layer are more favorable than those of the pure H_3BO_3 film. The thickness increases with the advancement of the reactions in the gas and on the surface of the boron acid layer. It would be difficult to determine the growth of the layer by calculation, but the layer thickness is easy to determine from the interference color of the film, which can be measured during the deposition process. The resulting deposition rates, gas flow rates, and water concentration are shown in Fig. 2 and 3, respectively.

If the gas mixing head is a simple tube, as shown in Fig. 1, and the substrate is not moved during the deposition, the variation of the deposition rate depends on the distance between the gas mixing head and the substrate (Fig. 4).

Examination of the Deposited Layers

The deposited layers to be used as a diffusion source for a small $4 \times 4 \mu m$ area have to be homogeneous of

max. $0.1 \mu m$ or less grain size. Figure 5 shows the layers to satisfy this requirement before diffusion. The method of thermal analysis has been applied for testing the water content of the boron acid layer. The water loss of the layers, that is, the $H_3BO_3 \rightarrow B_2O_3$ conversion, can be readily followed by thermogravimetry (TG), differential thermogravimetry (DTG), and differential thermal analysis (DTA). Results are shown in Fig. 6. The $HBO_2:H_3BO_3$ ratio determined from DTG (from $m =$ weight loss) in Fig. 6 was approximately 1:1. Because of the small quantity of material the error of the measurements was about $\pm 30\%$.

Diffusion from the Deposited Layers

The properties of the $B_2O_3 \times n H_2O$ layer diffusion sources from the aspect of the diffusion process differ only by their looser structure from those of B_2O_3 layers deposited at higher temperature. Therefore they are more hygroscopic and they contain more water. Be-

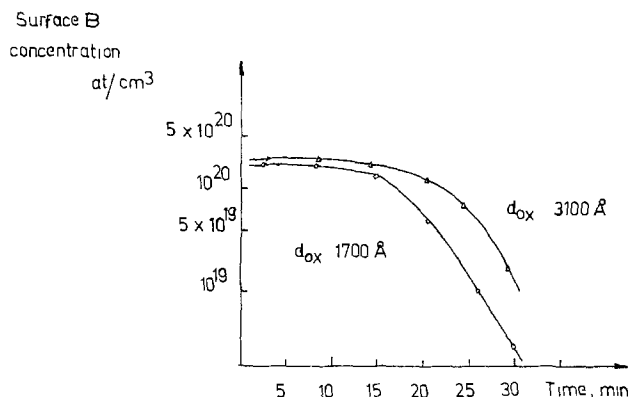


Fig. 7. Surface boron concentration in silicon vs. initial oxidation time for two different $B_2O_3 \times n H_2O$ thicknesses.

cause of their looser structure and higher water content they can be applied in a thicker layer without forming a so-called "boron skin." In the diffusion furnace these layers soften at about 500°C forming B₂O₃ melts similar to layers produced by other methods. Diffusion experiments have been performed with layers of various thicknesses on silicon substrates at 1100°C by first flowing dry oxygen and then nitrogen through the system.

The diffusion time was 30 min throughout. The surface boron concentration calculated from the Irvin curves vs. initial oxidation time is plotted in Fig. 7. The layers deposited by this method were used for the isolation diffusion of silicon bipolar integrated circuits and for special diffusions in opto-electronic devices.

Summary

A room temperature CVD method has been developed for producing B₂O₃ layers and layers for silicon diffusion sources. The properties of B₂O₃ *x* *n* H₂O

diffusion source layers have been investigated. From the aspect of appropriate surface concentration these layers are equivalent to B₂O₃ layers produced at a high temperature.

Manuscript submitted Oct. 3, 1977; revised manuscript received May 23, 1979.

Any discussion of this paper will appear in a Discussion Section to be published in the June 1981 JOURNAL. All discussions for the June 1981 Discussion Section should be submitted by Feb. 1, 1981.

REFERENCES

1. I. Ruge, "Halbleiter-Technologie," Springer-Verlag, Berlin, New York (1975).
2. W. Kern, *RCA Rev.*, **29**, 525 (1968).
3. W. Kern, and R. C. Heim; *This Journal*, **117**, 562 (1970).
4. W. Kern and A. W. Fischer, *RCA Rev.*, **31**, 715 (1970).



Anion Effects in the Stress-Corrosion Cracking of Copper and Brass

R. C. Newman* and G. T. Burstein**

Department of Metallurgy and Materials Science, University of Cambridge, Cambridge, England

Recently the stress-corrosion cracking (SCC) susceptibility of an admiralty brass has been studied in neutral electrolytes using slow strain rate and controlled potential (1). Transgranular SCC was observed in many electrolytes, and occurred most rapidly in the following order of severity with respect to anion:

$\text{NO}_2^- > \text{NO}_3^- > \text{ClO}_3^-$. Subsequently transgranular SCC of slowly strained copper was observed in aerated 1M NaNO_2 solution at open circuit (2), at present the only unambiguous instance of transgranular SCC in a pure metal. The present communication attempts to account for the severity of these anion effects.

Many copper alloys undergo SCC in ammoniacal environments. The potency of ammonia is associated with its ability to form stable soluble complexes with Cu(I) (3). In SCC of copper alloys, the rate of cracking is probably controlled by dissolution at bare metal surfaces. Localisation of the attack is ensured by a stable film on the crack walls (3), and the most severe cracking generally occurs when the repassivation of bare metal is slow but ultimately complete. The open circuit potential of cracking of copper in 1M NaNO_2 is +160-190 mV (nhe) (2): in this range the reaction $\text{Cu} = \text{Cu(II)}(\text{aq}) + 2\text{e}^-$ would rapidly approach equilibrium within the confines of a crack whether the soluble species is taken as $\text{Cu}^{2+}(\text{aq})$ (4) or $\text{CuNO}_2^+(\text{aq})$ (5). Thus the possible production of ammonia during the bare surface reaction has been investigated, as this would enable cracking to proceed by dissolution of copper as $\text{Cu(I)}(\text{aq})$ (3). The behaviour of ClO_3^- at bare copper and brass surfaces has also been examined.

Abrasion at open circuit was used together with qualitative and quantitative electrolyte analysis. Rods of copper and α -brass were abraded by hand for ~ 2 min in 6 ml pools of electrolyte lying on 120 grit emery paper, or immersed for 24 h without abrasion. Control electrolyte samples were obtained by abrading in doubly distilled water and by sampling the original electrolyte. The solutions used were high purity 1M NaNO_2 , NaNO_3 and NaClO_3 . After abrasion the electrolytes were filtered and tested quantitatively for ammonia using Nessler's reagent (6) and a set of standard NH_3 solutions, or qualitatively for Cl^- using acidified AgNO_3 solution. Both copper and brass produced high levels of ammonia from NaNO_2 and somewhat lower levels from NaNO_3 . For the Cu/NO_2 system, 500 single scrapes of a 0.2 cm^2 area produced $\sim 10^{-5}$ moles of NH_3 - even with a roughness factor of 10 for the rod and filings, this represents $\sim 10^{-8}$ moles NH_3 per cm^2 of bare surface, or ~ 5 monolayers of Cu dissolved as $\text{Cu}(\text{NH}_3)_2^+$. The process is therefore quite efficient. All control tests were negative for these solutions, and similar results were obtained by abrading with a sapphire blade. In NaClO_3 significantly higher levels of Cl^- were detected after abrasion of both metals than before: crude quantitative comparison suggested a somewhat less efficient reduction of the anion in this case.

*Electrochemical Society Student Member.

**Electrochemical Society Active Member.

The preliminary experiments described above highlight a possible role of anions which act both as cathodic reactants ($\text{NO}_2^- + 7\text{H}^+ + 6\text{e}^- = \text{NH}_3 + 2\text{H}_2\text{O}$; $\text{ClO}_3^- + 6\text{H}^+ + 6\text{e}^- = \text{Cl}^- + 3\text{H}_2\text{O}$) and as sources of complexants ($\text{Cu} + 2\text{NH}_3 = \text{Cu}(\text{NH}_3)_2^+ + \text{e}^-$; $\text{Cu} + 2\text{Cl}^- = \text{CuCl}_2 + \text{e}^-$) (5). The specificity of such processes to the bare surface may provide an additional localisation of attack which in the case of Cu/NO_2 is sufficient, and perhaps necessary, to cause SCC of a pure metal. Anions which complex directly (e.g. Cl^-) may well cause blunting of incipient cracks in pure metals but can cause SCC in alloys owing to additional features such as dealloying, coarse slip and grain boundary chemical heterogeneity. The Cu/NO_2 system is particularly favourable in that the open circuit potential lies in a potential range where the metal is in a borderline state of passivity; this may be another necessary condition for SCC to occur in a pure metal. The bare surface will undergo a negative pulse of potential in the presence of a local cathodic reactant, whether or not the potential is externally controlled, particularly in brass where transient dezincification current densities of $>10 \text{ A cm}^{-2}$ are possible (7) and must lead to large ohmic potential changes: this in itself will enhance the reduction of the anion to the aggressive complexant. It is significant that Devardas' alloy (Cu-45Al-52Zn) is used in analytical chemistry to reduce NO_2^- quantitatively to NH_4^+ . Prediction of other pure metal - environment combinations likely to exhibit SCC is in progress.

References

1. A. Kawashima, A.K. Agrawal and R.W. Staehle, Proc. Conf. 'Stress-Corrosion Cracking - the Slow Strain-Rate Technique', Toronto 1977, p 266. ASTM (1979).
2. S.P. Pednekar, A.K. Agrawal, H.E. Chaung and R.W. Staehle, J. Electrochem. Soc. **126**, 701 (1979).
3. T.P. Hoar and G.P. Rothwell, Electrochim. Acta **15**, 1037 (1970).
4. M. Pourbaix, 'Atlas of Electrochemical Equilibria in Aqueous Solutions', p.386. Pergamon Press, London (1966).
5. 'Stability Constants'. Chem. Soc. Special Publication no. 17. The Chemical Society, London (1964).
6. A.I. Vogel, 'Quantitative Inorganic Analysis', pp 306, 699. Longmans, Green & Co., London (1943).
7. R.C. Newman and G.T. Burstein, Corros. Sci. (1980, in press).

Acknowledgement

Financial support to R.C.N. from the British Petroleum Company Ltd. is gratefully acknowledged.

Manuscript received April 11, 1980.

Publication costs of this article were assisted by the University of Cambridge.

Analysis of the Gases Evolved during the Pitting Corrosion of Aluminum in Various Electrolytes

C. B. Bargeron and R. C. Benson

The Johns Hopkins University, Applied Physics Laboratory, Laurel, Maryland 20810

This paper contains a preliminary report of the composition of the gases evolved during the pitting corrosion of aluminum in aqueous electrolytes containing respectively KCl, KSCN, or NaNO₃. We believe the rather surprising results will bear positively on understanding pitting mechanisms and reactions. First, each electrolyte has a unique set of gases. Second, using a light microscope (1, 2), it was observed in each system that the gas evolution begins when the potential is increased above the pitting potential, E_p , and ceases when the potential is decreased below E_p . E_p has been determined to be about -0.8 V (all potentials are referred to the saturated calomel electrode) for 1 M Cl⁻ electrolytes by many investigators (e.g., 3-5). Galvele, et al have published pitting potentials of about 1.46 V and 0.96 V for 1 M NaNO₃ and 1 M KSCN, respectively (6, 7). Kaesche has observed that gas evolution occurs only above E_p for chloride electrolyte (8). Bargeron and Givens have observed blister formation, which requires gas production at the oxide-metal interface, as a step in the breakdown of the passivating oxide in chloride solutions (1, 2). As will be shown, the gases evolved from the NO₃⁻ and SCN⁻ electrolytes can only be explained by direct reaction of the anion with the metal. These results may also imply that Cl⁻ reacts directly with the metal.

The aluminum used for observations under the light microscope was 0.25 mm thick discs of purity 99.999 percent. The discs were placed in an electrode holder as described previously (1, 2). For the gas collection, aluminum of purity 99.99 percent was machined into a cylinder about 1 cm high and 1 cm in diameter. Samples were degreased in acetone and pickled briefly in 1 N NaOH. The samples used in the gas analysis experiments were screwed onto a Teflon holder which sealed the electrical connections from the electrolyte. Deionized water of resistivity 18 M Ω -cm and

A.C.S. reagents (highest purity available) were used to prepare electrolytes. The electrolytes were deaerated with high purity argon before gas collection. The gas collection apparatus (a glass tube with a bell-shaped piece on the end) was evacuated and filled with electrolyte. The evolved gases displaced the electrolyte in the tube, and 1-2 cm³ of gas was collected. Before entering the gas analyzer (VEECO Model SPI-10), the gases passed through a trap at -50°C (alcohol and dry ice) to remove water. After an experiment the trap was warmed to room temperature, and gases from it were analyzed. Only water was detected from the trap.

The sample potential was potentiostatically controlled. The reference electrode was a saturated calomel electrode connected by a bridge of the electrolyte through a Luggin capillary placed about 1 mm from the sample surface (the O.D. of the capillary was also about 1 mm).

The mass spectrum of the gas collected from pitting aluminum at a potential of 1.5 V in 1 M KCl is shown in Figure 1a. The spectrum shows the presence of H₂ and the deaeration gas Ar which is always present (Ar⁺ at m/e = 40 and Ar⁺⁺ at m/e = 20, where m/e is the mass-to-charge ratio). Potentials between -0.5 V and +1.5 V were investigated. The gas evolution increased with increasing potential (increasing current). For all potentials above E_p , only H₂ and Ar were detected. This is a surprising result since hydrogen production via the normal route of 2H⁺ + 2e → H₂ should be impossible at an anode potential of 1.5 V. Oxygen production (via 2H₂O → O₂ + 4H⁺ + 4e) is to be expected at this potential as assumed by others investigating pitting corrosion (9, 10). However in all cases O₂ was not observed above the weak background signal. Pickering and Frankenthal (11) also observed hydrogen evolution at controlled high potentials (1.2 V) during the pitting corrosion of iron and

Key words: gas evolution, pitting mechanism, pitting reactions, aluminum

stainless steels. Their explanation includes a high-resistance path resulting from a constriction in the pit caused by a gas bubble. Using a microelectrode they also measured much lower potentials within the pit.

The mass spectrum of the gas collected from pitting aluminum in 1 M KSCN at a potential of 1.2 V is shown in Figure 1b. The main components were H_2 and CH_4 (see Figure 1c for the cracking pattern of CH_4) with weaker peaks at 28, 32, 33, and 34 m/e. (It should be noted that the background signal was negligible at this sensitivity.) The distinctive odor of H_2S was present, and qualitative analysis of the solution after pitting was positive for sulfide (13). Hence, the 32-34 m/e peaks are probably due to the small amount of H_2S that escapes the water. The 28 m/e peak could be either N_2 or CO.

In Figure 1d the mass spectrum from gases evolved from pitting aluminum in 1 M $NaNO_3$ at a potential of 2.0 V is shown. In this case the gases are H_2 , N_2 , NO, and a peak at 44 m/e (likely N_2O). De Wexler and Galvele have previously noted briefly that gas is evolved during pitting in nitrate solutions and that the main component determined by gas chromatography was nitrogen. However, no further details are given (7). Adams, Eagle, and Foley have detected ammonia in mixtures of Cl^-/NO_3^- electrolytes in general corrosion tests (no potential control)(13). Qualitative analyses for NH_3 (12) in solution were positive. Ammonia is not present in the mass spectrum presumably because it is highly soluble in water.

The above results in which gas is evolved only at potentials above E_p strongly suggests that gas evolution is intimately involved in the pitting process. The mechanism by which these gases are formed is not known, but the fact that CH_4 , H_2S , N_2 , NO, and NH_3 are produced indicates that SCN^- and NO_3^- must interact directly with the metal. Furthermore, in the SCN^- and NO_3^- electrolytes, gas evolution only occurs above the pitting potentials of about +0.96 V and 1.46 V, respectively. Yet, in these instances there is concomitant H_2 production which requires a much lower potential. Thus, if H_2 is formed in the usual way, the potential difference across the electrified interface which controls the rate of the electrodic reaction (14) must fluctuate because of bubble constriction (11), even though the potential on the metal is constant.

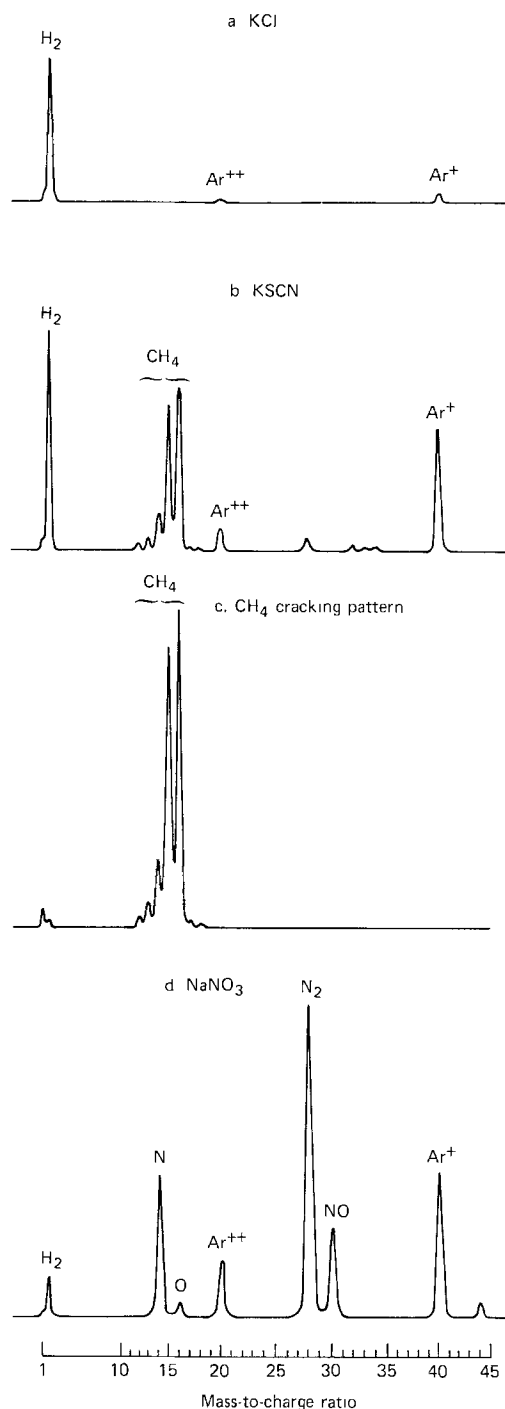


Figure 1

Mass spectra of the gases evolved during the pitting corrosion of aluminum under the conditions indicated: a) 1 M KCl at a potential of 1.5 V, b) 1 M KSCN at a potential of 1.2 V, c) cracking pattern of methane, and d) 1 M $NaNO_3$ at a potential of 2.0 V.

Regarding the metal-anion interaction, intermediate species may form which lead to gaseous products and metal dissolution. For example, in the pitting of aluminum in chloride solutions, aluminum chloride species have been proposed as intermediates (15, 16) which then hydrolyze. Similarly, during pitting in other solutions aluminum carbide, sulfide, or nitride species may be formed which then hydrolyze to CH_4 , H_2S , and NH_3 , respectively. (See *Handbook of Chemistry and Physics*.) Since these intermediate species are unstable in water, they would necessarily be formed on the metal surface which could provide some stabilization.

It should be noted that even the highest purity reagents that are commercially available contain chloride impurity. Therefore, it is possible that this Cl^- contaminant is involved in the H_2 production in the SCN^- or NO_3^- electrolytes. Experiments are being conducted to determine if trace amounts of chloride are significant.

In summary, the results reported here indicate that pitting of aluminum is accompanied by evolving gas which has a composition dependent on the anion and that a primary step in the pitting mechanism involves a direct interaction of the anion with the aluminum.

We wish to acknowledge the assistance of R. B. Givens.

REFERENCES

1. C.B. Barger and R.B. Givens, J. Electrochem. Soc., 124, 1845 (1977).
2. C.B. Barger and R.B. Givens, to be published in Corrosion.
3. J.R. Galvele and S.M. de De Micheli, Corr. Sci., 10, 795 (1970).
4. Z.A. Foroulis and M.J. Thubrikar, Werkst. und Korr., 26, 350 (1975).
5. B.N. Stirrup, N.A. Hampson, and I.S. Midgley, J. Appl. Electrochem., 5, 229 (1975).
6. J.R. Galvele, S.M. de De Micheli, I. L. Muller, S.B. de Wexler, and I.L. Alanis, in "Localized Corrosion," B.F. Brown, J. Kruger, and R.W. Staehle, Editors, p. 580, NACE-3, Houston (1974).
7. S.B. de Wexler and J.R. Galvele, J. Electrochem. Soc., 121, 1271 (1974).
8. H. Kaesche, Z. Phys. Chem. (N. F.), 34, 87 (1962).
9. J.A. Richardson and G.C. Wood, Corr. Sci., 10, 313 (1970). See especially p. 320, the second full paragraph.

10. K. Videm, Kjeller Report, KR-149, Institutt for Atomenergi, Kjeller, Norway, 1974. See especially p. 59, second column, the first full paragraph.
11. H.W. Pickering and R.P. Frankenthal, J. Electrochem. Soc., 119, 1297 (1972).
12. E.H. Swift and W.P. Schaefer, "Qualitative Elemental Analysis," W.H. Freeman and Co. (1962).
13. A.A. Adams, K.E. Eagle, and R.T. Foley, J. Electrochem. Soc., 119, 1692 (1972).
14. J.O'M. Bockris and A.K.N. Reddy, "Modern Electrochemistry," Plenum Press (1970), Vol. 2, p. 1142.
15. G. Sussek, M. Kesten, and H.-G. Feller, Metall (Berlin), 33, 1031 (1979).
16. F. Franz and P. Novak, in "Localized Corrosion," B.F. Brown, J. Kruger, and R.W. Staehle, Editors, p. 576, NACE-3, Houston (1974).

This work was supported by the Naval Sea Systems Command, U.S. Department of the Navy under Contract N00024-78-C-5384.

Manuscript submitted July 7, 1980; revised manuscript received Aug. 12, 1980.

Publication costs of this article were assisted by The Johns Hopkins University.

Cyclic Voltammetric and Spectroscopic Studies of SOCl_2 Solutions

H. V. Venkatesetty*

Honeywell Incorporated, Corporate Material Sciences Center, Bloomington, Minnesota 55420

The lithium-thionyl chloride (Li/SOCl_2) battery has the highest energy density of any known electrochemical system today (1-2). The solvent thionyl-chloride is also the cathode active material and this battery system has the potential for applications needing high rate discharge. Though the overall cell reaction is known to some extent, there is very little information on the reaction intermediates and the chemical reaction(s) following electrochemical reaction during the cell discharge process (3-6). The Li/SOCl_2 battery has shown a tendency to explode under a variety of conditions such as short circuit, forced over discharge and resistive load overdischarge (3,4,6). It has been postulated that during the discharge of SOCl_2 , the radical SO is formed according to $\text{SOCl}_2 + 2\text{Li} \rightarrow \text{SO} + \text{LiCl}$ and SO may dimerize and then decompose to S and SO_2 (7). $2\text{SO} \rightarrow (\text{SO})_2 \rightarrow \text{SO}_2 + \text{S}$. There is no definite experimental evidence for the formation of SO during electrochemical reduction and the following chemical reaction.

This paper presents cyclic voltammetric data on SOCl_2 carried out as a function of SOCl_2 concentration and scan rate in different aprotic organic solvents such as dimethylsulfite (DMSI), dimethylformamide (DMF) and acetonitrile (ACN) with lithium aluminum chloride and tetrabutylammonium hexafluorophosphate as supporting electrolytes. The cyclic voltammetric data have been treated using the diagnostic criteria of Nicholson and Shain (8) and the plots of current function versus voltage sweep rate are consistent with an irreversible charge transfer followed by chemical reaction. Studies have also been carried out using constant potential electrolysis and ultraviolet spectroscopy of solutions of SOCl_2 in acetonitrile with 0.1M tetrabutylammonium hexafluorophosphate.

Experimental Procedure.--The cyclic voltammetry and constant potential electrolysis

* Electrochemical Society Member,

Key words: Lithium battery, Thionyl chloride, cyclic voltammetry, chemical reactions

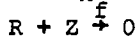
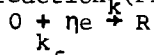
were carried out in a three compartment cell with fritted disc separator using a PAR 173 potentiostat/galvanostat and PAR 175 universal programmer and PAR 179 digital coulometer. The working electrode was glassy carbon, the counter electrode was platinum spiral and the reference electrode was lithium. The solvents DMF and ACN were Burdick and Jackson distilled in glass. The solvent DMSI was Eastman Kodak. All these solvents were redistilled using Perkin Elmer Spinning band column and the water content was found to be between 50 and 70 ppm as determined by an aquatest. Spectroscopic measurements were carried out using Beckman spectrometer. The supporting electrolytes were dried under vacuum and weighed inside a drybox. All experiments were carried out under dry and inert conditions.

Results and Discussion.--The cyclic voltammograms of 40 mM SOCl_2 in DMF containing 0.1M $(\text{C}_4\text{H}_9)_4\text{NPF}_6$ and 10 mM SOCl_2 in DMSI containing 0.1M LiAlCl_4 are shown in Figures 1 and 2 respectively. Similar voltammograms have been obtained with different concentrations of SOCl_2 . In the case of SOCl_2 reduction in DMSI with 0.1M LiAlCl_4 , there are three reduction peaks, peak I at 2.5V, peak II at 2.25V and a small peak III around 1.5V VS Li. On increasing the scan rate to 200mV/sec the peak at 2.5V becomes the shoulder of the large peak at 2.25V and the peak positions shift to more negative values. In the case of SOCl_2 reduction in DMF with 0.1M $(\text{C}_4\text{H}_9)_4\text{NPF}_6$, at slow scan rates, there are three peaks, one around 2.5V, the major peak around 2.1V and a small peak around 1.5V vs Li. Similar voltammograms are observed for SOCl_2 reduction in acetonitrile with LiAlCl_4 and $(\text{C}_4\text{H}_9)_4\text{NPF}_6$ supporting electrolyte. The reduction peaks I and II observed in these solvent systems are due to diffusion controlled processes as they show a linear relationship between the cathodic peak current versus square root of the voltage scan rate. The peaks I and II can be attributed to the two step reduction of SOCl_2 and the third peak around 1.5 can be attributed to the reduction of SO_2 .

A detailed mathematical analysis of the shape of the voltammograms for reversible and irreversible electrochemical reactions, preceded or followed by chemical reactions is given by Nicholson and Shain (8). One of the diagnostic criteria proposed by these authors is a plot of the current function

$$\frac{i_p}{\eta A F D^{1/2} v^{1/2} C^*}$$

against the voltage sweep rate V , where i_p is the peak current, D is the diffusion coefficient, V is the voltage scan rate and C^* is the concentration of SOCl_2 and η is the number of electrons transferred. F is the Faraday constant and A is the area of the working electrode. For uncomplicated charge transfer reactions such as reversible and irreversible charge transfer processes, horizontal straight lines are obtained (8). However, the plots of current function versus the voltage sweep rate for all the solutions studied in different solvents with different supporting electrolytes show that the reaction mechanism is consistent with results for an irreversible charge transfer followed by catalytic chemical reaction (Figures 3,4,5) (8).



Similar relationships have been found for different concentrations of SOCl_2 in DMF and DMSI containing 0.1M supporting electrolytes such as tetrabutylammonium hexafluorophosphate and tetrabutyl ammonium tetrafluoroborate.

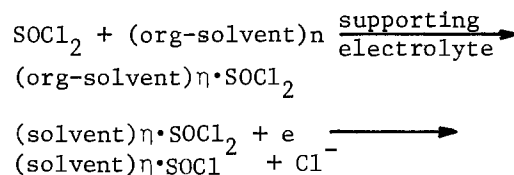
The ultraviolet spectrum of a freshly prepared solution of 0.1M tetrabutylammonium hexafluorophosphate in acetonitrile (UV grade) containing 5 mM SOCl_2 shows two medium intensity peaks at 232nm and 202nm. This solution, when left standing for several hours in the drybox, a new peak appears at 281nm whereas the peak at 232nm disappears and the peak at 202nm remains unchanged. On electrolyzing the solution using platinum electrodes at 1.75V vs Li the potential past the second reduction wave till most of SOCl_2 has been used up and examining the UV spectrum of the electrolyzed solution, three peaks are observed, a shoulder of medium intensity at 291nm, and two intense peaks, one at 256nm and the other at 202nm. The new high intensity peak at 256nm can be attributed to a new compound formed during electrolysis. Solutions of 0.1M tetrabutylammonium hexafluorophosphate in acetonitrile containing small amounts ($\approx 5\text{mM}$) of sulfur, sulfur monochloride (S_2Cl_2), Sulfur dichloride (SCl_2) and sulfurylchloride (SO_2Cl_2) were studied by UV spectroscopy. The solution containing sulfur shows four peaks, two medium intensity peaks at 277nm and 263nm and two high intensity peaks at 222.5nm and 206.5nm.

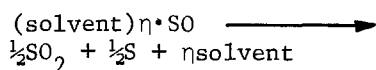
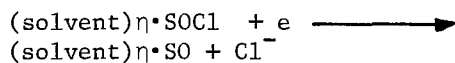
The solution containing S_2Cl_2 shows three peaks, two medium intensity peaks at 262.5nm and 201nm and a weak intensity peak at 305nm. The solution containing SCl_2 shows three peaks of medium intensity at 256nm, 242.5nm, and 202nm. The solution containing SO_2Cl_2 shows three intense peaks at 281nm, 239nm, and 214nm. The absorption spectra of the vapors of SCl_2 , S_2Cl_2 , SOCl_2 and SO_2Cl_2 have been investigated in the visible and ultraviolet regions (9). In the case of SCl_2 , there are two absorption peaks in the UV region appearing at 228nm and 261nm whereas S_2Cl_2 shows one absorption peak appearing at 258nm. SOCl_2 shows one absorption peak at 245nm and SO_2Cl_2 shows a continuous peak from 260nm to 108.6nm. These peak positions observed for the vapor state will be shifted generally to lower wavelength in solutions. The new medium intensity peak appearing at 256nm in electrolyzed solution of SOCl_2 can be attributed to the chlorides of sulfur SCl_2 and/or S_2Cl_2 produced during electrolysis.

The two step electrochemical reduction of SOCl_2 in solutions of organic aprotic solvents such as DMSI, DMF and ACN can be explained in terms of donor-acceptor approach. The ions and neutral species generated during electrochemical reduction process are expected to be stable in solvents of high donor strength.

The Donor Number (DN) of a solvent is a measure of the donor properties of the solvent and is defined as the numerical value of the heat of adduct formation between the donor molecule and the reference acceptor SbCl_5 in dilute 1,2-dichloroethane Solution (10). The Acceptor Number (AN) of a solvent is the ratio of the ^{31}P NMR Chemical Shift of triethylphosphine oxide (Et_3PO) in the solvent to that of 1:1 SbCl_5 Et_3PO in 1.2 dichloroethane multiplied by 100 (11-12).

The 'Donor Numbers' (DN) of thionylchloride, acetonitrile and dimethylformamide are 0.4, 14.1, and 26.6 and dimethyl sulfite is expected to show medium donor properties in comparison with the donor number of 15.3 for ethylene sulfite (10). Therefore, SOCl_2 is expected to form a donor-acceptor type complex with the aprotic solvents studied. A possible mechanism for the two step electrochemical reduction of SOCl_2 followed by chemical reaction can be written by the following reactions:





This kind of exothermic chemical reaction taking place following electrochemical charge-transfer process in Li/SOCl₂ battery may be important in relation to safety problems. Detailed investigations are in progress and will be reported in future papers.

Acknowledgement.--The author thanks D. J. Saathoff for technical assistance.

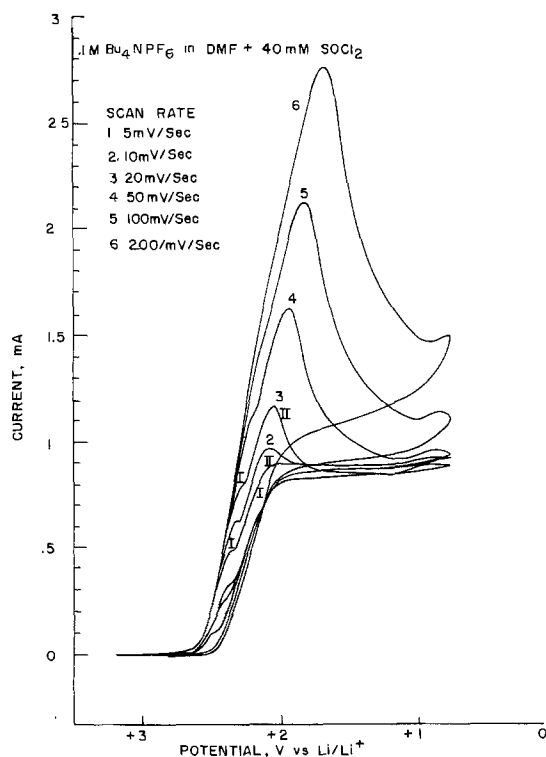


Fig. 1

REFERENCES

1. W. K. Behl, J. A. Christopoulos, M. Ramirez, and S. Gilman, *J. Electrochem. SOC.*, **120**, 1619 (1973).
2. J. J. Auburn, K. W. French, S. I. Lieberman, V. K. Shah, and A. Heller, *ibid.*, **120**, 1613 (1973).
3. A. N. Dey, *Proc. Symp. on Battery Design and Optimization*, S. Gross: Editor, The Electrochem Soc., NJ336 (1979).
4. D. L. Chua, S. L. Deshpande, and H. V. Venkatesetty, *ibid.*, 365 (1979).
5. W. Bowden and A. N. Dey, *J. Electrochem. SOC* **126**, 2035 (1979).
6. K. M. Abraham, G. L. Holleck and S. B. Brummer, *Proc. Symp. on Battery Design and Optimization*, S. Gross, Editor: The Electrochem. SOC, Inc., NJ (1979).
7. A. N. Dey, *J. Electrochem, SOC.*, **123**, 1262 (1976).
8. R. S. Nicholson and I. Shain, *Anal. Chem.* **36**, 706 (1964).
9. R. K. Asundi and R. Samuel; *Proc. Phys. Soc. (Lond)*, **48**, 28 (1936).
10. V. Gutmann, "The Donor-Acceptor Approach to Molecular Interactions", Plenum Press, New York-London (1978).
11. U. Mayer, *Pure. Appl. Chem.* **51**, 1697 (1979).
12. U. Mayer, V. Gutman and W. Gerger, *Monatsch Chem.* **106**, 1235 (1975).

Manuscript submitted June 3, 1980;
 revised manuscript received July 14, 1980.

Publication costs of this article
 were assisted by Honeywell Incorporated.

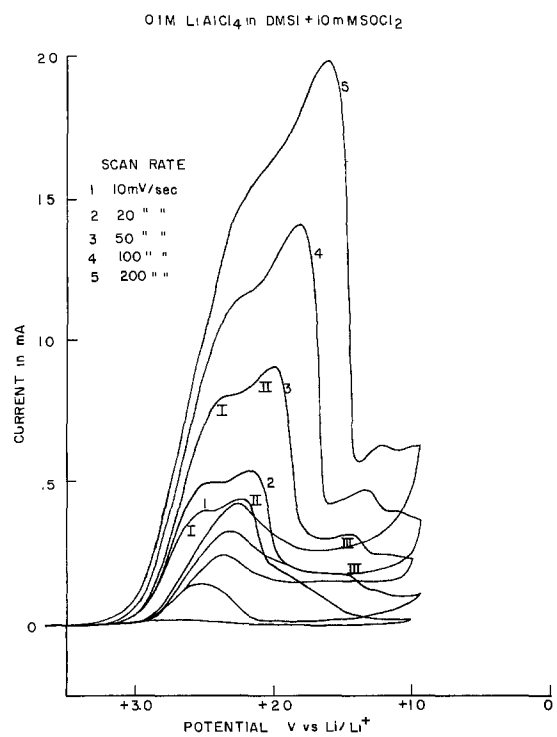


Fig. 2.

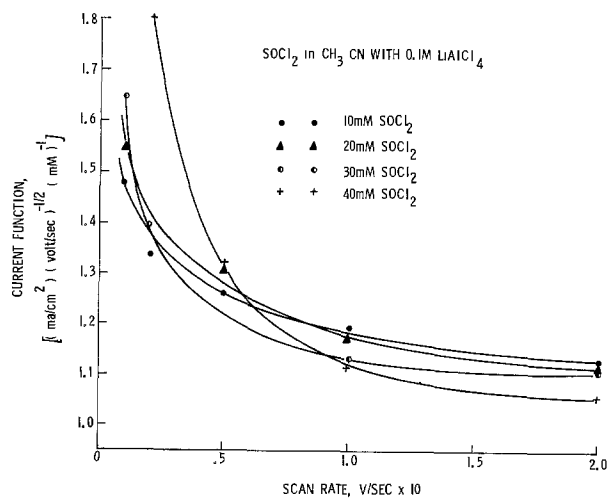


Fig. 3.

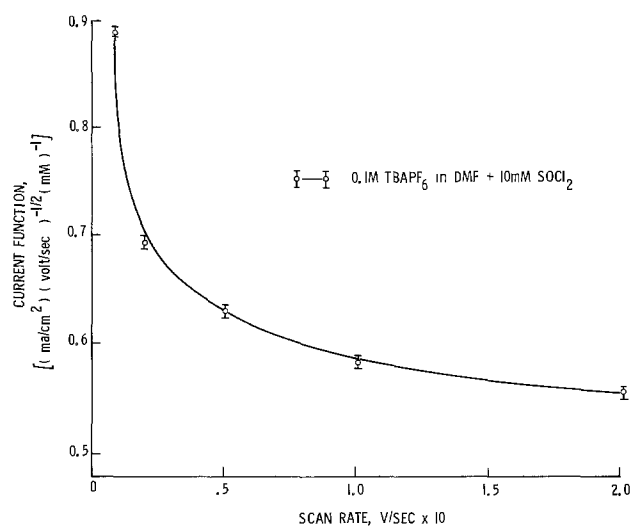


Fig. 4.

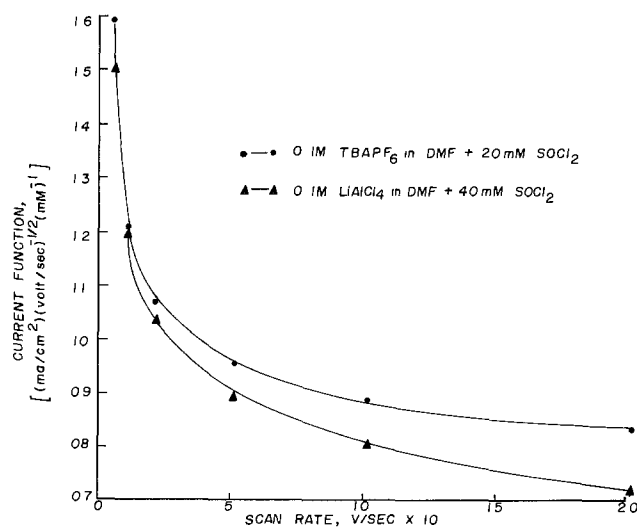


Fig. 5.



Electrochemical Aspects of the Cadmium Impregnation Process

T. Palanisamy*

University of Dayton Research Institute, Dayton, Ohio 45469

Y. K. Kao*

Department of Chemical and Nuclear Engineering, University of Cincinnati, Cincinnati, Ohio 45221

D. Fritts*

U. S. Air Force Aeropropulsion Laboratory, Wright-Patterson AFB, Ohio 45433

and J. T. Maloy*

Department of Chemistry, Seton Hall University, South Orange, New Jersey 07079

ABSTRACT

Electroanalytical methods have been employed to investigate the cathodic deposition of $\text{Cd}(\text{OH})_2$ on a nickel substrate from $\text{Cd}(\text{NO}_3)_2$ solution. Evidence for two distinctly different deposition products is given, depending on the potential of the deposition. At potentials positive of -0.6V vs. SCE a gray noncrystalline form of $\text{Cd}(\text{OH})_2$ appears to be deposited on the nickel substrate, presumably via a precipitation mechanism using the OH^- that is electrogenerated in the reduction of NO_3^- . At potentials negative of -0.8V vs. SCE , a black precursor to $\text{Cd}(\text{OH})_2$ is deposited. This black material forms at the same potentials as one of the further reduction processes of NO_3^- and NO_2^- that is reported herein; hence, it is believed to involve a cadmium complex of a nitrate reduction product. X-ray diffraction studies indicate that either of these materials is readily converted to crystalline hexagonal $\text{Cd}(\text{OH})_2$ during the electrochemical formation process. However, since the gray material is deposited with minimal concurrent gas evolution or metallic cadmium deposition, its utility in achieving high $\text{Cd}(\text{OH})_2$ loadings of a uniform material within the pores of nickel plaque material is stressed by this work. When low current densities (0.2 A/in.^2 plaque) are employed (such that the potential of the nickel substrate never becomes more negative than -0.65V vs. SCE) in the deposition; a high loading is achieved of a uniformly distributed product that requires no formation to reach maximum capacity. This work is supported by a series of scanning electron micrographs of impregnated plaque material. Some voltammetric evidence is presented that indicates somewhat reversible hydrogen adsorption on the negative cadmium-impregnated nickel electrode during overcharge.

The manufacturing methods for the cadmium electrodes used in alkaline cells which have been reported in the patent literature generally fall into two categories; vacuum deposition or electrochemical impregnation. In either method, porous ($>75\%$) nickel plaque material is employed as the electrode substrate. In the former method, the nickel plaque material is placed in a chamber and the chamber is evacuated. A cadmium salt solution is then allowed to flow into the chamber so that the plaque becomes immersed within it. The soaked plaque material obtained in this manner is removed from the chamber and immersed in an alkaline solution to precipitate cadmium hydroxide within the pores. This process is sometimes repeated to achieve higher $\text{Cd}(\text{OH})_2$ loadings than would be possible in a

single vacuum deposition cycle. In the latter method, a cadmium salt solution is reduced at the nickel plaque electrode to produce hydroxide ion which, in turn, precipitates cadmium hydroxide within the pores of the plaque material. Electrodes prepared by this single immersion process are generally less expensive than those prepared by the time-consuming vacuum deposition process, and they often exhibit superior performance characteristics with respect to cycle life and fading. However, the results obtained with electrochemically impregnated cadmium electrodes are not consistent and appear to be highly dependent on the experimental variables employed during the impregnation. These variables include the properties of the plaque material (thickness, porosity, and pore structure), the properties of the cadmium salt solution (composition, concentration, pH, and temperature), and

* Electrochemical Society Active Member.
Key words: voltammetry, deposition, electrode, films.

EST

the electrochemical parameters (applied voltage, current density, and time of electrolysis). A recent review (1) provides a compilation of some studies of these variables which have been undertaken by battery manufacturers. The basic electrochemistry of the cathodic deposition of cadmium hydroxide has not received much attention, even though this developed patent literature exists and emphasizes various control conditions of the cathodic process for nickel and cadmium electrodes [(1), and references contained therein]. This study was undertaken, then, to provide this fundamental electrochemical information about the cadmium process using the techniques that were employed in this laboratory during a recent investigation of the nickel process (2). Nickel microelectrodes were cathodized under controlled potential conditions to study the deposition process under various cadmium solution environments. Some cadmium hydroxide electrodes prepared in this manner (either by voltammetry or chronoamperometry) were also subjected to charge-discharge studies in 32% KOH. The information gained from these studies indicates that, even though the cadmium process is somewhat more complicated than the nickel process, the conditions for deposition may be controlled to produce cadmium electrodes that have consistently high utilization characteristics with minimum surface buildup. Because a thorough understanding of the mechanism of cathodic deposition of cadmium hydroxide is necessary to control these conditions properly, the elucidation of this mechanism which follows is believed to be essential to the further development of electrode fabrication technology.

Experimental

A Princeton Applied Research Model 170 Electrochemical System (PAR) was used in all electrochemical studies; digital chronocoulometry experiments were carried out using this instrument in conjunction with a Hewlett-Packard Model 2401C Integrating Voltmeter. All electrochemical experiments were conducted in quiescent deaerated solution contained in a covered 400 ml beaker under a maintained atmosphere of helium. The pH of the solution was controlled by adding the required amount of the acid of the cadmium salt employed in the experiment; no buffers were used. The nickel working electrode and saturated calomel reference electrode (SCE) used in these studies have been described previously (2). A 1.0×15.0 cm strip of cadmium was used as the counterelectrode. In some experiments a cadmium working electrode was used; this was made by imbedding a strip or wire of the desired metal in a sheath of Lucite or Teflon to form a microelectrode of area less than 0.1 cm^2 .

X-ray diffraction patterns were obtained using a Philips XRG-3000 diffractometer employing Ni-filtered $\text{CuK}\alpha$ radiation at a typical 2θ scan rate of $1^\circ/\text{min}$. Samples for these x-ray studies were prepared electrochemically on a 1.0×2.5 cm nickel foil that was used in place of the nickel microelectrode for this purpose; a correspondingly larger counterelectrode was employed with this nickel foil working electrode.

Scanning electron micrographs were obtained for cadmium electrodes which had been prepared by impregnating sintered nickel plaque material using the deposition technique that was suggested as a result of the microelectrode studies. (This method is outlined below.) The ETEC Scanning Electron Microprobe that was used for this purpose was equipped with a Kevex 5100C Analyzer for the x-ray energy dispersive analysis used to determine cadmium and nickel content. Gold-palladium sputtered samples were employed.

Results and Discussion

In a preliminary attempt to elucidate the mechanism of cadmium hydroxide cathodic deposition, cyclic voltammetry studies of 1M KNO_3 solutions in the presence and absence of $2\text{M Cd(NO}_3)_2$ were carried

out at controlled pH using both nickel and cadmium microelectrodes. The results of these preliminary studies at a nickel electrode are shown in Fig. 1. The upper multiscan voltammogram shows the processes that take place in a solution containing both cadmium and potassium nitrate when the electrode potential is scanned in a negative direction, reversed, and reversed again; the lower (background) curve shows at the same sensitivity those processes that occur in the absence of $\text{Cd(NO}_3)_2$. From this voltammetry it is clear that the participation of the cadmium ion is necessary for the electroactivity exhibited in the upper graph. The most prominent feature of this electroactivity is the large reduction wave at -0.63V vs. SCE that is obtained only during the initial negative scan. Plausible causes for this wave include the reduction of Cd^{+2} to electroplate metallic cadmium on the nickel surface or the reduction of a solution species to liberate OH^- in the presence of Cd^{+2} to precipitate a cadmium hydroxide on the electrode surface; evidence presented below indicates that the latter explanation is correct. When this portion of the sweep is followed by a further potential excursion into the background reduction process for the nitrate solution and then reversed, a second reduction process is observed at -0.62V vs. SCE during the reverse scan. Evidence presented below indicates that this wave is due to the reductive formation of metallic cadmium from some cadmium oxide or hydroxide that was deposited on the electrode surface during the forward scan. This contention is supported by the observation of the oxidation wave at -0.56V vs. SCE at the end of the first full cycle. This wave at the anodic stripping potential of cadmium is observed only if the preceding reduction wave is obtained in nitrate solution; therefore, it probably corresponds to the anodic stripping of the cadmium metal that is formed when the deposited material is reduced. That these processes (or one of them) effectively passivate the electrode to further electroactivity is evidenced by the lack of any significant reduction current at potentials positive of -0.75V vs. SCE during the second half-cycle. The reduction process at -0.63V causes a gray film to be deposited on the nickel electrode whereas the sweep past -0.75V results in the deposition of a black film. Evidence presented below indicates that the formation of the gray material at -0.63V vs. SCE is sufficient

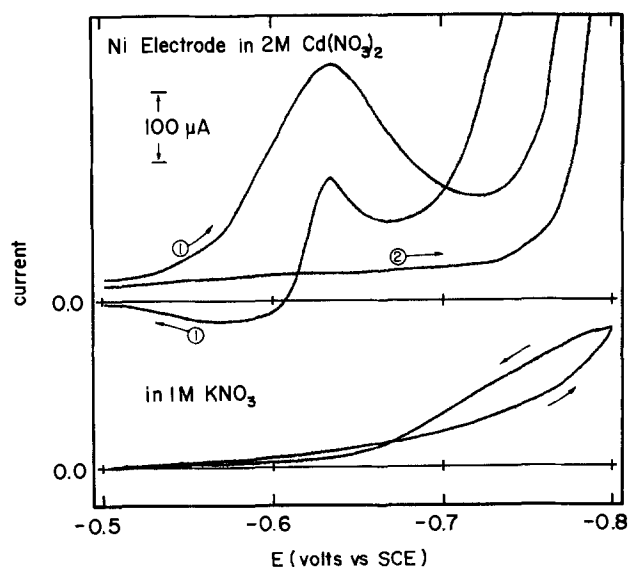


Fig. 1. Voltammetry of nitrate solutions at a nickel electrode. In addition to $2\text{M Cd(NO}_3)_2$ the solution used for the upper voltammogram contained 1M KNO_3 . In both runs $\text{pH} = 2.6$, $A = 0.013 \text{ cm}^2$, and $v = 0.1 \text{ V/sec}$. Scans were initiated at the solution rest potential (-0.15V vs. SCE , not shown, for the upper voltammogram).

to passivate the electrode to the extent exhibited during the second scan.

The corresponding voltammetry at a cadmium working electrode is shown in Fig. 2. As is evident from this figure, the large reduction wave that is present at -0.63V vs. SCE on nickel is absent on cadmium during the initial scan. If this wave on nickel is due to passive film formation, its absence on cadmium could indicate that this film is already present on the cadmium electrode at the start of the scan. In acid solution ($\text{pH} = 2.6$) the oxidation of cadmium metal is thermodynamically feasible. On the other hand, the absence of this wave on cadmium could be caused by the overvoltage of the species responsible for it being higher on cadmium than on nickel. Since the voltammetry of the KNO_3 solution in the absence of $\text{Cd}(\text{NO}_3)_2$ is essentially the same at either electrode, there is no evidence that the solution is reduced more readily on nickel than on cadmium. Thus, the pre-existence of a passivating film on cadmium in acid solution is presumed to be the reason for the absence of this wave on cadmium. This hypothesis is supported by the observation that the rest potential of a cadmium electrode in acidified $\text{Cd}(\text{NO}_3)_2$ solution is, at first, rather poorly defined. This suggests that spontaneous film formation begins to occur at the instant that the electrode is immersed in the solution and only ceases when the electrode is passivated to any activity at -0.63V vs. SCE .

The reversal of the initial scan on cadmium (following a potential excursion to -0.8V vs. SCE) reveals three additional reduction processes as opposed to the one observed on nickel. These are probably due to the reduction of different complexes of Cd^{+2} to metallic cadmium in the rapidly changing pH environment of the working electrode. Scan 2, which was begun without ever entering the potential region where anodic stripping of cadmium would occur, reveals a new reduction process at -0.68V . This probably corresponds to the same cathodic film formation that is observed on the initial scan at -0.63V on nickel. This

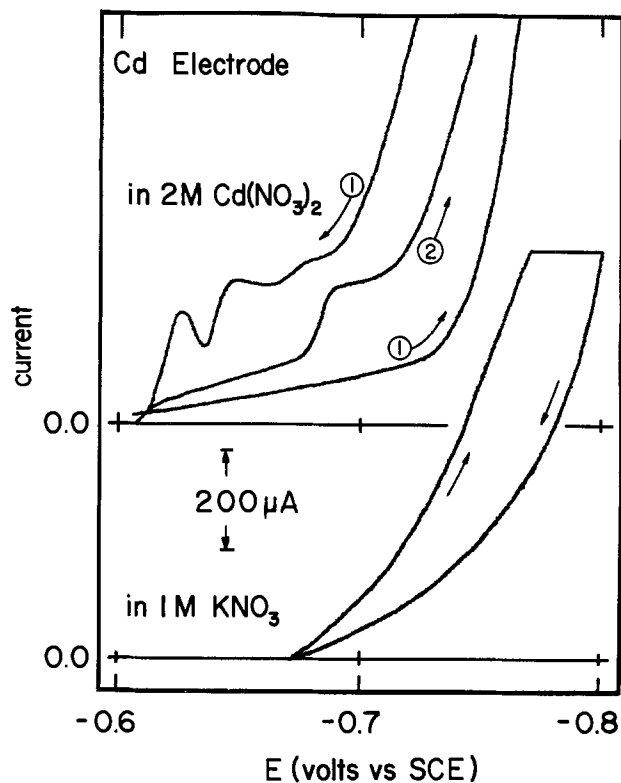
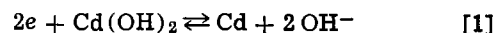


Fig. 2. Voltammetry of nitrate solutions at a cadmium electrode. Experimental conditions were identical to those given in Fig. 1 except that $A = 0.064\text{ cm}^2$. Potentials positive of -0.6V vs. SCE were avoided to prevent electrode oxidation.

explanation is plausible because the reduction processes observed at the end of the first scan probably deposit a fresh cadmium surface on the electrode so that it is no longer passivated to additional film growth.

The reductive formation of cadmium metal following potential excursions into cathodic background is supported by the upper voltammetry shown in Fig. 3. This voltammogram shows the effect of reversing the scan direction on the second half-cycle before reaching the potentials where anodic stripping of cadmium occurs. That the second scan exhibits a shoulder at -0.69V vs. SCE that is reminiscent of the wave seen at the start of the second scan on cadmium (see Fig. 2) indicates that the behavior of the nickel electrode is not unlike the behavior of a cadmium electrode under these conditions. Since this behavior is not at all like that seen during the second scan on nickel following anodic stripping (see Fig. 1), one can only infer that the reduction process at -0.62V on the reverse scan is responsible for the cadmium which forms on the electrode surface. Because this might appear to be contrary to the laws of thermodynamics, it is prudent at this point to rationalize this observation.

Let us assume that the species deposited on the electrode at -0.6V is $\text{Cd}(\text{OH})_2$. (X-ray evidence is presented below indicating that this species is a non-crystalline form of cadmium hydroxide.) This species could form on the electrode if the rate of solution decomposition is sufficiently fast to generate enough hydroxide ion to precipitate $\text{Cd}(\text{OH})_2$ ($K_{sp} = 1.2 \times 10^{-14}$) on the electrode surface, rather than allowing Cd^{+2} to be directly reduced. The reduction of $\text{Cd}(\text{OH})_2$ to metallic cadmium is pH dependent



and would occur more readily in acid medium. As the electrode potential is being swept in a positive direction from -0.8V vs. SCE where maximum hydroxide ion generation occurs, that is exactly what happens: the solution in the vicinity of the working

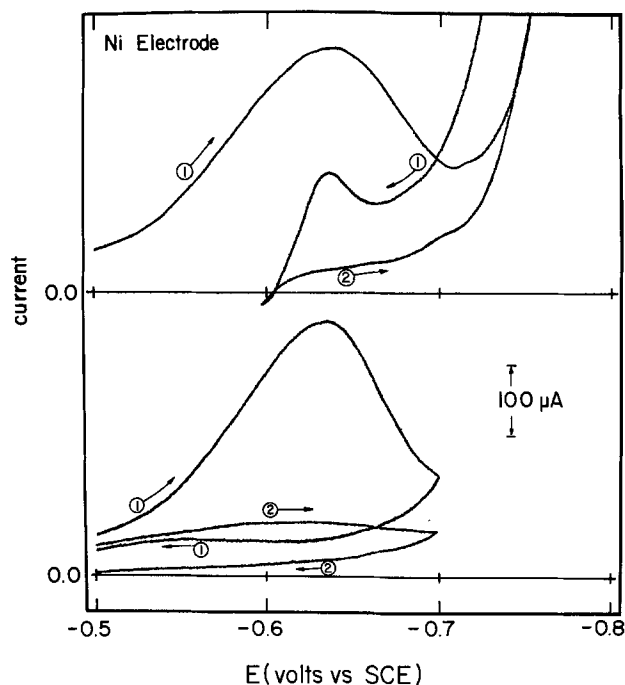


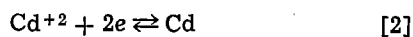
Fig. 3. The effect of potential variation in the voltammetry of $\text{Cd}(\text{NO}_3)_2$ solutions at a nickel electrode. Experimental conditions are given in Fig. 1. In the upper curve, the potential was swept from the rest potential to -0.8V vs. SCE , reversed, and reversed again at -0.6V . In the lower curve, each scan was initiated at the rest potential and reversed at -0.7V vs. SCE .

electrode approaches bulk acidity. At some potential, the generation of hydroxide ion diminishes to the point that reaction [1] may occur. When this happens, the cathodically deposited cadmium hydroxide is reduced to cadmium.

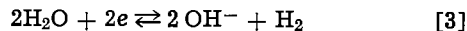
The lower voltammetry in Fig. 3 illustrates that the first reductive process that occurs at $-0.63V$ vs. SCE is sufficient to passivate the electrode to additional electroactivity at this potential. Because the scan direction was reversed before the onset of solution decomposition, the process occurring at $-0.63V$ is shown to be responsible for the passivation that is observed during the second scan. This process is believed to be the cathodic deposition of $Cd(OH)_2$.

This deposition occurs by a diffusion-controlled process, however. Evidence for this observation may be found in Table I which shows the linear sweep voltammetry $i_p/v^{1/2}$ data for the peak at $-0.63V$. The near constancy of this quantity over the range of given scan rates indicates that the rate of the deposition process is controlled by the diffusion of a solution species, at least in the early stages of the deposition (before film formation causes passivation).

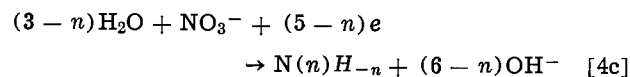
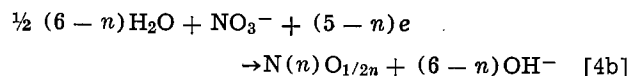
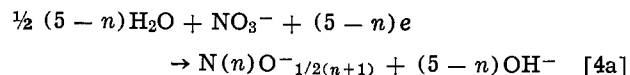
The pH dependence of this process is illustrated in Fig. 4. As the bulk solution becomes more acidic the reduction process that results in electrode passivation occurs at less negative potentials. In addition, even though the peak current is higher at pH 6.0 than it is at pH 1.5, there is a general decrease in area under the voltammetric peak with increasing pH (about 18% reduction in going from pH 1.5 to pH 6.0). This indicates that the reduction process occurs more readily in acid media and points to a pH-dependent redox reaction as a cause of this process. This data suggests that passivating film formation is not due to direct Cd^{+2} reduction in nitrate solution



Instead, it appears more likely that this wave is due to solution reduction coupled with $Cd(OH)_2$ precipitation. Solution reduction may occur either by solvent reduction



or by electrolyte reduction. In the latter case, the nitrate ion $N(V)O_3^-$ would either be reduced to another "mononegative" ion $N(n)O^{-1/2(n+1)}$ (such as NO_2^- or $N_2O_2^{2-}$) or to a molecular compound of nitrogen $N(n)O_{1/2n}$ or $N(n)H_{-n}$ (such as NO_2 , N_2O_3 , NO , N_2O , N_2 , NH_2OH , N_2H_4 , or NH_3) where n is the oxidation state of the nitrogen in the compound so formed. In general the electrode reaction for these NO_3^- reduction processes may be written



Either reaction [3] or [4] produces OH^- which may precipitate $Cd(OH)_2$

Table I. Current-scan rate data for linear sweep voltammetry at pH 3.5

Sweep rate v (mV/sec)	Peak current i_p (μA)	$i_p/v^{1/2}$
10	164	51.9
20	210	47.0
50	320	45.3
100	446	44.6
200	700	49.5

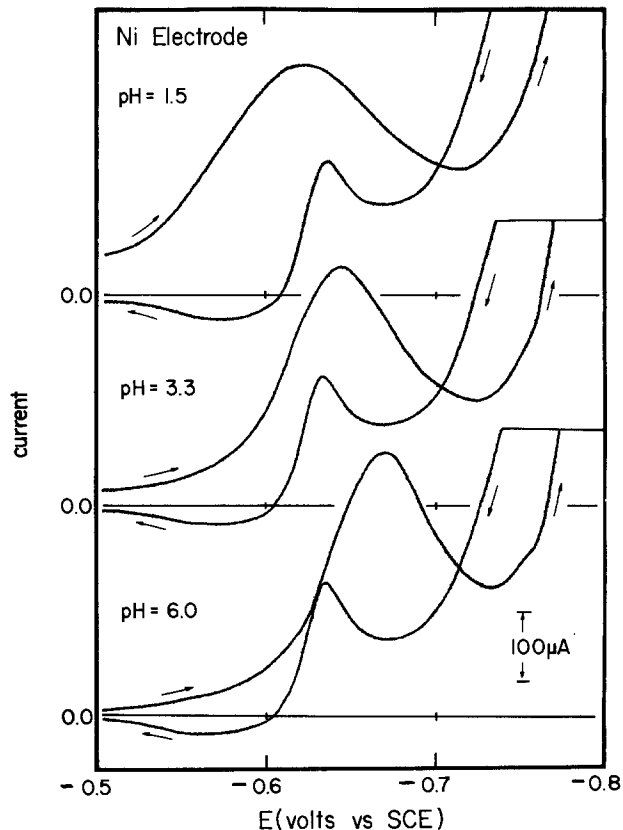
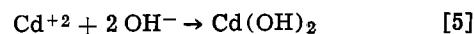
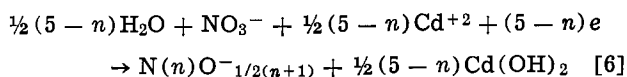


Fig. 4. The pH dependence of the voltammetry of $Cd(NO_3)_2$ solutions at a nickel electrode. Experimental conditions other than pH are given in Fig. 1.



on the electrode surface (or within the pores of the plaque material). Alternately, since the presence of the Cd^{+2} appears to be necessary to observe the NO_3^- reduction process, a concerted deposition reaction may be obtained by combining Eq. [3] or Eq. [4] with Eq. [5]. For example, by combining Eq. [4a] with Eq. [5]



is obtained. Comparison of this deposition stoichiometry with the charge-discharge stoichiometry (Eq. [1]) results in the conclusion that one equivalent of chargeable $Cd(OH)_2$ is deposited by each equivalent of charge passed during the concerted deposition represented by Eq. [6]. The different reduction products given in Eq. [3], [4b], and [4c] result in different concerted deposition stoichiometries, but in no case would more than two or less than one equivalent of chargeable $Cd(OH)_2$ be deposited by one equivalent of charge passed during deposition. Any of these deposition mechanisms would occur more readily in acid medium and exhibit the voltammetry of Fig. 4.

Voltammetric scans in the absence of NO_3^- , shown in Fig. 5, not only rule out reaction [2] as a source of OH^- , but also indicate that NO_3^- reduction is responsible for the behavior in question. The first three scans, done in 0.76M $CdCl_2$ at pH 2.0 adjusted with HCl show clearly that the onset of Cd^{+2} reduction is at potentials negative of $-0.7V$ vs. SCE. No electroactivity is observed between -0.6 and $-0.7V$ where the primary passivation wave occurs in nitrate solution. When the deposition threshold potential is crossed on the reverse scan, the anodic stripping of electro-deposited cadmium is observed. The behavior of 0.67M $CdSO_4$ at pH 2.0 adjusted with H_2SO_4 is essentially the same; this is shown in curve d. Only when nitrate ion is added (in the form of HNO_3 to maintain the pH in curves e and f) is there any electroactivity at poten-

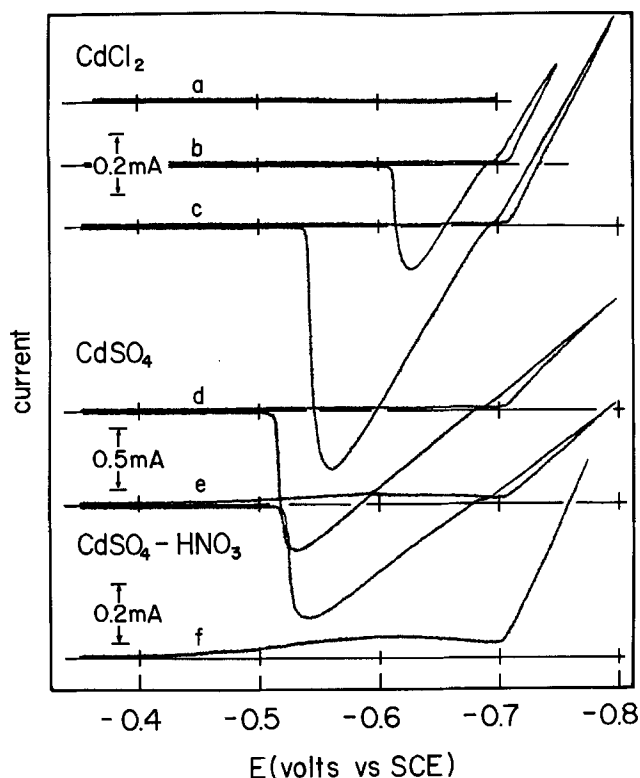


Fig. 5. Cadmium solution voltammetry in the absence of nitrate. Curves a, b, and c: 0.76M CdCl_2 at a nickel electrode; $v = 20$ mV/sec. Curves d, e, and f: 0.67M CdSO_4 at a nickel electrode; $v = 50$ mV/sec. The bulk pH was maintained at 2.0 using HCl for curves a, b, and c and H_2SO_4 for curve d; for curves e and f, this pH was maintained with HNO_3 .

tials positive of -0.7V vs. SCE . Even small quantities of NO_3^- (less than 0.01M), however, are sufficient to produce a discernible wave in the vicinity of -0.6V (see curve f). This experiment demonstrates conclusively that the wave observed at -0.63V vs. SCE on nickel in $\text{Cd}(\text{NO}_3)_2$ solution is due neither to the direct reduction of Cd^{+2} nor to the cathodic deposition of $\text{Cd}(\text{OH})_2$ from solvent decomposition. Instead, this work indicates that nitrate ion reduction followed by cathodic deposition of $\text{Cd}(\text{OH})_2$ (reactions [4] and [5]) is responsible for this wave.

The voltammetry of $\text{Cd}(\text{NO}_3)_2$ on cadmium at various levels of pH is shown in Fig. 6. These voltammograms confirm the absence of the cathodic deposition reaction on cadmium and illustrate variability of the rest potential in acidified nitrate solution. This suggests that the passive film forms spontaneously on cadmium immersed in nitrate solution at any pH studied. Regardless of pH, more electroactivity is observed on cadmium following excursions into cathodic background than is observed on nickel. These results merely tend to confirm the observations associated with Fig. 2.

These results indicate that it is electroanalytically possible to gain some information about the mechanism of cathodic deposition of a cadmium hydroxide film on a nickel electrode in nitrate solution. At potentials positive of -0.7V vs. SCE , the film is gray in color; it forms via nitrate reduction with little detectable gas evolution at a microelectrode; it effectively passivates the electrode to further film deposition; and it neither is metallic cadmium nor is it readily converted to metallic cadmium by making the electrode potential more positive (to decrease the local pH in vicinity of the film). At potentials negative of -0.7V vs. SCE , either a different kind of deposition occurs, or the film that was deposited at more positive potentials is transformed. At these potentials a black deposit forms on the surface of the electrode. Con-

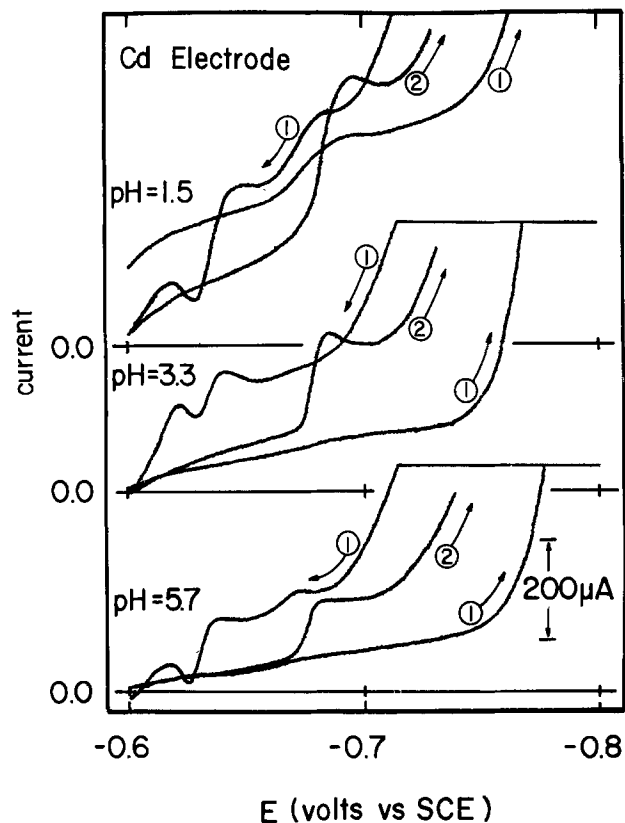


Fig. 6. The pH dependence of the voltammetry of $\text{Cd}(\text{NO}_3)_2$ solutions at a cadmium electrode. Experimental conditions other than pH are given in Fig. 2.

siderable gas evolution takes place concurrently with the deposition of the black film. Even though the electrode potential is sufficiently negative to deposit metallic cadmium at the potential of black film deposition, there is no evidence of cadmium deposition. Instead, metallic cadmium appears to be formed from the reduction of $\text{Cd}(\text{OH})_2$ that has been deposited on the electrode; this reduction seems to take place readily when the electrode potential is changed in a positive manner from the black film deposition potential so that the electrode experiences a rapid decrease in local pH. The black film is not nearly as effective as the gray film in passivating the electrode to further activity at the deposition potential. (Excessive gas evolution at the more negative potential may serve to suppress any uniform film growth on the electrode surface, thereby minimizing passivation.) Practitioners of the deposition art, then, have the ability to electrochemically deposit two different cadmium forms on a nickel substrate, depending on the potential of the deposition. Further investigations were carried out to characterize these two cadmium forms and to assess their utility as battery active material.

Macroelectrodes of the size necessary for x-ray diffraction studies were prepared potentiostatically from $\text{Cd}(\text{NO}_3)_2$ solution at -0.6 and -0.8V vs. SCE . During the deposition of the gray material at -0.6V (material A) minimal gas evolution was observed at the larger electrode; excessive gas evolution occurred with the deposition of the black material at -0.8V (material B). X-ray powder patterns for these two materials are given in Table II. The patterns for these materials were compared with ASTM reference patterns for hexagonal $\text{Cd}(\text{OH})_2$, metallic Ni, and metallic Cd (also given in Table II) and for several known cadmium compounds: monoclinic $\text{Cd}(\text{OH})_2$, CdO , $\text{Cd}(\text{O}_2)_{0.88}(\text{OH})_{0.24}$, $\text{Cd}(\text{NO}_3)(\text{OH}) \cdot \text{H}_2\text{O}$, and $\text{Cd}(\text{NO}_3)(\text{OH})$ (not given). Even though the patterns for materials A and B were in general poorly defined, it was clear from these comparisons that these materials could not be positively identified as any of these

Table II. X-ray powder diffraction data^a

Material A deposited at -0.6V	Material B deposited at -0.8V	Material A formed in 32% KOH	Material B immersed in H ₂ O	Hexagonal ^b Cd(OH) ₂	Ni ^c metal	Cd ^d metal
9.3(90)	7.73(15) 7.26(75) 5.23(20)					
4.70(30)	4.48(55) 3.767(100)	4.71(65)	4.74(56)	4.70(70)		
3.51(100)	3.534(15) 3.414(25) 3.273(15) 3.175(10)					
2.940(60) 2.814(40)		3.033(70)	3.028(59)	3.03(65)		2.809(65)
	2.755(40) 2.694(25)					
2.338(40)	2.362(35) 2.191(20) 2.101(10) 2.067(10) 1.957(10)	2.550(100) 2.350(5)	2.550(100)	2.550(100)		2.580(32) 2.340(7)
		2.036(40)	2.036(24)		2.032(100)	
	1.864(10) 1.843(10)	1.857(21)	1.859(27)	1.857(35)		1.901(32)
	1.728(20)	1.764(32) 1.749(21) 1.639(20) 1.512(7)	1.762(100+) 1.748(18) 1.639(48)	1.762(42) 1.748(20)	1.762(42)	
		1.442(10) 1.392(6)	1.443(13) 1.397(9)	1.441(8) 1.398(8)		1.516(26) 1.490(19)
		1.270(6)				1.404(3) 1.316(17) 1.290(2)
		1.248(19)			1.246(21) 1.062(20)	1.258(13)

^a d-spacings in Å (relative intensity).

^b ASTM Card 13-226.

^c ASTM Card 4-850.

^d ASTM Card 5-694.

known compounds. (Because material A has some characteristics in common with hexagonal Cd(OH)₂, it is believed to be a noncrystalline form of this compound.) Material A was then subjected to a few charge-discharge formation cycles in 32% KOH. Material B was allowed to stand in neutral water for 30 min. Either of these treatments produced a material having a pattern that agreed quite well with that of hexagonal Cd(OH)₂. Thus, either of these materials may be readily converted to the crystalline form of battery active hexagonal Cd(OH)₂. The ease with which material B is converted to Cd(OH)₂ suggests that it undergoes a simple redox or ligand exchange reaction when removed from the acid environment of the deposition solution and placed in neutral (or basic) water. The fact that the powder pattern of material B does not agree with the pattern of either of the reported nitrate complexes of Cd(OH)⁺ indicates that this material is not a nitrate complex, however.

To gain further insight as to the nature of the complex believed to be formed at -0.8V, the voltammetry of a dilute KNO₃-Cd(NO₃)₂ solution was carried out in the presence of saturated KCl supporting electrolyte. The presence of the KCl allowed for the proper assignment of voltammetric peak potentials for the nitrate reduction processes by eliminating the ionic migration effects observed in the absence of supporting electrolyte. In addition, as shown in Fig. 7, the KCl presence gave clear indication that two nitrate reduction processes are possible in this system, one occurring at -0.71V and the other occurring at -0.83V in the presence of supporting electrolyte. The wave at -0.71V corresponds to the wave at -0.62V in the absence of supporting electrolyte in Fig. 1. Note that by the tenth cycle, the electrode is passivated to further activity at this potential, just as is observed in two or three cycles on a more concentrated solution. The wave at -0.83V does not exhibit this effect. The product of this reduction appears to be relatively

stable and undergoes oxidation at -0.76V on scan reversal.

The appearance of this wave at -0.83V is observed in each of the three voltammograms shown in Fig. 8; again, fairly good stability of the reduction product is indicated by the corresponding oxidation wave. The curve a reduction wave at -0.71V, which is present only in nitrate solution, is believed to be the one associated with the deposition of Cd(OH)₂ from Cd(NO₃)₂ solution. If the reduction process associated with this

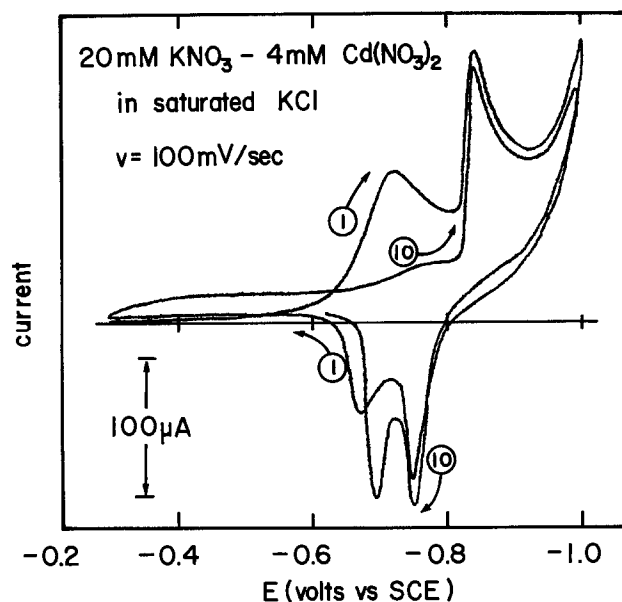


Fig. 7. Cyclic voltammetry of a dilute KNO₃-Cd(NO₃)₂ mixture in saturated KCl at a nickel electrode. The first and tenth cycles (as indicated by those numbers) are shown.

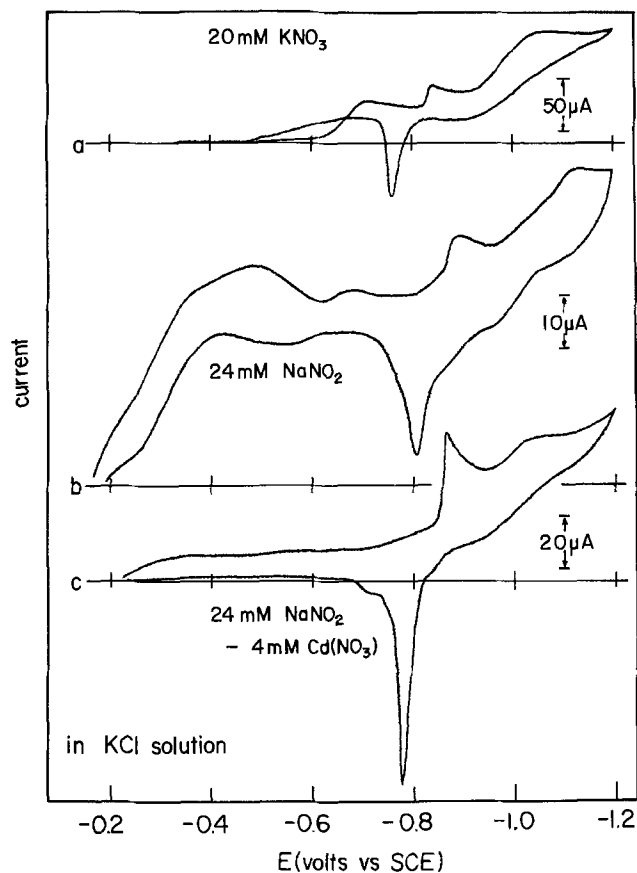


Fig. 8. Nitrate and nitrite voltammetry in saturated KCl. The composition of each solution is indicated in the figure. The scan rate was 10 mV/sec in each case.

wave leads to nitrite production, it is clear from the voltammetry in curve b that the NO_2^- produced in this manner will undergo further reduction at these potentials to some unspecified nitrogen product. This product of NO_2^- reduction is responsible for the wave at -0.83V which is common to all three voltammograms. It is possible that the product of this common reduction process is one of the molecular compounds mentioned above in the development of Eq. [4]. This would then be available in the vicinity of the electrode to form a complex cadmium hydroxide precipitate of the sort believed to be responsible for the black material formed at potentials negative of -0.8V in nitrate deposition solution. The voltammetry in curve c indicates that it may be possible to deposit the $\text{Cd}(\text{OH})_2$ from nitrite solutions, also. The presence of the Cd^{+2} in curve c appears to suppress the evolution of gaseous product that is believed to be responsible for the displaced voltammetry obtained in curve b.

This voltammetry suggests that the gray cadmium hydroxide material that is cathodically deposited from nitrate solution at potentials between -0.6 and -0.8V vs. SCE is caused by the reduction of NO_3^- to some product other than NO_2^- . Moreover, the black material which is deposited at potentials negative of -0.8V vs. SCE appears to be formed at potentials corresponding to a second reduction process common to products of both NO_3^- and NO_2^- reductions. The products of this reduction would be available to form a complex cadmium hydroxide on the electrode surface either by reaction with an existing $\text{Cd}(\text{OH})_2$ film or by complexation of Cd^{+2} followed by precipitation. Both materials are easily converted to crystalline hexagonal $\text{Cd}(\text{OH})_2$ by subjecting the electrode to formation cycles in KOH. However, since the gray material is deposited at less negative potentials with minimal concurrent gas evolution, a higher degree of $\text{Cd}(\text{OH})_2$ loading should be achieved within the nickel plaque

material under these conditions. This could be achieved by operating at low current density in a controlled current process. In addition, since the gray form of $\text{Cd}(\text{OH})_2$ is not readily converted to metallic cadmium at more positive (less basic) electrode potentials, current reversal techniques may be employed during the cathodic deposition, if the deposition is carried out at low current density. (Such reversal techniques are sometimes used to clean the counterelectrode or to aid in the introduction of fresh solution within the pores of the plaque material.) Reversal techniques could not be used at current densities high enough to produce the black precursor to $\text{Cd}(\text{OH})_2$; the metallic cadmium that is often formed when the electrode potential is made more positive during current reversal can be anodically stripped from the electrode during the reversal process unless careful potential control is exercised. Thus, this voltammetry indicates that it would be clearly self-defeating to employ current reversal techniques with any high current density cadmium deposition process.

Some experiments were also conducted to demonstrate that the low current density deposition product was battery active in concentrated KOH. A film of the gray $\text{Cd}(\text{OH})_2$ was deposited on the nickel working electrode from nitrate solution by sweeping the electrode potential from the rest potential to -0.6V vs. SCE and instantaneously ceasing the electrolysis. During this potential sweep the charge was measured and found to be 0.58 mC ; this is illustrated in Fig. 9. The electrode was then removed from the acidified $\text{Cd}(\text{NO}_3)_2$ solution, washed, and placed in 32% KOH where it was subjected to several charge-discharge formation cycles. Two of these are illustrated in Fig. 10. As shown in this figure, the electrode was charged potentiostatically for 500 sec at -1.4V vs. SCE and discharged potentiostatically at -0.21V vs. SCE for the same period. During the discharge, the current fell essentially to zero. As the electrode was subjected to repeated charge-discharge cycles, the current that passed during each half-cycle increased. By the fourth formation cycle, 95.6 mC passed during the charging half-cycle; this was indicative of the considerable amount of hydrogen evolution that was taking place at the charging potential. Of this charge, 29.3 mC were "recovered" on discharge. Since only 0.58 mC were used in the deposition of the $\text{Cd}(\text{OH})_2$ film, no more than 1.16 mC of active $\text{Cd}(\text{OH})_2$ could be available on the nickel substrate if the development associated with Eq. [4] and [5] is correct. Voltammetric investigations were carried out in an attempt to resolve this apparent discrepancy.

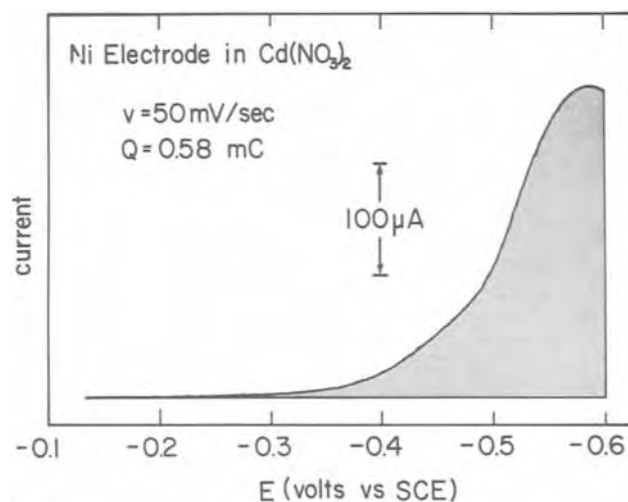


Fig. 9. Linear sweep voltammetry of the cathodic deposition of gray $\text{Cd}(\text{OH})_2$. The charge represented by the shaded area is given in the figure.

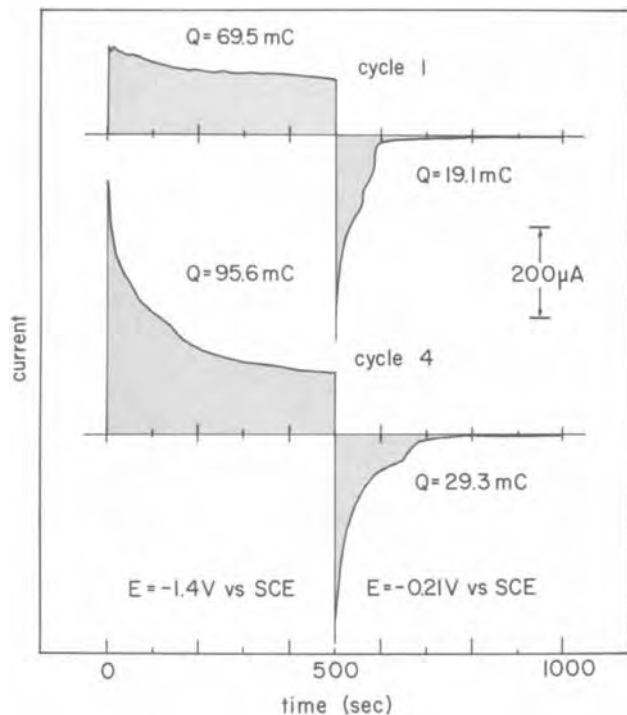


Fig. 10. Chronoamperometry of $\text{Cd}(\text{OH})_2$ in 32% KOH. The electrode used in these studies was the same one prepared by the cathodic deposition of Fig. 9. Charges represented by the shaded areas are given in the figure.

This slow scan voltammetry is shown in curve a of Fig. 11. Prominent in this voltammetry is a shoulder at -1.25V during the negative scan; this wave, which was concomitant with the hydrogen evolution process corresponds to the cadmium electrode charging process. After the potential scan direction was reversed, a broad discharge wave was obtained; this wave commences with a spike at -1.1V vs. SCE and continues with the passage of considerable current to -0.7V . The area under the spike corresponded to a discharge of 0.43 mC as shown in the figure. It is believed that this spike was caused by the discharge of the 0.58 mC of $\text{Cd}(\text{OH})_2$ that was deposited on the electrode in Fig. 9 and charged during the hydrogen evolution process of the forward scan. Based on the assumption that this admittedly crude current integration is an effective measure of the amount of deposited cadmium (by the reverse of Eq. [1]), the deposition process (represented by Eq. [4] and [5]) is seen to be between 37% and 74% efficient. That is, between 37% and 74% of the current that is used in the low current density deposition process goes to produce chargeable $\text{Cd}(\text{OH})_2$ on the microelectrode surface. However, the accurate measurement of this cadmium discharge is obscured by the broad discharge wave that accompanies it. Clearly, it is this secondary discharge that accounts for nearly all 29.3 mC of discharge that was observed during the second half of the fourth cycle of the chronoamperometry in Fig. 10. The amount of this secondary discharge current increases as the electrode is subjected to repeated charge-discharge cycles.

This may be seen in curve b of the same figure which was run on a $\text{Cd}(\text{OH})_2$ filmed nickel electrode that had not been subjected to any previous charge-discharge studies. The sweep rate used in obtaining curve b was ten times that used in curve a, so that the electrode was subjected to potentials negative of -1.2V vs. SCE for less than 10 sec. [When this is done, the relative amount of the secondary discharge process is greatly diminished, but the likelihood of completely charging the $\text{Cd}(\text{OH})_2$ film in this short time period is also decreased.] The near absence of the secondary discharge process in curve b, therefore, supports the

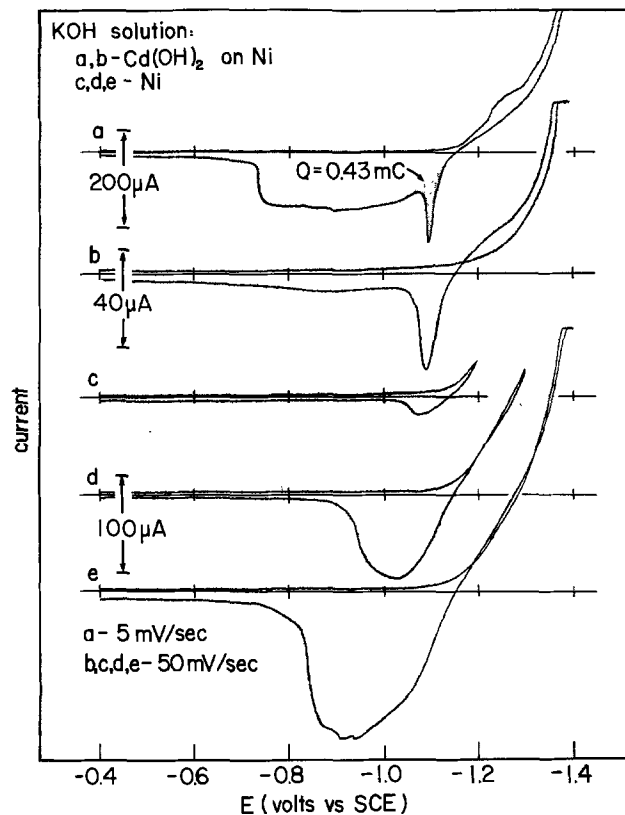


Fig. 11. Cyclic voltammetry studies in 32% KOH. The electrode used in curve a was the same one used in Fig. 9 and 10. Curve a was obtained after the fourth cycle of Fig. 10; curve b was obtained prior to any formation cycles on another $\text{Cd}(\text{OH})_2$ electrode; curves c, d, and e were run on a bare nickel electrode.

contention that it is related to the amount of time that the electrode experiences the overcharge condition, but this experiment does not suggest an easy electrochemical way to determine the quantity of deposited $\text{Cd}(\text{OH})_2$.

Evidence that the secondary discharge process is caused by the oxidation of hydrogen generated on overcharge is provided by curves c, d, and e, which were obtained on a nickel electrode in the absence of any $\text{Cd}(\text{OH})_2$ film. These three curves which have negative limits of -1.2 , -1.3 , and -1.4V vs. SCE , respectively, show that the oxidative current on reversal is dependent on the overcharge potential achieved. Even a brief excursion to -1.2V produces a significant oxidative current on scan reversal. This observation points out the difficulty in attempting to measure the amount of $\text{Cd}(\text{OH})_2$ deposited on the electrode surface by subjecting the electrode to charge-discharge studies: any potential that is sufficiently negative to charge the $\text{Cd}(\text{OH})_2$ will cause sufficient hydrogen evolution and adsorption on the nickel substrate to prevent the unambiguous determination of the amount of deposited cadmium through discharge current measurement. The adsorbed hydrogen will be oxidized either concurrently with the cadmium film or at potentials just positive of cadmium oxidation.

This voltammetry provides support for the hypothesis that the stepped discharge curve that is sometimes observed from cadmium-limited nickel-cadmium cells that have been subjected to considerable overcharge is due to the oxidation of adsorbed hydrogen on the negative plate during discharge (3). This oxidation takes place somewhat less readily than the oxidation of cadmium; thus, when the supply of cadmium is exhausted, the cell voltage would fall but the cell would continue to discharge until the adsorbed hydrogen was also used up. (The cell would operate as a nickel-hydrogen cell.) Other investigators have attributed this stepped discharge behavior to excessive carbonation

of the electrolyte (4) and to $\text{Ni}_5\text{Cd}_{21}$ alloy formation (5). While these processes may also contribute to a stepped discharge curve, it is clear from the voltammetry in Fig. 11 that hydrogen adsorption on overcharge would play a primary role in this behavior in cadmium-limited cells. Of course, in the more conventional nickel-limited cell composition, such behavior can be properly attributed to nickel electrode characteristics.

Applications

The information obtained in the studies above was used to suggest modifications in the procedure for the cathodic deposition of cadmium hydroxide in sintered nickel plaque electrodes. These observations and the corresponding suggestions for the manufacturing process are given below:

1. It is possible to deposit two distinctly different cadmium compounds for use as battery active material on nickel from $\text{Cd}(\text{NO}_3)_2$ solution depending on the deposition potential and the pH. The material deposited at less negative potentials (low current density in a controlled current process) appears to be deposited as a uniformly dense film. This is presumably due to the fact that the nitrate reduction process responsible for this deposition does not evolve any H_2 gas. The deposition at more negative potentials (high current density) may take place with H_2 gas evolution and probably involves cadmium complex formation with one of the products of NO_3^- reduction. Thus, the deposition at high current density is not only expected to be less dense, but also its pre-formation cadmium content is probably lower. For high loadings of a uniform $\text{Cd}(\text{OH})_2$ deposit, the deposition should be carried out at low current density so that the potential of the nickel electrode never becomes more negative than -0.65V vs. SCE .

2. The material deposited at low current density neither is metallic cadmium nor is it readily converted to metallic cadmium at less negative deposition bath electrode potentials. The material deposited at higher current densities may contain some metallic cadmium when the potential of the electrode is changed in a positive direction; this metallic cadmium can undergo anodic stripping when the electrode potential is changed in a positive manner as it would be in a current reversal deposition technique. Thus, if current reversal techniques are to be employed during the deposition either to introduce fresh solution within the pores of the nickel plaque material or to clean the surface of the electrodes, the low current density deposition is again recommended to avoid the build-up of strippable metallic cadmium on the electrode surface.

3. At low current density there is no H_2 gas evolution and the stoichiometry of the sequence given by Eq. [4] and [5] gives an approximation of the amount of active $\text{Cd}(\text{OH})_2$ that is actually deposited on the electrode surface. An exact determination of the efficiency of the cathodic deposition process cannot be made without further studies to identify the product(s) of the NO_3^- reduction process. However, if these products are mononegative ions or if they are molecular species containing nitrogen in a low positive or negative oxidation state, the number of equivalents of charge passed during deposition should nearly equal the maximum number of equivalents of $\text{Cd}(\text{OH})_2$ available for use in alkaline cell operation.

4. Either of the two materials investigated herein may be converted to battery active hexagonal $\text{Cd}(\text{OH})_2$ by subjecting the electrode to charge-discharge formation cycles in concentrated KOH. In either case, however, subjecting the electrode to a high overcharge either during formation or in actual use will produce deleterious results. Hydrogen evolved on overcharge is adsorbed on the nickel surface and is available for reaction when the cell is discharged. Unfortunately, this adsorbed hydrogen appears to dislodge the

$\text{Cd}/\text{Cd}(\text{OH})_2$ that is in contact with the nickel surface so that the amount of the available negative plate material is diminished. Care should be exercised during formation and use so as to minimize hydrogen evolution during the charging of the negative plate. If the electrode is to be used in the usual nickel-limited battery configuration, it might be advisable to eliminate any electrochemical formation whatsoever of the cadmium electrode.

In order to see if these recommendations could be related to the practical process, the cathodic deposition of $\text{Cd}(\text{OH})_2$ in some sintered nickel plaque material was attempted by controlled current techniques (6). A cadmium impregnation bath for porous nickel plaque was assembled as described by Pickett (7). The plaque material used in the deposition had a porosity of 78% and was 0.031 in. thick. The bath contained an SCE reference electrode so that the potential of the nickel plaque electrodes could be controlled by controlling the current density. It was found that a deposition potential positive of -0.65V vs. SCE could be maintained by not allowing the current density to exceed 0.2 A/in.^2 of single surface plaque area. (Deposition took place on both surfaces, however.) A high quality $\text{Cd}(\text{OH})_2$ electrode was obtained using this method. During the process, it was found to be useful (but not necessary) to alternate the direction of current flow for short periods of time to clean the surfaces of the electrodes. Cadmium electrodes prepared in this manner had a high initial capacity and did not have to be subjected to an electrochemical formation process to achieve a higher apparent capacity. This observation confirms the belief that an uncomplexed form of $\text{Cd}(\text{OH})_2$ is deposited at low current density so that the initial density of the active material is quite high.

This observation is supported by the scanning electron micrographs of a sample electrode shown in Fig. 12 and 13. These SEM results were obtained using an impregnated electrode prior to being subjected to any charge-discharge cycles in alkaline solution. Figure 12 shows the detail of the $\text{Cd}(\text{OH})_2$ that was deposited at low current density within the pores of the nickel sinter. Figure 13 is a composite of seven such micrographs that have been selected to show the cross-sectional distribution of the $\text{Cd}(\text{OH})_2$ from the outer surface of the impregnated plaque material to the nickel grid fracture surface in the center of the electrode. This composite shows the kind of loading that can be achieved by carrying out the deposition at low current density. The fact that larger $\text{Cd}(\text{OH})_2$ platelets are



Fig. 12. Scanning electron micrograph of nickel plaque impregnated with $\text{Cd}(\text{OH})_2$. Low current densities (0.2 A/in.^2) employed in this deposition never allowed the electrode to become more negative than -0.65V vs. SCE . $\text{Cd}(\text{OH})_2$ platelets are seen to be imbedded within the pores of the sintered nickel plaque material.

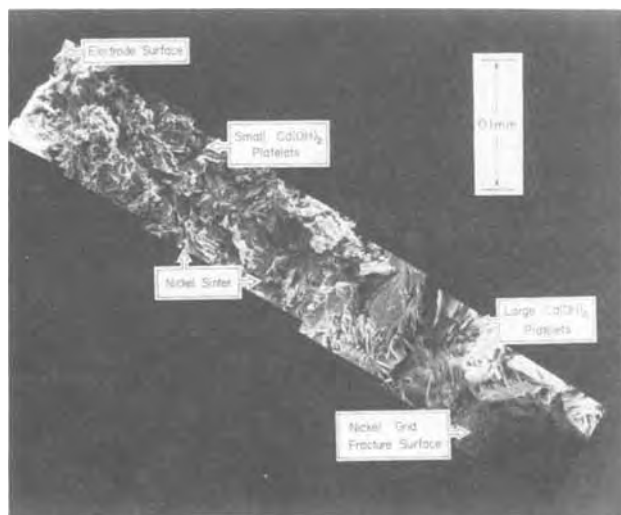


Fig. 13. Composite cross-section photomicrograph of $\text{Cd}(\text{OH})_2$ impregnated nickel plaque material. Seven different micrographs have been assembled to show this view of the fracture surface from outer electrode surface to the inner Ni grid wire contact. Larger platelets are evident in the interior of the plaque material.

found in the interior of the plaque material enforces the belief that deposition proceeds by a precipitation mechanism. Larger crystals are indicative of the slow crystal growth process that would occur in the diluted environment of unreacted cadmium ion that would be found in the solution in the interior. These concentration effects no doubt contribute to the minimal passive film formation that is observed on the highly irregular surface of the porous electrode material.

Figure 14 demonstrates that a uniform deposition of cadmium is achieved by this low current density method. This figure shows the impregnated plaque material in the vicinity of one of the nickel wires (shown in cross section) used in the support grid. In the upper left and right quadrants are the backscattered electron and secondary electron micrographs of this material. In the lower left and right quadrants are the x-ray energy dispersive analyses on the same material for cadmium and nickel, respectively. These results indicate clearly that cadmium-containing material is well distributed within the plaque, even deep in the interior. Electrodes having this characteristic are believed to resist capacity fading much better than electrodes having a high surface distribution of active material.

Electrodes prepared in this manner were also subjected to cycle life testing in cadmium-limited and conventional nickel-cadmium cells. The results of this testing are to be the topic of a future communication.

Acknowledgment

The technical assistance of John F. Leonard and helpful discussions with J. J. Lander are gratefully acknowledged. This work was supported by the Air Force Systems Command under contracts sponsored by the Air Force Aeropropulsion Laboratory and the Air Force Office of Scientific Research.

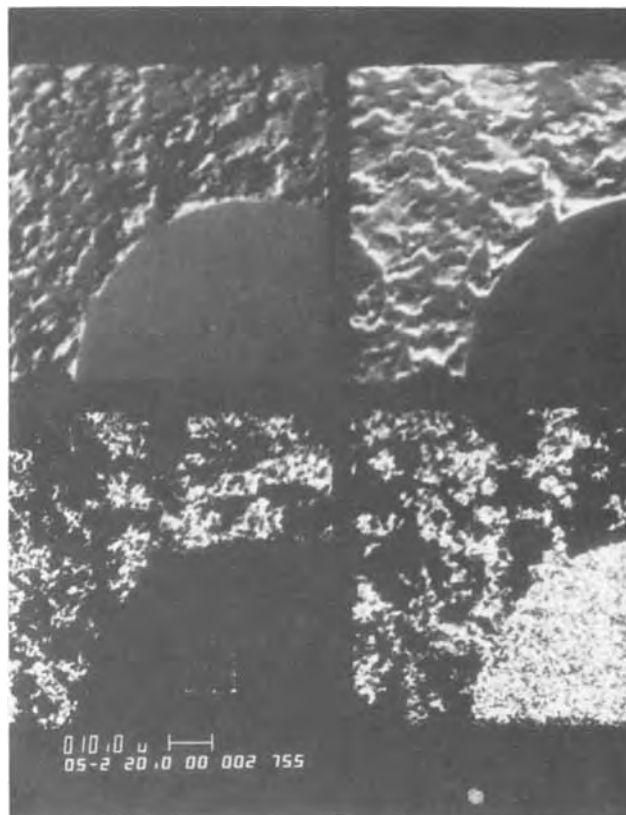


Fig. 14. SEM distribution studies of $\text{Cd}(\text{OH})_2$ impregnated nickel plaque material. Upper left quadrant clockwise: back-scattered electron micrograph; secondary electron micrograph; x-ray energy dispersive analysis for nickel; for cadmium. The same nickel grid wire is shown in cross section in each quadrant.

Manuscript submitted Feb. 13, 1980; revised manuscript received April 29, 1980. This was Paper 126 presented at the Los Angeles, California, Meeting of the Society, Oct. 14-19, 1979.

Any discussion of this paper will appear in a Discussion Section to be published in the June 1981 JOURNAL. All discussions for the June 1981 Discussion Section should be submitted by Feb. 1, 1981.

Publication costs of this article were assisted by the U.S. Air Force.

REFERENCES

1. S. Gross, Boeing Aerospace Technical Report under JPL Contract 953984, W.O. 342-46, August 1977; and references contained therein.
2. D. F. Pickett and J. T. Maloy, *This Journal*, **125**, 1026 (1978).
3. S. U. Falk, *ibid.*, **107**, 661 (1960).
4. D. L. Barney, A. J. Catotti, and S. F. Pensabene, in "Power Sources 3," D. H. Collins, Editor, chap. 7, Oriel, Newcastle upon Tyne, England (1970).
5. R. Bernard, G. T. Crickmore, J. A. Lee, and F. L. Tye, in "Power Sources 6," D. H. Collins, Editor, chap. 12, Academic Press, New York (1976).
6. D. H. Fritts, J. F. Leonard, and T. Palanisamy, U.S. Patent allowed April 1980.
7. D. F. Pickett, U.S. Pat. 3,873,368 (1975).

Moderate Temperature Sodium Cells

I. Transition Metal Disulfide Cathodes

K. M. Abraham,* L. Pitts, and R. Schiff

EIC Corporation, Newton, Massachusetts 02158

ABSTRACT

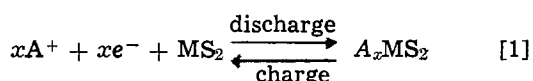
A moderate temperature, rechargeable Na cell having the configuration

Liquid Na/ β -Al₂O₃/Na⁺-conducting electrolyte/Transition metal disulfide

is described. The cell operates at ~130°C. Three transition metal disulfides, TiS₂, VS₂, and Nb_{1+x}S₂, have been evaluated as cathode materials. A 1M solution of NaI in 1,2-Bis(2-methoxy-ethoxy)ethane, (triglyme), served as the electrolyte. The mechanism of discharge in all the three cathode materials involves Na intercalation. Experimental results are presented on cathode capacity, rate capability, and rechargeability.

Recently, there has been considerable interest in high energy, secondary batteries with alkali metal anodes for applications such as electric vehicles, electrical load leveling and space modules. Secondary Li batteries utilizing transition metal chalcogenide (1, 2) or oxide (3) cathodes have shown considerable promise in this respect. A secondary sodium battery utilizing molten Na polysulfide cathode and operating at temperatures above 300°C is presently in advanced developmental stages (4). Recently, we described (5) a moderate temperature secondary Na cell which operates at the temperature range of 100°-150°C and utilizes a β -Al₂O₃ solid electrolyte in conjunction with a soluble S cathode. In the continued search for suitable cathode materials for this moderate temperature Na battery, we have evaluated several transition metal chalcogenides. In this paper our findings on TiS₂, VS₂, and Nb_{1+x}S₂ cathodes are reported.

The transition metal disulfides of interest here crystallize with layered structures (1). The unit building block of the disulfides consists of two hexagonally close-packed chalcogen layers between which reside the metal ions. The metal ions occupy either sites of octahedral (Oh) symmetry as in TiS₂ and VS₂ with 1T-CdI₂ structure (1) or trigonal prismatic (TP) symmetry as in 2H-NbS₂ (1). Bonding within the layers is strong, while between adjacent layers it is weak. Consequently, it is possible to form intercalation compounds under rather mild conditions by insertion of atoms, molecules, or ions between the weakly bound layers. It is the intercalation and deintercalation of the alkali metals (Eq. [1]) which form the basis of the cathode reactions in rechargeable cells



Lithium intercalation into the disulfides often proceeds with very little structural change in the host lattice (1) so that the reaction is readily reversible. A rechargeable cell based on the Li/TiS₂ couple has been shown to have very long cycle life (1, 2). While there have been several prior studies dealing with the structural chemistry of Na intercalates of TiS₂ (6, 7), VS₂ (8, 9, 10), and NbS₂ (11), very little is known about the reversibility of the reaction. The available structural data on the Na intercalates of these transition metal disulfides show that structural changes of the host lattice occur with Na intercalation. Often, in a given Na_xMS₂ ternary, more than one crystallographically distinct phase appears with the degree of intercalation (1, 6-11). A prior study (12) on the

ambient temperature electrochemical intercalation of Na into TiS₂ showed that the equilibrium potential-Na composition curve exhibits three plateaus which closely correlate with the three phases in the Na_xTiS₂ ternary at the Na composition ranges of 0.17 < x ≤ 0.33, 0.38 < x < 0.72, and 0.8 < x ≤ 1. The implication of these phase changes on the rechargeability of the cathode, especially at elevated temperatures, is unknown.

The three disulfides, TiS₂, VS₂, and Nb_{1+x}S₂, were evaluated as cathode materials in a cell of the configuration

Liquid Na/ β -Al₂O₃ / Na⁺-conducting electrolyte / Transition metal disulfide

The cell operates at ~130°C and utilizes as electrolyte a 1M solution of NaI in 1,2-Bis(2-methoxy-ethoxy)ethane, (triglyme).

Experimental

All the experiments were carried out in the absence of air and moisture using standard techniques employed for the manipulation of air-sensitive compounds (13). Wherever appropriate, the handling and transfer of reagents were also carried out in an argon-filled dry box (Vacuum Atmospheres Corporation).

Synthesis and Characterization of Metal Disulfides

TiS₂.—The disulfide was prepared by the direct reaction of stoichiometric amounts of Ti metal powder (–100 mesh, Ventron) and S (Ventron, random pieces) at ~700°C (14). The material was characterized by x-ray (1) and elemental analysis. Composition of the material was established as Ti_{1.02}S₂. Its x-ray pattern was consistent with the 1T-CdI₂ structure (1).

VS₂.—The compound was prepared by the reaction of either LiVS₂ (15, 16) or NaVS₂ (15) with CH₃CN/I₂ solution (16). Its x-ray data and elemental analysis confirmed material purity. X-ray data showed that the material had the 1T-CdI₂ structure (16).

Nb_{1.1}S₂.—The compound was synthesized by direct reaction of Nb powder (–60 mesh, Ventron) and S (random pieces, Ventron) at 950°C (17). The composition of the material was determined by combustion analysis as the oxide and found to be Nb_{1.1}S₂. X-ray pattern of the material showed that a major fraction belonged to the 3S-polytype (17).

Electrolyte Preparation

1,2-Bis(2-methoxy-ethoxy)ethane, (triglyme), obtained from Aldrich Chemical Company, (Cat. No. P-6952) was passed twice over Fisher neutral alumina. A 1M NaI solution was prepared by dissolving ultra-pure NaI (Ventron) at room temperature. The 1M NaI

* Electrochemical Society Active Member.
Key words: sodium cells, TiS₂, VS₂, Nb_{1.1}S₂.

solution has a specific conductivity of $2.55 \times 10^{-3} \Omega^{-1} \text{cm}^{-1}$ at 25°C and $4.5 \times 10^{-3} \Omega^{-1} \text{cm}^{-1}$ at 130°C . Infrared and visible-u.v. spectral analyses of electrolyte stored for 2 months at 130°C showed no evidence for decomposition. Also, the electrolyte exhibited no background current in the potential limits between 1 and 2.5V vs. Na^+/Na , the region of interest in the present study.

Electrochemical Measurements

The electrochemical cell incorporating $\beta\text{-Al}_2\text{O}_3$ tube was of the same type discussed previously (5). The transition metal sulfide cathodes were fabricated in the form of pressed electrodes. Initially an intimate mixture consisting of ~50 weight percent (w/o) metal sulfide powder, 40 w/o carbon (AGM-2100 graphite or Shawinigan 50% compressed carbon), and 10 w/o Teflon (du Pont 7A) was prepared in a blender. The mixture was then pressed onto an expanded Ni grid (Exmet Corporation, 5Ni5-5/0) at a pressure of ~5000 lb/in². The pressed electrode typically had an area of 8 cm²/side and a thickness of 0.60-1.0 mm. In some cells the electrodes were fabricated from a mixture of 90 w/o sulfide and 10 w/o Teflon without any carbon. The electrode areas were also varied in some cells. The pressed electrode was wrapped tightly around the $\beta\text{-Al}_2\text{O}_3$ tube and secured in position with another wrap of expanded Ni over the electrode. The wrap of expanded Ni over the electrode helped retain the active materials on the grid during cycling. The cell was completed by filling it with an appropriate amount of electrolyte. Before cycling, the cells were thermostated to 130°C . The cells were cycled galvanostatically or potentiostatically using standard instrumental techniques (2, 5).

Results and Discussion

The Sodium-Titanium Disulfide Cell

Galvanostatic tests.—The Na/TiS_2 cell has an open-circuit potential (OCV) of 2.15V at 130°C . Typical discharge curves are shown in Fig. 1. The first discharge corresponds to $0.85e^-/\text{moleTiS}_2$. The discharge curve is characterized by two plateaus spanning the Na composition (x) ranges at $0 < x \leq \sim 0.30$ and $0.37 < x \leq 0.8$. The end of discharge is indicated by a clear potential drop. There is a gradual decrease in discharge capacity in the early cycles (≤ 4) and this appears to result from an incremental inefficiency in cathode rechargeability in these cycles (vide infra). The first full cycle is shown in Fig. 2. There is a close similarity between the potential profiles of discharge and charge. Discharge/recharge reactions in-

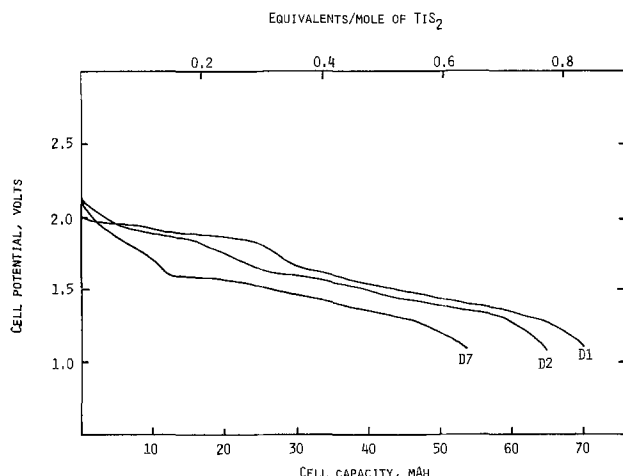


Fig. 1. Galvanostatic discharges of the cell, liquid $\text{Na}/\beta\text{-Al}_2\text{O}_3$ /triglyme/1M NaI, TiS_2 at 130°C . The cathode was fabricated from 50 w/o TiS_2 , 40 w/o C, and 10 w/o Teflon. Current, $i_d = i_c = 4$ mA. Current density = $0.5 \text{ mA}/\text{cm}^2$. Curves D1, D2, and D7 are the first, second, and seventh discharges.

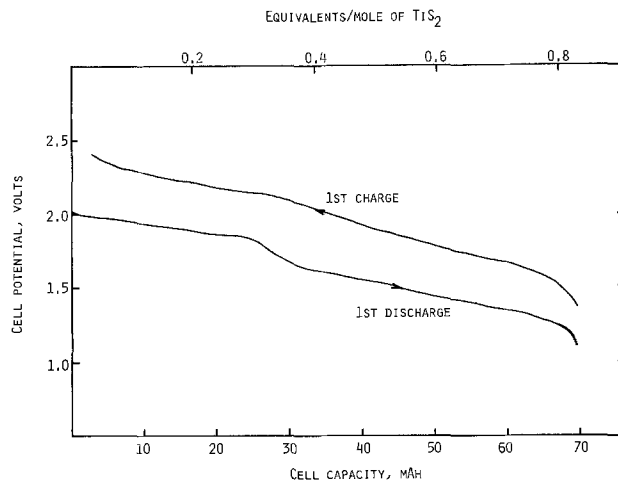
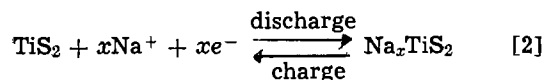


Fig. 2. The first full cycle of the TiS_2 cell shown in Fig. 1

volving intercalation and deintercalation of Na as shown in Eq. [2] could explain this type of behavior



This is substantiated by x-ray data on discharged cathodes. The C-lattice parameter of an electrochemically obtained Na intercalate of composition $\text{Na}_{0.8}\text{TiS}_2$ was found to be 6.68Å, in agreement with previous observations (6).

The phase diagram of the Na_xTiS_2 ternary has been described (6, 7). There are three phases as x is varied from 0 to 1. The first phase covering the Na composition range, $0.17 < x < 0.33$ is a second-stage trigonal prismatic (TP) phase with Na in trigonal prismatic and Ti in octahedral co-ordination sites. The Na occupies approximately every other layer in the crystal lattice. The second phase covering the region $0.38 < x < 0.72$ is a first-stage TP phase. The third phase for $0.8 < x \leq 1$ is trigonal antiprismatic (TAP) in which both Na and Ti occupy octahedral sites.

The two regions in the discharge curve (Curve D1, Fig. 1) appear to correlate with two TP phases. The sharp cutoff in the discharge curve at a Na composition of ~0.80 suggests that it is difficult to intercalate Na into the TAP phase at potentials above 1.0V vs. Na^+/Na . This is in agreement with the observations of Whittingham *et al.* (6) who found that in the preparation of Na_xTiS_2 from TiS_2 and Na-naphthalide, even with a large excess of the latter reagent, the ternary with the maximum Na content that could be prepared was $\text{Na}_{0.8}\text{TiS}_2$. The difficulty in obtaining Na_xTiS_2 with $x > 0.8$ is probably due to the lower diffusion coefficient of Na in the TAP phase (6). In the TAP phase, Na^+ has to pass through small 4 co-ordinate sites, whereas in the TP phase such sites are much larger, facilitating better Na diffusion.

Cathode rechargeability.—Figure 3 summarizes the capacities corresponding to the first and second phases in each discharge as a function of cycle number. The capacity in the second phase remains essentially constant whereas that in the first phase gradually decreases in the early cycles. At present we do not know why Na is only partially reversible in the first phase. However, it is noteworthy that the irreversibility is brought about gradually with cycling. This tends to suggest that under the conditions of the cathode cycling, a new phase is formed and irreversibly stabilized at low values of x in Na_xTiS_2 . It would be necessary to carry out a detailed study of the structural and electronic properties of Na_xTiS_2 at various stages of cycling. This is beyond the scope of the present work. The data suggest that in long-term cycling a fraction of the capacity in the first phase

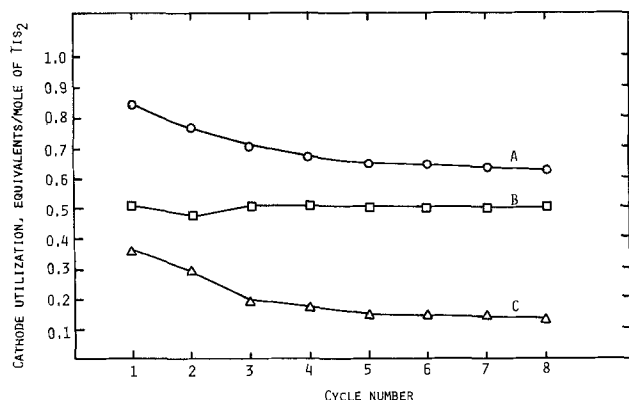


Fig. 3. Cathode utilization vs. cycle number for the TiS_2 cell shown in Fig. 1. Curve A represents the total capacity. Curve B represents the capacity in the second phase. Curve C represents the capacity in the first phase plus the transition region.

and all the capacity in the second phase would be rechargeable. A reasonable estimate for the average rechargeable capacity of the TiS_2 cathode is $\sim 0.65 e^-/\text{TiS}_2$.

The presence of carbon on the electrode matrix was found to be necessary for good cathode rechargeability. This was indicated by the cycling behavior of a cell in which the cathode composition was 90 w/o TiS_2 and 10 w/o Teflon. The first discharge corresponded to $0.8e^-/\text{TiS}_2$, as in the case of the cell with carbon. However, the capacity decreased rapidly in the next three cycles. Thus capacities of 0.64 , 0.45 , and $0.37e^-/\text{TiS}_2$ were obtained in the second, third, and fourth discharges, respectively. It was apparent from the discharge curves that the rapid loss in capacity in these cycles occurred from both of the phase regions. This seems to suggest that with cycling a fraction of the cathode material gets physically isolated in the electrode and not utilized electrochemically. The capacity loss was more gradual in subsequent discharges and was mostly attributable to the irreversibility in the first phase. Thus it was $0.33e^-/\text{TiS}_2$ in the fifth discharge and $0.26e^-/\text{TiS}_2$ in the seventh discharge. Evidently the isolation of the material occurs in the initial cycles. The TiS_2 crystallites show a largely reversible expansion and contraction upon intercalation and expulsion of Na. Thus an initially optimized electrode structure changes even after the first discharge-charge cycle, since bonded powder electrodes used in these studies do not show ideal elastic behavior. In the absence of C in the electrode matrix, a loss of particle to particle contact occurs, leading to diminished performance. We have observed a similar, but less drastic, phenomenon in the cycling of high capacity Li/TiS_2 cells (2).

Potentiostatic tests.—Potentiostatic discharge of TiS_2 cathode was carried out to obtain information on its rate capability. For discharge the potential was set at 1.3V and the current was monitored as a function of time. The current-time curves were incrementally integrated and Fig. 4 shows the capacity expressed as charge equivalents per mole of TiS_2 as a function of current density. At current densities $\leq 1 \text{ mA}/\text{cm}^2$, the cathode utilization is $\sim 0.8e^-/\text{TiS}_2$. A capacity of $0.48e^-/\text{TiS}_2$ has been obtained in the first 60 min of discharge during which time the minimum current density was $4.1 \text{ mA}/\text{cm}^2$. Since the cathode or the cell was not optimized for best performance, it appears that current densities higher than these with good utilization should be possible for the TiS_2 cathode.

The Sodium-Vanadium Disulfide Cell

Galvanostatic tests.—The Na/VS_2 cell has an OCV of 2.30V at 130°C . Typical discharge curves are shown in Fig. 5. The first discharge corresponds to a capacity

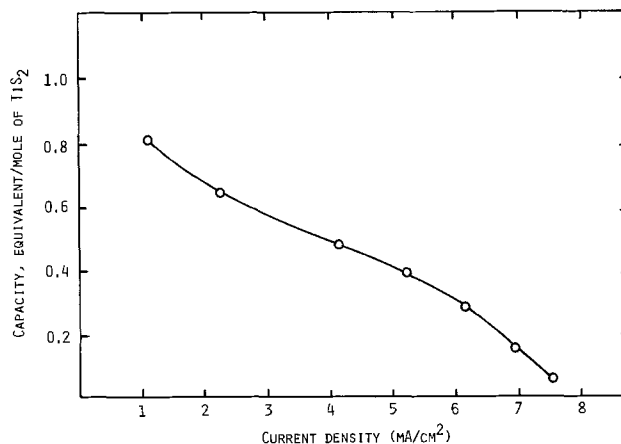


Fig. 4. Capacity vs. current density of TiS_2 cathode potentiostated at 1.3V. Temperature = 130°C .

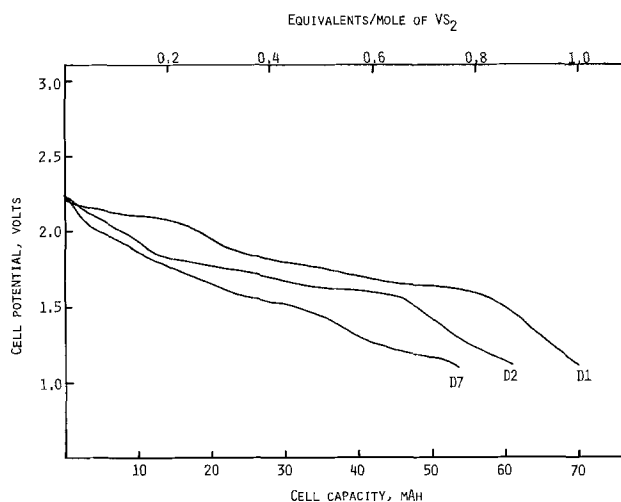


Fig. 5. Galvanostatic discharges of the cell, liquid $\text{Na}/\beta\text{-Al}_2\text{O}_3/\text{triglyme}/1\text{M NaI}, \text{VS}_2$ at 130°C . The cathode was fabricated from 50 w/o VS_2 , 40 w/o C, and 10 w/o Teflon. Current, $i_d = i_c = 4 \text{ mA}$. Current density = $0.5 \text{ mA}/\text{cm}^2$. Curves D1, D2, and D7 are the first, second, and seventh discharges.

of $1.0e^-/\text{VS}_2$. The discharge curve is mainly characterized by three regions, spanning the Na composition (x) ranges approximately at $0 < x \leq 0.28$, $0.3 < x \leq 0.85$, and $0.85 < x \leq 1$. There is a decrease in cathode utilization with cycle number, but much of this loss occurs in the second discharge and seems to mostly involve the capacity in the first plateau. The first full cycle is shown in Fig. 6. Apparently, the capacity encompassed in the first plateau is only fractionally recharged in the first charge.

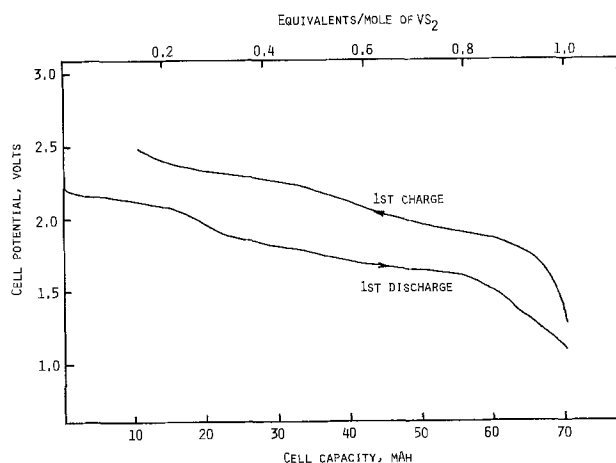


Fig. 6. The first full cycle of the VS_2 cell shown in Fig. 5

The x-ray diffraction pattern of a discharged cathode established that the mechanism of discharge involves Na intercalation into VS_2 . A discharged cathode of composition $\text{Na}_{\sim 1.0}\text{VS}_2$ exhibited a C-lattice parameter of 7.31Å as opposed to 5.72Å in VS_2 . Structural studies of Wiegiers (8) has shown that Na intercalation of VS_2 is accompanied by phase transformations as the Na composition is varied from 0 to 1. However, a precise phase diagram of the Na_xVS_2 ternary is not known. Rouxel has suggested (9), on the basis of a generalized model for the phase diagrams of Na_xMS_2 ternaries, where MS_2 has the 1T- CdI_2 structure as in VS_2 , that in the Na_xVS_2 ternary, there would be three phases spanning the Na compositions, x , at $0 < x < 0.3$ (second stage TP), $0.30 < x \leq 0.85$ (first stage TP), and $0.86 < x \leq 1.0$ (TAP). The three potential regions found in the first discharge of the Na/ VS_2 cell shown in Fig. 5 correlate fairly well with these phase regions. The structure of the ternary, $\text{Na}_{1.0}\text{VS}_2$, we have obtained from the electrochemical cell at the end of discharge appears to be identical to that of the TAP $\text{Na}_{1.0}\text{VS}_2$ described by Wiegiers with crystal lattice parameters of $a = 3.22\text{Å}$ and $C = 7.30\text{Å}$. We have further established Na intercalation by VS_2 from the x-ray patterns of Na_xVS_2 compositions prepared from VS_2 and Na-naphthalide (6). The C-lattice parameters for $\text{Na}_{0.4}\text{VS}_2$ and $\text{Na}_{0.8}\text{VS}_2$ intercalates have been found to be 7.08 and 6.94Å, respectively, in agreement with the observations of Wiegiers (8).

Cathode rechargeability.—Rechargeability of the VS_2 cathode was investigated by extended cycling of a cell with a pressed cathode (0.8m thick) containing 62 w/o VS_2 , 30 w/o C, and 8 w/o Teflon. Cathode utilization as a function of cycle number is shown in Fig. 7. An average capacity of $0.70e^-/\text{VS}_2$ was obtained in the first 40 cycles. The capacity then gradually decreased. The average capacity for the last 15 cycles was $0.6e^-/\text{VS}_2$. The 22nd cycle is shown in Fig. 8. Detailed analysis of the discharge curves suggests that the capacities involved in the second and third phases are rechargeable during extended cycling. However, it appears from the potential profiles of later discharges, for example the 22nd discharge shown in Fig. 8, that the structural differences between these two phases gradually disappear. The latter discharge curves exhibit more or less linear profiles. A possible reason for some of the decrease in capacity after the 40th cycle is mechanical loss of materials from the cathode matrix. This was evidenced by visual observations. The cycling data demonstrate that the Na/ VS_2 cell could deliver an average rechargeable capacity of $0.7e^-/\text{VS}_2$.

The cathode utilization in the first discharge of cells without carbon in the electrode matrix was only $\sim 0.70e^-/\text{VS}_2$. The potential profiles of the discharge curves suggested that Na intercalation into the third

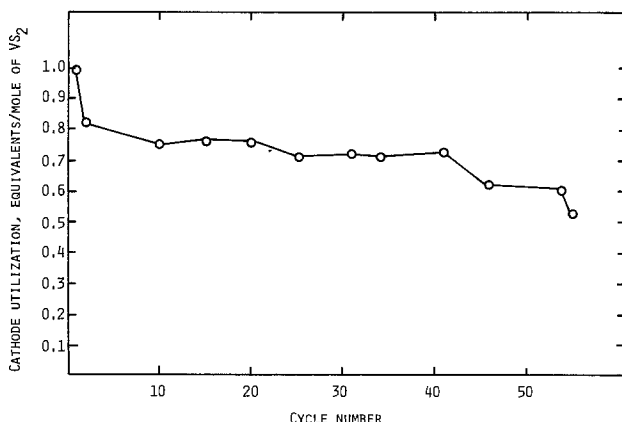


Fig. 7. Cathode utilization vs. cycle number for an Na/ VS_2 cell. Cathode = 62 w/o VS_2 , 30 w/o C, 8 w/o Teflon. Current $i_d = i_c = 4 \text{ mA}$. Current density = 0.5 mA/cm^2 .

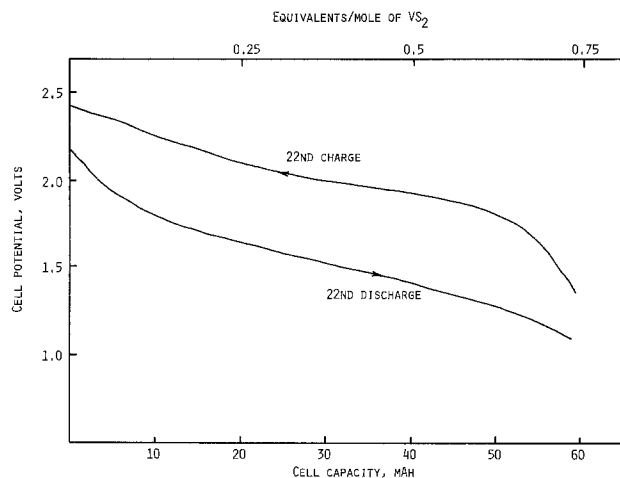


Fig. 8. The 22nd cycle for the VS_2 cell depicted in Fig. 7

phase was not achieved when carbon was absent. The resistivity data for VS_2 and Na_xVS_2 , $x = 0.65, 0.8$, and 1, shown in Table I, suggest that this may be due to decreased electronic conductivity of Na_xVS_2 compositions for $x \geq 0.8$. The data in Table I show that no significant increase in resistivity occurs until $x = 0.8$. When $x = 1$, the material becomes low conducting. The exact break-point to lower conductivity is not known, but may be associated with the TAP phase with $x \geq 0.8$. It has been shown by Wiegiers *et al.* (10) that $\text{Na}_{1.0}\text{VS}_2$ could exist in two crystallographic modifications, namely, the TP and TAP forms. The TAP modification is semiconducting, while the TP form is metallic. The x-ray data we have obtained for Na/ VS_2 samples prepared electrochemically are in good agreement with a TAP modification. These results seem to suggest that the capacity limiting factor in the TAP phase in VS_2 is electronic conductivity whereas that in TiS_2 is Na diffusion. The activation energy for Na intercalation usually decreases with increasing c/a ratio of the crystal lattice. The c/a ratio for the TAP phase in VS_2 is 2.26 whereas that for the TAP phase in TiS_2 , *i.e.*, in $\text{Na}_{0.8}\text{TiS}_2$, is 1.9 (6, 8).

In extensive cycling, rechargeable capacity of VS_2 cathode without carbon in the electrode matrix would be $\sim 0.4e^-/\text{VS}_2$.

Potentiostatic cycling of VS_2 .—A VS_2 cathode was potentiostatically cycled with the potential for discharge set at 1.3V and for charge at 2.3V. The cycling curves are shown in Fig. 9. The total integrated capacity in the first discharge corresponds to $0.95e^-/\text{VS}_2$. The capacities in the first charge and the second discharge are slightly lower than the capacity in the first discharge; however, they are about 10% higher than the values found in the corresponding galvanostatic cycles. Analysis of the first discharge curve shows a capacity of $0.58e^-/\text{VS}_2$ in the first 60 min of discharge during which time the minimum current density was 4.3 mA/cm^2 . The comparable rate capabilities of the VS_2 and TiS_2 cathodes are in conformity with their similar crystal structures.

The Sodium-Niobium Disulfide Cell

Typical galvanostatic cycles for a cell with $\text{Nb}_{1.1}\text{S}_2$ cathode are shown in Fig. 10. The open-circuit po-

Table I. Resistivity data for Na_xVS_2 ; $x = 0.0, 0.65, 0.8$, and 1.0

Compound	Resistivity, $\Omega \text{ cm}^{-1}$
VS_2	0.3
$\text{Na}_{0.65}\text{VS}_2^*$	1.2
$\text{Na}_{0.8}\text{VS}_2^*$	3.2
NaVS_2^*	208

* Prepared from VS_2 and Na-Naphthalide in THF.

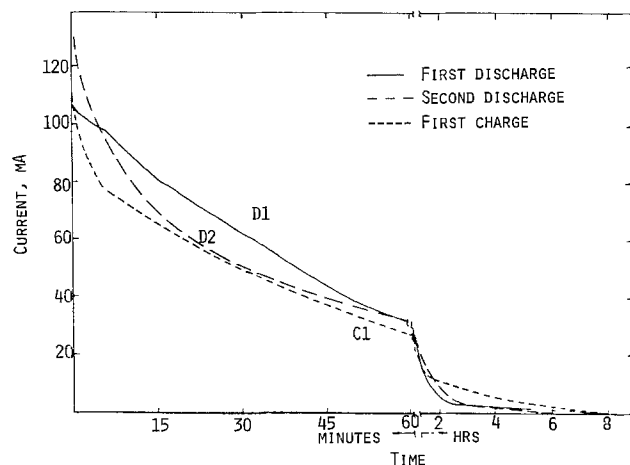


Fig. 9. Potentiostatic cycling curves for an Na/VS₂ cell at 130°C. Discharge potential = 1.3V. Charge potential = 2.3V. Cathode capacity = 103 mA-hr. Curves D1 and D2 are the first and second discharges. Curve C1 is the first charge.

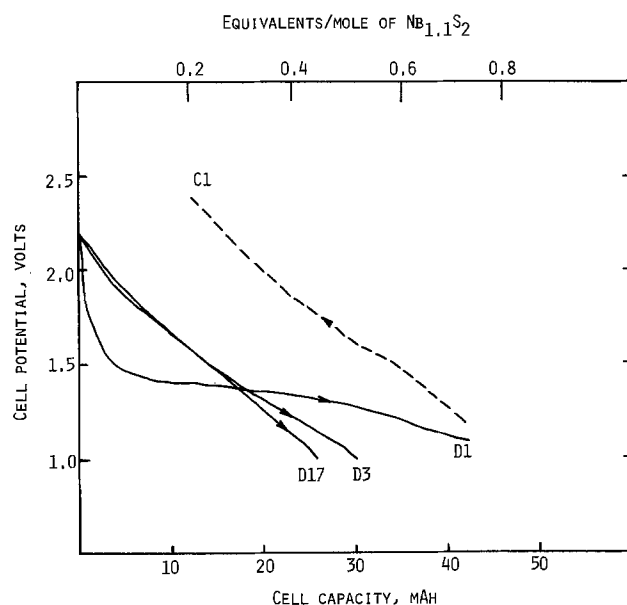


Fig. 10. Galvanostatic cycling curves for the cell, liquid Na/ β -Al₂O₃/triglyme/1M NaI, Nb_{1.1}S₂ at 130°C. The cathode was fabricated from 50 w/o Nb_{1.1}S₂, 40 w/o C, and 10 w/o Teflon. Current, $i_d = i_c = 4$ mA. Current density = 0.5 mA/cm². Curves D1, D3, and D17 are the first, third, and 17th discharges. Curve C1 is the first charge.

tential of the cell was 2.20V. However, the first discharge proceeds from 1.7V with the potential remaining at ~1.4V during most of the discharge. The first discharge corresponds to $0.72e^-/\text{Nb}_{1.1}\text{S}_2$. The first charge exhibits a more linear voltage-time behavior, with a much higher slope than the discharge. The charge corresponds to $0.54e^-$. All subsequent discharges and charges have slopes similar to the first charge. It appears that in the first discharge as Na is intercalated, Nb_{1.1}S₂ undergoes a phase change and the "new phase" retains the structures during subsequent cycling. Average cathode utilization in 17 cycles was $0.5e^-/\text{Nb}_{1.1}\text{S}_2$.

A wide variety of structural types are known in the Nb-S binary system (17). The x-ray pattern of our material of average stoichiometry Nb_{1.1}S₂ could not be indexed to a single homogeneous phase, although a considerable fraction of the material appeared to belong to the 3S-Nb_{1+x}S₂ structural type (17). A cathode was cycled once and then treated with CH₃CN/I₂ solution to remove all the residual Na. Its x-ray pattern appeared to be similar to that of the 2H-Nb_{1+x}S₂ structural type (17). It appears that intercalation of Na

Table II. Energy density of Na/MS₂ couples calculated from experimentally obtained capacities and voltages

Metal sulfide	Equiv./mole of MS ₂	Mid-discharge voltage	Specific energy (W-hr/kg)
TiS ₂	0.65	1.7	215
VS ₂	0.70	1.8	258
Nb _{1.1} S ₂	0.50	1.5	119

initially converts the 3S-Nb_{1+x}S₂ structure to the 2H-Nb_{1+x}S₂ structure which does not undergo further change with cycling. The potential profiles of the charge/discharge curves after the first discharge closely resemble the previously reported (18) EMF-Na composition curve of the Na_xTaS₂ ternary (18) where the parent disulfide belongs to the 2H-polytype.

Summary and Conclusions

Three transition metal disulfides, TiS₂, VS₂, and Nb_{1.1}S₂, have been evaluated as possible cathode materials for a moderate temperature rechargeable Na cell operating at ~130°C. Discharge and charge reactions in all the three cathodes involve Na intercalation and deintercalation, respectively. Our data seem to indicate that the cycling reactions proceed with phase transformations of the host lattice.

The first discharge of TiS₂ results in a capacity of 0.85 equiv./mole. It may be inferred from the discharge data that the Na_xTiS₂ ternary encompassing the Na compositional range, $0 < x \leq 0.85$ involves two phases. About half of the Na in the first phase spanning the Na compositional range, $0 < x \leq 0.30$ and practically all the Na in the second phase spanning the compositional range, $0.37 < x \leq 0.80$ are rechargeable.

Vanadium disulfide intercalates up to one mole of Na/mole of VS₂ in the first discharge. The resulting Na_xVS₂ ternary encompasses three phases at $0 < x \leq 0.28$, $0.3 < x \leq 0.85$, and $0.85 < x \leq 1$. Extended cycling data suggest that virtually all the Na in the last two phases are rechargeable. The Na involved in the first phase is practically irreversible.

Niobium disulfide appears to undergo a phase change in the first discharge. The new phase, however, retains the structure during subsequent cycling. The average rechargeable capacity in extended cycling of this cathode appears to be about 0.50 equiv./mole.

Energy densities of Na/MS₂ couples calculated from experimentally determined average capacities and mid-discharge voltages are presented in Table II. The energy density projection recently made by Rao (19) for an Na-TiS₂ cell is in close agreement with our results.

Acknowledgment

This work was supported by National Aeronautics and Space Administration under Contract No. NAS3-21726. Fruitful discussions with Dr. S. B. Brummer of EIC Corporation and Dr. Joseph Singer of NASA-Lewis Research Center, Cleveland, Ohio, are gratefully acknowledged.

Manuscript submitted Feb. 25, 1980; revised manuscript received June 18, 1980.

Any discussion of this paper will appear in a Discussion Section to be published in the June 1981 JOURNAL. All discussions for the June 1981 Discussion Section should be submitted by Feb. 1, 1981.

REFERENCES

- M. S. Whittingham, *Prog. Solid State Chem.*, **12**, 1 (1978).
- G. L. Holleck, K. M. Abraham, and S. B. Brummer, Paper 29 presented at the Electrochemical Society Meeting, Los Angeles, California, Oct. 14-19, 1979.
- D. W. Murphy and P. A. Christian, *Science*, **205**, 651 (1979).

4. S. A. Weiner and R. P. Tischer, Annual Report on the Ford Na-S Battery, Contract NSF-C805 (AER 73-07199) and references therein (1976).
5. K. M. Abraham, R. D. Rauh, and S. B. Brummer, *Electrochim. Acta.*, **23**, 501 (1978).
6. B. G. Silbernagel and M. S. Whittingham, *Mater. Res. Bull.*, **11**, 29 (1975).
7. A. Leblanc-Soreau, M. Danob, L. Trichet, and J. Rouxel, *ibid.*, **9**, 191 (1974).
8. G. A. Wiegers *et al.*, *ibid.*, **9**, 1261 (1974).
9. J. Rouxel, *J. Solid State Chem.*, **17**, 223 (1976).
10. G. A. Wiegers and C. V. Van Bruggen, *Physica*, **86-88B**, 1009 (1977).
11. W. P. F. A. M. Omloo and F. Jellinek, *J. Less Common Met.*, **20**, 121 (1970).
12. D. A. Winn, J. M. Shemilt, and B. C. H. Steele, *Mater. Res. Bull.*, **11**, 59 (1976).
13. D. F. Shriver, "The Manipulation of Air Sensitive Compounds," McGraw-Hill, New York (1969).
14. F. K. McTaggart and A. D. Wadsley, *Aust. J. Chem.*, **11**, 445 (1958).
15. B. Van Laar and D. J. W. Ijdo, *J. Solid State Chem.*, **3**, 590 (1971).
16. D. W. Murphy, C. Cros, F. J. DiSalvo, and J. V. Waszczak, *Inorg. Chem.*, **16**, 3027 (1977).
17. F. Jellinek, *Arkiv Kemi*, **20**, 447 (1963).
18. A. S. Nagelberg and W. L. Worrell, in "Electrode Materials and Processes for Energy Conversion and Storage," J. D. E. McIntyre, S. Srinivasan, and F. G. Will, Editors, p. 487, The Electrochemical Society Softbound Proceedings Series, Princeton, N.J. (1977).
19. B. M. L. Rao, in "Battery Design and Optimization," S. Gross, Editor, p. 457, The Electrochemical Society Softbound Proceedings Series, Princeton, N.J. (1979).

A Pulse Technique Employed for Studying Egress of Hydrogen from Iron Polarized Cathodically in As³⁺-Containing Solutions

P. Kedzierzawski, Z. Szklarska-Smialowska, and M. Smialowski*

Institute of Physical Chemistry, Polish Academy of Sciences, Warsaw, Poland

ABSTRACT

Triangular pulses were applied to one side of an iron membrane polarized cathodically in As³⁺-containing solution of 0.1N H₂SO₄ or 0.1N NaOH, and changes in the rate of the hydrogen ionization occurring at the diffusive side of the membrane were recorded. The results indicated that in both solutions the egress of hydrogen from iron at the polarized side of the membrane was hampered by some surface effects related to the presence of As³⁺ in the electrolyte. The probable nature of these effects is discussed.

In a study of the electrochemical extraction of hydrogen from iron membranes polarized cathodically on one side, Nanis and Namboodhiri (1) analyzed theoretically the transient current of hydrogen removal from iron following steady-state permeation. Two limiting conditions were considered: 1, the fastest possible decay caused by a rapid egress of hydrogen at both sides of the membrane; and 2, slow hydrogen removal occurring only at the diffusive side of the membrane. In case 1, the concentration of hydrogen at the input (polarized) side is considered to drop instantaneously to zero on polarization current interruption, whereas in case 2, the input side is thought to become impermeable to hydrogen removal. The theoretical analysis has shown that for the fastest possible decay (condition 1) the amount of hydrogen extracted at the diffusive side of the membrane is one-third of the total amount of hydrogen present at steady-state permeation. The remaining part of hydrogen diffuses out through the input side. In the second case (condition 2) the total quantity of hydrogen escapes at the diffusive side.

Experiments conducted with Armco iron membranes polarized cathodically in 0.1N H₂SO₄ or 0.2N NaOH solution proved (1) that after interruption of the charging current about 33% of the total quantity of hydrogen present at steady-state permeation escapes through the diffusive side indicating that condition 1 is fulfilled.

More generally, if v_{in} is the stationary rate of hydrogen ingress and v_{eg} is the rate of hydrogen egress

* Electrochemical Society Active Member.

Key words: cathodic polarization, iron, hydrogen diffusion, hydrogen permeation, hydrogen ionization.

at the polarized side of the membrane, then for condition 1

$$v_{in} \approx v_{eg} \gg \frac{C_H^\circ \cdot D}{L} \quad [1]$$

and for condition 2

$$v_{in} \approx \frac{C_H^\circ \cdot D}{L} \gg v_{eg} \quad [2]$$

where $(C_H^\circ \cdot D)/L$ is the rate of hydrogen permeation through the membrane.

In case 1 each variation of polarization conditions, for example of the cathodic current density i_c , induces immediately an appropriate change in C_H° . Therefore, changes in i_c and C_H° with time are determined by the same function. In case 2, however, variations of polarization conditions produce relevant changes in the value of $(\partial c/\partial x)_{x=L}$, i.e., of the concentration gradient of hydrogen at the entry side of the membrane.

Apart from the data reported by Nanis and Namboodhiri (1) there also are in the literature some other results suggesting that for sufficiently thick membranes charged with hydrogen evolved from acid or alkaline solutions condition 1 is satisfied. For example, on the basis of permeability measurements performed by Devanathan and Stachurski (2) on Armco iron membranes of different thicknesses polarized cathodically in 0.1N H₂SO₄ the following values were calculated: ¹ at $E = 600$ mV_{SCE} the stationary rate of hydrogen ingress was $v_{in} \approx 10^{-9}$ mole H/cm² · sec, and for $L = 0.77$ mm the steady-state permeation was 5.7×10^{-11} mole H/cm² · sec. At $E = 650$ mV_{SCE} the re-

¹ Calculations of v_{in} were made by extrapolating the steady-state permeation to zero thickness of the membrane ($L = 0$).

spective values were $\approx 10^{-9}$ mole H/cm² · sec and 8.3×10^{-11} mole H/cm² · sec. Similar experiments carried out by Kim and Wilde (3) on Ferrovac iron charged with hydrogen in 10^{-4} M NaOH led to following values: $v_{in} \approx 5 \times 10^{-10}$ mole H/cm² · sec and permeability through a 0.77 mm thick membrane = 6.2×10^{-11} mole H/cm² · sec.

The above results indicate that under stationary conditions of electrolytic charging of iron membranes with hydrogen evolved from pure, *i.e.*, promoter-free solutions, the permeability is by one to two orders of magnitude lower than v_{in} . Hence, in conformity with condition 1, v_{eg} is almost as high as v_{in} .

Similar conclusions follow from measurements performed by Kedzierzawski *et al.* (4). In their experiments high purity zone-refined Battelle iron was polarized with alternating currents in 0.1N H₂SO₄. The results indicated that the diffusivity of hydrogen calculated from either amplitude or phase relationships was independent of frequency. This led to the conclusion that at the input side of the iron membrane the current was in phase with C_H° ; hence again, condition 1 was fulfilled.

Different results were obtained for palladium membranes. Thus, according to Fullenwider (5), the permeability-time relationships obtained experimentally were close to those based on the assumption that each change in the potential applied to the Pd electrode induced an immediate change in the concentration gradient of hydrogen at the input side of the membrane; and Sekine (6) argued that in permeability measurements conducted with alternating currents the cathodic current was in phase with the concentration gradient of hydrogen at the input side of the Pd membrane. These results fit in with condition 2.

The present paper provides experimental evidence that in As³⁺-containing solutions pure iron behaves accordingly to condition 2.

It has been found in previous studies (7, 8) that compounds of arsenic, and also those of phosphorus, antimony, sulfur, selenium, and tellurium, promote the entry of hydrogen into iron only in such regions of the electrode potential and pH in which the hydrides of these elements coexist in trace amounts at the polarized cathode surface. On the other hand, it has been suggested (9) that in the presence of the compounds, which promote entry of hydrogen into metals, the reverse process, *i.e.*, the egress of hydrogen from the metal, is hampered.

In order to verify the above suggestion experimentally, a pulse technique was employed. The experiments were carried out by applying triangular pulses to the entry side of the iron membrane and measuring for each applied pulse the quantity of hydrogen ionized at the diffusive side of the membrane. This technique permitted evaluation to be made of the rate at which hydrogen egressed from iron at defined values of the electrode potential and current density applied to the entry side of the membrane. Also, measurements of the cathodic current after pulse application enabled conclusions to be drawn on the desorption of the promoting species from the cathode.

Theoretical Basis of the Method Employed

Changes in the ionization rate of hydrogen that occur at the diffusive side of the membrane when a potential pulse is applied to the polarized side can be analyzed considering that the egress of hydrogen at the latter side is controlled either by condition 1 (diffusion control), or by condition 2 (kinetic control).

The anodic current P at the diffusive side of the membrane is given by the expression

$$P(t) = DF \left(\frac{\partial c_H}{\partial x} \right)_{x=0} \quad [3]$$

To calculate $(\partial c_H / \partial x)_{x=0}$ it is necessary to know the concentration of hydrogen as a function of time and

space coordinates. For this, Fick's second law with defined initial and boundary conditions must be solved.

Case 1. Diffusion controlled process.—The system of equations to be solved is of the form

$$\frac{\partial^2 c_H}{\partial x^2} = \frac{1}{D} \frac{\partial c_H}{\partial t} \quad [4]$$

$$c_H(0, t) = 0 \quad [5]$$

$$c_H(L, t) = C_H^\circ + \lambda \delta(t) \quad [6]$$

$$c_H(x, 0) = \frac{C_H^\circ x}{L} \quad [7]$$

The use of Dirac's delta function $\delta(t)$ is justified by the fact that the duration of the pulse (both potential and current) is less than 0.1 sec, hence much shorter than the time during which permeation of hydrogen is recorded (10-100 sec).

By substituting $c = c_H - C_H^\circ x/L$ one obtains

$$\frac{\partial^2 c}{\partial x^2} = \frac{1}{D} \frac{\partial c}{\partial t} \quad [8]$$

$$c(0, t) = 0 \quad [9]$$

$$c(L, t) = \lambda \delta(t) \quad [10]$$

$$c(x, 0) = 0 \quad [11]$$

Above substitution eliminates the steady-state component of the permeation rate. Changes in the permeation rate ΔP registered in this work are related to the transient component of concentration c by

$$\Delta P = FD \left(\frac{\partial c}{\partial x} \right)_{x=0} \quad [12]$$

Equation [12] may be solved using Laplace's transformation method. By transforming both sides of [8] and for boundary conditions as above one gets

$$\frac{d^2 Y}{dx^2} - \frac{1}{D} sY = 0 \quad [13]$$

$$Y(0, s) = 0 \quad [14]$$

$$Y(L, s) = \lambda \quad [15]$$

where $Y = \alpha[c]$, $s =$ Laplace transformation parameter.

Equation [13] has a solution

$$Y = \frac{\lambda \sinh(x\sqrt{s/D})}{\sinh(L\sqrt{s/D})} \quad [16]$$

Inverse transformation of [16] gives

$$c = -\frac{2\pi D \lambda}{L^2} \sum_{n=1}^{\infty} (-1)^n n \sin \frac{n\pi x}{L} \exp\left(-\frac{n^2 \pi^2 D}{L^2} t\right) \quad [17]$$

and

$$\Delta P = FD \left(\frac{\partial c}{\partial x} \right)_{x=0} = -\frac{2\pi^2 D^2 \lambda F}{L^3} \sum_{n=1}^{\infty} (-1)^n n^2 \exp(-n^2 k) \quad [18]$$

where

$$k = \frac{\pi^2 D t}{L^2} \quad [19]$$

Therefore changes in the permeation rate with time are proportional to the factor

$$K_1 = -\sum_{n=1}^{\infty} (-1)^n n^2 \exp(-n^2 k) \quad [20]$$

The plot of K_1 vs. k is given in Fig. 1. Calculations indicate that in this case the half-peak width is equal to 1.4.

Case 2. Kinetically controlled process.—The system of equations to be solved has the form

$$\frac{\partial^2 c_H}{\partial x^2} = \frac{1}{D} \frac{\partial c_H}{\partial t} \quad [21]$$

$$c_H(0, t) = 0 \quad [22]$$

$$\frac{\partial c_H}{\partial x}(L, t) = \frac{C_H^\circ}{L} + \mu \delta(t) \quad [23]$$

$$c_H(x, 0) = \frac{C_H^\circ x}{L} \quad [24]$$

By substituting

$$c = c_H - \frac{C_H^\circ x}{L}$$

one obtains

$$\frac{\partial^2 c}{\partial x^2} = \frac{1}{D} \frac{\partial c}{\partial t} \quad [25]$$

$$c(0, t) = 0 \quad [26]$$

$$\frac{\partial c}{\partial x}(L, t) = \mu \delta(t) \quad [27]$$

$$c(x, 0) = 0 \quad [28]$$

As in the previous case the transient concentration component c is related to the transient component of the permeation rate by Eq. [12]. The above system of equations can again be solved using Laplace's transformation method. Transformation of both sides of [25] and of boundary conditions leads to the equation

$$\frac{d^2 Y}{dx^2} - \frac{1}{D} sY = 0 \quad [29]$$

with boundary conditions

$$Y(0, s) = 0 \quad [30]$$

and

$$\frac{dY}{dx}(L, s) = \mu \quad [31]$$

Equation [29] has the solution

$$Y = \frac{\mu \sqrt{D} \sinh(x \sqrt{s/D})}{\sqrt{s} \cosh(L \sqrt{s/D})} \quad [32]$$

Inverse transformation of [30] gives the expression for c

$$c = -\frac{2D\mu}{L} \sum_{n=1}^{\infty} (-1)^n \sin \frac{(2n-1)\pi x}{L^2} \exp \left[-\frac{(2n-1)^2 k}{4} \right] \quad [33]$$

Differentiation of [33] vs. x gives the expression for the transient component of the permeation rate

$$\Delta P = FD \left(\frac{\partial c}{\partial x} \right)_{x=0} = -\frac{\pi D^2 \mu F}{L^2} \sum_{n=1}^{\infty} (-1)^n (2n-1) \exp \left[-(2n-1)^2 k/4 \right] \quad [34]$$

Therefore changes in the permeation rates are proportional to

$$K_2 = - \sum_{n=1}^{\infty} (-1)^n (2n-1) \exp \left[-(2n-1)^2 k/4 \right] \quad [35]$$

The plot of K_2 vs. k is shown in Fig. 1. According to calculations, in this case the half-peak width is 4.3.

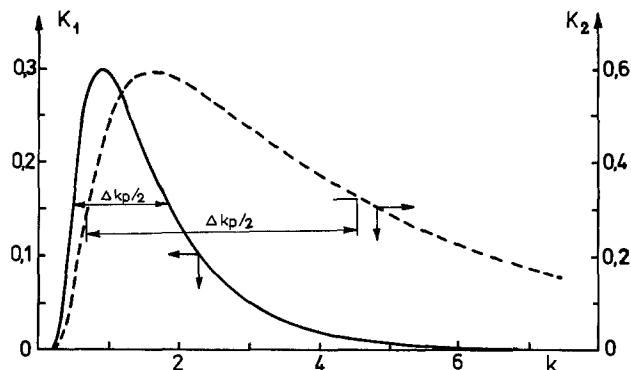


Fig. 1. Variations in K_1 and K_2 with k according to Eq. [20] (diffusion control, $\Delta k/2 = 1.4$; full line) and Eq. [35] (kinetic control, $\Delta k/2 = 4.3$; dashed line).

Experimental

A schematic drawing of the apparatus employed is shown in Fig. 2. The electrolytic permeability cell was based on the design similar to that used in Ref. (3). The Pt counterelectrode in the diffusion compartment, E_{p2} , was sheltered by a glass frit to minimize access of hydrogen from that source. As reference electrode, E_{02} , a Pt foil plated with Pt sponge bubbled with H_2 and immersed in 0.1N NaOH was used. The E_{01} reference electrode was either $Hg/HgSO_4/0.1N H_2SO_4$ or $Hg/HgO/0.1N NaOH$, this being dependent on the composition of the catholyte employed in the given experiments: either acid or alkaline.

The membranes were in shape of caps machined from a bar of Battelle ultrapure iron with 5 ppm non-metallic and 23 ppm metallic impurities. The cap's bottom, 0.8 cm in diameter, 0.077 cm thick, served as the membrane and its side part was clamped between the two compartments of the electrolytic cell which were made of Plexiglas. The membranes were ground with 600 grit abrasive paper, polished with diamond paste, degreased with benzene, heated in vacuo for 2 hr at 700°C, and furnace cooled. Before measurements the internal side of the cap which served as the diffusive side of the membrane was electroplated with a thin coat of palladium.

The measurements were performed at room temperature in either 0.1N H_2SO_4 or 0.1N NaOH. The solutions were pre-electrolyzed for several hours in an auxiliary cell between smooth Pt electrodes at a voltage of 1.6V.

As established in Ref. (7 and 8), in both acid and alkaline solutions the presence of arsenic compounds greatly increases the permeation rate of hydrogen

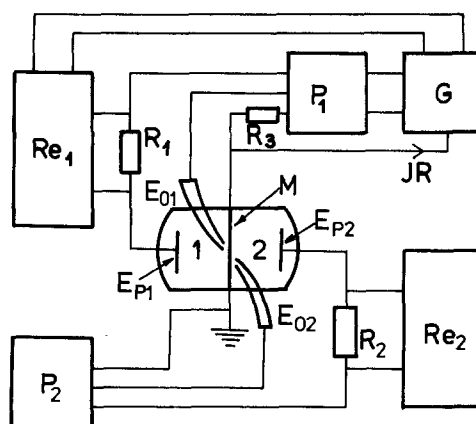


Fig. 2. Schematic drawing of the apparatus. M-iron membrane; E_{01} and E_{02} , reference electrodes; E_{p1} , E_{p2} , auxiliary electrodes; G, generator; R_1 , R_2 , R_3 , resistors; P_1 , P_2 , potentiostats; Re_1 , Re_2 , recorders; JR, ohmic resistance compensator; 1, polarization side; 2, diffusion side.

through iron polarized cathodically to potentials at which arsine is produced in trace amounts together with hydrogen evolution. The permeability of hydrogen increases with increasing As^{3+} concentration to a maximum at about 10^{-3}M and then decreases. The present experiments were carried out at 10^{-5}M or $5 \times 10^{-4}\text{M}$ As^{3+} .

Two types of experiments were performed: (i) measurements of polarization curves and permeabilities of hydrogen during galvanostatic polarization in As-free and As-containing solutions, and (ii) cyclic perturbation measurements in As-containing solutions.

Polarization and permeability measurements.—The iron membrane coated on one side with palladium was clamped between the two parts of the electrolytic cell. The cathodic polarization compartment was filled with either 0.1N H_2SO_4 or 0.1N NaOH , either without or with the addition of As_2O_3 at concentrations previously given. The diffusive compartment of the cell was filled with 0.1N NaOH and the potential of the membrane was set at $-70\text{ mV}_{\text{NHE}}$. Under these conditions all the hydrogen permeated through the membrane was ionized at the Pd-coated iron surface. Measurements of the cathodic polarization curves were made by changing the potential every 30 min by 50 mV in the negative direction. Simultaneously, the hydrogen ionization current was recorded.

Cyclic perturbation measurements.—These experiments were conducted only in As-containing solutions, because in the absence of As^{3+} the hydrogen ionization currents were too small to be recorded accurately enough.

Initially the polarized side of the membrane was kept at a constant "starting potential" E_i (Fig. 3) of either $-500\text{ mV}_{\text{NHE}}$ (in 0.1N $\text{H}_2\text{SO}_4 + \text{As}^{3+}$) or $-1300\text{ mV}_{\text{NHE}}$ (in 0.1N $\text{NaOH} + \text{As}^{3+}$). Under these conditions the cathodic current densities and the hydrogen ionization rates were recorded. After the steady state was established, a potential pulse, either cathodic or anodic, was applied to the entry side of the membrane. The triangular pulse lasted for $0.01\text{--}0.03\text{ sec}$. After attaining the peak at E_z (Fig. 3), the potential returned to its initial value of E_i . The change in the hydrogen ionization current occurring at the diffusive side in response to the potential pulse was recorded.

Results of Polarization and Permeability Measurements

Figures 4 and 5 show the cathodic polarization curves obtained for iron membranes exposed to As-free and As-containing electrolytes. It is seen that in the whole range of potentials examined the current density is less in the presence of As^{3+} than in its absence. This is probably due to adsorption of As and/or of its compounds on the cathode.

Figures 6 and 7 illustrate the dependence on potential of the steady-state ionization current of hydrogen permeating through the membrane polarized, respectively, in 0.1N H_2SO_4 and 0.1N NaOH with either 10^{-5}M or $5 \times 10^{-4}\text{M}$ of As^{3+} . In the range of potentials studied, higher permeabilities are observed for

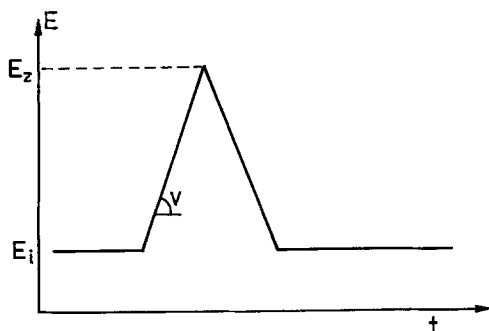


Fig. 3. Shape of the potential pulse applied. E_i , starting potential; E_z , reversal potential; $v = (dE/dt)$, sweep rate.

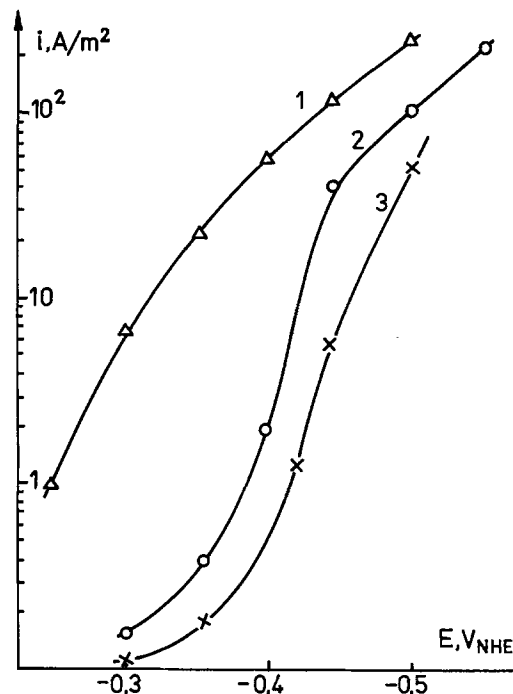


Fig. 4. Polarization curves for iron in 0.1N H_2SO_4 . Curve 1, without As^{3+} ; curve 2, with 10^{-5}M As^{3+} ; curve 3, with $5 \times 10^{-4}\text{M}$ As^{3+} .

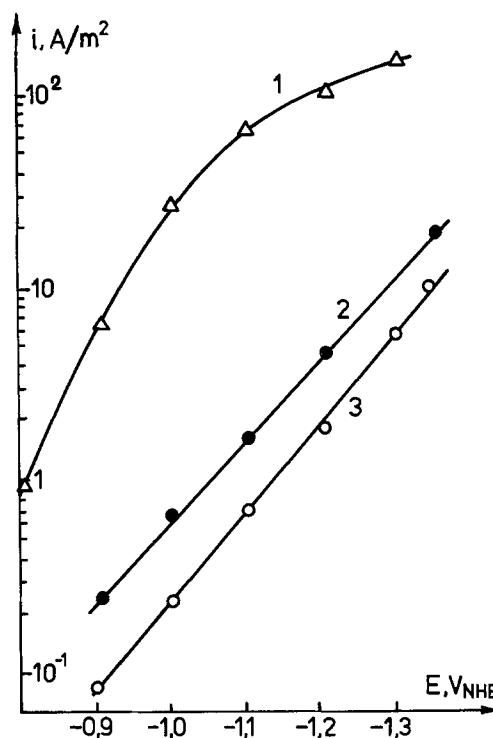


Fig. 5. Polarization curves for iron in 0.1N NaOH . Curve 1, without As^{3+} ; curve 2, with 10^{-5}M As^{3+} ; curve 3, with $5 \times 10^{-4}\text{M}$ As^{3+} .

both solutions at 10^{-5}M than at $5 \times 10^{-4}\text{M}$ As^{3+} . Also, higher permeabilities occur when iron is charged cathodically in acid than in alkaline solution. This fits in with the results found in Ref. (3 and 4).

Results of Perturbation Measurements

By recording the response of the hydrogen ionization current to the potential pulse one obtains P - t curves with maxima or minima, this being dependent on the direction of the pulse. As follows from theoretical considerations given above, the shape of the response curve, and especially the half-peak width,

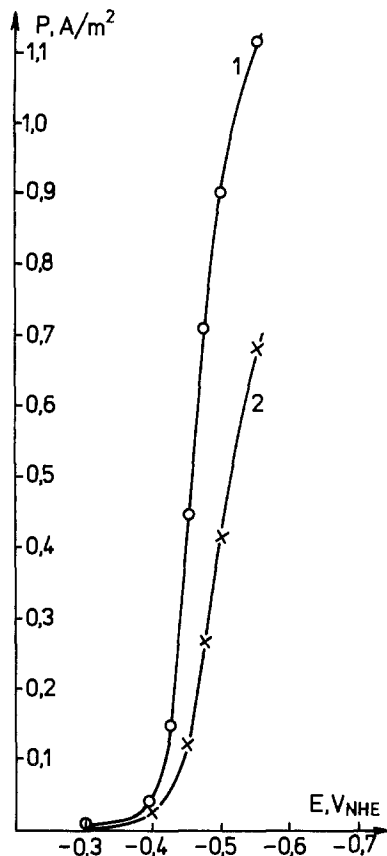


Fig. 6. Steady-state permeation rate vs. potential in 0.1N H₂SO₄. Curve 1, with 10⁻⁵M As³⁺; curve 2, with 5 × 10⁻⁴M As³⁺.

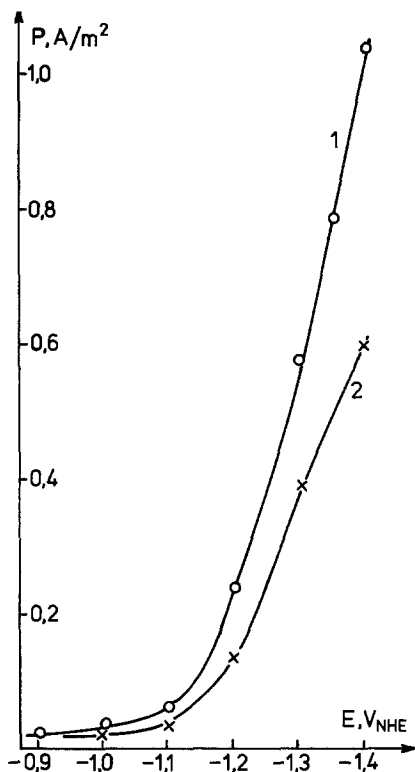


Fig. 7. Steady-state permeation rate vs. potential in 0.1N NaOH. Curve 1, with 10⁻⁵M As³⁺; curve 2, with 5 × 10⁻⁴M As³⁺.

permits conclusions to be drawn regarding kinetics of hydrogen extraction. Namely, if the removal of hydrogen were controlled by diffusion (condition 1), the dimensionless term

$$\Delta k_{P/2} = \frac{\pi^2 D}{L^2} \Delta t_{P/2}$$

would be equal to 1.4, whereas in the case of kinetic control (condition 2) this term would be equal to 4.3. By substituting $D = 8.3 \times 10^{-5}$ cm²/sec (6) and $L = 0.077$ cm one obtains for the diffusion controlled removal $\Delta t_{P/2} = 10.1$ sec and for the kinetically controlled removal 31.1 sec.

As shown in Fig. 8 and 9, in 0.1N H₂SO₄ + As³⁺ at E_z potentials less positive than 0.15 mV_{NHE}, and also in 0.1N NaOH + As³⁺ at E_z potentials more negative than -0.5 mV_{NHE} the time corresponding to the half-peak width is close to the value calculated for the kinetically controlled removal of hydrogen. At more anodic E_z potentials of the pulse wider peaks are observed.

Discussion

The above results indicate that the egress of hydrogen from iron exposed to As³⁺-containing solutions is hampered by some kinetic impediments dependent on the electrode potential.

Let us consider electrode processes which might be thought responsible for these effects.

Both in 0.1N H₂SO₄ + As³⁺ and 0.1N NaOH + As³⁺, at potentials at which, according to the previous results (7, 8), arsine occurs as a by-product of the hydrogen evolution reaction, the ingress of hydrogen into iron is accelerated (Fig. 6 and 7), but the egress of hydrogen from iron is restrained (Fig. 8 and 9). These effects are probably due to co-adsorption of arsenic hydride molecules or radicals with hydrogen

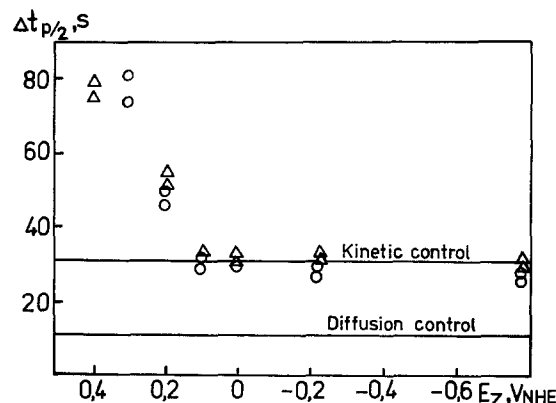


Fig. 8. Effect of reversal potential on width of half-peak of the ΔP - t curve for membranes polarized in 0.1N H₂SO₄. Circles, 10⁻⁵M As³⁺; triangles, 5 × 10⁻⁴M As³⁺.

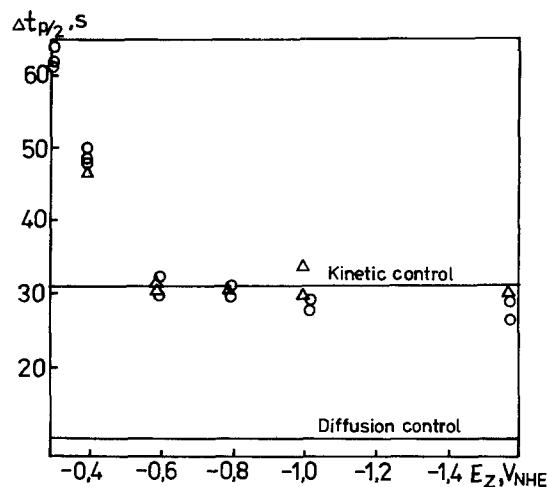


Fig. 9. Effect of reversal potential on width of half-peak of the ΔP - t curve for membranes polarized in 0.1N NaOH. Circles, 10⁻⁵M As³⁺; triangles, 5 × 10⁻⁴M As³⁺.

atoms at the metal surface. For some as yet unexplored reasons this promotes ingress of hydrogen into metal bulk and inhibits the reverse process.

At E_z potentials not exceeding $+150 \text{ mV}_{\text{NHE}}$ in $0.1\text{N H}_2\text{SO}_4 + \text{As}^{3+}$ (Fig. 8) or $-500 \text{ mV}_{\text{NHE}}$ in $0.1\text{N NaOH} + \text{As}^{3+}$ (Fig. 9), the duration of the half-peak width is about 31 sec, which corresponds to the value calculated for the kinetically controlled removal of hydrogen from iron (condition 2). Within the above E_z potential regions the cathodic current density has been found to return to its initial value. As follows from Fig. 10 and 11, more positive (or less negative) potential pulses result in longer times necessary to restore the initial current density. The higher E_z the slower is the return of the cathodic current to its initial value. Slower restoration and higher time lags are observed in alkaline than in acid electrolytes.

These effects are probably due to a rapid desorption of the promoting species (arsine?), which occurs if a relatively high anodic potential pulse is applied, followed by a slow re-adsorption of arsenic and/or of some of its compounds, the rate of these processes being dependent on E_z .

Because a part of the experiments was performed under conditions under which the entry side of the membrane was submitted to anodic potential pulses, a detailed analysis was undertaken to check whether anodic reactions, such as oxidation of iron, of arsenic, or of hydrogen, could affect the cathodic current density after the pulse was applied. However additional measurements of chronovoltammetric curves have shown that electric charges consumed by these reactions are about 10^3 times smaller than those found in the main series of our experiments. This indicates that the effect of these oxidation reactions is negligible and that the desorption of the promoting species is responsible for the increase of the cathodic current density observed after application of the anodic pulse.

Conclusions

A pulse technique was used to study the removal of hydrogen from iron membranes whose one side was polarized cathodically in the presence of small amounts of As^{3+} in either $0.1\text{N H}_2\text{SO}_4$ or 0.1N NaOH . In contrast

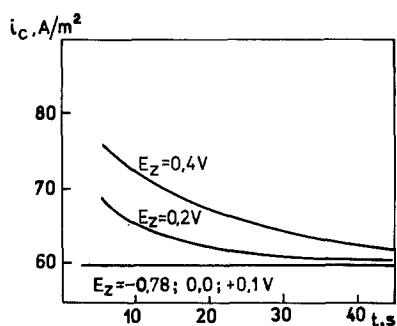


Fig. 10. Changes in cathodic current density with time after application of potential pulse in $0.1\text{N H}_2\text{SO}_4 + 5 \times 10^{-4}\text{M As}^{3+}$.

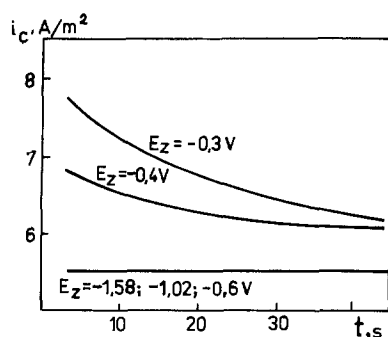


Fig. 11. Changes in cathodic current density with time after application of potential pulse in $0.1\text{N NaOH} + 5 \times 10^{-4}\text{M As}^{3+}$.

with the results of Nanis and Nambodhiri (1), and others (2-4), who found that in pure (*i.e.*, As^{3+} -free) solutions the egress of hydrogen from iron at the polarized side of the membrane was unhampered and almost as rapid as the ingress of hydrogen into iron, the results of the present study indicated that As^{3+} added to the catholyte at a concentration of the order of 10^{-3}M caused a nearly complete interception of the egress of hydrogen from iron. Under these conditions almost all the hydrogen which entered into iron at the polarized side of the membrane diffused out through its other side.

It is suggested on the basis of the present and previous (7, 8) results that arsine produced in trace amounts during the cathodic process promotes the entry of hydrogen into iron and inhibits the reverse reaction. These effects are probably related to co-adsorption of arsenic hydride molecules or radicals with hydrogen atoms on the surface of the cathode.

Acknowledgments

The authors gratefully acknowledge Dr. P. T. Wilson for valuable discussion and The Battelle Memorial Institute, Columbus, Ohio, for donation of ultrapure iron.

Manuscript submitted Feb. 27, 1980; revised manuscript received June 10, 1980.

Any discussion of this paper will appear in a Discussion Section to be published in the June 1981 JOURNAL. All discussions for the June 1981 Discussion Section should be submitted by Feb. 1, 1981.

LIST OF SYMBOLS

c_{H}	concentration of hydrogen in the metal
c_{H}°	concentration of hydrogen at the polarization side
c	nonstationary component of hydrogen concentration in metal
D	diffusivity of hydrogen in metal
E	electrode potential
E_i	starting potential
E_z	reversal potential
F	Faraday constant
i_c	cathodic current density
k	dimensionless parameter $= \pi^2 Dt/L^2$
K_1, K_2	sums of series of Eq. [20] and [35]
L	membrane thickness
P	ionization rate of hydrogen at the diffusive side of membrane
ΔP	nonstationary component of P
s	Laplace transformation parameter
t	time
v	sweep rate
v_{in} and v_{eg}	rates of ingress and egress of hydrogen at the polarized side, respectively
Y	$\alpha[c]$
λ, μ	proportionality coefficients
$\delta(t)$	Dirac's delta function
$\Delta t_{p/2}$	half-peak width of K_1, K_2 vs. k curve
$\Delta t_{p/2}$	half-peak width of ΔP vs. t curve

REFERENCES

- L. Nanis and T. K. G. Nambodhiri, *This Journal*, **119**, 693 (1972).
- M. A. V. Devanathan and Z. Stachurski, *ibid.*, **111**, 619 (1964).
- C. D. Kim and B. E. Wilde, *ibid.*, **118**, 202 (1971).
- P. Kedzierzawski, K. Benczek, and A. Sadkowski, *Bull. Acad. Pol. Sci., Ser. Sci. Chim.*, **24**, 595 (1976).
- M. A. Fullenwider, *This Journal*, **122**, 648 (1975).
- K. Sekine, *J. Res. Inst. Catalysis, Hokkaido Univ.*, **25**, 73 (1977).
- T. Zakroczymski, Z. Szklarska-Smialowska, and M. Smialowski, *Werk. Korros.*, **26**, 617 (1975).
- T. Zakroczymski, Z. Szklarska-Smialowska, and M. Smialowski, *ibid.*, **27**, 625 (1976).
- M. Smialowski, Proc. Intern. Conf. on Stress Corrosion Cracking and Hydrogen Embrittlement of Iron Base Alloys, France, June 1973, Publ. NACE 1977, p. 405.
- R. Bouraoui, Thesis, Paris VI University, 1974.

Auger Analysis of the Passivation of Gadolinium by Electropolishing

A. J. Bevolo, B. J. Beaudry, and K. A. Gschneidner, Jr.

Ames Laboratory and Departments of Physics and Materials Science and Engineering,
Iowa State University, Ames, Iowa 50011

ABSTRACT

A method of electropolishing has been developed at the Ames Laboratory which produces a shiny surface on gadolinium that remains untarnished for years at 20°C. Auger depth profiles have revealed the presence of a chlorine bearing layer on top of the native oxide after electropolishing with a chilled methanol-perchloric solution. Even though this passivating film is only a few monolayers thick it is continuous and stable for at least two years under room temperature air exposure.

Gadolinium metal does not turn completely into its oxide as the light rare earth metals do with extended exposure to air at room temperature, but it does tarnish so that within a period of weeks its original silvery metallic appearance is replaced by a darkened surface. At high temperatures >400°C gadolinium oxidizes more rapidly, exhibiting both linear and parabolic behaviors (1-4). A method of electropolishing has been developed at the Ames Laboratory (5) which produces a shiny surface on gadolinium which remains untarnished for years at 20°C. Auger electron spectroscopy was used in combination with ion beam sputtering to investigate the surface composition of electropolished gadolinium. We have been unable to find any Auger depth profiles of the native oxide of gadolinium in the literature. However, Farber and Braun (6) did investigate the effects of oxygen exposure up to 380 Langmuir (1L = 10⁻⁶ Torr-sec) on sputter-etched gadolinium.

A 1g sample was prepared from a batch of gadolinium metal which had the following impurities (all given in atomic parts per million): oxygen 2650, hydrogen 934, nitrogen 420, carbon 288, aluminum 8, silicon 8, chlorine 4, phosphorus 4, thorium <3, tantalum 2, copper 1, and zirconium 1. All other elements were below one ppm atomic. This sample was cut into two pieces with a low speed diamond saw. One piece was simply rinsed in acetone and no further treatment was done before its surface was analyzed. We call this the as-cut sample. The other piece was electropolished in a 6% perchloric acid solution in methanol held at -78°C and then rinsed in acetone.

The surface composition was analyzed by Auger electron spectroscopy in combination with ion beam sputtering to produce depth profiles. The Auger spectrometer utilized a Physical Electronics Incorporated Model 10-155 single pass cylindrical mirror analyzer with a coaxial electron gun. The electron beam had an energy of 3.0 keV with a total current of 10 μA into a spot size of about 50 microns and made an angle of 60° with the surface normal. The ion beam, which was produced by a 3M Minibeam I ion gun, was parallel to the sample normal and consisted of 2.5 keV Ar⁺ ions at a current of 50 nA. The ion beam spot size was approximately 0.3 mm in diameter and it was rastered over a 2 × 2 mm² area. The vacuum chamber, with a base pressure of 5 × 10⁻¹⁰ Torr, was backfilled to 7 × 10⁻⁵ Torr argon gas during the Auger depth profiles.

Figure 1 shows an Auger depth profile of the as-cut gadolinium sample through the native oxide. This profile was taken within a few days after the surface was exposed by the diamond saw and it still retained its high metallic luster. The data shown in Fig. 1 are the peak-to-peak amplitudes of the first derivative spectrum of the Gd(138), O(510), Cl(181), and C(272)

Auger transitions plotted vs. sputtering time. There is a very thin, low coverage chlorine layer at the very top of the sample surface (near zero sputter time) followed by a thicker carbon layer and then by the native oxide layer. We estimate the native oxide layer to be 200Å thick. The oscillations in the Gd(138) signal for sputter times longer than 25 min are reproducible and represent lineshape changes that occur as one proceeds through the oxide layer.

Figure 2 shows an Auger depth profile of the electropolished gadolinium sample taken under the same experimental conditions as those used for the as-cut sample. The major difference between the two samples is the presence of a high density of chlorine in the layer on the very top surface of the electropolished sample. We estimate that this chlorine bearing layer is 10Å thick and represents tens of percent of the surface composition at its maximum concentration. The

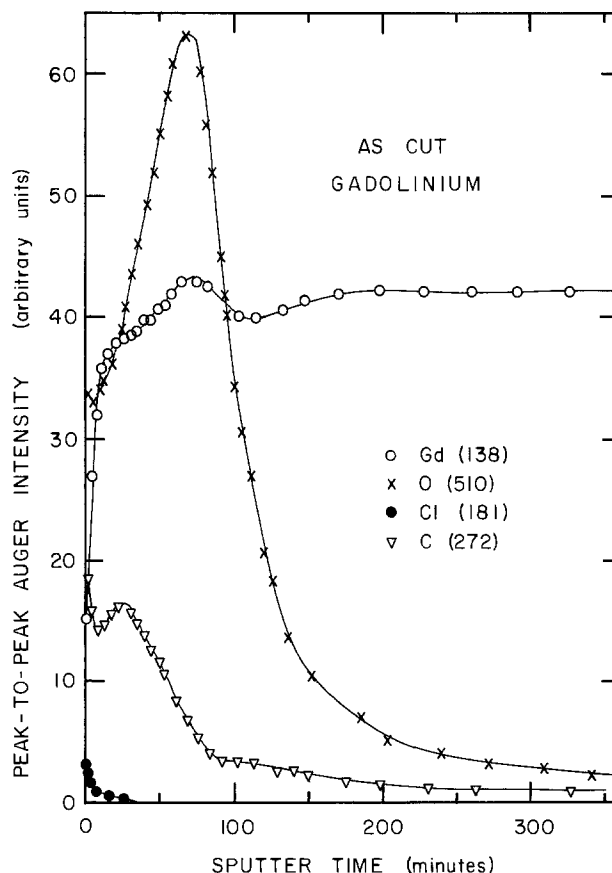


Fig. 1. Auger depth profile of the as-cut gadolinium sample

Key words: metals, electropolishing, AES.

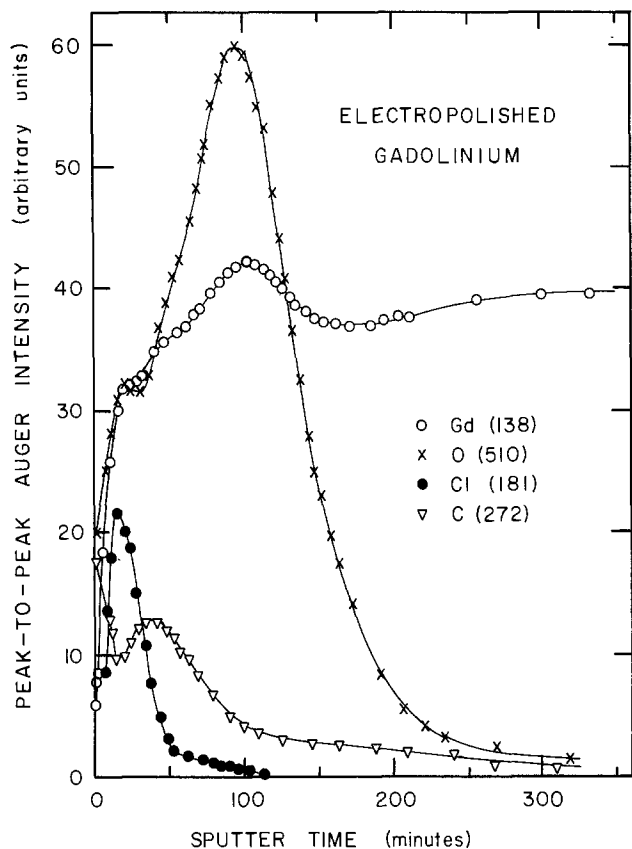


Fig. 2. Auger depth profile of the electropolished gadolinium sample with the chlorine bearing film occurring on top of the native oxide layer.

carbon and oxygen signals are nearly identical in both samples.

Both of these samples were Auger depth profiled again 22 months after their initial exposure to air. The electropolished sample had retained its high metallic luster (except at the site of the original ion bombarded area) while the surface of the as-cut sample had acquired a darkened surface coloration. Little change was found in the surface composition of the unsputtered electropolished sample. Specifically, the

thickness and compositions of the chlorine, carbon, and oxygen layers remained the same. On the other hand the as-cut sample exhibited an oxide layer that was five times thicker than that originally observed for this sample.

The results of this investigation permits the following conclusions. The tarnishing of the as-cut gadolinium is due to a slow but progressive oxidation of its surface. Electropolishing in the chilled methanol-perchloric bath suppressed this continuous air oxidation by forming a passivating chlorine bearing layer on top of the native oxide. This passivating layer is probably a gadolinium oxychloride phase. Although only a few monolayers thick this passivating film is continuous and stable for at least two years under air exposure. Finally, it is concluded that the methanol-perchloric electropolishing provides a viable technique for preventing continuous oxidation of gadolinium and should provide a useful procedure for those investigating the optical properties of gadolinium.

Acknowledgment

Ames Laboratory is operated for the U.S. Department of Energy by Iowa State University under contract No. W-7405-ENG-82. This research was supported by the Director of Energy Research, Office of Basic Energy Sciences, WPAS-KC-02-01 and WPAS-KC-02-02.

Manuscript submitted April 8, 1980; revised manuscript received ca. June 30, 1980.

Any discussion of this paper will appear in a Discussion Section to be published in the June 1981 JOURNAL. All discussions for the June 1981 Discussion Section should be submitted by Feb. 1, 1981.

Publication costs of this article were assisted by Ames Laboratory.

REFERENCES

1. B. Love and E. V. Kleber, *Mater. Design Eng.*, **52**, 134 (1960).
2. S. A. Dsouza, H. B. Mathur, and A. B. Biswas, *Ind. J. Chem.*, **2**, 307 (1964).
3. W. L. Phillips, Jr., *J. Less-Common Metals*, **7**, 139 (1964).
4. J. Brett and L. Seigle, *ibid.*, **10**, 22 (1966).
5. D. T. Peterson and E. N. Hopkins, "Electropolishing of Rare Earth Metals," IS-1036, Iowa State University, Ames Laboratory, Ames, Iowa (1964).
6. W. Farber and P. Braun, *Surf. Sci.*, **41**, 195 (1974).

Density Determination and Analysis of Porous Anodic Aluminum Surfaces Using MeV Ion Beams

D. G. Simons, C. R. Crowe, M. D. Brown, H. DeJarnette,* D. J. Land, and J. G. Brennan

Naval Surface Weapons Center, White Oak, Silver Spring, Maryland 20910

ABSTRACT

Densities of porous anodic aluminum oxide coatings have been measured to range from 1.1 to 2.2 g/cm³, values approximately 0.3-0.6 times those of bulk Al₂O₃. These measurements are obtained by using two independent techniques for determining film parameters, Rutherford backscatter (RBS) of MeV protons and alpha particles and optical or scanning Auger microscopy. The former gives areal densities in units of g/cm² and the latter two thicknesses in units of cm. Additional information on the composition of the films studied using ion-induced x-ray analysis simultaneously with RBS is: (i) the compositions are mainly Al₂O₃ with small amounts of SO₃ or CrO₃ for those anodic layers grown in H₂SO₄ or H₂CrO₄ electrolytes, respectively; (ii) sulfur is present as a contaminant in layers grown in H₂CrO₄ electrolytes; (iii) there is a reduction in the concentration of the alloying elements in anodized films grown on 7075 T-73 Al; (iv) atoms from the cathode are deposited on the film surfaces during anodization; (v) chlorine is present throughout the surface of alumina samples severely corroded in NaCl solutions.

The need to improve the corrosion resistance of aluminum parts and components is particularly important to naval applications in light of the corrosive salt-laden air and saltwater environments which are regularly encountered. The application of alumina coatings by anodization is one of the standard methods by which corrosion protection is provided. However, corrosion still occurs! Thus, there is a need to understand the corrosion process more fully in order to develop methods which may extend material lifetimes and reliability. In support of our metallurgical studies we have initiated a program of ion-beam analysis to investigate the composition and structure of anodized Al layers before and after exposure to corrosive salt environments. This investigation concentrates on the analysis of the composition of porous anodic oxide coatings which are obtained from chromic and sulfuric acid electrolytes. Although these coatings are softer and more porous than barrier-type anodic oxide films, they can be grown considerably thicker, and they can be sealed for added corrosion protection. These two characteristics have made them more desirable for naval applications.

Several ion beam and electron beam techniques are available for materials surface layer analysis. We have selected Rutherford backscattering spectroscopy (RBS) and positive ion-induced x-ray (PIX) techniques for this study. RBS allows in-depth profiling of relatively thick surface layers in which the stoichiometry for several material constituents are determined. Simultaneous PIX measurements permit specific elemental identification of high and middle atomic weight components in the film when RBS cannot uniquely determine the scattering atom because of limited mass resolution. This elemental identification is thus made on the same sample area used in the RBS analysis. In addition, trace element analysis is determined from the intensities in the x-ray spectra. Both techniques are nondestructive to the extent that removal of target matter by sputtering is negligible although areas the size of the beam diameter receive radiation damage.

Other techniques which are often used for surface analysis are secondary ion mass spectroscopy (SIMS), scanning Auger microscopy (SAM), scanning electron microscopy (SEM), and transmission electron micros-

copy (TEM). SIMS and SAM depend on the removal of target material by sputtering and hence destroy the target. They are often unreliable for the analysis of thick insulating targets such as the alumina layers studied here. In this case the charging of the insulating layer during sputtering can cause uncertainties in the measurement of the secondary ions emitted from the target. In addition, other uncertainties arise from the possibility of preferential sputtering rates from the components of a composite target, enhanced diffusion of the oxygen at the sputter site, or surface reoxidation during sputtering. SEM analyses are limited to thin surface layers while TEM techniques are limited to the study of thin self-supporting films. Moreover, TEM requires target destruction to produce specimens for study. The x-ray analysis associated with SEM (EDAX) has poor depth resolution. This drawback is also true for PIX, but EDAX is not as sensitive for trace element analysis as PIX because of the larger bremsstrahlung backgrounds encountered with electron beams.

Ion beam analysis has been used by various groups to study the growth of anodic films and the anodization process. RBS studies have been directed mainly to the determination of mobilities of ion implanted species during the anodization process (1-3). Investigations have also been made using SIMS to study the effects of ions in the growth of oxide layers (4). Those studies had been conducted mainly on thin anodic layers with areal densities of less than 0.05 mg/cm². The anodic films studied for this report had areal densities from 0.2 to 0.5 mg/cm².

The principal and unexpected result of this study has been the determination of film densities which are substantially less than previously reported. Whereas most density measurements are made from independent measurements of mass and volume, other techniques can be used. Independent measurements can be made of the areal density (units of g/cm²) and thickness (units of cm) of the anodic oxide films. The density is then determined by dividing the former by the latter. In RBS measurements areal densities are determined directly from the energy difference of positive ions scattered from the front and back surfaces of a thin film and from the stopping power [units of energy/(g/cm²)] for the projectile in the target material. The stopping power for the projectile in the anodized film is obtained from Bragg's

* Electrochemical Society Active Member.

Key words: corrosion, anodization, Rutherford backscatter, aluminum, anodization density.

rule by which energy loss is determined from the weighted average of the stopping power of the compound constituents. Since for high velocity protons this rule is valid to about 1% (5), differences between the stopping powers as determined for Al_2O_3 and an anodic film composed of the same proportions of Al and O are negligible. Independent measurements of film thicknesses are obtained directly from optical, SEM, or SAM techniques. The film densities obtained in this manner are approximately 0.3–0.6 times the density of bulk Al_2O_3 and are lower than densities of porous anodic oxide films reported by others (6, 7). This lower density is not consistent with the 15% porosity of the films grown.

Although information concerning chemical binding and composition is not obtainable in the ion beam analysis techniques used here, we are able to obtain general information on the stoichiometry of the anodic films. Results for the atomic composition of the films including pickup of the anions from the electrolyte, the reduction of the alloying elements of the bulk Al, and the presence of surface impurities from both the electrolyte and the cathode are reported.

Experimental Approach

Ion beams from NAVSWC's 2.5 MV Van de Graaff accelerator were used for the materials analysis. The backscatter spectra were obtained using both incident protons and ^4He ions. The protons have the advantage that their lower stopping power allows the analysis of thicker samples and in the targets studied here more clearly marks the interface between the anodic layer and the bulk Al. Helium has the advantage of better mass resolution for making stoichiometric determinations at the surface. The incident particles were collimated through 1.0 mm apertures and passed through an annular surface barrier detector which detected the particles after being scattered through 178.4° . In addition to the Rutherford backscattering measurements, the x-rays produced by these beams were simultaneously analyzed. The x-rays were detected by an Si(Li) x-ray detector with a 196 eV resolution of an ^{55}Fe source. It was mounted at 90° to the beam direction. The x-rays were collimated with a 2.5 mm aperture placed directly in front of the 25 μm Be detector window. In order to reduce the intensity of the low energy x-rays from the Al a 100 μm polyethylene absorber was placed in front of the window. The use of this absorber allows greater sensitivity for trace element analysis of elements with atomic number greater than Al but a considerably lower sensitivity for elements with atomic number less than Al. Both the backscatter spectra and the x-ray spectra were recorded simultaneously on a multichannel analyzer.

Anodic samples were prepared from both 7075 T-73 commercial Al and Marz grade (99.9995% pure) Al. In preparation for anodization all samples were polished mechanically with 600 grit SiC. They were then washed and rinsed in acetone or alcohol, etched for 30 sec in Keller's etch ($\text{HF} + \text{HNO}_3 + \text{HCl}$), and finally washed in deionized water. The anodization conditions given in Table I produce films which are approximately 2 μm thick with a porosity of approximately 15% (8).

Thickness measurements were obtained using three methods, optical, SEM, and SAM. Although these measurements destroy the specimen, it was possible to

Table I. Anodization conditions to produce $\sim 2 \mu\text{m}$ films. The anodic films were grown on 7075 T-73 and 99.9995% pure Al

Sample	Electrolyte	Voltage (VDC)	Time (min)	Current density (A/m^2)	Cathode
7075Al	H_2SO_4	13.5	4	130	Stainless steel
7075Al	H_2CrO_4	40	55	130	Pb
Pure Al	H_2CrO_4	40	55	130	Pb
Pure Al	H_2CrO_4	40	55	130	Pt

correlate the thickness obtained with these methods using samples prepared under identical conditions. The optical and SEM thickness measurements were made from an edgewise cross section of the anodized layer. The sectioning was done by carefully sawing the sample perpendicular to the surface with a slow speed cutoff wheel. The samples were then mounted in a room temperature curing epoxy containing alumina particles and polished metallographically for edge retention. The film thicknesses from the SAM measurements were obtained by knowing the sputter rate in A/min and the elapsed time at which a sharp increase in the Al concentration occurred. This increase is due to the increased Al concentration at the alumina/aluminum interface. The film thicknesses in both methods are measured in units of length.

Results and Discussion

A typical energy spectrum of 1.0 MeV protons scattered from pure Al anodized in H_2CrO_4 electrolytes is shown in Fig. 1. The position of the front surface of the anodized layer and the Al_2O_3 -Al interface can be identified from the energies of the protons scattered from both the aluminum and the oxygen. These energies are indicated in Fig. 1. Computer analyses by Niiler (9) were made on this spectrum and on a spectrum obtained from the same target with ^4He projectiles. Using a computer program by which film parameters are varied to reproduce the measured spectra, he obtained good fits to the data for a film 0.34 mg/cm^2 thick. The Bragg rule was used to determine the stopping power. The thickness measured optically with a microscope at $800\times$ magnification is 2.3 μm . The average film density must be 1.5 g/cm^3 for these two measurements to be consistent. This value is considerably lower than the density of bulk Al_2O_3 (3.5–3.9 g/cm^3) and the densities of alumina layers measured by others. Similar RBS studies by Bauer and Muskett (3) on anodic films produced in an aqueous solution of CP ammonium nitrate show that 48.4 $\mu\text{g}/\text{cm}^2$ films have a thickness of 1300 A . The resulting density of 3.72 g/cm^2 agrees with the bulk values. However, the film thus produced is a barrier-type film which is expected to be more dense than the porous films studied here.

Similarly, we determined densities of other films using proton RBS coupled with optical, SEM, or SAM measurements on the same alumina layers. The alumina films were made from 99.9995% pure or 7075

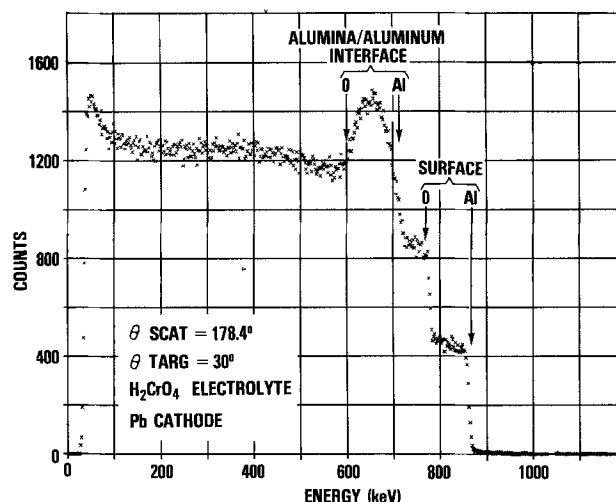


Fig. 1. Energy spectrum of 1.0 MeV protons RBS from 99.9995% pure Al anodized at 40 VDC in an H_2CrO_4 electrolyte for 55 min. Features due to scattering from O and Al at the front surface and at the alumina/aluminum interface are identified. The areal density is determined from the energy difference from scattering from the O or the Al at the front surface and at the interface and from proton stopping powers in Al_2O_3 .

T-73 Al anodized in H_2CrO_4 or H_2SO_4 electrolytes. The results of the density measurements are given in Table II. The densities range from 1.1 to 2.2 g/cm^3 . In those cases using 7075 Al two samples were made under similar conditions of current density, voltage, electrolyte concentration, electrolyte temperature, and target preparation (see Table I). One was then sealed in boiling water for 10-20 min. The densities of the sealed films are lower than those of their companion unsealed films although the differences obtained for those prepared in the H_2CrO_4 electrolyte are within the experimental error. The densities obtained for those samples whose thickness is determined optically and by SEM are more accurate than those for which SAM was used. We estimate an error in thickness of about 15% for the optical measurements and about 20% for SAM. For the measurement of the areal density using RBS we use the Bragg rule to obtain the proton stopping power for Al_2O_3 in which the stopping powers for aluminum and oxygen are given by Andersen and Ziegler (10). The resulting stopping powers are accurate to within 10%. Thick target calculations as described by Foti *et al.* (11) were followed. The determination of the energy differences for protons scattered from the front and back surfaces of the alumina films are also accurate to approximately 10%. The densities of the alumina layers as obtained from the RBS/optical combination have an error of 20% while those using the RBS/SAM combination have a 25% error. We determined these errors by accumulation in quadrature. The RBS measurements were made at three proton energies; 1.0, 1.2, and 1.4 MeV. The targets at three different tilt angles to the incident beam; 0°, 30°, and 45°. The film thickness for individual targets was found to be the same within experimental error for all angles and beam energies. Since the film thickness scales with angle, the pore size must play an insignificant role in these measurements.

An advantage of the ion beam studies described here is that they quickly yield a variety of information which ordinarily may require separate measurements to obtain. Thus, in addition to the average film densities, information concerning the surface stoichiometry and the presence and qualitative distribution of trace elements is obtained. To determine surface stoichiometry RBS spectra using 4He ions are used since better mass resolution and more accurate scattering cross sections are available. Typical spectra from 2 MeV 4He scattered from alumina layers produced from anodized pure Al in an H_2CrO_4 electrolyte are shown in Fig. 2. A Pb cathode was used during anodization. From the features of these spectra O, Al, S, Cr, and probably As can be readily identified to be on the surface of the samples. In addition traces of a high-Z material are seen, probably Pb from the cathode. The surface composition of the constituents of these samples was obtained using standard calculational tech-

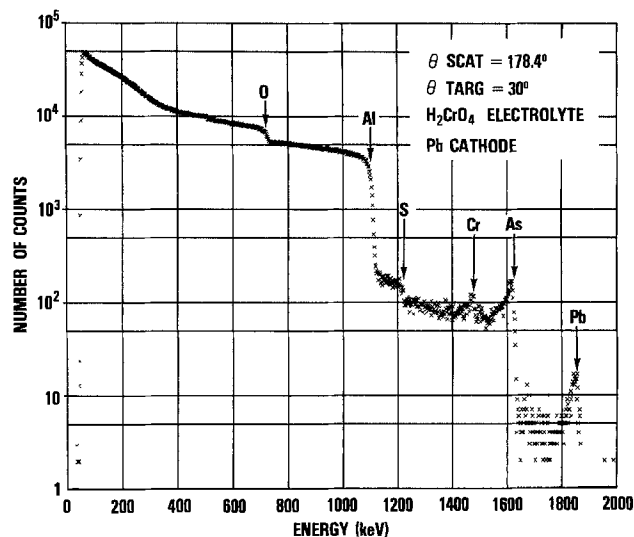


Fig. 2. Energy spectrum of 2.0 MeV 4He RBS from 99.9995% pure Al anodized in an H_2CrO_4 electrolyte. The identified elements appear at the front surface. The sample was anodized with a Pb cathode.

niques with Rutherford scattering cross sections and He stopping powers of Ziegler (12). The atomic fractions determined from these spectra along with those for other samples which will be discussed below are given in Table III. The computer analysis of Niiler (9) indicates that the Cr distribution is approximately uniform throughout the alumina film. The As and Pb appear as thin layers on the surface; their thickness is difficult to determine since the energy width is within the resolution of the detection system. Similar results are obtained for the films anodized in an H_2CrO_4 electrolyte using a Pt cathode instead of a Pb cathode.

The x-ray spectra obtained from this target by 1.2 MeV protons is shown in Fig. 3. This spectrum confirms that the feature which was attributed to As in the RBS spectra is indeed As, in addition to corroborating the existence of Al, S, and Cr in the target. The x-ray spectra from the films made with a Pt cathode also show x-rays from trace amounts P and Cl; the origin of these impurities is not known.

The anodized 7075 Al samples were corroded potentiostatically in 3.5 weight percent NaCl solutions. In those cases in which a small amount of corrosion occurred as indicated by the potentiostatic measurements, there was no appreciable change in the backscatter spectra. At this early stage of corrosion it is not possible to determine the corrosion site from the RBS spectra. The x-ray spectra, however, show the addition of Cl to the system. In the case of extreme corrosion, as observed visually by deep pits into the anodized layer, the uptake of Cl into the surface is

Table II. Summary of targets, areal densities, and thickness measurements for determination of film densities. The areal densities are obtained from RBS measurements. Samples joined by a bracket were prepared under identical conditions with one sealed in boiling water

Sample	Electrolyte	Sealed ^a	Areal density (mg/cm ²)	Thickness (μm)	Density (g/cm ³)
99.9995% Al ^b	H_2CrO_4	No	0.34	2.3 (SEM/optical)	1.5
99.9995% Al ^c	H_2CrO_4	No	0.21	1.3 (SEM/optical)	1.6
{ 7075T-73 Al }	H_2SO_4	No	0.33	1.5 (SAM) ^d	2.2
{ 7075T-73 Al }	H_2SO_4	Yes	0.35	2.6 (SAM)	1.4
{ 7075T-73 Al }	H_2CrO_4	No	0.39	2.7 (SAM) ^e	1.4
{ 7075T-73 Al }	H_2CrO_4	Yes	0.47	3.8 (SAM)	1.2
{ 7075T-73 Al }	H_2CrO_4	No	0.36	2.9 (SAM)	1.2
{ 7075T-73 Al }	H_2CrO_4	Yes	0.31	2.7 (SAM)	1.1

^a Targets were sealed in boiling water for 10-20 min.

^b Pb cathode.

^c Pt cathode.

^d Thickness in agreement with optical measurement on companion sample.

^e Thickness in agreement with growth rate vs. current density curve.

Table III. Surface composition of representative samples analyzed by ^4He RBS. Values are given in atomic fractions

Element	Al_2O_3	H_2CrO_4 electrolyte				H_2SO_4 electrolyte	
		99.9995% pure aluminum Pb cathode	99.9995% pure aluminum Pt cathode	7075 T-73	7075 T-73 corroded	7075 T-73	7075 T-73 corroded
O	0.604	0.624	0.635	0.627	0.683	0.616	0.456
Al	0.396	0.366	0.358	0.358	0.211	0.342	0.508
Cr	—	3.3×10^{-3}	3.6×10^{-3}	1.1×10^{-2}	—	—	—
Zn	—	—	—	3.1×10^{-3}	3.2×10^{-3}	3.0×10^{-3}	1.4×10^{-2}
S	—	5.1×10^{-3}	2.6×10^{-4}	—	—	3.9×10^{-3}	2.1×10^{-2}
As	—	2.4×10^{-3}	3.0×10^{-4}	—	—	—	—
Pb	—	6.2×10^{-5}	—	—	—	—	—
Pt	—	—	2.6×10^{-5}	—	—	—	—
Cl	—	—	—	—	0.102	—	—

quite apparent both from the RBS spectra and the x-ray spectra as shown in Fig. 4 and 5, respectively. The proton RBS spectrum of these heavily corroded samples no longer shows the existence of a thin alumina layer on a bulk aluminum substrate. Instead, the appearance is that of a bulk target containing O, C, Al, Cl, and the alloying additives of 7075 Al. All of these constituents appear to be uniformly distributed with regard to depth into the target.

Conclusions

The density of various porous aluminum films has been measured with values ranging from 1.1 to 2.2 g/cm^3 . These values are based on a combination of film thickness determinations using RBS with optical or SAM measurements. The densities obtained in this study are substantially lower than those which are based on Archimedes Principle. For instance, in studies by Mason (6) the mass and volume of alumina films are obtained from differences of mass and volume measurements made of alumina films on their aluminum substrates and from the aluminum substrates after the films had been stripped off. These measurements thus based on Archimedes Principle are obtained from the ratio of numbers each of which is a small difference of large numbers. The measurements reported here are made more directly from the alumina films *in situ*. Since the beam diameter of 1.0 mm is considerably larger than the size of the pores in these samples, the densities measured are averaged over many cell diameters. The thickness obtained by the RBS measurements scale with target angle with respect to the incident beam; hence the layers cannot have large porosity. The films studied here have approximately 15% porosity (8). Thus, it is concluded that the lower densities reported here are not accounted for by the porous nature of the films. The errors in the density which were de-

termined from the optical thickness is about 20% while the errors for those determined from the SAM thickness was larger (approximately 25%) due to reduced accuracies in the SAM measurement.

The surface compositions of representative samples analyzed by ^4He RBS are given in Table III. The values of the ratio of the atomic fraction of O to Al are greater than the expected value of 1.5 for Al_2O_3 . Our measurements on thin evaporated Al_2O_3 samples yield the proper ratio of O:Al. Thus, there is a larger fraction of oxygen in the anodized layers than expected from

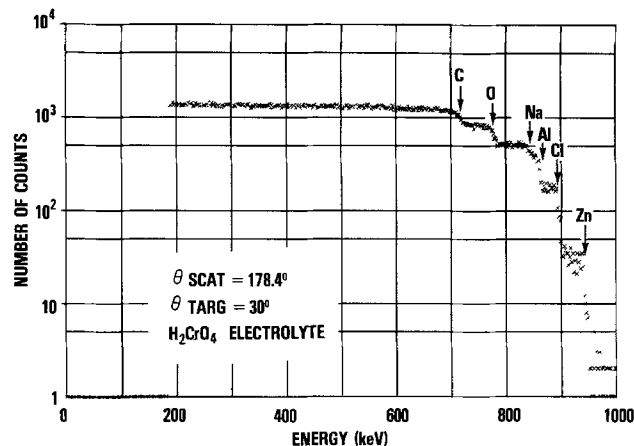


Fig. 4. Energy spectrum of 1.0 MeV protons RBS from anodized 7075 Al which had been heavily corroded in a 3.0 w/o NaCl solution. The identified elements appear at the target surface and are apparently distributed uniformly into the target to depths comparable to the proton range.

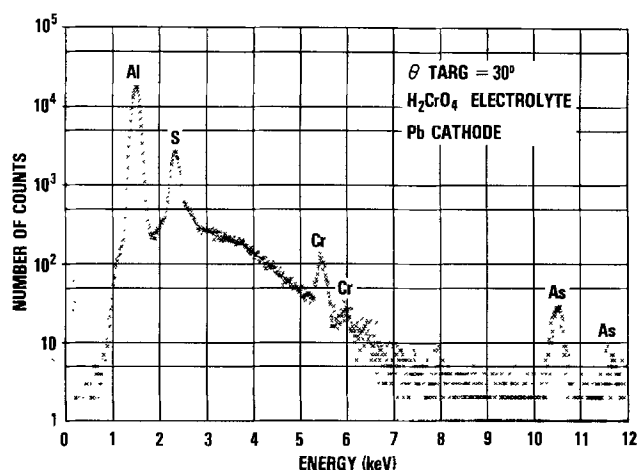


Fig. 3. X-ray spectrum induced by 1.2 MeV protons from pure Al anodized in an H_2CrO_4 electrolyte. The sample is the same one as shown in Fig. 2.

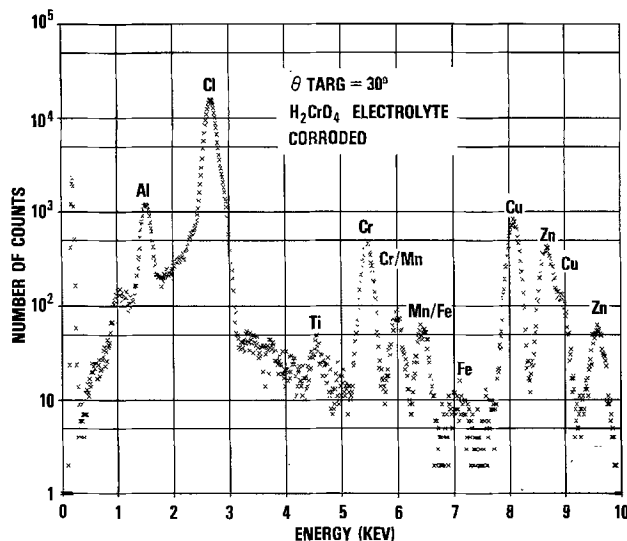


Fig. 5. X-ray spectrum induced by 1.0 MeV protons on the same target as shown in Fig. 4.

pure Al_2O_3 . Sulfur and chromium are also picked up into the alumina layers from their respective electrolytes. Their depth distribution appears to be uniform throughout the alumina layer. This result is in general agreement with those found by other methods (13). The amount of oxygen in excess of that needed to form Al_2O_3 is in the proper proportion for combination with the S (or Cr) in the films in the form of SO_3 (or CrO_3) anions. The films are thus composed mainly of Al_2O_3 with the addition of SO_3 (or CrO_3) anions from the electrolyte. This result is in agreement with those found by other methods (13). Additional conclusions on the composition of these films obtained from this analysis are: (i) There is a reduction of the atomic fraction of the alloying additives in the anodic layers by a factor of 5-10 as compared with those in the bulk aluminum. This value is obtained from the backscattering measurements on the concentration of the Zn additive and x-ray measurements which show that the relative x-ray production between the Zn and the other additives is the same in the alumina layers as in 7075 aluminum. This study does not indicate whether these additives are transported into the electrolyte or into the bulk aluminum during the growth of the oxide layer. From the ion implantation studies of Mackintosh *et al.* (1) and Towler *et al.* (2), it is more likely that they accumulate at the alumina/aluminum interface with some fraction being transported across the barrier interface as the layer growth continues. This model qualitatively accounts for a lower atomic fraction in the alumina layer.

(ii) The alumina layers also contain S which is present primarily when Pb (and to a lesser extent Pt) cathodes are used with H_2CrO_4 electrolytes. The atomic fraction is less by an order of magnitude from that when H_2SO_4 electrolytes are used.

(iii) Lead or platinum atoms from their respective cathodes are also transported to the anode surface (see Table III). The mechanism of transport for both S and the cathode atoms is not clear from this study.

(iv) Chlorine is picked up into the alumina layer after it has been corroded potentiostatically in an NaCl solution. In the cases of light corrosion (invisible to the eye), the addition of Cl is only apparent from the x-ray measurements, and it is not possible to determine its location from the RBS measurements. However, in the case of extreme corrosion, the structure of the alumina layer appears to be destroyed and Cl (10 atomic percent in the sample illustrated in Table III) is seen to extend from the surface of the corroded sample into the bulk Al. The proton RBS spectra indicate the removal of the alumina layer from the surface of the aluminum substrate and the incorporation of Cl into the aluminum to depths which are beyond the RBS analysis of protons (approximately 2-3 μm).

Acknowledgments

The authors would like to express their thanks to F. Rider for his work in preparing the anodized samples and to P. Cady for his assistance in taking the data. We are particularly thankful to Dr. A. Niiler, Army Ballistic Research Laboratory, for his computer calculations on the RBS spectra. The SAM measurements were made at the Naval Weapons Support Center, Crane, Indiana. This work was supported in part by the Naval Surface Weapons Center under the Independent Research Program and in part by NAVAIR Project No. SF54592.

Manuscript submitted March 10, 1980; revised manuscript received *ca.* July 15, 1980.

Any discussion of this paper will appear in a Discussion Section to be published in the June 1981 JOURNAL. All discussions for the June 1981 Discussion Section should be submitted by Feb. 1, 1981.

Publication costs of this article were assisted by the Naval Surface Weapons Center.

REFERENCES

1. W. D. Mackintosh, F. Brown, and H. H. Platner, *This Journal*, **121**, 1281 (1974); *ibid.*, **124**, 1168 (1977); F. Brown and W. D. Mackintosh, *ibid.*, **120**, 1096 (1973).
2. C. Towler, R. A. Collins, and G. Dearnaley, *J. Vac. Sci. Technol.*, **12**, 520 (1975).
3. W. Bauer and R. G. Muskett, *J. Appl. Phys.*, **44**, 2606 (1973).
4. M. F. Abd Rabbo, J. A. Richardson, G. C. Wood, and C. K. Jackson, *Corros. Sci.*, **16**, 677 (1976); M. F. Abd Rabbo, J. A. Richardson, and G. C. Wood, *ibid.*, **16**, 689 (1976).
5. W. K. Chu, J. W. Mayer, and M. A. Nicolet, "Backscattering Spectrometry," p. 44, Academic Press, New York (1978).
6. R. B. Mason, *Metal Finishing*, **55** (Aug. 1957).
7. C. Bürgers, A. Classen, and J. Zernicke, *Z. Phys.*, **74**, 593 (1932).
8. L. A. Cosgrove, *J. Phys. Chem.*, **60**, 385 (1956); G. Paloini, M. Masoero, F. Facchi, and M. Paganelli, *This Journal*, **112**, 32 (1965).
9. A. Niiler, Private communications.
10. H. H. Andersen and J. F. Ziegler, "Hydrogen, Stopping Powers and Ranges in All Elements," Pergamon Press, New York (1977).
11. G. Foti, J. W. Mayer, and E. Rimini, "Ion Beam Handbook for Material Analysis," J. W. Mayer and E. Rimini, Editors, p. 22, Academic Press, New York (1977).
12. J. F. Ziegler, "Helium, Stopping Powers and Ranges in all Elements," Pergamon Press, New York (1977).
13. G. C. Wood, V. J. J. Marson, and B. W. Lambert, *Nature*, **199**, 239 (1963); H. Ginsberg and K. Wofers, *Metall (Berlin)*, **17**, 202 (1963); R. C. Plumb, *This Journal*, **105**, 498 (1958).

The Chemical Nature of Aluminum Corrosion

III. The Dissolution Mechanism of Aluminum Oxide and Aluminum Powder in Various Electrolytes

T. H. Nguyen and R. T. Foley*

Department of Chemistry, The American University, Washington, D.C. 20016

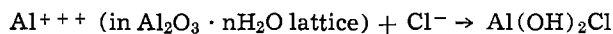
ABSTRACT

Attention was focused on the first steps in the pitting process, the adsorption of aggressive anions and the dissolution of aluminum oxide. The adsorption of chloride on alumina and aluminum powder are quite similar and show a saturation plateau at high chloride concentration; the amount of chloride adsorbed is proportional to the weight of alumina. The amount of "free" aluminum ions dissolved from alumina is inversely proportional to the chloride concentration while the amount dissolved from aluminum powder appears to be independent of chloride concentration. Nitrate ion is reduced by aluminum metal but not by alumina. Alumina will greatly reduce the amount of "free" aluminum in solutions of AlCl_3 , $\text{Al}(\text{NO}_3)_3$, and $\text{Al}_2(\text{SO}_4)_3$. These results support the idea that the first steps in aluminum pitting in aggressive solutions involve adsorption of the anion on the oxide film followed by chemical interaction to form a soluble species resulting in a thinning of the film and direct contact with the metal surface.

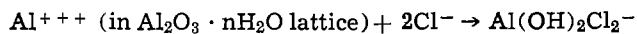
It is universally accepted that the exceptional corrosion resistance of aluminum depends to a great extent on the oxide film which is formed on its surface (1). When a fresh aluminum surface is exposed to air, it oxidizes rapidly (2), and, as a result, a compact, adherent protective film of aluminum oxide (alumina) is formed. In aqueous solutions, surface layers, which for the greater part consist of crystalline hydrates of alumina, are developed (3). Aluminum oxide is relatively inert chemically, and it is on this inactivity that the passive behavior of aluminum depends (4). If the oxide film dissolves, the metal corrodes uniformly and Lorking and Mayne (5, 6) have shown that corrosion was associated with the initial rate of solution of the anhydrous oxide. On the other hand, when the film is damaged under conditions that prevent normal self-repairing, localized corrosion ensues (7).

Pitting is one type of localized corrosion which appears on a metal surface that otherwise shows a very low dissolution rate. Its importance in the corrosion of aluminum, in particular, has been manifested by a number of investigations by various workers on this subject (8-10). Several explanations or theories have been proposed for the breakdown of the passive film (11, 12). However, there is not as yet a unanimously recognized explanation with respect to the mechanism by which an oxide film loses its protective character.

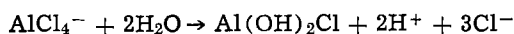
It has been postulated (13) that the initiation of pitting of aluminum in halide solutions proceeds in four consecutive steps, (i) the adsorption of the aggressive anion on the oxide film; (ii) the chemical reaction of the adsorbed anion with the Al^{+++} in the oxide lattice



or



the lower stoichiometric number (one or two) applicable to neutral solution; (iii) the thinning of the oxide film by dissolution; (iv) the direct attack of the exposed metal by the aggressive anion with the formation of transient complexes which rapidly undergo hydrolysis



* Electrochemical Society Active Member.
Key words: corrosion, films, oxidation.

In this mechanism the chemical properties of aluminum oxide proper, as distinguished from oxide-covered aluminum, assume major significance in the overall aluminum pitting reaction. The purpose of the present work is to investigate the reactivity of aluminum oxide toward an aggressive environment and compare it to the behavior of purified aluminum powder subjected to the same treatment.

Experimental

Adsorption-type alumina (Fisher A-540, Chromatographic grade α - Al_2O_3 , 80-200 mesh) and purified aluminum powder (Apache Chemical, 0093) were used throughout this work. Solutions were prepared with water doubly distilled from a quartz still and salts of reagent grade.

In a typical experiment, 100 ml of a salt solution was mixed with 10g of alumina or aluminum powder in a 150 ml flask. The mixture was shaken several times at constant intervals and then allowed to stand and settle for a fixed time (16 hr). The supernatant liquid was then filtered and analyzed for the presence of aluminum ions in solution. The quantitative analysis of aluminum ions was done spectrophotometrically with Eriochrome Cyanine-R as a dye reagent at the wavelength of 530 nm (14). This method is accurate to better than 6% in the absence of iron or manganese and the sensitivity is up to 1 μg per 50 cm^3 of solution. The concentration of chloride anions before and after adsorption was determined by the Mohr method with sodium dichromate as an indicator. At 25°C the sensitivity of 4 $\times 10^{-5}\text{N}$ silver is equal to the indicator blank. This corresponds to an excess of 0.08 ml of 0.1N silver nitrate in the titration of 100 ml of 0.1N NaCl or to an error of 0.08%. In our titration, an amount of 0.1 ml is subtracted from the volume of AgNO_3 read on the burette in order to account for the indicator correction. The reported concentration of chloride adsorbed is an average value of three different sets of NaCl solution. It is observed that the difference in the amount of chloride adsorbed between two different runs is around 10%.

Results and Discussion

Adsorption isotherm of chloride.—The uptake of chloride as a function of solution concentration is shown in Fig. 1. The plot in Fig. 2 shows that the amount of chloride adsorbed from a solution of 1N

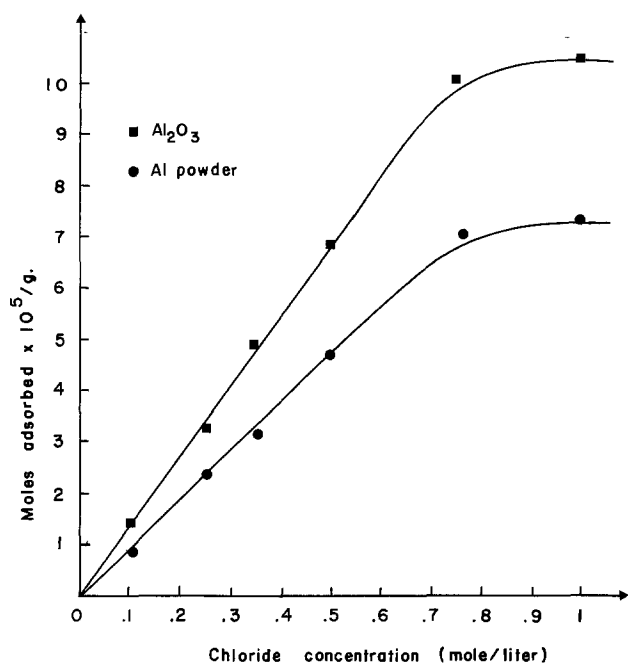


Fig. 1. Adsorption isotherm ($24^\circ \pm 1^\circ\text{C}$) of chloride on alumina, ■, on purified aluminum powder ●.

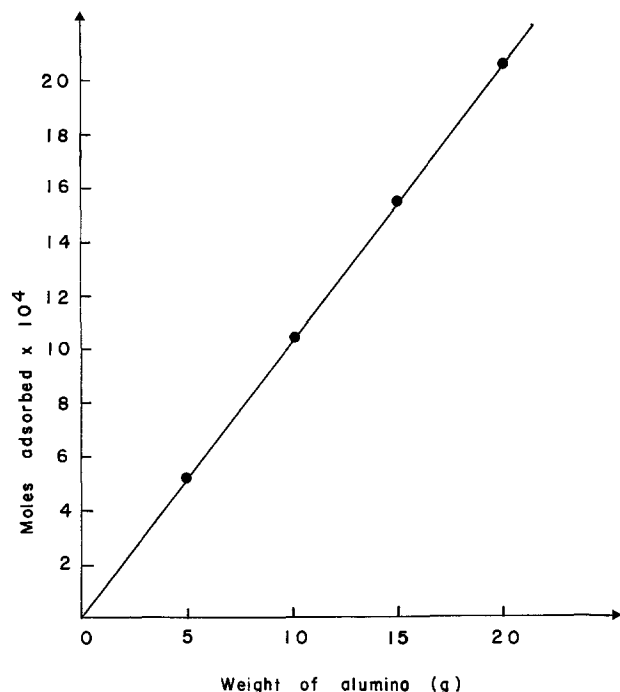


Fig. 2. Adsorption of chloride as a function of weight of alumina ($24^\circ \pm 1^\circ\text{C}$).

NaCl varies linearly with the weight of alumina present. It can be seen that the adsorption isotherm of chloride on aluminum oxide and on aluminum powder are quite similar. At low concentration adsorption is linear with concentration and, at high concentration, reaches a plateau on which adsorption is independent of concentration. These adsorption isotherms resemble characteristic Langmuir type isotherms but the mechanism must be different from that encountered in conventional chemisorption experiments involving ions on solid substrates which yield monolayers. First, is the question of available surface area. The "surface area" of the alumina or aluminum powder has no significance in the conventional sense, as established, for instance,

by a BET measurement. In contact with an aqueous solution the powder will hydrolyze to give a number of equilibrium and nonequilibrium species. These systems have been studied in some depth by Smith (15) who classifies the types of aluminum species as follows: Al^a as monomeric species, Al⁺⁺⁺, Al(OH)⁺⁺, Al(OH)₂⁺, and Al(OH)₄⁻; Al^b as polynuclear material containing 20-100 Al atoms; Al^c as large, solid Al(OH)₃ particles.

Thus, the "surface" of the powder must be seen as a dynamic, reacting system. An individual particle would very rapidly lose its original shape and surface area. The second important difference is the achievement of equilibrium. It has been established (15) that true equilibrium in these aluminum oxide systems is only achieved after several months or several years. The time frame in which we are working is that of a typical corrosion experiment that covers a few days or weeks. This means that the plateaus in Fig. 1 represent an approximate steady-state condition in which the particle interface is saturated with the product of the reaction between adsorbed chloride and aluminum oxide.

The initial surface charge on alumina is positive as shown by electrophoresis measurements and flocculation by a negatively-charged gold sol (15). The point of zero charge or the isoelectric point is about 8.9-9.2 and seems to be independent of the type of alumina in the absence of some drastic prior treatment being given the compound (16, 17). Table I shows the pH change of the solution before and after adsorption. The final pH in the chloride solution containing alumina is very close to the reported isoelectric point for alumina. The pH of the chloride solution in contact with the aluminum powder is approximately 8.0 independent of the chloride concentration. In the absence of chloride the pH is higher; approximately 10, but potentials of zero charge this high have been observed before and assumed to be caused by the adsorption of monomeric species (Al^a-type).

Solubility of aluminum oxide and purified aluminum powder.—The concentration of dissolved aluminum ions in solution from alumina and aluminum powder in the presence of different aggressive aqueous environments is reported in Table II and III. This analysis measures "free" aluminum, i.e., such species as Al⁺⁺⁺, Al(OH)⁺⁺, and Al(OH)₂⁺, but not aluminum tied up as a complex polymer with unit structure [Al(OH)₂Cl]. The concentration of such aluminum in H₂O solution is highest in the absence of electrolyte.

Table I. pH values of different test solutions before and after adsorption

Solution	Initial pH	Final pH in Al ₂ O ₃	Final pH in Al powder
0.1N NaCl	6.5	9.1	8.0
0.5N NaCl	5.9	8.9	8.0
1.0N NaCl	6.0	8.8	7.8
1.0N Na ₂ SO ₄	6.2	9.7	7.7
1.0N NaNO ₃	6.7	8.9	12.3
1N NaCl + 0.01N AlCl ₃	4.1	7.4	4.5
1N NaCl + 0.01N Al(NO ₃) ₃	4.1	7.8	4.5
H ₂ O	6.9	10.3	9.8

Table II. Amount of aluminum ions dissolved in 100 ml of different NaCl concentration solutions

Concentration of NaCl	Aluminum powder (10g)	Alumina (10g)
1.00N	41 ± 2 μg	231 ± 14 μg
0.75N	54 ± 3 μg	258 ± 15 μg
0.50N	65 ± 4 μg	322 ± 19 μg
0.35N	54 ± 3 μg	358 ± 21 μg
0.25N	54 ± 3 μg	433 ± 28 μg
0.10N	67 ± 4 μg	476 ± 28 μg

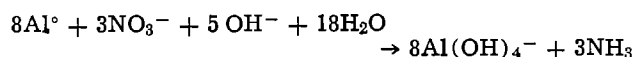
Table III. Amount of aluminum ions dissolved in 100 cm³ of different salt solutions

Solution	Al powder (10g)	Alumina (10g)
H ₂ O	247 ± 15 μg	1245 ± 74 μg
1N NaNO ₃	NH ₃ formation	230 ± 14 μg
1N Na ₂ SO ₄	169 ± 10 μg	308 ± 18 μg
1N NaCl + 0.01N AlCl ₃ (8.28 mg Al ³⁺)	14.00 ± 0.84 mg	329 ± 20 μg
1N NaCl + 0.01N Al(NO ₃) ₃ (8.30 mg Al ³⁺)	8.75 ± 0.52 mg	540 ± 32 μg
1N NaCl + 0.02N Al ₂ (SO ₄) ₃ (16.85 mg Al ³⁺)	19.16 ± 1.15 mg	211 ± 12 μg

At different concentrations of NaCl it is found that the apparent solubility of aluminum ions from alumina decreases with increasing concentration of NaCl. On the other hand the concentration of aluminum ion in solution from aluminum powder does not seem to follow any particular pattern and is practically the same regardless of the concentration of NaCl present. In the presence of water, aluminum oxide will undergo hydration and when chloride anions are available, the positive surface charge will attract chloride to form a soluble complex of the type Al(OH)₂Cl₂⁻ (18). With increasing chloride concentration the amount of chloride adsorbed increases. On the other hand, with increasing chloride concentration, the amount of "free" aluminum ion decreases. This suggests that the hydroxy-chloride species formed is a relatively stable species and probably remains attracted to the aluminum oxide lattice. This interaction is much more pronounced in the mixture with aluminum powder because of a possible reaction with the underlying aluminum metal.

Nitrate reaction.—Sodium nitrate has a surprising effect on aluminum powder. When a solution of NaNO₃ is brought in contact with aluminum powder, the formation of ammonia can be recognized after 16 hr. Upon shaking the suspension vigorously, the formation of NH₃ is quickly accelerated and within a few minutes, the heat generated by the reaction brings the whole solution to complete ebullition. Since there is no such formation of NH₃ in the case of alumina, it is concluded that NH₃ is the product of the chemical reaction between NO₃⁻ and the underlying aluminum metal.

It is known that nitrate is reduced by elemental aluminum in alkaline solution (19)



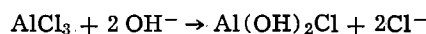
Alternately, NO₃⁻ can be reduced to NH₃ by nascent hydrogen, usually zinc and caustic soda is used (20). The reduction potential for the couple NO₃⁻/NH₄⁺ is only 0.47V (21).

In order to confirm the chemical role of the nitrate anion, a 0.5M solution of aluminum nitrate was mixed with aluminum powder. After 40 days of contact with regular shaking, there was still no perceptible odor of ammonia. However, when the mixture was shaken very vigorously for a while, the NH₃ odor became noticeable within the next day. And, after a few days, the aluminum powder was almost completely dissolved and a milky white precipitate was formed. The grinding process and perhaps even the abrasion between particles caused by the energetic stirring motion of the mixture will remove any protective film from the film surface and thus allow the reduction of NO₃⁻ by the suddenly unprotected aluminum metal. Whatever the mechanism, the reduction of NO₃⁻ to NH₃ is taken as evidence that the electrolyte is, at that point, in direct contact with the metal surface.

Adams, Foley, *et al.* (22, 23) have reported the formation of NH₃ in the accelerated corrosion of aluminum alloys 2024 and 7075 by certain mixtures of chloride and nitrate. It was concluded that the pres-

ence of Cu or Zn as alloying elements was necessary perhaps by the formation of a local alkaline cathodic site. Aluminum alloy 1199, which is essentially pure aluminum, does not exhibit the synergistic effect in which chloride promotes the dissolution of the film. Moreover, the existence of specific concentrations and anion ratios in which corrosion is accelerated is likely due to a competitive reaction between nitrate and chloride anions on the aluminum oxide leading to a formation of an inert (nitrate case) or labile (chloride case) hydrolyzed aluminum species. If the anion ratios are in favor of the formation of a labile complex, the synergistic effect will likely occur unless the nitrate anion present is too small. On the other hand, if there is a predominant formation of an inert complex at the surface to block the Cu or Zn reaction site, the synergistic effect will not be observed.

Mixtures of NaCl and aluminum salts.—The mixture of 1N NaCl with various aluminum salts has some interesting effects on the dissolution of alumina and aluminum powder. Table III shows that when a mixture of 1N NaCl and aluminum salt is in contact with alumina, the concentration of "free" aluminum ions in solution decreases considerably compared to the initial amount present. For example, the AlCl₃ solution contained 8.28 mg Al³⁺ initially in the 100 ml volume. After reaction with alumina the concentration dropped to 329 μg. Similar results were obtained with aluminum nitrate and aluminum sulfate. It was also observed that after the reaction ensued a heavy gelatinous precipitate was developed. On the other hand, the same solution in contact with aluminum powder greatly enhanced the solution of aluminum ions. The explanation for this difference in the two cases is that when aluminum salt is in contact with aluminum oxide it undergoes a hydrolysis reaction



According to Sillen (24), the nucleus Al(OH)₂Cl is the basis of the product of hydrolysis; other authors, by using Raman and NMR spectroscopy to study aqueous solutions of aluminum chlorides (25) have indicated an equilibrium between different forms of oxychlorides such as Al(OH)Cl₂, Al(OH)₂Cl, and Al₂(OH)₅Cl. Whatever the composition or structure of the product it is evident that the Al is tied up as a stable complexed species.

Conclusions

These experiments have shed some light on the first two steps in the aluminum corrosion process postulated above. They imply that the corrosive or noncorrosive state of a metal in a given environment depends on the stability of the complex species formed on the film and on the affinity of the anion present to react with the exposed metal. Nitrate is highly reactive with elemental Al to form ammonia. However, due to the ability of the complex species formed on the oxide film to remain attracted to the surface makes it behave in some cases like an inhibitor.

The ability of aluminum salts to activate the corrosion of aluminum have been reported by different authors (26, 27). This is a direct consequence of the hydrolysis of the salts by the hydroxyl from the aluminum oxide which help to accelerate the thinning process. However, it is not necessary that all aluminum salt solutions should activate the corrosion of aluminum. From step three it can be seen that it all depends on the ability of the anion to form a transient complex with the exposed metal. This is consistent with the idea that the hydrolysis reaction itself does not determine the corrosive nature of the solution (28).

As a result of this investigation, it can be concluded that the rate of dissolution or degree of passivity of a metal is directly correlated to the behavior and stability of the complex species formed, as predicted by the complex ion theory of corrosion (29).

Acknowledgment

The support of the Office of Naval Research under Contract N 00014-75-C-0799, NR 036-106, is gratefully acknowledged.

Manuscript submitted Feb. 29, 1980; revised manuscript received June 20, 1980.

Any discussion of this paper will appear in a Discussion Section to be published in the June 1981 JOURNAL. All discussions for the June 1981 Discussion Section should be submitted by Feb. 1, 1981.

Publication costs of this article were assisted by The American University.

REFERENCES

- U. R. Evans, "The Corrosion and Oxidation of Metals," p. 241, Arnold, London (1971).
- R. K. Hart, *Proc. R. Soc. London Ser. A*, **236**, 68 (1956).
- R. K. Hart, *Trans. Faraday Soc.*, **53**, 1020 (1957).
- H. P. Godard, W. P. Jepson, M. R. Bothwell, and R. L. Kane, "The Corrosion of Light Metals," John Wiley & Sons, New York (1967).
- K. F. Lorking and J. E. O. Mayne, *J. Appl. Chem.*, **11**, 170 (1961).
- K. F. Lorking and J. E. O. Mayne, *Br. Corr. J.*, **181** (1966).
- C. Edeleanu and U. R. Evans, *Trans. Faraday Soc.*, **47**, 1121 (1951).
- F. D. Bogar and R. T. Foley, *This Journal*, **119**, 462 (1972).
- Z. A. Foroulis and M. J. Thubrikar, *ibid.*, **122**, 1296 (1975).
- S. Dallek and R. T. Foley, *ibid.*, **123**, 1775 (1976).
- R. T. Foley, *Corrosion*, **26**, 58 (1970).
- J. Galvele, in Fourth International Symposium on Passivity, Airlie, Virginia, Oct. 17-21, 1977.
- T. H. Nguyen and R. T. Foley, *This Journal*, **126**, 1855 (1979).
- E. B. Sandell, "Colorimetric Determination of Traces of Metals," Interscience Publishers, Inc., New York (1950).
- R. W. Smith, Ph.D. Dissertation, Stanford University (1969).
- G. A. Parks, *Chem. Rev.*, **65**, 177 (1965).
- L. Campanella, F. Croce, and P. Mazzoni, *Oberflaeche-Surf.*, **19**, 224 (1978).
- K. Videm, Kjeller Report KR-149, Institute for Atomenergi (1974).
- W. Smith, *J. Soc. Chem. Ind.*, **22**, 132 (1903).
- P. C. L. Thorne and E. R. Roberts, "Fritz Ephraim Inorganic Chemistry," 5th ed., p. 620, Gurney and Jackson, London (1949).
- W. L. Latimer, "Oxidation Potentials," 2nd ed., p. 104, Prentice-Hall Inc., Englewood Cliffs, N.J. (1952).
- A. M. McKissick, Jr., A. A. Adams, and R. T. Foley, *This Journal*, **117**, 1459 (1970).
- A. A. Adams, K. E. Eagle, and R. T. Foley, *ibid.*, **119**, 1692 (1972).
- L. G. Sillen, *Acta. Chem. Scand.*, **8**, 299 (1954).
- A. P. Schut'ko, I. Ya. Mulik, and B. A. Geller, *Ukr. Chim. Zh.*, **42**, 993 (1976).
- T. Hagyard and J. R. Santhiapillai, *J. Appl. Chem.*, **8**, 323 (1959).
- K. Sotoudeh, T. H. Nguyen, R. T. Foley, and B. F. Brown, *Corrosion*, Submitted for publication.
- R. T. Foley, B. F. Brown, and A. H. Le, *ibid.*, Submitted for publication.
- R. T. Foley, *This Journal*, **122**, 1493 (1975).

Oxidation and Polarization Measurements on Zirconium and Zircaloy-2 in Molten Nitrite and Nitrates at 573°K

N. Ramasubramanian*

*Atomic Energy of Canada Limited, Materials Science Branch,
Chalk River Nuclear Laboratories, Chalk River, Ontario, Canada K0J 1J0*

ABSTRACT

Oxidation and polarization measurements were carried out on zirconium and Zircaloy-2 samples in molten $\text{KNO}_3\text{-NaNO}_3$, $\text{KNO}_3\text{-NaNO}_3\text{-NaNO}_2$, and NaNO_2 at 573°K. Good agreement between the rates of oxidation calculated from the weight gain and polarization data was found for zirconium and Zircaloy-2 samples in the three melts. The various steps leading to the oxide growth were identified as: (i) attainment of a highly negative immersion potential initially due to the existing thin insulating air-formed oxide film, (ii) lowering of the resistance of the oxide resulting from the growth of a doped conducting oxide film on the intermetallic and impurity precipitates and the shift in the sample potential in the anodic direction, and (iii) oxygen migration in the oxide under the driving force of the anodic shift in the potential.

Molten alkali nitrates and nitrites and their eutectics are simple and convenient media for oxidation studies on metals and alloys because (i) the oxide ion activity at temperatures $\geq 500^\circ\text{K}$ is sufficiently high and (ii) cathodic reduction of the anions occurs at potentials negative to -1V and anodic oxidation of the ions occurs at potentials positive to about 0.1V so that a potential span of at least a volt is available for polarization measurements during the oxidation.

The electroanalytical chemistry of the molten ni-

trates and nitrites has been investigated in detail recently. Such studies have been mainly concerned with the salt decomposition reactions and the effect of various additions to the melt on these reactions (1). Passivation and oxidation studies on iron, nickel, and mild steel in these melts have also been reported (2, 3). Here, the type of oxide grown was related to the reactions occurring at various potentials; but the rate of oxide growth from an independent measurement and its relation to the polarization behavior in the melt has not been explored. Unlike the oxides on the metals referred to in (2) and (3), the oxide grown

* Electrochemical Society Active Member.
Key words: fused salts, oxidation, polarization.

on zirconium and its alloys is highly resistive. Therefore, the potential applied during the polarization measurements might be expected to be mainly across the growing oxide and hence the measured currents are a consequence of charge transport in the oxide. Thus, the resistivity of the zirconia formed would also extend the available potential span to more than a volt during the polarizations.

In an earlier report, on the oxidation of Zircaloy-2 at 673° and 573°K in molten $\text{NaNO}_3\text{-NaNO}_2\text{-KNO}_3$ eutectic, an attempt was made to relate the oxidation currents obtained from the polarization data to the instantaneous oxidation rates calculated from the kinetics of weight gained (4). The results were inconclusive because of a lack of sufficient kinetic data, especially at the lower temperature of 573°K. We have, therefore, extended the investigation in the ternary nitrate-nitrite eutectic to oxidation and polarization measurements in NaNO_2 and the binary $\text{KNO}_3\text{-NaNO}_3$ eutectic. The rates of oxidation obtained from the polarization and kinetic data in the three melts are compared and related to the different reactions occurring in the melts.

Experimental

Paddle-shaped samples, with a surface area of $\approx 10 \text{ cm}^2$, were cut and prepared according to a standardized procedure of mechanical polishing followed by pickling in a bath of hydrofluoric and nitric acids. The zirconium and Zircaloy-2 samples were in the as-received (rolled and annealed) condition. The nitrates were 99.99% pure reagent grade chemicals and the nitrite was "chemically pure" at 97%. The molten salt baths, i.e., ternary eutectic $\text{NaNO}_2(40)\text{-NaNO}_3(7)\text{-KNO}_3(53)$, binary eutectic $\text{NaNO}_3(41)\text{-KNO}_3(59)$ and $\text{NaNO}_2(100)$ were made up without further purification of the chemicals; the numbers in the parentheses refer to percentages by weight.

The molten salt cell and the experimental apparatus used for current *vs.* potential measurements have been described in detail elsewhere (4). The only modification was the use of a Hewlett-Packard logarithmic converter so that semilog plots of current against voltage could be traced. Current *vs.* time transients were obtained using the pulse generator in the Universal Programmer, Model 175, supplied by Princeton Applied Research.

The kinetics of oxidation of a sample in a melt were followed. At predetermined times, the sample was polarized in the melt, withdrawn, washed, weighed, and returned to the melt for further oxidation. Oxidation and polarizations were carried out at 573°K and the polarization rate usually employed was 2 V/hr; the polarization always commenced with the cathodic forward and finished with the anodic reverse sweep. When tracing voltammograms, a rate of 15 mV/sec was used. A platinum wire fused in glass was used as a general reference electrode; its potential was frequently checked against an Ag/Ag^+ (0.07M in $\text{KNO}_3\text{-NaNO}_3$) reference electrode. All the potentials are quoted relative to this silver electrode. The oxidized samples were examined on a scanning electron microscope and characteristic x-ray energy spectra were also taken.

Results

Unalloyed zirconium.—Experiments were carried out in the binary and ternary eutectics. Hysteresis effects were observed mainly in the anodic portions of the polarization curves; therefore, the cathodic reverse and anodic forward portions in the curves were analyzed. A typical curve trace after 20 hr oxidation in the ternary melt is shown in Fig. 1. The linear anodic plateau was characteristic of all the polarizations carried out on zirconium. When the plateau was extrapolated to the rest potential, as shown by the dashed line in the figure, the equivalent amount of oxygen obtained from the current was found to be in agree-

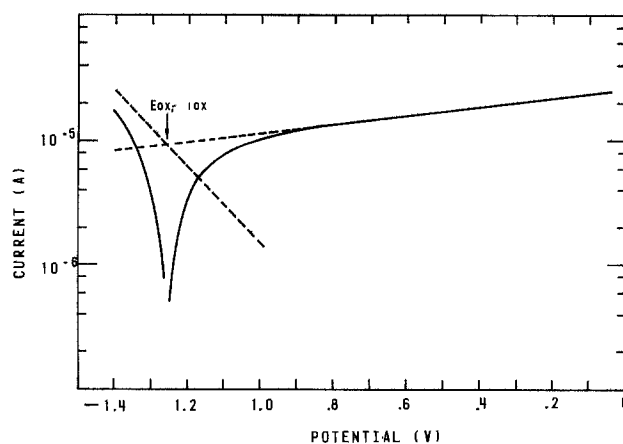


Fig. 1. Polarization curves for zirconium oxidized 20 hr and polarized in the ternary eutectic melt at 573°K; weight gain 1.2 mg/dm²; solid lines—curves obtained experimentally, dashed lines—curves obtained from analysis, E_{ox} —rest potential, and i_{ox} —oxidation current.

ment with the rate of oxidation calculated from the kinetic data. The rest potential was taken as the potential of zero current during the cathodic reverse and anodic forward sweep. This was slightly different, shifted towards anodic values, from the rest potential prior to the polarization. In Fig. 2, the oxidation rates calculated from the weight gain data are compared with the corresponding rates calculated from the oxidation currents (extrapolated currents at the rest potentials) obtained from the polarization data at various stages during the oxidation. The agreement is found to be generally good for oxidation in the binary as well as the ternary eutectics. The kinetics of oxidation also showed transitions similar to those in Fig. 2 and the oxidation of zirconium in the two melts was quite similar.

The cathodic portions obtained from analyzing the polarization curves traced, are shown in Fig. 3. When the two sets of curves are compared, a distinct difference in the rest potentials and the resistance to cath-

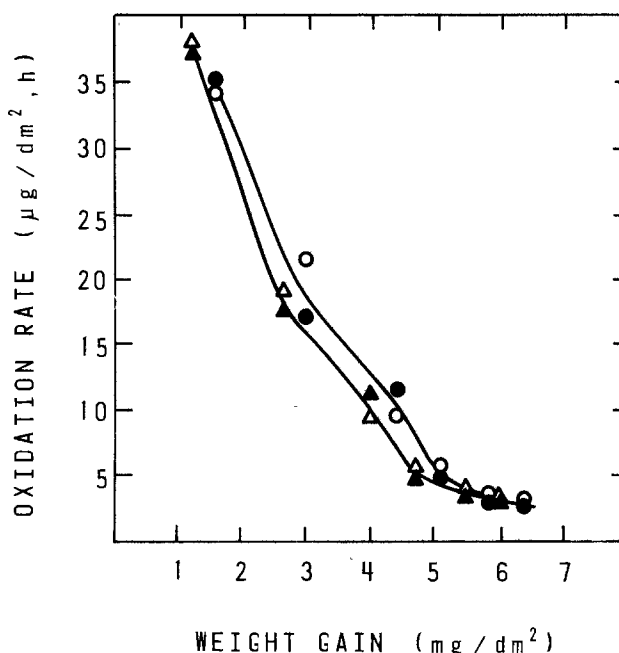


Fig. 2. Comparison of oxidation rates calculated from the kinetic and polarization data; zirconium oxidation in \circ : $\text{NaNO}_2\text{-NaNO}_3\text{-KNO}_3$ and \triangle : $\text{NaNO}_3\text{-KNO}_3$ melts at 573°K; solid symbols—kinetic and open symbols—polarization data.

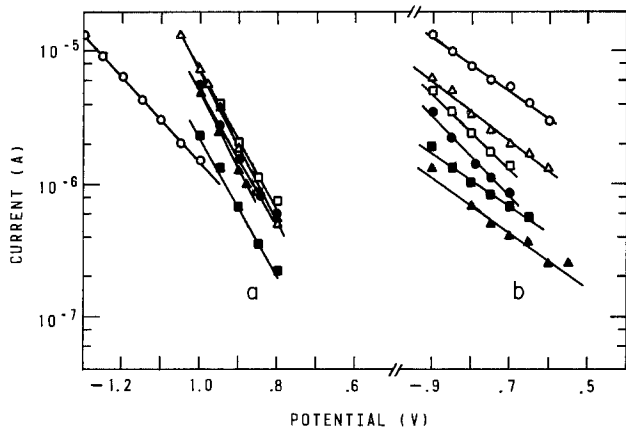


Fig. 3. Cathodic portions of the polarization curves after analysis; the corresponding weight gains are shown in Fig. 2 by the open or shaded points. Zirconium oxidized and polarized at 573°K in (a) the ternary eutectic and (b) the binary eutectic melts. Time of oxidation in hours: ○, 20; △, 86; □, 182; ●, 300; ▲, 500; and ■, 670.

odic current flow is seen; except for the curves corresponding to the 500 hr oxidation. In the case of the samples oxidized in the ternary melt the rest potential changed from -1.24 to -1.0 V initially and stayed steady at ~ -0.9 V during the rest of the oxidation; the resistance showed a decrease initially followed by a gradual increase with increasing oxidation. The rest potential stayed steady at ~ -0.85 V and the resistance increased gradually during the oxidation for samples oxidized in the binary melt.

Zircaloy-2.—Oxidation followed by polarizations were carried out in all the three melts. A typical set of polarization curves obtained in the three melts following a 24 hr oxidation is shown in Fig. 4. When compared to the curves shown in Fig. 1 for unalloyed zirconium, the anodic plateaus covered a shorter range of potentials and the rest potentials were more anodic; the curves obtained with the nitrite and ternary melts showed negative resistance regions in the cathodic portions. Such cathodic negative resistance (CNR) peaks were observed during the forward cathodic sweeps also and were present in the curves traced in both the nitrite containing melts, after various times of oxidation. The rates of oxidation calculated from the kinetic data and the corresponding rates from the oxi-

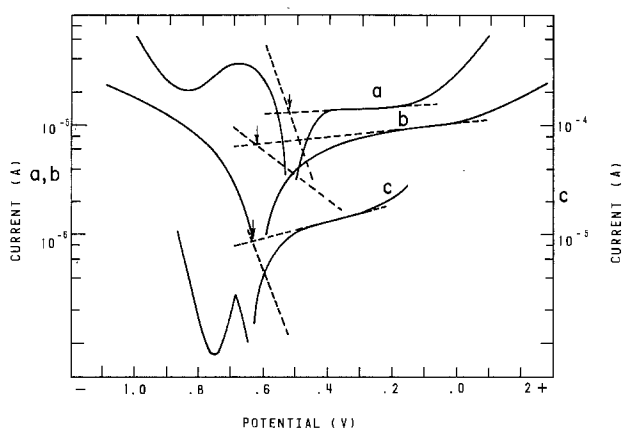


Fig. 4. Comparison of polarization curves obtained for Zircaloy-2 at 573°K in (a) NaNO_2 , (b) $\text{KNO}_3\text{-NaNO}_3$, and (c) $\text{NaNO}_2\text{-NaNO}_3\text{-KNO}_3$ following a 24 hr oxidation in the respective melt; solid lines—curves obtained experimentally and dashed lines—curves obtained from analysis. Note the curves "c" are moved down for clarity. Arrows locate the rest potentials and oxidation currents.

dation currents obtained from the polarization data are compared in Fig. 5. In each melt, the agreement between the two was quite good throughout the oxidation. The oxidation rates were different in the three melts in the initial stages but there was a tendency towards attaining a similar rate at high weight gains. In all the three melts, an increase in the oxidation rate was observed at the beginning; then the rates in the nitrite were nearly twice those in the other two melts. The amount of oxidation also varied as $\text{NaNO}_2 > \text{ternary} > \text{binary}$.

The cathodic portions of the analyzed polarization curves are shown in Fig. 6; unlike the curves shown in Fig. 3 for zirconium, the change in the resistance with increasing oxidation was small. In the case of the

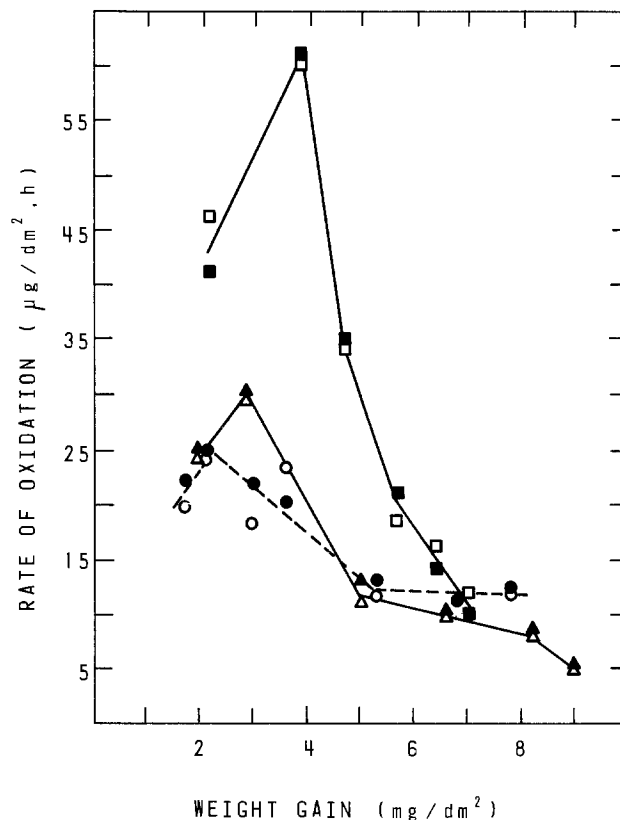


Fig. 5. Comparison of oxidation rates calculated from kinetics and polarization data. Zircaloy-2 oxidized and polarized at 573°K in: ○, ternary; △, binary; and □, sodium nitrite melts; solid symbols—kinetic and open symbols—polarization data.

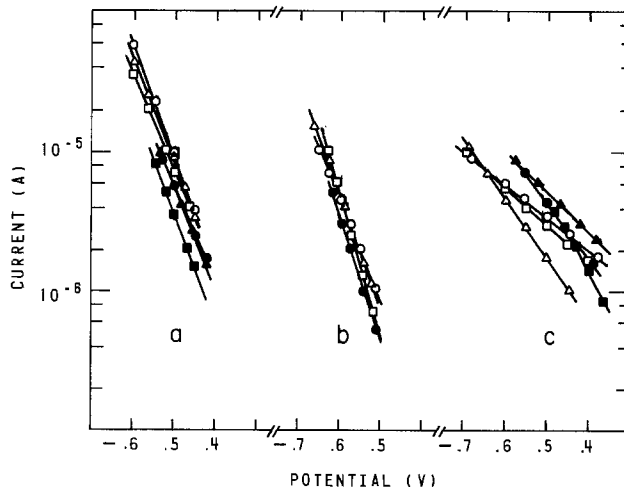


Fig. 6. Cathodic portions of the polarization curves after analysis. Zircaloy-2 is oxidized and polarized at 573°K in (a) sodium nitrite, (b) ternary, and (c) binary melts. Time of oxidation in hours: (a) ○, 24; △, 62; □, 85; ●, 135; ▲, 185; and ■, 255; (b) and (c) ○, 24; △, 72; □, 170; ●, 325; ▲, 500; and ■, 670.

samples oxidized in the nitrite and ternary melts, a slight increase in the resistance to the cathodic current flow is seen with increase in oxidation; the rest potentials have stayed nearly steady at about -0.5 and -0.6 V, respectively. A slight decrease in the resistance with increasing oxidation is noticed for samples oxidized and polarized in the binary melt; the rest potentials also showed a change from -0.65 to -0.45 V and a tendency to become steady towards the later stages of oxidation. In general, the oxides grown in the nitrite were found to be more conducting than those grown in the ternary and binary melts when their resistances to cathodic current flow were compared.

Ionic and electronic transport in growing zirconia films.—When the anodic portions of the polarization curves were plotted linearly, plateaus similar to those obtained on the semilogarithmic plots shown in Fig. 1 and 4 were obtained and the oxidation currents were also nearly identical to those from the latter curves. The immersion potentials of zirconium and Zircaloy-2 samples at the start of the oxidations varied from -1.8 V in the binary and ternary to -1.6 V in the sodium nitrite melt, and with oxidation, the rest potentials shifted in the anodic direction. Therefore, the ionic conductance of the growing oxide at any time during the oxidation was calculated from the ratio of the oxidation current, obtained from the corresponding polarization data, to the anodic shift in the rest potential relative to the immersion potential. The variation of the ionic conductivities, of the oxides grown on zirconium and Zircaloy-2, with weight gained is shown in Fig. 7. In the case of oxides grown in the binary and ternary melts on zirconium the conductivity values and their dependence on weight gain were almost the same, i.e., initially independent of weight gain with a gradual decrease to about a third of the initial value. On Zircaloy-2 the conductivities of the oxides grown in the binary and ternary melts were quite similar, whereas that of the oxide grown in the nitrite melt was two times higher than the former. The conductivities of the oxides grown on Zircaloy-2 in the three melts showed an increase initially, followed by a gradual decrease with oxide growth; a behavior similar to the variation of the oxidation rates with increasing oxidation shown in Fig. 5. There was a tendency, however, towards reaching more or less the same value at high weight gains.

During cathodic polarization, in nitrate and nitrite melts containing sodium ions, it is known that the precipitation of sodium oxide on the electrode surface inhibits the reduction reaction leading to the appearance of reduction peaks in the current-voltage curves (6, 7). When such voltammograms for a platinum wire elec-

trode in the three melts were compared, the cathodic reduction peak, located at ≈ -1.5 V, was most well defined in the ternary melt. Therefore, voltammograms were traced in the ternary melt for oxidized zirconium and Zircaloy-2 samples. A broad and well-defined reduction peak was observed at -1.4 to -1.6 V only in the case of the Zircaloy-2 samples; no systematic change in the size or the potential of the peak was observed with increasing oxidation and the voltammograms of samples oxidized in any of the three melts showed the presence of this reduction peak.

The ternary eutectic has a lower melting point than the binary and nitrite melts; therefore, current-time transients were obtained in the ternary melt on oxidized Zircaloy-2 samples at 573°K , the oxidation temperature, and at 473°K . D-C voltage pulses up to ± 30 mV relative to the rest potential and 20 sec in duration were applied and the resulting current-time transients were recorded. At 473°K the transients obtained on oxidized Zircaloy-2 samples, 8.5 cm^2 in area, were nearly identical to those on a platinum microelectrode, 0.1 cm^2 in area. At 573°K the curves for Zircaloy-2 were very different from those of platinum. On platinum the current decay was similar to that observed at 473°K , whereas on Zircaloy-2 the current decayed very slowly indicating that contributions from an ionic component were also present in the total current measured. A set of curves obtained for the platinum microelectrode and an oxidized Zircaloy-2 sample is shown in Fig. 8. From a comparison of the conducting area in oxidized Zircaloy-2 to that of platinum the density of the electronically conducting inter-

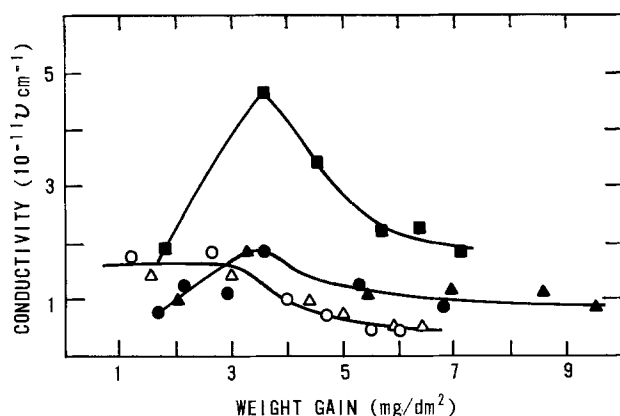


Fig. 7. Variation of ionic (oxygen ion) conductivity of zirconia films at 573°K with the weight gained during oxidation. Zirconia films grown on zirconium in \circ —ternary and \triangle —binary melts; on Zircaloy-2 in \bullet —ternary, \blacktriangle —binary, and \blacksquare —sodium nitrite melts.

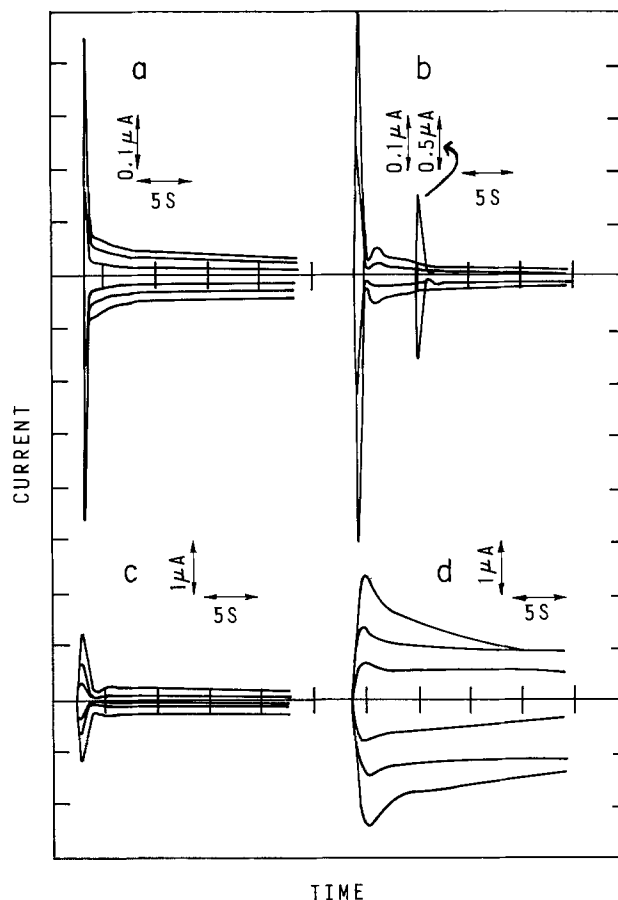
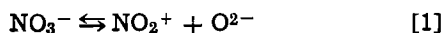


Fig. 8. Current vs. time transients obtained, on application of ± 10 , 20, and 30 mV d-c pulses 20 sec in width, for platinum 0.072 cm^2 in area and Zircaloy-2 8.5 cm^2 in area in the ternary melt. Zircaloy-2 was oxidized in the ternary melt and had a weight gain of 3.5 mg/dm^2 . Curves a and b traced at 473°K and c and d at 573°K ; curves a and c—platinum and b and d—oxidized Zircaloy-2. Note the 30 mV curves in b are shifted for clarity.

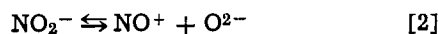
metallic precipitates in the alloy can be estimated as $1.6 \times 10^6/\text{cm}^2$, assuming an average diameter of $1 \mu\text{m}$ for the precipitates. This estimate is in good agreement with a density of $1 \times 10^6/\text{cm}^2$ obtained from optical examinations.

Discussion

Reactions in the molten salt.—In molten nitrite and nitrate the oxygen ions originate by self-dissociation according to the equilibria



and



The concentration of the oxygen ions can be calculated from the equilibrium constants; for example, at 573°K it is $\approx 10^{-12}$ mole/liter for reaction [1] (8). Marchiano and Arvia have worked out Pourbaix type potential *vs.* $p\text{O}^{2-}$ ($p\text{O}^{2-} = -\log [\text{O}^{2-}]$) diagrams for molten nitrite and nitrate (9). It is seen from these diagrams that, at such an oxygen ion concentration at 600°K , the various cathodic reactions leading to the formation of oxygen ions occur at potentials negative to -1V . The corrosion potentials during the oxidation of zirconium and its alloys were in the range of -1 to -0.4V ; therefore, cathodic reduction reactions of the nitrate and nitrite ions do not play a role in the oxidation. The oxygen ion concentration in the melts, at the oxidation temperature of 573°K used in the present study, would thus be extremely low. But the observation that the oxidation of zirconium and the alloys proceeds equally well in the three melts and the kinetics are comparable to those in other oxidizing media, indicates that the oxygen ion concentration and its mobility are not low enough to be rate limiting. The reactions leading to the oxidation of zirconium and the alloys are thus



followed by the cathodic reactions



Since the melts used in the present investigation were not extensively purified, water as a contaminant is very likely to be present; therefore, reduction of water to produce hydroxyl ions, reported to occur at $\approx -0.6\text{V}$, is another cathodic reaction to be considered in addition to reaction [5] (7).

During polarization measurements, at applied anodic potentials $\geq 0.1\text{V}$, anodic discharge of NO_2^- and OH^- is possible in addition to the reactions, discussed above, occurring during oxidation (7).

Anodic plateaus.—In the case of zirconium and Zircaloy-2 samples, anodic plateaus during the polarizations were observed throughout the period of oxidation. The currents obtained at the rest potentials corresponded to the kinetic rates derived from the weight gain data. These currents must therefore be the oxidation currents and the plateaus represent the variation of the ionic (oxygen ion) current flow, through the growing zirconia, with the applied potential. It is also implied that in the plateau region of the polarization curve, there is negligible contribution to the current from any other anodic or cathodic reaction and that the applied potential is across the growing zirconia. When compared to Zircaloy-2, the plateaus covered a wider range of potentials during polarization of oxidized zirconium. This can be attributed to the presence of intermetallic precipitates in the former, which act as electron conduction sites, as will be discussed later.

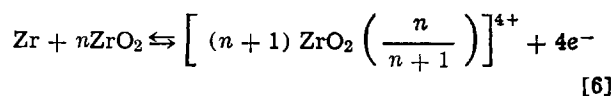
Under the conditions of temperature and oxide thickness investigated the ionic current would be expected to follow the low field approximation of the Tafel relation, and give a linear relationship with the potential (10). Anodic plateaus were indeed observed on linear current *vs.* voltage plots, though slightly

less well defined than on the semilog plots, and the oxidation currents were nearly identical to those obtained from the latter. However, for the sake of convenience and also because the other cathodic and anodic reactions (at the electron conduction sites in the oxide) obey a semilogarithmic relationship, the data are shown on semilog plots.

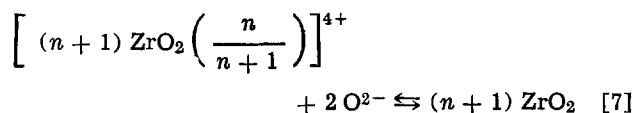
Electron conduction sites.—It has been established, from a comparison of the oxidation and polarization behavior of Zircaloy-2 in various metallurgical conditions and zirconium-tin and zirconium-iron binary alloys, that the oxidized intermetallic precipitates, mostly of zirconium and iron in Zircaloy-2, are localized high-conduction sites for electron transport during oxidation (4). This is further confirmed by the results of cathodic voltammograms and the current-time transients (Fig. 8) obtained in the present study. The inhibition by precipitated sodium oxide results in the formation of a broad peak at $\approx -1.5\text{V}$; a potential nearly the same as that observed for a number of other metals (5). The oxide on the intermetallics must therefore be a good conductor; otherwise, one would have expected this reduction peak to occur at a much more negative potential than -1.5V .

The current-time transients obtained at a temperature much lower than the oxidation temperature, where contributions from the ionic current flow through the oxide would be negligible, were nearly identical to those on platinum; another indication that the oxide grown on the intermetallics is a good electronic conductor. In the case of unalloyed zirconium, the cathodic voltammograms did not show reduction peaks; however, there is evidence for localized conduction sites (11). These are associated with impurities (*e.g.*, iron) in the material. These impurity sites are smaller in size, fewer in number, and less uniformly distributed than the intermetallic precipitates in Zircaloy-2. Thus, the intermetallic precipitates in Zircaloy-2 and impurity centers in unalloyed zirconium are the localized conduction sites for electron transport. The cathodic reduction of NO_2^+ , NO^+ , and H_2O during oxidation and polarization and in addition the anodic discharge of NO_2^- and OH^- during polarization, discussed previously, are facilitated by the electron transport at these sites. When the resistance to the cathodic current flow at these sites is compared (*e.g.*, Fig. 3 and 6) the impurity centers in zirconium are found to be more resistive than the intermetallics in Zircaloy-2. This may be due to differences in size, density, and distribution. With increasing oxidation, only slight changes in the resistance to cathodic current were observed on Zircaloy-2; occasionally, even a decrease was noticed. This may be attributed to the growth of a doped oxide, of increasing conductivity, on the intermetallic precipitates.

Mechanism of oxide growth.—A highly negative potential, $\sim -1.8\text{V}$, was attained by zirconium and Zircaloy-2 on immersion in molten alkali nitrates, nitrites, and their eutectics. The oxide growth during the first few minutes after immersion was estimated to be only about $0.2\text{--}0.4 \text{ nm}$, the higher value being in the nitrite melt. These values were obtained from extrapolations of the thin film growth in the initial stages monitored by observing the changes in the interference colors. The highly negative immersion potentials and negligibly small oxide growth on immersion indicate that the air-formed oxide film existing, prior to the oxidation in the molten salt, on all surfaces is highly resistive and remains so during the first few minutes following immersion. The reaction occurring at the metal-oxide interface is the oxidation and dissolution of zirconium in the air-formed oxide film



resulting in a positive space charge associated with the anion vacancies in the oxide and a negative charge, responsible for the immersion potential, on the metal or alloy. At the oxide-salt interface oxygen ions from the melt are incorporated into this modified air-formed oxide film, according to the reaction



This reaction reinforces the highly negative immersion potential attained by the metal or alloy. Electron flow from the latter could occur, to a small extent, by emission over the insulating zirconia barrier. Thickening of the air formed oxide film, by a few angstroms, occurs mainly by reactions [6] and [7].

The immersion potential measured may be nearly identical to $-E_a$, where E_a is the electrochemical potential associated with the anodic reaction [6] because of the condition that there is practically no oxide growth (12). The immersion potential will be, however, slightly anodic to $-E_a$ by an amount proportional to any IR drop across the oxide. Thus, the unique feature of the molten nitrates and nitrites, *viz.*, the availability of O^{2-} ions directly from the melt without recourse to a reduction step, and the high resistance of the air-formed zirconia films, enables the measurement of a potential close in value to E_a . With time of oxidation, however, the insulating oxides on the intermetallics and impurity precipitates become increasingly conducting due to doping by transition metal ions from the alloying additions or impurities. This results in a gradual lowering of the internal resistance of the cell, zirconium/Zircaloy-2-oxide-molten salt, and the rest potential shifts in the anodic direction with oxidation. The driving force for the ionic current flow through the growing zirconia is then the anodic shift in the rest potential from the initial immersion potential. Thus, the basic features are essentially the same as those proposed initially by Cox (5), *viz.*, the anodic reaction (oxygen-ion migration) occurs in the zirconia matrix and the electron transport for the cathodic reactions (which complete the oxidation) is localized at intermetallic and impurity sites.

Oxidation and polarization behavior.—During oxidation the metal or the alloy acquires a rest potential when the current due to electron transport at localized impurity or intermetallic sites is balanced by that due to the oxygen ions through the zirconia. It has been pointed out (13), and is also evident from the polarization curves reported here, that the anodic oxygen-ion current is more polarizable or less sensitive to a change in the potential than the cathodic electron current at the intermetallic sites. However, when comparing the oxidation behavior of zirconium and its alloys in a melt or different melts, the effect of a change in the rest potential and its relation to the rate of oxidation has to be considered in conjunction with the relevant resistances for ionic and electronic transport and their variation with oxide thickness. At comparable weight gains the electronic conductances of the oxides on zirconium are found to be less than those of the oxides on Zircaloy-2. Therefore, the rest potentials attained by zirconium are more negative and hence the rates of oxidation are less than those obtained for Zircaloy-2. Similarly, during polarization, because of a greater contribution to the current measured from the electron transport at the intermetallic sites, the anodic plateaus are shorter in the case of Zircaloy-2. When the oxidation of Zircaloy-2 in each of the three melts is compared, the rates in the nitrite melt are faster than those in the other two melts. This has to be related to the increased ionic conductivity of the zirconia grown in the nitrite melt because the rest potentials attained, the resistance to cathodic current flow, and the varia-

tion of these parameters with increasing oxide growth are similar in the three melts.

The reason for a higher ionic conductivity of zirconia grown in the nitrite melt is not clear. An important observation is that a large increase in the conductivity is seen when the oxide is 0.1–0.3 μm thick (1 mg/dm² weight gain \equiv 67.3 nm); therefore any mechanism proposed should also account for this dependence on the oxide thickness. The mechanism of oxide growth has been treated in detail by Cox (5). Oxygen-ions are transported mainly by a line diffusion process via the oxide crystallite boundaries and the oxide crystallites nucleate at the metal or alloy-oxide interface. Therefore, the cause for the increased ionic conductivity must originate at the oxide-salt interface. One possibility is the incorporation of impurities from the melt, in the outer layers of oxide, which inhibits the crystallite growth and imparts a high conductivity. Such impurity uptake might be dependent on the rest potential of the alloy. With increasing weight gain these outer oxide layers would form a diminishing proportion of the total oxide thickness. Therefore, an increase in the conductivity is observed in the initial stages and this is followed by a decrease at high weight gains.

The ionic conductance of zirconia was calculated from the ratio of the oxidation current to the anodic shift in the rest potential from the immersion potential because the low-field approximation, which assumes a linear relationship between the current and the potential, is expected to apply to films thicker than 0.1 μm (4). In calculating the ionic conductivities, the measured immersion potentials were used. However, there could be some minor differences between these measured values and the true values to be used due to one or more of the following reasons: (i) a depolarization caused by the thermal emission of electrons at the start of the oxidation might have lowered the immersion potential slightly; (ii) using an Ag/Ag^+ in KNO_3 - NaNO_3 as a reference electrode might have contributed to small potential differences, arising from junction potentials due to different solvents, in the nitrite melt; and (iii) during oxide growth Sn, Fe, Cr, and Ni in small quantities but varying amounts are oxidized along with Zr; these might correspond to small deviations from the immersion potential that is characteristic of pure zirconium.

Conclusions

When zirconium and Zircaloy-2 are oxidized in molten alkali nitrites, nitrates, and their eutectics, it is seen that (i) the rates of oxidation calculated from the kinetic data of weight gain are in good agreement with those calculated from the oxidation currents obtained from the polarization data; (ii) the oxides grown on the intermetallic and impurity sites are good conductors and the electron transport, completing the oxidation, occurs mainly at these sites; and (iii) the ionic (oxygen) conductivity of the zirconia grown in the nitrite melt is higher than in the other two melts. The electronic conductivity, per unit area of the samples, of the intermetallic precipitates in the alloy is higher than that of the impurity sites in the metal and the relative ease of transport of the ions and electrons determines the rest potentials. The molten nitrites and nitrates are thus convenient and suitable media for studying the mechanism of oxide growth on zirconium and Zircaloy-2.

Acknowledgments

The author gratefully acknowledges the many stimulating discussions with Dr. B. Cox and the assistance offered by Mr. V. C. Ling in sample preparation.

Manuscript submitted Dec. 3, 1979; revised manuscript received June 27, 1980.

Any discussion of this paper will appear in a Discussion Section to be published in the June 1981

JOURNAL. All discussions for the June 1981 Discussion Section should be submitted by Feb. 1, 1981.

Publication costs of this article were assisted by Atomic Energy of Canada Limited.

REFERENCES

1. K. W. Fung and G. Mamantov, in "Advances in Molten Salt Chemistry," Vol. 2, J. Braunstein, G. Mamantov, and G. P. Smith, Editors, p. 230, Plenum Press, New York (1973).
2. A. J. Arvia, J. J. Podesta, and R. C. V. Piatti, *Electrochim. Acta.*, **17**, 33 and 889 (1972).
3. A. Baraka, A. I. Abdel-Rohman, and A. A. El Mosary, *Br. Corros. J.*, **11**, 44 (1976).
4. N. Ramasubramanian, *J. Nucl. Mater.*, **55**, 134 (1975).
5. B. Cox, *ibid.*, **31**, 48 (1969), and "Advances in Corrosion Science and Technology," Vol. 5, M. G. Fontana and R. W. Staehle, Editors, p. 173, Plenum Press, New York (1976).
6. H. S. Swofford and H. A. Laitinen, *This Journal*, **110**, 814 (1963).
7. M. G. Sustersic, W. E. Triaca, and A. J. Arvia, *Electrochim. Acta*, **19**, 1 and 19 (1974).
8. R. N. Kust and F. R. Duke, *J. Am. Chem. Soc.*, **85**, 3338 (1965).
9. S. I. Marchiano and A. J. Arvia, *Electrochim. Acta*, **17**, 25 and 862 (1972).
10. L. Young, "Anodic Oxide Films," pp. 11-16, Academic Press, New York (1961).
11. N. Ramasubramanian, *This Journal*, **116**, 1237 (1969); Atomic Energy of Canada Limited Report, AECL-3082, March 1968.
12. D. H. Bradhurst, J. E. Draley, and C. J. Van Druenen, *This Journal*, **112**, 1171 (1965).
13. D. J. Norfolk, Central Electricity Generating Board, Berkeley Nuclear Laboratories, RD/B/N 4369, November 1978.

Electroplated Lead Collimator for Gamma Ray Imaging

Clinton J. Beuscher* and Christopher H. Tosswill

Galileo Electro-Optics Corporation, Sturbridge, Massachusetts 01518

ABSTRACT

A gamma-ray imaging collimator for the use in diagnostic radiology has been fabricated by applying electroplating techniques onto a glass structure. The substrates, an outgrowth of the microchannel plate technology, have a honeycomb geometry with hexagonal channels of 16 mm in length, 0.75 mm across opposing sides, and a surface area of 90×90 mm. The glass substrate was enveloped with a thin electroless nickel film followed with lead plating yielding a metal ratio of about 2:1.

The collimators to be described in this paper were prepared for the formation of gamma-photon images in the branch of radiology known as nuclear medicine. Gamma ray images are formed by photon selection in multi-channel collimators, because high energy radiation cannot be efficiently reflected or refracted. These images present the physician with two-dimensional projections of radionuclide distributions established within the patient under examination. The images are created by a collimator mounted in close proximity to an array of detectors responsive to gamma photons with wavelengths in the order of 0.1Å.

The typical collimator is a honeycomb structure with parallel walls of septa of a mass sufficient to absorb uncollimated incident photons. The assembled septa enclose a multiplicity of channels arranged in some regular pattern; the channel cross sections may be circular, square, or triangular, and in the main are chosen to simplify the task of construction. Collimator performance is measured in terms of spatial resolution, which depends upon the center-to-center dimensions of the channel structure; and of transmission efficiency, which depends upon the relative frontal areas of the septa and of the channels. The gamma-photon absorption coefficients of the elements grow very rapidly with rising atomic numbers; thus, making the ideal collimator an assemblage of very thin septa formed from one of the heaviest elements. Lead and steel collimators both have been widely used in nuclear medicine, but neither can be used with septa thinner than about 1 mm. Lead, despite its excellent absorption, is too soft, and steel is unsatisfactory because of its inferior absorption. A collimator with 1 mm septa affords an acceptable transmission level for center-to-center dimensions down to about 3 mm.

Until very recently the detector array to which the collimator was coupled took the form of a mosaic of photomultiplier tubes located behind a single massive crystal, usually of sodium iodide. The spatial resolution of this configuration was also 3 mm at best and there was obviously no great incentive to improve the collimator resolution without a matching improvement in detector resolution. This situation has now changed, because there are now in active development clinical radionuclide cameras employing semiconductor arrays, with both liquid-filled and gas-filled ionization detectors. All these new detector arrays will have intrinsic spatial resolution of the order of 1 mm, and will create a demand for collimators of at least equal performance.

Collimators with 1 mm resolution have recently been constructed by two very different techniques. In the first; a myriad of short pieces of small-bore tubing are stacked together and then cemented into a single rigid mass: although this procedure may not be practical for the assembly of full-size collimators, which require a total diameter of some tens of centimeters, successful small-area collimators have been assembled during the past year in this fashion. The second technique which the authors have developed, is based upon microchannel plate (MCP) technology, a process in which minute holes are etched through a thin glass disk.

MCP's were first developed to simplify electron fluxes in Night Vision image intensifier tubes. Glass, containing a small portion of lead was chosen to furnish the surface electrical conductivity and secondary electron emissivity necessary for electron multiplication within the channels, and fortuitously was an effective absorber of low energy x-rays and gamma-rays. Consequently, it was found that thick slabs cut from standard MCP boules could be used in some x- and gamma-ray collimator applications. To build a

* Electrochemical Society Active Member.

Key words: collimators, electroless plating, electroplated lead, microchannel plate (MCP), honeycomb structure, radiology.

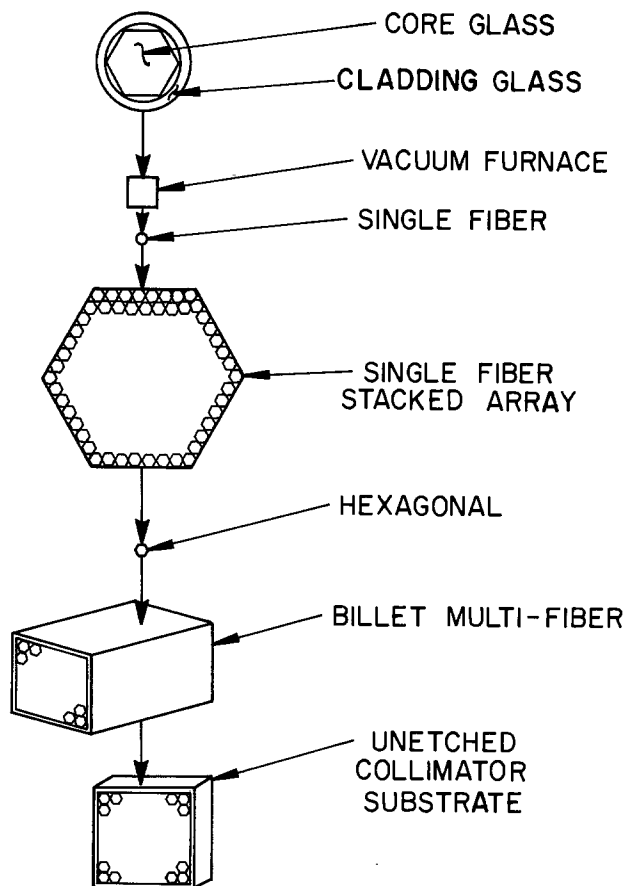
collimator which performs well across the entire clinical energy range (several hundred keV) a far higher proportion of lead, or of some other heavy element, is needed. Because the absorption process is related to the quantum levels of the inner electron shells, there are sharp discontinuities in the absorption energies and thus a lighter element may almost perform as well as a heavier one at some energy levels. In Fig. 1, tin comes close to matching lead at about 85 keV or tungsten at about 70 keV. However, tin does not span our range of interest.

Experimental

Collimator fabrication.—Collimator fabrication involves two distinctly different steps: (i) the manufacture of the glass capillary array substrate; and (ii) the metallization of the entire surface area of the substrate with a radiation absorbing layer.

The most obvious approach to obtain the collimator was to increase the lead content of the glass. Uncollimated radiation can readily pass through transparent glass, therefore, an absorbing type of glass such as Corning Glass Works 8161 (14% lead by volume; 51% lead by weight) was used. This glass can only absorb 10.2% of the radiation of an equivalent strip of lead of the same thickness. However, uncollimated stray radiation passing down the length of the glass column would be readily absorbed. Hexagonal microchannel plate geometry was selected for the matrix because of its inherently high, thin-walled strength and efficient packing density. The "staggering" of the channels aids to overcome the passage of uncollimated photons found in some collimator geometries. It is the author's belief that this approach offers a decided advantage over the previously described methods.

Microchannel plate manufacture is an outgrowth of fused fiber optic faceplate technology. A description of the various processes involved are found in the literature (2, 3). For those that are unfamiliar with this process Fig. 2 serves as an illustrative example.



HEXAGONAL DRAW

Fig. 2. Diagram of hexagonal draw

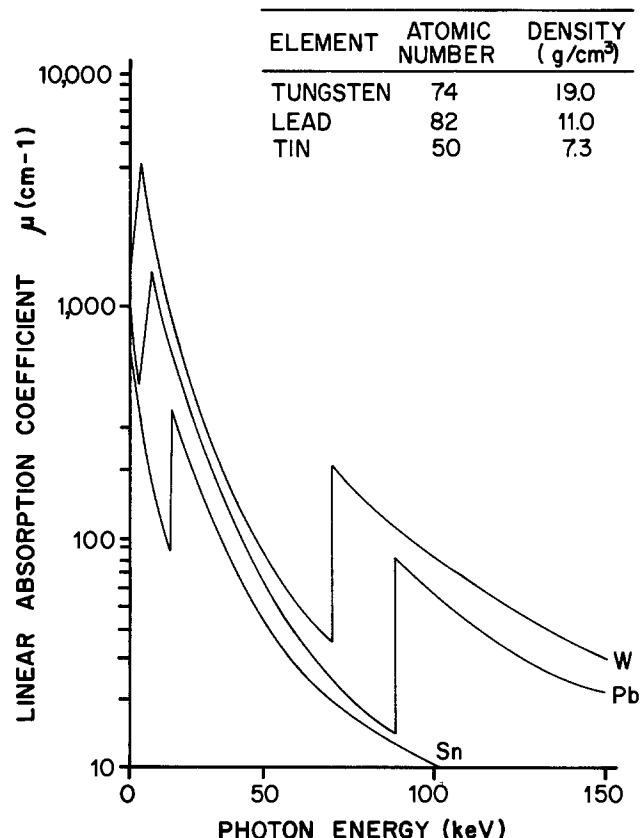


Fig. 1. Gamma photon absorption coefficients

MCP's and fiber optic plates are normally fabricated in a repetitive cycle of drawing, stacking, and fusing operations. The process begins with the passage into a drawing furnace of a single etchable glass rod within a nonetchable tube assembly. To produce the hexagonal geometry the combination is drawn through a vacuum furnace. Progressively larger numbers of smaller and smaller elements are heated and drawn down until the required dimensions are reached in the final boule. Channels less than 10 microns in diameter are readily achieved by this procedure, with dimensional uniformity of a few percent. Mosaics, thus fabricated, are wafered from the boules into slices 16 mm thick whose parallel surfaces are ground, but not polished, for good electroless plating adhesion. The substrate is etched in a 1.2M hydrochloric acid solution and dried for storage.

Electroless.—A dried glass substrate was mounted in a specially designed Teflon frame and was placed in a beaker of water and a vacuum drawn to fill the channels. The combination was then attached to the dunking unit as illustrated in Fig. 3. The variable speed unit was designed to have 8 cm of travel and a range of 2.5-60 rpm. It was found that 30 rpm produced an excellent exchange of solution through the holes and became the standard speed.

The electroless plating system was chosen over the various methods of coating nonconductors because of its excellent uniformity, high electrical conductivity, and plating solution compatibility. Shipley's CP-70 electroless copper system was initially tried. Film uniformity was satisfactory, however, adhesion to the 8161 glass was poor and peeled rather easily. The Enthone Ni-416 electroless nickel system adhered quite

TWIST-DUNK METHOD

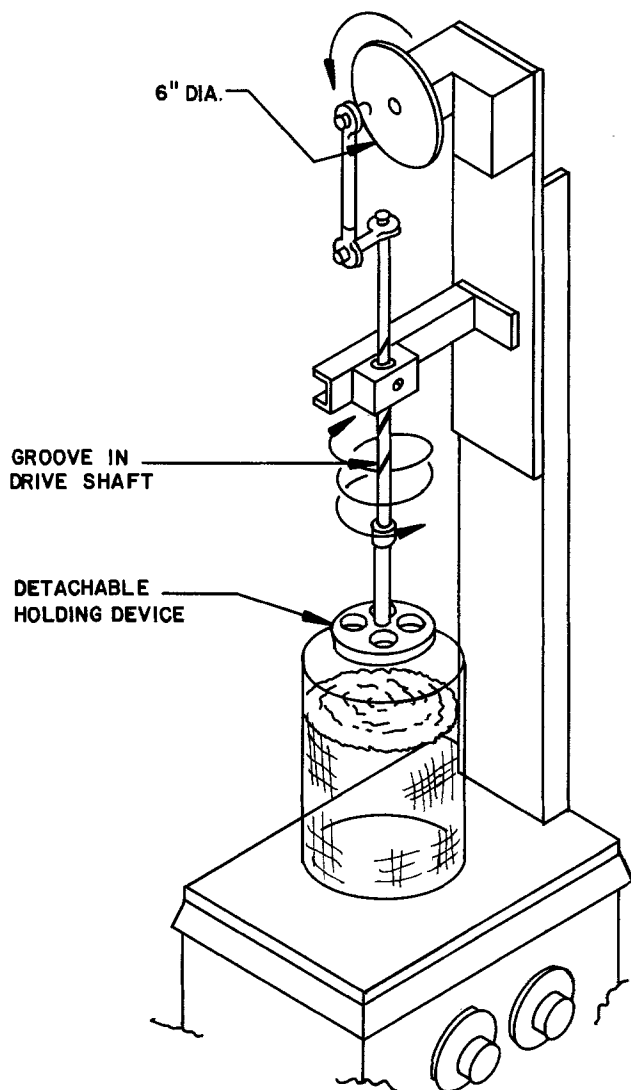


Fig. 3. Sketch of dunk-twist apparatus

well to the glass but their activators would not produce a continuous and uniform film.

A combination of the two systems gave excellent results and was used as follows:

1. Conditioner 1160 (19 parts deionized water, 1 part 1160) 3-5 min at room temperature (Shipley Company, Newton, Massachusetts).
2. Three 5 min deionized water rinses.
3. 15% hydrochloric acid (by volume) 2-3 min.
4. Catalyst 6F (2 parts deionized water, 3 parts hydrochloric acid, 1 part catalyst) 3-5 min at room temperature (Shipley Company, Newton, Massachusetts).
5. Three 5 min deionized water rinses.
6. Accelerator 19 (5 parts deionized water, 1 part catalyst) 3-5 min at room temperature (Shipley Company, Newton, Massachusetts).
7. Three 5 min deionized water rinses.
8. Electroless nickel (1 part Enthone Ni 416, 2 parts deionized water) raised to 80°C, pH 4.5-5.5. (Enthone Company, New Haven, Connecticut).

Applying these parameters, a deposit of between 5 and 8 microns of nickel was attained in 10-12 min. This was enough to provide a good conductive surface, yet not too much to interfere with absorption. The temperature of the final rinses was 80°C and the subsequent rinses were lowered in 20°C increments to prevent shock to the substrate.

Metal Absorbing Layer

In choosing a metal coating one is somewhat limited to the high *Z* numbered and high density metals. A list of the various candidates and appropriate parameters appears in Table I. All options were weighed in eliminating candidates from within this group. Cost, a major concern, eliminated gold and the noble metals. Tungsten was investigated and abandoned because of the difficulty in plating as reported by Sarojamma and Rama Char (4). Although tantalum tubes have been used to assemble small area collimators by hand it is a very difficult element to plate. Cadmium and tin, both very plateable and inexpensive were considered, but were borderline candidates for energy attenuation characteristics (range of interest being 50-140 keV). This left lead, an extremely good choice from the standpoint of energy attenuation range, plateability, and cost.

Electroplated lead has been used as a protective coating over steel, for bearings, on water pipes, for refrigeration tanks, and storage battery parts (5). Most of these coatings were on the order of 60 microns, or about half the amount anticipated for the collimator. The vast majority of lead plating work has been performed on flat or slightly curved surfaces, and, in a few cases slightly recessed surfaces. Very little lead plating effort has been directed towards channels except for a study reported by Greco (6) (in conjunction with 105 mm gun barrels).

It was apparent that the success of this undertaking might well lie in the throwing power and covering power of the lead plating bath selected. A careful review of the literature on throwing power (7-13) suggested that another exercise along this line was unnecessary. The theory has been well documented by Foulke and Kardos (14, 15).

The concerning factor of solution replenishment within the long channels was within the limits as suggested by Irvine (16). It became clear, however, that throwing and covering power were related to a number of parameters as recorded by numerous authors (17-21): (i) solution resistivity, (ii) current efficiency/current density relationship, (iii) cathode potential/current density relationship, (iv) primary and secondary current distribution. These parameters were easily adjusted by changing the tank geometry, plating bath formation, agitation, grain refiners, etc.

Seth (22) outlined 13 lead plating baths and gave compositions (acid, neutral, and alkaline) as well as comments on each. However, of these baths only the fluoborate has been universally used because of numerous advantages. The most important of these were thickness of deposit, numerous available specific grain refiners, high conductivity of solution, and ease of bath control.

Test Procedures

All of the experimental tests were run in a slightly enlarged Hull-type cell with 100% pure lead anodes. The work was performed at room temperature (22°-28°C) and the solution agitated using a magnetic stirrer. Brass tubing with various diameters (1.6, 2.5, and 4.5 mm) all cut in 16 mm lengths were used for test samples giving aspect ratios of 10.2, 6.2, and 3.5, respectively. As the throwing power was improved small sections of a round hole collimator (500 μ m diam) were used to extend the aspect ratios to 15 and 21.

A profiling system was adopted for the plated samples as shown in Fig. 4. One-half of the length of the interior of the brass tube is illustrated with one-half of the lead plate shown under the dashed line. The other half is shown with the solid line. The buildup of the plate on the ends and variation within the channel were easily discernible from the plots. The plating thickness was measured at 2 mm increments, starting at each end of the brass tube. A point 0.5 mm in from both ends was also plotted to check the "dog-bone" effect that generally occurs with

Table I. Possible elements for collimator layer

Element	Septa		Throwing power*	Plateable	Plating parameters			Usable Final candidate
	Density	Z			Control	Cost	Literature**	
Gold	19.3	79	10	Yes	Easy	Extremely expensive	+	No
Tungsten	19.0	74	2	Difficult	Difficult	Expensive	-	No
Tantalum	16.7	73	?	Difficult	Difficult	Expensive	0	No
Lead	11.0	82	4	Yes	Easy	Cheap	+	Yes
Cadmium	8.65	48	7	Yes	Easy	Moderate	+	No
Tin	7.3	50	3-6	Yes	Easy	Moderate	+	No

* Throwing power scale of 1-10 (gold being 10).

** +, an abundance of reports; -, a few reports; 0, one or two reports. Plating parameters are found in any plating manual or book on electroplating.

"in-hole" plating. In some cases the plating at the face of the sample had to be estimated because of the carry over of the plating to the exterior. For each bath, triplicate samples were run on three different test samples. The data gave us a spread from which we plotted the S/H (surface to center of hole thickness) ratio against T/D (substrate thickness to hole diameters) ratio.

A list of plating baths appears in Table II. The tin/lead bath was used to compare our data to Rothschild's (23), with the resultant curves fairly close. The amperage was lowered increasing the lead content, but no noticeable differences were observed in the throwing power. Hull cell testing was performed prior to each of the subsequent baths to provide a plating range for the best current density.

The initial test samples were the 4.5 mm tubes using baths No. 1 and No. 2 (24). Treeing and whiskering were more pronounced in bath No. 1. Periodic reverse (PR) plating was introduced and these baths were rerun, practically eliminating these faults. The efficiency cycle (25) was 78% and accounted for the small amount of treeing that appeared.

After experimenting with efficiency cycles ranging from 39 to 78% and plate to deplate time cycles of up to 4:1, a 50% efficiency cycle was established as the norm. The No. 2 bath was somewhat better in throwing power than the Sn/Pb bath, a decided increase in throwing power using the PR cycle. In baths No. 4, 5, and 6, peptone was added and the formulation altered. The results were not greatly different, although the No. 6 bath was the best of the three. The deposits were fairly fine grained and one can

see the buildup of the lead from the cross-sectioned 1.6 mm brass tube illustrated in Fig. 5.

In baths 7, 8, and 9, the peptone was replaced with Shinol LF-3 (26) along with variations in bath formulations. The No. 7 bath was made up to Harstan's specifications and yielded extremely fine grained, almost lustrous deposits. The bath exhibited excellent throwing power and displayed the narrowest spread for each of the test sample ranges. No noticeable improvement was observed in baths 8 or 9, although the latter was slightly cloudy during the test runs. Mechanical agitation was used in all baths, and the first 6 baths were filtered prior to use. In baths 7, 8, and 9, continuous filtering and agitation was used as suggested by the Harstan Company. From the test a metal ratio of 1.65:1 with a 21:1 aspect ratio was attained, and plotted with some of the other baths shown in Fig. 6. The solid lines represent our accumulated data, while the dashed lines represent the projected S/H ratio at an aspect ratio of 21:1. Our No. 2, 6, and 7 baths are shown along with Rothschild's Sn/Pb and acid gold data.¹

Collimator plating.—With the data gathered from the tests, general parameters were established to plate the collimators. A 7 liter container was used for the plating vessel. The bath was both constantly filtered and stirred, the anode/cathode distance was 10.5 cm, anode/cathode ratio was 1.5:1, and the work performed at room temperature. The hexagonal honeycomb structure with 75% open area, contains 2.5 times more sur-

¹ Reprinted with permission of The American Electroplaters Society Journal.

Table II. Lead bath formulations

Bath No.	Pb (g/liter)	HF ₄ (g/liter)	Sn (g/liter)	H ₃ BO ₃ (g/liter)	Grain refiner (g/liter)	Temp.	C.D. (A/dm ²)	Agitation	Comments
1	200	—	—	—	—	RT	0.5-2.1	Mech.	B&A formulation Treeing, whiskers
2	400	—	—	—	—	RT	0.5-2.1	Mech.	B&A formulation Better than No. 1
3	30	100	52	30	Peptone 5	RT	2.1-4.3	Mech.	Metal finishing handbook Ran at 2, 2.5, 3 A/dm ²
4	200	100	100	100	Peptone 5	RT	1-4.3	Mech. (filter)	Eliminated treeing Gray deposits Encouraging
5	200	200	—	30	Peptone 5	RT	1-6	Mech. (filter)	No treeing Dark deposits Slightly poorer than No. 4
6	100	200	—	30	Peptone 5	RT	1-6	Mech. (filter)	Better than No. 5 Light gray Fine-grained deposits
7	375	—	—	—	Shinol 20	RT	0.5-7	Mech. (filter)	Harstan formulation Smooth deposits Almost lustrous Used for collimators
8	200	100	—	20	Shinol 20	RT	0.5-9	Mech. (filter)	Our suggestion No improvement over No. 7
9	100	200	—	30	Shinol 20	RT	1-10	Mech. (filter)	No improvement Cloudy—rougher than No. 8

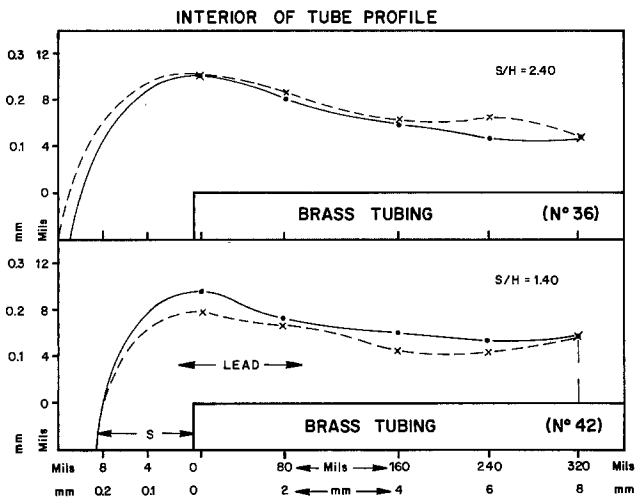


Fig. 4. Profile of plating in the tube cross section

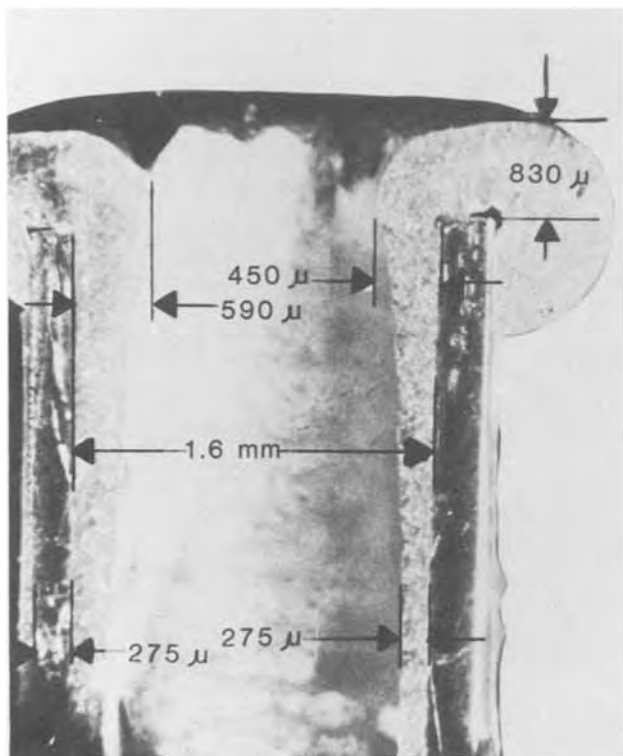


Fig. 5. Cross section of 2 mm brass tube with Sn/Pb plating

face area than the 500 μm round hole collimator samples. This structure has about 25 times greater surface area than a normal flat slice having the same exterior dimensions. The lead coating raised the mean fraction of lead within the collimator structure to approximately 50% by volume, and the performance of the collimator approached that of a homogeneous glass structure containing the same overall dimensions and fraction of lead. A calculation showed that a minimum of 5 times more lead, by weight, was needed than the total weight of the substrate materials. This afforded an easy control for our plating end point.

After the electroless nickel plate was accomplished an initial forward plate of 5 A/dm² completely enveloped the unit with lead in 30 min. The collimator was then removed and a lead plated copper "thief" was attached and a gap of 2 mm was allowed to separate the two. The substrate was then plated at an efficiency cycle of 50% using a current density of about 0.2 A/dm². The required amount of lead was deposited in about 42 hr.

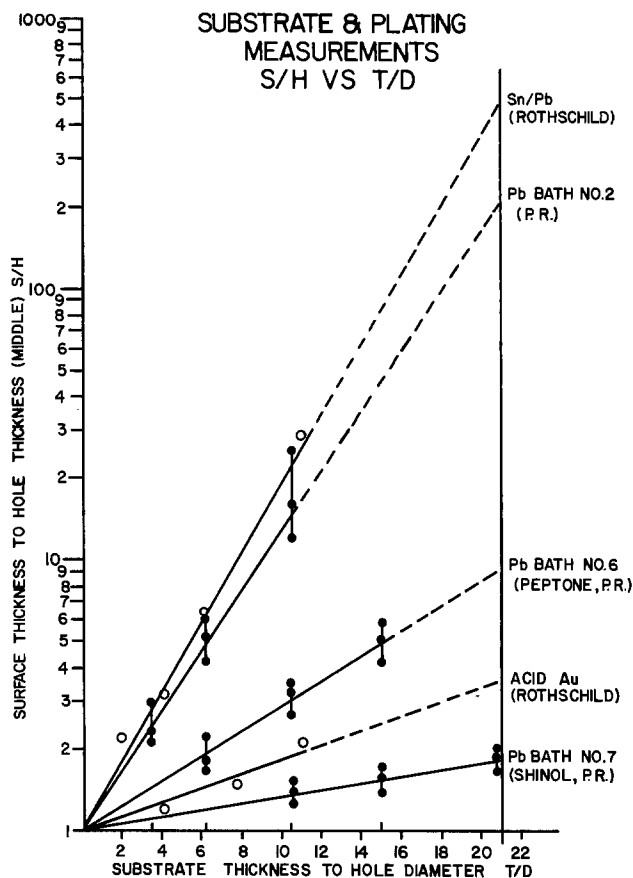


Fig. 6. Substrate thickness and plating measurements (S/H vs. T/D).

Figure 7 illustrates a transverse (perpendicular to the axis) cross section of the collimator with ideal dimensions. Figure 8 is an actual photograph of a similar cross section, the combined glass walls being about 145 μm while the metal plate is about 95-120 μm. Figure 9 shows a longitudinal (parallel to the axis) cross section, a different collimator section. Note the four plated channels visible; the channels closest to the center show the plating on the surface to be about 135 μm. The ends of the channels (on the photo) are less than half the distance to the midpoint, or about 3.25 mm long. The actual plating at the center of the channel was 105 μm for a metal ratio of 1.6:1.

A total of 8 collimators, 90 × 90 × 16 mm thick were plated, and from the best four, 75 mm squares were

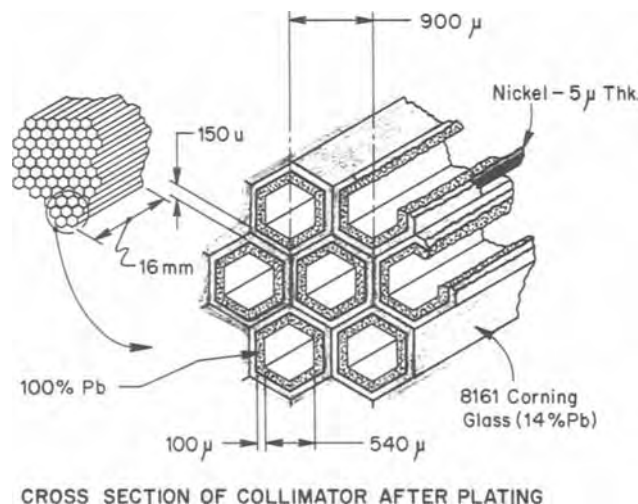


Fig. 7. Drawing of cross section of ideal collimator

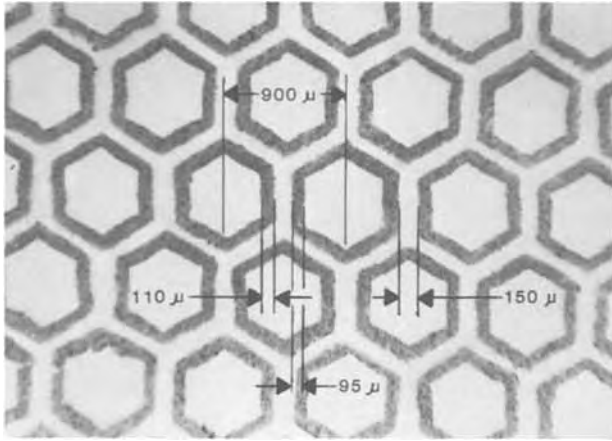


Fig. 8. Photograph of cross section of actual collimator (perpendicular to axis).

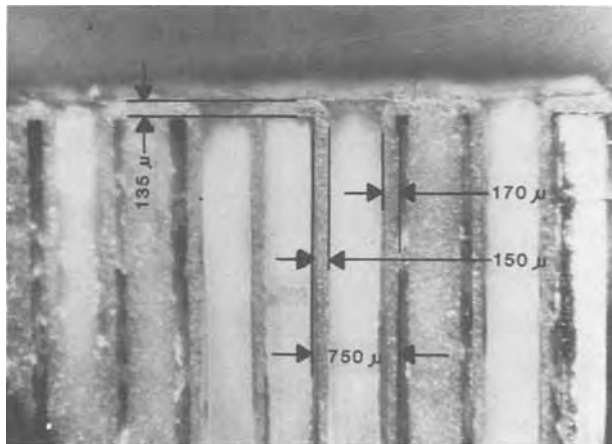


Fig. 9. Photograph of cross section of actual collimator (parallel to axis).

extracted from each. These four units had two surfaces milled square and were bonded together using an epoxy adhesive impregnated with tungsten powder 84% (by weight), to absorb stray radiation. The 15 cm square unit tested at The University of Florida exhibited the predicted resolution of about 1 mm using technetium 99^m as the radioactive source. A patent No. 4,125,776 entitled "Collimator for X and Gamma Radiation" was issued November 14, 1978.

Summary

A parallel hole, high resolution collimator for radionuclide cameras has been fabricated by combining microchannel plate technology with lead plating. The aspect ratio of 21:1 (length of hole to diameter) was obtained with a minimum of 0.10 mm of lead in the channel giving an average metal ratio of 1.85:1. This was accomplished by using a combination of periodic reverse plating with an efficiency cycle of 50% and

Shinol LF-3 (Harstan Company) grain refiner. Resolution at the face of the collimator was 0.9 mm, open area of 50%, sensitivity was 40% of a conventional high resolution collimator (which can resolve 3 mm) and septal penetration for 140 keV photons using technetium 99^m was 0.1%.

Acknowledgments

The authors wish to express their thanks to Mr. B. F. Rothschild of the Autonetics Strategic Systems of Rockwell International for helpful suggestions and the reproduction of his data. Acknowledgment is also due Mr. Ray Cochran and Mr. Peter Dowling for their laboratory assistance and Mr. Thomas J. Loretz for his helpful comments, all of Galileo Electro-Optics Corporation.

Manuscript submitted Jan. 30, 1980; revised manuscript received July 21, 1980. This was Paper 454A presented at the Los Angeles, California, Meeting of the Society, Oct. 14-19, 1979.

Any discussion of this paper will appear in a Discussion Section to be published in the June 1981 JOURNAL. All discussions for the June 1981 Discussion Section should be submitted by Feb. 1, 1981.

Publication costs of this article were assisted by Galileo Electro-Optics Corporation.

REFERENCES

1. Corning 8161 Glass, U.S. Pat. 2,964,414.
2. D. Washington *et al.*, *Acta Electron.*, **14**, 201 (1971).
3. J. W. Wiza, *Nucl. Instrum. Methods*, **162**, 592 (1979).
4. M. Sarojamma and T. L. Rama Char, *Metal Finishing*, **69**, 56 (1971).
5. R. Walker and S. Thorley, *ibid.*, **74**, 30 (1976).
6. R. P. Greco, *Metal Prog.*, **43**, 119 (1968).
7. A. Mankovich, *Metal Finishing*, **46**, 50 (1948).
8. D. T. Chin, *This Journal*, **118**, 818 (1971).
9. L. Serota, *Metal Finishing*, **55**, 68 (1957).
10. J. B. Mohler, *ibid.*, **54**, 53 (1956).
11. J. W. Dini, *Plating*, **51**, 119 (1964).
12. B. F. Rothschild and D. Sanders, *ibid.*, **56**, 1364 (1969).
13. W. Blum and G. B. Hogaboom, "Principles of Electroplating & Electroforming," 3rd ed., pp. 89-100, McGraw-Hill, New York (1949).
14. D. G. Foulke and O. Kardos, *Proc. Am. Electroplaters Soc.*, 172 (1956).
15. O. Kardos, *ibid.*, 181 (1956).
16. T. H. Irvine, *Metal Finishing*, **65**, 85 (1967).
17. R. Subramanian, *Electroplat. Met. Finish.*, **29** (Oct. 1969).
18. *ibid.*, **20** (Dec. 1969).
19. D. G. Foulke and D. C. Johnson, *Proc. Am. Electroplaters Soc.*, 167 (1956).
20. R. H. Rousselet, *Metal Finishing*, **59**, 57 (1961).
21. D. Landolt, *This Journal*, **119**, 708 (1972).
22. R. L. Seth, *Electroplat. Met. Finish.*, **5** (1972).
23. B. F. Rothschild, *Plating*, **53**, 437 (1966).
24. Baker and Adamson, General Chemical Division, Allied Chemical and Dye Corp., New York, N.Y., *Bulletin*, TA-38351.
25. A. K. Graham, "Electroplating Engineering Handbook," Vol. II, pp. 700-702, Rheinhold Publishing Co. (1962).
26. Harstan Chemical Corp., Brooklyn, N.Y., *Harstan Tech. Bull.* (Oct. 1972).

Variation of Contact Resistance of Electroless Ni-P on Silicon with the Change of Phosphorous Concentration in the Deposit

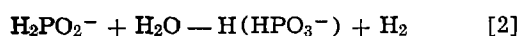
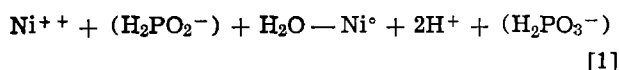
B. K. Singh and R. N. Mitra

Institute of Radio Physics and Electronics, Calcutta University, Calcutta 700009 India

ABSTRACT

Ohmic contacts to n-type silicon having resistivity of the order of 5 Ω -cm and orientation (111) by electroless Ni-P process were investigated under two different conditions, i.e., keeping operating temperature constant and pH variable and vice versa. It was found that the formation of Ni-P alloy during deposition resulted in low resistance ohmic contacts to silicon with increase of P-concentration and with heat-treatment after deposition in both cases.

Of the various methods used for making ohmic contact to silicon, the electroless nickel plating technique to achieve quick-to-solder and reliable low resistance ohmic contact is simple and economical. Basically, the process (1) is a type of chemical reduction of a metal salt such as nickel chloride to the metal with simultaneous oxidation of a reducing agent (sodium hypophosphite). The chemical reactions during electroless nickel plating are



Reactions [1] and [2] occur simultaneously. Reaction [1] is responsible for the nickel reduction and the formation of H^+ ions. As the H^+ ion concentration increases, nickel deposition stops when the pH falls below 3.0 (2). Therefore, in order to maintain the required pH some buffering and alkali agent are added. Reaction [2] is responsible for the evolution of molecular hydrogen which cleans the surface of the sample. The resulting deposit so obtained is not pure nickel but it is a mixture of nickel and phosphorous. It has been observed (2, 3) that the percentage of phosphorous in the nickel deposit is inversely proportional to pH containing about 3-15% phosphorous when the operating temperature of the bath is kept at about 95°C. It has been reported that the percentage of phosphorous in the deposit is directly proportional to the operating temperature of the bath if the pH of the same is kept constant. This observation was reported by Feldstein (4) who obtained about 2.5 and 5% phosphorous in the deposit when the bath was operated at 25° and 70°C, respectively. This means that by using electroless technique one might expect to obtain low resistance ohmic contact to n-type silicon if the conditions are such that more phosphorous can diffuse or alloy into silicon. Considering the advantage of the facts discussed above some attempts have been made to study the following observations: (i) variation of contact resistance (C_R) with sintering temperature keeping operating temperature of the bath constant and pH as parameter and (ii) variation of C_R with sintering temperature keeping pH constant and operating temperature as parameter. It has been observed that the contact resistance decreases as the phosphorous content in the deposit increases with the heat-treatment.

Experimental

n-Type silicon of resistivity 5 Ω -cm and orientation (111) were used. Samples were first lapped with 600 mesh carborundum powder, washed thoroughly with

deionized (DI) water, and then warmed in conc HNO_3 for a few minutes. Samples were then boiled in DI water, degreased in organic acids followed by washing in water. Next, samples were etched in caro's etch (5) for a few minutes. After washing, samples were treated in 48% HF solution for 1 min. Finally samples were rinsed. Immediately after this, samples were dipped first in sensitizing solution and then in activation solution (6) in steps for a few minutes. After each step samples were rinsed in water. It is believed that stannous ion reduces the palladous ion to metallic palladium, which act as palladium nuclei for electroless Ni-P deposition. Now, the samples were ready for deposition of nickel by immersing in the electroless plating bath. The compositions of the plating baths which were used in the present work are given in Table I. pH of the acidic and alkaline type of bath were maintained by adjusting the amount of HCL and NH_4OH , respectively. All the reported pH values were estimated to be within ± 0.5 . The optimum operating conditions for obtaining an adherent, bright, and dense deposit of nickel on silicon are also given in Table I. All chemicals used in this investigation were of laboratory grade except for sodium hypophosphite which was 99% pure.

Contact Resistance Studies

The electrical measurements were made by soldering leads to opposite faces of Ni-plated samples. The nickel plate was removed from all edges by grinding. The resistance of each sample was measured from its d-c V/I characteristics. Bulk resistance contributed by the silicon itself was calculated from silicon resistivity. The bulk resistance of the silicon plus the series resistance associated with the leads were deducted from the measured value which is called here the contact resistance (in Ω -cm²). All measurements were taken at room temperature.

Results and Discussions

The plated samples were sintered in N_2 atmosphere for about half an hour between the temperature range 500°-800°C. Sintering leads to the formation of a diffusion-like zone between silicon substrate and the plating. After sintering the samples were replated in order to facilitate taking the leads and measurements. Figure 1 shows the variation of contact resistance (C_R) with sintering temperature keeping operating temperature of the bath constant and pH as parameter and Fig. 2 shows the variation of C_R with sintering temperature keeping pH constant and operating temperature as parameter. For each temperature, three samples were used and the average value of C_R is plotted.

From Fig. 1, it is clear that as the pH of electroless bath decreases the P-concentration in Ni-P alloy increases, resulting in a decrease in contact resistance

Key words: resistivity, alloy, electroless Ni-P.

Table I. Compositions and operating conditions of baths

Bath used	Composition of the bath used	Operating conditions of the bath			
		pH	Temp. in °C	Immersion time in min	Control
Bath I	Solution A NiSO ₄ , 6H ₂ O—50 g/liter Na ₂ P ₂ O ₇ , 10 H ₂ O—100 g/liter NH ₄ OH—45 cm ³ /liter	10	25	30	pH was maintained by adding NH ₄ OH
		10	70	3-4	pH was maintained by adding NH ₄ OH
	Solution B NaH ₂ PO ₄ , H ₂ O—50 g/liter Solutions A and B were taken in the ratio 1:1				
Bath II	NiCl ₂ , 6H ₂ O—30 g/liter NaH ₂ PO ₄ , H ₂ O—10 g/liter (NH ₄) ₂ HCO ₃ —10 g/liter	3	95	60	pH was maintained by adding HCl and NH ₄ OH according to desired pH value
		4	95	45	pH was maintained by adding HCl and NH ₄ OH according to desired pH value
	5	95	10	pH was maintained by adding HCl and NH ₄ OH according to desired pH value	
	10	95	2-3	pH was maintained by adding HCl and NH ₄ OH according to desired pH value	

with sintering temperature. The contact resistance gradually decreases up to 700°C. In all cases the contact resistances were found to be minimum between the temperature range 600°-700°C. This minimum value decreases steadily with increase of phosphorous concentration. Beyond this, the contact resistance slightly increases. This increase in C_R is probably due to the out-diffusion of phosphorous during heat-treatment. Again, from Fig. 2, it can be seen that the contact resistance decreases as the operating temperature of the bath increases from 25° to 70°C because at high operating temperature (70°C) the deposited Ni-P alloy contains more phosphorous than the samples prepared at 25°C which contains low P-concentration.

Conclusion

Two electroless baths, I and II, were used in this work; when operated under two different conditions as described above they yield an adherent, bright, and dense deposit of Ni-P alloy which when sintered at higher temperature gives a low value of contact resistance. From the practical point of view for obtaining a low contact resistance, it may be concluded that the most favorable temperature range of heat-treatment is between 600°-700°C. Heat-treatment above 700°C slightly increases the contact resistance due to outdiffusion of P from Ni-P alloy.

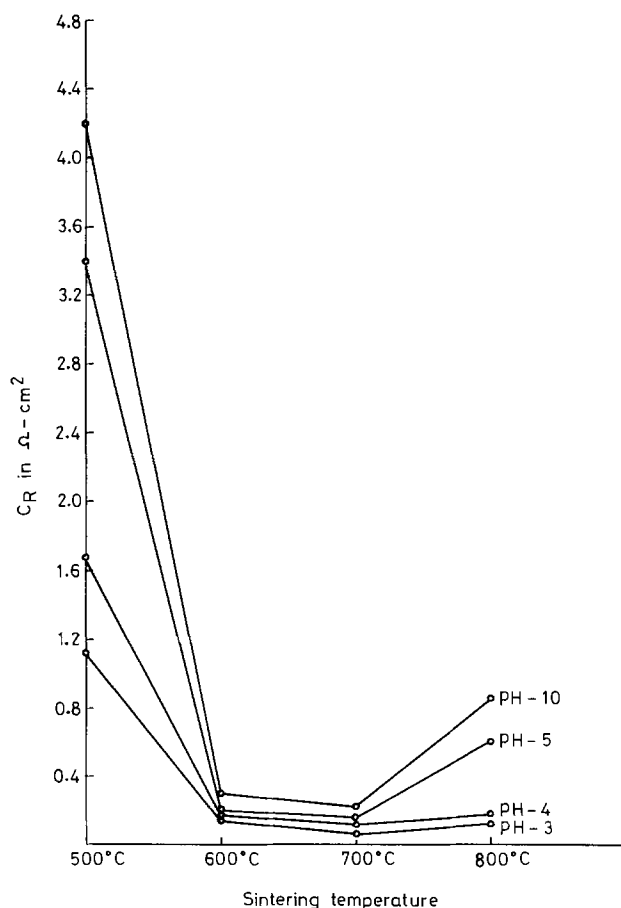


Fig. 1. Variation of contact resistance (C_R) with sintering temperature keeping operating temperature of the bath constant and pH as parameter.

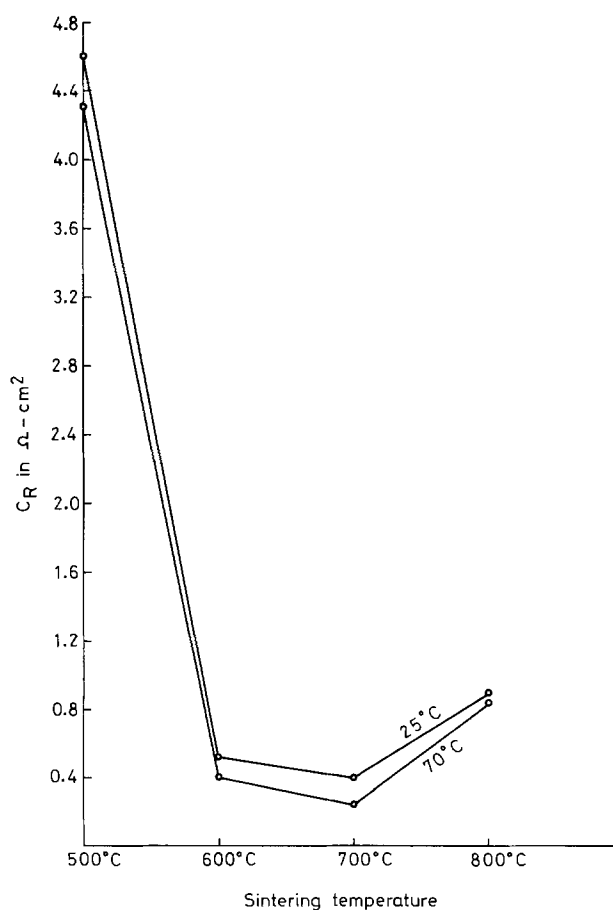


Fig. 2. Variation of contact resistance (C_R) with sintering temperature keeping pH constant and operating temperature as parameter.

Acknowledgments

The authors wish to thank Prof. M. K. Das Gupta, Head of the Department and Prof. A. N. Daw for constant encouragement in this work.

REFERENCES

1. E. B. Saubestre, *Metal Finish.*, **60**, 67 (1962).
2. P. Parikh and A. Subrahmanyam, *Res. Ind., New Delhi*, **15**, 157 (1970).
3. A. G. Van Nie, *Microelectron. Reliab.*, **15**, 221 (1976).
4. N. Feldstein, *RCA Rev.*, **31**, 317 (1970).
5. H. C. Card, in "Metal Semiconductor Contacts," p. 129, Proc. of Inst. of Physics, Conf. Series Number 22, Manchester (April 1974).
6. T. D. Schlabach and D. K. Rider, "Printed and Integrated Circuitry," p. 137, McGraw Hill Co., Inc., New York (1963).

Laser-Induced Photoelectrochemistry: Time-Resolved Coulostatic-Flash Studies of Photooxidation at n-TiO₂ Electrodes

S. P. Perone

Department of Chemistry, Purdue University, West Lafayette, Indiana 47907

J. H. Richardson and S. B. Deutscher

Lawrence Livermore Laboratory, University of California, Livermore, California 94550

and J. Rosenthal and J. N. Ziemer

Department of Chemistry, Purdue University, West Lafayette, Indiana 47907

ABSTRACT

Coulostatic-flash irradiation of semiconductor/liquid-junction cells with a pulsed laser source has allowed time-resolved measurements of photopotential transients in the submicrosecond time domain. In 1.0M electrolyte ~12 nsec rise times were observed with several different n-TiO₂ electrodes. The dependences of transient photopotentials on the initial potential, pulsed laser intensity, and nature of electrolyte have been studied, and the measurement limitations defined by experimental and instrumental parameters have been described. Most importantly, the time dependence of photopotential transients has been characterized. Four possible contributions to the transient behavior are discussed: electron-hole recombination, photoinduced charge transfer at the solution interface (oxidation), subsequent back-reaction of photo-products (reduction), and a transient expansion of the space charge layer due to rapid photoinduced charge injection.

A large number of studies have been conducted in recent years to characterize the photooxidation of water at n-type semiconductor electrodes (1-4). Most of this work has involved continuous irradiation with the purpose of determining final photoproducts, quantum yield, energy conversion efficiency, electrode durability, wavelength response, voltage dependence, intensity effects, etc. Photooxidation of water was first demonstrated at n-TiO₂ electrodes (5), but a wide variety of other electrode materials has been investigated in attempts to achieve improved performance. Recently, it has been shown that a solar-to-electrical conversion efficiency of ~12% could be obtained with n-GaAs electrodes using a regenerative Se_n²⁻/Se²⁻ redox couple for photooxidation (6). Such polychalcogenide solutions also generally enhance the durability of the electrode (*i.e.*, resistance to electrode photodissolution). On the other hand, the efficiency of the water-splitting photoprocess (leading to the production of hydrogen fuel), originally described by Fujishima and Honda (5), has been achieved with an overall solar energy conversion efficiency of only ~1% (1-4). The production of hydrogen has some very desirable attributes, obviously, in that a storable combustible fuel is produced. Thus, it is one goal of our studies to examine mechanistic aspects of the photooxidation pro-

cess which may dictate overall efficiency. To achieve a new perspective on these photoinduced electrode processes we have developed a time-resolved photoelectrochemical technique that allows meaningful measurements of photoeffects in a time domain several orders of magnitude shorter than previously reported.

We have reported previously on the limited time-resolution of potentiostatic photocurrents measured with pulsed irradiation (7, 8). At best, one can achieve resolution of ~500 nsec, with ~50 μsec more typical if correction for induced charging currents is made (8). Barker and co-workers (9) proposed coulostatic-flash measurements to obtain microsecond time resolution in photoemission studies with mercury electrodes. We recently achieved 200 nsec time resolution in coulostatic-flash mercury photoemission studies (10). The present work demonstrates that we can observe photopotential transients at semiconductor electrodes with at least 15 nsec time resolution. We have analyzed the electrical and electronic characteristics of photoelectrochemical cell and measurement circuitry to ensure the validity of short-time measurements; and we have suggested possible interpretations for the observed behavior. Our studies reported here have concentrated on observations with single crystal n-TiO₂ electrodes in various aqueous electrolytes, since such systems have been well characterized previously with CW light sources (1-4).

Key words: electrochemistry, semiconductor electrochemistry, photochemistry.

Experimental

Instrumentation.—The basic ingredients of the photoelectrochemical instrumentation have been described previously (10-13). A Princeton Applied Research Corporation (PAR) Model 174A polarograph was used for controlled-potential flash experiments as well as for cyclic voltammetry and voltage scans with CW irradiation. A 4-electrode cell was used (10), in which the fourth electrode is a platinum quasi-reference electrode. The pulsed laser source was a Moletron Model UV 1000 nitrogen laser (337 nm) with 10 nsec pulse width. The Moletron Model DL 200 dye laser was used to provide a pulsed source of subbandgap irradiation. The CW laser source was a Spectra-Physics Model 171 krypton ion laser (u.v. lines at 351/356 nm, visible lines at 531 and 647 nm). The coulometric-flash instrumentation has been described also (10), but some modifications to the measurement approach have been made for this study. They are as follows: (i) for photopotential transients in a time domain from 10 nsec to 10 μ sec, the working electrode and Pt quasi-reference electrode were directly connected (and a-c coupled) to a Tektronix Type 7A13 (105 MHz bandwidth) differential amplifier plug-in which was mounted in a Tektronix Model 7623A oscilloscope. All control/monitoring electronics were located inside the Faraday cage enclosing the cell. The y-axis output from the scope back panel was connected externally to a Type 7A19 (500 MHz bandwidth) plug-in amplifier (50 Ω input, a-c coupled), mounted in a Tektronix Model 7844 oscilloscope. (ii) For photopotential transients in the time domain from 1 μ sec to seconds, the Pt quasi-reference electrode was capacitively coupled (0.47 μ F) to the saturated calomel reference (SCE) electrode; the SCE and working electrode potentials were input to a wideband-pass (5 MHz) high input impedance ($10^{11}\Omega$) differential amplifier (4.6 \times), with d-c offset bias so that the d-c level of transients could be conveniently measured. Its output was in turn connected to a Tektronix Type 7A16-A amplifier plug-in, with 1 M Ω input impedance, and 225 MHz bandwidth. Traces were recorded photographically. The philosophy behind the above measurement approaches is documented elsewhere (10, 14). The important point is that the Pt quasi-reference electrode reflects accurately any transient changes in the cell potential in a time domain of <10 μ sec. Capacitive coupling of the two reference electrodes allows measurements of photopotential transients referenced to the SCE for times exceeding 1 μ sec. However, when only the magnitude of photopotential transients was required the quasi-reference electrode could be monitored directly, without coupling to the SCE.

A General Radio Model 1650-A impedance bridge was used to obtain cell impedance measurements for Mott-Schottky plots (15, 16). The cell bias voltage was provided by the polarograph, by connecting the working and counterelectrode terminals from the polarograph to the bias terminals of the bridge, through two 30 mH inductors. The reference electrode terminal of the polarograph was connected to the SCE in the cell. The working and counterelectrodes were connected to the "unknown" terminals of the bridge. The 1 kHz oscillator signal was used, with ~ 15 mV peak-to-peak amplitude. The cell equivalent circuit for the purpose of this measurement was assumed to be a simple series RC combination.

Cell impedance measurements were also made using a Hewlett-Packard Model 4800A Vector Impedance Meter. This instrument conveniently measures both the complex impedance and phase angle as a function of frequency (5 Hz to 500 kHz). Consequently the cell resistance R_s could be measured at high frequency where the cell capacitance has a negligible contribution to the total impedance. The resistance measured at high frequency is the more significant figure for calculating fast rise times. The values measured at

1 kHz compared favorably to those calculated from the bridge measurements made for the Mott-Schottky plots at 1 kHz.

Cell and electrodes.—The photoelectrochemical cell design is basically as described previously (10-13), except that the platinum counter and reference electrodes were constructed of a fine mesh. The Pt reference formed a cylinder of 1.7 cm in diameter and 1.5 cm in height around the working electrode; the Pt counterelectrode formed a half-cylinder around the Pt reference electrode, with the same surface area as the reference. The large surface area electrodes were desirable in these studies to help minimize cell impedance and hence minimize response delays related to the source impedance of the measurement circuit. In addition, for measurements to be related only to the interfacial capacitance of the working electrode, it is necessary that the counter and/or reference electrodes have much higher capacitance. The n-TiO₂ electrodes used in this work were prepared from a boule of single crystal TiO₂ (Commercial Crystal Laboratories, Incorporated, South Amboy, New Jersey). The procedure involved slicing the boule perpendicular to the c axis (with alignment by x-ray diffraction) with a diamond wafering blade. The resultant 1 mm slices were reduced in a hydrogen furnace at 500°C for varying times. The crystal slices were then boiled in concentrated H₂SO₄ for 1 hr, and indium metal was rubbed onto one side until a shiny metallic surface was obtained. Indium was melted onto the shiny surface and a 12 gauge copper wire was then silver-soldered to the surface. The entire assembly was then mounted to a glass tube with epoxy (Dexter Epoxi-patch), with care taken to expose only the flat crystal surface.

The electrodes were used unpolished.¹ Prior to each series of runs they were etched in 1:1 H₂O/H₂SO₄ for 10 min.² Four different electrodes were used, representing a range of resistivities and donor densities. These were designated as electrodes A-D, and their characteristics are summarized in Table I.

Photoelectrochemical procedures.—The coulometric-flash experimental procedure has been described in detail elsewhere (10). It involves first adjusting the cell voltage to the desired initial potential, E_i , for the semiconductor working electrode using the polarograph. A solid-state electronic switch which opens the cell circuit is triggered at 5 sec intervals. After ~ 30 μ sec time delay the pulsed laser is triggered and the open-circuit potential difference between the working and reference electrodes monitored as described above. After a 2 sec interval the cell circuit is closed again and the initial potential reimposed by the polarograph.

With CW irradiation the cell voltage is controlled or scanned with the polarograph. A-C photocurrent signals were measured by chopping the laser source at 500 Hz and using a PAR HR-8 Lock-in amplifier synchronized with the chopper. Details have been published elsewhere (10-13). D-C photocurrents were measured by monitoring the PAR 174A output directly.

Pulse photocurrent measurements were made directly from the PAR 174A polarograph as described previously (10-13).

All solutions were deaerated with high purity nitrogen for at least 10 min before photoelectrochemical studies were conducted. The nitrogen was allowed to flow over the solution surface during experiments.

Results and Discussion

Semiconductor electrode characteristics.—Table I summarizes the physical and photoelectrochemical features of the various n-TiO₂ electrodes used in this work. The Mott-Schottky (M-S) plots, from which much of the data are taken, were linear in every case over the range of -0.5 to $+1.0$ V vs. SCE in 1.0M KNO₃.

¹ Polishing is likely to introduce surface states (17).

² Etching of TiO₂ by concentrated H₂SO₄ is common in the preparation of photoelectrochemical electrodes, e.g., Ref. (18).

Table I. Summary of electrode characteristics. (n-TiO₂)

	Electrode			
	A	B	C	D
E_{FB} (M-S) vs. SCE, V	-0.4	-0.75	-0.53	-0.80
E_{TH} (CW/u.v./a.c.) vs. SCE, V*	-1.1	-1.1	-0.88	-0.93
E_{TH} (CW/u.v./d.c.) vs. SCE, V*	-0.8	-	-0.80	-0.70
E_{TH} (pulse i_p) vs. SCE, V*	-0.55	-	-0.50	-0.50
E_{TH} (C-F) vs. SCE, V†	-1.3	-1.3	-0.90	-1.1
N_D (M-S), cm ⁻³	1.6×10^{18}	3.0×10^{20}	1.4×10^{20}	1.5×10^{20}
C_s ($E = +1.0V$), μF	0.14	2.2	1.8	1.8
R_s ($E = +1.0V$), Ω	330	29	38	~86
Area, cm ²	0.11	0.14	0.20	0.21

All data obtained with 1.0M KNO₃ electrolyte. E_{FB} = flatband potential; E_{TH} = threshold potential; N_D = donor density; M-S = Mott-Schottky plot; CW/u.v. refers to photocurrent vs. E experiments with CW/u.v. laser source; a.c. refers to lock-in detection; d.c. refers to direct current measurements; C-F refers to coulometric-flash experiments; R_s , C_s refer to impedance bridge measurements of cell resistance and capacitance at 1 kHz.

* E_{TH} (CW/u.v.) and E_{TH} (pulse i_p) were obtained by extrapolating the rising portion of the i_p vs. E plot back to zero current.

† E_{TH} (C-F) was defined as the most negative potential at which a measurable negative photopotential transient was observed.

The magnitude and range of the features obtained from the M-S plots are both generally consistent with the observations of others (19). It should be pointed out, also, that the variation in donor density, N_D , was significant and deliberately created. There was also a corresponding range of resistance and capacitance of the electrodes at 1 kHz. Note that the value of R_s includes the solution resistance, which was $\sim 15\Omega$ for the 1.0M KNO₃; thus, the resistance of the semiconductor electrode alone can be calculated in each case. However, it is the total resistance, R_s , which affects the time response in coulometric and potentiostatic measurements, as discussed below. It is important to note that the measured values of R_s and C_s depend on the frequency used in the measurement. The values in Table I were taken from Mott-Schottky plots made at the usual frequency of 1 kHz. However, whenever pulse photocurrents or rapid coulometric measurements were interpreted, values of R_s and C_s obtained with the vector impedance meter at high frequency (>1 kHz) were used. The range of electrode characteristics exhibited in Table I was desired so that the effects on time-resolved photopotential/photocurrent transient behavior could be observed.

A significant observation in these characterization studies was that photoeffect threshold potentials usually did not agree with the flatband potential, E_{FB} , derived from Mott-Schottky plots (see Table I). Such discrepancy is not totally unexpected in correlating Mott-Schottky data to transient measurements. Some discussion of these discrepancies is presented below.

Photocurrent observations.—The dependence of photocurrent (i_p) on electrode potential with a continuous source irradiation is consistent with the previous literature (1-4). A typical curve is shown in Fig. 1. All electrodes behaved similarly, except for slight differences in E_{TH} (see Table I). Similar shapes were obtained for the a-c and d-c photocurrent, except a more noticeable "foot" was observed when monitoring the d-c photocurrent (Fig. 1). For the d-c current the rising portion of this lower intensity feature was extrapolated to zero current to yield E_{TH} (Table I). Finally, the quantum efficiency (photocurrent/incident photons) for d-c CW/u.v. experiments was approximately 0.1. This value is on the low side, probably because the high intensity laser source results in a lower fraction of photons absorbed in the depletion layer.

Thermal effects were easily distinguished by irradiating the electrode with subbandgap light (647/676 nm). The resulting a-c photorelated current observed was more than one order of magnitude lower in intensity and had a different shape (i_p vs. electrode potential) than the a-c photocurrent resulting from irradiation with u.v. light (351/356 nm). The corresponding d-c photorelated current was more than four orders of magnitude lower in intensity than the d-c photocurrent resulting from u.v. irradiation. In each

case the observed visible/u.v. photocurrent ratios were made using comparable laser intensities.

Photocurrent measurements with the pulsed laser source yield essentially the same type of photocurrent-potential behavior shown in Fig. 1. However, the time-resolved photocurrent pulse behavior is of primary interest here. As pointed out previously (7, 8), potentiostatic photocurrents with pulsed irradiation follow a time dependence dictated by the cell time constant ($R_s C_s$), as long as the pulse width is short compared to $R_s C_s$ and the photoinduced charge transfer processes are complete within a time frame short compared to $R_s C_s$. Figure 2 shows a typical photocurrent pulse. The decay times of these pulses compare favorably with the values of $R_s C_s$ obtained from Table I for each electrode. Thus, no information on the dynamics of

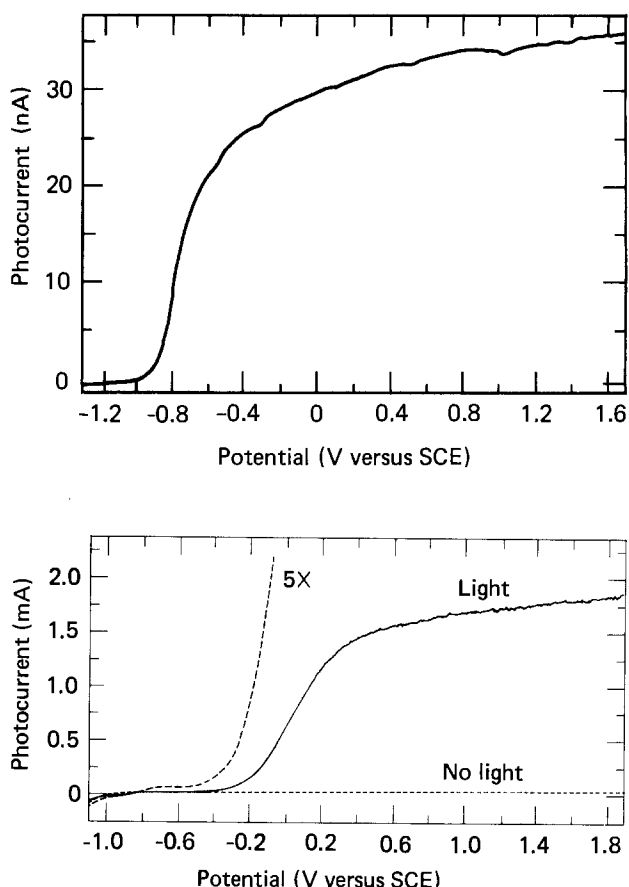


Fig. 1. Photocurrent-voltage curves with CW laser source. Electrode C; 1.0M KNO₃; wavelength = 351/356 nm; sweep rate = +20 mV/sec. (a, top) synchronous a-c detection, laser intensity = 0.15 mW/cm²; (b, bottom) d-c current, laser intensity = 270 mW/cm².

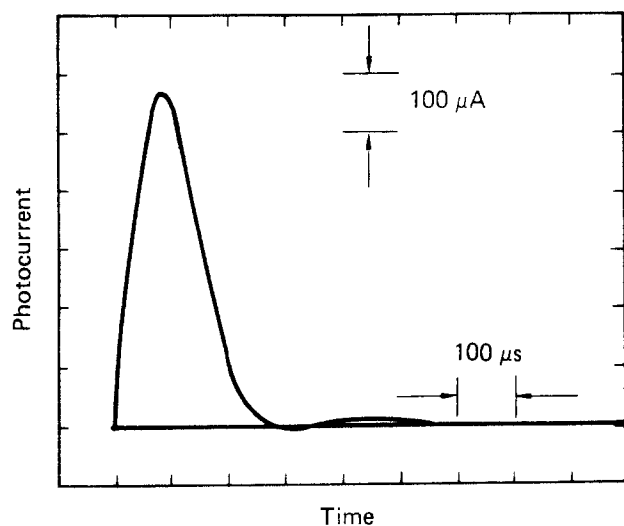


Fig. 2. Photocurrent-time behavior with pulsed laser source. Electrode C; $E_i = +1.5V$ vs. SCE; $1.0M$ KNO_3 ; light intensity = 10 kW/cm^2 .

photorelated processes can be obtained from pulse photocurrent measurements when $R_s C_s$ is long compared to the time frame of interest. However, it is possible to obtain a measure of the total photorelated charge (Q_p), simply by integrating the photocurrent pulse. Such information is useful, of course, for quantum efficiency calculations. It is also useful for determining the electrode capacitance by combination with coulostatic measurements, as discussed below.

The differences in E_{TH} (a-c i_p , d-c i_p , pulsed i_p , C-F) reflect the differences in the experimental measurement technique and the quantity being measured. For example, the pulsed i_p measurement has a longer time constant than the coulostatic-flash experiment (vide infra), and only measures the net charge transferred. The actual number of photons per pulse in the pulsed measurement is far less (by a factor of 10^{-4}) than the number of photons per second in the CW experiment; consequently the more positive E_{TH} observed for pulsed i_p may reflect a lower sensitivity or photon threshold.

Coulostatic-flash studies.—Time dependence.—In contrast to pulse photocurrent measurements, coulostatic (open-circuit) photopotential (E_p) measurements made with a pulsed laser source are not limited in response time by the cell time constant ($R_s C_s$) (9, 10). The response is limited by the RC time constant defined by the cell impedance (R_s) and the combined value of the interelectrode stray capacitance, the input capacitance of the measurement electronics, and cable capacitance. This combined value, C_M , is typically less than 100 pf. Thus, for electrodes A to D, respectively, $R_s C_M < 4, < 3, < 4, \text{ and } < 5$ nsec, where R_s is the value measured at high frequency with the vector impedance meter in $1.0M$ KNO_3 . These response time constants are comparable to or less than the pulse width of the laser source (10 nsec), thus allowing time-resolved studies in a time domain of ≥ 10 nsec as shown below.

Figures 3 and 4 show typical photopotential (E_p)-time behavior for coulostatic-flash experiments in $1.0M$ KNO_3 , using the nitrogen laser (337 nm). Irradiation with subbandgap energy light using the nitrogen pumped dye laser (520 nm) resulted in photopotential excursions at least four orders of magnitude lower (using comparable laser intensities).

Table II summarizes the time-dependent behavior of all four electrodes. Several features are worth noting. First of all, it is clear that the rise time ($t_{95\%}$) is ~ 12 nsec, which suggests that it is limited by the laser pulse-width and/or the bandwidth of the measurement electronics. The potential changes sharply in a

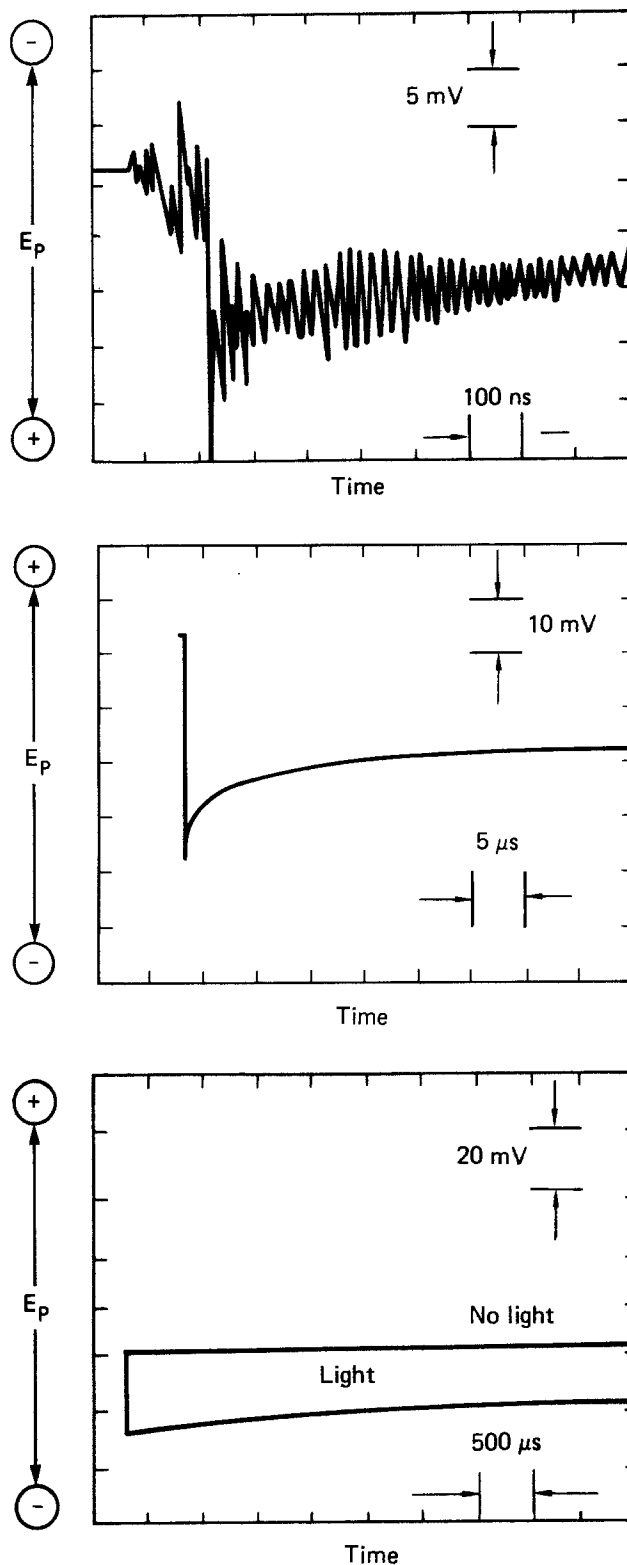


Fig. 3. Coulostatic-flash photopotential transients at positive potential for three different time domains. Electrode C; $E_i = +1.0V$ vs. SCE; $1.0M$ KNO_3 ; light intensity 10 kW/cm^2 . The 10 nsec laser pulse occurs at the onset of the negative potential transient; (a, top; b, center; c, bottom).

more negative direction, but then decays back toward the initial potential, E_i . When E_i is very positive of E_{FB} , the final photopotential, $(E_p)_F$, is reached after ~ 1 to 20 msec for the electrodes studied here. When E_i is near E_{FB} , not only is there a much smaller initial excursion of the photopotential, but $(E_p)_F$ approaches E_i ; also $(E_p)_F$ is reached in $< \sim 1$ msec.

The net magnitude of photopotential excursion achieved after the decay, $(\Delta E_p)_F$, is taken to be in-

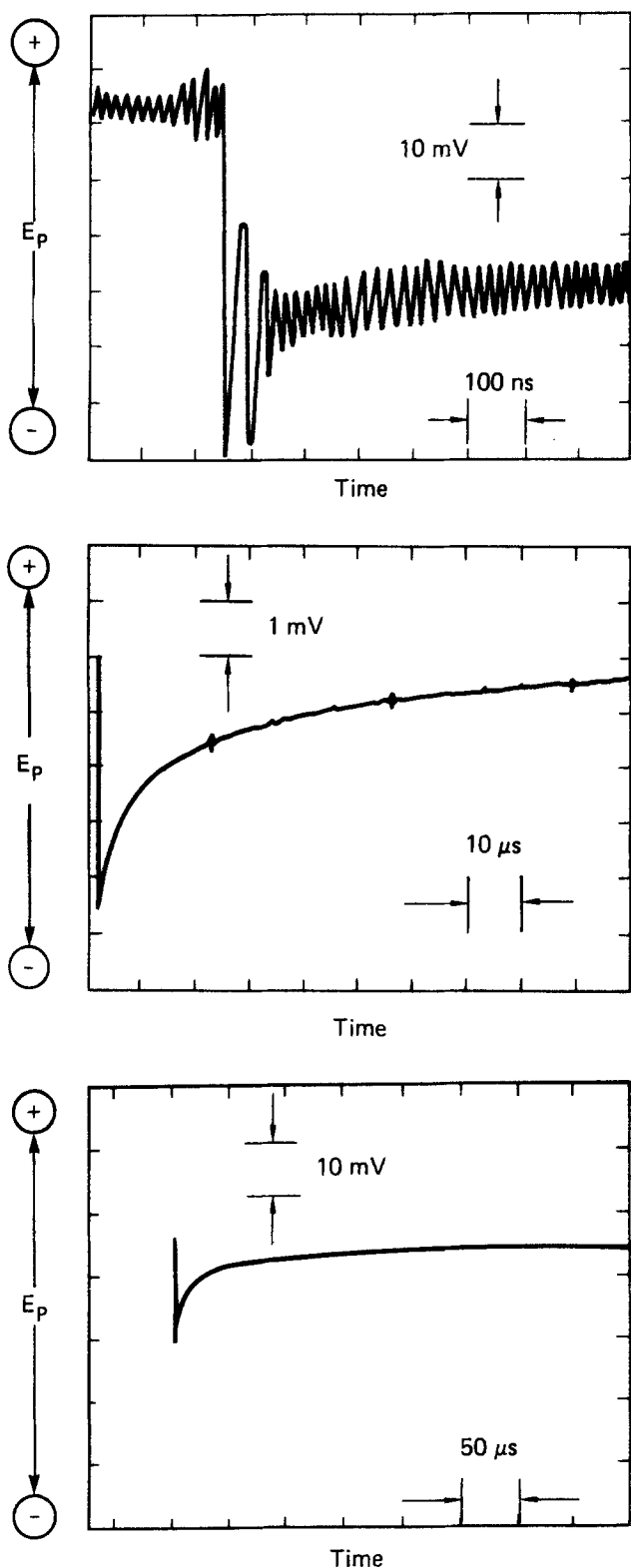


Fig. 4. Coulostatic-flash photopotential transients near E_{FB} for three different time domains. Electrode C; $E_i = -0.5V$ vs. SCE; $1.0M$ KNO_3 ; light intensity ≈ 10 kW/cm^2 . The 10 nsec laser pulse occurs at the onset of the negative potential transient; (a, top; b, center; c, bottom).

dicative of the net quantity of charge transferred, or "photocharge" (Q_p). Q_p can be calculated from the relationship, $Q_p = C_s \cdot (\Delta E_p)_F$. (In general C_s depends on the cell potential, so Q_p has to be calculated from the integral of C_s and E_p for large photopotential excursions). An indication of the efficiency of the photoelectrolysis process can be obtained from the ratio, Q_p/A , where A is the electrode area. The data in

Table II. Summary of time-dependent behavior of several n-TiO₂ electrodes with pulsed-laser coulostatic-flash experiments in $1.0M$ KNO_3

	Electrode			
	A	B	C	D
A. For $E_i = +1.5V$ vs. SCE				
τ , nsec*	12	10	15	12
t_F , msec	~ 20	~ 2.2	~ 1	~ 1
$(\Delta E_p)_F$	0.15	0.76	0.59	0.41
$(\Delta E_p)_{max}$				
Q_p/A , $\mu C/cm^2$ †	0.024	0.56	0.10	0.12
C_s , μF	0.12	1.96	1.56	1.46
B. For E_i near E_{FB} for each electrode				
τ , nsec*	12	10	12	12
t_F , μsec	~ 1000	~ 50	~ 175	~ 150
$(\Delta E_p)_F$	0.10	0.18	0.13	0.20
$(\Delta E_p)_{max}$				
Q_p/A , $\mu C/cm^2$ †	0.017	0.67	0.044	0.032
E_i , V vs. SCE, V	-0.7	-0.6	-0.5	-0.8
C_s , μF	0.53	3.5	3.1	3.4

* $\tau = t_{0.63}/0.63$ = rise time of photopotential in nsec, based on a smoothed fit to the rising portion of the curve.

† $Q_p = (\Delta E_p)_F \cdot C_s$; A = working electrode area in cm^2 . (The C_s value used was taken from M-S plots or was taken as the maximum measured value from the M-S plot when $E_i < E_{FB}$.)

Table II clearly show that electrode B is the most efficient and electrode A is the least efficient. By comparison with Table I, the trend in efficiency correlates well with the donor density. (However, because the laser pulse intensity varied $\pm 25\%$ due to optical alignment, and because N_D values for electrodes B, C, and D are similar, the efficiency trends can only be interpreted semiquantitatively.)

The times, t_F , required for the photopotential to decay to $(\Delta E_p)_F$ were only estimated from visual inspection of photographic traces, but do indicate a qualitative inverse correlation between t_F and the donor density. Finally, the quantum efficiency (Q_p /total photons incident) can be estimated to be $\sim 10^{-2}$. This value is somewhat low, but certainly includes the uncertainties in measuring the total charge transferred and the number of photons absorbed in the depletion layer during each 10 nsec laser pulse.

The nature of the E_p decay is certainly of interest (Fig. 5A). Several different factors may be involved (Fig. 5B-E). The first factor (Fig. 5B) is that the initial photopotential excursion is due to space charge layer contraction caused by electron-hole generation and separation. The narrower space charge layer has a larger capacitance, while the total charge remains the same, thus the excursion is toward E_{FB} . The subsequent decay is caused by electron-hole recombination (Fig. 5B). The rates of such processes in the bulk for highly doped semiconductor materials are typically found to be in the submicrosecond time domain (20). However, longer lifetimes might occur in the space charge region at a semiconductor/electrolyte interface (band bending at the interface facilitates the separation of electrons and holes).

The second factor (Fig. 5C) is oxidation (of either the solvent or species at the electrode surface) by holes migrating to the surface. Note that this process would tend to increase ΔE_p with time. An opposite effect would be due to the dark reduction of photo-products (Fig. 5D); i.e., the photopotential decay represents the dark back reaction of photooxidation products produced by the flash. We have some evidence from other controlled-potential, pulsed photocurrent studies (21) that such back reactions may occur, probably via surface states, even when the electrode potential is quite positive of E_{FB} . The rate (or efficiency) of the back reaction appears to increase as the potential is made less positive (21), and this is consistent with the observation here that the decay time constant decreases as E_i approaches E_{FB} (Table II).

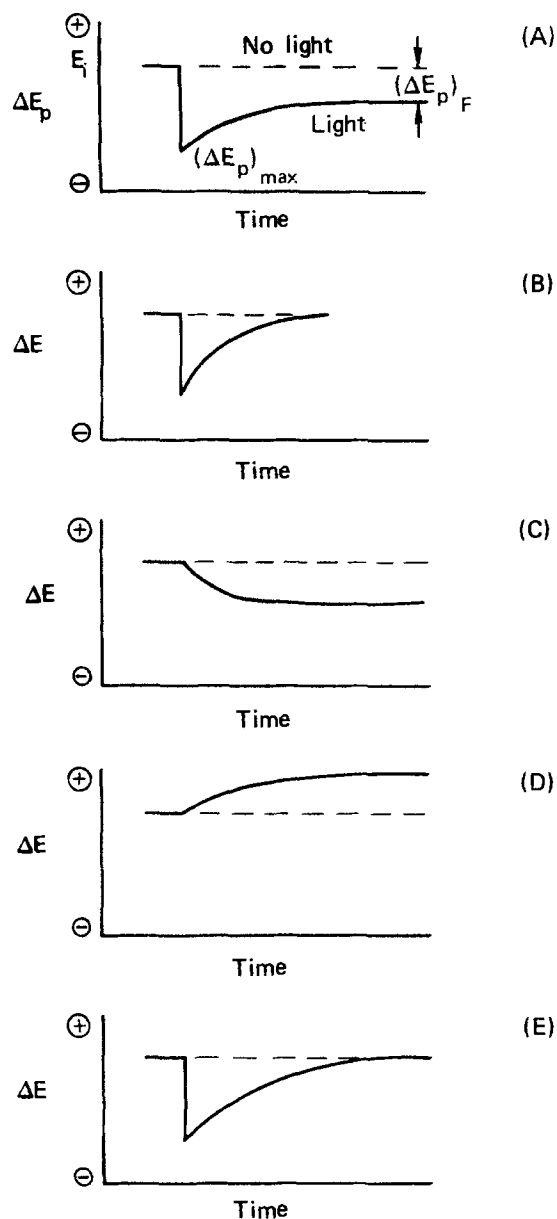


Fig. 5. Pictorial representation of four factors which may influence the observed transient photopotential: (A) experimentally observed behavior; (B) electron-hole separation and recombination; (C) photoinduced oxidation; (D) dark reduction; (E) expansion and relaxation of the space-charge layer. In all cases the vertical (ΔE) and horizontal (time) scales are arbitrary.

The fourth possible factor is that the very high rate of negative charge injection due to photooxidation caused by the intense 10 nsec laser pulse forces a transient nonequilibrium expansion of the space charge region in the semiconductor, followed by a relaxation back to its equilibrium dimensions, with associated overshoot and decay of the photopotential (Fig. 5E). (This decay may or may not involve hole-electron pair recombination, depending on the survival of excess surface holes.) Such a relaxation effect has been observed with coulometric electrical charge injection at a mercury/dilute-electrolyte interface (22, 23) and has been described theoretically (24-26) in terms of a transient overexpansion of the diffuse-double layer (interfacial) followed by a relaxation back to an equilibrium thickness, with corresponding changes in the measured double layer voltage analogous in nature and time dependence to those observed here.

The nature of steady-state photopotentials generated under conditions where charge transfer to solution is blocked has been described previously (27-29); and

experimentally observed instantaneous photovoltaic response has been described (30, 31). Gerischer (32) suggested that short light pulses should be used for these measurements to obtain a better characterization of the space charge region free from charge transfer and surface effects. However, no reliable measurements have been reported on a time scale comparable to our studies. The possibility that a transient photopotential overshoot and decay might be observed has been suggested previously (33, 34). Laser and Bard (35) also pointed out that the response of the semiconductor space charge layer to coulometric electrical charge injection is analogous to that predicted by Feldberg (26) for diffuse double layer relaxation, except that it should occur in a much shorter time domain. Unfortunately, the pulsed laser-induced photopotentiometry experiments performed here do not correspond exactly to the electrical coulometric charge injection situation described by Laser and Bard (35). Nor do the conditions agree with those used to simulate steady-state photopotentials (29) or to simulate the relaxation of photogenerated free carriers (33). However, Ref. (33) does demonstrate that distinct transient minima and maxima in the concentration-distance profiles of minority and majority charge carriers can be generated, perhaps leading to the kind of relaxation processes observed here. The time scale of the transient behavior predicted (33) is several orders of magnitude shorter than observed here. However, the conditions chosen for the simulations correspond to light fluxes and donor densities several orders of magnitude lower than those used here.

To investigate further the merits of the fourth possible factor influencing the photopotential decay (transient expansion and contraction of the space charge layer due to photocharge injection), the time dependence was compared to that predicted theoretically for diffuse double layer relaxation (26). In that case, assuming equal mobilities for positive and negative charge carriers, theory predicts that the observed double layer potential should follow a $t^{-2/3}$ dependence during the latter part of the decay when the potential is near E_{PZC} (potential of zero charge). By analogy, the same essential, theoretical concepts can be imposed on the response of the semiconductor space charge region to an instantaneous light-induced charge injection. Holes and electrons are considered to replace cations and anions, with their associated mobilities and concentrations; the thickness of the depletion layer replaces the double layer thickness, and E_{FB} replaces E_{PZC} .

The suggestion that double layer relaxation could also contribute to the time dependence observed here is of course appropriate. However, the effects have not been observed at mercury electrodes with concentrated electrolyte ($> \sim 0.05M$) and relatively small charge injection (22). Thus, we should not expect to see Helmholtz layer relaxation effects here, with $1.0M$ KNO_3 electrolyte and $Q_p/A < 1 \mu C/cm^2$.

A typical plot of E_p vs. $t^{-2/3}$ is shown in Fig. 6 for electrode D. The value of E_i for the experimental data in Fig. 6 was near E_{FB} . The data plotted are for only the latter part of the decay, where a linear dependence on $t^{-2/3}$ was observed. This behavior is analogous to double layer relaxation observations (22), where linear dependence of cell potential on $t^{-2/3}$ is predicted after coulometric charge injection when E_i is near E_{PZC} (26). The behavior shown in Fig. 6 was typical of all the electrodes used in these studies. Nonlinear dependence on $t^{-2/3}$ was observed at short times, as indicated in Table III. Nonlinear dependence on $t^{-2/3}$ was observed at all times when E_i was very positive of E_{FB} (e.g., at $+1.0V$ vs. SCE) for all electrodes; the slope of a linear least squares fit on a log-log plot of E_p vs. t becomes increasingly more positive as E_i becomes more positive of E_{FB} .

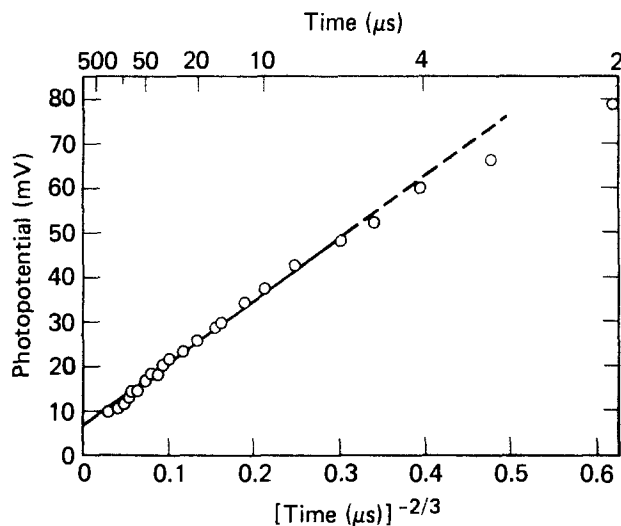


Fig. 6. Transient photopotential vs. $t^{-2/3}$ for E_i near E_{FB} . 1.0M KNO_3 , electrode D, $-0.5V$ vs. SCE, gain = 4.6.

In order to investigate further the observed time dependence of the transient photopotentials the slopes of the E_p vs. $t^{-2/3}$ plots were compared to the theoretical predictions of Feldberg (26). While an absolute correlation is not feasible without an accurate knowledge of the carrier mobilities and the internal potential gradient, it is possible to examine the observed slopes with regard to predicted correlations. Feldberg's theory predicts that the slope, S , is related to q , the injected charge density, C_z , the bulk concentration of charge carriers, and D , the diffusion coefficient of charge carrier, by a linear function shown in Eq. [1]

$$S = (\text{constant}) \cdot q^{5/3} \cdot C_z^{-3/2} \cdot D^{-2/3} \quad [1]$$

Because the diffusion coefficient in solution is analogous to the carrier mobility in a semiconductor, the relationship defined in [1] predicts that the product, $S \cdot C_z^{3/2} \cdot q_p^{-5/3}$, should be a constant for any particular semiconductor electrode, as q_p is varied experimentally. Thus, Eq. [2] defines a parameter, γ , which can be calculated for each electrode from the slope and intercept of various experiments where q_p is varied. ($q_p = (\Delta E_p)_F \cdot C_s/A$)

$$\gamma = S \cdot C_z^{3/2} \cdot q_p^{-5/3} \propto D^{-2/3} \quad [2]$$

(It should be pointed out that the values of q_p/C_z in our experiments are 1 or 2 orders of magnitude lower than what Feldberg found necessary for Eq. [2] to hold.)

The values of γ obtained from several different experiments are given in Table III. Note that the two values for electrode B agree reasonably well as q_p varies. Also, note that the magnitude of γ increases with the donor density from electrode to electrode.

Table III. Summary of $t^{-2/3}$ analysis of photopotential decay for E_i near E_{FB}

	Electrode				
	A	B	C	D	
E_i , V vs. SCE	-0.7	-0.6	-0.7	-0.5	-0.8
S , $V \cdot \mu\text{sec}^{-2/3}$ *	0.089	0.012	0.0025	0.027	0.013
t_s , μsec	~30	~4	~4	~15	~15
$(\Delta E_p)_F$, mV	3.6	2.7	0.78	2.8	2.0
q_p , $\mu\text{C}/\text{cm}^2$	0.017	0.067	0.021	0.044	0.032
C_z , $\text{cm}^{-3} (\times 10^4)$	0.027	5.0	5.0	2.33	2.5
$\gamma (\times 10^6)$	0.22	1.21	1.74	1.75	1.59

* S = slope of (ΔE_p) vs. $t^{-2/3}$ plot; t_s = time at which linear dependence on $t^{-2/3}$ begins; $(\Delta E_p)_F$ = intercept of (ΔE_p) vs. $t^{-2/3}$ as $t \rightarrow \infty$; q_p = photocharge density = $C_s \cdot (\Delta E_p)_F/A$ (see Tables I and II for C_s , A); $C_z = N_D/A_v$, where A_v = Avogadro's number = 6×10^{23} ; $\gamma = S \cdot C_z^{3/2}/q_p^{5/3}$.

This is consistent with the fact that the carrier mobility decreases with increasing donor density (20), and Eq. [1] predicts that the slope, S , should increase with decreased carrier mobility; thus, γ should increase with increased donor density, as indicated in Table III. Such results support our speculation that space charge relaxation is a possible factor in the observed transient time dependence of the photopotential.

Additional support is seen in the fact that the magnitude of the photopotential overshoot diminishes with increasing N_D (Table II-A). This behavior is consistent with Feldberg's theory (26). Moreover, the fact that lowering the solution electrolyte concentration does not change the long-term photopotential decay, but only increases the initial rise time (as discussed below), indicates that Helmholtz-layer relaxation is not contributing significantly to the observed potential excursions.

Potential dependence.—The dependences of $(\Delta E_p)_{\text{max}}$ and $(\Delta E_p)_F$ on E_i are shown in Fig. 7. The observed photopotential excursions were normalized with respect to the values obtained at the most positive potential for each electrode so that the responses for all electrodes could be plotted on the same vertical scale despite variations in laser intensity, optical alignment, and photoelectrolysis efficiency. The voltage axis uses the threshold potential ($E_{TH}(C-F)$) observed in coulostatic-flash experiments as the individual reference points for each electrode. Thus, the potential ref-

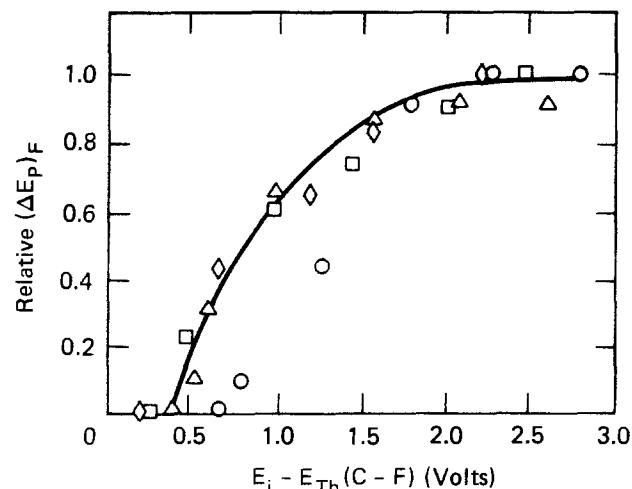
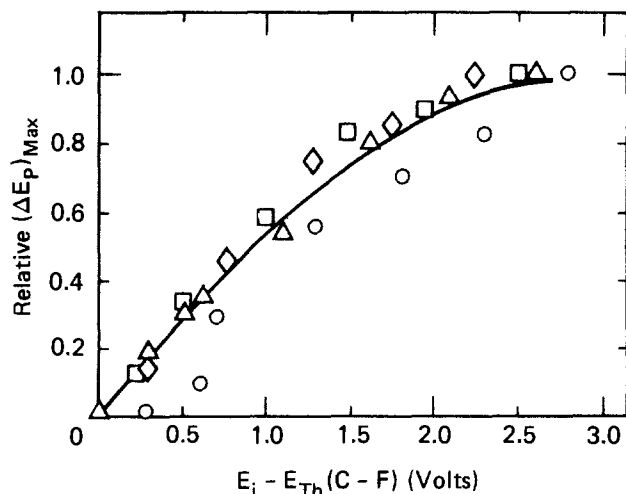


Fig. 7. Dependence of maximum (a, top) and final (b, bottom) coulostatic-flash photopotential on initial potential. 1.0M KNO_3 ; light intensity $\approx 10 \text{ kW}/\text{cm}^2$. Electrodes: A (Δ), B (\circ), C (\diamond), and D (\square).

erenced to the SCE for each electrode can be determined from Table I. Also, the relationships between $(\Delta E_p)_F$ and $(\Delta E_p)_{\max}$ at potentials near to, and very positive of E_{FB} can be obtained from Table II.

It is interesting to note from Fig. 7 that $(\Delta E_p)_F$ appears to achieve a plateau for $[E_i - E_{TH}(C-F)] > \sim 1.3V$, whereas $(\Delta E_p)_{\max}$ increases continuously with potential. This difference in dependence on potential is probably a reflection of the fact that $(\Delta E_p)_F$ is indicative of the net "photocharge" involved in the photoelectrolysis, whereas $(\Delta E_p)_{\max}$ would be related to all of the previously discussed factors which contribute to the initial photopotential excursion. Note also that the shape of Fig. 7B is similar to that seen for i_p (Fig. 1).

The fact that $(\Delta E_p)_F$ decreases as E_i approaches $E_{TH}(C-F)$ reflects a decrease in the efficiency of the photoelectrolysis process. This may be due to the occurrence of a dark back reaction, which becomes more favorable near E_{TH} . However, the back reaction must be very rapid, essentially complete before time, t_s , where the observed linear $t^{-2/3}$ dependence begins (Table III). We note that as E_i approaches $E_{TH}(C-F)$, the value of $(\Delta E_p)_F$ reaches zero before $(\Delta E_p)_{\max}$ (Fig. 6). That is, the observed photopotential pulse was not due, apparently, to a net photooxidation process for $(E_i - E_{TH}(C-F)) < \sim 0.5V$. This corresponds roughly to the potential region negative of E_{FB} . Thus, the apparent early thresholds ($E_{TH}(C-F)$) reported in Table I may be related to a transient laser-induced charge redistribution in the space-charge layer which allows minority carrier charge transfer to the solution, despite an equilibrium potential gradient opposing the flow of holes to the surface. The observation that $(\Delta E_p)_F$ approaches zero as E_i approaches E_{FB} suggests that the charge transfer is reversed as the equilibrium potential gradient in the space-charge region is approached. A similar argument may explain the early thresholds observed with chopped CW irradiation (Table I). The closer agreement between E_{TH} (pulse i_p) and E_{FB} may be attributed to the fact that the dynamics of the electrode process are not reflected in the pulse photocurrents, as discussed earlier. Of course, all of these observations at negative potentials must be tempered with the fact that for all four electrodes a gradual rise in background dark current was observed with cyclic voltammetry for E negative of $\sim -0.9V$ vs. SCE. It is not clear whether this influences the early threshold observations.

Intensity effects.—The effects of laser pulse intensity are summarized in Fig. 8. There is an apparent satura-

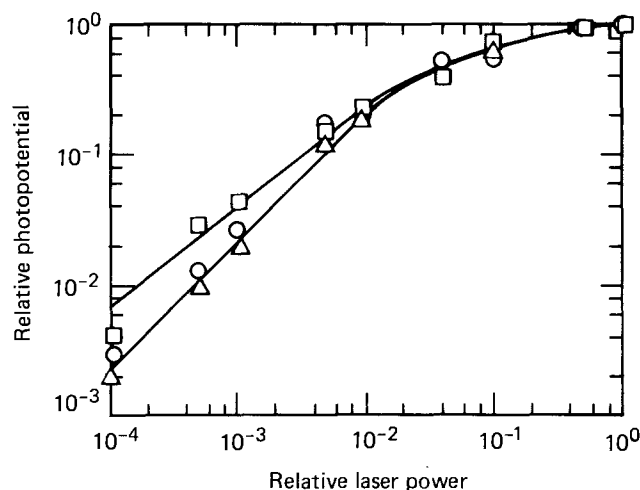


Fig. 8. Intensity dependence of photopotential $(\Delta E_p)_{\max}$ for coulometric-flash experiments. Electrode A; 1.0M KNO_3 ; $I_0 = 1$ MW/cm². $E_i = +1.0V$ vs. SCE (Δ); $E_i = 0.0V$ vs. SCE (\circ); $E_i = -0.6V$ vs. SCE (\square).

tion effect when the light intensity exceeds 10 kW/cm². Thus, all studies of potential and time dependence described here utilized a lower intensity laser pulse, as indicated in the figure legends and elsewhere. Another observation is that there is a somewhat different dependence of $(\Delta E_p)_{\max}$ and $(\Delta E_p)_F$ on light intensity. This different dependence is probably explained, as pointed out above, by the fact that $(\Delta E_p)_{\max}$ reflects the transient expansion of the space-charge layer as well as the net photoelectrolysis charge.

Electrolyte effects.—The effects of using a more dilute electrolyte, as well as using other electrolytes, have been examined. When more dilute electrolytes are used, the long-term time dependence remains the same, but the rise time of the transient increases. For example, for electrode C the observed rise times were ~ 12 , ~ 20 , and ~ 150 nsec, for 1.0, 0.1, and 0.01M KNO_3 solutions, respectively. Essentially the same trend in rise times was observed for all of the electrodes for various electrolyte concentrations. Thus, the rise time can be related primarily to the measurement limitations. That is, the rise time of the potentiometric circuitry is limited by $R_s C_m$, where R_s is the total cell resistance. [$t_{95\%} = 3(R_s C_m)$.] The value of C_m is estimated to be < 100 pf. R_s values were measured at high frequency using the vector impedance meter for the three different electrolyte concentrations. Thus, the rise times ($t_{95\%}$) are predicted to be < 8 , < 34 , and < 180 nsec for 1.0, 0.1, and 0.01M KNO_3 , respectively, based on R_s values of 26, 112, and 600 Ω for electrode C in these solutions. The trend is consistent with the observed data; in addition, using the observed rise times and R_s values, the calculated values of C_m are 60 and 80 pf, respectively, for 0.1 and 0.01M KNO_3 solutions (the measured value for 1.0M KNO_3 is limited by the laser pulse width and amplifier bandwidth).

The influence of other electrolytes was also studied. We observed no significant differences from all the above results of voltage, intensity, and time studies when 1.0M KCl or 1.0M Na_2SO_4 were substituted for 1.0M KNO_3 . With 1.0M NaOH there was an expected negative shift in the observed value of E_{FB} . Moreover, the expected trend in E_{FB} with pH was observed over the pH range of 1-13, as predicted by Eq. [3]

$$E_{FB} = E_{FB}(pH = 0) - (0.059)pH \quad [3]$$

It may be significant that unbuffered solutions were used; consequently local pH changes at the interface during photooxidation of H_2O may cause E_{FB} to vary. Further experiments need to be performed to see if buffering the solution has a significant effect and what buffers can be expected to respond rapidly enough to eliminate any contribution from a "pH jump" effect.

Correlation of flash photocurrent and photopotential measurements.—Another useful perspective on the photoinduced electrode process can be obtained by correlating the total photocharge in a photocurrent pulse obtained potentiostatically with the photopotential excursion observed coulometrically under the same conditions of laser pulse intensity, electrode potential, etc. The relationship, $Q_p/(\Delta E_p)_F = C_s$, should be approximately true.

For example, the value of C_s calculated in this way for electrode C with 1.0M KNO_3 , $E_i = 1.0V$ vs. SCE, was 3.5 μF . This value compares favorably with the value of C_s (3.3 μF) obtained from vector impedance meter measurements at 1.6 kHz (which is approximately the frequency of the photocurrent pulse, see Fig. 2). This agreement suggests that the interpretation of $(\Delta E_p)_F$ as relating to the net photooxidation charge transfer is correct.

Conclusions

These studies demonstrate for the first time that photoinduced electrode processes can be observed re-

liably in the nanoseconds to milliseconds time domains. The observed limitations on time resolution are consistent with those predicted. The time dependence of transient potentiostatic photocurrents is clearly related to the cell time constant (microseconds); whereas the time dependence of transient coulometric photopotentials can be studied with ~ 10 nsec time resolution. The fact that the rise time is ~ 12 nsec in 1.0M electrolyte may indicate that photoinduced transfer of charge to the electrolyte solution is essentially instantaneous with a 10 nsec laser pulse. While the pulsed experiment may only be accessing a monolayer or so on the surface, these initial experiments suggest that the electron transfer rate is proportional to the excitation rate. This observation is definitely a desired attribute for any stoichiometric photochemical process (e.g., solar energy conversion).

The observed subsequent photopotential decay may be related to a phenomenon of space charge relaxation which exhibits a decay time varying from ~ 1 to ~ 20 msec as the potential becomes more positive of E_{FB} . A significantly shorter and less dramatic decay is observed with increased doping density. Alternative explanations suggested here include photoproduct back reaction or hole-electron recombination. Because these other processes are known to occur to some extent, their possible contributions to the initial photopotential transient behavior should be investigated further.

These studies have provided a foundation on which to base further investigations of transient behavior with other semiconductor photoelectrodes and other photoelectrolysis processes. It should be possible to study the dynamics of redox stabilized photoelectrodes as well as dye-sensitized photoelectrolysis on a previously inaccessible time scale. Modification of the local environment (e.g., nonaqueous solvents) may be necessary to fully exploit this technique for studying chemical processes as opposed to processes inherent to the semiconductor electrode.

Acknowledgment

The authors wish to thank Jackson Harrar and Lloyd Steinmetz for their contributions to this study and Mark Wrighton for his critical review of the manuscript. Work performed under the auspices of the U. S. Department of Energy by the Lawrence Livermore Laboratory under Contract No. W-7405-Eng-48 and No. EG-77-5-02-4263, Purdue University.

Manuscript submitted March 17, 1980; revised manuscript received July 2, 1980. This was Paper 627 presented at the Los Angeles, California, Meeting of the Society, Oct. 14-19, 1979.

Any discussion of this paper will appear in a Discussion Section to be published in the June 1981 JOURNAL. All discussions for the June 1981 Discussion Section should be submitted by Feb. 1, 1981.

Publication costs of this article were assisted by the University of California.

REFERENCES

- M. S. Wrighton, *Acc. Chem. Res.*, **12**, 303 (1979).
- A. J. Bard, *J. Photochem.*, **10**, 59 (1979).
- A. J. Nozik, *Ann. Rev. Phys. Chem.*, **29**, 189 (1978).
- K. Rajeshwar, P. Singh, and J. DuBow, *Electrochim. Acta*, **23**, 1117 (1978).
- A. Fujishima and K. Honda, *Nature*, **238**, 37 (1972).
- B. A. Parkinson, A. Heller, and B. Miller, *Appl. Phys. Lett.*, **33**, 521 (1978).
- S. S. Fratoni and S. P. Perone, *Anal. Chem.*, **48**, 287 (1976).
- K. F. Dahnke, S. S. Fratoni, and S. P. Perone, *ibid.*, **48**, 296 (1976).
- G. C. Barker, A. W. Gardner, and G. Bottura, *J. Electroanal. Chem. Interfacial Electrochem.*, **45**, 21 (1973).
- J. H. Richardson, S. B. Deutscher, A. S. Maddux, J. E. Harrar, D. C. Johnson, W. L. Schmelzinger, and S. P. Perone, *ibid.*, **109**, 95 (1980).
- J. H. Richardson, S. M. George, J. E. Harrar, and S. P. Perone, *J. Phys. Chem.*, **82**, 1818 (1978).
- S. P. Perone, J. H. Richardson, B. S. Shepard, J. Rosenthal, J. E. Harrar, and S. M. George, in "New Applications of Lasers to Chemistry," G. M. Hieftje, Editor, ACS Symposium Series, Vol. 85, pp. 126-170, Washington, D.C. (1978).
- J. H. Richardson, L. J. Kovalenko, S. B. Deutscher, J. E. Harrar, and S. P. Perone, *J. Electroanal. Chem. Interfacial Electrochem.*, **106**, 263 (1980).
- C. C. Herrmann, G. G. Perrault, and A. A. Pilla, *Anal. Chem.*, **40**, 1173 (1968).
- V. Hofmann-Perez and H. Gerischer, *Z. Elektrochem.*, **65**, 771 (1961).
- L. A. Harris and R. H. Wilson, *Ann. Rev. Mater. Sci.*, **8**, 99 (1978).
- R. H. Wilson, Fourth DOE Solar Photochemistry Research Conference, University of Notre Dame, South Bend, Indiana (June 1980).
- M. S. Wrighton, D. S. Ginley, P. T. Wolczanski, A. B. Ellis, D. L. Morse, and A. Linz, *Proc. Nat. Acad. Sci. U.S.A.*, **72**, 1518 (1975).
- R. N. Noufi, P. A. Kohl, S. N. Frank, and A. J. Bard, *This Journal*, **125**, 246 (1978).
- S. M. Sze, "Physics of Semiconductor Devices," Wiley-Interscience, New York (1969).
- J. Rosenthal, A. D. Kupfer, J. Martin, and S. P. Perone, Unpublished work.
- F. C. Anson, R. F. Martin, and C. Yarnitzky, *J. Phys. Chem.*, **73**, 1835 (1969).
- C. Yarnitzky and F. C. Anson, *J. Phys. Chem.*, **74**, 3123 (1970).
- J. Newman, *J. Phys. Chem.*, **73**, 1849 (1969).
- R. P. Buck, *J. Electroanal. Chem. Interfacial Electrochem.*, **23**, 219 (1969).
- S. W. Feldberg, *J. Phys. Chem.*, **74**, 87 (1970).
- C. G. B. Garrett and W. H. Brattain, *Phys. Rev.*, **99**, 376 (1955).
- E. O. Johnson, *ibid.*, **111**, 153 (1958).
- D. Laser and A. J. Bard, *This Journal*, **123**, 1833 (1976).
- P. J. Boddy and W. H. Brattain, *ibid.*, **110**, 570 (1963).
- P. J. Boddy and W. H. Brattain, *Ann. N.Y. Acad. Sci.*, **101**, 683 (1963).
- H. Gerischer, in "Physical Chemistry an Advanced Treatise," Vol. IX-A, H. Eyring, Editor, chap. 5, p. 486, Academic Press, New York (1970).
- D. Laser and A. J. Bard, *This Journal*, **123**, 1837 (1976).
- R. K. Rhodes and R. P. Buck, *J. Electroanal. Chem. Interfacial Electrochem.*, **103**, 19 (1979).
- D. Laser and A. J. Bard, *This Journal*, **123**, 1828 (1976).

Voltammetric Evaluation of Zinc Electrowinning Solution Containing Nickel

Yar-Ming Wang

General Motors Corporation, Warren, Michigan 48090

and Thomas J. O'Keefe* and William J. James*

Materials Research Center, University of Missouri-Rolla, Rolla, Missouri 65401

ABSTRACT

The effect of nickel impurity in zinc sulfate electrowinning solutions was studied using voltammetry techniques. The reactions occurring at various points on the polarization curve are proposed and comparisons made for both pure electrolyte and those containing nickel. A nickel-activated hydrogen evolution peak was found to occur at low current densities during the anodic sweep portion of the curve, the height of which was found to be proportional to the nickel concentration in solution. The influence of certain operating parameters such as zinc ion concentration, potential scan limit, and scan rate on the nickel activated peak was also determined.

The primary industrial process for the production of metallic zinc is the electrolysis of acid sulfate solutions containing approximately 60 g/liter zinc ion and 200 g/liter H_2SO_4 (1, 2). Zinc has a rather negative potential ($-0.76V$ vs. SHE) but it also exhibits a high hydrogen overvoltage, thus making aqueous electrolysis possible. Unfortunately, the system is then very susceptible to the presence of any impurities with lower hydrogen overvoltages which might co-deposit with the zinc. Reductions in current efficiency will result if the concentration of certain impurities is too high, and extensive electrolyte purification is required prior to electrolysis to minimize this occurrence.

The problem is compounded by two factors. First, the levels of impurities that can affect deposition efficiency are very low, being in the range of 20 ppb to 10 ppm, depending on the impurity (3). In addition, synergistic interactions are common among various impurities, making it difficult to evaluate the quality of an electrolyte by chemical analysis alone. Both organic and inorganic compounds are added to assist in deposit growth control, which adds to the complexity of the solution chemistry (4). There have been numerous reports on the observed effects of impurities in zinc electrowinning (5-11) and inferences to the reasons for this behavior, but there is surprisingly little data on the more quantitative aspects of the mechanism involved.

Cyclic voltammetry techniques have been previously developed and successfully used to monitor the relative glue and antimony concentrations in zinc electrolytes (12, 13). During this research, it became apparent that other valuable information might also be derived from electrochemical testing of this type (14-17). One potential use of a more applied nature included the ability to evaluate the electrolyzability of a solution, i.e., to provide an indication of the concentration of active impurity present in solution. The process also offered interesting possibilities in establishing the fundamental behavior of many of the chemical species present in zinc electrolytes and of the zinc deposition process itself.

In order to determine the feasibility of this approach, studies were made on a "pure" or reference electrolyte and the results were compared with those obtained with nickel in solution. Nickel was chosen because it is one of the most common, harmful impurities found in zinc sulfate solutions. Furthermore, it has been extensively studied in previous electrolysis tests.

The objectives of this research were to determine the applicability of cyclic voltammetry to testing deposition efficiency in the presence of impurities such as Ni and to gain insight into the mechanism of impurity behavior in the zinc electrowinning process.

Experimental

The electrolyte was prepared by acidifying neutral, purified zinc sulfate (supplied by AMAX, Sauget, Illinois) with sulfuric acid to give a final composition of 60 g/liter Zn and 200 g/liter H_2SO_4 . For each experiment, 300 ml of electrolyte was introduced into a Pyrex "H" cell. When studying the effects of nickel additions, the desired amount of nickel sulfate was mixed with the electrolyte in a beaker before introducing it into the "H" cell.

The electrode was prepared by wet grinding on 600 grit paper, then water washed in an ultrasonic cleaner, rinsed and dried in an air stream, and immediately put into the "H" cell. An alternate preparation included a wheel polishing step using $0.05 \mu m$ γ -alumina following grinding on 600 grit paper. The cleaning and drying procedures were the same as described previously.

The cyclic voltammetry experiments were conducted in a Pyrex "H" cell, open to the atmosphere, and a three-electrode setup was used. The working electrode (test electrode) was Al (supplied by Cominco Limited, Trail, B.C., Canada), the exposed surface area of which was 1 cm^2 . The counterelectrode consisted of platinum gauze, and the reference electrode of Hg/Hg_2SO_4 (2M H_2SO_4). The entire cell assembly was immersed in a constant temperature water bath in order to maintain the electrolyte at the test temperature.

Cyclic voltammograms were obtained using a Petrolite Potentiodyne Analyzer M-4100. The current display is logarithmic which is useful in the microamp ranges encountered in the initial portion of the curve.

The cycle was set to begin at $-0.53V$ vs. SHE, with the upper cathodic limit set to a value capable of producing a total current of 50 mA (in some runs, 10 mA). At this point the process was reversed and driven anodically to the original potential. Figure 1 shows a zinc deposit obtained using parameters typical for those used in this study.

Results and Discussion

Voltammograms of a zinc electrolyte containing Ni^{+2} impurities.—Figure 2 shows the typical voltammogram of a zinc electrolyte which contains no nickel additions and Fig. 3 was obtained from an identical solution except for the addition of 5 ppm Ni^{+2} .

* Electrochemical Society Active Member.

Key words: electrowinning, zinc, voltammetry, impurities.

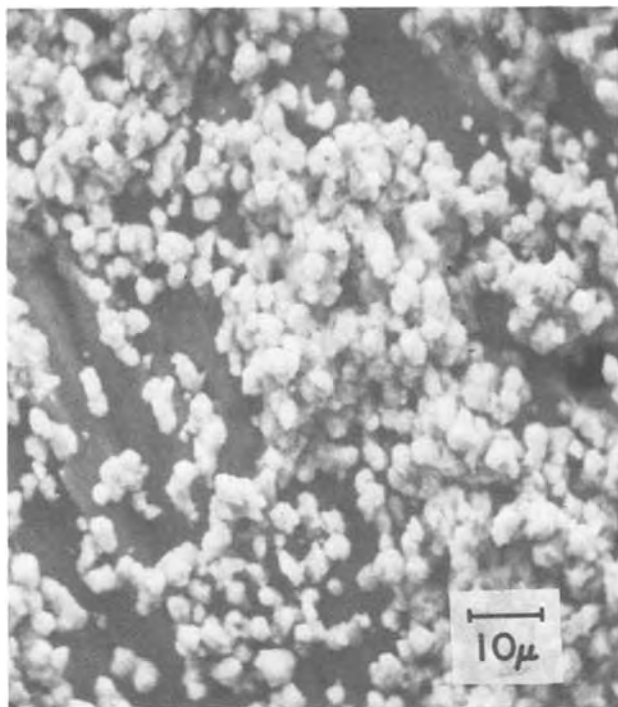


Fig. 1. SEM micrograph of a typical Zn deposit produced by cycling at 1 mV/sec to a current density of 50 mA/cm², reversing the scan until the 5 mA/cm² is attained and immediately removing from solution.

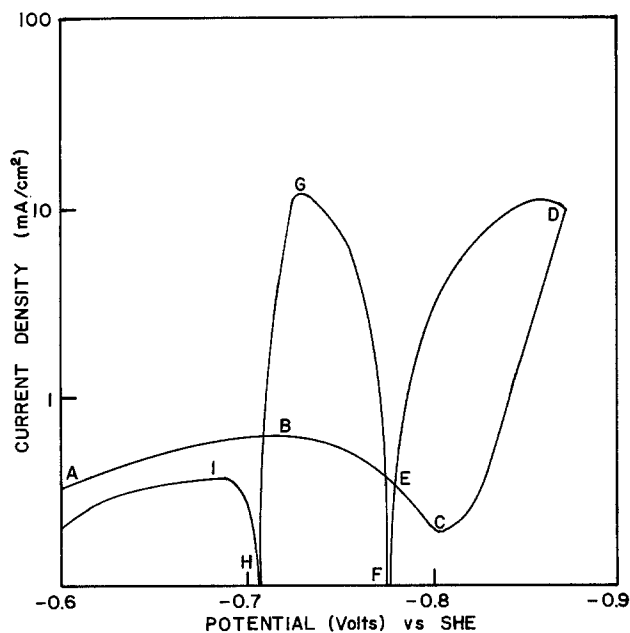


Fig. 2. Voltammogram for electrolyte containing 60 gpl Zn⁺⁺ and 200 gpl H₂SO₄. Aluminum cathode.

The more probable electrochemical reactions involved during the scan are proposed to be as follows

Cathodic reaction:

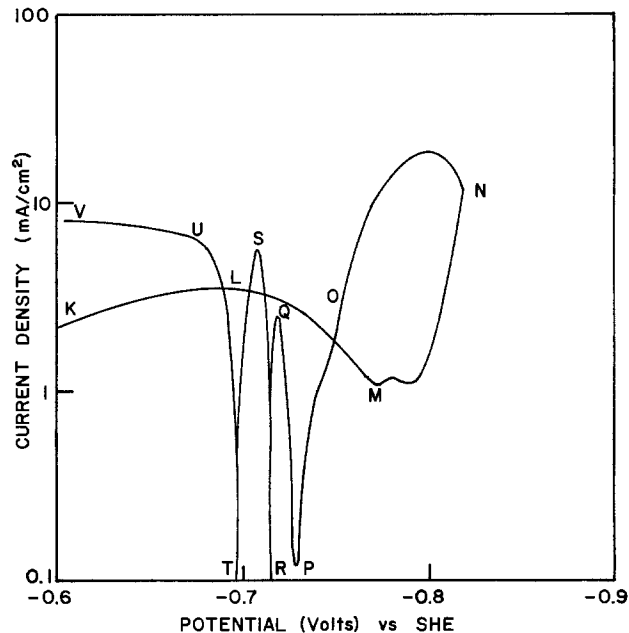
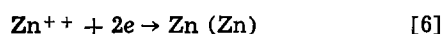
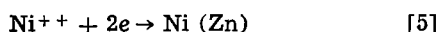
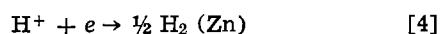
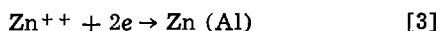
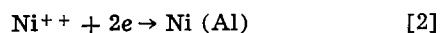
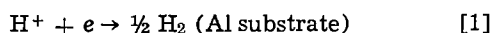
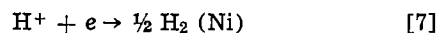
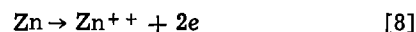


Fig. 3. Voltammogram for electrolyte containing 60 gpl Zn⁺⁺, 200 gpl H₂SO₄ and 5 mg/l Ni⁺⁺. Aluminum cathode.



Anodic reaction:



Since the Ni addition was less than 20 mg/liter, deposition of Ni should be diffusion controlled; i_2 and i_5 are the diffusion-limited currents.

The voltammogram for the electrolyte containing no Ni²⁺ is divided into 7 sections for the benefit of discussion. The numbered subscripts refer to the current for the reactions listed previously and i_c and i_a are net cathodic and anodic currents, respectively.

Region AB — ($i_c = i_1$).—Hydrogen ion reduction appears to be the main reaction occurring, but the magnitude of the current is affected by the chemical nature of the zinc solution. The potential of zero charge (PZC) for Al is approximately -0.6V (SHE). As the electrode potential becomes more negative, adsorption of zinc ions on the aluminum surface can occur. This blocks the access of H⁺ to the cathode for discharge. The hydrogen current for an electrolyte containing only H₂SO₄ (200 g/liter) is of a much higher value than for the same acid strength solution containing zinc ions. The effects of zinc ions on the initial hydrogen reduction current will be discussed in the latter part of this paper.

Region BC — ($i_c = i_1$).—Hydrogen ion reduction continues to be the dominant reaction until the potential where the minimum in current (point C) occurs. Some spot-checks have been conducted by holding the electrode at constant potential in this region for 20 min, removing it from the cell, and examining its surface with the scanning electron microscope (SEM) and energy dispersive x-ray attachment. There was no evidence of zinc deposition. As the electrode potential is made more negative, the contact adsorption (specific ion adsorption) of zinc ions becomes more pronounced. This surface blockage by zinc ions contributes to the decrease in hydrogen current.

Region CD — ($i_c = i_1 + i_3 + i_4 + i_6$).—The overpotential is sufficient to initiate zinc deposition at point C. From C to D, there is simultaneous reduction of zinc and hydrogen ions. The co-deposition occurs on both the aluminum and the freshly nucleated zinc, with the latter predominating with increasing potential.

Region DE — ($i_c = i_1 + i_3 + i_4 + i_6$).—At point D the scan direction is reversed. From D to E, zinc and hydrogen ions discharge on both Zn and Al surfaces. Zn deposited on Zn requires less activation overpotential, so the current is higher than that measured from the front sweep when compared at the same potential value. The cathodic current decreases with decreasing reduction potential. If a constant potential is maintained in the region D to E, the current will increase and reach a steady-state value. However, at point E (approximately 5–10 mV from the crossover potential for cathodic to anodic current) the current fluctuates. This instability is indicated by dissolution followed by partial deposition of zinc in a cyclic pattern. The exact pattern followed at this point is dependent on the purity and nature of the electrolyte. The potential at E can be considered as a type of reversible potential for Zn for the particular solutions under investigation.

Region EF — ($i_c = i_1 + i_4 - i_8$).—As the potential becomes less negative, i_8 , Zn dissolution increases. In the meantime, i_1 and i_4 decrease, so the net cathodic current i_c decreases. At point F, $i_1 + i_4 = i_8$ or $i_c = 0$; this condition is referred to as the crossover potential.

Region FGH — [$i_a = i_8 - (i_1 + i_4)$].—As the potential becomes more positive, i_8 increases and i_1 , i_4 decrease, so from F to G, Zn dissolution predominates but hydrogen ion reduction is still evident. As the anodic zinc process proceeds, the surface is eventually depleted, thus causing the drop of i_a from G to H. At point H, $i_a = 0$ and accordingly $i_8 = i_1 + i_4$.

Region HIJ — ($i_c = i_1 + i_4 - i_8$).—As the deposited zinc approaches complete dissolution, i_8 will approach zero, $i_c = i_1$, and the cathodic current results mainly from the hydrogen discharge reaction. Some notable changes in the curve occur when Ni^{2+} impurity is present in the solution, as shown in Fig. 3.

Region KL — ($i_c = i_1 + i_2$).— i_2 is very small and perhaps negligible, thus the amount of nickel deposited is insufficient to cause any increase in the hydrogen reduction current.

Region LM — ($i_c = i_1 + i_2$).—The drop of the hydrogen reduction current again is caused by the increasing coverage on the Al surface of zinc contact-adsorbed ions.

Region MNO — ($i_c = i_3 + i_1 + i_6 + i_4 + i_2 + i_5$).—Zinc starts to deposit at M. The surface area increases as the deposition process proceeds. As a result the nickel deposition current (the nickel diffusion current density is constant in this potential range) is higher. However, the nickel in the deposit is bridged over or covered by the massive deposition of zinc and is unable to serve as active sites for the hydrogen ion discharge reaction. The cathodic current from M to N increases with increasing negative potential. At point N the scan direction is reversed. From N to O the cathodic current becomes smaller as the potential becomes more positive. With the presence of nickel in the deposited layer, zinc dissolution begins at a more negative potential, O than the potential E when nickel ion is absent.

Region OPQR — ($i_c = i_7 + i_1 + i_4 - i_8$).—As the scan goes from O toward a more positive direction, partial dissolution of zinc begins from the outer layer, probably at selected imperfection sites. Nickel and hydrogen ions can also be discharged by a localized spontaneous displacement reaction. As some of the surface-layer zinc dissolves, the underlying nickel accumulated from the previous cathodic process is exposed to the solution. In this potential region, net zinc deposition stops, and zinc ion contact-adsorption becomes less severe due to the increasing positive potential. The presence of the additional active nickel sites and the reduction in blockage from the more massive deposition of zinc increases the hydrogen reduction current sharply from P to Q. From Q to R the decrease in cathodic current is due to the relative increase in zinc

dissolution compared to hydrogen evolution from the available nickel sites. At point R, $i_8 = i_7 + i_1 + i_4$, the net current is zero.

Region RST — [$i_a = i_8 - (i_7 + i_1 + i_4)$].—The net anodic current is due to the dominance of the zinc dissolution, but there is still considerable hydrogen reduction occurring.

Region TUV — ($i_c = i_1 + i_4 + i_7 - i_8$).—This part of the cathodic current is much higher than that from the front scan. There is an indication that some nickel still remains on the surface. However, when the cathode is left at open circuit for a few minutes and the second scan started, the hydrogen reduction current drops to a normal value. The probable cause is flushing or removal of the nickel deposits from the Al substrate surface by the hydrogen bubbles.

The presence of nickel is indicated by a cathodic current peak near the crossover potential at Q. Other findings for the voltammograms of electrolytes with Ni^{2+} additions (nickel voltammograms for short) are as follows:

1. The nickel peak appears only after some zinc has been deposited. If the cathodic sweep direction is reversed before the zinc deposition potential is attained, the nickel peak is not observed.

2. H_2 evolution is considerably more vigorous from the cathode surface at point Q on the voltammogram than for a comparable potential in the pure solution.

3. A continuous scan trace of the previous curve indicates that nickel does not accumulate nor remain on the Al substrate.

4. Table I shows the effects of zinc ion concentration on the nickel voltammograms. The nickel peak potential shifts toward less negative values with increasing Zn concentration in the electrolyte; the same trend holds for the Zn deposition potential. This indicates that the Ni peak potential is dependent on the Zn concentration in the electrolyte. Also the Ni peak current increases with decreasing Zn ion concentration.

Effects of test parameters on results.—The aims of the test parameter study were to develop procedures to maximize the nickel detectability in zinc electrolytes, and to investigate the behavior of nickel in zinc electrowinning processes.

Cathode surface preparation.—The height of the nickel peak current (point Q) is greater with a 600 grit polished electrode than for one which is wheel polished. The rougher surface, with higher effective area, enhances the effect of and sensitivity to the presence of the nickel impurity. Additional work on the cathode material and its preparation seems warranted, since it can influence the variations noted in polarization behavior in the presence of impurities.

Upper scan limit.—The results of this study are shown in Table II. There is a fivefold increase in the nickel peak current when the upper scan limit is raised from 1 to 10 mA/cm², but it remains fairly constant at higher limits, up to 50 mA/cm². The peak current is related to the Ni/Zn ratio in the deposit, and this ratio decreases with increased current density.

Scan rate.—Scan rates in the range of 0.1–10 mV/sec were studied and the results are tabulated in Table

Table I. Effects of zinc ion concentration on the nickel-type voltammograms, 200 g/liter H_2SO_4 , 20 ppm Ni^{2+} , Al cathode, 600 grit polished, 30°C, scan rate 0.5 mV/sec, upper scan limit 10 mA/cm²

Zinc ion concentration (g/liter)	Nickel peak potential V (SHE)	Nickel peak current (mA)	Zn deposition potential measured at 1.5 mA/cm ² on the cathodic sweep V (SHE)
20	-0.770	100	-0.841
60	-0.753	37	-0.823
100	-0.742	12	-0.805

Table II. Effect of upper scan limit on the nickel peak current densities, 60 gpl Zn, 200 gpl H₂SO₄, 5 mg/liter Ni²⁺, aluminum cathode, 600 grit-polished, 30°C, scan rate 0.5 mV/sec

Upper scan limit (mA/cm ²)	Ni peak height (mA/cm ²)
1	2.7
5	8.6
10	12.7
50	13.8

Table III. Effect of scan rates on the Ni voltammograms, 60 g/liter Zn, 200 g/liter H₂SO₄, 5 ppm Ni²⁺, Al cathode, 600 grit-polished, 30°C, upper scan limit 10 mA/cm²

Scan rate (mV/sec)	Ni peak height (mA/cm ²)	Time required for completing one cycle (min)
0.1	50	95
0.5	12	20
1.0	2	11
10.0	No Ni peak	1

III. The scan rate at 0.1 mV/sec gives the highest peak, and hence greatest sensitivity to the presence of nickel. The time for completion of a test approaches 2 hr at this scan rate, and would be too long if used for monitoring plant operations. However, for basic data generation it is acceptable and combinations of scan limits and rates must be tested to determine the optimum values for these parameters.

Electrolyte composition.—The effect of Zn ions on the voltammogram is shown in Fig. 4. The hydrogen discharge reaction appears to be depressed by the presence of Zn ions in the electrolyte. The adsorption of Zn ions on Al becomes pronounced at about 80 mV less cathodic than the Zn deposition potential. Also, the Zn deposition potentials shift to less negative potentials with increasing Zn ion concentration.

The effect of acid strength on Ni detectability was studied using a 60 g/liter Zn solution and the acid strength was varied from 50 to 200 g/liter. All solutions were doped with 3 mg/liter Ni, and the tests were conducted at 30°C. The voltammograms revealed

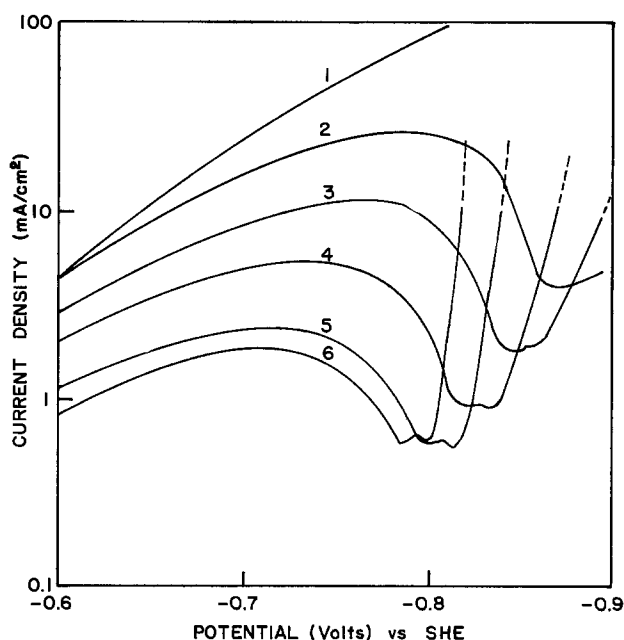


Fig. 4. Effect of Zn²⁺ content on voltammograms containing 200 gpl H₂SO₄ plus curve 1, no Zn²⁺; curve 2, 1 gpl Zn²⁺; curve 3, 5 gpl Zn²⁺; curve 4, 20 gpl Zn²⁺; curve 5, 60 gpl Zn²⁺; curve 6, 100 gpl Zn²⁺.

that the characteristic peak indicating the presence of Ni was present only at high acid contents (200 g/liter).

Electrolyte temperature.—Increasing the temperature did increase the sensitivity for Ni ion detection. With 1 mg/liter Ni in the electrolyte, no Ni peak appeared on the anodic sweep at 30°C. An Ni peak of 2 mA appeared at 55°C. Most Zn electro-winning plants operate in the temperature range of 30°–40°C.

Ni detectability study.—The detectable limit for nickel in the electrolyte of 60 g/liter Zn, 200 g/liter H₂SO₄ is 3 mg/liter at 30°C and 1 mg/liter at 45°C, using test parameters discussed previously. Values of the Ni potential and the Ni current as a function of Ni ion concentration are given in Table IV. It can be seen that the Ni peak potential is independent of the Ni²⁺ concentration, while the height of the Ni peak current density is proportional to Ni²⁺ concentration. A straight line relationship exists for the Ni peak current density vs. the Ni concentration as shown in Fig. 5. This indicates that the Ni deposition from the Zn electrolyte is a diffusion-controlled process.

Better detectability of nickel can be achieved by diluting the Zn ion concentration with 200 g/liter H₂SO₄. Starting from 60 g/liter Zn, 200 g/liter H₂SO₄ solution, the electrolyte was doped with 0.5 mg/liter Ni²⁺. Normally, 0.5 mg/liter would not show up on the voltammogram with the 60 g/liter Zn electrolyte; however, by one-tenth dilution with 200 g/liter H₂SO₄ solution, the Ni peak corresponding to 0.05 mg/liter appeared on the voltammogram as shown in Fig. 6.

The Ni concentration and peak current relationship for the 6 g/liter Zn electrolyte is shown in Table V.

Conclusions

By using cyclic voltammetry techniques, it is possible to elucidate the manner in which nickel is activated in zinc electrolytes. The behavior observed is also consistent with that found to occur for long term zinc deposition (6). Current efficiency decreases with increased nickel ion concentration, temperature, acid level, and time of deposition. The nickel peak current is shown to be sensitive to these parameters as well, and in the same approximate proportions, with higher nickel peaks indicating poorer efficiency. Once conditions on the electrode surface allow a critical content of nickel to be exposed, such as at the bottom of a recess in a rough deposit, preferred hydrogen evolution is initiated at this point. Zinc deposition is less

Table IV. Effects of Ni²⁺ concentrations on the nickel peak potential and current on the voltammograms, 60 gpl Zn, 200 gpl H₂SO₄, aluminum cathode, 600 grit-polished, 30°C, scan rate 0.5 mV/sec

Nickel concentration (mg/liter)	Ni peak potential V (SHE)	Ni peak current densities (mA/cm)
3	-0.750	6.6
5	-0.755	11.0
10	-0.756	23.0
15	-0.756	34.0

Table V. Nickel concentration, nickel peak current relationship observed from the voltammogram of 6 gpl Zn, 200 gpl H₂SO₄ electrolytes, 45°C, aluminum cathode, 600 grit-polished, scan rate 0.5 mV/sec

Ni concentration in the electrolyte (mg/liter)	Current measured at -0.796V (Ni potential) on the anodic sweep (mA/cm liter)	Peak current corrected from base electrolyte (mA)
0	1.9	0
0.05	2.9	1.0
0.10	3.7	1.8
0.20	6.1	4.2
0.30	8.0	6.1

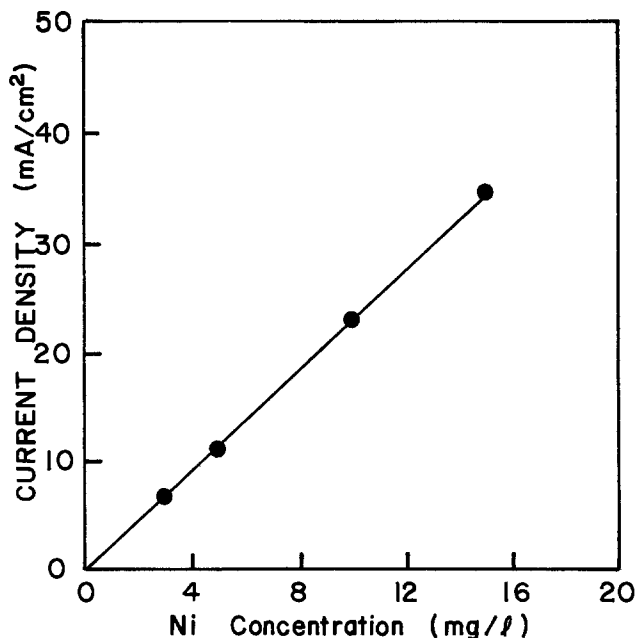


Fig. 5. Nickel concentration vs. nickel peak current taken from voltammograms for electrolyte containing 60 gpl Zn^{++} and 200 gpl H_2SO_4 . Aluminum cathode.

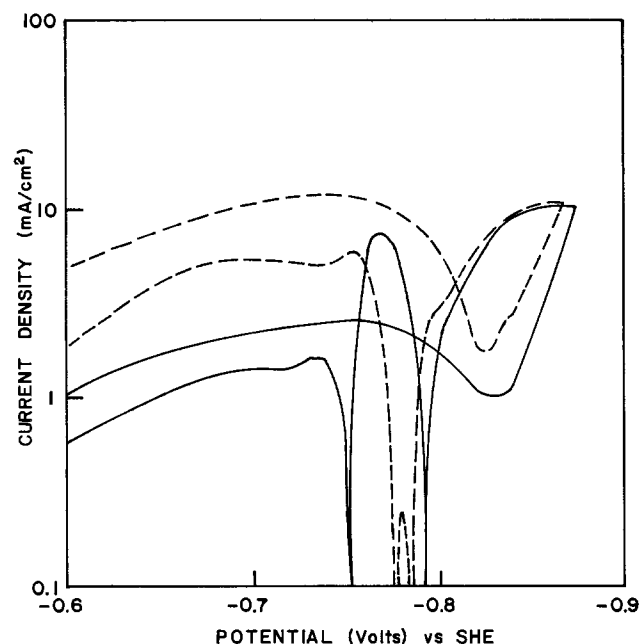


Fig. 6. Voltammograms for electrolyte containing 6 gpl Zn^{++} and 200 gpl H_2SO_4 (solid line) and 6 gpl Zn^{++} , 200 gpl H_2SO_4 plus 0.05 mg/liter Ni^{++} .

feasible, and an unstable condition is generated which allows zinc to dissolve. The condition is probably similar to a local cell reaction encountered in corrosion. It might also be expected that, with time, an autocatalytic reaction can occur, since even more nickel becomes exposed as the zinc dissolves. If such were the case, pitting might be expected, and although this was not investigated in these short time studies, pits have been noted in zinc deposits galvanostatically produced from electrolyte containing nickel.

In addition to providing for some insight into the mechanism for nickel behavior, this technique might also be used to monitor the level of nickel present

in solution. Additional tests would have to be conducted using other known detrimental impurities such as cobalt, copper, antimony, germanium, and arsenic. If there are common mechanisms involved in their behavior, it may be that only a total effect will be indicated, rather than a differentiation between individual impurities. This technique might also be used to advantage when attempting to find a means of combating the influence of nickel impurities. Screening tests could be run with the nickel peak height being used to indicate the effectiveness of the control method chosen.

The determination of the quality of zinc sulfate electrolyte prior to electrolysis has always been a major challenge in industrial operations. Polarization techniques of the type described appear to offer some promising opportunities to the solution of this problem and, if properly developed, might become a useful analytical tool in commercial practice.

Acknowledgments

The authors are particularly grateful for the contributions of Harlan Rice, Kenneth Allison, and Jack Smart during this investigation and the helpful technical discussions and suggestions of Dr. R. Kerby, Cominco Limited, and Dr. E. Cole, USDI, Bureau of Mines.

The financial and technical assistance of Cominco Limited and AMAX throughout this program is also acknowledged.

Particular thanks are extended to the U.S. Department of Interior, Bureau of Mines, for their continued support of this research under contract GO-264029.

Manuscript submitted Nov. 19, 1979; revised manuscript received ca. June 27, 1980.

Any discussion of this paper will appear in a Discussion Section to be published in the June 1981 JOURNAL. All discussions for the June 1981 Discussion Section should be submitted by Feb. 1, 1981.

Publication costs of this article were assisted by the University of Missouri.

REFERENCES

1. C. H. Mathewson, "Zinc, The Science and Technology of the Metal, Its Alloys and Compounds," pp. 217-224, Reinhold Publishing Company (1959).
2. C. L. Mantell, "Electrochemical Engineering," pp. 214-218, McGraw-Hill, New York (1960).
3. G. C. Bratt, Proc. Tasmania Conference, pp. 277-290 (1977).
4. D. J. Mackinnon and J. M. Brannen, *J. Appl. Electrochem.*, **7**, 451 (1977).
5. R. C. Kerby and T. R. Ingraham, Research Report R243, Department of Energy, Mines and Resources, Mines Branch, Ottawa.
6. H. H. Fukubayashi, T. J. O'Keefe, and W. C. Clinton, R17966, Bureau of Mines, U.S. Department of Interior, Washington, DC (1974).
7. I. W. Wark, Proc. First Aust. Conf. Electrochemistry, Sydney and Hobart (1963).
8. U. F. Turomshina and V. V. Stender, *Zhur. Prik. Khim.*, **28**, 372 (1955).
9. D. R. Fosnacht, Thesis, University of Missouri-Rolla (1978).
10. D. L. Cottey, Thesis, Columbia University (1976).
11. G. C. Bratt, *Electrochem. Technol.*, **2**, 323 (1964).
12. R. C. Kerby, H. E. Jackson, T. J. O'Keefe, and Y. M. Wang, *Metall. Trans.*, **8B**, 661 (1977).
13. B. A. Lamping and T. J. O'Keefe, *ibid.*, **8B**, 551 (1976).
14. M. Maja and P. Spinelli, *This Journal*, **118**, 1538 (1971).
15. O. Vennesland, H. Holtan, and S. Solhjill, *Acta. Chem. Scand.*, **27**, 846 (1973).
16. L. F. G. Williams, *This Journal*, **126**, 566 (1979).
17. D. Tench and C. Ogden, *ibid.*, **125**, 194 (1978).

Low Temperature Polarography of Alkyl Halides in Dimethylformamide

Adsorption onto Mercury of Complex Species Composed of Tetramethylammonium and Halide Ions

William F. Carroll, Jr.¹ and Dennis G. Peters

Department of Chemistry, Indiana University, Bloomington, Indiana 47405

ABSTRACT

At relatively negative potentials and at temperatures below -29°C , a prominent current minimum is observed in polarograms for the reduction of alkyl halides in dimethylformamide containing tetramethylammonium perchlorate. This minimum is attributed to the formation and subsequent adsorption onto mercury of complex ionic species which block reduction of the alkyl halide; these adsorbed species appear to be positively charged aggregates consisting of supporting electrolyte cations and halide ions released upon electrolysis of the starting material. If a small amount of tetramethylammonium halide is added to a solution of an electroactive substance other than an alkyl halide in dimethylformamide containing tetramethylammonium perchlorate, the same low temperature current minimum is seen. Further, in dimethylformamide containing only tetramethylammonium perchlorate at concentrations greater than 0.08*F*, there is evidence that a species derived from the supporting electrolyte itself is adsorbed onto mercury at temperatures lower than -33°C .

In three previous papers dealing with the electrochemistry of 1-halonorbornanes (1) and 1,4-dihalonorbornanes (2, 3) in dimethylformamide containing tetramethylammonium perchlorate, we have reported that low temperature polarograms exhibit unusual current minima. At temperatures below -29°C , a conspicuous depression of the current is observed on the diffusion plateau of the single polarographic wave for 1-iodonorbornane; this minimum becomes more severe as the temperature is lowered, obscuring a region of potentials as wide as 250 mV at -36°C . Similar behavior is seen for 1-bromonorbornane, although the polarographic minimum does not appear until the temperature reaches -33°C . Two polarographic waves are observed for 1,4-diiodonorbornane at room temperature, but at temperatures less than -28°C , the current corresponding to the second step of reduction is depressed to a level equal to that of the first wave. At -34°C the diffusion current for 1,4-dibromonorbornane is suppressed almost completely over more than a 200 mV range of potentials.

Phenomena responsible for these current minima, seen in low temperature polarograms for 1-halonorbornanes and 1,4-dihalonorbornanes only when tetramethylammonium perchlorate is employed as supporting electrolyte, manifest themselves in other ways. Thus, in the potential region corresponding to the polarographic minima, the shape of current-time curves for individual mercury drops is characteristic of adsorption onto the electrode surface of an electroinactive substance (4). Moreover, faradaic and capacitive currents observed by means of three-electrode, phase-sensitive a-c polarography (5) are likewise indicative of the adsorption of electroinactive species on the mercury cathode.

On the basis of the preceding kinds of experimental evidence, we conclude, as discussed in this paper, that when any of the aforementioned halogen-substituted norbornanes is reduced at low temperature in dimethylformamide containing the tetramethylammonium cation, the latter combines with the liberated iodide or bromide to form a complex ion aggregate

which is adsorbed onto mercury at certain potentials, thereby causing the anomalous polarographic minima. In addition, in the absence of an electroactive alkyl halide, it appears that a species derived from tetramethylammonium perchlorate itself may undergo adsorption at temperatures below -33°C .

Experimental

Reagents.—Dimethylformamide used as solvent and tetramethylammonium perchlorate employed as supporting electrolyte were handled as described in a previous paper (1). Modified procedures devised in our laboratory (1) were utilized for the synthesis of 1-bromonorbornane and 1-iodonorbornane, and the preparation of 1,4-dibromonorbornane and 1,4-diiodonorbornane was done according to a method outlined earlier (3). Commercially available 1-iododecane (Chemical Samples Company, 95%) and 1-bromodecane (J. T. Baker & Company, 97%) were purified by means of vacuum distillation; fractions used for electrochemical experiments were determined with the aid of gas chromatography to be greater than 99% pure (6).

Preparation of 1,10-diiododecane was accomplished by treatment of 1,10-dibromodecane with sodium iodide in acetone at 30°C . Sodium bromide precipitated immediately, and the reaction mixture was stirred until peaks due to bromine-containing compounds were absent from gas chromatograms. Upon recrystallization from pentane, the product was found to be identical to an authentic sample of 1,10-diiododecane purchased from ICN Pharmaceuticals, Incorporated, Plainview, New York.

Apparatus and procedures.—Figure 1 is a picture of the cell used for polarography. A nitrogen gas inlet tube and a reference electrode are mounted in horizontal 12/18 standard-taper ground-glass joints (A and B). An alcohol thermometer is inserted through a plastic adapter and sealed with a rubber O-ring into a screw-type glass joint (C). Extending from the bottom of the inner compartment of the cell are two standard-taper stopcocks (D); mercury drops can be trapped in the space between the stopcocks, and the lower stopcock can be opened to permit collection of the mercury.

¹ Present address: Firestone Plastics Company, Pottstown, Pennsylvania 19464.

Key words: adsorption, alkyl halides, 1,4-dihalonorbornanes, 1-halonorbornanes, low temperature polarography.

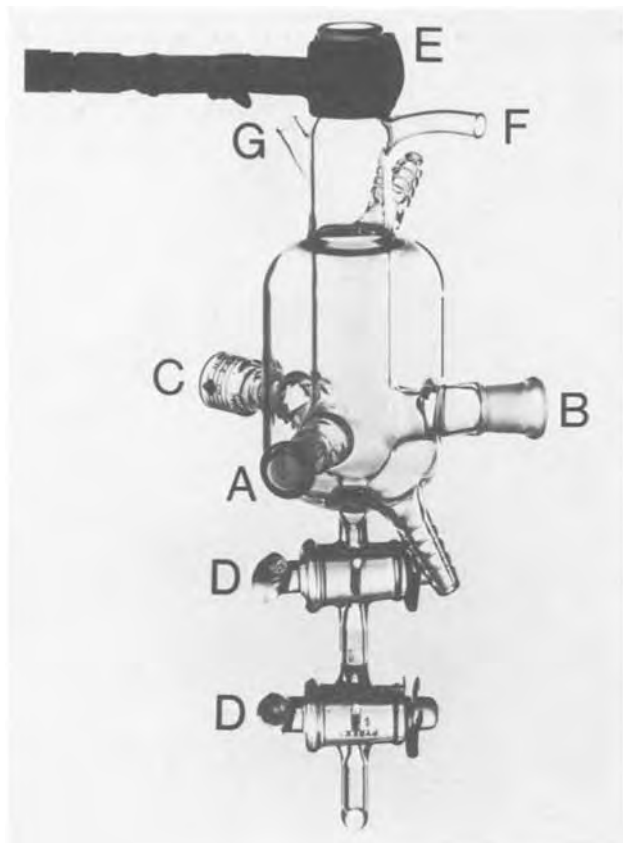


Fig. 1. Polarographic cell; see text for detailed discussion

A dropping mercury electrode is inserted through the 14/20 standard-taper ground-glass joint (E) at the top of the cell and is secured with a Teflon fitting. Nitrogen gas, used to stir and deaerate the solutions, escapes by way of a sidearm (F) near the top of the cell. A second sidearm (G) allows insertion of a platinum wire anode as well as introduction or removal of solution. To keep the temperature of the solution constant to within $\pm 0.1^\circ\text{C}$, a 1:1 methanol:water mixture was circulated through the jacket surrounding the cell by use of an FTS Systems, Incorporated, Stone Ridge, New York, MC-2-60 refrigerated bath equipped with FTS cryogenic pump and FTS TCH-1 controller. Polyurethane foam plumbing insulation was wrapped around both the polarographic cell and the solid polyurethane tubing used to carry the coolant.

Conventional d-c polarography was performed with the aid of a Princeton Applied Research Corporation (PAR) Model 175 Universal Programmer, a PAR Model 173 potentiostat/galvanostat, and a PAR Model 176 current-to-voltage converter capable of iR compensation. All of the a-c polarography was carried out by use of a PAR Model 174 Polarographic Analyzer equipped with a Krohn-Hite Model 5200A signal generator and a PAR Model 5101 lock-in amplifier; an a-c signal of amplitude 100 mV and frequency 600 Hz was used. All potentials are reported with respect to a reference electrode consisting of a saturated cadmium amalgam in contact with dimethylformamide saturated with cadmium chloride and sodium chloride (7, 8); this electrode has a potential of -0.750V vs. the aqueous saturated calomel electrode.

Results and Discussion

Low temperature polarography of alkyl halides.—Shown in Fig. 2 are polarograms recorded at various temperatures for the reduction of 1-iodonorbornane in dimethylformamide containing 0.1F tetramethylammonium perchlorate. Characteristic of the polarographic reduction of many alkyl halides at room

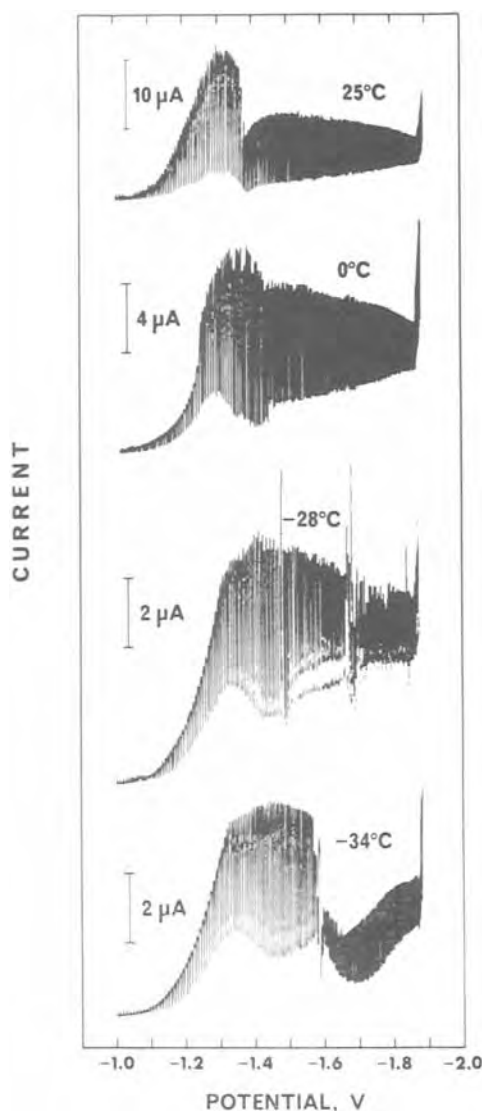


Fig. 2. Effect of temperature on polarograms for reduction of 0.0025M 1-iodonorbornane in dimethylformamide containing 0.1F tetramethylammonium perchlorate.

temperature is the appearance of a current maximum,² which diminishes in size and finally vanishes as the temperature is lowered. On the other hand, at temperatures below -29°C , the polarogram for 1-iodonorbornane exhibits a pronounced minimum which becomes more severe as the temperature is decreased. As revealed in Fig. 3, similar behavior is seen for 1,4-diodonorbornane. Figure 4 demonstrates that a low temperature minimum can be observed for alkyl bromides as well as for alkyl iodides, although temperatures below -32°C are needed to cause the phenomenon. A set of low temperature polarograms showing current minima for 1-bromodecane, 1-iododecane, and 1,10-diododecane is illustrated in Fig. 5, so the appearance of the minimum is not unique to norbornyl halides. Most significantly, the minima appear at low temperatures only when tetramethylammonium perchlorate is employed as supporting electrolyte.

Polarography of dimethylformamide solutions of tetramethylammonium perchlorate.—Even in the absence of an electroactive alkyl halide, solutions of tetramethylammonium perchlorate in dimethylformamide exhibit unusual polarographic behavior at low

² This polarographic maximum does not exhibit the usual response to added suppressors. Although further investigation of this phenomenon is underway, we believe that it is related to reduction of adsorbed alkylmercury radicals.

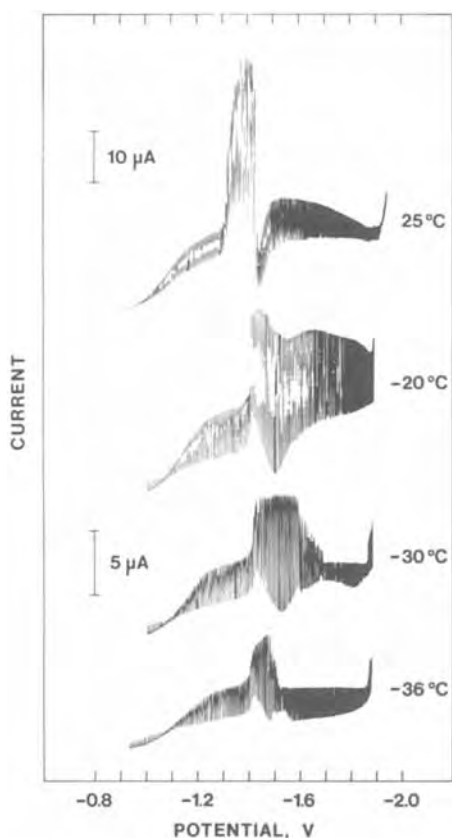


Fig. 3. Effect of temperature on polarograms for reduction of 0.0025M 1,4-diidonorborene in dimethylformamide containing 0.1F tetramethylammonium perchlorate; 10 μ A current scale applies to the upper polarogram and 5 μ A current scale applies to the three low temperature polarograms.

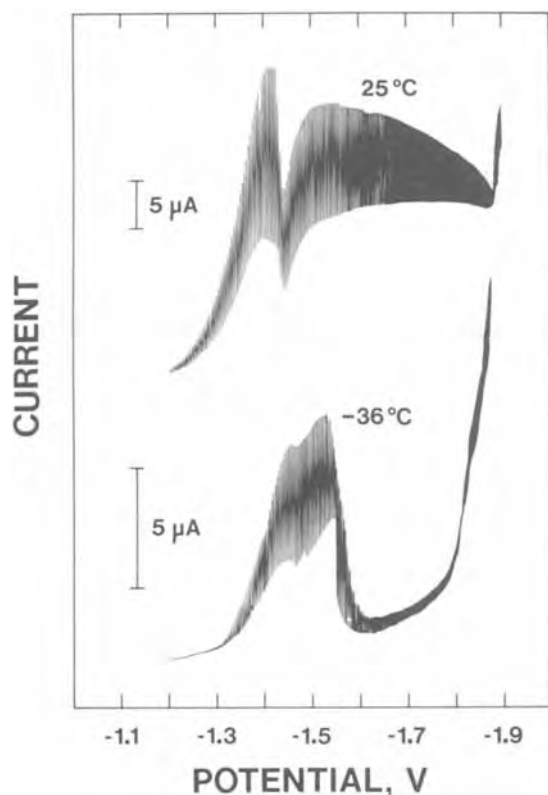


Fig. 4. Effect of temperature on polarograms for reduction of 0.0025M 1,4-dibromonorborene in dimethylformamide containing 0.1F tetramethylammonium perchlorate.

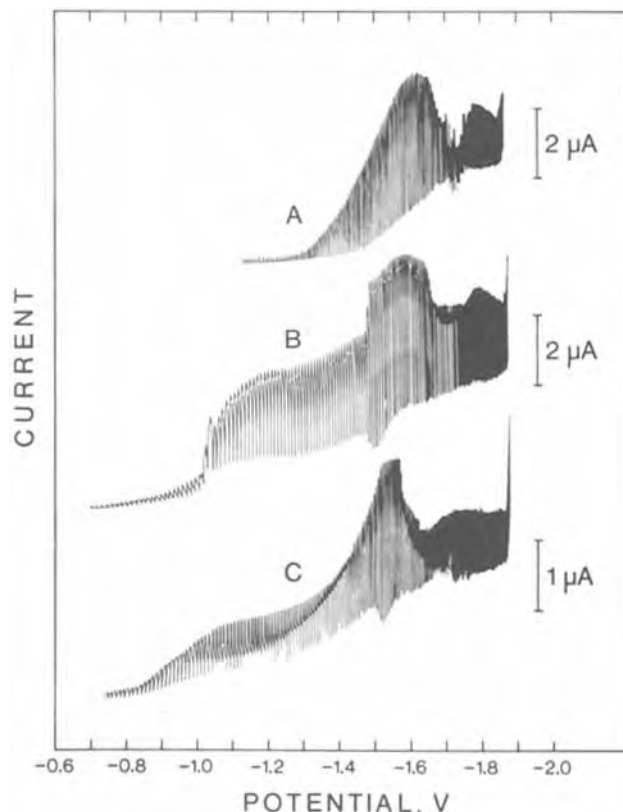


Fig. 5. Polarograms for reduction of alkyl halides in dimethylformamide containing 0.1F tetramethylammonium perchlorate at -33°C ; 2.2 mM 1-bromodecane (curve A), 3.0 mM, 1-iododecane (curve B), 0.8 mM 1,10-diiododecane (curve C).

temperature. A plot of mercury drop-time vs. potential for a 0.1F solution of tetramethylammonium perchlorate in dimethylformamide at -33°C is illustrated in Fig. 6A, in which the most notable feature is the sharp discontinuity at -1.64V . Presented in Fig. 6B are d-c polarograms for the same system that were recorded at two sensitivities; these residual-current curves show a depression in the region of potentials between -1.64 and -1.83V . Such a depression is seen more clearly both in the faradaic current ($\phi = 15^{\circ}$) and charging current ($\phi = 105^{\circ}$) monitored by means of phase-sensitive a-c polarography; the phase angles needed to optimize the effects depicted in Fig. 6B differ from the theoretically ideal values of 0° and 90° , respectively, undoubtedly because the resistance of the solution alters the desired phase relationships. These observations suggest that some species in solution, namely, the tetramethylammonium cation, tetramethylammonium perchlorate, or an ion aggregate derived from the supporting electrolyte, is adsorbed onto the surface of the mercury electrode at potentials between -1.64 and -1.83V .

Effects of temperature as well as the concentration of supporting electrolyte are shown in Fig. 7. An inspection of the faradaic and charging currents reveals that the anomalous depression is first observed in a-c polarograms recorded at -31°C and is fully developed at -33°C . Interestingly, when the concentration of tetramethylammonium perchlorate is decreased from 0.1 to 0.08F, a current depression is no longer seen at -33°C (Fig. 7E).

Tetramethylammonium and halide ions are both required to cause the low temperature polarographic minimum for alkyl halides.—Polarograms for a 0.003M solution of anthracene in dimethylformamide containing 0.1F tetramethylammonium perchlorate are depicted in Fig. 8A. At a temperature of -29°C , the d-c polarogram exhibits the expected two-step reduction, the half-wave potentials being -1.21 and -1.72V ,

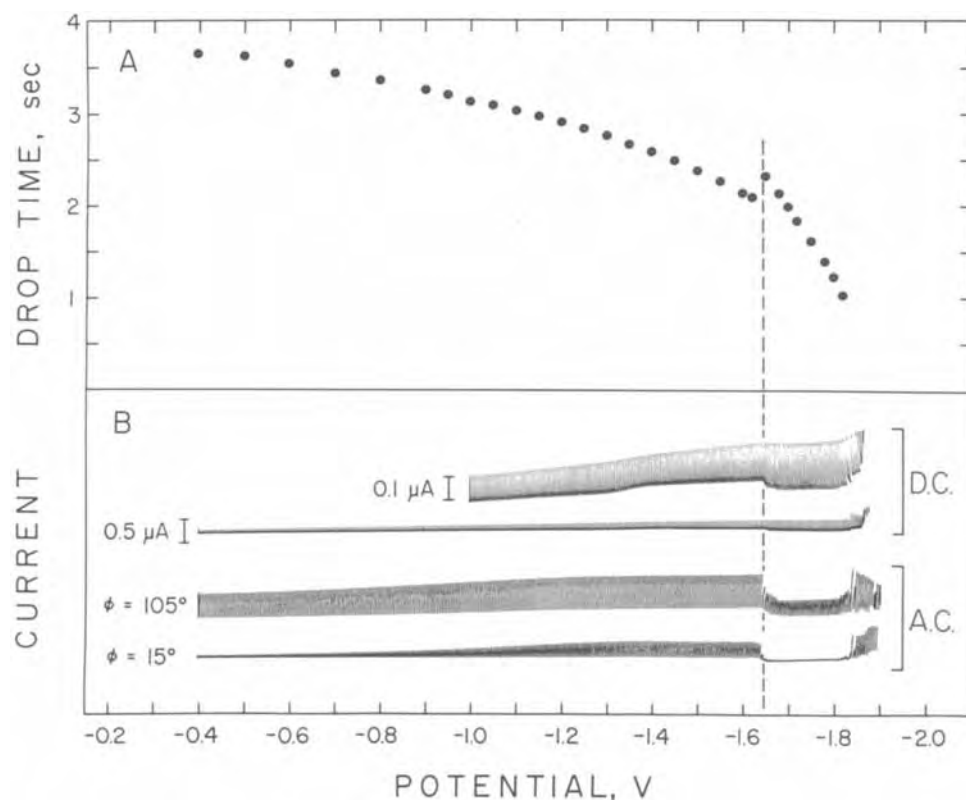


Fig. 6. Polarography of 0.1F tetramethylammonium perchlorate in dimethylformamide at -33°C . (A) Plot of mercury drop time vs. potential. (B) D-C and a-c polarograms.

respectively; a-c polarographic observations of the faradaic current at a phase angle of 6° and of the charging current at a phase angle of 96° are compatible with the d-c polarographic behavior of anthracene. When a small amount (0.0025F) of tetra-*n*-butylammonium iodide is dissolved in the anthracene-containing system, Fig. 8B reveals that the d-c and a-c polarograms change dramatically in the region of potentials from -1.64 to -1.86V ; the second stage of reduction is

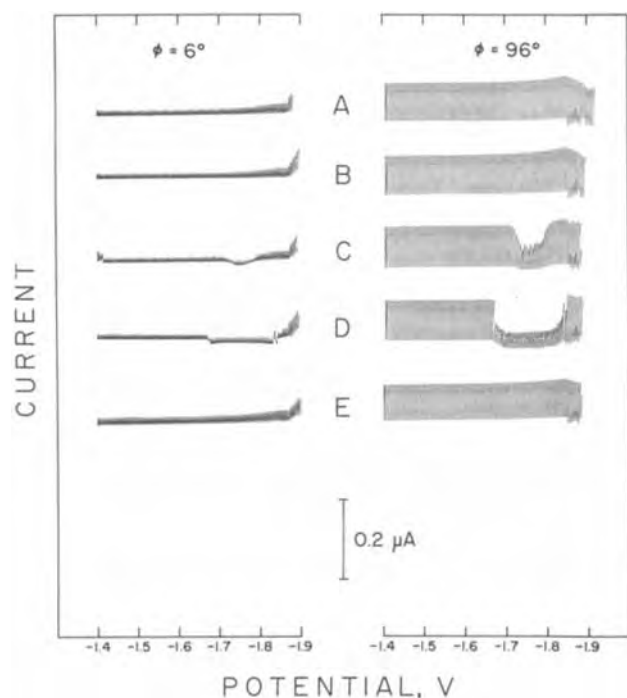


Fig. 7. Effects of temperature and of concentration of tetramethylammonium perchlorate on a-c polarograms. Temperatures are (A) -29°C , (B) -30°C , (C) -31°C , (D) -33°C , and (E) -33°C . Concentration of tetramethylammonium perchlorate is 0.1F for curves A through D and is 0.08F for curves E.

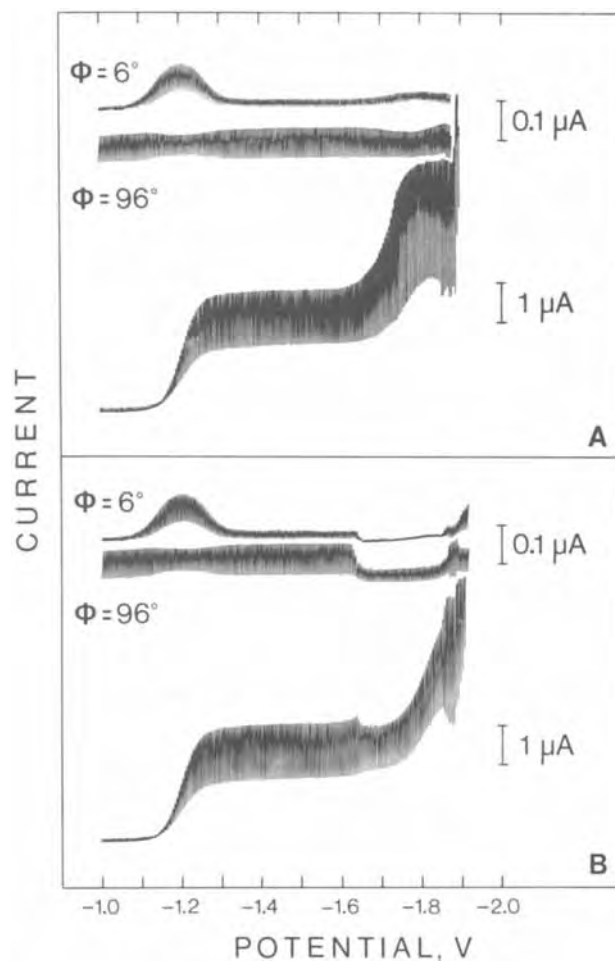


Fig. 8. D-C and a-c polarograms for reduction of 0.003M anthracene in dimethylformamide containing 0.1F tetramethylammonium perchlorate at -29°C . (A) no tetra-*n*-butylammonium iodide present. (B) 0.0025F tetra-*n*-butylammonium iodide present.

almost obliterated from the d-c polarogram, and pronounced depressions appear in the faradaic- and charging-current components of a-c polarograms. Clearly, these phenomena must be attributed to the presence of both the tetramethylammonium and the iodide ion, because the supporting-electrolyte cation alone does not cause such current depressions at -29°C , as is shown in Fig. 7A.

Additional evidence for the conclusion reached in the preceding paragraph is the set of polarograms in Fig. 9 for the reduction of 1-bromonorbornane in dimethylformamide containing 0.1F tetramethylammonium perchlorate. Figure 9A is a polarogram recorded at -33°C , showing the start of a wave at approximately -1.6V , but most of the rising portion of the wave between -1.66 and -1.86V is obscured by a current depression. As demonstrated by Fig. 9B, when the temperature is raised slightly to -30°C , the wave for reduction of the carbon-bromine bond is unmasked. However, if the temperature is kept at -30°C and if tetra-*n*-butylammonium iodide (0.0025F) is added to the solution, the polarogram in Fig. 9C is obtained. These observations confirm that at -30°C a small concentration of iodide, in combination with the tetramethylammonium cation, inhibits electron transfer to 1-bromonorbornane. Moreover, even the bromide ion released by reduction of 1-bromonorbornane interacts with the supporting-electrolyte cation to form a species, apparently adsorbed onto mercury, which can cause a current depression, although a lower temperature (-33°C) is needed to produce the effect.

Current-time curves for individual mercury drops change shape as a function of potential over the region corresponding to the polarographic minimum. Figure 10 shows some of these traces for the reduction of

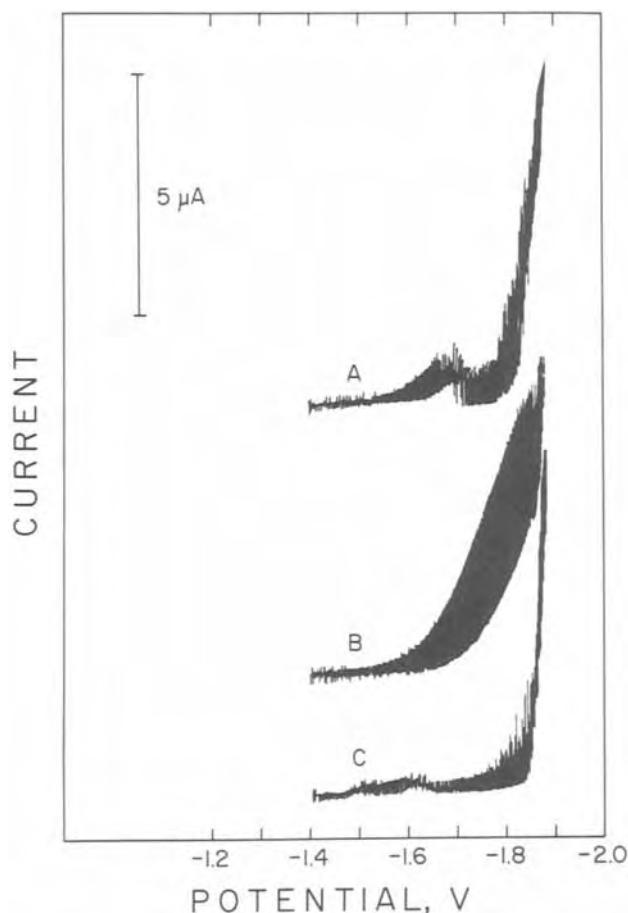


Fig. 9. Polarograms for reduction of 0.001M 1-bromonorbornane in dimethylformamide containing 0.1F tetramethylammonium perchlorate. (A) -33°C . (B) -30°C . (C) -30°C with 0.0025F tetra-*n*-butylammonium iodide present.

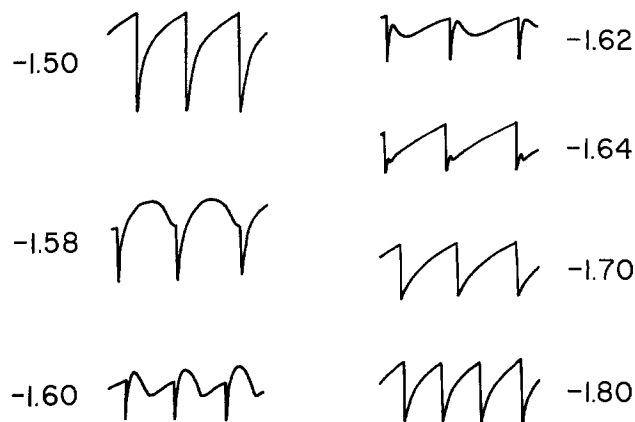


Fig. 10. Polarographic current-time curves for individual mercury drops as a function of potential for reduction of 0.0025M 1-iodonorbornane in dimethylformamide containing 0.1F tetramethylammonium perchlorate at -34°C .

1-iodonorbornane at -34°C . At a potential of -1.50V , which, as can be seen in Fig. 2, is before the beginning of the minimum, the current-time curves have a normal appearance. At a potential (-1.58V) near the onset of the minimum, the current decreases toward the end of each drop lifetime. Across the region of potentials corresponding to the polarographic minimum, the curves are characterized by an initial rise, severe depression, and eventual recovery of the current. At potentials more negative than the minimum, the current-time traces once again appear normal, but the final current is lower than that in a comparable electrochemical system which does not exhibit a polarographic minimum. For all curves in Fig. 10, the initial rise in current is due to reduction of the alkyl halide. Between approximately -1.58 and -1.64V , the temperature and solution composition are favorable for the formation of complex ionic species that are adsorbed onto the mercury drop; these adsorbed species block electron transfer to the alkyl halide, as evidenced by the decline in current which follows the initial rise. However, the adsorbed species appear to be imperfect insulators, because reduction of the alkyl halide resumes toward the end of the lifetime of a mercury drop.

Nature of the adsorbable species.—Adsorption of tetraalkylammonium ions onto mercury from aqueous media has been investigated extensively (9-14). Devanathan and Fernando (9) used a capillary electrometer to examine the behavior of several tetraalkylammonium iodides at 25°C and concluded, for tetramethylammonium iodide as well as the other salts, that there exists a mid-cathodic region of potentials within which the cation and anion are both specifically adsorbed and that the cations probably form "bridges" with the anions. In a later study by Piro, Bennes, and Bou Karam (10), tetramethylammonium bromide was observed to be less strongly adsorbed onto mercury than the iodide salt.

Although there have been no previous reports dealing with the adsorption of tetramethylammonium salts from dimethylformamide onto mercury, evidence offered in the present paper indicates that such species are adsorbed at low temperatures. In dimethylformamide containing only tetramethylammonium perchlorate, it appears as shown earlier (Fig. 6 and 7) that the low temperature polarographic minimum can be attributed to adsorption of the tetramethylammonium cation, tetramethylammonium perchlorate, or possibly an ion aggregate. However, when halide ions are either present initially or generated electrolytically, the phenomenon responsible for the minimum is more complicated.

Figure 11 illustrates conditions necessary for onset of the halide-induced current minimum for the polarographic reductions of 1-bromodecane and 1-iododecane

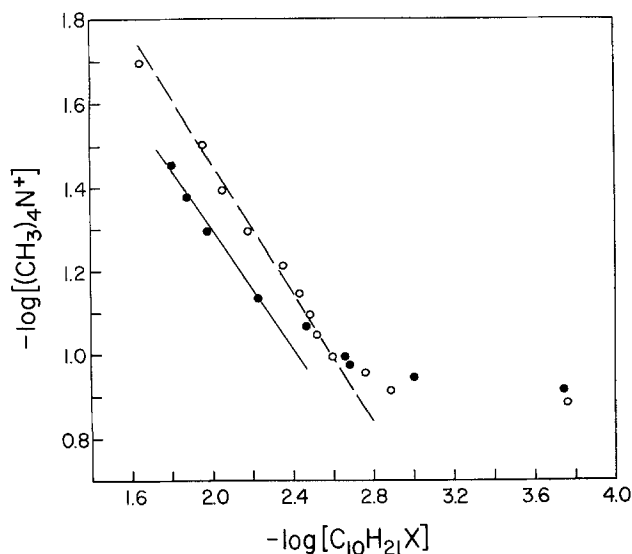


Fig. 11. Plot of logarithm of concentration of tetramethylammonium cation vs. logarithm of concentration of 1-bromodecane (filled circles) or 1-iododecane (open circles) needed to cause onset of polarographic minimum in dimethylformamide at -33°C .

at -33°C in dimethylformamide containing tetramethylammonium perchlorate. For these experiments, we varied the concentrations of supporting electrolyte and decyl halide to determine what combination of these parameters causes the minimum to appear; arbitrarily, we defined the onset of the minimum as a 10% diminution of the normal, unattenuated diffusion current. If the logarithm of the concentration of supporting electrolyte is plotted against the logarithm of the concentration of decyl halide, a linear correlation between these two variables is observed at intermediate concentrations of tetramethylammonium perchlorate. Graphical analysis of the slope of the line for each system indicates that the onset of the minimum is more highly dependent on the concentration of tetramethylammonium ion than of decyl halide. Moreover, if it is iodide or bromide ions liberated upon electrolytic reduction of a decyl halide which combine with the tetramethylammonium cation to form a surface-active species, we can conclude that the current minimum results from adsorption of one or more unipositive aggregates consisting of tetramethylammonium and halide ions in a ratio lying between 3:2 and 5:4.³ Such discrete species, if they exist, should be almost impossible to isolate and identify, especially because they might prevail only under the influence of a polarized electrode. Nevertheless, it is intriguing that the crude picture so far developed of the cooperative adsorption of tetra-

³ It can be shown (15) that the straight lines passing through the experimental data for 1-bromodecane and 1-iododecane in Fig. 11 fit the general relation $a \log[(\text{CH}_3)_4\text{N}^+] + b \log[\text{C}_{10}\text{H}_{21}\text{X}] = \text{constant}$ or $[(\text{CH}_3)_4\text{N}^+]^a [\text{C}_{10}\text{H}_{21}\text{X}]^b = \text{constant}$. For 1-bromodecane, a/b is 1.39 which lies between a ratio of 4:3 and 3:2; for 1-iododecane, a/b is 1.28 which lies between a ratio of 5:4 and 4:3.

methylammonium and halide ions onto mercury in dimethylformamide bears a remarkable resemblance to the model invoked by Devanathan and Fernando (9) in which halide ions and tetramethylammonium cations form bridged species adsorbed at the mercury-water interface.

Currently, we are completing the construction of a computer-controlled capillary electrometer, based on the design of Mohilner and co-workers (16). Our goal is to utilize this instrumentation to study in detail the electrical double layer at the mercury-solution interface in nonaqueous solvents containing various tetraalkylammonium salts in the presence and absence of electroactive organic compounds.

Acknowledgments

Appreciation is expressed to the donors of the Petroleum Research Fund, administered by the American Chemical Society, for financial support of this work. We thank Alan McQuarrie for assistance in recording polarograms as well as Brian Willett and Daniel La Perriere for many helpful discussions.

Manuscript submitted June 3, 1980; revised manuscript received July 16, 1980.

Any discussion of this paper will appear in a Discussion Section to be published in the June 1981 JOURNAL. All discussions for the June 1981 Discussion Section should be submitted by Feb. 1, 1981.

REFERENCES

- W. F. Carroll, Jr., and D. G. Peters, *J. Org. Chem.*, **43**, 4633 (1978).
- W. F. Carroll, Jr., and D. G. Peters, *Tetrahedron Lett.*, 3543 (1978).
- W. F. Carroll, Jr., and D. G. Peters, *J. Am. Chem. Soc.*, **102**, 4127 (1980).
- J. Heyrovský and J. Kůta, "Principles of Polarography," pp. 299-334, Academic Press, New York (1966).
- A. M. Bond, *Anal. Chem.*, **44**, 315 (1972).
- G. M. McNamee, B. C. Willett, D. M. La Perriere, and D. G. Peters, *J. Am. Chem. Soc.*, **99**, 1831 (1977).
- L. W. Marple, *Anal. Chem.*, **39**, 844 (1967).
- J. L. Hall and P. W. Jennings, *ibid.*, **48**, 2026 (1976).
- M. A. V. Devanathan and M. J. Fernando, *Trans. Faraday Soc.*, **58**, 368 (1962).
- J. Piro, R. Bennes, and E. Bou Karam, *J. Electroanal. Chem. Interfacial Electrochem.*, **57**, 399 (1974).
- J. B. Hayter and R. J. Hunter, *ibid.*, **37**, 71 (1972).
- J. B. Hayter and R. J. Hunter, *ibid.*, **37**, 81 (1972).
- E. Verdier, G. H. Naficy, and P. Vanel, *J. Chim. Phys.*, **70**, 160 (1973).
- E. Bou Karam, R. Bennes, and D. Bellostas, *J. Electroanal. Chem. Interfacial Electrochem.*, **84**, 21 (1977).
- W. F. Carroll, Jr., Ph.D. Thesis, Indiana University (1978).
- J. Lawrence and D. M. Mohilner, *This Journal*, **118**, 1596 (1971); H. Nakadomari, Ph.D. Thesis, Colorado State University (1974).

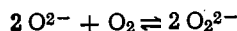
Voltammetric and Chronopotentiometric Studies of Na₂O-NaCl Melts

M. L. Deanhardt¹ and Kurt H. Stern*

Chemistry Division, Naval Research Laboratory, Washington, DC 20375

ABSTRACT

The oxidation of Na₂O in molten NaCl was studied in the presence of oxygen (<10 Torr) at 830°C by two electrochemical techniques: cyclic voltammetry and chronopotentiometry. The results indicate the following reaction pathway



The partial conversion of O²⁻ to O₂²⁻ in the melt results in two oxidizable species. Experimental data indicate that superoxide is absent from the Na₂O-NaCl melts.

In previous studies of the Na₂O-NaCl system (1), several types of experiments were reported which indicated that oxide ion (O²⁻) dissolved in molten NaCl is partially oxidized to peroxide (O₂²⁻) and perhaps to superoxide (O₂⁻). The motivation for this work was the previous finding (2) that O²⁻ is oxidized by two distinctly different kinds of reactions in molten nitrates: by molecular O₂ in oxygen-containing atmospheres and by the reduction of nitrate to nitrite in the (near) absence of oxygen. Since halide anions were considered difficult to reduce, it was thought likely that O²⁻ would be stable in NaCl in the absence of O₂. The results of manometric experiments, chemical analyses of quenched melts, and potentiometric studies with O²⁻-specific zirconia electrodes gave consistent results. When the atmosphere contained oxygen, Na₂O-NaCl melts take up O₂ reversibly, chemical analysis showed a species which reduces permanganate, and the potentiometric experiments indicated that a large fraction of any added Na₂O disappeared rapidly. These observations are all consistent with substantial conversion of O²⁻ to O₂²⁻, presumably by the reaction $\text{O}^{2-} + \frac{1}{2} \text{O}_2 \rightleftharpoons \text{O}_2^{2-}$. The experiments did not allow any conclusions to be drawn about O₂⁻ formation, but thermodynamic calculations indicate that its equilibrium concentration is much less than that of O₂²⁻.

Results in a low O₂ atmosphere were more puzzling. In a helium-filled glove box whose nominal O₂ content was 1-10 ppm, similar chemical and potentiometric studies also indicated peroxide formation, although at a slower rate. None of the several possible explanations examined appeared satisfactory.

The current work was therefore undertaken to (i) determine the number of species to which O²⁻ transforms and (ii) to shed further light on the remaining unresolved anomalies. Voltammetric and chronopotentiometric techniques had already been used successfully by several workers (3-6) to study oxide species in halide melts and were therefore used in this study.

Experimental

Apparatus.—The molten salt furnace, temperature controller, and helium-oxygen dry boxes have been previously described (1). High purity gold crucibles were used as containers for the melt.

Current-voltage and voltage-time curves were obtained with a Princeton Applied Research Corporation

Model 173 potentiostat/galvanostat. A triangle wave generator (PAR Model 175) was interfaced to the Model 173 to obtain cyclic sweep voltammograms. Fast voltammetric scan rates were recorded with a transient recorder (Biomation Model 802).

Electrodes.—The reference electrode consisted of a silver wire in contact with ~10 mole percent AgCl in NaCl. The reference melt was placed in a mullite tube which was immersed in the melt. The gold container served as the counterelectrode. Since gold is less susceptible to corrosion by the Na₂O-NaCl melt than is platinum, a gold wire (area ~0.50 cm²) was used as the working electrode.

Reagents.—Reagent grade NaCl was vacuum dried at 500°C before use. Reagent Na₂O (Alfa Inorganics) (94% Na₂O by analysis) containing ~2% Na₂O₂ impurity, and reagent Na₂O₂ were used without pretreatment. All weighing and transfer operations involving these substances were carried out in the dry box in which the experiments were done.

Procedure.—The temperature of the melt was maintained at 830° ± 5°C. Sodium oxide was added directly to the sodium chloride melt by means of a glass funnel and approximately 5 min were allowed for the oxide to dissolve before electrochemical measurements were made. Na₂O concentrations were kept as low as possible (<50 mM) in order to minimize corrosion effects on the electrodes and cell container. As will be discussed below, Na₂O is unstable at high oxygen pressures, resulting in the formation of Na₂O₂. Therefore studies were made at oxygen pressures generally below 10 Torr.

Results and Discussion

The oxidation of Na₂O in molten NaCl was studied by two electrochemical techniques, voltammetry and chronopotentiometry. Typical voltammograms of the oxidation of Na₂O are shown in Fig. 1. The reduction limit occurs at ~ -1.3V and the oxidation limit at ~ +0.3V (probably the oxidation of the gold electrode). Two oxidizable species are observed when Na₂O is added to the melt; the first anodic wave (wave I) occurs at -0.47V vs. the Ag/AgCl reference electrode and the second (wave II) occurs at ~ +0.12V. Additions of Na₂O immediately increase the peak current of wave I; therefore, this wave is attributed to the oxidation of oxide ions in the melt. Wave II does not immediately increase in peak current with added Na₂O; however, the peak current does increase with time as shown in Fig. 1, and is believed to be due to the oxidation of peroxide ions formed by the following

* Electrochemical Society Active Member.

¹ Present address: Chemistry Department, George Mason University, Fairfax, Virginia 22030.

Key words: fused salts, electrode, oxidation.

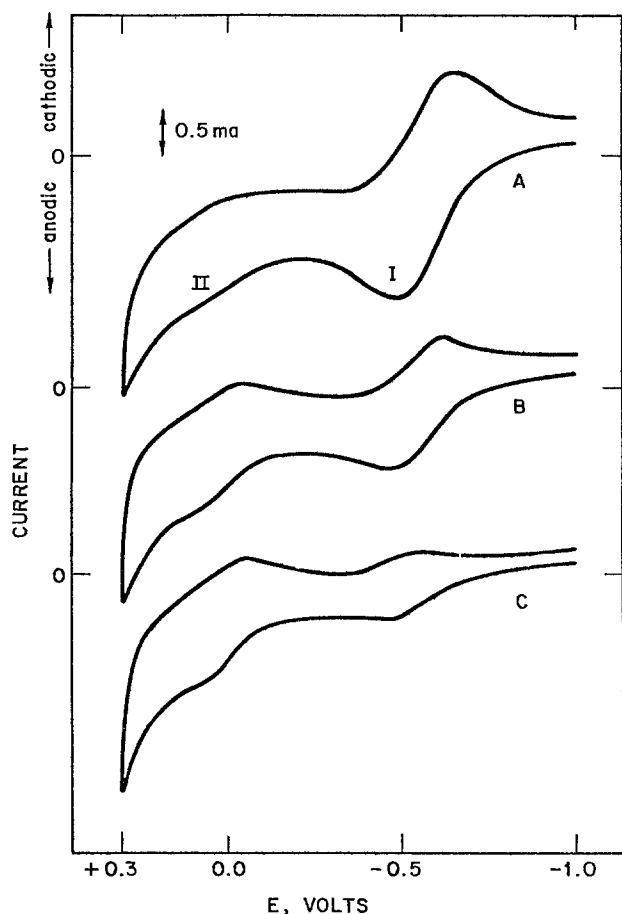
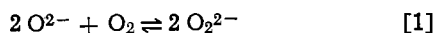


Fig. 1. Cyclic voltammograms for the oxidation of O_2^{2-} in molten NaCl. $[O_2^{2-}] = 7.2 \times 10^{-3}M$, Au working electrode ($A \approx 0.50 \text{ cm}^2$), $T = 830^\circ\text{C}$, O_2 pressure = 2.3 Torr, scan rate = 0.5 V/sec. Curve A: scan taken 8 min after addition of Na_2O . Curve B: scan taken 32 min after addition of Na_2O . Curve C: scan taken 59 min after addition of Na_2O .

reaction



The decrease in peak current of wave I with time can also be accounted for by reaction [1]. Measurement of this decrease indicated that the oxide concentration decreased in a first order fashion with a half-life of approximately 30 min.

The voltammogram in Fig. 2 was taken 2.3 hr after the first addition of Na_2O to the melt (at a higher total oxide concentration than in Fig. 1). This indicates that the O_2^{2-} concentration becomes appreciable when Na_2O remains in the melt for long periods of time. Loss of oxide ion and peroxide ion due to vaporization and reaction with container, electrodes, etc., also occurs in the melt but is a slow process that takes many hours (1). Attempts were made to enhance the peak current of wave II with additions of Na_2O_2 . The results were the same as for the addition of pure Na_2O . Most likely, solid Na_2O_2 decomposes to Na_2O before it dissolves in NaCl.

The reversibility of wave I was determined by measuring the separation of its peak and half-peak potential. $(E_p - E_{p/2})_a$ was found to be 120-135 mV at slow scan rates which is in reasonable agreement with the theoretical value of 105 mV for a reversible 2-electron process at 1103°K (7). The potential difference between wave I and its corresponding cathodic wave, $(E_p)_a - (E_p)_c$, was 125-150 mV which is also in reasonable agreement with the theoretical value of 105 mV for a reversible 2-electron process (7). The slightly higher experimental values could be attributed to quasi-reversible behavior; however the higher

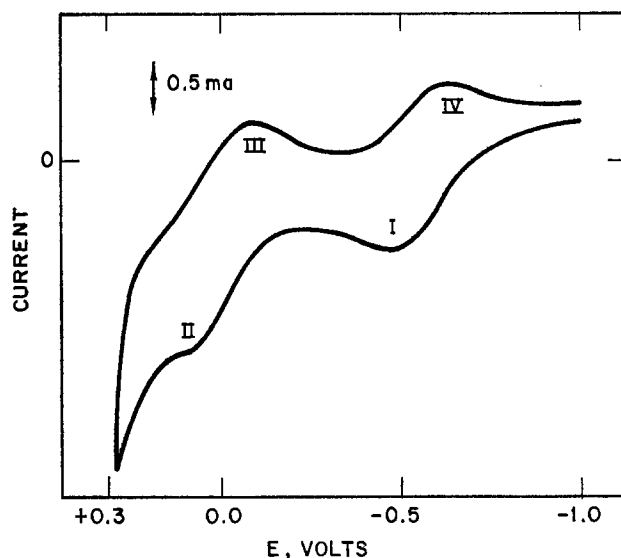


Fig. 2. Cyclic voltammogram for the oxidation of O_2^{2-} in molten NaCl. Cumulative $[O_2^{2-}] = 1.58 \times 10^{-2}M$, Au working electrode ($A \approx 0.50 \text{ cm}^2$), $T = 830^\circ\text{C}$, O_2 pressure = 2.3 Torr, scan rate = 0.5 V/sec, scan taken 2.3 hr after first addition of Na_2O .

values are probably due, in part, to uncompensated IR effects in the melt.

The peak potential of a reversible charge transfer should be independent of scan rate. The approximate constancy of peak potential with scan rate, ν , for wave I is shown in Table I. The peak potential changes only by ~ 50 mV for a hundredfold increase in scan rate. The shift in peak potential is probably due, in part, to larger IR drops at fast scan rates.

The second anodic wave (wave II) was not as well defined as the first anodic wave since it appears as a shoulder on the oxidation limit of the electrode. Therefore measurements of the peak potential of wave II were only approximate. Values of $(E_p - E_{p/2})_a$, $(E_p)_a - (E_p)_c$, and the constancy of peak potential with scan rate were similar to those of wave I and would suggest a 2-electron process for the oxidation of O_2^{2-} in the melt.

Chronopotentiometry was also used to study the oxidation of Na_2O in the melt. Typical anodic and current reversal chronopotentiograms for the oxidation of O_2^{2-} are shown in Fig. 3. Plots of E vs. $\ln \left(\frac{\tau^{1/2} - t^{1/2}}{t^{1/2}} \right)$

were linear with slopes ranging from -64 to -74 mV; the theoretical slope for a reversible 2-electron process is -48 mV (8). Using current reversal chronopotentiometry, t_i/τ_r values were found to be 3-4, which reasonably agrees with the theoretical value of 3 for a reversible electron transfer process (8). Chronopotentiograms for the oxidation of O_2^{2-} in the melt were ill defined due to their proximity to the oxidation limit of the melt. Therefore, no quantitative information was obtainable for the peroxide oxidation.

Based on these results and results reported earlier (1), we postulate the following reaction mechanism

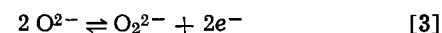
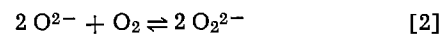


Table I. Variation of $(E_p)_a$ and $(E_{p/2})_a$ with scan rate for the oxidation of O_2^{2-} in molten NaCl $[O_2^{2-}] = 1.61 \times 10^{-2}M$

Scan rate (V/sec)	$(E_p)_a$ (mV)	$(E_p - E_{p/2})_a$ (mV)
0.1	-474	121
0.5	-475	135
1.0	-464	128
5.0	-431	156
10.0	-425	163

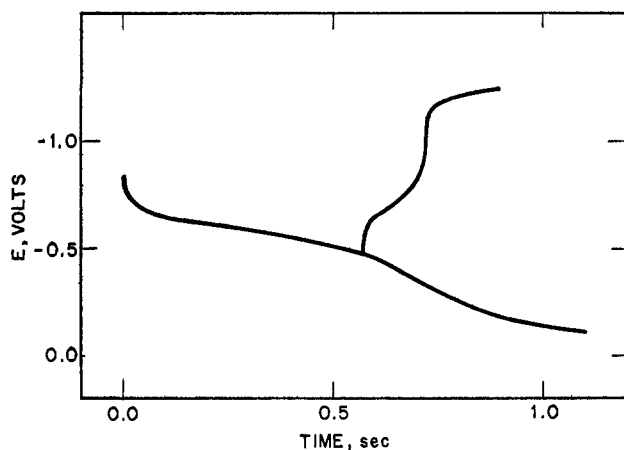
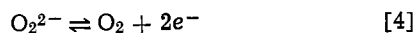


Fig. 3. Anodic and current reversal chronopotentiograms for the oxidation of O_2^{2-} in molten NaCl. $[O_2^{2-}] = 1.31 \times 10^{-2}M$, $T = 830^\circ C$, O_2 pressure = 2.3 Torr, forward current density = reverse current density = 36 mA/cm^2 .



Thus in Fig. 2, the first anodic wave (I) represents the oxidation of oxide to peroxide and the second anodic wave (II) represents the oxidation of peroxide to oxygen. On reversing the scan, the first cathodic wave (III) represents the reduction of oxygen and the second cathodic wave (IV) represents the reduction of peroxide.

The theory of cyclic voltammetry for multistep charge transfer systems has been derived and verified by Polcyn and Shain (8). When two electroactive species are reduced or oxidized at sufficiently different potentials ($\Delta E^\circ > 118/n \text{ mV}$), the multistep charge transfer reactions can be considered as resulting from separate reactions and will exhibit two separate voltammetric waves. The oxidation potentials for oxide and peroxide differ by several hundred millivolts and appear as uncomplicated charge transfer reactions as previously indicated.

Values of $i_p/\nu^{1/2}$ were measured as a function of scan rate to check for possible chemical reactions coupled to the multistep charge transfers. The invariance of $i_p/\nu^{1/2}$ with scan rate would indicate charge transfers with no chemical complication (7). Our mechanism proposes a chemical reaction, the oxide/peroxide equilibrium (Eq. [2]), coupled to multistep charge transfers, the oxidation of oxide to peroxide to oxygen (Eq. [3] and [4]). However the equilibrium reaction [2] appears to be a slow process so that essentially no chemical reaction takes place during the time interval of a voltammetric scan ($< 10 \text{ sec}$). In this case, charge transfer reactions [3] and [4] would occur with no chemical complications. Values of $i_p/\nu^{1/2}$ for the oxidation of oxide (wave I in Fig. 2) at various scan rates are listed in Table II. The times at which the voltammograms were measured with respect to the addition of Na_2O to the melt are also given. The initial decrease in $i_p/\nu^{1/2}$ is due to the loss of oxide in the melt. The decrease in i_p with time holding ν constant is illustrated in Fig. 1. Once the oxide/peroxide equilibrium is established, $i_p/\nu^{1/2}$ approaches a constant value within experimental error. Similar results were observed with the oxidation of peroxide (wave II in Fig. 2) except for an initial increase rather than decrease in $i_p/\nu^{1/2}$ due to the gain of peroxide in the melt. The results indicate that the multistep charge transfer reactions of

Table II. Variation of $i_p/\nu^{1/2}$ with scan rate for the oxidation of O_2^{2-} in molten NaCl; before addition, $[O_2^{2-}] = 2.67 \times 10^{-2}M$; after addition, $[O_2^{2-}] = 4.03 \times 10^{-2}M$

Scan rate (V/sec)	$i_p/\nu^{1/2}$ (mA/sec ^{1/2} /V ^{1/2})	Time elapsed after oxide addition (min)
0.5	3.4	9
1.0	3.2	12
2.0	2.9	15
5.0	2.9	20
10.0	3.0	22
20.0	3.0	25
0.5	2.8	57

oxide to peroxide to oxygen proceed with no chemical complications. This interpretation is further supported by the following observations: with voltammetry, the approximate constancy of peak potential with scan rate for both waves I and II; and with chronopotentiometry, the t_f/τ_r value of ~ 3 .

The presence of only two oxidizable species, O_2^{2-} and O_2 , would tend to rule out the presence of O_2^- in the melt. Increasing the O_2 pressure would tend to favor the formation of superoxide in the melt (1). Experiments were carried out in O_2 pressures as high as 60 Torr; however, no additional waves were observed.

According to reaction [2], the formation of peroxide should be minimal at low O_2 pressures. Experiments were carried out in He atmospheres containing less than 1 ppm O_2 . Voltammograms of the oxidation of Na_2O at this O_2 pressure were similar to those at higher O_2 pressures; however, the decrease in peak current of the first anodic wave was considerably slower than in the case of higher O_2 pressures. Since O_2 is produced by the oxidation of O_2^{2-} , it was impossible to study the formation of O_2^{2-} at very low O_2 pressures. The second anodic wave would produce O_2 in the vicinity of the electrode in the melt that would eventually react with O_2^{2-} to form O_2^{2-} .

In conclusion, we have shown that when Na_2O is dissolved in molten NaCl in the presence of oxygen, oxide ions react slowly with oxygen to form peroxide ions. The oxidation of oxide ion at a gold electrode results in two multistep charge transfers, the oxidation of oxide to peroxide followed by the oxidation of peroxide to oxygen.

Manuscript submitted Feb. 25, 1980; revised manuscript received May 26, 1980. This was Paper 344 presented at the Pittsburgh, Pennsylvania, Meeting of the Society, Oct. 15-20, 1978.

Any discussion of this paper will appear in a Discussion Section to be published in the June 1981 JOURNAL. All discussions for the June 1981 Discussion Section should be submitted by Feb. 1, 1981.

Publication costs of this article were assisted by the Naval Research Laboratory.

REFERENCES

- K. H. Stern, R. Panayappan, and D. R. Flinn, *This Journal*, **124**, 641 (1977).
- D. R. Flinn and K. H. Stern, *J. Electroanal. Chem. Interfacial Electrochem.*, **63**, 39 (1975).
- E. P. Mignonsin, L. Martinot, and G. Duyckaerts, *Inorg. Nucl. Chem. Lett.*, **3**, 511 (1967).
- D. Inman and M. J. Weaver, *J. Electroanal. Chem. Interfacial Electrochem.*, **51**, 45 (1974).
- Y. Kanzaki and M. Takahashi, *ibid.*, **58**, 339 (1975).
- D. L. Manning and G. Mamantov, *This Journal*, **124**, 480 (1977).
- R. S. Nicholson and I. Shain, *Anal. Chem.*, **36**, 706 (1964).
- D. S. Polcyn and I. Shain, *ibid.*, **38**, 370 (1966).

On the Short Time Solution for the Concentration Step at the Surface of a Rotating Disk

Daniel A. Scherson, Pier Filippo Marconi,* and John Newman*

Department of Chemical Engineering, University of California, Berkeley, California 94720

ABSTRACT

The first thirty coefficients of a proposed series solution for a fundamental problem in nonsteady diffusion to a rotating disk have been evaluated. The results obtained raise serious questions not only with respect to potential practical applications of such a solution, but also in regard to the claimed convergence character of the series. Certain difficulties related to the numerical determination of these coefficients are discussed in detail.

The use of transient techniques in conjunction with forced convection systems, such as a rotating disk, seems to be one of the most valuable tools in the analysis of electrode processes. In particular, the a-c impedance method has found a multitude of applications in the characterization and study of detailed mechanisms of electrochemical reactions.

From a theoretical standpoint, an expression for the Warburg impedance for a rotating disk was recently derived (1) by a formal space transformation of the solution for the step potential method. As a means of fully utilizing this particular property, previous mathematical treatments of the step potential problem, leading to analytic solutions, were carefully examined.

The transient concentration profile, under step potential conditions at the surface of a rotating disk electrode, has been investigated by Selman (2). Within the framework of approximations specified elsewhere (2,3), this author developed a series, up to third order, by means of a classical perturbation expansion. Krylov and Babak (3), on the other hand, have independently derived a generalized form of the same series by introducing parabolic cylinder functions. This latter approach allows a recurrence relation for the coefficients to be obtained without resorting to solving the resulting differential equations individually. Based on this solution, these workers arrived at an analytic expression for the flux at the surface and indicated that the series converged for any finite value of the dimensionless time.

In order to extend the accuracy of these results beyond the limits imposed by the first three coefficients reported, a numerical evaluation of the first thirty coefficients was performed. Given that the flux at the surface is intimately connected to the Warburg impedance through its Laplace transform, a series solution for the real and imaginary parts of the impedance can be easily obtained.

The purpose of this note is twofold. First, to report the results obtained and examine certain problems encountered in the calculations and second, to discuss, based on the former, the convergence character of the series in relation to potential practical applications.

Mathematical Formalism

A thorough derivation of the series under study will not be pursued here. Although the mathematical details are interesting in themselves only the results will be presented.

According to Krylov and Babak, the transient behavior of the flux at the surface is given by

$$j(\tau) = \frac{c_o(AD^2)^{1/3}}{\sqrt{\pi\tau}} \left\{ 1 - \pi \sum_{n=1}^{\infty} \sum_{k=-3n-1}^{3n-1} \frac{2^{k/2} b_k^{(n)}}{\Gamma\left(-\frac{k}{2}\right)} \tau^{3n/2} \right\} \quad [1]$$

where c_o and D are the bulk concentration and diffusion coefficient of the electrochemically active species, respectively. The dimensionless time τ , is related to the time t , the angular velocity Ω , and the kinematic viscosity of the solution ν by

$$\tau = (DA^2)^{1/3} t \quad \text{where } A = a \left(\frac{\Omega^3}{\nu} \right)^{1/2} \quad [2]$$

The double asterisk in the right upper corner of the summation sign in Eq. [1] indicates that "k" involves values which are only even, for odd n , or only odd, for even n .

The first four coefficients $b_k^{(1)}$ are given by

$$b_2^{(1)} = \frac{2}{3\sqrt{\pi}}, \quad b_0^{(1)} = \frac{1}{\sqrt{\pi}}, \quad b_{-2}^{(1)} = 0, \quad b_{-4}^{(1)} = \frac{-1}{\sqrt{\pi}} \quad [3]$$

which serve as a basis for calculating higher order coefficients through the recursion formulas specified below (for $n = 2, 3, 4, \dots$)

$$b_k^{(n)} = -\frac{2\sqrt{2}}{3n+k+1} [(k+1)(k+2)b_{k+1}^{(n-1)} + (2k+1)b_{k-1}^{(n-1)} + b_{k-3}^{(n-1)}] \quad \text{for } -3n+5 < k < 3n-5 \quad [4]$$

$$b_{3n-1}^{(n)} = -\frac{\sqrt{2}}{3n} b_{3n-4}^{(n-1)} \quad [5]$$

$$b_{3n-3}^{(n)} = -\frac{\sqrt{2}}{3n-1} [b_{3n-6}^{(n-1)} + (6n-5)b_{3n-4}^{(n-1)}] \quad [6]$$

$$b_{-3n+1}^{(n)} = -3\sqrt{2}(n-1)(3n-2)b_{-3n+2}^{(n-1)} \quad [7]$$

$$b_{-3n+3}^{(n)} = \frac{\sqrt{2}}{2} [(6n-7)b_{-3n+2}^{(n-1)} - (3n-5)(3n-4)b_{-3n+4}^{(n-1)}] \quad [8]$$

$$b_{-3n-1}^{(n)} = -\frac{3n}{2} \Gamma\left(\frac{3n}{2}\right) \sum_{k=-3n+1}^{3n-1} \frac{2^{(3n+k+1)/2}}{\Gamma\left(\frac{1-k}{2}\right)} b_k^{(n)} \quad [9]$$

* Electrochemical Society Active Member.
Key words: convection, diffusion, impedance.

Based on this formalism, the real and imaginary parts of the Laplace transform of the flux at the surface, $\mathcal{L}\{j(\tau)\}$, which prescribe the value of the Warburg impedance, are given by

$$\text{Re}[\mathcal{L}\{j(\tau)\}] = K^{1/2} \frac{\sqrt{2}}{2} - \frac{1}{\sqrt{\pi}} \sum_{n=1}^{\infty} \frac{\Gamma\left(\frac{3n+1}{2}\right)}{K^{1/2}(3n-1)} 3^n \sin \frac{1}{4} (3n-1)\pi \quad [10]$$

$$\text{Im}[\mathcal{L}\{j(\tau)\}] = K^{1/2} \frac{\sqrt{2}}{2} + \frac{1}{\sqrt{\pi}} \sum_{n=1}^{\infty} \frac{\Gamma\left(\frac{3n+1}{2}\right)}{K^{1/2}(3n-1)} 3^n \cos \frac{1}{4} (3n-1)\pi \quad [11]$$

where the coefficients Θ_n are defined by

$$\Theta_n = -\pi \sum_{k=-3n-1}^{3n-1} \frac{2^{k/2} b_k^{(n)}}{\Gamma\left(-\frac{k}{2}\right)} \quad n = 1, 2, 3 \dots \quad [12]$$

$$\Theta_0 = 1 \quad [13]$$

and $K = \omega\nu(3D/a\nu)^{2/3}/\Omega D$, is the dimensionless frequency.

Computation Method

Preliminary calculations based on Eq. [1] showed that even for small values of n , the computed coefficients, Θ_n , were appreciably altered by choosing π , arising from $\Gamma(k/2)$ for odd k , with an increasing number of significant figures. Moreover, noticeable changes were observed by merely performing the required arithmetic operations in a different order. This behavior was apparently induced by round-off errors, which may become extremely significant upon addition and subtraction of a collection of terms which are many orders of magnitude larger than the Θ_n itself.

This problem can be successfully overcome by multiplying the original $b_k^{(n)}$ coefficient by $\pi^{1/2}$, modifying the recursion formulas by a factor of $2^{1/2}$, and expanding the gamma functions. The newly generated set of $b_k^{(n)}$ coefficients can therefore be conveniently represented as the ratio of two integer numbers. Consequently, Θ_n or $\Theta_n\pi^{1/2}$, can be expressed in the same exact fashion, depending on whether n is even or odd.

Based on these considerations, a computer program which performs all the calculations by integer arithmetic was developed. Θ_n 's up to $n = 29$ were evaluated by effectively using up to 387 bits for storing the numerator and denominator of the $b_k^{(n)}$ coefficients. The results obtained, as well as the values for the flux at $\tau = 1$ are listed in Table I.

A comparison *a posteriori* indicated that floating-point representation and arithmetic could give reliable values of Θ_n up to $n = 7$ or $n = 16$ by using single-precision (48 bits exclusive of sign and exponent) or double-precision (96 bits) calculations, respectively.

Discussion and Conclusion

The different values for the flux at $\tau = 1$, obtained by taking an increasing number of terms in the Krylov-Babak series do not seem to improve the accuracy of the result. Actually, a careful inspection of Table I shows that an oscillatory departure from an arbitrary intermediate value is generated. Moreover, the fact that the coefficients do not seem to approach zero as n increases clearly suggests that the series diverges for all τ . This remark should be regarded as purely empirical, for no analytic proof of convergence has been

Table I. Values of the Θ_n coefficients, cumulative sum, and reduced flux at the surface for $\tau = 1$. [The exact value according to Nişancioğlu and Newman (4) is 0.639996.]

n	Θ_n^*	$\sum_{i=0}^n \Theta_i$	$\frac{j(1)}{[c_0(\Omega^2 D^3/\nu)^{1/3}]}$
0	1.000000E 00	1.000000	0.450832
1	4.431135E -01	1.443113	0.650601
2	1.666667E -02	1.459780	0.658115
3	-5.192736E -02	1.407853	0.634705
4	-1.085257E -03	1.406768	0.634215
5	1.962731E -02	1.426395	0.643064
6	2.110637E -04	1.426606	0.643159
7	-1.241360E -02	1.414192	0.637563
8	-8.280988E -05	1.414109	0.637525
9	1.101068E -02	1.425120	0.642489
10	5.129554E -05	1.425171	0.642512
11	-1.256595E -02	1.412606	0.636847
12	-4.389392E -05	1.412562	0.636828
13	1.753409E -02	1.430096	0.644732
14	4.813093E -05	1.430144	0.644754
15	-2.892067E -02	1.401223	0.631716
16	-6.451469E -05	1.401159	0.631687
17	5.504707E -02	1.456206	0.656504
18	1.023474E -04	1.456308	0.656508
19	-1.187551E -01	1.337353	0.603011
20	-1.877034E -04	1.337365	0.602927
21	2.863508E -01	1.623716	0.732023
22	3.909269E -04	1.624107	0.732199
23	-7.631807E -01	0.860926	0.388133
24	-9.117357E -04	0.860015	0.387722
25	2.227807E 00	3.087821	1.392088
26	2.354521E -03	3.090176	1.393149
27	-7.068859E 00	-3.978683	-1.793717
28	-6.670830E -03	-3.985354	-1.796724
29	2.422436E +01	20.239008	9.124387

* The exponential notation, E, represents powers of ten, i.e., 1.00E 00 = 1.0 x 10⁰.

presented. However, even if the series converged, the computational effort involved and the number of terms that would be required to obtain an acceptable answer, certainly make the use of this solution highly impractical.

Acknowledgment

This work was supported by a grant from Sandia Laboratories, Albuquerque, New Mexico.

Manuscript submitted Jan. 14, 1980; revised manuscript received June 24, 1980.

Any discussion of this paper will appear in a Discussion Section to be published in the June 1981 JOURNAL. All discussions for the June 1981 Discussion Section should be submitted by Feb. 1, 1981.

Publication costs of this article were assisted by the University of California.

LIST OF SYMBOLS

a	0.51023262 [see Ref. (5)]
A	$a(\Omega^2/\nu)^{1/2}$
$b_k^{(n)}$	coefficients of Krylov-Babak series
c_0	bulk concentration of reactant, mole/cm ³
D	diffusion coefficient of reactant, cm ² /sec
$j(\tau)$	flux at the electrode surface, mole/cm ² · sec
K	$\omega\nu(3D/a\nu)^{2/3}/\Omega D$, dimensionless frequency
t	time, sec
ν	kinematic viscosity, cm ² /sec
τ	dimensionless time
ω	frequency of alternating current, sec ⁻¹
Γ	gamma function
Θ	see Eq. [10]
Ω	rotation speed of disk, sec ⁻¹

REFERENCES

1. D. Scherson and J. Newman, Submitted to *This Journal*.
2. J. R. Selman, Ph.D. Thesis (UCRL-20557), University of California, Berkeley, California (1971).
3. V. S. Krylov and V. N. Babak, *Sov. Electrochem.*, **7**, 626 (1971); *Elektrokhimiya*, **7**, 648 (1971).
4. K. Nişancioğlu and J. Newman, *J. Electroanal. Chem. Interfacial Electrochem.*, **50**, 23 (1974).
5. E. Levart and D. Schuhmann, *Int. J. Heat Mass Transfer*, **17**, 555 (1974).

Voltammetric and Electrochromic Behavior of N-Heptylviologen on Chemically Modified Metal Oxide Electrodes

R. C. Cieslinski and N. R. Armstrong*

Department of Chemistry, University of Arizona, Tucson, Arizona 85721

ABSTRACT

Voltammetric and spectroelectrochemical results are presented for the one-electron reduction of n-heptylviologen dibromide on clean and silane-modified, tin oxide, and on indium tin oxide metallized-plastic optically transparent electrodes (MPOTE). The amount of n-heptylviologen dibromide reduced and the rate of coloration due to the formation of the cation-radical film can strongly be influenced by the state of the electrode surface. The initial 200-500 msec of viologen deposition are not mass transport controlled. Calculations for the amount of viologen deposited vary, depending on whether a spectrophotometric or coulometric estimated is used. Spectrophotometric data indicate that the amount of viologen deposited in the first 200 msec of chronoamperometric reduction from a concentrated viologen solution is ca. 10-14 monolayers and is increased at least 60% by the addition of a monolayer of the silane modifier to the electrode surface. In the case of the metallized plastic films, the increase in coloration rate may be attributed to the presence of nonpolar surface groups present at the surface of the conductive film.

Permanent attachment of various chemical species to electrode surfaces to change their surface properties is now widely recognized (1-19). These chemically modified electrodes have been tested for numerous reasons, with potential applications to electrocatalysis (9, 10, 13, 14, 19) and photosensitization (3, 4, 8). Their use as predictable and controllable electrochromic display materials is also another interesting possibility (17, 20). The present study presents the result of some spectroelectrochemical investigations of the reduction of a film-forming viologen on chemically-modified SnO_2 glass and $\text{In}_2\text{O}_3/\text{SnO}_2$ (ITO) metallized plastic films (21). The use of viologens (dialkyl and diaryl 4,4' bipyridinium compounds) in redox chromic displays is well known with a number of papers and patents discussing their use (22-27). The ability to vary the coloration rates of electrochromic reactions of these compounds through chemical modification of the electrode substrate will be demonstrated. The use of silanes to alter the behavior of an electrochemically adsorbed molecule is not new. Evidence that silane-modified SnO_2 electrodes exhibit appreciably different electrochemical behavior towards oxidation of xanthene-type dyes such as erythrosin and fluorescein has already been noted (3). With these xanthene dyes, where adsorption accompanies oxidation, anodic peak potentials have been shown to shift to lower overpotentials, and the total oxidative charge transferred increased at the silane-modified electrodes. The investigations reported here have shown that the silane-modified metal oxide surface probably promotes a higher surface concentration of nucleation sites for the viologen. In most cases, reduction of the viologen at the silanized SnO_2 electrode or ITO metallized plastic optically transparent electrodes (MPOTE) resulted in faster coloration rates. Occasionally several monolayers of the viologen were retained on the electrode surface following oxidation of the viologen film. Surface analysis studies indicated that increased coloration rates of the viologen films on the modified SnO_2 electrodes, and on the ITO MPOTE's resulted from an increase in the nonpolar nature of the electrode surface.

Experimental

A basic spectroelectrochemical cell design was used to measure the electrochromic properties. This design allows sandwich-like positioning of the electrodes to a Lucite body with a cell volume of approximately 5 ml. A circular brass contact recessed in the Lucite block and separated from solution by an O-ring allowed uniform distribution of current to the metal oxide electrodes. The geometric area of the electrode was 0.5 cm^2 . The cell was placed in a Baush and Lomb Spec 210 u.v.-visible spectrophotometer from which single beam or dual beam absorbance/time or transmittance/time measurements were made. The voltammetric measurements were performed using a potentiostat of conventional design. The recording instruments were either a Houston 2000 recorder, a Tektronix 5441 storage oscilloscope, or a PAR Model 4202 signal averager, used in the transient recorder mode.

In a typical double potential step chronoabsorbance experiment, absorbance or transmittance was monitored at the wavelength maximum for the viologen cation radical as a function of time while stepping to and from the deposition potential. During this time interval, both current and the total charge and the true potential of the working electrode *vs.* the reference electrode were recorded ($E_{\text{work}} - E_{\text{ref}}$).

N-heptyl viologen dibromide (1,1'-Diheptyl-4,4'-bipyridinium dibromide) was used as obtained from Aldrich Chemical Company. Reagent grade potassium bromide (Baker) was recrystallized twice from water which had been distilled three times from alkaline KMnO_4 . The deaerated electrolyte solutions were made just prior to investigation and stored under nitrogen. Toluene (Drake) was dried in magnesium sulfate and distilled from potassium metal under a nitrogen atmosphere prior to use. All silanes were purchased from Petrarch Systems Incorporated, and used as obtained from the manufacturer.

Fluoride-doped SnO_2 on glass was manufactured by Pittsburgh Plate Company. The electrodes were cleaned in an ultrasonic bath, using successive washings of alcoholic KOH, ethanol, and distilled water. Metallized plastic optically transparent electrodes (MPOTE) were obtained from Sierracin/Sylmar (Sylmar, California) under the trade name Intrex-K (indium-tin oxide,

* Electrochemical Society Active Member.
Key words: deposition, nucleation.

ITO) films (21). These electrodes were ultrasonically cleaned with ethanol and then with water before use. The sheet resistance of the SnO_2 electrodes was ca. 15-30 Ω/sq and that of the ITO films 100-300 Ω/sq .

For silane modification, the SnO_2 electrodes were refluxed in a 1-5% silane-dry toluene solution under nitrogen for 30 sec to 2 hr after which the excess silane was removed by rinsing the electrodes in dry toluene. The silanized electrodes were then stored in an inert atmosphere prior to use.

The presence of the silane or of n-heptyl viologen dibromide was confirmed by surface elemental analysis using either a GCA-McPherson ESCA 36 spectrometer (base pressure ca. 10^{-7} Torr) or a Physical Electronics, Incorporated (PHI) TFA Auger spectrometer (base pressure ca. 10^{-9} Torr).

Results and Discussion

Viologen deposition on unmodified SnO_2 electrodes.— A working model for redox processes of n-heptyl viologen films on transparent tin oxide (SnO_2) electrodes has been formulated by Jasinski (25, 26) and others (22-24). An initial cleaning/hydrolysis step with alcoholic KOH to remove carbonaceous material, generates hydroxyl-type entities on the surface. The next step calls for a modification of these entities, presumably through an ion exchange process with the viologen counter ion (Br^- in many cases), to produce a surface on to which the viologen may be deposited. The third step involves a nucleation of the radical cation film on these sites. After nucleation, the film grows at a rate limited by diffusion. The last step in the overall mechanism is equilibration of the radical cation salt deposited with the bulk of solution.

Some initial investigations of the viologen reduction indicated that diffusion control was achieved soon after (less than 100 μsec) the initiation of deposition (25, 26). Other reports (27) and the experiments described below, however, show that in a potential-controlled reduction of the viologen, diffusion control is not achieved instantly, and that the amount of viologen reduced in the first 100-500 msec can be strongly influenced by the state of the electrode surface. Figures 1 and 2 show the double potential step, current/time, charge/time, and transmittance (at 595 nm)/time measurements for a $1 \times 10^{-2}\text{M}$ solution of n-heptyl viologen dibromide in 0.5N KBr electrolyte. In these experiments, an SnO_2 electrode was biased between -0.7 and -0.8V vs. the Ag/AgCl reference electrode (just positive of the potential for reduction to the neutral viologen) and after approximately 3 sec (Fig. 1) the bias voltage was changed to $+0.4\text{V}$. The current/time profile, from 1 to 3 sec of reduction, shows that the growth of the n-heptyl viologen radical cation film on the tin oxide substrate appears diffusion controlled. The transmittance/time plot shows that the color change occurs through two distinct time regions, linear changes from 0 to 400 msec and then a nonlinear change from 1 to 3 sec. The behavior at longer electrolysis times is representative of spectroelectrochemical behavior for a diffusion-controlled process (28). A spectrophotometric assay of the deposited viologen concentration after 400 msec of deposition (assuming the molar absorptivity to be ca. $1.5 \times 10^4 \text{ M}^{-1} \text{ cm}^{-1}$, and a projected surface area of the viologen to be ca. 50Å^2) showed the surface excess to be ca. 15 monolayers. A coulometric assay at this same electrolysis time (corrected for charging current with or without viologen present) indicated a deposition of ca. 34 monolayers. The variation in the two numbers can be assumed to arise in an overestimation of the extinction coefficient for the viologen in the film or poor estimation of the projected area of the molecule.

When the bias voltage was changed to $+0.4\text{V}$ after 3.75 sec, the oxidative current was constant as a function of time during the first 500 msec of decoloration.

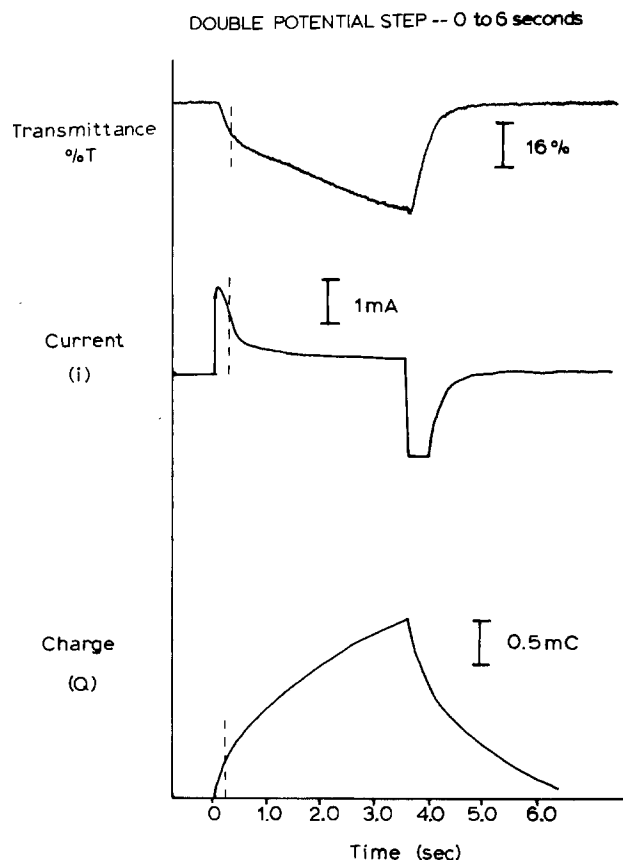


Fig. 1. Double potential step, transmittance (at 595 nm)/time, current/time, and charge/time measurements for a $1 \times 10^{-2}\text{M}$ solution of n-heptyl viologen dibromide in a 0.1N KBr at a clean SnO_2 electrode. Total elapsed time: 6 sec. Dashed line indicates the passage of 200 msec of electrolysis time (see Fig. 2).

Decoloration therefore appears to be kinetically limited. Measurement of $E_{\text{work}} - E_{\text{ref}}$ simultaneously in the chronoabsorptometric experiment indicated that the applied deposition or reduction potential (-0.8V) was reached within 10 μsec after initiation but that the oxidation potential ($+0.4\text{V}$) was reached only after 500-1000 msec, following application of that potential. We believe that this delay in controlled potential response is due to the inherent resistivity of the cation radical film (25-27) and the inability of the potentiostat to comply with the current/voltage characteristics necessary to achieve fast dissolution of the film. The resistivity of the viologen film toward oxidation may be due to low rates of electron transfer through the films, back to the electrode substrate. Saturation of this region with the newly formed dication may also impede electron transfer. The rectifying nature of the cation-radical film requires further study.

Reduction in the time region from 0 to 200 msec was examined in more detail with a series of double-potential step experiments shown in Fig. 2. Both the transmittance change and total reductive charge increased linearly over this time region. Absorbance change vs. $(\text{time})^{1/2}$ and charge vs. $(\text{time})^{1/2}$ plots therefore show a positive deviation from linearity. Even though potential control was achieved within 10 μsec , the reduction current was virtually constant with time throughout deposition. The deposition during the initial 200 msec is apparently not mass transport controlled (28). This initial reduction corresponds to approximately 1.8×10^{-9} moles/ cm^2 or ca. 6 monolayers (determined spectrophotometrically). The decoloration or stripping of viologen in this time interval is also resistively controlled similar to the longer time measurements. Since the first several monolayers of viologen are deposited at rates not controlled by mass

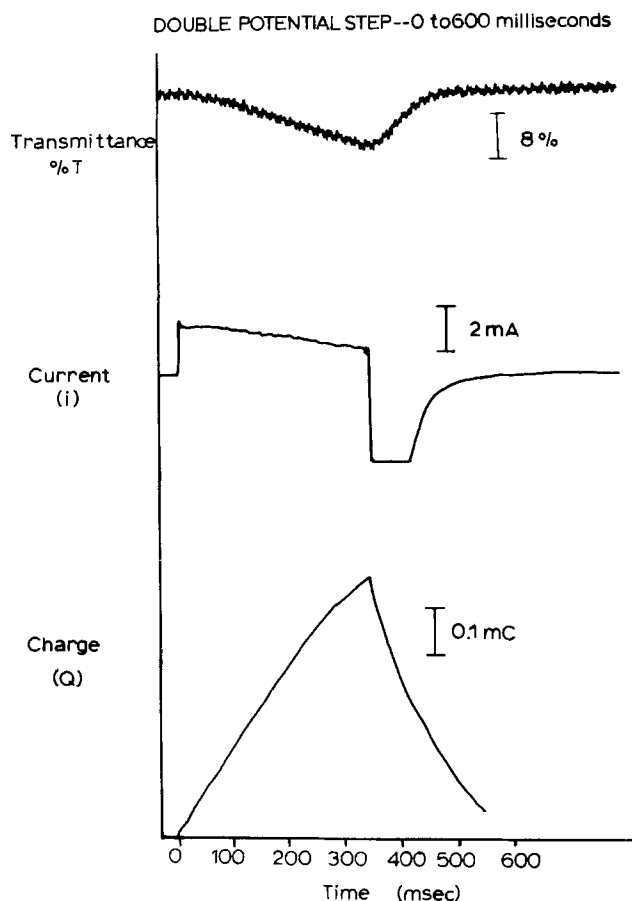


Fig. 2. Double potential step, transmittance (at 595 nm)/time, current/time, and charge/time measurements for a $1 \times 10^{-2} M$ solution of *n*-heptyl viologen dibromide in 0.1*N* KBr electrolyte at a clean SnO_2 electrode. Total elapsed time: 600 msec.

transport, we concur with Bruinink and Kregting (27) that nucleation of the cation-radical film is very important to film growth (22-26). Fletcher, Duff, and Barraclas have recently confirmed this nucleation hypothesis for the initial deposition of the cation-radical *n*-heptylviologen film on SnO_2 (29). Their results were obtained at low concentrations of the viologen (10^{-5} - $10^{-4} M$) where nucleation can be expected to be more dominant in the growth of the film than the results presented here. Similar conclusions have been reached regarding electrodeposition of metals (30). In our experiments, it appears that nucleation can be expected to dominate film growth from concentrated solutions of viologen for times up to 1 sec when reduction is carried out potentiostatically. This observation also leads to the conclusion that modification of the electrode surface should dramatically change the viologen deposition process by changing the number and type of nucleation sites.

Viologen deposition on chemically modified electrodes.—Most metal oxide electrodes have shown reactivity to silane coupling agents which can be used to alter the various electrochemical responses (1-8). We have found that those electrodes which possess short, nonpolar groups such as a dimethyl functionality (from dimethyldiethoxy silane, dmde-silane) or a phenyl functionality (from phenyltriethoxy silane, phensilane) or a metallized plastic film electrode (MPOTE) improve the coloration behavior of the *n*-heptyl viologen.

Preliminary results for dilute ($10^{-3} M$) solutions of *n*-heptyl viologen dibromide in 0.1*N* KBr had indicated an increase in coloration rates with increased nonpolar nature of the electrode surface (20). Unmodified SnO_2 electrodes were compared with amine-silane-modified SnO_2 electrodes and ITO metallized

plastic film electrodes. The amine-silanes included γ -aminopropyl triethoxy silane (pr-silane) and aminothiethylaminopropyl triethoxy silane (en-silane) both of higher molecular weight and chain length than in the studies reported here. A slight increase in current density for the reduction and oxidation waves of the cyclic voltammograms of *n*-heptyl viologen was noted on the modified SnO_2 electrode and the MPOTE. An increase of the coloration rate of the viologen film (1-30 sec) of up to 50% was noted on the modified SnO_2 electrode in chronoabsorptometric experiments. In the case of the SnO_2 electrodes, the increase in coloration rate was hypothesized to be due to the presence of the organic functionality on the electrode surface. In the case of the MPOTE electrodes, surface analytical data has indicated that the surface is carbon-rich, due to the admixture of the metal oxides and the polymer undercoating (21). Also of note was that the reduction prewave in the cyclic voltammograms of the viologen was missing on the chemically modified SnO_2 electrode. The prewave is typical of reactions where the product of the electroreduction is adsorbed on the electrode surface (31, 32). The absence of the prewave indicates the alteration of the adsorption surface site. Further exploration of this effect is necessary.

In spite of the encouraging results obtained with the pr- SnO_2 and en- SnO_2 electrodes, we found it difficult to control the surface concentration of the modifier so that optimum coloration and decoloration behavior was obtained. High surface concentrations of the modifier promoted excessive decoloration rates. It was decided that the propylamine or ethylamine-propylamine groups were not of the optimum type to promote a favorable change in the *n*-heptyl viologen deposition and dissolution. Dimethyl diethoxy silane and phenyltriethoxy silane were explored next, to add smaller, nonpolar functional groups to the SnO_2 surface.

Double potential step, transmittance/time plots, ($5 \times 10^{-2} M$ viologen, 0.1*N* KBr) from 0 to 5 sec, are shown in Fig. 3, comparing an unmodified SnO_2 electrode with a dmde-modified SnO_2 electrode. Several features are apparent in these plots. On the modified electrode surface the amount of coloration at 2 sec is ca. 30% greater than on the unmodified surface, consistent with the results presented previously for the more dilute solutions of viologen. On both electrodes, the initial viologen deposition (0-500 msec) is not mass transport controlled. On the modified surface in the first 500 msec of deposition the transmittance change is increased over that of the unmodified surface by ca. 60%. On both surfaces the rates of decoloration were kinetically controlled and were not significantly changed on the modified electrode surface. On those electrodes with large molecular weight silanes attached, or with surface concentrations of the silane consistent with a siloxane polymer (1, 2, 32), the decoloration rates were lengthened relative to the unmodified surface.

The effect of surface concentration of the silane on the electrochromic process is explored in more detail in Fig. 4. Cyclic voltammograms and chronoabsorbance behavior are shown for *n*-heptyl viologen ($10^{-3} M$) on unmodified SnO_2 , and SnO_2 electrodes exposed to dmde-silane at 20 and 100 min, respectively. The amount of silane found on the SnO_2 surface when examined by XPS is found to be a direct function of the exposure time of the SnO_2 electrode to the silane during modification. Both silanized electrodes show greater coloration rates when compared to an unmodified SnO_2 electrode, and the cyclic voltammograms show a greater current response due to the increase in surface concentration of viologens. The optimum coloration rate was achieved when the SnO_2 electrode was silanized for 20 min. Further exposure to silane solution caused a greater reduction current,

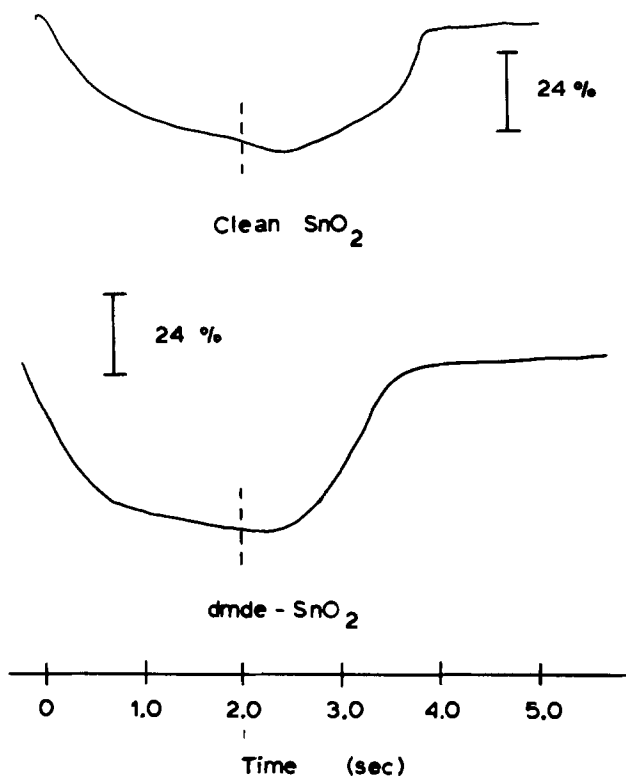


Fig. 3. Double potential step, transmittance (at 595 nm)/time plots comparing an unmodified SnO_2 electrode with a dmde-modified SnO_2 electrode for 5×10^{-2} solution of n-heptyl viologen dibromide in 0.1N KBr electrolyte. Total elapsed time: 5 sec. Dashed line indicates the point at which chronoabsorptometric behavior was compared.

but slowed down the coloration rate for that electrode. We believe that too much attached silane restricts the nucleation of viologen at the electrode surface and possibly forms an insulating surface layer (1, 2). This point is further illustrated in Fig. 5. Comparisons of unmodified dmde-modified and phen-modified SnO_2 electrodes and an ITO, MPOTE are shown. Upon potential cycling to and from the deposition potential, both the dmde- SnO_2 and the phen- SnO_2 electrodes show improved coloration rates after the 12th cycle.

Reaction Time of Silane

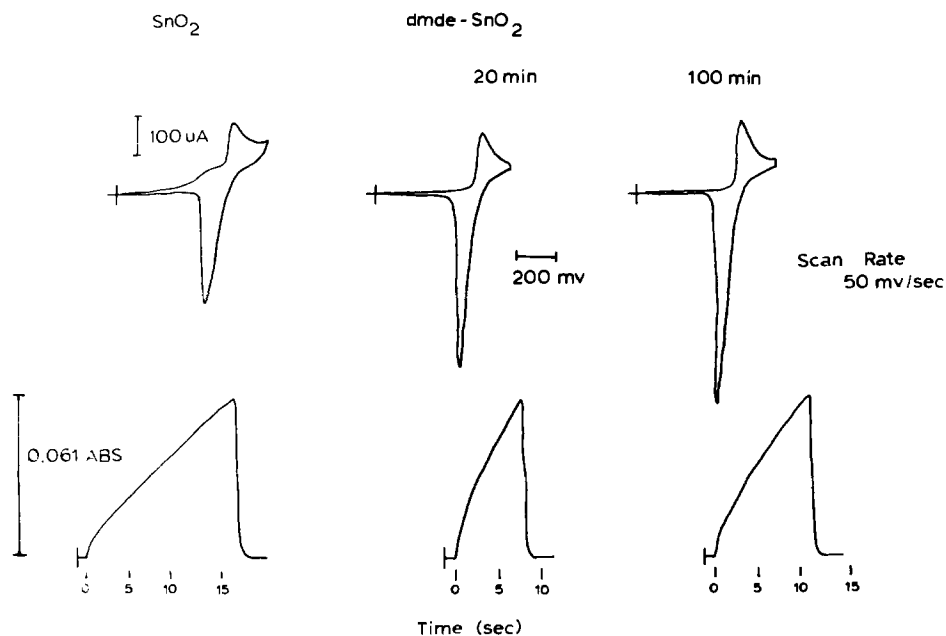


Fig. 4. Cyclic voltammograms and double potential step, chronoabsorbance curves for a 1×10^{-3} M solution of n-heptyl viologen in 0.1N KBr electrolyte on unmodified SnO_2 and SnO_2 exposed to dmde-silane at 20 and 100 min, respectively.

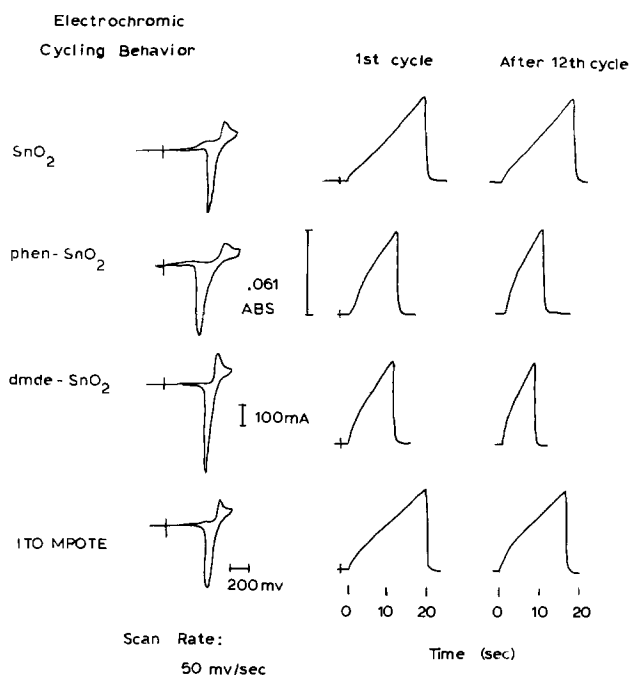


Fig. 5. Cyclic voltammograms and double potential step chronoabsorbance plots for a 1×10^{-3} M solution of n-heptyl viologen in 0.1N KBr electrolyte on clean unmodified SnO_2 electrode, SnO_2 electrodes modified with phenyl dimethoxysilane and dimethyldiethoxysilane, and an ITO metallized plastic electrode film. Behavior monitored as a function of number of times the electrode potential was cycled to and from the reduction potential.

This can be attributed to some activation of the modified electrode surface, possibly by electrochemical stripping of the unbound silane, or irreversible deposition of monolayers of viologen. No additional changes were noted for voltammetric cycles beyond the 12th cycle. Good stability of the film is apparent for 30-50 cycles. Further studies of film stability are in progress. Only minor amounts of improvement were observed upon potential cycling the SnO_2 and ITO MPOTE electrodes. Auger analysis of a surface removed from solution after the 12th cycle shows that the silane is still present on the surface, but its surface concentra-

tion is half that found after one cycle. Even after potential cycling the electrode, the coloration rates on the modified surfaces are still faster than on the unmodified electrodes.

Conclusions

It is clear that the amount of n-heptyl viologen electrochemically reduced and its rate of precipitation can be strongly influenced by the state of the electrode surface. Figure 6 is a schematic of the electrodeposition process for unmodified SnO_2 electrodes. The top picture represents an unmodified SnO_2 electrode whose surface is viewed to consist of hydroxyl groups which can be exchanged with a counter ion such as bromide (25, 26). Viologen undergoing electrochemical reduction precipitates in a configuration producing a partially conductive film. For chemically modified electrodes as shown in the bottom picture, the role of the counter ion is uncertain. Several recent studies have shown that only a fraction of the available surface hydroxyls are involved in silane bonding, so that ion exchange processes are still possible (33, 34). We believe that by providing a nonpolar site on the surface through attachment of the silane, that a more preferred nucleation site is obtained for the deposition of the first monolayers of viologen. The spectroelectrochemical data indicates that the amount of viologen deposited in the first 200-500 msec of the reduction is increased at least 60% by the addition of a monolayer concentration of the silane to the electrode surface. We have seen little effect on the reduction of methyl viologen using silane-modified electrodes and conclude that the heptyl group on the viologen is the major source of the interaction with the surface modifier. The role of the n-heptyl groups in the viologen reduction must be to reduce the solubility of the cation

radical and to increase the tendency toward aggregation of the deposited molecules. We picture the role of the silane modifier as a facilitator in the solvation of the nonpolar portions of the viologen. The surface functional groups cannot be too bulky, or the surface concentration of the modifier too large, to avoid excessive decoloration times for the viologen film. In the case of the metallized plastic films, it seems that the increase in coloration rate can be attributed to the presence of nonpolar surface groups which are present on the surface of the conductive film and interact with the viologen. XPS and AES analysis confirmed the higher surface concentration of carbon on these films compared to normal SnO_2 thin film electrodes (21, 36). Favorable nucleation sites are present on the MPOTE, but not of the same chemical type as those on the silane-modified SnO_2 surface.

Several questions remain under investigation regarding the viologen electrochromic reactions. The role of the anion in the deposition reactions is important and unexplored on the modified surfaces. Understanding of the nature of the interaction of Br^- with the metal oxide surface as well as other anions may lead to further optimization of the electrochromic response of the viologens. It would also be desirable to hold the viologen in a more rigid matrix next to the electrode surface to further enhance coloration rates, the stability of the viologen cation-radical film, and possibly reduce resistive effects on the decoloration process (37).

Acknowledgment

The authors would like to acknowledge the gift of the metallized plastic films from John Fenn, Sierracin/Sylmar. Partial support of this research came from a grant to N. R. Armstrong from the National Science Foundation, CHE 78-19959.

Manuscript submitted Dec. 21, 1979; revised manuscript received June 26, 1980.

Any discussion of this paper will appear in a Discussion Section to be published in the June 1981 JOURNAL. All discussions for the June 1981 Discussion Section should be submitted by Feb. 1, 1981.

Publication costs of this article were assisted by the University of Arizona.

REFERENCES

1. P. R. Moses, L. Wier, and R. W. Murray, *Anal. Chem.*, **47**, 1882 (1975).
2. N. R. Armstrong, A. W. C. Lin, and T. Kuwana, *ibid.*, **48**, 741 (1976).
3. D. D. Hawn and N. R. Armstrong, *J. Phys. Chem.*, **82**, 1288 (1978).
4. V. Rogers Shepard, Jr. and N. R. Armstrong, *ibid.*, **83**, 1268 (1979).
5. B. F. Watkins, J. R. Behling, E. Kariv, and L. Miller, *J. Am. Chem. Soc.*, **97**, 3549 (1975).
6. C. M. Elliot and R. W. Murray, *Anal. Chem.*, **48**, 1247 (1976).
7. J. R. Lenhard and R. W. Murray, *J. Electroanal. Chem. Interfacial Electrochem.*, **78**, 195 (1977).
8. J. C. Lennox and R. W. Murray, *ibid.*, **78**, 395 (1977).
9. J. F. Evans, T. Kuwana, M. T. Henne, and G. P. Rogers, *ibid.*, **80**, 409 (1977).
10. D. C. S. Tse and T. Kuwana, *Anal. Chem.*, **50**, 1315 (1978).
11. R. F. Lane and A. T. Hubbard, *J. Phys. Chem.*, **77**, 1401 (1973).
12. A. P. Brown, C. Koval, and F. C. Anson, *J. Electroanal. Chem. Interfacial Electrochem.*, **72**, 379 (1976).
13. J. P. Collman, M. Marrocco, P. Denisevich, C. Koval, and F. C. Anson, *ibid.*, **101**, 117 (1979).
14. A. Bettelheim, R. J. H. Chan, and T. Kuwana, *ibid.*, **99**, 391 (1979).
15. A. F. Diaz and K. K. Kanazawa, *ibid.*, **86**, 441 (1978).

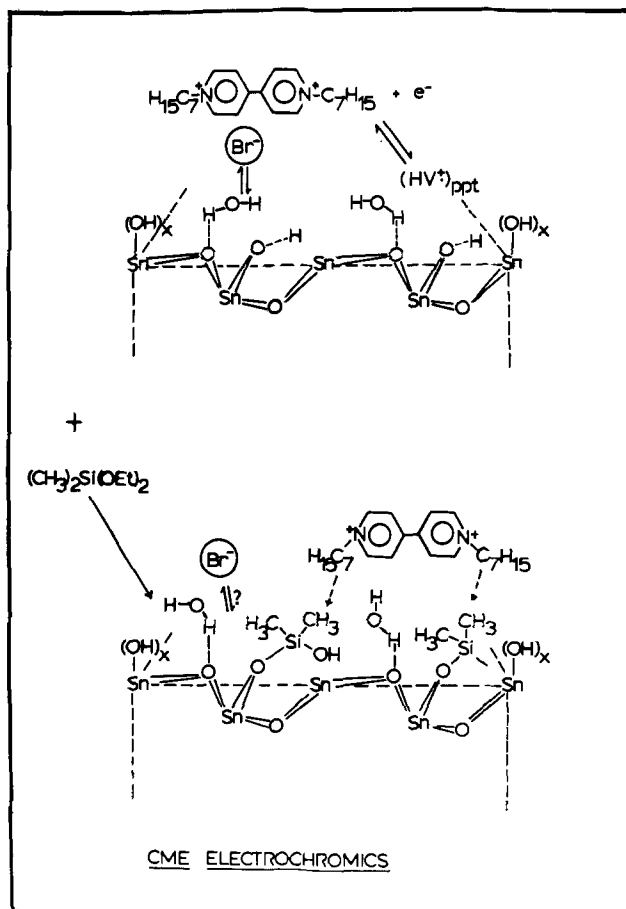


Fig. 6. Schematic representation of the viologen electrodeposition process on unmodified and chemically modified (CME) SnO_2 electrodes.

16. A. F. Diaz, U. Hetzler, and E. Kay, *J. Am. Chem. Soc.*, **99**, 6780 (1977).
17. F. B. Kaufman and F. M. Engler, *ibid.*, **101**, 547 (1979).
18. T. Osa and M. Fujihira, *Nature (London)*, **264**, 349 (1976).
19. M. R. Van DeMark and L. L. Miller, *J. Am. Chem. Soc.*, **100**, 3223 (1978).
20. R. C. Cieslinski and N. R. Armstrong, Paper 461A presented at The Electrochemical Society Meeting, Los Angeles, California, Oct. 14-19, 1979.
21. R. C. Cieslinski and N. R. Armstrong, *Anal. Chem.*, **51**, 565 (1979).
22. J. Bruinink, C. G. A. Kregting, and J. J. Ponjee, *This Journal*, **124**, 1854 (1977).
23. C. Schoot, J. Ponjee, H. van Dam, R. van Doorn, and R. Bolwijn, *Appl. Phys. Lett.*, **23**, 64 (1973).
24. J. Bruinink and P. van Zanten, *This Journal*, **124**, 1232 (1977).
25. R. Jasinski, *ibid.*, **125**, 1619 (1978).
26. R. Jasinski, *ibid.*, **126**, 167 (1979).
27. J. Bruinink and C. G. A. Kregting, *ibid.*, **125**, 1397 (1978).
28. N. Winograd and T. Kuwana, "Electroanalytical Chemistry," A. J. Bard, Editor, Vol. 7, Marcel Dekker, New York (1974).
29. S. Fletcher, L. Duff, and R. G. Barraclas, *J. Electroanal. Chem. Interfacial Electrochem.*, **100**, 759 (1979).
30. D. J. Astley, J. A. Harrison, and H. R. Thirsk, *Trans. Faraday Soc.*, **64**, 192 (1968).
31. R. H. Wopschall and I. Shain, *Anal. Chem.*, **39**, 1514 (1967).
32. W. M. Schwarz, Ph. D. Thesis, University of Wisconsin, Madison, Wisconsin (1961).
33. K. Itaya and A. J. Bard, *Anal. Chem.*, **50**, 1487 (1978).
34. N. R. Armstrong and V. R. Shepard, Submitted to *J. Phys. Chem.*
35. H. Finklea and R. W. Murray, *J. Phys. Chem.*, **83**, 353 (1979).
36. J. White, R. Cieslinski, and N. R. Armstrong, Manuscript in preparation.
37. R. Cieslinski and N. R. Armstrong, Work in progress.

An Investigation of Electrode Materials for the Anodic Oxidation of Sulfur Dioxide in Concentrated Sulfuric Acid

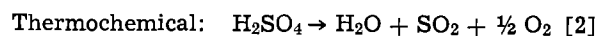
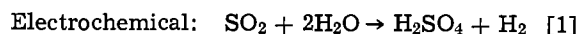
P. W. T. Lu* and R. L. Ammon

Westinghouse Electric Corporation, Advanced Energy Systems Division, Pittsburgh, Pennsylvania 15236

ABSTRACT

The kinetic studies and electrochemical evaluation of catalysts for the SO₂ oxidation reaction have been carried out in concentrated (50 weight percent) sulfuric acid solutions using the steady-state potentiostatic method and cyclic voltammetry. Palladium and palladium oxide have been identified to be better catalysts than platinum for this reaction. The polarization potential for SO₂ oxidation on a preanodized Pd anode decreases with increasing temperature, while the reaction mechanism is independent of temperature. The electrochemical oxidation of SO₂ commences at an anodic potential where the formation of adsorbed oxygen-containing species is initiated. On the Pt, Ru, Ir, and Rh anodes, the chemical transformation of the adsorbed species to metal oxides at higher potentials creates passivated layers which partially cover the electrode surface and inhibit the SO₂ oxidation reaction.

The sulfur cycle hydrogen production process is being developed for the electrolytic generation of hydrogen from water (1-4). This cycle is essentially composed of an electrochemical and a thermochemical reaction. In an electrolysis cell, sulfur dioxide dissolved in aqueous solutions is electrochemically oxidized at the anode while hydrogen gas is evolved at the cathode. Sulfuric acid produced in the electrolyzer is concentrated, using thermal energy from a high temperature heat source, and then catalytically decomposed to form sulfur dioxide, water, and oxygen. The hybrid cycle is completed by circulating the sulfur dioxide to the electrolyzer. The partial reactions for the cycle may be represented as follows



It has been noted (5) that the thermodynamic reversible potential for the reaction [1] is only 0.29V [in 50 weight percent (w/o) sulfuric acid at 25°C] as compared to 1.23V for water electrolysis. Conse-

quently, the sulfur-based cycle, through the anodic oxidation of sulfur dioxide (in place of the anodic evolution of oxygen), utilizes theoretically ~24% of electric energy required in the conventional water electrolysis.

In acid media, the electrochemical oxidation of sulfur dioxide has been intensively investigated on platinum (6-13), gold (8, 11, 14, 15), graphite (16), and platinum-gold alloys (14). In a view by Zhdanov (17), the mechanism of the SO₂ oxidation reaction has been discussed. Nevertheless, a majority of electrochemical studies on this reaction were carried out in dilute sulfuric acid solutions (less than 5 w/o). Quantitative information regarding the anodic oxidation of sulfur dioxide in concentrated electrolyte or on metals and alloys other than platinum and gold is sparse (12). As has been pointed out (2, 4, 18), however, high concentration of sulfuric acid solution in the electrolyzer is of crucial importance to maximize the overall energy efficiency of the cycle.

The objective of the present study is to understand the kinetics of the SO₂ oxidation reaction in concentrated sulfuric acid solutions. A number of candidate materials such as palladium, gold, ruthenium, rhenium, iridium, and rhodium, which are chemically stable in

* Electrochemical Society Active Member.

Key words: oxidation, catalysis, kinetics, depolarization, inhibition.

the electrolyte environment, were investigated as catalysts for this reaction. Effects of temperature on the electrode kinetic parameters were examined. In addition, cyclic voltammetric studies were conducted on smooth metal electrodes to determine the influence of oxygen-containing surface layers on the reaction kinetics. Attempts were also made to find alternate catalysts of low cost and promising activity to substitute for platinum in the electrochemical oxidation of sulfur dioxide in concentrated acid media.

Experimental

Electrode preparation.—A wire or rod of candidate materials was electrically connected to a platinum wire by spot welding. Each electrode was then sealed in a shrinkable Teflon tubing such that a surface area approximately 1 cm² was exposed to the electrolyte.

The porous carbon plates used in the fabrication of PdO_x/C electrodes were pretreated in concentrated (13.5*N*) nitric acid at 80°C for 4 hr, followed by ultrasonic cleaning. The resulting carbon substrates were rinsed thoroughly in distilled water and then dried in air at 125°C. An appropriate amount of aqueous PdCl₂ solution was applied to the pretreated carbon substrate by a vacuum filtration method. After thermal decomposition at 600°C under a hydrogen atmosphere, the catalyzed carbon electrode was oxidized at ~450°C in a stream of helium of gas containing 5 w/o oxygen. In preparing Pt-black/C electrodes, an aqueous solution of H₂PtCl₆ was applied and the oxidation process was eliminated. The catalyst loading of these electrodes was about 10 mg/cm².

Two dimensionally stable anodes (DSA), composed of RuO_x-TiO₂ and IrO_x-TiO₂, respectively, on titanium substrates, were obtained from Electrode Corporation. The PdO_x-TiO₂/Ti electrode was prepared by a thermal decomposition method. A flat titanium substrate was mechanically roughened, degreased, pickled (in 20 w/o oxalic acid at 90°C), and cleaned ultrasonically. An appropriate amount of the solution comprising palladium chloride (PdCl₂), titanium chloride (TiCl₃), isopropyl alcohol, and hydrochloric acid, was coated on the substrate. After a heat-treatment in air, a catalyst layer of mixed oxide was formed on the substrate. Prior to an experiment, each test electrode was degreased using acetone and then pretreated cathodically at 10 mA/cm² in SO₂-free sulfuric acid solutions for 10 min.

Electrolyte preparation.—The measuring solutions (50 w/o H₂SO₄) were prepared from Fisher analyzed reagent grade sulfuric acid and distilled water. With a view to minimizing impurities, each measuring solution was further purified by pre-electrolysis at a current density of about 2 mA/cm² on a Pt-gauze cathode for at least 24 hr, followed by bubbling a highly pure nitrogen gas to eliminate traces of oxygen and hydrogen dissolved in the electrolyte.

Apparatus.—Electrochemical studies were conducted in a three-compartment cell as described in the work by Miles and co-workers (19). A platinum spiral positioned in a small compartment served as a counter-electrode. A reversible hydrogen electrode (RHE) with sulfuric acid of the same concentration as the measuring solution was used as the reference. The working electrode was placed about 0.5 mm from the tip of a Luggin capillary. Electrochemical measurements were made using a PAR Model 371 potentiostat coupled with a PAR Model 175 programmer. While performing voltammetric studies, cyclic voltammograms were recorded on an X-Y recorder. A quartz tube furnace was used in the preparation of oxide and mixed oxide electrodes. The microstructures of these electrodes were examined by scanning electron microscopy (ISI Model SUPER IIIA).

Electrochemical measurements.—Tafel plots were determined for SO₂ oxidation on test electrodes in 50

w/o sulfuric acid solutions at 25°C, using the steady-state potentiostatic method. During each experiment, the electrolyte within the main compartment was a stirred solution deaerated with purified SO₂. At a constant polarization potential, the observed currents on the freshly prepared metal electrode gradually decayed with time. A similar phenomenon has also been reported in the literature (7). Therefore, each pretreated metal electrode was further potentiostated at 1.0V in SO₂-saturated solution for about 30 min. This preanodization process resulted in the formation of stable surface layers on the electrodes. Thus, steady currents were generally observed in the direction of decreasing potential. Electrochemical studies of the temperature effect on electrode kinetic parameters were performed on a smooth palladium electrode at temperatures of 25°, 50°, 70°, and 90°C.

Cyclic voltammetric studies were conducted on the smooth electrodes of Pt, Pd, Ru, Ir, and Rh. In the measuring solution, each freshly prepared electrode was initially potentiostated at 0.3V for 5 min. By applying a linear potential sweep of 100 mV/sec, the first ten traces of continuous cyclic voltammograms were recorded for a test electrode.

Results and Discussion

Kinetic studies on metal electrodes.—Electrocatalytic activities of preanodized electrodes of Pt, Pd, Au, Ru, Re, Ir, and Rh were investigated for SO₂ oxidation in 50 w/o sulfuric acid at 25°C and atmospheric pressure. As identified in an earlier analysis, the concentration of SO₂ in the saturated solution was approximately 1.2M under these conditions. Three separate studies were carried out on each electrode. It was found that the preanodization of a test electrode resulted in reproducible data. The potential-current density relationships shown in Fig. 1 represent the averaged results for the three individual studies. Well-defined Tafel regions were generally observed on these electrodes. Kinetic parameters such as Tafel slope, transfer coefficient, and limiting current density for SO₂ oxidation are summarized in Table I.

The performance characteristics of the Pt electrode is considered as a baseline for comparison. As illustrated in Fig. 1, Pd is a better catalyst than Pt for the SO₂ oxidation reaction. At 1 mA/cm², the polarization potential on the electrode is approximately 120 mV lower than on the Pt electrode. Under the identical experiment conditions, the Pd electrode exhibits a limiting current density of 4.0 × 10⁻² A/cm² as compared to 1.2 × 10⁻³ A/cm² for Pt (see Table I). In addition, Au and Ru show approximately the same catalytic activities as Pt. However, Ir, Re, and Rh electrodes were relatively inactive for the anodic oxidation of sulfur dioxide.

There have been a number of investigations on the reaction mechanism for SO₂ oxidation, with most of these studies being conducted in dilute sulfuric acid solutions (6-12). In concentrated acid media, Appleby and Pichon (12) first proposed a reaction mechanism

Table I. Electrode kinetic parameters for the SO₂ oxidation reaction on various candidate materials in 50 w/o H₂SO₄ solutions at 25°C

Electrode	Tafel slope (mV/decade)	Transfer* coefficient	Current density at 0.6V (A/cm ²)	Limiting current density (A/cm ²)
Pt	67	0.88	1.8 × 10 ⁻⁵	1.2 × 10 ⁻³
Pd	54	1.09	1.2 × 10 ⁻⁴	4.0 × 10 ⁻²
Au	63	0.94	2.8 × 10 ⁻⁵	2.0 × 10 ⁻³
Ru	63	0.94	2.0 × 10 ⁻⁵	1.6 × 10 ⁻³
Re	68	0.87	9.3 × 10 ⁻⁶	8.0 × 10 ⁻⁴
Ir	66	0.89	3.3 × 10 ⁻⁶	5.1 × 10 ⁻⁴
Rh	82	0.72	1.9 × 10 ⁻⁶	4.0 × 10 ⁻⁴

* Transfer coefficient = 2.303 RT/bF where b is the Tafel slope.

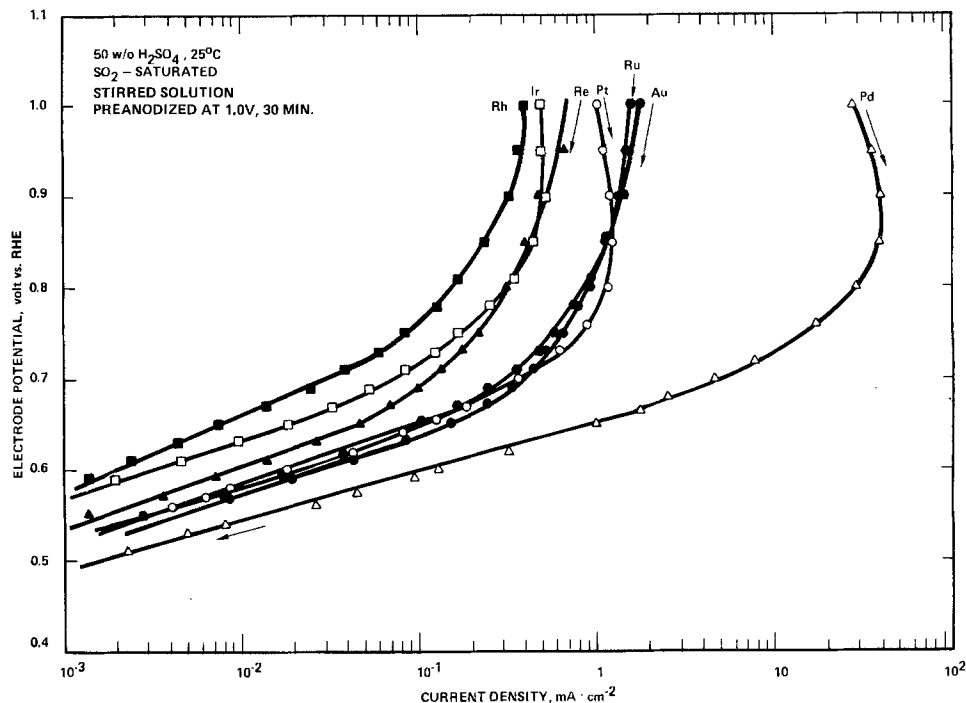
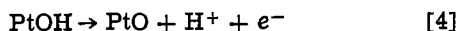
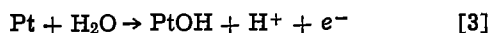


Fig. 1. Tafel plots for SO_2 oxidation on smooth electrodes of Pt, Pd, Au, Ru, Re, Ir, and Rh in 50 w/o sulfuric acid at 25°C.

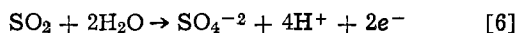
for Pt electrode which may involve the following steps



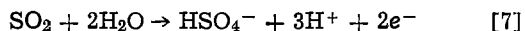
This reaction scheme is only applicable to interpret the SO_2 oxidation at potentials above 0.95V, the potential at which the formation of PtO film commences (20). As seen from Fig. 1, however, the linear Tafel regions for this reaction are normally found at potentials below 0.7V. Therefore, the measured kinetic parameters are not suitable for use to explain the oxidation mechanism by following the above reaction paths.

As shown in Table I, the observed Tafel slopes on the Pt, Pd, Au, Ru, Re, and Ir electrodes are close to RT/F (that is, transfer coefficients being close to unity). On the Rh electrode, a slightly higher Tafel slope of $\sim 1.4 RT/F$ is measured. By use of the observed Tafel slopes alone, it is difficult to determine uniquely the reaction mechanism. In 50 w/o sulfuric acid saturated with SO_2 , however, the measured open-circuit potentials at 25°C are ~ 0.49 and ~ 0.20 V on the Pt and Pd electrodes, respectively. Since the standard potential for the formation of $\text{H}_2\text{S}_2\text{O}_6$ is as high as 0.564V (17), it seems unlikely that in such a concentrated sulfuric acid, the SO_2 oxidation reaction takes place via the intermediate $\text{S}_2\text{O}_6^{2-}$ ions.

According to Robertson and Dunford (21), the measured concentrations of SO_4^{2-} and HSO_4^- ions in 50 w/o sulfuric acid are approximately 1.86 and 5.14M, respectively. It is thus highly uncertain (12) whether the overall electrochemical reaction for SO_2 oxidation is represented by



or



As a result, the reversible electrode potential for SO_2 oxidation cannot be obtained unambiguously. Thus, exchange current densities on the candidate materials are not determined from the observed Tafel plots. In Table I listed are the current densities at a polarization potential of 0.6V.

Temperature dependence of electrode kinetic parameters.—The effect of temperature on Tafel plots for

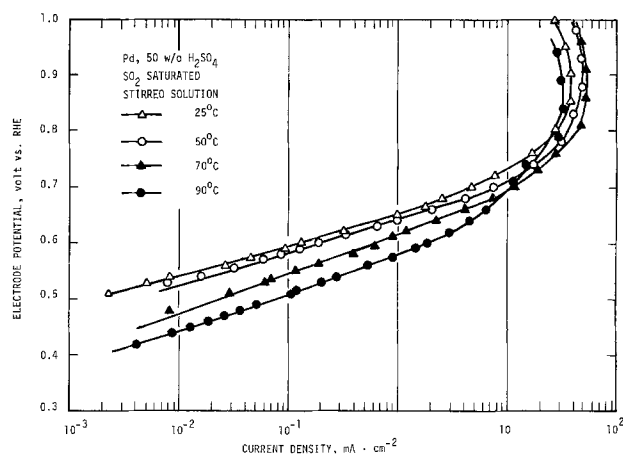


Fig. 2. Tafel plots for SO_2 oxidation on a smooth Pd electrode in 50 w/o sulfuric acid at temperatures of 25°, 50°, 70°, and 90°C.

SO_2 oxidation on a preanodized Pd electrode is shown in Fig. 2. Distinct linear Tafel regions of approximately three decades are observed at temperatures of this study. Electrode kinetic parameters for SO_2 oxidation at the four experimental temperatures are presented in Table II. The observed Tafel slopes (being close to RT/F) are approximately constant at various temperatures, indicating that the mechanism of the SO_2 oxidation reaction is independent of temperature.

There is very little or no improvement in the limiting current density arising from the temperature in-

Table II. Electrode kinetic parameters for the SO_2 oxidation reaction on preanodized palladium electrodes in 50 w/o H_2SO_4 solutions

Temperature (°C)	Tafel slope (mV/decade)	Transfer* coefficient	Current density at 0.6V (A/cm ²)	Limiting current density (A/cm ²)
25	54	1.09	1.2×10^{-4}	4.0×10^{-2}
50	59	1.09	2.0×10^{-4}	4.9×10^{-2}
70	72	0.92	6.0×10^{-4}	5.4×10^{-2}
90	70	1.03	1.9×10^{-3}	3.3×10^{-2}

* Transfer coefficient = $2.303 RT/bF$ where b is the Tafel slope.

crease. Under atmospheric pressure, the solubility of SO_2 in the electrolyte decreases significantly with increasing temperature (11, 12, 22, 23). Therefore, in the limiting current density region, any improvement in the electrode kinetics is probably marred by the reduction of SO_2 solubility. In the linear Tafel regions, however, the temperature increase results in a distinct decrease in the polarization potential. As illustrated in Fig. 2, an improvement of ~ 100 mV in the anodic overpotential at 1 mA/cm^2 is achievable by increasing temperature from 25° to 90°C . The current density for SO_2 oxidation at 0.6V increased by one order of magnitude from $1.2 \times 10^{-4} \text{ A/cm}^2$ at 25°C to $1.9 \times 10^{-3} \text{ A/cm}^2$ at 90°C (see Table II).

Electrochemical evaluation of alternate catalysts.—

A number of oxides and mixed oxides have attracted considerable attention for use as catalysts. Ruthenium oxide (RuO_x) on titanium, for instance, is highly active for the anodic evolution of chlorine and has found wide application as an electrocatalyst in the chlor-alkali industry (24–26). This DSA-type electrode also shows low anodic overpotentials for oxygen evolution from acid (27) and alkaline (28) media. In addition to metal electrodes, the present work has been extended to investigate oxides and mixed oxides as catalysts for SO_2 oxidation. The anode in an SO_2 -depolarized electrolyzer is normally operating at potentials below 0.7V vs. RHE (5). Apparently, a majority of noble metal oxides or mixed oxides are electrochemically stable under this operating condition.

The microstructure of a pretreated porous carbon plate used in the fabrication of PdO_x/C and Pt-black/C electrodes is illustrated in Fig. 3A. The mean pore diameter in this substrate is $\sim 9 \mu\text{m}$ prior to the pretreatment. Nevertheless, a maximum pore diameter $\sim 60 \mu\text{m}$ is observed in the scanning electron micrograph. A catalyst layer was applied to the surface of the pretreated carbon plate using a proprietary fabrication process. The microstructure of the resulting electrode is shown in Fig. 3B. Obviously, the density of catalyst particles on the PdO_x/C electrode is high and the particle distribution is rather uniform.

The potential-current density relationships for SO_2 oxidation on pure carbon, PdO_x/C and Pt-black/C electrodes are given in Fig. 4. The carbon substrate itself is extremely inactive for the anodic oxidation of SO_2 . The PdO_x/C electrode exhibits higher limiting current density and lower polarization potentials as compared to the Pt-black/C electrode. At 1 mA/cm^2 , for example, the anodic overpotential on the former is approximately 50 mV less than on the latter.

The $\text{PdO}_x\text{-TiO}_2$ electrode was prepared by a thermal decomposition method as described elsewhere (29). The microstructure of the electrode surface is shown in Fig. 5. The distribution of catalyst particles is uniform with a maximum particle size of $\sim 3 \mu\text{m}$. Illustrated in Fig. 6 is the electrochemical properties of the mixed oxide electrodes in SO_2 -saturated sulfuric acid solutions. The $\text{PdO}_x\text{-TiO}_2/\text{Ti}$ electrode exhibits an electrocatalytic activity quite comparable to the Pt-black/Ti electrode for the SO_2 oxidation reaction. A polarization potential of $\sim 0.60\text{V}$ was measured on this electrode at 10 mA/cm^2 . Ruthenium oxide and iridium oxide on titanium substrates are excellent catalysts for the anodic evolution of chlorine (24–26) and oxygen (27, 28). As seen from Fig. 6, however, both $\text{RuO}_x\text{-TiO}_2/\text{Ti}$ and $\text{IrO}_x\text{-TiO}_2/\text{Ti}$ electrodes are very ineffective for the electrochemical oxidation of SO_2 in acid media.

Cyclic voltammetric studies.—The voltammetric method has been extensively used to investigate the reaction mechanism of SO_2 oxidation on platinum (8–10, 14) and gold (8, 14, 15). The previous studies were, however, carried out only in dilute acid media. According to the work by Seo and Sawyer (8, 30), an activated electrode surface can be achieved by cycling the potential of a platinum or gold electrode between

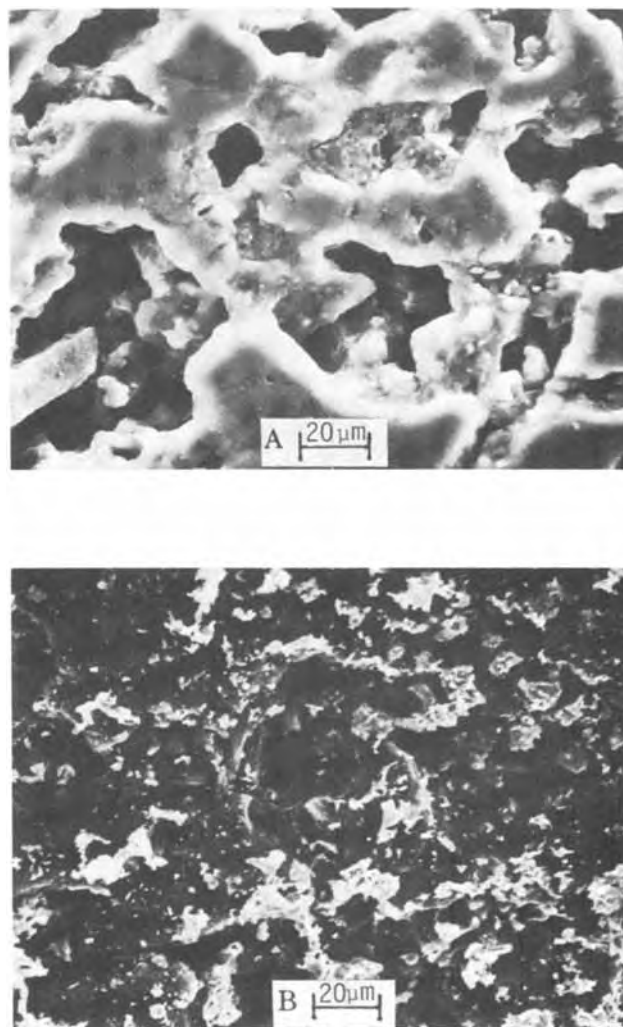


Fig. 3. Scanning electron micrographs of (A) a polished carbon substrate after treatment, and (B) a PdO_x -catalyzed carbon electrode (loading: $10 \text{ mg-PdO}_x/\text{cm}^2$).

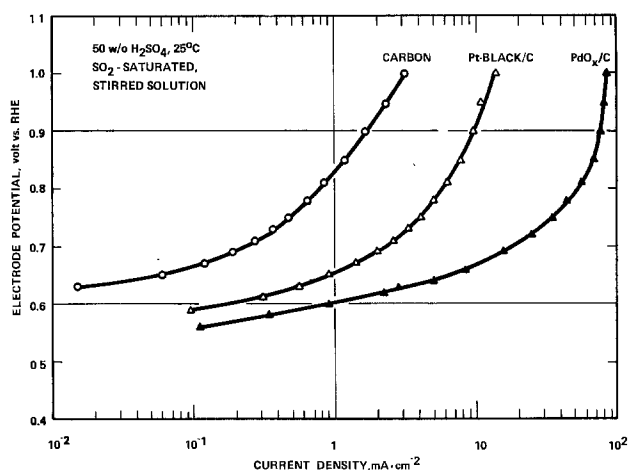


Fig. 4. Tafel plots for SO_2 oxidation on pure carbon, PdO_x/C and Pt-black/C electrodes in 50 w/o sulfuric acid at 25°C .

— 0.15 and 1.50V vs. SCE (saturated calomel electrode) directly in an SO_2 -containing electrolyte. In the cathodic sweep, the SO_2 -containing species in the solution is electroreduced in the potential region for hydrogen adsorption. As a result, the reduction reaction may lead to the formation of adsorbed sulfur and H_2S on the electrode surface (14, 31, 32). With a view to eliminating the adsorbed impurities, this study was carried

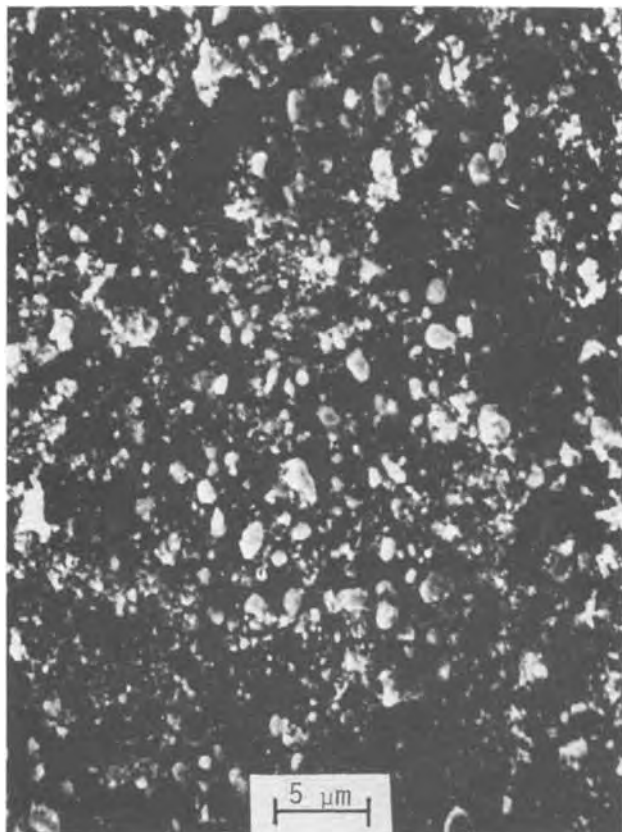


Fig. 5. Scanning electron micrograph of a $\text{PdO}_x\text{-TiO}_2/\text{Ti}$ electrode.

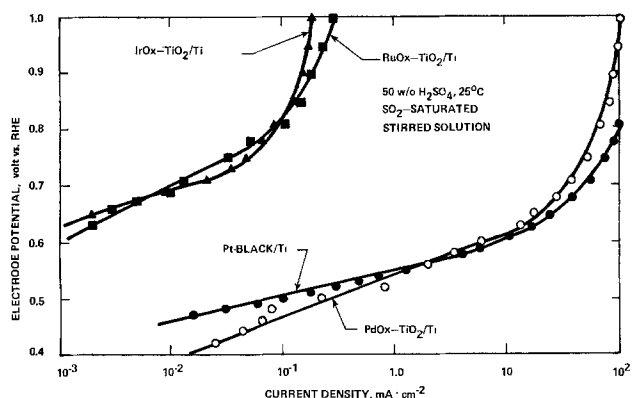


Fig. 6. Tafel plots for SO_2 oxidation on mixed oxide electrodes in 50 w/o sulfuric acid at 25°C .

out at potentials above 0.30V, where hydrogen adsorption does not occur.

Figure 7 shows the first traces of cyclic i -V curves on a freshly prepared Pt electrode in both SO_2 -free and SO_2 -saturated sulfuric acid solutions. It should be noted that the current density scales for the two voltammetric curves are significantly different. In the SO_2 -free electrolyte, the formation of adsorbed oxygen-containing species on the bare electrode surface commences at an anodic potential of $\sim 0.55\text{V}$ (see Fig. 7). Ellipsometric studies (20) indicated that starting at $\sim 0.95\text{V}$ in the 0.1N sulfuric acid, the adsorbed oxygen-containing species on a Pt anode is converted to platinum oxide, PtO, by the "place exchange mechanism" (33). Subsequently, the coverage and thickness of PtO species on the electrode surface increases with potential. It has been pointed out (34) that, in 2N sulfuric acid, the surface adsorbed oxygen is not converted to the so-called "dermasorbed oxygen," Pt-O, until potentials above 1.0V are reached. In this study, the

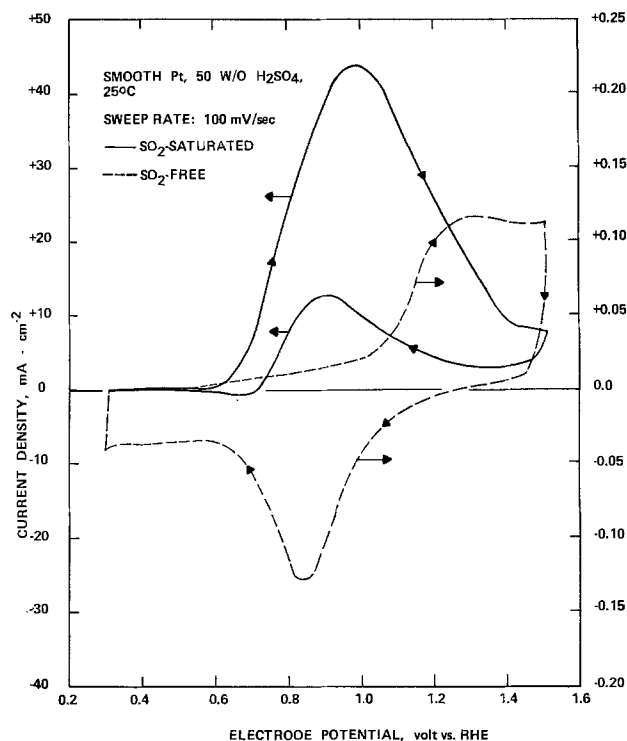


Fig. 7. Cyclic voltammograms on a smooth Pt electrode at 100 mV/sec in SO_2 -free and SO_2 -saturated sulfuric acid solutions at 25°C .

anodic and cathodic peaks observed at 1.30 and 0.83V, respectively, are probably attributed to the formation and reduction of the PtO film. According to the work by Thacker and Hoare (34), a complete layer of oxide film may be reached at about 1.6V.

In the SO_2 -saturated acid solution, the anodic and cathodic peaks corresponding to the formation and reduction of oxide film are entirely obscured by the relatively high currents for the SO_2 oxidation reaction. As shown in Fig. 7 this reaction commences at approximately the same potential ($\sim 0.55\text{V}$) as that for the formation of adsorbed oxygen-containing species. It is assumed that the presence of SO_2 -containing species in the electrolyte does not change significantly the potentials for the formation and chemical conversion of the surface film. In the anodic i -V curve, the observed current density decreases significantly with a further rising potential after reaching the peak maximum at $\sim 0.98\text{V}$. As discussed previously, the conversion of adsorbed oxygen-containing species to PtO film takes place at potentials above 0.95V (20). The appearance of the anodic peak is thus attributed to the formation of the PtO film, which partially covers the electrode surface, and the subsequent increase of its coverage with potential. At 1.40V, the observed current density is reduced to less than $\frac{1}{4}$ of the peak-maximum value.

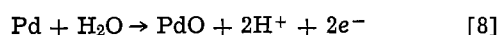
In the cathodic i -V curve, no detectable reduction peak is observed, indicating that the SO_2 oxidation reaction is highly irreversible. As seen from Fig. 7, the electroreduction of the PtO film in the cathodic sweep starts at $\sim 1.25\text{V}$. The complete reduction of the oxide film occurs at potentials below 0.6V. Nevertheless, on the partially reduced Pt electrode, an anodic peak for SO_2 oxidation appears at $\sim 0.90\text{V}$. It is noted¹ that, in the Tafel plots shown in Fig. 1, the measured current density on a preanodized Pt electrode increases slightly

¹ Ellipsometric results (20) revealed that the coverage of the PtO film on the Pt anode is much less than a monolayer at 1.0V. In oxygen-saturated acid solution, the measured coverage of oxide film on the surface of a Pt electrode is $\sim 30\%$ at the open-circuit potential of 1.06V (34). Therefore, on the Pt electrode preanodized at 1.0V, the SO_2 oxidation reaction takes place only at the active sites that are not covered by the PtO species.

with decreasing potential in the range of 0.85-1.0V, essentially due to the gradual reduction in the coverage of PtO species on the electrode surface. These observations indicate that the electrocatalytic activity of an oxide-covered Pt anode for the anodic oxidation of SO₂ is rejuvenated by the electroreduction of PtO film to adsorbed oxygen-containing species.

On the basis of voltammetric results, it is concluded that the electrochemical oxidation of SO₂ commences at the potential (~0.55V) where the first adsorbed oxygen-containing species appears on a bare Pt anode. At potentials higher than 0.98V, the adsorbed species is chemically converted to a passivating PtO film which partially covers the electrode surface and inhibits the SO₂ oxidation reaction.²

The first traces of cyclic *i*-V curves on a freshly prepared Pd electrode are illustrated in Fig. 8. In the SO₂-free electrolyte, two anodic peaks are detected at 1.03 and 1.14V. It has been found experimentally (35) that, in dilute acid solutions, palladium oxide, PdO, is formed on a bare Pd electrode at potentials above 0.79V by the following reaction



In addition, the standard potential for the formation of hydrated palladium oxide, Pd(OH)₂, is ~0.896V. Therefore, in the anodic sweep up to 1.2V, the chemical transformation of adsorbed oxygen-containing species to palladium oxide films should take place.

In the SO₂-saturated electrolyte, the cyclic voltammogram on the Pd electrode is somewhat different from that on the Pt electrode. On a bare Pd anode, the SO₂ oxidation reaction also commences at a potential where the formation of adsorbed oxygen-containing species is initiated (being ~0.60V as identified in Fig. 8). The observed current density for this reaction, however, increases distinctly with rising potential up

²There is possibly an alternative interpretation that the adsorbed SO₂ blocks the formation of PtO, which is a reaction intermediate for SO₂ oxidation (12). As a result, the overall SO₂ oxidation reaction is retarded by the gradual decrease of PtO species on the electrode surface. In this case, it is purely coincidental that the peak-maximum potential for SO₂ oxidation as shown in the anodic *i*-V curve in Fig. 7 is identical with the potential at which the formation of PtO species is initiated.

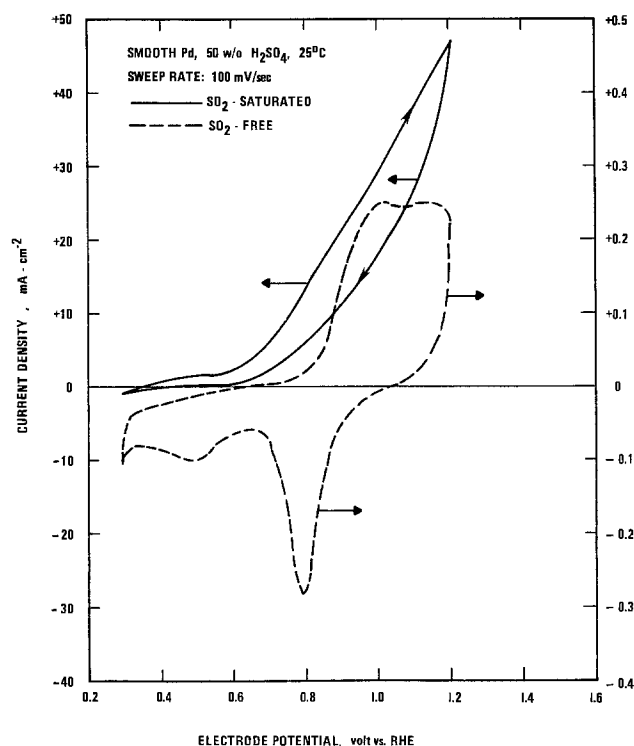


Fig. 8. Cyclic voltammograms on a smooth Pd electrode at 100 mV/sec in SO₂-free and SO₂-saturated sulfuric acid at 25°C.

to 1.2V and then decreases gradually with reducing potential. No oxidation peak is detected in either the anodic or the cathodic *i*-V curve. It is obvious that the formation of oxide films on the Pd anode does not inhibit the electrochemical oxidation of SO₂. More precisely, an oxide-covered Pd electrode exhibits high electrocatalytic activity for SO₂ oxidation.

Figure 9 shows the cyclic *i*-V curves on the freshly prepared electrodes of Ru, Ir, and Rh in SO₂-saturated sulfuric acid solutions. Like the Pt anode, broad anodic peaks are normally observed on these electrodes. At the potential sweep rate 100 mV/sec, the peak-maximum potentials on Ru, Ir, and Rh electrodes are approximately 1.12, 1.08, and 0.88V, respectively, in the anodic *i*-V curves. As observed on the Pt anode, the conversion of adsorbed oxygen-containing species to metal oxides on these electrodes also creates passivated surface layers which inhibit the SO₂ oxidation reaction.

Conclusions

For the anodic oxidation of SO₂, palladium and palladium oxide are better catalysts than platinum. The DSA-type electrodes such as RuO_x-TiO₂/Ti and IrO_x-TiO₂/Ti are inactive for this reaction. Increasing temperature results in remarkable improvements in the anodic overpotential for SO₂ oxidation on a pre-anodized Pd electrode. The reaction mechanism is, however, independent of temperature. In the anodic sweep, the SO₂ oxidation reaction commences at potentials where the formation of adsorbed oxygen-containing species is initiated. On most metal electrodes, the chemical transformation of the adsorbed species to metal oxides at higher potentials creates passivated surface layers which partially cover electrode surfaces and inhibit the SO₂ oxidation reaction. However, the oxide-covered Pd electrode exhibits high electrocatalytic activity for SO₂ oxidation.

Acknowledgment

The authors wish to thank G. H. Parker, R. W. Buckman, Jr., and G. H. Farbman for their constant interest and encouragement during the course of this study. Special thanks are due to E. R. Garcia and D. R. Zamba for performing the experimental work. This work was carried out under the auspices of the U.S. Department of Energy.

Manuscript submitted May 1, 1980; revised manuscript received July 9, 1980. This was Paper 653 presented at the Los Angeles, California, Meeting of the Society, Oct. 14-19, 1979.

Any discussion of this paper will appear in a Discussion Section to be published in the June 1981 JOURNAL. All discussions for the June 1981 Discussion Section should be submitted by Feb. 1, 1981.

Publication costs of this article were assisted by Westinghouse Electric Corporation.

REFERENCES

1. L. E. Brecher and C. K. Wu, U.S. Pat. 3,888,750 (1975).
2. G. H. Farbman and L. E. Brecher, in "Proceedings of the Tenth Intersociety Energy Conversion Engineering Conference," pp. 1199-1204, Newark, Delaware (1975).
3. G. H. Farbman and L. E. Brecher, in "Proceedings of the First World Hydrogen Energy Conference," T. N. Veziroglu, Editor, Vol. 1, 9A-29, Miami Beach, Florida (1976).
4. G. H. Farbman and G. H. Parker, in "Hydrogen: Production and Marketing," M. W. Smith and J. G. Santagelo, Editors, p. 359, American Chemical Society, Washington, D.C. (1980).
5. P. W. T. Lu and R. L. Ammon, in "Hydrogen Energy Progress," T. N. Veziroglu, K. Fueki, and T. Ohta, Editors, Vol. 1, p. 439, Pergamon Press, New York (1980).
6. K. I. Rozental and V. I. Veselovskii, *Zh. Fiz. Khim.*, **27**, 1163 (1953).
7. G. A. Bogdanovskii and A. I. Shlygin, *ibid.*, **32**, 418 (1958).

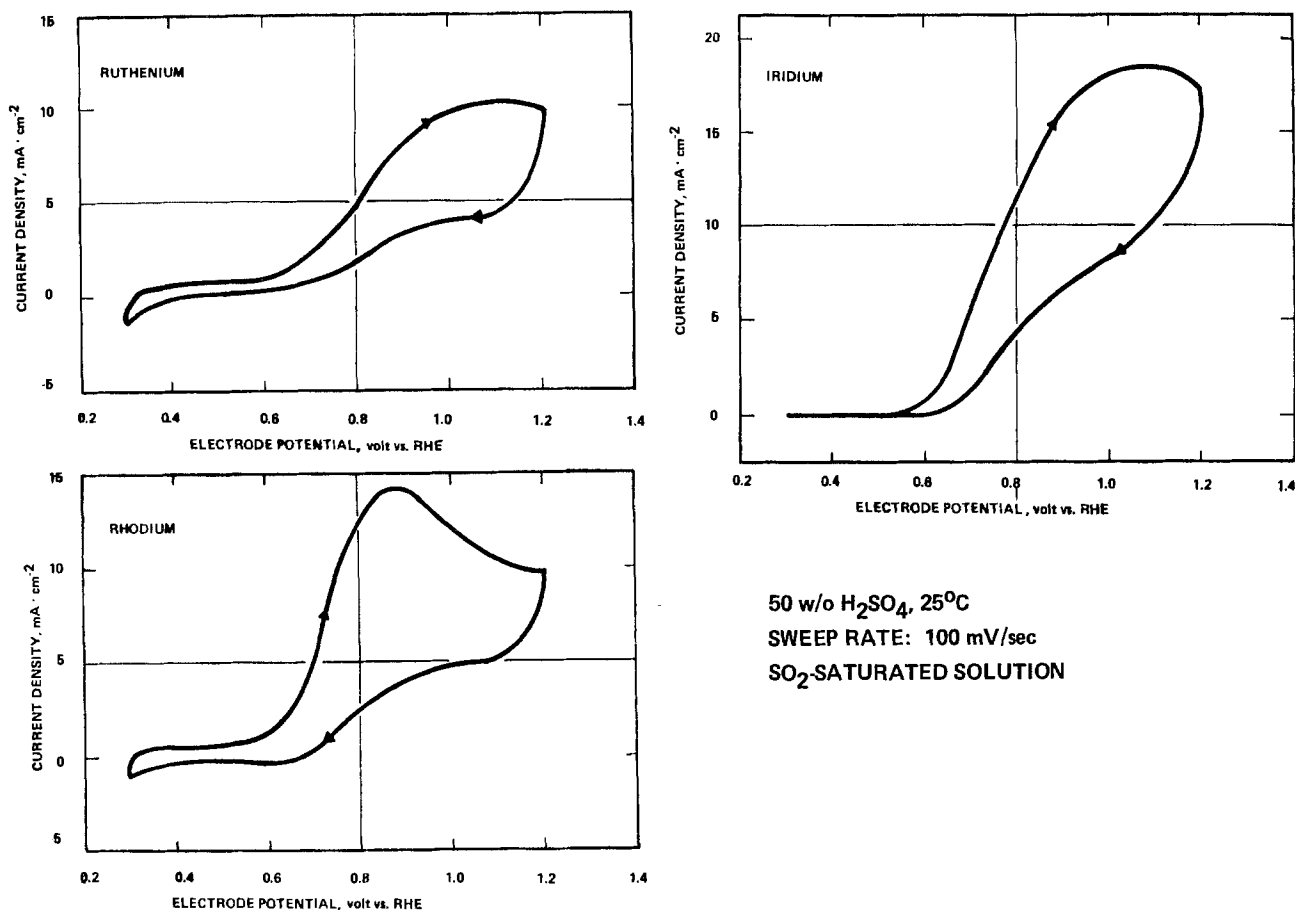


Fig. 9. Cyclic voltammograms on smooth electrodes of Ru, Ir, and Rh in SO₂-saturated sulfuric acid at 25°C

8. E. T. Seo and D. T. Sawyer, *Electrochim. Acta.*, **10**, 239 (1965).
9. M. Comtat and J. Mahenc, *Bull. Soc. Chim., Fr.*, **11**, 3862 (1969).
10. K. Wiesener, *Electrochim. Acta*, **18**, 185 (1973).
11. A. J. Appleby and B. Pichon, in "Hydrogen Energy Systems," T. N. Veziroglu and W. Seifritz, Editors., Vol. 2, p. 687, Pergamon Press, New York (1978).
12. A. J. Appleby and B. Pichon, *J. Electroanal. Chem. Interfacial Electrochem.*, **95**, 59 (1979).
13. C. Audry and M. Voinov, *Electrochim. Acta*, **25**, 299 (1980).
14. K. A. Lezhneva, T. I. Borisova, and M. G. Slin'ko, *Kinet. Katal.*, **2**, 854 (1964).
15. Z. Samec and J. Weber, *Electrochim. Acta*, **20**, 403, 413 (1975).
16. I. P. Voroshilov, N. N. Nechiporenko, and E. P. Voroshilova, *Elektrokhimiya*, **10**, 1378 (1974).
17. S. I. Zhdanov, in "Encyclopedia of Electrochemistry of the Elements," A. J. Bard, Editor, Vol. IV., pp. 273-360, Marcel Dekker, New York (1975).
18. S. S. Lin, Private communication.
19. M. H. Miles, G. Kissel, P. W. T. Lu, and S. Srinivasan, *This Journal*, **123**, 332 (1976).
20. A. K. N. Reddy, M. A. Genshaw, and J. O'M. Bockris, *J. Chem. Phys.*, **48**, 671 (1968).
21. E. B. Robertson and H. B. Dunford, *J. Am. Chem. Soc.*, **86**, 5080 (1964).
22. F. D. Miles and J. Fenton, *J. Chem. Soc.*, **117**, 59 (1920).
23. F. D. Miles and T. Carson, *ibid.*, 786 (1946).
24. R. R. Buker and R. G. Milner, *This Journal*, **117**, 9C (1970).
25. A. T. Kuhn and C. J. Mortime, *ibid.*, **120**, 231 (1973).
26. S. Puschaver, *Chem. and Ind.*, 236 (1975).
27. S. Trasatti and G. Buzzanca, *J. Electroanal. Chem. Interfacial Electrochem.*, **29**, App. 1 (1971).
28. W. O'Grady, C. Iwakura, J. Huang, and E. Yeager, in "Proceedings of the Symposium on Electrocatalysis," M. W. Breiter, Editor, pp. 286-297, The Electrochemical Society Softbound Proceedings Series, Princeton, N.J. (1974).
29. H. B. Beer, South Africa Pat. 680,834 (1968).
30. E. T. Seo and D. T. Sawyer, *J. Electroanal. Chem. Interfacial Electrochem.*, **7**, 184 (1964).
31. A. Q. Contractor and H. Lal, *ibid.*, **93**, 99 (1978).
32. G. L. Klyanina and A. I. Shlygin, *Zh. Fiz. Khim.*, **36**, 1849 (1962).
33. A. H. Lanyon and B. M. W. Trapnell, *Proc. R. Soc., London, Ser. A*, **227**, 387 (1955).
34. R. Thacker and J. P. Hoare, *J. Electroanal. Chem. Interfacial Electrochem.*, **30**, 1 (1971).
35. J. P. Hoare, *This Journal*, **111**, 611 (1964).

Effects of the Gaseous Environment on Propagation of Anodic Reaction Boundaries in Lutetium Diphthalocyanine Films

M. M. Nicholson* and F. A. Pizzarello

Rockwell International, Electronics Research Center, Anaheim, California 92803

ABSTRACT

Influences of the gaseous environment on the anodic oxidation of lutetium diphthalocyanine films contacted by aqueous Na_2SO_4 or KCl were investigated with a moving-boundary technique. Ambient water vapor was required to propagate the red/green boundary from both electrolytes. Oxygen was also required with the sulfate solution but not with the chloride. The results suggest that the diphthalocyanine oxidation product containing sulfate may bind oxygen reversibly at room temperature.

Recent papers from this laboratory have described color-boundary propagation in lutetium diphthalocyanine films due to anodic oxidation of the dye (1, 2). The film was supported on a strip of alumina, with the lower end immersed in an aqueous electrolyte and the upper end contacted by gold. Under constant applied current, the color conversion from green to red began at the dye/electrolyte interface and moved upward through the film. The electrochemical reaction was shown, approximately, to be a two-electron oxidation of the diphthalocyanine. Charge compensation occurred by migration of anions from the electrolyte through the red phase under the influence of the electric field. An ionic mobility of $4 \times 10^{-6} \text{ cm}^2/\text{Vsec}$ was determined in the solid oxidation products formed with both chloride and sulfate electrolytes. In radio-tracer experiments with Cl^{36} and S^{35} , the chloride product gradually lost chlorine and reverted to green in ambient air, but the sulfate product retained its red color and its radioactivity more than a month (2). It was also found that dry and moist elemental chlorine reacted immediately with lutetium diphthalocyanine films to form a red product (3).

In this paper, we report pronounced dependences of the faradaic boundary propagation on the composition of the gas in contact with the dye film. Specifically, the effects of water vapor and oxygen on the velocity of propagation from chloride and sulfate electrolytes were determined. The results are examined in relation to crystal structures of related actinide diphthalocyanines and the known abilities of certain phthalocyanines and porphyrins to form oxygen adducts. The interesting possibility of oxygen-carrier activity in diphthalocyanine derivatives is noted.

Experimental

Film specimens of lutetium diphthalocyanine $[\text{LuH}(\text{Pc})_2]$ were prepared by vacuum sublimation of the dye onto single-crystal sapphire strips 1.25 cm wide and approximately 5 cm long (1, 2). The film thickness was estimated from its optical density at 670 nm in the initial green state.

Quantitative measurements of the boundary position as a function of time were made with the cell shown in Fig. 1. The container was a Klett colorimeter cell, open at the top, with an inlet for blanketing the film with the selected gas. The electrolyte was 1M Na_2SO_4 or 1M KCl . In the sulfate solution, the reference and counterelectrodes were Pb/PbSO_4 ; in the chloride, they were Ag/AgCl .

Details of the cell assembly and measurement procedures were described previously (1). Constant

anodic currents were applied with a Princeton Applied Research (PAR) 173 galvanostat. The total voltage between the working and reference electrodes was monitored with a Keithley 610C electrometer and strip-chart recorder. With total applied currents in the microampere range, the current density through the cross section of the film ranged from approximately 20 to 50 mA/cm^2 . An open cell, illustrated in Fig. 2, was used to determine effects of the gases impinging directly on the red film. The container then was a Klett cell with a portion of the front wall removed, as indicated by the dashed line. In the open-cell experiments, the boundary was characterized as moving or stationary by observing it under a low power microscope, and the corresponding instantaneous voltages were noted.

The gases included in the study were ambient air, dry and wet oxygen, and dry and wet helium. In addition to cells with flowing helium, some of the partially enclosed cells were set up in a helium-atmosphere glove box where the oxygen content did not exceed a few ppm.

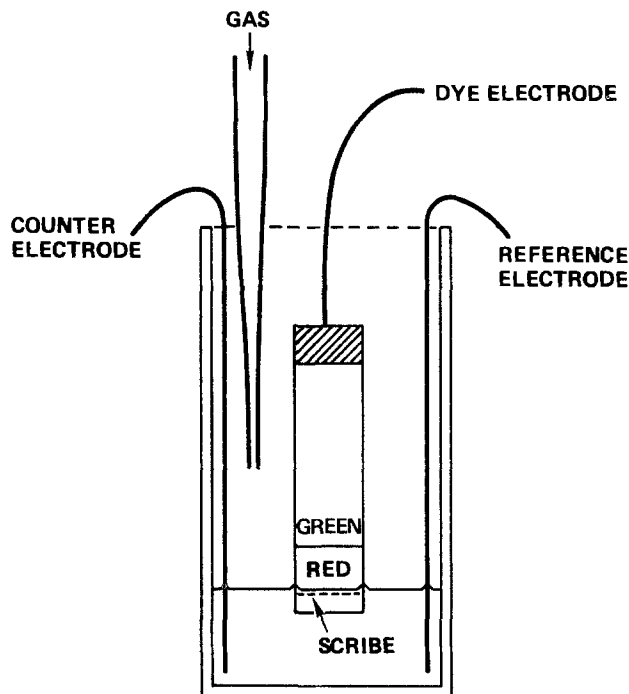


Fig. 1. Partially enclosed cell

* Electrochemical Society Active Member.

Key words: diphthalocyanines, moving boundary, oxygen, electrochromism.

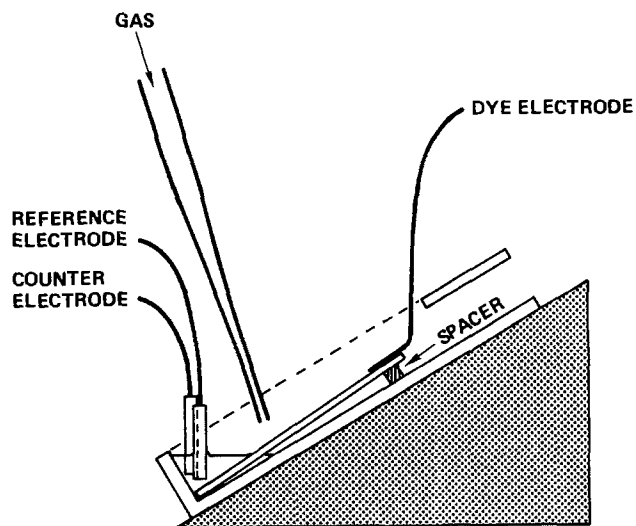


Fig. 2. Open cell

Results and Discussion

Qualitative observations of the boundary movement and voltage changes are summarized in Table I. The results were consistent through many experiments performed with a number of cells. Striking ambient effects occurred under certain conditions. For example, dry helium introduced above the sodium sulfate solution could drive the galvanostat to its full compliance of approximately 95V in a few seconds. Quantitative data for the two electrolytes in partially enclosed cells are presented in Fig. 3 and 4, where the propagation distances and voltages are plotted as functions of time.

It is apparent from the table that some water in the ambient gas was essential for propagation of the color change from both chloride and sulfate electrolytes; dry helium or dry oxygen impinging directly on the red film stopped the boundary movement in each case and caused a major increase in electrical resistance. Moreover, the water content of the film above the liquid could not be attributed to capillary action. The meniscus against the dye was nonwetting, and the previous tracer study had shown the uptake of anions to be stoichiometric (2). It is possible that water also

Table I. Summary of gaseous environment effects on boundary propagation^a

Electrolyte Ambient gas	1M Na ₂ SO ₄		1M KCl	
	Boundary movement	Voltage change ^b	Boundary movement	Voltage change ^b
Air	Yes	—	Yes	—
Dry helium open ^c	No	Increase	No	Increase
enclosed ^d	No	Increase	Yes	Slow increase
glove box (enclosed)	No	—	Yes	—
Wet helium open	No	None	Yes	None
enclosed	No	Slow decrease	Yes (slow)	Decrease
Dry oxygen open	No	Increase	No	Increase
enclosed	Yes	Slow increase	Yes	Increase
Wet oxygen open	Yes	Slight increase	Yes	None
enclosed	Yes	None	—	—

^a Current 0.2 μ A; optical density of green film 0.5-0.9 at 670 nm.

^b Initial change relative to voltage in ambient air.

^c Open cell as in Fig. 2.

^d Partially enclosed cell as in Fig. 1.

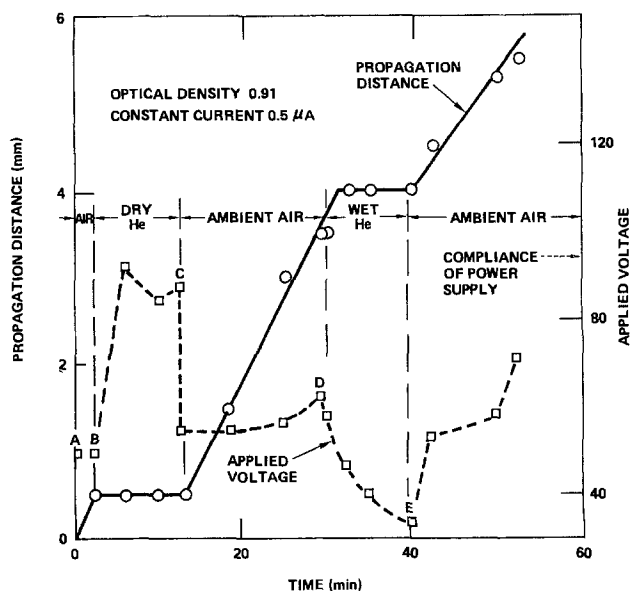
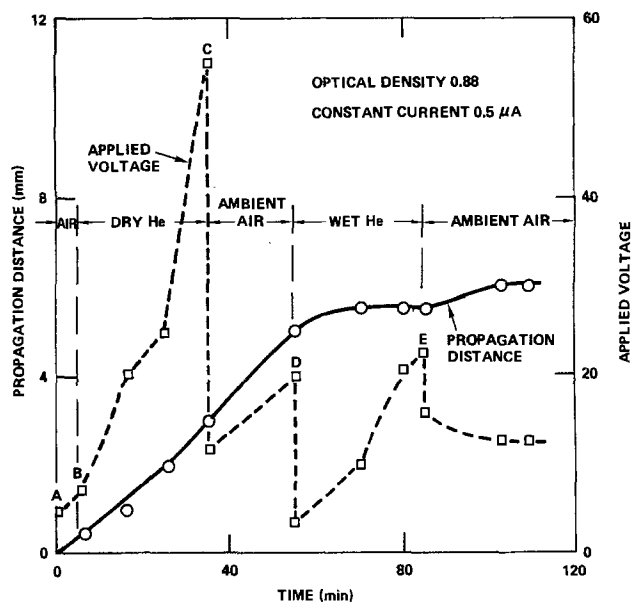
Fig. 3. Ambient effects on boundary propagation from 1M Na₂SO₄

Fig. 4. Ambient effects on boundary propagation from 1M KCl

combines with the dye stoichiometrically or that it accompanies the anion in some definite proportion.

The responses of the film to oxygen were quite different with the two electrolytes. Figure 3 represents the behavior in sodium sulfate. The boundary propagation, which had begun in air at point A, stopped completely on introduction of dry helium at B, and the voltage rose essentially to the compliance of the instrument. On addition of air at C, the voltage dropped abruptly, and normal propagation continued. Wet (water-saturated) helium, introduced at D, also arrested the boundary propagation, but the voltage then gradually fell instead of increasing as it did with dry helium. Again, the propagation resumed in the usual voltage range on addition of air at E. This figure establishes the important point that oxygen is necessary for propagation of the boundary from a sulfate solution. Although dry helium stopped all anodic processes, wet helium apparently transferred enough water to the outer surface of the film to support an electrolytic side reaction at low voltage. Oxidation of the dye was then effectively shunted by the lower faradaic resistance.

The contrasting results obtained with potassium chloride are illustrated by Fig. 4. Dry helium, introduced at point B, caused a gradual rise in voltage, but the boundary propagation still continued at the rate observed in ambient air (A-B and C-D). Wet helium, beginning at D, caused a sharp voltage drop and a pronounced decrease in the boundary velocity. This was attributed to electrolytic shunting by a film of water, as in the sodium sulfate experiment. The film in Fig. 4 probably remained somewhat wet, even after the final addition of air at point E.

In summary, an oxygen-containing atmosphere was required to propagate the boundary from sulfate solution, but not from chloride. Dry helium increased the resistance of the film system, and very dry oxygen or very dry helium could stop the boundary propagation from either electrolyte.

These points are borne out by observations of the initial reaction site under different conditions. Figure 1 shows a scribe line in the dye, which was placed just below the meniscus to limit any downward propagation of the red color. In sodium sulfate solution, the dye reaction always began at the meniscus. It then travelled upward with oxygen present, but with oxygen absent, it proceeded downward only and stopped at the scribe line. The dye reaction below the liquid level probably was sustained by anodically-formed oxygen. Any oxygen escaping into the gas phase was highly diluted, however, so that upward propagation was prevented. In the chloride electrolyte, the red color first appeared within the small submerged area and then continued upward, with or without oxygen present.

The effects of the gas environment were found to be associated almost entirely with the red region, rather than the green. This was apparent from the anion specificity in the case of oxygen. It was indicated in the case of water by Fig. 5, which shows a current-voltage plot determined on a strip of green dye film between two gold contacts. The relationship was ohmic in air to at least 93V (~20 V/cm). Wet and dry helium, passed over the film for more than an hour, produced significant resistance changes, but none approaching the magnitude of those in the propagation experiments. It should be noted in this context that other investigators have reported very large ambient effects of water and oxygen on electronic conduction in divalent-metal phthalocyanines (4). However, such compounds generally have resistivities several orders of magnitude higher than those of the rare-earth diphthalocyanines (5) and hence may be more susceptible to ambient effects.

We shall now consider the anodic reactions of the dye, some requirements for migration of anions into the film, and the possibility that the oxidation product containing sulfate could be an oxygen carrier at room temperature.

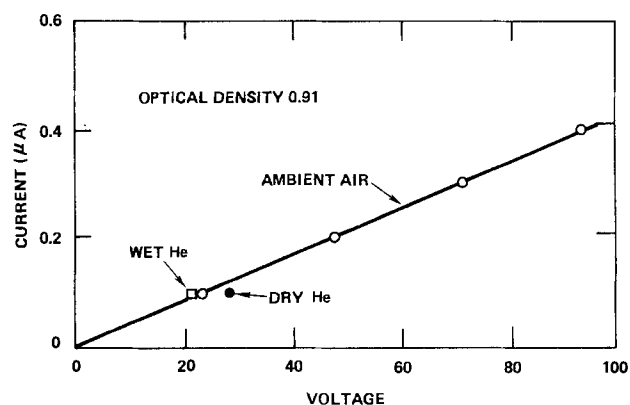
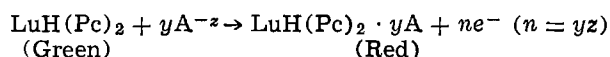


Fig. 5. Current-voltage characteristics of green film between two gold contacts.

Moskalev and Kirin originally suggested that the electrochromism of $\text{LuH}(\text{Pc})_2$ at anodic potentials in KCl was due to complexing with oxygen or water (6). It is now clear that both of these substances are involved with a sulfate electrolyte and that water, but not oxygen, is needed for the anodic process in chloride solution. In addition to any direct addition reactions, charge compensation must accompany the loss of electrons by the dye. Our previous work showed that this was accomplished by migration of anions A^{-z} into the film (1, 2)



The experimental n values were approximately 2 for KCl and Na_2SO_4 . Further work will be required to determine whether water and oxygen also participate stoichiometrically in the electrode process and how they are bonded within the organic structure.

The mobility of anions within the red phase may be examined in relation to the space available in the organic solid. The crystal structures of $\text{U}(\text{Pc})_2$ and $\text{Th}(\text{Pc})_2$ have been known for some time (7, 8), and that of a neodymium diphthalocyanine complex was recently investigated (9). These crystals contain open spaces great enough to accommodate unsolvated chloride ions, with a radius of 1.8Å. Hence it is plausible that oxidation of $\text{LuH}(\text{Pc})_2$ in a chloride electrolyte could occur and be reversed without a major change in lattice dimensions. This is in keeping with the high solid-state chloride-ion mobility of $4 \times 10^{-6} \text{ cm}^2/\text{Vsec}$.

The similar mobility of larger, polyatomic anions such as sulfate in the red phase seems to require further explanation. An attractive possibility, consistent with the ambient-atmosphere dependence, is the formation of an oxygen adduct by $\text{LuH}(\text{Pc})_2 \cdot \text{SO}_4$. It has long been known that certain organic crystals can expand on addition of oxygen. For example, Calvin *et al.* observed pronounced dimensional changes along one crystallographic axis in cobalt^{III}bis-(salicylaldehyde) ethylenediamine during cyclical absorption and desorption of oxygen (10). Such a lattice expansion of lutetium diphthalocyanine might provide the additional space needed for the sulfate ions. This mechanism requires the presence of oxygen throughout the red film, not just at the red/green interface. The very large voltage change that occurred on introduction of helium also suggests an effect in the bulk of the red film.

Thus it is quite possible, but not proved, that the sulfate oxidation product of $\text{LuH}(\text{Pc})_2$ is an oxygen carrier, *i.e.*, a compound that binds oxygen reversibly at room temperature. Although much work has been done in recent years on synthetic and natural oxygen carriers (11-15), this could be the first instance of carrier activity controllable by anions or (one may predict) by anion exchange. The natural hemoproteins achieve reversible oxygen binding by virtue of complicated structures attached to the porphyrin ring. Among simpler molecules, manganese(II) tetraphenylporphyrin forms a reversible dioxygen complex near -79°C in the presence of pyridine (13), but this is unstable at room temperature. However, manganese(II) phthalocyanine binds oxygen in pyridine at much higher temperatures (14, 15). Generally, it appears that oxygen-carrier behavior in the porphyrins and phthalocyanines results from a special balance of conditions that is not easily achieved. This balance may exist in a product such as $\text{LuH}(\text{Pc})_2 \cdot \text{SO}_4$ or in a solid hydrate of that product. Further investigations of the diphthalocyanine-oxygen systems are in progress.

Acknowledgment

This work was supported in part by the Office of Naval Research.

Manuscript submitted Jan. 21, 1980; revised manuscript received July 14, 1980.

Any discussion of this paper will appear in a Discussion Section to be published in the June 1981 JOURNAL. All discussions for the June 1981 Discussion Section should be submitted by Feb. 1, 1981.

Publication costs of this article were assisted by Rockwell International.

REFERENCES

1. M. M. Nicholson and F. A. Pizzarello, *This Journal*, **126**, 1490 (1979).
2. F. A. Pizzarello and M. M. Nicholson, *J. Electron. Mater.*, **9**, 231 (1980).
3. M. M. Nicholson, R. V. Galiardi, and G. A. Layman, Annual Technical Report for Period April 1, 1977 to March 31, 1978, Contract F49620-77-C-0074, C78-640/501, May 1978, Electronics Research Center, Rockwell International, Anaheim, California.
4. H. Tachikawa and L. R. Faulkner, *J. Am. Chem. Soc.*, **100**, 4379 (1978).
5. I. S. Kirin and P. N. Moskalev, *Russ. J. Phys. Chem.*, **41**, 251 (1967).
6. P. N. Moskalev and I. S. Kirin, *ibid.*, **46**, 1019 (1972).
7. A. Gieren and W. Hoppe, *J. Chem. Soc. Chem. Commun.*, 413 (1971).
8. I. S. Kirin, A. B. Kolyadin, and A. A. Lychev, *J. Struct. Chem.*, **15**, 415 (1974).
9. M. Tsutsui, Private communication.
10. A. E. Martell and M. Calvin, "Chemistry of the Metal Chelate Compounds," Chap. 8, Prentice-Hall, Englewood Cliffs, New Jersey (1952).
11. F. Basolo, B. M. Hoffman, and J. A. Ibers, *Acc. Chem. Res.*, **8**, 384 (1975).
12. J. P. Collman, R. R. Gagne, C. A. Reed, T. R. Halbert, G. Lang, and W. T. Robinson, *J. Am. Chem. Soc.*, **97**, 1427 (1975).
13. C. J. Weschler, B. M. Hoffman, and F. Basolo, *ibid.*, **97**, 5278 (1975).
14. L. H. Vogt, Jr., A. Zalkin, and D. H. Templeton, *Inorg. Chem.*, **6**, 1725 (1967).
15. A. B. P. Lever, J. P. Wilshire, and S. K. Quan, *J. Am. Chem. Soc.*, **101**, 3669 (1979).

Steady-State D-C Polarization Characteristics of the O₂, Pt/Stabilized Zirconia Interface

Turgut M. Gür, Ian D. Raistrick,* and Robert A. Huggins*

Department of Materials Science and Engineering, Stanford University, Stanford, California 94305

ABSTRACT

Four-probe d-c polarization studies were carried out on the Pt/stabilized zirconia interface between 600° and 900°C in the presence of 10⁻⁶-1 atm of oxygen partial pressure. Three types of polarization effects were observed. At high currents, the oxygen flux density is limited by diffusion of molecular oxygen in the gas phase through a boundary layer near the interface. At intermediate currents, porous Pt electrodes are almost completely non-blocking to oxygen, and the primary impedance present is due to ionic resistivity in the electrolyte. At low overvoltages, a limiting current plateau is observed at 600° and 700°C, which disappeared completely at 800°C and above. Two alternative mechanisms involving slow diffusion of either atomic oxygen or an electronic species are proposed to account for the observed behavior.

Although electrical conduction due to ionic motion was observed in oxides by Nernst (1) in 1899, the potential of the widespread use of solid oxides as electrolytes has been exploited only in the last two decades. Efforts have also only recently been made to better understand electrode/solid electrolyte interfaces and their polarization effects (2-5).

Early work on stabilized zirconia indicated that only ohmic polarization is present when suitable electrodes and current densities are used (6, 7). Further information on polarization effects under a broader range of conditions was obscured to a large extent by lack of proper characterization of the electrode/electrolyte interfaces being studied. This led to considerable variations in performance (8-12), even under apparently identical conditions. There is now sufficient evidence to believe that both the electrode material (10, 13) and the electrode morphology (14-22) play a very important role in the interface behavior. Experiments carried out in very oxygen deficient environments or under heavy polarization have resulted in readily observable structural changes, such as the "blackening" of the zirconia (19, 22-24).

Although the oxygen electrode/zirconia interface has been the subject of numerous investigations, there is considerable disagreement among them. This is seen in Table I, which summarizes the major studies in this field in chronological order.

* Electrochemical Society Active Member.

Key words: interface polarization, solid electrolyte, zirconia, porous electrodes, platinum.

The first attempt to rationalize these apparently conflicting results was by Kröger (30), who showed that the differences may be due to a change in the rate-limiting mechanism with changes in temperature, oxygen pressure, and electrode morphology. However, his calculations involved the use of the solubility product of oxygen in Pt estimated by Brook *et al.* (18). Recent measurements of this product by Velho and Bartlett (31) give values many orders of magnitude smaller, and thus Kröger's calculations may be misleading.

Pizzini *et al.* (29) and Casselton (21) contended that a limiting current proportional to [P_{O₂]^{1/2} is characteristic of cells operating at low temperatures with small electrode areas (14, 17-19, 28, 29). On the other hand, a limiting current proportional to P_{O₂} is often observed at high temperatures with larger electrode areas (9, 15, 21).}

Such attempts to resolve the disparate results were constrained by a lack of characterization of the electrode/electrolyte interface in many of the experiments to date. *In situ* determination of various parameters relating to the interphase morphology, such as the porosity, tortuosity, and pore size distribution of the electrode material and the effective area of the contact between the electrolyte and the electrode material, are certainly not easy. The physical situation is further obscured by time-dependent morphological changes induced by thermal and faradaic effects (22).

The earliest evidence of the importance of electrode morphology came from Karpachev and Filyaev (32).

Table I. Summary of d-c polarization studies with O₂-inert gas mixtures on stabilized zirconia

Reference	Electrolyte composition (m/o)	Electrode	Temperature range (°C)	O ₂ pressure range (atm)	I ₁ -P _{O₂} relation	Rate limiting mechanism
Tannenberger (7)	10% Yb ₂ O ₃	Porous Ag	650-800	1	—	O ₂ solution at O ₂ /ZrO ₂ then surface diffusion to Ag/ZrO ₂ interface
Kleitz (14)	12.5% CaO	Point Pt	700-1200	0.2-2 × 10 ⁻⁴	I ₁ αP _{O₂} ^{2/3}	Surface diffusion O _{ads} on ZrO ₂
Karpachev and Ovchinnikov (16)	12% Sc ₂ O ₃	Pt paste	800-1000	1-0.2	—	Mass transport in gas phase
Tedmon <i>et al.</i> (15)	10% Y ₂ O ₃	Porous PrCoO ₃	800-1200	5 × 10 ^{-1.5} × 10 ⁻³	I ₁ αP _{O₂}	Mass transport in gas phase
Bauerle (25) *	10% Y ₂ O ₃	Sp.† paste Pt	400-800	1-1.5 × 10 ⁻⁵	—	Dissociation of O ₂ /electron transfer
Yanagida <i>et al.</i> (19)	10% CaO	Porous Pt	560	1-10 ⁻³	I ₁ αP _{O₂} ^{2/3}	Diffusion of O through Pt
Gokshstein and Safonov (26)	15% Y ₂ O ₃	Pt disk	1400	0.2	—	Mass transport in gas phase
Etsell and Flengas (9)	10% CaO	Porous Pt	700-1100	1-10 ⁻³	I ₁ αP _{O₂}	Knudsen diffusion in Pt
Brook <i>et al.</i> (18, 27)	15% CaO	Foil, Sp.,† paste Pt	500-700	1-10 ⁻³	I ₁ αP _{O₂} ^{1/2}	Diffusion of O through Pt
Pizzini <i>et al.</i> (28, 29)	8% Y ₂ O ₃	Paste, bright Pt	700-1000	10 ^{-0.7} -10 ⁻⁵	I ₁ αP _{O₂} ^{1/2}	Surface diffusion of O on Pt
Pancharatnam (17)	8% Sc ₂ O ₃	Sp.,† paste, bright Pt	600-800	1-10 ⁻⁵	I ₁ αP _{O₂} ^{2/3}	Diffusion of O- through Pt
Casselton (21)	12% Y ₂ O ₃	Pt-13% Rh disk	800-1450	1-10 ⁻³	I ₁ αP _{O₂}	O ₂ + e' → O ₂ '
This work	8% Sc ₂ O ₃	Sp.† Pt	600-900	1-10 ⁻⁶	I ₁ αP _{O₂}	Boundary layer diffusion in gas phase

* A-C impedance.
† Sputtered.

They showed that cathodic overvoltages can significantly be reduced by scratching the surface of a Pt electrode, thus providing access for oxygen to a three-phase boundary. Similarly, Bauerle (25) utilized heavy current treatments on initially nonporous electrodes to induce artificial porosity which reduced electrode polarization effects.

Coupled effects of current and heat-treatments on Pt electrode morphology were demonstrated by Pizzini *et al.* (28, 29) using SEM. Current-voltage characteristics were found to be dependent on such morphological changes. More recently, Pizzini *et al.* (33) used model electrochemical cells and showed that the macroscopic polarization behavior also varies with cell geometry.

This work represents an attempt to further understand polarization effects pertinent to Pt/zirconia interfaces in an oxygen ambient by careful investigations made under a wide range of experimental conditions. Great care was given to the preparation of the interface.

Experimental Arrangements

Detailed descriptions of the experimental apparatus and procedures have been given elsewhere (34). A wide range of O₂-He mixtures was supplied to the interfacial region at a rate of 90-100 cm³/min. The oxygen content of the streaming gas was analyzed by two separate oxygen sensors, placed upstream and

downstream of the zirconia pump. Oxygen analysis was also independently made using a Varian Aerograph Model 142010 gas chromatograph. Excellent agreement was obtained between the two analytical techniques.

Mixtures of high purity He (Matheson) and zero grade oxygen (Air Products) were prepared in a lecture bottle by monitoring the oxygen pressure with a high precision Heise gauge. Traces of moisture and other possible impurities (*e.g.*, CO₂) in the streaming gases were removed by appropriate traps. The entire experimental system was evacuated (2 × 10⁻⁵ Torr) and lightly baked prior to each polarization experiment.

The oxygen sensors were made from one-end closed yttria-stabilized zirconia tubes (Zircoa) featuring gold paste (Hanovia, UR No. 01-FM) electrodes scratched to improve response time. The sensors were operated at 650°-700°C and the oxygen partial pressures were calculated using the Nernst equation.

The schematic design of the zirconia pump is shown in Fig. 1. A 12 × ½ in. OD calcia-stabilized zirconia (CSZ) tube (Zircoa) was used to support the 8 mole percent (m/o) Sc₂O₃ · ZrO₂ electrolyte disk (Applied Electrochemistry). The faces of the disk were polished with a 1 μm diamond paste. The CSZ tube and the disk were ultrasonically cleaned and then heated for a few hours in air at about 800°C.

Pt electrodes were deposited onto both faces of the disk by etch-sputtering. The disk was then sealed leak-

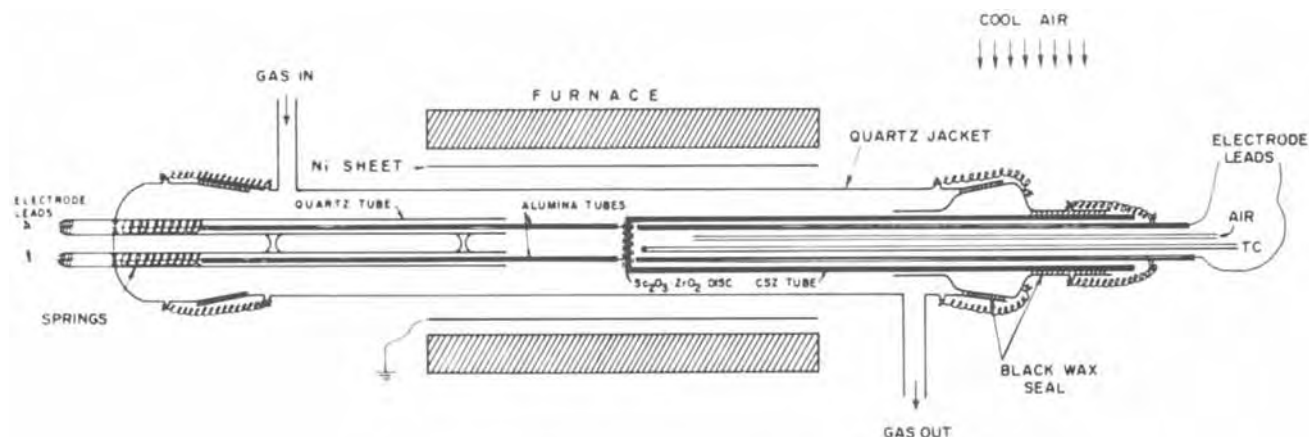


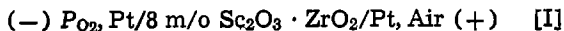
Fig. 1. Schematic design of the zirconia pump

tight on one end of the CSZ tube using a high temperature glass. Four electrode connections (two on each side of the disk) were made by spring-loaded Pt wires. Air was blown onto the inner electrode to avoid diffusional effects.

The basic electrical circuit used in the four-probe d-c experiments is shown in Fig. 2. Voltage across the electrolyte/electrode assembly was supplied by a d-c power supply. Current was measured by the voltage drop across a fixed resistor and a strip-chart recorder was employed to assess steady-state conditions. The applied, E_{app} , and monitored, E_{mon} , voltages and the open-circuit emf's of the two oxygen sensors were measured with a potentiometric microvoltmeter.

Polarization Experiments

Four-probe d-c polarization studies were carried out on the cell



between 600° and 900°C in the oxygen partial pressure range of 10^{-6} -1 atm. Scandia-stabilized zirconia was chosen for its superior ionic conductivity. Sputtered Pt electrodes 1 μ m thick and 0.66 cm² in area were used. These electrodes were initially essentially nonporous. Artificial porosity was generated by a novel progressive current treatment (22) which eliminates the possibility of blackening or mechanical failure of the electrolyte frequently observed when Bauerle's technique (25) is used. The new technique involves slowly cycling the potential of the cell between 0 and 2V at the highest working temperature using small voltage increments until no hysteresis is observed. The advantage of this technique is that it approximates a near-equilibrium process if sufficient time is allowed for the changes in surface morphology to keep up with variations in the faradaic current.

The results obtained in the polarization experiments following the progressive current treatment were completely reproducible. Data points on the polarization curves can easily be reproduced during ascending or descending voltages.

Results of D-C Polarization Experiments

Cathodic polarization.—Steady-state current-overvoltage characteristics of cell [I] were studied, with the overvoltage, η , defined as

$$\eta = E_{mon} - E^\circ - I_{ss}R_b$$

where, E_{mon} is the voltage drop across the electrolyte measured by a potentiometer in a circuit which carries no current, as opposed to E_{app} , where the external circuit carries the observed steady-state ionic current, I_{ss} ; R_b is the electrolyte bulk resistance obtained from a-c admittance measurements (35). Thus $I_{ss}R_b$ represents the voltage drop across the electrolyte and E° is the reversible potential of cell [I] given by the Nernst equation. Consequently, η represents the interfacial overvoltage.

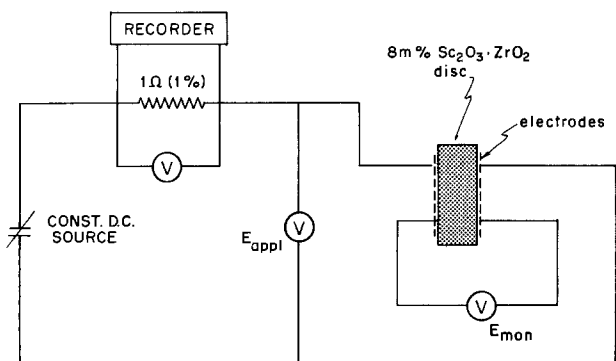


Fig. 2. Electrical circuit used in four-probe experiments

The steady-state current-overvoltage behavior of cell [I] between 600° and 900°C in the oxygen partial pressure range of 10^{-4} -1 atm is shown in Fig. 3 and 4. Two distinct characteristics at low η are immediately evident. At 600° and 700°C well-defined current plateaus extend to about $\eta = 250$ mV, above which the current increases rapidly in an exponential-like manner. The low overvoltage region at 600°C is expanded in Fig. 5 to show the limiting current plateau more clearly. The low η current plateaus, however, did not appear in the experiments at 800° and 900°C. This abrupt change in behavior occurs throughout the entire oxygen concentration range.

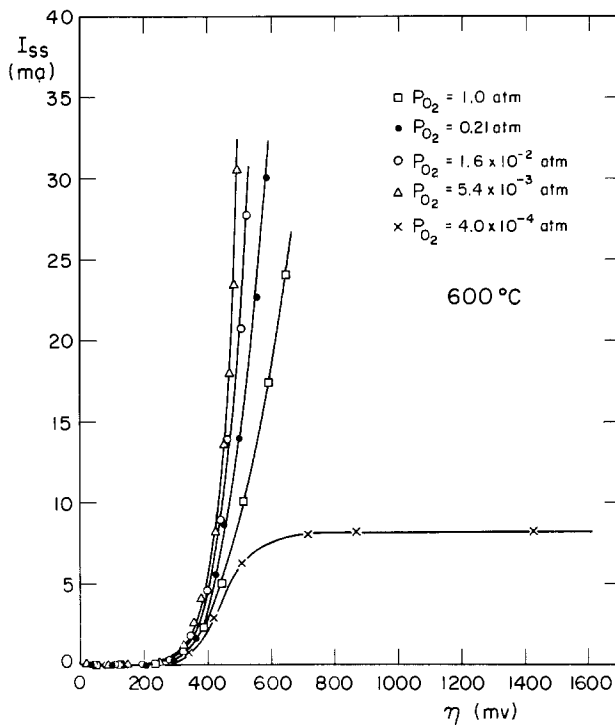


Fig. 3. Characteristic current-overvoltage behavior at 600°C

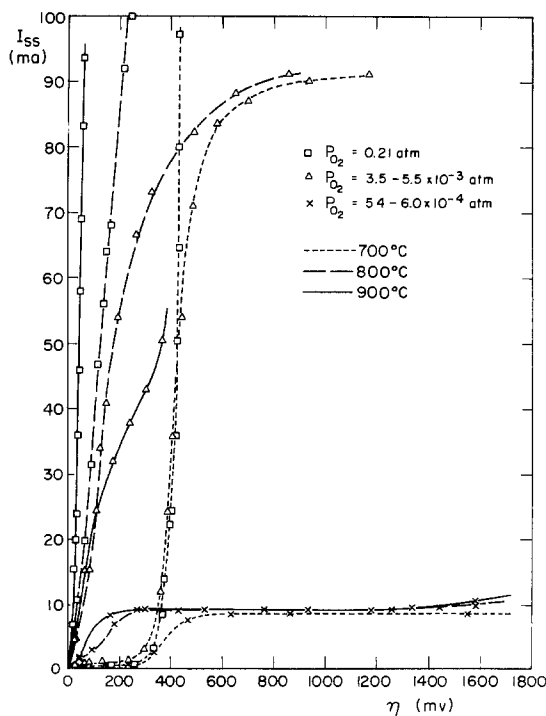


Fig. 4. Characteristic current-voltage behavior at 700°, 800°, and 900°C.

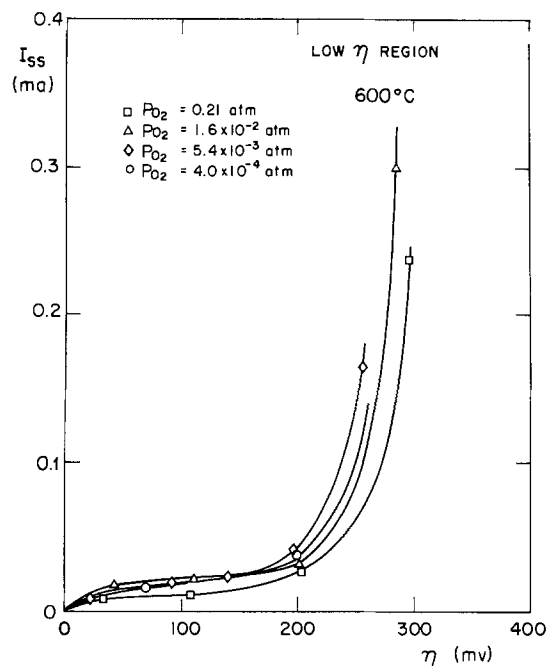


Fig. 5. Limiting current behavior in the low overvoltage region at 600°C.

The single plateau, observed at high temperatures and sufficiently low oxygen pressures, eventually gave way to mixed conductivity where the electronic contribution to the total current became more and more significant with increasing overvoltage. This situation is depicted in Fig. 6, where the ionic transference number t_i (calculated from oxygen sensor analysis) is plotted against voltage. At low temperatures (e.g., 600°C) all the observed current is predominantly ionic, whereas mixed conduction appears at large overvoltages at higher temperatures, as expected.

Effect of flow rate.—The double plateau phenomenon shown in the current vs. overvoltage plots (Fig. 3 and 4) has not previously been reported for the Pt/zirconia system. A survey of previous studies suggested that one of these plateaus might be due to mass transport constraint in the boundary layer in the gas. Thus a series of d-c experiments was conducted at different flow rates of the gas mixtures. If the mass transport involves diffusion through the solid electrode, no flow rate dependence of the limiting current plateaus should be observed. Conversely, if the rate is limited by mass

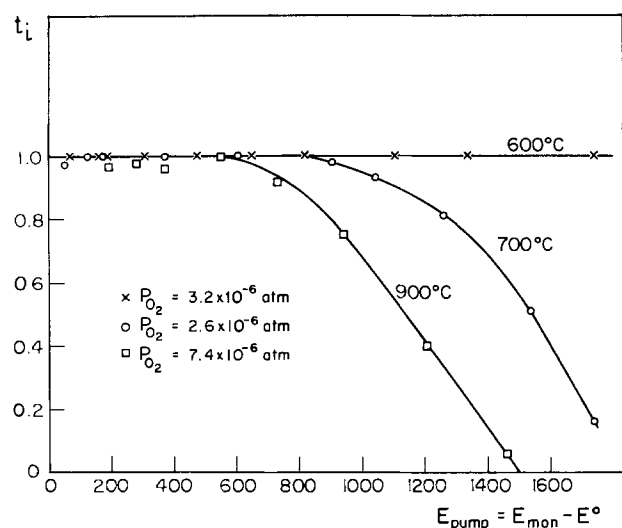


Fig. 6. Voltage and temperature dependence of ionic transference number, t_i , for oxygen.

transport in the gas phase, then it should be affected by the flow rate.

Figure 7 shows that the flow rate has virtually no effect on the low overvoltage limiting-current plateau, whereas it drastically affects upper plateaus in the higher overvoltage region. The latter effect is also observed at high temperatures. Gas chromatographic data indicated that the further increase in the current beyond the upper plateau region is due to the onset of electronic conduction as depicted in Fig. 8. Here the deviation from the predominantly ionic nature is given by the lateral distance between the solid and the dashed lines. The former represents the ionic current and the latter includes the electronic contribution, which increases rapidly with increasing overvoltage.

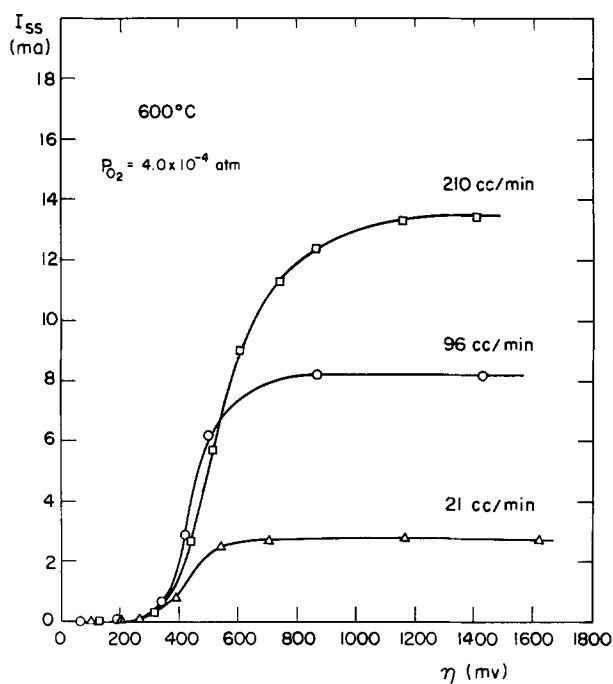


Fig. 7. Effect of flow rate on limiting current at 600°C

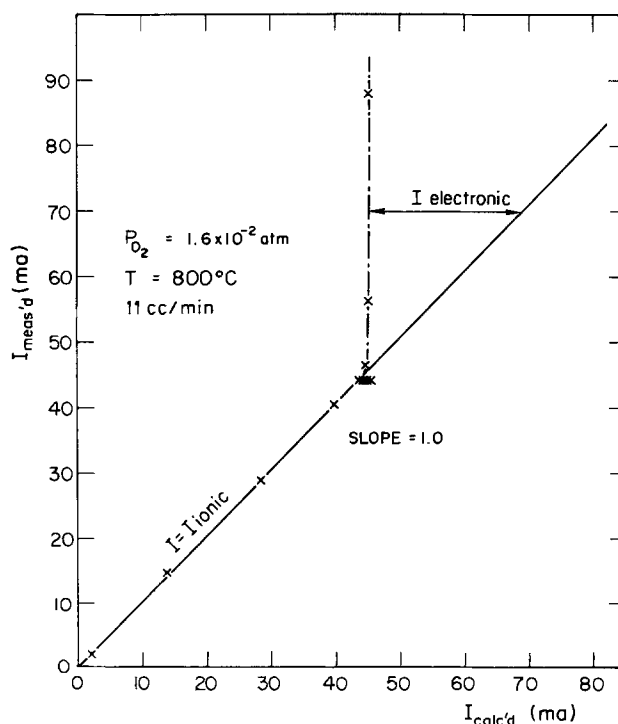


Fig. 8. Comparison of calculated ionic current with the experimentally measured current.

Effect of H₂O.—The influence of residual moisture is expected to be significant only when the $P_{\text{H}_2\text{O}}$ becomes comparable to or greater than the oxygen partial pressure.

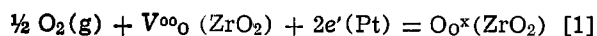
Studies carried out at 10^{-4} atm oxygen partial pressure with both wet and dry O₂-He mixtures indicated that the polarization behavior was not significantly altered by the presence of moisture.

The situation drastically changed for P_{O_2} values of 10^{-6} atm, where the limiting current plateau was raised to almost twice its dry mixture value by the presence of H₂O, as depicted in Fig. 9. Furthermore, the polarization curve for the dry gas mixture was predominantly ionic in nature, while the increased current in the presence of the wet mixture involved an electronic contribution.

Discussion

The characteristic current-overvoltage plots indicate three distinct regions of behavior at high, intermediate, and low overvoltage values. Throughout, it is assumed that the overall polarization behavior is governed by phenomena occurring at the cathode/electrolyte interface; the potential drop at the anode/electrolyte interface is assumed to be negligible (19, 21).

The overall cathode reaction for oxygen incorporation is



where V^{oo}_0 denotes an oxygen vacancy with an effective charge of +2, and O_0^{\times} is a normal oxygen species on an oxygen site in the electrolyte. Since this reaction involves species from all the three phases, it must occur at a site which is accessible to all of the reacting species. Therefore, this "electrochemical reaction site" (ERS) should be located at or near a boundary where the three phases meet.

Scanning electron microscope pictures of the cathode surface indicated that the electrode was quite porous. Huge voids, about 1-2 μm in width and up to 6 μm in length, exposed the zirconia surface directly to the gas phase.

Consequently, three possible paths can be visualized by which the oxygen can arrive at the ERS; namely, from the surface of the electrolyte or either through or along the surface of the platinum.

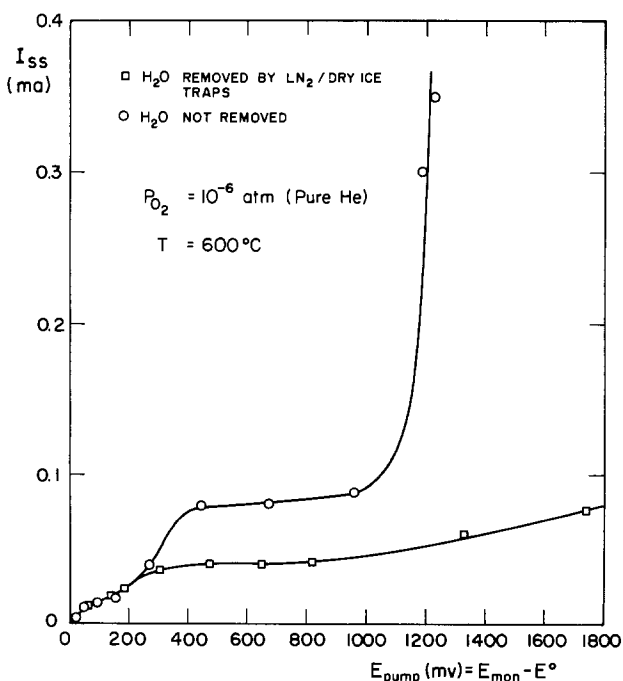


Fig. 9. Effect of H₂O on the limiting current at low oxygen partial pressures.

Mechanism of oxygen transport to ERS.—Information about surface diffusion of oxygen on zirconia is scarce. Smith (36) studied oxygen adsorption on pure zirconia at 400°-900°C. He concluded that 90-95% of the surface is covered with irreversibly adsorbed oxygen atoms and the remaining by weakly adsorbed mobile O₂' species. The "irreversibly adsorbed" oxygen was likely simply incorporated into the zirconia to make up for the stoichiometric loss (22, 34) due to the H₂ pretreatment given to the sample.

A rough estimate shows that surface diffusion of O₂' is not likely to be rate determining. At 900°C, the values of the surface exchange and bulk diffusion coefficients are about 4×10^{-6} cm/sec and 2×10^{-8} cm²/sec, respectively, (37). Assuming a surface density of 10^{15} sites/cm² and complete surface coverage, the limiting current density would be about 10^{-5} A/cm² for a diffusion distance of 1 μm . This agrees well with the value of 4×10^{-6} A/cm² estimated by Casselton (21). For 600°C, the limiting current density would be about 10^{-6} A/cm².

These values are much too low to account for the limiting current values observed in the present work.

If bulk diffusion of oxygen through the Pt were rate determining, the corresponding limiting current would be

$$i_{\text{lim}} = nFAJ_0 = nFAD_{\text{O,Pt}} \frac{C_{\text{s,O}}}{\delta} \quad [2]$$

where J_0 is the oxygen molar flux, $D_{\text{O,Pt}}$ is the diffusion coefficient of oxygen in Pt, $C_{\text{s,O}}$ is the molar oxygen concentration on the Pt surface, δ is the diffusion distance (taken as the thickness of the Pt layer, 1 μm), and A is the area (assumed to be equal to the geometric area of the electrode, i.e., 0.66 cm²).

The values of $D_{\text{O,Pt}}$ and $C_{\text{s,O}}$ at 900°C can be extrapolated from the data of Velho and Bartlett (31) to give 3×10^{-14} cm²/sec and 3×10^{-11} weight percent, respectively. Substitution into Eq. [2] gives a limiting current value of about 10^{-17} A at 900°C. Casselton (21) estimated limiting current densities of 10^{-10} A/cm² through 0.2 cm thick Pt electrodes at 1400°C.

Clearly, these estimated values are many orders of magnitude lower than those actually observed. Therefore, a transport path involving bulk diffusion through Pt is also improbable.

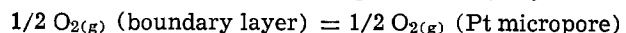
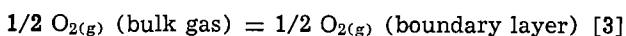
A third possibility is that oxygen arrives at the ERS primarily by adsorption and transport along the surface of the Pt. The surface diffusion coefficient for oxygen on Pt can be estimated to be about 10^{-6} cm²/sec at 900°C (38). For a diffusion area of $1 \times 1 \mu\text{m}$, a current density of about 10^{-1} A/cm² can be expected, assuming complete coverage of the surface, with 10^{15} sites/cm². This agrees well with the values observed in the present experiments.

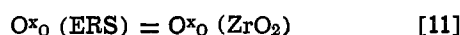
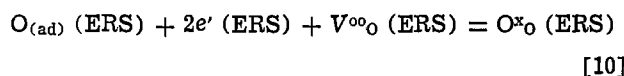
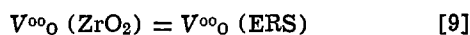
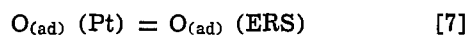
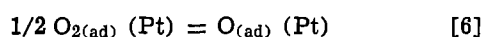
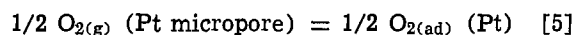
Thus, it is proposed that oxygen gets to the ERS by transport along the surface of the Pt rather than by either bulk diffusion through the Pt or by dissociation and surface migration on the electrolyte.

Possible rate-determining steps.—Thermodynamic studies by Ngo (39) established that Pt does not form a stable bulk oxide at elevated temperatures below 1 atm oxygen pressure. PtO₂, which is the most stable oxide of Pt, exists only up to 583°C at 1 atm oxygen pressure.

Oxygen, however, readily adsorbs on Pt with a low activation energy, about 3 kcal/mole (40, 41). The initial heat of adsorption for molecular oxygen is about 10-17 kcal/mole (38, 42, 43), and molecules readily dissociate into oxygen atoms, with a dissociative heat of adsorption of about 53-70 kcal/mole (44-46).

In view of the preceding considerations the overall cathode reaction can be divided into intermediate steps as follows





For reactions [9] and [11], only bulk transport conduction is assumed for the arrival and departure of $V^{\circ\circ\text{O}}$ and $\text{O}^{\times\text{O}}$ to and from the ERS. A unit reaction obviously cannot proceed unless the reaction product $\text{O}^{\times\text{O}}$ is removed from the ERS and is replaced by a $V^{\circ\circ\text{O}}$, so that the ERS is reset for the next unit reaction to take place.

Within the framework of this sequence of steps, the three overvoltage regions of interest will be discussed, and the most likely mechanism controlling the overall rate within each regime will be arrived at by a process of systematic elimination of the others.

High overvoltage region.—The applied voltages had to be kept below 2V in order to avoid electrolysis of the electrolyte [$E_{\text{decomp.}} = 2.27\text{V}$ at 900°C (50)]. One would expect to see a limiting current behavior below that voltage only when the oxygen partial pressure was sufficiently low that the rate of reaction at the ERS was limited by the rate at which oxygen arrived from the gas phase.

Assuming the ideal gas law, the rate of oxygen arrival at the ERS can be estimated from Fick's first law of the form

$$J_{\text{O}_2} = D_{\text{O}_2} \frac{\Delta[\text{C}_{\text{O}_2}]}{\delta} \\ = 7.5 \times 10^{-6} \frac{D_{\text{O}_2}}{\delta} [P_{\text{O}_{2(\text{g})}} - P_{\text{O}_2} (\text{ERS})] \quad [12]$$

for diffusion of molecular oxygen in the gas phase. Here D_{O_2} is the diffusion coefficient of molecular oxygen and δ is the diffusion length.

The molar oxygen flux, J_{O_2} , is also related to the current by Eq. [2], so that

$$i = 7.5 \times 10^{-6} nFA \frac{D_{\text{O}_2}}{\delta} [P_{\text{O}_{2(\text{g})}} - P_{\text{O}_2} (\text{ERS})] \quad [13]$$

where A is the cross-sectional area. Thus, it is clear that a constraint due to molecular oxygen transport will be inversely proportional to the oxygen partial pressure at constant temperature.

Similar equations can be written for the case of diffusion of atomic oxygen. The limiting current would then exhibit a $P_{\text{O}_2}^{1/2}$ dependence.

In order to assess the nature of the constraint at high voltages the limiting current is plotted against P_{O_2} in Fig. 10. The unit slope clearly indicates that gas phase diffusion of molecular oxygen causes this phenomenon, so that the phenomena related to Eq. [6]-[11] in the reaction sequence are not rate controlling in this regime. Similarly, Eq. [5] can also be eliminated because it represents a thermally activated process, whereas Fig. 10 virtually shows no temperature dependence (also see Fig. 11).

One expects that diffusion through the boundary layer would be strongly dependent on the gas flow rate and cell geometry, but independent of electrode morphology, whereas diffusion through micropores in the electrode structure should be dependent on the electrode morphology and the local P_{O_2} within the micropore, but practically independent of macroscopic flow rate.

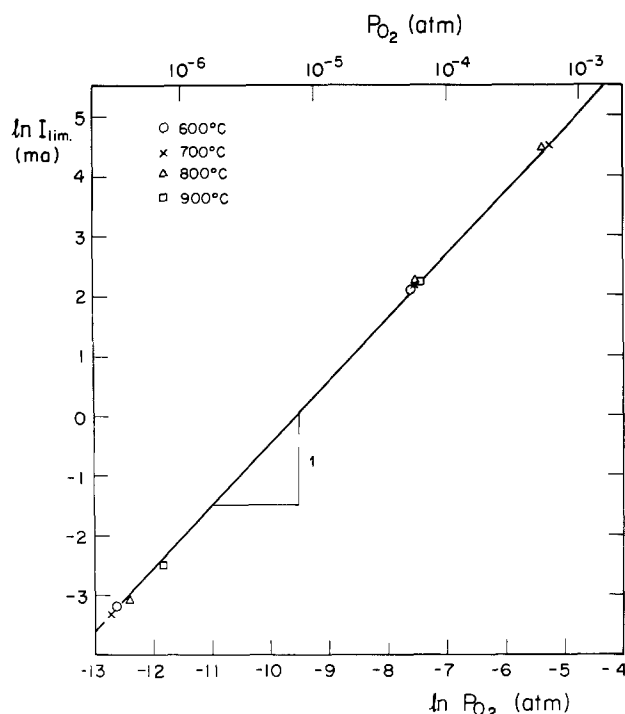


Fig. 10. Oxygen partial pressure dependence of high overvoltage limiting current.

The pronounced effect of flow rate on the high voltage limiting current was demonstrated in Fig. 7. A plot of limiting current vs. flow rate indicated a 0.6th power dependence. This is in good agreement with Bobb and Mason (47) who showed that a limiting current resulting from a slow diffusional process in a boundary layer should vary as the square root of the fluid velocity in a laminar flow system with stagnation flow geometry, similar to the conditions employed in the present work.

Consequently, the rate-determining mechanism in this overvoltage region is gas phase diffusion of molecular oxygen through the boundary layer (i.e., Eq. [3]), rather than diffusion within the micropores. This agrees with some of the findings reported in the literature (9, 15, 21).

The $P_{\text{O}_2}^{1/2}$ dependence of the limiting current observed by other authors (see Table I) has been attributed to oxygen bulk diffusion through Pt electrodes (17-19, 27). However, the activation energies of about 22-27 kcal/mole (17, 18, 27) for the limiting current are too low to account for bulk diffusion in Pt which involves 117 kcal/mole (31).

Actually, the measured temperature dependence is in much better accord with the activation energy of about 27-34 kcal/mole for surface diffusion of oxygen on Pt reported by Lewis and Gomer (38). The oxygen partial pressure dependence of surface diffusion also is consonant with the observed $P_{\text{O}_2}^{1/2}$ dependence. This, in fact, was proposed as the rate-determining mechanism by Kleitz (13, 14) and Pizzini *et al.* (28, 29) who reported activation energies of about 33-35 kcal/mole for the high voltage limiting current.

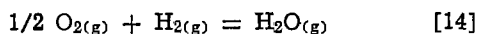
The effect of H_2O .—Although H_2 - H_2O mixtures have been used in various fuel cell applications (6, 51-54), little effort has been made to investigate their polarization behavior. There seems to be general agreement that ohmic polarization due to the ionic resistance of the ZrO_2 dominates the overall cell performance (6, 53), but the possibility of concentration overvoltage has also been reported (9).

The effect of water vapor would become noticeable only when $P_{\text{O}_2} \leq P_{\text{H}_2\text{O}}$ under conditions of gas phase polarization. It would, however, become important at much lower concentration levels if oxygen chemisorp-

tion were rate limiting, because it is known that water vapor and oxygen adsorb competitively on Pt (55).

The effect of H₂O on the limiting current was demonstrated by using dried and undried O₂-He mixtures. For P_{O₂} = 4 × 10⁻⁴ atm, the effect of H₂O was found to be insignificant, suggesting that the partial pressure of water vapor present was less than that of the oxygen. This is to be expected since diffusion of O₂ and H₂O in the boundary layer are comparable.

The situation, however, was quite different when pure He containing only a few ppm of O₂ was used. Undried He exhibited a significantly higher limiting current plateau than dried He, as depicted in Fig. 9. For this case P_{O₂} ≪ P_{H₂O} and the oxygen was present mainly in the form of H₂O molecules, owing to the large equilibrium constant, K_{H₂O}, for the reaction



which has a value of about 10¹² atm^{-1/2} at 600°C. This suggests that the rate-limiting mechanism in this case is due to the transport of H₂O rather than O₂.

If one assumes that chemisorption of H₂O is rate determining, one expects to see a lowering of the limiting current plateau due to competition between O₂ and H₂O, as observed by Pizzini *et al.* (29). If surface migration were rate determining, one should obtain a P_{O₂}^{1/2} dependence.

The observed behavior, however, was contradictory to both of these considerations. Thus, the rate-limiting mechanism was gas phase diffusion of water molecules through the boundary layer.

Intermediate overvoltage region.—At moderate voltages, and when P_{O₂} ≳ 10⁻³ atm, polarization curves showed a purely ohmic behavior, the current being determined by the bulk electrolyte resistance. Pancharatnam (17) also observed ohmic behavior with sputtered and paste Pt electrodes at intermediate voltages. Similar behavior has also been reported for other ionically conducting electrolytes (56).

There is, however, a slight oxygen partial pressure dependence of the ohmic slopes, especially at low temperatures (see Fig. 3). Theoretically, the bulk electrolyte resistance should be independent of P_{O₂} within the range of experimental conditions used in the present work.

A weak P_{O₂} dependence was also reported by Casselton (57) when the oxygen vacancy transport and ambient gas flow were not in the same direction. In the present work, gas flow and vacancy transport were in opposite directions. Thus, the observed P_{O₂} dependence is consistent with Casselton's results. However, the origin of this behavior is still unresolved.

Low overvoltage region.—The existence of double current plateaus was recently suggested by Fabry and Kleitz (58). They associated the first plateau with the depletion of adsorbed oxygen at the interface and the second plateau with the depletion of adsorbed CO₂. This may be valid in some cases but is obviously not applicable to the present situation.

The limiting current plateaus at low voltages are observed up to 700°C but disappear completely at higher temperatures (see Fig. 3 and 4). The plateaus are due to a process which is thermally activated and disappear, as the overvoltage is increased, into the ohmic region where the current remains entirely ionic. The temperature dependence of both the high and low overvoltage current plateaus are depicted in Fig. 11. The apparently high activation energy of about 61 kcal/mole associated with the low overvoltage limiting current agrees well with the activation energy value of >56 kcal/mole for the interface resistance obtained by the a-c admittance measurements (35). It matches, within experimental error, both the heat of molecular dissociation of oxygen on zirconia (36), about 58 kcal/mole, and on Pt (45, 46), 53-70 kcal/mole. No clear partial pressure dependence was found for the limiting current density in this low overvoltage region.

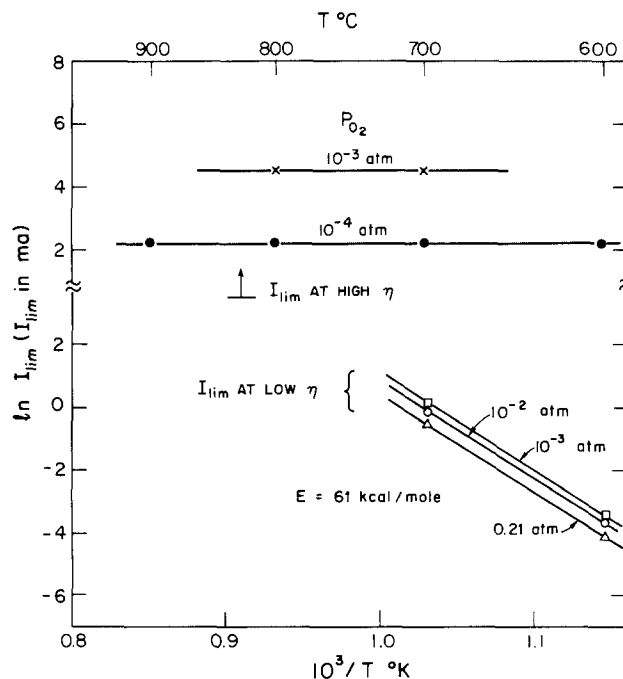


Fig. 11. Variation of limiting current with reciprocal of temperature.

Assuming that the current in this region is limited by the diffusion of some electroactive species, the available parameters do not allow an unambiguous assignment of the rate-determining step. Diffusion of oxygen on ZrO₂ itself or through Pt appear to allow too low a current density. Rate-limiting surface diffusion on the platinum [7], however, is of the right order of magnitude, and also predicts the correct temperature dependence when preceded by the molecular dissociation step [6]. This mechanism, also proposed by Kleitz (14), would predict a P_{O₂}^{1/2} dependence.

An alternative process might be the rate-limiting diffusion of an electronic species from the Pt electrode along the zirconia electrolyte toward the electrochemical reaction site represented by reaction [8]. It is implicitly assumed that the electrochemical reaction site is located in the first few atomic layers of the electrolyte, since oxygen vacancies can exist only in the zirconia side of the three-phase boundary. It is very likely that the electrochemical reaction sites are actually zones rather than restricted microscopic sites along the three-phase boundary. Otherwise, extremely large current densities would be involved. A rate-limiting mechanism involving diffusion of electronic species would predict a current independent of the oxygen partial pressure and may well explain the disappearance of the plateaus as the overvoltage is increased.

Little information is available in the literature regarding electron diffusion in zirconia. Weppner (48-50) reported activation energies of about 12.9 and 32.3 kcal/mole for electron and hole bulk diffusion coefficients in 10 m/o Y₂O₃ · ZrO₂ was found by the same author to be 94.5 kcal/mole. The comparable value for hole conductivity was 42.7 kcal/mole. These values are within 10% of those found by other investigators (59-61). None of these values, however, correspond to those observed experimentally in the present study.

The disappearance of the low voltage limiting current behavior beyond 700°C suggests a sudden change in the interface mechanism. A-C admittance measurements (35) conducted on cell [I] also indicated a sudden change at about 700°C in the activation energy of the interface resistance associated with the electrode

reaction. Pizzini (28) reported a significant decrease in charge transfer overvoltage around this temperature.

The shift in interface mechanisms around 700°C may be related to a characteristic behavior of the O₂/Pt system known as "surface reconstruction." This is commonly observed when a strongly exothermic surface reaction (e. g., chemisorption of oxygen) occurs on Pt (40), Ni or other metal surfaces (46). The reconstructed surface is composed of both Pt and chemisorbed oxygen atoms in periodic arrays (38). This raises the work function of Pt by 1.2 eV (46) thus imposing an additional barrier for electrons to leave the Pt electrode to participate in the charge transfer reaction. As the voltage across the cell is increased, the potential energy barrier can be distorted in such a way as to allow tunneling. However, the estimated limiting current density due to the "tunneling effect" is much too low to account for the low voltage current plateau.

Surface reconstruction can occur even at temperatures as low as 200°C, but the original Pt surface can be restored either by exposing the Pt to high temperatures (38, 41) or to H₂. The "restored" clean Pt surface is obviously more reactive. Strong evidence of this came from Ngo (39) who found a sudden increase of Pt catalytic activity toward NO₂ at 750°C and above. At this temperature the adsorbate on Pt becomes unstable and desorbs as O₂ or PtO₂ whereby the "restored" Pt surface becomes appreciably more active in decomposing NO₂.

So, it is possible that the transformation of the Pt electrode surface from a reconstructed to a restored state may be responsible for the disappearance of the lower current plateaus as the result of a change in interface mechanism above 700°C observed in the present work.

Conclusions

It has been shown that at high particle fluxes the current is limited by diffusion of molecular oxygen through the gas phase boundary layer. This has been substantiated by temperature, flow rate, and oxygen partial pressure dependence measurements. It has also been shown that the effect of water vapor on the polarization behavior in this regime becomes noticeable only when the partial pressure of water vapor is comparable to or greater than that of oxygen.

At intermediate rates, the interfaces are nearly non-blocking, and the major impedance is the ohmic resistance of the solid electrolyte to oxide ion migration.

In the low overvoltage region, current plateaus are observed at $T \leq 700^\circ\text{C}$ which disappear at higher temperatures. The disappearance may be due to a property of Pt surfaces in an oxygen environment which changes their surface structure from a reconstructed to a restored state around this temperature.

The physical phenomenon responsible for the observed limiting current behavior in this region could not be fully resolved. However, it seems like either electron diffusion through the ZrO₂ from Pt electrode to the ERS or oxygen surface diffusion on the Pt electrode may be rate determining.

Acknowledgments

The authors are indebted to Dr. J. Weissbart of Applied Electrochemistry, Incorporated, for kindly providing the scandia-stabilized zirconia samples. Financial support from the Environmental Protection Agency under Contract 5 R01 R 801337, as well as Stanford University, is also appreciated.

Manuscript submitted May 25, 1979; revised manuscript received June 9, 1980.

Any discussion of this paper will appear in a Discussion Section to be published in the June 1981 JOURNAL. All discussions for the June 1981 Discussion Section should be submitted by Feb. 1, 1981.

Publication costs of this article were assisted by Stanford University.

REFERENCES

- W. Nernst, *Z. Elektrochem.*, **6**, 41 (1900).
- L. Heyne, in "Mass Transport in Oxides," J. B. Wachtman, Jr., and A. D. Franklin, Editors, NBS Special Pub. 296, p. 149 (1968).
- A. D. Franklin, *J. Am. Ceram. Soc.*, **58**, 465 (1975).
- D. O. Raleigh, in "Progress in Solid State Chemistry," Vol. 3, H. Reiss, Editor, p. 83, Pergamon Press, New York (1967).
- D. O. Raleigh, in "Electroanalytical Chemistry: A Series in Advances," Vol. 6, A. J. Bard, Editor, p. 87, Marcel Dekker, Inc., New York (1973).
- J. Weissbart and R. Ruka, *This Journal*, **109**, 723 (1962).
- H. Tannenberger, Paper presented at the 154th Meeting of the American Chemical Society, Chicago (1967).
- A. D. Neumin, S. V. Karpachev, and S. F. Pal'guev, *Dokl. Akad. Nauk USSR*, **141**, 402 (1961).
- T. H. Etsell and S. N. Flengas, *This Journal*, **118**, 1890 (1971).
- H. H. Möbius and B. Rohland, *Z. Chem., Lpz*, **4**, 158 (1966).
- S. V. Karpachev, A. T. Filyaev, and S. F. Pal'guev, *Electrochim. Acta*, **9**, 1681 (1964).
- H. Binder, A. Köhling, H. Krupp, K. Richter, and G. Sanstede, *ibid.*, **8**, 781 (1963).
- P. Fabry and M. Kleitz, *Electroanal. Chem. Interfacial Electrochem.*, **57**, 165 (1974).
- M. Kleitz, Thesis, University of Grenoble (1968).
- C. S. Tedmon, Jr., H. S. Spacil, and S. P. Mitoff, *This Journal*, **116**, 1170 (1969).
- S. V. Karpachev and Yu. M. Ovchinnikov, *Sov. Electrochem.*, **5**, 181 (1969).
- (a) S. Pancharatnam, Ph.D. Dissertation, Stanford University (1974); (b) S. Pancharatnam, R. A. Huggins, and D. E. Mason, *This Journal*, **122**, 869 (1975).
- R. J. Brook, W. L. Pelzmann, and F. A. Kröger, *This Journal*, **118**, 185 (1971).
- H. Yanagida, R. J. Brook, and F. A. Kröger, *ibid.*, **117**, 593 (1970).
- C. B. Alcock and S. Zador, *J. Appl. Electrochem.*, **2**, 289 (1972).
- R. E. W. Casselton, *ibid.*, **4**, 25 (1974).
- T. M. Gür, Ph.D. Dissertation, Stanford University (1976).
- R. E. W. Casselton, J. S. Thorp, and D. A. Wright, *Proc. Brit. Ceram. Soc.*, **19**, 265 (1971).
- M. Guillou, J. Millet, and S. Palous, *Electrochim. Acta*, **13**, 1411 (1968).
- J. E. Bauerle, *J. Phys. Chem. Solids*, **30**, 2657 (1969).
- Ya. P. Gokhshtein and A. A. Safonov, *High Temp.*, **8**, 368 (1970).
- R. J. Brook and T. L. Markin, in "Fast Ion Transport in Solids," W. van Gool, Editor, North-Holland Publishing Co., Amsterdam (1973).
- S. Pizzini, in *ibid.*
- S. Pizzini, M. Bianchi, P. Colombo, and S. Torshio, *J. Appl. Electrochem.*, **3**, 153 (1973).
- F. A. Kröger, *This Journal*, **120**, 75 (1973).
- L. R. Velho and R. W. Bartlett, *Metal. Trans.*, **3**, 65 (1972).
- S. V. Karpachev and A. T. Filyaev, *Elektrokhimiya*, **2**, 1330 (1966).
- S. Pizzini, M. Bianchi, A. Corradi, and C. Mari, *J. Appl. Electrochem.*, **4**, 7 (1974).
- T. M. Gür and R. A. Huggins, *This Journal*, **126**, 1067 (1979).
- T. M. Gür, I. D. Raistrick, and R. A. Huggins, *Solid State Ionics*, **1**, 251 (1980).
- T. Smith, *This Journal*, **111**, 1020, 1027 (1964).
- L. A. Simpson and R. E. Carter, *J. Am. Ceram. Soc.*, **49**, 139 (1966).
- R. Lewis and R. Gomer, *Surf. Sci.*, **12**, 157 (1968).
- T. C. Ngo, Ph.D. Dissertation, Stanford University (1974).
- C. W. Tucker, Jr., *J. Appl. Phys.*, **35**, 1897 (1964).
- A. G. Stoll, Ph.D. Dissertation, University of California, Berkeley (1973).
- A. V. Sklyarov, I. I. Tretyakov, B. R. Shub, and S. Z. Roginskii, *Dokl. Phys. Chem.*, **189**, 829 (1969).
- W. H. Weinberg and R. P. Merrill, *Surf. Sci.*, **39**, 206 (1973).
- D. Brennan, D. O. Hayward, and B. M. W. Trapnell,

- Proc. R. Soc. London Ser. A*, **256**, 81 (1960).
45. O. D. Gonzalez and G. Parravano, *J. Am. Ceram. Soc.*, **73**, 4533 (1956).
 46. G. A. Somorjai, "Principles of Surface Chemistry," Prentice-Hall, New Jersey (1972).
 47. G. R. Bobb and D. M. Mason, *Electrochem. Technol.*, **2**, 129 (1964).
 48. W. Weppner, *Z. Naturforsch.*, **31a**, 1336 (1976).
 49. W. Weppner, *J. Solid State Chem.*, **20**, 305 (1977).
 50. W. Weppner, *Electrochim. Acta*, **22**, 721 (1977).
 51. H. H. Möbius and B. Rohland, *Rev. Energ. Primaire*, **2**, 27 (1966).
 52. V. N. Chebotin, M. V. Glumov, A. D. Neuimin, and S. F. Pal'guev, *Sov. Electrochem.*, **6**, 564 (1970).
 53. H. S. Spacil and C. S. Tedmon, Jr., *This Journal*, **116**, 1618, 1627 (1969).
 54. D. Yuan and F. A. Kröger, *ibid.*, **116**, 594 (1969).
 55. Y. L. Sandler and D. D. Durigon, *J. Phys. Chem.*, **72**, 1051 (1968).
 56. D. Hoeschen, Thesis, University of Gottingen (1966).
 57. R. E. W. Casselton, Thesis, University of London (1971).
 58. P. Fabry and M. Kleitz, in "Electrode Processes in Solid State Ionics," M. Kleitz and J. Dupuy, Editors, p. 331, D. Reidel Publishing Co., Dordrecht, Holland (1976).
 59. L. Heyne and N. M. Beekmans, *Proc. Br. Ceram. Soc.*, **19**, 229 (1971).
 60. J. W. Patterson, E. C. Bogren, and R. A. Rapp, *This Journal*, **114**, 752 (1967).
 61. L. D. Burke, H. Rickert, and R. Steiner, *Z. Phys. Chem., N.F.*, **74**, 146 (1971).

The Activation of Polycrystalline Gold to the Hydrogen Electrode Reaction Promoted with Repetitive Potentiodynamic Perturbations

R. Córdova O., M. E. Martins, and A. J. Arvía*

Instituto de Investigaciones Físicoquímicas Teóricas y Aplicadas, División Electroquímica, Sucursal 4, Casilla de Correo 16, 1900 La Plata, Argentina

ABSTRACT

The activation of gold electrodes toward the hydrogen electrode reaction is studied using the polycrystalline gold/1M H₂SO₄ interface at 25°C. The electrode activation is promoted by potentiodynamic aging in the potential range where the O-electrosorption/O-electrodesorption takes place. The activation effect is comparable to that earlier described when gold electrodes are cathodized for a relatively long time in the potential range of the net evolution of hydrogen. The activation effect is revealed through the appearance of a remarkable increase of current associated with the hydrogen ion discharge and an anodic current related to the electrooxidation of hydrogen. For the latter, different contributions are distinguished, namely, the molecular H₂ diffusion and those related to adsorbed and probably absorbed hydrogen. The electrochemical characteristics of the gold/1M H₂SO₄ interface are related to a large extent to the restructuring of the metal surface.

The energetic characteristic of the electrode surface is crucial in electrochemical kinetics. There are numerous experimental procedures described in the literature to activate particular metal electrodes such as the application of certain types of either current or potential pulses, the addition of traces of some particular species to the electrolyte solution, the production of electrodes with a determined size of particles, etc. Sometimes the activation or deactivation of metal electrodes depends to a large extent on the proper electrode history. This is the case of the mechanism of the hydrogen evolution reaction on gold which is very sensitive to the quality of the gold surface (1-3).

In this respect it has been recently shown that the surface structure of polycrystalline gold electrodes immersed in aqueous H₂SO₄ solutions changed when the electrochemical interface was subjected to several hundred potentiodynamic cycles in the 0-1.9V (NHE) range (4, 5). The electrochemical treatment transformed the originally disturbed surface into a structured surface with the appearance of grain boundaries and faceting (4-7) as in the thermal etching (8). It is clearly elucidated that crystal orientation of gold electrodes influences the capacity of the electrical double layer (4, 6, 9, 10). On the other hand, repetitive

polarization cycles in the -0.8 to 1.2V (vs. SCE) potential range produces a systematic and progressive change of the electrode surface from a (111) to a (110) structure as revealed through electron microscopy and electron diffraction and changes the potential of zero charge (4). The structural surface change is reflected in an increase of electrode activation of gold to the hydrogen electrode reaction (5-7, 11) as compared to the adsorption of hydrogen on non-activated gold (2, 12, 13). Values between 3% and 4% of a hydrogen adsorbed monolayer have been reported. The capacity maximum at about -0.2V (SCE) found at the (100) gold face, but not at the (110) face, was ascribed to hydrogen adsorption (6).

It has also been demonstrated that the surface restructuring requires the electrosorption and electrodesorption of oxygen on the metal surface (4, 5, 7, 11), but the influence of the perturbation variables on the efficiency of the electrode surface activation concerning the hydrogen electrode reaction is still not completely known. Therefore, in order to elucidate the problem of the gold electrode activation, the type of perturbation described in the literature to promote the potentiodynamic aging of layers of different species electrochemically formed on electrode surface (14-16), was systematically applied to the gold/1M H₂SO₄ interface. The corresponding results are relevant to understand, at least in part, the relationship between

* Electrochemical Society Active Member.

Key words: metals, electrocatalysis, voltammetry.

the electrode surface activation and the surface restructuring provoked by potential perturbations such as the combined complex repetitive triangular potential sweeps.

Experimental

The experimental procedure was based on that described in previous works (14, 15). The working electrode (0.38 cm² apparent area) consisted of a polycrystalline spectroscopic quality wire (Johnson, Matthey) mounted on a Teflon holder. The following electrode pretreatments were independently applied: (i) The gold electrode was polished with a 300 mesh Al₂O₃ powder-water suspension. The electrode was then immersed in 1:1 HNO₃-H₂SO₄ mixture and finally rinsed for a long time in water. (ii) The gold electrode was dipped without any polishing in a 5N HNO₃ solution. The first procedure gave the more reproducible results but the second one was particularly useful to emphasize the memory effect of the used electrodes which is described further on. The counterelectrode (7 cm² apparent area) was made with the same material and adequately separated to eliminate any diffusion of the products from the counterelectrode section of the cell to the working electrode compartment. An Hg/Hg₂SO₄ electrode properly protected to avoid Hg(I) diffusion into the electrolysis cell was used. Teflon tubing and stopcocks and joints lubricated with the electrolyte solution contained in the cell were employed. The electrode potentials are referred to the reversible hydrogen electrode (RHE).

The electrolyte was 1M H₂SO₄ solution prepared from triply distilled water and A.R. 98% H₂SO₄ (Merck). The distilled water was systematically tested to satisfy the purity requirements described in the literature (17). Platinum or any other possible electrode contaminant were carefully avoided. The experiments were made with purified gas saturation, either N₂ or H₂, and employing either quiescent or stirred electrolytes. The temperature was fixed at 25°C. The activation of gold electrodes to the hydrogen electrode reaction by means of the potentiodynamic aging in the O-electrosorption/O-electrodesorption potential range was studied by applying different potential/time perturbation programs. Runs were made covering different switching potentials ($E_{\lambda,a}$, $E_{\lambda,c}$, and $E'_{\lambda,c}$), potential sweep rates (v_a , v_c , and v_i) and durations (τ) of the intermediate perturbation. The subscripts a, c, and i stand for the positive going (anodic) and negative going (cathodic) potential excursions and for the intermediate repetitive triangular potential scan (RTPS), respectively. Both electrode handling and cell assembling were made taking precautions

to prevent any possible contamination through the laboratory atmosphere. The electronic circuitry is the same as employed in previous works (14, 15).

Results

Quiescent N₂-saturated electrolyte.—The E/I profiles resulting at 0.2 V/sec within $E_{\lambda,a} = 1.67V$ and $E_{\lambda,c} = -0.2V$, obtained with and without the potentiodynamic aging between $E_{\lambda,a}$ and $E'_{\lambda,c}$, are comparatively depicted in Fig. 1. The potentiodynamic aging at 0.2 V/sec was confined to a potential range ($E_{\lambda,a} = 1.67V$ and $E'_{\lambda,c} = 1.26V$), where about one-half of the O-containing layer was involved in each electrodesorption/electrosorption cycle. The potential sweep run immediately after the intermediate RTPS between $E_{\lambda,a} = 1.67V$ and $E_{\lambda,c} = -0.2V$ distinguishes the following features, as compared to the stabilized RTPS: (i) The shift of the O-electrodesorption current peak toward more negative potentials and its simultaneous slight increase in charge. The cathodic current peak becomes more symmetric and thinner than the corresponding current peak recorded in the stabilized RTPS. (ii) A remarkable increase of the hydrogen evolution current. (iii) A net anodic current in the 0.1-0.4V potential range which is attributed to the hydrogen electrooxidation (1, 5, 11). The potential of the anodic current peak recorded during the positive going potential sweep is located in the 0.120-0.165V range. The charge $Q_{H,a}$ related to the hydrogen electrooxidation under fixed values of $E_{\lambda,a}$, $E_{\lambda,c}$, and $E'_{\lambda,c}$ depends on the time τ and on the frequency of the intermediate RTPS (Fig. 2). The maximal $Q_{H,a}$ value is obtained at ca. 2 V/sec. Within the $E'_{\lambda,c}$ range indicated in the figure and within the 0-30 min range, $Q_{H,a}$ increases with τ . The $Q_{H,a}$ value recorded during the negative going potential sweep, reveals a composite current peak involving at least two contributions. The more positive contribution is in the 0.3-0.5V range, while the more negative one is in the 0.15-0.17V range. The potentials of the anodic current peak during successive potentials sweeps are reproducible within ± 10 mV.

The $Q_{H,a}$ value depends strongly on $E'_{\lambda,c}$ and correspondingly on the percentage of the O-containing species being removed during the intermediate RTPS (Fig. 3). The maximal $Q_{H,a}$ value results at ca. 80% of the electroadsorbed oxygen involved in the intermediate RTPS. This percentage is referred to the charge of the O-electrodesorption current peak in the stabilized E/I profile. The gold electrode, which became activated toward the hydrogen electrode reac-

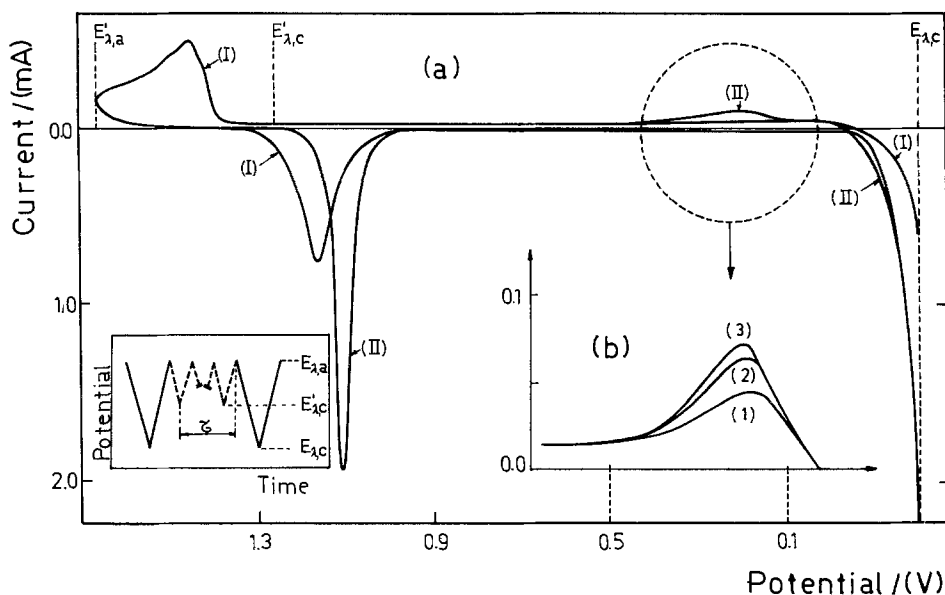


Fig. 1. Potentiodynamic E/I profile resulting from the potential/time perturbation program indicated in the figure. N₂-saturation. (a) (I) Stabilized RTPS E/I profile before the electrode activation. (II) First E/I display after the intermediate potentiodynamic perturbation. $v_a = v_c = v_i = 0.2$ V/sec. (b) Positive potential going scans at $v_a = 0.2$ V/sec after the intermediate perturbation during different τ . 1, 10 min; 2, 20 min; 3, 30 min.

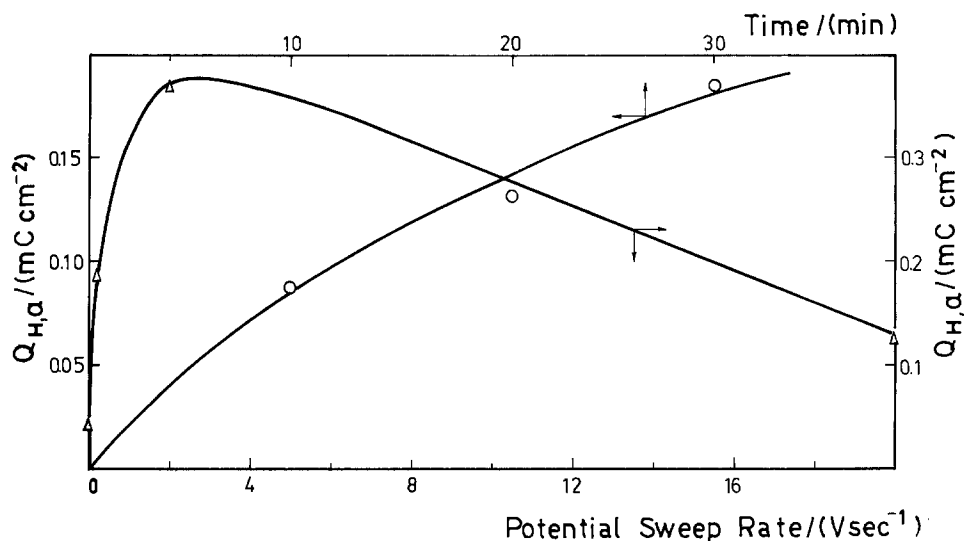


Fig. 2. Dependence of $Q_{H,a}$ on v_1 and on τ . N_2 -saturation. $E_{\lambda,a} = 1.7\text{V}$; $E_{\lambda,c} = -0.05\text{V}$; $E'_{\lambda,c} = 1.09\text{V}$; and $v_a = v_c = v_1 = 0.2 \text{ V/sec}$.

tion, progressively deactivates with a further potential cycling between $E_{\lambda,a}$ and $E_{\lambda,c}$.

The rate of decrease of the electrode activation can be followed through the change of the relative charge $(Q_{H,a})_n / (Q_{H,a})_1$ (Fig. 4) where $(Q_{H,a})_n$ is the hydrogen electrooxidation charge after the n th RTPS between $E_{\lambda,a}$ and $E_{\lambda,c}$ and $(Q_{H,a})_1$ refers to the same charge for the first potential sweep immediately after the intermediate RTPS carried out between $E_{\lambda,a}$ and $E'_{\lambda,c}$. The charge related to hydrogen electrooxidation decreases more rapidly when $E_{\lambda,a}$ becomes more negative than the potential which corresponds to the O-electrosorption. This result reveals the influence of the O-electrosorption on the activation for the hydrogen electrode reaction. For a constant set of perturbation conditions the charges $Q_{H,a}$ and $Q_{H,c}$ recorded during the triangular potential sweep run immediately after the electrode activation increase as $E_{\lambda,c}$ becomes more negative, but for a fixed $E_{\lambda,c}$, $Q_{H,a}$ is larger than $Q_{H,c}$ (Table I). There is, however, an optimal $E_{\lambda,c}$ value ($E_{\lambda,c} = -0.05\text{V}$ for $v_a = v_c = 0.2 \text{ V/sec}$ and $v_1 = 2 \text{ V/sec}$) at which $Q_{H,c}$ practically compensates $Q_{H,a}$.

On the other hand, under the same potentiodynamic aging conditions in the O-electrosorption region, $Q_{H,a}$ decays according to a rate law of the form $Q_{H,a} \sim t^x$ (Fig. 5) where the exponent x depends on the switching potentials of the triangular potential perturbation following the intermediate RTPS. Analogously $Q_{H,a}$ also decreases with τ_p , the time at which the electrode

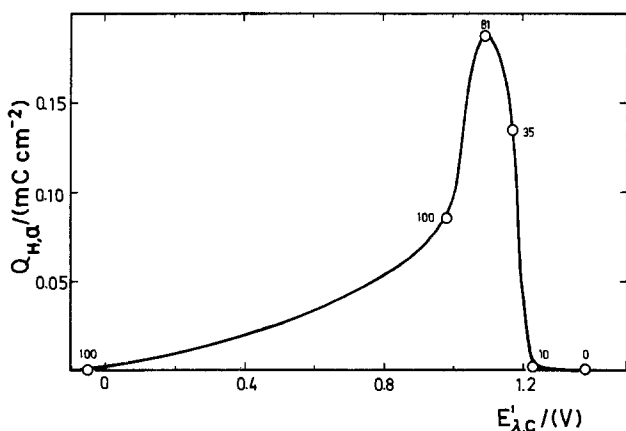


Fig. 3. Dependence of $Q_{H,a}$ on $E'_{\lambda,c}$. N_2 -saturation. $E_{\lambda,a} = 1.67\text{V}$; $E_{\lambda,c} = -0.05\text{V}$; $v_a = v_c = 0.2 \text{ V/sec}$; $v_1 = 2 \text{ V/sec}$; $\tau = 30 \text{ min}$. For each experimental point the percentage of the O-electrodesorption at $E'_{\lambda,c}$ in the first intermediate negative potential going sweep is indicated.

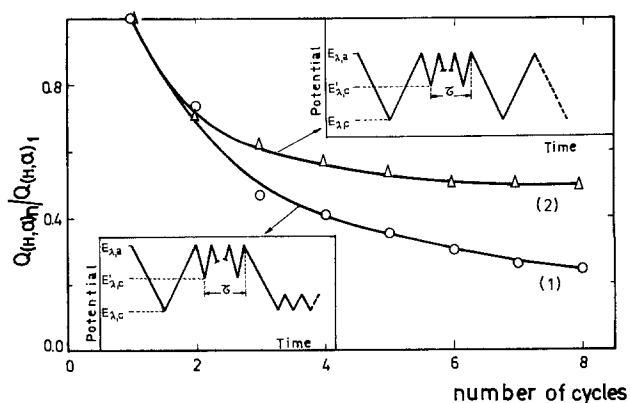


Fig. 4. Relative change of $Q_{H,a}$ as a function of the number of RTPS operating after the potentiodynamic aging. N_2 -saturation. $E_{\lambda,a} = 1.7\text{V}$; $E_{\lambda,c} = -0.05\text{V}$; $E'_{\lambda,c} = 1.09\text{V}$; $\tau = 30 \text{ min}$; $v_a = v_c = 0.2 \text{ V/sec}$. $v_1 = 2 \text{ v/sec}$. Curve 1, without covering the O-electrosorption potential range during the potential cycling. Curve 2, the O-electrosorption potential range is covered.

is held at $E_{\lambda,c}$ after its potentiodynamic activation. The decay of $Q_{H,a}$ fits a reasonable linear $Q_{H,a}$ vs. $\log \tau_p$ plot (Fig. 6).

Quiescent H_2 -saturated solution.—In the H_2 -saturated electrolyte the increase of $Q_{H,a}$ is already observed for $E_{\lambda,c} = 0.0\text{V}$, a potential at which no macroscopic H_2 gas evolution is produced (Fig. 7a and 7b). The electrode subjected to the potentiodynamic aging in the O-electrosorption/O-electrodesorption potential range exhibits an anodic current contribution in the negative potential going sweep before reaching $E_{\lambda,c}$, with two anodic current peaks at 0.39 and at 0.19V, respectively. The returning positive going sweep exhibits a single anodic current peak. During the triangular potential cycling as $Q_{H,a}$ decays, a gradual shift of the anodic current peak potential toward more negative potentials is observed. The heights of the anodic current peak decrease, particularly the one

Table I. Influence of $E_{\lambda,c}$ on the charges related to the hydrogen electrode reaction

$E_{\lambda,c}$ (V)	$Q_{H,a}/$ ($\text{mC} \times \text{cm}^{-2}$)	$Q_{H,c}/$ ($\text{mC} \times \text{cm}^{-2}$)	$Q_{H,a}/Q_{H,c}$
-0.20	0.58	9.97	0.06
-0.15	0.46	2.96	0.16
-0.05	0.37	0.40	0.94
-0.05	0.33	0.53	0.63
-0.05	0.17	0.20	0.84
-0.05	0.40	0.46	0.86

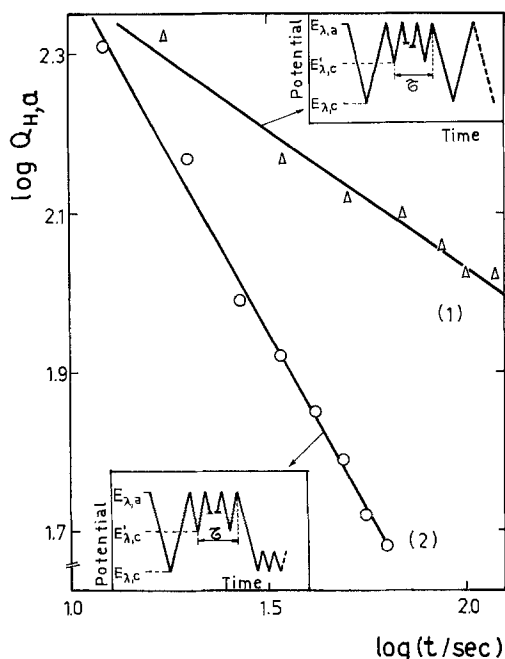


Fig. 5. Log-log plot for the $Q_{H,a}$ decay. N_2 -saturation. The time counting starts immediately after $\tau = 30$ min. $E_{\lambda,a} = 1.7V$; $E_{\lambda,c} = -0.05V$; $E'_{\lambda,c} = 1.09V$; $v_a = v_c = 0.2$ V/sec; $v_1 = 2$ V/sec. Curve 1, the O-electrosorption potential range is covered, $E_{\lambda,a} = 1.7V$. Curve 2, without covering the O-electrosorption potential range during the potential cycling.

located on the more positive potential side. A similar qualitative E/I response results when the electrode is held at $E_{\lambda,c} = 0.0V$ during $\tau_p = 30$ min (Fig. 7c) although the charge is smaller than that observed under the potentiodynamic aging.

The gold electrode activation in the H_2 -saturated electrolyte is greater than that observed in the N_2 -saturated electrolyte under comparable perturbation conditions.

Influence of the solution stirring.—The influence of stirring is determined under preset potential perturbation conditions. Thus, either for H_2 - or for N_2 -saturated stirred solution, the hydrogen-electrooxidation current gradually decreases when $E_{\lambda,c}$ is between 0.0 and $-0.2V$ and it increases again if the potential cycling continues and the stirring is interrupted.

Under the same potential perturbation conditions a remarkable decrease of $Q_{H,a}$ due to stirring is

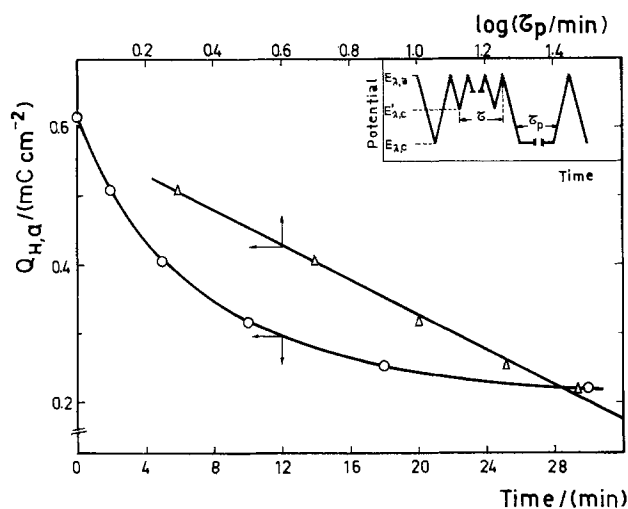


Fig. 6. Decay of $Q_{H,a}$ as a function of τ_p . N_2 -saturation. $E_{\lambda,a} = 1.7V$; $E_{\lambda,c} = -0.2V$; $E'_{\lambda,c} = 1.09V$; $\tau = 30$ min; $v_a = v_c = 0.2$ V/sec; $v_1 = 2$ V/sec.

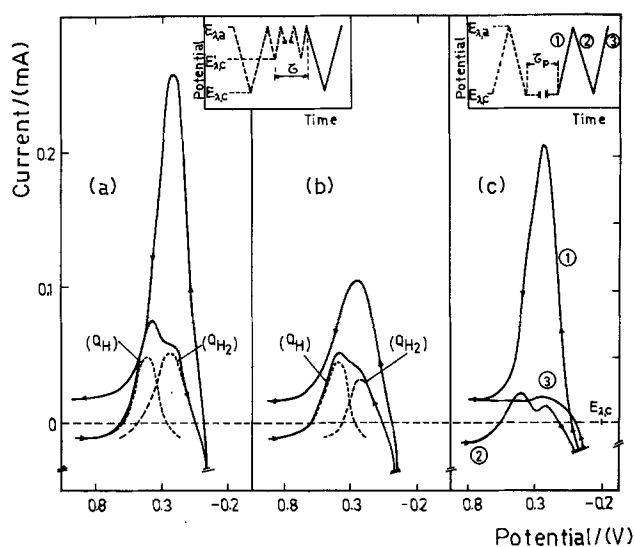


Fig. 7. Comparative E/I displays obtained after the electrode activation process with the potential/time perturbation programs indicated in the figure. H_2 -saturation. $E_{\lambda,a} = 1.7V$; $E_{\lambda,c} = 0.0V$; $E'_{\lambda,c} = 1.09V$; $v_a = v_c = 0.2$ V/sec; $v_1 = 2$ V/sec; $\tau = \tau_p = 30$ min. (a) The triangular potential sweep after the potentiodynamic aging initiates toward positive potentials. The dashed lines correspond to the estimated contributions of H-adatoms and H_2 in the E/I profile during the negative potential going half-cycle. Still solution. (b) The same as (a) but with solution stirring. (c) Comparative successive E/I displays (curves 1, 2 and 3) run with the electrode activated by holding the potential at $E_{\lambda,c}$ during τ_p . With solution stirring.

noticed in the E/I display run immediately after the potentiodynamic activation of the gold electrode. This effect, however, is significantly less in the negative going potential excursion than in the preceding positive going potential scan (Fig. 7a and 7b).

When the gold electrode activation is produced by cathodization at $E_{\lambda,c} = -0.2V$, the solution stirring produces a net decrease of the electrode activation. The decrease continues during the repetitive potential cycling, especially when $E_{\lambda,a}$ is more negative than the O-electrosorption/O-electrodesorption potential range. When $E_{\lambda,a}$ exceeds this value the E/I display recorded during the negative going potential scan then exhibits the anodic doublet previously reported (Fig. 7).

Memory effect.—Gold electrodes, which were repetitively activated through potentiodynamic aging followed by storing for a long period of time in a 5N HNO_3 solution, exhibit a residual activation when they were cycled by a triangular potential signal in quiescent, H_2 -saturated 1M H_2SO_4 solution between $E_{\lambda,c} = -0.2V$ and $E_{\lambda,a} = 1.3V$. Under these conditions, the positive going potential excursion shows an anodic current peak related to hydrogen electrooxidation. The negative going potential excursion after a progressive increase of $E_{\lambda,a}$ repeats the complex multiple E/I display previously described. The stable RTPS E/I profile is attained after about 10-15 cycles. The effect can be reversed simply by changing $E_{\lambda,a}$ to more negative potentials. Thus, the stable RTPS E/I profile of the activated electrode (Fig. 8a) changes to that shown in Fig. 8b when $E_{\lambda,a}$ decreases to 0.6V. Now the charge involved in the successive E/I profile in both directions decreases, as indicated by the arrows, to attain the new stable RTPS E/I profile shown in Fig. 8c (dashed line). Under these circumstances, an increase of $E_{\lambda,a}$ to 1.7V, the E/I profile first shows an increase of the current peaks up to a maximal value and afterward a slight decrease to attain again the stable profile depicted in Fig. 8d (dashed line). Finally,

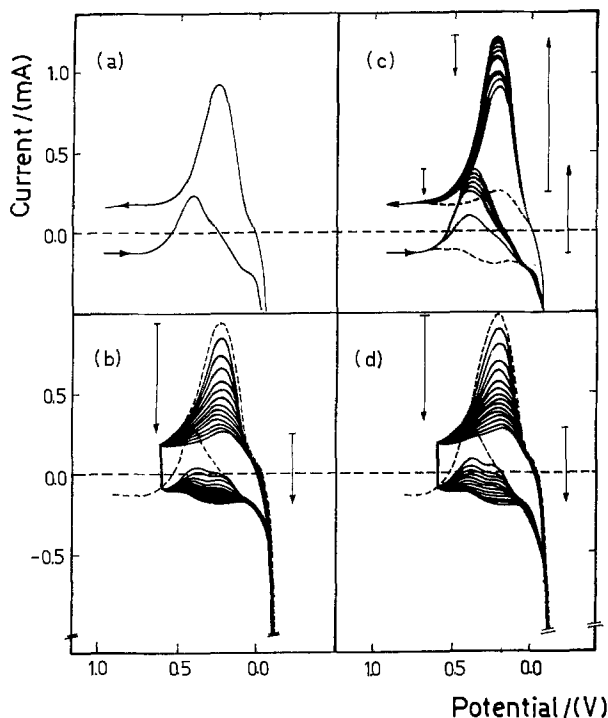


Fig. 8. Potentiodynamic E/I displays ($E_{\lambda,c} = -0.16V$; $v_a = v_c = 0.2$ V/sec; $\tau = \tau_p = 20$ min; H_2 -saturation) run according to the following sequence. (a) E/I profile run immediately after the potentiodynamic activation. (b) Stabilized E/I profile from (a) (dashed trace) and successive E/I displays after fixing $E_{\lambda,a} = 0.6V$ (full traces). (c) Stabilized E/I profile from (b) (dashed trace) and successive E/I displays after fixing $E_{\lambda,a} = 1.7V$ (full traces). (d) Stabilized E/I profile from (c) (dashed line) and successive E/I displays after fixing $E_{\lambda,a} = 0.6V$ (full traces).

a decrease of $E_{\lambda,a}$ from 1.7V back to 0.6V produces again a decrease of the electrode activation.

The memory effect disappears or it is appreciably attenuated after mechanically polishing the electrode with a water- Al_2O_3 suspension.

Discussion

The gold/aqueous acid interface can be activated for the electrooxidation of hydrogen under either potentiostatic cathodization or after potentiodynamic aging in the O-electrosorption potential range. In the former case, the effect depends on $E_{\lambda,c}$ and on τ_p (3-5) while in the latter it is influenced by $E_{\lambda,a}$, $E'_{\lambda,c}$, τ , and the frequency of the repetitive triangular potential perturbation between $E'_{\lambda,c}$ and $E_{\lambda,a}$. The values of $E_{\lambda,a}$ and $E'_{\lambda,c}$ determine the amount of electroadsorbed oxygen which is alternatively electroformed and electroreduced during the intermediate RTPS. The maximum effect corresponds to a charge which is about 80% of the O-monolayer charge on gold. Although both activation procedures give comparable results, the activation of the hydrogen electrooxidation on gold produced through the potentiodynamic aging is already noticed by holding the potential of the electrode at $E \approx 0V$.

The activation of the gold electrode toward the hydrogen electrode reaction implies both an increase of the overall cathodic current related to the evolution of hydrogen and the appearance of two anodic current peaks associated with the electrooxidation of hydrogen on gold. The possibility that the cathodic current increase is due to the increase of the electrode roughness is, in principle, disregarded because the charge related to the O-electrodesorption before and after the electrode activation remains practically the same.

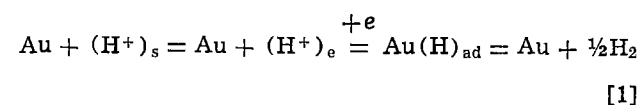
The two anodic current peaks present a different response to the solution stirring. Thus, the height of the main anodic peak located at more negative

potentials decreases strongly by stirring the solution, as one should expect for a diffusion-controlled redox reaction. This current peak should be related to the electrooxidation of molecular hydrogen, supersaturating the diffusion layer (18, 19). This local supersaturation is only observed with previously activated gold electrodes. The largest degree of H_2 supersaturation at the electrode surface is achieved through the cathodic potentiostatic activation and it depends both on the potential applied to the interface and on the time τ_p . The corresponding current peak potential is displaced toward the positive potential side from the H_2/H^+ equilibrium potential due to the irreversibility of the redox reaction. Most of the E/I profile recorded during the positive going potential scan after cathodic potentiostatic activation can be reproduced using the equation of a redox process (20) with the exchange current density, $i_0 \approx 10^{-5}$ A/cm² (2) and the estimated hydrogen supersaturation 10^{-1} mole/liter (19).

The smaller anodic current peak at ca. 0.3V appears as independent of the stirring of the solution. The E/I profile also indicates a possible third anodic current contribution at ca. 0.2V although it is mostly overlapped by the main diffusion-controlled current peak already discussed. The charge of the anodic current peak at ca. 0.3V as estimated from the negative potential going E/I display, is always less than the charge expected for the H-atom monolayer (210 $\mu C/cm^2$ for polycrystalline platinum) (21). This charge can be associated with the presence of H-adatoms whose surface concentration should depend on available active metal sites promoted on the surface by the potentiodynamic aging in the O-electrosorption potential range.

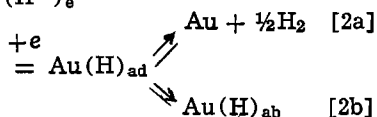
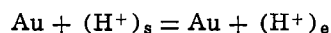
The gold electrode activation process for the hydrogen electrode reaction can be interpreted on the basis of the data reported for the dependence of the hydrogen overvoltage with the type of gold electrode used (2). The hydrogen overvoltage obtained with smooth gold electrodes are similar and rather high. They agree with calculation for $E_{Au-H} \approx 46$ kcal (22, 23). For a smooth gold electrode, the cathodic Tafel slope is ca. 0.1 V/decade or slightly higher and some evidence has been obtained for a lower slope at lower overvoltages (24, 25). Otherwise, for electrolytic gold deposits, smaller overvoltages and lower Tafel slopes are reported (24-26) especially for electrodes subjected to anodic-cathodic activations (1, 27). These results make it difficult to draw definite conclusions regarding the mechanism of the reaction under stationary conditions. But they correlate with the present data if one admits that the restructuring of gold electrode surfaces, which was demonstrated through optical methods (4-8), plays a significant role in defining their degree of activation.

To develop a qualitative formalism of the reactions at the gold electrode, let us first consider that it consists of a clean gold surface structure which remains practically unaltered during the potential perturbation and that no H_2 is dissolved into the electrolyte. Because of the (H)Au bond energy value, the hydrogen adatom concentration on the metal is probably very low. Therefore, the following reaction steps of the electrochemical process can be proposed



where s, e, and ad denote the bulk of the solution, electrode surface, and adsorbed species, respectively. The reaction sequence [1] has been considered to interpret earlier experimental results with the assumption that the concentration of adsorbed H is negligible and the adsorbed species is written as a postulated reaction intermediate (22). The rate-determining step under stationary conditions has been assigned to the

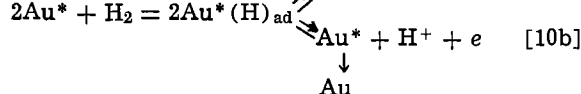
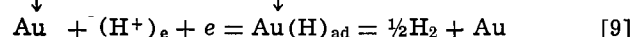
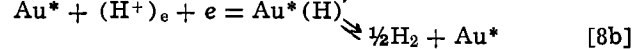
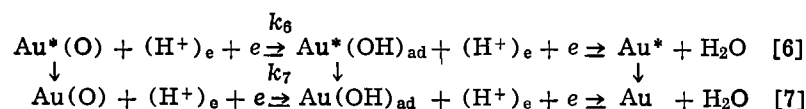
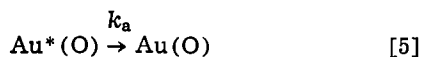
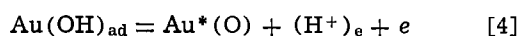
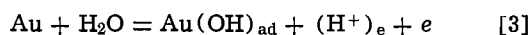
discharge plus H-desorption step. However, it is claimed that a fraction of the hydrogen atoms electrochemically produced can penetrate into the metal through a slow diffusion process. The diffusion coefficient of hydrogen in gold is estimated, at 25°C, equal to 4×10^{-12} cm²/sec (5). Then, this means that reaction sequence [1] should be written as follows



where ab stands for the adsorbed hydrogen. The electrooxidation of adsorbed hydrogen would occur through a reaction which may be either under activation or diffusion control.

The participation of sorbed hydrogen in the electrochemical process is appreciably influenced by the O-electrosorption/O-electrodesorption processes occurring at more positive potentials. These processes modify the crystallographic order at the first layers of the metal lattice (7, 14). Through the mobility of metal atoms out of the lattice assisted by their rearrangement during the O-electrodesorption stage and by the anisotropy of the surface energy due to the incomplete removal of the O-containing layer (7). These changes in the metal lattice should depend both on the frequency (ν) and duration (τ) of the intermediate RTPS and attains a maximal value for a particular set of perturbation variables as shown in Fig. 2 and 3.

The precedent discussion and the already reported data on the O-electrosorption/O-electrodesorption on gold (28) suggest that the overall processes occurring in the $E_{\lambda,a} - E_{\lambda,c}$ potential range on the activated gold electrode under potentiodynamic conditions can be ascribed by the following reactions



Reactions [3] to [5] explain the main processes involved in the potentiodynamic O-electrosorption/O-electrodesorption on gold (28). Reactions [3] and [4] are the initial steps related to the O-electrosorption occurring on the nonactivated gold electrode. Reaction [5] represents the aging of the O-electrosorbed species, k_a is the corresponding rate constant. This reaction plays an important role during the potentiodynamic aging covering the potential range of the O-electrosorption/O-electrodesorption processes. Reactions [3] to [5] imply at least the occurrence of two different surface sites, denoted as Au and Au*. Then, the O-electrodesorption may occur through the series of reactions [6] and [7] which also imply possible deactivation processes of the Au* species (dashed arrows). The relative surface concentration of Au and Au*

depend on the values of k_a , k_6 , k_7 , and the characteristics of the perturbation program applied to the electrode. The H₂-discharge reaction occurring on Au and Au* are explained by steps [8] and [9], respectively. The Au* sites are those which exhibit toward the hydrogen adatoms a reactivity higher than the Au sites. Reactions [8a] and [8b] should be responsible for the changes produced in the potentiodynamic E/I display after the potentiodynamic aging.

When the electrolyte layer adjacent to the electrode is saturated with H₂, the H₂ electrooxidation should preferentially occur at the Au* sites (reaction [10]). The presence of the Au* sites should favor the existence of hydrogen adatoms either electrochemically formed as well as produced from the dissociation of molecular hydrogen. Then, the surface concentration of H-adatoms should depend on the surface concentration of Au* sites. The potential of the corresponding electrooxidation current peak indicates a slight increase in the average Au*(H) bond energy as compared to that of the Au(H) bond. Under these circumstances the behavior of the activated gold electrode with respect to the hydrogen electrode reaction approaches that of the platinum electrode. The overall processes represented by reactions [3]-[10] under potentiodynamic conditions imply either the M-O and M-M or the M-H and M-M bonds changing simultaneously.

The effect of the activation process depends on the time spent to achieve it. Thus, when the activation process operates during a short time the electrode activation decays linearly with the logarithm of time (Fig. 5 and 6), a relationship commonly obtained in electrodesorption of different species from solids (29). This suggests that the activation effect is predominantly associated with the first layers of the metal lattice. On the other hand, when the time of the activation process is sufficiently large, the electrode acquires an activation memory with respect to the hydrogen electrode reaction which can be interpreted as a deeper and longer lasting change of the electrode surface structure resulting from the processes taking place over the O-electrosorption/O-electrodesorption potential range. This effect is probably assisted by

the possible accumulation of adsorbed oxygen in the metal as was suggested earlier to explain the discrepancy observed between the complex evolution of the optical properties of the metal associated with restructuring of its surface and the prediction of the simple faceting model (30). The resulting effects can be related to the penetration of hydrogen into the metal.

Acknowledgment

INIFTA is sponsored by the Consejo Nacional de Investigaciones Científicas y Técnicas, The Universidad Nacional de La Plata, and the Comisión de Investigaciones Científicas (Provincia de Buenos Aires). This work was partially supported by the Regional Program for the Scientific and Technological Development of the Organization of the American States.

Manuscript submitted May 16, 1979; revised manuscript received Feb. 19, 1980.

Any discussion of this paper will appear in a Discussion Section to be published in the June 1981 JOURNAL. All discussions for the June 1981 Discussion Section should be submitted by Feb. 1, 1981.

Publication costs of this article were assisted by the Instituto de Investigaciones Fisicoquímicas Teóricas y Aplicadas.

REFERENCES

- G. Gruneberg, *Electrochim. Acta*, **10**, 339 (1965).
- A. T. Kuhn and M. Byrne, *ibid.*, **16**, 39 (1971).
- G. Picq and P. Vennereau, *J. Electroanal. Chem. Interfacial Electrochem.*, **96**, 131 (1979).
- J. Lecoer, C. Sella, J. C. Martin, L. Tertian, and J. Deschamps, *C. R. Acad. Sci. Paris, Ser. C*, **281**, 71 (1975).
- F. Chao and M. Costa, *ibid.*, **284**, 603 (1977); *ibid.*, **284**, 639 (1977); *ibid.*, **284**, 763 (1977).
- G. M. Schmid and N. Hackerman, *This Journal*, **110**, 243 (1962).
- F. Chao, M. Costa, and A. Tadjeddine, *Surf. Sci.*, **46**, 265 (1974).
- J. Bénard, *Werks. Korrr.*, **21**, 107 (1970).
- C. Nguyen Van Huong, C. Hinnen, J. Lecoer, and R. Parsons, *J. Electroanal. Chem. Interfacial Electrochem.*, **92**, 239 (1978).
- C. Hinnen, C. Nguyen Van Huong, A. Rousseau, and J. P. Dalbera, *ibid.*, **95**, 131 (1979).
- R. Córdova, M. E. Martins, and A. J. Arvía, *Electrochim. Acta*, **24**, 469 (1979).
- M. Breiter, C. A. Knorr, and V. Volkl, *Ber. Bunsenges. Phys. Chem.*, **59**, 681 (1955).
- F. G. Will and C. A. Knorr, *ibid.*, **62**, 378 (1960).
- N. R. de Tacconi, J. O. Zerbino, M. E. Folquer, and A. J. Arvía, *J. Electroanal. Chem. Interfacial Electrochem.*, **85**, 213 (1977).
- M. E. Folquer, J. O. Zerbino, N. R. de Tacconi, and A. J. Arvía, *This Journal*, **126**, 592 (1979).
- A. J. Arvía, *Israel J. Chem.*, **18**, 89 (1979).
- B. E. Conway, H. Angerstein-Kozłowska, E. E. Criddle, and W. B. A. Sharp, *Anal. Chem.*, **45**, 1331 (1973).
- S. Shibata, *Bull. Chem. Soc. Jpn.*, **33**, 1635 (1960).
- S. Shibata, *ibid.*, **36**, 53 (1963).
- R. S. Nicholson and I. Shain, *Anal. Chem.*, **36**, 706 (1964).
- D. A. J. Rand and R. Woods, *J. Electroanal. Chem. Interfacial Electrochem.*, **31**, 29 (1971).
- L. I. Krishtalik, "Advances in Electrochemistry and Electrochemical Engineering," Vol. VII, P. Delahay and C. W. Tobias, Editors, Wiley-Interscience (1970).
- D. O. Haywood and B. M. W. Trapnell, "Chemisorption," Butterworths, London (1964).
- M. Breiter, H. Kammermaier, and C. A. Knorr, *Z. Elektrochem.*, **60**, 119 (1956); *ibid.*, **60**, 454 (1956).
- N. Pentland, J. O'M. Bockris, and E. Sheldon, *This Journal*, **104**, 182 (1957).
- J. O'M. Bockris and R. Parsons, *Trans. Faraday Soc.*, **44**, 860 (1948).
- S. Schuldiner and J. P. Hoare, *J. Phys. Chem.*, **61**, 705 (1957).
- C. M. Ferro, A. J. Calandra, and A. J. Arvía, *J. Electroanal. Chem., Interfacial Electrochem.*, **59**, 239 (1975); *ibid.*, **65**, 963 (1975).
- A. W. Adamson, "Physical Chemistry of Surfaces," Interscience Publishers, New York (1960).
- F. Chao, M. Costa, and A. Tadjeddine, *Bull. Soc. Chim. Fr.*, **7**, 2465 (1971).

Electrochemical Reactions at Multiple Interfaces

The Nickel Hydroxide Electrode Formed by Precipitation on a Platinum Surface

M. E. Folquer, J. R. Vilche,* and A. J. Arvía*

Instituto de Investigaciones Fisicoquímicas Teóricas y Aplicadas, División Electroquímica, Sucursal 4, Casilla de Correo 16, 1900 La Plata, Argentina

ABSTRACT

The formation of a multiple interface consisting of a platinum-base electrode covered by a chemically produced Ni(OH)₂ layer is investigated in alkaline electrolytes. The potentiodynamic response of the multiple interface is relatively complex but can be interpreted as the sum of two main contributions, namely, the processes related to the electrosorption and electrodesorption of hydrogen and oxygen on platinum and the conjugate redox processes related to the nickel hydroxide electrode. The mutual interference of the oxygen electrosorption and electrodesorption reactions with those of the nickel hydroxide electrode is inferred from the change of the aging characteristics of the oxygen electrodesorption process. The overall electrochemical reaction is interpreted through a reaction model involving two limiting planes dividing the electrochemical interface in two main regions associated with the two processes referred to above.

In a recent publication the concept of the multiple electrochemical interface was applied to explain the potentiodynamic behavior of iridium in different acid electrolytes (1, 2). A multiple electrochemical interface involves at least three different phases, namely, the base metal, the conducting or semiconducting film which covers the base metal either partially or totally, and the electrolyte. The cations or atoms of the metal in the film forming chemical species are different from those of the base metal electrode. Various electrochemical processes take place at the multiple electrochemical interface. The sites of each reaction within such an interface are differently located so that a reaction plane proper to each reaction can be as-

signed. During the electrochemical reaction the different planes move at rates which depend on the characteristics of the reactions, whether they refer to a corrosion of the base metal, a monolayer formation, a thickening of the anodic film, or a proton transfer process occurring through the film. The reaction model, which proved useful for interpreting the above-mentioned reaction, may have a more general application. In this sense, it is interesting to test it through coupling the characteristics of both the nickel hydroxide electrode and the platinum/alkaline solution interface and further to attempt to elucidate some of the questions regarding the kinetics of the former process.

Recent studies on the nickel hydroxide electrode have shown that the overall electrochemical reaction

* Electrochemical Society Active Member.
Key words: metals, potential, voltammetry.

involves complications previously disregarded since both the reactants and the products that usually enter electrochemical reactions correspond to composite mixtures of different species (3, 4). These species generally expressed in terms of simple limiting stoichiometries, involve different structures with their own energetic characteristics which are revealed through the electrochemical response under complex potentiodynamic conditions (5). In spite of the fact that the potentiodynamic results furnish information on the possible reaction pathways some important questions referring to these reactions are still unsolved. One of them concerns either the influence or the interference of the metal side of the interface on the overall electrochemical processes including the aging process which takes place in the composite nickel hydroxide film.

To achieve a stabilized hydroxide electrode, such as the nickel hydroxide electrode on an apparently inert base metal, the physicochemical properties of colloid films associated with proton transfer reactions are of special interest. These films may exist on the metal substrate with a sufficiently firm mechanical adhesion and a high electrochemical activity. The experimental data derived through the formation of a multiple electrochemical interface after the use of complex potentiodynamic perturbations indicate the mutual influence of the various processes assigned both to the nickel hydroxide electrode potential range and to the potential range where the platinum metal is covered with either an oxygen or a hydrogen electroadsorbed monolayer. This is clearly envisaged through the straightforward comparison of the electrochemical behavior of the multiple interface and the electrochemical characteristics of the separate interfaces.

Experimental

The experimental arrangement including the electrolysis cell, solution preparation, and perturbation techniques are the same as those previously described in different publications (3-5). The working electrode, in the present case, was a platinum wire (Johnson-Matthey, spec-quality) of 0.4 mm diam and 0.22 cm² apparent area.

The following electrolyte solutions were employed: 0.01N KOH + 0.66N K₂SO₄ (blank solution) or blank solution with Ni(OH)₂ saturation. The solutions were prepared from analytical grade Merck reagents and thrice distilled water. The Ni(OH)₂ saturation was achieved using the following different procedures. (i) By addition of 10⁻³N NiSO₄ to the blank solution and separation of the saturated solution from the precipitate. (ii) By addition of the NiSO₄ solution as indicated in (i) without separation of the precipitate. (iii) By forming the Ni(OH)₂ on the electrode outside the cell by alternatively and repetitively immersing first in the blank solution and then in a 10⁻²N NiSO₄ solution. After the preparation stage the electrode was immersed on the cell containing freshly prepared, previously deoxygenated blank solution. The ionic strength was kept practically constant and close to one. The nickel ion concentration in these solutions was of the order of 10⁻⁸M, since for Ni(OH)₂ at 25°C, $K_s = 1.5 \times 10^{-16}$ (mole/liter)³ (6, 7).

Experiments were run under different potential sweeps at 0.03 V/sec $\leq v \leq$ 0.30 V/sec and 25°C under 1 atm pressure N₂ gas saturation. The electrode potentials in the text are referred to the SCE scale.

The base platinum metal was prepared by using the two following different cleaning procedures. (i) Mechanical polishing with a fine grade pure alumina powder suspension in water to produce a mirror surface followed by immersion in an HNO₃ + H₂SO₄ (1:1) mixture for 15 min. (ii) Immersion in the acid mixture as indicated in (i).

Electrodes differently cleaned were tested with the blank solution by running repetitive triangular po-

tential sweeps (RTPS) in the potential range of the hydrogen and oxygen electroadsorption, between the anodic ($E_{\lambda,a}$) and the cathodic ($E_{\lambda,c}$) switching potentials. Procedure (i) requires a time longer than procedure (ii) to attain the stable E/I display at 0.3 V/sec. Although both procedures finally gave the same results, the latter was preferentially used.

Results

Preliminary information was obtained by comparing the potentiodynamic RTPS E/I displays run in the $E_{\lambda,c} = -0.90$ V to $E_{\lambda,a} = +0.65$ V potential range, at 0.3 V/sec, with the blank solution (Fig. 1) and with the solution containing Ni(II) after a previous potentiostatic cathodization of the platinum electrode at potentials ranging from -0.9 to -1.2 V during a fixed period of time ($1 \text{ min} \leq t \leq 5 \text{ min}$). Thus, for the Ni(II) containing solution, after a 5 min cathodization at -1.2 V (Fig. 2) the RTPS potentiodynamic run in the -0.9 to $+0.2$ V range repeats the main features already known for the blank solution, namely, the positive going potential excursion involves the anodic current peaks IHA and IIHA related to the electrodesorption of hydrogen adatoms and the IOA, IIOA, and IIIOA which correspond to the oxygen electroadsorbed layer on platinum. During the negative going potential excursion the following cathodic current peaks are recorded: IOC, pertaining to the electrodesorption of the oxygen layer, and IIHC and IHC related to the electroadsorption of the hydrogen adatoms. The charge related to the current peaks IHA + IIHA is approximately equal to the charge involved in current peaks IHC + IIHC. Those charges are of the order of the charge of one monolayer of hydrogen adatoms, which for a smooth polycrystalline platinum surface is taken as 210 $\mu\text{C}/\text{cm}^2$ (8-10). The same charge balance extends also to the sum of current peaks IOA + IIOA + IIIOA which equals that of IOC. At potentials higher than 0.25V, however, the E/I displays are different. The presence of the nickel hydroxide species on the platinum electrode is reflected in the conjugated redox couple characterized by the current peaks INiA and INiC, which are recorded in the 0.30-0.65V range.

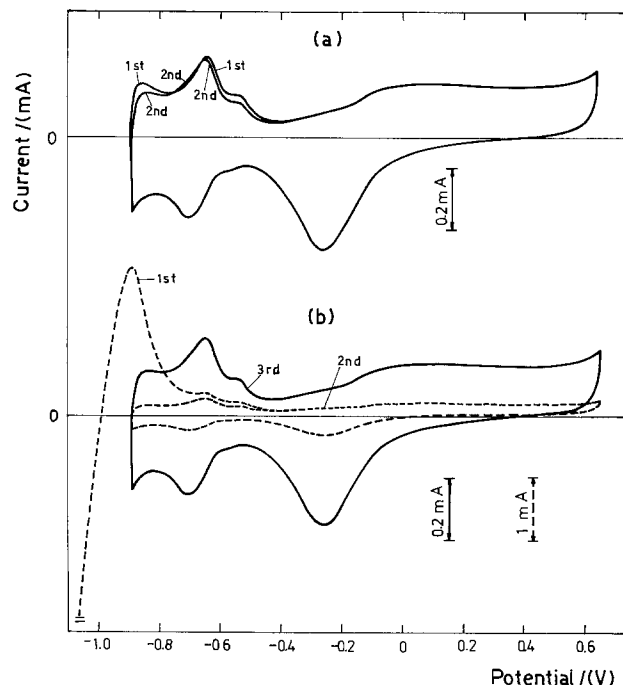


Fig. 1. Potentiodynamic E/I displays obtained under RTPS at 0.3 V/sec for platinum in the blank solution after a previous cathodization at different potentials. (a) 30 sec at -0.9 V; (b) 1 min at -1.1 V.

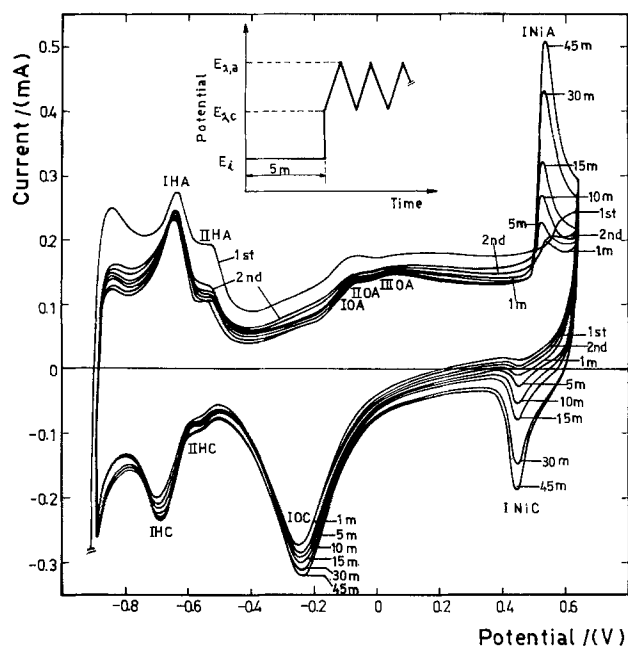


Fig. 2. Potentiodynamic displays run at 0.3 V/sec for platinum in the blank solution containing Ni(II) species after a previous cathodization at -1.2V during 5 min.

During the potential cycling obtained with a new electrolyte solution immediately after NiSO_4 additions the gradual change of the E/I profile is more noticeable in moving from the first to the second sweep, particularly in the positive going potential excursion. The latter exhibits a constant anodic current contribution throughout the whole potential range, but the currents of the redox couple related to the nickel hydroxide electrode are then more poorly defined. For the electrodes prepared according to either (i) or (ii), the potential of the anodic current peak is near 50 mV more positive than the peak potential in the stabilized E/I profile. The latter is recorded after about 60 min potential cycling and the corresponding charge, either anodic or cathodic, after the proper double layer charging and baseline corrections, is comparable to that of the hydrogen adatom current peaks. Within the -0.9 to $+0.4\text{V}$ range the E/I display reaches a stable situation much faster than the portion of the E/I display related to the nickel hydroxide electrode. But, although the charges of the hydrogen and oxygen electroadsorption regions remain unaltered during further potential cycling, the charge of the current peaks related to the nickel hydroxide electrode still increases to reach a constant value only after about 60 min.

When $0\text{V} \leq E_{\lambda,c} \leq 0.3\text{V}$, that is, $E_{\lambda,c}$ is more positive than the potential of the cathodic current peak IOC, the main effect produced in the E/I display is a slight shift of the anodic current peak potential INiA toward more positive value as $E_{\lambda,c}$ decreases (Fig. 3). Simultaneously, the cathodic current contribution of current peak IOC in the 0 to 0.3V range is appreciably reduced as $E_{\lambda,c}$ decreases. This corresponds to the potentiodynamic aging of the oxygen-containing monolayer on platinum already known (11).

The E/I profile of the nickel hydroxide redox couple is influenced by the anodic ($E_{\lambda,a}$) and cathodic ($E_{\lambda,c}$) switching potentials as depicted in Fig. 4. When $E_{\lambda,c}$ becomes more positive, within the potential range of current peak INiC, the positive going excursion exhibits the splitting of the anodic current peak INiA into two peaks. This behavior is the same as already described for the nickel hydroxide electrode on a nickel base which was attributed to the aging processes of the $\text{Ni}(\text{OH})_2$ species (4, 5). The stabilized E/I profile, particularly during the negative going

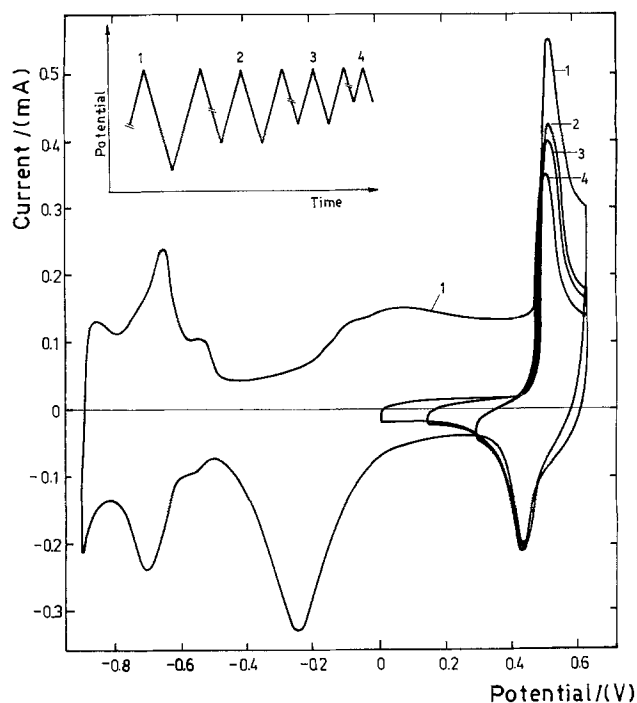


Fig. 3. Influence of the cathodic switching potential on the stabilized E/I profile at 0.3V/sec.

potential excursion, is slightly modified when $E_{\lambda,a}$ becomes more positive within the potential range exceeding that of the current peak INiA. The current peak INiC shifts toward more negative values as $E_{\lambda,a}$ increases. By further increasing $E_{\lambda,a}$ into the potential range of the oxygen evolution reaction one noticed that the latter reaction had no appreciable influence on the nickel hydroxide current peaks, with the ex-

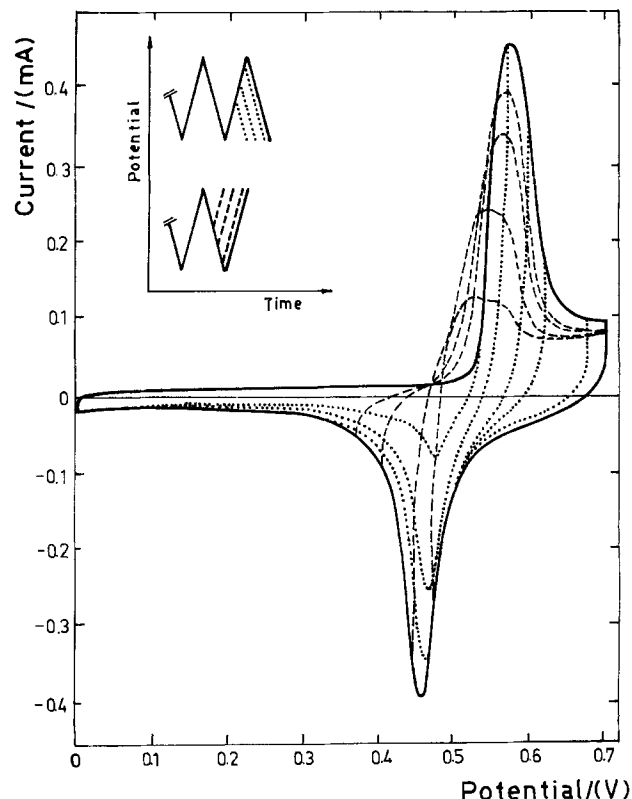


Fig. 4. Influence of the anodic and cathodic switching potentials on the E/I profile at 0.1 V/sec run with the platinum electrode in the potential range of the nickel hydroxide redox couple.

ception of changing the baseline cathodic current contribution predominantly in the potential region more negative than that of current peak INiC.

When platinum electrodes are left overnight in electrolyte solution in contact with the $\text{Ni}(\text{OH})_2$ precipitate the resulting E/I profiles show a poor electrochemical response associated with the nickel hydroxide redox couple. To decide whether the formation of the nickel hydroxide redox couple is due either to the deposition on the platinum surface of $\text{Ni}(\text{OH})_2$ out from the solution or to the $\text{Ni}(\text{OH})_2$ produced by the alkalization of the interface during cathodization in the presence of $\text{Ni}(\text{II})$ in solution, experiments were made with a freshly decanted $\text{Ni}(\text{OH})_2$ saturated solution and with a solution that had been decanted for three days. The E/I displays obtained with the fresh solution show only small current peaks while practically no current peaks are recorded with the latter. By adding to the fresh solution the previously separated $\text{Ni}(\text{OH})_2$ precipitate, small current peaks are observed but the charge corresponding to the nickel hydroxide electrode shows no further increase during the potential cycling. In contrast, after the addition of NiSO_4 solution to the electrolyte in the cell, the E/I profiles exhibit the features already described but without requiring the cathodization in the hydrogen evolution region.

The greatest charge contribution of the $\text{Ni}(\text{OH})_2$ redox couple is achieved when the NiSO_4 solution is added to the blank just in the vicinity of the electrochemical interface. Under these circumstances, if the $\text{Ni}(\text{OH})_2$ layer is now rapidly removed from the electrode and the latter is put back into the same solution without a further addition of NiSO_4 , the contribution of the nickel hydroxide current peaks are much lower than those previously observed. The first situation, however, can be reproduced by a further addition of NiSO_4 to the electrolyte. These experiments show, therefore, that the efficiency of the solution to produce $\text{Ni}(\text{OH})_2$ species on platinum, decreases relatively rapidly after the NiSO_4 addition. The precathodization of the interface seems to be less important than the nucleation and growth of the first $\text{Ni}(\text{OH})_2$ layer to accomplish the formation of the nickel electrode redox couple on the platinum electrode. To confirm those results the $\text{Ni}(\text{OH})_2$ film was prepared according to procedure (iii) (Fig. 5). The electrode was immersed for 15 min in the $\text{HNO}_3 + \text{H}_2\text{SO}_4$ mixture, then, washed in thrice distilled water, dipped for 5 min in the alkaline solution, and immediately afterward immersed in the NiSO_4 solution for another 5 min. Finally, the electrode was cathodized at -0.8V in the blank solution during 30 sec before running the RTPS between -0.8 and $+0.7\text{V}$. The first E/I display at 0.3 V/sec shows all the features already described, but the overall charge increases rapidly during the four first triangular potential sweeps. Later the rate of the charge increase diminishes to attain a stable charge after 5-10 min potential cycling. Further potential cycling produces net shifts of current peaks INiA, INiC, and IOC toward more positive values. The same effect is also observed on current peak IIHC and probably also on the baseline related to the oxygen evolution reaction. Furthermore, the longer the time of the potential cycling the larger the current peak INiA potential shift toward more positive potentials. If the INiA current peak involves the contribution of two current peaks whose separation is about 50 mV, then, initially the one at more negative potentials prevails while as the potential cycling continues the one at the more positive potential side becomes more important. The amount of charge playing a part in the nickel hydroxide electrode potential range attains a limiting value with the potential cycling as described above. The limiting charge slightly increases with the immersion time in the solutions involved in procedures (iii) (Fig. 6), but it increases dramatically with the

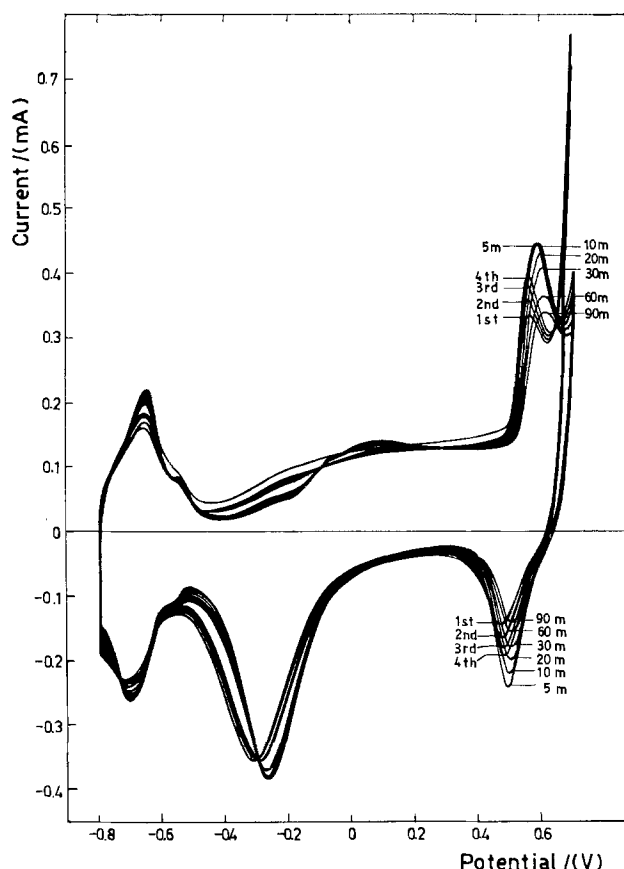


Fig. 5. Successive potentiodynamic E/I displays obtained under RTPS at 0.3 V/sec after a previous cathodization at -0.8V during 30 sec. The nickel hydroxide electrode was prepared by dipping the platinum electrode during 5 min in the blank solution and immediately afterward in the NiSO_4 solution for another 5 min.

number of the alternative immersions performed at a constant immersion time (Fig. 7). The charge increase is accompanied by shifts of the potentials of current peaks INiC and INiA. Although the potential shift of the INiC current peak follows no simple dependence on the number of immersions, that of peak INiA becomes more negative as the number of immersions increases. The charge increase of current peaks INiC and INiA has no appreciable influence on the rest of the potentiodynamic current peaks under the conditions depicted in Fig. 7.

The complexity of the E/I profile related to the nickel hydroxide electrode is also revealed by running stabilized RTPS potentiodynamic E/I profiles in the $0.3\text{--}0.7\text{V}$ range, at different potential sweep rates v (Fig. 8). The current peak heights, either INiA or INiC after correction for double layer charging and baseline effects, increase almost linearly with v . The charges involved are independent of v . The INiA current peak moves toward more positive values as v increases, but no definite shift is observed for current peak INiC. Nevertheless, the peak potential dependence on v is certainly more complex because of the composite characteristics of the potentiodynamic current peaks associated with the nickel hydroxide electrode (3-5).

The nickel hydroxide electrode prepared by any of the above described procedures remains active after having been removed from the electrolyte, washed with water, and again placed into the electrolysis cell.

Discussion

The potentiodynamic response of the platinum-nickel hydroxide-electrolyte multiple interface in the potential range of the electrochemical stability of water, reveals that there are three net potential ranges where

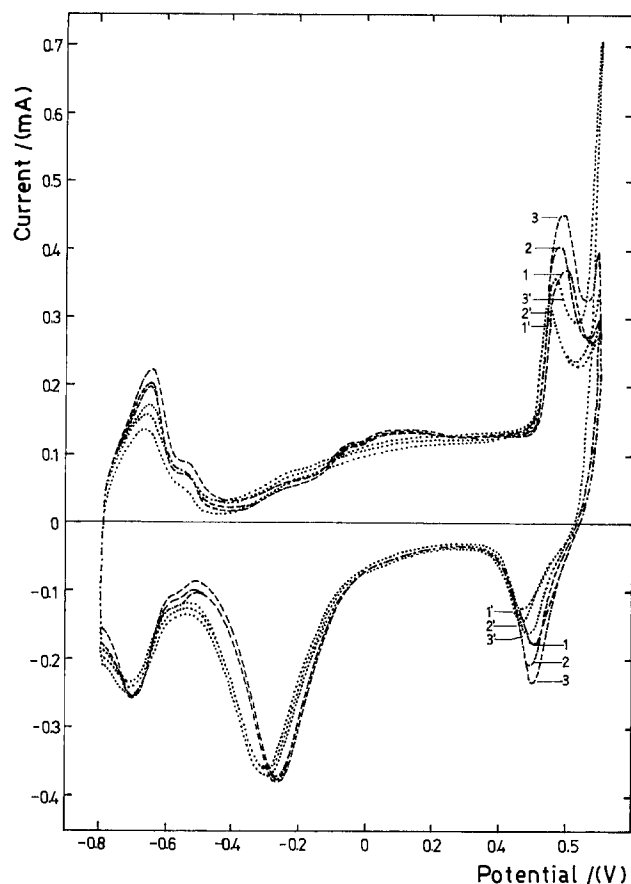


Fig. 6. Influence of the time (τ) spent during a single immersion of the platinum electrode in both the blank solution and the NiSO_4 solution on the potentiodynamic E/I displays run at 0.3 V/sec. The E/I displays 1, 2, and 3 are recorded during the second RTPS. The E/I displays 1', 2', and 3' are recorded after 5 min RTPS. $\tau = 10$ sec (1 and 1'). $\tau = 1$ min (2 and 2'). $\tau = 5$ min (3 and 3').

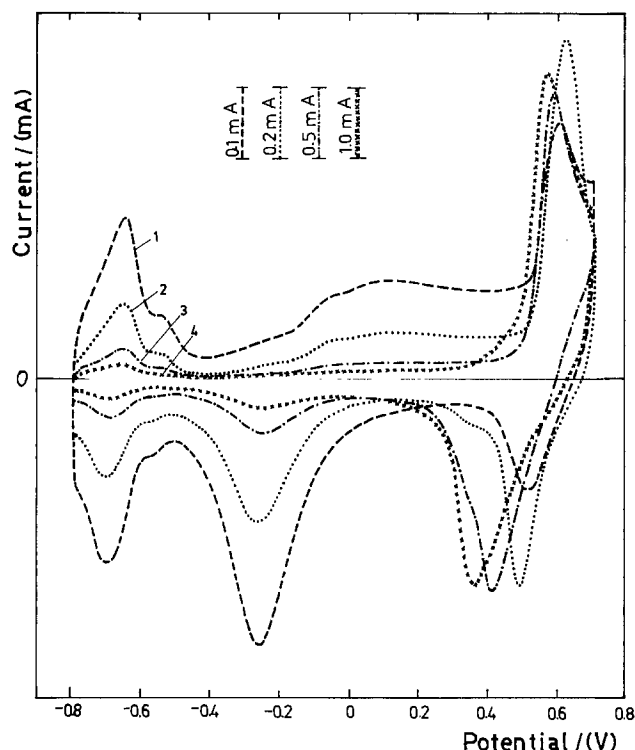


Fig. 7. Influence of the number of alternative immersions of the platinum electrode in the blank and in the NiSO_4 solution ($\tau = 10$ sec) on the potentiodynamic E/I displays run at 0.3 V/sec after 15 min RTPS. 1, 2, 3, and 4 correspond to a single, twice, ten times, and fifty times immersion in each solution, respectively.

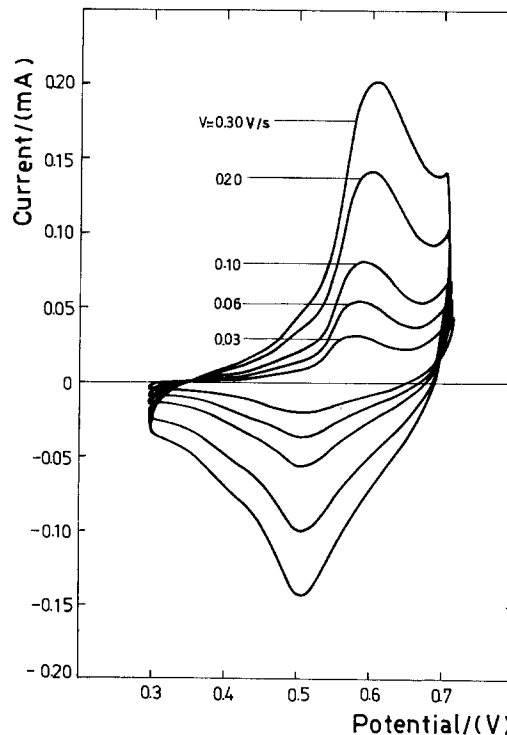
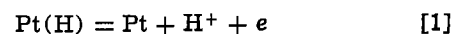


Fig. 8. Potentiodynamic E/I displays run with the stabilized nickel hydroxide electrode at different potential sweep rates.

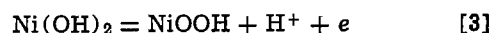
the following three conjugated electrode processes are successively taking place along with the progressive potential excursions. In the -0.8 to -0.5 V range



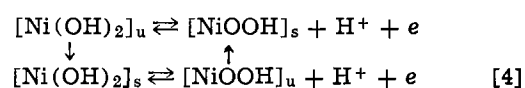
in the -0.5 to 0.2 V range



and in the potential range just preceding the electrochemical evolution of oxygen



Reactions [1] and [2] have been discussed in detail both in acid and alkaline electrolytes in numerous recent publications (11-19). They include, together with the proper electrochemical reactions, chemical and structural transformations of the various reactants and products participating in the overall reactions in both directions, which were described under the general term of aging processes. They exhibit time-dependent electrochemical spectra as expected for the gradual formation of species of more stable configuration on the electrode surface. Reaction [3] exhibits practically the same characteristics already described for the nickel hydroxide electrode on nickel, comprising the same type of splitting of the anodic and cathodic current peaks. Those splittings are assigned to the aging of both the Ni(OH)_2 and NiOOH species due to chemical transformations, so that at least two different Ni(OH)_2 species and two different NiOOH species participate in the electrochemical processes. The instantaneous ratio of the two species for both Ni(OH)_2 and NiOOH depends on the time elapsed since each species started to be either cathodically or anodically formed. This means that chemical transformations occur both under open-circuit conditions and also simultaneously with both electron transfer processes. So, the simplest reaction scheme can be put forward as follows



where u and s denote unstable and stable species, respectively. Reaction scheme [4], however, neglects the occurrence of crossed electrochemical reactions as recently reported under special perturbation conditions (20).

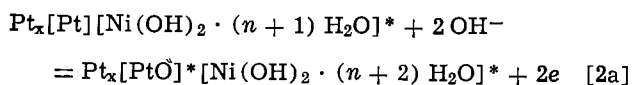
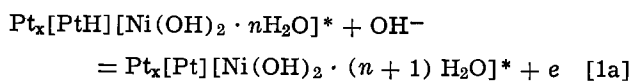
The present data, besides confirming recently reported results concerning reaction (4), are important for the interpretation of the nickel hydroxide conjugate reactions without the uncertainty of the changing roughness factor which occurs when the nickel hydroxide species are produced by corrosion of the nickel base metal. The roughness factor of the base platinum electrode is otherwise known either through the charge of the hydrogen adatoms monolayer or through the charge required to electrodesorb the oxygen layer formed on platinum, which for the switching potential limits of the present experiments, is exactly twice the charge of the former.

Two clearly different limiting cases can be distinguished depending on the overall charge involved in the potentiodynamic electroformation of the nickel hydroxide electrode. When the charge participating in the process is of the order of the hydrogen adatom monolayer the first potentiodynamic sweep depicts predominantly one anodic and one cathodic current peak associated with the conjugated nickel hydroxide reactions. The corresponding current peaks suggest then that the prevailing reaction is



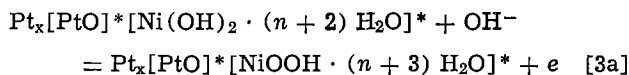
that is, the electrochemical reaction involves the more reactive $\text{Ni}(\text{OH})_2$ and NiOOH species. On the other hand, the transformation of the $[\text{Ni}(\text{OH})_2]_u$ species into the $[\text{Ni}(\text{OH})_2]_s$ species is facilitated when the charge involved in the nickel hydroxide electrochemical reaction gradually increases to exceed that of the hydrogen adatom monolayer. Hence, the present results demonstrate that under the conditions of a low surface coverage by the $\text{Ni}(\text{OH})_2$ species, the interpretation of the electrooxidation of $\text{Ni}(\text{OH})_2$ can be approached by the single electron transfer represented by reaction [5].

When the amount of nickel hydroxide exceeds several times the hydrogen adatom monolayer and the $\text{Ni}(\text{OH})_2$ species constitutes an actual phase, then its average composition depends on the type and time constants of the potential perturbation program applied to the interface. A comparison of the different E/I profiles during the successive potential cycling shows the increasing contribution of the reactions indicated in scheme [4]. In case (ii) the electron transfer reactions occurring in the multiple interface can be assigned to two different limiting reaction planes according to the model previously described (1). The plane related to the $\text{Pt}/\text{Ni}(\text{OH})_2$ (hydrated) interface is the site of reactions [1] and [2]. Another plane is ascribed to the $\text{Ni}(\text{OH})_2/\text{solution}$ interface. The proton (or OH^-) transfer process associated with reaction [3] occurs both through the latter plane and through the $[\text{Ni}(\text{OH})_2\text{-NiOOH}]$ layer located between the two limiting planes. For the latter reaction the oxidized platinum electrode surface acts mainly either as an electron source or an electron sink. Hence, the reactions taking place in the metal plane, when the positive going potential excursion starts from the hydrogen adatoms potential range up to the nickel hydroxide electrode potential range, can be put forward as follows

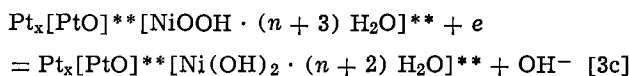


where n is the number of hydration water molecules in

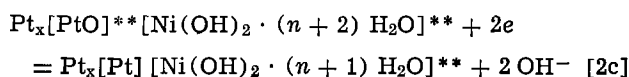
the nickel hydroxide layer and x refers to bulk platinum. At more positive potentials, in the nickel hydroxide layer



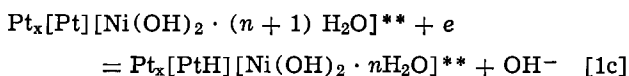
Analogously, during the negative going potential excursion within the same switching potential range, the complementary overall reactions can be written as follows. In the nickel hydroxide layer



and at the metal plane, at more negative potentials

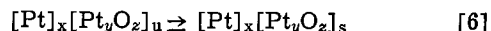


and



Reactions [1a]-[3a] and [3c]-[1c] also involve the corresponding OH^- ion transfer processes from the solution side of the interface to the multiple interface or the reverse, respectively. The brackets indicate the two different reaction regions, namely, the metal surface and the nickel hydroxide film. The single and double asterisks denote that the average energetic configuration of reactants and products, either in the anodic or the cathodic reactions, are different because of the aging processes.

The formation of the nickel hydroxide electrode on platinum produces a simultaneous decrease of the aging effect of the PtO species. This means that the PtO monolayer aging is coupled to some extent to the nickel hydroxide electrode reactions through a pseudostabilization of the PtO transient species with either the $\text{Ni}(\text{OH})_2$ or the NiOOH species on the electrode surface. The stabilization can be assisted through a structural unit such as either a $[\text{PtO} + \text{Ni}(\text{OH})_2]$ or a $[\text{PtO} + \text{NiOOH}]$ surface complex unit. These structures involve the innermost layer of the $[\text{Ni}(\text{OH})_2 + \text{NiOOH}]$ film which is just in contact with the PtO surface. According to recent results, the PtO aging is principally related to a surface reaccommodation process (11) formally written as



where x refers to the bulk metal and $z \leq y$ and $z \geq y$ when the monolayer is formed. Therefore, through a binding between $[\text{Pt}_y\text{O}_z]_u$ with either the $[\text{Ni}(\text{OH})_2]$ or the $[\text{NiOOH}]$ species different surface structures are achieved. Hence, the place exchange mechanism according to reaction [6] is partially impeded by the adsorption of either the $[\text{Ni}(\text{OH})_2]$ or the $[\text{NiOOH}]$ species on the Pt(O) surface. The stabilization of the surface species can be accounted for, at least in part, through the participation of hydrogen bonding.

The fact that the nickel hydroxide electrode on platinum is formed without requiring a simultaneous cathodization before running the potentiodynamic experiments and that the solution where $\text{Ni}(\text{OH})_2$ precipitates loses its property of generating the electrochemically active redox couple deserves a further comment in terms of the chemistry of the colloidal system involved. Those systems are unstable in the thermodynamic sense causing the accustoming of colloidal system (21), the coarsening or ripening of precipitates (22), as well as other aging effects (23, 24). All these effects are strongly dependent on the solution composition, pH, time of aging, nature of anions present and other topological transformation, and preparation conditions. Unfortunately, despite numerous investigations

little is still known about the mechanism of metal hydroxide and oxide precipitation. (23).

However, under the conditions prevailing during the Ni(OH)₂ precipitation on platinum one should recognize that most of those variables are also involved. Thus, it seems that the largest efficiency of the nickel hydroxide electrode, as measured through the charge involved in the *E/I* profile, is attained when the Ni(OH)₂ precipitation occurs from fresh solutions and as close as possible to the electrode surface. If the nucleation of the precipitate can occur either on the metal surface or in the bulk of the solution, the former situation is largely favored in the conditions where the greatest efficiency has been attained. The coarsening and aging of the precipitate adversely influence the yielding of the nickel hydroxide electrode formation. Therefore, besides the study of the proper electrode processes, the present results offer the possibility of establishing promising relations between the multiple interface electrode systems and the physicochemical characteristics of colloidal systems.

Acknowledgment

INIFTA is sponsored by the Consejo Nacional de Investigaciones Científicas y Técnicas, the Universidad Nacional de La Plata and the Comisión de Investigaciones Científicas (Provincia de Buenos Aires). This work was partially supported by the SENID (Navy Research and Development Service of Argentina) and the Regional Program for the Scientific and Technological Development of the Organization of the American States.

Manuscript submitted May 16, 1979; revised manuscript received ca. July 15, 1980.

Any discussion of this paper will appear in a Discussion Section to be published in the June 1981 JOURNAL. All discussions for the June 1981 Discussion Section should be submitted by Feb. 1, 1981.

Publication costs of this article were assisted by the Instituto de Investigaciones Fisicoquímicas Teóricas y Aplicadas.

REFERENCES

1. J. O. Zerbino, N. R. de Tacconi, and A. J. Arvia, *This Journal*, **125**, 1266 (1978).
2. J. O. Zerbino and A. J. Arvia, *ibid.*, **126**, 93 (1979).
3. J. R. Vilche and A. J. Arvia, in Proceedings of IVth International Symposium on Passivity, Arlie, Va. (1977).
4. R. S. Schrebler Guzmán, J. R. Vilche, and A. J. Arvia, *J. Appl. Electrochem.*, **8**, 67 (1978).
5. R. S. Schrebler Guzmán, J. R. Vilche, and A. J. Arvia, *This Journal*, **125**, 1578 (1978).
6. M. Pourbaix, in "Atlas of Electrochemical Equilibria," Pergamon Press, Oxford (1966).
7. W. Fischer, *Electrochim. Acta*, **21**, 1001 (1976).
8. S. Gilman, in "Electroanalytical Chemistry," Vol. 2, A. J. Bard, Editor, p. 111, Marcel Dekker, New York (1967).
9. T. Biegler, D. A. J. Rand, and R. Woods, *J. Electroanal. Chem. Interfacial Electrochem.*, **29**, 269 (1971).
10. A. T. Hubbard, R. M. Ishikawa, and J. Katekaru, *ibid.*, **86**, 271 (1978).
11. M. E. Folquer, J. O. Zerbino, N. R. de Tacconi, and A. J. Arvia, *This Journal*, **126**, 592 (1978).
12. K. Kinoshita, J. Lundquist, and P. Stonehart, *J. Catal.*, **31**, 325 (1973).
13. H. Angerstein-Kozłowska, B. E. Conway, and W. B. A. Sharp, *J. Electroanal. Chem. Interfacial Electrochem.*, **43**, 9 (1973).
14. H. Angerstein-Kozłowska, W. B. A. Sharp, and B. E. Conway, in "Electrocatalysis," M. W. Breiter, Editor, p. 94, The Electrochemical Society Softbound Proceedings Series, Princeton, N.J. (1974).
15. R. Woods, in "Electroanalytical Chemistry," Vol. 9, A. J. Bard, Editor, Arnold Press, London (1977).
16. V. I. Luk'yanycheva, A. V. Yuzhanina, M. R. Tarasevich, N. A. Shumilova, and V. S. Bagotskii, *Elektrokhimiya*, **13**, 506 (1977).
17. E. Yeager, W. E. O'Grady, M. Y. C. Woo, and P. Hagans, *This Journal*, **125**, 348 (1978).
18. S. Shibata, *J. Electroanal. Chem. Interfacial Electrochem.*, **89**, 37 (1978).
19. M. E. Folquer, N. R. de Tacconi, J. R. Vilche, and A. J. Arvia, *This Journal*, **126**, 257 (1979).
20. R. S. Schrebler Guzmán, J. R. Vilche, and A. J. Arvia, *J. Appl. Electrochem. Interfacial Electrochem.*, **9**, 183 (1979).
21. S. Voyutsky, "Colloid Chemistry," Chap. 9, MIR Publishers, Moscow (1978).
22. M. Kahlweit, *Adv. Colloid Interface Sci.*, **5**, 1 (1975).
23. E. Matijević and P. Scheiner, *J. Colloid Interface Sci.*, **63**, 509 (1978).
24. E. Matijević, in "Trends in Electrochemistry," J. O'M. Bockris, D. A. J. Rand, and B. J. Welch, Editors, p. 177, Plenum Press, New York (1977).

Some Electrochemical Properties of Strong Organic Acids for Use as Fuel Cell Electrolytes: Methane Sulfonic, Methane Di-sulfonic, Trichloroacetic, Chloro-Difluoroacetic, Pentafluoropropanoic, Benzoic, and Benzene Sulfonic Acids

N. Rebert, B. G. Ateya,¹ T. Poweigha, and L. G. Austin

Department of Materials Science and Engineering,
The Pennsylvania State University, University Park, Pennsylvania 16802

ABSTRACT

Several organic acids have been evaluated as possible electrolytes for the oxidation of hydrogen. The tests performed included electrical resistivity and vapor pressure measurements at various temperatures. Current-potential relations were obtained at both platinized-platinum rotating disk electrodes and Teflon-bonded, platinum-black gas diffusion electrodes. Most of the acids underwent chemical or electrochemical breakdown. Out of the electrolytes tested, the only one holding any promise as a fuel cell electrolyte is methane sulfonic acid. As a result of this work certain classes of compounds should be ruled out as candidates, *e.g.*, halogenated fatty acids and certain aromatic acids, *e.g.*, benzoic and benzene sulfonic acids.

This paper presents the results of a search for organic electrolytes which perform better than phosphoric acid as an electrolyte in fuel cells using H₂ or H₂-CO mixtures. There are several obvious requirements for the "ideal" electrolyte (1) as follows: (i) availability of suitable ions for fuel oxidation at the anode and oxygen reduction at the cathode, (ii) high ionic conductivity, (iii) good solvent, that is, high values of solubility-diffusivity products for fuel and oxidant, (iv) chemically inert toward fuel, oxidant, and reaction products (CO₂ and water), (v) stability over the voltage ranges involved, (vi) since water must be removed from the cell, the electrolyte must have a low vapor pressure (high boiling point) to avoid a complicated condensing-separation system, (vii) negligible absorbability on, and poisoning of, the electrode materials, and (viii) noncorrosive toward cell and electrode materials.

With the above requirements in mind, we performed a literature search which suggested a number of classes of organic acids as possible electrolytes on the basis of their melting and boiling points. Table I shows the properties of seven acids selected for study.

The tests performed include ionic conductivity and vapor pressure as a function of temperature and electrochemical performance with H₂ or H₂-3% CO as reactant. Two types of electrochemical tests were performed. Use of a gas diffusion electrode with the electrolyte gives a directly relevant measure of fuel performance. Tests with a rotating disk electrode in electrolyte saturated with H₂ indicate whether the reaction rate is controlled by mass transfer or by electron transfer kinetics.

Experimental Techniques

The resistivity of the various electrolytes was measured at various temperatures using a microconductivity cell (3403 Yellow Springs Company, cell constant = 1 cm⁻¹) and a digital conductivity bridge (Barnsted PM-70CB). The temperature was adjusted using an oil bath. The isoteniscope technique (2) was

chosen for measuring the saturated vapor pressure of the liquid.

The rotating disk electrode (RDE) assembly is shown in Fig. 1. The electrode was a disk of platinum force-fitted into the Teflon head. Best results were obtained with the disk lightly platinized. Double layer capacity measurements in 85% H₃PO₄ at 135°C in the range of 250-450 mV *vs.* a dynamic hydrogen electrode

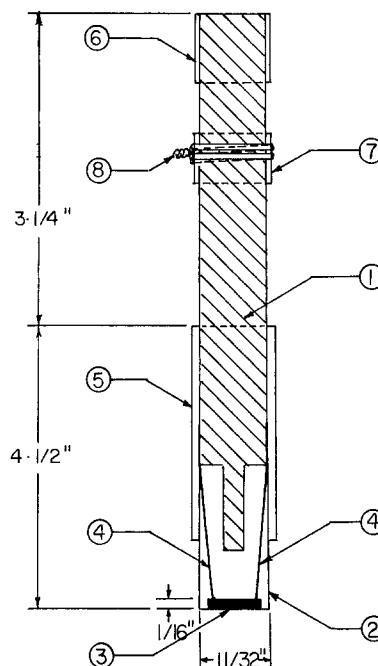


Fig. 1. Schematic of the rotating disk electrode. 1, Stainless steel rod; 2, Teflon head; 3, platinized Pt disk electrode force-fitted into the Teflon head; 4, Pt wires through the Teflon head; 5, heat shrinkable Teflon tubing; 6, electrical insulation to isolate the steel rod from motor chuck; 7, Cu tubing force-fitted on the stainless steel rod; and 8, Cu braid wound twice around the Cu tubing for electrical contact to the electrode.

¹ Present address: Chemistry Department, Faculty of Science, Cairo University, Cairo, Egypt.

Key words: resistivity, polarization, gas.

Table I. Melting and boiling points of selected electrolytes

Electrolyte	Formula	MP (°C)	BP (°C)	Manufacturer
Benzene sulfonic acid-hydrate	C ₆ H ₅ SO ₃ H · 1.5H ₂ O	45-46	—	Eastman Kodak
Methane disulfonic acid	CH ₃ (SO ₃ H) ₂	—	220	Eastman Kodak
Trichloroacetic acid	CCl ₃ CO ₂ H	54-58	196	Aldrich
Pentafluoropropanoic acid	C ₂ F ₅ CO ₂ H	—	96	ICN Pharmaceutical Incorporated
Chlorodifluoroacetic acid	ClCF ₂ CO ₂ H	24-26	122	Aldrich
Benzoic acid	C ₆ H ₅ CO ₂ H	118	249	Baker
Methane sulfonic acid	CH ₃ SO ₃ H	20	—	Eastman Kodak

(3) gave a capacity of $6.7 \times 10^3 \mu\text{F}/\text{cm}^2$, suggesting a surface roughness of about 270 (using $25 \mu\text{F}/\text{cm}^2$ for bright platinum). Rotation speed was measured with a phototachometer. The cell used with the gas diffusion electrode and the RDE (Fig. 2) was designed to meet the requirements: (i) small total volume (~ 15 ml) in view of the cost and availability of some of the electrolytes, (ii) separate compartments for the reference, working and auxiliary electrodes to prevent contamination of the electrolyte in the working electrode compartment with products of the reactions taking place in the other compartments, (iii) compatibility with an RDE assembly, with sufficient depth of electrolyte to avoid nonideal circulation of liquid to the rotating surface, (iv) ensurance of continuous saturation of the electrolyte with the fuel gas. The cell incorporated a dynamic hydrogen reference electrode (3) which is maintained at a small steady potential by passing a cathodic hydrogen evolution current of 1 mA cm^{-2} provided by an auxiliary circuit.

The designs of the porous gas-diffusion electrode and its holder were those described by Almaula and Austin for sulfuric acid (4). The electrode holder was made of two Teflon parts. The bottom part exposes one side of the electrode to the electrolyte and the other to the reactant gas. The top part has two concentric glass tubes through its length; the inner is the inlet of the gas (which is kept slightly above atmospheric pressure) and the outer is the outlet of the unreacted gas. The porous gas diffusion electrodes were made by pressing an homogenous paste of Pt-black and Teflon dispersion (du Pont 30) into a disk in a steel die to 18,000 psi for 2 min. It was dried at 50°C

for 1 hr, taken to 350°C over 5 min, and sintered for 2 min at 350°C . Electrodes prepared with a platinum screen were found to crack when heated in concentrated phosphoric acid at 135°C and gave irreproducible IR corrections. This has been attributed to the recrystallization of the Pt-black on the Pt screen (5, 6). More stable electrodes were obtained by pressing the Pt-black and Teflon paste onto a tantalum screen (45 U.S. mesh) (6).

Current densities at a desired potential between test and reference electrodes were measured with a Wenking or an Aardvark potentiostat. Corrections were made for the IR drop in the electrolyte path between the Luggin tip and the test electrode face by using the blanked-out portion of an oscilloscope trace after current interruption. The oscilloscope was connected to measure the test-reference potential at a steady current and the current interrupted with a rapid switching circuit which also triggered the trace.

Due to experimental difficulties encountered with obtaining reproducible results from phosphoric acid, and the differences in the properties of various electrodes, a comparison technique was used. Before each electrolyte was run at the desired temperature on a certain electrode, the electrode was tested with H_2 fuel in $1N \text{ H}_2\text{SO}_4$ at 25°C . This system gives well-defined limiting currents for Teflon-bonded electrodes which are not flooded (4). The ratio of the limiting current obtained in the particular electrolyte at a certain temperature to that obtained in sulfuric acid at 25°C was taken as a measure of the efficiency of the electrolyte. This ratio was found to be about 1.6 for $85\% \text{ H}_3\text{PO}_4$ at 135°C . Table II lists the properties of the various electrodes used in this work. Figure 3 shows the current-potential relations obtained in $1N \text{ H}_2\text{SO}_4$ at 25°C and in $85\% \text{ H}_3\text{PO}_4$ at 135°C using H_2 gas as fuel at the same electrode. The limiting current was taken to be the current at 500 mV vs. DHE .

Fuel gas was supplied to the cell through a train consisting of columns of Ridox (oxygen scavenger, Fisher Scientific), KOH, and Drierite. The phosphoric acid was purified using the H_2O_2 treatment recommended by Appleby (7), and the organic electrolytes were used as supplied.

Results and Discussion

Figure 4 shows the plots of log conductivity vs. $1/T$ for the electrolytes tested. Measurements were performed in both the ascending and descending direc-

Table II. Properties of the porous Teflon-bonded platinum black gas diffusion electrodes used in electrochemical measurements on H_2 oxidation

Code No.	Thickness (cm)	Porosity (calculated)	Pt loading (mg Pt black/cm ²)	i_L in $1N \text{ H}_2\text{SO}_4$ (mA/cm ² at 25°C)
E1*	0.050	0.47	130	310
E2	0.062	0.50	167	200
E3	0.029	0.21	249	950
E4	0.023	0.39	22	284
E5	0.036	0.40	102	167
E6	0.029	0.34	71	110
E7	0.030	0.35	74	49

* $i_L = 490 \text{ mA}/\text{cm}^2$ in $85\% \text{ H}_3\text{PO}_4$ at 135°C .

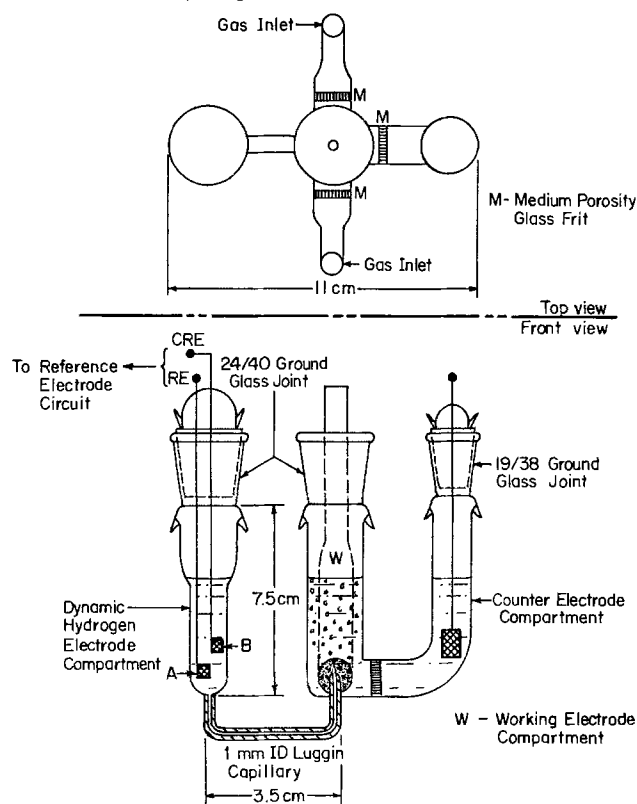


Fig. 2. Schematic of electrochemical cell

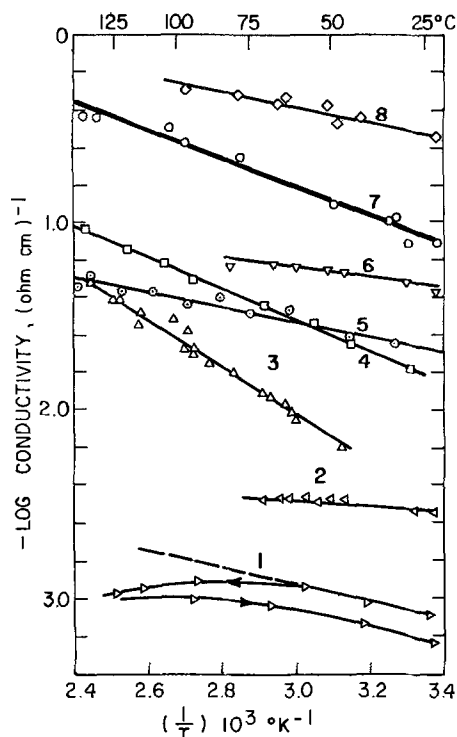


Fig. 3. Plot of log (conductivity of electrolyte) vs. reciprocal of absolute temperature. Curve 1, $\text{CCl}_3\text{CO}_2\text{H}$ (90 w/o); curve 2, $\text{C}_2\text{F}_5\text{CO}_2\text{H}\cdot\text{H}_2\text{O}$; curve 3, $\text{C}_6\text{H}_5\text{SO}_3\text{H}\cdot 1.5 \text{H}_2\text{O}$; curve 4, $\text{CF}_3\text{SO}_3\text{H}\cdot\text{H}_2\text{O}$; curve 5, $\text{CH}_3\text{SO}_3\text{H}$; curve 6, $\text{CCl}_3\text{CO}_2\text{H}$ (70 w/o); curve 7, 85 w/o H_3PO_4 ; and curve 8, $\text{CH}_2(\text{SO}_3\text{H})_2$ (50 w/o).

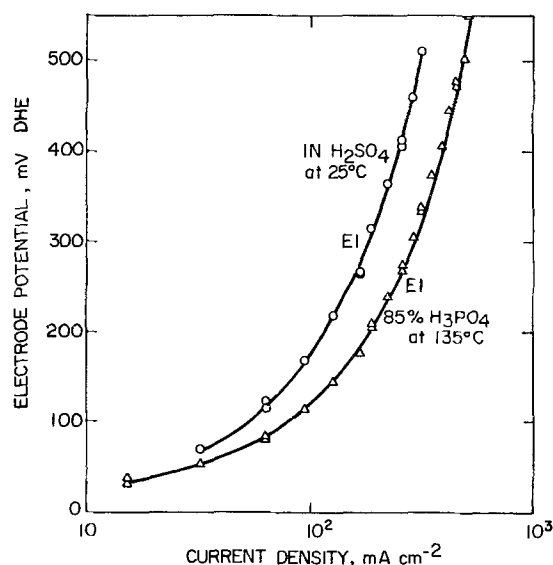


Fig. 4. Comparison of the current-voltage curves for H_2 oxidation at a Teflon-bonded gas-diffusion electrode in both 85% H_3PO_4 at 135°C and 1N H_2SO_4 at 25°C for the same electrode. The electrode porosity was 0.47 and catalyst loading was 133 mg Pt black cm^{-2} .

tions with respect to temperature. No significant hysteresis was observed except when significant amounts of water existed in the electrolyte and only when measurements were taken at high temperatures as, for example, with the 90% aqueous solution of $\text{CCl}_3\text{CO}_2\text{H}$. The straight lines shown are least squares correlations of the data. The results on the 85% H_3PO_4 agree well with the literature values (8). Table III lists the straight line equation, the correlation coefficient, and the temperature range over which the measurements were taken. In the case of the 90% aqueous solution

Table III. Least squares correlations of the data of log (conductivity) vs. reciprocal of absolute temperature for the electrolytes tested. The concentrations are in weight percent in an aqueous solution.

Compound	Conductivity equation (κ , $\Omega^{-1} \text{cm}^{-1}$)	Correlation coefficient	Temperature range ($^\circ\text{C}$)
$\text{C}_6\text{H}_5\text{SO}_3\text{H}$	$\log \kappa = 1.82 - 1.28 \times 10^3/T$	0.98	48-136
$\text{CH}_2(\text{SO}_3\text{H})_2$ (50%)	$\log \kappa = 0.68 - 0.351 \times 10^3/T$	0.95	23-97
$\text{CCl}_3\text{CO}_2\text{H}$ (70%)	$\log \kappa = 0.48 - 0.253 \times 10^3/T$	0.84	23-81
$\text{CCl}_3\text{CO}_2\text{H}$ (90%)	$\log \kappa = 1.57 - 0.453 \times 10^3/T$	0.98	24-126
$\text{C}_2\text{F}_5\text{CO}_2\text{H}$ (90%)	$\log \kappa = -1.97 - 0.165 \times 10^3/T$	0.81	24-71
$\text{CH}_3\text{SO}_3\text{H}$	$\log \kappa = -0.39 - 0.388 \times 10^3/T$	0.95	30-135
$\text{CF}_3\text{SO}_3\text{H}\cdot\text{H}_2\text{O}$	$\log \kappa = 1.00 - 0.835 \times 10^3/T$	1.00	29-138
H_3PO_4 (85%)	$\log \kappa = 1.28 - 0.702 \times 10^3/T$	0.95	23-138

of $\text{CCl}_3\text{CO}_2\text{H}$, hysteresis occurred due to loss of water, and the correlation is based on the low temperature results. It was concluded that methane disulfonic acid was the only electrolyte tested which had sufficient conductivity to compare with phosphoric acid.

The system for vapor pressure measurement was tested using benzoic acid, giving the result shown by curve 1 in Fig. 5. Although there is some scatter in the data points, the overall results agree with the accepted literature values, and the apparatus is considered adequate for the purpose of the present study.

Figure 5 also shows plots for benzene sulfonic acid, both 10% aqueous solution and anhydrous pentafluoropropanoic acid, and trichloroacetic acid. The results satisfactorily fit straight lines over the studied range of temperatures. Table IV summarizes the results.

Background Currents

Methane sulfonic acid gave the lowest background current of all the tested electrolytes (about 6% of the measured current at the limiting current at various temperatures for both the gas diffusion and the rotating disk electrodes). The corresponding percentages for the other electrolytes are: pentafluoropropanoic acid, 3% at low potentials increasing to 60% at the limiting current; chlorodifluoroacetic acid, 10% of the measured current at all potentials for both 23° and 50°C ; benzene sulfonic acid hydrate, 20% at 60°C ; methane disulfonic acid, less than 10%. All the acids tested (except one) gave anodic background currents. Trichloroacetic acid was the only acid which gave a

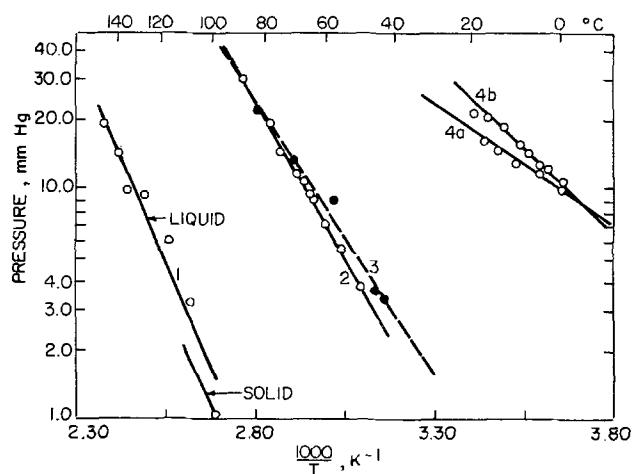


Fig. 5. Variation of the vapor pressure with the reciprocal of absolute temperature for: curve 1, benzoic acid (standard); curve 2, benzene sulfonic acid hydrate; curve 3, trichloroacetic acid (anhydrous); curve 4a, pentafluoropropanoic acid (90 w/o aqueous solution); and curve 4b, pentafluoropropanoic acid (anhydrous).

Table IV. Summary of vapor pressure results. The heat of vaporization ΔH_{vap} and the boiling point T_b were calculated using $\log(P/P_0) = -\Delta H_{\text{vap}}/2.303RT(1/T - 1/T_b)$, where $T = T_b$ at $P_0 = 760$ mm-Hg.

Electrolyte	BP ($^{\circ}\text{C}$), T_b		ΔH_{vap} (kcal/mole)		Vapor pressure at 135 $^{\circ}\text{C}$ (mm Hg)
	Expt.	Lit. (9)	Expt.	Lit. (9)	
Benzoic acid	246	249	16.3	16.29	10.3
Benzenesulfonic acid-hydrate	174	(d, 100)	12.4	—	209.0
Pentafluoropropanoic acid, 90 w/o	253	—	4.9	—	194.7
Pentafluoropropanoic acid anhydrous	132	96	7.2	—	(815.6)
Trichloroacetic acid	185	196	10.9	13.8	173.6

cathodic background current up to 500 mV DHE, increasing in magnitude with decreasing anodic potential.

The experimental results obtained on the various electrolytes are presented below, along with the relevant experimental observations. All the electrolytes were tested with H_2 and some were also tested with H_2 -3% CO to see whether CO poisoned the electrode. The results are as follows.

Pentafluoropropanoic acid (90 weight percent aqueous).—The ratio of limiting currents was less than 10^{-3} . The resistivity of this solution at 25 $^{\circ}\text{C}$ is 335 Ω cm. The electrolyte underwent polymerization on heating to 50 $^{\circ}\text{C}$. This electrolyte also had an undesirably high vapor pressure (see Fig. 5).

Trichloroacetic acid.—This electrolyte had to be diluted with water to give reasonable resistivity. The measured resistivities were 1240 and 23 Ω cm at 25 $^{\circ}\text{C}$ for the 90% and 70 weight percent (w/o) aqueous solutions, respectively. Figure 6 shows the current-potential relations obtained on the 70% acid solution at 25 $^{\circ}\text{C}$. The ratio of limiting currents is 0.22. It was noticed that chlorine gas evolved on heating this electrolyte. The acid itself (without dilution) also has an excessively high vapor pressure (see Fig. 5) and it is known to be hygroscopic.

Chlorodifluoroacetic acid.—Measurements were performed on this acid at 23 $^{\circ}$ and 50 $^{\circ}\text{C}$, see Fig. 6. The ratio of limiting currents was less than 10^{-3} . The decomposition of the acid leading to production of chlorine was also evident. The resistivities were 168 and 140 Ω cm at 23 $^{\circ}$ and 50 $^{\circ}\text{C}$, respectively.

Benzene sulfonic acid hydrate.—At 60 $^{\circ}\text{C}$ the limiting current ratio is 0.06, see Fig. 6. The acid resistivity was 108 Ω cm at 60 $^{\circ}\text{C}$ and the vapor pressure is fairly high. The acid decomposed, turning from the light brown color into a black color, on heating to higher temperatures in presence of the Pt-black electrode.

Methane disulfonic acid (50% aqueous).—Figure 7 shows the results obtained in this acid at two different

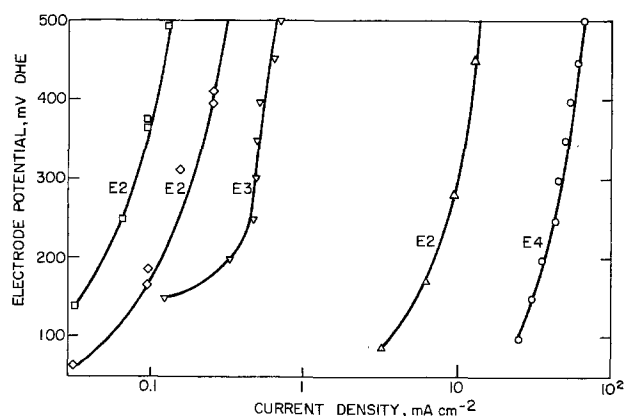


Fig. 6. Current-potential relations for H_2 oxidation at a platinum black, Teflon-bonded gas diffusion electrode in: E_2 chlorodifluoroacetic acid; at 23 $^{\circ}$ and 50 $^{\circ}\text{C}$, respectively; E_3 pentafluoropropanoic acid (90 w/o aqueous) at 26 $^{\circ}\text{C}$; E_2 benzene sulfonic acid hydrate at 60 $^{\circ}\text{C}$; and E_4 trichloroacetic acid (70 w/o aqueous) at 27 $^{\circ}\text{C}$ (see Table II).

temperatures for H_2 fuel. The limiting current ratios were 0.33 and 0.47 at 27 $^{\circ}$ and 54 $^{\circ}\text{C}$, respectively. The electrical resistivities were quite low; 3 and 2.5 Ω cm at 27 $^{\circ}$ and 54 $^{\circ}\text{C}$, respectively. Measurement at 80 $^{\circ}\text{C}$ gave irreproducible results due to the excessive loss of water. The nonaqueous acid is a very hygroscopic material which boils at 220 $^{\circ}\text{C}$. The only commercially available form is the 50% aqueous solution.

Benzoic acid.—Although this acid has a reasonable vapor pressure, it was ruled out because of its extremely high electrical resistivity; the values obtained were 2.1×10^7 , 2.0×10^7 , and 1.9×10^7 Ω cm at 135 $^{\circ}$, 141 $^{\circ}$, and 153 $^{\circ}\text{C}$, respectively. The acid is also insoluble in water.

Methane sulfonic acid.—This electrolyte was chosen on the basis of its low vapor pressure, 10 mm Hg at 167 $^{\circ}\text{C}$ (9), and relatively low resistivity of 66 Ω cm at 135 $^{\circ}\text{C}$. It is also available in reagent (>98%) and practical (>95%) grades, the latter being much cheaper than the former. Figure 8 shows the results obtained on the practical grade acid for the oxidation of both H_2 and H_2 -3% CO fuels at 50 $^{\circ}$, 90 $^{\circ}$, 135 $^{\circ}$, and 145 $^{\circ}\text{C}$. The limiting current ratios for H_2 oxidation are 0.14, 0.09, 0.55, and 3.7, respectively. Similar results were obtained with H_2 -3% CO, but the presence of CO poisoned the electrode surface and caused continuous decrease in the current. The results on H_2 -3% CO were obtained by allowing the electrode to rest at open circuit between each current and potential reading; the current was recorded before the start of the excessive drift.

There were several reasons for also using the rotating disk electrode technique in this work: (i) it clearly distinguishes between chemical and mass transfer-limited reactions and (ii) it provides for well-defined and reproducible hydrodynamic conditions at the electrode surface regardless of the electrolyte or the fuel gas used. For mass-transport limited reactions,

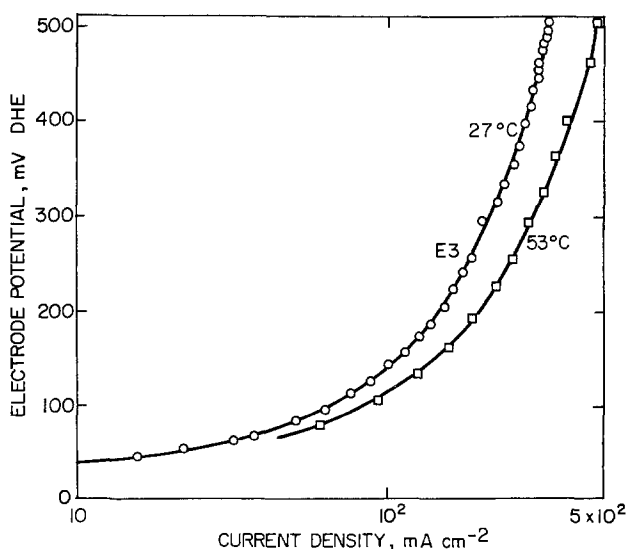


Fig. 7. Current-potential relations for H_2 oxidation at a gas diffusion electrode in methane disulfonic acid (50 w/o aqueous) at 27 $^{\circ}$ and 53 $^{\circ}\text{C}$; i_L (1N H_2SO_4) is 950 mA cm^{-2} .

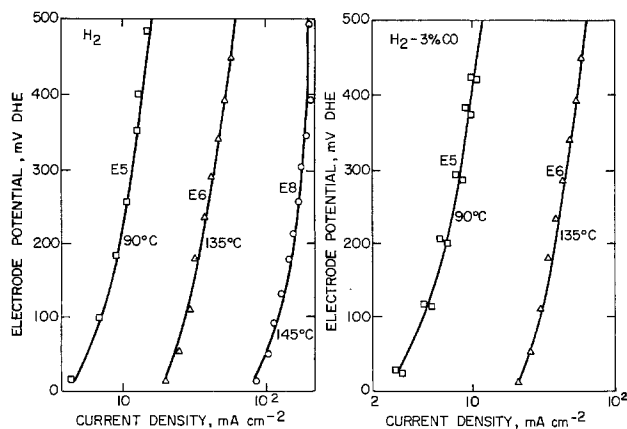


Fig. 8. Current-potential relations for the oxidation of H_2 and H_2 -CO in methane sulfonic acid at a gas diffusion electrode at 90° and 135°C, curves 1 and 2, respectively. Curves 1 are to be compared with an i_L (1N H_2SO_4) of 167 $mA\ cm^{-2}$.

it is possible to estimate the solubility-diffusivity product of the fuel gas in the particular electrolyte, using the Levich equation (10) and independent measurements of solubility and kinematic viscosity

$$i_L = 0.62 nFD^{2/3}\omega^{1/2}\nu^{-1/6}C$$

where i_L is the mass-transfer limiting current density, n is the number of electrons transferred per molecule, F is the Faraday constant, D is the diffusion coefficient, $\omega = 2\pi N$, where N is the number of rotations per second, ν is the kinematic viscosity, and C is the equilibrium concentration of the fuel gas in the electrolyte at the test temperature and gas pressure.

Figure 9 shows current-potential relations for H_2 oxidation at a platinum-platinum electrode at 135°C in both 85% H_3PO_4 and the technical grade methane sulfonic acid (MSA) at various rotation speeds. Clearly at the same potential and the same (or a comparable) rotation speed, methane sulfonic acid supports currents that are more than an order of magnitude higher than those obtainable in phosphoric acid. In fact, the currents obtainable at 500 mV in this acid at 35°C are

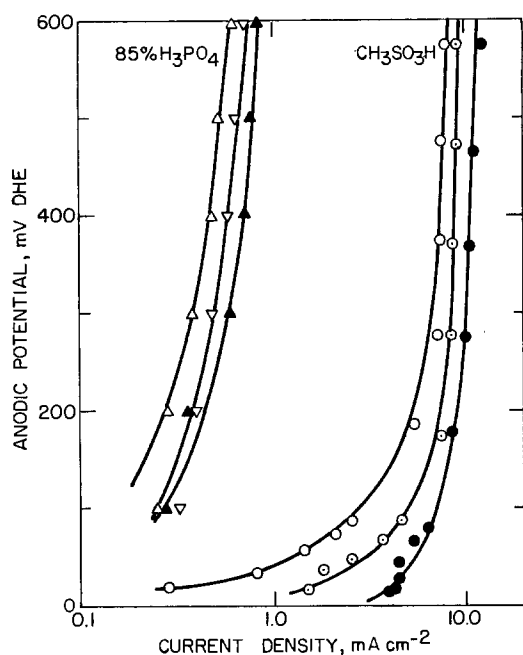


Fig. 9. Current-potential relations for the oxidation of H_2 at a platinum rotating disk electrode in both methane sulfonic acid (at 800, 1000, and 1650 rpm) and 85% H_3PO_4 (at 800, 1000, and 1500 rpm) both at 135°C.

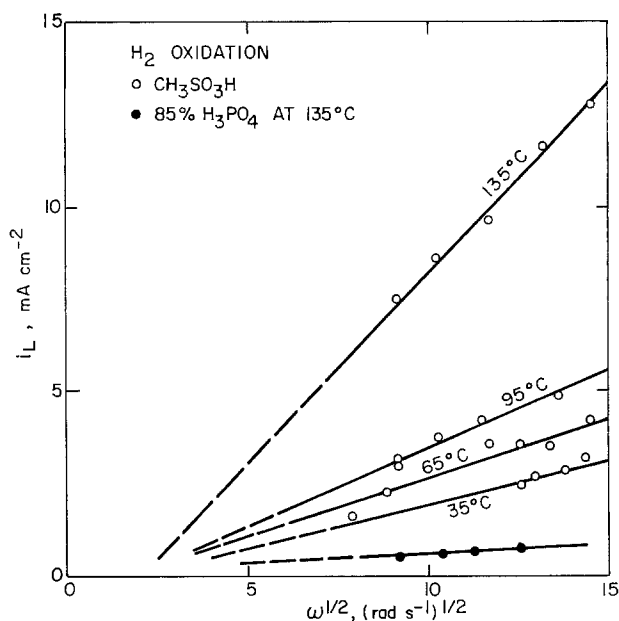


Fig. 10. Plots of the limiting current for H_2 oxidation at a platinumized Pt RDE in methane sulfonic acid at various temperatures and in 85% H_3PO_4 at 135°C.

comparable to those obtained in 85% H_3PO_4 at 135°C, see Fig. 10. This figure shows the results obtained in MSA at various temperatures and rotation speeds, plotted according to the Levich equation. Although satisfactory straight lines are obtained, extrapolation of the lines does not go through the origin as required by the Levich equation. This does not seem to be caused by the relatively small size of the cell as compared to the electrode diameter, since the same cell gave equivalent plots passing through the origin for the redox couple of ferri-ferrocyanide and for H_2 oxidation in 1N H_2SO_4 at 25°C. It is concluded that the limiting currents are a combination of mass transfer and chemical-limiting current effects.

Figures 11a and 11b show Arrhenius plots for the rates of hydrogen oxidation in MSA (a) for the ratio of limiting current densities at a porous gas-diffusion electrode and (b) for $i_L/\omega^{1/2}$ at an RDE. The error bars in Fig. 11b refer to the extent of the scatter of the data points obtained at 5 or 6 rotation speeds ranging from 700 to 2000 rpm. Both figures show regions of temperature where the rate of hydrogen oxidation is either: (i) insensitive to temperature changes (below 90°C), (ii) moderately temperature dependent (90°-135°C), or (iii) extremely temperature dependent (at and above 135°C). Figure 11b can be split into two regions: the first between room temperature and

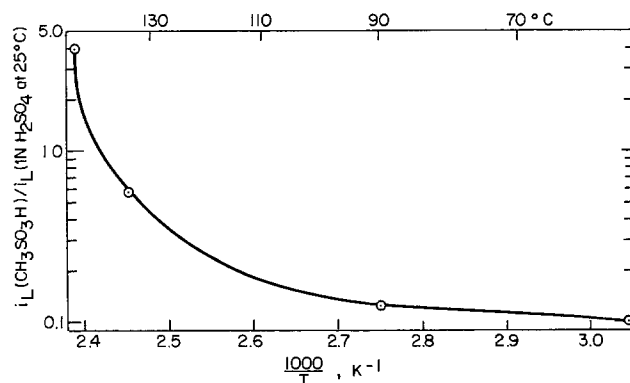


Fig. 11a. Arrhenius plot of the normalized limiting currents for H_2 oxidation in methane sulfonic acid at a Teflon-bonded Pt black gas diffusion electrode.

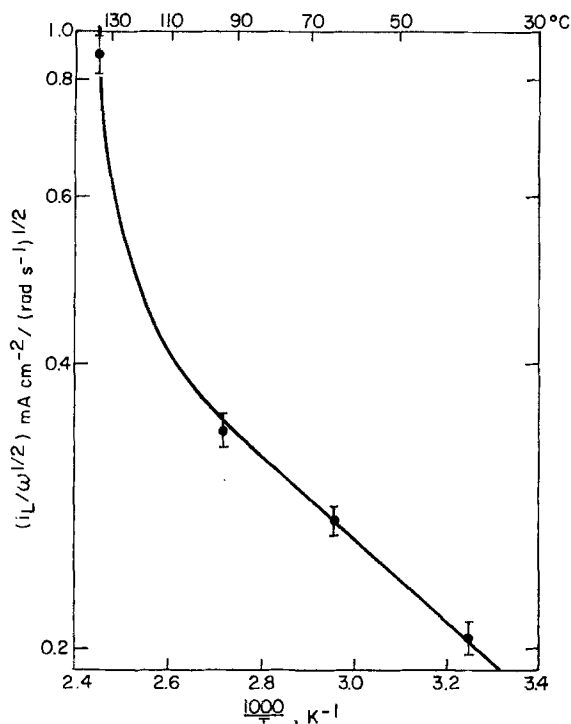


Fig. 11b. Arrhenius plot of the normalized limiting current for H_2 oxidation at an RDE. The error bars refer to the extent of the scatter of the data points obtained at 5 or 6 rotation speeds between 700 and 2000 rpm.

90°C where the slope of the Arrhenius plot gives an activation energy of 2.0 kcal/mole, which is characteristic of diffusion limited processes. Above 90°C, there is a steeper increase in reaction rate with temperature.

Conclusions

It is concluded that only methane sulfonic acid has any promise as a fuel cell electrolyte out of the

seven organic acids tested. The electrical resistivity and vapor pressure of the electrolytes vary with temperature according to the expected forms, but the mass transfer and electrochemical kinetics of H_2 oxidation at rotating platinized-platinum disk electrodes are not simple in these electrolytes. This could be due to impurities in the electrolytes, although the background currents in methane sulfonic acid were not significant compared to the measured currents (around 6% at the limiting current).

Acknowledgment

The authors gratefully acknowledge financial support of this work by the Department of Energy, under Contract No. EY-76-S-02-2927.

Manuscript submitted June 9, 1978; revised manuscript received Jan. 28, 1980.

Any discussion of this paper will appear in a Discussion Section to be published in the June 1981 JOURNAL. All discussions for the June 1981 Discussion Section should be submitted by Feb. 1, 1981.

REFERENCES

1. A. A. Adams and H. J. Barger, Jr., *This Journal*, **121**, 988 (1974).
2. G. W. Thompson, in "Techniques of Chemistry," Vol. 1, "Physical Methods of Chemistry," A. Weissberger, Editor, p. 23, Interscience, New York (1959).
3. J. Giner, *This Journal*, **111**, 376 (1964).
4. S. Almaula and L. G. Austin, *ibid.*, **114**, 927 (1967).
5. A. C. C. Tseung and S. C. Dhara, *Electrochim. Acta*, **20**, 681 (1975).
6. L. G. Austin, "Fuel Cells," SP-120, p. 73, NASA, Washington (1967).
7. A. H. Appleby, *This Journal*, **117**, 328 (1970).
8. J. R. Van Wazer, "Phosphorous and Its Compounds," Vol. 1, p. 484, Interscience, New York (1958).
9. C. M. Suter, "The Organic Chemistry of Sulfur," p. 99, John Wiley & Sons, Inc., New York (1944).
10. V. G. Levich, "Physicochemical Hydrodynamics," p. 69, Prentice-Hall, Englewood Cliffs, N.J. (1962).

DISCUSSION SECTION



This Discussion Section includes discussion of papers appearing in the *Journal of The Electrochemical Society*, Vol. 126, No. 5, 7, and 8, May, July, and August 1979 and Vol. 127, No. 1, 2, 3, 5, and 7, January, February, March, May, and July 1980.

The Stability of Trifluoromethane Sulfonic Acid as an Electrolyte in Fuel Cells

A. A. Adams and R. T. Foley (pp. 775-778, Vol. 126, No. 5)

V. B. Hughes and B. D. McNicol:¹ In this article Adams and Foley described the use of trifluoromethane sulfonic acid monohydrate (TFMSM) as an electrolyte in fuel cells using low relative molecular mass hydrocarbons as fuel. A reference therein to our paper² implied that we had concluded that the monohydrate was thermally unstable. This in fact is incorrect since our paper referred to the instability of TFMSM in aqueous solutions, in the presence of methanol. We were sur-

¹ Shell Research Limited, Thornton Research Centre, Chester, England CH1 3SH.

² V. B. Hughes and B. D. McNicol *et al.*, *J. Appl. Electrochem.*, **7**, 161 (1977).

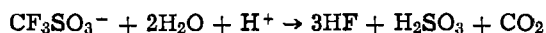
prised to read further that Adams and Foley ascribed the so-called instability observed by us as due to the source or purity of the acid or the use of a carbon counterelectrode in our system. Our paper had included a reasonable explanation for the instability of this aqueous acid under the particular conditions in which we were interested. We would therefore emphasize that we claimed instability only with respect to aqueous TFMSM systems and not with respect to the pure monohydrate. Furthermore, the instability was linked to specific concentrations [see Fig. 13 of Footnote 2]. Thus in the presence of methanol, at temperatures above 60°C using high activity catalysts, certain concentrations of aqueous TFMSM are unstable. Also, in pure aqueous solutions, at concentrations between 25-50 weight percent, and during potentiodynamic cycling, sulfur is produced (presumably during the cathodic sweep).

With regard to the pure monohydrate, we found no evidence for decomposition above 80°C but did imply that falloff in activity at temperatures in excess of 80°C

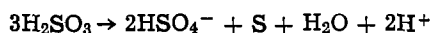
could perhaps be attributed to a reaction (as yet undefined) between the monohydrate and methanol.

That the source of our material should be called into question was surprising since it was stated in our paper that the acid was obtained for us by Fluorochem Limited, who bought it from the 3M Corporation, from whom Adams and Foley also obtained their material. The purity of our acid was also questioned yet in our paper we quite clearly recorded that the pure acid and the monohydrate were both triply distilled under nitrogen, showed correct boiling points, and in the case of TFMSM monohydrate showed the correct sharp melting point. The remarks concerning the purity of the acid used by us are therefore completely out of order.

Both graphite and platinum-gauze counterelectrodes were used in our studies and in both cases sulfur formation was found above 60°C with aqueous acid. At this point it should be emphasized (as we have done previously²) that the stability of TFMS is kinetic rather than thermodynamic and it is therefore perfectly feasible that in the presence of finely divided catalysts the temperature of decomposition could be lowered, especially if the agent responsible for the decomposition, *viz.* water, is present in significant quantities, *e.g.*



then



This reaction has been discussed in some detail by Fabes and Swaddle.³ Furthermore the role of methanol in promoting this decomposition is as yet unknown.

For the benefit of other readers, not already acquainted with our work, we are primarily interested in methanol electro-oxidation. As might be expected, the use of TFMSM monohydrate as an electrolyte for the methanol/air fuel cell resulted in low activities for both smooth and finely divided catalyst. This is perfectly understandable since there is simply not enough water available for the reaction (*cf.* methanol electro-oxidation in 96% H_3PO_4 which is also low⁴) and water is an important agent involved in the electro-oxidation of CH_3OH . Confirmation of this followed from our studies of aqueous systems which showed high activities, explained by us in terms of the higher water activity in such systems. Above 60°C, sulfur was formed from several possible sources, *e.g.*, the decomposition of the acid anion catalyzed by platinum as outlined above or from reaction with hydrogen at the counterelectrode (though both platinum and carbon counterelectrodes produced the same result).

In conclusion therefore we do feel that the reference to our work is completely out of context in this paper since (i) Adams' and Foley's paper does not deal with methanol electro-oxidation, and (ii) does not deal with aqueous TFMS solutions. We feel it is important therefore to emphasize these points in print.

A. A. Adams⁵ and R. T. Foley⁶ The reference to the Shell work⁷ was made because that laboratory was the only one to report chemical instability of trifluoromethanesulfonic acid, or its monohydrate, at temperatures as low as 60°C. This is implied for the monohydrate: "We found also that at temperatures higher than 80°C the activities of the catalysts decreased. A possible reason for this was decomposition of the electrolyte producing S species which could poison the catalyst. However, cyclic voltammetry studies showed

no evidence of sulfur poisoning of the catalysts (Fig. 4). Thus, for the moment the reason for the fall-off in performance above 80°C remains unclear."

Several other laboratories have worked with aqueous solutions of the acid over the temperature range of 60°-100°C but there has been no report of chemical instability. Appleby and Baker⁸ studied oxygen reduction at 62°C on Pt black electrodes in 1.1M solution. Full fuel cells have been run at 200 mA/cm² at 60°C in 6M TFMSA over 2000 hr.⁹ We have run half-cell tests in monohydrate at 135°C for weeks without a decrease in performance which would be very quickly seen if there was sulfur produced. Cells have been run with 6M electrolyte for months from 60° to 75°C without poisoning the catalyst electrode.¹⁰ There is no evidence to suggest that the chemical stability of aqueous solutions would differ from that of the monohydrate.

The importance or lack of importance, of methanol has not been resolved by the Shell reports. In the review by Howells and McCown¹¹ they mention "The exothermic reaction of alcohols with trifluoromethanesulfonic acid leads to esters, but ethers and olefins may also be formed." In our work with methanol we concluded that we did, in fact, see esterification but the Shell authors disputed our interpretation of NMR experiment on which we based the conclusion.

The proposed mechanism for the decomposition of the CF_3SO_3^- anion is difficult to accept for several reasons. The first step leading to the production of sulfur is the hydrolysis of the C-F bond. All the literature reports indicate that this does not occur under the conditions imposed here. (A more likely source of H_2SO_3 would be an SO_3 impurity in the original acid.) Apparently, the reaction proposed takes place only in methanol solution. But no role of methanol is indicated in either of the two steps given by these authors.

We suspect that the production of sulfur came from either (i) the reduction of trace amounts of SO_3 carried over from the original 97% acid, or (ii) voltage transients at the counterelectrode. The voltage transients would have to be greater than 1.5V (probably close to 2.0V) because we regularly cycle our electrodes to 1.5V to clean them before a voltammetry run.

Minority Carrier Lifetime: Correlation with IC Process Parameters

H. R. Huff and T. L. Chiu (pp. 1142-1147, Vol. 126, No. 7)

G. F. Cerofolini and G. Ferla¹² In this article, Huff and Chiu report an extensive correlation of minority carrier lifetime with IC process parameters.

Their results can be summarized as follows: lifetime is reduced by high temperature annealing; the higher the temperature, the sharper the decrease. Phosphorus diffusion alone is insufficient to increase lifetime. Phosphorus diffusion followed by "an extended *in situ* anneal and a subsequent additional proprietary nitrogen anneal" is very efficient to increase lifetime.

We wish to point out that similar results have been obtained by us by using a phosphorus diffusion followed by an anneal at moderate temperature.

These results have been extensively published¹³⁻¹⁷ and if the "proprietary anneal" quoted by Huff and

⁸ A. J. Appleby and B. S. Baker, *This Journal*, 125, 404 (1978).

⁹ M. George, Interim Technical Report on Contract No. DAAK70-78-C-0103, Energy Research Corporation, December 1979.

¹⁰ A. A. Adams, "Proceedings of the 29th Power Sources Conference," Atlantic City, N. J., June 9-12, 1980.

¹¹ R. D. Howells and J. D. McCown, *Chem. Rev.*, 77, 69 (1977).

¹² SGS-ATES, Milano, Italy.

¹³ L. Baldi, G. F. Cerofolini, G. Ferla, and G. Frigerio, *Phys. Status Solidi A*, 48, 523 (1978).

¹⁴ L. Baldi, G. F. Cerofolini, and G. Ferla, Paper 209 presented at The Electrochemical Society Meeting, Pittsburgh, Pennsylvania, Oct. 15-20, 1978.

¹⁵ L. Baldi, G. F. Cerofolini, and G. Ferla, *Surf. Technol.*, 8, 161 (1979).

¹⁶ G. F. Cerofolini and G. Ferla, Paper 492 presented at The Electrochemical Society Meeting, Los Angeles, California, Oct. 14-19, 1979.

¹⁷ L. Baldi, G. F. Cerofolini, and G. Ferla, *This Journal*, 127, 164 (1980).

³ L. Fabes and T. W. Swaddle, *Can. J. Chem.*, 53, 3053 (1975).

⁴ M. R. Andrew and B. D. McNicol *et al.*, *J. Appl. Electrochem.*, 7, 153 (1977).

⁵ U.S. Army Mobility Equipment Research and Development Command, Fort Belvoir, Virginia 22060.

⁶ Chemistry Department, The American University, Washington, D.C. 20016.

⁷ V. B. Hughes, B. D. McNicol, M. R. Andrew, R. B. Jones, and R. T. Short, *J. Appl. Electrochem.*, 7, 161 (1977).

Chiu is nitrogen anneal in the temperature range 700°-900°C, their results are confirmations to our theory.

The Potentiostatic Current Oscillations at Iron/Sulfuric Acid Solutions Interfaces

J. J. Podesta, R. C. V. Piatti, and A. J. Arvia
(pp. 1363-1367, Vol. 126, No. 8)

C. Gabrielli, M. Keddum, C. Rakotomavo, and H. Takenouti;¹⁸ In this paper J. J. Podesta *et al.* accumulated a number of quantitative data on the oscillations of the iron/H₂SO₄ interface. However, as far as, according to the authors themselves, emphasis is put on the "correlation of the potential range of the periodic effect to the passivity potential," their results and discussion deserve, we believe, the following remarks.

1. Although claimed to be coincident with literature, the *E/I* curves (their Fig. 1) are somewhat apart from data obtained under well-defined mass transport conditions (RDE). (i) Their *E/I* curves do not exhibit a clear diffusion plateau. (ii) Their *E/I* curves show a stable negative slope at the active-passive transition. (iii) Their *E/I* curves show an abnormally high passive current density, by one or two orders of magnitude when compared to the typical standard values under such conditions (5-10 μAcm⁻²).¹⁹

(i) and (ii) could be explained by the recording procedure itself, the stirring conditions being not elucidated. Did the authors use an RDE? (iii) is likely to arise from a poor contact between iron and the embedding material which induces an undermining active dissolution. Cl⁻ ions from the SCE can also be harmful to the passive layer. Did the authors use a Haber-Luggin capillary?

2. In spite of mentioning our work on localized attack [Ref. (21) in the paper under discussion], the authors completely disregard the accompanying Z-shaped *E/I* profiles involving a multiplicity of steady states (MSS).²⁰ Both effects were strictly correlated as established in a most recent interpretation.²¹ In view of the transition evidenced in the paper around 1.5N, our experiments previously performed in 2N H₂SO₄²⁰ were repeated in 1N solution. Figure 1 below shows the most typical features of the *E/I* curves recorded with an RDE. The primary electric field distribution keeps the ohmic resistance

(16Ω at a layer free surface) close to the working disk electrode. The reference electrode is located in the bulk of solution. The potential *E* actually measured between reference and working electrodes includes the ohmic drop *ReI*. The curves plotted by thin lines are obtained by means of a fast response potentiostat. By using a negative impedance converter (NIC) the working electrode can be grounded across an adjustable negative resistance ρ^{20} (see insert in Fig. 1), which counter balances the corresponding part of the electrolyte resistance. Under these conditions Z-shaped curves are recorded (bold lines), dotted lines indicate oscillations quite similar to those under discussion. This behavior is very close to that obtained previously in 2N H₂SO₄.²⁰ The potentiostatic curves exhibit a bistability (hysteresis) at the active-passive and passive-active transition. The plateau is diffusion controlled and obeys the Levitch law. These statements are also valid for 0.5N solution though the plateau is not so clearly seen. No fundamental change in the steady-state behavior and transport properties can be detected in this range of concentration. In fact, Fig. 2 and 4 of the paper under discussion show that the authors considered on both sides of 1.5N quite two different kinds of oscillations. The true passive state can be regarded as reached only in concentrated solutions (Fig. 2, 3, and Fig. 4, f through i) so that the comparison is hardly relevant.

3. Discussing the origin of oscillations in terms of steady-state behavior is certainly an extremely difficult task. However, the consideration of the respective positions of the *E/I* curve and of the load line imposed by the regulating device provides some clarification. The discussion of the stability can be restricted to the regions of the *E/I* profile where the system switches from one state to another. Figure 1b gives the steady-state polarization curve (Fig. 1a) near the point C with expanded current and voltage scales. During the passive part of the oscillation, the polarization point is located on the *E/I* curve at the potential *E*₀ controlled by the potentiostat. Triggering to the active state occurs suddenly when *M* reaches a position such as C where the load line becomes tangent to the *E/I* curves.²² Therefore, the succession of active and passive states and the slow increase of current during the passive period supports a periodic displacement of the Flade potential. Oscillations may occur if the potential is held within the narrow range of this displacement. However, as stated by Podesta *et al.*, the detailed mechanism is certainly far more complicated. Ohmic drop contribution can hardly be neglected as proved by the dependence of the frequency on both *E*₀ and ρ . Values of ρ locating the load line between PQ and PR (Fig. 1a) give the best conditions for obtaining sustained oscillations. In agreement with previous data,²³ potentiostatic oscillations were found difficult to reproduce, unless ohmic drop effects are partially compensated for by a Haber-Luggin capillary. As emphasized, FeSO₄ precipitated along with various hydrated oxides is likely to contribute in the relaxation process. More than one species should be considered in the transport phenomena to solve the apparent inconsistency between the hindrance of passivity leading to Z-shaped *E/I* curves and the cathodic shift of the passivation potential needed by the periodic effect.

J. J. Podesta, R. C. V. Piatti, and A. J. Arvia;²⁴ The main purpose of the paper is to present some phenomenological aspects related to periodic phenomena, in this particular case, the influence of electrolyte concentration is considered. The *E/I* curves were obtained both with iron wire electrodes under free convection

¹⁸ Groupe de Recherche No. 4 du CNRS "Physique des Liquides et Electrochimie," associé à l'Université Pierre et Marie Curie, 75230 Paris Cedex 05, France.

¹⁹ K. J. Vetter and F. Gorn, *Werkst. Korros.*, 21, 703 (1970).

²⁰ I. Epelboin, C. Gabrielli, M. Keddum, J. C. Lestrade, and H. Takenouti, *This Journal*, 119, 1632 (1972).

²¹ C. G. Law, Jr. and J. Newman, *ibid.*, 126, 2150 (1979).

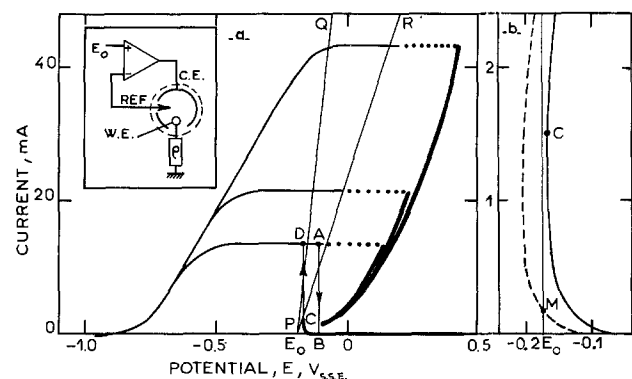


Fig. 1. Steady-state polarization curves: Fe disk (diameter 2 mm; Johnson-Matthey) 1N H₂SO₄, 25°C deoxygenated by Ar bubbling. Rotation speeds (1) = 0; (2) = 400, and (3) = 1600 rpm. SSE: saturated mercurous sulfate reference electrode. Insert: experimental setup (schematic): *E*₀, regulation potential referred to earth, $\rho = 0$, corresponds to the potentiostatic regulation (thin line *E/I*), and $\rho < 0$, NIC mode leads to bold line Z-shaped curves.

²² I. Epelboin, C. Gabrielli, M. Keddum, and H. Takenouti, Reprints of submitted paper "Kinetics of Physicochemical Oscillations," II, p. 297, Aachen (G.R.F.) (1979).

²³ Y. Torioe, *Denki Kagaku*, 35, 206 (1967).

²⁴ Instituto de Investigaciones Fisicoquímicas Teóricas y Aplicadas, División Electroquímica, 1900 LaPlata, Argentina.

and with iron RDE at rotation speeds from 168 to 425 rpm using the same type of perturbation technique already described in the literature. These curves allowed an adequate choice of the working potential region.

The magnitude of the passive current density cannot be attributed either to the undermining active dissolution or to the traces of chloride ion coming from the SCE. The Luggin-Haber capillary tip arrangement was used. The effect of chloride ion increases the frequency of the oscillations in the Fe/1N H₂SO₄ and Fe/1.5N H₂SO₄ interfaces under a potentiostatic step. The magnitude of the current density is referred to the apparent electrode area. The estimated electrode roughness factor is probably close to 10 as deduced from SEM data. Therefore, in this sense the coincidence between the *E*/*I* curves given in Fig. 1 and those reported in the literature is reasonably good within one order of magnitude. This is sufficient to evaluate the magnitude of the proper potential step to produce the periodic oscillations. There is a good correlation between the passive current density change with the H₂SO₄ concentration as given in Fig. 1 and 4.

The fact that no fundamental change of the Z-shaped *E*/*I* profiles involving a multiplicity of steady states is noticed in the 0.5-2.0N H₂SO₄ concentration range, does not preclude concentration effects on the *t_d*/*t_p* ratio as shown in Fig. 7 of the paper. Since both measurements correspond to a different time-scale, straightforward comparison is hardly relevant.

It is possible that the film involved during each period of the oscillating cycle is a nonstabilized film where the electric field assists the restructuring of iron oxides yielding more compact structures. But this situation which corresponds to an aging-type process is undistinguishable under the conditions of the paper in discussion, but it has to be considered in deriving conclusions from passive films formed under definite perturbation conditions that are involved in the periodic current oscillations.

Investigation of Two- and Three-Phase Fields in the Ga-As-Sb System

M. F. Gratton and J. C. Wooley (pp. 55-62, Vol. 127, No. 1)

Robert F. Brebrick:²⁵ The authors have made a valuable contribution to the experimental knowledge of the phase diagram for this ternary system. However, they have overlooked two references that are pertinent to the theoretical analysis they present. A systematic investigation of fits to III-V pseudobinaries,²⁶ made when the experimental data for Ga-As-Sb were less extensive, showed that a simple solution model with interaction coefficients linearly dependent upon *T* gave a calculated peritectic temperature at least 12° below the experimental value of 745°C. It was concluded at that time that, if the experimental peritectic temperature was correct, that a simple solution model for the pseudobinary solid is inadequate. This discrepancy still exists in the authors' analysis, in addition to the poor fit to the pseudobinary miscibility gap they mention, and the authors have correctly concluded a simple solution model for the pseudobinary solid is inadequate. In a later analysis of III-V binary systems,²⁷ including GaSb and GaAs, it was shown that the simple solution liquid model was inadequate in that it could not simultaneously provide an adequate simultaneous fit to the thermochemical data and liquidus lines. It was also shown that a liquid model in which the interaction coefficient was a linear function of both *T* and atom fraction was adequate in terms of the experimental data then available.

²⁵ Department of Mechanical Engineering, Marquette University, Milwaukee, Wisconsin 53233.

²⁶ R. F. Brebrick and R. J. Panlener, *This Journal*, 121, 933 (1974).

²⁷ R. F. Brebrick, *Metall. Trans. A*, 8, 403 (1977).

Table I.

AB	-ΔH° _f (J/mole AB)		-ΔS° _f (J/K-mole AB)	
	Calc	Exp.	Calc	Exp.
GaSb(s)	54,197	68,208	39.41	54.81
GaAs(s)	92,803	118,213	39.80	54.60

Thus the authors have used a liquid model that has been previously demonstrated to be inadequate. As one example of this inadequacy we cite the following. The zero Gibbs free enthalpy for the congruent melting of GaSb and GaAs leads to two equations for each binary (Eq. [13] and [14] of Footnote 27) which link the thermodynamic properties of the liquid phase with the enthalpy and entropy of formation, ΔH°_f and ΔS°_f, of the narrow homogeneity-range compound from its pure liquid elements and at its melting point. The values calculated for these latter quantities from the authors' liquid model parameters and the experimental values are shown in Table I above. Although the calculated values are of the right sign they are too small in magnitude by an amount that, in our opinion, exceeds the uncertainties in the experimental quantities.

The Warburg Impedance in the Presence of Convective Flow

Daniel A. Scherson and John Newman (pp. 110-113, Vol. 127, No. 1)

Eugène Levart²⁸ and **Daniel Schuhmann**²⁹ The aim of this paper was to establish approximate analytical expressions for the real and imaginary parts of the reduced Warburg impedance of an RDE, valid for very large Schmidt numbers only.

The results found at high frequencies are close to the numerically computed exact values. As correctly stated by the authors, they do not differ significantly from those reported by us [Ref. (7) in the paper under discussion]. Incidentally, it is to be pointed out that our expressions $\text{Re}(-1/\theta'(0)) = 1/\sqrt{2K} + 3/4K^2$ and $\text{Im}(-1/\theta'(0)) = -1/\sqrt{2K}$ are much simpler than Eq. [11]-[13] in the paper under discussion.

At low frequencies, the authors derive Eq. [14]-[16] in the form of an infinite series of the reduced frequency *K*, containing the known eigenvalues and the related coefficients of the Sturm-Liouville system. Their Table II summarizes the results found and compares them to the few exact values available to the authors (*K* ≳ 1.5) and to the values obtained by the Nernst layer approximation. This part of the paper requires some comments.

First of all, it should be recalled that in our previous paper [Ref. (5) in the paper under discussion] we have treated a very general case of the concentration impedance of an RDE. Series form solutions, valid for every finite value of the Schmidt number encountered in electrochemistry, have been given for all frequencies. The results relative to the limiting case *Sc* = ∞ at HF have then been developed in detail in Ref. (7) where it has been emphasized that our LF results agree perfectly with the exact solution from *K* = 0 to *K* = 30 at least. Surprisingly, in presenting their Table II, the authors make no mention of our LF solution. Perhaps because we used reduced quantities different from theirs, or because our Eq. [52] in Ref. (5) is not directly usable for *Sc* = ∞, or even because our Eq. [53] contained a small printing error (*μ* instead of *u*).

In any case, we take the opportunity to recall our Eq. [52] in Ref. (5) for the reduced impedance *M*°. For large values of *Sc* and in the absence of chemical

²⁸ Laboratoire d'Electrochimie Interfaciale du C.N.R.S., F 92190 Meudon-Bellevue, France.

²⁹ Groupe de Recherche Physico-Chimie des Interfaces—C.N.R.S., F 34033 Montpellier, France.

Table I. Low frequency solutions for the real and imaginary parts of $-1/\theta'(0)$

K	Scherson and Newman		Levart and Schuhmann (identical to the exact solution)					
			Sc = ∞		Sc = 1000		Sc = 100	
	Re	-Im	Re	-Im	Re	-Im	Re	-Im
0.0	0.89298	0	0.89298	0	0.92095	0	0.95703	0
0.05	0.89278	0.01134	0.89273	0.01331	0.92066	0.01470	0.95666	0.01666
0.1	0.89219	0.02266	0.89198	0.02659	0.91976	0.02937	0.95555	0.03327
0.2	0.88985	0.04516	0.88899	0.05286	0.91622	0.05845	0.95116	0.06615
0.5	0.87397	0.11010	0.86882	0.12850	0.89242	0.14119	0.92190	0.15871
0.7	0.85679	0.14988	0.84721	0.17408	0.86717	0.19034	0.89129	0.21244
1.0	0.82333	0.20229	0.80575	0.23271	0.81944	0.25214	0.83465	0.27774
1.5	0.75542	0.26748	0.72406	0.30195	0.72799	0.32147	0.73034	0.34565
2.0	0.68409	0.30641	0.64160	0.33934	0.63898	0.35526	0.63370	0.37365
3.5	0.51238	0.32695	0.45610	0.34736	0.44942	0.35185	0.44148	0.35585

reaction, this expression simplifies to its first term $m = 1$ and becomes

$$M^\circ(\text{Sc}, j\sigma) = \lambda_1^\circ(j\sigma)\text{Sc}^{-1/3} \quad [1]$$

Dividing Eq. [1] by the value of M° at zero frequency, $M^\circ(\text{Sc}, 0) = (3/0.510233)^{1/3}\Gamma(4/3)\text{Sc}^{-1/3}$ and replacing the ratio $M^\circ(\text{Sc}, j\sigma)/M^\circ(\text{Sc}/0)$ by its equivalent $-1/\theta'(0)\Gamma(4/3)$, we get

$$-1/\theta'(0) = \lambda_1^\circ(j\sigma)(3/0.51233)^{-1/3} \quad [2]$$

where $\sigma = K/3^{2/3}$ and λ_1° is a continued fraction of $j\sigma$

$$\lambda_1^\circ(j\sigma) = 1/(f_{1,0}^\circ + j\sigma/(f_{1,1}^\circ + j\sigma/(f_{1,2}^\circ + \dots))) \quad [3]$$

with known values of $f_{1,n}^\circ$, the coefficients $f_{m,n}^\circ$ having been computed and published for $m = 1$ to 4 and $n = 0$ to 14 [Ref. (5), Table II]. More precise values for $m = 1$ to 6 and $n = 0$ to 24 are also available on request from us. The number of divisions to be effected in Eq. [3] depends on σ and on the precision desired, but it is of the same order of magnitude as the number of terms in Scherson and Newman's series.

Table I above summarizes the results found using our LF solution and compares them to the corresponding values reported by Scherson and Newman. It is to be recalled once more that our results are identical to the exact values computed by the finite difference method over the range of K from 0 to 30 within 5 significant digits. These results overlap to a great extent the region of validity of the HF solutions which become exact within 5 digits for $K \geq 20$. In contradiction, the LF results given in the paper under discussion are noticeably different from these exact values which were not given by the authors.

We complete Table I above with the values computed for $\text{Sc} = 1000$ and $\text{Sc} = 100$, which make clear that the Scherson-Newman LF approximation is unable to describe the physical reality with an error smaller than about 5%. Like our Eq. [3] which is infinitely more precise, it requires the knowledge of a great number of numerical coefficients. The only apparent disadvantage of our equation is that it is not easily separable into analytical expressions for the real and imaginary parts of the impedance. However, such an objection is not serious because using modern computer techniques, operations on complex quantities are not more difficult than those on real numbers.

Investigation on the Kinetics of Electroreduction Processes at Dark TiO_2 and SrTiO_3 Single Crystal Semiconductor Electrodes

J. Vandermolen, W. P. Gomes, and F. Cardon
(pp. 324-328, Vol. 127, No. 2)

P. Salvador:³⁰ The authors postulate an interesting two-step mechanism involving bandgap surface states as intermediates of a process of electron transfer from the conduction band to the electrolyte oxidizing

³⁰ Instituto de Catálisis y Petroleoquímica, CSIC, Serrano 119, Madrid 6, Spain.

species. Under conditions of high enough concentration of the oxidizing agent the capture of C.B. electrons by surface states is shown to be the rate-limiting step of the overall reaction. Then a cathodic dark saturation current

$$J_{\text{sat}} = -eNk_1n_s \quad [1]$$

is reached, which is determined by the density of surface states, N , their coefficient of electron capture, k_1 , and the electron density at the semiconductor surface, n_s .

As shown by Morisaki *et al.*,³¹ an identical result is obtained from Nishida's theoretical treatment³² of the charge transfer, via surface states associated with the photoinduced evolution of oxygen, at the n-TiO₂/electrolyte interface, with the difference that in this case the process of charge transfer involved photogenerated holes from the valence band instead of conduction band electrons. According to Wilson,³³ we believe it is reasonable to assume that the same surface states are involved in both processes of charge transfer, since there is direct evidence that those surface states that are oxidized by valence band holes can also be reduced by conduction band electrons.

As predicted by Eq. [1], the saturation current is found to be independent of the oxidizing agent, but very sensitive both to the electrolyte pH and to the applied voltage, which is attributed to variations of n_s . However, the authors' conclusion that Nk_1 is a constant for a given material seems to us a little adventurous. In our opinion this statement might be correct in the case of preexisting surface states created, for instance, by pretreatment or semiconductor doping. Nevertheless, the possibility that surface states might result from the interaction of the semiconductor surface with the electrolyte must not be overlooked, in which case the density of surface states could be influenced by the electrolyte composition and pH.

From experimental values of J_{sat} , the authors estimate a density of surface states of $4 \times 10^{11} \text{ cm}^{-2}$ and 10^{10} cm^{-2} for TiO_2 and SrTiO_3 , respectively. These values are exceedingly low by comparison with that of about 10^{14} cm^{-2} corresponding to processes of charge transfer at TiO_2 , involving either conduction band electrons^{33,34} or valence band holes.³⁵ The discrepancy is due to the very high value assumed for the electron-capture cross section ($S_n = 10^{-12} \text{ cm}^{-2}$). In fact, from the quantitative analysis of the growth and decay of the peak corresponding to the reduction by conduction band electrons of bandgap surface states, Wilson³³ has been able to calculate the actual cross section of these states for interaction with electrons. He obtained a value of the order of 10^{-16} cm^2 , which is considerably smaller than the geometric cross section of a state localized on a single atom, probably

³¹ H. Morisaki, T. Baba, and K. Yazawa, *Phys. Rev. B*, **21**, 837 (1980).

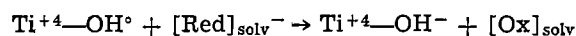
³² M. Nishida, *Nature (London)*, **277**, 202 (1979).

³³ R. H. Wilson, *This Journal*, **127**, 228 (1980).

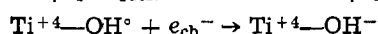
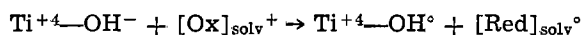
³⁴ B. Parkinson, F. Decker, J. F. Juiñó, H. Abramovich, and H. C. Chagas, *Electrochim. Acta*, **25**, 521 (1980).

³⁵ P. Salvador, Communication presented to the "Third International Conference on the Photoelectrochemical Conversion and Storage of Solar Energy," Boulder, Colorado (1980).

because of the poor electronic or phonon coupling between the surface state and the semiconductor.³³ On the other hand, there is indirect experimental evidence that surface hydroxyl groups are involved in the process of charge transfer through the interface semiconductor/electrolyte. For instance, Parkinson *et al.*³⁴ observed that surface pretreatment with a strong base enhanced the oxygen cathodic reduction via surface states at TiO₂. A similar effect is reported by Wilson³⁵ with respect to the enhancement of the peak corresponding to the reduction of the surface states by conduction band electrons when, instead of acidic electrolyte (H₂SO₄), a strongly basic one (KOH) is used. Wagner and Somorjai³⁶ also observed that the photocatalytic production of hydrogen on an illuminated surface of SrTiO₃ increased with the concentration of the NaOH solution surrounding the crystal. Finally, we have recently observed³⁵ that the quantum efficiency of water photo-oxidation at n-TiO₂ electrodes is noticeably dependent on the electrolyte pH. Surface OH⁻ groups probably act as centers for trapping and transfer of charge between the semiconductor and the electrolyte. For oxidation reactions involving valence band holes the mechanism could be



while, for conduction band electrons involving reduction reactions a simplified mechanism might involve the following steps



The position of the energy levels corresponding to active surface hydroxyls should be somewhere in the bandgap (*i.e.*, between the top of the valence band and the bottom of the conduction band). This requirement should be better fulfilled by the basic OH groups (bonded to one Ti atom) than by the acidic OH groups (bonded to two Ti atoms).

The surface density of OH⁻ active centers should depend on the electrolyte concentration of OH⁻ ions. The maximum density of basic surface hydroxyl groups in TiO₂ is of about 10¹⁴ cm⁻²,^{35,37} which is in good agreement with the density of surface states obtained by several authors for different oxidation and reduction reactions.³³⁻³⁵ From structural considerations this value should be, in general, lower for SrTiO₃ than for TiO₂, which agrees with Vandermolen *et al.*'s observation that for a given n_s value J_{sat} is lower for SrTiO₃ than for TiO₂.

This charge transfer model involving surface OH⁻ groups predicts, therefore, a new effect of the electrolyte pH upon the behavior of the cathodic current density, which is ascribed to the variations of N . However, this effect is masked by that due to the variations of n_s , since $dn_s/dpH \gg dN/dpH$.

The experimental fact that surface hydroxyls play a decisive role in TiO₂ and SrTiO₃ photochemistry at the gas/solid interface,³⁷⁻³⁹ gives support to the identification of surface OH groups with the surface states involved both in photoassisted and dark reactions at the electrode/electrolyte interface.

J. Vandermolen, W. P. Gomes, and F. Cardon:⁴⁰ It is indeed interesting to remark that our experimental value of the product NS_n for TiO₂ is roughly in agreement with Wilson's recent results⁴¹ which lead to the conclusion that, in his experiments, a nearly complete

coverage of the surface by acceptor-type centers is involved. Hence, it might well be that the same centers are responsible for the cathodic current in both cases. In contrast to Salvador's statement, we did not estimate N to be 4×10^{11} cm⁻², but merely used this number to illustrate, by the example of a donor-type center, the fact that the observed saturation current is quantitatively interpretable on the basis of a charge transfer mechanism through surface states.

In our opinion, a kinetic study like the one under discussion does not allow the determination of the chemical nature of the centers participating in the proposed mechanism. It may be remarked in this context that Salvador's suggestion, that these centers might originate from the interaction between the semiconductor surface and the electrolyte, is not supported by our experimental results, since they do not exhibit any significant dependence of Nk_1 on the nature of the oxidizing agent or on pH. Therefore, we think that independent studies would be needed in order to establish whether surface hydroxyl groups are indeed involved in the process discussed.

High Rate Discharge Characteristics of Li/SOCl₂ Cells

K. A. Klinedinst and M. J. Domeniconi
(pp. 539-544, Vol. 127, No. 3)

M. H. Miles:⁴² The authors present an interesting study relating to the discharge of Li/SOCl₂ cells at high current densities. The results show that higher discharge voltages and discharge capacities can be obtained with cells containing pure AlCl₃ rather than the conventional LiAlCl₄ electrolyte. The authors point out that the direct reaction of Li with SOCl₂ deposits a protective LiCl film on the anode that, in turn, reacts with AlCl₃ to produce soluble LiAlCl₄. These reactions continue until either Li, SOCl₂, or AlCl₃ is exhausted. The formation of LiAlCl₄ by these reactions accounts for sufficient electrolyte conductivity to support the cell discharge. How long, approximately, does it take in terms of time per unit volume of SOCl₂ per unit area of exposed lithium for the reactions of Li, SOCl₂, and AlCl₃ to produce sufficient conductivity? The authors mention a 10 min stand on open circuit before beginning cell discharge experiments.

Although the cell discharge was cathode limited due to LiCl precipitating within the cathode pores, it would be interesting to know the coulombic efficiency for the lithium anode in the pure AlCl₃ electrolyte. What is the ratio of Li reacting electrochemically *vs.* that reacting directly with SOCl₂? This may be a critical factor in designing practical batteries since considerable heat may be produced by the direct reaction of Li with SOCl₂ as well as by I²R heating that takes place during cell discharge. The direct reaction of Li with SOCl₂ could also greatly decrease the energy density obtained from such cells. Using the reported 0.75 mm thickness for Li and assuming a 1 cm² area (Fig. 1 in the paper under discussion suggests an even larger anodic area), the results for 4.5M AlCl₃ in Fig. 4 in the paper under discussion indicate that less than 4% of the Li present reacts electrochemically. It is realized that the authors purposely used large excesses of both Li and SOCl₂; nevertheless, data regarding the relative amounts of Li reacting electrochemically *vs.* that reacting directly with SOCl₂ is needed to judge the practicality of such cells. The anode efficiency is an important parameter in any cell that uses an oxidizing electrolyte. In thermal battery cells utilizing molten nitrates as the oxidizing electrolyte, direct reaction of the electrolyte with the calcium anode occurs.^{43,44} In thermal battery systems, however, the

³⁶ F. T. Wagner and G. A. Somorjai, *Nature (London)*, in press.
³⁷ G. Munuera, V. Rives-Arnau, and A. Saucedo, *J. Chem. Soc. Faraday Trans I*, 75, 736 (1979).

³⁸ A. H. Boonstra and C. H. H. A. Mutsaers, *J. Phys. Chem.*, 79, 2025 (1975).

³⁹ H. Van Dame and W. K. Hall, *J. Am. Chem. Soc.*, 101, 4373 (1979).

⁴⁰ Rijksuniversiteit Gent, Krijgslaan 271, B-9000 Gent, Belgium.

⁴¹ R. H. Wilson, *This Journal*, 127, 228 (1980).

⁴² Naval Weapons Center, Chemistry Division, China Lake, California 93555.

⁴³ M. H. Miles, D. A. Fine, and A. N. Fletcher, *J. Electrochem. Soc.*, 125, 1209 (1978).

⁴⁴ M. H. Miles and A. N. Fletcher, *J. Appl. Electrochem.*, 10, 251 (1980).

heat generated by the direct reaction might be useful in maintaining the high temperature of the molten salt.

K. A. Klinedinst⁴⁵ and M. J. Domeniconi⁴⁶ The authors wish to thank M. H. Miles for a very thoughtful response to this paper. With regard to the use of pure AlCl_3 rather than LiAlCl_4 to form the Li/SOCl_2 electrolyte, it should first be pointed out that such AlCl_3 solutions are suitable only for batteries to be operated in the reserve mode. Thus, the cell is filled with the AlCl_3 solution just before the beginning of its discharge. Tests have shown that, when Li/SOCl_2 cells are activated by the addition of a 4.5M AlCl_3 solution, between 1 and 2 sec are required to reach acceptable operating voltages (for cells discharged at room temperature with a 30 mA/cm² discharge rate). It is clear, therefore, that enough LiAlCl_4 is formed immediately to sustain a moderately high discharge rate.

It is presumed that the further direct reaction between dissolved AlCl_3 , SOCl_2 , and Li to produce LiAlCl_4 is primarily controlled by the rates of diffusion of AlCl_3 to the anode surface and of the reaction products away from the anode surface. We presently have no data on the coulombic efficiency for the lithium anode in pure AlCl_3 electrolyte. It is important to note that this efficiency will be a function of both the rate of discharge and the operating temperature. It is also noted that the heat resulting from the production of the LiAlCl_4 by this direct reaction may help to attain a somewhat elevated temperature which will provide even a greater efficiency of operation of the battery. Alternatively, some solid LiCl may be stored within the battery (e.g., within the porous separator or cathode). The presence of such solid LiCl would hasten the achievement of the minimum LiAlCl_4 concentration required to support a high rate discharge, and the heat produced by the LiAlCl_4 formation reaction could be used to attain the desired operating temperature.

A Study on Activation and Acceleration by Mixed $\text{PdCl}_2/\text{SnCl}_2$ Catalysts for Electroless Metal Deposition

Tetsuya Osaka, Hideki Takematsu, and Kohji Nihei
(pp. 1021-1029, Vol. 127, No. 5)

Rudolph J. Zeblysky⁴⁷ This paper evaluated the characteristics of mixed $\text{PdCl}_2/\text{SnCl}_2$ catalysts used in electroless plating, and concluded that catalytic activity is exhibited only by colloidal systems. A major reason for this conclusion was spectrophotometric data (Fig. 3 in the paper).

I have also conducted similar spectrophotometric measurements on these $\text{PdCl}_2/\text{SnCl}_2$ catalysts solutions and have additional information that assists in understanding the nature of these solutions. My spectrophotometric measurements of $\text{PdCl}_2/\text{SnCl}_2$ catalyst solutions diluted with water similar to Osaka *et al.* produced the same spectra as that described in the paper. I also found that these water-diluted catalysts were unstable and were no longer effective for catalyzing plastics for electroless metal deposition. This would indicate that the water diluted catalyst solutions had decomposed and were no longer representative of the original catalyst solutions.

It is not possible to measure the spectra of undiluted commercial solutions due to spectra intensity. From the above it is clear that the dilution procedure is an important consideration. I have found that the stability of these $\text{PdCl}_2/\text{SnCl}_2$ catalysts is dependent on their environment. Therefore as outlined in several

U.S. patents,⁴⁸ they require sufficient excess chloride ions, excess stannous ions, and acid to maintain solubility and stability of the catalyst complex. Even local or temporary dilution with water can cause catalyst instability and some decomposition. To avoid this decomposition it is usual to use an acidic chloride solution,⁴⁸ e.g., HCl or an acidic chloride stannous solution^{49,50} HCl-Sn^{++} prepolymer to avoid the drag-in of water, which would result in decomposition of the catalyst solution.

In addition to maintaining the stability and solubility of the $\text{PdCl}_2/\text{SnCl}_2$ catalyst, the hydrolysis^{48,50,51} of excess tin compounds present in the catalysts must be avoided to prevent precipitates which will interfere with spectrophotometric measurements. Insoluble tin compounds can form at a pH of about 2 depending on the tin compound present, excess chloride ion, oxygen concentration, and other factors. Water dilution of catalysts can raise the pH, and cause hydrolysis of tin. The dissolved oxygen in the water can also oxidize the Sn(II) to Sn(IV) reducing the excess Sn(II) and chloride ion concentration of the catalysts which cause precipitates in the diluted samples.

Therefore, in order to determine the spectra of $\text{PdCl}_2/\text{SnCl}_2$ solution, I diluted $\text{PdCl}_2/\text{SnCl}_2$ catalyst solutions using the principles outlined in U.S. Patents 3,672,923 and 3,672,938 to maintain catalyst stability. A blank was prepared with the identical composition of the catalyst less the palladium component. A diluting solution consisting of 215 g/liter NaCl and 10 ml/liter HCl (37%) was used to dilute the catalyst and the blank. The PdCl_2 concentration in the diluted sample was 0.01 g/liter. The diluted catalyst produced very sharp, well-defined absorption peaks at 310, 340, and 410 nm, using a Perkin Elmer 552 spectrophotometer. The diluted catalyst also proved effective for catalyzing plastic for subsequent electroless copper deposition, with longer immersion times of 30 min to compensate for the dilution.

In view of the retention of both sharp, well-defined peaks in the spectrophotometric measurements and the catalytic effectiveness of the diluted catalyst, I feel that the nature of the catalyst is different than the results indicated in the paper. The additional work reported here indicates that it is possible to dilute the catalysts and still retain the complex nature of the $\text{PdCl}_2/\text{SnCl}_2$ complex. I propose that the loss of absorption peaks in the water diluted samples was due to decomposition of the catalyst complex in an unstable environment.

T. Osaka⁵² Dr. Zeblysky discussed the spectrophotometric data shown in Fig. 3 of the paper. He claims that the water diluted catalyst solutions do not give the true nature of the catalysts because of their giving no longer catalyst activity.

We have obtained additional information about the spectrophotometric measurements as shown in Fig. 1. Catalysts A, B, and C which show lower catalytic activity became unstable, close to greenish brown color solutions, and finally colorless solutions after several hours when they were diluted 100 or 200 times with 1M HCl . Absorption spectra of samples A, B, and C diluted 200 times with 1M HCl are shown in Fig. 1 as 1, 2, and 3, where the absorption spectra are measured within 1 hr after dilution. They lost the feature of high extinction coefficient conditions and the spectra of 1 and 3 showed wavy curves which seemed to contain very small absorption peaks around 320 ~ 330, 410 ~ 430, and 610 ~ 620 nm. The spectrum of 2 diluted with HCl , which decomposed the fastest, gave a clear ab-

⁴⁸ R. J. Zeblysky, U.S. Pat. 3,672,923 and 3,672,938.

⁴⁹ L. Roger, R. S. Vincent, and H. Wilson, U.S. Pat. 3,627,558.

⁵⁰ A. Rantell and A. Holtzman, *Trans. Inst. Metal Finish.*, 52, 31 (1974).

⁵¹ A. Rantell and A. Holtzman, *Plating*, 61, 326 (1974).

⁵² Department of Applied Chemistry, Waseda University, Tokyo 160, Japan.

⁴⁵ GTE Laboratories, Waltham, Massachusetts 02154.

⁴⁶ Altus Corporation, Palo Alto, California 94306.

⁴⁷ Kollmorgen Corporation, PCK Technology Division, Glen Cove, New York 11542.

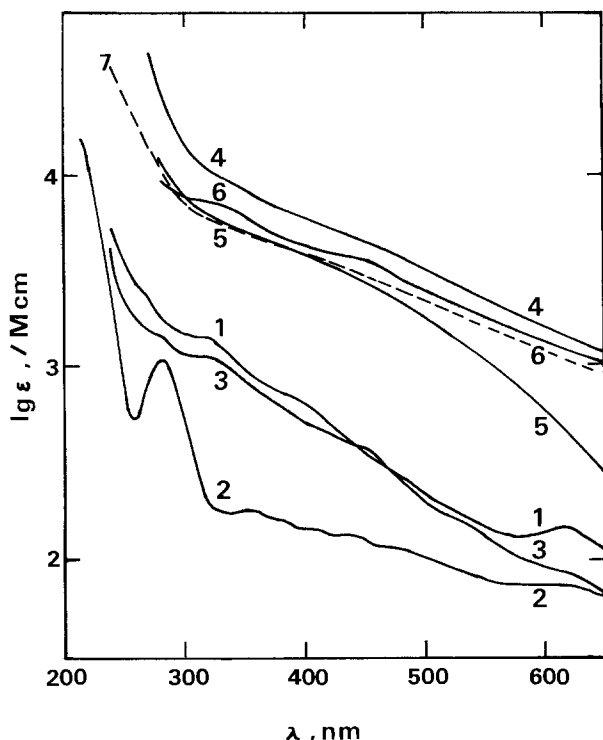


Fig. 1. Absorption spectra of $\text{PdCl}_2/\text{SnCl}_2$ catalysts diluted with various conditions. Curve 1, catalyst A diluted 200 times with 1M HCl (i.e., PdCl_2 0.005 g/liter); curve 2, catalyst B diluted with 1M HCl (i.e., PdCl_2 0.00125 g/liter); curve 3, catalyst C diluted with 1M HCl (i.e., PdCl_2 0.005 g/liter); curve 4, catalyst D diluted 100 times with distilled water (i.e., PdCl_2 0.01 g/liter); curve 5, catalyst D diluted 100 times with 1M HCl (i.e., PdCl_2 0.01 g/liter); curve 6, catalyst D diluted 100 times with 215 g/liter NaCl and 10 ml HCl (37%) (i.e., PdCl_2 0.01 g/liter); curve 7, (dashed line) catalyst D diluted 200 times with water (the same as D in Fig. 3 of the paper).

sorption peak of 280 nm with lasting high extinction coefficient. Samples A, B, and C, however in the case of water dilution, gave the linear high extinction coefficient as shown in Fig. 3 of the paper.

In the case of catalyst D which has higher catalytic activity, the solutions of three different dilution (shown as 4, 5, and 6 in Fig. 1) are stable in contrast to those of samples A, B, and C and their absorption spectra show the feature of high extinction coefficient absorption similar to those of Fig. 3 of the paper (data in the paper are diluted 200 times with water). The high extinction coefficient absorption spectrum of 6 which is diluted with the same dilution solution as that of Dr. Zeblicky seems to contain small absorption peaks around 320 ~ 330 and 420 ~ 430 nm. The sample D solution diluted with HCl or (NaCl + HCl) was stable until about one day and after one day the solution decomposed completely and gave the colorless solution (in this case the precipitates were not noticed because of small amount of palladium concentration). The water diluted catalyst D solution gave the same conditions as dark brown color solution with high extinction coefficient absorption for a long time.

As for the results of the functionality test of the diluted catalysts using electroless nickel deposition (bath composition was already shown in the paper), the HCl or (NaCl + HCl) diluted sample D solution (5 or 6 in Fig. 1) initiated the nickel deposition after immersion time of 10 min with HCl acceleration of 30 sec on copper sheet and also glassy epoxy plastic board. The water diluted sample D solution did not activate the nickel deposition as pointed out by Dr. Zeblicky using electroless copper plating. We found, however, very interesting results that the catalytic activity of water diluted sample D solution is restored by the addition of several drops of HCl (37%) even

though HCl is added after one day and that the water diluted solution with the addition of HCl initiates the nickel deposition.

The water diluted catalyst solution is considered to no longer give the catalytic activity because of the formation of stannous or stannic hydroxide on colloidal particle surfaces due to the change of solution pH, but the addition of HCl is considered to activate the water diluted catalyst solution because of the dissolution of stannous or stannic hydroxide on colloidal particle surfaces which covers the active core. It is concluded from the above results that a large excess of Cl^- ion environment accelerates the decomposition of the dark brown intermediate and the reformation of green intermediate, and that it finally enhances the formation of black precipitate of palladium metal. The data of the absorption spectrum by Dr. Zeblicky which produces well-defined absorption peaks at 310, 340, and 410 nm are considered to result from the solution conditions where both the green and dark brown intermediates coexist. This is also supported by the fact that the solution color of catalyst changes immediately from dark brown to greenish brown when the catalyst solution is diluted with HCl. Since the freshly prepared catalyst B, which has greenish dark brown color and gradually becomes dark brown with several minutes, showed much lower catalytic activity in our functionality test, the green color intermediate may have lower catalytic activity, and it is also the other possibility in the long time immersion experiment of diluted catalyst solution by Dr. Zeblicky that the palladium metal particles of precipitate which are produced by long-term immersion accelerate the metal deposition.

The functionality test of acidic mixed $\text{PdCl}_2/\text{SnCl}_2$ solution was reported by Nagai *et al.*⁵³ using electroless copper plating and they concluded that the intermediate with dark brown color gives active sites rather than that with green color whose absorption spectrum shows three or four peaks at 290, 325, 420, and 640 nm,⁵⁴ where the absorption peak at 290 nm is due to palladium ions. We also investigated this catalyst system using electron diffraction analysis⁵⁵ and found that the particle sizes adsorbed on substrate become larger with the aging process which enhances the catalyst activity (cf., the difference of catalyst preparations between A and D).

Therefore, we can conclude that the catalyst solution having higher activity is relatively stable against environment and that the feature of absorption spectrum with high extinction coefficient, which is observed in all cases of water, HCl, and (NaCl + HCl) diluted catalyst D solutions, informs the true nature of the catalyst solution with dark brown color which gives the higher catalytic activity, and we can finally conclude that the dark brown intermediate should be colloidal states and that the colloidal particles adsorbed on substrate give active sites rather than soluble complexes. The above final conclusion can also be supported by the fact that the aging process, which is an important procedure in the preparation to enhance the catalytic activity, produces the distribution of well-defined larger colloidal particles in solution.

Mixed Potential Analysis of Sulfation of Molten Carbonate Fuel Cells

Dan Townley, Jack Winnick, and H. S. Huang
(pp. 1104-1106, Vol. 127, No. 5)

Thomas E. Tang⁵⁶ and J. R. Selman⁵⁷ Townley *et al.* present a thermodynamic model to estimate the effect

⁵³ M. Kose, T. Kishi, H. Yamamoto, and T. Nagai, *Kinzoku Hyomen Gijutsu (J. Metal Finish. Soc. Jpn.)*, 24, 203 (1973).

⁵⁴ M. Tsukahara, T. Kishi, H. Yamamoto, and T. Nagai, *ibid.*, 23, 83 (1972).

⁵⁵ T. Osaka, H. Nagasaka, and F. Goto, *This Journal*, 127, 2343 (1980).

⁵⁶ Institute of Gas Technology, Chicago, Illinois 60616.

⁵⁷ Department of Chemical Engineering, Illinois Institute of Technology, Chicago, Illinois 60616.

of H₂S on molten carbonate fuel cell performance. They make use of six experimental data points reported by the Institute of Gas Technology [IGT, Ref. (2)] and by United Technologies Corporation [UTC, Ref. (1)].

We would like to point out that several experimental results in these reports clearly invalidate the assumptions used by Townley *et al.* We refer in particular to the following.

1. Thermodynamic equilibrium relations (Eq. [39-c]) are used to calculate the potential shifts due to H₂S in the anode gas, at a given current load. Not only is this logically inconsistent, it is also in contradiction to experimental observations. The open-circuit potential of the anode is negligibly affected by moderate H₂S levels in the fuel gas, however, anode overpotential (polarization) is strongly affected [see, for example, Ref. (1) of the original paper, pp. 5-22 and Ref. (2), pp. 5-12]. This points not to thermodynamic, but to kinetic or mass-transfer limitations, which cannot be interpreted in a physically meaningful way by shifts in equilibrium ("mixed") potential and a pseudo-thermodynamic Henry coefficient for H₂S.

2. Sulfation of the electrolyte is assumed to be mainly responsible for the effect of H₂S. The sulfate [6a] and sulfide [6b] equilibria, if applied consistently in a thermodynamic reaction model, may indeed predict a considerable degree of sulfation (>75%) of the carbonate electrolyte, as Townley *et al.* indicate in their Table III. The conditions which favor sulfation have been discussed extensively in the IGT and UTC reports referenced by the authors (3, 4 of the original paper). However in actual fuel cells such a high degree of sulfation is simply not found; see, for example, Table 3-3 of Ref. (3). Therefore, it appears groundless to ascribe the potential loss upon introduction of H₂S to an equilibrium sulfation process.

We conclude that the concept of a pseudo-Henry coefficient put forward by Townley *et al.* is of very limited utility for predicting performance loss. Certainly, much more extensive data than they used (Fig. 1) would be necessary to verify the concept. That the applicability of a pseudo-constant to the experimental data may have an entirely different cause, is suggested by the similarity of the Nernst relations [39-c] and the Tafel relation written for constant current density

$$\eta = \text{constant} - \frac{RT}{\alpha_a F} \ln i_0$$

Here i_0 (of hydrogen oxidation) may be assumed to depend on $p_{\text{H}_2\text{S}}$. For example, the IGT data presented in Fig. 1 are correlated quite well by

$$\eta_{\text{H}_2\text{S}} (\text{mV}) = -47.5 + 91.5 \log p_{\text{H}_2\text{S}} (\text{ppm})$$

which would suggest a reaction mechanism with $\alpha_a = 2$ and $i_0 (\text{H}_2) \sim p_{\text{H}_2\text{S}}^{-1}$.

Our intention here is not to speculate about such a reaction mechanism but to caution against "simple," but equally speculative, correlations and models which ignore important experimental information. Also, more systematic experimental work is needed to make analysis fruitful.

Furthermore, we believe that the term "mixed potential" should remain reserved for the potential of an electrode at which multiple electrode reactions proceed, each at a finite rate. The potential analyzed by Townley *et al.* is the common equilibrium potential of electrode reactions [29-c].

Finally, the free energy changes for the sulfation reactions [6a] and [6b], quoted as taken from an IGT report [Ref. (3) of original paper], are not correct. The IGT data (3) are, for [6a] + 20.5 kcal/mole, and for [6b] - 0.6 kcal/mole ($M = \text{Na}$). This is substantially different from, respectively, + 7.7 kcal/mole

and -1.7 kcal/mole. It is nowhere mentioned that these and other data are for 923 K (650°C) only.

Dan Townley,⁵⁸ Jack Winnick,⁵⁸ and H. S. Huang:⁵⁹

The main criticism of Tang and Selman (TS) relates to the fact that our treatment predicts a high sulfur-species thermodynamic activity at the anode. Yet chemical analysis has found little in the electrolyte from fuel cells run with H₂S contaminant at ppm levels. As we suggested the activity may be strongly affected by the presence of the electrode and matrix materials, neither of which were present during the equilibrium measurements. The condition of interest is that at the electrolyte-electrode-gas interface. In a recent study Energy Research Corporation (ERC), following a sulfur tolerance test, analyzed the bulk electrolyte, the layer adjacent to the anode, and the electrolyte within the anode structure.⁶⁰ The total quantity of sulfur found is not great. However, they find a gradient in sulfur species, increasing as the anode is approached. No technique has yet been capable of analyzing the material in the immediate vicinity of the actual interface. Here it is expected that, under closed-circuit conditions, the gradient is very steep and the interfacial electrolyte has a high sulfur-species activity.

In the ERC chemical analysis, furthermore, little insoluble (*i.e.*, Ni or Co) sulfide was found.⁶⁰ These sulfides are expected if the anode material, composed of metallic Ni and Co, were being sulfided by the H₂S present in the fuel gas. This information provides even more support for the conclusion that the main cause of the loss of voltage is the alteration of the electrolyte at the interface.

The observation that the open-circuit potential is unaffected by H₂S is entirely consistent with our treatment. As stated in our note, the value of H^{-1} calculated is a function of the current density. This dependence is based on the diffusion of reacting species to and from the interface. The gas diffusion portion of H^{-1} can be removed by finding, as a function of current density, the partial pressures of the reacting species at the interface. Wilemski *et al.*⁶¹ have developed a sophisticated model of the processes occurring at the anode. We have used their gas-phase physical property data as well as their effective diffusivities through the electrode to carry out these calculations. These values for the partial pressures are then used in our Eq. [1], [3a-c], and [4] to calculate a value of H^{-1} which does not depend on current density. A much smaller value is found and the calculations then show little effect of H₂S at open-circuit conditions.

For example, at a current density of 160 ASF, for 75% utilized low BTU fuel, the ratios of activities at the surface, a_e , and in the bulk, a_b , for hydrogen and water, are calculated at about

$$(a_{\text{W,e}}/a_{\text{W,b}}) = 1.2 \quad \text{and} \quad (a_{\text{H}_2\text{e}}/a_{\text{H}_2\text{b}}) = 0.5$$

The electrolyte composition is seen to be strongly dependent on the partial pressures of hydrogen and water. The activity of carbonate ion, as expressed in Eq. [3a-c] and [4], depends upon $(a_{\text{H}_2\text{e}}/a_{\text{W,e}})^4$. The above calculated values cause this ratio to be around 3% of the ratio in the bulk gas. At open circuit, however, the ratios are identical. The net effect of this calculation is to show that very little sulfation of the electrolyte occurs at open circuit, in complete agreement with experiment.

TS's criticism of the free energy values used for reactions [6a] and [6b] is more puzzling. Those preferred by Tang and Selman are taken from the JANAF tables

⁵⁸ Georgia Institute of Technology, Atlanta, Georgia 30332.

⁵⁹ Argonne National Laboratory, Argonne, Illinois.

⁶⁰ A. Pigeaud, Energy Research Corporation, Quart. Report, DOE Contract TE AC 03 ET11304 (July 1980).

⁶¹ G. Wilemski, T. Wolf, D. Bloomfield, M. L. Finson, E. R. Pugh, and K. L. Wray, "Performance Model for Molten Carbonate Fuel Cells, Final Report for 5 July 1979," Physical Sciences, Incorporated, Woburn, Massachusetts August 1979.

for $M = \text{Na}$. These values do not agree with the experimental results reported on pages 3-11 in the same reference for $M = 0.62 \text{ Li}, 0.38 \text{ K}$. These free energies were obtained by bubbling the gas through free electrolyte. In an operating cell there are two additional phases, LiAlO_2 and the electrode, which we feel may alter the activity coefficient of the H_2S through surface effects. Furthermore, as stated in the note, the free energy changes used for the reactions need not be accurate to predict the proper $\eta_{\text{H}_2\text{S}}-P_{\text{H}_2\text{S}}$ curve. They do have a large effect on the calculated activities of sulfide and sulfate in the electrolyte and on H^- , but very little effect on the calculated $\eta_{\text{H}_2\text{S}}$. All data used are indeed for 650°C .

Finally, we agree with TS that, in many instances of limited experimental information, a kinetic interpretation may yield a description equivalent to a thermodynamic one. That however, is not the case here. Our treatment involves but one empirical parameter to adequately characterize two independent sets of data, run with quite different fuel utilizations. On the other hand, a kinetic expression, uniquely defined in terms of H_2S concentration, can characterize only that one data set from which its two empirical parameters are determined.

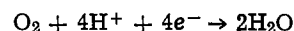
Voltage Losses in Fuel Cell Cathodes

R. P. Iczkowski and M. B. Cutlip (pp. 1433-1440, Vol. 127, No. 7)

Philip N. Ross, Jr.⁶² The authors are to be commended for the scope of the analysis of transport processes in polytetrafluoroethylene (PTFE)-bonded air cathodes, particularly the use of the Stefan-Maxwell equations for multicomponent gaseous diffusion. Their analysis is also the first to include the possible variation in Galvani potential within the electrolyte-filled agglomerates due to the effective resistivity of the electrolyte. As the authors show in Fig. 4, the resistive component is the largest component of voltage loss in a particular electrode to which they applied their analysis. They have, however, done very little to justify the physical model of the electrode structure to which their mathematical analysis was applied. The importance of establishing the physical validity of the model is appreciated by the authors who state: "This model is useful to evaluate how much voltage loss is caused by each of the basic transport processes . . . identification of the most important sources of voltage loss allows research and development efforts to be directed towards the minimization of these voltage losses." The model will be useful in directing structure development only if the adjustable parameters of the model are truly related to real physical characteristics of the structure. Otherwise the model is just another example of parametric curve-fitting. The authors have done both themselves and electrochemical science an injustice by not properly exercising the model. Instead of applying the model to a single electrode (whose structural characteristics are not described), the model should have been applied to electrodes of variable structure and electrolytes of variable conductivity to determine whether the adjustable parameters relate to physical properties in a meaningful way. For example, Klinedinst *et al.*⁶³ have shown that the structure of the PTFE-carbon black composite, *i.e.*, the radius of flooded agglomerates, can be controlled by variation of the weight fraction of PTFE solids and the curing time and temperature. One would expect, for example, that as the weight fraction of PTFE solids varies, the effective agglomerate radius would change, and the voltage loss due to dissolved oxygen diffusion in the agglomerate should vary proportionately. Klinedinst

*et al.*⁶³ have also demonstrated analytical methods for independently measuring the effective agglomerate radius. In a Vulcan XC-72R/TFE-30 composite containing 50 w/o TFE solids cured at 610 K the independently measured⁶³ agglomerate radius is *ca.* 10^{-6}m . It would be of great interest to know whether the value of r_a determined by application of the model to polarization curves from this type of electrode is of the correct magnitude. According to the model, changing the conductivity of the electrolyte should decrease the "ohmic" component of the voltage loss. Again, exercising the model with the same electrode in phosphoric acid of variable concentration, and therefore variable conductivity, would provide a more adequate test for validity of the analysis, particularly the suspect treatment of ionic conduction in the catalyst layer.

The treatment of ionic conduction within the agglomerate, and its effect on electrode polarization, is over-simplified and the conclusions related to it misleading. The authors simply write Ohm's law to relate the Galvani potential in solution (in their notation E_1) to the ionic current, and then assume the electrochemical reaction rate depends only on $(E_e - E_1)$, the catalyst-solution Galvani potential difference. This treatment is incorrect. Physically, the process they attempt to describe is actually an ionic diffusion polarization due to the absence of excess supporting electrolyte. Hydrogen ion is consumed at the catalyst surface via the reaction



The appropriate diffusion equation is that for a binary electrolyte where one of the two ionic species is electroactive. For this case, it can be shown⁶⁴ that the gradient in hydrogen ion concentration is related to the ionic current by

$$-I_1(z) = n_+ \left(1 + \frac{n_+}{|n_-|} \right) D_+ F \frac{dC_+}{dz} \quad [1]$$

where z is the spatial variable in the author's Eq. [33] and [34], n_+ and D_+ are the hydrogen ion valence and diffusivity, respectively, n_- is the anion valence, and C_+ the hydrogen ion concentration. The ionic concentration at any point is related to the Galvani potential in solution from the equilibrium condition of the (inert) anions

$$\bar{\mu}_- = \mu_- + RT \ln C_- + |n_-| F E_1 = \text{constant} \quad [2]$$

and the electroneutrality condition

$$n_+ C_+ = |n_-| C_- \quad [3]$$

Equations [1]-[3] must be solved simultaneously with the diffusion equations for the dissolved neutral species and the kinetic rate equation. It is also important to note the coupling between hydrogen ion concentration and reaction rate was neglected. In fact, the rate of oxygen consumption at any point z in the agglomerate is given by⁶⁵

$$N_1(z) = \left(\frac{K}{4F} \right) (C_+) \exp [-(E_e - E_1)/T_s] \quad [4]$$

where C_+ , E_e , and E_1 are functions of z , and not by the simpler expression used by the authors

$$N_1(z) = \left(\frac{K'}{4F} \right) \exp [-(E_e - E_1)/T_s] \quad [5]$$

The stronger coupling of ionic conductivity with the oxygen consumption rate implied in Eq. [4] *vs.* Eq. [5] would mean, in principal, an even larger effect of internal resistance on the total polarization for an electrode than would be computed in the model presented.

⁶² Lawrence Berkeley Laboratory, Materials and Molecular Research Division, Berkeley, California 94720.

⁶³ K. Klinedinst, W. Vogel, and P. Stonehart, *J. Mater. Sci.*, **11**, 794 (1976).

⁶⁴ K. J. Vetter, "Electrochemical Kinetics," pp. 166-170, Academic Press, New York and London (1967).

⁶⁵ A. Damjanovic, D. Sepa, and M. Vognovic, *Electrochim. Acta*, **24**, 887 (1979).

In work at our laboratory, we have used the current ratios for varying oxygen partial pressure to separate ionic diffusion losses from molecular diffusion losses in air cathodes. We have found⁶⁶ that ionic diffusion losses of 5-10 mV per 100 mA/cm² current density are observed only when the acid concentration exceeds 98 w/o, e.g., 99 w/o acid shows a 7.5 mV resistance polarization at 200 mV/cm² but only ca. 2 mV is observed in 95 w/o acid. We postulate that the dramatic appearance of this internal resistance polarization is due to a change in the majority proton species from [H₉O₄]⁺ to [H₄PO₄]⁺ in this region of concentration.

In their discussion on optimum electrode thickness, the authors express a very interesting rationale for the variations in voltage loss with PTFE content (at fixed Pt loading). In their model increasing PTFE content increases E_a , the agglomerate tortuosity factor, reducing diffusion losses (see Eq. [28] of the paper) but increasing voltage loss due to the "ohmic" component. Too little PTFE results in large diffusion losses and too much PTFE results in excessive "ohmic" loss, the optimum PTFE probably occurring at the crossover point for these competing effects. The conventional wisdom concerning the increase of voltage loss with PTFE content above the optimum has been that the structure has "dry" catalyst above a certain PTFE level. The authors present a new and more compelling explanation.

Finally, two assumptions were made in applying the model to phosphoric acid fuel cell cathodes that appear questionable, and further affect the general applicability of the breakdown of the losses shown in Fig. 4. Inside the gas pore, water vapor is assumed to be in equilibrium with the electrolyte at every point z .

⁶⁶ P. Ross, Lawrence Berkeley Laboratory Report, Materials and Molecular Research Division, LBL-10799 (May 1980).

If this were always the case, the polarization curve at zero oxygen utilization would not depend on the partial pressure of water in the bulk air stream (in back of the substrate). This is in fact not the case, as we have observed that polarization curves for purely dry oxygen and for oxygen presaturated to the water vapor pressure of the bulk electrolyte are significantly different, e.g., the dry gas curve shows lower polarization. The magnitude of the diffusion losses determined by application of this model to polarization curves will depend critically on the kinetic parameters for oxygen reduction that are used, particularly the Tafel slope. The breakdown of voltage losses shown in Fig. 4 were produced by use of a 90 mV/decade Tafel slope, referring to the work of Kunz and Gruver⁶⁷ as having determined this parameter independently. Careful reading of the cited article reveals a circular argument, since PTFE-bonded electrodes were used in the cited work to arrive at the 90 mV/decade Tafel slope with transport modeling employed to "deduce" this kinetic parameter. The definitive determination of the kinetic parameters for smooth platinum in concentrated H₃PO₄ appears to be the recent work by Yeager and co-workers,⁶⁸ and shows that the Tafel slope is 120 mV/decade. For platinum clusters dispersed on carbon black, we have found⁶⁹ that the true Tafel slope depends on the microstructure of the clusters (105-115 mV/decade), but for a catalyst like that used by Kunz and Gruver the true Tafel slope is 105 ± 5 mV/decade, instead of 90 mV/decade. It would be of interest to know how the analysis of losses in real fuel cell electrodes changes in light of these new kinetic parameters.

⁶⁷ H. Kunz and G. Gruver, *This Journal*, 122, 1279 (1975).

⁶⁸ J. Huang, R. Sen, and E. Yeager, *ibid.*, 126, 786 (1979).

⁶⁹ P. Ross, Abstract 190, p. 508, The Electrochemical Society Extended Abstracts, Los Angeles, California, Oct. 14-19, 1979.

Erratum

In the paper "The Solubilities of NiO, Co₃O₄, and Ternary Oxides in Fused Na₂SO₄ at 1200°K" by Dilip K. Gupta and Robert A. Rapp which appeared on pp.

2194-2202 in the October 1980 JOURNAL, Vol. 127, No. 10, Fig. 1 and 2 should be as follows:

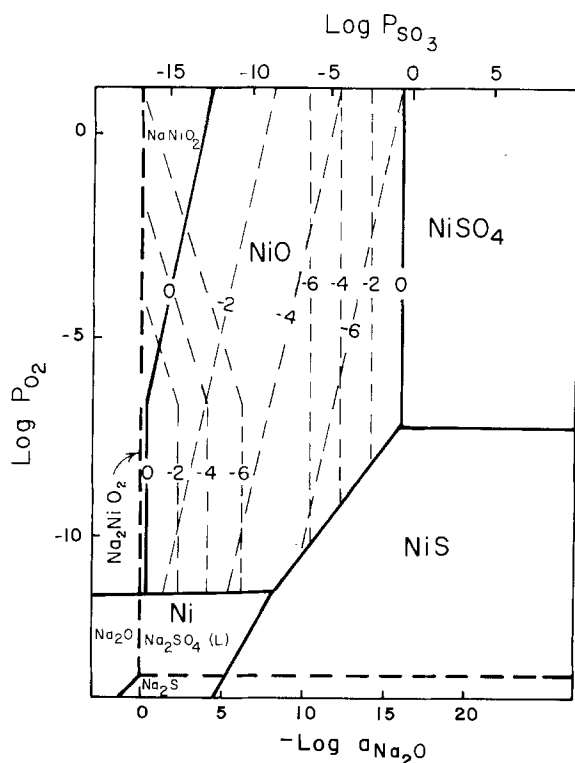


Fig. 1. Thermodynamic phase stability for Na-Ni-S-O system at 1200°K.

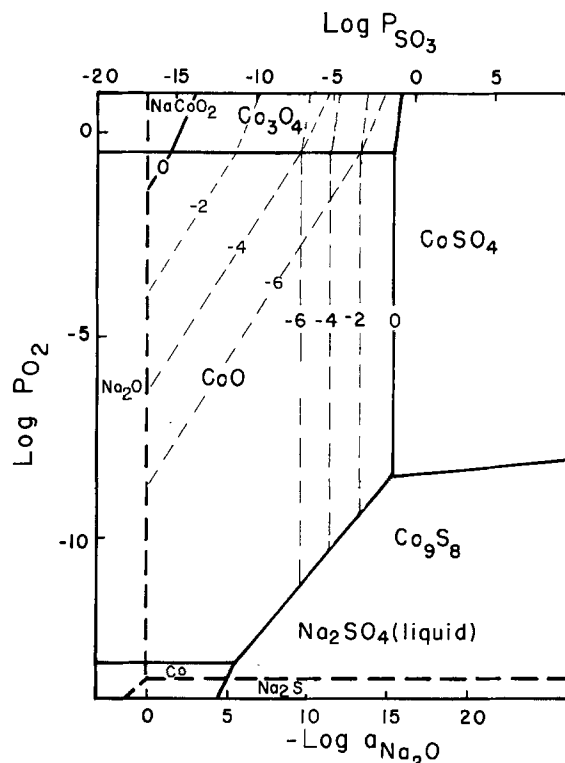


Fig. 2. Thermodynamic phase stability for Na-Ca-S-O system at 1200°K.



A Titanium Dioxide Hydrogen Detector

L. A. Harris

General Electric Company, Corporate Research and Development Center, Schenectady, New York 12301

ABSTRACT

Sputtered films of titanium dioxide several thousand angstroms thick and sandwiched between a layer of titanium and a layer of platinum are highly selective detectors of hydrogen. The resistance of the device decreases on exposure to hydrogen. At concentrations above 0.5% H_2 in air, the response is rapid and limited by lead resistance. At lower concentrations the response is proportional to concentration but relatively slow at room temperature. Moderate increases in temperature quicken the response. The detectors may be used as effective alarm devices at room temperature, with a-c or d-c circuitry that requires negligible power in the absence of hydrogen.

It is well known that reducing gases can donate an electron to the conduction band of some normally insulating oxides, thereby greatly increasing the conductivity of the oxide (1-7). This principle has formed the basis of several solid-state detectors for a variety of gases (5-12). Most of these detectors exhibit changes in conductivity along their surface due to surface adsorption of the reacting gas and thus frequently respond to a variety of gases.

If the detector response depended on diffusion of a particular species within the solid then it could be made specific for those gases that give rise to the diffusing species. A case in point is titanium dioxide (TiO_2) in its rutile form, in which the diffusion of hydrogen (protons) is a much studied phenomenon (13-16). Here, H atoms can enter the lattice and in doing so become ionized to produce a mobile interstitial proton and a conduction electron, a process that can readily occur even at room temperature (3, 4).

For these reasons, and encouraged by an earlier suggestion of Johnson *et al.* (16), some simple experimental crossed-film detectors were constructed and tested. This paper describes some of the characteristics of these devices in which the current flows through, instead of along the surface of, the thin insulating or semiconducting film.

Construction

The devices were made by successive depositions of thin films on standard glass microscope slides. The first film was a 3000Å layer of TiO_2 sputter deposited onto the clean slide. This layer was covered by a 1000Å film of Ti metal which, in turn, was covered by a second sputter deposited layer of TiO_2 in thicknesses ranging from 500 to 3000Å. The sputtering was done in an rf system in argon for Ti and in 50% argon, 50% O_2 for TiO_2 . The gas pressure was approximately 2.5 Pa (18-20 microns) and the rf power was 500W. With the target voltage raised to 1700V the deposition rate was approximately 90 Å/min. The slides rested on a water-cooled support which kept plasma heating of the substrates to about 200°C. X-ray diffraction showed the films to be principally anatase, with a trace of rutile.

Key words: titanium dioxide, hydrogen detectors, hydrogen sensors, gas detectors, instruments, sensors, indicators.

All of the above films covered the entire slides except for two small areas of Ti metal left uncovered near the ends of the slide for contacts to that film.

A coating of lacquer (Hunt Waycoat negative photoresist) was painted by hand over the second TiO_2 layer except for a 2-3 mm strip down the center of the slide and the two Ti contact areas. This configuration was chosen as the simplest one that would prevent gas-induced conduction on the TiO_2 surface between the Ti contacts and the Pt cross strips to be applied later. These cross strips, 200Å thick and 1 mm wide, were electron-beam evaporated after the lacquer was thoroughly dried and polymerized by exposure to u.v. light. Figure 1 shows schematically the disposition of the various layers comprising the detector slide.

The first film of TiO_2 was included to balance the stresses on the base metal layer (Ti) after earlier attempts using noble metals (Au and Pt) on glass

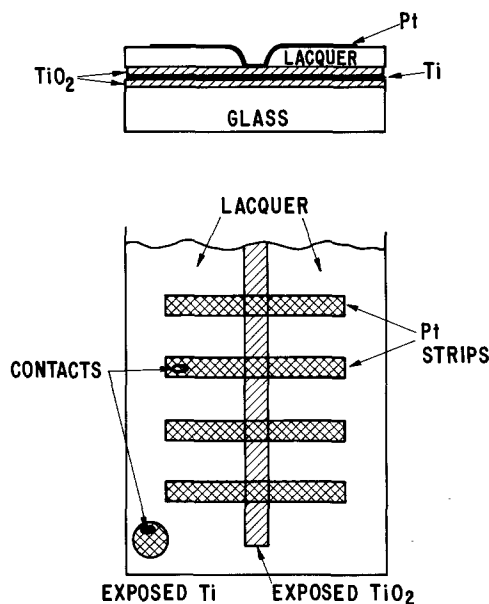


Fig. 1. Schematic illustration of hydrogen detector construction

failed by peeling. The TiO_2 layer improved the situation, but noble metals were still unstable. Ti and Cr films were found to be stable, but Cr films showed no sensitivity to hydrogen, presumably because of the highly insulating layer of Cr_2O_3 on its surface. With Ti films it may be possible to omit the first TiO_2 layer.

Platinum was chosen for the top film for its ability to dissociate molecular hydrogen to the atomic form that can diffuse into the TiO_2 .

Detectors made in this way were not uniformly successful. On some slides most of the junctions had excessive conductance even at very low voltages, while other junctions exhibited extremely low conductances. The junctions tested were selected from the latter group having typical junction conductances of the order of 10^{-7} mhos or less, measured in the absence of hydrogen.

Experimental

Samples were tested by attaching leads to the Ti and Pt films with indium solder, after first applying contact pads of silver paint. A potentiostat (Pine Instruments Company RDE 3) acted as a regulated power supply and current converter. For logarithmic current plots, a Keithley Model 26000 Logarithmic Picoammeter in series with a resistor measured the output voltage of the potentiostat's current indicator. The voltages (V) applied for testing were scaled roughly with TiO_2 layer thickness (d) to keep the average field (V/d) less than about 10^5 V/cm. In what follows the voltage or bias is that of the Pt film with respect to the Ti film.

The detector slides were mounted inside a jar or a small metal oven through which the test gas could be flowed and then vented to air. When the oven was used, the slide rested on a thin stainless steel tray to which a Chromel-Alumel thermocouple was attached.

The test gas was made by mixing hydrogen with air or nitrogen through a two-stage dilution system consisting of the valves and flowmeters indicated in Fig. 2. The mixed gas passed through a drying (Drierite) tube and a small three-way valve mounted near the test chamber. This arrangement allowed the gas flow to be diverted to the room while it was adjusted to the desired mixture, and after the feed lines had equilibrated the gas was directed to the test chamber. Usually hydrogen was mixed with air because it was found that the current decreased only very slowly after hydrogen removal if oxygen was not present in the ambient gas.

To the extent possible the flow rate through the test chamber was held at about 2.5 SCFH (≈ 20 cm³/

sec) as indicated by the flowmeters. At this rate the largest test chamber had a complete change of gas in about 12 sec. The concentrations of H_2 in air quoted in this paper are only approximate because of instabilities in the gas flow and the imprecise nature of the small plastic meters and their associated valves. An approximate correction for the flow of H_2 through flowmeter B (Fig. 2) was applied after measuring flow rates with a bubble meter.

Qualitative tests of the sensitivity of detectors to gases other than H_2 were made by flowing undiluted chemically pure gases from lecture bottles through the test chamber and noting any change in response from that for dry air.

Some brief experiments were done in a humidity chamber to assess the value of these devices as humidity sensors. Though some response was obtained, it was so slight as not to warrant further investigation.

Except for one test, all of the measurements were made under d-c or slow sweep conditions (100 mV/sec). In that one case the complex admittance of the detector was measured with a Hewlett-Packard Model 3042A Network Analyzer at frequencies from 100 Hz to 10 MHz both in air and in pure H_2 at room temperature.

Results

The volt-ampere characteristics of a detector with a 3000Å (TiO_2) thickness are shown in Fig. 3, both in the absence and in the presence of hydrogen. Generally similar results were obtained with thinner specimens, but the slope or conductance of the curve at the origin tended to increase as the thickness decreased. Owing to the variability of junctions even on the same slide it is not possible to quantify any thickness dependence reliably.

Notable features of Fig. 3 are the asymmetrical or rectifying nature of the curves both with and without H_2 present, the marked hysteresis of the positive segment of the curve with H_2 present, and of course the very large increase in current for H_2 for both polarities. (Note the scale change indicated on Fig. 3.) All of these features are discussed in the section to follow.

Figure 4 shows the current response and recovery times for exposure of a 1000Å detector to pure H_2 for several negative and positive biases. The rapid current onset and the delay in current fall after H_2 flow ceased suggest that the current response is triggered by much lower partial pressures of H_2 than the atmospheric pressure used in this test.

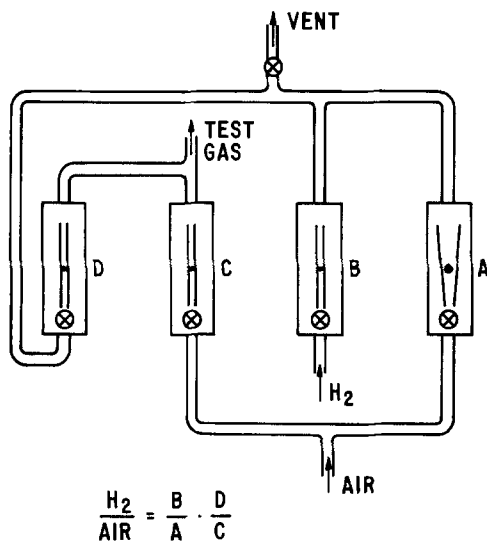


Fig. 2. Arrangement of valves and flowmeters for two-stage dilution of hydrogen in air.

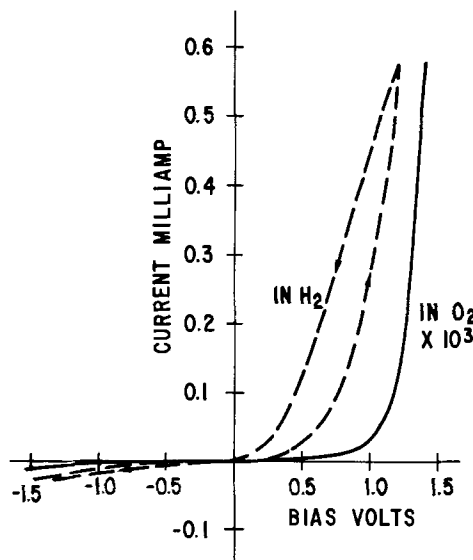


Fig. 3. Current-voltage characteristics of detector 4A, 3000Å thick, in oxygen and in hydrogen. Voltage scan rate was 100 mV/sec.

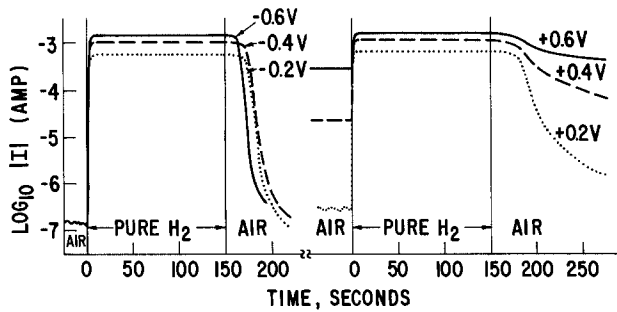


Fig. 4. Response and recovery of detector 2B, 1000 Å thick, to 100% hydrogen for several negative (left) and positive (right) bias voltages at room temperature.

Figure 5 shows the corresponding responses of the same device to 4500 ppm (0.45%) of H₂ in air. About the same saturation values are reached as for 100% H₂, but the response time is longer and the recovery time shorter, consistent with more rapid dilution to subsaturation levels of H₂. Figure 5 shows more clearly than does Fig. 4 that the response when H₂ is introduced is quicker for positive bias than for negative, but the converse is clearly true with respect to recovery.

The saturation currents in Fig. 4 and 5 correspond to a total device resistance of roughly 350Ω. If the resistance of the thin Pt film between the contact and the overlap area is estimated by taking half the measured resistance of the Pt film from the contact to its other end a similar magnitude is obtained. This crude correspondence suggests that with H₂ present most of the device resistance is associated with the Pt connection and not with the TiO₂ layer between Pt and Ti.

The slow response to lower concentrations of H₂ (900 ppm in air) at room temperature is more dramatically shown in Fig. 6. Although the response with positive bias is notably faster, in neither case does it give a meaningful indication of H₂ concentration in reasonable observation times (less than 10-15 min). The momentary drop in current for positive bias at about 20 sec on the time scale is related to the internal

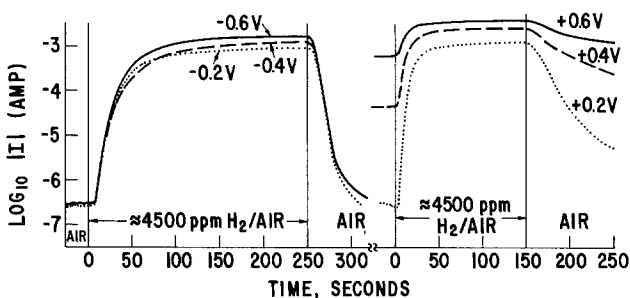


Fig. 5. Response and recovery of detector 2B to 0.45% H₂ in air at room temperature.

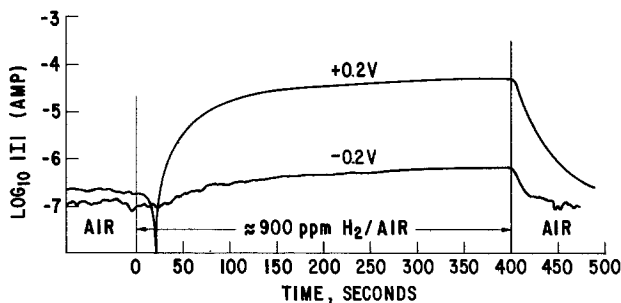


Fig. 6. Response of detector 2B to 0.09% H₂ in air at room temperature.

fields in the TiO₂ layer and is discussed in the section to follow.

Response and recovery times might be expected to depend on thickness and temperature. As noted above it was not possible to make reliable quantitative measures of thickness dependence, but some qualitative features may be noted. There appeared to be little significant difference in rates or saturation levels with thickness though the thickest films 3000 Å may have been somewhat slower. The principal result of increasing thickness was a lowering of the background current, which in effect lowers the threshold of detectable current changes. Thus, given enough time, a 3000 Å detector gave an observable response to as little as 20 ppm H₂ in air, when the background current in air was about 10⁻⁹A.

In contrast to thickness, temperature had a dramatic effect on the speed of responses. Figure 7 shows how the risetime decreased as temperature was raised, even for the low concentration of 900 ppm H₂ in air (cf. Fig. 6) and for a small negative bias. (The data of Fig. 7 were obtained from a different junction from the one used in Fig. 6, but both were nominally 1000 Å thick.) So far as can be judged, given the rough reproducibility of the gas mixture from test to test, the steady-state response of the detector was relatively independent of temperature. It was observed to shift quite readily with minor adjustments of the gas mixture.

This steady-state response, now observable at elevated temperature, was approximately linearly dependent on H₂ concentration, as Fig. 8 shows, down to about 500 ppm below which the response was not

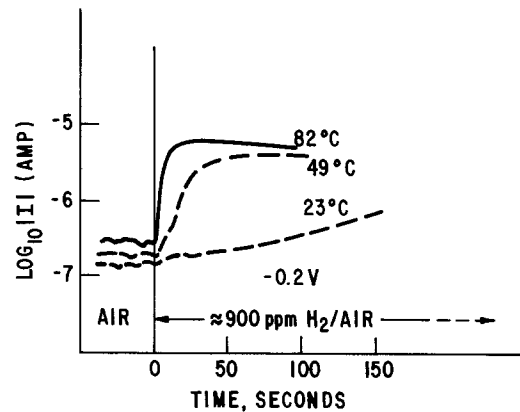


Fig. 7. Response of detector 11B, 1000 Å thick, to 0.09% H₂ in air at several temperatures.

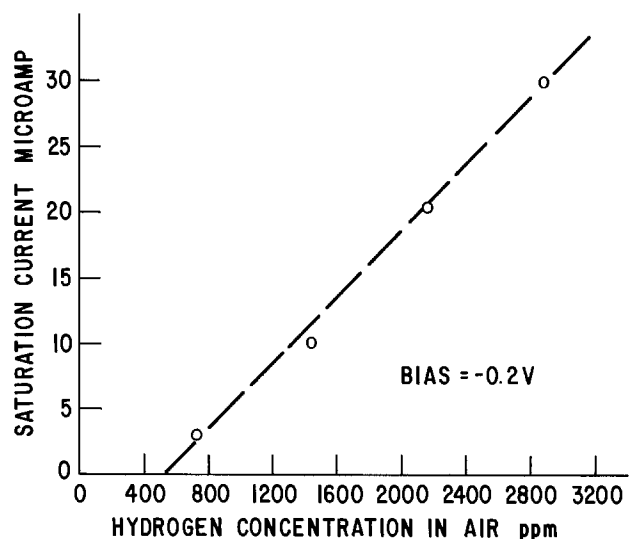


Fig. 8. Dependence of saturation current on hydrogen concentration in air for detector 11B, with -0.2V applied, at 82°C.

detectable. These data were obtained with negative bias only, as that was judged to be the more useful mode of operation.

Failure of the detector current to recover from H₂ exposure in the absence of oxygen was noted earlier. This behavior is illustrated in Fig. 9, in which pure H₂ was used for about 58 sec followed by pure N₂ for another 172 sec, at which time the gas was changed to pure O₂ and the current returned to its base value of 4×10^{-7} A.

In order to clarify some features of detector operation its photoresponse was observed both in the absence and presence of hydrogen. Similar results were obtained with bright light from a xenon lamp and with the 350 nm component of that light obtained from a monochromator. Figure 10 shows the volt-ampere characteristics observed with the detector dark and illuminated for both kinds of ambient gas.

The results of the a-c admittance test noted in the previous section are shown in Fig. 11. Interpretation of these results is deferred to the following section.

Response of the detectors to gases other than H₂ was observed qualitatively using pure gases, alternating with O₂ to flush the test chamber while maintaining a negative bias to ensure restoration of the normal background current. These tests were done at room temperature and at 71°C with both positive and negative biases. The results are summarized in Table I. They show that at room temperature and negative

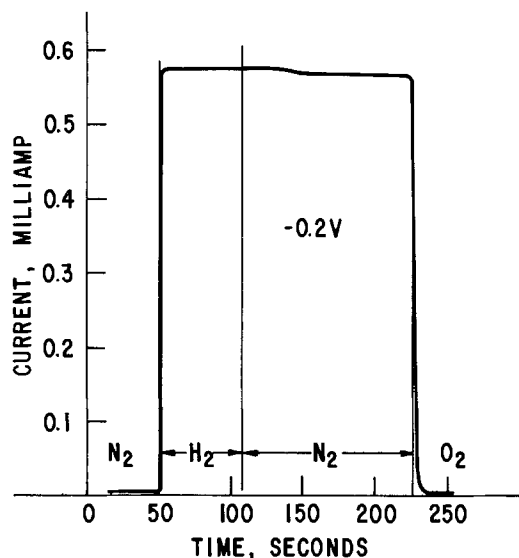


Fig. 9. Illustrating the need for oxygen to reduce electron current after exposure to hydrogen. Detector 11B, -0.2 V, room temperature.

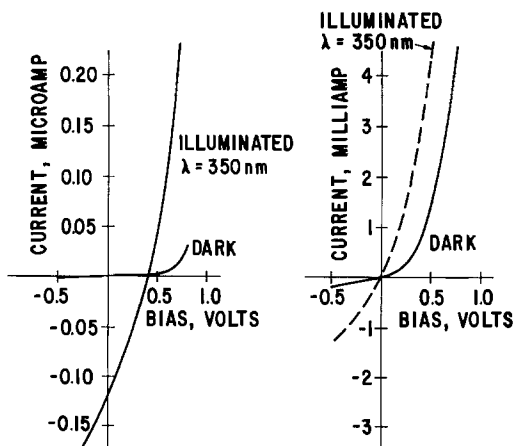


Fig. 10. Photoresponse of detector 2A, 3000Å thick, in the absence of H₂ (left) and in the presence of H₂ (right).

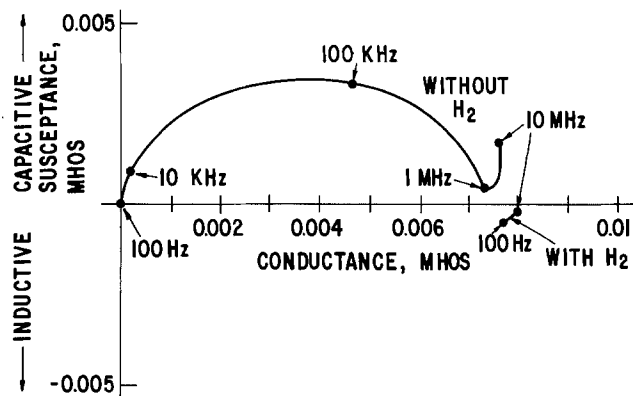


Fig. 11. Locus of complex admittance of detector 2B as frequency is varied, with and without hydrogen at room temperature. Applied signal amplitude is approximately 0.14V peak.

bias the response to most of the gases tested is negligible compared to that for H₂, though H₂S does provide a clearly measurable effect. With positive bias, CO, CO₂, and H₂O respond very weakly while NH₃ and H₂S have moderate responses (5-10% of that for H₂). At elevated temperatures the detector is not so selective, and it responds much more strongly to most gases when biased positively.

Discussion

Sputtered TiO₂ films, which are polycrystalline, largely anatase, and highly disordered, differ markedly from the single crystal rutile on which many diffusion studies have been made. Despite these differences the behavior of these hydrogen detectors is generally consistent with that deduced from earlier electrochemical and other observations using the single crystal material.

According to this view, H₂ is dissociated on the Pt top layer into H atoms, some of which cross the interface into the TiO₂. Once inside the TiO₂, the H atoms ionize to produce a conduction electron and an interstitial proton (3). Depending on the direction of the field at the TiO₂-Pt interface and other factors, either electrons or protons are driven toward the Ti base layer while the other carrier is driven back to the interface.

The photoresponse of the device in the absence of H₂, particularly its displacement from the origin (Fig. 10, left) indicates the existence of a Schottky barrier at the Pt-TiO₂ interface. Figure 12 (left) shows a presumed band structure when no bias is applied and no H₂ is present. Band bending within the TiO₂ pro-

Table I. Response of detectors to various gases, compared to that with O₂

Gas	I_{gas}/I_{O_2}			
	Room temperature		71°C	
	+	-	+	-
O ₂	1	1	1	1
N ₂	—	1.2 ^a	88 ^a	4 ^a
CO ₂	2.5 ^b	1 ^a	3.8 ^a	1.2 ^a
CO	2 ^b	1 ^a	113 ^a	4 ^a
CH ₄	1 ^b	1 ^a	—	—
C ₂ H ₆	1 ^b	1 ^a	75 ^a	3 ^a
C ₄ H ₁₀	1 ^b	1.2 ^a	75 ^a	3 ^a
NH ₃	20 ^a	1.3 ^a	625 ^a	117 ^a
H ₂ S	660 ^b	50 ^b	—	—
H ₂ O	1.5 ^c	—	2.6 ^d	—
H ₂	11200 ^e	3540 ^e	—	—

^a Detector 11B, 1000Å, bias ± 0.2 V.

^b Detector 4A, 3000Å, bias swept between ± 1 V.

^c Detector G3, 2000Å, bias + 0.5V, $I_{90^\circ/O_2RH}/I_{120^\circ/O_2RH}$, 20°C.

^d Detector G3, 2000Å, bias + 0.5V, $I_{90^\circ/O_2RH}/I_{120^\circ/O_2RH}$, 50°C.

^e Detector 2B, 1000Å, bias ± 0.4 V, I_{H_2}/I_{O_2} .

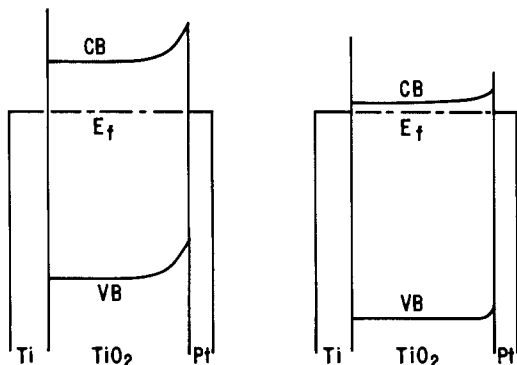


Fig. 12. Presumed band pattern of detector with zero applied voltage, in the absence of H_2 (left) and with H_2 (right).

vides a field at the interface which may not be overcome by a small positive bias. The momentary drop in current noted in connection with Fig. 6 can be attributed to a reverse current of conduction electrons from the first H atoms to enter the TiO_2 film. These are moved toward the base layer by the built-in field of the depletion region, but as we shall see this field does not persist as more H enters the insulator.

When H_2 is present, the intercept of the current with illumination (Fig. 10, right) shifts to zero bias, suggesting that the Schottky barrier is no longer effective (17). This situation might be represented by the band structure shown on the right of Fig. 12. The change in band structure can be expected because the H atoms are electron donors converting the poorly conducting TiO_2 to an n-type semiconductor. The Fermi level of the TiO_2 is thus moved closer to its conduction band and electron transfer between the Pt and TiO_2 is greatly facilitated. In thick films or crystals of TiO_2 nonuniform distributions of H can result in significant band bending and internal fields due to this effect, and these fields can complicate the resultant electron and proton flow rates (2, 13).

The increased current due to illumination, even when H_2 is present, may be attributed to photoconductivity of the TiO_2 . The light absorbed in the TiO_2 produces both mobile holes and electrons which move in opposite directions as determined by the field in the material.

The comparable sensitivities observed with bias of either polarity suggest that the principal conduction mechanism is electronic rather than ionic. With sufficient negative bias, protons are held near the Pt side of the TiO_2 layer so ionic conduction cannot play a significant part, but the electronic conductivity arises from the presence of ions in this layer.

The ionic current contribution can be seen in cases of positive bias when H_2 is present. The significant hysteresis in the positive portion of the curve of Fig. 3 with H_2 may be attributed to the motion of protons into the TiO_2 during the positive voltage excursion. The 10 sec duration of the 1V upward sweep in Fig. 3 provides some notion of the rate at which ions can enter the TiO_2 and move within it. The recovery times (Fig. 4-6) are considerably longer, but they are governed by the rate at which H atoms can be removed from the surface, as discussed below, as well as by proton motion toward the surface. This motion is enhanced by negative bias and retarded by positive bias.

The a-c admittance measurements shown in Fig. 11 are consistent with this view of electronic conductivity. The approximately semicircular locus of admittance with frequency roughly corresponds to an equivalent circuit consisting of a 135Ω resistance in series with a 0.016 μ f capacitance (8). These values correlate with the approximate measured resistance of the Pt film and the capacitance of the junction area if a dielectric constant of 62 is assumed for the TiO_2 . When the

detector is exposed to H_2 its admittance locus collapses to a virtually constant value corresponding to the lead resistance, suggesting that the capacitor has been shunted by a very high conductance that is essentially independent of frequency.

Even when the current is primarily electronic and not ionic, it arises from electrons donated by H atoms to the conduction band. This current must therefore be related to the density and distribution of protons within the TiO_2 layer. These quantities are governed by the applied and internal fields in the material, the concentration gradients of protons, and the surface boundary concentration, which is determined by the rates at which H atoms are supplied to and removed from the surface.

The principal source of H atoms is dissociation of H_2 molecules, with lesser contributions from other dissociable molecules, e.g., H_2O , H_2S , NH_3 . On recovery after H_2 exposure, accumulation of protons near the surface from within the bulk of the TiO_2 also provides H atoms. The sinks for H atoms are diffusion into the bulk, reaction with oxygen to form water, or recombination to form H_2 . In the presence of oxygen, the formation of water is undoubtedly predominant.

Bearing these competitive processes in mind, it is easy to understand why the recovery rate is negligible in the absence of oxygen (Fig. 9), why the response is faster and the recovery slower with positive bias (Fig. 5 and 6), and why increasing temperature accelerates the response significantly.

These considerations lead us to expect a dependence of sensitivity and response time on the carrier gas. Indeed it was observed that for a given concentration of H_2 the sensitivity and speed of response was least in O_2 , somewhat greater in air, and greater still in N_2 . By the same token we might expect a high relative humidity to increase the sensitivity and response speed, not because the water vapor dissociates (which it does only very slowly) but because it shifts the reaction away from water formation.

Optimum thicknesses of the TiO_2 and Pt layers have not been determined in this work. It seems clear, however, that excessively thin TiO_2 layers are not advantageous because they have relatively high background currents and high threshold levels of detection thus limiting their dynamic range. Excessive thickness, on the other hand, will eventually result in slowed response and recovery.

The saturation current of the detectors described in this work was determined by the Pt lead resistance, the resistance of the TiO_2 layer becoming negligible at about 0.5% H_2 in air. The saturation current, and with it the measurable H_2 concentration range, might be raised by reducing the resistance of Pt film. This course might carry with it the danger of thermal damage to the detector due to higher current in localized "hot spots." The existence of thin spots or localized regions of higher conduction is strongly suggested by the generally higher background currents observed with thinner TiO_2 layers, even with constant applied field.

Conclusions

The TiO_2 devices described here are effective detectors of hydrogen at concentrations of a few hundred parts per million in air, though some units have detected less than 1/10 of this value with slower response. The preferred mode of operation is with the Pt film negative with respect to the base film of Ti because this provides a greater dynamic range and considerably faster recovery when hydrogen is removed. This polarity also makes the detector virtually unresponsive to other gases at room temperature, and almost so even at higher temperatures.

Air or oxygen is generally needed to remove hydrogen from the detector once the source of H_2 is cut off. The response rate but not the sensitivity is strongly increased by a moderate rise in temperature.

The d-c voltages applied in this work are generally smaller than those available from batteries, so that appropriate series resistors, doubling as current sensing elements, would be needed if the detectors are battery operated. Nevertheless low and moderate frequency a-c methods are also applicable so that a considerable variety of instrumentation circuitry can be devised.

At very low hydrogen concentrations the detector responses can be quantitative, but they saturate at concentrations above about 0.5% H₂ in air, making them excellent alarm devices specific to hydrogen. (Though the detector does not respond to pure CH₄, natural gas apparently has sufficient hydrogen in it to produce a strong response.)

The operation of the device depends on the relative rates of hydrogen dissociation and reformation, hydrogen atom diffusion into and out of the dielectric, and reaction between hydrogen and ambient oxygen to form water vapor, all of which are catalyzed by the platinum film.

The diffusion of hydrogen into and out of the detector appears to be quite reversible, at least for the duration of the experiments reported here. It is not known, however, what the lifetime of these devices might be and how it would be affected by temperature. Temperatures above about 300°C might come dangerously close to effecting a permanent reduction of the TiO₂ to a highly conducting state (4).

Significant advantages of this detector are its effectiveness as an alarm for hydrogen operable at room temperature and requiring simple circuitry that uses negligible power in the absence of hydrogen.

Acknowledgment

The author is grateful to R. H. Wilson for useful discussions, to J. Briant for the admittance measurements, and to R. O. Carlson for assistance with humidity measurements. Construction of the detectors was accomplished through the work of A. Golab and I. Mullin.

Manuscript submitted May 20, 1980; revised manuscript received July 10, 1980.

Any discussion of this paper will appear in a Discussion Section to be published in the June 1981 JOURNAL. All discussions for the June 1981 Discussion Section should be submitted by Feb. 1, 1981.

Publication costs of this article were assisted by General Electric Company.

REFERENCES

1. A. vonHippel, J. Kalnajs, and W. B. Westphal, *J. Phys. Chem. Solids*, **23**, 779 (1962).
2. J. W. DeFord and O. W. Johnson, *J. Appl. Phys.*, **46**, 1013 (1975).
3. L. A. Harris, M. E. Gerstner, and R. H. Wilson, *This Journal*, **126**, 850 (1979).
4. L. A. Harris and R. Schumacher, *ibid.*, **127**, 1186 (1980).
5. T. Seiyama, A. Kato, K. Fjuiishi, and M. Nagatani, *Anal. Chem.*, **34**, 1502 (1962).
6. T. Seiyama and S. Kagawa, *ibid.*, **38**, 1069 (1966).
7. P. J. Shaver, *Appl. Phys. Lett.*, **11**, 255 (1967).
8. C. M. Svensson, L. S. Lundkvist, K. I. Lundstrom, and M. S. Shivaraman, U.S. Pat. 4,058,368 (1977).
9. J. M. Ruths, S. J. Fonash, and T. E. Sullivan, Paper 241 presented at The Electrochemical Society Meeting, Pittsburgh, Pennsylvania, Oct. 15-20, 1978.
10. H. Windischmann and P. Mark, *ibid.*, **126**, 627 (1979).
11. S. Kanefusa, M. Nitta, and M. Haradome, *J. Appl. Phys.*, **50**, 1145 (1979).
12. H. Taguchi, Jpn. Pat. 45-38200.
13. O. W. Johnson, S-H. Paek, and J. W. DeFord, *J. Appl. Phys.*, **46**, 1026 (1975).
14. G. J. Hill, *J. Physics D*, **1**, 1151 (1968).
15. J. V. Cathcart, R. A. Perkins, J. B. Bates, and L. C. Manley, *J. Appl. Phys.*, **50**, 4110 (1979).
16. O. W. Johnson, W. D. Ohlsen, and P. I. Kingsbury, Jr., *Phys. Rev.*, **175**, 1102 (1968).
17. K. Ito, Abstract C2-3 International Conference on Solid Films and Surfaces, Tokyo, Japan (1978).
18. J. E. Bauerle, *J. Phys. Chem. Solids*, **30**, 2657 (1969).

A Model on the Mechanism of Room Temperature Interfacial Intermixing Reaction in Various Metal-Semiconductor Couples: What Triggers the Reaction?

Akio Hiraki

Department of Electrical Engineering, Osaka University, Suita, Osaka 565, Japan

ABSTRACT

Metal films such as Al, Au, Cu, and Pd exhibit an intermixing reaction at room temperature with semiconductors of energy gaps (E_g) of less than ~ 2.5 eV or dielectric constants (ϵ) larger than ~ 8 . The semiconductors are mostly covalent ones. A model of the mechanism, especially the triggering mechanism, of this room temperature interfacial intermixing reaction is proposed. One of the bases of the model is the consideration of the role of metal on the covalent semiconductor from the theoretical view point to induce instability in the cohesive mechanism resulting in facilitating the reaction. The other is our slow deposition experiment of Au film onto Si (111) surface in ultrahigh vacuum.

We previously found and reported (1, 2) that when metal films ($\sim 500\text{\AA}$) such as Al, Au, Cu, and Pd are vacuum evaporated onto clean surfaces of semiconductors with energy gaps (E_g) less than 2.5 eV or dielectric constants (ϵ) larger than ~ 8 , they react

Key words: films, semiconductor, metals.

and intermix at the interfaces with each other readily even at room temperature, as summarized in Table I. However, insulators like SiO₂ and NaCl, which do not satisfy the above criterion, exhibit no reaction. As a result of the intermixing reaction, a very thin alloyed layer is introduced irrespective of the deposited metal

Table I. Summary of the room temperature interfacial reaction in various metal-semiconductor couples studied by Hiraki *et al.* (1, 2)

Semiconductors	E_g (eV)	Interface reaction	Surface atom(s)	Dielectric constant
Ge	0.67	Yes	Ge	16
InSb	0.18	Yes	In,Sb	15.2
Si	1.11	Yes	Si	12
GaAs	1.35	Yes	Ga	10.5
InP	1.26	Yes	In,P	9.5
GaP	2.24	Yes	Ga	8.4
SiC	2.9	No		6.4
SiO ₂	6.5	No		3.5
NaCl	7.7	No		2.5

forming with the semiconductor stable compounds (like Si-Pd) or not (Si-Au). Then the reaction is called the room temperature interfacial intermixing reaction. In many cases the constituent atoms of the semiconductors are released from the alloyed interfacial region and they migrate through the metal films to accumulate on the top of the films under high vacuum. As an example, Fig. 1 demonstrates the surface accumulation of In and P atoms on Au film observed in an InP-Au couple.

Since most of the semiconductors (listed in Table I) which readily intermix with the metals are classified as covalent semiconductors with fairly large bond energy (the bond energy of Si, for example, is ~ 2 eV/bond), without the presence of such an effect of metal as to induce instability in the bonding (or cohesive) character of the semiconductor adjacent to the metal, the above interfacial intermixing reaction can hardly occur.

We postulate that the physical origin of this instability is due to the ability of metal to screen Coulomb interaction by its mobile free electrons. Although there may be other possible mechanisms of the present room temperature interfacial intermixing reaction, we think the above postulated possibility of the metal induced instability in the semiconductor bonding character is very likely from the following experimental facts and theoretical considerations.

Using ELS, AES, LEED, and ion sputtering techniques, Okuno *et al.* (3) of our group performed the experiment on the slow deposition (~ 0.1 monolayer/min) of Au film onto clean Si(111) surface with 7×7 LEED structure at ultrahigh vacuum ($\sim 5 \times 10^{-10}$ Torr). As illustrated schematically in Fig. 2, the results indicate an abrupt onset of the room temperature interfacial intermixing or alloy-forming reaction between the deposited Au film and the Si substrate at the thickness of ~ 4 monolayers, the presence of a critical film-thickness for the reaction. Namely, 1-2 monolayers of Au induce no intermixing reaction either at room temperature or at an elevated temperature of $\sim 800^\circ\text{C}$, although the ELS signal shows that the deposited Au atoms eliminate the surface states indicating that the atoms relax the reconstruction existing on the Si(111) clean surface. However,

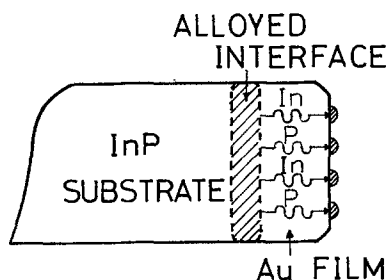


Fig. 1. Schematic illustration of the room temperature accumulation of In and P atoms on top of Au film caused by the interfacial intermixing reaction between InP and Au.

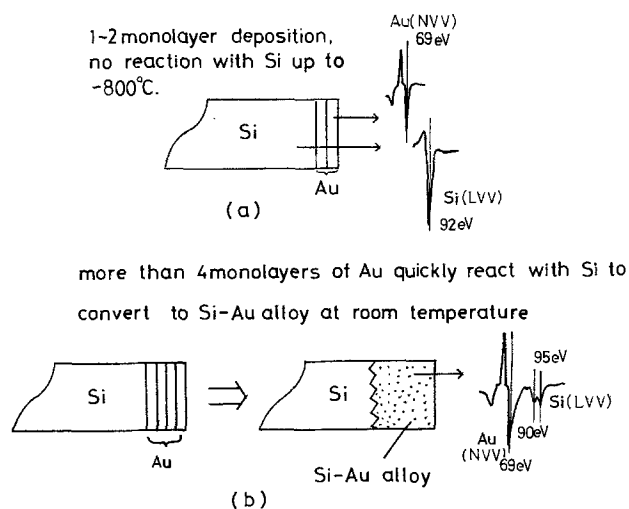


Fig. 2. Schematic illustration of the results on the slow deposition experiment by Okuno *et al.* (3) of Au film on clean Si(111) surface under ultrahigh vacuum.

more than four monolayers of Au immediately react with the substrate and the Au film intermixes with Si to convert into a layer of amorphous Si-Au alloy which can be clearly identified from the definite chemical shift of the Si(LMM) Auger signal with characteristic double peaks at 90 and 95 eV [Fig. 2(b)] (4). The amorphous layer thus produced is unstable against temperature rise and easily decomposes into Au and Si grains at $\sim 200^\circ\text{C}$. This is an obvious contrast to the tough thermal stability of two monolayers of Au film up to $\sim 800^\circ\text{C}$ which is far above the Si-Au eutectic point ($\sim 370^\circ\text{C}$).

Similar experimental results were reported for the AES-LEED study on the first stage condensation of Au film on Si(111) surfaces by Le Lay *et al.* (5). Also the recent result of the MeV He⁺ ion backscattering/channeling study by Narusawa *et al.* (6) on Si(111) and Si(100)-Au systems under ultrahigh vacuum is consistent with our observation (Fig. 2). They observed a steep increase of the surface peak intensity of Si at ~ 4 monolayers of Au and interpreted that this was due to the abrupt appearance of an amorphous gold silicide film as a result of the intermixing reaction.

We interpret the above facts on our slow deposition experiment as follows. For Au film to function as a metal, a highly polarizable medium which is expected, as mentioned already, to induce instability in the covalent bonding of Si at the interface, its thickness must be more than four monolayers, the critical thickness: this criterion is generally accepted for most of metal films to behave as intrinsic metal. On the other hand, 1-2 monolayers of Au do not act as metal in the above sense but as nonmetal, probably due to covalent interaction with underlying covalent Si through the dangling bonds: this statement is in agreement with both the ELS and AES studies on monolayer Ga on Si by Rowe *et al.* (7) and monolayer Al on Si by Kobayashi *et al.* (8).

Moreover, the definitive role of an intrinsic metal to trigger the interfacial intermixing reaction can be demonstrated by the following experiment. We deposited onto a clean Si surface 500 Å of nonmetallic (or covalent) Ge film in high vacuum and heated the specimen up to $\sim 500^\circ\text{C}$ and detected no intermixing reaction by RBS (9). But, if we convert this nonmetallic film into metallic by depositing ~ 2000 Å of thick Au film on the thinner (~ 500 Å) Ge film followed by heat-treatment at $\sim 200^\circ\text{C}$ to produce metallic Ge-Au alloy, Si reacts with the metal (or Ge-Au alloy) readily and consequently metallic Si-Ge-Au alloy appears. These results are schematically shown in Fig. 3.

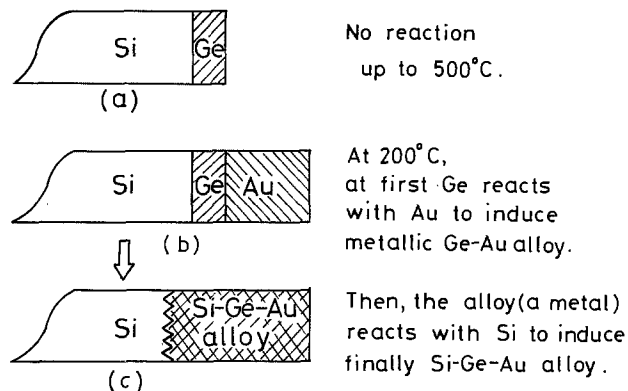


Fig. 3. Schematic illustration of the results on the experiment by Hiraki *et al.* (9) to show that Ge(nonmetal) does not react with Si, but metallic Ge-Au alloy does to produce Si-Ge-Au alloy.

The modification or instabilization of bonding character in covalent semiconductors by metal has been investigated theoretically by Phillips (10), Inkson and Anderson (11) to understand the metal-independent Schottky barrier height in place of the familiar concept of Bardeen's surface state. Okiji *et al.* (12) using the Hubbard model took the effect of metal into account on narrow gap nonmetal whose gap is caused by the many body effects or electron correlation.

Inkson and Anderson's calculation suggests the band closure of covalent semiconductor energy gap in the region of 2-3 monolayers of semiconductor side in contact with the metal and therefore the region converts to metal from semiconductor (11). Theory by Okiji *et al.* also concludes the possibility of the transition of nonmetal to metal in several layers (12). Figure 4 is a schematic illustration of the proposals of these theories, where S and M denote semiconductor (or nonmetal) and metal, respectively. In the figure, to avoid confusion, the temperature is set at $\sim 0^\circ\text{K}$ [Fig. 4(b)], because we already know that by the metal (or M) deposition even at room temperature S reacts immediately to induce S-M alloyed layer [Fig. 4(c)]: however, due to the presence of activation energy for the interfacial intermixing reaction as evidenced by our previous experi-

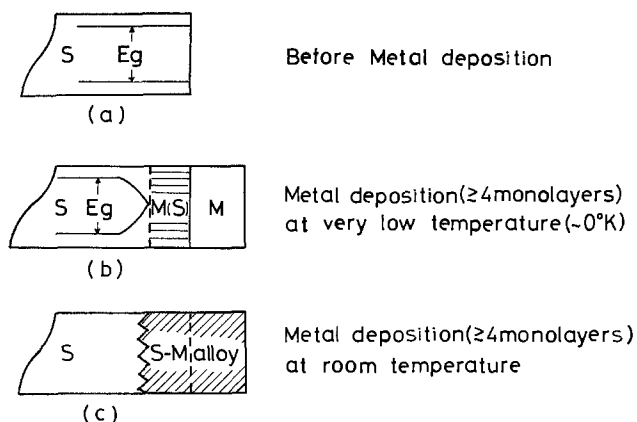


Fig. 4. Schematic illustration of the effect of metal (M) deposition on covalent semiconductor (S) to provide situation for easy S-M interfacial reaction. (a) Before metal deposition; S with energy gap ($E_g \lesssim 2.5$ eV). (b) Metal deposition (≥ 4 monolayers) at very low temperature ($\sim 0^\circ\text{K}$). Band closure of several monolayers of S to convert to metal [M(S)] due to presence of M (≥ 4 monolayers), see text for the reason for setting the temperature to 0°K . (c) Metal deposition at room temperature. Converted metal layer [M(S)] readily reacts with M at room temperature to induce S-M alloy.

ment on GaP-Au couple at 22°C and 200°C (1), only very low temperature (or $\sim 0^\circ\text{K}$) may guarantee the unreacted but converted (to metal from S) layer designated by M(S) of 2-3 monolayers thick.

From our slow deposition experiment illustrated in Fig. 2, we know that four monolayers of Au induce the interfacial intermixing reaction and the cause can be attributed to the effect of intrinsic metal. This effect of metal is expected by the above theories to convert S into M(S) which is schematically illustrated in Fig. 4(b). So the next question may be the reason why once a part of S converts to M(S) as Fig. 4(b) shows, it reacts and intermixes with M to form an alloyed interface at such a low temperature as room temperature. Before answering this question, it may be more convincing to refer to experimental data indicating ready low temperature intermixing or interdiffusion in metal-metal (M-M) couples (13). The most important factor to facilitate the low temperature M-M intermixing may be the cohesive mechanism of metal which is quite different from that of the covalent semiconductor (14), since from the consideration of the cohesive mechanism of metals, both in the metal films and at the interface, we can expect the ready atomic motion which is requisite for the intermixing or interdiffusion reaction to take place. In other words, the cohesive energy of metal, roughly speaking, is determined mostly by the density of its mobile free electron or electron gas, and so long as the atomic motion of metal ions does not increase the electron density, the Fermi energy of the electron gas exerts no restriction against the atomic motion. Therefore, it is understandable that for the metal layer M(S) to intermix with M through the atomic motion is in general far easier than in the case where the region of S adjacent to M does not convert into M(S) and still stays as covalent semiconductor (or nonmetal).

The resistance against the atomic motion in metal films is due mainly to atomic size, perfection of the films, and so on, to suggest that in or into defect-rich metal films, such as evaporated films, atomic motion may be quite easy. So the easiness of the intermixing reaction which proceeds from atomic motion is expected to greatly depend on the perfectness of the deposited metal layer and, therefore, deposition condition. Many complicated factors control the deposition condition and then determine the perfectness of the deposited films. They are deposition rate, deposition temperature, surface geometry (such as, orientation and lattice spacing) of the substrate, surface energy and so on.

Therefore, with a few exceptions, it is not possible to deposit defect-free or single crystalline metal film (M) on the semiconductor substrate (S). Consequently, almost all room temperature metal (M) deposition on S helps low temperature interdiffusion between M(S) and M to take place inducing the S-M alloy as shown in Fig. 4 and resulting in the interfacial intermixing reaction of the S-M couple.

However, we must point out that on GaAs(001) it has been reported that it is possible to deposit Al film epitaxially (15) suggesting no mutual intermixing. In this GaAs(001)-Al case, in addition to the suitable geometrical fitness, *i.e.*, lattice matching and so on, for epitaxial growth to be satisfied in the couple, both a high enough deposition temperature and slow enough deposition rate may be generally necessary to allow deposited Al atoms to arrange themselves into a perfect epitaxial layer.

Also it may be crucial and relatively easier to control if this arrangement of Al atoms is perfect in the first two monolayers so defects are not induced which would assist intermixing between Al and GaAs to occur when the Al film thickness exceeds more than four monolayers. As mentioned and illustrated already in connection with Fig. 2(a), 1-2 monolayers of de-

posited Al film are expected not to intermix with GaAs substrate as in the case of Si-Au couple. Otherwise, epitaxial deposition of Al on GaAs is impossible: we already know the GaAs(111) intermixes even readily with deposited Al film ($\sim 500\text{\AA}$) when the evaporation is performed with the conventional deposition rate at room temperature (2). Such determinative role of defects or the perfection of the deposited film in the low temperature interdiffusion or interfacial intermixing reaction in metal-metal couples is clearly shown by Kirsch *et al.* in the case of an Ag-Au couple (16).

More detailed description of the present model on the role of intrinsic metal triggering the low temperature interfacial intermixing reactions taking place in S-M couples will be published elsewhere soon (9) with experimental and theoretical discussion.

Manuscript submitted Dec. 12, 1979, revised manuscript received April 16, 1980. This was Paper 349 presented at the Los Angeles, California, Meeting of the Society, Oct. 14-19, 1979.

Any discussion of this paper will appear in a Discussion Section to be published in the June 1981 JOURNAL. All discussions for the June 1981 Discussion Section should be submitted by Feb. 1, 1981.

Publication costs of this article were assisted by Osaka University.

REFERENCES

1. A. Hiraki, K. Shuto, S. Kim, W. Kammura, and M. Iwami, *Appl. Phys. Lett.*, **31**, 611 (1977).
2. A. Hiraki, S. Kim, W. Kammura, and M. Iwami, *Surf. Sci.*, **86**, 706 (1979).
3. K. Okuno, T. Itoh, M. Iwami, and A. Hiraki, *Solid State Commun.*, **34**, 493 (1980).
4. T. Narusawa, S. Komiya, and A. Hiraki, *Appl. Phys. Lett.*, **20**, 272 (1972).
5. G. Le Lay and J. P. Faurie, *Surf. Sci.*, **69**, 295 (1977).
6. T. Narusawa, K. Kinoshita, W. M. Gibson, and A. Hiraki, *J. Vac. Sci. Technol.*, **18** (1981), To be published.
7. J. E. Rowe, G. Margaritondo, and S. B. Christman, *Phys. Rev.*, **B15**, 2195 (1977).
8. K. L. Kobayashi, Y. Shiraki, and Y. Katayama, *Proceedings of the 14th Conference on Physics of Semiconductors*, p. 211, Edinburgh (1978).
9. A. Hiraki, K. Shuto, K. Okuno, T. Itoh, and M. Iwami, *Jpn. J. Appl. Phys.*, To be published.
10. J. C. Phillips, *Solid State Commun.*, **12**, 861 (1973).
11. P. W. Anderson, in "Elementary Excitations in Solids, Molecules and Atoms," Part A, p. 1, Nato Advanced Study Institute Series, Plenum Press (1974).
12. A. Okiji, H. Kasai, and S. Terakawa, *J. Phys. Soc. Jpn.*, **44**, 1275 (1978).
13. See for example, "Thin Films: Interdiffusion and Reactions," J. M. Poate, K. N. Tu and J. W. Mayer, Editors, John Wiley & Sons, Inc., New York (1978).
14. A. Hiraki, in "Progress in Point Defects," M. Doyama and S. Yoshida, Editors, p. 393, University of Tokyo Press (1977).
15. A. Y. Cho and D. Dernier, *J. Appl. Phys.*, **49**, 3328 (1978).
16. R. G. Kirsch, J. M. Poate, and M. Eibschutz, *Appl. Phys. Lett.*, **29**, 772 (1976).

Plasma-Developed X-Ray Resists

Gary N. Taylor* and Thomas M. Wolf

Bell Laboratories, Murray Hill, New Jersey 07974

ABSTRACT

A novel plasma-development method using an oxygen plasma and new materials which optimize sensitivity have been evaluated as x-ray resists at the 4.37\AA $\text{Pd}_{L\alpha}$ wavelength. Both negative and positive tone images can be obtained upon plasma development. To date, negative tone images are more technologically important. X-ray absorbing host polymers and moderately volatile guest monomers are used. Images are developed after exposure and low temperature fixing under vacuum by differential development in an oxygen plasma. Examples are presented for monomers which are locked by free radical and cationic mechanisms. One composition which has optimum properties is a mixture of 81 weight percent poly(2,3-dichloro-1-propyl acrylate) and N-vinyl carbazole. With it features as small as $0.3\ \mu\text{m}$ were resolved for a short 1.5 min exposure time. These resists and processes are suitable only for multilevel resist processing schemes which are demonstrated.

One of the fundamental problems of high resolution lithography using polymeric negative resist materials is the limit to resolution caused by swelling of the polymeric resist during solution development of the exposed pattern (1). Positive resists of either the novolac-quinonediazide type (2) or of the poly(methacrylate) family (3) are virtually free of swelling problems. Both classes of materials appear to develop in an etch-like manner by selective dissolution of material in the exposed areas. For the novolac-quinonediazide resists the difference in wetting properties of the exposed and unexposed areas and the very small size of the host novolac resin and quinonediazide sensitizer molecules minimizes swelling. For the poly(methacrylates) the unique mobility of the chain segments associated with the methacrylate structure is believed to control and minimize developer permea-

tion leading to swelling and dissolution (4) even though the molecular weight of polymer in the exposed areas is still high. For these reasons positive resists are considered to have far superior resolution.

For conventional solution-developed negative resists, swelling is a necessary consequence of the development process in which uncrosslinked material is dissolved in unexposed areas and is extracted from crosslinked gel in the exposed areas. The crosslinked gel is itself swelled by the developing solvent. Swelling can be minimized by a judicious choice of developer and rinsing solvents and conditions (5). However, resolution is still limited to about $2\ \mu\text{m}$ (gap) in 5000\AA final resist thickness for many negative resists. Recent results by Feit (6) with poly-(chlorostyrene) electron resist have indicated that improved resolution to $\sim 1.0\ \mu\text{m}$ can be achieved if resist contrast is sufficiently high ($\gamma > 2.0$). Moran and Taylor have shown that higher resolution can be achieved with a negative

* Electrochemical Society Active Member.

Key words: oxygen plasma, high resolution lithography.

x-ray resist mixture containing 92.5 weight percent (w/o) poly(2,3-dichloro-1-propyl acrylate) and poly(glycidyl methacrylate-co-ethyl acrylate) when it is exposed in the presence of trace amounts of oxygen (7). However, resolution is at best only 1 μm in 5000Å final resist thickness.

Clearly, it would be very useful if negative resists could be developed which would not be swelled during the development process. Hofer, Kaufmann, and Kramer have recently described one new type of negative resist which minimizes swelling. This involves conversion of the resist to a highly ionic state by electron or x-ray irradiation of charge-transfer organic metalloid polymers (8). Herein we describe another new means to avoid limitations due to swelling. These are new negative x-ray resist materials and development processes which develop the resist image by plasma etching. The materials are mixtures of a host polymer and a moderately volatile monomer which is locked into the host by the impinging radiation. Pattern development is accomplished by subsequent heating (fixing) and exposure to an oxygen plasma. Recently a similar process has been described for photoresist compositions by workers from Motorola (9, 10). However, no chemical details of their process were presented.

Experimental

Materials.—Poly(vinyl chloride) (Aldrich), poly(chloroprene) (du Pont), and poly(epichlorohydrin) (Hercules) were used as received. Poly(butene-1 sulfone) was obtained from Mead Chemical Company. The chlorinated acrylates and methacrylates were prepared in house using techniques analogous to those previously reported (22). Monomers were obtained from either Monomer-Polymer Laboratories, Poly-science, or Aldrich. 2-(1-naphthyl)ethyl acrylate and methacrylate were prepared in house.

Equipment.—X-ray exposures were conducted with a Pd L_{α} exposure system which was previously described (17). X-ray masks were of the polyimide membrane type. Fabrication details have also been disclosed (23). All x-ray exposures were conducted under a nitrogen atmosphere. Plasma development was accomplished in an oxygen plasma contained in a Dionics, Incorporated, Model 2005T plasma etcher at 0.40 Torr and 100W without a Faraday cage.

Results and Discussion

Initial results.—While investigating x-ray resist mixtures of poly(2,3-dichloro-1-propyl acrylate), DCPA, and poly(glycidyl methacrylate-co-ethyl acrylate), COP, we observed an interesting phenomenon. When a 1 μm thick film of the polymer mixture on an Si wafer was exposed to 10-20 mJ/cm² of Pd L_{α} x-radiation and was then heated at 100°C and 50 mTorr pressure for 1-2 hr, a faint relief image was visible. No image was evident immediately after exposure. The relief image was shallow, of the order of several hundred angstroms, and appeared to be thinner where the resist had been exposed. The relief image appeared to be an exact copy of the gold absorber pattern on the x-ray mask although submicron dimensions could not be measured accurately because of low optical resolution. In order to establish the dimensions more accurately, the sample was placed in a barrel-type plasma etching apparatus. The polymeric film was removed by etching in an oxygen plasma until the bare Si substrate surface was first reached. Surprisingly, the substrate was first cleared of polymeric material in the unirradiated regions which had initially been thicker than the irradiated regions. The final resist thickness in the irradiated regions was approximately 500Å.

These results indicated that the irradiated regions had etched more slowly than the unirradiated regions and that the enhanced relief image was the result of different removal rates for polymer in the two regions. Attempts to increase the final relief image either by

increasing the x-ray dose, the heating time, or changing the composition proved unsuccessful. However, it was possible to obtain thicker films after heating in vacuum and oxygen plasma etching when the COP was replaced by a moderately volatile polymerizable monomer containing aromatic functionality.

Polymer host: monomer guest mixtures.—Our choice of moderately volatile aromatic polymerizable monomers in a polymeric host binder as x-ray resist compositions having the possibility of high resolution was derived from several inputs. First, Broers and co-workers (11) had demonstrated extremely high resolution ($\sim 80\text{Å}$) by contamination writing in a scanning transmission electron microscope. They "locked" extremely small amounts of "monomer" pump oil contaminants as very thin films on gold and used the fine resist lines thereby created as a mask for the ion milling of the fine patterns into the thin gold film contained on a carbon foil substrate.

Their results prompted us to think of a more practical method of locking monomers. The basis for this lies in two articles by Chandross and co-workers (12) who made optical waveguide circuits, directional couplers, and grating couplers by photolocking 2-(1-naphthyl)ethyl acrylate into a 1:1 copolymer of methyl methacrylate and glycidyl methacrylate, functionalized with cinnamic acid or monoethyl fumarate, by exposure to ultraviolet and visible radiation. For x-ray locking the analogous processes are radiation grafting and polymerization (13). One example is the high energy electron irradiation of mixtures of poly(vinyl chloride) and multifunctional acrylic and methacrylic monomers now used in the manufacture of telephone frame wire (14).

A third input was the general knowledge that resist materials containing aromatic functionality are generally more resistant to plasma etching than their aliphatic analogues. This coupled with our observations of differential removal of exposed and heated conventional x-ray resist mentioned above suggested that the locking process, followed by a fixing step using heat and vacuum to remove unreacted monomer, would provide a film having different types and amounts of chemical bonds in the irradiated and unirradiated regions which would be removed at different rates when a plasma was applied. Since oxygen plasma etching is utilized to strip resist materials (15) we have found it very useful in achieving differential removal of the imaged and nonimaged regions. Recently we reported relative rates of removal for 40 polymers in an unshielded oxygen plasma (16). We have used the data generated to design resist compositions which would hopefully optimize differential removal in the plasma treatment (development) step.

The process which has been realized experimentally for resists exposed to x-rays is schematically outlined in Fig. 1. In the first step, exposure of a mixture of monomer m and polymer P in the region indicated by the impinging radiation designated by the vertical arrow, presumably causes locking by chemical reactions as grafted (P-m bonds) and polymerized (m-m bonds) material. The second step, fixing, is accomplished by heating the exposed resist under vacuum thus removing the unreacted monomer chosen to have moderate volatility. Since more material is removed in the unirradiated regions a relief image is generated. In the third step plasma treatment removes material from the imaged and nonimaged areas. However, because of the different chemical nature of the two regions the rates of removal can be substantially different. In the case of plasma A, which is typically an oxygen plasma, the imaged regions are removed at a lower rate than the nonimaged regions thus enhancing the initial relief image obtained after fixing and affording a fully developed negative tone pattern when the substrate is bared. For plasma B the unimaged regions are removed at a significantly lower rate than the imaged regions thus inverting the tone obtained at the

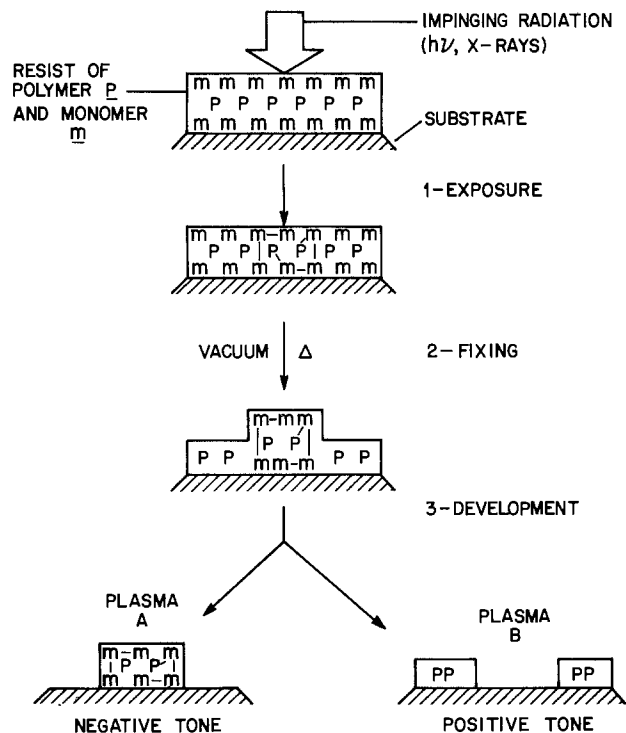
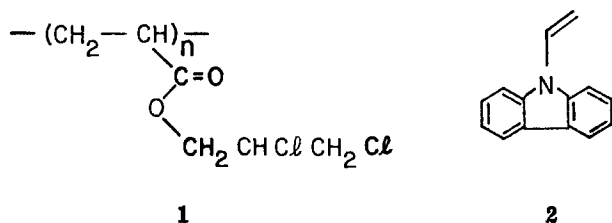


Fig. 1. Schematic diagram of plasma-developed resist showing the resist film composed of polymer host P and moderately volatile monomer m. The three processing steps are (a) exposure which locks monomer in place by grafting and polymerization, (b) fixing which removes unlocked monomer from all regions, (c) plasma development where plasma A is an oxygen plasma. Plasma B will be described elsewhere (18).

fixing stage and providing a positive tone pattern upon complete development when the substrate surface is reached.

Experimental realization of these processes is provided in Fig. 2. Photomicrograph 2A shows a shallow relief image seen immediately after exposure of a 1.0 μm thick film comprised of 80 parts by weight poly(2,3-dichloro-1-propyl acrylate) 1 and 20 parts by weight N-vinyl carbazole 2



The patterned regions were exposed to 12 mJ/cm² of Pd_{L α} x-radiation [4 min exposure on a 4 kW x-ray exposure system described by Zacharias and co-workers (17)]. Photomicrograph 2B shows the enhanced relief image obtained after fixing by heating at 75°C and 0.05 Torr for 1 hr. The resist thickness in the exposed regions was 8700Å and in the unexposed regions was 7800Å. The relief image was, therefore, 900Å. Upon treatment with an unshielded 100W O₂ plasma at 0.55 Torr generated in a Model 2005T Plasma Etcher obtained from the International Plasma Division of Dionics, Incorporated, the resist was completely removed in the unexposed regions by etching for approximately 3 min thus affording the magnified patterns of 1 and 2 μm lines and spaces 3200Å thick shown in Fig. 2c. A comparison of identical features on the x-ray mask is shown in Fig. 2E. Figure 2D shows a similar pattern but with the positive resist tone obtained after treatment with other plasmas. The resist thickness in 2D was 6400Å in the unexposed regions compared to bare substrate in the exposed regions. The

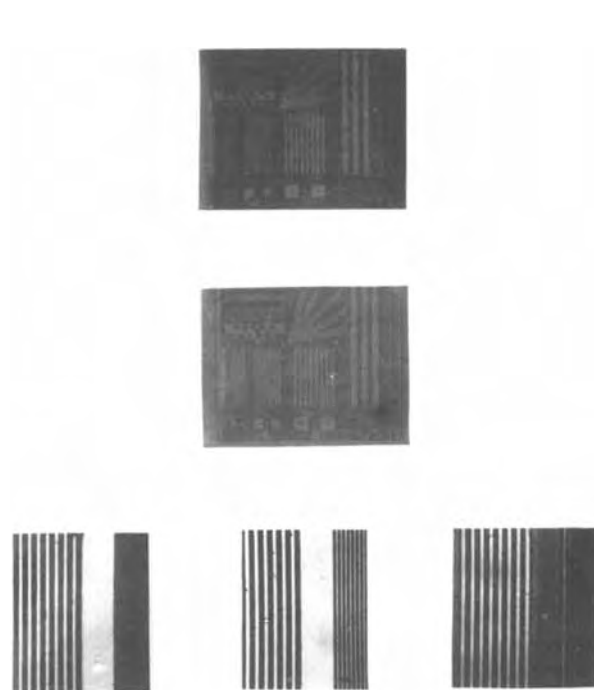


Fig. 2. Photomicrographs of plasma-developed resist patterns in 80 w/o poly(2,3-dichloro-1-propyl acrylate) and 20 w/o N-vinyl carbazole at various processing steps: (a, top) immediately after exposure for 2.5 min, (b, middle) after fixing at 90°C and 0.10 Torr for 1 hr, (c, bottom left) 2500Å negative-tone image after O₂ plasma treatment of magnified 1 and 2 μm lines and spaces, (d, bottom right) 6400Å positive-tone image obtained after treatment with plasma B, (e, bottom middle) corresponding features on the mask.

details of the positive tone process will be presented elsewhere (18). The remainder of the present report is concerned with the negative tone process.

In order to discuss our results we must first define several terms relating to sensitivity. This is necessary since the usual terms employed to define the sensitivity of solution-developed negative resists, D_g^i and $D_g^{0.5}$, no longer apply since plasma-developed resists are not gelled or crosslinked by the low doses of incident radiation used. We find that plots of normalized thickness vs. log dose for both the relief and plasma developed images to be useful aids in examining resist properties as a function of composition. Such plots are presented in Fig. 3 for an 85:15 mixture by weight of poly(2,3-dichloro-1-propyl acrylate) and N-vinyl carbazole.

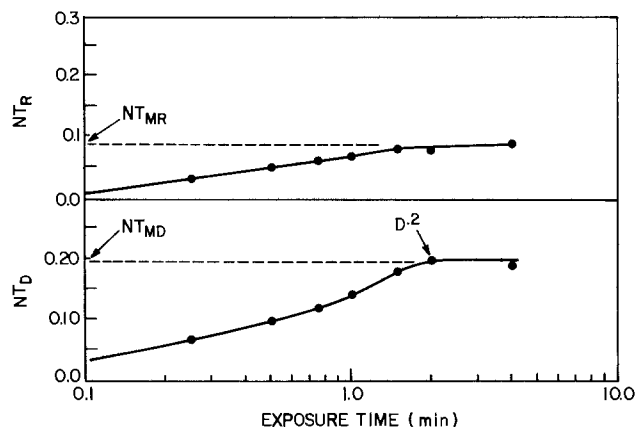


Fig. 3. Sensitivity curves for an 85:15 mixture by weight of poly(2,3-dichloro-1-propyl acrylate) and N-vinyl carbazole. The top curve plots normalized relief image thickness NT_R obtained after fixing vs. log exposure time (dose). The lower curve plots normalized thickness of the plasma-developed image NT_D vs. log dose.

Here NT_R is the normalized thickness of the relief image

$$NT_R = NT_{RE} - NT_{RU} \quad [1]$$

and NT_{RE} and NT_{RU} are the normalized thickness of the exposed and unexposed regions after fixing, respectively. In the lower portion of the plot NT_D is the normalized thickness of the plasma-developed image

$$NT_D = NT_{DE} - NT_{DU} \quad [2]$$

where NT_{DE} and NT_{DU} are the normalized thickness of the exposed and unexposed regions after plasma development, respectively. Plasma development is continued until the substrate is bared or $NT_{DU} = 0$ such that

$$NT_D = NT_{DE} \quad [3]$$

At all points on the lower curve resolution is equal and usually closely approximates the features on the mask. The slope of the linear portion of the lower curve is called γ , the contrast. Another parameter which we employ is $D^{0.2}$ or the dose required to give $NT_D = 0.2$. This is useful because starting from a 1.5 μm film we obtain 3000Å final thickness which is typically the minimum required for subsequent trilayer processing (22).

Several additional parameters are instructive. Certain compositions such as that shown in Fig. 3 exhibit plateaus at high doses for both NT_R and NT_D . These maximum normalized thicknesses we call NT_{MR} and NT_{MD} . In all cases we find that NT_{MR} is less than the theoretical NT_R expected for the case in which all monomer initially present is locked. The theoretical NT_R is assumed to be given by $1 - NT_{RU}$ for zero exposure time. One parameter not given in Fig. 3 is the differential removal rate for oxygen plasma treatment called R_D . It is given by

$$R_D = (NT_{RU} - NT_{RE} + NT_D)/t = (NT_D - NT_R)/t \quad [4]$$

where t is the plasma etching time required to clear the unexposed regions. This value is dependent on dose since the x-ray mask permits exposure beneath the nominally masked regions. Thus, longer etch times are required at higher doses. Typical differential removal rates for the 85:15 mixture are 220 Å/min for a 2 min exposure and 140 Å/min for a 1 min exposure.

We have examined a large number of monomer-polymer mixtures as x-ray resists. In Table I we present data for ten monomers in poly(2,3-dichloro-1-

propyl acrylate) host. They can be divided into two classes. Monomers 1-5 are polymerized by both cationic and free radical initiators whereas monomers 6-9 are polymerized only by free radical initiators. Monomer 10, N-phenyl maleimide, is presumably locked not by polymerization but by a free radical chain-transfer process.

Within each class the monomers are ordered according to sensitivity. With the exception of N-vinyl carbazole the two classes of materials have comparable locking efficiencies as judged by the NT_R values for the 2.5 min exposure time (5.5 mJ/cm²). 9-vinylanthracene is observed to have an abnormally low NT_R value. This arises because the NT_{RE} and NT_{RU} values are >0.90 indicating that thermal locking during the fixing step is overwhelming that due to the radiation locking.

Comparing NT_D to NT_R we observe that the inclusion of aromatic functionality reduces plasma removal rate and optimizes the differential removal rate. The exceptions are examples 7 and 8. Both monomers are locked efficiently. This is particularly true for 8 which contains chlorine functionality and hence absorbs the Pd_{L α} x-rays efficiently. A reason for the low differential removal rates is not apparent. Since the acrylate corresponding to 8 behaves in an identical manner the lower rates do not appear to result from the presence of methacrylic functionality. Also, the methacrylate ester of 9 does have the protective property expected of aromatic groups.

The dependence of properties on monomer concentration is detailed for N-vinyl carbazole, naphthylethyl methacrylate and acrylate, and N-phenyl maleimide. The complete sensitivity curves are given in Fig. 4-6, respectively. For 5 the sensitivity is observed to increase with increasing N-vinyl carbazole concentration. At high doses a plateau is reached in each case. The NT_{MR} values in the plateau region for the various N-vinyl carbazole concentrations are always less than the theoretical NT_R values expected if all monomers were locked in each case. For example, in Fig. 2 NT_{MR} is 0.08 or about 53% of the theoretical amount. This implies that only a certain fraction of monomer is present in reactive sites and suggests a microscopic incompatibility which is not observed at 0.1 μm dimensions in patterned samples. Above 20 w/o the mixture becomes macroscopically incompatible and crystallization results. Similar phenomena occur for acenaphthalene and hydroquinone dimethacrylate above 20 w/o monomer.

Table I. Properties of poly(2,3-dichloro-1-propyl acrylate)-monomer mixtures

Monomer	State	Monomer (w/o)	Exposure ^a time (min)	NT_R	NT_D	$D^{0.2}$ (mJ/cm ²)	γ
1. 9-Vinylanthracene	s	15	2.5	Trace	0.04	—	—
2. N-vinyl phthalimide	s	20	2.5	0.05	0.10	—	—
3. Acenaphthalene ^b	s	20	2.5	0.04	0.14	—	—
		30		Monomer crystallized		—	—
4. 2-Vinylnaphthalene ^b	l	15	2.5	0.05	0.17	—	—
5. N-vinyl/carbazole	s	5	1.0	0.03	0.08	17.5	0.13
		10	1.0	0.04	0.11	10.0	0.13
		15	1.0	0.06	0.14	4.6	0.16
		20	1.0	0.07	0.18	3.1	0.14
		25		Monomer crystallized		—	—
6. Ethylene glycol dimethacrylate	l	20	2.5	0.04	0.04	—	—
7. Hydroquinone dimethacrylate	s	12.5	2.5	0.08	0.09	—	—
		25		Monomer crystallized		—	—
8. Pentachlorophenyl methacrylate and acrylate	s	25	2.5	0.10	0.13	—	—
9. 2-(1-naphthyl)-ethyl methacrylate and acrylate	l	10	2.5	0.05	0.12	15.6	0.16
		20	2.5	0.02	0.06	20.9	0.24
		30	2.5	Trace	0.03	29.6	0.21
10. N-phenyl maleimide	s	5	2.5	0.02	0.12	10.7	—
		10	2.5	0.03	0.16	8.4	0.18
		20	2.5	0.02	0.15	9.0	—
		30	2.5	Trace	0.10	11.0	—

^a Pd_{L α} flux was 2.9 mJ/cm²/min.

^b Monomer rapidly exuded from the film.

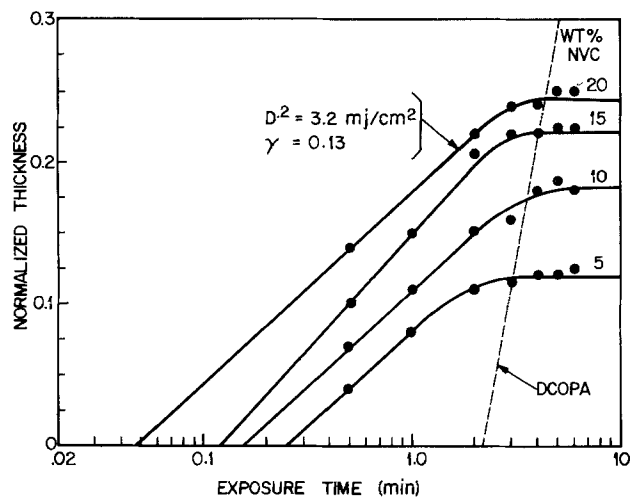


Fig. 4. Sensitivity curves for mixtures by weight of poly(2,3-dichloro-1-propyl acrylate) and N-vinyl carbazole.

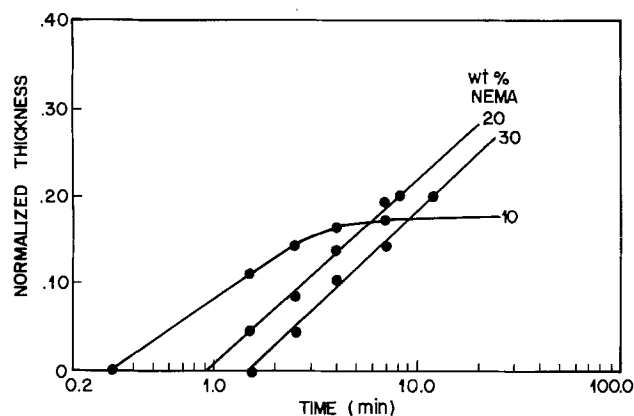


Fig. 5. Sensitivity curves for mixtures by weight of poly(2,3-dichloro-1-propyl acrylate) and 2-(1-naphthyl)ethyl acrylate.

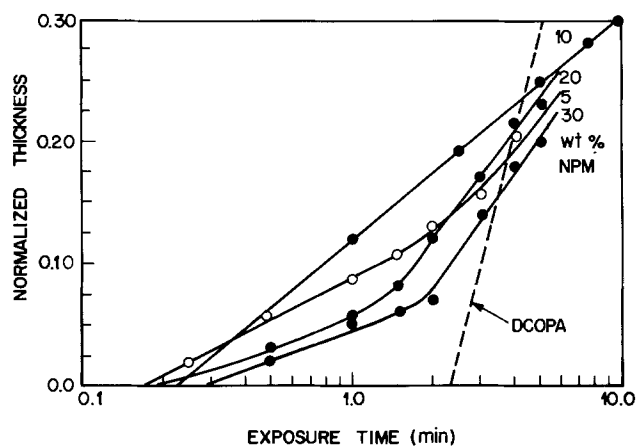


Fig. 6. Sensitivity curves for mixtures by weight of poly(2,3-dichloro-1-propyl acrylate) and N-phenyl maleimide.

Monomer volatility can also be a problem. Both acenaphthalene and 2-vinylnaphthalene exude too rapidly from spun films. Others such as 1,3-dimethoxystyrene, phenyl acrylate, and 4-chlorostyrene are also too volatile, while materials such as bis-phenol-A-dimethacrylate are too involatile and are partially polymerized during the higher temperature fixing step required. As a general rule of thumb we have found that monomers having a molecular weight ranging from 190-350 g/mole have appropriate volatility when mixed with poly(2,3-dichloro-1-propyl acrylate). The lower end of the range can be extended if a suitable glassy

host polymer were used or if a highly polar monomer or a monomer containing hydrogen bonding groups were used. An example of the polar monomer case is N-phenyl maleimide, molecular weight 173 g/mole, which is less volatile than N-vinyl carbazole. Conceivably the upper part of the range could be extended by the use of monomers which are less subject to thermal polymerization.

The dependence on monomer concentration exhibited by N-vinyl carbazole is not mimicked by examples 9 and 10 for which free radical species are presumably involved. In other cases a maximum sensitivity is observed at about 7.5 w/o monomer. Similar results are obtained for many other materials locked by free radical mechanisms. It appears that these monomers are self-inhibiting, i.e., less monomer is locked at high monomer content. This is in part due to the monomer's low x-ray absorption. However, at 30 w/o monomer, estimates based on calculated mass absorption coefficients predict only a 27% reduction in absorbed dose. This contrasts with a 75% reduction in sensitivity observed for 9 and a 40% reduction for 10. Since reduced absorption cannot account for these results, significant chemical quenching must be occurring.

We note that N-vinyl carbazole and 2-(1-naphthyl)-ethyl methacrylate exhibit nearly identical differential removal rates for equivalent NT_R values. In contrast, N-phenyl maleimide is locked least efficiently but exhibits the highest differential removal rates. At 10 w/o composition $NT_D > 5NT_R$ for it whereas $NT_D \approx 3NT_R$ for N-vinyl carbazole and naphthylethyl methacrylate for $NT_R = 0.02$.

For all three monomers the contrast γ given by the slopes in Fig. 4-6 is low. However, resolution is high because of the differential removal process. It appears limited mainly by the mask and the electron range of secondary electrons produced in the resist. Unlike conventional wet-developed resists resolution is identical for all points along each sensitivity curve. The linewidth appears to be independent of exposure.

For comparison purposes in Fig. 4-6 we present the sensitivity curve for a high speed conventional wet-developed negative resist termed DCOPA. It is a 92.5:7.5 w/o mixture of poly(2,3-dichloro-1-propyl acrylate) and poly(glycidyl methacrylate-co-ethyl acrylate). Its properties were recently described by Moran and Taylor (7). For present x-rays masks with 6000Å Au and 1000Å Ta and a 25°-30° sloped edge, the proper exposure for 1 μ m resolution and good linewidth control occurs at $D_g^{0.5}$, the 50% dose. For slightly lower doses resolution is adequate but linewidth is less than desired. For exposures at $<D_g^{0.4}$ resolution is inferior. For exposure $>D_g^{0.55}$ both resolution and linewidth control are worse. With plasma-developed resists underexposure or overexposure results in a shorter or longer plasma development time, respectively. Although final resist thickness is altered resolution remains identical. For N-vinyl carbazole and N-phenyl maleimide the sensitivity is higher for exposure to $D_g^{0.2}$. These materials thus offer considerable sensitivity advantages. Resolution also is much improved.

To date the most reactive monomer we have investigated is N-vinyl carbazole. We have studied it in a variety of polymer hosts which are absorbing at the $Pd_{L\alpha}$ wavelength. Our results are presented in Table II and are listed in order of increasing sensitivity. Results are given for that monomer composition which afforded optimum sensitivity. Sulfur, bromine, and chlorine containing host polymers were studied. A broad range of sensitivities is observed. They are dependent on the specific bonding and polymer phase. The importance of polymer phase is best seen by comparing poly(2,3-dichloro-1-propyl acrylate) and the corresponding methacrylate. Both polymers are removed in an oxygen plasma at an identical high rate. The locked compositions exhibit nearly identical differential removal rates. The considerable difference in

Table II. Influence of polymer host on the properties of plasma developed negative x-ray resist containing N-vinyl carbazole monomer

Polymer	Phase ^a	Relative ^b plasma removal rate	Monomer (w/o)	Exposure time (min)	NT _R	NT _D	D ^{0.2} (mJ/cm ²)	γ
Poly(vinyl chloride)	G	12.96	20	Incompatible	—	—	—	—
Poly(chloroprene)	R	13.33	20	9	0.01	0.02	—	—
Poly(butene-1 sulfone)	G	7.11	25	9	0.02	0.07	—	—
Poly(epichlorohydrin)	R	21.50	20	9	0.04	0.12	—	—
Poly(2,3-dibromo-1-propyl acrylate)	R	3.04	20	9	0.12	0.04	—	—
Poly(2,3-dichloro-1-propyl methacrylate)	G	12.96	20	4	0.06	0.13	20.1	0.16
Poly(2-chloroethyl acrylate)	R	11.67	10	2.5	0.05	0.13	13.2	0.19
Poly(2,2,2-trichloroethyl acrylate)	G	11.90	30	2.0	0.09	0.20	5.8	0.10
Poly(1,3-dichloro-2-propyl acrylate)	R	11.85	20	2.0	0.06	0.22	4.0	0.34
Poly(2,3-dichloro-1-propyl acrylate)	R	12.22	20	1.0	0.07	0.18	3.2	0.14

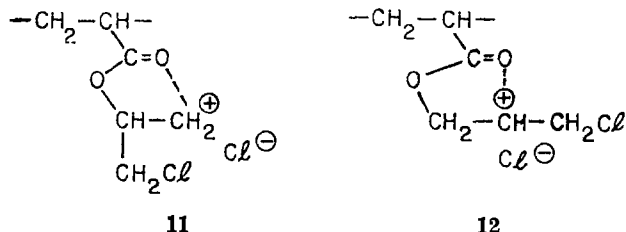
^a G = glass and R = rubber.

^b Relative to the removal rate for poly(styrene) in an oxygen plasma (270Å/min) at 35°C.

sensitivity thus appears to be related solely to the locking efficiency which is four times less efficient for the harder glassy methacrylate.

Locking efficiency also appears to be controlled by the type of chemical bonds present. Most striking is the very long exposure time required to lock monomer into poly(2,3-dibromo-1-propyl acrylate). This is further aggravated by the tendency of the locked portions of the film to etch faster than the unlocked regions thus providing the sole example for which $NT_D < NT_R$. Perhaps in this case locked carbazole sensitizes the decomposition of the brominated acrylate.

Vinyl chloride found in poly(chloroprene) appears to have low locking efficiency whereas aliphatic C-Cl bonds have much greater reactivity which is highly dependent on structure. The most sensitive compositions appear to be those which can form the most stable carbonium ion intermediates. The 1,3- and 2,3-dichloro-1-propyl acrylate polymers can both yield such stabilized species. In the case of the 1,3-isomer the primary carbonium ion can be stabilized by intramolecular participation with the carbonyl oxygen as depicted below (11). The 2,3-isomer can be similarly



stabilized (12) but in addition is a more stable secondary ion. Its expected greater stability could be responsible for the initiation of N-vinyl carbazole locking by a cationic polymerization mechanism.

Poly(2,3-dichloro-1-propyl acrylate)-N-vinyl carbazole mixtures.—Our best results to date have been obtained using a mixture of 81 parts by weight poly(2,3-dichloro-1-propyl acrylate) (DCPA) and 19 parts by weight N-vinyl carbazole (NVC). The sensitivity curve for this composition is given in Fig. 7. An exposure time of 1 min affords a normalized thickness of 0.14-0.15 when developed in an oxygen plasma. The sensitivity curve is independent of thickness for 3 μm or less initial thickness films. Figure 8 plots final resist thickness vs. initial thickness for a 1 min exposure time. The linear plot is equivalent to a constant normalized thickness of 0.18. It results from the very nearly uniform absorption of x-rays by the resist having an absorption of 11%/μm at the 4.37Å Pd_{Lα} line. Resolution for each point is identical. Thus, although the normalized thickness is rather low, the final thickness can have a practical value which of course is obtained by using a film having a greater initial thickness.

The reader may have noticed that the NT_D at 1 min exposure time for Fig. 7 is lower than that obtained in

Fig. 8. This results from slight environmental and processing variations which can be both controlled and optimized. First, exposure to ambient fluorescent light causes resist exposure with consequent locking of significant NVC in nominally unexposed regions and affords a reduction in sensitivity. This results from absorption of light below 3700Å by the N-vinyl carbazole as shown in Fig. 9. DCPA is not absorbing at wavelengths >2300Å. The locked product, Fig. 9c, also is absorbing at the longer wavelengths. From the difference in absorbance of curves 9b and 9c at 3440Å we calculate that a 2.5 min exposure followed by fixing locks approximately 20% of the total monomer present assuming no variation in the extinction co-

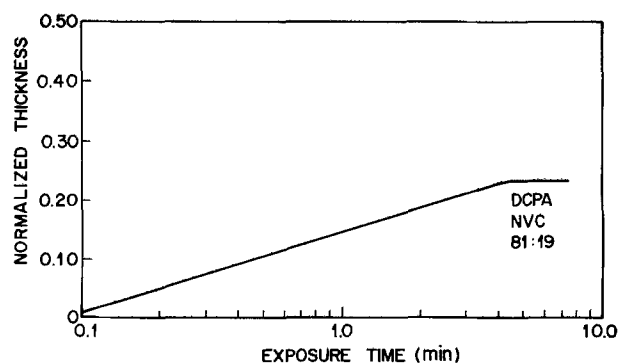


Fig. 7. Sensitivity curve for a mixture by weight of 81 parts poly(2,3-dichloro-1-propyl acrylate) and 19 parts N-vinyl carbazole.

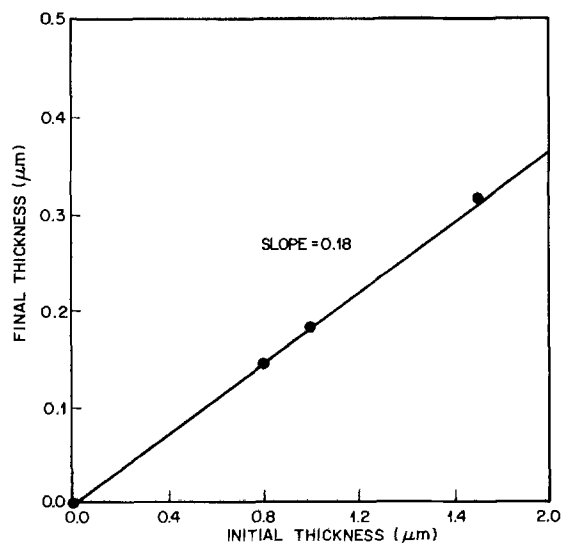


Fig. 8. Plot of final plasma-developed resist thickness vs. initial film thickness for the resist mixture detailed in Fig. 7 and exposed for 1.0 min.

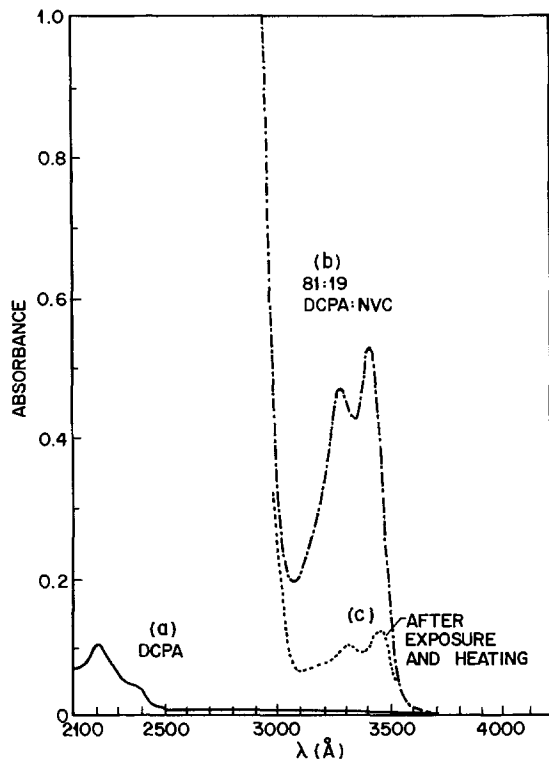


Fig. 9. Absorbance as a function of wavelength for (a) poly(2,3-dichloro-1-propyl acrylate), (b) 81 parts (a) and 19 parts N-vinyl carbazole, (c) (b) after 2.5 min exposure and fixing for 1 hr at 90°C and 0.1 Torr.

efficient for monomer and polymer. Use of yellow safelights and black wafer handling boxes has eliminated problems arising from ambient light exposures.

A second factor is fixation temperature and fixation time, a time temperature superposition. Results of a study of NT_D for a 1.5 min exposure as a function of fixing conditions are given in Table III for a 1.5 μm initial thickness film. The ultimate vacuum in the vacuum oven was 0.1 Torr. At the lowest temperature (23°) NT_D in large patterned areas was very high. However, development was microscopically nonuniform. Large unpatterned areas cleared before small unpatterned features. This was minimized by vacuum treatment for much longer time at 23° or by fixing at higher temperatures. At the highest temperature, NT_D values were lower than the optimum value obtained at 70°. Presumably, at the higher temperatures thermal locking of NVC becomes significant during the time required for removal of the unlocked NVC thus leading to a smaller difference in etch rates in the exposed and unexposed regions. A complete explanation of the phenomenon occurring at lower temperatures is not yet apparent.

Table III. Affect of fixing conditions on final thickness for 81:19 DCPA-NVC

Temp (°C)	Fixing time (hr)	Final ^a thickness (μm)	Remarks
23	0.50	0.47	Very nonuniform development
23	1.00	0.53	Very nonuniform development
23	16.00	0.36	Slight nonuniform development
45	0.50	0.32	Slight nonuniform development
60	0.50	0.30	Very slight nonuniform development
70	0.75	0.30	Uniform development
83	0.50	0.28	Uniform development
118	0.25	0.25	Uniform development
118	1.00	0.25	Uniform development

^a The initial thickness was 1.5 μm and the exposure time was 1.5 min.

A third factor is loss of NVC from spun films by slow exudation of this slightly volatile material. A plot of spun thickness vs. time is given in Fig. 10 for the 81:19 mixture and a 1 μm initial film thickness. Thickness loss became significant for standing times longer than 4 hr at which time <5% of the NVC was lost. After 8 hr 12.5% was lost. In thicker films the rate of loss of NVC was less. At long setting times (≥ 16 hr) microcrystal formation was observed. After exposure the wafer may sit for times as long as 2 days before fixing. However, immediate processing is recommended.

A fourth factor constitutes the influence of plasma processing conditions on developed image thickness, uniformity, and quality. Center-of-table-mounted single 3 in. wafer samples were developed most uniformly at 0.40 Torr. Thickness uniformity across the wafer was 500 \AA . At lower and higher pressures uniformity was worse. At low pressure (0.10 Torr) the center of the wafer cleared first whereas the edges cleared first at 1.00 Torr. The NT_D values were optimum at 0.40 Torr. Temperature variations from 25°-70°C did not appear to affect NT_D . The combination of high temperature and high pressure did lead to deposition of polymer on the wafer which was worst at wafer edges. At high temperatures the film removal rate was at least a factor of 2 greater than at 25°C. At the optimum pressure of 0.40 Torr, power variations by $\pm 200\%$ had little effect on NT_D but did alter film removal rate and uniformity. The optimum power was 100W in the 13 in. barrel reactor.

These variations with plasma conditions are a consequence of the well-known loading effect in plasma etching (19). It is observed when the lifetime of the reactive intermediates responsible for etching is long, as is the case with oxygen atoms thought to be responsible for the oxygen plasma stripping of photoresists (20). Uniformity of plasma development is essential in order to maintain both adequate resist thickness for further etching steps as well as to maintain linewidth control. In the hope of achieving better development uniformity, patterns were developed using a radial flow plasma reactor with floating bias. Results with the radial flow etcher were worse than those obtained with the barrel reactor. Uniformity was at best 1200 \AA and NT_D values were lower.

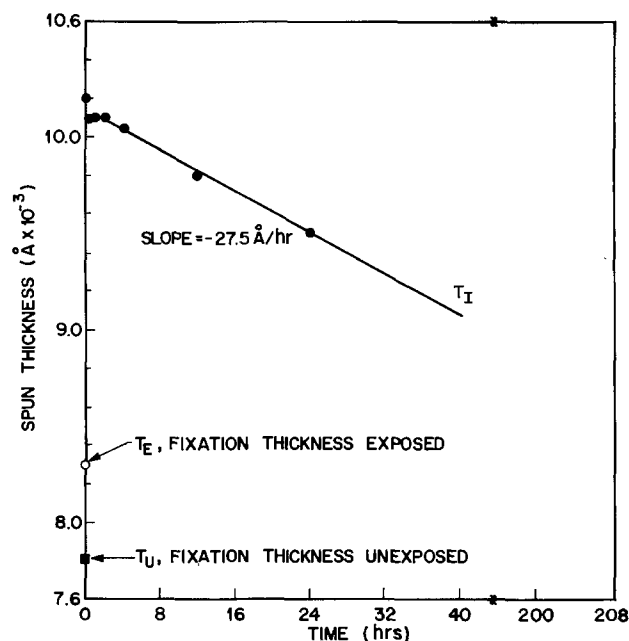


Fig. 10. Spun film thickness vs. standing time after coating of 81:19 DCPA-NVC.

Etch gas composition also has a considerable affect. Of all the gases and gas mixtures with and without oxygen that we have studied, only oxygen gave superior results. The other gases tried included CF_4 , CHF_3 , CF_3Cl , C_2F_6 , N_2 , He, Ar, NO_2 , and CO_2 . At low oxygen pressures traces of background air and pump oil hydrocarbons reduced NT_D . Thus plasma development afforded significant differential development only for oxygen containing plasmas.

A final factor is host molecular weight. Unlike many conventional negative resists in which sensitivity is dependent on the reciprocal of \overline{M}_w , we find no similar dependence for plasma-developed resists since crosslinking is not involved. Identical sensitivity curves were obtained for DCPA host having $[\eta] = 2.05$ and 0.80 dl/g. Thus, the molecular weight of the host can be designed to optimize processing properties. To date DCPA with molecular weight considerably lower than that used in conventional resist formulations has been found to be superior. Present DCPA properties are: $[\eta] = 0.80$ dl/g in ethyl acetate at 30°C , $\overline{M}_w = 764,000$ g/mole, $\overline{M}_n = 244,000$ g/mole, $P = 3.13$, and weight percent solids = 12 in chlorobenzene. Unlike conventional, negative crosslinking resists polydispersity has no influence on resist contrast.

Resolution.—In principle, the resolution of plasma-developed resists should be superior to that of conventional negative resists because of the absence of solvent-induced swelling. Consistent with this, we find that the resolution is better than $0.5 \mu\text{m}$. SEM photomicrographs of thin (2500\AA) patterns on silicon are shown in Fig. 11. The $0.5 \mu\text{m}$ gap is resolved including the proximity effect variations on the mask at the end of the gap. Resolution appears equally good in the partially developed $1 \mu\text{m}$ lines and spaces shown in Fig. 11d. Patterns in 6000\AA thick resist are shown in Fig. 12. The lines are undersized in the line and space features

due to overexposure in the mask resulting in greater gap widths as seen in the $0.5 \mu\text{m}$ gap (Fig. 12d) which is $1 \mu\text{m}$ wide in the print. Different masks were used to make the prints in Fig. 11 and 12.

Comparison of the pictures in Fig. 13 establishes the lower limit of resolution. SEM photomicrographs were taken of plasma-developed patterns exposed to 1.5 min of x-irradiation and further processed by trilevel techniques (21) to give high aspect ratio structures (Fig. 13a, 13b, and 13c). The exactly corresponding patterns in the x-ray mask are shown in Fig 13d, 13e, and 13f. It was necessary to destroy the mask and remove the topmost protective organic layer on it by plasma etching in order to obtain samples for SEM evaluation. The resist patterns are negative images of the mask pattern. Note that the particular mask chosen had very poor $0.5 \mu\text{m}$ features and only fair $1.0 \mu\text{m}$ features. Evaluation of resist resolution must be examined by comparison to the poorly resolved mask features having corrugated edges. In this regard, the fine structure at mask feature edges appears to be well resolved. This fine structure was copied to a great extent with about $0.1 \mu\text{m}$ of additional edge roughness being introduced. During pattern transfer to the intermediate 1200\AA SiO_2 layer, only 300\AA of the protective resist was lost. The change in linewidth from this loss is too small to measure by the techniques used here. The conventional DCOPA negative x-ray resist is not capable of resolving the poor $0.50 \mu\text{m}$ features on this mask. The plasma developed resist can resolve these features if development is continued for slightly longer time. This causes a 500\AA thinning of resist and a consequent loss of linewidth for the larger features which is within the linewidth variation desired for the larger features.

This type of resolution can only be achieved on flat surfaces. On a surface having topography, the spun resist film will not cover all features to a uniform thickness. Consequently, during development the thinnest regions will clear first and the thickest regions last. The thickness difference due to topography may approach $0.70 \mu\text{m}$ in the worst case. In such cases plasma-developed resists having the present composition will be completely removed in the thinner regions thus offering no protection during subsequent process-

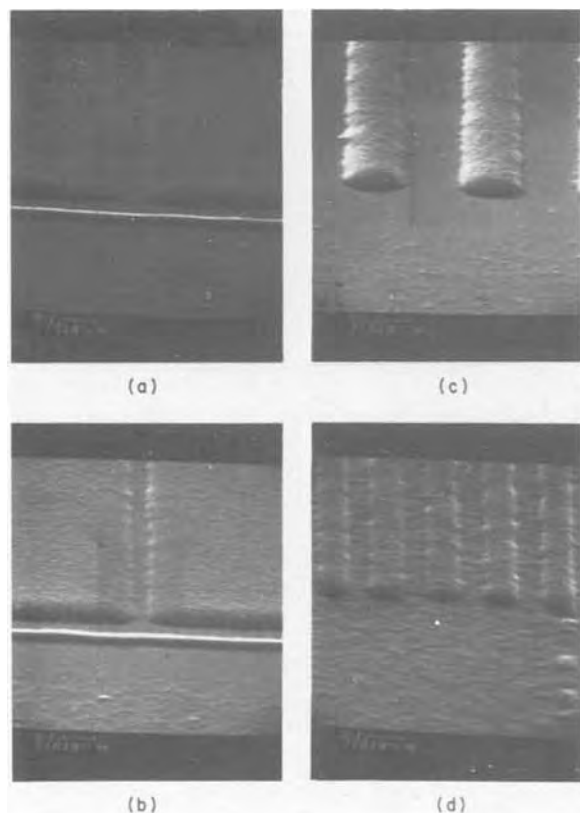


Fig. 11. Plasma-developed resist patterns from 81:19 DCPA-NVC in 2500\AA thick resist after exposure for 1.5 min and plasma development. Initial thickness was $1.5 \mu\text{m}$. Fully-developed patterns are shown in (a), (b), and (c). A 2000\AA thick partially developed pattern is shown in (d).

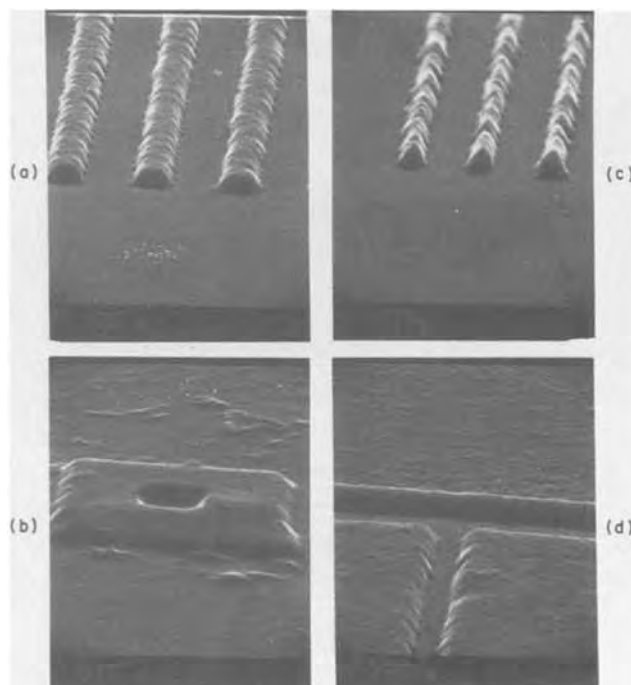


Fig. 12. 6000\AA thick plasma developed resist patterns in 81:19 DCPA-NVC. The initial thickness was $3 \mu\text{m}$ and the exposure time was 1.5 min.

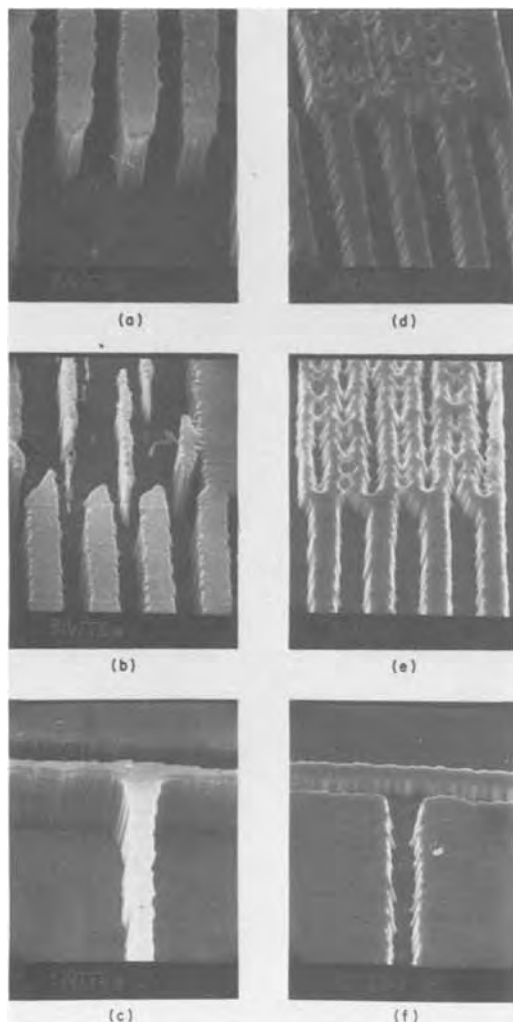


Fig. 13. Comparison of trilevel resist pattern resolution in $2.0 \mu\text{m}$ thick resist obtained from a plasma-developed resist top layer (a), (b), (c) to the exactly corresponding mask patterns in 7000\AA thick Au (d), (e), (f). The limit to resolution seen by matching up the sharpest edges in the resist and mask patterns is about $0.3 \mu\text{m}$.

ing steps. For reduced topographic variations, linewidth control will suffer. The trilevel process provides a means for circumventing the above difficulty. Using it and a higher resolution mask, line and space features as small as $0.3 \mu\text{m}$ should be resolved. Thus, it appears that plasma-developed x-ray resists are readily capable of submicrometer resolution.

General processing properties.—It was mentioned previously that the 81:19 DCPA-NVC composition provided a very good mask for etching the SiO_2 film used in the trilevel process. It also functions as an excellent etch mask for the dry etching of Si_3N_4 using 92% CF_4 and 8% O_2 . Less than 500\AA was lost in the latter case when 1200\AA of Si_3N_4 was etched. Plasma etch resistance has not been evaluated for plasma etching conditions used to etch P-glass, polysilicon, and aluminum since trilevel resist processing must be used in conjunction with pattern transfer operations on these substrates.

In general, plasma developed resists have better processing properties than conventional negative x-ray resists. The former are easily filtered through $0.2 \mu\text{m}$ pores. The present formulation of 81:19 DCPA-NVC using $764,000 \bar{M}_w$ DCPA affords excellent spun $1.5 \mu\text{m}$ initial thickness films by coating at 2450 rpm. A complete spin curve is given in Fig. 14. At spin speeds less than 2200 rpm a nonuniformity of the coating is observed which becomes worse at lower spin speeds. The nonuniformity appears as thickness variations of as

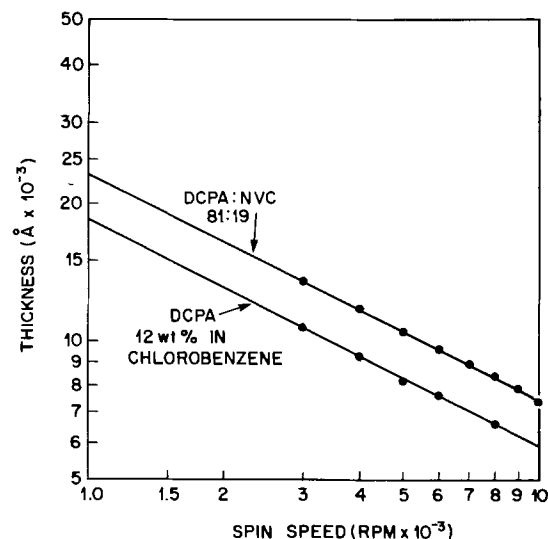


Fig. 14. Log-log plot of coated thickness in angstroms vs. spin-coating speed in rpm for 12 w/o $764,000 \text{ g/mole}$ DCPA in chlorobenzene and the same solution admixed with NVC to give 81:19 DCPA-NVC solution by weight.

much as 1000\AA over areas as large as $2500 \mu\text{m}^2$ and results in ragged feature edges. We believe it arises from channel formation in the very rubbery intermediate phase formed as the solvent plasticizer exudes from the film during spin drying. At high spin speeds the lifetime of this semifluid phase is probably short enough to preclude formation of the regions with undulating thickness.

Conclusions

We have shown that it is possible to obtain sensitive negative x-ray resists that are developed by oxygen plasma etching. They do not suffer from the limitations to resolution imposed by distortions caused by wet solvent development of conventional negative resists. The differential removal of exposed and unexposed regions amplifies the initial relief images obtained by radiation locking moderately volatile monomers into a host polymer. The host polymer serves as a container and binder for the monomer and also functions as the main x-ray absorber and polymerization initiator. It has a high removal rate in an oxygen plasma. The most preferred monomer, N-vinyl carbazole, is not highly absorbing, but is readily polymerized presumably by a cationic mechanism. It has a volatility which offers optimum processing characteristics. The optimum 81:19 w/o composition of DCPA and NVC provides final resist thicknesses of $0.30 \mu\text{m}$ for a 1.5 min exposure time and submicrometer resolution. Flat substrate surfaces are required for good thickness and linewidth control. The resist is thus ideally suited to sequential trilevel processing. Total sequential processing by dry methods has been demonstrated for trilevel processed wafers.

Optimum and reproducible developed thickness has been found to be dependent on ambient light, fixing conditions, and plasma processing conditions as well as resist composition. All of these processes can be readily controlled thus assuring excellent reproducibility. Presently, initial spun thickness uniformity, etch uniformity, and end point control limit resolution to the submicrometer regime. Because the mechanism of action of this new type of resist is different, it is possible to tailor the molecular weight of the host polymer to give optimum processing properties. Low molecular weights are desired.

We believe that plasma developed x-ray resists offer superior properties relative to those of solution-developed resists. The most important of these are resolution, sensitivity, latitude of molecular parameters, and perhaps ultimate cost.

Acknowledgment

We thank E. A. Chandross, D. Maydan, and C. J. Mogab for helpful discussions and the latter for use of his plasma processing apparatus.

Manuscript submitted April 16, 1980; revised manuscript received June 10, 1980.

Any discussion of this paper will appear in a Discussion Section to be published in the June 1981 JOURNAL. All discussions for the June 1981 Discussion Section should be submitted by Feb. 1, 1981.

Publication costs of this article were assisted by Bell Laboratories.

REFERENCES

1. R. D. Heidenreich and G. W. Kammlott, *Polym. Eng. and Sci.*, **17**, 377 (1977).
2. J. Kosar, "Light-Sensitive Systems," pp. 143-146, John Wiley & Sons, Inc., New York (1965).
3. M. Hatzakis, *This Journal*, **116**, 1033 (1969).
4. A. C. Ouano, *Polym. Eng. and Sci.*, **18**, 306 (1978).
5. E. D. Feit, M. E. Wurtz, and G. W. Kammlott, *J. Vac. Sci. and Technol.*, **15**, 944 (1978).
6. E. D. Feit and L. E. Stillwagon, *Polym. Eng. and Sci.*, To be published.
7. J. M. Moran and G. N. Taylor, *J. Vac. Sci. and Technol.*, To be published.
8. D. Hofer, F. Kaufman, and S. Kramer, Proc. Reg. Technical Conf., Mid-Hudson Sect., Soc. Plastics Eng., Ellenville, N.Y., Oct. 12, 1979, pp. 245-247.
9. *Electronics News*, May 28, 1979, p. 99.
10. J. N. Smith, H. G. Hughes, J. V. Keller, W. R. Goodner, and T. E. Wood, *Semiconductor International*, No. 10, 41 (1979).
11. A. N. Broers, "Proceedings of 1st International Conference on Electron and Ion Beam Science and Technology," R. Bakish, Editor, p. 191, John Wiley & Sons, Inc., New York (1964); R. B. Laibowitz, A. N. Broers, J. M. Viggiano, J. J. Cuomo, and W. W. Molzen, *Bull. Am. Phys. Soc.*, **23**, 357 (1978).
12. E. A. Chandross, C. A. Pryde, W. J. Tomlinson, and H. P. Weber, *Appl. Phys. Letters*, **24**, 72 (1974); **25**, 303 (1975).
13. J. E. Wilson, "Radiation Chemistry of Monomers, Polymers, and Plastics," chap. 9, Marcel Dekker, Inc., New York (1974).
14. W. A. Salmon and L. D. Loan, *J. Appl. Polym. Sci.*, **16**, 671 (1972).
15. R. L. Bersin, *Solid State Technol.*, **13**, 39 (1970).
16. G. N. Taylor and T. M. Wolf, *Polym. Eng. and Sci.*, To be published.
17. J. R. Maldonado, M. E. Poulson, T. E. Saunders, F. Vratny, and A. Zacharias, *J. Vac. Sci. and Technol.*, To be published.
18. G. N. Taylor and G. P. Schwartz, To be published.
19. C. J. Mogab, *This Journal*, **124**, 1260 (1977).
20. J. F. Battey, *ibid.*, **124**, 147 (1977); R. F. Reichelderfer, J. M. Welty, and J. F. Battey, *ibid.*, **124**, 1924 (1977).
21. J. M. Moran and D. Maydan, *Bell Syst. Tech. J.*, **58**, 1027 (1979).
22. G. N. Taylor, G. A. Coquin, and S. Somekh, *Polym. Eng. and Sci.*, **17**, 420 (1977).
23. D. Maydan, G. A. Coquin, H. J. Levinstein, A. K. Sinha, and D. N. K. Wang, *J. Vac. Sci. and Technol.*, To be published.

Chemical Vapor Deposition of Single Crystalline β -SiC Films on Silicon Substrate with Sputtered SiC Intermediate Layer

Shigehiro Nishino, Yoshikazu Hazuki, Hiroyuki Matsunami, and Tetsuro Tanaka¹

Department of Electronics, Faculty of Engineering, Kyoto University, Kyoto 606, Japan

ABSTRACT

A single crystal of β -SiC was grown by chemical vapor deposition using an $\text{SiH}_4\text{-C}_2\text{H}_2\text{-H}_2$ system on a silicon substrate with a sputtered layer. The grown layer of 4 μm thickness was confirmed as a single crystal by examination with reflection electron diffraction and x-ray diffraction. To reduce the large mismatch between β -SiC and a silicon substrate, a sputtered β -SiC layer was employed as a buffer layer. Even though the sputtered layer was polycrystalline, the subsequent layer deposited by CVD was a single crystal. The crystallinity of the deposited layer was strongly affected by the thickness of the sputtered layer, the substrate temperature during sputtering, and the temperature of chemical vapor deposition.

Silicon carbide (SiC) is an interesting material for electronic and optical device applications because of its high temperature stability and large energy gap. The cubic form, β -SiC, has a bandgap energy of 2.35 eV (1) at room temperature, an electron mobility of 1000 $\text{cm}^2/\text{V}\cdot\text{sec}$ (2), and a drift velocity of 2.7×10^7 cm/sec (at 2×10^5 V/cm) (3). These properties are particularly attractive for minority carrier as well as majority carrier device applications. However, a large area substrate is not available because of the difficulty of crystal growth. Crystals of β -SiC obtained by a sublimation process (Lely method) have small size and irregular shapes, thus complicating wafer processing for device fabrication. In order to

obtain β -SiC single crystals of large area, it is desirable to grow β -SiC on foreign substrates.

Epitaxial growth of β -SiC on foreign substrates has been reported by many investigators with chemical vapor deposition (CVD) (4-6), chemical conversion (7-9), evaporation (10), or rf sputtering methods (11-13). They, however, reported only very thin films of β -SiC. By the chemical conversion method, Nakashima *et al.* (9) have obtained single crystal films of β -SiC less than 100 nm thick on an Si substrate. Examination with reflection electron diffraction (RED) showed the change of the crystal structure from single crystal to polycrystal with increasing film thickness. Rohan *et al.* (5) showed oriented β -SiC layers grown on sapphire substrates by CVD and reported that the growth of single crystal films was not possible because of relatively large lattice mismatch.

¹ Present address: Takuma Radio Technical College, Takuma, Mitoyo-gun, Kagawa 769-11, Japan.

Key words: silicon carbide, CVD, epitaxial films, thin films, sputtering.

Difficulty with heteroepitaxial growth comes from the lattice mismatch between the grown layer and the substrate (a_{SiC} : 4.358Å, a_{Si} : 5.430Å, a_{sapphire} : 4.75Å, c_{sapphire} : 12.95Å). One of the approaches to overcome this difficulty is to introduce a buffer layer between substrate and deposit. This approach is well known in the crystal growth of III-V compounds by liquid phase epitaxy. A few examples are reported for CVD systems such as GaP/evaporated P/Si (14), ZnO/sputtered ZnO/sapphire (15), β -SiC/evaporated Ni/ α -SiC (16), and α -SiC/sputtered AlN/W (17).

We previously reported the preparation of β -SiC on Si substrates by a sputtering method and suggested that the sputtered β -SiC layer might be attractive as a substrate in the CVD process (18). In the CVD process, we reported the optimum conditions for epitaxial growth of β -SiC on Si substrates with an SiCl_4 - C_3H_8 - H_2 system (19). In this report, chemical vapor deposition of single crystal β -SiC films on Si substrates with sputtered β -SiC intermediate layers is described. Chemical vapor deposition was carried out using an SiH_4 - C_3H_8 - H_2 system. The crystallinity of the deposited layer was found to be strongly affected by the thickness and the crystalline structure of the sputtered layer. The surface morphology and crystallinity of the layer grown by CVD are described. The growth mechanism of β -SiC is also discussed.

Experimental

Sputtering.—Thin films of β -SiC were deposited on Si substrates by rf sputtering. The target material was an SiC disk from Union Carbide Company. The distance between the target and the substrate was 4.5 cm. The Si substrate was heated by a molybdenum strip heater and the temperature was measured by means of an optical pyrometer.

After preliminary evacuation of the reaction chamber to 1×10^{-6} Torr, argon gas was introduced up to a pressure of 1×10^{-2} Torr. Rf power of 200W (peak voltage of 2 kV and frequency of 13.5 MHz) was applied. Substrate temperatures were varied between 800° and 1000°C. Sputtering time was varied from 100 sec to 60 min. The thickness of the thin film was determined by using an interference microscope at a step made by masking a portion of the substrates during sputtering.

Chemical vapor deposition.—The deposition of β -SiC by pyrolysis of silane (SiH_4) and thermal decomposition of propane (C_3H_8) in a hydrogen flow system was carried out using the apparatus shown in Fig. 1. The reaction tube of 30 mm ID and 440 mm length was made of clear fused quartz with a water-cooled jacket. The thickness of the sputtered layer was 30–80 nm. After being rinsed in acetone and dried, the substrate was put on an SiC-coated graphite susceptor ($24 \times 5 \times 30 \text{ mm}^3$). To obtain a uniform grown layer, the susceptor was tilted at an angle of 10° from the horizontal. The linear velocity (defined

as the ratio of the carrier gas flow rate to the cross section of the reaction tube) of the system was approximately 2 cm/sec. The temperature was measured by observing the Si substrate through the water-cooled wall of the reaction tube with an optical pyrometer. The measured temperature was calibrated taking account of the emissivity of Si, but no correction was made for absorption by the water-cooled quartz jacket. The entire system was evacuated by a rotary pump and backfilled with H_2 . After H_2 flowed for 10 min, the substrate was heated externally by an rf generator and kept at 1000°C for 5 min before deposition of β -SiC.

The deposition of the β -SiC was carried out at a substrate temperature in the range of 1000°–1360°C with the standard gas composition: H_2 -750 cm^3/min , SiH_4 -0.6 cm^3/min , C_3H_8 -0.2 cm^3/min , Si/H_2 -0.7 $\times 10^{-3}$, and $\text{Si}/\text{C} = 1$. The deposition time was usually 30–180 min. The thickness of the deposited β -SiC films was determined by direct observation of the cross section of fractured specimens with a scanning electron microscope (SEM). To study the crystallinity of the β -SiC films, the grown layers were examined by reflection electron diffraction with an acceleration voltage of 80 kV. The lattice parameters of the grown layers were determined from a spot pattern using the diffraction pattern of gold as a reference.

Experimental Results

Preparation of substrates.—The relation between the thickness of the sputtered SiC film and sputtering time is shown in Fig. 2. The sputtering rate depends on the substrate temperature. The higher the substrate temperature, the lower the sputtering rate obtained. The temperature dependence is explained by a reduced sticking coefficient of sputtered atoms at high substrate temperatures, or by decreased sputtering yield resulting from high target temperature due to thermal radiation from the heated substrate (20).

Since the substrate with the sputtered layer is kept at high temperature during the CVD process, the crystallinity of the sputtered layer could be changed by the heating process. Consequently, the crystallinity of the sputtered layer before and after annealing was examined by RED analysis. Thermal annealing was carried out in an Ar ambient at 1270°C for 30 min. Diffraction patterns of the sputtered layer before and after annealing are shown in Fig. 3. Before annealing, every RED pattern showed haloes which implies an amorphous state. This was true even if a high substrate temperature was employed during sputtering, as shown in Fig. 3(b) and (c). After annealing, the RED pattern showed Debye rings which imply a polycrystalline state. The Debye rings became stronger

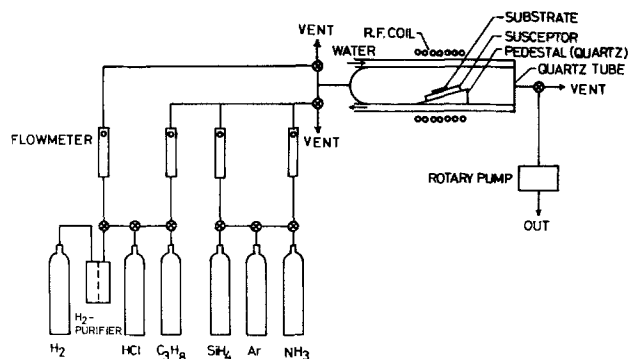


Fig. 1. A schematic diagram of the reaction tube and CVD system.

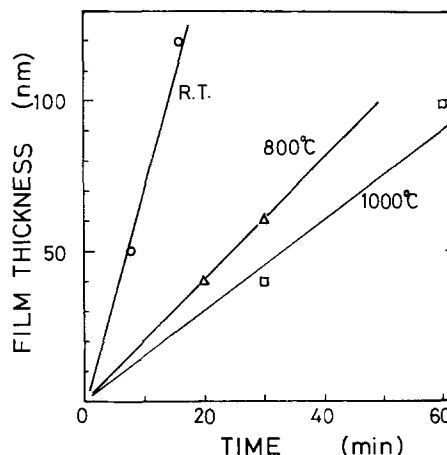


Fig. 2. Relation of film thickness and deposition time for sputtered films prepared at various substrate temperatures: ○, room temperature; △, 800°C; □, 1000°C.

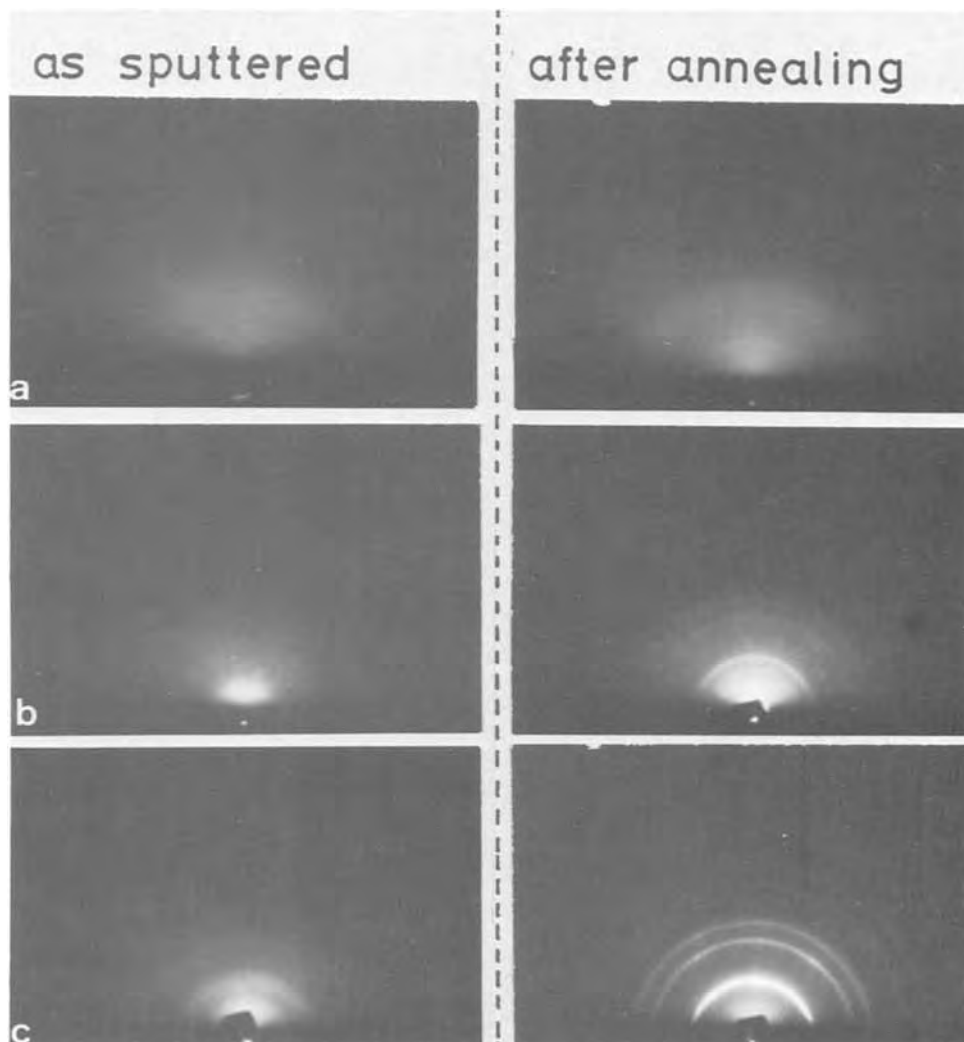


Fig. 3. Reflection electron diffraction patterns from layers as-sputtered and annealed at 1270°C for 30 min in Ar ambient. Substrate temperatures during sputtering were (a) room temperature, (b) 800°C, and (c) 1000°C.

when the substrate was kept at high temperature during sputtering. The sputtered layer was verified as being polycrystalline β -SiC by analyzing the RED pattern.

Temperature dependence of the CVD growth rate.—The growth rate as a function of the substrate temperature is plotted in Fig. 4. Vertical bars in the figure define the thickness difference from run-to-run. The mole ratio of the reactant gas (SiH_4 , C_3H_8 , $\text{Si}/\text{C} = 1$) to hydrogen is shown in the figure. The open circles indicate a higher mole ratio than that for the solid circles. While the higher mole ratio gave higher growth rate, it also gave an irregular surface and poor crystallinity, so the layer grown with the higher mole ratio is not favorable for device applications. The lower mole ratio gave a smooth surface and good crystallinity; therefore the ratio represented by a solid circle in Fig. 4 was chosen as a standard gas composition. The growth rate is expressed by an exponential function of the reciprocal substrate temperature above 1200°C, which indicates that the growth rate is limited by surface reaction. The activation energy for the formation of β -SiC calculated from the slope of the line is about 15 kcal/mole. An activation energy of 20–25 kcal/mole was obtained for the growth of β -SiC on an Si substrate without a sputtered layer when using the SiCl_4 - C_3H_8 - H_2 system (19). Two reasons may be given for the two activation energies. First, the growth of β -SiC on an Si substrate is heteroepitaxial growth, while the growth of β -SiC on a buffer layer (polycrystalline β -SiC) is homoepitaxial growth to some extent. The activation energy

for homoepitaxial growth is generally smaller than that for heteroepitaxial growth. Second, SiCl_4 was used for the Si source in the previous work (19), while SiH_4 was used in this work. Since the temperature of decomposition of SiH_4 is lower than that of SiCl_4 , a smaller activation energy might be expected.

The growth rates appear to be constant at substrate temperatures lower than 1200°C. The deposition mech-

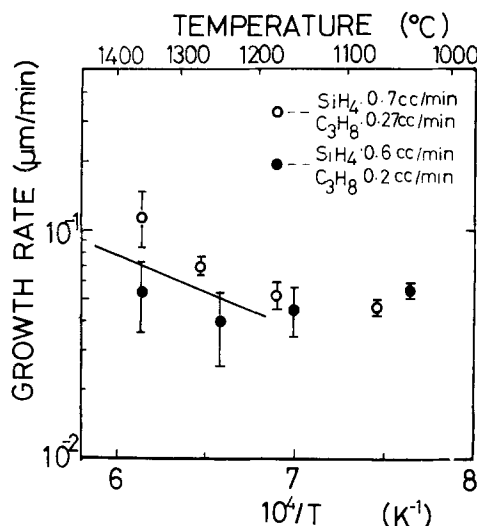


Fig. 4. Temperature dependence of the CVD growth rate

anism might be different in the high substrate temperature and low substrate temperature regions. Although the sputtered layer originates many nucleation sites for subsequent CVD growth, the layers grown by CVD at low temperatures tend to be polycrystalline because of short migration length of adatoms on the surface.

Surface morphology.—Surface morphology of the layers grown at three substrate temperatures is shown in Fig. 5. When the deposition was done at 1070°C, the surface was covered with rounded grains of size less than 0.2 μm . On the surface grown at 1250°C, the size of the rounded grains became larger. When the film was deposited at 1360°C, the surface was strongly influenced by the crystal habit of the sub-

strate. Although the size of the grains became larger at a substrate temperature lower than 1360°C, the layer showed a bumpy surface resulting from incomplete coalescence of the grains. When the substrate temperature was above 1360°C, coalescence of the grains was fully developed and a replica of the crystal habit of the substrate appeared in the grown layer. Figures 6(a) and (b) show surface morphology of the layer grown at 1360°C. Square crystallites with a side of 1 μm were observed on the layer grown on the (100)Si substrate, while triangular crystallites with a side of 2 μm were observed on the layer grown on the (111)Si substrate.

Crystalline properties of β -SiC films.—The crystallinity of growth obtained by the CVD process was strongly affected by the thickness of the sputtered SiC layer and the substrate temperature during sputtering. The layer grown by CVD was not a single crystal when the sputtered layer was thicker than 100 nm, even if a high substrate temperature was employed during sputtering. When the sputtering was done at a substrate temperature lower than 800°C, the subsequent layer grown by CVD was not a single crystal in spite of keeping the substrate at high temperature during the CVD process. From these experiments, it was found that the Si substrate should have a sputtered β -SiC overlayer with a thickness of 30-80 nm prepared at a substrate temperature of 1000°C.

The growth temperature for CVD is one of the important parameters which determines the crystallinity of the grown layer. The crystallinity of a layer of about 4 μm thickness was examined by the RED method. The diffraction pattern of β -SiC prepared at 1160°C showed so-called Debye rings which indicate a polycrystalline structure. Spots were superimposed

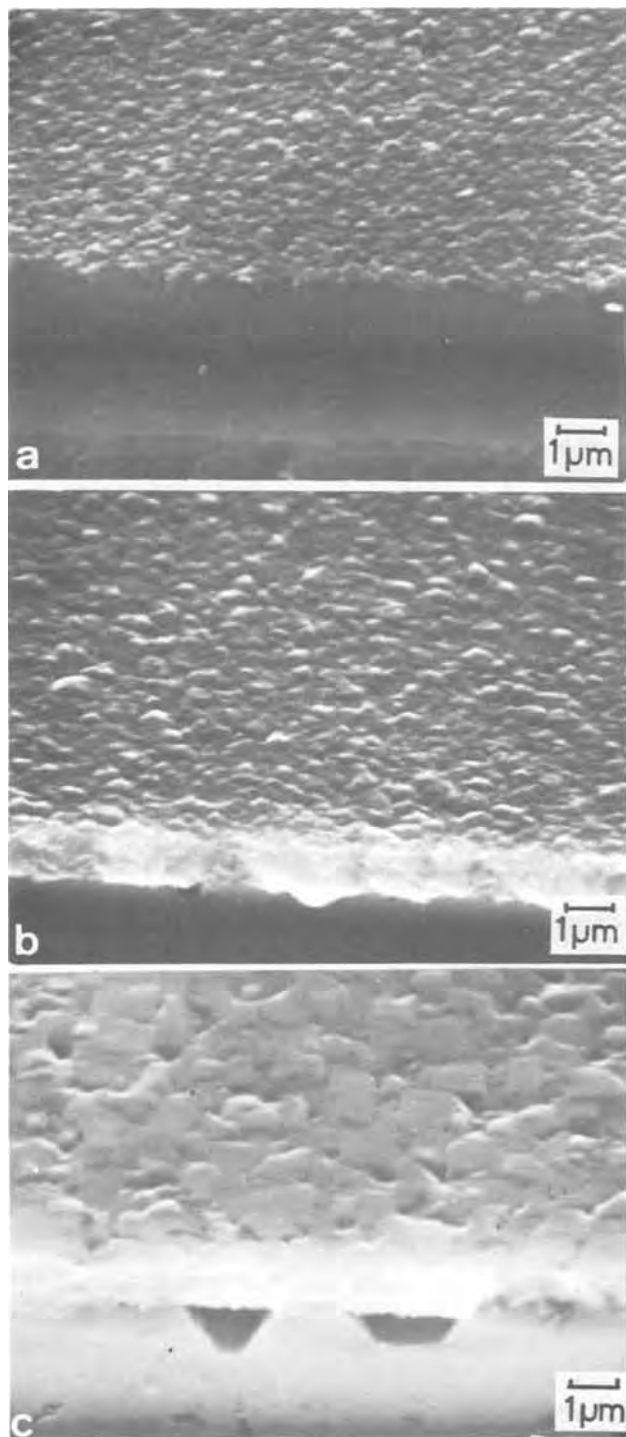


Fig. 5. Morphology of the grown layer for different substrate temperatures: (a) 1070°C, (b) 1250°C, (c) 1360°C.

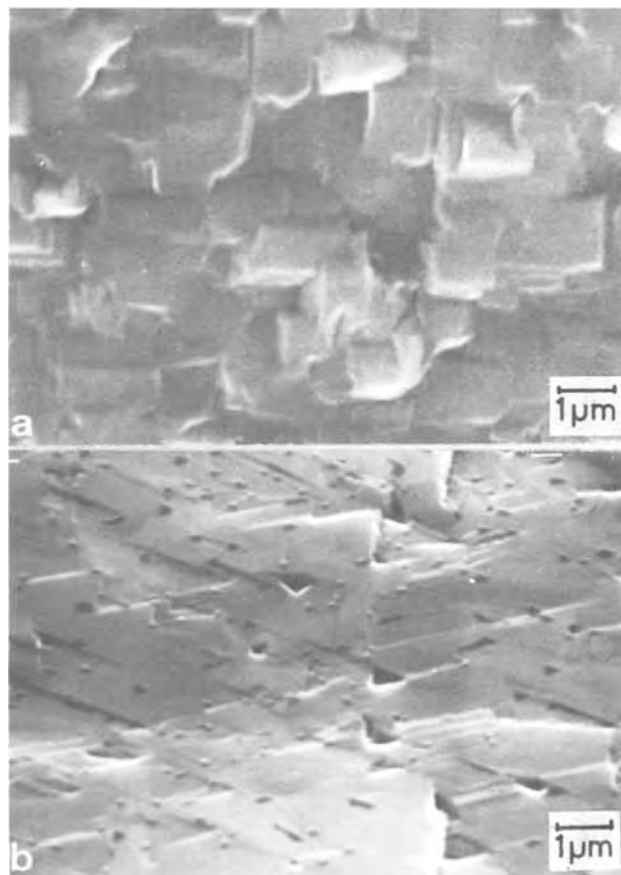
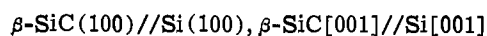
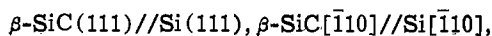


Fig. 6. Morphology of the grown layer reflecting the crystal habit of the substrate. (a) Layer grown on (100)Si substrate with a sputtered layer. (b) Layer grown on (111)Si substrate with a sputtered layer.

on the faint Debye rings for the film prepared at 1250°C, but the diffraction pattern was not changed when the direction of the incident electron beam was changed. The grown layer was therefore considered to have a preferred orientation. For the film prepared at 1360°C, the diffraction pattern consisted of strong spots. Consequently, it may be concluded that a change from polycrystalline to single crystal structure occurred with increasing substrate temperature. Good single crystals seem to be obtained at approximately 1360°C.

To investigate the substrate-orientation dependence of the growth, substrates with (111) or (100) surface planes were used. The CVD growth of β -SiC was carried out on the two substrates simultaneously using the standard gas composition at 1360°C. The diffraction patterns from the layers grown on the two substrates are shown in Fig. 7. Strong spots indicate that the layers are single crystalline. The orientation relationship between the overgrowth and the substrates is as follows



Since the RED measurement gives information on crystallinity very near the surface, the layer was examined by x-ray diffraction with a copper target for further crystal analysis. Figure 8 shows typical diffraction charts for the β -SiC layers. A strong peak appeared at $2\theta = 41.40^\circ$ for the layer grown on the (100) substrate. A peak for the Si substrate also appeared due to the thin β -SiC layer. A strong peak also appears at $2\theta = 36.65^\circ$ for the layer grown on the (111) substrate. Furthermore, the β -SiC film without a substrate was also examined by x-ray transmission Laue method. The Si substrate was removed by chemical etching using an HNO_3 -HF solu-

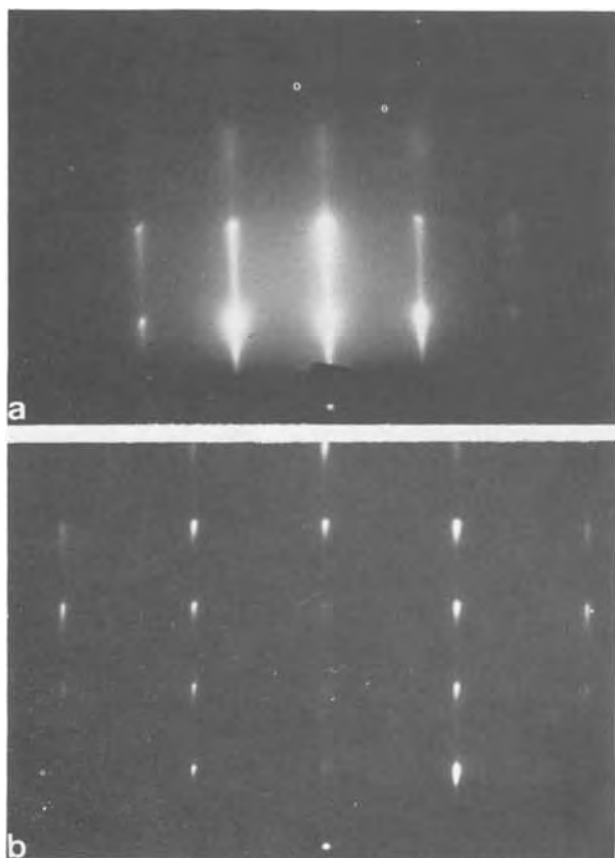


Fig. 7. Reflection electron diffraction patterns from layers grown on (a) (100)Si and (b) (111)Si substrates with sputtered layers.

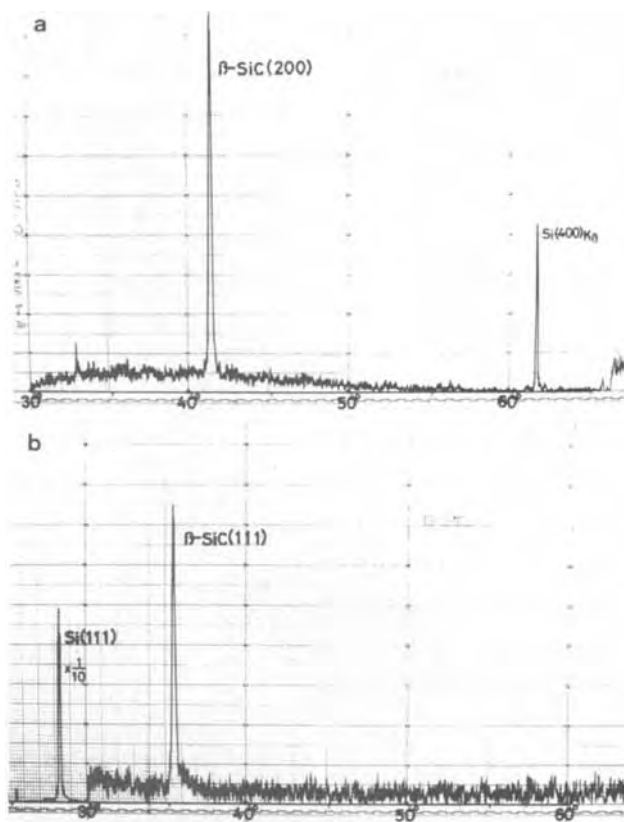


Fig. 8. X-ray diffraction spectrum obtained from layer grown on (a) (100)Si and (b) (111)Si substrates with sputtered layers.

tion. The Laue photographs are shown in Fig. 9 for the layers grown on the (100) and (111) substrates. The Laue pattern for the layer grown on the (100) substrate shows fourfold symmetric spots with faint Debye rings as shown in Fig. 9(a). The Laue pattern for the layer grown on the (111) substrate shows threefold symmetry with diffuse spots and faint Debye rings, as in Fig. 9(b).

The faint Debye rings are found to arise from the polycrystalline layer contiguous to the Si substrate. The underside of the β -SiC film was observed by SEM and examined by RED. A triangular morphology was observed on the underside surface of the layer grown on the (111) substrate, as shown in Fig. 10(a). In this figure, the length of the side of the triangles was scattered from 0.1 to 0.4 μm . The RED pattern from the underside of the layer shows Debye rings of polycrystalline β -SiC, as shown in Fig. 10(b).

Discussion

When a β -SiC film is deposited directly on an Si substrate, it is difficult to grow single crystals of β -SiC thicker than 100 nm, as reported by most researchers. The difficulty arises from the large lattice mismatch and stresses between the grown layer and the substrate. In this work, by introducing an intermediate layer as a buffer layer, stresses caused by the lattice mismatch could be released. The buffer layer should have an appropriate film thickness and crystallinity, because the crystal field of the substrate must be transferred through the buffer layer.

We speculate that the nature of the polycrystalline β -SiC layer obtained by sputtering is different from the one obtained by CVD. In the CVD system, the grown layer is formed under a condition of thermodynamic equilibrium, so that nucleation and growth are strongly dependent on the surface treatment of the substrate. The initial stage of growth is influenced by parameters difficult to control, such as surface roughness and dislocations. An adatom moves toward favorable sites of the substrate, so the density of nu-

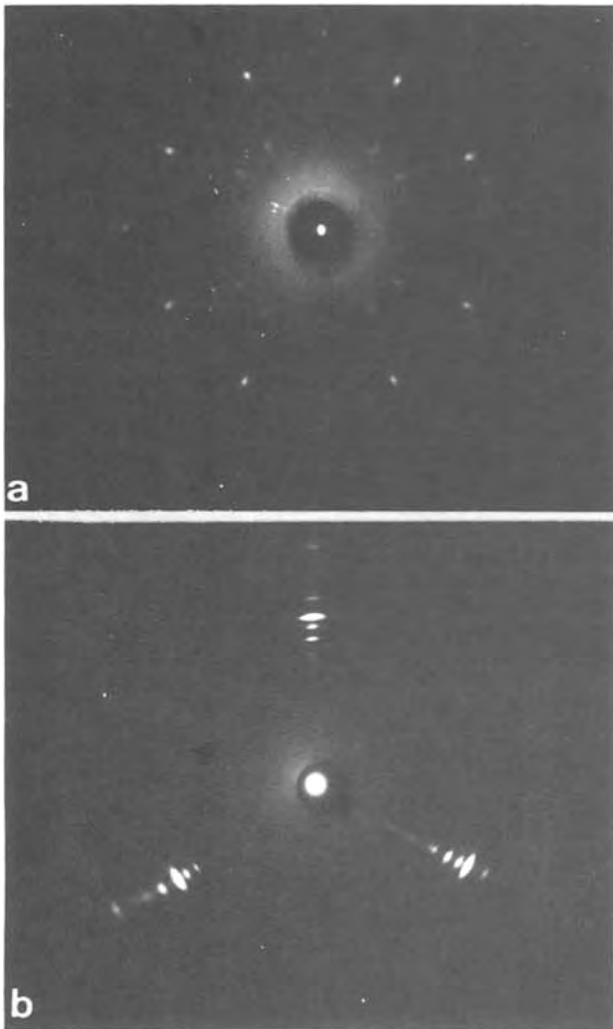


Fig. 9. X-ray transmission Laue photographs of the grown layer removed from (a) (100)Si and (b) (111)Si substrates with sputtered layers.

cleation on the surface might be nonuniform atomically. As a result, single crystal growth of β -SiC on an Si substrate by the CVD process needed careful preparation including SiC coating of the susceptor and etching of the substrate before the crystal growth. Furthermore, reproducibility of single crystal growth was not good. In the sputtering method, deposition is carried out under a nonequilibrium condition. Sputtered atoms uniformly hit the whole area of the substrate and nucleation may occur more uniformly over the surface. Therefore, the intermediate layer of β -SiC prepared by sputtering can be more uniform than that by CVD. Consequently, the initial stage of growth in the subsequent CVD process is not strongly dependent on the surface and single crystals of β -SiC are reproducibly obtained. When the CVD deposition was done at a substrate temperature higher than 1360°C, single crystalline β -SiC was also obtained in cases where the film thickness was less than 4 μm .

Conclusion

Single crystals of β -SiC were obtained reproducibly by CVD at a substrate temperature of 1360°C on Si substrates by using sputtered SiC layers as buffer layers. Crystallinity of the β -SiC layer so grown was examined by the RED and x-ray diffraction transmission Laue methods. The epitaxial relation between the β -SiC film and the Si substrate was obtained. Sputtering should be done at a substrate temperature between 800° and 1000°C. To obtain a single crystal by

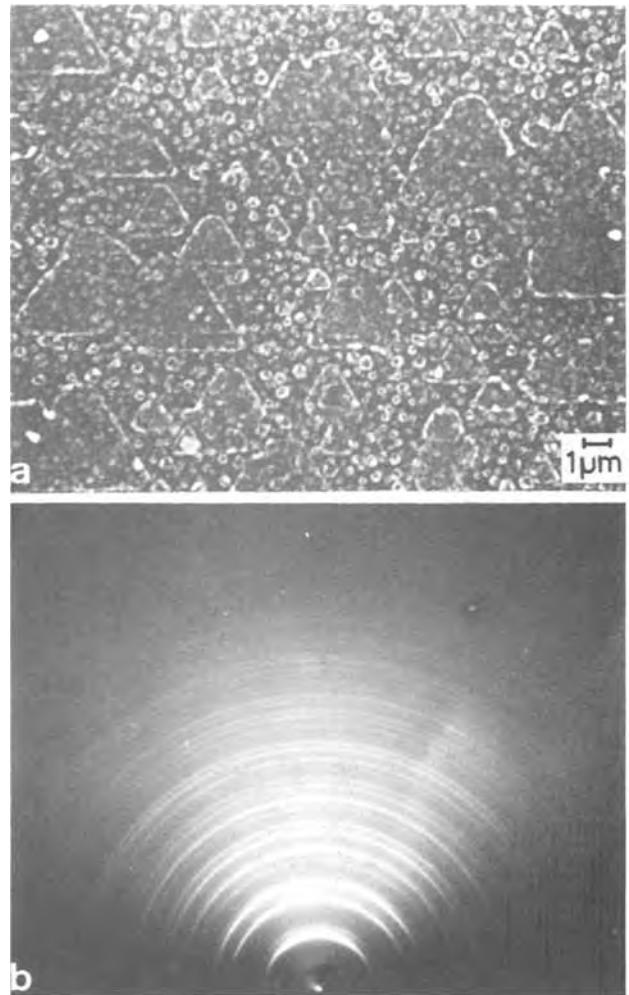


Fig. 10. Crystal structure of the underside of β -SiC after removal of the Si substrate. (a) SEM photograph and (b) RED pattern.

CVD, the thickness of the sputtered layer must be less than 100 nm. It is speculated that the growth of the single crystalline β -SiC was controlled by the crystal field of the Si substrate through a polycrystalline intermediate layer formed by sputtering.

Acknowledgment

This work was partially supported by the Grant-in-Aid for Scientific Research from the Ministry of Education of Japan and by the N.S.G. Foundation for Research and Development on Materials Technology.

Manuscript submitted April 4, 1980; revised manuscript received May 21, 1980.

Any discussion of this paper will appear in a Discussion Section to be published in the June 1981 JOURNAL. All discussions for the June 1981 Discussion Section should be submitted by Feb. 1, 1981.

REFERENCES

1. D. S. Nedzvetskii, B. V. Novikov, N. K. Prokofeva, and M. B. Reifman, *Sov. Phys.-Semicond.*, **2**, 914 (1969).
2. W. J. Silva *et al.*, in "Silicon Carbide-1973," R. C. Marshall, J. W. Faust, Jr., and C. E. Ryan, Editors, p. 673, University of South Carolina Press, Columbia (1974).
3. D. K. Ferry, *Phys. Rev. B*, **12**, 2361 (1975).
4. D. M. Jackson, Jr. and P. W. Howard, *Trans. Met. Soc. AIME.*, **223**, 488 (1965).
5. J. J. Rohan and J. L. Sampson, *J. Phys. Chem. Solids, Suppl. No. 1*, 523 (1967).
6. K. Kuroiwa and T. Sugano, *This Journal*, **120**,

- 138 (1973).
7. W. G. Spitzer, D. A. Kleinman, and C. J. Frosch, *Phys. Rev.*, **113**, 133 (1959).
 8. N. C. Tombs, J. J. Commer, and J. F. Fitzgerald, *Solid State Electron.*, **8**, 835 (1965).
 9. H. Nakashima, T. Sugano, and H. Yanai, *Jpn. J. Appl. Phys.*, **5**, 874 (1966).
 10. Y. Onuma, *ibid.*, **8**, 401 (1969).
 11. K. E. Haq and A. J. Learn, *J. Appl. Phys.*, **40**, 430 (1969).
 12. A. J. Learn and I. H. Khan, *Thin Solid Films*, **5**, 145 (1970).
 13. I. Berman, R. C. Marshall, and C. E. Ryan, in "Silicon Carbide-1973," R. C. Marshall, J. W. Faust, Jr., and C. E. Ryan, p. 42, University of South Carolina Press, Columbia (1974).
 14. M. Kishi and T. Katoda, *J. Jpn. Assoc. Cryst. Growth*, **5**, 8 (1978) (in Japanese).
 15. S. Ohnishi, Y. Hirokawa, T. Shiosaki, and A. Kawabata, *Jpn. J. Appl. Phys.*, **17**, 773 (1978).
 16. I. Berman and J. J. Commer, *Mater. Res. Bull.*, **4**, 107 (1969).
 17. R. F. Rutz and J. J. Cuomo, in "Silicon Carbide-1973," R. C. Marshall, J. W. Faust, Jr., and C. E. Ryan, Editors, p. 72, University of South Carolina Press, Columbia (1974).
 18. S. Nishino, H. Matsunami, M. Odaka, and T. Tanaka, *Thin Solid Films*, **40**, 27 (1977).
 19. H. Matsunami, S. Nishino, and T. Tanaka, *J. Cryst. Growth*, **45**, 138 (1978).
 20. V. A. Labunov and V. E. Borisenko, *Sov. Phys.-Solid State*, **20**, 712 (1978).

Application of the Langmuir Probe in Sputtering Techniques

H. Norström, R. Olaison, S. Berg, and L. P. Andersson*

Institute of Technology, Uppsala University, S-751 21 Uppsala, Sweden

ABSTRACT

During sputtering the plasma potential of the glow discharge may be influenced by unprotected electrodes situated in the vicinity of the plasma region. A positive electrode potential (V_a) is known to shift the plasma potential by a value of V_a in the positive potential direction. A negative electrode potential has no such influence on the plasma potential. A consequence of this behavior of the plasma potential is that all grounded parts of the vacuum system will establish a substantial ($\sim V_a$) negative potential with respect to the plasma if a positive electrode is introduced. This effect may cause excess contamination of the sputtered films since sputtering during this condition takes place both from the grounded vessel surfaces and from the sputtering target. Also, grounded substrates will then be subjected to unintended bombardment by energetic ions. This is especially important to consider in planar magnetron sputtering, where no energetic bombardment of substrates is supposed to take place. Introducing a negatively biased Langmuir probe into the plasma makes the probe current very sensitive to plasma conductance without affecting plasma potential conditions during sputtering. It is thus possible to monitor the sputter-cleaning of targets. During cleaning of an Al target the secondary emission factor of electrons caused by ion impact changes considerably. Thus the conductance of the plasma changes. This is detected by the Langmuir probe.

Numerous papers have been published in the field of Langmuir probe studies of glow discharges (1-3). We will restrict ourselves to the region of interest during sputtering. It has been reported that during sputtering of Ta and TaO it is necessary to reproduce not only pressure and bias conditions but also plasma conditions in order to obtain reproducible results.

This points out the importance of knowing and understanding plasma conditions during sputtering. It is well known that the plasma potential follows the potential of a positive electrode introduced into the plasma. In this way Holland (4) used the effect for treating and passivating vacuum systems. Coburn and Kay (5) measured the energy of ions extracted from a plasma and showed that the ion energy increased by the same value as a positive bias applied to an electrode exposed to the plasma. Both of these observations strongly confirm that the plasma I - V characteristic is indeed affected by an extra electrode introduced into the plasma in a sputtering system.

In some plasma applications it is very important to avoid any possible sputter bombardment of the substrates. If such bombardment takes place it may ruin the performance of the device. We are going to point

out some possible sources causing such (unintended) bombardment of the substrates during sputtering.

Experimental Results and Discussion

A system such as that shown in Fig. 1 was used during the probe I - V measurements. A single Langmuir planar probe was inserted into the sputtering plant. The upper electrode in Fig. 1 formed the cathode and consequently operated as the target during sputtering. A metal screen was inserted inside the glass bell jar. This metal screen was insulated from ground and a positive or negative voltage may be applied.

Consider the experimental I - V characteristics shown in Fig. 2. Here the Langmuir probe characteristics have been measured under different conditions where voltage is applied to the metal screen inside the vacuum chamber during sputtering. The I - V characteristic clearly shifts to more positive potentials with a value equal to that applied to the metal screen. Since the plasma is quite conductive, the plasma potential V_p follows the potential of the positive metal screen as expected. The implication of this effect is clearly demonstrated by applying a very high positive value to the metal screen. If so, a "dark space" region is observed over grounded areas inside the vacuum cham-

* Electrochemical Society Active Member.

Key words: sputtering, discharge, plasma potential.

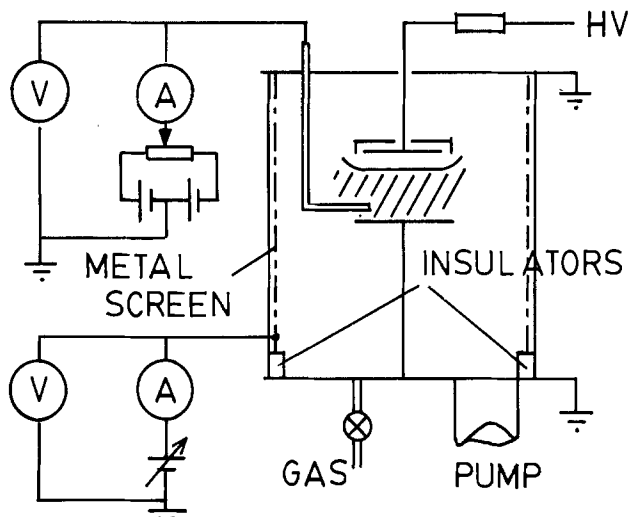


Fig. 1. Schematic of the experimental d-c-sputtering system with the probe inserted.

ber. These areas are then subjected to sputter bombardment of argon ions. This effect has earlier been used by several authors, e.g., Holland (4) to clean grounded stainless steel vacuum chambers. It is also a well-known fact that this effect causes outgassing of the system (6) and speeds up pumping time. This coupling of the plasma potential to the most positive potential in the vacuum chamber also exists in a planar magnetron system. Figure 3 shows the photograph of the *I-V* characteristics of the Langmuir probe in a magnetron sputtering equipment. Figure 3 clearly demonstrates the described coupling effect. Since many commercially available magnetron plants are equipped with a positive anode ring it is important to realize the effect of this anode on the plasma potential. In certain applications this positive anode may cause unintended bombardment of grounded substrates

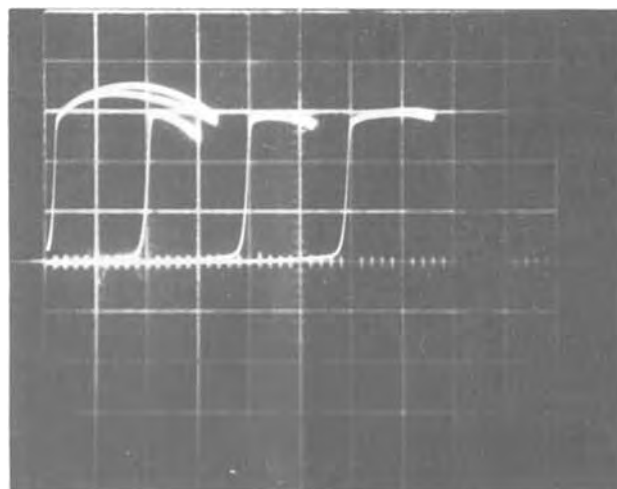


Fig. 3. Experimental *I-V* characteristics of the Langmuir probe during planar magnetron sputtering for different metal screen potentials (5, 10, 20, and 30V). x-axis, 5 V/div; y-axis, 0.5 mA/div.

by energetic ions. If a positive bias is applied the ground to plasma potential difference may exceed the threshold value for sputtering. The yield is of course still low, but this effect may under severe circumstances cause excess film contamination from chamber walls.

This is in accordance with the results from Coburn and Kay (5) who showed by mass spectrometric studies that grounded areas really are bombarded by energetic particles if the plasma potential is raised by introducing a positive electrode.

We also want to report on a quantitative way to make use of the Langmuir probe. We have found that the probe operates as an end-point detector in sputter-etching experiments. The probe was used with a negative bias of 15V so as to collect only ions, not influenc-

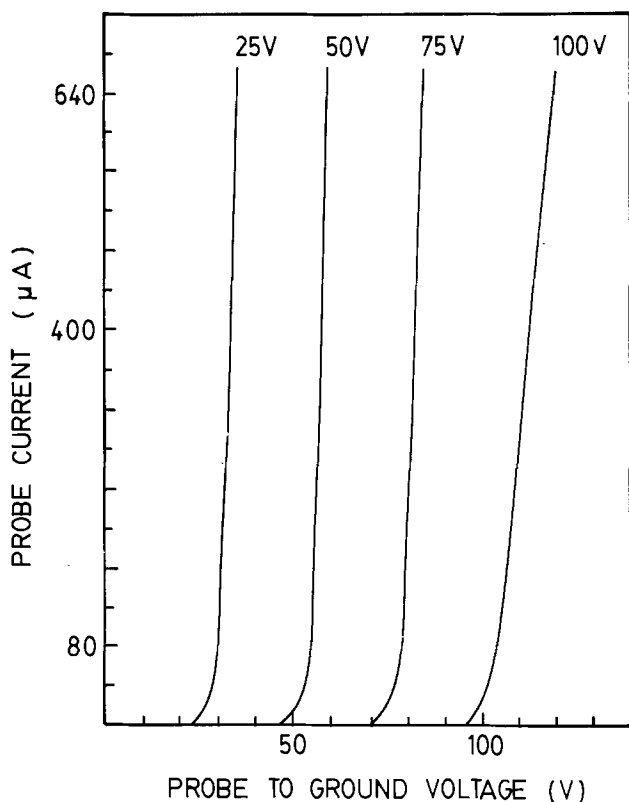


Fig. 2. Experimental *I-V* characteristics of the Langmuir probe showing the influence of large positive bias on the metal screen.

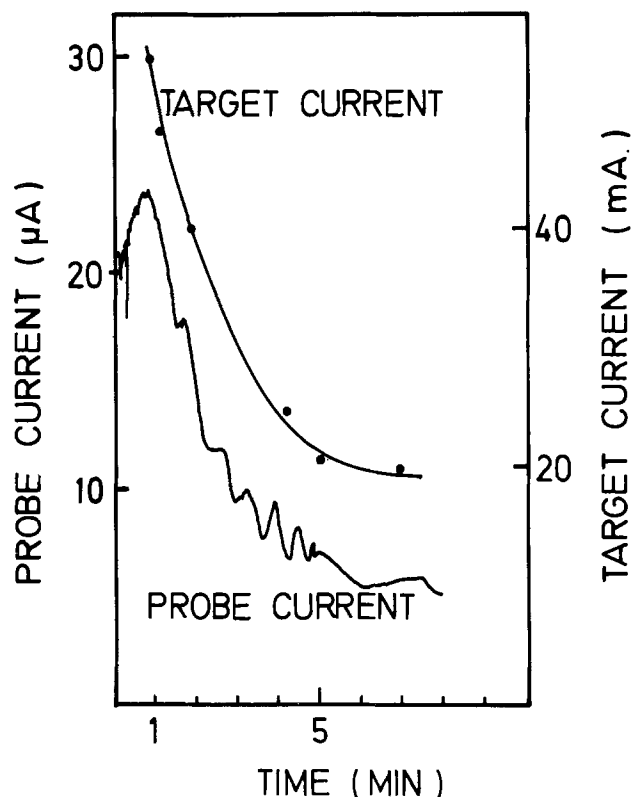


Fig. 4. Probe and target current vs. time during sputter cleaning of an Al target. Probe voltage = -15V, target potential -2.0 kV, argon pressure 50 mTorr, and target diameter 3 in.

ing the sputter conditions. In Fig. 4 the collected ion-current to the probe is monitored during cleaning of an Al target in d-c-sputtering equipment. Here the ion-current vs. time is shown to decrease to a steady-state level. In the same figure the cathode current of the Al target is also recorded. These two curves have a very strong correlation. What is demonstrated is that Al_2O_3 is removed from the surface. The secondary electron coefficient by ions is lower for Al than for Al_2O_3 . Thus the target current decreases. Since fewer secondary electrons are generated at the target surface when the oxide is removed, the conductance of the plasma decreases. Thus the ion concentration in the plasma will be smaller. The ion-current collected by the probe thus decreases, indicating that the oxide is removed. The Langmuir single planar probe thus offers the possibility of simple end-point detection in a d-c-sputtering system.

Preliminary results on rf-sputtering and on d-c-magnetron sputtering showed no such simple and reliable results. The reason why end-point detection cannot be observed by a single Langmuir probe under these conditions is probably due to the differences in ionization mechanisms compared to simple d-c-sputtering. Here the ionization is not directly dependent on the target electron secondary emission coefficient. Instead plasma conductance depends on frequency, magnetic flux, etc. Thus the change in plasma conductance may be too small to be ensured. However further work will be carried out to investigate the usefulness of Langmuir probe as end-point detectors.

Summary

The plasma potential in d-c-sputtering equipment will be determined by the most positive electrode exposed to the plasma. This may cause unintended bombardment of grounded substrates by energetic ions. The plasma conductance changes when an oxide is removed from an Al-target in a d-c-sputtering system. This effect is used to detect target cleaning with a single Langmuir planar probe.

Manuscript submitted Dec. 26, 1979; revised manuscript received May 23, 1980. This was Paper 128 presented at the St. Louis, Missouri, Meeting of the Society, May 11-16, 1980.

Any discussion of this paper will appear in a Discussion Section to be published in the June 1981 JOURNAL. All discussions for the June 1981 Discussion Section should be submitted by Feb. 1, 1981.

Publication costs of this article were assisted by Uppsala University.

REFERENCES

1. J. A. Thornton, *J. Vac. Sci. Technol.*, **15**, 188 (1978).
2. R. M. Clements, *ibid.*, **15**, 193 (1978).
3. E. Eser and R. E. Ogilve, *ibid.*, **15**, 199 (1978).
4. L. Holland, *Vacuum*, **26**, 97 (1976).
5. Coburn and Kay, *J. Appl. Phys.*, **43**, 4965 (1972).
6. O. Christensen and B. Klein, *J. Phys. E. Sci. Inst.*, **7**, 261 (1974).

Electrostriction in Anodic Oxides: Comparison with Macroscopic Theory

Jack L. Ord*

Department of Physics, University of Waterloo, Waterloo, Ontario, Canada N2L 3G1

ABSTRACT

Optical studies of the anodic oxidation of tantalum, niobium, and tungsten have recently found that application of the anodizing field increases the oxide film thickness by between 0.1 and 1% and decreases both the optical and low frequency dielectric constants by about the amount predicted by the Clausius-Mossotti relation between dielectric constant and density. These results are shown to contradict the predictions of the macroscopic theory of electrostriction, and the reasons for the conflict are examined. Energy conservation is shown to require the dielectric constant to have an explicit dependence on the electric field, and this requirement invalidates both the Clausius-Mossotti relation and the form of the energy density used in the macroscopic theory. A modified theory using an energy density of the form used in the theory of ferroelectrics is shown to give results consistent with all of the experimental results including the observation that at large strains the dependence on field is not quadratic.

The current physics literature on electrostriction is characterized by complaints from experimentalists that "disagreements exist as to the proper form of the (Maxwell) stress tensor in material media" (1), and complaints from theoreticians that "there exists very little information on detailed numerical values of the electrostrictive tensor ... most references are very old ..." (2). The problem has been that electrostrictive effects in most materials are so small that they are of little interest to the experimentalist, and as a consequence there are insufficient data available to test competing theories.

The electrochemical literature, on the other hand, contains a small but growing number of recent papers (3-10) which report extraordinarily large electrostrictive effects in anodic oxide films. Although there is some disagreement concerning the form of the field dependence, there is no argument about the three main features of the results: (i) the strains are very large, as large as 1%, (ii) the strains are positive, i.e., film thickness increases with field, and (iii) the effects appear to be universal, having been observed directly in the anodic oxides of tantalum, niobium, and tungsten, and indirectly in the anodic oxides of vanadium (11) and molybdenum (12). Although no explanation has been offered for the occurrence of a large positive strain instead of the small negative strain expected to

* Electrochemical Society Active Member.

Key words: dielectrics, capacitance, ellipsometry, ferroelectricity.

result from coulomb attraction between the opposing charge layers, the optical and low frequency dielectric constants have been shown to vary with field in approximately the manner predicted by the Clausius-Mossotti relation between dielectric constant and density.

In this paper we begin by summarizing the experimental results and outlining the development of the macroscopic or phenomenological theory of electrostriction. We then show that the experimental results contradict the predictions of the theory, and we examine the reasons for the disagreement. Finally we show how the theory can be brought into agreement with the results of experiment, and we discuss the physical significance of the modifications required.

The Experimental Results

The anodic oxides of tantalum and niobium have a number of properties which make them ideal from an experimental viewpoint for a study of electrostriction: (i) they support high electric fields without appreciable leakage current; (ii) they have high dielectric constants; (iii) they can be studied over a wide range of film thickness; (iv) they are insoluble in the electrolytes of interest; (v) the high-field growth process keeps their thickness uniform. Further, they have two properties which make them ideal also from a theoretical point of view: (vi) their vitreous structure is isotropic at zero applied stress and field; (vii) the massive metal substrate applies the boundary condition that the transverse strain be zero. The anodic oxides of tungsten, vanadium, and molybdenum are progressively less ideal, and metals such as iron which cannot be anodized beyond the oxygen evolution potential have anodic oxides which are far too thin for direct optical strain measurements. The only way in which the anodic oxides of tantalum and niobium differ significantly from ideal films of elastic dielectric is a consequence of the fact that they are grown in a high electric field. The large-scale atomic migration during film growth tends to relax stress in the film and when the field is removed the film is not left in a stress-free state, whereas all simple models assume that the film starts out in a stress-free state at zero field. We will deal no further here with this problem nor with the related problem of stress relaxation beyond noting that both introduce uncertainties into the analysis of the optical data.

The main experimental technique used to study electrostriction in anodic oxides is ellipsometry. This optical technique, based on the analysis of the change in polarization produced on reflection of light incident at an oblique angle on a film-covered interface, is capable of measuring and distinguishing between small changes in refractive index and film thickness. The two laboratories which have been involved in the optical studies of electrostriction in anodic oxides use similar self-nulling ellipsometers linked along with the anodization circuitry to minicomputer systems. Although the original study (3) treated the oxide films as optically isotropic, in all of the more recent work (4-6, 9, 10) the analysis takes account of the field-induced birefringence.

In all of our investigations the optical measurements have been complemented by measurements of the field dependence of the dielectric constant of the oxide film. In our original work (3) we used an a-c technique similar to that used on tantalum film capacitors (7, 8), but recently (9, 10) we have used a technique based on the analysis of open-circuit transients (13). This latter technique is primarily an analysis of the ionic conductivity of the oxide film and is based on the assumption that the logarithm of the ionic current density is proportional to the product KE , where E is the electric field in the oxide film and K is its dielectric constant. The technique was developed more as a test of the influence of electrostriction on the ionic con-

ductivity than as a technique for determining the field-dependence of the dielectric constant. If the electrical equation of state relating the dielectric constant of the oxide to its density is known, the dielectric constant data can be used to calculate a relation between strain and field which can be compared directly with the optical data. The equation of state which we have used in all of our work is the Clausius-Mossotti relation which "gives the correct dependence of K on density for a wide class of solids and liquids" (14)

$$(K - 1)/(K + 2) = A\rho \quad [1a]$$

where A is a constant and ρ is the density of the oxide. If the transverse strain is zero, the relation can be rewritten in the form

$$u = 3(K_0 - K)/((K_0 + 2)(K - 1)) \quad [1b]$$

where K_0 is the value of K when u , the strain in the field direction, is zero. For large values of K , Eq. [1b] can be rewritten, to a very good approximation, in a form which shows that the Clausius-Mossotti relation "amplifies" the effect of strain by a factor of $K_0/3$

$$K_0/K = 1 + (K_0/3)u \quad [1c]$$

Although the Clausius-Mossotti relation can be used to link dielectric constant measurements to optical strain measurements, it is of no direct use in the analysis of open-circuit transient or a-c data where one needs instead a relation between dielectric constant and field. In our analysis of open-circuit transient data (9, 10) we have fitted the data to the empirical form

$$K = K_0(1 - \gamma(E/E_1)^n) \quad [2]$$

where γ is the fractional change in K when the field is raised from 0 to E_1 , the oxidation field. An expression of this form can be used in the analysis of a-c data also provided one is careful to take account of the fact that the a-c technique involves the derivative of the dielectric constant. In fitting our original a-c data (3) to Eq. [2] for inclusion in the figures which follow, we had insufficient information to determine all three parameters, and were forced to assume a value for n . Since our most recent values (10) for n were 1.85 for niobium and 1.75 for tungsten, we took their average, 1.8, and applied it to the a-c data from original study.

The experimentally determined dependences of strain on field for the anodic oxides of tantalum, niobium, and tungsten are shown in Fig. 1, 2, and 3. All of the optical results plotted in the figures were obtained by analysis techniques which take account of the birefringence induced in the oxide film by the field, and the source of the data is indicated in each case. The dielectric constant data were all obtained in our laboratory, and strains were calculated from them using the Clausius-Mossotti relation as described above. Although we shall see that the Clausius-Mossotti relation is not actually applicable to our data, it does provide a convenient means of reducing dielectric constant data to a dimensionless, frequency-independent form suitable for comparison with strain data.

Although the tantalum system was the first one to be studied, it has received little recent attention because the electrostrictive effects are smaller than in the other two systems. The optical results plotted in Fig. 1 were taken directly from the paper by Cornish and Young (4), and the dielectric constant data for the second curve were calculated from our original a-c capacitance data (3) using the procedure described above.

The niobium system has received more attention than the others because it combines large electrostrictive effects with ideal electrochemical behavior. The results of optical studies by Yee and Young (5), Wang (6), and Ord and Lushiku (10) are shown in Fig. 2. In the case of niobium, both a-c (3) and open-circuit

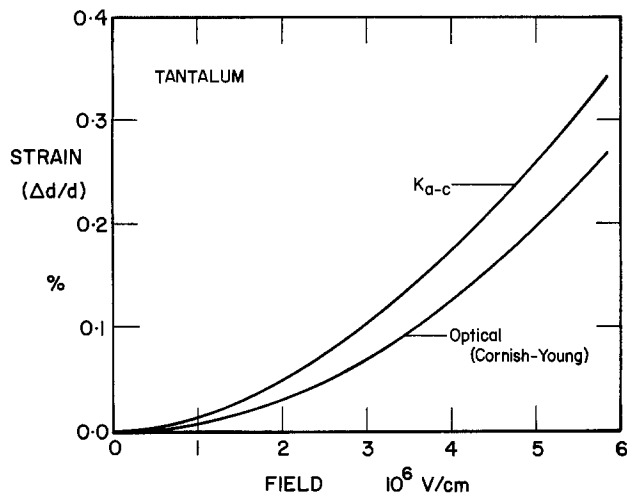


Fig. 1. The dependence of strain on field for the anodic oxide of tantalum as measured optically and as calculated from a-c dielectric constant data using the Clausius-Mossotti relation.

transient (10) dielectric constant data are available for strain-field calculations, and the two curves are shown in the figure.

The tungsten system exhibits larger electrostrictive effects than do the tantalum or niobium systems, but the solubility of the oxide in the low-resistance electrolytes convenient for electrical measurements, and the relatively low breakdown potential combine to make it a more difficult system to study. Figure 3 shows the results of the one optical study which has been undertaken (9) and curves calculated from a-c (3) and open-circuit transient (10) dielectric constant data.

There is little one need say about Fig. 1, 2, and 3 because the results speak for themselves, establishing the large positive strains and corresponding changes in dielectric constant as experimental facts for which the theory of electrostriction must account.

The Macroscopic Theory

Traditional textbook treatments of electrostriction (15) write the stress due to electrical forces exerted on the surface of a dielectric slab in a parallel-plate capacitor as the sum of three terms: (i) the internal pressure in the dielectric created by the field, (ii) the stress on the surface polarization charge layer, and

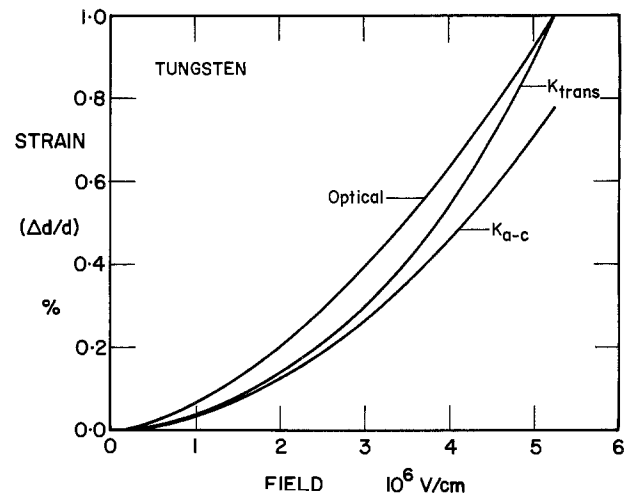


Fig. 3. The dependence of strain on field for the anodic oxide of tungsten as measured optically and as calculated from a-c and open-circuit transient dielectric constant data using the Clausius-Mossotti relation.

(iii) the stress on the charge layer on the surface of the plate in contact with the dielectric. The internal pressure is calculated by relating the force on a dipole in a nonuniform field to the pressure gradient in the dielectric. Since the force involves the field gradient, both expressions can be integrated directly, and the internal pressure in a uniform field is found to be $\sigma_p E/2$, where E is the field in the dielectric, and σ_p is the polarization charge density on surfaces perpendicular to the field. The stress on the surface polarization charge, if there is a gap between the slab and the plates, is $\sigma_p (E_0 - E)/2$, where E_0 is the field in the gap, and hence the internal pressure and the stress on the polarization charge sum to give a tensile stress equal to $\sigma_p E_0/2$ or $K(K - 1)\epsilon_0 E^2/2$ on the surface of the dielectric. For a slab not in contact with the plates, the stretching along the field lines in response to this tensile stress is known as electrostriction, and is quadratic in the field. If, as is the case in our system, the slab is in contact with the plates, the stress on the surface charge layer, $K^2\epsilon_0 E^2/2$, is transmitted to the dielectric, and the net stress on the surface of the dielectric is a compressive stress equal to $K\epsilon_0 E^2/2$. If the slab has a stiffness constant c , the strain, u , which results from the compression exerted by the electrical forces is

$$u = -K\epsilon_0 E^2/2c \quad [3]$$

The small compressive strain predicted by this expression was what was expected before large strains of the opposite sign were found experimentally. As we shall see, the more advanced theoretical treatment of electrostriction fares no better when compared with experiment.

The treatment of electrostriction outlined above neglects effects due to the variation of the dielectric constant with density, and hence cannot be expected to apply to high dielectric-constant materials which are expected to be quite sensitive to density variations. The variation of dielectric constant with density can be dealt with by introducing an additional stress, but in order to determine the form of the stress we must formulate the problem in terms of energy rather than in terms of force. There is considerable controversy in the literature over what constitutes a proper non-linear theory of the elastic dielectric, but fortunately we can avoid the controversy because all of the competing treatments give identical results when applied to a system as simple as the one we are studying. The simplicity of our system results from the fact that to a very good approximation the field is uniform and confined to the oxide film. We get the same results

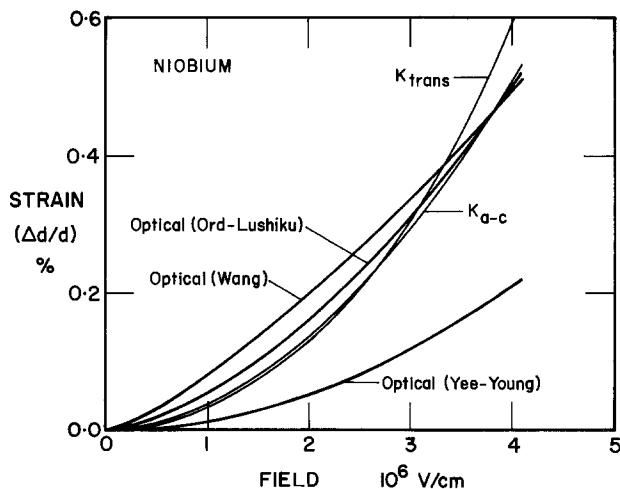


Fig. 2. The dependence of strain on field for the anodic oxide of niobium as measured optically and as calculated from a-c and open-circuit transient dielectric constant data using the Clausius-Mossotti relation.

using a model with a thin spherical dielectric shell on a massive metal sphere as we get using a model with a thin slab constrained to have zero transverse strain, but the slab model is much simpler mathematically, and is the one we use here.

We can extract a solution for our system from a more general solution (16) by setting numerous tensor components equal to zero, but we get a better picture of what is involved by restricting our attention to the isotropic slab with zero transverse strain at the outset, and following through the steps in the solution. Grindlay (17) and Juretschke (2) have published treatments of the dielectric slab problem which attempt to present the theory in a form which treats the coupling between elastic and dielectric effects properly, yet is free of cumbersome mathematics. Grindlay's treatment, which emphasizes the variational technique used to solve the problem, is more suitable for our purposes than Juretschke's treatment which emphasizes the tensor nature of the coupling. Grindlay's treatment, however, is not self-contained, and we must refer to his more general treatment of electrostriction (16) for an explicit expression for the energy density.

In order to set up a problem for a solution based on energy considerations, it is usually necessary to have an expression for the energy density at all points in space, but in our system the field is confined to the slab, and the substrate is unstrained, so we need only an expression for the energy density in the dielectric. In order to avoid having to distinguish between energy density per unit volume and per unit mass, we will write instead an expression for the internal energy, U , of a square slab of side l and unstrained thickness z . The internal energy is represented by a power series in the strain, u , and the electric displacement, D , carried to fourth order in D (assuming u of order D^2).

$$U = [cu^2/2 + (q + b/2)uD^2 + bD^2/2]zl^2 \quad [4]$$

where c and q are the elastic stiffness and electrostrictive constants of the oxide film, and $b = 1/K_0\epsilon_0$. This expression for the internal energy reduces to the correct form for a capacitor with a vacuum between the plates when q and c are zero, and it can be used to describe a capacitor with a spring between the plates when q is zero and c is nonzero. [Note that if $q = 0$, $(1 + u)$ can be factored out of the entire expression since the elastic energy term is unchanged to second order in u when it is divided by $(1 + u)$.] The internal energy does not contain the fourth-order term in D used in the theory of ferroelectrics, and as a consequence we will find that the dielectric constant depends on the density but not on the field, a result which is consistent with the Clausius-Mossotti relation.

The fundamental relation in Grindlay's treatment is the principle of conservation of energy

$$\delta U = \delta W \quad [5]$$

where δU is the change in internal energy when charge δQ is added to the capacitor, changing the electric displacement by $\delta D = \delta Q/l^2$ and the strain by δu , and δW is the external work done. In charging a capacitor with no externally applied stress, the only external work done is the electrical work $V\delta Q$, where V is the potential difference across the capacitor. If we expand δU in terms of δu and δD , Eq. [5] takes the form

$$\{[cu + (q + b/2)D^2]\delta u + [(2q + b)uD + bD] \delta D\}zl^2 = Ez(1 + u)l^2\delta D \quad [6a]$$

where E is the electric field in the oxide film. Collecting terms in δu and δD , we can rewrite Eq. [6a] in the form

$$[cu + (q + b/2)D^2]\delta u = [E(1 + u) - (2q + b)uD - bD]\delta D \quad [6b]$$

In a variational calculation, δu and δD are treated as arbitrary independent variations, and hence their coefficients in Eq. [6b] must vanish, yielding

$$u = -(2q + b)D^2/(2c) \quad [7]$$

$$E(1 + u) = [(2q + b)u + b]D \quad [8a]$$

These equations constitute a complete solution to the dielectric slab problem. Equation [7] gives the dependence of the strain on the electric displacement, and Eq. [8a] is an electrical equation of state which defines the dielectric constant. The equation of state can be compared with the Clausius-Mossotti relation by rewriting Eq. [8a] in the form of Eq. [1c]

$$K_0/K = 1 + (2q/b)u \quad [8b]$$

Note that if q equals zero, the dielectric constant is independent of density, and the expression for the strain in Eq. [7] reduces to the expression given earlier in Eq. [3]. On the other hand, if the Clausius-Mossotti relation is valid, q must equal $1/6\epsilon_0$, and the strain will be larger by a factor of $(1 + K_0/3)$ than predicted without taking the variation of dielectric constant with density into account.

We can use the results we have obtained to write our original internal energy expression in three alternate forms which will be useful in the discussion which follows

$$U = [cu^2/2 + (1 + u)ED/2]zl^2 \quad [9a]$$

$$U = (cu^2/2)zl^2 + QV/2 \quad [9b]$$

$$U = [bD^2/2 - (2q + b)2D^4/8c]zl^2 \quad [9c]$$

Comparison Between Theory and Experiment

The electrostrictive constant q , unlike the elastic stiffness c , can be either positive or negative, and we might expect the choice of sign to provide the degree of freedom needed to fit theory to experiment, but this is not the case. Equation [7] can account for the observed positive strain if q is negative and sufficiently large, but Eq. [8b] which must account for the observed decrease in dielectric constant with increasing field involves the product qu and requires that q be positive to agree with experiment.

We can see how this conflict arises by considering the implications of using the internal energy expression given in Eq. [9b] to describe the charging of a capacitor whose dielectric constant varies during the charging process. Equation [9b] states that the internal energy is the sum of the electrostatic term $QV/2$ and an elastic term $(cu^2/2)zl^2$. There is nothing unreasonable about this statement, and it is something we might well have assumed at the outset. It does, however, dictate the shape of charging curves. Figure 4 shows charging curves for capacitors with the same low-field dielectric constants and same total charge, but whose dielectric constants (a) remain unchanged, (b) increase by 25%, and (c) decrease by 25% during the charging process. The external work done in each case is the area under the charging curve, and the electrostatic term in the internal energy is the area under the line joining the endpoints of the charging curve. If the dielectric constant does not change during the charging process, the external work done and the electrostatic energy stored are equal, and hence the elastic energy is zero. If the dielectric constant increases during the charging process, the charging curve will curve toward the charge axis, the external work done will exceed the stored electrostatic energy, and the difference will be stored as elastic energy. This is the prediction of our theory, and it is the direction of the change in dielectric constant which is critical, not the sign of the strain which appears squared in the elastic energy term.

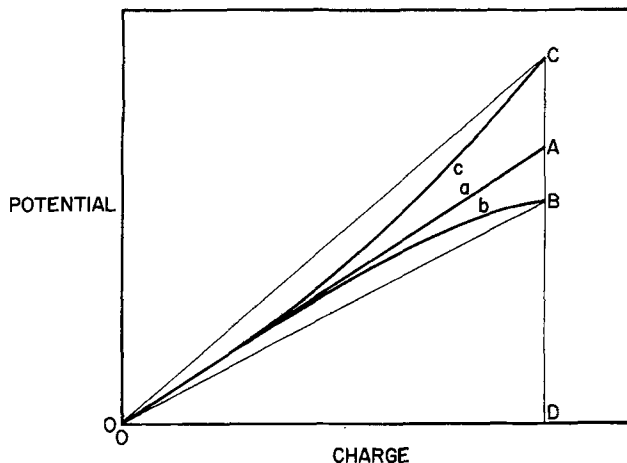


Fig. 4. Charging curves for capacitors with dielectrics whose dielectric constants have the same low field value, but (a) remain unchanged, (b) increase by 25%, (c) decrease by 25% during charging.

If the dielectric constant decreases during the charging process, the charging curve will curve away from the charge axis, and the external work done will be less than the electrostatic energy stored—a clearly impossible situation because the elastic energy cannot be negative. This then is the extent to which theory and experiment disagree: the apparently reasonable expression we derived for the internal energy of a capacitor makes it impossible for the experimentally observed decrease in the dielectric constant to occur without violating the principle of energy conservation. Since the principle of energy conservation is not seriously open to question, there must be something wrong either with the experimental results or with the theory.

All experimental results can be questioned, and more measurements correlating dielectric constant variation with strain need to be made, but it is unlikely that an effect which has been seen in both *in situ* anodic oxidation studies at room temperature and tantalum film capacitor studies at liquid nitrogen temperature will prove to be an artifact of the widely different measurement techniques. If we accept as fact the experimental observation that the dielectric constant can decrease when the field is applied, then we must reject the theory we derived in the previous section. We could, of course, argue that our theory constitutes a definition of electrostriction, and that other effects may mask its experimental observation, but a theory of electrostriction which applies to neither electrolytic nor film capacitors is sterile at best.

The conflict between theory and experiment can be resolved by looking carefully at what both theory and experiment are saying. If we look at the charging curve in Fig. 4 for a capacitor whose dielectric constant decreases on charging, we can, without assuming a form for the internal energy, determine whether or not the decrease is a consequence of the strain in the film. If the decrease in dielectric constant results from the strain, then if we clamp the capacitor and charge it without allowing the film thickness to change, the charging curve will be linear, and the external work will be less than for charging a free capacitor. If we disconnect the charging supply before releasing the clamp, the external work done during the release will be negative no matter what the sign of the strain because the force exerted by the clamp must oppose the displacement to the strained state. Hence the external work done in charging a clamped capacitor then releasing it is less than the work done by the free capacitor when it is subsequently discharged. Conservation of energy therefore forces us to conclude that if the dielectric constant decreases during charging it

cannot be due to strain in the film, no matter what its sign. We can, in fact, conclude that more work must be done to charge a clamped capacitor than a free one, and hence the effect of strain must actually oppose the observed decrease in the dielectric constant, not produce it.

We can reach the same conclusions without reference to the experimental results simply by requiring that the theory apply to large electrostrictive effects as well as small. (Perhaps "large" is an inadequate term to apply to effects which are many orders of magnitude larger than anticipated.) The solution we derived in the previous section is only stable if the effects are small, and hence we should not be surprised that it conflicts with the experimental results on anodic oxides. The instability shows up clearly both in the internal energy expression and on a charging curve. The internal energy expression in Eq. [9c], which was obtained by substituting the solution for the strain back into the original internal energy expression, is the sum of a positive term in D^2 and a negative term in D^4 . (The sign of the D^4 term is inherent to the theory and does not depend on the sign of q .) This means that although the energy increases with D at small D , as D gets larger it decreases without bound. This effect shows up in a different way on the charging curve in Fig. 4 for a capacitor whose dielectric constant increases on charging. The curve is drawn for a quadratic dependence on D with an overall change of 25% in the dielectric constant. Note that the charging curve is almost flat at its top end, and if charging is continued the potential across the capacitor will actually begin to decrease as additional charge is added. Hence the increase in the dielectric constant required by the theory guarantees its instability, and the experimentally observed decrease in the dielectric constant is actually a necessity if the system is to be stable.

Once the stability problem is recognized, and it is realized that the decrease in the dielectric constant cannot be due to the strain in the film, it is not difficult to modify the theory to ensure stability at high fields. Our expression for the internal energy is a power series in even powers of D with a lead term of second order, and fourth-order terms of the form u^2 and uD^2 . As we noted at the outset, there is the additional explicit fourth-order term, and this term is needed for a stable fourth-order theory. If we write the internal energy in the form

$$U = [cu^2/2 + (q + b/2)uD^2 + gD^4/4 + bD^2/2]zI^2 \quad [10]$$

and follow the same procedure we used in the last section, our expression for the strain in Eq. [7] remains unchanged, but Eq. [8b] which defines the dielectric constant becomes

$$K_0/K = 1 + (2q/b)u + (g/b)D^2 \quad [11]$$

and Eq. [9c] for the internal energy becomes

$$U = [bD^2/2 + (g/4 - (2q + b)^2/8c)D^4]zI^2 \quad [12]$$

For stability we require the coefficient of D^4 in Eq. [12] to be positive, and hence

$$g > (2q + b)^2/2c \quad [13]$$

As we expected, the sign of q does not affect stability, and we are free to choose q negative a fit the sign of the observed strain. Equation [11] bears out the conclusion we reached by considering a clamped capacitor: the decrease in dielectric constant is due to an explicit field-dependence, and the strain in the film acts to oppose the change in dielectric constant. If it were not for the sign of the strain term, Eq. [11] could be thought of as an extension of the Clausius-Mossotti relation to allow for field-dependent polarizability, but with the sign as it is, we are forced to conclude that the Clausius-Mossotti relation is simply not valid

for the valve-metal oxides. We reach this conclusion reluctantly, for we have made extensive use of the Clausius-Mossotti relation in the past to relate dielectric constant variation to strain, but the conclusion is a direct consequence of energy conservation applied to the observed decrease in dielectric constant with increasing field, and is inescapable.

The quadratic dependence of strain on displacement predicted by the theory serves to resolve the minor controversy in the literature over the form of the field dependence. A quadratic dependence on KE will appear quadratic in E up to fields at which the decrease in K becomes significant, and beyond this point the dependence on E will appear slower than quadratic. For tantalum, therefore, the dependence should appear quadratic almost all the way to the anodizing field, but for niobium and tungsten the dependence should appear quadratic over no more than half the region to their anodizing fields. This prediction is consistent with our experimental findings and with the different ranges used to fit the reported quadratic dependences for tantalum (4) and niobium (5).

Acknowledgment

The work received partial support from the Natural Sciences and Engineering Research Council Canada under Grant No. A-1151. The author would like to thank Dr. John Grindlay for providing extensive reference material on the theory of the elastic dielectric.

Manuscript received April 1, 1980.

Any discussion of this paper will appear in a Discussion Section to be published in the June 1981

JOURNAL. All discussions for the June 1981 Discussion Section should be submitted by Feb. 1, 1981.

Publication costs of this article were assisted by the University of Waterloo.

REFERENCES

1. G. B. Walker and G. Walker, *Can. J. Phys.*, **55**, 2121 (1977).
2. H. J. Juretschke, *Am. J. Phys.*, **45**, 277 (1977).
3. J. L. Ord, M. A. Hopper, and W. P. Wang, *This Journal*, **119**, 439 (1972).
4. W. D. Cornish and L. Young, *Proc. R. Soc. London Ser. A*, **335**, 39 (1973).
5. K. K. Yee and L. Young, *Appl. Opt.*, **14**, 1316 (1975).
6. W. P. Wang, Thesis, University of Waterloo (1975).
7. P. W. Wyatt, *This Journal*, **122**, 1660 (1975).
8. P. W. Wyatt, *ibid.*, **123**, 667 (1976).
9. J. L. Ord, J. C. Clayton, and K. Brudzewski, *ibid.*, **125**, 908 (1978).
10. J. L. Ord and E. M. Lushiku, *ibid.*, **126**, 1374 (1979).
11. J. C. Clayton and D. J. DeSmet, *ibid.*, **123**, 1886 (1979).
12. D. J. DeSmet, *Electrochim. Acta*, **21**, 1137 (1976).
13. J. L. Ord, J. C. Clayton, and W. P. Wang, *This Journal*, **124**, 1671 (1977).
14. W. K. H. Panofsky and M. Phillips, "Classical Electricity and Magnetism," p. 39, Addison-Wesley, Reading, Mass. (1962).
15. L. Page and N. I. Adams, "Principles of Electricity," p. 48, Van Nostrand, New York (1931).
16. J. Grindlay, *Phys. Rev.*, **160**, 698 (1967).
17. J. Grindlay, "An Introduction to the Phenomenological Theory of Ferroelectricity," p. 165, Pergamon Press, Elmsford, N.Y. (1970).

Bilayer Taper Etching of Field Oxides and Passivation Layers

Lawrence Keith White

RCA Laboratories, David Sarnoff Research Center, Princeton, New Jersey 08540

ABSTRACT

As geometries and design rules become more stringent for multilayer devices, precise taper control is essential to insure high reliability products. A bilayer process appears to provide precise taper control and the ability to adjust the taper angle as various IC designs may require. The taper control layer of a bilayer process minimizes the effect of the photoresist-oxide interface properties on the tapering process. Control of the taper is determined by the etch rate of the underlying layer's etch rate to the taper control layer's etch rate. Examples presented here show that thermal SiO_2 can be tapered with control layers of CVD SiO_2 and 6% densified PSG can be tapered with an undensified PSG layer of similar phosphorus concentration. Optimum control layer thickness ranges from 500 to 1000Å. Taper angles are relatively insensitive to etch temperature and buffer composition changes for buffered HF etchants. Taper slopes were estimated by a combination of Tencor Alpha-Step profilometry or interference fringes obtained from optical microscopy. SEM analysis was used to verify these results.

Properly tapered steps for multilayered devices are essential for high reliability products. Smooth and gradually sloped steps for field oxides, and for under metal passivation layers promote good metallization coverage and minimize buried channel and void formation. One tapering process used now for IC production is undercutting at the photoresist-oxide interface. The process is based on photoresist adhesion and is highly sensitive to environmental factors that influence the photoresist-oxide interface properties, such as temperature, humidity, photoresist lot, and surface

Key words: etching, slope angle, silicon dioxide, phosphosilicate, CVD.

contamination. Although this process is workable, precise control of taper angle is difficult. Precise control of taper angle is becoming more critical for the anticipated reduced geometries and tighter design rules for IC's.

Tapering processes were investigated that had the potential to provide tighter control for thermal oxides or passivating PSG layers. The processes are based on good photoresist adhesion, as this variable appears easier to control than varying degrees of poor adhesion. Consequently, a photoresist primer, hexamethyldisilazane (HMDS), has been used for all these studies. The literature describes several techniques

that can be used to taper steps during chemical pattern etching. These include etch temperature variation (1-3), buffer composition variation (2-4), ion-implant techniques (5, 6), and bilayer control process (7-9). In many respects the ion-implant technique is similar to a bilayer process. The ion-implant process step can be viewed as a way of producing a fast-etching taper control layer on top of a field oxide. Although ion-implant techniques would appear to provide excellent taper control, according to the literature, the economics of the process would appear to be unattractive and control of ion-implant parameters could be difficult. Thus, our efforts have concentrated on etch temperature variation, HF buffer composition, and the bilayer control processes. Early in our study, it became apparent that both the etch temperature and HF buffer composition tapering techniques depended on interface properties. Since these properties are inherently difficult to control, most of the work here deals with the bilayer tapering process.

The determination of the average taper is not trivial. Several methods were used to monitor the performance of the tapering process. They include Tencor profilometry, interference microscopy, and SEM analysis. Comments on the use and applicability of these methods in a production environment are included.

Experimental

A number of dielectric layers were deposited or grown on polished, single crystal silicon wafers. The methods for each type of layer are summarized as follows: (i) Thermal SiO_2 was grown at 1000°C in steam at (atmospheric) pressure to a thickness of $1\ \mu\text{m}$. (ii) CVD SiO_2 used for taper control layers was deposited from a silane-oxygen-nitrogen gas mixture at 450°C . (iii) PSG layers were deposited from a silane-phosphine-oxygen-nitrogen gas mixture at 450°C , and in some instances at 300°C .

Densification of CVD SiO_2 and PSG were carried out in a nitrogen ambient for 30 min at the desired densification temperature. Thicknesses of CVD SiO_2 , CVD PSG, and thermal oxide films were measured with a Tencor Alpha-Step Profilometer. Etch rate measurements and pattern etching were done in a constant temperature bath controlled within $\pm 0.2^\circ\text{C}$. Pattern etching times through field oxide or passivating layers were determined by observing the repellency point of the etchant on the underlying silicon of an unpatterned control sample or from previously determined etch rate and thickness measurements. The etchants used for these studies were all buffered HF compositions that were made from reagent grade 40% aqueous NH_4F and 49% aqueous HF. Volume to volume compositions of the NH_4F and HF solutions used for these studies ranged from 6:1 to 30:1.

Photoresist masking for pattern etching was done with Kodak 747 negative photoresist. The adhesion promotion priming treatment consisted of a 5 min immersion in neat (100%) HMDS.

The determination of average taper for patterned etched samples is discussed in a following section. A combination of SEM analysis, Tencor profilometry, and interference optical microscopy was used.

Temperature and Buffer Composition Taper Etching Studies

Initial taper etching studies examined the effects of the etch temperature and buffer composition. These effects have been examined in the literature by Parisi *et al.* (1). Since both these methods of tapering are based on enhanced etch rates at the photoresist-oxide interface, careful control of interface properties is necessary to produce meaningful results. These experiments have been repeated with the use of an adhesion primer to insure that the photoresist-oxide interface has good adhesion. A single type of negative photoresist, Kodak 747, was used throughout the

study. These experiments were structured to determine whether enhanced etching of the interface was still operative even with good photoresist adhesion.

Figure 1a and b display a schematic of the expected taper for conditions of "good" and "poor" photoresist adhesion at the interface. If adhesion is "good," an isotropic etchant etches at the same rate in every direction. The classic quarter circle profile for the step is the expected result (Fig. 1a). Although the taper at the bottom of this step is smooth, the top portion of the step is sharp and steep, and thus undesirable. In practice, the full quarter circle profile is not usually observed, because most etching processes employ some degree of overetching. Under overetch conditions, the arc of the profile is less than that of a quarter circle giving steeper and still less desirable average tapers. If adhesion is "poor," enhanced etching occurs at the interface, and the etch rate in the lateral direction is greater than that in the vertical direction, producing a smooth taper both at the top and bottom of the step. The taper angle is determined by the increased magnitude of the lateral etch rate relative to the vertical etch rate. Because the magnitude of the lateral etch rate is highly sensitive to interface properties, the slope of the taper is difficult to predict or reproduce.

Figure 2 plots the average taper for thermal oxide as estimated from interference microscopy *vs.* the HF buffer composition. The estimated average tapers displayed here are not necessarily smooth. Taper profiles approaching a quarter circle are expected for the steeper slopes. The average taper displayed here is more a relative measure than an absolute measure of the taper profile. A discussion of estimation of average taper is presented in a later section of this report. The compositions of the various volume-to-volume mixtures of 40% NH_4F and 49% HF have been converted to molarity of HF. The 6:1, 10:1, and 20:1 compositions are marked on the HF axis. The "[HF]" concentration shown is not the actual composition of the etchant, since other etching species are present, notably HF_2^- . Figure 2 shows that higher etching temperatures and higher buffer compositions produce shallower tapers for the oxide step. An exact comparison of our results to the Parisi study (1) is difficult, since average taper angles were not reported for every etching condition and their evaluation methods were somewhat different. However, the present results appear to be in reasonable agreement with Parisi. It should be emphasized that the results dis-

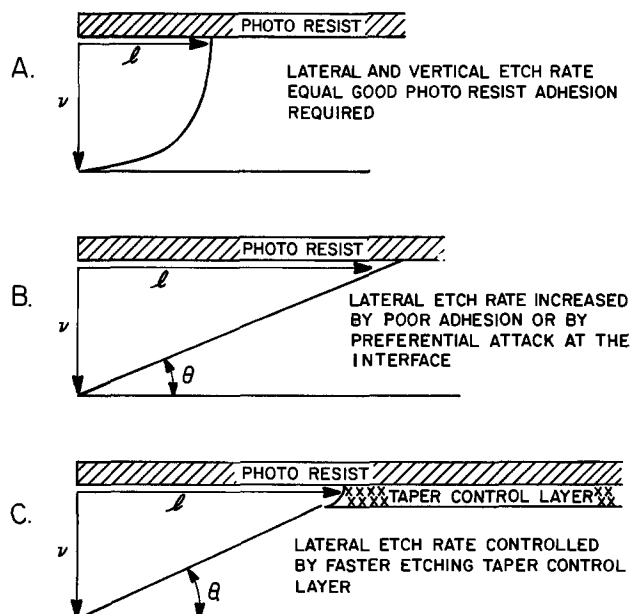


Fig. 1. Tapering processes

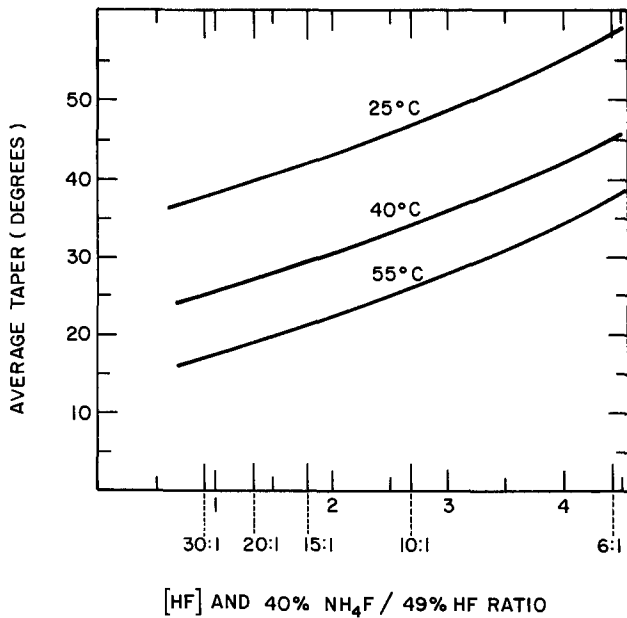


Fig. 2. Observed taper vs. HF buffer composition

played in Fig. 2 should not be considered exact or reproducible. A different photoresist lot or somewhat different processing conditions could dramatically change the observed taper. For example, on occasion the degree of lateral undercut has been observed to increase by factors of two to three times with no intentional or obvious change in processing conditions.

The results shown in Fig. 2 illustrate that the taper of field oxide can be varied through variations in the etchant composition or the etching temperature. Both these processes can provide some degree of taper control, but both are still based on the properties of the photoresist-oxide interface. Obviously, etchant temperature changes influence the etchant composition or the interface properties to vary the undercutting (i.e., the lateral etch rate at the interface). Buffer composition changes also have a similar effect.

Both of these processes are still subject to variations in interface properties. After all, at constant buffer composition, temperature changes affect the taper angle and vice versa. Even in the presence of good adhesion, some preferential attack at interfaces occurs under a variety of conditions. Also, these results demonstrate that etch temperature and buffer composition variation can be used to determine how sensitive a tapering process is to interface properties and photoresist undercutting. The studies of the bilayer taper control process make use of similar experiments to test the sensitivity of the taper angle to interface properties and undercutting effects. Taper processes that do not rely on interface properties should be easier to control.

Bilayer Taper Control Process

Multilayer processing of IC's requires that top layers etch faster than underlying layers to produce a smooth taper. The bilayer taper process investigated here makes use of this observation to taper individual field oxide or under-metal passivating layers. A faster etching taper control layer is deposited on the layer to be tapered. Several literature reports (7-9) have used this technique to taper steps of a variety of compositions.

Figure 1c shows a schematic of the bilayer process. The taper control layer is deposited on top of the underlying layer to be pattern etched. The ratio of the etch rate of the taper etched layer to that of the control layer determines the taper angle. Our initial study used a CVD SiO₂ taper control layer deposited at 450°C to taper etch thermal oxide. To test the

process sensitivity to photoresist-oxide interface properties and undercutting, several experiments were done varying the etching temperature and the etchant buffer composition.

Figure 3 summarizes etch rate data for 450°C deposited CVD SiO₂ and thermal SiO₂ as a function of etchant composition. Data was collected for two etching temperatures, 25° and 40°C. Note that, as previously described, the buffer composition is expressed as an HF concentration and 6:1, 10:1, and 20:1 compositions are marked on the axis. Assuming that the relative etch rates of the control layer to the underlying layer (i.e., the etch ratios) determine taper angles, some change in taper angle may be expected just from the etch ratio variations. Figure 4 plots the etch rate ratio of various CVD control layers on thermal oxide against buffer composition. The changes in the etch ratio are slight, even for different etching temperatures. Thus, the taper slope using a CVD SiO₂ control layer is expected to be relatively insensitive to etch temperature and buffer composition, provided that undercutting effects at the interface are insignificant. Comparisons of tapers obtained using the bilayer process show that variations of the temperature or buffer composition do not change the observed taper significantly. Figure 5 displays interference fringes for a thermal oxide etched at 25° and 40°C. The change in the distance from bottom of step to

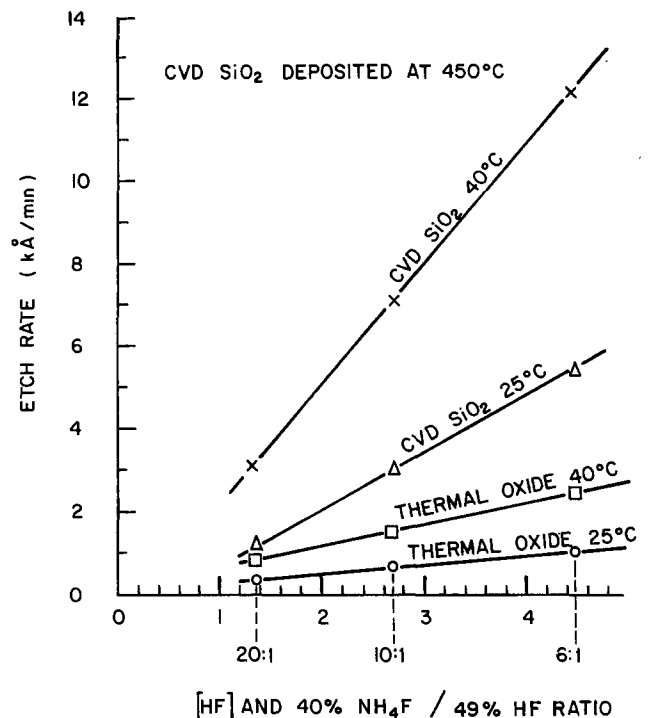


Fig. 3. Etch rate vs. HF buffer composition

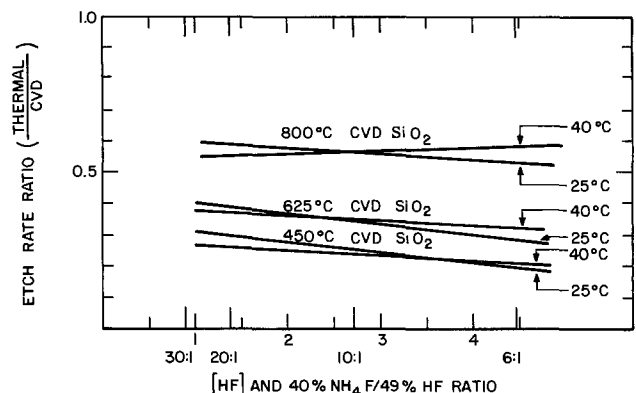


Fig. 4. Etch ratio vs. HF buffer composition

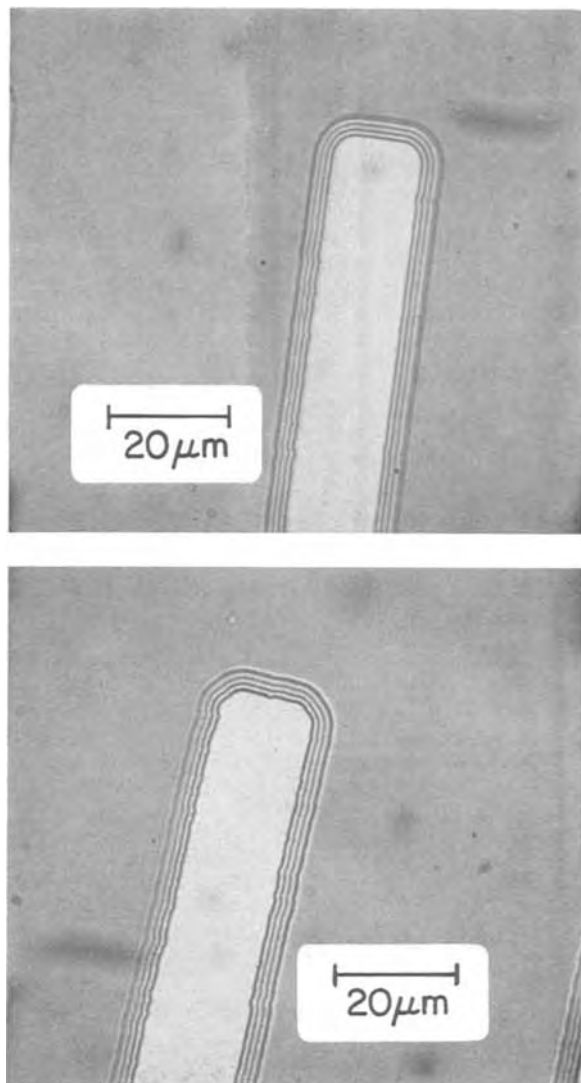


Fig. 5. Interference fringes for tapered thermal oxide. a (top) 6:1 buffered HF 25°C, CVD SiO₂ deposited at 450°C over thermal oxide. b (bottom) 6:1 buffered HF 40°C, CVD SiO₂ deposited at 450°C over thermal oxide.

top of step is small, indicating only minor changes in the taper angle have occurred. Similar results have been obtained using various etchant compositions. This insensitivity to environmental factors that normally produce taper angle changes in the absence of a control layer indicates that the effects of interface properties and undercutting are indeed insignificant or small for the bilayer tapering process. Evidently, control of the tapering process has been transferred from the photoresist-oxide interface to the taper control layer. In addition, contrary to undercutting processes, we do not expect the average taper angle produced from a bilayer process to be significantly affected by the degree of overetching.

The effect of the thickness of the taper control layer on the taper slope of the step was also examined. CVD SiO₂ taper control layers ranging in thickness from 1 to 20 kÅ were deposited on a 10 kÅ thermal oxides. Profiles of the pattern etched slopes were recorded on a Tencor Alpha-Step Profilometer. These results are displayed in Fig. 6. Two slopes are apparent in the profile, one corresponding to the thermal oxide and the other to the taper control layer. The slopes of steps with taper control layer thicknesses less than 2000Å appear smooth. However, this observation is an artifact of the Tencor Alpha-Step Profilometer. SEM's of these samples do detect a small lip for the taper control layer. Figure 7 shows an example of

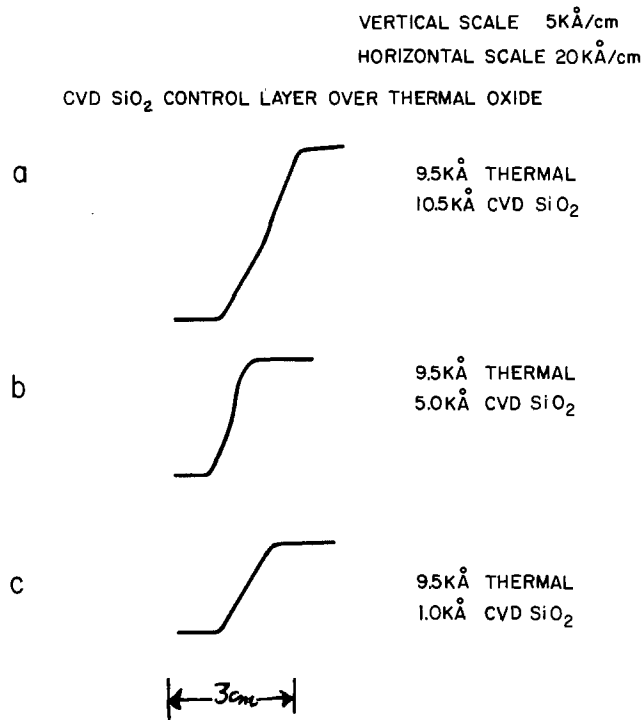


Fig. 6. Tencor traces of tapered profiles

the lip for a 1000Å SiO₂ CVD layer on top of a 10 kÅ thermal oxide layer.

Generally, the slope of the taper control layer is steeper than that of the underlying field oxide. An etch profile of an arc less than a quarter circle is expected for the control layer, while the ratio of the etch rates should determine the slope of the underlying oxide. The Tencor traces and interference fringe analysis indicate that the taper of the underlying oxide is relatively insensitive to the control layer's thickness.

The lip produced by the taper control layer could interfere with metallization coverage. Thinner taper control layers produce less substantial and less noticeable lips. Thus, thin taper control layers are more desirable. A taper control layer of 500-1000Å thickness should provide good coverage of the underlying oxide and keep the control layer's lip small. We also believe that this thickness is sufficient to insure that the undercutting and interface attack have minimal effect on the taper angle. Should the small lip on the taper control layer present coverage problems, dip etching can be employed to completely remove the taper control layer. Since the bilayer taper con-

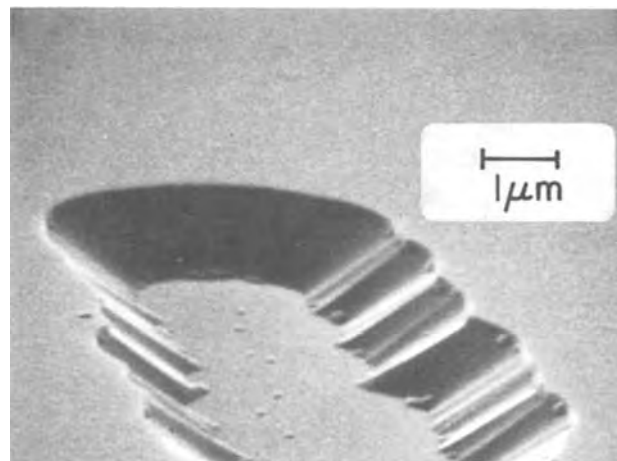


Fig. 7. Taper control layer on thermal oxide, 1 kÅ CVD SiO₂, 10 kÅ thermal oxide, SEM angle 80°.

control process is insensitive to taper control layer thickness, etch temperature, and buffer composition, some other parameter must be used to alter the taper angles. The etch rate properties of control layer can be modified to control the angle of the taper slope. Two examples of a bilayer process are presented here that use various methods to vary the etch rate of the control layer.

Bilayer Etching Results

The etch rate of the CVD SiO_2 control layer used to taper etch patterned thermal oxide can be altered by densification at the appropriate temperature. Figure 8 plots the etch rate of CVD SiO_2 deposited at 450°C vs. densification temperature, where the densification is carried out in dry nitrogen for 30 min. The etch temperature is 25°C and buffered HF (6:1 v/v 40% NH_4F :49% HF) is the etchant. The etch rate of thermal SiO_2 is included for a reference. Figure 9a, b, c, show SEM's of the taper of the field oxide for the various CVD SiO_2 control layers. The tapers estimated from interference optical microscopy are 13° for the 450°C CVD SiO_2 (as deposited), 24° for the 625°C densified CVD SiO_2 , and 37° for the 800°C densified CVD SiO_2 . Figure 10 plots these estimated tapers vs. densification temperature.

Etch rate data for the control layer and underlying oxide can provide some predictive ability for the expected taper angle. The arc tangent of the etch rate ratio would appear a reasonable approximation. The predicted taper from etch rate data is also shown in Fig. 10. The arc tangent function consistently predicts lower taper angles than those estimated for our experiments. Also, the maximum theoretical angle possible is 45° . This maximum angle would correspond to the average slope of the quarter circle profile, but the estimated average angle could be much steeper. Since the bottom of the step has a shallow taper, optical detection methods may not discern the true bottom of the step. This difficulty could lead to estimated average tapers steeper than the actual average slope for the quarter circle profiles. Also, the quarter circle implies zero overetch; in practice, an overetch time must be used and thus angles greater than 45° are likely.

Literature references (1, 10) report that the arc sine of the etch ratio can be used to approximate the observed taper. The predicted taper using the arc sine function is also displayed in Fig. 10. Although some improvement for predicting our estimated aver-

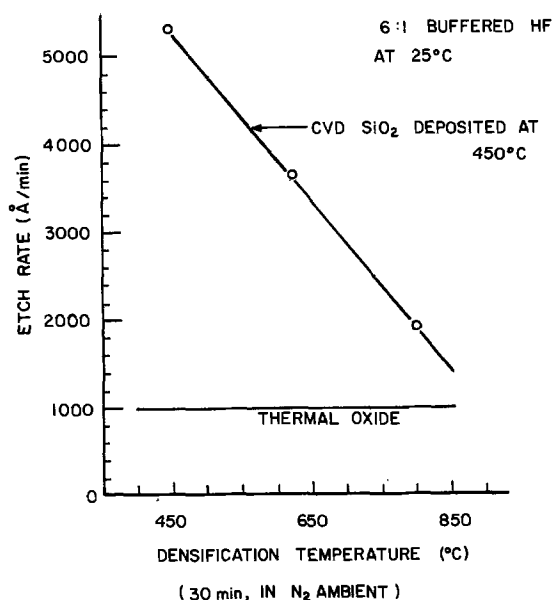


Fig. 8. Etch rate vs. CVD SiO_2 densification temperature

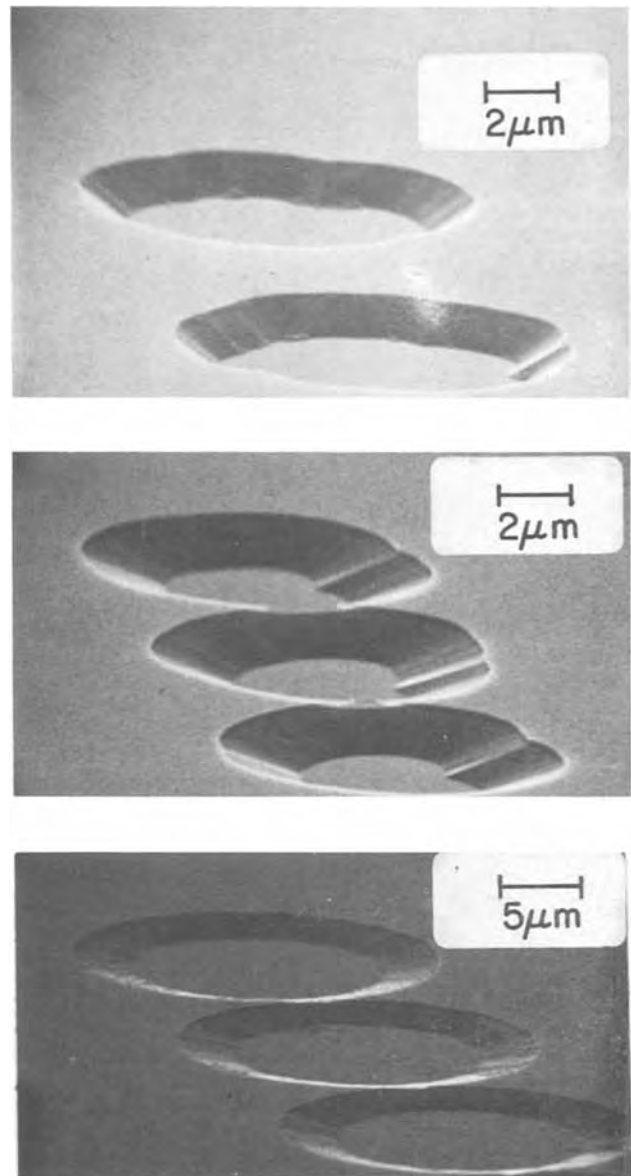


Fig. 9. SEM of taper produced from various CVD control layers. a (top) 6:1 buffered HF at 25°C CVD SiO_2 control layer densified at 800°C . b (center) 6:1 buffered HF at 25°C , CVD SiO_2 control layer densified at 625°C . c (bottom) 6:1 buffered HF at 25°C , CVD SiO_2 control layer deposited at 450°C .

age tapers is apparent, particularly for the steeper tapers, our estimated taper angles still are higher than the predicted ones. This discrepancy is not thoroughly understood. Uneven taper slopes and the experimental error for the estimated average taper may account for part of the discrepancy. However, other factors may play a role. Etchant depletion in occluded regions produced during pattern etching could lead to variations in the vertical and lateral etch rates. Oxide thickness and the extent of pattern delineation could influence the etchant depletion within occluded regions. In spite of these apparent discrepancies between the predicted and observed average taper slopes, the arc sine functional form appears to be a good starting point for predicting taper angles for untried control layers from etch rate data alone. After initial taper determinations, adjustments in the etch rate to alter the taper slope can be made as required.

Phosphosilicate glasses are being used more frequently in device fabrication for their gettering capability or flow properties. Taper etching of these glasses may require taper control layers that etch

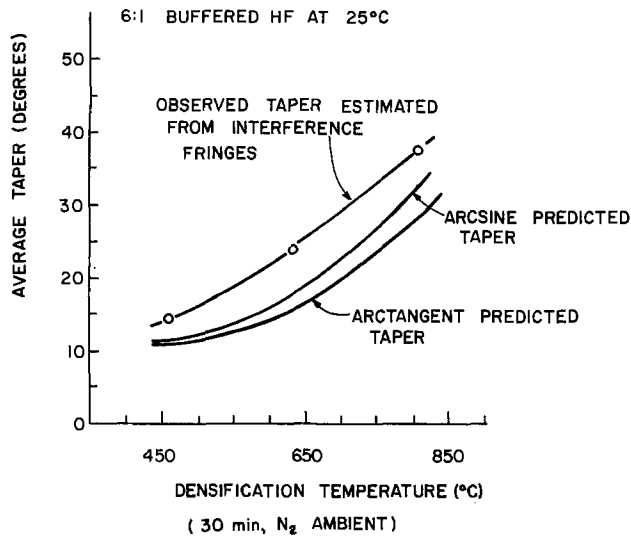


Fig. 10. Average taper vs. CVD SiO₂ densification temperature

faster than a CVD SiO₂. PSG passivating layers are typically densified before pattern etching. Thus, faster etching undensified PSG can be used as a taper control layer. Densified 6% PSG has been tapered with an undensified PSG layer of similar phosphorus composition (deposited at 450° or 300°C). Figure 11 displays SEM photographs of some tapers obtained using an undensified control PSG layer of similar phosphorus composition in buffered HF at 25°C. Suitable tapers are obtained using the undensified PSG control layer (10). Phosphorus composition of the layer or the deposition temperature can be used to vary the etch rate of the taper control layer. If, however, a phosphorus content greater than 6% is used, or if the 6% taper control layer is not subsequently densified, the layer should be removed before metallization to reduce susceptibility to metal corrosion (11).

The previous examples show that a bilayer process can be tailored into specific IC designs to provide the desired taper. The transfer of the taper control from the photoresist-oxide interface to the taper control layer makes it possible to alter the taper angle. CVD deposited layers, however, are only one possible candidate for a taper control layer. Since the taper angle is largely controlled by the etch rate of the control layer relative to the underlying layer to be patterned etch, several types of taper control layer compositions and deposition techniques appear possible. LPCVD deposited layers show promise as taper control layers. These rapidly deposited, uniform layers will provide scale-up production advantages over the conventional atmospheric pressure CVD deposition.

Determination of the Taper Angles

Accurate and rapid determination of the taper angle for a process in a production environment is not a trivial task. The taper angle is not necessarily smooth, as pointed out in previous discussions. In the classic quarter circle profile for pure isotropic etching, the taper angle ranges from 0° at the bottom of the step to 90° at the top of the step. Small lips encountered for the bilayer process, and for various undercutting processes, also produce deviations from a smoothly tapered step. In spite of these excursions from a smooth taper angle, we believe that an average taper of a step provides a simple and useful characterization of a tapering process.

Since most thin-film layers used in IC manufacture have thicknesses of one micron or less, average taper angle determinations require the measurement of distances of a similar magnitude. Both the thickness of the step and the span between the top and bottom of the step need to be estimated to obtain an average

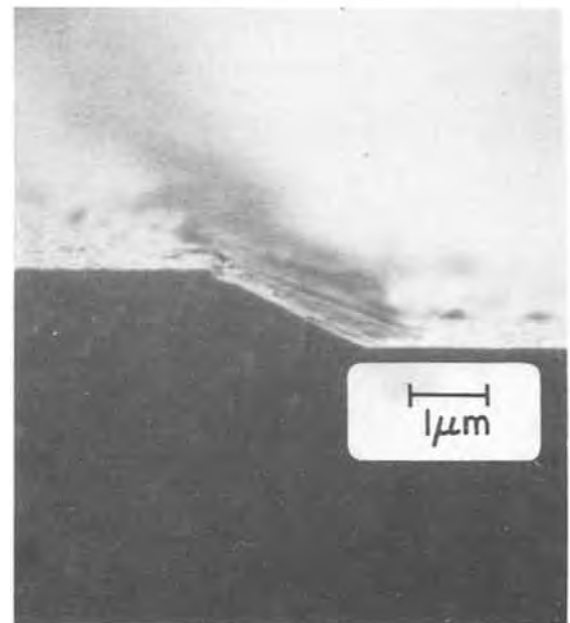
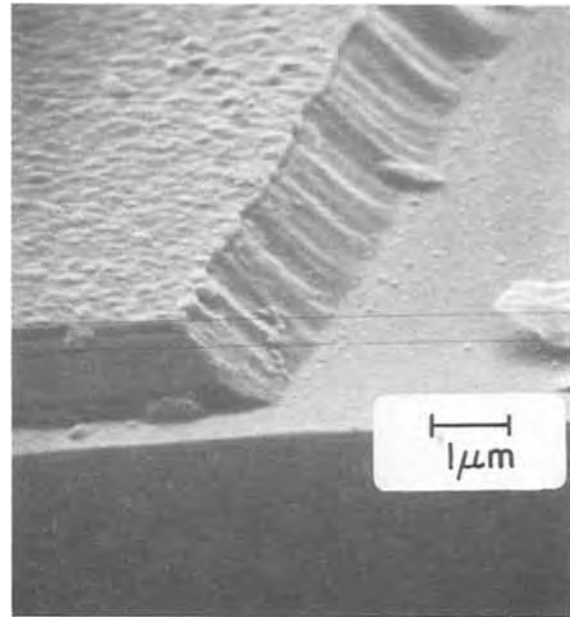


Fig. 11. SEMs of tapered 6% densified PSG layers. a. 6:1 buffered HF at 25°C, undensified 6% PSG, control layer deposited at 450°C. b. 6:1 buffered HF at 25°C, undensified 6% PSG, control layer deposited at 300°C.

taper angle. Two rapid methods of taper estimation were used in our studies: interferences fringes obtained from optical spectroscopy and Tencor Alpha-Step profilometry. SEM photographs at low angles were used to check the accuracy of our taper angle determination.

The Tencor profilometry technique involves the use of a stylus to trace the profile of the step. The vertical step is expanded and an excellent thickness determination is obtained. The lateral distance determination going up the step is on a less expanded scale and can be distorted by the point of the stylus (12).

Profiles have been examined using styli of different radius (12). The smaller radius styli points produce profiles that are less sensitive to distortions produced by the stylus point. The smallest stylus available, nominally a 2 micron stylus radius, can detect differences in the profile slope provided the slope is less than 35° for a 1 μm step. This technique cannot measure any slopes greater than 35°, and taper angles

approaching this angle are not detected with good sensitivity, due to the effect of the stylus radius (12). Also, the maximum detectable taper angle decreases as the step height decreases (12).

The use of interference fringes obtained with an optical microscope has different disadvantages. The fringe count for a layer of known refractive index can be used to determine the thickness. Also, the distance from the bottom fringe to top fringe is usually a good measure of lateral distance from the top to bottom of the step. The accuracy of the thickness determination is reduced from that obtained of a profilometer, since a single fringe represents $\sim 1900\text{\AA}$ for most SiO_2 -type thin films. Fractions of a fringe are difficult to determine. Steep tapers present more serious problems. Fringes begin to overlap and it becomes virtually impossible to measure the layer thickness from a fringe count. The distance from top to bottom of a step is more difficult to determine, because a fraction of a millimeter difference at $760\times$ microscope power is necessary to obtain accurate taper measurements. However, for tapered layers of known thickness, we have been able to estimate lateral distances for one-micron steps corresponding to an estimated average taper $\sim 55^\circ$. Either the Tencor Alpha-Step Profilometer with $2\ \mu\text{m}$ stylus radius or interference fringes obtained from optical microscopy alone can be used to estimate average tapers of 35° or less for a $1\ \mu\text{m}$ step. Tapers greater than this can be estimated using interference fringes provided the thickness of the layer is known accurately. The Tencor profilometer could provide this thickness determination with relative ease. A combination of both instrumental techniques could be used to estimate average tapers above 35° up to about 60° .

Conclusions

As geometries and design rules become more stringent for multilayer devices, precise taper control is essential to insure high reliability products. A bilayer process appears to provide precise taper control and the ability to adjust the taper angle as various IC designs may require. The taper control layer of bilayer process minimizes the effect of photoresist-oxide interface properties on the taper process. Control of the taper is determined by the etch ratio of the underlying layers etch rate to the taper control layers etch rate. Examples presented here show that thermal oxide can be tapered with control layers of CVD SiO_2 , and 6% densified PSG can be tapered with an undensified PSG layer of similar phosphorus concentration. Adjustments in the taper slope can be made for the thermal oxide through etch rate ratio changes produced by different densification temperatures for the CVD SiO_2 control layer. Taper adjustments for a 6% densified PSG layer can be made by varying the phosphorus content or deposition temperature of the PSG control layer. Optimum control layer thick-

nesses range from 500 to 1000\AA . The apparent advantages of the bilayer process include: precise control of the taper angle through the etch rate of the control layer, minimal effects on the taper angle from undercutting at the photoresist-oxide interface, and the taper angle's relative insensitivity to etch temperature and HF buffer composition. Although a taper control layer does introduce additional processing steps, this disadvantage does not appear serious. Only the etching properties of the layer are important. Precise control of the layer thickness is not critical. Removal of the taper control layer is accomplished with a dip etch.

Estimation of the average taper for $1\ \mu\text{m}$ steps can be accomplished for tapers less than 35° using either Tencor Alpha-Step profilometry or interference fringe microscopy alone. Interference fringe microscopy can be used to estimate taper greater than 35° and up to 60° provided that the thickness of the step is known accurately.

Acknowledgment

The author thanks George Schnable and Werner Kern for critically reviewing the manuscript and for many valuable technical discussions. The technical assistance provided by Robert Vibronek is also deeply appreciated.

Manuscript submitted April 22, 1980; revised manuscript received June 23, 1980.

Any discussion of this paper will appear in a Discussion Section to be published in the December 1981 JOURNAL. All discussions for the June 1981 Discussion Section should be submitted by Feb. 1, 1981.

Publication costs of this article were assisted by RCA Laboratories.

REFERENCES

1. G. I. Parisi, S. E. Haszko, and G. A. Rozgonyi, *This Journal*, **124**, 917 (1977).
2. J. S. Judge, *ibid.*, **118**, 1992 (1971).
3. J. Lawrence, Abstract 191, p. 466, The Electrochemical Society Extended Abstracts, Miami Beach, Florida, Oct. 8-13, 1972.
4. R. A. Haken, I. M. Baker, and J. D. E. Beynon, *Thin Solid Films*, **18**, 53 (1973).
5. P. D. Parry and S. P. Bristol, *J. Vac. Sci. Technol.*, **15**, 664 (1978).
6. J. A. North, T. E. McGahan, D. W. Rice, and A. C. Adams, *IEEE Trans. Electron Devices*, **ed-25**, 809 (1978).
7. L. H. Hall and D. L. Crosthwait, *Thin Solid Films*, **9**, 447 (1972).
8. B. A. Boxall, *Solid State Electron.*, **21**, 1173 (1978).
9. W. Kern, J. L. Vossen, and G. L. Schnable, in Proceedings of the 11th Annual Reliability Physics Conference, p. 214 (1973).
10. T. Yanagawa and I. Takekoshi, *IEEE Trans. Electron Devices*, **ed-7**, 964 (1970).
11. R. B. Comizzoli, *RCA Rev.*, **37**, 483 (1976).
12. L. White, Unpublished results.

On Predicting the Maximum Efficiency of Phosphor Systems Excited by Ionizing Radiation

D. J. Robbins

Royal Signals and Radar Establishment, Great Malvern, Worcestershire, England WR14 3PS

ABSTRACT

A model allowing theoretical prediction of the maximum possible efficiency for any cathode-ray or x-ray phosphor is proposed, based on an earlier statistical analysis of e-h pair generation by van Roosbroeck. The model is independent of the detailed band structure of a particular solid, and predicts the limiting yield of e-h pairs, Y , in terms of an energy loss ratio for energetic particles $K = (\text{energy lost to phonons per ionization event/ionization energy})$. The novelty of the model lies in the emphasis placed on competitive phonon losses during the carrier avalanching process, and it is probably successful because of the dominant role played by carriers with energies a few times greater than threshold where electrons and holes may be expected to behave similarly. A quantitative estimate of the average energy per e-h pair in a particular phosphor can be made by reference to an index of efficiency \mathcal{Q} , which is proportional to van Roosbroeck's parameter K but which is defined in terms of accessible physical constants of the phosphor host lattice: ϵ_s , ϵ_i , E_g , and ω_{LO} . The predicted efficiencies η_{\max} are in good agreement with measured values for widely different phosphor types, suggesting that the model is quite generally applicable and may be used in a predictive fashion in the search for new and efficient phosphor systems. Finally, the relationships between the present theory and previous approaches involving plasmon excitation are discussed.

The past forty years have seen intensive development of a wide variety of phosphor systems, for both consumer and professional applications (1-3). However there is still no theory which can explain in a satisfactory manner the relative power efficiencies observed for different CRT or x-ray phosphor materials. Empirical "rules of thumb" are legion; for example it is known that the efficiencies of CRT phosphors tend to decrease in the order: sulfides > oxysulfides > oxides, and that there is some (rather obscure) relationship between the limiting efficiency of a particular phosphor host lattice and its bandgap. The reasons for these observations are not known, and yet a successful theory capable of explaining such observations could clearly have great value. In the first place, it would allow prediction of those solids likely to generate efficient phosphor hosts, thereby facilitating the search for new materials and eliminating considerable empirical development work. Secondly, it would provide an estimate of the maximum efficiency for a particular host-activator combination, allowing development to terminate as soon as optimum performance had been achieved. Clearly the difficulties involved in developing a reliable predictive theory of this kind are considerable, not least because of the very wide variety of rather complex solids which can be used as phosphor host lattices. However it is the purpose of this paper to make an initial attempt in this direction by putting forward a semi-empirical treatment of phosphor efficiency which is at least capable of rationalizing the relative limiting efficiencies of a wide range of phosphor systems in a consistent way. As will be seen, the theory appears to give sufficiently good correlation between calculated and observed efficiencies for known phosphor systems that it may be used in a cautiously predictive fashion.

The excitation mechanisms for both cathode-ray (CR) and x-ray (XR) phosphors are similar in that high energy ionizing radiation is absorbed by the phosphor lattice, giving rise to an avalanche of secondary carriers which ultimately excite the luminescent activator (4). In what follows we shall concentrate on CR phosphor systems, but the theory is also ap-

plicable to XR materials. It is well known that the power conversion efficiencies of CRT phosphors decrease at high power densities (4), but we neglect all such saturation effects and consider only the efficiency at lower loadings where the response is linear. We shall also adopt the generally accepted model (4) of the phosphor excitation process which assumes that the energy of the incident high energy radiation is rapidly converted into thermalized electron-hole (e-h) pairs, and that the recombination energy of these pairs is transferred to the activator center where it is finally emitted as a photon. One e-h pair can therefore give rise to one quantum of radiation emitted by the activator. With these assumptions the efficiency of the CRT phosphor system can be written as follows (4-6)

$$\eta = (1 - \tau_b) \cdot \left(\frac{h\nu_m}{\xi} \right) \cdot S \cdot Q \quad [1]$$

where τ_b is the primary back scattering coefficient, $h\nu_m$ is the mean energy of the luminescent photons, ξ is the average energy required to generate one e-h pair, S is the efficiency for transfer of carrier recombination energy to the activator emitting state, and Q is the quantum efficiency for the final luminescent process.

The efficiency of the energy transfer process, S , has been discussed in earlier publications from this laboratory (7-9). The backscattering coefficient τ_b depends on the average atomic number of the phosphor material and on the morphology of the phosphor layer; we shall assume that this factor does not vary greatly amongst practical phosphor systems. The maximum efficiency for any host-activator combination will therefore be reached when conditions can be adjusted to that $S = Q \sim 1$ in Eq. [1] i.e.

$$\eta_{\max} \sim \text{constant} \cdot \left(\frac{h\nu_m}{\xi} \right) \quad [2]$$

The key to calculating this maximum limiting efficiency for different phosphor systems is clearly the parameter ξ , the average energy per e-h pair generated in the lattice by high energy radiation. This energy is greater than the bandgap energy E_g , as can be seen from Fig. 1, which illustrates schematically the

Key words: cathodoluminescence, solids, x-rays.

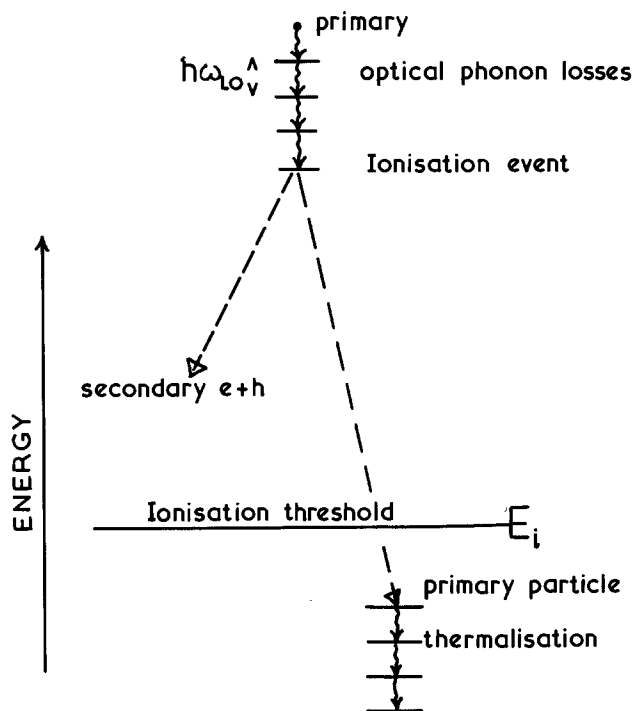


Fig. 1. Schematic sequence of energy loss processes for an energetic electron or hole as it nears the ionization threshold. Particles falling below E_i can lose further energy only by phonon emission or recombination.

energy loss processes for a primary particle (e or h) with an energy in excess of the ionization threshold. The fast particle can lose energy either by creation of optical phonons or by impact ionization. As soon as its energy falls below the ionization threshold E_i it is unable to create further secondaries and simply emits phonons until equilibrium with the lattice is established. The average energy required to produce each e-h pair therefore includes various phonon losses in addition to the intrinsic pair recombination energy. For semiconductor radiation counters, in which the same mechanisms operate, it has been found empirically that the following relationship holds over a range of semiconductor materials (10)

$$\xi = \beta E_g \quad [3]$$

with $\beta \sim 3$.

Theoretical estimates of ξ have been made by a number of workers, including Shockley (11), Klein (10), and van Roosbroeck (12). These calculations generally assume a simple parabolic band structure with equal masses and equal division of excess energy between secondary electrons and holes generated in the ionization process. The average energy per pair can then be written as the sum of three terms (see Fig. 1)

$$\xi = E_i + E_{op} + 2E_f \quad [4]$$

where E_{op} is the average energy lost to optical phonons for each ionization event during the avalanching process and E_f is the average energy of a carrier when first it falls below threshold and cannot produce further ionization. In order to calculate E_f both Shockley (11) and Klein (10) assume an initially uniform distribution of carriers in momentum space up to the threshold energy E_i , which leads to the conclusion that phonon losses during final thermalization are more significant than optical phonon generation by particles above threshold. On the other hand the statistical analysis by van Roosbroeck (12) suggests that for realistic optical phonon loss rates the distribution of carriers as they fall below threshold is not uniform, but is peaked at low energy. This implies that optical phonon loss by

ionizing particles may be more significant than suggested by Shockley or Klein, and that the competition between phonon generation and ionization for fast particles will be important in governing the average energy per pair, ξ .

Lehmann (6) has used Eq. [1] and [3] to estimate the parameter β for a range of phosphor materials, not restricted to the more covalent elemental and binary semiconducting compounds for which Eq. [3] was established. However he found that this " $3 \times E_g$ " rule is quite inadequate for many phosphor systems, especially for oxide materials where β can take values in the range 4-13 when fitting measured efficiency data to Eq. [1]. In order to tackle this problem Klein (13), Kingsley and Ludwig (5), and subsequently Rothwarf (14), have discussed ionization in semiconductors and phosphors in terms of plasmon creation by fast particles. These workers have pointed out that the electron energy loss function is not uniform above threshold, and should be peaked at the zero in the dielectric function corresponding to the frequency of the collective valence-electron plasmon oscillation

$$\omega_p = \left(\frac{4\pi n_v e^2}{m} \right)^{1/2} \quad [5]$$

where n_v is the valence electron density. Phonon losses were neglected in the calculations of Kingsley and Ludwig and of Rothwarf and it was suggested that differences in efficiency for phosphor materials could be correlated with the calculated plasmon frequency. The reasoning is that if the high energy particles lose energy primarily by plasmon creation, and the plasmons then decay into e-h pairs, one expects the average energy per pair, ξ , to be determined by the plasmon energy. Some correlation between η and $(\omega_p)^{-1}$ was observed, but only for a limited number of phosphor materials. However the usefulness of the plasmon concept is open to question in the wider-gap phosphor materials, where the energy of the single-particle excitations is comparable to the calculated plasmon energy. The distinction between these excitations then becomes blurred, and in fact, when the calculated frequencies ω_p are replaced by measured plasmon energies for some of the more efficient phosphor systems, the correlation between η and $(\omega_p)^{-1}$ disappears (15, 16).

Thus none of the theories so far advanced has proved capable of rationalizing the relative efficiencies of the full range of phosphor systems. Attempts to modify the " $3 \times E_g$ " rule have emphasized differences in the ionization process for different materials by introducing the plasmon concept, but have neglected any competitive phonon losses. On the other hand the majority of e-h pairs are generated near the end of the branching process, by particles with energies only a few times the ionization threshold. For such particles optical phonon losses can constitute a significant fraction of their total excess energy, and any realistic model must take into account the competition between optical phonon generation and ionization in the overall de-excitation of these fast particles. Clearly as the ratio (energy lost to optical phonons/energy lost in ionization) increases then the yield of secondary e-h pairs must fall and the average energy per pair, ξ , must rise.

Fortunately van Roosbroeck's statistical treatment of e-h pair generation in solids (12) takes account of this competitive energy loss in a natural way, and allows prediction of the secondary yield in terms of an energy loss ratio K . The model is independent of details of band structure and quite general in its application; it will therefore be used as the starting point in estimating the parameter ξ for a range of phosphor materials. We shall show that η_{max} calculated according to Eq. [2] using the theory developed here correlates well with the observed efficiencies for many

optimized phosphor systems. In the next section the basis of van Roosbroeck's "crazy carpentry" model will be outlined. In the section "The Loss Parameter K " a method is developed for calculating the loss ratio K in terms of the physical properties of a phosphor host material. This parameter is used in the section "The Average Energy per e-h Pair Generated by Ionizing Radiation" to calculate the average energy per pair, ξ , for typical phosphor host lattices. In the section "The Maximum Efficiency of CRT Phosphors" the measured efficiencies of a number of optimized phosphor systems are compared with the calculated values, and in the last section the relationship between the present theory and the results of previous treatments is discussed.

The "Crazy-Carpentry" Model (12)

Van Roosbroeck has called his statistical treatment of e-h pair generation the "crazy-carpentry" model because it can be formulated in terms of the equivalent problem of cutting boards of a given length (see Fig. 2). We begin with a board of length L (in units of E_i), and the rules are as follows. For all boards greater than unit length, remove with probability r a length $x_r \ll 1$. This represents creation of an optical phonon, so that $x_r = (h\nu_{LO}/E_i)$. With a probability $(1 - r)$ remove a length unity, to represent e-h pair generation, and then make a random cut in the remainder (at Z in Fig. 2). The random length Z now represents energy remaining in the primary particle after ionization, and the excess energy transmitted to the secondaries (represented by the right-hand length $L - Z - 1$) is equally divided between the electron and hole, giving each a KE equal to $(L - Z - 1)/2$. These steps are repeated for all remaining pieces of greater than unit length, and boards shorter than unity are discarded. The number of boards of unit length produced at the end of this process represents the number of e-h pairs produced by the initial particle of energy $(L \times E_i)$. The limiting yield of e-h

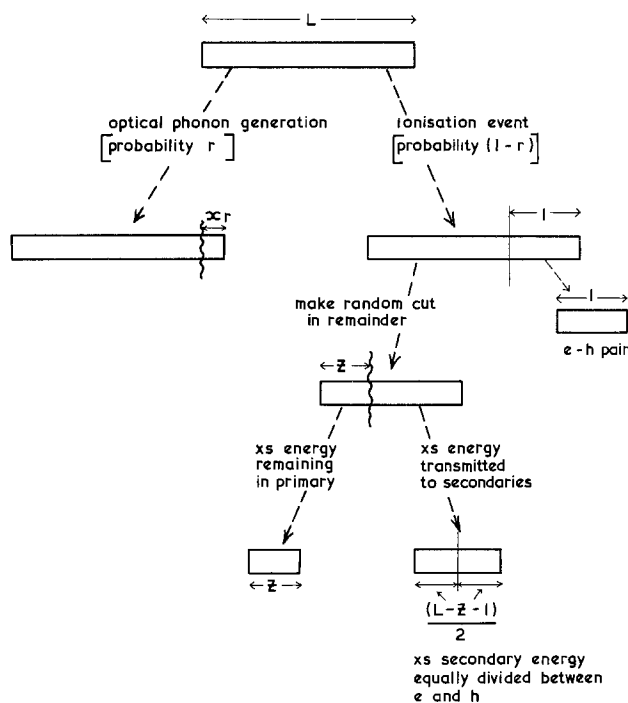


Fig. 2. Competitive energy loss processes for energetic particles formulated in terms of the "crazy-carpentry" model of van Roosbroeck [Ref. (12)]. The initial board length L is defined in units of the ionization threshold E_i . Each board of unit length produced in this way represents the generation of one e-h pair by impact ionization. The equal division of excess kinetic energy between secondary electrons and holes is a simplification which is discussed in the text.

pairs, Y , is defined for large L

$$Y = \frac{(\text{No. of boards of unit length})}{L} \quad [6]$$

$$= \frac{(\text{No. of e-h pairs}) \times E_i}{\text{initial particle energy}}$$

The average energy required to produce a e-h pair, ξ , is given by

$$\xi = \frac{E_i}{Y} \quad [7]$$

$$= E_i + KE_i + 2L_f E_i \quad [8]$$

where L_f is the average length of a waste board ($L_f < 1$) (or the energy of a particle when first it falls below threshold)

$$K = Nx_r \quad [9]$$

and

$$N = \frac{\tau}{(1 - r)} \quad [10]$$

$$= \frac{\lambda_i}{\lambda_{op}}$$

the ratio of the mean free path for ionization to the mfp for optical phonon generation.

The limiting yield can be obtained from the crazy-carpentry model either analytically or by Monte Carlo techniques. The yield Y is determined largely by the parameter K , although it would be modified to some extent by assuming a different division of excess energy between secondary carriers produced in an ionization event. K is essentially a ratio of energy loss rates for a fast particle

$$K = \frac{\text{rate of energy loss to optical phonons}}{\text{rate of energy loss in ionization}} \quad [11]$$

and the term KE_i in Eq. [8] represents the average energy lost to optical phonons for each ionization event during the avalanching process. The yield Y is plotted as a function of K in Fig. 3, using data taken from van Roosbroeck's paper.

The crazy-carpentry model should be quite generally applicable to the problem of excitation by high energy radiation as long as "all the incident unreflected energy is ultimately accounted for by secondary electrons and holes, and by phonons" (12). Of course it involves a number of idealizations. The random cutting involved in division of energy between primary and

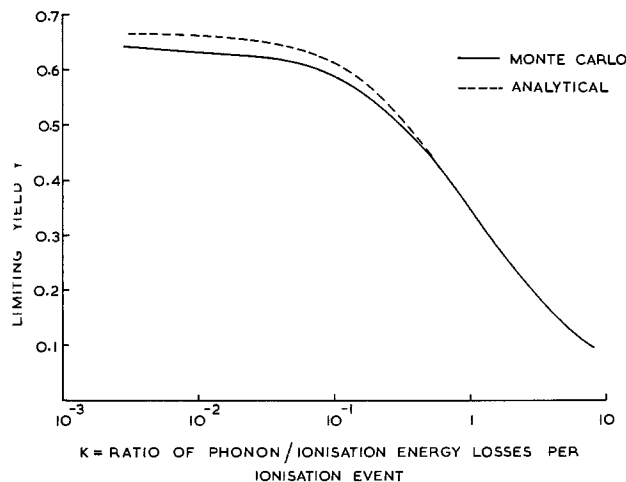


Fig. 3. The e-h pair limiting yield, Y , plotted as a function of the energy loss ratio $K = rx_r/(1 - r)$ for the "crazy-carpentry" model illustrated in Fig. 2. Solid line: Monte Carlo results. Broken line: analytic solution [after van Roosbroeck, Ref. (12)].

secondary particles at each ionization event assumes a uniform probability distribution for excitation, and neglects discrete loss processes such as plasmon creation. Equal division of excess energy between secondary electrons and holes is also open to question, since a narrow valence band would limit the energy of mobile holes. In addition the probability of optical phonon loss, r , is assumed constant for all particle energies $> E_i$, and this is unlikely to be strictly true (17). The saving grace lies in the fact that the limiting yield Y is approached rapidly for initial particle energies $\gtrsim 4E_i$. This means that the overall yield is determined largely by particles with energies only a few times E_i , where electrons and holes might be expected to behave somewhat similarly and the assumption of constant r may not be too bad. Clearly the phonon loss rate becomes very significant in determining the ionization yield when the particle energies approach the threshold E_i .

The Loss Parameter K

The average energy per e-h pair, ξ , can be obtained from Eq. [7] when Y and E_i are known. It is therefore necessary to calculate a value of the loss parameter K for a given material, so that Y can be read from the theoretical curve in Fig. 3. The loss parameter K can be written as

$$K = \frac{\text{optical phonon generation rate}}{\text{ionization rate}} \cdot \frac{(\hbar\omega_{\text{opt}})}{E_i} \quad [12]$$

In order to calculate K we make a number of simplifying assumptions. These are simply stated here, and will be discussed further below: (i) the particle energies are sufficiently large and the lattice temperature sufficiently low that only phonon generation need be considered, and phonon absorption from the lattice neglected; (ii) the fast charged particles couple principally to the LO phonon modes; (iii) phonon dispersion is neglected; (iv) the ionization rate for particles appreciably above threshold is assumed constant for all materials; (v) the energetic electrons and holes above threshold are well-removed from the band extrema and are therefore assumed to have the free electron mass; and (vi) the ionization threshold $E_i = 1.5 E_g$. With these assumptions the loss parameter reduces to

$$K \sim \frac{(\text{optical phonon generation rate})}{\text{constant}} \cdot \frac{(\hbar\omega_{\text{LO}})}{1.5E_g} \quad [13]$$

We estimate the phonon generation rate in the following way. A free primary or secondary charged particle in a solid polarizes the lattice atoms in its vicinity, the particle and polarization cloud propagating as a single quasi-particle, the polaron (18). In the limit of narrow bandwidth and very polar materials with strong short-range forces the polarization may be so strong as to induce self-trapping, as in the V_k center in alkali halides (19). In general, however, the particle will remain mobile in the lattice, but will exhibit an increased effective mass. At any instant the polarization surrounding a low-energy particle near the band extrema can be considered as a cloud of virtual phonons (20), the average number of phonons in the cloud being of the order $\sim \alpha/2$, where α is the polaron coupling constant appropriate for a polar material

$$\alpha = \frac{e^2}{\hbar} \cdot \left(\frac{1}{\epsilon_\infty} - \frac{1}{\epsilon_s} \right) \left(\frac{m}{2\hbar\omega_{\text{LO}}} \right)^{1/2} \quad [14]$$

and where ϵ_∞ , ϵ_s are the high frequency and static dielectric constants, respectively. For the higher energy charged particles of interest here we shall assume that the instantaneous deformation of the lattice can again be described by the polaron coupling constant, but that now the fast particle loses energy by the creation of

real phonons at a rate proportional to the coupling constant multiplied by the phonon frequency, i.e.

$$\begin{aligned} (\text{optical phonon generation rate}) &\propto \frac{\alpha\omega_{\text{LO}}}{2} \\ &= \text{constant} \cdot \frac{1}{\epsilon} (\hbar\omega_{\text{LO}})^{1/2} \quad [15] \end{aligned}$$

where

$$\frac{1}{\epsilon} = \left(\frac{1}{\epsilon_\infty} - \frac{1}{\epsilon_s} \right) \quad [16]$$

and we have used the free electron mass $m = m_e$ for the charged particle, which is now well removed from the band extrema. Introducing Eq. [15] into [13] gives the expression for the relative energy loss parameter K which we are seeking

$$K \sim \text{constant} \cdot \frac{1}{\epsilon} \cdot \frac{(\hbar\omega_{\text{LO}})^{3/2}}{1.5E_g} \quad [17]$$

The rate of energy loss to optical phonons included in this expression contains the same functional dependence on phonon frequency and effective dielectric constant as that given by Ulbrich (21) for the loss rate averaged over a Maxwellian distribution of hot electrons for which the electron temperature $T_e \gg (\hbar\omega_{\text{LO}}/k)$.

From Eq. [17] it is possible to calculate the loss parameter, K , and hence the e-h pair yield Y , in terms of four physical constants of any material: (i) the LO phonon frequency, ω_{LO} ; (ii) the bandgap (or absorption edge), E_g ; (iii) the static dielectric constant, ϵ_s ; (iv) the high frequency dielectric constant, ϵ_∞ (or the refractive index at optical frequencies in a region of negligible absorption, when $\epsilon_\infty = n^2$). Before going on to this stage, however, it is necessary to justify some of the assumptions made in establishing Eq. [17].

The restriction to LO phonon modes is commonly made in polaron coupling theory, and since these are among the highest energy phonons in a solid they are likely to dominate the rate of phonon energy loss. The assumption of a constant ionization rate for all energetic particles (electrons and holes) is more sweeping, but fortunately some insight can be obtained from studies of carrier avalanching in semiconductor devices such as avalanche photodiodes and IMPATT diodes (22, 23). The problem here is to obtain a carrier distribution function in an applied field in order to calculate the ionization rate. Baraff (24) has developed a theory for the ionization rate per unit distance traveled in the field which rests on the following assumptions: (i) the energy bands are parabolic; (ii) optical phonon generation is the only important dissipative process for the hot carriers which competes with ionization; (iii) a single phonon energy for the optical modes; (iv) the mfp for optical phonon scattering (λ_{op}) is independent of carrier energy; (v) the mfp for ionization (λ_i) is a step function, rising at the threshold E_i and constant for energies $> E_i$. These assumptions are similar to those made earlier in this section.

Much of the experimental work on avalanche multiplication in a range of semiconductor materials has been fitted using Baraff's theory (22, 23), with the assumption that the ionization rate for electrons, α_e , is equal to the ionization rate for holes, β_i . More recent work (25) has indicated that at low fields ($\leq 4 \times 10^5$ V cm^{-1}) in GaAs the ionization rates are sensitive to band structure; β_i is roughly isotropic, but α_e varies strongly with the crystallographic direction along which the field is applied. At high fields ($> 5 \times 10^5$ V cm^{-1}), however, it is apparent that $\alpha_e \sim \beta_i$ in all directions, a result confirmed by Ito *et al.* (26). Similar ionization rates for both electrons and holes are observed in Si and GaP at comparable fields (27). The fact that $\alpha_e \sim \beta_i$ at high fields, where a larger fraction of carriers have energies appreciably above

threshold, supports the idea that details of band structure or differences in effective mass for carriers near the band extrema are not significant in determining ionization rates for more energetic particles. A similar conclusion may be drawn from the work of Kane (28), who calculated the pair production rate in Si using pseudopotential energy bands and wavefunctions. For electron energies >8 eV above the VB the calculated ionization rate approaches the value calculated using a free-electron approximation with an electron density appropriate for Si. If carrier energies are measured from midgap the calculated hole ionization rate gives a curve almost identical to that obtained for energetic electrons. The implication is that for particle energies appreciably above threshold the ionization rates are not very sensitive to details of band structure, density-of-states, or carrier masses. Since a free-electron approximation gives a good estimate of the ionization rate for energetic particles in Si, the assumption of a constant ionization rate for hot carriers in the solids of interest here is probably not unreasonable.

At first sight it might appear surprising to suggest that hot electrons and hot holes can be treated similarly. A hole is simply the absence of an electron, and if created in a deep core band level it will be immobile with an essentially atomic-like wavefunction. It cannot therefore cause ionization directly by propagation through the lattice, like a hot electron of the same energy. However the energy of the core hole is stored as useful potential energy which can be released by subsequent relaxation of the atom, for example by x-ray fluorescence or by emission of an Auger electron. This energetic secondary particle (photon or electron) has only a small probability of escaping from the lattice, and the bulk of this secondary energy will be reabsorbed in creating lower energy (but still hot) e-h pairs. This relaxation will continue until the potential energy of the original core hole is converted into the energy associated with holes in the valence band and electrons in the conduction band. At this stage the hot VB holes have sufficient mobility to create further secondaries by impact ionization. Thus the relaxation of a very high energy immobile hole can be considered to take place through intermediate electron states, until its potential energy is converted partly into the energies of electrons and holes a few times greater than the ionization threshold, and partly into phonons generated during the relaxation process. Taken overall, therefore, the relaxation of a core hole proceeds via processes which are essentially similar to those for a high energy electron, and it is not unreasonable as a first approximation to treat energy losses for these two kinds of particles in the same way. Towards the end of the relaxation process, in an energy range a few times above threshold, the competitive phonon losses

assume greatest significance and then the assumption of similar ionization behavior for electrons and holes receives support from the fitting of experimental data to Baraff's theory.

The best value of the ionization threshold in fitting avalanche data to Baraff's theory is generally found to be $E_i = 1.5 E_g$, as assumed in the derivation of Eq. [17] (22, 23). This is actually the calculated threshold for a direct gap material with simple parabolic bands and equal carrier masses; the boundary conditions which set the minimum threshold are that the group velocities of the three final particles in the ionization event should be equal, and that energy and momentum are conserved (25). As noted above the details of band structure are important when the carrier distribution is peaked well below threshold, but for higher carrier energies a threshold which is independent of such specific material properties gives adequate description of the experimental results.

The Average Energy per e-h Pair Generated by Ionizing Radiation

In Table I are collected together the physical constants necessary to calculate the relative loss parameter K for a range of phosphor materials of interest. In column 6 is shown the value of the material coefficient \mathcal{R} , defined as

$$\mathcal{R} = \left(\frac{1}{\epsilon_s} - \frac{1}{\epsilon_\infty} \right) \frac{(\hbar\omega_{LO})^{3/2}}{1.5E_g} \quad [18]$$

From Eq. [17] \mathcal{R} is seen to be proportional to K , and we shall therefore use this as an index of relative efficiency for phosphor host materials. In order to obtain the constant of proportionality between \mathcal{R} and K use is made of experimental evidence which suggests that the archetypal phosphor host materials, ZnS and CdS, obey the " $3 \times E_g$ " rule (4, 6, 10). For such materials, with $\xi = 3E_g$ and $E_i = 1.5E_g$, we deduce from Eq. [7] that

$$Y = 0.5 \quad [19]$$

and hence, using the Monte Carlo values of yield in Fig. 3, that

$$K = 0.30 \quad [20]$$

Setting the mean value of \mathcal{R} for ZnS and CdS (i.e., $\mathcal{R} = 1.23 \times 10^{-4}$) equal to this value gives

$$K = (0.244 \times 10^4) \mathcal{R} \quad [21]$$

This constant of proportionality will be used for all phosphor hosts, in accordance with [17]. The choice of ZnS and CdS as reference compounds is natural because of our particular interest in the relative efficiencies of phosphor materials, but is somewhat arbitrary in that other semiconducting compounds (such

Table I. Physical constants for materials of interest

	$\hbar\omega_{LO}$ (eV)	E_g (eV)	ϵ_∞	ϵ_s	$\mathcal{R} (\times 10^4)$	β
GaAs (29)	0.036	1.4	10.9	12.85	0.45	2.6
GaP (29)	0.050	2.3	8.46	10.28	0.68	2.7
CdTe (29)	0.021	1.6	7.21	10.23	0.52	2.6
CdS (29)	0.038	2.6	5.3	8.4	1.33	3.0
ZnS (29)	0.044	3.8	5.14	8.0	1.13	2.9
CaS (30)	0.047	4.8 (6)	4.5	8.1; 6.7	1.35; 1.0	2.9-3.0
CsI (29)	0.011	6.4 (16)	3.09	6.4	0.20	2.5
NaI (29)	0.022	5.9 (16)	3.08	6.9	0.67	2.7
La ₂ O ₃ S	0.057 (31)	4.4 (32)	[4.67] (33)	18 (34)	3.26	3.9 _s
CaO	0.068 (35)	7.7 (16)	[3.38] (36)	11.8 (37)	3.24	3.9
ZnO (29)	0.073	3.44	4.0	8.15	4.9	4.7 _s
MgO (39)	0.091 (38)	8	2.95	9.8	5.3	4.8 _s
Y ₂ O ₃	0.068 (40)	5.6 (16)	[3.61] (41)	17 (42)	4.6	4.6
Al ₂ O ₃ (43)	0.112	8.7 (44)	3.2; 3.1	9.5; 11.64	6.0-6.8	5.2-5.6
Y ₃ Al ₅ O ₁₂ (45)	0.105	6.3	3.65	11.7	6.8	5.6
Zn ₂ SiO ₄	0.130 (46)	5.5 (16)	[2.92] (36)	6 (47)	9.8	6.8
CaWO ₄ (48)	0.112	4.6 (49)	3.4; 3.5	10.4; 9.7	9.9-10.7	6.8-7.1
YVO ₄ (50)	0.116	3.7 (51)	3.98; 4.04	9.7; 14.4	10.6-12.7	7.1-7.9

Bracketed values for ϵ_∞ are obtained from the square of the refractive index at $\sim 1 \mu\text{m}$.

as GaAs and GaP) might equally well have been chosen. However the principal conclusions would not be greatly affected by a change of reference since the yield Y does not vary strongly with K (or \mathcal{R}) in the range covering this group of binary semiconductors.

In Fig. 4 is shown a plot of β vs. \mathcal{R} , where β is defined from Eq. [3] and [7] as

$$\beta = \frac{\xi}{E_g} = \frac{3}{2Y} \quad [22]$$

and Y is obtained from Fig. 3 via Eq. [21]. The average energy per e-h pair can be obtained from Eq. [3] by making use of the data in Table I. For small phonon losses ($\mathcal{R} \rightarrow 0$) the factor β tends to a limiting value ~ 2.35 . The magnitude of β initially increases only slowly with \mathcal{R} as the relative losses to phonons become more significant, but the increase is much more rapid when $\mathcal{R} > 1 \times 10^{-4}$ corresponding to a relative phonon loss parameter $K \sim 0.25$. At the top of Fig. 4 are indicated the values of \mathcal{R} appropriate to materials of phosphor interest. As expected, the binary semiconductors for which the " $3 \times E_g$ " rule was established cluster in the center of the curve, with values of β in the range 2.6-3.0. It should be noted that CaS, although being highly ionic, is predicted to behave in a manner analogous to the IIB-VI compounds ZnS and CdS since it has similar dielectric properties and a comparable LO phonon frequency.

For the conventional phosphor materials it can be seen that β increases in the order sulfides < oxysulfides < oxides. Since phosphor efficiency $\eta \propto \beta^{-1}$ this ordering of the phosphor hosts according to the index \mathcal{R} is clearly consistent with the observations made in the introduction to this paper. It is worth noting that the alkali halides CsI and NaI fall at the LH side of the diagram mainly because of their low frequency phonon modes; conversely the "molecular" oxides such as Zn₂SiO₄, CaWO₄, and YVO₄ have the largest values of the index \mathcal{R} principally because of the high vibrational frequencies introduced by the strong intramolecular bonding in the [MO₄] tetrahedra within the lattice structure. In such materials excitation of these high frequency modes carries away a greater proportion

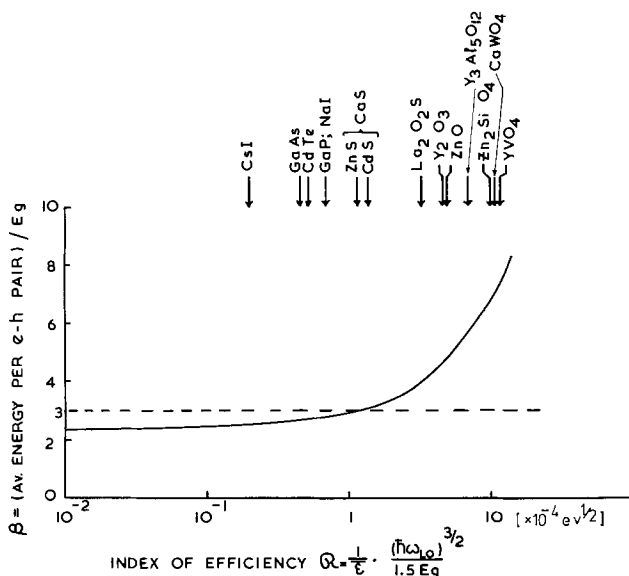


Fig. 4. The parameter $\beta = \xi/E_g$ as a function of the index of efficiency \mathcal{R} defined in Eq. [18]. The index \mathcal{R} depends on basic physical constants of a particular material and is proportional to the energy loss ratio K in Fig. 3: $K = (0.244 \times 10^4) \mathcal{R}$. The line $\beta = 3$ corresponding to the " $3 \times E_g$ " rule for the average energy per e-h pair is indicated. At the top of the diagram values of \mathcal{R} for several phosphor host materials are shown. The average energy per pair for oxides is predicted to be much higher than that for the sulfides.

of the particle energy near the end of the avalanching process and greatly reduces the e-h pair yield.

The data in Table I for GaAs and GaP also lend support to the assumption that details of band structure can be neglected in estimating the energy loss parameters. The mean free paths for optical phonon generation in the low temperature limit obtained from fitting ionization data to Baraff's theory are $\lambda_{op} = 58$ and 42\AA for GaAs and GaP, respectively (52). The same parameter is applicable for both electron and hole scattering in each material. Assuming similar velocities for energetic carriers in the two materials λ_{op} is inversely proportional to the optical phonon generation rate, so that the ratio of mfp's $\lambda_{op}(\text{GaAs})/\lambda_{op}(\text{GaP})$ can be obtained from Eq. [15] and Table I. This calculated ratio is ~ 1.75 , compared with the experimental ratio (52) ~ 1.38 under conditions in which only phonon creation is significant. Applying this reasoning to the oxide materials in Table I suggests $\lambda_{op} \sim 3\text{-}5\text{\AA}$, i.e., a distance on the order of a unit cell or between the tightly bound MO₄ units in the lattice.

The Maximum Efficiency of CRT Phosphors

The maximum efficiency which might be expected from any host activator combination, η_{max} , was defined in Eq. [2] in terms of the mean luminescence photon energy, $h\nu_m$, and the e-h pair energy parameter, ξ . In Table II η_{max} is calculated for a number of important phosphor systems, neglecting backscattering and using values of β and E_g from Table I. Figure 5 compares these calculated values of η_{max} with measured values of efficiency reported in the literature for the same phosphor systems.

It is gratifying to find that the experimental points cluster about the line of perfect correlation in Fig. 5. There are many reasons why the measured efficiency for a particular phosphor might fall below the predicted value η_{max} (for example the neglect of backscattered primaries, or a reduction in the energy transfer efficiency S or the quantum efficiency Q in Eq. [1]), but it does appear that the best reported values correlate well with the theoretical predictions. The most serious deviation occurs for CaS:Ce, which has a much higher reported efficiency than we predict (6); the behavior of CaS:Mn and CaS:Pb on the other hand is more consistent with the theory. In some cases, notably Zn₂SiO₄, there is a lack of reliable physical data so that certain parameters have been estimated in evaluating the index \mathcal{R} . Agreement between predicted and measured efficiencies may be improved when better data are available.

For most phosphors there is good agreement between the efficiencies measured under CR and XR excitation. An exception to this rule is CaWO₄, which has an XR efficiency $\sim 8\%$ but an optimum CR efficiency of only half this value (56). As one might expect, theory predicts a maximum efficiency close to the higher of the measured efficiencies, $\eta_{max} \sim 9\%$. The reasons for the lower limit to the CR efficiency are not clear, but may

Table II. The maximum power conversion efficiency, η_{max} (Eq. [2], [3])

	$h\nu_m$ (eV)	E_g (eV)	β	η_{max}
ZnS:Ag	2.75	3.8	2.9	0.25
ZnS:Cu	2.3	3.8	2.9	0.21
CaS:Ce	2.3	4.8	3.0	0.16
CaS:Mn	2.1	4.8	3.0	0.15
CaS:Pb	3.4	4.8	3.0	0.24
CaO:Mn	2.1	7.7	3.9	0.07 ₀
CaO:Pb	3.45	7.7	3.9	0.11
CaWO ₄	2.9	4.6	7.0	0.09
ZnO:Zn	2.4	3.44	4.8	0.14 ₅
NaI:Tl	3.02	5.9	2.7	0.19
CsI:Tl	2.25	6.4	2.5	0.14
Y ₃ Al ₅ O ₁₂ :Tb	2.3	6.3	5.6	0.06 ₅
Zn ₂ SiO ₄ :Mn	2.4	5.5	6.8	0.06 ₅
YVO ₄ :Eu	2.0	3.7	7.5	0.07 ₂
Y ₂ O ₃ :Eu	2.0	5.6	4.6	0.07 ₈
La ₂ O ₂ S:Eu	2.0	4.4	3.9	0.12

- | | |
|--|-------------|
| 1. Zn ₂ SiO ₄ : Mn | 9. CsI: Tl |
| 2. Y ₃ Al ₅ O ₁₂ : Tb | 10. ZnO: Zn |
| 3. CaO: Mn | 11. CaS: Mn |
| 4. YVO ₄ : Eu | 12. CaS: Ce |
| 5. Y ₂ O ₃ : Eu | 13. NaI: Tl |
| 6. CaWO ₄ | 14. ZnS: Cu |
| 7. CaO: Pb | 15. CaS: Pb |
| 8. La ₂ O ₂ S: Eu | 16. ZnS: Ag |

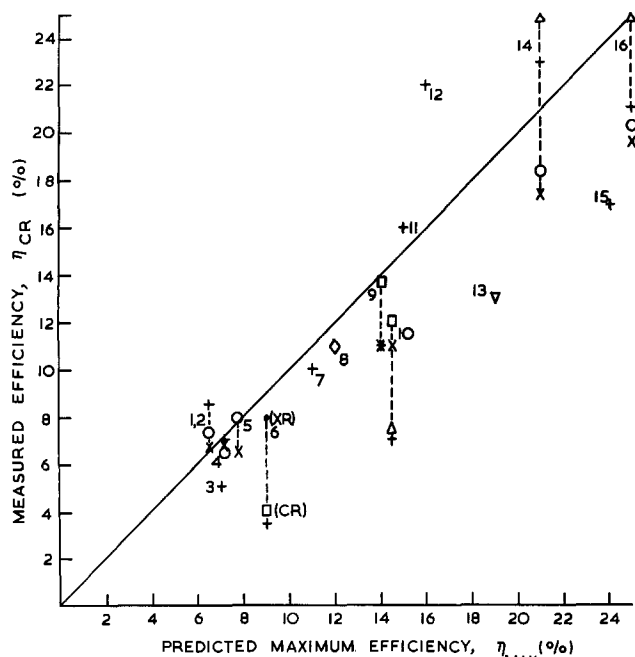


Fig. 5. The correlation between measured values of phosphor efficiency and the theoretical maximum efficiency predicted by the model. The measured value for a particular phosphor will fall below the line of perfect correlation if the energy transfer and radiative processes in the phosphor are not optimized. However the best reported values of efficiency for a wide range of phosphor types show good agreement with the predictions. Data points: Δ [Ref. (53)]; \circ [Ref. (54)]; $+$ [Ref. (6)]; \times [Ref. (55)]; ∇ [Ref. (4)]; \bullet [Ref. (56)]; \square [Ref. (57)]; $*$ [Ref. (58)]; \diamond [Ref. (59)].

for example reflect the increased importance of surface deactivation for the less-penetrating electron radiation.

Discussion

A calculation of the maximum efficiency to be expected from particular host-activator phosphor combinations has been made using a model which is very idealized, but which should be quite general in its application. The theory draws heavily on van Roosbroeck's statistical analysis of the e-h pair generation problem in semiconductors (12), but in the context of phosphor materials the approach adopted in this paper is novel in emphasizing the competitive phonon loss processes which occur during the carrier ionization cascade. The relative phonon loss parameter K appearing in van Roosbroeck's analysis is here translated into an index of efficiency, \mathcal{R} , which can be calculated from accessible physical constants of a particular material: ω_{LO} , E_g , ϵ_∞ , ϵ_s . The many simplifications in the model are probably successful because the yield of secondary e-h pairs, which is a critical factor in the limiting efficiency, is determined largely by carriers with energy only a few times greater than the ionization threshold, E_i . In this energy range, covering higher valence and conduction band states, the ionization rates are governed by excess particle energy and are insensitive to details of band structure or carrier charge and mass. In the final analysis, however, it is the good agreement between measured phosphor efficiencies and the maximum value η_{max} calculated from the theory which must be considered the principal

justification for the many assumptions made during the development.

The degree of correlation with experiment evident in Fig. 5 suggests that the index \mathcal{R} may prove a useful tool in the search for new and efficient phosphor host materials. The model should be applicable generally to those polar semiconducting and insulating materials for which polar optical mode scattering is expected to dominate the phonon energy dissipation, and this includes the materials of primary interest as phosphor hosts. If the index \mathcal{R} is calculated for any potential phosphor lattice according to Eq. [18], the average energy per e-h pair for these materials can be read from Fig. 4 and the limiting efficiency estimated using Eq. [2]. However it must be realized that this maximum efficiency represents only one ingredient in the recipe for a useful phosphor system (it is also necessary that the lattice have the requisite damage-resistance), and that an efficient activator center can be incorporated so that the parameters S and Q in Eq. [1] are optimized.

At a somewhat simpler level it is clear from Fig. 4 that the index places the more common phosphor hosts in an order which is in satisfying agreement with experience; the more efficient sulfides to the left hand, the oxysulfides in the center, and the less efficient oxides to the right of the figure. The important parameters which determine \mathcal{R} are the effective dielectric constant $\bar{\epsilon}$ (defined in Eq. [16]) and the LO phonon frequency (or at least the ratio $\hbar\omega_{LO}/E_g$). The effective dielectric constant $\bar{\epsilon}$ arises from relaxation of the lattice atoms alone, and relates the lattice polarization field to the electric displacement associated with the free charge carriers (18)

$$\bar{P}_{lattice} = \frac{1}{4\pi\bar{\epsilon}} \bar{D} \quad [23]$$

If $\bar{\epsilon}$ is large the lattice deformation induced by the free carriers is relatively small, and the phonon coupling is reduced. Both oxides and alkali halides have small values for $\bar{\epsilon}$; phonon coupling is therefore strong, but in the case of the heavier halides the LO phonon frequency is low so that the total energy carried away by phonons is small and the index \mathcal{R} as a whole is reduced. This is consistent with the well-known use of the heavier alkali halides as the host lattices for efficient scintillator devices (4). In the majority of oxides, on the other hand, the combination of the light O atom and tighter, more covalent bonding produces high phonon frequencies and therefore larger values for the index \mathcal{R} . The large pair energy ξ , and the corresponding modest efficiency, for oxide-based materials are therefore to be understood as the consequences of a low effective dielectric constant $\bar{\epsilon}$ coupled with a high lattice phonon frequency.

As a final point it is worthwhile to consider the relationship between the present theory and previous attempts to rationalize the relative efficiencies of different phosphor materials. Alig and Bloom (16) have emphasized that the correlation between CR efficiency η and the inverse plasmon frequency $(\omega_p)^{-1}$ originally proposed by Kingsley and Ludwig (5) is only valid when calculated plasmon frequencies are used; no correlation exists for measured values of ω_p . From Eq. [5] it is therefore clear that the foundation of Kingsley and Ludwig's observations must lie in a correlation between η and $(n_v)^{-1/2}$, where n_v is the valence electron density. For those phosphor lattices which can be considered to have a similar ratio of ionic to covalent bonding (i.e., specifically neglecting the alkali halides) Alig and Bloom have demonstrated that there is indeed a relationship between η and n_v ; in fact they have plotted η vs. $(n_v)^{-1}$ and have shown that some degree of correlation does exist between these quantities.

In this work we predict an inverse relationship between η and the index $\bar{\epsilon}$, i.e., from Eq. [18] we expect some positive correlation between η and the product of the quantities $\bar{\epsilon}$ and $(\hbar\omega_{LO}/E_g)^{-1}$. The observations discussed in the previous paragraph would therefore be understandable if there exists a correlation between $\bar{\epsilon}$ and/or $(E_g/\hbar\omega_{LO})$ and the inverse valence electron density $(n_v)^{-1}$. These quantities are listed in Table III and plotted in Fig. 6 using the reported values of n_v ; this figure demonstrates that both $\bar{\epsilon}$ and the ratio $(E_g/\hbar\omega_{LO})$ do indeed vary as $(n_v)^{-1}$, and that the correlation with their product is even stronger. The reasons for this dependent behavior are as follows. The quantity $(n_v)^{-1}$ tends to be larger for lattices containing the bigger anions, such as S^{2-} and Se^{2-} , than for the oxides. The presence of heavy ions in a lattice reduces the vibrational frequency $\hbar\omega_{LO}$, so that the ratio $(E_g/\hbar\omega_{LO})$ also tends to be larger for the sulfides and selenides. As noted previously this ratio is particularly low for oxides containing tightly bound molecular anions. The effective dielectric constant can be rewritten as

$$\bar{\epsilon} = \frac{\epsilon_\infty}{(1 - \epsilon_\infty/\epsilon_g)} \quad [24]$$

and for the more polar materials of interest here it is most sensitive to variation in the high frequency dielectric constant ϵ_∞ . According to the Clausius-Mossotti relation (60) ϵ_∞ increases with the electronic polarizability of the ions in the lattice. Since the anion polarizability is dominant, and for the chalcogenides has the order $Se^{2-} > S^{2-} > O^{2-}$, it is again apparent that $\bar{\epsilon}$ will be larger for those compounds containing the bigger anions for which $(n_v)^{-1}$ is also larger.

We therefore suggest that the explanation of the earlier observations of Kingsley and Ludwig and of Alig and Bloom is as follows. For a particular phosphor host our theory predicts a positive relationship between the maximum phosphor efficiency η_{max} and the product of two quantities, $\bar{\epsilon}$ and $(E_g/\hbar\omega_{LO})$. As long as we restrict our attention to compounds with similar bonding properties, e.g., the chalcogenides, we find that both these quantities tend to increase with increasing anion size, for reasons discussed above. For lattices containing the larger anions the inverse valence electron density, $(n_v)^{-1}$, is also large. Hence the previously reported appearance of correlation between η and $(n_v)^{-1}$ [and implicitly between η and $(\omega_p)^{-1}$] arises simply because for the compounds of interest the product of the effective dielectric constant $\bar{\epsilon}$ and the energy ratio $(E_g/\hbar\omega_{LO})$ for a particular compound tends to be large in those lattices containing the larger anions, for which $(n_v)^{-1}$ is also larger.

Acknowledgments

The author is grateful to a number of colleagues, particularly Dr. P. J. Dean, for valuable comments on this work.

Table III. The inverse valence electron density [Ref. (16)], the effective dielectric constant, $\bar{\epsilon}$, and the ratio $(E_g/\hbar\omega_{LO})$ for selected phosphor host lattices

	$(n_v)^{-1}$ (\AA^3)	$\bar{\epsilon}$	$(E_g/\hbar\omega_{LO})$
ZnF ₂	2.16	3.5	—
CaWO ₄	2.44	5.3	62
YVO ₄	2.49	6.1	48
Zn ₂ SiO ₄	2.72	5.7	64
ZnO	2.98	7.9	71
Y ₂ O ₃	3.11	4.6	123
CaO	3.47	4.7	169
La ₂ O ₃ S	4.12	6.3	116
ZnS	4.95	14.3	130
ZnSe	5.68	20	141
CaS	5.75	11.9	154

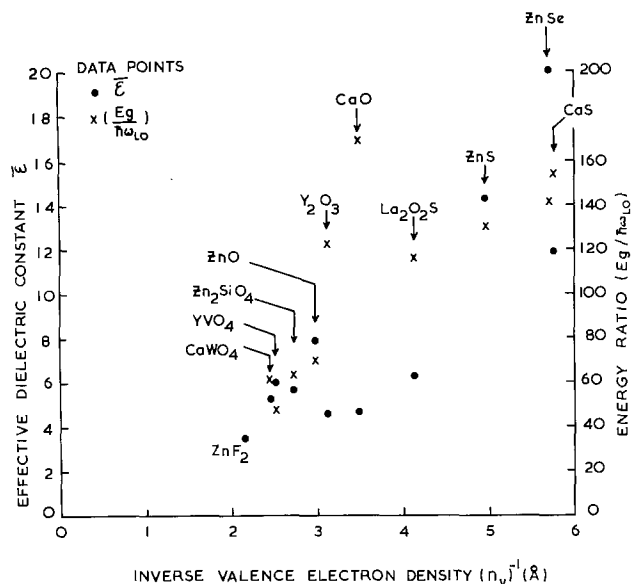


Fig. 6. The effective dielectric constant $\bar{\epsilon}$ and the ratio $(E_g/\hbar\omega_{LO})$ for a number of phosphor host materials plotted against the inverse valence electron density $(n_v)^{-1}$ taken from Ref. (16). A positive relationship between phosphor efficiency η and the product $\bar{\epsilon} (E_g/\hbar\omega_{LO})$ is expected on the basis of the theory developed in this paper. The evident correlation between these quantities and $(n_v)^{-1}$ is the origin of a previously noted correlation between η and the calculated plasmon frequency $\omega_p = (4\pi n_v e^2/m)^{1/2}$.

Manuscript received April 1, 1980. This was Paper 207 presented at the St. Louis, Missouri, Meeting of the Society, May 11-16, 1980.

Any discussion of this paper will appear in a Discussion Section to be published in the June 1981 JOURNAL. All discussions for the June 1981 Discussion Section should be submitted by Feb. 1, 1981.

REFERENCES

- S. Larach and A. E. Hardy, *Proc. IEEE*, **61**, 915 (1973).
- A. L. N. Stevels, *J. Lumin.*, **12**, 13, 97 (1976).
- E. Banks, *This Journal*, **125**, 415C (1978).
- G. F. J. Garlick, in "Luminescence of Inorganic Solids," Chap. 12, P. Goldberg, Editor, Academic Press, New York (1966).
- J. D. Kingsley and G. W. Ludwig, *This Journal*, **117**, 353 (1970).
- W. Lehmann, *ibid.*, **118**, 1164 (1971).
- D. J. Robbins and P. J. Dean, *Adv. Phys.*, **27**, 499 (1978).
- D. J. Robbins, B. Cockayne, J. L. Glasper, and B. Lent, *This Journal*, **126**, 1221 (1979).
- D. J. Robbins, B. Cockayne, B. Lent, and J. L. Glasper, *ibid.*, **126**, 1556 (1979).
- C. A. Klein, *J. Appl. Phys.*, **39**, 2029 (1968).
- W. Shockley, *Solid State Electron.*, **2**, 35 (1961).
- W. van Roosbroeck, *Phys. Rev. A*, **139**, 1702 (1965).
- C. A. Klein, Proc. Int. Conf. Phys. Semicond., Kyoto: (1966), *J. Phys. Soc. Jpn.*, **21**, Supplement, 307.
- A. Rothwarf, *J. Appl. Phys.*, **44**, 752 (1973).
- H. Yamamoto and A. Tonomura, *J. Lumin.*, **12**, 13, 947 (1976).
- R. C. Alig and S. Bloom, *This Journal*, **124**, 1136 (1977).
- E. M. Conwell, "High Field Transport in Semiconductors" in "Solid State Physics," Suppl. 9, Chap. 3, Academic Press, New York (1967).
- "Polarons and Excitons," C. G. Kuper and G. D. Whitfield, Editors, Oliver and Boyd, Edinburgh, (1963).
- M. N. Kabler, in "Point Defects in Solids," Chap. 6, J. H. Crawford Jr. and L. M. Slifkin, Editors, Plenum Press, New York (1972).
- D. Pines, in "Polarons and Excitons," Chap. 2, C. G. Kuper and G. D. Whitfield, Editors, Oliver

- and Boyd, Edinburgh (1963).
21. R. Ulbrich, *Phys. Rev. B*, **8**, 5719 (1973).
 22. G. E. Stillman, Proc. 6th Int. Symposium on GaAs and Related Compounds, Edinburgh (1976); *Inst. Phys. Conf. Ser. A*, **33**, 185 (1976).
 23. W. Monch, *Phys. Status Solidi*, **36**, 9 (1969).
 24. G. A. Baraff, *Phys. Rev.*, **128**, 2507 (1962).
 25. T. P. Pearsall, *Solid State Electron.*, **21**, 297 (1978).
 26. M. Ito, S. Kagawa, T. Kaneda, and T. Yamaska, *J. Appl. Phys.*, **49**, 4607 (1978).
 27. S. M. Sze, "Physics of Semiconductor Devices," Wiley & Sons, New York (1969).
 28. E. O. Kane, *Phys. Rev.*, **159**, 624 (1967).
 29. E. Kartheuser, in "Polarons in Ionic Crystals and Polar Semiconductors," J. T. Devreese, Editor, p. 717, North Holland, Amsterdam (1972).
 30. M. Drofenik and A. Azman, *J. Phys. Chem. Solids*, **33**, 761 (1971).
 31. K. A. Wickersheim, R. A. Buchanan, and E. C. Yates, in "Proc. 7th Rare Earth Research Conference," p. 835, NSF (1968).
 32. C. W. Struck and W. H. Fonger, *Phys. Rev. B*, **4**, 22 (1971).
 33. L. E. Sobon, K. A. Wickersheim, R. A. Buchanan, and R. V. Alves, *J. Appl. Phys.*, **42**, 3049 (1971).
 34. Value estimated as the mean of ϵ_s for Y_2O_3 and BaS.
 35. D. H. Saunderson and G. E. Peckham, *J. Phys. C*, **4**, 2009 (1971).
 36. CRC Handbook of Physics and Chemistry," 58th ed., R. C. Weast, Editor, CRC Press Inc., Cleveland, Ohio (1977).
 37. "Am. Inst. Phys. Handbook," 3rd Ed., D. E. Gray, Editor, McGraw-Hill, New York (1972).
 38. M. J. L. Sangster, G. E. Peckham, and D. H. Saunderson, *J. Phys. C*, **3**, 1026 (1970).
 39. A. E. Hughes and B. Henderson, in "Point Defects in Solids," Chap. 7, J. H. Crawford, Jr. and L. M. Slifkin, Editors, Plenum Press, New York (1972).
 40. L. A. Riseberg and H. W. Moos, *Phys. Rev.*, **174**, 429 (1968).
 41. W. Heitmann, *Appl. Opt.*, **12**, 394 (1973).
 42. C. K. Campbell, *Thin Solid Films*, **6**, 197 (1970).
 43. A. S. Barker, *Phys. Rev.*, **132**, 1474 (1963).
 44. W. R. Hunter and S. A. Malo, *J. Phys. Chem. Solids*, **30**, 2739 (1969).
 45. J. P. Hurrell, S. P. S. Porto, I. F. Chang, S. S. Mitra, and R. P. Bauman, *Phys. Rev.*, **173**, 851 (1968).
 46. Vibrational frequencies of SiO_4^{2-} obtained from K. Nakamoto in "IR Spectra of Inorganic and Co-ordination Compounds," Wiley and Sons, New York (1963).
 47. Value for ϵ_s for Mg_2SiO_4 used: "CRC Handbook of Tables for Applied Engineering Science," R. Bolz and G. L. Tuve, Editors, CRC Press Inc., Cleveland, Ohio (1970).
 48. A. S. Barker, *Phys. Rev. A*, **135**, 742 (1964).
 49. R. Grasser, E. Pitt, A. Scharmann, and G. Zimmerer, *Phys. Status Solidi B*, **69**, 359 (1975).
 50. A. Armbruster, *J. Phys. Chem. Solids*, **37**, 321 (1976).
 51. J. D. Kingsley and G. W. Ludwig, *J. Appl. Phys.*, **41**, 370 (1970).
 52. C. R. Crowell and S. M. Sze, *Appl. Phys. Lett.*, **9**, 242 (1966).
 53. A. Bril and H. A. Klasens, *Philips Res. Rep.*, **7**, 401 (1952).
 54. V. D. Meyer, *This Journal*, **119**, 920 (1972).
 55. G. W. Ludwig and J. D. Kingsley, *ibid.*, **117**, 348 (1970).
 56. J. A. de Poorter and A. Bril, *ibid.*, **122**, 1086 (1975).
 57. G. W. Ludwig, *ibid.*, **118**, 1152 (1971).
 58. A. L. N. Stevels, *Medica-Mundi*, **20**, 12 (1975).
 59. P. N. Yocom and R. E. Shrader, Proc. 7th Rare Earth Res. Conf., p. 601 (NSF, 1968).
 60. C. Kittel, "Introduction to Solid State Physics," 4th ed., Chap. 13, Wiley and Sons, New York (1971).

Investigation of Contact Metallization Systems for Solar Cells

R. B. Campbell and A. Rohatgi

Westinghouse Advanced Energy Systems Division, Pittsburgh, Pennsylvania 15236

ABSTRACT

In conventional solar cells, evaporated Ti-Pd-Ag metallization system has been found reliable. However, for low cost terrestrial applications, its cost effectiveness may be questioned. Electroplated Ag and Cu have been investigated as replacements for evaporated Ag and have given results comparable to the evaporated Ti-Pd-Ag system.

Reliable contact systems are required if solar cells are to meet the operating lifetime goal. Evaporated Ti-Pd-Ag is the most widely used contact system due to its overall satisfactory performance and it has been qualified for space cells. However, this system may not be cost effective due to: (i) the use of expensive Ag, (ii) vacuum techniques, and (iii) inefficient use of evaporated material. A second problem, relating to operating life, is the interaction between the interconnect strap and the contact metallization. If these are different metals, there could be problems arising from galvanic corrosion effects and formation of intermetallics.

In this paper we will describe several alternate contact systems which ease processing, are suitable for a single metal interconnect system, and which are less costly than the evaporated Ti-Pd-Ag system.

Key words: solar, electroplating, metallization.

Systems Studied

The following contact systems were studied: (i) evaporated Ti-Pd-Ag (baseline system); (ii) evaporated Ti-Pd + electroplated Ag; (iii) evaporated or electroplated Cu; (iv) evaporated Pd + electroplated Cu; and (v) evaporated Ti-Pd + electroplated Cu.

Evaporated Ti-Pd-Ag was used as a baseline contact system against which all other systems were evaluated. The evaporated Ti-Pd electroplated Ag system (No. ii) should be more cost effective than No. i since the Ag is deposited only on the well-defined grid area. The evaporated Ti-Pd electroplated Cu system (No. iii) has the advantages of No. ii as well as using a less expensive metal. In addition, a system with a top layer of copper may permit a single metal contact-interconnection system using copper foils. The Pd-Cu system was investigated to determine the role of the diffusion barrier metal, Ti, in the system. The evaporated Cu on Si sys-

tem was studied to show that even at very moderate operating conditions copper on silicon is unsatisfactory.

These contact systems were studied by fabricating 1×1 cm $n^+ p p^+$ solar cells on either float zone or dendritic web silicon. The base material was 10-15 Ω -cm boron-doped. The cell parameters were determined by a combination of dark and lighted I - V measurements. The open-circuit voltage (V_{oc}), short-circuit current (I_{sc}), fill factor (FF), and cell efficiency were determined for the AM1 spectrum using a quartz-iodine simulator. The bulk and junction responses were determined by transforming the measured dark I - V data by removing the effects of series and shunt resistances as described by Davis *et al.* (1). The upper segment of the transformed I - V curve (Fig. 1) represents the bulk performance (ideality factor of unity) and the lower segment is indicative of the junction response. If the upper segment moves to the left it indicates a loss of bulk lifetime and the upward movement of the lower segment suggests increased recombination in the junction or junction recombination current (2, 3). The lifetime was determined by the open-circuit decay (OCD) technique using 20 mA current. The junction current (I_j) dominates at low voltages and is indicated in this paper by the current in the lower segment at $V \approx 0.3V$. The junction excess current can reduce the fill factor and cell performance if it becomes appreciable in relation to the current at the operating point.

Experimental Results and Discussion

Table I shows a comparison of the evaporated Ti-Pd-Ag system *vs.* the evaporated Ti-Pd electroplated Ag system. These data were obtained by removing the evaporated Ag from the samples in the first column and then electroplating an Ag layer. The data show no essential difference between the two systems. The electroplated Ag system will be less costly since the Ag is deposited only on the grid structure, and not over the entire cell (as in the evaporation technique).

The evaporated copper system resulted in extremely poor yields. The main failure mechanism was a low shunt resistance of the order of few ohms as compared to the normal 30 $k\Omega$ or greater. This was most probably due to the Cu diffusing into the silicon, and shunting the junction. This occurred at the moderate processing temperatures of about 100°C.

Table II shows a comparison of the baseline system with evaporated Pd-electroplated Cu. The specific data

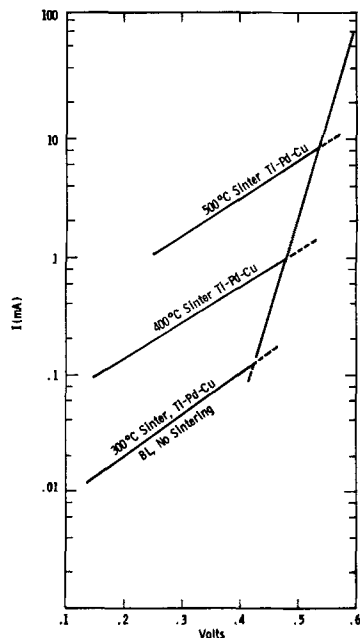


Fig. 1. Transformed I - V curves of baseline system and Ti-Pd-Cu system.

Table I. Evaporated Ti-Pd-Ag vs. evaporated Ti-Pd-plated Ag

	Evaporated Ag	Plated Ag
η (%)	14.4	14.3
I_{sc} (mA)	34.6	35.1
V_{oc} (V)	0.572	0.578
FF	0.749	0.73
R_s (Ω)	0.5	0.7
R_{sh} ($k\Omega$)	300	300
I_j at 0.3V (mA)	0.04	0.05
τ_{ocd} (μ sec)	21	22
FZ cells AR coating		
AM-1; 100 MW/cm ²		

In the above table, the cell parameters are defined as: η (%)—cell efficiency; I_{sc} (mA)—short-circuit current; V_{oc} (V)—open-circuit voltage; FF —curve form factor; R_s (Ω)—series resistance in cell measured at the I_{sc} point; R_{sh} (Ω)—shunt resistance, measured at $-1V$ reverse bias; I_j (mA)—junction excess current, measured at 0.3V; τ_{ocd} (μ sec)—open-circuit decay lifetime with injected current of 20 mA.

Table II. Evaporated Ti-Pd-Ag vs. evaporated Pd-plated Cu

	Ti-Pd-Ag	Pd-Cu	Pd-Cu 150°C sinter	Pd-Cu 300°C sinter
η (%)	14.4	14.5	13.97	1.5
I_{sc} (mA)	34.7	35.0	34.3	0.2
V_{oc} (V)	0.572	0.574	568	13.1
FF	0.749	0.751	0.740	0.49
R_s (Ω)	0.45	0.35	0.35	0.3
R_{sh} ($k\Omega$)	300	2	2	2
I_j at 0.3V (mA)	0.04	0.29	0.31	51.5
τ_{ocd} (μ sec)	21	19.5	19.5	—

FZ cells, AR Coating
AM-1; 100 MW/cm²

in Table II is for a Pd layer of 0.03 μ m, although layers from 0.08 to 0.3 μ m were tested with the same results. The unsintered Pd-Cu system is equivalent to the baseline system. However, the system cannot withstand sintering as shown in the last two columns. The sintering was carried out in H_2 at the noted temperature for 15 min. The degradation is due to an increase in the junction excess current, again presumably due to the Cu diffusing through the Pd to the junction.

Although not indicated in the table, the experiments were repeated using sintered Pd as a base for plating the Cu. Pd layers from 0.08 to 0.3 μ m were studied. In these tests the Pd was sintered for 15 min at 300°C to form Pd silicides prior to plating 4 μ m of Cu. Initial cell characteristics were good but when these samples were sintered at 300°C they showed the same degradation as the cells in Table II, *i.e.*, excess junction current. We, therefore, conclude that Pd, either sintered or unsintered, does not serve as a barrier to Cu.

Table III shows the comparison of evaporated Ti-Pd-Ag system and the evaporated Ti-Pd electroplated Cu system. All cells were fabricated on dendritic web silicon. As seen from the table, this system is equivalent to the baseline system and can be sintered to

Table III. Evaporated Ti-Pd-Ag vs. evaporated Ti-Pd-plated Cu

	Ti-Pd-Ag	Ti-Pd-Cu	Ti-Pd-Cu 300°C sinter	Ti-Pd-Cu 400°C sinter	Ti-Pd-Cu 500°C sinter
η (%)	14.0	14.1	14.2	13.2	10.6
I_{sc} (mA)	33.6	33.3	33.4	33.7	29.6
V_{oc} (V)	0.572	0.580	0.580	0.574	0.544
FF	0.74	0.754	0.76	0.731	0.667
R_s (Ω)	0.5	0.6	0.45	0.5	0.5
R_{sh} ($k\Omega$)	2.5	2.5	2.5	2	1.1
I_j at 0.3V (mA)	0.044	0.044	0.040	0.27	1.4
τ_{ocd} (μ sec)	11	11.5	11.5	10	6

Web cells AR coating
AM-1, 100 MW/cm²

above 300°C. There is only a slight decrease in performance when sintered at 400°C, but a significant degradation when sintered at 500°C. The degradation was due to increased junction current with no significant effect on the bulk properties.

This is indicated in Fig. 1 which shows the transformed *I-V* curves of the Ti-Pd-Ag baseline system (unsintered) and the Ti-Pd electroplated Cu system after sintering at 300°, 400°, and 500°C. As the sintering temperature is increased, the cell degrades by an increase in the junction current until at 500°C it noticeably affects the cell parameters. For example, the efficiency drops from 14 to 10.5%. This increase in junction current can be due to impurities or defects in the depletion region, such as Cu precipitates.

These data indicate that evaporated Ti-Pd electroplated Cu is a promising contact system from both a performance and cost standpoint. Its long term reliability under realistic cell operating conditions has not been determined.

Conclusions

From the data given we conclude:

1. Electroplated Ag can be used instead of evaporated Ag to reduce the use of expensive Ag.
2. Pd-Cu is not a suitable system since it cannot withstand sintering.
3. Ti-Pd electroplated Cu behaves essentially the same as the baseline system.
4. Ti and not Pd acts as a diffusion barrier.

Acknowledgments

We wish to acknowledge helpful discussions with P. Rai-Choudhury. We also acknowledge the technical assistance of E. J. Seman, H. Abt, and D. Schmidt. The dendritic web was grown by the Crystal Sciences Department. This paper presents results of research performed for the Low-Cost Silicon Solar Array Project, Jet Propulsion Laboratory, California Institute of Technology, sponsored under an Interagency Agreement between the U.S. Department of Energy and the National Aeronautics and Space Administration.

Manuscript submitted Oct. 1, 1979; revised manuscript received May 23, 1980.

Any discussion of this paper will appear in a Discussion Section to be published in the June 1981 JOURNAL. All discussions for the June 1981 Discussion Section should be submitted by Feb. 1, 1981.

Publication costs of this article were assisted by Westinghouse Electric Corporation.

REFERENCES

1. J. R. Davis, A. Rohatgi, P. Rai-Choudhury, P. Blais, R. H. Hopkins, and J. R. McCormick, "Conf. Record of the 13th Photovoltaic Specialists," p. 490, (1978).
2. R. J. Stirn, "Proc. 9th IEEE Photovoltaic Specialists Conf.," p. 72, Silver Springs (1972).
3. H. J. Hovel, "Semiconductor and Semimetals," Vol. II, Solar Cells, Academic Press, New York (1975).

Laser Interferometer Bevel Angle Measurement for Spreading Resistance Profiling

D. C. D'Avanzo,¹ C. Clare, and C. Dell'Oca*

Hewlett Packard Laboratories, Palo Alto, California 94304

ABSTRACT

A laser interferometer system is utilized to automatically measure bevel contours for spreading resistance profiling. Comparative results demonstrate the system's ability to measure angles between 0.2° and 2° with better than 10% consistency. The effects of bevel rounding are investigated by incorporating the complete bevel contour into a multilayer data analysis algorithm. Both rounding and three-dimensional effects are shown to contribute to the near-surface depletion of spreading resistance impurity profiles.

Spreading resistance measurements are widely used to determine the impurity profiles of diffused, implanted, and epitaxially grown layers (1). The method is capable of profiling an extensive range of resistivities and profile shapes and is relatively rapid and convenient. The procedure begins by beveling the sample at a shallow angle to achieve high spatial resolution. Spreading resistance is measured between two probes which are stepped along the beveled surface (Fig. 1). The impurity profile extracted from the measurement data is highly dependent on the bevel angle measurement which establishes the actual depth into the sample. As can be seen in Fig. 1, the perpendicular distance, *y*, from the original surface is the product of the sine of the bevel angle, θ , and the distance traveled in the *x* direction. An accurate bevel angle measurement is therefore essential for an accurate profile measurement.

Existing angle measurement techniques average the slope of the bevel over the entire beveled plane, result-

ing in significant error when the beveled surface is rounded. In order to minimize this error, considerable time and effort must be dedicated to sample preparation. In addition, these angle measurement techniques are usually made independent of the resistance measurement further increasing the total measurement time.

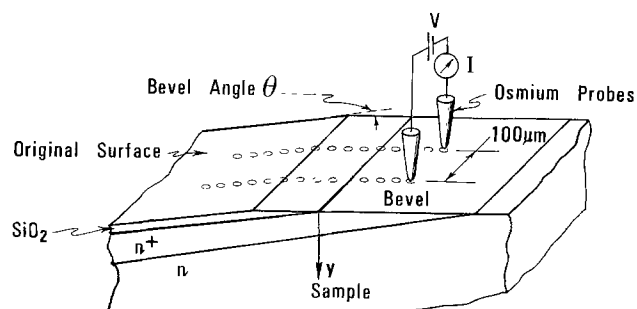


Fig. 1. Schematic diagram of a spreading resistance measurement on a beveled sample.

* Electrochemical Society Active Member.

¹ Present address: Hewlett Packard, Santa Rosa, California 95404.

Key words: impurity profile measurement, two-point probes, multilayer analysis, bevel rounding, near-surface concentration.

In this work, a laser interferometer has been employed to measure the vertical displacement of one of the probes as it moves along the beveled surface. The probe serves as a profilometer so that the actual surface contour is measured. Furthermore, both the resistance measurement and the angle measurement are recorded simultaneously and automatically, reducing the measurement time and minimizing the need for operator interpretation. The laser system and optimization of the laser measurement are discussed in the next section. Comparative results are presented in the third section, and finally, bevel rounding and its effect on the corrected impurity profile are considered in the fourth section.

Laser Interferometer System

Figure 2 is a schematic of the laser interferometer system² (2) used in conjunction with the spreading resistance probe.³ The helium-neon laser uses Zeeman splitting to produce a coherent beam composed of two slightly different optical frequencies of opposite circular polarization. The two components are split in an interferometer where one is reflected internally, while the other is reflected from a mirror mounted on the back of a probe arm. The two reflected beams interfere in the interferometer, producing a difference frequency. Relative motion of the probe arm results in a proportional Doppler shift in the difference frequency which is detected by the receiver and processed by the accompanying electronics. Displacements of approximately one-fortieth of the optical wavelength or 150Å can be detected.

Both the laser and spreading resistance systems are interfaced to a Hewlett-Packard Series 1000 21MX computer. The laser data is processed by the computer and a bevel contour is constructed. The raw spreading resistance data is combined with the contour information and analyzed by multilayer theory (3, 4) to produce a concentration profile for the sample.

Maximum laser resolution is difficult to obtain in practice due to the effects of mechanical vibrations, changes in air density, and thermal expansion of the supports. Vibrations are minimized by mounting the system on an isolation table while changes in air density introduced by turbulence are reduced by enclosing the beam in a protective column.

The third source of error, thermal expansion of the support structure, can lead to considerable inaccuracy if not compensated. The 10 in. aluminum structure supporting the interferometers expands at a rate of 7 microns per degree centigrade. The ambient temperature changes by approximately 0.1°C during a mea-

²The laser source, optics, and electronics, System 5501A, are commercially available from Hewlett Packard Company, Palo Alto, California.

³The spreading resistance system, the ASR 100, is produced by Solid State Measurements, Monroeville, Pennsylvania.

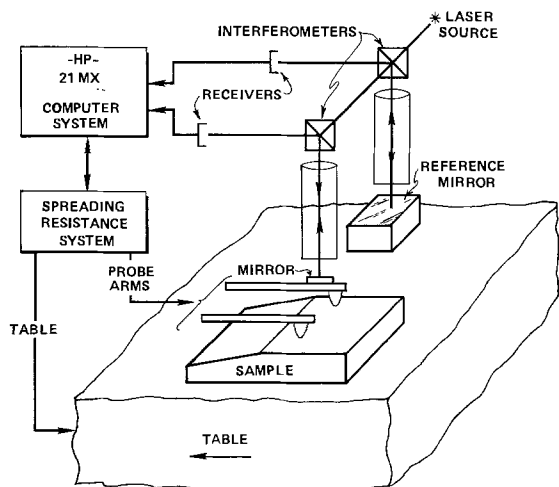


Fig. 2. Laser interferometer and spreading resistance system

surement resulting in a 6000Å expansion. Compensation has been achieved by measuring the path length between a reference mirror located near the sample and a reference interferometer mounted on the support structure close to the primary interferometer, Fig. 2. Changes in the reference path length are interpreted as displacement of the interferometer due to expansion of the supports. This displacement is subtracted from the probe arm displacement. A typical result is reproduced in Fig. 3. In this experiment the probe arm was allowed to rest on the surface of a stationary sample. The change in path lengths to the probe arm and the reference mirror were measured every 30 sec for 15 min. Without compensation the probe appears to have moved over a micron. When compensation is included the apparent displacement is eliminated. The reduction in the noise level to a 300-400Å ripple is sufficient to accurately determine the bevel angles commonly used for spreading resistance profiling.

Results

Bevel angle determination.—During each spreading resistance measurement cycle the probe is slowly lowered to the sample surface where it remains for several seconds while the resistance measurement is made, and then is lifted to allow the sample to be moved horizontally. Figure 4 shows the height of the probe throughout a measurement cycle. The local height of the sample surface is determined by averaging a burst of laser measurements while the probe is resting on the surface. The data selection interval is shown in Fig. 4. The standard deviation associated with the average value is usually less than 100Å. The averaging procedure is repeated each time the probe is lowered to the sample surface. The probe height is recorded as a

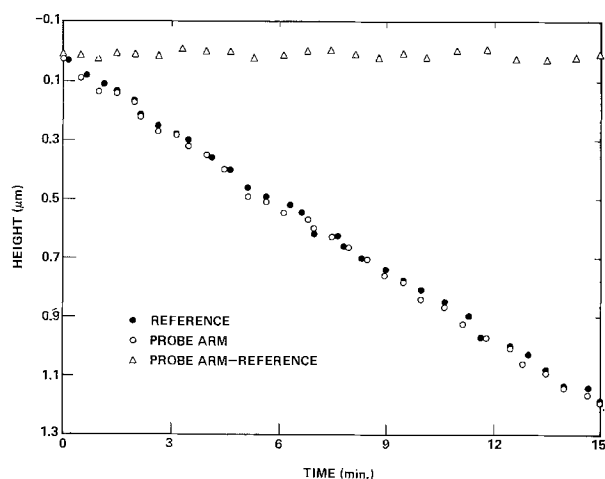


Fig. 3. Reference mirror compensation for thermal expansion

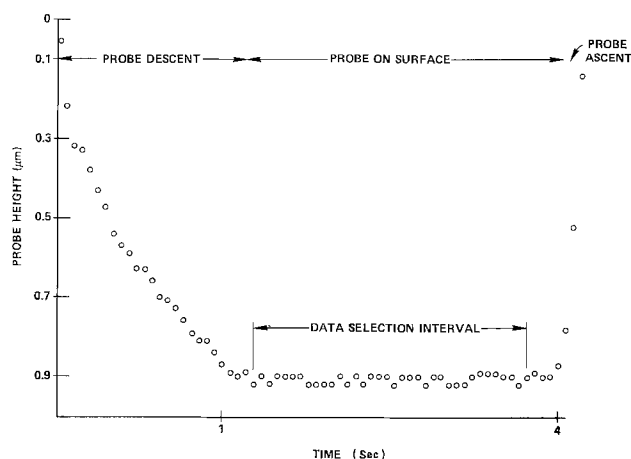


Fig. 4. Probe height during a measurement cycle

function of horizontal travel to recreate the bevel contour. Figure 5 shows a typical result for a nominal $1^{\circ}9'$ bevel block. The bevel angle is determined by fitting two lines to the measurement data; one on the beveled silicon surface and one on the original surface.

To evaluate the accuracy of the laser technique bevels between 0.15° and 2.8° were measured and the results were compared to the angles determined by multibeam interference using an interference attachment in an optical microscope. The bevel angle can be related to the angle formed by the interference fringes as they pass over the bevel edge. The absolute accuracy of the multibeam technique is difficult to evaluate since the fringe bending is measured manually. Repeatability of the method is typically between 5% and 10%.

The comparative results are shown in Fig. 6 where the ratio of the laser angle to the multibeam angle is plotted as a function of the laser angle. For angles over 0.2° (12 min) the agreement is always better than 10% and improves slightly as the angle increases. The apparent range over which reliable laser measurements can be made includes all the nominal bevel angles normally used for spreading resistance profiling which are between $16'$ and 5° .

The ability of the laser technique to reproducibly measure junction depths is demonstrated in Fig. 7. The npn structure has junction depths of 0.5 and 2 μm . Each concentration profile was measured on a different chip taken from the same wafer. The triangles were extracted from a nominal $16'$ bevel with 10 μm stepping, while the circles were measured on a $34'$ bevel at 5 μm

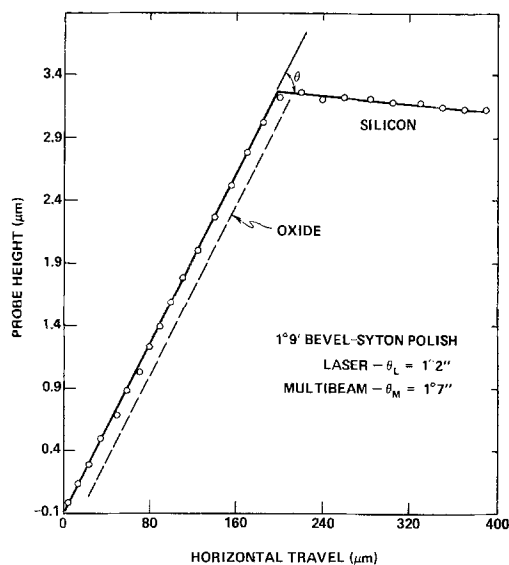


Fig. 5. Laser interferometer measurement of a beveled surface

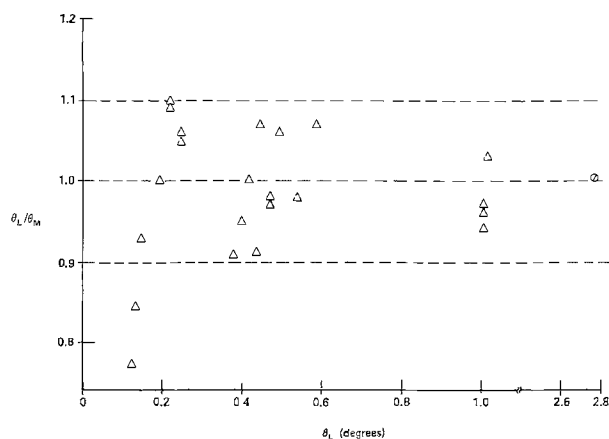


Fig. 6. Comparison of laser interferometer, θ_L , and multibeam, θ_M , angle measurement.

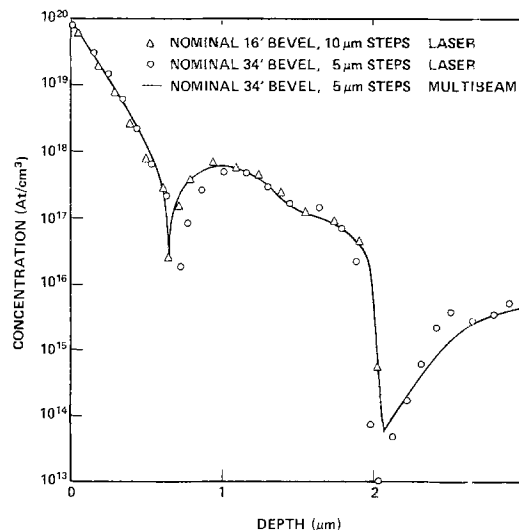


Fig. 7. Comparison of impurity profiles using laser angle measurements on $16'$ and $34'$ bevels and multibeam measurement on a $34'$ bevel.

stepping to maintain the same approximate vertical resolution. (For comparison, the solid line in Fig. 7 was derived from a $34'$ bevel at 5 μm steps and a multibeam angle measurement. The agreement in junction depths is within 500 \AA , which is the approximate spatial resolution for these particular angles and stepping distances.) The angles for both samples were determined by the laser interferometer and are shown in Fig. 8(a) and (b).

Up to this point the discussion has been limited to the ability of the laser interferometer to accurately and reproducibly measure bevel angles. The next section explores the potential of the laser technique to quantify the detailed contour of the beveled surface and demonstrate corresponding effects on corrected impurity profiles.

Bevel contour determination and effects.—For the analysis of spreading resistance data the beveled surface is usually assumed planar so that the distance between each measurement point is constant and equal to the product of the sine of the beveled angle and the stepping distance. In practice, the beveled surface can be rounded as has been shown qualitatively with surface profilometer measurements (4). Rounding will introduce nonuniformity in the actual distance between measurement points and may lead to erroneous concentration profiles if the effect is not included in the data analysis scheme. A rounded bevel is one possible cause for the previously reported (4, 5) anomalous depletion of impurities at the surface of diffused samples where none is expected. Since the laser interferometer technique measures the probe height at each point along the sample surface, the actual vertical distance between spreading resistance measurements can be determined and incorporated in the data analysis algorithm.

An example of a laser measurement on a rounded bevel is shown in Fig. 9. The rounded portion of the surface extends through the oxide and over 8000 \AA vertically into the silicon. The procedure for quantifying the contour measurement is schematically diagrammed in Fig. 10. A parabolic fit approximates the data in the rounded portion of the bevel while linear fits are sufficient outside the rounded area. The vertical distances between measurement points, the h_i , are calculated from the approximating functions. As can be seen in Fig. 10, rounding causes the vertical steps to increase with distance away from the original surface approaching a constant value equal to that derived from an angle measurement. The particular effect on the corrected impurity profile will depend on the data analysis algorithm but, in general, a decrease in h_i will result in an increased concentration, since the

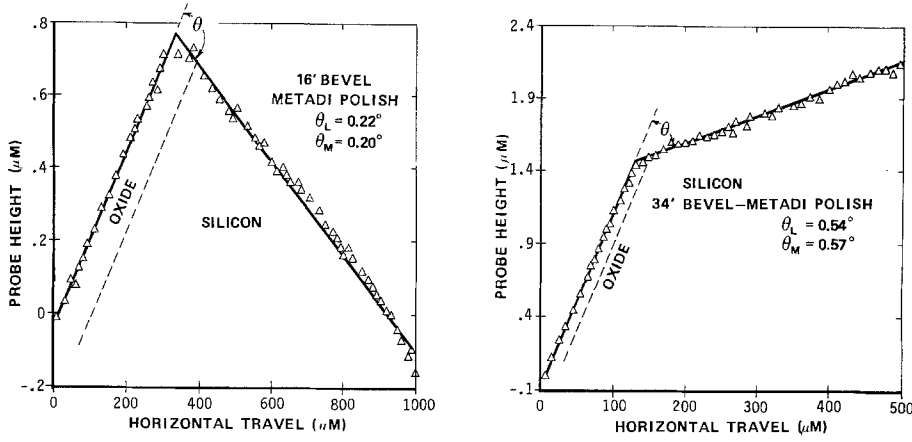


Fig. 8. Laser level contours for nominal 16' (a, left) and 34' (b, right) bevels.

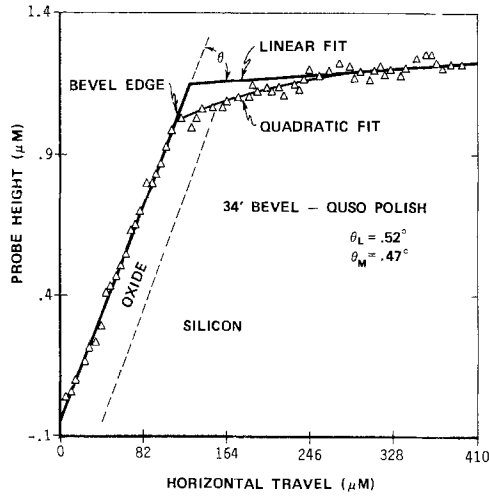


Fig. 9. Laser contour measurement demonstrating bevel rounding

concentration is roughly proportional to the local slope of the resistance data. Therefore, incorporation of the actual bevel contour will increase the near-surface concentration.

A typical result for a phosphorus predeposition is reproduced in Fig. 11. The laser data and corresponding linear and quadratic approximations to the bevel contour are shown in Fig. 11(a), and the resulting profiles determined by multilayer analysis are shown in Fig. 11(b). The circles are obtained when a planar bevel or uniform resolution is assumed while the triangles result when bevel rounding is included. Other measurement techniques and diffusion theory have confirmed that the solid solubility phosphorus redeposition should not deplete near the surface. The observed depletion of impurities is apparently an artifact introduced by the spreading resistance technique. Comparison of the two profiles indicates that the quantification

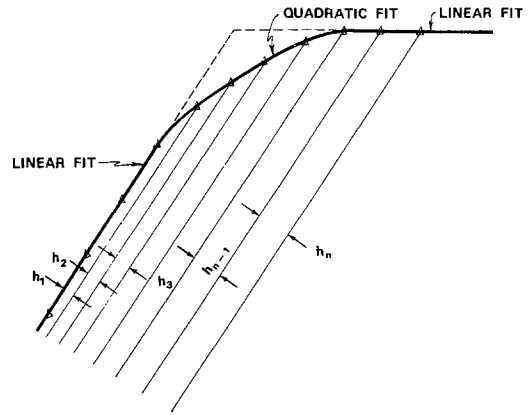


Fig. 10. Schematic of a rounded bevel contour and approximating functions.

and incorporation of bevel rounding improves the near-surface profile shape but fails to completely resolve the apparent anomaly.

To continue the investigation, the surface oxide was removed and both the spreading resistance and bevel contour were remeasured, Fig. 12. As expected, the spreading resistance (circles in Fig. 12) remained at a constant value far from the bevel edge in the original sample surface but begin to increase as the surface is approached. The accompanying surface contour clearly shows that the increase occurs before the bevel has penetrated the sample surface. It appears that the presence of the bevel influences the electric field distribution and hence the measured spreading resistance when the distance between the probes and bevel edge is approximately equal to the probe separation (100 micrometers for this measurement).

Exact analysis of the bevel influence on the measured resistance would require a three-dimensional solution

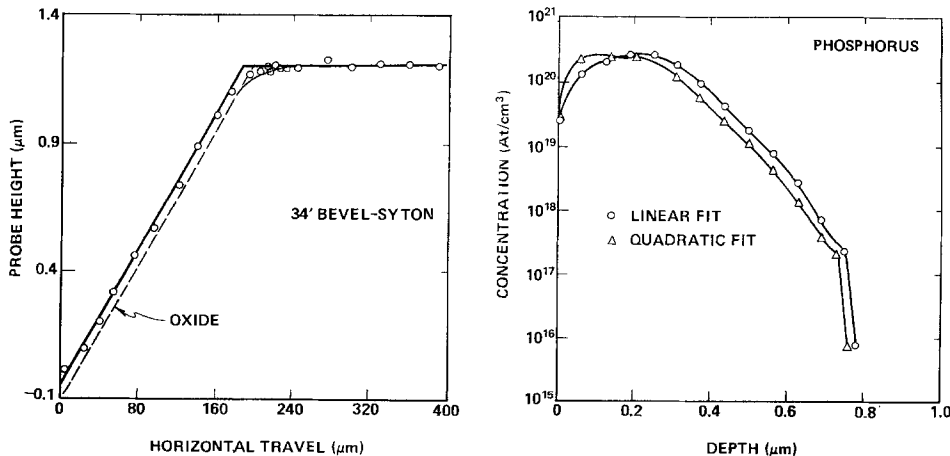


Fig. 11. Laser contour measurement (a, left) and resulting impurity profiles with and without bevel rounding (b, right).

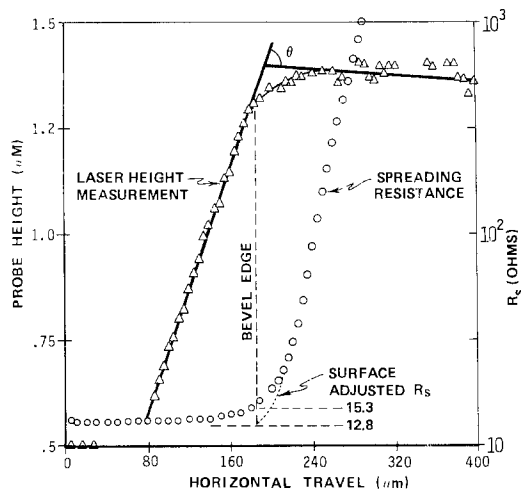


Fig. 12. Laser contour measurement and corresponding spreading resistance measurement after oxide removal.

of Laplace's equation. An empirical approach was adopted in order to estimate the relative effect of the three-dimensional geometry on the corrected impurity profile. This was accomplished by setting the spreading resistance at the bevel edge equal to the constant value measured on the original surface and adjusting the near-surface resistance values to obtain a smooth curve (the dashed line in Fig. 12). The adjusted spreading resistance values were analyzed first with uniform resolution, and then including the effect of bevel rounding. The results are compared in Fig. 13. Adjusting the surface resistance, assuming a planar bevel (the triangles), improves the surface concentration, but the most realistic profile is obtained when both the adjusted surface resistance and bevel rounding are included (the circles in Fig. 13). It appears that the anomalous depletion of impurities at the surfaces of spreading resistance profiles is influenced both by nonuniform spatial resolution due to bevel rounding and by the effect of the three-dimensional bevel geometry on the potential distribution.

The latter effect can be minimized by reducing the probe separation. Figure 14 compares spreading resistance measurements on a phosphorus diffusion with 100 and 25 μm probe separation. The difference between the resistance at the bevel edge and the constant value on the unbeveled surface decreases significantly with decreased probe separation.

Conclusion

A laser interferometer system has been successfully applied to the measurement of shallow bevel contours

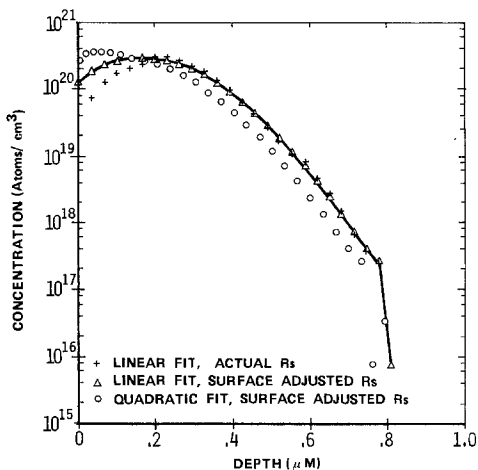


Fig. 13. Impurity profiles demonstrating the effects of bevel rounding and three-dimensional field distortion.

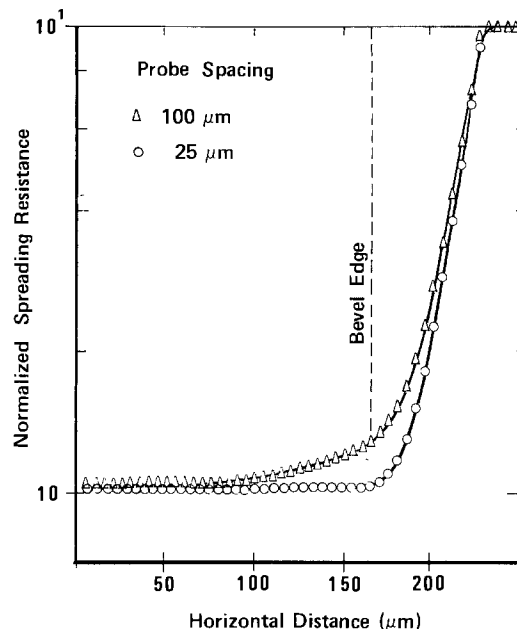


Fig. 14. Normalized spreading resistance measurements on a phosphorus diffusion with 25 and 100 μm probe separation.

for spreading resistance profiling. The new technique provides an automatic determination of bevel angles as well as a quantitative measure of the bevel contour. With adequate compensation for thermal expansion angles as small as 0.2° are accurately measured.

The quantitative contour information has been utilized to study the effects of bevel rounding on spreading resistance impurity profiles. The results imply that the apparent depletion of impurities at the sample surface is only partially caused by rounding. In addition, the three-dimensional bevel geometry tends to increase the spreading resistance near the bevel edge, resulting in lower impurity concentrations. Improved results are obtained when the quantitative bevel contour is taken into account and the near-surface spreading resistance is empirically adjusted.

Acknowledgments

The authors wish to thank Lynette Martinez, Bob Schuchard, Phil Nygren, Bob Stockwell, Gary Leo, Dan Struckman, Hee Gook Lee, and Skip Rung for contributions to this work.

Manuscript submitted Nov. 9, 1979, revised manuscript received June 18, 1980. This was Paper 292 presented at the Seattle, Washington, Meeting of the Society, May 21-26, 1978.

Any discussion of this paper will appear in a Discussion Section to be published in the June 1981 JOURNAL. All discussions for the June 1981 Discussion Section should be submitted by Feb. 1, 1981.

Publication costs of this article were assisted by the Hewlett Packard Laboratories.

REFERENCES

1. R. G. Mazur and D. H. Dickey, *This Journal*, **113**, 3 (1966).
2. R. R. Baldwin, G. B. Gordon, and A. F. Rudé, "Remote Laser Interferometry," *Hewlett Packard Journal*, **23**, No. 4 (December, 1971).
3. P. A. Schumann and E. E. Gardner, *This Journal*, **116**, 87 (1969).
4. D. C. D'Avanzo, R. D. Rung, A. Gat, and R. W. Dutton, *ibid.*, **125**, 1170 (1978).
5. G. A. Lee, in "Spreading Resistance Symposium," J. R. Ehrstein, Editor, NBS Special Publication 400-10 (June 1974).

Stabilization of n-CdSe Photoanodes in Nonaqueous $\text{Fe}(\text{CN})_6^{3-/4-}$ Electrolytes

Rommel Noufi,* Dennis Tench,* and Leslie F. Warren

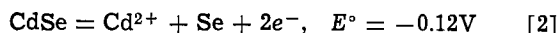
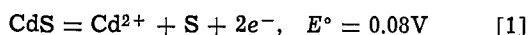
Rockwell International, Electronics Research Center, Thousand Oaks, California 91360

ABSTRACT

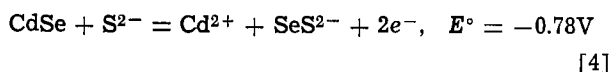
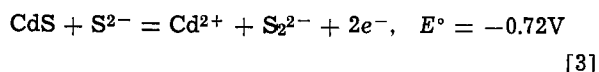
The systematic development of a nonaqueous ferro-ferricyanide electrolyte for stabilization of n-CdSe photoanodes is described. Selection of the solvent is discussed in terms of inherent stability provided, the rate of the redox reaction, the tendency toward specific adsorption of the redox species, and the equilibrium potential of the redox couple with respect to the flatband potential (attainable open-circuit voltage). Results are presented for cells of the type n-CdSe/methanol/ $\text{Fe}(\text{CN})_6^{3-/4-}$ /Pt which have been operated for up to 700 hr at 6 mA/cm² with no detectable degradation in either the electrode surface or the photoresponse.

It is generally recognized that the key problem with electrochemical solar cells is photodissolution of the required narrow-bandgap semiconductor anode material. To date, the best stability in such cells has been attained with n-type cadmium chalcogenide (CdX, where X = S, Se, or Te) (1-5) and n-GaAs (6, 7) electrodes stabilized by chalcogenide/polychalcogenide redox couples (e.g., $\text{Se}^{2-}/\text{Se}_x^{2-}$) in aqueous electrolytes. Photogenerated holes, which would otherwise lead to destruction of the semiconductor lattice, are preferentially consumed in the redox reaction. Unfortunately, the photocurrents in such systems, at least for CdX electrodes, still deteriorate slowly with time, especially at higher light intensities. In the case of CdX, this has been shown to involve chalcogenide exchange between the electrolyte and the electrode surface, possibly via photo-oxidation followed by reprecipitation (8-12).

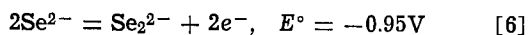
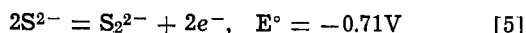
Suppression of the photodissolution of n-CdX anodes in aqueous systems by X^{2-} ions appears to result primarily from specific adsorption of X^{2-} at the electrode surface and concomitant shielding of the lattice ions from the solvent molecules, rather than from rapid annihilation of photogenerated holes. This is apparent from the dramatic shift in the dissolution potentials for electrolytes containing sulfide¹ (4, 13), i.e.



compared with²



Because of these shifts (which presumably also occur for Se^{2-} and Te^{2-}), X^{2-} oxidation has practically no energetic advantage compared to CdX dissolution in competing for photogenerated holes, i.e.



As a consequence of X^{2-} specific adsorption and the fact that the $\text{X}^{2-}/\text{X}_n^{2-}$ couples involve a two-electron

* Electrochemical Society Active Member.

Key words: electrochemical solar cells, stabilizing redox systems, methanol, ferro-ferricyanide.

¹ Note that a similar shift is expected for CdTe dissolution, but data do not appear to be available for this reaction.

² Note that these reactions are written as oxidations so that dissolution proceeds from left to right, but the E° values are reduction potentials (in agreement with accepted electrochemical practice). All voltages are referred to the saturated calomel electrode (SCE).

transfer, the overall redox process (adsorption/electron transfer/desorption) is also slow, which limits the degree of stabilization that can be attained in such systems. In addition, the type of interaction of the S^{2-} ions with the electrode surface which produces the shifts in the decomposition potentials also favors anion substitution in the lattice and the concomitant degradation of the photoresponse.

On the basis of these observations, fast one-electron redox couples which do not involve strong specific adsorption³ on the electrode surface appear to be the best candidates for stabilization of n-CdX electrodes against photodissolution. The importance of kinetics in the competition for photogenerated holes is evident from the fact that the $\text{Fe}(\text{CN})_6^{3-/4-}$ couple ($E^\circ = +0.12\text{V vs. SCE}$) partially quenches the photodissolution of n-CdS in water (14, 15) even though its reaction is thermodynamically unfavorable compared to dissolution ($E^\circ = +0.08\text{V}$). Of course, it is also evident from this example that fast electron transfer by itself is not sufficient to ensure stabilization. Added stability can be attained, however, through the use of nonaqueous solvents (16) which, in general, are inherently less ionizing than water, and also provide flexibility in gaining an energetic advantage for the redox reaction over photodegradation of the semiconductor.

In the present work, various nonaqueous ferro-ferricyanide electrolytes were evaluated for use in stabilizing n-CdSe photoanodes. This evaluation included determination of the inherent stability provided by each solvent, as well as the relevant kinetic and thermodynamic characteristics of the redox reaction in each system. The methanol/ $\text{Fe}(\text{CN})_6^{3-/4-}$ electrolyte chosen on the basis of these data was shown to completely stabilize n-CdSe photoanodes. This electrolyte also has the distinct advantage of being practically transparent to most of the solar spectrum, i.e., light energies below 2.6 eV.

Experimental Details

Solvent purification.—Reagent grade solvents (Baker Analyzed) were further purified under inert atmosphere before use. Alcohols were refluxed over Mg, and then fractionally distilled. Acetonitrile was stirred over calcium hydride, refluxed over P_2O_5 , distilled, and then stored over activated alumina. DMF (N,N-dimethylformamide) was stirred over activated alumina, then distilled under reduced pressure. Propylene carbonate was dehydrated over 4A molecular sieves.

Electrolyte preparation.—The tetraethylammonium cation was used as the counterion for the redox species

³ It should be mentioned, however, that some interaction between the redox species and the electrode surface may be desirable if it results in a negative shift in the flatband potential so that the open-circuit voltage of the cell is increased.

and the supporting electrolyte. With the smaller tetramethylammonium cation, solubilities are inadequate, whereas the larger tetrabutylammonium cation produces a negative shift in the E° value of the redox reaction (17). The perchlorate supporting electrolyte used in acetonitrile, ethanol, and dimethylformamide was obtained from Southwestern Analytical Company (Austin, Texas). The tetraethylammonium fluoroborate used in the methanol and propylene carbonate solvents was precipitated from a solution of Et_4NBr and HBF_4 in ethanol by addition of isopropanol, and was then recrystallized twice from ethanol.

Tetraethylammonium ferrocyanide was prepared by *in situ* electrochemical reduction of the ferricyanide species using Pt electrodes ($\sim 10 \text{ cm}^2$ each) in individual compartments of a Pyrex glass cell separated by a medium glass frit. During the electrolysis, which was performed in an inert atmosphere dry box, the cathode potential remained constant at about -0.45 V vs. SCE (saturated calomel electrode) and the current density was typically $3\text{--}5 \text{ mA/cm}^2$. The desired catholyte redox composition was attained by controlling the amount of charge passed. The tetraethylammonium ferricyanide starting material was prepared by a literature method (17).

Electrodes.—Reference electrodes were always isolated in a separate compartment which was connected to the main cell through a medium glass frit. Reference electrode potentials were checked periodically against that of the ferrocene-ferricenium reaction on Pt, which was found to be independent of the solvent ($0.40 \pm 0.02 \text{ V vs. SCE}$). The nonaqueous Ag/Ag^+ reference was used in acetonitrile. In the other solvents, both aqueous Ag/AgCl and saturated calomel reference electrodes were used with comparable results.

The Pt disk electrode (0.13 cm^2) used to study the kinetics of the $\text{Fe}(\text{CN})_6^{3-/4-}$ reaction was mounted concentric and flush with the end of a 12 mm diam Kel-F cylinder by hot pressing. After mounting, the electrode was polished on successively finer aqueous alumina powder slurries to $1 \mu\text{m}$ particle size, and was then cleaned ultrasonically in water. Before each use, the electrode was further cleaned by immersion in boiling concentrated nitric acid.

The n-CdSe electrodes ($0.18 \text{ cm}^2 \times 1 \text{ mm}$ thick) were cut from rods supplied by Cleveland Crystals (Cleveland, Ohio) and had from 10^{17} to 10^{18} carriers/ cm^3 . Ohmic contacts were made with an In-Ga alloy. Before use, n-CdSe electrodes were polished to $0.05 \mu\text{m}$ particle size, then etched in 3M nitric acid or a 1:25 mixture of concentrated nitric and hydrochloric acids (with comparable results). For long-term studies, n-CdSe electrodes were mounted in Kel-F by hot-pressing. Results for electrodes mounted in silicone adhesive/sealant (Dow Corning Corporation, Midland, Michigan) were comparable.

Electrochemical measurements.—All electrochemical measurements were made in Pyrex glass cells inside an inert atmosphere dry box using a PAR Model 173 Potentiostat/Galvanostat in conjunction with a PAR Model 175 Universal Programmer. The effects of solution resistance were always eliminated by electronic IR compensation. The a-c impedance of n-CdSe electrodes was determined from the current response to a small a-c voltage (5 mV rms) measured by an Ithaco Dynatrac III Lock-In Analyzer. Electrodes were illuminated by a tungsten-halogen lamp through a quartz window. The illumination intensity was measured with a Pyroelectric Radiometer (Molelectron, Sunnyvale, California).

Results and Discussion

Inherent electrode stability.—The inherent stability of n-CdSe electrodes in various solvents was investigated by following the photocurrent at the same degree of band bending as a function of time under illumination at constant intensity in the absence of redox

species in the electrolyte. Data are shown in Fig. 1. Since in the absence of electrode photodegradation the rate of charge carrier recombination should be high, lower initial photocurrent and fast decay are taken as indications of intrinsic stability. Based on these criteria, Fig. 1 indicates that the resistance of CdSe to photodecomposition increases in the order: water \ll methanol \cong ethanol $<$ N,N-dimethylformamide $<$ propylene carbonate \cong acetonitrile.

Kinetic considerations.—The kinetics of the $\text{Fe}(\text{CN})_6^{3-/4-}$ redox reaction in the various solvents were investigated using a rotating Pt disk electrode (18). Typical voltammograms obtained in methanol, ethanol, acetonitrile, and propylene carbonate are shown in Fig. 2. The plateau currents observed for both the anodic and cathodic branches were found to be diffusion limited in all cases. As shown in Table I, the equilibrium potential for the $\text{Fe}(\text{CN})_6^{3-/4-}$ reaction correlates well with the solvent acceptor number (17), which reflects the stabilization of the iron(II) complex by outer-sphere solvent interactions. Note that there is no correlation with the dielectric constant. The equilibrium potential can be varied almost continuously through the use of mixed solvents. Because of the extremely negative E° value for the $\text{Fe}(\text{CN})_6^{3-/4-}$ couple in dimethylformamide, which ensures a low open-circuit voltage, since based on the photocurrent onset the flatband potential is about -1.1 V , this solvent was not considered further.

The $\text{Fe}(\text{CN})_6^{3-/4-}$ reaction is generally reversible as indicated by the voltammograms in Fig. 2, and linear kinetic plots (19) of the type shown in Fig. 3 for the methanol electrolyte were generally obtained. The current function plotted in Fig. 3 includes corrections for the back reaction and mass transport for both the reactant and product; i = current, i_f and i_b = the diffusion-limiting currents for the forward and back reactions, respectively, E = electrode potential, and E_r = rest potential. When the redox reaction is reversible and specific adsorption does not occur, the slope of the kinetic plot ("Tafel" slope) should be 120

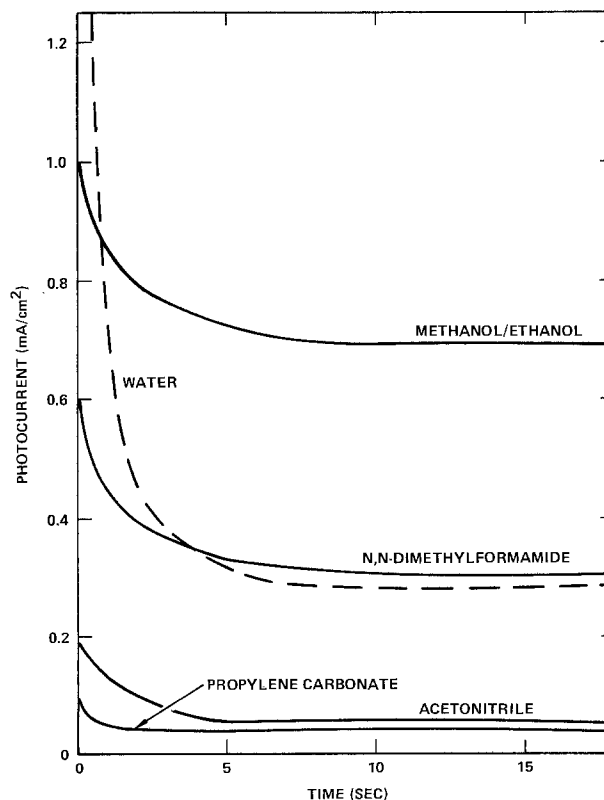


Fig. 1. Photocurrent decay for n-CdSe photoanodes in various solvents at 0.9V positive of the flatband potential.

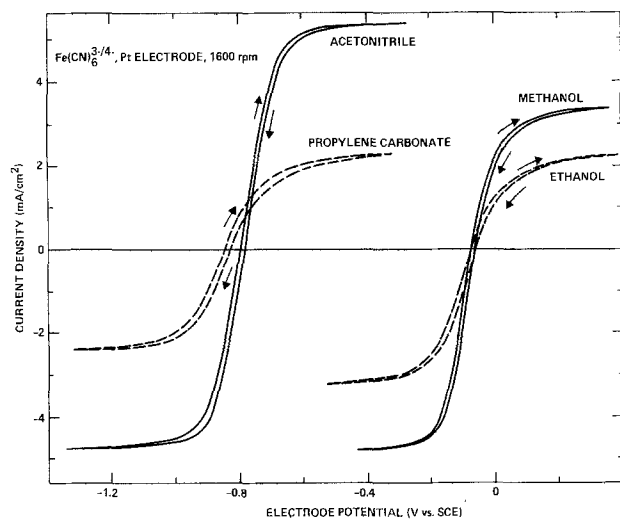


Fig. 2. Cyclic voltammograms at 100 mV/sec for a Pt disk electrode rotating at 1600 rpm in various solvents containing 0.01M tetraethylammonium ferro- and ferricyanide, and 0.1M tetraethylammonium supporting electrolyte (perchlorate in acetonitrile and ethanol, fluoroborate in methanol, and propylene carbonate).

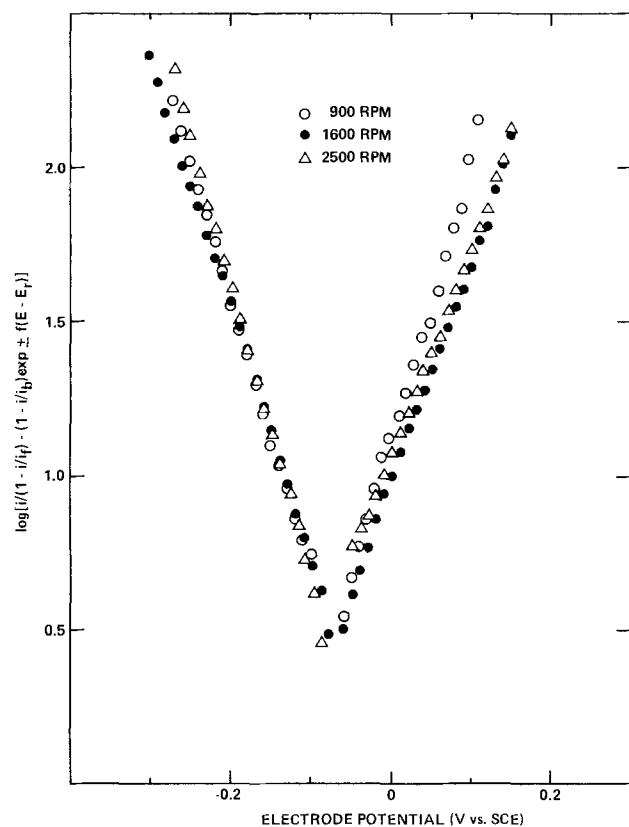


Fig. 3. Kinetic plots for the $\text{Fe}(\text{CN})_6^{3-}/4-$ redox reaction on a rotating Pt disk electrode in a methanol electrolyte (conditions same as Fig. 2).

mV/decade (assuming that the symmetry factor, α , is 0.5) and extrapolation to the rest potential yields the apparent exchange current (and consequently the apparent rate constant). When specific adsorption occurs, the "Tafel" slope is generally higher.

Kinetic data for the $\text{Fe}(\text{CN})_6^{3-}/4-$ couple on Pt are summarized in Table II. The electron transfer rate decreases with the solvent in the order methanol > ethanol > acetonitrile > propylene carbonate, by about a factor of 1/3 in each case. The Tafel slopes for ethanol and propylene carbonate of 130 mV/decade for the cathodic branch and 170–180 mV/decade for the

Table I. Correlation of the $\text{Fe}(\text{CN})_6^{3-}/4-$ redox potential with the solvent acceptor number

Solvent	Dielectric constant	Acceptor number*	Equilibrium potential (V vs. SCE)
Methanol	32.7	41.3	-0.08
Ethanol	24.5	37.1	-0.10
Acetonitrile	38.8	18.9	-0.78
Acetonitrile-10% methanol	—	—	-0.50
Propylene carbonate	69.0	18.3	-0.82
Dimethylformamide	36.7	16.0	-1.08

After G. Gritzner et al. (17).

Table II. Kinetic data for the ferri-ferricyanide couple at a rotating Pt disk electrode in nonaqueous solvents containing tetraethylammonium as the cation

Solvent	Anodic Tafel slope (mV/decade)	Cathodic Tafel slope (mV/decade)	Apparent rate constant (cm/sec)
Methanol	120	120	3.2×10^{-3}
Ethanol	170	130	1.3×10^{-3}
Acetonitrile	120	~120	0.4×10^{-3}
Propylene carbonate	180	130	0.1×10^{-3}

anodic branch suggest increasing specific adsorption at more anodic potentials in these solvents, which is reasonable for a highly charged anionic redox species.

These Pt data are indicative of the inherent kinetic limitations of the $\text{Fe}(\text{CN})_6^{3-}/4-$ couple in each solvent, but caution must be exercised in extrapolating to n-CdSe electrodes. For example, it should be kept in mind that specific adsorption effects may vary with the electrode material. Nonetheless, the trends observed for Pt should also be valid for n-CdSe.

Thermodynamic considerations.—Flatband potentials were determined for n-CdSe in the various solvents [containing $\text{Fe}(\text{CN})_6^{3-}/4-$] from a-c impedance measurements. A typical Mott-Schottky plot is shown in Fig. 4. The results are summarized in Table III.

System selection.—Although methanol provides the lowest inherent stability of the solvents investigated, this is more than compensated by fast electron transfer, no specific adsorption, and a favorable flatband potential, so that this solvent appears to be the most promising for stabilization of CdX photoanodes with the ferro-ferricyanide couple. If high inherent stability were weighted more heavily, acetonitrile would then appear most attractive. The choice of methanol seems to be vindicated by cyclic voltammetric data at 200 mV/sec for static n-CdSe electrodes under illumination at low light intensities in methanol and acetonitrile electrolytes containing 0.1M $\text{Fe}(\text{CN})_6^{3-}/4-$ and 0.1M supporting electrolyte. For methanol, a stable anodic photocurrent plateau is observed from -0.7 to 0.1V vs. SCE, which indicates that photogenerated holes are collected at high efficiency over a wide potential range. For acetonitrile, the photocurrent begins to increase (above the plateau level) at about -0.5V, which indicates that some of the holes are not being collected by the redox couple. Furthermore, $\text{Fe}(\text{CN})_6^{4-}$ is reported to be unstable in acetonitrile solution (17).

Table III. Solvent dependence of the flatband potential and photocurrent onset for n-CdSe

Solvent	Flatband potential (V vs. SCE)	Photocurrent onset (V vs. SCE)
Acetonitrile	-1.2	-1.1
Propylene carbonate	-1.1	-1.0
Acetonitrile/10% methanol	-1.0	-1.0
Methanol	-0.9	-0.8
Ethanol	-0.9	-0.8

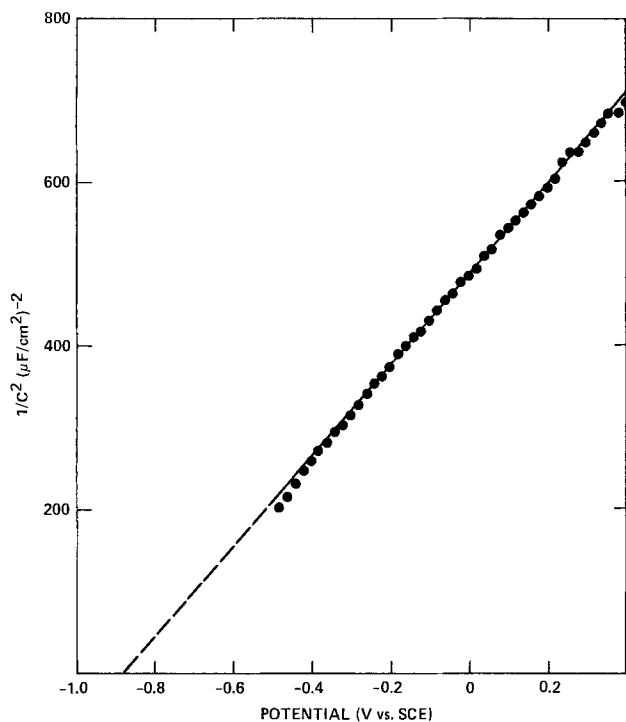


Fig. 4. Mott-Schottky plot for n-CdSe in methanol/0.01M $\text{Fe}(\text{CN})_6^{3-/4-}$ /0.1M Et_4NBF_4 solution.

Evaluation of the n-CdSe/methanol/ $\text{Fe}(\text{CN})_6^{3-/4-}$ system.—The long-term stability of n-CdSe photoanodes in the methanol/ferro-ferricyanide system was investigated using tungsten-halogen illumination of about 85 mW/cm^2 intensity. The current at single crystal n-CdSe photoanodes remained constant at 6 mA/cm^2 (conversion efficiency of $\sim 3.5\%$) for as long as 700 hr in a stirred methanol electrolyte containing 0.4 M each of tetraethylammonium $\text{Fe}(\text{CN})_6^{3-/4-}$ plus 0.1 M tetraethylammonium fluoroborate. No deterioration of the electrode surface or weight loss was detected although the charge passed was equivalent to 81 times the weight of the crystal. Since these studies were designed to demonstrate stability, no attempt was made to optimize the cell performance characteristics which were undoubtedly diminished because of the high carrier concentration of the n-CdSe electrodes (10^{17} – $10^{18}/\text{cm}^3$). A current-cell voltage curve for this system with a Pt counterelectrode is given in Fig. 5. It was also demonstrated that the stability of n-CdSe photoanodes in methanol/ferro-ferricyanide is not sensitive to traces of water, as shown in Fig. 6.

Work is currently underway to optimize performance of the n-CdSe/methanol/ $\text{Fe}(\text{CN})_6^{3-/4-}$ system for both single crystal and polycrystalline electrodes. Considerable attention is focused on the electrolyte. At higher redox couple concentrations, ion pairing, specific adsorption, and impurity effects become more important. This necessitates development of better methods of preparing and purifying materials, and consideration of alternate counterions (e.g., dications) and solvent mixtures. With redox electrolytes prepared by a new chemical method, sustained photocurrents at n-CdSe electrodes of about 17 mA/cm^2 have recently been attained. These results, which will be elaborated upon in a future publication, illustrate the potential of this system.

Conclusions

The thermodynamic and kinetic considerations outlined here seem to provide a rational basis for development and evaluation of new redox systems for stabilization of semiconductor anodes against photo-degradation. These considerations include the inherent stability provided by the solvent, the rate of the redox reaction, the tendency of the redox species to spe-

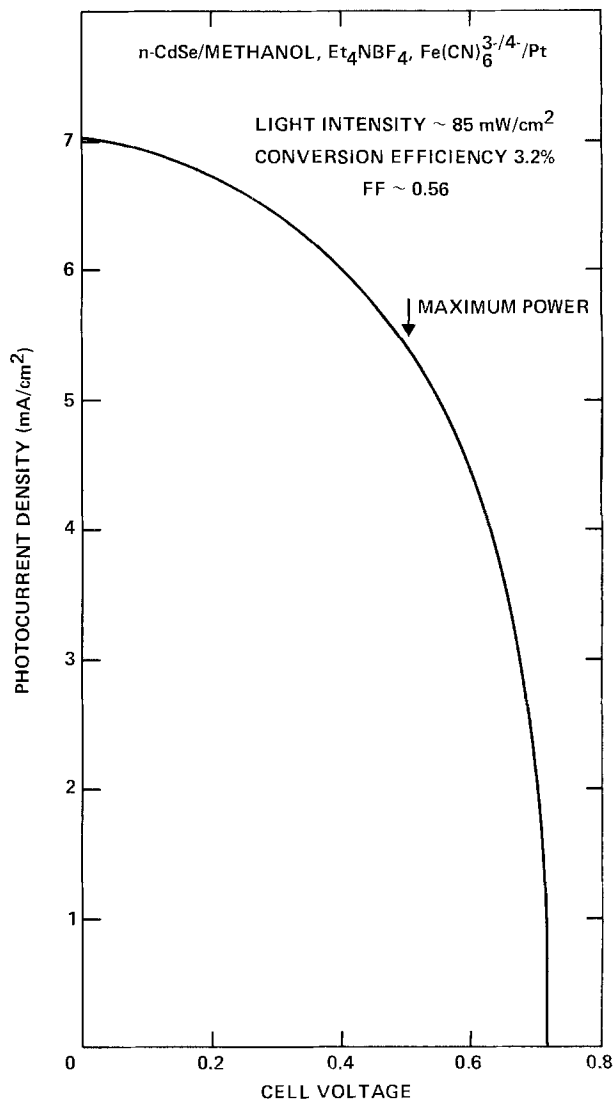


Fig. 5. Photocurrent density vs. voltage for the cell n-CdSe/methanol/0.4M $\text{Fe}(\text{CN})_6^{3-/4-}$ /0.1M Et_4NBF_4 /Pt under illumination at 85 mW/cm^2 .

cifically adsorb, and the equilibrium potential of the redox couple with respect to the flatband potential.

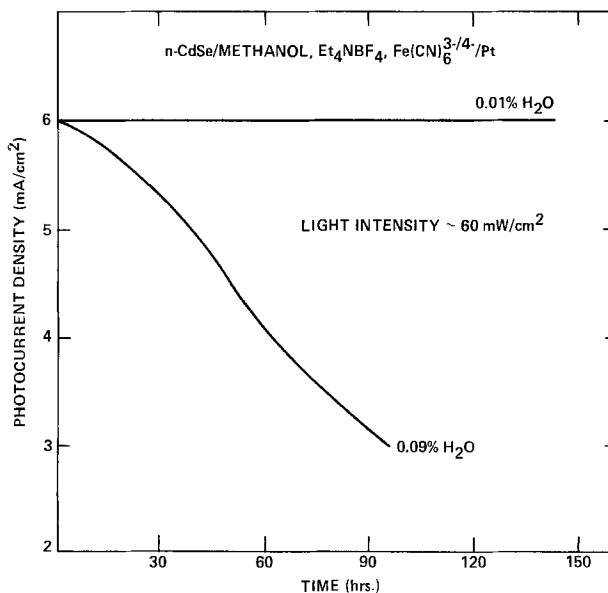


Fig. 6. Photocurrent density as a function of time for the cell described in Fig. 5 after addition of water.

Stabilization of n-CdSe photoanodes has been attained in the methanol/ $\text{Fe}(\text{CN})_6^{3-/4-}$ system.

Acknowledgments

The authors gratefully acknowledge support of this work by the Department of Energy through subcontract number XP-9-8002-1 from the Solar Energy Research Institute.

Manuscript submitted April 7, 1980; revised manuscript received May 15, 1980.

Any discussion of this paper will appear in a Discussion Section to be published in the June 1981 JOURNAL. All discussions for the June 1981 Discussion Section should be submitted by Feb. 1, 1981.

Publication costs of this article were assisted by Rockwell International.

REFERENCES

1. A. B. Ellis, S. W. Kaiser, and M. S. Wrighton, *J. Am. Chem. Soc.*, **98**, 1635, 6418, 6855 (1976).
2. G. Hodes, J. Manassen, and D. Cahen, *Nature (London)*, **261**, 403 (1976).
3. B. Miller and A. Heller, *ibid.*, **262**, 680 (1976).
4. A. B. Ellis, S. W. Kaiser, J. M. Botts, and M. S. Wrighton, *J. Am. Chem. Soc.*, **99**, 2839 (1977).
5. A. Heller, K. C. Chang, and B. Miller, *This Journal*, **124**, 697 (1977).
6. K. C. Chang, A. Heller, B. Schwartz, S. Menezes, and B. Miller, *Science*, **196**, 1097 (1977).
7. B. A. Parkinson, A. Heller, and B. Miller, *This Journal*, **126**, 954 (1979).
8. H. Gerischer, *J. Electroanal. Chem. Interfacial Electrochem.*, **82**, 133 (1977).
9. H. Gerischer and J. Gobrecht, *Ber. Bunsenges. Phys. Chem.*, **82**, 520 (1978).
10. A. Heller, J. P. Schwartz, A. G. Vadinsky, S. Menezes, and B. Miller, *This Journal*, **125**, 1156 (1978).
11. D. Cahen, G. Hodes, and J. Manassen, *ibid.*, **125**, 1623 (1978).
12. R. Noufi, P. Kohl, J. Rogers, Jr., J. White, and A. J. Bard, *This Journal*, **126**, 949 (1979).
13. W. M. Latimer, "Oxidation Potentials," 2nd ed., Prentice Hall Inc., Englewood Cliffs, New Jersey (1952).
14. H. Gerischer, *J. Electroanal. Chem. Interfacial Electrochem.*, **58**, 263 (1975).
15. T. Inoue, T. Watanabe, A. Fujishima, K. Honda, and K. Kohayakawa, *ibid.*, **124**, 719 (1977).
16. P. A. Kohl and A. J. Bard, *This Journal*, **126**, 603 (1979).
17. G. Gritzner, K. Danksagmuller, and V. Gutmann, *J. Electroanal. Chem. Interfacial Electrochem.*, **72**, 177 (1976).
18. V. G. Levich, "Physicochemical Hydrodynamics," Prentice-Hall, Englewood Cliffs, New Jersey (1962).
19. P. Delahay, "Double Layer and Electrode Kinetics," p. 171, Interscience, New York (1965).

Band Bending and Passivation Studies of GaAs Grain Boundaries

J. W. McPherson, W. Collis, E. Stefanakos, A. Safavi, and A. Abul-Fadi

School of Engineering, North Carolina Agricultural and Technical State University,
Greensboro, North Carolina 27411

ABSTRACT

The zero-bias band-bending properties of grain boundary (g-b) interfaces showing pronounced rectifying characteristics in polycrystalline GaAs were investigated both experimentally and theoretically. A strongly rectifying g-b presents a potential barrier to the majority carrier leading to a large g-b resistance R_B . R_B for individual g-b's was determined by passing a constant current normal to the g-b and monitoring the voltage drop, as a function of temperature, associated with the thermionic current. The band-bending $e\phi_b$, as a function of donor density N_D , was obtained from a plot of the activation energy $k_B(TR_B)$ vs. $(1/T)$. A theoretical fit of the $e\phi_b$ vs. N_D curve gave a dominant density of defect acceptor states at the g-b interface: $\sigma_1 = 5.2 \times 10^{11}/\text{cm}^2$ at 0.41 eV and $\sigma_2 = 9.0 \times 10^{11}/\text{cm}^2$ at 0.90 eV below E_c . These acceptor levels have been tentatively identified with the dangling bonds of A- and B-type dislocations which normally occur at III-V compound-semiconductor g-b's. In addition, the use of potassium as a grain boundary passivating dopant is discussed. After diffusing K into the g-b, a lower R_B and reduction in the g-b rectifying properties were noted.

The use of GaAs for large scale generation of electrical power depends on being able to grow thin layers ($\cong 1 \mu\text{m}$) of GaAs on a cheap foreign substrate. Without a recrystallization effort, present growth techniques (1, 2) have produced only fine grain polycrystalline films with an average grain size $d \leq 1 \mu\text{m}$, well below the required average grain size of $10 \mu\text{m}$ (3). The grain boundaries (g-b's) severely limit collection efficiency (best reported efficiency for polycrystalline GaAs is 6.3%) (4) for two reasons: (i) the g-b serves as a recombination region thereby reducing the short-circuit current and (ii) the high conductivity along the g-b can produce a shunting

of the device with a reduction in open-circuit voltage. Since the g-b's so severely limit the collection efficiency, it was felt that a better understanding of GaAs g-b physics might lead to possible passivation ideas, and this was the impetus for the research.

Our experimental studies closely parallel the earlier works of Seto (5) and Seager and Castner (6) on the electronic properties of polycrystalline silicon films. We have chosen to use bicrystalline GaAs samples so that single g-b characterization could be facilitated. In the following section we describe sample preparation and characterization of the GaAs bicrystalline samples. There, we report the electrical resistance measurements conducted on the samples and

Key words: GaAs grain boundary interface states.

present the band bending *vs.* donor density data. Next, we discuss some of the underlying physics of *g-b*'s in GaAs and present a *g-b* density of defect states calculation based on the band-bending data for strongly rectifying grain boundaries. *G-B* passivation efforts are reported. The article is concluded with a discussion of results.

Experimental Studies

Sample preparation and grain boundary characterization.—The large grain polycrystalline GaAs wafers used in the experiments were supplied by Morgan Semiconductors. The wafers ($>10 \text{ cm}^2$) were cut from *n*-type, boat-grown, undoped and Si-doped crystals. The ingots were intended to be single crystals but a few independent nucleation centers in the boule produced a very large grain (some wafers contained only 5 or 6 grain boundaries) polycrystalline material. The use of large grain material allowed the carrier concentration to be determined by calculating the resistivity of single-grain filament sections and referring to published data on resistivity *vs.* carrier concentration for GaAs (14).

The samples used for *g-b* investigations were in the form of bars, approximately $0.1 \times 0.05 \text{ cm}^2$ in cross-sectional area, cut with a wire saw from the large grain polycrystalline GaAs wafers. Included in the sample's length was a single *g-b* running transverse to the long dimension of the sample, as shown in Fig. 1. The sawed and lapped surfaces of the bar-like samples were degreased, then polished by etching in $5\text{H}_2\text{SO}_4:1\text{H}_2\text{O}_2:1\text{H}_2\text{O}$ for 2 min. Ohmic contacts were formed on the *n*-type GaAs by alloying Sn dots at 450°C for 1 min in a hydrogen atmosphere. As shown in Fig. 1, the two dots on the same single-grain region could be used to verify the ohmic nature of the contacts. To insure that the samples were bicrystals, both cathodoluminescence (CL) and electron beam induced current (EBIC) studies were performed using a scanning electron microscope (SEM).

Due to problems of poor contrast on a smoothly polished GaAs surface, *g-b*'s can be difficult to detect in the normal secondary-electron mode of SEM operation and, if detected, give no information about the electrical characteristics of the *g-b*. However, by using a CL detector (8), regions of nonradiative recombination can be contrasted and resolved as is shown in the *g-b* micrograph of Fig. 2. The main advantage with CL is the fact that no electrical contacts to the sample are needed. The main problem encountered using CL microscopy is its dependence on surface morphology and electron beam penetration depth R ($R = 0.027E_b^{1.46} \mu\text{m}$, where the electron beam energy is in kV) (9). Light emitted from a depth R can be absorbed before reaching the surface or, the light upon reaching a rough surface, can be scattered thus limiting resolution. These problems are avoided using EBIC. Here the electron beam is scanned over the sample generating electron-hole pairs up to a depth R . A space charge region in the crystal can serve to separate the pairs for collection. The resulting current can be amplified and used for imaging. Using the space charge region associated with a *g-b* to perform the separation, we show in Fig. 3 an EBIC micrograph taken of one of the bicrystals.

After the bicrystalline nature of the samples was established using CL and EBIC, preliminary characterization of the filamentary samples included the observation of the current (*I*)-voltage (*V*) character-

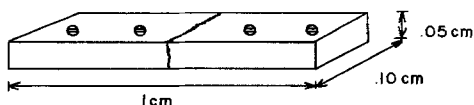


Fig. 1. The typical bar-like bicrystalline samples and the ohmic contact configuration used in the electrical measurements.

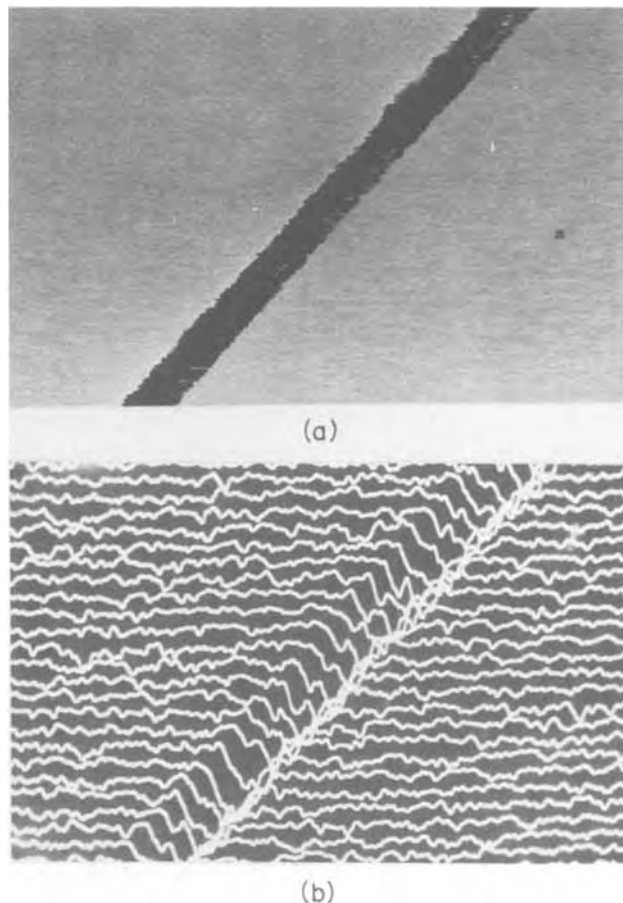


Fig. 2. CL and CL intensity line-scan micrographs of a single *g-b* ($500\times$). (a) Shows CL imaging with the *g-b* appearing as a very dark diagonal line of nonradiative recombination. (b) Shows the reduction in intensity of the CL signal as the electron beam is rastered over the *g-b* region.

istics of the *g-b*'s. *I-V* curves for several bicrystalline samples taken from different regions of the same wafer showed a remarkable difference in rectifying characteristics. Figure 4 shows the *I-V* curves for three *g-b*'s taken from the same wafer. Figure 4(a) indicates that this *g-b* has ohmic characteristics, indicative of scattering as the majority carriers traverse the *g-b* interface. Figure 4(b) shows a slight rectification indicating that a weak potential barrier must be negotiated by the majority carrier. Figure 4(c) shows that the rectification is large, indicating a significant *g-b* potential barrier.

Some of the ohmic *g-b*'s could be explained, at least qualitatively, in terms of an extended Read dislocation model for *g-b*'s in GaAs as presented by McPherson *et al.* (10). According to dislocation theory, at donor levels $\cong 10^{16}/\text{cm}^3$ the space charge cylinder surrounding the dislocation core is expected to be of radius $R_0 \cong 0.1 \mu\text{m}$. For low angle *g-b*'s, the spacing between dislocations D is greater than $2R_0$. A carrier approaching such a *g-b* may traverse the interface by scattering, without having the required energy to go over the potential barrier. To substantiate the model, the dislocation spacing was observed experimentally.

A sample showing ohmic-like characteristics was etched with an inhibited Schell's reagent ($200 \text{ HNO}_3:600 \text{ H}_2\text{O}:1 \text{ butylamine}$) (11) for 15 min at 80°C . An optical micrograph of the *g-b* (Fig. 5) after etching reveals a low angle *g-b* structure, *e.g.*, individual dislocation etch pits could be resolved with a spacing of $D \cong 1 \mu\text{m}$. This large value for D would indicate that the dislocation space charge cylinders do not overlap leading to a porosity in the *g-b* interface. Not all observed ohmic-like *g-b*'s, with random grain

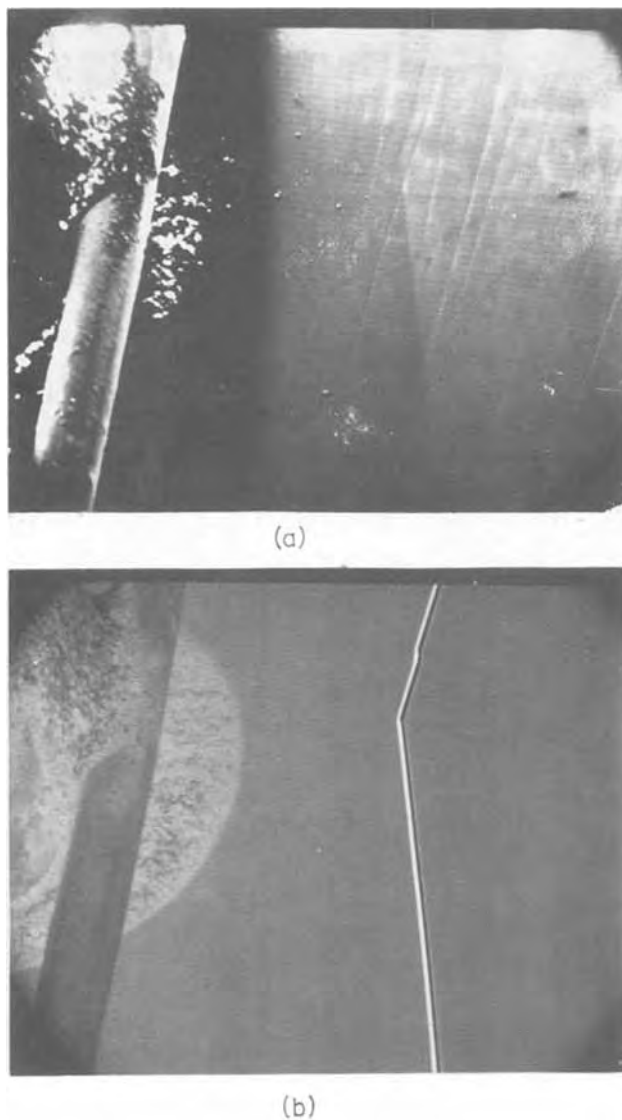


Fig. 3. SEM and EBIC-SEM micrographs of the same g-b ($200\times$). (a) Shows an SEM micrograph of the g-b (to the right of contact and lead wire) and illustrates the problem of poor contrast on polished GaAs. (b) EBIC-SEM micrograph of the same area makes the g-b clearly discernible.

orientation, could be tested for their assumed low angle nature because of the reactive nature of the etchant, *i.e.*, the etchant reveals dislocations only on low index planes (12), in particular the (111) and $(\bar{1}\bar{1}\bar{1})$. The dislocation density determination could be made only on a few samples with proper orientation in an effort to extract a qualitative understanding of why at least some of g-b's have ohmic-like characteristics.

We expect that the slightly rectifying g-b's are of higher angle thus leading to a partial overlap of the space charge cylinders and that in the case of the highly rectifying g-b's the overlap is complete ($D \ll 2R_0$). However, this point could not be verified by a dislocation density determination because the etchant tended to etch the rectifying g-b's uniformly so that individual dislocation etch pits could not be resolved.

This research was focused on the highly rectifying g-b's. The quantitative analysis of our g-b band bending results relied on the theory as presented by Seager and Castner (15) for g-b band bending in polycrystalline silicon. Since this theory does not depend explicitly on dislocation densities and tilt angles, these parameters were not pursued further.

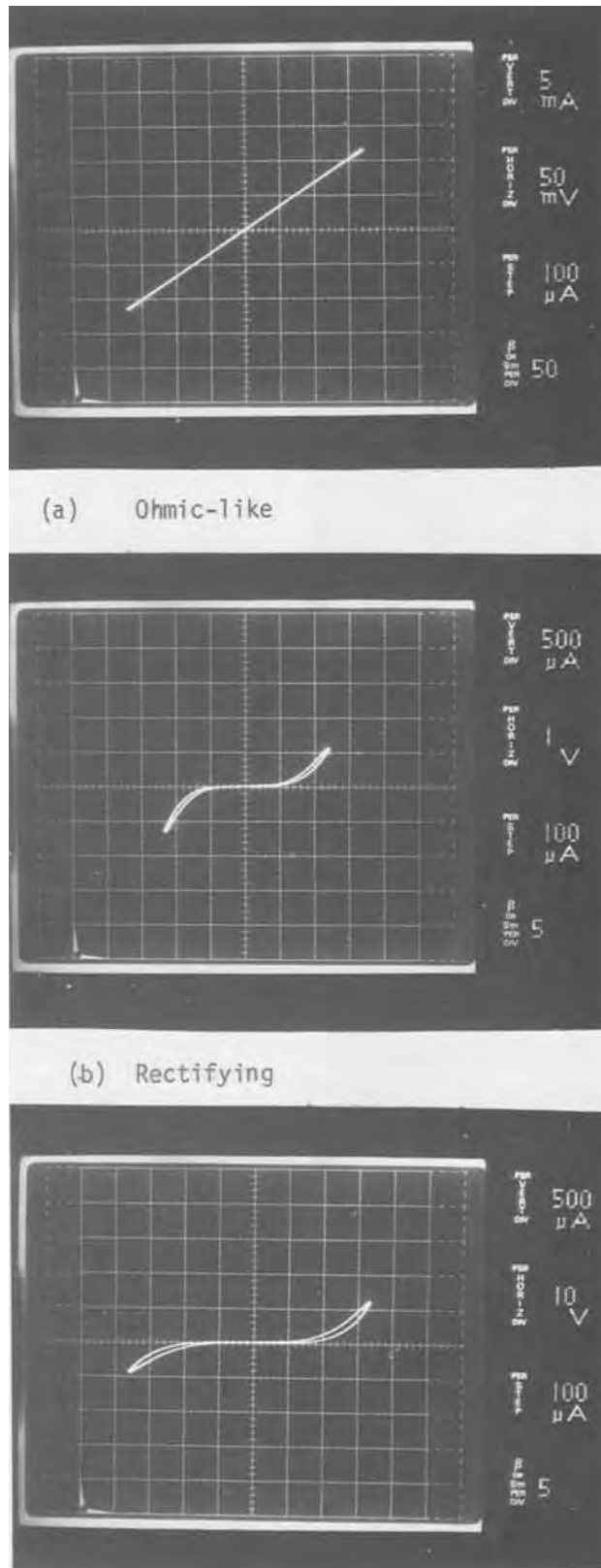


Fig. 4. *I-V* characteristics of a variety of g-b's taken from the same GaAs wafer. (a) Shows the *I-V* characteristics of an ohmic-like g-b (5 mA per vertical division, 50 mV per horizontal division). (b) Shows the *I-V* characteristics of a rectifying g-b (500 μ A per vertical division, 1V per horizontal division). (c) Shows the *I-V* characteristics of strongly rectifying g-b (500 μ A per vertical division, 10V per horizontal division).

Grain boundary band-bending studies.—Due to the disruption of the crystalline matrix, a g-b in an n-type semiconductor generally produces deep acceptor states associated with the distorted or broken bonds (13).

As the electrons leave the Fermi level to take up residence on the g-b, a space charge region develops in the grains adjacent to the g-b. This space charge separation produces a bending of the bands such as to make the addition of the next electron to the g-b more difficult. Electrons are added to the g-b until the work required, to add an additional one, produces a free energy change $\cong 0$. The band bending produced by a g-b is schematically represented in Fig. 6.

The bent bands present a potential barrier to the majority carrier leading to a large g-b resistance R_B . R_B for individual g-b's was determined by passing a constant current (0.01 μA through the outer two contacts shown in Fig. 1) and monitoring (inner two contacts) the voltage drop associated with the thermionic current density J_{th} (14, 15)

$$J_{th} = A^* T^2 \exp\left(\frac{-e\Phi_b'}{k_B T}\right) \left[\exp\left(\frac{eV}{k_B T}\right) - 1 \right] \quad [1]$$

with A^* the Richardson constant, T the temperature, $e\Phi_b'$ the barrier height, and V the applied voltage.

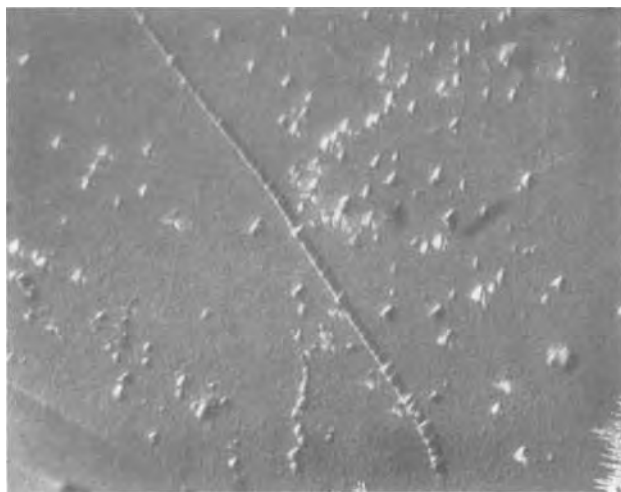


Fig. 5. Optical micrograph (400 \times) of an etched ohmic-like g-b. The micrograph reveals that the individual dislocation etch pits along the g-b are separated approximately 1 μm .

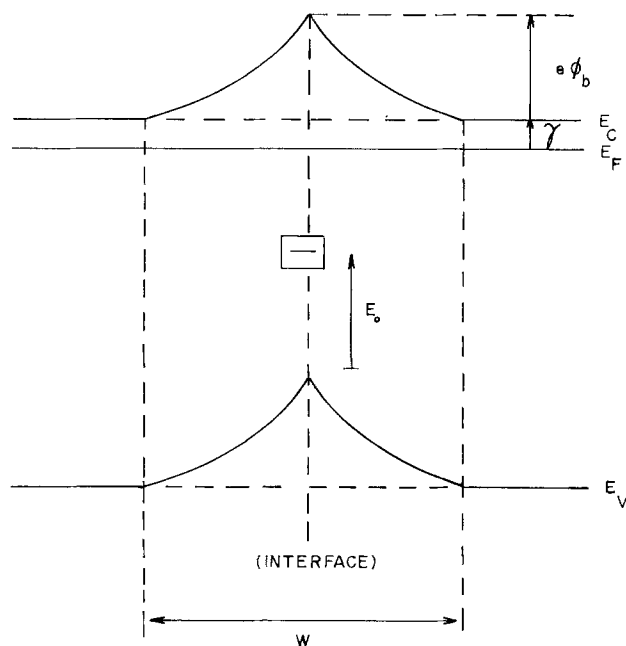


Fig. 6. Band bending $e\Phi_b$ which occurs at a g-b due negative charge accumulation at the interface.

Here it is assumed that only those carriers with sufficient thermal energy to surmount the potential barrier can contribute to the current. (Tunneling is expected to be negligible in the donor range ($<10^{18}/\text{cm}^3$) of samples investigated.) Expanding the last equation with $eV \ll k_B T$, we can write the g-b resistance as

$$R_B = \frac{V}{J} = \left(\frac{k_B}{eA^*} \right) [\exp(-e\Phi_b'/k_B T)/T] (\Omega \cdot \text{m}^2) \quad [2]$$

Rewriting Eq. [2] in an activation energy form, we have

$$k_B \frac{\partial \ln(TR_B)}{\partial \left(\frac{1}{T}\right)} = e \left[\Phi_b' - T \frac{\partial \Phi_b'}{\partial T} \right] \quad [3]$$

The relationship between the barrier height Φ_b' and band bending Φ_b is given by

$$\Phi_b' = \Phi_b + \gamma = \Phi_b + k_B T \ln(N_c/N_D) \quad [4]$$

From this, we obtain

$$k_B \frac{\ln(TR_B)}{\partial \left(\frac{1}{T}\right)} = e \left[\Phi_b - T \frac{\partial \Phi_b}{\partial T} \right] \quad [5]$$

We note that the band bending is equal to the activation energy only at $T = 0$.

The data taken for two samples is shown in Fig. 7. From this data, we note that over the temperature range, kept small due to instrument limitations and the theoretical requirement that $eV \ll k_B T$, the experimental points are fit quite well by a straight line. Also, we note that the slope is a sensitive function of donor density N_D . The $T = 0$ band bending $e\Phi_b$ vs. the donor density N_D for the highly rectifying g-b's is shown in Fig. 8. $e\Phi_b$ decreases from 1.03 eV at $N_D = 4.5 \times 10^{15}/\text{cm}^3$ to 0.19 eV at $5.0 \times 10^{17}/\text{cm}^3$. The theoretical curve and the density of defect states calculation is presented in the next section.

Theoretical Studies

Physics and chemistry of GaAs grain boundaries.—When two separately nucleated grains are mated at the g-b, the lack of long-range order produces dangling (13) or severely stretched bonds at the g-b. These disturbed bonds are fairly well localized at the interface, i.e., the disturbed bond region extends into the grains from the interface on the order of 10 \AA (16). These disrupted interfacial bonds generally lead to

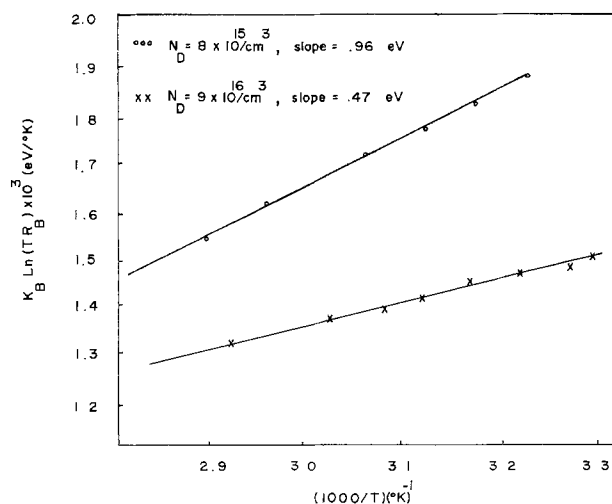


Fig. 7. G-B resistance R_B data taken for two strongly rectifying g-b's. It should be noted that the data is fit well by a straight line approximation.

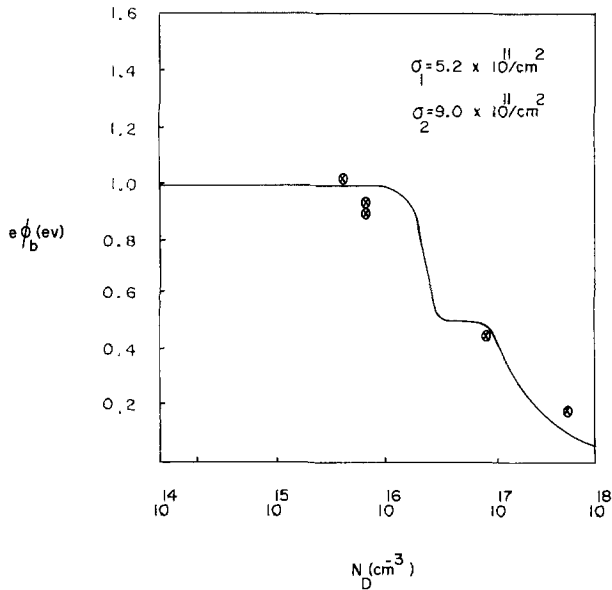


Fig. 8. $T = 0$ band bending $e\Phi_b$ vs. donor density N_D for strongly rectifying g-b's in GaAs. The experimental points were determined from the activation energy studies.

deep acceptor levels in semiconductors. The presence of deep levels at the g-b is manifested in the band bending and space charging associated with such an interface.

Models for g-b's have evolved from dislocation theory, e.g., see McPherson *et al.* (10). Evidence for a dislocation model of a g-b is extensive and has been accumulated for more than two decades [a review of the subject through 1970 can be found in Matare (17)]. Currently, the experimental evidence is still very supportive for such a model, e.g., Syutkin *et al.* (16) reported from a field-ion microscopic study of the atomic structure of g-b's that the interface is dominated by the appearance of extra atomic rows which can be interpreted as the emergence of dislocations. This study also indicated the lack of evidence for an amorphous-like structure at g-b's. A g-b interface is thus substantially different from a free surface. The atoms will tend to restructure as one moves from the interior toward the free surface of a crystal. The restructuring of the atoms is associated with the crystal's effort to lower its high surface energy subject to the constraint that the crystal's total free energy be at a minimum. However, at a g-b, the grains are competing for periodicity in the lattice. This competition between grains freezes the extra atomic half-planes (dislocations) into metastable states at the interface.

The predominant slip system in GaAs (18, 19) is $\{111\}$ with slip occurring in the $\langle 110 \rangle$ direction with Burger's vector $\vec{b} = a_0/2 \langle 110 \rangle$ where $a_0 = 5.65 \text{ \AA}$ is the lattice constant. With the dislocation core running at 60° to the slip vector, such dislocations are referred to as 60° dislocations. Due to its high mobility (20), 60° dislocation dominance (21) at the g-b is assumed. This places the dangling bonds along the core of the dislocation some 4 \AA apart.

Grain boundary modeling in GaAs is complicated by the fact that the dislocations may be formed either by terminating the extra atomic half-plane on a row of Ga atoms (A(s) $\equiv \alpha$ dislocation) (22) or on a row of As atoms (B(s) $\equiv \beta$ dislocation). Therefore, we can have A dislocations whose cores consist of a row of Ga dangling bonds and/or B dislocations whose cores consist of a row of As dangling bonds. The physics and chemistry of Ga and As dangling bonds are somewhat different, as evidenced by the

different chemical properties of the (111) and $(\bar{1}\bar{1}\bar{1})$ surfaces (12).

A single dangling bond can accommodate up to two electrons. The first electron is added more easily than the second due to the electrostatic repulsion of two electrons in the same sp^3 orbital. Thus, as Mueller and Jacobson (23) assumed for InSb, two distinct energy levels are assumed for a single dangling bond, i.e., separate one-electron and two-electron flow levels are used. Since the dangling bonds are only 4 \AA apart on the 60° dislocation cores, some wavefunction overlap is expected leading to a broadening of these levels as depicted in Fig. 9. The one-electron flow band for the A dislocation is shown $3/4$ filled in the neutral state. This is dictated by the fact that Ga has three valence electrons which are spread over four sp^3 orbitals. However, the one-electron flow band is filled and the second-electron flow band is $1/4$ filled for a B dislocation in the neutral state because As has 5 valence electrons which are spread over four sp^3 orbitals.

With the Fermi level above the neutrality level in n-type material, electrons will leave the Fermi level and take up a quasi-localized residence on the dislocation core. (Quasi-localized in a sense that while the electrons are confined to the g-b interface, some mobility along the dislocation cores at the interface is expected). This accumulation of excess negative charge at the g-b interface leads to a region of positive ionized donors (depletion width W) adjacent to the g-b and an electrostatic potential (band-bending $e\Phi_b$) associated with the space-charge distribution. The bands are bent such that they limit the amount of excess negative charge that can be placed on the g-b interface.

The exact energy level location of A and B neutrality levels are unknown. However, on the basis of results reported for InSb (24) and GaAs (25), selective dislocation production by four-point bending indicated that the A level is above midgap and the B level is below. Spencer *et al.* (26) report that two dominant g-b acceptor levels associated with atomic disorder were observed from deep level transient spectroscopy (DLTS) studies of GaAs bicrystals. These acceptor levels were located at 0.41 and 0.90 eV below the conduction band and were believed to be associated with atomic disorder.

Theory of GaAs grain boundary band bending.—As electrons leave the donors to take up residence on the g-b acceptor states, a region of positive donor ion density N_D develops in each grain adjacent to the

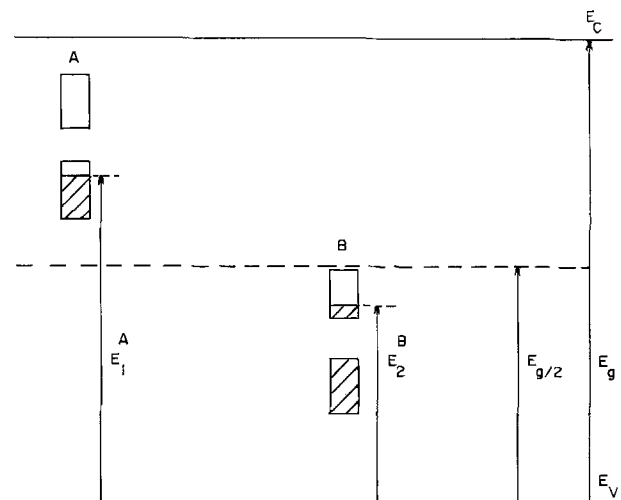


Fig. 9. Proposed flow level diagram for A- and B-type dislocations in GaAs with neutrality levels indicated. The flow band widths are exaggerated.

g-b. This positive space charge region is assumed to extend from the interface into each grain a distance L . To model the band bending, we assume that the excess negative charge added to the g-b is spread uniformly over an interface plane with a surface density of Q_s . Choosing the y, z axes in the plane and x normal to it, the one dimensional Poisson's equation to solve is of the form

$$\frac{d^2\Phi}{dx^2} = \frac{-\rho(x)}{\epsilon_s} \quad [6]$$

with

$$\rho(x) = eN_D - eQ_s\delta(x) \quad (-L \leq x \leq L)$$

The solution of Eq. [6] gives the depletion width $W (=2L)$ as a function of the band bending $e\Phi_b$ at the interface, as

$$W = \left(\frac{8\epsilon_s\Phi_b}{eN_D} \right)^{1/2} \quad [7]$$

A relationship between W and Q_s is obtained by invoking charge neutrality

$$WN_D = Q_s \quad [8]$$

which yields

$$Q_s = \left(\frac{8\epsilon_s N_D \Phi_b}{e} \right)^{1/2} \quad [9]$$

Another expression for Q_s can be obtained by integrating over the density of states times the probability of that state being occupied

$$Q_s = \int_0^{E_c} n(E) f(E, e\Phi_b, E_F) dE \quad [10]$$

where f is the occupational probability. f is a function of flaw level position E , band bending $e\Phi_b$, and Fermi level location E_F in the grains adjacent to the g-b. In Ref. (6), the g-b occupational probability is written as

$$f(E, e\Phi_b, E_F) = F(E + e\Phi_b, E_F) - \gamma \quad [11]$$

where

$$F(E + e\Phi_b, E_F) = \frac{1}{1 + \exp(E + e\Phi_b - E_F)} \quad [12]$$

and γ is the g-b occupational probability in the neutral condition. γ is given by $\gamma = F(E, E_{FB})$ with E_{FB} the neutral g-b Fermi level location.

DLTS measurements (26) indicate that the density of g-b interface states in GaAs is discrete, i.e.

$$n(E) = \sum_i \sigma_i \delta(E - E_i) \quad [13]$$

where σ_i is the number of flaw states per unit area of g-b interface with energy location E_i above the valence band. Substituting Eq. [11] and [13] into [10] gives

$$Q_s = \sum_i \sigma_i [F(E_i + e\Phi_b, E_F) - \gamma_i] \quad [14]$$

The self-consistent equation for band bending is obtained by equating Eq. [9] and [14], giving

$$\sum_i \sigma_i [F(E_i + e\Phi_b, E_F) - \gamma_i] = \left(\frac{8\epsilon_s N_D \Phi_b}{e} \right)^{1/2} \quad [15]$$

Equation [15] is a transcendental equation. Given the flaw level positions, flaw densities, and neutrality conditions, we can solve for the band bending as a function of donor density, or conversely, given the band bending vs. donor density we can elicit information about the flaw levels.

Theoretical analysis of experimental results.—For our numerical calculations, we wanted to solve Eq. [15] for the band bending in an effort to better understand its dependence on the g-b interface density of flaw

levels σ , neutrality occupation γ , temperature T , and donor density N_D . We have used the following experimental data (26): two dominant discrete acceptor levels associated with atomic disorder at $E_1 = 1.01$ eV and $E_2 = 0.53$ eV (above the valence band) with respective equivalent volume densities of $N_1 > 1 \times 10^{16}/\text{cm}^3$ and $N_2 > 6 \times 10^{16}/\text{cm}^3$, and a high level of copper segregation with multivalent acceptor levels located at $E_3 = 0.15$ eV and $E_4 = 0.44$ eV with an equivalent volume density of $N_3 = N_4 > 8 \times 10^{15}/\text{cm}^3$. The copper contaminated g-b's are expected for the bulk grown polycrystalline samples.

The best-fit theoretical curve shown in Fig. 8 for the $T = 0$ band bending $e\Phi_b$ vs. donor density N_D was obtained using the two levels associated with atomic disorder, $\sigma_1 = 5.2 \times 10^{11}/\text{cm}^2$ at E_1 and $\sigma_2 = 9.0 \times 10^{11}/\text{cm}^2$ at E_2 , and with an assumed g-b copper segregation of $\sigma_3 = 4.4 \times 10^{11}/\text{cm}^2$. The neutral g-b Fermi level E_{FB} was pinned at 0.46 eV above the valence band. This value of E_{FB} effectively excludes the importance of the copper segregation on the ($T = 0$) $e\Phi_b$ vs. N_D curve because the copper traps are filled even when the g-b is in a neutral condition. However, as discussed shortly, the values of E_{FB} and σ_3 , used in the calculation, were necessary to produce a nearly temperature-independent activation energy which was experimentally observed.

The ($T = 0$) $e\Phi_b$ vs. N_D curve shown in Fig. 8 has two plateaus. The higher plateau at 0.99 eV occurs due to the filling of the E_2 trap as the donor density N_D increases. At $N_D \cong 10^{16}/\text{cm}^3$, the E_2 trap is filled and $e\Phi_b$ decreases as $(N_D)^{-1}$. At $e\Phi_b = 0.51$ eV the E_1 level, which had effectively been frozen out by the severe band bending at the lower donor levels, is now starting to be filled. The asymptotic behavior for $N_D > 10^{17}/\text{cm}^3$ occurs as N_D^{-1} .

The parameter values used to fit the ($T = 0$) $e\Phi_b$ vs. N_D data were tested to verify that this particular set of values could reproduce the nearly temperature-independent activation energy which was experimentally observed. First, using Eq. [15], we show in Fig. 10 the temperature dependence of the band bending as a function of N_D . It should be noted that a substantial temperature dependence exists, especially at the lower donor levels, and that the temperature dependence closely parallels the temperature dependence of E_F . However, for comparison, Fig. 11 shows the calculated activation energy, using Eq. [5] in conjunction with

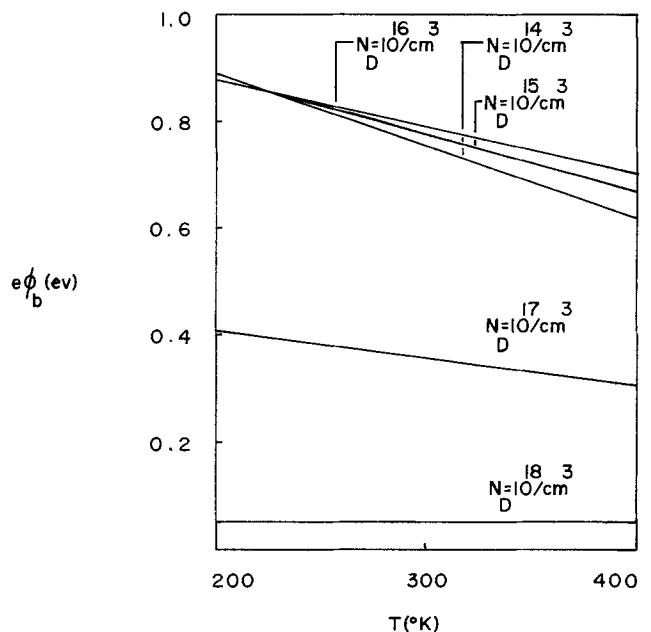


Fig. 10. Predicted temperature dependence of the band bending

Eq. [15]. We note that the activation energy is nearly temperature independent throughout the donor range for the set of parameter values used.

The number of flaw states per unit area ($\cong 10^{12}/\text{cm}^2$) presented here for g-b's in GaAs agree favorably with that reported by Seto (5) and Seager and Castner (6) for polycrystalline silicon grain boundaries.

GaAs G-B Passivation Efforts

Generally, the electronic properties of g-b's in photovoltaic devices are dominated by: (i) a tendency of the g-b to serve as a sink for the minority carrier leading to a high interfacial recombination velocity and (ii) a high sheet conductance along the g-b interface. While the high interfacial recombination velocity is a direct consequence of the band bending, the high sheet conductance may or may not depend on the band bending. For example, in n-type ($N_D = 10^{16}/\text{cm}^3$) bicrystalline samples of Ge and InSb the g-b sheet conductance is due to holes (27, 28). The hole conductivity in g-b's arises from the fact that the valence bands are bent above the Fermi level, i.e., a degenerate inversion layer produces the observed high p-type sheet conductance.

In Si, the g-b band bending is only 0.4 eV at $N_D = 10^{16}/\text{cm}^3$ and one might expect conductance is due to electrons. However, in GaAs, the band bending is more severe (0.99 eV at $N_D < 10^{16}/\text{cm}^3$) and one might expect the conduction along the g-b to be due to both electrons and holes in low donor material.

In contrast to single crystal behavior, the g-b hole mobility may be greater than the g-b electron mobility. The g-b electrons are assumed to move along the g-b interface via dislocations. The dangling bonds are located only 4Å apart on the dislocation core and some wavefunction overlap occurs. However, a low electron mobility is expected for two reasons. First, the dangling p-orbitals are dangling transverse to the dislocation core and a small wavefunction overlap is expected (30). Second, in a real g-b, the one dimensional periodicity of the dislocation core is disrupted by jogs, kinks, impurity precipitation, and vacancy precipitation. A relatively high hole mobility is expected since the hole region is adjacent to the g-b interface (17) where lattice disruptions are expected to be minimal.

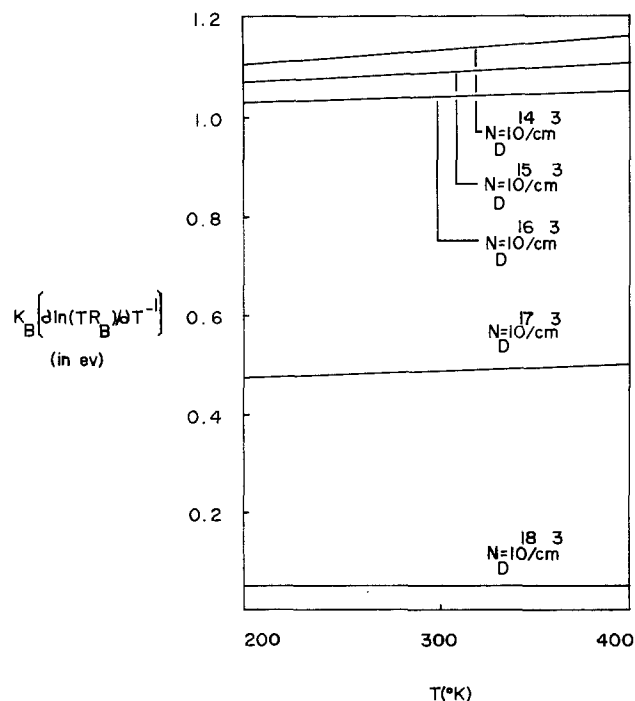


Fig. 11. Predicted weak temperature dependence of activation energy.

Since the g-b recombination is directly dependent on $e\Phi_b$, and the g-b sheet conductance may depend on $e\Phi_b$, it seems most natural to try to eliminate, or at least reduce, the band bending in order to improve photovoltaic efficiency. Approaches reported (31, 32) for Si g-b passivation have centered around hydrogenation. Monatomic hydrogen is introduced to the g-b via a plasma discharge. Located at the g-b, it is expected that the H covalently bonds to the dangling bond. Presumably, this lowers the dangling bond's energy and removes it from the bandgap. This eliminates many of the traps at the g-b and leads to a smaller band bending.

An approach, other than hydrogenation, is to add simple donors to the g-b interface. This tends to fill up the traps locally without the space charging and associated band bending. This would dramatically improve the short-circuit current due to a smaller recombination velocity. In addition, if the sheet conductance is primarily p-type, due to the bending of the bands, the sheet conductance may also decrease leading to an improved open-circuit voltage.

In an effort to add donors to the interface, one might be tempted to heavily dope the polycrystalline film with donors and then anneal the sample thereby diffusing many of the donors to the g-b interface. However, whether an element serves as a donor or acceptor depends on the crystal-field environment in which the given element is placed, e.g., an amphoteric dopant can serve as a donor or acceptor depending on the lattice position. Thus, if either a IV element donor (at a Ga site) or a VI element donor (at an As site) diffuses to the g-b, the donor properties may not be conserved. In fact, if either of the substitutional donor elements chemically combines with a dangling bond, the electronic octet configuration is not completed and acceptor-like properties may be expected from the impurity-dangling bond complex.

In searching for donor candidates for g-b diffusion, the following requirements seem necessary: (i) the impurity must serve as a donor at the interface, (ii) the impurity must diffuse rapidly into the g-b's but not into the grains during diffusion cycle, and (iii) the passivating impurity must remain localized at the interface for long-time stability requirements. The alkaline metals seem to be excellent candidates for g-b diffusion.

Due to their compensating properties, every effort is made to eliminate the alkaline metals from single crystal growths. An element such as Li sits interstitially in the lattice at low concentrations and serves as a simple donor (35). However, as the concentration of the Li increases, the lattice energy associated with this interstitial impurity rises. To relieve the stress, a Ga atom (of smaller radius than Li) will hop out of its lattice site. The Li then proceeds to complex with the Ga vacancy (short three electrons). The Li will donate its electron, but to the complex not to the conduction band. Since the complex is still short some two electrons, the complex will serve as a deep acceptor in GaAs. It is this tendency of the alkaline metals to always donate their weakly bound s^1 electron, independent of crystal-field environment, which make them attractive candidates for g-b diffusion.

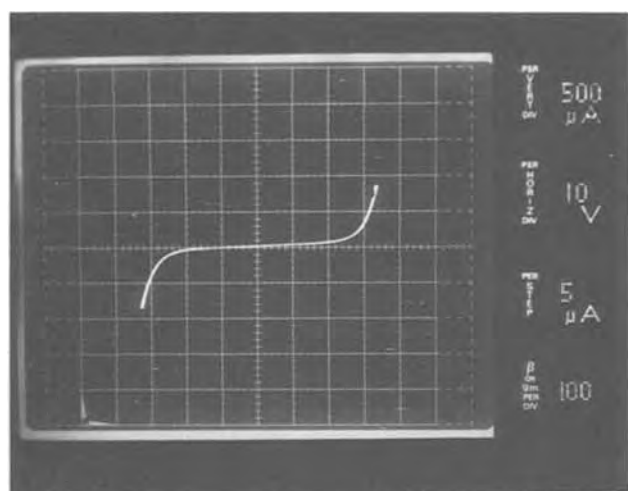
For our diffusion experiments we have used potassium (K). K has a larger radius than Li and this is expected to minimize intragrain diffusion during the diffusion process. However, the impurity is still expected to diffuse freely into the g-b due to the much higher diffusion constant associated with a g-b. To separate the effects of K diffusion from the thermal anneal, two bicrystalline samples (as described above) were cut from adjacent regions of the same g-b with one serving as a control sample.

In the diffusion process, a small amount of K was transferred in a nitrogen purged glove bag into one of the two Pyrex ampuls containing the GaAs bi-

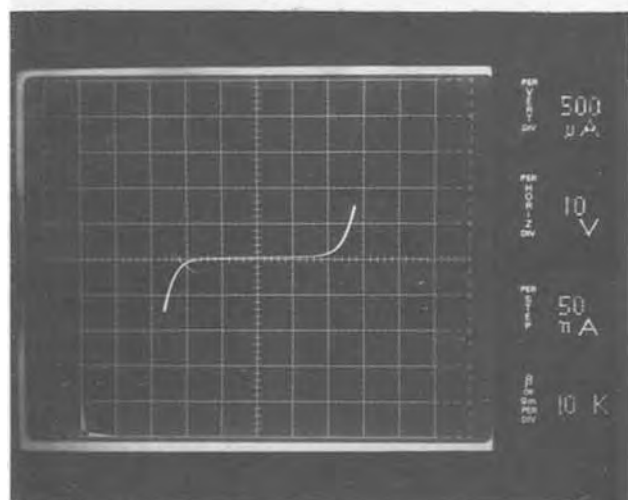
crystalline samples. The ampuls were then evacuated, sealed, and heated in an oven for 75 min at 140°C. The samples were then removed, cleaned in HCl, and tin contacts are alloyed as described above.

The I - V characteristics of a bicrystalline sample (a) before diffusion and (b) after diffusion are shown in Fig. 12. We notice that to produce 500 μA of current in the virgin sample, 32V were required. However, to produce 500 μA in the sample after diffusion, only 26V were needed. To insure that the increased conductivity was due to g - b passivation and not due to improved intragrain conduction, intragrain resistivity measurements were conducted before and after diffusion with no appreciable change noted. This would indicate that the large radius of K prevents intragrain diffusion during the cycle. When the control sample was investigated, no changes were detected in either the rectifying properties of the grain boundary or the g - b resistance. This is somewhat expected for a low temperature (140°C) quick (75 min) anneal of the bulk-grown material.

A plot of the g - b resistance $k_B \ln(R_B T)$ vs. $(1/T)$ before and after diffusion (Fig. 13) reveals a reduction in grain boundary resistance. We also note that before diffusion the points are fitted quite well by a straight line. However, after the diffusion, the behavior is non-Arrhenius and the data could not be fitted with a straight line.



(a)



(b)

Fig. 12. I - V characteristics of a single g - b . (a) Before diffusion and (b) after diffusion (500 μA per vertical division and 10V per horizontal division).

To ascertain the extent of passivation, Fig. 14 shows, using a set of common axes, the I - V curves for another sample before diffusion, after diffusion, after diffusion and after etching. Before diffusion the g - b shows strong rectifying properties due to a large band bending (experimentally we obtain $\phi_b = 0.87\text{V}$). After diffusion, the strong blocking property of the g - b has diminished. Even after etching away some 20 μm of the surface, we still find evidence of partial passivation. The fact that the passivation may extend at least 20 μm is very important with respect to thin film passivation.

Discussion of Results

On the basis of our measurements on bulk grown GaAs polycrystalline material, it appears that the highly rectifying (bad) g - b 's have an interface density of trapping states on the order of $10^{12}/\text{cm}^2$. This interface density agrees well with that reported for bulk and vapor phase grown, polycrystalline Si. An interface density of $10^{12}/\text{cm}^2$ would correspond to intrinsic (free from impurity precipitation) g - b 's with a rather low tilt angle of less than 1° . Why g - b 's with larger angles were not observed is unclear. Perhaps in the higher angle g - b 's, either the dangling bonds are partially compensated extrinsically (by impurity precipitation) or else the severe lattice strain leads to a very brittle interface which cannot withstand the sample preparation (a few of the samples were observed to break at the g - b during the cutting and handling).

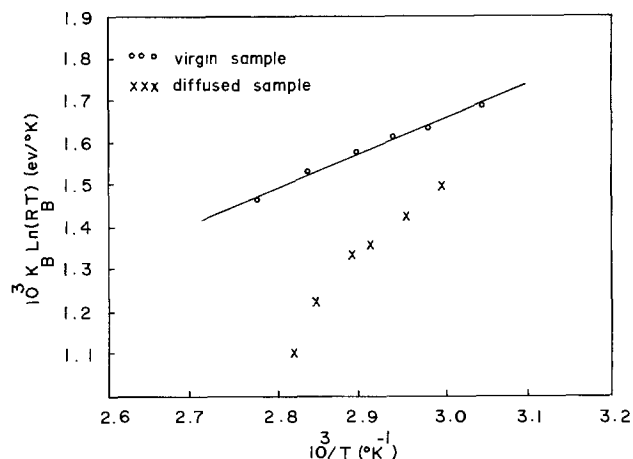


Fig. 13. Change in g - b resistance R_B of a single g - b after diffusion.

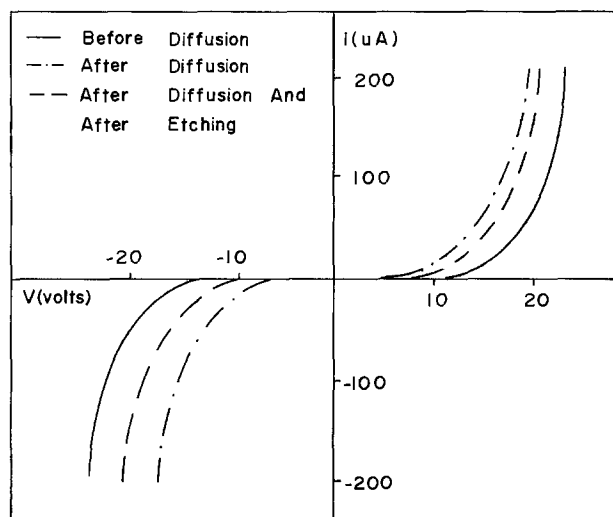


Fig. 14. I - V characteristics of a single g - b before diffusion, after diffusion, after diffusion and after etching.

Also, we found that the g-b resistance was lowered and the strong rectifying characteristics diminished after an introduction of K into the g-b via vapor phase diffusion. This is believed to be a result of a band-bending reduction due to the K ions serving as localized interfacial donors. However, while the g-b electrical characteristics changed after K diffusion, the intragrain properties were unchanged. This would indicate that intragrain diffusion of K during the diffusion cycle was not a problem.

With respect to polycrystalline solar cell applications, a reduction in the g-b band bending would improve the short-circuit current in the photovoltaic device due to a smaller g-b recombination velocity. Whether the K will lead to a higher sheet conductance (resulting in a smaller open-circuit voltage) depends on the conduction mechanism (holes or electrons) along the interface.

Acknowledgment

This work was supported by the U.S. Department of Energy under Contract No. XS-9-8032-1.

Manuscript submitted Feb. 25, 1980; revised manuscript received May 30, 1980. This was Paper 317 presented at the St. Louis, Missouri, Meeting of the Society, May 11-16, 1980.

Any discussion of this paper will appear in a Discussion Section to be published in the June 1981 JOURNAL. All discussions for the June 1981 Discussion Section should be submitted by Feb. 1, 1981.

Publication costs of this article were assisted by North Carolina Agricultural and Technical State University.

REFERENCES

1. P. D. Dapkus, R. D. Dupuis, R. D. Yinging, J. J. Yang, W. I. Simpson, L. A. Moudy, R. E. Johnson, A. G. Cambell, H. M. Manasevit, and R. O. Ruth, in Thirteenth IEEE Photovoltaic Specialists Conference, p. 960, Washington, D.C. (June 1978).
2. S. S. Chu, T. L. Chu, and H. T. Yang, in *ibid.*, p. 956.
3. H. C. Hovel, in *Proc. IEEE Photovoltaic Spec. Conf.*, 12th, Baton Rouge, La. (1976).
4. S. S. Chu, T. L. Chu, and H. T. Yang, *Appl. Phys. Lett.*, **32**, 557 (1978).
5. J. W. Y. Seto, *J. Appl. Phys.*, **46**, 5247 (1975).
6. C. H. Seager and T. G. Castner, *ibid.*, **49**, 3879 (1978).
7. The wafers were cut from bulk grown GaAs ingots and supplied to us by Morgan Semiconductors.
8. The secondary-electron detector can be used as a cathodoluminescence detector provided that:
 - (i) the scintillator is removed from the head assembly of the secondary electron detector and
 - (ii) the photomultiplier tube is sensitive in the infrared ($0.8 \mu\text{m}$). Our best micrographs were obtained when we used, in connection with the light pipe, a 2-64 Corning filter with a 50% transparency at $0.67 \mu\text{m}$.
9. W. D. Johnston, Jr., *This Journal*, **127**, 90 (1980).
10. J. W. McPherson, G. Filatovs, E. Stefanakos, and W. Collis, *J. Phys. Chem. Solids*, Accepted for publication.
11. A. L. Esquivel, S. Sen, and W. N. Lin, *J. Appl. Phys.*, **47**, 2588 (1976).
12. M. S. Abrahms and C. J. Buiocchi, *ibid.*, **36**, 2855 (1965).
13. W. Shockley, *Phys. Rev.*, **91**, 228 (1953).
14. S. M. Sze, "Physics of Semiconductor Devices," Wiley-Interscience, New York (1969).
15. C. H. Seager and T. G. Castner, *J. Appl. Phys.*, **49**, 3879 (1978).
16. N. N. Syutkin, E. G. Fedorova, and N. N. Vyatkin, *Sov. Phys. Solid State*, **20**, 1134 (1978).
17. H. F. Matare, "Defect Electronics in Semiconductors," Wiley-Interscience, New York (1971).
18. H. C. Gatos, *J. Appl. Phys.*, **32**, 1232 (1961).
19. D. Laister and G. M. Jenkins, *J. Mater. Sci.*, **8**, 1218 (1973).
20. H. Booyens, J. S. Vermaak, and G. R. Proto, *J. Appl. Phys.*, **49**, 5435 (1978).
21. N. S. Belyatskava, S. P. Grishina, M. B. Mil'vidski, V. B. Osvenski, and V. G. Fomin, *Izv. Akad. Nauk USSR Neorg. Mater.*, **3**, 1347 (1967).
22. The notation used here conforms to that suggested in Journal de Physique, Colloque C6, 1979—Foreword by Alexander, Haasen, Labusch and Schroter. The (s) used in the notation refers to the so-called shuffle set of {111} pairs of planes.
23. R. K. Mueller and R. L. Jacobson, *J. Appl. Phys.*, **33**, 2341 (1962).
24. R. L. Bell and A. F. W. Willoughby, *J. Mater. Sci.*, (1970).
25. A. L. Esquivel, S. Sen, and W. N. Lin, *J. Appl. Phys.*, **47**, 2588 (1976).
26. M. Spencer, R. Stall, L. F. Eastman, and C. Wood, *ibid.*, **50**, 8006 (1979).
27. Y. Matukura and S. Tanaka, *J. Phys. Soc. Jpn.*, **16**, 833 (1961).
28. R. K. Mueller and K. N. Maffitt, *J. Appl. Phys.*, **35**, 734 (1964).
29. Y. Matukura, *J. Phys. Soc. Jpn.*, **16**, 842 (1961).
30. T. Figielski, *Solid-State Electron.*, **21**, 1403 (1978).
31. C. H. Seager and D. S. Ginley, *Appl. Phys. Lett.*, **34**, 337 (1979).
32. D. R. Campbell, M. H. Brodksy, C. M. Hwang, R. E. Robinson, and M. Albert, *Bull. Am. Phys. Soc.*, **24**, Abstract Jk8, p. 435 (1979).
33. J. A. McMillan and E. M. Peterson, *J. Appl. Phys.*, **50**, 5238 (1979).
34. W. T. Read, *Philos. Mag.*, **45**, 775 (1954).
35. A. G. Milnes, "Deep Impurities in Semiconductors," Wiley-Interscience, New York (1973).

Direct Evidence for 1 nm Pores in "Dry" Thermal SiO₂ from High Resolution Transmission Electron Microscopy

J. M. Gibson¹ and D. W. Dong

IBM Corporation, Thomas J. Watson Research Center, Yorktown Heights, New York 10598

ABSTRACT

Thin films of thermally grown SiO₂ have been studied by high resolution bright-field electron microscopy. Contrast phenomena observed in images from 9 nm thick "dry" films are consistent with the existence of 1 nm pores, typically 10 nm apart. Similar films grown in a wet oxidizing ambient do not display this contrast. A pore structure had previously been suggested to explain differences in growth behavior and electrical properties between "wet" and "dry" SiO₂. The reliable detection of such pores or voids in electron micrographs from amorphous materials is not straightforward and a novel approach which has been successfully applied to these films is described. A simple model which explains the appearance of pores only in "dry" films is proposed and is related to the trapping behavior of thicker films.

Some properties of thermally grown SiO₂ are substantially affected by the presence of water in the oxidizing atmosphere (1). Incorporation of 2000 ppm H₂O into an oxidizing ambient of N₂ and O₂ has been shown to increase the mean dielectric breakdown voltage of 15 nm thick thermal SiO₂ layers by 30% (1). Furthermore, the value of film thickness at which the growth *vs.* time behavior starts to follow the linear-parabolic law (2) [typically several tens of nm for "dry" films (3)] decreases almost to zero (4).

The parabolic nature of the growth kinetics arises from a reduction in free oxygen concentration at the oxide-Si interface as the thickness through which O₂ must diffuse increases. On the other hand, the linear nature is characteristic of a thickness independent growth, *i.e.*, a free surface effect. The above observation that diffusion is almost immediately a limitation for the "wet" films has been interpreted by Irene (1) as evidence for pores or voids in "dry" films which are not present in "wet" films. Thus the "dry" film growth follows a linear law up to several tens of nm because O₂ has rapid access to the oxidizing interface through such pores. "Wet" films, which are more uniform, rapidly protect the virgin Si from further oxidation.

Irene's first observation, concerning dielectric breakdown, is also consistent with this hypothesis. He noted that while "dry" films follow a broad statistical distribution of number of breakdown events *vs.* applied field, the "wet" films follow much more closely the behavior expected from uniform dielectric layers, *i.e.*, a delta function at the field strength E_0 which pulls the valence electrons from the Si-O bond. He proposed that the spread in breakdown field (always less than E_0) found for "dry" films occurs because the pores lead to fluctuations in the internal field which in some places can sufficiently exceed the applied field E_a to cause breakdown, even though $E_a < E_0$.

Current measurements through SiO₂ made while ramping an applied voltage are known to exhibit a linear Fowler-Nordheim regime which is displaced on retracing after a short time (5). This displacement is caused by a reverse field from charged traps. The magnitude of this shift was measured by Irene for both types of film. It is too small to explain the dielectric breakdown differences and is in any case similar for both "wet" and "dry" oxides.

Thus it was concluded that the significant difference between "wet" and "dry" films, when less than 20 nm

thick, lies in the density of electrically inactive defects such as pores. Other workers (6, 7) have observed that "wet" SiO₂ contains many more electrically-active traps than "dry" SiO₂ at thicknesses greater than 20 nm, which would suggest that any pores must be in general electrically inactive. This point will be commented on in more detail later.

Irene made various transmission electron microscope (TEM) studies of these films in an attempt to find direct evidence for such pores. However, the resolution of his instrument and the conventional imaging methods he was obliged to use were not able to distinguish directly between the films or to resolve any defects down to 5 nm in size. By decoration and etching experiments he concluded that defects smaller than 5 nm may exist in either type of film.

In the present paper direct high resolution TEM evidence for 1 nm scale pores or voids in the "dry" films is presented. These have not been seen in images from "wet" films. The interpretation of high resolution TEM images from amorphous samples is complicated and one of the authors (JMG) has developed a new approach for the very purpose of locating very small voids in such specimens. This method has previously been described rather briefly (8, 9) and a more detailed account will be published separately. In this paper, the main aim of which is to present the results for the SiO₂ system, the technique will be elaborated only in necessary but sufficient detail. The provision of some background information about high resolution TEM of amorphous materials was also felt to be valuable as an aid to understanding the approach taken by the authors of this paper.

High Resolution TEM of Amorphous Materials

A good recent review of this subject is given by Howie (10). The principal points which we wish to emphasize here are: images are not simply related to the object (although they can appear deceptively so such as "lattice plane" images from crystals) because image contrast arises from complex electron wave interference; also the imaging mode to be used in any study of amorphous materials should be carefully considered to suit the information which is required. It is not always sensible to form an image utilizing the highest resolution of the microscope and containing the maximum information. This is because there is a considerable amount of meaningless signal which comes from random effects in a disordered sample and which can drown out nonrandom effects of interest. If one has a firm idea of what one is looking for one can

¹ Present address: Bell Laboratories, Murray Hill, New Jersey 07974.

Key words: voids, thin films, oxidation, silicon, electrical breakdown.

use an imaging mode which "homes in" on the meaningful information at the expense of random signal (which could be labelled "noise").

Not only will it be shown in this paper that such consideration is essential for the detection of small voids but it has previously been demonstrated to be very useful in locating small regions of long-range order in amorphous samples (11). These two types of "defect" encompass all the high resolution information which one could expect to obtain from TEM images of amorphous materials at present, i.e., from the projected atomic density (on which images depend) one can only pick up either intense features (characteristic of voids) or weaker periodicities arising from atomic ordering. Therefore the approach to high resolution TEM imaging of which this paper is representative is felt by the authors [and for example, Howie (10)] to be the most fruitful one for high resolution real-space imaging of disordered materials.

Neglecting multiple scattering and assuming the independence of instrumental effects from scattering within the specimen, the emergent electron wave which results from plane-wave illumination (wave-vector \mathbf{k}) of a thin sample is

$$\psi_0(\mathbf{r}) = (1 + i\phi(\mathbf{r})) \exp(i\mathbf{k}\cdot\mathbf{r}) \quad [1]$$

where $\phi(\mathbf{r})$ is proportional to the projected atomic potential in the \mathbf{k} direction (12). It can be seen from [1] that to a first approximation the incident-wave is simply phase-shifted by an amount proportional to ϕ and is therefore refracted. [These approximations are valid for weakly-scattering amorphous specimens < 20 nm thick, particularly in view of the qualitative nature of the conclusions to be made, but not for strongly scattering crystalline samples (13).]

A perfect microscope imaging system would display no contrast in the image plane, since all electron detectors are phase-insensitive. To obtain phase-contrast one must introduce a defect-of-focus (defocus) which causes a scattering-angle dependent phase-shift. Such a phase-shift gives rise to amplitude variations in the image plane (much like a hologram) where the scattered beams interfere with the unscattered reference beam. In the axial-bright-field (ABF) mode this leads to an image plane intensity given by

$$I(\mathbf{r}) = 1 + \phi(\mathbf{r}) \circ t(\mathbf{r}) \quad [2]$$

where \circ denotes convolution and

$$t(\mathbf{r}) = \text{Fourier Transform}\{\exp[-i\gamma(s)]a(s)E(s)\}$$

$\gamma(s)$ is the Scherzer aberration function (14) which takes account not only of defocus z but also of spherical aberration C_s which is present in all electron lenses

$$\gamma(s) = -\pi\lambda(zs^2 + C_s\lambda^2s^4) \quad [3]$$

λ is the electron wavelength and s is the Fourier coordinate (spatial frequency) $= 1/d$, where d is a spatial period in the object. $a(s)$ allows for the presence of a microscope objective aperture of radius s_{ap} such that $a(s < s_{ap}) = 1$ and $a(s > s_{ap}) = 0$. $E(s)$ is an envelope function which takes account of limited spatial and temporal coherence in the illuminating wave (15).

One can see that $t(\mathbf{r})$ describes the response of the instrument to a point object and is consequently known as the "point-spread" function. The relation between ABF images and the object is more obviously revealed by Fourier transforming $I(\mathbf{r})$ to give the image power spectrum

$$P(\mathbf{s}) = \delta(\mathbf{s}) + \tilde{\phi}(\mathbf{s}) \sin[\gamma(\mathbf{s})] E(\mathbf{s}) a(\mathbf{s}) \quad [4]$$

It can thus be seen that the object's Fourier transform $\tilde{\phi}(\mathbf{s})$ is simply filtered by the function $\sin \gamma E(\mathbf{s}) a(\mathbf{s})$ which is known as the contrast transfer function (CTF). This function determines how strongly and with which sign a given object spatial frequency is reproduced in the image. Figure 1 displays plots of

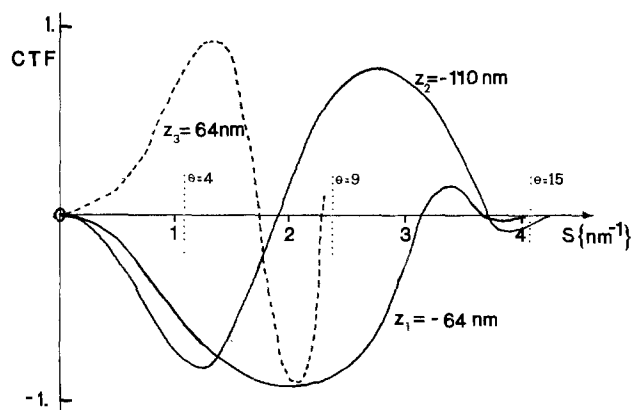


Fig. 1. The contrast transfer function (CTF) for three values of the defocus z . Microscope parameters are $C_s = 1.1$ mm, angular illumination spread 1.2 mrad, and source energy spread 0.9 eV. These are values appropriate to the Philips 301 TEM with biological pole piece which was used in this study. z_1 is known as the Scherzer defocus at which the point-to-point resolution of the instrument is at its highest value (0.31 nm). The effect of an objective aperture is to cut this function abruptly off at $s_{ap} = \theta/\lambda$ where θ is the half-angle subtended by the aperture. Three values of θ (in mrad) are marked on the s -axis.

the CTF for typical instrumental parameters which are appropriate to the Philips 301 TEM used in this study. At the Scherzer defocus there is a broad band-pass out to approximately 3.2 nm^{-1} (the reciprocal of which is the point-to-point resolution of the instrument: 0.31 nm). By increasing the defocus one can image higher spatial frequencies (higher spatial resolution) but now with reversed contrast beyond 1.9 nm^{-1} . Obviously image interpretation is not simple when the object's power spectrum extends over oscillations in the CTF (such as the diffraction from amorphous materials).

The other imaging mode of relevance to this discussion is tilted-illumination dark-field (TIDF). In this mode the reference or main beam is excluded from the image by an objective aperture ($a(0) = 0$). The image intensity is no longer linear in $\phi(\mathbf{r})$ but depends on ϕ^2 . Therefore this mode particularly emphasizes atomic superpositions in projection against the background. In consequence TIDF is well suited for detecting ordered regions (16). However random superpositions yield a speckle pattern which can be misleading (17). It has been shown that spatial incoherence in the illumination can reduce the random contribution to the speckle, thus enhancing the visibility of small crystals (11). Incoherent dark field may also have application to the imaging of small voids due to its direct representation of projected thickness fluctuations with reduced confusion from interference effects, but this has so far been unexplored.

The above was a brief outline of the standard theory of high resolution TEM imaging of thin specimens, which originates from Born and Wolf's treatise on optics (18). Now we can go on to consider the specific problem of observing voids or pores in amorphous materials.

Detection of Small Voids

The following discussion of image contrast from small voids in amorphous materials applies equally well to any defect which gives rise to a variation in the projected potential, e.g., an interstitial or vacancy cluster. The normal method for imaging such defects in crystalline materials (19), which utilizes the bending of lattice planes from long-range stress fields, is not appropriate to amorphous materials because of the lack of long-range order and the associated high oscillating strain field. Small voids in crystalline materials, which exhibit very little strain contrast, have often been detected by the ABF phase-contrast method,

described above and pioneered in this context by Rhule (20). They produce a fluctuation in the projected potential which can be imaged out-of-focus. One can see from Eq. [3] and [4] that the CTF for small s and large z has the same sign as z . So with a small objective aperture which excludes high spatial frequencies (reduced resolution), spherical aberration has negligible effect and a void will reverse its image contrast when the defocus is changed in sign (with no contrast in focus). This is often called, rather misleadingly, Fresnel contrast because large voids exhibit Fresnel fringes around their edges. For small voids at low defocus the fringes degenerate to a simple white or black spot (21). This method (or perhaps more accurately, concept) can be simply extended to large voids in thick amorphous specimens where the projected potential from the amorphous sample is effectively constant compared with the fluctuation due to the void. However, as the void size decreases to less than (say) 2 nm in a 10 nm thick film, the statistical fluctuations in projection of a random network become comparable in size to the effect from the void. When these two are of the same order it is impossible from one 2-D projection to sensibly identify the void.

One can estimate this absolute limit rather simply. Let the smallest resolvable feature in the image be of dimension R . Then in the film it defines a column of volume $\pi R^2 T$ in which there are $N = \pi R^2 T / \Omega$ atoms. (T is the film thickness and Ω its atomic volume.) For $N \gg 1$ in a random film this number exhibits gaussian fluctuations with standard deviation \sqrt{N} . This is a simple estimate of the magnitude of the random fluctuation in an image with resolution R and with unit CTF out to $s_{ap} = 1/R$. For the void to be statistically distinguishable it must produce a decrease in N which is of magnitude at least $2\sqrt{N}$ (say). In the optimal condition that $R = d_{min}$, the diameter of the smallest detectable spherical void, one obtains the condition that

$$d_{min} > 1.8 (\Omega T)^{1/4} \quad [5]$$

which for SiO_2 of 9 nm thickness (as examined in this study) gives $d_{min} \cong 1$ nm. Given this fundamental limit it is still no simple task to identify such small features in an image, without perhaps a sophisticated statistical analysis of image intensity/area.

It should be noted that specimen tilting is one way of improving on this fundamental limit, which applies only to one 2-D projection. In an analogous way it has been pointed out that specimen (16) or beam (11) tilting differentiates between localized order and random superpositions which arise from typically larger volumes. Thus a fluctuation which is visible in two independent projections can be more clearly identified as nonrandom. At present this type of analysis has not been achieved due to the difficulty of identifying the same area on a featureless sample after tilting and specimen-stage stability problems.

The better imaging mode for the detection of voids in amorphous materials is ABF. This is because the nonlinear nature of TIDF emphasizes atomic superpositions very strongly. Thus M atoms in the film which happen to line up appropriately in projection can yield M^2 times the contribution from one atom in a TIDF image. On the other hand M atoms missing from the film can on average only change the mean intensity by M times one atomic contribution (neglecting effects from reconstruction of the surrounding atoms). Since the TIDF image from a disordered material is dominated by the "speckle" produced by many atoms superimposing constructively, a small unreconstructed void would be invisible in comparison. Even though interesting features have been seen in TIDF images from amorphous specimens which have the shape one might expect from voids (22), these are unlikely to originate from unreconstructed voids because of their high intensity. So it is better to use the linear ABF imaging mode where objects that do not exist give

comparable intensity to those which do. This rule-of-thumb does not apply to crystals, however, where in TIDF atoms may be arranged to scatter very weakly into the aperture because of their long-range periodicity. Then a defect which destroys or removes this order can yield a much greater intensity than the background. This is the basis of the so-called elastic-diffuse-scattering imaging method (23).

The ABF conditions which lead to maximum signal-to-noise ratio from voids in amorphous samples are not in fact the best with which to detect them visually. In the Rhule technique for crystalline specimens and from the above discussion one would expect to use the smallest possible objective aperture to reduce unwanted high-frequency "noise." Thus the objective aperture size $s_{ap} = 1/d$. Under these circumstances it will be found that in order to observe the contrast reversal with focus from a void it is necessary to have

$$|z| > C_s \lambda^2 s_{ap}^2$$

from Eq. [3] and [4]. Then it is obvious that the whole image will reverse in contrast identically, since the only difference between the contrast from the void and the random effects is in intensity. This regime of aperture size and defocus is known as the projected-charge-density (PCD) approximation because it is to this which the image intensity is proportional (24).

Contrast reversal arises in PCD because the transfer function ($\sin(\gamma(s))a(s)$) is cut off at a low value of s and exhibits approximate mirror symmetry in the s -axis when the sign of z is flipped. This can be seen in Fig. 1 for $z = \pm 64$ nm (z_1 and z_3) if $\theta = 4$ mrad. However, with θ much greater than this the mirror symmetry breaks down and image behavior when the sign of z is changed becomes less obvious. Low spatial frequencies will still reverse contrast, of course, but some higher frequencies will remain with the same sign of contrast or may even be extinguished on reversal of z , depending on their magnitude. Image features with a "white noise" (uniform) power spectrum will then look increasingly unrelated on either side of $z = 0$ as the objective aperture is increased in size. The exact values of aperture size and defocus at which an image appears to behave unpredictably like this cannot be analytically determined. Numerical simulations from thin amorphous specimens, generated from Eq. [2] using two fast Fourier transforms for the convolution integral, are very useful in this context.

Figure 2 shows computed images of this type. A totally random distribution of atoms corresponding to a 9 nm thick amorphous SiO_2 film was used as the object in the calculation. For this discussion of contrast from voids and pores, interatomic correlations are not significant, except perhaps to enhance the scattered intensity due to reconstruction on the void surface [an effect which would be much more important in TIDF (21) where atomic superpositions are nonlinear]. If the local power spectrum in image 2(b) were sufficiently distorted by the presence of (say) a void then the transfer function would be principally sampled in its "symmetrical" region yielding cross-correlation, untypical of the rest of the image. This will be seen in the next set of computations.

Figure 3(a) shows the same image pair as in 2(a) but with a 0.8 nm diam spherical void cut from the middle of the object. Although the void produces a slightly more intense image than the background, its contrast reversal does not uniquely identify it. One can see from these images that it is hopeless to try to identify the exact shape and size of a void from high resolution TEM micrographs and statements about these properties must be rather qualitative in comparison to the information that could be determined if the atomic-structure around the defect were exactly known (as in a crystal).

Figure 3(b) shows the same image pair with an intermediate-sized objective aperture. Now the void is identifiable qualitatively as the only reverse-

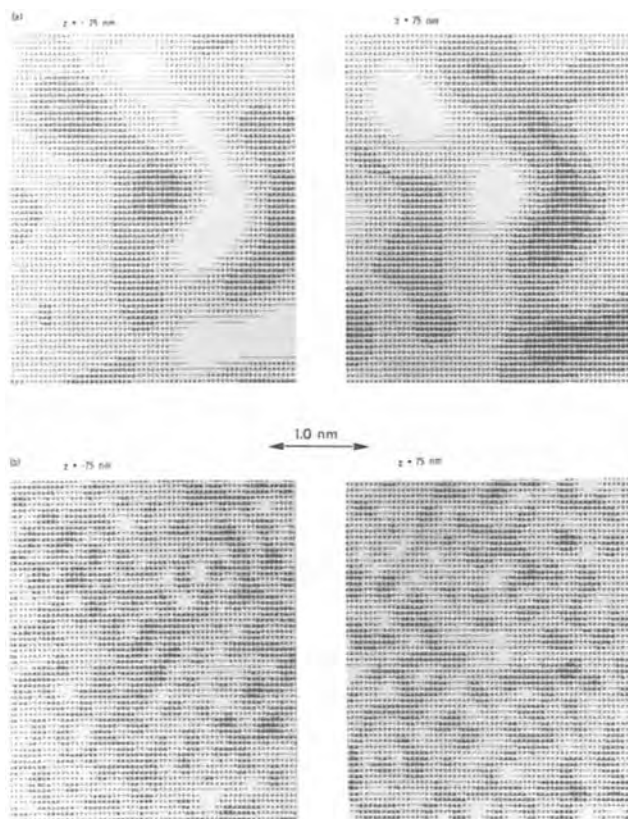


Fig. 2. Computed ABF images from a random distribution of atoms equivalent in projection to a 9 nm thick amorphous SiO_2 film. Complete reversal of image contrast with the sign of defocus (z) can be seen for a 4 mrad objective aperture (a) which limits the resolution to 0.6 mrad. With a 15 mrad objective aperture (b), the images display higher resolution and no simple behavior with the sign of z . (Seven gray levels were generated by overprinting. The intensity scale is arbitrarily adjusted to make all images of similar appearance, as one usually does in photographic printing.)

correlating object in a randomly-behaving background. If one increases the objective aperture size too much as in 3(c) [same size as in 2(b)], then the void itself becomes less distinct. In these computations the microscope parameters (including partial coherence) were the same as those used to compute the CTF's of Fig. 1. The critical objective aperture size will depend on the coherence. Some random cross-correlation will always be noticed but in this study, which involves comparison of two films, striking differences in the density of cross-correlating areas are seen which can be reliably attributed to nonrandom effects.

Note that it is not spatial extent in the image plane but the intensity (which comes from spatial extent in the beam direction) which this method is designed to reveal. Thus a column-shaped void in the beam direction may be clearly seen but could be invisible if its long axis were parallel to the image plane.

Of course this method, since it relies only on image projection, is unable to distinguish between a void and a surface pit. We emphasize that it shows up statistically unlikely fluctuations in the projected potential. Having said this, one can certainly identify the absence of voids or pores on the 1 nm scale with this technique. Furthermore it can give corroborative evidence when the presence of pores is suspected. For maximum information one should compare two films of identical thickness and structure using identical imaging conditions where the only suspected difference is the presence of voids or pores in one of the films. Thermal SiO_2 is thus an ideal system to examine, as we shall see. One simply compares image pairs while increasing the objective aperture size and looks for the

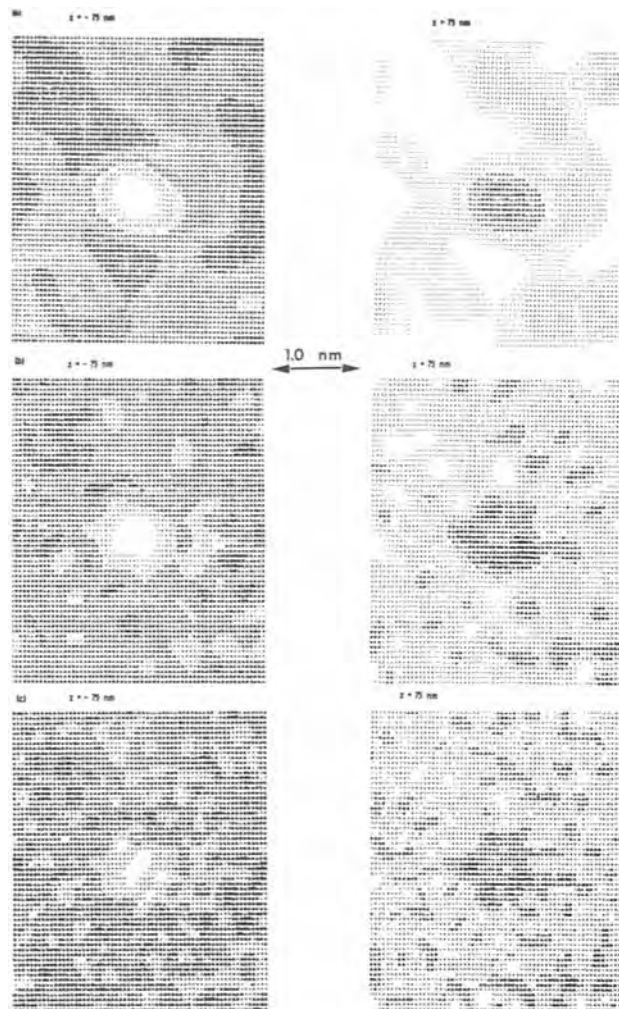


Fig. 3. (a) Same image pair as Fig. 2(a) but with a 0.4 nm radius spherical void cut from the center of the object. The void produces a slightly more intense fluctuation than the random effects but its image contrast behaves identically with reversal of z . (b) With a 9 mrad objective aperture the void is now qualitatively distinguishable in the images as the only feature which reverses contrast with z . (c) With a 15 mrad objective aperture the void is beginning to disappear. The void size was chosen by inspection as the smallest detectable by this method.

onset of random image behavior with reversal of defocus. This identifies the critical aperture size at which the films should be compared for the presence of nonrandom fluctuations in projected potential. One practical point concerning the optimum objective aperture size: the coherence envelope function $E(s)$ effectively acts as an aperture in that it can prevent high spatial frequencies s from reaching the image. For this reason it will often suffice, depending on the electron-source coherence, to use no aperture at all for the optimal void imaging condition. The 15 mrad aperture used in these experiments was similar in effect to the 9 mrad aperture in the simulations because the real coherence was a little poorer than the values used in computation. Accurate figures for the microscope coherence parameters are not known and depend critically on condenser lens settings.

Experimental Details

All substrates were (100) oriented $10 \Omega \text{ cm}^{-1}$ p-type Si wafers. Irene has shown (4) that resistivity type and value in the range $2\text{--}10 \Omega \text{ cm}^{-1}$ has negligible effect on the oxidation process. Dry oxidations were carried out in O_2 containing less than 1 ppm water. For wet oxidation, H_2O was added to N_2 by passing the gas through a clean silica vessel containing deionized water.

The H_2O vapor pressure was approximately 10^4 ppm. Oxide thickness was measured with an automated optical ellipsometer system (25) which gives better than 0.3 nm accuracy averaged over 2 mm^2 . The films described in this TEM study were both $9 \pm 0.3 \text{ nm}$ thick deduced from ellipsometric measurements.

Samples were prepared for TEM observation by jet etching from the back side of the wafer, the oxide surface being protected by beeswax. The acid mixture was 3 HF:5 HNO_3 :3 CH_3COOH . Specimens were etched just until the formation of a tiny hole at which point several thin areas where the SiO_2 film was exposed were usually found. Although thinning with this acid mixture is a little more fortuitous than using an Si-preferential etch [such as pyrocatechol (26)] for the last few μm 's, it is less likely to accentuate Si/ SiO_2 interface roughness which could be confused with a pore structure in projection. Since the ellipsometric technique measures only average film thickness and acid attack may also change local SiO_2 layer thickness, another method was used to check the actual film thickness in the areas studied with TEM. With a small objective aperture in place in the TEM, there is a decrease in the average intensity due to scattering out of the aperture, which can be readily measured from a photographic plate. From knowledge of the scattering properties of the film, thickness can be deduced (27). In this case no absolute measurements of thickness were made, but the wet and dry films were found to be within 10% of the same thickness in the areas examined.

High resolution TEM images were taken with a Philips EM 301 electron microscope which was fitted with a biological high resolution fixed pole piece for this study. The pole piece has a spherical aberration of 1.1 mm at 100 kV operating voltage which gives a maximum point-to-point resolution (inverse of cutoff frequency at the Scherzer defocus) of 0.31 nm. Cross-correlation of defocal series was carried out very primitively using transparent tracing paper. An edge or some similar feature was always used to aid exact location of the same area on different plates. A more sophisticated but still relatively simple method would be to make positive and negative transparent prints from each member of the series. A positive taken at $z = -x \text{ nm}$ when superimposed on a negative at $z = +x \text{ nm}$ would show up reverse correlating features as bright dots when held up to a strong light source. However this is not really necessary except as a neat demonstration of the results. One of the main advantages of this TEM imaging technique is that it allows easy visual identification of voids without image processing. This can be achieved while viewing the image on the microscope screen by simply reversing the sign of the defocus under the conditions described above. Then any voids should catch the eye because of their simple contrast reversal behavior.

Results

Figure 4 shows ABF images from a "dry" film at $\pm 75 \text{ nm}$ defocus with a 5 mrad semi-angle objective aperture in place. This small aperture restricts the point-to-point resolution to 0.7 nm and puts these images in the PCD regime. Thus exact contrast reversal with defocus can be seen. Nothing can be qualitatively deduced from these images because of this restricted regime. Similarly a "wet" film displays this effect in Fig. 5. These are the imaging conditions which would be recommended for imaging small voids in crystals and as discussed above they are obviously inappropriate for amorphous materials. (It should be noted that most crystals have amorphous oxide or contamination layers on their surface and the detection of the tiniest voids or point-defect clusters reverts to this same problem.) The images in Fig. 4 and 5 are analogous to the numerical simulations of Fig. 2(a) and 3(a). Any voids present in either film are not readily visible under these imaging conditions.

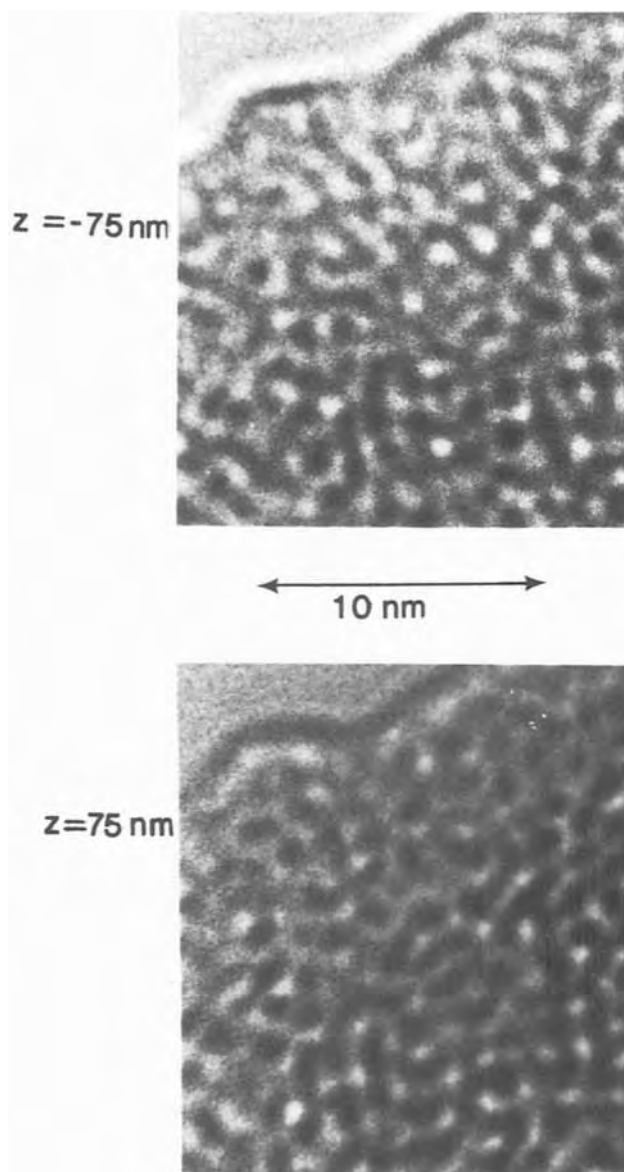


Fig. 4. ABF images from a 9 nm thick "dry" SiO_2 film with a 5 mrad objective aperture. Image reversal with sign of z is observed everywhere under these conditions. The defoci quoted in all experimental figures are accurate to $\pm 25 \text{ nm}$.

The images in Fig. 6 were formed with a 15 mrad semi-angle objective aperture from the "wet" film. Now there is no extensive correlation found on reversal of defocus from $+75$ to -75 nm . This is as predicted from the simulation in Fig. 2(b) where only random effects predominate. However, the "dry" film although generally exhibiting no simple behavior with reversal of z , does show isolated features which reverse correlate, some of which are indicated in Fig. 7. From our previous discussion these can be interpreted as arising from large nonrandom fluctuations in the projected potential. Furthermore the sign of these fluctuations can be inferred from the sign of the contrast at negative defocus—they are generally reductions in the projected potential. These observations are commensurate with voids or pores in the "dry" film of typical size 1 nm and typical separation 10 nm. This yields a density of 10^{12} cm^{-2} .

Krivanek and co-workers have looked at the interface between Si and "dry" SiO_2 at high resolution using samples prepared in cross section (28). They saw no surface roughness on a scale which would yield the fluctuations which we see in the projected potential, so that this effect can be ruled out.

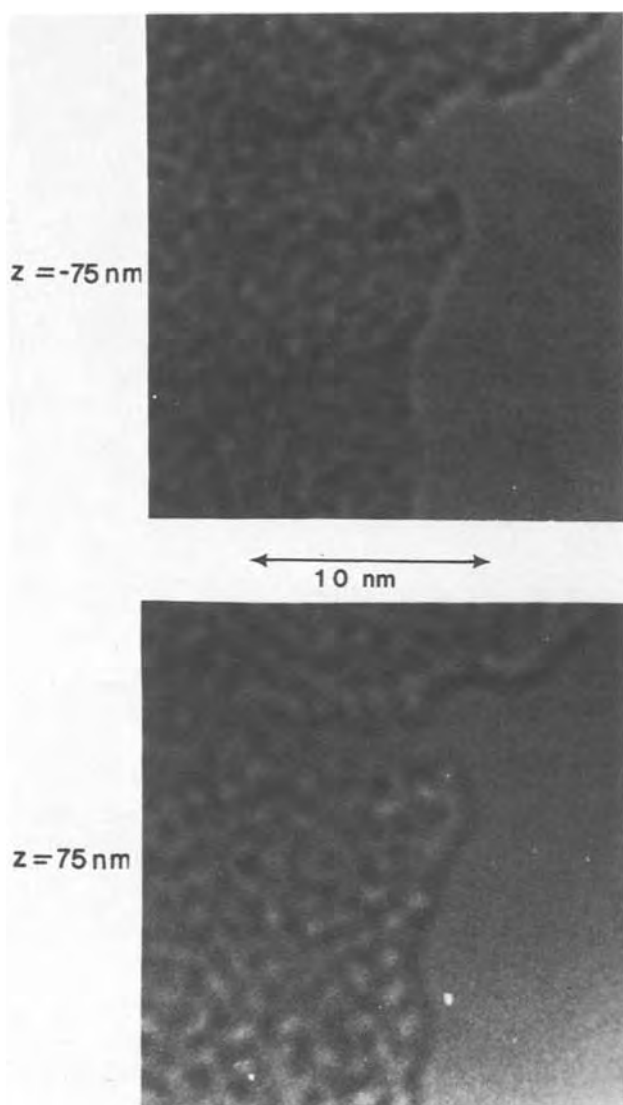


Fig. 5. ABF images from a 9 nm thick "wet" SiO_2 film which similarly show total reversal of contrast with sign of z because the objective aperture half-angle is only 5 mrad.

It has also been checked that in focus ($z = 0$) the image contrast in both films is very much less than out-of-focus. This confirms that the contrast phenomena observed with nonzero defoci are indeed of the phase-type discussed above. Amplitude effects, which could for example arise from heavy atom contaminants on the film surfaces, can be dismissed as they would show up just as prominently in focus.

Discussion

The contrast phenomena observed in high resolution images from the "dry" film agree well with the previous data and hypothesis of Irene (1). We have estimated that these defects have a density of about 10^{12} cm^{-2} . From Irene's I - V measurements it is clear that the trapping behavior does not explain the breakdown effect, which is no doubt caused by the nonuniformity of the potential introduced by these pores. Although the contrast features observed could conceivably arise from other thinning effects such as surface roughness caused by the thinning process, they are very consistent with Irene's previous data and obviously add considerable weight to the pore hypothesis.

Unfortunately, one cannot conclude directly that the voids which are observed here in high resolution TEM images are interconnected or shaped in such a way as to form pores through the whole thickness of the film. However, considering the limited image-plane spatial

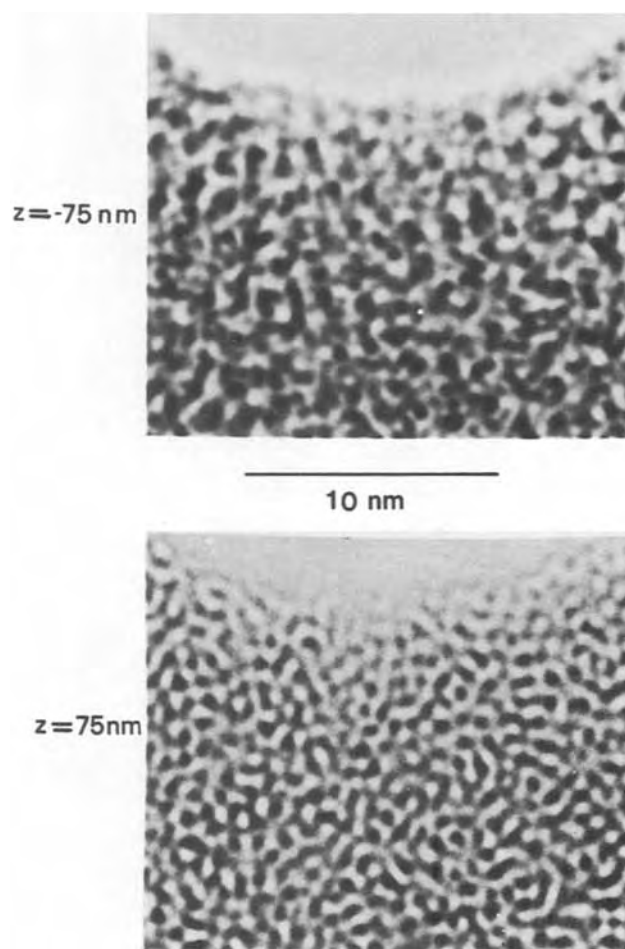


Fig. 6. ABF images from the "wet" film with a 15 mrad objective aperture. In general no simple contrast reversal is seen on changing the sign of z . This tells us that there are no statistically significant fluctuations in the projected potential on the 1 nm scale.

extent of the voids and the fact that they must arise from density fluctuations of at least 25% of the film thickness (from Eq. [5]), one can conclude that they are in general elongated in the substrate (100) direction. Although the electrical data would be explained by the presence of unconnected voids, the growth behavior suggests that they are connected to form pores. High resolution images, of the type we have described, from samples prepared in cross section may help to resolve this question. If the voids are columnar in shape, as seems most likely, when viewed side-on they will probably not produce significant contrast to be detectable. Thus a null result in the cross-section samples from "dry" SiO_2 would actually confirm the pore hypothesis. Of course, if the voids are in general spherical-like, they would be just as visible in any direction.

Why should pores form in the growing "dry" films? The observation could be simply explained, in our view, if the structure of the films is not a true continuous random network (CRN) as is the case for vitreous silica (29). Let us suppose that the structure, although basically similar to the CRN, actually nucleates at first in a slightly different configuration from the bulk-metastable CRN structure. This sort of idea has been proposed by Gaskell (30), among others, for tetrahedrally-bonded amorphous materials and leads to a cluster-radius dependent strain field. As the radius reaches a critical size the introduction of breaks or pores is inevitable. The critical size estimated from the pore spacing would be about 10 nm, which is of the same order as the size of Gaskell-type cluster which

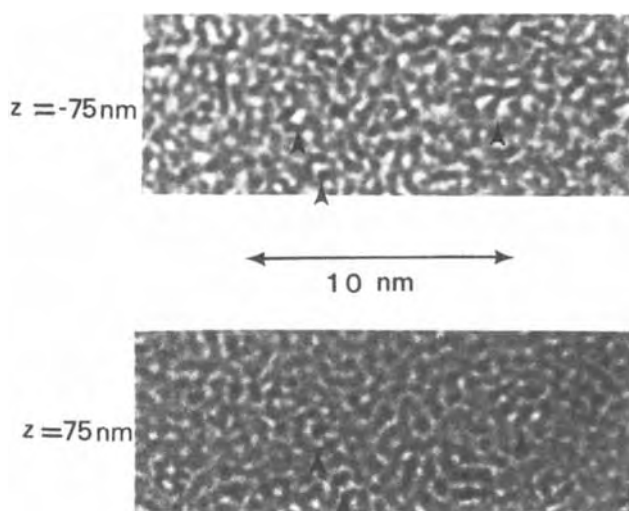


Fig. 7. ABF images from the "dry" film with a 15 mrad objective aperture. Although reverse correlation is not generally observed between the image pair, there are several arrowed features which do exhibit this behavior. These correspond to large non-random fluctuations in the projected potential which probably arise from pores or voids. Their size or shape cannot be accurately estimated but the typical image plane dimension is in the region of 1 nm or less.

was calculated to be necessary to fit radial-distribution-function and elastic-strain energy-density measurements for amorphous Si (31).

Why then do the wet films not exhibit this pore structure? There are two possibilities consistent with the above hypothesis. The first is that the OH (or another water-related) radical in some way reduces the strain in the random network as it is growing, leading to a much less prominent void structure (perhaps just at a much lower density because the "critical radius" becomes greater). Hetherington *et al.* (32) have shown that the viscosity of SiO₂ films decreases as the water content goes up, which is consistent with this suggestion. Alternatively, the pores may still exist at the same density but may be "plugged" by OH-type bonding. [It is known that micropores exhibit large capture cross sections and form strong bonds with foreign atoms (33).] This would essentially block them as pipes for rapid oxygen diffusion to the oxidizing interface and would explain the growth-kinetic phenomena. It may also explain the breakdown phenomena because the potential fluctuation from water-filled pores would be less than from empty ones. The induced charge density would then be similar for both "wet" and "dry" films when very thin, and that density is close to the measured pore density in the "dry" films. As the film thickness increases the pores may be annihilated (they tend to be near the interface) in the "dry" films but the water may stabilize them in the "wet" films, explaining the observed (ref) higher trapping density in thick "wet" films. Finally, the TEM results would still be consistent because the fluctuations in projected potential from the filled pores in the "wet" oxide would be of much smaller magnitude than from the unplugged pores in the dry films.

The authors are in the process of attempting to differentiate between these last two hypotheses by using microdiffraction in a scanning TEM. This facility allows diffraction patterns to be obtained from 1 nm² areas on a thin specimen, and so any radius-dependent structural effects on the 10 nm scale should be detectable. Samples of thermal SiO₂ are also being thinned using other preparation techniques to identify any artifacts (which in any case must arise from genuine differences between the "wet" and "dry" oxide) introduced by this processing step.

Acknowledgments

The authors would like to thank E. A. Irene and D. R. Young for useful discussions and critical reading of the manuscript. One of us (JMG) would also like to gratefully acknowledge many past discussions with A. Howie, W. M. Stobbs, and A. B. Mistry from the University of Cambridge on the subject of imaging voids in amorphous thin specimens.

Manuscript submitted May 2, 1980; revised manuscript received June 12, 1980.

Any discussion of this paper will appear in a Discussion Section to be published in the June 1981 JOURNAL. All discussions for the June 1981 Discussion Section should be submitted by Feb. 1, 1981.

Publication costs of this article were assisted by IBM Corporation.

REFERENCES

1. E. A. Irene, *This Journal*, **125**, 1708 (1978).
2. B. E. Deal and A. S. Grove, *J. Appl. Phys.*, **36**, 3770 (1965).
3. E. A. Irene and Y. J. Van der Muelen, *ibid.*, **123**, 1380 (1976).
4. E. A. Irene, *ibid.*, **121**, 1613 (1974).
5. P. Solomon, *J. Appl. Phys.*, **48**, 3843 (1977).
6. E. H. Nicollian and C. N. Berglund, *ibid.*, **42**, 5654 (1971).
7. D. R. Young, E. A. Irene, D. J. DiMaria, R. F. DeKeersmaecker, and H. Z. Massoud, *ibid.*, **50**, 6366 (1979).
8. J. M. Gibson, in "Proc. of the 37th. Ann. Meeting of EMSA," p. 540, Claitor's, Baton Rouge, Louisiana (1979).
9. J. M. Gibson, *Inst. Phys. Conf. Ser.*, **52**, 149 (1980).
10. A. Howie, *J. Non-Cryst. Sol.*, **31**, 41 (1978).
11. J. M. Gibson, A. Howie, and W. M. Stobbs, *Inst. Phys. Conf. Ser.*, **36**, 275 (1977).
12. F. Lenz, in "Electron Microscopy in Materials Science," p. 540, Academic Press, New York (1971).
13. J. M. Crowley and A. F. Moodie, *Acta Crystallogr.*, **10**, 609 (1957).
14. O. Scherzer, *J. Appl. Phys.*, **20**, 20 (1949).
15. J. Frank, *Optik*, **38**, 519 and 582 (1973).
16. J. M. Gibson, *Inst. Phys. Conf. Ser.*, **52**, 273 (1980).
17. A. Howie, O. L. Krivanek, and M. L. Rudee, *Philos. Mag.*, **27**, 235 (1973).
18. M. Born and E. Wolf, "Principles of Optics," Pergamon, Oxford (1959).
19. P. B. Hirsch, A. Howie, R. B. Nicholson, D. W. Pashley, and M. J. Whelan, "Electron Microscopy of Thin Crystals," Butterworth's, London (1965).
20. M. R. Rhule, in "Radiation-Induced Voids in Metals," p. 255, USAEC Office of Information Series, Washington, D.C., (1972).
21. P. M. Field and J. M. Cowley, *Acta Crystallogr.*, **A34**, 103 (1978).
22. W. M. Stobbs and J. M. Gibson, *Inst. Phys. Conf. Ser.*, **36**, 279 (1977).
23. A. L. J. Chang, W. Krakow, and S. L. Sass, *Acta Metall.*, **24**, 29 (1976).
24. D. F. Lynch, A. F. Moodie, and M. A. O'Keefe, *Acta Crystallogr.*, **A31**, 300 (1975).
25. Y. J. Van der Muelen, *This Journal*, **119**, 530 (1972).
26. R. M. Finne and D. L. Klein, *ibid.*, **114**, 965 (1967).
27. L. A. Freeman, A. Howie, A. B. Mistry, and P. H. Gaskell, in "The Structure of Non-Crystalline Materials," p. 245, Taylor and Francis, London, (1976).
28. O. L. Krivanek, T. T. Sheng, and D. C. Tsui, *Appl. Phys. Lett.*, **32**, 437 (1978).
29. R. J. Bell and P. Dean, *Nature*, **212**, 1354 (1966).
30. P. H. Gaskell, *Philos. Mag.*, **32**, 211 (1975).
31. P. H. Gaskell, J. M. Gibson, and A. Howie, in "The Structure of Non-Crystalline Materials," p. 181, Taylor and Francis, London (1976).
32. G. Hetherington and K. H. Jack, *Phys. Chem. Glasses*, **3**, 129 (1962).
33. e.g., S. J. Gregg and K. S. W. Sing, "Adsorption, Surface Area and Porosity," p. 19, Academic Press, New York (1967).

Molecular Beam Epitaxy of GaAs and InP with Gas Sources for As and P

M. B. Panish*

Bell Laboratories, Murray Hill, New Jersey 07974

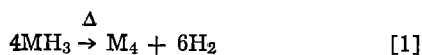
ABSTRACT

Arsine and phosphine were decomposed in a high temperature leak-source to provide As₂ and P₂ molecular beams for molecular beam epitaxy of GaAs and InP. Reasonable growth rates (0.5-1.5 μm/hr) were achieved for both semiconductors. The studies demonstrated that with this method, MBE of GaAs can be done with the substrate temperature as high as 700°C. The maximum growth temperature obtained for InP was approximately 600°C. A reasonable increase in leak rate at the source should permit GaAs-MBE at 750°C and InP-MBE at 650°C.

Conventional molecular beam epitaxy of III-V compounds is usually done with a source for the group V element that consists of a condensed phase in an effusion oven (1). Usually the condensed phase is the solid element itself, although many studies have been done in which it is a solution of the group V elements in liquid group III element. Effusion sources utilizing the solid group V elements have several disadvantages. They are rapidly depleted and the surface area of the condensed phase may change. Thus beam flux varies with time, in the nonideal effusion ovens used for MBE. Solid phosphorus may cause beam intensity control problems because the solid red phosphorus source generally consists of an ill-defined mixture of allotropic phases having different vapor pressures (2). When the liquid solution of group V in group III element is used the source is initially the III-V compound in contact with the liquid as the result of preferential loss of group V element at the source temperature. At a given temperature these sources will provide a constant flux of As₂ or P₂ as long as solid III-V compound remains. Such sources are usually exhausted quickly because it is inconvenient and expensive to maintain a large volume of source III-V compound at the high temperatures required. Furthermore, for such sources, the group V element beam intensity cannot be varied independently of the group III element beam intensity.

Several studies (3, 4) have demonstrated that the quality of MBE material, at least for GaAs and Al_xGa_{1-x}As, improves with increasing substrate temperature during growth. Furthermore there is an increasing interest in III-V solid solutions containing both As and P. At higher substrate temperatures the efficiency with which the group V element is used decreases rapidly as the result primarily of its rapidly increasing partial pressure over the III-V compound. A source is needed that does not require frequent replenishment. For MBE of the III-V solid solutions containing As and P, a source that provides precise control over the group V element beam intensities is needed.

In this work, AsH₃ and PH₃ were thermally decomposed in a "leak-source" at sufficiently high temperatures for the reaction



to go to completion in a "high pressure" section at approximately 1/2 to 3 atm. An "effusion section" of the source is intended to thermalize the beam to yield a cosine distribution and cause the reaction



to occur. This gas source for the group V elements does not require replenishment inside the vacuum system. The group V element beam intensity can be precisely controlled simply by exercising control over gas pressures at about 1 atm in a simple gas handling system; and, if necessary, mixed sources can be used to provide constant group V element ratios in the molecular beam.

Experimental

The MBE system used to demonstrate gas-source MBE is a modified vacuum system that was used for early MBE studies in 1970. Because of the necessity to pump rather large volumes of hydrogen, the original ion pumping system was replaced with a 6 in. oil diffusion pumping stack consisting of a 6 in. gate valve, an efficient liquid nitrogen cooled trap, and then the diffusion pump. The lowest pressure the system could achieve was about 5×10^{-9} Torr. The arrangement of the group III and group V element sources is illustrated in Fig. 1. Minimal cryopaneling was provided and the system was clearly not suitable for growth of extremely high purity material (even without oil diffusion pumping). However, it was adequate to permit definition of conditions under which GaAs and InP can be grown with gas source MBE.

The effusion sources for the group III elements were of conventional construction (1) with a pyrolytic boron nitride crucible to contain the group III element and most heated metal parts of molybdenum to preclude

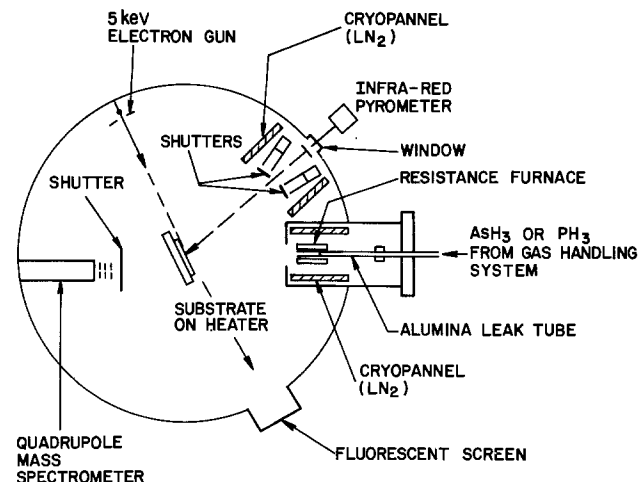


Fig. 1. Schematic representation of the MBE apparatus used for this work.

* Electrochemical Society Active Member.

Key words: semiconductor, arsine, phosphine, crystal growth.

their reaction with H_2 . The source for the group V elements (Fig. 2) consisted of an alumina tube with a leaky end seal having a leak rate such that with the pumping stack used, and with the pressure in the gas handling system at about 3 atm, the vacuum system pressure did not exceed $\sim 5 \times 10^{-5}$ Torr during a run. Several centimeters of the end of the alumina tube were heated by a resistance furnace that was maintained at 800°-900°C during a run. As illustrated in Fig. 2, the alumina furnace tube protruded about 2 cm beyond the alumina tube seal to provide an effusion section for the source.

For the studies reported in this paper only one leak-source-furnace combination was used. This source was calibrated for As_2 and P_2 beam flux distribution at the substrate by having the beam impinge on a liquid nitrogen cooled Si wafer masked with a wire grid. The deposited arsenic layer was dense and metallic in appearance, with a surface that mirrored the surface of the Si substrate. Layer thickness was determined with profilometer scans across the masked and unmasked regions of the surface. For the determination of P_2 beam flux distributions, a similar procedure was followed. The only modification to the procedure was that a thin protective layer of As was deposited immediately following the phosphorus deposition. The thickness of the As layer was determined from the previous As runs, and the profilometer thickness measurement for the composite structure then yielded the phosphorus layer thickness.

Epitaxial layers of GaAs were grown on (100) GaAs substrate surfaces that were chemically polished with a Br_2 -methanol solution and then briefly etched with a peroxide- H_2SO_4 solution. The InP epitaxial layers were grown on (100) InP substrates that were chemically polished only with a Br_2 -methanol solution. During growth the substrate wafers were "glued" to the Mo heating block with indium. The oven orifice of the leak source was 9 cm from the substrate and the group III element source-to-substrate distances were about 12 cm. The group III beam intensities were regulated by monitoring and varying the effusion cell temperature with conventional thermocouple controlled regulators. Nominal effusion cell temperatures ranged from 900° to 1000°C for Ga and 800° to 840°C for In.

For both GaAs and InP epitaxy, the growing crystal surface was monitored by observing the reflection-high energy electron diffraction (RHEED) pattern for electrons diffracted at a glancing angle (1, 5) as illustrated in Fig. 1. In addition, the condition of the crystal surface was monitored visually and the temperature of the wafer surface was monitored with an infrared pyrometer. Calibration for the pyrometer was obtained for GaAs surfaces by observing the Si-Al eutectic transition at 577°C (6) for a partially Al-coated silicon wafer mounted on the heater block with the GaAs wafer. Similarly for InP, the Ge-Al eutectic temperature at 424°C (6) was used for calibration. It

was assumed that the calibration corrections were constant over the temperature ranges studied.

Results and Discussion

The leak-effusion source.—The use of AsH_3 and PH_3 as sources for As_2 and P_2 beams requires that the hydrides be thermally decomposed before introduction into the vacuum system. This was done at 800°-900°C with pressures in the range 1/2 to 3 atm on the high pressure side of the leak. Virtually complete decomposition of the hydrides occurred. In the leak-source As_4 or P_4 plus H_2 molecules leak from the high pressure region at about 1 atm into the effusion section of the leak-source heater where the pressure is in the milli-Torr range. Within the leak path there should be a transition from hydrodynamic to molecular flow. The leak is essentially a free jet (7), and in the ideal case, would produce a shock wave in the low pressure region. The shock wave is expected to rethermalize the velocity distribution so that the species emitted from the effusion section would have the cosine distribution expected from an effusive source. Since the walls of the effusion section are at 800°-900°C, decomposition to the binary species (Eq. [2]) is also expected.

The measurements of the beam distribution suggest that for the very simple arrangement of Fig. 2, the jet is only partly rethermalized. In Fig. 3 a typical relative distribution for As actually measured at the substrate location is compared to the intensity curve expected for a cosine distribution from the source. Clearly the beam is much more sharply peaked than the cosine distribution and thus still retains some of the character imposed by hydrodynamic flow. This will be corrected in future experiments. However, the source was adequate for delineating the MBE conditions with small (~ 1 cm²) substrate crystals used in this work.

The actual As_2 flux at the target under various AsH_3 input pressures was determined from the thickness of the As layers on the Si calibration targets. Similar experiments were done with the P_2 beams. However, while the As appeared metallic and fully dense, the thin P layers protected by As were less readily observed. The usual α (white) phosphorus that is found when P_4 vapor condenses is a lattice of P_4 molecules (2). It is unlikely that solid would result from the condensation of P_2 molecules on a cold surface. It is more probable that the condensed phosphorus phase is amorphous with a less open structure and a higher density than the P_4 based α phosphorus. The densities of the various allotropic forms of phosphorus range from 1.83 g/cm³ for white phosphorus to 2.7 g/cm³ for the high pressure induced black crystalline modification. The amorphous black and red, and crystalline red forms have densities from 2.2 to 2.5 g/cm³. Not knowing the density of the solid it is necessary to resort to our knowledge of the As_2 beam flux to determine that for P_2 .

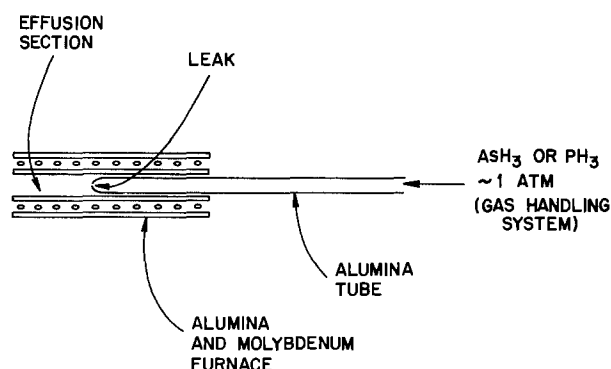


Fig. 2. The leak source

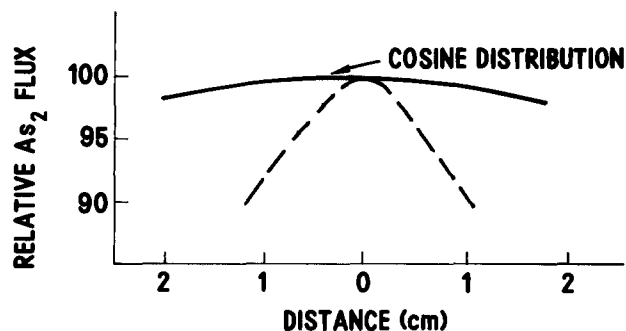


Fig. 3. Approximate relative As_2 flux distribution across the center of the substrate. Pressure on the high pressure side of the source was at about 1 atm. The curve is normalized to unity at the target center. Also illustrated is a cosine distribution.

The leak source under the pressure conditions of this experiment is, in the ideal case, expected to behave like a free jet that is formed by the expansion of a gas through a nozzle into a zero pressure region. For such a source the total flow rate will be linear with pressure and inversely proportional to the half power of the average molecular weight of the gas mixture on the high pressure side (7). In Fig. 4 the dependence of the As_2 beam flux on source input pressure is linear as expected. The dashed curve shows the P_2 flux calculated from the As_2 flux assuming free jet conditions at the leak. The rectangular data points show measured P_2 flux on the assumption that the density of the solid P is 2.7 g/cm^{-3} , the same as the most dense crystalline form. While these ways of arriving at the P_2 flux are certainly very approximate, the agreement in Fig. 4 suggests that the plotted curve is probably correct to within $\pm 25\%$. That curve is used in the balance of this work.

Gas source MBE of GaAs.—Cho (5) has shown that, depending upon the As_2/Ga flux ratio in the impinging molecular beam, a number of RHEED patterns may be observed during MBE. The easiest to study are those obtained on the (100) surface with the electron beam along the $[1\bar{1}0]$ azimuth. Summarizing much previous work, at the start of MBE, surface smoothing accompanied by the appearance of diffraction patterns characteristic of the growth conditions is observed (5, 8). These patterns result from diffraction by several different two-dimensional surface structures for the atoms constituting the crystal surface. These patterns, obtained when the diffracted electron beam strikes a phosphorescent screen, are a series of streaks with characteristic spacing. At relatively high As_2/Ga flux ratios a pattern with streak spacing one-half that of the bulk (1×1) crystal structure is observed. This is the one-half order or As-stabilized C (2×8) structure (1). With very clean substrates and vacuum systems extremely smooth layers of GaAs have been grown in the As-stabilized regime.

At relatively low As_2/Ga flux ratios a diffraction pattern having three equally spaced streaks between the bulk (1×1) streaks is obtained. This is the 1/4 order or Ga-stabilized C (8×2) structure. In the Ga-stabilized regime the crystal surface and diffraction pattern gradually degrade as the result of Ga droplet formation on the growing surface. Cho (5, 8) has also observed that in a plot of As_2/Ga flux ratio against $1/T$ the Ga and As stabilized growth regimes are separated by a transition region in which the (1×1) or faint transitional diffraction patterns exist. The boundaries of the different regions shifted, depending upon whether the transition was induced by heating or cooling. In this work the Ga and As-stabilized regimes were readily observed. However, they occur without

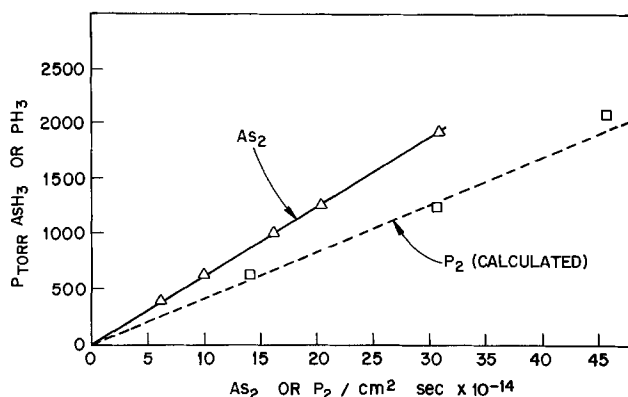


Fig. 4. Flux of As_2 (measured) and P_2 (estimated) at the target center as a function of P_{AsH_4} or P_{PH_3} on the high pressure side of the leak source. The square points were obtained upon the assumption that the density of the deposited phosphorus layer was 2.7 g/cm^{-3} .

hysteresis and, as shown in Fig. 5, at appreciably higher temperatures.

In experiments with much lower (but unspecified) Ga beam flux, Chang *et al.* (9) observed transitions between the Ga-stabilized, the transitional (3×1) , and the As-stabilized structures at temperatures intermediate between those reported by Cho (8) and those reported here for As_2/Ga flux ratios in the same range. With comparable Ga beam intensities, but very low As_2/Ga flux ratios that overlap those reported here only at $As_2/Ga = 1$, the data of Chang *et al.* for the transition from the As-stabilized to the (3×1) or 1/3 order transitional structure are at slightly higher temperature. They also report a significant variation of surface transition temperature with absolute beam intensity.

The data of Fig. 5 cover a growth range of $0.45\text{--}1.5 \mu\text{m GaAs/hr}$, corresponding to an absolute Ga beam flux at the sample ranging from 2.75 to $9.15 \times 10^{14} \text{ Ga/cm}^2 \text{ sec}$. Transitions from the 1/3 to 1/2 order pattern were gradual, over about a 10° temperature range, without a very precise transition temperature. Transitions to and from the 1/4 order structure were rapid. There seemed to be a region between the 1/3 order and 1/4 order regimes where only the (1×1) pattern could be observed. It should be pointed out that with the 5 kV electron gun used in this work the transition (3×1) pattern could only be observed under ideal conditions and actually may extend further toward the other regimes. The scatter in the data does not seem to depend upon Ga flux, but is probably related to the As_2 beam nonuniformity. In fact, the slope of the curves appear to become much shallower at $As_2/Ga < 1$ so that because of the beam nonuniformity shown in Fig. 3 different portions of the crystal surface were in different surface structural regimes. For that reason no attempt was made to study growth for $As_2/Ga < 1$ in this work.

At the highest As_2/Ga ratio studied, ~ 10.2 , smooth GaAs epitaxy without surface defects was obtained with the substrate temperature as high as 700°C . The transition to nonsmooth (i.e., Ga-droplet coated) surfaces occurred slowly within the transition region and rapidly as soon as the diffraction pattern characteristic of the Ga-stabilized structure appeared. A

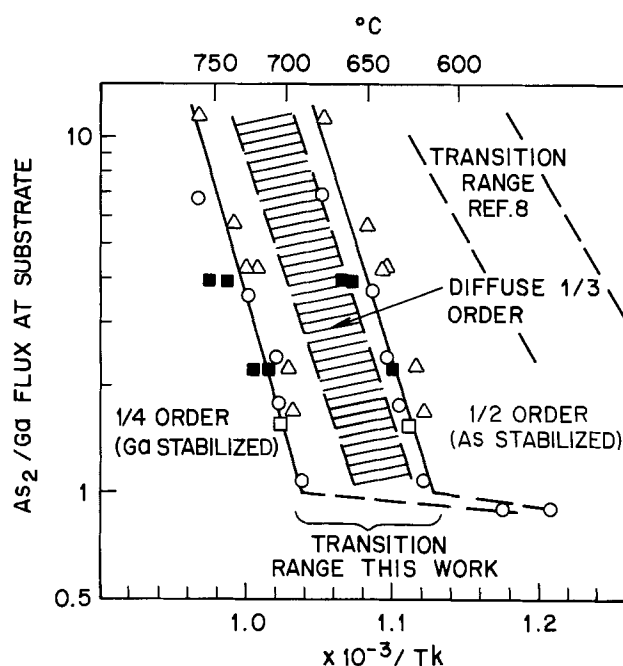


Fig. 5. As_2/Ga molecular beam flux ratio as a function of temperature for transitions between surface structures during MBE of GaAs. The growth rates were: Δ , $0.45 \mu\text{m/hr}$; \circ , $0.8 \mu\text{m/hr}$; \blacksquare , $1.25 \mu\text{m/hr}$; and \square , $1.5 \mu\text{m/hr}$.

clear demarcation from smooth to matte growth was not observed in the transition region. However, the way the experiments were done, changing temperature at a given As_2/Ga flux ratio and then repeating the experiment at different ratios after resmoothing the surface with As-rich growth, made it inconvenient to attempt to observe slow or very subtle surface appearance changes.

Since the apparatus was not designed to give high purity growth, little attempt was made to electrically characterize the grown layers. Several layers were grown on Cr-doped semi-insulating substrates. These samples were deliberately doped with Sn from a separate Sn-containing effusion oven. Hall and several photoluminescence measurements were made. For most of the samples studied ($N_D - N_A$) was in the range $2-4 \times 10^{17} \text{ cm}^{-3}$ and Hall mobilities were about $3000 \text{ cm}^2 \text{ V}^{-1} \text{ sec}^{-1}$ at room temperature. This is about 15% lower than would be expected for the best mobilities for GaAs at that electron concentration. A few samples had mobilities as good as the best reported [e.g., $4200 \text{ cm}^2 \text{ V}^{-1} \text{ sec}^{-1}$ at $(N_D - N_A) = 1.5 \times 10^{17} \text{ cm}^{-3}$]. For these the room temperature photoluminescence peak intensity was as high as that obtained here for equivalently doped liquid epitaxy layers.

Gas source MBE of InP.—Indium phosphide layers were grown on (100) InP surfaces with the same leak source that was used for GaAs growth. During growth RHEED patterns were observed with the electron beam along the $[\bar{1}\bar{1}0]$ azimuth. The 1/2 order C (2×8) pattern could readily be observed on the surface after heating to 550°C with a P_2 flux of $\sim 5 \times 10^{15} \text{ P}_2/\text{cm}^2 \text{ sec}$ to remove oxide. Opening the shutter to the In oven started growth and the diffraction pattern usually became sharper and completely streaked. The sample surface during growth was visually observed while temperature was increased at a given P_2 and In beam intensity.

Usually a rapid change in gross surface morphology from smooth to matte could be observed with no change in diffraction pattern. The change in the temperature for this smooth-to-matte surface transition as a function of P_2/In flux ratio is given in Fig. 6 for InP growth rates ranging from 0.7 to $1.3 \mu\text{m/hr}$ ($3.75-7.3 \times 10^{14} \text{ In/cm}^2 \text{ sec}$). With no In beam and a P_2 beam at $7.5 \times 10^{15} \text{ P}_2 \text{ cm}^{-2} \text{ sec}$, the smooth-to-matte transition occurred at $600^\circ \pm 10^\circ\text{C}$. The 1/4 order, C(8×2) pattern could only occasionally be observed when the wafer was rapidly heated to a regime where liquid In was generated on the crystal surface.

In all cases studied the smooth-to-matte transition represented the formation of In droplets on the crystal surface. The surfaces of several InP crystals are shown with phase contrast microscopy in Fig. 7. Figure 7(a) shows the surface of an InP sample heated to 605°C with the P_2 flux at $5 \times 10^{15} \text{ P}_2 \text{ cm}^{-2} \text{ sec}^{-1}$ for several minutes. Etching of the surface and In droplet formation are clearly visible. The crystal shown in Fig. 7(b) is that used for the experimental point at the molecular beam flux ratio $\text{P}_2/\text{In} = 4.6$ in Fig. 6. The run was ended immediately after the smooth-to-matte transition. Figure 7(c) and (d) are micrographs of two locations at opposite ends of the $\sim 1.5 \text{ cm}$ wide crystal used for the experimental point at $\text{P}_2/\text{In} = 1.0$ in Fig. 6. The 10-20% variation in the P_2/In flux ratio across the crystal as the result of P_2 beam inhomogeneity (Fig. 3) and tilting of the sample relative to the In oven (Fig. 1) yield the differences in morphology at the relatively P_2 -rich end [Fig. 7(d)] and the relatively In-rich end, Fig. 7(c). Figures 7(c) and (d) show the great sensitivity of the surface morphology to flux ratio near the smooth-to-matte transition. For several layers grown on the right side of the curve on Fig. 6, surfaces were extremely smooth with some structure barely visible with phase contrast microscopy but at too low a contrast to be photographed. No electrical or optical characterization of the InP layers was done.

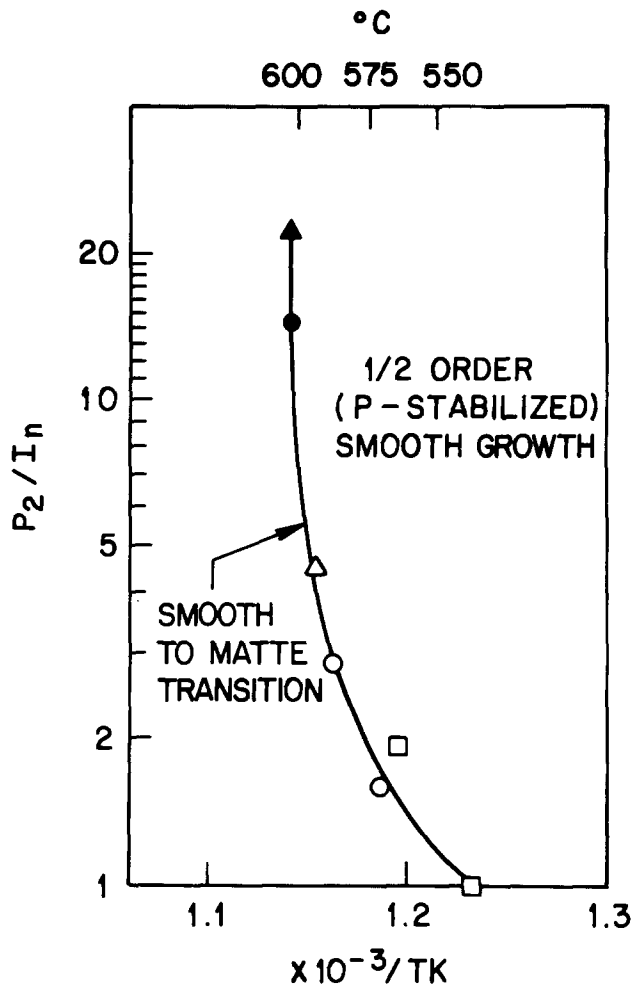


Fig. 6. P_2/In molecular beam flux ratio as a function of temperature for the observed transition from growth of InP with a smooth to growth with a matte surface.

The data of Fig. 6 and the morphological studies represented by Fig. 7 suggest that the limitation represented by the smooth-to-matte transition is simply the more rapid loss of P than In from the crystal lattice at the surface. In other words, the data of Fig. 6 represent the liquidus curve for the In plus P liquid in contact with the InP solid under the P_2 and In flux conditions of the experiment. Since each two impinging In atoms consume one P_2 molecule, the P_2 flux, less half of the In flux, represents the excess flux of P_2 molecules that are equivalent to a partial pressure of P_2 over the InP. The flux F of a vaporizing species can be related to its equilibrium partial pressure P by means of the Langmuir relation

$$F = \frac{P\alpha}{(2\pi mkT)^{1/2}} \quad [3]$$

where α is the accommodation coefficient. If α is taken as constant with T , a plot of $\log [(F_{\text{P}_2} - 1/2 F_{\text{In}}) T^{1/2}]$ against $1/T$ should be equivalent to a plot of $\log P_{\text{P}_2}$ against $1/T$ and should be linear. The data of Fig. 6 are replotted in Fig. 8. The factor of $T^{1/2}$ is almost constant over the temperature range under consideration and has been omitted. For comparison, the partial pressure of P_2 in equilibrium with the In-P liquidus (10) against $1/T$ is also given in Fig. 8. The two curves appear to be equivalent.

Since the smooth-to-matte transition is actually the liquidus-partial pressure boundary, Fig. 8 represents the maximum InP-MBE growth temperature at any P_2 flux. A leak source with a flux ten times that of the source used in this work is feasible and from Fig. 8 would have an upper InP growth temperature limit of

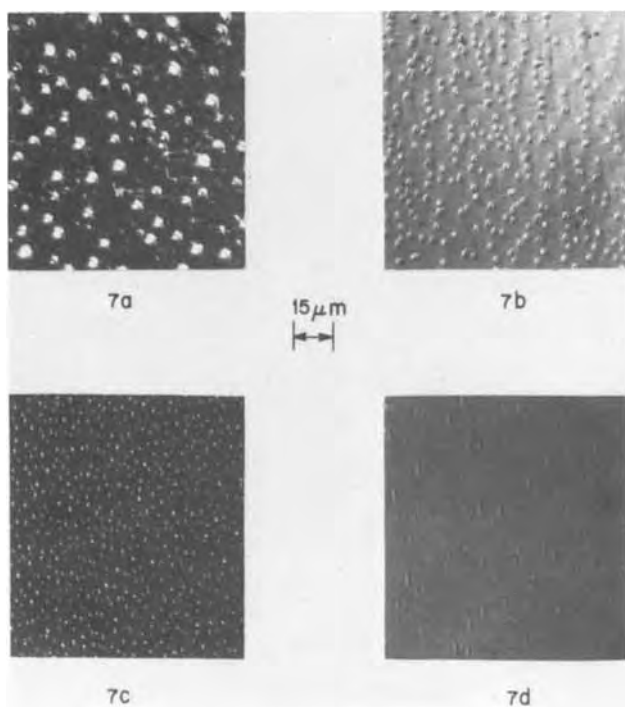


Fig. 7. (a) InP surface after several minutes at 605°C with a P_2 molecular beam flux of $5 \times 10^{15} P_2/cm^2$ sec. The smooth-to-matte transition occurred between 600° and 605°C. (b) InP surface after the smooth-to-matte transition during MBE at a P_2/In molecular beam flux ratio of 4.6. (c) and (d) InP surface at two different locations after the smooth-to-matte transition during MBE at a P_2/In flux ratio of 1.0.

650°C at infinitely small growth rate. A small additional P_2 flux with the appropriate In flux would then yield InP growth.

Conclusion

A series of experiments have demonstrated that with an appropriate input device and vacuum system, AsH_3 and PH_3 could be used to generate As_2 and P_2 beams for molecular beam epitaxy of GaAs, InP, and by extension, crystalline solid solutions of GaAs and InP. The leak source devised for this work permitted sufficiently intense beams that GaAs and InP could be grown at temperatures as high as 700° and 600°C, respectively. For InP this is higher than previously reported for MBE of these semiconductors. For GaAs, Gossard and Wiegmann (11) have obtained growth to approximately 750°C by generating an As_2 beam with an auxiliary heater on the end of a solid As source effusion cell. The limitation on the growth temperature of InP, and probably also GaAs by this technique appears only to be the formation of the liquidus as the result of a higher vaporization than flux rate of the group V element at the crystal surface. With modified sources to yield a factor of ten greater flux it is expected that growth at 750°C for GaAs and 650°C for InP could be achieved. Probably more important is the ease of control over beam flux that can be achieved with the gas source. Such a source will be useful for the growth of mixed crystals containing both As and P.

Acknowledgments

The author would like to thank G. Kubiak, J. Robinson, and S. Sumski for their help in building and running the MBE apparatus, and M. Cardillo, A. Y. Cho, and J. C. Bean for their advice and discussions during the course of this work.

Manuscript received May 5, 1980.

Any discussion of this paper will appear in a Discussion Section to be published in the June 1981

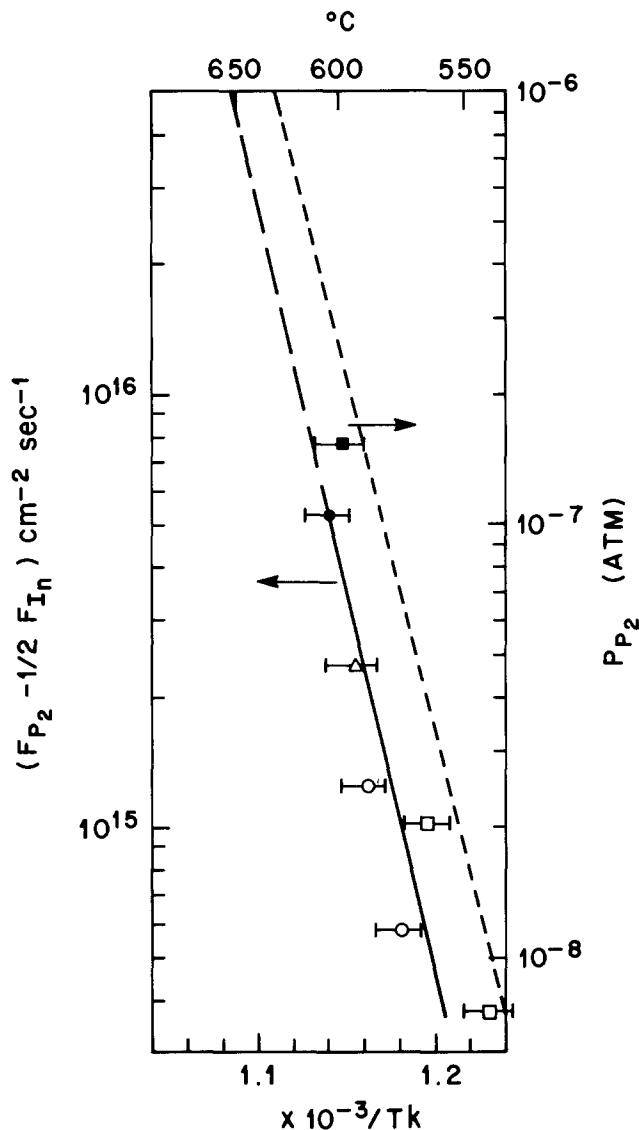


Fig. 8. Excess P_2 flux $(F_{P_2} - 1/2 F_{In})$ and equilibrium P_2 partial pressure against $1/T$ at the smooth-to-matte transition during MBE of InP. Except for \blacksquare which is for a P_2 beam only, the experimental points are those of Fig. 6.

JOURNAL. All discussions for the June 1981 Discussion Section should be submitted by Feb. 1, 1981.

Publication costs of this article were assisted by Bell Laboratories.

REFERENCES

1. A. Y. Cho and J. R. Arthur, in "Prog. Solid State Chemistry," Vol. 10, G. Somorjai and J. McCal-din, Editors, p. 157, Pergamon, New York (1975).
2. "Phosphorus: Properties of the Element and Some of its Compounds," T. D. Farr, Editor, Tennessee Valley Authority, Chemical Engineering Report No. 8, Muscle Shoals, Alabama (1950).
3. H. C. Casey, Jr., A. Y. Cho, and P. A. Barnes, *IEEE J. Quant. Electron.*, **qe-11**, 467 (1975).
4. W. T. Tsang, *Appl. Phys. Lett.*, **34**, 473 (1979).
5. A. Y. Cho, *J. Appl. Phys.*, **47**, 2841 (1976).
6. M. Hansen and K. Anderko, "Constitution of Binary Alloys," McGraw-Hill, New York (1958).
7. J. P. Anderson, in "Molecular Beams and Low Density Gas Dynamics," P. P. Wegener, Editor, p. 1, Marcel Dekker, New York (1974).
8. A. Y. Cho, *J. Vac. Sci. Technol.*, **8**, 531 (1971).
9. L. L. Chang, L. Esaki, W. E. Howard, R. Ludeke, and G. Schul, *ibid.*, **10**, 655 (1973).
10. M. B. Panish, *J. Cryst. Growth*, **27**, 6 (1974).
11. A. C. Gossard and W. Wiegmann, Private communication.

Phosphorus Silica Glass as Dopant Source

M. L. Polignano, P. Picco, and G. F. Cerofolini

Divisione MOS, SGS-ATES, 20041 Agrate, Milano, Italy

ABSTRACT

The behavior of phosphorus silica-glass (PSG) as a silicon dopant source has been studied by measuring PSG etch rate, depth, and resistivity of the junction formed after diffusion. Our results are in agreement with known data concerning phosphorus diffusion in a flat region.

The system formed by a silicon surface covered by a layer of doped oxide is not yet well characterized. This is due both to an insufficient knowledge of the properties of the oxide and to the difficulties of a mathematical description of the diffusion from one phase to another. In the past ten years we have seen several efforts to set up reliable systems for measuring the dopant (phosphorus and boron) level in the oxide (1-4) as well as to solve the diffusion problem (5-8). However, the diffusion problem has satisfactorily been solved only for phosphorus concentrations below 5% (5, 7, 8), when the high-concentration-PSG/silicon system was considered, only under 5% concentration in PSG agreement between the model and experimental results is obtained.

Barry, for instance, presented conclusions which though they claim to show linearity, actually evidence high concentration effects (7). He found [Fig. 5 of Ref. (7)] that the linearity predicted by his model between surface concentration C_0 and phosphorus concentration in the oxide holds true only for $C \lesssim 4 \times 10^{20}$ P atoms/cm³ (≈ 1 m/o).

In this work, we have undertaken the study of diffusion from high concentration (≈ 10 m/o) PSG, in order to verify whether the oxide characteristic induces a phosphorus profile in silicon as complex as the one described by Fair and Tsai [kink effect (10)], and in view of a possible use of this phosphorus source to form source and drain regions of n-channel MOS transistors.

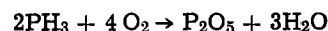
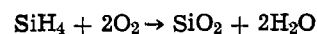
Key words: diffusion, junction, resistivity.

The techniques used in this work are conventional V/I and x_j measurements of the layers formed after diffusion on p-type samples, and etch-rate measurement of the oxide, in order to characterize diffusion within it.

Experimental and Results

P-type, 3 in., (100) oriented, 1.7-2.6 Ω -cm (corresponding to a substrate concentration 8×10^{15} B atoms/cm²) Si slices were used in this work.

PSG was deposited in an open-tube reactor at 420°C by simultaneous oxidation of silane and phosphine

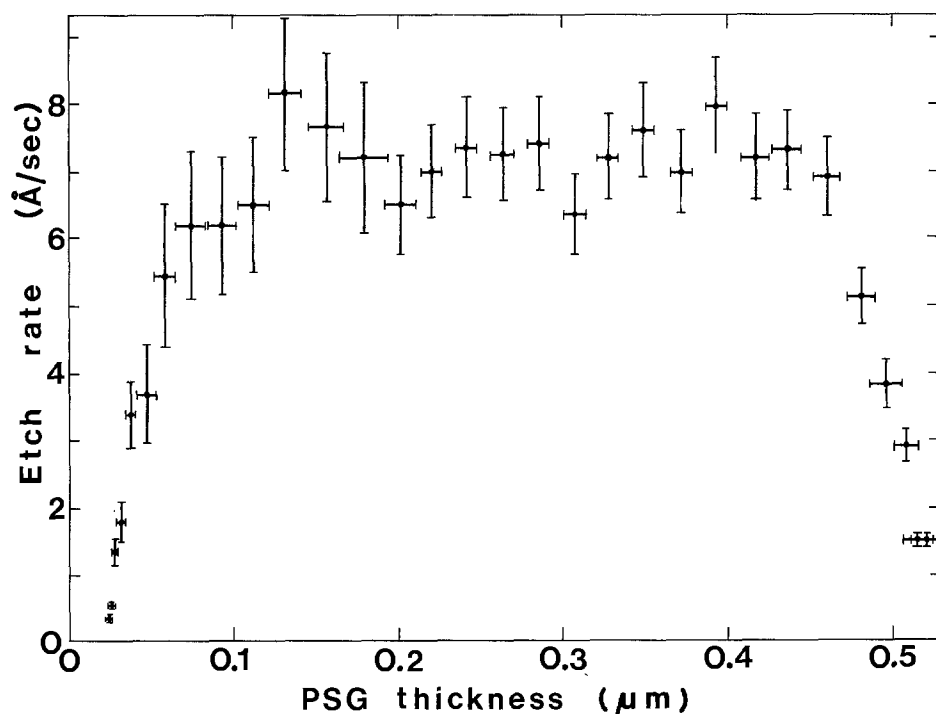


in the proportion required to have a P_2O_5 molar concentration of about 10% ($\approx 3.9 \times 10^{21}$ P atoms/cm³) and for a time sufficient to grow a thickness of about 5000Å.

After a moderate annealing (N_2 , 800°C, 30 min), the wafers were partitioned in several groups and were treated at three different temperatures (940°, 1000°, 1050°C) for three lapses of time (0.25, 1, 2.25 hr) in a combined way. Measurements of V/I and junction depth x_j were carried out on all samples.

The etch rate profile was determined at 15°C only on the samples treated for 2.25 hr by using a P-etch solution (17 cm³ 49% HF, 10 cm³ 70% HNO₃, 300 cm³ H₂O) diluted in five parts of H₂O to increase sensitivity and accuracy.

Fig. 1. Etch-rate profile for PSG after 2.25 hr annealing at 940°C. The shape is qualitatively the same for all the considered temperatures. Profiles obtained by successive etching of the doped oxide film. Etch rate is defined as $v(x_i) = (x_i - x_{i+1})/\Delta t_i$ (x_i , film thickness before the single etching; x_{i+1} , film thickness after the single etching; Δt_i , etching time). The last point is chosen as the last point keeping a physical meaning (i.e., satisfying the condition $v \geq v_0$). This point corresponds to a total asportation of the oxide on about 25% of the wafer surface, owing to lack in uniformity of the PSG film: for this it does not coincide with the origin.



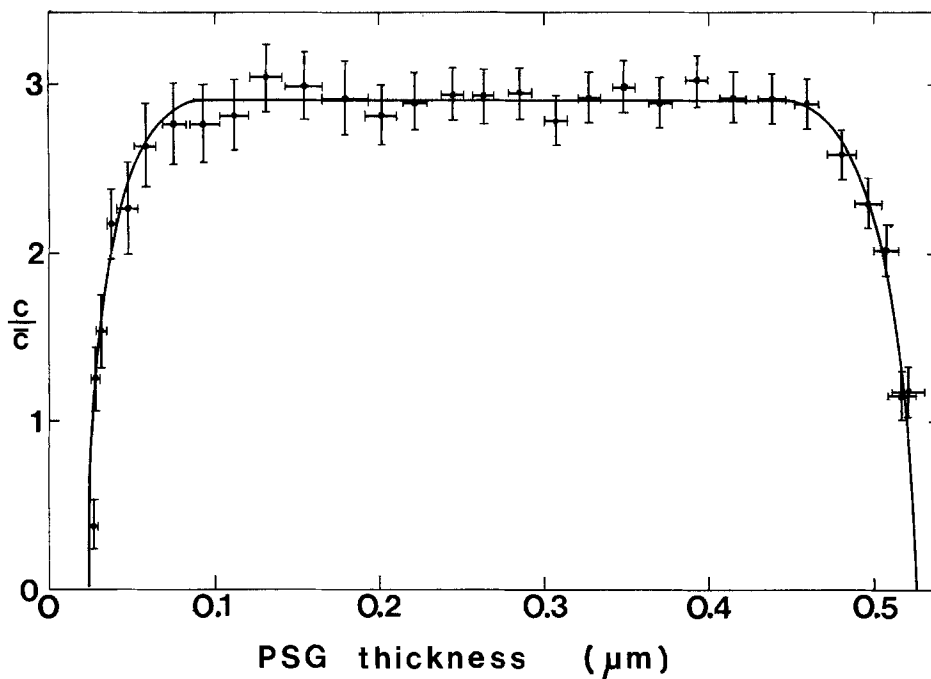


Fig. 2. Phosphorus concentration profile in PSG after 2.25 hr annealing at 940°C. The profile does not extrapolate to the origin for what was reported in Fig. 1. The estimated extrapolation to $C = 0$ is used for Q^{Si} calculations.

All our etch rate profiles have the same qualitative shape: the one annealed at 940°C for 2.25 hr is shown in Fig. 1. It is known (1, 2), and we have verified by measuring the etch rate of nondensified samples of calibrated concentration (measured by neutron activation analysis) that the etch rate of PSG in P-etch v depends upon phosphorus concentration c according to

$$v(c) = v_0 \exp(c/\bar{c}) \quad [1]$$

where $v_0 = v(0)$ and \bar{c} is a suitable concentration. Because of its physical meaning v_0 can be measured on "undoped PSG" (our readers will excuse this contradiction) and has been found to depend upon thermal treatment; on the contrary, \bar{c} has been found to be a constant. Table I confirms this statement.

Equation [1] allows us to transform kinetic profiles into concentration profiles: one of them is shown in Fig. 2. These profiles allow the estimate of the thickness x_d of the two phosphorus-depleted PSG layers, both next to silicon (x_d^{Si}) and facing vacuum (x_d^v); moreover, via a numerical integration, the total amount of phosphorus diffused into silicon (Q^{Si}) or toward vacuum (Q^v) are easily computed.

Table II reports these quantities and shows that $x_d^{Si} \approx x_d^v$, $Q^{Si} \approx Q^v$; this is an evidence that in the considered system the rate-determining step is the diffusion process in the oxide.

Figures 3 and 4 show the results of V/I and x_j measurements. All the presented data can be used to test different hypotheses on concentration profile of phosphorus in silicon. To this aim, a choice of diffusion coefficient D , which depends on concentration, and/or a determination of surface concentration C_0 are implied ($Q \propto C_0 \sqrt{Dt}$).

Table I. Etch rate parameters in diluted P-etch after 2.25 hr annealing (V_{max} determined from the flat zone of the etch rate profile; v_0 measured on samples of undoped oxide; \bar{c} follows from Eq. [1])

Temperature (°C)	V_{max} (Å/sec)	v_0 (Å/sec)	\bar{c} (10^{21} cm $^{-3}$)
940	7.1 ± 0.3	0.38 ± 0.02	1.33 ± 0.05
1000	6.2 ± 0.2	0.33 ± 0.03	1.32 ± 0.05
1050	5 ± 0.3	0.28 ± 0.02	1.36 ± 0.07

Let us consider the hypothesis of erfc or gaussian profile. The surface concentration C_0 can be determined with the aid of Irvin curves (9).

With such C_0 , using the value for D given by Fair and Tsai (10), relative to the flat region, and considering it valid for the whole diffusing phosphorus, much higher Q with respect to the measured ones (Q^{Si}) are obtained (see Q_e and Q_G in Table III) (here and in the following, Q will indicate the generical phosphorus dose injected in silicon, Q^{Si} our experimental value of it, Q_e , Q_G , and Q_b the doses compatible with V/I and x_j measurements, relative to erfc, gaussian or box profile, respectively).

Trying to avoid this disagreement, a lower diffusion coefficient must be chosen. The intrinsic value for D can be considered (10, 11) but unreasonably high C_0 results, calculated from x_j values. The intermediate (and correct) possibility to test the erfc or gaussian profile hypothesis is to use the diffusion coefficient which fits Q^{Si} values, assuming again C_0 is known (from V/I and x_j). The result is a diffusion coefficient decreasing with increasing temperature.

In scheme 1 this whole discussion is summarized. The hypothesis of erfc or gaussian profile must then

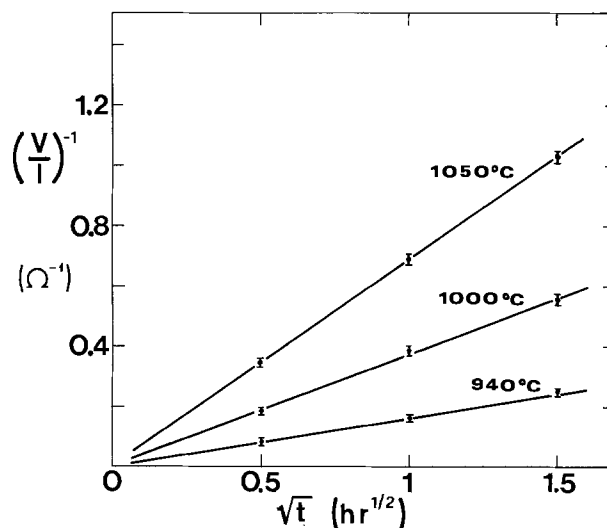


Fig. 3. V/I vs. time. V/I measured with a four-point probe

Table II. x_d and Q values after 2.25 hr annealing

Temperature (°C)	x_d^{Si} (Å) ($\pm 100\text{Å}$)	x_d^v (Å) ($\pm 100\text{Å}$)	$\frac{x_d^{Si} - x_d^v}{x_d^{Si}}$	Q^{Si} (10^{16} cm^{-2}) ($\pm 10\%$)	Q^v (10^{16} cm^{-2}) ($\pm 10\%$)	$\frac{Q^{Si} - Q^v}{Q^{Si}}$
940	600	720	0.2	0.51	0.58	0.12
1000	1260	1140	0.1	0.79	0.74	0.06
1050	1720	1550	0.1	1.0	1.0	0

Table III. Total amounts of phosphorus in silicon: measured and deduced by different doping profiles. Q_G^{Si} , Q_e^{Si} , and Q_b^{Si} refer to the amounts respectively deduced by gauss, erfc, and box profiles.

Temperature (°C)	Q^{Si} (10^{16} cm^{-2}) ($\pm 10\%$)	Q_e^{Si} (10^{16} cm^{-2}) ($\pm 10\%$)	Relative error $ \frac{Q_e^{Si} - Q^{Si}}{Q^{Si}} $ (%)	Q_G^{Si} (10^{16} cm^{-2})	Relative error $ \frac{Q_G^{Si} - Q^{Si}}{Q^{Si}} $ (%)	Q_b^{Si} (10^{16} cm^{-2})	Relative error $ \frac{Q_b^{Si} - Q^{Si}}{Q^{Si}} $ (%)
940	0.51	0.42	18	0.39	24	0.35	31
1000	0.79	2.99	278	2.26	186	0.82	4
1050	1.0	13.42	1242	11.24	1024	1.61	61

be ruled out. The same holds true for any other profile for which $Q > Q^{Si}$.

The problem, "Does a profile exist for which $Q \leq Q^{Si}$, for the given V/I and x_j ?" arises. An affirmative answer is vital for the consistency of our data. Formally stated, this means we must first look for the profile $C(x)$ that, for given V/I and x_j , minimizes Q , which is then to be compared to Q^{Si} .

The variational calculus shows that such a profile is the box-function one, corresponding to the minimum dose Q_b . If Q_b were higher than our measured value Q^{Si} , an unresolvable contradiction would result. If it were lower, it would mean we are in presence of electrically nonactive phosphorus in our system, but no indication would arise about concentration profile.

But in this case good agreement results between the box-type value Q_b and Q^{Si} (see Table III): this

is a strong indication for the existence of a flat region in phosphorus profile, since a box-type profile is the one which has a zone, near the surface, where $C(x)$ ranges in a region of nearly constant mobility (12), and in which the most part of the dopant is contained.

Discussion

At the first sight the results of our work seem to be in such a striking disagreement with previous observation to deserve a more accurate analysis. This seeming disagreement can be removed by invoking the diffusion properties of phosphorus at high concentration, i.e., the profile of phosphorus in silicon [flat region near the surface, then a sudden decrease (kink), followed by a typical complementary error function behavior (tail)] are to be ascribed to the sufficiently high surface concentration of phosphorus, independently of the type of phosphorus source.

It is well known that conductivity and phosphorus amount of the whole diffused region are almost exclusively given by the flat region (plateau), while kink and tail position determine the junction depth.

According then to Fair and Tsai formulas (10), the total amount of phosphorus diffused into silicon after a time t is given by

$$Q = \frac{1}{2} C_0 x_0 \quad [2]$$

where

$$C_0 = \frac{1}{2} n_s (1 + 2.04 \times 10^{-41} n_s^2) \quad [3]$$

$$x_0 = 2(D_1 = (n_s/n_i)^2 h t)^{1/2} \quad [4]$$

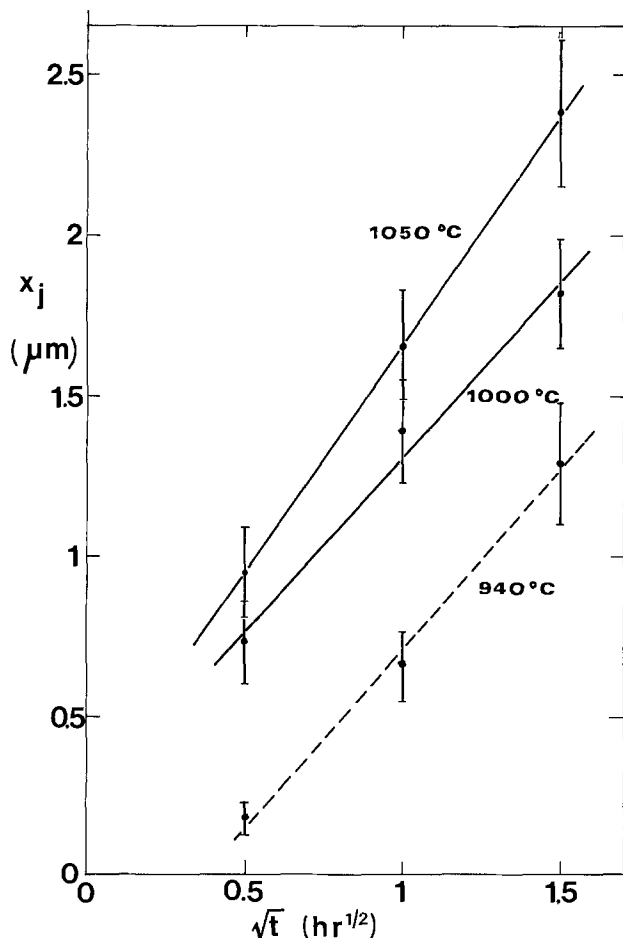
n_s being the electrically active surface concentration, n_i the intrinsic electron concentration, D_1 the intrinsic diffusion coefficient of the E-center with doubly ionized vacancy, h (≈ 2) the electric field enhancement factor. Inserting Eq. [3] and [4] in Eq. [2] and solving for n_s allows determination of x_0 and C_0 .

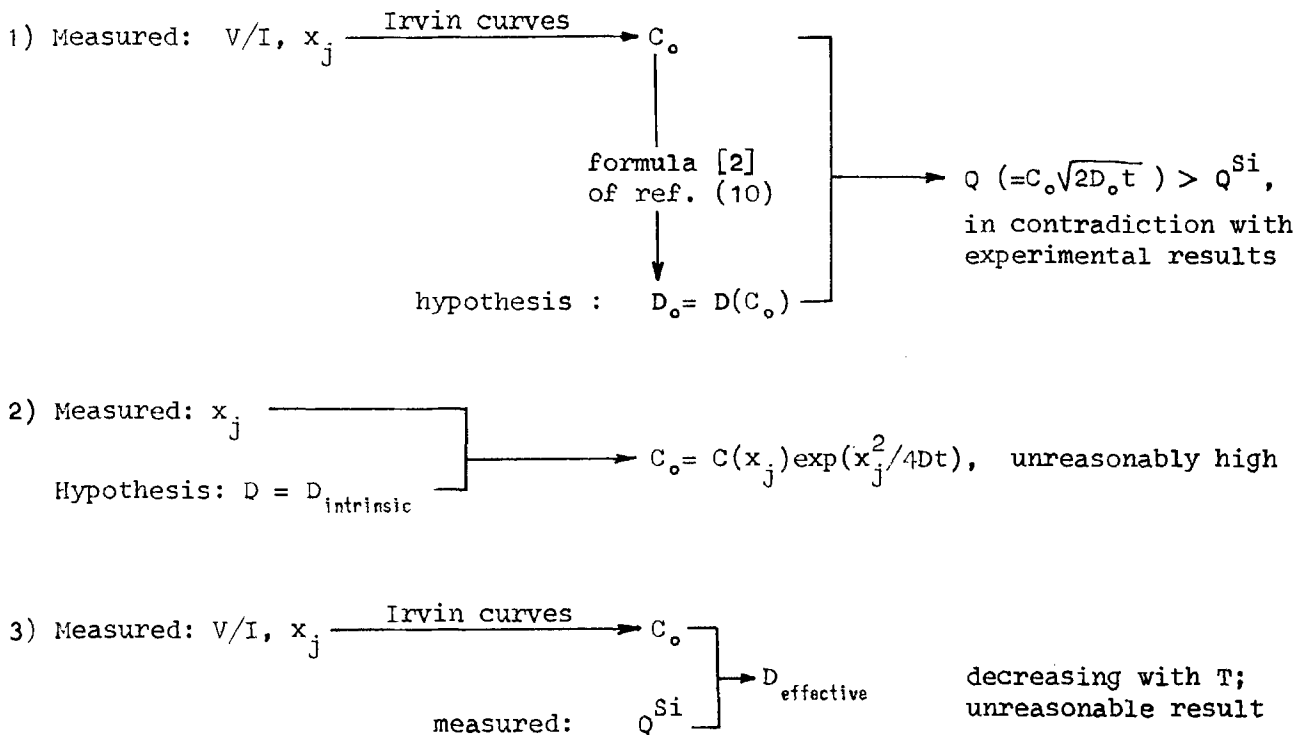
The results are reported in Table IV and show that C_0 decreases as diffusion temperature increases; this because the rate-determining step is the diffusion process in the oxide. Since x_0/x_j ranges from 0.36 to 0.50 (see Table IV) the concentration profile approaches the box-type one as temperature increases.

This fact may be the cause of the large disagreement between Q_e^{Si} (or Q_G^{Si}) and the experimental data at high temperature. The following conclusion may be

Table IV. Surface concentration and depth of the flat region as follows from (10, 11) for the measured Q^{Si}

Temperature (°C)	Q^{Si} (10^{16} cm^{-2})	C_0 (10^{20} cm^{-3})	x_0 (μm)	x_0/x_j
940	0.51	2.2	0.46	0.36
1000	0.79	1.9	0.83	0.46
1050	1.0	1.7	1.18	0.50

Fig. 4. Junction depth x_j vs. time



Scheme 1. Why gaussian (and erfc) profiles have been rejected.

drawn. The PSG etch rate in P-etch has been characterized as a function of the annealing temperature; measurements of the parameters v_o and \bar{c} in formula [1] clearly showed that only v_o depends on annealing temperature, while \bar{c} is constant in the considered temperature interval.

The behavior of high concentration (10%) PSG films also as dopant sources has been studied. It has been confirmed that this behavior is determined by diffusion in oxide. Moreover, for the first time consistency tests between the measured quantities (Q^{Si} , x_j , V/I) and different possible phosphorus concentration profiles have been performed. It has been found that at the considered PSG concentrations kink effect takes place.

Addendum

After the first submission of this paper, a referee put forward a criticism to value and limit of our experimental data in interpreting the diffusion mechanism. In particular, he showed that "the method used to reach the conclusions is . . . an indirect one, and the results, although self-consistent with the experimental data, must be considered speculative in nature."

The criticism is sound and so we have modified the text to present our conclusions according to their speculative character, but we have also measured a profile to verify the conclusions. This profile has been measured by determining x_j after annealing at 1050°C for 2.25 hr on substrates of different resistivities.

The profile is shown in Fig. 5. Although the experimental points do not directly give information about the flat region, however they support our conclusion mentioned earlier and agree with Fair and Tsai results.

Indeed, the three experimental points at lowest concentrations align along an erfc type profile with $D = 8.6 \times 10^{-14}$ cm²/sec. The extrapolation to the surface (dashed line) gives as previously said, unreasonably high C_o value.

The experimental point F fortuitously corresponds to the x_o value; at the point K, according to Eq. [2], [3], and [4] of Ref. (11), with our C_o (see Table IV),

phosphorus concentration deviates from the erfc-type profile.

These considerations are supported by the following consistency test between our results and Fair and

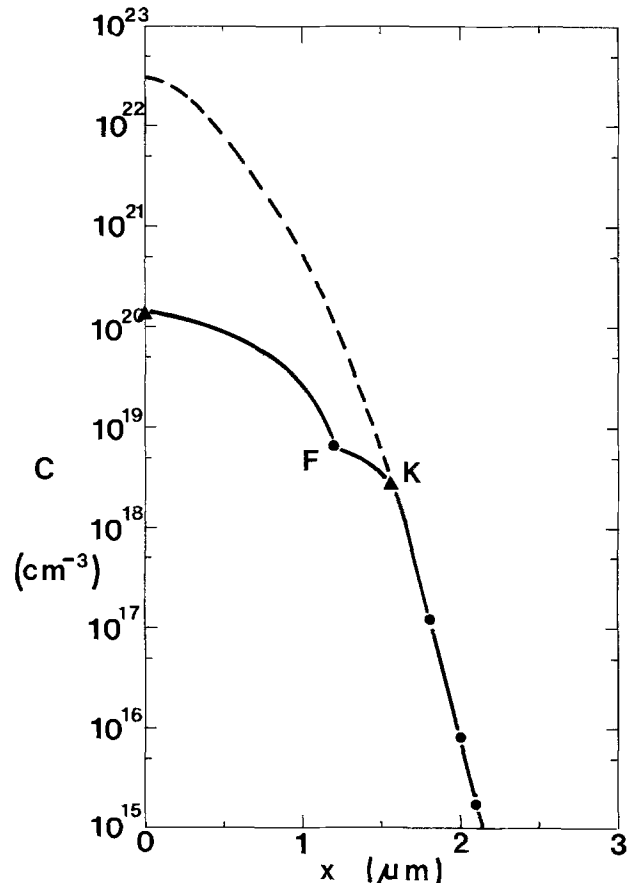


Fig. 5. Phosphorus concentration profile in silicon, after 2.25 hr annealing at 1050°C. Dashed line, extrapolation to the surface of the erfc-type part of the profile.

Tsai model. This model establishes a relation between diffusion coefficient in tail region, D_{TAIL} , and phosphorus surface concentrations C_o . Then a measure of D_{TAIL} is an independent, though indirect, measure of C_o .

We have measured diffusion coefficient in the tail region, and we then can compute $C_o:C_o = 1.2 \times 10^{20} \text{ cm}^{-3}$ results, consistent with the value $C_o = 1.7 \times 10^{20} \text{ cm}^{-3}$ (see Table IV) obtained in the last section of the paper.

Manuscript submitted Feb. 29, 1980; revised manuscript received June 11, 1980.

Any discussion of this paper will appear in a Discussion Section to be published in the June 1981 JOURNAL. All discussions for the June 1981 Discussion Section should be submitted by Feb. 1, 1981.

Publication costs of this article were assisted by SGS-ATES.

REFERENCES

1. W. Kern, *RCA Rev.*, **37**, 3; 78 (1976).
2. A. C. Adams and S. P. Murarka, *This Journal*, **126**,

- 334 (1979).
3. A. C. Adams, C. D. Capio, S. E. Haszko, G. I. Parisi, E. I. Povilonis, and Mc D. Robinson, *ibid.*, **126**, 313 (1979).
4. A. N. Saxena and R. A. Powell, in "The Physics of SiO₂ and Its Interfaces," S. T. Pantelides Editor, p. 195, Pergamon Press, New York (1978).
5. R. N. Ghoshtagore, *Solid-State Electron.*, **17**, 1065 (1974).
6. M. L. Barry and P. Olofsen, *This Journal*, **116**, 854 (1969).
7. M. L. Barry, *ibid.*, **117**, 1405 (1970).
8. K. M. Mar, *ibid.*, **126**, 1252 (1979).
9. J. C. Irvin, *Bell Syst. Tech. J.*, **41**, 387 (1962).
10. R. B. Fair and J. C. C. Tsai, *This Journal*, **124**, 1107 (1977).
11. R. B. Fair, *ibid.*, **125**, 323 (1978).
12. G. Masetti, D. Nobili, and S. Solmi in "Semiconductor Silicon 1977," H. R. Huff and E. Sirtl, Editors, p. 648, The Electrochemical Society Softbound Proceedings Series, Princeton, N.J. (1977).

Auger Electron Spectroscopy Study of the Chemisorption of Iodine on Zirconium

Gopala N. Krishnan, Bernard J. Wood, and Daniel Cubicciotti*

SRI International, Menlo Park, California 94025

ABSTRACT

Auger electron spectroscopy was used to observe the relative coverage of iodine on the surface of a zirconium crystal exposed to a flux of iodine gas molecules. The zirconium was heated to temperatures of 1000-1300 K, and the iodine pressures corresponded to 10^{-4} - 10^{-6} Pa (10^{-9} - 10^{-11} atm). Iodine was found to chemisorb on the surface; the isotherms corresponded to the Temkin model. Isotherms derived from these isotherms showed a logarithmic dependence of pressure on reciprocal temperature. The slopes of the isotherms indicated an enthalpy of formation of the surface layer of about 60 kcal/mole. The thermodynamics of formation of an iodine adspecies on a zirconium surface were compared with the thermodynamics of formation of zirconium monoiodide, the lowest solid iodide of zirconium.

The iodine-induced stress corrosion cracking (SCC) of zirconium involves chemical reactions between clean zirconium surface and iodine-containing species (1). That is, in the SCC process, fresh metal surface is created as cracks grow. The freshly formed surface apparently reacts with iodine-containing species in the system as evidenced by the fact that the topography of the cracks formed in the metal and the stresses required to form and extend the cracks are different in an iodine-containing environment than in a noniodine-containing environment. Consequently adsorption of iodine-containing species at the crack tip is likely to be the critical chemical reaction in the SCC process. Such a surface reaction would weaken the Zr-Zr bonds in certain crystallographic planes in the metal, leading to the observed effects of iodine on the failure process.

The reaction of iodine-containing species with clean zirconium surfaces is therefore central to the mechanism of iodine-induced SCC of zirconium alloys; however, no studies have been made of this reaction. The rates of reaction of iodine with zirconium have been studied but only under conditions in which the metal was covered by surface layers of zirconium iodides (1-3).

In the present study, Auger electron spectroscopy (AES) was used to monitor the surface of a clean zirconium foil exposed to a flux of iodine vapor. The AES technique provided a quantitative measurement of the concentration of iodine chemisorbed on the surface as a function of zirconium temperature and iodine flux. The conditions of this AES study are different from those present in an SCC crack during formation and propagation; however the pertinent results are the demonstration of chemisorption of iodine on clean zirconium and the thermodynamic stability of the chemisorbed state.

Experimental Program

AES is a surface-sensitive analytical technique that has been used extensively to study gas-metal interactions at the monolayer levels (4). During AES analysis, the specimen is bombarded with a medium energy (~3 keV) electron beam, which causes secondary electron emission from the specimen. Some of these secondary electrons consist of Auger electrons arising from electronic transitions in the atoms present in the specimen. The technique is surface sensitive because of the limited escape depth of the Auger electrons. For electron energies from 50 to 500 eV, the range of interest in this study, the analysis depth varies from 0.5 to 1 nm.

* Electrochemical Society Active Member.

Key words: surfaces, adsorption, stress corrosion.

The concentration of a particular elemental component in the near-surface atomic layer of a specimen determines the amplitudes of the peaks in its Auger spectrum. But the proportionality factor relating concentration to peak amplitude, frequently referred to as the Auger yield, is a complex quantity that cannot be precisely evaluated from first principles (4). However, changes in concentration of a component can be followed with good precision by measuring the growth or decay of an Auger peak.

Apparatus and materials.—All experiments were conducted in an ultrahigh vacuum system capable of attaining 10^{-8} Pa base pressure. The AES analyses were performed with a Varian cylindrical mirror analyzer with an integral electron gun. The incident electron beam was ~ 100 μm in diameter at the specimen and was normally operated at 3000 eV and 5 μA . The total pressure in the system was measured with an ionization gauge, and the partial pressures of gas components were determined with a quadrupole mass spectrometer. A rastered, 3-keV argon ion beam was used to clean the specimen surface. The arrangement of the various components with respect to the specimen is shown in Fig. 1.

The specimen used in this study was a high purity zirconium foil 0.0127 cm thick and ~ 0.3 cm wide. The strip was resistively heated, and its temperature was monitored by a Chromel-Alumel thermocouple spot-welded to the back of the specimen at its midpoint. A 0.01 cm diam area in the center of the specimen was analyzed by the Auger electron spectrometer.

Iodine was introduced into the vacuum chamber through a glass-lined stainless steel capillary tube¹ (~ 0.4 mm ID \times 90 cm long). The upstream end of the capillary tube was attached to a Pyrex glass manifold by means of a Cajon ultra-Torr stainless steel vacuum

¹ Supplied by Scientific Glass Engineering, Incorporated, Austin, Texas 78759.

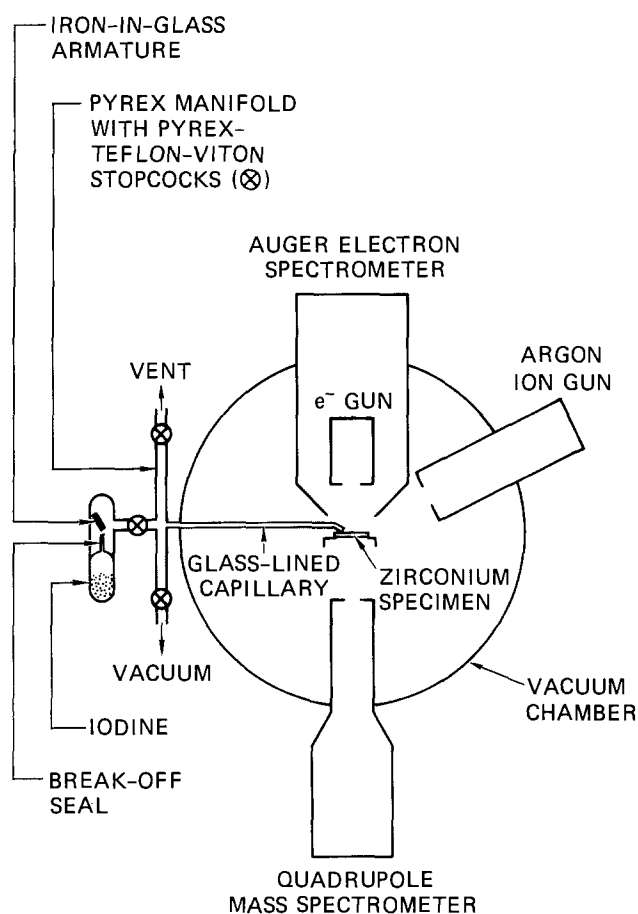


Fig. 1. Schematic diagram of apparatus

connector. This small connector was the only metal surface in contact with the iodine vapor. The iodine reservoir could be isolated from the capillary by means of a Viton sealed glass valve. The iodine manifold was heated when necessary by a heating tape and could be evacuated through a liquid nitrogen-cooled, molecular sieve trap into a mechanical pump. Before the experiment began, the iodine reservoir was filled with resublimed iodine by vacuum distillation through a molecular sieve trap to remove traces of water. The reservoir, equipped with a break-seal tubulation, was pulled off from the distillation manifold and subsequently attached to the capillary inlet manifold. Immediately before the experiment began, the break seal was fractured to admit iodine into the manifold.

The outlet end of the capillary tube was pointed at the specimen and situated about 0.2 cm from its surface. On the basis of our measurements with oxygen with a similar arrangement (5), we estimate that 70% of the gas molecules leaving the capillary tube strike the specimen

Procedure.—The mass flow rate of iodine through the capillary tube was determined by the pressure of iodine in the manifold and by the conductance of the capillary tube. The pressure of iodine in the manifold was controlled by immersing the reservoir in various freezing bath mixtures designed to maintain constant subambient temperatures. The baths used and the attained temperatures are listed in Table I. The iodine manifold and the capillary tube were initially degassed at 400 K overnight. The iodine reservoir was kept at the bath temperature for 2 hr before the iodine valve was opened to admit iodine to the manifold and to the vacuum chamber.

The zirconium specimen surface was cleaned by a combination of argon ion sputtering and high temperature treatment. After initial sputtering, we found that holding the specimen at 1200 K was sufficient to maintain a relatively clean surface as observed from AES spectra. During the start of the experiment, the specimen was cooled or heated from 1200 K to the selected reaction temperature, and the capillary inlet valve was opened to admit iodine to the specimen surface. After a steady-state coverage was attained, the temperature of the specimen was increased to a higher temperature while a constant iodine reservoir temperature was maintained.

The iodine pressure near the specimen can be computed from the mass flow rate, \dot{m} , of iodine passing through the capillary tube by the following equation derived from kinetic theory of gases

$$\bar{P} = \frac{4k\dot{m}RT}{a\bar{c}} \quad [1]$$

where a = area of the specimen, \dot{m} = mass flow rate, \bar{P} = equivalent pressure, \bar{c} = mean molecular velocity, T = gas temperature, and k = fraction of molecules leaving the capillary that strike the specimen surfaces.

Table I. Temperature of iodine bath and equivalent iodine pressure near the specimen

Bath	Bath temperature (K)	Iodine vapor pressure (Pa)	Mass flow rate through capillary Pa · liter sec ⁻¹	Iodine pressure at the specimen* (Pa)
CCl ₄ solid-liquid	252.7	4.34	3.04×10^{-6}	5.9×10^{-6}
Saturated KCl-ice	263.7	11.9	8.31×10^{-6}	1.6×10^{-5}
Ice-water	273.2	26.9	1.83×10^{-4}	3.6×10^{-5}
p-dioxane solid-liquid	281.2	48.4	3.39×10^{-4}	6.6×10^{-5}

* Pressure equivalent of collision rate averaged over area of specimen that intercepts 70% of iodine molecules leaving the capillary.

The mass flow rate of iodine through the capillary tube is proportional to its conductance and to the pressure at the inlet end

$$\dot{m} = P \cdot c \quad [2]$$

where P = manifold pressure and c = capillary conductance.

The iodine pressure in the manifold is equal to the vapor pressure of iodine at the reservoir bath temperature. The conductance of the capillary was determined in a separate experiment in which the manifold was connected to a Validyne stainless steel diaphragm pressure gauge. Iodine was introduced from the reservoir into the manifold of calibrated volume, V , up to a chosen pressure, P , and then the reservoir valve was shut off. From the observed rate of pressure decrease, dP/dt , due to iodine flowing through the capillary tube, the conductance, c , of the capillary was calculated from the following relation

$$c = \frac{V}{P} \frac{dP}{dt} \quad [3]$$

the conductance of the capillary tube was found to have a constant value of 6.4×10^{-6} liters sec^{-1} over an iodine pressure range of 13.3-66.7 Pa.

Results and Discussion

Auger electron spectra in the range of 70-570 eV were recorded at suitable intervals at various specimen temperatures and iodine pressures. Table II summarizes the Auger peaks and transitions of interest (6). Figure 2 shows representative Auger spectra at different specimen temperatures. The major peaks of iodine at 504 and 515 eV closely bracket the major oxygen peak at 510 eV. Hence, if oxygen is a significant component on the specimen surface, overlap would occur between the oxygen peak and these iodine peaks. To eliminate oxygen interference, we used high specimen temperatures at which oxygen accumulation on the surface was minimal (5), as confirmed by the absence of the AES oxygen peak under these conditions. Examining the ratios of the iodine peak heights provided further evidence. (Peak heights are represented by the symbol: A element, energy.) We found that values of the ratios $A_{I\ 504}/A_{I\ 515}$ did not change significantly with variations in the iodine pressure and the specimen temperature. Thus, any contribution of oxygen to the iodine 504-eV peak was negligible under our experimental conditions.

The zirconium and iodine Auger peaks do not appear to shift in energy with iodine coverage on the surface (Fig. 2). The absence of any energy shifts suggests that the iodine observed on the zirconium surface, at the high temperatures and the low iodine pressures used, is present in a chemisorbed state, in contrast to being combined in a surface or bulk compound.

Table II. Auger electron energies^a

Element	Transition	Kinetic energy (eV)
Zr	$M_5N_2N_{2,3}$	92
	$M_5N_{2,3}N_{2,3}$	117
	M_4N_5V	127
	$M_4N_{2,3}N_{4,5}$	147
	$M_5N_{4,5}N_{4,5}$	175
	$M_5N_1N_{4,5}$	369
I	$M_4N_1N_{4,5}$	389
	$M_4N_2N_{4,5}$	434
	$M_2N_{4,5}N_{4,5}$	507
	$M_4N_{4,5}N_{4,5}$	515
	$M_5N_5N_7$	560
	$M_4N_5N_7$	570
O	KL_1L_1	475
	KL_1L_2	490
	KL_2L_2	510
C	KL_2L_2	274

^a Ref. (6).

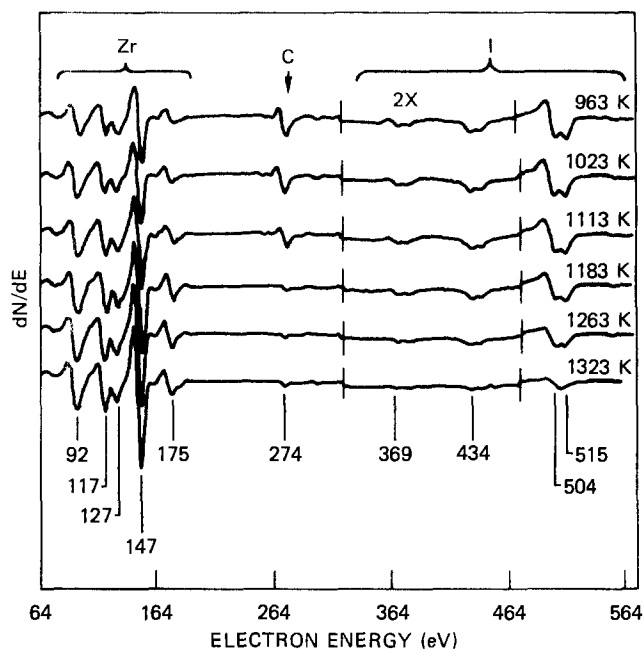


Fig. 2. Typical Auger electron spectra of zirconium foil exposed to iodine vapor at various temperatures.

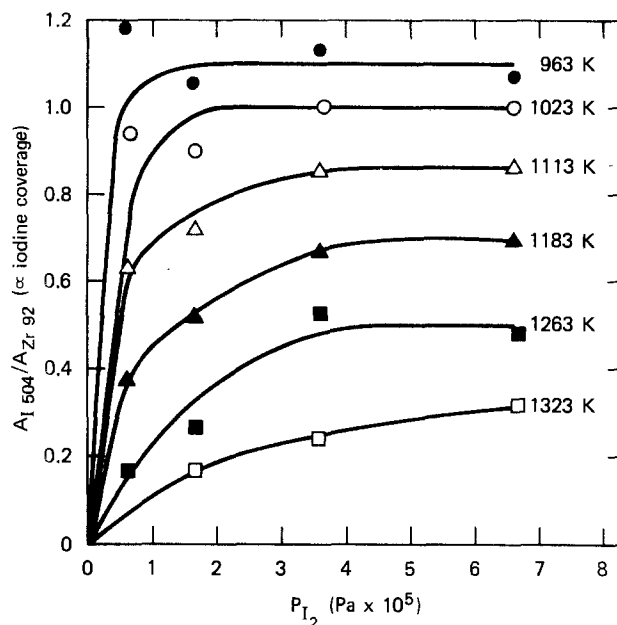


Fig. 3. Adsorption isotherms for iodine on zirconium

Figure 3 illustrates the change in the ratio $A_{I\ 504}/A_{Zr\ 92}$ as a function of iodine pressure at different specimen temperatures. This ratio of iodine to zirconium peak heights is a relative measure of the coverage of iodine on the surface. Normalization of the iodine peak to this stable core-level zirconium peak compensates for random variations in instrumental parameters such as incident electron beam current, electron multiplier gain, and the position of the specimen with respect to the focal point of the electron energy analyzer. As the temperature was decreased, the normalized iodine signal appeared to approach an asymptote with a value of $A_{I\ 504}/A_{Zr\ 49} \approx 1.2$, suggesting an upper limit in coverage. Under the high temperatures and low iodine pressures used in these experiments, such a coverage limit is likely to be less than a monolayer of the adspecies.

We attempted to establish unequivocally an iodine signal intensity that corresponded to monolayer coverage by taking the Zr crystal to much lower temperatures while exposing it to a high iodine flux. Our

effort was thwarted by the appearance of a significant oxygen signal at temperatures below 960 K. Carbon also appeared on the surface and increased significantly at lower temperatures. We concluded that these impurities originated in the bulk of the specimen because the background pressure in the vacuum chamber was too low ($\sim 10^{-8}$ Pa) to populate the surface to the observed impurity levels within the duration of the experiments. Although the general appearance of the curves in Fig. 3 is similar to the Langmuir isotherm, a critical plot of the data showed they deviated significantly from the Langmuir equation. That is, a plot of $A_{I\ 504}/A_{Zr\ 92}$ divided by pressure of iodine vs. pressure of iodine was not linear as it would be for the Langmuir form of isotherm (7). The results in the temperature range 1023–1323 K, however, were equally well fit by the Freundlich equation (7) [proportionality of $\log(A_{I\ 504}/A_{Zr\ 92})$ vs. $\log P(I_2)$] and by the Temkin equation [proportionality of $(A_{I\ 504}/A_{Zr\ 92})$ vs. $\log P(I_2)$]. Figure 4 shows the results of the Temkin plot.

The smooth isotherms of Fig. 4 were used to obtain the pressures of iodine in equilibrium with three different surface coverages, corresponding to $(A_{I\ 504}/A_{Zr\ 92})$ of 0.2, 0.4, and 0.8. Graphs of the log of iodine pressure vs. reciprocal of absolute temperature for

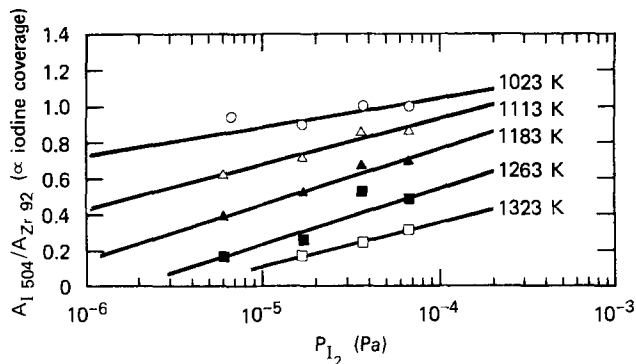


Fig. 4. Adsorption isotherms, Temkin plot

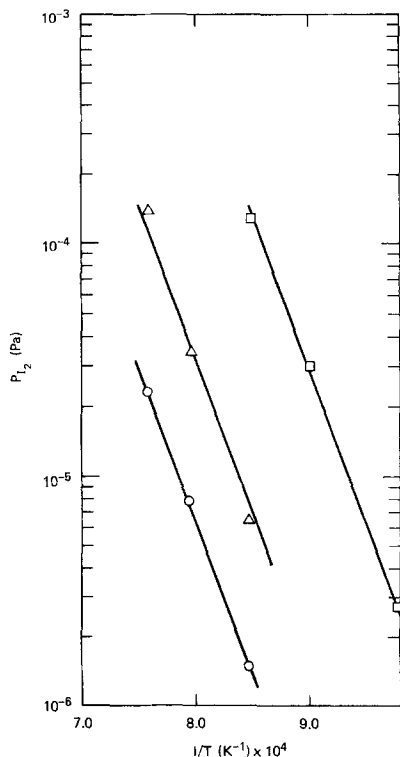


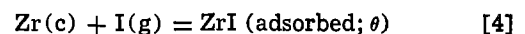
Fig. 5. Adsorption isotherms, I_2/Zr . Points taken from curves of Fig. 4 at three values of $A_{I\ 504}/A_{Zr\ 92}$: \circ , 0.2; \triangle , 0.4; \square , 0.8.

these isosteres are shown in Fig. 5 to be straight lines.

On the basis of the experimental results, we postulate that the interaction between gaseous molecular iodine and metallic zirconium involves the following mechanistic model. At the gas pressures (10^{-4} Pa or less) and surface temperatures (1000–1300 K) used, thermodynamic data (8) predict that monatomic iodine will be several orders of magnitude more abundant than molecular iodine. Hence the iodine molecules that strike the metal surface and become thermalized will dissociate; therefore the iodine can be assumed to be monatomic in its interaction with the zirconium. The iodine striking the surface either adheres to form an adsorbed layer on the metal or is evaporated into the gas. The iodine that adheres to the surface forms a chemisorbed layer from which volatile species can then evaporate. Such a model is consistent with the results of studies of the evaporation of halides from metal surfaces exposed to halogen gases (9, 10). It has been shown that the processes can be represented by the following steps: (i) the incident molecules adsorb dissociatively, (ii) surface reactions occur between the adsorbed species and surface metal, and (iii) the reaction products evaporate. The atom ratios of the species that evaporate were found to be in good accord with values calculated from equilibrium thermodynamics for several transition metal-halide systems (9–12).

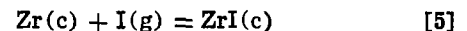
To apply this model to the present system requires an evaluation of the equilibrium partial pressures of the gaseous species. The thermodynamic information required (13–16) to evaluate the partial pressures in equilibrium with zirconium metal are available (9). The calculation shows that the predominant species is monatomic iodine. At the lowest temperature (1000 K) and highest pressure (10^{-4} Pa) considered, there was a small contribution by ZrI_4 gas, which amounted to about 0.1% of the iodine atom pressure. The pressures of all other species were smaller.

The interaction model and the equilibrium gas pressures calculation show that it is now reasonable to treat the system in terms of the equilibrium between monatomic iodine gas and a chemisorbed layer of iodine on the zirconium surface. Thus, the data presented in Fig. 5 relate to the equation



in which θ represents surface coverage and is proportional to $A_{I\ 504}/A_{Zr\ 92}$, referred to below as θ' .

The solid zirconium iodide in equilibrium with zirconium metal has the composition $ZrI_{1.05}$, which can be considered to be the monoiodide (ZrI) (17). Its enthalpy of formation has been evaluated, and its absolute entropy has been estimated so that for equilibrium



the standard free energy change ΔG° is

$$\Delta G^\circ = -59,500 + 30.5T \text{ (kcal/mole)} \quad [6]$$

Thus the equilibrium partial pressure of monatomic iodine is

$$\log P(I, \text{atm}) = -13,000/T + 6.67 \quad [7]$$

Interestingly, the coefficient of the reciprocal temperature term (proportional to the enthalpy change for the reaction) is the same as the slope of the lines drawn through the data points in Fig. 5. Thus the enthalpy change for reaction [4] is the same as that for reaction [5] and we write the following equations from the data in Fig. 5

$$\log P(I, \text{atm}) = -13,000/T + 2.44 \quad (\text{for } \theta' = 0.8) \quad [8]$$

$$\log P(I, \text{atm}) = -13,000/T + 1.20 \quad (\text{for } \theta' = 0.4) \quad [9]$$

$$\log P(I, \text{atm}) = -13,000/T + 0.51 \quad (\text{for } \theta' = 0.2) \quad [10]$$

Thus, for the three levels of iodine coverage, the enthalpy change for chemisorption, considered in terms of formation of surface ZrI, is the same as the enthalpy of formation of solid ZrI. The differences in the thermodynamics of formation of the solid and the chemisorbed state lie in the entropies of the reactions and indicate that the chemisorbed ZrI species have substantially larger absolute entropies than the crystalline solid.

These results show that iodine chemisorbed on zirconium is thermodynamically more stable than combined in the zirconium iodides. The free energy of transfer of a gram atom of iodine from the lowest solid iodide (namely ZrI) to a partially covered zirconium surface can be evaluated from Eq. [7] and [10] to be

$$\begin{aligned}\Delta G(\text{iodine transfer}) &= (6.67-0.51) \times 4.57 \times T \\ &= 28T \text{ cal/mole}\end{aligned}$$

Thus there can be a significant thermodynamic driving force for such a transfer. In the overall process of iodine-induced SCC of zirconium alloys this has the following significance. Iodine can initially react with exposed zirconium surface and the solid iodides formed can act as a source of iodine available to be transferred at a later time to fresh zirconium surface that might be formed when the metal is strained. The mechanism by which iodine can be transferred is not elucidated by these thermodynamic considerations, but surface diffusion of iodide species or vapor transport as ZrI₄ gas are possibilities.

Conclusions

We have shown from Auger electron spectroscopy measurements that a heated zirconium surface exposed to iodine vapor acquires a chemisorbed layer of iodine. The variation with iodine pressure of fractional coverage of the zirconium surface can be fitted to a Temkin model. Interpreted in terms of an equilibrium thermodynamic model, the results suggest that chemisorption of iodine on zirconium at high temperatures involves the formation of a ZrI surface compound.

Acknowledgment

This research was supported by the Office of Basic Energy Science of the U.S. Department of Energy under Contract EY-76-S-03-1339.

Manuscript submitted April 10, 1980; revised manuscript received July 16, 1980.

Any discussion of this paper will appear in a Discussion Section to be published in the June 1981 JOURNAL. All discussions for the June 1981 Discussion Section should be submitted by Feb. 1, 1981.

Publication costs of this article were assisted by SRI International.

REFERENCES

1. B. Cox and J. C. Wood, in "Corrosion Problems in Energy Conversion and Generation," C. S. Tedmon, Jr., Editor, p. 275, The Electrochemical Society Softbound Proceedings Series, Princeton, New Jersey (1974).
2. L. N. Shelest, E. K. Safrnov, and A. S. Mikhailova, *Russ. J. Inorg. Chem.*, **18**, 9 (1973).
3. R. M. Horton and R. L. Kinney, in "Metal-Slag-Gas Reactions and Processes," Z. A. Foroulis and W. W. Smeltzer, Editors, p. 217, The Electrochemical Society Softbound Proceedings Series, Princeton, New Jersey (1975).
4. C. C. Chang, in "Characterization of Solid Surfaces," P. F. Kane and G. B. Larrabee, Editors, p. 537, Plenum Press, New York (1974).
5. G. N. Krishnan, B. J. Wood, and D. Cubicciotti, To be published.
6. Y. E. Strausser and J. J. Uebbing, "Chart of Auger Electron Energies," Varian Associates, Palo Alto, Calif. (1971).
7. F. C. Tomkins, "Chemisorption of Gases on Metals," p. 93, Academic Press, London (1978).
8. B. R. Stull and H. Prophet, "JANAF Thermochemical Tables," U.S. National Bureau of Standards, NSRDS-NBS 37, June 1971.
9. J. L. Philippart, J. Y. Caradec, B. Weber, and A. Cassuto, *This Journal*, **125**, 162 (1978).
10. B. Weber, J. L. Philippart, and A. Cassuto, *Surf. Sci.*, **52**, 311 (1975).
11. J. Y. Caradec, J. L. Philippart, B. Weber, and A. Cassuto, *ibid.*, **54**, 593 (1976).
12. J. C. Batty and R. E. Stickney, *J. Chem. Phys.*, **51**, 4475 (1969).
13. P. D. Kleinschmidt, D. Cubicciotti, and D. L. Hildenbrand, *This Journal*, **125**, 1543 (1978).
14. D. Cubicciotti, K. H. Lau, and M. J. Ferrante, *ibid.*, **125**, 972 (1978).
15. D. Cubicciotti and K. H. Lau, *ibid.*, **126**, 771 (1979).
16. D. Cubicciotti and K. H. Lau, *ibid.*, To be published.
17. R. H. Lamoreaux and D. Cubicciotti, *ibid.*, To be published.

Rapidly Quenched Tungstate and Molybdate Composition Containing Lithium: Glass Formation and Ionic Conductivity

K. Nassau, A. M. Glass, M. Grasso, and D. H. Olson

Bell Laboratories, Murray Hill and Holmdel, New Jersey 07974

ABSTRACT

Extended glass-forming regions were found by twin-roller quenching in the systems of Li_2O with WO_3 and/or MoO_3 . The crystallization of the glasses was studied by DTA and x-ray analysis; a new metastable crystalline phase was observed for $\text{Li}_2\text{W}_2\text{O}_7$. The glasses exhibited lithium ion conductivities in the 10^{-5} - 10^{-6} ($\Omega\text{-cm}$) $^{-1}$ range at room temperature which were in all cases much greater than the conductivity of the polycrystalline phases after crystallization. The corresponding Li^+ diffusion coefficients in the low lithium content tungstates in the glassy and crystallized phases are comparable to the values reported for the grain boundaries and grains of fine grained polycrystalline WO_3 electrochromic films.

The formation of oxide glasses by twin-roller quenching (1, 2) has permitted the preparation of a wide variety of new glasses and metastable crystalline phases. Of particular interest to us is the observation that many of the glasses prepared with alkali oxides exhibit reasonably high alkali ion conductivities (3-5), a characteristic which makes these materials of possible interest as battery cathodes or solid electrolytes. Our previous studies have dealt with the preparation (2, 6) and properties of niobate and tantalate glasses (2, 3), as well as systems of Li_2O with Al_2O_3 , Ga_2O_3 , and Bi_2O_3 (4, 7). In this paper we continue our survey of glass formation and alkali ion conductivity in oxide system formed by rapid quenching of Li_2O with the oxides of tungsten and molybdenum. In both of these systems extended glass forming regions were determined by differential thermal analysis (DTA) and x-ray diffraction studies. Previous work on glasses in limited parts of the alkali molybdate and tungstate systems has been summarized by Gossink (8).

We find that all the glasses within these systems exhibit lithium ion conductivities considerably greater than do the polycrystalline phases which are produced by heating the glass through the crystallization temperature, a result which could have practical implications if tungstates are to be used as cathodes in lithium batteries (9).

Lithium ion transport in WO_3 has already attracted considerable attention in connection with electrochromic devices (10). In this case the lithium is introduced by insertion into evaporated or sputtered WO_3 films. The results reported here may shed light on the nature of the diffusion mechanism in these materials.

Experimental

The twin-roller quenching technique (2), giving quenching rates of about 10^7 deg/sec (6), the identification of glass in the product (2, 6), and the a-c conductivity measurement technique using blocking electrodes (3) have been described previously in detail. The preparation and quenching parameters are given in Tables I and II. Reagents used were Apache Chemicals Incorporated 5N Li_2CO_3 , J. T. Baker Chemical Company reagent grade tungstic acid, and Fisher Scientific Company, reagent grade MoO_3 . Throughout this work the lithium content of the material is expressed as the Li cation fraction in the starting material, i.e.

Key words: quenched glasses, ionic conductivity, lithium tungstate glasses, lithium molybdate glasses, lithium tungstate, metastable.

$$\text{Li} = [\text{Li}] / ([\text{Li}] + \Sigma[\text{M}])$$

where M represents all other cations present. Chemical analyses have shown that there is no significant change in composition on melting or quenching. Many of the glasses, particularly the high Li-content ones, were quite hygroscopic, so all specimens were stored in a desiccator. Although significant ionic conductivity can derive from moisture present (11), optical absorption and thermal annealing experiments showed that this did not contribute significantly to the measured ionic conductivities.

Glass Formation and Metastable Phases

Six tungstate, one mixed tungstate-molybdate and five molybdate compositions were quenched as outlined in Tables I and II. Essentially pure glass was obtained with a lithium content of 0.6 or less except for the two lowest tungstate compositions, where mixed glass and crystals occurred. Above 0.667 only crystalline material was observed. At an Li content of 0.667 no glass was detected by DTA but a small peak observed in the ionic conductivity measurements indicated traces of glass. Trace amounts of glass can sometimes be observed in conductivity measurements by studies of selected flakes of material since the glass occurs as a continuous phase in the spaces between crystallites. Since the glass phase usually has a higher conductivity than the crystal, a decrease of conductivity is observed at the crystallization temperature. In the tungstate system the crystallization paths on heating the glass were worked out in full detail and are given in the last column of Table I.

Li_2O - WO_3 compositions.—Parts of the Li_2O - WO_3 phase diagram have been studied by various workers (12-18). There is almost unanimous agreement that Li_2WO_4 (Li = 0.667) and $\text{Li}_2\text{W}_2\text{O}_7$ (Li = 0.50) melt congruently. A noncongruent melting WO_3 -rich compound is either $\text{Li}_2\text{W}_4\text{O}_{13}$ (12, 13, 17) (Li = 0.333), $\text{Li}_2\text{W}_5\text{O}_{16}$ (14, 15) (Li = 0.285), or $\text{LiW}_4\text{O}_{13}$ (18) (Li = 0.20). Additional compounds reported include noncongruent $\text{Li}_6\text{W}_2\text{O}_9$ (15, 16) and also Li_4WO_5 and Li_6WO_6 (13, 15, 17) (Li = 0.75, 0.80, and 0.857, respectively). The existence of a metastable crystalline compound in the Li_2O - WO_3 system during low temperature reaction has been mentioned without any detail (19).

The compositions quenched were chosen so that some corresponded to congruent melting compounds (Li = 0.50 and 0.667), some to possible incongruent compounds (Li = 0.333 and 0.75), and two near probable eutectics (Li = 0.25 and 0.60). The occurrence of

Table I. Quenched specimens in the $\text{Li}_2\text{O}-\text{WO}_3$ system

Li content	Compound	Number of quenches and temp. ($^{\circ}\text{C}$)	Nature and color	Composition and transformations* ($^{\circ}\text{C}$)
0.25	—	1, 1350	Green opaque glass	$\text{G} + (\text{WO}_3)/340/\text{WO}_3 + \text{G}/430/\text{WO}_3 + \text{Li}_2\text{W}_2\text{O}_7/\sim 700$
0.333	$(\text{Li}_2\text{W}_2\text{O}_7?)$	1, 1600	Yellow green opaque glass plus crystal	$\text{WO}_{2.9} + (\text{G})/350/\text{WO}_3 + (\text{G})/430/\text{WO}_3 + \text{Li}_2\text{W}_2\text{O}_7/\sim 700$
0.50	$\text{Li}_2\text{W}_2\text{O}_7$	1, 925	Colorless transp. glass	$340\ddagger\text{G}/370/\text{metastable } \text{Li}_2\text{W}_2\text{O}_7/430/\text{Li}_2\text{W}_2\text{O}_7/\sim 700$
0.60	—	1, 975	Colorless transp. glass	$325\ddagger\text{G}/340/\text{glass}/430/\text{Li}_2\text{WO}_4 + \text{Li}_2\text{W}_2\text{O}_7\ddagger/470/\text{Li}_2\text{WO}_4 + \text{Li}_2\text{W}_2\text{O}_7/\sim 670$
0.667	Li_2WO_4	3, 950-1025	Colorless opaque crystal trace glass	$\text{Li}_2\text{WO}_4/\sim 700$
0.75	$\text{Li}_6\text{W}_2\text{O}_9$	2, 975	Beige opaque crystal	$\text{Li}_6\text{W}_2\text{O}_9/\sim 600$

* Sequence gives observed or deduced phases, exothermic transformation temperatures in $^{\circ}\text{C}$ underlined for strong exotherms. Last temperature is the initial endotherm (melting or eutectoid). G is glass.

† Glass transition temperature.

‡ Broad diffraction lines.

Table II. Quenched specimens in the $\text{Li}_2\text{O}-\text{MoO}_3$ system and Li_2MoWO_7

Li content	Compound	Number of quenches and temp. ($^{\circ}\text{C}$)	Nature and color	Composition and transformations* ($^{\circ}\text{C}$)
0.33	$\text{Li}_2\text{Mo}_4\text{O}_{13}$	1, 1000	Blue transp. glass	$\text{G}/275/\text{a}/320/\text{b}/\sim 560$
0.40	—	2, 1000, 1150	Tan transp. glass	$230\ddagger\text{G}/260/\text{c}/\sim 420/\text{d}/\sim 530$
0.50	$(\text{Li}_2\text{Mo}_2\text{O}_7)$	2, 950, 1000	Tan transp. glass	$240\ddagger\text{G}/270/\text{e}/300/\text{f}/530$
0.667	Li_2MoO_4	2, 975, 1000	Beige cryst. tr. glass	$\text{Li}_2\text{MoO}_4/\sim 680$
0.75	—	1, 1250	Yellow opaque cryst.	$\text{Li}_2\text{MoO}_4 + \text{Li}_2\text{MoO}_5/\sim 430$
(0.50)	Li_2MoWO_7	2, 1675, 1700	Brown transp. glass	$290\ddagger\text{G}/310/\text{G}/350/\sim 560\ddagger$

* Sequence gives observed or deduced phases, exothermic transformation temperatures in $^{\circ}\text{C}$, underlined for strong exotherms. Last temperature is the initial endotherm (melting or eutectoid). G is glass, "a" thru "f" indicate unidentified x-ray diffraction patterns.

† Glass transition temperature.

‡ Same structure as $\text{Li}_2\text{W}_2\text{O}_7$.

glass does not appear to be related to any of these characteristics.

In the WO_3 -rich compositions some WO_3 [the powder x-ray diffraction pattern matched JCPDS Card No. 20-1324 (20) or $\text{WO}_{2.9}$ (JCPDS 18-1417)] was present together with the glass formed. In the $\text{Li} = 0.25$ composition, the first exotherm at 340°C appears to correspond to the crystallization from the glass of additional WO_3 and the second at 430°C to the formation of $\text{Li}_2\text{W}_2\text{O}_7$ (JCPDS 24-664) as shown in Table I. In the case of $\text{Li} = 0.333$, the $\text{WO}_{2.9}$ formed converted to WO_3 (possibly simultaneously with some WO_3 crystallizing from the glass) and $\text{Li}_2\text{W}_2\text{O}_7$ again formed subsequently. In neither case was pure glass obtained, nor were any of the other expected compounds, particularly the $\text{Li} = 0.333$ one, observed.

Essentially pure glass was obtained at $\text{Li} = 0.5$ and 0.6 , with glass transitions at 340°C and 325°C , respectively, as shown in Fig. 1. In the first of these compositions, a metastable phase was observed on crystallization at 370°C ; this subsequently transformed to the expected stable $\text{Li}_2\text{W}_2\text{O}_7$ at 430°C . The x-ray diffraction patterns for this transformation sequence are shown in Fig. 2. The x-ray diffraction peaks of the metastable $\text{Li}_2\text{W}_2\text{O}_7$ formed by heating the glass to 420°C are given in Table III; indexing was not possible in the absence of single crystals. At $\text{Li} = 0.60$, however, there was an exotherm at 340°C above which no crystalline phase could be observed by x-ray diffraction. Subsequently, the expected mixture of Li_2WO_4 (JCPDS 12-760) plus stable $\text{Li}_2\text{W}_2\text{O}_7$ formed at 430°C , with a possible minor phase change at 470°C .

At $\text{Li} = 0.667$ and 0.75 only the expected Li_2WO_4 and $\text{Li}_6\text{W}_2\text{O}_9$ (JCPDS 25-503) crystalline phases were observed by x-ray diffraction and no glass crystallization exotherm by DTA, although the conductivity measurements indicated a trace of glass at $\text{Li} = 0.667$.

Li₂O-MoO₃ and mixed compositions.—Parts of the $\text{Li}_2\text{O}-\text{MoO}_3$ phase diagram have been studied by various workers (12-15, 21-22). There is only agreement on the congruently melting Li_2MoO_4 ($\text{Li} = 0.667$) and noncongruent $\text{Li}_2\text{Mo}_4\text{O}_{13}$ ($\text{Li} = 0.333$). There are also

Table III. Powder x-ray diffraction pattern* of metastable $\text{Li}_2\text{W}_2\text{O}_7$

d(A)†	I
6.06	w
4.59	vwv
4.02 v broad	vwv
3.167 sharp	vs
2.46	m
2.06	w
1.82	m
1.64	w
1.576	w
1.50	vwv
1.46	vwv

* Using Ni-filtered Cu radiation at 30 kV and 10 mA in a Rigaku Corp. Miniflex Diffractometer at $2^{\circ}/\text{min}$.

† All lines broad, about $1^{\circ} 2\theta$ half width except as indicated.

possible noncongruent $\text{Li}_2\text{Mo}_4\text{O}_{13}$ (21), noncongruent $\text{Li}_2\text{Mo}_3\text{O}_{10}$ (12, 21), congruent $\text{Li}_4\text{Mo}_3\text{O}_{17}$ (22), and congruent $\text{Li}_2\text{Mo}_2\text{O}_7$ (12-14, 21); an Li_4MoO_5 has also been mentioned (15) ($\text{Li} = 0.333, 0.40, 0.444, 0.50$, and 0.80 , respectively). Here too a metastable crystalline phase occurring during low temperature reaction has been mentioned without any detail (19).

In this system, glass was obtained at four compositions ranging from $\text{Li} = 0.333$ to 0.50 as shown in Table II. The intermediate crystalline phases produced on heating gave complex diffraction patterns and no extended effort was made to interpret these; they are designated "a" to "f" in Table II. At $\text{Li} = 0.667$ the conductivity measurement indicated a trace of glass.

One composition, Li_2MoWO_4 ($\text{Li} = 0.50$) was quenched in the mixed tungstate molybdate system and essentially pure glass was obtained. The final crystalline phase formed on heating had an x-ray diffraction pattern very similar to that of $\text{Li}_2\text{W}_2\text{O}_7$ (JCPDS 24-664), although one report (15) had indicated that solid solution probably did not extend to the center of the $\text{Li}_2\text{Mo}_2\text{O}_7-\text{Li}_2\text{W}_2\text{O}_7$ pseudobinary.

Baynton *et al.* (23) prepared a glass near LiMoO_4 by cooling milligram-size samples on platinum foil.

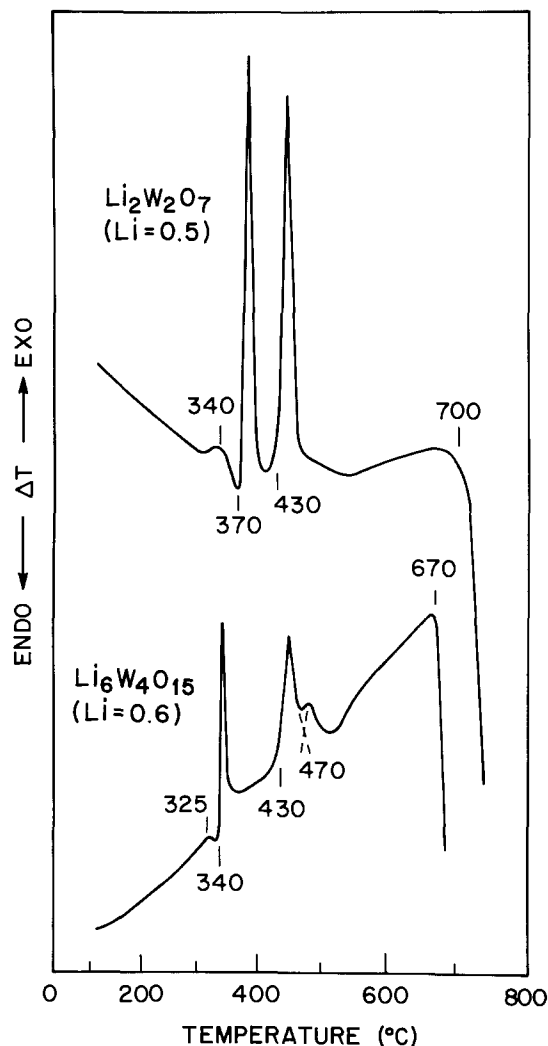


Fig. 1. DTA of quenched $\text{Li}_2\text{W}_2\text{O}_7$ ($\text{Li} = 0.50$) and $\text{Li}_6\text{W}_4\text{O}_{15}$ ($\text{Li} = 0.60$) in flowing N_2 at $20^\circ\text{C}/\text{min}$.

Stevls and co-workers used the same system to study parts of the alkali tungstate (24) and molybdate systems (21), including determination of the critical cooling rate (ccr) for glass formation to occur. The lowest ccr in the $\text{Li}_2\text{O}-\text{WO}_3$ system (24) was found near $\text{Li} = 0.53$ as about $2000 \text{ deg}/\text{sec}$ with only a very small range of glass formation from $\text{Li} = 0.51$ to 0.54 , extended by Gossink (8) down to 0.47 . For the $\text{Li}_2\text{O}-\text{MoO}_3$ system

(21) the minimum was near the same composition but at a ccr of about $25 \text{ deg}/\text{sec}$; glasses were obtained from about $\text{Li} = 0.33$ to 0.62 , extended by Gossink (8) down to 0.17 . Pure glassy MoO_3 had been previously reported by Sarjeant and Roy (25). The early workers (21, 24) appear to have been limited in their ccr to less than $10^4 \text{ deg}/\text{sec}$, while Gossink used splat cooling at about $10^6 \text{ deg}/\text{sec}$. Gossink measured a ccr of about $250 \text{ deg}/\text{sec}$ in the mixed Li_2MoWO_7 composition.

The crystallization temperature was determined by Gossink (8) as the visual onset of crystallization, and his values were generally much higher than those in Tables I and II, indicating that he probably did not detect the initial crystallization but some later, advanced stage in the crystallizing process. These workers (8, 21, 24) also reported infrared spectra and discussed the possible structural aspects of glass formation in these systems.

The range of glass-formation in the $\text{Li}_2\text{O}-\text{MoO}_3$ system obtained in this report is consistent with these previous studies, but we have extended the range from the previous $\text{Li} = 0.47-0.54$ to $0.25-0.60$ for the $\text{Li}_2\text{O}-\text{WO}_3$ system, this being consistent with our higher cooling rate of about $10^7 \text{ deg}/\text{sec}$.

Conductivity Measurements

The electronic conductivity, measured at d.c. with ionically blocking gold electrodes varied considerably from one flake to another, from values as high as $10^{-4} (\Omega\text{-cm})^{-1}$ down to $10^{-10} (\Omega\text{-cm})^{-1}$. Conductivities as high as $10^{-2} (\Omega\text{-cm})^{-1}$ could be achieved by heating the flakes in hydrogen at temperature over 300°C , well below the crystallization temperature. Flakes with higher conductivities had a blue color due presumably to reduced tungsten or molybdenum ions. Only flakes having electronic conductivities below 1% of the total a-c conductivity were selected for ionic conductivity measurements with gold blocking electrodes.

Results, taken as a continuous function of temperature at 1 kHz , are plotted in Fig. 3 as $\log \sigma$ vs. $1/T$. In all cases the results fall on straight lines up to a temperature about 50° below the crystallization temperature. At the crystallization temperature T_{cryst} all compositions showed a maximum in the ionic conductivity indicating that the glass phase was more conductive than the polycrystalline phase. Typical data recorded by heating the sample through T_{cryst} followed by slow cooling in the crystalline phase is shown in Fig. 4. The peak in conductivity is much broader than the exotherm seen in Fig. 1 for the same material and no distinctive feature is observed at the temperature corresponding to the second exotherm. At room temperature the conductivity of the glass phase is some five

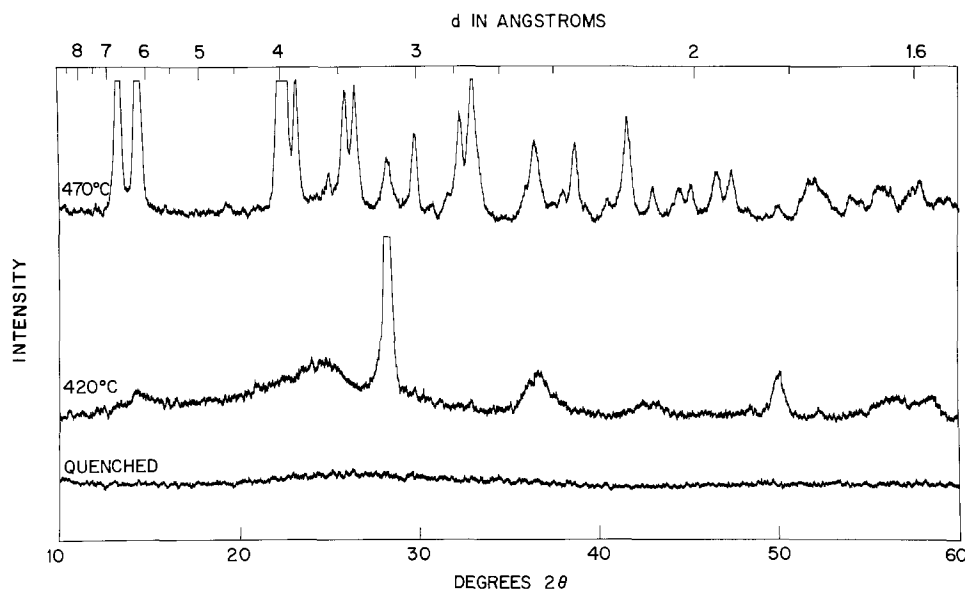


Fig. 2. Powder x-ray diffraction patterns of $\text{Li}_2\text{W}_2\text{O}_7$ as quenched, metastable crystalline phase after heating to 420°C , and as the stable crystalline phase after heating to 470°C .

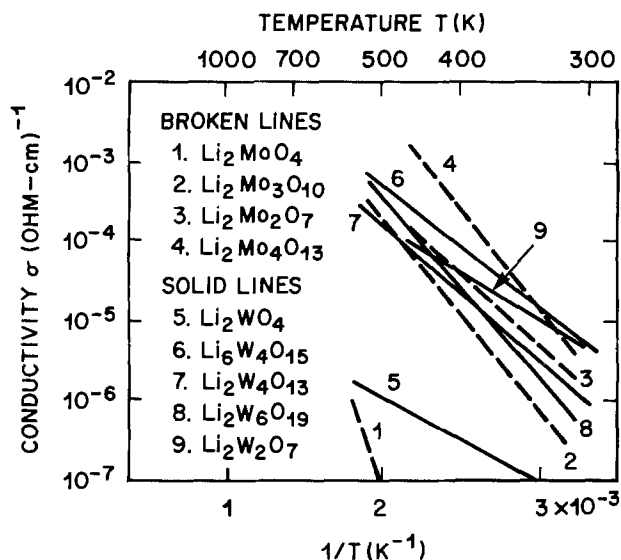


Fig. 3. Ionic conductivity of quenched lithium molybdates and tungstate glasses. Samples were pure glass except for 1 and 5, which were primarily crystalline. (In Ref. (4), line 6 was inadvertently drawn $10\times$ too low). Also see note added in proof.

orders of magnitude greater than that of the same material after crystallization (extrapolated to room temperature).

The data in Fig. 3 show remarkably little variation of ionic conductivity with fractional Li ion content between 0.25 and 0.6. This is emphasized in Fig. 5 where conductivity is plotted as a function of Li ion content at two different temperatures. (The points at 0.667 cation percent are omitted since they were taken on primarily crystalline material so these values cannot be compared with the pure glass values.) These results are in marked contrast with the results for $\text{Li}_2\text{O}-\text{Al}_2\text{O}_3$, $\text{Li}_2\text{O}-\text{Ga}_2\text{O}_3$, and $\text{Li}_2\text{O}-\text{Bi}_2\text{O}_3$ glasses (4) in which the conductivity changed by several orders of magnitude over the same composition range. Furthermore, there does not seem to be any systematic varia-

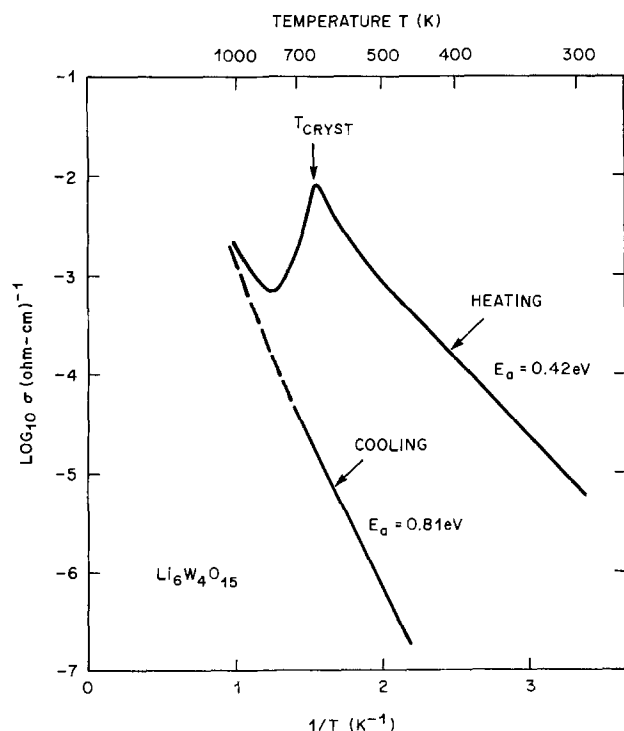


Fig. 4. Temperature dependence of the ionic conductivity of $\text{Li}_6\text{W}_4\text{O}_{15}$, measured at 1 kHz, upon heating through the crystallization temperature followed by slow cooling of the crystallized material.

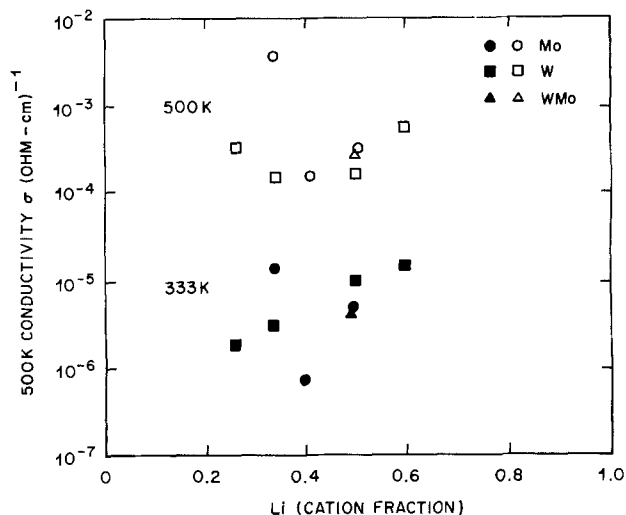


Fig. 5. Variation of the ionic conductivity at 500 K with the lithium content of quenched molybdate and tungstate glasses.

tion of the activation energy with Li ion content. Since the measured conductivity is just the product of the total concentration of Li ions, the ionic charge, and the average ionic mobility (averaged over all Li ions in the disordered structure), this result shows that the average mobility of the ions is not greatly affected by their concentration.

It is interesting to compare the diffusion coefficient of Li ions obtained from these conductivity measurements with apparent values in dry WO_3 films prepared by evaporation or sputtering (26). Films prepared in this way were found to be microcrystalline (26, 27) with up to 25% by volume of disordered material in grain boundary regions (10). There is some indication from the electrochromic behavior of the films that Li insertion proceeds by rapid diffusion along grain boundaries followed by slower diffusion into the crystallites. Using this model and the measured total diffusion coefficient, the estimated diffusion coefficient within the grain boundaries is (10, 26)

$$D \sim 10^{-11} \text{ to } 10^{-12} \text{ cm}^2/\text{sec}$$

and in the bulk (27)

$$D \sim 10^{-15} \text{ to } 10^{-16} \text{ cm}^2/\text{sec}$$

The diffusion coefficient obtained from conductivity measurement on bulk stoichiometric, electronically insulating lithium tungstate glasses may not be equivalent to lithium ion insertion into WO_3 where charge compensation occurs by simultaneous electron injection, in view of the differing oxygen content and higher electronic conductivity. The comparison is nevertheless interesting in view of the insensitivity of the ionic mobility to composition. Using the Nernst relation and the data of Fig. 4

$$\sigma = \frac{Ne^2D}{fkT}$$

where N is the concentration of lithium ions of charge e , we find that, if we take the correlation factor f for the glass phase at room temperature to be (28) 0.5, then

$$D \sim 10^{-11} \text{ cm}^2/\text{sec}$$

and after crystallization

$$D \sim 10^{-16} \text{ cm}^2/\text{sec}$$

Both these values are remarkably similar to those quoted above and are clearly in support of the two phase model for electrochromic films.

The conductivity data for the lithium molybdate glasses also shown in Fig. 3 and 5 are quite similar to those of the tungstate. The mixed composition Li_2MoWO_7 exhibited essentially the same conductivity

as the $\text{Li}_2\text{Mo}_2\text{O}_7$ composition. There was some variation of the ionic conductivity between glass samples quenched from the same melt (up to a factor of four) so that small differences in conductivity cannot be considered too significant.

To determine the effect of network forming additives to $\text{Li}_2\text{O}-\text{WO}_3$ glasses, 20 mole percent SiO_2 , GeO_2 or B_2O_3 were added to the $\text{Li}_2\text{O}:2\text{WO}_3$ and the $5\text{Li}_2\text{O}:8\text{WO}_3$ compositions. In all cases pure glass was obtained, but no measureable difference of the ionic conductivity, within the experimental errors, due to the network forming additive could be detected.

Conclusions

Extended glass forming regions of the $\text{Li}_2\text{O}-\text{WO}_3$ and $\text{Li}_2\text{O}-\text{MoO}_3$ system have been found by using cooling rates of about 10^7 deg/sec. A new metastable phase which follows crystallization of the $\text{Li}_2\text{W}_2\text{O}_7$ composition is reported.

Lithium ion conductivities of all the molybdate and tungstate glasses studied are reasonably high, falling in the 10^{-5} - 10^{-6} ($\Omega\text{-cm}$) $^{-1}$ range at room temperature. Since the glasses can be made electronically conducting by suitable reduction of the material, these materials may be of interest as cathodes in lithium batteries. The measured conductivities yield lithium ion diffusion coefficients about 10^{-11} cm^2/sec in the glass phase and 10^{-16} cm^2/sec in the crystallized material which lends support to the grain boundary diffusion model for electrochromic WO_3 films.

Acknowledgments

We are grateful to W. C. Dautremont-Smith for valuable discussions concerning WO_3 electrochromic films.

Manuscript submitted March 3, 1980; revised manuscript received May 26, 1980.

Any discussion of this paper will appear in a Discussion Section to be published in the June 1981 JOURNAL. All discussions for the June 1981 Discussion Section should be submitted by Feb. 1, 1981.

Publication costs of this article were assisted by Bell Laboratories.

Note Added in Proof: Measurements of the ionic conductivity as a function of frequency similar to those of Fig. 2 of Ref. (3), indicate that some blocking effects are already present at 1 kHz in the higher temperature regime ($> 200^\circ\text{C}$). Data taken at 1 MHz suggest that the true ionic conductivities may be up to one order of magnitude greater than those shown in Fig. 3. The relative behavior of different compositions remains unchanged.

REFERENCES

1. T. Susuki and A. Anthony, *Mater. Res. Bull.*, **9**, 745 (1974).
2. K. Nassau, C. A. Wang, and M. Grasso, *J. Am. Ceram. Soc.*, **62**, 74 (1979).
3. A. M. Glass, K. Nassau, and T. J. Negran, *J. Appl. Phys.*, **49**, 4808 (1978).
4. A. M. Glass and K. Nassau, *ibid.*, **51**, 3756 (1980).
5. A. M. Glass, K. Nassau, and D. H. Olson, in "Proceedings of the International Conference on Fast Ion Transport in Solids," P. Vashishta, J. N. Mundy, and G. K. Shenoy, Editors, p. 707, North Holland Pub. Co., New York (1979).
6. K. Nassau, C. A. Wang, and M. Grasso, *J. Am. Ceram. Soc.*, **62**, 503 (1979).
7. K. Nassau, M. Grasso, and A. M. Glass, *J. Non-Cryst. Solids*, **34**, 425 (1979).
8. R. G. Gossink, *Philips Res. Rep. Suppl.*, No. 3, 1 (1971).
9. H. K. Cheng and M. S. Whittingham, Paper presented at The Electrochemical Society Meeting, Los Angeles, Calif., October 14-19, 1979.
10. See for instance, M. Green, W. C. Smith, and J. A. Weiner, *Thin Solid Films*, **38**, 89 (1976); W. C. Dautremont-Smith, M. Green, and K. S. Kang, *Electrochim. Acta*, **22**, 751 (1977).
11. R. M. Biefeld and R. T. Johnson, *This Journal*, **126**, 1 (1979).
12. F. Hoermann, *Z. Anorg. Allg. Chem.*, **177**, 145 (1928-1929).
13. J. M. Réau and C. Fouassier, *Bull. Soc. Chim. France*, **1971**, 398 (1971).
14. M. Parmentier, J. M. Réau, C. Fouassier, and C. Gleitzer, *ibid.*, **1972**, 1743 (1972).
15. D. Gloekler, F. Jeannot, and C. Gleitzer, *J. Less-Common Met.*, **36**, 41 (1974).
16. M. Parmentier, C. Gleitzer, and J. Aubry, *C.R. Acad. Sci., Paris*, **274**, 1681 (1972).
17. J. Hauck, *J. Inorg. Nucl. Chem.*, **36**, 2291 (1974).
18. L. L. Y. Chang and S. Sachdev, *J. Am. Ceram. Soc.*, **58**, 267 (1975).
19. E. K. Belyaev and V. F. Annopol'skii, *Russ. J. Phys. Chem.*, **48**, 1418 (1974).
20. JCPDS Powder Diffraction File, International Centre for Diffraction Data, Swarthmore, PA (1977).
21. J. C. Th. G. M. Van der Wielen, H. N. Stein, and J. M. Stevels, *J. Non-Cryst. Solids*, **1**, 18 (1968).
22. W. S. Brower, H. S. Parker, R. S. Roth, and J. L. Waring, *J. Cryst. Growth*, **16**, 115 (1972).
23. P. L. Baynton, H. Rawson, and J. E. Stanworth, *Nature*, **178**, 910 (1956).
24. R. J. H. Gelsing, H. N. Stein, and J. M. Stevels, *Phys. Chem. Glasses*, **7**, 185 (1966).
25. P. T. Sarjeant and R. Roy, *J. Am. Ceram. Soc.*, **50**, 500 (1967).
26. M. Green, W. C. Dautremont-Smith, and K. S. Kang, Proc. of the Second International Meeting on Solid Electrolytes, St. Andrews, Scotland (1978).
27. M. Green and K. S. Kang, *Thin Solid Films*, **40**, 119 (1977).
28. R. Terai and R. Hayani, *J. Non-Cryst. Solids*, **18**, 217 (1975).

Technical Notes



The Chemical Vapor Deposition of Polycrystalline InP

Masahide Inuishi and Bruce W. Wessels*

Materials Research Center and Department of Materials Science and Engineering,
Northwestern University, Evanston, Illinois 60201

Heterojunctions involving indium phosphide have been suggested as possible candidates for solar cells

because of the optimal match of the bandgap of indium phosphide with the solar spectrum (1). Moreover, since indium phosphide has a direct bandgap and a large absorption coefficient, it appears feasible to

* Electrochemical Society Active Member.

Key words: thin films, polycrystalline semiconductors.

prepare indium phosphide photovoltaics in thin film form.

Recently, the preparation of thin films of indium phosphide for use in polycrystalline solar cells has been investigated. Deposition techniques that have been studied include planar reactive deposition (2), chemical vapor deposition (CVD) from organometallics (3), and phosphorus trichloride (4, 5). In this paper experiments on the chemical vapor deposition of polycrystalline indium phosphide onto molybdenum substrates using an alternative method are examined. It is shown that using In/HCl/PH₃/H₂ system homogeneous thin films of InP can be deposited at temperatures as low as 410°C.

Experimental Conditions

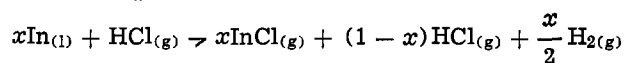
The system used for the preparation of InP was similar to that described previously for the deposition of other III-V compounds from hydrides (6, 7). Reactant gases included electronic grade HCl, a 5% mixture of electronic grade phosphine in ultrahigh purity hydrogen, and palladium-diffused hydrogen as the carrier gas. Elemental indium of 5 nines' purity was the metallic source. Thin films of indium phosphide were deposited onto molybdenum substrates which were 0.1 mm × 100 mm² in size and had a (100) preferred orientation. Before deposition the substrates were ultrasonically cleaned in trichloroethylene and methanol, subsequently etched in a 1H₂SO₄-1HNO₃-3H₂O solution. In some experiments the Mo substrates were mechanically abraded in order to improve film nucleation (8).

Typical growth conditions consisted of an indium source temperature of 750°C and substrate temperatures of 410°-620°C. The phosphine and hydrogen chloride flow rates were 3.5 and 3.0-7.5 cm³/min, respectively. The hydrogen flow rate over the In source was 180 cm³/min, with a total hydrogen flow rate through the system of 280 cm³/min.

The thickness of the deposited layers was obtained from the weight gain of the substrate and by optically measuring the cross sections for films with thicknesses of greater than 2 μm. In order to determine the degree of preferred orientation of the as-deposited films, relative x-ray intensity was measured with an x-ray diffractometer and subsequently compared to an ASTM standard. Correction for film thickness on the x-ray intensities was neglected as it was observed to have a negligible contribution.

Results

Growth kinetics.—Homogeneous growth of InP on molybdenum substrates was obtained only with careful control of the indium transport efficiency. Previous studies have shown that indium transport is extremely sensitive to gas flow conditions (9). The theoretical transport efficiency can be obtained by considering the source reaction



where x the transport efficiency is defined as

$$x = \frac{n_{\text{InCl}}}{n_{\text{HCl}}}$$

the mole fraction of HCl converted to InCl.

Theoretically predicted conversion efficiency was obtained by adjusting flow conditions by the addition of baffles into the gas stream between the source and the substrate. For a source temperature of 750°C, the indium transport rate was linear with HCl input pressure as shown in Fig. 1. At total linear gas flow rates of 1 cm/sec the transport efficiency observed was 0.98, which is a good agreement with theoretical analyses (9).

The temperature dependence of the growth rate of polycrystalline indium phosphide was found to decrease exponentially with decreasing temperature

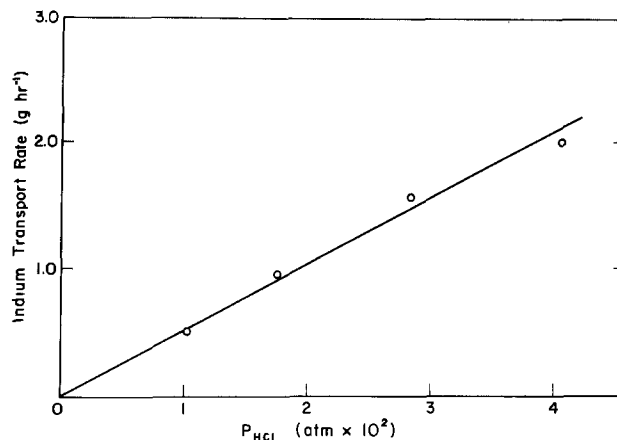


Fig. 1. Indium transport rate as a function of HCl input pressure. The source temperature is 750°C. Solid line indicates theoretically predicted rate.

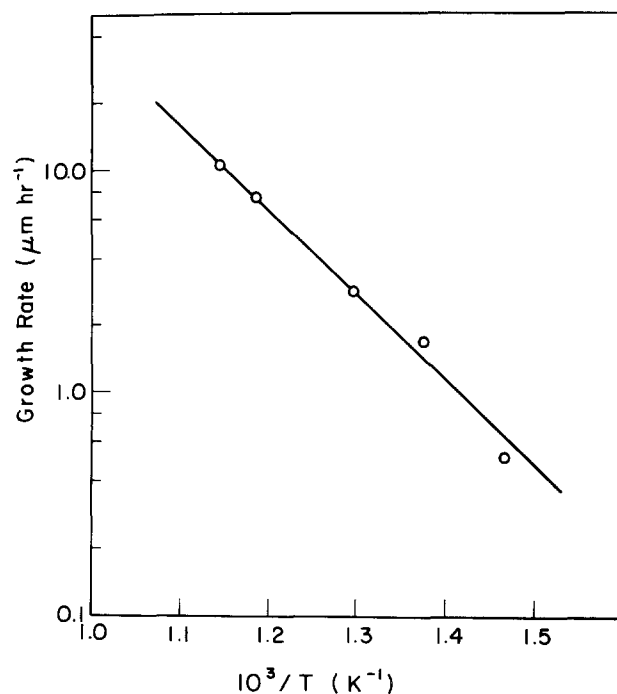


Fig. 2. Temperature dependence of growth rate for InP deposition. The HCl and PH₃ partial pressures were 1.6×10^{-2} and 1.0×10^{-2} atm, respectively.

(Fig. 2). Thus the growth of the InP films by CVD is an activated process. An Arrhenius plot of the deposition rate indicates an activation energy of 17.7 kcal/mole. This agrees well with the 15 kcal/mole observed by Saitoh *et al.* (4) for InP deposition using the PCl₃/In/H₂ reactant system. It should be noted that in the present study films were deposited at temperatures as low as 410°C, 250°C lower than that normally used in InP chemical vapor deposition. Low substrate temperatures are of course desirable to minimize film contamination by the substrate as a result of interdiffusion.

The kinetic model for the activated deposition process was established from the effect of PH₃/HCl reactant ratio on growth rate. For PH₃/HCl reactant ratios of less than 0.33 it was observed that the growth rate was strongly dependent upon the partial pressure of phosphine. For higher PH₃ pressures the growth rate saturated to a limiting value of 15 μm/hr as shown in Fig. 3. This dependence of film growth rate on phosphine pressure suggests that adsorption of phosphorus or a phosphorus-containing species by a Langmuir-

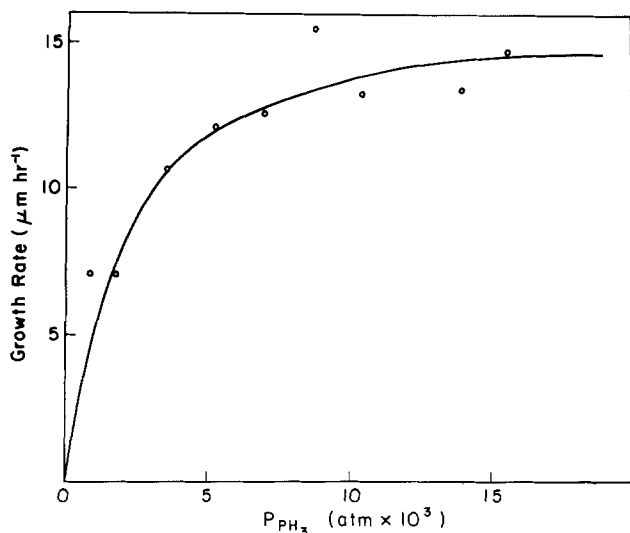


Fig. 3. The effect of PH_3 partial pressure on growth rate. The substrate temperature is 620°C and the partial pressure of HCl is 2×10^{-2} atm.

type mechanism is the rate-limiting step for indium phosphide film growth.

The proposed kinetic model was confirmed by plotting the data on the indium phosphide growth rate vs. phosphine pressure in an alternate form. If the InP growth rate G depends on the adsorption of a monolayer of phosphorus, then G should follow the Langmuir adsorption equation

$$y = K\theta = \frac{aP}{1 + bP} \quad [1]$$

where y is the amount of phosphorus adsorbed per unit area and is proportional to the surface coverage θ in Eq. [1]. The quantity P is the pressure, a and b are constants. By equating G to y and rearranging Eq. [1] we obtain

$$\frac{P}{y} = \frac{1}{a} + \frac{bP}{a} \quad [2]$$

or

$$\frac{P_{\text{PH}_3}}{G} = \frac{1}{a'} + \frac{b'P_{\text{PH}_3}}{a'} \quad [3]$$

Since a' and b' are constants, plotting P_{PH_3}/G vs. P_{PH_3} should yield a straight line as shown in Fig. 4. Good agreement between Eq. [3] and experimental observations over an order of magnitude of phosphine pressure variation is noted, supporting the conclusion that adsorption of phosphorus plays a key role in the growth of InP films by chemical vapor deposition.

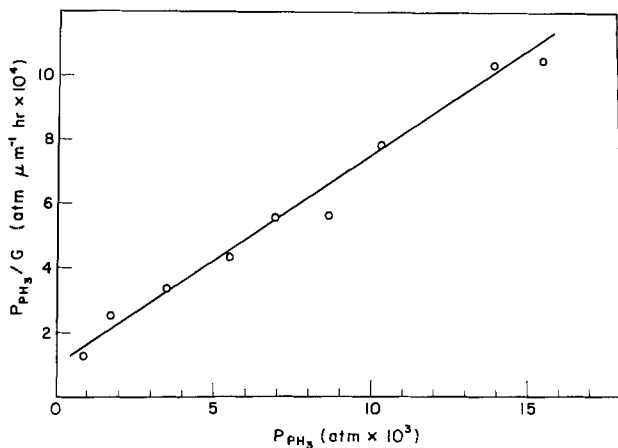


Fig. 4. Application of Langmuir equation to the growth of InP on Mo at 620°C .

Adsorption of phosphorus was also found to be important in the planar reactive deposition of InP at the sub-atmospheric pressures (10^{-4} Torr), Fraas *et al.* (2) observed that in order to obtain stoichiometric films, it was necessary to prepare the films under excess phosphorus conditions. Thus vapor deposition of indium phosphide is apparently controlled by the same type of surface reaction mechanisms at both high and low pressures.

Film structure.—Using x-ray diffractometer techniques the phases and the preferred orientation of the as-grown InP were analyzed. Films grown under stoichiometric as well as phosphorus-rich conditions are single phase and have diffraction lines characteristic of cubic indium phosphide. As shown in Fig. 5, at substrate temperatures below 500°C the films had predominantly a $\{111\}$ texture, though as the substrate temperature was increased other orientations appeared including the $\{200\}$ $\{220\}$ $\{331\}$ $\{311\}$ planes. Nevertheless, the $\{111\}$ remained the dominant orientation. Even for films as thin as $1 \mu\text{m}$, preferred orientation was still prevalent.

The indium phosphide film morphology was observed by using optical and scanning electron microscopy. Films were found to be continuous over the entire 100 mm^2 area. The grain size of the as-deposited films also depended on temperature. For material grown at 620°C , the average grain size was $6 \mu\text{m}$; whereas for films grown at temperatures of less than 500°C , the grain size was less than $1 \mu\text{m}$ (Fig. 6). Increased surface roughness coincided with the decrease in the preferred orientation.

Conclusions

These studies demonstrate that homogeneous InP polycrystalline thin films can be grown at temperatures as low as 410°C , using the hydride deposition technique. Films prepared at temperatures below 500°C have a preferred $\{111\}$ orientation. Grain size of the films varied from $6 \mu\text{m}$ to less than a micron

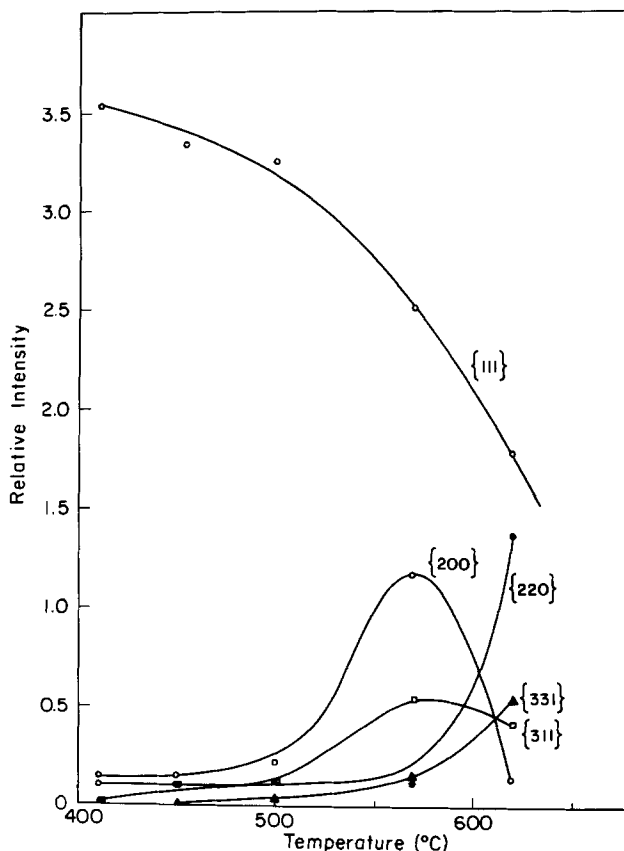


Fig. 5. The dependence of relative x-ray intensity for several crystal planes on substrate temperature.

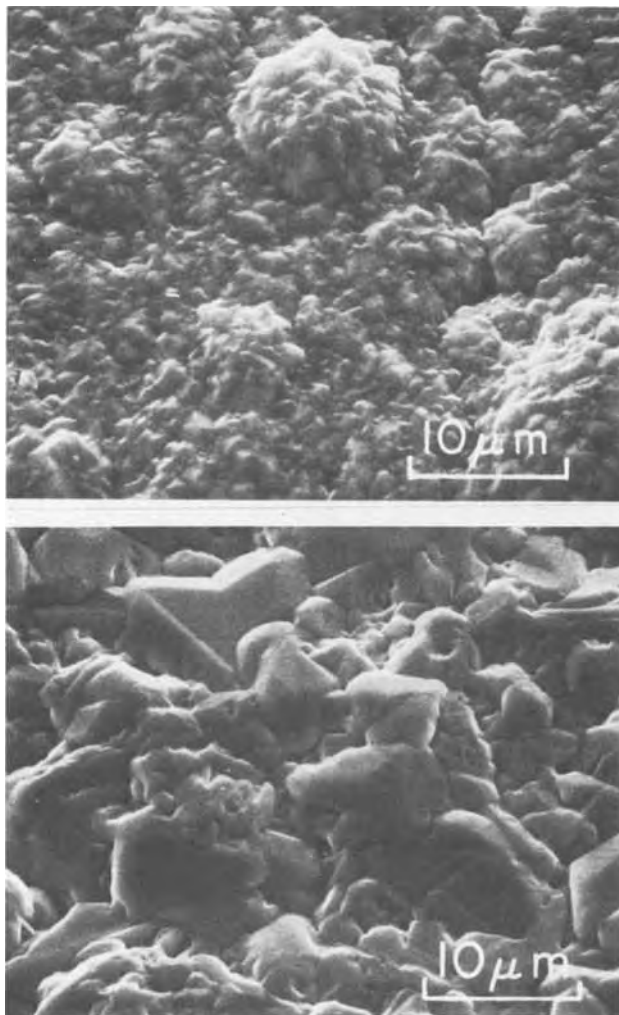


Fig. 6. Scanning electron micrographs of as-deposited InP films: (a, top) $T_{\text{substrate}} = 500^{\circ}\text{C}$; (b, bottom) $T_{\text{substrate}} = 620^{\circ}\text{C}$.

depending on the deposition temperature. Kinetic studies support that adsorption of phosphorus via the Langmuir mechanism controls the growth rate of the polycrystalline InP films over the temperature range studied.

Acknowledgment

This work was supported by the NSF-MRL program through the Materials Research Center of Northwestern University (Grant DMR76-80847). A grant of CVD equipment from the General Electric Company is greatly appreciated.

Manuscript submitted August 9, 1979; revised manuscript received ca. July 7, 1980.

Any discussion of this paper will appear in a Discussion Section to be published in the June 1981 JOURNAL. All discussions for the June 1981 Discussion Section should be submitted by Feb. 1, 1981.

Publication costs of this article were assisted by Northwestern University.

REFERENCES

1. S. Wagner, J. L. Shay, K. T. Bachmann, and E. Buehler, *Appl. Phys. Lett.*, **26**, 229 (1975).
2. L. M. Fraas, K. Zanio, and M. Shibata, *Appl. Phys. Lett.*, **28**, 415 (1976).
3. H. M. Manasevit, K. L. Hess, P. D. Dapkus, R. P. Ruth, J. J. Wang, A. G. Campbell, R. E. Johnson, L. A. Moudy, R. H. Bube, L. B. Fabick, A. L. Fahrenbruch, and M. J. Tsai, in Proc. 13th IEEE Photovoltaic Specialists Conference, p. 165 (1978).
4. T. Saitoh, S. Matsubara, and S. Minagawa, *This Journal*, **123**, 403 (1976).
5. K. J. Bachmann, E. Buehler, J. S. Shay, S. Wagner, and M. Bettini, *ibid.*, **123**, 1509 (1976).
6. A. G. Sigai, C. J. Neuse, R. E. Enstrom, and T. Zamerowski, *ibid.*, **120**, 947 (1973).
7. B. W. Wessels, *ibid.*, **122**, 402 (1975).
8. T. Saitoh, S. Matsubara, and S. Minagawa, *Thin Solid Films*, **48**, 339 (1978).
9. V. S. Ban and M. Ettenberg, *J. Phys. Chem. Solids*, **34**, 119 (1973).

Miniature Cantilever Beams Fabricated by Anisotropic Etching of Silicon

Richard D. Jolly¹ and Richard S. Muller

Department of Electrical Engineering and Computer Sciences and the Electronics Research Laboratory, University of California, Berkeley, California 94720

Anisotropic etching of single crystal silicon was shown to be capable of producing ultrasmall three-dimensional micromechanical devices (1). Petersen has used thin, metal-coated, SiO₂ cantilever beams made by this technique in light-modulator arrays (2), and for miniature switches (3). Roylance (4) and Ross-vold (5) etched cantilever beams in silicon diaphragms to construct piezoresistive accelerometers.

Different beam structures are required for the most effective use of micromechanics with piezoelectric field-effect transducers (PI-FET's) (6). Preferred for this purpose is a beam in which thermal oxide separates one conducting electrode from another. Strain-induced charge in a piezoelectric can then be inhibited from relaxation so that a response to a d-c-applied strain is possible.

¹ Present address: Hewlett-Packard Laboratories, Palo Alto, California 94304.

Key words: mechanics, membrane, capacitance, composites.

This paper describes the construction of such beams as well as other beams with useful cross sections. The fabrication process is compatible with ion-implanted MOS planar technology.

Fabrication

The anisotropic etching of silicon makes use of ethylenediamine, pyrocatechol, and water (EDP) (7). The etchant can remove the silicon from below a layered structure consisting of SiO₂ and heavily-doped p-type silicon. We have used this process to construct four types of miniature cantilever beams having the cross sections sketched in Fig. 1. The beams consist of cantilevers: (i) with thin (100 nm) SiO₂ layers covering 200 nm of bulk p⁺ silicon; (ii) with thin SiO₂ on bulk p⁺ silicon isolated from the substrate by a thick oxide beam (800 nm); (iii) formed of 200 nm thick p⁺ silicon; (iv) formed of 800 nm thick SiO₂.

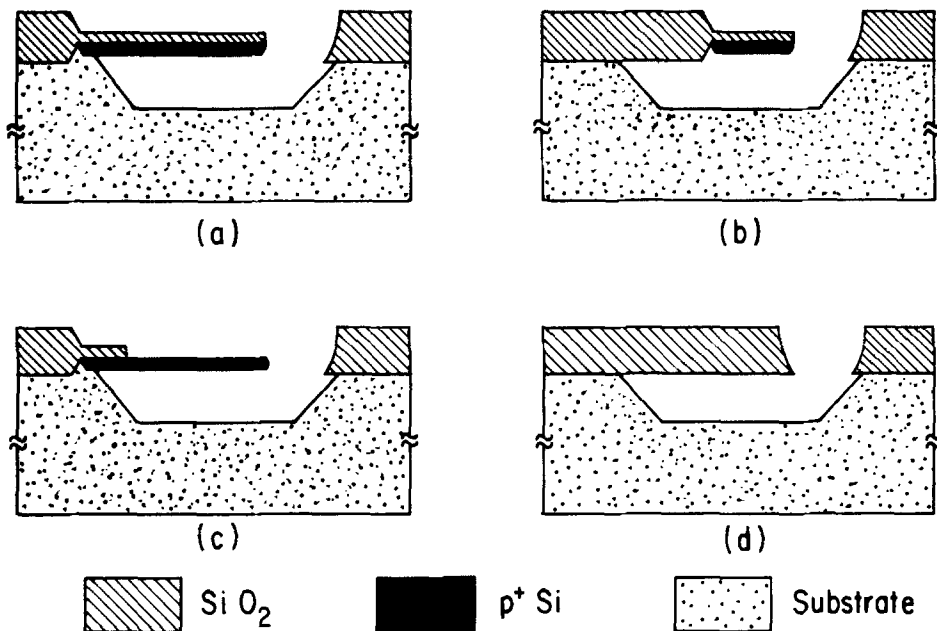


Fig. 1. Cross sections of the four types of miniature cantilever beams.

Each of the four types of beams were processed in widths varying from 5 to 40 μm , at lengths varying from 15 to 160 μm . The size of the cavity under the cantilevers is a function of the etch time—it is typically between 15 and 50 μm in depth.

All beams were fabricated on both p- and n-type substrate material. The starting wafers were B-doped, 4 $\Omega\text{-cm}$ $\langle 100 \rangle$ -oriented Si for the p-substrate and P-doped, 6 $\Omega\text{-cm}$ $\langle 100 \rangle$ -oriented Si for the n-substrate. To process the wafers, first a thick (800 nm) oxide is grown in a steam atmosphere at 1100°C followed by a 20 min anneal at the same temperature in N_2 . Next, the oxide is patterned with buffered HF, and 100 nm of oxide is grown in a dry O_2 -TCE ambient for 32 min at 1100°C. This step is also followed by a 20-min anneal at 1100°C in N_2 . The p+ region is formed using an ion implant of BF_2^+ at 180 keV with a dose of 10^{16} cm^{-2} . An anneal at 600°C in N_2 and O_2 for 6 hr follows, after which the dopants are activated at 950°C in N_2 for 40

min. A computer simulation [using SUPREM (8)] predicts that this process results in a B concentration greater than roughly 10^{20} cm^{-3} in a layer extending about 0.4 μm downward from the Si-SiO₂ interface. Below this, the B concentration drops very steeply.

The beams are formed using EDP anisotropic etchant (8 ml water: 17 ml ethylenediamine: 3g pyrocatechol) at a temperature of 110°C using a glass refluxing system. The etch rate for the (100) plane is approximately 50 $\mu\text{m/hr}$.

Discussion

Figure 2 collects data about the micro-beams on a map with coordinates equal to the beam thickness t and the beam width w . The data points marked with an x represent beams which were broken or else so severely bent as to be useless as mechanical cantilevers. These failures in fabrication may result from the excessive stress present because of mismatched mechanical properties at the Si-SiO₂ interface.

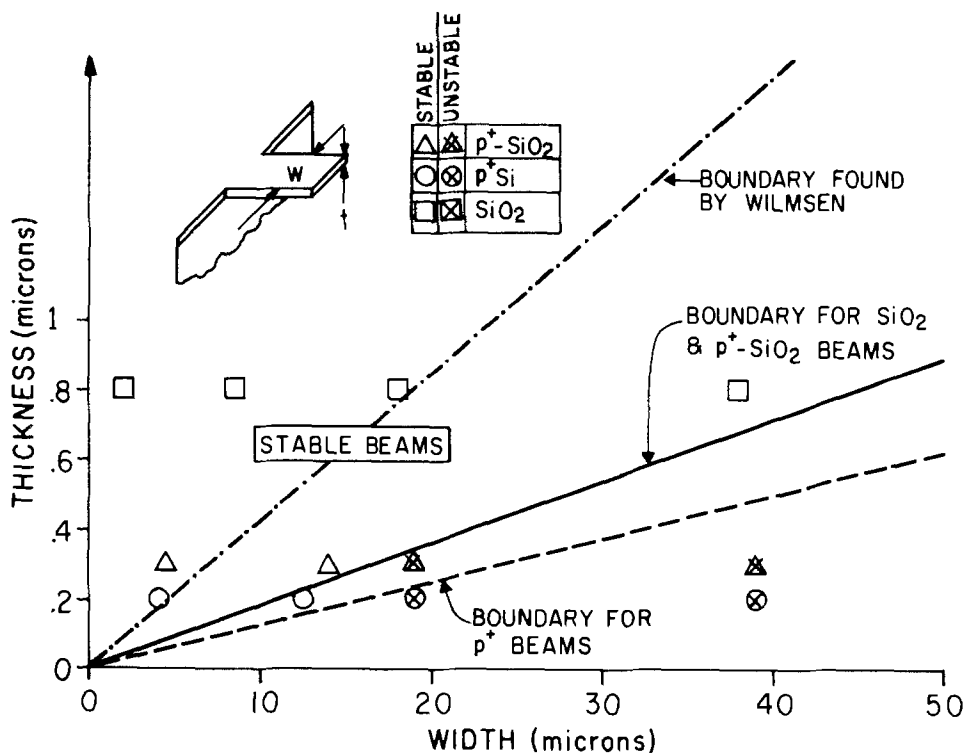


Fig. 2. "Map" of thickness vs. width of successful beam fabrications. The sloped lines indicate the lower bounds for t/w ratios that were produced: (i) solid line for oxide and composite Si-oxide beams, (ii) double dashed line for pure Si beams, and (iii) dot-dash line for unsupported SiO₂ windows as found by Wilmsen et al. (9).

Because the coefficient of thermal expansion for Si is greater than that for SiO₂, films formed by thermal oxidation are compressed when the processed wafer is cooled after oxidation. Wilmsen, Thompson, and Meissner (9) have discussed the effect of this energy on the buckling and fracture of unsupported SiO₂ windows. By applying elasticity theory, they show that it is not possible to obtain a stable oxide film if the ratio of its thickness to the window dimension t/w is made too small. The lower permissible limit for the t/w ratio is related to the difference in the coefficients of thermal expansion for Si and SiO₂ and to the change in temperature. By considering most and least restrictive boundary conditions, Wilmsen was able to show that the lower limit on t/w should be bounded according to Eq. [1]

$$0.52 \sqrt{\Delta\alpha\Delta T} < t/w < 1.2 \sqrt{\Delta\alpha\Delta T} \quad [1]$$

where $\Delta\alpha$ is the difference between the coefficients of thermal expansion for the SiO₂, and ΔT is the change in temperature. Wilmsen *et al.* fabricated stable windowed structures for $t/w > 0.7 \sqrt{\Delta\alpha\Delta T}$. This boundary is indicated by the dot-dash line on Fig. 2.

The cantilevered structures we studied are freed of stress on three sides and therefore not strictly comparable to the SiO₂ windows examined in Ref. (9). However, qualitatively similar results on SiO₂ film stability were obtained in this study. As seen in Fig. 2, the apparent lower bound for t/w for these cantilever beams is $0.4 \sqrt{\Delta\alpha\Delta T}$ for stable SiO₂ beams [Fig. 1(d)] and stable SiO₂ on p⁺ Si beams [Fig. 1(a)]. Stable p⁺ Si beams were obtained for $t/w > 0.27 \sqrt{\Delta\alpha\Delta T}$. These boundaries are also shown on Fig. 2. For our process, the oxide growth was carried out at 1100°C so ΔT is roughly 1075°C. For Si and SiO₂, $\Delta\alpha$ is 2×10^{-6} , so that $\sqrt{\Delta\alpha\Delta T} = 0.046$.

The differing thermal expansions for Si and SiO₂ are also responsible for bending observed in composite beams. When a cantilever of Si and SiO₂ is formed, it can be expected to bend downward as the tension in the Si and the compression in its oxide seek accommodation. However, cantilevers formed of one homogeneous material should not be bent in either direction unless there is some reconfiguration caused by the release of stored strain energy.

Figures 3 through 7 are SEM photographs of the cantilever beams. The beams were coated with roughly 20 nm of gold to avoid charging by the SEM electron beam. This coating had no appreciable effect on the mechanical loading of the structures. Figure 3 shows examples of three types of beams, all constructed with a mask dimension for the width of 10 μm and for the length of 30 μm. Bending in two of the beams may have resulted from the thermal-mismatch stress. As expected, the oxide-silicon beam bends downward. The bending in the thin Si beam may have resulted from plastic deformation of one surface or from inhomogeneity of mechanical properties due to processing. Petersen (1) observed similar effects on some beams.

Figure 4 shows an 800 nm SiO₂ beam (lower structure), as shown in Fig. 1(d), adjacent to a beam composed of 100 nm of SiO₂ overlaying roughly 200 nm of p⁺ silicon. This two-layer beam has the p⁺ silicon underneath the oxide extending beyond the SiO₂ edge to facilitate inspection. The thickness of the p⁺ layer has been estimated using these photographs and the known magnification of the SEM. When inspected with an optical microscope, the p⁺ layer causes characteristic color fringes below the SiO₂ film.

Figure 5(a) shows a Fig. 1(b)-type beam (lower cantilever) next to an 800 nm thick oxide beam [Fig. 1(d)]. In Fig. 5(b), the tip of the lower beam of Fig. 5(a) has been magnified to show the p⁺ Si projecting from beneath the 100 nm oxide. Figure 6 is an SEM

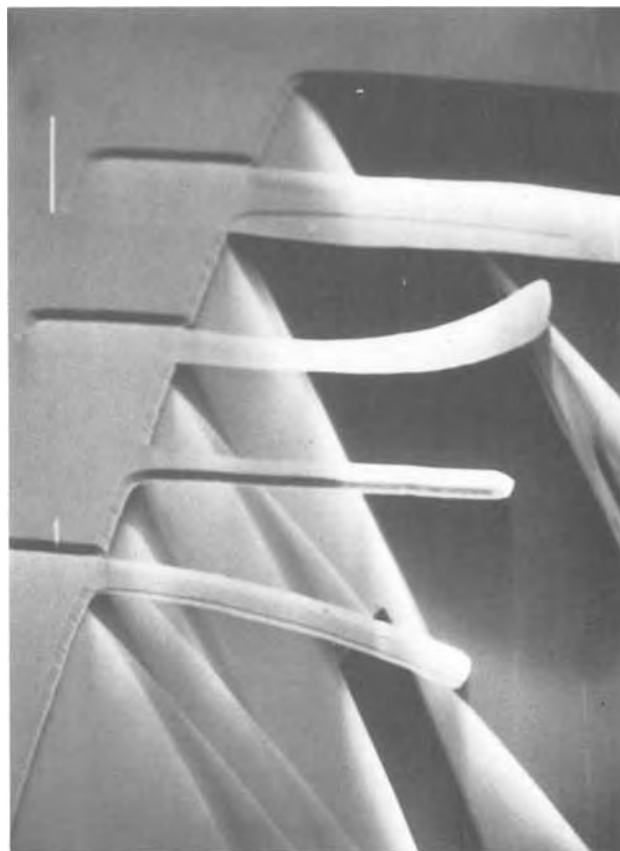


Fig. 3. SEM photograph of 3 types of miniature cantilever beams. From bottom to top: thin SiO₂ on p⁺ Si [as in Fig. 1(a)], thick SiO₂ [as in 1(d)], thin p⁺ Si [as in 1(c)], SiO₂ on p⁺ Si (magnification 2000×, specimen angle 72°). The uppermost beam has 7 μm of extended p⁺ Si and is incompletely etched.

photograph of a cantilever of thin p⁺ Si [similar to Fig. 1(c)] below a beam of thick oxide [Fig. 1(d)].

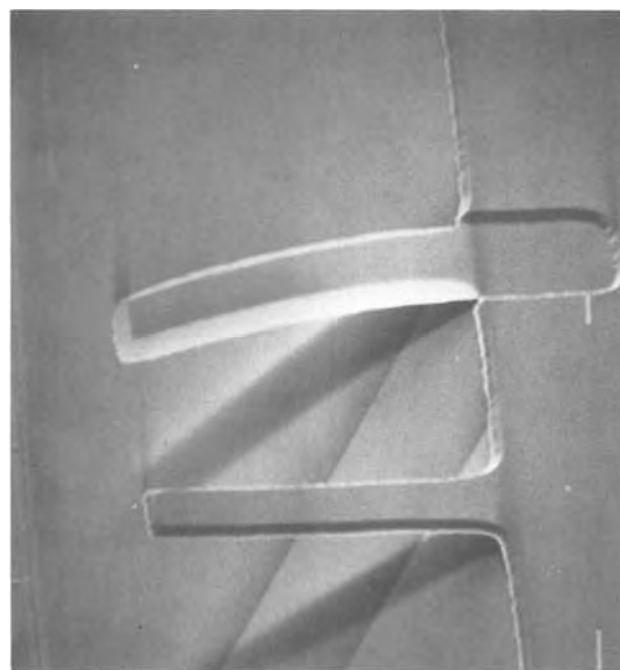


Fig. 4. SEM photograph of an SiO₂ beam (lower structure) and an SiO₂ on p⁺ Si beam [Fig. 1(a)] (2000×, 50°).

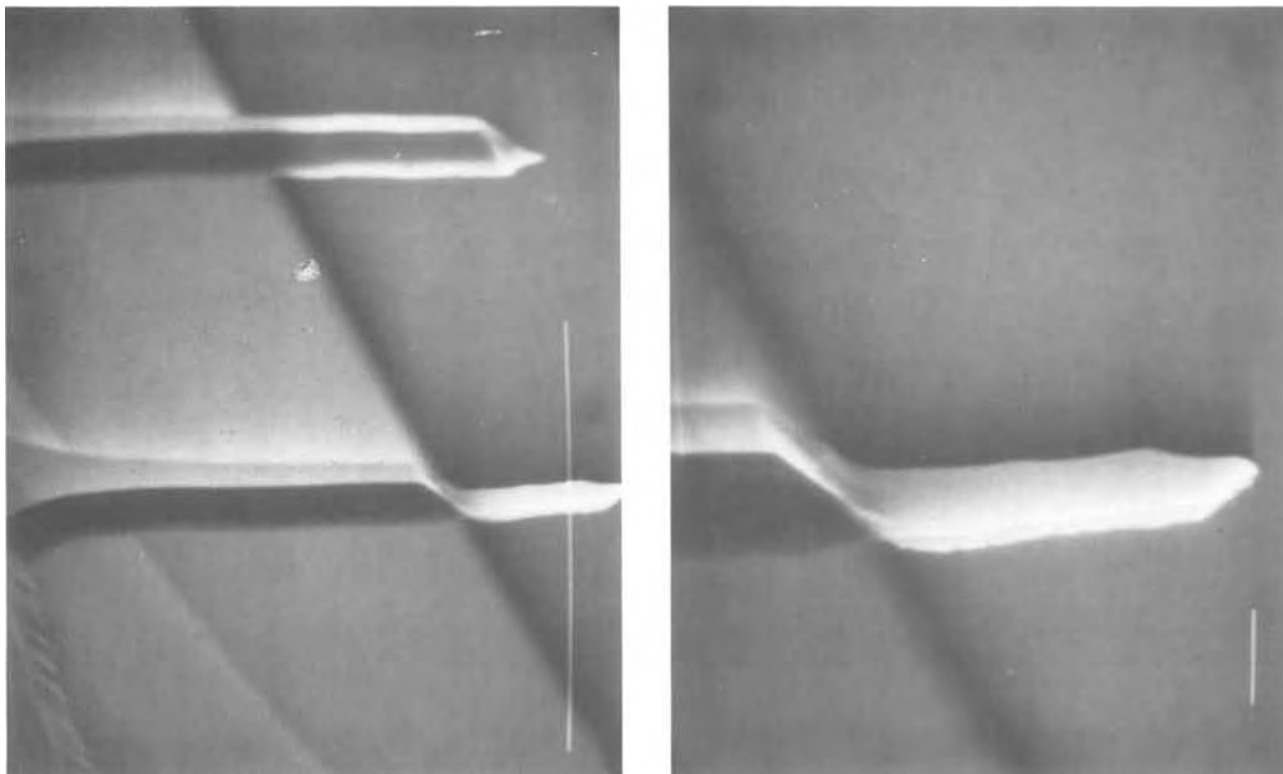


Fig. 5. (a, left) SEM photograph of a beam of SiO_2 on p^+ Si isolated by a beam of thick SiO_2 [Fig. 1(b)] ($7500\times$, 75°), (b, right) an enlargement of the tip of the beam shown in (a) ($20,000\times$, 75°).

Samples of all types of beams were fabricated without mechanical damage in widths ranging from 4 to $12\ \mu\text{m}$ at lengths of 15-40 μm . Widths greater than $12\ \mu\text{m}$ were only successfully constructed with the 800 nm SiO_2 films unless a stiffening technique was employed as in the cantilever shown in Fig. 7. A thicker oxide

ridge (800 nm) has been left on the periphery of the cantilever to form a stiffer and more rugged beam.

Conclusions

The methods demonstrated in this work may apply to a number of electronic systems. Of particular importance is the fabrication of conducting layers underneath thermally-grown SiO_2 . With this construction, the beam itself can be an electrical capacitor with very low leakage. It might be used to isolate a piezoelectric thin film on top of the beam, allowing direct reading of the surface charge on the piezoelectric. Other applications in the transducing area are also of interest

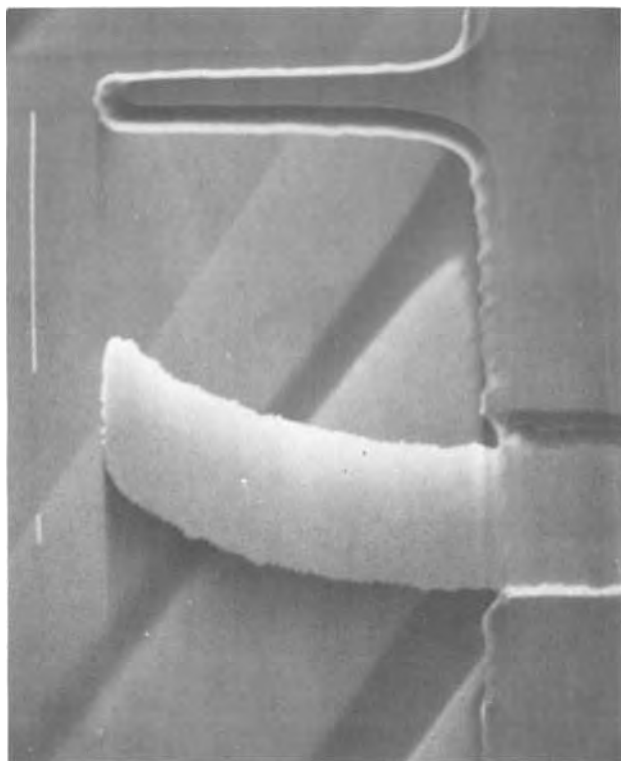


Fig. 6. SEM photograph of a beam of thin p^+ Si (lower beam) ($5000\times$, 30°), the upward-bending of this cantilever is unexpected, but observed on some beams.

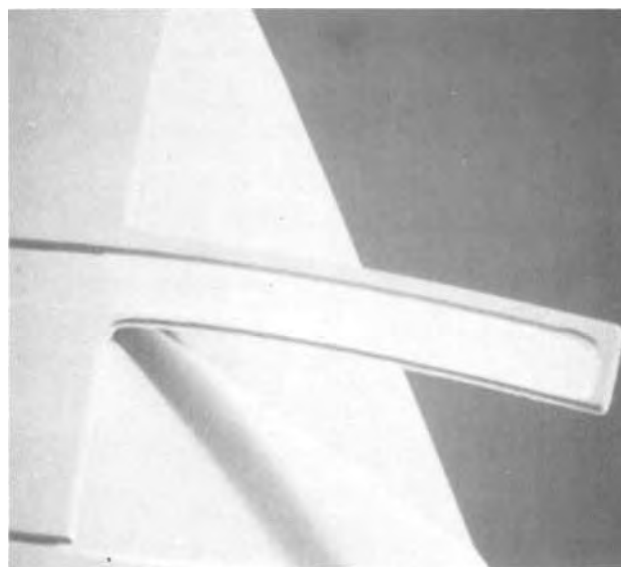


Fig. 7. SEM photograph of a thin SiO_2 on p^+ Si beam [Fig. 1(b)]. The beam is $20\ \mu\text{m}$ in width and has been reinforced by a thick rib of SiO_2 .

wherever the electrical isolation of one material from another is desired.

Although we studied only cantilever structures, doubly-supported beams consisting of SiO₂ supporting thin p⁺ silicon could be built. Such beams could have applications to silicon integrated circuits in the production of transmission lines with very low capacitance per unit length. The transmission lines would be composed of the p⁺ silicon layers overlain with insulating oxide suspended above cavities etched from the silicon by EDP.

Acknowledgment

This research was supported by the National Science Foundation under grant Eng-7822193 and partially by contract DASG60-79-C-0021 from BMD-ATC administered by the Rockwell International Science Center.

Manuscript submitted March 10, 1980; revised manuscript received May 22, 1980.

DISCUSSION SECTION



This Discussion Section includes discussion of papers appearing in the *Journal of The Electrochemical Society*, Vol. 127, No. 1 and 3, January and March 1980.

Observation and Analysis of Surface States on TiO₂ Electrodes in Aqueous Electrolytes

R. H. Wilson (pp. 228-234, Vol. 127, No. 1)

J. F. Julião,¹ Franco Decker,² and M. Abramovich:² In a paper recently published³ and coauthored by B. A. Parkinson, H. C. Chagas, and ourselves, a very similar effect on TiO₂ electrodes was reported and discussed on the basis of different electrochemical techniques. The potential of the peak observed by Wilson, the dependence of the peak height on the scan rate, and the effect of alkaline solutions on the phenomenon are very similar to that observed in our work. Our reduction peak, however, was observed in the dark, without previous u.v. illumination (therefore with no oxygen in the cell) and was reversible under cyclic voltammetry. No peak was seen unless the sample was previously held in contact with concentrated KOH or NaOH solutions for a few hours.

The presence of surface states is a reasonable explanation for such phenomena. However, it has been shown by Tomkiewicz⁴ that with a proper surface treatment such states can be avoided on TiO₂, and straight 1/C² vs. voltage plots result as a consequence. We have recently observed a correlation between the reduction peak, straight 1/C² vs. voltage plots and surface treatment.

TiO₂ samples (001 surfaces) freshly polished with 0.25 μm diamond paste or polished and subsequently etched at 240°C for 30 min in a concentrated solution of sulfuric acid and ammonia sulfate (1:1) did not show the reduction peak in the cathodic region of the *i* vs. *V* curves, when phosphate buffer, 1M Na₂SO₄, or 1M H₂SO₄ were used as electrolytes. The 1/C² vs. volt-

Any discussion of this paper will appear in a Discussion Section to be published in the June 1981 JOURNAL. All discussions for the June 1981 Discussion Section should be submitted by Feb. 1, 1981.

REFERENCES

1. K. E. Petersen, *IEEE Trans. Electron. Devices*, ed-25, 1241 (1978).
2. K. E. Petersen, *Appl. Phys. Lett.*, 31, 521 (1977).
3. K. E. Petersen, *IBM J. Res. Dev.*, 23, 376 (1979).
4. L. M. Roylance and J. B. Angell, *IEEE Trans. Electron Devices*, ed-26, 1911 (1979).
5. W. Rossvold, AF Avionics Laboratory Tech. Report 77-152, Cantilever Accelerometer (September, 1977). Signetics Report.
6. S. H. Kwan, Ph.D. Thesis, Univ. of California, Berkeley, California (1978).
7. R. M. Finne and D. L. Klein, *This Journal*, 114, 965 (1967).
8. D. Antoniadis and R. W. Dutton, *IEEE Trans. Electron Devices*, ed-26, 490 (1979).
9. C. W. Wilmsen, E. G. Thompson, and G. H. Meissner, *ibid.*, ed-19, 122 (1972).

age plots for the same samples were linear for potentials up to 1.5V positive of the flatband potential (Fig. 1 of this discussion).

After these samples were immersed for 16 hr in 5M KOH two behaviors were observed: the etched samples showed the same behavior as before, while the polished ones showed now the reduction peak and nonlinear 1/C² vs. voltage plots. A mechanical polishing, however, restored the same characteristics as prior the KOH treatment. The flatband potential as measured from capacitance plots had a Nernstian dependence on pH for the freshly prepared or repolished samples, while the samples aged in KOH had a much steeper slope (see Fig. 2 of this discussion), a behavior also observed by Wilson on page 232 for his samples.

Our experiments show that surface states are easily created on TiO₂, but can also be removed by proper treatments. Therefore, we believe it is very important to characterize the surface preparation of TiO₂ electrodes, due to its influence on the results. The relevance of surface states for photoelectrolysis, however,

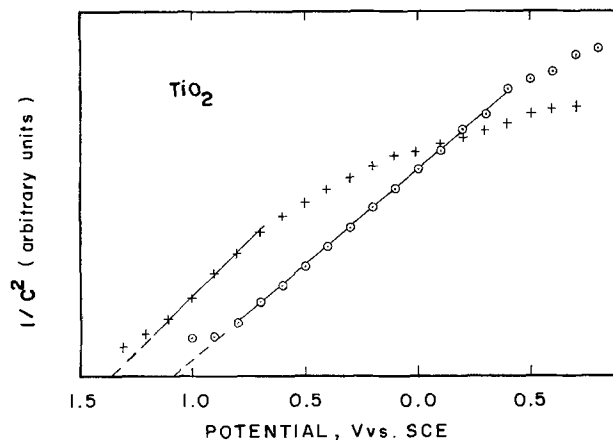


Fig. 1. 1/C² × *V* plots of TiO₂ electrodes in a phosphate buffer solution, pH = 11. The circles are for a freshly polished sample. The crosses are for a KOH-aged sample.

¹ Instituto de Física, UNICAMP, Campinas, (SP), Brazil (Present address: Depto de Física, Univ. Fed. do Ceará, CP 1262, 60.000 Fortaleza, CE, Brazil).

² Instituto de Física, UNICAMP, Campinas, (SP), Brazil.

³ B. A. Parkinson, F. Decker, J. F. Julião, M. Abramovich, and H. C. Chagas, *Electrochim. Acta*, 25, 521 (1980).

⁴ M. Tomkiewicz, *This Journal*, 126, 1505 (1979).

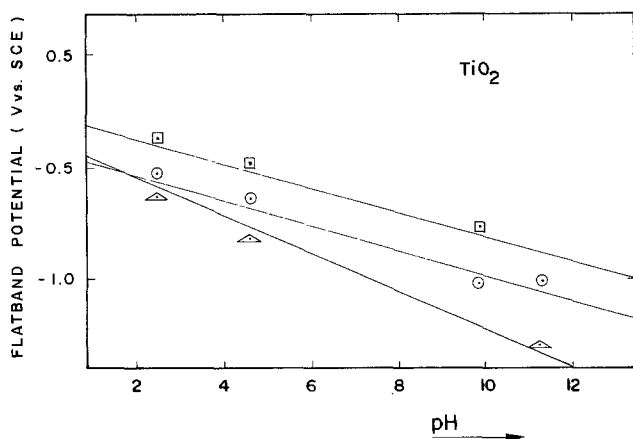


Fig. 2. Flatband potential as a function of pH for a TiO_2 sample after three different surface treatments: circles: freshly polished; triangles: aged in KOH; squares: repolished.

is still a big question. Actually, there is probably no relationship between the kind of surface states we observed and photoelectrolysis, since the photo-current-potential curves we measured (*i vs. V* plots in the anodic region, with illuminated electrode) were very much the same both for the fresh and for the KOH-aged samples.

R. H. Wilson:⁵ The comments by Julião *et al.* are interesting but have very little to say about the principal observations and conclusions in the paper under discussion. The potential of the reduction peak described in my paper and its dependence on illumination demonstrate that it is not the same peak discussed by Julião *et al.*

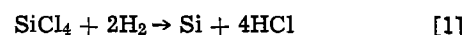
While the observations reported by Julião *et al.* are interesting, they must be interpreted with care. The near surface bulk properties of TiO_2 can be affected by electrochemical exposure and by mechanical polishing.^{6,7} These can change the capacitance-voltage behavior as observed in differential capacitance measurements as well as in capacitive currents observed during a voltage sweep. These possible changes in bulk properties have not been considered by Julião *et al.* in interpreting their observations.

Silicon Deposition on a Rotating Disk

R. Pollard and J. Newman (pp. 744-752, Vol. 127, No. 3)

Michael L. Hitchman:⁸ In deriving theoretical transport-controlled growth rates for CVD processes the effect of the temperature gradient close to the reaction surface is usually neglected in order to obtain a simple analytical treatment, and values of gas properties corresponding to some average temperature are taken. A simple consideration of the differential equations for fluid flow and heat and mass transfer shows⁹ that one might expect the steep temperature profile commonly encountered at a susceptor surface to lead to a considerable distortion of the diffusion boundary layer and hence of the growth rate. Nevertheless, the agreement between theory based on constant gas property conditions and experiment for various reactor geometries is usually reasonable.⁹ However, in order to make use of this approximate approach one still has to obtain an exact solution to the constant property problem, and although this is simpler than for the

variable property case it is not always easy, especially for those instances where there is distortion of boundary layers by, for example, reactor walls. Therefore the one-dimensional rotating disk system which has been such a powerful tool for studies with solutions could be expected to be equally valuable for the investigation of CVD processes. The paper under discussion extends the theory of fluid dynamics and transport of a disk rotating in an isothermal medium to one in nonisothermal medium. The analysis should allow one to take account of the variation with distance from the surface of a heated disk of the physical properties of the medium and of the change of equilibria and kinetic rates for homogeneous processes. A more exact comparison between theory and experiment than the approximate approach allows should then be possible for CVD processes, such as the epitaxial deposition of silicon quoted in the paper



However, there is a fundamentally important difference between the more usual case of a disk electrode, for example, rotating in a liquid and a heated disk rotating in a gas mixture for a CVD process. This difference is that whereas in the first case the solution is essentially stationary and the hydrodynamic flow pattern, and hence the mass transport, are imposed by the disk rotating, in the second case one has a gas mixture being continuously fed to the reactor with the result that the fluid dynamics and heat and mass transport can be determined not just by the rotating disk but by the inlet gas flow as well. This distinction does not seem to have been appreciated either by Pollard and Newman, or by Sugawara¹⁰ in the paper from which the authors have taken results in order to test their theoretical analysis. Unfortunately, Sugawara does not explicitly state what gas flow was used during the silicon deposition, but a flow of 40 liter/min⁻¹ is implied since he says "the quartz tube was fixed, 40 liters/min of H_2 was inserted, and rf heating was effected. After reaching the set temperature for the epitaxial reaction, a 5 min interval was taken before feeding SiCl_4 together with H_2 ." If such a high flow rate was employed during the deposition then it is very probable that the flow characteristics would have been largely determined by the inlet gas flow rather than the disk rotating. The reported weak dependence of growth rate on rotation speed would then simply be a reflection of this and not of rate control by homogeneous gas phase kinetics. Strong evidence in support of this conclusion is given by results we have obtained from studies of the rotating disk system for CVD processes in general and, with a reactor very similar to that described by Sugawara, for the deposition of silicon by reduction of SiCl_4 in particular.^{11,12} Detailed results will be published shortly,^{13,14} but we can briefly summarize the main findings here.

We have monitored the temperature profile with a small thermocouple probe on the axis of a rotating disk heated to 1200°C in a hydrogen gas flow. These measurements clearly show that the thickness of the thermal boundary layer is very sensitive to the inlet gas flow. For example, with a rotation speed of 500 rpm and a gas flow of 1.9 liter/min⁻¹ the thermal boundary layer thickness (obtained by extrapolation of the linear portion of the temperature profile at the surface to intercept the horizontal portion corresponding to the bulk temperature) is ~ 20 mm, while

¹⁰ K. Sugawara, *This Journal*, 119, 1749 (1972).

¹¹ M. L. Hitchman, B. J. Curtis, H. R. Brunner, and V. Eichenberger, in "Physicochemical Hydrodynamics—V. G. Levich Festschrift," Vol. II, D. B. Spalding, Editor, pp. 1021-1029, Advance Publications Ltd., London (1977).

¹² M. L. Hitchman and B. J. Curtis, Abstract 219, p. 586, The Electrochemical Society Extended Abstracts, Pittsburgh, Pennsylvania, Oct. 15-20, 1978.

¹³ M. L. Hitchman in "Progress in Crystal Growth and Characterization," B. R. Pamplin, Editor, Pergamon Press, Oxford, To be published.

¹⁴ M. L. Hitchman and B. J. Curtis, Results to be published.

⁵ General Electric Company, Research and Development Center, Schenectady, New York 12301.

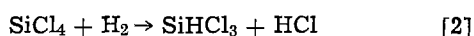
⁶ R. H. Wilson, L. A. Harris, and M. E. Gerstner, *This Journal*, 126, 844 (1979).

⁷ L. A. Harris, M. E. Gerstner, and R. H. Wilson, *ibid.*, 126, 850 (1979).

⁸ Department of Chemistry and Applied Chemistry, University of Salford, Salford, England M5 4WT.

⁹ M. L. Hitchman, *J. Cryst. Growth*, 48, 394 (1980).

with a gas flow of 6 liters/min⁻¹ it is ~ 12 mm. Also with a rotation speed of 1000 rpm and 1.9 liters/min⁻¹ of hydrogen the boundary layer thickness of ~ 18 mm is not significantly different from that at 500 rpm under the same conditions. It is evident, therefore, that before one can use the rotating disk for studies of CVD processes analogous to those made with isothermal disks in solution, the effect of the gas flow on the mass transport must be compensated for. We have done this by setting up, at a given disk temperature, conditions with the carrier gas alone which give experimental temperature profiles in accordance with those expected on the basis of theory;¹⁵ this theory is, admittedly, only approximate and does not take account of the physical property variations with distance from the disk surface, but the indications are that this does not lead to errors which are too serious.¹⁶ Then we have carried out epitaxial deposition of silicon under the same conditions and measured the growth rate. If the growth rate is truly transport controlled one would expect a dependence on the square root of the rotation speed (Ω), whereas for kinetic control a smaller dependence would be expected, as pointed out by Pollard and Newman. We find at 1200°C, for example, a linear dependence of growth rate on $\Omega^{1/2}$ at low rotation speeds (< 300 rpm) with a lower dependence at higher speeds (> 300 rpm), thus indicating a transition from mass transfer control to reaction rate control. A complete analysis of the results for growth rate against temperature over the range 900°-1300°C with a two parameter fit to an expression for combined kinetics and transport allows the activation energy and pre-exponential term for the kinetic rate constant of the rate-determining step to be obtained. An activation energy of ~240 kJ mole⁻¹ is required to fit the experimental points and this is considerably higher than the values in the range 120-170 kJ mole⁻¹ commonly reported in the literature for the reaction [1]; the low literature values are obtained from the linear portion of an Arrhenius type plot at temperatures below ~1100°C, and it can be shown¹¹ that transport has a significant effect on the overall growth at temperatures down to 1000°C or less. The pre-exponential term needed to fit the data is ~10¹⁰ cm sec⁻¹ which, when due allowance is made for surface concentrations, can be converted to an equivalent homogeneous first-order rate constant of ~10¹⁰ sec⁻¹. Both the kinetic parameters determined from fitting the data are in reasonable agreement with those found experimentally for the reaction¹⁷



which is described by

$$d[\text{SiHCl}_3]/dt = 7 \times 10^9 [\text{SiCl}_4] \exp(-230 \times 10^3/RT)$$

for a hydrogen pressure of 1 atm. Thus the rate-determining step in the silicon deposition would appear to be reaction [2] which is, in fact, the same process postulated by Pollard and Newman, albeit on the erroneous basis of earlier published results.

In conclusion, it may be said that the rotating disk is as potentially useful a tool for the study of CVD reactions as it has been for reactions at an interface

in contact with a liquid, and the analysis of Pollard and Newman should allow a more exact comparison between theory and experiment than is possible with less rigorous approaches. However, as our results clearly show, whether one uses an exact or approximate analysis of the mass transport problem it is essential to ensure that due consideration is given to the effect of inlet gas flow on the mass transfer.

R. Pollard¹⁸ and J. Newman¹⁹ Hitchman suggests that the weak dependence of growth rate on rotation speed reported by Sugawara²⁰ is caused by high inlet gas flow rates. However, if bulk gas flow increases the mass transfer rate, the observation of deposition rates below the mass transfer limit at high rotation speeds can only be explained by a transition to reaction rate control, as Hitchman's own data indicate. Certainly, distortion of the velocity profile by passage of gas through the reactor could be an additional reason for discrepancies between experimental results and theoretical predictions, but this only emphasizes the need for careful experimental procedure.

The influence of bulk gas velocity cannot be properly accounted for by simply "adding on" the effect of carrier gas as Hitchman proposes. A rigorous treatment would necessitate a complete solution of the partial differential equations of motion, subject to the appropriate boundary conditions. The von Kármán transformation would no longer apply, even with the assumption of constant physical properties, and the attractiveness of the rotating disk, as a system with mass transfer and fluid flow characteristics that can be predicted accurately, would be lost. Similarly, attempts to account properly for natural convection and radial diffusion would make the mathematical formulation far less tractable and would introduce radial dependences that could cloud the interpretation of experimental data.

Application of the present analysis to chemical vapor deposition of silicon shows that the large physical property variations across the boundary layer can significantly affect the predicted behavior. Simplifications to the model (that Hitchman needs to account for large inlet gas velocities in a simple manner) immediately raise questions concerning the choice of the most appropriate diffusion coefficient, density, viscosity, and other physical properties. Naturally, values can be chosen to give the best fit between experiment and theory, but this has no theoretical basis and makes the predicative capability of the model questionable. The need to resort to analyses of this type can only be regarded as a retrograde step.

Alternatively, the use of large, downward-facing disks and long gas residence times could minimize the uncertainties associated with radial diffusion, natural convection, and inlet gas flow rates, in a quantitative manner. With carefully chosen experimental conditions, the rigorous model presented for the rotating disk may be used with confidence to predict reaction mechanisms and fundamental kinetic parameters for chemical vapor deposition processes.

If external factors dictate the need for large inlet gas velocities, it may be more appropriate to use an alternative to the rotating disk, such as the impinging jet system, in the laboratory.

¹⁵ E. M. Sparrow and J. L. Gregg, *Trans. ASME J. Heat Transfer*, **81**, 249 (1959).

¹⁶ S. Ostrach and P. R. Thornton, NACA Technical Note 4320, NACA, Washington (1958).

¹⁷ D. J. Ashen, G. C. Bromberger, and T. J. Lewis, *J. Appl. Chem.*, **18**, 348 (1968).

¹⁸ Chemical Engineering Department, University of Houston, Houston, Texas 77004.

¹⁹ Chemical Engineering Department, University of California, Berkeley, California 94720.

²⁰ K. Sugawara, *This Journal*, **119**, 1749 (1972).



Universal Ending of a Technological Quartz Furnace Tube

Andrzej Hejduk

*Instytut Technologii Elektronowej Politechniki Wrocławskiej,
Wybrzeże St. Wyspiańskiego 27, 50-370, Wrocław, Poland*

Basic high - temperature processes of planar silicon technology /i.e. semiconductor doping, making of SiO_2 films, heating in various technological stages/ are performed mainly in large diameter quartz tubes. Necessary components of the working atmosphere are supplied to the tube in the gaseous phase through a tube ending. Such an ending is a section of a quartz tube closed at one end, with short, thin quartz pipes soldered in /gas line supplies are installed to them/.

The ending is connected to the main tube through a conic, quartz, ground tube [1]; in particular cases the ending is formed on the main tube itself. The construction of the whole-glass ending described here has some basic disadvantages:

- the ending is hard to make, what makes it expensive,
- due to the brittleness of quartz, the ending is easy to damage, especially during gas line supplies installing,
- the quantity of the gas line supplies is determined by a particular technological process being performed in the tube, therefore adaptation of such an ending to the requirements of another process cannot be made easy.
- exchange of a damaged tube or ending often requires grinding of newly selected set of connection tubes.

The disadvantages described above make exploitation of the whole-glass ending a difficult task, especially when it is used in the research work.

Therefore a new construction of the ending is developed [2].

The ending is made from acid-resistant steel and polytetrafluoroethylene, securing the high purity of the working atmosphere in the tube.

The scheme of the design is shown in figure 1.

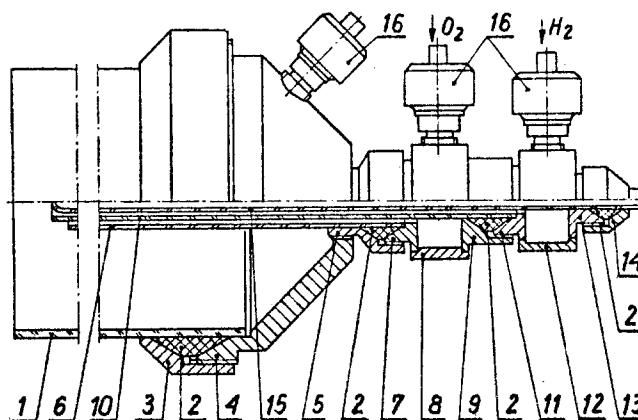


Fig. 1. Schematic section of a quartz tube end with fastened ending, and with an oxygen-hydrogen blowpipe producing steam.

Easiness of the fastening of the ending to the tube 1, which is out straight, is being the greatest advantage of this construction. Connection of the ending to the pipe 1, which is both mechanically resistant and very tight, is obtained due to the mating of an elastic annular connector 2 made from polytetrafluoroethylene with correspondent seats in the nut 3 and in the ending body 4. Holes, in which the gas line supplies are screwed, are situated in a way as to make the gas stream coming into the tube move along a screw line. Such a shape of the stream improves the homogeneity of the working atmosphere. The ending may be easily adapted to the requirements of a specific technological process by screwing a proper amount of gas lines 16 into the body 4 /holes not used are to be closed by proper pins/.

An idea of an oxygen-hydrogen blowpipe [3] is also shown in figure 1.

Two basic disadvantages of a whole-glass quartz blowpipe [4] are avoided in this construction: high price and vulnerability.

In the new construction, principle of quartz pipe fastening is the same as in the construction of an ending described above. Working gases are supplied to the tube 1 through two nozzles: 6 /oxygen/ and 10 /hydrogen/. The temperature is controlled by means of a thermocouple secured by pipe 15. Concentric setting of pipes 6, 10, and 15 is made due to the mating particular pipes with annular connectors 2 compressed by elements 5, 7 /oxygen nozzle/, elements 9, 11 /hydrogen nozzle/, and in the case of thermocouple pipe 15, by elements 13 and 14. Supply of the working gases to the blowpipe is made through deliveries 16 screwed into the oxygen chamber /composed of elements 7, 8, 9, 10/ and into the hydrogen chamber /composed of elements 11, 12, 13, and 14/.

Process of oxidation of silicon substrates can be made with the use of the oxygen-hydrogen blowpipe in the atmosphere of both dry oxygen and steam; humidity of the oxidating medium can be regulated by changing the proportion of hydrogen to oxygen. It is to be underlined that the steam produced by the blowpipe is of the highest purity, and is being mainly determined by the quality of supplied gases.

SUMMARY Designs of the technological tube ending and of the oxygen-hydrogen blowpipe producing steam of the highest purity, are described in this paper. In the construction shown here, disadvantages of well-known whole-glass quartz designs are eliminated. The basic advantages of a new designs are: easy adaptation of the ending to the requirements of different high-temperature processes and its resistance to mechanical damage. These advantages make the research work easier, especially in the field of semiconductor devices and integrated circuits technology.

REFERENCES

[1] Heraeus catalog, for example Q-B3/112

- [2] A. Hejduk, A. Zyderkiewicz, Końcówka rury technologicznej, Zgłoszenie pracowniczego projektu wynalazczego, Politechnika Wrocławska, 1980
- [3] A. Hejduk, A. Zyderkiewicz, Konstrukcja palnika wodorowo-tlenowego, Zgłoszenie pracowniczego projektu wynalazczego, Politechnika Wrocławska, 1980
- [4] Thermoc catalog card, Quartz H₂ Injector - 04-466-75

Manuscript submitted April 14, 1980;

revised manuscript received June 20, 1980.

Azide Photoresists for Deep U.V. Lithography

T. Iwayanagi, T. Kohashi, and S. Nonogaki

Hitachi Limited, Central Research Laboratory, Kokubunji, Tokyo, Japan

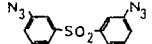
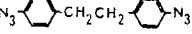
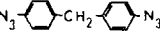
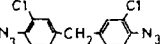
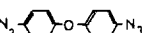
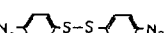

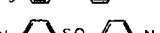
Deep UV lithography utilizing wavelengths in the 200-300 nm region has become of interest in recent years, since it provides a means of defining 1-2 μm patterns in the microfabrication of solid-state devices (1,2). A reflecting 1:1 projection printer, VL-MR1, was recently developed for a deep UV exposure system (3). One problem with deep UV lithography is the lack of high power light sources, which places the requirement of high sensitivity on deep UV resists (4). Methacrylate resists such as PMMA (polymethyl methacrylate) (1,5) and sensitized PMIPK (polymethyl isopropenyl ketone) resists (6) have so far been used for deep UV applications. However, the sensitivity of these resists is not sufficient to achieve practical exposure times for scanning type deep UV projection printers such as VL-MR1 (3). In this paper, we report highly sensitive azide photoresists suitable for deep UV lithography.

Current negative resists in conventional photolithography consist of cyclized polyisoprene and photosensitive diazide compounds. The most commonly used diazide is 2,6-di(4'-azidobenzal)-4-methylcyclohexanone (7), with an absorption maximum at 355 nm. Therefore, resist composed of this diazide and cyclized polyisoprene has maximum sensitivity at about 360 nm (8) and is not well suited for deep UV applications. Diazides for deep UV resists should possess the following absorption properties: (I) wavelength of absorption maximum lying between 200 and 300 nm to give high sensitivity to deep UV radiation; and (II) sharp cut-off in the longer wavelength region. Aromatic diazides without conjugation between the two benzene rings would satisfy the above requirements. Such diazides were synthesized from parent diamines by the established method (Table I). Resists consisting of the diazides and cyclized polyisoprene were evaluated as negative deep UV

resists. These resists are insensitive to ordinary white fluorescent lamps and are hence abbreviated as WR (White Resist).

Cyclized cis-1,4-polyisoprene was obtained from Tokyo Ohka Kogyo Co. (OBC-83, Mw 150,000, degree of cyclization 70%). Cyclized polyisoprene was dissolved to 10 weight percent (wt.%) in xylene and then 0.2-10 wt.% of diazide based on the polymer was added to the solution. The resist films were spin coated on silicon wafers with thicknesses of 0.7-1.2 μm and prebaked at 60°C for 20 min. All exposures were carried out in air with Xe-Hg lamps. After exposure, the films were developed by dipping in a 70 vol.% n-heptane/30 vol.% xylene mixture for 2 min at 25°C and then rinsed in n-butyl acetate for 1 min.

Table I Melting Points and Wavelengths of Absorption Maximum for Diazides and Exposure Times for Cyclized Polyisoprene-Diazide Resists

Diazide	m.p. (°C)	λ_{max} (nm)	Exposure Time*(sec)
A 	116	240	0.6
B 	80	254	0.3
C 	44	256	0.5
D 	128	258	0.5
E 	77	264	0.2
F 	37	266	0.7
G 	90	273	0.1
H 	163	284	0.3

* Exposure time required for 50% remaining film thickness for resist consisting of cyclized polyisoprene and diazide (1.0 wt.% based on polymer).

Key words: Negative photoresist, Deep UV resist, Deep UV lithography

The sensitivity of WR containing 1.0 wt.% diazide (based on polymer weight) was measured. The resist films were exposed at a fixed light intensity (120 mW/cm^2) for various exposure times using a 600 W Xe-Hg lamp (Canard Hanovia Inc.) in conjunction with quartz optics and a 4 cm water filter. The exposure times for WR required to give a 50% remaining film thickness after development are given in Table I. An exposure time of 45 sec is required for PMMA under the same exposure conditions; hence WR is approximately 60-450 times more sensitive than PMMA. The use of diazide G (4,4'-diazido-diphenyl sulfide) for WR resulted in the highest sensitivity, as shown in Table I. Therefore, it was decided to select diazide G from the various diazides listed in Table I.

The sensitivity of WR with diazide G (WR-G) was measured with the deep UV projection printer VL-MR1, equipped with a 2 kW Xe-Hg lamp (Ushio Electric Inc.) and a cold mirror CM-290 (Canon Inc.) (3). The exposure characteristics of WR-G resists were examined with varied concentrations of diazide G. The sensitivity increased by a factor of three as the diazide G content increased from 0.5 to 3.0 wt.%, while concentrations above 3 wt.% did not enhance the sensitivity any further. With concentrations of 2.0 wt.% or above, the resist patterns were found to be subject to swelling and deformation during development unless the resists were overexposed. On the other hand, with concentrations of 0.5 wt.% or below, a marked decrease in film thickness after development was observed upon projection exposure in air. This is due to the oxygen

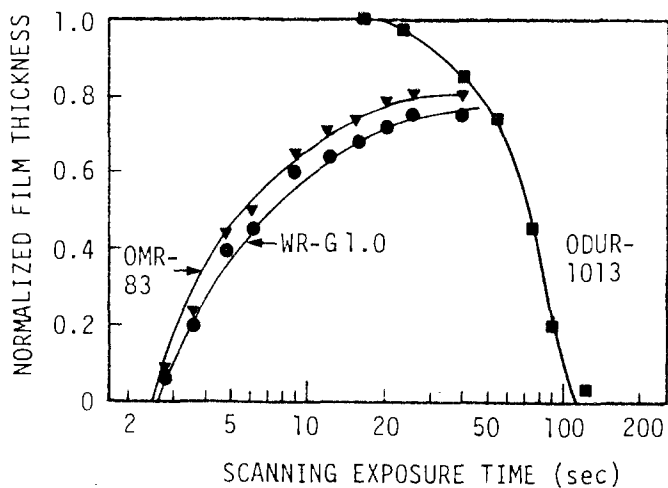


Figure I Exposure Characteristics for Deep UV Resists (1:1 projection printer VL-MR1 with 2 kW Xe-Hg lamp and cold mirror CM-290).

effect often encountered in diazide photoresists (8-10). From these results, it was concluded that WR-G 1.0 which contains 1.0 wt.% diazide G based on cyclized polyisoprene would be most suited for deep UV projection printing. Exposure characteristics for WR-G 1.0 are compared with those for a sensitized PMIPK (ODUR-1013 of Tokyo Ohka Kogyo Co.) and a current negative photoresist OMR-83 (Tokyo Ohka Kogyo Co.) in Figure I. A practical scanning exposure time of about 20 sec can be achieved for WR-G 1.0. OMR-83 is slightly more sensitive than WR-G 1.0 under the stated exposure conditions. The cold mirror used for these exposures is known to permit the transmission of some light with wavelengths above 300 nm (3). If the OMR-83 resist were evaluated in a system which eliminated the light with wavelengths longer than 300 nm, then its sensitivity would be reduced.

The resolution and lithographic performance of WR-G 1.0 will be described in a subsequent paper.

ACKNOWLEDGMENT

The authors are grateful to Y. Hatano for his preliminary study of this work. They would like to thank S. Iwamatsu and K. Asanami for deep UV exposure by VL-MR1.

REFERENCES

1. B. J. Lin, *J. Vac. Sci. Technol.*, **12**, 1317 (1975).
2. B. J. Lin, *IBM J. Res. Develop.*, **20**, 213 (1976).
3. S. Iwamatsu and K. Asanami, *Solid State Technol.*, **23** (5), 81 (1980).
4. M. J. Bowden and L. F. Thompson, *Solid State Technol.*, **22** (5), 72 (1979).
5. Y. Mimura, T. Ohkubo, T. Takeuchi, and K. Sekikawa, *Japan J. Appl. Phys.*, **17**, 541 (1978).
6. M. Tsuda, S. Oikawa, Y. Nakamura, H. Nagata, A. Yokota, H. Nakane, T. Tsumori, Y. Nakane, and T. Mifune, *Photogr. Sci. Eng.*, **23**, 290 (1979).
7. J. J. Sagura and J. A. Van Allan, U. S. patent, 2,940,853 (1960).
8. M. S. Htoo, *Kodak Photoresist Proceedings*, p 25 (1968-Vol. I).
9. T. Kohashi, M. Akagi, S. Nonogaki, H. Hashimoto, N. Hayashi, and T. Tomita, *Photogr. Sci. Eng.*, **23**, 168 (1979).
10. S. Shimizu and G. R. Bird, *This Journal*, **126**, 273 (1979).

Manuscript submitted June 10, 1980;

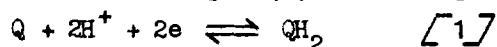
revised manuscript received Sept. 3, 1980.

A Reversible Redox Couple in Quinone-Hydroquinone System in Nonaqueous Medium

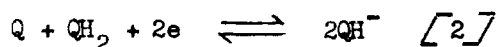
V. J. Koshy, V. Swayambunathan, and N. Periasamy

Chemical Physics Group, Tata Institute of Fundamental Research, Bombay 400 005 India

In aqueous acidic solutions an equimolar mixture of a quinone and the corresponding hydroquinone forms the well-known quinhydrone reversible redox couple (1). In nonaqueous



solvents quinone and hydroquinone are not electrochemically coupled as the reduction potential of the quinone and the oxidation potential of the hydroquinone occur at potentials separated by more than one volt (1, 2). It is reported (3) that in pyridine the electrochemical reduction of p-benzoquinone (BQ) is not affected by the presence of p-benzohydroquinone (BQH₂). In acetonitrile, however, it is observed (4) that BQH₂ acts as a proton donor affecting the electrochemical reduction of BQ. Complexities in the chemical and electrochemical reactions of 'quinhydrone' solutions have been observed (4) and the mechanism has not been understood. We report here our preliminary results on the study of quinone-hydroquinone systems in a nonaqueous solvent. Our results suggest the existence of the following quasi-reversible redox couple:



Such a redox couple has not been previously reported for a quinone-hydroquinone system in nonaqueous solvents.

The cyclic voltammogram of anthraquinone (AQ) (1.7×10^{-3} M) in 1,2-dimethoxyethane (DME) containing the supporting electrolyte, tetra-n-butyl ammonium perchlorate (TBAP) is shown in Fig. 1A. The vacuum electrolysis cell used in the experiment consists of a Pt wire (test electrode), a Pt mesh (counter electrode) and a silver wire (quasi reference electrode). The solution was degassed on a vacuum line ($< 10^{-4}$ Torr) by freeze-pump-thaw cycle method. As shown in Fig. 1A, AQ is

reduced in two steps, $AQ + e \rightleftharpoons AQ^{\cdot -}$ and $AQ^{\cdot -} + e \rightleftharpoons AQ^{2-}$, and the reduction peak potentials (waves I and II) of the two redox reactions in DME are -0.97 and -1.62 V vs SCE, respectively.

Anthrahydroquinone (AQH₂) is an oxygen (air) sensitive substance and the following method was adopted to prepare a solution of AQ and AQH₂ in DME for the cyclic voltammetric experiment. A solution of AQ (2.1×10^{-3} M) and TBAP (0.2 M) in isopropyl alcohol (IPA) was taken in the vacuum electrolysis cell and degassed on a vacuum line. The solution was transferred to a side arm of quartz tube and UV (300 - 400 nm) photolysed for one minute. Facile photoreduction of AQ to AQH₂ occurs in IPA (5) as indicated by the strong green fluorescence of AQH₂. Approximately 80% of AQ was converted to AQH₂ after the photolysis for one minute. IPA was expelled from the electrolysis cell and DME was distilled into

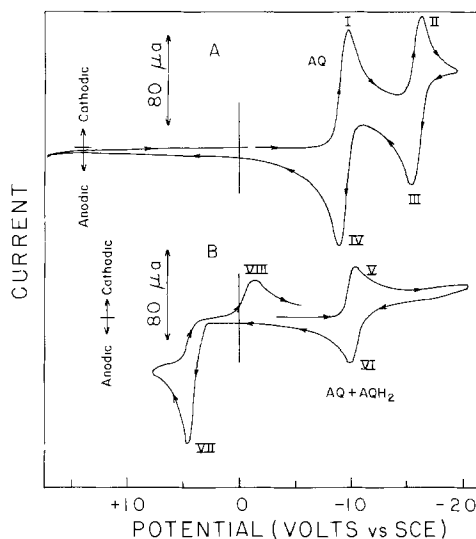


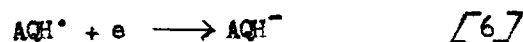
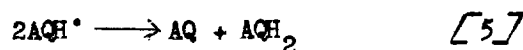
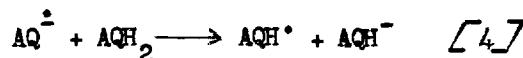
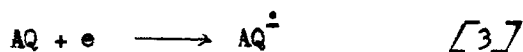
Fig. 1 Cyclic voltammograms in DME: (A) AQ (1.7×10^{-3} M), (B) AQ and AQH₂ ($[AQH_2] > [AQ]$, $[AQ] + [AQH_2] = 2.1 \times 10^{-3}$ M). $[TBAP] = 0.2$ M. Sweep rate = 145 mV/sec. iR compensation has been given.

Key words: Quinone, Hydroquinone, Redox couple, Nonaqueous medium, Cyclic voltammetry

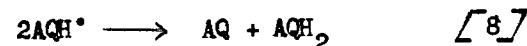
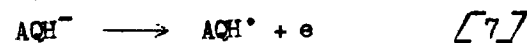
the cell on a vacuum line to make a solution of AQ and AQH₂ whose total concentration is 2.1×10^{-3} M.

The cyclic voltammogram of AQ and AQH₂ in DME is shown in Fig.1B. It is significant to note that the waves II and III which correspond to the second electron redox reaction, $AQ^{\cdot-} + e \rightleftharpoons AQ^{2-}$, are absent showing that AQ^{•-} is consumed in a chemical reaction. And more importantly, an oxidation wave VI (E_p = -0.96V) appears in the reverse anodic scan which cannot be attributed to $AQ^{\cdot-} \rightleftharpoons AQ + e$, as one would interpret the wave IV to be in Fig.1A. Wave VII (E_p = 0.48V) is attributed to the oxidation of AQH₂ and wave VIII (E_p = -0.12V) may be attributed to the reduction of AQH[•] or AQ/H[•] (4). AQH₂ was oxidised to AQ by admitting air (oxygen) into the vacuum cell. The solution was then degassed and the cyclic voltammogram of this solution was identical to that shown in Fig.1A.

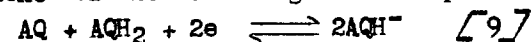
These results are interpreted as follows. The electrogenerated AQ^{•-} undergoes proton transfer reaction with AQH₂ and wave V (E_p = -1.02V) in Fig.1B is interpreted to be the result of the following electrode and chemical reactions:



The semiquinone radical, AQH[•] is known to disproportionate fast (6, 7) and AQH⁻ is the only stable species formed in the reactions (3) - (6). Spectroelectrochemical investigation of this system using Pt OTE confirms the formation of AQH⁻ (8). The absence of the second electron reduction wave of AQ^{•-} in Fig.1B indicates that the reaction (4) is sufficiently fast in the time scale of the experiment. The appearance of wave VI in the reverse anodic scan is attributed to the oxidation of AQH⁻, followed by the disproportionation of AQH[•].



The appearance of the reduction wave V and the oxidation wave VI with a peak potential separation of 50 mV and less suggests the possible existence of the following redox couple:



Such a thermodynamic quasi-reversible redox couple is possible if the reactions (3) - (8) are sufficiently fast. It is observed that an increase in the concentration of AQH₂ relative to that of AQ decreases the peak separation of waves V and VI approaching the theoretical value of 29 mV for the reversible 2e redox couple.

The electrochemical behaviour of BQ - BQH₂ system in DME is found to be identical to that of AQ - AQH₂ system when the concentration of BQ is low. The cyclic voltammogram of BQ (1.2×10^{-4} M) in DME is shown in Fig. 2A. The reduction waves I and II are attributed to the 1e reduction of BQ and BQ^{•-}. Addition of BQH₂ (1×10^{-2} M) (Fig.2B) to this solution completely suppresses the second electron reduction wave II and the reduction peak current of wave V is nearly twice that of wave I. The appearance of the oxidation wave VI in the reverse anodic scan is attributed to the oxidation of BQH⁻. The peak separation of waves V and VI is 50 mV or less. The following quasi reversible redox couple is suggested in this system also:

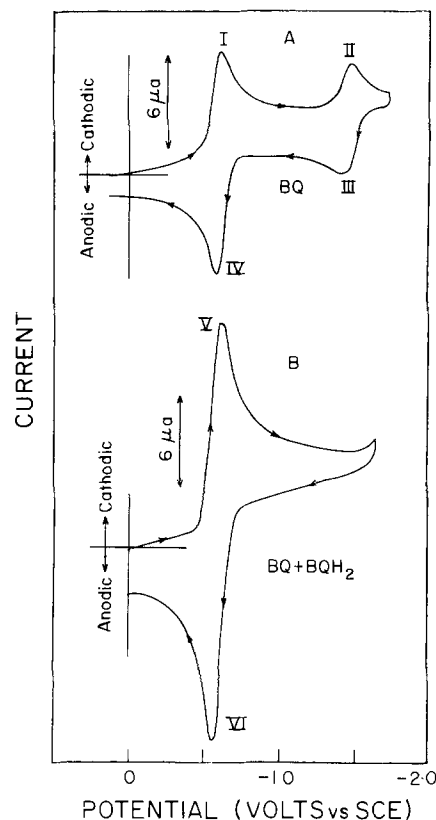
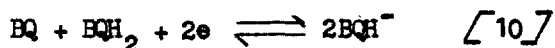


Fig.2 Cyclic voltammograms in DME: (A) BQ (1.2×10^{-4} M), (B) BQ (1.2×10^{-4} M) and BQH₂ (1×10^{-2} M). [TBAP] = 0.2M Sweep rate = 145 mV/sec. IR compensation has been given.



The complexities in the electrochemical reduction of BQ in the presence of BQH₂ in acetonitrile, observed by Eggins and Chambers (4) is also observed in DME when the concentration of BQ is increased to 1 x 10⁻³M or more. These complexities are explained (8) to be due to the electrode deposition of BQH⁻ (as salt), presumably due to the low solubility of BQH⁻ in nonaqueous solvents (4, 9).

REFERENCES

1. S. Wawzonek, R. Berkey, E.W. Blaha and M.E. Runner, This Journal, 103, 456 (1956).
2. C.K. Mann and K.K. Barnes, "Electrochemical Reactions in Nonaqueous Systems", Chapter 6, Marcel Dekker, Inc., New York (1970).
3. W.R. Turner and P.J. Elving, This Journal, 112, 1215 (1965).
4. B.R. Eggins and J.Q. Chambers, This Journal, 117, 186 (1970).
5. K. Tickle and F. Wilkinson, Trans. Faraday Soc., 61, 1981 (1965).
6. S.K. Wong, W. Sitnykh and J.K.S. Wan, Can. J. Chem., 50, 3052 (1972).
7. I.V. Khudyakov and V.A. Kuzmin, (Uspekhi Khimii) Russ. Chem. Rev. (Eng.), 44, 801 (1975).
8. To be published.
9. J. Badoz-Lambling and G. Demange-Guerin, Anal. Lett., 2, 123 (1969).

Manuscript submitted April 29, 1980;

revised manuscript received Aug. 25, 1980.



Microlithography—Key to Solid-State Device Fabrication

C. A. Deckert* and D. L. Ross

RCA, David Sarnoff Research Center, Princeton, New Jersey 08540

Over the past twenty years or so, expressions such as "solid-state circuitry" and "electronics revolution" have become increasingly familiar to the American consumer. The birth and growth of the solid-state industry has been responsible for increased reliability, availability, miniaturization, complexity, and cost reduction of consumer electronics items (1).

The solid-state device, or chip, consists of patterned thin films of one or more metals, dielectrics, and semiconductors on a monolithic substrate, usually a silicon or sapphire wafer as large as 100 mm in diameter. An individual chip varies from about 4 to 15 mm on a side, and may contain from one to 250,000 discrete components (usually transistors).

The fabrication of these devices depends on controlled deposition and removal of the various thin film and substrate materials (2). In order to produce the desired patterns in the solid-state device, a process called microlithography is employed. At various stages in the fabrication process, whenever a new pattern must be defined in the device, a temporary, stencil-like pattern in a thin film covering the surface is defined by techniques related to photography, and selective etching (or, in some cases, deposition) takes place in the unprotected areas. The temporary film known as a "resist" material is then removed and processing continues (3).

This image-forming process is clearly the key to producing complex, patterned, multilayer solid-state devices. Because of its functional similarity to photolithographic operations used in graphic arts, and because of the fine patterns involved, the overall process is known as photolithography, or, more generally, microlithography.

The Historical Development of Modern Microfabrication Techniques (4, 5)

Techniques directly related to microlithography have been widely used in the graphic arts industry for over 100 years. The term "lithography" (literally, writing on stone) is actually a misnomer as applied to the process described here. Lithography is a printing method that utilizes a flat-surfaced, normally water-receptive, plate or stone on which the image areas have been made water-repellant and ink-receptive by photochemical or other means. The surface is wet with water and a greasy ink is applied which adheres only to the image areas. The ink is transferred from the surface to the paper (sometimes via an intermediate rubber surface) by pressure. The procedures developed by the printing trade that are the true antecedents for today's electronics microfabrication industry relate to the manufacture of printing plates, usually of metal, on which a surface relief pattern is produced by removal of material through

chemical etching.¹ In the process called gravure printing, ink is transferred to paper from small "wells" that have been etched into the surface of a plate. Photogravure processes are well established in graphic arts. Thus, "microgravure" might be a more accurate term to apply to the subject of this article.

The development of photoetching techniques represents an example of the impact of the Industrial Revolution on fields that had traditionally been the province of artisans. Chemical technology was substituted for the meticulous hand labor involved in the cutting away of portions of the surfaces of plates (woodcuts, engravings) used to print pictorial images. The invention of lithography in the last decade of the 18th century by the Bavarian, Alois Senefelder, was perhaps the first step in this process. The key events leading to the discovery of an integrated process for chemically etching a relief printing plate with the use of a photoresist have been well documented and can be outlined as follows:

1782: Jean Senebier, a Swiss, studied the influence of light on a variety of materials (including silver compounds) and found that certain naturally occurring resins change color on exposure to sunlight.

ca. 1814: Joseph Nicéphore Niépce (French) wished to capture the images produced by the *camera obscura* without the labor involved in tracing them on paper. He began experiments on light-sensitive materials. By about 1824, he had found that a natural asphalt, "bitumen of Judea," when exposed to light, became less soluble in certain organic solvents. Niépce made the first photograph by coating a polished pewter plate with a thin layer of the asphalt, exposing it (for 8 hours!) in a camera, and developing the image. Within the next several years (ca. 1826), he had used the insolubilized asphalt pattern as a resist and etched the metal (pewter, copper) with acid to produce a relief plate. [Niépce went on to collaborate with Louis Jacques Mandé Daguerre who discovered (ca. 1837) how to make permanent images on the surfaces of silvered copper plates which had been sensitized with iodine vapors (the daguerreotype).]

1832: Gustav Suckow (German) published his observations that mixtures of organic substances with potassium dichromate change color on exposure to light.

1839: Alfred Donné (French) etched daguerreotypes with acid, producing relief printing plates.

1839: Mungo Ponton, a Scot, found that paper soaked in potassium dichromate was light sensitive. When the paper was washed in water following exposure, the unexposed regions washed clean while the exposed pattern remained orange-brown.

¹In the graphics arts, a distinction is made between relief plates, from which the ink is transferred to the paper from the raised portions of the surface (examples: letterpress, woodcuts), and intaglio plates, from which the ink is transferred from those portions cut below the surface (engravings, etchings, gravure plates).

* Electrochemical Society Active Member.

1840: Edmund Becquerel (French) investigated Ponton's findings and determined that the starch sizing in the paper played an important role in the image formation.

1841: Joseph Dixon (American) employed the fact that a mixture of dichromate and natural gum, on exposure to light, changed its surface properties (the exposed areas become ink-receptive while the unexposed areas remain water-receptive) to produce lithographic printing plates. He used such plates to counterfeit bank notes.

1852: W. H. Fox Talbot (English) discovered that exposing films of dichromated natural colloids (e.g., gelatin) to light produced sufficient solubility reduction to permit the unexposed regions to be selectively washed away with water. He patented the use of these materials in photoengraving. This was the first use of a synthetic (man-made) photoresist.

Thus, by the mid-1800's, the groundwork had been laid for today's sophisticated microelectronics fabrication techniques.² It is interesting to note that, with the exception of Suckow and Becquerel, who were university professors, all of the above investigators were amateur inventors.

Dichromated colloid resists suffer from a number of practical shortcomings including a relatively short "pot life," "dark-hardening" (the unexposed coating gradually loses its solubility on storage), excessive dependence of solubility (developability) properties on environmental factors such as ambient humidity, and poor resistance against the strong etchants used for microelectronics materials. In spite of this, dichromated colloids remained the workhorse photoresists of the printing industry until after World War II. Even today, the television industry uses substantial quantities of these materials for the printing of phosphor screens in kinescopes and for the etching of shadow masks for color picture tubes.

Photoengraving techniques were first employed by the electronics industry in the fabrication of copper printed circuits shortly after the war. The application of this technology to transistor fabrication in the early 1950's depended on the development of new classes of entirely synthetic photoresists.

Resists: Chemical Principles (3, 6)

All the resist materials used for microelectronics depend on radiation-induced changes in the solubility of a synthetic organic polymer in some selected developer solvent. Resist materials are classified as either positive-working or negative-working, depending on whether solubility in the developer increases (positive) or decreases (negative) upon exposure to irradiation (Fig. 1). Polymers are universally used for preparing resists because of their excellent film-forming and coating properties and the ease with which such properties can be influenced by synthetic techniques. The polymers usually employed are linear and have molecular weights ranging from a few thousand to several hundred thousand. When dissolved in easily evaporated solvents, the viscosity of their solutions are such that films of useful thickness can be obtained by spin-coating. The molecular structures of the polymers are chosen to permit good spreading and wetting behavior on metal and oxide surfaces. Polymers used to prepare positive resists, where the "stencil" is comprised of unexposed (and, therefore, chemically unchanged) material, must possess the physical and chemical robustness and adhesion to the substrate necessary to withstand subsequent processing steps (or be capable of having these properties imparted to it by a simple post-development step, such as baking).

² In fact, by about 1870, optical equipment had been developed that permitted photoreduction of images by a factor of 1/300 to produce pellicles in silver halide emulsions. These precursors of microfilm and photoreticles were used by the French with the help of pigeons, to communicate with the outside world during the siege of Paris.

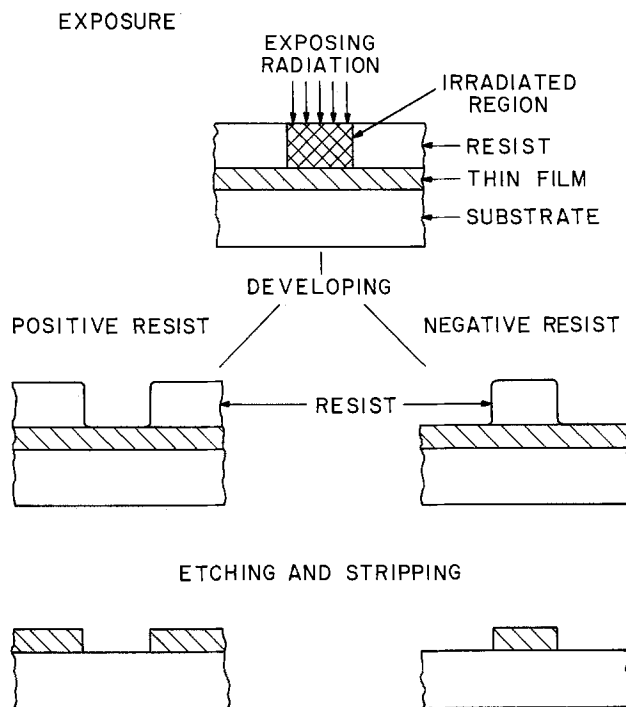


Fig. 1. Schematic diagram of the microlithographic process

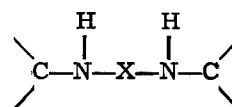
To act as a resist, the polymer must be capable of absorbing the radiation used to expose it, and it must contain, either as components of its molecular composition, or as a second constituent mixed with it, species that will chemically react in carefully selected ways when excited by the absorbed radiant energy. These chemical reactions bring about the desired changes in solubility.

Photoresists must absorb light in order to react. It usually is necessary for the light to be absorbed directly by the molecular species that are to undergo the desired chemical reactions. This is accomplished by choosing conjugated unsaturated systems as the reactive species so as to provide molecular energy levels capable of undergoing electronic transitions corresponding to optical wavelengths in the near ultraviolet (350-450 nm).

The applications of these principles to modern resist technology are outlined below.

Photoresists

Negative-working.—There is only one general type of negative photoresist presently of significance to microelectronics fabrication. Exposure to light causes cross-linking of the polymer molecules. This cross-linking produces an increase in molecular weight, reducing the solubility. Eventually, a three-dimensional network of interconnected polymer molecules (a gel) forms that is totally insoluble. The resist is prepared by mixing with a suitable polymer a polyfunctional, light-sensitive additive that, when excited by the absorption of light, can attach itself to at least two sites on the polymer molecule. Modern negative resists of this class use difunctional azides, N_3-X-N_3 , in which X contains aromatic groups as part of a conjugated system so as to place the optical absorption band in a useful region of the spectrum. On excitation, these compounds lose two molecules of nitrogen and form species known as nitrenes $:N-X-N:$. These highly reactive, short-lived intermediates can react with the C-H bonds (Fig. 2) of a polymer to form the desired cross-links



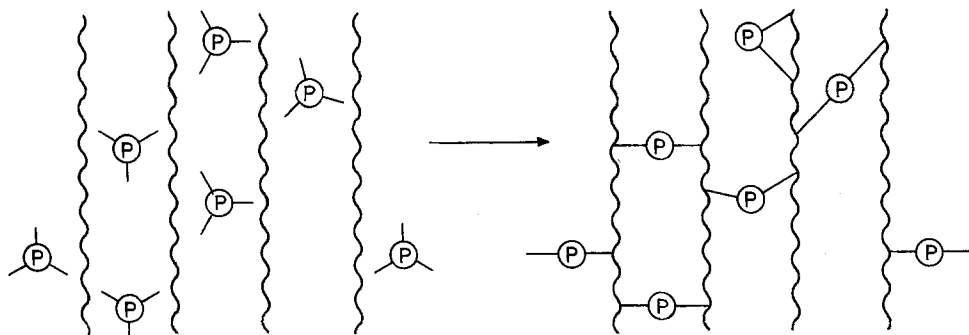


Fig. 2. A typical negative-working photoresist is a mixture of polymer molecules (represented by the wavy lines) and molecules of a light-sensitive, polyfunctional additive (symbolized by the P's). When excited by the absorption of light, the additive reacts with several sites on the polymer chains, causing the polymer to cross-link and, thus, decrease in solubility in the developer solvent.

The polymers used for azide-based resists are usually aliphatic, rubber-like materials based on poly(isoprene). Some closely related resists have been described in which monofunctional aromatic azides are attached to the polymer chains. The patent literature suggests that certain organic compounds act as photochemical sensitizers for azide systems. These compounds absorb some of the incident light and are raised to electronically excited states from which energy can be transferred to the azide molecules which then react as though they had been directly excited. By this means, the sensitivity of these systems can be extended to wavelengths beyond those at which the reactive sites themselves absorb.

While their solutions, and coatings made from them, have considerably better stability and life than dichromated colloids, and their processing is relatively insensitive to environmental factors, all of the negative photoresists currently used for microelectronics suffer from several shortcomings. Two are inherent to all conventional negative resists: (i) Because adhesion of the image areas to the substrate depends on the photo-crosslinking reaction, the exposure required must be adequate to penetrate to and produce some minimum amount of cross-linking at the substrate-resist interface. This sometimes makes it difficult to achieve adequate adhesion without overexposure of the resist (line broadening); (ii) Although the cross-linking reactions render the polymer insoluble in the developer, they cannot completely prevent the exposed resist from solvent-induced swelling. This causes very fine patterns ($\sim 2 \mu\text{m}$) to distort in size and shape and, in extreme cases, to lift from the substrate. Defects known as "stringers" and bridging can be produced by such processes.

In addition, the azide-based resists are sensitive to oxygen which can compete with the desired photo-crosslinking reaction by reacting with the nitrene intermediates. This can lead to "reciprocity law failure": the amount of insolubilization produced by a given total exposure is dependent on the rate at which the exposure is delivered, since the kinetics of the oxygen-based reactions depend on the rate with which oxygen molecules can diffuse in the resist film. When exposure and pattern definition are very critical, films of these resists are generally purged of oxygen prior to exposure by flooding with an inert gas (nitrogen, CO_2).

Positive-working.—All positive photoresists in current use are based on the photochemical conversion of an ortho-diazoketone to a carboxylic acid (Fig. 3). This reaction converts a neutral, organic-soluble molecule to one that is readily soluble in weakly alkaline aqueous developer solvents. These resists are usually formulated from a mixture of a relatively low-molecular weight, hydrophobic, phenolic polymer (which, itself, has some alkali solubility) and a diazoketone (about 15% by weight) derived from an aminonaphthol sulfonic acid, such as is illustrated in Fig. 3. In other closely related systems, the diazoketone is attached directly to the polymer molecules. As a result of association between the polymer and

the diazoketone, the solubility of the mixture in the alkaline developer is inhibited. The hydrophobic nature of the polymer further inhibits attack by the developer. On exposure to light, the diazoketone liberates a molecule of nitrogen and undergoes a molecular rearrangement to the alkali-soluble acid. The formation of the polar carboxyl groups in the exposed areas also renders the film less hydrophobic and, thus, more easily attacked by the aqueous developer (7).

One of the most significant advantages of this family of resists is the fact that, instead of swelling the film and leaching out the solubilized materials, the developer removes the exposed areas by an etching process. As a result, no swelling-induced pattern deformation occurs, and images of extremely high resolution ($< 0.25 \mu\text{m}$) can be formed. Because the adhesion to the substrate is not influenced by the photochemistry, the exposure and development conditions can be adjusted strictly in terms of the relief pattern geometry desired.

The diazoketone resists do not respond to photochemical sensitizers and are not affected by the presence of oxygen.

"Deep-U.V." resists.—The pattern resolution achievable by photoresists is ultimately limited by the wavelengths of the light used to expose them. During the last several years, in attempts to define patterns 1.0–1.5 μm in size, work has been carried out with new light sources and special (quartz) optics to permit exposure systems to utilize wavelengths in the 200–250 nm region. While some conventional photoresists respond adequately to these wavelengths, many do not because the polymers from which they are derived absorb strongly enough to block the transmission of the exciting radiation. The use of these shorter wavelengths makes the task of designing the reactive sites somewhat easier because simpler systems can be used (long conjugated systems are unnecessary). Because of the limitations of negative resists discussed above, most of the new resists being developed for deep-u.v. applications are positive-working and are based on polymers that will undergo a reduction in molecular weight (and, thus, an increase in solubility)

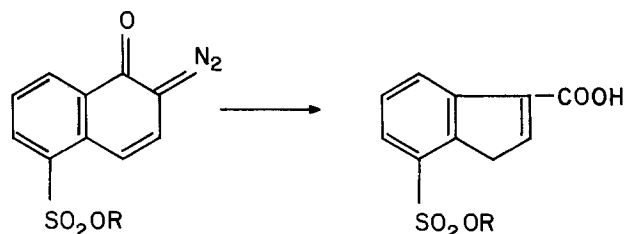


Fig. 3. The molecular structure of a 2-diazo-1-naphthol-5-sulfonic acid ester. Compounds of this type are mixed with phenolic polymers to prepare positive-working resists. When excited by the absorption of light, the normally alkali-insoluble compound loses a molecule of nitrogen and is converted to a carboxylic acid. This causes an increase of the solubility of the mixture in the aqueous alkaline developer.

as a result of photo-induced main-chain scission. Work in this field is in its infancy. The degree to which it flourishes will depend on systems evaluations comparing this approach to higher resolution with those involving electron beam and x-ray exposure schemes.

Electron Beam and X-Ray Resists

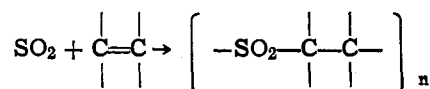
With the ability to focus electron beams to very small diameters (below 1000Å), and the very short wavelengths of soft x-rays (5-50Å), the pattern resolution obtainable when resists are exposed to this kind of radiation is no longer primarily dependent on the exposure means. The fundamental limitations are now a function of the scattering of electrons (or, in the case of x-rays, the range of the photoelectrons produced on absorption of the radiation) in the resist material, or the scattering of electrons reflected from the substrate. During the last 10-15 years, electron beam exposure schemes for the defining of sub- μm patterns in resist materials have been examined at several electronics companies (8). At RCA, the impetus was the mastering of the VideoDisc for which it was desired to record relief patterns having wavelengths of ca. 0.5 μm (9). At Bell Laboratories and IBM, the application was the fabrication of chrome master masks and direct exposure of IC wafers. More recently, research done at MIT Lincoln Laboratories demonstrated that soft x-rays could also be used to expose appropriate resist materials. The electron beam techniques employ a scanned, sharply focused beam as a "pencil" to delineate the desired patterns while the x-ray scheme uses a flood exposure through a patterned mask. In both cases, the interaction of energetic electrons with the resist material brings about the solubility-altering chemical reactions.

The principal difference between these materials and photoresists lies in the fact that, here, the incident energy is absorbed more or less indiscriminately by all functional groups in organic polymer molecules rather than being selectively absorbed at specific reactive sites. The primary chemical event induced by exposure is the breaking of covalent bonds to produce free radicals or ions. As a consequence, the chemical changes brought about are more analogous to those produced by heat than by light. The fate of the ions or radicals determines whether the resist is negative- or positive-working: if these species react with one another to form new covalent bonds, the polymer can increase in molecular weight and/or cross-link; while, if the fragmentation leads to backbone scission, the molecular weight will decrease.

The major emphasis in the search for negative resists is the identification of materials that have the highest practical sensitivity and the best edge definition in the face of the usual swelling problems. Of course, the usual requirements, outlined above, of good adhesion, etch resistance, etc., must be met. Currently, the most widely used negative electron beam resist is a copolymer of ethyl acrylate and glycidyl methacrylate ("COP") developed at Bell Laboratories. The epoxy groups provide a highly sensitive route for cross-linking. It is interesting to note that the cross-linking reactions in this material proceed for a time following the electron exposure. Thus, exposed substrates must be kept in the vacuum chamber of the exposure apparatus for some 20-40 min after exposure is completed to obtain uniform results.

The most useful classes of polymers for positive resists are those known to degrade in molecular weight by thermal processes. The first, and still widely used, positive electron beam resist is poly(methyl methacrylate), long known to be capable of "cracking" back to monomer by destructive distillation. Although a factor of 10-50 lower in sensitivity than is required by today's electron beam exposure systems, it has very high resolution and good etch resistance. An-

other class of polymers known to undergo efficient thermal degradation is the poly(olefin sulfones) (10). These materials are synthesized by the copolymerization of SO_2 and unsaturated monomers



A wide variety of these has been examined at RCA and Bell Laboratories. One, the copolymer of butene (polybutene sulfone, "PBS"), is currently used in the production of chrome masters in MEBES (11). With these polymers, cleavage of the backbone can lead to a chain depolymerization reaction from which the comonomers are regenerated. This introduces considerable "gain" into the exposure process and can produce excellent separation of molecular weight (and, thus, good differential solubility in developers) between exposed and unexposed regions of the resist film. In some materials, the depolymerization process is so efficient that relief patterns are produced directly by evaporation of the reaction products in the vacuum chamber of the exposure apparatus without the need for a separate development step. PBS suffers from several shortcomings: its development characteristics are very dependent on the effects of moisture and ambient humidity; it cannot be used in coatings that are as thick as are needed for step coverage in wafer fabrication; and it has poor resistance against the "dry etching" procedures to be discussed below.

Because the phenolic polymers have low sensitivity to electron-beam-induced cross-linking and because the diazoketones can also undergo heat-induced molecular rearrangement, certain formulations related to typical positive photoresists can function usefully as electron beam resists. At RCA, over a thousand VideoDisc masters were fabricated by electron beam recording using "Mark II" resist, a proprietary material of this type.

While the field of x-ray resists is quite new, it can be predicted that most of the findings relevant to electron beam sensitive materials will apply here. Many of the materials that function well as electron beam resists show similar behavior on x-ray exposure. Considerable emphasis is placed on the incorporation of high Z-value elements in the polymer structure so as to increase the absorption of incident soft x-ray energy.

Microlithographic Processing—Overview

In the fabrication of solid-state devices, the photolithographic process is constantly pushing the limits of the state of the art. Many of the requirements for producing today's complex chips would have been considered impossible just a few years ago, and this trend appears to be continuing unabated (1, 12, 13), as shown in Fig. 4.

The most important resist properties required for producing a microlithographic pattern are resolution, contrast, freedom from defects, uniformity, high sensitivity to the exposing radiation, ease of processing, adhesion to the substrate, resistance to degradation by the etchant, and subsequent ease of removal (3).

The resolution requirement in particular has increased rapidly over recent years. It is important to distinguish between best possible resolution achievable over a small-area unpatterned substrate under carefully controlled laboratory conditions, and best resolution achievable at reasonable yields over large areas in a production environment when various levels must be accurately aligned and precise dimensions maintained. In this paper, unless otherwise stated, the term "resolution" will be taken to mean the smallest feature on a chip that can be imaged economically on 3 in. wafers under production conditions. For example, RCA's 16K RAM SOS devices, the MWS-5114, requires four-micrometer resolution. This chip

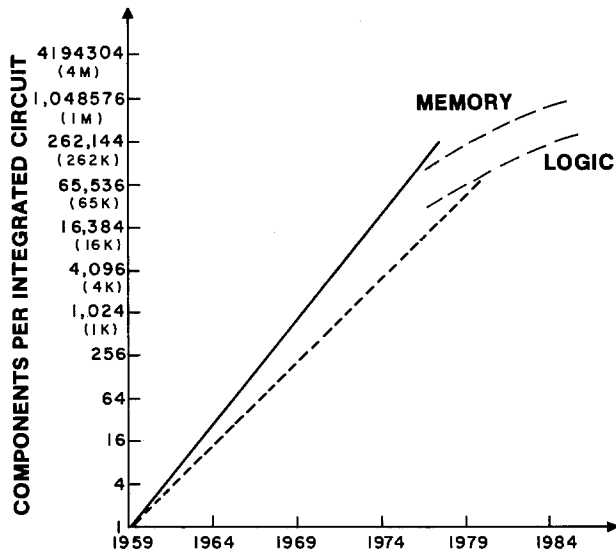


Fig. 4. Number of components per chip has been increasing at a geometric rate since 1959, when the planar transistor was developed. Solid line Ref. (1); short dashes, Ref. (12); long dashes, Ref. (13) (prediction).

is illustrated in Fig. 5. It is thought that the current practical limit for production using conventional photolithographic methods is no better than $3\ \mu\text{m}$ (14). On the other hand, surface structures as small as 80\AA have reportedly been defined in the laboratory (15). Some examples of the recording of high resolution on resists, not from the solid-state industry, include RCA's VideoDisc masters (9), which were formerly fabricated using electron beam recording, and Holo-tape® (16), relief-phase holograms which were recorded using a He-Ne laser. In both these cases, illustrated in Fig. 6 and 7, resolution of $0.25\ \mu\text{m}$ was routinely achieved over a large-area substrate.

In order to fulfill the requirements of microlithography, some steps of the process have become more or less standardized (3), while at most steps, a compromise between high performance and cost is reached. Control of the environment and the choice of resist

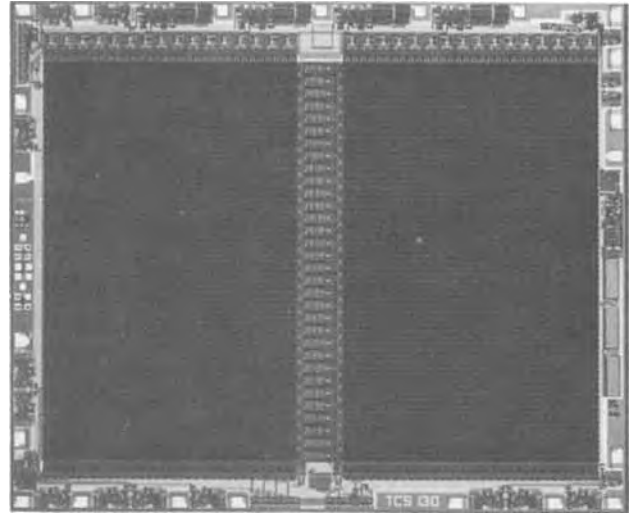


Fig. 5. A complex chip, RCA's 16K RAM SOS device illustrated here, requires four- μm resolution. Even finer dimensions will be required on next-generation circuits.

material itself are other factors where choice is dependent on process requirements.

"Microlithography," as used in electronic device fabrication, designates the successive steps of: preparing the substrate, (e.g., a silicon wafer); applying a thin (usually less than $5\ \mu\text{m}$) film of radiation-sensitive polymeric composition (the "resist") to the surface of the substrate; prebaking the resist coating; exposing the film to a pattern of electromagnetic radiation (light, electron beams, x-rays) so that chemical reactions take place in the film that change its solubility in certain solvents ("developers"); bathing the film in a developer solvent that selectively removes either the exposed ("positive-working") or unexposed ("negative-working") areas thereby creating a patterned stencil in the resist film; postbaking the resist; selectively removing material from or depositing material on those areas of the substrate which have been uncovered by the development step;

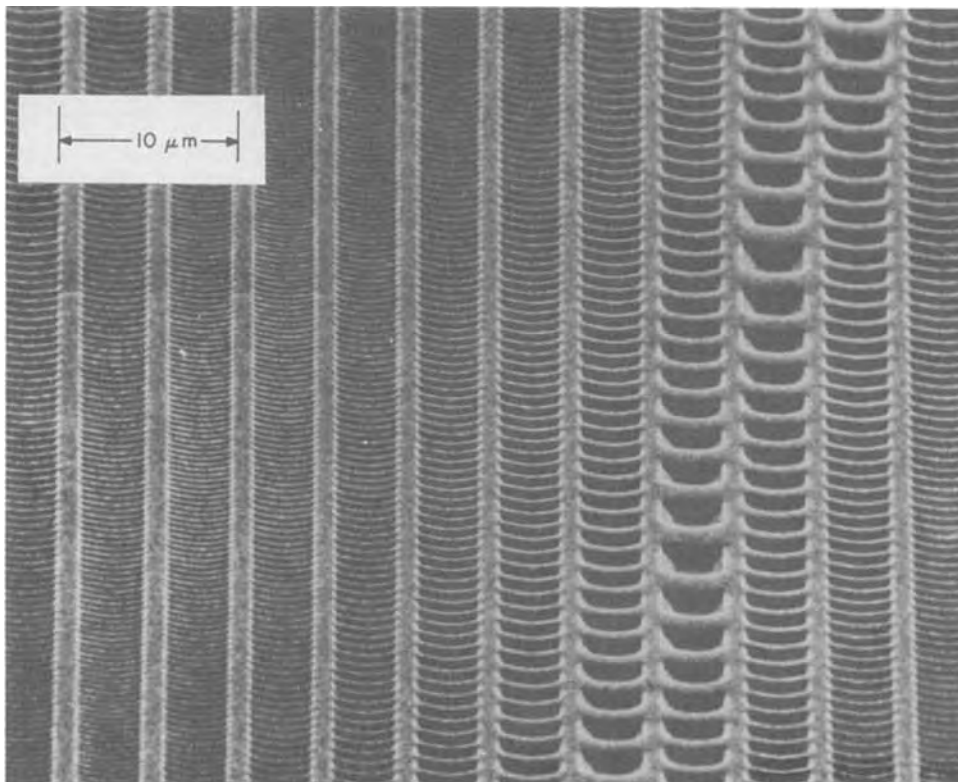


Fig. 6. The masters for RCA's VideoDisc were formerly recorded in a resist material using electron beam exposure.

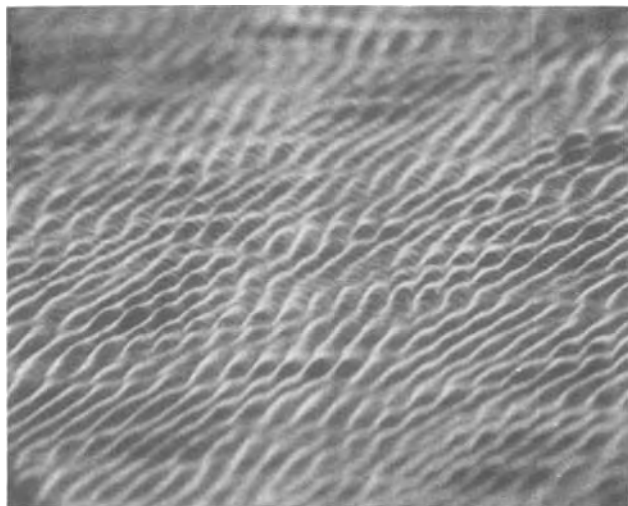


Fig. 7. This Fraunhofer hologram was recorded in a resist material using an He-Ne laser. The pattern exhibits 1 μm periodicity.

and finally removing the remaining resist pattern ("stripping").

Substrate Preparation

Preparation of the substrate may involve film growth or deposition, diffusion or implantation of impurities, or cleaning procedures. If the wafers have been exposed to the ambient for more than a few minutes, contamination is probable (3), and a high temperature bake ($\sim 200^\circ\text{C}$) and/or application of an adhesion promoter are employed. In many wafer processing areas, these steps are routinely used regardless of the time lapse. The importance of cleanliness in solid-state processing cannot be overemphasized. Surfaces must be scrupulously cleaned and kept clean. Contamination, in some form or another, is probably the principal cause of day-to-day processing problems in fabrication areas. For this reason, environmental control (particle count, air flow and quality, clothing, humidity level) is a major factor in determining yields of good chips. A defect which can be traced to surface contamination is shown in Fig. 8.

Coating and Prebaking

Microlithographic processes usually employ liquid resist materials rather than dry film resists³ because of the higher resolving power of the former. The method of application is nearly always a spin-on technique, which offers very good uniformity at a low processing cost. Resist solutions are formulated so that during the application and spinning process, the solvent(s) evaporate at a rate optimum for producing a non-"skinned" coating of uniform thickness (17). In order to remove the last traces of solvent from the resist film and to promote adhesion to the substrate, a prebake step is next carried out, usually at a moderate temperature ($70^\circ\text{--}90^\circ\text{C}$).

Exposure

Exposure is probably the single most important step in the microlithographic process. Resolution and pattern uniformity are determined at this step, and the exposure equipment and operation must be maintained at the precise optimum level to ensure good image production.

The most common type of exposure system involves near-u.v. exposure of the resist-coated wafer through a patterned (photographic emulsion, chrome, iron oxide) glass mask with which it is in contact; however, several other types of exposure systems are now available or under development. These various systems,

³ Dry film resists are nonsolvent-containing photoresist films, as thin as 25 μm (one mil), supplied in a laminated form, and used primarily in the printed circuit board industry.

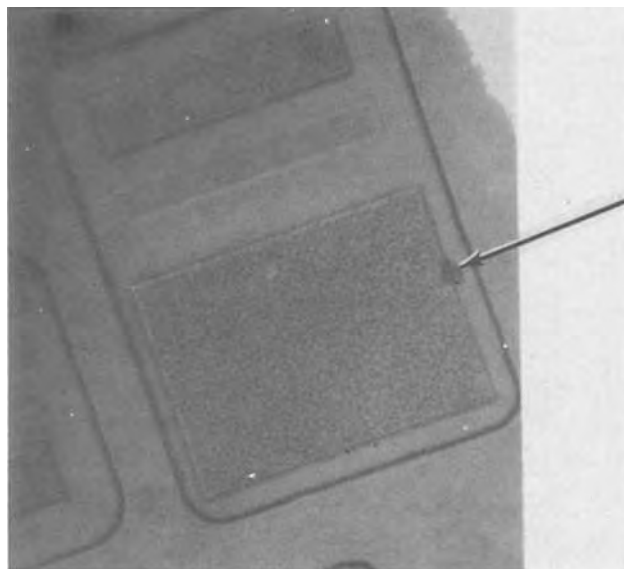


Fig. 8. A foreign particle, either on the surface or in the resist, produced the defect seen in this photoresist pattern. (Light gray areas bear resist material.)

as well as their respective advantages and disadvantages, will be discussed below.

Development

Following exposure, the resist film is developed, i.e., treated by a solvent in which either the unexposed (negative resist) or exposed (positive resist) areas are soluble. Development is carried out either by a spray or immersion technique. As discussed previously, certain types of resists are treated in a rinse solvent to remove residual developer and to reduce any swelling. Some types of resist pattern defects can be detected by inspection at this point, as illustrated in Fig. 9.

Recently, a "dry-developable" negative resist has been prepared (Motorola), thus permitting use of an entirely dry photolithographic process (18).

Postbake

After developing, the patterned resist films are postbaked to drive off any remaining developer or rinse solutions and to maximize the film/substrate adhesion. Typical postbake temperatures are $120^\circ\text{--}135^\circ\text{C}$. It is thought that best adhesion is obtained by baking at as high a temperature as possible just below the softening point of the resist.

Etching

In most cases, the photolithographic process is subtractive, and the next step involves etching the unprotected areas of the wafer. Either wet or dry etching processes may be used. Wet, or chemical, etching is the traditionally used method, in which the wafers are immersed in liquid etchant (gas phase etching is also included in this category) (19). Wet etching is simple and inexpensive, and this method was used almost exclusively until the past few years, when it became evident that the sloped edges inherent in isotropic wet-etching processes would limit control of the feature size. In addition, the lack of perfect adhesion of photoresist film to the substrate during wet etching leads to "undercutting," a failure mechanism in which very highly sloped edges occur (19, 20) (Fig. 10). In certain instances, a sloped edge is preferred so that the material to be subsequently deposited will cover the edge uniformly and completely. In order to achieve controlled undercutting, a very thin layer of material which dissolves in the etchant more rapidly than does the substrate film may be deposited prior to resist application. Equipment is now available for "dry etching"

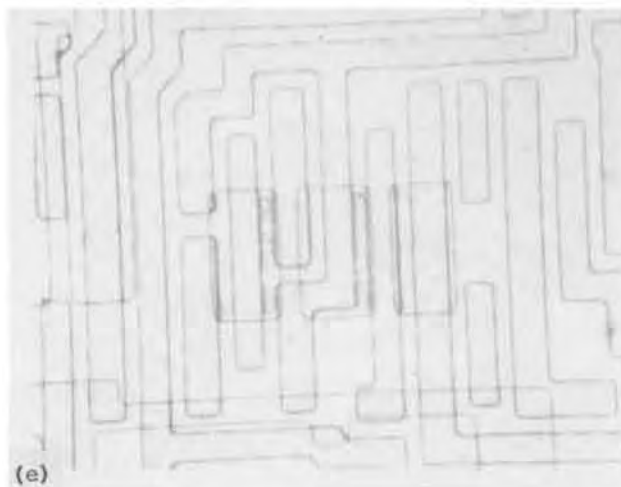
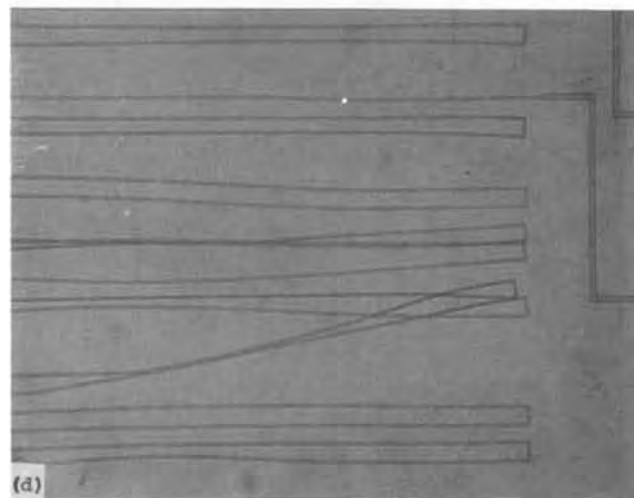
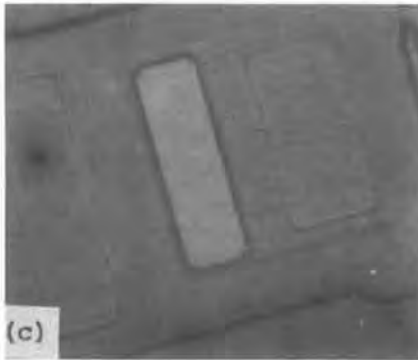
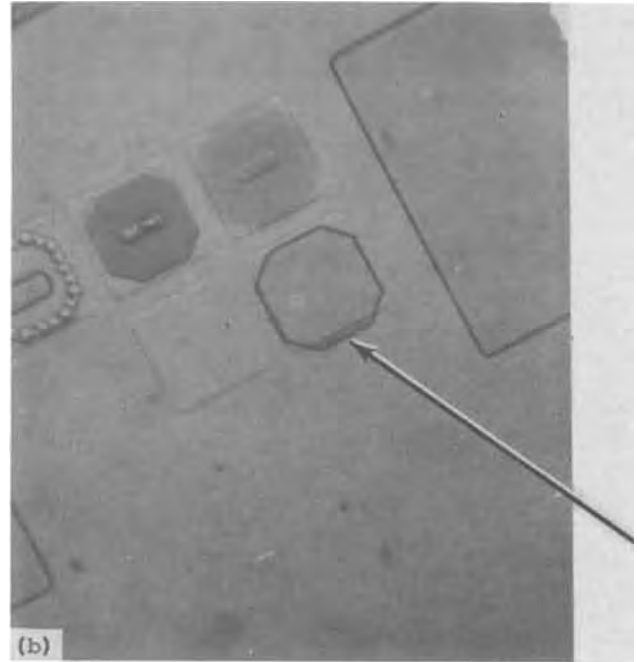
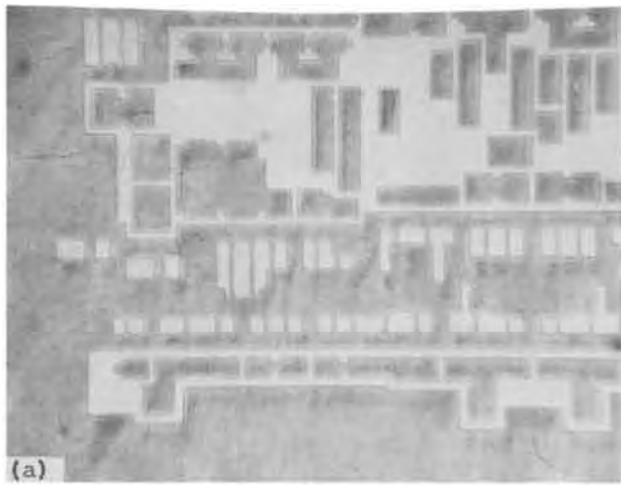


Fig. 9. Various types of photoresist pattern defects observed after development. (a) "Orange peel" is a common occurrence when negative resists are underexposed; (b) the photoresist pattern is slightly misaligned in this pattern test key, since the octagon-shaped resist image does not coincide perfectly with the underlying substrate image; (c) imperfect contact between mask and wafer caused the inward notching at the corners of this photoresist pattern (gray areas are covered with resist); (d) poor adhesion of the photoresist to the substrate can lead to lifting of the resist image during development; (e) Bridging of the resist across open areas can be due to either substrate contamination, poor contact during exposure, or underdevelopment.

(plasma etching) (21) of wafers reproducibly, at high resolution, and in production volumes. Photoresist adhesion is much less critical in dry etching processes, and very high aspect ratios can be achieved in planar systems (22) as illustrated in Fig. 11.

Deposition

In those cases where an additive photolithographic process is employed, the substrate is not etched, but rather, an evaporation, ion implantation, or plating step is carried out at this point. In the trimetal (Ti-

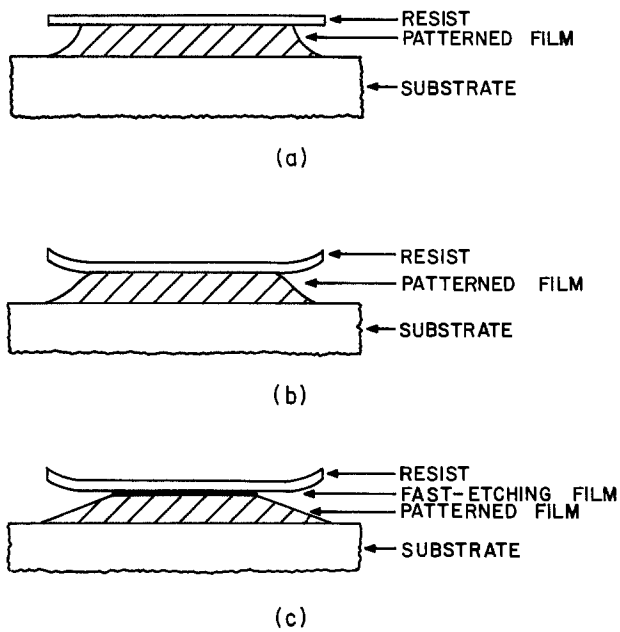


Fig. 10. Different edge profiles produced from various degrees of undercutting (a) good resist-to-film adhesion produces this type of edge; (b) undercutting has occurred at resist-film interface; (c) use of a fast-etching film to achieve controlled undercutting.

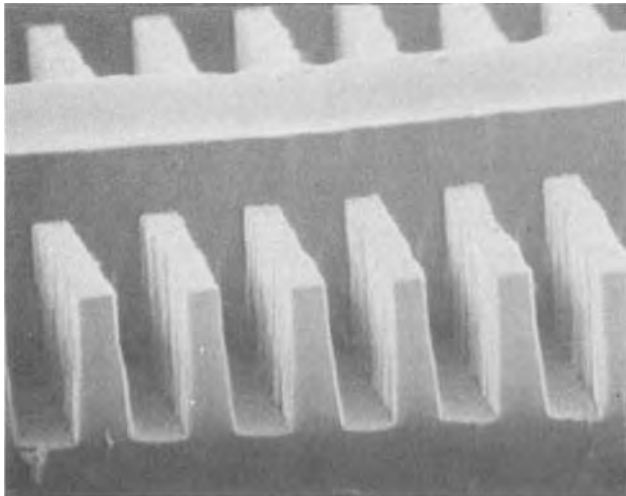


Fig. 11. Photoresist pattern over grating in fused quartz. Thickness of resist layer from top of lines = $1\ \mu\text{m}$. Periodicity of grating in SiO_2 = $1.4\ \mu\text{m}$; periodicity of grating in photoresist = $10\ \mu\text{m}$ ($5\ \mu\text{m}$ line width). A reactive sputter etching procedure in a fluorocarbon gas was used to etch the SiO_2 .

Pt-Au or Ti-Pd-Au) process (23), for example, the gold layer is electroplated through openings in the photoresist onto the Pt or Pd layer on the substrate. In this case, poor resist adhesion leads to "underplating," an example of which is shown in Fig. 12.

Resist Removal

Finally, the resist material must be stripped before the next level of the device can be defined. A variety of acids, bases, and solvents are used for stripping, as is a plasma stripping procedure. Removal of the last traces of resist residue, however, can be rather difficult to achieve (24). An example of incomplete resist removal is shown in Fig. 13.

Quite relevant to a discussion of processing is the procedure of inspecting wafers and masks. Operator inspection using an optical microscope is the traditional inspection method, but for masks, in particular, several types of highly sensitive and accurate, automatic

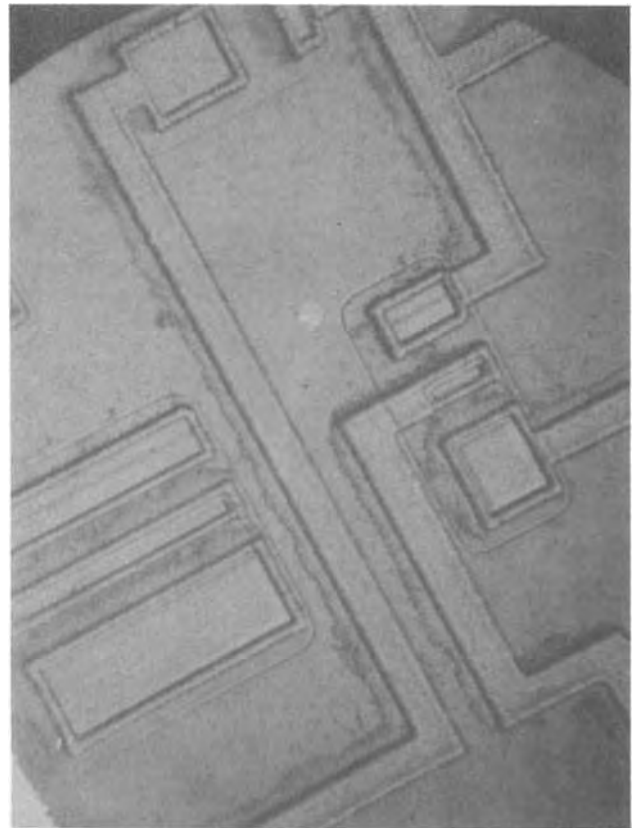


Fig. 12. Gold has been electroplated into the open (interconnect) areas of the photoresist pattern. Poor photoresist adhesion has led to plating under the resist film pattern edges.

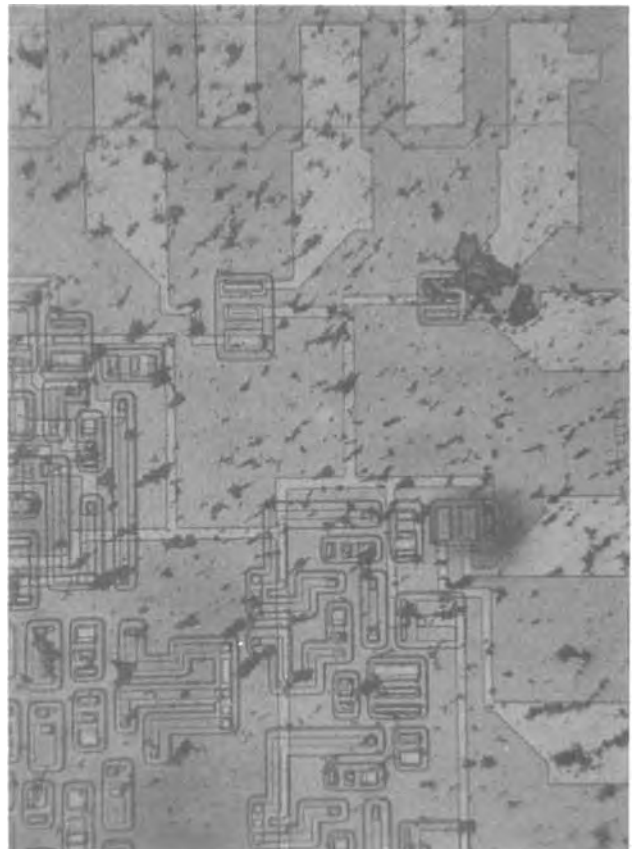


Fig. 13. An extreme case of incomplete photoresist removal

inspection instruments have recently been developed (25, 26). Some very simple mask inspection techniques, such as optical examination using a collimated light

beam, either at a glancing angle or from behind the substrate, can also be very sensitive to defects.

Exposure Techniques are Crucial to the Microlithographic Process

As discussed above, exposure is often considered the most crucial step in the photolithographic process. It is at this point that the resolution, uniformity, and image fidelity of the device are determined. Because of the interaction of the mask, the exposure equipment, and the resist material, the choice of an exposure system must consider all these elements. Trade-offs in terms of resolution, cost, and throughput will determine which system is chosen.

Masks

Masks which are either in current use or will be used in developmental systems include photomasks, electron-beam masks, photo-reticles, and electron-beam reticles. [Photomasks and electron-beam masks bear an array of patterns whose magnification is the same as the pattern to be defined on the device wafer; a reticle, on the other hand, bears a single pattern whose magnification is larger (usually 5 or 10 times) than that to be defined on the wafer.] In addition, applications not requiring a mask, for example, the use of direct E-beam writing on a wafer, are under consideration. Masks are typically fabricated of silver halide emulsions, chromium (reflective or nonreflective), or iron oxide patterned onto a glass substrate. Emulsion masks are lowest in cost, but resolution and durability are limited. Iron oxide masks offer the advantage that the operator can see through them for easy pattern alignment. However, most high quality masks are now fabricated of chromium with a thin surface layer of oxide which makes the metal film nonreflective. Exceedingly complex and/or large masks, such as a CCD mask [Fig. 14(a)], and masks to be used in noncontact exposure systems may be generated by contact printing from an electron-beam master (11), or an optically generated step-and-repeat (S&R) master may be used directly. Very fine geometry ($<2 \mu\text{m}$) masks can be fabricated directly by electron-beam recording. Masks which are to be used with deep (far) u.v. exposure systems require quartz substrates, and x-ray exposure systems utilize a heavy metal (e.g., gold) pattern on a thin substrate such as beryllium, silicon, silicon carbide, or an organic polymer (27).

Systems and Equipment

Various types of wafer exposure systems may be used. These include u.v. flood exposure (contact or proximity), u.v. exposure (projection), u.v. S&R reduction exposure (projection), x-ray flood exposure (proximity), or electron-beam scan exposure (direct writing). The various combinations of mask types and wafer exposure systems which are in use or are being developed are shown in Fig. 15, along with a summary of some features of each type.

Near u.v. flood exposure (contact mode) is the traditional method of photolithographic exposure. This method affords very good resolution; in production, about $3 \mu\text{m}$ can be achieved on the newest instruments (14), and throughput is usually high. On a laboratory scale, square wave gratings with micron and submicron periodicities and etch depths up to $3 \mu\text{m}$ have been achieved (21) (Fig. 11 and 16). Hard contact (thousands of grams force between mask and wafer) causes short mask life, however; as a result, very expensive masks, such as electron-beam generated masters, or very complex masks where very low defect levels are required, cannot be used economically.

Near-u.v. flood exposure using soft contact (only a few grams force between mask and wafer) or proximity (wafer separated from mask by tens of micrometers) is another exposure scheme. The resolution capability is somewhat lower than for hard contact, but improved mask life can make this a feasible process in certain cases. Power transistors, for example, use relatively coarse geometries and often have mask-damaging "bumps" on the wafer surface.

Projection near-u.v. exposure has become quite popular in the microelectronics industry over the past 3-4 years because of the advent of accurate, relatively high resolution 1:1 projection alignment instruments (Perkin-Elmer Corporation). These instruments are highly cost effective because they afford essentially infinite mask life and can achieve resolution down to about $2.5 \mu\text{m}$. Because of the long mask life, expensive masks, such as electron-beam generated masters, can be used.

Under typical factory conditions, existing near-u.v. exposure systems are limited in resolution by factors such as photomask accuracy and dimensional stability, runout, and wafer flatness (28). The advent of commercial S&R reduction u.v. exposure systems (14, 29), using a single 5 or $10\times$ photo- or E-beam-generated reticle as the photomask, is of considerable interest at

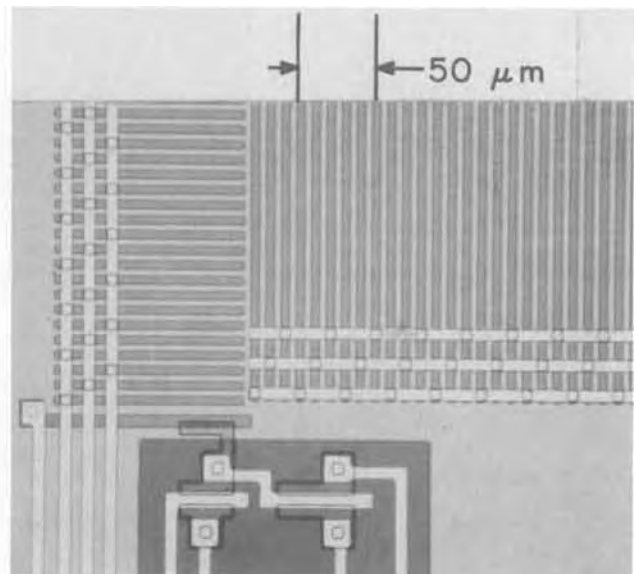
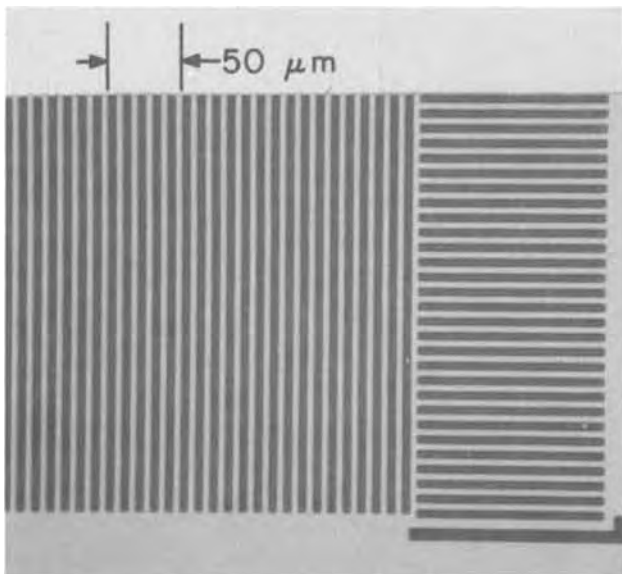


Fig. 14. RCA's CCD requires essentially perfect photolithographic patterning over a large area ($10 \text{ mm} \times 15 \text{ mm}$). A small portion of the pattern is shown here. (a, left) E-beam generated chrome master for the polysilicon gate level; (b, right) completed CCD.

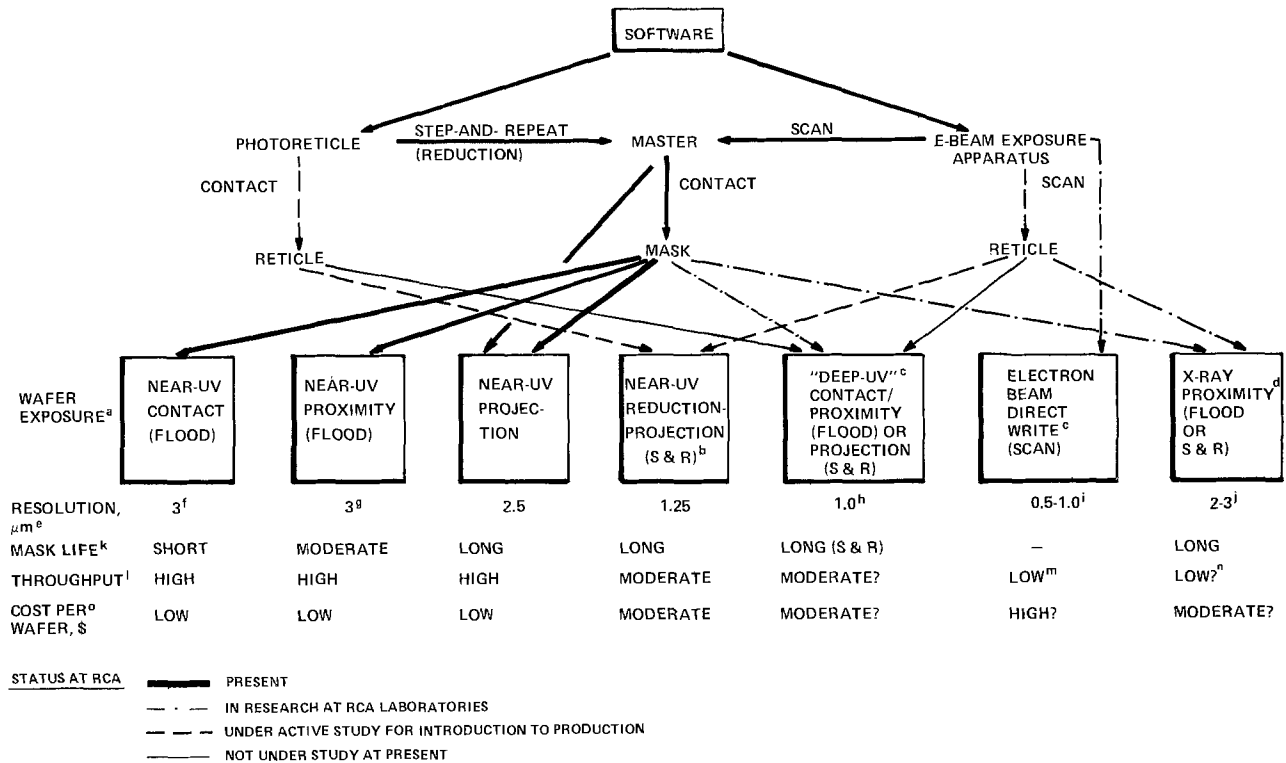


Fig. 15. Wafer exposure processes and parameters. Notes: (a) much of the data in this chart was updated by us from information assembled by R. Epifano of Central Engineering, RCA Solid State Division, in mid-1978; (b) using 10 \times reticle; (c) only a few prototype systems available; (d) first commercial system prototype (Cobilt) using proximity flood exposure now being tested. S&R systems not commercially available; (e) factory conditions, 3 in. wafers assumed. For near-u.v. exposure, resolution quoted is for positive photoresist. Near-u.v. exposed negative resist resolution about 30% larger; (f) one μm resolution possible on small flat substrates; (g) at 20 μm mask-to-wafer spacing, the minimum acceptable to avoid frequent mask-to-wafer contact; (h) estimate for a projection S&R system; (i) using MEBES (Manufacturing Electron-Beam Exposure System, ETEC Corporation), raster scan. Vector scan can resolve 0.1 μm ; (j) resolution limit on prototype system, limited by manual alignment accuracy. Bell Labs proprietary resist and equipment can resolve 0.5 μm ; (k) short, 100-150 exposures; moderate, 150-1500; long, 1500-5000 or more; (l) low, <25 3 in. wafers per hour; moderate, 25-50; high, 50-100; (m) MEBES could print <2 3 in. wafers per hour. IBM EL-1 can do 22 2 $\frac{1}{4}$ in. (or 12 3 in.) wafers per hour; (n) Bell Labs resist and equipment can do 15 3 in. wafers per hour. Information not available for Cobilt system; (o) based on ratio of capital equipment cost to wafer throughput only.

present (GCA Mann, Electromask Corporation). Some features of these systems are high resolution (1.25 μm), virtually no runout over the wafer, automatic focusing at each step, long mask life, and relative insensitivity to dust on the mask (because of the reduced image size).

The eventual use of deep u.v. exposure may extend the useful wavelength range of conventional photolithography and thus allow somewhat higher resolution

(30). A few domestic commercial deep u.v. systems are now reportedly being tested.

No x-ray exposure systems are commercially available as yet, but an experimental model (Cobilt), offering 2-3 μm resolution capability, is reportedly now being tested. This method, using flood exposure in a proximity mode (Fig. 17), appears quite promising in terms of resolution (limited by alignment, by dimensional stability of mask and wafer, by the resolving power of the resist, and by accuracy of defining the mask pattern) and anticipated moderate cost per wafer (14, 27, 29).

Use of an electron beam for wafer fabrication appears to be limited to direct writing by a computer-

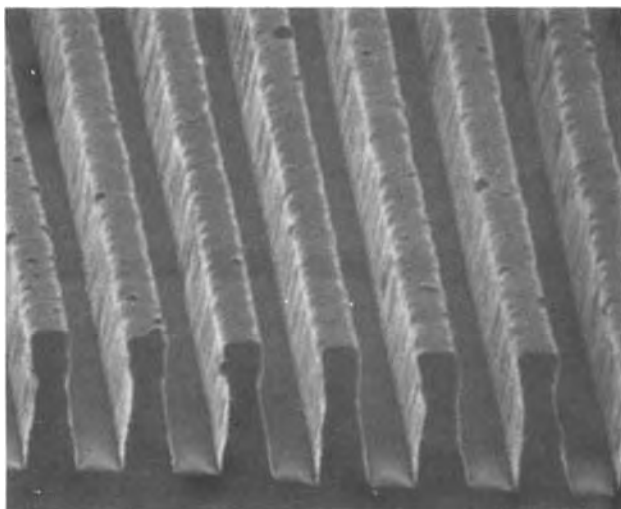


Fig. 16. Photoresist pattern on (111)-Si, thickness of resist layer, 1.5 μm ; 1.4 μm periodicity grating.

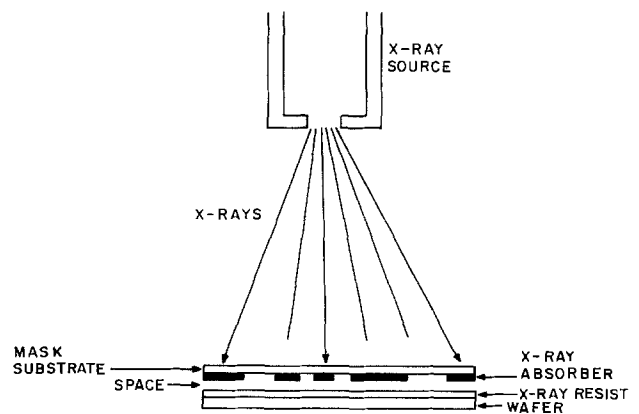


Fig. 17. Schematic diagram of x-ray proximity flood exposure system.

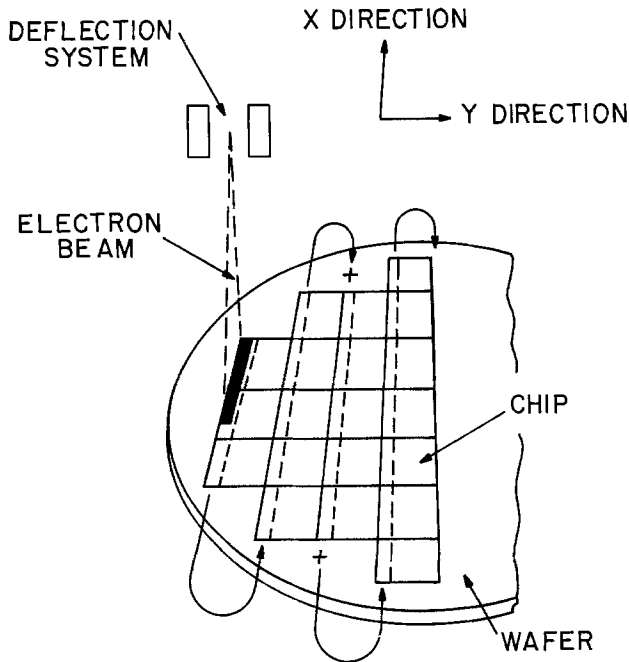


Fig. 18. A raster scan technique may be used for wafer fabrication by direct electron beam exposure.

controlled scanning method (29, 31) (Fig. 18). At present, this procedure is not commercially feasible because of low throughput, but improved system design and the advent of very large scale integrated (VLSI) circuits may bring the method into use in the 1980's (14).

An alternative method for fabricating devices by an electron beam is E-beam projection (29, 32), whereby a special thin film photomask is bombarded with electrons, and resultant emission of electrons from the mask projects the mask image onto the wafer. However, because of numerous problems, this approach will require considerable improvement before commercial application is practical.

Resist Material

The type of resist material chosen depends on the type of exposure system used. In general, photoresists cannot be used in electron-beam or x-ray exposure systems, but there are exceptions. For example, certain of the diazoquinone-type positive resist materials can be used in either deep u.v. or E-beam systems as well. In all areas of microlithography, more sensitive resist materials are constantly being sought, particularly in x-ray lithography, where low source intensity is a particular problem.

As mentioned previously, liquid resists are used almost exclusively, even in relatively low resolution applications. Conventional u.v./contact exposure processes have traditionally used negative photoresists, both for historical reasons and because of their greater process latitude (33), better adhesion, and lower costs relative to positive photoresists. Proper exposure and use of nonxylene developers can permit definition of dimensions down to $\sim 2 \mu\text{m}$ with negative resists, but the relative ease of achieving very fine resolution with positive photoresist materials has led to a shift throughout the microelectronics industry over the past several years, as more and more highly complex chips are designed.

Conclusion and a Look Ahead

The field of microlithographic processing for producing integrated circuit devices has evolved so far from classical lithographic procedures that a comparison is hardly possible. Requirements for producing the next generations of devices, such as 1M RAM's, will surely bring about more developments of high

sophistication and capability. Minimum geometries of $2 \mu\text{m}$ by 1980 and $1.3\text{--}1.5 \mu\text{m}$ by 1982 are estimated (14, 34), and thus future trends in the solid-state industry will include such processes as x-ray and electron-beam exposure of wafers, and increased use of dry etching processes. However, the wide range of device requirements will surely ensure continued use of conventional photolithographic processes in many areas as well.

Acknowledgments

The authors are very grateful to various individuals within RCA who have assisted in preparing this article, either by consultation, by critical review of the manuscript, or by assistance in gathering the illustrations. These individuals include R. A. Bartolini, W. Bösenberg, D. A. Doane, R. Epifano, R. Geshner, N. Goldsmith, W. Henry, W. Hobson, R. Hollingsworth, H. Lehmann, D. L. Matthies, M. S. Miller, C. Musser, D. A. Peters, J. H. Reisner, G. L. Schnable, and J. L. Vossen.

Manuscript submitted July 23, 1979; revised manuscript received Oct. 15, 1979.

Any discussion of this paper will appear in a Discussion Section to be published in the December 1980 JOURNAL. All discussions for the December 1980 Discussion Section should be submitted by Aug. 1, 1980.

Publication costs of this article were assisted by RCA, David Sarnoff Research Center.

REFERENCES

1. R. N. Noyce, *Sci. Am.*, **237**, 63 (1977).
2. "Thin Film Processes," J. L. Vossen and W. Kern, Editors, Academic Press, New York (1978).
3. W. S. DeForest, "Photoresist Materials and Processes," McGraw-Hill, New York (1975).
4. J. M. Eder, "History of Photography" (translated from 4th German edition of 1932 by E. Epstein), Columbia University Press, New York (1945).
5. H. Gernsheim and A. Gernsheim, "The History of Photography" (revised and enlarged edition), Thames and Hudson, London (1969).
6. J. Kosar, "Light-Sensitive Systems," John Wiley and Sons, Inc., New York (1965).
7. D. Meyerhofer, "Photosolubility of Diazo-Quinone Resists," Submitted to *IEEE Trans. Electron Devices*, cf., M. Kaplan and D. Meyerhofer, *RCA Rev.*, **40**, 166 (1979).
8. L. F. Thompson and R. E. Kerwin, *Annu. Rev. Mater. Sci.*, **7**, 267 (1977).
9. E. O. Keizer, *RCA Rev.*, **39**, 60 (1978).
10. R. J. Himics, M. Kaplan, N. V. Desai, and E. S. Poliniak, *Poly. Eng. Sci.*, **17**, 406 (1977).
11. R. A. Geshner, *RCA Eng.*, **24**, 47 (1978).
12. Annual Report, AT&T (1978).
13. T. A. Longo, Kodak Microelectronics Seminar, San Diego, California, October 1-3, 1978.
14. R. P. Capece, *Electronics*, p. 111, November 23, 1978.
15. Anon., *Ind. Res.*, **19**, 19 (1977).
16. R. A. Bartolini, N. Feldstein, and R. J. Ryan, *This Journal*, **120**, 1408 (1973).
17. D. Meyerhofer, *J. Appl. Phys.*, **49**, 3993 (1978).
18. Anon., *Solid State Technol.*, **22**, 78 (1979).
19. W. Kern and C. A. Deckert, in "Thin Film Processes," J. L. Vossen and W. Kern, Editors, p. 399, Academic Press, New York (1978).
20. C. A. Deckert and D. A. Peters, in "Proc. Kodak Microelectron. Seminar," p. 3, Eastman Kodak Company, Rochester, New York (1978).
21. C. M. Melliar-Smith and C. J. Mogab, in "Thin Film Processes," J. L. Vossen and W. Kern, Editors, p. 497, Academic Press, New York (1978).
22. H. W. Lehmann and R. Widmer, *J. Vac. Sci. Technol.*, **15**, 319 (1978).
23. E. D. Winters, *Plat. Surf. Finish.*, **66**, 61 (1979).
24. D. A. Peters and C. A. Deckert, Abstract 237, p. 637, The Electrochemical Society Extended Abstracts, Pittsburgh, Pennsylvania, Oct. 15-20, 1978; *This Journal*, **126**, 883 (1979).
25. Y. Goto, Y. Furukawa, and T. Inagaki, *J. Vac. Sci. Technol.*, **15**, 953 (1978).
26. D. Angel, P. H. Johnson, and M. B. Vye, Kodak Microelectronics Seminar, San Diego, California, October 1-3, 1978.

27. E. Spiller and R. Feder, in "Topics of Applied Physics," Vol. 72, Chap. 3, H. J. Queisser, Editor, Springer-Verlag, New York (1977).
28. C. S. Kim and W. E. Ham, *RCA Rev.*, **39**, 565 (1978).
29. B. P. Piwczyk, *Elec. Pkg. Prod.*, p. 36 (May, 1978).
30. B. J. Lin, *J. Vac. Sci. Technol.*, **12**, 131 (1975); B. J. Lin, *IBM J. Res. Dev.*, **20**, 213 (1976).
31. A. N. Broers, in "Proc. Internat. Conf. on Micro-lithography," p. 21, Paris, June 21-24, 1977.
32. T. W. O'Keefe, J. Vine, and R. M. Handy, *Solid State Electron.*, **12**, 841 (1969).
33. C. A. Deckert and D. A. Peters, *Solid State Technol.*, **23**, 76 (1980).
34. A. C. Tobey, *Solid State Technol.*, **21**, 49 (May, 1978).

Interfaces in Electrochemistry

Roger Parsons²

The news of the award of the Olin Palladium medal was a great surprise to me and I am very conscious of the honor which represents the regard of my friends and colleagues in electrochemistry. It is an unexpected honor in view of the eminence of the previous holders of the medal as well as of the many distinguished electrochemists who deserve it, but have not yet had the good fortune to be honored in this way. For this I would like to thank the members of the Selection Committee. I am also very grateful to Fred Anson for his kind introduction. I spent an enjoyable year in his laboratory twelve years ago, where I was able to confirm my belief that what people called "electro-analytical chemistry" was just as interesting and exciting as what people call "electrochemistry."

It is true of practically every research worker in the modern world that he works as part of a team. My own work could not have been done without the help and stimulation of my friends. Almost all my career has been spent in universities, the largest part in Bristol, and I am a firm believer in the informal collaboration of the small university research group as an efficient generator of new science. My co-workers have been mostly undergraduates, graduate students, post-doctoral fellows, and visitors from a wide variety of countries. I am glad to say that without exception they worked together harmoniously and I am glad to acknowledge the major part which they have played in my work. I have learned in this sort of environment that illumination may come from unexpected places and that the fresh approach of a beginner may be as helpful as the insight of a savant.

The title of my lecture could be taken in several ways. Electrochemistry has important interfaces with many other subjects, such as engineering, biology, physics, etc. . . . Nowadays the properties of the interface between our experimental systems, their electronic controls, and computers play an increasingly important part in our research lives. However I propose to use the term in its original sense and to describe some of the progress made in the study of junctions between chemical phases, mainly between a metal and an electrolyte and to talk about structure and kinetics.

I began my research career 33 years ago in just such a university group which John Bockris started at Imperial College. It was his undergraduate lectures which stimulated my interest in electrochemistry and his energy which kept me in the subject. I was in fact the first of a very long line of Ph.D.'s who graduated under his detailed supervision. Only those who had contact with the earlier atmosphere of physical chemistry at Imperial College (1) can fully appreciate the impact of John Bockris on the research there. I shall always be grateful to him for starting me off so well in electrochemistry, with the classical problem of hydrogen overpotential which still plays an important part in electrochemistry even if it is far from being as dominant as it was then. The flavor of electrochemical research at that time can be judged very well by looking at the reports of the Faraday Society Discussion on Electrode Processes (2) held in Manchester in April 1947 which my friend and contemporary Brian Conway recalled in his excellent profile on electrode kinetics recently (3). As he implies, this discussion marked a watershed in the subject. One can see, side by side, work pointing towards the

future and work which nowadays seems to be part of the dark ages. It was unfortunate that some of the most stimulating papers, those by Frumkin, Levich, and Ershler could not be presented by the authors and so played much less part in the actual meeting than they deserved. The work of Frumkin and his colleagues had already been brought to the attention of our group by Bockris and it has played an important part in my scientific development as it must for any electrochemist of my generation.

After my Ph.D. I began to work on interfacial structure because it seemed essential to know more about this in order to understand the kinetics of processes which occur in the interphase. The power of methods developed in the nineteenth century to solve these problems still fascinates me and although remarkable techniques have been developed to apply these methods, the basic principles are still yielding useful results in competition with those based on more recently developed ideas.

For example the Lippmann electrometer which is 104 years old is still yielding useful results of high precision which are analyzed by the powerful thermodynamic methods developed by Willard Gibbs shortly afterwards. (It is perhaps surprising to remember that one of the first to recognize the power of Gibbs' work and to publicize it was James Clerk Maxwell who died a century ago this year. Of course his other contributions have overshadowed his role as Gibbs' advocate.) I remain astonished that classical thermodynamics (which is, after all, a rigorous method of rearranging experimental information in a perhaps more comprehensible form) can give use so much insight into the minute regions of space occupied by electrochemical and other interfaces.

The concept of the electrical double layer in such systems was first clearly expressed by Helmholtz (4) also a century ago. Although the essential principles were laid down so long ago and much important application of them was made by Gouy and by Frumkin, systematic study of the metal/electrolyte interface really began in the nineteen forties when David Grahame (5) showed how precision measurements of the capacity of the double layer could be made using the dropping mercury electrode. I have no doubt that if it had not been for his early death, he would have been a Palladium medallist and would have continued to make important contributions to electrochemistry. The whole modern picture of the electrical double layer is founded on the work of Frumkin, Stern, and Grahame, and largely on the detailed study of the mercury electrode. Using essentially classical thermodynamics one can build up a reliable picture of the composition, and to some extent deduce information about the orientation of molecules, in the interface. Figure 1 shows a sketch of the probable molecular arrangement at a structureless metal surface.

I would like to recall a few simple examples of this type of approach. The fact that one can measure only surface excesses leads to a method of estimating the thickness of the inner part of the double layer, that is the distance of closest approach of solvated ions to the metal surface (6-8).

We consider a perfectly polarized electrode and assume that the adsorption of ions from a binary 1:1-electrolyte is due entirely to electrostatic forces. The adsorbed ions then populate the diffuse layer described by Gouy-Chapman theory (9, 10). Owing to the finite size of the ions and possibly to a difference in the solvent structure near the electrode there is

²Olin Palladium Medal Address delivered October 16, 1979 at the Los Angeles, California Meeting of The Electrochemical Society. The medal was struck from palladium supplied by the International Nickel Company, 67 Wall Street, New York, New York 10005.

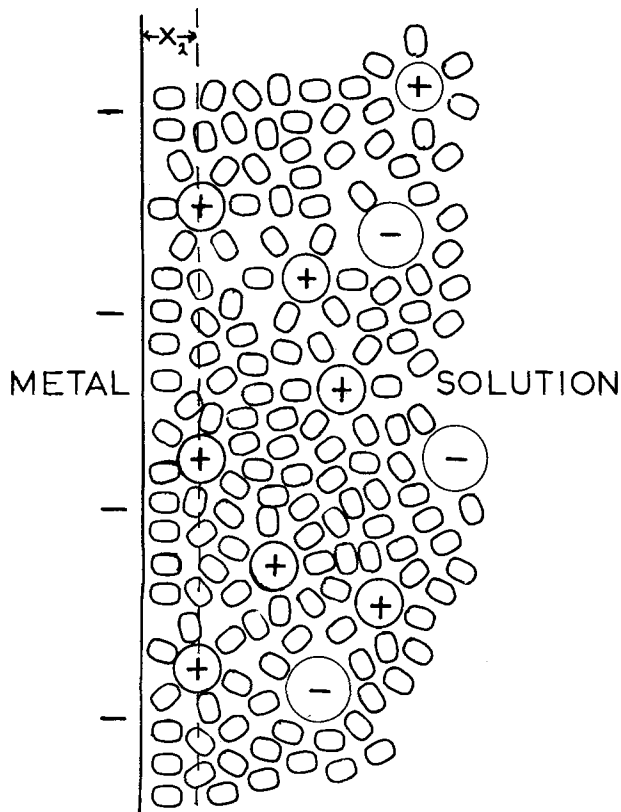


Fig. 1. Schematic picture of the structure of the electrical double layer at a uniform metal surface.

a region between the metal and the diffuse layer in which there are no ions (8). Thus the distribution of ions is similar to that shown in Fig. 2.

If we assume that the system consists of an aqueous solution of MX in contact with a mercury electrode then we may obtain the quantity $\Gamma_{M+(H_2O)}$ from experiment

$$\Gamma_{M+(H_2O)} = \Gamma_{M+} - (x_{MX}/x_{H_2O})\Gamma_{H_2O} \\ = \Gamma_{M+} - (n_{MX}^b/n_{H_2O}^b)\Gamma_{H_2O} \quad [1]$$

where n_i denotes the concentration of species i in the bulk of the solution.

If the local concentrations of M^+ and of H_2O are n_{M+} and n_{H_2O} , respectively, then the surface excess can be expressed as

$$\Gamma_{M+(H_2O)} = \int_0^\infty \{n_{M+} - (n_{M+}^b/n_{H_2O}^b)n_{H_2O}\}dx \quad [2]$$

where $x = 0$ corresponds to the physical interface and positive x is towards the solution. The integral should more accurately have a lower limit of $-\infty$ but if we can assume that neither component is present in the metal phase the contribution from $-\infty$ to 0 is zero. If the distance of closest approach of the ions is x_2 , then we may split the integral into two parts

$$\Gamma_{M+(H_2O)} = \int_0^{x_2} \{- (n_{M+}^b/n_{H_2O}^b)n_{H_2O}\}dx \\ + \int_{x_2}^\infty \{n_{M+} - (n_{M+}^b/n_{H_2O}^b)n_{H_2O}\}dx \quad [3]$$

The second term on the right-hand side of [3] can be evaluated from Gouy-Chapman theory if it is assumed (as it is in G-C theory) that the solvent concentration is independent of x , i.e., $n_{H_2O} = n_{H_2O}^b$. This term then becomes

$$\Gamma^{2-s_{M+(H_2O)}} = \int_{x_2}^\infty (n_{M+} - n_{M+}^b)dx \quad [4]$$

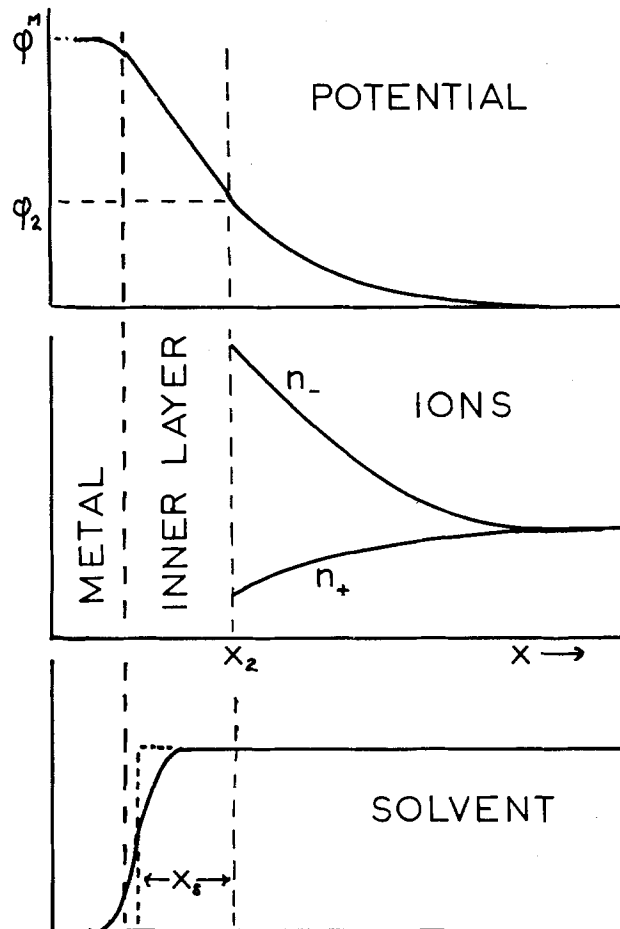


Fig. 2. Schematic diagram of potential and concentration distribution in the electrolyte near the electrode. The x coordinate is perpendicular to the interface and positive in the direction of the solution. The physical interface is assumed to be at the origin. x_2 is the distance of closest approach of the ionic species in solution; at this distance and at $x > x_2$ the only interaction between the ions and the electrode is assumed to be the simple electrostatic force due to their charges. (a, top) shows the distribution of potential Φ averaged in planes parallel to the interface. Φ^M is the potential at the metal surface due to free charges; Φ_2 that at x_2 . The potential in the bulk of the solution as $x \rightarrow \infty$ is taken as zero. The charge on the metal is assumed to be positive. (b, middle) shows the distribution of cations corresponding to the situation described above. n_- is the local concentration of anions, n_+ that of cations averaged in planes parallel to the interface. (c, bottom) shows the supposed distribution of the concentration of water (solvent) molecules. The real concentration (full line) can be replaced by an equivalent rectangular distribution (dotted line) as described in the text leading to Eq. [6].

and this can be evaluated using the G-C theory (5) to obtain

$$\Gamma^{2-s_{M+(H_2O)}} = (2n_{M+}^b/k) \{ \exp(-e\Phi_2/2kT) - 1 \} \quad [5]$$

This quantity can be evaluated since Φ_2 is obtained from σ^s , the charge on the solution given by the Lippmann equation $\sigma^s = (\partial\gamma/\partial E)\mu_{MX}$ again using G-C theory.

The other part of the integral can be evaluated if we assume that the actual distribution of water in the inner layer can be replaced by a distribution consisting of a constant concentration up to a plane at x_w and a zero concentration at $x < x_w$ (Fig. 2c). Then

$$- \int_0^{x_2} (n_{M+}^b/n_{H_2O}^b)n_{H_2O}dx = - \int_{x_w}^{x_2} n_{M+}^b dx \\ = - n_{M+}^b (x_2 - x_w) \quad [6]$$

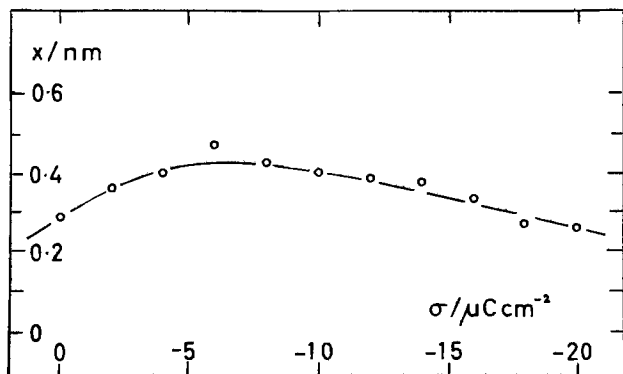


Fig. 3. Experimental determination of the thickness of the inner layer ($x_2 - x_w$) as a function of charge on the electrode.

Thus the experimental surface excess is given by

$$\Gamma_{M+(H_2O)} = -n^b_M + (x_2 - x_w) + 2(n^b_M + \kappa) \{ \exp(-e\Phi_2/2kT) - 1 \} \quad [7]$$

The first term on the right-hand side can be found by finding the difference between the experimental surface excess and that calculated from G-C theory (second term on the right-hand side). If it is verified that it is linear in the ionic concentration the value of $x_2 - x_w$ may be obtained. This result depends on a model, that of Gouy and Chapman, which is stretched to its limits, but we have other evidence which suggests that in this type of use the result is not very model-sensitive. The result obtained (8, 11) (Fig. 3) is in the region of 0.3 nm, which corresponds to the thickness of one water molecule and so seems reasonable. It is remarkably close to a very early estimate of the double layer thickness given by William Thomson (Lord Kelvin) and quoted in Helmholtz's 1879 paper (4).

An alternative route to the dimensions of the inner layer come from the use of a parallel plate condenser model with an approximate measure of the effective permittivity (ϵ). This can be done by measuring the potential shift (ΔE) produced by a small molecule (thiourea) adsorbed in this layer if the perpendicular component of its dipole moment (p) is assumed to be known (12, 13). Use of the Helmholtz equation

$$\Delta E = -p\Gamma/\epsilon$$

leads to values of ϵ in the region of $8\epsilon_0$ to $10\epsilon_0$, where ϵ_0 is the permittivity of free space, and hence again a thickness of about the same magnitude as the diameter of a water molecule.

The low value of the permittivity in the inner layer, compared with that in the bulk solvent, had been fore-

shadowed by Frumkin from a comparison of results in several solvents (14), and it enabled an explanation (15) of the remarkable independence of the capacity of negatively charged mercury of the nature of the cation in solution discovered in Grahame's work. In a system with a rather sharp change in permittivity, almost all the potential drop occurs in the region of low permittivity (the inner layer) and the capacity is insensitive to the precise position of the counter charge provided it is present in the high permittivity region.

More detailed models of the solvent in the inner layer were developed by Macdonald (16), Watts-Tobin (17), Bockris, Devanathan, and Muller (18), Levine (19), Frumkin and Damaskin (20) and this led to a semi-quantitative explanation (21) of the temperature dependence observed by Grahame (Fig. 4) as well as of the shapes of the capacity curves in nonaqueous solutions (22). More recent work by Fawcett (a former post-doc. at Bristol) and Levine has refined this model and removed some of its inconsistencies.

Although these classical methods remain useful, it is, naturally, important to use other independent methods to examine the interface. One of the most promising is the group which includes reflection spectroscopy and ellipsometry, because the possibility of measuring very precisely the state of polarization of visible light allows the small changes due to a monolayer or less to be detected and their refractive index and mean thickness to be determined. In a complicated adsorption system such as that of β -quinoline (23) this allows the orientation of molecules to be followed in close comparison with the amount adsorbed (Fig. 5).

Unfortunately so far we have not succeeded in following the orientation of solvent molecules which would be so desirable for comparison with the models. However, Bewick and Robinson (24) showed that reflection spectroscopy can reveal a change in the density of water in the inner layer which can amount to about 5%. This has recently been extended at Meudon to gold, both polycrystalline (25) and single crystals (26). The results for polycrystalline gold are similar to those for lead and mercury although it is possible in this case to see effects at both charge extremities (Fig. 6). The results at single crystal surfaces are particularly interesting (Fig. 7) because they show the effect of surface structure. In particular the (110) surface which has an asymmetric structure of "rails"; parallel to these "rails" the apparent change is similar to that on the "smooth" (111) surface indicating that the molecules can move equally freely along the rails as on a smooth surface. On the other hand if the electric vector is perpendicular to the "rails" the apparent change in concentration is very much less, indicating that the movement of molecules is more restricted in this direction.

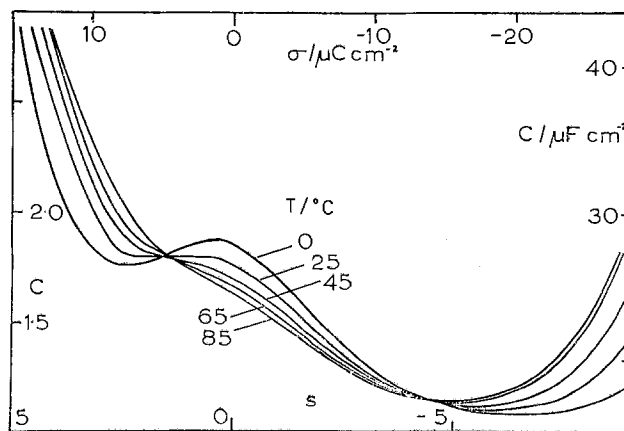
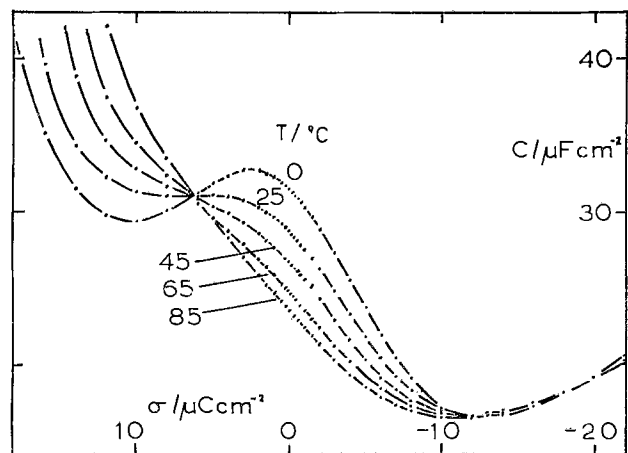


Fig. 4. (a, left) Capacity of the inner layer as a function of temperature measured by D. C. Grahame. (b, right) Curves calculated using the simple four position model.

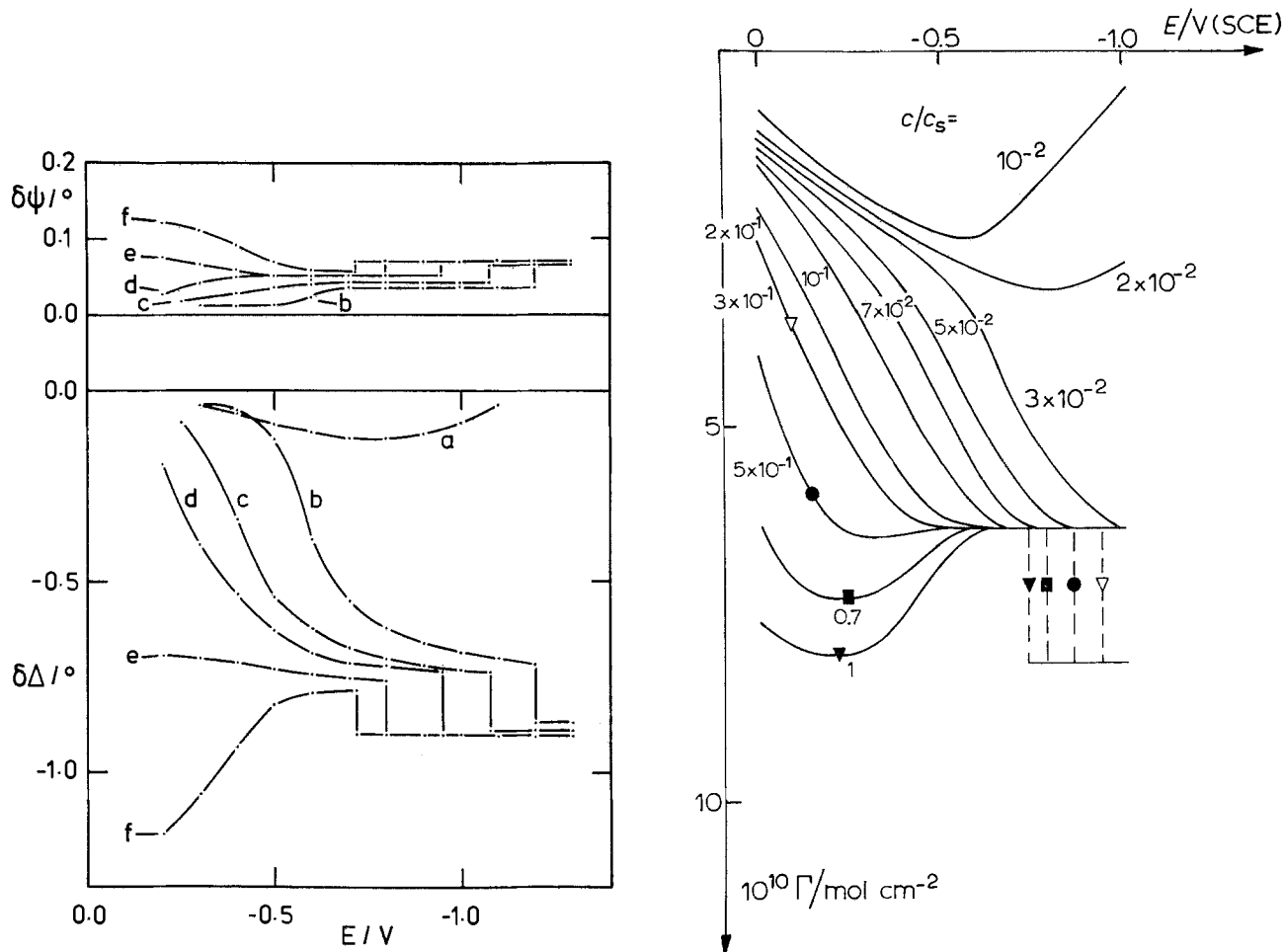


Fig. 5. (a, left) Adsorption of β -quinoline at the mercury-aqueous 0.5M NaOH interface. The charge of the ellipsometric parameters $\Delta\Psi$ and $\delta\Delta$ is shown as a function of electrode potential E (vs. SCE) for several adsorbate concentrations (a) 0.3 mM, (b) 1.5 mM, (c) 3.0 mM, (d) 6.0 mM, (e) 15 mM, (f) saturated solution (~ 30 mM). Angle of incidence 70° , wavelength 546.1 nm, temperature $25^\circ \pm 1^\circ\text{C}$ except curve (b) 22°C . (b, right) Surface excess of β -quinoline at a mercury electrode 0.5M Na_2SO_4 (data of N. Van Laethem, C. Herman, and L. Gierst).

We hope soon to extend this type of approach to silver electrodes to help to explain the spectacular capacity peak which has been observed with single crystals (27). It seems to be due to reorientation of individual water molecules but is structure-sensitive at positive charges which suggests strong silver-water interactions.

The electroreflectance spectrum of the metal itself shows remarkable features. On gold (28) it is strongly dependent on the structure of the face being observed. Present models of surface electronic structure do not seem to be able to account for this, but theoretical de-

velopments seem imminent. Such experiments show promise for the *in situ* study of solid surfaces. We have a great deal to learn about the behavior of solid surfaces in contact with liquids and the prospects for the immediate future are exciting.

I want now to turn to the problems of the kinetics of electrode reactions. As I mentioned earlier, my Ph.D. work with John Bockris was mainly on hydrogen overpotential. In a written comment to the 1947 Faraday Discussion, Frumkin remarked, "It is noteworthy that in the case of a mercury electrode, the value of the coefficient $b = RT/\alpha F$ in the term containing $\log i$ in Tafel's equation, corrected for the influence of the ψ_1 term, gives for α the value $1/2$ with an accuracy up to 0.01. It must be conceded that, up to date, no one has

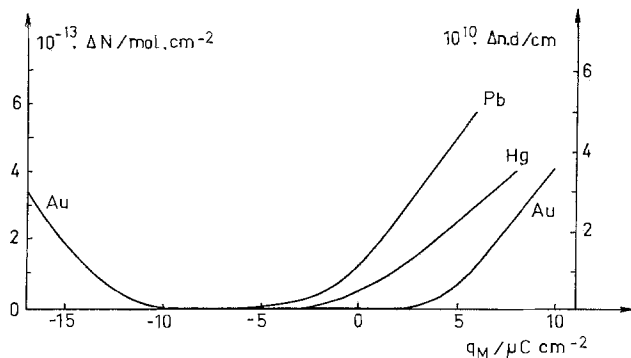


Fig. 6. Change of concentration of water in the inner layer of mercury and polycrystalline lead [data from Bewick and Robinson, Ref. (24)] and also for polycrystalline gold [data from Hinnen et al., Ref. (25)].

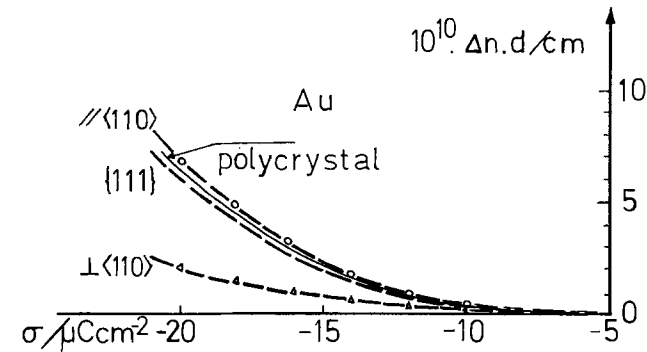


Fig. 7. Change concentration of water in the inner layer of single crystal gold [data from Hinnen et al., Ref. (26)].

been able to explain why α , in this case at least, is so close to $\frac{1}{2}$ and remains constant over such a wide range of potentials. It appears to the author that since the paper by Horiuti and Polanyi, no considerable progress has been made in the interpretation of the coefficient α . Not being so conscious of my limitations as I am now, I rushed in to solve this problem. I took what was essentially Butler's theory (29) and worked it out quantitatively using Morse curves and showed (in my thesis) that this gave not only about the right rate for the process but also a reasonably constant value of α over the range of potential which was used experimentally. Unfortunately this was not the final answer; the problem of α is still with us. Most people know that the models of simpler electrode processes involving only electron transfer yield in the first approximation a linear dependence of α on potential. Rudy Marcus mentioned in his opening lecture that we attempted to verify this model using the slow $\text{Cr}^{3+}/\text{Cr}^{2+}$ reaction (30). We appeared to have good success but the accuracy of the fit was rightly criticized by Fred Anson (31) although the theory has been largely vindicated by later work in respect of the potential dependence of α (32).

Work on the hydrogen reaction led first to an attempt to construct a general framework for electrode reactions so that it was possible to see more clearly what was useful to measure and how the purely kinetic problems might be disentangled from the changes in the double layer structure. This was originally written as a large single paper but was split into two for publication. The first considered the situation when a single elementary step is rate-determining (33) while the second considered the possibility of simultaneous control of the rate by two elementary steps and suggested that this could occur only over rather narrow regions of potential (34). It is interesting that the separation of this work has resulted in the first part being much better known than the second and illustrates the necessity for publishing in the right place.

After this rather formal approach a somewhat more practical kinetic problem was presented. How can one predict the optimum catalyst for a given reaction? Of course the answer to this problem depends on a number of factors but since heterogeneous catalysis depends on the bonding of the reactant to the catalyst, it seems that the most important factor is likely to be the energy of this bond. The consequences of this simplification were worked out for the hydrogen reaction (35) and led to the "volcano" curve previously predicted by Balandin for gas phase catalytic reactions, using a thermochemical argument. The same simple kinetic argument is applicable in principle for both gas phase and electrochemical catalysis (36) and the general predictions are borne out for many of the former (37) and a few of the latter notably of course the hydrogen reaction (38).

Nevertheless this model is at best a first approximation, and, in an attempt to find the way in which it might be extended under more complicated conditions, we made a study of the oxidation of formic acid on a series of metals (39). Here it seems appropriate to show the result on palladium electrodes, which, as it happens, is the simplest type of behavior found for this reaction. That is, the oxidation current observed (Fig. 8) in a cyclic voltammogram is independent of the direction of the sweep. This indicates that the oxidation of formic acid on Pd is an irreversible surface reaction, occurring with the absence of any substantial concentration of blocking intermediates. Nevertheless, the presence of a maximum in the current-voltage curve is remarkable. It appears that the simplest mechanism which can account for this type of behavior is one involving three partial reactions and two transient adsorbed intermediates, the second occupying more sites than the first (40). These may be present at rather low concentrations and they have not yet been detected

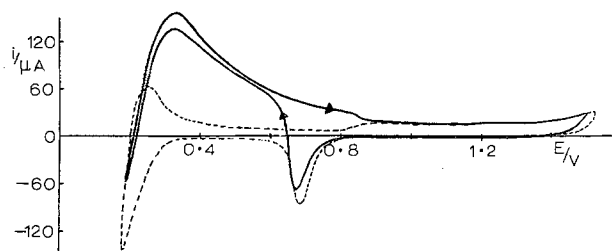


Fig. 8. Cyclic voltammogram for palladium electrode in (.....) $0.5\text{M H}_2\text{SO}_4$, (—) $0.5\text{M H}_2\text{SO}_4 + 0.1\text{M HCOOH}$. Sweep speed 70 mV sec^{-1} . Potential E on the hydrogen scale. Temperature 25°C .

so that the mechanism remains hypothetical. Even with such a simple mechanism the prediction of the effect of the nature of the metal on the binding of the two species and hence on the kinetics takes us beyond present knowledge. If the interactions between adsorbed species and the heterogeneity of the surface are to be considered then at best only rather formal solutions can be found.

There is now some sign that the problem of preparing clean well-defined surfaces for electrochemical studies is approaching a reasonable solution at least for some surfaces. To show that work on this type of fundamental problem can still produce exciting results on systems thought to be simple and relatively well understood, I should like to finish by showing some very recent work on platinum single crystals done in my laboratory at Meudon by Clavilier together with some research workers in another C.N.R.S. laboratory at Grenoble (41). Clavilier has developed a simple and effective method of preparing clean metal surfaces and putting them into an electrolytic cell. Their cleanliness is verified by parallel Auger experiments and by the fact that the cyclic voltammogram is stable from the first cycle. Most striking results are obtained on the (111) surface which in sulfuric acid gives the curve a of Fig. 9 which is stable, provided that the positive potential limit is kept below 1.2V (no formation of oxide layer). However extension of the potential limit to 1.5V yields a remarkable change in the hydrogen adsorption region indicating loss of the high energy hydrogen adsorption sites presumably by a reconstruction of the surface. If the surface is deliberately slightly contaminated the voltammogram a of Fig. 10 is obtained. Up to 20 cycles are required to decontaminate the surface but at the same time it is reconstructed to yield curve b which is essentially the same as curve a in Fig. 9. Thus, with a contaminated surface the high energy adsorption of Fig. 9a is never seen. This high energy adsorption is very sensitive to the nature of the anions in solution and curves obtained in the presence of HClO_4 (Fig. 11) which is less strongly adsorbed show this hydrogen adsorbing at even more positive potentials. Addition of increasing amounts of SO_4^{2-} causes the high energy adsorption region to shift towards more negative potentials until the curve of Fig. 9a is reached. Results on the (110) plane are notably less sensitive and are in good agreement with those found in other laboratories. One important conclusion from this work is that electrochemistry can provide results which are extremely sensitive to surface structure and conversely this underlines the importance of surface structure in electrochemical reaction.

The work I have just described is an illustration of the development of electrochemistry in that it depends on an essentially modern way of thinking about surfaces and surface structure as well as modern techniques while using a basically simple technique of the measurement of current and voltage.

The increasing interest in the molecular and atomic structure of the interface in electrochemistry parallels the similar development in physical chemistry in general and in solid-state physics notably, of course, in the

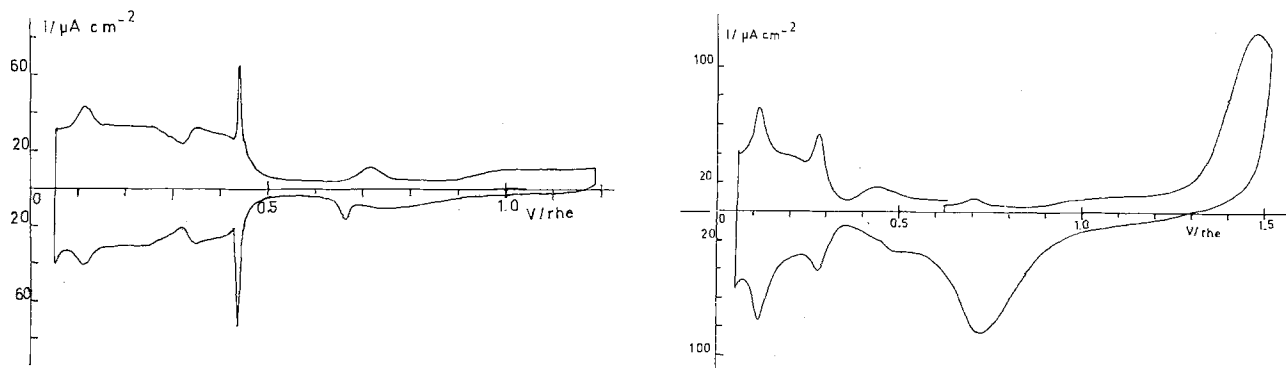


Fig. 9. (a, left) Voltammogram for Pt (111) in 0.5M H_2SO_4 after annealing. Sweep rate 50 mV sec^{-1} . Potential on the hydrogen scale. (b, right) The same but first cycle in which the limit at positive potentials was 1.5V (RHE).

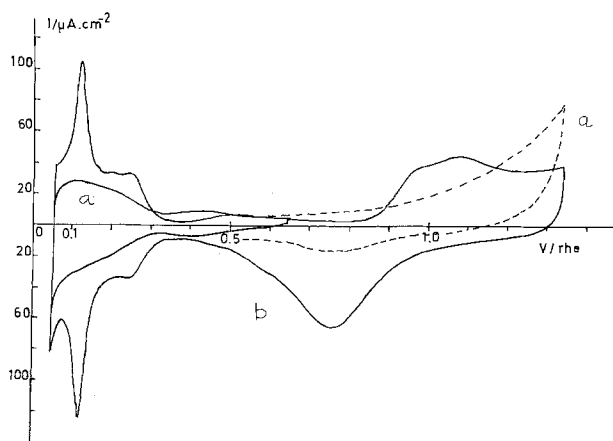


Fig. 10. (a) Voltammogram for Pt (111) in 0.5M H_2SO_4 annealed and then contacted with laboratory atmosphere for a few minutes. (b) The same after 20 cycles.

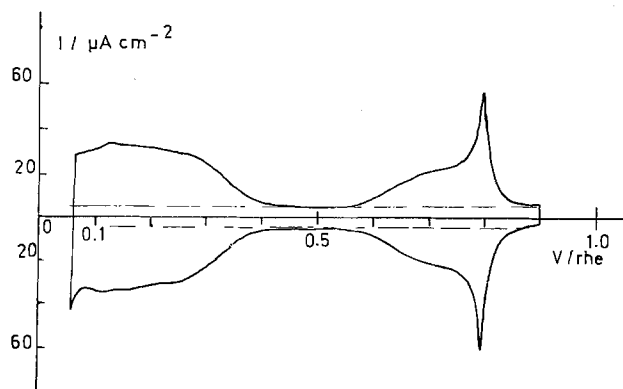


Fig. 11. Voltammogram for Pt (111) in 1M $HClO_4$ after annealing. Sweep rate 50 mV sec^{-1} .

shift of interest from bulk properties to surface properties which has accelerated in the past few years. The tendency in the past has been to attempt a molecular-quantum interpretation of experiments which were still based on averaged properties whether thermodynamic or kinetic. Too often the comparison between theory and experiment of this type is unspecific and cannot reveal much about the true nature of the system. Experiments which are themselves more directly based on molecular properties are now being done, notably in the study of the interaction of light with electrodes as so brilliantly described by Heinz Gerischer in his Palladium medal lecture. I believe that we are on the threshold of the transformation to a real molecular understanding of electrified interphases and con-

sequently that we are now at an exciting interface in electrochemistry.

REFERENCES

1. R. Parsons, *R. Coll. Sci. J.*, **29**, 28 (1949).
2. *Discuss. Faraday Soc.*, **1** (1947).
3. B. E. Conway, *This Journal*, **124**, 410C (1977).
4. H. von Helmholtz, *Ann. Phys. Chem.*, **7**, 337 (1879).
5. D. C. Grahame, *J. Am. Chem. Soc.*, **63**, 1207 (1941); **68**, 301 (1946); *Chem. Rev.*, **41**, 441 (1947).
6. Z. A. Iofa and A. N. Frumkin, *Acta Physicochim. URSS*, **10**, 473 (1939).
7. D. C. Grahame and R. Parsons, *J. Am. Chem. Soc.*, **83**, 1291 (1961).
8. R. Parsons, and F. G. R. Zobel, *J. Electroanal. Chem.*, **62**, 3511 (1966).
9. M. Gouy, *J. Phys.*, **9**, 457 (1910).
10. D. L. Chapman, *Philos. Mag.*, **25**, 425 (1913).
11. J. A. Harrison, J. E. B. Randles, and D. J. Schiffrin, *J. Electroanal. Chem. Interfacial Electrochem.*, **25**, 197 (1970).
12. F. W. Schapink, M. Oudeman, K. W. Leu, and J. N. Helle, *Trans. Faraday Soc.*, **56**, 415 (1960).
13. R. Parsons, *Proc. R. Soc. London, Ser. A*, **261**, 79 (1961).
14. A. N. Frumkin, *Z. Phys. Chem.*, **103**, 43 (1923).
15. N. F. Mott, R. Parsons, and R. T. Watts-Tobin, *Philos. Mag.*, **15**, 483 (1962).
16. J. R. Macdonald, *J. Chem. Phys.*, **22**, 1857 (1954).
17. J. Watts-Tobin, *Philos. Mag.*, **6**, 133 (1961).
18. J. O'M. Bockris, M. A. V. Devanathan, and K. Müller, *Proc. R. Soc. London, Ser. A*, **274**, 55 (1963).
19. S. Levine, G. M. Bell, and A. L. Smith, *J. Phys. Chem.*, **73**, 3634 (1969).
20. B. B. Damaskin and A. N. Frumkin, *Electrochim. Acta*, **19**, 173 (1974).
21. R. Parsons, *J. Electroanal. Chem. Interfacial Electrochem.*, **59**, 229 (1975).
22. R. Parsons, *Electrochim. Acta*, **21**, 681 (1976).
23. M. W. Humphreys and R. Parsons, *J. Electroanal. Chem. Interfacial Electrochem.*, **82**, 369 (1977).
24. A. Bewick and J. Robinson, *ibid.*, **60**, 163 (1975); **71**, 131 (1976).
25. C. Hinnen, C. Nguyen Van Huong, A. Rousseau, and J. P. Dalbera, *ibid.*, **95**, 131 (1979).
26. C. Hinnen, C. Nguyen Van Huong, A. Rousseau and J. P. Dalbera, *ibid.*, **106**, 175 (1980).
27. G. Valette and A. Hamelin, *ibid.*, **45**, 301 (1973).
28. C. Nguyen Van Huong, C. Hinnen, J. Lecoer, and R. Parsons, *ibid.*, **92**, 239 (1978).
29. J. A. V. Butler, *Proc. R. Soc. London, Ser. A*, **157**, 423 (1936).
30. R. Parsons and E. Passeron, *J. Electroanal. Chem. Interfacial Electrochem.*, **12**, 524 (1966).
31. F. C. Anson, N. Rathjen, and R. D. Frisbee, *This Journal*, **117**, 477 (1970).
32. J. M. Saveant and D. Tessier, *J. Phys. Chem.*, **81**, 2192 (1977).
33. R. Parsons, *Trans. Faraday Soc.*, **47**, 1332 (1951).
34. R. Parsons, *J. Chim. Phys.*, **49**, C82 (1952).
35. R. Parsons, *Trans. Faraday Soc.*, **54**, 1053 (1958).
36. R. Parsons, *Trans. Soc. Adv. Electrochem. Sci. Technol.*, **10**, 91 (1975).

37. A. A. Balandin, *Adv. Catal.*, **19**, 1 (1969).
38. S. Trasatti, *J. Electroanal. Chem. Interfacial Electrochem.*, **39**, 163 (1972).
39. A. Capon and R. Parsons, *ibid.*, **44**, 239 (1973); **45**, 205 (1973).
40. A. Capon and R. Parsons, *ibid.*, **65**, 285 (1975).
41. J. Clavilier, R. Faure, G. Guinet, and R. Durand, *ibid.*, **107**, 205 (1980).



Report of the Electrolytic Industries for the Year 1979¹

K. E. Woodard, Jr.*

Olin Corporation, Chemicals Group, Charleston, Tennessee 37310

and E. J. Rudd*

Diamond Shamrock Corporation, T. R. Evans Research Center, Painesville, Ohio 44077

Chlorine-Caustic Soda

Production and capacity.—U.S. production of chlorine in 1979 rose 11% to 12,271,519 tons. Industry capacity increased less than 1%, from 39,165 tons/day to 39,279 tons/day, during the year. Production rates exceeded 90% of capacity at the end of the year, up significantly from the beginning of the year (1-3).

Estimates of the production capacity of individual U.S. producers are shown in Table I (4).

Expansions completed in early 1979 by BASF Wyandotte and Georgia Pacific are included in Table I.

Pennwalt completed two expansions during 1979, raising its capacity to 464,000 tons/year of chlorine.

During 1979 several acquisitions occurred: Linden Chemicals and Plastics acquired three chlor alkali plants from Allied Chemical, raising their capacity from 450 tons/day to 1150 tons/day (5, 6). Vulcan Materials Company purchased a chlor alkali plant located at Port Edwards, Wisconsin from BASF Wyandotte Corporation, increasing their capacity 200 tons/day to 1340 tons/day (8-10).

New plant expansions and modernizations are shown in Table II (11).

During 1980, PPG plans to complete the 750 tons/day second phase of its Lake Charles, Louisiana, plant doubling capacity. Hooker will increase the capacity of its Tacoma, Washington, plant to 675 tons/day. Fort Howard Pulp and Paper will start up a 12.5 tons/day membrane cell plant in Muskogee, Oklahoma. In early 1981 Convent Chemical will start up its 800 tons/day unit in Convent, Louisiana. Dow will add an increment to its Freeport, Texas, plant in 1980 or 1981 (4, 12).

Average annual chlorine capacity is estimated to be 16,435,000 tons/year and consumption is estimated to be 12,820,000 tons in 1982 (13).

Caustic soda production was 12,313,848 tons, up 14.6% from 1978. Production of caustic soda may increase to 13,000,000 tons in 1980. Plant capacity for caustic soda was 15.5 million tons/year in the first quarter of 1980 (14, 15).

Canadian production capacity increased 650,000 tons/year in 1979, to 1,650,000 tons/year. Canadian Industries

The Industrial Electrolytic Division is grateful for the support received from the Vittorio de Nora-Diamond Shamrock Fund in assisting with the publication costs of this report.

¹ This report is sponsored by the Industrial Electrolytic Division of The Electrochemical Society. It represents a summary of the published information on production, plant capacities, consumption, markets and trends, prices, raw materials, new developments, health and environmental aspects in the electrolytic and related industries.

The material presented herein has been obtained from many sources, as noted in the reference list, and does not necessarily represent the opinions of the authors.

increased the capacity of their Becancour, Quebec, facility 150,000 tons/year.

Dow Chemical of Canada increased the capacity of their Fort Saskatchewan, Alberta, facility 500,000 tons/year. Production nameplate capacity of the Canadian producers is shown in Table III (16-26).

Total Canadian chlorine production is forecast to be 1220.5 kilotons by 1983 (16).

The amount of salt used to manufacture chlorine and caustic soda increased as the chlorine production increased. Chlorine and caustic soda production is the largest single salt consumer, comprising 41% in 1978. Some supply problems were encountered during 1979 as a result of hurricane David "melting" solar salt crops, and production problems encountered in the Louisiana rock salt mines. Expansion of salt production was announced by Cargill, Incorporated and Great Lake Minerals and Chemicals Corporation (27-31).

Markets and prices.—World demand for chlorine from the U.S. increased during 1979. Energy prices helped exports of energy intensive chlorine derivatives. Chlorine prices gained strength on the booming market for ethylene dichloride export. Price increases during the year resulted in \$10-20 increase in chlorine, up to \$135 to 150, and caustic soda up to \$160 to 175/ton (32).

Reduced world wide demand for chlorine has led to a tightening in the caustic soda market. Price increases in early 1980 increased prices for caustic soda up to \$25/ton (33-44).

Table I. U.S. chlorine producers 1000 tons/year of chlorine

Allied Chemical	350
Aluminum Co. of America	200
BASF Wyandotte	488
Diamond Shamrock	1234
Dow Chemical	4650
DuPont	479
Ethyl Corporation	176
FMC Corporation	350
Georgia Pacific	513
Goodrich Chemical	110
Hooker	1161
ICI Americas	170
International Minerals & Chemical	119
Kaiser Aluminum & Chemical	205
Linden Chemicals & Plastics	166
Olin Corporation	930
Pennwalt Corporation	409
PPG Industries	1250
Shell Chemical	105
Stauffer Chemical	380
Vulcan Materials Company	410
Weyerhaeuser Company	140
Others	403
Total	14,398

Table II. New plant expansions and modernizations in the United States

Location	Producer	Project	Status	Projected completion	Notes
Louisiana	Convent Chemical Co.	800 tons/day Diamond MDC 55	Building	1st Quarter 1981	¹
Lake Charles	PPG Industries, Inc.	Phase 2, 750 tons/day, (bipolar)	Building	2nd Quarter 1980	¹
Oklahoma	Fort Howard Paper Co.	12.5 tons/day Hooker MX (membrane)	Building	2nd Quarter 1980	¹
Muskogee					
Oregon	Pennwalt Corp.	Expansion 310-410 tons/day	Building	1st Quarter 1980	¹
Portland		Expansion 410-570 tons/day (diaphragm)	Engineering	1981	
Texas	Dow Chemical USA	Expansion, Dow (diaphragm)	Continuing	1980-1981	¹
Freeport					
Washington	Hooker Chems. & Plastics Corp.	Expansion 400-675 tons/day	Engineering	3rd Quarter 1980	¹
Tacoma		Hooker H-4			
		Expansion 200-250 tons/day	Building	1st Quarter 1980	¹

Note: All Dow USA locations—conversion to metal anodes scheduled to have started in late 1979.

¹ Electrolytic plant producing caustic soda, chlorine, and hydrogen from brine.

U.S. producers claimed chlorine was still under priced, despite price hikes (45).

Chlorine burning to produce HCl is forecast to increase at 10% annual growth rate in the early 1980's (46).

Ethylene dichloride had a good year in 1979 but will probably not have as good a year in 1980 (47).

Chlorinated solvents remain under the pollution gun. Demand for these chlorine derivatives appears likely to have little growth prospect (47).

The pattern of chlorine and caustic end use is shown in Table IV, and Table V (48).

Membrane cells.—Akzo Zout Chemie Netherland BV announced plans to build the first world scale membrane cell chlor alkali plant, 250,000 tons/year chlorine, in June 1979. Akzo chose Asahi Chemicals membrane technology because of the performance of the Asahi cells and the fact that the technology is more advanced than any other in the field. The plant is due on stream in 1982 (49-60).

Table III. Canadian chlorine producers (16)
(kilotons/year of chlorine)

	Capacity
Canadian Industries (CIL)	388
Canadian Occidental (Hooker)	134
Cansco Chemicals	18
Dow Chemical of Canada	918
FMC Chemicals	33
Prince Albert Pulp	33
Reed	14.5
Stanchem (PPG Industries)	116
Total	1654.5

Table IV. End use patterns of chlorine

Derivative	Percent
Vinyl chloride monomer	18
Chlorinated methanes	8
Chlorinated ethanes	10
Other chlorinated organics	20
Pulp and paper	12
Inorganic chemicals	15
Water and waste treatment	6
Miscellaneous	11

Table V. End use patterns of caustic soda

Derivative	Percent
Chemical processing	40
Pulp and paper	20
Petroleum	4
Aluminum	4
Soap and detergents	4
Textiles	2
Rayon and cellophane	3
Miscellaneous	6
Exports	17

Sweden's A.B. Celleco (Stockholm), established to sell membrane cell technology developed by Ionics using duPont Nafion membranes, is supplying Celleco's process package to Elkem Spigeverk. The 25 tons/day chlorine plant will cost \$4.5 million and is due on stream in mid 1980 (61-63).

Udhe GmbH will supply the Hooker MX type electrolysis cells to Tofte Cellulose Fabrikk of Hurum, Norway. The 14,000 tons/year plant is scheduled to be on stream in July 1980, at Tofte on the Oslo Fjord. Caustic soda will be a 15% solution, virtually salt free (63-67).

Diamond Shamrock Corporation licensed its diaphragm cell chlor alkali technology to the Peoples Republic of China. A 625 tons/day plant will be built at Shengli in Shantung Province (68-71).

Diamond Shamrock Corporation licensed a 22 metric tons/day caustic membrane cell plant to Nigerian National Paper using its bipolar membrane cells, and a 24.5 metric tons/day membrane cell plant using its new DM-14 monopolar membrane cells to Paek Kwang in South Korea (72).

Asahi Glass Company has constructed a pilot plant at its Chiba factory for the production of ion exchange membranes. The company has decided to construct a full-fledged plant for the production of ion exchange membranes. Construction time, startup, and capacity have not been disclosed (73).

During 1979 Asahi Glass Company has continued to sell its membrane technology: Imperial Chemical Industries, ICI, concluded an agreement for the evaluation of Asahi Glass' membrane technology. The agreement cost ICI \$500,000 (74, 75). Udhe GmbH reached an agreement for full disclosure of Asahi's ion exchange membranes and electrolytic cells and appointed Udhe sole agent for their manufacturing and sales. A demonstration plant of 3,000 tons/year will be constructed. Asahi Glass will also supply ion exchange membranes to Bayer & Hoechst (76, 77). Nippon Carbide Industries will switch its (1,450 tons/year) mercury process to an ion exchange membrane process plant using Asahi Glass Company's membrane technology by November 1980. Nippon Carbide is the first to announce the switch over (80). P. N. Soda Waru in Indonesia and the Paper Industries Corporation of the Philippines have also licensed plants of undisclosed capacity from Asahi Glass Company (81).

Asahi Chemical Company has licensed its ion exchange membrane cell technology to N. Z. Forest products of New Zealand. The plant will produce 10,000 tons/year caustic soda (78, 82).

The world membrane cell plants are listed by technology utilized in Table VI.

Performance of the leading Japanese membrane cell technology is detailed in Table VII (83).

Tokuyama Soda has increased the caustic concentration from its process from 20 to 27% without

Table VI. Membrane cell plants

I.	Asahi Chemical Company Technology	
1.	Asahi Chemical Company 1975 Nobeoka, Japan	80,000 Mtons/ year
2.	Prince Albert Pulp Company 1978 Saskatoon, Sask., Canada	30,000 Mtons/ year
3.	St. Anne-Nackawic Pulp & Paper 1979 Nackawic, New Brunswick	10,000 Mtons/ year
4.	Denki Kagaku Company 1976 Ohmi, Japan	60,000 Mtons/ year
5.	Akzo Zout Chemie Netherland BV 1982 Hengelo	280,000 Mtons/ year
6.	N.Z. Forest Product Ltd. 1981 New Zealand	10,000 tons/year NaOH
II.	Hooker & Uhde Technology	
1.	Reed Paper 1975 Dryden, Ontario	12,000 Mtons/ year
2.	Ft. Howard Pulp & Paper 1980 Ft. Howard, Arkansas to be expanded	4,500 Mtons/ year 9,000
3.	Tofte Cellulose Fabrikk 1980 (Hurum) Norway	16,500 Mtons/ year
III.	Diamond Shamrock Technology	
1.	Muscle Shoals 1975	3,000 tons/year
2.	Uddeholms AB 1978 Skoghall, Sweden	20,000 tons/year
3.	Aracruz Cellulose 1980 Victoria, Brazil to be expanded	13,000 tons/year 38,000 tons/year
4.	Nigerian National Paper	8,000 Mtons/ year
5.	Paek Kwang South Korea	9,000 Mtons/ year
6.	Korea Potassium South Korea	12,000 Mtons/ year KOH
IV.	Ionics & Cellico Technology	
1.	Elkem Spigeverk 1980 Bremanger, Norway	10,000 tons/year 72 Mtons/ day KOH
2.	ROT Chimica Monterey, Mexico	2,600 Mtons/ year
V.	Asahi Glass Company Technology	
1.	Asahi Glass Company 1978 Kansai, Japan	10,000 tons/year
2.	P.N. Soda Waru Indonesia	Undisclosed
3.	Paper Industries Corp. of Phillipines	Undisclosed
4.	Uhde GmbH West Germany	3,000 tons/year
5.	Nippon Carbide Industries, Inc. Japan	1,450 tons/year
VI.	Tokuyama Soda Company Technology	
1.	Tokuyama Soda 1977 Yamaguchi, Japan	10,000 tons/year
VII.	Allied Chemical Corp.	
1.	Allied Chemical 1976 Syracuse Pilot Plant	2,000 tons/year

increasing its power consumption. Tokuyama Soda plans to begin construction of a commercial plant in fiscal year 1981 (79).

Allied's technology utilizes a patented series catholyte flow for optimized production of low strength 10-20% NaOH. Power consumption is 10% below a parallel flow unit when producing 16.5% NaOH. A six tons/day commercial prototype has been in operation since early 1978 (84).

Developments.—A nonelectrolytic chlorine process has been patented by Battelle Memorial Institute. The process recovers chlorine from hydrochloric acid by oxidation in a molten salt containing vanadium oxide and alkali metal sulfates and pyrosulfates. The work is reportedly still at the laboratory stage, and further development would require an industrial sponsor (85-87).

Conradty GmbH and Great Lakes Carbon have formed a joint venture company called Grelcon to market electrodes. Conradty's subsidiary Metallelektroden developed technology for coating electrodes which have been sold in Europe for many years (88).

Asahi Glass, PPG, and De Nora have agreed to the joint development of a new caustic soda manufacturing process called SPE, Solid Polymer Electrolyte. The process features 20% lower electric power consumption than the latest ion exchange membrane processes. Asahi Glass Company has recently launched its own R&D program on the SPE separately from the joint undertaking with PPG and De Nora (89-91).

New energy saving cathodes are being developed for diaphragm and membrane chlor alkali cells. Tokuyama Soda has announced that its new cathode is being applied successfully in its 10,000 tons/year membrane cell plant, reducing cell voltage from 3.5 to 3.3V (92).

Diamond Shamrock expects to save \$2 million/year at its Houston plant where high surface area nickel cathode coatings on its steel diaphragm cell cathodes reduces hydrogen overvoltage 120-140 mV. A commercial facility to produce coated cathodes for other chlor alkali producers has been constructed (93, 94).

Hooker Chemicals and Plastics Company and Lurgi discussed cathode coatings at the Society of the Chemical Industry Conference on the Advances in Chlor Alkali Technology, which should be commercially available in 1980 for diaphragm cells (95).

D. H. Porter of Hooker Chemicals and Plastics Company discussed the reduction in energy consumption of the Hooker diaphragm cells at the Society of the Chemical Industry Symposium on Advances in Chlor Alkali Technology. Power consumption reduction of 20% using a new microporous diaphragm, a lower brine gap, and new electrode coatings, along with greatly increased surface area in the same basic cell design, was discussed. Power consumption was reduced from 2900 kW-hr/ton chlorine to 2300 kW-hr/ton chlorine (95).

General Electric has developed and commercially operates a catalytic system to remove 85-97% of the sodium chlorate from its diaphragm cell caustic soda. Product quality of less than 30 ppm sodium chlorate can be obtained (96).

Mercury cells.—The Japanese mercury cell plants must discontinue operations by the end of 1984. MITI has proposed a plan to divide the 21 mercury process companies into two groups. MITI will urge the first group of three companies, Asahi Chemical Industry Company, Asahi Glass Company, and Tokuyama Soda Company to complete the switch to ion exchange membrane technology within 2 years. Each company has developed its own technology. The remaining medium and small scale producers will be required to convert the technology within 5 years. The program also calls for a closure of 423,000 tons/year of capacity, 290,000 tons/year mercury and the remainder in diaphragm production capacity. A total of 1,360,000 tons

Table VII. Performance parameters Japanese membrane cell technology

	Current efficiency	Voltage	Current density	Power consumption	HCl consumption	Caustic concentration	Cell temperature
Asahi Chemical Co.	93.4-94.8	3.81-3.90	4 kA/m ²	2698 to 2776 kW-hr/ MT NaOH	132 to 146 kg/MT NaOH	40%	90°C
Asahi Glass Co.	92.0-95.5	3.80-3.87	2 kA/m ²	2667 to 2781 kW-hr/ MT NaOH	None	38.5-40.8%	85°-90°C
Tokuyama Soda	94	3.50	2 kA/m ²	2496 kW-hr/MT NaOH	40 kg/MT NaOH	20%	85°C
	NaCl depletion	Cell type	Size of membrane	Source of membrane	Source of anode		
Asahi Chemical Co.	70%	Bipolar	1.2m x 2.4m	Self supply	Self supply	Self supply	
Asahi Glass Co.	46-56%	Monopolar	1m x 2m	Self produced	Purchase	Purchase	
Tokuyama Soda Co.	40-50%	Bipolar	270 dm ²	Self supply	Purchase	Purchase	

of capacity will be converted to ion exchange membrane technology (97-99).

The EEC Commission has made two proposals to limit the mercury content of effluent from mercury cell chlor alkali plants. The first proposed directive limits the mercury content of the effluent from chlor alkali plants:

Mercury in effluent g/ton of chlorine capacity

	Recycle brine process	Brine discharge process
July 1, 1983	1.5	8
July 1, 1986	1.0	5
July 1, 1989	0.5	2.5

The second directive covers fresh water after receiving the effluents:

Fresh water	0.5 mg/m ³
Seawater	0.05 mg/m ³

Mercury concentration in fish cannot exceed 0.3 mg/m³. Industry is dissatisfied with the proposals, particularly the water quality and imposition only to the chlor alkali industry (100, 101).

Health and environment.—Dow is planning to build a 30 million pound a year bromine-chloride plant for use in disinfecting municipal and industrial waste water. Bromine-chloride is considered environmentally safer and as effective as chlorine (102).

OSHA has set a ceiling limit of 1 ppm for the workplace exposure to chlorine. NIOSH has developed a criteria document calling for 0.5 ppm ceiling limit to protect the worker from acute eye and respiratory irritation. The stay by OSHA in February 1979 was lifted on July 17, 1979, resulting in the Chlorine Industry's petition of the Court of Appeals. On March 7, 1980, the Fifth Circuit Court of Appeals affirmed OSHA's position relative to the chlorine standard (103-111).

Studies by an Italian research team have concluded that trichloroethylene is not carcinogenic, a direct contradiction of the U.S. National Cancer Institute findings issued in a 1976 report. The research team says the epichlorohydrin used as a stabilizer was responsible for the NCI findings and that Montedison trichloroethylene is free of any epichlorohydrin (112, 113).

Asbestos regulations are being considered by the U.S. EPA and Consumer Product Safety Commission. EPA advanced Notice of Proposed Rulemaking for Asbestos Regulation under TSCA. Its entire asbestos control program is expected to become effective between 1985-95, but commercial and industrial uses are targeted for ruling in the fall of 1980, and promulgation in the summer of 1981 (111, 114, 115).

Derailment of a 106-car Canadian Pacific freight train in Mississauga, Ontario, 20 miles southwest of Toronto, resulted in evacuation of 220,000 people due to a leaking chlorine car. Evacuation occurred because it was feared additional explosions of propane cars could cause dangerous concentrations of chlorine in the surrounding area. The largest evacuation in North American history turned out to be a valuable opportunity to test a theoretical disaster plan. Emergency planners, civil defense people and government representatives from all over the world have asked Mississauga for their plan. A seminar package, including eight hours of color videotape is in the process of being developed (111, 116).

Other Alkaline or Chlorine Compounds

Caustic potash.—Domestic caustic potash production totaled 284,258 short tons in 1979, an increase of 18.1%

over 1978. Production during the 4th quarter of 1979 exceeded the 4th quarter of 1978 by over 72% (117).

The domestic price of liquid caustic potash, 45% solution, increased \$15/ton (in September 1979) to \$200/short ton for standard grade and to \$205/short ton for low chloride grade (118).

The sole Canadian supplier of 45% KOH solution, Canadian Industries, announced expansion of the output of caustic potash at Cornwall, Ontario, by 50% before the end of 1979 (119, 120).

The first North American membrane cell plant to produce potassium hydroxide started production at ROT Quimica Monterey, Mexico. Ionics "Cloromat" membrane cell technology is used in the 2000 tons/year plant (121).

Diamond Shamrock has confirmed the licensing of its monopolar membrane cell technology for production of potassium hydroxide to Korea Potassium Chemical Company, South Korea. The plant will initially produce 32 metric tons/day of KOH (122, 123).

Domestic production of potash increased 1% in 1979 to about 2.24 million metric tons (K₂O content). U.S. demand increased 6% to about 6.6 million tons (124).

The world potash supply is estimated to be 32.3 million short tons K₂O in 1979. World demand for potash is at record levels. Production capacity increases are expected to increase the world supply to 43.2 million tons by 1985 (125).

The average domestic price of muriate of potash, excluding soluble and chemical grades, increased from \$76 to \$96/metric ton during the year (124).

Soda ash.—Early projections predicted a modest increase of perhaps 3% in the production of soda ash in the United States in 1979, but the estimated total of 8.17 million short tons represented a decrease of over 1%. This decline has been largely attributed to the closing in 1978 of two plants, one in Corpus Christi, Texas (PPG Industries, Incorporated) and the other the facilities of BASF Wyandotte Corporation in Michigan, which effected a loss in production of synthetic soda ash of over one million short tons (126-128).

Continued growth in the production of natural soda ash in the United States is forecast through 1985. Confidence in the availability of markets, both at home and abroad, is mirrored in the announced expansions to existing facilities and construction of new plants. It is interesting to note that the replacement of synthetic soda ash with the natural product has in fact been a major change in the industry. This change is almost complete in the United States, where synthetic soda ash is produced only by Allied Chemicals in Syracuse, New York (127, 129-136).

The United States is the principal source of natural soda ash, with a total output of approximately 7.3 million short tons in 1979, from: (i) trona ore deposits (a sodium sesquicarbonate), located in Green River, Wyoming; and (ii) brine, e.g., Searles Lake, California.

In the free world today, there are only two other sources of natural soda ash capable of supporting commercial production. At one of these locations, in Kenya, the Magadi Soda Company (a subsidiary of ICI) is both expanding and upgrading its existing facility and building a new plant, to thereby essentially double its output by 1983 (137).

A multimillion dollar development program to commercialize new solution mining and processing techniques for natural soda ash has been undertaken by FMC Corporation in the Green River Basin in Wyoming. The company has stated that the new technology substantially reduces costs and improves the basic economics of soda ash production relative to conventional dry mining techniques (135, 136, 138).

PQ, a privately-owned U.S. company, is seeking participants in the joint development of its deposits of trona ore in Wyoming. Itself a major use of soda ash, PQ estimates that approximately 100 million short tons of natural soda ash could be produced from its lease holdings. The cost of the overall venture is predicted to be approximately \$300 MM and it may be 7-8 years before the project is "off the ground" (136).

Texasgulf Chemicals Company is planning a major expansion of its natural soda ash plant also in Green River, Wyoming, thereby increasing the company's output to approximately two million short tons per year. Permission for the expansion, to be granted by the American EPA and Wyoming authorities, will depend upon the results of environmental and socio-economic studies undertaken this year (130).

Tenneco Oil Processing and Marketing Company announced that construction of a plant for the mining and processing of trona ore had begun. Scheduled for completion in mid-1982, the facility is designed to produce one million short tons of high purity soda ash per year (134).

Exports of soda ash from the United States had shown steady overall growth since 1975, but decreased approximately 6% to 730,000 short tons this year (127, 129).

Year	Total exports (1000 short tons/year)
1975	530
1976	645
1977	760
1978	780

A factor in this unexpected reversal is that the major manufacturers of soda ash in Europe appear to have succeeded in securing their market shares in the face of the U.S. imports. Early in 1979, the European soda ash industry was closely scrutinized on two counts: (i) the proposed importation into Belgium of natural soda ash from the United States, a situation that was resolved in favor of Solvay, and (ii) the inquiry into the pricing policies of ICI, which again was resolved in favor of the European Company (139).

Furthermore, imports of low-priced light soda ash from the Soviet Union into Europe were curbed by the imposition of a provisional antidumping duty, effective November 24, 1979 (140).

However, it is anticipated that the demand for American natural soda ash will climb rapidly in the export market in the next few years, particularly as the old European plants (producing synthetic soda ash) become economically unattractive and environmentally unacceptable (132).

Late in the year, Stauffer Chemical Company, Allied Chemical Company, and Kerr-McGee Chemical Company raised the price of soda ash, following the initiative of Texasgulf. The year-end price for bulk dense soda ash varied from \$66 per ton (FMC) to \$76 per ton. Kerr-McGee raised its price for the product to \$90 per ton (141).

The average price for synthetic soda ash at the end of 1979 was \$111-112/ton (141).

Sodium chlorate.—Domestic production of sodium chlorate decreased 3.2%, down to 248,073 tons, from the 1978 level of 256,320 tons (142).

There are now ten sodium chlorate producers in the U.S. Production capacity is estimated in Table VIII (143).

Four U.S. sodium chlorate plants started up: Erco 25,000 tons/year plant in Monroe, La; IMC's 40,000 tons/year plant in Orrington, Me; Georgia Pacific Corporation's 27,000 tons/year plant in Plaquemine,

Table VIII. Sodium chlorate 1979 estimated annual capacity
Thousands short tons

Brunswick Chemical	8
Erco	25
Georgia Pacific	31
Hooker Chemicals	149
Huron Chemicals	11
IMC	40
Kerr-McGee	67
Olin	26
Pacific Engineering	6
Pennwalt	80
Total	443

La; and Olin's 20,000 tons/year plant in McIntosh, Alabama (144-148).

Brunswick Pulp and Paper has announced it will build a 25,000 tons/year crystal and solution sodium chlorate plant at Brunswick, Georgia, replacing the old 8,000 tons/year plant. Krebs NC electrolytic cell process will be used. The plant is estimated to cost \$12-15 million, with completion in late 1980 (149-151).

Domestic sodium chlorate prices firmed up to \$345/ton during the year (152-157).

Canadian production capacity is expected to increase 30% to 303,000 tons/year during the 1979-1980 period. Canadian manufacturers' production capacities are detailed in Table IX.

QueNord Incorporated opened its \$17 million 25,000 tons/year plant at Magog, Quebec (159-161).

St. Anne Chemical began operations, while Tidal ceased operations (162).

The \$8.5 million 15,000 tons/year plant to be built by Saskatoon Chemicals has an expected completion date of mid 1980. Start-up of the Saskatoon Chemicals plant could coincide with yet another shutdown of Canadian Oxy's Brandon Manitoba facility (163-166).

Erco will become the world's largest producer of sodium chlorate, 172,000 tons/year once the Thunder Bay expansion is completed (167-174).

New Canadian producer price schedules effective January 1, 1980 increased the cost of solution chlorate to \$353/ton, up 17.7%, and crystal grade chlorate to \$408/ton, up 16.6% (175, 176).

Metals

Aluminum.—Domestic production of primary aluminum rose an estimated 4% to 5 million short tons. Domestic consumption increased to 6.2 million tons. Imports decreased to 0.9 million tons (177).

At the beginning of 1979 all the aluminum potlines in the Pacific Northwest were operating, but by the

Table IX. Canadian manufacture of sodium chlorate (158)

Company and location	Capacity (000 tons/ year)
<i>Merchant</i>	
Canadian Occidental, Brandon, Manitoba	11
Squamish, British Columbia	11
Erco Industries, Buckingham, Quebec	63.5
North Vancouver, British Columbia	54.5
Thunder Bay, Ontario	13.5
Stanchem, Beauharnois, Quebec	30
<i>Captive</i>	
BC Chemicals, Prince George, British Columbia	24.5
Canso Chemicals, Abercrombie, Nova Scotia	8.5
Huron Chemicals, Marathon, Ontario	1.5
Reed Chemical, Dryden, Ontario	4.5
Tidal Chemicals, Saint John, New Brunswick*	11
<i>Under Construction</i>	
Erco Industries, Thunder Bay, Ontario	+ 18
QueNord Chemicals, Magog, Quebec	25
St. Anne Chemical, Nackawic, New Brunswick	10
Saskatoon Chemicals, Saskatoon, Saskatchewan	13.5
Stanchem, Beauharnois, Quebec	+ 3

* Scheduled to close September 1, 1979.

end of the year 162,500 tons, 3.1% of the total U.S. capacity, had been idled due to power cutbacks. Potlines in Texas that were idle at the beginning of the year had been restarted by the end of the year. Kaiser restored 20,000 tons/year of idled capacity in January 1980 in anticipation of improved power production (178, 194).

Uncertain power situations face the six U.S. aluminum producers in the Pacific Northwest where 31% of the U.S. primary aluminum capacity is located. Power cost increases of 95% occurred on December 20, 1979, increasing from 3.12 to 6.095 mills/kW-hr, adding approximately 2.4¢/lb to the cost of producing aluminum (195).

Power contracts also expire in the 1984 to 1988 time frame when the Bonneville Power Administration is expected to be deficient in meeting power obligations.

Some of the northwest producers are converting production to new energy saving technology that can reduce energy consumption by an estimated 20% (195).

Martin Marietta plans to expand its primary aluminum production from 65,000 tons/year to 185,000 tons/year by the end of 1981. The project will utilize the energy saving Sumitomo technology and is expected to cost \$125 million. Energy consumption could be 25% less than the old potlines (196-199).

Kaiser Aluminum and Chemical Corporation cancelled its \$66 million program to revamp the Baton Rouge, Louisiana, aluminum refinery, due to uncertainties over construction costs and energy prices (200, 201).

Kaiser Aluminum and Chemical Corporation will spend \$30 million plus as the initial phase to upgrade its primary aluminum plants at Tacoma, Washington, and Chalmette, Louisiana (202).

Alumax may still build a 186,300 tons/year smelter at Umatilla, Oregon, despite environmental and energy costs (195).

A 200,000 tons/year primary aluminum smelter may be built at Clarendon, North Carolina, by a Middle East consortium of metal users and investors. The project is estimated to cost \$400 million and be on stream by the end of 1982. Much of the smelter's production will be exported (203, 204).

The Alumax 197,000 tons/year 400 million dollar primary smelter at Berkley, South Carolina, is expected to start pots late in the summer of 1980. Reports of a new primary smelter being constructed by Alcoa in Kentucky have not been confirmed by the company (204).

U.S. prices for 99.5% aluminum ingot ranged from 55 to 57.5 cents/pound. Price increases by the producers at various times during the year advanced prices to 66 to 66.5 cents/pound. Merchant spot prices exceeded published prices all year long and reached nearly 80 cents/pound at year end (205).

Total domestic aluminum demand had begun to fall in the last half of 1979 and is projected to become weaker in 1980. Some forecasters predict at least a

2% decline of 144,000 tons, others predict 5.6-15% decline in U.S. consumption (206-208).

Reynolds Aluminum Recycling Company announced a record 75 million pounds of aluminum recycled during the first six months of 1979, an increase of 7%. Payment for recycle aluminum beverage cans was increased to 23 cents/pound, an increase of 3 cents (209, 210).

Reynolds Metals Company's Recycling and Reclamation Division plans to build a scrap metal separations plant to separate aluminum and other nonferrous metals from automotive shredder residues. The facility located in Sheffield, Alabama, is expected to recover more than 10 million pounds of aluminum during its first year of operation (179, 181).

Recycling aluminum requires only 5% of the energy needed to produce aluminum from ore. In November 1979 Howmet Aluminum in Rockwall, Texas, completed a 75 million pounds/year plant that will produce high quality aluminum from 100% recycled material. Martin Marietta Aluminum is building a scrap recycling processing plant that can produce up to 240 million pounds of sheet ingot for their steel mill. "A Way of Life," a color film on aluminum recycling and energy is available on free loan from Modern Talking Picture Service, 1901 L Street NW, Washington, DC 20036 (212).

Ford Motor expects to increase aluminum usage in its cars from its 1980 model year content of 140 pounds/car to 190-200 pounds by 1985. Other auto producers also expect to achieve 190-200 pounds/car. Aluminum castings are expected to be the major portion of the growth (213, 214).

The aluminum industry succeeded in 1978 in achieving the U.S. Department of Energy goal of 10% reduction in energy by 1980. Additional new ideas in processing and materials promise significant energy savings in the next decade. (215-218).

A study of aluminum smelting processes carried out by Arthur D. Little, Incorporated for the Department of Energy through Argonne National Laboratory, reached a major conclusion that the only alternative technology at present to the Hall Heroult cell for the production of primary aluminum is the Alcoa chloride electrolysis process, with the sulfide and nitride electrolytic processes offering potential advantages in the future. Titanium diboride cathodes may achieve significant energy consumption reductions in the Hall Heroult cell (179, 180).

Alcoa continues the development of its low energy process, called the Alcoa smelting process (ASP), that began in 1973. Redesign, construction, and testing of a new segment of the chemical plant is expected to take 3-4 years additional development. The ASP system is viewed as holding promise for a 30% reduction in the smelting energy perhaps, to 4.5 kW-hr/pound, down from 6 kW-hr/pound in the most efficient Hall's cells (220-224).

Direct reduction (DR) that produces an aluminum and silicon alloy is being studied by Alcoa in a small pilot reactor with partial funding by the U.S. Department of Energy. Commercial scale demonstration may occur in 1990 after formidable technical obstacles are overcome (224).

Technology to produce aluminum metal and chemicals from kaolin via alumina and aluminum chloride will be the joint development of Pullman Kellogg and Toth Aluminum Corporation. Success could lessen U.S. dependence on imported bauxite (225, 226).

Kaiser Aluminum will install 10 prototype aluminum reduction cells that will use in-house "prebake" technology to effect significant improvements in the plants energy efficiency and work environment (215).

Oak Ridge National Laboratory is evaluating a commercial sized plant to process 1 million tons/year of fly ash to recover 98% of the aluminum and over 90% of the other metals. This plant is based on the

Table X. Northwest aluminum producer power contract expiration dates (195)

	Smelter capacity (tons/year)	Expiration date
Alcoa, Vancouver, Washington	115,000	June 1978
Wenatchee, Washington	205,000	June 1987
Anaconda, Columbia Falls, Montana	180,000	Dec. 1986
Intalco, Ferndale, Washington	265,000	Oct. 1984
Kaiser, Mead, Washington	220,000	Oct. 1986
Tacoma, Washington	81,000	Oct. 1986
Martin Marietta, The Dalles, Oregon	90,000	Feb. 1988
Goldendale, Oregon	120,000	Feb. 1988
Reynolds, Troutdale, Oregon	210,000	Dec. 1986
Longview, Washington	130,000	Dec. 1986
Total	1,616,000	

process called Calsinter that Oak Ridge National Laboratory developed (227-229).

New aluminum structural materials made from aluminum and silicon carbide whiskers are being tested by Lockheed Georgia Company for application in aircraft structures.

Alcan Aluminum Corporation's new super plastic aluminum alloy, containing zinc and calcium, offers lightness, strength, and corrosion resistance and has potential in limited production vehicles. A thermoforming process using compressed air can be used to form complex shapes, allowing more economical production than traditional stamping techniques (231, 232).

Free world primary aluminum production increased to 13.2 million short tons in 1979, an increase of 409,000 short tons. Changes in the free world primary aluminum capacity in 1979 are shown in Table XI.

Australia plans to become a major aluminum exporter by the mid '80's. Five projects are expected to add 585,500 metric tons/year to the existing 280,000 metric tons/year.

Domestic production of bauxite was estimated at 1.7 million metric tons in 1979, the same level as 1978. Jamaica, Guinea, and Surinam remain the principal sources of bauxite. Imports of dried and calcined bauxite declined slightly in 1979, totaling approximately 14 million tons. Imports of alumina increased, reaching a record level of 4.1 million metric tons of which three fourths came from Australia (177).

Alumina capacity of the free world rose to 34,436,000 short tons/year, up 1.9%. Alumina production rose 4.1% to 29.4 million short tons in 1979. Free world production of bauxite was 89.9 million short tons, an increase of approximately 10 million short tons (233).

Development of non-bauxite routes to aluminum originally designed to reduce the U.S. dependence on imported bauxite have stalled, due to changes in the IBA, International Bauxite Association, that has resulted in a brighter future for the bauxite supply picture. The U.S. produces about one-third of the world's aluminum but imports more than 90% of the raw materials. Originally, ten domestic alumina consumers and the U.S. Bureau of Mines funded a program to evaluate a hydrochloric acid/clay process. Now participation has dwindled to four producers and the pilot plant costing 52 million cannot be built due to the level of cost participation necessary by the remaining few producers (234, 235).

Beryllium.—Production and consumption of beryllium ores in the United States in 1979 were essentially unchanged from that in 1978. In fact, there has been no significant growth in this industry over the last several years. There are two major beryllium ores. (i) Bertrandite, which is produced in Mallard County, Utah

by Brush-Wellmann, Incorporated. Future demand for this ore is expected to increase in light of the announced expansion in the extraction of beryllium from bertrandite by a major U.S. consumer of beryllium metal. (ii) Beryl, approximately 80% of which was imported from Brazil and Argentina. The average value of the imported beryl in 1979 was \$574/ton (236).

Beryllium metal is used in the aerospace industry because of its high strength and rigidity yet light weight, and in the nuclear industry, where both low thermal-neutron absorption and high neutron-scatter cross section are required. However, in the free world, a more important end-use for this metal is in the production of beryllium-copper alloys; the addition of approximately 4% beryllium significantly improving the strength, as well as the fatigue and corrosion resistance of the copper. The volatility of the copper market in 1979 led to a new pricing system for beryllium-copper alloys being introduced by Kawecki Berylco Industries during the fourth quarter. This company also increased the base price of beryllium-copper products in the fourth quarter, so that, effective January 1980 the price of strip (number 25) will be \$5.54/lb; of bar, rod and wire (number 25) will be \$5.80/lb; and the master alloy will be \$90/lb. It was also stated that size extras and "adders" for special treatment, such as mill hardening and cadmium plating, have been adjusted in accordance with the cost content of specific operations (237).

The carcinogenic properties of beryllium and beryllium compounds led to the introduction of standards by OSHA that the industry maintained were impossible to achieve economically. Additional studies and commentary were initiated during 1977-1978, the results of which were expected to support the Government's position, but no reports have been published in 1979 (238).

Although not necessarily related to the environmental regulations, Kawecki Berylco Industries (a wholly owned subsidiary of Cabot Corporation and one of only two producers of beryllium in the free world) announced that it will phase out production of the metal. It was stressed that the change in business direction is not expected to affect the production of beryllium ores (239).

As of November 30, 1979, the Government stockpile inventories were as follows:

Beryl (11% BeO equivalent)	17,987 short tons
Be/Cu master alloy (~4% Be)	7,387 short tons
Beryllium metal	229 short tons

Chromium.—Domestic demand for chromium was strong in 1979, primarily due to a high level of stainless steel output. Domestic consumption of chromite increased 19%, totaling 1.2 million tons, with the major increase occurring in the metallurgical industry:

	1978	1979
Metallurgical	53%	61%
Refractory	23%	18%
Chemical	24%	21%

Consumption of chromium alloys increased almost 5% to nearly 526,000 tons (240, 241).

Domestic producers of chromium alloys exceeded the record year of 1974, producing about 280,000 tons of chromium alloys. Chromium alloy imports were expected to substantially decrease from 1978 levels. The Republic of South Africa continued to be the leading supplier, accounting for 66% of the imports. (240).

Published year-end chromite prices were close to year-end 1978. South African high-iron chromite remained at \$54-58/metric ton, high chromium. Turkish chromite increased \$5 to \$110 per long ton, and the price of Russian chromite was suspended. Prices for chromium alloys fluctuated as shown in Table XII.

Table XI. Additions to free world primary aluminum reduction capacity in 1979 (233)

Country	Company	Amount (short tons/ year)
U.S.	Anaconda	60,000
Brazil	Pocos de Caldos	33,000
	Aluminas	16,000
Brazil	Cia Brasileira de Alumínio (CBA)	30,000
Venezuela	Industria Venezolana de Aluminio SA	235,000
France	Pechiney Ugine Kuhlmann	25,000
Spain	Aluminio Espanol	150,000
South Africa	Alusaf	6,000
Japan	Closed a total of	75,000
Bahrain	Alba	5,000
Dubai	—	15,000
India	Bharat Aluminum (Balco)	25,000
Australia	Alcan Australia	50,000
	Total	725,000

Table XII. Chromium alloy pricing during 1979
(Cents per pound of chromium)

	Beginning	End
Ferrochromium silicon	29.3-29.5*	43-44.5*
Low Carbon ferrochromium	74	95
Imported 50-55% charge chromium	40-44	43-44.5
Producer 50-55% charge chromium	43-44	46-49
Electrolytic chromium metal	299	350

* Units—cents/pound of alloy.

The United States removed economic sanctions against Southern Rhodesia in mid-December 1979, allowing resumption of the import of chromium materials (240).

Boycott action by the International Longshoremen's Association against USSR vessels, in protest of the Afghanistan invasion by the Soviets, could affect the U.S. ferrochrome industry in the second half of 1980. Inventories of chromite, estimated to be 500,000 tons, potentially a years supply, are held by U.S. ferroalloyers. This situation could shift the use of chromite ore from high grade to low grade, increasing the imports from South Africa. A total and sustained curtailment of Soviet chrome imports will almost certainly be translated into higher prices. U.S. companies produce about one-half of the U.S. stainless steel industry requirements (242).

PPG and Harrison & Cranfield, a United Kingdom based company, agreed in principle for the sale of PPG's chrome chemicals business for around \$15-20 million (243, 244).

Airco sold its ferroalloy operations in Niagara Falls, New York, and Calvert City, New York, to Satra Corporation; its operations in Charleston, South Carolina, to Macalloy Corporation; and its operations in Sweden to Vargon Alloy AB (245, 246).

A platinum-chrome mine may be developed by Texasgulf Incorporated, based on a new process developed for Foster Wheeler Corporation by Tetronics Research and Development in the United Kingdom. The plasma process produces a temperature of 2000°C, achieving a fine melt and facilitates recovery (247).

A process for regeneration and recycle of spent chromium solutions produced from plating and finishing printed circuit boards, and other surface treatment operations, has been developed by scientists at the Bureau of Mines, Rolla Metallurgy Research Center. The process utilizes an electrolytic cell with Nafion® 427 membrane to oxidize the chromium in the anode compartment, while other metal ions migrate to the cathode compartment. Energy use is 3-4 kW-hr/pound of regenerated etchant (248).

Copper.—The major copper producing and consuming countries, including the United States, held three meetings in 1979 under the auspices of the United Nations Conference on Trade and Development (UNCTAD). The primary objectives of the conference were to continue to examine the causes of market instability and to consider possible solutions to the problem. Special attention was directed to the feasibility and desirability of using buffer stocks to stabilize prices. Further meetings are expected in 1980 (249).

The significant improvement in the copper industry shown in 1977 and 1978, after several years of a depressed market and oversupply of the metal, was maintained in 1979. The consumption of refined copper in the United States increased again (~1%) to 2.2 million tons, approximately equal to the record high level realized in 1973 (249).

Production of copper from mines in the United States was estimated to be 1.57 million short tons, showing an increase of 5% over 1978 production. The rapid escalation in the price of copper in the market place during 1979, resulted in a substantial increase

(~45%) in the value of the copper produced, its being estimated at \$2.9 billion. This improved outlook for marketing copper and the increased value of the metal prompted the reopening of several mines that were closed following the slump in demand in 1975. Principal states for the production of copper were Arizona (65%), Utah (13%) and New Mexico (12%).

The average estimated price for refined copper in 1979 on the London Metal Exchange (LME) was 92 cents/pound, showing approximately a 50% increase relative to 1978 prices. Producer prices in the United States for refined copper increased similarly; the average price in 1979 being 93 cents/pound (249).

A comprehensive study, sponsored by the United Nations, has concluded that the free world countries must increase their capacity to produce copper metal to meet the demand projected through 1990. The analysis predicted that the consumption of refined copper will grow at approximately 4% per year over the fifteen year period 1977-1992. (Although the increase in consumption was only approximately 1% in 1979, the combined increase over 1978 and 1979 agrees with this prediction.) This forecast, when translated into the required mine capacity, projected a cost of \$46.5 billion (1977 prices) to expand the copper capacity in the free world (249-251).

Kennecott Copper Corporation has announced plans to expand and upgrade its mining properties over the next five years at an estimated cost of approximately \$700 million. In particular, Kennecott intends to extensively improve the Chino Mines Division in New Mexico, to make the mine "one of the lowest-cost copper properties in the United States." The introduction of new concentrator facilities at the Utah Copper Division will cost about \$300 million, and a project for low-cost recovery of copper concentrates from existing tailings ponds is also planned at the Nevada Mines Division (252).

Kaiser Engineers Incorporated has been awarded a contract by Asarco Incorporated (New York) to provide engineering and procurement services for a \$50 million plant to concentrate copper to be built near Troy, Montana. This unit will be adjacent to a new underground mine being developed by Asarco and will produce approximately 60,000 tons of copper per year from copper sulfide ore. Production is scheduled to begin in mid-1981 (253).

Texasgulf plans to construct a copper smelter and refinery in Kidd Creek, Ontario. The production of copper at the new plant is estimated to be 65,000 tons/year and the projected cost of construction is \$200 million (254).

It has been reported that Israel Chemicals will reactivate the Timna Copper mines near Eilat and build a plant to produce copper salts and manganese metal on-site. The mines were closed about three years ago following the decline in the world markets for copper (255).

Acceleration of the development of the vast Duluth Gabbro mineral lode in Minnesota is being seriously considered by several of the mining companies, in particular Amax Incorporated, the world's largest producer of nonferrous metals. The mineral lode is regarded as a future source of copper, cobalt, and nickel, which will become economic when richer ores worldwide have been exhausted. Amax Incorporated estimates that the vein of copper-nickel sulfides is worth \$50 billion (1979 prices) and would support mining for 50 years, increasing the U.S. copper reserves by 25%. However, the deposits lie in a region that is today perhaps the most actively protected environmentally. The chief concerns of the environmental lobby are: (i) that toxic metals from mine waste will be leached into the water table and the lakes of the Boundary Waters Canoe Area, and; (ii) the pollution associated with smelting, i.e., the production of sulfur gases and, therefore, "acid rain." An extensive study of the en-

vironmental and economic impacts of mining the Duluth Gabbro mineral lode was completed in September 1979 and the State legislature is presently conducting hearings upon the results (256).

Total spending by the U.S. copper industry in order to meet environmental, safety, and health regulations by 1987 will be \$3.5 billion (1974 dollars) according to a comprehensive survey released by the Commerce Department in April. The report also highlighted several "probable shutdowns" of copper smelting facilities as a result of the inability of the plants to economically meet future environmental standards. In this respect, the copper industry appears to be one of the hardest-hit of the mineral industries. It is evident that the application of new technology and large capital investments will be required to either modify existing pyrometallurgical practices or adopt new chemical processing techniques (257, 258).

On October 30, the Federal Trade Commission amended the consent order negotiated with Atlantic Richfield Company (ARCO) in February, deleting provisions that brought sharp protests from leading U.S. copper producers, especially Asarco Inc. The consent order requires ARCO to divest itself of certain copper properties acquired in 1976 in a merger with Anaconda Company, but: (i) prohibits purchase by any company with more than 10% of U.S. copper mine production (eliminating Kennecott, Phelps Dodge, and Newmont Mining); (ii) stipulates that companies with 5-10% of the market must seek FTC approval before bidding on any Anaconda properties (which applies to Asarco, Duval, and Cyprus Mines); (iii) requires that the four biggest integrated copper producers seek prior FTC approval of any joint ventures (which affects Asarco, Kennecott, Phelps Dodge, and Newmont Mining (256)).

An electrolytic process utilizing a fluidized particle-bed has been developed by Akzo Zout Chemie (Netherlands) and is applicable to the removal of copper from the waste streams from vinyl chloride monomer plants. The metal is deposited onto cathodically charged particles, which then sink and are discharged from the cell. Concentrations of metal particles in wastewater streams can be reduced from 100 to 0.1 ppm. The first commercial unit using this process has been in operation for several months at an Enka plant in Wuppertal, West Germany (259, 260).

The recovery of copper metal from industrial waste streams has been the subject of considerable research and development. Several new processes are claimed to show promise in both laboratory and pilot-plant trials, e.g., the use of ion exchange resins and leaching with solutions containing chloride ions (261-263).

A new metal electrowinning process, involving the oxidation of a slurry of coal rather than water as the anodic process, is claimed to significantly reduce the power consumption for the recovery process. Electrowinning is presently an important source of chromium, cobalt, nickel, copper, zinc, and cadmium in the United States. In laboratory experiments the electrodeposition of copper in this new cell required approximately 66% less electrical power than the conventional electrodeposition process (264).

Lithium.—World wide lithium chemical consumption increased 6% over that of 1978, with the largest increases occurring in Western Europe and South America.

No new producers of lithium chemicals or ores emerged in 1979 (265).

Lithium Corporation of America, a subsidiary of Gulf Resources and Chemical Corporation, began construction of a new plant in the United Kingdom, near Liverpool, to produce an alkyl lithium catalyst, important in production of high performance synthetic rubber products for European markets. Initial capacity

Estimated 1979 world consumption
of lithium metal and chemicals
(Tons Li₂CO₃ equivalent)

North America	12,500
Western Europe	5,500
Japan	2,350
South America	1,900
Other Countries	3,000
TOTAL	25,250
USSR (est.)	4,000-6,000

of 200,000 pounds/year is expected to start up in late 1980 (265-267).

The production capacity of the domestic producers is estimated to be (265):

	Tons LiCO ₃ equivalent		
	1979	1980	1981
Lithium Corp. of America			
Bessemer City,			
North Carolina	14,000	18,000	22,500
Foote Mineral Company			
Silver Peak, Nev.	8,000	8,000	8,000
Kings Mtn.,			
North Carolina	7,000	7,000	7,000
	15,000	15,000	15,000
Estimated total U.S. capacity	29,000	33,000	37,500

World production capacity of lithium mineral is estimated to be 10,200 short tons of contained lithium in 1979 and is forecast to be 17,400 short tons by 1985 (268).

Foote Mineral Company has completed the feasibility study for a 6000 tons/year lithium carbonate plant from brine in Northern Chile (265).

Tantalum Mining Corporation jointly owned by the Manitoba government, 25%, Hudson Bay Mining Company, 37.5%, and Kawecky Berylco Industries, 37.5%, is conducting a feasibility study for a 7,500 to 10,000 tons/year lithium carbonate plant at Bernic Lake, Manitoba (265).

Lithium chemical prices increased approximately 11% on October 1, 1979. New schedule prices are:

Technical grade lithium carbonate	\$1.15 per/pound
Lithium carbonate pellets	\$1.19
Lithium hydroxide monohydrate	\$1.53
Anhydrous technical lithium chloride	\$1.85 (269, 270)

Lithium metal prices were \$15.20-\$15.65/pound for ingot, and \$24.80-\$25.25/pound for rod (271).

Demand for lithium chemicals and metal is forecast to have a probable average annual world growth rate of 6.2% through the year 2000. New uses not yet commercialized or not yet discovered are expected to approximate one quarter of the total end use of lithium by the year 2000. Probable demand for lithium chemicals and metal in the U.S. is estimated to be 13,600 short tons of contained lithium by the year 2000. End uses are projected to be

Aluminum production	37%
Ceramics and glass	11
Lubricants	7
Other	15
New uses	30 (272)

Lithium batteries can deliver 1.5-10 times the power of conventional batteries of the same volume, and 3-5 times those of the same weight. Virtually all pacemakers, over 250,000 installed in the last 7 years, are powered by lithium batteries (273).

Magnesium.—Based upon data collected by the International Magnesium Association, the domestic production of primary magnesium metal was estimated to be 160,000 short tons for the period from January to September in 1979. Although data for the total production of magnesium metal are not yet available, it is clear that it will substantially exceed that produced in 1977 and 1978. Exports of the primary metal, valued at \$98.9 million, were actually more than ten times the amount imported, which also represents a significant increase to the metal industry (274, 275).

Consumption of the metal in North America is estimated to be 115,000 short tons for the year. At the end of 1979, the quoted prices were as follows.

Magnesium ingots	\$1.09/pound	
Magnesium die-casting alloy	\$1.07/pound	(274)

In contrast to the mediocre performance from 1973 to 1977, when the annual consumption of magnesium appeared to reflect the worldwide economic slowdown, there has been a sharp increase in the use of magnesium in 1978 and 1979. It has been projected that by 1985 an annual growth rate of approximately 5% will be achieved by the industry. Furthermore, with the continued increase in the production of magnesium in North America through 1985, the industry is confident that supply will continue to significantly exceed this increased demand (276-278).

The major producers of magnesium metal in the United States are: NL Industries, Incorporated (Rowley, Utah), Dow Chemical Company (Freeport, Texas); and Northwest Alloys, Incorporated (Addy, Washington). Despite the optimistic forecast for magnesium, NL Industries announced plans to sell a magnesium facility at Salt Lake City. This plant, which produces approximately 15% of the total U.S. magnesium, has operated at a loss since it was opened in 1972. It is expected that the plant will continue to operate at least until the end of 1980 (279).

The largest single application for magnesium is in the production of an aluminum-magnesium alloy, essentially half of the total production being used in this way. Other important markets for the metal are die-casting (~16% of production) and chemical uses, such as Grignard reagents, production of pyrotechnics and antiknock additives for leaded gasoline (~15% of production).

It is projected that a major increase in the use of magnesium will be for the desulfurization of iron. Apparently anticipating this, Dow Chemical Company has authorized the construction of a 20 million pounds/year plant for the production of magnesium metallurgical granules, due to be "on-stream" in mid-1980 at Freeport, Texas. The product is specifically for use in the blast furnaces, offering several advantages over calcium carbide or other forms of magnesium in terms of energy savings, improved productivity and better control of sulfur (278-280).

du Pont has recently announced the development of an aluminum-magnesium composite, incorporating 55% alumina fiber, which has structural properties superior to steel. The reinforcement is a continuous web of polycrystalline α -alumina fiber and outlets in both the aerospace and automobile industries are foreseen (281).

Certainly the demand for fuel-efficient automobiles is likely to be an important factor in the growth of the magnesium industry. Until recently the high price of magnesium relative to aluminum, has excluded it from being considered as a replacement for zinc and iron in automobile castings. However, recent projections indicate that the price of aluminum will approach that of magnesium, making the latter metal economically attractive to the auto industry (276, 277, 282).

Ford Motor Company has pioneered the use of magnesium in automobiles, already having used the metal to cover side-mirrors for some 1980 models. Two additional components fabricated from magnesium will be introduced later this year (1980). Larger components are presently being considered, since the auto industry has now gained experience with this highly flammable metal.

In order to gain full advantage of any competitive edge it is essential that the cost of production of magnesium be reduced. Thus, Dow Chemical Company is developing a new process that is claimed to reduce overall energy consumption by 35%. More economical methods of fabrication are being explored by the various companies, e.g., Black and Decker Manufacturing Company. It is also recognized that safe working practices, particularly in any large scale manufacturing process, are of primary importance (282).

Manganese.—No production or shipment of manganese ore containing 35% or more manganese occurred in the U.S. during 1979. Lower grade manganese ores continue to be produced in Minnesota, New Mexico, and South Carolina (283).

Manganese ore consumption increased but was less than one quarter of that imported in 1970. Imported ferromanganese was brought in to make up the deficit. Domestic production of ferromanganese increased in 1979. Major shifts in ownership of U.S. ferromanganese production occurred in 1979 as a result of sale of the 40,000 metric tons/year plant of Circo, Incorporated at Mobile, Alabama, to Mexico's Cia. Mineia Autlan. Aircor's Calvert City, Kentucky manganese ferroalloy plant was sold to Germany's SKW Alloys, Incorporated, a wholly owned subsidiary of SKW Trostberg, AG. Roane Limited, a subsidiary of South African Manganese Amcor Limited, (SAMANCOR) purchased Engelhard Mineral and Chemicals Roane Electric Furnace Company at Rockwood, Tennessee, which produces ferromanganese and silicomanganese. Preliminary ruling by the U.S. Treasury Department against Brazil and Spain for subsidizing ferromanganese and silicomanganese exports to the U.S. would allow countervailing duties to be imposed (283, 284).

Prices for metallurgical ore containing a minimum of 48% manganese were \$1.36 to 1.42/long ton unit (ltu) on contract during 1979. Annual contract negotiations for 1980 have suppliers asking \$1.80 to \$1.83/ltu, an increase of 29 to 33%, primarily due to rapidly escalating ocean freight costs (284, 285).

Union Carbide Corporation expanded and modernized its Marietta, Ohio, electrolytic manganese metal facility, increasing capacity approximately 10-15% to 10,000 tons/year (286).

Electrolytic manganese metal prices were increased 4 cents/pound to 62¢, up 7% during the last quarter of 1979 by U.S. producers, Union Carbide, Foote Mineral, and Newmont. The increases were expected by the industry due to rising energy costs (284, 287-289).

U.S. produced high carbon ferromanganese (78% Mn) were \$440/long ton (lt) in early 1979, moving upward in stages to \$490/lt by May. Union Carbide increased prices to \$530/lt on November 1. Imported alloys of the same grade were quoted at \$375-420 at the beginning of the year and went through a high of \$450-490 in the summer and declined to \$440 to \$450 during November. LeNickel Incorporated, sales agent for SAMANCOR, announced effective December 31, a price of \$485/long ton (283,290).

World manganese production is steady at 23-25 million metric tons/year. The USSR accounts for about 40% of the world total. Eight countries supply 95% of the world total (284).

Total dependence of the U.S. on imported ore and ferromanganese have led to controversy over world manganese ore reserves. Fran R. Dykstra, who testified before a Senate subcommittee, projected supply

and demand crossover in manganese resulting in a world pinch on manganese in the late 80's. He disagrees with the Bureau of Mines estimation of Russian reserves. He urged passage of legislation to enable the U.S. to begin harvesting sea floor manganese nodules (291).

Manganese ore reserves are estimated to be:

Manganese ore reserves

	(million short tons contained Mn)
USSR	1,350
South Africa	1,680
Australia	175
Gabon	100
Mexico	15
Brazil	70
China	34
Other	176
Total	3,600 (284)

The Bureau of Mines issued Report of Investigations No. 8330, "Catalytic Properties of Natural and Rare-Earth-Promoted Manganese Nodules." After study of small samples from both the Atlantic and Pacific Oceans, it was concluded that the deep-sea nodules have sufficient potential as oxidation catalysts for control of air pollution to warrant more extensive investigation after commercial production of the nodules has begun. Report of Investigations No. 8383, "Properties of Manganese-Copper Alloys Prepared From Metal Powders," reported on Bureau research, demonstrating that high-damping manganese-copper alloys can be made by powder metallurgy techniques (286).

The U.N. Law of the Sea conference is still stumbling over taxation questions related to mining manganese nodules. Mining tests conducted by Ocean Minerals Company (OM Co.) which used the Glomar Explorer have, it is believed, gone to lesser scale efforts to mine these nickel cobalt manganese nodules from the ocean floor. The other four consortiums have maintained a low level of activity in 1979. Expectations of 1990 nodule mining operations are fading. Japan has launched a new \$19 million nodule exploration vessel and the 35 company Deep Ocean Mining Associate expects nodule mining by 1990 (284).

The USEPA lifted its ban temporarily on manganese gasoline additive, MMT, to stretch gasoline supplies (284).

Nickel.—Production of the only domestic nickel mine was about 14,000 tons, a slight decline from 1978, while primary nickel consumption was 201,000 tons, an increase of 11%. Total nickel demand was 271,000 tons, the third highest year on record. Labor strikes in Canada and curtailed production caused producer stocks to decline during the first half of the year (292).

Smelter production, with the ore supplied by the single domestic mine in Oregon, totaled 11,000 tons of nickel in ferronickel, and about 1,000 tons were recovered as by-product from primary copper operations (292).

AMAX Nickel, Incorporated's facility at Port Nickel, Louisiana, produced 25,000 tons of nickel. An hourly work stoppage which continued for four months impaired production (292-294).

Nickel was consumed in three principal primary forms showing minor change from 1978:

Unwrought	68%
Ferronickel	21%
Nickel oxide	8%

Product line consumption of nickel varied slightly:

	1978	1979
Stainless and alloy steel	44%	47%
Nickel and copper base alloys	33	33
Electroplating	17	16
		(292, 295)

Nickel recovered from scrap increased in total tonnage in 1979 but remained at 17% of total demand (292).

Nickel inventories declined significantly below normal levels as revealed by Inco, the world's largest nickel producer:

	Year end
1977	89 million pounds
1978	141 million pounds
1979	341 million pounds
Normal level	120 million pounds

Most producers are operating at 60-70% of capacity and share Inco's light inventory situation.

List prices of \$2/pound for melting nickel were regained in February 1979 and successive, almost monthly, increases raised the price \$3.20 by years end. Producer nickel price profile is shown in Table XIII.

OPEC oil price hikes of \$8 per barrel may further increase producer prices 15-50 cents/pound, especially for energy intensive lateritic nickel which makes up half the world supply (298).

World nickel production rose 12% above 1978 levels to 1.04 billion pounds. Inventories dropped with finished nickel production for 1979 corresponding to approximately 70% of capacity utilization. 1980 nickel production is expected to increase to about 1.2 billion pounds with an increase in producer inventories. Over the long term, through 1985, production is expected to rise to about 80% capacity utilization (299).

Current free world nickel industry capacity is estimated to be 1.6 billion pounds per year, growing to 2 billion pounds by 1985. Free world consumption of 1.3 billion pounds in 1979 is expected to reach 1.58-1.65 billion pounds in 1985. Costs of adding nickel capacity have tripled since 1970, from \$3.00 to \$11.00/pound. Increased oil prices have added a \$1/pound to the cost of producing nickel from lateritic ores since 1973. These escalating costs will put upward pressure on nickel prices over the next decade (300).

Table XIII. Producer nickel price profile (297)

Inco (eff. Dec. 4)	
Cathode (1x1, 2x2), S-rounds	\$3.25
Cathode (4x4, up), pellets, 123 powder	\$3.20
Sinter 75, Incomet, utility shot/pig	\$3.11
	(Europe) \$3.08
Falconbridge (eff. Dec. 10)	
Cathode (1x1, 2x2), crowns	\$3.25
Cathode (4x4, up)	\$3.20
Ferronickel (37% nickel)	\$2.19
SLN (eff. Dec. 3)	
Electroplating cathode	\$3.25
HP cathode	\$3.20
FN-1 ferronickel	\$3.29
FN-3 ferronickel	\$3.26
FN-C ferronickel	\$3.24
SLN 25 granules	\$3.23
FN-4 ferronickel	\$3.22
Western Mining (eff. Dec. 6)	
Briquettes	\$3.20
Steelmaking briquettes, steelmaking powder	\$3.11
Hanna (eff. Dec. 11)	
Ferronickel (50% nickel)	\$3.15
Sherritt Gordon (eff. Dec. 5)	
Briquettes, S-grade powder	\$3.20
Larco (eff. Dec. 12)	
Ferronickel (25% nickel)	\$3.22
Amax (eff. June 11)	
Briquettes	\$3.00
Nickel corrugates	\$2.97
Steelmaking powder	\$2.93

The London Metal Exchange began trading pure nickel class I material on contracts for six (6) metric tons, 13,228 pounds, in April. During the last half of the year 2,500 tons of nickel reached consumers at 25-45 cents/pound below producer prices (292, 301).

General Motors claims to have cleared a major technological obstacle to the introduction of electric powered vehicles in the mid-1980's with its zinc-nickel oxide battery developments. Energy storage of 2-2.5 times the level of lead acid batteries is claimed. Production of 100,000 Electrovettes (converted Chevrolet Chevette) would consume 1.5% of the nickel industries current annual production (302-304).

The Department of Energy has said that at least 200 of the 700 demonstration vehicles to be purchased in 1980 will be powered by nickel-zinc or nickel-iron batteries (305).

AMAX continues with the evaluation of the Duluth gabbro copper-nickel deposits. A multiagency report concluded that the large resource could be mined with proper precautions to protect the environment (292).

Work continues on a demonstration plant evaluation to extract cobalt and nickel from western laterites using a new hydrometallurgical process (292).

A Japanese consortium announced construction of an ocean survey vessel, scheduled for operation in July 1980, which is specifically equipped to survey for manganese nodules in the promising area south-east of Hawaii (292).

Sodium.—No references to metallic sodium were found for the year 1979.

Titanium.—With respect to both production and consumption of titanium, 1979 was a strong year and the trends established in 1977 and 1978 were maintained (306-308).

The strong market for titanium metal results primarily from the demands of the aircraft industry and the purchase of airplanes, such as the Boeing 747 and 767, Lockheed L1011, and McDonnell-Douglas DC10, with relatively high titanium content. It is predicted that the market for titanium will continue to grow, since aging fleets of jetliners need to be replaced by planes having lower fuel consumption, smaller engines, and lower noise levels (307).

Boeing Commercial Airplane Company is considering the use of trans-beta-titanium alloy in the construction of new 767 airliners. Studies carried out at the Boeing Central Technical Center indicate that the alloy is superior to other titanium alloys, offering significant weight savings and therefore reduced costs. The alloy is a proprietary interest of Timet Incorporated, one of four companies engaged to fabricate parts from the material. Other companies involved are Alcoa, Ladish Company, and Wyman-Gordon (309).

The new Pratt and Whitney jet engine JT8D-209, utilizing titanium "in new ways," will be incorporated in the McDonnell-Douglas DC-9 Super 80 twin jet. The engine is claimed to use approximately 10% less fuel than the older JT8D engines. Furthermore, noise levels are significantly reduced as a consequence of the use of an alloy, Ti-6Al-2Sn-4Zr-Mo-Si, developed by Timet Incorporated and Pratt and Whitney specifically to withstand the high temperatures of the jet exhaust (310).

According to the Bureau of Mines the production of titanium ingots remained stable over the four quarters of 1979 and totaled 37,000 short tons, an increase of 18% over 1978 production levels. Although the total production of titanium ingot (plus approximately 400 short tons that were imported) was sufficient to meet the market demand both at home and abroad, there was a small decrease in the industry's stockpile. Similar trends were shown in the production and consumption of titanium sponge. Domestic production increased 22% relative to that in 1978

and there was a significant increase in imports (from 1500 short tons in 1978 to 2500 short tons), primarily from Japan (306, 311).

The limited supplies of titanium throughout 1979 led to controversy between purchasers (primarily the aircraft industry) and the mill suppliers over conditions of long term contracts. Titanium Metals Corporation of America (TIMET) and RMI Company of Niles, Ohio, began to demand contracts for supply of titanium over the next three years with substantial penalties for cancellation (312).

This continuing shortage of titanium has led producers, both in the United States and abroad, to increase production capacity. For example, Howmet Turbine Components Corporation announced the purchase of a titanium ingot plant at Reno, formerly operated by a division of Whittaker Corporation, but idle since 1976. The facility contains three vacuum arc melting furnaces, with an annual capacity of approximately 2000 short tons of ingot, according to Howmet. The Reno plant, which is the second ingot facility for the company, is expected to begin production early in 1980 (313).

Shotton, Wales, has been selected as the site for the construction of a \$55 million plant to produce approximately 5500 tons of titanium metal granules per year. The plant will be operated as a joint venture of Britain's National Enterprise Board, IMI Limited and government-owned Rolls-Royce Limited (314, 315).

Considerable emphasis is also being placed on increased production of titanium sponge. New technology and expansion plans already underway, announced or under consideration, could raise the total annual capacity in the United States to 34,000 short tons by 1985. The current U.S. capacity for the production of titanium sponge is shown below, together with the process and producer (306, 307).

Company	Current capacity	Process
Timet Incorporated	14,000 short tons	Kroll
RMI Company	7,500 short tons	Hunter
Oregon Metallurgical Corporation	2,500 short tons	Kroll
Totals	24,000 short tons	

Dow Chemical Company and Howmet Turbine Components Corporation (a subsidiary of Pechiney Ugine Kuhlmann Incorporated) have announced a joint venture agreement to commercialize an electrolytic process for the production of titanium sponge. The process is based upon work by the Bureau of Mines in the mid-1960's, which has been subsequently developed by Dow and by Homet. Electrolytic reduction of titanium tetrachloride yields a titanium sponge which can be melted to give the pure metal or used to make titanium alloys. If successful, it is anticipated that a production-scale operation will be "on-stream" by the mid 1980's. At present, virtually all titanium is produced by either the Kroll process (reduction of $TiCl_4$ using magnesium) or the Hunter process (the reducing agent being sodium metal). According to Dow, the energy requirements for the electrolytic process are approximately one-half those of the conventional processes. Furthermore, the titanium product is of a higher quality with respect to consistency of both size and purity (316-318).

RMI Company is expanding its main plant in Niles, Ohio, to increase the output of mill products approximately 25%. Earlier in the year RMI had announced a \$3.5 million expansion of the company's sponge facility at Ashtabula, Ohio. Both expansions are scheduled for completion by the third quarter of 1980 (318, 319).

Cometals Incorporated, has agreed to import titanium sponge from China in amount described as "significant" relative to that imported from Japan, the Soviet Union and the United Kingdom (320).

Production of titanium ores in the United States is summarized in tabular form below (306):

Ore	Production (short tons/year)
Ilmenite	550,000, a decrease of 7% from 1978 production levels
Rutile	No domestic production

The heavy minerals operation at Boulougne in Florida, which produced a bulk titanium concentrate containing rutile, was closed down in November because of depleted reserves. The only U.S. plant producing synthetic rutile, located in Alabama, is expected to resume production early in 1980 (306).

Imports of ilmenite, essentially all from Australia, was estimated to be 280,000 short tons, a decrease of approximately 9% from 1978. There was a substantial decrease (approximately 37%) in the amount of natural rutile imported in 1979, but in sharp contrast, a fourfold increase in the imports of the synthetic rutile. The major sources of the synthetic ore were Australia (69%) and Taiwan (21%) (306).

Sierra Rutile Limited, owned by subsidiaries of Bethlehem Steel Corporation (85%) and Nord Resources Corporation (15%), began to mine rutile in Sierra Leone from the Mogbwemo deposit, about 80 miles from Freetown. It is anticipated that in 1980 Sierra Rutile will ship 110,000 short tons of the ore (318).

Associated Minerals Consolidated, a subsidiary of Consolidate Goldfields of Australia, announced that it will expand the capacity of the plant at Capel (producing synthetic rutile) to 60,000 tons/year. It was also reported that the company, the world's largest producer of rutile, plans an eventual increase in total capacity to 120,000 tons/year (321).

Reports indicate that NL Industries will sell its subsidiary, Titanium Alloy Manufacturing Company Pty. Limited (Tamco) to Utah Mining Australia, Limited (321, 322).

The spot price of rutile at the year end was \$375-400 per short ton f.o.b. Atlantic and Great Lakes ports; the price f.o.b. Australia increased approximately 40% during the year to \$348-369 per short ton (306).

Zinc.—According to the Bureau of Mines, U.S. Department of the Interior, in 1979 the mine production of zinc in the United States was only 286,000 short tons, the lowest level since 1932 and a decrease of 14% from the production in 1978. Several prolonged strikes were largely responsible for the observed decrease in production. The year long strike at the Balmat-Edwards mine (St. Joe Zinc Company) was settled in July, but production for the remainder of the year was only 50% of capacity. Production at both the Azark Lead Company mine in Missouri and the New Market Mine (Asarco Incorporated) was interrupted by strikes, the latter mine having been reopened in January 1979. Workers at the Young mine in Tennessee struck in September and the mine has remained idle through the remainder of the year (323-325).

The Shullsburg mine in Wisconsin closed indefinitely due to problems meeting environmental regulations and the unfavorable conditions of the zinc market (326).

The production of approximately 540,000 tons of zinc metal in 1979 by U.S. primary and secondary smelters represents an increase of 22% over that of 1978. The new electrolytic plant in Tennessee, owned by Jersey Miniere Zinc Company, operated almost at capacity for the whole year, producing approximately 82,000 tons of zinc metal (323).

In November, St. Joe Zinc Company announced the closing of its electrothermic zinc smelting facilities in Monaca, Pennsylvania (capacity 200,000 tons/year). The increasing cost of energy, labor demands, and the large capital investments required to meet the environmental regulations, were cited as the primary reasons for the shutdown. It was stated that the joint venture of SNC/Dravo had been engaged by St. Joe Zinc Company to design a new electrolytic refinery to be built at one of several possible locations. In the meantime, St. Joe will meet customer demand for zinc slab with tolled metal produced from its zinc concentrates and with purchased metal (323, 327, 328).

Exxon Minerals Company, U.S.A. continued to explore the zinc-copper deposit at Crandon, Wisconsin. Furthermore, the company anticipated the start of an underground sampling program in 1980 at the properties in New Mexico, properties which have been estimated as a deposit of 7 million tons, grading 2% copper, 3% zinc, and recoverable quantities of silver and gold (323).

Cominco Limited announced plans for the immediate development of the "Polaris" zinc-lead ore deposit of Arvik Mines Limited. The cost of the development program is estimated at approximately \$150 million and the mine is expected to produce almost 190,000 short tons of zinc concentrate annually. Agreement has been reached with the Government of Canada with respect to the conditions under which the Polaris mine can be developed and production of the zinc concentrate (and lead concentrate) should begin early in 1982 (329).

A joint venture of Louisiana Land and Exploration Company and Superior Oil Company have reported that if technical and environmental studies are favorable the development of the Bald Mountain property in Maine could begin in 1984 (323).

A new study conducted by the Commerce Department has concluded that by the year 2000 minerals found in the deep ocean floor, including copper, cobalt, manganese, and zinc, will be critical not only to the industrial and economic strength of the United States, but also to its national security. This is perhaps made more significant by the recent discovery of massive deep-sea deposits of ore-grade zinc, copper, and iron sulfides by a team of French, American, and Mexican geologists. The discovery also confirms a geochemical theory that such deposits were formed when seawater rapidly cooled the lava (330-332).

Noranda Exploration Incorporated exercised its option to acquire an interest in the Ontario mine of Park City Ventures in Utah. The company announced plans to reopen this mine in 1980 (323).

The consumption of slab zinc in 1979 decreased 3% (relative to 1978) to approximately 1 million tons, apparently due to significantly decreased demand for zinc in die-casting, rolled zinc, and zinc oxide (323, 333).

Use	Consumption (tons/year)	% of total consumption
Galvanizing	411,000	45
Zinc-base alloys	282,000	31
Brass and bronze	139,000	15
Rolled zinc	22,000	2
Zinc oxide	36,000	4
Miscellaneous (includes batteries, zinc dust)	30,000	3

The demand for zinc in 1980 is expected to continue to decrease, particularly that for die-cast metal. However after 1980 the market is expected to strengthen the demand increasing at probably 2-3% per year for several years (334).

A new zinc alloy, ZA-12 (containing 12% aluminum) is claimed to have improved casting properties and can be used to replace bronze, cast-iron, and heat-treated aluminum. The alloy, developed by Pittsburgh Cast Products Incorporated, is approximately 30% lighter and stronger than either cast iron or bronze and offers significant savings in both materials and machine costs (335).

The average price of prime western grade zinc in 1979 was 37.4 cents/pound, an increase of approximately 20% relative to 1978 prices. On the Long Metal Exchange the average price was 33.2 cents/pound, maintaining the smaller difference between the European and U.S. prices observed late in 1978 (323, 336).

Imports of zinc in ore and concentrates were essentially unchanged from 1978 and major sources were again Peru, Bolivia, Mexico, and Honduras. It was noted that several of the countries supplying zinc to the United States are politically unstable and may pose a threat to future supply of the metal (323, 337).

In contrast, the major supplier of zinc metal to the United States is Canada, total imports in 1979 decreasing to 510,000 tons, 18% lower than in 1978 (323).

Confrontation between several U.S. producers of lead and zinc (St. Joe Minerals Corporation, New Jersey Zinc, Anaconda, Asarco Incorporated) and the Council on Wage and Price Stability (COWPS) occurred throughout 1979, following the announcement by the Council that unlike copper these metals were not exempt from the voluntary guidelines. Discussions led to the Council agreeing to consider special guidelines in which the U.S. prices for zinc and lead would be related to the world market prices on the London Metal Exchange (338, 339).

The Electrical Industry

The once-placid, investor-owned electric utility which produces 77% of all electrical power in the United States, finds itself caught in a spiral of uncertainties: the energy crisis, regulation, and inflation (340).

The slower growth in energy sales in recent years was initially regarded as a "short-term aberration" by executives of the utility companies and it is, of course, well known that the industry responds slowly to changes. Furthermore, stringent environmental regulations and inflation have made new construction appear prohibitively expensive. It was recently reported by the Edison Electric Institute that the average capital cost of a coal-fired plant has increased from \$144 per kilowatt hour (kW-hr) in 1970 to \$1096 kW-hr for a plant to come "on-stream" in 1987. For a nuclear power plant the comparable costs are \$165 and \$1861. Of necessity then many utilities are delaying and/or canceling new construction (340).

The cumulative woes of the electrical industry are exemplified by the present position of San Diego Gas and Electric Company. Faced with a projected growth of 5% per year in customer demand for electricity, the utility cannot afford to build any new capability. A major problem has been the rapid escalation in the cost of producing power, costs that have increased approximately 250% in the last five years, while increases in customer rates have been limited to only approximately 140% over the same time period. This has resulted in lower bond ratings, restrictions on the utilization of current debentures, and the inability to sell new stock. San Diego Gas and Electric Company has cancelled plans to upgrade a fossil-fired unit (projected cost \$60 million) and to construct a \$50 million 45 MW geothermal plant in Imperial Valley in California (340).

The Energy Crisis.—In a recent review of sources of energy available to the United States in the near

term (1985-2000), it was pointed out that the growth in production and sales of energy has diminished and will probably level off in the 1990's. The production of oil and gas in the U.S. peaked approximately seven years ago and it is claimed that there is no reasonable basis to justify predictions of increased yields. Estimates of undiscovered petroleum liquid resources in this country are presently placed at 100 billion barrels, and it is evident that the U.S. resources of conventional oil will be seriously depleted within 20-25 years (341-343).

Since the early predictions of expansion and growth the development of nuclear energy has suffered a series of setbacks and consequently diminished expectations. This has in part been due to environmental and sociological constraints, and it has become evident that nuclear power may not be regarded as the major future source of energy in the United States (341, 344).

According to the Bureau of Mines, recent estimates indicate that there are 437 billion tons of coal in deposits in the United States that can be mined under present economic conditions and using current technology. Furthermore, it is projected that coal will be available in increasing quantities, sufficient to meet increased demand for energy and allow transition to a society that is able to use energy more efficiently and/or alternative abundant sources such as solar and geothermal energy. Thus despite the present environmental and sociological constraints, coal is the only domestic energy resource capable of substantial expansion (341, 345).

Environmental regulations, health, and safety.—It has been estimated that in 1990 additional revenues amounting to 16% of the electric plant base costs would be required to meet federal air, water, and nuclear regulations. This is an indication that federal regulation itself represents "a massive industry" and that the cost of compliance is rapidly becoming prohibitively expensive (346).

To bring existing facilities up to the pollution control standards (effective January 1979), it was estimated that the total cost to the U.S. business was \$27.2 billion. The expenditures of two industries, the electric utilities and the petroleum industry, account for 44% of the cost of all planned pollution-control modifications. Also for most industries and businesses, modest increases are forecast in planned spending for antipollution measures over the next 3-5 years whereas for the electric utilities expenditures of \$4 billion have been projected (see Table XIV) (347).

According to the method chosen by Department of Energy for classification of power plants as "new" or "existing" under the Fuel Use Act (FUA), as of May 8, 1979 a new power plant was prohibited from burning oil or gas. An existing plant may continue to burn oil although conversion may be ordered in certain cases. In order to be classified as an "existing" plant a utility must indicate that it will suffer a "substantial financial penalty" or impairment of reliability if it is not. In response to many objections, the act was revised and the Economic Regulatory Administration

Table XIV. Expenditures for pollution control 1978, 1979 and 1982 (347)

Industry	Air pollution			Water pollution		
	1978	1979	1982	1978	1979	1982
Gas utilities	21	31	76	31	18	54
Aerospace	26	38	20	11	15	21
Rubber	76	50	69	9	10	16
Paper	135	249	211	136	184	164
Mining	231	231	243	113	171	97
Chemicals	211	287	280	281	292	458
Iron and steel	278	395	254	144	264	138
Petroleum	354	808	442	377	291	277
Electric utilities	1785	1883	1542	935	1032	2311

of the Department of Energy will now "take into consideration any financially related factor that is considered appropriate" (348).

The Tennessee Valley Authority (TVA) is now implementing a \$1 billion program to reduce air pollution at its coal-fired power plants. Thus TVA emerges as the costly pacesetter for many of the nation's utilities, and it is clear that the Environmental Protection Agency (EPA) intends to use the performance of TVA to push into line utilities that are not presently in compliance with the clean-air regulations. In a series of modifications that will be fully implemented by 1982 it is predicted that sulfur dioxide emission will be reduced 42% at ten TVA plants. It is also predicted that particulate emission at ten TVA plants will be reduced 22% (349).

A controversy involving Dow Chemical Company, the EPA, and the State of Michigan concerned the chemical company's innovative pollution control system at its Midland plant. The EPA has yet to approve the amendments introduced by the state of Michigan and is charging Dow with violation of the standards outlined in the Clean Air Act. Although some agreements were recently reached several major issues remain:

1. Can a company be forced to spend \$22 MM to switch fuels for boilers that will be obsolete in 3-4 years?

2. Can the EPA deny the State's amendments to the state implementation plan?

3. Is there sufficient flexibility in the Clean Air Act for the EPA to allow controls that meet the spirit, if not the letter, of the law?

Dow Chemical Company has also argued that conversion to total oil would consume an additional 7000 barrels/day and result in an additional \$22-25 MM outlay for fuel. (350).

For several years, officials of the State of Ohio have struggled to prevent imposition of sulfur dioxide emission standards on the electric utilities in their state. Recent air control plans outlined by the State were rejected in October of 1979, but at the same time the EPA has eased the requirements for the major utilities in Ohio. As a result many of the power plants will continue to burn high-sulfur coal without the addition of costly pollution-control equipment. A major winner in the confrontation was Cleveland Electric Illuminating Company, since the EPA agreed to fourfold relaxation in the emission limits for two large plants at Avon Lake and Eastlake. It was estimated that installation of scrubbers to meet the original standards would have cost approximately \$524 MM (351, 352).

The moratorium on new construction permits and operating licenses for nuclear plants imposed by the Nuclear Regulatory Commission has created considerable unhappiness in the electrical industry. It was pointed out that with today's high rates of inflation any delays were extremely costly. The announcement of the indefinite delay in licensing surprised TVA, which had planned to begin fuel loading at Sequoyah unit 1 in mid-November. Financial officials of the company estimated that the delay will cost \$10 MM per month and would cost residential customers an additional \$1.20 per month. Southern California Edison

Company is also concerned, pointing out that within the next 12 months 15 nuclear units, representing an aggregate capacity of 15,450 MW, will require operating licenses. Extended delays would be costly and would strain the summer capacity reserves, particularly in the southeast (353).

The chemical affinity of neoprene for PCB's, which has previously been a definite drawback, has been adapted to provide a system to remove PCB's from oil insulating fluids. Introduced by RTE Corporation as a disposable filter the neoprene "gravel" effectively reduces the levels of PCB in transformer fluids to less than 50 ppm (354).

It is reported that the investor-owned electrical utilities in the United States plan to spend \$413 MM on health and safety of employees, placing the utilities third among all U.S. industries surveyed by the McGraw-Hill Department of Economics. These expenditures represent 1.4% of total capital spending by the electric industry, slightly lower than the 1978 level of 1.8% (355).

The electrical industry has shown that significant effort is expended to make transmission rights-of-way (ROW) esthetically pleasing. A utility's vegetation manager plays a major role in developing ROW's that will be assets physically to the general public as well as functionally to the industry. In general, three distinct components contribute to the structural makeup of the vegetation. By evaluating these components on a variety of ROW's, sites can be created that blend harmoniously with their surroundings (356).

Power generation in the United States.—Sales of electrical energy increased only 2.85% in 1979, to a total of 2075 billion kilowatt-hours (kW-hr), significantly lower than forecast. A sharp decrease in the growth of sales of electrical power to residential users (see Table XV) probably reflects the surging inflation rate and the demand for national energy conservation. This is certainly supported by the decrease in the average use for residential power (Table XVI) from 8849 to 8820 kW-hr, only the second decrease in a decade. However, with the average rate for electrical power for the residential user escalating to 4.32 cents/kW-hr the average annual bill actually increased approximately \$25 in 1979. Data for commercial and industrial power are also shown in Table XVI (357, 358).

A survey released by the National Utilities Service Incorporated (New York) showed that over a period of fifteen months (January 1978 to March 1979) rate increases were moderate. The average rate increase for the nation's 24 largest utilities was 7.5%. It is of interest to note that for utilities heavily dependent upon nuclear energy, e.g., Connecticut Light and Power

Table XV. Electric utility sales, 1977, 1978, and 1979 (357)
(Billions of kW-hr)

	Residential	Industrial	Commercial	Other	Total
1977	652.3	757.2	469.2	72.1	1950.8
1978	679.2	782.1	480.7	75.8	2017.8
1979	693.4	812.5	493.6	75.9	2075.4
% Change					
1977-1978	4.1	3.3	2.3	1.3	3.5
% Change					
1978-1979	2.1	3.8	2.7	—	2.85

Table XVI. Average annual use, electric rate, and utility bill 1977, 1978, and 1979 (357)

	Residential			Commercial			Industrial		
	Average use, kW-hr	Average bill		Average use, kW-hr	Average bill		Average use, kW-hr	Average bill	
		Per kW-hr	Annual		Per kW-hr	Annual		Per kW-hr	Annual
1977	8693	3.78¢	\$328.6	52,892	3.84¢	\$2031	1,722,567	2.33¢	\$40,105
1978	8849	4.03¢	\$356.6	53,085	4.10¢	\$2176	1,702,939	2.59¢	\$44,156
1979	8820	4.32¢	\$381.5	53,184	4.36¢	\$2332	1,707,768	2.85¢	\$48,614

Company, rate increases were unusually moderate (359).

The capability of the electrical industry to generate power grew modestly (approximately 4%) in 1979, increasing to 597,523 MW, vis-a-vis a capability of 574,365 MW as of November 30, 1978. As can be seen in Table XVII the dependence upon fossil fuels has strengthened, with the use of coal dominant (in terms of kW-hr of generated power) (357).

Perhaps as a consequence of the limited U.S. reserves and the inflated world market prices, the electrical industry consumed significantly less oil in 1979 (see Table XVIII), the preliminary estimates showing a decrease of 17.6% from 635.8 to 523.5 millions of barrels (357).

The present and projected generating capability for the industry is shown as Table XIX. Although the planned capability includes a substantial amount (108,491 MW) from nuclear power-plants, it can be seen that the strong dependence upon fossil fuels will be maintained (357).

Total revenues for the investor-owned electric utility industry were \$68 billion in 1979, which represents a record high for the industry. Although total expenses have increased, the overall performance closely matches that achieved by the industry in 1978. It was reported that 88 electric utilities announced increased dividends in 1979, the net increase for the industry being 6.2% (357).

According to data compiled by the Ebasco Business Consulting Company, electricity rates were increased by 80 utilities, amounting to an increase in revenues of \$4.57 billion, which is substantially larger than that obtained in 1977 or 1978 (see Table XX) (357).

Table XVII. Energy generated and source, 1977, 1978, and 1979 (357)

	(Billions of kW-hr)				
	Coal	Oil	Gas	Nuclear	Total
1977	985.2	358.2	305.5	251	1899.9
1978	976.6	364.2	305.4	276.4	1922.6
1979	1075.5	303	329.5	255.4	1963.4
% Change 1978-1978	+10.1	-17	+7.9	-7.6	+2.1

Table XVIII. Fuel consumption by the electrical industry (357)

	Coal, millions of tons	Oil, millions of barrels	Gas, millions of ft ³
1977	477	624.2	3191.2
1978	481.6	635.8	3188.4
1979	529	523.5	3490.3
% Change 1977-1978	+7.3	-17.6	+9.4

Table XIX. Electric power industry capability, MW (357)

Fuel type	Capability December 1979	Additional capability planned be- yond 1980	Total
Hydro (including pumped storage)	75,326	24,020	99,346
Fossil fuel	412,399	125,129	537,528
Nuclear	53,744	108,491	162,235
Internal combustion	5,492	696	6,188
Combustion turbine	50,562	5,322	55,884
Industry total	597,523		

Table XX. Electric rate increases in 1977, 1978, and 1979 (357)

	Increases granted		Applications pending	
	Number	Revenue (\$)	Number	Revenue (\$)
1977	88	2636.8 MM	61	2518.0 MM
1978	73	2362.7 MM	59	3458.9 MM
1979	80	4567.0 MM	70	4715.4 MM

Capital expenditures primarily for generation, transmission, and distribution of electricity in the United States were \$35.2 billion in 1979, and forecasts again indicate increased capital outlay in 1980. In particular, the capital required for nuclear power plants is expected to amount to \$13.7 billion, an increase of approximately 11% from the level of expenditure in 1979. Comparable outlay is anticipated for fossil-fuel plants. It is of interest that because of several factors, including a higher forced-outage rate, long-range load-forecasting difficulties financing, land-use and the selection of suitable sites, construction of large power plants (approximately 3000 MW capacity) is being re-examined and reevaluated. The sequential construction of smaller plants allows much shorter lead-times for design and construction (357, 358, 360).

Energy from fossil fuels.—The amount of power generated in the United States utilizing fossil fuels has varied only slightly over the last three years, being 86.8% in 1977, 85.6% in 1978, and 87% in 1979 (see Table XVII). On the other hand, there has been a significant change in the consumption of particular fossil fuels, especially in 1979 when there was a substantial decrease in the consumption of oil (see Table XVIII). As has been mentioned previously, coal continued to strengthen its position in the national energy picture.

With respect to capability beyond 1980, planned additions would utilize fossil fuels to generate 47.5% of the electrical power, which is now slightly higher than that forecast earlier (361).

Oil shale.—A new oil shale extraction process, using radio-frequency electric fields to heat the deposits, is being jointly developed by Texaco, Raytheon, and Badger. In this process both liquid and gaseous hydrocarbons are produced *in situ*, eliminating the need for mining, retorting, and waste disposal. At this time, no economic assessment of the process has been carried out, and it is believed that by the end of 1980 only feasibility will have been demonstrated (362, 363).

A cost-sharing agreement also to produce oil-shale *in situ* is being considered by Occidental Petroleum and the Department of Energy. It is planned to construct two retorts at the Loga-Walsh test site near Debeque, Colorado, at a cost of approximately \$24 MM. The expected agreement represents the second phase of a \$45 MM pact between the two organizations signed in 1977 (363).

Under an agreement with the Aero-Propulsion Laboratory of the U.S. Air Force, the Process Division of UOP, Incorporated, will evaluate a new technique for the conversion of shale-oil to transportation fuels, primarily jet fuel. The contract with UOP covers a four-phase effort for a total of \$1.87 MM, the whole program extending over two and one-half years (364).

Coal gasification and coal liquefaction.—Two projects to liquefy coal, one a joint venture between Air Products and Chemicals and Wheelabrator-Frye and the other a U.S./West German/Japanese plant, will be supported by the U.S. Government, Department of Energy. The former venture, projected to cost \$625 MM and to be located in Kentucky, is expected to be operating in 1984, converting 6000 tons of coal/day into 20,000 barrels/day of oil. The plant will use a combination of a solvent refining process (SRC-1) and a catalyst hydrocracking process. The other project involves a plant to be located in Morgantown, West Virginia, and uses the SRC-II process developed by Gulf Mineral Resources. Initial plans are also to process 6000 tons/day of coal (365).

The first commercial coal-gasification project in the United States has been given approval by the Federal Energy Regulatory Commission. The \$1.2 billion project, to be located in Beulah, North Dakota, will convert 4.5 MM tons/year of lignite into high-Btu pipeline gas,

using the Lurgi gasification process. Called the Great Plains Coal Gasification Project, the undertaking is owned by a consortium of American Natural Resources Company and four other firms (366).

In October 1979, the Department of Energy and Gulf Science and Technology (the research arm of Gulf Oil) began a test-burn in Rawlins, Wyoming, as part of the first demonstration of coal gasification in a steeply slanted coal seam. This phase is part of the agreement established between Gulf Oil and the Department of Energy in 1976 (363).

Fluor Engineers and Constructors (Irvine, California), a subsidiary of U.S. Fluor Corporation, and Sasol (Johannesburg, South Africa) have agreed to market coal-conversion technology (developed by Sasol) in the United States. Sasol has been using the Fischer-Tropsch process to make a range of fuels and chemicals from coal since 1955. Fluor Engineers and Constructors have completed Sasol-2, a \$2.8 billion complex with an estimated capacity of 1.7 million short tons/year of fuel products, 170,000 short tons/year of ethylene, 110,000 short tons of ammonia and 220,000 short tons/year of coal-tar derivatives. The complex plant incorporates thirty six gasifiers that consume 30,000 tons/day of coal (367).

Texaco and Southern California Edison announced plans to construct a coal gasification unit capable of treating 1000 tons/day of coal. The products will feed gas and steam turbines to generate 90-95 MW of electric power. The new unit is to be located northeast of Los Angeles and the joint project will be supported by the Electric Power Research Institute (Palo Alto, California) (368).

A demonstration plant, utilizing a chemically activated fluidized-bed process for producing low-sulfur, low Btu gas from high-sulfur coal or lignite, came on-line mid-year. This plant, located at San Benito, Texas, is the culmination of gasification research project jointly undertaken by Central and Southwest Corporation (Dallas), Foster Wheeler Energy Corporation (New Jersey), and the federal EPA (369).

Exxon has developed a catalytic process for coal gasification that is claimed to overcome many of the problems associated with the fluidized-bed process. The use of alkali metal compounds enables the gasification reactions to occur at significantly lower temperatures than in the normal process. The predevelopment phase has been completed and Exxon is preparing to start up a 1 ton/day development unit in Baytown, Texas (368).

Coal.—The demonstrated annual production capacity from coal-mining operations in the United States is approximately 900 MM tons and of this the electric utilities burned 529 MM tons to produce electricity (see Table XVIII). The characteristics of specific classifications of available coal shows: (i) The Eastern and mid-Western coals, which represent 70% of the total U.S. recoverable reserves, are mostly high sulfur (2.8% and above) and high Btu (12,600-14,000 Btu/lb) coals and the majority is deep-mined. (ii) The Western coals, which represent only 20% of the total U.S. recoverable reserves, are low sulfur (0.8% and less) but low Btu coals.

The demand for the low-sulfur Western coal has recently increased substantially, probably as a consequence of the Amendments to the Clean Air Act in 1977. Blending of the low-sulfur coals with the high-sulfur, high Btu coals from the East and mid-West has been effective in meeting pollution standards in many states. Alternatively, coal-washing processes or flue-gas desulfurization techniques allow use of the Eastern coals. As discussed earlier (see the section on Environmental Regulations, Health, and Safety), Ohio faced a serious problem with respect to the air pollution standards imposed on its electric utilities, e.g., Cleveland Electric Illuminating, Toledo Edison, Ohio Edison, and Dayton Power and Light, and anticipated purchase

of significant quantities of out-of-state coal. Such action could have resulted in a depression in the coal industry in eastern Ohio but relaxations in the EPA regulations late in 1979 allowed the utilities to continue to burn the high-sulfur coal (370-372).

To meet the goal of the production of 1.1 billion tons/year of coal by 1985, the goal announced by President Carter in 1977, the railroads have embarked on programs to increase and improve their coal-hauling capabilities. The Chessie System, the largest coal-hauling system in the United States, is presently installing 16,000 new open-top hopper coal cars and has increased the number of available locomotives. Conrail is involved in an extensive long-term rehabilitation program estimated to cost \$6 billion. In the West, the Burlington Northern has undertaken a program of coal-related expenditures that may exceed \$1.5 billion between 1979 and 1983. This program calls for the relaying or replacing of 2300 miles of track and the construction of over 400 miles of new track and siding (371).

The cost of coal shipments by rail is presently a subject of concern to the electric utilities. Present controversies include (372): (i) the railroad deregulation bill pending in the Senate; (ii) a house committee investigation of freight-rate increases for the Tennessee Valley Authority; (iii) an alleged restraint-of-trade suit in Montana involving two railroads and a mining company.

The Edison Electric Institute favors deregulation for competitive rail traffic, but opposes it for captive-coal traffic. The Potomac Electric Power Company are concerned that full deregulation would lead to substantial increases in railroad rates and, therefore, increases in consumer electric rates.

The Tennessee Valley Authority is so concerned with the recent increases in freight-rates imposed by Louisville and Nashville Railroad that it is "seriously considering" joining utilities studying the construction of a pipeline for coal-slurry, running from eastern Kentucky through Tennessee and Georgia into Florida (372).

Poland is eastern Europe's major producer of anthracite coal. Although it is within the Soviet block, Poland does enjoy relative independence in the technological development, use, and export of this coal, even to the United States. Tampa Electric Company is currently importing Polish coal, the utility receiving 700,000 short tons of coal in 1978. New England Electric Power Company and Baltimore Gas and Electric Company have also utilized coal from Poland (373).

Energy from Nuclear Fuels.—The accident at Unit 2 of Metropolitan Edison Company's Three Mile Island Nuclear Plant on March 28, was caused by a combination of human and design errors and equipment failure. In a preliminary report, staff on the Nuclear Regulatory Commission listed several major errors that contributed to the accident (374, 375).

1. The failure to keep spare auxiliary feedwater pumps on-line. Only one of four was operational on March 28, leaving no margin for safety when the accident began.

2. A relief valve in the primary coolant loop opened during the accident, as it should have, to release overheated water. Then it failed to close, causing a dangerous drop in pressure.

3. At least one water level indicator on the pressurizing system appears to have given a faulty reading, causing a technician to think the system was full of water when it was not.

4. When the emergency core cooling system came on automatically, which only happens under serious circumstances, another automatic system designed to contain radioactive leaks failed to operate.

5. Technicians in the control room turned off the

emergency and primary cooling pumps. No one knows why they were stopped.

The results of what is the worst commercial nuclear power plant accident in U.S. history were the discharge of radioactive gases into the air and substantial damage to the plant and nuclear core. No one was injured or killed by the accident (374).

For Metropolitan Edison and General Public Utilities, the costs associated with the accident are large. In an effort to conserve resources to meet the total costs that will be incurred, General Public Utilities has announced suspension of all construction projects involving additional generating and transmission facilities. It has also stopped all, except the most critical, construction programs on existing stations and postponing all nonessential maintenance activities (374).

The three owners of Unit 2, Metropolitan Edison (50%), Jersey Central Power and Light (25%), and Pennsylvania Electric (25%), have an investment of \$780 million in the plant, including the nuclear core. It is believed that the major part of the cost of cleanup and repair will be covered by insurance. The cost of replacement power is obviously not (374).

Radiation dosage claimed much of the attention of the media. It has been shown that for the fifteen days following the accident no one in the vicinity of the nuclear plant received any unusual radiation. Very little radioactive iodine was found in the milk in the area (that found being well below allowable limits), and none was detected in the vegetation or in the soil (374, 375).

The antinuclear demonstration in Washington on May 6, provided a strong message to members of Congress and increased the pressure for a nuclear moratorium (imposed later in the year as is discussed in a section on Environmental Regulations, Health, and Safety). For the nuclear industry and the electric utilities the demonstration heralded future uncertainty, particularly with respect to the regulatory issues. Despite significant review and investigation, the risks associated with nuclear technology are still uncertain. A recent report written by radiological experts from the National Academy of Sciences appeared to make nuclear power an attractive source, but did not adequately consider the hazards posed by terrorism, leaks from waste storage areas, and obviously leaks from a major nuclear power plant (376, 377).

In mid-1979, the General Accounting Office issued a report examining the implications and trade-offs should the growth of nuclear power be limited. The report concluded that without severe reductions in the total demand or increased use of coal, the generation of electricity by nuclear technology would be essential to avoid power shortages in the 1980's. The report further indicated that, even with steady growth in coal production in the United States to 2 billion tons/year by the year 2000, over the mid-term (1985-2000) the combined demands on coal to: (i) displace oil and gas from electricity generation and (ii) meet the growth in demand for energy would seriously constrain expansion of nonelectrical uses for coal, e.g., coal gasification, synthetic fuels, chemicals (378).

Officials of the Arizona Public Service Company stated that without nuclear power the company could not possibly meet the energy needs of the state in the mid-1980's and beyond. Unlike the Northeastern United States, electricity shortfalls in the West cannot be supplemented by surpluses from neighboring states. In the long-term, the utilities believe that extensive coal-fired generation and possibly solar power systems will adequately provide electrical power (379).

Energy from other sources.—Seattle City Light and Tacoma City Light, in order to protect future generating capability, are jointly going to develop six low head hydro plants along approximately 1000 miles of irrigation canals in the eastern part of the state of

Washington. The six plants are expected to produce 100 MW of electricity at an estimated cost of only 1.5¢/kW-hr, which is substantially lower than power produced by either coal-fired plants or nuclear plants (382).

Most development effort being expended on ocean thermal energy conversion (OTEC) is concerned with closed-cycle systems. The most common working fluid in these systems is ammonia and there is little doubt that the first generation of OTEC plants will be closed-cycle systems. However, there are indications that significant improvements are possible with open cycles based on water. In one of the new approaches, a research group at Carnegie-Mellon University has made use of the thermodynamic properties of foams generated from water and a surfactant. A variation of the foam system has been proposed by engineers at the University of California (Los Angeles), this being a "mist-lift" system involving a vertical concentric pipe riding in the ocean (383).

The first demonstration plant to utilize heat energy from the ocean has been put into operation in Hawaii. This is a closed-cycle system, using ammonia as the working fluid, and has an output of 50 kW. One of the sponsors of the project, Lockheed Missiles and Space Company, is confident that this small demonstration unit will point the way to much larger OTEC plants (384).

Malfunctions delayed the start-up of Magma Power Company's 11 MW demonstration binary-cycle geothermal unit at East Mesa in California. It is expected that the unit will use geothermal heat to power a gas-expansion turbine generator and the \$15 MM installation is wholly financed by Magma. The company has a two year contract to sell the power to the San Diego Gas and Electric Company for 25 mills/kW-hr (385).

It is reported that San Diego Gas and Electric Company may resurrect plans for a 50 MW, \$50 MM geothermal binary-cycle unit if the Department of Energy is able to provide financial support. The utility shelved the project in July 1978 when the DOE selected Public Service Company of New Mexico for demonstration funding for a similar project (385).

Southern California Edison Company and San Diego Gas and Electric Company have completed initial discussions with the Mexican government-owned utility Commission Federal de Electricidad for the purchase of 600 MW of surplus geothermal power from Mexico's Baja California region. To furnish the power Mexico will have to expand its 150 MW flash process geothermal generating facility at Cerro Prieto at an estimated cost of approximately \$480 MM. The American utilities will build 28 miles of 230 kV transmission lines with the first interconnection to be completed in 1981 (386).

Working in cooperation with Pacific Gas and Electric Company at the Geysers in California, EIC (Newton, Massachusetts) has recently demonstrated the feasibility of a new process for effectively removing approximately 95% of the hydrogen sulfide from the geothermal steam. It is predicted that the new process will allow substantial expansion in the electrical output from the Geysers (387).

Magnetohydrodynamics (MHD) is an alternative way to produce electric power that promises dividends in energy efficiency and environmental protection. MHD has remained a laboratory curiosity since the first generator was built by Avco Corporation in 1958, but present economic conditions have led to significant government support for its development. The University of Tennessee received a five-year, \$37 MM contract to continue development of a coal-fired flow concept for a magnetohydrodynamic system. Independent of government funding, a small company in Pittsburgh, Roldiva Incorporated, has acquired the backing of Southern California Edison Company to

build a commercially operating MHD facility. The unit, scheduled for completion in 1985, will be attached to a conventional, 125 MW steam turbine generator at Fontana (California) and will produce an additional 60 MW of power (388, 389).

Engineers at General Electric's research and development center in Schenectady (New York) have successfully tested the key component of an advanced superconducting generator. Fabricated from thousands of niobium-tantalum filaments, bound into a copper matrix by a special vacuum epoxy-impregnation process, the superconductor spins a 13 foot long, 1.5 ton rotor at 3600 rpm in liquid helium at 4°K. When completed in 1981, it is estimated that the experimental generator will produce 18 MM watts of alternating current (390).

A commercial superconducting generator will be designed and built by Westinghouse Electric Company under a \$19 MM, five-year contract awarded by the Electric Power Research Institute, Palo Alto (California). The generator will be rated at 300 MW and once in commercial operation will supply enough electricity for some 90,000 homes (391).

Wind turbine generators are increasing in importance in the production of electricity. Southern California Edison is a leader in the development and commercialization of this technology. A three-bladed unit, called a Schachle, is currently under construction at SoCal Edison's Wind Turbine Test site. Other designs of wind turbines are also being developed by General Electric Company for the Department of Energy (392).

Industrial applications for solar energy systems are becoming more attractive. In 1978 an industrial solar process for generation of hot water, developed by General Electric Company was installed to heat water for an open fabric-dyeing vat at a textile plant in La France, South Carolina. The energy savings are estimated to be approximately 8 MM equivalent barrels of oil per year. A second system will provide high temperature steam to a pasteurizing unit in an orange-juice processing plant (Tropicana Products) in Florida. General Electric, under a \$235,000 contract from the Department of Energy, will design this system (393).

PFR Engineering Systems Incorporated are designing a \$13.5 MM solar-powered primary reformer for a 600 tons/day ammonia plant operated by Valley Nitrogen Producers Incorporated (394, 395).

Florida Power is joining Sea World Incorporated and General Electric Company in the design of a 300 kW photovoltaic concentrator solar plant to be located adjacent to Sea World. The federal government is participating on a cost-share basis in the nine-month study (396).

A low cost route to high purity silicon has been developed at SRI International (Menlo Park, California). If commercialized, SRI claims that it would reduce the cost of silicon for solar cells to about \$5/kg, more than meeting the goals set by the Department of Energy. The new process involves the heating of sodium metal and sodium fluorosilicate in the presence of a catalyst (394).

Instrument maker Ametek, Incorporated (Paoli, Pennsylvania) has filed for several patents on thin-film semiconductor materials that the company thinks can be used to make low-cost photovoltaic solar cells. The new cells are claimed to be close to realizing the DOE price goal (1986) of 70¢/peak watt of generated power. Ametek credits its lower costs to two factors: material cost is low because the film is only 1-2 micrometers thick and the coating is produced at essentially ambient temperatures (397).

The probability that a commercially successful electric vehicle will be developed by 1990 is claimed to be greater than 75%. The leading battery contenders for electric cars remain those that have shown promise

for the past several years, i.e., lead-acid, nickel-iron, and nickel-zinc batteries for development by 1985, and the zinc-chlorine, lithium-metal sulfide and sodium-sulfur batteries by the year 2000. Few other candidates are likely to be successfully commercialized by the end of the century without major technical breakthrough (398).

In this light, General Motors Corporation claimed to have achieved a "long-elusive breakthrough" in the development of a zinc-nickel oxide battery for vehicle propulsion. The energy density of the new GM battery is stated to be 27 W-hr/pound (cf. lead acid batteries have an energy density of 12 W-hr/pound) and further development is expected to increase that to 32 W-hr/pound. The R&D programs supported by GM during fifteen years has cost approximately \$33 MM (399, 400).

Gulf and Western Industries (New York) claims to have progressed significantly in the development of a zinc-chlorine battery for off-peak power storage. Limited production is expected to begin in 1980. The company has also been developing a similar battery system for vehicle propulsion but commercial application is stated to be "a few years away" (401).

General Electric Company and EPRI will jointly develop an advanced storage-battery system to help the utilities to conserve oil and natural gas and to manage peak energy demands. GE will design, fabricate, and test 2000 cells (sodium-sulfur system) and will assemble four 100 kW-hr capacity modules (402).

Fume-free nickel/cadmium batteries are presently being used as a source of reserve power in the Bureau of Reclamation's Central Valley hydroproject computer-control system. The use of these batteries (as opposed to lead-acid batteries) eliminates the need for extensive ventilating systems, fluid drains and safety equipment (403).

REFERENCES

1. Chlorine Statistical Report, United States Chlorine Institute, Inc., Nov. 1979.
2. Chlorine Statistical Report, United States Chlorine Institute, Inc., Jan. 1980.
3. *Journal of Commerce*, p. 3, Feb. 8, 1980.
4. *Chemical Week*, p. 30, March 14, 1979.
5. *Chemical Week Newswire Service*, Item 11590, Dec. 18, 1979.
6. *European Chemical News*, p. 6, Jan. 7, 1980.
7. *Chemical Marketing Reporter*, p. 5, 19, Feb. 4, 1980.
8. *Chemical Week Newswire Service*, Item 11777, Feb. 4, 1980.
9. *Chemical Marketing Reporter*, p. 3, 15, Feb. 11, 1980.
10. *European Chemical News*, p. 26, Feb. 11, 1980.
11. North American Chlor Alkali Industry Plants & Production Data Book, Chlorine Institute Pamphlet 10, Jan. 1980.
12. *European Chemical News*, International Project Review Supplement, p. 28, 30, Feb. 25, 1980.
13. *Chemical Purchasing*, p. 69, Nov. 1979.
14. *Chemical and Engineering News*, p. 12, April 7, 1980.
15. Current Industrial Reports, Inorganic Chemicals, U. S. Department of Commerce, Bureau of Census, January through December 1979.
16. Chlorine, CPI Product Profile, Dec. 15, 1979.
17. *Canadian Chemical Processing*, p. 42, 43, 47, 48, Nov. 14, 1979.
18. CPI Management Service, Vol. 11, No. 9, p. 1, March 5, 1979.
19. *Ibid.*, Vol. 11, No. 11, p. 1, March 19, 1979.
20. *Ibid.*, Vol. 11, No. 11, Sept. 24, 1979.
21. *Electrochemical Progress*, p. 5, Nov. 1979.
22. *Chemical Engineering*, p. 81, Oct. 22, 1979.
23. *Chemical Week*, p. 41, Oct. 10, 1979.
24. *Chemical Marketing Reporter*, p. 7, Oct. 8, 1979.
25. *Chemical Week Newswire Service*, Item 11248, Sept. 28, 1979.
26. CPI Management Service, p. 2, Aug. 20, 1979.

27. Salt in 1979, Mineral Industry Surveys, U.S. Department of the Interior, Bureau of Mines, Annual Preliminary, Dec. 31, 1979.
28. *Chemical Marketing Reporter*, p. 7, 69, Sept. 17, 1979.
29. *World Salt Journal*, p. 38, Sept. 28, 1979.
30. *Chemical Marketing Reporter*, p. 7, Oct. 22, 1979.
31. Chemical Products Synopsis, Sodium Chloride, Mannsville Chemical Products, June 1979.
32. *Journal of Commerce*, p. 3, Feb. 28, 1980.
33. *Purchasing*, p. 11, March 28, 1979.
34. *Chemical Marketing Reporter*, p. 32, April 16, 1979.
35. *Purchasing*, p. 18A5, April 11, 1979.
36. *Chemical Marketing Reporter*, p. 7, March 19, 1979.
37. *Ibid.*, p. 32, March 26, 1979.
38. *Purchasing*, p. 10, July 25, 1979.
39. *Chemical Week*, p. 65, Sept. 5, 1979.
40. *European Chemical News*, p. 12, Sept. 10, 1979.
41. *Chemical Week*, p. 20, Sept. 12, 1979.
42. *Ibid.*, p. 40, Nov. 28, 1979.
43. *Ibid.*, p. 13, Feb. 20, 1980.
44. *European Chemical News*, p. 13, 28, March 3, 1980.
45. *Journal of Commerce*, p. 5, Oct. 24, 1979.
46. *Chemical and Engineering News*, p. 9, July 2, 1979.
47. *Ibid.*, p. 10, 11, April 7, 1980.
48. *Chemical Purchasing*, p. 51, Oct. 1979.
49. *European Chemical News*, p. 27, April 30, 1979.
50. *Chemical Age*, p. 10, June 1, 1979.
51. Chemical Week Newswire Service, July 5, 1979.
52. *Chemical and Engineering News*, p. 19, July 9, 1979.
53. *European Chemical News*, p. 28, July 16, 1979.
54. *Chemical Marketing Reporter*, p. 7, 51, July 23, 1979.
55. *Japan Chemical Week*, p. 7, July 12, 1979.
56. *Patents and Licensing*, p. 23, Aug. 1979.
57. *European Chemical News*, p. 4, Dec. 3, 1979.
58. *Ibid.*, p. 4, Jan. 14, 1979.
59. *Ibid.*, p. 28, Jan. 21, 1980.
60. *Ibid.*, p. 6, Jan. 21, 1980.
61. *Ibid.*, p. 8, April 9, 1979.
62. *Chemical Age*, p. 7, Aug. 24, 1979.
63. *Chemical Engineering*, p. 64, Nov. 5, 1979.
64. *Chemical Marketing Reporter*, p. 33, July 9, 1979.
65. *European Chemical News*, p. 35, July 23, 1979.
66. *Chemical and Engineering News*, p. 16, Aug. 6, 1979.
67. *Chemical Age*, p. 12, Sept. 14, 1979.
68. *European Chemical News*, p. 31, Jan. 22, 1979.
69. *Chemical Marketing Reporter*, p. 4, Feb. 19, 1979.
70. *European Chemical News*, p. 36, Feb. 26, 1979.
71. *Chemical Purchasing*, p. 78, March 1979.
72. Private Communication from Roland Horvath, Diamond Shamrock Corporation, March 3, 1980.
73. *Japan Chemical Week*, p. 6, Oct. 11, 1979.
74. *Ibid.*, p. 3, July 5, 1979.
75. *Chemical Age*, p. 3, Aug. 1979.
76. *Chemical Daily (Kagaku Kogyo Nippo)*, Jan. 24, 1980.
77. *European Chemical News*, p. 28, Feb. 11, 1980.
78. *Patents and Licensing*, p. 30, Feb. 1980.
79. *Japan Chemical Week*, p. 7, Feb. 14, 1980.
80. *Ibid.*, p. 7, Nov. 15, 1979.
81. *Ibid.*, p. 9, Nov. 1, 1979.
82. *Ibid.*, p. 6, Feb. 14, 1980.
83. "Appraisal of the Ion Exchange Membrane Process," June 13, 1979, Commission for Promotion of Conversion of Soda Industrial Manufacturing Method, Technical Expert Commission for Technical Appraisal of Ion Exchange Membrane Method.
84. *Chemical Age*, p. 19, June 1979.
85. *Journal of Metals*, p. 16, April 1979.
86. *Mechanical Engineering*, p. 20, May 1979.
87. *European Chemical News*, p. 23, March 26, 1979.
88. *Chemical Week*, p. 34, March 28, 1979.
89. *Japan Chemical Week*, p. 1, June 28, 1979.
90. *Chemical Age*, p. 15, July 6, 1979.
91. *Japan Chemical Week*, p. 7, Dec. 6, 1979.
92. *Ibid.*, p. 7, June 14, 1979.
93. *Chemical Engineering*, p. 106, Feb. 11, 1980.
94. *Canadian Chemical Processing*, p. 39, Nov. 14, 1979.
95. *European Chemical News*, p. 24, 32, June 25, 1979.
96. *Chemical Engineering*, p. 88, 89, Feb. 26, 1979.
97. *Japan Chemical Week*, p. 11, Sept. 27, 1979.
98. *Ibid.*, p. 2, Oct. 11, 1979.
99. *Chemical Age*, p. 14, June 6, 1979.
100. *European Chemical News*, p. 28, July 23, 1979.
101. *Electrochemical Progress*, p. 4, July/August 1979.
102. *Chemical Marketing Reporter*, p. 7, 35, Oct. 22, 1979.
103. *Chemical and Engineering News*, p. 18, Feb. 19, 1979.
104. *Chemical Week*, p. 13, Feb. 21, 1979.
105. Chlorine Bulletin 8, The Chlorine Institute, Inc., p. 1, March 1979.
106. *Chemical Regulation Reporter*, Vol. 3, No. 16, Section 1, July 20, 1979.
107. *Chemical Marketing Reporter*, p. 5, 29, July 23, 1979.
108. *Chemical Week*, p. 23, July 25, 1979.
109. News Release, The Chlorine Institute, July 25, 1979.
110. Chlorine Bulletin 10, The Chlorine Institute, Inc., p. 1, 2, Aug. 8, 1979.
111. Chlorine Bulletin 12, The Chlorine Institute, Inc., p. 1, March 1980.
112. *Chemical Marketing Reporter*, p. 7, 31, March 5, 1979.
113. *European Chemical News*, p. 19, March 5, 1979.
114. *Chemical Marketing Reporter*, p. 4, 37, Oct. 22, 1979.
115. *Business Week*, p. 98D, H, L, Dec. 3, 1979.
116. *Chemical and Engineering News*, p. 8, Nov. 19, 1979.
117. Current Industrial Reports, Inorganic Chemicals, U.S. Department of Commerce, Bureau of the Census, January thru December 1979, p. 3.
118. Chemical Week Newswire, Item 11162, Sept. 11, 1979.
119. *European Chemical News*, p. 36, Feb. 26, 1979.
120. CPI Management Service, p. 4, Jan. 22, 1979.
121. *European Chemical News*, p. 42, June 11, 1979.
122. Personal Communication, Roland Hovath, Diamond Shamrock Corporation, March 3, 1980.
123. *Japan Chemical Week*, p. 7, March 29, 1979.
124. Potash in 1979 Annual Preliminary Mineral Industry Survey, Bureau of Mines, U.S. Department of the Interior, Dec. 31, 1979.
125. *Engineering and Mining Journal*, p. 85, March 1980.
126. *Chemical and Engineering News*, p. 14, Feb. 26, 1979.
127. Sodium Compounds in 1979, Annual Preliminary, Mineral Industry Surveys, Bureau of Mines, U.S. Department of the Interior, Dec. 1979.
128. Report of the Electrolytic Industries for the Year 1978, p. 19.
129. G. Innes, Paper presented at the AIME Annual Meeting, Feb. 1980, Preprint #80-13.
130. *European Chemical News*, p. 32, June 25, 1979.
131. *Ibid.*, p. 27, Dec. 17, 1979.
132. *Business Week*, p. 132, April 16, 1979.
133. *Chemical Marketing Reporter*, p. 7, Dec. 10, 1979.
134. *Ibid.*, p. 3, Oct. 22, 1979.
135. *Chemical Week*, p. 35, Aug. 15, 1979.
136. *European Chemical News*, p. 27, Aug. 20/27, 1979.
137. *Ibid.*, p. 23, July, 2, 1979.
138. *Chemical and Engineering News*, p. 28, Dec. 10, 1979.
139. *European Chemical News*, p. 13, Nov. 5, 1979.
140. *Ibid.*, p. 12, Dec. 10, 1979.
141. *Chemical Marketing Reporter*, p. 34, Dec. 17, 1979.
142. Inorganic Chemicals Current Industrial Reports, U.S. Department of Commerce Bureau of Census, January thru December 1979, p. 3.
143. *Chemical Purchasing*, p. 60, July 1979.
144. *Paper Journal*, p. 56, April 15, 1979.
145. *European Chemical News*, p. 16, Feb. 26, 1979.
146. *Chemical Purchasing*, p. 15, March 1979.
147. *Chemical Engineering*, p. 274, March 26, 1979.
148. *Pulp and Paper*, p. 225, May 1979.
149. *Chemical Marketing Reporter*, p. 4, 43, Oct. 1, 1979.
150. *Electrochemical Progress*, p. 5, Oct. 1979.
151. *Chemical Age*, p. 15, Dec. 7, 1979.
152. *Chemical Marketing Reporter*, p. 30, March 12, 1979.
153. *Ibid.*, p. 26, March 19, 1979.
154. Chemical Week Newswire, Item 11223, Sept. 24, 1979.

155. *Chemical Marketing Reporter*, p. 57, Sept. 24, 1979.
156. *Chemical Week Newswire*, Item 11553, Dec. 10, 1979.
157. *Chemical Marketing Reporter*, p. 35, Dec. 17, 1979.
158. CPI Management Service, p. 1, June 11, 1979.
159. *Pulp and Paper*, p. 195, Dec. 1979.
160. *Paper Journal*, p. 71, Nov. 30, 1979.
161. *Canadian Pulp and Paper*, p. 9, Nov. 1979.
162. CPI Product Profile, Sodium Chlorate, June 15, 1979.
163. CPI Management Service, p. 2, June 11, 1979.
164. *Chemical Purchasing*, p. 16, Oct. 1979.
165. *Canadian Chemical Processing*, p. 43, Sept. 5, 1979.
166. *Chemical Marketing Reporter*, p. 5, 21, Aug. 20, 1979.
167. CPI Management Service, p. 1, March 19, 1979.
168. *Chemical Marketing Reporter*, p. 5, 29, March 19, 1979.
169. *European Chemical News*, p. 28, March 26, 1979.
170. *Chemical and Engineering News*, p. 13, April 2, 1979.
171. CPI Management Service, p. 2, Oct. 15, 1979.
172. *Chemical Marketing Reporter*, p. 4, Oct. 15, 1979.
173. *European Chemical News*, p. 16, Oct. 15, 1979.
174. CPI Management Service, p. 2, Jan. 21, 1980.
175. CPI Management Service, p. 3, Nov. 12, 1979.
176. CPI Management Service, Nov. 26, 1979.
177. Aluminum & Bauxite in 1979, Mineral Industry Surveys, U.S. Department of the Interior, Bureau of the Mines, Annual Preliminary, Dec. 31, 1979.
178. *Metals Week*, p. 1, Feb. 26, 1979.
179. *Chemical Marketing Reporter*, p. 5, March 26, 1979.
180. *Ibid.*, p. 3, 33, March 5, 1979.
181. *Ibid.*, p. 7, Aug. 13, 1979.
182. *Chemical Week Newswire Service*, Item 10996, Aug. 16, 1979.
183. *Metals Week*, Aug. 13, 1979.
184. *Electrochemical Progress*, p. 7, Sept. 1979.
185. *Chemical Week Newswire*, Item 11696, Jan. 15, 1980.
186. *Chemical and Engineering News*, p. 9, March 12, 1979.
187. *Engineering and Mining Journal*, p. 19, Dec. 1979.
188. *Chemical Marketing Reporter*, p. 5, 22, March 17, 1980.
189. *Metals Week*, p. 3, Dec. 24, 1979.
190. *Ibid.*, p. 3, Sept. 17, 1979.
191. *Ibid.*, p. 1, Dec. 17, 1979.
192. *Chemical Marketing Reporter*, p. 3, Jan. 28, 1980.
193. *Metals Week*, p. 3, Jan. 28, 1980.
194. *Chemical Week Newswire Service*, Item 11751, Jan. 28, 1980.
195. *Metals Week*, p. 9, 10, Nov. 12, 1979.
196. *Electrochemical Progress*, p. 5, Oct. 1979.
197. *Journal of Metals*, p. 10, Nov. 1979.
198. *Metals Week*, p. 5, Sept. 3, 1979.
199. *Chemical Marketing Reporter*, p. 31, Sept. 3, 1979.
200. *Chemical Week Newswire Service*, Item 11295, Oct. 10, 1979.
201. *Chemical Week*, p. 17, Oct. 19, 1979.
202. *Ibid.*, p. 9, Aug. 1, 1979.
203. *Chemical Marketing Reporter*, p. 3, 28, March 17, 1980.
204. *Metals Week*, p. 1, March 17, 1980.
205. *Engineering and Mining Journal*, p. 76, March 1980.
206. *Metals Week*, p. 7, Aug. 6, 1979.
207. *Ibid.*, p. 3, Feb. 4, 1980.
208. *Ibid.*, p. 5, Feb. 18, 1980.
209. *Journal of Metals*, p. 9, Nov. 1979.
210. *Ibid.*, p. 13, Oct. 1979.
211. *Chemical Week Newswire Service*, Item 11091, Aug. 27, 1979.
212. *Journal of Metals*, p. 55-62, Feb. 1980.
213. *Metals Week*, p. 4, Oct. 15, 1979.
214. *Chemical Engineering*, p. 45, Dec. 3, 1979.
215. *Ibid.*, p. 85, Aug. 13, 1979.
216. *Journal of Metals*, p. 10, Jan. 1979.
217. *Engineering and Mining Journal*, p. 57, June 1979.
218. *Chemical Engineer*, p. 94, 96, 98, Oct. 22, 1979.
219. A Survey of Potential Processes for the Manufacture of Aluminum, Arthur D. Little, ANLOEPM 79-4, p. iii, Dec. 1979.
220. *Chemical Marketing Reporter*, p. 5, 25, May 28, 1979.
221. *Chemical and Engineering News*, p. 8, June 4, 1979.
222. *Inside R&D*, p. 3, June 6, 1979.
223. *Electrochemical Progress*, p. 9, Sept. 1979.
224. *Engineering and Mining Journal*, p. 11, Jan. 1980.
225. *Chemical and Engineering News*, p. 23, April 30, 1979.
226. *Chemical Marketing Reporter*, p. 5, 31, April 23, 1979.
227. *Chemical and Engineering News*, p. 19, Oct. 29, 1979.
228. *Chemical Week Newswire Service*, Item 11374, Oct. 26, 1979.
229. *Chemical Engineering*, p. 107, Feb. 11, 1980.
230. *Chemical and Engineering News*, p. 22, Nov. 26, 1979.
231. *Auto News*, p. 8, 19, April 30, 1979.
232. *Journal of Metals*, p. 18, June 1979.
233. *Engineering and Mining Journal*, p. 77, March 1980.
234. *Chemical Engineering*, p. 53-58, Dec. 3, 1979.
235. *Business Week*, p. 36F, H, Feb. 19, 1979.
236. Beryllium in 1979, Annual Preliminary, Mineral Industry Surveys, U.S. Department of the Interior, Bureau of Mines, Dec. 31, 1979.
237. *American Metal Market/Metal Working News*, p. 29, Dec. 17, 1979.
238. Report of the Electrolytic Industries for the Year 1978, p. 32.
239. *Journal of Metals*, p. 17, Aug. 1979.
240. Chromium in 1979, Mineral Industry Survey, U.S. Department of the Interior, Bureau of Mines, Annual Preliminary, Jan. 21, 1980.
241. Chromium in December 1979, Mineral Industry Survey, U.S. Department of the Interior, Bureau of Mines, Chromium Monthly, March 5, 1980.
242. *Metals Week*, p. 1, Feb. 4, 1980.
243. *Chemical Age*, p. 23, May 25, 1979.
244. *Chemical Week Newswire Service*, Item 10643, May 17, 1979.
245. *Chemical and Engineering News*, p. 9, Jan. 22, 1979.
246. *Engineering and Mining Journal*, p. 103, 104, March 1980.
247. *Ibid.*, p. 150, Aug. 1979.
248. *Electrochemical Progress*, p. 11, July/Aug. 1979.
249. Copper in 1979 Annual Preliminary, Mineral Industry Survey, Bureau of Mines, U.S. Department of the Interior, Jan. 1980.
250. *American Metal Market/Metal Working News*, p. 25, July 9, 1979.
251. Report of the Electrolytic Industries, 1978, p. 36.
252. *Chemical Marketing Reporter*, p. 7, July 2, 1979.
253. *Chemical Engineering*, p. 276, March 26, 1979.
254. *Ibid.*, p. 135, Oct. 22, 1979.
255. *Chemical Week*, p. 56, Dec. 12, 1979.
256. *Business Week*, p. 54J-54Q, Nov. 19, 1979.
257. *Chemical Marketing Reporter*, p. 7, April 30, 1979.
258. *Business Week*, pp. 134D-134H, May 7, 1979.
259. *Chemical and Engineering News*, p. 21, Sept. 17, 1979.
260. *European Chemical News*, p. 27, Sept. 10, 1979.
261. R. R. Grinstead, *Journal of Metals*, p. 13, March 1979.
262. K. C. Jones and R. A. Pyper, *ibid.*, p. 19, April 1979.
263. L. E. Murr, Z. Annamalai, and P. C. Hsu, *ibid.*, p. 26, Feb. 1979.
264. *Chemical and Engineering News*, p. 28, Sept. 10, 1979.
265. *Engineering and Mining Journal*, p. 131, March 1980.
266. *Chemical Week Newswire Service*, Item 10651, May 18, 1979.
267. *European Chemical News*, p. 42, May 21, 1979.
268. Lithium Mineral Commodity Profile Bureau of Mines, U.S. Department of Interior, p. 4, Sept. 1979.
269. *Chemical Marketing Reporter*, p. 36, Oct. 1, 1979.
270. *Chemical Week Newswire Service*, Item 11213, Sept. 21, 1979.
271. *Metals Week*, p. 6, June 25, 1979.

272. Lithium Mineral Commodity Profile Bureau of Mines, U.S. Department of Interior, Sept. 1979, p. 22, 23.
273. *Electronics Products Magazine*, p. 75, Nov. 1979.
274. Magnesium and Magnesium Compounds, Annual Preliminary, Mineral Industry Surveys, U.S. Department of the Interior, Bureau of Mines, Dec. 31, 1979.
275. Report of the Electrolytic Industries for the Year 1978, p. 42.
276. *American Metal Market/Metal Working News*, p. 23, July 2, 1979.
277. *Journal of Metals*, p. 17, April 1979 and p. 6, Dec. 1979.
278. *Chemical and Engineering News*, p. 15, July 23, 1979.
279. *European Chemical News*, p. 8, Dec. 10, 1979.
280. *Chemical and Engineering News*, p. 10, June 25, 1979.
281. *Ibid.*, p. 19, July 9, 1979.
282. *Business Week*, p. 94G, Dec. 17, 1979.
283. Manganese in 1979, Annual Preliminary Mineral Industry Surveys, U.S. Department of Interior, Bureau of Mines, p. 1.
284. *Engineering and Mining Journal*, p. 149, 150, March 1980.
285. *Metals Week*, p. 1, Jan. 14, 1980.
286. Manganese in 1979, Annual Preliminary Mineral Industry Surveys, U.S. Department of Interior, Bureau of Mines, p. 2.
287. *Metals Week*, p. 1, Sept. 17, 1979.
288. *Ibid.*, p. 6, Oct. 22, 1979.
289. *Ibid.*, p. 5, Nov. 19, 1979.
290. Manganese Monthly Mineral Industry Surveys, U.S. Department of the Interior, Bureau of Mines, Nov. 1979.
291. *Purchasing* p. 65, June 6, 1979.
292. Nickel in 1979, Mineral Industry Surveys, U.S. Department of the Interior, Bureau of Mines, Annual Preliminary, Dec. 31, 1979.
293. Nickel Monthly, July 1979, Mineral Industry Surveys, U.S. Department of the Interior, Bureau of Mines, Oct. 25, 1979.
294. Nickel Monthly, November 1979, Mineral Industry Surveys, U.S. Department of the Interior, Bureau of Mines, Feb. 5, 1980.
295. Report of the Electrolytic Industries for the Year 1978, p. 47.
296. *Metals Week*, p. 3, Feb. 11, 1980.
297. *Ibid.*, p. 6, Dec. 17, 1979.
298. *Ibid.*, p. 1, Jan. 14, 1980.
299. *Engineering and Mining Journal*, p. 167, March 1980.
300. *Metals Week*, p. 6, Nov. 26, 1979.
301. *Ibid.*, p. 1, April 9, 1979.
302. *Chemical Marketing Reporter*, p. 4, Oct. 1, 1979.
303. *Metals Week*, p. 1, Oct. 1, 1979.
304. *Chemical Week*, p. 19, Oct. 3, 1979.
305. Nickel Monthly, Mineral Industry Surveys, U.S. Department of the Interior, Bureau of Mines, Nickel in June 1979, Aug. 30, 1979.
306. Titanium in 1979, Annual Preliminary, Mineral Industry Surveys, Bureau of Mines, U.S. Department of the Interior, Dec. 1979.
307. L. E. Lynd. *Journal of Metals*, p. 22, May 1979.
308. Report of the Electrolytic Industries for the Year 1978, p. 50.
309. *American Metal Market/Metal Working News*, p. 10, April 30, 1979.
310. *Journal of Metals*, p. 9, Nov. 1979.
311. Titanium in the Fourth Quarter, 1979, Titanium Quarterly, Mineral Industry Surveys, Bureau of Mines, U.S. Department of the Interior.
312. *American Metal Market/Metal Working News*, p. 1, Nov. 12, 1979.
313. *Ibid.*, p. 19, Dec. 24, 1979.
314. *Chemical Marketing Reporter*, p. 65, Dec. 10, 1979.
315. *European Chemical News*, p. 26, Sept. 3, 1979.
316. *Chemical and Engineering News*, p. 8, May 14, 1979.
317. *European Chemical News*, p. 30, May 21, 1979.
318. Titanium in the Second Quarter, 1979, Titanium Quarterly, Mineral Industry Surveys, Bureau of Mines, U.S. Department of the Interior, Sept. 1979.
319. *Chemical Engineering*, p. 277, March 26, 1979.
320. *American Metal Market/Metal Working News*, p. 33, Sept. 17, 1979.
321. Titanium in the Third Quarter, 1979, Titanium Quarterly, Mineral Industry Surveys, Bureau of Mines, U.S. Department of the Interior, Dec. 1979.
322. *Chemical Week*, p. 13, Oct. 3, 1979.
323. Zinc in 1979, Annual Preliminary, Mineral Industry Surveys, Bureau of Mines, U.S. Department of the Interior, Jan. 1980.
324. Zinc Production, Monthly, Mineral Industry Surveys, Bureau of Mines, U.S. Department of the Interior, Nov. 1979.
325. Zinc Production, Monthly, Mineral Industry Surveys, Bureau of Mines, U.S. Department of the Interior, Feb. 1980.
326. Zinc Production, Monthly, Mineral Industry Surveys, Bureau of Mines, U.S. Department of the Interior, Jan. 1980.
327. *Chemical Marketing Reporter*, p. 4, Dec. 3, 1979.
328. *American Metals Market/Metal Working News*, p. 5, Nov. 19, 1979.
329. *Chemical Marketing Reporter*, p. 4, Nov. 19, 1979.
330. *Chemical and Engineering News*, p. 15, April 16, 1979.
331. *Nature*, pp. 277-523, 1979.
332. *Chemical and Engineering News*, p. 16, March 5, 1979.
333. Zinc Industry, Monthly, Mineral Industry Surveys, Bureau of Mines, U.S. Department of the Interior, March 10, 1980.
334. *American Metal Market/Metal Working News*, p. 28, Nov. 26, 1979.
335. *Ibid.*, p. 41, Dec. 10, 1979.
336. Report of the Electrolytic Industries for the Year 1978, p. 52.
337. *Business Week*, p. 38M, May 14, 1979.
338. *Ibid.*, p. 24, Feb. 19, 1979.
339. *Ibid.*, May 21, 1979.
340. *Ibid.*, p. 108, May, 28, 1979.
341. *Science*, Vol. 203, p. 233, Jan. 19, 1979.
342. B. M. Miller *et al.*, "Geological Estimates of Undiscovered Recoverable Oil and Gas Resources in the United States," U.S. Geological Survey, Circular 725, 1975.
343. J. F. Schanz, Jr. "Oil and Gas, Welcome to Uncertainty," Resources for the Future, Washington, D.C., 1978.
344. *Electrical World*, p. 71, Jan. 14, 1979.
345. Mineral Facts and Problems, U.S. Bureau of Mines, Bulletin 667, 1975.
346. *Electrical World*, p. 4, Jan. 1, 1979.
347. *Ibid.*, p. 27, July 15, 1979.
348. *Ibid.*, p. 58, May 1, 1979.
349. *Business Week*, p. 106C, Feb. 26, 1979.
350. *Chemical Week*, p. 48, Oct. 31, 1979.
351. *Business Week*, p. 54T, Nov. 19, 1979.
352. *Electrical World*, p. 27, Oct. 15, 1979.
353. *Ibid.*, p. 19, Dec. 15, 1979.
354. *Ibid.*, p. 106, Oct. 15, 1979.
355. *Ibid.*, p. 25, Sept. 1, 1979.
356. *Ibid.*, p. 73, Feb. 15, 1979.
357. *Ibid.*, pp. 49-80, March 15, 1980.
358. *Ibid.*, pp. 69-84, Sept. 15, 1979.
359. *Business Week*, p. 108, May 28, 1979.
360. *Electrical World*, p. 36, July, 1, 1979.
361. Report of the Electrolytic Industries for the Year 1978, p. 66.
362. *European Chemical News*, p. 33, Nov. 5, 1979.
363. *Chemical Week*, p. 24, Oct. 24, 1979.
364. *Chemical Marketing Reporter*, p. 17, Aug. 27, 1979.
365. *European Chemical News*, p. 32, Oct. 8, 1979.
366. *Chemical Week*, p. 46, Nov. 21, 1979.
367. *Ibid.*, p. 45, Sept. 12, 1979.
368. *Ibid.*, p. 32, Aug. 8, 1979.
369. *Electrical World*, p. 71, Jan. 15, 1979.
370. *Ibid.*, p. 16, Jan. 1, 1979.
371. *Ibid.*, p. 60-82, Oct. 15, 1979.
372. *Ibid.*, p. 17, Aug. 1, 1979.
373. *Ibid.*, p. 37, Sept. 1, 1979.
374. *Ibid.*, p. 29, May 1, 1979.
375. *Science*, Vol. 204, p. 280, April 20, 1979.
376. *Ibid.*, Vol. 204, p. 715, May 18, 1979.
377. *Ibid.*, Vol. 204, p. 714, May 18, 1979.
378. *Chemical and Engineering News*, p. 17, June 11, 1979.

379. *Electrical World*, p. 95, Oct. 15, 1979.
380. *Ibid.*, p. 43, Nov. 1, 1979.
381. *Ibid.*, p. 9, Dec. 15, 1979.
382. *Ibid.*, p. 19, Feb. 1, 1979.
383. *Chemical and Engineering News*, p. 24, Sept. 3, 1979.
384. *Chemical Week*, p. 48, Sept. 12, 1979.
385. *Electrical World*, p. 20, Oct. 1, 1979.
386. *Ibid.*, p. 32, May 1, 1979.
387. *Chemical and Engineering News*, p. 29, Dec. 3, 1979.
388. *Business Week*, p. 126T, May 21, 1979.
389. *Chemical and Engineering News*, p. 16, Aug. 20, 1979.
390. *Ibid.*, p. 24, Nov. 12, 1979.
391. *Ibid.*, p. 20, Jan. 22, 1979.
392. *Electrical World*, p. 22, Nov. 15, 1979.
393. *Ibid.*, p. 104, Jan. 15, 1979.
394. *Chemical Week*, p. 76, Sept. 5, 1979.
395. *Ibid.*, p. 27, Sept. 12, 1979.
396. *Electrical World*, p. 52, Jan. 1, 1979.
397. *Chemical Week*, p. 47, Nov. 7, 1979.
398. *Chemical and Engineering News*, p. 20, May 7, 1979.
399. *Chemical Marketing Reporter*, p. 4, Oct. 1, 1979.
400. *Chemical Week*, p. 19, Oct. 3, 1979.
401. *Ibid.*, p. 34, Nov. 28, 1979.
402. *Electrical World*, p. 65, Dec. 15, 1979.
403. *Ibid.*, p. 61, March 1, 1979.



The Invention and Industrial Development of Metal Anodes¹

Henri Bernard Beer

Scientific Research Society, NV, 2190 Essen, Belgium

Madame President, ladies and gentlemen, I should like to begin by expressing my gratitude to the Board of Directors of The Electrochemical Society for the honor of having been elected to receive the Vittorio de Nora-Diamond Shamrock medal and prize for 1980. I could never have dreamed that such an award would be bestowed on me when I first began to attend your meetings. It is indeed a great honor and pleasure for me to speak here today about the inventions and the industrial development of the activated metal anodes, or "DSA"^R as they are usually called nowadays.

Let me start by telling you how the invention of these anodes was brought about and accomplished.

I had already been searching for a better anode material to replace the customary graphite, magnetite etc. for about 20 years, without success, when between the years 1954 and 1957 it happened that I was experimenting with a new method to manufacture magnetic oxide materials as, e.g., ferrites by means of an electrolytic process. For this purpose I used metals like iron, nickel, cobalt, etc. which were anodically dissolved and then chemically coprecipitated without causing any changes in the electrolyte. Then on a certain day in 1956 someone asked me to prepare ferrotitanate according to this method. I did not expect difficulties in doing this by means of an iron and a titanium anode, but I soon found out that I could not dissolve the titanium anodically in my usual chloride containing electrolyte, because the titanium became inert by the formation of a unique oxide layer, which prevented completely the passage of the electric current to the electrolyte. I then tried out various other electrolytes with more or less the same result. It was this phenomenon that brought me to the idea that this titanium might be an ideal and economical base metal for among other things, anodes to be used in the chlorine-alkali electrolysis, if it could be coated with an electrical conducting and electrocatalytic active, chemically inert material which itself would not become nonconductive under anodic conditions. The oxide layer which is formed anodically on the titanium prevents the current to flow to the electrolyte, but is conductive to another electrical conductive material as for instance the platinum metals etc. On those spots where the platinum metals might be porous or where they had been worn off, the titanium substrate will anodically protect itself against further corrosion by forming an oxide layer. In this way the substrate of the titanium anode is "self-healing."

It was therefore between 1956 and 1957 that I became aware that on account of its special properties,

titanium was exceptionally suitable for use as a base metal for the manufacture of anodes to be used, e.g., in the chlorine-alkali electrolysis.

After that a long searching activity began, to find an appropriate and reliable electrocatalyst for the production of chlorine. The reason why the production of chlorine was chosen, was that this product is being produced on a large scale by means of an electrochemical process and that consequently a new and better type of anode might be of great technical and economical importance. The first coatings I was experimenting with were made of metals of the platinum group which were galvanically deposited on the titanium. Most of these coatings were subject to too great a loss of platinum metals and especially of platinum per se per ton chlorine produced. Besides, on account of an excessive overvoltage of these coatings during the electrolysis of brine, the energy consumption was too high so that in this respect there was no real saving in comparison with the existing graphite anodes. On top of this, the platinum coating had the tendency to become passive during operation.

I also found out then that the pretreatment of the titanium was very important if one wished to apply on it an active layer with good adhesive properties. Therefore the titanium was first thoroughly degreased chemically and electrolytically and all other products like oxides etc. removed.

After this the titanium was etched in such a way that the total surface area of the anode had at least trebled, while after the etching and even after rinsing following the etching bath, preferable a titaniumhydride remained on the surface which protected the underlying titanium metal during a few hours against air oxidation. Upon this surface the active layers were applied. According to the type of coating to be used, the enlargement of the surface area of the titanium can in some cases be increased by mechanical treatment, such as sand-blasting whereafter the titanium may be treated by a short acid-etch. I also found out that the crystal structure of the titanium is of importance, because this has a great influence on the passivation of this metal when used under anodic conditions in chloride-containing solutions. Both problems, the passivation and the excessive loss of platinum metal were solved by the addition of iridium to the platinum in a ratio of about 20 to 30 weight percent.

Instead of applying these layers galvanically, a thermochemical process was developed by dissolving the desired metals as their salts in an organic liquid which solution was then applied to the etched titanium, either by immersion or by painting with a brush, after which the solvent was evaporated. By increasing the temperature under alkaline reducing conditions the platinum metal salts were then decomposed and

¹The Vittorio de Nora-Diamond Shamrock Award Address delivered May 13, 1980 at the St. Louis, Missouri, Meeting of the Society.

thus a metal deposit was formed on the titanium with good adhesion and electrocatalytic properties.

In practice it became evident, however, that the use of platinum, either alone or in combination with other platinum metals, as an active layer on titanium for the production of chlorine in mercury cells was not economical. The main reason is that in mercury cells it is practically impossible to prevent the formation of the so-called mercury-butter in the mercury amalgam on account of impurities in the mercury.

This mercury-butter keeps on growing until it reaches the anode surface and through contact with it, the electrocatalytic layer of platinum metals on the titanium is damaged and partly or totally removed. As the formation of this mercury-butter and the unavoidable contact with the anode will inevitably occur several times when the cell is in operation, it became obvious that metal anodes, that is to say those made of titanium coated with platinum metals, would never give a satisfactory performance in mercury cell operation.

For those amongst you who are not familiar with the mode of operation of the chlorine-alkali electrolysis, it may be useful to explain briefly the basic principles of this process.

Chlorine is being produced mainly by an electrochemical process, in cells through which an aqueous solution circulates of about 30% sodium chloride, called brine, having a pH of 2-4 and a temperature of 75°-90°C. By conducting through this brine a direct electrical current chlorine is generated at the anode.

In principle there exist three main cell types for the electrolysis of brine: (i) the mercury cell, (ii) the diaphragm cell, and (iii) the membrane cell, which is the latest development.

In the modern mercury cell, anodes are used made of titanium rods or mesh coated with stabilized oxides of ruthenium and titanium as the active catalytic coating. The cathode consists of liquid mercury in which the sodium ions are reduced to sodium. This sodium is dissolved into the mercury and forms with it an amalgam. The amalgam is transported outside the cell to the decomposer or denuder, where the sodium-amalgam is decomposed into sodium-ions and hydrogen-gas through contact with water and pieces of carbon. The result is a very pure and highly concentrated aqueous sodium hydroxide solution. The mercury, now free from sodium, is recirculated through the cell and is used again.

In the diaphragm and membrane cells the cathode and anode are placed vertically in 2 compartments, separated one from the other by a diaphragm or by a membrane. The diaphragm, which consists generally of asbestos and additives, is a separator through which ion transport and electrolyte flow from the anodic compartment to the cathodic compartment is possible, on account of hydrostatic pressure. The diaphragm cell produces therefore a caustic of lesser quality, because it always contains some sodium chloride. Contrary to this a membrane only allows ions to pass, so that the catholyte and the anolyte are completely separated. During the reaction, the anolyte is diluted, but is continuously replenished with sodium chloride. At the anode chlorine is evolved.

In general, plain steel cathodes are used in these cells, or else steel cathodes with for instance a nickel coating, in order to obtain a lower hydrogen overvoltage and all through the reaction the aqueous catholyte is enriched with sodium hydroxide. This solution is called "lye" or caustic.

In membrane cells, lye of a high purity grade is formed, but at the moment the concentration cannot be so high as for instance in mercury cells, because back-diffusion might occur through the membrane from the cathode to the anode compartment by the osmotic pressure. Therefore, unlike the mercury cells, which produce a concentrated product directly, the

membrane cells need extra energy to obtain the desired concentration of the lye, which naturally increases the general costs. The first chlorine plants which were equipped with membrane cells have been installed during the last two years.

In membrane cells the use of graphite anodes would have been practically impossible as the membranes get clogged entirely by the loose graphite particles which drift about in the electrolyte as a result of the oxidation and disintegration of the graphite anodes. The industrial development of the membrane cells can therefore be mainly attributed to the invention of the DSA^R anodes.

For the sake of completeness I should like to say something about the commercial experience I gained in the beginning and also later on with these anodes in my contacts with the industry. Though I knew a good deal about electrochemistry in general, my knowledge about the chlorine-alkali industry was limited. My visits to various industrial firms, were therefore of an exploring nature. I wanted to find out what the producers would expect and require from a new type of anode. Any alterations to the existing graphite anodes had hardly ever been considered during the last 50 years as their deficiencies had simply been accepted and the industry had learned to live with them.

It is true, of course, that changing over to a new type of anode was not easy for the chlorine manufacturers, as the consequences which would be attached to it were great. In the event of a failure, the consequences would be considerable. Most industries in Europe which manufactured chlorine, did so for their own captive use in the production of all kinds of chemical products. Hence, a possible even short stagnation of the chlorine production, might paralyze the whole line with serious economic losses.

For the relatively few factories supplying merchant chlorine to third parties, a stagnation was just as inconvenient as they generally had contractual obligations.

Moreover, a change from graphite anodes to metal anodes was extremely costly for some producers, when not only the anodes had to be replaced, but also because the old cells for which a switch to metal anodes would be made, had to be partly rebuilt in order to obtain the best possible results. For some mercury cells the current density could be increased considerably in order to justify the new anodes.

It was further necessary that the gap between the anode and cathode be as small as possible, without increasing the chance of a short circuit. The assessment of this gap could not be made any more in the usual manner as with the graphite anodes, by provoking a slight short circuit, but had to be made in a different way. For the mercury cells there were some reasons to object against these new anodes and understandably the objections were mostly of an economical nature.

For the diaphragm cells some constructional readjustments were necessary as well, to adapt them to the use of metal anodes, such as the purchase of copper bases.

In any case it can be said that the opposition lay sometimes in the difficulty to accept that an outsider should be able to bring about such a substantial innovation in so exclusive and secret an industry as the chlorine manufacture. I often felt that the "not invented here" syndrome may have played a prominent part in this too.

Reverting to the technical development of the anodes, some of the problems which arose in connection with the mercury cells could be solved towards the end of 1965 through the development of my new generation of titanium anodes in which oxides of the metals of the platinum group were used, either alone or with oxides of nonprecious metals.

In these anodes the overpotential for the chlorine process is reduced to practically its theoretical value even at very high current densities, on account of which a considerable saving in energy per ton chlorine produced, can be obtained and at the same time a near-doubling of the chlorine production capacity can be achieved with practically no increase in unit power consumption.

Moreover, I had found out in the meantime that it was possible to use also the cheapest of the platinum metal oxides for the coating, namely ruthenium oxide. This too accounted for an important reduction of the cost of the anodes, as ruthenium costs only a fraction of the price of platinum or iridium.

Nevertheless, there were still a few problems left for the use of these oxide anodes in mercury and other cells and that because of the following:

1. The sodium-amalgam as well as the mercury-butter which are formed in mercury cells during the electrolysis are strong reducing agents and a direct contact with one or both, reduces again the platinum oxides (or the mixture of these with some oxides of other metals) to their metallic state. As a result the oxide coating is lost through further contact with the amalgam or mercury-butter, just as it happens with the original metal coatings.

2. The anodes coated with the oxides of platinum metals were rather sensitive to the current reversal occurring whenever the cell is short-circuited, which happens from time to time when cleaning the cell or doing other maintenance work. This also causes losses of platinum oxides which are considered to be too high.

When I speak of platinum oxides, this means the oxides of all the platinum metals like rhodium, palladium, ruthenium, and iridium.

I succeeded in solving these problems also in my following generation of anodes in the year 1967. In that period the oxides of the platinum group could be stabilized by the addition of titanium oxide or one or more oxides of the other valve metals like tantalum, niobium, or zirconium to the coating mixture and by coprecipitating these oxides thermochemically on the titanium from a solvent. These are the anodes which have been registered by Diamond Shamrock under the trademark DSA^R.

The catalytically stabilized oxides of the metals of the platinum group like platinum, rhodium, iridium, ruthenium, and palladium with the oxides of valve metals like tantalum, zirconium, niobium, etc. can be used for other applications than for the production of chlorine.

It is, however, the ruthenium oxide plus titanium oxide stabilized coatings on titanium which presents such an extraordinary electrocatalytic activity for the production of chlorine, that this type of coating is generally used nowadays for the chlorine-alkali electrolysis in either mercury, diaphragm, or membrane cells.

Very large chlorine plants with a capacity of up to 1500 metric tons per day, using diaphragm cells provided with dimensionally stable anodes, have now been installed in the United States and elsewhere and are run by fewer operators than those needed with graphite anodes. DSA^R-type anodes have been in use in diaphragm cells for more than 10 years and are still in good condition. They will certainly last another few years.

Graphite anodes even of improved quality have a life of only about 1-2 years according to the current density and other operating conditions. On account of the fact that the graphite is burned off constantly, the electrical resistance in the cell increases and causes the cell voltage to rise. The consequence is that the energy consumption of a cell with graphite anodes is gradually increasing.

Also the performance of diaphragms in cells is greatly improved by use of DSA^R anodes on account

of prolonging their life and making them more dimensionally stable. The use of the improved diaphragms became possible only after the introduction of the DSA^R.

The dimensionally stable anodes of the present day, by which about 60% of the chlorine output in the western part of the world is produced, are generally fabricated from titanium rods or from expanded metal, provided with an electrocatalytic coating of stabilized ruthenium oxides and titanium oxides. The rods are mounted on a titanium substructure to build a solid unit and also to provide good electrical conductivity.

These anodes are mounted in the cells in such a way that they are placed on a distance of only a few mm from the cathode. In mercury cells they are fixed in a horizontal position, in diaphragm and membrane cells in a vertical position. Especially at high current densities the geometric configuration of metal anodes favors the release of gas bubbles from the anode surface and prevents "gas bubble effect" which lowers the efficiency of the cell.

The replacement of graphite anodes by dimensionally stable anodes in the chlorine-alkali cells has brought about a considerable saving of energy since they were first introduced and applied in the United States in 1968. Since 1970 up to the end of 1979 the savings of electric energy in North America which can be attributed directly to the use of DSA^R, in 70 different plants, totals considerably over 19 billion kW-hr. The energy savings in North America for 1979 in these plants is estimated at about 3 billion kW-hr.

Whenever mercury cells might become forbidden on account of the mercury pollution, the switch from mercury cells to membrane cells might be a perfect alternative.

The massive change-over to metal anodes, called DSA^R, has opened the possibility to embark on a great volume of research and development work in various directions.

Another field where the DSA^R is applied on a large scale and which is in full development is the production of sodiumhypochlorite solutions, used in great quantities for disinfection purposes. These hypochlorite solutions are employed as a means to prevent fouling of the cooling systems of power stations due to growth of aquatic organisms, by blocking the biological activity in the cooling water during supply and drainage.

Water, sterilized by hypochlorite solutions is also used to be injected into oil and gas-containing strata to compensate the decrease in pressure of the oil wells and to boost it up in order to raise the oil production.

Hypochlorite solutions are also applied for the destruction of the cyanide used in the galvanizing industry, for the disinfection of potable water from seawater, for bleaching paperpulp and textiles, for the sterilization of water in swimming pools, and for treating sewage.

Since hypochlorite solutions have the tendency to deteriorate with time and are also difficult to transport in large quantities, it is now becoming popular for users to produce their own hypochlorite solutions by means of small cells placed right at the point of use, by the direct electrolysis of brine or seawater. Many types of these cells are offered and are generally electrolyzers of bipolar design, available in different sizes ranging from an electrolyte-flow rate of 0.5-100 cubic meters per hour to produce a hypochlorite solution with a concentration from 1 to 8 g/liter.

The use of these hypochlorite generators, equipped with DSA^R, right on the point of use, avoids the problems arising when chlorine is used for the above purposes, since the storage of chlorine is dangerous and the dosage of chlorine to the liquid to be treated is not an easy matter, because it has to be carefully

controlled. Moreover, some countries have restricted the transportation of chlorine on public roads.

The most used electrocatalytic coating on titanium anodes for the preparation of hypochlorite solutions, consists of stabilized mixed oxides of ruthenium and titanium.

For all these and other purposes, the coatings can be modified by the addition of other metals or metal oxides such as tin, antimony, and noble metals to improve their catalytic activity and life. The field of application of these anodes, apart from the chlorine-alkali electrolysis, is constantly expanding. Such is the case for example in the electrowinning of metals from aqueous solutions of metal chlorides or metal sulfates, where the dimensionally stable anodes have met with great success, as they permitted a more economical winning of metals from ores having a low concentration of metals.

Here again the dimensionally stable anodes have brought considerable improvements to this field. They may be summarized as follows: (i) lower half-cell potential, (ii) use of higher current densities, (iii) lower gas bubble effect through special anode designs, (iv) no loss of anode material, keeping the electrolyte pure, (v) no contamination of the cathode deposits on the cathode, (vi) high current efficiency, and (vii) simple cell constructions. The electrowinning of cobalt on an industrial scale by means of dimensionally stable anodes has been initiated in Sweden a few months ago.

Since my invention of the dimensionally stable metal anodes with stabilized coatings of mixed oxides in 1967, these anodes have been widely accepted in the industrial world, for use in all kinds of electrolytic processes and has consequently spurred much research activity in the whole world.

Unquestionably the invention of the dimensionally stable anodes has stimulated the general interest for electrochemistry and has drawn the attention again on its importance for the industry in many different fields. Scientific reports and patents relating to electrochemistry have been increasing yearly.

A result of this is that recently much research is being done on cathodes, diaphragms, membranes, cell constructions etc. all of which have contributed to savings in energy and capital investments.

It was in April 1957 that I handed in my first patent application for the protection rights regarding titanium metal coated with one of the platinum metals for use as an anode, in the first place with a view to the electrolysis of brine. Towards the end of 1965 I claimed protective rights for titanium anodes coated with oxides of platinum metals alone or together with oxides of nonprecious metals such as lead oxide, iron oxide, copper oxide, etc.

In 1967 I sought protection regarding the use of electrocatalytic materials on titanium, tantalum, etc. which consisted of stabilized mixed oxides of platinum metals and the oxides of the so-called valve metals such as titanium, tantalum, zirconium, etc.

My patent application of 1965 was submitted in 26 countries, in all of which it was granted. The application of 1967 was presented in 44 countries and granted in all of them with the exception of one or two.

The patent priority of the anodes coated with simple oxides therefore dates back to 1965, while that of the stabilized mixed oxides as for example $\text{RuO}_2/\text{TiO}_2$ dates from 1967.

The fact that some of these patents, as, e.g., in the United States, have only been granted in 1972 does not alter the fact that the inventions were made and claimed in 1965 and 1967, respectively, and have priority patent protection from that time on. In some countries, as for instance in the United States, supplementary patents of third parties have been granted earlier than these basic patents of the oxide anodes. This has to be attributed to the longer period needed

for the examination of the original basic patent applications of 1965 and 1967 which therefore were granted on a later date. Since 1956, the beginning of the first generation of titanium anodes, until the year 1970, I have applied for more than 400 patents in this field, spread over various countries. Practically all of these have been granted.

I would like to add that the invention of stabilized electrocatalytic oxides on titanium for use in electrochemical reactions came just at the right time, but its success would not have been so great and its worldwide application not so rapid without the contribution of Vittorio de Nora. His profound knowledge of electrochemistry and his vision of the future revolutionary applications of DSA^{R} , particularly to the chlorine and electrometallurgical industry, made him sure (probably the only one at that time) that my electrodes, presently known as DSA^{R} , could work with great advantages in substitution of graphite anodes with enormous savings in energy and that they would permit the design of a new generation of cells. He was sure of the success and had the enthusiasm and perseverance to reach this success.

But in doing so he had the full support of his brother Oronzio and the backing of his company "Impiati Electrochimici S.A." which for many years had supplied chlorine cells to the United States, Japan, France, and other countries, as well as that of Diamond Shamrock with its unique position of supplier of electrochemical technology and one of the world's biggest chlorine producers. Bill Bricker, chairman of Diamond Shamrock did understand the importance of this new technology and acquired the world rights for this technology, which is continuously being improved, thanks to the great research efforts for which he gives the financial support and personal encouragement of his company.

I remember that when I began to experiment with platinized titanium back in 1957 there was very little interest for metal coated anodes in the industry. Of course nobody could foresee the energy crisis and the costs of labor were no special difficulty at that time. Consequently there was in the first ten years hardly any interest on the part of, e.g., the chlorine-alkali industry. Luckily it was different for the installations for cathodic protection systems, electroplating industries, and other minor industrial fields where these anodes could at once solve existing technical problems. This kept me going more or less financially through all those years.

The chlorine-alkali industry did not generally struggle with problems, which urgently needed a solution or with any major technical difficulty. In this particular branch the industry had learned to live with some inconveniences connected with the operation of their plants. But in 1967 the upcoming of DSA^{R} with its improved catalytic coatings of stabilized mixed oxides, at once filled a vacuum in the chlorine-alkali industry, created by the sharp rise in energy costs, labor, and because the experts began to believe in the advantages of DSA^{R} .

DSA^{R} should not be looked upon as an integral system of its own, the effect of which can be measured at a glance and therefore might be easily accepted. Rather it should be considered as one of the components in a very complicated system as for instance the chlorine-alkali process and the intricate function of the cells in which it takes place.

Vittorio de Nora has been successful in convincing the greatest chlorine producers of the enormous advantages which these new anodes would have for their industries and he persuaded them to try out these anodes in their plants. This was by no means an easy job, as industrial firms are often rather skeptical when it comes to the introduction of new technologies in their plants especially when it would require an in-

vestment of millions of dollars and might be a big failure.

Especially the idea not to sell but to lease the anodes to customers and guarantee their performance, has to a great extent, contributed to this successful enterprise, with the result that these anodes could be commercialized on a large scale and did not remain a laboratory curiosity.

As you have heard in the beginning of my paper, the invention of the metal anode has been made quite accidentally. I may say, by a lucky chance, but after that followed a long time of research, testing, negotiating, and commercializing. But many inventions have been made in this way in the past and many examples from earlier times can prove it. But even in our days it still happens rather often. A recent example is the award of the two Nobel prizes for organic chemistry last year to Herbert C. Brown and Georg Wittig. Their discovery also was made quite accidentally and it became their point of departure for their eventual successful results.

Professor Wittig himself said the following about this: "The paths of research rarely lead in straightforward fashion from starting point to desired goal. Although intention predisposes the route, chance or occurrences along the way often enforce a change of course. Just such an interplay of intent and chance has dominated my chemical career, begun approxi-

mately 50 years ago." (Chemical & Engineering News, Oct. 22, 1979.)

That is the reason why in research work, it is so important to give full attention to the smallest details especially the most unexpected ones, and to examine them thoroughly, because once fully developed, they may prove to be more important than the original target of the research program.

I should like to finish my paper by emphasizing the great importance of the savings in energy and the contribution of pollution control which are being obtained by the application of dimensionally stable anodes, especially in the chlorine-alkali electrolysis.

It has recently been calculated that all energy savings in this field in the United States of America, taken together, from the year 1973 until now, would make it possible to supply 2 million houses of middle-sized families with electricity for a whole year. Taking into account that in the States almost half of all the western-world production of chlorine is being manufactured, it would mean more than twice as much for the total western hemisphere and three times for the entire world. This is the contribution of the dimensionally stable anodes to the energy problem.

At the end of this paper I should like to express my gratitude to all those who have assisted me in the past morally, technically, commercially, and financially to bring this venture to a good end.

I thank you for your attention.

Reports on Electrochemical Society Summer Fellowship Awards

During the summer of 1979 the following graduate students received \$1,875, \$1,575, and \$1,050, respectively, representing the three Summer Fellowship Awards of The Electrochemical Society.

Mr. Lawrence A. Bottomley, The University of Houston, Houston, Texas, was awarded the Edward Weston Fellowship.

Mr. John D. Porter, Carleton University, Ottawa, Canada, was designated as the recipient of the Colin Garfield Fink Fellowship.

Mr. Bradley R. Karas, University of Wisconsin-Madison, Madison, Wisconsin, received the Joseph W. Richards Fellowship.

The Summer Fellowship Awards are made "without regard to sex, citizenship, race, or financial need, to a fellow or teaching assistant pursuing work between the degrees of B.S. and Ph.D. on a subject in a field of interest to The Electrochemical Society." They are intended to cover a period during which the recipient has no financial support for the continuance of his or her work.

The Edward Weston Summer Fellowship Report

Mr. Bottomley's report is given below.

An Electrochemical Investigation of Several μ -Nitrido Iron Porphyrin Dimers

To date, there are a limited number of complexes known in which two heme centers exist in close proximity. The most well characterized of these is the μ -oxo dimer (1) in which the Fe atoms of two porphyrin or Schiff base complexes are bound to a single O atom. Crystallographic evidence (2) has shown that the μ -oxo dimer of tetraphenylporphyrinatoiron, (TPPFe)₂O¹, has a nearly linear Fe-O-Fe bond. Theoretical work has predicted this bond to be bent, and such is the case for μ -oxo Schiff base complexes which do not

have steric factors in opposition to the bending forces in the molecule (3). In the case of (TPPFe)₂O, both Fe atoms are antiferromagnetically coupled and are displaced from the porphyrin plane toward the O atom by 0.50Å. The distance between the two mean porphyrin planes is 4.40Å. This system has been the subject of detailed infrared, Mössbauer and NMR spectroscopic (1) investigations. Recent electrochemical studies (4) have shown that the parent [TPPFe(III)-O-Fe(III)TPP] complex can be oxidized to form the mixed valence [TPPFe(IV)-O-Fe(III)TPP]⁺ or reduced to form the mixed valence [TPPFe(II)-O-Fe(III)TPP]⁻ complex. In all three complexes, the formal O²⁻ bridging moiety does not permit axial coordination of Fe atoms by any additional ligands.

Summerville and Cohen (5) have reported that the thermal decomposition of hemin azide produces a second type of hematin dimer, μ -nitrido-bis-[$\alpha,\beta,\gamma,\delta$ -tetraphenylporphyrinatoiron], (TPPFe)₂N. This was the first complex reported in which two first row transition metal complexes were bridged by a single N atom. Crystallographic results (6) have shown that both Fe atoms are displaced from the porphyrin plane by 0.32Å toward the N atom. In addition, the distance between the two mean porphyrin planes is 4.15Å, 0.25Å shorter

¹ Abbreviations used in this report are as follows: μ -oxo-bis($\alpha,\beta,\gamma,\delta$ -tetraphenylporphyrinatoiron), (TPPFe)₂O; μ -nitrido-bis($\alpha,\beta,\gamma,\delta$ -tetraphenylporphyrinatoiron), (TPPFe)₂N; (chlorato) (meso-tetraphenylporphyrinatoiron), TPPFeCl; (perchlorato) (meso-tetraphenylporphyrinatoiron), TPPFeClO₄; tetrabutylammonium perchlorate, TBAP; 1,2-dichloroethane, EtCl₂; dichloromethane, CH₂Cl₂.

than the distance observed for the μ -oxo hematin dimer. Each Fe atom was formally assigned a $+3\frac{1}{2}$ valence state. This formalism was preceded by the earlier assignment of -3 for the bridging N atom from studies on second and third row transition metal systems (7).

A recent electrochemical investigation by Kadish and co-workers (8) has demonstrated that the neutral $[(\text{TPPFe}(\text{III})\frac{1}{2})-\text{N}-\text{Fe}(\text{III})\frac{1}{2})\text{TPP}]$ dimer can be oxidized to form the mixed valence $(\text{TPPFe}(\text{III})-\text{N}-\text{Fe}(\text{IV})\text{TPP})^+$ dimer or reduced in a one electron transfer to form $[(\text{TPPFe}(\text{III})-\text{N}-\text{Fe}(\text{III})\text{TPP})]^-$ complex, isoelectronic with the μ -oxo dimer. Both Fe atoms of the parent complex were shown to be equivalent on the XPS time scale (9). From this data, the electronic configuration about each Fe atom was unambiguously assigned as low spin. This was only the second case of a five coordinate Fe porphyrin complex designated as such (10): thus the uniqueness of this complex prompted the electrochemical investigation of possible ligand binding by nitrogenous bases to the μ -nitrido dimer.

Experimental Section

Materials.— $(\text{TPPFe})_2\text{N}$ was the generous gift of Professor Irwin Cohen. The supporting electrolyte, TBAP, was purchased from Eastman Chemical and dried *in vacuo* prior to use. EtCl_2 was obtained from Mallinckrodt as reagent grade. Ethanol, added by the manufacturer as a stabilizing agent, was removed by extraction with an equal volume of concentrated H_2SO_4 followed by a distilled water wash and then extraction with an equal volume of 5% KOH solution. The solvent was then distilled from P_2O_5 and stored over 4Å molecular sieves prior to use. All ligands used were obtained from Aldrich Chemical. Pyridine, py, was distilled from CaO and stored over 4Å molecular sieves prior to use. 3-Pic and 4-Pic were distilled from KOH pellets and stored in the dark. 3-CN Py and 4-CN Py were recrystallized from benzene and dried *in vacuo* prior to electrochemical titrations. The remaining ligands listed in Table I were used as received.

Instrumentation.—Cyclic voltammetric measurements were made with an EG & G Princeton Applied Research (PAR) Model 173 potentiostat/galvanostat driven by a PAR Model 175 universal programmer. Scans were recorded with a Houston Omnigraphic 2000 X-Y recorder or with a Tektronix Model 5111 storage oscilloscope. A conventional three-electrode system was utilized. A Pt button served as the working electrode and a Pt wire was used as the counterelectrode. A commercial saturated calomel electrode (SCE) was utilized as the reference electrode. Current-voltage curves were measured at 0.02–10 V/sec while all titrations were recorded either at 0.05 or 0.10 V/sec. At faster scan rates IR loss was held to a minimum by the use of a positive-feedback device built into the Model 176 current follower. All solutions were made

Table I. Formation constants for the addition of selected ligands to $(\text{TPPFe})_2\text{N}$

Ligands ^a	σ^b	$\log \beta_2^{c,d}$
3,5-dichloropyridine	0.75	3.8 ± 0.2
3-cyanopyridine	0.56	4.35 ± 0.2
4-cyanopyridine	0.66	4.74 ± 0.15
3-chloropyridine	0.37	5.8 ± 0.2
3-bromopyridine	0.39	5.6 ± 0.1
3-acetylpyridine	0.38	6.90 ± 0.17
4-acetylpyridine	0.50	6.65 ± 0.25
Pyridine	0.00	7.62 ± 0.04
3-picoline	-0.07	7.8 ± 0.2
4-picoline	-0.17	8.10 ± 0.09
3,4-lutidine	-0.24	8.6 ± 0.2

^a See footnote 1 for explanation of abbreviations.

^b Taken from A. J. Gordon and R. A. Ford, "The Chemist's Companion," pp. 144–147, John Wiley & Sons, New York, N.Y.

^c Measured in EtCl_2 , 0.1M TBAP.

^d Temperature = $23^\circ \pm 1^\circ\text{C}$.

0.1M in TBAP and were deoxygenated by bubbling solvent-saturated N_2 through the solution for 10 min. For all electrochemical measurements the SCE was separated from the bulk of the solution with a fritted-glass bridge filled with solvent and supporting electrolyte. Stability constants were determined from the shifts of half-wave potentials as a function of ligand concentration. The method of calculation has been described in previous publications (12, 13). All potentials are reported in volts vs. the SCE. Half-wave potentials were measured as $E_{1/2} = \frac{1}{2}(E_{pa} + E_{pc})$ as determined from cyclic voltammetric data.

Results

$(\text{TPPFe})_2\text{N}$ was dissolved in EtCl_2 , which was 0.1M in TBAP and its redox behavior studied by cyclic voltammetric methods at a Pt button. The redox mechanism previously reported (8) for electrooxidation reduction in CH_2Cl_2 was identical to that observed in EtCl_2 . In the absence of any nitrogenous base, $(\text{TPPFe})_2\text{N}$ was reduced at $+0.17$ and -1.19V vs. SCE to form $[(\text{TPPFe})_2\text{N}]^-$ and $[(\text{TPPFe})_2\text{N}]^{2-}$, respectively. Additions of aliquots of substituted pyridines produced negative shifts in potential for the first reduction of $(\text{TPPFe})_2\text{N}$. A typical plot of $E_{1/2}$ for the reduction of $(\text{TPPFe})_2\text{N}$ vs. the bulk concentration of added ligand is presented in Fig. 1. Similar potential dependences on added ligand concentration were observed for all ligands investigated. In contrast, potentials for the second reduction of $(\text{TPPFe})_2\text{N}$ were invariant over the ligand concentration ranges studied. The potential shifts observed were consistent with complexation of the starting material, $(\text{TPPFe})_2\text{N}$, by two ligand molecules, but not of the reduced species, $[(\text{TPPFe})_2\text{N}]^-$. From the shifts in $E_{1/2}$ stability constants were calculated and are listed in Table I.

Discussion

The complexation of the μ -nitrido dimer reported herein is the first evidence of six coordinate dimeric

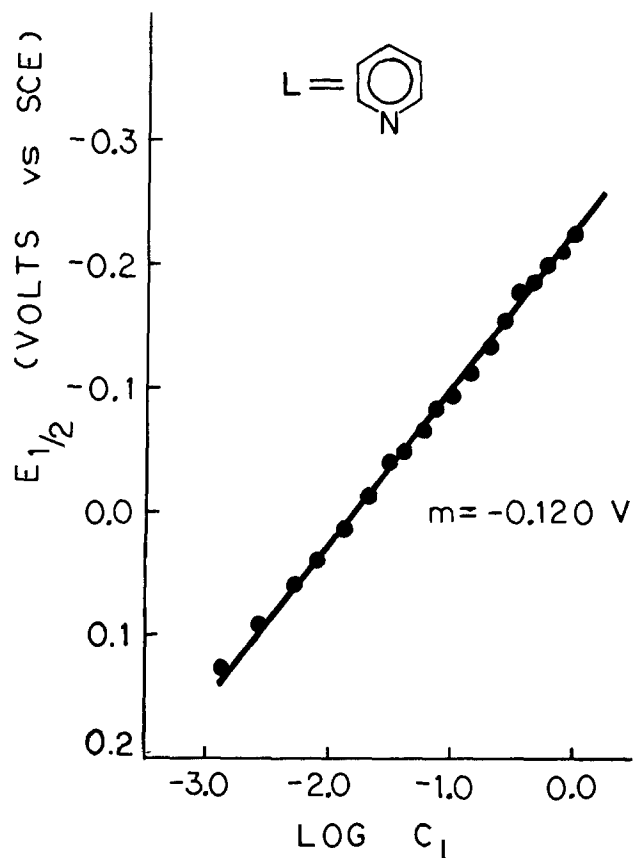


Fig. 1. Half-wave potential dependence upon the bulk concentration of pyridine.

Fe porphyrin species. The coordination of the dimer is intriguing when compared to the behavior of the μ -oxo dimer in the presence of similar complexing agents. There is currently no evidence of any axial coordination of the μ -oxo dimer by substituted pyridines. Ostfeld (14), however, has reported that the μ -oxo dimer is cleaved by the addition of imidazole in nonaqueous media to form the bis imidazole complex of TPPFe^+ . The stability of the μ -nitrido dimer adducts may be attributed, in part, to the increased charge on the bridging N^{3-} atom when compared to O^{2-} . However, a knowledge of the factors responsible for this increased stability is unknown at the present time. Theoretical modeling studies are currently underway in an attempt to explain the observed chemistry (15).

Of special note is the magnitude of β_2 (see Table I). Previous measurements of the affinity of TPPFeCl (16) and TPPFeN_3 (17) for pyridine have yielded values of $\beta_1 = 0.2$ and 1.75M^{-1} , respectively. It is tempting to consider the complexation of each Fe atom in the dimer as a monomeric species with $(\text{N-FeTPP})^-$ as the counterion, in an analogous fashion to Cl^- or N_3^- . However, stepwise addition of the ligands to the μ -nitrido dimer is not observed. Secondly, comparison of the formation constant magnitudes makes any attempts at such a formulation fortuitous.

A linear free energy relationship has been constructed in Fig. 2 comparing the formation constant magnitudes with the respective electron donating or withdrawing substituents on the coordinating ligand. From the slope of $\log \beta_2$ vs. 2σ , a $\rho = -2.38$ was computed. This value is similar to that observed for monomeric iron porphyrin complexes and implies that electron donating substituents on the pyridine facilitate the formation of the complex (see Table II).

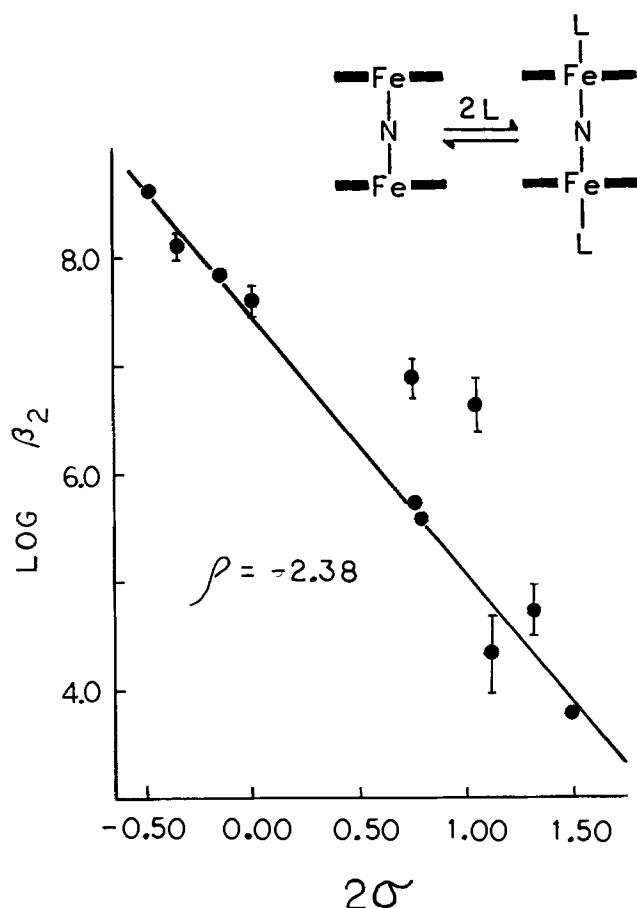


Fig. 2. Linear free energy relationship for addition of two substituted pyridine molecules to $(\text{TPPFe})_2\text{N}$ in EtCl_2 .

Table II. Linear free energy relationships for substituted pyridine complexes of various iron tetraphenylporphyrins

Complex	Formal oxidation state	Solvent	ρ^a
TPPFeL_2	II	CH_2Cl_2	-1.25 ^b
$[\text{TPPFeL}_2] + \text{ClO}_4^-$	III	CH_2Cl_2	-4.19 ^b
$(\text{TPPFeL})_2\text{N}$	III $\frac{1}{2}$	EtCl_2	-2.38

^a Calculated from plots of $\log \beta_2$ vs. 2σ .

^b Calculated from data in Ref. (11).

The reactivity of the μ -nitrido dimer towards imidazole and substituted imidazoles is being studied and will be reported in a subsequent communication.

Acknowledgments

The support of The Electrochemical Society through the Edward Weston Fellowship is gratefully acknowledged. In addition, the author wishes to thank Professor Karl M. Kadish for his support and guidance and Professor Irwin A. Cohen for his gift of the μ -nitrido dimer. Partial support of this research from the National Institutes of Health (Grant GM 25172-02) is also acknowledged.

REFERENCES

- M. A. Torrens, D. K. Straub, and L. M. Epstein, *J. Am. Chem. Soc.*, **94**, 4160 (1972); I. A. Cohen, *ibid.*, **91**, 1980 (1969); G. N. LaMar, G. R. Eaton, R. H. Holm, and F. A. Walker, *ibid.*, **94**, 3620 (1972); D. A. O'Keefe, C. H. Barlow, G. A. Gmythe, W. H. Fuchsman, T. H. Moss, H. R. Lilienthal, and W. S. Caughey, *Bioinorg. Chem.*, **5**, 125 (1975); J. O. Alben, W. H. Fuchsman, C. A. Beaudreau, and W. S. Caughey, *Biochemistry*, **8**, 534 (1969).
- E. B. Fleischer and T. S. Srivastava, *J. Am. Chem. Soc.*, **91**, 2403 (1969); A. B. Hoffman, D. M. Collins, V. W. Day, E. B. Fleischer, T. S. Srivastava, and J. C. Hoard, *ibid.*, **94**, 3620 (1972).
- K. S. Murray, *Coord. Chem. Rev.*, **12**, 1 (1974).
- K. M. Kadish, G. Larson, D. Lexa, and M. Momen-teau, *J. Am. Chem. Soc.*, **97**, 282 (1975).
- D. A. Summerville and I. A. Cohen, *ibid.*, **98**, 1747 (1976).
- W. R. Scheidt, D. A. Summerville, and I. A. Cohen, *ibid.*, **98**, 6623 (1976).
- W. P. Griffith, *Coord. Chem. Rev.*, **8**, 369 (1972).
- K. M. Kadish, J. S. Cheng, I. A. Cohen, and D. A. Summerville in "Electrochemical Studies of Biological Systems," Chap. 5, D. T. Sawyer, Editor, ACS Symposium Series, No. 38, American Chemical Society, Washington, D.C. (1977).
- K. M. Kadish, L. A. Bottomley, J. Brace, and N. Winograd, *J. Am. Chem. Soc.*, **102**, 4341 (1980).
- The first case was TPPFeNO as reported by W. R. Scheidt and M. E. Frisse, *J. Am. Chem. Soc.*, **97**, 17 (1975).
- K. M. Kadish and L. A. Bottomley, *Inorg. Chem.*, **19**, 832 (1980).
- K. M. Kadish, L. A. Bottomley, and D. Beroiz, *ibid.*, **17**, 1124 (1978).
- K. M. Kadish, L. A. Bottomley, and J. S. Cheng, *J. Am. Chem. Soc.*, **100**, 273 (1978).
- D. Ostfeld and J. A. Colfax, *Inorg. Chem.*, **17**, 1796 (1978).
- K. Tatsumi, R. Hoffman, and M. H. Whangbo, *J. Chem. Soc. Chem. Commun.*, 509 (1980).
- F. A. Walker, M. Lo, and M. T. Ree, *J. Am. Chem. Soc.*, **98**, 5552 (1976).
- K. M. Adams, P. G. Rasmussen, W. R. Scheidt, and K. Hatano, *Inorg. Chem.*, **18**, 1892 (1979).

The Colin Garfield Fink Summer Fellowship Report

Mr. Porter's report is given below.

Two-Dimensional Electrocrystallization at Low Overpotentials

Detailed, quantitative studies of the potential dependences of two-dimensional electrocrystallization processes at low overpotentials are lacking. Frequently, experimental results are analyzed in terms of the Fleischmann-Thirsk (FT) geometric model of growth at constant potential (1), which states that the composite rate (k^2Z_n) is related to the transient maximum parameters t_m and i_m (see List of Symbols). Data are collected at individual potentials, and are routinely fit (sometimes implicitly) to empirical equations of the form

$$\log t_m = a_t \eta + b_t \quad [1a]$$

$$\log i_m = a_i \eta + b_i \quad [1b]$$

} for $(t_m, i_m)_{\eta=\text{constant}}$

The geometric FT model demands that $a_t \equiv -a_i$, and consequently the absolute value of either a_t or a_i is usually all that is reported, although the nucleation order n [$n \equiv 0$ for instantaneous nucleation and $n \equiv 1$ for progressive nucleation (2)] is sometimes given as well.

Equations [1a] and [1b] were critically tested in the present study, along with the ability of the FT geometric model to quantitatively describe experimental responses to both potential step and (in an extended form) linear potential ramp perturbations. A self-consistent analysis of transient responses to these perturbations as well as to galvanostatic perturbations was developed for that purpose, and in this scheme experimental results are analyzed in terms of surface coverage. The details of the surface coverage analysis are presented elsewhere (2).

Experimental investigations were performed on the formation of calomel at 22° and -5°C on mercury (2, 3), the formation of thallos chloride at -6.3°C (2, 4), and the formation of thallos bromide at -3.0°C (4), both on thallium amalgam. For reasons of brevity, only the results concerning the formation of thallos chloride will be presented here in any detail.

Experimental

Thallium shot (m6N, Alfa Inorganics) was combined directly with electronic instrument grade mercury (m5N8, Alfa Inorganics) under dry nitrogen to form the 2.1 atom percent (a/o) amalgam used in the present study. The base electrolyte was 0.1M HCl (AristaR, B.D.H.) and oxygen was purged using purified nitrogen. The reference half-cell was the 2.1 a/o Tl(Hg)/TlCl couple in the same base electrolyte and maintained at the same temperature as the working electrode compartment (-6.3° ± 0.1°C). Potentials are quoted either with respect to the reversible potential of the bulk couple or with respect to the reversible potential of the monolayer phase, whichever is appropriate. Careful attention was paid to cell design in order to minimize instrumental limitations to a negligible level. The entire cell assembly was enclosed in a light-tight Faraday cage, which was mounted on a vibration-damped platform.

The potentiostat used in the experiments reported here was a Wenking Model 70 HP 10, and potential perturbations were supplied by a PAR 175 Universal Programmer through a wideband 10:1 divider. Responses to potential perturbations were recorded on a Tektronix 503 x-y/y-t oscilloscope and a Biomation 805 transient recorder, which allowed data to be obtained in a digital format.

Results

General features of the Tl(Hg)/TlCl system.—The anodic electrocrystallization of thallos chloride on thallium amalgam was found to follow the general scheme: (i) simultaneous dissolution and specific adsorption of chloro-thallos complexes, (ii) formation of the first crystalline monolayer of thallos chloride, probably of (110) orientation, (iii) formation of the second crystalline monolayer, probably of (100) orientation, (iv) formation of the third monolayer, (v) formation of the thick layer of bulk thallos chloride. This sequence of events can be seen in Fig. 1, which presents an illustrative current transient recorded in response to a potential step to a high overpotential with respect to the bulk couple. Completely analogous responses were observed to linear potential ramp perturbations. The same pattern was recorded for the formation of thallos bromide (4).

Previous studies performed using thallium amalgam electrodes failed to report the formation of three distinct monolayer phases (5-7), although indications of a third peak in triangular sweep experiments were reported for the case of TlCl formation on solid thallium (6). The reversible potential for the first monolayer has been reported to be at -38 mV with respect to the reversible potential of the bulk couple at 25°C (8), i.e., at underpotential with respect to the bulk phase. This result was confirmed in the present work, a value of (-31 ± 1) mV being routinely observed at -6.3°C.

The experimental procedures reported in a widely quoted early study (5) involved the application of a double potential step, where the intermediate potential was the "rest potential" with respect to the bulk Tl(Hg)/TlCl couple. It is clear that the formation of the first layer could not have been observed in this study under the reported experimental conditions; consequently, the reported formation (5) of two monolayers prior to the formation of the bulk phase, at posi-

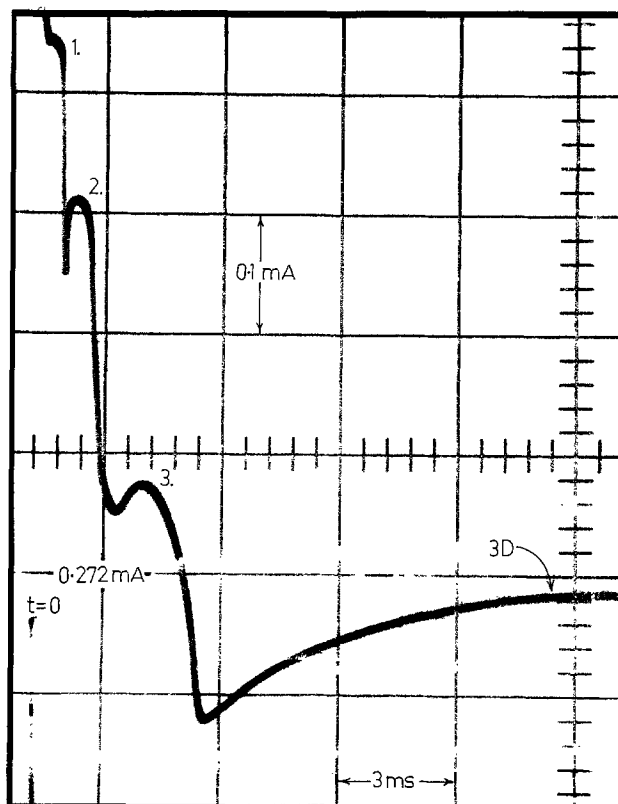


Fig. 1. Representative current transient obtained in response to a potential step to high overpotentials with respect to the bulk phase Tl(Hg)/TlCl couple. The successive formation of three monolayers prior to thick film formation can be seen. $\eta = 143.7$ mV, $T = -6.3^\circ\text{C}$, electrode area = 9.13×10^{-3} cm².

tive overpotentials with respect to the bulk phase, must represent the formation of the second and third monolayers. The crystallographic assignment of (100) orientation for the first of these (5) is consistent with the results obtained for the second monolayer as it is defined in the present study. The crystallographic assignments made here are based upon precise determinations of monolayer charges at their reversible potentials (see Table I), experimental data being compared with crystallographic values (9). Crystalline monolayers of TlBr formed on mercury from aqueous Tl^+ , Br^- solutions have been assigned (110) orientations based upon monolayer charges (10, 11).

The first monolayer was observed to remain both kinetically and thermodynamically distinguishable from bulk phase thallos chloride (and bromide) at all times, even in the presence of a thick film. A separate and distinctive peak was observed for the reduction of the first monolayer subsequent to the reduction of the bulk phase during triangular linear potential ramp perturbations. The unusual property of "underpotential electrocrystallization" observed for the first monolayer of thallos bromide (4) and thallos chloride (8) allowed the formation of the monolayer to be studied in detail, completely separate from the formation of subsequent layers, over a wide potential range. The results of such a kinetic investigation for the case of the formation of the first monolayer of thallos chloride on thallium amalgam are reported below.

Potential step perturbation.—Transient responses were obtained at a series of low overpotentials with respect to the reversible potential of the first monolayer. For reasons of clarity, individual transients were analyzed in terms of surface coverage and quantitatively compared with model curves of $i_r(S)$ (2). Surface coverages were obtained by the numerical integration of current transients using the relationship

$$S(t) = \frac{\int_0^t i \cdot dt}{\int_0^{t_x} i \cdot dt} = \frac{q(t)}{q_x} \quad [2]$$

where $q_x \rightarrow q_{tot}$ as $t_x \rightarrow \infty$. Quantitative agreement between individual experimental transients and model curves was observed regardless of overpotential, provided that the transients were recorded under conditions of low instrumental distortion. A nucleation order $n = 0$, corresponding to instantaneous nucleation of N_0 nuclei, was observed to be in force. The FT geometric model of two-dimensional electrocrystallization appeared to be a quantitatively useful one, therefore, and a more detailed analysis of experimental data based upon the application of this model seemed to be justified. The same conclusion was drawn in the case of the other systems investigated.

However, the parameter q_{tot} was found to be a uniform function of overpotential, again in every case investigated (i.e., for the first monolayers of Hg_2Cl_2 , $TlCl$, and $TlBr$), in direct violation of one of the fundamental assumptions of the FT geometric model. For the case of the first monolayer of $TlCl$, q_{tot} was observed to closely obey an empirical equation of the form

$$\log q_{tot} = \log q_1 - a_q \eta \quad [3]$$

where a_q was determined to be $(10.8 \text{ mV})^{-1}$. This dependence is too high to be due to a potential dependent variation of the crystallographic lattice parameters, despite the excellent agreement between the model and experimental reduced variable curves. A more likely explanation in this case is that the apparent variation in layer charge is due to the potential dependence of $\theta_{Tl(I)}$, where $Tl(I)$ represents specifically, randomly adsorbed thallium (I) species [likely neutral $TlCl$ units (7, 10, 11)]. The "equilibrium" value of $\theta_{Tl(I)}$ is likely to be rapidly established at short times during the falling "dissolution" component of the current transient. Electrocrystallization would then occur, drawing proportionally from the adsorbed reservoir of $Tl(I)$ species and from the $Tl^0(Hg)$ species through further charge transfer; only the latter process contributes to the value of q_{tot} as it was determined in the present study.

This is apparently the first time that uniform variations in the observed "electrocrystallization charges" of two-dimensional layers have been reported. The vital consequence of this observation is that experimental transient maximum parameters may not be converted directly to fundamental kinetic parameters in these cases. Hence, kinetic analyses of systems which exhibit this apparent charge variation, based upon the direct application of the geometric FT model to experimental transient maximum parameters, are invalid unless the effects of the apparent charge variation are eliminated.

The potential dependences of the transient maximum parameters t_m and i_m were investigated carefully in the light of this observation. Both parameters were observed to be extremely potential dependent at "low" overpotentials. Equations [1a] and [1b] were found to be excellent representations of both t_m and i_m , respectively, down to overpotentials as low as 0.2 mV. Least squares values of the empirical constants of Eq. [1a] and [1b] are presented in Table II. One incidental side effect of these extreme, but uniform and well-characterizable potential dependences, was to force an alteration of traditional concepts of overpotential "magnitude" in the author, when electrocrystallization process was being considered. It was often found to be useful to think of potentials in terms of units of a_t or a_i , i.e., to translate potential differences into orders-of-magnitude of observed rate differences.

When plotted in logarithmic form, both $\log t_m(\eta)$ and $\log i_m(\eta)$ were observed to exhibit curvature beginning abruptly at overpotentials "moderately" removed from zero ($\eta \gtrsim 1.5 \text{ mV}$). A quantitative analysis of this curvature will be presented in a section below.

Consistent with the observation of q_{tot} being a function of potential, the parameters a_t and a_i were not observed to be equal and opposite. For those values of overpotential where [1a] and [1b] represent the data well, $(d \log q_{tot}/d\eta) = a_t + a_i$ (2); the least squares data yield a value of $-0.097 \text{ mV}^{-1} = (-10.3 \text{ mV})^{-1}$. This agrees well with the empirical value of a_q , which is valid as well for overpotentials where [1a] and [1b] do not hold. A model-based value for q_1 may be calculated from the empirical b parameters (2), and they give a value of $79.6 \mu\text{C cm}^{-2}$ which agrees well with the experimental and crystallographic values presented in Table I.

Because of experimental limitations, reliably precise measurements were difficult to make at overpotentials less than about 0.2 mV. Down to that limit, however, there was no evidence of a "linear" region where t_m and/or i_m were proportional to η . Strictly expo-

Table I. Integrated monolayer charges† at the monolayer reversible potentials

Salt	Crystallographic*			Experimental	
	$q(100)$	$q(110)$	$q(111)$	q_1	q_2
TlCl	108.99	77.07	125.85	76	103
TlBr	101.65	71.88	117.38	77	102

† In $\mu\text{C cm}^{-2}$.
* Ref. (9).

Table II. Least squares derived constants for Eq. [1a] and [1b], TlCl

$$\begin{aligned} a_t &= -1.110 \text{ mV}^{-1} = (-0.901 \text{ mV})^{-1} & b_t &= -0.130 \\ a_i &= 1.013 \text{ mV}^{-1} = (0.987 \text{ mV})^{-1} & b_i &= -1.186 \end{aligned}$$

potential behavior of those parameters with overpotential was universally observed at the lowest limits of overpotential experimentally accessible. In direct consequence, no nucleation-growth rates lower than the extrapolated values at $\eta = 0$ could be investigated using this technique at the time of the investigation.

Linear potential ramp perturbation.—The analysis of individual transient responses to linear potential ramp perturbations was performed in terms of surface coverage in an analogous manner to the analysis of potential step data, *i.e.*, in terms of $i_r(S)$. Experimental data were compared with model reduced variable curves generated using an extended form of the geometric FT model (2), which is based upon a strictly exponential potential dependence of the combined rate (k^2Z_n). The curves were observed to be encouragingly similar at low potential ramp gradients, but there were some significant differences between the experimental and model responses at surface coverages less than about $\frac{1}{2}$ (2). These differences are reflected in the values of $S_m:S_m \sim 0.56$ (observed) *cf.* $S_m = 0.63$ (model). It is postulated that the differences observed between the extended model and experiment could be due to: (i) growth occurring, at least partly, in potential regions where equations [1a] and [1b] are poor representations of the potential step data, (ii) the presence of effects due to the form of $\theta_{TlCl}(E)$, *i.e.*, the phenomenon manifested as the apparent "electrocrystallization charge" variation in the potential step experiments.

The numerical simulations showed clearly that sets of $(\eta_m, i_m)_\nu$ data obtained in response to linear potential ramp perturbations at a variety of ν , could also be analyzed to yield kinetic information about the electrocrystallization processes, equivalent to that obtained through the analysis of sets of $(t_m, i_m)_\eta$ data obtained in response to potential step perturbations at a series of η values (2). That observation was tested experimentally in the present investigation, and was found to be valid. Kinetic data derived from transient data obtained in response to the two potential perturbation techniques are compared below.

Transient maximum currents were characterized in terms of linear potential ramp gradient as shown in Fig. 2. When plotted in \log vs. \log format, the data could be described best by a series of linear segments. Table III lists their gradients and intersection points. Two important observations can be made: (i) at no time is the observed gradient equal to one, the value demanded by theory and numerical simulation (2, 12), (ii) the gradients decrease as $\log \nu$ increases, again in opposition to theory (12). Similar piecewise-linear behavior was observed both for TlBr formation (4, 12)

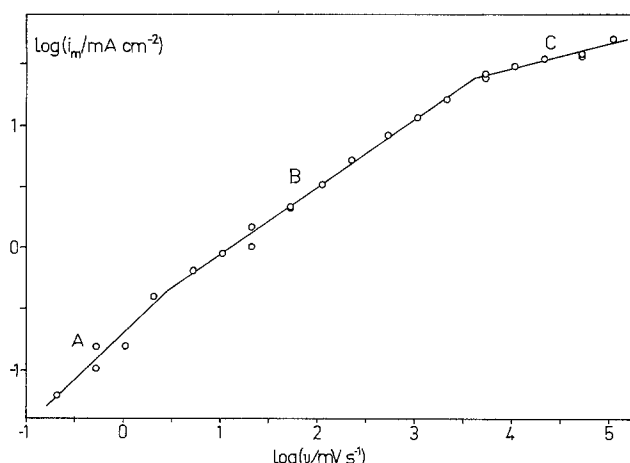


Fig. 2. The dependence of the current maximum observed for the formation of the first monolayer of TlCl on linear potential ramp gradient. The data are represented well by three linear segments (see Table III).

Table III. Analysis of linear potential ramp current maximum data

Section†	Gradient	$\log \nu$ (low)	$\log \nu$ (high)
A	0.758	(-1)*	0.47
B	0.550	0.47	3.62
C	0.202	3.62	(5)*

† See Fig. 2.

* Experimental, not phenomenological limit.

and Hg_2Cl_2 formation (3, 12), and has been recorded for other 2D systems as well (12). In the case of TlBr formation the apparent charge variation effects are comparatively much smaller and the observed gradient was approximately equal to one in the limit of low ν . Correction of the data at low ν for apparent charge variation in the Hg_2Cl_2 data (directly) and the TlCl data (approximately, via Eq. [3]) gave gradients of 0.95 and 0.85, respectively. A value of $(d \log \nu / d \eta_m) = 1.007 \text{ mV}^{-1}$ was observed for TlCl at $\log \nu$ values less than about 0.5. The gradient corresponds well with a_i , obtained from the potential step data.

Potential dependence of derived kinetic parameters.—The FT geometric model states that the transient maximum parameters t_m and i_m , observed in response to a potential step perturbation, are related to the more fundamental composite rate (k^2Z_n) in the following manner, regardless of the form of $(k^2Z_n) = f(\eta)$

$$t_m = ((n+1)^2 \rho^2 / 2\pi M^2 (k^2Z_n))^{1/(n+2)} \quad [4a]$$

$$i_m = (2\pi(zFh)^{(n+2)} (\rho(n+1)/M)^n (k^2Z_n))^{1/(n+2)}$$

$$\exp(-n/(n+2)) \quad [4b]$$

In regions of overpotential where Eq. [1a] and [1b] represent the potential step data well, then the following form of $(k^2Z_n) = f(\eta)$ is implied

$$(k^2Z_n) = K_n \exp(a'\eta) \quad [5]$$

where $K_n = (k^2Z_n)_{\eta=0}$ and a' is an empirical constant. It can be demonstrated that a' and K_n are related to the a and b parameters of Eq. [1a] and [1b] in a direct fashion (2). Using the data presented in Table II, standard values for physical constants (13) and correcting for the apparent charge variation when necessary, values for K_0 and $(a'/2.303)$ were calculated to be: $(2.5 \times 10^{-4}) \text{ mole}^2 \text{ cm}^{-6} \text{ sec}^{-2}$ and 2.220 mV^{-1} from the t_m data, and $(9.1 \times 10^{-4}) \text{ mole}^2 \text{ cm}^{-6} \text{ sec}^{-2}$ and 2.211 mV^{-1} from the i_m data, giving mean values of $\log K_0 = (-3.32 \pm 0.28)$ and $(a'/2.303) = (2.22 \pm 0.01) \text{ mV}^{-1}$. If an absolute upper bound for N_0 at $\eta = 0$ is assumed to be $6.8 \times 10^{14} \text{ cm}^{-2}$, which corresponds to a critical nucleus size of one TlCl unit in a (110) plane, then an absolute lower bound for $k(\eta = 0)$ can be calculated to be $\sim 8.4 \times 10^{-10} \text{ mole cm}^{-2} \text{ sec}^{-1}$. The corresponding linear potential ramp data yielded a value of $(a'/2.303) = 2.20 \text{ mV}^{-1}$, in good agreement with the mean value given above. Two sets of data are given in Fig. 3, the least squares slope giving $(a'/2.303) = 2.21 \text{ mV}^{-1}$.

Quantitative analysis of the data which occur in the curved region of $\log(k^2N_0)$ vs. η plots was also performed. The data derived from both perturbation techniques were found to be well described by an empirical equation of the form

$$(k^2N_0) = \overset{1}{K}_0 \exp(\alpha'\eta^{1/2}) \quad [6]$$

This is shown in Fig. 4. The best-fit value of α' appeared to be dependent upon the perturbation technique used to obtain the data ($\alpha' = 5.64 \text{ mV}^{-1/2}$ for the potential step data and $\alpha' = 4.70 \text{ mV}^{-1/2}$ for the linear potential ramp data, their ratio being 0.83). It is possible that a more precise correction for apparent charge variation would yield better agreement of the linear potential ramp data with the potential step

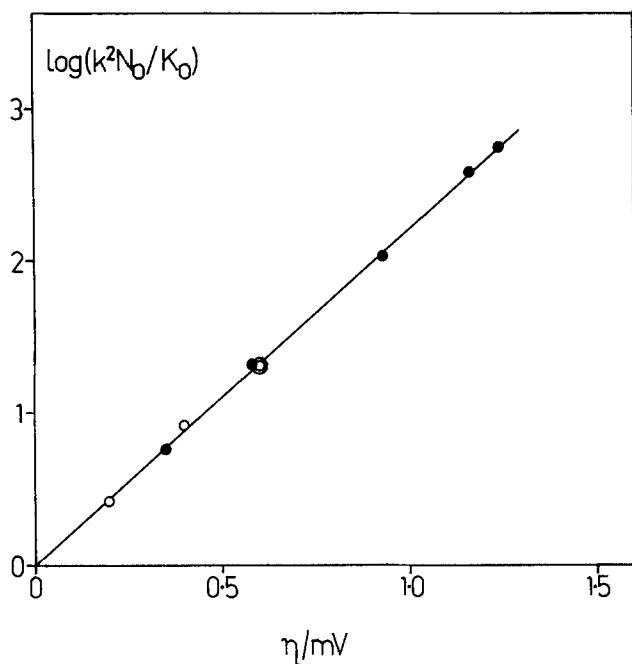


Fig. 3. The potential dependence of the composite rate (k^2N_0) for the formation of the first monolayer of TlCl is illustrated in the "exponential" region where the empirical equation (5) approximates the data well. Rates are derived from (●) potential step and (○) linear potential ramp perturbation responses.

data. Certainly the close correspondence observed between the two sets of data can be considered to be indicative of the quantitative usefulness of the linear potential ramp technique for investigating electrocrystallization processes.

Conclusions

The electrocrystallization of thallos chloride on thallium amalgam was found to follow the sequence: (i) simultaneous dissolution and specific adsorption of Tl(I) species, (ii) formation of the first monolayer of (110) orientation, (iii) formation of the second monolayer of (100) orientation, (iv) formation of the third monolayer, (v) formation of the thick three-dimensional film. The electrocrystallization of thallos bromide was found to follow the same scheme. The first monolayers of TlCl and TlBr are deposited at underpotential with respect to the reversible potential of the bulk phase, and hence their formation could be studied in detail, relatively free from interference. The results for TlCl are presented here.

The FT geometric model of two-dimensional nucleation-growth at constant potential was tested by experimental data analyzed in terms of surface coverage. It was found to be a quantitatively useful model with which to describe the formation of the first monolayers of TlCl, TlBr, and Hg_2Cl_2 using the potential step perturbation technique. An apparent variation in the electrocrystallization charge with overpotential was noted in all three cases. It was strictly necessary to correct characteristic transient parameters for the apparent charge variation before a meaningful kinetic analysis could be performed.

Transient responses to linear potential ramp perturbations proved amenable to quantitative analysis as well, yielding kinetic information which compared favorably with that obtained using the potential step technique. The functional form of the composite rate (k^2N_0) = $f(\eta)$ was determined empirically. At low overpotentials, $\log(k^2N_0)$ was found to be strictly linear with respect to η ; at higher overpotentials $\log(k^2N_0)$ was found to be linear with respect to $\eta^{1/2}$, the transition being abrupt.

The unusual dependence of $\log i_m$ obtained in re-

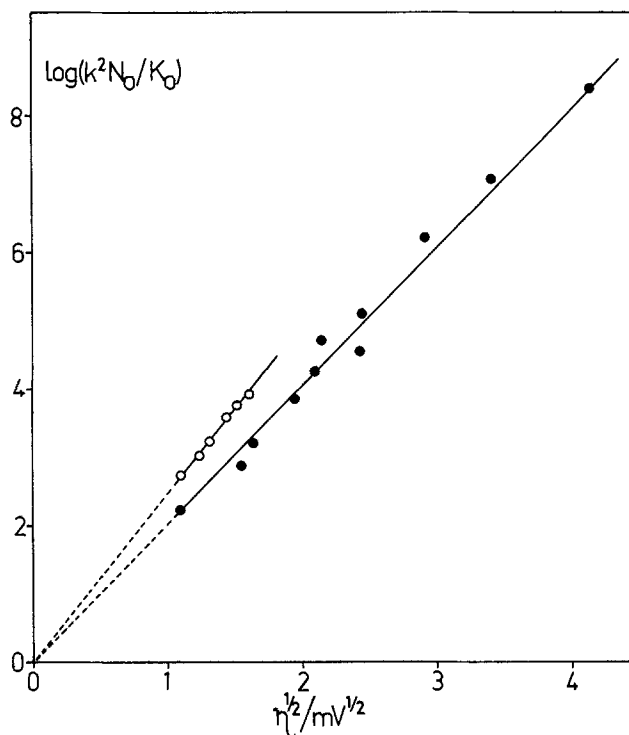


Fig. 4. The potential dependence of the composite rate (k^2N_0) for the formation of the first monolayer of TlCl is illustrated in the "parabolic exponential" region where the empirical equation (6) describes the data well. Rates are derived from (○) potential step and (●) linear potential ramp perturbation responses. The data of Fig. 3 occur in the region of the dotted lines.

sponse to a linear potential ramp perturbation as a function of $\log \nu$ may be rationalized as being due to a combination of factors. In potential regions where $\log(k^2N_0) \propto \eta^1$, the gradient is approximately one as predicted by theory and simulation; where $\log(k^2N_0) \propto \eta^{1/2}$, the gradient is strictly less than one. The effects of potential-dependent charge variation are complex in this case but, overall, this phenomenon serves to decrease the experimentally observed values of $(d \log i_m / d \log \nu)$.

Acknowledgments

The author would like to thank Miss Lilah Moore for her invaluable assistance in obtaining the experimental data presented in this paper. He would also like to thank Professor R. G. Barradas for providing the facilities of his laboratory and for his continuing supervision and encouragement. The receipt of the Colin Garfield Fink Summer Fellowship (1979) of The Electrochemical Society is also most gratefully acknowledged.

LIST OF SYMBOLS

a_t, a_i, a_q, a'	empirical constants, mV^{-1}
A	normalized limiting nucleation rate, $cm^{-2} sec^{-1}$
b_t, b_i	empirical constants
h	monolayer height, cm
i_r	reduced current, $i_r = i/i_m$
k	lateral spreading rate, $mole\ cm^{-2}\ sec^{-1}$
m	refers to transient maximum
M	gram formula weight, $g\ mole^{-1}$
n	nucleation order, $n = 0$ instantaneous, $n = 1$ progressive
N_0	number of nucleation sites per cm^2
q_j	charge density of j th monolayer at its reversible potential, $\mu C\ cm^{-2}$
q_{tot}	integrated monolayer charge density, $\mu C\ cm^{-2}$
S	surface coverage
z	number of electrons
Z_n	nucleation parameter, $Z_0 = N_0, Z_1 = A$
α'	empirical constant, $mV^{-1/2}$
η	overpotential, mV

$\theta_{\text{Tl(I)}}$	fractional surface coverage of adsorbed Tl(I) species
ν	linear potential ramp gradient, mV sec ⁻¹
ρ	density, g cm ⁻³

REFERENCES

1. M. Fleischmann and H. R. Thirsk in "Advances in Electrochemistry and Electrochemical Engineering," Vol. 3, P. Delahay, Editor, p. 123, Interscience, N.Y. (1963).
2. R. G. Barradas and J. D. Porter, *J. Electroanal. Chem. Interfacial Electrochem.*, in press.
3. R. G. Barradas and J. D. Porter, in preparation.
4. R. G. Barradas, L. A. Moore, and J. D. Porter, in preparation.
5. M. Fleischmann, J. Pattison, and H. R. Thirsk, *Trans. Faraday Soc.*, **61**, 1256 (1965).
6. R. D. Armstrong, L. J. Pierce, and H. R. Thirsk, *Electrochim. Acta*, **14**, 949 (1969).
7. R. D. Armstrong, W. T. Race, and H. R. Thirsk, *J. Electroanal. Chem. Interfacial Electrochem.*, **23**, 351 (1969).
8. R. D. Armstrong and J. D. Milewski, *ibid.*, **21**, 547 (1969).
9. R. W. G. Wyckoff, "Crystal Structures," Interscience, N.Y. (1948).
10. C. M. Elliott and R. W. Murray, *J. Am. Chem. Soc.*, **96**, 3321 (1974).
11. C. M. Elliott and R. W. Murray, *Anal. Chem.*, **48**, 259 (1976).
12. R. G. Barradas and J. D. Porter, *Electrochim. Acta*, Submitted.
13. R. C. Weast, Editor, "Handbook of Chemistry and Physics," 54th ed., CRC Press, Cleveland (1973).

The Joseph W. Richards Summer Fellowship Report

Mr. Karas' report is given below.

Temperature Effects on Excited-State Deactivation in Luminescent Photoelectrochemical Cells Employing Tellurium-Doped Cadmium Sulfide Electrodes

Photoelectrochemical cells (PEC's) have received widespread attention recently, owing to their ability to convert optical energy directly into electricity (1). A typical PEC consists of an n-type semiconductor, a counterelectrode, and an electrolyte. The key element of the PEC is the semiconductor, which serves as both photoreceptor and electrode.

The excited state is efficiently formed by the semiconductor's absorption of an ultrabandgap energy photon to generate a conduction band electron and valence band hole ($e^- - h^+$ pair) (2). We consider deactivation of the semiconductor excited state by three routes: $e^- - h^+$ separation leading to photocurrent, radiative $e^- - h^+$ recombination, and non-radiative $e^- - h^+$ recombination (heat). Thus far, only a few studies have dealt with radiative recombination in PEC's (3-5).

To date, we have determined the general characteristics of Te- and Ag-doped CdS-based PEC's (6-8). The stability of Te- and Ag-doped CdS (CdS:Te, CdS:Ag) photoelectrodes was demonstrated by lack of weight loss and surface damage after prolonged PEC operation. Both CdS:Te and CdS:Ag resemble undoped CdS in their ability to sustain the conversion of ultrabandgap (≥ 2.4 eV; $\lambda \lesssim 500$ nm) light into electricity. The novel feature of these doped electrodes is the luminescence observed while they function in an operating PEC. Luminescence in this context signifies that radiative recombination of $e^- - h^+$ pairs occurs in direct competition with $e^- - h^+$ separation leading to photocurrent.

Emission from CdS:Te and CdS:Ag involves intra-

bandgap states. Tellurium is thought to substitute for S to yield states ~ 0.2 eV above the valence band edge (9-11). Because of its smaller electron affinity, Te can trap a hole which can then coulombically bind an electron to form an exciton. Radiative collapse of the exciton is the source of luminescence ($\lambda_{\text{max}} \sim 600$ nm for 100 ppm CdS:Te). The mechanism by which CdS:Ag emits is more complex and depends on the presence of additional impurities and on whether Ag substitutes at Cd sites or interstitially (15-17).

The emissive properties of CdS:Te- and CdS:Ag-based PEC's were exploited by assembling the cell in the emission compartment of a spectrofluorometer. Inclining the semiconductor photoelectrode at $\sim 45^\circ$ to both the Ar ion laser excitation source and the emission detection optics allows for sampling of front-surface emission during PEC operation. PEC parameters such as excitation wavelength (457.9-514.5 nm) and intensity (≤ 30 mW/cm²), the presence of composition of (poly)chalcogenide electrolytes, and applied potential ($-0.3V$ vs. SCE to the onset of cathodic current) only perturb the emission intensity, not its spectral distribution. For ultrabandgap excitation ($\lambda \lesssim 500$ nm), increasingly negative bias decreases the driving force for $e^- - h^+$ separation and increases the luminescence intensity by ~ 15 -1400% in passing from $-0.3V$ vs. SCE to open circuit. Over this same potential range the photocurrent progressively declines to zero. With bandgap edge illumination (514.5 nm) the luminescence intensity is almost independent of electrode potential (6-8). These observations are likely due to the difference in penetration depth between ultrabandgap and bandgap edge photons.

The temperature coefficient for the CdS bandgap edge is $\sim -5 \times 10^{-4}$ eV/ $^\circ\text{K}$ (12). As the temperature is raised, the absorption onset should red shift, and a marked change in penetration depth for 514.5 nm excitation should occur. Our goal was to investigate the effect of elevated temperature on the emission intensity, spectral distribution, and photocurrent as a function of voltage, excitation wavelength, and electrolyte composition.

Experimental

Single crystal plates of vapor-grown 100 ppm CdS:Te and undoped CdS were obtained from Cleveland Crystals, Incorporated, Cleveland, Ohio. The $\sim 5 \times 5 \times 1$ mm samples were oriented with their 5×5 mm face perpendicular to the c-axis. Electrode and electrolyte preparation as well as electrochemical and optical instrumentation have been described previously (8, 13).

Results and Discussion

As stated above, a diminution of the CdS:Te bandgap is expected with increasing temperature; however, the effect on the CdS:Te emission spectral distribution will depend on the relative positions of the valence band, conduction band, and the intrabandgap tellurium states. In (di)selenide electrolyte between 20 $^\circ$ and 100 $^\circ\text{C}$, little or no change in the emission spectrum occurs. The emission spectrum is also independent of whether 501.7 or 514.5 nm excitation is used and independent of electrode potential between +0.7V vs. Ag (pseudoreference electrode, PRE) and the onset of cathodic current (13). To facilitate emission intensity measurements a single wavelength was monitored, generally λ_{max} .

A decrease in emission intensity obtains with increasing temperature over the range 20 $^\circ$ -100 $^\circ\text{C}$. Figure 1(a) displays the open-circuit emission intensity monitored at 600 nm for 501.7 and 514.5 nm excitation. It is apparent that the rates of decline (a factor of ~ 10 -20) are comparable for both excitation wavelengths. In addition, the effect of potential on the emission intensity is shown in Fig. 1(b) and (c) which present emission-temperature plots for 514.5 and 501.7 nm ex-

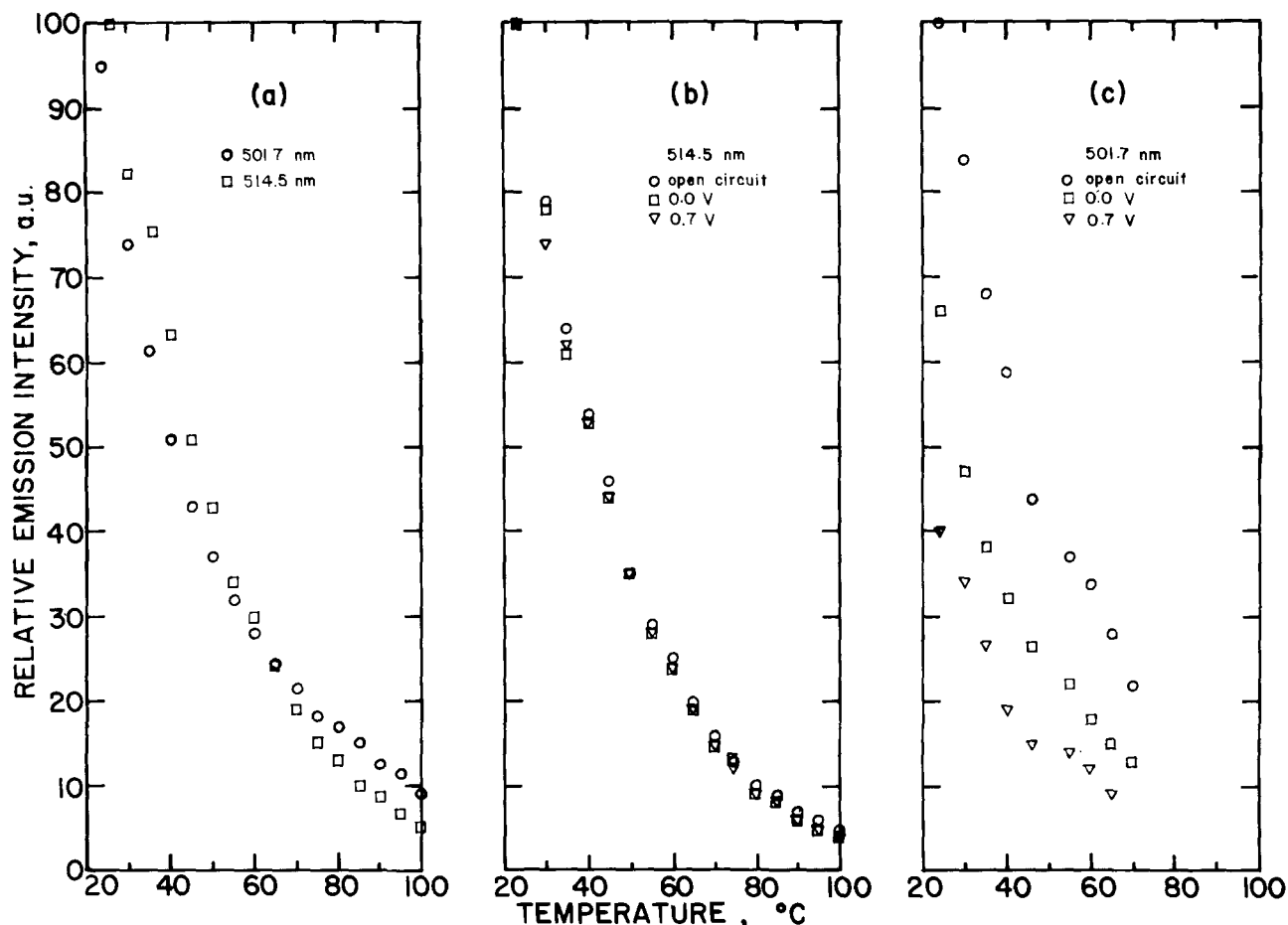


Fig. 1. (a) Relative emission intensity monitored at 600 nm vs. temperature in polyselenide electrolyte ($5M OH^-/0.09M Se^{2-}/0.001M Se_2^{2-}$) of CdS:Te excited at open circuit with 501.7 nm (circles) and 514.5 nm (squares) light. The excitation intensity at 501.7 nm is $6\times$ that at 514.5 nm in order to approximately match emission intensity at room temperature; (b) relative emission intensity vs. temperature for 514.5 nm excitation of a CdS:Te electrode [different sample than in (a)] in polyselenide electrolyte ($5M OH^-/0.02M Se^{2-}/0.001M Se_2^{2-}$) at three potentials. Circles, squares, and triangles correspond to open circuit, 0.0V, and 0.7V vs. Ag (PRE), respectively; (c) relative emission intensity vs. temperature for the same electrode and geometric configuration as in (b), but now excited with an equivalent number of 501.7 nm photons as in (b). The point "100" on the emission scale is \sim one-fifth the corresponding point in (b). The symbols in (c) have the same significance in terms of potential as in (b). Typical photocurrent behavior at 0.7V accompanying the emission changes shown in (b) and (c) is given in Fig. 2(a).

citation, respectively, at three potentials: open circuit, 0.0V, and 0.7V vs. Ag (PRE). The rate of decline in both figures is roughly independent of potential. This is most easily seen in Fig. 1(b) where little potential dependent emission occurs until high temperatures are reached. However, even with potential dependent emission (ultrabandgap 501.7 nm excitation) in Fig. 1(c), roughly parallel rates of decline are observed. These data demonstrate that the emission intensity declines at a rate which is basically independent of excitation wavelength (501.7 and 514.5 nm) and potential (0.7V vs. Ag (PRE) to open circuit).

The room temperature photocurrent for 501.7 nm excitation of a CdS:Te photoelectrode is \sim 15-20 times greater than for bandgap edge 514.5 nm light [Fig. 2(a)]. In (di)selenide electrolyte between 20° and 100°C, the 514.5 nm photocurrent increases by an order of magnitude, reaching 50-100% of the room temperature 501.7 nm value. Over the same temperature excursion 501.7 nm photocurrent increases modestly by \sim 20%. A similar photocurrent-temperature profile for undoped CdS is shown in Fig. 2(b).

Simultaneous measurement of current, luminescence, and voltage (iLV curve) as a function of temperature is shown in Fig. 3. Equivalent intensities (ein/sec) of 501.7 and 514.5 nm excitation were used at both room temperature and elevated temperatures (49°C for 501.7 nm, 86°C for 514.5 nm). The iLV curves may be summarized as follows: photocurrent at 23°C is \sim 18 times

greater for 501.7 nm excitation (curve A vs. curve B) and emission intensity is \sim 5 times smaller (A' vs. B'). The ratio of the open-circuit to the in-circuit [0.7V vs. Ag (PRE)] emissive quantum efficiencies (ϕ_{r0}/ϕ_r) is 1.0 for 514.5 nm (B') and 3.5 for 501.7 nm light (A'). Increasing the temperature to 49°C increases the 501.7 nm photocurrent by \sim 15% (C) and reduces the emission intensity by a factor of 2. However, a similar value of ϕ_{r0}/ϕ_r of 3.4 obtains (C'). At 86°C the 514.5 nm photocurrent increases by a factor of almost 8 (D). For the first time with 514.5 nm excitation and despite its lower absolute intensity, potential dependent emission was observed and a ϕ_{r0}/ϕ_r value of 1.27 recorded (D', note $10\times$ scale expansion). All of the aforementioned changes were reversible upon returning to lower temperature. Similar photocurrent and emissive trends are observable in OH^-/S^{2-} electrolyte.

Observation of an increased photocurrent quantum yield (ϕ_x) and a nonunity ϕ_{r0}/ϕ_r value for 514.5 nm excitation provided insight into a correlation of ϕ_x with ϕ_{r0}/ϕ_r . These relationships is described in detail elsewhere (13, 14).

Acknowledgment

I am grateful to The Electrochemical Society for its support through the Joseph W. Richards Summer Fellowship. In addition, the author wishes to thank Professor Arthur B. Ellis for his continued support and guidance; David J. Morano and Daniel K. Bilich are

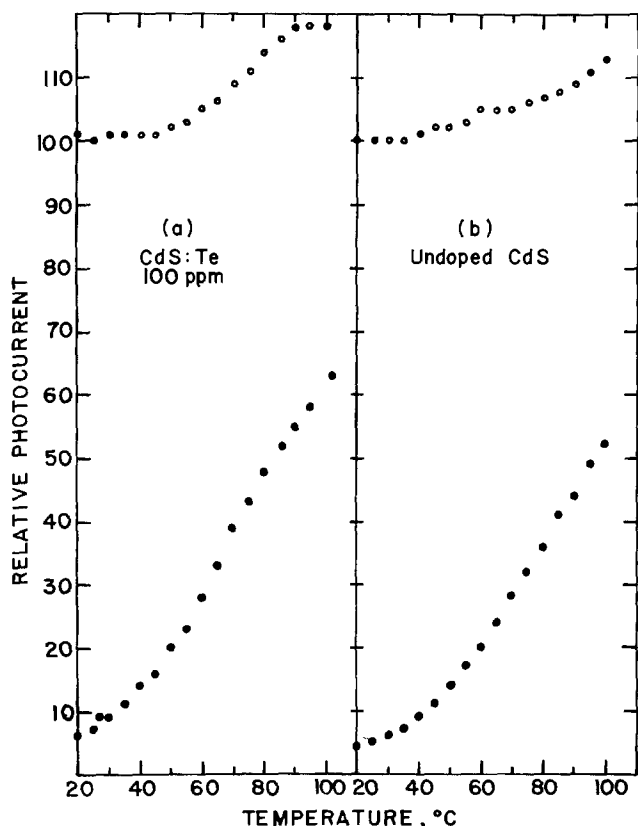


Fig. 2. (a) Relative photocurrent vs. temperature for a CdS:Te electrode in aqueous polyselenide electrolyte ($5M OH^-/0.02M Se_2^{2-}/0.001M Se_2^{2-}$) excited with equivalent photons of 514.5 nm (filled circles) and 501.7 nm (open circles) light at 0.7V vs. Ag (PRE). The scale is such that the photocurrent at 25°C from 501.7 nm excitation has been arbitrarily set at 100 and corresponds to a current density of $\sim 0.36 \text{ mA/cm}^2$ and a quantum yield for electron flow, ϕ_{ex} of ~ 0.50 ; (b) relative photocurrent vs. temperature for an undoped CdS electrode in the same electrolyte as in (a), excited with an equivalent photon flux of 514.5 nm (filled circles) and 501.7 nm (open circles) light. Again, "100" has been arbitrarily set as the 25°C photocurrent from 501.7 nm excitation and represents a current density of $\sim 0.44 \text{ mA/cm}^2$ and a ϕ_{ex} of ~ 0.60 .

acknowledged for their assistance with some of the measurements.

REFERENCES

- (a) A. J. Bard, *Science*, **207**, 139 (1980); (b) M. S. Wrighton, *Acc. Chem. Res.*, **12**, 303 (1979); (c) A. J. Nozik, *Ann. Rev. Phys. Chem.*, **29**, 189 (1978).
- H. Gerischer, *J. Electroanal. Chem. Interfacial*

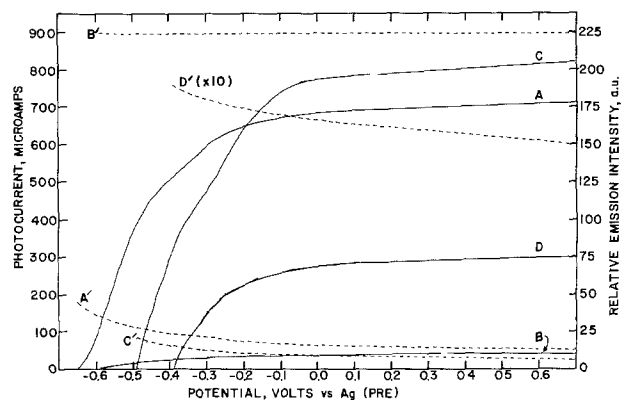


Fig. 3. Current-luminescence-voltage (*iLV*) curves for a CdS:Te electrode in polyselenide electrolyte. Unprimed, solid line curves are photocurrent (left-hand scale) and primed, dotted line curves are luminescence intensity (right-hand scale) monitored at $\lambda_{max} \sim 600 \text{ nm}$. A and A' were obtained from excitation at 501.7 nm, 23°C; B and B' from 514.5 nm, 23°C; C and C' from 501.7 nm, 49°C; D and D' from 514.5 nm and 86°C. Note that the ordinate of D' has been expanded by a factor of 10. Equivalent numbers of 501.7 and 514.5 nm photons were used in identical PEC geometric configurations. The exposed electrode area is $\sim 0.41 \text{ cm}^2$ and the estimated ϕ_{ex} for 501.7 nm excitation at 23°C and 0.7V vs. Ag (PRE) is ~ 0.50 , uncorrected for reflection losses and solution absorbance.

Electrochem., **58**, 263 (1975).

- G. Petermann, H. Tributsch, and R. Bogomolni, *J. Chem. Phys.*, **57**, 1026 (1972).
- B. Pettinger, H.-R. Schöppel, and H. Gerischer, *Ber. Bunsenges. Phys. Chem.*, **80**, 849 (1976).
- K. H. Beckmann and R. Memming, *This Journal*, **116**, 368 (1969).
- A. B. Ellis and B. R. Karas, *J. Am. Chem. Soc.*, **101**, 236 (1979).
- A. B. Ellis and B. R. Karas, *Adv. Chem. Ser.*, **184**, 185 (1980).
- B. R. Karas and A. B. Ellis, *J. Am. Chem. Soc.*, **102**, 968 (1980).
- J. D. Cuthbert and D. G. Thomas, *J. Appl. Phys.*, **39**, 1573 (1968).
- D. M. Roessler, *J. Appl. Phys.*, **41**, 4589 (1970).
- A. C. Aten, J. H. Haanstra, and H. deVries, *Philips Res. Rep.*, **20**, 395 (1965).
- R. H. Bube, *Phys. Rev.*, **98**, 431 (1955).
- B. R. Karas, D. J. Morano, D. K. Bilich, and A. B. Ellis, *This Journal*, **127**, 1144 (1980).
- A. B. Ellis, B. R. Karas, and H. H. Streckert, *Faraday Discuss. Chem. Soc.*, Submitted for publication.
- K. Colbow and K. Yuen, *Can. J. Phys.*, **50**, 1518 (1972).
- H. H. Woodbury, *J. Appl. Phys.*, **36**, 2287 (1965).
- J. Lambe and C. C. Klick, *Phys. Rev.*, **98**, 909 (1955).



Photochemical Selective Activation for Electroless Metal Deposition on Nonconductors

Milan Paunovic*

Kollmorgen Corporation, PCK Technology Division, Glen Cove, New York 11542

ABSTRACT

The photochemical methods for selective activation of nonconductors for electroless metal deposition have been classified in this review on the basis of kinetic scheme involved. There are three general kinetic schemes for the formation of catalytic metallic nuclei on nonconductors: photoelectrochemical, photoelectron, and intramolecular photoreduction. Photoelectrochemical scheme involves a photochemical reaction which is followed by an electrochemical reaction. The photochemical reaction is used to produce or deactivate the reducing agent. Catalytic metallic nuclei are formed in the subsequent electrochemical reaction. In the photoelectron method, electrons necessary for the formation of catalytic metallic nuclei M from metallic cations M^{n+} are generated in the direct absorption process of a photon by a semiconductor crystal, which results in the generation of an electron and a hole. In the intramolecular photoreduction kinetic scheme catalytic metallic nuclei are formed in the intramolecular ligand to metal electron transfer process. This review surveys fundamental photochemical principles and discusses problems and prospects of the above processes.

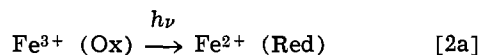
Photochemical processes have been used to produce catalytic metallic nuclei in three ways, each characterized by a different kinetic scheme: photoelectrochemical, photoelectron, and intramolecular kinetic scheme.

Photoelectrochemical method.—In this method the catalytic metallic nuclei M are generated in an electrochemical oxidation reduction process



where Red is the reduced and Ox the oxidized form of a substance and M^{n+} the metallic ion.

The reducing agent (Red) necessary for the reduction of M^{n+} into M according to reaction [1] can be generated in a photochemical process, e.g., the Fe^{2+} (Red) reducing agent is generated in the photochemical process



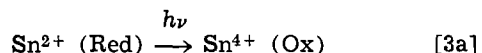
or, in general



Alternatively, the photochemical reaction



can be used to deactivate Red in the area where reaction [1] is not desired (background area), e.g., the Sn^{2+} (Red) reducing agent is deactivated in the photochemical reaction

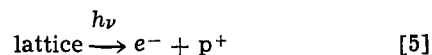


Photoelectron method.—In the photoelectron method, electrons (e^-) necessary for the formation of the cata-

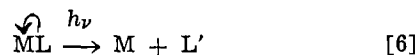
lytic metallic nuclei M according to the reaction



are generated in the direct absorption process of a photon by a semiconductor crystal which results in the generation of an electron and a hole p^+



Intramolecular photoreduction method.—Catalytic metallic nuclei M can also be formed in the intramolecular ligand to metal charge transfer



where $h\nu$ designates a quantum of absorbed energy (photon), L a ligand, L' the reaction products originating from L, and the arrow above the molecule ML the direction of the electron transfer. The term ligand is taken here in its most general definition: an atom, ion, or molecule capable of functioning as the donor in a coordinate bond.

This review will survey fundamental photochemical principles and basic steps of major processes for the photochemical selective activation of nonconductors for electroless metal deposition. Emphasis will be on the mechanism of image formation since understanding the mechanism of these processes may contribute to the solutions for remaining practical problems and the development of new processes.

Description of Kinetic Schemes

Photoelectrochemical Method

The photoelectrochemical method for the formation of catalytic metallic nuclei on nonconductors (1, 2) has three basic steps: (i) sensitization, (ii) latent image formation, and (iii) activation.

* Electrochemical Society Active Member.

Key words: absorption, catalysis, energy transfer, nucleation.

According to the redox theory: (1) the catalytic metallic nuclei M on a nonconductor are formed in the third step, activation, which is interpreted as the electrochemical process represented by the general equation

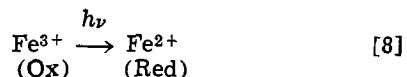


where Red represents a reducing agent (e.g., Fe^{2+} , Sn^{2+} , Ti^{3+} , Pb^{2+}) for the metallic cation M^{n+} (e.g., Pd^{2+}) and Ox is the oxidation product of Red; (2) the function of the first and the second step is to produce a latent image that consists of the active sites of the reducing agent Red in the pattern area.

Sensitization.—In the first step a photosensitive salt is applied on the surface of the nonconductor. The photosensitive salt can be in its electrochemically active (with respect to reaction [7]), lower oxidation state, Red form, or it can be in its electrochemically inactive, higher oxidation state, Ox form.

An example for the sensitizer which is initially active in the electrochemical step is SnCl_2 , Stannous ion Sn^{2+} can reduce Pd^{2+} ions into palladium metal. A typical sensitizer solution is 0.044M SnCl_2 in 0.1M HCl (3, 4).

An example for the sensitizer initially inactive in the electrochemical step is ferric oxalate, $\text{Fe}_2(\text{C}_2\text{O}_4)_3$. Ferric ion cannot act as a reducing agent, Red, in reaction [7]. However, the reducing agent Fe^{2+} (Red) can be formed from ferric oxalate, $\text{Fe}_2(\text{C}_2\text{O}_4)_3$, the Ox form, in the photoreduction reaction



The photogenerated reducing agent Fe^{2+} can reduce Pd^{2+} ions into Pd metal. The two preferred sensitizer solutions (2) of this type are 0.1M to 0.5M $\text{Fe}_2(\text{C}_2\text{O}_4)_3$ or 0.1M to 0.5M $\text{Hg}_2\text{C}_2\text{O}_4$.

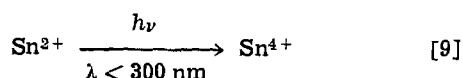
Thus, there are two types of sensitizers in the photoelectrochemical method of formation of catalytic metallic nuclei: (i) initially electrochemically active and (ii) initially electrochemically inactive sensitizers.

Sensitizers can be applied on the surface of a nonconductor selectively, the pattern sensitizing technique, or the entire surface can be covered by the sensitizer, the panel sensitizing technique. In the first case, the pattern printing technique (5), a rubber stamp having the desired pattern can be used to transfer sensitizer from the stamp pad to the nonconductor. The amount of stannous chloride applied to a surface by this technique is found to be in the order of $\mu\text{g}/\text{cm}^2$ (5).

In the second case, the panel sensitizing technique, the sensitizer is applied on the entire surface of the nonconductor using roller coating or immersion technique (2). The amount of the SnCl_2 sensitizer in the sensitized layer was determined by the x-ray fluorescence to be in the order of $\mu\text{g}/\text{cm}^2$ (5).

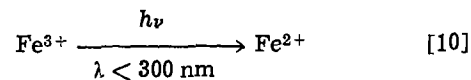
Thus, the result of the sensitization process is a nonconductor having a layer of a sensitizer in the pattern areas or on the entire surface. If the sensitizer is applied in the pattern areas only, and if the sensitizer is of the initially electrochemically active type (Sn^{2+}), the result of the sensitization process is a latent image of the pattern and the nonconductor is ready for the third, activation step. If the panel technique for sensitization is used, the latent image is formed in the second, photochemical step, which is followed by the third, activation step.

Image formation.—Positive version.—The starting material in this process (1) is a nonconductor covered with a layer of the electrochemically active sensitizer, SnCl_2 . The pattern is formed by exposing the sensitized layer to the photochemically active radiation in the background areas leaving pattern areas not exposed. The photochemical reaction is



The result of this photochemical process is that only the pattern area contains Sn^{2+} and the background area Sn^{4+} ions. Since only Sn^{2+} ions can form catalytic active species with Pd^{2+} (e.g., Pd metal, according to reaction [1]), only the pattern area can be subsequently activated to produce catalytic Pd nuclei.

Negative version.—The starting material in this process (2) is a nonconductor covered with the layer of an electrochemically inactive sensitizer, $\text{Fe}_2(\text{C}_2\text{O}_4)_3$. In this case the pattern is formed by exposing the pattern area to the photochemically active radiation leaving background areas unexposed. The photochemical reaction in the exposed area is



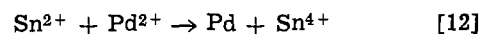
As the result of this process electrochemically active Fe^{2+} ion is generated in the pattern area only, while the background area contains inactive Fe^{3+} ions. Since only Fe^{2+} ions can reduce Pd^{2+} into catalytic Pd metal sites, only the pattern area can subsequently be provided with catalytic metallic nuclei.

Activation.—The activation step consists of exposing a nonconductor containing the latent image of a pattern to an activator solution in order to produce catalytic metallic nuclei according to the general equation

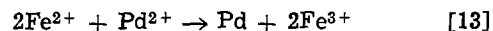


where M represents catalytic metallic nuclei in the pattern area on the nonconductor surface. The activator usually contains salts of noble metals, PdCl_2 , PtCl_2 , or AgNO_3 , that can be reduced in the pattern areas by the reducing species Red.

Specifically, for the positive process (1, 3, 6, 7) using Sn^{2+} as the sensitizer, the activation process is described by the equation¹



and for the negative sensitizing process (2) using Fe^{3+} as a sensitizer, by the equation



Ions present in the background areas, Sn^{4+} in the positive process and Fe^{3+} in the negative process, are inactive in the activator solution. However, Sn^{4+} , under certain conditions, can be chemically active in the activator solution (4, 8-13).

A solution can be prepared that contains both the sensitizer and the activator, for the negative process, in one and the same solution (2). The sensitizer and the activator components will react at the surface on the nonconductor when exposed to the photochemically active radiation in the pattern area. However, one-step tin-palladium solution cannot be used for the positive process (4).

Thus, at the end of the activation process the nonconductor surface contains catalytic metallic nuclei in the pattern area. These nuclei are capable of catalyzing electroless metal deposition.

Mechanism of image formation.—In this review only one mechanism of each kinetic scheme will be discussed.

Negative version. General: photochemistry of coordination compounds.—Understanding the mechanism of photochemical processes requires knowledge of the absorption spectrum of the molecule under consideration. A typical absorption spectrum of a coordination compound consists of several broad bands in the ultraviolet and visible spectrum, each of which is associated with one or more electronic transitions.

¹In some cases this is a simplified presentation of a very complex system. Details are given by R. L. Cohen and K. W. West, *This Journal*, 120, 502 (1973) and R. L. Meek, *ibid.*, 122, 1476 (1975).

Spectra of coordination compounds can be interpreted on the basis of the molecular orbital (MO) theory (14, 15). The ligand-metal bonding system of a coordination compound is mutually interacting in such a degree that one cannot consider excited states of isolated bonds or groups but rather the excited states of the molecule.

Molecular orbitals for a metal complex can also be constructed by the LCAO (linear combination of atomic orbitals) method. These orbitals are given by the Ψ function

$$\Psi = a \Psi_M + b \Phi_{Lig} \quad [14]$$

where Ψ_M is the metal ion orbital, Φ_{Lig} a normalized combination of ligand orbitals, and a and b are the coefficients that determine relative contribution of Ψ_M and Φ_{Lig} to Ψ .

In general, a molecular orbital Ψ formed from two component orbitals, Ψ_A and Ψ_B , includes a larger contribution from that component orbital which is closer to it in energy.

In the first approximation some molecular orbitals Ψ of a metal complex are predominantly metal Ψ_M orbitals, and some ligand orbitals Φ_{Lig} , in character. This localization of states on the central metal ion or on the ligand is only a very rough approximation. The degree of this delocalization of the electron is determined by the values of the coefficients a and b , Eq. [14]. When $a \gg b$ the orbital Ψ is largely localized on the metal and the orbital is a metal-localized orbital. When $a \ll b$ the orbital Ψ is largely localized on the ligand and the orbital is a ligand-localized orbital. This description of the molecular orbitals should be taken as a first approximation only. The molecular orbital diagram for a hypothetical octahedral transition metal complex is shown in Fig. 1.

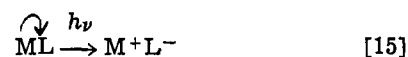
On the basis of the molecular orbital theory one can classify the electronic transitions in coordination compounds into three types.

Ligand field transition (or $d \rightarrow d$ transitions).—These are electronic transitions between MO's mainly localized on the central metal ion (d orbitals).

Intra-ligand transitions.—In the internal ligand transitions electronic transitions occur between MO's mainly localized on the ligand.

Charge transfer (CT) or electron transfer transitions.—In the charge transfer transitions the transfer of electronic charge occurs between MO's mainly localized around the ligand and MO's mainly localized on the central metal.

Depending on the origin of the excited electron one distinguishes two basic types of the charge transfer. (i) Excited electron originally localized on central metal. [Metal \rightarrow Ligand ($M \rightarrow L$) Charge Transfer (MLCT, or CTTL)] In this transition the electron transfer occurs from the metal to a ligand. MLCT can be schematically represented as



where the arrow above the molecule ML shows the direction of the charge transfer.

(ii) Excited electron originally localized on ligand(s). [Ligand \rightarrow Metal ($L \rightarrow M$) Charge Transfer (LMCT or CTTM)] In this transition the electron moves from the ligand toward the central metal. LMCT can be schematically represented as



where the arrow above the molecule ML shows the direction of the charge transfer.

Thus, in both cases, MLCT and LMCT, the absorption of electromagnetic radiation results in an oxidation-reduction process. The ligand to metal charge transfer processes ($L \rightarrow M$) are of central interest in our discussion of the formation of catalytic nuclei on nonconductors.

MLCT and LMCT can be classified as internal charge transfers, charge transfers within a molecule. Another type of charge transfer can occur which can be classified as intermolecular charge transfer. In this type of charge transfer the electron is transferred from either a ligand or the complex as a whole to the solvent, CTTS. In this case the electron is lost to the solvent.

Irradiation of different absorption bands produces different excited states which result in different reaction products and yields. Thus, an interpretation of the absorption spectrum of a photosensitive molecule is necessary in order to be able to conduct a photochemi-

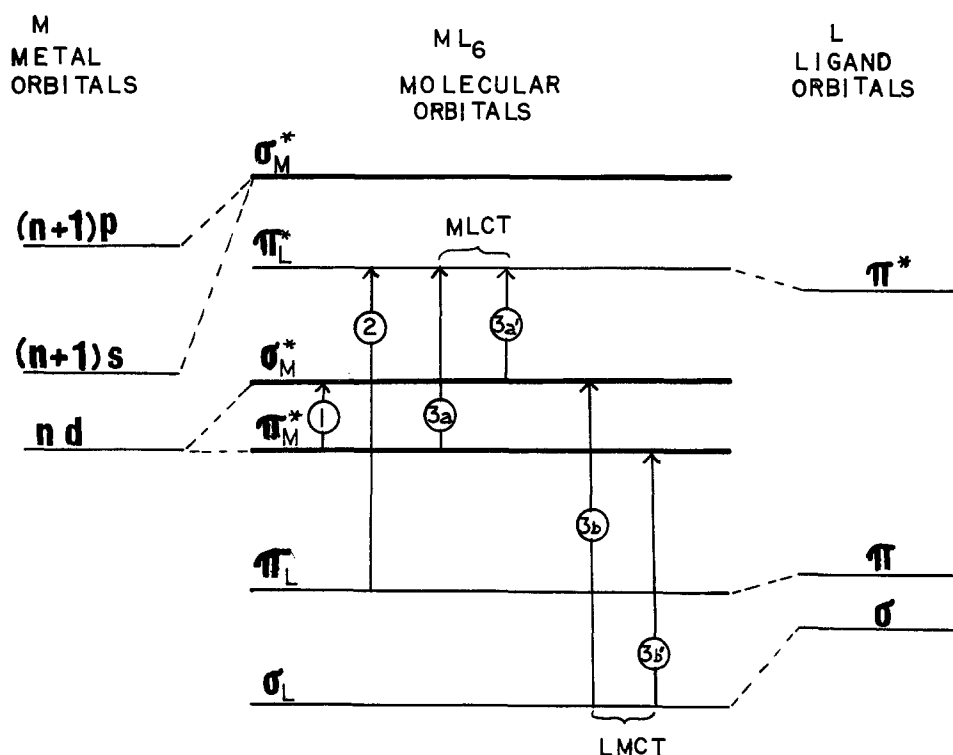
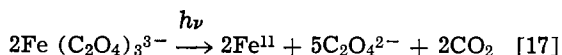


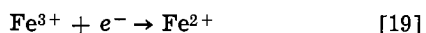
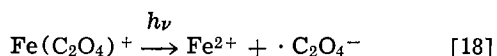
Fig. 1. The molecular orbital diagram for a hypothetical octahedral transition metal complex in which ligands have σ and π orbitals. A molecular orbital which is in the first approximation associated with a ligand orbital is shown in thin-line and molecular orbital associated with the central metal is shown in thick line. Arrows: 1, ligand field transition; 2, intra-ligand transition, 3a, 3a', MLCT; 3b, 3b', LMCT transition.

cal reaction in a direction of production of specific, desired products.

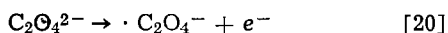
Photochemical reduction of complexed ferric ions.—The redox photolysis of the trisoxalato ferrate(III) in the solid state and in the solution (16, 17) proceeds in such a way that the tripositive Fe^{3+} ion is reduced to the dipositive Fe^{2+} ion and oxalate is oxidized to carbon dioxide, according to the overall reaction



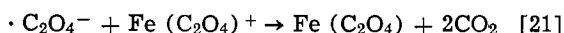
The net primary photochemical reduction reaction of monoxalatoiron(II) ion is, according to Cooper and De Graff (18), the ligand to metal charge transfer



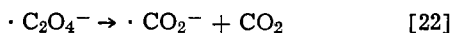
where Fe^{3+} is reduced to Fe^{2+} and the oxalate ion is oxidized to the oxalate radical $\cdot\text{C}_2\text{O}_4^-$



The oxalate radical generated in the primary photochemical process reduces monoxalatoiron(III) ion in a secondary reduction reaction

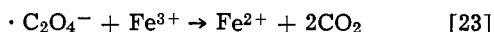


It was proposed (19) that the oxidized ligand, the oxalate radical, can dissociate to give the $\cdot\text{CO}_2^-$ radical and CO_2

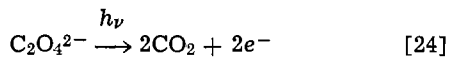


The radical $\cdot\text{CO}_2^-$ can react with the monoxalatoiron(III) ion in a reaction analogous to reaction [20].

In the presence of an excess of Fe^{3+} ions, the oxalate radical can reduce Fe^{3+} ions into Fe^{2+}



Thus, the overall reaction of oxidation of $\text{C}_2\text{O}_4^{2-}$ is



A similar mechanism was proposed for the photochemical reduction of dioxalate and tris-oxalato ferrate (20-23). In the primary photochemical process the electron transfer occurs, resulting in generation of either $\cdot\text{C}_2\text{O}_4^-$ or $\cdot\text{CO}_2^-$ followed by the secondary reactions of these radicals with ferrioxalate or itself, or both.

Positive version. Photochemistry of the Sn(II) sensitizer.—D'Amico, Litt, and DeAngelo (7) postulated that the role of the light is to generate electron hole pairs, in the SnO-SnO_2 sensitized layer, which can participate in the Sn(II) oxidation into Sn(IV). The side reaction in the oxidation of Sn(II) is the reduction (3) of Sn(II) to Sn.

This photochemical reaction needs more study.

Photoelectron Method

In the photoelectron method the catalytic nuclei on nonconductors are formed in two basic steps: (i) sensitization and (ii) image formation. A latent image in this process consists of metallic nuclei M, where M can be Pd, Pt, Au, Ag, or Cu.

Sensitization.—The sensitized nonconductor contains in the surface a pair of substances: a photosensitive substance reacting according to reaction [5] and a reducible metal ion salt reacting according to reaction [4]. These substances are usually (24, 25) applied in two separate steps.

Application of a photosensitive layer.—Titanium dioxide is applied to the surface of a nonconductor in the form of a homogeneous dispersion of fine solid particles ranging in size from 0.02 to 0.2 μm in an adhesive (25). The adhesive serves as the medium in

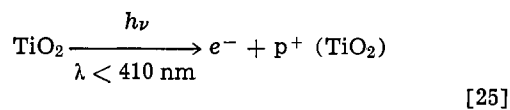
which the photosensitive compound is dispersed. In this photosensitive layer the TiO_2 particles are completely enveloped with a thin layer of adhesive.

The encapsulation of TiO_2 particles by adhesive ensures the adhesion between photosensitive layer and substrate. However, the encapsulation makes TiO_2 particles inaccessible to the second compound of the sensitizer, the aqueous solution of salts of metal ions such as Pd^{2+} , Pt^{2+} , Au^+ , Ag^+ , and Cu^{2+} , which are necessary for the formation of a metallic, latent image according to reaction [4]. TiO_2 particles are therefore made accessible by etching the surface of the adhesive layer thus partially uncovering the upper layer of TiO_2 particles and rendering them accessible to the aqueous metal ion solution. In order to ensure good adhesion the thickness of the adhesive layer after etching should be at least 5 μm .

In a modification of this procedure (25) TiO_2 particles are incorporated into the substrate during its fabrication. For a glass-epoxy-based material, TiO_2 particles are intermixed with the epoxy-resin before impregnating the glass-cloth. The impregnation and the lamination of the glass-epoxy based substrate are performed in such a way that the final laminate has a glassless top layer ($> 40 \mu\text{m}$) of epoxy-resin.

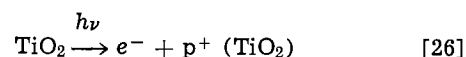
Application of metal ion salts.—The sensitization process is completed by treatment of the TiO_2 -adhesive-coated substrate having exposed TiO_2 particles with a dilute aqueous solution of a metal ion salt. Salts of Pd^{2+} , Pt^{2+} , or Au^+ are used when the electroless plating of Cu, Ni, or Co is desired. Cu^{2+} salts may be used when the electroless plating is restricted to copper.

Image formation.—The latent (or printout) image of the desired pattern on a sensitized nonconductor is formed in the following sequence of reactions



where $\text{Pd}_{\text{ads}}^{2+}$ designates the Pd^{2+} ions adsorbed on TiO_2 (24-26). In the exposed areas Pd^{2+} ions are converted into Pd metallic nuclei in the activation step. Nonexposed areas contain Pd^{2+} ions. When the substrate is sensitized with Pt^{2+} , Au^+ , Ag^+ , or Cu^{2+} salts, metallic nuclei of Pt, Au, Ag, or Cu are formed, respectively.

Mechanism of image formation.—Photoelectron processes are based on the photophysical properties of titanium dioxide (26). Absorption of a photon by a solid TiO_2 promotes an electron e^- from the filled (2p) valence band to the vacant (3d) conduction band, when the energy of the photon is equal to or greater than the bandgap energy (27, 28). Result of this absorption is generation of a free electron in the conduction band and a free hole p^+ in the valence band. This process can be represented by the simplified kinetic scheme



resulting in the formation of a hole-electron pair.

Mobile electrons, e^- , generated in the process [26] can be captured by a species adsorbed on TiO_2 , e.g., a metal ion M^{n+} , which is thus reduced into metal M



where n is the number of electrons, and subscripts s and ads designate surface and adsorbed species, respectively.

Metallic nuclei M formed in the reduction step [27] can catalyze electroless metal deposition. M may be Pd, Pt, Au, Ag, or Cu (24, 25).

Photoholes p^+ , generated in the process [26], can be trapped (26) by the surface O^- ions and form O_2 , recombined with electrons, or participate in the destruction of the metallic phase (M) to form metal ions (M^{n+}).

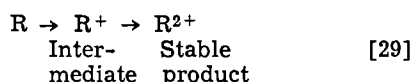
For the case when M is Ag and Pd it was found that quantum yield for Ag formation is dependent on the silver ion concentration in the solution and independent of light intensity (26, 29, 30). Kinetic data for TiO_2 in solutions of different $AgNO_3$ concentrations obey the Stern-Volmer mechanism

$$\Phi = \Phi_{lim} C_{Ag^+} / (k + C_{Ag^+}) \quad [28]$$

where Φ is the yield at silver concentration C_{Ag^+} , Φ_{lim} is the limiting yield at high C_{Ag^+} , and k is a constant.

Quantum yield for reaction [26], and thus Φ_{lim} in reaction [28], can be increased by the use of photosensitizers. In this case TiO_2 is excited by the sensitizer (30).

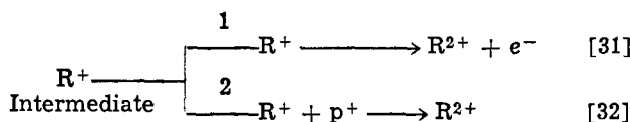
Reaction [27] can be catalyzed by multiequivalent reducing agents (31-36). If a two equivalent reducing agent R is adsorbed on TiO_2 a two-step sequence occurs upon irradiation



In the first step the reducing agent R is oxidized by a photogenerated hole p^+



producing the intermediate R^+ . The intermediate R^+ can be oxidized into the stable species R^{2+} in two alternative pathways



In the pathway 1, reaction [31], R^+ is oxidized by the release (injection) of an electron to the conduction band while in the pathway 2, reaction [32], R^+ is oxidized by a hole. The pathway 1 is the preferred one.

In the case when M^{n+} is present on the surface of TiO_2 , simultaneously with R, the pathway 1 consists of the electron transfer from R^+ to M^{n+} resulting in the reduction of M^{n+} , i.e., catalysis of reaction [27].

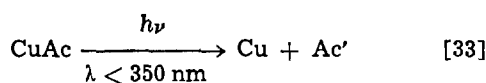
Catalyzed reduction of Pd^{2+} on TiO_2 can be achieved by R = methanol, ethanol, and 1-propanol (35).

Intramolecular Photoreduction Method

Intramolecular photoreduction method has two basic steps: (i) sensitization and, (ii) image formation.

Sensitization.—The sensitizer layer applied on a nonconductor in the intramolecular photoreduction method contains three principal components: cupric acetate, cupric bromide, and anthraquinone-2,6-disulfonic acid, disodium salt (37, 38). In the panel sensitizing technique the sensitizer is applied using roller coating.

Image formation.—The latent, or printout, image is formed in the photochemical reaction



where Ac' stands for the oxidation products of acetate ion Ac . Thus, the pattern area in this process is composed of catalytic copper nuclei. Images containing Pd, Pt, Au, or Ag can be made using this method.

Mechanism of image formation.—As far as we know there is no published study on the mechanism of photoreduction of cupric ions in the system of cupric acetate, cupric bromide, and anthraquinone-2,6-disulfonic

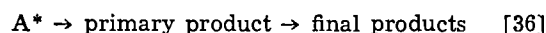
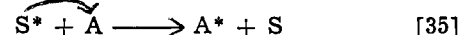
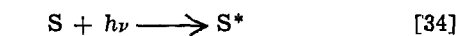
acid, disodium salt. The following mechanisms are suggested for the formation of catalytic metallic nuclei in the intramolecular photoreduction method.

Mechanism of photoreduction of cupric acetate.—On the basis of mechanistic studies (39) on photoreduction of acetatopentaamminecobalt (III) the following mechanism is proposed for the photoreduction of cupric acetate. In the case of cupric acetate, $[Cu_2(OCOCH_3)_4] \cdot 2H_2O$, a dimer in the crystalline state (40, 41), irradiation of the charge transfer band results in the electron transfer from the acetato ligand to the copper ion center. The excited electron, originally localized on the ligand, is predominantly on the central copper ion. The result of this charge-transfer process is the oxidation of the acetato ligand (39) to an oxidized ligand free radical and the reduction of Cu^{2+} ions to Cu^+ or Cu.

Mechanism of photoreduction of cupric bromide.—The mechanism of photolysis of cupric bromide can be discussed on the basis of the band theory of the solid state or on the basis of theories of photochemical reactions in solution. Since the sensitizer layer in this process contains a considerable amount of water molecules we feel that the interpretation in terms of photochemistry of solutions can provide useful insights (42-46). In this case, in the primary photochemical process of photolysis of cupric bromide, the light is absorbed by the hydrated bromide ion resulting in the formation of solvated electron, e_{aq}^- . The solvated electron then reacts with Cu^{2+} to produce the copper nuclei. Reduction of Cu^{2+} ion in cupric bromide can occur also in a direct "intramolecular," ion pair process.

Mechanism of photosensitized reduction of copper ions.—So far we have considered interaction of electromagnetic radiation with a single molecule or a collection of molecules of one type. In this section we will consider interaction of electromagnetic radiation with a system of two distinct molecules separated in space, or a collection of molecules of two distinct types. In this system a photosensitized reaction can occur (47, 48).

A photosensitized reaction proceeds in three basic steps



In the first step photons are absorbed by the sensitizer molecule S resulting in the production of the electronically excited molecule S^* . The second step is the energy transfer step in which the energy is transferred from the excited sensitizer molecule S^* to molecule A with production of the excited molecule A^* and the ground state of the sensitizer molecule, S. In the third step the electronically excited molecule A^* is deactivated in a photochemical reaction. It is proposed that for the discussed process the anthraquinone-2,6-disulfonic acid, disodium salt is the sensitizer S (the energy donor) and the copper acetate molecule the energy acceptor A (the quencher).

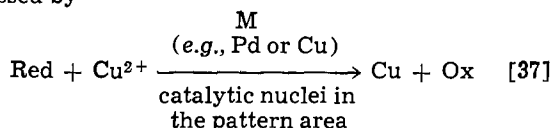
Energy transfer from S^* to A may occur by two mechanisms: resonance transfer and electron transfer mechanism (20, 49-53).

Image Development

In all three kinetic schemes the catalytic metallic nuclei are used to initiate electroless metal deposition in the image development process. Prior to development the background is desensitized by removing the components of the sensitizing solution. Background desensitization is achieved by rinsing with water (54) or other solvents, or with solutions of complexing agents suitable to remove metallic cations (55, 56). Developers used in the electroless (physical) development contain a developing (reducing) agent, a metal

salt, and usually a complexing agent for metal ions, in a water solution at a pH depending on the developing and the complexing agent (20, 37, 38, 57, 58).

The general reaction of development or amplification of the latent and printout images of copper can be expressed by



where Red and Ox are the reduced and oxidized form of the developer, respectively.

Processes of electroless copper deposition are well known and will therefore not be discussed here (59, 60). Image composed of Pd nuclei can be developed in the electroless Cu, Ni, Pd, or Co bath. Electroless metal deposition bath used as a developer should be formulated in such a way that it deposits only on the photoimage areas and not on the background. Background areas can be catalytic for processes in a developer, due to incomplete removal of sensitizer.

Discussion

We will discuss characteristic problems of individual processes and prospects for the photochemical selective activation of nonconductors, in general.

Photoelectrochemical Method

Positive version.—Characteristic problems of this method are: (i) stability of the Sn^{2+} sensitizer solution, and (ii) the short u.v. radiation (220–300 nm) in the image formation step.

The most important characteristic of aqueous SnCl_2 solutions relevant to the process of sensitizing is "aging." Freshly made SnCl_2 sensitizing solution consists of about 95% Sn^{2+} ions complexed with Cl^- ions and 5% Sn^{4+} ions complexed with OH^- and Cl^- ions (61). The "aging" of the stannous chloride sensitizing solution can be described as a two-step process. In the first step Sn^{4+} ions are produced in the solution as a result of exposure of Sn^{2+} ions to the atmospheric oxygen. In the second step the produced Sn^{4+} ions (i) precipitate on the existing colloid particles, or (ii) nucleate new colloidal particles (62, 63). This instability of the sensitizer is certainly a drawback in the positive version of the photoelectrochemical method.

The short u.v. radiation (220–300 nm) used in the image formation step can be hazardous and requires special shielding for the protection of production personnel.

Negative version.—The latent image in the pattern area in this process is composed of Fe^{2+} ions. The Fe^{2+} latent image is unstable since Fe^{2+} ions are easily oxidized into Fe^{3+} ions. This instability of image is a problem in the negative version of the process.

Photoelectron Method

The background is the major problem in this method. It was found (35) that in the $\text{TiO}_2/\text{PdCl}_2$ system Pd^{2+} ions remain in nonexposed areas of the surface even after thorough rinsing with water. The remaining Pd^{2+} ions in the background areas cause fogging during the development, since Pd^{2+} can be reduced to Pd by the reducing agent present in electroless plating solution, giving rise to catalytic Pd nuclei and thus the extraneous deposition of metal present in the developer as metal ions (e.g., Cu, Ni, Co). The amount of palladium salt adsorbed on TiO_2 , or the surface in general, in the nonexposed areas, can be considerably reduced if the rinsing is assisted by treating with an aqueous solution of a strong complexing agent for Pd^{2+} ions. Effective complexing agents are, e.g., aminoacetic acid and triethanolamine (35).

An advantage of the photoelectron method over other photochemical methods is the long u.v. (410 nm) radiation.

Intramolecular Photoreduction Method

The background desensitization, after image development, is the major problem in this process. The compounds present in the background are: cupric acetate, cupric bromide, and anthraquinone-2,6-disulfonic acid, disodium salt. If not removed, the compounds present in the background may react with components of the developing solution, thus causing nonselective deposition of electroless metal over the entire surface.

An advantage of this method is that it involves the nonnoble metal nuclei (Cu).

Photochemical Selective Activation: Prospects

Major activities in the field are related to the two common problems in the development step: (i) the nonselective, extraneous deposition of electroless metal over the background, and (ii) the lateral growth of the pattern (the vertical/horizontal growth ratio).

The extraneous deposition in the background area can be hindered by specific additives in the image development solution. This type of additive should preferentially adsorb on the background, the adhesive layer of the surface, but not on the metallic nuclei in the pattern area. Search for additives of these properties is a very active area of research, see, for example, Ref. (64).

The problem of hindering the horizontal (lateral) growth is approached in the same way. Specific additives can block the lateral growth (65), causing the development of the photo image to proceed in the vertical direction only. The ratio between the vertical and the lateral growth rate is the determining factor for line resolution in the printed circuit boards production.

Resolution for the photochemical selective activation methods depends on the wavelength of the electromagnetic radiation used and the particle size of sensitizer on the surface of the nonconductor. Since the wavelengths are of the order of 350 nm and less (u.v. range), and since the particle size is of the order of 100 nm and less (1, 25), the expected resolution is about 1 μm . In practice, pattern lines with width of 3–4 μm have been made (1, 24).

Production resolution limits, with good yield, for the manufacture of printed circuit boards are: linewidth and spacing 175, 125, and 75 μm for the copper thickness of 35, 25, and 20 μm , respectively.

Solutions to the background and the lateral growth problems are essential for the successful application of the discussed kinetic schemes in the selective activation of nonconductors for the production of printed circuit boards.

Summary

Fundamental aspects of photochemical selective activation can be summarized in three major points.

1. Three types of photochemical reactions can result in activation of nonconductors: (i) catalytic metallic nuclei can be generated in an intramolecular electron transfer resulting from photon absorption. In this case catalytic nuclei are of the same metal as the photosensitive compound. Intramolecular charge transfer can be a primary or a sensitized photochemical reaction. (ii) Catalytic metallic nuclei can be formed in an interaction of a metallic compound and photoelectrons generated in the absorption of photons by a semiconductor crystal. (iii) Catalytic metallic nuclei can be formed in the oxidation reduction process where the reducing agent is generated in a photochemical reaction.

2. Wavelengths of photochemically active electromagnetic radiations for the above reactions are in the range of 220–410 nm.

3. Nonconductors can be activated photochemically with Pd, Pt, Au, Ag, or Cu catalytic nuclei. These nuclei are catalytic for electroless metal deposition.

Technological aspects can be summarized as follows.

1. Pattern lines with a width of 3-4 μm have been made.

2. Production limits, with good yields, for the manufacture of printed circuit boards are: linewidth and spacing 175, 125, and 75 μm for the copper thickness of 35, 25, and 20 μm , respectively.

3. Catalytic nuclei of noble (Pd, Pt, Au, Ag) and nonnoble metals (Cu) can be photochemically generated in the pattern areas on a nonconductor.

Acknowledgments

Discussions with Dr. K. Egerer and Messrs. D. Frisch, J. McCormack, and J. Polichette are gratefully acknowledged.

Manuscript submitted Nov. 26, 1976; revised manuscript received April 14, 1980. This was Paper 470 presented at the Los Angeles, California, Meeting of the Society, Oct. 14-19, 1979.

Any discussion of this paper will appear in a Discussion Section to be published in the June 1981 JOURNAL. All discussions for the June 1981 Discussion Section should be submitted by Feb. 1, 1981.

Publication costs of this article were assisted by the Kollmorgen Corporation.

REFERENCES

- D. J. Sharp, *Plating*, **58**, 786 (1971).
- M. A. DeAngelo and D. J. Sharp, U.S. Pat. 3,562,005 (1971).
- J. F. D'Amico, M. A. DeAngelo, J. F. Henrickson, J. T. Kenney, and D. J. Sharp, *This Journal*, **118**, 1695 (1971).
- J. F. D'Amico and M. A. DeAngelo, *ibid.*, **120**, 1469 (1973).
- D. R. Turner, Abstract 137, p. 368, The Electrochemical Society Extended Abstracts, Detroit, Mich., Oct. 5-9, 1969.
- R. L. Cohen, J. F. D'Amico, and K. W. West, *This Journal*, **118**, 2042 (1971).
- J. F. D'Amico, F. A. Litt, and M. A. DeAngelo, *ibid.*, **119**, 956 (1972).
- S. L. Chow, N. W. Hedgecock, M. Schlesinger, and J. Rezek, *ibid.*, **119**, 1013 (1972).
- M. Schlesinger, *ibid.*, **121**, 667 (1974).
- B. K. W. Baylis, A. Busuttill, N. E. Hedgecock, and M. Schlesinger, *ibid.*, **123**, 1376 (1976).
- B. K. W. Baylis, A. Busuttill, N. E. Hedgecock, and M. Schlesinger, *ibid.*, **123**, 348 (1976).
- B. K. W. Baylis, N. E. Hedgecock, and M. Schlesinger, *ibid.*, **124**, 346 (1977).
- B. K. W. Baylis, G. C. Huang, and M. Schlesinger, *ibid.*, **126**, 394 (1974).
- A. W. Adamson, W. L. Waltz, E. Zinato, D. W. Watts, P. D. Fleischauer, and R. D. Lindholm, *Chem. Rev.*, **68**, 541 (1968).
- V. Balzani, and V. Carassiti, "Photochemistry of Coordination Compounds," Academic Press, New York (1970).
- H. E. Spencer, *J. Phys. Chem.*, **73**, 2316 (1969).
- C. A. Parker, *Trans. Faraday Soc.*, **50**, 1213 (1954).
- G. D. Cooper and B. A. DeGraff, *J. Phys. Chem.*, **76**, 2618 (1972).
- H. Taube, *J. Am. Chem. Soc.*, **70**, 1216 (1948).
- T. H. James, Editor, "The Theory of the Photographic Process," 3rd ed., The McMillan Co., New York (1966).
- G. D. Cooper and B. A. DeGraff, *J. Phys. Chem.*, **75**, 2897 (1971).
- C. Parker and C. Hatchard, *ibid.*, **63**, 22 (1959).
- D. J. Ingram, W. E. Hodgson, C. A. Parker, and W. T. Rees, *Nature*, **176**, 1223 (1955).
- C. J. G. F. Janssen, H. Jonker, and A. Molenaar, *Plating*, **58**, 42 (1971).
- J. F. Mansveld and J. M. Jans, *Plating Surf. Finish.*, **66**, 14 (1979).
- F. Mollers, H. J. Tolle, and R. Memming, *This Journal*, **121**, 1160 (1974).
- C. Kittel, "Introduction to Solid State Physics," John Wiley and Sons, Inc., New York (1976).
- N. B. Hannay, Editor, "Semiconductors," Am. Chem. Soc., Chap. 14, Reinhold Publishing Co., New York (1959).
- P. D. Fleischauer, H. K. A. Kan, and J. R. Shepherd, *J. Am. Chem. Soc.*, **94**, 283 (1972).
- P. D. Fleischauer, in "Concepts of Inorganic Photochemistry," A. W. Adamson and P. D. Fleischauer, Editors, Chap. 9, John Wiley & Sons, New York (1975).
- H. Yoneyama, Y. Toyoguchi, and T. Tamura, *J. Phys. Chem.*, **76**, 3460 (1972).
- J. Cunningham and H. Zaimal, *ibid.*, **76**, 2362 (1972).
- R. Memming, in "Electrocatalysis," M. W. Breiter, Editor, p. 178, The Electrochemical Society Soft-bound Proceedings Series, Princeton, N.J. (1974).
- S. R. Morrison and T. Freund, *J. Chem. Phys.*, **47**, 1543 (1967).
- J. J. Kelly and J. K. Vondeling, *This Journal*, **122**, 1103 (1975).
- W. P. Gomes, T. Freund, and S. R. Morrison, *ibid.*, **115**, 818 (1968).
- J. Polichette and E. J. Leech, U.S. Pat., 3,772,078 (1973).
- J. Polichette and E. J. Leech, U.S. Pat. 3,959,547 (1979).
- E. R. Kantrowitz, M. Z. Hoffman, and J. F. Endicott, *J. Phys. Chem.*, **75**, 1914 (1971).
- J. K. Kochi and R. V. Subramanian, *Inorg. Chem.*, **4**, 1527 (1965).
- F. A. Cotton and G. Wilkinson, "Advanced Inorganic Chemistry," p. 918, Interscience Publishers, New York (1966).
- M. S. Matheson, W. A. Mulac, and J. Rabani, *J. Phys. Chem.*, **67**, 2613 (1963).
- J. Jortner, M. Ottolenghi, and G. Stein, *ibid.*, **67**, 1271 (1963).
- J. Jortner, M. Ottolenghi, and G. Stein, *ibid.*, **68**, 247 (1964).
- R. Devonshire and J. J. Weiss, *ibid.*, **72**, 3815 (1968).
- M. J. Blandamer and M. F. Fox, *Chem. Rev.*, **70**, 59 (1970).
- A. W. Adamson and P. D. Fleischauer, Editors, "Concepts in Inorganic Photochemistry," pp. 72, 404, John Wiley & Sons, New York (1975).
- N. J. Turro, "Modern Molecular Photochemistry," The Benjamin Cummings Publishing Co., Inc., Menlo Park, Calif. (1976).
- G. M. Burnett and A. M. North, Editors, "Transfer and Storage of Energy by Molecules," Vol. 1, John Wiley & Sons, New York (1969).
- W. F. Berg, M. Mazzucato, H. Meier, and G. Semerano, Editors, "Dye Sensitization," Symposium Bressanone, Focal Press, New York (1970).
- H. Meier, "Spectral Sensitization," Focal Press, New York (1968).
- F. Wilkinson, in "Advances in Photochemistry," Vol. 3, J. Wiley & Sons, New York (1964).
- G. W. Robinson and R. P. Frosch, *J. Chem. Phys.*, **38**, 1187 (1963).
- J. F. Polichette and E. J. Leech, U.S. Pat. 3,930,963 (1976).
- R. V. Dafter, U.S. Pat. 4,084,023 (1978).
- H. Tabei, S. Nara, and K. Matsuyama, *This Journal*, **121**, 67 (1974).
- W. Jaenicke, in "Advances in Electrochemistry and Electrochemical Engineering," H. Gerischer and C. Tobias, Editors, Vol. 10, John Wiley & Sons, New York (1977).
- T. H. James, "Advances in Catalysis," Vol. 2, Academic Press, New York (1950).
- M. Paunovic, *Plating*, **55**, 1611 (1968).
- M. Saito, *Met. Surf. Technol.*, **16**, 300 (1965).
- R. L. Cohen and K. W. West, *This Journal*, **119**, 433 (1972).
- S. Meibuhr and P. R. Carter, *Electrochem. Technol.*, **2**, 267 (1964).
- J. S. Johnson and K. A. Kraus, *J. Am. Chem. Soc.*, **63**, 440 (1959).
- E. Sholtens, A. Molenaar, J. E. A. M. Van Den Meerakker, and J. Boven, Abstract 471, p. 1183, The Electrochemical Society Extended Abstracts, Los Angeles, California, Oct. 14-19, 1979.
- S. T. Rao and R. Weil, *Trans. Inst. Met. Finish.*, **57**, 97 (1979).



Theory of Electrochemical Memory

Application to Short-Circuit Memory in Electrochromic Displays

G. Beni

Bell Laboratories, Holmdel, New Jersey 07733

ABSTRACT

We introduce the concept of electrochemical memory and discuss it in relation to electrochromism. We show that the electrochemical memory could be created by the dynamics of the ion-electrolyte interaction during the ion-insertion process. To calculate the electrochemical memory we introduce a small-polaron model of ion transfer at the electrochemical interface and derive general, analytical expressions for the probability of transitions. We apply these expressions to a Langmuir-type macroscopic model of the electrochromic reaction. Under these assumptions, we establish lower limits of the breakdown voltage necessary for short-circuit memory with threshold in an electrochromic display cell. We also derive a simple expression for the maximum memory in terms of the intrinsic response time of the electrochromic cell. For response times ~ 10 msec and breakdown voltages $\sim 2V$, the maximum memory would be ~ 20 min at room temperature. Finally, we calculate the electrolyte reorganization energy required to achieve the maximum memory. Its value lies in the range $1.5 \leftrightarrow 2.0$ eV. In applying these results to displays, we find that the number of lines which could be sequentially matrix addressed in an electrochromic display matrix spans the range $10 \leftrightarrow 10^5$. In contrast to the current notion, this proves that direct matrix addressing of electrochromic displays is theoretically possible.

Electrochromics are promising display materials (1). Unlike liquid crystals, they have open-circuit memory and an unrestricted viewing angle. Although early electrochromics degraded rapidly (2), the recently discovered (3-8) anodic iridium oxide films (AIROF's) are highly stable. They have been tested for $\sim 10^6$ cycles with no detectable degradation. In addition, all-solid-state display cells have been demonstrated (9) and reactive-sputtering techniques (10) have simplified considerably the fabrication of practical devices. Thus, electrochromics promise to play a significant role in new passive-display technologies.

Even so, displays consisting of many electrochromic elements are considered impractical. When the number of display elements in a matrix exceeds ~ 100 it becomes essentially impossible to drive each element individually. Instead, rows and columns of the display matrix must simultaneously be driven according to a scheme known as "matrix-addressing" (11). But the possibility of direct (12) matrix-addressing of electrochromic displays has been ruled out. Indeed, electrochromics have been regarded as "fundamentally unsuited for matrix-addressing" (13) and, consequently, fundamentally unsuited for any but the simplest multielement displays. In contrast, this paper shows how, by appropriate choice of the electrolyte, electrochromic displays might be matrix-addressed. Large matrixes of electrochromic elements might then become a practical possibility.

The paper is organized as follows. The remaining part of this section is devoted to a more precise description of memory in electrochromic cells and of the problems of matrix-addressing. In particular, the

concept of short-circuit memory is introduced and it is shown that matrix-addressing requires electrochromic cells with short-circuit memory. The following section discusses, in general, the concept of electrochemical memory: how it relates to the free energy of the electrochromic reaction and to the concepts of metastability, hysteresis, and relaxation. It is shown that the free energy barrier of the electrochromic reaction is the essential element for electrochemical memory. The physics of the free energy barrier is the subject of the section "Microscopic Model." A microscopic model for the charge transfer at the electrolyte-electrochromic interface is presented. Analytical results yield the probability of charge transfer as a function of the potential difference across the interface. The section "Macroscopic Model" is devoted to the macroscopic model of the electrochromic reaction. Using the microscopically calculated probability of transition, the macroscopic model yields general results (e.g., upper limits) on the electrochemical memory. Specific numerical results are given in the Results section where the properties of the electrolyte are related to the size of the memory and to the maximum number of elements in an electrochromic display matrix. The last two sections discuss the approximations involved in the calculations, compare various types of electrochromic memories, and summarize the results.

Broadly defined, electrochromism is a persistent but reversible color change induced electrochemically. Although electrochromism is a widespread phenomenon, here we consider only electrochromism of ion-insertion materials. An ion-insertion material (14) is a mixed conductor (i.e., electronic and ionic) in which ions can be rapidly and reversibly inserted. Of course, for charge neutrality, an electron

* Electrochemical Society Active Member.

Key words: displays, electrochemical kinetics, electrochromism.

is also inserted (extracted) whenever an anion is extracted (inserted) or whenever a cation is inserted (extracted). Examples of ion-insertion materials are Li_xTiS_2 and $\text{Li}_x\text{V}_2\text{O}_5$ which are used as electrodes in lithium-insertion batteries (15). Electrochromics are ion-insertion materials whose optical properties depend strongly on the number of inserted ions. Thus, they may be regarded also as storage batteries with a visible state of charge.

An important property of an ion-insertion material is its internal electromotive force (emf). In order to define it, consider first the "capacity" of the ion-insertion material. This is the maximum number N_{max} of ions that can be inserted in a unit volume. When N ions per unit volume are inserted in the material, the "relative ion-occupancy" $q = N/N_{\text{max}}$ determines the chemical potential $\mu(q)$ of an ion in the ion-insertion material. In turn, the chemical potential is related to the internal emf ϵ by $\epsilon(q) = -e\mu(q)$, where e is the electron charge. Obviously $\epsilon(q)$ varies with the temperature; at a given temperature the function $\epsilon(q)$ is usually referred to as an "isotherm" of the ion-insertion material. Isotherms of electrochromics are measurable and have been studied extensively (16-20). They are the most fundamental properties characterizing the ion-insertion material.

Let us consider now the symmetric cell shown in Fig. 1a. 1 and 5 are electronic conductors. 2 and 4 are ion-insertion mixed conductors. 3 is the electrolyte. For simplicity let 1,5 and 2,4 be identical. Let us assume also that the relative ion-occupancies q_4 of 4 and q_2 of 2 are such that $q_2 + q_4 = 1$. The potential difference between 1 and 5 is $\Delta\epsilon = e[\mu(q_4) - \mu(q_2)]$. Thus, if 1 and 5 are externally connected, and if $q_2 \neq q_4$, ions will be transferred between 4 and 2 across the electrolyte 3 until $q_2 = q_4 = 1/2$ and $\Delta\epsilon = 0$. The cell is in thermodynamic equilibrium. The cell can be displaced from equilibrium by applying an external voltage between 1 and 5. If, by application of the appropriate voltage, a configuration q_2, q_4 ($q_2 + q_4 = 1$) is obtained, this configuration persists after opening the external circuit since charge cannot be transferred unless 1 and 5 are connected. This property of the cell is referred to as open-circuit memory.

Open-circuit memory is a useful property of an "electrochromic" cell, i.e., a cell where 2 and 4 are electrochromic materials. Typically in such a cell, 1 is a transparent conductor e.g., SnO_2 and 3 a white-pigmented electrolyte. If 2 is transparent for $q_2 = 0$ and is blue for $q_2 = 1$ then, when viewed from above, the display cell appears either white or blue depending on the applied potential. The color persists even after disconnecting 1 and 5 from the applied voltage. This open-circuit memory is clearly useful in many applications, but it cannot be used for matrix-addressing.

Matrix-addressing is a technique used to drive a large number of display elements. Figure 2 shows schematically, for a 2×3 matrix, how this technique works. The top electrodes, 1, are connected in rows and the bottom electrodes, 5, are connected in columns. For illustration, assume the existence of a voltage V_A such that, [see Fig. 1(b)], for any elements: (a) $q_2 = 1$ ($q_4 = 0$) if $V_1 - V_5 \geq V_A$ where $V_1 - V_5$ is the potential difference between top and bottom electrodes; and (b) $q_2 = 0$ ($q_4 = 1$) if $V_1 - V_5 \leq -V_A$.

In an actual device, only the upper part, 1, 2, 3, of any display element is visible, whereas 4 and 5 are hidden from view. Thus, in (a), the display element appears colored and, in (b), it appears bleached.

The information to be displayed on the matrix is multiplexed onto the columns which are addressed with bias $+3V_A$ or $+V_A$. The rows, instead, are

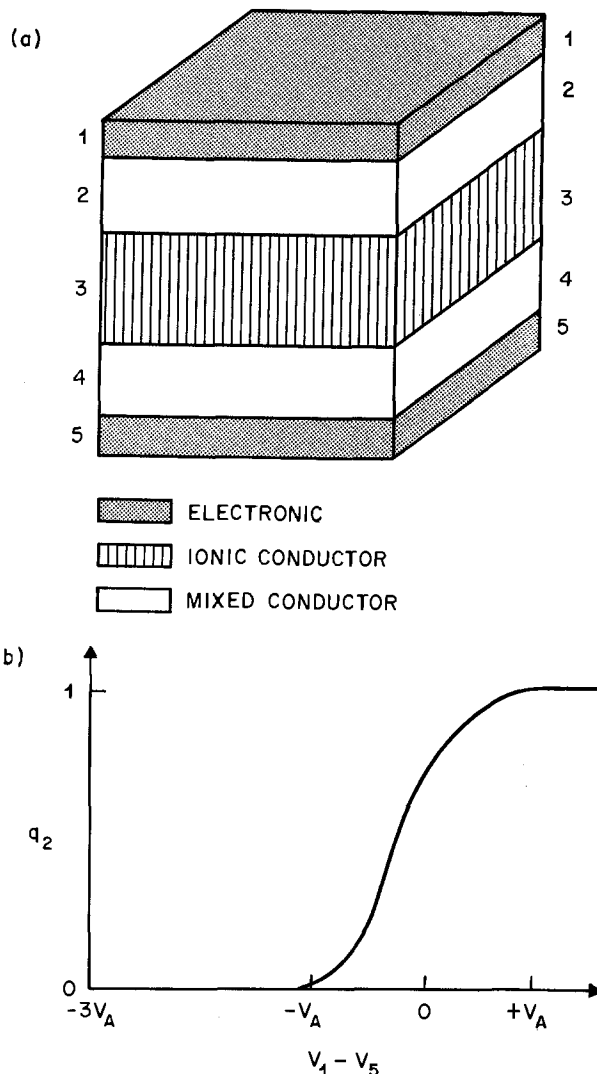


Fig. 1. (a) Schematic structure of an ion-insertion cell. 1 and 5 are electronic conductors. 2 and 4 are mixed conductors and, more specifically, ion-insertion materials. 3 is the electrolyte, i.e., an ionic conductor. In a typical electrochromic cell, 1 is a transparent conductor such as SnO_2 , 2 is the electrochromic material, and 3 is a white-pigmented electrolyte. 4 and 5 are hidden from view. (b) Example of relative ion-occupancy q_2 of the ion-insertion material 2 as a function of the voltage difference $V_1 - V_5$ applied between the electrodes 1 and 5. In this example, the relative ion occupancy is negligible for $-3V_A \leq V_1 - V_5 \leq -V_A$ and increases gradually to 1 at $V_1 - V_5 = +V_A$. Thus, $-V_A$ is the threshold voltage.

addressed sequentially (i.e., only one row is selected in a given interval) by bias pulses of amplitude $+2V_A$ and duration Δt . This kind of addressing colors the ij display element if, and only if, the j th column is biased at $+V_A$ during the i th row selection interval. Thus, for the particular addressing example shown on the right-hand side of Fig. 2, the display elements 12, 13, and 21 become colored whereas 11, 22, and 23 remain bleached.

This example is easily generalized to an $n \times m$ matrix. For an $n \times m$ matrix, driving each display element individually requires $n \times m$ inputs whereas matrix-addressing requires only $n + m$ inputs. Thus, matrix-addressing greatly simplifies the circuitry of multielement displays.

Many variations of the basic matrix-addressing scheme exemplified in Fig. 2 are possible. But every scheme requires two essential properties of the display cell: (i) threshold response and (ii) short-circuit memory.

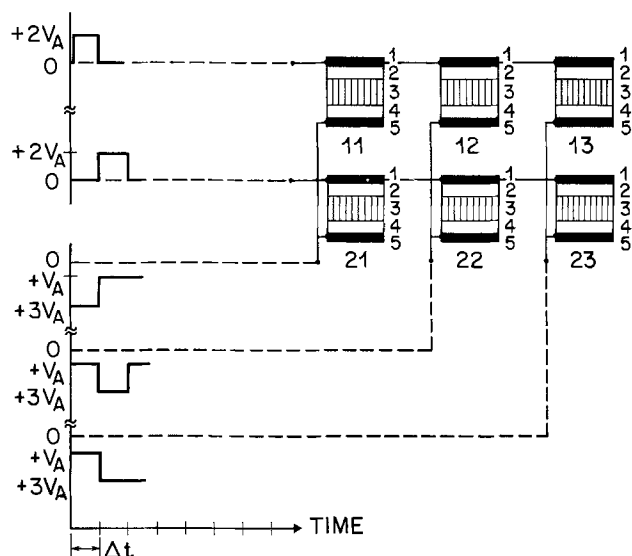


Fig. 2. Schematic matrix-addressing for a 2×3 array of electrochromic cells. The vertical numbers have the same meaning as in Fig. 1(a). The numbers underneath each cell are simply labels. Each cell is assumed to have threshold at $-V_A$ [see Fig. 1(b)]. Rows are addressed one at a time with voltage pulses of amplitude $+2V_A$ and duration Δt . Columns are addressed with either $+3V_A$ or $+V_A$. The addressing voltages shown on the left-hand side give rise to "coloration" of cells 12, 13, and 21, whereas 11, 22, and 23 remain "bleached."

Threshold response.—In the example of Fig. 2, we assumed the existence of a voltage V_A satisfying the conditions (a) and (b). This is not a restrictive assumption for most electrochromics. The addressing voltages, however, impose strict requirements on the electrochromic cell. In the example, addressing voltages vary from $+3V_A$ to 0 corresponding to the potential differences $-3V_A \leq V_1 - V_5 \leq +V_A$. If, for any voltages in the interval $[-3V_A, -V_A]$, the electrochromic cell is unstable (e.g., because of side reactions such as gas evolution, degradation etc.), then matrix-addressing is precluded. Thus, it is imperative that the electrochromic cell remains essentially inert during the scan $-3V \leq V_1 + V_5 \leq -V_A$. In general, regardless of the particular value of V_A , this threshold response of the electrochromic cell is necessary for any matrix-addressing scheme. A second essential requirement is short-circuit memory.

Short-circuit memory.—In Fig. 2, let us consider the closed circuit formed by cells 11, 12, 21, and 22. The voltage-scans in the example color 12 and 21. Thus, these four cells form a series with a total emf of $+4V_A$. Current will flow until the four cells are in equilibrium at $q_2 = \frac{1}{2}$, all of them being half-colored. This example illustrates the general problem of "cross-talk" among the electrochromic cells in a matrix. Since colored electrochromic cells are basically charged batteries, they can discharge through the connecting circuits and thus partially color other cells. This happens essentially because the cells lack short-circuit memory. In fact, if in a cell $q_2 \neq \frac{1}{2}$ and its electrodes 1, 5 are short-circuited, then q_2 quickly relaxes to $\frac{1}{2}$ while the cell loses any memory of the displayed information.

Thus, both threshold-response and short-circuit memory are essential for matrix-addressing. Early electrochromics lacked both (21). The recently discovered AIROF's have a fairly sharp threshold which is satisfactory for matrix-addressing. AIROF's in common aqueous electrolyte, however, have no intrinsic short-circuit memory. In the following sections we shall see how this problem can be overcome.

Electrochemical Memory

Strictly speaking, no electrochromic cell has zero short-circuit memory. When an electrochromic cell is short-circuited, it relaxes to equilibrium in a characteristic time t_M determined by its internal emf and its internal resistance. However, to avoid "flickers" in the display-matrix, t_M must satisfy the condition $t_M \geq n\Delta t$ where $n\Delta t$ is the matrix total scanning time. An obvious way to increase t_M is to increase the resistivity of the electrolyte. This method, however, besides requiring high driving voltages, would correspondingly increase the response time t_R and thus, necessarily, Δt . The maximum number n_{\max} of addressable rows would remain constant, since $n_{\max} \sim t_M/t_R$. So, increasing the electrolyte resistivity does not solve the short-circuit memory problem. Similar considerations apply to any scheme based on increasing the circuit impedances within the display matrix.

We will investigate a different method by which a useful short-circuit memory might be built into the electrochromic cell. The method discussed in this paper takes advantage of the unique properties of electrochemical interfaces. Since the electrochemical interface is the physical basis for this type of short-circuit memory we shall refer to it as electrochemical memory. Let's now discuss its general character.

Figure 3(a) shows a schematic free energy diagram of a model system. Each curve refers to one particular value of the external variable x (e.g., temperature, pressure, applied field etc.). Let $x_1 \leq x' \leq x'' \leq x_2$. The abscissa indicates the internal variable y (e.g., volume, charge density, magnetization etc.). For a classical system at absolute zero, $y = y_1$ at $x = x_1$. As x increases, y does not change until $x = x_2$. At $x = x_2$, where no energy barrier separates $F(y_1)$ from $F(y_2)$, y switches from y_1 to y_2 . Similarly, in reversing the path, $y = y_2$ for $x > x_1$. At $x = x_1$, y switches from y_2 to y_1 . Thus, at x_1 , $y = y_1$ and, at x_2 , $y = y_2$, but, for $x_1 < x < x_2$, y is either y_1 or y_2 depending on the history of the system. This phenomenon is well known (23) and is usually referred to as supersaturation or metastability. In general, a system exhibits metastability if, by exchanging the external variable $x_1 \leftrightarrow x_2$, the corresponding change of the internal variable $y_1(x_1 \leftrightarrow y_2(x_2))$ occurs, for $x_1 \rightarrow x_2$, along a path A and, for $x_2 \rightarrow x_1$, along a path B \neq A [see Fig. 3(b) upper graph].

Metastability is at the basis of hysteresis, relaxation, and memory. It is important, however, to distinguish carefully between these various concepts. Hysteresis is exhibited by a system composed of a large number of subsystems (domains) with metastability and with slightly differing switching points randomly distributed around their average values x_1, x_2 . In the metastability "loop" [Fig. 3(b) upper graph], at least some of the states are metastable (dashed lines) and/or nonreproducible (dotted lines), whereas in the hysteresis loop [Fig. 3(b) middle graph] all points are stable and reproducible (solid lines). Thus, in a hysteretic loop (but not in a metastability loop), the internal variable is a genuine double-valued thermodynamic function of the external variable. And, therefore, a hysteretic system has infinite memory.

On the other hand, a metastable system may or may not have infinite memory. The classical system of Fig. 3(a) has infinite memory at absolute zero. Similarly, this system has infinite memory above zero temperature if the free energy barrier between y_1 and y_2 may be regarded as infinite for some values of x . Apart from these two special cases, however, a metastable system does not have infinite memory since its metastable states will eventually decay to lower energy states in a characteristic

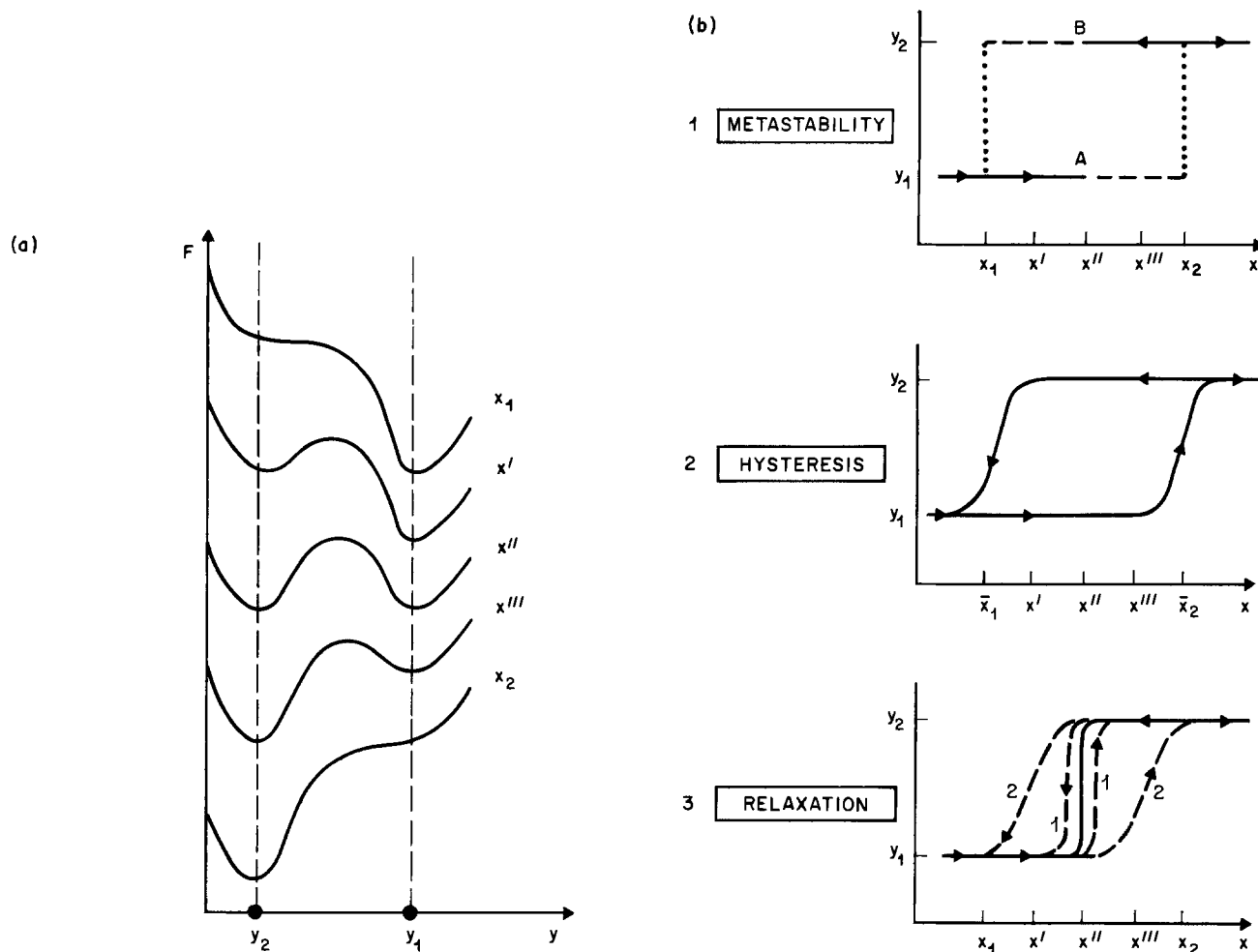


Fig. 3. (a) Schematic free energy diagram of a metastable system characterized by an internal variable y , for 5 different values ($x_1 < x' < x'' < x''' < x_2$) of the external variable x . (b) Internal variable y vs. external variable x for: 1. a metastable system with infinite equilibration time. Solid lines are metastable states and dotted lines are nonreproducible states. 2. A system composed of a large collection of metastable domains with switching points randomly distributed around their averages \bar{x}_1, \bar{x}_2 . All states in the loop are stable and reproducible. In this case the system exhibits hysteresis. 3. A metastable system with finite equilibration time. This system exhibits relaxation. The size of the relaxation loop depends on the rate of change of x . Loop 1 corresponds to a lower rate than loop 2. The solid line refers to an infinitely slow change of x .

time t which depends on the temperature and on the free energy barrier height. Even so, such a system may have a large finite memory. If the rate of change of the external variable x is very small, then the states at y_1 and y_2 are always in equilibrium and thus there is no memory. [Fig. 3(b) lower graph, solid line.] But, as dx/dt increases, the states at y_1 and y_2 do not have time to equilibrate so that the system exhibits memory. In this case, the internal variable $y(x)$ becomes double-valued and so the $y(x)$ plot shows a loop. [Fig. 3(b) lower graph, dashed lines.] This phenomenon (24) is referred to as time-dependent hysteresis or simply relaxation. The size of the relaxation loop depends on t and on dx/dt . All points on the loop correspond to metastable states (except for $dx/dt \rightarrow 0$) but are all reproducible. To sum up, a metastable system may have infinite, finite, or zero memory depending on t and on the rate of change of the external variable. In any case, the required characteristic for metastability and, thus, memory is that the free energy diagram have 2 valleys in the direction of the internal variable and that each valley turn over to its neighbor at a point of inflection.

This characteristic is inherent in the most fundamental electrochemical reaction, *i.e.*, the charge transfer at the electrolyte-electrode interface. In fact, the schematic free energy diagram of the charge transfer reaction [Fig. 4(a)] has the same basic fea-

tures as the free energy diagram of Fig. 3(a). According to Fig. 4(a), the ion is in the electrolyte when the electrode potential is at V_1 and in the electrode when the potential is at V_2 . At the intermediate potentials, however, the ion is in the electrode or in the electrolyte depending on the history of the system. (For simplicity we assume that the energy level in the electrolyte does not change with the applied voltage.) Unlike other chemical reactions, an electrochemical reaction is ideal for inducing relaxation phenomena since the free energy level in the electrode can be easily changed by the applied voltage. The rate of change of the applied potential and the height of the free energy barrier determine the size of the relaxation loop [Fig. 4(b)]; and, correspondingly, the size of the electrochemical memory.

The same size of electrochemical memory can be obtained: (a) with a low free energy barrier and a high potential scanning rate or (b) with a high free energy barrier and a low potential scanning rate. To obtain a significant short-circuit memory in an electrochromic cell we must resort to case (b), since short circuit is equivalent to essentially zero scanning rate. Therefore, for short-circuit memory, it is necessary to have a high free energy barrier at the electrolyte-electrochromic interface.

It is important to note that the effect of a high free energy barrier at the electrochemical interface

is not equivalent to the effect of an electrolyte with high resistance. The electrochemical interface with a high free energy barrier is equivalent to a large resistance only when the free energy difference between electrode and electrolyte is zero. By changing the electrode potential, this resistance drops to zero at a given voltage which depends on the barrier height. At this voltage, the intrinsic response time is unaffected by the barrier. Thus, the electrochemical interface acts, in effect, as a voltage-controlled resistor. And this is precisely what is required to provide the cell with short-circuit memory without altering the intrinsic response time of the cell. There remains to see how a high free energy barrier can be built into an electrochemical interface, without altering the response time. This is discussed in the next section.

Microscopic Model

So far, we have considered only the macroscopic aspects of the electrochemical interface. Microscopically, the electrochemical interface has an extremely complicated structure which is very poorly understood (25). Even more complex is the dynamics of charge transfer across the interface. The free energy barrier of Fig. 4(a) is obviously an oversimplified way to characterize the probability of transition across the interface.

The probability of transition depends on many factors which can be classed into three groups: (i) nature of the transferred particle; (ii) nature of the electrode, and (iii) nature of the electrolyte. Here, we shall not be concerned with (i) and (ii). These factors should be taken into account in a general discussion of electrochemical memory, but, in this paper, we are basically trying to answer the question: "given an ion-insertion electrochromic material, how can we design an electrochromic cell with short-circuit memory?" Thus, the nature of the electrode and of the transferred ion are fixed at the outset. Therefore we restrict our attention to the dependence of the probability of transition from the electrolyte.

As in other fields of chemical kinetics, a satisfactory *a priori* theoretical evaluation of rate constants for electrochemical reactions is still an elusive goal. Many models have been proposed and the field is still controversial (26). However, in the early sixties, and continuing to the present, a major thrust in interpretation was made by Marcus (27) and by Levich, Dogonadze, and Kuznetsov (LDK) (28). Their theories contain the most widely accepted model of charge transfer at the electrochemical interface.

These theories are based on two main concepts.

1. The electrolyte is represented as a continuous polarizable medium characterized by a frequency ω and a "reorganization energy" E_R . The latter is a measure of the change in the solvation structure of the ions in the electrolyte when an electron, or ion, is transferred across the electrochemical interface. A detailed discussion of ω and E_R is given in Ref. (28).

2. The charge transfer across the interface is determined primarily by thermal fluctuations in the electrolyte.

In general, the problem of charge transfer at the electrochemical interface has much in common with the polaron (29) problem. In fact, it was pointed out (30) by the author that, for electron transfer, the results of the LDK theory could be easily derived from the small-polaron theory (31). Indeed, the small-polaron theory yields more general results than the LDK theory.

Less studied is the case of ion transfer across the electrochemical interface. The LDK theory, in this case, becomes quite complex and it has been

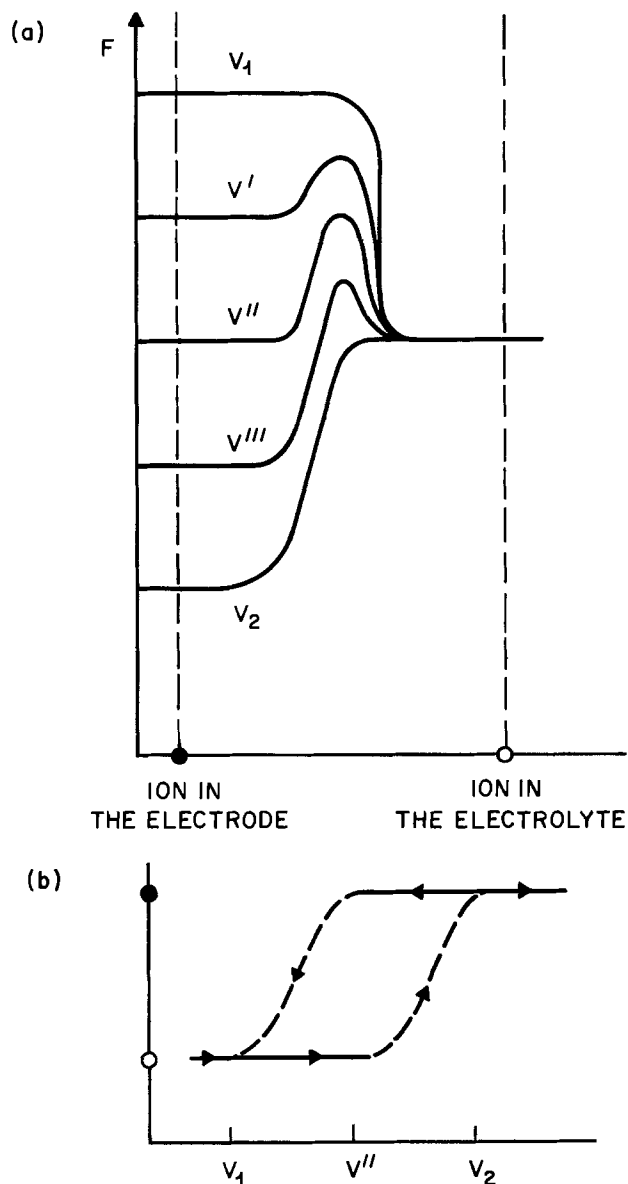


Fig. 4. (a) Schematic free energy diagram for charge transfer in an ion-insertion reaction. The five curves correspond to five different values of the electrode voltage. The open circle corresponds to a state of the ion in the electrolyte and the full circle to a state of the ion in the electrode. (b) Schematic relaxation loop for an ion-insertion reaction. The size of the loop depends on the voltage-scanning rate.

worked out only for proton transfer. As for the small-polaron theory, very few extensions beyond electron transfer have been developed (32), even outside electrochemistry. Recently, however, Emin *et al.* (33) have applied successfully the small-polaron theory to the motion of interstitials in solids. In this section we extend the small-polaron theory to the transfer of ions across the electrochemical interface.

The small-polaron theory describes the motion of a particle between adjacent sites in response to fluctuations of the medium of propagation (characterized by a frequency ω). Since, in this work, we are mainly concerned with room temperature effects, we consider only the high temperature limit. For $k_B T \gtrsim \hbar \omega$ (T is the temperature; k_B the Boltzmann constant, and $\hbar = 1$ throughout the paper), the dynamics of transfer reduces to a two-site problem and the medium may be viewed as classical. The thermal fluctuations of the medium create temporary degeneracies between two adjacent energy levels (coincidence events). During each coincidence event,

the particle has a finite probability of transferring to the adjacent level. The probability depends on ν , the time derivative, evaluated at coincidence, of the energy difference between the two adjacent energy levels. The rate of transfer W is given by

$$W = \int_0^{\infty} \langle P_c(\nu) \rangle P_t(\nu) d\nu \quad [1]$$

where $\langle \dots \rangle$ means thermal average, $P_c(\nu)$ is the probability of a coincidence event and $P_t(\nu)$ is the probability of transfer during the coincidence event. Holstein (31) has shown that

$$P_t = \frac{(1 - e^{-\alpha})}{(1 - (1/2)e^{-\alpha})} \quad [2]$$

where $\alpha = 2\pi J^2/|\nu|$ and J is the transfer integral at coincidence.

Let us now extend this general approach to the electrochemical interface. Two main aspects distinguish this case from the classic small-polaron problem.

1. Only one of the two sites is inside the fluctuating medium, i.e., the electrolyte. The other energy level (i.e., the energy level of the ion in the electrode) is not affected by the fluctuations in the electrolyte.

2. The energy difference between the two levels, besides fluctuating thermally, can also be changed by the applied electrode potential. Taking these two features into account, let us calculate the probability of ion transfer using Eq. [1] and Eq. [2].

First, let us establish the basic parameters and the restrictions of the theory. Besides ω the electrolyte is characterized by the reorganization energy E_R . To define E_R and to illustrate its physical meaning, let us recall that, at $k_B T \gtrsim \omega$, we regard the electrolyte as a classical polarizable medium, i.e., as a collection of classical oscillators. When an ion transfers from the electrode into the electrolyte, the potential energy of one of its oscillators changes from

$$E(X) = (1/2)kX^2 \quad [3]$$

(X is a generalized coordinate; k the "spring constant") to

$$E(X) = (1/2)kX^2 - AX \quad [4]$$

(assuming linear coupling with coupling constant A). Equation [4] can be rewritten as

$$E(X) = (1/2)k(X - X_0)^2 - E_R \quad [4a]$$

($X_0 = A/k$; $E_R = A^2/2k$) which defines the reorganization energy E_R as the "polaron binding energy" of the ion in the electrolyte.

The validity of the small-polaron theory is restricted by the conditions $J/E_R \ll 1$ and $J^2/E_R k_B T \ll 1$. These two conditions however are easily satisfied in the electrochemical case since, typically, $J < k_B T$ and $E_R > 1$ eV.

To calculate the rate of transfer from Eq. [1] and [2] we need to calculate $\langle P_c(\nu) \rangle$. If no potential difference exists across the electrochemical interface, a coincidence event occurs when $X = 0$, in accordance with the Franck-Condon principle. The probability to satisfy this condition, for a given value of ν , e.g., $\nu = \nu'$, is

$$P_c(\nu') = \langle \delta(X) \rangle \langle \delta(\nu - \nu') \rangle \nu' \quad [5]$$

where $\delta(\)$ is the Dirac delta function. $\langle \delta(X) \rangle$ and, thus, $P_c(\nu')$, depend on whether the ion is in the electrolyte or in the electrode. When the ion is in the electrolyte, i.e., coupled to the oscillator

$$\begin{aligned} \langle \delta(X) \rangle &= \frac{\int_{-\infty}^{+\infty} dX e^{-[(1/2)kX^2 - AX]/k_B T} \delta(X)}{\int_{-\infty}^{+\infty} dX e^{-[(1/2)kX^2 - AX]/k_B T}} \\ &= \frac{A e^{-E_R/k_B T}}{(4E_R k_B T \pi)^{1/2}} \quad [6a] \end{aligned}$$

Whereas when the ion is in the electrolyte

$$\begin{aligned} \langle \delta(X) \rangle &= \frac{\int_{-\infty}^{+\infty} dX e^{-(1/2)kX^2/k_B T} \delta(X)}{\int_{-\infty}^{+\infty} dX e^{-(1/2)kX^2/k_B T}} \\ &= A / (4E_R k_B T \pi)^{1/2} \quad [6b] \end{aligned}$$

On the other hand, $\langle \delta(\nu - \nu') \rangle$ is, in either case, given by

$$\begin{aligned} \langle \delta(\nu - \nu') \rangle &= \frac{\int_{-\infty}^{+\infty} d\nu e^{-(1/2)k\nu^2\omega^{-2}/k_B T} \delta(\nu - \nu')}{\int_{-\infty}^{+\infty} d\nu e^{-(1/2)k\nu^2\omega^{-2}/k_B T}} \\ &= \left(\frac{k}{2\pi k_B T \omega^2} \right)^{1/2} e^{-\frac{k\nu'^2}{2k_B T \omega^2}} \quad [7] \end{aligned}$$

Finally, from Eq. [1], [2], [5], [6a], [6b], and [7], we obtain the transition rates

$$W_{23}^{\rightarrow} = \frac{\omega}{2\pi} g(\gamma) \quad [8a]$$

$$W_{32}^{\rightarrow} = \frac{\omega}{2\pi} g(\gamma) e^{-E_R/k_B T} \quad [8b]$$

where, in conformity to the notation of Fig. 1(a), the subscripts 2 and 3 stand for electrode and electrolyte, respectively; and

$$\gamma = \frac{J^2 \pi}{\omega (2E_R k_B T)^{1/2}} \quad [9a]$$

and

$$g(\gamma) = 1 - \int_0^{\infty} dz \frac{ze^{-z^2}}{1 - (1/2)e^{-\gamma/z}} \quad [9b]$$

The function $g(\gamma)$ is plotted in Fig. 5. For $\gamma \ll 1$ (nonadiabatic limit), $g(\gamma) \sim \gamma\pi^{1/2}$ and, for $\gamma \gg 1$

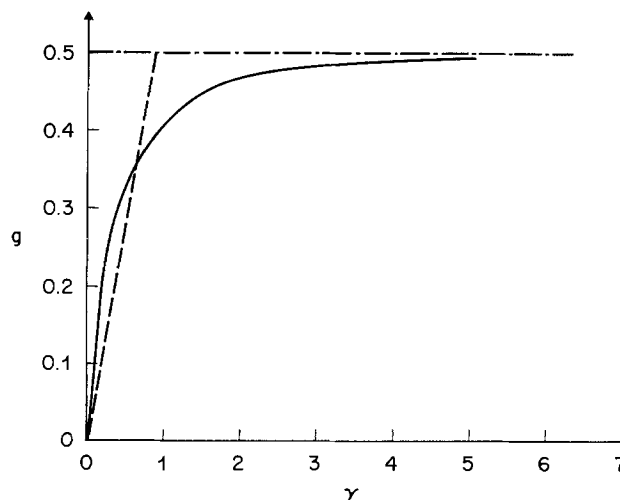


Fig. 5. Dependence of the function g (defined in Eq. [9b]), on the adiabaticity parameter ν (defined by Eq. [9a]). The dashed line refers to the nonadiabatic limit, whereas the dot-dashed line refers to the adiabatic limit.

(adiabatic limit), $g(\gamma) \sim 1/2$. When a potential difference V is applied across the interface, the Franck-Condon condition for coincidence becomes $AX = V$ and the probability of satisfying this condition for $\nu = \nu'$ is given by

$$P_c(\nu') = \left\langle \delta \left(X - \frac{V}{A} \right) \right\rangle \langle \delta(\nu - \nu') \rangle \nu' \quad [10]$$

Following a procedure analogous to the one followed from Eq. [5] to Eq. [8], we obtain

$$W_{23}^{\rightarrow}(V) = \frac{\omega}{2\pi} g(\gamma) e^{-\frac{V}{2k_B T} \left(1 - \frac{V}{4E_R} \right)} \quad [11a]$$

$$W_{32}^{\rightarrow}(V) = \frac{\omega}{2\pi} g(\gamma) e^{-\frac{V}{2k_B T} \left(1 + \frac{V}{4E_R} \right)} \quad [11b]$$

Equations [11a] and [11b] are the general expressions for the transfer rate across the interface and constitute the main result of this section. In order to apply them to our electrochromism problem, however, it is convenient to introduce a few simplifying approximations.

1. Since we are assuming $E_R > 1$ eV and $J < k_B T$, ω , we have $\gamma \ll 1$ and thus we may use the nonadiabatic limit value of g , i.e., $g(\gamma) = \gamma\pi^{1/2}$.

2. For $V \lesssim E_R$ we may simplify Eq. [11] by neglecting the $V/4E_R$ term in the exponential. Thus

$$W_{23}^{\rightarrow} \sim \frac{\omega}{2} \gamma\pi^{-1/2} e^{V/2k_B T} \quad [12a]$$

$$W_{32}^{\rightarrow} \sim \frac{\omega}{2} \gamma\pi^{-1/2} e^{-E_R/k_B T} e^{-V/2k_B T} \quad [12b]$$

3. The symmetric cell of Fig. 1(a) has two electrochemical interfaces: 2|3 and 3|4. Assuming that the applied voltage $V_1 - V_5$ divides equally at the two interfaces, and assuming fast transport across the electrolyte, we obtain the effective probabilities of transition between 2 and 4

$$W_{42}^{\rightarrow} = (W_{43}^{\rightarrow} W_{32}^{\rightarrow})^{1/2}$$

$$= \sqrt{\pi/8} \frac{J^2}{\sqrt{E_R k_B T}} e^{-E_R/2k_B T} e^{-\frac{V_1 - V_5}{2k_B T}} \quad [13a]$$

$$W_{24}^{\rightarrow} = W_{42}^{\rightarrow} e^{-\frac{V_1 - V_5}{k_B T}} \quad [13b]$$

Equations [11]-[13] establish that E_R determines the electrochemical memory. In fact, from Eq. [13], we see that, at short-circuit (i.e., $V_1 = V_5$), the transfer rate is independent of ω and varies as $\sim \exp[-E_R/(2k_B T)]$, corresponding to an effective free energy barrier $\sim E_R/2$. An increase in the reorganization energy from an initial value E_{Ri} to a final value E_{Rf} , results in a decrease of the short-circuit transfer rate by a factor $(E_{Ri}/E_{Rf})^{1/2} \exp[(E_{Ri} - E_{Rf})/(2k_B T)]$, which is independent of J and, obviously, is very sensitive to $E_{Rf} - E_{Ri}$. So, to increase the electrochemical memory we need to choose an electrolyte with a larger reorganization energy. Reorganization energies of many different electrolytes have been calculated and measured (34). This makes it possible, in practice, to tailor the electrolyte in order to obtain the appropriate electrochemical memory. The quantitative relationships between reorganization energy, electrochemical memory, response time, and size of the electrochromic display matrix are established in the next two sections.

Macroscopic Model

So far, we have established that we can increase the electrochemical memory by increasing the re-

organization energy of the electrolyte. There is a limit, however, to this process. The limit is set by the breakdown voltage of the electrolyte. In fact, the larger E_R (and, thus, the free energy barrier at the interface), the larger must be the applied voltage to lower the barrier to zero and thus allow charge transfer [cf. Fig. 4(a)]. Clearly, a high voltage is not desirable in the driving circuitry. But, more fundamentally, a high enough applied voltage eventually decomposes the electrolyte. Moreover, it is found frequently that it is impossible to drive the electrochromic cell even at voltages lower than the breakdown voltage because of side reactions such as gas evolution, electrode corrosion, and so on. Thus, for each electrochromic reaction there is a finite "window" that can be reversibly scanned by the applied voltage. The amplitude of the window, $2V_0$, limits the maximum value of E_R and, thus, the maximum value of the electrochemical memory.

To calculate the maximum electrochemical memory, let us consider the simplest model of electrochromic reaction in an electrolyte of scanning window $2V_0$. The simplest electrochromic reaction can be written as



where the atom A resides in the electrode and the ion A^{\pm} in the electrolyte. (+ and - refer to cation and anion electrochromism, respectively.)

The rate-determining step for most electrochromic reactions has not been established yet. Regardless of the initial rate-determining step, however, once the free energy barrier at the interface has been established by increasing E_R , the rate-determining step becomes the rate of charge transfer at the electrochemical interface. For a reaction of the type of Eq. [14], in its simplest case, the rate of charge transfer across the electrochemical interface [e.g., 2/3 of Fig. 1(a)] is given by

$$\dot{q}_2 = W_{32}^{\rightarrow} (1 - q_2) - W_{23}^{\rightarrow} q_2 \quad [15]$$

where W_{23}^{\rightarrow} and W_{32}^{\rightarrow} are given by Eq. [11a] and [11b]. For a symmetric cell, using Eq. [13a] and [13b], with $V_1 - V_5 = V$, $W_{42}^{\rightarrow} = W \exp(V/2k_B T)$ and $q_2 = q$, $q_4 = 1 - q$ we get

$$\dot{q} = W [e^{V/2k_B T} (1 - q) - e^{-V/2k_B T} q] \quad [16]$$

which is of the Butler-Volmer type (25) with symmetric transfer coefficients.

The solution of Eq. [16] depends on the form of the scanning voltage. For triangular scanning, i.e., for periodic scanning with waveform

$$V(t) = \mp V_0 \pm st \quad [17]$$

(upper signs for $0 \leq t \leq 2V_0/s$; lower signs for $2V_0/s \leq t \leq 4V_0/s$) the equation can be easily solved. This choice of the voltage scanning wave form is used in cyclic voltammetry (35). An equation of the form [16] appears in the theory of electrochemical adsorption kinetics (36)—a process which has been studied extensively by cyclic voltammetry. In this context, Eq. [16] (with W as a free parameter) has been discussed first by Srinivasan and Gileadi (37). In our case we focus on the role of $2V_0$ —the voltage scanning window—which, in Eq. [17], we have assumed to be symmetric around $V = 0$. This assumption, which is generally not satisfied by real systems, is introduced here for simplicity. It will be relaxed later, after we have obtained some general results qualitatively independent of this assumption.

From Eq. [17] and the initial condition $q(t = 0) = 0$, the solution of Eq. [16] can be written in terms of a simple one-dimensional integral as

$$q = fe^{-2f \sinh(V/2k_B T)} \int_{-V_0/2k_B T}^{V_0/2k_B T} dz e^{z+2f \sinh z} \quad [18]$$

where $f = 2k_B T W/s$. It is important to note that: (i) q depends on the time only through V ; and (ii) q depends on the scanning rate s and the probability of transition W only through f , i.e., only through their ratio. Physically, this is consistent with the discussion about Fig. 4(a). Namely, the same amount of charge is transferred between the two levels either by a high scanning rate through a low barrier or by a low scanning rate through a higher barrier.

Analytical solutions of Eq. [18] are easily obtained in 2 special cases: (i) at quasi-equilibrium, i.e., for $f \rightarrow \infty$. In this case

$$q = (1 + e^{-V/k_B T})^{-1} \quad [19]$$

(ii) Whenever the backward reaction can be neglected, i.e., for $f \rightarrow 0$. In this case

$$q = 1 - e^{(e^{-V_0/2k_B T} - e^{V/2k_B T})f} \quad [20]$$

Clearly, for very small f , not all the charge can be transferred during a voltage scan, i.e., $q(+V_0) < 1$. But full coloration in a practical electrochromic cell usually requires full ion-occupancy, i.e., $q = 1$. From Eq. [18], we can easily determine the minimum value of f which satisfies this condition. Setting $q = 1$ and $V = V_0$ in Eq. [18] and solving numerically, we obtain

$$f_m \sim \pi [\sinh(V_0/2k_B T)]^{-1} \quad [21]$$

with an accuracy of $\sim 0.2\%$.

For $f = f_m$, the numerical solution of Eq. [18] yields the relaxation loops showed in Fig. 6 (dashed lines 2 and 3) for $V_0 = 20k_B T$ and $V_0 = 40k_B T$. At room temperature, these values of V_0 correspond to 0.5 and 1.0 eV, respectively, which are realistic voltage limits for electrochromic cells.

Figure 6(b) shows the "pseudocapacitance" $q(2k_B T/s)$ corresponding to the ion-occupancy curves of Fig. 6(a). The pseudocapacitance is the quantity which is measured by cyclic voltammetry.

Two features of these figures are worth noting: (i) both curve 2 and 3 have excellent threshold. Even in the least favorable case, i.e., for $V_0 = 20k_B T$, the ion-occupancy at $V_0/2$ is only a few percent. (ii) The size of the loops is closely related to V_0 and, thus, to f_m . Indeed it is easy to show that the inflection points in the $q(V)$ curves (i.e., the maxima and minima of the pseudocapacitance) occur (if $V_0 \gtrsim 20k_B T$) at

$$V_{\text{Max}} = \pm 2k_B T \log f_m \quad [22]$$

Thus, f_m is a measure of the maximum size of the relaxation loops.

Actually, f_m is basically a measure of the maximum free energy barrier that can be established at

the electrochemical interface, without altering the response time of the cell. In fact, let t_R be the cell intrinsic response time, i.e., the response time at 0 free energy barrier. This time sets the minimum voltage scanning speed at

$$s_m \sim V_0/2t_R \quad [23]$$

Thus, the minimum probability of charge transfer W_m across the interface is

$$W_m = \frac{f_m s_m}{2k_B T} \sim \frac{f_m V_0}{4t_R k_B T} \quad [24]$$

and the maximum free energy barrier $\sim f_m^{-1}$.

Now, let us use as a practical definition of "maximum electrochemical memory" the time t_M necessary to reduce by 1% the relative ion occupancy, following a voltage excursion $0 \rightarrow +V_0 \rightarrow 0$. With this definition, using Eq. [21] and [24], it is easy to obtain

$$t_M = \frac{2 \times 10^{-2}}{\pi} \left(\frac{k_B T}{V_0} \right) t_R e^{V_0/2k_B T} \quad [25]$$

Another way of looking at the memory time is as follows: Let us determine the maximum value f_M of f for which at $V = 0$, the ion occupancy is ~ 0 . Numerically (0.3% accuracy), we find (for $V_0 \gtrsim 20k_B T$)

$$f_M \sim \pi 10^{-2} \quad [26]$$

For $W = W_m$, this value of f corresponds to a scanning rate $s_M = f_m V_0 / 2f_M t_R$. Thus, if we define the memory time t_M as $t_M = k_B T / s_M$, we obtain

$$t_M \sim \frac{2f_M k_B T}{f_m V_0} t_R \sim 2 \times 10^{-2} e^{V_0/2k_B T} \frac{k_B T}{V_0} t_R$$

which is identical to Eq. [25]. This equation relates the maximum electrochemical memory to the intrinsic response time and to the electrolyte breakdown voltage. For example, for $V_0 = 1.0\text{V}$ and $t_R = 10$ msec, the maximum memory at room temperature is ~ 20 min.

In the opposite limit, i.e., for large f at the same scanning rate, the memory is zero. Curves 1 of Fig. 6(a) and 6(b) are obtained for $f \gtrsim \pi$. This is the so-called reversible limit of cyclic voltammetry. In this limit, the pseudocapacitance is symmetric about V , the charge is a single-valued function of V , and the electrochromic cell has no memory.

In this section, then, we have seen that, starting from the reversible limit and decreasing W we can increase the electrochemical memory up to a maximum determined by f_m and, thus, by V_0 . Since, as shown in the previous section, W is determined primarily by E_R , we have now all the elements to relate the performance of an electrochromic display matrix to the microscopic properties of the electrolyte. The results are presented in the next section.

Results

From the results of the two previous sections we can obtain a lower limit on the reorganization energy necessary to achieve the maximum electrochemical memory compatible with response time t_R and scanning voltage window $2V_0$. In fact, from Eq. [13], [21], and [23], with $J \lesssim k_B T$, we obtain

$$E_R \gtrsim V_0 + 2k_B T \log \left[\left(\frac{k_B T}{E_R} \right)^{1/2} \left(\frac{k_B T}{V_0} \right) \frac{k_B T t_R}{\pi} \right] \quad [27]$$

From Eq. [27], the lower value of E_R is plotted in Fig. 7(a) as a function of V_0 for $t_R = 10$ msec and for $t_R = 100$ msec. It is clear that E_R practically scales with V_0 but is not too sensitive to t_R . The magnitude of E_R is approximately $2V_0$, which is the amplitude of the scanning window. The range of values of E_R ,

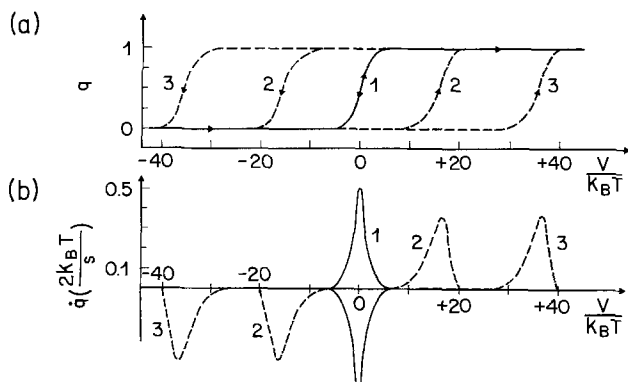


Fig. 6. Relative ion-occupancy (a) and pseudocapacitance (b) of the electrochromic electrode as a function of the applied voltage for no-memory conditions (solid lines 1) and for two different values of the memory parameter f_m . Loop 2: $f_m = \pi(\sinh 10)^{-1}$. Loop 3: $f_m = \pi(\sinh 20)^{-1}$.

i.e., 1.5-2.0 eV are realistic numbers for the reorganization energy of various electrolytes. And, from Fig. 6 (curves 2 and 3), it is clear that, within this range, the relaxation loops are large enough to exhibit a distinct threshold in $q(V)$.

Having established the range of E_R suitable for memory with threshold, it is possible to relate E_R to the maximum number of display elements that can be matrix addressed. As discussed in the introduction, the short-circuit memory t_M of the electrochromic cells in the matrix must be such that $t_M \gtrsim n\Delta t$, where n is the number of rows and Δt the duration of each biasing pulse. Since $\Delta t \gtrsim t_R$, we have, from Eq. [25], $n \leq t_M/t_R \sim 10^{-2}(k_B T/V_0)e^{V_0/2k_B T}$. In turn, V_0 and E_R are related through Eq. [27], which establishes a relationship between the maximum number of addressable rows and the reorganization energy of the electrolyte. The relationship is shown graphically in Fig. 7(a) and 7(b). We see that, for $1.5 \text{ eV} \leq E_R \leq 2.0 \text{ eV}$, n spans the range $10 \leftrightarrow 10^5$, which encompasses any practical size of display matrices.

We remark that the results obtained so far, apply to: (i) a symmetric electrochromic cell and, (ii) to an electrochromic reaction occurring at the center of the scanning voltage window. Both restrictions were adopted for simplicity of exposition and can now be relaxed.

An electrochromic display needs only one electrochromic electrode [e.g., 2 in Fig. 1(a)]; the counterelectrode (e.g., 4 in Fig. 1(a)) needs simply be an ion-insertion material. Moreover, the ions inserted in 2 and 4 may be different. In fact, if the electrolyte conducts via both anions and cations, a frequent circumstance, then the electrode 2 could, e.g., exchange anions with the electrolyte, while the counterelectrode 4 exchanges cations. In practice, it is convenient to have a counterelectrode with fast ion-exchange and with "flat" isotherms, i.e., with $\epsilon(q)$ almost independent of q . In this case, the counterelectrode may essentially be ignored, and the memory of the cell depends only on the 2/3 electrochemical interface. This, in a sense, is the opposite limit of the symmetric cell considered previously.

In this asymmetric cell, the rate of charge transfer across the 2/3 interface can be calculated from Eq. [15] with W_{32} and W_{23} given by Eq. [12]. It is convenient to rewrite Eq. [15], for the asymmetric cell, in the symmetric form

$$q_2 = W \left[e^{\frac{V - E_R}{2k_B T}} (1 - q_2) - e^{\frac{E_R - V}{2k_B T}} q_2 \right] \quad [28]$$

By comparing Eq. [28] and [16] it is clear that the asymmetric case yields the same results as the symmetric case, but with V replaced by $V - E_R$. Actually, in Eq. [28], we have tacitly assumed that, by increasing the voltage, anions are inserted. If, instead, by increasing the voltage, cations are extracted, then it is easy to see that the transfer rate is the same as in the symmetric case, but with V replaced by $V + E_R$.

From the previous results, it is clear that, if the electrochromic reaction is not centered in the middle of the voltage window, it will be convenient to use an asymmetric cell, so that the center of the memory loop will be displaced by E_R or $-E_R$. Naturally, the actual amount of asymmetry to be built into the cell depends on the position of the electrochromic reaction in the voltage window.

There is, then, a substantial degree of flexibility in creating the short-circuit memory of electrochromic cells. The value of E_R necessary to create the memory does not have to be specified exactly, but only within a range of typical values; and if, in the electrolyte with the appropriate E_R , the electro-

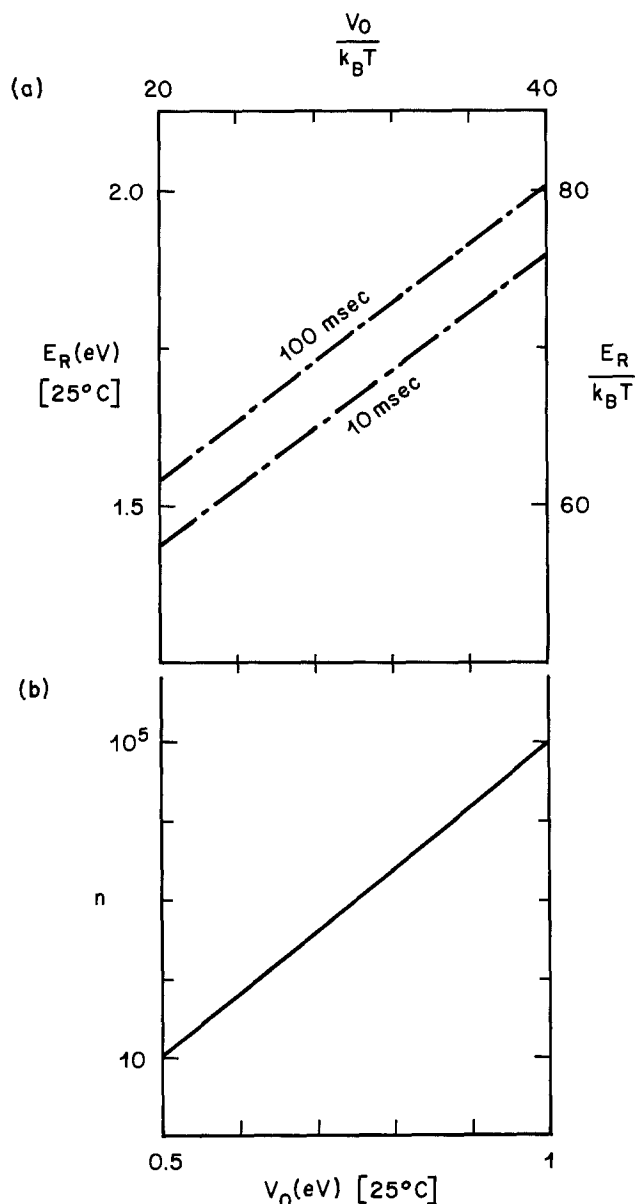


Fig. 7. (a) Reorganization energy E_R as a function of V_0 for two different response times. (b) Maximum number of rows that can be matrix addressed in a display-matrix consisting of electrochromic cells with scanning window $2V_0$. By combining (a) and (b) n is related to the reorganization energy of the electrolyte.

chromic reaction does not occur at the center of the voltage window, then the counterelectrode can be modified to keep the relaxation loops within the window.

Discussion

The main conclusions of this work rest on the physical basis of electrochemical memory and thus do not depend on the particular models chosen. We have in effect, introduced the simplest possible models and solved them in the simplest possible cases. These simplifications have facilitated the task of proving the main point of the paper, i.e., that electrochromic display cells can have short-circuit memory. They have also allowed us to show a general method to design electrochromic cells suitable for matrix-addressing. The details of our results, however, depend on several assumptions and approximations.

The major assumption is the choice of the microscopic model. As already stressed in the section "Microscopic Model," the problem of ion transfer at the electrochemical interface has not been given a general quantitative solution yet. The small-polaron

approach is the simplest treatment of electron transfer at the electrochemical interface. In this paper we have extended this treatment, for the first time, to ion transfer. Thus, this theory is still experimentally untested. It is hoped that the results presented here may stimulate further work in this direction.

In addition, although we obtain general expressions, *i.e.*, Eq. [11], for the probability of ion transfer, we have subsequently introduced the simplifying assumption of large E_R , *i.e.*, $V/4E_R \ll 1$. This is not an unreasonable approximation. In fact its validity is confirmed, *a posteriori*, by the results presented in the Results section, *i.e.*, $E_R \sim 2V_0$, which is also consistent with the choice of the transfer probability.

The most restrictive assumption of the macroscopic model is the form of the equation describing the electrochromic reaction, *i.e.*, Eq. [15]. This equation leads to simple Langmuir (38) isotherms. In general, however, the electrochromic isotherms (18) are more complicated. In fact, an improved macroscopic model would use an equation leading to the experimentally observed electrochromic isotherms. It is interesting to note, however, that, for AIROF's, the electrochromic isotherms are indeed of a generalized Langmuir type. That is

$$\epsilon(q) = pk_B T \log(q/(1-q)) \quad [29]$$

with $p = 2$ or 3 , whereas, for Langmuir isotherms, $p = 1$. Thus, our choice of the electrochromic reaction equation is of the same general form as the experimentally observed ones.

Implicitly, we have also made two assumptions on the physical properties of the electrolyte. First, we have neglected its internal resistance. Clearly, if the electrolyte with the appropriate E_R has a high resistivity, it would slow down the response of the electrochromic cell. But a large E_R is not necessarily associated with a high resistivity of the electrolyte. In fact, E_R depends on the binding to the electrolyte of the ion involved in the electrochromic reaction, whereas the electrolyte conductivity depends either on the mobility of a different ionic species or on the mobility of the complex to which the ion is bound. An example of fast ion transport of a bound ion-complex is provided by proton-insertion electrochromics—here the transferred ion is H^+ , but the mobility depends on H_3O^+ . Thus, it is not inconsistent with our model to neglect the electrolyte resistivity.

We have also implicitly assumed that the probability of charge transfer at zero free energy barrier, *i.e.*, J , is independent of E_R . In general, however, a different E_R is associated with different interfacial structures. Thus, J could depend on E_R . But how sensitive J is to E_R remains an open question since no experimental or theoretical study of this relation has been carried out yet.

Finally, for a symmetric cell, we have assumed that the applied voltage is divided equally between the two interfaces. This is generally not so since the impedance of the electrochromic material may depend on q . In such cases, it is straightforward to relax this assumption, the results remaining qualitatively unchanged.

Having discussed the approximations, let us now look at our results from a different perspective. It has recently been pointed out (39) that nickel hydroxide films are electrochromic and exhibit a hysteretic voltammogram. Obviously, an electrochromic with large hysteresis in $\epsilon(q)$ has short-circuit memory and thus could be suitable for matrix-addressing. There are, however, two major problems with nickel hydroxide films. First, the electrochromic reaction occurs in the region of oxygen gas evolution, so that the electrode is basically unstable. Second, although

the isotherms are hysteretic, they have no threshold. Thus, nickel hydroxide cannot be used for matrix-addressing. Similar considerations apply to all the known group VIII oxide exhibiting hysteresis.

On the other hand, a hysteretic ion-insertion material could be used as a counterelectrode in an electrochromic cell to provide the necessary short-circuit memory. The counterelectrode should: (i) be compatible with the electrolyte; (ii) have fast kinetics; and (iii) exhibit hysteresis with threshold.

This approach to short-circuit memory may be advantageous, but it has not been explored yet. Obviously, the main difficulty is finding or designing a counterelectrode with the required characteristics. In contrast, our approach to short-circuit memory does not require modifications of the properties of the electrode or counterelectrode—the electrochromic memory being based primarily on the properties of the electrolyte.

In a sense, the concept of electrochemical memory may be regarded as the antithesis of the concept of electrocatalysis. The central problem of electrocatalysis is to lower the barrier at the interface in order to increase the exchange current and reaction rate. The opposite is true in the electrochemical memory problem. The barrier at the interface should be as high as possible to prevent charge transfer at short circuit. Ultimately, both electrocatalysis and electrochemical memory depend on the structure of the electrochemical interface and on the kinetics of the transfer across it. Thus, further study of the electrochemical memory may shed some light on the fundamental nature of electrochemical kinetics.

Summary

Electrochromics, although promising display materials, have been regarded as unsuitable for matrix addressing because of their lack of threshold and short-circuit memory. In this paper we have shown that threshold and short-circuit memory of an electrochromic display cell depend on the electrolyte. If an appropriate electrolyte can be found, the threshold and short-circuit memory of the electrochromic display cell might become sufficient to matrix-address multielement electrochromic displays of practically any size.

To reach this conclusion, first we have introduced the concept of electrochemical memory. In general, the memory of an ion-insertion electrode can be defined as the memory of its relative ion-occupancy following an excursion of its internal emf. In a hysteretic electrode, the memory has a thermodynamic origin. In a nonhysteretic electrode (such as AIROF) the memory has a kinetic origin, arising from the dynamics of charge transfer at the electrochemical interface. This type of memory we have referred to as electrochemical memory.

We have shown that the electrochemical memory is created by the interaction of the transferred ion with the electrolyte. This interaction is measured by the electrolyte reorganization energy E_R .

To calculate the electrochemical memory, we have introduced a small-polaron model of ion transfer at the electrochemical interface. We have obtained general expressions for the probability of transition in terms of the properties of the electrolyte. In the limits of interest, the probability of transition depends exponentially on E_R and on the cell potential (Eq. [13]).

Then, we have introduced a macroscopic model of the electrochromic reaction, based on Langmuir-type isotherms. Coupled with the transition probability expressions obtained from the microscopic model, the rate equation for the reaction turns out to be of the Butler-Volmer type with symmetric transfer coefficients (Eq. [16]). We have solved this equation as a function of the electrolyte breakdown

voltage, $2V_0$. From its solution, we have established the lower limit of the electrolyte breakdown voltage necessary for threshold and short-circuit memory.

Next, we have found a simple expression, Eq. [25], for the magnitude of the maximum short-circuit memory with threshold in terms of the breakdown voltage and the cell response time t_R . For $t_R \sim 10$ msec and for $V_0 \sim 1$ eV, the maximum memory is ~ 20 min.

Finally we have determined the value of the reorganization energy required to obtain the maximum short-circuit memory with threshold. The calculated values of E_R lie in the range $1.5 \leftrightarrow 2$ eV, which are realistic numbers for many electrolytes. These values of E_R , in turn, correspond to a range of matrix addressable lines $10 \leftrightarrow 10^5$ which encompasses all practical cases. Thus, there is no intrinsic theoretical limitation to matrix-addressing large matrixes of electrochromic display cells.

Naturally this conclusion has been reached by introducing assumptions and approximations. However we have seen that neither are very restrictive so that the main results are not qualitatively affected by them.

We have also remarked that, unlike the electrochemical memory discussed here, the hysteretic memory of the kind exhibited by, e.g., nickel hydroxide, is unsuitable for matrix addressing because of its lack of threshold.

Finally, we have pointed out that electrochemical memory and electrocatalysis are opposite limits of the same general concept.

Acknowledgments

I am grateful to J. L. Shay for his valuable comments and his constant interest. I wish to thank also W. C. Dautremont-Smith, C. E. Rice, and L. M. Schiavone for many stimulating discussions.

Manuscript submitted Dec. 26, 1979; revised manuscript received April 7, 1980.

Any discussion of this paper will appear in a Discussion Section to be published in the June 1981 JOURNAL. All discussions for the June 1981 Discussion Section should be submitted by Feb. 1, 1981.

Publication costs of this article were assisted by Bell Laboratories.

REFERENCES

- See, e.g., "Non Emissive Electrooptic Displays," A. R. Kmetz and F. K. Von Willisen, Editors, Plenum Press, New York (1976).
- J. P. Randin, *J. Electron. Mater.*, **7**, 47 (1978).
- S. Gottesfeld, J. D. E. McIntyre, G. Beni, and J. L. Shay, *Appl. Phys. Lett.*, **33**, 208 (1978).
- G. Beni and J. L. Shay, *ibid.*, **33**, 567 (1978).
- J. L. Shay, G. Beni, and L. M. Schiavone, *ibid.*, **33**, 942 (1978).
- S. Gottesfeld and J. D. E. McIntyre, *This Journal*, **126**, 742 (1979).
- G. Beni and J. L. Shay, Proc. of Int. Conf. on Fast Ion Transport in Solids, Lake Geneva, Wisc. (May 1979).
- J. L. Shay and G. Beni, *IEEE Trans. Electron Devices*, ed-26, 1138 (1979).
- W. C. Dautremont-Smith, G. Beni, L. M. Schiavone, and J. L. Shay, *Appl. Phys. Lett.*, **35**, 563 (1979).
- L. M. Schiavone, W. C. Dautremont-Smith, G. Beni, and J. L. Shay, *ibid.*, **35**, 823 (1979).
- "Non Emissive Electrooptic Displays," A. R. Kmetz and F. K. Von Willisen, Editors, p. 261, Plenum Press, New York (1976).
- A "refreshed" matrix-addressed electrochromic display has been discussed by A. Arellano, G. S. Keller, P. J. Melz, M. D. Shattuck, and C. V. Wilbur, 1978 SID Intern. Symp.-Digest Tech. Papers, L. Winner, p. 22, Coral Gables (1978).
- Non Emissive Electrooptic Displays," A. R. Kmetz and F. K. Von Willisen, Editors, p. 282, Plenum Press, New York (1976).
- For a recent general reference see "Proc. of Int. Conf. on Fast Ion Transport in Solids," Lake Geneva, Wisc. (May 1979).
- See, e.g., D. W. Murphy and P. A. Christian, *Science*, **205**, 651 (1979).
- R. S. Crandall, P. J. Wojitowicz, and B. W. Faughnan, *Solid State Commun.*, **18**, 1409 (1976).
- R. S. Crandall and B. W. Faughnan, *Phys. Rev. B*, **16**, 1750 (1977).
- M. L. Hitchman, *J. Electroanal. Chem. Interfacial Electrochem.*, **85**, 135 (1977).
- G. Beni and J. L. Shay, *Phys. Rev. B*, **21**, 364 (1980).
- G. Beni, C. E. Rice, and J. L. Shay, *This Journal*, **127**, 1342 (1980).
- B. W. Faughnan, R. S. Crandall, and P. M. Heyman, *RCA Rev.* **36**, 177 (1975).
- See, e.g., K. J. Vetter, "Electrochemical Kinetics," Academic Press, New York (1967).
- A good discussion is given by D. H. Everett and W. I. Whitton, *Trans. Faraday Soc.*, **48**, 749 (1952), for a recent analysis see D. R. Knittel, S. P. Pack, S. H. Lin, and L. Eyring, *J. Chem. Phys.*, **67**, 134 (1977).
- See, e.g., D. H. Everett and F. W. Smith, *Trans. Faraday Soc.*, **50**, 187 (1954).
- See, e.g., J. O'M. Bockris and A. K. N. Reddy, "Modern Electrochemistry," Plenum Press, New York (1970).
- See, e.g., B. E. Conway, *This Journal*, **124**, 410C (1977).
- R. A. Marcus, *J. Chem. Phys.*, **24**, 966 (1956); **37**, 1835 (1962); **41**, 2624 (1964); **43**, 679 (1965).
- The theory has been reviewed by V. G. Levich, in "Physical Chemistry, An Advanced Treatise," H. Eyring, D. Henderson, and W. Jost, Editors, Vol. 98, Academic Press, New York (1970).
- See, e.g., C. Kittel, "Quantum Theory of Solids," Wiley, New York (1963).
- G. Beni, in "Semiconductor Liquid-Junction Solar Cells," A. Heller, Editor, The Electrochemical Society Softbound Proceedings Series, Princeton, N.J. (1977).
- T. Holstein, *Ann. Phys.*, **8**, 325 (1959); **8**, 343 (1959).
- C. P. Flynn and A. M. Stoneham, *Phys. Rev. B*, **10**, 3966 (1970).
- D. Emin, M. I. Baskes, and W. D. Wilson, *Phys. Rev. Lett.*, **42**, 791 (1979).
- V. G. Levich, *Advances in Electrochem. Electrochem. Eng.*, **4**, 249 (1965).
- A. Sevcik, *Coll. Czech. Chem. Commun.*, **13**, 349 (1948).
- F. G. Will and C. A. Knorr, *Z. Elektrochem.*, **64**, 258 (1960); **64**, 270 (1960).
- S. Srinivasan and E. Gileadi, *Electrochim. Acta*, **11**, 321 (1966).
- A. Clark, "The Theory of Adsorption and Catalysis," Academic Press, New York (1970).
- J. D. E. McIntyre, W. F. Peck Jr., and G. P. Schwartz, Paper presented at the 21st Electronic Materials Conf., Boulder, Co., June 27-29, 1979.